ULPGC
Universidad de
Las Palmas de
Gran Canaria

grres ULPGC
group for the research on renewable energy systems

Proceedings of ECOS 2023

36th International Conference on Efficiency, Cost, Optimization, Simulation and Environmental Impact of Energy Systems

Proceedings Book 2 - Preliminary Version

June 25 - 30, 2023
LAS PALMAS DE GRAN CANARIA
SPAIN

ECOS2023

SUPPORTED BY:

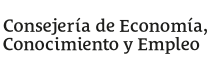

Proceedings of ECOS 2023
36th International Conference on Efficiency, Cost, Optimization, Simulation and Environmental Impact of Energy Systems

Proceedings Preliminary Version
Juny 2023

By
Ana María Blanco-Marigorta, Beatriz Del Rio Gamero, Noemí Melián Martel, Nenna El Kori.

Publisher by: ULPGC – Juan de Quesada, 30 35001 Las Palmas de Gran Canaria
www.ulpgc.es

Conference chairs
Ana María Blanco-Marigorta, ULPGC, Spain
Georte Tsatsaronis, TU-Berlin, Germany
Sotiris Karellas, NTU, Greece
Brian Elmegaard, DTU Technical University of Denmark, Lyngby, Denmark

Honorary chairs
Richard Gaggioli
Ozer Arnas

Local organizing committee
Ana María Blanco-Marigorta
Pedro Jesús Cabrera Santana
Fabián Déniz Quintana
José Antonio Carta González
Julieta Schallenberg Rodríguez
Alexis Lorenzo Medina
Noemí Melián Martel
Baltasar Peñate Suárez
Beatriz del Rio Gamero
Carlos Alberto Mendieta Pino
Sergio Velázquez Medina
Nenna El Kori
Nestor Rubén Florido Suárez
Graciliano Nicolás Marichal Plasencia
Deivis Ávila Prats

ECOS 2023 Scientific Committee Members

Abel Hernandez-Guerrero, Mexico
Adriano Sciacovelli, UK
Alojz Poredoš, Slovenia
Ana María Blanco Marigorta, Spain
Andrea Lazzaretto, Italy
Anna Stoppato, Italy
Antonio Valero Capilla, Spain
Asfaw Beyene, USA
Assaad Zoughaib, France
Brian Elmegaard, Denmark
Daniel Favrat, Switzerland
Eden Mamut, Romania
Edson Bazzo, Brasil
Enrico Sciubba, Italy
Erwin Franquet, France
François Maréchal, Switzerland
George Tsatsaronis, Germany
Giampaolo Manfrida, Italy
Gordana Stefanović, Serbia
Jean-Pierre Bedecarrats, France
José Carlos Teixeira, Portugal
Lydia Stougie, Netherlands
Mauro Reini, Italy
Michel Feidt, France
Na Zhang, China
Noam Lior, USA
Ofira Ayalon, Israel
Ozer Arnas, USA
Pascal Stouffs, France
Rene Hofmann, Austria
Ron Zevenhoven, Finland
Ryohei Yokoyama, Japan
Senhorinha Teixeira, Portugal
Silvia Nebra, Brazil
Silvio de Oliveira Júnior, Brazil
Soteris Kalogirou, Cyprus
Sotirios Karellas, Greece
Sylvain Quoilin, Belgium
Tetyana Morosuk, Germany
Umberto Desideri, Italy
Vittorio Verda, Italy
Vladimir Stevanović, Serbia
Wojciech Stanek, Poland
Yoshiharu Amano, Japan
Young Duk Lee, Korea
Zornitza Kirova-Yordanova, Bulgaria

ULPGC
Universidad de
Las Palmas de
Gran Canaria

grres ULPGC
group for the research on renewable energy systems

J. Energy-waters nexus, desalination, waste water treatment

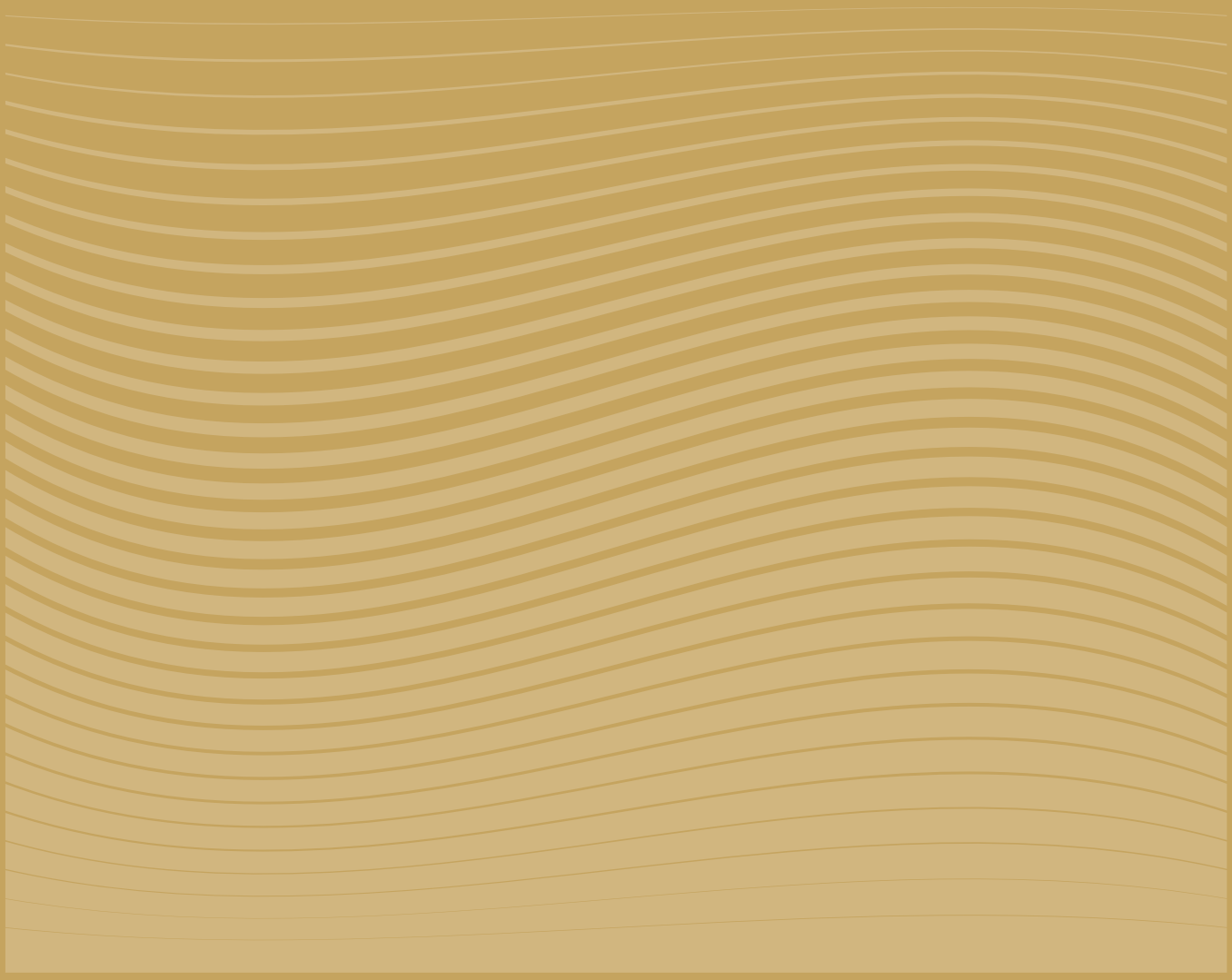

ECOS2023

Feasibility study of renewable energy systems to supply energy to desalination plants.

Deivis Avila Prat[a], Felipe San Luis Gutiérrez [a], Ángela Hernández López [a], José Ángel Rodríguez Hernández [a] and G. Nicolás Marichal Plasencia[a]

[a] Polytechnic School of Engineering (EPSI), University of La Laguna
Tenerife, Spain, nicomar@ull.edu.es

Abstract:

In this research, a renewable energy hybrid system (PV-Wind) is modeled to compare different design options based on their economic and technical features. The energy requirements of a RO desalination plant located on the island of Tenerife with a water production capacity of up to 20,000 m³/day will be considered. The system will be connected to the electricity grid.

The HOMER software has been used to produce optimum strategies for renewable energy. The assumptions input into the model were: the technical specifications of the devices, electricity demand of the desalination plant, as well as the solar radiation and the wind speed potentials. Numerous arrangements have been considered by the software. The optimal results have been obtained based on the use of renewable energy. The data used in the study were recorded in Tenerife in the Canary Islands. The experience of this research could be transferred to other Atlantic islands with similar conditions.

Keywords:

Renewable Energy; Desalination; Reverse Osmosis; Canary Islands

1. Introduction

The Canary archipelago is a pioneer in seawater desalination due to its experience in applications with dissimilar technologies. Currently, the Islands have 330 desalination plants, which produce around 214.6 hm³ of fresh water per year [1,2].

In two of the seven main islands that make up the archipelago (Lanzarote and Fuerteventura), desalinated water accounts for 99% and 86%, respectively, of the water used to supply the population and tourism [1,2,3].

The main problem with desalination is the energy required, which is harmful to the atmosphere due to the growing pollution caused by the burning of fossil fuels. The isolated electrical grid of the Canary Islands poses a problem in its optimization, as does the high dependence on imported fuel [3-7].

The use of renewable energies to procure fresh water from seawater for human consumption is beneficial for the environment, since it reduces pollution.

On the island of Tenerife, wind speed and solar radiation are generally high and allow for the optimal use of renewable energy systems (RES) to produce energy. An example of this are the eight solar plants belonging to the "Technological Institute of Renewable Energies" (ITER), with a total of 44.3 MW of installed photovoltaic systems and 65.7 MW of wind energy, installed in different wind farms [8,9].

The groundwater in Tenerife is under threat due to severe overuse. In recent years, desalination from sea water has increased to around 26.64 hm³/year, accounting for 14.0% of freshwater production, and is likely to continue increasing in the medium-term [10].

In this paper, different RES based on wind energy and photovoltaic (PV) systems connected to the electrical grid are modeled in order to assess different designs based on their technical and economic properties. The power needs for a reverse osmosis desalination plant could be guaranteed up to a water production capacity of up to 20,000 m³/day.

The Hybrid Optimization Model for Electrical Renewable (HOMER) [11] has been used to achieve the most optimal designs of RES to supply Reverse Osmosis (RO) systems.

The starting assumptions were: the electrical needs of the RO plant, technical specifications, and the sources of renewable energy (wind speed, solar radiation) on the island. HOMER models the RES with a grid connection, and the RES will always try to deliver the highest power required by the RO plant.

HOMER has been used in numerous studies carried out in many regions of the world, with the objective of finding options to replace part of the conventional energy with RES. Some examples may be found in islands

of the Atlantic Ocean [6,7], in Oceania [12], in Eurasia [13], North American [14,15], Asia [16-22], the Arabian Peninsula [23-27], Southeast Asia [28], the north Pacific Ocean [29] and in Australia [30].

Tenerife was selected for this study due to the rising annual water demands on the island, the high tourism industry, the agricultural operations on the island, the decline of groundwater and the exceptional renewable energy sources on the island.

The main objective of this study is to determine the best renewable energy systems (RES) with connection to the electricity grid to ensure the energy needs of RO plants for the production of fresh water on the island of Tenerife. The research is carried out taking into consideration the best technical-economic configuration. This research can be extrapolated to other regions with similar circumstances of water scarcity and with good sources of renewable energy.

This research is arranged into five sections. Following this introduction is a presentation of Tenerife, its population and the status and production of its water. Section 3 provides the materials and methods that will be used in the study, and defines the principal input variables of the HOMER software. The results and discussions are reported in Section 4. Lastly, Section 5 shows the most significant conclusions of the study.

2. Contextualization of Tenerife Island

The Canary Islands is an archipelago situated on the Atlantic Ocean, in Macaronesia. The archipelago is composed of seven main islands: La Gomera, El Hierro, La Palma, Tenerife, Gran Canaria, Fuerteventura, and Lanzarote (Figure 1). The islands' population is over 2 million. The number of tourists received in the islands in 2022 was in excess of 12 million [26]. The only way to supply this service sector on an island with high water scarcity is by using efficient RO desalination systems [3,4,6,31].

Tenerife is the largest and most inhabited island in the Canary Islands, with around 42.5% of the archipelago's inhabitants. Every single year, more than 5.5 million tourists visit Tenerife, which is why it is considered the most popular island in the Canaries [31].

The largest volume of this tourist population is received in the south of the island, generating a great demand for fresh water, more than 300 liters/day-tourist [32,33]. This water demand is covered in large part by desalinated water.

2.1 Desalination water in Tenerife

Desalination is nothing more than the method of removing salts from brackish or marine water to make it useful for agricultural, industrial or human consumption. In the Canary Islands, desalination provides a significant percentage (19%) of the water supply in many sectors such as agriculture, the tourism industry and the population [3,6,34].

Currently, there are 29 reverse osmosis (RO) seawater desalination plants (EDAM) in Tenerife. The most important plants by water production capacity are shown in Table 1, two of which are located in the south of the island and the other in Santa Cruz de Tenerife, the island's capital. Figure 1 shows the locations of these three desalination plants in Tenerife [10].

Table 1. Fresh water production in three RO seawater desalination plants (EDAM), Tenerife.

RO desalination plant EDAM	Capacity of water production (m^3/day)	Energy consumption (kWh/m^3)
Adeje-Arona	30,000	4.51
Caleta de Adeje	10,000	4.29
Santa Cruz de Tenerife	21,000	4.6

The EDAM with the lowest energy consumption is Caleta de Adeje, due to the improved energy recovery technology used in the desalination process. The RO desalination plant in Adeje-Arona went into operation in 1998, with a total water production capacity of 10,000 m^3/day. Due to the increasing water demand in the region, this water plant's current capacity is 30,000 m^3/day [10]. All these plants supply the demand of the population and tourists.

Figure 1. Map of Tenerife showing the locations of desalination plants, wind farms, meteorological stations and selected locations.

Figure 1 shows the distribution of the wind farms on Tenerife, which are located in those places on the island with the most wind potential, almost all of which are in the south of the island, especially in the region of Granadilla de Abona.

According to the Spanish Wind Observatory [34], on Tenerife wind farms, the preferred wind turbines in both current and new projects are GAMESA, ENERCON, VESTAS and MADE, including the repowering of old wind turbines.

Renewable energy systems such as wind turbines and photovoltaic systems, as well as reverse osmosis desalination, are all mature technologies that can be combined in different arrangements. However, only some desalination plants are currently powered by RES due to the large initial investment required, with no more than 1.0% of the desalination plants on the planet being powered by RES [35,36].

On the island of Tenerife, there is no isolated or connected RES to supply the total energy of a desalination plant, which could reduce the environmental consequences of desalination due to its enormous energy consumption from traditional sources.

All the energy used in the desalination process on the island proceeds directly from the electrical network. That is the reason behind this research, to propose the optimal renewable energy system with network connection.

3. Materials and Methods

After evaluating the state of desalination on the island of Tenerife, identifying the main plants, their production capacities and energy consumption, we decided to consider a maximum production of 20,000 m^3/day for the study, with a maximum energy consumption of 4.50 kWh/m^3 of desalinated water, although this consumption may be lower depending on energy recovery.

An analysis of Figure 1 and the study conducted by the "*Cabildo Insular del Agua de Tenerife"* (Tenerife Water Council) [37] reveal that many desalination plants are located in regions with a high solar and wind potential.

Taking this analysis into consideration, two possible locations for the study were selected, the first in the extreme south of the island, near the Montaña Roja Nature Reserve, and the second in Santa Cruz, the capital of Tenerife (Figure 1). Both locations have a high solar and wind potential and are close to meteorological stations and existing infrastructure (roads, workshops, electrical substations, equipment and supplies, etc.).

3.1. Input variables to HOMER Software

On islands like Tenerife, with high renewable energy resources and water stress, the combination of desalination plants and RES can provide a solution to the large energy consumption of the desalination industry. Combining the desalination and electrical industries requires an optimal design and consistency, and also that it be sustainable.

Taking these objectives into account, we must first propose the selection and sizes of the possible elements of the RES to power the desalination plant. The HOMER software was selected to achieve the most satisfactory design. This software can carry out the simulation, optimization, and sensitivity analyses of the RES (PV-Wind) to determine the energy needs of the desalination plants in question [6]. Figure 2 shows the suggested RES for the simulation. These devices can involve PV modules in combinations of various wind turbines, all connected to the electrical grid.

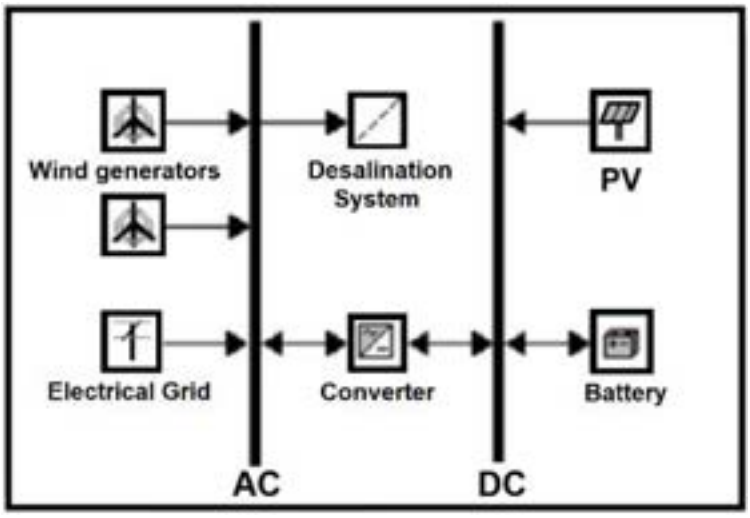

Figure 2. Renewable Energy Systems HOMER model, with electrical grid connection

3.2. Electrical loads

In order to carry out this research it was assumed a desalination plant with a production of 20,000 m^3/day, with a possible energy expenditure of 4.50 kWh/m^3 of desalted water. According to HOMER, the energy consumption of the installation can reach 89,225 kWh/day. The average electricity demand will be 3,719 kW, which may increase to 6,113 kW at peak hours. Figure 3 displays the annual distribution of electrical energy consumed, the average, and the minimum and the maximum consumption per each month.

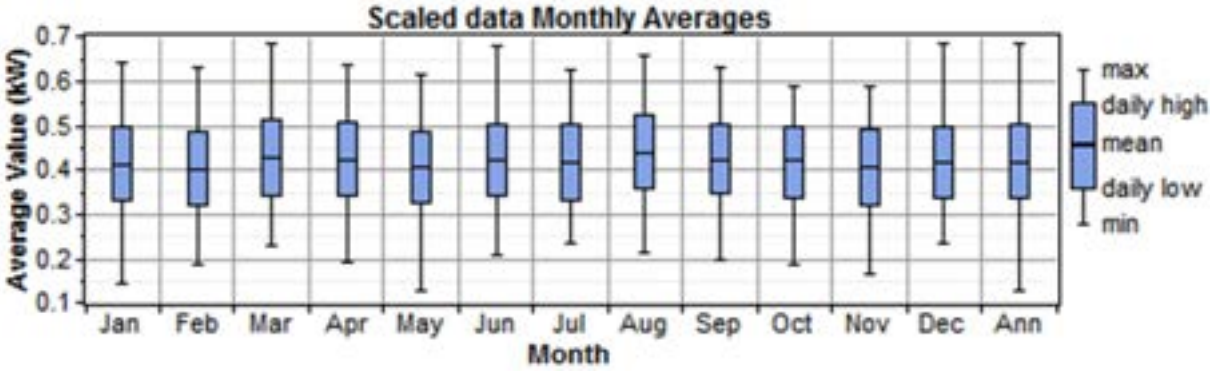

Figure 3. Annual distribution of electrical energy consumed

3.3. Solar radiation

HOMER takes the monthly solar radiation directly from NASA data. Figure 1 shows the meteorological stations used in the study for each location selected, which in this research were the South Airport (*Reina*

Sofía) (C4291) meteorological station for the Montaña Roja Nature Reserve, and the Santa Cruz de Tenerife (C449C) station to study the case in the island's capital. The coordinates used for the study on the island are shown in Table 2.

Table 2. Coordinates of the Meteorological stations

Meteorological stations	**Coordinates** *(Latitude and Longitude)*	**Altitude (m)** *(above sea level)*
South Airport *(Reina Sofía)* **(C429I)**	*Latitude:* 28° 2' 51'' N *Longitude:* 16° 33' 39'' W	64
Santa Cruz de Tenerife **(C449C)**	*Latitude:* 28° 27' 48'' N *Longitude:* 16° 15' 19'' W	35

3.4. Wind speeds

The monthly average wind speeds were taken from the two meteorological stations whose coordinates are shown in Table 2. The first one, located at the Reina Sofia Airport, has a database of more than 35 years and an average annual wind speed of 6.1 m/s. The second is located in Santa Cruz de Tenerife, where the average annual wind speed is 3.0 m/s, according to figures dating back over 85 years. The simulation performed by HOMER uses the Weibull probability density function.

3.5. PV system

When the model of the photovoltaic system is designed, the HOMER software does not take into account the temperature and voltage to which the system is subjected during operation. HOMER assumes that the direct current (DC) output of the PV panel is linearly proportional to the incident radiation [38]. Table 3 shows the cost of the photovoltaic panels used in the research. The photovoltaic panel is assumed to have a useful life of 20 years.

Table 3. Economic data

Components	**Initial capital cost (ICC_{PV})$**	**Replacement cost (RC)$**	**O&M cost ($)**	**Lifetime**
PV panels	7000 ($/kW)	7000 ($/kW)	(0.015)x(ICC_{PV})	20 years
Wind Turbines	1200 ($/kW)	(0.85) x (ICC_{Wind})	(0.025)x(ICC_{Wind})	25 years

3.6. Wind turbine system

Manwell, McGowan and Rogers state in [39] that a standard procedure is used to model wind turbines, assuming that the kinetic energy of the wind turbine is converted to electricity based on a specific power curve. HOMER computes the average wind turbine power (*Pwind*) using the Weibull distribution.

Figure 4 shows the power curves of the wind generators selected for the study, which are manufactured by ENERCON, GAMESA and VESTAS. All these machines were tested in different wind farms on Tenerife. The initial economic data for the wind generators and photovoltaic systems are shown in Table 3.

Table 4 shows the characteristics of the proposed wind turbines, with nominal powers of 800, 850 and 2000 kW.

Table 4. Commercial characteristics of wind generators (*Source:* [40-43]).

Characteristics	**E48**	**E82**	**G52**	**G90**	**V52**	**V80**
Nominal Power (kW).	800	2,000	850	2,000	850	2,000
Hub height (m)	55	78	55	78	55	78
Rotor diameter (m).	48	82	52	90	52	80
Cut-in wind speed (m/s)	3.0	2.0	4.0	3.0	4.0	4.0
Cut-out wind speed (m/s)	25	25	25	21	25	25

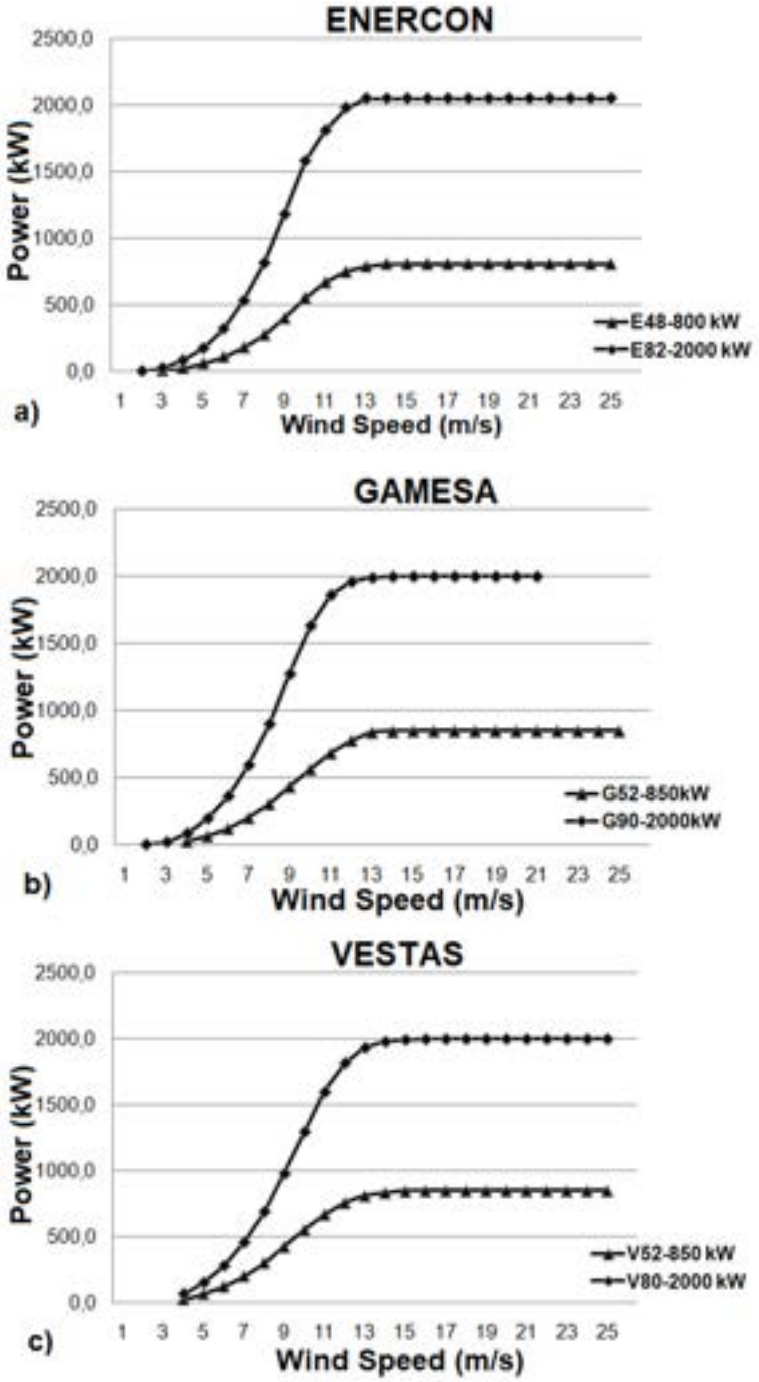

Figure 4. Power curves of the wind generators. a) ENERCON, E48-800 kW and E82-2,0 MW; b) GAMESA, G52-850 kW y G90-2,0 MW; c) VESTAS, V52-850 kW y V80-2,0 MW (Source: [40-43]).

3.7. Economic analysis

Typically, conventional electric systems have a lower initial capital cost than RES, while the cost of operation is higher in thermoelectric plants. In the optimization process, the HOMER software compares the economic characteristics between renewable energy systems and the traditional electrical system to recommend the most economical system [38].

The tools used by HOMER to perform the economic analysis are the “Levelized Cost of Energy” (COE), which calculates the average (cost/kWh) of the electricity produced by the system, and the “Total Net Present Cost” (NPC) ($), which computes the cost to install and operate any system [3,6].

4. Results and discussions

The main problem when designing any RES, whether hybrid or not, is to determine its components and the size of each, which is conditioned by the renewable energy sources in the region where it is installed.

The HOMER software is an excellent tool to use in this situation, since it allows simulating numerous system arrangements. For example, the NPC makes it possible to sort values that are in the viable range and discard those that are unviable.

The results of the technical-economic simulation carried out by HOMER are shown below. The cost of electricity from renewable energy is assumed to be $0.15/kWh; the cost of electricity purchased from the grid is $0.10/kWh; the desalination process is assumed to consume 4.50 kWh/m^3 of desalinated water; and the maximum production capacity of the proposed desalination plant is 20,000 m^3/day.

4.1. Optimization results in Santa Cruz de Tenerife

After modeling the technical-economic aspects with RES based on PV and wind systems from different manufacturers, such as ENERCON, GAMESA and VESTAS, connected to the electrical grid in Santa Cruz de Tenerife to supply energy to a desalination plant, we can state that the optimal energy system to supply energy to a desalination plant in the capital is the grid, with an approximate consumption of 32,666,286 kWh/year and an approximate cost of $3,266,629/year.

This is mainly due to the low wind speeds in the region analyzed, the high costs of photovoltaic systems and the lack of land in the capital to install a solar farm.

4.2. Optimization results in Special Nature Reserve “Montaña Roja”

Tables 5 and 6 show the result of the technical-economic and energy simulation and optimization carried out for the Montaña Roja Nature Reserve area by the HOMER software, using the data set from the Reina Sofía Airport meteorological station. The RES used in this model is the same as that used to model the system in Santa Cruz de Tenerife (PV-wind systems from different manufacturers such as ENERCON, GAMESA and VESTAS connected to the electrical grid).

Table 5. Technical-economic optimization results for the RES (PV-Wind- electrical grid) in the Montaña Roja Nature Reserve.

Turbine Model	No. of Turbines	Initial capital cost ($)	O&M cost ($/year)	Total NPC ($)	COE ($/kWh)
G90	2	4,800,000	1,730,579	26,922,606	0.064
E82	2	4,800,000	1,750,828	27,181,456	0.065
V80	2	4.800.000	1,932,697	29,506,358	0.071

Table 6. Energy optimization results for the RES (PV-Wind- electrical grid) in the Montaña Roja Nature Reserve.

Turbines Model	No. of Turbines	Energy consumption (kWh/year)	Energy purchased (kWh/year)	Energy produced (kWh/year)	Renewable fraction(%)	Energy Sold (kWh/year)	Energy Sold Fraction(%)
G90	2	32,666,340	17,213,290	16,190,625	48.5	737,575	4.5
E82	2	32,666,340	17,555,310	15,941,763	48.0	830,733	5.2
V80	2	32,666,340	18,932,300	14,270,080	43.0	536,040	3.8

Table 5 shows that an initial capital cost of $4,800,000 is considered, which is the same for all possible wind farms connected to the electrical grid. The COE for the different wind turbine models varies between $0.064 and $0.071/kWh, with the system with two G90 wind turbines being the one with the lowest cost/kWh.

The percentage of renewable energy that can be injected into the electrical grid varies between 43.0 and 48.5%, with the system with two G90 wind turbines being the largest producer of renewable energy, followed by the system with two E82 wind turbines (48, 0%). In the latter, up to 5.2% of the total renewable energy produced in a year can be sold.

After analyzing the systems with G90 wind turbines, the energy required for the desalination system totals 32,666,340 kWh/year, of which 15,453,050 kWh/year (47.3%) come from the 4.0 MW wind farm, and the rest (17,213,290 kWh/year) from the electricity grid.

4.3 Polluting gas emissions

Table 7 shows the amounts of polluting gas emissions that can be avoided by wind farms with two G90 wind turbines. This scenario is for the combination with the highest energy production from renewable sources, with a total production of 16,190,625 kWh/year. During the year, only 4.5% of this energy has to be sold to the electricity grid due to excess production, meaning the scenario can be regarded as successful, since 95.5% of the energy is used for desalination (Table 6).

Table 7. Pollutants avoided by the Wind System.

Wind farm	Pollutant	Avoided emissions (kg/year).
2 Turbines (G90)	Carbon dioxide (CO_2)	8,732,130
	Sulfur dioxide (SO_2)	81,390
	Nitrogen oxides (NO_x)	39,710

The RES proposed to supply the maximum possible energy from renewable sources to a desalination plant with a maximum production of 20,000 m^3/day can avoid releasing into the environment 8,732,130 kg/year of CO_2, 81,390 kg/year of SO_2 and 39,710 kg/year of Nitrogen Oxides.

5. Conclusions

The following conclusions can be drawn from the technical-economic analyses conducted for the possible installation of an RES to supply the maximum possible energy from renewable sources to a desalination plant on the island of Tenerife. The places on the island under consideration were the Montaña Roja Nature Reserve and Santa Cruz de Tenerife.

The first technical-economic analysis was carried out for the capital, Santa Cruz de Tenerife, and yielded the finding that an RES cannot be installed in this location to supply energy to a desalination plant due to insufficient wind speed and lack of available land to install a solar farm.

The second technical-economic analysis was carried out for the Montaña Roja Nature Reserve, which has good wind potential. Wind turbines from different manufacturers, such as ENERCON, GAMESA and VESTAS, were analyzed, all of them connected to the electrical grid, which yielded very good results, with the G90 wind turbines being the systems that can inject the greatest amount of energy into the electrical system, with a total of 16,190,625 kWh/year, of which 15,453,050 kWh/year (47.3% the energy required) is used directly in the desalination plant, with the remaining 4.5% being sold to the electricity grid. These RES avoid releasing into the atmosphere 8,732,130 kg/year of CO2, 81,390 kg/year of SO2 and 39,710 kg/year of NOx. The results of this study show that the strategy proposed could be appropriate to be used in similar locations in the Macaronesia region or in other parts of the North Atlantic Ocean.

Acknowledgments

This research has been co-funded by FEDER funds, INTERREGMAC 2014–2020 Programme of the European Union as part of the E5DES project (MAC2/1.1a/309).

References

[1] [1]. ACIISI (Canarian Agency for Research, Innovation and Information Society). Tecnoagua Project. Final inform, 2011, Available at: <https://issuu.com/cienciacanaria/docs/evaluaci__n_de_tecnolog__as_potenci > [accessed 16.7.2022].

[2].ITC (Instituto Tecnológico de Canarias), (Canary Islands Institute of Technology). Plan de ECOGESTIÓN en la producción y distribución de agua de Canarias (2014-2020); 2013, p. 7- 30, Available at: https://oic.itccanarias.org/files/PLAN_ECOGESTIoN_DEL_AGUA.pdf [accessed 16.7.2022].

[3].D. Avila, G. N Marichal, A. Hernández, & F. San Luis. Hybrid renewable energy systems for energy supply to autonomous desalination systems on isolated islands. In A. T. Azar & N. A. Kamal (Eds.), Design, Analysis, and Applications of Renewable Energy Systems. Academic Press, 2021: 23–51.

[4].HCh. Gils, S. Simon, Carbon neutral archipelago-100% renewable energy supply for the Canary Islands. Appl. Energy 2017; 188: 342–355.

[5]. D.Avila, G.N. Marichal, R. Quiza, San F. Luis. Prediction of wave energy transformation capability in isolated islands by using the Monte Carlo method. Journal of Marine Science and Engineering 2021;9: 980.

[6]. I. Padrón, D. Avila, G.N. Marichal, J.A. Rodríguez. Assessment of Hybrid Renewable Energy Systems to supplied energy to Autonomous Desalination Systems in two islands of the Canary Archipelago. Renewable and Sustainable Energy Reviews 2019; 101: 221–230.

[7].I. Padrón, M.D. García, G.N. Marichal, D. Avila. Wave Energy Potential of the Coast of El Hierro Island for the Exploitation of a Wave Energy Converter (WEC). Sustainability 2022;14: 12139.

[8].ITER (Instituto Tecnológico y de energías Renovables), (Renewable Energies Technological Institute). Photovoltaic installations. Available at: https://www.iter.es [accessed 23.8.2022].

[9].ITER (Instituto Tecnológico y de energías Renovables), (Renewable Energies Technological Institute). New wind parks. Available at: https://www.iter.es [accessed 23.8.2022].

[10]. CIATF (Insular Council of Water of Tenerife). General study of the hydrographic demarcation of the Tenerife Island. 2018. Available at: http://aguastenerife.org/images/pdf/PHT3erCiclo/PHT3erCiclo.pdf [accessed 2.9.2022].

[11]. HOMER Software (2.72), HOMER Energy; 2012, Available at: http://homerenergy.com/ [accessed 13.9.2022].

[12]. K. Alphen, W. Sark, M.P. Hekkert. Renewable energy technologies in the Maldives—determining the potential. Renewable and Sustainable Energy Reviews 2007; 11:1650–1674.

[13]. A. Demiroren, U. Yilmaz. Analysis of change in electric energy cost with using renewable energy sources in Gökceada, Turkey: An island example. Renewable and Sustainable Energy Reviews 2010; 14:323–333.

[14]. Iqbal MT. A feasibility study of a zero energy home in Newfoundland. Renewable Energy 2004; 29: 277–289.

[15]. M.J. Khan, M.T. Iqbal. Pre-feasibility study of stand-alone hybrid energy systems for applications in Newfoundland. Renewable Energy 2005; 30: 835–854.

[16]. M.D. Alam, M. Denich. Assessment of renewable energy resources potential for electricity generation in Bangladesh. Renewable and Sustainable Energy Reviews 2010; 14: 2401–2413.

[17]. K.Y. Lau, M.F.M. Yousof, S.N.M. Arshad, M. Anwari, A.H.M. Yatim. Performance analysis of hybrid photovoltaic/diesel energy system under Malaysian conditions. Energy 2010; 35: 3245-3255.

[18]. T.M.I. Mahlia, P.L. Chan. Life cycle cost analysis of fuel cell based cogeneration system for residential application in Malaysia. Renewable and Sustainable Energy Reviews 2011; 15: 416–426.

[19]. A. Al-Karaghouli, L.L. Kazmerski. Optimization and life-cycle cost of health clinic PV system for a rural area in southern Iraq using HOMER software. Solar Energy 2010;84: 710–714.

[20]. M.A.A Rahmat, A.S. Abd-Hamid, Y. Lu, M.A.A. Ishak, S.Z. Suheel, A. Fazlizan, A. Ibrahim. An Analysis of Renewable Energy Technology Integration Investments in Malaysia Using HOMER Pro. Sustainability, 2022, 14, pp. 13684. Available at: https://doi.org/10.3390/su142013684 [accessed 12.9.2022].

[21]. A. Singh, P. Baredar, B. Gupta. Computational Simulation and Optimization of a Solar, Fuel Cell and Biomass Hibrid Energy System Using HOMER Pro Software. Procedia Engineering 2015; 127:743 – 750.

[22]. G. Ali, H. H. Aly and T. Little, "Using HOMER software to investigate, size and apply renewable energy sources in a convention center in Sabratha, Libya," 2021 International Conference on Electrical, Communication, and Computer Engineering (ICECCE), Kuala Lumpur, Malaysia; 2021: 1-6.

[23]. S. Rehman, et al. Feasibility study of hybrid retrofits to an isolated off-grid diesel power plant. Renewable and Sustainable Energy Reviews 2007; 11: 635–653.

[24]. S. Rehman, L. Al-Hadhrami. Study of a solar PV-diesel-battery hybrid power system for a remotely located population near Rafha, Saudi Arabia. Energy 2010; 35: 4986-4995.

[25]. S.M. Shaahid, M.A. Elhadidy. Technical and economic assessment of grid-independent hybrid photovoltaic–diesel–battery power systems for commercial loads in desert environments. Renewable and Sustainable Energy Reviews 2007; 11: 1794–1810.

[26]. S.M. Shaahid, M.A. Elhadidy. Economic analysis of hybrid photovoltaic–diesel–battery power systems for residential loads in hot regions—A step to clean future. Renewable and Sustainable Energy Reviews 2008; 12: 488–503.

[27]. S.M. Shaahid, I. El-Amin. Techno-economic evaluation of off-grid hybrid photovoltaic–diesel–battery power systems for rural electrification in Saudi Arabia—A way forward for sustainable development. Renewable and Sustainable Energy Reviews 2009;13: 625–633.

[28]. J. R. Balbin, J. R. T. Bautista, E. J. S. Manalansan and J. P. Tumaliuan, "Hybrid Renewable Energy System Model Using HOMER as Support to the Power Crisis in the Philippines," 2020 IEEE 12th International Conference on Humanoid, Nanotechnology, Information Technology, Communication and Control, Environment, and Management (HNICEM), Manila, Philippines, 2020:1-6,

[29]. K. Burman, J. Keller. B. Kroposki, P. Lilienthal, R. Slaughter, J. Glassmire. Renewable Power Options for Electrical Generation on Kaua'i: Economics and Performance Modeling. Technical Report. NREL/TP-7A40-52076. Contract No. DE-AC36-08GO28308; 2011.

[30]. G.J. Dalton, D.A. Lockington, T.E. Baldock. Feasibility analysis of stand-alone renewable energy supply options for a large hotel. Renewable Energy 2008; 33: 475–1490.

[31]. ISTAC (Instituto Canario de Estadística), (Canarian Statistic Institute); 2022, Available at: http://www.gobiernodecanarias.org/istac [accessed 26.10.2022].

[32]. J. Chenoweth. Minimum water requirement for social and economic development. Desalination 2007; 229: 245–25.

[33]. S. Gössling, et al. Tourism and water use: Supply, demand, and security. An international review. Tourist Management 2012; 33: 1-15.

[34]. Wind Observatory, Hard times for wind energy in Spain Energies Renewables 2011; 98: 34-40. ISSN: 1578-6951.

[35]. G. Micale, A. Cipollina, L. Rizzuti. Seawater desalination for freshwater production.In: Cipollina A, Micale G, Rizzuti L, editors. Seawater desalination, green energy and technology. Berlin: Springer-Verlag; 2009. p. 1–26. [ISBN: 978-3-642-01150-4].

[36]. MEDA. Water, ADIRA handbook, a guide to autonomous system concepts. 2007. p. 14–20. Available at: https://nmwaterconference.nmwrri.nmsu.edu/wp-content/uploads/2011/Relevant-Papers/2008_adira_handbook.pdf [accessed 14.12.2022].

[37]. Insular Water Council of Tenerife. General Study of the Hydrographic Demarcation of the Island of Tenerife. 2008.

[38]. T. Lambert, P. Gilman, P. Lilienthal. Micropower modeling system. 2006. pp.379–417. Available at: http://www.pspb.org/e21/media/HOMERModelingInformation.pdf [accessed 14.12.2022].

[39]. J.F. Manwell, J.G. McGowan, A.L. Rogers. Wind energy explained: theory, design and application. 2nd ed. John Wiley and Sons, 2009. p. 23–89. [ISBN: 978-0-470-01500-1]. Available at: http://www.worldcat.org/title/wind-energy-explained-theory-designand-application/oclc/431936159 [accessed 15.12.2022].

[40]. ENERCON, 2012. Gama de aerogeneradores ENERCON. Available at: http://www.enercon.de/p/downloads/EN_PUE_es_web.pdf [accessed 20.12.2022].

[41]. Gamesa, 2007. GAMESA G52-850 kW. Available at: https://tecnologia4eso.wikispaces.com/file/view/G52castellano.pdf [accessed 16.12.2022].

[42]. Gamesa, 2008.Gamesa G90-2.0 MW. Available at: http://www.unizar.es/jmyusta/wpcontent/uploads/2010/06/G90-castellano3.pdf [accessed 16.12.2022].

43]. Vestas Wind Systems, 2011. Gama de aerogeneradores VESTAS. Available at: http://www.vestas.comshould [accessed 16.12.2022].

A comprehensive review of water distillation technologies for green hydrogen production

Rolando Argandona[a], Assaad Zoughaib[b] and Rasha Mustapha[c]

[a] Mines Paristech, Paris, France, rolando.argandona_villavicencio@mines-paristech.fr, CA
[b] Mines Paristech, Paris, France, assaad.zoughaib@mines-paristech.fr
[c] STEM, Paris, France, rasha@stem-tech.fr

Abstract:

The use of low-carbon hydrogen is called to be one of the key vectors for the decarbonization of the energy sector and industry. In that regard, green hydrogen, which is produced through the electrolysis of water using renewable sources of electricity, is the process that offers the most advantages. In order to operate efficiently, water electrolysis technologies require a water source of near-ultrapure quality. To achieve this, a preceding water treatment stage is necessary, and reverse osmosis technology is currently the most widely used. This pressure-driven technology has reached maturity, but it still has certain technological limitations and energy consumption to be considered. This paper presents a comprehensive literature review of water distillation technologies currently available for obtaining the water quality required by green hydrogen electrolyzers. The comparison between mature and innovative water distillation processes showed that membrane distillation is one of the most promising technologies and that it has proved its effectiveness in the desalination sectors, but it has yet to be exploited to produce green hydrogen. This technology uses hydrophobic membranes and can be powered by a low-temperature heat source (between 40 °C and 90 °C), which provides opportunities to use alternative sources of heat, such as solar, geothermal, and even low-quality waste heat. This presents a great opportunity for energy integration with water electrolysis processes, as they generate a low-temperature waste heat flow (around 80 °C) during operation, which is compatible in quality and quantity with membrane distillation process requirements.

Keywords:

Water Distillation; Green Hydrogen; Membrane distillation; Energy Integration.

1. Introduction

It is well-known that the fight against climate change and environmental degradation has intensified in recent years. In that regard, the energy sector has proposed solutions for its decarbonization, with hydrogen (H_2) playing an important role as a possible alternative to the use of fossil fuels [1]. Among the main advantages of the use of H_2 is that it is abundant, non-toxic [2], and has one of the highest energy densities among the well-known fuels [3] (reaching a low heat capacity of 120 MJ/kg [4]). Additionally, H_2 only emits water as a by-product during combustion [2], is much easier to store and transport than electricity [3] and is flexible enough to be used in sectors such as power generation and buildings [5], as well as being a potential solution for the decarbonization of sectors difficult to electrify, such as transport [3].

Although the use of H_2 has increased to a global consumption of almost 90 Mt of H_2 in 2020 [6], there is still no accurate projection of its demand in the years to come. Several authors [3,5,7–10] have taken different base scenarios to make their projections, stating that it will be required from 50 Mt/y of H_2 [10] to 2.3 Gt/y by 2050 [9]. Despite the lack of homogeneity in the projections, a considerable amount of H_2 would be required, and therefore it would be necessary to find a reliable source from which to obtain it.

It should be noted that H_2 is an energy vector, not an energy source, so its veritable contribution to carbon neutrality will depend on how it is produced [1] since it can derive from fossil fuels as from electricity [11]. Therefore, a color-coding system is often used to describe the level of "cleanliness" depending on the type of source and technology used for obtaining the H_2 [4]. The most commonly used colors for H_2 are grey (obtained by steam methane reforming, SMR), blue (obtained by SMR with carbon capture and storage), turquoise (obtained by methane pyrolysis), and green (obtained by water electrolysis) [12].

Almost all types of H_2 mentioned above are considered pollutants to some degree [13] since they are obtained using fossil energies as their primary source. Only the green one is considered a clean source of H_2 [4,14] since the electricity required comes from low-carbon sources such as renewable energy sources (RES) [13]. However, it should be noted that H_2 is currently mainly produced by SMR systems of natural gas (48% of the

total) or using other fossil sources (48%) [2]. This means that only 4% of the total H_2 produced corresponds to green H_2 [15].

Therefore, boosting the production of H_2 through water electrolysis using RES presents great potential to decarbonize the energy sector [3] and could be crucial in addressing the climate crisis [16–18]. In addition, coupling the production of green H_2 with electricity generated from RES (which are considered unstable in terms of generation) is one of the best methods for storing the excess energy from RES, known as power-to-gas storage [2]. Other benefits of green H_2, and its direct relationship with RES, include its compactness, the possibility of being independent of the existing electrical infrastructure, and its attractiveness towards emerging markets [19].

However, it should be noted that the production of green H_2 is still under development, therefore it is currently more expensive than the production methods based on fossil fuels [2]. Nevertheless, it is expected that the use of green H_2 electrolyzers with extended operating hours will enable them to reach competitive costs [20]. Furthermore, due to the many advantages listed above, as well as the fact that the price of RES electricity continues to decrease [16], it is estimated that its production will expand to reach at least 22% of the total H_2 produced in 2050 [2].

The production of green H_2 is defined by two main components: the use of RES and the use of water electrolyzers [19]. The latter are electrochemical devices that separate water molecules (H_2O) into H_2 and oxygen by passing an electric current through them [20]. In order to operate efficiently, water electrolysis technologies require to be fed by a water source of near-ultrapure quality [16]. Consequently, they require a previous water treatment (distillation) stage to protect the electrochemical process. This paper presents a comprehensive literature review of the water distillation technologies currently available for obtaining the water quality required by electrolyzers to produce green H_2, as well as other developing processes that show considerable potential for entering this market.

2. Electrolyzers

Currently, there are several electrolyzer technologies already developed, all of which share the same fundaments: water separation in the electrodes, allowing the transport of ions (H^+ and OH^-) through liquid electrolytes or solid membranes [20]. The two main commercial varieties are alkaline water electrolyzers (AWE) and proton exchange membrane electrolyzers (PEME) [16].

AWE technology has been developed since the 1920s [21], making it the most mature and well-established technology on the market [2]. This technology uses aqueous solutions of KOH or NaOH as electrolytes and typically operates at temperatures between 60 °C and 90 °C [22] and pressures below 30 bar. Its costs are significantly lower than those of other technologies because it does not require the use of expensive catalysts [23] and utilizes simple stainless-steel electrodes [22]. This technology presents a response to sudden changes in power supply in the order of seconds [23], although very abrupt changes can cause soda-like eruptions in the electrolyte [22]. On the other hand, its H_2 purity level is slightly lower than those of other technologies (in the order of 99.95% [19]), due to the use of a relatively permeable separator that can sometimes allow bubbles to pass through [2]. Its feed water quality requirements are slightly more flexible than those of other technologies; however, if impurities are present, they can clog the device and contaminate the electrolyte [22]. Additionally, very low-quality water feed can lead to faster equipment deterioration. Impurities such as Fe, Cr, Cu, Si, AL, and B have the greatest impact on the performance of the system [20].

On the other hand, PEME technology began its history in the early 1950s [16] and is now close to its full technological development [19]. This system features a compact modularity thanks to the membrane-electrode assembly (MEA) concept, which allows easy downsizing [2]. Unlike AWE technology, this system only requires the supply of pure water (no electrolyte is necessary), thus its service life is longer, due to the absence of KOH-induced corrosion [16]. The electrolyte is formed by a solid polymer that allows high conduction of H^+ protons [22]. Its operating temperature is lower than AWE, being able to operate in a range between 50 °C and 80 °C and at pressures below 70 bar [20]. One of its key points is its flexible operation with a fast response time (in the order of milliseconds) [23], which allows it a suitable solution for coupling with RES electricity.

Additionally, the H_2 obtained through PEME presents a high purity, typically around 99.99% [19,24]. This technology, however, has the disadvantage of being more costly than AWE due to the high-cost catalysts [2] and other noble materials, such as Pt or Ir [25], used in the electrolyzer. Furthermore, the precision required for the bipolar dishes due to the MEA system contributes to the increased cost of production [22]. In terms of purity requirements in the water supply, PEME is one of the most demanding technologies as it is quite sensitive to the presence of impurities [22] and this is one of the main reasons for its failure [26]. The components most vulnerable to impurities are the solid membrane, the catalyst, and the porous transport layers [20]. Among the most harmful elements for the system is the presence of Mg_2 and Ca_2, as they generate precipitates on the cathode side [27], which can lead to irreversible damage.

Today, the industry is shifting towards the use of PEME systems due to their compact design, fast response to dynamic changes, and high purity in the generation of H_2 [23,24]. However, AWE systems still have a significant market presence due to their lower cost.

3. Water requirements

3.1. Quality requirements

As can be seen, water electrolysis technologies require a minimum degree of water purity to function properly and avoid damaging their components [26]. However, detailed studies on the required water quality for each type of electrolysis technology are not available [28].

Nevertheless, the industrial standard adopted for this purpose is the ASTM standard specification for Reagent Water [29]. In this sense, it is recommended to use pure water with a minimum quality of type II of the ASTM standard, being preferred type I (ultrapure) for PEME systems [16], as they are more sensitive to impurities. Table 1 summarizes the ASTM water quality types. It can be seen that the purity requirement for electrolyzer feedwater is quite high, considering that commercially sold distilled water typically has a conductivity lower than 10 µS/cm [30].

Table 1. ASTM water quality standard [29].

Parameter	Type I	Type II	Type III	Type IV
Conductivity, min µS/cm (25 °C)	0.056	1	0.25	5
Resistivity, min MΩ-cm (25 °C)	18	1	4	0.2
TOC, max µg/l	50	50	200	No limit
Sodium, max µg/l	1	5	10	50
Silica, max µg/l	3	3	500	No limit
Chloride, max µg/l	1	5	10	50
pH value (25 °C)	-	-	-	5-8

3.2. Quantity requirements

Stoichiometric theory indicates that 9 kg of input water are required for each kg of H_2 produced [20]. In reality, considering the inefficiencies in the electrochemical reaction, this water demand is typically higher, being commonly used an average value of 15 kg of water per kg of H_2 [3,8]. Given the maximum projected H_2 demand of 2.3 Gt/y by 2050 [9], and assuming that all the production relies on generating green H_2, the total direct water consumption for this projected demand would be around 34.5 Gt/y of H_2O [8].

However, it should be noted that this water demand only considers the direct consumption by the electrolysis process; the indirect consumption of the system, which comes from upstream and includes the water consumption for power generation and secondary equipment (mainly water treatment process and cooling water requirements) [3], can be up to 20 times higher than the direct consumption [11]. A maximum value of 126 kg of water per kg of H_2 is currently used for global system estimations [11].

It must be considered that the production of green H_2 will interlock the energy-water-nexus in unpredictable ways given its direct relation [3]. This relationship, together with the significant water demand, has raised doubts about the viability of a green hydrogen-based economy in certain authors [8,31], considering that there are already water shortages (of fresh water), and this demand may pose greater water stress in certain already affected areas [3].

4. Water resource

The world's total water resources are about 1.4 billion km^3 [32], from which 97.5% is sea and ocean saltwater and only 2.5% is fresh water [33]. However, of this total, only 0.27% is accessible for direct use [34], approximately 94500 Gm^3, with the rest being ice and groundwater. Therefore, the projected water requirement for direct electrolyzation feed is relatively small in comparison [3]. Despite this, the idea is not to sum any additional burden to freshwater use, considering that certain areas of the planet already have limited or no access to fresh water supply [8].

It must be taken into account that population growth and increased water demand per capita are among the main factors contributing to the problem of water scarcity. Additionally, it should be noted that the effects of climate change act in synergy with these two factors to increase water stress [35].

The water stress index (WSI) measures the amount of water used relative to the amount of water available [35]. However, it should be noted that the WSI only considers the physical availability of the resource. To gain a more comprehensive understanding of water security, the inclusion of economic and social indices is suggested. In this regard, Gain et al. [36] presented a global water security index (GWSI) that considers criteria such as availability, accessibility, security and quality, and resource management. The results of their analysis indicated that some regions, particularly in the South, are beginning to experience a water safety problem.

Moreover, projected scenarios of water scarcity have been generated, estimating that by 2025, the number of people facing this problem will reach 2.8 billion, and by 2050 it could reach 4 billion [35]. Similarly, the World Water Program estimates that by 2030, only 60% of the world's required water will be available, and according to the OECD, this will drop to 55% by 2050 [32]. These factors have prompted a debate on the need to seek

new sources of fresh water [32]. Given that, in the context of global water distribution, saltwater is the most abundant resource [33], and in light of the other aquatic stressors mentioned above, the possibility of using seawater as a source for obtaining fresh water has been encouraged [37].

Furthermore, in the context of H_2 production, marine environments could be a source of renewable energy for green H_2 [38]. Moreover, recent decades have seen some researchers [1,16,22,26] consider the possibility of generating H_2 through direct electrolysis of seawater. In this sense, efforts have been made to develop electrolyzers, membranes, and catalysts that can operate with seawater without prior purification [26]. However, most studies have come to the same conclusion: a seawater desalination process and subsequent feeding of a classic electrolyzer is much cheaper than a potential direct seawater electrolysis process [1,16,22,26]. This is mainly because the costs of water desalination, which is estimated to be around 0.1 $/kg H_2 in the case of using a reverse osmosis (RO) process [1], are minimal compared to the other costs associated with a classic water electrolysis process, such as the cost of energy consumed [16]. Additionally, the expensive materials needed for direct seawater electrolysis and its technical uncertainties [16], made this technology economically non-attractive [16,26,28].

Therefore, as seawater desalination processes have already reached a level of maturity and are now considered reliable water sources [39], it is recommendable to focus efforts on the technical and economic improvement of these processes [16].

5. Seawater desalination processes

The first desalination technologies date back to World War II and have since been gaining traction around the globe in response to the increasing demand for water [40,41]. As of now, the global desalination capacity is 115 Mm^3/d [42], with 65% of that total capacity located in the Middle East, particularly in the Persian Gulf [32]. The global distribution of different water sources used to supply desalination systems demonstrates that 60% of production uses seawater due to its abundance, while brackish water is the second most used resource, with nearly 21% of the share [43].

There are currently 16876 desalination plants [44] utilizing various technologies to carry out the process. Figure 1 illustrates the global desalination plant distribution. It is evident that RO technology is the most prevalent on the market today, as it consumes less energy than thermal systems and has seen tremendous progress in membrane technology [45] since the 1960s [46]. It is worth noting, however, that in some regions such as the Middle East (which accounts for 47.5% of the overall market [47]), thermal technologies, including multi-stage flash distillation (MSF), are the most widespread [46] and are used in thermal cogeneration.

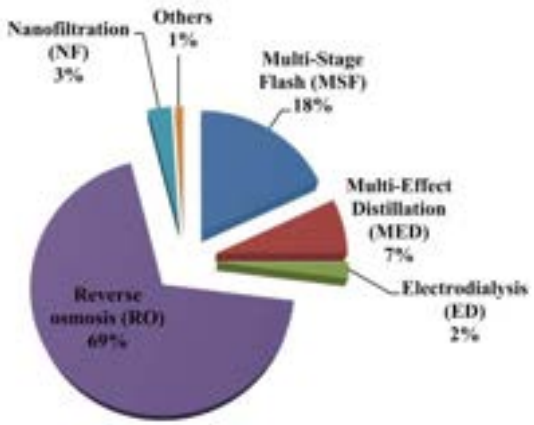

Figure. 1. Worldwide water desalination processes distribution [32].

In general, technologies are currently classified into two major groups: thermal desalination processes and membrane desalination processes [48].

5.1. Thermal desalination processes

In synthesis, thermal desalination processes are phase change techniques [49] that involve heating the feed liquid, under certain temperature and pressure conditions, to create a water vapor that will separate it from the salts and other non-volatile components in the feed stream. This vapor is then condensed to produce a stream of distilled water [50]. The most used thermal desalination processes today include MSF and multi-effect distillation (MED).

As noted above, MSF is based on the principle of boiling seawater (or other feed fluid) at a temperature below its normal boiling point, due to the “flashing effect” [40]. An external heat source, usually steam [41], is required to heat the feed fluid between 90°C and 115 °C [33]. The feed fluid passes through several stages, where the temperature and pressure of each stage decrease compared to the preceding stage [32]. As it passes through

the stages, some of the heated fluid will evaporate due to the stages being at a pressure lower than their vapor pressure. The vapor formed is then condensed on the outer surface of heat exchange tubes where low-temperature salinized water passes [40], and therefore, a distilled condensate could be collected. MSF facilities can consist of 4 to 40 stages [51].

Among thermal desalination technologies, MSF is the most widely used method due to its lower maintenance costs and longer service life [52]. MSF systems, however, face important technological challenges, such as the precipitation of Ca and Mg salts on the tubes of the heat exchanger [53], corrosion [40], and high thermal energy consumption [40,49]. Despite these issues, MSF systems provide good-quality desalinated water [54]. Although the conductivity values of the desalinated product are scarce at the literature level, Deghani et al. [55] demonstrated through experimentation the production of distillate with less than 30 µs/cm from a feed flow with 73 mS/cm.

For its part, MED technology is older than MSF [40] and operates on a similar principle (using a series of vessels at pressures lower than ambient). The main difference between them is that MED generates steam by spraying the feed water in the form of a thin film [40] onto heat exchanger tubes (evaporator), where steam from the previous stage passes [32]. Generally, MED has between 4 to 14 effects [40] and has the advantage of working at temperatures and pressures lower than those of MSF, requiring the heating of salinized water to only 66 °C [51], thus consuming less energy [40]. MED is suitable for small to medium size plants but is subject to corrosion [40] and high maintenance costs due to the utilization of spraying water systems [52]. Their desalinated water quality is comparable to that of MSF, given their similar processes [52].

In general, the operating principle of thermal distillation technologies is simple, but their operating and maintenance costs are high due to the high pressures and temperatures needed to operate them. Moreover, they have low desalination efficiency [56] and require large amounts of energy for the evaporation of water which needs sensitive and latent heat [47], making it difficult to implement them on a large scale [57].

5.2. Membrane desalination processes

Membrane technologies utilize various types of permeable membranes to separate and isolate salts and impurities on one side of the membrane, thereby achieving salt-water separation [56]. The most common membrane processes are RO, nano-filtration (NF), and electrodialysis (ED). The membrane characteristics required for effective separation, such as pore size and mechanical strength, will depend on the type of process.

The RO process is the most widely used membrane technology, and it involves forcing seawater through a semi-permeable membrane (water permeable, but not salt permeable) using a pumping system that requires an electrical supply. The hydraulic pressure applied must be higher than the osmotic pressure, which is related to the concentration of salts in the feed stream [57]. Therefore, the salt concentration directly affects the electrical energy consumption of the system and thus its operating cost (which is one of its main operating costs) [40]. Typically, these systems operate at pressures between 54 bar and 83 bar for seawater desalination [40].

Despite the development of energy-efficient RO systems, as well as energy recovery devices, which have resulted in decreasing the capital and operating costs of the system [16], the increased electrical energy demand to process high salinity solutions remains one of their primary challenges [50]. Additionally, the presence of fouling, defined as the process in which an undesirable material (foulant) adheres to the surface or pores of the membrane [58], is another issue that must be addressed as it can lead to blockage of the membrane and, eventually, complete plugging of the system [40]. Therefore, in order to maintain a constant permeate flow, an increase in the operating pressure will be required, resulting in higher operating costs [59] and reduced process efficiency. This will ultimately impact the overall performance of the process.

For this reason, RO systems typically require a pre-treatment stage, both physically and chemically [16], to ensure their proper operation and to reduce the risks posed to the membrane [57]. However, this also carries environmental risks due to the use of chemicals to control fouling, which could have an adverse impact on the sea [60,61]. For example, the use of coagulants such as ferric salts can cause the coloring of the outlet stream (called red brine) and thus increase the turbidity and reduce the light penetration in the water [62]. In terms of water quality, the distillate produced will depend on the initial quality of the feed stream, the membrane properties, and the operating pressure of the system [52]. However, it has been demonstrated that the quality of desalinated water tends to be lower than that obtained from thermal systems [63], and therefore in many cases a second desalination stage or supplementary process is required.

NF is a pressure-driven process with certain similarities to RO (in fact, its operation is between that of RO and ultrafiltration [64]) but it is capable of operating at lower pressures, higher flow rates, and with lower investment costs [65]. NF has a membrane pore structure that is larger than that of RO, allowing more salts to pass through it [66]. Generally, it has a high rejection rate for divalent ions (around 98%) [64], however, there are certain issues when it comes to the total removal of NaCl in desalination processes [59]. Despite this, some studies [67] have achieved quality results comparable to those of RO when used with salinized water. Ultimately, the choice between NF and other water treatments will depend on the quality requirements, the

quality of the input water, and the capacity required [67]. As is the case with RO, NF also presents problems with fouling control and difficulty in controlling the pore size of the membrane [68].

Another membrane process is the ED, which is an electro-membrane process in which ions are transported from one solution (the feed) to another via a membrane, due to the application of an electrical potential difference [66]. It should be noted that the cost of the process is proportional to the number of salts transported to the membrane, so it is recommended to use it for fluids with a low concentration of solids (between 8 g/L and 10 g/L) [49]. Furthermore, other membrane-based processes, such as microfiltration and ultrafiltration, are not recommended for desalination processes. Nevertheless, these technologies have found a market as a pre-treatment process for RO systems [49].

5.3. Problems of current desalination technologies

As has been seen, the increasing demand for fresh water coupled with its scarcity has led to the use of desalination technologies as one of the main solutions. Although these technologies have already reached a certain level of maturity, they still have challenges to overcome, particularly those related to the discharge of brine [49], high investment costs [56], and high energy consumption [45]. Concerning the latter, it has been noted that desalination processes can consume from 8 to 20 times more energy (thermal or electrical, depending on the process) than conventional surface water treatments [69]. For example, the current consumption of electric energy by desalination processes is 56 TWh, however, it is estimated that by 2040, this consumption would become the second-largest energy-intensive process in the entire water sector with 345 TWh, only surpassed by the water supply energy demand [70]. In addition, high energy consumption is often accompanied by increased greenhouse gas emissions [46]. This is especially true because many desalination systems are still powered by fossil fuels [71]. It is estimated that, overall, 23 kg of CO_2/m^3 of desalinated water are currently being released [63].

Moreover, the technologies mentioned above are designed to be economically viable in large-scale operations (in most cases, the scale is the most influential factor when it comes to capex). For example, in the case of RO, a typical current plant produces 0.1 Mm^3/d of water [72], while commercial electrolyzers do not exceed a power of 10 MW, which is equivalent to the use of approximately 125 m^3/d of water [26]. This illustrates the significant difference in scale between the two processes.

Therefore, it is necessary to find alternative desalination processes with reduced greenhouse gas emissions, lower energy requirements and that can be powered by renewable sources or waste heat [37], in order to sustainably meet the world's growing demand for fresh water and feed water for electrolyzers. In this regard, forward osmosis (FO), reverse electrodialysis (EDR) and membrane distillation (MD) are the principal emerging technologies on the market (the 1% of others, as seen in Figure 1).

FO consumes less energy than RO, since it does not require external hydraulic pressure and has a lower fouling tendency [50]. However, it still poses certain technological challenges in extracting water from the draw solution to regenerate the cyclic process [47]. For its part, EDR works similarly to ED (see section 5.2) but with the added capability of reversing the polarity of its electrodes during specific time intervals, enabling it to minimize fouling and remove deposited materials [47]. However, like ED, its energy consumption depends on the feed concentration, making it more suitable for solutions with low salinity. Finally, MD doesn't require a high electrical consumption and has the potential to be more energy efficient than other processes when valorising waste heat or renewable heat sources, which make it one of the most promising technologies to date for desalination.

5.4. Membrane distillation technology

MD is a non-isothermal membrane process that is based on the generation of a steam phase in a hot solution stream, close to the surface of a membrane [34]. The vapor will be able to pass through the membrane (the hot side of the system) and then condenses onto the cold side of the system, where cold distilled water circulates. This process is made possible by the use of hydrophobic membranes, which allow only the passage of steam, and volatile compounds, while retaining the liquid part in the hot stream (which contains dissolved salts and other non-volatile compounds) [73]. In this way, a permeate (distilled water) can be obtained on the cold side of the system. Figure 2 shows a diagram of a counter-current MD system.

The driving force of MD is the difference in partial vapor pressure between the hot and cold side of the system. This difference is responsible for converting some of the molecules in the supply liquid into vapor [48], thus initiating the mass transfer process described above. MD systems are considered thermal-driven since the partial pressure difference is related to the temperature gradient on the membrane sides [74]. In order for MD to be effective, a temperature difference of at least 20 °C must exist between the two sides of the system [75].

The membrane material and its characteristics are among the most important parameters for the successful operation of MD systems. As the physical barrier between the hot and cold side of the system, its properties will influence the heat and mass transfer. Generally, MD membranes have a pore size between 0.2 μm and 1 μm [76], with a porosity between 65% and 85% [77], a tortuosity regularly assumed to be 2 [78], and a thickness between 0.04 mm and 0.25 mm [79]. Polymers such as PTFE, PP, and PVDF are commonly used for the

fabrication of MD membranes [61], due to their ability to be modulated in terms of intrinsic properties and low surface tension [77].

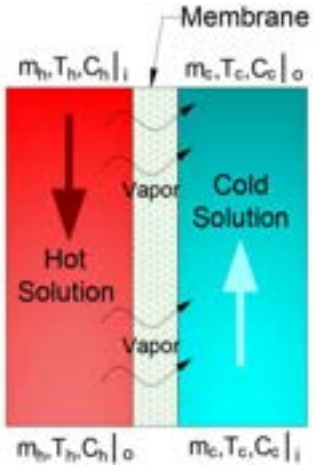

Figure. 2. Diagram of a counter-current MD system.

In addition to the previously mentioned points, MD technology has other advantages. For instance, it is almost insensitive to the initial concentration of the feed stream, which causes problems in other distillation systems [61], and has a high rejection factor, with leads to a theoretically complete separation [80]. Additionally, MD systems are robust, compact, and modular [73], thus reducing investment costs [34].

On the other hand, the main drawbacks of MD technology are its low permeate flow and high energy consumption [50] (cf. 5.4.1). The low permeate flow can be attributed to the air trapped in the membrane, which introduces resistance to the mass transfer [80], with a greater effect than on pressure-driven processes. The high energy consumption is due to MD being a phase change process, which requires a large amount of thermal energy [74], but at a low temperature.

Studies [39,81–84] have shown that distillates produced through MD technology can have electrical conductivities ranging from 2 and 5 µS/cm, with high salt rejection (higher than 99.7%). Furthermore, a second MD distillation stage can improve the purity of the distillate, reaching values near 0.7 µS/cm [81]. It has been found that the quality of the distillate is not affected by the initial operating conditions (temperatures, flows, concentrations) [39,82], due to the membrane, which does not allow for the passage of liquid. However, it is important to note that the operating conditions will influence the time required to achieve low-conductivity distillates since MD technology tends to start its operation producing distillates with high conductivity, which will decrease over time (generally taking a bit less than an hour) [82].

5.4.1. Comparison with other technologies

Table 2 shows a comparison of parameters between the main water desalination technologies used to date and MD technology.

Table 2. Comparison of water desalination technologies.

Parameter	RO	MSF	MED	MD
Electric consumption (kWh/m^3) [63]	3.7 - 8	2.5 - 5	2 - 2.5	0.6 - 1.8
Thermal energy consumption (kWh/m^3) [49]	-	190-390	230-390	100 - 800
Water quality (ppm TDS) [63]	200 - 500	10	10	10
Unit product cost (USD/m^3) [49]	0.52-0.56	0.52-1.75	0.52-1.01	No information
Maximal feed salinity (g/L) [43]	70	180	180	350
Water composition changes tolerance [57]	Very low	Medium - High	High	High
Fouling [57]	High	-	-	Low - Medium
CO_2 emissions (kgCO_2/m^3) [51]	1.75 - 2.79	5.56 -25	4.38 - 17.6	No information

Table 2 reveals that MD technology has several advantages over conventional technologies, and a comparison with the dominant technology in the market, the RO, reveals even more advantages. For example, MD is not limited by a maximum osmotic pressure [85], and the hydrostatic pressure required is much lower than that of RO systems [80], which allows for the use of less resistant materials. Additionally, the membrane required for MD is simpler and has a larger pore size, which reduces the risk of fouling [48], resulting in improved cost recovery [74].

In addition, focused on obtaining adequate water quality to feed water electrolyzers, it can be seen that RO yields the lowest quality among the compared technologies, due to its reliance on the quality of the input water.

Typically, at the industrial level, at least two RO stages are needed to achieve acceptable quality. On the other hand, thermal technologies, MED and MSF, yield better-quality water, albeit with somewhat higher conductivity than with MD [55,82].

Even though the amount of thermal energy needed for MD is much higher than for other systems, there is a critical point to consider: the thermal energy required differs in quality from the thermal systems. Conventional thermal systems require energy sources with temperatures above 90 °C for MSF and at least 70 °C for MED, while MD systems require flexible low-temperature heat, in the 40 °C to 90 °C range [86], making it more economically attractive [63]. Furthermore, the quality of the required heat provides opportunities to use alternative sources of heat, such as solar, wind, geothermal, or even waste heat, making the MD technology more environmentally attractive.

5.4.2. Potential use of waste heat

In this regard, the use of waste heat is versatile due to its various forms (liquid, gaseous or diffuse) and temperatures, which are specific to the industrial process from which they originate [71] and gives it different valorizations. However, its ease of use depends on aspects such as continuity, temperature range, heat transfer modes, and location between source and place of use [87]. Despite these barriers, there is immense potential for this resource to be exploited in various ways [87].

Estimating the existing total waste heat is complicated by the fact that it is difficult to quantify with certainty due to the constant changes in the overall energy mix [88] and changes and variations in the processes that generate this heat. Few studies have sought to quantify the potential of the waste heat field, yet, some estimations indicate that the total waste heat released at a global level would be between 68.2 PWh [87] and 72.7 PWh [88]. It is also estimated that the waste heat could reach 89.4 PWh by 2030 [88].

However, it should be noted that these projected values only reflect the amount of waste heat, not the amount of energy that can be converted into work, known as exergy [87]. Thus, an exergy analysis, taking into account the quality factors, known as the Carnot factor [88], related to the source temperature, is necessary to quantify the true potential of the waste heat that can be used [87]. To this end, it is necessary to recognize different temperature scales at which waste heat occurs. For example, according to the quantification of Forman et al. [87], 20.6% of the waste heat is above 300 °C (high quality), 16% is between 100 °C and 300 °C (medium quality) and the rest is below 100 °C (low quality). By applying the corresponding Carnot factors for each temperature range, and for each sector from which the waste heat originates, the authors obtained a theoretical waste heat potential of 13400 TWh, which is only about 20% of the total waste heat that can be recovered and used.

As can be seen, there is an abundance of waste heat resources that can be recovered and exploited. Moreover, when using this heat source, it is considered that its utilization will not add CO_2 emissions to the balance, as there is no additional fuel needed [71]. However, it is worth noting that it is not entirely free energy (although some studies consider an investment of 0 to simplify the calculations) since its use entails costs related to collection, transportation, processing, and operation, which in some cases may make the use of conventional energy sources more feasible [89]. For this reason, a technical-economic analysis should be carried out in each case of study to ensure the usefulness of the exploitation of this resource.

5.4.3. Potential coupling with hydrogen electrolyzers

The coupling of MD systems and green H_2 generation systems also presents multiple opportunities for exploiting waste heat. The electrochemical reaction of the electrolyzers generates residual heat, due to their inefficiencies [90], which is usually dissipated by a cooling water circuit. The operating temperature of the electrolyzers is typically between 50 °C and 90 °C (depending on the type of electrolyzer) [91,92], which has already been shown to be useful to powered district heating networks when the urban area is close to the electrolization plant [90,93].

Therefore, the heat dissipated by the electrolyzer has a quality that can be used by an MD system, which can be energetically powered by the cooling water of the system. Additionally, the regular configurations of electrolyzers AWE and PEME have certain heat exchangers (for refrigeration) [20] with potentially usable dissipated heat. Some examples are the KOH cooling system in the electrolyzer stack (in AWE systems) or the inter-stage cooling system in the hydrogen compression process.

Some studies have detailed figures on the heat dissipated during the operation of water electrolyzers. Tiktak [90] reported 171 MW of heat dissipated at a temperature of 77 °C while operating at a nominal production rate of 5.25 kg/s of H_2. Similarly, Burrin et al. [91] estimated 0.31 kW of heat at 75 °C during the generation of 18.7 kg/h of H_2. When taking into consideration the equivalence of kg of water required per kg of H_2 (as discussed in Section 3.2), it can be estimated that the electrolysis systems release 604 and 1120 kW/m^3 of required water, respectively. The potential to use this heat in MD systems can be clearly appreciated when compared with the energy demand values presented in Table 2. Despite the potential presented, the MD-green H_2 coupling has not been studied yet, so it is essential to promote these projects to dispel the uncertainties of these systems.

6. Conclusions

The present study conducted a comprehensive literature review of water distillation technologies oriented towards producing hydrogen using water electrolyzers that are powered by renewable electric energy (green H_2). These devices require water of a quality bordering on ultrapure to operate without the risks associated with their electrochemical reaction. Therefore, considering the projections of water requirements for a future green H_2 market, the most viable form of water treatment appears to be seawater desalination.

In this regard, today two large groups of technologies dominate the market: thermal technologies (25%) and membrane technologies, where the main and dominant is RO (69%). However, these technologies still present technical and economic challenges, including high investment costs, high energy consumption (either electrical or thermal), and carbon emissions (linked to the use of fossil fuels).

For this reason, several new technologies are being proposed as potential solutions to these challenges. Among them, membrane distillation technology presents the greatest potential, due to the quality of water it produces, its flexibility with different feed fluids, and its low-quality heat requirement, which opens the possibility of working with renewable heat sources and waste heat. The latter opens the door for the coupling of MD systems with green H_2 generation systems, as there is potential waste heat, in quantity and quality, during the electrochemical reaction on the electrolyzers that could be used to power the MD process. Nevertheless, this technology is still under development, and the study of being coupled with green H_2 generation systems has yet to be conducted, so there remain uncertainties to address.

References

[1] Gao F-Y, Yu P-C, Gao M-R. Seawater electrolysis technologies for green hydrogen production: challenges and opportunities. Curr Opin Chem Eng 2022;36:100827.

[2] Jang D, Kim J, Kim D, Han W-B, Kang S. Techno-economic analysis and Monte Carlo simulation of green hydrogen production technology through various water electrolysis technologies. Energy Convers Manag 2022;258:115499.

[3] Woods P, Bustamante H, Aguey-Zinsou K-F. The hydrogen economy - Where is the water? Energy Nexus 2022;7:100123.

[4] Dawood F, Anda M, Shafiullah GM. Hydrogen production for energy: An overview. Int J Hydrog Energy 2020;45:3847–69.

[5] Simoes SG, Catarino J, Picado A, Lopes TF, di Berardino S, Amorim F, et al. Water availability and water usage solutions for electrolysis in hydrogen production. J Clean Prod 2021;315:128124.

[6] IEA. Global Hydrogen Review 2021 – Analysis. Paris: 2021.

[7] Nnabuife SG, Ugbeh-Johnson J, Okeke NE, Ogbonnaya C. Present and Projected Developments in Hydrogen Production: A Technological Review∗. Carbon Capture Sci Technol 2022;3:100042.

[8] Beswick RR, Oliveira AM, Yan Y. Does the Green Hydrogen Economy Have a Water Problem? ACS Energy Lett 2021;6:3167–9.

[9] Oliveira AM, Beswick RR, Yan Y. A green hydrogen economy for a renewable energy society. Curr Opin Chem Eng 2021;33:100701.

[10] Lane B, Reed J, Shaffer B, Samuelsen S. Forecasting renewable hydrogen production technology shares under cost uncertainty. Int J Hydrog Energy 2021;46:27293–306.

[11] Shi X, Liao X, Li Y. Quantification of fresh water consumption and scarcity footprints of hydrogen from water electrolysis: A methodology framework. Renew Energy 2020;154:786–96.

[12] Hermesmann M, Müller TE. Green, Turquoise, Blue, or Grey? Environmentally friendly Hydrogen Production in Transforming Energy Systems. Prog Energy Combust Sci 2022;90:100996.

[13] Mulder M, Perey PL, Moraga JL. Outlook for a Dutch hydrogen market: economic conditions and scenarois. Groningen: Centre for Energy Economics Research, University of Groningen,; 2019.

[14] Zhao G, Nielsen ER, Troncoso E, Hyde K, Romeo JS, Diderich M. Life cycle cost analysis: A case study of hydrogen energy application on the Orkney Islands. Int J Hydrog Energy 2019;44:9517–28.

[15] Shiva Kumar S, Himabindu V. Hydrogen production by PEM water electrolysis – A review. Mater Sci Energy Technol 2019;2:442–54.

[16] Khan MA, Al-Attas T, Roy S, Rahman MM, Ghaffour N, Thangadurai V, et al. Seawater electrolysis for hydrogen production: a solution looking for a problem? Energy Environ Sci 2021;14:4831–9.

[17] van Renssen S. The hydrogen solution? Nat Clim Change 2020;10:799–801.

[18] Papadis E, Tsatsaronis G. Challenges in the decarbonization of the energy sector. Energy 2020;205:118025.

[19] Nasser M, Megahed TF, Ookawara S, Hassan H. A review of water electrolysis–based systems for hydrogen production using hybrid/solar/wind energy systems. Environ Sci Pollut Res 2022;29:86994–7018.

[20] IRENA. Green Hydrogen Cost Reduction: Scaling up Electrolysers to Meet the 1.5°C Climate Goal. Abu Dhabi: International Renewable Energy Agency,; 2020.

[21] IEA. The Future of Hydrogen. Paris: International Energy Agency; 2019.

[22] d'Amore-Domenech R, Santiago Ó, Leo TJ. Multicriteria analysis of seawater electrolysis technologies for green hydrogen production at sea. Renew Sustain Energy Rev 2020;133:110166.

[23] Schmidt O, Gambhir A, Staffell I, Hawkes A, Nelson J, Few S. Future cost and performance of water electrolysis: An expert elicitation study. Int J Hydrog Energy 2017;42:30470–92.

[24] Buttler A, Spliethoff H. Current status of water electrolysis for energy storage, grid balancing and sector coupling via power-to-gas and power-to-liquids: A review. Renew Sustain Energy Rev 2018;82:2440–54.

[25] Bhandari R, Trudewind CA, Zapp P. Life cycle assessment of hydrogen production via electrolysis – a review. J Clean Prod 2014;85:151–63.

[26] Farràs P, Strasser P, Cowan AJ. Water electrolysis: Direct from the sea or not to be? Joule 2021;5:1921–3.

[27] O'Brien TF, Bommaraju TV, Hine F. Chemistry and Electrochemistry of the Chlor-Alkali Process. In: O'Brien TF, Bommaraju TV, Hine F, editors. Handb. Chlor-Alkali Technol., Boston, MA: Springer US; 2005, p. 75–386.

[28] Hausmann JN, Schlögl R, Menezes PW, Driess M. Is direct seawater splitting economically meaningful? Energy Environ Sci 2021;14:3679–85.

[29] Atlas High Purity Solutions. ASTM and ISO Water Quality Standards for Laboratory-Grade Water 2019 – Available at:<https://forum.atlashighpurity.com/blog/astm-and-iso-water-quality-standards-for-laboratory-grade-water> [accessed 14.02.2023].

[30] The distilled water company. Distilled Water Quality and Production – Available at:<https://www.thedistilledwatercompany.com/distilled-water-quality> [accessed 27.02..2023].

[31] Webber ME. The water intensity of the transitional hydrogen economy. Environ Res Lett 2007;2:034007.

[32] Esmaeilion F. Hybrid renewable energy systems for desalination. Appl Water Sci 2020;10:84.

[33] Salman HH, Aswad ZS. Desalination methods and their role in solving and managing the problem of salinization in Iraqi water resources. IOP Conf Ser Earth Environ Sci 2022;1002:012004.

[34] Shirazi MMA, Kargari A. A Review on Applications of Membrane Distillation (MD) Process for Wastewater Treatment. J Membr Sci Res 2015;1:101–12.

[35] Kucera J. Introduction to Desalination. Desalination Water Water, John Wiley & Sons, Ltd; 2019, p. 1–49.

[36] Gain AK, Giupponi C, Wada Y. Measuring global water security towards sustainable development goals. Environ Res Lett 2016;11:124015.

[37] Narayan A, Pitchumani R. Analysis of an air-cooled air gap membrane distillation module. Desalination 2020;475:114179.

[38] Astariz S, Iglesias G. The economics of wave energy: A review. Renew Sustain Energy Rev 2015;45:397–408.

[39] Kayvani fard A, Manawi Y. Seawater Desalination for Production of Highly Pure Water Using a Hydrophobic PTFE Membrane and Direct Contact Membrane Distillation (DCMD). Int J Environ Ecol Geol Mar Eng 2014;8:391–9.

[40] Nair M, Kumar D. Water desalination and challenges: The Middle East perspective: a review. Desalination Water Treat 2013;51:2030–40.

[41] Li C, Goswami Y, Stefanakos E. Solar assisted sea water desalination: A review. Renew Sustain Energy Rev 2013;19:136–63.

[42] Dhakal N, Salinas-Rodriguez SG, Hamdani J, Abushaban A, Sawalha H, Schippers JC, et al. Is Desalination a Solution to Freshwater Scarcity in Developing Countries? Membranes 2022;12:381.

[43] Panagopoulos A. Water-energy nexus: desalination technologies and renewable energy sources. Environ Sci Pollut Res 2021;28:21009–22.

[44] Eke J, Yusuf A, Giwa A, Sodiq A. The global status of desalination: An assessment of current desalination technologies, plants and capacity. Desalination 2020;495:114633.

[45] Al-Mutaz IS. The continued challenge of capacity building in desalination. Desalination 2001;141:145–56.

[46] Subramani A, Jacangelo JG. Emerging desalination technologies for water treatment: A critical review. Water Res 2015;75:164–87.

[47] Elsaid K, Taha Sayed E, Yousef BAA, Kamal Hussien Rabaia M, Ali Abdelkareem M, Olabi AG. Recent progress on the utilization of waste heat for desalination: A review. Energy Convers Manag 2020;221:113105.

[48] Noamani S, Niroomand S, Rastgar M, Azhdarzadeh M, Sadrzadeh M. Modeling of Air-Gap Membrane Distillation and Comparative Study with Direct Contact Membrane Distillation. Ind Eng Chem Res 2020;59:21930–47.

[49] Do Thi HT, Pasztor T, Fozer D, Manenti F, Toth AJ. Comparison of Desalination Technologies Using Renewable Energy Sources with Life Cycle, PESTLE, and Multi-Criteria Decision Analyses. Water 2021;13:3023.

[50] Ahmed FE, Khalil A, Hilal N. Emerging desalination technologies: Current status, challenges and future trends. Desalination 2021;517:115183.

[51] Mezher T, Fath H, Abbas Z, Khaled A. Techno-economic assessment and environmental impacts of desalination technologies. Desalination 2011;266:263–73.

[52] Tayyeban E, Deymi-Dashtebayaz M, Dadpour D. Multi objective optimization of MSF and MSF-TVC desalination systems with using the surplus low-pressure steam (an energy, exergy and economic analysis). Comput Chem Eng 2022;160:107708.

[53] El Din AMS, Mohammed RA. Brine and scale chemistry in MSF distillers. Desalination 1994;99:73–111.

[54] Prajapati M, Shah M, Soni B, Parikh S, Sircar A, Balchandani S, et al. Geothermal-solar integrated groundwater desalination system: Current status and future perspective. Groundw Sustain Dev 2021;12:100506.

[55] Deghani M, Nourmoradi H, Hashemi, Azimi AA, Doleh M, Vafaee R. An evaluation of physical, chemical and biological quality of influent and effluent water obtained by reverse osmosis and multistage flash processes for drinking consumption. Res Med 2013;36:36–42.

[56] Wei H, Zhao S, Zhang X, Wen B, Su Z. The future of freshwater access: functional material-based nano-membranes for desalination. Mater Today Energy 2021;22:100856.

[57] Mehta D, Gupta L, Dhingra R. Forward Osmosis in India: Status and Comparison with Other Desalination Technologies. Int Sch Res Not 2014;2014:1–9.

[58] Wang Z, Lin S. Membrane fouling and wetting in membrane distillation and their mitigation by novel membranes with special wettability. Water Res 2017;112:38–47.

[59] Nthunya LN, Bopape MF, Mahlangu OT, Mamba BB, Van der Bruggen B, Quist-Jensen CA, et al. Fouling, performance and cost analysis of membrane-based water desalination technologies: A critical review. J Environ Manage 2022;301:113922.

[60] Geng H, Wu H, Li P, He Q. Study on a new air-gap membrane distillation module for desalination. Desalination 2014;334:29–38.

[61] He Q, Li P, Geng H, Zhang C, Wang J, Chang H. Modeling and optimization of air gap membrane distillation system for desalination. Desalination 2014;354:68–75.

[62] Lattemann S, Höpner T. Environmental impact and impact assessment of seawater desalination. Desalination 2008;220:1–15.

[63] Gopi G, Arthanareeswaran G, Ismail A. Perspective of renewable desalination by using membrane distillation. Chem Eng Res Des 2019;144:520–37.

[64] AlTaee A, Sharif AO. Alternative design to dual stage NF seawater desalination using high rejection brackish water membranes. Desalination 2011;273:391–7.

[65] Zhou D, Zhu L, Fu Y, Zhu M, Xue L. Development of lower cost seawater desalination processes using nanofiltration technologies — A review. Desalination 2015;376:109–16.

[66] Anand Tularam G, Ilahee M. Environmental concerns of desalinating seawater using reverse osmosis. J Environ Monit 2007;9:805–13.

[67] Wafi MK, Hussain N, El-Sharief Abdalla O, Al-Far MD, Al-Hajaj NA, Alzonnikah KF. Nanofiltration as a cost-saving desalination process. SN Appl Sci 2019;1:751.

[68] Yadav D, Karki S, Ingole PG. Current advances and opportunities in the development of nanofiltration (NF) membranes in the area of wastewater treatment, water desalination, biotechnological and pharmaceutical applications. J Environ Chem Eng 2022;10:108109.

[69] Voutchkov N. Energy use for membrane seawater desalination – current status and trends. Desalination 2018;431:2–14.

[70] IEA. Water Energy Nexus. Paris: International Energy Agency, 2017.

[71] González D, Amigo J, Suárez F. Membrane distillation: Perspectives for sustainable and improved desalination. Renew Sustain Energy Rev 2017;80:238–59.

[72] Caldera U, Breyer C. Learning Curve for Seawater Reverse Osmosis Desalination Plants: Capital Cost Trend of the Past, Present, and Future. Water Resour Res 2017;53:10523–38.

[73] Duong HC, Ansari AJ, Hailemariam RH, Woo YC, Pham TM, Ngo LT, et al. Membrane Distillation for Strategic Water Treatment Applications: Opportunities, Challenges, and Current Status. Curr Pollut Rep 2020;6:173–87.

[74] Moejes SN, van Wonderen GJ, Bitter JH, van Boxtel AJB. Assessment of air gap membrane distillation for milk concentration. J Membr Sci 2020;594:117403.

[75] Drioli E, Ali A, Macedonio F. Membrane distillation: Recent developments and perspectives. Desalination 2015;356:56–84.

[76] Zhang J, Dow N, Duke M, Ostarcevic E, Li J-D, Gray S. Identification of material and physical features of membrane distillation membranes for high performance desalination. J Membr Sci 2010;349:295–303.

[77] Onsekizoglu P. Membrane Distillation: Principle, Advances, Limitations and Future Prospects in Food Industry. In: Zereshki S, editor. Distill. - Adv. Model. Appl., IntechOpen; 2012.

[78] El-Bourawi MS, Ding Z, Ma R, Khayet M. A framework for better understanding membrane distillation separation process. J Membr Sci 2006;285:4–29.

[79] Camacho LM, Dumée L, Zhang J, Li J, Duke M, Gomez J, et al. Advances in Membrane Distillation for Water Desalination and Purification Applications. Water 2013;5:94–196.

[80] Alkhudhiri A, Darwish N, Hilal N. Membrane distillation: A comprehensive review. Desalination 2012;287:2–18.

[81] Marzo E, Gali A, Lefevre B, Bouchy L, Vidal A, Cortina JL, et al. Hydrogen and Oxygen Production using Wastewater Effluent Treated with Ultra-Filtration and Membrane Distillation (Greenlysis). Procedia Eng 2012;44:1744–6.

[82] Ruiz-Aguirre A, Andrés-Mañas JA, Zaragoza G. Evaluation of Permeate Quality in Pilot Scale Membrane Distillation Systems. Membranes 2019;9:69.

[83] Guillén-Burrieza E, Zaragoza G, Miralles-Cuevas S, Blanco J. Experimental evaluation of two pilot-scale membrane distillation modules used for solar desalination. J Membr Sci 2012;409–410:264–75.

[84] Winter D, Koschikowski J, Wieghaus M. Desalination using membrane distillation: Experimental studies on full scale spiral wound modules. J Membr Sci 2011;375:104–12.

[85] Pangarkar BL, Sane MG, Parjane SB, Guddad M. Status of membrane distillation for water and wastewater treatment—A review. Desalination Water Treat 2014;52:5199–218.

[86] Khalifa A, Lawal D, Antar M, Khayet M. Experimental and theoretical investigation on water desalination using air gap membrane distillation. Desalination 2015;376:94–108.

[87] Forman C, Muritala IK, Pardemann R, Meyer B. Estimating the global waste heat potential. Renew Sustain Energy Rev 2016;57:1568–79.

[88] Firth A, Zhang B, Yang A. Quantification of global waste heat and its environmental effects. Appl Energy 2019;235:1314–34.

[89] Thomas N, Mavukkandy MO, Loutatidou S, Arafat HA. Membrane distillation research & implementation: Lessons from the past five decades. Sep Purif Technol 2017;189:108–27.

[90] Tiktak J. Heat Management of PEM Electrolysis: A study on the potential of excess heat from medium- to large-scale PEM electrolysis and the performance analysis of a dedicated cooling system 2019.

[91] Burrin D, Roy S, Roskilly AP, Smallbone A. A combined heat and green hydrogen (CHH) generator integrated with a heat network. Energy Convers Manag 2021;246:114686.

[92] Contreras Bilbao D. Valorization of the waste heat given off in a system alkaline electrolyzer-photovoltaic array to improve hydrogen production performance: Case study Antofagasta, Chile. Int J Hydrog Energy 2021;46:31108–21.

[93] Li J, Lin J, Song Y, Xing X, Fu C. Operation Optimization of Power to Hydrogen and Heat (P2HH) in ADN Coordinated With the District Heating Network | IEEE Journals & Magazine | IEEE Xplore. IEEE Trans Sustain Energy 2019;10:1672–83.

NICEST - Master study proposal on Next generation Industrial Control Engineering for Sustainable water system Treatment

R. Vilanova[a], M. Meneses[a], M. Dominguez[b] A.M. Blanco[c] M. Barbu[d] D. Selistanu[e] A. Visioli[f] A. Capodaglio[g] N. Andritsos[h] P. Samaras[i] and K. Plakas[j]

[a] Universitat Autonoma Barcelona, Bellaterra, Spain, {Ramon.Vilanova, Montse.Meneses}@uab.cat
[b] Universidad de Leon, Leon, Spain
[c] Universidad de Las Palmas de Gran Canaria, Las Palmas de Gran Canaria, Spain,
[d] "Dunarea de Jos" University of Galati, Galati, Romania
[e] University of Craiova, Craiova, Romania
[f] University of Brescia, Brescia, Italy
[g] University of Pavia, Pavia, Italy
[h] University of Thessaly, Thessaly, Greece
[i] UInternational Hellenic University in Thessaloniki, Thessaloniki, Greece
[j] Centre for Research and Technology-Hellas, Thessaloniki, Greece

Abstract:
In this paper a collaborative experience towards the development of a new joint master degree is presented. The design of the curriculum has as main pillars: a) to provide an interdisciplinary view and approach to advanced water treatment solutions, and b) the development of the curriculum is done according to the new challenges for Higher Education in Europe, therefore providing references of good practices with this respect. The experience is worth to be shared as in an immediate future the expected collaboration among Higher Education Institutions in Europe is to increase if an integrated and high quality Higher Education Area is to be developed. The ongoing reviewing/re-structuring process of higher education programmes provides the opportunity to promote new types and levels of learning new technologies and practices in and through pan-European collaboration. The proposal that is motivated by the need for a green approach to water treatment. Like many other industries, water and wastewater treatment plants also face the problem of a staffing shortage. Efficient and productive workers that are skilled in the business are necessary to properly manage water systems. Automation may be a potential solution to this shortage. Not only will it fill in the gaps of needed employment, but it will also put less stress on existing workers. To this aim the Next generation Industrial Control Engineering for Sustainable water system Treatment (NICEST) project is presented in this paper.

Keywords:
Water Engineering, Control Technology, .Higher Education

1. Introduction

There is by now (almost) no doubt that to establish joint collaborative experiences on curriculum design and the establishment of joint degrees in particular is one of the major challenges of the forecasted European Higher Education Area. [6] In particular to work for a joint degree puts on the table existing differences both on academic conception of courses and on established procedures for administrative matters. In fact, Feel Europe!! This could be a possible synthetic way of expressing one of the major characteristics asked for to the newly developed study programmes at European Level. Integration of parts of the curriculum to be offered by leading institutions (therefore taking advantage of acquired expertise) as well as offering the possibility of realising the different cultural experiences both from academic and social points of view.

To overcome these differences is not an easy task. It is the author's opinion that an actual barrier that avoids having a large number of experiences is the lack of knowledge on how to tackle such an interdisciplinary project or, even not knowing what are the problems that the consortium will need to face with.

This communication's aim is to present what the authors experienced as the road taken in order to establish an international joint master degree. It is intended to be a guideline both for the kind of problems that arise on such projects and suggestions for strategies that will help to face them. Different faces of the overall process are presented, highlighting the strategies to follow and the important points to take into account that may be possible source of problems.

Regarding the scope of the study programme, this is motivated by the need for a green approach to water treatment [1]. In fact, the water sector is a key one where digital innovation plays a key role looking forward to the European Green Deal challenge. The Water Sector is at the core of the environmental debate. Water is, quite simply, the most essential natural resource on the planet. Global water challenges affecting water resources, such as climate change, population growth, increasing urbanization and ageing infrastructure, continue to intensify. The European Green Deal is that response. It will drive us forward to climate neutrality by 2050 and at the same time focus on adaptation. The key strategy for the period 2019-2024 is and will be the Twin Transition to a green and digital economy firmly grounded in the objectives of the European Green Deal. No attempt to establish a Green Economy can be successful if it does not involve the water sector in all its facets. Like many other industries, water and wastewater treatment plants also face the problem of a staffing shortage. Efficient and productive workers that are skilled in the business are necessary to properly manage water systems. Automation may be a potential solution to this shortage. Not only will it fill in the gaps of needed employment, but it will also put less stress on existing workers. The ongoing reviewing/re-structuring process of higher education programmes provides the opportunity to promote new types and levels of learning new technologies and practices in and through pan- European collaboration. Currently, there is no programme offered in Europe similar to the one being proposed, nor to modern control systems technology nor with its application to the operation of water systems. The prospective master degree is expected to fulfil the demand for well-qualified personnel required with an enhanced capability for solving many of the water supply problems foreseen in the next 20 years.

On the basis of the two broad issues above, the rest of the paper presents first the rationale; in Section 2.; and innovative and added value of the intended study programme in Section 3.. The rest of the sections are aimed to provide a road-*like* view to help understand as well as to serve as starting point/reference for those that want to undertake a project like this one. Accordingly, Section 4. will present the three general axes to be considered. Those are developed in the corresponding subsections. Additional considerations regarding economic management, student services and transversal issues are reflected in Sections 6., 7. and 8., respectively. The paper end with some conclusions.

2. The topic: NICEST rationale

This study programme is motivated by the need for a green approach to water treatment. In fact, the water sector is a key one where digital innovation plays a key role looking forward to the European Green Deal challenge. The European Green Deal was stated as one of the six ambitions/objectives for Europe described by Ursula von der Leyen in 2019 [1]. The increase in global temperature, the depletion of natural resources and continued biodiversity loss, undermine our security and prosperity. The Water Sector is at the core of the environmental debate [2]. Water is, quite simply, the most essential natural resource on the planet. Global water challenges affecting water resources, such as climate change, population growth, increasing urbanization and ageing infrastructure, continue to intensify. The European Green Deal is that response. It will drive us forward to climate neutrality by 2050 and at the same time focus on adaptation. The key strategy for the period 2019-2024 is and will be the Twin Transition to a green and digital economy firmly grounded in the objectives of the European Green Deal. No attempt to establish a Green Economy can be successful if it does not involve the water sector in all its facets. An important advance towards such progress faithfully reflects the second factor of the Twin Transition: Digitalization.

The problem of diminishing clean fresh-water resources facing Southern Europe and most other parts of the world is very serious. Water is essential for life and is central to both industry and agriculture. The demands on water infrastructure are increasing and have to deal with population growth and climate change. Furthermore, in all Mediterranean and Middle Eastern countries, the scarcity of conventional freshwater resources poses a serious threat to their sustainable socio-economic development. In planning for water uses in various human activities, especially in such arid areas, a primary objective should be sustainable development. This target transcends national boundaries, demanding that society should utilize available water resources in a way that will ensure their availability for generations to come. In addition to political vision, water availability problems need technological know-how for their solution. Moreover, specific efforts are focused on water reclamation and reuse while the recovery of added value products and energy represents a challenging option under the water-energy concept. It is not surprising that both the United Nations and the US National Research Council indicated wastewater reuse as a yet untapped available water source. Water reuse is an integral element of sustainable water management, keeping a viable resource in the natural cycle, and allowing its preservation for future uses, at the same time meeting present supply requirements. According to UNESCO, improved wastewater treatment and increase in water reuse, as called for in Sustainable Development Goals Target 6.3 (Clean Water and Sanitation), will support the global transition to a sustainable circular economy. Hence, a selective approach for wastewater recovery to provide water at specific quality standards for different reuse objectives (industrial, agricultural and even potable) is nowadays desirable and technologically feasible. This ”fit-for-purpose” approach to water reuse could both save water and would reduce production cost and energy

demand by eliminating unnecessary treatment and long-range conveyance, as it typically aims at local reuses, but it requires appropriate plant and control configurations.

All of these issues, and the global challenges that lie ahead of us in the next few decades, mean that Environmental Engineering will rapidly become one of the most important areas of Engineering. Water resources protection, efficient water uses and recycling, air and soil pollution and materials and energy recovery from effluents and wastes are just a few of the problems that need to be tackled in order to assure sustainable growth of the world economy and ecosystem stability. These problems are relevant in both industrialized countries, where solutions are already being found and implemented, albeit not always at the necessary pace, and in developing countries, where interventions according to the state of the art of technology should be concurrent with ongoing development.

Many environmental problems are related to large scale, geographically distributed control system problems: the regional management of water and wastewater resources at basin scale are conceptually and technologically comparable to the management of a regional or national High Voltage Transmission system. The daily management and operation of a large wastewater treatment facility can be compared to a medium-scale industrial process, where optimization and real-time control can contribute to increased productivity and opportunities for water reuse (better effluent quality) and lower costs (mainly energy and process requirements). A similar situation can be found in waste incinerators with recovery of electrical and thermal energy. Unfortunately, this combination of knowledge has seldom crossed the realm of applied research and has never become part of an academic curriculum, except occasionally at taught postgraduate level.

Digital monitoring solutions can help to optimise the management and control of wastewater treatment plants, which may result in higher degrees of energy efficiency as well reductions in chemicals used and carbon or other gas emissions achieving at the same time an effluent of high quality; such an approach is becoming significant considering the variable composition of the influents and the strong effect of environmental conditions to the operation. Nevertheless, the achievement of an effluent of constant quality will allow for its reuse in various applications requiring safe water. Employing such tools, digital process information can be used to simulate possible configurations of a plant for varying design parameters (e.g. inflow conditions) in order to identify the optimal configuration of wastewater management and reuse systems at different scales and to determine the potential for extraction of valuable materials. With regards to data reporting processes, digital solutions can provide valuable input, with regards, for example, to water quality monitoring designed to support the implementation of the Water Framework Directive (WFD). Green innovative technology has been improving the way we treat water so that the environmental footprint left by wastewater treatment plants is smaller and less impactful. With automation and innovation moving forward, we can continue to expand on these ecofriendly technologies to make wastewater treatment greener.

All the previous issues and scenarios, moved us towards the need for the development of a Joint Degree Master Programme entitled Next generation Industrial Control Engineering for Sustainable water system Treatment (NICEST) according to the European Higher Education principles. The objective of this Master Programme is to fill a rapidly developing gap that is emerging for graduates that are trained in key processes and management associated with water supply and reuse. There is great demand for such graduates at the

3. NICEST added value

Innovations in the water domain are fragmented and often experimented at small scales. Thus, there is a need to strengthen the innovation capacity of the water industry. Even a 1% increase in the growth rate of the water industry could create up to 20,000 new Jobs - from Water Reuse in Europe - Relevant guidelines, needs for and barriers to innovation, Publications Office of the European Union: JRC92582).

There is a wide variety of master's degrees in various aspects of environmental engineering outside Europe coming from the USA and with small but developing groups in Asian counties. From a review carried out by this Consortium, as well as from other sources, we can conclude that conventional water treatments are well covered in EU degrees, either from the technology or the management viewpoint. However, there is a real and urgent need for specialised and regular training in newly developed technologies and areas not covered by the current schemes. There are several MSc programmes covering conventional municipal and industrial water treatment. Some of the programmes are aimed at the science and technology of water provision, while others are more focused on the water management systems.

However, curricula analysis demonstrates a clear skills mismatch related to the employers' expectations. The current master-level curricula in water seldom involve Big Data, IoT or other digitalisation approaches or results, and on some occasions, process simulations. The industry is also occupied with further development of conventional solutions. It is important to bridge the historical gap between control engineers and process specialists in order to overcome the many technological and physical challenges in the sector and support the existing EU research and innovation initiatives.

The NICEST scheme offers a unique programme of education in Desalination and Water Treatment Technologies. It addresses the major developing areas of the subject giving the prospective student state of the art knowledge and opportunities to specialise in the major areas of the subject, Desalination, Water Reuse and Wastewater Control Systems. These are key areas of technology and infrastructure in a developing world that will be required to deal with the threats of climate change and help with conflict resolution based on resources. The Master's degree will fulfil the demand for well-qualified personnel required with an enhanced capability for solving many of the water supply problems foreseen in the next 20 years. It will also support these rapidly developing commercial areas of water technology worldwide. Currently, there is no programme offered in Europe similar to the one being proposed.

Because of the approach an also because the water thematic field is at the forefront of the EU and local governments agenda, the project is aligned with European policies:

- supports strengthening the competitiveness of EU water business through talent and innovation in higher education according to the Strategic framework for European cooperation in education and training [6]. It also addresses revitalisation of educational focus towards the growing mismatch between the digital skills water specialists acquire and the demand on the labour market accounting the water digitalisation trend and supporting development towards Digital Single Market.
- focuses on digital technology for teaching and learning, developing digital competences and skills and improving education through better data analysis and foresight meeting the goals of the EU Digital Education Action plan. [8]
- is designed to support the implementation of the European policy agenda for growth, jobs, equity and social inclusion referring to the importance of education and employment. This will transform the teaching and learning of digital skills in a lifelong learning perspective. This will further develop digital skills for the digital economy, e.g. upskilling and reskilling workers and jobseekers, career advice and guidance.

4. Joint Study Programme elements

The road presented arises from an international experience in new Curriculum Development from the perspective of the new challenges for Higher Education in Europe, and with an interdisciplinary approach to content design [3], [7]. One of the factors stressed in the communication is the need for collaborative work among academic and administrative staff. To run an international joint degree implies different procedures than the ones actually running on standard national degrees.

Different faces of the overall process are presented, highlighting the strategies to follow and the important points to take into account that may be possible source of problems:

- Curriculum Structure: topics like the following ones, among others, should be taken into consideration: ECTS adopted as the central concept on the curriculum structure; Mobility designed as an integral part of the curriculum; Integration Actions to let the students know the corresponding local cultures; Teaching and Learning methods are programmed as a mixture of classical (frontal teaching) and modern (read e-learning and web based) methods.
- Curriculum definition management: Adopted roles and procedures: (i) the use of tools for collaborative work is showed to play a central role in the sharing of information and in the development of coordination and communication aspects among partners, (ii) creation of Committees (steering, admission, quality) to tackle the different management aspects and assuring all partners are involved in the different tasks, etc
- Academic, Administrative Procedures and legal aspects: with no doubt different legislations will go into conflict. People coming from academia are not generally aware of all the pinpoints concerning these issues. In addition to put together administrative staff from the different partner members, joint and collaborative work with administrative staff is a must in order to guarantee the success of the experience. The authors are a representative of this collaborative work.

On a broad sense, the idea is to expose on a clear way the implications of this kind of ventures trying to identify the cornerstones of the process in order to assure as much as possible the success of the experience. The sections that follow are organised in such a way that constitute a first step towards a practical guide of the different aspects to be considered. It is a fact that the actual lack of homogeneity among different national legislations and national degrees structure across Europe constitute a continuous source for difficulties and barriers that are to be solved. This situation constitutes an extra reason for a clear as possible guided road to the establishment of an international joint degree.

4.1. Curriculum Structure

The definition of the curriculum should be done from a holistic point of view. It is a usual practice just to put together modules offered at the partner universities in order to generate the global master offer. This usually provides a curriculum with no added value. One of the important points the consortium has to be able to highlight is the added value of the joint degree with respect to the individual courses offered at the partner universities: something that cannot be done by the partners on their own way.

The design of the curriculum is intended to be done on a top-down basis. Starting from the general goals that the consortium is committed to meet and melting down to de details of each one of the integrating modules.

There are some basic questions the consortium has to fix. Even sometimes they seem too basic and obvious it is important to agree on every point from the very beginning. They can by classified on the basis of the aforementioned top-down manner. General Questions at degree level:

- Degree offered (Joint degree, double degree): It should become clear from the very beginning if all partner institutions can award a joint degree (it may depend on local regulations and on each country legal framework) or if double degree awarding is needed. All EHEA countries are supposed to adapt their legal frameworks according to the Bologna process standards prior 2010. To obtain a Joint Degree, a minimum of one semester mobility has to be done to another partner institution (host university/ies).
- Diploma Supplement: Will the Diploma supplement be used? If so the form and content should be agreed.
- What will be the Language of instruction? Use of local languages will introduce the need for deep knowledge of different languages on the students. It is therefore natural to ask for a common language for instruction even local languages are to be introduced in order to help the introduction of local culture settings and to help students
- What will be the mode of study? (full time basis, distance learning based, ...)
- What will be the duration of study? 12 months, 24 months.

These questions can be identified as operational aspects. However, the consortium has also to be able to answer content related questions like: What is the added value of the programme with respect to existing studies? What are the learning outcomes/competences/skills? Professional Qualifications?

With respect to the course structure it is important to think on mobility aspects. What kind of curriculum is desired?

- Will the student we allowed to choose a path from the very beginning? This means the initial hosting institution may not be the same for all the students.
- Will there be the possibility of taking the same modules in more than one institution? This situation will introduce elements of choice based on geographical location more than on educational content. Therefore an unbalanced flow of students may be generated.

Advantage of the local expertise of the partners should be taken and the corresponding specialisations or elective options offered.

At module level, the description suggested from the ECTS User's guide [3] is to be employed. A common module description has to be adopted by all partners in order to facilitate both, coherent information to students as well as transfer of grading and student records information.

4.1.1. Local Constraints

When defining the global structure of the study programme it should be beard in mind that local approvals will be needed from each partner institution (and, in some cases from the local governments). This raises the point that the final structure of the programme should accomplish with local constraints:

- Do all the partners understand and apply the ECTS under the same terms?
- What is the number of elective credits to be offered?
- Is it mandatory to assign a minimum number of credits to the Master Thesis?
- Should the programme assure methodological and/or local culture credits?

The existing local regulations at national level will establish if the awarded degree can be a joint degree or a double degree. For a joint degree it will be needed that all partners be in disposition to award a joint degree.

4.2. Curriculum definition management

4.3. Academic, Administrative Procedures and legal aspects

Admission to the programme is one of the important points the consortium has to agree on. Possibly, each partner institution will have its own procedures and selection criteria. The possible conflicts have to be detected as early as possible. Therefore, each partner has to provide a detailed description of the procedures, required information and documentation the student has to provide as well as the minimum requirements; according to the corresponding national legislation; for a student to access to the degree. Therefore:

- Common standards for admission should be established: mandatory admission requirements. These standards have to accomplish with all institutions requirements. Required documents have to be legalised by at least one of the participating institutions embassies, and the rest should recognise them. It is also advisable that all institutions accept documents officially translated in English or any other agreed language. All these recognitions will make easier the legal procedures that non-EU students will have to follow.
- Common application procedure should be agreed and put in place by the coordinating institution as the consortium secretariat has to be the contact and entering point to the study programme. Note this means that just one application form will be available and that this application form may not be that of any partner
- Joint student selection procedure should be organised by the coordinating institution. The criteria on the basis the applicants will be ranked should be clear and agreed. This will allow to create an applicant scale on the basis of; for example; Accepted / Waiting List / Accept to Waiting List / Cannot Accept

During the entire admission process, staff from the consortium secretariat should be in touch with the candidate and inform him/her on actions to be taken, missing / incomplete documents etc. In addition, dates and timing for application have to be announced. Once the Admission Committee has reached its decision, it is recommended that successful candidates are put in touch with local accommodation offices so that suitable accommodation can be arranged in a timely manner.

Special attention should be put into the troubles some third country students may have in getting the corresponding visas in order to enter to the partner institutions countries. For example, the visa may only be for 6 months. In addition the student may be required to be in their home country to get the visa. This is not a problem for the firs country he/she is to visit. However if the mobility requires the visit to another country this may imply an extra travel. Therefore to be taken in to account in order to minimize foreign student travel.

In case the master is going to deliver a double/multiple degree, every institution will need a certified copy of all admission and registration documents, having to update the academic transcript of all those students that are going to receive the degree issued by their institution (those spending at least one semester).

5. Academic Management

Academic management will be one of the major tasks coordinated by the consortium secretariat and will encompass a sequence of tasks that will follow the life of the student within the programme from its very beginning.

The Consortium's Secretariat will keep the full student record in order to monitor progress, to help the preparation of the Diploma Supplement and other actions requiring the full students' record. On the other hand, host institutions will provide the Secretariat with the corresponding semester qualifications, so that it can update students? academic files. This way the consortium secretariat will be in charge of providing the agreed degree and Diploma Supplement.

As the Consortium's Secretariat is to centralise the student's records, at the end of each semester the marks of each student should be communicated to the Secretariat. For this matter, the definition of the Examination Boards facilitates a communication framework among local institutions and Secretariat. The local Examination Boards will be the local committee that gives validity to the marks obtained by the students during the semester and officially communicates (by using a common agreed form) the results to the Secretariat.

6. Economic Management

As the access point to the programme, the consortium secretariat is the appropriate body to be in charge of the economic management of the consortium. This way the consortium secretariat will receive the agreed fees form the students and distribute them to the partner institutions according to the local costs per enrolled student.

When calculating the registration and administration fees, the consortium has to be sure that the amount will cover official fees at each institution. It is a must that all European students pay the same fee. Third country students' fees may differ.

Different national/local rules concerning fees should be solved at consortium level. This way it is preferable that the student.

In order to avoid problems, it is advisory to establish, on a yearly basis:

- What are the fees to be transferred from the secretariat to the partner universities (by student per semester) depending n the amount of ECTS credits. - Is there any fixed amount devoted to cover administration costs? - Regular meetings of the different meetings are also to be covered. They need to be included into the cost provision. - Publicity and web hosting - Language courses

An interesting option that has also to be considered is the provision of study grants directly from the consortium. If there is the possibility of having sponsors from industry the consortium may consider the possibility of granting some students per year.

7. Student Services

It is important to provide the students with a minimum level of services that guarantee a smooth integration into the local social life as well as facilitate enrolment and development of the lecturing and study activities while the stay in one of the institutions.

The members of the consortium should engage themselves in helping students with incoming procedures such as finding housing and ensure that students will have access to language courses, libraries and canteens as well as to the services of the respective International Offices.

Before any mobility, consortium institutions have to provide legal advice to students, regarding visa requirements to destiny country: how long in advance they have to ask for the visa, required documents, etc. Every European country has its own legislation and requirements, and students needs at least a 6 months stay permit.

In addition it is encouraged to provide a personal faculty advisor, chosen from the teaching staff, which will be assigned to each student. The advisor will help the student for particular needs in the curriculum and in the everyday life. In addition, non academic counselling will be provided by trained counsellors form the student support services

8. Transversal and Good Practice Considerations

The elaboration of joint ventures provides a framework for the application of intercultural integration. Therefore, it is desired for the partners to promote the creation of integrated language programmes and cultural integration. This way the students will undertake other activities for improving their language skills and their knowledge of culture of the host country. Typically these classes will include the written and spoken language and/or the culture and civilization of the host country.

A practical way of helping foreign students integration is to provide them with a manual with information on each university / surrounding, structures, procedures, assistance, language tuition, etc

It is also advisable to have a Master website where all this information can be facilitated.

The implemented procedures should guarantee equal opportunities and rights between male and female. Likewise, it is important to assure easy accessibility to any disabled scholars and students.

9. NICEST Curriculum Structure

The NICEST degree programme aims to provide the student with a thorough knowledge in the field of advanced water treatment and particularly in technologies such as saline water desalination and wastewater treatment and reuse. The programme will comprise different teaching approaches, expertise and research competencies of the participating institutions. It reflects the specific experiences of the involved departments, realises important synergies, and gives preference to the best available and most-up-to-date modules in each field.

The determination of the final academic programme with the detail of the modules to be offered and specific syllabus is one of the purposes of this EMDM project. However, because of the expertise contributed by each partner member, an initial structure of the curriculum has been outlined. It exploits the expertise and international reputation of each one of the consortium partner members, so each partner will contribute to the design of the NICEST curriculum by bringing specific competences and skills corresponding to their area of expertise. In some specific cases, for the benefit of accounting for the best specialists and in favour of a rich consortium, academic collaboration between two institutions is expected during the common first semesters.

The structure of the academic programme is reflected in Figure (1). The overall view shows the two years structure, with the academic semesters and interlaced events such as the integration week, summer school and graduation event.

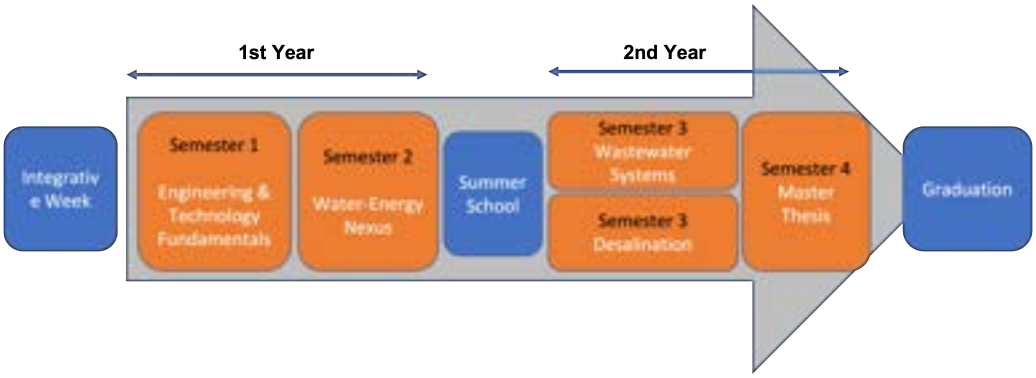

Figure 1: Curriculum degree overview

- Wellcome Integration days: This will provide the first contact of the students with the NICEST Consortium. It is proposed to take place in one place that is not mandatory on the curricular itinerary. This way students will have the possibility can get in touch with the partner and get knowledge about the local facts. The new students will get the opportunity to meet the alumni from the previous cohort who are graduating at the same time.
- Summer School: This will be intended to provide a transition between the fundamental, more generic courses, of the first year to the second year specialisations. It will be organised on a partner institution different from the welcome, integration week. The Summer School will allow for presenting specific topics related to water treatment, also some topics not covered within the study programme (legal issues for example) with the participation of invited guest speakers.
- Graduation event: The graduation ceremony will be organised after the Master's Thesis defence. As previously commented, the idea is to make it coincident, or at least to overlap somehow, with the integration week in order to favour the interaction of recently graduating and newcomers.

Intended structure is:

- Common first year where the basics of Industrial Control, process engineering, sustainability and environmental management, biological processes and aspects related to industrial communication systems and cybersecurity are covered. This first year will be delivered at UAB (Barcelona, Spain) and ULE (Leon, Spain). The second semester will concentrate on what we called the water-energy nexus. This is intended to cover aspects related to energy usage and renewable energies for water treatment. This is a transversal issue that becomes more and more important whatever the water sector we can refer. This second semester will be delivered in Greece with UTH & IHU (Greece) with the research centre CERTH as an associate partner.
- The second year is characterised, at each institution, by the focus on project/specialist work, with courses that reflect the different areas of special expertise of each of the partner institutions. The following specialisation courses are identified at this stage: wastewater treatment UGA & CRA (Romania) and Desalination Engineering ULPGC (Las Palmas, Spain)
- Master project according to the expertise but including co-supervision with an external advisor that complements with needed engineering and technological aspects.

Figure (2) summarises the degree structure and prospective list of modules.

10. Conclusions

In this communication a rough description of the aspects concerned when addressing the conception and design of an international joint degree has been presented. The sections have been structures in order to classify the main points to be addressed and questions to be tackled. The description is by no means far from complete but can be taken as a global picture, therefore a starting point.

11. Acknowledgements

The authors would like to acknowledge the European Commission for his support to this project under the Erasmus+ Erasmus Mundus Design Measure project ERASMUS-EDU-2022-EMJM-DESIGN 101082541. The European Commission support for the production of this publication does not constitute an endorsement of the contents which reflects the views only of the authors, and the Commission cannot be held responsible for any use which may be made of the information contained therein.

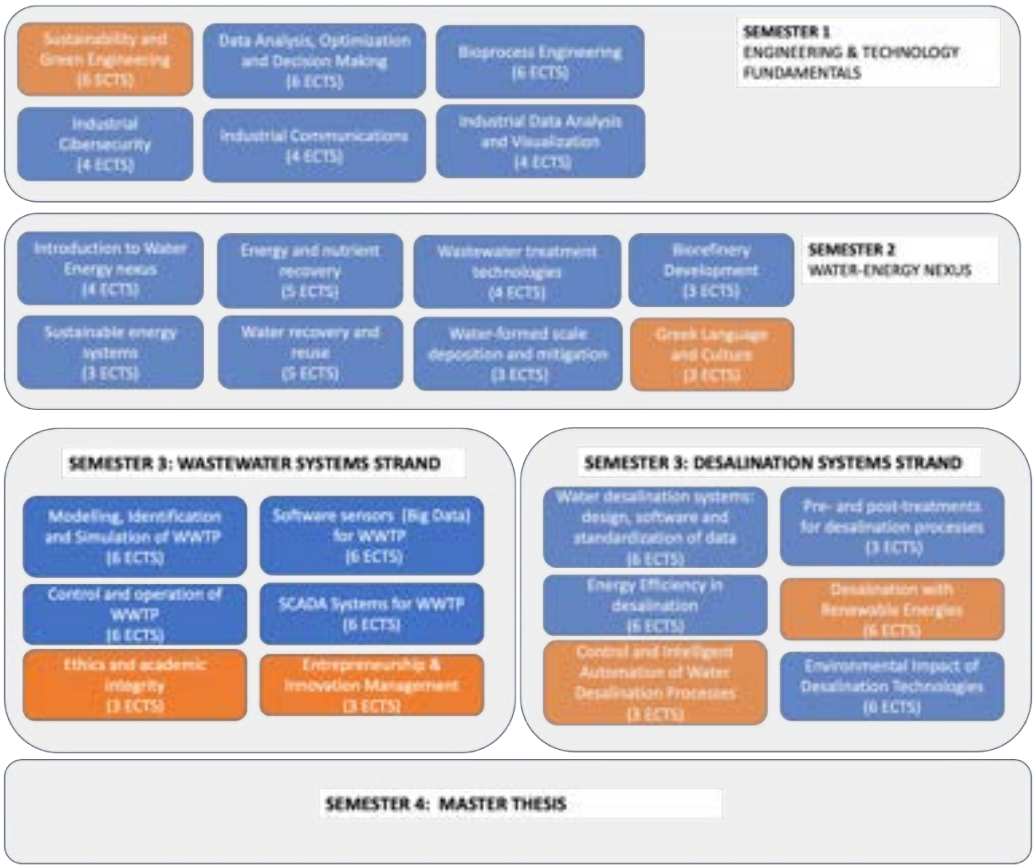

Figure 2: Curriculum detail. Modules and semester content

References

[1] Von der Leyen U, A Union that strives for more. My agenda for Europe. 2019

[2] IPCC 2013, Climate Change 2013: The Physical Science Basis. Working Group I Contribution to the IPCC 5th Assessment Report, IPCC, Cambridge, United Kingdom and New York, NY, USA.

[3] Capodaglio A.G., Katebi R., Butler D., Mikkelsen P.S. , Jeppsson U., Vilanova R. Papageorgiu M. Integrated water quality management in river basins through an innovative integrated educational approach, Proceedings, Agua 2005 ?From Local Action to Global Targets?, Cali, Colombia, October 2005

[4] Juhlke R., Unger M., Erasmus Mundus Joint Master Graduate Impact Survey 2020/21 Comprehensive report of results. Survey conducted in cooperation with the Erasmus Mundus Students and Alumni Association, 2021.

[5] EHEA, European Higher Education Area Ministerial Conference, 2020: Rome Ministerial Communique.

[6] European Commission, ET2020 - Strategic framework for European cooperation in education and training.

[7] EACEA, European Education and Culture Executive Agency of the European Commission (EACEA) (2020): Implementing joint degrees in the Erasmus Mundus action of the Erasmus+ programme.

[8] European Comission, Digital Education Action Plan 2021-2027, Resetting education and training for the digital age

Innovative low-grade sorption desalination technology for application on board of vessels

A. Frazzica[a,*], Y. Zhang[a], A. Bonanno[a], V. Palomba[a], V. Brancato[a], W. Mittelbach[b]

[a] Istituto di Tecnologie Avanzate per l'Energia "Nicola Giordano", CNR ITAE, Messina, Italy.
andrea.frazzica@itae.cnr.it
[b] Sorption Technologies GmbH, Freiburg, Germany

Abstract:

This study aims to develop a high-water-yield adsorption desalination system by sorbents screening and lab-scale prototype testing, for future application on board of vessels. For sorbents optimization, silica gel-30%LiCl and vermiculite-45%LiCl composites were developed. The sorption isobars and sorption kinetics were measured and the results contributed to further calculations of SDWP (Specific Daily Water Production). Silica gel-30%LiCl composite was chosen as the optimized one with the highest SDWP. Afterwards, the ad/desorption dynamics of the adsorber made of finned flat-tubes heat exchanger and silica gel-30% LiCl composites were tested in a T-LTJ (thermal large temperature jump) adsorption apparatus. The obtained results were used to calculate the SDWP and optimized cycle time and to evaluate the performances of three system designs (2-reactors, 3-reactors and 4-reactors). The design of 3-reactors was selected, which can reach an SDWP as high as 69 m^3/tonne/day under the condition of $T_{eva/cond}$=20 °C and T_{de}=80 °C.

Keywords:

Adsorption desalination; Silica gel; LiCl; Water uptake; Sorption dynamics.

1. Introduction

Water scarcity was listed as the top 5 global risks in terms of potential impact by the World Economic Forum since 2012 [1]. Desalination has served as the governing technology to provide potable water since the 1980s [2]. Although commercial desalination plants like the multi-stage flash (MSF) are developing rapidly, their drawbacks of high energy consumption and negative environmental impacts [3] lead to the requirement of developing new desalination technologies. Adsorption desalination technology is proposed as a novel desalination method, where the sorbents extract water vapour from the saline water in the sorption process, and such adsorbed water will be released and condensed into potable water in the desorption process. Its dominant advantages are the utilization of renewable and waste heat energy and high-quality produced water [4].

The adsorption desalination technology is still in the early research stage, and the previous research interest lies in verifying the validity of freshwater production [5,6] and proposing advanced system configurations like the 2-evaporator cycle and multistage reactors [7,8]. Despite a large number of sorbents have been fully studied in other adsorption-based systems (adsorption cooling, thermal energy storage, etc.), only limited types of sorbents have been studied. Silica gel and zeolite are the most utilized sorbents for adsorption desalination systems by now, they have good hydrothermal stability, but their cyclic water uptake is lower than chemical sorbents and composite sorbents and the obtained SDWP in the system is generally lower than 15 m^3/tonne/day [9]. Composite sorbents [10] are regarded as the most promising sorbents for their high water uptake amount and tailored sorption properties. However, composite sorbents have not been widely studied for desalination applications. Besides the sorbents, the investigation of the performances in practical systems is also significant. Ad/desorption dynamics are critical to evaluate the operation performance, which is also not so extensively studied in previous publications. Thus, this study developed two types of LiCl-based composite to select the optimized one, whose ad/desorption dynamics in practical desalination systems were experimentally studied, resulting in the development of a high-water-yield system. The optimization of a composite sorbent for desalination purposes is here reported in details from the material development up to the lab-scale testing.

2. Materials synthesis and characterizations

2.1. Materials synthesis

The dry impregnation method was used to develop the silica gel-30%LiCl and vermiculite-45%LiCl composites. Briefly, the dry silica gel (pore size 8.377 nm, particle size 0.5-0.8 mm) or expanded vermiculite (pore size >20 nm, particle size 1.7-2.4 mm) was mixed with LiCl aqueous solution (its volume equals the total pore volume of the matrix and the contained salt mass equals the objective required amount) drop by drop, then composites were obtained after drying in an oven.

2.2. Sorption isobars and sorption kinetics

The sorption isobars of the sorbents were measured by the dynamic vapor sorption (DVS) instrument. The adsorption isobars under 17.21, 23.60 and 42.83 mbar were tested, the results are shown in Figure. 1. It shows that both composites experience multistage sorption process, including physisorption, hydration reaction + deliquescence and solution absorption. A hysteresis loop appears for silica gel-30%LiCl in the full range except for the solution absorption, possibly caused by the capillary phenomenon. No hysteresis loop appears for vermiculite-45%LiCl since its macropores have negligible impacts on the sorption behavior of the LiCl. Generally, the sorption amount increases with the increased vapor pressure or the decreased temperature. Vermiculite-45%LiCl can obtain higher sorption capacity than silica gel-30%LiCl under the same operation condition, owning to its higher salt concentration. The D-A (Dubinin–Astakhov) equation derived from the Polanyi theory was utilized to better describe the equilibrium sorption capacity under various operation conditions:

$$w = w_0 \, e^{-(k \, \Delta F^n)} \qquad [\mathrm{g/g}] \tag{1}$$

where w_0 [g/g] is the maximum sorption capacity, both k [s^{-1}] and n are fitting parameters. ΔF is the free sorption potential and can be calculated by:

$$\Delta F = R \, T \ln\left(\frac{p_{sat}}{p}\right) \qquad [\mathrm{kJ/kg}] \tag{2}$$

The parameters of Eqn.(1) and (2) were summaried in our previous publication [11].

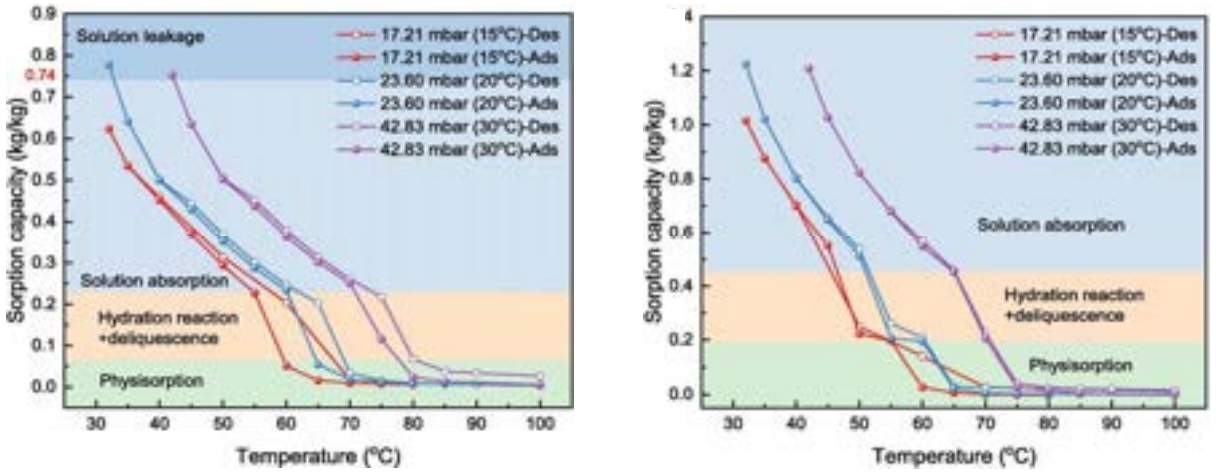

Figure. 1. The sorption isobar curves of (a) silica gel-30%LiCl and (b) vermiculite-45%LiCl composite [11].

Besides sorption equilibrium, sorption kinetic represents another important aspect to evaluate the achievable sorption properties, and it can be used to calculate the SDWP altogether with sorption equilibrium data. The ad/desorption kinetics at different temperature jump at 8.79, 17.21 and 31.98 mbar were measured by the DVS instrument. Partial results are depicted by Figure. 3. The commonly utilized linear driving force (LDF) model [12] is used to obtain the kinetics coefficient (k) for the evaluation of the sorption/desorption rate:

$$\frac{dw}{dt} = k \, (w_\infty - w) \qquad [\mathrm{g/(g \cdot s)}] \tag{3}$$

In general, the sorption rates of silica gel-30%LiCl and vermiculite-45%LiCl composites are much slower than the ones achieved by pure physical adsorbents commonly used in adsorption machines, such as silica gel and zeolites. This is due to the slower reaction rate of the salt-water hydration reaction as well as to the higher sorption capacity of the composites. Nevertheless, looking at the results reported in Figure. 2, a clear difference can be identified also between composites. Indeed, thanks to the mesoporous structure of the silica gel, the crystal size of the embedded salt is much smaller than the one inside the macropores of the vermiculite. This causes a much faster reaction in silica gel-based composite.

Accordingly, for a lab-scale comparison, the composite embedding LiCl into silica gel was selected to be compared against the reference microporous silica gel, usually applied in adsorption chillers.

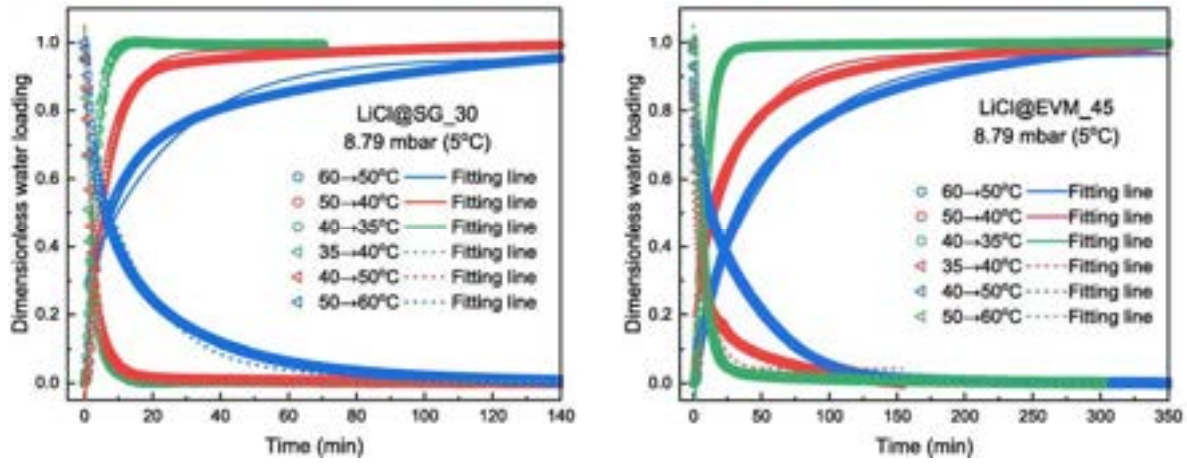

(a) (b)

Figure. 3. The ad/desorption kinetics curves of (a) silica gel-30%LiCl and (b) vermiculite-45%LiCl composite [11].

3. Lab-scale adsorption desalination system

3.1. Experimental apparatus and methods

The lab-scale testing was performed aiming at investigating the adsorption kinetic performance of a small-scale adsorber, thus deriving the achievable performance in terms of cooling and desalination capacity.

The applied testing apparatus is reported in the literature as thermal large temperature jump (T-LTJ) (see Figure. 4a). It consists of a vacuum chamber, an evaporator/condenser, four thermostats and a vacuum pump. A finned flat-tubes aluminum heat exchanger (see Figure. 4b) serves as the ad/desorber, and 74.4 g sorbent particles were packed between the fins. Fast temperature jumps/drops are operated by quickly switching the valves after reaching desorption/adsorption equilibrium, aiming to simulate practical adsorption and desorption process.

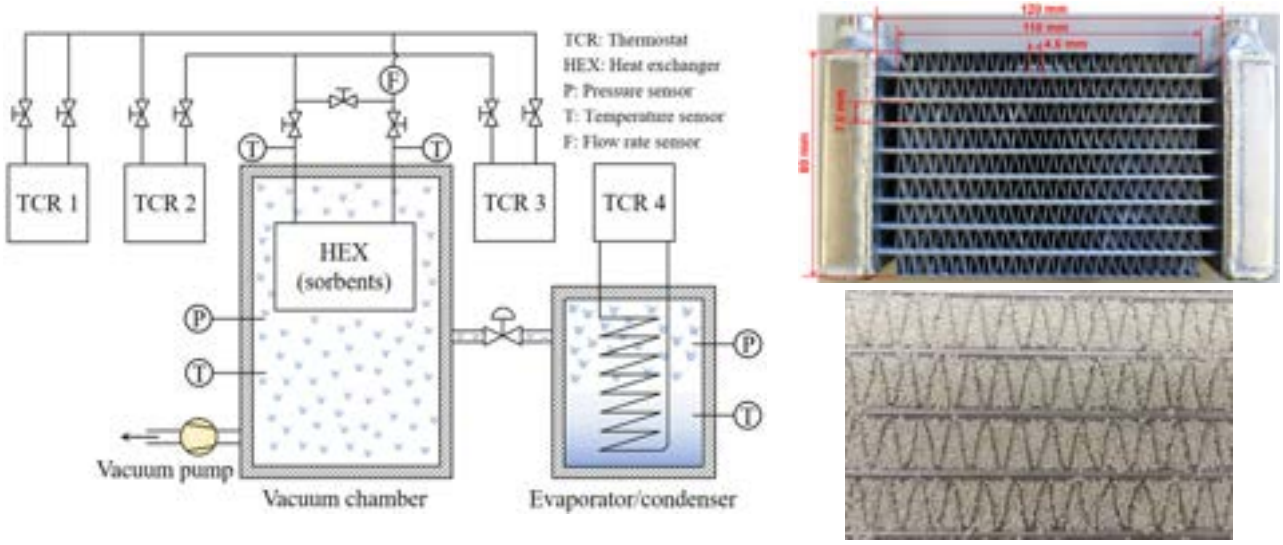

(a) (b)

Figure. 4. (a) Schematic diagram of the T-LTJ testing system and (b) pictures of the blank heat exchanger and the heat exchanger packed with silica gel-30% LiCl [13].

The testing approach is based on the evaluation of the temperature difference measured at the inlet and the outlet of the adsorber during reference adsorption cycles. Due to the exothermic reaction of the adsorption process, the heat transfer fluid shows a temperature increase at the beginning of the test, due to the high sorption rate, followed by a continuous decreasing caused by the reduction of the sorption rate due to the saturation of the material occurring.

The sorption kinetic rate is then evaluated by analysing the decay (often exponential) of the ΔT measured and deriving typical parameters, such as the characteristic times and the average power, that can be employed to compare different materials and heat exchanger configurations. An uncertainty analysis of the method showed an accuracy in the range between 5% and 8% depending on the operating conditions.

3.2. Experimental results

Following the above introduced description of the methodology,the $\Delta T_{ad/de}$ contributed by the ad/desorption process is calculated by:

$$\Delta T_{ad/de}(t)=\Delta T_{ov}(t)-\Delta T_{bl}(t) \quad (4)$$

where ΔT_{ov} identifies the temperature differences of the inlet and outlet heat transfer fluid of the adsorber under ad/desorption mode, and ΔT_{bl} is this temperature difference of the related blank test, which is needed to depurate the test by the sensible heating and cooling effect of the inert masses (such as the metal of the heat exchanger and the sorbent material thermal capacity).

As demonstrated in previous publications [13], the $\Delta T_{ad/de}$ curves can be well fitted using the exponential function under most operation conditions:

$$\Delta T_{ad/de}(t) = \Delta T_{\infty} + \Delta T_0 \cdot \exp(-\frac{t}{\tau_{ad/de}}) \quad (5)$$

Both adsorption and desorption tests were carried out over the adsorber filled with the composite and the microporous silica gel. For the sake of brevity, only some of the results obtained on the composite sorbent are reported below.

Figure. 5a reports a comparison among different adsorption kinetic curves obtained while testing the composite sorbent, varying the reference desorption temperature. As expected at high temperature the adsorption capacity and thus the measured ΔT is higher, but, overall, the adsorption kinetic is comparable when the reference desorption temperature is varied.

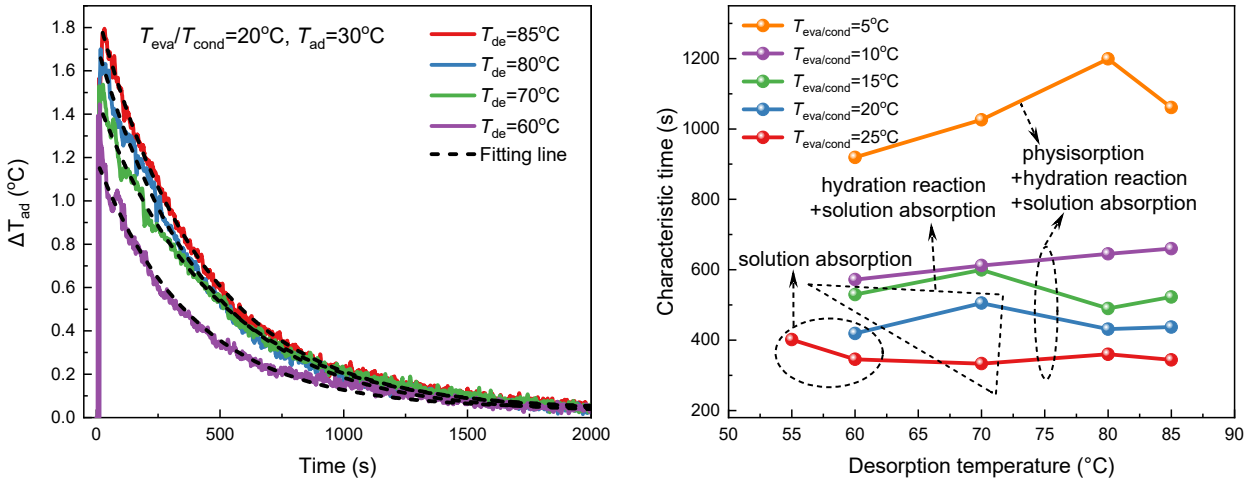

Figure. 6. (a) Comparison of different adsorption runs measured over the composite sorbent and (b) comparison of the achieved characteristic times for all the tests performed [14].

To investigate the effect of the boundary conditions over the kinetic performance, a large set of tests varying different boundaries were performed, and the characteristic times were calculated. Figure. 7b compares the different characteristic times as a function of the reference desorption temperature and evaporation/condensation temperature. As highlighted, the desorption temperature does not play a critical role, while the main difference is obtained by varying the evaporation/condensation temperature. Indeed, the kinetic performance increase by increasing the evaporation/condensation temperature. This can be justified by the higher absolute water vapor pressure inside the testing chamber at higher evaporation/condensation temperature. This reduces the mass transfer resistance across the material packed between the fins of the heat exchanger, thus minimizing the time to reach the equilibrium (i.e. maximizing the kinetics).

Figure. 8a compares the achievable desorption kinetic for two different desorption temperatures, namely, 60 °C and 80 °C, at the same evaporation/condensation temperature, 20 °C. As expected, there is a clear increase in the measured temperature difference passing from 60 °C to 80 °C, due to the higher degree of reaction between water vapor and embedded salt. Similarly, a comparable effect can be highlighted when the evaporation/condensation temperature increases, as reported in Figure. 9b.

Overall, from a direct comparison of adsorption and desorption kinetic performance under similar conditions, usually the desorption run is between 2 and 3 times faster than the adsorption run. This can be ascribed to the

higher pressure gradient occurring between the adsorber and the condenser during the desorption phase, compared to the same existing during the adsorption between evaporator and adsorber, that reduces the mass transfer resistance, thus allowing the vapor leaving the adsorber quickly.

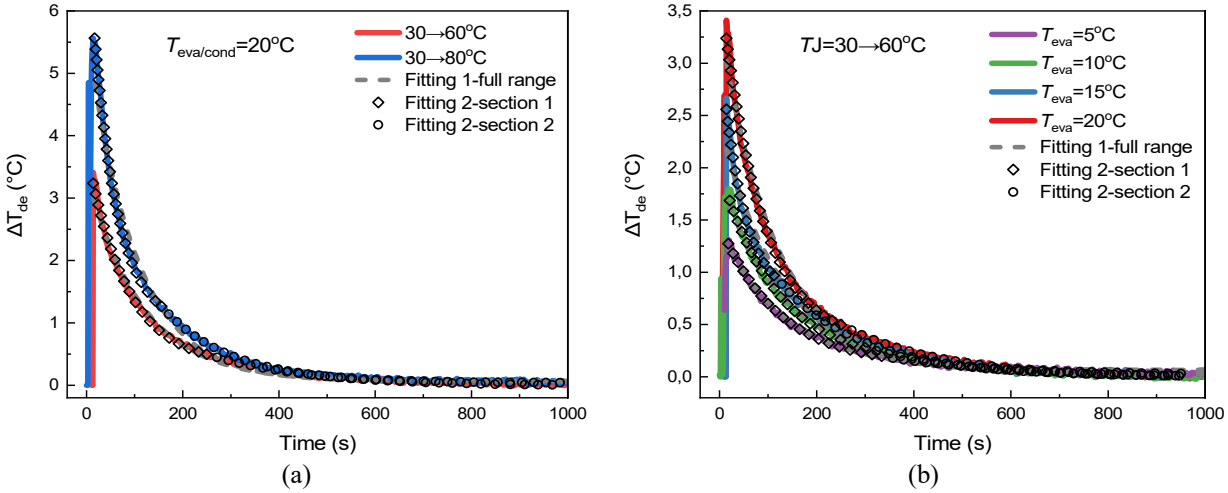

Figure. 10. (a) Effect of the desorption temperature on the sorption kinetic for the composite sorbent and (b) effect of the condensation temperature for the same configuration [14].

3.3. SDWP calculation and preliminary design for a large-scale desalination unit

As already mentioned, one of the most relevant performance indicators to be considered for an adsorption desalination unit is the specific daily water production (SDWP), namely, the volume of desalinated water produced daily per mass of adsorbent material employed, as reported below.

$$SDWP = \frac{86400\left[\frac{s}{day}\right]}{t_{cycle}}(w_{ad} - w_{de})\left[\frac{\frac{m^3}{tonne}}{day}\right] \quad (6)$$

This performance is strongly depending on the adsorption equilibrium difference processed during the cycle (w_{ad}-w_{de}) as well as on the sorption kinetic which is influencing the operating cycle time. Increasing the sorption difference and decreasing the cycle time lead to an overall SDWP enhancement.

Starting from the small-scale testing in the lab, the SDWP for the composite silica-gel/LiCl was calculated for all the conditions tested, as summarized in Table. 1. As it can be highlighted, the SDWP is quite limited at low evaporation/condensation temperatures and it is also almost unaffected under these conditions by the desorption temperature. Differently, as soon as the evaporation/condensation temperature overcomes a certain threshold, i.e. 15 °C, the SDWP increases and shows a relevant difference when the desorption temperature raises from 60 °C and 80 °C. This is justified by the higher amount of water vapor exchanged which does not affect negatively the sorption kinetic.

In general, the composite sorbent can guarantee a SDWP increase in a range from 25% to 50% compared against the standard microporous silica gel, thus confirming the potentiality of reducing the size of adsorption desalination units, which is of utmost importance in mobile applications such as the naval one.

Table. 1. SDWP calculated for all the testing conditions measured at lab scale.

Rererence cycle	$T_{eva/cond}$ 5 °C	$T_{eva/cond}$ 10 °C	$T_{eva/cond}$ 15 °C	$T_{eva/cond}$ 20 °C
$T_{ads/des}$ 30-60 °C	14	25	25	40
$T_{ads/des}$ 30-80 °C	11	24	40	57

The reported calculations were carried out considering a standard 2-adsorbers desalination unit design. Nevertheless, looking at the kinetic testing results, it is clear that, since the desorption process is much faster, it could be reasonable to increase the number of adsorbers, thus being able to re-allocate the adsorption/desorption phases, optimizing the overall performance and exploiting the sorption properties of the material at their maximum level. Preliminary calculations showed that having a 3-adsorbers design can help in further increasing the SDWP in a range from 10% to 15% compared to the 2-adsorbers design.

On this basis, the first large scale setup for testing in the lab is under design, for further investigation before being realized in larger scale for validation on board of a demo vessel.

4. Conclusions

The development of innovative, high efficiency and compact adsorption-based desalination machines requires investigation at materials and components levels. In this paper new innovative composite sorbents were developed and tested both from the equilibrium and kinetic point of view. The most efficient one, based on LiCl embedded inside mesoporous silica gel, was manufactured in large scale and tested in a lab-scale device developed for characterizing sorption kinetic properties under real operating conditions for desalination and cooling applications. A small-scale finned-flat tubes aluminium heat exchanger was used to embed the grains of the composite as well as a reference material (i.e. microporous silica gel). The results demonstrated that the water vapor mass transfer across the adsorber is limiting the kinetic performance, thus affecting the achievable SDWP. Moreover, the desorption kinetic resulted being 2 to 3 times faster than the corresponding adsorption process.

Starting from the obtained results, the estimation of the SDWP of this configuration against the one employing microporous silica gel was carried out, showing a performance increase ranging from 25% up to 50%. Moreover, the possibility of using a 3-adsorbers based adsorption machine resulted the most appropriate one, to manage the difference kinetic performance of adsorption and desorption phases.

This investigation will represent the basis of the design of a lab-scale adsorption desalination machine to be tested in the lab and subsequently on board of a demo vessel.

Acknowledgments

This project has received funding from the European Union's Horizon Europe research and innovation programme under grant agreement No 101056801 (ZHENIT)

References

[1] World Economic Forum. The Global Risks Report 2020. 2020.

[2] Shahzad MW, Burhan M, Ybyraiymkul D, Ng KC. Desalination Processes' Efficiency and Future Roadmap. Entropy 2019;21:84. https://doi.org/10.3390/e21010084.

[3] Ihsanullah I, Atieh MA, Sajid M, Nazal MK. Science of the Total Environment Desalination and environment : A critical analysis of impacts , mitigation strategies , and greener desalination technologies. Sci Total Environ 2021;780:146585. https://doi.org/10.1016/j.scitotenv.2021.146585.

[4] Riaz N, Sultan M, Miyazaki T, Shahzad MW, Farooq M, Sajjad U, et al. A review of recent advances in adsorption desalination technologies. Int Commun Heat Mass Transf 2021;128:105594. https://doi.org/10.1016/j.icheatmasstransfer.2021.105594.

[5] Wu JW, Hu EJ, Biggs MJ. Thermodynamic cycles of adsorption desalination system. Appl Energy 2012;90:316–22. https://doi.org/10.1016/j.apenergy.2011.04.049.

[6] Zhang H, Ma H, Liu S, Wang H, Sun Y, Qi D. Investigation on the operating characteristics of a pilot-scale adsorption desalination system. Desalination 2020;473:114196. https://doi.org/10.1016/j.desal.2019.114196.

[7] Riaz N, Sultan M. Investigation of Adsorption and Desorption Characteristics of Metal-Organic Frameworks for The Development of Desalination Systems. Proc Int Exch Innov Conf Eng Sci 2021;7:261–7. https://doi.org/10.5109/4739231.

[8] Mitra S, Kumar P, Srinivasan K, Dutta P. Simulation study of a two-stage adsorber system. Appl Therm Eng 2014;72:283–8. https://doi.org/10.1016/j.applthermaleng.2014.04.023.

[9] Zhang Y, Palomba V, Frazzica A. Understanding the effect of materials , design criteria and operational parameters on the adsorption desalination performance – A review. Energy Convers Manag 2022;269:116072. https://doi.org/10.1016/j.enconman.2022.116072.

[10] Aristov YI, Restuccia G, Cacciola G, Parmon VN. A family of new working materials for solid sorption air conditioning systems 2002;22:191–204. https://doi.org/10.1016/S1359-4311(01)00072-2.

[11] Zhang Y, Palomba V, Frazzica A. Development and characterization of LiCl supported composite sorbents for adsorption desalination. Appl Therm Eng 2022;203:117953. https://doi.org/10.1016/j.applthermaleng.2021.117953.

[12] Glueckauf E, Coates JI. 241. Theory of chromatography. Part IV. The influence of incomplete equilibrium on the front boundary of chromatograms and on the effectiveness of separation. J Chem Soc 1947:1315–21. https://doi.org/10.1039/JR9470001315.

[13] Palamara D, Palomba V, Calabrese L, Frazzica A. Evaluation of ad/desorption dynamics of S-PEEK/Zeolite composite coatings by T-LTJ method. Appl Therm Eng 2022;208:118262. https://doi.org/10.1016/j.applthermaleng.2022.118262.

[14] Zhang Y, Palamara D, Palomba V, Calabrese L, Frazzica A. Performance analysis of a lab-scale adsorption desalination system using silica gel/LiCl composite. Desal 2023;548:116278. https://doi.org/10.1016/j.desal.2022.116278

Solar Energy Drier for Algae with Water Recovery for Island Applications

Eden Mamut[a], Laurențiu Oancea[b] and Marcel Ionescu[c]

[a] *Ovidius University of Constanța, Constanta, Romania, e-mail: emamut@univ-ividius.ro, CA*
[b] *Ovidius University of Constanta, Constanta, Romania, e-mail: loancea@univ-ovidius.ro*
[c] *Europlastic Ltd, Bucharest, Romania, e-mail: marcelionescu2008@yahoo.com*

Abstract:

The paper is presenting the results of the evaluation of a model to address the water-food-energy-ecosystem security nexus on islands from the perspective of structuring circular aquatic bioeconomy loops. The scientific research activities have been based on the achievements made in the ROMANA project on the establishment of a methodology for hierarchical EEA in some geographical control volumes. Specifically, there were taken into consideration two scales as the National economy of Romania and the regional economy of the Constanta County that is part of the Dobrogea Region. Using the results and the validation of the multi-scale approach from ROMANA project, in the present paper, there are presented the results of the possible extrapolation of the method for the case of a country with islands like it is the case of Spain.

Keywords:

Solar Energy Drier, Algae Processing, Water Recovery, Island.

1. Introduction

In the current context of the population growth, degradation of the habitat, the evolution of the accumulation of Green House Gases (GHG) in the atmosphere and trends in the climate change, the situation of the islands and especially of the small islands, is one of the most vulnerable. There are several approaches to address the complexity of the factors that are affecting of mid and long term the socio-economic situation of the islands and the water-food-energy-ecosystem security nexus approach, as [1] demonstrates, is a holistic and well-structured one for their sustainable development.

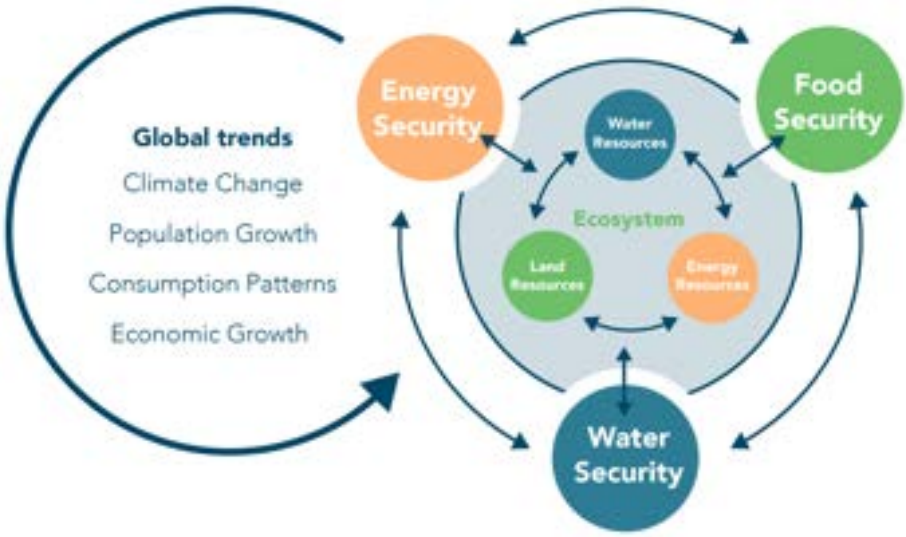

Figure. 1. The interdependences in the Water, Food, Energy and Ecosystem security Nexus [1].

As Austen et al [2] demonstrate, ecosystem valuation must be considered as part of this approach that has to help the achievement of objectives and targets of the environmental policies such as the Good Environmental Status (GES) of the island riparian sea or ocean waters.

As it is mentioned in [3], seaweed and microalgae are responsible of 50% of photosynthesis on Earth and using algae in the Circular Economy concept, the efficiency of solar-to-chemical energy conversion via algal photosynthesis is 4% – 10% compared to 0.5% - 2.2% in land-based farming crops.

In this context, algae harvesting on islands is considered a significant and beneficial activity, particularly if the islands are in areas with abundant algal growth. Algae are photosynthetic organisms that can be found in

marine, freshwater, or terrestrial environments. They play a crucial role in various ecosystems and have numerous applications in industries such as food, pharmaceuticals, cosmetics, and biofuels.

Besides of appropriate selection of algae species and aspects of sustainability and environmental impact, a very important attention must be given to processing and utilization. Once harvested, algae can be processed for various applications. This may involve drying, extraction of specific compounds, or further refinement for specific industries. It's important to have appropriate processing facilities in place to maximize the value and utility of the harvested algae. The economic viability of algae harvesting depends on the costs associated with harvesting, processing, and transportation. Identifying potential markets and customers for the harvested algae products is essential to ensure profitability and sustainability in the long term.

Algae harvesting on islands can provide economic opportunities, promote sustainable practices, and contribute to the local economy. However, it's crucial to balance these activities with the preservation and protection of the island's ecosystems to ensure long-term environmental and economic benefits.

1.1. Humidity content and nutrient value of algae

Algae are considered an extremely heterogeneous group of organisms, very difficult to define. Without being able to consider algae as a single taxon, they could be defined as photosynthetic autotrophic organisms, with a very simply organized vegetative apparatus, called "thal", which can be microscopic, unicellular, or macroscopic, multicellular and which can be found in various habitats, from sufficiently moistened terrestrial ones, to aquatic ones. They are particularly important primary producers for living value chains, the only ones in the seas and oceans, also providing the oxygen necessary for the aquatic life. Macrophytes are also found in continental waters (fresh, salty, or brackish). The estimated net primary production of seaweeds in natural environment by vegetation type is reproduced in figure 2 after [3].

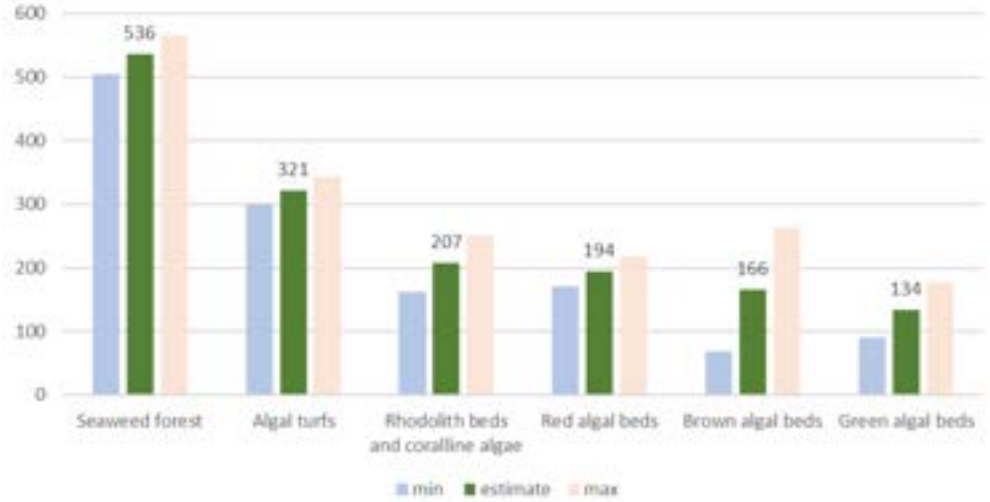

Figure. 2. The net primary production in natural environment by vegetation type, excluding floating algae (in $gC/m^2/year$) [3]

There are three large groups of algae as followings:

- The group of chlorophytes, characterized by the presence of A and B chlorophyll, represents a fundamental phylogenetic line within which the autotrophic terrestrial plants were differential.
- The group of rhodophytes, characterized by the presence of A and D chlorophyll, as well as of phycobilin and especially of phycoerythrin, which gives them the aspect of red colour.
- The group of chomophytes is distinguished by the presence of A and C chlorophyll, along with which there are different types of carotenoid pigments that determine their varied colour as: yellowish, brown – red and red.

As it is mentioned in [4], the total harvested output in the World was reported in 2019 as 34.7 million tonnes of farmed seaweed and 1.1 tonnes of wild-harvested seaweed.

The biochemical composition of seaweed varies depending on the species, geographical space, season, water temperature. Seaweed is valuable for its chemical and biochemical composition having a high content in minerals (magnesium, calcium, phosphorus, potassium, and iodine), micronutrients and carbohydrates. The quality of lipids and proteins is comparable to that of terrestrial plants due to the high content of essential amino acids and the relatively high level of unsaturated fatty acids.

According to Mamut and Ionescu [5], seaweed contains polysaccharides in the range of 30 to 50% of the dry matter content whose structure differs depending on the species. The fraction of soluble fibre is 51 –56% of the total fibres in green and red algae and 67-87% of brown algae. Macrophytes contain considerable amounts of polysaccharides: alginates in brown algae, carrageen, and agar in red algae. In smaller quantities there are xylenes (in red and green algae), ulvans (in green algae) and fucoidans (in brown algae).

Macroalgae extract from the sea an extraordinary wealth of mineral elements. The mineral substance of some macrophytes can reach up to about 36% of the dry matter. Seaweed is a source of iodine and calcium. Only one gram of dried brown seaweed provides 500 to 8 000 µg of iodine, and green and red algae from 100 to 300 µg. Red and green algae, although they have a lower iodine content than brown ones, it is still superior to terrestrial plants. The calcium content in macrophytes accounts for approximately 4 to 7 % of the dry matter.

Macrophyte algae are a natural source of vitamins, polyphenols, and carotenoids with antioxidant properties. The extracts from brown algae are distinguished by the high content of fucoxanthin, β-carotene and violaxanthin. In red algae the main carotenoids are α- and β-carotene and their derivatives, zeaxanthin and lutein. The composition of carotenoids in green algae is similar to vegetal: anteraxanthin, zeaxanthin, neoxanthin, β-carotene, lutein and violaxanthin.

The harvested algal biomass is a raw material with high content of humidity and nutrients, which begins to degrade almost immediately after harvesting. For this reason, the algal biomass is requiring a solution for stabilization if it is not processed within a few hours of harvesting. The raw algal biomass can suffer of up to 20% dry matter losses within a week because of biochemical and microbial degradation.

Reducing the moisture content below 15% is a common conservation strategy for lignocellulosic biomass and is likely to be sufficient for the conservation of algal biomass. With few exceptions, drying experiments conducted in various studies were continued until the algae/terrestrial biomass mixtures reached humidity content below 10% at which point they were considered stable. In [6], there are also presented the results of drying temperatures of the algal biomass and the impact on the conservation of the most important components.

1.2. Algae solar drying

In general terms, biomass drying is a preservation technique that involves reducing the moisture content of biomass to prevent microbial growth, degradation, and spoilage during storage. By reducing moisture, the biomass can be stored for longer periods without compromising its quality or value.

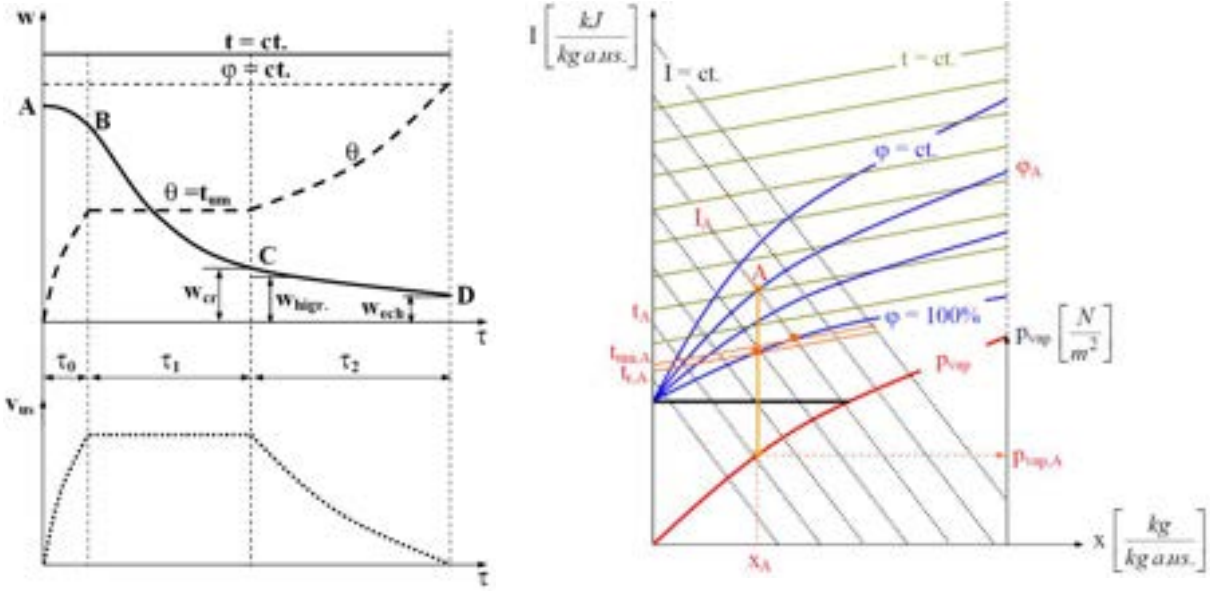

A B

Figure. 3. The general process of drying of biomass by using thermal energy: A - Moisture reduction, feedstock temperature evolution and drying speed, B – Drying air humidity evolution during the drying process.

The removal of water from algae can be done with various techniques as: mechanical pressing or centrifugal processing, hot air drying, drum drying, solar drying, microwave drying, as well as freeze drying, spray draying or solvent extraction.

In Figure 3 there are presented the kinetics and main parameters of the hot air-drying process. An alternative of the hot air-drying process is the solar drying process.

Algae solar drying as the process of using solar energy to remove moisture from harvested algae, is an important step in various industries where algae are used, such as biofuel production, animal feed, and food supplements. Solar drying offers an environmentally friendly and cost-effective method for reducing the moisture content of algae.

The classical phases in solar drying of algae are as followings:

- Harvesting: Algae are typically harvested from ponds, tanks, or bioreactors when they have reached the desired growth stage.

- Pre-treatment: Before drying, the harvested algae may undergo pre-treatment processes such as filtration, centrifugation, or dewatering to remove excess water and impurities.
- Drying beds or trays: The algae biomass is spread out in thin layers on drying beds or trays. These surfaces should be designed to maximize exposure to sunlight.
- Solar exposure: The trays or drying beds are placed in an open area where they can receive direct sunlight. The solar energy heats the algae and evaporates the water content.
- Turning and flipping: To ensure uniform drying, the algae biomass needs to be periodically turned or flipped to expose all sides to sunlight. This promotes consistent drying and prevents the growth of moulds or bacteria.
- Protection: During the drying process, it is essential to protect the algae from rain, dust, and contaminants that can degrade the quality of the final product. This can be done by covering the drying beds or trays with a mesh or protective covering.
- Monitoring: The drying process should be regularly monitored to assess the moisture content of the algae and determine when it reaches the desired level of dryness. Moisture meters or visual inspections can be used for this purpose.
- Storage: Once the algae biomass has reached the desired moisture content, it is removed from the drying beds or trays and stored in suitable containers to prevent rehydration.

The drying time will depend on various factors such as the type of algae, thickness of the biomass layer, ambient temperature, humidity, and solar radiation. In the classical installations, the drying process can take several days to weeks, and it may be necessary to cover the drying beds during the night or in unfavourable weather conditions to protect the algae.

Solar drying offers a sustainable and energy-efficient method for algae drying, utilizing readily available solar energy and minimizing the use of fossil fuels or electricity. This method is particularly suitable for regions with abundant sunlight, where it can significantly reduce the energy costs associated with conventional drying methods.

2. Characterization of algae samples

2.1. Algae sampling and characterization

The evaluation of algae drying processes have been developed for the harvested algae from the Black Sea coast. On the basis of the samples collected from the Black Sea shore and from the continental waters, the physico-chemical properties regarding the moisture content were determined, using conventional drying methods: by using as reference the natural drying for 24h and by using an oven and determining the humidity content. Also, the humidity and ash content of the algae were determined using thermogravimetric analysis methods.

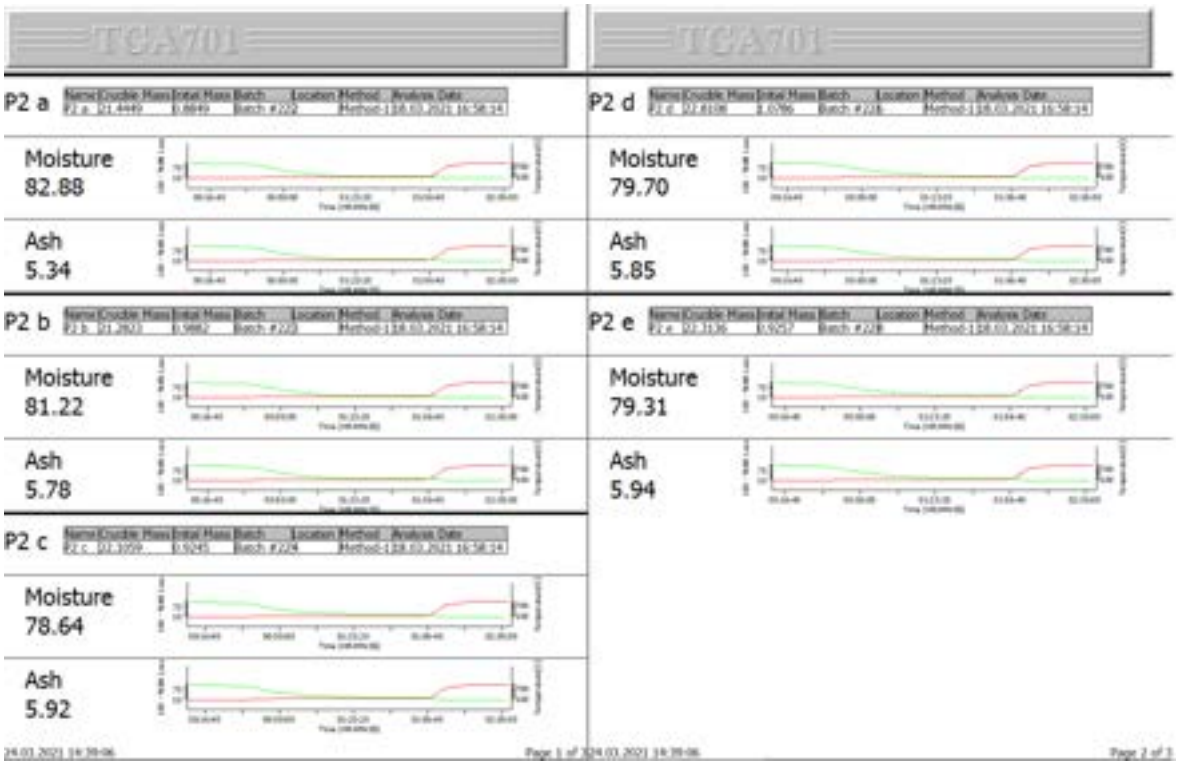

Figure. 4. Water and inorganic matter content of algae samples collected from sea water.

For collected algal samples, the humidity and total solids content have been determined according to ASTM E1756-01 and T412 man-02.

The samples were weighed before being placed in the oven at a temperature of 60°C for 24h. After keeping them 24h in the owen, the samples were weighed, and the difference between the initial and the final mass of each sample is the loss of humidity.

For the samples of algae that were collected from the water and dried naturally for 24h, the average moisture content was 80,35 %. The average content of inorganic substances in water samples of algae was 5,76 %.

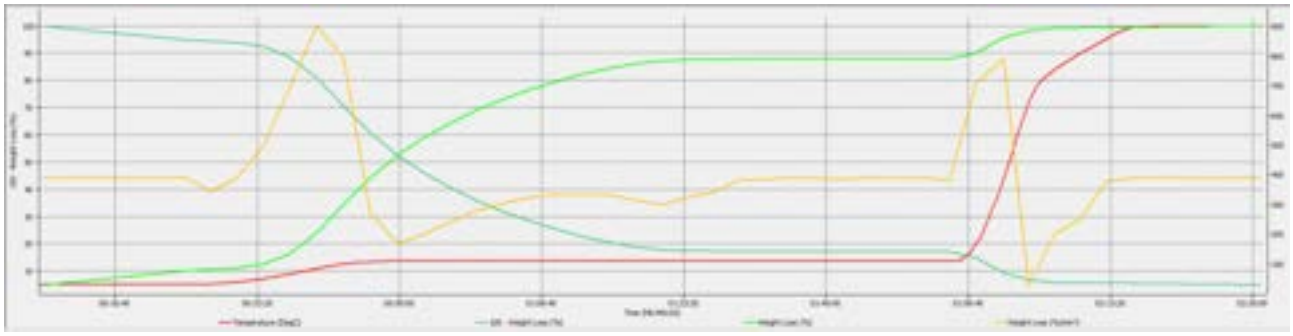

Figure. 5. Graph of the loss of weight in relation to the increase in temperature for algae taken from water.

According to the graph presented in Figure 5, the weight loss was recorded in relation to the increase in temperature. In the temperature range 30 – 45°C the weight loss of the sample was of 7,5%. In the temperature range 45 – 75°C the lost weight of the sample was 15%, and in the temperature range 75 – 90°C, the weight loss of sample was of 23.43%.

For seaweed samples taken from the beach and dried naturally, the average moisture content was 8,34 %. The average content of inorganic matter present in algae samples collected from the beach was 33,05 %.

2.2. Synthesis of the results

As a result of the performed experimental investigations, the dynamics of the weight loss was observed in relation to the increase in temperature.

In the temperature range 30 – 45°C the weight loss of the sample was of 0,98%. In the temperature range 45 – 75°C the weight loss was of 4.05%, and in the temperature range 75 – 90°C, the weight loss of was of 6.2%.

Table 1. Table with the synthesis of the algae sample analyses.

Sample code	Oven Temperature (°C)	Drying period (h)	Initial weight (g)	Final weight (g)	Weight loss (g)	Percentage (%)
P1 a	60	24	5,06	4,62	0,44	8,7
P1 b	60	24	4,96	4,51	0,45	9,1
P1 c	60	24	5	4,67	0,33	6,6
P1 d	60	24	5,07	4,65	0,42	8,29
P1 e	60	24	5,06	4,73	0,33	6,53
P3 a	60	24	5,16	2,46	2,7	52,33
P3 b	60	24	5,14	2,19	2,95	57,4
P3 c	60	24	4,95	2,73	2,22	44,85
P3 d	60	24	5,38	3,13	2,25	41,83
P3 e	60	24	5,04	3,03	2,01	39,89

Following the thermogravimetric analysis of samples collected from water, the following results were obtained:

- the average value of the moisture content of the samples was 5,51 % for the samples of algae collected from the water;
- the average value of the moisture content of the samples was 3,3 % for seaweed samples collected from shore;
- the average value of the total solids content of the samples was 36,43 % for samples of algae collected from the water;
- the average value of the total solids content of the samples was 43,79 % for seaweed samples collected from the shore.

Based on the performed analyses, it was found a weight loss of samples depending on temperature range, as followings:

- in the temperature range 30 to 45 ^{o}C, the weight loss was 0.22%;
- in the temperature range 45 to 75 ^{o}C, the weight loss was 2.55%;
- in the temperature range 75 to 90 ^{o}C, the weight loss was 4.43%.

As it may be seen in the table above, depending on temperature range, the following results were obtained:

- in the temperature range 30 to 45 ^{o}C, the weight loss was 0.14%;
- in the temperature range 45 to 75 ^{o}C, the weight loss was 1.3%;
- in the temperature range 75 to 90 ^{o}C, the weight loss was 2.1%.

3. Drying equipment

3.1. Reference concepts

The reference concepts of driers that have been used for the development of the innovative solution are presented in Figure 6. It has been started from the reference concept of solar drier for algae as may be seen in figure 6 A (adapted after [7]). The solar radiation is heating air in the solar collector located in the bottom side and when the drying temperature is reached, the access valve allows the passage of hot air that is flowing over the fixed bed wet biomass absorbing the humidity and evacuating it by natural convection from the one-way evacuation exit located on the top side of the drier.

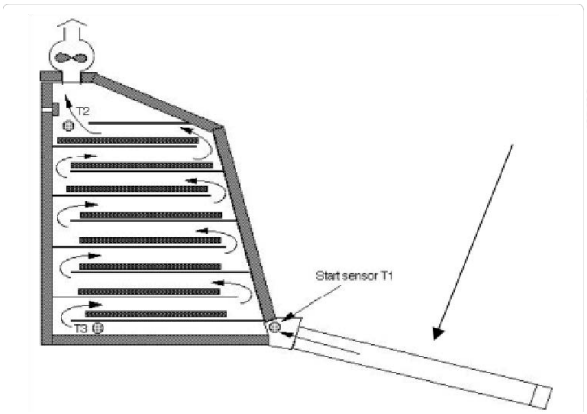

A

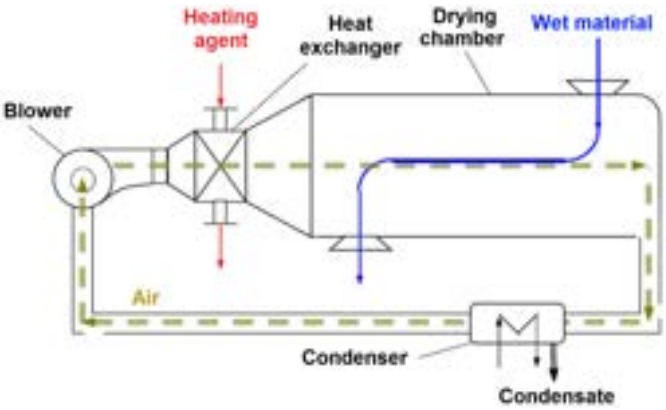

B

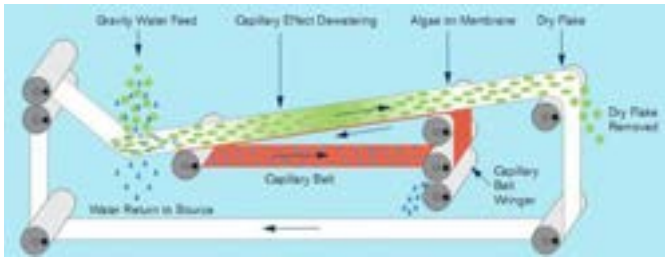

C

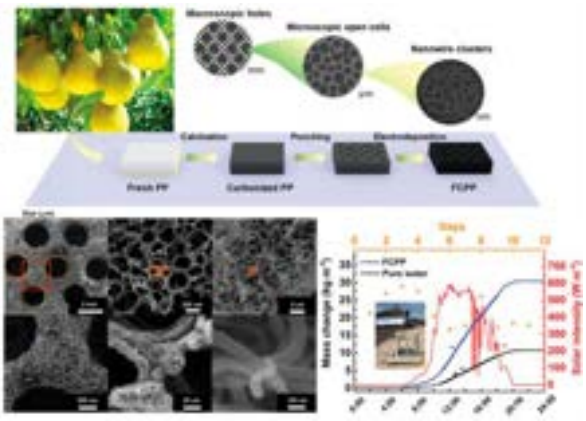

D

Figure. 6. The reference concepts of driers that has been used for the development of the innovative solution of solar algae drier: A – batch solar drier for small quantities of algae (adapted after [7]), B – continuous drying chamber with the recuperation of water condensate, C – drying booster based on a capillary belt (adapted after [8]), D - hierarchically structured nanostructured materials (adapted after [9]).

The solution has been adapted for a continuous drier concept as presented in figure 6 B. It consists of a drying chamber where there is a belt on which from the top side it is fed continuously the wet biomass. The hot air is circulated from the chamber absorbing the humidity of the wet biomass and after drying, the algae is evacuated from the bottom side of the chamber. The high humidity air is recirculated from the condenser and the excess water is recovered as condensate from the bottom side of the graph. The air is further recirculated and reheated before entering in the drying chamber.

To avoid the critical regime (point C in figure 3 A) in the drying process, the innovative concept has been developed by adding a capillary belt as presented in figure 6 C (adapted after [8]). The capillary belt is pressed to the conveyor belt transporting the wet biomass and by the very high hydrophobicity of the capillary material, absorbing the humidity from the bottom and giving a boost to the drying process.

The superhydrophobic material of the capillary belt has been developed as a hierarchically structured nanostructured material like the example presented in figure 6 D (adapted after [9].

3.2. Solar drier concept for continuous processing of wet algae

The concept of the drier has been developed based on a methodology of innovation that started from the definition of the requirements, collection of related information, development of new ideas to address the requirements, co-design of alternative solutions, modelling, testing validation and optimization of the solutions and finally, the selection of the final design by a Multi-Criteria Decision-Making process.

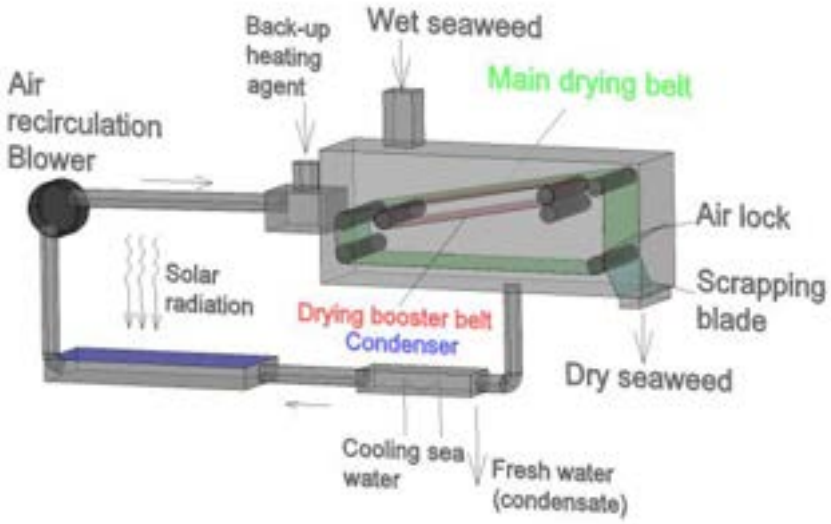

Figure. 7. Innovative concept of drier using solar energy and producing dried seaweed and fresh water.

The solution that has been developed, consists of a continuous belt drier using hot air. The thermal energy is obtained from a solar air collector. The air is circulated in a closed loop that includes a condenser for collecting fresh water resulting from the drying process of algae. As backup thermal energy source, for balancing the intermittence of the solar energy, it has been included a pellet boiler heater.

To avoid the critical drying regime and to improve the efficiency of the drying process, the installation includes a drying booster belt using a fabric that integrates super hydrophilic nanostructured powder for absorbing the humidity from the wet biomass by contact on the bottom side of the main drying conveyor belt.

Therefore, the innovative installation is processing the wet seaweed collected from the sea or the beach, to produce dry algae as a stable, high value concentrate of minerals, vitamins, and other important substances. At the same time, the installation is producing fresh water by the condensation of water vapours from the drying air. As condensing coolant is used the sea water.

The solar energy collectors have been developed by integrating an absorber of solar radiation with a paint integrating Multi Wall Carbon Nanotubes (MWCNT). For the improvement of the convective heat transfer from the absorber to the air stream, a special design architecture has been developed.

4. Hierarchically Multiscale Modelling

The proposed innovative approach is based on the Extended Exergy Accounting - EEA.

The EEA method [10], [11] and [12] is based on the idea that the three Externalities (Labour, Capital and Environmental Cost) can be assigned “equivalent primary exergy values”, under a set of assumptions derived from an exergy budget of the region in which the process is located. EEA is based on a series of assumptions that concern the control volume used for the analysis: since it is necessary to exactly quantify the mass- and energy streams flowing in- and out of a given economic system, the most proper „control volume” to use is at the Country or at the Regional level (like the EU or a sub-regions of Member Countries), where sufficiently disaggregated data are available from reliable sources. Thus, every EEA analysis ought to begin by considering the material, energy and economic balance of the entire Country. Once these global data have been extracted, manipulated and processed, EEA most convenient applications are at intermediate and low (highly disaggregated) levels, down to a single production line. The theory requires that two conversion functionals, the equivalent primary exergy of the unit of monetary circulation, ee_K [J/€], and the equivalent primary exergy of the workhour, ee_L [J/workhour], be calculated at the regional level, and they require the acquisition of two econometric parameters that contain global economic, social and exergetic data [11].

The EEA method begins with the subdivision of the region in which the process is located, in 7 Sectors: Domestic (DO), Extraction (EX), Conversion (CO), Industrial (IN), Transportation (TR), Tertiary (TE) and Agricultural (AG). Each Sector exchanges material and immaterial fluxes with other sectors, with the environment and/or with another conventional -fictitious- system called "Abroad" that accounts for the import/export fluxes. Similarly, every single (material or immaterial) process S taking place in the region exchanges physical fluxes with some of the sectors: all of these fluxes can be converted to extended exergy (i.e., their primary exergetic equivalent) by means of the two above functionals. In particular, EE_{L} is assumed to be originated only in DO, and EE_{K} in TE. Imported commodities are handled through TE.

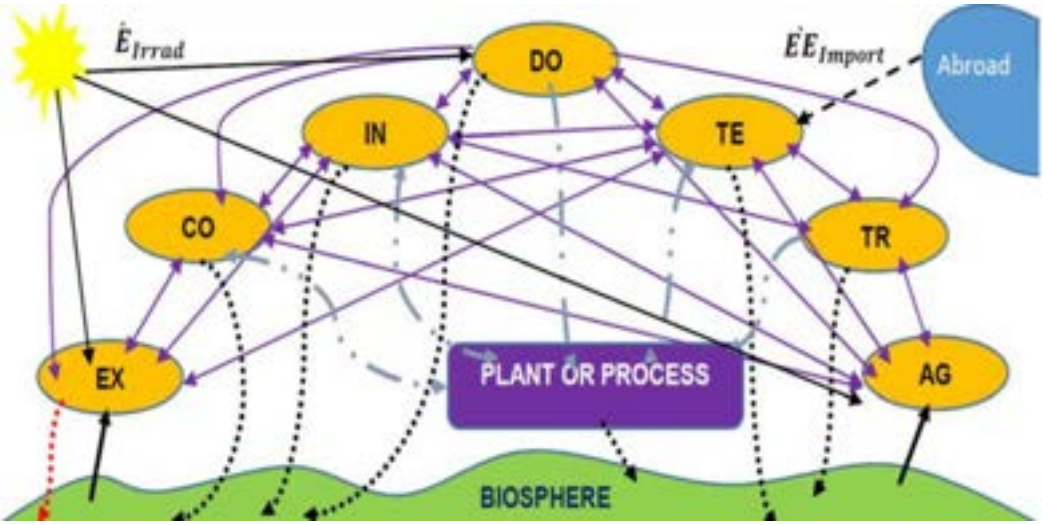

Figure. 8. Structuring the activities in a certain control volume in 7 Sectors: Domestic (DO), Extraction (EX), Conversion (CO), Industrial (IN), Transportation (TR), Tertiary (TE) and Agricultural (AG) (adapted from [12])

Once the above quantities are known, a balance for the EE_j is performed, resulting in a specific extended exergy cost, ee_c [$J_{primary\ exergy}$/unit] that reflects the total amount of primary resources consumed for the production of 1 unit of product X: a genuine exergy cost.

Notice that the EEA method is perfect tool for the assessment of medium- and long range scenarios: since it clearly identifies the contributions from renewable and non-renewable sources, it provides useful quantitative indications about the progress of a process, a technological line, an industrial sector, a Region or a Country along the so-called "transitional path to sustainability".

The calculation of the ee_c requires that highly disaggregated data are available for the Region under analysis. It also requires that updated technical information is available for all feasible technical treatment processes of each pollutant. Additionally, labour and monetary statistics at regional level are necessary to calculate two econometric coefficients, called α and β [7,8] needed for the calculation of ee_K and ee_L. Procedures to calculate these econometric coefficients for a multiscale approach have been validated in the Project ROMANA that is in final phase of implementation at Ovidius University of Constanţa. EEA-based procedures were developed for the integrated evaluation of energy efficiency at Country Level – Romania, county level – Constanţa, and process level for the District Heating System in the Constanţa Municipality.

4.1. Drier scale modelling

For the evaluation of the main energy and commodity flows, at the scale of the drying installation as it is presented in fig. 7, the following values have been calculated:

- required heat for drying,
- absorbed solar radiation energy,
- the resulting flows of water and dry matter the process.

At the drier scale, the conservation equations are as followings:

- specific heat in the convection heat transfer between air and wet biomass

$$q = \alpha\left(t_m - t_f\right) \quad (1)$$

- mass balance equation

$$\dot{m}_1 = \dot{m}_2 + \dot{W} \quad (2)$$

- humidity balance in the drying installation

$$\dot{m}_1 \frac{w_1}{100} + Lx_0 = \dot{m}_2 \frac{w_2}{100} + Lx_2 \quad (3)$$

- thermal balance in the drying process

$$q = l(I_2 - I_0) = 1.006(t_1 - t_0) + 1.863x_1(t_1 - t_0) \quad (4)$$

The modelling equations (1) – (4), were written by taking into consideration theoretical conditions, without considering losses from the walls, chemical reactions, and the transportation losses.

The calculated streams of energy and commodities have been integrated in the EEA calculation toolbox.

4.2. Island scale modelling

The scientific research activities that have been developed under ROMANA project, have been concentrated on the establishment of a methodology for hierarchical EEA in some geographical control volumes. Specifically, there were taken into consideration two scales as the National economy of Romania and the regional economy of the Constanta County that is part of the Dobrogea Region. Using the results and the validation of the multi-scale approach from ROMANA project, in the present paper, there are presented the results of the possible extrapolation of the method for the case of a country with islands like it is the case of Spain.

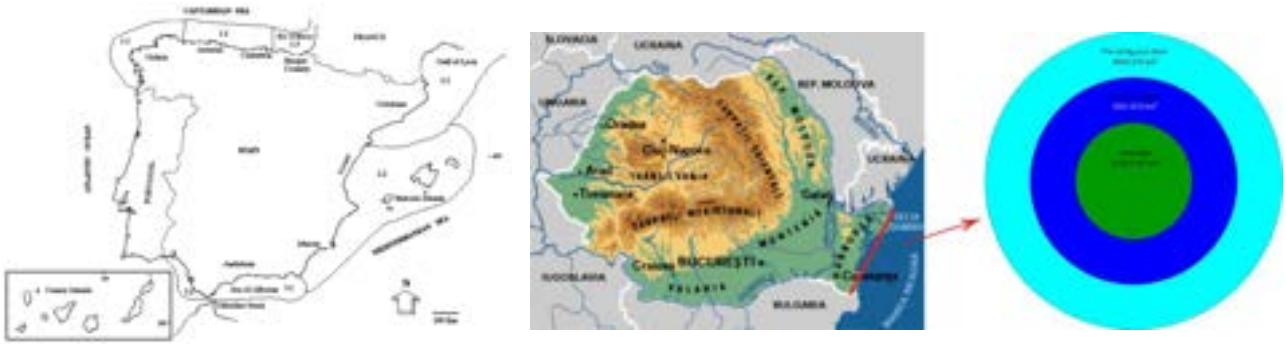

A B

Figure. 8. Equivalent Island model for the yields of algae from the sea waters. A – Regions of Spain that are active in the aquatic bioeconomy [13]. B – Conventional model for structuring a coastal region as an island.

It has to be mentioned that the Dobrogea region has a specific characteristic consisting on the geographical boundaries established by the Lower Danube in the West, Danube Delta in the North and the Black Sea in the East. For this reason, it has been considered the shoreline to the Black Sea and a possible structuring of it as a conventional island shoreline as presented in the fig. 8 B. This offered the possibility to define an equivalent land surface for estimating the specific input of solar energy that could be used for calculating EEA in relation with aquatic bioeconomy inputs. At the same time, offering the possibility to define a reference surface for the associated coastal waters including the equivalent surface of territorial waters and contiguous zone according to the current international laws.

Using the above-mentioned assumption, an equivalent conventional island has been generated and used to apply the EEA method for the evaluation of the relation between the solar energy potential, the aquatic bioeconomy inputs and the outputs in terms of dried seaweed and fresh water, by using the data collected for the Dobrogea region.

5. Experimental results

The estimation of the annual yields of seaweed has been carried out for the conditions in the South-East region of Romania, where the collection season starts in June and ends in October.

A B

Figure. 9. Collection of the seaweed yields: A – Collection from water; B – Collection from the beach

There is a specialized company that is organized for collecting algae both from the sea shallow waters and from the beaches. The total shoreline is of 180 km and the average annual yield is of 40.000 tonnes.

By comparing the SE region of Romania with other regions, it has to be underlined the importance of the contribution of the Danube River exit to the Black Sea. The high concentration of nutrients transported by the Danube has a major role in supporting the production of algae yields.

The validation of the model of the solar air collector has been done by using a 1:1 physical model that is presented in the Figure 10 A. The solar collector integrates an absorber that was developed using a special paint with MWCNT. The absorption rate of solar radiation that was measured on the experimental prototype was 98.8%.

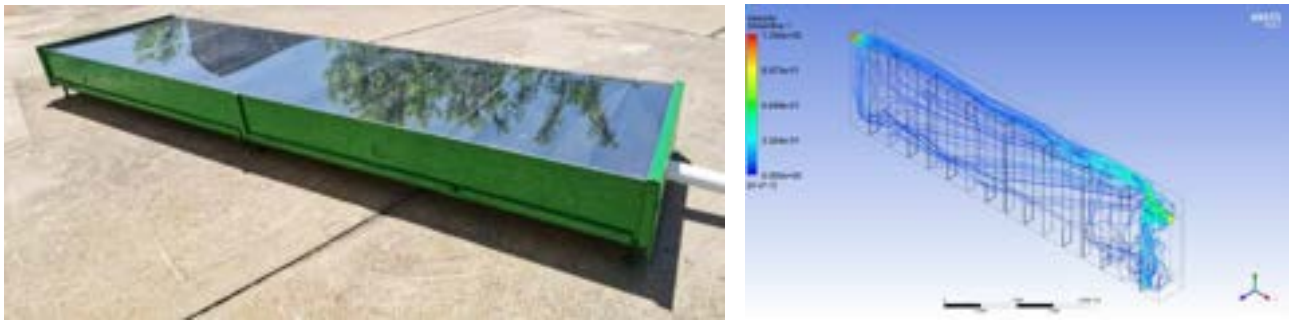

A B

Figure. 10. Solar air collector validation: A – Experimental validation prototype; B – ANSYS Fluent thermofluidic analysis and optimization model.

An ANSYS Fluent model has been developed for the study of the thermofluidic processes in order to improve the convective heat transfer properties and to define an optimal flow architecture for highest convection heat transfer coefficient.

Considering the annual yield of wet algae collected from water in the range of 40.000 tonnes with an average humidity of 80%, using the model described in paragraph 4.1, it has been calculated the total required heat for the drying process, in the amount of 28.000 MWh/year.

The calculated heat resulted for the estimated final humidity of the dry algae of 10%. The total quantity of dry algae is estimated at 12.000 tonnes.

The by-product obtained from the drying process is fresh water in an amount of 28.000 tonnes/year.

The price for dry algae was estimated at 200 Euro/tonne and the price for fresh water is 2 Euro/tonne.

The total income for the installation has been estimated at 2.4 million Euro for the dry algae and 56.000 Euro for water.

The operational costs included the following items:

- labour costs in an amount of 72.000 Euro
- energy costs (including cost of transport) in an amount of 168.000 Euro
- overheads in an amount of 24.000 Euro

Total operational costs have been estimated at 264.000 Euro.

The investment costs include the following items:

- Solar air collectors – 2.400.000 Euro
- Dryer – 400.000 Euro
- Ancillary equipment and construction works – 280.000 Euro

Total investment cost – 3.080.000 Euro.

Considering a depreciation period of 15 years, with a fix rate of depreciation, it has been obtained a yearly depreciation of 205,333.3 Euro.

From the economic point of view, the investment payback period is of 7.6 years.

But the benefits of exploitation of the seaweed yields are much more complex and include the avoidance of the GHGs that are resulting from the natural decomposition of the biomass. In this respect, it has been developed an EEA model for the evaluation of the energy efficiency in the hierarchical model that has been presented in paragraph 4.

Two configurations were compared: the first one uses a CH_4-fuelled drier, and the second one is the solar drying configuration described above.

The exergy flows of the two processes were analysed first, and the Solar configuration showed a slightly better efficiency: 0.68 vs. 0.66. But the EEA analysis, that includes in the “product cost” the primary exergy flow equivalent to the externalities (Labour and Capital in this case), provided a different picture. Table 2 shows the extended exergy cost ee_c for the two co-products, dry biomass and desalinated water: considering that the exergy cost of Reverse Osmosis desalination is about 0.01 kWh/kg, the process is not a convenient

desalinator. But the primary exergy cost ee_c for the dried biomass is about one third of that of natural gas (3 vs. 15.88 kWh/kg), which makes the biomass very convenient both as a secondary biofuel or as a raw material input for the chemical industry.

Table 2. Extended Exergy Cost ee_c [kWh/kg] of the two co-products.

	Dried biomass	Desalinated water
Natural gas-fired drier	5.61	1.12
Solar drier	5.81	1.16

The calculated quantity of GHG equivalent of CO_2 that is saved in the case the solar drier, is of 4453 tonnes/y. Considering a price per CO_2 certificate of 100 Euro/t the total value of the certificates is 445,300 Euros.

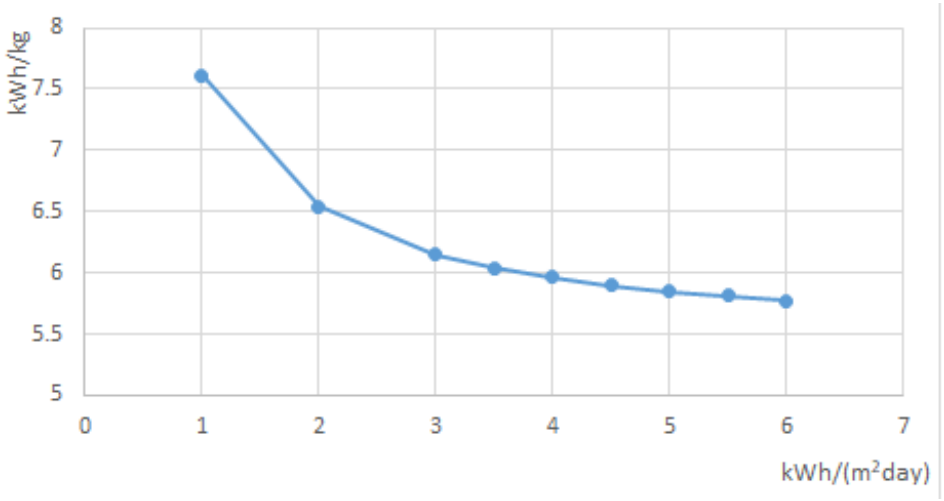

Figure. 11. The impact of solar irradiation of the extended exergy cost of the biomass

In fig. 11, it is presented the influence of the solar irradiation on the extended exergy cost of the dried biomass. It may be seen that the increase of the irradiation is reducing the extended exergy cost based on the reduction of the investment on solar panels.

A similar analysis must be done on the aspects referring to the primary exergy of the dry algae. Depending on the quality of the algae the price is varying between 200 and 1200 Euro/t. In the EEA model that has been used for the present study, the price was used as 200 Euro/tonne.

6. Conclusions

The water-food-energy-ecosystem security nexus approach is a holistic and well-structured model addressing the complexity of the factors that are affecting on mid and long term the socio-economic situation of the islands and for their sustainable development.

The scientific research activities have been presented in the paper were obtained based on the achievements made in the ROMANA project on the establishment of a methodology for hierarchical EEA in some geographical control volumes. Specifically, there were taken into consideration two scales as the National economy of Romania and the regional economy of the Constanta County that is part of the Dobrogea Region. Using the results and the validation of the multi-scale approach from ROMANA project, in the present paper, there are presented the results of the possible extrapolation of the method for the case of a country with islands like it is the case of Spain.

The innovative solution that is presented in the paper is efficient and taking into account only the commercial values for OPEX and CAPEX, the investment payback period is of 7.6 years

But the benefits of exploitation of the seaweed yields are much more complex and include the avoidance of the GHGs that are resulting from the natural decomposition of the biomass. In this respect, at present, there is under development the EEA model for the evaluation of the energy efficiency in the hierarchical model that has been presented in paragraph 4.

Acknowledgments

This work was supported by a grant of the Romanian Ministry of Education and Research, CNCS - UEFISCDI, project number PN-III-P4-ID-PCE-2020-2738, within PNCDI III.

Nomenclature

q heat, J/kg

t temperature, °C

$\dot{m}$ mass flow rate, kg/s

$\dot{W}$ mass flow rate, kg/s

w specific humidity, kg/kg$_{\text{wet biomass}}$

L air flow rate, kg/s

l specific air flow rate, kg/kg$_{\text{humidity}}$

x air humidity content, kg/kg$_{\text{dry air}}$

I enthalpy, kJ/kg$_{\text{dry air}}$

Greek symbols

α heat transfer coefficient, W/(m^2 K)

Subscripts and superscripts

m mean value

f fluid

0 air inlet section

1 biomass inlet section

2 dry biomass exit section

References

[1] M. van der Geest, D. Slijkerman. Nexus interventions for small tropical islands: case study Bonaire, WUR, 2019, https://edepot.wur.nl/471566

[2] M.C. Austen, P. Andersen, C. Armstrong, R. Doring, S. Hynes, H. Level, S. Oinonen, A. Ressureicao, J. Coopman, Valuing Marine Ecosystems. Taking into account the value of ecosystem benefits in the Blue economy, Future Science Brief, No. 5, April 2019.

[3] Blue Bioeconomy Report, EUMOFA, 2023 January

[4] European Commission (2023), The EU Blue Economy Report, 2023, Publications Office of the European Union, Luxembourg

[5] E. Mamut, M. Ionescu, LD 2.1 Research report on the processing system experimental model of the residual biomass from different types of bioresources, Project "Scientific Research on the Development of Advanced Materials and Multiscale Optimization by Integrating Nano-structured Materials in Advanced Energy Systems - MultiScale", contract no. 8 / 01.09.2016, ID: P_40_279, MySMIS code 105531, Competitiveness Operational Program, Priority Axis 1 - Research, Technological Development and Innovation (RDI) in Support of Economic Competitiveness and Business Development, Action: 1.2.3 Project type Partnerships for Knowledge Transfer. The project is co-financed by the European Regional Development Fund through the Competitiveness Operational Program, 2021.

[6] A.L. Augusto, P.M. Nunes, S.L. Mendes, C.N. Afonso and T.M. Mouga. Effect of different drying temperatures on the moisture, content of phytochemical constituents and technological properties of Peniche coast seaweed. Front. Mar. Sci. Conference Abstract: IMMR | International Meeting on Marine Research 2016. doi: 10.3389/conf.FMARS.2016.04.00011.

[7] M. Musrady Mulyadi, N. Rusdi, The forced convection biomass and solar collector dryer for drying seaweed using exhaust fan, AIP Conference Proceedings 1977, 060011 (2018); https://doi.org/10.1063/1.5043023

[8] T. A. Burke, Modification and Validation of a Novel Solid-Liquid Separation Technique Using a Microscreen and Capillary Belt System, MSc Thesis, Russ College of Engineering and Technology of Ohio University, 2012.

[9] W. Chen, L. Gan and J Huang, Design, Manufacturing and Functions of Pore-Structured Materials: From Biomimetics to Artificial, Biomimetics 2023, 8, 140. https://doi.org/10.3390/biomimetics8020140

[10] E. Sciubba, 1998: A novel exergetic costing method for determining the optimal allocation of scarce resources, Proc. Contemporary Problems in Thermal Eng., Gliwice, Rudnicki et al. Eds., 311-324

[11] E. Sciubba, 2001: Beyond Thermoeconomics? The concept of Extended Exergy Accounting and its application to the analysis and design of Thermal Systems, IJEx v.1, n.1, 68-84

[12] A.Biondi, E.Sciubba, 2021: Extended Exergy Analysis (EEA) of Italy, 2013–2017. Energies 14, 2767.

[13] P. A. Sosa, J. L. Gómez Pinchetti, J. A. Juanes, 2006. The seaweed resources of Spain. Chapter in Book: Critchley, AT, Ohno, M, Largo, DB (Eds.) World Seaweed Resources, An authoritative reference system. http://mdc.ulpgc.es/cdm/singleitem/collection/DOCULPGC/id/3801/rec/54

A tool for effluent characterization and design of Natural Treatment Systems for Wastewater (NTSW) for livestock farms with high organic load in isolated island environments.

Tania Garcia-Ramirez, Carlos A. Mendieta-Pino, Saulo Brito-Espino, Alejandro Ramos-Martin and Federico Leon-Zerpa

Department of Process Engineering, Institute for Environmental Studies, and Natural Resources (i-UNAT), University of Las Palmas de Gran Canaria (ULPGC), tania.garcia@ulpgc.es

Abstract:

The high organic load of the effluent generated in these farms has an important environmental impact, which is amplified in insular or isolated territories. The application of natural treatment systems of wastewater (NTSW) has demonstrated their suitability in these environments, but their design lacks proper characterization and sizing tools for their adequate operation. This work proposes a series of strategies and tools for the design and characterization of NTSW. As an application, an inventory, characterization, sizing, and design is carried out in 9 pig farms with a high environmental impact located on the island of Gran Canaria (Spain). The proposed tools in this work are based on a collection of experimental data over a five-year period of application of NTSW in real farms. This work contributes to facilitate the design and implementation of NTSW in farms located in isolated, island or similar size environments.

Keywords:

Wastewater treatment; natural systems; livestock farms; characterization.

1. Introduction

1.1. Waste generation and characterization overview

Livestock wastes in general, and pig wastes in particular, is made up of a dry part, formed by animal excrement, food remains, bedding, and a liquid part. This mixture is called slurry [1, 2]. Pig slurry is a source of multiple mineral constituents: primary macroelements or nutrients (N, P, K), secondary macroelements (Mg, Ca, Na) and trace elements (Cu, Zn, Mn, Fe, S, B, Mo). The availability of macroelements in slurry for crops is good (N, P) and even comparable to that of mineral fertilizers [3], [4].

The new Spanish legal framework establishing basic rules for the management of intensive and extensive pig farms can be found in Royal Decree 306/2020, of February 11. This Royal Decree (hereinafter referred to as RD306) focuses on environmental issues with respect to the protection of water, soil and air, and on the fight against climate change. Livestock farm effluent with a high organic load has a strong environmental impact that 35 is amplified in island territories.

In turn, slurry may have different properties at any given time due to various factors inherent to production, such as the number of heads, number of sows, piglet, fattening pig. As well as, the form of exploitation, type and management of the farmer, varied diet, cleanliness, the season of the year, emptying of the reception pits and the climate [5– 7].

This is the reason for the interest in developing a characterization tool bases on historical data on the operation of these systems in livestock farms. As indicated by [8, 9], an interesting basic characterization is carried out based on one or several parameters that are easy to determine in situ, leaving other more complex parameters for the laboratory. Likewise, the excessive or unfavourable application of slurry on land can lead to losses of nitrogen and phosphorus by percolation and runoff into surface and subsurface water bodies [8]–[10]. Excess phosphorus and nitrogen in the form of ammonium (NH_4^+), nitrate (NO_3^-) and nitrite (NO_2^-), in waters can accelerate the aging of aquatic ecosystems [11–15]. Ammonia (NH_3) is recognized as one of the most important toxic gases present in swine facilities and has profound effects on pig performance [16] and responds to its toxicity by altering in the barriers and defence mechanisms of the respiratory tract, facilitating the entry of pathogens, and increasing the likelihood of respiratory diseases [17].

Therefore, for a basic characterization of the effluent that allows the sizing of the treatment plant by means of NTSW, the flow rate (Q), chemical oxygen demand (COD), conductivity (EC), total nitrogen (TN) and ammonia (NH_3) are defined.

However, when it comes to dimensioning these systems, there are no tools applicable to agricultural and livestock farms in isolated territories, and they are limited to adaptations based on experience in small communities and rural settlements [29 -30].

1.2. Treatment systems for wastewater

Different slurry treatment systems have been proposed with the aim of reducing the pollutant load so that the treated waste can be reused as fertilizer or safely discharged into the sewage system [18, 19].

Conventional systems involve treating the effluent by means of concentrated physicochemical and biological processes in which the hydraulic retention time (HRT) is relatively short, and a stable operation can be ensured within preestablished and carefully controlled parameters. These have been implemented with varying degrees of success, but numerous problems have been reported, associated especially but not exclusively with the modes of operation and the costs of the system [18, 20–25].

Many pig farms have very tight profit margins and have few human resources due to direct competition with other more suitable production sectors, making on-farm effluent treatment necessary [19, 22, 26 - 27].

Natural treatment systems of wastewater (NTSW) employ effluent storage with a longer HRT which depends on the load applied and the climatic conditions, with the organic matter degraded though the activity of heterotrophic bacteria present in the natural environment. The treatment is carried out by passing the effluent through various types of ponds, artificial wetlands and anaerobic digesters, each of which facilitates a series of natural processes. Such systems have been successfully applied in rural community settings and small settlements with a population equivalent below 1000 [1, 2, 28].

However, when it comes to sizing such systems, there are no tools available for agricultural and livestock farms in isolated territories, with sizing limited to adaptations based on local farmer experience [29 - 30].

1.3. Geographic and primary sector overview

The island of Gran Canaria has a total 136 pig farms, the majority of which are small and family production. However, 10% of these farms account for more than 90% of the census and are industrial farms, in some cases close to environmental protection zones and are shown in Figure 1. For many years, livestock waste has been used as fertilizer in fields or farmland. However, in recent years, the gradual disappearance of these small farms and the increase in intensive livestock farming, the high number of animals per farm and the abandonment of traditional systems have led to a greater fluidity and dilution of the waste generated, thus increasing its volume, but there is not always enough arable land for its correct disposal [30].

Figure 1. Study pig farms in Gran Canaria

According to the applicable Spanish legislation, which establishes basic rules for the management of intensive pig farms, farms can be classified according to their productive capacity, which can be self-consumption farms, reduced farms and industrial farms, a self-consumption farm is considered a farm when it is used for the breeding of animals exclusively for family consumption, with a maximum production per year of 3 fattening pigs and without having a breeding farm; a reduced farm is one that houses a maximum number of 5 breeding animals, being able to keep a number of no more than 25 fattening animals.

This legislation also establishes standards for the management of livestock waste on the farm and the production of manure (theoretical maximum) by livestock unit (LSU). This unit is established for purposes of comparison between livestock species, classifying farms according to this value. By way of example, the corresponding LSU is 0.30 for boars with a waste production of 6.12 m^3/place/year, 0.96 for closed cycle sows with a waste production of 17.75 m^3/place/year, and 0.02 for piglets from 6 to 20 kg with a waste production of

0.41 m^3/place/year. This classification distinguishes between family farms, which may not house more than the equivalent of 5 LSUs, and industrial farms, which are farms with a capacity of up to 120 LSUs.

1.4. Objective

The objective and the novelty of this work is the proposal of a series of strategies and tools for the design and characterization the effluents of NTSW in livestock farms. As an application, an inventory, characterization, and sizing will be carried out for the pig farms with the greatest impact located on the island of Gran Canaria.

2. Materials and Methods

2.1. Model

In this article, the methodology was adapted from that shown and applied [18], in which a study of the water-energy-waste nexus is developed, considering parameters of waste generation, consumption and occupied surface. The integral model is shown in Figure 2, for the evaluation of livestock farms in Gran Canaria, also considering the parameters of greenhouse gas emissions (GHG).

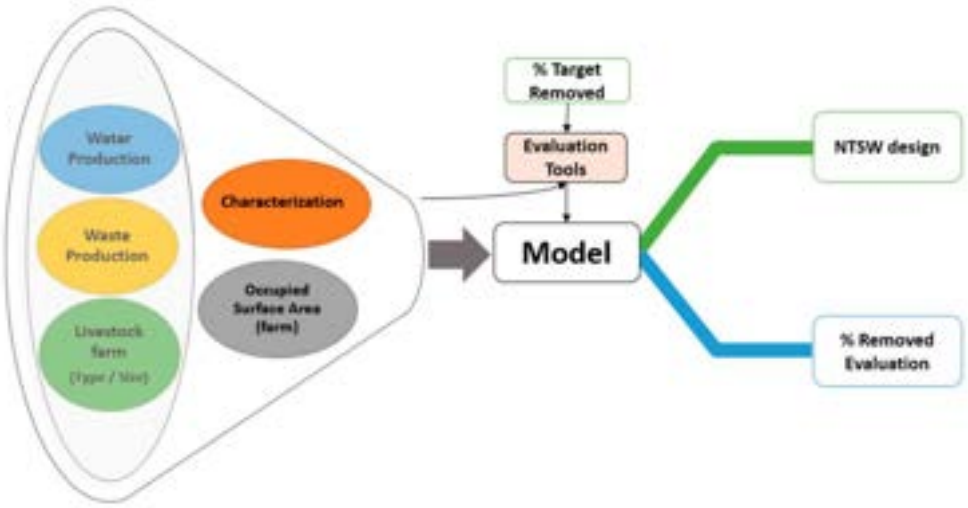

Figure 2. Model

2.2. Waste generation and characterization

Numerous authors have indicated the need to have tools to characterize livestock waste and to monitor parameters that are easy to apply and measure on the farm itself [1, 31–33].

Therefore, the waste generated in each farm was characterized considering the following variables: Q, COD, EC, TN and NH_3 from historical data.

The Q has been characterized by means of the correlation between the effluent flow rate and the number of sows with a correlation coefficient of 0.976 [2]. On the other hand, it was carried out according to Royal Decree 306/2020, of February 11, which includes the manure production (theoretical maximum) by type of livestock. As for COD, the correlation between input COD and Q; with a correlation coefficient of 0.575 [2].

For EC there is no significant correlation between conductivity and Q or COD, but there is a significant correlation with organic matter (Morg). For this reason, Morg was characterized by the correlation between Morg and COD with a correlation coefficient of 0.945 [2]. On the other hand, conductivity was calculated by the correlation between EC and Morg with a correlation coefficient of 0.938 [2].

Finally, the TN generated was characterized by correlation with an r=0.74 [31,34] and the generated NH_3 was characterized by the correlation with a correlation coefficient of 0.91 [31, 34].

Variable	unit	Correlation
Q	m^3/day	$Q=4.425+3.029\times10^{-7}\cdot(No.Sow)^3$
COD	mg/L	$COD=7{,}995.901+360.593\cdot(Q)^2-10.134\cdot(Q)^3$
Morg	mg/L	$Morg=162.505+0.273\cdot(COD)$
EC	dS/m	$EC\ (dS/m)=0.009\cdot(Morg)-8.4\times10^{-7}\cdot(Morg)^2$
TN	mg/L	$TN=83.79\cdot EC^{1.25}$
NH_3	mg/L	$NH_3=39.89\cdot EC^{1.343}$

2.3 Livestock farms.

The 9 selected farms on the island of Gran Canaria have from 15 to 220 sows (3.75 a 55 UGM), the farms total 4,442 animals, representing 94% of the total census on the island [35]. The farms have between 1,180 and 82, 065 m^2 of available land [36].

2.4 Natural Treatment Systems.

For the application of the NTSW, the starting point was the articles [1, 28] which study three livestock farms, one of which is our reference farm [2]. The criteria used for the design were the characteristics of the farms, Q, COD and EC.

2.5 Initial characterization and design of the treatment system.

For the application of the NTSW, the same rotary sieve (50mm) has been applied (and in the case of the digester and ponds plus wetlands, based on the data obtained in these articles, their behavior has been studied according to the needs of the farms studied [1, 2, 28]. The digester is more suited for a high removal of COD 2.33 %/day and ponds plus wetlands system is more suitable for a removal of EC 1.5%/day [2, 28]. To start, set the number of sows of the farm, set a depuration target (measured in COD and EC reduction) and characterize the waste generated, Q, COD, EC, NT, NH_3. A mechanical separation system is applied [21] and we study the behavior it has on the waste. With this final waste, we start to design the digester starting from 1 chamber with the desired volume (22, 10 and 5 m^3) [2, 28], considering the Q of the farm, with a % removal of COD and EC according to the volume of the chamber. As digester data we obtain COD, EC, hydraulic retention time (HRT) and total volume (V_{dig}) and we check if the livestock farm, due to its location and available surface, it is possible and necessary to apply a pond + wetland. For the application of a pond plus wetland we start from the criterion of the location of the farm, considering if it has a nearby population, since this process releases bad odours, and if it is in areas with a high percentage of rainfall and high altitude, being open systems more influenced by climatic conditions (temperature, humidity, rainfall, and evaporation). If it is not possible to design the pond, it is observed whether the results obtained meet the objective. If so, the digester is designed, if not, another chamber is added to the digester and so on.

In terms of its design, it is based on a 15-day HRT, thus setting the maximum volume of the basin (V_{Lag}), a COD removal rate of 1.34 %/day and an EC removal rate of 1.51 %/day [2]. With the results obtained we check if it meets the target. If the COD is high to the target, The volume of the digester would be increased by adding a chamber and so on, if the EC is high to the target we would increase the volume of the pond + wetland. The decision tree is shown in Figure 3, to characterize the natural depuration systems of livestock farms in Gran Canaria.

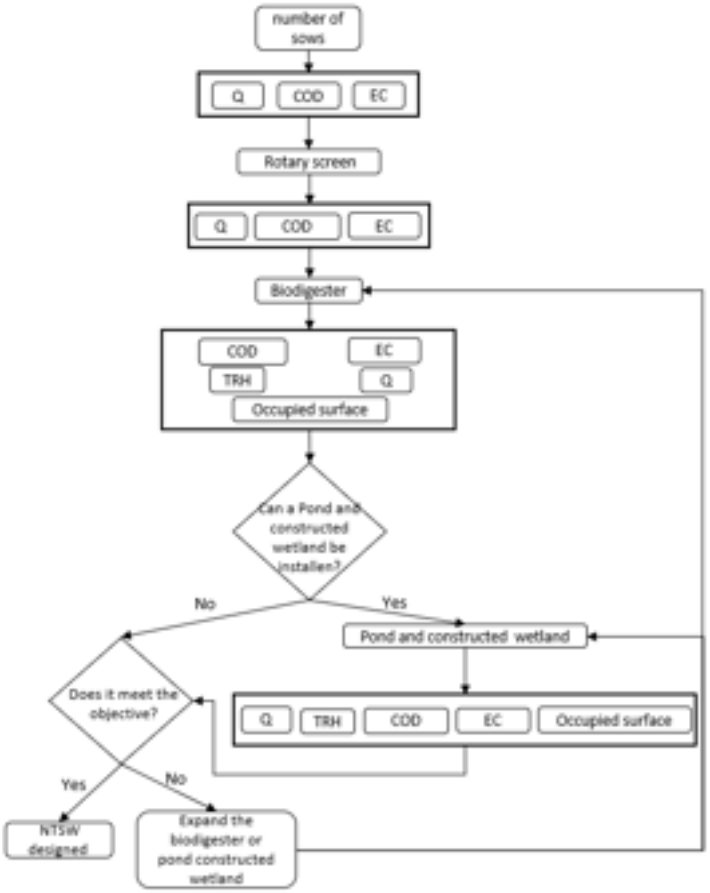

Figure 3. Decision tree.

3. Results and discussion

3.1. Types of farms and waste

This study has focused on 9 farms which, due to their characteristics, type of farm and number of sows, require a treatment system. From the farms studied, the waste generated was characterized, obtaining COD values between 24,078 and 8,049 mg/L, EC between 23 and 16 dS/m and between 2,625 and 1,704 mg/L of NH_3 generated. The selected farms have an available plot between 1,180 and 82,065 m^2, with different soil types and according to the Gran Canaria 2017 management plan could be built on the evaluated soils. By size and type of soil an NTSW can be implemented in the farms. These data are reflected in Table 1.

As mentioned above, to propose a natural depuration treatment system, it is necessary to know the waste generated in each farm, i.e., the slurry Q, COD, EC, TN NH_3.

The slurry flow rate was characterized by two criteria, by correlation and/or by Royal Decree 306/2020, February 11. The choice of one method or the other was based on the type of farm (intensive-confined or semi-confined) and the number of sows. These criteria are since an intensive-confined farm stores more manure than a semi-confined farm. However, intensive-confined farms have been characterized according to the Royal Decree. The reason for this choice is because, although they are industrial farms, the number of sows is lower than the other farms and in the case of using the criterion of number of sows, an error of 62-92% is made, resulting in over-dimensioning the capacity of the NTSW of the farms.

The COD values obtained are in the range between 24,078 and 7,999 mg/L. The mean value is within the range of the observed values of 5,000 and 25,000 mg/L [37], between 28,000 y 13,200 mg/L [38], between 14,200 y 9,400 mg/L [32].

The EC values found are in the range between 16,3 y 23 dS/m. Previous studies have found values, among 13.2 y 33.2 dS/m [31] and from to 9.9 y 25 dS/m [32] hence these results are considered valid.

Table 1. Characterization of farms and livestock wastes

Farm	X	Y	Z	Available area (m^2)	Type of farms	UGM (unit)	Q (m^3/day)	COD (mg/L)	Morg (mg/L)	EC (dS/m)	NT (mg/L)	NH_3N (mg/L)
1	458,08	3,091,56	249.26	18,935	intensive-confined	109.45	7.52	24078.48	6699.93	22.59	4127.14	2625.67
2	455,82	3,084,34	119.28	58,642	intensive-confined	84.5	5.15	16186.60	4545.45	23.55	4347.77	2776.77
3	446,11	3,102,56	705.20	4,516	intensive-confined	70.13	4.62	14705.19	4141.02	22.86	4189.40	2668.25
4	456,59	3,086,37	248.09	1,180	semiconfined	32.13	1.76	9056.79	2599.01	17.72	3045.65	1894.32
5	446,85	3,110,52	330.13	6,885	semiconfined	18.32	1.00	8346.36	2405.06	16.79	2847.08	1761.95
6	440,65	3,096,39	1216.72	10,089	intensive-confined	32.05	1.67	8953.96	2570.94	17.59	3017.58	1875.57
7	457,82	3,085,47	97.72	82,065	intensive-confined	50.95	2.60	10262.17	2928.08	19.15	3356.81	2103.01
8	434,67	3,081,32	202.11	5,931	semiconfined	14.8	0.81	8228.20	2372.80	16.63	2813.02	1739.31
9	445,53	3,097,59	1026.85	35,541	semiconfined	7.27	0.39	8049.96	2324.14	16.38	2761.10	1704.84

Finally, the TN generated was characterized by giving values between 2,746 y 4,347 mg/L and the NH_3 generated between 1,694 y 2,625 mg/L. The results obtained from the calculations performed high values of ammonia, which may affect health and productivity as described by several authors. [39 – 43], It is necessary to adequately manage livestock waste. Table 1 shows the results obtained in this study in the different farms.

3.2 Natural treatment system.

From [2, 28] the characteristics of the farms, where they are located, flow, COD, EC and according to current local legislation sets a maximum discharge target of 1600 mg/L COD and 2500 µS/cm EC the NTSW sizing has been proposed for each farm.

For farm 1, an NTSW consisting of a rotary screen, homogenizer tank and digester has been proposed. In the case of the sieve, it has been designed the same as that of the reference farm, giving a reduction percentage of 45% and an EC reduction percentage of 7.5%. As for the digester, starting with 4 chambers and a chamber

volume of 22 m^3, with a COD reduction percentage of 30%, a necessary volume of 96.82 m^3 and a hydraulic retention time of 13 days was obtained. However, the result of this design did not meet the objective. For this reason, 6 more chambers were added, increasing the COD reduction percentage to 77% and an HRT of 33 days.

In the case of farm 2, the same criteria are used, and the digester is also increased to a HRT of 26 days and a COD reduction percentage of 59.84%. In these two farms it was decided to increase the digester instead of installing a pond and wetlands, like the reference plant, because the digester has a higher percentage of COD reduction than the pond plus wetlands and because the area where these farms are located has low precipitation and therefore does not favour the degradation of organic matter in the pond.

For farms 4, 5, 6, 6, 7, 8 and 9, a NTSW consisting of a rotary screen, homogenizer tank and digester has also been designed. In these cases, the screen is the same for all, but the digester varies in terms of number of chambers, chamber volume and HRT, depending on the effluent conditions. All farms with an average of 25 HRT and an average COD reduction % of 61% meet the discharge criteria. However, farms 5, 6 and 9, due to their location, could be equipped with pond with wetlands. Therefore, for these farms it would be recommended to install a pond and wetland, even if they meet the objective, since this would improve the final discharge conditions. Appendix A shows the results obtained in this study in the different farms.

4. Conclusions

- The characterization of the parameters Q, COD, EC, NT, NH_3
- of the farms studied in Gran Canaria indicates the importance of adequate treatment in the farm itself to minimize the environmental impact that this activity supposes for the environment.
- NTSW are suitable and provide a viable treatment alternative for the livestock waste produced.
- There is no single NTSW model for all pig farms as the type, flow, organic load, location and climatic conditions of each one will dictate the conditions of its design.
- The proposed decision strategy tools for the design of NTSW have proven to be a useful tool for the sizing of the farms considered in the study.

5. Nomenclature

Q	flow rate
COD	chemical oxygen demand
EC	electrical conductivity
TN	total nitrogen
NH3	ammonia
GHG	greenhouse gas emissions
Morg	organic matter
N_o Sow	number of sows
LSU	livestock unit
HRT	hydraulic retention time

Author Contributions: Conceptualization, T.G.-R, C.A.M.-P, S.B.-E, F.L.-Z and A.R.-M; Data curation, T.G.-R, C.A.M.-P, , F.L.-Z and A.R.-M ; Formal analysis, T.G.-R and C.A.M.-P ; Funding acquisition, C.A.M.-P and S.B.-E ; Investigation, T.G.-R, C.A.M.-P, S.B.-E and A.R.-M; Methodology, T.G.-R and C.A.M.-P ; Project administration, A.R.-M; Resources, T.G.-R, C.A.M.-P, F.L.-Z and S.B.-E; Software, T.G.-R, C.A.M.-P and A.R.-M; Supervision, C.A.M.-P; Validation, T.G.-R, and C.A.M.-P; Visualization, T.G.-R, F.L.-Z and C.A.M.-P ;Writing—original draft, T.G.-R and C.A.M.-P ; Writing—review & editing, T.G.-R and C.A.M.-P .All authors have read and agreed to the published version of the manuscript.

Funding: This research has been co-funded by the INTERREG V-A Cooperation Spain–Portugal MAC (**Madeira-Azores-Canarias) program MITIMAC project MAC2/1.1a/263.**

Acknowledgments: This research work has been carried out within the Livestock Industry Modernization Program of the Cabildo de Gran Canaria (Government of the island), and with the in-estimable help of the farmers and the technical staff of the Agrarian Extension and Agricultural Development Service, Agrofood and Phyto pathological Laboratory of the Cabildo de Gran Canaria and Analytical Control of Environmental Sources (CAFMA), Institute for Environmental Studies and Natural Resources (i-UNAT) of the University of Las Palmas de Gran Canaria.

Conflicts of Interest: The authors declare no conflict of interest.

Appendix A

Table 2. Proposed NTSW design.

	Effluent			Solid-liquid separation						Biodigester					
Farm	**Q (m^3/day)**	**COD (mg/L)**	**EC (dS/m)**	**% removal COD (%)**	**% removal EC (%)**	**COD (mg/L)**	**EC (dS/m)**	**% removal COD (%/day)**	**% removal EC (%/day)**	**HRT_{dig} (day)**	**$V_{chamber}$ (m^3)**	**V (m^3)**	**Chambers (units)**	**COD (mg/L)**	**EC (dS/m)**
1	7.520	24,078.48	22.59	45	7.45	13,243.16	20.91	2.3	0.2	33	22	96.8	10	1,341.49	20.25
2	5.154	16,186.60	23.55	45	7.45	8,902.63	21.80	2.3	0.2	26	22	66.4	5	1,625.21	21.05
3	4.624	14,705.19	22.86	45	7.45	8,087.85	21.16	2.3	0.2	18	22	59.5	3	2,165.91	20.42
4	1.759	9,056.79	17.72	45	7.45	4,981.23	16.40	2.3	0.2	25	22	22.7	1	925.22	15.56
5	1.000	8,346.36	16.79	45	7.45	4,590.50	15.54	2.3	0.2	35	22	12.9	1	391.03	14.45
6	1.670	8,953.96	17.59	45	7.45	4,924.68	16.28	2.3	0.2	26	22	21.5	1	879.70	15.43
7	2.604	10,262.17	19.15	45	7.45	5,644.19	17.72	2.3	0.2	21	22	33.5	2	1,290.86	16.97
8	0.812	8,228.20	16.63	45	7.45	4,525.51	15.39	2.3	0.2	25	10	10.5	1	849.63	14.61
9	0.389	8,049.96	16.38	45	7.45	4,427.48	15.16	2.3	0.2	26	5	5.0	1	806.52	14.38

Table 3. Proposed NTSW design.

	Pond + constructed wetlands							NTSW		
Farm	**HRT (day)**	**% removal COD (%/day)**	**COD (mg/L)**	**% removal EC (%/day)**	**EC (dS/m)**	**V (m^3)**	**Surface (m^2)**	**V (m^3)**	**Surface (m^2)**	**HRT (day)**
1	-	-	-	-	-	-	-	96.83	83.61	33.35
2	-	-	-	-	-	-	-	66.36	44.12	25.68
3	15	1.34	1,730.56	1.51	15.79	69.37	46.24	128.91	73.42	33.00
4	-	-	-	-	-	-	-	22.65	14.88	25.38
5	15	1.34	312.43	1.51	11.18	15	10	27.88	21.63	49.88
6	15	1.34	702.88	1.51	11.93	25.04	16.7	46.54	31.20	41.05
7	-	-	-	-	-	-	-	33.53	18.51	21.32
8	-	-	-	-	-	-	-	10.45	6.82	25.19
9	15	1.34	644.41	1.51	11.12	5.84	3.89	10.85	7.23	40.72

References

[1] C. A. Mendieta-Pino, A. Ramos-Martin, S. O. Perez-Baez, and S. Brito-Espino, “Management of slurry in Gran Canaria Island with full-scale natural treatment systems for wastewater (NTSW). One year experience in live-stock farms,” J Environ Manage, vol. 232, pp. 666–678, 2019, doi: https://doi.org/10.1016/j.jenvman.2018.11.073.

[2] C. A. Mendieta-Pino, S. O. Pérez-Báez, A. Ramos-Martín, F. León-Zerpa, and S. Brito-Espino, “Natural treatment system for wastewater (NTSW) in a livestock farm, with five years of pilot plant management and monitoring,” Chemosphere, vol. 285, p. 131529, Sep. 2021, doi: 10.1016/J.CHEMOSPHERE.2021.131529.

[3] H. G. V. Penha et al., “Nutrient accumulation and availability and crop yields following long-term application of pig slurry in a Brazilian Cerrado soil,” Nutr Cycl Agroecosyst, vol. 101, no. 2, pp. 259–269, 2015, doi: 10.1007/s10705-015-9677-6.

[4] M. C. Villar, V. Petrikova, M. Díaz-Raviña, and T. Carballas, “Recycling of organic wastes in burnt soils: combined application of poultry manure and plant cultivation,” Waste Management, vol. 24, no. 4, pp. 365–370, 2004, doi: https://doi.org/10.1016/j.wasman.2003.09.004.

[5] B Riaño and M C García-González, “On-farm treatment of swine manure based on solid-liquid separation and biological nitrification-denitrification of the liquid fraction,” J Environ Manage, vol. 132, 2014.

[6] W. Antezana et al., “Composition, potential emissions and agricultural value of pig slurry from Spanish commercial farms,” Nutr Cycl Agroecosyst, vol. 104, no. 2, pp. 159–173, Sep. 2016, doi: 10.1007/S10705-016-9764-3.

[7] M. Sánchez and J. L. González, “The fertilizer value of pig slurry. I. Values depending on the type of operation,” Bioresour Technol, vol. 96, no. 10, pp. 1117–1123, Jul. 2005, doi: 10.1016/j.biortech.2004.10.002.

[8] C. P. Dionisi et al., “Monitoring of physicochemical parameters of soils after applying pig slurry. Analysis of its application in short and long periods in the province of Córdoba, Argentina,” Microchemical Journal, vol. 159, p. 105545, Dec. 2020, doi: 10.1016/j.microc.2020.105545.

[9] O. Thygesen, J. M. Triolo, and S. G. Sommer, “Indicators of Physical Properties and Plant Nutrient Content of Animal Slurry and Separated Slurry,” Biol Eng Trans, vol. 5, no. 3, pp. 123–135, 2012, doi: 10.13031/2013.42273.

[10] A. Cavanagh, M. O. Gasser, and M. Labrecque, “Pig slurry as fertilizer on willow plantation,” Biomass Bioenergy, vol. 35, no. 10, pp. 4165–4173, Oct. 2011, doi: 10.1016/j.biombioe.2011.06.037.

[11] Y. Hou, G. L. Velthof, J. P. Lesschen, I. G. Staritsky, and O. Oenema, “Nutrient Recovery and Emissions of Ammonia, Nitrous Oxide, and Methane from Animal Manure in Europe: Effects of Manure Treatment Technologies,” Environ Sci Technol, vol. 51, no. 1, pp. 375–383, Jan. 2017, doi: 10.1021/acs.est.6b04524.

[12] O. Oenema, D. Oudendag, and G. L. Velthof, “Nutrient losses from manure management in the European Un-ion,” Livest Sci, vol. 112, no. 3, pp. 261–272, Dec. 2007, doi: 10.1016/j.livsci.2007.09.007.

[13] S. O. Petersen et al., “Recycling of livestock manure in a whole-farm perspective,” Livest Sci, vol. 112, no. 3, pp. 180–191, Dec. 2007, doi: 10.1016/j.livsci.2007.09.001.

[14] N. Ramankutty et al., “Trends in Global Agricultural Land Use: Implications for Environmental Health and Food Security,” Annu Rev Plant Biol, vol. 69, no. 1, pp. 789–815, Apr. 2018, doi: 10.1146/annurev-arplant-042817-040256.

[15] G. Li, G. Huang, H. Li, M. K. van Ittersum, P. A. Leffelaar, and F. Zhang, “Identifying potential strategies in the key sectors of China’s food chain to implement sustainable phosphorus management: a review,” Nutr Cycl Agroecosyst, vol. 104, no. 3, pp. 341–359, Apr. 2016, doi: 10.1007/s10705-015-9736-z.

[16] R. Zimmerman, “La Higine de las naves es la clave para reducir el amoníaco,” 3tres3. 2000. [Online]. Available: https://www.3tres3.com/articulos/la-higiene-de-las-naves-es-la-clave-para-reducir-el-amoniaco_337/

[17] M. R. Muirhead and T. J. L. Alexander, Managing Pig Health: A Reference for the Farm, 2nd, ilistra ed. 2013.

[18] S. Lopez-Ridaura, H. van der Werf, J. M. Paillat, and B. le Bris, “Environmental evaluation of transfer and treatment of excess pig slurry by life cycle assessment,” J Environ Manage, vol. 90, no. 2, pp. 1296–1304, Feb. 2009, doi: 10.1016/j.jenvman.2008.07.008.

[19] X. Flotats, A. Bonmatí, B. Fernández, and A. Magrí, “Manure treatment technologies: On-farm versus central-ized strategies. NE Spain as case study,” Bioresour Technol, vol. 100, no. 22, pp. 5519–5526, Nov. 2009, doi: 10.1016/j.biortech.2008.12.050.

[20] X. Font, N. Adroer, M. Poch, and T. Vicent, “Evaluation of an Integrated System for Pig Slurry Treatment,” Journal of Chemical Technology & Biotechnology, vol. 68, no. 1, pp. 75–81, Jan. 1997, doi: 10.1002/(SICI)1097-4660(199701)68:1<75::AID-JCTB593>3.0.CO;2-C.

[21] M. Hjorth, K. v. Christensen, M. L. Christensen, and S. G. Sommer, “Solid—liquid separation of animal slurry in theory and practice. A review,” Agron Sustain Dev, vol. 30, no. 1, pp. 153–180, Mar. 2010, doi: 10.1051/agro/2009010.

[22] J. Alvarez, “Characterization of pig slurry and their treatment efficiency in central Spain,” 2006.

[23] C. León-Cófreces, M. C. García-Gonzalez, M. Acítores, and M. P. Pérez-Sangrador, “Development of a pig slur-ry treatment system with SBR and MBR technology,” 2006.

[24] L. Deng, C. Cai, and Z. Chen, “The treatment of pig slurry by a full-scale Anaerobic-Adding Raw Wastewater-Intermittent Aeration Process,” Biosyst Eng, vol. 98, no. 3, pp. 327–334, Nov. 2007, doi: 10.1016/j.biosystemseng.2007.08.001.

[25] L. M. Ferreira, “Pilot scale experience of anaerobic co-digestion of pig slurry with fruit wastes on site operation in a pig farm with a mobile plant,” 2009.

[26] W. Antezana et al., “Composition, potential emissions and agricultural value of pig slurry from Spanish commercial farms,” Nutr Cycl Agroecosyst, vol. 104, no. 2, pp. 159–173, Mar. 2016, doi: 10.1007/s10705-016-9764-3.

[27] Y. Hou et al., “Stakeholder perceptions of manure treatment technologies in Denmark, Italy, the Netherlands and Spain,” J Clean Prod, vol. 172, pp. 1620–1630, Jan. 2018, doi: 10.1016/j.jclepro.2016.10.162.

[28] C. A. Mendieta-Pino, T. Garcia-Ramirez, A. Ramos-Martin, and S. O. Perez-Baez, “Experience of Application of Natural Treatment Systems for Wastewater (NTSW) in Livestock Farms in Canary Islands,” Water (Basel), vol. 14, no. 14, 2022, doi: 10.3390/w14142279.

[29] M. A. Belmont, E. Cantellano, S. Thompson, M. Williamson, A. Sánchez, and C. D. Metcalfe, “Treatment of domestic wastewater in a pilot-scale natural treatment system in central Mexico,” Ecol Eng, vol. 23, no. 4–5, pp. 299–311, Sep. 2004, doi: 10.1016/j.ecoleng.2004.11.003.

[30] L. Vera, G. Martel, and M. Márquez, “Two years monitoring of the natural system for wastewater reclamation in Santa Lucía, Gran Canaria Island,” Ecol Eng, vol. 50, pp. 21–30, Jan. 2013, doi: 10.1016/j.ecoleng.2012.08.001.

[31] A. Suresh, H. L. Choi, D. I. Oh, and O. K. Moon, “Prediction of the nutrients value and biochemical characteristics of swine slurry by measurement of EC – Electrical conductivity,” Bioresour Technol, vol. 100, no. 20, pp. 4683–4689, Oct. 2009, doi: 10.1016/j.biortech.2009.05.006.

[32] R. Moral, M. D. Perez-Murcia, A. Perez-Espinosa, J. Moreno-Caselles, C. Paredes, and B. Rufete, “Salinity, organic content, micronutrients and heavy metals in pig slurries from South-eastern Spain,” Waste Management, vol. 28, no. 2, pp. 367–371, 2008, doi: 10.1016/j.wasman.2007.01.009.

[33] R. Moral, J. Moreno-Caselles, M. D. Perez-Murcia, A. Perez-Espinosa, B. Rufete, and C. Paredes, “Characterization of the organic matter pool in manures.,” Bioresour Technol, vol. 96, pp. 153–159, 2005.

[34] A. Suresh and H. L. Choi, “Estimation of nutrients and organic matter in Korean swine slurry using multiple regression analysis of physical and chemical properties,” Bioresour Technol, vol. 102, no. 19, pp. 8848–8859, Oct. 2011, doi: 10.1016/j.biortech.2011.06.087.

[35] ISTAC, “ISTAC Instituto Canario de Estadística.” [Online]. Available: www.gobiernodecanarias.org/istac

[36] “IDE Canarias visor 4.5.1.” [Online]. Available: https://visor.grafcan.es/visorweb/

[37] J. E. Hall, “Nutrient Recycling : The European Experience - Review -,” Asian-Australas J Anim Sci, vol. 12, no. 4, pp. 667–674, Jun. 1999, doi: 10.5713/ajas.1999.667.

[38] C. A. Mendieta Pino, “Evaluación y modelización de sistemas de tratamiento no-convencional o natural para efluentes procedentes de explotaciones ganaderas de porcino en la isla de Gran Canaria,” 2015.

[39] T. D. Hamilton, J. M. Roe, C. Hayes, and A. J. Webster, “Effects of ammonia inhalation and acetic acid pretreatment on colonization kinetics of toxoginec Pasteurella multocida within upper respiratory tracs of swine.,” j. Clin. Microbiol, vol. 36,1260–12, 1998.

[40] T. Arango, R. Besteiro, V. G. Souto, M. R. Rodríguez, and M. D. Fernández, “Concentración de NH3 en relación con otras variables ambientales en alojamientos para lechones de 6 a 20 kg de p.v.,” VIII Congreso Ibérico de Agroingeniería, 2015.

[41] K. J. Donham, “Effects on Swine Health, Productivity, Human Health and the enviroment,” Toxicology, vol. 16, 2000.

[42] L. Fraile, A. Alegre, R. López-Jiménez, M. Nofrarías, and J. Segalés, “Risk factors associated with pleuritis and cranio-ventral pulmonary consolidation in slaughter-aged pigs,” Veterinary Journal, vol. 184, no. 3, pp. 326–333, 2010, doi: 10.1016/j.tvjl.2009.03.029.

[43] T. Wang, Q. He, W. Yao, Y. Shao, J. Li, and F. Huang, “The variation of nasal microbiota caused by low levels of gaseous ammonia exposure in growing pigs,” Front Microbiol, vol. 10, no. MAY, pp. 1–14, 2019, doi: 10.3389/fmicb.2019.01083.Table 4. Proposed NTSW designThis Appendix describes the Direct

A triple solar desalination system integrated with a biomass-fuelled SCO2 power cycle: Thermodynamic modelling

Hamed Ghiasirad[a,*], Towhid Gholizadeh[b], Saeed Rostami[c], Bartosz Stanek[d], Anna Skorek-Osikowska[e], and Lukasz Bartela[f]

[a] *Silesian University of Technology, Gliwice, Poland, hamed.ghiasirad@polsl.pl*
[b] *Silesian University of Technology, Gliwice, Poland, Towhid.gholizadeh@gmail.com*
[c] *Sharif University of Technology, Tehran, Iran, rostami.sae@gmail.com*
[d] *Silesian University of Technology, Gliwice, Poland, bartosz.stanek@polsl.pl*
[e] *Silesian University of Technology, Gliwice, Poland, anna.skorek@polsl.pl*
[f] *Silesian University of Technology, Gliwice, Poland, Lukasz.bartela@polsl.pl*

Abstract:

Numerous methods are invented to capture the dissipating heat from different sectors, among all, the combination of power generation and fresh water units in the form of integrated systems based on renewable energy has received less attention. In traditional systems, not only was energy wasted to the environment, but fossil fuels caused serious damage to the environment. To overcome this problem, a new solar-biomass driven integrated system is devised in this investigation. Instead of wasting the energy of sCO2 into the environment, a novel system is proposed to increase EUF. Meanwhile, the use of HDH-TVC-RO along with the MED unit increases the amount of freshwater rate. The results indicated that the fresh water rate, GOR, and EUF are 29.36 kg/s, 14.38, and 3.372, respectively. Hence, the total GOR of the devised system is constant with the alteration of input vapor pressure to HDH-TVC; in contrast, the total GOR is increased with the increase of the pressure ratio of compressors. In addition, the behaviour of the EUF is linear in the presence of alteration of both parameters of input vapor pressure parameters to HDH-TVC and the pressure ratio of compressors.

Keywords:

Parabolic trough collector, biomass gasification, SCO2, MED desalination, HDH-TVC-RO.

1. Introduction

Water and power are two essential resources necessary for human survival and the functioning of modern society. Unfortunately, the scarcity of these resources is a growing concern worldwide, particularly in areas with growing populations, increased industrialization, and changing weather patterns. Access to clean and safe drinking water is a fundamental human right, yet many people in developing countries still lack primary access to this resource. Furthermore, power outages and unreliable energy sources can disrupt daily life, especially in countries with limited infrastructure. As the world population grows, there is an urgent need to address these issues and find sustainable solutions to ensure that everyone has access to these vital resources. On the other hand, the production of water and power with fossil fuels has significant environmental impacts that damage the planet. The combustion of fossil fuels releases carbon dioxide and other greenhouse gases into the atmosphere, contributing to global climate change [1]. In addition to climate change, extraction, transportation, and burning of fossil fuels can cause air and water pollution, habitat destruction, and soil degradation. For example, coal-fired power plants produce large amounts of air pollutants such as sulphur dioxide, nitrogen oxides, and particulate matter, contributing to respiratory problems and other health issues[2]. Production of water using fossil fuels can also lead to environmental degradation. Given these negative impacts, there is an urgent need to transition towards cleaner and more sustainable alternatives to produce water and power, such as renewable energy sources such as solar, wind, and biofuels.

Today, the use of Integrated Systems using renewable resources (ISRR) is a very efficient cure to overcome the problems of water and power shortage due to increased efficiency, cost savings, enhanced resilience, reduced environmental impact, and increased flexibility. Over the past decade, several investigations have pivoted the limelight on the all-round usage of the ISRR via proposing various renewable energies such as wind, solar and biofuels (for employing its producing heat) or recommending different thermal-driven

desalination systems (for producing drinking water). Xia et al. [3] proposed a solar-powered supercritical carbon dioxide (sCO_2) cycle for reverse osmosis (RO) desalination. The recommended integrated system includes a sCO_2 power cycle, solar collectors, RO, and LNG subsystem. They employed thermodynamics analysis and maximized the rate of produced drinking water by using a genetic algorithm for parametric optimization. They found an optimal value for the turbine input pressure of the sCO_2 cycle to obtain the maximum exergy efficiency. Under optimal conditions, a proposed ISRR reached the daily exergy efficiency of 4.90% and produced 2537.33 m^3 of drinking water per day. In 2016, Kouta et al. [4] conducted an investigation on ISRR comprised of a solar tower, a sCO_2 subsystem (for power generation), and multiple effect desalination with thermal vapor compression (MED-TVC) (for freshwater production). They compared two sCO2 cycles consisting of regeneration and recompression. ISRR was analysed from thermodynamic and exergoencomic points of view; the result showed that the solar tower generated more than 80% of the total entropy in both configurations, followed by the MED-TVC system, and the sCO_2 subsystem. A case study for different cities in Saudi Arabia was conducted and these results were extracted that the cities of Yanbu, Khabt, and Al-Ghusn achieved the lowest cost, respectively. The Yanbu LCOE was 0.0826 $/kWh and 0.0915 $/kWh for the recompression and regeneration solar cycles at a fraction of 0.5, respectively. Then, Sharan et al. [5] found the optimal feed flow in a cogeneration system consisting of a MED and sCO_2 for the production of electricity and freshwater simultaneously. The results showed that the forward feed is an optimum configuration compared to the parallel/ cross one. Consequently, the forward feed configuration reduced the distilled cost by 2.6% and increased the distilled production by 7.5%. In the same year, Alharbi et al. [6] compared two integrated systems consisting of sCO2 as a power supplier combined with multi-effect desalination coupled with mechanical vapor compression (MED-MVC) and conventional MED. Since the efficiency of the MED system is higher in the forward feed configuration[5], they invented both integrated systems with forward feed configuration. It was generally perceived that the performance of the conventional MED system in universal performance ratio, total water price, and specific power consumption for MED systems was better than that of the MED-MVC system. In 2019, Sharan et al. [7] invented an innovative concept to reduce the cost of distilled water. In this regard, they introduced an ISRR which includes a sCO_2 Brayton cycle that uses its dissipating heat to run a MED system. Concentrating solar power (CSP) plants were responsible for supplying energy to the integrated system. Due to the intermittency of solar radiation, the system included tanks for storing solar energy. Optimization of the storage tank led to reduction of the cost of distilled water by 19% and increase of the capacity of MED system from 46% to 75%. In addition, they compared the MED and RO systems from the point of view thermoeconomic, the comparison revealed that the use of MED can decrease the cost of distillation by 16%. In order to compare the distillation methods in the ISRR systems, Rostamzadeh et al. [8] conducted a cost comparison in two different ISRR systems. They juxtaposed the hybrid HDH-RO system and the solo-RO system, both of them driven by dissipating heat of the wind turbine. The results revealed that the drinking water production using a solo RO unit is cheaper than one using a hybrid HDH-RO desalination unit. Exergic analysis and operation simulations of the concentrated solar-driven power and desalination (CSPD) system are carried out by Wang et al. [9]. They showed that the efficiency of the sCO_2 cycle could be 36.6%, while the distilled water and output power produced by CSPD are 4050.8 t/day and 50.1 MW/day, respectively. In order of thermodynamic metrics, the results pointed out that two highest energy destruction and two minimum exergy efficiency are related to heat exchanger of the desalination system and solar tower receiver. They concluded that the CSPD systems are economically feasible since the system has levelized cost of water (LCOW) of 1.15 $/t and LCOE of 0.059 $/kWh. Since the use of sCO_2 can reduce the cost of solar power generation, Yuan et al. [10] used sCO_2 in the ISRR combined with the MED unit. One of the concerns about the combination of the sCO_2 cycle with the MED unit was the possibility of a decrease in the efficiency of the sCO_2 cycle, which they showed that such a combination does not reduce the efficiency of the sCO_2. They showed in the low split ratio (the ratio of the mass flow rate of the main compressor to the total mass flow rate), approximately less than 0.6, that the amount of freshwater produced decreases with the increase of the split ratio. For values greater than 0.6 the freshwater rate is increased with the increase in the split ratio. In the optimal state, the LCOE is 0.081 $/kWh and the LCOW is 0.81 $/$m^3$. Using the five-effect distillation system, the freshwater results indicated that the rate is 459 m^3/day. Realizing that the heat dissipating from an CSP-sCO_2 can be used for free but with slightly reduced thermal efficiency, Omar et al. [11] invented a new ISRR based on CSP, a CO_2 cycle, and Cascade MED system. The results indicated that four-MED systems can maximize freshwater production, with 57% dissipating heat energy recovery compared to 26% waste heat recovery using a single-MED system. In another study, khanmohammadi et al. [12] proposed an ISRR system consisting of a solar collector, a humidification and dehumidification (HDH) unit. The system is surveyed using environmental simulation and thermodynamic modelling. The results indicated that an increase in the compressor pressure ratio leads to a decrease in COP and freshwater flow. Similarly, freshwater production and exergy efficiency decrease with an increase in the outlet pressure. Although the authors used a solar collector to supply the heat needed for the HDH system, they could use a sCO_2 system to increase the efficiency of the system and supply the energy by using dissipating the heat of the sCO_2 unit.

The use of clean energy to prevent serious damage to the environment is not limited to solar and wind energy. In several scholars, attention has been paid to biomass to supply the heat needed for ISRR

consisting of the sCO_2 cycle. Balafkandeh et al. [13] proposed a biomass-based heating, power, and cooling system configuration consisting of sCO_2.The system was analysed from thermodynamic exergoeconomic viewpoints, in addition an environmental analysis is carried out to evaluate the CO_2 emission of the proposed system. Cao et al. [14] introduced a biomass-fueled integrated cycle to generate adequate power. The invented system includes two Brayton cycles with working fluids of sCO2 and nitrogen. An economic and thermodynamic investigation is performed. To seek the optimum from the exergoeconomic viewpoint, multi-criteria optimization is conducted. The results indicated that the exergetic efficiency reach 43.51% and the power cost leads 19.78 $/GJ in state of optimal point. Finally, in 2023, Hai et al. [15] combined a biomass-fueled SCO2 cycle with a MED desalination system to product power and freshwater simultaneously with the highest efficiency and without harming the environment.

1.1. Scientific Gaps

According to the authors of the above-reviewed works, it can be understated that there are considerable scientific gaps in previous studies dealing with the integration of the sCO_2 cycle with a desalination unit as a bottoming cycle for the production of power and drinking water, simultaneously. Although it has been shown in the above literature that various sources of clean energy including solar, wind and biomass can be used to supply the required heat of the bottoming cycle (e.g., MED unit), each of them has shortage. To date, no one has used the combination of two renewable resources for driving one of the desalination methods. It has been indicated that using the MED unit as the bottoming cycle of the sCO2 system driven by a biofueled heat source is carried out by Hai et al. [15]. However, they did not pay attention to the fact that the fresh water produced by the MED unit has a high temperature compared to the ambient temperature. In this case, by slightly increasing the temperature of the produced water, it can be used as an energy supplier in low-temperature cycles such as HDH unit. Furthermore, it is obvious that the drinking water distillated from a MED unit is more expensive than an HDH unit due to Khalilzadeh and Nezhad [16]reported a high value of 16.16 $/kWh for the cost of fresh water.

1.2. Novelties

Integration of the Rankine cycle with a distillation system can increase the operating pressure of the condenser (in the Rankine cycle), which leads to an increase in the heat-rejection temperature. Still, such a combination reduces the efficiency of the power plant's efficiency[5]. To eliminate the defect of reducing efficiency, it is possible to utilize the sCO_2 Brayton cycle because it has high efficiency compared to the Rankine cycle. On the other hand, the sCO_2 cycle has high-temperature rejection that is suitable for driving an MED system[7]. As mentioned, the biomass-fueled integration of the sCO_2 and MED unit was investigated in 2023. But in the present study, to increase the amount of freshwater production, the freshwater produced by the MED unit, which has a relatively high temperature, was redirected to a new subsystem consisting of HDH-TVC-RO. Solar collectors are used to increase the temperature of the redirected freshwater that drives the HDH-TVC-RO unit. All in all, the primary purpose of this study is multifaceted and is pinched as follows:

- Proposing a novel integrated system using biomass and solar energy as primary sources.
- Using MED, HDH, and RO desalination unit and sCO_2 cycle in the solar biomass-based multigeneration unit.
- investigating a comprehensive study assessing the impacts of vital parameters on the performance of the invented integrated system.

2. Description of the setup

A schematic diagram of the proposed system is shown in Fig. 1. The system consists of five subsystems: gasifier, supercritical CO2 cycle, Multi-effect desalination system, Parabolic Trough Solar and varied pressure humidification-dehumidification system coupled with reverse osmosis. In the gasification process, biomass (68) and environmental air (69) are fed to the gasifier where syngas is produced. Syngas is then fed to the combustion chamber (CC) together with the hot air exiting from the Air pre-heating (76). The high-temperature combustion products (71) are directed to the reactor to supply the energy for the supercritical CO2 cycle, which is used to increase the turbine inlet temperature (TIT) in the S–CO2 cycle (2). The SCO2 power cycle is actually a combination of the Power system and the MED (multi-effect desalination) so that the heat rejected in the gas cooler1 of the S–CO2 system is utilized to run the MED which is used to produce fresh water in the MED system.

Some of the water produced by the MED system increased pressure by the water pump (62). The high-pressure water then takes its initial energy through the PTC (Parabolic Trough Collector) system, and the high-pressure water is converted into steam by the evaporator, which obtains this energy from the exhaust gas. The high-pressure steam (46) by thermal vapor compressor enters a humidification-dehumidification system coupled with reverse osmosis to produce more water.

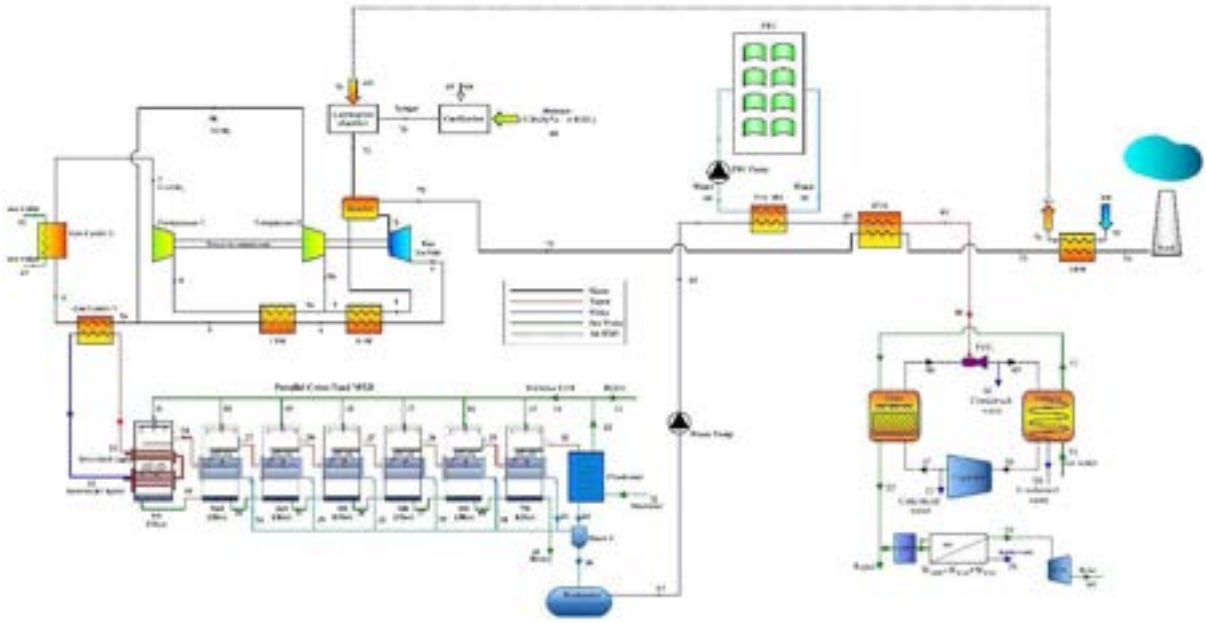

Figure 1: Schematic of the devised solar-biomass-driven power/desalination unit.

3. Materials and Methods

3.1. Thermodynamic assumptions

To analyse the proposed solar-biomass integrated system, below assumptions are developed:

- All Governing equations and thermodynamic process are advanced under steady-state condition.
- The freshwater temperature is assumed as the average temperature of the air in the closed loop of HDH unit.

In addition, other required thermodynamic data for the devised system is illustrated in Table 1.

Table 1: Set of input parameters for thermodynamic simulation of the devised system.

The input data	Unit	Value	Ref.
Ambient temperature	K	298.15	[17]
Ambient press	bar	1.013	[17]
Gasifier and combustion reactions			
Type of biomass feedstock		$Wood\ CH_{1.44}O_{0.66}$	[18]
Biomass flow rate	Kg, s^{-1}	1.115	[19]
Moisture content	%	20	[18]
Gasification temperature	K	1073.15	[18]
Outlet temperature of combustion chamber	K	1520	[20]
Pressure ratio of compressors		3	[21]
Temperature output of gas cooler 2	C	35	[22]
Temperature of Reactor	C	550	[21]
Compressor efficiency	%	0.9	[21]
Turbine efficiency	%	0.85	[21]
Epsilon LTR	%	0.86	[22]
Epsilon HTR	%	0.86	[22]
Pressure output Turbine	bar	74	[22]
Temperature difference of Gas cooler 1	C	10	[22]
Number of effects		7	[23]
Seawater salinity	gr/kg	35	[23]
Condensation temperature of the 1st effect	K	344.15	[23]
Temperature difference between effects	K	3.3	[24]
Temperature difference condenser	K	0.7	[24]
Feed/seawater mass flow rate ratio at states 13 and 14		0.415	[24]
Number of PTC		3	
Pressure of PTC water	bar	15	[25]

DNI ptc	W/m^2	1000	[25]
Fluid work		Water	[25]
Temperature difference PTC_hex	K	10	
Inlet Temp of PTC	C	70	[25]
Mass flow rate of PTC	Kg/s	0.8	[25]
Vapor Pressure inlet TVC	bar	50	[26]
Seawater salinity	g/kg	35	[27]
Humidifier effectiveness	%	85	[27]
Dehumidifier effectiveness	%	85	[27]
Expander efficiency	%	50	[26]
TVC efficiency	%	30	[26]
TVC pressure ratio		1.2	[26]
Pump efficiency	%	70	[27]
Heat capacity rate ratio		1	[26]
Recovery ratio	%	0.3	[28]
Salt rejection percentage		0.9944	[28]
Fouling factor		0.85	[28]
Element area	m^2	35.4	[28]
Number of elements		7	[28]
Number of pressure vessels		42	[28]

3.2. Energy analysis

Conservation equations including energy and mass can be articulated as [29]:

Mass balance Eq.:

$$\sum \dot{m}_{in} - \sum \dot{m}_{out} = 0 \tag{16}$$

Energy balance Eq.:

$$\dot{Q}_{c.v.} - \dot{W}_{c.v.} = \sum (\dot{m}h)_{out} - \sum (\dot{m}h)_{in} \tag{17}$$

Salinity balance Eq.:

$$\sum (\dot{m}S)_{in} - \sum (\dot{m}S)_{out} = 0 \tag{18}$$

The desalination flow ratio (MR) of the HDH unit is expressed as follows [23]:

$$MR = \frac{\dot{m}_{seawater}}{\dot{m}_{dryair}} \tag{19}$$

The effectiveness of humidifier/dehumidifier (ε) is expressed as below [23]:

$$\varepsilon = \frac{\Delta \dot{H}}{\Delta \dot{H}_{max}} \tag{20}$$

The energy, mass and salinity relations for each component of the invented system are showed in Table 2.

Table 2: Mass, Salinity, and Energy balance equations for each component of the proposed system.

Component	Mass and energy balance equations
Reactor	$\dot{Q}_{Rect} = \dot{m}_{71}(h_{71} - h_{72}) = \dot{m}_2(h_2 - h_1)$
Gas Turbine	$\dot{W}_{Gastur} = \dot{m}_2(h_2 - h_3), \quad \eta_{Gastur} = \frac{h_2 - h_3}{h_2 - h_{3S}}$
HTR	$\dot{Q}_{HTR} = \dot{m}_3(h_3 - h_4) = \dot{m}_1(h_9 - h_1)$
LTR	$\dot{Q}_{LTR} = \dot{m}_4(h_4 - h_5) = \dot{m}_8(h_9 - h_8)$
Compressor 1	$\dot{W}_{comp\,1} = \dot{m}_7(h_8 - h_7), \quad \eta_{comp\,1} = \frac{h_7 - h_{8S}}{h_7 - h_8}$
Compressor 2	$\dot{W}_{comp\,2} = (x)\dot{m}_5(h_9 - h_5), \quad \eta_{comp\,2} = \frac{h_5 - h_{9S}}{h_5 - h_9}$
Gas cooler 1	$\dot{Q}_{GC1} = \dot{m}_6(h_5 - h_6) = \dot{m}_{22}(h_{22} - h_{23})$
Gas cooler 2	$\dot{Q}_{GC2} = \dot{m}_6(h_6 - h_7) = \dot{m}_{10}(h_{67} - h_{10})$
Effects	$T_{V,out} = T_{\mathrm{B,out}} = T_{\mathrm{V,in}} - \Delta T_{Eff}$

	$\dot{m}_{\mathrm{SW}} + \dot{m}_{\mathrm{B,in}} = \dot{m}_{V,out} + \dot{m}_{\mathrm{B,out}}$ $\dot{m}_{B,in} S_{\mathrm{B,in}} + \dot{m}_{\mathrm{SW}} S_{\mathrm{SW}} = \dot{m}_{B,out} S_{\mathrm{B,out}}, \quad \dot{m}_{\mathrm{SW}} = \frac{\dot{m}_{14}}{N_{Eff}}$ $\dot{m}_{\mathrm{FW}} h_{\mathrm{FW}} + \dot{m}_{V,out} h_{V,out} + \dot{m}_{\mathrm{B,out}} h_{\mathrm{B,out}} = \dot{m}_{\mathrm{SW}} h_{\mathrm{SW}} + \dot{m}_{V,in} h_{V,in} + \dot{m}_{B,in} h_{\mathrm{B,in}}$
condenser	$\dot{Q}_{Cond} = \dot{m}_{12}(h_{12} - h_{11}) = \dot{m}_{42}(h_{42} - h_{44})$
Mixer	$\dot{m}_{26} h_{26} + \dot{m}_{29} h_{29} + \dot{m}_{32} h_{32} + \dot{m}_{35} h_{35} + \dot{m}_{38} h_{38} + \dot{m}_{41} h_{41} = \dot{m}_{45} h_{45}$
Water Pump	$\dot{W}_{WPump} = \dot{m}_{61}(h_{62} - h_{62}), \quad \eta_{WPump} = \frac{h_{61} - h_{62}}{h_{61} - h_{62S}}$
PTC HX	$\dot{Q}_{PTC,Hex} = \dot{m}_{62}(h_{63} - h_{62}) = \dot{m}_{65}(h_{65} - h_{66})$
Evaporator	$\dot{Q}_{Eva} = \dot{m}_{63}(h_{64} - h_{63}) = \dot{m}_{72}(h_{72} - h_{73})$
Air preheater	$\dot{Q}_{APH} = \dot{m}_{74}(h_{74} - h_{73}) = \dot{m}_{76}(h_{76} - h_{75})$
Dehumidifier	$\dot{m}_{Air}(h_{49} - h_{50}) = \dot{m}_{51}(h_{52} - h_{51}) + \dot{m}_{54} h_{54}$ $\dot{m}_{54} = \dot{m}_{Air}(w_{50} - w_{49})$ $\varepsilon_{dhum} = max\left\langle \left(\frac{h_{49} - h_{50}}{h_{49} - h_{50.ideal}}\right) . \left(\frac{\dot{m}_{52} h_{52} - \dot{m}_{51} h_{51} + \dot{m}_{54} h_{54}}{\dot{m}_{52} h_{52,ideal} - \dot{m}_{51} h_{51} + \dot{m}_{54} h_{54,ideal}}\right)\right\rangle$
Humidifier	$\dot{m}_{52} h_{52} - \dot{m}_{53} h_{53} = \dot{m}_{Air}(h_{48} - h_{47})$ $\dot{m}_{53} = \dot{m}_{52} - \dot{m}_{Air}(w_{48} - w_{47})$ $\varepsilon_{hum} = max\left\langle \left(\frac{h_{48} - h_{47}}{h_{48.ideal} - h_{47}}\right) . \left(\frac{\dot{m}_{52} h_{52} - \dot{m}_{53} h_{53}}{\dot{m}_{52} h_{52} - \dot{m}_{53} h_{53.ideal}}\right)\right\rangle$
TVC	$\eta_{TVC} = \frac{\dot{m}_{st,rev}}{\dot{m}_{st}}, \quad \dot{m}_{st} = \dot{m}_{46}$ $\dot{m}_{st,rev} s_{46} = \dot{m}_{Air}\left(s_{rev,49} - s_{48}\right) + \dot{m}_{56} s_{56}$ $\dot{m}_{st,rev} h_{46} = \dot{m}_{Air}\left(h_{rev,49} - h_{48}\right) + \dot{m}_{56} h_{56}$
Expander	$\eta_{TVC} = \frac{\dot{m}_{Air}(h_{50} - h_{47}) - \dot{m}_{55} h_{50}}{\dot{m}_{Air}\left(h_{50} - h_{s,47}\right) - \dot{m}_{55} h_{50}}$ $\dot{W}_{exp} = \dot{m}_{50} h_{50} - \dot{m}_{47} h_{47} - \dot{m}_{55} h_{55}$
High Pressure Pump	$\dot{W}_{hpp} = \dot{m}_{57}(h_{57} - h_{53})$ $\dot{W}_{hpp} = \dot{W}_{exp} + \dot{W}_{ert}, \quad \eta_{pu} = \frac{h_{57s} - h_{53}}{h_{57} - h_{53}}$
Energy recovery turbine	$\dot{W}_{ert} = \dot{m}_{59}(h_{59} - h_{60}), \quad \eta_{ert} = \frac{h_{360} - h_{60}}{h_{60} - h_{60}}$

3.3. Performance Criteria

The net power of the gas turbine is articulated as follows.

$$\dot{W}_{net,GT} = \dot{W}_{Gastur} - \dot{W}_{comp\ 1} - \dot{W}_{comp\ 2} \qquad (31)$$

where, $\dot{W}_{Gastur}$, $\dot{W}_{comp\ 1}$, and $\dot{W}_{comp\ 2}$ are the produced power by gas turbine, Power consumed by compressors 1 and 2. The net output power of the devised system can be written as follows.

$$\dot{W}_{net,total} = \dot{W}_{net,GT} - \dot{W}_{WPump} \qquad (32)$$

The gain output ratio (GOR) of the HDH-TVC-RO unit, MED unit, and the proposed integrated system is expressed as [23]:

$$GOR_{HDH-TVC-RO} = \frac{\dot{m}_{54} + \dot{m}_{55} + \dot{m}_{56} + \dot{m}_{58}}{\dot{m}_{46}} \qquad (35)$$

$$GOR_{MED} = \frac{\dot{m}_{45}}{\dot{m}_{22}} \qquad (35)$$

$$GOR_{total} = \frac{\dot{m}_{45} - \dot{m}_{61}}{\dot{m}_{22}} + \frac{\dot{m}_{54} + \dot{m}_{55} + \dot{m}_{56} + \dot{m}_{58}}{\dot{m}_{46}} \qquad (35)$$

Another important metric in the setup is the Recovery Ratio (RR) which is which is defined as follows for the HDH-TVC-RO unit, the MED unit, and the proposed integrated system [23].

$$RR_{HDH-TVC-RO} = \frac{\dot{m}_{54} + \dot{m}_{55} + \dot{m}_{56} + \dot{m}_{58}}{\dot{m}_{51}} \qquad (36)$$

$$RR_{MED} = \frac{\dot{m}_{45}}{\dot{m}_{11}} \quad (36)$$

$$RR_{total} = \frac{\dot{m}_{45} - \dot{m}_{61} + \dot{m}_{54} + \dot{m}_{55} + \dot{m}_{56} + \dot{m}_{58}}{\dot{m}_{11} + \dot{m}_{51}} \quad (36)$$

Finally, the Energy Utilization Factor (EUF) is defined as [27]:

$$EUF = \frac{\dot{W}_{net,total} + (\dot{m}_{45} - \dot{m}_{61})h_{45,fg} + \dot{m}_{54}h_{54,fg} + \dot{m}_{55}h_{55,fg} + \dot{m}_{56}h_{56,fg} + \dot{m}_{58}h_{58,fg}}{(\ LHV_{biomass} \times \dot{m}_{biomass} + \dot{Q}_{PTC,Hex}\ )} \quad (36)$$

4. Results and discussion

4.1. Model Comparison

In this subsection, a comparison between devised system (shown in Fig. 1) and the five different studies is carried out, and the results are illustrated in Table 3.

In the current research, we explore the utilization of solar energy and biomass gasifier as the primary energy sources, while employing the SCO_2 power cycle for efficient electricity generation. Moreover, we have incorporated multiple units, namely the MED, HDH-TVC, and RO, which collectively yield a substantial amount of freshwater. The proposed cycle exhibits impressive performance, with a power output of 4250 kW and a freshwater production rate of 29.36 kg/s. Notably, the recovery ratio, GOR, and EUF are reported as 23.74%, 14.38, and 3.372, respectively.

Comparatively, our findings demonstrate superior efficiency when contrasted with previous works. Table 3 illustrates that the GOR values and EUF values of prior studies range from 6.3 to 10.2 and from 0.516 to 0.884, respectively, further highlighting the enhanced performance of our present work.

Table 3: Model comparison between the reference system and the devised WT/HDH-MED-MVC system.

Ref.	Similar subsystems	Net output power (kW)	Freshwater rate (kg/s)	Recovery ratio (%)	GOR	EUF
Present study	Solar biomass, SCO2-MED, HDH-TVC-RO	4250	29.36	23.74	14.38	3.372
[8]	HDH-RO	4459	0.59	13.1	-	-
[30]	Solar, MED	419.2	6.8	26.01	8.5	0.884
[31]	SCO2-MED	290960	214.9	-	6.3	0.516
[32]	Biomass, GT, MED	220.4	0.48	-	-	0.55
[33]	Solar, MED-TVC	-	34.72	-	10.2	-

4.1. Basic results

For a base form of the study, the thermodynamic metrics of the devised system are presented in Table 4. The most important metrics include the mass flow rate of biomass, total freshwater distilled from the system, total GOR and EUF.

Table 4: Main thermodynamic metrics evaluated for the devised system.

$\dot{m}_{biomass}$	1.155 kg/s
$\dot{W}_{net,total}$	4250 kW
$\dot{m}_{fw,med}$	7.361 kg/s
$\dot{m}_{fw,HDH-TVC-RO}$	24.38 kg/s
$GOR_{HDH-TVC-RO}$	10.23
GOR_{MED}	6.133
GOR_{total}	14.38
RR_{MED}	26.73%
$RR_{HDH-TVC-RO}$	25.36%
RR_{total}	23.74%
EUF	3.372

4.1. Parametric Evaluation

In this section, the impact of the input vapor pressure to HDH-TVC and the compression pressure ratio are investigated on the main impressed performance criteria such as GOR, net output power and EUF for HDH-TVC-RO unit MED unit, and whole invented system.

4.1.1. Impact of the input vapor pressure to HDH-TVC on the system

Fig. 2 shows an alteration of the GOR, net output power, and EUF versus the input vapor pressure to HDH-TVC. As Fig. 2 (a) illustrates, in two subsystems of HDH-TVC-RO and MED, and in the entire system, the GOR is slightly increased with the increase in the input vapor to HDH-TVC. In the entire range of input vapor pressure to HDH-TVC changes from 40 to 60, the GOR value for the HDH-TVC-RO unit is higher than for the MED unit. Fig. 2 (b) shows the net output power as well as EUF versus the input vapor to HDH-TVC. As the input vapor pressure of HDH-TVC increases, the EUF value also increases almost linearly. Accordingly, the EUF value is almost 3.31 in input vapor pressure to HDH-TVC value of 40 and the value EUF increases until it reaches 3.42 at the input vapor pressure to HDH-TVC value of 60. On the other hand, the behaviour of net output power is parabolic in relation to the input vapor pressure to HDH-TVC. In this sense, as the input vapor pressure for HDH-TVC increases to 50, the net output power decreases and then increases.

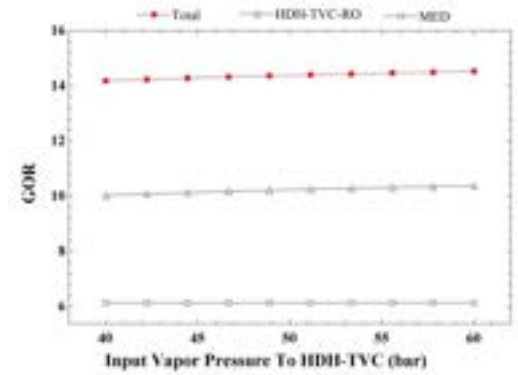

(a)

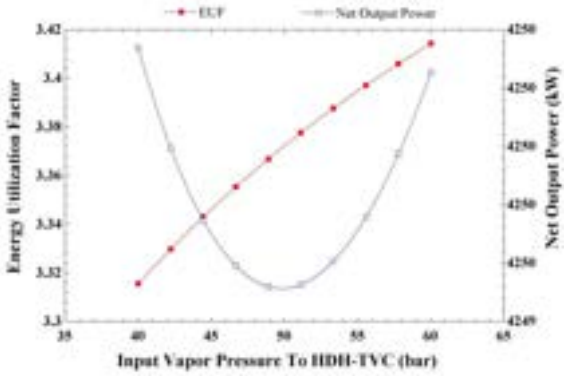

(b)

Figure 2: Impact of the input vapor pressure on HDH-TVC on the: (a) GOR, (b) EUF and net output power.

4.1.1. Impact of the pressure ratio of compressors on the system

Fig. 3 displays an alteration of the GOR, net output power, and EUF versus the pressure ratio of the compressors. As Fig. 3 (a) shows, the GOR of the MED subsystem remains almost constant and its value is equal to 6. In HDH-TVC-RO subsystem, the GOR remains constant and its value is equal to 10, similar to what we saw in MED subsystem. It is clear that in general the GOR of the HDH-TVC-RO subsystem is higher than that of the MED subsystem in the entire range of the pressure ratio of compressors. First, the total GOR increases with increasing pressure ratio of compressors. Its value reaches 15 at the pressure ratio of the compressors value of 3.7, then its value remains constant. Fig. 3 (b) shows the net output power as well as EUF versus pressure ratio of the compressors. The effect of pressure ratio changes on EUF is almost linear and the EUF is increased with increase of the pressure ratio of compressors. The EUF increases from 3.1 to 3.55, while the pressure ratio of the compressors varies from 2.2 to 4. The behavior pattern of net output power with the pressure ratio of compressors change is parabolic. The net output power starts from 4050 kW at the pressure ratio of compressors value of 2.2, and the net output power increases until it reaches its maximum (4250 kW) at the pressure ratio of compressors value of 3. Then the net output power decreases until it reaches 4125 kW at a compressor pressure ratio of 4.

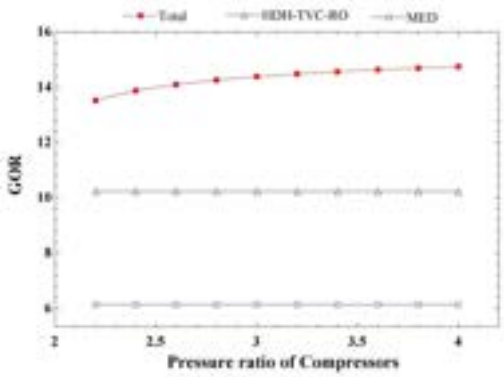

(a)

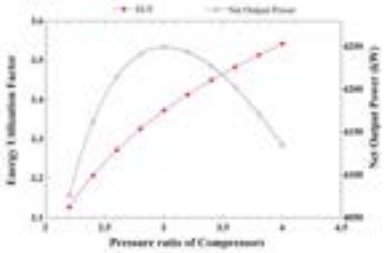

(b)

Figure 3: The impact of pressure ratio of compressors on the: (a) GOR, (b) EUF and net output power.

5. Concluding remarks

An integrated system with renewable resources is a matured solution to tackle the problems arising during the use of fossil fuels. On the other hand, to increase power production, SCO_2 cycles can be used, which have higher efficiency and the ability to drive a MED system. Consequently, in the present study, in addition to using the MED unit, the HDH-TVC-RO unit has also been used in the configuration. In regard to that, the following concluding points can be drawn:

- In the base mode, the fresh water rate, the GOR, and the EUF are 29.36 kg/s, 14.38, 3.372, respectively.
- The GOR of the HDH-TVC-RO unit is 40% higher than that of the MED unit, regardless of the value of input vapor pressure to HDH-TVC and pressure ratio of compressors.
- The total GOR of the developed system is constant and equal to 14.38 by changing vapor pressure to HDH-TVC.
- The total GOR enhances by increasing the pressure ratio of compressors
- The power generation process exhibits an interesting characteristic where an optimal point is reached when the pressure ratio of compressors is set to 3.
- The Energy Utilization Factor (EUF) experiences a notable improvement of 13.5% as the pressure ratio of compressors increases from 2.25 to 4.
- The EUF of the proposed cycle demonstrates a remarkable achievement, being nearly four times higher than that of previous works.

Nomenclature

Symbols		**Subscripts and superscripts**	
GT	Gas turbine	B	Brine
HTR	High Temperature Recuperator	CV	Control volume
LTR	Low Temperature Recuperator	da	dry air
MED	Multi effect desalination	Dhum	dehumidifier
RR	Recovery Ratio	Eff	Effect
EUF	Energy Utilization Factor	en	energy
LHV	Low Heat value $(kJ.kg^{-1})$	F	fuel
RO	Reverse Osmosis	FW	freshwater
HTR	High Temperature Recuperator	Hum	humidifier
LTR	Low Temperature Recuperator	in	inlet

GOR	Gained-Output-Ratio	max	maximum
h	specific enthalpy $(kJ.kg^{-1})$	net	net value
RO	Reverse Osmosis	out	outlet
$\dot{m}$	mass flow rate $(kg.s^{-1})$	pum	pump
N	Number of effects	ert	Energy recovery turbine
P	pressure (bar)	s	constant entropy
S	Salinity $(g.kg^{-1})$	SW	seawater
s	specific entropy $(kJ.kg^{-1}.K^{-1})$	tot	total
T	temperature (K)	v	vapor
TTD	terminal temperature difference(K)	w	work
$\dot{W}$	power (kW)	r	rated
$\dot{Q}$	Heat (kW)	rev	reversible
Greek Symbols		exp	Expander
ω	humidity ratio	hpp	High Pressure Pump
ε	Effectiveness (%)		
η	Efficiency (%)		

Acknowledgement

The present work was funded by the Silesian University of Technology for the beginning of scientific activities in a new research topic within the framework of project no. 32/014/SDU/10-22-37.

References

[1] A. Skorek-Osikowska, L. Bartela, D. Katla, and J.-L. Galvez-Martos, "Characteristic of a system for the production of synthetic natural gas (SNG) for energy generation using electrolysis, biomass gasification and methanation processes," May 2019.

[2] M. A. Gonzalez-Salazar, T. Kirsten, and L. Prchlik, "Review of the operational flexibility and emissions of gas- and coal-fired power plants in a future with growing renewables," *Renewable and Sustainable Energy Reviews*, vol. 82, pp. 1497–1513, Feb. 2018, doi: 10.1016/j.rser.2017.05.278.

[3] G. Xia, Q. Sun, X. Cao, J. Wang, Y. Yu, and L. Wang, "Thermodynamic analysis and optimization of a solar-powered transcritical CO2 (carbon dioxide) power cycle for reverse osmosis desalination based on the recovery of cryogenic energy of LNG (liquefied natural gas)," *Energy*, vol. 66, pp. 643–653, Mar. 2014, doi: 10.1016/j.energy.2013.12.029.

[4] A. Kouta, F. Al-Sulaiman, M. Atif, and S. bin Marshad, "Entropy, exergy, and cost analyses of solar driven cogeneration systems using supercritical CO2 Brayton cycles and MEE-TVC desalination system," *Energy Convers Manag*, vol. 115, pp. 253–264, May 2016, doi: 10.1016/j.enconman.2016.02.021.

[5] P. Sharan, T. Neises, and C. Turchi, "Optimal feed flow sequence for multi-effect distillation system integrated with supercritical carbon dioxide Brayton cycle for seawater desalination," *J Clean Prod*, vol. 196, pp. 889–901, Sep. 2018, doi: 10.1016/j.jclepro.2018.06.009.

[6] S. Alharbi, M. L. Elsayed, and L. Chow, "Thermo-Economic Analysis of an Integrated Supercritical CO2 Brayton Cycle and Multiple Effect Desalination Systems," in *International Mechanical Engineering Congress and Exposition*, American Society of Mechanical Engineers, Nov. 2018. doi: 10.1115/IMECE2018-88409.

[7] P. Sharan, T. Neises, J. D. McTigue, and C. Turchi, "Cogeneration using multi-effect distillation and a solar-powered supercritical carbon dioxide Brayton cycle," *Desalination*, vol. 459, pp. 20–33, Jun. 2019, doi: 10.1016/j.desal.2019.02.007.

[8] H. Rostamzadeh, S. Rostami, M. Amidpour, W. He, and D. Han, "Seawater Desalination via Waste Heat Recovery from Generator of Wind Turbines: How Economical Is It to Use a Hybrid HDH-RO Unit?," *Sustainability*, vol. 13, no. 14, Jul. 2021, doi: 10.3390/su13147571.

[9] G. Wang, B. Dong, and Z. Chen, "Design and behaviour estimate of a novel concentrated solar-driven power and desalination system using S–CO2 Brayton cycle and MSF technology," *Renew Energy*, vol. 176, pp. 555–564, Oct. 2021, doi: 10.1016/j.renene.2021.05.091.

[10] L. Yuan, Q. Zhu, T. Zhang, R. Duan, and H. Zhu, “Performance evaluation of a co-production system of solar thermal power generation and seawater desalination,” *Renew Energy*, vol. 169, pp. 1121–1133, May 2021, doi: 10.1016/j.renene.2021.01.096.

[11] A. Omar, D. Saldivia, Q. Li, R. Barraza, and R. A. Taylor, “Techno-economic optimization of coupling a cascaded MED system to a CSP-sCO2 power plant,” *Energy Convers Manag*, vol. 247, p. 114725, Nov. 2021, doi: 10.1016/j.enconman.2021.114725.

[12] S. Khanmohammadi, S. Razi, M. Delpisheh, and H. Panchal, “Thermodynamic modeling and multi-objective optimization of a solar-driven multi-generation system producing power and water,” *Desalination*, vol. 545, p. 116158, Jan. 2023, doi: 10.1016/j.desal.2022.116158.

[13] S. Balafkandeh, V. Zare, and E. Gholamian, “Multi-objective optimization of a tri-generation system based on biomass gasification/digestion combined with S-CO2 cycle and absorption chiller,” *Energy Convers Manag*, vol. 200, p. 112057, Nov. 2019, doi: 10.1016/j.enconman.2019.112057.

[14] Y. Cao *et al.*, “Techno-economic investigation and multi-criteria optimization of a novel combined cycle based on biomass gasifier, S-CO2 cycle, and liquefied natural gas for cold exergy usage,” *Sustainable Energy Technologies and Assessments*, vol. 52, p. 102187, Aug. 2022, doi: 10.1016/j.seta.2022.102187.

[15] T. Hai, M. A. Ali, A. Alizadeh, S. F. Almojil, A. I. Almohana, and A. F. Alali, “Reduction in environmental CO2 by utilization of optimized energy scheme for power and fresh water generations based on different uses of biomass energy,” *Chemosphere*, vol. 319, p. 137847, Apr. 2023, doi: 10.1016/j.chemosphere.2023.137847.

[16] S. Khalilzadeh and A. Hossein Nezhad, “Utilization of waste heat of a high-capacity wind turbine in multi effect distillation desalination: Energy, exergy and thermoeconomic analysis,” *Desalination*, vol. 439, no. October 2017, pp. 119–137, 2018, doi: 10.1016/j.desal.2018.04.010.

[17] J. Bezaatpour, H. Ghiasirad, M. Bezaatpour, and H. Ghaebi, “Towards optimal design of photovoltaic/thermal facades: Module-based assessment of thermo-electrical performance, exergy efficiency and wind loads,” *Appl Energy*, vol. 325, Nov. 2022, doi: 10.1016/j.apenergy.2022.119785.

[18] Z. A. Zainal, R. Ali, C. H. Lean, and K. N. Seetharamu, “Prediction of performance of a downdraft gasifier using equilibrium modeling for different biomass materials,” *Energy Convers Manag*, vol. 42, no. 12, pp. 1499–1515, Aug. 2001, doi: 10.1016/S0196-8904(00)00078-9.

[19] A. Shokri Kalan, S. Heidarabadi, M. Khaleghi, H. Ghiasirad, and A. Skorek-Osikowska, “Biomass-to-energy integrated trigeneration system using supercritical CO2 and modified Kalina cycles: Energy and exergy analysis,” *Energy*, vol. 270, p. 126845, May 2023, doi: 10.1016/j.energy.2023.126845.

[20] T. Gholizadeh, M. Vajdi, and H. Rostamzadeh, “Exergoeconomic optimization of a new trigeneration system driven by biogas for power, cooling, and freshwater production,” *Energy Convers Manag*, vol. 205, p. 112417, Feb. 2020, doi: 10.1016/j.enconman.2019.112417.

[21] H. Ghiasirad, H. Rostamzadeh, and S. Nasri, “Design and Evaluation of a New Solar Tower-Based Multi-generation System: Part II, Exergy and Exergoeconomic Modeling,” in *Integration of Clean and Sustainable Energy Resources and Storage in Multi-Generation Systems*, Cham: Springer International Publishing, 2020, pp. 103–120. doi: 10.1007/978-3-030-42420-6_6.

[22] H. Ghiasirad, H. Rostamzadeh, and S. Nasri, “Design and Evaluation of a New Solar Tower-Based Multi-generation System: Part I, Thermal Modeling,” in *Integration of Clean and Sustainable Energy Resources and Storage in Multi-Generation Systems*, Cham: Springer International Publishing, 2020, pp. 83–102. doi: 10.1007/978-3-030-42420-6_5.

[23] S. Rostami, H. Ghiasirad, H. Rostamzadeh, A. S. Kalan, and A. Maleki, “A wind turbine driven hybrid HDH-MED-MVC desalination system towards minimal liquid discharge,” *S Afr J Chem Eng*, vol. 44, pp. 356–369, Apr. 2023, doi: 10.1016/J.SAJCE.2023.03.007.

[24] H. Rostamzadeh, H. Ghiasirad, M. Amidpour, and Y. Amidpour, “Performance enhancement of a conventional multi-effect desalination (MED) system by heat pump cycles,” *Desalination*, vol. 477, p. 114261, Mar. 2020, doi: 10.1016/j.desal.2019.114261.

[25] B. Stanek, W. Wang, and Ł. Bartela, “A potential solution in reducing the parabolic trough based solar industrial process heat system cost by partially replacing absorbers coatings with non-selective ones in initial loop sections,” *Appl Energy*, vol. 331, p. 120472, Feb. 2023, doi: 10.1016/j.apenergy.2022.120472.

[26] F. A. Al-Sulaiman, G. Prakash Narayan, and J. H. Lienhard, “Exergy analysis of a high-temperature-steam-driven, varied-pressure, humidification–dehumidification system coupled with reverse osmosis,” *Appl Energy*, vol. 103, pp. 552–561, Mar. 2013, doi: 10.1016/j.apenergy.2012.10.020.

[27] H. Ghiasirad, N. Asgari, R. Khoshbakhti Saray, and S. Mirmasoumi, “Thermoeconomic assessment of a geothermal based combined cooling, heating, and power system, integrated with a humidification-

dehumidification desalination unit and an absorption heat transformer," *Energy Convers Manag*, vol. 235, p. 113969, 2021, doi: https://doi.org/10.1016/j.enconman.2021.113969.

[28] A. Shekari Namin, H. Rostamzadeh, and P. Nourani, "Thermodynamic and thermoeconomic analysis of three cascade power plants coupled with RO desalination unit, driven by a salinity-gradient solar pond," *Thermal Science and Engineering Progress*, vol. 18, p. 100562, Aug. 2020, doi: 10.1016/j.tsep.2020.100562.

[29] A. S. Kalan, H. Ghiasirad, R. K. Saray, and S. Mirmasoumi, "Thermo-economic evaluation and multi-objective optimization of a waste heat driven combined cooling and power system based on a modified Kalina cycle," *Energy Convers Manag*, vol. 247, Nov. 2021, doi: 10.1016/j.enconman.2021.114723.

[30] E. D. Kerme *et al.*, "Energetic and exergetic performance analysis of a solar driven power, desalination and cooling poly-generation system," *Energy*, vol. 196, p. 117150, Apr. 2020, doi: 10.1016/j.energy.2020.117150.

[31] S. Alharbi, M. L. Elsayed, and L. C. Chow, "Exergoeconomic analysis and optimization of an integrated system of supercritical CO2 Brayton cycle and multi-effect desalination," *Energy*, vol. 197, p. 117225, Apr. 2020, doi: 10.1016/j.energy.2020.117225.

[32] Z. K. Mehrabadi and F. A. Boyaghchi, "Exergoeconomic and exergoenvironmental analyses and optimization of a new low-CO2 emission energy system based on gasification-solid oxide fuel cell to produce power and freshwater using various fuels," *Sustain Prod Consum*, vol. 26, pp. 782–804, Apr. 2021, doi: 10.1016/j.spc.2020.12.041.

[33] A. Khouya, "4E assessment of a hybrid RO/MED-TVC desalination plant powered by CPV/T systems,"CPV / T systems', *Energy Convers Manag*, vol. 277, p. 116666, Feb. 2023, doi: 10.1016/j.enconman.2023.116666.

4E analyses of integration of microbial desalination cell, humidification-dehumidification and reverse osmosis desalination to produce sustainable freshwater based on solar and wind energies

Mohammad Hassan Khoshgoftarmanesh [a], Sepehr Davadgaran[b], Seyed Alireza Mousavi Rabeti[c] and Ana M Blanco-Marigorta[d]

[a] Energy, Environment and Biological Systems Research Lab (EEBRlab), Division of Thermal Sciences and Energy Systems, Department of Mechanical Engineering, Faculty of Technology & Engineering, University of Qom, Qom, Iran, m.khoshgoftar@qom.ac.ir, mh.khoshgoftar@gmail.com
[b] Energy, Environment and Biological Systems Research Lab (EEBRlab), Division of Thermal Sciences and Energy Systems, Department of Mechanical Engineering, Faculty of Technology & Engineering, University of Qom, Qom, Iran, sepehrdavadgaran@gmail.com
[c] Energy, Environment and Biological Systems Research Lab (EEBRlab), Division of Thermal Sciences and Energy Systems, Department of Mechanical Engineering, Faculty of Technology & Engineering, University of Qom, Qom, Iran, mousavi.sayed20@gmail.com
[d] Department of Process Engineering, Universidad de las Palmas de Gran Canaria, Las Palmas de Gran Canaria, Spain, anamaria.blanco@ulpgc.es

Abstract:

Over time, the water shortage crisis will have irreparable effects on the lives of many organisms, including humans. As a small contribution to alleviate the problem, the present work presents an innovative cogeneration system based on solar and wind renewable energies for sustainable production of freshwater, power, and wastewater treatment. To produce freshwater and treat wastewater in this system, the integration of a Microbial Desalination Cell with a Humidification-Dehumidification and Reverse Osmosis water desalination unit has been used. These systems obtain the required heat from solar energy to produce freshwater, and when solar radiation is unable to provide this heat, a hydrogen internal combustion engine driven with wind energy is used. Excess heat from the internal combustion engine is fed into the organic Rankine cycle with the working fluid R141B to generate power, to reduce the system waste heat and to increase the efficiency. To check the performance of the proposed system, energy, exergy, exergeoeconomic, and exergoenvironmental (4E) analyses have been carried out. The results of the analysis of the integrated system show that this system can produce 720 kW of electricity and 5.36 m^3/h of freshwater. The energy efficiency of the system is 22.09%, and its overall cost rate and overall environmental impact rate are 540.33 $/h and 17.37 Pts/h, respectively.

Keywords:

Microbial Desalination Cell (MDC); Humidification-Dehumidification (HDH); Hydrogen Internal Combustion Engine (HICE); Solar and wind energy; Cogeneration.

1. Introduction

In today's world, the crisis of freshwater scarcity has become one of the main problems that are exacerbated in many regions of the world due to the continuous reduction of water resources and population growth. According to the World Health Organization statistics [1], only 30,000 m^3 of freshwater worldwide are accessible for human use, and the largest amount of freshwater exists as precipitation and polar ice caps in the North and South Poles, which are difficult to access. Producing freshwater through various methods has been proposed as one of the effective solutions for the optimal management of water resources. One of these methods is the use of cogeneration cycles for producing freshwater, wastewater treatment, and power generation simultaneously. In these systems, it is possible to increase efficiency and benefit from water, energy, and environmental resources.

To increase the efficiency of these systems in freshwater production, the HDH (Humidification-dehumidification) system can be used. In this system, by using air humidification and passing this air through

a cold surface, water humidity can be recovered and fresh water can be produced [2]. Due to the lack of need for external energy sources and simple operation, as well as the benefits of low maintenance and capital costs, HDH has been proposed as an efficient method in freshwater production [3]. In this regard, zubair et al [4]. have investigated that the HDH desalination system integrated with solar evacuated tubes, in various locations, can produce freshwater in the range of 16,430 to 19,445 l with costs ranging from 0.032 to 0.038 US$ per litter. Furthermore, Khoshgoftar Manesh et al [5]. proposed a cycle along with HDH for the production of power, hydrogen, hot water, and freshwater. Their results indicate that the energy and exergy efficiencies, as well as the overall annual cost and environmental impacts of the system, are 23.87%, 28.21%, 0.144 kWh/$, and 0.024 Pts/kWh, respectively. In addition, it is possible to simultaneously generate electrical power, remove salt from water, and treat wastewater using Microbial Desalination Cell (MDC) systems [6]. The features of MDC are perfectly aligned with our goals in freshwater cogeneration cycles, wastewater treatment, and power generation. Furthermore, to prevent energy loss and increase freshwater production, the integration of HDH technology with RO (Reverse Osmosis) is used. By integrating HDH and RO technologies, Ravajiri et al [7]. produced a total of 184.3 m^3/h of freshwater.

There are various methods available for recovering heat used in the freshwater production process. Khoshgoftar Manesh et al [8]. explored a recovering heat process for freshwater production in a proposed system based on an integrated solid oxide fuel cell-gas turbine-organic Rankine cycle-multi effect distillation system. The optimized hybrid system was capable of producing 5000 cubic meters of freshwater per day with five effects on MED-TVC. Various sources such as internal combustion engines, turbines, and solar panels are utilized for heat recovery. However, among them, heat recovery from internal combustion engines is one of the best methods for freshwater production processes, considering the simultaneous production of power and heat as well as the high rate of heat entry into the system by the engines [9]. In addition, various fuels such as gasoline, diesel, and hydrogen can be used in internal combustion engines [10]. The use of hydrogen in these engines results in minimal carbon dioxide emissions and minimizes its pollutants [11]. Furthermore, due to its high atomic energy, the use of hydrogen provides very high efficiency in heat recovery [12]. Nikitin et al [13]. used HICE (Hydrogen Internal Combustion Engine) in a multi-generation system based on solar and wind energy. The dynamic results of HICE have been reported in several different cities, showing an average return ranging from 21.82% to 24.76%.

In cogeneration systems, renewable energies such as solar and wind energy can be utilized. The addition of these renewable energies to cogeneration systems provides numerous benefits for the cycle [14]. One of the greatest benefits of using renewable energies in cogeneration systems is the reduction in production costs [15]. These types of energies are obtained directly from nature, and the costs of fuel, maintenance, and installation of power and heat generation systems from these energies are much lower [16]. Moreover, the use of these energies leads to a reduction in environmental impacts due to the decrease in greenhouse gas emissions [17]. Khoshgoftar Manesh et al [18]. investigated the most important renewable energy-based polygeneration systems for producing fresh water using thermal desalination and membrane processes. The most promising options include the integration of thermal and membrane desalination technologies such as Multi-Stage Flash (MSF), Multi-Effect Distillation (MED), Humidification-Dehumidification (HDH), and Reverse Osmosis (RO). makkeh et al [19]. in another study, investigated a combined system of solar collectors and wind turbines for generating power and freshwater. They reported that this configuration reduces the cost of freshwater production by up to 23%.

Studies indicate that the use of various water desalination methods is essential for mitigating the water scarcity crisis. On the other hand, given the limitations of each water desalination method, integrating different desalination techniques can be effective in improving the efficiency of desalination plants. In this regard, the present work proposes a co-generation system for desalination, power generation, and wastewater treatment based on solar and wind energy. In this system, the scenario of freshwater production is evaluated for the first time by integrating MDC-HDH-RO. Solar energy is utilized to provide the required heat for the system. During possible periods of radiation reduction or at night, an internal combustion engine based on hydrogen produces simultaneous power and heat. Reducing engine losses and recovering its heat is essential for increasing efficiency, and the presence of an Organic Rankine Cycle (ORC) can greatly address this issue. In the end, energy, exergy, economic, and environmental analyses have been utilized in the present study to analyze the efficiency of using such a system from various perspectives. The innovations involved in the present work are as follows:

- Integration of MDC-HDH-RO desalination systems has been utilized for freshwater production.
- A combination of solar and wind energy has been employed to minimize the system's emissions.
- A hydrogen-based internal combustion engine has been utilized to simultaneously generate power and heat.

2. System description

The present work proposes a cogeneration system based on solar and wind energy for freshwater production, power generation, and wastewater treatment in Tehran, Iran. Tehran city is located between 51 degrees 6 minutes to 51 degrees 38 minutes east longitude and 35 degrees 34 minutes to 35 degrees 51 minutes north latitude. The average wind speed and solar radiation in Tehran are 4.5 m/s and 514.05 W/m^2, respectively [20].

To produce freshwater in the current system, MDC-HDH-RO desalination units have been integrated. The saline water is initially introduced into the MDC and desalination using anion exchange membranes (AEM) and cation exchange membranes (CEM) as well as the potential difference between the cells. This process leads to the pre-treatment of wastewater and power generation while producing freshwater. The saline water, after the primary desalination by MDC, enters the Flat Plate Collectors (FPC) and receives the required heat before being directed to the HDH desalination unit for further freshwater production. In HDH, the air is humidified under standard environmental conditions and, as a result of a collision with hot water, heat, and mass transfer occur. Following this, some amount of saline water enters the air as humidity and is transferred to the dehumidifier, where it undergoes mass and heat transfer in the presence of freshwater, resulting in increased production of freshwater. RO integration has been utilized at the outlet of HDH to increase efficiency and further enhance freshwater production.

Because solar energy varies throughout the day and to ensure stable production of fresh water, the use of an internal combustion engine allows for heat recovery in the freshwater production system. To reduce the environmental impact of ICE, hydrogen fuel has been considered for this equipment, which is produced using a PEM electrolyzer.

The power consumption of the PEM electrolyzer is supplied using renewable wind energy. Furthermore, wind turbines are also used to supply the electricity required for RO. The remaining power produced by the wind turbines is injected into the grid.

Finally, to reduce the thermal losses of the studied system, the use of an organic Rankine cycle with R141B as the working fluid has been considered. The proposed system is shown in Fig. 1.

The following assumptions have been made for this system:

- The system has been analyzed in a steady-state condition.
- Changes in potential and kinetic energies are negligible.
- The temperature, pressure, and relative humidity of Tehran city are considered to be 25℃, 1.01 bar, and 30%, respectively.
- Heat losses have been disregarded in all heat exchangers and water desalination units.
- An isentropic efficiency of 85% is considered for the organic turbine and an isentropic efficiency of 80% is considered for the organic pump.
- An isentropic efficiency of 85% is assumed for the RO pump.
- The salinity concentration of the feedwater to the MDC is 35000 mg/l [6].
- Artificial wastewater containing 1000 mg/L of acetate has been used as the feed for the MDC [6].
- The HDH packings are made of polypropylene and have a specific surface area of 320 m^2/m^3 [21].
- Only variations in the air in the x-direction and variations in water in the z-direction have been considered in the HDH desalination process.
- The LTW77 wind turbine model with a capacity of 1 MW has been considered [21].
- The temperature and pressure in the PEM electrolyzer are assumed to be constant at 80 ℃ and 1 bar, respectively [22].
- The air-to-fuel ratio for the internal combustion engine has been considered to be 34.3 [23].
- A 4-cylinder inline internal combustion engine model has been considered.

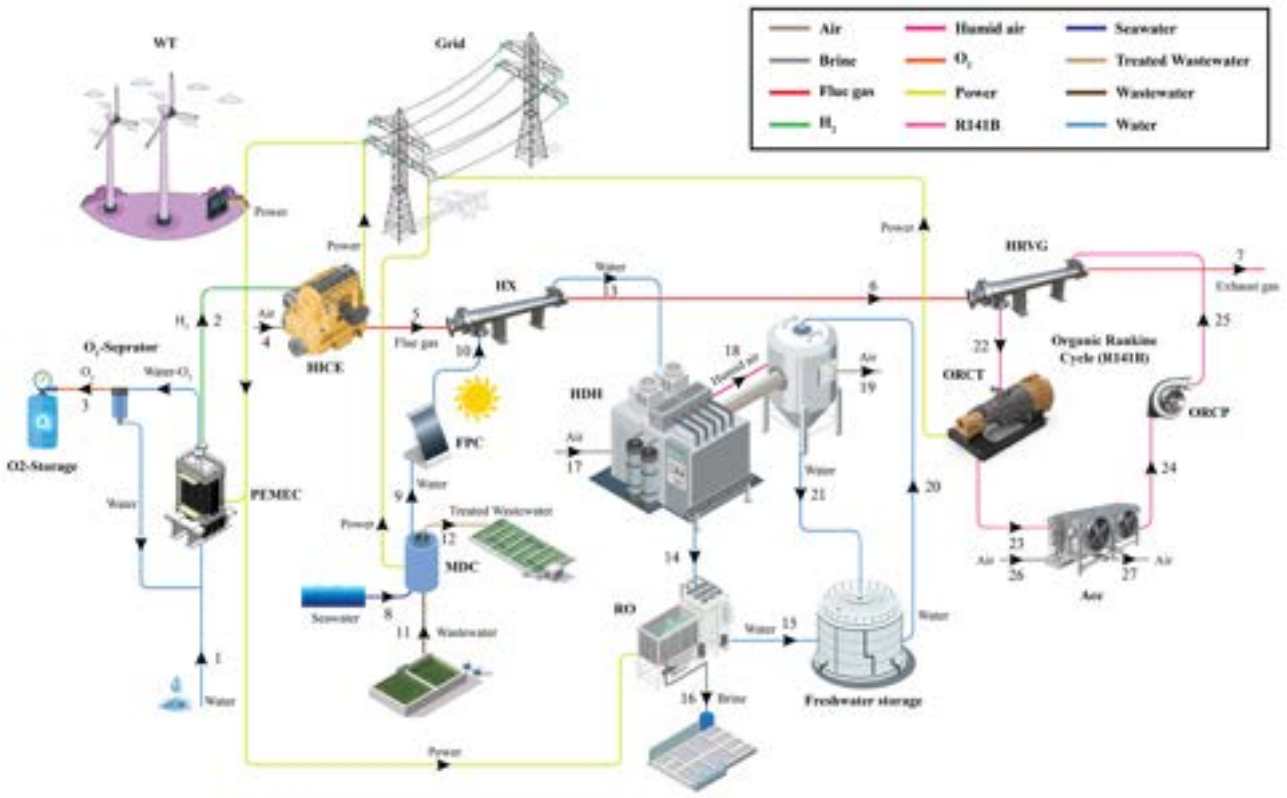

Figure. 1. Schematic of proposed cogeneration for production of desalination, power, and wastewater treatment based on solar and wind energy.

3. Governing equations

The mass and energy balance of equipment is generally calculated using the following equations [24]:

$$\sum_{i=0}^{n} m_{in} - \sum_{i=0}^{n} m_{out} = \left(\frac{dm}{dt}\right)_{system}, \quad (1)$$

$$Q - W + \sum_{i=0}^{n} m_{in}\left(h + \frac{V^2}{2} + gz\right)_{in} - \sum_{i=0}^{n} m_{out}\left(h + \frac{V^2}{2} + gz\right)_{out} = \left(\frac{dE}{dt}\right)_{system}, \quad (2)$$

The concepts of m which means mass flow rate, Q which means heat transfer, and W which means exchanged power is used in the above equation. In Equation 2, the terms within the summation represent the energy flows at the inlet and outlet of the control volume, associated with the energy of the flows. Terms containing V or Z are considered to be zero due to neglecting the kinetic and potential energies. Also, h represents the specific enthalpy. It should be noted that for open systems operating under steady-state conditions, Equations 1 and 2 can be defined in the following form: d/dt=0. However, in many pieces of equipment, it is necessary to create equations to improve their modelling. For example, for flat plate solar collectors, their specific surface area for absorbing solar energy needs to be calculated. Therefore, the heat transfer equations related to this type of equipment should be considered [25]. Moreover, for modelling a PEM electrolyzer, it is necessary to calculate the power consumption by specifying the produced hydrogen flow rate and the potential equations of this electrolyzer [22]. Modelling an RO desalination system requires taking into account the equations related to osmotic and mechanical pressure. Then, the amount of produced freshwater and the pump power consumption of the RO system can be calculated through the recovery ratio [26]. Continuing, for modelling an internal combustion engine based on hydrogen, the amount of recovered heat is calculated by knowing the engine's nominal power [27, 28]. Additionally, to model a wind turbine based on the wind speed of the study area, the equations presented in the references [19, 29] have been used. To model an MDC system, the differential equations presented in the reference [6] have been used. These equations consist of mass balance equations for substrate and microorganisms in the anode compartment, mass balance equations for salt in the desalination compartment, anode compartment, and cathode compartment, in addition to equations for the current generation, which all must be solved simultaneously. The MDC inputs have been obtained from the references [6, 30]. The differential equations for modelling HDH consist of heat and mass transfer equations for water and air in the dehumidifier and humidifier [31]. These equations must also be solved simultaneously.

It is not entirely possible to assess the quality of energy processes in terms of reversibility. Therefore, by adding the concept of exergy to energy analysis, a more comprehensive view of entropy generation and evaluation of

the irreversibility of energy processes can be obtained. Thus, exergy is defined as the useful work capacity and its calculation is relative to a dead reference. The overall exergy balance for all energy systems operating in steady-state can be defined by the following equation [32]:

$$E\ x_Q - E\ x_W + \sum_{i=1}^{n} E\ x_{in} - \sum_{i=1}^{n} E\ x_{out} + E\ x_D = 0, \quad (3)$$

In the above equations, Ex_Q refers to thermal exergy, Ex_W refers to power exergy, and Ex_D refers to the destruction of exergy, which is created as a result of entropy production. The expressions within the summation sign correspond to the flow exergy at the input and output of exergy systems.

Given that the capital payback period and profitability are crucial in system planning, after examining the energy aspects of the system, its economic aspects should also be considered. The economic balance of steady-state energy systems with an exergy approach is defined as follows [33]:

$$C_Q - C_w + \sum_{i=1}^{n} C_{in} \sum_{i=0}^{n} C_{out} + Z_k = 0, \quad (4)$$

In the above equations, C_Q means the heat cost, C_W means the power cost, and Z_k means the equipment purchase rate of the energy system, which is calculated based on references [21, 33].

Life cycle assessment (LCA) is a method for evaluating the environmental pollutants released during the life cycle of a system, from raw material extraction to transportation, construction, and disposal. In the current research, environmental analysis based on LCA, which is defined based on exergy analysis, has been used. Environmental balance is defined for systems operating in a steady state as follows [33]:

$$B_Q - B_w + \sum_{i=1}^{n} B_{in} \sum_{i=0}^{n} B_{out} + Y_k = 0, \quad (5)$$

In the above equations, B_Q means the environmental impact of heat, B_W means the environmental impact of power, and Y_k means the rate of environmental impacts of energy system equipment, which can be calculated using the equations from references [5, 33]. In addition, the constants used in this study are as follows: a 10% interest rate, a maintenance factor of 1.06, a 20-year lifespan for the power plant, 3500 operating hours for FPC, 6000 operating hours for WT, and 8000 operating hours for other equipment [33]. It should be noted that for economic and environmental calculations, the investment cost and equipment weights were obtained from references [5, 21].

4. Results

Table 1 shows the extent of the exergy destruction, costs, destruction costs, environmental impacts, and environmental destruction effects associated with each piece of equipment used in the proposed system. The results of this section indicate that exergy destruction in wind turbines is higher than in other equipment in the system. The reason for this is the higher power production in wind turbines compared to other equipment in the system. After the wind turbine, the internal combustion engine has the highest exergy destruction due to irreversibilities and chemical reactions within it. Regarding the cost destruction, it should be noted that the cost destruction associated with the internal combustion engine is calculated to be higher than other equipment due to the chemical reactions occurring within it. After the internal combustion engine, the PEM electrolyzer has the highest cost destruction. Systems that operate with renewable energy sources (WT, FPC, MDC) have no cost destruction. The results regarding environmental degradation are similar, with the difference that the heat exchanger after the internal combustion engine has the highest environmental degradation.

In Table 2, the results of the 4E analysis of the proposed system are presented. Based on these results, the net power generation, cogeneration exergy efficiency, overall cost rate, and overall environmental impact rate of the system are 0.72 MW, 4.55%, 540.33 $/h, and 17.37 Pts/h, respectively.

Fig. 2 represents the change in humid air temperature inside HDH desalination. In Fig. 2(a), temperature changes in humidification are shown. As expected, the air in contact with warmer saltwater gets hotter. The modelling results also demonstrate these temperature changes with an increase in the length of humidification. In Fig. 2(b) as well, these changes are shown for dehumidification, which operates in reverse. That means the temperature of the humid air decreases in the vicinity of cooler freshwater. These results are also consistent with the modelling.

Fig. 3 shows the absolute humidity change of the air in the HDH desalination. The results of Fig. 3(a) indicate that after the air enters the device, it interacts with salty water and its absolute humidity increases. This result is consistent with the modelling. On the other hand, in Fig. 3(b), in the dehumidification process, water is absorbed from the air, which causes the air to become drier and its absolute humidity to decrease. This process, due to mass transfer with water, leads to the production of freshwater.

Table 1. The main result of exergy, exergoeconomic, and exergoenvironmental analysis for all components of the proposed system

Component	$\dot{E}x_D\ (MW)$	$\dot{Z}\left(\frac{\$}{h}\right)$	$\dot{C}_D\left(\frac{\$}{h}\right)$	$\dot{Y}\left(\frac{mPts}{h}\right)$	$\dot{B}_D\left(\frac{mPts}{h}\right)$
WT	10.25	378.40	0.00	16647.37	0.00
PEMEC	2.84	123.69	133.54	80.92	5875.12
HICE	5.11	5.98	424.39	2.06	14091.21
Hx	0.03	0.07	17.97	0.05	5897.87
HRVG	0.08	0.34	53.82	0.20	1765.90
ORCT	0.01	0.62	16.08	406.27	178.47
ACC	0.02	0.04	--	0.00	--
ORCP	0.00	0.01	0.60	0.01	21.61
MDC	0.22	0.02	0.00	63.84	0.00
FPC	0.99	15.28	0.00	16.77	0.00
HDH	0.02	1.25	25.13	0.00	491.53
RO	0.01	14.65	8.85	149.62	178.47

Table 2. Overall results of the analysis.

Parameters	value
Net power generation (MW)	0.72
Total freshwater production (m^3/h)	5.36
Cogeneration energy efficiency (%)	22.09
Total exergy destruction (MW)	18.73
Cogeneration exergy efficiency (%)	4.55
Overall cost rate ($/h)	540.33
Overall environmental impact rate (Pts/h)	17.37
Levelized cost of electricity ($/kWh)	0.75
Levelized environmental impact of electricity (Pts/kWh)	0.02
Number of wind turbine	23
Solar field area (m^2)	3000

Fig. 4 shows the change in water temperature in the HDH desalination. In humidification, considering that the incoming water has a higher temperature than the air, it is expected that due to the heat and mass transfer, the temperature of the outlet water is lower. This expectation is consistent with the results of the modelling shown in Fig. 4(a). In this plot, as we move upwards, the water temperature decreases. In dehumidification, conversely, humid air interacts with sweet water and causes the outlet water to become warmer. Therefore, it is expected that the outlet water has a higher temperature than the incoming water. This expectation is consistent with the Fig. 4(b) plot, in a way that as we move upwards in the plot, the water temperature increases.

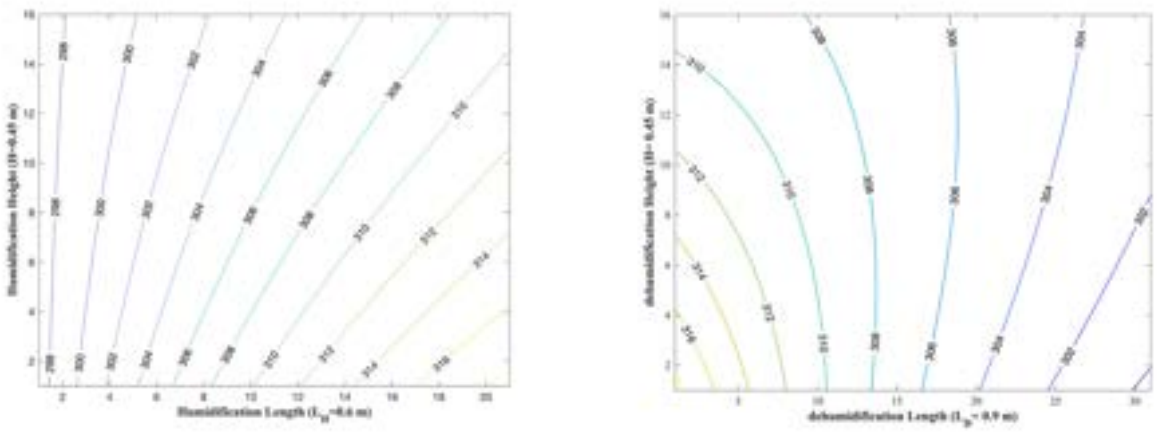

(a) (b)

Figure. 2. Humid air temperature change in HDH Desalination.

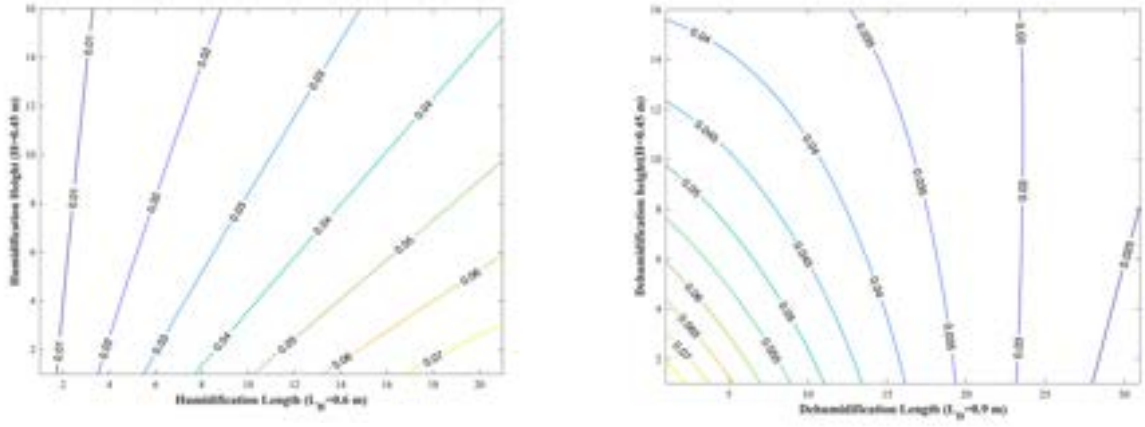

(a) (b)

Figure. 3. Absolute humidity change in HDH Desalination.

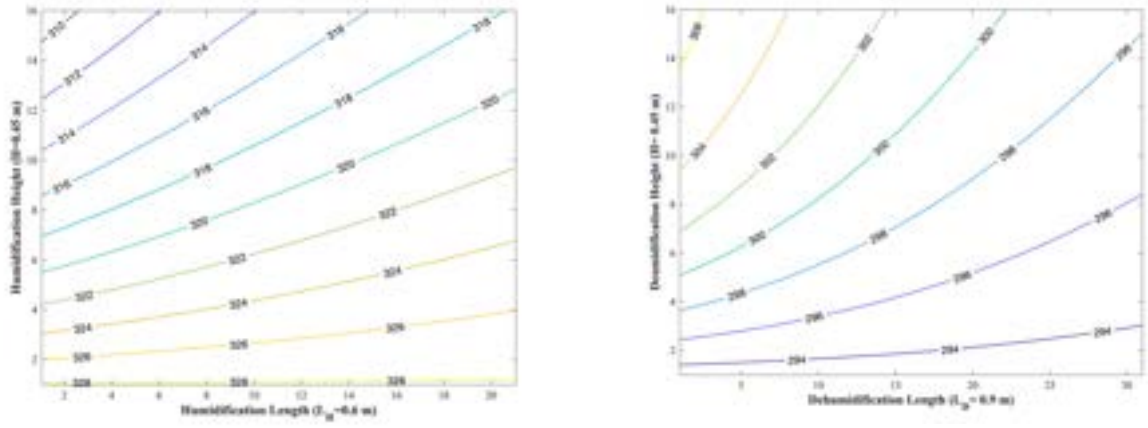

(a) (b)

Figure. 4. Water temperature change in HDH Desalination.

Fig. 5 illustrates the change in water mass flow rate in HDH desalination. In humidification, the water mass flow rate decreases and is added to the ambient air humidity, which its variations are observable. In other words, as we move upwards in plot Fig. 5(a), the water mass flow rate decreases, and the humidity of the ambient air increases. In Fig. 5(b), these changes can be observed conversely for dehumidification.

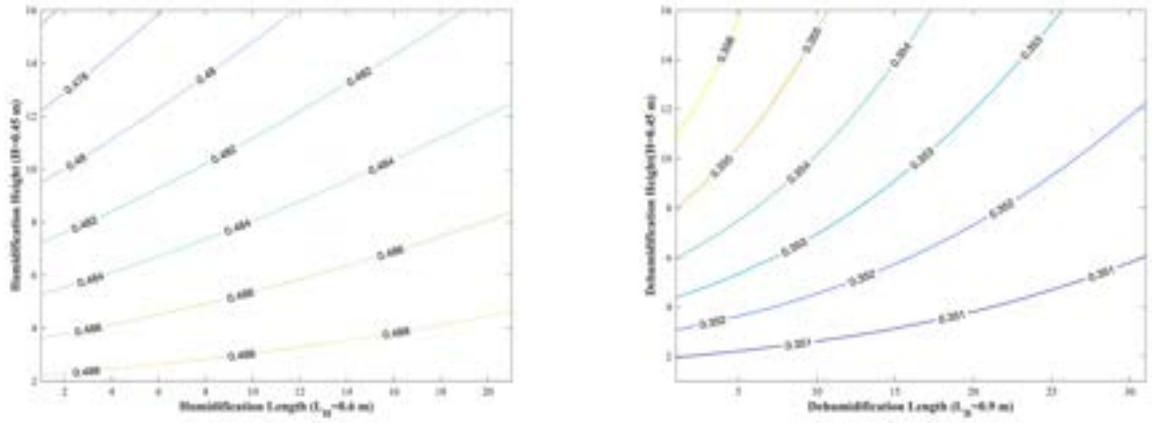

(a) (b)

Figure. 5. Specific water mass flow rate change in HDH Desalination.

Fig. 6(a) displays the changes in salt concentration over time in the intermediate chamber for different initial salt concentrations. The results indicate that for the initial salt concentration of 35g/l, desalination was achieved by a considerable amount of 65.85%. In Fig. 6(b), the effect of changes in the salt solution flow rates on the variation of salt concentration in the intermediate chamber has been investigated. The results indicate that a higher percentage of desalination can be achieved by decreasing the salt solution flow rates. In other words, desalination has increased from 19.28% at a flow rate of 20 l/day to 77.82% at a flow rate of 0.05 l/day.

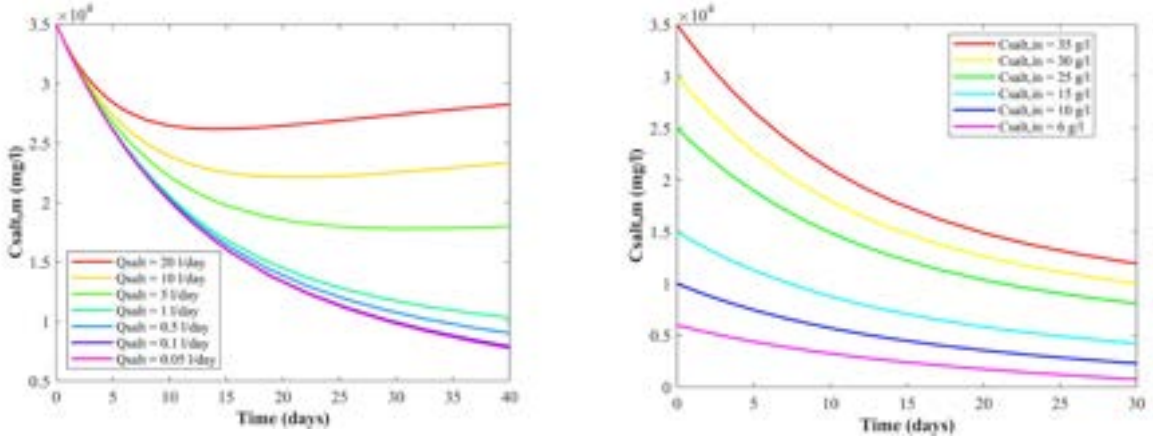

(a) (b)

Figure. 6. The salt concentration in the desalination compartment with time for (a) different salt solution flow rates, (b) different initial salt concentrations (when Q_{salt} = 0.1 l/day).

Fig. 7 illustrates that as the growth rate of methanogenic bacteria increases, the current generation decreases and ultimately experiences maximum enhancement when the rate of methanogenic production is equal to zero. Thus, the results confirm that methanogenic bacteria lead to a reduction in the current generation.

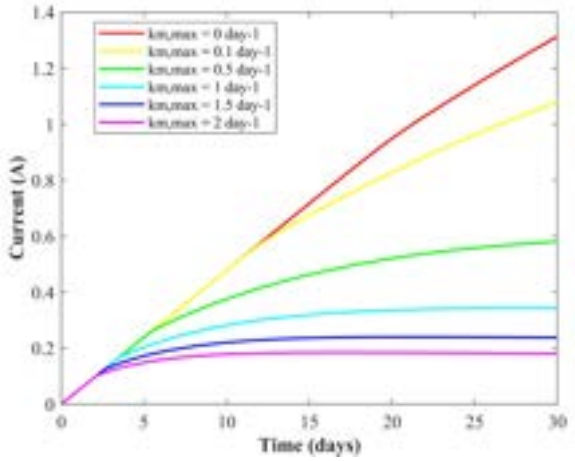

Figure. 7. The relationship between the current production and methanogenic growth rate.

5. Conclusions

The present work presented a cogeneration system for the production of power, freshwater, and wastewater treatment based on solar and wind energy. For freshwater production, the integration of MDC with HDH and RO systems was investigated. The required heat of the complex was combined using FPC and HICE based on solar and wind energy. Energy, exergy, exergeoeconomic, and exergoenvironmental (4E) analyses were used for the integrated system. The overall results obtained indicate that the integrated system can produce 0.72 MW power and 5.36 m^3/h freshwater. Also, the overall cost rate and overall environmental impact rate of the whole system were calculated as 540.33 $/h and 17.37 Pts/h, respectively. A series of other results of the system are as follows:

- In addition to wastewater treatment and power production, the MDC has been able to reduce the concentration of dissolved salt in water by 20 g/kg.
- The RO desalination plant has produced 1.42 kg/s of freshwater using 6 kW of power.
- The highest exergy destruction is related to WT and HICE, respectively.
- The most destructive of costs and destruction of environmental impacts are related to HICE.
- WT has the highest production environmental impacts and the highest investment cost.

In the end, it should be mentioned that the presented system can be used to meet the needs of greenhouses, industrial factories, residential areas, and military barracks. But it is necessary to examine the feasibility of using such a system from various aspects such as safety risk, controllability, etc.

Acknowledgments

This research has been co-funded by ERDF funds, INTERREG MAC 2014-2020 programme, within the E5DES project (MAC2/1.1a/309). No funding sources had any influence on study design, collection, analysis, or interpretation of data, manuscript preparation, or the decision to submit for publication.

References

[1] Invest in climate action for health: cut emissions, clean our air, save lives. World Health Organization. Available at: <https://www.who.int/director-general/speeches/detail/invest-in-climate-action-for-health-cut-emissions-clean-our-air-save-lives> [accessed 23.9.2019].

[2] Jamil, M. A., Elmutasim, S. M., & Zubair, S. M. Exergo-economic analysis of a hybrid humidification dehumidification reverse osmosis (HDH-RO) system operating under different retrofits. Energy Conversion and Management 2018; 158, 286-297.

[3] Ding, P., Yuan, Z., Shen, H., Qi, H., Yuan, Y., Wang, X., ... & Sobhani, B. Exergoeconomic analysis and optimization of a hybrid Kalina and humidification-dehumidification system for waste heat recovery of low-temperature Diesel engine. Desalination 2020; 496, 114725.

[4] Zubair, M. I., Al-Sulaiman, F. A., Antar, M. A., Al-Dini, S. A., & Ibrahim, N. I. Performance and cost assessment of solar driven humidification dehumidification desalination system. Energy Conversion and Management 2017; 132, 28-39.

[5] Manesh, M. K., Rabeti, S. M., Nourpour, M., & Said, Z. J. S. E. T. Energy, exergy, exergoeconomic, and exergoenvironmental analysis of an innovative solar-geothermal-gas driven polygeneration system for

combined power, hydrogen, hot water, and freshwater production. Sustainable Energy Technologies and Assessments 2022; 51, 101861.

[6] Khaled, H., Zrelli, A., Hamed, M., & Chaouachi, B. Modelisation and Optimization of a Microbial Desalination Cell System. Journal of Sustainable Bioenergy Systems 2021; 11(3), 118-130.

[7] Ravajiri, E. S., Jalali, A., & Houshfar, E. Multi-objective optimization and 4E analysis of an integrated system based on waste-to-energy, solar PV, power-to-gas, and HDH-RO desalination. Energy Conversion and Management 2023; 277, 116677.

[8] Manesh, M. H. K., Ghorbani, S., & Blanco-Marigorta, A. M. Optimal design and analysis of a combined freshwater-power generation system based on integrated solid oxide fuel cell-gas turbine-organic Rankine cycle-multi effect distillation system. Applied Thermal Engineering 2022; 211, 118438.

[9] Reitz, R. D., Ogawa, H., Payri, R., Fansler, T., Kokjohn, S., Moriyoshi, Y., ... & Zhao, H. IJER editorial: The future of the internal combustion engine. International Journal of Engine Research 2019; 21(1), 3-10.

[10] Martins, J., & Brito, F. P. Alternative fuels for internal combustion engines. Energies 2020; 13(16), 4086.

[11] Shadidi, B., Najafi, G., & Yusaf, T. A review of hydrogen as a fuel in internal combustion engines. Energies 2021; 14(19), 6209.

[12] Tsujimura, T., & Suzuki, Y. The utilization of hydrogen in hydrogen/diesel dual fuel engine. International journal of hydrogen energy 2017; 42(19), 14019-14029.

[13] Nikitin, A., Deymi-Dashtebayaz, M., Baranov, I. V., Sami, S., Nikitina, V., Abadi, M. K., & Rumiantceva, O. Energy, exergy, economic and environmental (4E) analysis using a renewable multi-generation system in a near-zero energy building with hot water and hydrogen storage systems. Journal of Energy Storage 2023; 62, 106794.

[14] He, Y., Guo, S., Zhou, J., Wu, F., Huang, J., & Pei, H. The many-objective optimal design of renewable energy cogeneration system. Energy 2021; 234, 121244.

[15] Brown, M. A., & Herrera, V. S. Combined heat and power as a platform for clean energy systems. Applied Energy 2021; 304, 117686.

[16] Gonzalez, A., Riba, J. R., Esteban, B., & Rius, A. Environmental and cost optimal design of a biomass–Wind–PV electricity generation system. Renewable energy 2017; 126, 420-430.

[17] Zhao, Z. Y., Chen, Y. L., & Thomson, J. D. Levelized cost of energy modeling for concentrated solar power projects: A China study. Energy 2017; 120, 117-127.

[18] Khoshgoftar Manesh, M. H., & Onishi, V. C. Energy, exergy, and thermo-economic analysis of renewable energy-driven polygeneration systems for sustainable desalination. Processes 2021; 9(2), 210.

[19] Makkeh, S. A., Ahmadi, A., Esmaeilion, F., & Ehyaei, M. A. Energy, exergy and exergoeconomic optimization of a cogeneration system integrated with parabolic trough collector-wind turbine with desalination. Journal of Cleaner Production 2020; 273, 123122.

[20] Alamdari, P., Nematollahi, O., & Mirhosseini, M. Assessment of wind energy in Iran: A review. Renewable and Sustainable Energy Reviews 2012; 16(1), 836-860.

[21] Khani, N., Manesh, M. H. K., & Onishi, V. C. 6E analyses of a new solar energy-driven polygeneration system integrating CO2 capture, organic Rankine cycle, and humidification-dehumidification desalination. Journal of Cleaner Production 2022; 379, 134478.

[22] Ahmadi, P., Dincer, I., & Rosen, M. A. Energy and exergy analyses of hydrogen production via solar-boosted ocean thermal energy conversion and PEM electrolysis. International Journal of Hydrogen Energy 2013; 38(4), 1795-1805.

[23] Akal, D., Öztuna, S., & Büyükakın, M. K. A review of hydrogen usage in internal combustion engines (gasoline-Lpg-diesel) from combustion performance aspect. International journal of hydrogen energy 2020; 45(60), 35257-35268.

[24] Cengel, Y. A., Boles, M. A., & Kanoğlu, M. Thermodynamics: an engineering approach New York: McGraw-hill; 2011.

[25] Bellos, E., & Tzivanidis, C. Performance analysis and optimization of an absorption chiller driven by nanofluid based solar flat plate collector. Journal of cleaner production 2018; 174, 256-272.

[26] Zhou, W., Song, L., & Guan, T. K. A numerical study on concentration polarization and system performance of spiral wound RO membrane modules. Journal of Membrane Science 2006; 271(1-2), 38-46.

[27] Wang, J., Wu, J., & Wang, H. Experimental investigation of a dual-source powered absorption chiller based on gas engine waste heat and solar thermal energy. Energy 2015; 88, 680-689.

[28] Norani, M., & Deymi-Dashtebayaz, M. Energy, exergy and exergoeconomic optimization of a proposed CCHP configuration under two different operating scenarios in a data center: Case study. Journal of Cleaner Production 2022; 342, 130971.

[29] Rokni, M. M. Power to hydrogen through polygeneration systems based on solid oxide cell systems. Energies 2019; 12(24), 4793.

[30] Pinto, R. P., Srinivasan, B., Manuel, M. F., & Tartakovsky, B. A two-population bio-electrochemical model of a microbial fuel cell. Bioresource technology 2010; 101(14), 5256-5265.

[31] Zamen, M., Amidpour, M., & Firoozjaei, M. R. A novel integrated system for fresh water production in greenhouse: Dynamic simulation. Desalination 2013; 322, 52-59.

[32] Dincer, I., Rosen, M. A., & Ahmadi, P. Optimization of energy systems. John Wiley & Sons; 2017.

[33] Cavalcanti, E. J. C. Exergoeconomic and exergoenvironmental analyses of an integrated solar combined cycle system. Renewable and Sustainable Energy Reviews 2017; 67, 507-519.

ULPGC
Universidad de
Las Palmas de
Gran Canaria

grres ULPGC
group for the research on renewable energy systems

K. Energy policy and planning

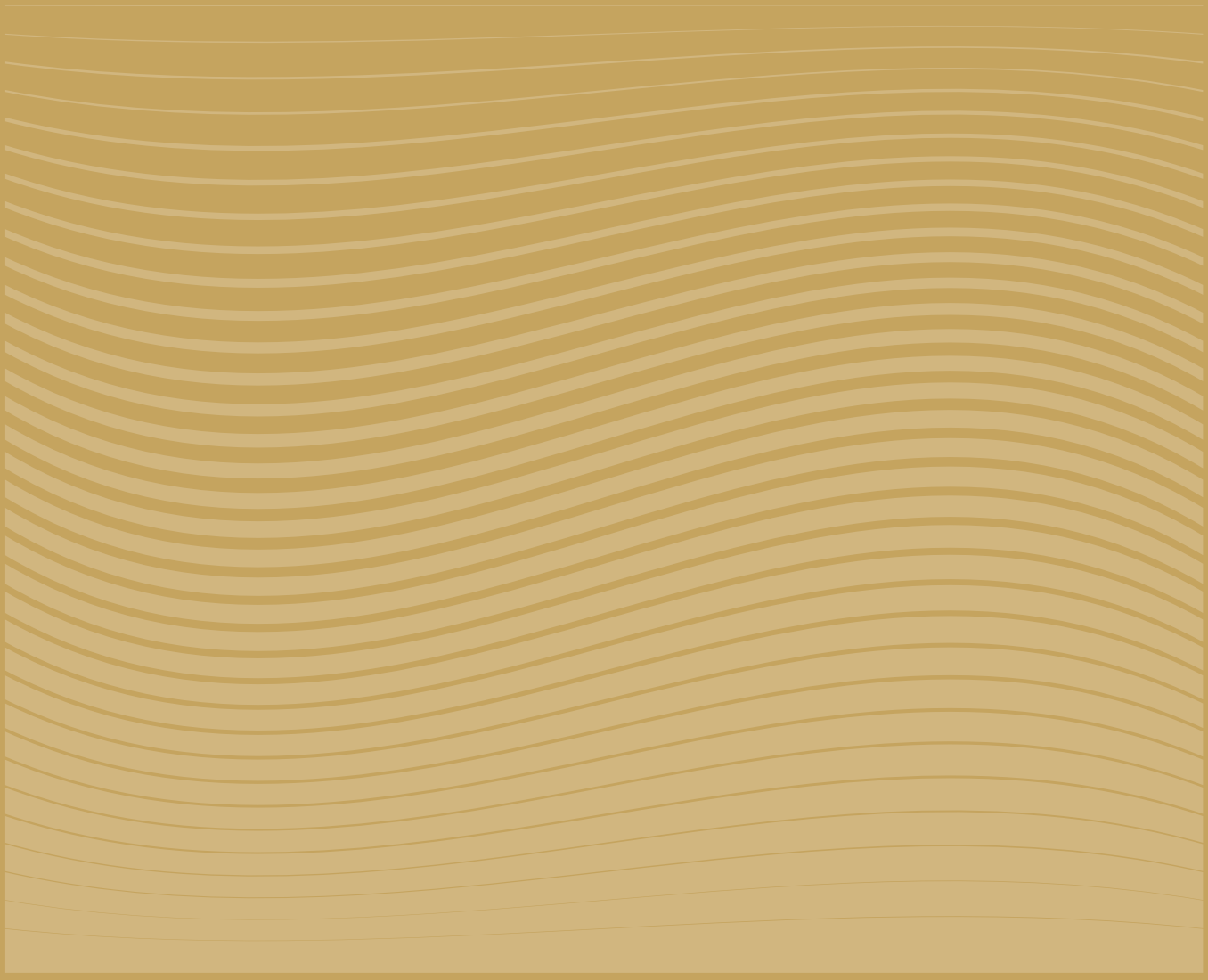

ECOS2023

PROCEEDINGS OF ECOS 2023 - THE 36TH INTERNATIONAL CONFERENCE ON
EFFICIENCY, **C**OST, **O**PTIMIZATION, **S**IMULATION AND ENVIRONMENTAL IMPACT OF ENERGY SYSTEMS
25-30 JUNE, 2023, LAS PALMAS DE GRAN CANARIA, SPAIN

Cost sensitivity analysis on Swiss energy transformation towards net-zero target

Xiang Li [a,b,*], Matthieu Souttre [a,c,*], and François Maréchal [a]

[a] IPESE, Ecole Polytechnique Fédérale de Lausanne, Sion, Switzerland
[b] E4S, Ecole Polytechnique Fédérale de Lausanne, Lausanne, Switzerland
[c] CIRAIG, Polytechnique Montréal, Montréal, Canada
[*] The authors contribute equally to this work.
Correspondence: xiang.li@epfl.ch

Abstract:
Energy technology costs and fuel prices play a critical role in the energy transition towards carbon neutrality. Despite its straightforwardness in comparing standalone technologies, the widely-used levelized cost of energy (LCOE) is not able to estimate the activation condition for low-carbon technologies due to lack of systematic assessment of the complexities in energy systems. In this study, we analyzed the impact of energy cost uncertainties for the deployment of renewables and carbon capture technologies for Switzerland based upon Energyscope, a systematic energy planning platform optimizing both investment and operational strategies for electricity, heat, and mobility. The results show that carbon capture becomes competent to renewable technologies when its cost drops below approximately 70 USD/tCO2. Furthermore, synthetic natural gas (NG) is promising to substitute fossil NG when the import price of the latter rises to above 0.1 USD/kWh level. These discoveries can be helpful for long-term planning, especially in the context of increasing geopolitical concerns on energy supply security.

Keywords:
Energy system, Cost sensitivity, Long-term planning.

1. Introduction

The 2022 United Nations Climate Change Conference (COP27) in Egypt [1] highlights that the global energy crisis, in addition to the impact of climate change, are challenging the efforts to achieve energy security. It calls on the essence of increasing the renewables' share in the energy mix and encourages the continued efforts to phase out fossil fuels. As indicated by [2–4], a radical transformation of the energy sector is mandatory. However, such rapid transition is triggering a series of social-economic concerns, especially in terms of the transition cost, which is commonly regarded as capital-intensive [5–7]. For instance, IEA [7] claims that the investment into clean energy should at least be doubled and triple by 2030 in the announced pledges scenario and the net-zero emission scenario respectively, with respect to 2022 levels (i.e., USD 1.4 trillion).

With the decreasing trends of renewable costs in the last decades, as illustrated in Figure 1, it is likely that renewable costs have already dropped below, or might become competitive to fossil energies, depending on geographical and meteorological conditions (solar irradiation, wind speed etc.). However, it is very difficult to predict the energy costs. On one hand, IRENA [8] emphasizes that most renewable energy technologies benefit from learning-by-doing, thus allowing the decrease of their investment costs at the global scale over time. For instance, the global capacity-weighted average total installed cost of utility-scale solar PV and onshore wind projects in 2021 decreased by 81% and 35% respectively with respect to 2010 values. On the other hand, IEA [7] observed that highly unpredictable exogenous events, such as the Russo-Ukrainian war, may have dramatic consequences on the cost of energy technologies, especially resources, like natural gas (NG) in the case of the Ukrainian conflict. Thus, taking into account learning trends while accounting for uncertainty that may come from exogenous events is key for making plausible decisions in order to achieve energy transition towards carbon neutrality.

Across the current energy research, one common practice is using the Levelized Cost Of Energy (LCOE) [10–12] to compare the energy costs. LCOE is calculated by the ratio of the total cost (investment and operational costs) and total energy output during the lifetime of a technology. By definition, the LCOE metric focuses only on a standalone technology, which is not able to capture the synergies and conflicts occurring between energy technologies among the highly interconnected energy systems. As a result, the conclusion of

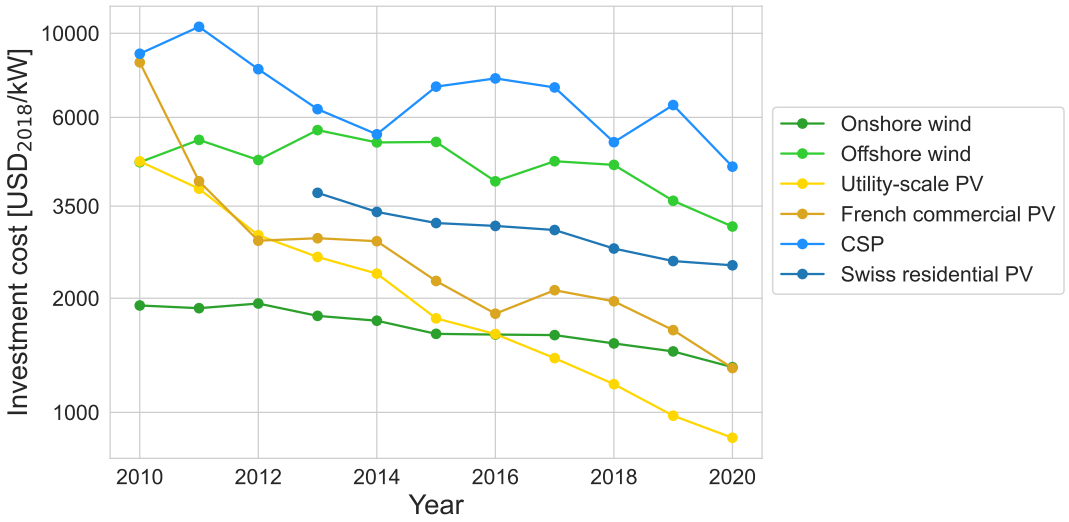

Figure 1: Historical cost trends for the main renewable energy technologies. Data taken from IRENA [9]. The costs are global-averaged data, except for the residential and commercial PV.

”cheap” or ”expensive” based upon simply comparing LCOE may become unreliable in the field of long-term energy planning. For instance, even if the LCOE of a photovoltaic (PV) panel drops below a gas power plant, the system may still keep using the gas, taking into account additional costs for deploying the PV such as the storage (e.g. by battery) and backup technologies. More specifically, Hansen [13] compared the LCOE with Energy System Analysis (ESA) for assessing the cost of integrating an energy technology into an energy system by using the simulation model EnergyPLAN which accounts for systemic perspectives. The results show that the two methods lead to different energy technologies priorities and confirm that the LCOE method lacks to consider crucial systemic dimensions. Ueckerdt et al. [14] proposed a new version of LCOE, namely the Systemic LCOE, that considers both the integration and generation costs. The results show that integration costs may become within the same range as generation costs in the case of high wind shares, thus confirming the possible poor reliability of LCOE without having a systemic view. Consequently, it is important to apply system-level models with a holistic representation of the interactions of energy technologies, to analyze the impact of energy cost variation on the energy transition.

However, the majority of energy models are based upon cost-minimization, or profit maximization assumptions. As emphasized by Trutnevyte [15], costs are a key driver of the energy transition, but there are many others (e.g., social impacts) that may lead to non-rational decision. For instance, the electricity system transition of UK from 1990 to 2014 was not cost-optimized, by a 9-23% deviation according to Trutnevyte [15]. Nevertheless, cost-optimization models such as Energyscope [16] are needed, not for exactly predicting how the future energy system will look like, but as a systemic decision-making tool for generating a series of possible scenarios allowing for uncertainty analysis in order to evaluate potential trade-offs among heterogeneous pathways.

This work aims at unveiling the sensitivity of the future energy system as a function of the of the key energy technologies costs within their uncertainty ranges, while accounting for the interdependence between the different technologies. The sensitivity of the energy system is mainly reflected by the variation of annual energy output (in terms of GWh) for each technology. This paper is organized as below: Section 2 introduces the methodology of our study; Next, some preliminary results are presented and analyzed in Section 3; Finally, we summarize the major novelties of this work and possible future research direction in Section 4.

2. Methodology

2.1. Modelling framework

This research is conducted upon Energyscope, a bottom-up energy system model based on cost-optimization, designed for decision-making in the field of energy transition. It has been originated by Moret [16] as a so-called *snapshot* model. *Snapshots* describe an energy system at a given time mainly in terms of energy technologies installation [MW] and utilization [GWh/year] as well as the investment and operation costs that are associated to these. To generate those results, Energyscope is based on a Mixed-Integer Linear Programming (MILP) optimization problem, that is constituted by a set of energy conversion technologies (including

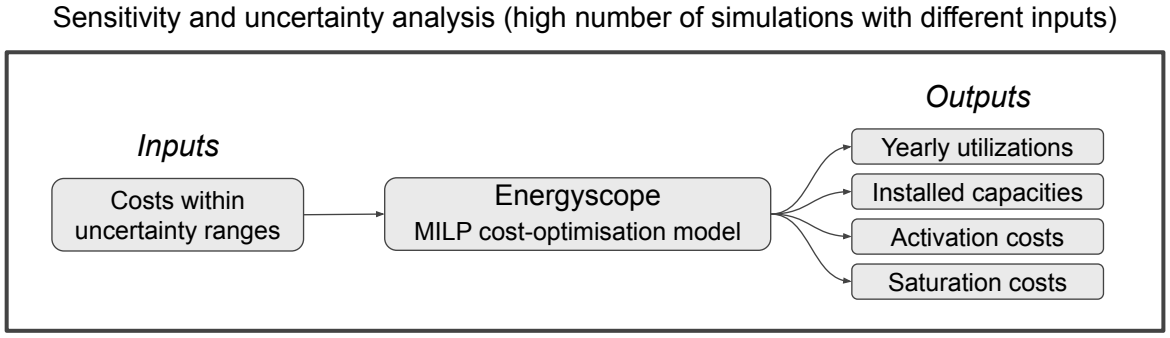

Figure 2: Scheme of the methodology

storage technologies), energy resources as well as the energy end-use demand (EUD). Each energy conversion technology is characterized according to a: 1) reference size [MW], 2) investment cost [USD/kW], 3) maintenance cost [USD/kW/year], 4) Global Warming Potential (GWP), 5) lifetime [year], 6) capacity factor [-], 7) minimum installed capacity [MW] and 8) maximum installed capacity [MW]. This model is working with a monthly granularity in order to account for time-dependent parameters (e.g., EUD, solar irradiation, wind power etc.) that are occurring over a year.

Whereas other energy system models may be proprietary, computationally expensive and only integrating the electricity sector, Energyscope is open-source, has a small computation time (sec) due to its *snapshot* design and both models the electricity, heat and mobility sectors. Its short computation time allows to use this model for sensitivity and uncertainty analysis, which typically requires several thousands of iterations. The modelling of the entire energy system ensures that the interactions between the different energy sectors are taken into account in the results and thus in the decision-making process. The heat sector EUD is further divided between low temperature and high temperature heating needs, whereas the mobility sector EUD is divided between passenger mobility [Mpkm] (itself divided between public and private mobility) and freight mobility [Mtkm] (itself divided between road and rail freight).

The objective function of the MILP optimization problem to minimize is the system total cost, defined by Eq. 1, subject to mass and energy balances, as well as storage behaviours. The optimization variables (written in **bold**), and thus the output of the model, are the energy conversion technologies installed capacities [MW] and yearly productions [GWh/year], the centralised and decentralised heat supply shares, the public and private mobility shares as well as the freight rail and road shares. The complete optimization problem can be found in [16]. We added a modelling of carbon flows [17] by identifying carbon sources, carbon conversion technologies and carbon sinks. This is allowing to model a carbon circular economy within the context of a highly interconnected energy system due to increasing deployment of biomass and carbon capture, use and storage (CCUS) technologies.

$$\min \ \mathbf{C_{tot}} = \sum_{j \in TECH} (\mathbf{C_{inv}}(\mathbf{j}) \cdot \tau(j) + \mathbf{C_{maint}}(\mathbf{j})) + \sum_{i \in RES} \mathbf{C_{op}}(\mathbf{i}) \tag{1}$$

where:

$$\tau(j) = \frac{i_{rate}(1 + i_{rate})^{n(j)}}{(1 + i_{rate})^{n(j)} - 1} \tag{2}$$

$$\mathbf{C_{inv}}(\mathbf{j}) = c_{inv}(j) \cdot \mathbf{F}(\mathbf{j}) \tag{3}$$

$$\mathbf{C_{maint}}(\mathbf{j}) = c_{maint}(j) \cdot \mathbf{F}(\mathbf{j}) \tag{4}$$

$$\mathbf{C_{op}}(\mathbf{i}) = \sum_{t \in T} c_{op}(i, t)\mathbf{F_t}(\mathbf{i}, \mathbf{t})t_{op}(i) \tag{5}$$

The above equations are mainly cost-relevant formulations. More detailed mathematical framework of Energyscope is available in [17, 18]. Next, we define scenarios and vary the model inputs, in order to analyze the corresponding variation of utilization of resources.

2.2. Scenario definition

Two scenarios are defined in this study, namely:

- Scenario (a): State-of-the-art, based upon the Swiss energy system in 2020. This implies all the model parameters and variables, including technology costs, fuel costs, installed capacities, and energy supply, are fixed with the real values in 2020. As the price of natural gas had a significant change before/after the Russia-Ukraine war, we conducted a specific sensitivity analysis on the utilization of natural gas as a function of natural gas cost.
- Scenario (b): Net-zero scenario, based upon the cost projection data (as of 2050) from a variety of sources, such as IEA [5–7] and IRENA [19–21] databases. Built on the future energy system, we perform Monte Carlo simulation in order to explore how robust a net-zero emission system is against cost uncertainty.

Based upon the definition of scenario (b), one interesting topic is to assess the competition between renewables and carbon capture: both are beneficial to realize the climate target, but which condition one might be more widely used compared to the other ? Furthermore, we analyze the simultaneous effects of both carbon capture cost and fuel price on the energy system.

3. Preliminary results

Figure 3 shows the results for scenario (a), illustrating the variation of natural gas utilization as a function of its price. It is observed that NG is not used anymore when the price rises above 90 USD/MWh; when the price drops below 50 USD/MWh (critical point), it begins to be largely used, probably replaced by a massive penetration of wind turbines, as reflected by the green line. In correspondence, the total cost of the energy system becomes almost invariant when NG cost is above the critical point.

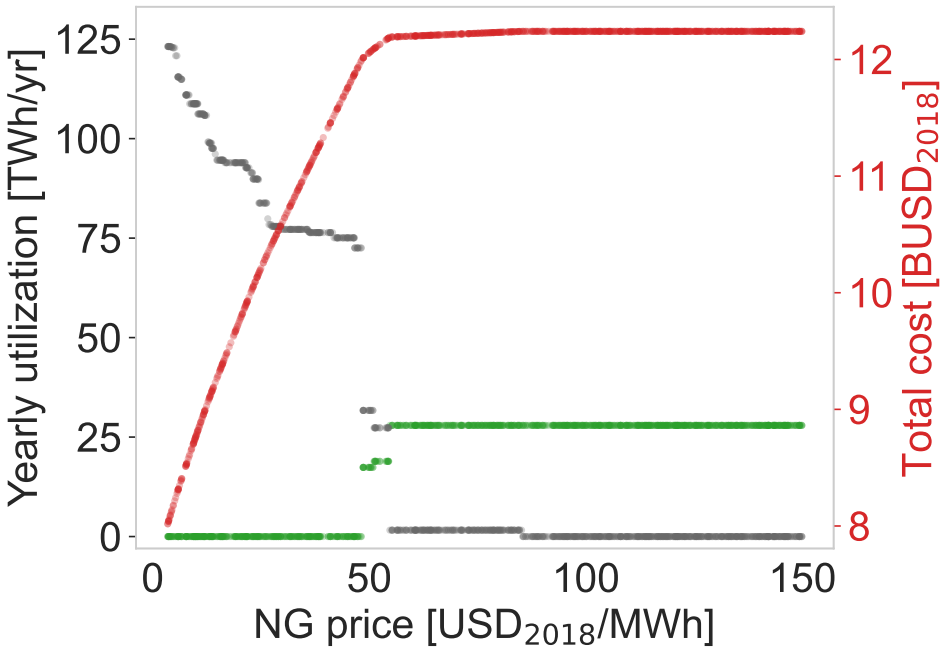

Figure 3: Sensitivity of natural gas consumption (grey dots), wind energy (green dots), and system total cost (red dots) as a function of NG price signal. Other costs are fixed to their 2020 values.

Furthermore, Fig. 4 reflects the impacts of NG price and carbon capture cost on the utilization of NG, Synthetic NG (SNG), and the total cost of the energy system in the net-zero scenario. From Fig. 4 (a), the utilization of natural gas is highly sensitive to the carbon capture cost when NG price remains low. In the most extreme case where the NG price is close to zero, the carbon capture cost has to be surpass 70 USD/tCO2 in order to maintain the NG utilization below 50 TWh/year. When the NG price stays the same as of 2020, i.e., around 30 USD/MWh, a carbon capture cost close to 100 USD/tCO2 can stop the utilization of NG. In practice, these results can be linked to carbon tax and thus conductive to defining effective energy measures.

Figure 4 (b) and (c) serve as supplementary of (a), showing the substitution of NG by SNG and the variation of the total cost of the energy system respectively. When the natural gas cost rises above 45 USD/MWh in the condition of zero carbon capture cost, SNG becomes competitive to NG. A high carbon capture (100 USD/tCO2) cost can even further halve the NG cost for activating SNG facilities. Finally, Fig 4 (c) reflects the corresponding maximal variation of the energy system cost is within $[-10\%, 20\%]$ range assuming the NG price staying the level 2020 and no carbon capture technologies.

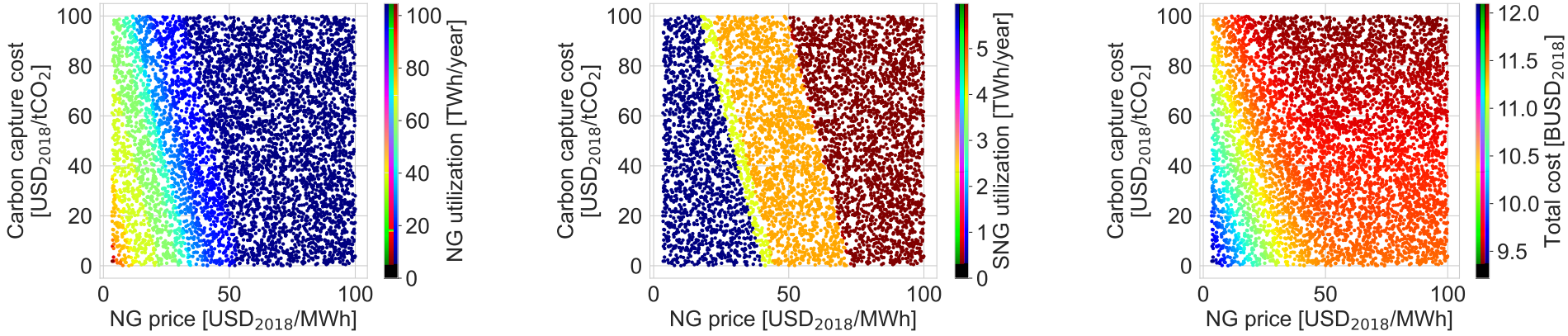

(a) NG (b) SNG (c) Total cost

Figure 4: Sensitivity of NG and SNG utilization as well as total cost as a function of both carbon capture cost and NG price. Other costs are fixed to their 2050 value.

4. Conclusion

This study performed sensitivity analyses on the impact of cost on the energy transition, allowing for quantifying the activation cost and saturation cost for different energy technologies and resources. All the results are obtained from a system-level model instead of simply comparing the LCOE, thus improving their plausibility. We believe these results can be easily understood by policy makers and other energy stakeholders, thus contributing to rational decision making, in particular for enacting energy policies.

This paper is dedicated to sharing our research idea. A complete paper with detailed data and more results are in preparation.

References

[1] COP27, "Climate Change Conference." https://cop27.eg/#/, 2022.

[2] D. Bogdanov, J. Farfan, K. Sadovskaia, A. Aghahosseini, M. Child, A. Gulagi, A. S. Oyewo, L. de Souza Noel Simas Barbosa, and C. Breyer, "Radical transformation pathway towards sustainable electricity via evolutionary steps," *Nature Communications*, vol. 10, p. 1077, Mar. 2019.

[3] J. Markard, F. W. Geels, and R. Raven, "Challenges in the acceleration of sustainability transitions," *Environmental Research Letters*, vol. 15, p. 081001, Aug. 2020.

[4] M. M. Vanegas Cantarero, "Of renewable energy, energy democracy, and sustainable development: A roadmap to accelerate the energy transition in developing countries," *Energy Research & Social Science*, vol. 70, p. 101716, Dec. 2020.

[5] IRENA, "World Energy Transitions Outlook 2022: 1.5℃ Pathway," p. 352, 2022.

[6] IEA, "The cost of capital in clean energy transitions," 2021.

[7] IEA, "World Energy Outlook 2022," p. 524, 2022.

[8] IRENA, "Renewable Power Generation Costs in 2021," p. 204, 2022.

[9] IRENA, "Renewable Power Generation Costs 2020," tech. rep., 2021.

[10] G. Glenk, R. Meier, and S. Reichelstein, "Cost Dynamics of Clean Energy Technologies," *Schmalenbach Journal of Business Research*, vol. 73, pp. 179–206, June 2021.

[11] G. R. Timilsina, "Are renewable energy technologies cost competitive for electricity generation?," *Renewable Energy*, vol. 180, pp. 658–672, Dec. 2021.

[12] M. Ligus, "An analysis of competitiveness and potential of renewable energy technologies in poland," *Energy & Environment*, vol. 26, no. 8, pp. 1247–1269, 2015.

[13] K. Hansen, "Decision-making based on energy costs: Comparing levelized cost of energy and energy system costs," *Energy Strategy Reviews*, vol. 24, pp. 68–82, Apr. 2019.

[14] F. Ueckerdt, L. Hirth, G. Luderer, and O. Edenhofer, "System LCOE: What are the costs of variable renewables?," *Energy*, vol. 63, pp. 61–75, Dec. 2013.

[15] E. Trutnevyte, "Does cost optimization approximate the real-world energy transition?," *Energy*, vol. 106, pp. 182–193, July 2016.

[16] S. Moret, *Strategic Energy Planning under Uncertainty*. PhD thesis, EPFL, 2017.

[17] X. Li, T. Damartzis, Z. Stadler, S. Moret, B. Meier, M. Friedl, and F. Maréchal, "Decarbonization in Complex Energy Systems: A Study on the Feasibility of Carbon Neutrality for Switzerland in 2050," *Frontiers in Energy Research*, vol. 8, p. 549615, Nov. 2020.

[18] S. Moret, V. Codina Gironès, M. Bierlaire, and F. Maréchal, "Characterization of input uncertainties in strategic energy planning models," *Applied Energy*, vol. 202, pp. 597–617, Sept. 2017.

[19] IRENA, "Electricity storage and renewables: Costs and markets to 2030," tech. rep., 2030.

[20] IRENA, "Renewable Power Generation Costs 2020," tech. rep., 2020.

[21] IRENA, "Renewable solutions in end-uses: Heat pump costs and markets," p. 57, 2022.

Using PyPSA-Earth to address energy systems modelling gaps in developing countries. A case study for Bolivia

Carlos A. A. Fernandez Vazquez [a], Sergio Balderrama [b] and Sylvain Quoilin [c]

[a] Université de Liège (ULiege), Liège, Belgium, caa.fernandez@uliege.be, (CA)
[b] Universidad Mayor de San Simón (UMSS), Cochabamba, Bolivia, s.balderrama@umss.edu,
[c] Université de Liège (ULiege), Liège, Belgium, squoilin@uliege.be

Abstract:

Bolivia is a developing country in South America which is slowly starting its energy transition towards more renewable technologies. However, at this moment, Institutions in charge of regulating, operating, and planning the development of the sector are still working with “black box” (or licensed) models, which are costly and less transparent, and are highly dependent on external expertise to formulate national plans. A proper transition will arguably require endogenous know-how and resources to be sustainable, affordable, and sovereign for the country.

In this context, open-source energy models are increasingly used in Bolivia, mostly by academic and non-profit institutions. These are used to study alternative development scenarios, quantify environmental impacts and/or define potential techno-economic requirements.

Previous works have focused on the development of dispatch models that analyse the stability and operation over short-terms and on energy-balance models to study impacts over long-term scenarios. However, while operation and planning aspects are somewhat covered independently, the combination of both is still missing (i.e. high time and spatial resolution and long-term horizon perspectives).

To bridge this gap the PyPSA-Earth model was identified and used to derive a model specific for the Bolivian context using a dedicated workflow. The model is adapted to run and provide country-specific outputs regarding generation capacities, grid expansion and sector-specific demands, which are later compared with historical information to assess its accuracy and capabilities.

Modelling results provide inputs regarding the characteristics of the tool and quantify deviations of its outputs compared to the Bolivian system in 2020. Based on these, it is concluded that the flexibility of the model, combined with its transparent structure, show great potential for implementation.

Keywords:

Energy modelling; Open-source; Bolivia; Energy systems; PyPSA-Earth; Developing countries.

1. Introduction

1.1. General context

Energy modelling has been an extensively researched topic for several decades, particularly in the context of studying energy systems and their components, such as power generation systems, dispatch mechanisms, demand analysis, coverage, and operational capacities at the transmission and distribution levels. Because of this, a diverse range of models can be found in the literature and, depending on the study's focus, models can be classified based in several ways. The paradigm of data utilization, the solving approach, the spatial-scale, and the time-frame studied, among others, are examples of what this classification can be based on [1].

Nevertheless, even among different taxonomies, overarching objectives in energy modelling include enhancing the energy system's characteristics, supporting design and planning efforts, improving the understanding of system components and their interactions, and examining the relationships between various critical aspects. These aspects are mostly related to technology availability, cost reductions, environmental impacts, social factors, and policy implementation [2].

Over time, modelling tools have proliferated and evolved, primarily in industrialized/developed countries, where they were developed to address specific behavioural conditions and technical/operational characteristics. However, these models are subject to significant limitations when applied to developing countries, as they assume high standards of system operation, exhibit inflexibility in the parameters/factors considered, and may

assume data availability, all of which often conflict with the reality of developing countries [3]. Furthermore, these tools were initially developed as closed and proprietary systems by large institutions, which had no obligation or incentive to make their tools publicly available. Consequently, there is a growing need for more open, flexible, transparent, and accessible modelling tools [4].

In the case of Latin America & the Caribbean, a region comprised mostly by developing countries, modelling requirements are driven by the region's characteristics [5]:

- a rapidly increasing energy demand;
- a strong correlation between energy consumption and economic growth;
- highly variable energy intensity consumption;
- increasing energy production costs;
- increasing penetration of non-flexible renewable powerplants;
- large heterogeneity in power systems across neighboring countries;
- the need to achieve universal access;
- improve networks stability at transmission/distribution level;
- dealing with outdated subsidization policies for fossil fuels.

1.2. Previous work and modelling experience in Bolivia

Although the energy sector has a distinct organizational structure in each country, with clearly defined actors and responsibilities, developing economies often lack the resources (technical, human or economic) to invest in their own capabilities. Bolivia is a prime example of this, as outsourced companies and tools have consistently been used for the formulation of planning efforts and strategic documentation [6], specifically for the electric sector [7]. However, due to the nature of the relation between institutions, most of the information provided is provided solely as results generated through black-box models and, reports that don't provide insights into the tools used.

Experience with energy modelling at the institutions in charge of the sector shows a big reliance on licensed tools, such as:

- SDDP (Stochastic Dual Dynamic Programming), a unit commitment hydrothermal dispatch model [8], developed by the company PSR [9];
- PowerFactory, a power system analysis model developed by DIgSILENT [10], used for studying the transmission network, among other uses [11];
- HOMER (Hybrid Optimization of Multiple Energy Resources), a modelling software owned by UL [12], that is used to design and study small hybrid power systems (isolated communities or microgrids) [13].

From a governmental and institutional perspective, outsourcing institutions for the analysis of the power system, with their own licensed modelling tools, can provide some advantages. For instance, that they can provide fast results and simplified information to decision makers, a highly trained technical team and proven experience. However, this practice has its downsides. First, it does not foster the development of local capacities in the institutions that require them, resulting in an overreliance on external know-how. Second, the costs of contracting external personnel, consulting companies, or acquiring licenses for private software are usually high. Third, planning efforts can only cover short to mid-term periods, as long-term scenarios are not flexible enough to be continuously and consistently adapted [14].

To tackle these problems, which aren't unique for the Bolivian case, an array of new open-source modelling tools have started to appear as efforts from various research institutions [4]. These models, which come on a wide array of alternatives, are currently being used to analyse energy systems across the world and seem to be able to answer some relevant questions linked to the design, operation and planning of the sector [15].

Particularly in Bolivia, open-source modelling tools have been started to be used by researchers to develop case studies for the electrical sector with a wide range of approaches: studying the dispatch capabilities of the interconnected electric system (Dispa-SET) [16]; analysing the electrification process based on grid expansion and microgrids for isolated communities (OnSSET - Open Source Spatial Electrification Tool) [17]; analysing energy demands consumption in rural communities (RAMP – Remote Areas Multi energy load Profiles generator) [18]; the optimization of design of microgrids (MicroGridsPy) [19]; or analysing evolution of investments based on policy implementation and sustainable development scenarios in the long-term (OSeMOSYS - Open Source energy MOdelling SYStem) [20].

1.3. PyPSA-Earth

PyPSA-Earth, as many other models, has the general objective of exploring the development of energy systems by considering a set of techno-economic components and optimization functions. However, unlike the studies mentioned before, PyPSA-Earth provides a complementary look of the energy system from the power network perspective by analysing power flows in the system [21]. Additionally, the modelling tool can combine a high spatial resolution representation of the network (missing in OSeMOSYS), optimization functions for expansion of the system (missing in Dispa-SET) and focusing simultaneously on generation and grid components (missing from OnSSET) [22]. Additionally, the model's workflow structure is designed based on the PyPSA-Eur model, an open model dataset for the European region and used for operational and transmission expansion studies [23].

Both PyPSA-Eur and PyPSA-Earth are derived from PyPSA (Python for Power System Analysis), an open-source modelling framework tool designed for simulating and optimizing power systems focusing on the physics of the power flows over multiple periods (typically a full year) and optimizing the total system costs given techno-economic characteristics and constraints of its components [24].

PyPSA's structure considers a representation of power systems based on nodes, which correspond to buses or network elements (generators, loads, and transformers), and edges, which represent transmission lines or cables. The network is described using a linear and nonlinear equations, including Kirchhoff's laws, Ohm's law, and the power flow equations. These equations are used, using numerical optimization techniques such as Newton-Raphson or interior-point methods, to obtain the steady-state operating conditions of the system. PyPSA also includes a range of optimization algorithms for capacity expansion planning, unit commitment, and optimal power flow, which are used to optimize the system's economic and environmental performance under different scenarios and constraints [24].

The PyPSA-Earth model (previously PyPSA meets Africa) has been tested for Africa and a country-specific case, achieving close representations of the system compared to information available on international sources such as the World Bank (networks), Open Street Maps (substations and generation), IRENA (renewable resources) and Our World in Data (energy dispatched), among others [22]. In this sense, although the PyPSA-Earth tool has been proven valuable, its potential for implementation is still to be fully exploited due to its novelty and need for validation in other countries and regions. Because of this, and the fact that no open-source models haven't been used to analyse the Bolivian power network, the opportunity of testing a complementary tool for already existing models and efforts is worth being explored.

1.3. Aim of the paper

While the experiences presented are a good first step in addressing the national necessities for understanding and representing Bolivia's energy sector, the models used must be further developed and validated to ensure they can accurately represent national conditions. This, coupled with a continuous process of exploring new complementary tools, could eventually make the country self-sufficient in terms of know-how and analysis capabilities in the long-term.

One particular gap identified in the existing modelling toolkit developed for Bolivia is the lack of a model that focuses on network representation and expansion. Therefore, the present work aims to address this gap by deriving a country-specific model for Bolivia's power network from PyPSA-Earth, a new open-source modelling tool, and analyse its potential for application, explore requirements for guarantying future work, and identify possibilities for further contribution.

2. Methodology and calculations

Given the open-source characteristics of the model information required for running the model for particular cases is available online, in their github repository and their documentation webpage [25]. Using this information and the current version of the model, the following methodology was applied to derive a model for Bolivia based on PyPSA-Earth:

1. Workflow adaptation: The existing workflow framework for PyPSA-Earth was configured so that scripts and parameters are capable of running a "testing" version of the Bolivian case with its corresponding country-specific conditions.
2. Consistency analysis: In order to assess the accuracy of the model, an optimization scenario is run for the year 2020. This scenario considered variations of relevant parameters such as the number of buses/clusters considered or the time aggregation periods. Results from the optimization process and intermediate stages of the workflow, focused mostly in the representation of networks, generators and energy produced, are later compared with national historical data for the same year.

3. Identification of model's potential and development opportunities: Based on the results obtained in the previous step, a more in-depth analysis is conducted to explore future usage and implementation of the model for the Bolivian case, as well as opportunities for further development of the tool and contribution opportunities to enrich the code.

2.1. Case Study: The Bolivian energy system

Bolivia has undergone significant changes in the development of its energy/electricity system over the years. The Electricity Law of 1994 transferred state-owned companies to the private sector through a process called "capitalization." Prior to this, approximately 70% of electricity came from hydroelectric sources. The law aimed to promote intensive use of natural gas as the primary energy source for electricity generation, as large volumes of Natural Gas (NG) were unused at the time, by establishing a special price for NG used for electricity generation, below international prices [26]. Ever since, low natural gas prices have effectively blocked the development of new hydroelectric and renewable energy in the country, changing the situation so that by 2006, 70% of the generation was generated by NG thermal plants [27].

In 2006, with the arrival of a new left government, the energy policy changed. The electricity sector, along with the hydrocarbon sector, was nationalized, and the National Electricity Company (ENDE) was restructured into a vertically integrated corporation, a "national strategic and corporate public company" [28]. ENDE now has 12 subsidiary companies. ENDE, together with the CNDC (National Committee for Charge Dispatch), as the main coordinator for power dispatch, and AETN (Supervision Authority for Electricity and Nuclear Technology), as the main entity in charge of regulating the electric system, have been stablished as the key institutions that manage the large majority of the electric system in Bolivia [29].

In the last ten years, there have been three notable developments: the creation of the Vice Ministry of Electricity and Alternative Energies (VMEEA), the approval of a Policy on Alternative Energies for the Electricity Sector [30], and the installation of photovoltaic parks and wind farms for larger populations. These, together with newly published documents like the its national development plan (PDES 2021-2025) [31] or the updated NDC (Nationally Determined Contributions) [32], demonstrate the government's willingness to shift the previous paradigm regarding renewable technologies and incorporate them into the electricity sector. In both documents expressed goals are mentioned in which the country should achieve over 75% participation of renewable technologies in its electric system by 2030.

In 2020 Bolivia's National Interconnected System (SIN) recorded a capacity of 3,228.61 MW in its generation mixed and total production of 8,897.3 MWh [33], with conventional thermal plants (NG) being the main contributor with 63.3% of the share, followed by hydroelectric providing 32.3%, and a combination of solar, wind, and biomass power plants for the rest [34]. Currently, the installed capacity in the country is twice the amount required due to large efforts to expand and develop the power generation system to open a potential offer of electric energy to neighboring countries.

Finally, according to the 2020 yearly memoires of the sector's national institutions, Bolivia's power network was composed of high voltage transmission lines operating at 230, 115 and 69 kV, with an accumulated amount of 94 substations and 6340 km of powerlines across the SIN, in 8 of the 9 departments of the country [35]. In the generation aspect, 36 power plants, each with several generation units, are currently being operated [36].

2.2. PyPSA-Earth's Workflow for the Bolivian case

The general structure of PyPSA-Earth is comprised by a workflow with the following main stages: Automated data retrieval from open-source data bases (downloading data for the pre-defined case); data pre-processing and inputs generation (specific data filtering processes used for representative variables); base network generation (inputs are used to create a network model with PyPSA); network optimization for given conditions (solving the desired problem). Following these steps, a post-processing stage is required, in which results have to be explored [37]. While these stages of the workflow can be straightforward, several internal/intermediate processes are considered in each step, amassing to over 20 specific python scripts that deal with each of the tasks required to run the model. The automated handling of these tasks is done with the use of Snakemake, a workflow management tool [38].

Depending on the configuration of the model, what commands are run and their interdependency, rules can be considered or ignored by snakemake. This configuration of the model/simulation is made on an specific file (config.yaml) that works as the main framework definition section, which enables which rules are to be taken into account as well as global parameters considered in the model: number of clusters/buses used to simplify the model, optimizing the network based costs and/or line's volume, emission limits, time resolution and others.

While the PyPSA-Earth model can run easily with a predefined configuration, it is a relatively general model, which needs to be enriched when "zooming" on a particular country. To optimize processing times between runs, a testing-version is set-up considering most of the default configurations, half a year period analysis, 10 clusters to aggregate information of the system and time steps of 8 hours.

After an adaptation process, a running version of the model was achieved for which the case-specific workflow for Bolivia is represented in **Figure. 1.** Additionally, the following changes represent the biggest modifications required to create an operative case for similar countries in the region:

- Specific weather data for South America was considered during the extraction process of online repositories (Copernicus Climate Data Store) [39].
- Landcover data retrieved from the predefined data bundle has been manually replaced by landcover maps for the South America (ProtectedPlanet) [40].
- Offshore wind turbines have not been taken into account in the model to facilitate the execution of the workflow during the creation of renewable availability profiles for offshore wind resources, because of Bolivia's condition as a landlocked country.

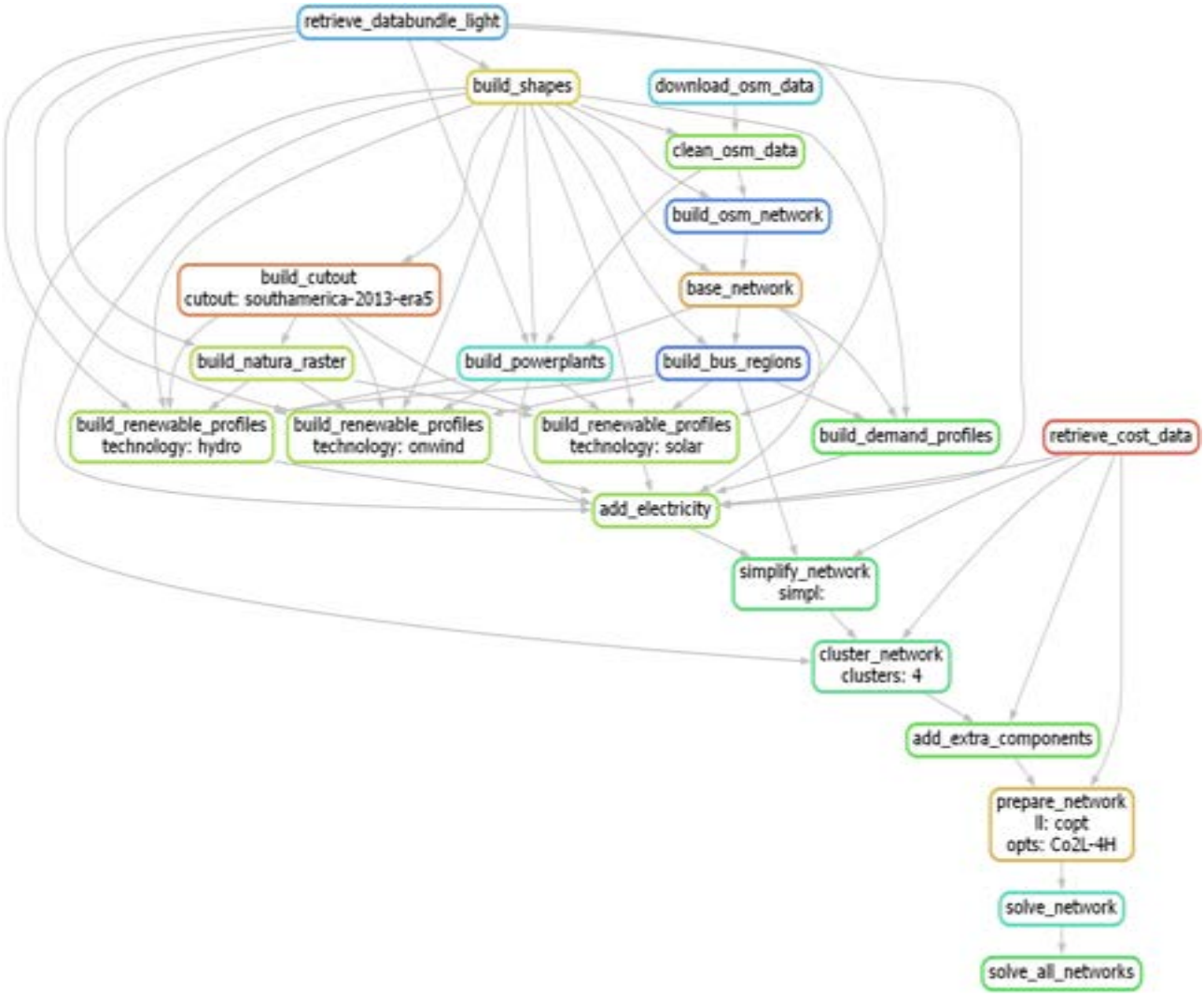

Figure. 1. Case-Specific workflow considered for Bolivia based on PyPSA-Earth.

For the sake of transparency and following the good practice of open-source modelling, a version control of the model can be found on a github repository: https://github.com/carlosfv92/pypsa-earth-BO, where relevant files, details of changes made on scripts and steps taken to run the Bolivian case are available.

2.3. Validation scenarios

Given the characteristics of the model, simulations use a predefined set of data sources to extract bundles of georeferenced information for a given country/region. Information extracted from these sources, combined with some precalculated datasets, allows the workflow to generate the databases required for creating the base network and optimizing its expansion. A list of the most relevant sources and the information they provide is available in **Table.1.**

Table. 1. Relevant data sources for the PyPSA-Earth workflow.

Source	Information extracted
Open Street Maps [41]	Network topology and components
Copernicus Climate Change Service [42]	Climate and weather data
HydroSHEDS [43]	Environmental variables
DRYAD [44]	Economic parameters
Shared Socioeconomic Pathways [45]	Global energy demand projections

After the model is setup for the Bolivian case a validation scenario is considered to study the outputs that can be obtained with the model, taken into account the following characteristics:

- Optimization of the system based on operational costs
- Operation of an entire trial year (2020)
- Time aggregation of 6 hours
- Non existing practical upper limit for emissions
- No restriction regarding the usage of emitting or renewable technologies
- Weather data based on historical information (year 2013)
- Default data sources from online repositories

To have a general grasp of the model's capabilities the analysis on results was focused on three aspects: network representation, powerplants installed capacity and energy demand coverage. For the first case, a major focus is given to how the model recognizes and processes available information regarding substations and transmission lines by modifying clustering values in the configuration and running different cases to compare them to with the existing Bolivian grid. For the second and third case, using a 4-node clustered version of the network, the optimized installed capacities and energy production are revised and compared to the existing operational conditions of the power system.

3. Results and discussion

3.1. Bolivia's transmission network simulation

To compare the capacities of the model to properly represent the Bolivian network in 2020, the model was run with different clustering objectives. Utilizing the plotting functions of networks generated with the PyPSA package and the intermediate results from the workflow, it's possible to explore different states and conditions of the system.

Some examples of what can be analysed are: The base network that the model creates after downloading and filtering default data, which assumes the totality of "usable" data, meaning properly georeferenced, defined and tagged elements (lines, substations and generators); Clustered networks created based on the defined number of buses that are given to simplify the network and the rest of characteristics of the model structure; The optimized network, which results from the final stage of solving the objective function of the system and can include additional or complementary elements in the buses, depending on the technical capacities of the system and their costs.

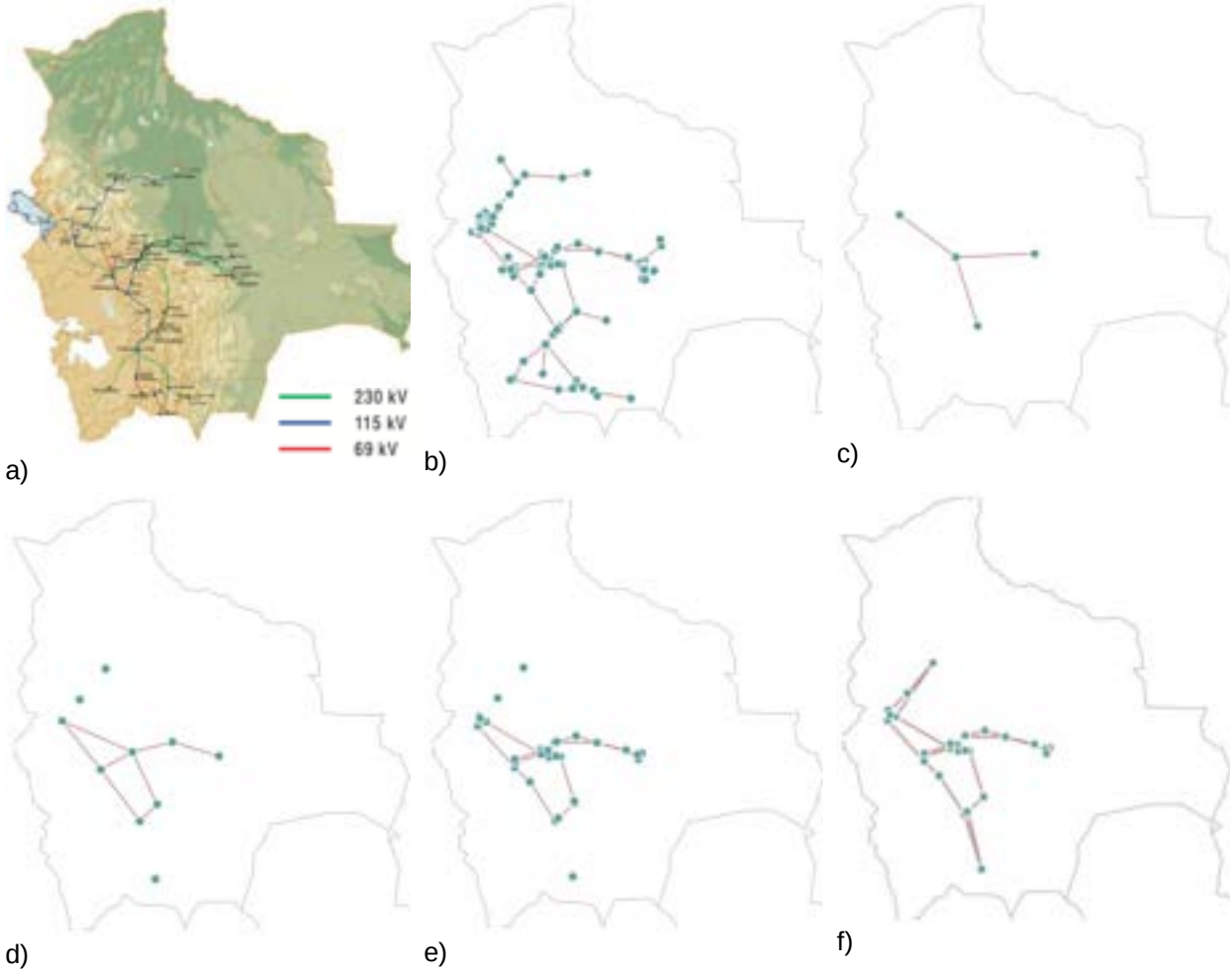

Figure. 2. Network recognition and clustering for Bolivia based on PyPSA-Earth: a) Bolivian transmission network in 2015 according to sectorial development plan *[6]*; b) Representation of the base network and lines pre-simplification and optimization; c) 4-node optimized version of the Bolivian network; d) 10-node optimized version of the Bolivian network; e) 37-node optimized version of the Bolivian network; f) 37-node optimized version of the Bolivian network with forced augmentation of powerlines.

A mix of these different cases, and the way they graphically represent the network, is available in **Figure. 2.** When comparing the real network in 2015 (a) with what is available from online repositories (b), it can be seen that most of the network's elements are considered and most of the relevant characteristics can be found in both cases like the connection rings in the south and central parts of the STI (Backbone Network System), as well as most of its 69, 115 and 230 kV lines. When the model is later clustered and optimized to a four node simplification (c), results are consistent with the 4-zone aggregation that the Bolivian network uses in their planning efforts: the southern area, central area, oriental area and northern area [29]. This representation, even though simplified, provides an overall good understanding of how the energy is used in the country and has already being used in previous studies focused on dispatch to simulate the Bolivian system [16].

After this minimal clustering, increasing numbers of nodes in the system are run (d), however, a limit was found at 37 nodes (e). This limit of nodes representation is derived by the simplification process of the available data into the base network used by PyPSA-Earth before the optimization, which aggregates the system considering only high-voltage components of the system (recognizing only 37 usable points to represent buses).

Because of this same reason, only lines above 30 kV are considered in the analysis, dropping several of the lower voltage lines, which leads to the assumption of several nodes as isolated from the rest of the grid. While this condition might seem problematic, it is important to take into account the scale for which PyPSA-Earth was created (regional and international analysis), therefore high voltage lines were given priority [22]. In this sense, this would represent a great opportunity for future work, given that if the scope/array of lines considered

is modified, this could help study and represent potential integration strategies for isolated communities, which is a major focus according to national policies [32].

Finally, an alternative way to impose the model to consider power flows between nodes can be achieved by forcing the optimization to include a minimum number of interconnections to allow a better representation (f). However, the forced creation of new networks would already represent predefined discrepancies that could affect the rest of the analysis, especially when comparing historical years.

To avoid the creation of isolated nodes and avoid forcing the model to create already existing lines, the 4-nodes representation is used for the rest of the analysis, and, even though this configuration provides a simplified version of the network, it can still be comparable to “existing” conditions.

3.2. Energy demand aggregation and simulated installed capacities

Results from the optimization of the system with the 4-node clustering configuration of the system, show an expected energy demand of 7,558.73 GWh for the entire year, distributing it as shown in **Figure. 3.** These results are in agreement with the total historical energy demand in Bolivia in 2020, according to the Bolivian authorities [29], presenting a discrepancy of 13.5%. Regarding the distribution of energy demands, the representation of the areas in the model is properly encapsulated, showing the same pattern of aggregation of energy consumption in the buses as the one provided in official documentation of the country, with the biggest outlier being the oriental area, having a deviation of 25.2% between the modelled data and the historical values.

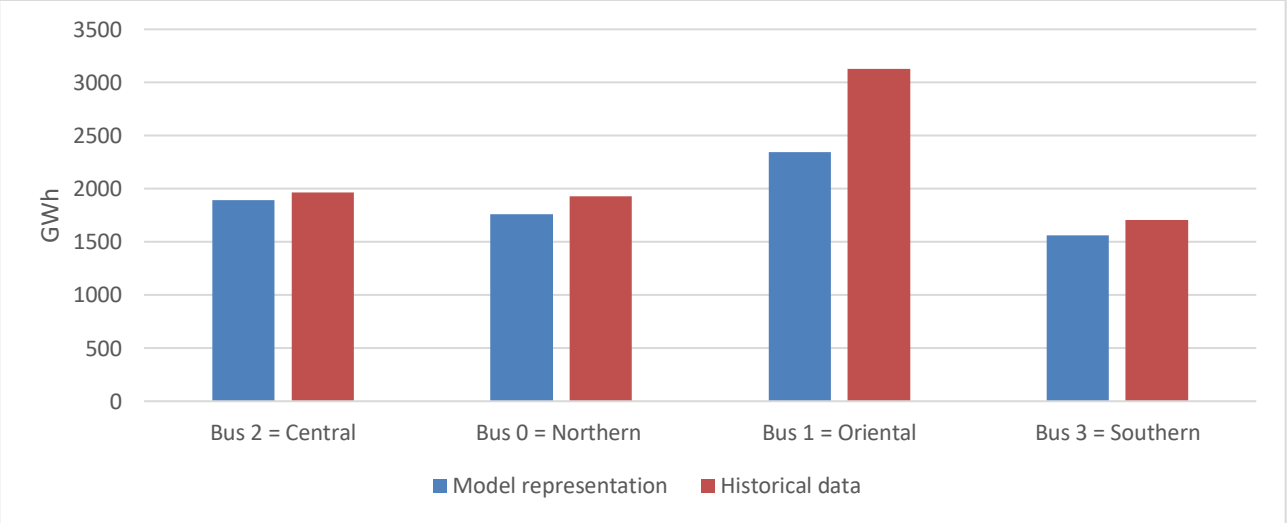

Figure. 3. Comparison of estimated energy demand by node in the model and registered energy demand in Bolivia for the year 2020.

These differences can be explained by the use of aggregated data at a global scale, which assume average growth trends in different scenarios but not at regional or country specific cases [45]. Bolivia in particular, seems a very atypical country due to a large period of sustained economic growth since 2010, where its GDP has had an average yearly value of over 3.5% [46]. This value is significantly larger than what was registered in the rest of the Latin-American region, with and average growth of lower than 2% in the last 10 years [47]. However, making data closer to historical values can be somewhat addressed in the model by adapting some sections in the configuration file. These changes should allow to increase the scaling factor of the referential time series data, by modifying data files used by the model or by including an additional section on the workflow for using country specific trends.

On the other hand, the analysis of installed capacity and its optimization shows structural discrepancies regarding the information used. **Table. 2.** Presents the details of the composition of the available powerplants according to the model and online data sources (Available capacity), the optimized values to cover the 2020 demands (Optimized capacity), as well as the actual data registered for 2020 in Bolivia (Real capacity):

Table. 2. Modelling results for the installed capacities in the Bolivian power system for 2020.

Carrier	Available capacity [MW]	Optimized capacity [MW]	Real capacity (2020) [MW]
OCGT	914.34	1099.40	1029.05
CCGT	-	-	1239.83
Oil	33.99	33.99	31.58
Onwind	25.52	25.52	27.00
Ror	344.00	344.00	-
Res	-	-	734.83
Solar	119.22	119.22	115.07
Biomass	-	-	51.25
Total	1437.07	1622.13	3228.61

Results regarding power generation show that the automated workflow using online data sources underestimates the existing capacities in the model in the year 2020. This is clear when comparing the total Available capacity with the total Real capacity, which is almost twice the value that online data sources take into account. Additionally, other relevant characteristics regarding how technologies are defined in the model can be found, compared to historical information from the national entities:

1) All the NG turbines are considered only as Open Cycle Gas Turbines (OCGT), which is not currently the case, given that several units and centrals are currently operating in the system with Combined Cycles (CCGT);
2) Hydropower in the Bolivian case is mostly composed by small reservoir units (Res), however, all available hydro units are recognized as run-off river powerplants (Ror) in PyPSA-Earth;
3) While not critically significant in terms of capacity, biomass powerplants (Biomass) are not being taken into account in the model, when in reality there is a small installed capacity available.

These discrepancies can be explained by two reasons. The first one being that, for older powerplants, information might not be fully or properly updated in the online data sources like Open Street Maps or PowePlantMatching. This is consistent with the fact that newer plants such as solar or onshore wind (Onwind) are accounted for, while large capacities in the other cases (thermal and hydro) are absent. The second reason would be the lack of proper tagging in the newer centrals, which have been created as expansions from other plants or where several units have been adapted or have grown over time.

Clear examples of these two cases are powerplants with two phases but the same name, like the hydro centrals San Jose 1 & San Jose 2, or the OCGT in Warnes, which were converted into CCGT with additional installed capacities [29]. Both of these issues can be sorted out by considering a country-specific set of data to replace the one generated by the model, however, while this functionality is currently available, there are some mismatching problems that have to be tuned to properly be used.

Finally, when analyzing the optimized capacities proposed by the model to cover power demands in the system, values are quite similar to the historical peak capacity covered in Bolivia, with a value of 1,565,80 MW [34]. This would mean that, while the mix of powerplants used by the model can vary between optimized and historical values, its capacity to optimize the system in order to cover future demands operates properly. The main reason for this variation is that the model does not have the same initial generation (legacy) capacities available in order to operate them, and the current over capacity installed in Bolivia [35], which was enforced mostly due to political reasons rather than technical requirements.

4. Conclusions and future work

Open-source tools are a valuable asset for countries and institutions immersed in energy system modelling. While this topic has been historically worked and developed by private entities and their own private tools, with their current growth, it can be expected that open-source models will eventually be able to replace licensed/black-box software used in energy system modelling.

A key example of this type of tools is PyPSA-Earth, a modelling tool that was developed within an open and transparent framework that allow its developers (and users) to generate simplified representation of the power system network of regions or countries in the world. Some of the novelties of this modelling tool are the integration of georeferenced information into the power flow analysis, the use of predefined online data sources, an optimization approach linked to the operation of the power system and the use of a detailed time resolution.

In this sense, the model was adapted to run the country-specific case of Bolivia for the year 2020 and it outputs were later compared to historical data to assess the capabilities of the model. Results show a high potential for its implementation in the future given that its scope and results are complementary to already developed tools. This would help filling gaps in the modelling requirements and capabilities for a better comprehension of the country's power system.

However, it is also important to address that the work done here is an introductory process to study the capabilities and conditions of the tool in order to assess its applicability in developing countries, with Bolivia being only a case study. Aside of the previous results obtained, several additional, configurations and outputs should also be explored in future work. These aspects are mostly linked to fine tuning of the model in order to allow the change of certain default data files to local-based information in order to improve the capabilities of the tool to represent country-specific cases in a manner closer to reality.

In parallel, particularities of the model's capabilities found in this work should be followed through and developed. For instance, adapting the model to include and focus on additional high voltage lines (voltage levels of 69 and 115 kV for example), would represent a relevant change in the tool and a potential big contribution to the PyPSA-Earth model. Doing this would allow the model to better represent smaller scale systems, as it is not possible to make the assumption that the grids behave or have the same topology as the ones in developed countries

Another example would be to update or further develop the process and adaptations required in the model to use customized data sets of information regarding generators and alternative energy demand projections. Both of these would allow the model to increase the flexibility of PyPSA-Earth by improving its capacities to work in countries with less reliable data in the online sources.

Finally, another potential aspect to exploit in future work would be to develop feedback loop processes between modelling tools developers, users with detailed information and online data providers. This would allow to improve capacities on all fronts at the same time as promoting the open-source philosophy, enhance contribution among researchers and transparency between users of the model and its results.

Acknowledgments

The Belgian cooperation ARES is acknowledged for the financial support for this work, in the framework of the PRD Project: Tailored energy system models for energy planning in Bolivia.

Acronyms

SDDP	Stochastic Dual Dynamic Programming
HOMER	Hybrid Optimization of Multiple Energy Resources
OnSSET	Open Source Spatial Electrification Tool
RAMP	Remote Areas Multi energy load Profiles generator
OSeMOSYS	Open Source energy MOdelling SYStem
PyPSA	Python for Power System Analysis
NG	Natural Gas
ENDE	Empresa Nacional De Electricidad (National Electricity Company)
CNDC	Comite Nacional de Despacho de Carga (National Committee for Charge Dispatch)
AETN	Autoridad de Fiscalización de Electricidad y Tecnología Nuclear (Supervision Authority for Electricity and Nuclear Technology)
VMEEA	Viceministerio de Electricidad y Energias Alternativas (Vice Ministry of Electricity and Alternative Energies)
SIN	Sistema Interconectado Nacional (National Interconnected System)
STI	Sistema Troncal de Interconexion (Backbone Network System)
OCGT	Open Cycle Gas Turbines
CCGT	Combined Cycle Gas Turbines
Ror	Run-off river powerplants
Res	Reservoir
Onwind	Onshore wind

References

[1] Pandey R., Energy policy modelling: agenda for developing countries. Energy Policy, vol. 30, no. 2, pp. 97–106, Jan. 2002, doi: 10.1016/S0301-4215(01)00062-3.
[2] Bhattacharyya S. C., Timilsina G. R., A review of energy system models. International Journal of Energy Sector Management, vol. 4, no. 4, pp. 494–518, Nov. 2010, doi: 10.1108/17506221011092742.
[3] Urban F., Benders R. M. J., and H. C. Moll, “Modelling energy systems for developing countries,” Energy Policy, 2007.
[4] Pfenninger S., et al., Opening the black box of energy modelling: Strategies and lessons learned. Energy Strategy Reviews, vol. 19, pp. 63–71, Jan. 2018, doi: 10.1016/j.esr.2017.12.002.
[5] Balza L. H., Espinasa R., Serebrisky T., Energy Needs in Latin America and the Caribbean to 2040.
[6] Viceministerio de Electricidad y Energías Alternativas, Plan Eléctrico del Estado Plurinacional de Bolivia 2025. 2014.
[7] Ministerio de Hidrocarburos y Energia, Plan Optimo de Expansion del Sistema Interconectado Nacional. 2012.
[8] Philpott A., On models for estimating the effect on prices of CO2 charges. 2004.
[9] Software | PSR – Energy Consulting and Analytics, Software | PSR – Energy Consulting and Analytics, Available at: https://www.psr-inc.com/softwares-en/ (accessed May 10, 2023).
[10] PowerFactory - DIgSILENT. Available at: https://www.digsilent.de/en/powerfactory.html (accessed May 10, 2023).
[11] Olasunkanmi O. G., Deng Z., Todeschini G., Load Flow Analysis of the Nigerian Transmission Grid Using DIgSILENT PowerFactory, 56th International Universities Power Engineering Conference (UPEC), Middlesbrough, United Kingdom: IEEE, Aug. 2021, pp. 1–6. doi: 10.1109/UPEC50034.2021.9548253.
[12] HOMER - Hybrid Renewable and Distributed Generation System Design Software. Available at: https://www.homerenergy.com/ (accessed May 10, 2023).
[13] Mahmud N., Hassan A., Rahman M. S., Modelling and cost analysis of hybrid energy system for St. Martin Island using HOMER, International Conference on Informatics, Electronics and Vision (ICIEV), Dhaka, Bangladesh: IEEE, May 2013, pp. 1–6. doi: 10.1109/ICIEV.2013.6572678.
[14] IRENA, Summary Report - IRENA Regional Workshop on Long-term Energy Planning - Buenos Aires 2017. 2017.
[15] Oberle S., Elsland R., Are open access models able to assess today’s energy scenarios?. Energy Strategy Reviews, vol. 26, p. 100396, Nov. 2019, doi: 10.1016/j.esr.2019.100396.
[16] Navia M., Orellana R., Zaráte S., Villazón M., Balderrama S., Quoilin S., Energy Transition Planning with High Penetration of Variable Renewable Energy in Developing Countries: The Case of the Bolivian Interconnected Power System, Energies, vol. 15, no. 3, p. 968, Jan. 2022, doi: 10.3390/en15030968.
[17] Peña Balderrama J. G., et al., Incorporating high-resolution demand and techno-economic optimization to evaluate micro-grids into the Open Source Spatial Electrification Tool (OnSSET). Energy for Sustainable Development, vol. 56, pp. 98–118, Jun. 2020, doi: 10.1016/j.esd.2020.02.009.
[18] Sanchez C., et al., The Energy Sufficiency Concept and Its Impact on Energy Demand Estimation in Rural Communities from Developing Countries, 2022.
[19] Balderrama S., Lombardi F., Riva F., Canedo W., Colombo E., Quoilin S., A two-stage linear programming optimization framework for isolated hybrid microgrids in a rural context: The case study of the ‘El Espino’ community. Energy, vol. 188, p. 116073, Dec. 2019, doi: 10.1016/j.energy.2019.116073.
[20] Fernandez Vazquez C. A. A., Brecha R. J., Fernandez Fuentes M. H., Analyzing carbon emissions policies for the Bolivian electric sector. Renewable and Sustainable Energy Transition, vol. 2, p. 100017, Aug. 2022, doi: 10.1016/j.rset.2022.100017.
[21] Parzen M., et al., PyPSA-Earth. A New Global Open Energy System Optimization Model Demonstrated in Africa. arXiv, Sep. 10, 2022. Accessed: Mar. 14, 2023. [Online]. Available: http://arxiv.org/abs/2209.04663
[22] Kirli D., et al., PyPSA meets Africa: Developing an open source electricity network model of the African continent, in 2021 IEEE AFRICON, Arusha, Tanzania, United Republic of: IEEE, Sep. 2021, pp. 1–6. doi: 10.1109/AFRICON51333.2021.9570911.
[23] Hörsch J., Hofmann F., Schlachtberger D., Brown T., PyPSA-Eur: An open optimisation model of the European transmission system. Energy Strategy Reviews, vol. 22, pp. 207–215, Nov. 2018, doi: 10.1016/j.esr.2018.08.012.
[24] Brown T., Hörsch J., Schlachtberger D., PyPSA: Python for Power System Analysis. JORS, vol. 6, no. 1, p. 4, Jan. 2018, doi: 10.5334/jors.188.

[25] pypsa-meets-earth/pypsa-earth: PyPSA-Earth: An Python-based Open Optimisation Model of the Earth Energy System. Available at: https://github.com/pypsa-meets-earth/pypsa-earth (accessed May 10, 2023).
[26] Bolivia: Ley de Electricidad, 21 de diciembre de 1994. 1994.
[27] Ministerio de Hidrocarburos y Energia, Balance Energetico Nacional 2006-2020. 2022.
[28] E. M. Ayma, Bolivia: Decreto Supremo Nº 29644, 16 de julio de 2008. 2008.
[29] CNDC, Memoria Anual 2020. 2021.
[30] Ministerio de Hidrocarburos y Energia, Política de Energías Alternativas para el Sector Eléctrico en el Estado Plurinacional de Bolivia. 2012.
[31] Ministerio de Planificacion del Desarrollo, Plan de Desarrollo Economico y Social 2021-2025. 2022.
[32] Ministerio de Medio Ambiente y Aguas, Nationally Determined Contribution (NDC) of the Plurinational State Of Bolivia. 2022.
[33] AETN, Anuario estadistico 2020. 2021.
[34] AETN, Memoria anual 2020. 2021.
[35] ENDE Transmision, Memoria Anual 2021. 2022.
[36] "COMITE NACIONAL DE DESPACHO DE CARGA - CNDC. Available at: https://www.cndc.bo/agentes/generacion.php (accessed Mar. 19, 2023).
[37] The structure — PyPSA-Earth 0.1.0 documentation. Available at: https://pypsa-earth.readthedocs.io/en/latest/structure.html (accessed Mar. 16, 2023).
[38] Mölder F., et al., Sustainable data analysis with Snakemake, F1000Res, vol. 10, p. 33, Jan. 2021, doi: 10.12688/f1000research.29032.1.
[39] Climate Data Store. Available at: https://cds.climate.copernicus.eu/#!/home (accessed Mar. 17, 2023).
[40] Protected Areas (WDPA), Protected Planet. Available at: https://www.protectedplanet.net/en/thematic-areas/wdpa?tab=WDPA (accessed Mar. 17, 2023).
[41] OpenStreetMap, OpenStreetMap. Available at: https://www.openstreetmap.org/about (accessed Mar. 18, 2023).
[42] Hersbach H., et al., The ERA5 global reanalysis. Q.J.R. Meteorol. Soc., vol. 146, no. 730, pp. 1999–2049, Jul. 2020, doi: 10.1002/qj.3803.
[43] HydroBASINS. Available at: https://www.hydrosheds.org/products/hydrobasins (accessed Mar. 18, 2023).
[44] Kummu M., Taka M., Guillaume J. H. A., Gridded global datasets for Gross Domestic Product and Human Development Index over 1990–2015. Sci Data, vol. 5, no. 1, p. 180004, Feb. 2018, doi: 10.1038/sdata.2018.4.
[45] Riahi K., et al., The Shared Socioeconomic Pathways and their energy, land use, and greenhouse gas emissions implications: An overview. Global Environmental Change, vol. 42, pp. 153–168, Jan. 2017, doi: 10.1016/j.gloenvcha.2016.05.009.
[46] Crecimiento del PIB (% anual) - Bolivia | Data. Available at: https://datos.bancomundial.org/indicador/NY.GDP.MKTP.KD.ZG?end=2021&locations=BO&start=2010 (accessed Mar. 21, 2023).
[47] Crecimiento del PIB (% anual) - Latin America & Caribbean | Data. Available at: https://datos.bancomundial.org/indicator/NY.GDP.MKTP.KD.ZG?end=2021&locations=ZJ&start=2010 (accessed Mar. 21, 2023).

PROCEEDINGS OF ECOS 2023 - THE 36TH INTERNATIONAL CONFERENCE ON
EFFICIENCY, **C**OST, **O**PTIMIZATION, **S**IMULATION AND ENVIRONMENTAL IMPACT OF ENERGY SYSTEMS
25-30 JUNE 2023, LAS PALMAS DE GRAN CANARIA, SPAIN

The impact of spatial resolution on optimal renewable energy portfolios

Aina Maimó-Far[a], Victor Homar[a]

[a] Universitat de les Illes Balears, Palma, Spain, aina.maimo@uib.cat, CA

Abstract:

Efforts in the energy planning department are required to achieve the target levels of renewable energy penetration and electricity demand in the European Union. Mean-variance analysis is commonly used to identify the optimal deployment of variable renewable energy sources. By using it, we can determine the most effective ways to increase renewable energy penetration and minimise supply risks through varying spatial and technological deployments. In this study, we investigate the effectiveness of optimising capacities at the scale of climate data grid points, rather than administrative regions, which is a common approach due to data availability and computation costs. We find that a finer description of climate resources and variable renewable energy capacity factors results in a better exploitation of complementarities and offers increased degrees of freedom in optimisation. Our analysis reveals that better describing local conditions results in two advantages over lower resolution approaches: higher average capacity factors and generation combinations with lower covariances. Additionally, we find that higher resolution approaches significantly reduce variability in daily and annual climate frequencies in renewable generation under the optimal scenario. These results highlight the importance of accounting for detailed climate information when identifying optimal renewable deployment scenarios and can provide valuable support for stakeholders and policy makers in making sustainable commitments.

Keywords:

Climate energy assessment model; High-resolution energy modeling; Mean-variance analysis; Renewable energy system planning; Spatial resolution.

1. Introduction

The shift towards low-carbon energy systems is a current and future challenge, with the EU setting goals for decarbonization by 2050 [1]. In turn, each country must establish specific measures to achieve these goals. In Spain, there are multidisciplinary plans in place to mitigate climate change [2] and promote renewable energy [3], which emphasize the need for research and the installation of new renewable energy sources, while also recognizing the challenges associated with integrating them into the electricity system.

Solar photovoltaic (PV) and wind energy are the main variable renewable energy (VRE) sources driving the transition towards a highly renewable future, aiming to cover half of the Spanish energy demand due to their improving technology and decreasing costs [4,5]. Spain has seen a significant increase in the installed capacity (IC) of these sources in recent years, with a 156% increase in PV and a 17% increase in wind IC from the end of 2018 to the end of 2020, compared to only a 1% increase in the previous five years for both technologies [6–8]. By the year 2020, the two sources combined reached a mean penetration level of 30%, and installations are planned to grow even further.

While solar radiation and wind drive the energy generation by PV cells and wind turbines, several factors other than the generation potential are involved in planning these installations, including capital and operation costs. Classical approximations follow atlas-derived average capacity factors to estimate the levelized costs of energy for a given technology and location. However, these factors fail to account for the risk posed by the intermittent nature of the resource and the complementarity between different components of the system. This consideration should not be ignored, as taking advantage of the complementarity of the system is crucial in order to minimize electricity supply risks and meet the demand [9, 10]

To ensure renewable energy systems meet certain requirements, optimization methods are commonly used, but the many factors that can vary from one optimization to another emphasize the importance of configuration in planning renewable energy deployment [11] These factors can include constraints, time span, optimization method, and region. In this article, we apply a common approach to optimize the deployment of VRE sources by simultaneously maximizing the mean and minimizing the variance through modifications to the spatial distribution of IC for each VRE source. This straightforward method helps us identify the scenarios with the lowest variance, which serves as a proxy for supply risk, for a given level of penetration and provides optimal scenarios for multiple penetration levels.

The way generation and demand data are processed and represented is key when applying mean-variance analysis or similar portfolio-based methods. Some studies (e.g. [12, 13]) use regionally aggregated electricity and climatic data in conjunction with portfolio theory to optimize the deployment of VRE across countries or large regions, by using various metrics. However, these results only provide information about optimal deployment for very large areas and do not offer guidance on specific installation locations within those areas. Another approach [14] consists on fixing the total regional IC through an optimization, and then identifying possible deployment locations within each region. This specific allocation of VRE sources uses criteria such as climatic potential and socioeconomic constraints. However, this type of methods could follow initial large-scale distributions that are made under possibly non-representative average conditions.

The process of aggregating different renewable energy generation sites and technologies can lead to a smoothing effect on the generation curve. However, there are alternative approaches to optimization that do not rely on this aggregation, such as using grid-based models or considering existing generation farms as installation points [15, 16]. Despite the more precise description of the system of these methods, they are quite uncommon in the literature [17]. Additionally, obtaining high-resolution data on electricity generation and demand can be challenging, particularly at very high resolutions where the network topology becomes relevant. Nevertheless, the resolution used for optimization is crucial, especially when dealing with highly heterogeneous regions [18, 19].

There is limited research on how different spatial aggregation approaches impact the optimization of renewable energy deployment. Previous studies have looked at a specific form of aggregation, but have not specifically investigated the effects of changes in resolution on the optimal solutions. More extensive research [17] has been done on optimization models, methodologies, and constraints, but there are still no clear answers to the challenges that arise with different levels of resolution.

This article builds upon previous research [20] that investigated the impact of spatial granularity or resolution on renewable energy deployment optimization. However, instead of using administrative regions, this study explores the effects of arbitrary divisions of space on the optimization results, representative of changing resolution. Through a thorough analysis of experiments at varying levels of resolution, we observe the mechanisms that occur as resolution increases and interpret them in relation to the simplifications and underlying drivers of the renewable energy system.

This article is structured as follows: section 2. gives an overview of the methods and data used, section 3. shows and discusses the main results, and finally section 4. summarizes the main conclusions derived from this study.

2. Methods and data

When it comes to implementing renewable energy sources while guaranteeing a stable supply to the network, the challenge can be reduced to a bi-objective optimization problem. This problem involves maximizing the penetration of renewable sources while minimizing the risks of supply failure. To solve this problem, a mean-variance optimization scheme can be used, where the risk is considered as the square root of variance. The resulting set of optimal solutions defines a Pareto front, which represents the minimum variance/risk squared for a fixed mean. In order to optimize renewable energy deployment, the decision variable is the vector of installed capacities of PV and wind at each location, and each location is associated with a specific capacity factor for renewable energy generation. The capacity factor quantifies the percentage of the potential maximum technical production that is actually generated over a period of time. The national demand is also considered, as the primary objective is to determine the optimal generation curve that best matches the demand and its fluctuations, rather than targeting an average specific level of generation.

To optimize the deployment of renewable energy sources, the ratio of national hourly VRE generation to national hourly demand is defined as hourly. However, the model does not constrain the adequacy between generation and demand. This is because the purpose of the mean-variance analysis is to prevent the need to model non-VRE producers that would also contribute to meeting the demand. The mean penetration is then defined as the time average of the hourly penetration series, and risk is defined as its standard deviation. The only constraint set to the capacities is to be non-negative.

We use the e4clim model [21] as our tool, with the consideration of predictable and unpredictable risk [22]. We use ERA5 [23] as the climatic data source, also functioning as out highest resolution grid, and include a nation-wide calibration of generation and demand with electricity data from Red Eléctrica de España (REE). ERA5 has an effective spatial resolution of around 25 km at the latitudes of mainland Spain, with an hourly time step (see Fig. 1a for a reference on the grid and the administrative regions considered). We perform this experiment over a 7-year period with overlapping electricity and climate data, ranging from the years 2014 to 2020. We take the electricity mix at the end of 2020 as a reference, establishing a reference mean penetration of 30%.

We conducted a series of experiments to investigate how the spatial resolution affects the identification of optimal scenarios for renewable energy deployment. Instead of using traditional administrative regions, we created evenly divided artificial regions across the domain, ranging from the full climatic grid resolution to just four total regions. It should be noted that by considering the regions approach, we assume each of them to be homogeneous and capacity to be evenly distributed. We gradually decrease the resolution of the model by aggregating grid points into larger regions (averaging capacity factors and summing installed capacities) and analyze the impact on optimization results. We then compute a Pareto front for each level of resolution. As the resolution of the model increases, so does the ratio of penetration-risk in the system, resulting in steeper Pareto front slopes (Fig. 1b for the fronts using the whole grid and the administrative regions).

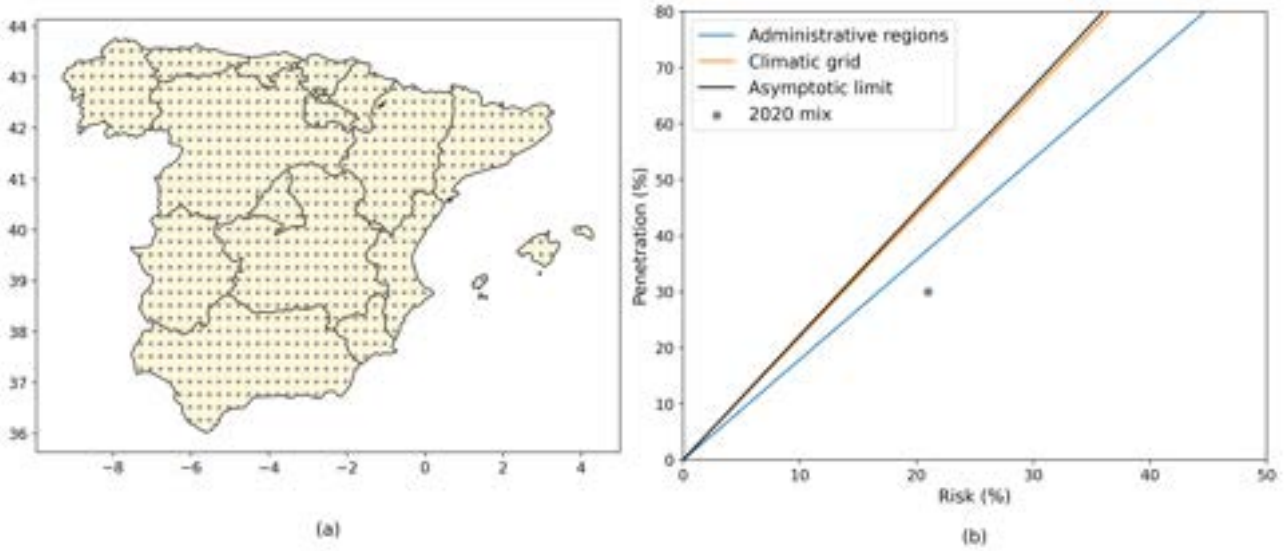

Figure 1: Reference for the administrative regions and full climatic grid approaches in the map (a) and penetration-risk diagram (b). The map (a) shows the full climatic grid over the administrative regions over which they are commonly aggregated. The penetration-risk diagram (b) presents the Pareto fronts for the approaches with administrative regions (blue) and the climatic grid (orange), and for the asymptotic Pareto front (black). The grey dot indicates the location of the 2020 mix.

The Pareto front for each of these experiments is linear in the mean penetration-risk space (fig. 1b). For an arbitrary fixed level of penetration, a minimization of the risk returns the associated capacity distributions for PV and wind. Changing the level of penetration simply introduces a scaling factor to these distributions, which remain the same in relative terms. Therefore, the slope of the Pareto front is constant for each specific resolution, and defines what we call the penetration-risk ratio (PRR).

3. Results and discussion

On a first analysis, we observe that as the resolution of the model increases, there is a corresponding increase in the PRR, with the highest ratio marked by the scenario that uses the full climatic grid. Since the system is powered by climate resources, the extent to which this ratio can increase is limited by the degree to which these resources match the demand. This bounded, increasing behavior indicates the existence of an asymptotic Pareto front, which represents an intrinsic property of the climate driving the system. In this case, ”intrinsic” implies that it is not influenced by the resolution used in the optimization, but it may be affected by the resolution of the climate model used, or the nature of the climate and electricity data that was introduced into the model.

The evolution of the PRR (Fig. 2a) shows a very steep increase at low resolutions, implying that small increments in resolution bring large improvements to the optimization, as the precision in the description of climatic features drastically increases. Once a certain level of resolution is reached, virtually no information is added with increasing resolution because the large climatic modes are already mostly represented, and therefore the PRR practically stabilizes. This implies that the majority of information added at such high resolutions is either redundant, insignificant in relation to the big signals already described, or lacks further resolution from the climatic data. In order to include an analytical dimension that allows us to diagnose the asymptotic behavior of the PRR, we propose a parameterized curve to fit:

$$\mathrm{PRR}(N) = a + \frac{b}{N - c} \tag{1}$$

where N is the number of spatial divisions over the domain, and representative of the resolution, given that the domain remains unchanged. *a*, *b*, and *c* are parameters to be fitted by the known values of PRR and N at varying resolutions. By definition, the asymptotic Pareto front has the largest PRR possible (as $N \to \infty$), which takes the value of $a = 2.22$, and would return lower risk for any level of penetration (or higher penetration for any level of risk) than any other possible configuration with a lower resolution (see Fig. 1a). This value describes the best optimal configuration that could exist under the climate conditions as described by ERA5, but changes in the climatic resolution would not necessarily identify the exact same value.

However, we are not interested only in the asymptotic behavior of the PRR, but in the specific impacts on the optimization of a changing resolution. A first approach is to analyze the total installed capacity for each technology at the 30% penetration level and how they change with resolution (Fig. 2b). At low resolutions, high amounts of capacity are needed to reach a fixed level of penetration, even though they produce higher levels of risk. In a directly opposite behavior to the PRR, the capacity necessary to reach a fixed level of penetration decreases with increasing resolution, reaching a similarly asymptote-like behavior on the lowest necessary capacity to install. This behavior stems from the underlying assumption of homogeneity and even installation that is made in the consideration of regions. Since no additional information is given on the specific locations of installations, it is likely that they fall on suboptimal regions within the area, since the optimization used regional divisions. Through this effect, it is also illustrated that considering low resolution aggregated regions can in turn lead to an overestimation of the necessary capacity by nearly 100%, as the decisions on capacity installation are not accounting for the actual climatic potential.

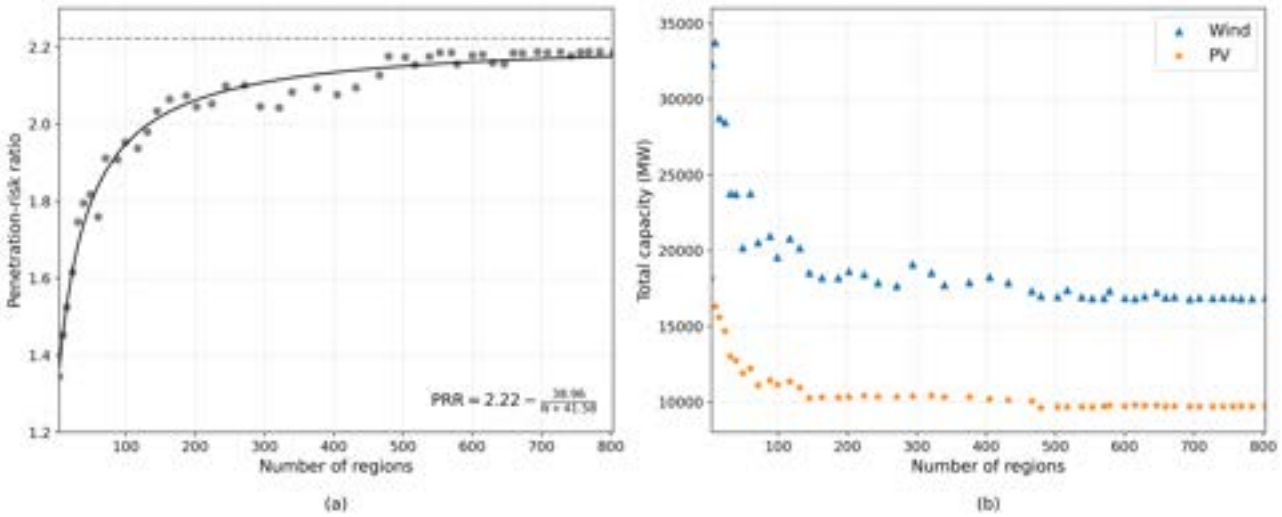

Figure 2: Change with the number of regions of the penetration-risk ratio (a) and total installed capacity per technology at the 30% mean penetration level (b). In (a), the penetration-risk ratio for each number of regions is indicated by a grey dot, the fitting of the points is shown by the solid black line, with the dashed grey line indicating the asymptotic value. The equation for the black line is annotated in the graph, with N the number of regions. For the evolution of capacity (b), the blue triangles indicate the wind capacity, and the orange stars represent the PV installed capacity.

The overestimation of the total installed capacity is an issue that appears in the general vision of the results and that can stem from different causes linked to resolution. In addition to the impacts on total required installed capacity, resolution may also play a role on the spatial distribution of optimal scenarios, which would reveal a significant degrading effect of the regional averaging of the climatic source on the optimization results. An effective method to analyze the spatial dispersion of these distributions is to count the regions with installed capacity exceeding a certain threshold.

Upon analyzing the number of regions with installed capacity exceeding 100 MW at the 30% penetration level, we identify two differentiated behaviors for PV and wind. PV installations (Fig. 3a) are concentrated in a single region across most resolutions, showing no apparent dependence on resolution tendency. This behavior responds to the cyclic nature of PV, which presents little variability across the domain, and is therefore not strongly affected by the averaging process. Indeed, the high covariant component observed in all PV production series within the domain indicates a limited potential for favorable generation complementarities.

The results for wind capacity (Fig. 3b) show a different pattern compared to PV. With increasing resolution, there is a clear tendency for the distribution of installed capacity to spread across a greater number of regions. This suggests that a higher resolution allows for the emergence of more favorable low-covariance combinations

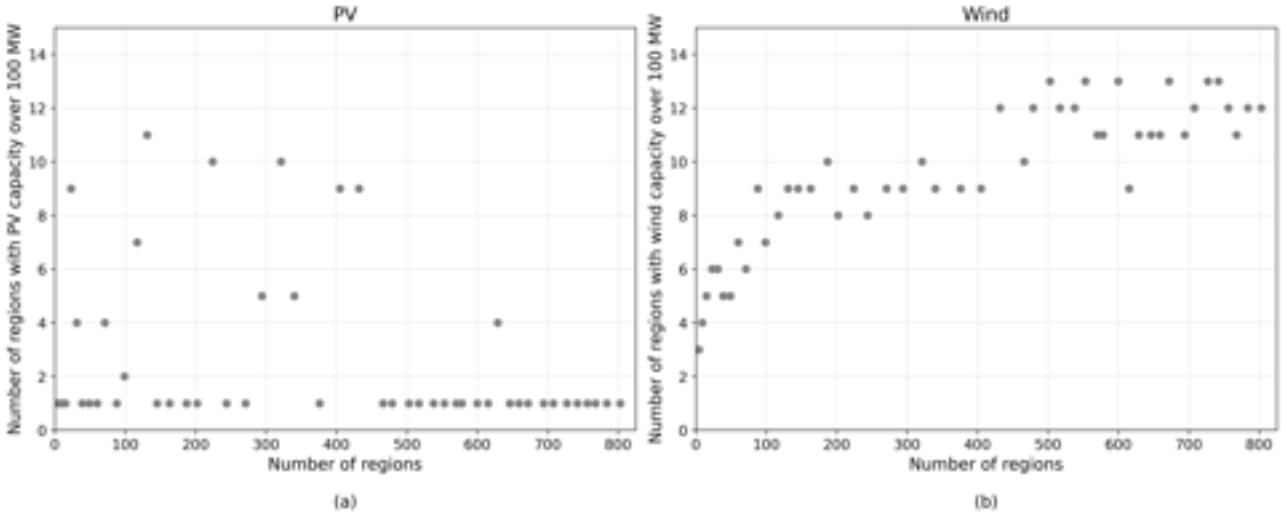

Figure 3: Number of regions exceeding 100MW of installed capacity at a penetration level of 30% at each level of resolution for PV (a) and wind (b).

of wind capacity across different locations. In fact, whereas PV is mostly covariant within the domain, wind resource presents higher variability, and an increased chance for low covariances or even anticovariances to occur is higher. Therefore, using a high enough resolution to capture the potential of favorable low-covariance combinations is key to achieving the maximum actual potential for renewable generation of any given domain.

Thus far, two conclusions that complement the asymptotic PRR results have been drawn. Firstly, the capacity required to achieve a specific level of penetration decreases with resolution, along with the associated risk, due to the better representation of the climatic resource. Secondly, for PV, the capacity tends to be concentrated in a single region, regardless of the modeling resolution, whereas for wind, it spreads across more regions as the resolution increases. These two effects derive from the cyclic quality of PV (following similar patterns all over the domain), and the non-cyclic variable nature of wind.

Therefore, in order to explore the impact of resolution on optimal renewable energy deployment scenarios, the spatial distribution of three resolution levels - low, middle, high - for the 30% penetration target is examined in detail (Fig. 4 a-b, c-d, and e-f, respectively).

The distribution of installed capacity for PV is concentrated in the same region across all three resolution levels, as previously discussed. This suggests that the points that determined the selection of regions in the middle and low resolution scenarios were primarily those located in the region identified by the high resolution scenario. Due to the limited variability of PV, the averaging process does not degrade the results. Additionally, higher resolutions require less capacity in a given region because the optimization more accurately identifies the area with the highest capacity factors and lowest variability, and thus exploits the available climate resources more effectively.

The behavior of wind capacity exhibits two distinct patterns. In the western half of the domain, wind installations behave as PV series in the sense that the entire region follows a similar pattern driven by a substantial influence of sustained strong Atlantic winds. This results in the high resolution wind installations contained within the regions of the middle and low resolution optimal scenarios. On the other side, the eastern half of the domain presents different response. Despite some strong northern winds in the islands and some mountain-influenced winds in the northeast regions, the eastern side of the domain presents very variable patterns, which may not arise at the low and middle resolutions. This is coherent with the more variable Mediterranean climate.

Despite not presenting any installed capacity at the low resolution, the southeastern quadrants of the wind capacity distributions have a region contained in it entering the mix at the middle resolution, and then again presenting zero installed capacity at the high resolution. The capacity allocated at low resolution in the northeast quadrant of the domain, is reallocated differently in the middle and high resolution resulting scenarios. This effect arises from the unique characteristics of each high resolution region being smoothed out when resolution is lowered. The high resolution enables greater detail in the spatial characterization of the climatic resource, allowing previously obscured areas to become visible in the optimal mix. Conversely, areas that were included in the optimal mix at the middle resolution due to the mean, were no longer competitive at the high resolution. The cause behind this is the reduction in region size associated to the increase in resolution. This effect allows high potential areas to stand out without the smoothing effect of the mean, and contrarily considers regions that may stand out only in terms of the mean but that may not contain any smaller areas

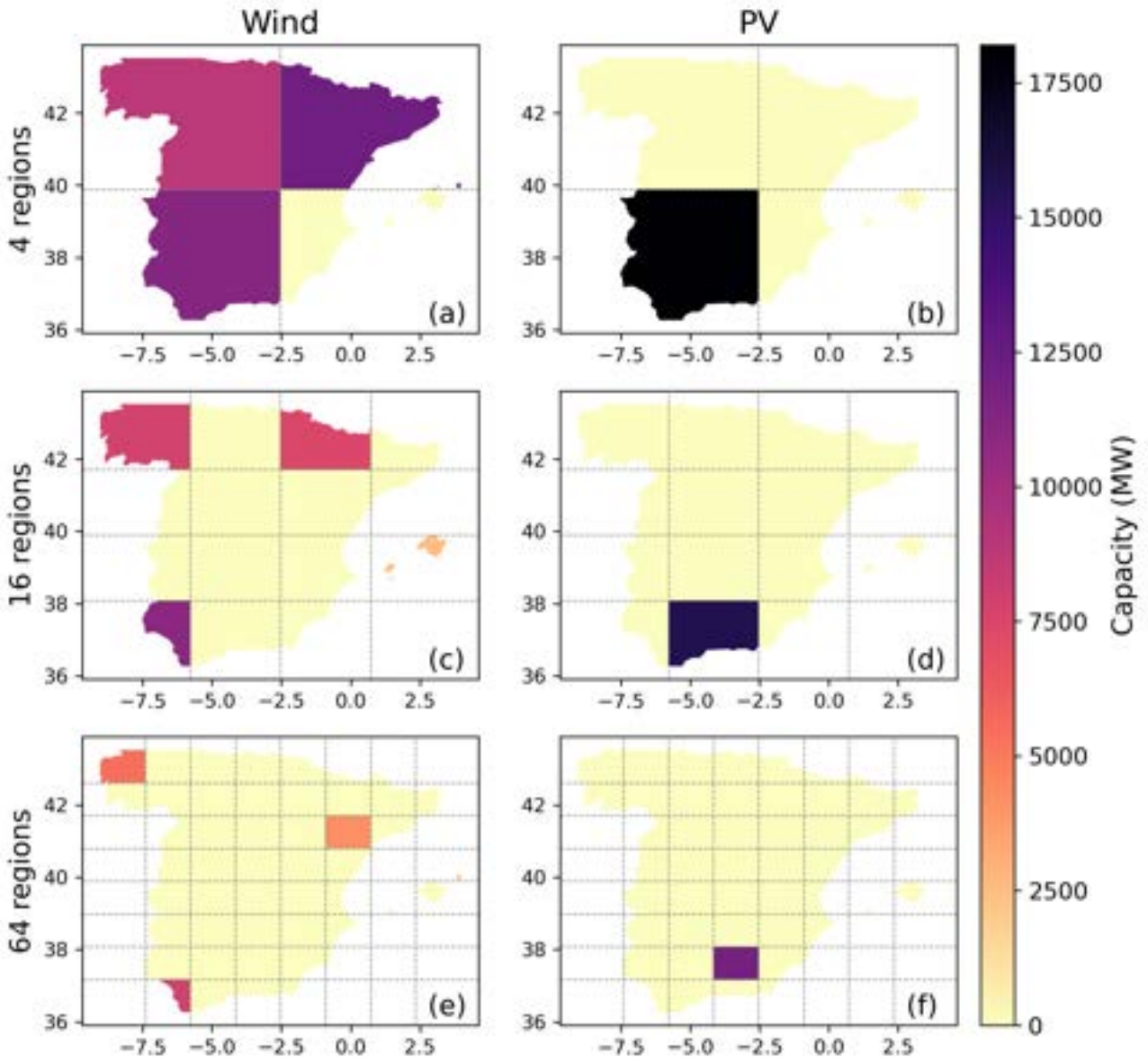

Figure 4: Optimal distribution of installed capacity for wind (a,c,e) and PV (b,d,f) for the configurations with 4 (a, b), 16 (c, d), and 64 (e, f) regions at the 30% penetration level.

of particular potential. This proves key, especially considering that any renewable installation will exploit the corresponding local climatic resource, and not some averaged value.

4. Summary and conclusions

In this article, we determined and analyzed the impacts of resolution on the results of optimization models for VRE deployment. By simple asymptotic reasoning, the absolute limit in penetration-risk ratio for a certain spatio-temporal distribution of climate resource and electricity demand is derived and represented by the asymptotic Pareto front of the system.

The usable resolutions in renewable energy deployment optimization models are primarily bounded by climate data resolution. The intrinsic limit of the attainable penetration-risk ratio can be represented by the asymptotic Pareto front, which provides an estimate of the upper limit in terms of renewable penetration-risk payoff given the available resource. The illustrative example of Spain renders a penetration-risk maximum payoff of 2.22, and therefore the Spanish VRE system should assume a minimum risk threshold of 45% in order to achieve 100% penetration. This front is independent of the resolution used for the optimization, but not necessarily independent of the climate data and its resolution. We find that the frontier reached when using the full climate grid optimization closely approximates the asymptotic behavior of increasing resolution, with minimal differences in penetration and/or risk under 1% at any given level.

Both PV and wind technologies exhibit similar patterns in terms of the total installed capacity, and with in-

creases in penetration, the necessary capacity decreases while also lowering the risk, as a result of more accurate descriptions of the real climatic reality. However, they show different behaviors when the actual distributions of capacity are considered. PV tends to have all its capacity concentrated in one region. By its nature, PV follows a similar pattern over the whole domain (i.e., the predictable daily and seasonal cycles), which implies that the potential benefits of combining different installation location are small. Contrarily, wind presents a more varying nature over the territory, which in turn favors instances where combining wind resources is beneficial to the overall system. As a result of this changing quality, wind capacity distribution varies with the changing resolution due to some high-potential areas being averaged out across regions, as well as some regions having better averaged values than their individual components. However, in areas with strong sustained wind patterns, wind capacity follows a similar behavior to PV.

The use of higher resolution data can prevent overestimations of necessary capacity. The usage of the highest possible resolution helps identify the synergies between different locations for installation. In turn, these synergies allow for smaller amounts of installed capacity to reach high penetration levels. Lower resolution approaches limit the possible combinations and the precision of their components, which presents a reduced representation of reality that is detrimental both in terms of return and in terms of necessary capacity.

Acknowledgments

This research is framed within the TRAMPAS (PID2020-113036RB-I00/AEI/10.13039/501100011033) project. Author A. Maimó-Far received funding from the Spanish Ministerio de Ciencia Innovación y Universidades (FPU18/00520).This research made use of e4clim, an open source software, developed in the frame of the Energy4Climate Interdisciplinary Center (E4C) of Institut Polytechnique de Paris and École des Ponts ParisTech and supported by the 3rd Programme d'Investissements d'Avenir [ANR-18-EUR-0006- 02] and by the Foundation of École Polytechnique (Chaire Défis Technologiques pour une Énergie Responsable).

References

[1] European Commission. A Clean Planet for All. A European strategic long-term vision for a prosperous, modern, competitive and climate neutral economy. Brussels; 2018. COM/2018/773 final.

[2] Ministerio para la transición ecológica y el reto demográfico. Plan nacional de Adaptación al Cambio Climático 2021-2030. Spain; 2020.

[3] Ministerio para la transición ecológica y el reto demográfico. Plan Nacional Integrado de Energía y Clima (PNIEC) 2021-2030. Spain; 2020.

[4] IEA. World Energy Outlook 2019. France; 2019. ISBN:978-92-64-97300-8.

[5] Victoria M, Zhu K, Brown T, Andresen GB, Greiner M. Early decarbonisation of the European energy system pays off. Nature communications. 2020;11(1):1-9.

[6] Red Eléctrica de España. The Spanish Electricity System 2013 Report. Madrid; 2014.

[7] Red Eléctrica de España. The Spanish Electricity System 2018 Report. Madrid; 2019.

[8] Red Eléctrica de España. The Spanish Electricity System 2020 Report. Madrid; 2021.

[9] Sun W, Harrison GP. Wind-solar complementarity and effective use of distribution network capacity. Applied Energy. 2019;247:89-101.

[10] Weschenfelder F, Leite GdNP, da Costa ACA, de Castro Vilela O, Ribeiro CM, Ochoa AAV, et al. A review on the complementarity between grid-connected solar and wind power systems. Journal of Cleaner Production. 2020;257:120617.

[11] Deng X, Lv T. Power system planning with increasing variable renewable energy: A review of optimization models. Journal of Cleaner Production. 2020;246:118962.

[12] Holttinen H, Meibom P, Orths A, Lange B, O'Malley M, Tande JO, et al. Impacts of large amounts of wind power on design and operation of power systems, results of IEA collaboration. Wind Energy. 2011;14(2):179-92.

[13] Castillo CP, e Silva FB, Lavalle C. An assessment of the regional potential for solar power generation in EU-28. Energy policy. 2016;88:86-99.

[14] Jerez S, Thais F, Tobin I, Wild M, Colette A, Yiou P, et al. The CLIMIX model: A tool to create and evaluate spatially-resolved scenarios of photovoltaic and wind power development. Renewable and Sustainable Energy Reviews. 2015;42:1-15.

[15] Santos-Alamillos FJ, Brayshaw DJ, Methven J, Thomaidis NS, Ruiz-Arias JA, Pozo-Vázquez D. Exploring the meteorological potential for planning a high performance European electricity super-grid: optimal power capacity distribution among countries. Environmental Research Letters. 2017;12(11):114030.

[16] Xu D, Bai Z, Jin X, Yang X, Chen S, Zhou M. A mean-variance portfolio optimization approach for high-renewable energy hub. Applied Energy. 2022;325:119888.

[17] Martínez-Gordón R, Morales-España G, Sijm J, Faaij A. A review of the role of spatial resolution in energy systems modelling: Lessons learned and applicability to the North Sea region. Renewable and Sustainable Energy Reviews. 2021;141:110857.

[18] Aryanpur V, O'Gallachoir B, Dai H, Chen W, Glynn J. A review of spatial resolution and regionalisation in national-scale energy systems optimisation models. Energy Strategy Reviews. 2021;37:100702.

[19] Raventós O, Dengiz T, Medjroubi W, Unaichi C, Bruckmeier A, Finck R. Comparison of different methods of spatial disaggregation of electricity generation and consumption time series. Renewable and Sustainable Energy Reviews. 2022;163:112186.

[20] Maimó-Far A, Homar V, Tantet A, Drobinski P. The effect of spatial granularity on optimal renewable energy portfolios in an integrated climate-energy assessment model. Sustainable Energy Technologies and Assessments. 2022;54:102827. Available from: https://www.sciencedirect.com/science/article/pii/S221313882200875X.

[21] Tantet A, Stéfanon M, Drobinski P, Badosa J, Concettini S, Cretì A, et al. E4CLIM 1.0: The energy for a climate integrated model: Description and application to Italy. Energies. 2019;12(22):4299.

[22] Maimó-Far A, Tantet A, Homar V, Drobinski P. Predictable and Unpredictable Climate Variability Impacts on Optimal Renewable Energy Mixes: The Example of Spain. Energies. 2020;13(19):5132.

[23] Hersbach H, Bell B, Berrisford P, Hirahara S, Horányi A, Muñoz-Sabater J, et al. The ERA5 global reanalysis. Quarterly Journal of the Royal Meteorological Society. 2020;146(730):1999-2049.

Towards CO2 valorization in a multi remote renewable energy hub framework

V. Dachet[a], A. Benzerga[b], R. Fonteneau[c], D. Ernst[de]

*[a] University of Liège, Liège, Belgium, victor.dachet@uliege.be **CA***
[b] University of Liège, Liège, Belgium, abenzerga@uliege.be
[c] University of Liège, Liège, Belgium, raphael.fonteneau@uliege.be
[d] University of Liège, Liège, Belgium, dernst@uliege.be
[e] Telecom Paris, Institut Polytechnique de Paris, Paris, France, damien.ernst@telecom-paris.fr

Abstract:

In this paper, we propose a multi-RREH (Remote Renewable Energy Hub) based optimization framework. This framework allows a valorization of CO2 using carbon capture technologies. This valorization is grounded on the idea that CO2 gathered from the atmosphere or post combustion can be combined with hydrogen to produce synthetic methane. The hydrogen is obtained from water electrolysis using renewable energy (RE). Such renewable energy is generated in RREHs, which are locations where RE is cheap and abundant (e.g., solar PV in the Sahara Desert, or wind in Greenland). We instantiate our framework on a case study focusing on Belgium and 2 RREHs, and we conduct a techno-economic analysis. This analysis highlights, among others, the interest of capturing CO2 via Post Combustion Carbon Capture (PCCC) rather than only through Direct Air Capture (DAC) for methane synthesis in RREH. By doing so, a notable reduction of 9.2% is observed in the total cost of the system under our reference scenario. In addition, we use our framework to derive a carbon price threshold above which carbon capture technologies may start playing a pivotal role in the decarbonation process of our industries. For example, this price threshold may give relevant information for calibrating the EU Emission Trading System so as to trigger the emergence of the multi-RREH.

Keywords:

CO2 Valorization, Energy Hub, Multi-Energy Systems, Optimization of Energy Systems, Sector Coupling.

1. Introduction

While the whole world is engaged in a process to decrease greenhouse gas emissions, capturing CO2 appears more and more as a crucial element to limit global warming. Once it is captured, CO2 may be either stored (CCS - Carbon Capture and Storage), either valorized (CCU - Carbon Capture and Utilisation), for instance through synthetic methane generation. In this article, we focus on CCU, where CO2 is seen as a required ingredient in the process of generating synthetic methane, together with *green* hydrogen, i.e. hydrogen obtained from renewable energy-based electrolysis.

In this paper, we build on top of the Remote Renewable Energy Hub (RREH) approach [3] to propose a multi-hub, multi CO2 sources approach. CO2 is captured using both Post-Combustion Carbon Capture (PCCC) and Direct Air Capture (DAC) technologies. Hydrogen is produced from electrolysis using renewable energy in a RREH which is particularly well-suited for producing cheap and abundant renewable energy (e.g., solar energy in the Sahara desert, or wind energy in Greenland). The RREH concept also relies on the following idea: some locations show large amount of energy consumption while not having lots of renewable energy resources (e.g., Europe). On the opposite, some places have abundant renewable energy while having almost no energy demand. In its original formulation, the RREH concept suggests to use DAC technologies to feed the CO2 demand at the RREH. In this paper, we include PCCC technologies as an alternative to DAC technologies: in addition or replacement to being captured in the atmosphere, CO2 emitted in energy intensive locations may be transported to the RREHs to be combined with green hydrogen for producing neutral synthetic methane.

We propose a methodology for assessing the technico-economic feasibility of exporting CO2 into RREH where synthetic CO2-neutral methane would be generated using locally produced green H2. We formalise an optimisation problem where CO2 sources are in ”competition” to provide CO2 to the methanation units in the RREHs. This methodology is based on a linear program modelling of Belgium energy system, including gas and electricity demand, and main CO2 emitters. We rely on previously published approaches to develop our approach Berger et al. [3], and, in particular, we use the GBOML language Miftari et al. [17] to model the energy system and to optimize it.

Our methodology is evaluated in the Belgian context: we consider Belgian CO2 emissions and Belgian gas and electricity demand. CO2 may be captured using Post Combustion Carbon Capture (PCCC) in Belgium or DAC in RREH locations. CO2 neutral synthetic methane will be produced in a remote energy hub from where it would be shipped back to serve the Belgian gas demand. We derive a CO2 emission cost in order to have a neutral emission system. We also determine a value of lost load (*i.e.* a price associated with a lack of energy service) in order to serve the energy demand at all times. Several scenarios are studied with different prices of CO2 emissions, allocation or not of unserved energy and forcing of a given RREH.

2. Related Work

This work is mainly related with the following topics that may play an important role in the deep decarbonation of our societies: (i) global grid approaches, (ii) power-to-X technologies, multi-energy systems and and energy hub approaches, and (iii) CO2 quotas markets.

Global Grid (GG) approaches [7], [25], sometimes referred to as Global Energy Interconnection approaches [16], are related with the idea of harvesting renewable energy from abundant and potentially remote renewable energy fields to feed the electricity demand in high demand centres. These approaches have mainly been oriented towards solutions using the electricity vector to repatriate energy from energy hubs, and have received a growing interest starting from the DESERTEC concept [23] that focuses on Sahara solar energy resources from the Sahara desert to serve the European electricity demand. More recently, wind from Northern Europe and Greenland has also been identified as a promising resource to be valued within the GG context [21]. Resource and demand configurations combining several types of resources as well as demand time zones show better results [25].

Multi-energy systems approaches [19, 20] exploit the benefits of integrating energy demand and generation, as well as infrastructure. Power-to-X technologies, in particular power-to-CH4 technologies using hydrolysis and renewable energy for producing H2 [15], offer a CO2 neutral solution to serve gas demand, but also a way to store vast quantities of energy issues from renewable sources [5]. Recently, Berger et al. have proposed a modeling framework [3] for assessing the techno-economics viability of carbon-neutral synthetic fuel production from renewable electricity in remote areas where high-quality renewable resources are abundant. Let us mention that the idea of energy hubs was preexisting the work of Berger et al. [14, 18, 22], however the contribution of Berger et al. is the introduction of remote energy production, far from the demand. Our contribution is in line with the latter.

As this work aims to enhance the value of CO2, it is closely linked to the European Union Emissions Trading System (EU ETS). The EU ETS system, which is described on the European Commission's website [1] and in [6], is a 'cap and trade' program. The system sets a cap on the total amount of certain greenhouse gases (GHG) that can be emitted by the facilities covered by the ETS. Within the cap, facilities are given emissions allowances, which can be traded with one another. The total number of allowances available is limited to ensure that they have value, and the cap is gradually reduced over time to lower total emissions. If a facility fails to cover its emissions fully, it faces substantial fines. Conversely, if a facility reduces its emissions, it can either retain the surplus allowance for future use or sell it to another facility that has not succeeded in covering its own emissions. This trading mechanism aims to reduce GHG emissions as soon as it becomes the most cost-effective solution and encourage investments in low GHG emissions solutions.

3. CO2 Valorisation in a Multi-Remote Renewable Energy Hubs Approach

The Remote Renewable Energy Hub concept was first introduced in [3] where the authors proposed a hub for synthesizing CH4 based on hydrogen and CO2 captured from the air thanks to a methanation unit. This concept has emerged within the context of global grid [7] and multi-energy systems approaches. These approaches aim at optimising the generation and utilisation of renewable energy (RE) by both (i) looking for abundant and cheap RE fields, (ii) taking advantage of daily/seasonal complementary of RE, as well as (iii) using power-to-gas technologies for better addressing RE generation fluctuations and meet e-fuels demand to act as a substitute for molecules derived nowadays from fossil fuels.

In the original article [3], the methanation unit was supplied with CO2 by a Direct Air Capture unit, and the energy demand was fulfilled by a single RREH located in Algeria. However, in this paper, we propose to investigate the feasibility of valorizing CO2 captured through Post Combustion Capture techniques at the energy demand center (EDC). Additionally, we deviate from the original paper by introducing a multi-RREH approach, wherein the EDC serves as a CO2 provider to a set of multiple RREHs, denoted as $RREH_1, \dots, RREH_h$. Each hub $RREH_i (1 \leq i \leq h)$ has its unique characteristics, such as renewable energy type, potential, distance from the EDC, and means of CO2 transport from the EDC, which can affect its competitiveness.

In order to illustrate the concepts discussed above, we have developed a model for a multi-RREH system

[1] https://climate.ec.europa.eu/eu-action/eu-emissions-trading-system-eu-ets_en

based on the following assumptions: (i) the EDC is Belgium, encompassing its gas and electricity demands as well as its CO2 emissions, (ii) there are two RREHs: one situated in the Sahara desert with access to solar and wind resources, and another in Greenland benefiting from the high-quality wind fields in the region. A detailed schematic of the resulting system is shown in Fig. 1. Similar to [3], we employed the GBOML language [17], a recently developed language tailored for energy system optimization (refer to section 4. for more information), to model the system.

We note that the GBOML model code with two RREHs and one EDC system is available online[2] and can be easily extended to add additional RREHs and EDCs.

4. Modelling

This section provides insight into the optimization framework that underlies the multi-energy system model proposed in this work. The GBOML language introduced in [17], a recently developed language dedicated to modeling graph-based optimization of multi-energy systems, is utilized to build this model. The optimization problem can be viewed as optimization on graphs, where a multi-energy system is considered as a set of nodes $\mathcal{N}$ that contribute to the (linear) objective and local constraints, and hyperedges $\mathcal{E}$ are used to model the constraints between nodes, such as those between RREHs and the EDC in our context.

The formalism employed in this work follows that introduced in [3]. The entire system is defined by sets of nodes $\mathcal{N}$ and hyperedges $\mathcal{E}$. The optimization horizon is denoted by T, with time-steps indexed by $t \in \mathcal{T}$, where $\mathcal{T} = \{1, \dots, T\}$.

A node $n \in \mathcal{N}$ is defined by internal X^n and external Z^n variables, where internal variables describe the specific characteristics of the unit, such as the nominal power capacity installed in the asset. Equality constraints $h_i(X^n, Z^n, t) = 0$ with $i \in \mathcal{I}$ and inequality constraints $g_j(X^n, Z^n, t) \leq 0$ with $j \in \mathcal{J}$, are employed for each $t \in \mathcal{T}$ to model operational constraints.

Each node n has an associated cost function $F^n(X^n, Z^n) = \sum_{t=1}^{T} f^n(X^n, Z^n, t)$ that typically represents the capital expenditure and operational expenditure, i.e., CAPEX and OPEX, respectively.

Finally, equality and inequality constraints on hyperedges can be defined as $H^e(Z^e) = 0$ and $G^e(Z^e) \leq 0$ with $e \in \mathcal{E}$ to model the laws of conservation and caps on given commodities.

One can read this type of problem as:

$$\begin{aligned} \min \quad & \sum_{n=1}^{N} F^n(X^n, Z^n) \\ \text{s.t.} \quad & h_i(X^n, Z^n, t) = 0, \forall n \in \mathcal{N}, \forall t \in \mathcal{T}, \forall i \in \mathcal{I} \\ & g_j(X^n, Z^n, t) \leq 0, \forall n \in \mathcal{N}, \forall t \in \mathcal{T}, \forall j \in \mathcal{J} \\ & H^e(Z^e) = 0, \forall e \in \mathcal{E} \\ & G^e(Z^e) \leq 0, \forall e \in \mathcal{E}. \end{aligned} \tag{1}$$

The main assumptions underlying our model are the following:

- Centralised planning and operation: In this framework, a single entity is responsible for making all investment and operation decisions.
- Perfect forecast and knowledge: It is assumed that the demand curves, as well as weather time series, are available and known *in advance* for the entire optimisation horizon, i.e., $\forall t \in \{1, \dots, T\}$.
- Permanence of investment decisions: Investment decisions result in the sizing of installation capacities at the beginning of the time horizon. Capacities remain fixed throughout the entire optimisation period, i.e., $\forall t \in \{1, \dots, T\}$.
- Linear modelling of technologies: All technologies and their interactions are modelled using linear equations within this framework.
- Spatial aggregation: The energy demands and generation at each node are represented by single points. The topology of the embedded network required to serve this demand locally is not modelled in this approach. This can be viewed as an extension of the copper plate modelling approach used in electrical power systems.

In our problem, all cost functions and constraints are affine transformation of the inputs. More details on the constraints of each technology can be found in [2], [3]. Additionnaly, the local objective function corresponding

[2] https://gitlab.uliege.be/smart_grids/public/gboml/-/tree/master/examples

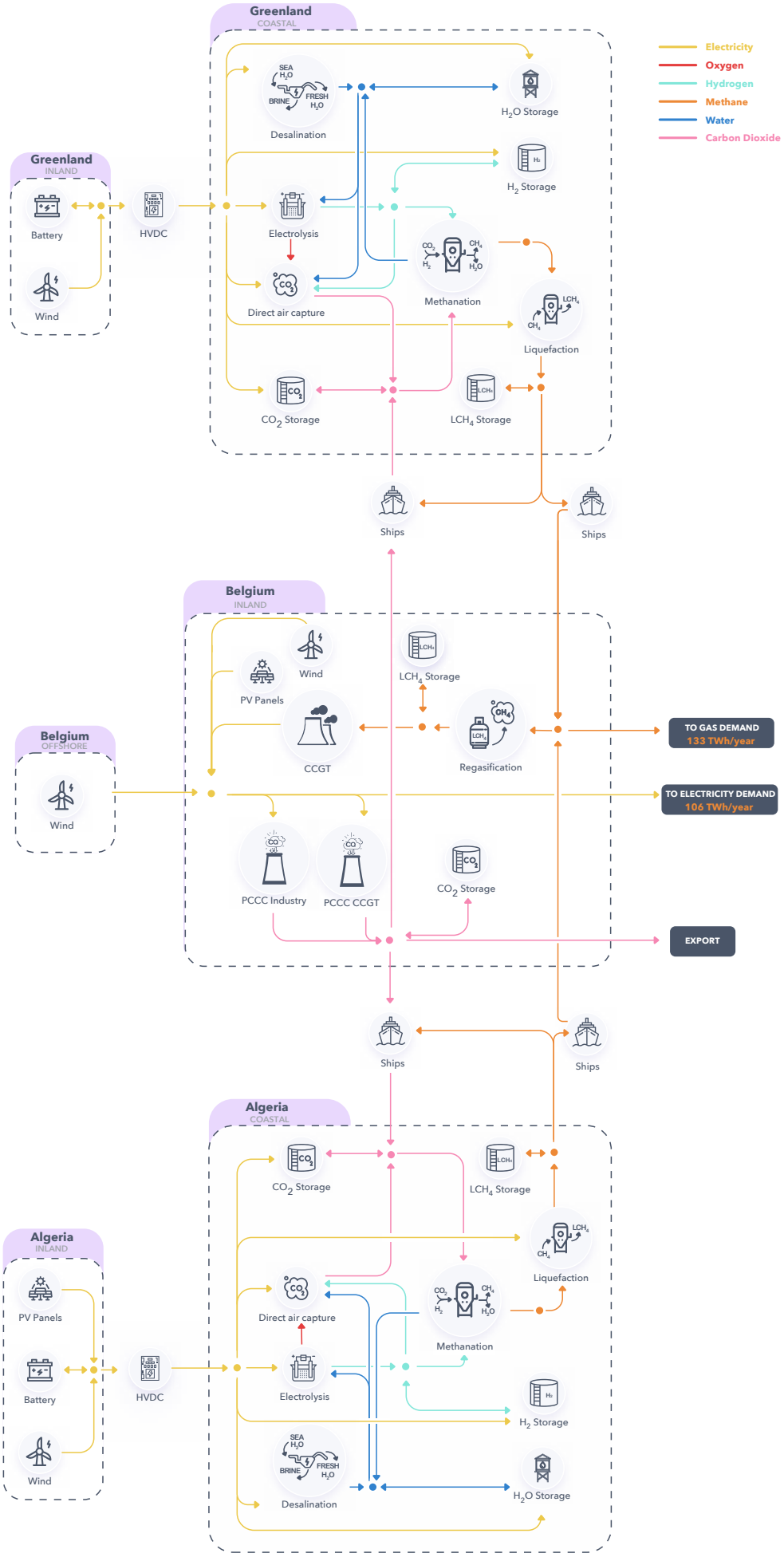

Figure 1: A schematic illustration of the remote energy hub. CO2 being captured, it may be used to synthesize fuel either locally either in a remote energy hub where renewable energy may be cheaper and more abundant.

to the CAPEX is modelled with a uniform weighted average cost of capital (WACC) of 7% for each technology. Thus, the CAPEX is computed using the following formula:

$$\zeta^n = \text{CAPEX}_n \times \frac{\text{w}}{(1-(1+\text{w})^{-\text{L}_n})} \tag{2}$$

with L_n the lifetime of technology n and w the WACC. Hence, ζ^n represents the annualised cost of investing in technology n.

Moreover, a cap on the net CO2 emissions (*i.e.* release in minus captured from the atmosphere) is added to the model. This latter is defined as

$$\sum_{t\in\mathcal{T}}(\sum_{a\in\mathcal{A}} q^a_{co2,t} - \sum_{c\in\mathcal{C}} q^c_{co2,t}) \leq \kappa_{co2}\nu \tag{3}$$

with $\mathcal{A}$ and $\mathcal{C}$ representing the sets of technologies that release CO2 into the atmosphere and those that capture CO2 directly from the atmosphere, respectively, κ_{co2} represents the CO2 cap in kilotons per year, and ν represents the number of years covered by the optimization horizon. The shadow price, or marginal cost, which is the dual variable associated with (3) allows for the derivation of a CO2 cost in €/t. A detailed explanation of dual variables as marginal costs in linear programming can be found in [4, Chapter 4].

5. Case Study: Belgium

This case study is focused on Belgium with two remote renewable energy hubs: one located in Algeria and another one located in Greenland. We will analyse the techno-economic feasibilty of the system while responding to an energy demand composed only of electricity and gas in Belgium.

5.1. Data

The data cover 2 years: 2015 and 2016. It is used to characterize energy demand as well as load factors for renewable energy sources.

Renewable generation profiles

In order to determine the generation profiles of variable energy sources in Belgium we use the data from the transmission system operator (TSO) of Belgium [11]. The profiles for the RREH located in Algeria are extracted with the same methodology as in [3]. For the RREH situated in Greenland, the profiles of renewable energy are extracted thanks to the MAR model [12] and given a power curve for an offsore wind turbine MHI Vestas Offshore V164-9.5MW.

Energy consumption

The energy consumption data is collected for two energy vectors: gas ([13]) and electricity ([10]) with the same methodology as in [2]. In Fig. 2, the data corresponding to the two years is represented, where the signal is daily aggregated. In some cases, gas usage is shifted towards electricity needs, as described in [2, section 4.2.2]. This shift is due to the use of heat pumps, which can help decarbonize heating in Europe. For both energy vectors, industrial and heating demands are taken into account.

The peak power demand is equal to 60.13 GWh/h for both gas and electricity. The energy demand for electricity ranges from 6.42 to 20.29 GWh/h, while that for gas ranges from 5.51 to 39.84 GWh/h. The total energy demand is on average 106.45 TWh/year and 132.65 TWh/year for electricity and gas, respectively.

5.2. Model Configuration

Our model consists of three main components (see Fig. 1): the energy demand center located in Belgium and two Remote Renewable Energy Hubs (RREHs) situated in Algeria and Greenland. The RREH in Algeria is modeled as described in [3] with the same techno-economic parameters. The distinction is made with the inclusion of the CO2 connection between Belgium and Algeria. The RREH in Greenland is similarly modeled, with the exception of the removal of the photovoltaic potential and the modification of the high-voltage direct current (HVDC) line to a length of 100 km rather than 1000 km.

The transportation of CO2 is achieved through the use of boats, which have a CAPEX of 5M€/kt, a lifespan of 40 years, and an average daily energy consumption of 0.0150 GWh/day. CO2 transport data was obtained from [1]. The loading and traveling time for these boats are assumed identical to those for liquefied methane carriers [3], *i.e.* 24 and 116 hours, respectively. In order to fill the tank of CO2 carriers with fuel (liquefied methane), these tanks are loaded when unloading the CO2 at the RREH. Indeed, at the RREH, synthetic CH4 is available without having undergone any additional transport-related losses. Except for the storage facilities, liquefaction of CO2 has been excluded from the model. Sideways analyses have confirmed that this assumption has a negligible impact on the optimal objective.

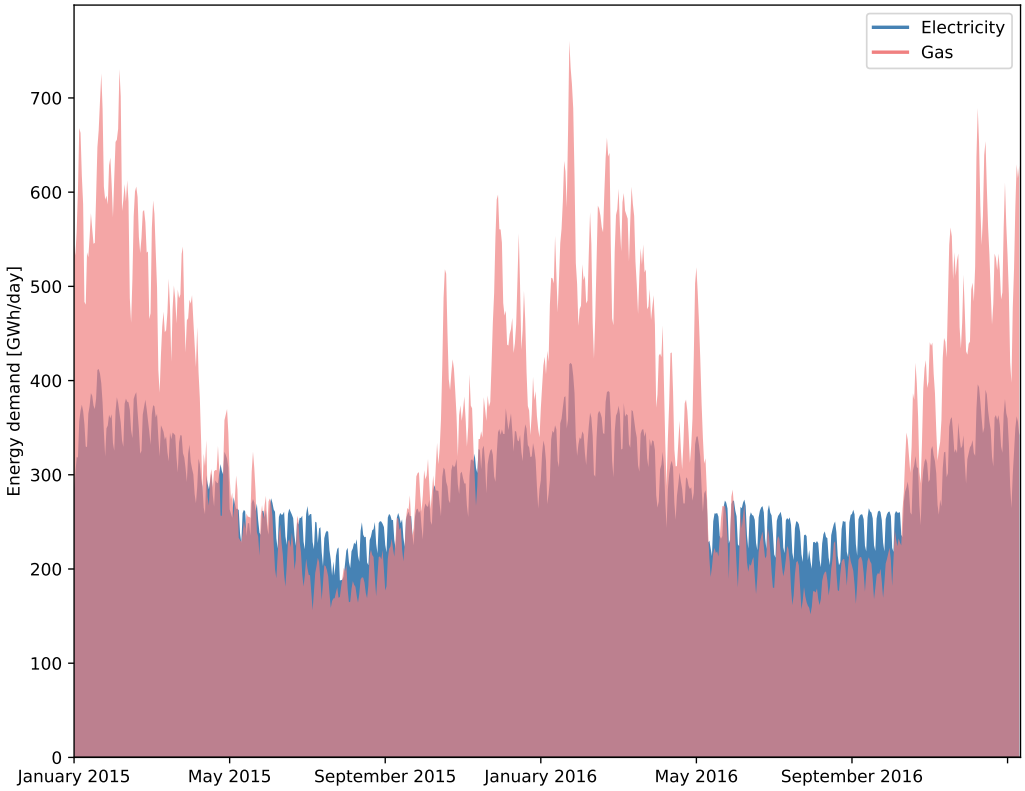

Figure 2: Daily aggregated profiles of electricity and natural gas demand covering the years 2015 and 2016 spanned by the optimisation.

Belgium is modeled with an electricity and gas demand as depicted in Fig. 2, with various means of production, including wind power, solar power, and a combined cycle gas turbine. The solar potential is limited to 40GW. The wind potential is equal to 8.4 GW and 8 GW for onshore and offshore capacities, respectively. The techno-economic parameters of each technology deployed in Belgium follow those in [2].

We have also added a CO2 source that is equivalent to 40Mt CO2/year, which corresponds to the energy sectors and industrial processes greenhouse gases in Belgium in 2019 [8, Table 4.1.1 (pp. 165- 166)]. We assume that we can install post-carbon capture technologies (PCCC) in these sectors.

In terms of carbon capture technologies, the model has access to direct air capture installed at the RREHs, as well as a PCCC in Belgium on the 40Mt of CO2 per year and a PCCC installation on the CCGT.

As stated in [2], the cost of PCCC is 3150M€/kt/h of CAPEX. The variable operating and maintenance costs (VOM and FOM) have been neglected in this analysis. However, a demand of $0.4125 GWh_{el}/kt_{CO2}$ of electricity is required. The expected lifetime is assumed to be 20 years.

Similarly, according to [3], the cost of DAC is equal to 4801.4 M€/kt/h of CAPEX. Similar to PCCC, VOM and FOM are ignored. The operational requirements for DAC are $0.1091 GWh_{el}/kt_{CO2}$ of electricity, $0.0438 kt_{H2}/kt_{CO2}$ of di-hydrogen, and $5.0 kt_{H20}/kt_{CO2}$ of water. The expected lifetime is assumed to be 30 years.

5.3. Results

In this section, we explore several scenari. We describe the variables that are used to differentiate the scenari

1. Cost or Cap on CO2: either a cap is set of 0 t/year or a price at 80€/t or 0€/t
2. Cost of energy not served (ENS): either energy not served is not allowed or a penalty of 3000€/MWh is imposed for each unit of unproduced energy.
3. Forcing or not the use of a given RREH.

Scenario	Cap on CO2 (kt)	Cost of CO2 (M€/kt)	ENS	Cost ENS (€/MWh)	Objective (M€)
1	0.0	0.0	No	-	83742.61
2	0.0	0.0	Yes	3.0	80778.02
3	No	0.08	Yes	3.0	78872.94
4	No	0.0	Yes	3.0	76323.94
5	0.0	0.0	No	-	111209.95

Table 1: Scenari parameters.

The results are generated with 5 scenari:

Scenario 1: This scenario seeks to avoid energy scarcity, whatever the cost. Therefore, no ENS is allowed. In addition, a hard constraint is set on CO2 emissions: a cap on CO2 is set.

Scenario 2: This scenario follows the same assumptions as scenario 1 except that it leverages the constraint on energy not served. The cost associated to electricity not served is equal to 3000€/MWh, which is a standard value in the electricity context [24].

Scenario 3: This scenario leverages the constraint on CO2 emissions, and does not force the avoidance of energy not served but is penalized by 3000€/MWh not served. A penalty is associated with any CO2 emission in the atmosphere in the form of a fee equal to 80€/MWh - a value that reflects the current price of CO2 in the EU-ETS trading system [9].

Scenario 4: This scenario follows the same assumptions as scenario 3, with the difference that the cost of CO2 is equal to 0€/MWh. The aim is to showcase the system's configuration in the absence of any considerations for CO2 emissions.

Scenario 5: This scenario follows the same assumptions as scenario 1, with the difference that the only available RREH is in Greenland.

These scenari summarized in Table 1 vary in their degree of constraint. Scenario 1 is the most restrictive, with a cap on CO2 emissions and no allowance for energy not served. Scenario 2 allows for energy not served, while scenarios 3 and 4 remove the cap and replace it with CO2 prices of 80€ and 0€ per ton, respectively. Finally, scenario 5 requires the use of the RREH in Greenland, with parameters identical to those of scenario 1.

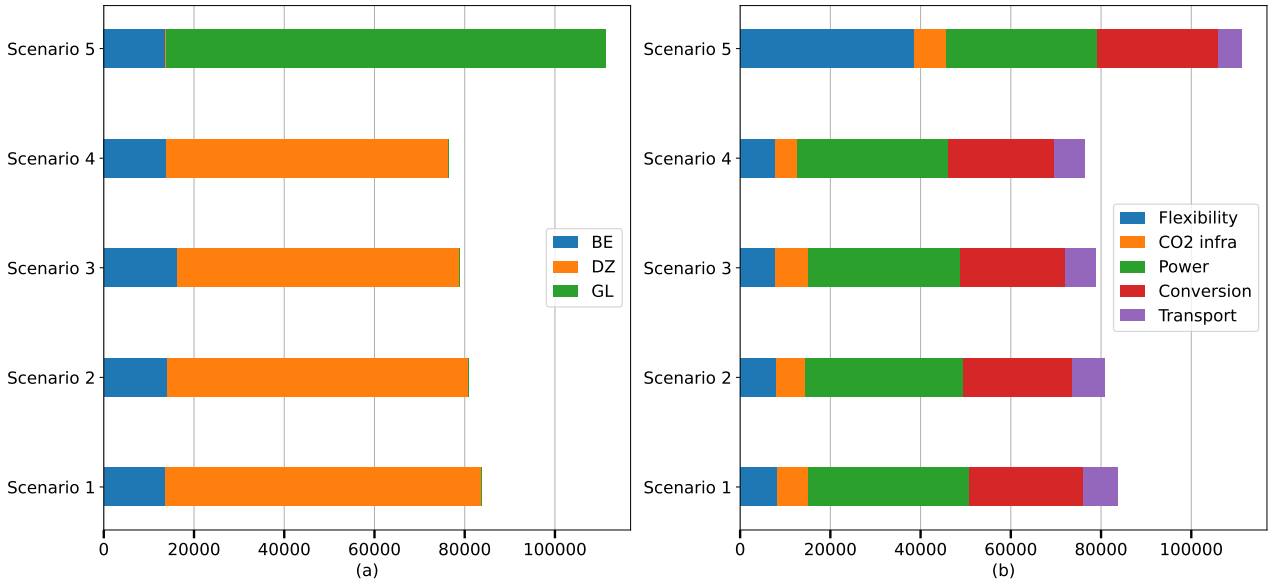

Figure 3: (a): Breakdown of costs per scenario and per cluster (Belgium (BE), Algeria (DZ), and Greenland (GL)). (b): Breakdown of costs per scenario per asset function. Flexibility covers storage capacities, CO2 Infra covers CO2 capture, storage, and transport, Power covers means of electricity production, Conversion covers all assets that convert one commodity into another and Transport HVDC lines and CH4 carriers.

5.4. Analyses and Discussion

In this section, we introduce and discuss the results in detail. We choose to present a cross-scenario analysis in the light of key indicators and statistics extracted from the model.

Total cost.

The results indicate that the costs associated with enabling the hub in Algeria are substantially lower than those in Greenland, as depicted in Fig. 3 (a) where nothing is built in the Greenland hub from scenarios 1 to 4, despite it being available for use. This disparity in costs can be attributed to the over-dimensioning of flexibility assets, particularly the storage capacities, as illustrated in Fig. 3 (b). This is mainly explained to electricity generated solely through wind available in Greenland, whereas both solar and wind electricity are obtainable in Algeria. This implies that the flexibility assets have to take the lead in maintaining a minimum of electricity delivery required in the electrolysis power plant.

Furthermore, a reduction in total costs is observed in the first four scenarios with respect to the objective. This is explained with the order on the scenari based on their degree of constraint with scenario 1 being the most constrained and scenario 4 being the least.

Power installation capacities.

All power capacities installations are displayed in Table 2.

The potential in Belgium of solar energy is never reached while for both wind offshore and onshore the potential is reached in all scenari.

From scenario 1 to scenario 2, the only difference being the allowance of ENS, there is an increase in the installation of controllable energy production assets. Indeed, there is a shift in capacity from CCGT to solar energy in Belgium between the first scenario and the second.

Comparing scenario 1 and 5, solar energy in Belgium is more expensive than importing CH4 from the RREH in Algeria. Importing from Greenland is more expensive and leads to an increase in power capacity installation in Belgium for solar, but it does not reach the maximum potential.

Another interesting comparison can be made with the work of [3], where the capacity installation in the hub for the reference scenario is 4.3GW of solar and 4.4GW of wind. In our case, the reference scenario 1 displays 100.51GW and 103.62GW, respectively. The power installation capacity is multiplied by approximately 23 while providing, on average, 282TWh/year of gas (HHV) to serve the gas demand and part of the electricity demand in Belgium, which is 28.2 times the gas production in the original paper.

Scenario	Wind onshore BE	Wind offshore BE	Solar BE	CCGT BE	Wind GL	Wind DZ	Solar DZ
1	8.40	8.00	10.56	22.69	0.00	103.62	100.51
2	8.40	8.00	15.35	17.95	0.00	98.43	95.47
3	8.40	8.00	14.95	17.83	0.00	93.32	90.32
4	8.40	8.00	14.72	17.82	0.00	93.28	90.28
5	8.40	8.00	17.48	19.58	129.43	0.00	0.00

Table 2: Total Power installation in GW per scenario.

CO2 installations (transport, capture).

In Table 3, the capacities of the CO2 capture units and the installations of transport capacity per scenario are displayed. Each time PCCC is activated, we recall that capturing CO2 is the only means to create gas in our system, and thus a minimum installation is required to support the demand. On the other hand, the DAC is only activated when a CO2 cap is set. PCCC has an efficiency of CO2 capture set to 90%, which means that a direct air capture technology asset is necessary to recover the remaining 10% of emissions in the atmosphere. This leads to a direct consequence, which is that when the DAC is available, the capacity of transport decreases because CO2 is locally available in the hub. However, the cost of CO2 capture by PCCC added to transport of CO2 is cheaper than the cost of DAC in the RREH. The only way to put PCCC out of business would be to have a distance between the hub and the energy demand center so long that the transport cost would increase too much.

Due to the higher concentration of CO2 in manufacturing smoke compared to the air, PCCC will likely always be cheaper than DAC, even with significant improvements in the DAC process. As a result, the operational costs associated with the energy required for PCCC will be lower than those of DAC.

Cost of CO2 derived and Cap of CO2.

From the first, second, and fifth scenarios, we are able to derive a shadow price thanks to the CO2 cap constraint. These correspond to approximately 162.77€/tCO2 for the first and second scenarios and 235.65€/tCO2

Scenario	PCCC	PCCC CCGT	DAC DZ	DAC GL	Carrier DZ	Carrier GL
1	4.11	2.62	1.30	0.00	8.030	0.000
2	4.11	2.07	1.47	0.00	7.142	0.000
3	4.11	1.80	0.00	0.00	9.694	0.000
4	3.76	2.06	0.00	0.00	9.701	0.000
5	4.11	2.40	0.00	1.35	0.000	7.564

Table 3: Capacity, in kt/h, of CO2 capture technology and transport by hub and per scenario.

for the fifth scenario. This shows that given the system considered, i.e., Belgium and RREHs, putting a price of CO2 equal to 162.77€ would avoid these emissions in the atmosphere and activate the export of CO2 to Norway for storage purposes. In scenario 3, where a price of 80€/tCO2 is set, there is a net balance in the atmosphere of approximately 15Mt/year. In scenario 4, where no price is fixed, there is a net balance in the atmosphere which is equivalent to 16Mt/year.

We would like to emphasize that the CO2 cap in our model only considers the emissions from the industrial and energy sectors, which are fully modeled. It does not account for a part of the emissions resulting from the gas demand served. Of this demand, 32% is attributed to industrial needs, which are included in the statistics of the 40 Mt of CO2 emitted per year (see subsection 5.2.), while the remaining 68% is due to heating and is not covered by our cap. This heating gas demand translates to approximately 12.3 Mt of CO2 emitted per year.

Cost of CH4 derived

To estimate the cost of CH4 production, we first subtract from the optimal objective function the cost of the means of electricity production in Belgium (PV, on/off shore wind, CCGT), the cost of unserved energy (when applicable), and the cost related to export of CO2 for sequestration. All of these costs are substracted because they do not refer directly to the cost of producing synthetic methane. Then, we divide the obtained cost by the total energy content (HHV) in CH4 produced at the output of the regasification power plant in Belgium.

These methane costs, listed in Table 4, are compared to the price of 147.9€/MWh of methane (HHV) obtained by [3]. Our scenarios achieve a lower cost for gas production (except for Greenland). This demonstrates that PCCC, which uses smoke with a high concentration of CO2 combined with transport, is more cost-effective than having only access to a DAC unit, as previously mentioned.

In our system, no fossil gas is available for import to Belgium; only synthetic gas produced from CO2 capture is used. If fossil gas were still available for import, our model would seek to minimize costs and import as much cheap gas as possible while staying within our carbon budget.

Scenario	1	2	3	4	5
[€/MWh]	136.00	137.19	133.89	129.27	192.00

Table 4: Estimation of methane price by retrieving the costs of power installations in Belgium, costs of unserved energy, and costs of exporting CO2 for storage purposes.

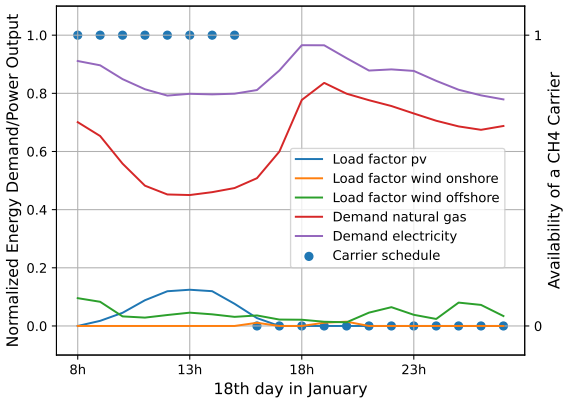

Figure 4: Evening of January 18th leading to the maximum shadow price associated with the hard constraint on energy not served in scenarios 1 and 5.

ENS cost discussion

The cost of unserved energy is a fixed parameter in scenarios 2, 3, and 4, but not in scenarios 1 and 5. Instead, a hard constraint is imposed to ensure that electricity demand is always met, resulting in a shadow price associated with the constraint. The maximum shadow price values for scenarios 1 and 5 are 913,640€/MWh and 1,075,913€/MWh, respectively. This is attributed to the peak in electricity and gas demand observed on January 18th at 18:00 (as shown in Figure 4), where renewable energy load factors were low. Thus, all energy demand had to be supplied by the Combined Cycle Gas Turbine (CCGT) and gas resources.

6. Conclusion

In this work, we present our framework of multi remote energy hubs with capture of CO2 enabled in an energy demand center and its valorization by synthesizing methane in remote renewable energy hubs. We demonstrate the feasibility of serving the energy demand at the horizon 2050 of an entire country with only renewable energy and gas power plant fueled by synthetic methane while decarbonizing the energy and industry sectors on a case study implying Belgium as energy demand center and two RREHs: Greenland and Algeria. Our reference scenario exhibits a gas price of 136.0€/MWh instead of 149.7€/MWh in [3] where only direct air capture was available in the RREH in order to feed CO2 into the methanation process. This shows the potential of Post Combustion Carbon Capture installations in the context of remote renewable energy hubs supply chains. We also derive a cost of CO2 of 163€ per ton in order to avoid any emission in the industrial and energy sector in Belgium. Finally, our model effectively captures the ”competition” between different RREHs and is able to select exactly in which investments should be prioritized. In our simulations, the investments were made only for the RREH located in Algeria. In this respect, it would be interesting to study further how the different devices structuring the RREH in Greenland should be modified to become competitive with the RREH located in Algeria. This could be done for example by modifying the wind turbines selected for the Greenland hub so that they can operate with higher nominal wind speeds and higher cut-off speeds in order to better exploit the strong winds in this area.

7. Acknowledgements

The authors would like to thank Jocelyn Mbenoun for the templates and the useful conversations about energy, as well as Bardhyl Miftari and Guillaume Derval for their useful help with shadow pricing. The authors extend also their thanks to Julien Confetti for his precious help in the elaboration of script for generating the multi-hub picture. This research is supported by the public service of the Belgium federal government (SPF Économie, P.M.E., Classes moyennes et Energie) within the framework of the DRIVER project. Victor Dachet was supported by the Walloon region (Service Public de Wallonie Recherche, Belgium) under grant n°2010235 – ARIAC by digitalwallonia4.ai.

Appendix A Glossary

BE	Belgium
CAPEX	Capital Expenditure
CCGT	Combined Cycle Gas Turbine
DAC	Direct Air Capture
DZ	Algeria
EDC	Energy Demand Center
ENS	Energy Not Served
ETS	Emission Trading System
GBOML	Graph Based Optimzation Modeling Language
GL	Greenland
HHV	Higher Heating Value
OPEX	Operational Expenditure
PCCC	Post Combustion Carbon Capture
PV	Photovoltaic
RE	Renewable Energy
RREH	Remote Renewable Energy Hub
RES	Renewable Energy Sources

Nomenclature

Sets and indices

$\mathcal{E}, e$ set of hyperedges and hyperedge index

$\mathcal{G}$ hypergraph with node set $\mathcal{N}$ and hyperedge set $\mathcal{E}$

$\mathcal{I}^n, i$ set of external variables at node n, and variable index

$\mathcal{N}, n$ set of nodes and node index

$\mathcal{T}, t$ set of time periods and time index

Parameters

$\nu \in \mathbb{N}$ number of years spanned by optimisation horizon

$\kappa_i \in \mathbb{R}_+$ maximum flow capacity of commodity i

$\zeta^n \in \mathbb{R}_+$ annualised CAPEX of node n (flow component)

Variables

$q_{it}^n \in \mathbb{R}_+$ flow variable i of node n at time t

References

[1] Danish Energy Agency. Technology data for carbon capture, transport and storage, 2023. URL https://ens.dk/en/our-services/projections-and-models/technology-data/technology-data-carbon-capture-transport-and.

[2] Mathias Berger, David Radu, Raphaël Fonteneau, Thierry Deschuyteneer, Ghislain Detienne, and Damien Ernst. The role of power-to-gas and carbon capture technologies in cross-sector decarbonisation strategies. *Electric Power Systems Research*, 180:106039, 2020. ISSN 0378-7796. doi: https://doi.org/10.1016/j.epsr.2019.106039. URL https://www.sciencedirect.com/science/article/pii/S037877961930358X.

[3] Mathias Berger, David-Constantin Radu, Ghislain Detienne, Thierry Deschuyteneer, Aurore Richel, and Damien Ernst. Remote renewable hubs for carbon-neutral synthetic fuel production. *Frontiers in Energy Research*, 2021. doi: 10.3389/fenrg.2021.671279.

[4] Dimitris Bertsimas and John N. Tsitsiklis. *Introduction to Linear Optimization*. Athena Scientific, 1997. ISBN 978-1886529199.

[5] Herib Blanco and André Faaij. A review at the role of storage in energy systems with a focus on power to gas and long-term storage. *Renewable and Sustainable Energy Reviews*, 81:1049–1086, 2018. ISSN 1364-0321. doi: https://doi.org/10.1016/j.rser.2017.07.062. URL https://www.sciencedirect.com/science/article/pii/S1364032117311310.

[6] Howarth N. Brohé A., Eyre N. *Carbon Markets*. Routledge, 2009. doi: https://doi.org/10.4324/9781849770699.

[7] Spyros Chatzivasileiadis, Damien Ernst, and Göran Andersson. The global grid. *Renewable Energy*, 57: 372–383, 2013.

[8] European Commission and Directorate-General for Energy. *EU energy in figures : statistical pocketbook 2021*. Publications Office of the European Union, 2021. doi: doi/10.2833/511498.

[9] Trading Economics. EU carbon permits, 2023. URL https://tradingeconomics.com/commodity/carbon.

[10] Elia. Load and load forecasts – total load, 2022. URL https://www.elia.be/en/grid-data/load-and-load-forecasts.

[11] Elia. Power generation, 2022. URL https://www.elia.be/en/grid-data/power-generation.

[12] X. Fettweis, J. E. Box, C. Agosta, C. Amory, C. Kittel, C. Lang, D. van As, H. Machguth, and H. Gallée. Reconstructions of the 1900–2015 Greenland ice sheet surface mass balance using the regional climate MAR model. *The Cryosphere*, 11(2):1015–1033, 2017. doi: 10.5194/tc-11-1015-2017. URL https://tc.copernicus.org/articles/11/1015/2017/.

[13] Fluxys. Flow data – ex-post domestic exit point information, 2022. URL https://gasdata.fluxys.com/fr/transmission-ztp-trading-services/flow-data/.

[14] Martin Geidl, Gaudenz Koeppel, Patrick Favre-Perrod, Bernd Klockl, Goran Andersson, and Klaus Frohlich. Energy hubs for the future. *IEEE power and energy magazine*, 5(1):24–30, 2006.

[15] Manuel Götz, Jonathan Lefebvre, Friedemann Mörs, Amy McDaniel Koch, Frank Graf, Siegfried Bajohr, Rainer Reimert, and Thomas Kolb. Renewable power-to-gas: A technological and economic review. *Renewable Energy*, 85:1371–1390, 2016. ISSN 0960-1481. doi: https://doi.org/10.1016/j.renene.2015.07.066. URL https://www.sciencedirect.com/science/article/pii/S0960148115301610.

[16] Zhenya Liu. *Global energy interconnection*. Academic Press, 2015.

[17] Bardhyl Miftari, Mathias Berger, Hatim Djelassi, and Damien Ernst. GBOML: Graph-Based Optimization Modeling Language. *Journal of Open Source Software*, 7(72):4158, 2022. doi: 10.21105/joss.04158. URL https://doi.org/10.21105/joss.04158.

[18] Mohammad Mohammadi, Younes Noorollahi, Behnam Mohammadi-Ivatloo, and Hossein Yousefi. Energy hub: From a model to a concept–a review. *Renewable and Sustainable Energy Reviews*, 80:1512–1527, 2017.

[19] Marie Munster, Daniel Moller Sneum, Rasmus Bramstoft, Fabian Buhler, Brian Elmegaard, Spyros Giannelos, Goran Strbac, Mathias Berger, David-Constantin Radu, Damian Elsaesser, Alexandre Oudalov, and Antonio Iliceto. Sector coupling: Concepts, state-of-the-art and perspectives. Technical report, January 2020. URL https://www.etip-snet.eu/sector-coupling-concepts-state-art-perspectives/.

[20] Mark O'Malley, Benjamin Kroposki, Bryan Hannegan, Henrik Madsen, Mattias Andersson, William D'haeseleer, Mark F McGranaghan, Chris Dent, Goran Strbac, Suresh Baskaran, et al. Energy systems integration. defining and describing the value proposition. Technical report, National Renewable Energy Lab.(NREL), Golden, CO (United States), 2016.

[21] David Radu, Mathias Berger, Antoine Dubois, Raphaël Fonteneau, Hrvoje Pandžić, Yury Dvorkin, Quentin Louveaux, and Damien Ernst. Assessing the impact of offshore wind siting strategies on the design of the european power system. *Applied Energy*, 305:117700, 2022.

[22] Hadi Sadeghi, Masoud Rashidinejad, Moein Moeini-Aghtaie, and Amir Abdollahi. The energy hub: An extensive survey on the state-of-the-art. *Applied Thermal Engineering*, 161:114071, 2019.

[23] Tobias Samus, Bastian Lang, and Holger Rohn. Assessing the natural resource use and the resource efficiency potential of the desertec concept. *Solar Energy*, 87:176–183, 2013.

[24] Thomas Schröder and Wilhelm Kuckshinrichs. Value of lost load: An efficient economic indicator for power supply security? A literature review. *Frontiers in Energy Research*, 3, 2015. ISSN 2296-598X. doi: 10.3389/fenrg.2015.00055. URL https://www.frontiersin.org/articles/10.3389/fenrg.2015.00055.

[25] J. Yu, K. Bakic, A. Kumar, A. Iliceto, L. Beleke Tabu, J.L. Ruaud, J. Fan, B. Cova, H. Li, Damien Ernst, Raphaël Fonteneau, M. Theku, G. Sanchis, M. Chamollet, M. Le Du, Y. Zhang, S. Chatzivasileiadis, David-Constantin Radu, Mathias Berger, M. Stabile, F. Heymann, M.A. Dupré La Tour, Miguel Manuel de Villena Millan, and M. Ranjbar. Global electricity network - feasibility study. Technical report, October 2019. URL https://e-cigre.org/publication/775-global-electricity-network-feasibility-study.

PROCEEDINGS OF ECOS 2023 - THE 36TH INTERNATIONAL CONFERENCE ON
EFFICIENCY, **C**OST, **O**PTIMIZATION, **S**IMULATION AND ENVIRONMENTAL IMPACT OF ENERGY SYSTEMS
25-30 JUNE 2023, LAS PALMAS DE GRAN CANARIA, SPAIN

Development of an optimization-based methodology for subsidy programs of residential buildings

Nico Fuchs[a], Jonas Baumgärtner[b], Dominik Hering[c] and Dirk Müller[d]

[a] RWTH Aachen University, E.ON Energy Research Center (ERC), Institute for Energy Efficient Buildings and Indoor Climate (EBC), Aachen, Germany, nico.fuchs@eonerc.rwth-aachen.de, CA
[b] RWTH Aachen University, ERC, EBC, Aachen, Germany, jonas.baumgaertner@eonerc.rwth-aachen.de
[d] RWTH Aachen University, ERC, EBC, Aachen, Germany, dominik.hering@eonerc.rwth-aachen.de
[e] RWTH Aachen University, ERC, EBC, Aachen, Germany, dmueller@eonerc.rwth-aachen.de

Abstract:
The success of the energy transition in the building sector depends not only on the technical feasibility but also on the economic viability of energy modernization measures. Subsidy programs for building owners and energy prices exert a strong influence on this economic viability and thus on the spread of low-emission building energy systems. Against this background, this study presents a bi-level optimization approach to determine cost-efficient subsidy strategies. At the upper stage, the government aims to reduce subsidies to reach CO_2 targets. At the lower stage, individual building models optimize their total costs by modernizing the heat conversion technology or insulating the building shell. To achieve solvability, the lower model is implemented into the upper model as a discrete set, resulting in a single-stage problem. The model determines the minimal subsidy rates that make the purchase of the technologies and measures worthwhile for the building owner, depending on a CO_2 target aimed by the government. Results show that the introduction of subsidy programs has a considerable steering effect on emission savings. The targeted promotion of low-emission heat supply technologies, such as HPs, with up to 40 % subsidy quota in combination with subsidies for insulation measures contributes significantly to their installation in existing buildings and thus to the achievement of climate protection goals, if the future expansion of renewable energies in the electricity mix is taken into account. With the current costs and emission factors of pellet, the promotion of pellet heating can further contribute to strong emission savings.

Keywords:
Bi-level optimization, energy-efficient buildings, building optimization, subsidy optimization, Subsidy programs for energetic modernization, Residential buildings

1. Introduction

The European Union is committed to decreasing greenhouse gas emissions by a minimum of 55 % by 2030 and achieving climate neutrality by 2050 [1]. These ambitious targets necessitate significant efforts across all energy consumption sectors. As the building sector is accountable for 36 % of European greenhouse emissions [2], it plays a crucial role in achieving emission reductions. The European Commission has reported that 75 % of the European building stock is energy inefficient [3], highlighting the necessity for energy retrofitting. To lower building-related emissions, the European Union intends to double the current retrofit rate, which is currently less than 1 % per year. In practice, the decision of building owners to renovate their buildings is primarily driven by economic considerations. The installation of building envelope insulation or the utilization of low-emission heating technologies entail significant capital expenditures and may not be economically viable in every case. To overcome these financial barriers and promote retrofits, various policy instruments have been developed. According to Vedung [4], there are three general types of policy instruments: regulations, economic means, and information dissemination. Regulations establish energy efficiency standards and partially limit the choice of heating technology in the building sector. Subsidy programs, on the other hand, affect the economic viability of low-emission energy systems. Information flow is critical to educating building owners about sensible renovation measures. Among these policy instruments, Ruparathna et al. [5] identify financial incentives as essential means to encourage the energy retrofitting of bRegulationsuildings. Among these, direct capital grants for retrofit works are the most common financial incentives in Europe [5].

1.1. Subsidy programs in optimization models

In recent years, numerous research papers have incorporated subsidy programs into models for designing and optimizing energy systems for individual residential buildings to quantify their effects. Asadi et al. [6] formulate a multi-objective optimization model that optimizes renovation decisions for discrete insulation measures and

the installation of solar thermal collectors. The Mixed-Integer Linear Program (MILP) minimizes investment costs, taking into account investment grants, while maximizing energy savings. Ashouri et al. [7] present a MILP for the design optimization of a building energy system. The authors model a large portfolio of heat conversion technologies, plants for renewable energy production and different thermal and electrical storage types. The target function minimizes total costs, including investment grants and feed-in tariffs, and a penalty term punishing thermal comfort violations. The works of Harb et al. [8], Renaldi et al. [9], and Schütz et al. [10] show further examples of the integration of incentives in MILPs for building energy system design optimization. All three models minimize the total costs of the building owner but differ in the portfolio of modernization strategies considered and incentive schemes. Harb et al. [8] focus on CHP systems and feed-in tariffs for CHP electricity. Renaldi et al. [9] consider hybrid systems with HP and implement remunerations for heat generated by HP. Schütz et al. [10] integrate all building-relevant German subsidies in their MILP, including investment grants for single measures, subsidies for reaching efficiency standards, as well as feed-in tariffs for PV and CHP electricity. All models demonstrate that subsidies effect the economic viability of modernization measures and thus the investment decision. While most of the models simplify the conditions of the subsidy programs and omit the constraints under which support is granted, Schütz et al. [10] integrate a significant portion of the funding measures available in Germany along with their restrictions into the model.

1.2. Optimization models for the improvement of subsidy programs

While building owners aim to minimize total costs through modernization, funding agencies aim to enhance the energy performance of buildings while minimizing the costs of subsidies. The goal of the funding agency is to allocate subsidies effectively to individual buildings, providing incentives to undertake energy-efficient retrofitting and achieve emission savings. Different research papers attempt to formulate optimization models to model the relationship between the funding agency and energy systems with the goal to improve subsidy programs from the perspective of a funding agency. Liu et al. [11] present an optimization model for multi-energy systems on an urban scale. The model is formulated as a Stackelberg competition, commonly used in game theory. In this case, the state as funding agency aims to minimize total subsidies while meeting an emission reduction target or achieving a share of renewable energy. The upper level perspective is modeled as a mixed-integer linear program (MILP) with binary variables determining the minimum size of plants required for subsidies. Subsidies include investment grants and remuneration for renewable energy production. At the lower level, a city determines how to meet its energy demand at the lowest possible total annual cost (TAC). The lower problem is modeled as a linear program (LP) with plant size and operation as continuous decision variables. Both perspectives result in a bi-level optimization problem (BiOP). In order to solve the BiOP, Liu et al. reformulate the original problem. Since the lower problem is modeled with continuous variables and linear inequalities, it is continuously differentiable, and the Karush-Kuhn-Tucker (KKT) conditions can be applied to include the lower problem in the upper problem. By reformulating the resulting non-linear terms through discretization of variables and the use of the Big-M method, Liu et al. are able to reformulate the BiOP into a single-stage MILP. Martelli et al. [12] introduce a model to determine optimal incentives and CO_2 prices to achieve emission reduction targets for a multi-energy systems on a district scale. The upper problem of the BiOP minimizes incentives for produced renewable heat and electricity while maximizing the income from CO_2 prices. The overall budget and emissions are constrained, and the costs for the lower problem must not exceed a maximum value. The lower level problem minimizes the TAC to cover the energy demand of the district. Technology choices on the lower level are implemented with binary variables resulting in a MILP. As the problem is not continuously differentiable, a problem reformulation by means of the KKT conditions is not possible, and the problem is solved with a gradient-free direct search algorithm (Particle-Generating Set-Complex Algorithm) which was developed by the authors and is not open source available. Prada et al. [13] determine the influences of investment grants in Italy by formulating a BiOP. Both levels are solved separately for different investment grants, and the solution of both problems is compared. At the upper level, the funding agency aims to minimize the primary energy demand of the building stock and its own investment, resulting in a multi-objective target function. The lower level model minimizes the primary energy demand and the TAC. By comparing variations, the originally formulated problem is not necessarily solved to optimality. Another example of solving a BiOP to determine optimized subsidy programs in energy science is the work of Zhou et al. [14] . The model minimizes subsidies for renewable electricity production on the upper level while achieving a minimum share of renewables in a electricity production system. The lower level minimizes the total cost of the portfolio and is modeled as a graphical flow problem with nodes for producers as well as consumers and with discrete technology choices resulting in a MILP. The authors solve the BiOP by a combination of a modified CPA on the lower level and a heuristic approach on the upper level.

1.3. Rationale of the work

The aforementioned approaches demonstrate the potential of subsidy programs to influence investment decisions and present various models for determining optimized subsidies. The studies utilize BiOPs to optimize investment grants and remunerations for renewable energy production. To ensure solvability, the BiOPs are ei-

ther reformulated into a single-level problem if possible or solved using heuristics at the upper level. The BiOPs presented in the studies focus on connected urban and multi-energy systems. Prada et al.'s BiOP [13] takes the single building perspective into account but is not solved to optimality. Therefore, the following aspects have been identified as research gaps based on the findings of the literature review:

- How can subsidies be optimally allocated from the perspective of a funding agency to reduce building stock emissions, while considering individual investment decisions at the level of single residential buildings?

The formulation of a BiOP based on the literature presented shows promise. However, compared to previous works on multi-energy systems, the consideration of building stocks requires the inclusion of multiple entities in the lower-level problem. It is not sufficient to assume, as in Liu et al. [11], that every technology is chosen at the lower level resulting in a linear programming problem. As a result, the main contribution of this work is to address this challenge by:

1. Formulating a BiOP to determine the minimum subsidies required for individual modernization measures to achieve an emission reduction target.
2. Integrating the perspectives of multiple building owners into the BiOP for optimized subsidy allocation.
3. Reformulating the BiOP as a single-level optimization problem and presenting an approach to solve it using deterministic optimization methods.

The paper is organized as follows: The second section describes the methodology and model formulation and illustrates the use of the German single-family-house building stock as a case study as well as the input data used. The third section analyzes the results, and the fourth section constitute the conclusion.

2. Methodology

To determine optimized subsidy schemes, a BiOP is utilized in this study. At the lower level, individual building entities aim to minimize their costs, while on the upper level, a funding agency aims to encourage energy-efficient modernizations by disbursing subsidies to achieve an emission reduction target. The method employed in this paper is designed for this two-stage approach. Subsection 2.1. outlines the model used on the lower level, while Subsection 2.2. formulates the BiOP. In Subsection 2.3., the application of the method is presented through a case study of the German residential single-family house building stock, including the necessary input data. Figure 1 gives an overview about the methodology in this paper.

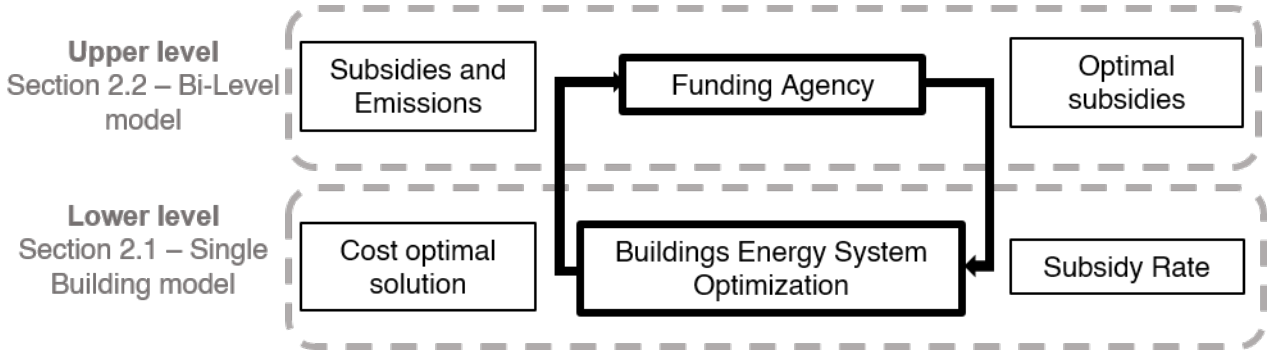

Figure 1: Overview over the Bi-Level approach with the funding agency on upper level and individual buildings on lower level

2.1. Single Building model

At the lower level, we use a mixed-integer linear programming (MILP) design optimization model developed by Schütz et al [10]. The model's detailed features can be found in Schütz et al. [10]. We present only the main features and adaptations of the model for this work. The model selects the optimal energy system in terms of total annualized costs considering available system technologies and insulation measures. The paper considers gas boilers (GAS), electrical air-source heat pumps (HP) with electrical heaters (EH) as backup heaters, and pellet boilers (PEL) as heat generators. Photovoltaic collectors (PV) and solar thermal collectors (STC) are available as solar energy harvesting options. Additionally, batteries (BAT) and thermal energy storages (TES) are included as possible energy storage options. In addition, we consider the insulation of the building's outer wall (WALL), roof (ROOF), ground floor (FLORR) and window replacement (WIN) as possible measures.

The optimization program offers two retrofit scenarios, retrofit and advanced retrofit, to reduce the building's energy demand. As the model's input were updated compared to the original version of Schütz et al., section 2.3.2. describes the updated input data. To reduce computing time and to consider extreme days, we implement a k-MILP clustering [15] algorithm to represent the annual profiles of weather data, domestic hot water (DHW), and electricity demand through eight weighted type days complemented by two extreme days. The target function minimizes the total annualized costs (TAC) for the building owner, which are calculated based on the VDI 2067 [16] standard. The cost function includes annualized investments (c^{inv}), demand costs (c^{dem}), and revenues from the sale of surplus electricity ($r^{el,sell}$) or subsidies (r^{sub}).

$$\min(c^{inv} + c^{dem} - r^{el,sell} - r^{sub}) \tag{1}$$

If the observation period exceeds the service life of a system, the residual value is calculated based on a replacement investment. The investment is comprised of acquisition costs for the system technology and renovation costs for building envelope measures. Demand costs and profits from surplus electricity fed into the grid are annualised using a dynamic factor and annuity factor. Binary variables x are utilised to map system selection, and to bound the nominal heat output Q^{nom}_{dev} of a heat generator *dev* with its minimum and maximum size.

$$\dot{Q}^{nom}_{dev} \leq \dot{Q}^{nom}_{max,dev} \cdot x_{dev} \quad \text{and} \quad \dot{Q}^{nom}_{dev} \geq \dot{Q}^{nom}_{min,dev} \cdot x_{dev} \tag{2}$$

For the PV and STC systems, the integer variable z specifies how many modules are installed on the roof. The area of all installed solar modules must not exceed the maximum roof area A^{roof}_{max}.

$$\sum_{sol \in \{STC,PV\}} z_{sol} \cdot A_{sol} \leq A^{roof}_{max} \tag{3}$$

For the building envelope components, the decision variable $x^{retrofit}$ represents whether the component is retrofitted and to which retrofit level. The retrofit levels considered are standard (strd), retrofit (retrofit) and advanced retrofit (adv). The *strd* level is associated with no costs and each component of the building envelope has to select one level.

$$\sum_{i \in \{strd,retrofit,adv\}} x^{retrofit}_{shell,i} = 1, \forall \text{ shell in Building Shell} \tag{4}$$

The heat demand is calculated according to DIN EN 12831 [17] and includes the heat required for room heating and DHW production. The DHW demand is considered by time series as a fixed input parameter, while the space heating demand is computed based on the building envelope renovation and the difference between indoor and outdoor temperatures. The resulting heat demand must be provided at each time step. Further details on the modeling of heat generators and technical devices can be found in Schütz et al [10] . This study focuses on the impact of investment subsidies for individual retrofit measures. Under the German subsidy scheme for individual measures, a percentage of the investment costs is subsidized for the installation of HP, PEL, PV, STC, BAT, or for retrofitting components of the building shell to a maximum heat transfer coefficient U^{max} (WALL: 0.2 $\frac{W}{mK}$, WIN: 0.95 $\frac{W}{mK}$, ROOF: 0.14 $\frac{W}{mK}$, FLOOR: 0.25 $\frac{W}{mK}$).

2.2. Bi-Level model

To determine optimized subsidy schemes for modernization measures, a model is described which includes the objectives and goals of the funding agency as well as the funding recipients. Between the funding agency and the funding recipient exists a dynamic behaviour and their decision making process is intertwined. Within the studies of game theory in economics, this market situation is known as the Stackelberg Competition. The game consists of a leader and a group of follower. The leader makes an action which can be observed by all followers. After that, the followers react with an action best suited for their needs. With regard to the optimization of federal subsidy funding, the state takes the position as leader who decides about subsidy shares for different renovation measurements and building owners are the followers who use the provided subsidy share to minimize their total annualized costs.

As an assumption, the funding agency aims to minimize its use of paid subsidy funds and thus its costs. At the same time, a CO_2 goal is defined for the considered building stock and the funding agency has to provide at least as much subsidy funds as needed to achieve the CO_2 goal.

The decision variables of the funding agency are the funding shares provided for a device or a building shell modernization measure and are denoted with ϕ^{inv}. The individual buildings decide for their best investment strategy with the variables c^{inv}(y) which derives from the solution of the lower problem (LowP). In addition, the variable *em*(*y*) obtained from the LowP is the amount of CO_2 emitted, which must not exceed the parameter em^{lim}.

This results in the following form of the upper problem (UppP):

$$\begin{aligned} \mathit{UppP}: \quad & \min \quad \phi^{inv} \cdot c^{inv}(y) \\ & \text{s.t.} \\ & \qquad em(y) \quad \leq \quad em^{lim} \\ & \qquad\quad y \quad \in \quad \text{argmin}(\mathit{LowP}(\phi)) \end{aligned} \tag{5}$$

In the above formulation, the decision variables of the UppP and LowP are multiplied and thus constitute a non-linearity. To avoid this non-linear terms, the linearization following the approach of Liu et al. [11] is applied. For this purpose, the variable ϕ^{inv} is mapped as a discrete interval *KX* with a step length *KM* and the binary variable δ_k and the continuous auxiliary variable CX_k are introduced. The equations describing the linearization are displayed in equations 6a - 6e.

$$\sum_{k \in KX} \delta_k \leq 1 \tag{6a}$$

$$CX_k \leq \delta_k \cdot M \quad , \forall k \in KX \tag{6b}$$

$$c^{inv} - CX_k \leq (1 - \delta_k) \cdot M \quad , \forall k \in KX \tag{6c}$$

$$CX_k \leq c^{inv} \quad , \forall k \in KX \tag{6d}$$

$$\phi^{inv}_{min} + (\phi^{inv}_{max} - \phi^{inv}_{min})/KM \sum_{k \in KX} k \cdot \delta_k = \phi^{inv} \tag{6e}$$

Using equation 6e, the auxiliary variable δ_k can be translated back to the original variable ϕ^{inv}. The UppP of the BiOP can be represented using only linear terms and can be stated as follows:

$$\begin{aligned} \mathit{UppP}: \quad & \min \quad \phi^{inv}_{min} \cdot c^{inv} + (\phi^{inv}_{max} - \phi^{inv}_{min})/KM \sum_{k \in KX} CX_k \\ & \text{s.t.} \\ & \qquad\qquad em(y) \quad \leq \quad em^{lim} \\ & \qquad \text{Equations (6a)} \quad - \quad \text{(6e)} \\ & \qquad\qquad\quad y \quad \in \quad \text{argmin}(\mathit{LowP}(\phi)) \end{aligned} \tag{7}$$

As there are still binary variables present in this model, a reformulation of the BiOP to a single-stage optimization program using the KKT condition is not possible. Instead, the solution space of the LowP is discretized and included in the UppP to formulate the optimization problem as a single-level model.
The result of a single-building optimization can be roughly divided into energetic renovation measures of the building envelope, which improve the heating load of the building, and technology for heat generation, which covers the heating load. Three levels are considered as renovation measures for the building components WALL, WIN, ROOF and FLOOR. The heating load can be covered either by GAS, HP with back up EH or PEL. Furthermore, the roof can be used for PV or STC. As a simplification, the roof area is divided into the discrete steps no usage, half usage, or full usage. Within the cases of full usage PV, a further distinction is made between the possibility to buy BAT or not. For the discretization of the solution space, all combinations between the components are calculated and stored. The single building model is then reformulated making use of the discrete combinations. A binary variable λ_i for each possible combination *i* indicates whether the combination *i* is chosen as the optimal solution. Using the TAC_i and the investment c^{inv}_i of the combination *i*, the optimization program of the single building model can thus be represented as follows.

$$\begin{aligned} \mathit{LowP}: \quad & \min \quad \sum_{i \in \mathcal{K}} \lambda_i (TAC_i - c^{inv}_i \cdot \phi^{inv}) \\ & \text{s.t.} \\ & \qquad \sum_{i \in \mathcal{K}} \lambda_i \quad = \quad 1 \\ & \qquad\quad \phi^{inv} \quad \in \quad \text{argmin}(\mathit{UppP}(\lambda_i)) \end{aligned} \tag{8}$$

We use the following approach to resolve the bi-level structure of the BiOP: If only the constraints of the LowP are included in the UppP, the optimizer selects a package of measures, thereby minimizing the funding agency's objective function. However, the selected package of measures is not necessarily the preferred solution for the single building. To reflect this, equations are added using the Big M method to ensure that the selected measures are also optimal for the single building with the current solution of the UppP. Assuming that

a combination i_1 from the set of combinations $\mathcal{K}$ can be considered as the optimal set of measures. Then the total cost minus the subsidies of combination i_1 must be less than or equal to the total cost minus the subsidies of any other possible combination i_2 in $\mathcal{K}$. Generalizing this constraint for any i_1, i_2 in $\mathcal{K}$ yields:

$$TAC_{i_1} - c_{i_1}^{inv} \cdot \phi^{inv} - (1 - \lambda_{i_1})M \quad \leq \quad TAC_{i_2} - c_{i_2}^{inv} \cdot \phi^{inv} \quad , \forall i_1, i_2 \in \mathcal{K} \tag{9}$$

From equation 9 follows that λ_{i_1} can only take the value 1 if no other combination $i_2 \in \mathcal{K}$ exists for which there is a lower cost under the current solution ϕ^{inv}. Although equation 9 ensures that the optimal package of measures is selected for the individual building, this formulation of constraints is not efficient. Since the set $\mathcal{K}$ is iterated over twice, the number of constraints is quadratic to the possible combinations in $\mathcal{K}$ leading to high computation time to generate the constraints of the optimization model. To counteract this, we use a Cutting Plane Algorithm (CPA) and systematically add only the constraints that restrict the solution space. The optimization problem is first initialized without equation 9 and a branch-and-bound algorithm (B&B) is started. If an admissible solution is found, the combination i for which λ_i takes the value 1 is determined. If another combination $j \in \mathcal{K}$ exists for which the total cost is lower than with i, the specific constraint is added, by which the current solution i is no longer admissible. The flow of the CPA is outlined in algorithm 1.

Algorithm 1 CPA for iterative restricting the solution space

```
Initialize B&B
Solve LP-relaxation
if Solution i ∈ ℤ then
    if TAC_i − c_i^inv · φ^inv ≤ TAC_j − c_j^inv · φ^inv, ∀j ∈ 𝒦 then
        Solution accepted
    else
        for j ∈ 𝒦 : TAC_j − c_j^inv · φ^inv ≤ TAC_i − c_i^inv · φ^inv do
            Add constraint:
            TAC_i − c_i^inv · φ^inv − (1 − λ_i)M ≤ TAC_j − c_j^inv · φ^inv
        end for
    end if
end if
```

Since the funding agency wants to achieve a CO_2 target for a stock consisting of different buildings, the set $\mathcal{B}$ is defined which includes the different building types. Using the discretization of the single building optimization presented in equations 10, the CPA presented in algorithm 1 and considering a building stock defined by the set $\mathcal{B}$, the BiOP can be reformulated as a single stage MILP by the following equations 10.

$$\begin{aligned}
\min \quad & \sum_{b \in \mathcal{B}} \Big(\sum_{i \in \mathcal{K}_b} (\phi_{min}^{inv} \cdot \lambda_{i,b} \cdot c_{i,b}^{inv}) + (\phi_{max}^{inv} - \phi_{min}^{inv}) / KM \sum_{k \in KX} CX_{k,b} \Big) & & & \\
\text{s.t.} \quad & & & & \\
& \sum_{i \in \mathcal{K}_b} \lambda_{i,b} & = & 1 & , \forall b \in \mathcal{B} \\
& \sum_{b \in \mathcal{B}} \Big(\sum_{i \in \mathcal{K}_b} \lambda_{i,b} \cdot em_{i,b} \Big) & \leq & em^{lim} & \\
& \sum_{k \in KX} \delta_{k,b} & \leq & 1 & , \forall b \in \mathcal{B} \\
& CX_{k,b} - \delta_{k,b} \cdot M & \leq & 0 & , \forall k \in KX, b \in \mathcal{B} \\
& \sum_{i \in \mathcal{K}_b} \lambda_{i,b} \cdot c_{i,b}^{inv} - CX_{k,b} - (1 - \delta_{k,b}) \cdot M & \leq & 0 & , \forall k \in KX, b \in \mathcal{B} \\
& CX_{k,b} - \sum_{i \in \mathcal{K}_b} \lambda_{i,b} \cdot c_{i,b}^{inv} & \leq & 0 & , \forall k \in KX, b \in \mathcal{B} \\
& \lambda_{i,b}, \delta_{k,b} & \in & \{0,1\} & , \forall i \in \mathcal{K}_b, k \in KX, b \in \mathcal{B}
\end{aligned} \tag{10}$$

2.3. Application at case study

2.3.1. Building stock data

The focus of this study is on the residential single-family house stock in Germany. The European TABULA [18] project provides 12 archetypes that classify the German residential building stock based on the building's energetic quality, with each archetype representing a specific age class of buildings. Since buildings constructed after 2001 are assumed to already have good energy performance, they are not included in this study. To achieve comparability, all buildings are assumed to have a heated net floor area of 150 m^2 and three occupants per household. The building geometry is parameterized based on the TABULA database, using relation

factors between net floor area and buildings shell components similar to Lauster et al [19]. Potsdam is chosen as the location to represent a typical moderate German climate.

2.3.2. Inputs on building level

Different technical and economical inputs as well as time series data are necessary inputs on single building level: Typical modernization measures and heat transfer coefficients for the different archetypes originate from the TABULA typology [18]. Technical device efficiencies are obtained from manufacturer data, while the HP's behavior is modeled according to DIN V 18599 [20]. Emission factors of the energy sources originate from [21] and [22]. General economic parameters are based on the past 10-year development and are presented in Table A.2. Energy prices are scenario dependend and explained in section 1. Investment costs for building shell retrofitting are obtained from IWU [23] and include fixed and area-related costs. Installation costs for heating technologies are sourced from BDEW [24], while costs for PV and STC are from the online construction database Sirados [25]. Device investment costs are derived from market research and include fixed and power-related (for heating technologies) or area-related (for PV and STC) costs. Operation and maintenance costs are presented as percentages of component costs. Hourly time series data for outdoor temperature and solar radiation are obtained from the German Meteorological Service (DWD) [26] to account for the interaction with the outdoor climate. Load profiles for domestic hot water and electricity demands are generated using the RichardsonPy [27] tool and serve as hourly input data. These inputs are summarized in Appendix A.

2.3.3. Scenarios

Two scenarios are considered to estimate the impact of future changes in energy prices and emission factors. The transition to renewable energy sources is expected to change the electricity mix, leading to fluctuations in electricity prices and emission factors. Additionally, the pellet market is affected by demand changes and the use of wood in other sectors. Therefore, scenario A represents the current market situation in Germany, while scenario B considers prognosed energy prices and emission factors for the year 2030 [28]. For scenario A, the emission factors for 2021 are based on current data, while for scenario B, the emission factor for electricity is expected to decrease according to the German climate targets for the energy sector. A linear regression model is used to extrapolate an emission factor for electricity from the grid in 2030. The emission factor for pellets in scenario A is based on sustainable forestry practices in Germany [21]. However, Röder et al. [29] found that the production conditions highly influence the emission factor of pellets. To account for possible increased demand effects and non-sustainable forestry practices, scenario B assumes an emission factor of 100 $\frac{g_{CO_2}}{kWh}$ for pellets. Table 1 summarizes the assumptions for both scenarios.
Pehnt et al. [30] propose a system of emission classes to rate buildings based on their maximum CO_2 emissions relative to their living space. These classes range from A+++ for buildings emitting less than -10 $\frac{kg_{CO_2}}{m^2}$ to H for those emitting more than 60 $\frac{kg_{CO_2}}{m^2}$. To incentivize PV electricity feed-in, the system offers an emission credit that can result in negative emissions. In this study, we adopt Pehnt et al.'s emission classes and investigate the minimum required subsidies to attain classes A to C in average over all buildings. Therefore, the area-related climate targets are multiplied by the living space and the numbers of buildings in the considered building stock. Table 1 shows the resulting emissions targets A,B and C, which are the same for both scenarios.

Table 1: Energy prices Emissions factors in different scenarios

		Scenario A	**Scenario B**
Energy prices in $\frac{EUR}{kWh}$	Electricity	0.400	0.327
	El. HP	0.350	0.246
	Pellet	0.104	0.110
	Gas	0.120	0.125
Emission factors in $\frac{g_{CO_2}}{kWh}$	Electricity	420	164
	Pellet	36	100
	Gas	202	202
Emission targets in Mil. t_{CO_2}	A	6.9	6.9
	B	16.6	16.6
	C	27.6	27.6

3. Results

The optimized subsidy strategy yields different outcomes based on the desired climate target of the funding agency. Figure 2 (a) summarizes the optimized subsidy shares for individual measures for the emission targets A, B, and C for both scenarios A and B. In addition to the subsidy rates, an analysis of the investments indicates

the effects of the subsidy schemes. Therefore, Fig. 2 (b) shows the annualized investment costs per emission target and scenario divided into a bar for plant technology and a bar for shell measures.

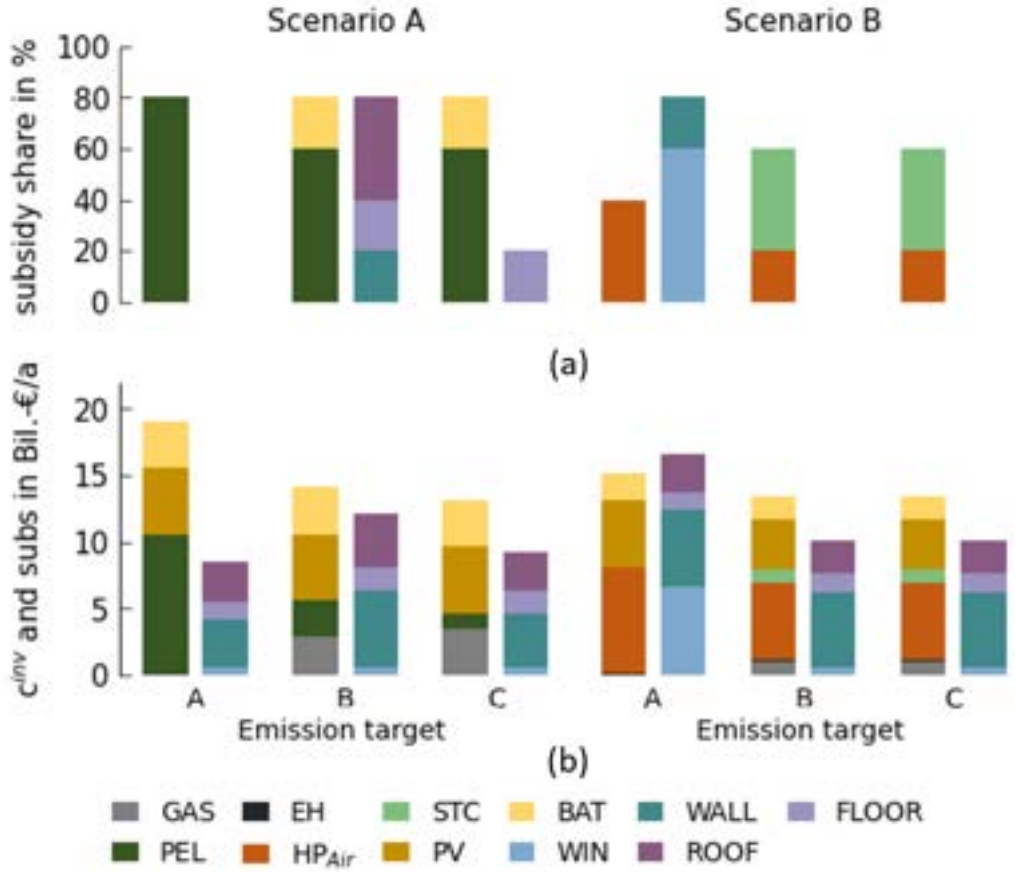

Figure 2: Investment costs for plant technology (left bar) and insulation measures (right bar) for different emission targets and scenarios

In the case of emission target A and parameters of scenario A, the unique subsidized technology is PEL with an investment grant of 80 %. Under this funding rate, all building entities install PELs as their heat conversion technology, making the investment in PELs the highest cost position for emission target A in scenario A. Pellets are nearly climate neutral and given the emission factors of scenario A, lead to a significant CO_2 reduction. Compared to the heat generation by HP, pellet heat supply is cheaper, given the price assumptions of scenario A. Moreover, due to the higher emissions factor of the current German electricity mix, the heat supply by pellet leads to lower emissions per kWh than an alternative supply by HP. Besides the investment in PEL, Fig. 2 shows high investments in PV and BAT systems. Installing PV and BAT is advantageous in all buildings due to the high electricity prices, resulting in cost savings in electricity supply by the means of PV and BAT. Therefore, no subsidies for PVs and BAT are required. The investment in PELs leads to a decrease in emissions even without any subsidies for shell modernization measures due to the low pellet emission factor. Even without incentives, measures on the roof and ground floor are chosen in old buildings as they come with comparatively low investment costs. In old buildings with poor insulation standards, the insulation of the outer wall is favorable under the high energy prices of scenario A even without subsidy. Newer buildings refrain from modernizing the building shell. However, the results of high penetration of PELs should be considered with regard to demand effects and the associated increases in the pellet price and emission factor, as shown in scenario B (see section 1). In scenario B, the optimal solution is to promote HPs with a 40 % investment grant, while also providing subsidies for window replacement (60 % share) and wall insulation measures (20 % share). The differences to scenario A can be explained by the lower electricity prices and emission factors and the increased pellet emission factor making the HP the best option in terms of CO_2 avoidance costs. Figure 2 shows high investments in HPs and PVs in this scenario. Electrification of the energy system of each building achieves the emission target for emission target A. Investments in PV's and BAT reduce costs from the building owner's point of view. To reach the ambitious emission target, investments in the insulation of the building shell are necessary as Fig. 2 demonstrates. As wall insulation is highly effective in heating demand reduction, it should be promoted to retrofit old building ages with poor insulation standards. As window replacement is

expensive in relation to energy and cost savings, its implementation must be promoted with subsidies of 60 %. The results show that the subsidies for the building shell lead to modernization in older buildings with poor insulation standards, while buildings with higher insulation standards refrain from renovation measures.

Optimization results for emission target B show similarities with regard to the subsidised technologies but differ in subsidy shares and promoted renovation measures. In scenario A, the investment in PELs should be promoted with a 60 % investment grant. Compared to emission target A, Fig. 2 demonstrates that the total investment in PELs for emission target B is only a quarter of the investment in PELs for emission target A. The PEL subsidy share of 60 % leads to PELs only being used in modern buildings, where the outer wall is not retrofitted after the optimization. These modern buildings initially have a better insulation standard than older buildings. In buildings with retrofitted outer wall, the investment in a GAS is preferred to the choice of a PEL due to the low investment costs in combination with only slightly higher demand related costs. PVs and BAT are again, like in all scenarios, chosen even without subsidies and lead to high emissions savings. Instead of stimulating the investment in low-emission heat conversion technologies on a large scale, the energetic modernization of the outer wall, the ground floor and the roof is promoted for emission target B in scenario A. The increased subsidies lead to higher investments in insulation measures, especially for the insulation of outer walls and the roof. Scenario B shows a different subsidy strategy for emission target B compared to emission target A: HPs are promoted with a 20 % investment grant and STC with a 40 % investment grant. This subsidy scheme leads to HPs being installed in all buildings except for old buildings with a low insulation standard, where they operate with lower efficiency than in better insulated buildings. The reduction of the investment in HPs amounts to 25 %. In older buildings with low insulation standards, GAS are installed. STC supports the heat supply in buildings with GAS, where they can achieve relevant emission savings.

For emission target C in scenario A, the results show an optimized subsidy share of 60 % for PEL and 20 % for FLOOR. In this scenario, the PEL only supplies older buildings with poor insulation standard, that do not modernize the outer wall. The investments in PELs, therefore, decrease by more than half compared to the results for emission target B. The lower share of PELs is replaced by GAS, resulting in lower investment costs but higher emissions. The investments in PVs and BAT are the same as for emission target B. A subsidy share of 20 % for floor measures ensures that all buildings undertake a floor modernization. The subsidy strategy and investments for emission target C in scenario B are exactly the same as for emission target B. No feasible solution seems to lie between emission target C and B.

Examining the amount of subsidies disbursed and the consequent emission avoidance cost can provide insights into the efficient utilization of subsidy funds. Figure 3 illustrates the total annualized subsidies and the CO_2 avoidance costs for emission targets A, B, and C under both scenarios A and B. It is apparent that the

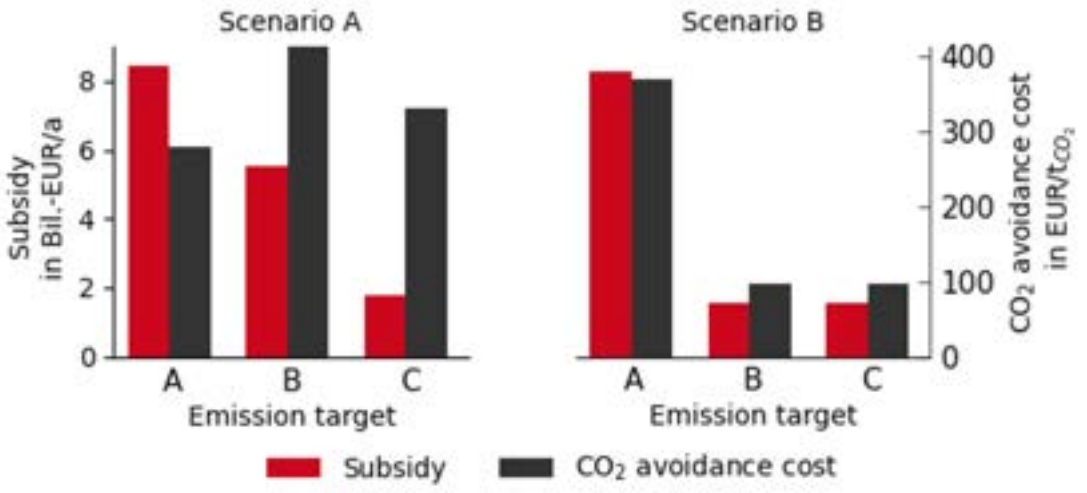

Figure 3: Total amount of annualized subsidies and emissions for different emission targets and scenarios

required subsidies increase significantly with more ambitious climate objectives. In scenario A, complete decarbonization of the building stock is achieved for emission target A, even if the climate target permits higher emissions. The low emission factor of pellets in combination with an emission credit for electricity fed into the grid, results in a balance of approximately zero emissions for the building stock. Compared to emission targets B and C, the CO_2 avoidance cost for target A are comparatively low due to the high emission savings. For emission target B, the building stock's emissions rise to 16.3 million tons of CO_2 per year, while subsidies

decrease by 30 %. When aiming for emission target C, the emissions increase by one-third compared to class B, while the costs decrease by two-thirds, leading to lower CO_2 avoidance costs. Lower climate targets are found to be more cost-effective in terms of emission savings. In scenario B, the emission targets B and C are achieved with significantly lower CO_2 avoidance costs than in scenario A. The use of heat pumps in combination with lower emission factors of electricity leads to cost-efficient emission reductions. In the region between the emission targets C and B, only one optimal solution prevails over all others and leads to the same subsidy strategy. The inference that ambitious objectives necessitate significant subsidies can also be drawn from the results of scenario B.

4. Conclusion

This study introduces a BiOP for the optimal allocation of subsidies to achieve emission targets in a building stock. The method is applied to the residential single-family house building stock of Germany. Results show that an optimized strategy depends on aimed emission targets, energy prices, and emission factors of energy sources. If sustainable forestry can supply pellets with low emission factors, the best strategy is to promote PELs with high subsidy shares of up to 80 %. In combination with PV systems PELs can contribute to the decarbonization of the building stock. As the investment in PELs and the associated investment grant is comparatively expensive, the optimized subsidy strategy for less ambitious climate targets provides lower subsidy shares for PEL and additional subsidies for insulation measures for outer wall and floor insulation amounting to 20 %. If the electricity mix improves as aimed by the government and predicted by recent forecasts, the subsidy of HPs will be optimal in terms of minimized subsidy cost for emission reduction. High emission reductions must be promoted with a subsidy share of 40 % for HPs and accompanied by the promotion of window replacement with 60 % and outer wall insulation with 20 %. For lower emission targets, the promotion of insulation measures is not necessary. A subsidy rate of 20 % for HPs and 40 % for STCs which are combined with GAS achieves significant emission savings. With the progressive expansion of renewable energies in the electricity mix, funding agencies are advised to promote the electrification of heat supply through HP. These incentives should be accompanied by incentives for building insulation in poorly insulated old buildings.

The method presented allows a detailed technical examination of the investment decision of different building entities and proposes an approach for reformulating a bi-level problem with a lower-level MILP. The consideration of MILP at both levels of the bi-level problem and the application to a stock of individual buildings, each with its own decisions, is a novelty in the literature. The optimization program presented supports the decision-making process for subsidizing various energy-related measures and can facilitate the decision-making process of a funding strategy. When reformulating the problem into a one-stage problem, the solution space had to be discretized. This discretization could lead to inaccuracies in the problem solution. In addition, a very simple approach to mapping the building stock is used in this work. For the demonstration of the methodology, this seems justified. Future work should attempt to achieve a more accurate spatially resolved mapping and map the current state of modernization in buildings. A temporal resolution of the refurbishment process as well as the inclusion of limited resources such as investment budgets or craftsmen's capacities can be achieved by the method. Demand effects, which could lead to rising energy prices, can only be taken into account by the method through parameter variations.

Acknowledgments

We gratefully acknowledge the financial support by Federal Ministry for Economic Affairs and Climate Action (BMWK), promotional reference EA4400.

Appendix A Economical and technical Inputs

Table A.2: General Economical parameters and energy prices

Variable	Value	Unit	Variable	Value	Unit
Observation period	15	a	Yearly inflation	1.014	-
Interest rate	0.02	-	Energy tax gas	0.0055	EUR/kWh
Yearly el. price change	1.0388	-	Gas grid connection costs	118.7	EUR/a
Yearly gas price change	1.001	-	El. grid connection costs	96.0	EUR/a
Yearly pel. price change	1.0158	-			

Table A.1: Economical Parameters Devices

Device	Installation Cost	Fix Investment Costs	Variable Investment costs	OM Cost
GAS	3,500 EUR	2,781.20 EUR	94.86 EUR/kW	2.5 %
HP Air	6,020 EUR	2,072.20 EUR	677.5 EUR/kW	2.5 %
Pellet	7,700 EUR	8,308.20 EUR	146.42 EUR/kW	5 %
STC	4,300 EUR	0.00 EUR	245.22 EUR/m^2	1.5 %
PV	8,000 EUR	0.00 EUR	95.42 EUR/m^2	1%
TES	0 EUR	460.00 EUR	608.6 EUR/m^3	2%
BAT	0 EUR	2,500.00 EUR	709.4 EUR/kW	1%
EH	100 EUR	111.00 EUR	8.00 EUR/kW	3%
WALL	Included in Fix.	3.3 EUR/(m)	112.2 EUR/(m^2m)	0 %
WIN	Included in Fix.	-2.7 EUR/(m)	876.1 EUR/(m^2)	0 %
ROOF	Included in Fix.	2.8 EUR/(m)	39.1 EUR/(m^2m)	0 %
ROOF	Included in Fix.	1.8 EUR/(m)	63.0 EUR/(m^2m)	0 %

Nomenclature

Abbreviations

BAT Battery

BiOP Bi-Level Optimization Program

DHW District Hot Water

FLOOR Ground floor insulation

HP Heat pump

GAS Gas boiler

KKT Karush-Kuhn-Tucker

MILP Mixed-Integer Linear Program

PEL Pellet boiler

PV Photovoltaic collector

ROOF Roof insulation

STC Solar thermal collector

TAC Total Annual Cost

WALL Outer Wall insulation

WIN Window replacement

BES Building energy system

Variables

A_{sol} solar module area

c^{dem} demand cost

c^{inv} invest cost

$r^{el,sell}$ revenue from feed-in electricity

r^{sub} revenue from subsidy

$\dot{Q}^{nom}_{dev}$ nominal heat output

x purchase decision variable

$x^{retrofit}_{shell}$ decision variable for renovation measure

ϕ^{inv} subsidy share

λ decision variable for measure pattern

References

[1] European Commission. A Renovation Wave for Europe -greening our buildings, creating jobs, improving lives. 2020. Available from: https://eur-lex.europa.eu/resource.html?uri=cellar:0638aa1d-0f02-11eb-bc07-01aa75ed71a1.0003.02/DOC_1&format=PDF.

[2] European Commission, Directorate-General for Communication. European green deal : delivering on our targets; 2021. Available from: https://data.europa.eu/doi/10.2775/373022.

[3] European Commission. Energy Efficiency in Buildings. MDPI; 2020. Available from: https://commission.europa.eu/system/files/2020-03/in_focus_energy_efficiency_in_buildings_en.pdf.

[4] Vedung E. Policy Instruments: Typologies and Theorie. In: Carrots, Sticks, and Sermons: Policy Instruments and Their Evaluation; 1998. p. S. 21 28.

[5] Ruparathna R, Hewage K, Sadiq R. Economic evaluation of building energy retrofits: A fuzzy based approach. Energy and Buildings. 2017;139:395-406.

[6] Asadi E, da Silva MG, Antunes CH, Dias L. Multi-objective optimization for building retrofit strategies: A model and an application. Energy and Buildings. 2012 Jan;44:81-7.

[7] Ashouri A, Fux SS, Benz MJ, Guzzella L. Optimal design and operation of building services using mixed-integer linear programming techniques. Energy. 2013 Sep;59:365-76.

[8] Harb H, Reinhardt J, Streblow R, Müller D. MIP approach for designing heating systems in residential buildings and neighbourhoods. Journal of Building Performance Simulation. 2015 Jun;9(3):316-30.

[9] Renaldi R, Kiprakis A, Friedrich D. An optimisation framework for thermal energy storage integration in a residential heat pump heating system. Applied Energy. 2017 Jan;186:520-9.

[10] Schütz T, Schraven MH, Remy S, Granacher J, Kemetmüller D, Fuchs M, et al. Optimal design of energy conversion units for residential buildings considering German market conditions. Energy. 2017 Nov;139:895-915.

[11] Liu Z, Wang S, Lim MQ, Kraft M, Wang X. Game theory-based renewable multi-energy system design and subsidy strategy optimization. Advances in Applied Energy. 2021 may;2:100024.

[12] Martelli E, Freschini M, Zatti M. Optimization of renewable energy subsidy and carbon tax for multi energy systems using bilevel programming. Applied Energy. 2020 jun;267:115089.

[13] Prada A, Cappelletti F, Gasparella A. Optimization of government subsidization strategies for building stock energy refurbishment. International Association of Building Physics (IABP); 2018.

[14] Zhou Y, Wang L, McCalley JD. Designing effective and efficient incentive policies for renewable energy in generation expansion planning. Applied Energy. 2011 Jun;88(6):2201-9.

[15] Zatti M, Gabba M, Freschini M, Rossi M, Gambarotta A, Morini M, et al. k-MILP: A novel clustering approach to select typical and extreme days for multi-energy systems design optimization. Energy. 2019;181:1051-63.

[16] VDI. Wirtschaftlichkeit gebäudetechnischer Anlagen: VDI 2067; 2012.

[17] Deutsches Institut für Normung e V . DIN EN 12831 - Heizungsanlagen in Gebäuden - Verfahren zur Berechnung der Norm-Heizlast;. Abgerufen am 16.07.2022. Available from: https://www.beuth.de/de/norm-entwurf/din-en-12831-1/215479737.

[18] Loga T, Diefenbach N, Stein B, Born R. TABULA - Scientific Report Germany: Further Development of the National Residential Building Typology. 2012.

[19] Lauster M, Constantin A. Verification of a Low Order Building Model for the Modelica Library AixLib using ASHRAE Standard 140. In: Proceedings of Building Simulation 2017: 15th Conference of IBPSA. Building Simulation Conference Proceedings. IBPSA; 2017. .

[20] DIN. Energetische Bewertung von Gebäuden - Berechnung des Nutz-, End- und Primärenergiebedarfs für Heizung, Kühlung, Lüftung, Trinkwarmwasser und Beleuchtung: DIN V 18599; 2018.

[21] Bundesamt für Wirtschaft und Ausfuhrkontrolle. Informationsblatt CO_2-Faktoren; 2021.

[22] Petra Icha, Dr Thomas Lauf. Umweltbundesamt, editor. Entwicklung der spezifischen Treibhausgas-Emissionen des deutschen Strommix in den Jahren 1990 - 2021;.

[23] Koch T, Achenbach S, Müller A. Anpassung der Kostenfunktionen energierelevanter Bau- und Anlagenteile bei der energetischen Modernisierung von Altbauten auf das Preisniveau 2020; 2021.

[24] Mailach O. BDEW, editor. BDEW-Heizkostenvergleich Altbau 2021;.

[25] SIRADOS. SIRADOS Baudaten; 2023. Available from: https://www.sirados.de.

[26] Deutscher Wetterdienst. Ortsgenaue Testreferenzjahre von Deutschland für mittlere, extreme und zukünftige Witterungsverhältnisse; 2017. Available from: https://www.bbsr.bund.de/BBSR/DE/forschung/programme/zb/Auftragsforschung/5EnergieKlimaBauen/2013/testreferenzjahre/try-handbuch.pdf?__blob=publicationFile&v=6.

[27] Richardson I, Thomson M, Infield D, Clifford C. Domestic electricity use: A high-resolution energy demand model. Energy and Buildings. 2010 Oct;42(10):1878-87.

[28] PROGNOS. VBW, editor. Strompreisprose; 2022.

[29] Mirjam Röder, Carly Whittaker, and Patricia Thornley. How certain are greenhouse gas reductions from bioenergy? In: Biomass and Bioenergy. vol. 79;. p. S. 50-63.

[30] Pehnt M, Mellwig P, Lempik J, Darup BS, Schöffel W, Drusche V. Neukonzeption des Gebäudeenergiegesetzes (GEG 2.0) zur Erreichung eines klimaneutralen Gebäudebestandes; 2021.

PROCEEDINGS OF ECOS 2023 - THE 36TH INTERNATIONAL CONFERENCE ON
EFFICIENCY, **C**OST, **O**PTIMIZATION, **S**IMULATION AND ENVIRONMENTAL IMPACT OF ENERGY SYSTEMS
25-30 JUNE 2023, LAS PALMAS DE GRAN CANARIA, SPAIN

Electricity demand forecasting for rural communities in developing countries: Calibrating a stochastic model for the Bolivian case

Claudia Sanchez[a,c], Pietro Di Betta[b], Nicolo Stevanato[b], Sergio Balderrama[c], Emanuela Colombo[b] and Sylvain Quoilin[a]

[a] Universite de Liege, Liege, Belgium, clsanchez@uliege.be,CA
[b] Politecnico di Milano, Milano, Italy,
[c] Universidad Mayor de San Simon, Cochabamba, Bolivia,

Abstract:

The world crusade to close the electrification gap is coming to an end in most regions of the world. In recent years the research in the area has concentrated on the development of planning methods to minimise the cost of implementation. Although successful, the lack of focus on the complex dynamics that govern electricity demand lead to over/under-sizing of technical solutions resulting in waste of resources and missed developing opportunities. In this sense, this paper aims to propose an electricity demand model for rural communities in Bolivia, based on an open-source bottom-up stochastic tool for load profile computation. The "energy sufficiency" concept is used to ensure that people's basic needs for energy are met in all the analysed cases. Information from various sources, such as on-site surveys, databases and national reports were used to characterise the main geographical areas in Bolivia and the relative specific categories of users. Specific load curves generated with the model were used as inputs in a micro-grid sizing tool and the results were compared with an approach using a demand analysis in less detail. Main results show that the model obtained is capable of generating stochastic demand curves for single or multiple rural communities according to contextual particularities. Notably, the geographic location and the socio-economic characteristics have a significant impact in the peak loads and the total demand. Considering small industries as an income generating activity can increase in the peak load by about 45%, consequently, there is an economic impact when investing in the solution.

Keywords:

Rural electrification, developing countries, energy sufficiency, energy demand

1. Introduction

The global effort to close the electrification gap has made significant progress in recent years moved by the Sustainable Development Goal 7 [1]. However, much of the research in this area has focused on minimizing the cost of implementation, often at the expense of considering the complex dynamics that govern electricity demand in rural communities [2]. This narrow focus has led to the implementation of technical solutions that are either oversized or undersized, leading to resource wastage and missed opportunities for development. [3, 4]. Therefore, it is crucial to develop planning methods that consider the specific contextual factors influencing electricity demand in rural communities [5]. This approach ensures that technical solutions are adequately sized and effectively meet the basic energy needs of the population [6]. In order to achieve this, the selection of the optimal electricity supply strategy and the capacity of the local generation and storage system heavily rely on the anticipated electricity usage. This demand is determined by both the shape and height of the hourly load curve, as well as the overall energy consumption, as evidenced in [7].

According to the literature, there is a wide range of energy modelling tools with different scopes and capabilities to support energy planning at different scales. However, it is clear that there are still challenges related to the demand side, that need to be addressed [8]. Energy System models have demonstrated limited representativity of societal transformations such as behaviour of actors, transformation dynamics on time and heterogeneity across and within societies, that could potentially have impacts in the demand side [9, 10]. Regarding to demand estimation tools, [11] concludes that deterministic models for energy demand estimation are simpler to comprehend and use, but the results they generate are inflexible and have limited information. Conversely, stochastic methods require more resources and complex mathematical models but offer a more precise understanding of demand scenarios. In [12], the authors incorporated high-resolution demand estimation to an energy planning process, however, there is still room to improve the level of detail in the estimation in sectors such as productive activities.

Although there is no universally recognized definition for energy access, the literature frequently uses the term to describe a scenario in which individuals have access to modern energy sources and affordable end-use technologies [13, 14]. It is worth noting that while facilitating access to improved energy carriers is essential, it alone is inadequate for achieving broad-based poverty reduction and promoting socioeconomic development [14]. In this regard, recent studies have examined the impact of incorporating energy sufficiency scenarios in the context of electricity demand in Bolivia to estimate the amount of energy rural communities might need [15]. The current research aims to contribute to this effort by calibrating a bottom-up stochastic tool that can effectively capture the distinctive characteristics of the electricity demand in a developing country context.

2. Methodology

This section outlines the methodology employed to achieve the proposed objective. The approach encompasses four primary stages, as illustrated in Figure 1. In the first stage, an analysis was conducted on the database containing historical electricity consumption per household situated in rural areas where the rural communities already possess access to electricity. Through this analysis, significant variables that affect residential electricity consumption and typical monthly aggregate consumption ranges for each region were identified.

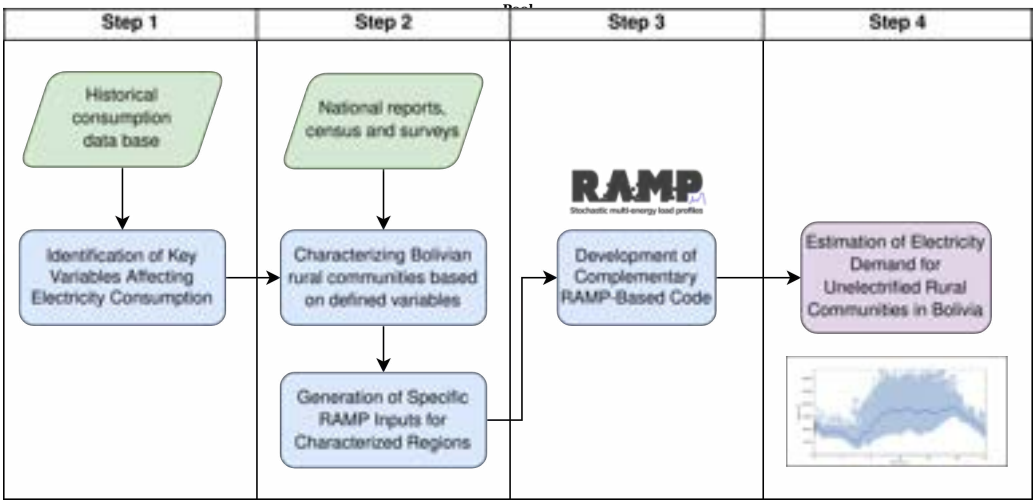

Figure 1: Flowchart of the four-step methodology

The second stage involved developing tailored inputs for the RAMP model for the region under study. This was achieved by considering the different sectors of energy consumers in the rural communities. The inputs for the RAMP model were created using the data obtained from in site surveys from previous studies, which were then cross-checked and replicated closely with the monthly aggregate consumption data acquired in the preceding stage. National reports and standards were employed to construct the RAMP inputs for the remaining sectors.

The third stage focuses on the development of a tool for village load formulation based on RAMP model, to utilize the tailored inputs created in the previous stage to generate stochastic load curves that are appropriate for specific scenarios. The model is designed to incorporate the most critical variables identified in the first stage. In the final stage of the study, the model is employed to generate load curves for rural communities in developing countries based on different established scenarios. These scenarios involve communities with different characteristics, thereby providing insights into how demand varies across diverse contexts.

2.1. A bottom-up stochastic tool for estimation of energy demand: RAMP

The RAMP tool is a stochastic model that operates from the bottom-up and is capable of generating load curves based on user behavior. It is a valuable tool for exploring the demand of remote communities and as an initial step towards sizing appropriate energy systems. The tool is built upon three layers: users, user types, and appliances. The top layer involves defining various User types (such as households, commercial activities, public offices, hospitals, etc.) based on the modeller's discretion. The level of detail for each User type can vary depending on the available information, for example, households can be divided into income classes or building types for greater precision. The second layer involves determining the number of individual Users associated with each User type, while the third layer focuses on the Appliances owned by each User. This three-layer structure enables independent modeling of the behavior of each Appliance and the creation of a unique load profile for each individual User within a given User type. Aggregating all independent User profiles generates a total load profile that is different for each model run, replicating the unpredictability of

users' behavior and producing a range of daily profiles. Further information about the model can be found [16]. In order to approach the reality of a community or region as accurately as possible, it is essential to conduct a detailed characterization of its users. This is particularly important when studying the electricity demand of communities that have yet to gain access to electricity, and it represents a significant challenge.

3. Case of study

3.1. The Bolivian Context

Bolivia, a South American nation, is yet to achieve complete electrification coverage across its entire territory. However, universal access to electricity has been set as a national target to be achieved by 2025. As of 2018, the country had registered a national electricity coverage of 93 %, with 99% of urban areas and 80% of rural areas covered [17]. According to a previous study, rural communities with fewer than 50 households were mainly low-income and might not generate enough demand to make micro-grids economically feasible. Furthermore, the dispersed nature of some of these communities complicates the installation of a local grid [18].

3.2. Main regions of geographic importance

The rural communities in Bolivia are distributed throughout the country's three geographic regions: lowlands, valleys, and highlands. The National Agricultural Compendium [19] describes the characteristics of these regions. The lowlands span over an area of 670,000 km2 and exhibit a diverse mixture of land uses, tenure systems, and actors ranging from indigenous peoples to small-scale farmers and agro-businesses. The valleys are situated between 1800 and 3000 meters above the sea level and are known for their narrow valleys, rough terrain, and moderate climate. The highlands are defined as regions situated at an altitude exceeding 3000 meters above sea level, primarily located in the western part of the country, and inhabited by numerous remote indigenous communities. Agriculture is a significant activity in all three regions, with temperature, precipitation, and altitude serving as fundamental factors in determining the productive potential and production systems. It is noteworthy that cultural disparities exist among these regions, which could potentially impact individuals' attitudes and practices towards electricity consumption.

3.3. Rural community structure

The structure of the rural communities in Bolivia has been previously defined in [15], which comprises a residential consumption sector (RS), a community services sector (CS) and an income generating activities sector (IGA).

The Electricity Authority's 2020 Statistical Yearbook [20] indicates that the residential sector represents the largest portion of national electricity demand (both in the National Interconnected System and in the Isolated Systems), accounting for 43.56% of the total. This is followed by the industrial sector at 22.2%, the general category at 18.8%, mining at 6.4%, and public lighting and other sectors at 9%. The 2016 National Demographic and Health Survey in Bolivia [21] reveals the prevalence of various electrical appliances in households across different regions of the country that are notably different. Community services aim to provide education, health services, and clean water to the population, and common infrastructure for this purpose includes hospitals, schools, drinking water supply systems, and sports facilities.

Income-generating activities (IGA) in Bolivian rural areas are primarily agricultural and livestock-based, with 78% of the employed population working in this sector [22]. However, non-agricultural activities also contribute to the income of rural households, with 22% of the population engaged in manufacturing, sales and repairs, and construction. Livestock activities are important sources for improving the income of rural households, with more than 12% of rural household income coming from livestock activity and derived products. Agricultural production has low productivity and generally faces low prices in the market, but self-consumption of agricultural products provides food security for rural households [23, 24]. Different types of irrigation are used for agricultural activities, and the transformation of agricultural products is an important form of economic diversification in rural communities. Non-agricultural IGA's vary by region, reflecting the characteristics of local idiosyncrasy. Energy needs for IGA should not be neglected, as access to electricity can impact rural economies, with the transformation processes of agricultural products representing an opportunity for growth and diversification.

4. Results and discussion

The results obtained from the characterization of rural communities and their energy consumer groups, which were incorporated into the design of the tool, are presented in this section. Subsequently, the analysis of the demand profiles generated with the model is presented.

4.1. Generation of tailored inputs for RAMP

The findings of the initial phase of the investigation reveal the impact of certain variables on electric power consumption in rural communities that are connected to the main grid. The analysis of the database was

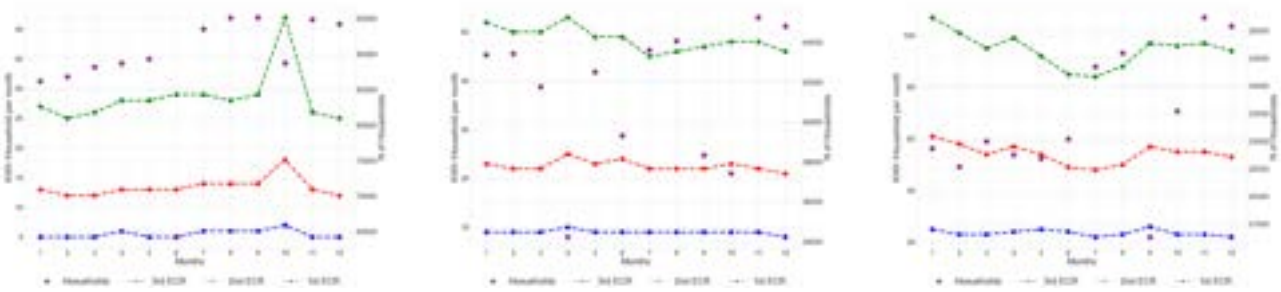

(a) Highlands (b) Valleys (c) Lowlands

Figure 2: Quartiles of electricity consumption of electrified households in rural areas.

initially developed by filtering the data of consumers in rural areas, classified in the three defined regions. A correlation analysis was performed using variables such as percentage of poverty, geographic location, proximity to roads, among others, corresponding to the municipality to which these residential consumers belong. The results of this analysis show that the variables of impact on electricity consumption at a residential level are: the geographic location or altitude and the household income.

To characterize and generate taylored inputs for RAMP, a range of information sources were utilized, including site surveys, national reports, and databases. Site surveys conducted specifically for the purpose of generating RAMP inputs for previous studies [25–27] were used as a point of reference, conducted in rural communities such as El Espino, La Brecha, El Sena, and Raqaypampa, located in distinct geographical regions across the country. Additionally, the 2012 Census national database [28] was employed, with demographic data projected through 2025. To determine the variables with the most significant impact on energy consumption at the national level, the electricity consumption database from [29] was utilized to validate variables that influence electricity consumption.

4.1.1. Residential sector

The 2016 National Demographic and Health Survey in Bolivia [21] reveals the prevalence of various electrical appliances in households across different regions of the country. Radios, televisions, and cellphones are the most commonly used appliances in both low and high poverty municipalities, which are predominantly rural communities. Refrigerators are more commonly used in low poverty regions of the lowlands compared to the highlands, where temperatures are lower. Radios are more frequently used than TVs in high poverty regions. Access to modern appliances is limited in high poverty regions [30]. Although different types of family composition have been recorded among the communities, the average number of persons per household in rural areas of Bolivia is 3.1, according to the 2016-2017 Household Survey [31].

To gain an overview of residential electrical consumption, it was possible to perform an statistical of the monthly electricity consumption ranges that represent general behavior over the course of a year, using the mentioned data base from [29]. This was achieved by computing the median of all percentile threshold values for each month. By identifying the most representative consumption ranges in this way, as showed in figure 2, it is possible to use them to characterize the electrical consumption patterns of low, middle, and high-income households in all three regions under consideration.

Figure 2 highlights the significant regional disparities in electricity consumption. The harsh living conditions in the highlands result in the lowest consumption rates. Conversely, the valleys have much higher electricity usage than the highlands, typically consuming twice as much across all consumption ranges. However, it is in the lowlands that the most substantial impact on overall electricity consumption is present, with values almost twice as high as those of the valleys. The reason behind this effect relies on tend to use appliances to improve the comfort due to high temperatures. Moreover, the use and energy consumption of refrigerators are also influenced by these temperatures, as demonstrated in [32, 33].

The findings of the study highlight the importance of taking into account the unique characteristics of different regions when modeling electricity usage in rural communities. By doing so, it becomes possible to more accurately capture the diverse needs and behaviors of households across the country. However, it was found that the difference in consumption between households was mainly driven by one appliance, namely refrigerators. Therefore, the study focused on only two categories of residential users, high-consumption and low-consumption, based on their overall electricity usage. The RAMP appliance configuration used in the study was designed to adequately represent these behaviors, which were consistent with the results of on-site surveys. This approach can help researchers and policymakers make informed decisions about energy planning

and management in rural communities, taking into account the specific characteristics and needs of different regions.

4.1.2. Community Services Sector

To deliver community services, appropriate infrastructures are needed including hospitals, schools, drinking water supply systems, sport facilities, public lighting and churches. government-mandated norms and standards for the community sector are uniform across the country, and as a result, altitude don't have any effect on the composition and characteristics of the energy users of this sector. This means that the list of appliances and the usage patterns associated with each service will remain unchanged. The only variation across different regions considered is in the behaviours of thermal appliances, which is determined by the average temperature of the targeted area.

Therefore, the selection of various types of facilities took place using specific criteria for different services. The criteria assumed for this methodology are described in the following sections for each type of facility considered and summarized in Table 1a.

Table 1: Criteria for the allocation of a) community services infrastructure and b) IGAs in rural communities according the population size of the communities

(a)

Infrastructure	Criteria
1 Health post	if 500-1000 inhab.
1 Health center	if more than 1000 inhab.
1 Public lighting post	per every 10 HH
1 Sport field	if more than 500 inhab.
1 Church	if more than 500 inhab.
1 Water supply system	per every 100 HH
1 School A	if less than 100 inhab.
1 School B	if 100-500 inhab.
1 School C	if more than 500 inhab.

(b)

Activity	HL	VA	LL
1 Irrigation system	30HH	22HH	18HH
1 Transformation activity	200HH	200HH	200HH
1 Grocery store	25HH	25HH	30HH
1 Restaurant	30HH	30HH	30HH
1 Workshop	80HH	70HH	60HH
1 Entertainment center	100HH	80HH	60HH

4.1.2.1 Health facilities

For this infrastructure, the "National Norm for the Characterization of Primary Health Care Facilities" [34] sets guidelines and standards for its availability in rural areas, including infrastructure and equipment requirements. For communities with a population between 500 and 1000, a "health post" is mandated, while for those with between 1000 and 10,000 inhabitants, a "health centre" with the capacity for hospitalization is required. If a community has fewer than 500 residents, it must be within a two-hour driving distance from both low and high-capacity healthcare facilities. The equipment ownership data per facility type was collected from the norm as well.

4.1.2.2 Educational facilities

With regards to education, three types of schools have been identified as the most common in rural areas, based on community size. Type A schools are small multi-level establishments located in the smallest and most remote communities with a population of less than 100 people. Type B schools have a larger number of classrooms and offer a range of instruction from primary to secondary education, with double-shift operation for communities with a population between 100 and 500. Type C schools are well-equipped educational institutions that can accommodate a greater number of students, typically in larger villages near cities or major roads when the population exceeds 500 [34]. Access to educational facilities remains a significant challenge for those living in rural areas. For example, education coverage still stands at 73-83% in the lowlands, indicating that significant improvements are still possible despite recent progress [34].

4.1.2.3 Drinking water supply systems

The type and characteristics of drinking water systems are influenced by the availability of water resources and the terrain in which the community is located. However, a standard water supply system has been chosen for each type of community in this study [35], as the modeling of these systems is not the primary focus. Future research could aim on doing a more in-depth characterization of water supply systems, as they are crucial for the health and well-being of rural communities, as emphasized by the Sustainable Development Goal 6 (SDG 6).

4.1.2.4 Public lighting and other community services

The presence of streetlights in rural communities is guided by the standards set forth in a document published by the energy ministry [35], which provides guidelines for the implementation of energy access projects. Accordingly, the guideline states that a streetlight must be installed for every 10 households in a community.

In recent years, the availability of sports facilities in rural communities has increased due to government health policies, as the Supreme Decree No. 1868 of the 2014 testifies [36]. As a result, in this work is considered that communities with a certain number of inhabitants will have this kind of community services.

4.1.3. Income Generating Activities

Income generating activities are defined as responsible for income increase or productivity growth. Neglecting the energy needs of IGA increases the risk of energy marginalization in rural communities, leading to greater energy inequality and a significant underestimation of the communities' total energy needs [37]. This sector is divided into agricultural and non-agricultural activities. Non-agricultural activities include grocery stores, restaurants, workshops, and entertainment businesses , while agricultural activities encompass irrigation systems and the processing of agricultural products.

As already done for the other two sectors, it is fundamental to explore how the three drivers influence the modelling of IGAs. Naturally, agricultural activities are substantially influenced by altitude as it serves as a crucial determinant for the viable sustenance of various plant and animal species [38]. Consequently, irrigation and transformation activities are affected.

Non-agricultural IGAs are reflect the local idiosyncrasies of each region. For instance, certain areas in the lowlands, like the Beni region, have a higher concentration of recreational and food businesses [39]. Taking into account these regional variations is crucial for modelling, but it can also be a complex task due to the limited availability of this type of data. For this reason, the empirical formulas presented in Table 1b are an estimation that aims at capturing the frequency of appearance of these businesses, based on [39], [40], [41].

The level of UBN in a community determines the composition of its energy sectors. As already mentioned, based on a specified level of poverty, the selection of IGA energy users follows the rules outlined in 2. Consequently, each community IGA user will be included in the community structure only if a certain UBN threshold is met.

In the other hand, the number of IGA users is influenced by specific regional criteria, but the overall number is also considered proportional to the total population, which is calculated using an empirical formula. For example, in the highlands, there is one grocery store for every 25 households, while in the lowlands, there is one grocery store for every 30 households. The criteria assumed for this methodology are explained in the following sections for each type of IGA considered and summarized in Table 1b.

4.1.4. Irrigation systems

In rural areas, there are various types of irrigation systems, some of which require electricity while others do not. Most of the irrigation relies on flood-gravity techniques, which cover around 97% of the irrigated land. However, there has been an increasing adoption of modern irrigation methods such as sprinkler or drip irrigation, which account for the remaining portion. Based on the "Irrigation Development National Plan" [42], the majority of requested irrigation projects in rural areas are of micro or small typologies. To simplify the analysis, it is assumed that rural villages are more likely to have small or micro systems that include an electric pump and a drip irrigation system. It is also assumed that each system can cover up to ten acres of cultivated land.

The total number of irrigation systems is determined by a function of the population, taking into account the number of households and the region they belong to. This correlation is derived from a simple analysis of irrigation system databases, specifically by studying the distribution of irrigation systems across Bolivia [43]. The variation in the number of irrigation systems aims to reflect differences in climatic conditions and rainfall volume, as well as the significance of the agribusiness industry in the region. However, as the primary focus of this study is not on modelling these systems, and due to the potential complexity of such task, it is suggested that future research could explore deeper into characterizing these systems.

4.1.5. Transformation activities

Agricultural product transformation can boost economic growth, diversifying the source of income while increasing the electricity consumption due to the need of processing equipment and machinery [44]. Among governmental and non-governmental support programs, the provision of equipment is often included to support the processing. However even after access to electricity, the thriving of processing products remains challenging.

In this context, one processing activity has been selected for each region and will only be introduced once the energy sufficiency status is achieved. Extensive analysis, based on [38], was conducted to select relevant

processing activities for each region and for the national context. Therefore, Quinoa processing was selected for the highlands, cereal processing for the lowlands, and a small-scale dairy industry for the valleys.

The seasonal behaviour of quinoa and cereals must be taken into account for these processing activities, and therefore these activities are only modelled during the harvest period, which typically spans from July to October [38]. Additionally, to determine the number of processing units, it was decided to introduce one unit for every 200 households, based on [44], with the exception of the milk dairy industry, which has a fixed assumed number of one unit. The details of all users defined and characterized for each zone, the appliances associated with each of them and their use characteristics can be found in the repository `https://github.com/CIE-UMSS/RAMP_Bolivia.git`

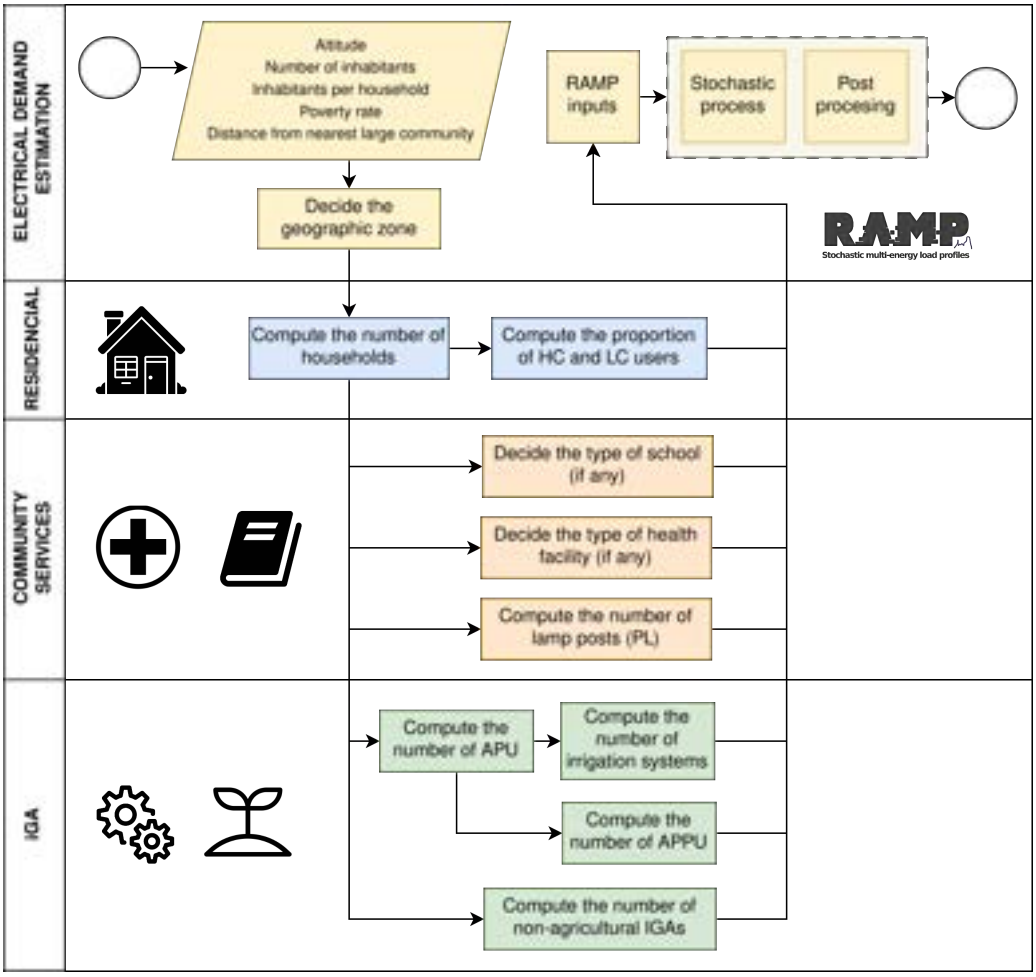

Figure 3: RAMP inputs creation per community

4.2. Estimation of Electricity Demand for Unelectrified Rural Communities in Bolivia

The model, which is based on RAMP, enables the generation of load curves for remote communities situated within Bolivian territory. The inputs for the model include community size, altitude (which determines the region in which the community is located), the proportion of high and low consumption (defined by the UBN), the average number of people of a family. A summary of how the complementary model works to calculate energy demand based on the mentioned data is shown in figure 3

The electricity demand for a year was simulated for four different scenarios in each region. The characteristics provided by the complementary model for these scenarios, in the form of RAMP inputs, can be seen in the Table 2, which represent four different states that theoretically improve living conditions since the percentage of poverty decreases and the availability of community services is greater. Likewise, economic diversification improves. The four archetypes where simulated for a community of 500 inhabitants in each one of the three important regions.

Figure 4 illustrates the computed annual electricity demand for each scenario. The aggregate demand and the participation of each sector within it can be observed. Notably, annual aggregate demand is higher in the lowlands and decreases at lower altitudes. This is partly due to the behavior of residential demand, described in section 4.1.1., and to the predominance of this sector's demand in overall demand. On the other hand,

Table 2: Four scenarios considered for each community size.

N°	Poverty (%)	Community Services	Agricultural IGA's	Non-agricultural IGA's
1	96	No community Services	No irrigation or transformation	No commerce
2	90	Public lighting + water supply system	No irrigation or transformation	Grocery stores + restaurants
3	70	Public lighting + water supply system + school	Irrigation	Grocery stores + restaurants
4	53	Public lighting + water supply system + school + hospital + other community services	Irrigation + transformation	Grocery stores + restaurants + workshops + entertainment business

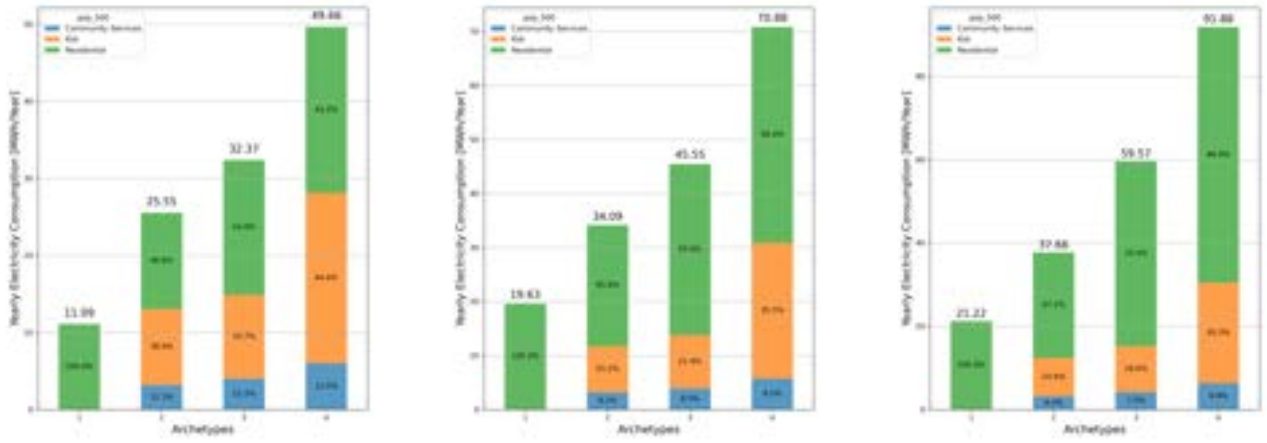

(a) Highlands (b) Valleys (c) Lowlands

Figure 4: Simulated yearly demand for rural communities of 500 inhabitants in the highlands, valleys and lowlands of Bolivia

it can be observed that the share of IGAs in the aggregate consumption of the highlands reaches a higher share because the production and transformation processes of typical products of these regions tend to be more costly in terms of energy consumption. The demand corresponding to the community services sector experiences a slight increase from region to region due to the thermal appliances owned by users within this group.

Analyzing the peak loads showed in Figure 5, it can be observed that in the lowlands, the peak load reaches about 28KW as opposed to the lowlands, where it reaches around 25KW. However, the main contribution in both cases is made by the activities related to the transformation of products. Again, in the case of the IGAs in the highlands, the contribution to the peak is higher due to the complexity of the equipment required in the processes selected for the region.

Figure 6 shows an example of a load curve generated for a community in the lowlands using RAMP. It is possible to appreciate the stochasticity with which the 365 daily profiles (one year) are generated, from which an average daily load curve is computed. The peak load range is observed between 12 noon and 6 p.m. in this case.

5. Conclusion

The estimation of electricity demand in remote communities is a crucial yet challenging task for energy planning. This study aimed to calibrate a bottom-up stochastic tool to generate load curves for rural communities in Bolivia. Although previous research has recognized the need to improve demand analysis processes, they

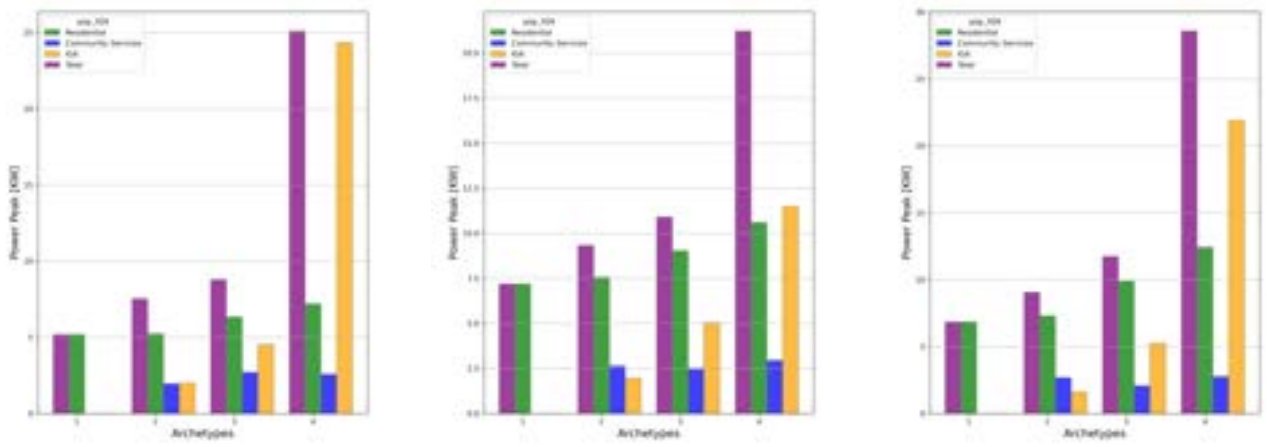

(a) Highlands (b) Valleys (c) Lowlands

Figure 5: Simulated peak loads for rural communities of 500 inhabitants in the highlands, valleys and lowlands of Bolivia

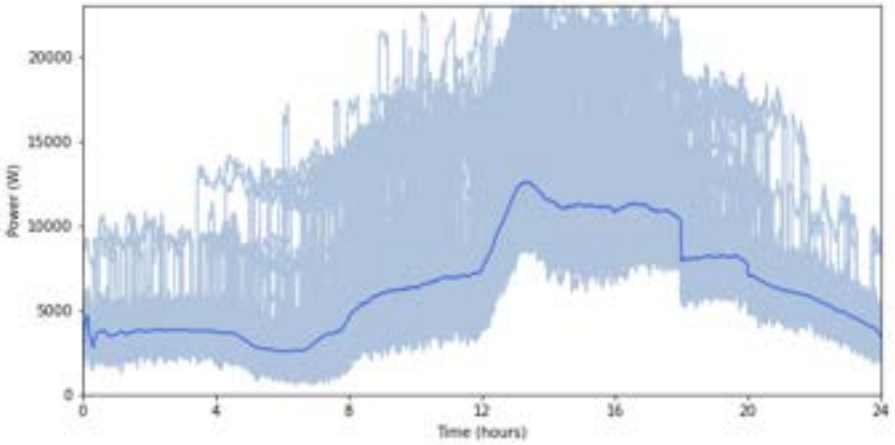

Figure 6: Average load curve computed with RAMP for a community with a population of 500 people in the LL, with scenario 4 characteristics (according Table 2)

have rarely considered energy use related to income-generating activities. Additionally, demand phenomena are strongly linked to contextual factors, requiring careful calibration and adjustment processes. However, the RAMP tool proved to be a powerful tool in capturing specific features of the zones under study to formulate adequate load curves. The biggest challenge remains obtaining accurate calibration information.

Exploring energy demand across consumer sectors and rural communities can provide useful insights for energy planning towards universal access. The proposed model enables the calculation of rural communities' demand using critical characteristics such as size, poverty rate and altitude. The study successfully simulated demand for rural communities from various regions of Bolivia, capturing the particular characteristics that highlight the main differences between the regions in terms of peak loads and aggregated demand. This study emphasized the high impact of geographical location on energy use and the electricity needs for productive uses, which depend on regional potential. Future work includes improving the model for serial computation of the demands of multiple rural communities.

Acknowledgments

The ACADÉMIE DE RECHERCHE ET D'ENSEIGNEMENT SUPÉRIEUR (ARES) is acknowledged for the financial support for this work in the framework of the Research Project for Development "Tailored energy

system models for energy planning in Bolivia".

Nomenclature

LL	Lowlands,
VA	Valleys,
HL	Highlands,
IGA	Income Generating Activities,
PL	Public Lighting,
RS	Residential sector,
RS	Community Services,
UBN	Unsatisfied Basic Needs
HH	Households,

References

[1] UN News Centre. Transforming our world: The 2030 Agenda for Sustainable Development. United Nations Department of Economic and Social Affairs. 2015. Available from: http://www.un.org/en/development/desa/news/sustainable/un-adopts-new-global-goals.html#more-15178.

[2] Bisaga I, Parikh P. To climb or not to climb? Investigating energy use behaviour among Solar Home System adopters through energy ladder and social practice lens. Energy Research and Social Science. 2018 Oct;44:293-303. Publisher: Elsevier Ltd.

[3] Ulsrud K, Winther T, Palit D, Rohracher H, Sandgren J. The Solar Transitions research on solar mini-grids in India: Learning from local cases of innovative socio-technical systems. Energy for Sustainable Development. 2011;15(3):293-303. Publisher: International Energy Initiative. Available from: http://dx.doi.org/10.1016/j.esd.2011.06.004.

[4] Riva F, Tognollo A, Gardumi F, Colombo E. Long-term energy planning and demand forecast in remote areas of developing countries: Classification of case studies and insights from a modelling perspective. Energy Strategy Reviews. 2018;20:71-89. Publisher: Elsevier Ltd. Available from: https://doi.org/10.1016/j.esr.2018.02.006.

[5] Klaniecki K, Duse IA, Lutz LM, Leventon J, Abson DJ. Applying the energy cultures framework to understand energy systems in the context of rural sustainability transformation. Energy Policy. 2020;137(October 2019):111092. Publisher: Elsevier Ltd. Available from: https://doi.org/10.1016/j.enpol.2019.111092.

[6] Riva F, Ahlborg H, Hartvigsson E, Pachauri S, Colombo E. Electricity access and rural development: Review of complex socio-economic dynamics and causal diagrams for more appropriate energy modelling. Energy for Sustainable Development. 2018;43:203-23. Publisher: International Energy Initiative. Available from: https://doi.org/10.1016/j.esd.2018.02.003.

[7] Balderrama S, Lombardi F, Riva F, Canedo W, Colombo E, Quoilin S. A two-stage linear programming optimization framework for isolated hybrid microgrids in a rural context: The case study of the "El Espino" community. Energy. 2019;188:116073. Publisher: Elsevier Ltd. Available from: https://doi.org/10.1016/j.energy.2019.116073.

[8] Ringkjøb HK, Haugan PM, Solbrekke IM. A review of modelling tools for energy and electricity systems with large shares of variable renewables. Renewable and Sustainable Energy Reviews. 2018;96(August):440-59. Publisher: Elsevier Ltd. Available from: https://doi.org/10.1016/j.rser.2018.08.002.

[9] Trutnevyte E, Hirt LF, Bauer N, Cherp A, Hawkes A, Edelenbosch OY, et al. Societal Transformations in Models for Energy and Climate Policy: The Ambitious Next Step. One Earth. 2019;1(4):423-33.

[10] Krumm A, Süsser D, Blechinger P. Modelling social aspects of the energy transition: What is the current representation of social factors in energy models? Energy. 2022;239:121706. Publisher: Elsevier Ltd. Available from: https://doi.org/10.1016/j.energy.2021.121706.

[11] Herraiz-Cañete Ribó-Pérez D, Bastida-Molina P, Gómez-Navarro T. Forecasting energy demand in isolated rural communities: A comparison between deterministic and stochastic approaches. Energy for Sustainable Development. 2022 Feb;66:101-16. Publisher: Elsevier B.V.

[12] Peña Balderrama JG, Balderrama Subieta S, Lombardi F, Stevanato N, Sahlberg A, Howells M, et al. Incorporating high-resolution demand and techno-economic optimization to evaluate micro-grids into the Open Source Spatial Electrification Tool (OnSSET). Energy for Sustainable Development. 2020 Jun;56:98-118. Publisher: Elsevier B.V.

[13] Spalding-Fecher R, Winkler H, Mwakasonda S. Energy and the World Summit on Sustainable Development: What next? Energy Policy. 2005;33(1):99-112.

[14] Pachauri S, Brew-Hammond A, Barnes DF, Bouille DH, Gitonga S, Modi V, et al. Energy Access for Development. Global Energy Assessment (GEA). 2012:1401-58.

[15] Sanchez C, Betta PD, Stevanato N, Andersen L, Guzmán G, Quoilin S, et al. The Energy Sufficiency Concept and Its Impact on Energy Demand Estimation in Rural Communities from Developing Countries. SDEWES LA 2022 Proceedings. 2020.

[16] Lombardi F, Balderrama S, Quoilin S, Colombo E. Generating high-resolution multi-energy load profiles for remote areas with an open-source stochastic model. Energy. 2019;177:433-44. Publisher: Elsevier Ltd. Available from: https://doi.org/10.1016/j.energy.2019.04.097.

[17] ENDE. Memoria Anual 2018. Empresa Nacional de Electricidad; 2018.

[18] Peña Balderrama JG, Balderrama S, Lombardi F, Stevanato N, Sahlberg A, Colombo E, et al. Incorporating an automated methodology to evaluate mini-grid solutions into the Open Source Spatial Electrification Tool (OnSSET). In Press. 2020.

[19] MDRyT, VDRA. Compendio Agropecuario: Observatorio Agroambiental y Productivo; 2012.

[20] AETN. Anuario Estadístico 2020; 2020.

[21] INE, Ministerio de Salud. Encuesta de Demografia y Salud 2016; 2019.

[22] Jiménez W, Lizárraga S. Ingresos y Desigualdad en el Área Rural de Bolivia. UDAPE. 2003.

[23] Salazar C, Jimenez E. Ingresos familiares anuales de campesinos e indigenas rurales en Bolivia; 2018.

[24] Valencia H, Vera D. Diversificación de ingresos en el Área Rural : Determinantes y Características. Banco Central de Bolivia; 2010.

[25] Lombardi F, Balderrama S, Quoilin S, Colombo E. Generating high-resolution multi-energy load profiles for remote areas with an open-source stochastic model. Energy. 2019;177:433-44.

[26] Soto A, Balderrama Subieta SL, Cardozo E, Fernandez M, Zambrana J, Quoilin S. Exploring the Tradeoff between Installed Capacity andUnserved Energy in Rural Electrification. 2021. Available from: https://orbi.uliege.be/handle/2268/261913.

[27] Fuentes MF, Cardozo E, Zambrana J, Peña G, Balderrama S, Sánchez C, et al. Electrificación rural en Bolivia: Propuestas accionables; 2020.

[28] INE. Censo Nacional 2012; 2012. Available from: https://www.ine.gob.bo/index.php/censos-y-banco-de-datos/censos/.

[29] Andersen LE, Branisa B, Calderón F. Estimaciones del PIB per cápita y de la actividad económica a nivel municipal en Bolivia en base a datos de consumo de electricidad. La Paz: CIS; 2019.

[30] GIZ. Estudio de caracterización sobre el consumo eléctrico en hogares y las potencialidades relacionadas con eficiencia energética; 2020.

[31] INE INdE. Encuesta integrada de hogares 2016- 2017. 2019:545.

[32] Saidur R, Masjuki HH, Choudhury IA. Role of ambient temperature, door opening, thermostat setting position and their combined effect on refrigerator-freezer energy consumption. Energy Conversion and Management. 2002;43(6):845-54. ISBN: 6037959528.

[33] Harrington L, Aye L, Fuller B. Impact of room temperature on energy consumption of household refrigerators: Lessons from analysis of field and laboratory data. Applied Energy. 2018;211(December 2017):346-57. Publisher: Elsevier. Available from: https://doi.org/10.1016/j.apenergy.2017.11.060.

[34] de salud y deportes M. Norma Nacional De Caracterización De Establecimientos De Salud De Primer Nivel. Ministerio de salud y deportes; 2013.

[35] de Hidrocarburos y Energía M. Manual de elaboracion y evaluation de proyectos de electrification rural. Ministerio de Hidrocarburos y Energía; 2014.

[36] Morales GE. Bolivia: Decreto Supremo Nº 1868, 23 de enero de 2014;. Available from: http://www.gacetaoficialdebolivia.gob.bo/year={2014-01-23}.

[37] O'Sullivan K, Golubchikov O, Mehmood A. Uneven energy transitions: Understanding continued energy peripheralization in rural communities. Energy Policy. 2020;138:111288.

[38] Vásquez V, Gallardo G. Compendio Agropecuario; observatorio agroambiental y productivo 2012. Ministerio de Desarrollo Rural y Tierras, Estado Plurinacional de Bolivia, La Paz, Bolivia. 2012:403.

[39] Vargas LFF. MICRO-GRIDS LOADS EVOLUTION: TRENDS IN RURAL BOLIVIA CLIMATE ZONES. Politecnico di Milano; 2020.

[40] National rural electric cooperative association U. Evaluación Del Impacto Socioeconómico Proyecto De Electrificación Para El Desarrollo Alternativo En Los Yungas. National rural electric cooperative association, USAID; 2007.

[41] National rural electric cooperative association S. Evaluación de Impacto Socioeconómico Programa "USDA" de Electrificación. National rural electric cooperative association, SNV; 2011.

[42] de medio ambiente y agua M. Plan nacional de desarollo del Riego " para Vivir Bien" 2007-2011. Ministerio de medio ambiente y agua; 2007.

[43] de medio ambiente y agua M. Inventario national the de sistemas de riego 2012. El estado plurinacional de Bolivia; 2012.

[44] Jaime Sologuren GG. Impactos (2005 – 2010) Proyecto EnDev GIZ Bolivia – Acceso a Energía. GIZ; 2011.

PROCEEDINGS OF ECOS 2023 - THE 36TH INTERNATIONAL CONFERENCE ON
EFFICIENCY, **C**OST, **O**PTIMIZATION, **S**IMULATION AND ENVIRONMENTAL IMPACT OF ENERGY SYSTEMS
25-30 JUNE 2023, LAS PALMAS DE GRAN CANARIA, SPAIN

Landlord-Tenant Dilemma: How Does the Conflict Affect the Design of Building Energy Systems?

Larissa Kühn[a], Lars Braun[b], Nico Fuchs[c], Laura Maier [d] and Dirk Müller [e]

[a] RWTH Aachen University, E.ON Energy Research Center (ERC), Institute for Energy Efficient Buildings and Indoor Climate (EBC), Aachen, Germany, larissa.kuehn@eonerc.rwth-aachen.de, CA
[b] RWTH Aachen university, ERC, EBC, Aachen, Germany, lars.braun@eonerc.rwth-aachen.de
[c] RWTH Aachen university, ERC, EBC, Aachen, Germany, nico.fuchs@eonerc.rwth-aachen.de
[d] RWTH Aachen university, ERC, EBC, Aachen, Germany, laura.maier@eonerc.rwth-aachen.de
[e] RWTH Aachen university, ERC, EBC, Aachen, Germany, dmueller@eonerc.rwth-aachen.de

Abstract:
To achieve the climate goals, the European Union needs to increase the renovation rate of buildings from 1 to 3 %. In owner-occupied buildings, financial incentives for renovation are motivated by energy cost savings. However, 30 % of all Europeans live in rented property, where conflicting stakeholder interests arise. Landlords are responsible for renovation decisions on the building envelope and the energy system as well as the corresponding investments. Tenants, for their part, face rising rents as investments are apportioned and only slightly benefit from falling utility costs. Literature calls this conflict the landlord-tenant dilemma. However, existing publications lack a precise quantification of the conflict, and little is known about the effects on technology choices and the heat transition. To address this gap, we incorporate the different perspectives of landlords and tenants in a model-based approach for optimized technology choice in form of a mixed-integer linear program. We compare optimal individual technology choices against the total cost optimum for renovations decisions. Additionally, we examine how changes in the regulatory framework affect the landlord's technology choice. Thereby, we consider the regulatory framework of Germany because of a comparatively low home ownership rate of 49 %. On this basis, we assess the technology choice of different stakeholders in terms of its impact on costs and emissions. Our study reveals that total costs and emissions are up to 29 % and 143 % higher for landlords deciding for rented houses compared to owner-occupied properties. Current approaches to solve the dilemma, such as tenant electricity and an energy-differentiated reference rent, could lead to the replacement of technical equipment and favor the development towards a climate-friendly energy system. However, the renovation of the building envelope is only partly considered in decisions of landlords, and operating costs are completely disregarded. As a result, tenants are the most burdened within the transition to a climate-neutral building stock.

Keywords:
Landlord-tenant dilemma; Renovation; Multi family houses; Optimization; MILP; Emissions; Costs.

1. Introduction

The building sector is responsible for 36 % of the greenhouse gas emissions in the European Union (EU) [1]. To achieve the set climate goals, e.g., a climate-neutral building stock by 2050, an increase of the renovation rate of buildings is required. While the European Commission is aiming for an increase in the renovation rate from an average of 1 % to 2 % [2], recent studies assume a minimum renovation rate of 3 % necessary to achieve the climate targets [3]. In addition to the renovation of the building envelope, a transformation of the building energy system is needed to defossilize the heating sector.

This transformation involves considerable costs for renovation measures, and the question of who pays for the heat transition arises. Especially in rented property, where 30 % of all Europeans live [4], conflicting stakeholder interests and the challenge of an appropriate cost distribution between the landlord (owner) and the tenant (user) arises. Landlords are responsible for the renovation decisions on the building envelope and the energy system, as well as the corresponding investment, but will not benefit from future energy cost savings. On the other side, tenants face raising rents and often only slightly decreased energy costs. This causes the so-called *landlord-tenant dilemma*, which involves two major challenges concerning the landlord's decisions:

1. Missing incentives to invest in renovation measures
2. No interest in renovation decisions that lower operating costs for tenants

Based on these issues, a third problem arises:

3. Lack of emission reductions and incentive to reach the climate targets

To achieve the climate targets, it is therefore essential to resolve these challenges. This means incentivizing investment decisions by landlords that simultaneously contribute to a favorable solution for tenants and, furthermore, do not contradict the climate goals.

In comparison with other EU countries, Germany has the largest rental share in the residential building stock of 51 % [4]. In regard to the *landlord-tenant dilemma*, Germany has introduced a retrofitting fee (RF). This fee is supposed to refinance the investments in renovation measures by allocating a proportion of the investment to the tenants. However, the RF leads to further problems, as its determination is only cost-based and the profitability depends strongly on the development of market rents [5]. In addition, the cost-based calculation results in an increase in base rents (rent without energy costs) for which tenants are not necessarily compensated with reduced energy costs [6].

As a further step, Germany has introduced the Tenant Electricity (TEL) Act in practice, which is intended to simplify the sale of self-generated electricity from landlords to tenants. In addition, literature proposes different approaches to resolve this dilemma. A promising solution is an energy differentiated (ED) local reference rent (LRR) [6–8]. According to the German Civil Code (BGB) landlords in Germany have the right to increase the rent up to the LRR, irrespective of any renovation decision. Taking into account energy related attributes of buildings within an ED LRR could lead to renovation decisions that actually reduce energy demand and green house gas emissions and therefore, simultaneously costs.

Although this approach seems promising, most publications focus on qualitative studies on the *landlord-tenant dilemma* and its solutions and lack precise quantification of it. Therefore, little is known about the associated technology choices of landlords and the consequences for tenants. This further implies, literature has not yet investigated the specific impact of the dilemma on the heat transition. To address this gap, we develop a model-based approach in from of a mixed-integer linear program (MILP) to perform a holistic investigation of the conflict and the possible solutions by TEL and an ED LRR.

The developed optimization model is based on an existing MILP, that includes renovation measures of the building envelope and the building energy system [9]. As Germany is the country with the highest share of rented property in Europe, we extend the model by the respective legal framework of Germany for this study. Additionally, we incorporate the different perspectives of the stakeholders and compare individual technology choices with the total cost optimum and emissions of an owner-occupied building. With this framework, we close the current research gap by answering the following questions:

- How does the building owner's renovation decision differ between owner-occupied and rented buildings based on current regulations?
- Do TEL or an ED LRR solve the dilemma?
- What is the impact of the *landlord-tenant dilemma* on the heat transition?

2. State of the art

2.1. Landlord-tenant dilemma in literature

The *landlord-tenant dilemma* has been studied in various research disciplines, whereby economic, legal, and social science as well as engineering approaches can be identified. Table 1 provides an overview of the different research disciplines and their consideration of relevant aspects related to the *landlord-tenant dilemma*. The evaluation reveals three relevant aspects - building calculation, rental law and other legal framework. With regard to the building calculation, the literature overview denotes whether the studies consider renovations of the building envelope and the building energy system and the studies' level of detail in the building modeling. The area of rental law focuses on whether rent payments and the RF or the LRR and therein specifically ED features are considered. Furthermore, the overview lists whether requirements from the Building Energy Act (GEG), subsidies, CO_2 price allocation, feed-in tariffs and TEL are taken into account.

Studies from economics [7, 8, 10, 11] and legal science [6, 12, 13] focus on the current rental law and neglect a precise building calculation. The analyses from social science mostly show a detailed consideration of the stakeholder's willingness to pay and some individual aspects of rental law, but strong simplifications in other aspects [14–17]. Engineering approaches represent actual refurbishment options on the building envelope and building energy systems with varying degrees of accuracy in building modeling [18–20]. However, these models widely disregard the applicable rental law. In addition, all considered publications only occasionally address aspects of other related legal frameworks (e.g., GEG or CO_2 price allocation).

This literature review demonstrates that scientific publications so far mostly focuses on individual topics instead of combining all relevant aspects related to the *landlord-tenant dilemma*. For instance, Braeuer et al. [19] examine TEL in terms of its profitability for the landlord, but neglect rental payments. Henger et al. [5, 8] and Mellwig et al. [11] extensively address the rental law and further combine it with subsidies, but disregard

Table 1: *Landlord-tenant dilemma* in literature.

Considered in publication: ○ not ◔ hardly ◑ partly ◕ almost ● fully			Building calculation			Rental law (BGB)				Other legal framework				
			Building envelope	Building energy system	Building modeling	Rent payments	Retrofitting fee (RT)	Local reference rent (LRR)	Energetic differentiation (ED)	Buildings Energy Act (GEG)	Subsidies	CO_2 price allocation	Feed-in tariffs	Tenant electricity (TEL)
Economic science	2022	Ahlrichs et al.	●	○	◑	◔	●	○	○	○	○	○	○	○
	2021	Henger et al.	○	○	○	●	●	●	●	○	●	◔	○	○
	2020	Henger et al.	○	○	○	●	●	●	●	○	●	◔	○	○
	2019	Mellwig et al.	◑	○	○	●	●	◑	○	○	●	○	○	○
	2016	Kossmann et al.	○	○	◔	●	●	●	●	○	○	○	○	○
Legal science	2019	Gaßner et al.	○	○	○	●	●	●	●	○	○	○	○	○
	2011	Neitzel et al.	◔	◔	○	●	●	●	●	○	○	○	○	○
	2009	Ekardt et al.	○	○	○	●	●	○	○	○	○	○	○	○
Social science	2022	Taruttis et al.	◕	◕	◑	●	◔	◔	●	○	○	◔	○	○
	2022	März et al.	◔	◔	○	●	○	○	●	○	○	○	○	○
	2021	Lang et al.	○	○	○	◑	○	○	◑	○	○	○	○	○
	2019	März	◔	◔	○	●	●	●	●	○	◑	○	○	○
Engineering	2022	Petkov et al.	●	●	◕	●	○	○	○	○	○	○	●	○
	2022	Braeuer et al.	○	●	◔	○	○	○	○	○	○	○	●	●
	2015	Steinbach	●	●	●	◔	●	○	○	○	○	○	◔	○

a specific examination of the building and some regulations (e.g. GEG and TEL). Since these topics are interdependent we close this gap by developing a comprehensive optimization model taking into account all mentioned aspects within this study.

2.2. Solutions to the landlord-tenant dilemma

In 2017, the TEL Act came into force in Germany with the aim of creating incentives for landlords to invest in systems for the self-generation of electricity. Moreover, the reviewed literature proposes a variety of further possible ways to resolve the *landlord-tenant dilemma* (see Tab. 2). The most frequently referenced solutions in literature are an adjustment of the current RF, an ED LRR, and the so-called one-third model.

For an adjusted RF, literature suggests an RF that is no longer solely dependent on the cost, but rather on energy savings. The aim is to prevent landlords from benefiting from increasing the costs of renovations. The ED LRR aims for a similar goal. A higher LRR for climate-friendly energy systems is intended to create incentives for renovation decisions that are favorable for all stakeholders and the climate targets. The one-third model was first presented by Mellwig et al. [11]. The model states that the costs of an energy-efficient renovation should be equally allocated between landlords, tenants, and the state.

Among the suggested solutions ED LRR is the only proposed solution that already has a legal basis in the context of the rental law in Germany. Moreover, current political efforts with a law to reform the rent index law indicate that LRRs will play a central role in the future. However, in the reviewed literature, ED LRRs have not been quantitatively addressed yet. Therefore, we contribute to literature by applying the developed optimization model to address the question on whether or not an ED LRR represents a possible solution to the *landlord-tenant dilemma*. Also, very few have examined the impact of TEL on the landlord's renovation decision [19]. Therefore, we combine both solutions to show their effects and dependencies.

Table 2: Overview of presented solutions for the landlord-tenant dilemma

Approach	Source
Adjustment of the retrofitting fee (RF)	[7], [8], [10], [13], [12], [17]
Energy differentiated local reference rent (ED LRR)	[7], [8], [6]
One-third model	[11], [8], [12], [17]
Energy and climate fund model	[5], [8]
Separate surcharge on cold rent	[6], [12]
Differentiation of subsidies by landlord type	[17]
Obligation to renovate	[17]

3. Method

3.1. Optimization framework

We extend an existing MILP for design and operational optimization of residential buildings. For a complete documentation of the initial model, we refer to Schütz [21]. Figure 1 presents all aspects of the extended MILP.

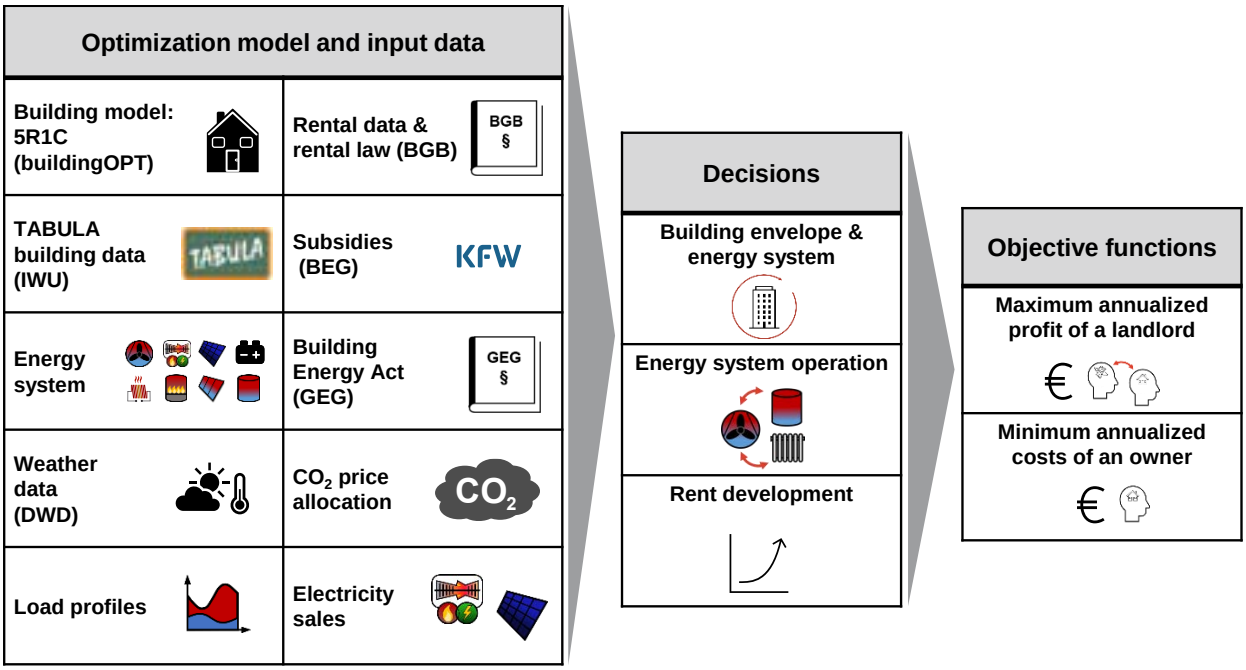

Figure 1: Overview of the optimization model and its decisions and objectives.

3.1.1. Objective functions

The objective of the model is to find a cost-optimal technology choice at the beginning of a specified time period from different perspectives. The annuity serves as economic metric [22]. Table 3 illustrates the relevant financial contributions for the respective stakeholders. Costs are marked with a minus sign (-), revenues with a plus sign (+) and no consequences with an empty field ( ). Investments, installation costs and subsidies are incurred at the beginning of the period under consideration. Maintenance costs, consumption costs, emission costs, metering costs, feed-in revenues, rental payments and TEL payments are incurred annually. A price-dynamic present value factor is determined to reflect price changes, except for rental payments. For the latter the cost for tenants for each year (y) are obtained by multiplying variable specific rental payments c_y^{rent} with the living area (A) and discounting it to the starting point by q. The annualized rental payments $c_{\text{ann}}^{\text{rent}}$ are then determined by applying the capital recovery factor (CRF) to the sum of yearly rent payments over the considered time period T (1).

$$c_{\text{ann}}^{\text{rent}} = \left(\sum_{y \in (1,\ldots,N)} \frac{c_y^{\text{rent}} \cdot 12 \cdot \text{A}}{q^y} \right) \cdot \text{CRF} \tag{1}$$

Table 3: Overview of the costs of the objective function

Category	Owner-occupied	Landlord	Tenant
Investment	-	-	
Installation	-	-	
Maintenance	-	-	
Consumption	-	-	-
Emissions	-	-	-
Metering	-		-
Feed-in/ self-consumption surcharges	+	+	
Subsidies	+	+	
Rent		+	-
TEL*		(+)	(-)

*only if TEL is applied

3.1.2. Decision variables

As a result of the optimization, the model decides on the cost-optimal combination of the building envelope and the energy system design and operation. Thereby, we consider various renovation measures, which can be combined in any way. For the facade, the roof and the windows four levels with increasing insulation standard can be selected independently. Regarding the energy system we consider boilers (BOI), combined heat and power engines (CHP), air source heat pumps (HP), electric heaters (EH), solar thermal collectors (STC), photovoltaics (PV), thermal energy storages (TES) and batteries (BAT). In case of optimized costs in a landlord-tenant relation, the MILP also determines how the rent can be increased according to regulations. For the rent development, the two rent increase mechanisms LRR and RF are available (see subsubsection 3.1.3.).

3.1.3. Optimization model and input data

Building and energy system

The building and energy system models are provided by the existing MILP. The thermal behavior of the building is described by a 5R1C model based on DIN EN ISO 13790 [23]. The 5R1C model summarizes the entire building into one thermal capacity and five thermal resistances. The whole building is modeled as one thermal zone with central heating. Building data for the initial building standard is taken from TABULA typologies [24]. To determine the size of the initial energy system, the standard heating load according to DIN EN 12831-1 is used with with a set indoor temperature of 20 °C.

To derive the external influences due to ambient heat and solar irradiation, local weather data from the Germany's National Meteorological Service are applied [25]. In this work, hourly resolved ambient temperatures and solar irradiances for average years are used. The method of Richardson et al. serves as a basis for the definition of electricity demand profiles [26]. Profiles for domestic hot water are retrieved by combining the presence profiles according to Richardson et al. with the domestic hot water profiles according to Beausoleil-Morrison [27]. In each case, the load profiles take into account that the peak demand grows degressively with the number of households, since a temporal distribution of the loads takes place.

Regulations and economic boundary conditions

With regard to the rental law, we implement regulations for rent increase, specifically the allowed rent increase mechanisms for the LRR according to § 558 BGB and for the RF according to § 559 BGB. The combination of both mechanisms is integrated based on a German Federal Court of Justice ruling [28]. For both mechanisms, we only consider existing tenants, as more extensive regulations apply to new tenants (e.g., rent control - see § 556d BGB). The RF allows the costs of renovation measures to be passed on to the tenant in the amount of 8 % of the investment. The LRR, which is determined every two years, is specified in rent indices and reflects the rent for comparable residential spaces. The landlord may increase the rent in accordance with the housing characteristics in particular location, size, type, features and quality.

The review of current literature reveals an ED LRR as one promising solution for the *landlord-tenant-dilemma*. To evaluate the impact, we implement an LRR with ED and without ED. The ED LRR in this work is based on the final energy demand for heating and domestic hot water as defined for the building energy pass (§§ 79-88 GEG). Other types of energy differentiation are possible and used in practice [29,30]. However, the final energy demand must be determined after renovation measures and allows for a standardized comparison of buildings. The binary variable x_{lev} indicates which LRR level (lev) has to be applied based on the achieved final energy demand $Q^{\text{fin}}_{\text{tot}}$ (4). Thereby, each energy quality level has a maximum final energy demand Q^{fin}_{lev} and only one energy level can be chosen (4). The corresponding LRR c^{lrr}_{y} is selected from the available LRRs $c^{\text{lrr}}_{y,lev}$ (3). The variable x^{switch}_{y} indicates whether the LRR is applied in the respective year if the RF was previously used. The switch is only possible once since the RF becomes part of the newly determined rent (5).

$$Q^{\text{fin}}_{\text{tot}} \leq \sum_{lev \in L} Q^{\text{fin}}_{lev} \cdot x_{lev} \tag{2}$$

$$c^{\text{lrr}}_{y} = \sum_{lev \in L} c^{\text{lrr}}_{y,lev} \cdot x_{lev} \quad \forall\, y \in (1, ..., T) \tag{3}$$

$$\sum_{lev \in L} x_{lev} \leq 1 \tag{4}$$

$$x^{\text{switch}}_{y} \leq x^{\text{switch}}_{y+1} \quad \forall\, y \in (1, ..., T-1) \tag{5}$$

For the allowed combination of the LRR and the RF, we distinguish whether a switch from the RF to the LRR has occurred using the big-M method with the binary x^{switch}_{y}. If the RF is applied, the base rent is the rent of the previous year c^{rent}_{0} (year 0 before the start of the period under consideration) or the initial LRR of the unrenovated state $c^{\text{lrr,init}}_{1,lev}$ and the RF is charged on top (6). Alternatively, the rent can be increased according to the LRR of the refurbished condition (7). The calculation of the RF c^{rf} is based on 8 % of the investment minus received subsidies.

$$c_y^{\text{rent}} \leq c^{\text{rf}} + max(c_0^{\text{rent}}, c_{1,lev}^{\text{lrr,init}}) + M \cdot x_y^{\text{switch}} \quad \forall\, y \in (1, ..., T) \tag{6}$$

$$c_y^{\text{rent}} \leq x_y^{\text{lrr}} + M \cdot (1 - x_y^{\text{switch}}) \quad \forall\, y \in (1, ..., T) \tag{7}$$

For both rent increase mechanisms, independent capping limits must be respected. The capping limit for the LRR consists of a maximum percentage rent increase within three years (§ 558 Art. 3 BGB). The capping percentage $c_{\text{limit}}^{\text{lrr}}$ depends on the local housing market (8). The capping limit of the RF consists of an absolute rent increase value per m^2 (§ 559 Art. 3a BGB). The capping limit $c_{\text{limit}}^{\text{rf}}$ is dependent on the rent before the application of the RF (9) and is constrained by (10). By (11) and (12) we take into account the independence of both capping limits.

$$c_{\text{limit}}^{\text{lrr}} = \begin{cases} 0.15 & \text{if} \quad \text{tense market} \\ 0.20 & \text{if} \quad \text{no tense market} \end{cases} \tag{8}$$

$$c_{\text{limit}}^{\text{rf}} = \begin{cases} 2\ \frac{€}{\text{m}^2} & \text{if} \quad max(c_0^{\text{rent}}, c_{1,lev}^{\text{lrr,init}}) \leq 7\ \frac{€}{\text{m}^2} \\ 3\ \frac{€}{\text{m}^2} & \text{if} \quad max(c_0^{\text{rent}}, c_{1,lev}^{\text{lrr,init}}) > 7\ \frac{€}{\text{m}^2} \end{cases} \tag{9}$$

$$c^{\text{rf}} \leq c_{\text{limit}}^{\text{rf}} \tag{10}$$

$$c_y^{\text{rent}} \leq c^{\text{rf}} + c_{\text{limit}}^{\text{lrr}} \cdot c_{y-3}^{\text{rent}} + M \cdot x_y^{\text{switch}} \quad \forall\, y \in (1, ..., T) \tag{11}$$

$$c_y^{\text{rent}} \leq c_{\text{limit}}^{\text{lrr}} \cdot c_{y-3}^{\text{rent}} + M \cdot (1 - x_y^{\text{switch}}) \quad \forall\, y \in (1, ..., T) \tag{12}$$

For the modeling of the basic structure of the subsidies, we refer to the original model [21]. In this study, some new regulations are added and existing parameters are changed according to current standards. Thereby, we take into account current subsidies for efficient buildings from BEG in form of single measures and the overall building efficiency. The BEG single measures, among other measures, subsidizes the installation of HPs, STCs, TESs and the insulation of the facade, the roof and the windows. Regarding the overall building efficiency, BEG subsidizes the achievement of certain efficiency house levels based on specified values for the annual primary energy demand and the specific transmission heat loss. Further, GEG prescribes U-values for the facade, the roof and windows that must be achieved as a minimum in the case of renovations (§ 48 GEG). Alternatively, limit values for the annual primary energy demand and the specific transmission heat loss after renovation must be met (§ 50 GEG).

Since 2023 the CO_2 costs of fossil energy solutions are split between landlord and tenant based on a distribution scheme considering the specific emissions [31]. The higher the CO_2 emissions relative to the heated living space, the higher the landlord's share of the costs.

Owners can profit from the feed-in and the self-consumption of PV and CHP power. According to the Renewable Energy Sources Act (EEG), PV feed-in is remunerated for 20 years (§ 25 Art. 1 EEG) depending on the installed capacity (§ 48 Art. 2 EEG). CHP feed-in is regulated by the CHP Act (KWKG) and remunerated for 30,000 full load hours (§ 8 Art. 1 KWKG) depending on the installed capacity (§ 7 Art. 1 KWKG). The CHP remuneration includes the average price for base-load electricity (CHP-index) [32] in addition to the federal surcharges. For the self-consumption of PV power, we consider the option of a TEL between landlord and tenant. In this case, the German Energy Act (EnWG) states that the landlord acts as the electricity supplier for the tenant with a price cap of 90 % of the respective basic supply tariff (§ 42a Art. 4 EnWG). In addition, the federal tenant electricity surcharge is granted (§ 48a EEG). The CHP self-consumption is remunerated regardless of a tenant electricity contract (§ 7 Art.2/3 KWKG).

3.2. Use case

We apply the developed model for two typical multi family houses (MFHs) according to TABULA. Table 4 presents the specifications for both buildings, which mainly differ in the construction age and thus also in their energetic quality (e.g., heat demand and building envelope). The energy system of the initial building consist of a gas BOI with low efficiency (82 %) based on data from TABULA. Since Hamburg is considered a good example in Germany for the implementation of an ED LRR as described in 3.1.2., we choose Hamburg as the location for our study [33]. Here, LRR levels are determined by dividing the final energy demand into five levels (0-4). MFH D (MFH H) is classified into level 0 for a final energy demand above 167.7 kWh/m^2 (84.3 kWh/m^2) and in the highest level 4 for final energy demands below 121.0 kWh/m^2 (48.5 kWh/m^2). This results in an LRR dependent on the energetic level between 7.06 and 9.88 €/m^2 (6.30 and 10.30 €/m^2). Table 5 provides information about energy tariffs and assumptions about revenues from feed-in electricity. General economic parameters, e.g., for energy prices developments, and prices for all considered technologies are listed in the appendix A. For improved solving times, we apply a k-medoid clustering after Domínguez-Muñoz et al. [34] and solve the problem for four representative days with a MIP gap of 0.5 %.

Table 4: Use case: MFH D and MFH H from TABULA

	MFH D	MFH H
Construction period	1949-1957	1984-1994
Living area	575 m^2	707 m^2
Apartments	9	10
Annual heat demand	210 kWh/m^2	115 kWh/m^2
Nominal heat load	61 kW	43 kW

	MFH D	MFH H
BOI	74,2 kW	52,0 kW
TES	45,6 kWh	56,1 kWh
Facade (F)	1,2 W/(m^2K)	0,6 W/(m^2K)
Roof (R)	1,6 W/(m^2K)	0,4 W/(m^2K)
Window (W)	3,0 W/(m^2K)	3,0 W/(m^2K)

Table 5: Energy prices from the end of 2022 (Scenario 1) and predictions for 2030 (Scenario 2) [35] (left). Assumptions for feed-in of CHP and PV electricity (right).

Prices		Scenario 1	Scenario 2	Unit
Gas price		0.2004	0.125	€/kWh
El. price		0.4007	0.327	€/kWh
CO_2 price		0.03	0.105	€/kg
Revenue landlord*	MFH D	35240	33238	€/year
	MFH H	43181	42327	€/year
Cost tenant*	MFH D	69467	64240	€/year
	MFH H	70150	66735	€/year

*initial state

Revenues	Scenarios	Unit
CHP index feed-in	0.1928	€/kWh
CHP feed-in	0.044 - 0.016*	€/kWh
CHP self-consume	0.015 - 0.08*	€/kWh
PV feed-in	0.082-0.109*	€/kWh
PV self-consume	0.0167-0.0267*	€/kWh

*dependent on the installed power

4. Results

4.1. Effects of the landlord-tenant dilemma

In a first step, we analyze how the renovation decision of the building owner differs between owner-occupied and rented buildings. Therefore, we first consider the use case without any of the suggested solutions to the *landlord-tenant dilemma* (ED LRR or TEL). Figure 2 compares total annual costs and emissions of the initial state with the owner-occupied building and a landlord-tenant relation for MFH D (left) and MFH H (right). For comparability, only the costs that correspond to the owner-occupied building are shown (see Tab. 3), hence rent payments, although they are considered in the landlord's decision, are not illustrated. It becomes obvious that for both buildings the landlord's decision is worse than the decision in an owner-occupied building in terms of costs and emissions. For MFH D for example, the owner of an owner-occupied building chooses a HP in combination with an EH and a PV. Further, the decision leads to an increased insulation of the roof (R), which lowers the total energy demand by around 16.7 % compared to the initial state. In contrast, the landlord of a rented property chooses a hybrid system consisting of a BOI, a HP and an EH. Compared to the owner-occupied building this is not only more expensive when comparing total costs (+29 %) over the considered lifetime, but also causes higher emissions (+123 %). Instead of a hybrid system, the landlord of MFH H only chooses a BOI, which leads to increased costs (+22 %) and high emissions (+143 %) compared to the respective owner-occupied building.

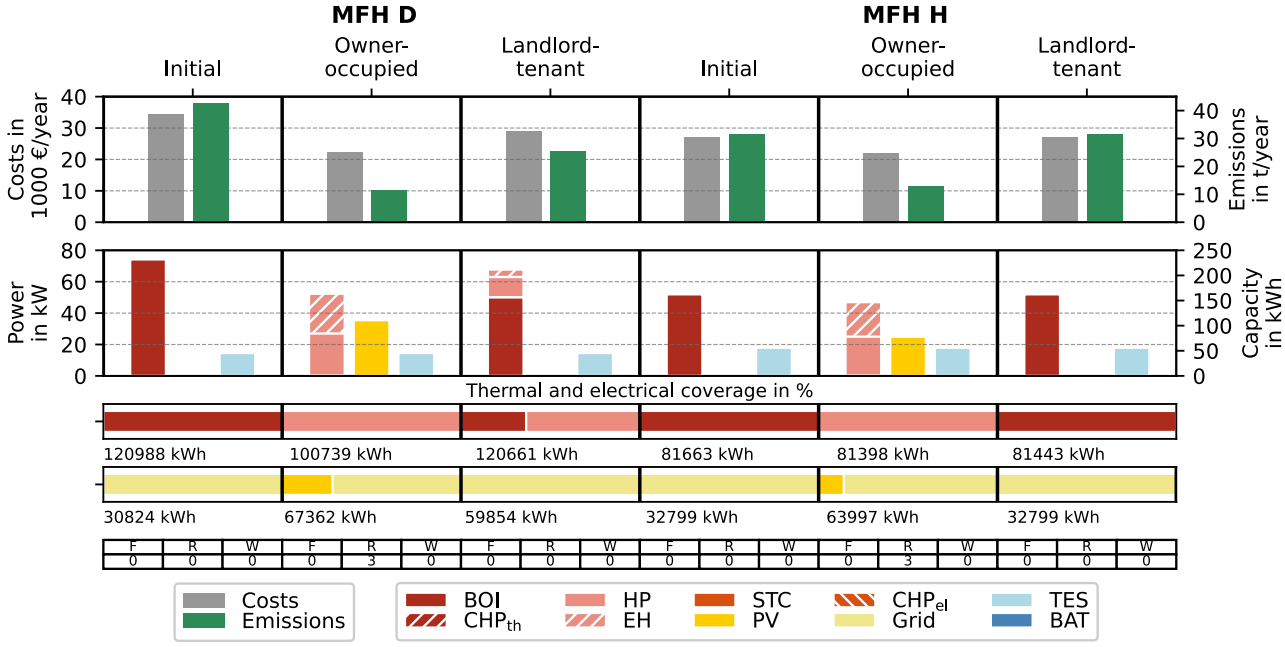

Figure 2: Renovation decisions for owner-occupied and rental buildings within price scenario 1.

Regarding the *landlord-tenant dilemma*, it can be concluded that although the landlord decides to replace the energy system, the favorable renovation of the roof is omitted for both considered use cases. This illustrates that there is no incentive for a landlord to invest in the building envelope and thus to decrease the energy demand (problem 1). Moreover, our results show that for both buildings the landlord decides on an energy system, which is not optimal in terms of total annual costs and emissions compared to the total cost optimum of an owner-occupied building (problem 2 and 3).

4.2. Solutions to the landlord-tenant dilemma

Based on the depiction of the *landlord-tenant dilemma*, we examine solutions proposed in the literature and, in some cases, already used in practice. Figure 3 shows the effect of an ED LRR without the application of TEL for two pricing scenarios for 2022 and 2030 (1 and 2). We find that in all scenarios with ED (w ED) compared to the scenarios without ED (w/o ED) an electrification of the energy system takes places by choosing an EH and/or an HP instead of a BOI or a CHP. This leads to decreased emissions, ranging from savings of only 1.6 % for MFH D to 51.9 % for MFH H in price scenario 1 (2022). Besides the different energy systems, in case of MFH H, the landlord also decides to renovate the roof to the highest energetic standard.

In terms of costs, the results show differences in revenues for the landlord and costs for the tenants compared to the respective initial status. Because of the ED, landlords can increase the rent more if a lower final energy demand is achieved. Thus, in scenarios with ED the landlord decides on renovation measures that lead to the highest level of energetic quality (level 4), enabling the highest rent increase. This results in higher revenues for the landlord, as well as higher cost for tenants, since the rent increase is not compensated for by lower energy costs, within all scenarios. Within price scenario 2 (2030), we can observe the highest increase in revenues for MFH D (+100.8 %) and in costs for MFH H (+54.3 %).

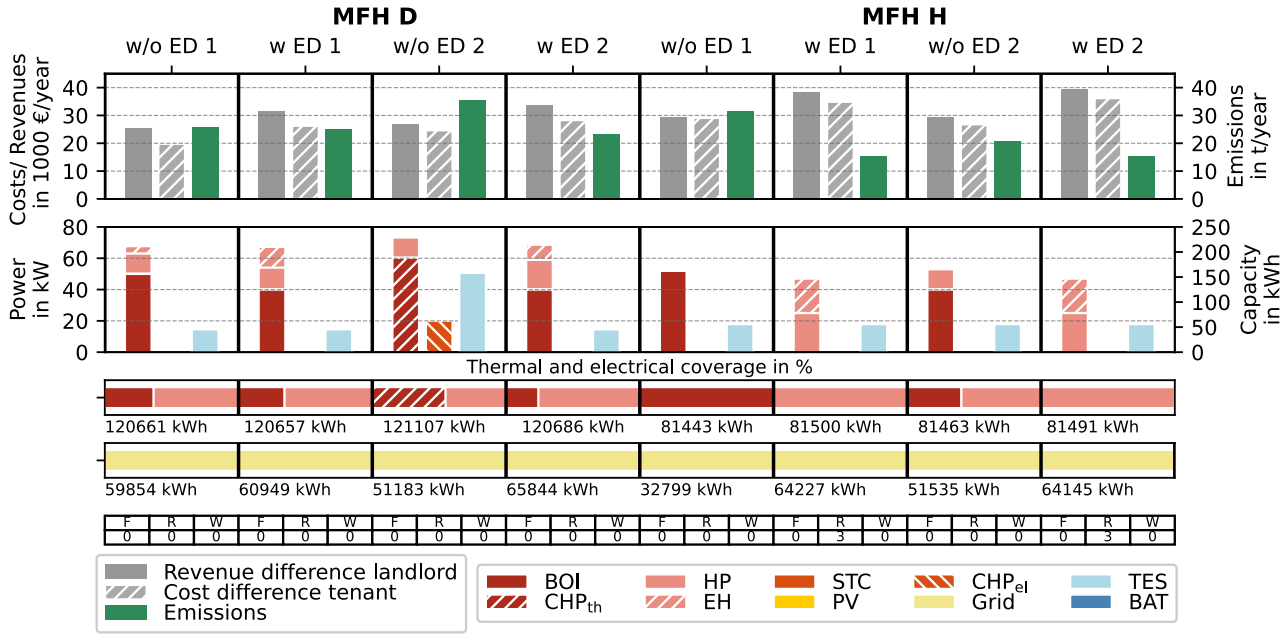

Figure 3: Renovation decisions in a landlord-tenant relation without (w/o) and with (w) ED LRR for price scenarios 1 and 2 (without TEL).

Regarding the *landlord-tenant dilemma* we see a slight reduction in the severity of the first problem of missing incentives for investments of the landlord, e.g., partly renovation of the roof of MFH H. In addition, the landlord invests in climate-friendly technologies (problem 3). However, due to high electrification combined with only minor measures on the building envelope, this could lead to an overload in the power grid during peak loads in the future. Referring to the second level of the dilemma, the tenant is burdened with significantly higher costs. Thus we can even observe an intensification of the second problem.

Finally, Fig. 4 presents the combination of ED LRR with TEL. In contrast to Fig. 3, the results reveal that TEL leads to the investment in PV in all considered scenarios. However, in the scenarios without ED (w/o ED) the owner's decision leads to mainly fossil based technologies for the remaining energy system. The energy system of MFH D, besides a small HP, mainly consists of a CHP as the landlord is able to sell the produced electricity to the tenants. In the case of MFH H, the landlord solely chooses a BOI. Although all scenarios have a PV, compared to the results without TEL that leads to higher emissions of up to 40.8 % for MFH D in price scenario 1 (2022).

Combining TEL with ED LRR, again a defossilization of the energy system takes place. Compared to Fig. 3 the emissions in the scenarios with ED are only higher for MFH D in price scenario 2 (+3.1 %). For all other

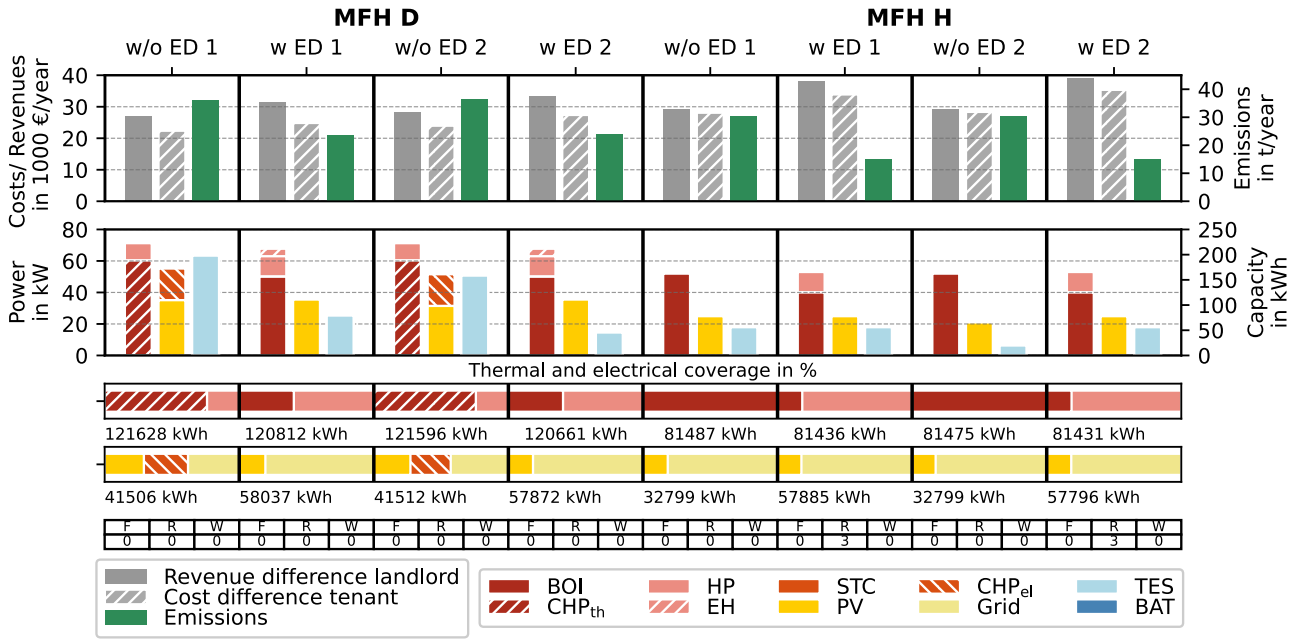

Figure 4: Renovation decisions in a landlord-tenant relation without (w/o) and with (w) ED LRR for price scenarios 1 and 2 (with TEL).

scenarios the combination of both solutions leads to favorable results in terms of emissions (up to 5.6 % for MFH D in price scenario 1) compared to the single approach of ED LRR. In terms of cost allocation, revenues for the landlord and costs for tenants are again significantly increased under the combined approach compared to the initial state. However, in comparison with the exclusive application of energy differentiated LRR, the landlord's revenues and the tenant's costs are slightly reduced (up to 0.3 % and 1.5 %).

Regarding the *landlord-tenant dilemma*, we find that TEL incentivizes the investment of landlords in PV. On the other hand, for the heating system, TEL rather favors CHP than a HP, which is consistent with the findings of Braeuer et al. [19]. In combination with the ED LRR, the decision of the landlord is again favorable for a more climate-friendly solution, adressing the first and the third problem of the dilemma. However, the second level of the conflict is only marginally improved, since the ED only considers the final energy demand, not the operating costs.

5. Discussion

In the optimization framework, we assume that the operation of the energy system is always optimal as we have a perfect foresight, allowing e.g., load shifts. That means that we likely underestimate operational costs in the MILP. This is particularly relevant for the operation of the HP in the owner-occupied building (see subsection 4.1.). Since the operation of the HP is highly dependent on the outdoor temperature and covers the entire heat demand within the considered period (see Fig. 2). This could mean that in practice the results are closer to each other and the second level of the landlord-tenant dilemma might be slightly less severe than presented. On the other hand, within the landlord-tenant relation, tenants are the ones burdened with operating costs. This means an underestimation of the operational cost, could also intensify the second level of the *landlord-tenant-dilemma*. Besides the operation of the energy system, in practice the heating behavior of the tenants might look different, too. For now, all apartments are assumed to be heated to 20 °C. Future studies should consider user behavior and related effects such as rebound and prebound effects as this could have a great impact on the results [36].

6. Conclusion

We extended a MILP for renovation decisions on the energy system and the building envelope to analyze the *landlord-tenant dilemma*. The dilemma consists of two levels. First, the landlord's missing incentives to invest in renovation measures, and second, increasing costs for tenants due to the landlord's decisions. To examine these two levels, we integrated the different perspectives and cost shares of landlords and tenants into the model and the objective function. The extension included the regulatory framework from Germany, in particular the rental law, but also, for example, the allocation of emission costs between landlords and tenants. Based on this, we implemented TEL and an ED LRR as possible solutions to the conflict. As a use case we chose two comparable typical buildings from the German city Hamburg with different construction ages.

The analysis without any of the proposed solutions confirmed both levels of the dilemma. The results showed

that for rented buildings the landlord's decisions are unfavorable in terms of total costs (29 %) and emissions (143 %) compared to an owner-occupied building. The application of TEL pushed investments in PV, but on the other hand, also led to a more fossil based heating system. In case of ED LRRs, we observed greater incentives of the landlord to invest in climate-friendly technology and, in some cases, in an advanced roof insulation. However, for both solutions, alone and combined, the *landlord-tenant dilemma* was only partially resolved for the first level. With regard to the second level, we found increasing costs for the tenants compared to the initial state for all considered scenarios. Thus, we deduce that the concept of ED LRRs needs to be extended and should not only be limited to the final energy demand.

In order to transfer these results further, additional building types and influences of different boundary conditions (e.g. location, price developments) should be investigated in the future. Furthermore, the operation of the energy system and user behavior should be modeled more precisely.

Appendix A Economical assumptions

Table A.1: General economical parameters and price developments [35]

General parameters		**Price development**	**Scenario 1**	**Scenario 2**
Observation period	20	Yearly el. price change	0.969	0.981
Interest rate	0.035	Yearly gas price change	0.960	0.992
Yearly inflation	1.02	Yearly CO_2 price change	1.08	1.02

Table A.2: Economical parameters for devices from manufacturer sheets and [37]

Device	**Power/ Capacity**	**Investment Costs**	**Installation Cost**	**OM Cost**
BOI	15 - 240 kW	2,158 - 13,516 €	5,000 €	3 %
HP	6 - 27 kW	7,800 - 18,315 €	1,530 €	2.5 %
CHP	2.5 - 293 kW	15,293 - 199,363 €	5,800 €	5 %
STC	continuous	245.22 €/m^2	6,500 €	1.5 %
PV	continuous	900 €/kWp	250 €/kWp	1 %
TES	0,116 - 7.3 m^3	756 - 6,973 €	500 €	0 %
BAT	5.5 - 66.24 kWh	7,638 - 47,785 €	2,500 €	0 %
EH	continuous	245 + 19 €/kW	2,000 €	0 %
Fasade	4 insulation levels	2.8484 €/(cm)	98.1968 €	0 %
Window	4 u-value levels	-226.8908 €/(W/m^2K)	736.18 €	0 %
Roof	4 insulation levels	4.1645 €/(cm)	105.5533 €	0 %

Nomenclature

Abbreviations

BAT Battery

BGB German Civil Code

BOI Boiler

CHP Combined heat and power engines

EEG Renewable Energy Sources Act

ED Energy differentiated

EH Electric heater

EM single measures

EnWG German Energy Act

EU European Union

GEG Building Energy Act

HP Air source heat pump

KWKG Combined Heat and Power Act

LRR local reference rent

MILP Mixed-integer linear program

PV Photovoltaic

RF retrofitting fee

STC Solar thermal collectors

TEL Tenant electricity

TES Thermal energy storage

WG Overall building efficiency

Variables

c_{ann}^{rent} annualized rent per month and m²

C_y^{rent} annual rent

c_y^{lrr} LRR per year

$c_{y,lev}^{lrr}$ LRR per year and level

c_{limit}^{lrr} LRR capping limit

c^{rf} RF

c_{limit}^{rf} RF capping limit

q interest rate

Q_{tot}^{fin} final energy demand

Q_{lev}^{fin} final energy demand of respective level

x_y^{switch} binary to switch between RF and LRR

x_y^{lrr} binary variable for the LRR level

x_{lev} binary variable for the energetic level

References

[1] European Commission. In focus: Energy efficiency in buildings. Brussels; 2020.

[2] European Commission. A Renovation Wave for Europe - greening our buildings, creating jobs, improving lives. Brussels; 2020.

[3] Buildings Performance Institute Europe. On the way to a climate-neutral Europe – Contributions from the building sector to a strengthened 2030 climate target; 2020.

[4] Eurostat. Verteilung der Bevölkerung nach Wohnbesitzverhältnissen, Haushaltstyp und Einkommensgruppe - EU-SILC Erhebung; 2022. [accessed 15.3.2023]. Available from: `https://ec.europa.eu/eurostat/databrowser/view/ilc_lvho02/default/table`.

[5] Henger R, Krotova A. Auflösung des Klimaschutz-Wohnkosten-Dilemmas? Förderung energetischer Modernisierungen mit dem Energie- und Klimafonds. Cologne; 2020.

[6] Neitzel M, Dylewski C, Pelz C. Wege aus dem Vermieter-Mieter-Dilemma: Konzeptstudie. Bochum; 2011.

[7] Kossmann B, von Wangenheim G, Gill B. Wege aus dem Vermieter-Mieter-Dilemma bei der energetischen Modernisierung: Einsparabhängige statt kostenabhängige Refinanzierung; 2016.

[8] Henger R, Köhler B, Braungardt S, Meyer R. Potsdam-Institut für Klimafolgenforschung, editor. Wer zahlt für den Klimaschutz im Gebäudesektor? Reformoptionen der Modernisierungsumlage. Potsdam; 2021.

[9] Schütz T, Schiffer L, Harb H, Fuchs M, Müller D. Optimal design of energy conversion units and envelopes for residential building retrofits using a comprehensive MILP model. Applied Energy. 2017;185:1-15.

[10] Ahlrichs J, Rockstuhl S. Estimating fair rent increases after building retrofits: A max-min fairness approach. Energy Policy. 2022;164:112923.

[11] Mellwig P, Pehnt M. Sozialer Klimaschutz in Mietwohnungen: Kurzgutachten zur sozialen und klimagerechten Aufteilung der Kosten bei energetischer Modernisierung im Wohnungsbestand. Heidelberg; 2019.

[12] Gaßner H, Viezens L, Bechstedt A. Faire Kostenverteilung bei energetischer Modernisierung – rechtliche Rahmenbedingungen einer Umwandlung der Modernisierungsumlage gemäß § 559 BGB in ein sozial gerechtes und ökologisches Instrument. Berlin; 2019.

[13] Ekardt F, Heitmann C. Energetische Sanierung im Altbestand und das EEWärmeG: Kann das Investor-Nutzer-Dilemma ökologisch-sozial aufgelöst werden? Recht der Energiewirtschaft; 2009.

[14] Taruttis L, Weber C. Inefficient markets for energy efficiency - Empirical evidence from the German rental housing market. SSRN Electronic Journal. 2022.

[15] März S, Stelk I, Stelzer F. Are tenants willing to pay for energy efficiency? Evidence from a small-scale spatial analysis in Germany. Energy Policy. 2022;161:112753.

[16] Lang M, Lane R, Zhao K, Tham S, Woolfe K, Raven R. Systematic review: Landlords' willingness to retrofit energy efficiency improvements. Journal of Cleaner Production. 2021;303:127041.

[17] März S. Warum sollte ich meine Mietimmobilie energetisch sanieren? Analyse und Multi-Level-Governance quartiersbezogener und individueller Rahmenbedingungen zur Steigerung der energetischen Sanierungstätigkeit privater Kleinvermieter. DuEPublico: Duisburg-Essen Publications online, University of Duisburg-Essen, Germany; 2019.

[18] Petkov I, Mavromatidis G, Knoeri C, Allan J, Hoffmann VH. MANGOret: An optimization framework for the long-term investment planning of building multi-energy system and envelope retrofits. Applied Energy. 2022;314:118901.

[19] Braeuer F, Kleinebrahm M, Naber E, Scheller F, McKenna R. Optimal system design for energy communities in multi-family buildings: the case of the German Tenant Electricity Law. Applied Energy. 2022;305:117884.

[20] Steinbach J. Modellbasierte Untersuchung von Politikinstrumenten zur Förderung erneuerbarer Energien und Energieeffizienz im Gebäudebereich [Dissertation]. Fraunhofer-Institut für System- und Innovationsforschung; 2015.

[21] Schütz T. Optimale Auslegung von Energiewandlungsmaschinen und Gebäudehüllen in Wohngebieten. RWTH Aachen University; 2018.

[22] Verein deutscher Ingenieure. VDI Richtlinie 2067 Blatt 1 - Wirtschaftlichkeit gebäudetechnischer Anlagen: Grundlagen und Kostenberechnung; 2012.

[23] DIN Deutsches Institut für Normung e V . DIN EN ISO 13790 Energieeffizienz von Gebäuden: Berechnung des Energiebedarfs für Heizung und Kühlung. Berlin: Beuth Verlag GmbH; 2008.

[24] Loga T, Stein B, Diefenbach N, Born R. Typology approach for building stock energy assessment, EPISCOPE - Energy performance indicator tracking schemes for the continous optimisation of refurbishment processes in European housing stocks. 2nd ed. Darmstadt: IWU; 2015.

[25] Koppe, Christina. Deutscher Wetterdienst, editor. Klimaberatungsmodul. Offenbach; 2022. Available from: https://kunden.dwd.de/obt/.

[26] Richardson I, Thomson M, Infield D, Clifford C. Domestic electricity use: A high-resolution energy demand model. Energy and Buildings. 2010;42(10):1878-87.

[27] Beausoleil-Morrison I. The Simulation of Building-Integrated Fuel Cell and Other Cogeneration Systems (COGEN-SIM). Hertfordshire; 2013.

[28] Bundesgerichtshof. Urteil des VIII. Zivilsenats vom 16.12.2020;. [accessed 15.3.2023]. Available from: https://juris.bundesgerichtshof.de/cgi-bin/rechtsprechung/document.py?Gericht=bgh&Art=en&az=VIII%20ZR%20367/18&nr=113751.

[29] Knissel J, v Malottki, Christian, Alles R. Bundesinstitut für Bau-, Stadt- und Raumforschung (BBSR) im Bundesamt für Bauwesen und Raumordnung (BBR), editor. Integration energetischer Differenzierungsmerkmale in Mietspiegel; 2010.

[30] Bundesministerium für Verkehr, Bau und Stadtentwicklung. Bundesministerium für Verkehr, Bau und Stadtentwicklung, editor. Hinweise zur Integration der energetischen Beschaffenheit und Ausstattung von Wohnraum in Mietspiegeln; 2013.

[31] Bundesregierung. Entwurf eines Gesetzes zur Aufteilung der Kohlendioxidkosten: CO2KostAufG;. [accessed: 15.3.2022]. Available from: https://www.bmwk.de/Redaktion/DE/Downloads/Gesetz/20220525-entwurf-eines-gesetzes-kohlendioxidkosten.pdf?__blob=publicationFile&v=8.

[32] European Energy Exchange AG. KWK Index; 2023. [accessed: 15.3.2023]. Available from: https://www.eex.com/de/marktdaten/strom/indizes.

[33] Freie und Hansestadt Hamburg Behörde für Stadtentwicklung und Wohnen. Hamburger Mietenspiegel 2021. Hamburg; 2021. [accessed: 15.3.2023]. Available from: https://www.hamburg.de/mietenspiegel/.

[34] Domínguez-Muñoz F, Cejudo-López JM, Carrillo-Andrés A, Gallardo-Salazar M. Selection of typical demand days for CHP optimization. Energy and Buildings. 2011;43:3036-43.

[35] vbw – Vereinigung der Bayerischen Wirtschaft e V , Prognos AG Berlin. Strompreisprognose. München; 2022.

[36] Osterhage T. Messdatengestützte Analyse und Interpretation sanierungsbedingter Effizienzsteigerungen im Wohnungsbau [Dissertation]. Technische Universität Dortmund; 2018.

[37] Figgener J, Haberschusz D, Zumühlen S, Sauer DU. Speichermonitoring BW - Abschlussbereicht - RWTH Aachen Institut für Stromrichtertechnik und Elektrische Antriebe. 2021.

GHG mitigation in the electricity production system in Canary Islands. A proposal for a management and optimization tool in generation.

Juan Carlos Lozano Medina [(1)], Vicente Henríquez-Concepción [(1)], Alejandro Ramos-Martín [(1,2)], Fabian Alberto Déniz Quintana [(3)], Carlos Alberto Mendieta-Pino [(1,2)]

(1) Department of Process Engineering. University of Las Palmas de Gran Canaria (ULPGC)
(2) University institute for Environmental Studies and Natural Resources (i-UNAT), (ULPGC)
(3) University Institute of Intelligent Systems and Numeric Applications in Engineering (SIANI) (ULPGC)
+34609153268 juancarlos.lozano@ulpgc.es

Abstract:

The penetration of renewable energies in island environments poses a series of challenges such as stability, demand response and guarantee of supply, among others. Throughout this work, a study methodology will be presented based on the current conditions of electricity demand in the Canary Islands and their electricity production system to mitigate the emission of greenhouse gases and improve the penetration of renewable energies in island electricity systems. Based on the initial data, a tool will be proposed that optimizes the energy production system through combustion technology (non-renewable) and combines it with the production of energy through renewables that meet expectations both in dynamic response, safety, scaling and integration with renewable energy systems, in terms of efficiency and power. Resulting in a series of cases, under different operating conditions, providing different scenarios and an expansion of up to 36.78% of the renewable installed capacity in the Canary Islands (70% in Gran Canaria) with a reduction of 65.13% of tCO_{2eq} and a reduction in fuel consumption of 71.45%.

Keywords:

Thermodynamics; Energy; Canary; Generation; Island; Electric.

1. Introduction

1.1. Energetic overview.

All abound in the need for decarbonization [1], [2][3], [4][5], [6][7], in the need to increase the penetration of renewable energies, in the need for a broader vision of the management of our resources with better management of our technologies. The Canary electricity systems face challenges of environmental, economic, and social sustainability, largely dependent on imported fossil fuels for electricity generation [8]–[10]; this leads to an increase in the cost of electricity and CO_2 emissions; a reduction can be made using more renewable energy sources [11]–[13]. The penetration of renewable energies is in the phase of being the great challenge to become a half reality [14]–[16]. With the passage of time, environmental awareness has increased, this has driven the mobilization of island governments (promoting wind farms, and encouraging the installation of solar panels, etc.) and the mobilization of the end user of energy, with the installation of solar panels, use of electric vehicles, etc. [17]–[19]. This reality faces another not so beneficial environmentally in the production of energy and the age of the existing power generation equipment in the Canary Islands, with more than 30 years, as well as the type of fuel, Fuel Oil, Diesel, and Diesel Oil, and ignoring Natural Gas [20] [21][22]. For this study, energy data have been available until 2020, in this last year it is observed that the primary energy consumption of 3,541,855 toe (-27.49%) and 2,504,547 toe (-31.85%) of final energy, is not representative, that is why this article will refer to the data at a general level to the year 2019, last reference year before the COVID-19 pandemic [23].

It is about finding a balance between type of combustion energy production technologies, types of fuels, renewables and demand behavior that take us to the most optimal point of energy production to meet demand. That is, to produce energy through renewable energies, to make it as much as possible by optimizing and expanding all renewable systems, and for the production of energy through combustion technologies, that this is the lowest possible, with the lowest possible GHG emission, and with the least number of tons of fuel consumed possible and trying to make the fuel used the least polluting. We establish a tool that relates all these variables to us and inspect the situation with different hypotheses.

1.2. GHG emissions overview

In relation to the emission of GHGs due to electricity generation, they are mainly due to the gases formed in combustion, so that, for these purposes, CO_2 and NO_2 emissions are considered. The emission factors provided by "Red Eléctrica de España" use the GWP (Global Warming Potential) value included in the IPCC Fifth Assessment Report (AR5) and shown in [24][25]**Table 1**.

Table 1. Emissions according to generation technologies in Spain.

Technology	CO_2 emissions *(tCO_2/MWh)*	NO_2 emissions *(tCO_2/MWh)*	*Non-peninsular territories system Greenhouse gas emissions ($tCO_{2\text{-}eq}/MWh$)*	Peninsular territories system Greenhouse gas emissions *($tCO_{2\text{-}eq}/MWh$)*
Combined cycle (diesel)	0.60	0.00	0.60	-
Combined cycle (natural gas)	0.41	0.00	0.41	0.37
Diesel (diesel, fuel oil)	0.65	0.03	0.68	-
Steam turbine (fuel oil)	0.90	0.00	0.90	0.77
Steam turbine (coal)	-	-	-	0.95
Steam turbine (nuclear)	-	-	-	0.00
Gas turbine (diesel)	1.12	0.00	1.12	-
Gas turbine (natural gas)	0.84	0.00	0.84	-
Solar-Photovoltaic	0.00	0.00	0.00	0.00
Wind	0.00	0.00	0.00	0.00

In the Spanish electricity systems of the island territories (Canary Islands and Balearic Islands) these CO_2 emission factors are basically the same as those used to determine the remuneration for costs of emission rights of generation groups and which is included in national legislation in Royal Decree 738/2015, which regulates the activity of electricity production and the procedure for dispatch in the electricity systems of the non-peninsular territories. Emissions per electricity consumption, in 2019, are 0.331 $kgCO_{2\text{-}eq}$./kWh Final Energy and 2.368 $kgCO_{2\text{-}eq}$./kWh Primary Energy for the peninsular system, and 0.776 $kgCO_{2\text{-}eq}$./kWh Final Energy and 2.994 $kgCO_{2\text{-}eq}$./kWh Primary Energy in insular systems (IDAE, 2016). In the Canary Islands, the mix of conventional technologies makes the average emission of 0.694 $tCO_{2\text{-}eq}$./MWh, by comparison for 2019, the average emission of Spain was 0.190 $tCO_{2\text{-}eq}$./MWh.

2. Energy situation in the Canary Islands in 2019.

2.1. Energy and environmental values.

The participation of the different sources and technologies in the coverage of electricity demand in terms of gross energy in the Canary Islands in 2019, by island and technology is shown in **Appendix A.** Note that the penetration of renewables is 15.9%.

In 2019 the Canary Islands had an installed capacity of 3,320.03MW, of which 623.67MW are renewable sources and 2,696.36MW are non-renewable sources. The installed power is shown in **Appendix B**.

Fuel consumption for electricity generation in the Canary Islands in 2019 was 1,702,166.0 MT (57.6% fuel oil, 41.2% diesel oil and 1.2% diesel-oil). By technologies, the steam units consumed 595,170 mt of fuel oil and 515 mt of diesel, the diesel units 384,935 mt of fuel oil and 18,826 mt of diesel and 21,259 mt of diesel-oil, the gas turbine units 12,995 mt of diesel and the combined cycle units 294,378 mt of diesel, all of which are substitute fuels as the design fuel in these units was natural gas. Fuel consumption and GHG emissions for 2019 are shown in **Appendix C** and are represented in the following graphs.

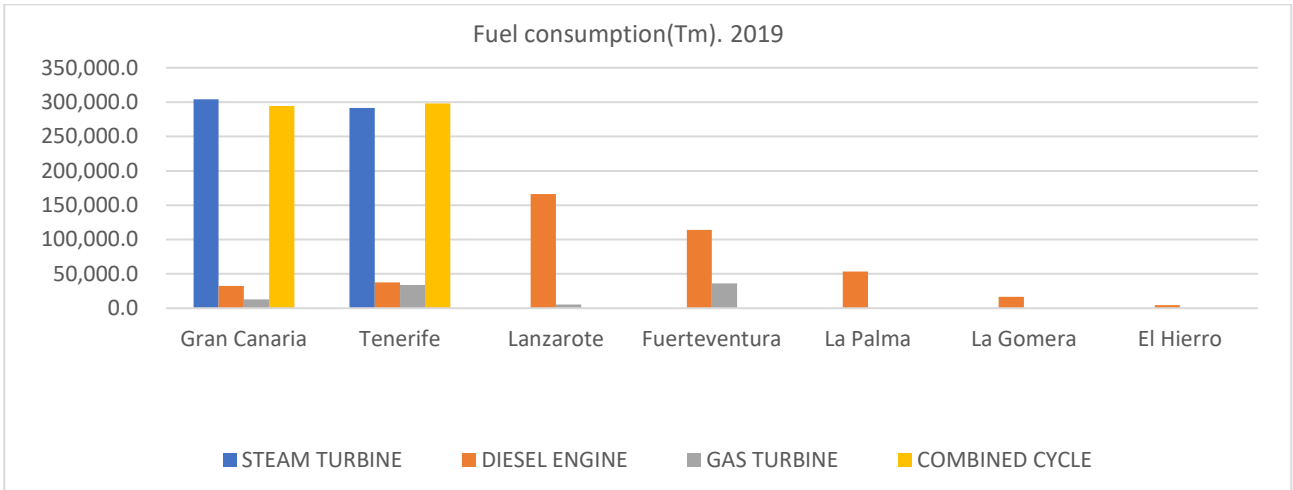

Figure1. Fuel consumption by islands and technology in the Canary Islands. Source: Canary Islands Energy Yearbook 2019.

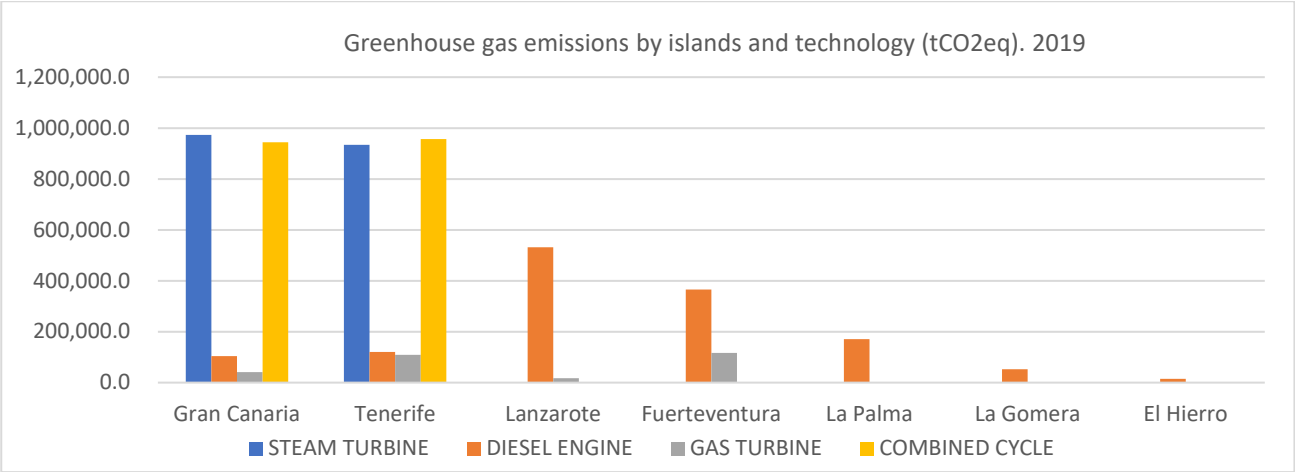

Figure2. Greenhouse gas emissions by islands and technology in the Canary Islands. Source: Canary Islands Energy Yearbook 2019.

As for emissions, for 2019 in the Canary Islands it was 5,454,911 $tCO_{2\text{-eq}}$. Of these, 99.7% was CO_2, 0.1% CH_4 and 0.2% NO_2. As for the emission factor ($tCO_{2\text{-eq}}$./MWh) calculated based on the energy produced, the results are shown in **Appendix D,** differentiated by islands and power equipment. It is worth mentioning the high emission factor of gas turbines and the fall of this factor in El Hierro due to renewable energies.

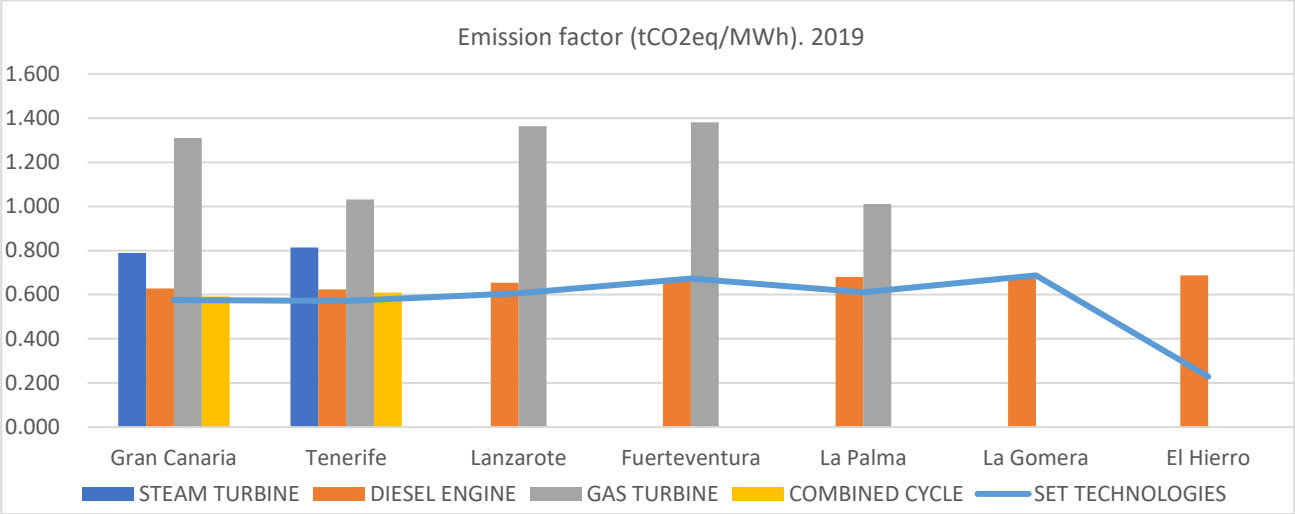

Figure3. Emission factor by islands and technology in the Canary Islands. Source: Canary Islands Energy Yearbook 2019.

The lowest emission factor is that of combined cycle power plants (0.601 $tCO_{2\text{-eq}}$./MWh) and diesel engines (0.656 $tCO_{2\text{-eq}}$./MWh). An overall emission factor for the Canary Islands, including renewable production, is estimated at 0.584 $tCO_{2\text{-eq}}$./MWh. **Table 2** shows the date and time of highest demand by islands in 2019.

Table 2. Demand peaks. Source: Canary Islands Energy Yearbook 2019.

Island	date	hour	MW
Gran Canaria	02/10/2019	20:58	537.00
Tenerife	02/10/2019	20:21	576.00
Lanzarote	31/12/2019	19:06	139.00
Fuerteventura	17/08/2019	20:53	113.00
La Palma	19/08/2019	21:36	43.00
La Gomera	17/08/2019	21:59	12.10
El Hierro	20/08/2019	21:27	8.10

Specifically, in Gran Canaria, the moment of greatest demand was on October 2, 2019 (20:58h,) with emissions of 0.631 $tCO_{2\text{-eq}}$ MWh-1 and a peak of 537.0 MW (**Figure 4**). The demand curve is very similar to the rest of the days except for small fluctuations produced by particular cases. In turn, the different groups are programmed to meet that demand curve. That is why it is necessary to carry out a good programming for a correct functioning of the network. It is also worth emphasizing the difficulty of predicting the curve correctly, and the validity of the data obtained to provide the necessary power and specifically in systems based on renewable energies (wind and solar) existing on the island.

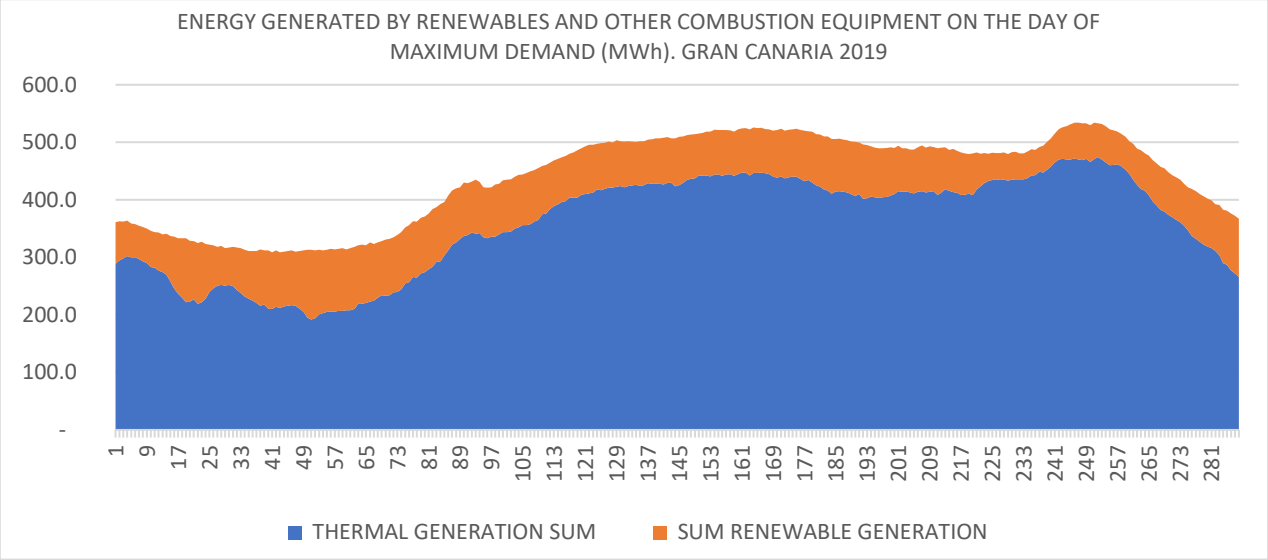

Figure 4. Demand curve Gran Canaria. Peak demand 2019. Thermal and renewable generation. Source: Canary Islands Energy Yearbook 2019.

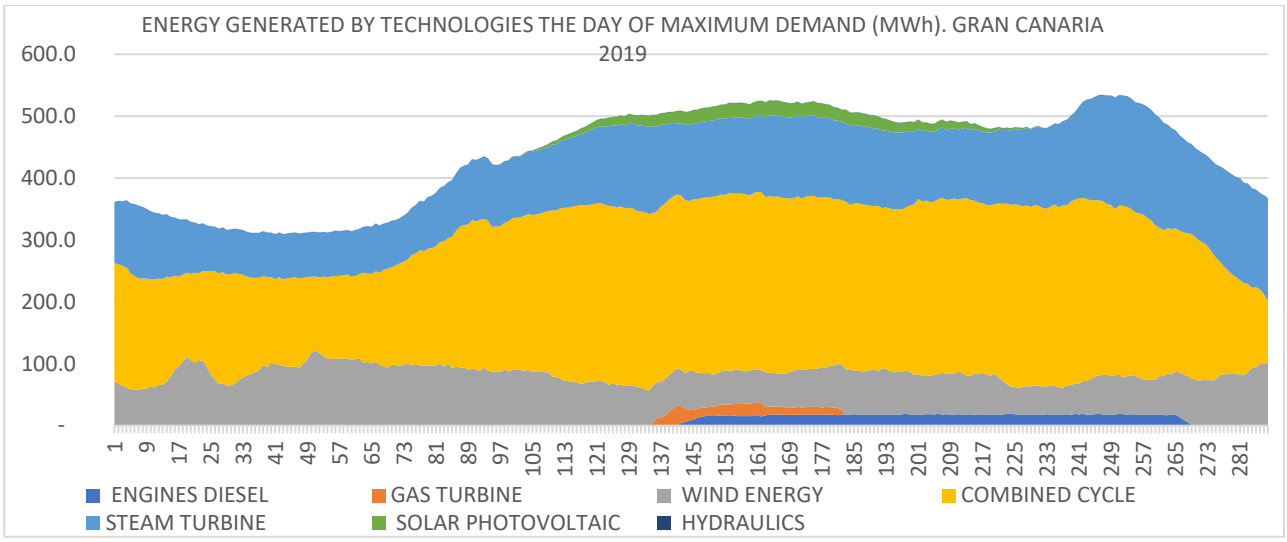

Figure 5. Demand curve Gran Canaria. Peak demand 2019. Generation differentiating technologies. Source: Canary Islands Energy Yearbook 2019.

For the peak demand day, the steam turbine and combined cycle groups contribute 33.35% and 51.28% of the electricity to the grid, leaving the Diesel and gas turbine groups for the tips and being the contribution of renewables (wind) of 11.83% (**Figure 5**).

2.2. Penetration values of renewable energies in the Canary Islands.

The data collected start from 2004, in that year, the Canary Islands had 138.22 MW installed and for Gran Canaria 75.85 MW. In this time horizon, with an average annual growth of 8%, two specific years stand out where there were very significant increases in installed capacity compared to the previous year, years 2008 and 2018, in the case of Gran Canaria, the technology that drove the development of the sector was wind generation. It is observed how the penetration of renewable energies has been slow during the years studied. As indicated above, the penetration of renewables in 2019 was 15.9%.

3. Material and methods. Non-renewable production system alternatives based on the expansion of the penetration of renewables and optimization of existing equipment.

3.1. Tool.

A tool is proposed that helps to regulate and optimize the energy production equipment and describes the different existing combinations in achieving an energy production that meets the demand, all this optimizing fuel consumption, reducing GHG emissions, increasing the penetration of renewables and reducing the CO_2

emission factor, (tCO_{2eq}/MWh). The following list has been defined that covers all the possibilities of operation of energy production equipment in the Canary Islands. With this ratio it is possible to obtain, for the different operating conditions, the power produced, GHG emissions, fuel consumption, etc.

$$E=\{[ax\alpha1+a´x(1-\alpha1)]xA+[bx\alpha2+b´x(1-\alpha2)]xB+[cx\alpha3+c´x(1-\alpha3)]xC+[dx\alpha4+d´x(1-\alpha4)]xD\}x(1+\beta)$$

where:

Table 3. Definition of parameters.

Technologies				Definition of parameters.
Steam turbine	Engines diesel	Gas turbine	Combined cycle	
a´	*b´*	*c´*	*d´*	Studied value of this technology running on 100% usual fuel
a	*b*	*c*	*d*	Studied value of this technology running on 100% natural gas
α1	*α2*	*α3*	*α4*	% use of natural gas in this technology
A	*B*	*C*	*D*	% of operation of this technology
Renewable		*β*		% contributed from this technology calculated on the total contributed by the rest of technologies not including renewables.
		R		% contributed from this technology calculated on the total contributed by all technologies, including renewables.

A variation of this expression, also interesting since it is a function of the percentage of penetration of renewables in the system (R), is:

$$E=\{[ax\alpha1+a´x(1-\alpha1)]xA+[bx\alpha2+b´x(1-\alpha2)]xB+[cx\alpha3+c´x(1-\alpha3)]xC+[dx\alpha4+d´x(1-\alpha4)]xD\}/(1-R)$$

The indicator "CO_2 *GREEN"* has also been defined. This indicator evaluates the status or situation of the objective " $tCO_{2\text{-eq}}$ *ZERO*", the cancellation to 100% of the $tCO_{2\text{-eq}}$. In short, it is the amount of $tCO_{2\text{-eq}}$ that has stopped being emitted into the atmosphere in the energy production process per person. This percentage increase in the *$tCO_{2\text{-eq}}$/inhabitant* that are no longer emitted, causes environmental damage to decrease in the same proportion, as well as damage to people's health.

3.2. Starting values 2019.

For this we start from the base that in 2019 as indicated we have in the Canary Islands the following indices:

Greenhouse gas emissions 5.454.911,00 tCO_{2eq}, Emission factor 0,584tCO_{2eq}/MWh and Fuel consumption estimation 1.702.166,00 Tn.

3.3. Procedure.

With this relationship we establish several hypotheses with the aim of reducing emissions, fuel consumption, and increasing the penetration of renewables. Applying the relationship established for the existing situation in 2019 for Gran Canaria, we obtain:

Fuel consumption =a´xA+b´xB+c´xC+d´xD = 643.814,00 Ton

Energy production ={a´xA+b´xB+c´xC+d´xD}x(1+β) = {a´xA+b´xB+c´xC+d´xD}/(1-R) = 3.581.933,00 MWh

Greenhouse gas emissions =a´xA+b´xB+c´xC+d´xD = 2.063.911,00 tCO2eq

It has been contemplated that there is no Natural Gas in 2019 in Gran Canaria and the respective data have been entered:

Table 4. Data for the situation in Gran Canaria 2019

	Steam turbine		Engines diesel		Gas turbine		Combined cycle	
	a´	*a*	*b*	*b´*	*c*	*c´*	*d*	*d´*
Fuel consumption estimation (Tn)	604.618,4	528.898,2	144.308,2	144.308,2	619.815,9	479.656,8	745.377,9	576.825,5
Energy Produced (MWh)	2.452.800	2.452.800	735.840	735.840	1.519.422	1.519.422	4.044.754	4.044.754
Greenhouse gas emissions (tCO2eq)	1.936.141	1.421.637	462.166	462.166	1.989.295	1.648.313	2.392.330	1.982.216
	α1	*A*	*α2*	*B*	*α3*	*C*	*α4*	*D*
Gran Canaria 2019	0,00%	50,24%	0,00%	22,50%	0,00%	2,09%	0,00%	39,49%

Being β= 18.29% and R= 15.46% for energy production.

3.4. Proposal of hypotheses of operation of equipment preserving the current type of fuel.

3.4.1. HYPOTHESIS 1: Reordering power plants with historical annual maximums. Penetration of renewables: 15.9%.

In this hypothesis, we proceed to work with the least polluting equipment in the different production centers of the islands, bringing them to a production ceiling marked by the maximum annual historical productions. The

historical annual maximums of combined cycle plants (3,418,748MWh) and diesel engines (2,390,736.2MWh) which are the least polluting have been studied, proportionally rearranging the rest of the equipment. Preserving the penetration of renewables (1,480,634MWh, 15.9%). This results in an overall emission factor of 0.563 $tCO_{2\text{-}eq}$/MWh.

Table 5. Hypothesis 1.

Technology	Energy Produced (*MWh*)	Greenhouse gas emissions (tCO_{2eq})	Emission factor (tCO_{2eq}/MWh)	Fuel consumption estimation (*Tn*)
Steam turbine	2.045.977,0	1.641.421,5	0,802	512.582,8
Diesel engine	2.390.736,2	1.562.556,1	0,654	488.206,3
Combined cycle	3.418.748,0	2.052.294,4	0,600	639.433,0
Renewable (15,9%)	1.480.634,0	-	-	-
Total	9.336.095,2	5.256.271,9	0,563	1.640.222,1

3.4.2. HYPOTHESIS 2: Rearrangement of power plants working exclusively with the least polluting. Penetration of renewables: 15.9%.

In this hypothesis, we proceed to continue working with the least polluting equipment in the different production centers of the islands, but we work exclusively with them, ignoring the rest of the equipment. All this entails producing 5,428,740.4MWh in the combined cycle plants and 2,426,720.8MWh diesel engines, which are the least polluting, leaving the rest of the equipment in disuse or as reserves. Preserving the penetration of renewables (1,480,634MWh, 15.9%). All this results in an overall emission factor of 0.519 $tCO_{2\text{-}eq}$/MWh.

Table 6. Hypothesis 2.

Technology	Energy Produced (*MWh*)	Greenhouse gas emissions (tCO_{2eq})	Emission factor (tCO_{2eq}/MWh)	Fuel consumption estimation (*Tn*)
Diesel engine	2.426.720,8	1.585.013,5	0,653	495.218,0
Combined cycle	5.428.740,4	3.259.874,3	0,600	1.015.678,5
Renewable (15,9%)	1.480.634,0	-	-	-
Total	9.336.095,2	4.844.887,8	0,519	1.510.896,4

3.4.3. HYPOTHESIS 3: Reorganization of power plants working exclusively with the least polluting, but incorporating the Chira-Soria project. Penetration of renewables: 29.5%-36.8%.

In this hypothesis, we proceed to continue working with the least polluting equipment in the different production centers of the islands, but we work exclusively with them, ignoring the rest of the equipment. The Chira-Soria power plant is incorporated. With this addition, a global penetration in renewables in Gran Canaria is expected between 51% and 70%.

If we estimate 51% in Gran Canaria **(HYPOTHESIS 3a),** which affects the overall figure of penetration of renewables in the Canary Islands, rising to 29.1%. All this entails producing 4,307,822.1MWh in the combined cycle plants and 2,310,552.60MWh diesel engines, which are the least polluting, leaving the rest of the equipment in disuse or as reserves. The penetration of renewables would be (2,717,720.5MWh, 29.1%). This results in an overall emission factor of 0.440 $tCO_{2\text{-}eq}$/MWh.

Table 7. Hypothesis 3a.

Technology	Energy Produced (*MWh*)	Greenhouse gas emissions (tCO_{2eq})	Emission factor (tCO_{2eq}/MWh)	Fuel consumption estimation (*Tn*)
Diesel engine	2.310.552,6	1.512.050,4	0,654	472.435,9
Combined cycle	4.307.822,1	2.596.890,5	0,603	809.112,7
Renewable (29,1%)	2.717.720,5	-	-	-
Total	9.336.095,2	4.108.940,9	0,440	1.281.548,5

If we estimate 70% in Gran Canaria **(HYPOTHESIS 3b),** which affects the overall figure of penetration of renewables in the Canary Islands, rising to 36.8%. All this entails producing 3,658,707.6 in the combined cycle plants and 2,243,280.5MWh diesel engines, which are the least polluting, leaving the rest of the equipment in disuse or as reserves. The penetration of renewables would be (3,434,107.1MWh, 36.8%). This yields an overall emission factor of 0.394 $tCO_{2\text{-}eq}$/MWh.

Table 8. Hypothesis 3b.

Technology	Energy Produced (*MWh*)	Greenhouse gas emissions (tCO_{2eq})	Emission factor (tCO_{2eq}/MWh)	Fuel consumption estimation (*Tn*)
Diesel engine	2.243.280,5	1.469.798,2	0,655	459.242,9
Combined cycle	3.658.707,6	2.212.962,0	0,605	689.492,2
Renewable (36,8%)	3.434.107,1	-	-	-
Total	9.336.095,2	3.682.760,2	0,394	1.148.735,1

3.4.4. Summary of these 5 hypothesis:

The following is a summary of the improvements produced by these 4 variants of hypothesis:

Table 9. Summary and comparison of the hypotheses planted

Hypothesis	% Renewable penetration	Greenhouse gas emissions (tCO_{2eq})	Emission factor (tCO_{2eq}/MWh)	Fuel consumption estimation (Tn)	% improvement	Green CO_2 (tCO_{2eq}/inhabitant year)
2019	15,86%	5.454.911	0,58	1.702.166	-	2,50
1	15,86%	5.256.271	0.56	1.640.222	-3,8%	2,41
2	15,86%	4.844.887	0.52	1.510.896	-12,6%	2,22
3a	29,11%	4.108.940	0.44	1.281.548	-32,8%	1,89
3b	36,78%	3.682.760	0.39	1.148.735	-48,1%	1,69

Logically, we improve the green CO_2 index by incorporating more renewables and stop producing CO_2. It is worth mentioning the significant improvement with the entry of the Chira-Soria project. If we compare green CO_2 between islands and by hypothesis we obtain:

Table 10. Island Green CO_2 (tCO_{2eq}/inhabitant year)

Hypothesis	Gran Canaria	Tenerife	Lanzarote	Fuerteventura	La Palma	La Gomera	El Hierro	Canarias
2019	2,42	2,28	3,52	4,02	2,06	2,42	1,25	2,50
1	2,34	2,21	3,46	3,51	2,06	2,42	1,25	2,41
2	2,11	1,98	3,46	3,51	2,06	2,42	1,25	2,22
3a	1,25	1,98	3,46	3,51	2,06	2,42	1,25	1,89
3b	0,75	1,98	3,46	3,51	2,06	2,42	1,25	1,69

We can see that the worst situation is in terms of Green CO_2 is on the island of Lanzarote and Fuerteventura and the best in El Hierro. Gran Canaria approaches El Hierro from the 3rd hypothesis and Tenerife in the 4th hypothesis, like the rest of the islands.

3.5. Proposal of hypotheses of operation of equipment changing the type of current fuel.

We continue with more Hypotheses, but now we make a variant on the previous Hypotheses. This variant consists of the modification of the fuel. As far as possible and allowed the equipment will move to use Natural Gas.

Natural gas produces CO_2 emissions 40-50% lower than those of coal and 25-30% lower than those of fuel oil. As for NOx, the nature of the gas (its combustion takes place in the gas phase) allows to achieve a more perfect mixture with the combustion air which leads to complete and more efficient combustion, with less excess air. Methane, which is the main component of natural gas, is a more potent cause of the greenhouse effect than CO_2, although methane molecules have a shorter lifetime in the atmosphere than CO_2. De according to independent studies, direct losses of natural gas during extraction, transport and distribution worldwide, they have been estimated at 1% of the total gas transported, the CO_2 emission in the combustion of Natural Gas is 58 $kgCO_2/GJ$ compared to that of Fuel Oil or Diesel which is 79 $kgCO_2/GJ$ and 70 $kgCO_2/GJ$ respectively. On the other hand, we have that the calorific value of natural gas is higher than that of the other fuels usually used in the Canary Islands.

Table 11. Calorific power.

Fuel type	Higher calorific power (Kcal/Kg)	Lower calorific power (Kcal/Kg)
Fuel	10.430,00	9.850,00
Diesel	9.265,00	8.713,00
Diesel oil	10.790,00	10.140,00
Natural gas	12.474,00	11.259,00

All this makes the convenience of using Natural Gas double since we need to burn less fuel to produce the same electricity and less CO2 is generated by electricity produced. The distribution of fuel for the current situation (starting situation) where all equipment except diesel engines switch to Natural Gas is as shown in **Appendix E** as well as the new emission distribution ($tCO_{2\text{-}eq}$) expected for this new situation. As a result of the change of fuel we managed to reduce emissions of polluting gases by 16.17%, from 5,454,911.4 tCO2-eq to 4,573,053,30 $tCO_{2\text{-}eq}$ and reduced fuel consumption by 13.44%, from 1,702,166.00 tons to 1,473,468.48 tons. The new emission factor is 0,490 tCO_{2eq}/MWh.

3.5.1. NG-HYPOTHESIS 1: Rearrangement of power plants with historical annual maximums. Penetration of renewables: 15.9%.

As already indicated above, in this hypothesis we proceed to work with the least polluting equipment in the different production centers of the islands, bringing them to a production ceiling marked by the maximum annual historical productions. The historical annual maximums of combined cycle plants (3,418,748MWh) and diesel engines (2,390,736.2MWh) which are the least polluting have been studied, proportionally rearranging

the rest of the equipment. Preserving the penetration of renewables (1,480,634MWh, 15.9%). With all this we obtain a global emission factor of 0.563 $tCO_{2\text{-}eq}$/MWh to 0.479 $tCO_{2\text{-}eq}$/MWh.

Table 12. NG-Hypothesis 1.

Technology	Energy Produced (*MWh*)	Greenhouse gas emissions (tCO_{2eq})	Emission factor (tCO_{2eq}/MWh)	Fuel consumption estimation (*Tn*)
Steam turbine	2.045.977,0	1.205.228,3	0,589	448.391,4
Diesel engine	2.390.736,2	1.562.554,0	0,654	488.206,3
Combined cycle	3.418.748,0	1.700.472,5	0,497	494.837,9
Renewable (15,9%)	1.480.634,0	-	-	-
Total	9.336.095,2	4.468.254,7	0,479	1.431.435,6

3.5.2. NG-HYPOTHESIS 2: Rearrangement of power plants working exclusively with the least polluting. Penetration of renewables: 15.9%.

In this hypothesis, we proceed to continue working with the least polluting equipment in the different production centers of the islands, but we work exclusively with them, ignoring the rest of the equipment. All this entails producing 5,428,740.4MWh in the combined cycle plants and 2,426,720.8MWh diesel engines, which are the least polluting, leaving the rest of the equipment in disuse or as reserves. Preserving the penetration of renewables (1,480,634MWh, 15.9%). With all this, we went from a global emission factor of 0.519 tCO2-eq/MWh to 0.459 $tCO_{2\text{-}eq}$/MWh.

Table 13. NG-Hypothesis 2.

Technology	Energy Produced (*MWh*)	Greenhouse gas emissions (tCO_{2eq})	Emission factor (tCO_{2eq}/MWh)	Fuel consumption estimation (*Tn*)
Diesel engine	2.426.720,8	1.585.011,2	0,653	495.218,.0
Combined cycle	5.428.740,4	2.701.038,7	0,498	786.002,9
Renewable (15,9%)	1.480.634,0	-	-	-
Total	9.336.095,2	4.286.049,9	0,459	1.281.220,9

3.5.3. NG-HYPOTHESIS 3: Reorganization of power plants working exclusively with the least polluting but incorporating the Chira-Soria project. Penetration of renewables: 29.5%-36.78%.

In this hypothesis, we proceed to continue working with the least polluting equipment in the different production centers of the islands, but we work exclusively with them, ignoring the rest of the equipment.

The Chira-Soria power plant is incorporated. With this addition, a global penetration in renewables in Gran Canaria is expected between 51% and 70%.

If we estimate 51% in Gran Canaria **(GN-HYPOTHESIS 3a),** which affects the overall figure of penetration of renewables in the Canary Islands, rising to 29.1%. All this entails producing 4,307,822.1MWh in the combined cycle plants and 2,310,552.60MWh diesel engines, which are the least polluting, leaving the rest of the equipment in disuse or as reserves. The penetration of renewables would be (2,717,720.5MWh, 29.1%). With all this, we went from an overall emission factor of 0.440 $tCO_{2\text{-}eq}$/MWh to 0.392 $tCO_{2\text{-}eq}$/MWh.

Table 14. NG-Hypothesis 3a.

Technology	Energy Produced (*MWh*)	Greenhouse gas emissions (tCO_{2eq})	Emission factor (tCO_{2eq}/MWh)	Fuel consumption estimation (*Tn*)
Diesel engine	2.310.552,6	1.512.048,9	0,654	472.435,9
Combined cycle	4.307.822,1	2.151.709,3	0,499	626.147,9
Renewable (29,1%)	1.480.634,0	-	-	-
Total	9.336.095,2	3.663.758,3	0,392	1.098.583,8

If we estimate 70% in Gran Canaria **(NG-HYPOTHESIS 3b),** which affects the overall figure of penetration of renewables in the Canary Islands, rising to 36.8%. All this entails producing 3,658,707.6 in the combined cycle plants and 2,243,280.5MWh diesel engines, which are the least polluting, leaving the rest of the equipment in disuse or as reserves. The penetration of renewables would be (3,434,107.1MWh, 36.8%). With all this, we went from an overall emission factor of 0.394 $tCO_{2\text{-}eq}$/MWh to 0.354 $tCO_{2\text{-}eq}$/MWh.

Table 15. NG-Hypothesis 3b.

Technology	Energy Produced (*MWh*)	Greenhouse gas emissions (tCO_{2eq})	Emission factor (tCO_{2eq}/MWh)	Fuel consumption estimation (*Tn*)
Diesel engine	2.243.280,5	1.469.797,0	0,655	459.242,9
Combined cycle	3.658.707,6	1.833.597,1	0,501	533.577,2
Renewable (36,78%)	3.434.107,1	-	-	-
Total	9.336.095,2	3.303.394,1	0,354	992.820,1

3.5.4. Summary hypothesis, production with teams working with natural gas:

As a summary of these 4 new hypotheses, a summary of the improvements produced by these 4 variants of hypotheses is shown below:

Table 16. Summary and comparison of the hypotheses planted

Hypothesis	% Renewable penetration	Greenhouse gas emissions (tCO_{2eq})	Emission factor (tCO_{2eq}/MWh)	Fuel consumption estimation (Tn)	% improvement	Green CO_2 (tCO_{2eq}/inhabitant year)
2019	15,86%	5.454.911	0,58	1.702.166	-	2,50
NG 2019	15,86%	4.573.053	0,49	1.473.468,48	-	2,10
NG-1	15,86%	4.468.254	0,48	1.431.435,58	-2,3%	2,05
NG-2	15,86%	4.286.049	0,46	1.281.220,92	-6,7%	1,97
NG-3a	29,11%	3.663.758	0,39	1.098.583,77	-24,8%	1,68
NG-3b	36,78%	3.303.394	0,35	992.820,10	-38,4%	1,52

Logically, the trend shown of improvements without the incorporation of Natural Gas increases with the incorporation of this fuel. We improve the green CO_2 index by incorporating more renewables and stop producing CO_2. It is worth noting the significant improvement with the entry of the project Chira-Soria. If we compare the green CO_2 between islands and by hypothesis we obtain:

Table 17. Island Green CO_2 (tCO_{2eq}/inhabitant year)

Hypothesis	Gran Canaria	Tenerife	Lanzarote	Fuerteventura	La Palma	La Gomera	El Hierro	Canarias
2019	2,42	2,28	3,52	4,02	2,06	2,42	1,25	2,50
NG 2019	1,92	1,81	3,50	3,85	2,06	2,42	1,25	2,10
NG-1	1,89	1,78	3,46	3,51	2,06	2,42	1,25	2,05
NG-2	1,79	1,68	3,46	3,51	2,06	2,42	1,25	1,97
NG-3a	1,06	1,68	3,46	3,51	2,06	2,42	1,25	1,68
NG-3b	0,63	1,68	3,46	3,51	2,06	2,42	1,25	1,52

We can see that the worst situation is still in terms of Green CO_2 that of the island of Lanzarote and Fuerteventura and the best in El Hierro. Gran Canaria approaches the Iron and improves from the GN-Hypothesis 3ª and Tenerife in the 4th Hypothesis, like the rest of the islands.

3.6. Results.

As a summary of the results we have:

Hypothesis 2: this approach is what offers immediate results at the lowest cost. As indicated in its approach, it consists of working exclusively with the least polluting equipment in the different production centers of the islands, combined cycle and Diesel engines. We subject this equipment to greater mechanical stress, but bearable with good maintenance according to its use. The most affected would be the combined cycles of Gran Canaria and Tenerife that their use would be 67.83% and 67.10%, and the Diesel Engines of Fuerteventura and Lanzarote that their use would be 67.35% and 55.57%. The rest of the equipment would have a use of less than 45%. With all this we lower total GHG emissions ($tCO_{2e}q$) by 12.59% and fuel consumption (Ton) by 12.66% and the economic and temporary cost is practically zero.

Execution Time: Immediate; Economic cost: Minimum; Decrease in total GHG emissions (tCO2eq):12.59%; Decrease in fuel consumption (Ton):12.66%; Renewable penetration: 15.86%.

NG Hypothesis 2: this second approach described in the GN. hypothesis2, consists of working exclusively with the least polluting equipment in the different production centers of the islands, combined cycle and Diesel engines, but we also change the fuel used in the combined cycle, going from diesel to natural gas.

We subject these teams to a mechanical stress like that of the previous hypothesis, although it is somewhat lower in the combined cycle. As a result, we obtain:

Execution Time: Average; Economic cost: medium; Decrease in total GHG emissions (tCO2eq):2 2.08%; Decrease in fuel consumption (Ton):1 8.91%; Renewable penetration: 15.86%.

Hypothesis 3a: third approach for our objective is the one described in hypothesis3a, to work exclusively with the least polluting equipment in the different production centers of the islands, combined cycle and Diesel engines, with their usual fuel, but we also incorporate the Chira-Soria project that incorporates the Chira-Soria plant and that foresees a penetration in renewables overall in Gran Canaria between 51% and 70%. In this hypothesis, 51% was estimated in Gran Canaria (the minimum expectation of this project), which affects the overall figure of penetration of renewables in the Canary Islands, rising to 29.1 1%.

Execution Time: Medium-High; Economic cost: medium-high; Decrease in total GHG emissions (tCO2eq):3 2.76%; Decrease in fuel consumption (Ton): 32.82%; Renewable penetration: 29.11%.

NG Hypothesis 3a: a fourth approach to our objective is that described in the GN. hypothesis3a, to work exclusively with the least polluting equipment in the different production centers of the islands, combined cycle and Diesel engines, changing the fuel of the combined cycle to natural gas, but we also incorporate the Chira-

Soria project that incorporates the Chira-Soria plant with a penetration in renewables global in Gran Canaria between 51% in Gran Canaria (the minimum expectation of this project), which affects the overall figure of penetration of renewables in the Canary Islands, rising to 29.1 1%.

Execution Time: Medium-High; Economic cost: medium-high; Reduction of total GHG emissions (tCO2eq): 48.89%; Decrease in fuel consumption (Ton):54.94%; Renewable penetration: 29.11%.

NG Hypothesis 3b: a fifth approach and the most optimal of all for our objective is the one described in the GN. hypothesis3b, working exclusively with the least polluting equipment in the different production centers of the islands, combined cycle and diesel engines, changing the fuel of the combined cycle to natural gas, but we also incorporate the Chira-Soria project that incorporates the Chira-Soria plant with a penetration in renewables global in Gran Canaria between 70% in Gran Canaria (the maximum expectation of this project), which affects the global figure of penetration of renewables in the Canary Islands, rising to 36.78%.

Execution Time: Medium-High; Economic cost: medium-high; Reduction of total GHG emissions (tCO2eq):65.13%; Decrease in fuel consumption (Ton): 71.45%; Renewable penetration: 36.78%.

3.7. Conclusions.

There are several measures that can be taken because of the result of this study through the tool proposed to achieve our environmental objective. All these measures to be taken depend in turn on several factors:

Economic factor: The measures to be taken can be very expensive with a satisfactory result or less expensive and obtain to a lesser degree a satisfactory result. Although not always the investment is directly proportional in a linear way to the result.

Temporal factor: If we take into account this factor, we can find several situations ranging from the immediacy of the actions to be taken or the other extreme that is to go to several years of delay in achieving completion of that action, and of course all intermediate situations are also valid.

The results will improve as these two factors grow, that is, we have more time and more investment.

Appendix A

TableA.1. Energy produced (MWh). Source: Canary Islands Energy Yearbook 2019.

Technology	Gran Canaria	Tenerife	Lanzarote	Fuerteventura	La Palma	La Gomera	El Hierro	Canarias
Steam turbine	1.233.316	1.146.979						2.380.295
Diesel engine	1.657.552	192.784	813.663	552.146	251.332	76.696	20.738	2.072.911
Gas turbine	31.758	105.645	12.791	841.585	603			235.382
Combined cycle	1.597.427	1.569446						3.166.873
Renewable	553.880	696096	79.623	80.108	29.081	154	41.692	1.480.634
Total	3.581.933	3710950	906.077	716.839	281.016	76.850	62.430	9.336.095

Appendix B

Table B.1. Installed capacity (MW). Source: Canary Islands Energy Yearbook 2019.

Technology	Gran Canaria	Tenerife	Lanzarote	Fuerteventura	La Palma	La Gomera	El Hierro	Canarias
Steam turbine	280,00	240,00						520,00
Diesel engine	84,00	84,00	166,76	107,92	82,84	21,17	14,91	564,60
Gas turbine	173,45	265,70	62,50	79,10	22,50			603,25
Combined cycle	461,73	456,80						918,53
Refinery-Cogen.	24,88	65,10						89,98
Renewable	199,92	314,54	32,41	41,42	12,18	0,37		623,67
Total	1.223,98	1.426,14	264,67	228,44	117,52	21,54	22,83	3.320,03

Appendix C

Table C.1. Fuel consumption in the thermal power plants of the Canary Islands (Ton) and greenhouse gas emissions (tCO_{2eq}) per fuel used. Source: Canary Islands Energy Yearbook 2019.

Technology	Fuel consumption (Ton)				Greenhouse gas emissions (tCO_{2eq})			
	Fuel	Oil	Dieseloil	Total	Fuel	Oil	Diesel oil	Total
Steam turbine	595.170	515	-	595.685	1905.884	1.652		1.907.536
Diesel engine	384.935	18.826	21.259	425.020	1.232.665	60.423	67.103	1.360.191
Gas turbine	-	88.944	-	88.944	-	285.467		285.467
Combined cycle	-	592.517	-	592.517	-	1.901.715		1.901.715
Total	980.105	700.802	21.759	1.702.166	3.138.549	2.249.257	67.103	5.454.909

Appendix D

Table D.1. Greenhouse gas emissions (tCO_{2eq}) by type of technology in the thermal power plants of the Canary Islands and emission factor (tCO_{2eq}/MWh). Source: Canary Islands Energy Yearbook 2019.

Technology	Energy Produced (MWh)	Greenhouse gas emissions (tCO_{2eq})	Emission factor (tCO_{2eq}/MWh)
Steam turbine	2.380.295,0	1.907.536,0	0,801
Diesel engine	2.072.911,0	1.360.192,0	0,656
Gas turbine	235.382,0	285.468,0	1,213
Combined cycle	3.166.873,0	1.901.715,0	0,601
Renewable	1.480.634,0		-
Total	9.336.095,2	5.454.911,0	0,584

Appendix E

Table E.1. Estimation of fuel consumption in the thermal power plants of the Canary Islands (Ton)

Technology	Fuel consumption (Ton)				
	Natural gas	Fuel	Oil	Diesel oil	Total
Steam turbine	521.086,4	-	-	-	521.086,4
Diesel engine	-	384.935,0	18.826,0	21.259,0	425.020,0
Gas turbine	68.831,1	-	-	-	68.831,1
Combined cycle	458.531,0	-	-	-	458.531,0
Total	1.048.448,5	384.935,0	18.826,0	21.759,0	1.473.468,5

Table E.2. Estimation total greenhouse gas emissions (tCO_{2eq}) per fuel used.

Technology	Greenhouse gas emissions (tCO_{2eq})				
	Natural gas	Fuel	Oil	Diesel oil	Total
Steam turbine	1.400.625,8	-	-	-	1.400.625,8
Diesel engine	-	1.232.665,0	60.423,0	67.103,0	1.360.191,0
Gas turbine	236.529,8	-	-	-	236.529,8
Combined cycle	1.575.706,7	-	-	-	1.575.706,7
Total	3.212.862,3	1.232.665,0	60.423,0	67.103,0	4.573.053,3

References

[1] Y. Qiblawey, A. Alassi, M. Zain ul Abideen, and S. Bañales, “Techno-economic assessment of increasing the renewable energy supply in the Canary Islands: The case of Tenerife and Gran Canaria,” *Energy Policy*, vol. 162, p. 112791, 2022, doi: https://doi.org/10.1016/j.enpol.2022.112791.

[2] M. Uche-Soria and C. Rodríguez-Monroy, “Energy planning and its relationship to energy poverty in decision making. A first approach for the Canary Islands,” *Energy Policy*, vol. 140, p. 111423, 2020, doi: https://doi.org/10.1016/j.enpol.2020.111423.

[3] C. Vargas-Salgado, C. Berna-Escriche, A. Escrivá-Castells, and D. Alfonso-Solar, “Optimization of the electricity generation mix using economic criteria with zero-emissions for stand-alone systems: Case applied to Grand Canary Island in Spain,” *Progress in Nuclear Energy*, vol. 151, p. 104329, 2022, doi: https://doi.org/10.1016/j.pnucene.2022.104329.

[4] C. Berna-Escriche, C. Vargas-Salgado, D. Alfonso-Solar, and A. Escrivá-Castells, “Can a fully renewable system with storage cost-effectively cover the total demand of a big scale standalone grid? Analysis of three scenarios applied to the Grand Canary Island, Spain by 2040,” *J Energy Storage*, vol. 52, p. 104774, 2022, doi: https://doi.org/10.1016/j.est.2022.104774.

[5] L. Sigrist, E. Lobato, L. Rouco, M. Gazzino, and M. Cantu, “Economic assessment of smart grid initiatives for island power systems,” *Appl Energy*, vol. 189, pp. 403 – 415, 2017, doi: 10.1016/j.apenergy.2016.12.076.

[6] P. Stenzel, A. Schreiber, J. Marx, C. Wulf, M. Schreieder, and L. Stephan, “Renewable energies for Graciosa Island, Azores – Life Cycle Assessment of electricity generation,” *Energy Procedia*, vol. 135, pp. 62–74, 2017, doi: https://doi.org/10.1016/j.egypro.2017.09.487.

[7] E. Dallavalle, M. Cipolletta, V. Casson Moreno, V. Cozzani, and B. Zanuttigh, “Towards green transition of touristic islands through hybrid renewable energy systems. A case study in Tenerife, Canary Islands,” *Renew Energy*, vol. 174, pp. 426–443, 2021, doi: https://doi.org/10.1016/j.renene.2021.04.044.

[8] C. Berna-Escriche, C. Vargas-Salgado, D. Alfonso-Solar, and A. Escrivá-Castells, “Can a fully renewable system with storage cost-effectively cover the total demand of a big scale standalone grid? Analysis of three scenarios applied to the Grand Canary Island, Spain by 2040,” *J Energy Storage*, vol. 52, p. 104774, 2022, doi: https://doi.org/10.1016/j.est.2022.104774.

[9] H. C. Gils and S. Simon, “Carbon neutral archipelago – 100% renewable energy supply for the Canary Islands,” *Appl Energy*, vol. 188, pp. 342–355, 2017, doi: https://doi.org/10.1016/j.apenergy.2016.12.023.

[10] S. Maas and M. Attard, “Policies to promote cycling in Southern European island cities: challenges and solutions from three ‘starter’ cycling cities,” *Transportation Research Procedia*, vol. 60, pp. 52–59, 2022, doi: https://doi.org/10.1016/j.trpro.2021.12.008.

[11] D. Groppi, A. Pfeifer, D. A. Garcia, G. Krajačić, and N. Duić, “A review on energy storage and demand side management solutions in smart energy islands,” *Renewable and Sustainable Energy Reviews*, vol. 135, p. 110183, 2021, doi: https://doi.org/10.1016/j.rser.2020.110183.

[12] H. Meschede, M. Child, and C. Breyer, “Assessment of sustainable energy system configuration for a small Canary island in 2030,” *Energy Convers Manag*, vol. 165, pp. 363–372, 2018, doi: https://doi.org/10.1016/j.enconman.2018.03.061.

[13] J. Barrera-Santana and R. Sioshansi, “An optimization framework for capacity planning of island electricity systems,” *Renewable and Sustainable Energy Reviews*, vol. 171, p. 112955, 2023, doi: https://doi.org/10.1016/j.rser.2022.112955.

[14] I. Bonilla-Campos, Fco. J. Sorbet, and D. Astrain, “Radical change in the Spanish grid: Renewable energy generation profile and electric energy excess,” *Sustainable Energy, Grids and Networks*, vol. 32, p. 100941, 2022, doi: https://doi.org/10.1016/j.segan.2022.100941.

[15] G. Barone, A. Buonomano, C. Forzano, G. F. Giuzio, and A. Palombo, “Increasing renewable energy penetration and energy independence of island communities: A novel dynamic simulation approach for energy, economic, and environmental analysis, and optimization,” *J Clean Prod*, vol. 311, p. 127558, 2021, doi: https://doi.org/10.1016/j.jclepro.2021.127558.

[16] A. Abramic, A. García Mendoza, and R. Haroun, “Introducing offshore wind energy in the sea space: Canary Islands case study developed under Maritime Spatial Planning principles,” *Renewable and Sustainable Energy Reviews*, vol. 145, p. 111119, 2021, doi: https://doi.org/10.1016/j.rser.2021.111119.

[17] Y. Qiblawey, A. Alassi, M. Zain ul Abideen, and S. Bañales, “Techno-economic assessment of increasing the renewable energy supply in the Canary Islands: The case of Tenerife and Gran Canaria,” *Energy Policy*, vol. 162, p. 112791, 2022, doi: https://doi.org/10.1016/j.enpol.2022.112791.

[18] D. V. Pombo, J. Martinez-Rico, and H. M. Marczinkowski, “Towards 100% renewable islands in 2040 via generation expansion planning: The case of São Vicente, Cape Verde,” *Appl Energy*, vol. 315, p. 118869, 2022, doi: https://doi.org/10.1016/j.apenergy.2022.118869.

[19] P. Arévalo, A. Cano, and F. Jurado, “Mitigation of carbon footprint with 100% renewable energy system by 2050: The case of Galapagos islands,” *Energy*, vol. 245, p. 123247, 2022, doi: https://doi.org/10.1016/j.energy.2022.123247.

[20] K. Matsumoto and Y. Matsumura, “Challenges and economic effects of introducing renewable energy in a remote island: A case study of Tsushima Island, Japan,” *Renewable and Sustainable Energy Reviews*, vol. 162, p. 112456, 2022, doi: https://doi.org/10.1016/j.rser.2022.112456.

[21] G. N. Psarros and S. A. Papathanassiou, “Generation scheduling in island systems with variable renewable energy sources: A literature review,” *Renew Energy*, vol. 205, pp. 1105–1124, 2023, doi: https://doi.org/10.1016/j.renene.2023.01.099.

[22] D. V. Pombo, J. Martinez-Rico, S. V Spataru, H. W. Bindner, and P. E. Sørensen, “Decarbonizing energy islands with flexibility-enabling planning: The case of Santiago, Cape Verde,” *Renewable and Sustainable Energy Reviews*, vol. 176, p. 113151, 2023, doi: https://doi.org/10.1016/j.rser.2023.113151.

[23] Gobierno de Canarias, “Anuario energético de canarias 2019.” Consejería de Transición Ecológica Lucha contra el cambio climático y Planificación Territorial, 2020.

[24] Red Eléctrica España (REE), “CO2 emissions of electricity generation in Spain,” 2021.

[25] IPCC, “IPCC, 2014: Climate Change 2014: Synthesis Report. Contribution of Working Groups I, II and III to the Fifth Assessment Report of the Intergovernmental Panel on Climate Change,” 2015.

Spatial national multi-period long-term energy and carbon planning scenarios, including temporal network security analysis. Complementing renewable energy and hydropower due to climate change

Ben Cevallos[a] and Javier Urquizo[b]

[a] Escuela Superior Politécnica del Litoral, Guayaquil, Ecuador, benceval@espol.edu.ec
[b] Escuela Superior Politécnica del Litoral, Guayaquil, Ecuador, jurquizo@espol.edu.ec

Abstract:

As emerging countries work to balance the energy trilemma and provide secure, affordable, and environmentally sustainable energy, the link between energy, water and food and the rising demands for all are stressing the supply resource. The Republic of Ecuador is withinside the method of improvement a residential, industries and commercial demand plan which ends up in an supply call for increase, with a populace of 17.08 million population for 2018, it affords an strength boom of about 7.13% annual common until 2027, this means that our mounted strength supply should be capable of deliver all of the demand for and its annual increase, it is miles because of this that during our research we are able to examine the incorporation of recent and proposed plant life deliberate to fulfil the call for of the residential, commercial and industries in tiers that the country is planning to make bigger way to the renewable energy withinside the efficient energy matrix, withinside the equal manner the export of energy to neighbouring international locations Colombia and Peru is proposed. However, to reap this incredible alternate we pose numerous hypotheses that describe the hypothetical demand of residential, industries and commercial call for and in addition to the development of recent renewable technology plant life. Traditional and unconventional taking gain of renewable sources in abundance which include capacity water strength, wind strength, sun strength amongst others to generate electric supply and because of the modern-day state of affairs, deepen a public and private funding settlement to reap our objective, on this manner, pleasing our biggest hypothetical cases, we are able to be capable of deliver all of the energy needs for the year 2035, making sure a strong interconnected country wide grid with its enough reserve potential and making sure that each one the residential call for is included plus the projected commercial and industry call for pleasing the big emblematic projects, that the sizable majority will directly generate new jobs, financial boom and we are able to develop as a global industrialized nation.

Keywords:

Energy planning; Electric power; Renewable energies; Ecuadorian energy matrix.

1. Introduction

This paper reviews the current state of the Ecuadorian Electric Sector, defining its structure, production, energy consumption and the legal framework on which the future expansion of the Generation System through private investment is based, as well as the concession model of certain awarded projects to the present date. The Generation planning in the Ecuadorian Electric System is based on different programs at the state level such as the Electricity Master Plan (2018-2027) [1] and the National Energy Efficiency Plan, its general objectives being to increase the generation capacity of electrical energy in an efficient and clean manner with the environment, which the Ministry of Energy and Non-Renewable Natural Resources has called 'The change of the energy matrix'.

1.1. Electricity sector main actors

The Ecuadorian electricity sector is made up of legal entities dedicated to the activities of generation, self-generation, transmission, distribution and commercialization, public lighting, import and export of electrical energy, as well as natural or legal persons who are considered consumers or end users [2, p. 20-21].

1.1.1 Generation.

Generation and/or Self-generation activities in the country are carried out by public and private companies, which must pass certain requirements to be authorized by the competent authority. Generating companies

are those that have permission for the economic operation of one or more plants and deliver their production to one or more points of the National Transmission System, Distribution System, or isolated points. Self-generating companies are those dedicated to an industrial or commercial activity, whose electricity generation is used to supply their demand, and if applicable, the surplus can be made available to the sector. In 2019 there were 129 generation plants, of which 77 correspond to public companies and 52 plants to private companies. Now, the Electric Corporation of Ecuador Public Company maintains the largest amount of electricity production. Of the national installed generation capacity of 7,320 MW by 2020, 86% corresponds to CELEC EP, that is, 6,366.2 MW, which is distributed as follows: 27 Power Plants that correspond to 90% of the thermal park, 14 Hydroelectric Power Plants with 89% and an installed capacity of 4,498.73 MW and finally a wind power plant with 9% of a capacity of 16.5 MW.

1.1.2 Transmission.

CELEC EP - Transelectric Business Unit oversees the planning, operation, maintenance, and expansion activities of the National Transmission System, based on the energy policies established by the Ministry of Energy and Non-Renewable Natural Resources (MEM).

1.1.3 Commercial and Distribution units.

The distribution and commercialization of electrical energy is carried out by state companies corresponding to eleven (11) Business Units of the National Electricity Corporation Public Company, additionally there are nine (9) companies established as public limited companies, which act according to current regulations. The energy consumption of the distribution companies in 2019 can be seen in Figure 1.

1.1.4 International links

The Ecuadorian Electric System currently has two International Interconnections of a legal nature, one with Colombia through a 230 kV link, and another with Peru through charge block transfers.

1.2. Structure of the electricity sector

Figure 2 shows the interrelation of the actors in the electricity sector with the other control agencies. The Ecuadorian electricity sector is made up of a governing body that is the MEM, which through the Vice-Ministry of Electricity and Renewable Energy, is the entity responsible for meeting the country's electricity energy needs, through the formulation of the pertinent regulations, development plans and sectoral policies for the efficient use of its resources.

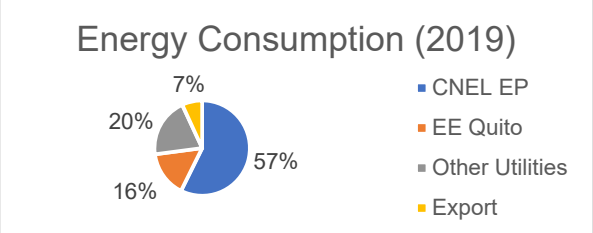

Figure 1 Energy consumption 2019 [1]

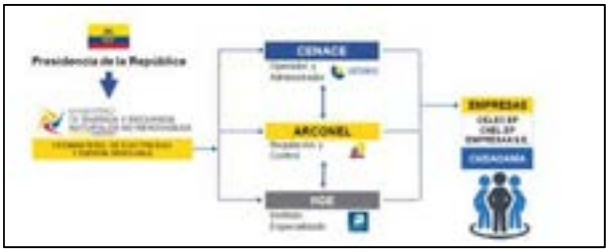

Figure 2. Structure of the Ecuadorian electricity system [1].

The National Electricity Operator (CENACE) is a strategic technical body attached to the MEM, which will act as technical operator of the National Transmission System (NTS) and is the commercial administrator of the energy block transactions, and responsible for the continuous supply of electricity at the lowest possible cost, preserving the global efficiency of the sector [2].

Executive Decree 1036 issued by the Presidency of the Republic of Ecuador established the merger of the Mining Regulation and Control Agency (ARCON), the Hydrocarbons Regulation and Control Agency (ARCH) and the Electricity Regulation and Control Agency (ARCONEL) [3] into one single entity called: Agency for the Regulation and Control of Energy and Non-Renewable Natural Resources (ARC) since July 1, 2020. By provision of the Organic Law of 'Public Electricity Service' (PES), it corresponds to ARCONEL, in its legal nature (Art. 14) regulate and control the activities related to the public electric power service and the general public lighting service, safeguarding the interests of the consumer or end-users, having among its attributions the issuance of the regulations to which the electric companies; CENACE and consumers or end users; whether these are public or private, observing the energy efficiency policies, for which they are obliged to provide the information that is required, the same that are previously approved and issued by its Board of Directors.

The Geological and Energy Research Institute (IIGE), created by Executive Decree No. 399 of May 15, 2018, through the merger of two institutes focused on research into energy efficiency, renewable energy, geology, mining, and metallurgy. With the creation of the IIGE, scientific research regarding earth sciences is strengthened, which will improve institutional capacities by generating a specialized human and technical resource, with greater scope for scientific work, technological development, and local innovation.

Electricity Corporation of Ecuador (CELEC EP) is a public company, dependent on the MEM, which was born in 2009 after the nationalization and unification of various companies in the sector. Its objective is the generation and transmission of Electric Power. National Electricity Corporation (CNEL EP) is a public company established in 2008, to provide public services of distribution and commercialization of electrical energy.

1.3. Energy production

According to the CENACE [2], in 2019 the Gross Energy produced in 2019 was 27,733.96 GWh. By origin, around 88.39% (24,513.99 GWh) was obtained from hydraulic sources, 10.14% (2,811.52 GWh) from thermal sources, and 1.45% (402.62 GWh) from renewable generation, and the remaining 0.02% (5.83 GWh) to international interconnections, as shown in Figure 3. The energy produced [2] from hydraulic sources has increased from 71.6% in 2017 to 88.39% in 2019. The Renewables gross production is distributed in 62% for Biomass, 20% Wind, 10% for Biogas and 8% for Photovoltaic Generation, as shown in Figure 4.

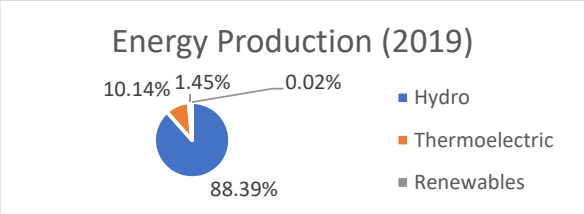

Figure 3. Energy Production by source in year 2019

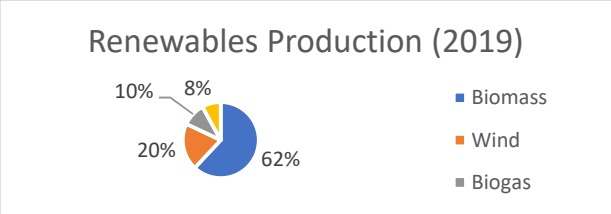

Figure 4. Renewables production in year 2019

1.4. Energy demand

The growth in energy demand in 2019 reached 8.12% compared to 2018. Table 1 includes a monthly comparative table of the energy demands of the Ecuadorian electricity sector between 2018 and 2019.

Table 1. Energy demand (GWh) 2018 and 2019 [2]

Month	2018	2019	Percent change %
January	2,064.02	2,096.56	1.58
February	1,764.59	1,946.52	10.31
March	1,970.88	2,150.00	9.09
April	1,970.93	2,117.26	7.42
May	1,999.55	2,162.90	8.17
June	1,838.77	2,000.16	8.78
July	1,862.94	2,042.18	9.62
August	1,867.16	2,034.04	8.94
September	1,845.81	1.974,23	6.96
October	1,891.27	2,040.53	7.89
November	1,870.50	2,059.80	10.12
December	1,947.52	2,129.05	9.32
Total	22,893.94	24,753.23	8.12

The per capita consumption of electricity in 2017 was 1,157.99 kWh/inhabitant, according to the National Institute of Statistics and Censuses of Ecuador.

1.5. Private Investment Opportunities

The legal framework where the opportunity for private investment in the electricity sector is based are:

- Concession Contracts (Art. 25 et seq. PES and 18 et seq. of its regulations) through MEM public selection processes.
- Projects under the Public-Private Association modality are delegated Management Contracts (PES incentives for public-private associations).
- Associative capacity of public companies to fulfil their business goals and objectives. Any type of association, strategic alliances, mixed economy companies with public or private sectors at the national or international level or within the popular and solidarity economy sector. (Art. 35 and following of the Organic Law of Public Companies).

In December 2020, through a public selection process for the concession to the private electricity generation, the renewable projects Villlonaco II and III wind farms and El Aromo photovoltaic systems (PV), with an installed capacity of 110 MW, and 200 MW, respectively, were awarded to the Spanish companies Consortium Cobra Zero-E Villonaco and Solarpackteam. These awards involve the design, construction, operation, and maintenance of new power generation projects located in the provinces of Loja (wind) and Manabí (PV).

This research contains a number of preliminary research questions that have not been previously explored in detail, and that do not have definitive answers regarding the impact that generation projects would have on the Ecuadorian electricity sector, (i) what will Ecuador's energy planning be like and the income of the different generation projects to satisfy the energy demand during the period from 2020 to 2035?, (ii) what will be the energy production supplied by the renewable blocks in the Ecuadorian Electric System during the period from 2020 to 2035?, (iii) what will be the best scenario to satisfy the energy demand in the period 2020 to 2035?, (iv) will it be possible to supply the demand for electrical energy without having Cardenillo and Santiago hydroelectric projects?

2. Methodology

2.1. Data availability

In this chapter we will review the technical information available by the control agencies of the Ecuadorian electricity sector such as MEM, CENACE and ARC, which will serve as input data for our modelling in the Long Emissions Analysis Platform (LEAP).

For the operational data, the CENACE 2019 Annual Report was used, for the forecast load and generation projection, the Electricity Master Plan 2018-2027 issued by the MEM was used, for certain specific data the System Data (SISDAT) Database was used, and the Annual and Multiannual Statistics of the Ecuadorian Electricity Sector 2018, Resolution ARCONEL – 069/16.

2.2. Historic production

The historical production for the year 2019 of the generation plants of the Ecuadorian Electric System was obtained from the CENACE Annual Report 2019, specifically in annex 2.3 (Net production by generation company [GWh] 2019). As shown in Table 2.

Within the report issued by CENACE, the power plants or generation units whose historical production in 2019 is zero have not been considered. This situation occurs because the effective capacity in hydroelectric generation that Ecuador currently has increased considerably in recent years, causing the lower capacity thermal plants to not be required in daily dispatches, other plants do not have the authorization of the governing bodies to participate in the Ecuadorian electricity sector, even though these plants are currently operational, additionally there is another group of plants that are intervened by the Ecuadorian state, whose equipment and components are deteriorating due to lack of operation and maintenance. Table 3 shows a summary of the companies with the drawbacks.

2.3. Energy Capacity

The energy capacity of the power plants and/or generation units was obtained by means of the Statistical Information Reports of the Ecuadorian Electricity Sector available in the SISDAT database of ARC as shown in Table 4.

Table 2. Production by generation company [2]

Power Plant	Jan.	Feb.	March	April	May	June	July	Aug.	Sept	Oct.	Nov.	Dec.
C. F. Altgenotec	0.09	0.09	0.1	0.1	0.09	0.07	0.09	0.11	0.08	0	0	0
C. F. Brineforcorp	0.11	0.12	0.14	0.13	0.1	0.07	0.06	0.09	0.09	0.07	0.1	0.13
C. H. Minas San Francisco	28.57	14.42	38.89	52.63	7.29	6.49	38.39	38.49	12.88	17.95	25.09	25.6
C.H. Minas San Francisco	21.28	40.52	26.09	21.72	43.64	11.21	28.39	38.49	12.88	17.95	25.09	25.6
C. H. Coca Codo Sinclair	565.86	483.61	544.62	536.66	533.94	524.1	370.12	524.1	550.7	572.52	584.541	591.15
C. H. Manduriacu	12.95	16.73	20.39	15.14	18.24	14.65	11.95	11.31	7.66	5.28	14.36	19.3
C.H. Manduriaco	12.35	16.73	19.23	14.72	17.92	14.9	9.1	4.17	5.85	12.89	13.48	19.37
C. E. Villonaco	6.52	4.59	6.21	4.84	4.93	8.74	9.68	11.49	8.8	5.31	3.28	4.25
C. H. Delsitanisagua	39.84	19.68	19.13	0	11.12	12.7	8.68	0	0	23.15	28.08	33.71
C. H. Delsitanisagua	27.88	26.9	17.02	14.71	16.83	11.13	12.29	0	0	23.61	31.35	35.03
C. H. Delsitanisagua	21.25	14.61	13.71	31.51	13.35	17.63	11.92	0	0	22.44	25.74	31.84
C. H. Alazán	1.14	2.54	2.68	2.64	1.76	1.5	2.61	2.16	2.82	2.8	2.19	2.16
C. T. Jaramijó	20.99	19.05	21.29	22.35	21.32	21.14	22.92	19.13	13.04	24.15	9.38	9.38
C. T. Manta 2	2.96	3.06	3.16	4.54	5.23	4.02	4.39	3.44	2.38	4.15	4.06	4.52
C. T. Miraflores	0	0.01	0	0	0	0	0.01	0	0	0.01	0	0.01
C. T. Miraflores	0.13	0.3	0.24	0.21	0.3	0.1	0	0.01	0.01	0.02	0.02	0.01
C. T. Miraflores	0.14	0.36	0.29	0.26	0.29	0.1	0	0.01	0.01	0.02	0.02	0.01
C. T. Miraflores	0	0.01	0	0	0	0	0.01	0	0	0.01	0	0.01
C. T. Miraflores	0.04	0.23	0.22	0.05	0.23	0.01	0	0	0.01	0.02	0.02	0.01
C. T. Miraflores	0.04	0.15	0.14	0.23	0.19	0.03	0	0.01	0.01	0.02	0.02	0.01

It was considered that the reports are of high quality and contain the fundamental information of the Ecuadorian Electric System, this information will be useful for our modelling in the LEAP software in the ‘Exogenous Production’ section.

Table3. Companies with problems in their legalization

Company	Nominal Power [MW]	Fuel
Termoguayas Generation	150	Fuel Oil 6
Electroquil	180	Diesel Gas Turbine
Intervisa Trade	105	Diesel Gas Turbine
Ulysseas	30	Naphtha

In accordance with the provisions of the Electricity Master Plan, the expansion of generation will be carried out with the following objective: Guarantee the supply of electricity in Ecuador through the optimal expansion of the electric power generation stage, in the short, medium and long term, with criteria of efficiency, sustainability, quality, continuity and security; promoting the use of renewable energy resources, in an area of sufficiency, energy sovereignty, social and environmental responsibility; considering technical, economic, financial and administrative aspects.

Table 5 details the Electricity Generation projects that are under construction, Table 6 details the Electric Power Generation projects with Enabling Titles. Table 7 details the hydroelectric projects with more than 500 MW that have a final study and design, and Table 8 presents the summary of the generation projects for the case of the productive matrix that are additional to the Base case, detailing the most probable date of commercial operation, the name of the generation project, the company or institution in charge, the current state (construction, studies, etc.), if the project is financed with public or private funds, the type of technology (hydroelectric, thermoelectric, Non-Conventional Renewable Energies, among others), the nominal power (MW), and the estimated average annual energy (GWh/year).

2.4 Generators factors of maximum availability

Resolution No. ARCONEL-069/16, in its literal 4, defines the referential availability factors:

> "*…the referential availability factors are detailed by type of technology of the generating plants, which will serve for the comparison of the monthly average availability factor; and, for the liquidation of the fixed charge or annuity*."

These Values are presented in Table 9. The referential maximum availability values indicated by the resolution do not consider the Generation systems with renewables, for this reason due to the availability of their primary energies such as wind and solar energy, in our modelling we will enter the value of 100%. for this type of technology.

Table 4. Energy Capacity of National Grid Generators

Company	Investment	Power Plant	Type	Power subtype	Energy Type	Nominal Power (MW)	Effective Power (MW)	Nominal Power to public service (MW)
Algenotec	Private	Algenotec	Solar	Fotovoltaic	Renewable	0.936	0.936	0.936
Brineforcorp	Private	Brineforcorp	Solar	Fotovoltaic	Renewable	0.999	0.999	0.999
CELEC–Coca Codo Sinclair	Public	Manduriacu	Hydro	Hydro	Renewable	63	65	63.36
CELEC–Coca Codo Sinclair	Public	Coca Codo Sinclair	Hydro	Hydro	Renewable	1,500	1,476	1,500
CELEC- Electroguayas	Public	Trinitaria	Thermoelectric	Turbovapour	Non-renewable	133	133	133
CELEC- Electroguayas	Public	Gonzalo Zevallos (Vapour)	Thermoelectric	Turbovapour	Non-renewable	146	140	146
CELEC- Electroguayas	Public	Gonzalo Zevallos (Gas)	Thermoelectric	Turbogas	Non-renewable	26.265	20	26.265
CELEC- Electroguayas	Public	Enrique Garcia	Thermoelectric	Turbogas	Non-renewable	102	96	102
CELEC- Electroguayas	Public	Santa Elena II	Thermoelectric	Internal Combustion motor	Non-renewable	90.1	65.025	90.1
CELEC- Electroguayas	Public	Santa Elena III	Thermoelectric	Internal Combustion motor	Non-renewable	41.7	40.002	41.7
CELEC-Gensur	Public	Villonaco	Wind	Wind	Renewable	16.5	16.5	16.5
CELEC-Gensur	Public	Delsitanisagua	Hydro	Hydro	Renewable	180	180	180
CELEC_Hidroagoyán	Public	Pucará	Hydro	Hydro	Renewable	73	73	73
CELEC_Hidroagoyán	Public	Agoyán	Hydro	Hydro	Renewable	160	156	160
CELEC_Hidroagoyán	Public	San Francisco	Hydro	Hydro	Renewable	230	212	230
CELEC_Hidroazoguez	Public	Alazán	Hydro	Hydro	Renewable	6.23	6.23	6.23
CELEC-Hidronación	Public	Marcel Laniado	Hydro	Hydro	Renewable	213	213	213
CELEC-Hidronación	Public	Baba	Hydro	Hydro	Renewable	42.2	42	42.2
CELEC-Sur	Public	Molino	Hydro	Hydro	Renewable	1075	1,100	1,075
CELEC-Sur	Public	Mazar	Hydro	Hydro	Renewable	170	170	170
CELEC-Sur	Public	Sopladora	Hydro	Hydro	Renewable	486.99	486.9	486.99
CELEC-Sur	Public	Minas San Francisco	Hydro	Hydro	Renewable	270	270	270
CELEC-Termoesmeraldas	Public	Esmeraldas I	Thermoelectric	Turbovapour	Non-renewable	132.5	125	132.5
CELEC-Termoesmeraldas	Public	La Propicia	Thermoelectric	Internal Combustion motor	Non-renewable	10.5	8.5	10.5

Table 5. Electricity Generation Projects under Construction [1]

Project/Power Plant	Company	Public or private	Type	Power [MW]	Average Energy [GWh/year]
Toachi - Pilatón	CELEC EP - Hidrotoapi	Public	Hydro	254.40	1,120
Machala Gas Ciclo Combinado	CELEC EP – Termogas Machala	Public	Thermoelectric	110	690
Machala Gas Tercera Unidad	CELEC EP – Termogas Machala	Public	Thermoelectric	77	510
Minas de Huascachara	Elecaustro S.A.	Public	Wind	50	119
Quijos	CELEC EP – Coca Codo Sinclair	Public	Hydro	50	355
Piatúa	San Francisco Genefran S.A.	Private	Hydro	30	210
Sabanilla	Hidrelgen S.A.	Private	Hydro	30	210.5
Rio Verde Chico	Hidrosierra S.A.	Private	Hydro	10	74.3
Chalpi Grande	EPMAPS EP	Public	Hydro	7.59	36
Mazar-Dudas: Dudas	CELEC EP - Hidroazogues	Public	Hydro	7.38	41.4
Mazar-Dudas: San Antonio	CELEC EP – Hidroazogues	Public	Hydro	7.19	44.9
San José de Minas	Hidroeléctrica San José de Minas S.A.	Private	Hydro	5.95	48
Chorrillos	Hidrozamora EP	Public	Hydro	4	23.2
Ulba	Hidroulba S.A.	Private	Hydro	1.02	8.4
TOTAL				**644.5**	**3,490.6**

Table 6. Power Generation projects with Enabling Titles [1]

Project/Power Plant	**Company**	**Public or private**	**Type**	**Power [MW]**	**Average Energy [GWh/year]**
Ibarra Fugúa	Hidro Ibarra Fugúa	Private	Hydro	30	208.4
El Salto	Hidroequinoccio EP	Public	Hydro	30	247
La Magdalena	Hidroequinoccio EP	Public	Hydro	20	167
Soldados Yanuncay, Central Yanuncay	Elecaustro S.A.	Public	Hydro	14.6	79.5
Pilaló 3	Qualitec Comercio e Industria Cía. Ltda.	Private	Hydro	9.3	68.7
Maravilla	Hidroequinoccio EP	Public	Hydro	9	61.6
Chalpi Grande	EPMAPS EP	Public	Hydro	7.59	36
Soldados Yanuncay, Central Soldados	Elecaustro S.A.	Public	Hydro	7.2	39.2
Pichacay II	EMAC-GBP	Mixed	Biogas	1	3.5
El Laurel	CBS Energy	Private	Hydro	0.97	6.8
TOTAL				**130**	**918**

Table 7. Hydroelectric projects with more than 500 MW [1]

Project	**Technology**	**Power [MW]**	**Average Energy [GWh/year]**
Santiago	Hydro	2,400	14,613
Cardenillo	Hydro	596	3,409
TOTAL		**2,996**	**18,022**

Table 8. Summary of Electricity Generation projects [3]

Year of entry into operation	**Project**	**State**	**Public or private investment**	**Type**	**Power [MW]**	**Average Energy [GWh/year]**
2018	Normandía	In operation	Private	Hydro	49.6	350.3
2018	Delsitanisagua	In operation	Public	Hydro	180	1,411
2019	Minas – San Francisco	In operation	Public	Hydro	274.5	1,290.8
2019	Pusuno	In operation	Private	Hydro	39.5	216.9
2019	Rio Verde – Chico	In operation	Private	Hydro	10	74.3
2020	San José de Minas	In construction	Private	Hydro	5.95	48
2020	Machala Gas Tercera unidad	In construction	Public	Thermoelectric	77	510

2020	Mazar – Dudas: San Antonio	Paralyzed	Public	Hydro	7.19	44.9
2020	Minas de Huascachaca	In construction	Public	Wind	50	119.0
2021	Machala Gas Ciclo Combinado	In construction	Public	Thermoelectric	110	680
2021	Piatúa	In construction	Private	Hydro	30	210
2021	Chalpi Grande	In construction	Public	Hydro	7,59	36
2021	Toachi – Pilatón (Sarapullo 39 MW, Alluriquín 205.4 MW)	In construction	Public	Hydro	254.4	1,120
2021	La Magdalena	Operation authorization	Public	Hydro	20	167
2021	Maravilla	Operation authorization	Public	Hydro	9	61.6
2021	Ibarra - Fugúa	Concession contract	Private	Hydro	30	208.4
2021	Mazar – Dudas: Dudas	Paralyzed	Public	Hydro	7.38	41.4
2021	Sabanilla	In construction	Private	Hydro	30	210.5
2022	El Salto	Operation authorization	Pubic	Hydro	30	247
2022	Chorrillos	Paralyzed	Public	Hydro	4	23.2
2022	Soldados Yanuncay, Central Soldados	Operation authorization	Public	Hydro	7.2	39.2
2022	PV Aromo and Wind: Villonaco II and III.	Structured public selection process	Private	Renewables	500	1,700
2023	Soldados Yanuncay, Central Yanuncay	Operation authorization	Public	Hydro	14.6	79.5
2023	Quijos	Paralyzed	Public	Hydro	50	355
2023	Bloque Ciclo Combinado I	Structured by public selection process	Public	ERNC	400	3,000
2023	Bloque ERCN II	In studies	Private and/or public	Thermoelectric	400	1,400
2023	Bloque Ciclo Combinado II	In studies	Private and/or public	Thermoelectric	600	4,500
2024	Santa Cruz	Minig self-generation in process	Private	Hydro	100	560
2025	Bloque de Proyectos Hidroelectricos I	In studies	Private and/or public	Hydro	150	850
2026	Bloque de Proyectos Hidroelectricos II	In studies	Private and/or public	Hydro	150	850
2026	Bloques de Proyectos Geotérmicos	In studies	Private and/or public	Geothermic	50	380
2026	Paute - Cardenillo	In public selection process	Private	Hydro	595.6	3,409
2026	Santiago (G8), Fase I	In public selection process	Private	Hydro	1,200	9,874
2027	Santiago (G8), Fase II	In public selection process	Private	Hydro	1,200	4,739
	Total				**6,644**	**38,816**

Table 9. Factors of maximum availability [2]

Type	Technology	AF_{ref}
Hydro	Reservoir	0.92
Hydro	Run-of-the river	0.90
Thermal	Vapour	0.80
Thermal	Gas	0.80
Thermal	Internal Combustion motor	0.80

2.5. Other considerations

Within this study, the following special aspects must be considered, referring to the generation projects that will enter in the following years:

- The Paute-Cardenillo Hydroelectric Project is the last project to be built for the development of the Paute River Complex and will work jointly with Sopladora, Mazar and Molino. It will have an installed capacity of

596 MW. The referential investment of the project has a cost of USD 1.3 billion and will be awarded to the private company that will be responsible for the design, construction, implementation, administration, operation, and maintenance of the project.

- The Santiago hydroelectric project is in the southeaster region of Ecuador, it is located on the river of the same name within the Amazon hydrographic region, in the Tiwintza, Limón Indanza and Santiago de Méndez cantons, in the province of Morona Santiago, it will have an installed capacity of 3,600 MW. Due to its size, it will be executed in phases. This project will also be concessioned to a private company.
- The renewable blocks corresponding to technologies such as hydroelectric, wind, solar and biomass are projects that will be in different sectors of the country, and that will be concessioned to private companies according to the structured legal framework.
- The Chespi, Chontal, Tortugo and Tigre Hydroelectric Generation projects with a total capacity of 943 MW have the following investment time: Chespi (48 months, USD 793 million), Chontal (60 months, USD 435 million), Tortugo (50 months, USD 471 million) and Tigre (54 months, USD 215 million) are considered in our modelling.

Additionally, for the analysis of the demand, it is necessary to consider the hypotheses raised in the Master Plan, where the industrial city of Posorja is considered and from 2030 it will be a normal scenario of demand growth, the needs are projected for 12,000 GWh energy and 3,000 MW power.

Within the operational planning of the electrical system, there must be a rolling reserve that can act in the event of possible dynamic scenarios or sudden increases in demand, according to what is established by the Master Plan, this reserve is around 20% in the Ecuadorian Electrical System. Which considers the technical reserve, the primary frequency regulation, and the secondary frequency regulation.

Additionally, the cold reserve must be considered, unlike the rolling reserve, this is not available immediately. The cold reserve is the part of the non-rolling reserve (hydraulic or thermal) that can come into service and reach its available power in a time of no more than 15 minutes, which are within a merit list, to cover the deficit of generation reserve caused by various contingencies that occur in the system.

The cold reserve amount will be determined based on a reliability study, while in the case of the NTG it has been technically determined. The maximum value of the cold reserve according to the dispatch and operation procedures (of CENACE) must be equal to the generation unit with the highest power dispatched, thus preventing way the probable loss of the largest generation of the system.

3. Results

This section details the results to carry out the modelling of our Ecuadorian Electric System, for which we use the LEAP program [4], obtaining an analysis of the planning of electric power generation systems. The planning of electrical power systems represents a great economic development, for this reason it is necessary to define strategies for its expansion in the medium and long term, within this scenario the forecasted load plays an important role, for this reason we will follow the approaches determined in the Master Plan. The analysis carried out exclusively involves the expansion of generation and its attention to the scheduled demand, the expansion of the Transmission and Distribution Systems that require additional investments is not being considered, although the power losses did were considered.

The Hypotheses that we will present below are those found in the Master Plan where three study hypotheses are proposed that generated seven projection scenarios in LEAP, of which six were inherited from a trend scenario of energy demand. The study hypotheses will allow the construction of scenarios that will manage to articulate the policy of productive development, energy efficiency and basic industries (Master Plan). To make a projection from 2020 to 2035, the possible trends in the short, medium, and long term were entered with the aim of being able to determine the energy needs in the stages of generation and transmission of Electric Power. From 2030 to 2035, a normal increase in demand growth has been considered; needs of 12,000 GWh and 3,000 MW are projected. To enter the data of the demand 2030 to 2035 in the LEAP program in the base scenario we must create a folder in the Demands branch that we will call 2030 loads where an ‘energy-intensive technologies" will be created, when selecting the reference case, we locate the variable ‘Final Energy Intensity’. In this scenario, it contemplates what is the upward growth trend of users of industrial, commercial, and residential consumption. An average annual growth of 5.44% is estimated from 2018 to 2027, reaching 33,840 GWh in 2027 (Master Plan chapter 3 Electricity Demand, page 84) considering the average annual growth of 2.43% in users, reaching 6.48 million of users in 2027.

Hypothesis 1 corresponds to the projection baseline, which considers the trend growth of electricity demand; it incorporates econometric models, analysis of previous periods and analytical schemes. Hypothesis 2 results from incorporating into the projection baseline Hypothesis No. 1, the singular loads of the industrial group, which are linked to mining, cement, steel, oil, transportation, among others; energy efficiency projects, the load of the agricultural and agro-industrial community of Ecuador and to the Connection of the NTG with the Interconnected Petroleum Electric System (SEIP), with the purpose of optimizing the use of energy resources in an integral way (Master Plan, Chapter 3 page 92). The singular loads correspond to the electrical demand of industries that are expected to grow or expand. The singular loads were classified as:

singular loads in operation and projected. The data for each classification can be found in the Electricity Master Plan in Chapter 3, page 94. Due to its importance, in the projection of electricity demand, the incorporation of new technologies that are commercialized in the future were considered, the incorporation of which foresees significant electricity requirements. These projects are the Quito (capital city) Metro, the Cuenca (third city) Tram, electromobility (mass transportation) and the entry of electric vehicles. (Master Plan Chapter 3 page 95). For the hypothesis No. 3, in addition to all mentioned in hypothesis 2, the incorporation of the demand corresponding to Basic Industries, thereby obtaining the power and energy requirements of the electrical system in all functional stages, this scenario is what is called the Productive Matrix Case for the elaboration of the expansion studies of generation and transmission. (PME Chapter 3 page 96).

The Master Plan proposes the construction of two emblematic hydroelectric projects Cardellino and Santiago with an installed capacity of 596 MW and 3,600 MW, respectively. The decision of how to include the Central Santiago to the NTG is complex because within the planning there are many important variables that are currently not clearly defined regarding the concession, adjudication, construction timeline, operating stages and in how many years would be the most beneficial for its commissioning and operation, for this reason five additional scenarios inherited from hypothesis 3 are proposed.

Scenario 1 where the Renewable Blocks and the Hydroelectric Plants made up of Chespi, Chontal, Tortugo and Tigre are included to the NTG, but the contribution of Santiago and Cardenillo is not considered. Scenario 2 corresponds to the inclusion of Cardenillo (2026), does not consider the contribution of Santiago. Scenario 3 which includes Santiago with a power of 3,600MW in the following possible phases of operation: (i) phase 1: 1,800 MW (2026) and phase 2: 1,800 MW (2030); (ii) phase 1: 2,400 MW (2026) and phase 2: 1,200 MW (2030); and phase 1: 1,200 MW (2026), phase 2: 1,200 MW (2028) and Phase 3: 1,200 MW (2030).

This section shows the results of the LEAP simulations regarding the demand and energy generated by the power plants modelled in each of the scenarios proposed with their respective hypotheses. This Section is organized as follows: Section 3.2 corresponds to the demand results for each of the hypotheses of the proposed scenarios. In Section 3.3 is the energy planning of the system for each of the proposed scenarios.

3.1 Demand

The demand for electricity is presented with a growth of 5.44% for the period from 2020 to 2035, confirming an entry of singular loads projected in operation from 2020 to 2035, the entry of the transportation load corresponding to transportation in year 2020, the export of energy is maintained in the same current terms, the development of the industrial city of Posorja from 2023 and from 2030 the demand increases by 12,000 GWh. The demand results for hypothesis (number 3) are shown in Figures 5 (graph) and 6 (tabular), respectively.

Figure 5. Graph - demand results for Hypothesis 3

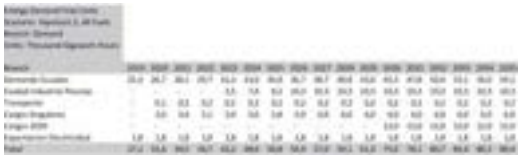

Figure 6. Tabular - demand results for Hypothesis 3

For Hypothesis 2, the demand presents a growth of 5.44% for the period between 2020 and 2035, transport charges and singular charges are considered from the year 2020, we maintain electricity exports and energy requirements from of 2030. The results obtained are shown below in Figures 7 and 8. For Hypothesis 1, demand presents a growth of 5.44% for the period from 2020 to 2035, we maintain electricity exports and energy requirements from 2030. The results obtained are shown below in Figures 9 and 10.

3.2. Generation

3.2.1. Hypothesis 1

For Hypothesis 1, in the final year of the analysis, 2035, there is a generated energy of 75,058 GWh and an estimated demand of 72,896 GWh. The maximum installed generation capacity is given in the year 2028 with 11,605 MW. In Figure 11 we observe the energy supplied by the generation plants.

3.2.2. Hypothesis 2

For Hypothesis 2 in the year 2035 there is an energy of 81,442 GWh and an estimated demand of 79,096 GWh. The maximum installed generation capacity occurs in the year 2028 with 11,605 MW. In Figure 12 we observed the energy supplied by the generation plants.

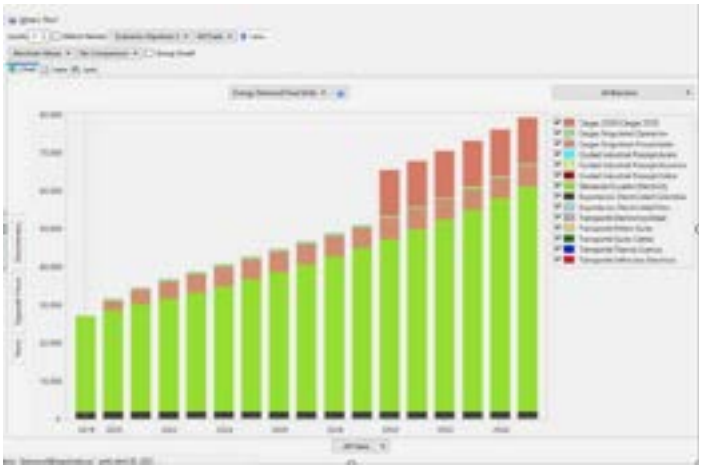

Figure 7. Graph - demand results for Hypothesis 2

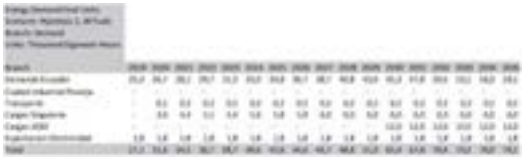

Figure 8. Tabular - demand results for Hypothesis 2

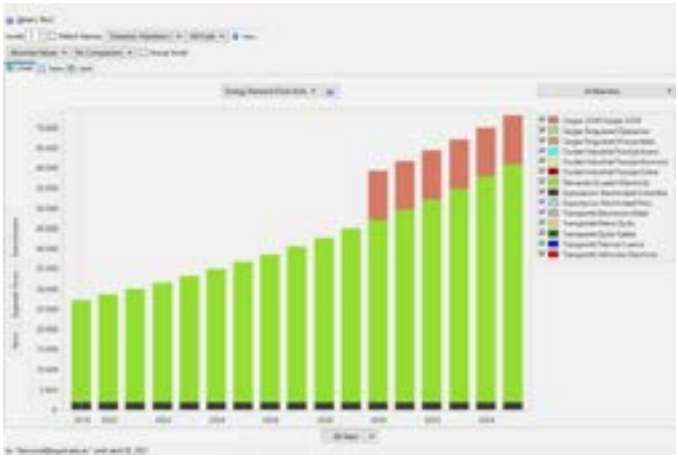

Figure 9. Graph - demand results for Hypothesis 1

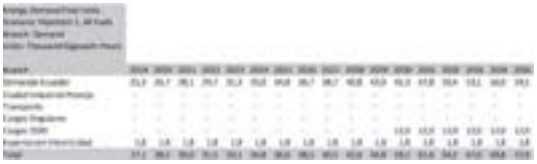

Figure 10. Tabular - demand results for Hypothesis 1

3.2.3. Hypothesis 3

For Hypothesis 3 in the year 2035 there is a generated energy of 89,320 GWh and an estimated demand of 89,380 GWh. The maximum installed generation capacity is given in the year 2028 with 11,605 MW. In Figure 13 we observed the energy supplied by the generation plants.

3.2.4. Hypothesis 3 – Cardenillo

For Hypothesis 3 and entry of the Cardenillo Power Plant in 2026, in 2035 there is a generated energy of 91,690.4 GWh, an estimated demand of 89,380 GWh and an installed capacity of 11,261 MW. The maximum installed generation capacity occurs in the year 2028 with 12,201 MW. In Figure 14 we observed the energy supplied by the generation plants.

3.2.5. Hypothesis 3 – Santiago A

For Hypothesis 3 and the entry of the Santiago Power Plant in 2026 with 1,800 MW, there is an installed capacity in the system of 13,601 MW. When the second phase of 1,800 MW enters in 2030, there is the capacity maximum installed in the system of 15,801 MW., and in the year 2035 we have a generated energy of 92,031 GWh and an estimated demand of 89,380 GWh. In Figure 15 we observed the energy supplied by the generation plants.

3.2.6. Hypothesis 3 – Santiago B

For Hypothesis 3 and entry of the Santiago Power Plant in the year 2026 with 2,400 MW., there is an installed capacity in the system of 13,661 MW., when entering the second phase of 1,200 MW in the year 2030, there is the maximum capacity in the system of 15,801 MW., and in the year 2035 we have a generated energy of 92,031 GWh and an estimated demand of 89,380 GWh. In Figure 16 we observed the energy supplied by the generation plants.

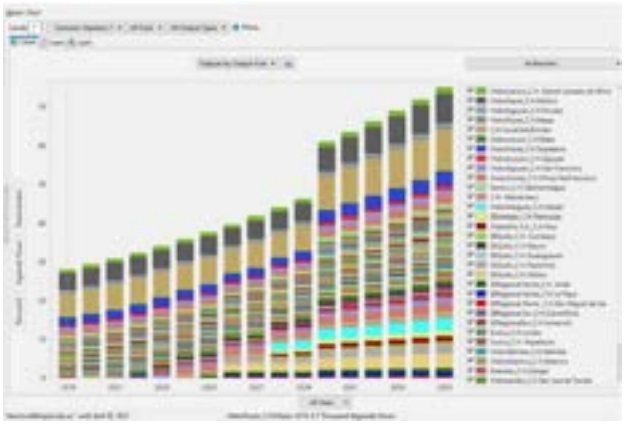

Figure 11. Energy supplied by the Generation Plants - Hypothesis 1

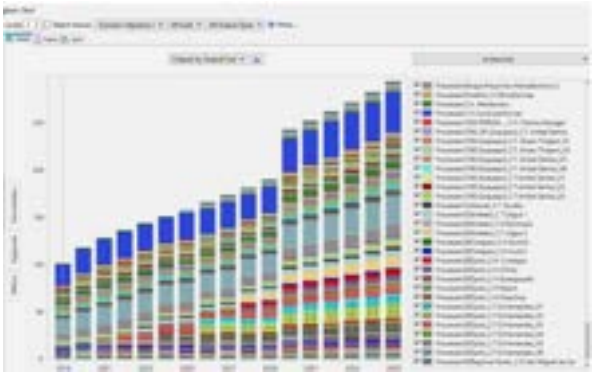

Figure 12. Energy supplied by the Generation Plants - Hypothesis 2

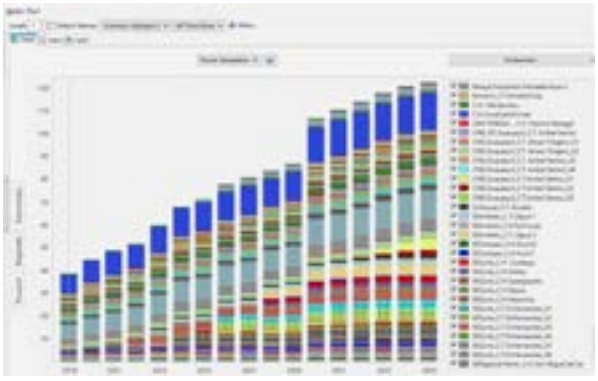

Figure 13. Energy supplied by the Generation Plants - Hypothesis 3

Figure 14. Energy supplied by the Generation Plants – Cardenillo

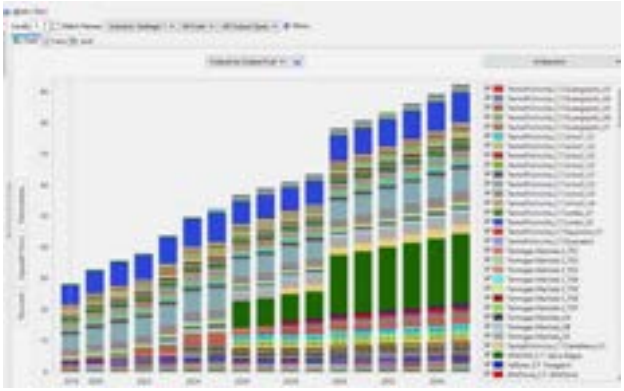

Figure 15. Energy supplied by the Generation Plants - Santiago A

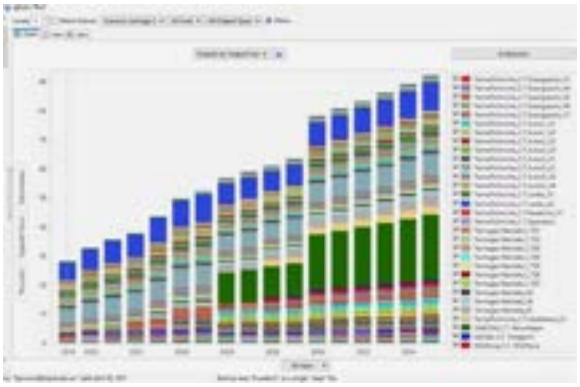

Figure 16. Energy supplied by the Generation Plants - Santiago B

3.2.7. Hypothesis 3 – Santiago C

For Hypothesis 3 and the entry of the Santiago Power Plant in 2026 with 1,200 MW, there is an installed capacity in the system of 12,461 MW. When the second phase of 1,200 MW enters in 2028, we have an installed capacity of 14,601 MW., and when entering the final phase of 1,200 MW in the year 2030, we have the maximum capacity in the system of 15,801 MW., in the year 2035 we have a generated energy of 92,031 GWh and an estimated demand of 89,380 GWh. In Figure 17 we observed the energy supplied by the generation plants. Regarding renewables, we can see the importance of this group, Figures 18 shows where we see its growth from the projects awarded recently, which would be the beginning of a group of projects that will be fundamentally for the energy development of the country contributing additionally to minimizing CO_2 emissions.

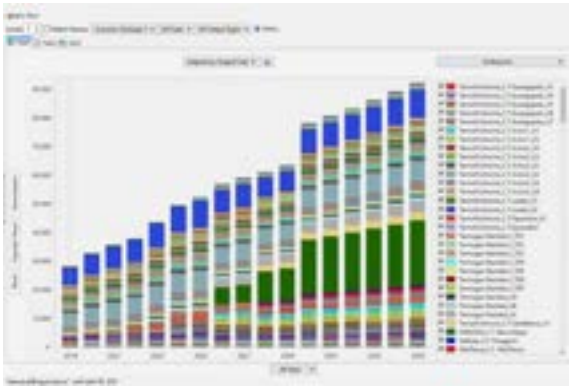

Figure 17. Energy supplied by the Generation Plants - Santiago C

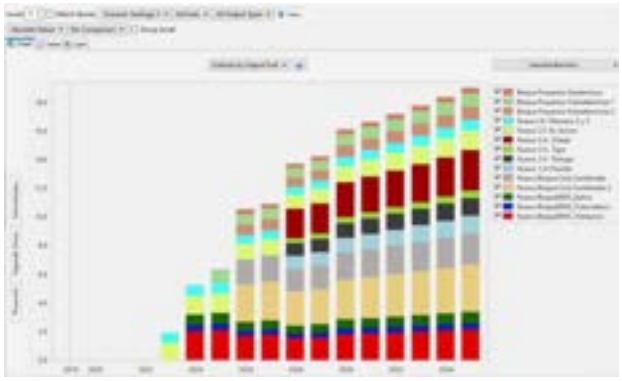

Figure 18. Graph - Energy supplied by the Renewables Hypothesis 3 - Santiago C

4. Discussion

Although in this paper the authors has carried out a systematic and brief review of what corresponds to the Ecuadorian Electric Sector reviewing its regulations and energy planning for the period 2020-2035, we have to indicate that the results of the simulations for each scenario indicate how the generation will be distributed over time, although we guarantee that the different loads are attended in all the periods analysed, there will always be maintenance, contingencies and other internal and external eventualities to which one must be prepared, as the success of continuing to have generation that meets our demand, as well as possible energy exports to neighbouring countries depends exclusively on the continuation of the energy policies carried out by the current National Government.

There will be many criteria that differ specifically with the inputs of specific generation, with the way in which the expansion of the system is proposed, energy policies, cost of energy, etc., but there is a point in which all the technicians and officials of the In the electricity sector we converge, attention to demand and avoid energy rationing in the near future, we must maintain this perspective, for years we have seen how the electricity sector has not had the continuity that is required and the results are in history and as in a previous era, there was a severe impact on the electricity supply. Additionally, we could optimize the income of new projects by applying non-traditional methods for their study where costs have their own decision scenario. The updating of the data as well as the useful life of the equipment proposes a vision of reengineering and replacement of generators that due to useful life must be replaced in the future.

5. Conclusion

The analysis of the demand and the energy planning of the generation was carried out in different scenarios, for this reason the values proposed in the available technical information were used, it is necessary over time to be able to guarantee that the hypotheses proposed for the demand can be met or adjustments must be made that lead to a rescheduling in relation to long-term energy projects. The Santiago hydroelectric project becomes essential for the country's energy development. It has been shown that the National Electric Power System would not be able to supply the demand for electricity when the industrial city of Posorja is under development.

If we want to maintain Ecuador's electricity trade balance as an Electricity exporting country, we must continue with the energy investment plans currently issued by the MERNNR, otherwise we will once again need imports from the existing binational electrical interconnections with Colombia and Peru.

The production of renewables in the Ecuadorian Electric System will have a substantial increase from 2023 with the concession of the EL Aromo and Villonaco projects (II and III).

Once the analysis of the different scenarios of the phases in which the Santiago hydroelectric project could be put into operation, it can be concluded that the best option is to divide it into three phases of 1,200 MW each and that revenues should be in 2026, 2028 and 2030 respectively. In this way, it could be supplied without the projection of the most critical demand raised by the MEM.

References

[1]. Ecuadorian Electricity National Masterplan [Plan Maestro de Electricidad], Ministerio de Energía y Recursos Naturales No Renovables, 2019

[2]. Annual National Report [Informe Anual] CENACE (Operador Nacional de Electricidad), 2019

[3]. Annual National Report [Informe Anual] ARCONEL (Agencia Nacional de Regulación y Control. [Online] Available:https://sisdatbi.regulacionelectrica.gob.ec/

[4]. Heaps, C.G., *LEAP: The Low Emissions Analysis Platform.* [Software version: 2020.1.20] Stockholm Environment Institute. Somerville, MA, USA. https://leap.sei.org, 2020

Decarbonisation & Optimization Strategies in Distributed Energy Community characterized by Demand of Electricity, Cooling, and Heating

Stefano Mazzoni[a], Greta Magnolia[a], Michela Vellini[a] and Marco Gambini[a]

[a] Department of Industrial Engineering, University of Roma Tor Vergata, Rome, Italy
[*]CA: stefano.mazzoni@uniroma2.it

Abstract:
The global call for an environmentally friendly, sustainable and reliable distributed energy community is gaining traction nowadays, pushing the scientific community to explore novel multi-energy system layouts for highly decarbonised design. The complexity of highly integrated systems resides in selecting the components optimal capacities and establishing the demands for electricity, cooling and heating. While traditional fossil-based centralised distribution is not affected by intermittencies of renewables, highly decarbonized decentralised energy communities need to cope with the variability – in the short and long term – of renewables and the end-users demands. The scientific community addresses this problem by integrating various energy storage technologies in the energy community, but the selection of the most suitable technology and the related optimal capacity requires advanced optimisation tools capable of simulating years of the system operations, including stochastics factors that affect prices, costs and carbon taxes and regulations. The authors developed over the last five years the DECAPLAN™ Digital Platform capable of solving master-planning and optimal dispatch strategy problems. DECAPLAN™ includes hybrid heuristic/deterministic algorithms, based on a Genetic/MINLP solver, for establishing the optimal energy community design in respect of financial indicators, such as NPV, ROI and CO2 per year. In the paper, the authors present a real case in the Mediterranean Tropic region, showing a sensitivity analysis of the effect of environmental policies on the whole system design. Results in terms of energy community optimal component selection and optimal dispatch strategy are presented together with a sensitivity analysis on the effect of fuel and CO2 tax prices variability over the next decade.

Keywords:
Decarbonization, Master-Planning, DECAPLAN™, Distributed Energy Community, Optimization

1. Introduction

Scientists are calling for an energy transition [1] which must confront the limitations of reality , and specifically address the inadequate infrastructures that currently exist. The electricity sector is the primary focus of this transition, as evidenced by the significant increase in the installation of electric renewables over the past two decades [2], which has largely been achieved through a centralized approach that involves connecting new renewable energy power plants to the grid. While this has reduced the Primary Energy Factor of the Power Grid, it has also placed additional stress on the grid due to the influx of new energy production [3]. To address the balancing issues that result from the mismatch between energy demand and production, storage facilities have been included, but their limited size and high costs have impacted the grid's operation [3, 4, 5]. In light of this, it is necessary to consider the energy balance at the national level as the sum of smaller-scale energy balances, highlighting the crucial role of local Distributed Energy Communities (DECs) [16] in achieving a more balanced and sustainable energy mix [7, 8, 9]. By reducing changes and stress on the grid infrastructure, local energy communities can focus on local emission factors linked to energy mixes [10], leading to a decentralized search for renewable energy plants and the establishment of Renewable Energy Communities codified in the EU Directive REDII. Additionally, incentive schemes supporting Self-Consumption aim to provide community members with shared added value in terms of environmental and financial impacts throughout the energy chain [12, 13].

Solar PV and Solar Collectors on the roof, hot water storage, electric batteries in the basement are the most used tools made available to the citizens to participate to this new entity. Beside them, innovative technologies are taking place such hydrogen energy systems. Similarly, centralized approach for assisting the Grid is taking place first even with the limitations in size and impact due to the high costs. Later, small scale hydrogen energy

systems are seeing interest thanks to devices like the reversible fuel cells offering the production and utilization of hydrogen as a service for the buildings and in cooperation with other sectors like the mobility.

The integration of DECs in the existing infrastructure is a challenge faced by the scientific community in the last decade and affects the large scale DECs development due to some limitation such as the Capital Investment Cost, the Intermittency and variability of the renewable energy resources, the limited capacity related to the site-specific conditions and also on the technical challenge of integrating DECs into the existing grid. Indeed, to accommodate the DECs power generation it could be required to upgrade the grid infrastructure and may involve significant regulatory and policy changes.

Furthermore, in order to answer the call for higher decarbonization DECs, the integration of multi-energy highly integrated systems allows for drastically reduction in CO2 emissions but not necessarily in a easy-to-implement techno-economic manner. Accordingly, the selection of the most suitable technology and the related optimal capacity requires advanced optimisation tools capable of simulating years of the system operations, including stochastics factors that affect prices, costs and carbon taxes and regulations. The authors developed DECAPLAN™ digital platform capable of solving master-planning and optimal dispatch strategy problems. DECAPLAN™ includes hybrid heuristic/deterministic algorithms, based on a Genetic/MINLP solver, for establishing the optimal DEC design in respect of financial & environmental indicators, such as NPV, ROI and CO2 emitted per year. In the paper, the authors present a real case in the Mediterranean Tropic region, showing results in terms of energy community optimal component selection and optimal dispatch strategy, together with a comparative analysis on the achievable Operating Cost (OPEX) savings and CO2 emission reductions related to DEC configuration complexity.

2. Technical Background

The role of citizens regarding energy consumption and production has progressively changed during the last years. From passive energy consumers, they have become “prosumers” or active energy consumers because they both consume and produce energy, mainly through the installation of photovoltaic (PV) panels on their rooftops [14]. Renewable Distributed Energy Communities (DEC) can be defined as a group of prosumers composed of diverse users (e.g. individual households, municipal bodies, private businesses etc.) who share power plants for the generation and self-consumption of electricity, cooling and heating from renewable energy sources [15]. The diffusion of Renewable DECs produces benefits in terms of sustainability, costs and safety [16, 17] because DECs show:

- Localized generation of highly decarbonized electricity, cooling and heating, concurrently reducing CO_2 emissions, fuel poverty and energy losses during distribution.
- reduced grid fees and energy costs;
- flexibility of the energy usage due to the integrations of energy storage technologies for allowing peak shaving operations at DECs level.

DECs are also characterized by social innovation because they reinforce support between citizens and encourage their participation towards climate neutrality and energy transition through a democratic control over energy investments [18].

2.1. Existing Distributed Energy Community and the reference case

Renewable Distributed Energy Communities are progressively spreading in Europe, mainly in Germany, Denmark and Netherlands [18]. Italy is still characterized by a much lower number of active communities, equal to around 20 [19, 20].

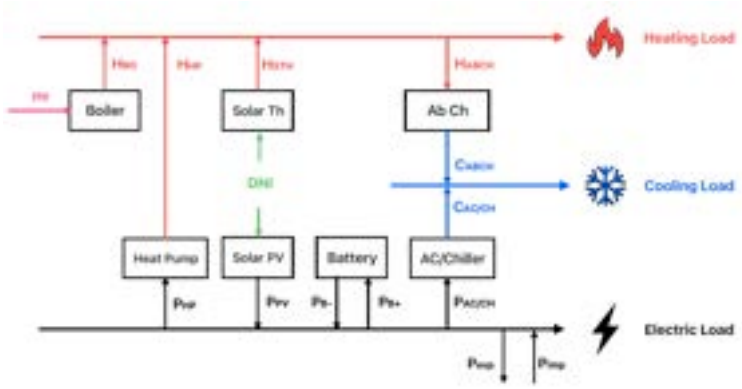

Figure 1. Schematic representation of the Renewable DEC of this study

According to literature [18 - 21], solar technologies are the most common used in Renewable DECs. Indeed, solar panels and solar collectors allows for quick and easy-to-customize installations suitable for rooftops of different buildings such as households, public buildings, and farms. Another important characteristic of existing energy communities is in the local production and consumption of energy, combined - when possible - with a variety of end-user uses of energy with the aim to match demand and generation, minimizing energy import/export from/to the power grid.

In this paper, the authors model and investigate the environmental and economic viability of different configurations of a Renewable DEC located in the Mediterranean Tropic region (latitude of around 37° 35' 59.9784"), where solar availability is relatively huge. The Renewable DEC is made up taking the main features of a real DECs and the overall demands of heat, domestic hot water, electricity, and cooling into consideration. The DEC account for a real municipality of around 350-400 inhabitants

The load demands of electricity, heating and cooling have been evaluated by considering that the DEC serves different types of users. Indeed, specific load profiles for different destination of usage have been combined, and mainly are related to:

- a shopping center with a supermarket, a coffee bar and a chemist's.
- a sport club.
- a town hall.
- 200 households

The authors present different DEC configurations (case studies A1 – E5), based on the DEC layout given in figure 1, varying the equipment technology and related installed capacity for supplying the end-users needs.

The DEC layout modelled by the authors and adopted for running the simulations is depicted in figure 1 together with the equipment providing for the generation and consumption of the required end user demands in terms electricity, heating and cooling. Indeed, the system has been modelled in buses as described below:

- Electricity Bus: Solar PV (P_{PV}), Battery Discharge (P_{B-}) and Power imported from the grid (P_{imp}) are the positive contribution for the positive terms for the electric load generation, while Heat Pump (P_{HP}), Battery Charge (P_{B+}), Air-condition/Chiller System ($P_{AC/CH}$) and power exported to the grid (P_{exp}) are negative ones.
- Heat Bus: Natural Gas fed Boiler (H_{BO}), Heat Pump (H_{HP}) and Solar Thermal Collector (H_{STH}) are contributing to the satisfaction of the Heat Load demand (H_{Load}), while Absorption Chiller (H_{ABCH}) is reducing the H_{Load} generation, for supplying the Cooling Load (C_{Load}).
- Cooling Bus: the C_{Load} is supplied by AC/Chiller ($C_{AC/CH}$) and by the Absorption Chiller (C_{ABCH}) cooling generation equipment.

The DEC can import and export electricity from or to the grid in case of lack or excess of production from the installed plants in the community, as shown in Figure 1.

2.2. The sensitive Parameters characterizing DECs

As mentioned in Paragraph 2, DEC can serve different kinds of end-consumers and related needs. Accordingly, the load demands of electricity, domestic hot water, cooling, and heat of the community are obtained by combining each of the load demands related to the various end-users in the DEC. Indeed, each consumer has specific load demands [22], which vary on the basis of the time period of the day and of the week (e.g. working days and holidays), the month of the year and the season. Other factors impacting on the load curves are [23, 24]:

- building size and architecture, looking at gross floor area (GFA) (m^2) and volumetric extension (m^3);
- building energy class and the related energy efficiency policies for planning;
- differentiation between regions and countries in terms of climate (e.g. DNI, ambient temperature, relative humidity), economic conditions and Technology Level (e.g. developed countries have a lower number of people per household).

In previous scientific works, the authors presented a deep analysis of the load demands from industrial [25, 26], commercial and domestic users [27-29]. In this study, the total demand of the DEC is evaluated by taking both the in-situ analyses performed in previous works and the available data referred to European municipalities located at the same latitudes of the DEC [25-29] into consideration.

Figure 2 shows - the normalized electricity load profiles of a typical winter working day related to the different users for being part of the proposed DEC. The type of user determines different trends: the shopping centre shows a practical constant load during the day, both the sports club and the households have the load peak during the evening, while the town hall shows his peak in the morning.

The DEC is modelled according to available data of real municipalities in the Mediterranean tropic region in terms of number, floor area and volumetric extension of households, buildings and facilities [30, 31].

The generation side is evaluated considering the values of temperature and solar irradiance at the latitudes of the DEC [32, 33]. An optimization of the design of the community structure is executed grouping diverse types of users with the aim of matching demand and generation curves, reducing energy export to the external grid.

The assumptions and the DEC architectural features are presented to perform the analysis to evaluate the load demands (electricity, cooling, and heating) of the DEC, it is important to understand how the boundary conditions (namely temperature and DNI) and the buildings/infrastructure configuration influences the heat/cold gain of the system and as well the electrical consumption. Indeed, based on the general specific daily load profile given in section 2, in the specific case scenario the DEC serves four diverse types of users, namely households, a shopping centre, a sports centre and a town hall, supplying electricity, domestic hot water, heat and cooling. According to the proposed case study located in the Mediterranean area, the authors have summarized in Table 1 the main characteristics of the community's buildings, while in Table A.2 shows the number of families with the number of family members living in the community.

The yearly temperature and DNI distribution for the given location, have been retrieved by MARRA-2 Data base. The yearly curves for the different load demands and different type of user are evaluated thanks to DECAPLAN™ Digital Platform by finetuning the parameters on the basis of the data derived from literature [34], that account for the variability of the demands supply during the day, week and month. As an example, the aggregated load demands of electricity, cooling and heating for a typical week during the winter (January) and during the summer (July) have been presented in figure 3 by the authors.

Table 1. DEC Buildings Architectural Characteristic

Type of building	Floor surface [m^2]	Volumetric extension [m^3]
Real estate district	13,590 – 13,600	40,770 – 40,780
Shopping centre	820 – 830	2,900 – 2,910
Sports centre	710 – 720	2,140 – 2,150
Town hall	230 - 240	700 - 710

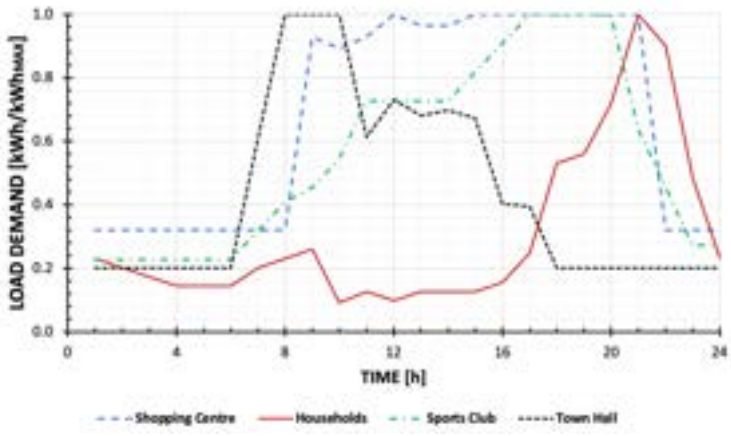

Figure 2. Electricity Load Demands for different DEC user during a typical winter working

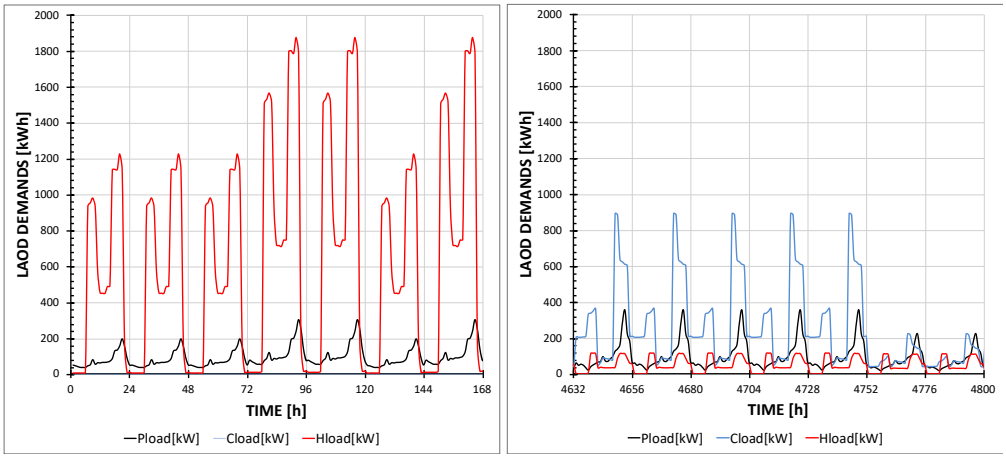

Figure *3.* Typical Load Demands Profile during winter (left) and summer (right) for reference case study.

3. Materials and Methods

In this section, the methods used for data collection, modeling and analysis are described. The DECAPLAN™ digital platform [34-37] is proprietary software of MEDS Venture Global Pte Ltd start-up company spin-off of Nanyang Technological University. The DECAPLAN™ Digital Platform has been developed by the authors over the last five years for designing power plants, microgrids, and industrial and building estates characterised by high energy mix by establishing the best plant arrangement and choosing among database (DB) the most suitable commercially available components. The DECAPLAN™ allows for concurrently optimising the best multi-energy plant design and operation by solving the energy dispatch (unit commitment) problem for given electricity, cooling and heating demands. In this paper, the optimal solution is addressed to minimise the primary energy consumption and the greenhouse pollutant emissions (CO_2) by minimizing them at the same time. The mathematical formulation of the DECAPLAN™ objective function enables the digital platform to search for the best solutions taking the Operational Expenses (OPEX), the Localized Cost of Electricity (LCOE), the Return of the Investment (ROI), and other parameters into consideration. More details on the modelling approach and the optimisation strategy are given in the next section. The proposed system layout includes several DEC components such as Solar PV, Solar Cooling, Heat Pumps, Chillers, Energy Storage Technologies (namely battery in the specific DEC) and others as well as their part-load off-design maps for optimized asset management.

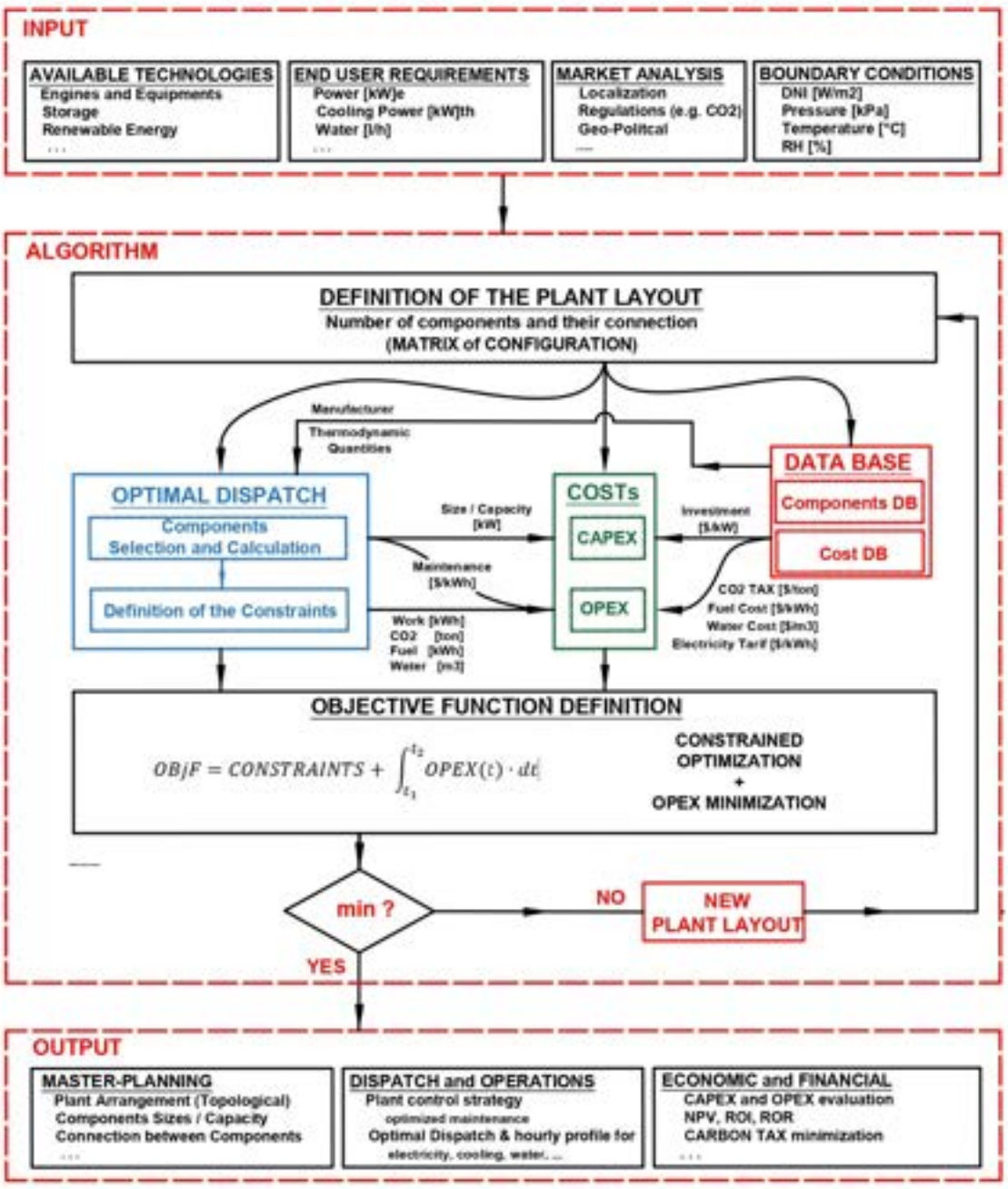

Figure 4. The functional block diagram of DECAPLAN™ digital platform

Details on the mathematical formulation for the Master Planning (MP) and the Optimal Dispatch Planning (ODP) are discussed by the authors in [36, 37], while for purposes of this work the functional scheme with the description of the main features of the DECAPLAN™ digital platform is summarized below. The simulation tool for the DEC system was developed using a modular approach at the component level. To set up the DEC simulator, steady-state 0-D component models were adopted as per the method proposed by the DECAPLAN™ digital platform algorithm. The DECAPLAN™ includes various solvers such as quadratic programming, mixed-integer linear programming (MILP), and mixed-integer non-linear programming (MINLP).

Research has shown that the mixed-integer quadratic programming technique used by the DECAPLAN™ digital platform is robust and efficient, as demonstrated by comparisons with a hybrid heuristic algorithm based on GA and PSO solvers [36, 37] and other mathematical approaches [35 - 37]. Additionally, the use of stochastic algorithms has been found to potentially lead to suboptimal results in master-planning problems [65-67]. Figure 4 provides a complementary block diagram to understand the optimization process flow that the end-users need to perform, specifically the optimal dispatch block diagram DECAPLAN™.

The algorithm consists of three parts: the *input layer*, where conditions such as temperature, DNI, and precipitation profiles, as well as plant demands and costs, are inputted; the *optimal dispatch layer*, where the algorithm matches and connects components, ensuring that conservation equations are not violated; and the *output layer*, where the optimal dispatch strategy for the power plant and its associated costs are presented. Additionally, the algorithm uses a modular approach to simulate power systems and incorporates a database of component performance maps to evaluate costs, degradation, and maintenance. Accordingly, the authors have developed ad-hoc thermal components for the specific scientific work, including solar cooling, heat pumps and thermal solar.

3.1 DEC Main Component Modelling

Solar PV: is modelled by adopting lumped performance features. The scheme of the PV model is presented in figure 6-A. The generated power PPV is calculated as (eq.1):

$$P_{PV} = DNI \cdot S_{PV} \cdot \eta_{PV} \quad (1)$$

Where DNI, SPV and η_{PV} are the direct normal irradiance (DNI), the solar PV surface and the solar PV efficiency. The η_{PV} in the actual conditions is established by the adoption of normalized maps developed by the authors that relates the solar PV reference efficiency, the DNI and PV cell temperature (typically referring to the panel type and to the manufacturer testing conditions) to the actual DNI and cell temperature T. The lower the cell temperature, the higher the efficiency. Typically, DB provides 0 °C as the minimum value. Accordingly, η_{PV} is expressed functionally by (eq.2):

$$f\left(\frac{\eta_{PV}}{\eta_{PV_R}}, \frac{DNI}{DNI_R}, \frac{T}{T_R}\right) = 0 \quad (2)$$

Solar Thermal Collector: is modelled similarly to the Solar PV module, but as the output useful quantity is the Heat Power (H_{STH}) defined in (eq.3), where η_{STH} is the STC efficiency, evaluated in similarities with the procedure of eq.2.

$$H_{STH} = DNI \cdot S_{STH} \cdot \eta_{STH} \quad (3)$$

Heat Pumps: the characteristic equation allowing for evaluating the useful effect H_{HP} is given in (eq.4), and the details of the modelling approach are given in [35, 37], as well as per the absorption chiller and vapour compression chiller details. Off-design curves are also discussed in [35,37]

$$H_{HP} = COP_{HP} \cdot P_{HP} \quad (4)$$

Chillers Systems: the AC/Chiller system and the absorption chiller equations are summarized in (eq.5) and (eq.6), and the full model details can be found in [37]

$$C_{ABCH} = COP_{ABCH} \cdot H_{ABCH} \quad (5)$$

$$C_{ACCH} = COP_{ACCH} \cdot P_{ACCH} \quad (6)$$

Fuel Boiler: the model allows for evaluating the useful effect H_{BO} (eq.7) based on the routine described in [37] for evaluating the complete combustion details of the process together with exhaust gas composition, carbon emitted.

$$H_{BO} = m_{fBO} \cdot \eta_{BO} \cdot LHV_f \quad (7)$$

Battery: the entire description of the model is described by the authors in [37], the main equation required for solving the ODP is given in (eq.8), where the battery energy capacity at the time-step *t+1* is evaluated as

function of the optimized control strategy of the battery and the capacity at the time-step *t.* For ensuring the energy conservation equation during the whole period of the battery operation, an equality constraint is introduced (eq.9).

$$E_{BATT}(t+1) = E_{BATT}(t) + P_{B+} \cdot \Delta t - P_{B-} \cdot \Delta t \quad (8)$$

$$E_{BATT}(t = t_{START}) = E_{BATT}(t = t_{END}) \quad (9)$$

3.2 Environmental Techno-Economic Indicators

The overall CO2 emissions are evaluated by taking into consideration the specific emission factors of the different energy generation processes, in the specific case from the import of the electricity from the national grid and from the combustion process in the fuel fed boiler. At DEC level the production of electricity from RES and export to the national grid could be expressed as a negative/avoidance of CO2 emitted and included in the evaluation. For accounting this term, that can or not included in the Scenario evaluation, the authors have adopted a (δ = 0 or δ =1) variable in the formulation. According to the above, the CO2 emissions per year are expressed by (eq.10

$$CO_2 = \sum_{t=1}^{8760} (Pimp - \delta \cdot Pexp) \cdot \Delta t \cdot f_{CO2_{grid}} + mf \cdot \Delta t \cdot f_{CO2_{fuel}} \quad (10)$$

The overall operating cost O_{PEX} is evaluated as the sum of the running costs (e.g. cost of the electricity imported and fuel), maintenance cost, renting cost of the surface where installing DEC equipment and by the carbon tax, expressed by (eq.11). Accordingly, the overall OPEX, fully described in [35,37] is sinthetically expressed by (eq.12):

$$O_{CO2_{TAX}} = CO_2 \cdot TAX_{CO2} \quad (11)$$

$$O_{PEX} = O_{RUN} + O_{MAIN} + O_{RENT} + O_{CO2_{TAX}} \quad (12)$$

3.3 Power Constraints, Objective Function and Optimization Strategy

The solution of ODP consists of two main steps such as the minimisation or maximisation of the objective function (*ObF*) and satisfying of the equality constraints, namely electricity and cooling power flow (electricity and cooling bus load demands). From a numerical perspective, the adopted solver is based on simultaneous solutions; this means that concurrent to the equality constraints satisfaction, the *ObF* is also optimised. In the current work, the *ObF* to be maximised has been set to be the linear combination of the OPEX and CO2 emissions reduction of the k-th scenario, versus the OPEX and CO2 emissions of the reference case (REF) NPV, expressed by (eq.13).

$$ObF - Search\ MAX\ of:\ CF_k + \Delta CO2 = \left(OPEX_{REF} - OPEX_{k_{th}}\right) + \left(CO2_{REF} - CO2_{k_{th}}\right) \quad (13)$$

The satisfaction of the energy flows (operational constraints) for the economic dispatch on the electric bus is expressed by (eq.14), on cooling bus by (eq.15) and on heating bus by (eq.16).

$$P_{Load} \cdot \Delta t = P_{imp} \cdot \Delta t + P_{pv} \cdot \Delta t + P_B^- \cdot \Delta t - P_B^+ \cdot \Delta t - P_{exp} \cdot \Delta t - P_{ACCH} \cdot \Delta t - P_{HP} \cdot \Delta t \quad (14)$$

$$C_{Load} \cdot \Delta t = C_{ACCH} \cdot \Delta t + C_{ABCH} \cdot \Delta t \quad (15)$$

$$H_{Load} \cdot \Delta t = H_{HP} \cdot \Delta t + H_{BO} \cdot \Delta t + H_{STH} \cdot \Delta t - H_{ABCH} \cdot \Delta t \quad (16)$$

The formulation of the optimisation problem has been fully described by the objective function and constraints structure definition. In the next section, the test case and the analysis of the results are presented.

4. CASE STUDIES

The schematic representation of the Renewable DEC presented by the authors in figure 2 allows to generate multiple case studies in respect of the components included in the DEC layout and of the capacity. Furthermore, the different case studies can also be contextualized in different energy policy scenarios where Incentives, Carbon Certificates and Financial Rewards for CO2 avoidance and power generation in the DEC can be taken into consideration. According to the above, the authors have explored five DEC configurations (Layout) A, B, C, D and E, and for each of the configuration varied the number of Solar PV (0, 250, 500 and 1000), according to the maximum allowable gross floor area available for the PV installation. For the configuration C, the authors have selected the maximum number of Solar Thermal Collector of 500 unit. The matrix of the configuration generated and optimized by DECAPLAN™ Digital Platform is given in Table 3. Looking at the number in Table 2, since some of the equipment such as Heat Pumps, NG fed Boilers AC/Chiller unit splitter are specific of each unit of each building, the authors have assumed that if the component exist (N = 1) while if not (N = 0).

Table 2. Case Studies – DEC Configuration Matrix

CASE STUDIES	A1 - REF	A2	A3	A4	B1	B2	B3	B4	C1	C2	C3	C4	D1	D2	D3	D4	E1	E2	E3	E4
	1	2	3	4	5	6	7	8	9	10	11	12	13	14	15	16	17	18	19	20
nPV [-]	0	250	500	1000	0	250	500	1000	0	250	500	1000	0	250	500	1000	0	250	500	1000
nAC/CH [-]	1	1	1	1	1	1	1	1	1	1	1	1	1	1	1	1	1	1	1	1
BATT [kWh]	0	0	0	0	0	0	0	0	0	0	0	0	2000	2000	2000	2000	20000	20000	20000	20000
nHP [-]	0	0	0	0	1	1	1	1	1	1	1	1	1	1	1	1	1	1	1	1
nBOf [-]	1	1	1	1	0	0	0	0	0	0	0	0	0	0	0	0	0	0	0	0
nSTH [-]	0	0	0	0	0	0	0	0	500	500	500	500	0	0	0	0	0	0	0	0

Table 3. Case Studies – DEC Assumption for the Optimization

Parameter	Value	Unit of Measure
Fuel (Price, LHV)	(1.00, 50.0)	(Euro/kg, MJ/kg)
Electricity tariff (Buy/Sell)	Refer to Figure A.3	Euro/kWh
PV (Peak Capacity, Surface, Efficiency)	(550, 2.584,21.1)	(Wp, m^2, %)
STH (Surface, Efficiency)	(2.0, 40.0)	(m^2, %)
COP (HP, VCCH, ABCH)	(2.6, 5.5, 0.7)	(-)
*Battery (*RTE, SOC_M, SOC_m*)*	(93, 95, 5)	(%)
Carbon Tax	80.0	Euro/Ton
DEC Emission Factor	0.212	$kgCO_2$/kWh electric
Natural gas Emission Factor	0.192	$kgCO_2$/kWh fuel

For the battery component instead, it is assumed that it can serve the entire DEC and so introduced with the nominal capacity, expressed in kWh.

On top of these 20 case studies (A1 – E4), the authors have also investigated three policy scenario related to the qualifications in terms of CO2 carbon credit and financial gain of selling the excess of electricity generated by the DEC to the National grid. The results of the scenario analysis will be deeply presented in the result section, by differentiating the colours of the candle stick bars charts. Accordingly, the three scenarios are considering that the yearly exported electricity (kWh exp):

- Scenario 1 (Blue): allow CO2 Certificate Recognition and exported electricity is reward.
- Scenario 2 (Red): NOT allow CO2 Certificate Recognition and exported electricity is reward.
- Scenario 3 (Green): NOT allow CO2 Certificate Recognition and exported electricity is NOT reward.

Price of electricity bought and sold are 230 and 70 euro/MWh.

4.1 Assumptions

According to the DEC building specifications given in section 2, to the ambient condition given by MARRA Database, and to the yearly load profiles for electricity, cooling and hearting shown in figure 3, the main assumptions required for the calculations have been presented in table 3. Indeed, main components specification such as nominal capacity, surface of each module, efficiency, and performance indexes such the Coefficient of Performance (COP) are fundamental parameters to perform the optimization process thanks to DECAPLAN™ Digital Platform.

To perform the environmental techno-economic analysis, prices of electricity (sell and buy) and cost of the carbon tax are also needed. Accordingly, since it has been considered power can be imported (Pimp) and exported (Pexp) from and to the National grid, buy & sell prices are 230 and 70 euro/MWh, respectively. Furthermore, to assess the overall yearly production of pollutant emissions in terms of Ton of CO2/year from the DEC, the emission factors of the system and associated to the combustion of the natural gas into fuel fed boilers have also been included in the optimization and thus included in table 3.

Once boundary conditions and assumptions have been set, the authors have been able to run the optimization and the scenario analysis above-mentioned thanks to DECAPLAN™ Digital Platform. Accordingly, results of the optimization together with discussion and consideration are given in section 5.

5. RESULTS & DISCUSSION

In this section, the authors present the results of the environmental techno-economic optimisation carried out by the DECAPLAN™ Digital Platform, taking the different DEC configuration and scenarios into considering. The case study A1 (order number 1) is the reference case study and represent the scenario in which all the electricity is imported from the national grid, all the cooling load is satisfied by the generation of air conditioning from individual unit splitters and the heat load is supplied by the heat power generated through the Heat Pump. In this configuration, the yearly CO2 emitted by the DEC is of 732 Ton/year and the overall OPEX are of about 540,000 euro/year. These two numbers are very important because they become the benchmark/baseline to

compare all the other case studies and scenarios. Looking at the same DEC configuration A4 equipped with 1000 Solar PV modules, it can be observed by the charts given in figures 5 and 6, that for the scenario 1, where the amount of kWh exported to the grid is accounted in the overall CO2 emission per year, the year CO2 emissions drop of 21% to 575 Ton/year and the yearly OPEX decreases of 22% to 420,000 euro/year. This trend is justified by the fact that the integration of the solely Solar PV in the DEC configuration does not modify the load allocation of the other loads, such as cooling and heating. When A4 configuration is instead compared among the three scenario 1, 2 and 3, it can be clearly be observed that cCO2 credit mechanism of the scenario 1, does not allow in case 2 and 3 to achieve the same CO2 emissions reduction. Indeed, in case 2 (and equivalently in case 3) the maximum CO2 reduction is of 57 Ton/year, corresponding to about -9% CO2 emission reduction. On the OPEX side instead, scenario 2 shows 427,000 euro/year and scenario 3 shows 452,000 euro/year. The evaluation of the scenario B4, where the generation from the NG fed Boiler is swap with the Heat Pump system, shows an interesting trend among CO2 and OPEX. Indeed, given the marginal cost of the electricity from the grid and of the fuel and the different emissions factors, the solution B4 reduces the CO2 emissions of 65% leading to a yearly emitted value of only 254 Ton/year, with a corresponding OPEX of 460,000 euro/year, that is anyway a saving of 14.8% in the OPEX of the DEC. The introduction of 500 Solar Thermal Collector for the generation of heating and cooling in case C4, keep the reduction of the CO2 emissions practically unchanged, up to 66%, corresponding to an absolute value of 249 Ton/year, and reduces the OPEX of 15.0%, leading to a yearly OPEX of 457,000 euro. The scenarios D4 and E4 are characterized of the introduction of 2000 kWh and 20000 kWh battery capacity in the DEC. In the case of the smaller battery, D4, the CO2 emission reduction is of 64.5%, while the OPEX reduction is of up to 28%, corresponding to a yearly operating cost of 385,600 euro. In case of the large battery instead, E4, the CO2 emissions reduction is 64.0 %, while the OPEX reduction is up to 33.2%, corresponding to a 359,000 euro/year DEC operating cost. The reason behind the massive reduction on the OPEX due to the integration of the battery in the design of the DEC is because it allows to perform the peak shaving procedure and allow to reduce the dependency of the DEC from the National Grid. On the CO2 emissions perspective instead, the fact that each charging/discharging operation is characterized by a loss (round trip efficiency) leads to increase the demand of electricity (energy) in the DEC and consequently to a marginal increase of the CO2 emitted, in comparison between the case without battery. It is worthy of note, that the reduction is anyway very considerable and for sure – the OPEX cost massive reduction will justify the solution. An important consideration related to the introduction of the battery system into the layout are related to the fact that the exported power – in the case of 20000 kWh capacity – is almost zero along the entire year. This is an important consideration since grid complexity and regulation would rather prefer the DEC to be independent from the grid to ensure stability on the frequency of the electricity generated by the DEC system.

Indeed, by comparing the charts given in figures 7 and 8, that represents configurations D4 and E4, it is possible to observe how the capacity of the battery influences different aspects. The red chart representing the power imported from the National grid allows to understand how the dependency from the Nation Grid is much lower in case E4. Looking at the summer period, the DEC is fully independent from the National Grid and furthermore, the electric work exported to the grid is practically zero for the entire year. On the battery duty cycle operations, the grey chart in figures 7 and 8, it can be observed that the case D4 equipped with the smaller capacity, the battery system is adopted in day-to-day operations, accounting for supplying the DEC in case of intermittency of RES in the short term. When the capacity of the battery increases up to 20000 kWh, the storage solution become and interesting tool for planning long term operations, for ensuring flexibility and grid independence of the DEC system.

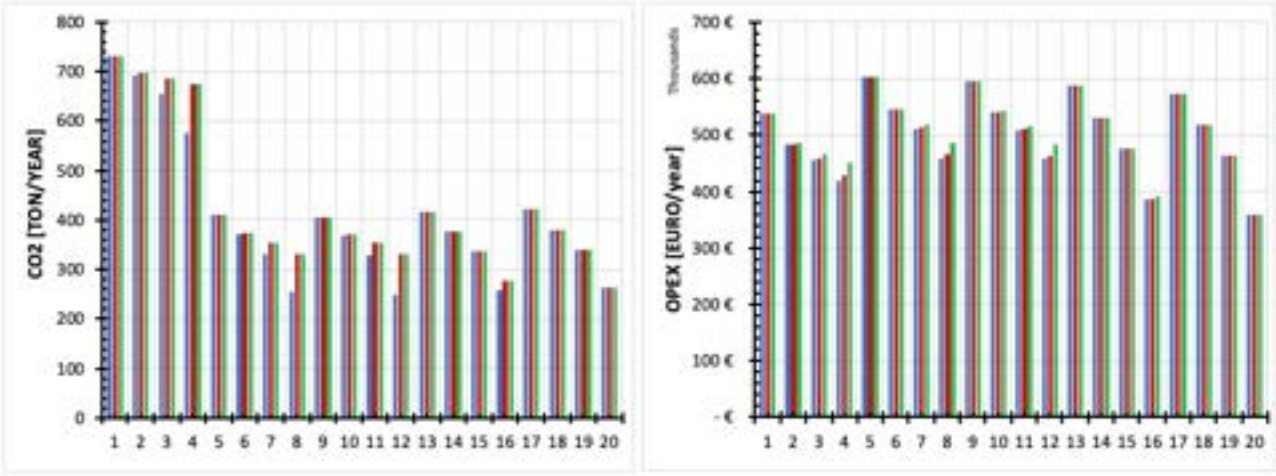

Figure 6. CO2 and OPEX comparison among (A1 – E4) configuration and Scenarios 1,2 and 3

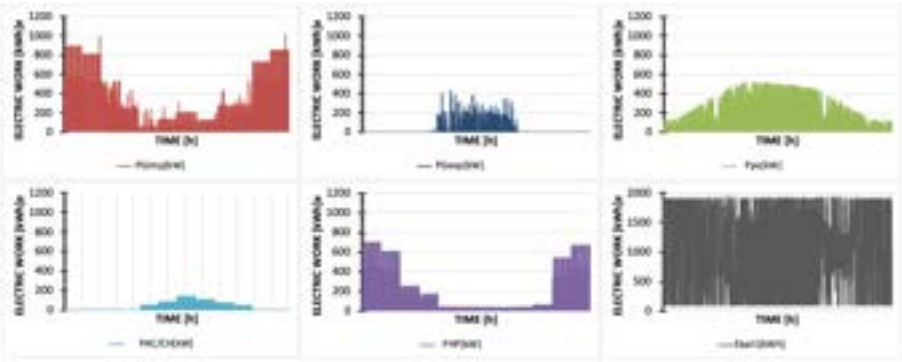

Figure 7. Configuration D4 – Dispatching Profile on the electric load.

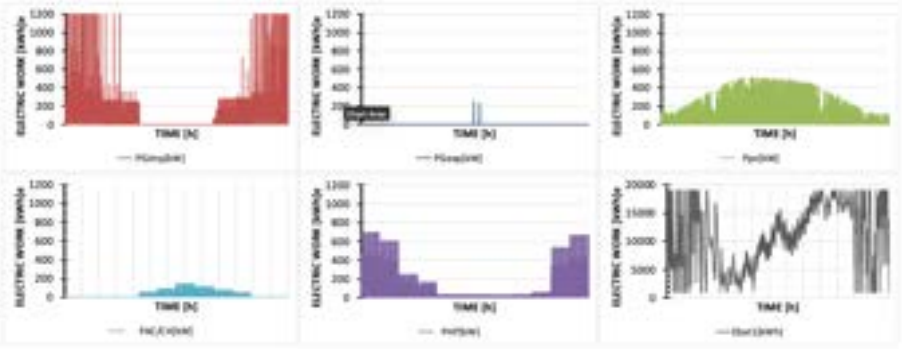

Figure 8. Configuration DE – Dispatching Profile on the electric load.

6. CONLCUSIONS

The paper investigated the promising topic of Renewable Distributed Energy Communities and their role in achieving environmental techno-economic alternatives in the pathway towards decarbonization. The concurrent requirements from the DEC users of electricity, cooling and heating make the design of optimal DEC a complex process, since multitude of variables are involved in the optimization process. The authors have developed a digital platform – DECAPLAN™- that can solve Master-Planning and Optimal Dispatch Problems of highly integrated DEC. Thanks to the modular approach proposed and to the optimization algorithm the authors have ranked the best DEC configurations in terms of potential in CO2 emissions and OPEX reduction. It has been demonstrated that an optimal designed DEC with Solar PV, Heat Pumps and Solar Thermal Collectors is capable to reduce of up to 65.1% the CO2 emissions yearly, when compared to the case in which all the assets are generated via fossil fuel sources (boilers and import from national grid). Indeed, the CO2 Emissions drop from 732.6 Ton/year to just 249.5 Ton/year, reducing the environmental impact of the DEC and reducing the cost associated to the carbon tax (savings of almost 40,000 euro per year of CO2 Tax). The maximum saving from the OPEX perspective – instead – takes place when the DEC is equipped with a large capacity electrochemical energy storage system, with capacity ranging between 2,000 and 20,000 kWh). Indeed, the CO2 reduction comparted to reference case is still very high – with 64% reduction, corresponding to 259.4 Ton/year, but the OPEX drop from 537,000 euro/year to about 385,000 euro/year, that leads to about 28.2% savings yearly, in the case of the 2,000 kWh battery. The authors decided to consider at the day of today the smaller battery as the most easy-to-implement solution for DEC since a much larger battery of 20,000 kWh would also imply to account for thermal management problems and surely much higher CAPEX. It is worth of note, that the larger energy storage capacity simulated in the paper as an electrochemical energy storage system, could also be simulated by alternative storage solutions and plant configurations, based on Hydrogen solutions.

For concluding, the authors have not considered the impact of the CAPEX in the optimal design of the system and for sure it will be the next brick the authors will integrated in the analysis for fully understanding and assessing the environmental techno-economic viability of DEC, in the holistic perspective, accounting for the entire lifetime of the DEC.

Acknowledgments

The authors acknowledge and thank the Department of Industrial Engineering of University of Roma Tor Vergata and the Italian Ministry of University and Research (MUR) for the support.

Nomenclature

H Heating Power, W

C Cooling Power, W

P Electric Power, W

$\dot{m}$ mass flow rate, kg/s

t temperature, °C, timestep, h

η efficiency

δ binary variable (0,1)

Subscripts and superscripts

BO Fuel Boiler

PV Photovoltaic

STH Solar Thermal Collector

$ABCH$ Absorption Chiller

AC/CH Air Condition Unit / Chiller Unit

HP Heat Pumps

$BATT$ Battery

References

1. Şiir Kılkış, Goran Krajačić, Neven Duić, Marc A. Rosen, Moh'd Ahmad Al-Nimr, Effective mitigation of climate change with sustainable development of energy, water and environment systems, Energy Conversion and Management, Volume 269, 2022, 116146, ISSN 0196-8904, https://doi.org/10.1016/j.enconman.2022.116146
2. IEA World Energy Outlook 2022 report, https://www.iea.org/reports/world-energy-outlook-2022 [Accessed January 8th, 2023]
3. Anya Castillo, Dennice F. Gayme, Grid-scale energy storage applications in renewable energy integration: A survey, Energy Conversion and Management, Volume 87, 2014, Pages 885-894, ISSN 0196-8904, https://doi.org/10.1016/j.enconman.2014.07.063
4. Arduin I, Andrey C and Bossmann T. What energy infrastructure will be needed by 2050 in the EU to support 1.5°C scenarios? [version 1; peer review: 2 approved]. F1000Research 2022, 11:387 https://doi.org/10.12688/f1000research.109399.1
5. Bethani Turley, Alida Cantor, Kate Berry, Sarah Knuth, Dustin Mulvaney, Noel Vineyard, Emergent landscapes of renewable energy storage: Considering just transitions in the Western United States, Energy Research & Social Science, Volume 90, 2022, 102583, ISSN 2214-6296, https://doi.org/10.1016/j.erss.2022.102583
6. Stian Backe, Sebastian Zwickl-Bernhard, Daniel Schwabeneder, Hans Auer, Magnus Korpås, Asgeir Tomasgard, Impact of energy communities on the European electricity and heating system decarbonization pathway: Comparing local and global flexibility responses, Applied Energy, Volume 323, 2022, 119470, ISSN 0306-2619, https://doi.org/10.1016/j.apenergy.2022.119470
7. Yinghao Ma, Mengyuan Zhang, Hejun Yang, Xuli Wang, Jiayin Xu, Xudong Hu, Decentralized and coordinated scheduling model of interconnected multi-microgrid based on virtual energy storage, International Journal of Electrical Power & Energy Systems, Volume 148, 2023, 108990, ISSN 0142-0615, https://doi.org/10.1016/j.ijepes.2023.108990
8. Hui Chen, Shangheng Yao, Kun Peng, Saiqun Zhou, Peipei Tian, Grid emission factors: The key to greenhouse gas emission accounting, Resources, Conservation and Recycling, Volume 190, 2023, 106846, ISSN 0921-3449, https://doi.org/10.1016/j.resconrec.2022.106846
9. Keiko Hori, Jaegyu Kim, Reina Kawase, Michinori Kimura, Takanori Matsui, Takashi Machimura, Local energy system design support using a renewable energy mix multi-objective optimization model and a co-creative optimization process, Renewable Energy, Volume 156, 2020, Pages 1278-1291, ISSN 0960-1481, https://doi.org/10.1016/j.renene.2019.11.089
10. Poul Alberg Østergaard, Neven Duic, Younes Noorollahi, Soteris Kalogirou, Renewable energy for sustainable development, Renewable Energy, Volume 199, 2022, Pages 1145-1152, ISSN 0960-1481, https://doi.org/10.1016/j.renene.2022.09.065
11. Italian Ministry of Economic Development Decree 16 September 2020 Codification and incentives of Self Consumption, https://www.gazzettaufficiale.it/eli/id/2020/11/16/20A06224/sg [Accessed on January 5th, 2023]

12. European Union, Clean energy for all Europeans package Eur Community (2019) https://ec.europa.eu/energy/topics/energy-strategy/clean-energy-all-europeans_en [Accessed January 11th, 2023]

13. Valeria Casalicchio, Giampaolo Manzolini, Matteo Giacomo Prina, David Moser, From investment optimization to fair benefit distribution in renewable energy community modelling, Applied Energy, Volume 310, 2022, 118447, ISSN 0306-2619, https://doi.org/10.1016/j.apenergy.2021.118447

14. European Parliament, Electricity "Prosumers," (2016). https://www.europarl.europa.eu/thinktank/en/document/EPRS_BRI(2016)593518.

15. European Environment Agency, Energy prosumers in Europe — Citizen participation in the energy transition, (2022). https://www.eea.europa.eu/publications/the-role-of-prosumers-of.

16. F. Ceglia, P. Esposito, E. Marrasso, M. Sasso, From smart energy community to smart energy municipalities: Literature review, agendas and pathways, Journal of Cleaner Production. 254 (2020) 120118. https://doi.org/10.1016/j.jclepro.2020.120118.

17. ENEA, La Comunità Energetica, (2021). https://www.enea.it/it/seguici/pubblicazioni/pdf-volumi/2021/opuscolo-comunita-energetica.pdf.

18. E. Caramizaru, A. Uihlein, Energy communities: an overview of energy and social innovation, JRC Publications Repository. (2020). https://doi.org/10.2760/180576.

19. RSE, Fondazione Utilitatis, Orange Book22, Le Comunità Energetiche in Italia, (2022).

20. Legambiente, Comunità Rinnovabili, (2021).

21. ENEA, Le Comunità Energetiche In Italia, (2020).

22. M. Noussan, B. Nastasi, Data Analysis of Heating Systems for Buildings—A Tool for Energy Planning, Policies and Systems Simulation, Energies. 11 (2018) 233. https://doi.org/10.3390/en11010233.

23. T. Gallo Cassarino, E. Sharp, M. Barrett, The impact of social and weather drivers on the historical electricity demand in Europe, Applied Energy. 229 (2018) 176–185. https://doi.org/10.1016/j.apenergy.2018.07.108.

24. International Energy Agency, Performance Assessment of Residential Cogeneration Systems in different Italian climatic zones, (2007).

25. M. Gambini, M. Vellini, T. Stilo, M. Manno, S. Bellocchi, High-Efficiency Cogeneration Systems: The Case of the Paper Industry in Italy, Energies. 12 (2019) 335. https://doi.org/10.3390/en12030335.

26. M. Vellini, M. Gambini, T. Stilo, High-efficiency cogeneration systems for the food industry, Journal of Cleaner Production. 260 (2020) 121133. https://doi.org/10.1016/j.jclepro.2020.121133.

27. M. Vellini, J. Tonziello, Hydrogen Use in an Urban District: Energy and Environmental Comparisons, Journal of Energy Resources Technology. 132 (2011). https://doi.org/10.1115/1.4003032.

28. M. Gambini, M. Manno, M. Vellini, Hydrogen use in an urban district: energy and environmental impact evaluation (part A), in: 2007 20th International Conference on Efficiency, Cost, Optimization, Simulation and Environmental Impact of Energy Systems, Padova, 2007: pp. 563–574. https://art.torvergata.it/handle/2108/50162.

29. M. Gambini, M. Manno, M. Vellini, Hydrogen use in an Urban District: Energy and environmental impact evaluation (part B), in: 2007 20th International Conference on Efficiency, Cost, Optimization, Simulation and Environmental Impact of Energy Systems, Padova, 2007: pp. 563–574. https://art.torvergata.it/handle/2108/255110.

30. Home - Eurostat, (n.d.). https://ec.europa.eu/eurostat/?lang=en.

31. Statista - The Statistics Portal, Statista. (n.d.). https://www.statista.com/.

32. JRC Photovoltaic Geographical Information System (PVGIS) - European Commission, (n.d.). https://re.jrc.ec.europa.eu/pvg_tools/en/tools.html.

33. SunSim website, (n.d.). http://www.sunsim.it/.

34. DECAPLAN™ https://www.medsventure.com/digital-platform/ [Accessed on March 22nd, 2023]

35. Rémy Rigo-Mariani, Sean Ooi Chea Wae, Stefano Mazzoni, Alessandro Romagnoli, Comparison of optimization frameworks for the design of a multi-energy microgrid, Applied Energy, Volume 257, 2020, 113982, ISSN 0306-2619, https://doi.org/10.1016/j.apenergy.2019.113982

36. Cerri, G., Chennaoui, L., Giovannelli, A., & Mazzoni, S. (2014). Expander models for a generic 300 MW F class gas turbine for IGCC. Proceedings of the ASME Turbo Expo, 2C(June). https://doi.org/10.1115/GT2014-26493

37. Mazzoni, S., Ooi, S., Nastasi, B., & Romagnoli, A. (2019). Energy storage technologies as techno-economic parameters for master-planning and optimal dispatch in smart multi energy systems. Applied Energy, 254, 113682. https://doi.org/10.1016/j.apenergy.2019.113682

PROCEEDINGS OF ECOS 2023 - THE 36TH INTERNATIONAL CONFERENCE ON
EFFICIENCY, **C**OST, **O**PTIMIZATION, **S**IMULATION AND ENVIRONMENTAL IMPACT OF ENERGY SYSTEMS
25-30 JUNE, 2023, LAS PALMAS DE GRAN CANARIA, SPAIN

Techno-economic optimization of a multimodal energy system for a fully renewable energy-supplied Danish island

Tao Yang [a,*], Konstantin Filonenko [b], Benjamin B. L. Larsen [a], Vinusan Jeyarajah [a], Cecilie Larsen [c], Muhyiddine Jradi [a], Christian Veje [d]

[a] Center for Energy Informatics, University of Southern Denmark, Odense, Denmark
[b] DTU compute, Technical University of Denmark, Lyngby, Denmark
[c] Municipality of Aero, Aero, Denmark
[d] Department of Mechanical and Electrical Engineering, University of Southern Denmark, Odense, Denmark,
** taoy@mmmi.sdu.dk*

Abstract:

Accelerating the green energy transition is of great importance in fighting global climate change. Currently, the Danish island Aero utilizes a large amount of fossil fuel-based energy resources in the electricity, heating, and transport sectors. In line with the holistic green transition initiatives in Denmark and the holistic goal of the fossil-fuel free Danish energy sector by 2050, this study aims to find a feasible solution for the island to be fully sustainable relying solely on renewable energy sources, operating in island mode. To that end, different approaches are investigated including the electrification of the transport sector, installing energy storage systems, increasing renewable energy production capacities, energy production planning, and demand side management. Using linear programming, a hybrid scenario combining these energy approaches is developed and an hourly optimization is conducted to balance the island's energy production and demand. The proposed hybrid scenario is compared to the island's current energy system operation (base scenario) via a techno-economic approach, where dimensioning of the technologies is evaluated and the overall system cost is projected. The results showed that the hybrid scenario achieves higher renewable energy contribution (100%) and lower system cost (1625.9 DKK/month/person) compared to that of the base scenario (55.77% and 1689.6 DKK/month/person respectively). In connection to the hybrid scenario, a sensitivity analysis is carried out to investigate the impact of specific modifications to the hybrid scenario on the system's technical and economic performance. The results showed that installing an additional ferry is the most beneficial approach to improve the hybrid scenario's performance.

Keywords:

Energy planning, sector coupling, island mode, optimization, demand side management

1. Background and motivation

To mitigate climate change and global warming, Denmark has set an ambitious goal to phase out fossil fuels and achieve CO_2 neutrality by 2050 [1]. Complying with the holistic goal of this fossil-fuel free Danish energy sector, Danish island Aero aims to be CO_2 neutral and self-sufficient in renewable energy by 2025 [2]. Aero has long been stepping towards green energy transition and the CO_2 emissions have been reduced by 38% in the period from the year 2008-2019. However, the current energy systems in Aero still rely on a large amount of fossil fuel-based energy resources in the three main sectors, i.e. the electricity, heating, and transport sectors.

Aero has already equipped wind turbines and PVs for green electricity production, the transport and heating sectors are responsible for the major CO_2 emissions on Aero. This is largely due to the use of fossil fuel-based cars and buses for transportation as well as oil burners for individual heating. To make it sustainable, the transport sector will be completely electrified by substituting fossil fuel-based vehicles with electric vehicles, and the oil burner will be replaced by district heating and electric water heating. However, these measures will lead to an increase in electricity demand. In addition, Aero aims to operate in island mode in the future without importing or exporting electricity, which poses a big challenge for the energy balance between supply and production. To address this issue, the current Aero energy systems need upgrades to be fully sustainable relying solely on renewable energy sources and operating in island mode.

`

Possible solutions for the energy system upgrading encompass electricity generation expansion and electricity storage. In this paper, several different green energy technologies suitable for the conditions of the island have been selected. However, there are remaining questions to be answered in order to find the most feasible solution for a green energy system operation for the island of Aero:

- What is the optimal capacity of the energy system?
- How to optimally operate the energy systems to balance energy production and supply?

The multi-energy systems characterize energy systems on Aero as an energy hub where energy production, storage and usage by end-users are involved. Many studies in the literature apply mathematical optimization to find the optimal design and operation of energy systems.

Pazouki et al. [3] investigated the optimal planning and scheduling of an energy hub consisting of CHP, boiler, wind turbine, and electric and thermal energy storage systems. They formulated a mixed-integer linear programming (MILP) strategy for optimizing the energy hub under different season scenarios and analyzed the functionality of each subsystem in the energy hub in terms of delivering electricity and heat demand. Wang et al. [4] developed the energy hub model consisting of PV, CHP, boiler, HP, battery, and thermal energy storage systems. The proposed MILP optimization achieves a significant reduction of energy cost and CO_2 emissions as compared to the system without optimization. Some other similar works on the mathematical modeling and optimization of multi-energy systems can be found in [5]–[7]. An optimization study was done before for the Danish island of Bornholm, where the energy system was simulated both on an hourly basis and then from second to second [8]. Apart from optimizing energy system operation, some studies also apply mathematical optimization to optimize the capacity of different kinds of production [9]–[11].

The objective of the paper is to achieve self-sufficiency in renewable energy and operate in island mode on Aero by 2025. In this regard, this paper proposed a hybrid scenario devising a roadmap for upgrading the current energy system. The proposed hybrid scenario combines different approaches ranging from the electrification of the transport sector, installing energy storage systems, increasing renewable energy production capacities, energy production planning, to demand-side management. Furthermore, a mathematical optimization model for hour-to-hour balancing energy supply and demand is developed to find the optimal capacities for renewable energy production units and optimal dispatching schedules for various energy systems.

The rest of the paper is structured as follows: Section 2 describes the methodology and formulation of the optimization problem. Section 3 presents and discusses the optimization results for different scenarios. Lastly, the conclusions and contributions of the work are highlighted in Section 4.

2. Methodology and problem formulation

In this section, we present the formulation of the hourly optimization problem for a one-year simulation, which is applied to the energy system on Aero to find the most feasible solution for a green energy system operation by 2025. The mathematical models of the energy system associated with their operational constraints are described first, followed by objective functions for different scenarios and collected data for simulation. The energy system models described below contain both current existing energy systems and perspective energy systems to be installed in the hybrid scenario. The selection of the perspective energy systems relies on the preliminary study carried out in [12].

2.1. Model constraints

Energy balance

The balance between electricity production and demand is constrained in Eq.(1). Likewise, the balance between heating production and demand is constrained in Eq.(2),

$$P_{T,EL}^{t} = D_{T,EL}^{t}\,, \forall t \tag{1}$$

$$P_{T,H}^{t} = D_{T,H}^{t}\,, \forall t \tag{2}$$

2.1.1. Electricity sector

Interconnection to the main grid

The electricity interconnection to the island today has a limited capacity of 100 MW. This constraint only applied to the current energy systems while the future energy systems operating in island mode will not involve the use of the interconnection.

$$-I_C \le I^t \le I_C\,, \forall t \tag{3}$$

Where the value I^t is positive during import, and negative during export.

Wind turbine

$$0 \le P_W^t \le P_{Wmax}^t \cdot F_W\,, \forall t \tag{4}$$

$$1 \le F_W \tag{5}$$

`

Where F_W is the scaling factor of the current wind capacity, allowing optimize wind turbine capacity suitable for the future energy system.

Photovoltaics (PV)

$$0 \leq P_{PV}^t \leq P_{PVmax}^t \cdot F_{PV}\,, \forall t \quad (6)$$

$$1 \leq F_{PV} \quad (7)$$

Where $F_{PV}$is the scaling factor of the current PV capacity, allowing optimize PV capacity.

Organic Rankine cycle (ORC)

The ORC has a certain capacity for heat and power, which are constrained in Eq.(8) and Eq.(9) respectively. Eq.(10) defines the maximum ratio between power and heat production.

$$0 \leq P_{ORCEl}^t \leq P_{ORCElmax}\,, \forall t \quad (8)$$

$$0 \leq P_{ORCH}^t \leq P_{ORCHmax}\,, \forall t \quad (9)$$

$$P_{ORCEl}^t \leq P_{ORCH}^t \cdot ORC\eta_{El/H}\,, \forall t \quad (10)$$

Biogas

Biogas turbine is the potential energy generation system to be installed, which makes use of biomass on Aero to produce electricity. Additionally, this requires installing a biogas plant that converts biomass to biogas first. In Eq.(11), the model is constrained so the model only uses the manure available on the island, and thus emissions in connection with the transport of biomass from outside the island are also avoided.

$$\frac{\sum_{n=1}^{8760} P_{Bio}^t}{\eta_{Bio}} \leq C_{Bio}\,, \forall t \quad (11)$$

$$0 \leq P_{Bio}^t \leq C_{Bio,C}\,, \forall t \quad (12)$$

The space heating, electric water heating and refrigerator described below are demand response unit that integrates consumers into the electricity system.

Space heating

An air-to-water heat pump is used for space heating. Eq.(13) is the model for indoor temperature dynamics, while Eq. (14) represents the constraint of the electric power of the heat pump. Eq. (15) is the indoor temperature constraint.

$$\theta_i^{t+1} = \theta_i^t - \frac{1}{C \cdot R}\left(\theta_i^t - \theta_0^t + R \cdot D_{Sp}^t \cdot COP^t\right), \forall t \quad (13)$$

$$0 \leq D_{Sp}^t \leq D_{Sp,C}\,, \forall t \quad (14)$$

$$\theta_{i,min}^t \leq \theta_i^t \leq \theta_{i,max}^t\,, \forall t \quad (15)$$

Electric water heating

Similarly, Eq.(13) is the model of water temperature in the tank.

$$\theta_{EWH}^{t+1} = \theta^t + \frac{1}{C}(-\alpha(\theta_{EWH}^t - \theta_i^t) - v^t + COP^t \cdot D_{EWH}^t), \forall t \quad (16)$$

$$0 \leq D_{EWH}^t \leq D_{EWH,C}\,, \forall t \quad (17)$$

$$\theta_{EWH,min}^t \leq \theta_{EWH}^t \leq \theta_{EWH,max}^t\,, \forall t \quad (18)$$

Refrigerator

The electricity is used in the refrigerator of each household to main favorable temperatures for food storage. The temperature inside the refrigerator has to satisfy the constraints in Eq.(19) and Eq.(21). The maximum electrical power of the refrigerator is constrained in Eq (20).

$$\theta_{ref}^{t+1} = \epsilon \cdot \theta_{ref}^t + (1-\epsilon)\left(\theta_i^t - R \cdot D_{ref}^t \cdot \eta\right), where\ \epsilon = e^{-\frac{\Delta t}{R \cdot C}},\ \forall t \quad (19)$$

$$0 \leq D_{ref}^t \leq D_{ref,C}\,, \forall t \quad (20)$$

$$\theta_{ref,min}^t \leq \theta_{ref}^t \leq \theta_{ref,max}^t\,, \forall t \quad (21)$$

There is no electricity storage available on Aero currently, the potential electricity storage considered are Li-ion battery, high temperature thermal storage and hydrogen storage. As the constraints are similar for the three storage systems, here only the constraints for Li-ion battery storage are elaborated in detail.

Li-ion battery storage

In a battery, the state of charge (SOC) must be kept consistent with the in- and outputs, which is constrained in Eq.(22). The charge and discharge are constrained in Eq.(25) and Eq.(26) to ensure the battery does not charge or discharge too quickly. In Eq.(23) the SOC is constrained between 0 and the maximum value.

`

Constraint in Eq.(24) is to ensure the SOC at the first hour of the year and last hour of the year is consistent, enabling running the storage for multiple years.

$$SOC_b^{t+1} = SOC_b^t + Ch_b^t - Dis_b^t, \forall t \quad (22)$$

$$0 \leq SOC_b^t \leq SOC_{b,C}, \forall t \quad (23)$$

$$SOC_b^1 = SOC_b^{8760} \quad (24)$$

$$0 \leq Ch_b^t \leq Ch_{b,C}, \forall t \quad (25)$$

$$0 \leq Dis_b^t \leq Dis_{b,C}, \forall t \quad (26)$$

High-temperature thermal storage

High temperature thermal storage (HTTS) belongs to both the electricity and heating sectors. It is charged with electricity, which is used to heat rocks or minerals to very high temperatures, as high as 600 °C. The heat is then used to generate steam, which runs through a turbine to produce electricity and heat.

$$SOC_{HTTS}^{t+1} = SOC_{HTTS}^t + Ch_{HTTS}^t - Dis_{HTTS}^t, \forall t \quad (27)$$

$$0 \leq SOC_{HTTS}^t \leq SOC_{HTTS,C}, \forall t \quad (28)$$

$$SOC_{HTTS}^1 = SOC_{HTTS}^{8760} \quad (29)$$

$$0 \leq Ch_{HTTS}^t \leq Ch_{HTTS,C}, \forall t \quad (30)$$

$$0 \leq Dis_{HTTS}^t \leq Dis_{HTTS,C}, \forall t \quad (31)$$

Hydrogen storage

Hydrogen storage consists of three parts, an electrolyzer, a hydrogen tank and a fuel cell. The surplus electricity production can be stored in the form of hydrogen via electrolyzing water. The stored hydrogen can be used to produce electricity in need through fuel cells.

$$SOC_{Hyd}^{t+1} = SOC_{Hyd}^t + D_{Elec}^t \cdot \eta_{Elec} - D_{FC}^t, \forall t \quad (32)$$

$$0 \leq SOC_{Hyd}^t \leq SOC_{Hyd,C}, \forall t \quad (33)$$

$$0 \leq D_{Elec}^t \leq D_{Elec,C}, \forall t \quad (34)$$

$$0 \leq D_{FC}^t \leq D_{FC,C}, \forall t \quad (35)$$

$$SOC_{Hyd}^1 = SOC_{Hyd}^{8760} \quad (36)$$

$$D_{FC}^t = P_{FC}^t / \eta_{FC}, \forall t \quad (37)$$

2.1.2. Heating sector

On Aero, approximately a third of the households are heated with individual heating, while the rest are heated with district heating.

Solar collector

Solar collectors are very similar to wind turbines and PVs in that they are limited by the solar flux and the installed capacity. However, for solar collectors, the amount of installed capacity cannot be changed, as there are already a lot of solar collectors on Aero.

$$0 \leq P_{SC}^t \leq P_{SC,C}^t, \forall t \quad (38)$$

Straw boiler

$$0 \leq P_{DHB}^t \leq P_{DHB,C}^t, \forall t \quad (39)$$

District heating heat pump

$$0 \leq P_{DHHP}^t \leq P_{DHHP,C}^t, \forall t \quad (40)$$

$$D_{DHHP}^t \cdot COP_{DHHP}^t = P_{DHHP,}^t, \forall t \quad (41)$$

Seasonal heat storage

Aero currently equips a pit thermal storage for seasonal heat storage. The pit storage is a water reservoir and it uses a heat pump to discharge the heat. The maximum state of charge ($SOC_{SS,C}$) of the seasonal heat storage is 6.638 MWh.

$$SOC_{SS}^{t+1} = SOC_{SS}^t + Ch_{SS}^t - Dis_{SS}^t - H_L, \forall t \quad (42)$$

$$0 \leq SOC_{SS}^t \leq SOC_{SS,C}, \forall t \quad (43)$$

$$SOC_{SS}^1 = SOC_{SS}^{8760} \quad (44)$$

`

$$0 \leq Ch_{SS}^{t} \leq Ch_{SS,C}\ , \forall t \quad (45)$$

$$0 \leq Dis_{SS}^{t} \leq Dis_{SS,C}\ , \forall t \quad (46)$$

2.1.3. Transport sector

Passenger electric vehicles and electric buses are not installed in Aero currently, while E-ferry is already running. They all serve as electric batteries with specific charging and discharging patterns.

Passenger electric vehicles

The specific electric car "Renoult Zoe" is used, which has a 53 kWh battery and a 400 km driving distance. All cars are assumed to be in use every morning at 7 am, when people go to work, and ready for charging again from 5 pm when they get home, until the next morning. It is assumed that 20% of cars drive 5 km twice every day and the owners have a charging box at home, with a capacity of 11 kW.

$$SOC_{AllEV}^{t+1} = SOC_{AllEV}^{t} + D_{AllEV}^{t} - Dis_{AllEV}^{t}, \forall t \quad (47)$$

$$0 \leq D_{AllEV}^{t} \leq D_{AllEV,C}\ , \forall t \quad (48)$$

$$0 \leq SOC_{AllEV}^{t} \leq SOC_{AllEV,C}\ , \forall t \quad (49)$$

Buses

Two public buses on Aero run the same route but from mirrored starting points. Each route takes approximately one hour and there is time for the buses to charge for 5 minutes after the completion of each route. The buses can charge completely during the night.

$$SOC_{bus}^{t+1} = SOC_{bus}^{t} + D_{bus}^{t} - Dis_{bus}^{t}, \forall t \quad (50)$$

$$0 \leq D_{bus}^{t} \leq D_{bus,C}\ , \forall t \quad (51)$$

$$0 \leq SOC_{bus}^{t} \leq SOC_{bus,C}\ , \forall t \quad (52)$$

Electric ferry (E-ferry)

The ferry starts at 6 in the morning, makes six round trips per day, and has 32 mins in Aeroskoebing between trips to charge if needed, returning to Aeroskoebing at midnight. The e-ferry has a large battery of 4.3 MWh. The charger in Aeroskoebing has a capacity of 4.2667 MW.

$$SOC_{EF}^{t+1} = SOC_{EF}^{t} + D_{EF}^{t} - Dis_{EF}^{t}, \forall t \quad (53)$$

$$0 \leq D_{EF}^{t} \leq D_{EF,C}\ , \forall t \quad (54)$$

$$0 \leq SOC_{EF}^{t} \leq SOC_{EF,C}\ , \forall t \quad (55)$$

2.2. Objective functions

This section details objective functions for various scenarios investigated in this paper. Overall, the objective functions are the same targeting minimizing the cost, enabling comparison of different scenarios. But they are subject to different constraints in accordance with the considered technologies for a specific scenario.

Business as usual (BAU) scenario

In order to compare the proposed hybrid scenario with the current energy systems on Aero, a business as usual (BAU) scenario was created resembling the current system, which will be the reference scenario for performance evaluation. The objective function of the BAU scenario is to minimize the costs consisting of variable costs, fixed operational costs and investment costs.

$$minimize \sum_{n=1}^{N} (C_V^n \cdot U^n) + \sum_{n=1}^{N} (C_I^n + C_F^n) \cdot C^n$$

$$s.t.\ Eq.(1-4), (6), (8-10), (13-21), (38-46), (53-55)$$

Where *n* denotes different technology, the variable costs (C_V^n) for each technology are multiplied by the use (U^n) of that technology. The fixed operational costs (C_F^n) and investment costs (C_I^n) for each technology are multiplied by the capacity (C^n) of that technology.

Hybrid scenario

As compared to BAU scenario, hybrid scenario has expanded wind turbines and PVs capacity, installed biogas turbines, electrified all buses and personal vehicles, eliminate the use of cable for connection to the mainland grid, added new energy storage systems including Li-ion battery storage, high temperature thermal storage and hydrogen storage. The objective function of hybrid scenario is to minimize the costs as well, which is the same as that of BAU scenario.

`

$$minimize \sum_{n=1}^{N}(C_V^n \cdot U^n) + \sum_{n=1}^{N}(C_I^n + C_F^n) \cdot C^n$$

$$s.t.\ Eq.(1-2),(4-55)$$

Furthermore, extensions of the hybrid scenario were also investigated to see how the system changes under different conditions. Among them, the second ferry, exporting surplus electricity, and PtL technology are investigated.

Hybrid+2Ferry scenario

Currently, Aero has several ferry routes to the mainland and other islands, but there is only one electric ferry available between Soeby and Fynshavn. Therefore, it is interesting to investigate the possibility of replacing more of them with e-ferries. In hybrid+2Ferry scenario, the objective function is still minimizing the costs, subject to the same constraints in hybrid scenario, except that additional constraints for the second ferry are added.

Hybrid+Export scenario

Though Aero aims to operate energy systems in island mode, it is still worth investigating the potential economic benefits of selling surplus renewable electricity production to the mainland grid. In hybrid+Export scenario, the objective function is the same as that of the hybrid scenario, and the constraint for interconnection is included, allowing the export of electricity.

Hybrid+PtL scenario

The hybrid scenario does not consider green fuels for heavy transport since it is not yet the goal for the municipality by 2025. In continuation of this, complete sustainability is the aim for 2030, where elements like heavy transport must be considered through the Power-to-Liquid process. Hybrid+PtL share the same objective function as that of the hybrid scenario, but is subject to additional constraints for jet fuel and methanol production as shown in Eq. (56-63):

$$D_{FT}^t \cdot \eta_{FT} = P_{FT}^t\ ,\ \forall t \tag{56}$$

$$\sum_{t=1}^{T} P_{FT}^t = D_{jet}^{Annual} \tag{57}$$

$$0 \le P_{FT}^t \le P_{FT}^{max},\ \forall t \tag{58}$$

$$0 \le P_{FT}^{max} \tag{59}$$

$$D_{MeOH}^t \cdot \eta_{MeOH} = P_{MeOH}^t,\ \forall t \tag{60}$$

$$\sum_{t=1}^{T} P_{MeOH}^t = D_{MeOH}^{Annual} \tag{61}$$

$$0 \le P_{MeOH}^t \le P_{MeOH}^{max},\ \forall t \tag{62}$$

$$0 \le P_{MeOH}^{max} \tag{63}$$

2.3. Data collection and implementation

To perform optimization, some essential data needs to be collected apart from the data for technology size and operating limitations. These data are outdoor temperature, solar irradiance, wind data profile, the electricity spot price, electricity demand and heating demand. One-year data (in the year 2018) is collected in a resolution of an hour. Note that the hourly electricity demand and heating demand for Aero cannot be found specifically. Hence, the electricity demand was estimated by scaling down the total electricity demand for Denmark to fit the size of Aero, and the heating demand was estimated by scaling down the total heating demand for Odense to fit the size of Aero. Figure 1 illustrates the derived electricity and heating demand.

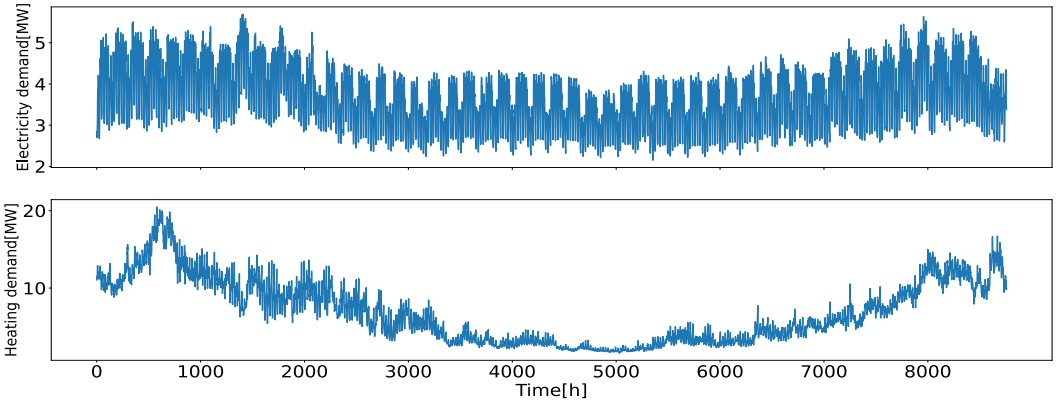

Figure. 1. Electricity and heating demand for Aero.

`

The optimization was implemented in Matlab [13] using the package Yalmip [14], and the optimization problem was solved using “Linprog” solver for linear programming.

The expected outcomes of the optimization are the optimal capacity for existing PV and wind turbine expansion, the optimal capacity of the potential energy units, and the optimal dispatching schedule for each energy system involved.

3. Results and discussions

In this section, the optimization results of different scenarios are presented. Table 1 summarizes the main capacities of different energy systems in the investigated scenarios. As shown in the BAU scenario, the current wind turbine and PV capacities are 12 MW and 1.232 MW, respectively, while their capacities increase in the other four scenarios due to the increasing electricity demand. To better visualize the energy flows from the production side to the storage and end-user side, the corresponding Sankey diagram for each scenario is provided and discussed.

Table 1. Capacity overview of different scenarios

Capacity	Unit	BAU	Hybrid	Hybrid+2Ferry	Hybrid+Export	Hybrid+PtL
Interconnection (Import/Export)	[MWh]	11273/16305	/	/	Export: 519814.8	/
Wind capacity	[MW]	12	15.8	18.7	153.2	37.1
Wind production	[MWh]	38499	28568.4	30771.1	386351.0	115051.1
PV capacity	[MW]	1.232	15.4	18.9	164.0	34.7
PV production	[MWh]	1642.9	13813.4	16228.6	178797.1	39673.5
Li-ion capacity	[MWh]	/	4.4	5.6	0.28	0.20
HTTS capacity	[MWh]	/	0	0	0	0
Hydrogen capacity	[MWh]	/	0	0.45	0	0
Biogas turbine	[MW]	/	3.9	4.1	4.3	4.5
Jet fuel production capacity	[MW]	/	/	/	/	2.22
Methanol Production capacity	[MW]	/	/	/	/	5.99

3.1. BAU scenario

As shown in Figure 2, the current energy systems in Aero consume a large amount of fossil fuels for personal vehicles and household heating. The heating sector in Aero consists of around 1/3 individual heating and 2/3 district heating. The straw boiler, solar collector, ORC unit and seasonal storage supply a lot of district heating. District heating is close to using 100% renewable energy sources, depending on whether the electricity consumed in the heat pump comes from renewable energy sources or the mainland grid.

In BAU scenario, the importing and exporting of electricity happen frequently throughout the year to secure an hour-to-hour balancing of electricity demand and production. The total exporting electricity is higher than the total importing electricity, indicating there are many situations of having excess renewable electricity production, which necessity electricity storage for flexibility.

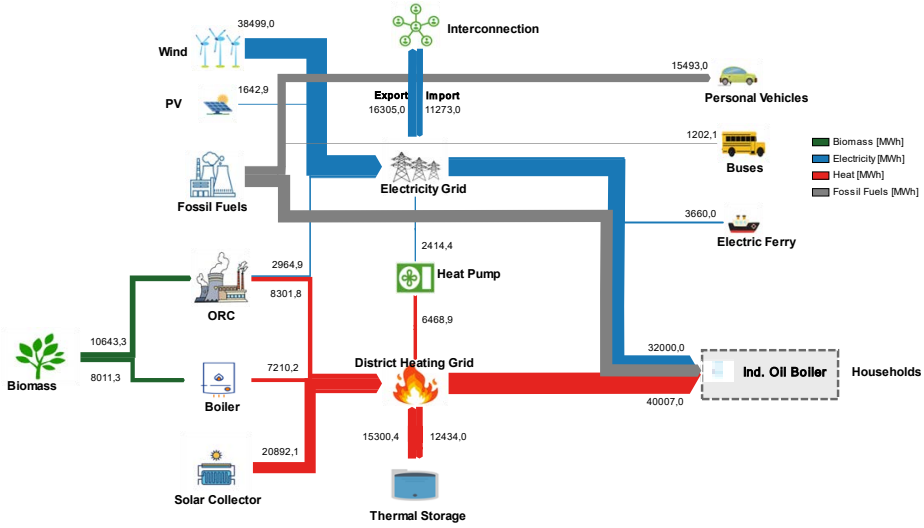

Figure. 2. Energy flows in BAU scenario.

`

3.2. Hybrid scenario

Figure 2 illustrates the energy flow in hybrid scenario. As compared to BAU scenario, the interconnection is no longer available in hybrid scenario. The wind turbine capacity increases slightly, while the PV capacity increases more than 10 times. Hybrid scenario recommends installing a biogas turbine with a capacity of 3.9 MW. Concerning storage, a 4.4 MW Li-ion battery is included while the HTTS and hydrogen storage are not used. To run primarily on RES and storage, a very large amount of storage is needed for long periods when production is needed. However, this can be done far more easily with controllable production, in this case, the biogas turbine. This is far better since the storage of biogas or manure is far easier than storing hydrogen or electricity in a battery.

The demand for vehicles and individual heating is lower in hybrid scenario than that of BAU scenario. This is because the efficiencies of combustion engines and boilers used in BAU scenario are much lower than electric motors and heat pumps used in hybrid scenario, resulting in larger fuel demand.

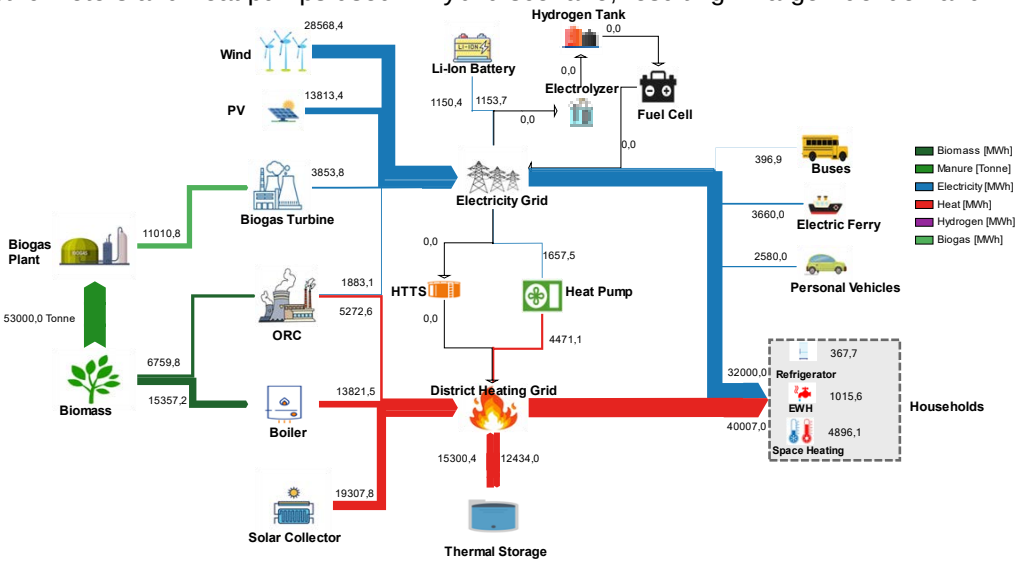

Figure. 3. Energy flows in hybrid scenario.

3.3. Hybrid+2Ferry scenario

The energy flow in the scenario with an additional e-ferry is seen in Figure 4, and the capacities can be seen in Table 1. The new ferry requires some extra electricity demand, leading to an increase in the capacity and production from renewable energy sources (RES) as compared to hybrid scenario. Furthermore, this increased demand also means that more long-term storage is suddenly needed, which means that hydrogen storage is included in a small capacity (0.45MWh). It is the only scenario that hydrogen storage is used among the investigated five scenarios and the Li-ion storage capacity also increases slightly compared to hybrid scenario. The barely used hydrogen storage in most scenarios is due to the high investment and operational cost, which is economically cost-ineffective.

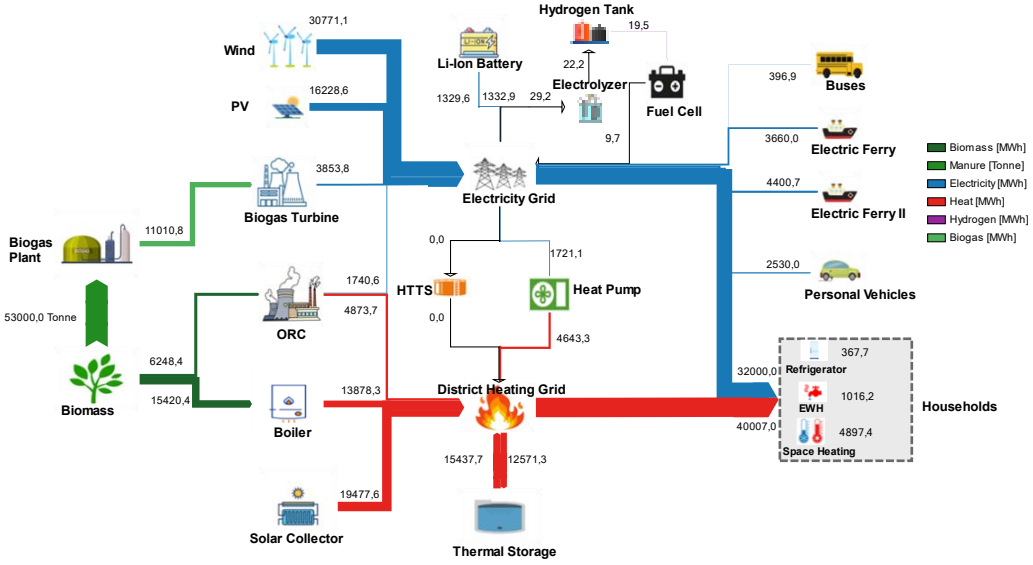

Figure. 4. Energy flows in hybrid+2Ferry scenario.

`

3.4. Hybrid+Export scenario

It is clear from Table 1 and Figure 5 that allowing exporting surplus electricity changes the system significantly, and that making money from selling excess production to the grid is very much possible for most of the hours of the year. The RES capacities can be extremely high because production can be exported, and they can cover most of the demand. However there are still hours without wind or sun, therefore the battery, ORC unit and biogas turbine are necessary. The battery storage is used less than in other scenarios as the system prioritizes selling the surplus electricity for profits, resulting in a very small battery capacity (0.28MWh).

Hybrid+export scenario seems good as it benefits from selling electricity, but the model is based on current electricity prices. In the future, there will be an increasing amount of RES in the Danish system, which will most likely decrease the possibilities for profits from selling it. Furthermore, Aero is a small island with attractive nature and vacation homes, which creates a lot of resistance to building objects that damage the view, it is, therefore, infeasible to build that much wind turbine and PV capacity.

The hybrid+Export does not comply with the goal of island mode operation on Aero by 2025. But in the case that the demand on the island is met and there is still potential to produce a lot of green electricity, it would be ideal to export this electricity. In this way, the national main grid will benefit from the green electricity that would otherwise have been lost.

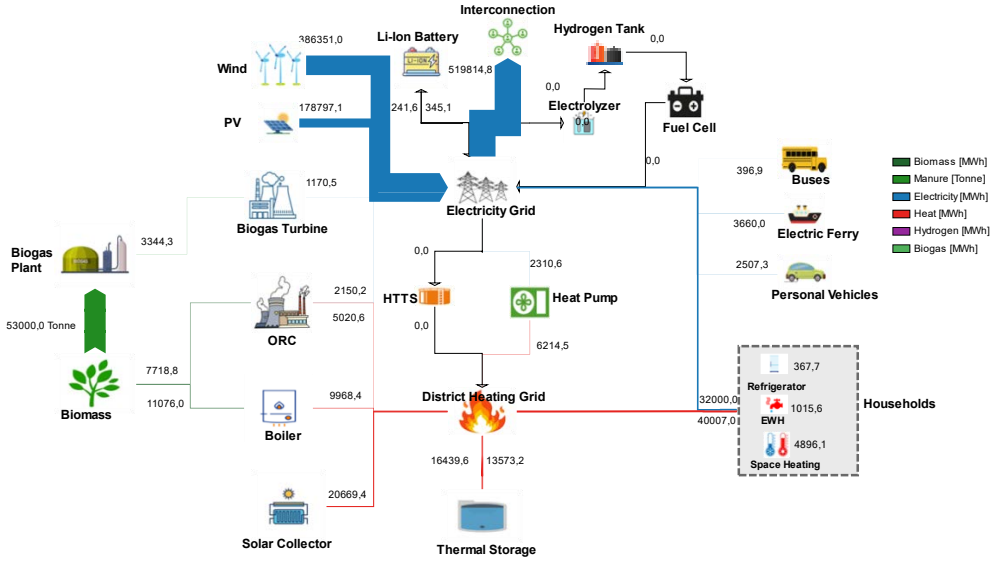

Figure. 5. Energy flows in hybrid+Export scenario.

3.5. Hybrid+PtL scenario

As shown in Figure 6 and Table 1, involving Power to Liquid in the system changes the system considerably as compared to hybrid scenario, though the changes are not as significant as hybrid+Export scenario. Since the efficiency of PtL process is low, the demand for electricity increases substantially. The RES production needs to fit the high demand. Therefore, a huge capacity of RES is needed in this scenario.

Hybrid+PtL scenario has no HTTS, no hydrogen storage, and a small Li-ion battery storage (0.2MWh), indicating the RES capacities in this scenario are almost fully utilized by end-users. This is because the PtL can almost always use the produced electricity. The PtL capacities are also relatively large. The results show that the PtL is not only an extra demand but is very useful for balancing the system.

3.6. Techno-economic evaluations

To quantitatively evaluate the technical feasibility and economic benefits of each scenario before real implementation in practice, the two key performance indicators (KPIs) are calculated and presented in Table 2. The metric of renewability is defined in Eq. (64), which reflects the share of renewable energy production over the total energy input for the island. It is assumed that the imported electricity is 100% based on fossil fuels. For Hybrid, Hybrid+2Ferry, Hybrid+Export, and Hybrid+PtL scenarios, the term "$I_{Imp} + P_{fossil}$" is zero, resulting in 100% renewability. However, only 55.77% of energy demand is supplied by renewable energy sources for the BAU scenario, which justifies applying a hybrid scenario to realize self-sufficiency in renewable energy.

$$Renewability\ \% \ = \ 1 - \frac{I_{Imp}+P_{Fossil}}{I_{Imp}+P_{Fossil}+P_{Wind}+P_{Bio}+P_{PV}+P_{ORCel}+P_{ORCheat}+P_{Boiler}+P_{SC}} \quad (64)$$

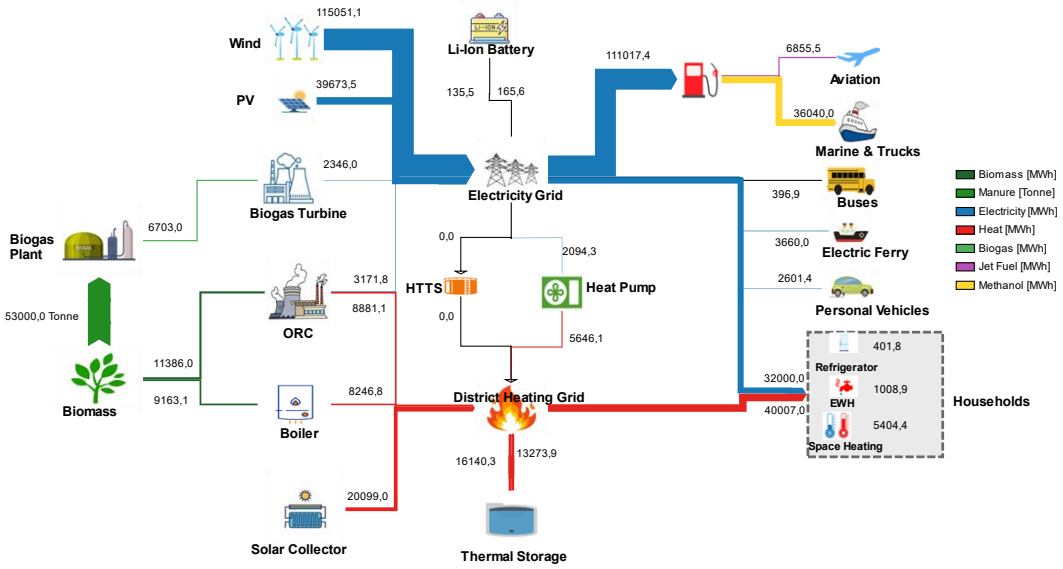

Figure. 6. Energy flows in hybrid+PtL scenario.

The total cost is calculated based on the annualized investment costs considering its lifetime, variable costs, and fixed operational costs. Then, the individual cost [DKK/month/person] is calculated and presented in the table, corresponding to what each citizen on Aero must pay to run the system.

As shown in Table 2, the lowest cost is achieved in the hybrid scenario, while hybrid+PtL exhibits the highest cost due to the expensive Power-to-Liquid unit. Therefore, the hybrid scenario is the final recommended scenario for the energy system upgrade roadmap for Aero by 2025 considering both technical feasibility and economic benefits.

Figure 7 shows the cost breakdown for each system. It can be seen that infrastructure cost accounts for the major part of total cost in all investigated scenarios except for the hybrid+Export scenario, where cost by renewable energy production predominates. This is because hybrid+Export scenario encourages selling electricity to the mainland grid for earnings, resulting in higher RES production and high cost for RES facility expansion. Note that infrastructure is an aggregate item consisting of several elements such as expenses for electric vehicles, buses, ferry, individual heating, and demand response units.

The results show that installing an additional ferry is the most beneficial approach to improve the hybrid scenario's performance among hybrid+2Ferry, hybrid+Export, and Hybrid+PtL scenarios. Even though hybrid+Export results in less cost, it is not advised as it violates the goal of island mode operation.

Table 2. Summary of the KPIs for different scenarios

KPIs	Unit	BAU	Hybrid	Hybrid+2Ferry	Hybrid+Export	Hybrid+PtL
Renewability	[%]	55.77	100	100	100	100
Cost	[DKK/month/person]	1689.6	1625.9	2035.6	1680.3	2430.3

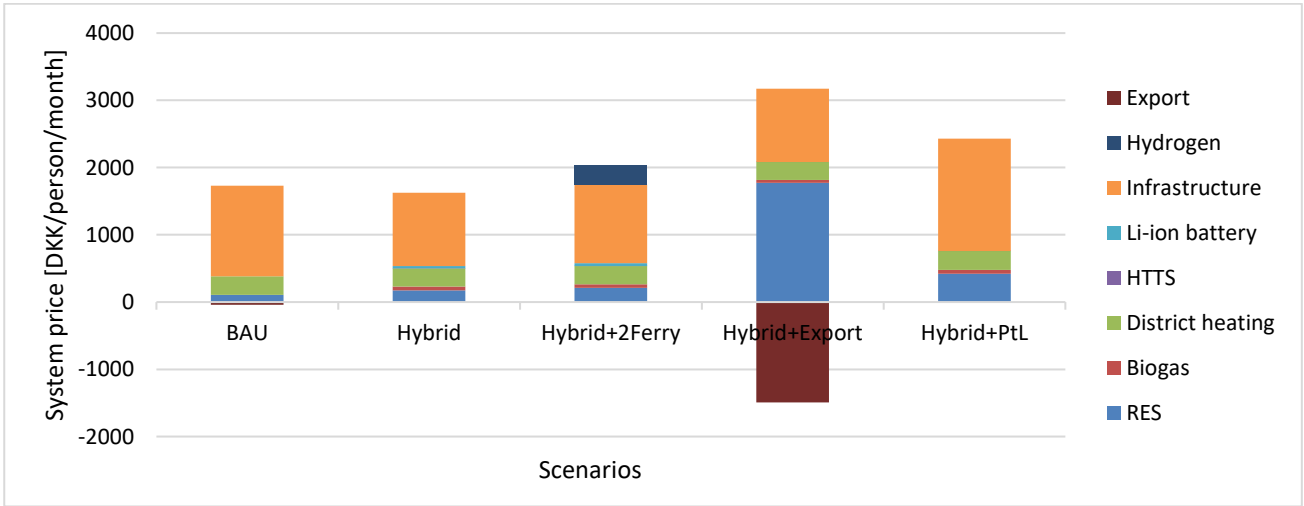

Figure. 7. Cost breakdown for all scenarios

`

4. Conclusion

This paper aims to find a feasible solution for a Danish island Aero to be fully sustainable relying solely on renewable energy sources and operating in island mode by 2025. To that end, a hybrid scenario, as a combination of different technologies including electrification of the transport sector, installing energy storage systems, expanding renewable energy production capacities, energy production planning, and demand-side management, is proposed. A linear programming optimization problem is formulated in accordance with the hybrid scenario to optimize the energy system capacity and energy system operation.

The proposed hybrid scenario performance is analysed and compared to a business-as-usual (BAU) scenario, where the energy system remains unchanged but the energy system operation is optimized. A techno-economic approach is used to quantitatively evaluate the system's performance in terms of renewability and costs. The hybrid scenario yields 100% renewability and 1625.9 DKK/month/person, while the BAU scenario achieves 55.77% renewability with a higher cost of 1689.6 DKK/month/person. Thus, the established hybrid scenario should be seen as an achievable green energy system for the island in 2025, with various options for development. Among them, extensions of the hybrid scenario by including the second ferry, exporting excess electricity, and installing Power-to-Liquid units are investigated and compared, the results show that including the second ferry is the most beneficial approach to improve the hybrid scenario's performance, with a cost of 2035.6 DKK/month/person.

Acknowledgments

This work is financed by Interreg North Sea Region (European Regional Development Fund) of EU through the Zero Emission Ports North Sea (ZEM Ports NS) project.

Nomenclature

P	energy production, MW
D	energy demand, MW
I	interconnection to the main grid, MW
F	scaling factor, -
SOC	state of charge, -
COP	coefficient of performance, -
ORC	the Organic Rankine Cycle unit
C	thermal capacitance, J/K
R	thermal resistance, K/W
v	hot water consumption, MW
Ch	charge power, MW
Dis	discharge power, MW

Greek symbols

η	efficiency, -
θ	temperature, °C

Subscripts and superscripts

t	number of hours during a year
i	indoor air
W	wind turbine
C	maximum capacity
PV	photovoltaics
Sp	space heating
EWH	electric water heating
ref	refrigerator

`

$ORCEL$	electricity output of the Organic Rankine Cycle
$ORCH$	heat output of the Organic Rankine Cycle
Bio	biogas turbine
b	li-ion battery
$HTTS$	high temperature thermal storage
Hyd	hydrogen storage
FC	fuel cell
$Elec$	electricity demand of the electrolyzer
SC	solar collector
DHB	district heating straw boiler
$DHHP$	district heating heat pump
SS	seasonal heat storage
EF	electric ferry

References

[1] "World Energy Outlook 2021 – Analysis - IEA." [Online]. Available: https://www.iea.org/reports/world-energy-outlook-2021. [Accessed: 28-Dec-2021].

[2] "Energi-, Forsynings- og Klimaudvalget - 01-09-2016 : Energi-, Forsynings- og Klimaudvalget besøger Ærø / Folketinget." [Online]. Available: https://www.ft.dk/udvalg/tidligere-udvalg/efk/rejser/26987/index.htm. [Accessed: 26-Mar-2023].

[3] S. Pazouki and M. R. Haghifam, "Optimal planning and scheduling of energy hub in presence of wind, storage and demand response under uncertainty," *International Journal of Electrical Power & Energy Systems*, vol. 80, pp. 219–239, Sep. 2016.

[4] H. Wang, H. Zhang, C. Gu, and F. Li, "Optimal design and operation of CHPs and energy hub with multi objectives for a local energy system," in *Energy Procedia*, 2017, vol. 142, pp. 1615–1621.

[5] Z. Hashemi, A. Ramezani, and M. P. Moghaddam, "Energy hub management by using decentralized robust model predictive control," *2016 4th International Conference on Control, Instrumentation, and Automation, ICCIA 2016*, pp. 105–110, Jun. 2016.

[6] M. Arnold, R. R. Negenborn, G. Andersson, and B. De Schutter, "Model-based predictive control applied to multi-carrier energy systems," *2009 IEEE Power and Energy Society General Meeting, PES '09*, 2009.

[7] J. F. Marquant, R. Evins, and J. Carmeliet, "Reducing Computation Time with a Rolling Horizon Approach Applied to a MILP Formulation of Multiple Urban Energy Hub System," *Procedia Computer Science*, vol. 51, no. 1, pp. 2137–2146, Jan. 2015.

[8] J. R. Pillai, K. Heussen, and P. A. Østergaard, "Comparative analysis of hourly and dynamic power balancing models for validating future energy scenarios," *Energy*, vol. 36, no. 5, pp. 3233–3243, May 2011.

[9] B. Zakeri, S. Syri, and S. Rinne, "Higher renewable energy integration into the existing energy system of Finland – Is there any maximum limit?," *Energy*, vol. 92, no. Part 3, pp. 244–259, Dec. 2015.

[10] M. G. Rasmussen, G. B. Andresen, and M. Greiner, "Storage and balancing synergies in a fully or highly renewable pan-European power system," *Energy Policy*, vol. 51, pp. 642–651, Dec. 2012.

[11] R. Jing *et al.*, "Balancing the Energy Trilemma in energy system planning of coastal cities," *Applied Energy*, vol. 283, p. 116222, Feb. 2021.

[12] Benjamin B. L. Larsen, Vinusan Jeyarajah. A Techno-Economic Modeling & Optimization of an Energy System Operation Towards a Renewable Island Power System for Aero in 2023 [Master thesis]. Odense, Denmark: University of Southern Denmark, 2021.

[13] T. M. Inc., "MATLAB version: 9.13.0 (R2022b)." The MathWorks Inc., Natick, Massachusetts, United States, 2022.

[14] J. Löfberg, "YALMIP: A toolbox for modeling and optimization in MATLAB," *Proceedings of the IEEE International Symposium on Computer-Aided Control System Design*, pp. 284–289, 2004.

Modelling financing schemes for energy system planning: a mini-grid case study

Giacomo Crevani[a], Castro Soares[b], Emanuela Colombo[c]

[a] Politecnico di Milano, Department of Energy, Milan, Italy, giacomo.crevani@polimi.it (CA)
[b] Fundo de Energia (FUNAE), Maputo, Mozambique,
Politecnico di Milano, Department of Energy, Milan, Italy, castro.soares@polimi.it
[c] Politecnico di Milano, Department of Energy, Milan, Italy, emanuela.colombo@polimi.it

Abstract:
Energy modeling has been playing a crucial role in defining solutions for effective energy planning. Bottom-up energy system planning models, namely those models characterized by high technological detail, typically present exogenous techno-economic parameters which rely on data gathered by the user, from specific costs to efficiencies. However, poor to no attention has been given to the date to the financial parameters of energy models, which are often assumed and barely justified (e.g., “discount rate equal to 10%”, full stop). Still, model outputs are drastically sensitive to variations of finance-related parameters and must provide the financing structure that a decision-maker should implement for funding the advised energy planning strategies. This results particularly crucial for mini-grid sizing in sub-Saharan African countries, where the challenge of the energy transition entails the construction of massive new capacities to improve energy access rates and tiers of service, demanding an enhanced collaboration between private and public sectors. The case study, applied on an off-grid mini-grid in Mozambique, proposes a comparison between scenarios with increasing financial detail and a possible conceptualization of the hard link between detailed financial modelling and a bottom-up energy model for mini-grid optimization. Different financing schemes are modelled and their impact on the energy modelling outputs assessed. Project finance hence emerges as a useful approach that could upgrade the financing structure of domestic power projects in African countries. This may lead to many benefits: more sustainable and affordable interest rates where corporate finance is missing, improved risk management, diversified funding mix, and facilitated financial support from international institutions.

Keywords:
Mini grid; energy planning; financing schemes; access to energy; Mozambique; project finance.

1. Introduction

The electrification of rural areas in developing countries is a critical challenge for achieving sustainable development goal 7 (SDG7) of United Nations’ Agenda 2030 [1], aimed to assure access to electricity and to clean fuels and technologies for all by 2030. Despite the significant progress that has been made in recent years, with global access to electricity rising from 83% in 2010 to 91% in 2020, still the 80% of world’s people without access to electricity lived in rural areas in 2020 [2]. This results in limiting the ability to develop local economies and reducing their chances of improving living standards. On the one hand, new technological solutions for decentralized generation such as mini-grids are increasing their viability for last-mile electrification [3], providing high standards of service for densely populated rural areas [4]. The use of such solutions grew significantly between 2010 and 2019: the number of people with access to decentralized solutions, including solar home systems and mini-grids, more than tripled, rising from 12 million in 2010 to 39 million in 2019 [2]. Alongside this, a large community of energy modellers specifically focused on the optimal sizing of decentralized solutions has raised in the last decade, bringing to several models and approaches for their effective planning [5,6]. On the other hand, new business models [7] and financing schemes [8] are emerging, evidencing the need of private sector involvement for fostering off-grid electrification. According to several scholars [5,9] and international organisations [10–12], the profitability and the attractiveness of investment in mini-grid solutions still remains one of the key barriers for their definitive market upscaling in developing countries, characterised by limited resource, governance and infrastructure. Moreover, as sub-section 1.3 will detail, there is an increasing interest, both at academic research and at international institutions levels, to understand to which extent assumptions on financial parameters affect the ouput of energy modelling scenarios. In fact, these parameters are crucial to provide the financing structure that a public or private decision-maker should implement for funding the advised energy planning strategies.

This paper proposes a modelling exercise able to test the suitability of different financing structures for triggering virtuous financing markets for mini grids in Mozambique. The methodology adopted will advance a possible conceptualization of the hard link between financing structures and a bottom-up energy model for

mini-grid sizing, thus assessing the impact of financial parameters on the energy modelling outputs. The first introductory sub-sections of the work have the scope of framing the problem of mini-grid financing in relation to mini-grid sizing. First, the state-of-art of mini-grid financing in Africa is briefly investigated, providing references and a non-exhaustive overview of the trends of the sector. Existing financing structures are hence introduced into the discussion. Second, sub-section 1.2 is devoted to summarising the state-of-art of energy modelling for mini-grid sizing in African contexts. The research gap is then identified in sub-section 1.3, where claims from recent literature are reported to push for the increase of financial detail in energy modelling research. The rest of the paper is structured as follows: section 2 details the modelling methodology adopted, inclusive of energy and financial modelling; section 3 draws the case study of Ndoro village in the Caia district of Sofala Province Mozambique; results are then discussed critically in section 4; finally; section 5 concludes the work providing outlooks derived from the exercise.

1.1. Financing mini grids in Africa

Even though mini-grids already represent a least-cost option for delivering high tiers of energy services in many contexts [4], the existing mini-grid sector in sub-Saharan Africa (SSA) is characterized by early-stage market fragmentation, lack of competition, high transaction costs, perceived investment risks, and high cost of capital. According to a market report by the Mini-grids Partnership [13], in 2020 a total of 5544 mini-grid projects have been mapped as installed and operative among Asia (60% of the total), SSA (39%), Island nations (1%) and Latin America (0.4%). Of these, more than 60% were powered by solar or solar-hybrid energy, the 21% exclusively by hydropower, the 11% by fossil-fuels and the remaining by biomass, wind, or other energy sources. Despite the very reduced current market, the suitability of mini-grid solutions towards universal access to electricity has been reproved by the International Energy Agency (IEA) in the Sustainable Africa Scenario (SAS) of the last Africa Energy Outlook [11]. In this scenario, aimed to give access to electricity to 90 million people in Africa each year on average from 2022 to 2030, the 32% of the new connections are established via renewable mini-grids and the 21% via renewable stand-alone systems. The Outlook shows how mini-grid systems could constitute a profitable business for small private companies in small and isolated communities, which would remain out of electrification policies planned by the national grid operators. However, according to Williams et al. [9], there are three main financial challenges for their definitive market upscaling: revenue insecurity, due to the capital-intensive nature of electrification investments and to the associated high costs of unincentivized energy tariffs, unaffordability to consumers, related to the spread inability to pay, and reduced access to finance, due to the poor local investment climate mostly associated to perceived risks.

The immaturity of the mini-grid market in Africa is reflected by the typical structure of financing of these systems. Traditional financing of power projects, including plans for off-grid electrification, usually sees the participation of the national government, through its national energy ministry or agency, as the major funder. The main source of the investment usually comes from the governmental development budget or from aided borrowing by multilateral and bilateral development agencies. In the current situation, the participation of the private sector is therefore very limited: it is involved at the stages of construction and first running of the power plant, but the property (and the associated risk of investment) is still owned by a national public utility, in most of the cases. In general, two types of financing can be employed in the mini-grid market for structuring a new investment:

Table 1. Types of financing in the African mini-grid market.

Type of financing	Description
Debt	Debt financing consists in the mini-grid developer borrowing capital from lenders such as banks, privates, or other financial institutions to fund the project. Debt must then be repaid at an agreed cost, called return on debt or interest rate, and within a certain time horizon, called maturity of debt. Debt repayment is generally independent from the performance and prioritary to equity repayment. As Smith summarises in his book [14], debt lenders that currently invest in African countries markets can be grouped into: private commercial lenders (domestic or international), foreign countries, African state-owned firms, multilateral commercial banks, and export-import banks. However, debt financing remains widely untapped in the mini-grid market due to its low attractiveness and bankability. As a result, rates of return on debt are still high: locally sourced debt often reaches interest rates up to 20% in SSA [9], but for the mini-grid market this figure can increase up to 30% for countries such as Sudan and Somalia [15].

Equity	Financing by equity means that the mini-grid developer invests his own capital available (i.e., the residual cash flows from existing assets) into a new asset, namely the mini-grid infrastructure. Equity can also be supported by project promoters such as local banks who, in case of attractive projects, can enter the investment as shareholders. Equity is therefore derived from the company's shareholders' capital, which will be repayed according to a rate of return on investment called return on equity. Apart from private capitals, equity investors in mini-grids market in developing countries are mainly development finance institutions (DFIs) and impact investors [13]. It is worth mentioning that the return on private equity is usually high since it embeds several upfront uncertainties on the success of the investment, especially for high-risk projects such as mini grids in developing countries. For this reason, it is usually supported in blended finance with grants.

Grant financing can support both equity and debt. Donors (international institutions, regional development banks, governments through national cooperation agencies, private foundations, etc.) provide grants in highly concessional forms, meaning to null (donation) or negligible rate of return. This is the most common type of funding for the mini-grid sector in SSA and can subsidize the investment in various ways: reducing the upfront capital requirements, ensuring revenues and limiting their volatility, and reducing the interest owned to the debt provider [16], in case of blended commercial lending. Currently, two types of grants are adopted in mini-grid financing structures [13]: upfront grants (usually blended with equity from the developer or shareholders) and result-based financing grants (a type of public-private partnership including a commercial lender as third party between a public institution and private developer).

Finally, it is relevant to highlight that the technical solution chosen for a local electrification plan strongly influences the cost of capital and the possible financing structure. As Agutu et al. [15] argued, mini grid solutions represent a infrastructure-based system and imply a high initial investment. Their strong dependence on the local regulatory framework and on the political setting of the country makes them perceived as riskier with respect to stand-alone systems, thus requiring longer maturities and higher return rates and costs of capitals. Moreover, the specific components that constitute a mini grid system (i.e., PV panels, diesel generators, battery banks, hydropower turbines, wind turbines, etc.) have very diverse cost structures [17]: renewable energy technologies imply high initial investment cost, whereas fossil fuels-powered technologies will have greater operation and maintenance costs. As this study will reprove, the least-cost sizing of the mini-grid is relevantly affected by the cost structure of its components and especially by how the associated investment and operating costs will be paid back (i.e., by the financing structure chosen).

1.2. Energy modelling for off-grid planning

Energy modelling has proved, over the last 20 years, to be growing in relevance on providing evidence based and scientifically solid insights for energy strategy formulation [18]. Thanks to energy modelling it is possible to develop energy scenarios, assess the potential impact of the penetration of technologies in the market and identify optimal strategies to achieve energy related goals. However, as Debnath et al. highlighted in 2018 [19], the entirety of the existing energy system models originated in developed countries, and for this reason, some key issues that affect the developing world's energy systems are not considered in such models. Among such issues, the author's identifies lack of reliable data, and the issue of access to energy, urging for more attention dedicated to modelling suppressed demand and the socio-political feedbacks of developing countries.

Especially when it comes to mini-grid sizing and off-grid energy planning, a more specific set of challenges exists [5], the main reason for that being that off-grid energy system are not purely a technological challenge, but above all a social challenge, as the main goal of developing off-grid systems for access to energy is to trigger local development [20], which is complex phenomenon to include into modelling frameworks [21]. A set of specific models has been developed along the years for supporting off-grid energy planning [22], and can be classified into two categories: i) Off-Grid Strategy Selection Models, and ii) Off-Grid System Sizing Models. As for the second category of models, Akbas et al. [22] categorise them into models aiming to provide: optimal system configuration and unit sizing, optimal power dispatch strategy, and optimal network design. The present study specifically addresses the first two issues, involving the selection of types of energy resources and least-cost sizing of mini grid system components, which become crucial when considering costs and impacts of a project for rural electrification. Optimal power dispatch will come together with system configuration since the optimization will be run on the hourly availability of resources.

1.3. Research gap and article's scope

Recent literature has been highlighting how energy models must be tailored to the african specific context [19,23], specifically highlighting the diffused disregard of the cost of capitals for financing energy access

options in the energy modelling discipline [5,15,24,25]. This absence brings to a general neglection of the impacts of financial parameters on the outputs of energy modelling exercises and eventually devaluates the research evidence that may outcome to support policy and decision makers. A contribution by Lonergan et al. [26] critically reviewed how the cost of capital is accounted in existing energy system models and found that, even though most existing models still rely on own assumptions and on expert elicitation for selecting an exogenous cost of capital, the literature trend is directing towards academic reference values, project data and financial data. This encouraging trend suggests that the energy modelling community is becoming more and more aware of the impact of the cost of capital to the model results. The International Energy Agency (IEA) is also moving in this sense: a "cost of capital observatory"[1] has been launched in 2022 to collect and update data on the cost of capital of renewable energy projects, with a specific focus on some developing countries. This work has the scope of complementing the existing literature providing a simple approach to expand the hard link between energy and financial modelling on the local scale. A new hybrid modelling methodology is hence proposed to reflect the financing structures of a mini grid investment.

2. Modelling methodology

2.1. Financial modelling approach

The financial modelling approach adopted in this work introduces some essential features of financial analysis for pushing beyond the traditional approach present in energy modelling. The modelling of the cost of capital is here presented to substitute the discount rate with the Weighted Average Cost of Capital (WACC). From this parameter, scenarios on the financing structures of the investments are produced.

2.1.1 Weighted Average Cost of Capital (WACC) and Leverage (L)

This parameter represents the cost of capital invested in the project averaged on its financing structure and can be intended as the minimum return over which the investment becomes profitable, given a certain structure. It must hence be minimized as much as possible. It is here defined as in Steffen [27] formulation:

$$WACC = R_D * (1 - t) * \frac{D}{D+E} + R_E * \frac{E}{D+E} \quad (1)$$

Where the following definitions and units of measure hold:

D	Total level of debt	[kUSD]
E	Total level of equity	[kUSD]
R_D	Cost of debt (i.e., the interest rate)	[-]
R_E	Cost of equity (i.e., the return required by the equity shareholders)	[-]
t	Corporate tax deduction (debt is assumed as tax deducible)	[-]

Two complementary definitions follow in Eq. (2) and Eq. (3). To this work, the total asset value of the investment is defined as the sum of debt and equity invested in the project:

$$V = D + E \quad (2)$$

An additional parameter to be introduced is the Leverage ratio, also known as the debt-to-equity ratio. This parameter gives a proxy of the risk perceived by investors, or viceversa as the attractiveness of the investment to external debtors.

$$L = D/E \quad (3)$$

The Leverage ratio varies between 0 (the project is fully financed by equity) and +∞ (the project is fully financed by debt). According to the definitions provided in Eq. (2) and Eq. (3), Eq. (1) can be reformulated as a function of the Leverage ratio, thus bringing to Eq. (4):

$$\begin{cases} \frac{D}{D+E} = \frac{1}{1+\frac{E}{D}} = \frac{1}{1+\frac{1}{L}} = \frac{L}{1+L} \\ \frac{E}{D+E} = \frac{1}{1+\frac{D}{E}} = \frac{1}{1+L} \end{cases}$$

[1] https://www.iea.org/data-and-statistics/data-tools/cost-of-capital-observatory

$$WACC = R_D * (1-t) * \frac{L}{1+L} + R_E * \frac{1}{1+L} \quad (4)$$

$$WACC = f(L)$$

Eq. (4) represents the Weighted Average Cost of Capital as a function of the Leverage ratio (or debt-to-equity ratio), varying between 0 and 1. This explicit formulation allows to represent R_D, R_E and t as parameters, while L will be kept as the only variable of the financial model. It is worth noticing that being the leverage L in a [0; +∞) domain, WACC varies depending on the parameters above mentioned, and can be qualitatively depicted as in **Figure 1**.

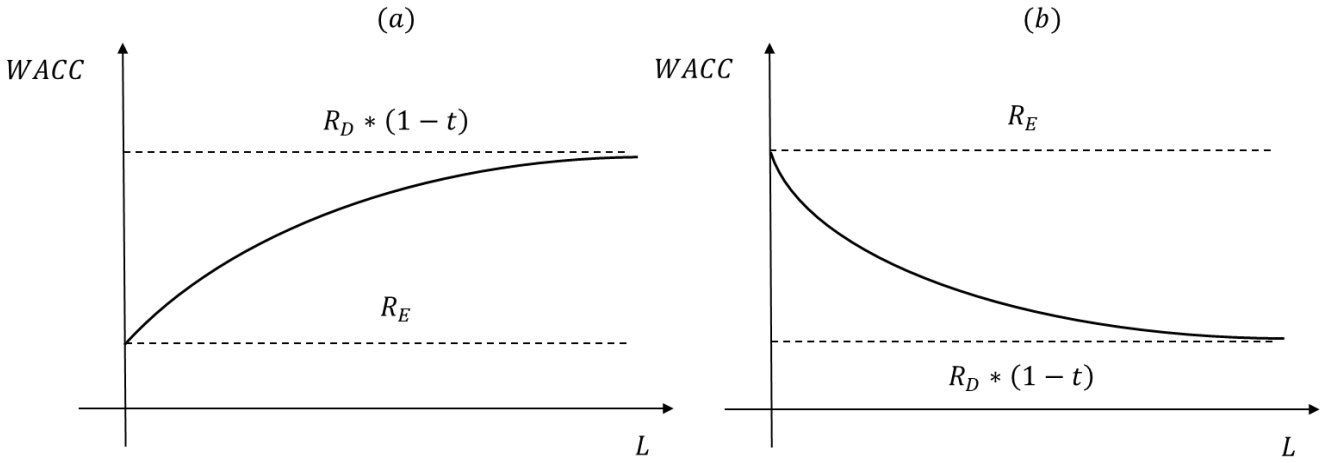

Figure 1. WACC as function of the leverage, for different values of return on equity and return on debt. In (a), the return on debt discounted of taxes is higher than the return on equity, and the WACC. The opposite works for (b).

In general, the higher the equity E is invested in a project, the less risk is perceived by new lenders and the more the cost of borrowing external capitals can reduce over the time, pushing for an increase of D. Consequently, as the above graphs reflect, the WACC can be minimized by:

(a) maximizing the level of equity E (i.e., minimizing L) in the case that the rate of return on debt (R_D) discounted of taxes (t) results greater than the rate of return on equity (R_E); or
(b) maximizing the level of debt D (i.e., maximizing L) in the case that the rate of return on equity (R_E) results greater than the rate of return on debt (R_D) discounted of taxes (t).

In the case of this study, the WACC will be minimized according to the scenario of interest, referring to configuration (a) or (b). Finally, it is worth mentioning that the figures of R_D and R_E strongly depend on the financing structure adopted for the project. As will be advanced in the following sections, a structure built with a project finance approach can help in maximizing the leverage while keeping the return on debt low, if the solidity of future cash flows is assumed [28].

2.1.2 Scenario setting

Three scenarios are here considered, stemming from the ones proposed by Agutu et al. [15]. As already mentioned, the leverage is generally high in SSA power projects, but the return rates on debt are still high, thus bringing to high costs of capital if borrowed through debt. The scenario setting must hence start from the consideration that, in the current mini grid sector in SSA, the most common condition is represented by the rate of return on debt (R_D) discounted of taxes (t) resulting greater than the rate of return on equity (R_E).

The first scenario represents a common *status-quo* situation for the mini grid sector, in which the whole costs are assumed to be covered by public funded equity (i.e., granted at very low rate of return). However, this situation hinders the participation of private lenders or shareholders and does not therefore contribute to develop the sector market, for the reasons already mentioned. For this, a second scenario is introduced, called *increasing private participation* scenario. In this scenario, the shifting from a 20% to a 100% debt-financed mini grid is represented, while keeping the rates of return fixed to the current condition. Finally, the third scenario foresees a *public intervention* in which the regulator intervenes to substantially increase the corporate tax discount (t) and to produce a rate of return on debt (R_D) discounted of taxes (t) lower than the return on equity (R_E). Sensitivity analyses, corresponding to different financing structures, will be performed to understand the impact of these parameters on the modelling outputs.

2.1.3 Assumptions

It is worth mentioning that the financial modelling approach above introduced entails two main assumptions that are far from being negligible in the context of this study. These are:

(i) the source of financing for the investment will provide 100% of the investment on due time, disregarding the upstream sources and markets, and

(ii) the investment will be paid back in its entirety, with assured revenues over the lifetime of the project.

2.2. Energy modelling approach

The open-source energy modelling approach applied in this work emulates the one adopted by Stevanato et al. [29]. It couples an open-source bottom-up energy planning model, MicrogridsPy [30], with an open-source stochastic load demand generator, RAMP [31].

MicrogridsPy is a two-stage linear stochastic mini-grid optimization software developed in python (pyomo) by several authors in the years (original version in 2019 by Balderrama et al. [30]; multi-energy system optimization by Stevanato et al. [32]; multi-year capacity expansion, or MicrogridsPy-MYCE, by Stevanato et al. [29]; last published version in Stevanato et al. [33]). MicrogridsPy requires as inputs: the load demand with hourly resolution, the time series of the variable renewable energy sources with the same time resolution of the demand, and other parameters of techno-economic and financial nature. Both the inputs and the outputs are meant to be user-friendly, being written in intuitive excel sheets. The most advanced version of MicrogridsPy (2.0, March 2023, published at [33]) allows the user to:

- choose the objective function of MicrogridspPy between economic ones (minimum Net Present Cost or non-actualized Operation Costs) or environmental ones (minimum CO2 emissions), or a weighted combination of the two (multi-objective optimization),
- implement stochastic optimization,
- implement multi-year evolving load demand and multi-step capacity expansion,
- account for possible future connection to the main national grid,
- account for existing capacity already installed (brownfield optimization),
- deal with data paucity issues by mean of built-in load archetypes for rural users and endogenous calculation of renewable energy sources production from NASA-Power database.

The code, available in GitHub [34] and in constant updating, is open-source under the EUPL v1.1 license and needs an external solver for the model resolution. The compatibility of MicrogridsPy with a stochastic load profile generator such as RAMP (Remote-Areas Multi-energy systems load Profiles, [31]) has been already tested in existing literature [29,35]: the coupling of the two models provides a powerful energy planning tool to account for stochasticity both on input and design sides of the problem, thus producing more robust modelling results. According to the financial modelling approach introduced in the previous section, some input parameters as well as structural equations of MicrogridsPy have been modified to realise the hard linking with the financial modelling and run the scenarios introduced. The updated code is available in a new branch of MicrogridsPy 2.0 [36]. The user is now allowed to insert the input parameters of **Table 2** in the "Model_data.dat" file.

Table 2. New input parameters to MicrogridsPy.

Parameter and default value	Comment
`param: WACC_Calculation := 1;`	`# 1 to select Weighted Average Cost of Capital calculation, 0 otherwise`
`param: cost_of_debt := 0.11;`	`# Cost of debt, i.e., rate of return on loaned debt capital`
`param: cost_of_equity := 0.12;`	`# Cost of equity, i.e., rate of return on equity capital from shareholders`
`param: tax := 0.02;`	`# Corporate tax to be discounted from loaned debt`
`param: equity_share := 0.10;`	`# Total level of equity as a share of the total investment cost [-]`
`param: debt_share := 0.90;`	`# Total level of debt as a share of the total investment cost [-]`
`param: Discount_Rate := 0.02;`	`# Generic discount rate to be applied if WACC_Calculation is not selected`

The parameters are hence used in a pre-processing function that computes the leverage and the WACC as in Eq. (4). Moreover, all the functions including any actualization of costs have been updated to use WACC instead of Discount_Rate, including the Levelized Cost of Electricity (LCOE). Above all, the objective function will be the minimization of the Net Present Cost (NPC), now defined as:

$$NPC = \sum_{y}^{N} \frac{Inv_y + Fix_y + Var_y - Salvage}{(1+WACC)^y} \quad (5)$$

3. Case study: Ndoro village

3.1. Mozambique off-grid energy context

According to the World Bank [37], Mozambique is among the top 20 access-deficit countries (7th in the world), with 22 million people lacking access to electricity in 2020. This share, corresponding to the 38% of the national population, is mostly located in rural areas under extreme poverty caused by lack of electricity, income, education, and healthcare [38]. Mini-grids are not a new phenomenon in the country: since almost more than 25 years, the public services have owned and operated off-grid diesel generators for remote villages [39,40]. Off-grid electrification via renewable-based or hybrid mini-grids is increasing in the region but at insufficient pace to meet economic and demographic growth [16, 18], because of several barriers that are being investigated in disciplinary literature and reports. Among these, Baruah and Coleman [42] indentify economic and financial barriers such as: high cost of capital from local banks (i.e., associated to high interest rates), short maturity of lending, underdeveloped microfinance options, reduced attractiveness for foreign capitals, and no national-led incentives to mobilize low-cost finance to private-sector led off-grid projects. As Soares et al. [43] proved in their recent investigation, private sector stakeholders in the mini-grid sector of Mozambique consider economic factors as the most limiting ones for the enabling of the national market. Particularly, the authors highlight how the five economic factors, including general economic stability, cost of investment, and positive economic environment, are mostly equally important, according to the stakeholders interviewed.

3.2. Materials

3.2.1 Ndoro village

The village of Ndoro is situated in the Administrative Post of Ndoro, in the Caia district of Sofala Province, at the geographical coordinates of 34°56'35.6"E 18°6'59.5"S, located 62 kilometers away from the nearest national electrical network. This distance has resulted in a lack of access to electricity for over 19,161 residents of the Ndoro community. The current village's energy sources are primarily dependent on diesel generators, solar panels, wood, dung, charcoal, waste, candles, kerosene, portable electric torches, and batteries (see **Table 3**). Due to the dispersed population of the village, it is difficult to plan and execute initiatives for installing a mini grid. The absence of electricity has resulted in numerous difficulties for the community, including limited access to education and healthcare, lack of communication facilities, and decreased economic opportunities. The community's reliance on traditional sources of energy has also contributed to environmental degradation and pose health hazards. Efforts to address this problem and bring sustainable electricity to Ndoro are underway, including the installation of solar home systems However, due to the challenges posed by the village's reduced economic opportunities and geographical location, these initiatives lack extensive planning and resources. Nonetheless, providing reliable and sustainable energy to the people of Ndoro remains crucial for their overall development and wellbeing.

Table 3. General information of Ndoro village

Location (lat., lon.)	Lat. - 18°6'59.5"S Lon. - 34°56'35.6"E; 62 km from Caia district, Sofala province, where the nearest national electricity grid is located
Population	19’161
Number of users interviewed	69
Social services	Hospitals, Schools, Church, Police office, Administrative post
Productive activities	Bars, Tents, Barbershops, Tailor workshop, Mills
Sources/devices used	Lighting – candles, kerosene, portable electric torches, and small lithium batteries Heating and cooking – wood, dung, residues, and charcoal

During the site visits, between 2019 and 2020, it was possible to collect data from households, public institutions, and commercial infrastructures, reaching an overall of 69 potential users. The local energy needs were investigated in two ways: first, through the field visit, which allowed for the observation of the village's actual condition; and second, through meetings with focus groups involving institutions and the local leadership. This second step allowed to define tailored scenarios of demand evolution, too. During the on-field visit, it was also possible to assess the viability of local renewable energy sources for generating electricity. The solar energy resource is unbounded, and its huge potential is freely available with few topological constraints. Relevant hydropower resource is absent. The load demand estimated from the data collected and the correspondent scenarios have been organized in a shared Zenodo repository, accessible at [44]. The following sub-section aims to detail the inputs that are provided to the model.

3.2.2 Model definition

Energy resource assessment

First, the potential of each energy source available in Ndoro has been evaluated. As for fossil fuels, the on-field visit confirmed the availability of diesel in the local market to supply diesel generators, provided by local sellers at a roughly constant price of 1.1 USD per litre. As for renewable energy assessment, the built-in feature for renewable energy assessment of MicrogridsPy 2.0 has been adopted to build the hourly resolution time series to provide as input. The solar resource potential found was characterized by annual average global horizontal irradiation of about 1712.72 kWh/m^2, with daily average of 400 Wh/m^2 and peaks of almost 1000 Wh/m^2. The potential of wind was evaluated at 23 m of height from the soil with the peak values over 14 m/s, and the yearly average wind speed of 4.055 m/s, in which is considered too low for efficient power generation.

Load demand definition

Even tough the current situation of Ndoro is far from being energy intensive, growth scenarios contained in [44] detail the perspective provided by local focus groups. High growth scenario has been chosen for the scope of this analysis, due to the willingness of investigating financing structures for a >100 kW of peak power capacity mini grid. In fact, this represents the most suitable case for a commercial-alike study. The output of RAMP software is depicted in **Figure 2**, showing the estimated evolution of Ndoro yearly load duration curves along the modelling horizon (2022-2041).

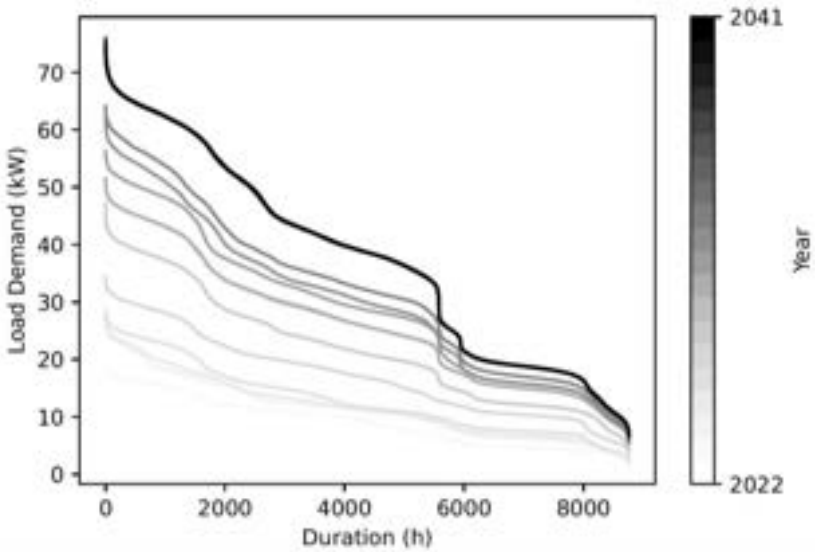

Figure 2. Estimated load duration curve evolution in Ndoro village.

Technology selection and techno-economic parameters

The model considers the possible technologies that could be employed for the construction of a 3rd generation hybrid mini grid [10]: solar PV panels, wind turbines, diesel generators and lithium-ion batteries. The techno-economic parameters for the definition of these technologies are available at [45].

Financial parameters and financing structures

The sensitivity analysis has been conducted on the parameters that characterize the scenarios drawed according to the rationale previously introduced. The combinations of these parameters correspond to a specific financing structure. Values for Mozambique market have been taken and adapted to the case study from the publication by Agutu et al. [15]. A summary and critical description of the financing structures are proposed in **Table 4**.

Table 4. Summary of financing structures associated to the scenarios considered.

Scenario	Description	R_D	R_E	t	D [%]	E [%]	WACC
Status quo	The scenario represents the business-as-usual case, characterised by total absence of private capital participation. The resulting WACC is low, due to the low rate of return required by public funding.	0.26	0.13	0.02	0	100	0.13

Increasing private participation	The scenario represents an increasing of private capital participation from a partially public funded to a non-funded mini grid. However, since the market is assumed to be static, the rates of return are fixed to the status quo boundaries, and the overall WACC increases as D increases. The return on equity in this scenario is slightly increasing with respect to the status quo, due to the participation of private shareholders in the equity market, too.	0.26	0.17	0.02	20	80	0.187
					40	60	0.204
					60	40	0.221
					80	20	0.238
					100	0	0.255
Public intervention	The scenario shows how a substantial increase of t, consisting in a massive public incentivizing scheme, brings to a $(1-t)*R_D$ lower than R_E. This changes the slope of the WACC curve (see Figure 1.) and makes the increase of D functional to the reduction of the WACC, thus pushing for the participation of the private sector.	0.26	0.17	0.4	20	80	0.167
					40	60	0.164
					60	40	0.162
					80	20	0.159

4. Results and discussion

The extent of impact of the financing structure is assessed observing the modelling outputs of the mini grid, i.e., the values taken by the decision variables of the model. The comparison of the results makes sense at scenario level and broader considerations can be made to provide an outlook for the research.

Table 5. Summary of results associated to the scenarios considered.

Scenario	WACC	PV [kW]	Diesel genset [kW]	Battery bank [kWh]	LCOE [USD/kWh]	NPC [kUSD]
Status quo	0.130	83.42	41.94	138.49	0.271	330.201
Increasing private participation	0.187	48.96	41.94	54.62	0.313	247.892
	0.204	38.3	60.21	12.91	0.321	227.569
	0.221	32.45	70.85	0.08	0.328	209.055
	0.238	28.98	74.17	0.05	0.335	192.876
	0.255	26.01	74.25	0.03	0.341	178.748
Public intervention	0.167	64.75	74.31	107.08	0.299	273.146
	0.164	65.93	46.79	107.42	0.297	277.203
	0.162	66.77	46.68	107.67	0.296	279.968
	0.159	68.55	46.6	111.97	0.294	284.196

In the *status quo* scenario the WACC has been taken at a value of 0.13 from [15], considering 100% equity financing sourced from public fund. As already debated in different literature, this scenario is not advisable since it excludes the participation of private capitals. However, the relatively low WACC provides high PV and battery bank capacity, corresponding to the greater NPC of all the scenarios.

As for the *increasing private participation* scenario, the resulting installed capacities are depicted in Figure 3. The five values of WACC considered correspond to a variation of the debt share from 20% to 100%. It is already evident from the depicted results how the PV technology, as well as the LCOEs, benefit from lower discount rates, in this case related to the lower debt shares. It is worth mentioning that the proposed configuration cannot raise debt penetration, being the return on debt still too high compared to the return on equity. Conversely, the *public intervention* scenario shows how in the case of a massive incentivizing intervention (t) by the regulator, the increase of debt share D can reduce the WACC. In this case, the modelling outputs are much less sensitive due to the reduced range of variation of the WACC.

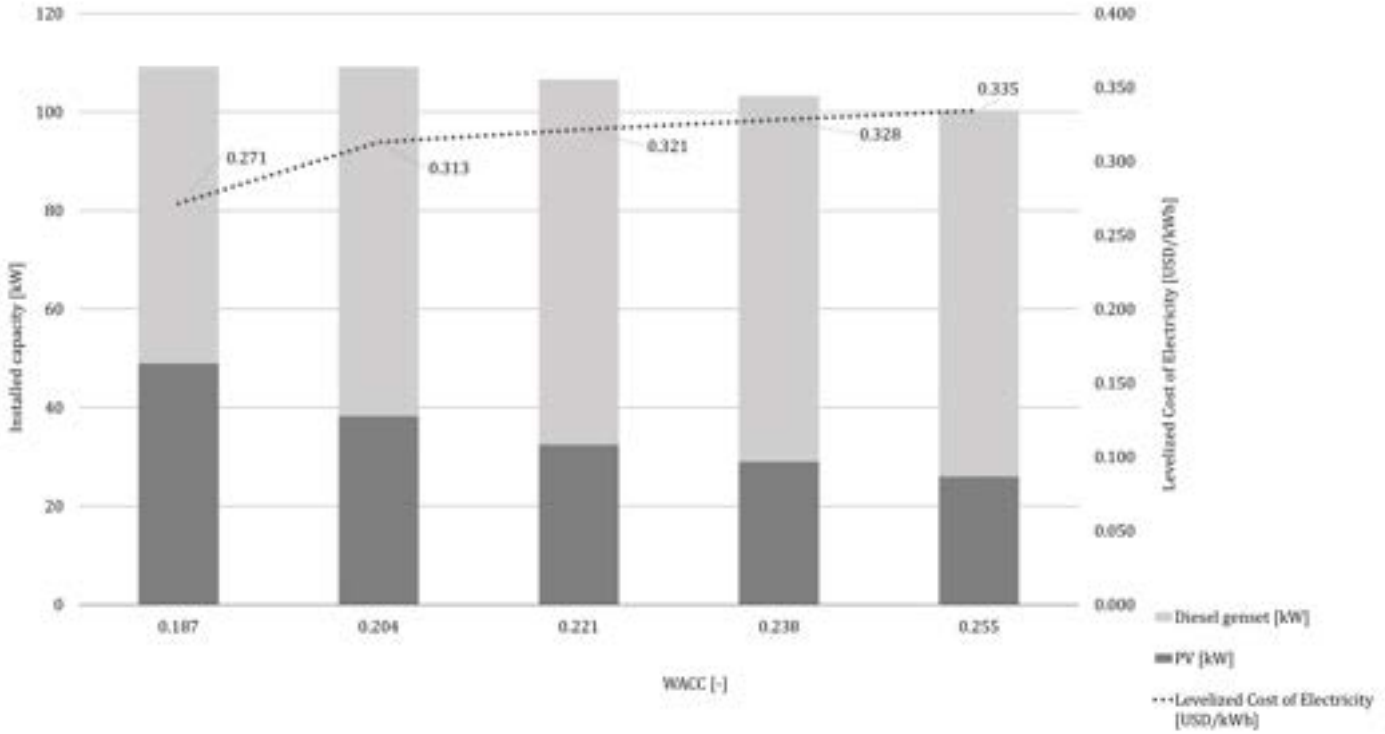

Figure 3. Capacities and LCOE as function of WACC in the *Increasing private participation* scenario.

All the above results are derived from scenarios with current rates of return, which are provenly inefficient and unattractive from a market perspective. The *public intervention* scenario moves in the sense of changing the slope of the WACC as function of the leverage L by varying the (1 – t) factor, i.e., switching from configuration (a) to (b) in **Figure 1**. On the one hand, this proves that, from the regulator perspective and to the goal of enhancing private participation, it would be more efficient to facilitate through a tax discount rather than through equity public funding. On the other hand, such a massive incentivizing intervention (correspondent to 40% of sourced debt) is far from being possibly realised in Mozambique.

5. Conclusion

The study conducted and the results proposed have some limitations to highlight. The limitations are strictly related to the assumptions already commented; for instance, the willingness to accept and wilingness to pay for the service have been assumed, granting that the capitals invested will be paid back. However, as Dibaba et al. [46] highlight, the effective financial sustainability of an off-grid solution cannot neglect the business model that interfaces with the users. Moreover, the financial modelling approach adopted in this study has disregarded the technolgy-specific rates of return, though national and scenario-related values for the costs of capitals have been taken. Out of the results obtained and referring to **Figure 1**, a massive public intervention would be needed to reach an efficient mini grid market in which the increase of the leverage L produces lower WACCs and higher penetration of renewables. The installation of renewables, characterised by lower variable costs and higher initial investment costs, is in fact favoured by lower WACCs in the actualization procedure. Another option to produce this effect is to directly tackle the rates of return and reduce R_D. To this scope, new financial approaches can be introduced. Project finance has been pointed out as a possible tool to upgrade the financing structure of domestic power projects in developing countries [28] and maximise the leverage while diversifying the sources. Such an approach could help in sourcing from climate finance, too, as suggested by Rai et al. [47], thus merging advantages of multiple investment streams while reducing the rates of return. In the case of mini grid financing, project finance is still almost unexplored and could be adopted for financing portfolios of several mini grids, able to ensure more solid cash flows and to mitigate the risk perceived by investors [13]. From the modelling perspective, this requires a more detailed representation of the cash flows and, possibly, a net present value-oriented optimization, able to account for the payback maturity and conditions of the different sources of financing.

Acknowledgments

Financial support from the European Commission H2020 funded project LEAP-RE (Long-Term Joint EU-AU Research and Innovation Partnership on Renewable Energy), Grant Number 963530 is gratefully acknowledged.

References

[1] UN. Transforming our world: the 2030 Agenda for Sustainable Development. vol. 25. 2010. https://doi.org/10.1163/157180910X12665776638740.
[2] IEA, IRENA, UNSD, WB, WHO. Tracking SDG7: The Energy Progress Report. Washington, DC: WB; 2022.
[3] Mandelli S, Mereu R. Distributed Generation for Access to Electricity: "'Off-Main-Grid"' Systems from Home-Based to Microgrid. Renewable Energy for Unleashing Sustainable Development, Springer International Publishing; 2013, p. 75–97. https://doi.org/10.1007/978-3-319-00284-2_10.
[4] Nerini FF, Broad O, Mentis D, Welsch M, Bazilian M, Howells M. A cost comparison of technology approaches for improving access to electricity services. Energy 2016;95:255–65. https://doi.org/10.1016/j.energy.2015.11.068.
[5] Peters J, Sievert M, Toman MA. Rural electrification through mini-grids: Challenges ahead. Energy Policy 2019;132:27–31. https://doi.org/10.1016/j.enpol.2019.05.016.
[6] Trotter PA, McManus MC, Maconachie R. Electricity planning and implementation in sub-Saharan Africa: A systematic review. Renewable and Sustainable Energy Reviews 2017;74:1189–209. https://doi.org/10.1016/j.rser.2017.03.001.
[7] Pérez-Arriaga I. New regulatory and business model approaches to achieving universal electricity access. Papeles de Energia 2016:7–48.
[8] Falchetta G, Michoud B, Hafner M, Rother M. Harnessing finance for a new era of decentralised electricity access: A review of private investment patterns and emerging business models. Energy Research & Social Science 2022;90:102587. https://doi.org/10.1016/j.erss.2022.102587.
[9] Williams NJ, Jaramillo P, Taneja J, Ustun TS. Enabling private sector investment in microgrid-based rural electrification in developing countries: A review. Renewable and Sustainable Energy Reviews 2015;52:1268–81. https://doi.org/10.1016/j.rser.2015.07.153.
[10] ESMAP. Mini Grids for Half a Billion People: Market Outlook and Handbook for Decision Makers. Executive Summary. Energy Sector Management Assistance Program (ESMAP) Technical Report 014/19. 2019.
[11] IEA. Africa Energy Outlook 2022. Paris: 2022.
[12] UNIDO. Clean Energy Mini - Grid Policy, Development Guide. UNIDO; 2020.
[13] BloombergNEF, SE4ALL. State of the Global Mini-grids Market Report 2020 - Trends of renewable energy hybrid mini-grids in Sub-Saharan Africa, Asia and island nations. Mini-grids partnership; 2020.
[14] Smith G. Where credit is due: how Africa's debt can be a benefit, not a burden. New York, NY: Oxford University Press; 2021.
[15] Agutu C, Egli F, Williams NJ, Schmidt TS, Steffen B. Accounting for finance in electrification models for sub-Saharan Africa. Nat Energy 2022;7:631–41. https://doi.org/10.1038/s41560-022-01041-6.
[16] Gatti S. Introduction to the Theory and Practice of Project Finance. Project Finance in Theory and Practice, Elsevier; 2018, p. 1–42. https://doi.org/10.1016/B978-0-12-811401-8.00001-5.
[17] Barbieri J, Simonet E. Technologies for Power Generation in Rural Contexts. Renewable Energy for Unleashing Sustainable Development, Springer International Publishing; 2013. https://doi.org/10.1007/978-3-319-00284-2_6,.
[18] Fodstad M, Crespo del Granado P, Hellemo L, Knudsen BR, Pisciella P, Silvast A, et al. Next frontiers in energy system modelling: A review on challenges and the state of the art. Renewable and Sustainable Energy Reviews 2022;160:112246. https://doi.org/10.1016/j.rser.2022.112246.
[19] Debnath KB, Mourshed M. Challenges and gaps for energy planning models in the developing-world context. Nature Energy 2018;3:172–84. https://doi.org/10.1038/s41560-018-0095-2.
[20] Riva F, Tognollo A, Gardumi F, Colombo E. Long-term energy planning and demand forecast in remote areas of developing countries: Classification of case studies and insights from a modelling perspective. Energy Strategy Reviews 2018;20:71–89. https://doi.org/10.1016/j.esr.2018.02.006.
[21] Riva F. Modelling endogenous complexities in rural electrification: on the local dynamics of growth and the planning of off-grid systems. PhD thesis. Polytechnic Univesity of Milan, 2019.
[22] Akbas B, Kocaman AS, Nock D, Trotter PA. Rural electrification: An overview of optimization methods. Renewable and Sustainable Energy Reviews 2022;156:111935. https://doi.org/10.1016/j.rser.2021.111935.
[23] Mulugetta Y, Sokona Y, Trotter PA, Fankhauser S, Omukuti J, Somavilla Croxatto L, et al. Africa needs context-relevant evidence to shape its clean energy future. Nat Energy 2022. https://doi.org/10.1038/s41560-022-01152-0.
[24] Ameli N, Dessens O, Winning M, Cronin J, Chenet H, Drummond P, et al. Higher cost of finance exacerbates a climate investment trap in developing economies. Nat Commun 2021;12:4046. https://doi.org/10.1038/s41467-021-24305-3.
[25] Egli F, Steffen B, Schmidt TS. Bias in energy system models with uniform cost of capital assumption. Nat Commun 2019;10:4588. https://doi.org/10.1038/s41467-019-12468-z.

[26] Lonergan KE, Egli F, Osorio S, Sansavini G, Pahle M, Schmidt TS, et al. Improving the representation of cost of capital in energy system models. Joule 2023:S2542435123000739. https://doi.org/10.1016/j.joule.2023.02.004.
[27] Steffen B. Estimating the cost of capital for renewable energy projects. Energy Economics 2020;88:104783. https://doi.org/10.1016/j.eneco.2020.104783.
[28] Baker R, Benoit P. How project finance can advance the clean energy transition in developing countries. Oxford Institute for Energy Studies; 2022.
[29] Stevanato N, Lombardi F, Guidicini G, Rinaldi L, Balderrama SL, Pavi M, et al. Long-term sizing of rural microgrids: Accounting for load evolution through multi-step investment plan and stochastic optimization. Energy for Sustainable Development 2020;58:16–29. https://doi.org/10.1016/j.esd.2020.07.002.
[30] Balderrama S, Lombardi F, Riva F, Canedo W, Colombo E, Quoilin S. A two-stage linear programming optimization framework for isolated hybrid microgrids in a rural context: The case study of the “El Espino” community. Energy 2019;188:116073. https://doi.org/10.1016/j.energy.2019.116073.
[31] Lombardi F, Balderrama S, Quoilin S, Colombo E. Generating high-resolution multi-energy load profiles for remote areas with an open-source stochastic model. Energy 2019;177:433–44. https://doi.org/10.1016/j.energy.2019.04.097.
[32] Stevanato N, Rinaldi L, Pistolese S, Luis S, Subieta B, Quoilin S, et al. Modeling of a Village-Scale Multi-Energy System for the Integrated Supply of Electric and Thermal Energy. MDPI - Applied Sciences 2020;10.
[33] Stevanato N, Pellecchia G, Sangiorgio I, Shendrikova D, Soares CA, Mereu R, et al. Planning Third Generation Minigrids: multi-objective optimization and brownfield investment approaches in modelling village-scale on-grid and off-grid energy systems. Renewable and Sustainable Energy Transition 2023:100053. https://doi.org/10.1016/j.rset.2023.100053.
[34] SESAM-Polimi. MicrogridsPy - v2.0 n.d.
[35] Stevanato N, Balderrama S, Lombardi F, Quoilin S, Colombo E. Open source stochastic methodology for the sizing of off-grid energy systems in a rural context. open energy modelling initiative, 2019.
[36] Crevani G. MicroGridsPy-SESAM/ECOS23_WACC // Available at: https://github.com/SESAM-Polimi/MicroGridsPy-SESAM/tree/ECOS23_WACC n.d.
[37] WB. World development indicators n.d.
[38] Uamusse MM, Tussupova K, Persson KM, Berndtsson R. Mini-grid hydropower for rural electrification in mozambique: Meeting local needs with supply in a nexus approach. Water (Switzerland) 2019;11. https://doi.org/10.3390/w11020305.
[39] African Development Bank. Mini Grid Market Opportunity Assessment: Mozambique. SEforALL Africa Hub African Development Bank; 2017.
[40] Come Zebra EI, van der Windt HJ, Nhumaio G, Faaij APC. A review of hybrid renewable energy systems in mini-grids for off-grid electrification in developing countries. Renewable and Sustainable Energy Reviews 2021;144:111036. https://doi.org/10.1016/j.rser.2021.111036.
[41] George A, Boxiong S, Arowo M, Ndolo P, Chepsaigutt-Chebet, Shimmon J. Review of solar energy development in Kenya: Opportunities and challenges. Renewable Energy Focus 2019;29:123–40. https://doi.org/10.1016/j.ref.2019.03.007.
[42] Baruah P, Coleman B. Country Brief: Mozambique - Off-grid solar power in Mozambique: opportunities for universal energy access and barriers to private sector participation. Seoul: Global green growht institute; 2019.
[43] Soares CA, Shendrikova D, Crevani G, Silinto B, Colombo E. Enabling factors for the development of mini-grid solutions in Mozambique: A PESTLE-based analysis. Energy Strategy Reviews 2023;45:101040. https://doi.org/10.1016/j.esr.2022.101040.
[44] Crevani G, Soares C. Ndoro village load demand dataset 2023. https://doi.org/10.5281/ZENODO.7681579.
[45] Crevani G. Ndoro - input files for MicrogridsPy 2.0 // Available at: https://github.com/GiacomoCrevani/ECOS23_Ndoro_inputs n.d.
[46] Dibaba H, Demidov I, Vanadzina E, Honkapuro S, Pinomaa A. Feasibility of rural electrification and connectivity—A methodology and case study. Applied Energy 2022;315:119013. https://doi.org/10.1016/j.apenergy.2022.119013.
[47] Rai N, Best S, Soanes M. Unlocking climate finance for decentralised energy access. London: IIED; 2016.

Impact of Detailed Hydropower Representation in National Energy System Modelling

M. Catania[a], F. Parolin[b], F. Fattori[c] and P. Colbertaldo[d]

[a] Department of Energy, Politecnico di Milano, Milan, Italy, matteo.catania@polimi.it, CA
[b] Department of Energy, Politecnico di Milano, Milan, Italy, federico.parolin@polimi.it
[c] Dipartimento di Scienze Teoriche e Applicate, Università degli Studi dell'Insubria, Varese, Italy, fabrizio.fattori@uninsubria.it
[d] Department of Energy, Politecnico di Milano, Milan, Italy, paolo.colbertaldo@polimi.it

Abstract:

Renewables are becoming more and more important due to the ambitious decarbonization targets. In this scenario, the improved integration of hydropower can play a crucial role thanks to its programmable operation, which is a valuable feature. In some countries it is a primary alternative to fossil resources, for example Italy, where hydro currently covers roughly half of the renewable power generation. Hydropower flexibility poses considerable modelling challenges due to the scarce availability of data. This work aims at addressing this research gap, by analysing the impact of hydropower details on energy system models. Using open-source information, a detailed dataset of Italian hydroelectric programmable plants (pumped hydro and reservoirs) is created. For each plant, storage capacity, geographical location, and nominal power are available. The multi-annual historical operational data are exploited to derive a precipitation inflow timeseries for each electricity market bidding zone, which is then distributed on power plants aggregated by administrative region. This new set of data is applied to a multi-node, multi-sector, and multi-vector energy system model, which optimises the design and operation of a carbon-neutral Italian energy system, looking at a 2050 framework with assigned energy vectors demand. Results are compared to those of a fixed-hydropower operation case, thus being able to assess how the modelled flexibility impacts the optimal solution. The analysis favours an improved understanding of future energy systems, helping to shape properly integrated systems with a great amount of non-programmable sources.

Keywords:

Hydropower; Energy dispatch; Integration; Energy system modelling.

1. Introduction

The focus on decarbonization has been increasing steadily over the years, permeating every aspect of society. Within the energy sector, this trend has spurred the growing importance of renewable energy sources (RES), stimulated by ever-more ambitious targets. This demanding path is pushing each technology to find new ways to improve efficiency and economic viability. The European Union has exemplified this trend through initiatives such as FitFor55 [1] and REPowerEU [2], which provide substantial public funds to improve investments and enhance the energy security of the region.

Such initiatives offer an exceptional opportunity for EU countries to gain greater control over their energy supply, thus enhancing their economic stability and security. This could help to mitigate the impact of global energy market fluctuations, which is particularly important for countries with high dependence on imported energy sources. For instance, Italy suffered significant economic consequences in 2022 as a result of its heavy reliance on gas and oil imports. Renewable energy sources, on the other hand, offer countries the necessary autonomy. This is particularly true when the manufacturing of RES-based technologies is not reliant on critical materials, which may otherwise hinder the achievement of climate targets.

Within this framework, hydroelectric power generation is a crucial asset, since it is a clean energy source that does not require the use of rare or strategical elements for its construction. In addition, unlike solar and wind sources, its operations can be programmed to fit the needs of the grid. Accordingly, its smart integration can lead to an important reduction of CO_2 emissions and to a better design of the energy system reducing the duty of other storage options.

Even if the flexibility of hydropower is relevant for realistic analyses, its accurate integration in Energy System Models (ESMs) is often challenging. This can be attributed to the absence of a unified dataset that lists all

hydroelectric plants and their corresponding rated power and storage capacity. Hydropower modelling in ESMs typically relies on the Joint Research Center (JRC) database [3], which provides data on hydroelectric power generation at a plant-specific level and is continuously updated over the years. However, numerous plants are not included in the database, and energy capacity data of reservoir systems are often unavailable. Looking at a country or continental scale, the available hydroelectric power and energy capacities result considerably underestimated. This data deficiency is common also to Italy, and it is also compounded by the difficulty in obtaining precipitation inflow profiles for each hydroelectric plant. As a result, aggregated data are often utilized, leading to higher levels of uncertainty in the results.

This work aims at addressing this research gap, by analysing the impact of hydropower flexibility on carbon-neutral integrated energy systems, focusing on the case of Italy. Using open-source information, a detailed dataset of Italian hydroelectric programmable plants (pumped hydro and reservoirs) is developed. This provides the storage capacity, geographical location, and nominal power of each plant, as well as the inflow time series by region (NUTS-2 areas). Such database is exploited to investigate the impact of hydropower operation in the Italian energy system using OMNI-ES, a multi-node, multi-sector, and multi-vector ESM, which optimizes the total annual cost, under the constraint of net-zero CO_2 emissions for a target year with assigned demand of energy vectors. To conclude, results are compared to a case with fixed hydropower operation based on historical hydroelectric power generation profiles. The structure of this work is the following: Section 2 describes the methodology developed for the gathering and elaboration of the required data. The model used is presented in Section 3, where also the scenario description and the assumption for the simulation are presented. The main results are then shown and discussed in Section 3, and finally, the key conclusions are summed up in Section 4.

2. Methods and data

This section introduces the methodological approach of the analysis. This includes the development of the Italian hydropower database (Section 2.1), the description of the OMNI-ES model (Section 2.2), the design of the assessed scenario (Section 2.3), and the modelling of hydroelectric plants (Section 2.4).

2.1. Hydro power generation and storage data in Italy

Hydroelectric power plants can be divided into three main technologies: run-of-river (RoR), hydro water reservoir (HWR), and pumped hydro storage (PHS). The first takes water from the flow of the rivers to generate electricity, thus representing a non-programmable source. HWR plants, instead, use dams to create basins that enable long-term energy storage. PHS is analogous, but it offers the possibility to pump water back to the upstream basin, allowing for cyclic operation. Accordingly, HWR and PHS guarantee dispatchable electricity, and their operation can be optimised according to the need of the grid.

To investigate the role of HWR and PHS in decarbonised scenarios, this work develops a detailed database of the existing plants in Italy. Hydroelectric power generation has historically been a relevant source of energy in Italy due to the country's favourable natural conditions. However, the construction of dams in almost all the suitable locations has already taken place, leaving limited scope for new installations. Consequently, hydroelectricity is expected to have lower relevance in the Italian energy system in future scenarios compared to solar photovoltaic and onshore wind [4], which feature a significantly larger potential of capacity expansion [5]. Although hydroelectric power generation faces limited opportunities for expansion, it could still provide a crucial contribution to the energy system, offering the opportunity to perform long-term storage (from weekly and monthly to seasonal) avoiding investments for new installations and reducing the risk of curtailment of solar and wind electricity. The existing databases of the national transmission system operator (TSO) [6] and ENTSO-E [7] are characterised by a poor spatial resolution, as data are aggregated either at national or bidding zone level. However, recent studies have shown that in systems where renewables dominate, grid dispatchability cannot be guaranteed, thus requiring a higher level of spatial resolution to incorporate possible congestion limits [5,8]. In addition, the available open-source databases lack information on the energy storage capacity of HWR and PHS plants. To fill these gaps, this works develops a comprehensive dataset of Italian HWR and PHS systems, providing the energy capacity and location of each plant.

The analysis starts from the JRC hydropower database [3], which provides reliable data for what concerns the plants name and power capacity. However, only few of them feature the information about the energy capacity, and the comparison with the number of plants provided by the Italian TSO *Terna SpA* [6] shows that a significant number of plants is absent in the JRC database. Specifically, the TSO reports a total of over 4000 plants, whereas the JRC database lists approximately 300 plants. As a result, the JRC database underestimates the national power capacity of hydro by over 20% (19.4 GW_e compared to 24.7 GW_e). Accordingly, a dedicated and detailed search has been carried out to complete the list of plants and to retrieve the energy capacity. The analysis relies on freely accessible sources, largely derived from the websites of plant owners and of the Italian Ministry of infrastructures and transport [9]. In particular, the latter provides the volume of the basins. In the cases for which the storage capacity (C) is absent, it is evaluated as:

$$C = \eta \cdot C_{water} \cdot H \quad (1)$$

where η is the turbine efficiency, assumed equal to 87% considering a reference value for a plant featuring a Pelton turbine. Such assumption is in many cases conservative, as it is applied also to plants where the more efficient Francis turbines are installed. The water capacity of the basin is expressed by C_{water}, while H represents the head (in m) from the dam to the turbine where the conversion into electricity occurs. In the cases for which the plant head is not explicitly provided, it is estimated from topological data.

Values at the plant level are then aggregated to have a regional detail, in order to comply with the resolution of the ESM (see Section 2.2). The final values are represented in Figure 1, and are used as input to the model to define the maximum capacity of each region.

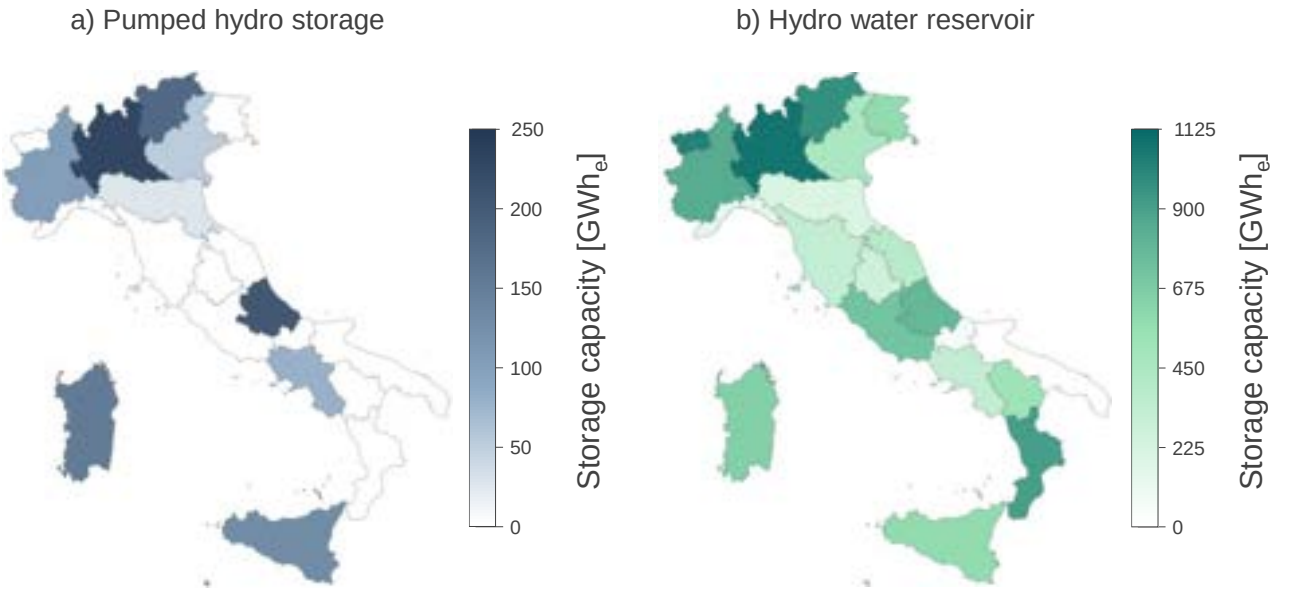

Figure 1. Energy storage capacity by region for (a) pumped hydro storage and (b) hydro water reservoir plants.

After having defined the capacities for each region, the water inflow is computed. This depends on the precipitations occurred in the watershed connected to each plant. However, detailed inflow data at a plant level are unavailable, and it is difficult to link a specific dam to the precipitation in the upstream portion of the watershed over a specific time period. Accordingly, the analysis considers the aggregate inflow by region.

The time series of the aggregate filling rate of HWR and PHS plants provided by ENTSO-E [7] is the starting point to derive the precipitation inflow. In particular, data represent the weekly-resolved estimation of the stored energy value (SEV) aggregated by bidding zone. The inflow time series is computed as:

$$Inflow_i = SEV_{i+1} - SEV_i + \sum_{j=1}^{168} (E_{HWR,j} + E_{PHS_{gen},j} - E_{PHS_{cons},j}) \quad (2)$$

where $E_{HWR,j}$, $E_{PHS_{gen},j}$, and $E_{PHS_{cons},j}$ are respectively the energy generated by reservoirs plants, the one generated by pumped storage plants, and the pumping consumption of pumped storage plants. Profiles of these quantities are available from ENTSO-E with an hourly resolution [10], so they are summed over each week of the year to be consistent with the SEV data. The *i* subscripts indicate the weeks in the year while the *j* ones represent the hours. To be consistent with the TSO inputs, a change in the ENTSO-E profiles is required. Indeed, since in the TSO data HWR are higher in terms of capacity, a compensation regarding the overall energy generated by them is needed not to underestimate the inflow. Consequently, the ENTSO-E profiles are scaled to match the overall generation by bidding zone provided by the TSO. The difference between the two data providers is due to different classification criteria regarding the type of hydropower plants. These are classified according to the time in which the overhead basin is filled by water stream. Specifically, the TSO sets as threshold between RoR and HWR a filling time of 2 hours, while ENTSO-E considers a value of 24 hours.

The resulting profiles represent what is assumed to be the charging or discharging of the bidding zone basins due to only the natural contributions (i.e., precipitations, evaporation, icing). As an example, Figure 2 shows the inflow profiles of two bidding zones (i.e., Centre-North and Sardinia). The inflow profiles clearly show that the distinct bidding zones feature seasonally different precipitation profiles. This is especially noticeable comparing northern and southern regions, where the basins are used as seasonal water storage to compensate the absence of rain during summer. Figure 2 also shows how, depending on the season, the inflow may also feature negative ones. These may result from evaporation and ice formation, or may be due

to maintenance of dams, which can require to empty the whole basin. Another reason may be the minimal vital flow that each river must provide and that, in the case it is regulated artificially, must be preserved through the spilling of water from reservoirs, especially in periods where no precipitations occur and the power plants are turned off. These data also show how in some regions (e.g., Sardinia) precipitations are extremely concentrated in time, highlighting importance of artificial basins for the river flow regulation.

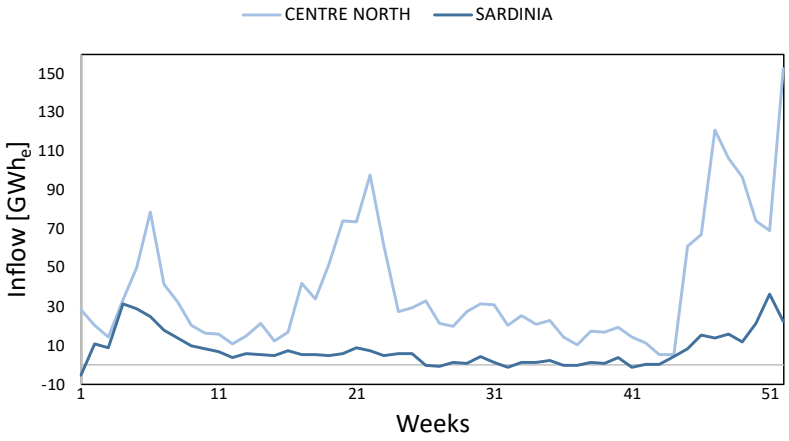

Figure 2. Inflow profiles of the Centre-North and Sardinia bidding zones.

The obtained inflow profiles must be distributed over the two different technologies (i.e., HWR and PHS) and over the regions that constitute each bidding zone. This is attained by dividing the inflow proportionally to the regional energy capacity of HWR and PHS plants (as previously derived). This is equivalent to assuming that plants with larger capacity benefit from a proportionately greater share of the bidding zone inflow.

2.2. Model description

The Italian energy system is modelled with the OMNI-ES model described in Ref. [5]. Considering a target year (2050 in this work), the model optimizes the national energy system by minimizing the total annual cost (including both capital and operational expenditures), covering all end-use sectors (residential and services, industry, road mobility, aviation, and navigation) and considering capacity expansion for all the included technologies adopting a brownfield approach. OMNI-ES is based on a multi-node formulation with a regional (NUTS-2) resolution and solves the energy balances on an hourly basis, adopting a perfect foresight approach. As

Figure **3** shows, the model encompasses a multiplicity of energy vectors (electricity, methane, hydrogen, liquid fuels – fossil, biogenic, or hydrogen-based) and the related transport networks, enabling the possibility to exploit the existing gas grid to deliver a blend of methane and hydrogen. In addition, OMNI-ES tracks the CO_2 flows considering carbon sources, sinks, and uses, in order to introduce a net-zero emission constraint.

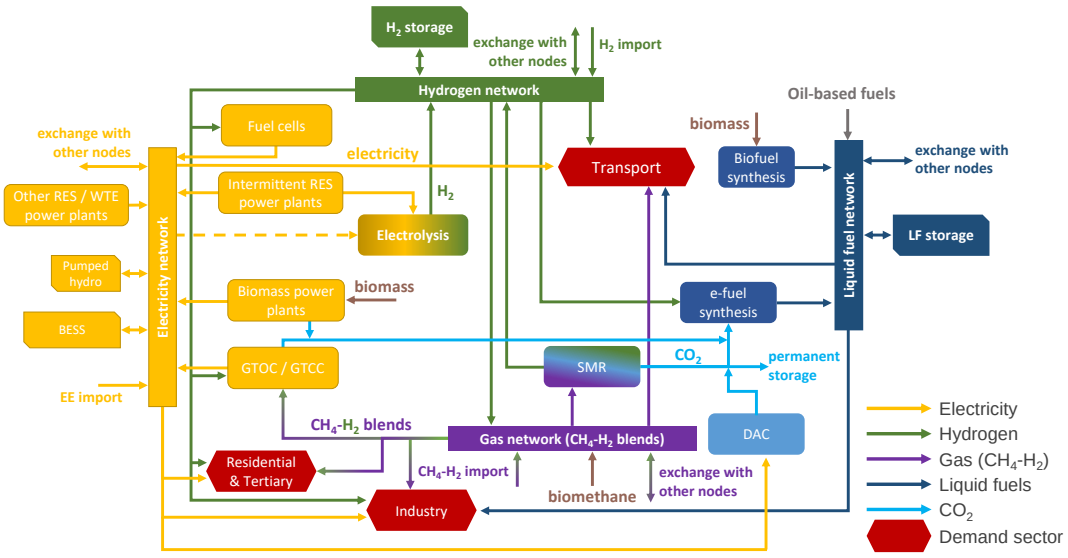

Figure 3. Schematised structure of the OMNI-ES model: nodal balances of energy vectors and CO_2 [5].

2.3. Scenario definition

This work applies the OMNI-ES model to investigate the role of hydroelectricity in a long-term scenario for Italy, considering 2050 as target year and enforcing the achievement of economy-wide carbon neutrality.

OMNI-ES requires as exogenous input the demand quantity and hourly profiles of each energy vector. Specifically, the analysis considers the evolution of all end-use sectors towards the adoption of decarbonized options. The resulting sectorial energy vector demand is summarized in Figure 4, considering the share by energy vector and the total annual demand by sector. The underlying assumptions are briefly presented in the remainder of this section, while a detailed discussion may be found in Ref. [5].

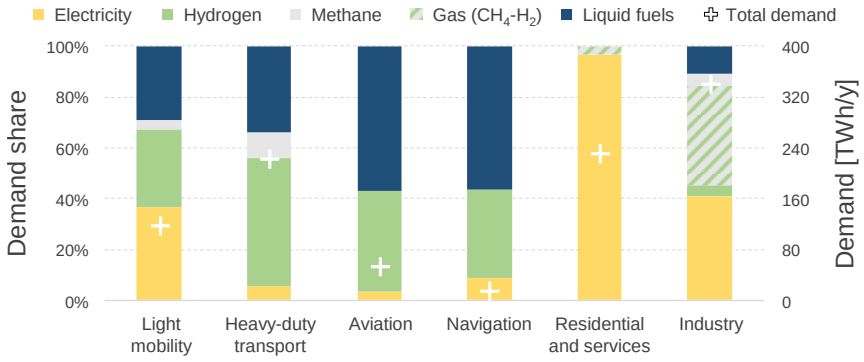

Figure 4. Demand of energy vectors by sector: shares on energy basis (left axis) and annual quantity (right axis).

The electric load encompasses the projection of the conventional consumers demand based on population and gross domestic product (GDP) growth and increased electrification in households, as assumed by the transmission system operators [11], and the additional demand from the electrification of building heating, transport, and industrial heat generation. The gas demand is assumed to be satisfied with a CH_4-H_2 blend with unconstrained hydrogen fraction, and takes into account the projected consumers demand as defined by the transmission system operator [11], a residual use of gas systems for heating of buildings, and high-temperature industrial heat generation. Pure hydrogen uses encompass applications in the transport sector and in industry, while liquid fuels are used in transport, considering the possibility to exploit carbon-neutral fuels in internal combustion engines, aviation, and navigation, and industry as chemical feedstocks.

In the heating sector, 75% of the thermal demand is assumed to be covered via electric heat pumps, 15% via district heating, 5% via gas absorption heat pumps, and 5% via biomass boilers. Cooling introduces an additional electricity demand, defined accounting for thermal comfort needs. The corresponding hourly-resolved profiles for each technology are determined following the methodology presented in Refs. [12–14].

Demand shares in transport are defined on the basis of recent long-term estimations for the sector [15,16]. The stock share assumptions for road transport (reported in Table 1) consider a massive presence of battery electric vehicles (BEVs) in light mobility, while hydrogen-powered fuel cell electric vehicles (FCEVs) and internal combustion engine vehicles (ICEVs) fed with liquid fuels (LF) are more relevant in heavy transport. The analysis also maintains the current reliance of part of road transport on pure CH_4, with use of either natural gas or biomethane. For aviation and navigation, demand shares are assigned considering the national consumption as reported in Figure 4, taking into account both passenger and freight transport.

Table 1. Road transport stock share assumptions.

Category	ICEV-LF	ICEV-CH_4	BEV	FCEV
Passenger cars	10%	-	75%	15%
Light-duty vehicles	20%	5%	50%	25%
Heavy-duty vehicles	20%	10%	10%	60%
Buses	15%	-	50%	35%

The industrial demand of energy vectors is built from historical consumptions [17], considering the adoption of decarbonized technologies. In particular, the analysis assumes the complete electrification of low-temperature (< 100 °C) process heat generation (excluding the systems already based on biomass, geothermal, and solar energy), while medium- and high-temperature (> 100 °C) heat generation based on oil derivatives and solid

fuels is considered to be converted to gas boilers fed by a CH_4-H_2 blend with hydrogen fraction up to 100%. Regarding the chemical industry, all fossil-based feedstocks are assumed to be converted to carbon-neutral options. This involves the replacement of natural gas in ammonia and methanol production with hydrogen, and the substitution of naphtha in high-value chemicals (HVC) and BTX (benzene, toluene, and xylenes) with carbon-neutral methanol [18]. Primary steelmaking is assumed to switch to Direct Reduction of Iron ore (DRI) and Electric Arc Furnaces (EAF), considering that, as DRI feed, half of the production relies on methane and half on hydrogen. The implementation of carbon capture and storage (CCS) is imposed for the methane-based production. Carbon capture and permanent sequestration is considered also in cement production.

The potentials for renewable energy sources are determined based on Ref. [5]. The solar photovoltaic potential is estimated to 405 GW_e, considering both rooftop- and ground-based plants, while the available wind speed and the geomorphological features of the territory limit the onshore wind potential to 224 GW_e. Considering areas with suitable wind intensity and seabed morphology for piled foundations [19], the offshore wind potential is set to 9.5 GW_e. For thermoelectric power generation, the analysis considers the revamping of combined-cycle gas turbines (CCGTs) and open-cycle gas turbines (OCGTs) with the installation of high-efficiency devices fuelled by CH_4-H_2 blend, as well as the phase out of oil- and coal-based plants. The maximum capacity of CCGTs and OCGTs is set 50% higher than current values (resulting in 83 GW_e for CCGTs and 5 GW_e for OCGTs), as revamping generally involves larger machinery. The biomass-based power generation potential is assumed equal to today's installed capacity (4 GW_e), as biomass availability is the main constraints for its exploitation. In accordance with national strategies, the operation of Waste-to-Energy (WtE) plants is kept unvaried (the installed capacity is currently 1 GW_e) [20]. As most available areas have already been exploited, only a slight increase of geothermal (+10%, reaching 1 GW_e) and run-of-river (+20%, reaching 7 GW_e) capacity is considered. For the same reason, the installed capacity of HWR and PHS is assumed unvaried (see Section 2 for the discussion on the current status of hydroelectric power generation).

Regarding domestic sources, the upper boundary for domestic gas production is set to the 2019 value, equal to 47 TWh_{LHV}/y, taking into account both onshore and offshore wells [21]. A biomass availability of 52 TWh_{LHV}/y is determined considering waste and residual solid biomass exclusively [22], while a biomethane production potential of 55 TWh_{LHV}/y is estimated considering the upgrading of biogas produced from livestock residues and biodegradable waste [22,23]. Finally, an annual storage capacity of 20 Mt_{CO2}/y is assumed as upper boundary for permanent CO_2 sequestration, corresponding to the lower boundary of the range indicated in the national long-term strategy [4].

2.4. Modelling of hydroelectric power generation

Based on the description provided, the aim is to analyze the impact of flexible hydropower operation on the national energy system in long-term scenarios with high levels of renewable energy penetration. To this end, two scenarios are investigated. The first does not enable hydropower flexibility of reservoir plants, assigning the operation of HWR plants based on historical generation profiles. The second scenario differs from the previous one in the way in which the reservoir plants are modelled. Here, the model selects the optimal plant operation, according to the equation:

$$Q_{HWR}^{r,t+1} = Q_{HWR}^{r,t} + \tilde{q}_{inflow,HWR}^{r,t} - \frac{q_{\mathrm{otp},HWR}^{r,t}}{\tilde{\eta}} \tag{3}$$

where, referring to the generic region r and time step t, $Q_{HWR}^{r,t}$ is the energy storage content of HWR plants, $\tilde{q}_{inflow,HWR}^{n,t}$ is the inflow as determined in Section 2.1, and $q_{\mathrm{otp},HWR}^{r,t}$ is the output power generation of HWR plants. Specifically, the inflow $\tilde{q}_{inflow,HWR}^{n,t}$ is an exogenous input data, while the storage content $Q_{HWR}^{r,t}$ and the power output $q_{\mathrm{otp},HWR}^{r,t}$ are model variables endogenously optimised.

The database developed in Section 2.1 provides the hourly profiles of natural inflow and the available storage capacity of HWR plants, which bounds the storage content in each region. To provide a realistic assessment, the initial level of the basins is imposed equal to the historical one at the first hour of the year. The level at the end of the year is instead imposed to be greater than or equal than the minimum value between the initial storage content and the historical end-of-year level. For this analysis the reference year, from which the historical data are derived, is the 2019. The choice is made to be consistent with the data used in Ref. [5], which considered 2019 as reference weather year. In addition, 2019 represents an average year for what concerns precipitations and basins filling levels. To conclude, the operation of pumped hydro storage plants is optimised in both scenarios, and run-of-river plants are modelled with assigned profiles equal to the historical ones, assuming a 20% capacity increase to account for new installations.

3. Results and discussion

Given the model description, the main assumptions, and the input data, the analysis compares the cost-optimal energy system configuration in a scenario with assigned HWR plant operation based on historical profiles (considered as reference) and in one with optimised flexible HWR operation.

Figure 5 shows the HWR duration curve comparison between the flexible and the assigned operation scenarios. The curve of the reference scenario features a smoother trend, as hydroelectricity has traditionally provided base load generation. When enabling flexible operation, HWR plants exhibit a peaking behavior, as the operating hours do not cover the whole year and the profile is shifted towards higher power values.

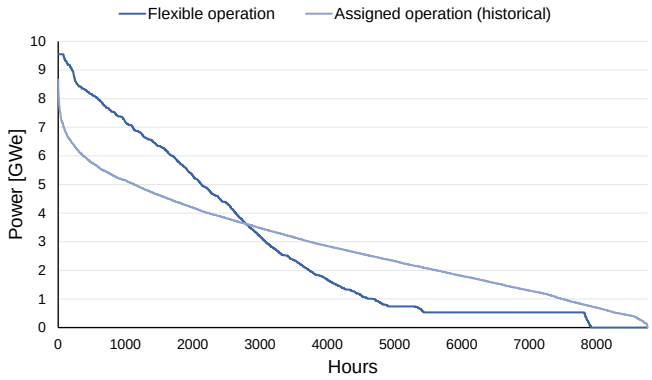

Figure 5. Duration curves of hydropower reservoir (HWR) plants in the flexible and in the reference scenarios.

Figure 6 shows the comparison of the storage energy value by bidding zone in both scenarios, following the geographical division of 2019. Specifically, the curve of the reference case is derived from historical data from ENTSO-E for the year 2019. In contrast, the flexible scenario aggregates results from individual regions across the bidding zones.

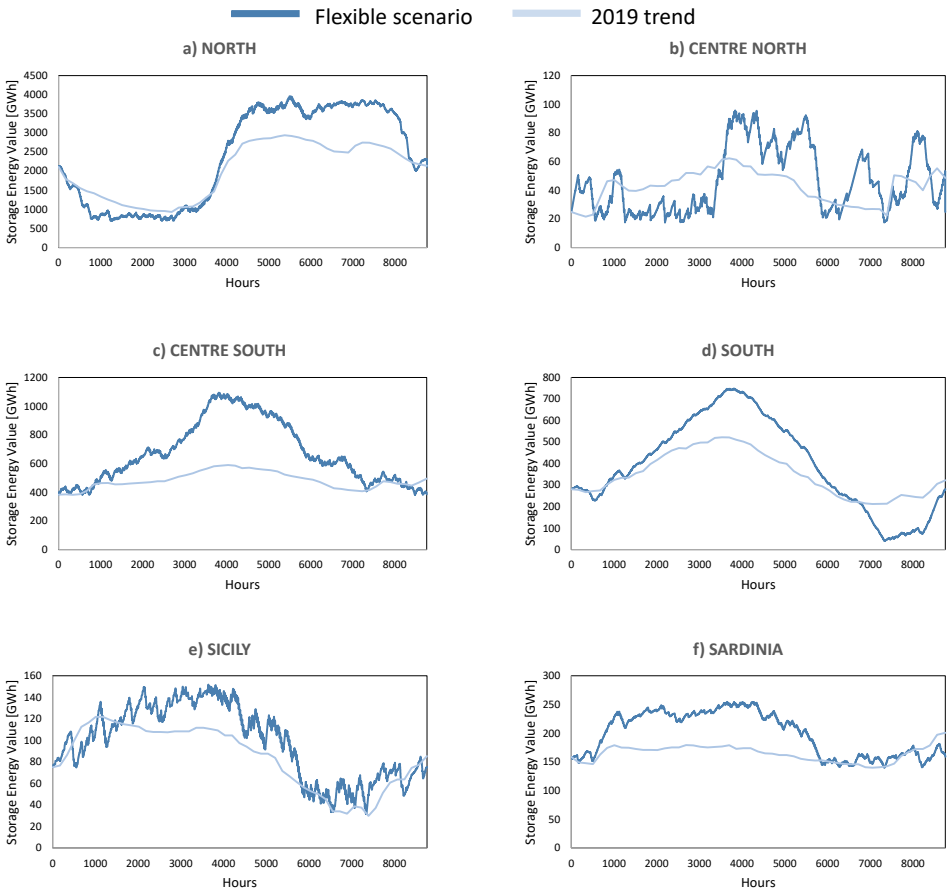

Figure 6. SEV comparison between the flexible scenario output and the 2019 profiles, for the aggregation of HWR and PHS basins in each bidding zone.

The model is allowed to vary between the maximum capacity of the basins, determined by the analysis illustrated in Section 2, and a minimum storage content, set equal to the historical minimum basin level. In some bidding zones (e.g., Sicily) the difference between the two lines is less marked, showing that using the assigned historical profiles does not represent a great difference, as HWR power generation is mostly driven by the availability of inflow. Instead, the curves are more distinct in bidding zones (e.g., Centre-South) resulting in a higher amount of energy stored during summer to be then discharged in autumn when photovoltaic generation is lower. Results reveal that the North bidding zone, which represents nearly 65% of the national value in terms of capacity, exhibits a trend similar to the historical one. However, it features a more pronounced seasonality, reaching differences of the energy stored during summer in the order of 1000 GWh_e.

These results show how hydroelectric basins operation can be assimilated to storage systems and that HWR detailed modelling can lead to a different optimal system configuration. In this regard, Table 2 shows the variation of the installed capacities of the most relevant technologies between the two scenarios. The introduction of HWR flexibility significantly impacts on the installation of battery energy storage systems (BESS), which feature a sensibly lower capacity in the flexible scenario. This is due to the possibility to exploit existing assets (i.e., hydroelectric plants) as storage systems, reducing the need for new installations that would represents an extra cost for the system. Indeed, the optimised use of HWR replaces BESS role in balancing short-term oscillations of renewable power generation. The availability of investment-free storage options enables a larger deployment of solar photovoltaic, which is the RES power generation technology with the lowest lower levelized cost of electricity, while the wind capacity undergoes a corresponding decrease. To avoid curtailment, the system relies on a larger hydrogen storage capacity, which is also used to compensate the greater seasonal unbalances that result from the additional PV installations. Gas turbine-based power generation capacity decreases by 22 %, as the flexible operation of HWR plants guarantees dispatchable electricity to assist the grid in hours where non-programmable sources are not available.

Table 2. Installation of main technologies.

Technologies	Reference scenario	Flexible scenario	Variation
Solar photovoltaic [GW_e]	311	338	+8%
Wind [GW_e]	130	127	-2%
Gas turbine-based power generation [GW_e]	17	15	-13%
Battery energy storage [GWh_e]	106	81	-24%
H_2 storage [GWh_{LHV}]	944	1212	+28%

Figure 7 focuses on the integration between PV and hydro reservoirs in the flexible operation scenario. The black line represents the cumulative duration curve of these two technologies, while stacked columns represent the share of HWR (in light blue) and photovoltaic (yellow) on the generated power in each hour. The figure shows a complementarity relation between solar PV and HWR, as the latter is used when solar radiation is scarce or not available. Indeed, the share of hydro reservoir generation starts to appear only at low power, increasing significantly in the right part of the chart.

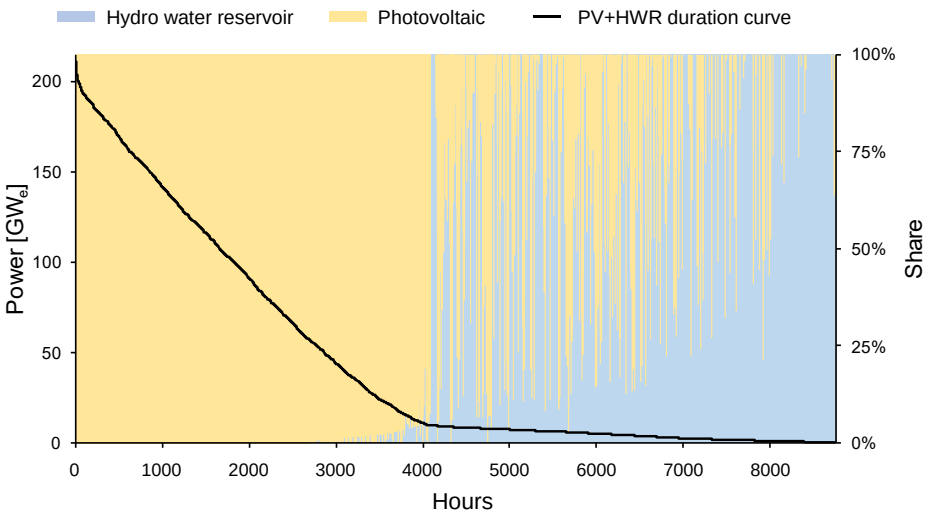

Figure 7. Cumulative PV and HWR duration curve (left axis) and hourly share on generated power (right axis).

Such behavior is also evident in Figure 8, which highlights that hydro reservoirs are adopted to compensate for the lack of PV generation during nighttime or low-solar-radiation days. The operation of the two systems features a strong daily pattern, with HWR covering the load in the early morning and late afternoon and PV taking over the central hours of the day. Consistent with the trend highlighted in Figure 5, HWR plants often operate at peak power. A certain degree of seasonal complementarity is also observed, as HWR generation in the central hours of the day intensifies in periods with low availability of solar radiation, such as the end of January, November, and December. Figure 8 also provides insights on the effect that the optimised management of hydroelectric systems has on reducing the need for BESS capacity, with the former compensating short-term renewable generation deficits.

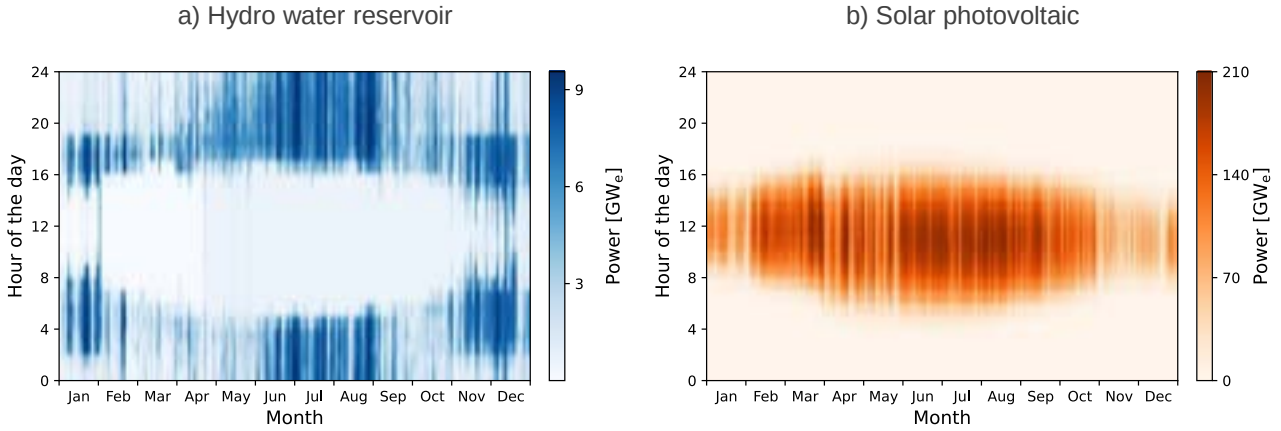

Figure 8. Hourly-resolved power generation profiles of hydro water reservoir (a) and solar photovoltaic (b).

4. Conclusions

The study presented in this work investigated the impact of hydropower flexibility on the Italian energy system, by introducing detailed hydropower data in a multi-node, multi-sector, and multi-vector energy system model. A comprehensive dataset of the programmable hydroelectric plants (pumped hydro and reservoirs) in Italy was created using open-source information. Compared to the available hydropower data sources, the developed dataset includes a complete list of plants, providing the nominal power and the energy storage capacity, which is typically unavailable in both national and European databases. Data have been aggregated to the regional level (NUTS-2) to compute the natural inflow profiles of HWR and PHS systems. The OMNI-ES energy system model was adopted to investigate the role of hydropower in economy-wide carbon-neutral scenarios. Adopting a perfect-foresight approach, the model application compared a flexible HWR operation scenario with optimised management of HWR plants, and an assigned operation scenario with HWR generation profiles based on historical data. The year 2019 was considered as reference for all the time series, while sensitivity analyses on the impact of the weather year are left to future assessments.

Results show that hydropower operation shifts from baseload to peak generation, thus acting as compensation of the intermittent generation of non-programmable sources. Accordingly, the system avoids the installation of additional flexibility elements, such as battery energy storage and gas turbine-based power generation, which feature a 24% and 13% capacity reduction compared to the assigned-operation scenario, respectively. Correspondingly, the optimised hydropower operation enables the deployment of additional solar photovoltaic capacity (+ 8%), leveraging its LCOE. Overall, the system is positively impacted by the possibility to perform both short-term and seasonal storage exploiting already existing assets, improving the integration of intermittent renewable sources in the energy system. Further developments of the work will involve the assessment of the impact of the reference climate year, considering different historical time series characterised by higher or lower precipitation. The effect of climate change will also be addressed, investigating the change of hydropower resources caused by global warming.

Nomenclature

Acronyms

BESS	Battery Energy Storage System
BEV	Battery Electric Vehicle
CCGT	Combined Cycle Gas Turbine
CCS	Carbon Capture and Storage
EAF	Electric Arc Furnaces

ESM Energy System Model
FCEV Fuel Cell Electric Vehicle
GDP Gross Domestic Production
HVC High Valuable Chemicals
HWR Hydro Water Reservoir
ICEV Internal Combustion Engine Vehicle
JRC Joint Research Centre
LF Liquid Fuels
OCGT Open Cycle Gas Turbine
PHS Pumped Hydro Storage
PV Photovoltaic
RES Renewable Energy Sources
RoR Run of River
SEV Storage Energy Value
TSO Transmission System Operator
WtE Waste to Energy

Symbols

C	Electric energy storage capacity
C_{water}	Water volume of hydropower basins
$E_{HWR,j}$	Energy generated by hydro water reservoir plants at hour j
$E_{PHS_{gen},j}$	Energy generated by pumped hydro storage plants at hour j
$E_{PHS_{cons},j}$	Energy consumed by pumped hydro storage plants at hour j
H	Head of hydropower plants
$Inflow_i$	Inflow to hydro water reservoir and pumped hydro storage plants in week i
SEV_i	Storage energy value of hydro water reservoir and pumped hydro storage plants in week i
$\tilde{q}_{inflow,HWR}^{r,t}$	Inflow to hydro water reservoir plants in region r and time step t
$Q_{HWR}^{r,t}$	Storage content of hydro water reservoir plants in region r and time step t
$q_{\mathrm{otp},HWR}^{r,t}$	Power output of hydro water reservoir plants in region r and time step t
η	Conversion efficiency of hydropower plants

References

[1] European Commission, COMMUNICATION FROM THE COMMISSION TO THE EUROPEAN PARLIAMENT, THE COUNCIL, THE EUROPEAN ECONOMIC AND SOCIAL COMMITTEE AND THE COMMITTEE OF THE REGIONS “Fit for 55”: delivering the EU’s 2030 Climate Target on the way to climate neutrality, 2021.

[2] European Commission, COMMUNICATION FROM THE COMMISSION TO THE EUROPEAN PARLIAMENT, THE EUROPEAN COUNCIL, THE COUNCIL, THE EUROPEAN ECONOMIC AND SOCIAL COMMITTEE AND THE COMMITTEE OF THE REGIONS REPowerEU: Joint European Action for more affordable, secure and sustainable energy, 2022.

[3] European Commission, Joint Research Centre, JRC Hydro-power database, (2019).

[4] Ministero dell’Ambiente e della Tutela del Territorio e del Mare, Ministero dello Sviluppo Economico, Ministero delle Infrastrutture e dei Trasporti, Ministero delle Politiche agricole Alimentari e Forestali, Strategia Italiana Di Lungo Termine Sulla Riduzione Delle Emissioni Dei Gas a Effetto Serra, 2021.

[5] P. Colbertaldo, F. Parolin, S. Campanari, A comprehensive multi-node multi-vector multi-sector modelling framework to investigate integrated energy systems and assess decarbonisation needs, Submitt. to Energy Convers. Manag. (2023).

[6] Terna, Terna: statistics 2019, (2019).

[7] ENTSO-E, Water Reservoirs and Hydro Storage Plants, (n.d.).

[8] F. Neumann, E. Zeyen, M. Victoria, T. Brown, Benefits of a Hydrogen Network in Europe, Preprint. (2022).

[9] Ministry of infrastructures and transport, Direzione generale per le dighe e le infrastrutture idriche, (n.d.).

[10] ENTSO-E, Actual Generation per Production Type - 2019, (n.d.).

[11] Terna, Snam Rete Gas, Relevant Scenario Report (Documento di Descrizione degli Scenari), 2022.
[12] M. Pozzi, G. Spirito, F. Fattori, A. Dénarié, J. Famiglietti, M. Motta, Synergies between buildings retrofit and district heating. The role of DH in a decarbonized scenario for the city of Milano, Energy Reports. 7 (2021) 449–457. https://doi.org/10.1016/j.egyr.2021.08.083.
[13] A. Dénarié, F. Fattori, G. Spirito, S. Macchi, V.F. Cirillo, M. Motta, U. Persson, Assessment of waste and renewable heat recovery in DH through GIS mapping: The national potential in Italy, Smart Energy. 1 (2021). https://doi.org/10.1016/j.segy.2021.100008.
[14] B. Dehghan B., T. Toppi, M. Aprile, M. Motta, Seasonal performance assessment of three alternative gas-driven absorption heat pump cycles, J. Build. Eng. 31 (2020) 101434. https://doi.org/10.1016/j.jobe.2020.101434.
[15] IEA, Net Zero by 2050, Paris, 2021.
[16] IRENA, Reaching Zero With Renewables, 2020.
[17] L. Mantzos, N. Matei, E. Mulholland, M. Rózsai, M. Tamba, T. Wiesenthal, The JRC Integrated Database of the European Energy System, European Commission, 2018.
[18] A.M. Bazzanella, F. Ausfelder, Low carbon energy and feedstock for the European chemical industry, 2017.
[19] P. Colbertaldo, S. Cerniauskas, T. Grube, M. Robinius, D. Stolten, S. Campanari, Clean mobility infrastructure and sector integration in long-term energy scenarios: The case of Italy, Renew. Sustain. Energy Rev. 133 (2020) 110086. https://doi.org/10.1016/j.rser.2020.110086.
[20] Decreto del Presidente del Consiglio dei Ministri 10 agosto 2016, Gazz. Uff. Della Repubb. Ital. (2016).
[21] Ministry of Economic Development, Data Book 2020, (2020).
[22] R. Pudelko, M. Borzecka-Walker, A. Faber, The feedstock potential assessment for EU-27 + Switzerland in NUTS-3. Deliverable D1.2 of the BioBoost project, 2013.
[23] Ministry of Health, Livestock Database, (2019).

PROCEEDINGS OF ECOS 2023 - THE 36TH INTERNATIONAL CONFERENCE ON
EFFICIENCY, **C**OST, **O**PTIMIZATION, **S**IMULATION AND ENVIRONMENTAL IMPACT OF ENERGY SYSTEMS
25-30 JUNE 2023, LAS PALMAS DE GRAN CANARIA, SPAIN

Comparative analysis of dynamic and linear programming energy systems models applied to the Bolivian power system

Alizon Huallpara[a*], Marco Navia[b], Isaline Gomand[c], Sergio Balderrama[d], Matija Pavičević[e] and Sylvain Quoilin[f]

[a,d] Universidad Mayor de San Simón, Cohabamba, Bolivia, alizon.huallpara@fcyt.umss.edu.bo, CA
[b,c,f] University of Liege, Liege, Belgium,
[e] UC Louvain, City, Louvain-la-neuve Belgium

Abstract:
Energy system models are indispensable tools for energy planning and decision making. They identify the most cost-effective way of delivering energy to the final consumer. No one tool that addresses all the energy system-related issues. Every model has its own strengths and limitations and serves a different purpose. This paper aims to compare the capabilities of two different model formulations to model both the hydro scheduling and the short-term dispatch problems in hydro-dominated power systems. On the one hand, SDDP, a commercial model for hydrothermal generation scheduling with a representation of the transmission network, has been used by the Bolivian system operator for dispatch simulations. Conversely, Dispa-SET, an open-source unit commitment and economic dispatch model with mid-term hydrothermal coordination capability, has been used previously in several Bolivian case studies. In this paper, both models were applied to the same input dataset of the Bolivian electric system considering probabilistic results for 43 weather years from 1984 to 2021. SDDP optimizes the system under all weather years, while Dispa-SET optimises under one full year, for which 43 runs were made. The results show that SDDP generation, reservoir level and spillage fall into the ranges of Dispa-SET results. Some differences that are present mainly lie in the conceptualization of the methods of both models. SDDP prioritizes the dispatch of hydro units, while Dispa-SET, with a higher temporal and technical resolution, maximizes the use of non-dispatchable units such as variable renewables and run-of-river.

Keywords:
Dispa-SET Bolivia; Energy system modelling; SDDP; Hydro scheduling.

1. Introduction

The Paris Agreement and Sustainable Development Goals (SDGs) are crucial global frameworks addressing environmental and development challenges, requiring changes in every country. The Paris Agreement commits countries to achieve net-zero greenhouse-gas emissions by the middle of the century, while the SDGs consist of 17 SDGs and 169 targets for Prosperity, People, Planet, Peace, and Partnership [1]. SDG7 aims to ”Ensure access to affordable, reliable, sustainable and modern energy for all” [2]. For this, renewable generation expansion is critical in helping to mitigate global warming. These agreements have significant implications for national development plans for developed and developing countries [3]. Bolivia’s Nationally Determined Contribution (NDC) [4], consistent with the Paris Agreement, presents climate goals and actions aligned with emission reduction and adaptation to the impacts of climate change. Bolivia aims to achieve a transition in electricity generation towards renewable energy and targets 79 % renewable energy consumption and 50 % of renewable installed capacity by 2030. Bolivia’s alternative energy goal by 2030 is to reach 19 % energy consumption from Biomass, Solar, Wind and Geothermal energy, contributing to SDGs 7,8,12, and 13.

Energy models are essential analytical tools that can support SDG goals by analyzing potential energy project impacts [5]. Energy models’ quantitative analysis supports much of academic research and energy policy-making [6]. There is a wide variety of models, each with its unique blend of paradigms, techniques and solutions. Each model’s extensive range of choices makes it unlikely that a single model could incorporate them all at once [7]. While most models’ source code is not available for public access or modification, open-source models allow users to access and modify the model code. According to Pfenninger [6], open-access models improve the quality of science, allow more effective collaboration across the science-policy boundary, increase productivity through collaborative burden sharing and allow profound relevance to societal debates. In Energy models, when solving the hydrothermal scheduling problem (HTSP) in a system with a large share of hydro generation, such as Bolivia, water inflows play an essential role in the decision-making process. The scheduling of generators must consider various future possibilities, and if a cascade system exists, water

availability is influenced by decisions made in upstream reservoirs. These issues complicate the HTSP, and when an optimization model is designed for it, the decision variables that must be considered include the turbined water used for generation, storage, and spillage [8].

The models of interest for this study are a Stochastic dual dynamic programming model (SDDP) and a Mixed-Integer Linear Programming model (MILP), both bottom-up and dynamic energy models. The Brazilian engineering company PSR has used SDDP algorithm in its software bearing the same name, which has been applied in operations studies in more than 30 countries, including Bolivia. On the other hand, the Dispa-SET model, which uses the MILP algorithm, is an open-source model that has been applied in previous research in different countries, including Bolivia. Both models analyze the components and interconnections between different energy sectors, allowing the comparison of the impact of different technologies on the energy system and finding the best future alternative [9]. They can also find optimal solutions for energy systems under predefined constraints [10]. SDDP and Dispa-SET models have been used in previous research for hydro-thermal scheduling. For example, Gjerden et al. [11] applied SDDP for the Norwegian hydropower system, with 500 hydropower modules applying a stochastical time resolution of one week, showing that the statistical properties of the inflow model significantly impacts the model performance and that the accuracy of SDDP-based models are dependent on the number of inflow series. In [12] the soft-linking between two models was done, where Dispa-SET is used for mid-term hydrothermal coordination, optimal unit commitment and power dispatch over the whole African continent. In this article, the water-energy nexus was analyzed, whose indicators reveal that the water stress induced by power generation activities is problematic in some power pools. Zarate et al. [13] modelled the Bolivian power system on Dispa-SET, focusing on hydropower to assess the effects of different rainfall years on the ability of hydropower to generate and store electricity in the Bolivian electric system.

In this paper, these two energy models are compared, applied to the Bolivian electric system for the year 2026, where renewable energy projects are planned to be implemented. The paper is structured as follows: Section 2 provides an overview of the Bolivian case study; Section 3 describes the methodology that was followed for the model mapping and the simulation configuration; Section 4 presents the modelling results and comparison between the two models; Section 5 concludes.

2. Case study - The Bolivian energy system

The Bolivian electric system consists of the National Interconnected System (SIN) and the Isolated System, which provide electricity to main cities and remote places, respectively. This study focuses on the SIN, which is divided into four zones: North (La Paz and Beni), Oriental(Santa Cruz), Central(Oruro and Cochabamba) and South (Potosí, Chuquisaca and Tarija) (Fig.1). In 2021, SIN energy production was 9628.93 GWh, 33.24% from hydro, 62.31% from thermal (mainly gas), 3.52% from solar PV and 0.93% from wind power plants. [14]

Figure 1: The Bolivian National Interconnected System zones: North (La Paz and Beni), Oriental(Santa Cruz), Central(Oruro and Cochabamba) and South(Potosí, Chuquisaca and Tarija), with the new transmission lines scheduled to be implemented by 2026 [15].

The Bolivian electric plan 2025 [16], proposes expanding the electrical infrastructure and gradually incorporating the Isolated System into the SIN. The plan targets 70 % hydroelectric generation and 4 % alternative energy generation [16]. The plan includes the incorporation of Miguillas power plant with two generation units, Umapalca with 83 MW and Palillada with 116 MW, both located in La Paz; Ivirizu power plant with two generation units, Sehuencas with 194 MW and Juntas with 89 MW of installed power located in Cochabamba, and Condor with 1,4 MW in Potosi. The renewable generation projects to 2025 consider the incorporation of 2 wind farms, La Ventolera, with 23 MW of power, located in Tarija, and Warnes-2, with 20 MW of power, located in Santa Cruz [16] [15]. The total installed capacity in 2022 was 3495 MW, and it is planned to increase to 4036 MW with the hydroelectric and renewable energy projects for 2025. Figure 2 shows the current installed capacity for each zone (2022) and the projected installed capacity for 2025 by zone, with new additions mostly in the form of hydro, VRE and biomass. The existing VRE installed capacity is 29.4% in 2022 and is expected to grow to 38.8% by 2026. The new VRES projects are mainly in the form of hydro and wind.

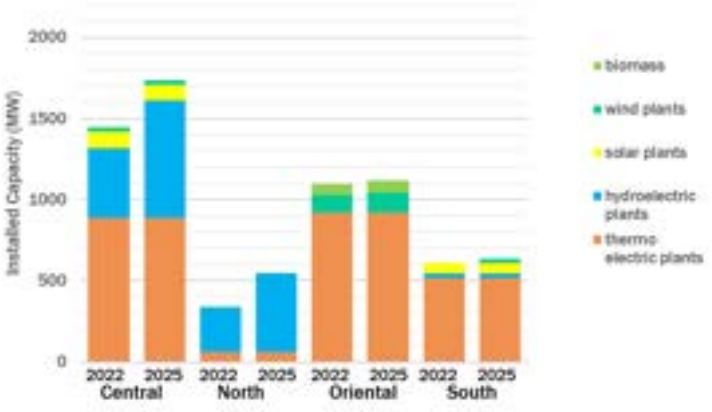

Figure 2: Current (2022) and projected (2025) total installed capacity (MW) by zone. New additions are mostly in the form of hydro, VRE and biomass.

The expansion of the electrical transmission infrastructure between the neighbouring zones by 2026 includes [17] [15].:

- A new transmission line between Central and Oriental zone with the Carrasco-Brechas line of 500 KV, which in the future will be part of the exporting lines to neighboruring countries.
- A new transmission line of 230 KV between Central and North zone with Santivañez-Miguillas line
- A new line between the Central and South zone with 230 KV in the line Mizque-Sucre.

3. Methodology

The work presented in this paper is a continuation of previous Dispa-SET studies for the Bolivian energy system [18] [19], with the novelty of probabilistic analysis of results. The input data for Dispa-SET was obtained from the Bolivian electric system of SDDP software, which is used by CNDC (Comité Nacional de despacho de carga) and ENDE Corporation, to ensure consistency and compare simulation results for 2026 after incorporating new generation and transmission infrastructure.

3.1. Stochastic dual dynamic programming model

SDDP model is used to optimize the expected value of a benefit function or a cost function over a given planning horizon involving weeks or months stages [20]. The optimization problem in this model is solved using dynamic programming, and the solution is used to update a set of dual variables [**?**]. SDDP breaks down the multistage nonlinear problem into a series of stage linear problems (assuming that the overall problem is convex). The dual variables are then used to formulate and solve a linear programming problem that generates a new set of feasible solutions. Rougé et.al. [20] says: " The basic idea behind SDDP is to approximate the convex benefit-to-go function by Benders cuts, mathematical objects that can be thought of as hyperplanes. The algorithm then simulates reservoir operation decisions by using these hyperplanes approximating the true benefit-to-go functions".

SDDP software is a hydrothermal dispatch model with a detailed representation of the transmission network. SDDP considers hydro plants operations, thermal plant modelling, spot markets, supply contracts, hydrological uncertainty, transmission network, and load variations to find the least-cost operating policy of a proposed

hydro system. The main outputs from SDDP are hydro and thermal generation, thermal operation costs, energy interchange, fuel consumption, deficit risks and energy not supplied, short-run marginal costs and marginal capacity benefits.

3.2. Mixed-Integer linear programming model

Dispa-SET, a deterministic dynamic programming algorithm, is an open-source unit commitment and economic dispatch (UCED) model, developed within the Joint Research Centre of the EU Commission. It is a multi-sectoral energy model that represents the short-term operation of large-scale power systems with a high level of detail to assess the flexibility needs of systems with a high share of VRES, solving the UCED problem. Dispa-SET is expressed as a Mixed-Integer-Linear-Program (MILP), written in python and solved in GAMS. The model's objective function is to minimize the total operational system cost [21].

Dispa-SET includes a Mid-Term Scheduling (MTS) module, a relaxed formulation of the core hydro thermal MILP formulation, executed in the pre-processing phase, enabling fast and efficient pre-allocation of the State of charge (SOC) of all storage units present in the system. Since Dispa-SET simulations are performed for a whole year with a time step of one hour, the problem dimensions are not computationally tractable if the optimization is done at once [12]. Therefore, in the unit commitment and power dispatch module (UCM), the problem is split into smaller optimization problems that are run recursively throughout the year. The initial values of the optimization for any given day are the final values of the optimization of the previous day. A look-ahead period is included and then discarded to avoid issues linked to the end of the optimization period. This optimal hydro allocation is particularly relevant in systems with a high share of hydro dams and pumped hydro reservoirs [12]. Results from MTS are used as guidance curves of the reservoir levels, which are then used as minimum level constraints in the UCM module.

3.3. Comparison between model capabilities

Both Dispa-SET and SDDP are dynamic, partial equilibrium, hydro scheduling models. The summary of modelling features between SDDP and Dispa-SET is shown in Table 1. Dispa-SET is a model that needs accurate input data that can be run in parallel on several historical weather years. The results from such analysis can be statistically processed and presented in a probabilistic format. SDDP is a stochastic model that needs a significant amount of historical data to calibrate the inputs, considering uncertainties of parameters. Dispa-SET is an open-source model, while SDDP is a commercial model. Dispa-SET has a higher temporal and technical resolution than SDDP, taking into account the variability and uncertainty of renewable energy sources, as well as the demand variability and network congestion.

Table 1: Comparison between SDDP and Dispaset models

	SDDP	Dispa-SET
Type	Stochastic	Deterministic/Probabilistic
Open Source	X	✓
Therm	Mid-term	Mid-term
Geographical area	National/Regional	Regional/National/Continental
Optimization	Dynamic LP	Dynamic MILP/LP
hydro scheduling	✓	✓
Unit Commitment and Power Dispatch	Limited	Full
Resolution	5 blocks/week	hourly/15 min
Equilibrium	Partial	Partial
Multisectorial	Gas/hydrogen/electricity/water	Any
Renewables representation	5 blocks/week	Per hour/ 15 min
Reserves	predefined	co-optimization
Network	DC Power flow	NTC/DC Power flow
Curtailment	X	✓
Shed Load	✓	✓

The inflow modules of the two models are different. The deterministic model (Dispa-SET) tries all possible historical inflows individually. SDDP, on the other hand, uses a stochastic inflow model (periodic auto-regressive model) that, based on the available historical data, generates synthetic inflows (mapping the unknown future with an unlimited amount of possible inflows) in an attempt to match the inflow profile of the historical data [22].

3.4. Model mapping

In this study, SDDP and Dispa-SET models were applied to the same input dataset of the Bolivian electric system to evaluate it for the year 2026 with the new infrastructure projects. Figure 3 presents the link between

SDDP and Dispa-SET models. In the inputs section, the parameters from SDDP are shown next to the equivalent parameters of Dispa-SET, for which conversion scripts written in python were used to have an automatic input data mapping. SDDP does the simulations of the system operation considering weekly stages with five demand blocks (Peak, Semi Peak, Intermediate, Medium and Low). To use the SDDP database for Dispa-SET, the weekly time step resolution was converted to an hourly resolution based on the five hourly demand blocks (Fig. 4) approved by AETN (Autoridad de Fiscalización y Control Social de Electricidad) [23].

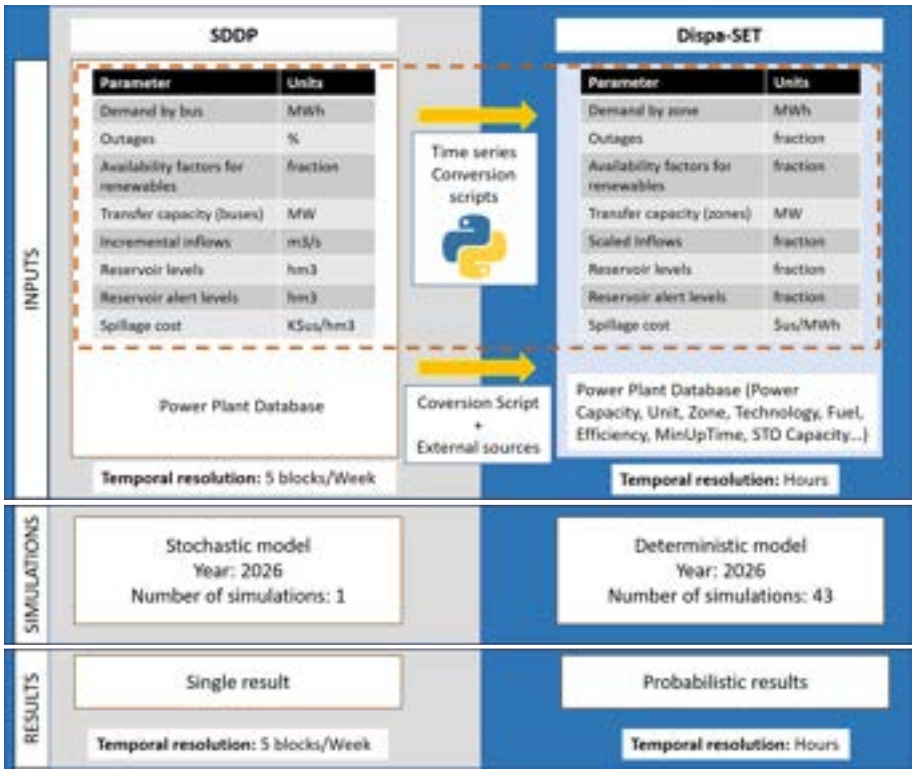

Figure 3: Link of SDDP databases to Dispa-SET for the input data and differences in the simulation configuration and results

Three types of data mapping were done:

- 1-1: Direct mapping of power plant data.
- 1-N: Time series mapping from five blocks per week to an hourly resolution, for parameters such as Outages and Availability factor.
- N-1: Time series mapping from five blocks per week to an hourly resolution, where the parameters described by bus in the SDDP database, such as demand and transfer capacity, were grouped by zone for Dispa-SET.

For Power Plant Database, besides the information from SDDP, external sources of information were needed for the operational parameters of generation units.

Day/Hour	1	2	3	4	5	6	7	8	9	10	11	12	13	14	15	16	17	18	19	20	21	22	23	24
Saturday	B	B	B	B	B	B	B	M	M	M	M	M	M	M	M	M	M	M	I	I	I	I	M	M
Sunday	B	B	B	B	B	B	B	B	B	B	B	B	B	B	B	B	B	B	M	I	I	M	M	B
Monday	B	B	B	B	B	B	B	M	M	M	M	M	M	M	M	M	M	M	I	S	S	I	M	M
Tuesday	B	B	B	B	B	B	B	M	M	M	M	M	M	M	M	M	M	M	I	P	S	I	M	M
Wednesday	B	B	B	B	B	B	B	M	M	M	M	M	M	M	M	M	M	M	I	P	S	I	M	M
Thrusday	B	B	B	B	B	B	B	M	M	M	M	M	M	M	M	M	M	M	I	P	S	I	M	M
Friday	B	B	B	B	B	B	B	M	M	M	M	M	M	M	M	M	M	M	I	P	S	I	M	M

Block	Hours	
Peak	4	P
Semi peak	6	S
Intermediate	16	I
Medium	81	M
Low	61	B

Figure 4: Hourly demand blocks approved by AETN, which show in which hours and days of a week each demand block is present [23].

Most Bolivian hydropower plants are part of a cascade system, where downstream water availability relies on

the usage of the unit upstream. Though weekly mean incremental inflow data is available, approximations of inflows and outflows for each unit are required. Three hydro inflow approximation hypotheses were conducted:

- The first one summing the inflows of the unit above plus the external inflows to each unit.
- The second approximation was applied for units that do not have generation capacity but gather or provide flows, using an approximation function to obtain its outflow and spillage.
- The third approximation was applied to Corani, the largest hydro dam, with 2958 storage hours. For this unit, the outflows were considered as the average of the total yearly inflows, considering that Corani has an almost constant generation during the year.

Approximations for each unit's historical weather years (1979 to 2021) were computed, and a statistical analysis was done with the expected generation of the computed inflows. For some units, the variation range between the weather years is particularly high, for example, Sehuencas, with an absolute difference of 1.335 TWh between the lowest and highest values. The approximation was compared to the generation plus spillage of SDDP data for the year 2026. Figure 5 shows that SDDP generation for each hydro unit fits into the range of the expected generation of the Dispa-SET model, proving the hydro inflow approximation hypothesis above-mentioned.

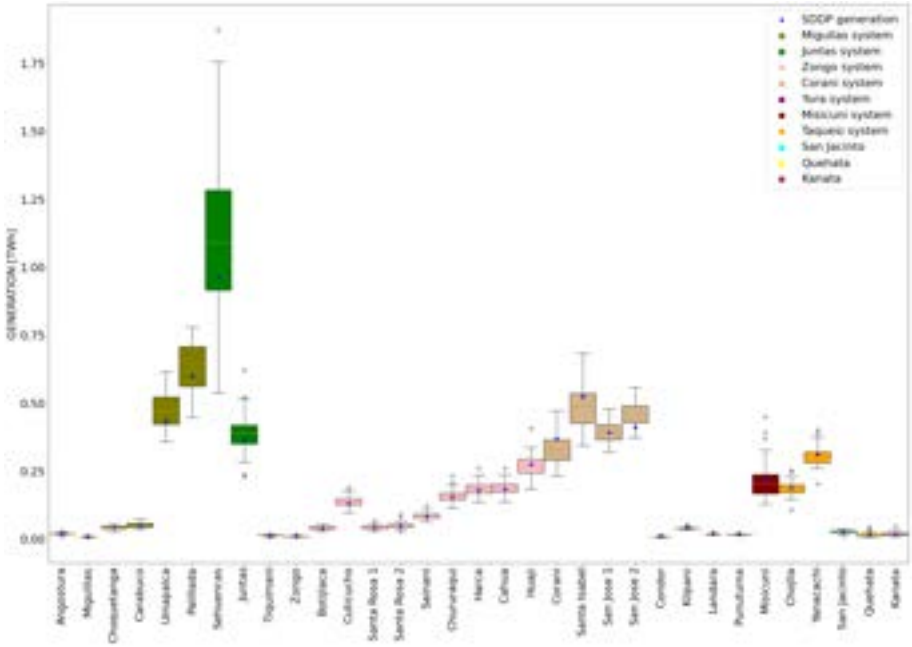

Figure 5: Comparison of SDDP and Dispa-SET generation based on inflows

Bolivia's SDDP simulation begins on the 1st of April, while Dispa-SET's starts on the 1st of January. Various parameters were influenced by the distinction in starting dates, particularly reservoir levels, alert levels, and initial reservoir volumes. Reservoir levels were derived from SDDP runs in Dispa-SET, and the initial reservoir volume inputted in SDDP simulations was adjusted the 1st of April in Dispa-SET.

3.4.1. Reservoir level constraints

The goal of the unit commitment problem is to minimize the total power, transportation system operational cost. The objective function of Dispa-SET is therefore, to minimize the total generation cost over the optimization period (Eq. (1)). In this study, the model has been expanded by the following constraints: Reservoir Alert Level and Spillage cost by unit, as proposed in Eq. (2), where the total system cost is defined as the sum of different cost items such as fixed, variable, ramping, start-up and shut-down, shed load, and the Cost of "storage Alert Level" and "Cost of Spillage" that have been added. In this equation, "i" stands for a subset of simulated hours for one iteration.

$$\underset{i \in I}{\text{minimize}} \left\{ SystemCostRollingHorizon = \sum_{i} SystemCost_i + StorageLevelViolationCosts_i \right\} \quad (1)$$

$$
\begin{aligned}
SystemCost_i = {} & FixedCost_i \cdot TimeStep + StartUpShutDownCosts_i \cdot TimeStep \\
& + VariableCost_i \cdot TimeStep + RampingCost_i \cdot TimeStep + CurtailmentCosts_i \cdot TimeStep \\
& + TransmissionCosts_i \cdot TimeStep + EnergyNotServedCosts_i \cdot TimeStep \\
& + CostStorageAlert_i \cdot LL_StorageAlert \cdot TimeStep + CostSpillage_i \cdot Spillage \\
& + CurtailedPower_i \cdot CostCurtailment \cdot TimeStep
\end{aligned} \tag{2}
$$

The constraint Cost of Storage Alert prevents the reservoir level to go below Storage Alert Level, which will only be violated to avoid power rationing and is set to the equal 1,1* Marginal Cost of the most expensive unit in the system, as in proposed in (3), where ”s” is the set of all storage units (with reservoir).

$$
\begin{aligned}
& StorageCapacity_s \cdot Nunits_s \cdot min\left(StorageAlertLevel_{s,i}, AvailabilityFactor_{s,i}\right) \\
& \qquad \leq StorageLevel_{s,i} + LL\_StorageAlert_{s,i}
\end{aligned} \tag{3}
$$

3.5. Simulation configuration

To consider different future possibilities based on water availability, 43 simulations were run in Dispa-SET. Each simulation reflected the inflows from a different historical weather year (1979-2021). During the historical weather years, 1984 was the wettest year, and 2016 was the driest (Fig 6). In Dispa-SET, all units are considered individually for each hydro plant to be observed in the results. The constraint ”Reservoir Alert Level” is considered in both models for particular hydro dams such as Corani, Miguillas, Angostura, Zongo, San Jacinto and Misicuni.

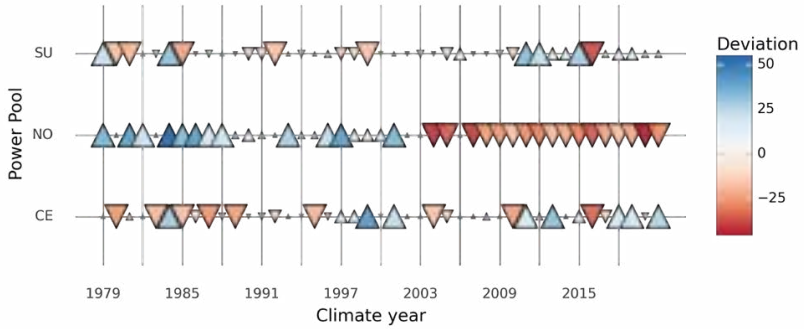

Figure 6: Annual variability (percentage deviation from the mean) of inflows in the 43 climate years. The size of the triangles indicates the inter-annual variability, the direction highlights the increase or decrease compared to the mean, and the colour indicates the intra-annual variability.

From a computational point of view, the variability of the inflows (from 1979 to 2021) directly impacts the simulation times. The simulation time was ranged from 2 hours up to 25 hours for the year 2001, which is the year with excessively high inflows that might not be historically accurate.

4. Results and Discussion

This section presents the expected configuration of the Bolivian electric system for the year 2026. All new VRES and hydro projects are included.

4.1. Energy mix

Figure 7 shows the share of renewable generation for 2026 from all the simulations ordered from the highest to the lowest share of renewable generation. Bolivian electricity production from renewable energy is expected to range between 45.9 % and 65.2 % in 2026. The share of renewable energy in Bolivia in the Stochastic model is 59%, which fits in the range of Dispa-SET share. The North zone is expected to have the highest share of renewable generation with 98 % due to the new hydro projects planned to be installed in this zone. The Central zone is expected to share between 60.3 % to 79 % of renewable energy. Oriental and South zones are expected to still rely more on natural gas to produce electricity than renewable energy. Despite the connections between zones, Bolivia is expected to still depend on natural gas to generate electricity.

In the Bolivian electric plan 2025, VRE was planned to reach 74 % of the total production. From the probabilistic results of the MILP model, it can be seen that with the addition of new power plants, VRE could reach between

45.9% and 65.2 % of the total generation, where biomass is excluded, whereas, in SDDP the VRE share represent 59%.

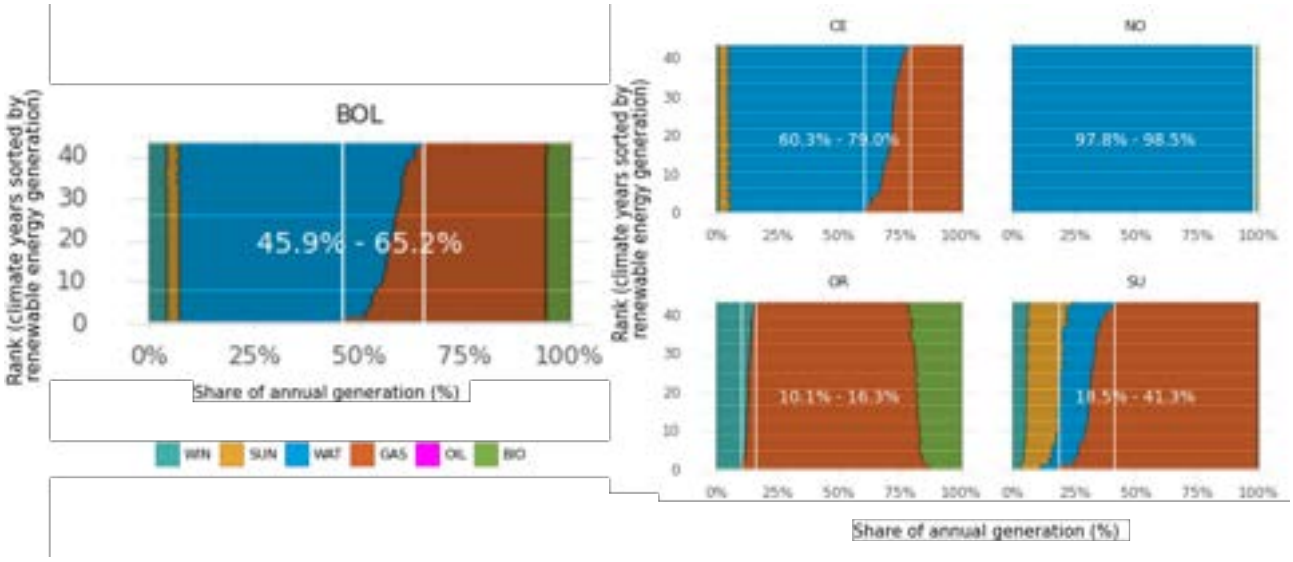

Figure 7: Generation mix and renewables share for the considered climate years of Bolivia and by zone for 2026 from the 43 simulations results, ordered by the share of renewable generation. White lines indicate minimum and maximum shares of renewable generation.

The difference in the total hydro generation between SDDP and Dispa-SET (an average weather year) is 5 %, the Central zone has a difference of 0.1%, the North zone has a difference of 11%, and the South zone has a difference of 7 %. The hydro units with the highest impact on the total generation are Sehuencas, Palillada and Santa Isabel, with a share of 14.5%, 10.6% and 9.3% of the total generation, respectively.

4.2. Power dispatch

The year 2026 power dispatch was analyzed per zone using inflows closest to the average weather year (Fig 8). Bolivia experiences dry months from May to October when the electric system relies on thermo-electric units. During the wet season (December to April), North and Central zones primarily utilize hydroelectric plants. In the dry season, the Central zone uses gas and hydro plants, exporting energy throughout the year to the North, Oriental, and South zones. Conversely, the North zone imports energy during the dry season but exports during the wet season due to hydroelectric production. Oriental and South zones import energy during the wet season but generate electricity from natural gas in the dry season. While the Oriental zone can export its gas-generated production, the South zone still needs to import energy. In all zones, the grid is stable, and there is no congestion in the transmission lines. As for the reservoir levels, they are filled during the wet season.

4.3. Reservoir Levels and generation

The largest Bolivian hydro dams in the Central zone are Corani (with 2958 storage hours), Misicuni (with 2779 storage hours), Miguillas (that will be implemented by 2026 with 1072 storage hours), Angostura (with 525 storage hours), Sehuencas (a new power plant with 257 storage hours); and in the South zone is San Jacinto (with 730 storage hours).

The variation in water supply affects these units' generation, reservoir level and spillage. Simulations results for all these units are presented in Fig. (9), where the black line is the median of the results of all the historical data, the regions with darker colour show that 20% of the results are in that range. The lighter colour shows that 100% of the results are in that range. From the inflows plots, it can be seen that for some years, the inflows are extremely high compared to the median, which indicates the long simulation time, which for some years took up to 25 hours.

The Reservoir levels were compared between the two models. SDDP reservoir level results are plotted as a grey dashed line. The reservoir alert level was included as a solid red line. The inflows are higher during the wet season, and reservoir levels do not go below the reservoir alert level. Sehuencas hydroelectric plant does not have an alert level, but its reservoir level follows a similar tendency to SDDP results. Angostura hydroelectric plant has an alert level and a defined volume for the 1st of April (green cross). For this unit, the reservoir level of SDDP is higher than the median of Dispa-SET in the dry season. However, it's still in the range of the results

of Dispa-SET. The reservoir level of Miguillas hydroelectric plant follows a similar tendency to SDDP. Corani reservoir level in SDDP simulation goes up from 0,3 to 0,54 the last week of December. However, given the available inflows, this would not happen, so for this unit, Dispa-SET results are more reliable.

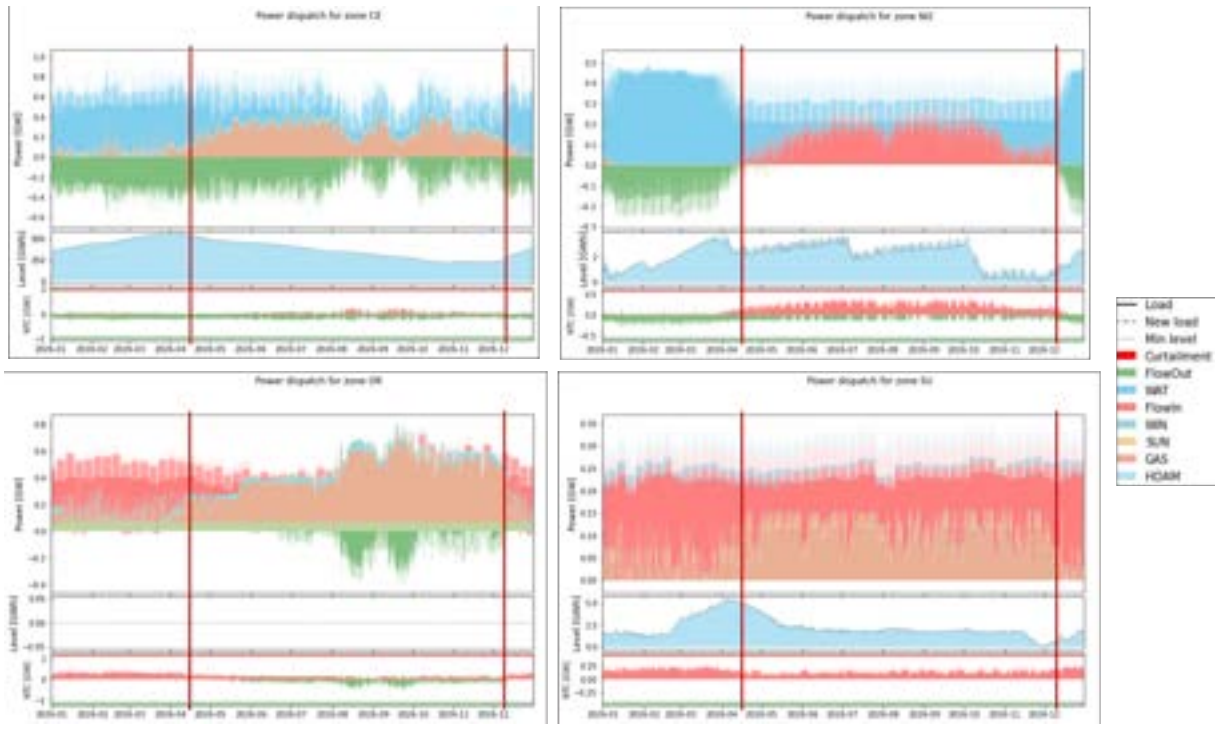

Figure 8: Power dispatch by zone for 2026 based on an average year (2003). The red vertical lines show the limits for the dry season, from April to December

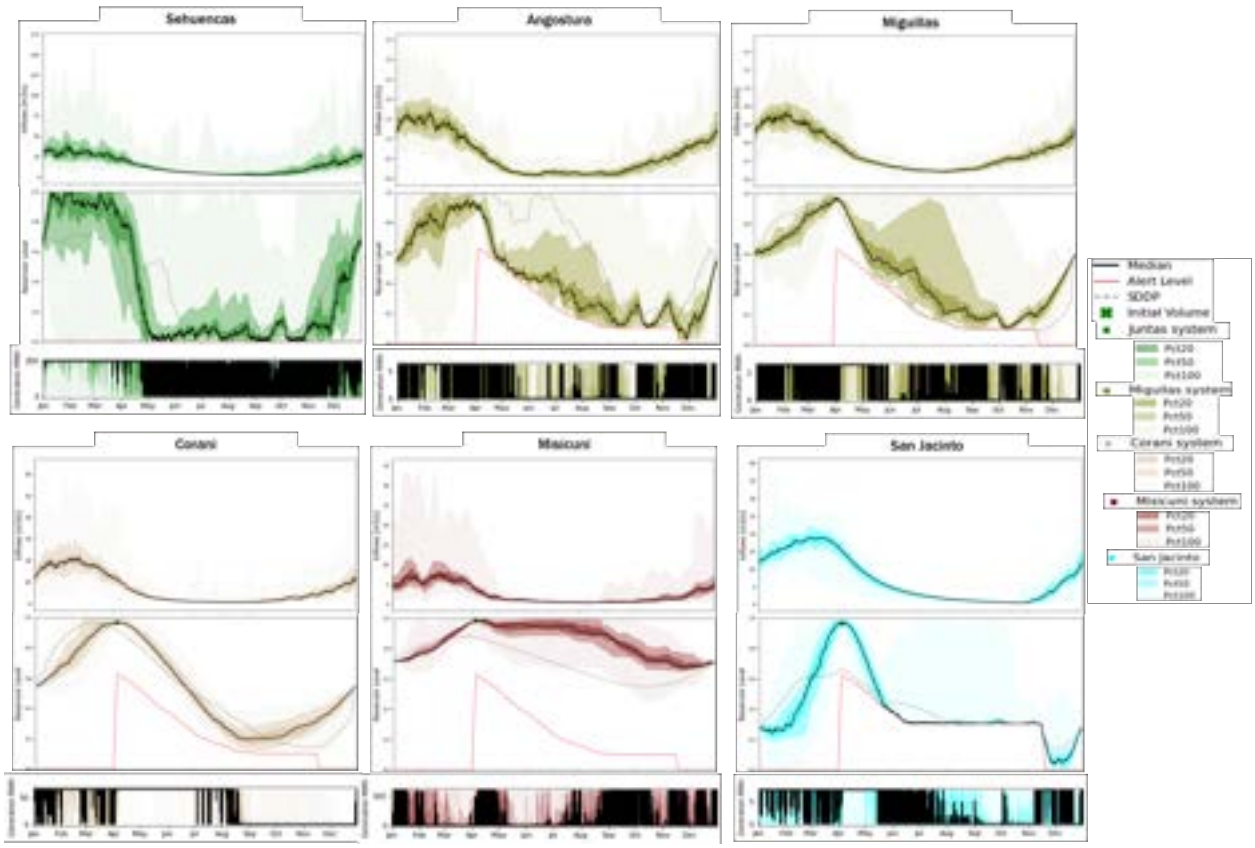

Figure 9: Inflows, Generation and Reservoir Levels from the 43 runs for the biggest hydro dams of Bolivia.

The maximum generation variation range between the weather years was found for Sehuencas, with an absolute difference of 0.941 TWh between the lowest and highest generation (for years 2020 and 1985, respectively). The difference in SDDP generation related to the weather years is 44% compared to the lowest value, 5.7% compared to the median, and 53% compared to the highest value.

4.4. Spillage

Spillage results for both models were compared (Fig.10). Dispa-SET's range of spillage for 43 years is shown in a boxplot for each unit, while blue dots represent SDDP's spillage results. The spillage results from SDDP fit into the range of the results obtained in Dispa-SET. The units Kanata, Zongo, Tiquimani, Kilpani and Punutuma in Dispa-SET do not have any spillage for any year, while in SDDP, there is some spillage. The variation range between the weather years is exceptionally high for Sehuencas, with an absolute difference of 0.54 TWh between the lowest and highest values. The difference in Sehuencas' SDDP spillage related to the weather years is 100% compared to the lowest value, 15.6% compared to the median and 260% compared to the highest value.

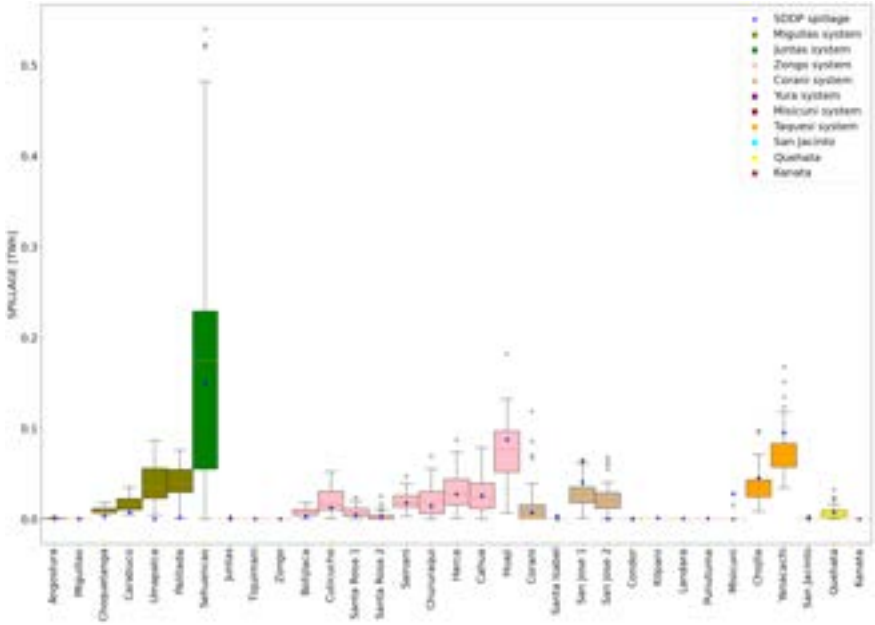

Figure 10: Spillage comparison for 2026 from SDDP (blue dots) and Dispaset (boxplot)

4.5. Water value

The expected marginal value of water, referred as storage shadow price, expresses the opportunity cost of water [24]. Figure 11 shows the Storage Shadow price for the main hydroelectric dams for a wet year (1984), a dry year (2016) and an average year (2003). The storage shadow price, dependent on the water value, is higher in the dry season than in the wet season. For the wet year, the Corani storage shadow price reaches 1500 from September to December, while in the dry year, the price reaches that value one month earlier. Comparing this with the reservoir level (9), the median reaches the lowest level in September. For San Jacinto, the shadow price is higher in December when the reservoir level reaches a lower value. In general, for the dry year, a high shadow price is present during more hours than the wet and average year since water availability is lower.

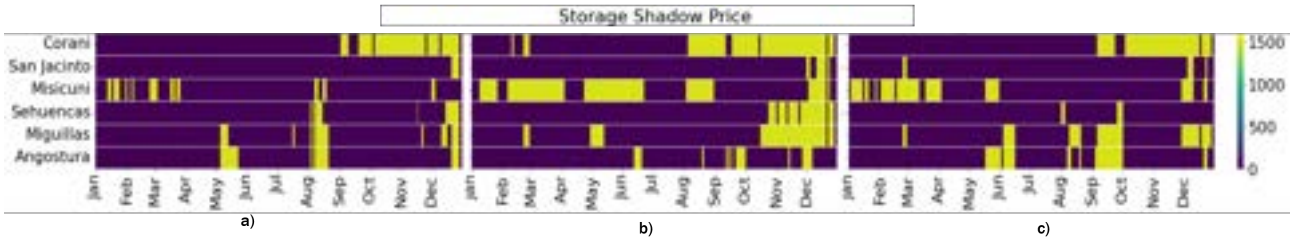

Figure 11: Storage shadow price for the main hydro dams a) for a wet year (1984) b) for a dry year (2016) c) for an average year (2003)

5. Conclusions

The article compares the results obtained by two model formulations, SDDP and MILP, applying the same input data and constraints to analyze the Bolivian electric system to 2026. In the MILP formulation, 43 simulations were done to obtain probabilistic results since the Bolivian electric system is highly dependent on hydropower, and its generation varies during the year and year by year. These results were then compared with SDDP. The novelty of this work is the probabilistic way to show the likelihood of certain events happening, such as the distribution of the State of charge (SOC) for each hydro dam, dispatch of each hydro unit, spillage and generation distribution.

The automatic input data mapping from SDDP to the MILP model was successfully implemented. For the inflows of hydroelectric power plants in a cascade system, an approximation was made for each unit for all the historical weather years. We show that SDDP values are within the MILP model range. Furthermore, in the objective function of the MILP model, constraints have been added for the reservoir level (reservoir level alert) and the spillage cost.

Simulation results indicate that the two models' power generation is in the same range. The maximum variation ranges between the weather years are found for the Sehuencas hydropower plant, which is the unit that has the highest impact on the power system, comprising 14.5% of the total generation. The maximum generation variation between the weather years for Sehuencas is 44% compared to the lowest generation value, 5.7% compared to the median and 53% compared to the highest generation.

The reservoir levels obtained in the probabilistic results follow a similar tendency to the reservoir levels of SDDP, except for some minor deviations, especially in small units with low storage hours. Spillage from SDDP falls between Dispa-SET ranges. Sehuencas power plant has the maximum spillage variation ranges between the weather years. The difference in Sehuencas' SDDP spillage related to the weather years is 100% compared to the lowest spillage value, 15.6% compared to the median and 260% compared to the highest spillage value.

The MILP and SDDP formulations can be used as complementary models for decision-making on the Bolivian electric system operation, taking advantage of their strengths and compensating for their limitations. SDDP has a greater detail in the representation of the electric network, and it takes into account uncertainties of the input parameters. Incontrast, the MILP formulation has a higher time resolution that can provide a more detailed and accurate resolution for renewable energy and has probabilistic results that provide statistical analysis. Low-resolution models, like SDDP, may exhibit deviations from more detailed modelling, especially for renewable systems, not considering the dependency of VRE on weather conditions that vary throughout the day. On the other hand, high-resolution models capture the system's dynamic due to the change in weather conditions.

Acknowledge

The authors acknowledge ENDE Corporation for their support and access to SDDP simulation results. We are acknowledged for the Swedish International Development Cooperation Agency financial support.

References

[1] J. D. Sachs, G. Schmidt-Traub, M. Mazzucato, D. Messner, N. Nakicenovic, and J. Rockström, "Six transformations to achieve the sustainable development goals," *Nature Sustainability*, vol. 2, no. 9, p. 805 – 814, 2019. Cited by: 574.

[2] A. Papavasiliou, Y. Mou, L. Cambier, and D. Scieur, "Application of stochastic dual dynamic programming to the real-time dispatch of storage under renewable supply uncertainty," *IEEE Transactions on Sustainable Energy*, vol. 9, no. 2, p. 547 – 558, 2018. Cited by: 63.

[3] C. Allen, G. Metternicht, and T. Wiedmann, "National pathways to the sustainable development goals (sdgs): A comparative review of scenario modelling tools," *Environmental Science and Policy*, vol. 66, p. 199 – 207, 2016. Cited by: 149; All Open Access, Green Open Access.

[4] M. de Medio Ambiente y Aguas Autoridad Plurinacional de la Madre Tierra, "Nationally determined contribution (ndc) of the plurinational state of bolivia: Ndcs update for the 2021-2030 period within the framework of paris agreement," 2021.

[5] S. Pfenninger, A. Hawkes, and J. Keirstead, "Energy systems modeling for twenty-first century energy challenges," *Renewable and Sustainable Energy Reviews*, vol. 33, pp. 74–86, 2014.

[6] S. Pfenninger, J. DeCarolis, L. Hirth, S. Quoilin, and I. Staffell, "The importance of open data and software: Is energy research lagging behind?," *Energy Policy*, vol. 101, pp. 211–215, 2017.

[7] L. M. Hall and A. R. Buckley, "A review of energy systems models in the uk: Prevalent usage and categorisation," *Applied Energy*, vol. 169, pp. 607–628, 2016.

[8] A. R. de Queiroz, “Stochastic hydro-thermal scheduling optimization: An overview,” *Renewable and Sustainable Energy Reviews*, vol. 62, pp. 382–395, 2016.

[9] M. G. Prina, G. Manzolini, D. Moser, B. Nastasi, and W. Sparber, “Classification and challenges of bottom-up energy system models - a review,” *Renewable and Sustainable Energy Reviews*, vol. 129, 2020. Cited by: 93; All Open Access, Green Open Access, Hybrid Gold Open Access.

[10] J. Priesmann, L. Nolting, and A. Praktiknjo, “Are complex energy system models more accurate? an intra-model comparison of power system optimization models,” *Applied Energy*, vol. 255, p. 113783, 2019.

[11] K. S. Gjerden, A. Helseth, B. Mo, and G. Warland, “Hydrothermal scheduling in norway using stochastic dual dynamic programming; a large-scale case study,” in *2015 IEEE Eindhoven PowerTech*, pp. 1–6, IEEE, 2015.

[12] M. Pavičević, M. De Felice, S. Busch, I. Hidalgo González, and S. Quoilin, “Water-energy nexus in african power pools – the dispa-set africa model,” *Energy*, vol. 228, p. 120623, 2021.

[13] S. Zarate, M. Villazón, M. Navia, S. L. Balderrama Subieta, and S. Quoilin, “Modeling hydropower to assess its contribution to flexibility services in the bolivian power system,” 2021.

[14] C. N. de Despacho de Carga, “Memoria anual 2021,” 2022.

[15] C. N. de Despacho de Carga, “Programación de mediano plazo en el sistema interconectado nacional,” 2022.

[16] M. de Hidrocarburos y Energía, “Plan eléctrico del estado plurinacional de bolivia 2025,” 2014.

[17] E. Transmisión, “Memoria anual 2021,” 2022.

[18] R. A. Rojas Candia, S. L. Balderrama Subieta, J. A. Araoz Ramos, V. Senosiain Miquélez, J. F. H. Peña Balderrama, J. G., and S. Quoilin, “Techno-economic assessment of high variable renewable energy penetration in the bolivian interconnected electric system,” *International Journal of Sustainable Energy Planning and Management*, vol. 22, 2019.

[19] M. Navia, R. Orellana, S. Zaráte, M. Villazón, S. Balderrama, and S. Quoilin, “Energy transition planning with high penetration of variable renewable energy in developing countries: The case of the bolivian interconnected power system,” *Energies*, vol. 15, no. 3, 2022.

[20] C. Rougé and A. Tilmant, “Using stochastic dual dynamic programming in problems with multiple near-optimal solutions,” *Water Resources Research*, vol. 52, no. 5, pp. 4151–4163, 2016.

[21] M. Pavičević, A. Mangipinto, W. Nijs, F. Lombardi, K. Kavvadias, J. P. Jiménez Navarro, E. Colombo, and S. Quoilin, “The potential of sector coupling in future european energy systems: Soft linking between the dispa-set and jrc-eu-times models,” *Applied Energy*, vol. 267, p. 115100, 2020.

[22] G. G. Pétursson, K. Jónasson, E. Benedikt Hreinsson, and Linnet, “A comparison of two hydro scheduling algorithms, sddp and lpsim,” in *2013 48th International Universities’ Power Engineering Conference (UPEC)*, pp. 1–5, 2013.

[23] A. de Fiscalización y Control Social de Electricidad, “Resolución ae nº 0216/2012,” 2012.

[24] A. Helseth, M. Fodstad, M. Askeland, B. Mo, O. B. Nilsen, J. I. Pérez-Díaz, M. Chazarra, and I. Guisández, “Assessing hydropower operational profitability considering energy and reserve markets,” *IET Renewable Power Generation*, vol. 11, no. 13, pp. 1640–1647, 2017.

Towards low-carbon energy systems: The case of Bolivia until 2035

Pablo Jimenez Zabalaga[abc], Sergio Balderrama[c], Matija Pavičević[a], Evelyn Cardozo[c], Paolo Thiran[a], Gauthier Limpens[a] and Hervé Jeanmart[a]

[a] Institute of Mechanics, Materials and Civil Engineering, Université Catholique de Louvain, Louvain-la-Neuve, Belgium, pablo.jimenez@uclouvain.be, CA
[b] Departamento de Mecánica, Universidad Mayor de San Simón, Cochabamba, Bolivia
[c] Centro Universitario de Investigaciones en Energías, Universidad Mayor de San Simón, Bolivia

Abstract:
Energy is vital to reduce poverty and improve social and economic development. For more than a century, modern economies have based their growth on fossil fuels, which has led to global warming, environmental pollution, and social problems. In accordance with the Paris Agreement (2015), governments have committed to evaluating their energy systems to seek appropriate solutions to support their decarbonization and keep global warming well below 2^{o}C. In order to achieve this objective, developing countries are making considerable efforts, among which is considered a shift to the use of renewable energy sources to satisfy their growing demand. Despite the current development and planning for the sector, there is room for improvement within the long-term planning and evaluation of energy systems. This paper analyses the difference between fossil-based and renewable-based growth in terms of economics, technical and environmental effects in Bolivia. To do so, all the country's energy sectors, including electricity, heat, and mobility, are covered and optimized through the open-source energy system modeling framework EnergyScope. Results showed a sustainable energy scenario in 2035, which accounted for 66% of renewable share and 44.64 €/t$CO_{2\text{-eq.}}$ related to a compensation value for the difference with the business-as-usual scenario based on future government plans. This work demonstrated that a Bolivian energy system with a high share of renewable resources is possible, leading to energy sovereignty addressing climate change.

Keywords:
Bolivia, Sustainable growth, Renewable energy, Energy system modeling, Energy development.

1. Introduction

Poverty reduction, industrial activities, and improvement of education and healthcare services are strongly related to the energy a society can consume. Nonetheless, the availability of energy supply is not the only objective, but also to achieve sustainability to maintain an ecological balance, social equity, and economic vitality [1]. The use of fossil fuels has led to global concern about the emissions of greenhouse gases (GHG). Therefore, one hundred and ninety countries have pledged to the Paris Climate Agreement to limit the global average temperature increase to 1.5℃ or well below 2℃ and have established clear goals to be fulfilled by the years 2030 and 2050 [2]. Decarbonization exploits pressure on all nations globally, but even more low and middle-income countries, which in most cases, have planned to rely on fossil fuels to achieve development [3]. Although Bolivia possesses a relatively low contribution to global GHG emissions (0.21% of the total 48.6 GtonCO_2eq registered in 2021) [4], it was the 43th country with the highest emissions per capita in 2021 (9.6 tonCO_2eq/person) [5]. Thus, Bolivia has signed the agreement and is putting significant efforts to meet the commitment and also become a primary net exporter of electricity in South America [6].
According to the information provided by the Ministry of Hydrocarbons and Energy (MHE), Bolivia's total primary energy supply (TPES) in 2021 was 202.9 TWh, based mostly on fossil fuels (80.7% and 11.9% of the energy coming from fossil gas (FG) and oil, respectively). From this value, 58% corresponded to gas export (117.4 TWh) [7]. Related to other sources, such as biomass, hydro, solar, and wind energy, reached 7.4%. Similarly, the power sector has relied heavily on fossil gas for the last two decades. The Bolivian power grid is divided into the National Interconnected System (SIN) and the Isolated Systems (SAs). For instance, the country's total installed electricity generation capacity was 3.72 GW for 2021, of which 71.03% comes from thermoelectric power plants, 20.36% from hydropower plants, and 8.60% from other renewable sources such as wind energy and photovoltaic systems [6]. Moreover, fossil fuel-based electricity generation is subsidized by approximately 46.63 €/MWh for diesel [8], and 3.95 €/MWh for FG (Supreme Decree No. 29510) [9]. In this context, the government has established policy guidelines, including universal electricity access, reducing the consumption of petroleum derivatives, and increasing renewable energy use for electricity generation [10].

Nevertheless, most of Bolivia's energy objectives and projections are based on 2007 statistics and extend until 2030. Recent expansion plans for the sector are described in the Patriotic Agenda for 2025 [11] and the update of the Intended Nationally Determined Contribution (INDC) [2]. For instance, the Electrical Plan of the Plurinational State of Bolivia (PEEBOL2025) presented by the MHE stipulated the installation of 183 MW of renewable energy by 2025 [12], and the Alternative Energy Development Plan (PDEABOL2025) included a simple estimation of the renewable energy potential of the country [13]. Recent projections from the National Electricity Company (ENDE) indicate that 74% of the newly installed and existing capacity will be hydropower (Hydro dam and hydro run-of-river), 4% other renewable, 12% combined cycle plants, and 10% thermal power plants. Nonetheless, only the SIN is accounted for in these forecasts. So, electrification plans for rural communities that cannot be included in the SIN are also required [12].
Furthermore, Bolivia aims to become an electricity exporter to neighboring nations. With the new large hydropower capacity inclusion, the electricity exports could account for up to 21% of total electricity exports in South America [14]. Besides the estimated hydroelectric potential of 39.86 GW related to the watercourses of the large rivers that surround Pando, Beni, and the strip that goes from the Yungas of La Paz in the north of the country to Tarija in the south, Bolivia holds a high RE potential, which is distributed throughout its territory. Thus, the country has a high solar energy potential due to its position south of the equator line and high altitude above sea level (higher than the international solar radiation average). Practically, 97% of all the national territory is suitable for solar energy, and the remaining 3% have been identified as areas of dense cloudiness located to the east of the Andes region [15]. According to Bolivia's Atlas of global solar radiation, the existing solar radiation in the country's lowlands (Santa Cruz, Beni, Pando, and north of La Paz) reaches a maximum of 5.1 kWh/m^2/day. At the same time, in the sector of the valleys (Cochabamba, Chuquisaca, and Tarija), this value can vary between 5.1 and 6.7 kWh/m^2/day and in the Altiplano (La Paz, Oruro, and Potosí), the radiation is between 6.7 and 9.5 kWh/m^2/day [16]. The most robust wind resource is located in the southern and western regions of the department of Santa Cruz, in the southwestern sector of the department of Potosí, in a strip to the west and south of La Paz and Cochabamba [17]. Furthermore, twenty-one potential geothermal resources have been detected in the country's western mountain range, eastern mountain range, and Altiplano, near the departments of Potosí, Oruro, and La Paz [15]. Significant biomass resources are available in the country, likewise. For instance, forest biomass such as firewood and logs can be extracted in the Amazon region principally. In 2005, Bolivia possessed a wood stock of 317 million m^3 in its forested area. It was estimated that the sustainable production capacity of the Bolivian forest was 20 million m^3 of wood stock per year [15, 18]. Due to the country's unique natural circumstances, Bolivia produces various agricultural products. According to the agricultural census conducted by the National Institute of Statistics, the six most important crops grown in Bolivia are sugarcane, soy, sorghum, corn, rice, and sunflower, with the Department of Santa Cruz being the primary producer [19]. Morató et al. estimated that approximately 3.7 Mton/year of sustainable biomass on a dry basis is available in Santa Cruz [20]. Even though agricultural and forest residues are abundant in Bolivia, they are not utilized as a low-cost energy source to increase the proportion of renewable energy in the energy mix and reduce fossil fuel consumption.
The Bolivian energy sector is the second largest contributor to the country's GHG emissions (After agriculture, forestry, and other land uses). Although the country lacks rigorous emissions reduction targets, the INDC, presented by the authorities to United Nations Framework Convention on Climate Change (UNFCCC), projected a decrease in GHG emissions from 0.41 tonCO_2eq/MWh in 2015 to 0.04 tonCO_2eq/MWh in 2030 in the country's power sector [2, 21]. Additionally, the Global Climate Risk Index (IGRC) of 2021 ranked Bolivia as the most affected and the tenth most vulnerable country in the world [2]. This highlights Bolivia's need for strategic energy policies and carbon reduction goals to protect its most vulnerable communities and rich biodiversity. Thus, the energy system will allow renewable energy (RE) to be competitive, cope with subsidies, and deal with the absence of negative GHG emission pricing. Therefore, the focus of this study is to model a fully sustainable transition for Bolivia across all energy sectors and assess the feasibility of such a transition in terms of economics, technical and environmental effects to help shape future Bolivian society's energy behavior and reach the objectives for a long-term sustainable energy system with low-carbon emissions. The remainder of the paper is structured as follows. Section 2 describes the methods of the EnergyScope model. Section 3 presents the current Bolivian energy system and information about resources, demand, and technologies. Section 4 provides results by sector for each scenario. These results and main limitations are discussed in Section 5. The main conclusions are summarised in Section 6, then recommendations for future works are made.

2. Methods

The present research relies on *EnergyScope TD*, a bottom-up linear programming modeling framework for the long-term planning of energy systems, including a high share of RE and representing the heating, mobility, and electricity sectors equally [22]. It has already been applied to develop energy transition scenarios for European countries such as Switzerland [22, 23], Belgium [24], Italy [25], as well as Uganda [26]. Given demands in the different sectors and resources, the model identifies a design and an hourly operation optimisation of

the conversion technologies to minimize the overall system cost, considering a constraint on greenhouse gas emissions. The main input data of EnergyScope TD are founded on three elements: resources, technologies (energy conversion, storage and infrastructure), and demand, as depicted in Fig. 1. Furthermore, it involves typical days (TD) to reduce the computational time (around one minute on a personal laptop) while keeping a simple and straightforward formulation. The reconstruction method by Gabrielli et al. enables consideration of seasonal phenomena [27]. In this application, twelve TDs have been used, which was shown to be a good trade-off between accuracy and computation time [24]. Moreover, the version utilized is the one that corresponds to Limpens' thesis [26]. Even though the original model accounted already for more than 100 options for technologies, resources and demands, an adaptation was required for the present study. The main additions were:

- Resources: Liquefied petroleum gas (LPG).
- Demand: Heat demand for cooking.
- End-use categories: Cooking and mobility freight air.
- Technologies: Open cycle gas turbine (OCGT), diesel genset, biomass combustion power plant, syngas combustion power plant, firewood stove, LPG stove, FG stove, oil stove, electric stove, aircraft, biomass fermentation to bioethanol, esterification to biodiesel, diesel engine, LPG burner and gasoline bus.

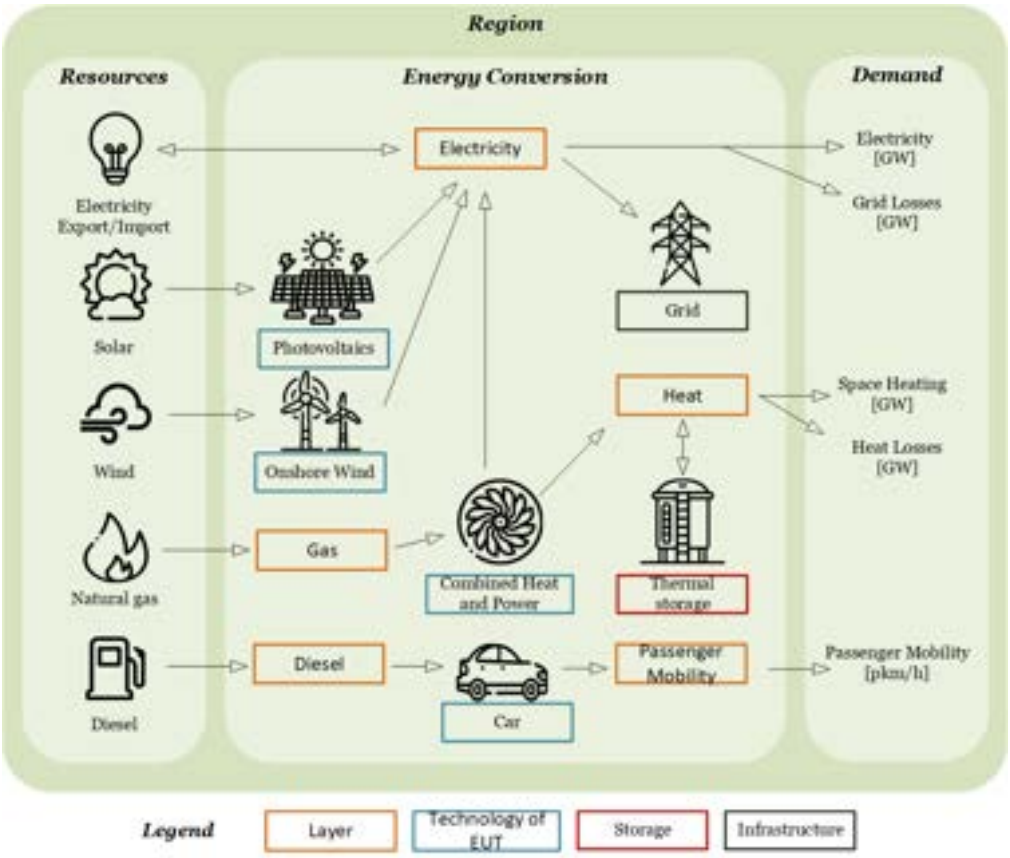

Figure 1: Conceptual representation of an energy system: Resources are converted by technologies to supply end-use type (EUT) demands related to electricity, mobility, and heating. Layers, such as *Electricity and Heat*, require to be balanced in each period. This figure is inspired from [22].

3. Case study: Bolivia

This section presents an overview of the Bolivian energy system based on the last national energy balance presented by the Ministry of Hydrocarbures and Energy (MHE) for the year 2021 [28,29], and the main techno-economic information to perform the optimisation for the year 2035.

3.1. Demonstration for the year 2021

Primary energy consumption in Bolivia for the year 2021 reached 94.28 TWh, with an approximate population of 11.84 million inhabitants [30]. Regarding sources, fossil fuels (FG, diesel, gasoline, LPG, and light fuel oil (LFO)) represented 87.0% of the country's final energy demand. In this context, the participation of renewable

energy sources was limited to less than 14% of the total: wet and woody biomass with 9.1%, hydropower with 3.4%, and others (solar and wind) with a proportion of 0.5%. This data was assembled and summarized in a Sankey diagram, Fig. 2.

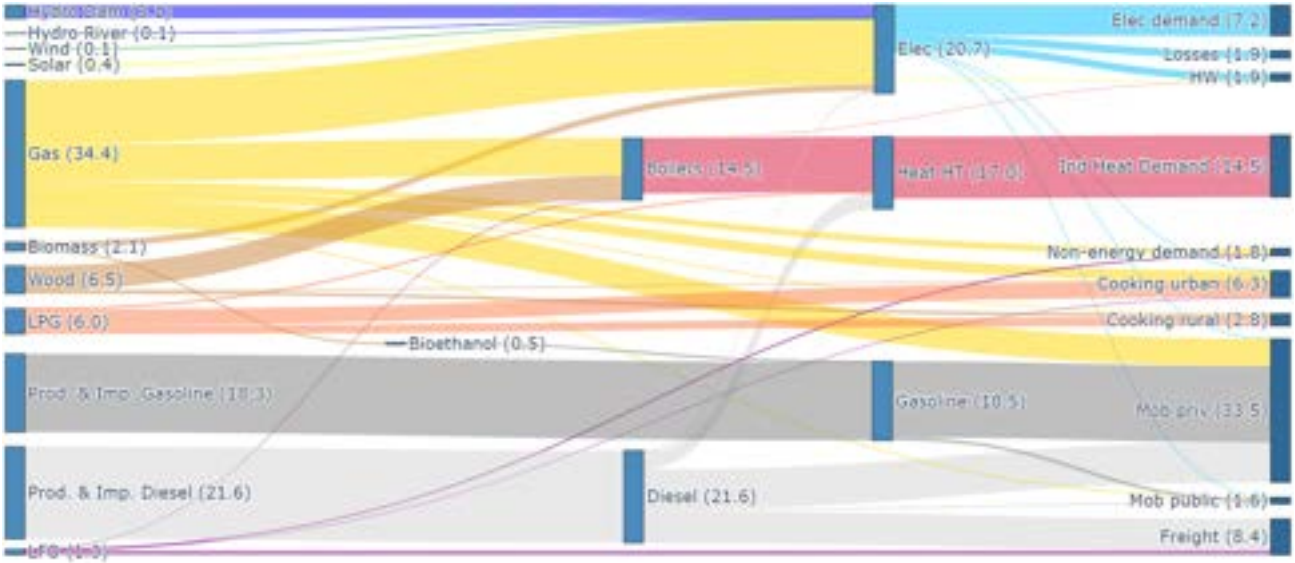

Figure 2: Energy flows of the modeled Bolivian energy system for 2021 (Units: TWh). The left side integrates all the resources while the right side retrieves the final energy consumption. The conversion technologies are in between. Energy exports are not represented. Abbreviations: mobility (mob), private (priv), electricity (Elec), liquefied petroleum gas (LPG), light fuel oil (LFO), industrial (Ind), domestic hot water (HW), low temperature (LT), high temperature (HT), importation (Imp), production (Prod).

As shown in Fig. 2, the present landscape of energy utilization in Bolivia could be divided into electricity, transport, and heat. The electricity generation was mainly covered by gas turbines (open-cycle and combined-cycle technologies), which represented around 59.7% of the total amount, followed by hydropower (29.7%), biomass (4.2%), photovoltaic (3.2%), diesel gensets (2.1%), and wind (1.1%) [6, 29]. The mobility sector was split into public transport with diesel, gasoline, gas buses, and electric aerial tramways. On the other hand, private transport comprised light vehicles fueled by gasoline, diesel, fossil gas, and electricity [31, 32]. Trucks contributed the most to freight transportation. Still, there were also rail, boat, and air transport options. Heat use was subdivided into three major demands: cooking, domestic hot water (HW), high-temperature heat (HT) from industrial processes such as manufacturing (foods and beverages, textiles, no metallic, and metallic), cement production, mining, and quarrying [31]. Residential and commercial cooking demand in Bolivia was mainly based on LPG (approximately 73.6%), followed by fossil gas (23.2%), woody biomass (2.5%), electric (0.4%), and LFO stoves (0.3%). A division between cooking in rural and urban areas was made, as the gas network does not cover the entire country. Likewise, the industry also relied on FG [28]. Overall, the EnergyScope TD model accurately portrayed the final energy consumption (FEC) of the Bolivian energy sector and its associated GHG emissions for the year 2021. The assessment of the present state of the system revealed 94.19 TWh/y in terms of primary energy consumption, differing only 0.1% from the country's energy balance [28]. Similarly, regarding CO_2 emissions related to the energy sector and waste, the model calculated 24.51 $MtCO_{2\text{-eq.}}$/y whereas CAIT country greenhouse gas emissions reported 23.17 $MtCO_{2\text{-eq.}}$/y [4, 33, 34].

3.2. Scenario in 2035

Due to a vast array of modern technologies and a rapid expansion of the economy, the energy system of Bolivia may undergo significant changes. So, this section presents the resources and technology potentials and forecast demands for Bolivia in 2035, a period that allows for substantial transformations yet close enough to know the available technologies at that time.

3.2.1. Energy resources

The resources available for the Bolivian energy system could be divided into fossil and renewable.

3.2.1.1 Fossil resources

Bolivia holds FG reserves (2 729, 1 009, and 1 485 TWh of proven, probable and possible reserves in 2018) [29]. Furthermore, the economy of the country relies to a great extent on fiscal revenues and tax collection from FG exports. In 2021, nearly 72% of its total FG production was exported (75.45 and 48.22 TWh of FG to Brazil and Argentina, respectively). Those accounted for 20.5% of Bolivia's total exports (around 1 924

M€) [35]. Nonetheless, oil extraction is limited (14.09, 89.00, and 220.25 TWh of crude oil, natural gasoline, and condensate proven reserves in 2018, respectively) [29]. Consequently, the government has to import diesel, gasoline, and other oil-based products. Since 2001, Bolivia has subsidized those fuels in the energy sector, intending to pass on affordable prices (46.63, 53.48, 35.45, 3.95 €/MWh related to diesel, gasoline, LFO and FG subsidized prices, respectively) [36]. For comparison, the prices used in this article correspond to the ones without the subsidy (Table 1). Moreover, the estimated prices of fossil fuels for the horizon of 2035 in Bolivia are based on the projection of the U.S. Energy Information Administration (EIA), expressed in the reference case of the Annual Energy Outlook 2022 (153.91, 163.21, 139.10, 15.03, 33.27 €/MWh for diesel, gasoline, LFO, FG, and LPG, respectively) [37].

3.2.1.2 Renewable resources

Renewable energies are essential to the energy transition; consequently, their deployment is crucial. Real weather data and scaled inflows were used to model solar, wind, and hydro resources to account for temporal variations in availability. For each hour, average capacity factors for wind and solar were computed using the open-source Renewables Ninja database [38–40]. For hydropower plants, hourly water inflows were used. The Electric Load Dispatch Committee (CNDC) supplied these hydrological data; values are publicly available in [41]. The biomass and waste yearly resources could be summarized as follows: 17.81 TWh of wet biomass from agricultural residues [42], 5.2 TWh of wet biomass from the 2010 approximated value of organic municipal solid waste [30, 43], 4.5 TWh of wet biomass used to generate electricity in 2021 [29], 5.7 TWh of wet biomass used to reach the maximum volume mentioned in the agreement by the government and the bioethanol producers until 2025 [44], 1.2 TWh of wet biomass from elephant grass of the two future biomass power plants planned by the government [45] and 28.6 TWh of wet biomass from the three future biodiesel production facilities planned to be built until 2025 [46]. Unfortunately, no information about woody biomass resources such as forest residues has been reported. So, only firewood for cooking was considered in this article, accounting for the sustainable production of wood as a limit [18]. The potential geothermal estimates were determined according to Gawell et al. [47], besides the planned Laguna Colorada geothermal power plant, which is currently a pilot plant [48]. Table 1 summarizes the resource potential described previously.

Table 1: Energy resources and their potential.

	Sources	TPES in 2021 (TWh)	Availability (TWh/y)	Price in 2021 (€/MWh)	References
Fossil fuels	Gasoline	18.54	(no limit)	124.12	[29]
	Diesel	21.72		111.31	
	LFO	1.07		85.12	
	FG	34.43		10.66	
	LPG	6.03		21.58	
Biomass	Woody	0.78	150	16.98	[18, 29]
	Wet	2.07	63	10.32	[29, 30, 42–46]

3.2.2. Energy demand

The Latin American Energy Organization (OLADE) published a report offering future energy projections of the Andean zone. Those numerical values included the yearly FEC by fuel based on future expansion plans of the energy sector, energy balances, and gross domestic product (GDP) growth of Bolivia, Colombia, Ecuador, Perú, and Venezuela until 2050 [49]. The yearly end-use demand (EUD) was estimated and used as an input parameter in the model based on this final energy demand. Besides, cooling demand was not specified due to the lack of information on the consumption of residential, commercial, and industrial subsectors. Nonetheless, as in other developing countries, refrigeration, food conservation, and air conditioning (AC) requirements in Bolivia are usually covered by electricity [50]. Therefore, it is already included in electricity demand. For instance, AC is seldom used in the households of the Altiplano and the valley regions. On the other hand, electric fans and AC systems utilizing liquid refrigerants are commonly employed in the country's lowlands urban areas. These can account for up to 40% of the total energy demand in an urban household in Santa Cruz during a hot summer day [51, 52]. Moreover, commercial and home refrigerators and other complex industrial systems in the country usually comprise electric compressors [50]. Table 2 illustrates the differences between the end-use demand in 2021 and 2035.

Table 2: Comparison of energy end-use demand for 2021 and 2035. Abbreviations: temperature (Temp.), passenger (pass.), tons(t).

		Units	2021	2035	Δ	References
End-use demand	Electricity	(TWh)	7.2	10.1	+2.9	[28, 49]
	Heat High-Temp. [a]	(TWh)	14.5	19.9	+5.4	
	Heat Low-Temp. [a]	(TWh)	1.8	2.5	+0.7	
	Cooking [a]	(TWh)	5.1	6.9	+1.8	
	Mobility pass. [a]	(Gpass.-km)	73.7	101.0	+27.3	
	Freight [a]	(Gt-km)	15.5	21.2	+5.7	
	Non-energy [a]	(TWh)	1.8	2.4	+0.6	

[a] In [49], the FEC is provided instead of the EUD; hence own calculations were performed to estimate these values.

The forecast given in Table 2 shows an increase in all types of demands of around +37%. Electricity increase was the most important (+42%). The increase in energy demand was related to the projected economic growth of the country at an average annual GDP growth of 2.7% since 2024 [49] and the population growth with an average rate of 1.33% for the 2020-2040 period [53]. In addition to yearly demands, an hourly time series is used to dispatch the variable demand over the year. Thus, the electricity demand series was obtained from CNDC [54], and the mobility demand was adapted from [55].

3.2.3. Energy technologies

The technologies utilized in this study can be divided into three categories: conversion, storage, and network. Conversion refers to transforming one energy carrier into another with conversion efficiency. Storage devices can store energy over time, characterized by input/output efficiency and losses. Lastly, networks permit the transport of certain energy carriers across the nation, such as the gas or electrical grid. The networks are characterized by transmission losses. In this case, the one for the electricity grid is set at its historical value of 17.2% [28, 29]. Future technologies were based on local commercial availability [51, 53], government plans, and trends in Bolivia, so hydrogen-based, carbon-capture, heat pumps, and seasonal storage technologies were not considered. Table 3 shows different technologies' installed capacity and potential.

4. Results

In the following section, the model was applied to prospect the energy system at the horizon of 2035. The data used were listed in Section 3.2. First, the Business As Usual (BAU) projected scenario based on the future power plants [12] and biodiesel production facilities [61], planned by the government until 2025 was presented 4.1.). Then, a renewable-based scenario was proposed and compared to the BAU one (see 4.2.).

4.1. Business As Usual (BAU) case

The Business As Usual case was based on the characterization of the Bolivian energy system without GHG constraints, leading to a scenario without considering major changes in consumption trends or policies that alter the behavior of the system components. Hence, a minimum capacity for power plants, the technologies for producing biodiesel and bioethanol, and the share between the different mobility technologies were maintained.

4.1.1. Major trends in energy consumption

Optimisation results stated a FEC of 142.08 TWh per year, representing an increase of 50.8% compared to the year 2021. Figure 3 illustrates the energy balance over the year 2035 from primary to final energy consumed for this solution. As can be seen, the system still relied heavily on FG (around 42.9% of the total demand), which was consistent with the regional policies of extraction, production, and use of this resource. Furthermore, the national reserves were sufficient to supply the mentioned demand besides the significant growth and the export volumes of the current contracts (Approximately 2 619.1 TWh of total gas demand from 2021 to 2035). Related to renewable resources, there was a massive increment of biomass to produce biodiesel and bioethanol in this scenario according to the government plans. Regarding GHG emissions, the system produced 25.74 $MtCO_{2\text{-eq.}}$ (around 1.81 $tCO_{2\text{-eq.}}$ per capita), during its yearly operation, which represented a 5.0% increase compared to the system of 2021, and 66% smaller than the Belgian cost optimum BAU scenario for 2035 [24].

4.1.2. Power sector

Electricity generation was dominated by hydro dam power plants (6.24 TWh), followed by combined cycle gas turbines (3.34 TWh), Photovoltaic plants (PV) (1.75 TWh), geothermal plants (0.80 TWh), wind turbines (0.61 TWh), hydroelectric run-of-river power units (0.30 TWh), open cycle gas turbines (0.27 TWh), and bioenergy steam turbines (0.51 TWh). Aside from the planned power plants established in PEEBOL2025, only one

Table 3: Installed capacity of technologies and their potential.

	Technology	Capacity in 2021	Initial capacity in 2035	Max. Potential	References
Electricity generation ($GW_{elec.}$)	Combined cycle gas turbine	1.05	1.05	(no limit)	[6]
	Open cycle gas turbine	1.06	1.06		
	Diesel genset	0.47	0.47		
	Photovoltaic	0.17	0.18	40 000	[6, 12, 56]
	Onshore wind	0.13	0.21	260	
	Hydro run-of-river	0.03	0.07	39.9	[6, 12, 57]
	Conventional hydro dam	0.71	2.34	39.9	
	Biomass steam turbine	0.15	0.19	0.85	[6, 45]
	Syngas steam turbine	0.001	0.001	0.32	
	Geothermal	0	0.10	0.89	[12, 47, 48, 58]
Heat generation ($GW_{thermal}$)	Boiler gas (Industry)	0.97	0.97	(no limit)	[6, 28]
	Boiler woody biomass (Industry)	0.63	0.63		
	Boiler oil (Industry)	0.002	0.002		
	LPG burner (Industry)	0.02	0.02		
	Diesel engines (Industry)	0.18	0.18		
	Boiler gas (HW)	0.005	0.005		
	Electric shower (HW)	0.20	0.20		[6, 52]
	Solar thermal (HW)	0.007	0.01		[6, 28, 59]
Cooking ($GW_{thermal}$)	Firewood stove	0.01	0.01	(no limit)	[6, 28]
	LPG stove	0.42	0.42		
	FG stove	0.13	0.13		
	Oil stove	0.002	0.002		
	Electric stove	0.01	0.01		
Mobility (Gpass.-km) (Gt-km)	FG bus	1.3	1.3	(no limit)	[29, 32, 60]
	Diesel bus	1.5	1.5		
	Gasoline bus	2.5	2.5		
	Aerial tramway	0.4	0.4		
	Electric car	0.05	0.05		
	FG car	16.5	16.5		
	Diesel car	19.6	19.6		
	Gasoline car	32.0	32.0		
	Diesel train freight	0.2	0.2		
	Diesel boat freight	0.02	0.02		
	Diesel truck	13.2	13.2		
	LFO aircraft	2.1	2.1		
Storage (TWh)	Battery of electric vehicles	0.01	0.01	(no limit)	[29]

energy technology represented a cost-effective solution and experienced an increment. PV installed capacity rose from 0.18 GW to 0.88 GW.

4.1.3. Heat sector

Heating demands (HW, HT, and cooking) were projected to increase from 21.40 TWh in 2021 to 29.32 TWh in 2035. Regarding HT demand, gas-based heating remained nearly the sole technology (Almost 99.9% of total demand). HW demand was provided by gas boilers (with 99.2%) and solar thermal (around 0.8%). The latter's share was based on the current installation ratio of these technologies in Bolivia (500 systems/y), according to Noël [59] and Fernandez [52]. Finally, the cooking demand was covered by FG (68.4%), electric (16.2%), and LPG stoves (15.4%) in the urban areas and by FG (81.7%) and LPG (18.3%) in rural areas. Moreover, biomass and kerosene stoves were reduced from the solution, covering only 0.1 MWh of the cooking demand. The share of the different fuels used for cooking was projected based on the information presented by the National Statistics Institute of Bolivia (INE) in 2021 [62].

4.1.4. Transport sector

The final energy demand for public and private passenger transportation was based on FG (42.5%), gasoline (34.1%), diesel (20.9%), and electricity (2.4%). Moreover, electric tramways for public transport showed an

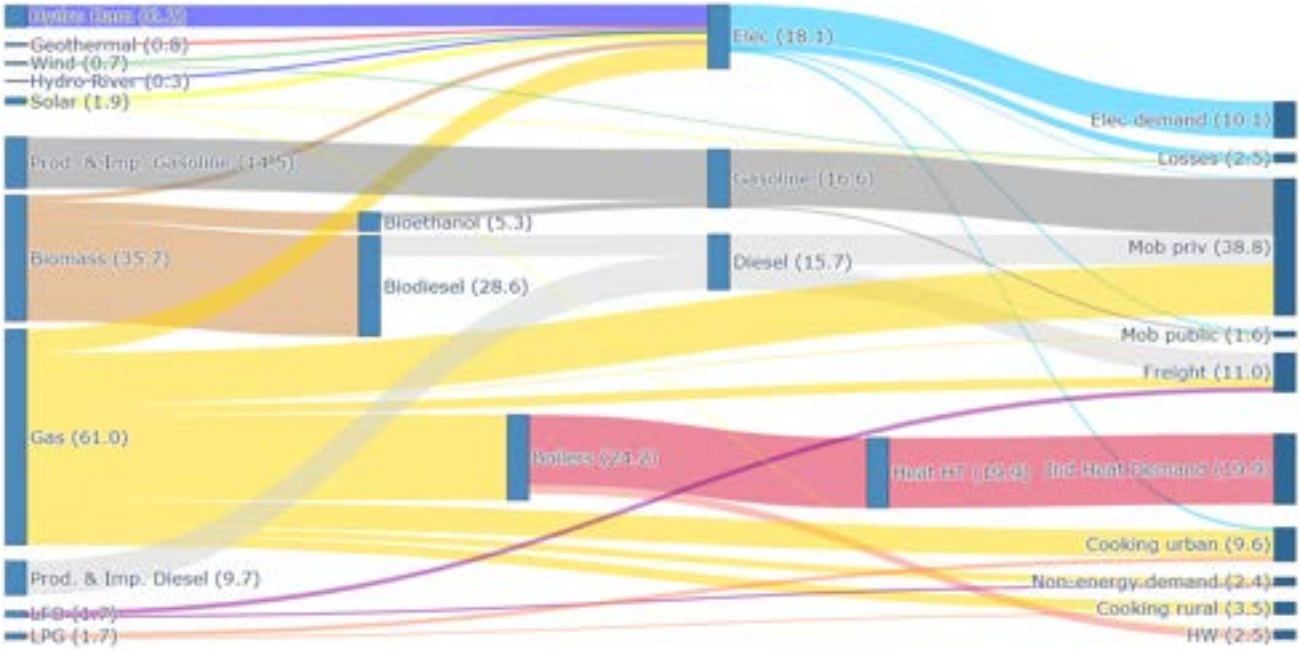

Figure 3: Energy flows of the modeled Bolivian energy system for 2035 BAU scenario (Units: TWh). The left side integrates all the resources while the right side retrieves the final energy consumption. The conversion technologies are in between. Energy exports are not represented. Abbreviations: mobility (mob), private (priv), electricity (Elec), liquefied petroleum gas (LPG), light fuel oil (LFO), industrial (Ind), domestic hot water (HW), low temperature (LT), high temperature (HT), importation (Imp), production (Prod).

increase. Those technologies resulted in an installed capacity of 0.81 GW. On the other hand, fossil fuels technologies (FG, diesel, and LFO) almost completely covered freight transport demand (63.2%, 23.0%, and 13.8% of diesel vehicles, FG vehicles, and aircrafts, respectively). Furthermore, freight share was 85.0% of transportation by road, 13.8% of transportation by air, 1.1% of transportation by rail, and 0.1% of transportation by boat. Even though the demand for liquid fossil fuels was considerable, approximately 12.7% of all gasoline and 38.3% of all diesel were produced from biofuels such as bioethanol and biodiesel.

4.2. Renewable energy (RE) case

In this scenario, the system was simulated considering the minimum GHG constraint that allowed finding a feasible optimisation solution, determining whether total growth based on renewable resources was achievable, and seeking a low carbon emission case.

4.2.1. Major trends in energy consumption

In contrast to the BAU scenario, the system depended on biomass as the principal primary energy source (40.5 TWh and nearly 29.5% of TPES). Nonetheless, biofuel production remained the same due to a lack of information on the maximum production limit. For instance, the government created a program in 2022 to promote oil production of oil species such as African palm, jatropha, macororó, and soybean (Supreme Decree No.4764). Those energy crops are expected to be farmed, reaching an approximate production of 638 344 m^3/y of biodiesel [63]. Moreover, an agreement with local ethanol producers has established a maximum purchase of 380 000 m^3/y of bioethanol by 2025, an amount which will be used as blended fuel with gasoline (Law No. 303/2017-2018) [44]. As shown in Figure 4, FG was still present but reduced (around 78.7 % less than the BAU scenario). Regarding CO_2 emissions, the system produced 12.50 $MtCO_{2\text{-eq.}}$/y, representing a 49% of decrement compared to the 2021 case.

4.2.2. Power sector

Electricity generation was dominated by PV (25.03 TWh), followed by wind turbines (15.75 TWh), hydro dam power plants (6.54 TWh), geothermal plants (2.38 TWh), bioenergy steam turbines (1.93 TWh), and hydroelectric run-of-river power units (0.31 TWh), and limited production of combined cycle and open cycle gas turbines (2.66 MWh). In terms of total installed capacity, PV arrays reached 12.70 GW, wind power 4.98 GW, bioenergy steam turbines 0.65 GW, and geothermal plants 0.30 GW.

4.2.3. Heat sector

The energy supply for the heat sector was extensively electrified. To illustrate, HT demand was based on direct-electric heating (around 77% of total demand), followed by gas boilers (23%). Also, the HW demand

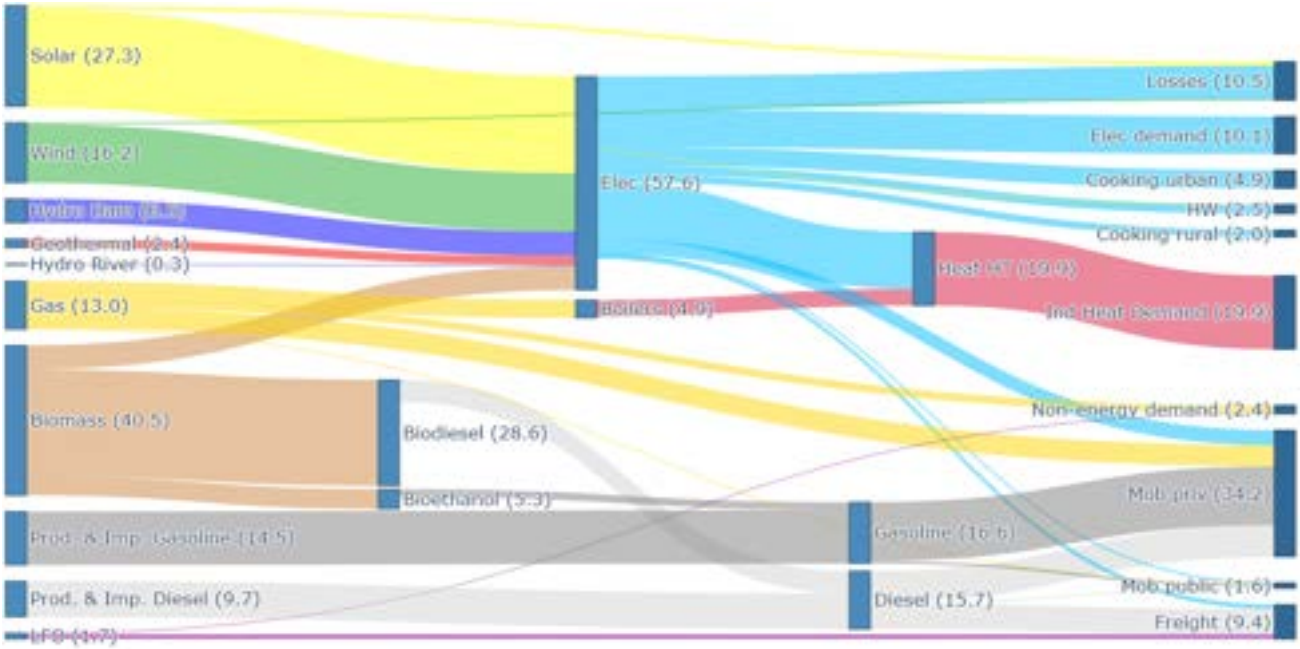

Figure 4: Energy flows of the modeled Bolivian energy system for 2035 RE scenario (Units: TWh). The left side integrates all the resources while the right side retrieves the final energy consumption. The conversion technologies are in between. Energy exports are not represented. Abbreviations: mobility (mob), private (priv), electricity (Elec), liquefied petroleum gas (LPG), light fuel oil (LFO), industrial (Ind), domestic hot water (HW), low temperature (LT), high temperature (HT), importation (Imp), production (Prod).

was provided by electric heating (99.2%), and the rest corresponded to solar thermal (around 0.8%). Finally, the cooking demand was almost completely covered by electricity in urban and rural areas.

4.2.4. Transport sector

Regarding the transport sector, there was a limited electrification share. The mobility demand for public and private passenger transportation was covered by gasoline (34.1%), electricity (27.4%), diesel (20.9%), and FG technologies (17.6%). Similar to the BAU scenario, electric tramways ended up with an installed capacity of 0.81 GW. The demand for freight transportation was covered by diesel-based vehicles (63.2%), electric trucks (23.0%), and aircraft (13.8%). The share between rail, boat, road, and aviation freight transport remained the same as the BAU scenario.

5. Discussion

This section highlights key insights and trends from the preceding sections. Finally, the limitations of the work were enumerated.

5.1. Comparison of scenarios

In 2035, according to the BAU scenario results, the Bolivian energy system is still fossil-based, with traditional fuels accounting for 62% of the TPES. Most of the primary energy goes to mobility (51.4 TWh), whereas heating and industrial processes are the second sector (24.2 TWh), electricity the third one (18.1 TWh), and cooking the last one (13.0 TWh). In contrast, the RE scenario is only 28% fossil-fuel dependent on the TPES. Moreover, the electricity sector represents 56.5 TWh in terms of primary energy due to the high electrification of the scenario, followed by the mobility sector with 45.1 TWh, heating and industrial processes with 22.7 TWh, and cooking with 6.9 MWh. Regarding the system's annualized total cost, the BAU scenario shows a lower value than the RE scenario (6 925 and 7 516 M€ per year for BAU and RE scenarios, respectively). Nonetheless, the RE solution reduces 49% of GHG emissions from 2021 (51% fewer emissions than the BAU scenario), which is equivalent to 44.64 €/$tCO_{2\text{-eq.}}$ of compensation. Moreover, it is essential to highlight that the mobility sector is a main constraint to the system transition, as the majority of the vehicles throughout the 14 years of analysis remain in the system due to the permissive laws and regulations in Bolivia. Nearly 8% of the total vehicle fleet in 2021 was composed of vehicles manufactured in 1885 or below, according to INE [62]. Moreover, the importation of new vehicles is still under the Euro II emissions standard [64].

5.2. Limits of the study

The energy system optimisation model was intended for developed economies with well-established networks and accounting for all users with electricity access. Moreover, more studies are required to confirm the dispatchability of various resources, such as agricultural and industrial residues, municipal solid waste, biofuels, or power for cooking. Furthermore, decentralized energy systems like microgrids, a significant component of Bolivia's power sector, should be accounted for. Additionally, a model for cooling demand could be determined and evaluated to estimate this consumption and associated technologies. Also, a more thorough market analysis is required to evaluate the costs of the existing technologies, their evolution, and the introduction of others. Energy policies could be evaluated especially for the transport sector and account for an increase in the share of public mobility. Finally, this study does not address the socioeconomic effects of the transition based on fossil fuels or renewable energy.

6. Conclusions

The Bolivian energy system is going to experience a transition from a fossil fuel-based supply to one with a high share of renewable resources to fulfill the commitment of the Paris Agreement and future governmental plans. Nowadays, the country is going through strong population and economic growth, which is reflected in future energy demand projections. In this context, the energy system was assessed utilizing the EnergyScope TD framework in order to gain a comprehensive understanding of its reality. The adapted version of the model for Bolivia is freely available at [65].

The case study consistency was verified by applying the energy system optimisation for the national energy balance of 2021, showing a high similarity between the reported and simulated values. Furthermore, the highest energy demand in the mentioned year was related to the transport sector, mainly supplied by gasoline (18.5 TWh), diesel (17.2 TWh), and fossil gas (6.7 TWh). This is followed by heat demand for industries, agriculture, and mining, mostly based on FG (8.7 TWh). Electricity demand was covered principally by FG (14.9 TWh), and finally, cooking demand was based on LPG (5.8 TWh), FG (2.5 TWh), and wood (0.8 TWh). The latter was more used in rural populations.

A projection of the energy system by 2035 allowed to identify difficulties and opportunities. With the current subsidies for fossil fuels, the system would economically prefer to experience growth based on fossil energies. For this reason, a optimisation was carried out including future plans, fuel prices, and technologies costs from the government's point of view. The latter scenario being called the business-as-usual scenario. It represents a share of 32% renewable sources related to the final energy consumption and a 5% rise of greenhouse gas emissions compared to the 2021 case. Furthermore, this scenario could not meet the emissions target of the INDC (0.18 ton$CO_{2,eq}$/MWh).

On the other hand, a sustainable scenario with a constraint in greenhouse gases emissions to reach a low-carbon system showed a renewable resources share of 66%. Although this latter was a bit more expensive, it showed a 49% decrement of CO_2 emissions during its operation from the base case, which is also equal to 44.64 €/t$CO_{2\text{-eq.}}$ of compensation. This growth driven by renewable energy required the electrification of heat and transportation systems, as well as enhancing renewable electricity generation using solar, wind, biomass, and geothermal technologies. Finally, this work has demonstrated that a Bolivian energy system with a high share of renewable resources could meet a significant increase in energy demand for all sectors at every hour throughout the year. Yet, to achieve this change, national policies must set ambitious goals for the transportation and heat sectors. Future studies should consider the pathway to assess the complete transition of the system, including more policy scenarios for different sectors.
Moreover, an improvement of the technical resolution is required, assessing the potential of microgrid systems such as PV-battery systems necessary to generate electricity, especially in remote areas, and addressing the extension of the electricity and gas network around the country.

References

[1] Karekezi S, McDade S, Boardman B, Kimani J, Lustig N. Energy, poverty, and development. Global Energy Assessment–Toward a Sustainable Future [Johansson, TB, N Nakicenovic, A Patwardhan, and L Gomez-Echeverri (eds)] Cambridge University Press, Cambridge, United Kingdom and New York, NY, USA and the International Institute for Applied Sys. 2012:151-90.

[2] Estado Plurinacional de Bolivia. Nationally Determined Contribution (NDC) of the Plurinational State of Bolivia; 2022.

[3] Bradley S, Lahn G, Pye S. Carbon Risk and Resilience. Chatham House, London. 2018.

[4] World Resources Institute. Climate Watch; 2022. Available from: `https://www.climatewatchdata.org`.

[5] Jones MW, Peters GP, Gasser T, Andrew RM, Schwingshackl C, Gütschow J, et al.. National contributions to climate change due to historical emissions of carbon dioxide, methane and nitrous oxide. Zenodo;. Available from: https://zenodo.org/record/7636699.

[6] Autoridad de Fiscalización de Electricidad y Tecnología Nuclear (AETN). Anuario Estadístico 2021. La Paz; 2021. Available from: https://sawi.aetn.gob.bo/docfly/app/webroot/uploads/.

[7] Latin American Energy Organization (OLADE). Latin American and Caribbean Energy Information System (sieLAC); 2022. Available from: https://sielac.olade.org/default.aspx.

[8] Banco Interamericano de Desarrollo (BID). Evaluacion Financiera y Economica del Proyecto Electrificacion Rural con Energıa Renovable (BO-X1013). Cochabamba, Bolivia; 2013.

[9] Sauer IL, Escobar JF, da Silva MFP, Meza CG, Centurion C, Goldemberg J. Bolivia and Paraguay: A beacon for sustainable electric mobility? Renewable and Sustainable Energy Reviews. 2015;51:910-25.

[10] Ministerio de Hidrocarburos y Energías (MHE). Plan de Desarrollo energetico - Análisis de Escenarios: 2008-2027. La Paz, Bolivia; 2009.

[11] Ministerio de Planificación del Desarrollo. Agenda Patriótica 2025; 2014.

[12] Ministerio de Hidrocarburos y Energías (MHE). Plan Electrico del Estado Plurinacional de Bolivia 2025. La Paz, Bolivia; 2014.

[13] Viceministerio de Electricidad y Energías Alternativas. Plan para el Desarrollo de las Energías Alternativas 2025. La Paz, Bolivia: Ministerio de Hidrocarburos y Energía; 2014.

[14] de Moura GNP, Legey LFL, Balderrama GP, Howells M. South America power integration, Bolivian electricity export potential and bargaining power: an OSeMOSYS SAMBA approach. Energy strategy reviews. 2017;17:27-36.

[15] Fernandez M, Fernandez C, Rodriguez G. Situación Energética de Bolivia y Desafíos. Cochabamba; 2020.

[16] Fernandez M, Periódico Digital PIEB. Estudio sostiene que la energía solar es factible en el 97% del territorio nacional. Cochabamba; 2012.

[17] 3TIER. Atlas Eólico de Bolivia. Transportadora de Electricidad [TDE]; 2009.

[18] Malky Harb A. Sector Forestal en Bolivia; 2005.

[19] Instituto Nacional de Estadistica (INE). Censo Agropecuario Estado Plurinacional de Bolivia; 2013.

[20] Morató T, Vaezi M, Kumar A. Techno-economic assessment of biomass combustion technologies to generate electricity in South America: a case study for Bolivia. Renewable and Sustainable Energy Reviews. 2020;134:110154.

[21] Balderrama JGP, Alfstad T, Taliotis C, Hesamzadeh MR, Howells M. A sketch of Bolivia's potential low-carbon power system configurations. The case of applying carbon taxation and lowering financing costs. Energies. 2018;11(10).

[22] Limpens G, Moret S, Jeanmart H, Maréchal F. EnergyScope TD: A novel open-source model for regional energy systems. Applied Energy. 2019;255:113729.

[23] Limpens G, Moret S, Guidati G, Li X, Maréchal F, Jeanmart H. The role of storage in the Swiss energy transition. In: Proceedings of the 32nd International Conference On efficiency, Cost, Optimization, Simulation and Environmental Impact of Energy Systems, Wroclaw, Poland; 2019. p. 23-8.

[24] Limpens G, Jeanmart H, Maréchal F. Belgian energy transition: what are the options? Energies. 2020;13(1):261.

[25] Borasio M, Moret S. Deep decarbonisation of regional energy systems: A novel modelling approach and its application to the Italian energy transition. Renewable and Sustainable Energy Reviews. 2022;153:111730.

[26] Limpens G, Thiran P, Lara E, Pavičević M, Quoilin S. Competitiveness of economic growth based on renewable energy: the case of Uganda to 2035. In: 2022 IEEE PES/IAS PowerAfrica. IEEE; 2022. p. 1-5.

[27] Gabrielli P, Gazzani M, Martelli E, Mazzotti M. Optimal design of multi-energy systems with seasonal storage. Applied Energy. 2018;219:408-24.

[28] Organización Latinoamericana de Energía (OLADE). Sistema de Información Energética de Latinoamérica y el Caribe (OsieLAC); 2021.

[29] Ministerio de Hidrocarburos y Energías (MHE). Balance Energético Nacional 2006 – 2021; 2022.

[30] Instituto Nacional de Estadistica (INE). Proyección de Población Total e Indicadores Demográficos, 2012-2022. La Paz, Bolivia: Instituto Nacional de Estadistica (INE); 2023.

[31] Balderrama JGP, Broad O, Sevillano RC, Alejo L, Howells M. Techno-economic demand projections and scenarios for the Bolivian energy system. Energy strategy reviews. 2017;16:96-109.

[32] Instituto Nacional de Estadistica (INE). Estadísticas del Parque Automotor 2003-2021; 2022.

[33] Gütschow J, Jeffery ML, Gieseke R, Gebel R, Stevens D, Krapp M, et al. The PRIMAP-hist national historical emissions time series. Earth System Science Data. 2016;8(2):571-603.

[34] Gütschow J, Pflüger M. The PRIMAP-hist national historical emissions time series v2.4 (1750-2021); 2022.

[35] Instituto Nacional de Estadistica (INE). Exportaciones según actividad económica y Producto por Año y Mes, 1992-2022; 2022.

[36] Agencia Nacional de Hidrocarburos (ANH). Precios Internacionales de Hidrocarburos 2010-2020; 2021.

[37] Energy Information Administration (EIA). Annual energy outlook 2022. Washington: US Energy Information Administration. 2022.

[38] Pfenninger S, Staffell I. Long-term patterns of European PV output using 30 years of validated hourly reanalysis and satellite data. Energy. 2016;114:1251-65.

[39] Staffell I, Pfenninger S. Using bias-corrected reanalysis to simulate current and future wind power output. Energy. 2016;114:1224-39.

[40] Pfenninger S, Staffell I. Renewables Ninja;. Available from: https://www.renewables.ninja/.

[41] Comité Nacional de Despacho de Carga (CNDC). Datos Hidrólogicos Previstos; 2021. Available from: https://www.cndc.bo/estadisticas/index.php.

[42] Morato T, Vaezi M, Kumar A. Assessment of energy production potential from agricultural residues in Bolivia. Renewable and Sustainable Energy Reviews. 2019;102:14-23.

[43] Dirección General de Gestión Integral de Residuos Sólidos. Diagnóstico de la Gestión de Residuos Sólidos en Bolivia. La Paz, Bolivia: Ministerio de Medio Ambiente y Agua (MMAyA); 2010.

[44] Kempff Bacigalupo R. Los biocombustibles pueden ayudar a mejorar la economía. La Paz, Bolivia; 2020.

[45] Fundación Solón. Biomasa: Del bagazo de caña al pasto de Uganda; 2020.

[46] Agencia Boliviana de Información (ABI). Planta de Biodiésel 1 se construirá con Sus 40 millones y prevén que inicie operaciones en 2023. La Paz, Bolivia; 2022.

[47] Gawell K, Reed M, Wright PM. Preliminary report: Geothermal energy, the potential for clean power from the earth. Washington, DC: Geothermal Energy Association. 1999.

[48] Empresa Nacional de Electricidad (ENDE). Proyecto: Construcción Planta Piloto Geotérmica Laguna Colorada; 2023.

[49] Organización Latinoamericana de Energía (OLADE). Panorama energético de América Latina y el Caribe 2022. Quito, Ecuador: Organización Latinoamericana de Energía (OLADE); 2022.

[50] Villarroel Schneider J. Combined energy solutions applied to dairy farming in Bolivia and Latin America. KTH Royal Institute of Technology; 2023.

[51] Proyecto EnDev Bolivia. Guía de Eficiencia y Ahorro Energético para el Área Rural de Bolivia; 2020.

[52] Fernández Fuentes M. Tecnología Termosolar Situación en Bolivia. ENERGÉTICA; 2011.

[53] Fernandez Vazquéz C, Rodriguez Cáceres G, Fernandez Fuentes M. Modelamiento del Sistema Energético Boliviano al 2040 según metas del IPCC: Un Primer Enfoque a los Modelos de Transición y las Políticas de Gestión de Emisiones de Carbono. Cochabamba, Bolivia: ENERGÉTICA; 2020.

[54] Comité Nacional de Despacho de Carga (CNDC). Despacho de carga realizado; 2021.

[55] McGuckin N, Fucci A. Summary of Travel Trends. National Household Travel Survey, Washington DC USA. 2017.

[56] Cheng C, Gutierrez NP, Blakers A, Stocks M. GIS-based solar and wind resource assessment and least-cost 100 % renewable electricity modelling for Bolivia. Energy for Sustainable Development. 2022;69:134-49.

[57] Organización Latinoamericana de Energía (OLADE), Empresa Nacional de Electricidad (ENDE). Evaluación de los Recursos Hidroenergéticos de Bolivia. La Paz, Bolivia; 1984.

[58] Jorquera C. Avanza construcción de primera planta geotérmica de Bolivia; 2022.

[59] Solar Platform America Latina (SOPELIA). Solar Thermal Bolivia; 2016.

[60] Instituto Nacional de Estadistica (INE). Estadísticas del Parque Automotor 2017. La Paz, Bolivia: Instituto Nacional de Estadistica (INE); 2017.

[61] Flores Y. Con la planta de biodiesel se prevé reducir 100 MM de dólares en importación de diésel. La Paz, Bolivia; 2023.

[62] Instituto Nacional de Estadistica (INE). Bolivia: Hogares según área y tipo de combustible usado para cocinar, 2011-2021. La Paz, Bolivia: Instituto Nacional de Estadistica (INE); 2021.

[63] Agencia Boliviana de Información (ABI). Biodiésel: Bolivia apunta a importar plantas aceiteras de tres países y tiene identificadas zonas de potencial producción. La Paz, Bolivia; 2022.

[64] Ministerio de Obras Públicas SyVM. Comunicado 16-08-2021. La Paz, Bolivia; 2021.

[65] Jimenez Zabalaga P, Thiran P, Limpens G, Jeanmart H. Bolivian EnergyScope TD Model;. Available from: https://github.com/pablojimenezzabalaga/EnergyScopeBOL/.

ULPGC
Universidad de
Las Palmas de
Gran Canaria

grres ULPGC
group for the research on renewable energy systems

L. Energy storage

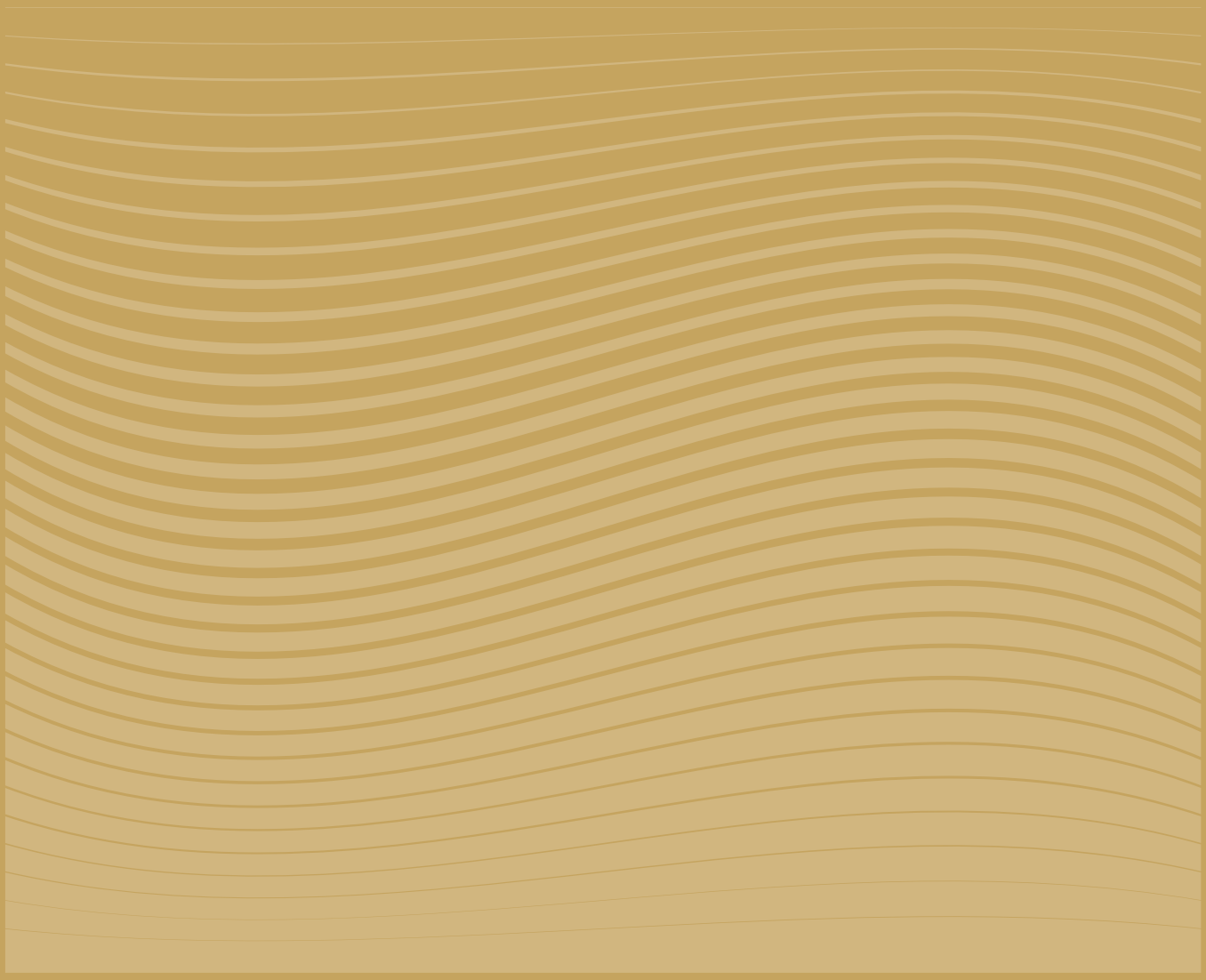

ECOS2023

PROCEEDINGS OF ECOS 2023 - THE 36TH INTERNATIONAL CONFERENCE ON
EFFICIENCY, **C**OST, **O**PTIMIZATION, **S**IMULATION AND ENVIRONMENTAL IMPACT OF ENERGY SYSTEMS
25-30 JUNE 2023, LAS PALMAS DE GRAN CANARIA, SPAIN

Off-design analysis of a TES-based electricity storage system

Alberto Benato[a], Matteo Pecchini[b], Francesca De Vanna[c] and Anna Stoppato[d]

[a] Department of Industrial Engineering, University of Padova, Padova, Italy, alberto.benato@unipd.it, CA
[b] Department of Industrial Engineering, University of Padova, Padova, Italy, matteo.pecchini@phd.unipd.it
[c] Department of Industrial Engineering, University of Padova, Padova, Italy, francesco.devanna@unipd.it
[d] Department of Industrial Engineering, University of Padova, Padova, Italy, anna.stoppato@unipd.it

Abstract:

Carnot battery is considered one of the most promising technologies for large-scale electricity storage. Among the available configurations, the so-called Integrated Energy Storage System (I-ESS) developed by the University of Padova research group allows the use of components of unused gas turbine power generation units for storage purposes. In particular, during low-demand hours, the electricity generated in surplus by, e.g., wind and solar, is used in an electric heater to heat up the air sucked by a fan. When air passes through the tank composed of a packed bed of solid material, it heats the bed itself. Therefore, excess electricity is stored as sensible heat in the storage material. Air then leaves the tank and is released into the atmosphere. During peak demand hours, the heat stored in the packed bed is extracted and converted again into electricity using a modified gas turbine in which the combustion chamber is bypassed and replaced by the storage tank. Having established that the I-ESS configuration can compete with the other large-scale storage technologies, the focus of this work is on the I-ESS off-design performance during the discharge phase. An investigation that still lacks in the literature. To predict the behaviour of the plant in part-load, the characteristic curves of the turbine and the compressor are implemented into the mathematical model of the I-ESS. In this way, the influence of key parameters such as pressure ratio, turbine inlet temperature, and generated power is analysed for the different state of discharge of the tank. The parameter that most affects the discharge time is the temperature of the tank. In fact, for a temperature of 1200 K, the total discharge time is up to 35 h. The discharge efficiency reaches 25.3%.

Keywords:

Renewable Energy, Thermal Energy Storage, Off-design, Part-load analysis, Carnot battery.

1. Introduction

Reducing CO_2 emissions from human activities is one of the most urgent challenges in our society, and the electricity sector is one of the most impactful in terms of greenhouse gas emissions. For this reason, the production of power from renewable energy sources (RES) is of crucial importance to boost the sector decarbonisation. However, variability and unpredictability, the distinctive traits of renewables such as wind and solar, are pushing the need to develop and install energy storage units (ES) to avoid mismatch between electricity supply and demand. Various ES technologies have been developed over the years, each with its features in terms of power, capacity, response time, etc. Due to these differences, ES technologies can be classified according to their role in grid regulation, the way adopted to store the electricity, the amount of storable energy, etc.

Among large-scale technologies, electrochemical (flow batteries, FBs) and mechanical storage (pumped hydro storage (PHS) and compressed air energy storage (CAES)) are considered mature and commercially available solutions. However, FBs suffer from a short lifespan, whereas PHS and CAES are subjected to stringent geographical constraints. In addition, CAES needs a fossil fuel stream, whereas PHS requires an almost constant water flow rate. Furthermore, the vast exploitation of suitable PHS installation sites (especially in Europe and the United States), coupled with the drawbacks mentioned above, limits the further spread of this mature technology.

In fact, in recent years, due to the need for new types of grid-scale ES, researchers have begun to look at *thermomechanical* storage. Among these technologies, there are liquid air energy storage (LAES) systems and the so-called *Carnot batteries* (CBs). The latter is one of the most promising solutions in the field of large-scale electricity storage, as underlined by both Vecchi et al. [1] and Lampasi et al. [2]. The general working principle of a CB is as follows: during the charge, electricity is converted into heat and stored as thermal energy. When power is requested from the grid, thermal energy is converted back into electricity and delivered to the grid.

Several types of CB have been studied over the years (i) using sensible and latent thermal energy storage (TES), (ii) performing the charge by direct electric heating, heat pumps and low-temperature waste heat, and (iii) discharging the system by means of different thermodynamic cycles such as the Rankine, Brayton-Joule, and Kalina cycles [3]. Despite the proposals, the most studied CB plant arrangement is the one named Pumped Thermal Energy Storage (PTES).

PTES is characterised by a high energy density, low self-discharge rate, no geographical limitations, and a small installation footprint. It is based on a high temperature heat pump cycle, which converts the off-peak electricity into thermal energy and stores it inside two man-made thermally isolated tanks (usually called 'thermal energy storage' (TES)): one hot (storing temperature from 500°C to 1000°C) and one cold (storing temperature ranging from -150°C to -70°C). During high-demand hours, the system is discharged. In this phase, a thermal engine cycle is adopted to convert stored thermal energy into electricity. The working fluid is a gaseous medium, air, or argon, while electricity is stored as sensible heat using inexpensive and solid materials such as concrete, gravel, or other common minerals [4–6]. In addition, PTES allows the use of components from existing out-of-market fossil-based thermal power plants.

The latter is the motivation that led the authors of this work to develop the Integrated Energy Storage System (I-ESS): a storage unit that can be embedded in unused or currently being decommissioned fossil-based power plants, as well as at the same installation site for wind and solar plants [7, 8].

Briefly, the plant stores electricity as sensible heat in a high-temperature artificial tank consisting of a packed bed. The I-ESS plant is an open cycle that adopts air as a working fluid in both the charging and delivery modes. The charging scheme consists of a high-temperature tank, a fan, an electric heater, an electric motor, and a heat exchanger, while the delivery unit is made up of a compressor, a turbine, an electric motor/generator and the same high-temperature tank. In practise, the power train is a gas turbine in which the high-temperature tank replaces the combustion chamber.

Compared to PHS and CAES, I-ESS does not suffer from geographical constraints and does not require a stable water flow, such as PHS, or a natural gas stream such as CAES. Unlike FBs, the I-ESS plant is characterised by a longer cycle life, whereas, compared to PTES, the I-ESS layout features a lower complexity. Despite the previously conducted studies demonstrated the feasibility of the I-ESS plant (see, e.g., [7, 8]), and its ability to be coupled with a variable renewable-based facility to smooth its variable production (see, e.g., [9]), it is necessary to investigate the off-design behaviour of the system during the discharge phase. This is a critical phase due to the need for fast matching the grid requirements; a fact that forces the I-ESS plant to operate in off-design conditions.

To this end, the mathematical model of the I-ESS is improved by implementing the performance maps of the turbomachines and a tailor-made control strategy in order to make the mathematical model able to predict the off-design behaviour of the I-ESS during the discharge. To investigate only the discharge phase, the starting point of the TES tank is an isothermal condition.

The rest of the work is organised as follows. Section 2. describes the I-ESS layout, while Section 3. presents the off-design mathematical model of the I-ESS storage unit. Section 4. summarises the most interesting outcomes of the numerical investigation, while Section 5. states the conclusions.

2. Integrated Electricity Storage System (I-ESS)

The storage plant investigated in this work is based on the configuration developed and tested by Benato et al. [7, 8]. The arrangement is named Integrated Energy Storage System; a thermomechanical unit for storing electricity in the for of sensible heat that allows the use of components of existing unused or in-decommissioning fossil power plants. In this way, the system provides flexibility to the grid without installing additional capacity.

The layout of the plant is sketched in Figure 1.

During charge, a fan guarantees the circulation of air in the storage charging circuit. Air is the heat transfer fluid. After being sucked by the fan, the air is preheated in a heat exchanger (HX) using the energy content of the air leaving the storage tank and then heated up by a resistive electric heater (EH). Hot air leaving the electric heater is at a high temperature and enters the TES tank. Air heats the solid material that constitutes the thermal energy storage tank. Therefore, electricity is stored as sensible heat because of an increase in the temperature of the storage material. The power input during the charging phase is in the fan and in the electric heater. The adoption of an EH allows the air temperature to be maintained at the input of the packed bed at a fixed value independently of the other operating conditions.

Note that in a PTES system, the storage inlet temperature is an independent variable only if the compressor's inlet conditions are constant. This is guaranteed by a heat exchanger; a component that is the source of high losses.

The discharge cycle is based on the Brayton-Joule thermodynamic cycle. In terms of components, the discharge arrangement is a gas turbine, where thermal storage replaces the combustion chamber or an air bot-

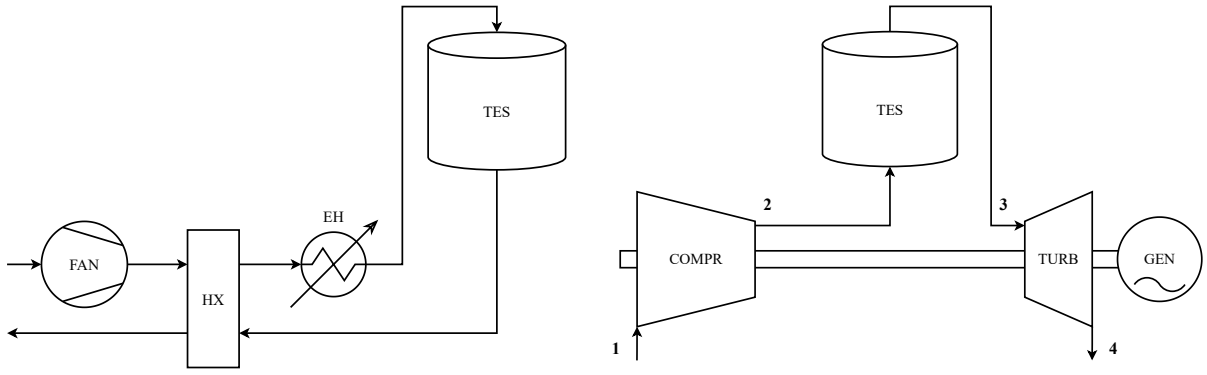

(a) *Charge phase* (b) *Discharge phase*

Figure 1: Layout of the I-ESS system in (a) charge and (b) discharge modes.

toming cycle in which the heat exchanger is replaced with the TES tank.

The air under ambient conditions is sucked and compressed by a compressor. Then it is heated in high-temperature TES. Consequently, the temperature of the material that makes up the TES decreases with increasing of the discharge time. Finally, the hot air expands through a turbine and returns to the atmosphere. The mechanical power generated by the turbine is converted into electricity through the electric generator. In this way, excess electricity generated by renewable sources and not requested by the grid is stored as sensible heat and then reinjected into the grid when required.

In the I-ESS configuration, the compressor and the turbine can be radial and axial turbomachines depending on the plant nameplate power. In this case, the devices are axial turbomachines that work at a constant rotational speed.

Although the layout of both working conditions is shown in Figure 1, only the discharge phase is investigated. The reason for this choice is as follows. In previous studies, it was shown that, despite poor efficiency, the investment costs of I-ESS are really competitive with other ES technologies [7]. Furthermore, a proper selection of the type and shape of solid storage material allows the plant to reduce costs, as well as design a storage facility that can store a different amount of energy in the same volume [8]. A feature that intrinsically guarantees the scalability of the plant based on the needs of the network. However, an in-depth analysis of plant behaviour under off-design conditions is still lacking. To fully understand the potential of the proposed storage system and develop custom management strategies, the decrease in turbomachine efficiency under part-load conditions must be taken into account. For these reasons, this work is focused on off-design modelling of the I-ESS system with an in-depth description of the compressor and the turbine through the use of performance maps.

3. The I-ESS off-design numerical model

During the delivery phase, the thermal reservoir temperature profile changes continuously. This means that the turbine inlet temperature (TIT), which is the driving parameter in calculating the equilibrium point of the system, also changes continuously. This fact leads to two important consequences. On the one hand, unlike a conventional power plant, the I-ESS never works under design conditions. Therefore, it is important to build an ad hoc mathematical model to describe its off-design behaviour. However, the system operates in a continuous transient state. Therefore, the steady-state working point does not exist.

In the already available I-ESS mathematical model, only the thermal reservoir one is dynamic, whereas the rest of the components, as well as the control strategy, are treated with a steady-state approach. This means that the model is built on the hypothesis that the time constant of the thermal phenomena is higher than the time constant of the mechanical one. With this approach, a pseudo-steady-state equilibrium point is computed at each time step.

Obviously, this way of modelling the turbomachinies is widely adopted and guarantees to describe in an appropriate manner the behaviour of the system, especially if the simulation time involves the entire year. However, to predict the step response and the start-up/shut-down of the storage unit, a proper dynamic model of the whole system must be built, but this is beyond the objectives of this work because it is focused on the discharge arrangement.

The system consists of two axial turbomachines and a packed-bed thermal reservoir. The power regulation of the plant takes place by managing the angle of the variable inlet guide vanes (VIGV) at the compressor inlet, while the rotational speed of the shaft remains constant. The model is built in a Matlab environment, while the

thermophysical properties of both air and storage material are taken from the *NIST* databases.

3.1. The I-ESS off-design model

3.1.1. The air compressor model

Turbomachines are modelled with a zero-dimensional approach. In fact, the behaviour of both the compressor and the turbine is described through their performance maps. Standard maps are taken from the database of commercial software [10] and then scaled according to the design point. The working point, which is characterised by a certain combination of pressure ratio (pr), mass flow rate ($\dot{m}$) and isentropic efficiency (η_{is}), is expressed as a function of rotational speed (N) and auxiliary coordinate β (see Equation 1).

$$\{pr, \dot{m}, \eta_{is}\}_c = f(\beta_c, N_c) \tag{1}$$

Due to the maps' interpolation, these values can be derived. Then, providing as input the inlet pressure and temperature, it is possible to compute the outlet conditions using Equation 2 and Equation 3.

$$p_2 = p_1 \cdot pr_c \tag{2}$$

$$T_2 = T_1 \cdot \left(1 + \frac{1}{\eta_{is,c}} \cdot \left(pr_c^{\frac{\gamma-1}{\gamma}} - 1\right)\right) \tag{3}$$

During off-design operating conditions, the I-ESS management system varies the VIGV angle (α_{IGV}) to keep the rotational speed constant. The laws that describe the modification of the compressor working point as a function of α_{IGV} are as follows.

$$a_{VIGV} = \frac{\partial \dot{m}\,[\%]}{\partial VIGV\,[^\circ]} \tag{4}$$

$$b_{VIGV} = \frac{\partial (pr_c - 1)\,[\%]}{\partial VIGV\,[^\circ]} \tag{5}$$

$$c_{VIGV} = \frac{\partial \eta_{is}\,[\%]}{\partial VIGV\,[^\circ]} \tag{6}$$

The values of the coefficients a, b, and c are set equal to 1, 1 and 0.01 as suggested in Ref. [11]. The positive values of α_{IGV} correspond to the closure of the variable inlet guide vanes. In contrast, negative values mean an opening of the VIGV compared to the design position ($\alpha_{IGV,des} = 0$).

3.1.2. The turbine model

The turbine is also modelled using standard maps scaled according to the design values of the pressure ratio and the corrected mass flow. As given for the compressor, the values of the mass flow rate, the pressure ratio and the isentropic efficiency are expressed as a function of the rotational speed and the auxiliary coordinate β (Equation 7).

$$\{pr, \dot{m}, \eta_{is}\}_t = f(\beta_t, N_t) \tag{7}$$

The turbine geometry is fixed, and there are no variable inlet guide vanes. The outlet temperature and pressure are calculated as given in Equation 8 and Equation 9.

$$p_4 = \frac{p_3}{pr_t} \tag{8}$$

$$T_4 = T_3 \cdot \left(1 - \eta_{is,t}\left(1 - \left(\frac{1}{pr_t}\right)^{\frac{\gamma-1}{\gamma}}\right)\right) \tag{9}$$

3.1.3. The thermal energy storage with packed bed mathematical model

The thermal energy storage tank is the key component of the I-ESS plant because it allows the storage of electrical energy in the form of sensible heat.

Several models can be found in the literature for the description of the thermal reservoir [12] but, in this case, the TES-PD model developed by Benato et al. [13] is adopted. The TES-PD model is a 1D model in which

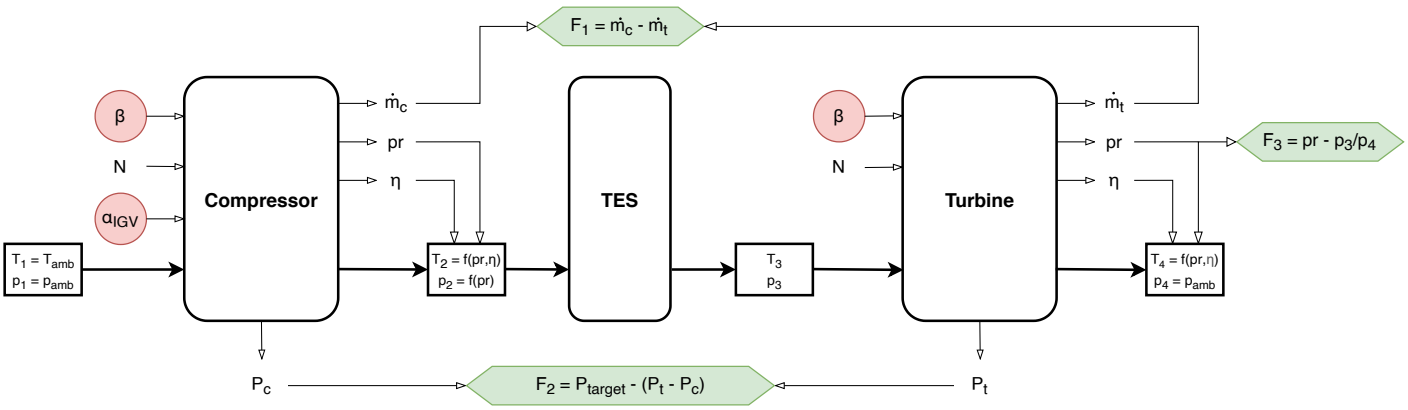

Figure 2: Scheme of the calculation for the matching procedure. The matching variables are highlighted in red, while the functions are highlighted in green.

the tank is discretised into *n* layers characterised by the same dimension. The influence of the number of discretisations on both the computation time and the accuracy in the calculation of the temperature profile has been thoroughly investigated in Ref. [13]. One of the peculiarities of the model is its ability to take into account the variability of the thermophysical properties of both the solid material that makes up the packed bed and the heat transfer fluid (air). For more details, the interested reader can refer to [13].

3.2. Components matching

The I-ESS model calculates pseudo-steady-state points, where the turbomachines are supposed to instantaneously adapt to the thermal behaviour of the reservoir. This means that for each time step, the power and the mass balance are fulfilled.

In this scenario, finding the equilibrium point of the system requires solving a system of non-linear equations of dimension three [14]. The procedure is based on the gradient-based `fsolve` algorithm available in the *Matlab* suite. It employs a variant of the Powell method (trust-region algorithm [15]). In Equation 10, δx is the vector that contains step changes of the matching variables, J is the Jacobian matrix, and F is the vector with errors. The matching variables are β_{compr}, α_{IGV} and β_{turb}, while the errors come from the check of the turbine pressure ratio, the mass continuity, and the power balance, as shown in Figure 2.

$$J \cdot \delta x = -F \tag{10}$$

At each iteration k, the new variables are calculated as $x_k = x_{k-1} + \delta x$. The system is solved when $F = 0$. The final values of β_{compr}, α_{IGV}, and β_{turb} are those that meet the equations of mass and power balance and give a net power equal to that set as input.

3.3. The I-ESS model setup

Being the aim of the work to study the off-design behaviour of the I-ESS system during the discharge process to improve the accuracy of the plant behaviour prediction, the design parameter of the system must be defined. To evaluate in future work the advantages in terms of accuracy of using compressors' and turbines' maps instead of simplified models, the I-ESS design parameters are the same as those in the work presented in Ref. [9].

In particular, the thermal storage volume is equal to 250 m^3, while its height is 6.6 m. The packed bed is made up of spheres of aluminium oxide (Al_2O_3). The density, void fraction, and diameter of the spheres are summarised in Table 1.

The design power of the power train is set at 0.8 MW, while the compressor pressure ratio and the polytropic efficiency of both turbomachines are set at 8.5 and 0.85, respectively.

Based on the design characteristics of the gas turbine used to build the I-ESS power train, the thermal reservoir design temperature, which is equal to the turbine inlet temperature, is set at 1200 K while the air mass flow during discharge is 4.42 $kg \cdot s^{-1}$.

The turbomachines have an axial arrangement. Therefore, for the compressor and the turbine, an axial map is selected from the commercial software database. Subsequently, the selected maps are scaled according to the design values. Note that this is common practise in the case of a lack of information on the performance maps of the machines considered [16].

To properly study the delivery phase, the discharge investigation is carried out starting from a TES tank under

Geometry	packed-bed	
Material	Al_2O_3 (allumina)	
Shape	spheres	
TES volume	250	m^3
TES height	6.6	m
Al_2O_3 density	3990	$kg\,m^{-3}$
Void fraction	0.4	$-$
Spheres diameter	50	mm

Table 1: Design characteristics of the TES.

isothermal conditions (1200 K).

4. Results and discussion

After model validation (see, [7, 8]), a preliminary investigation is conducted with the aim of finding the technical minimum of the system. As said, for simplicity, the reservoir starts in an isothermal condition.

At the beginning of the discharge phase, the I-ESS-deliverable power is set to the nameplate one. However, in the progress of the discharge, the temperature of the packed bed decreases and, consequently, the turbine inlet temperature. Therefore, the I-ESS management system is not able to maintain both the power and the rotation speed at the design value. Then, since the control strategy is devoted to maintaining a constant rotational speed, the power delivered to the grid is reduced with the decrease in the state of charge of the TES (see Figure 3). The power reduction continues until the system can no longer provide power by maintaining a constant rotational speed. This condition corresponds to a power equal to about 40% of the design one. Taking into account the safety margin, the I-ESS technical minimum is set equal to 50% of the gas turbine nameplate power.

The analysis of the discharge phase from the full charge to the technical minimum reveals that, as the TIT changes, the equilibrium point of the system also changes. Therefore, to maintain the rotational speed constant, the angle of the VIGVs must be continuously adjusted (Figure 3). The initial value of α_{IGV}, when the VIGVs are in the design condition, is $\alpha_{IGV} = 0$. Initially, to maintain the rated power, the VIGVs have to slightly open to counterbalance the decrease in the TIT. Then, when the power is scaled, α_{IGV} suddenly increases to a positive value (Figure 4).

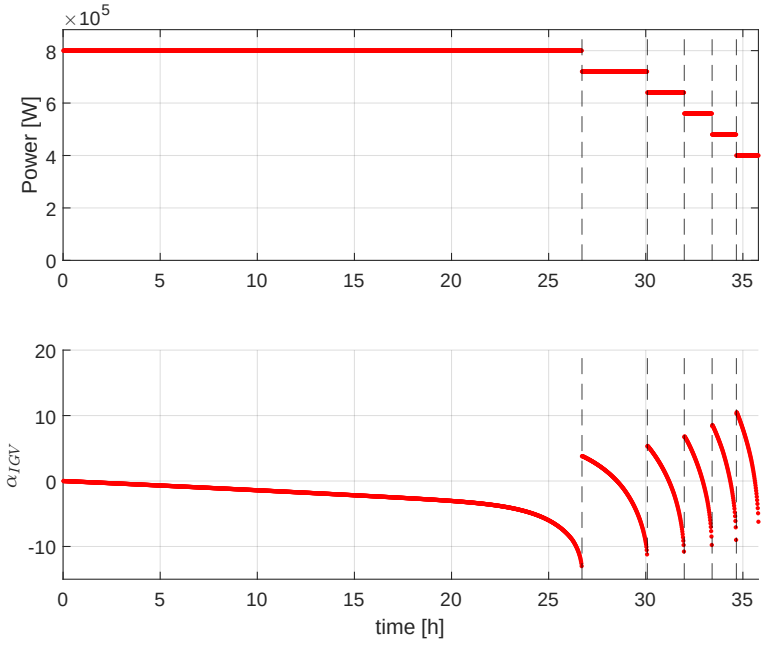

Figure 3: Power trend and α_{IGV} trend over time.

As said, during the delivery phase, the temperature of the packed bed decreases. Figure 5 shows the temperature trend of some layers over time. It is interesting to note that the temperature of the first layers quickly drops to 600 K, which is the compressor outlet temperature. The first layer is slightly heated after some time

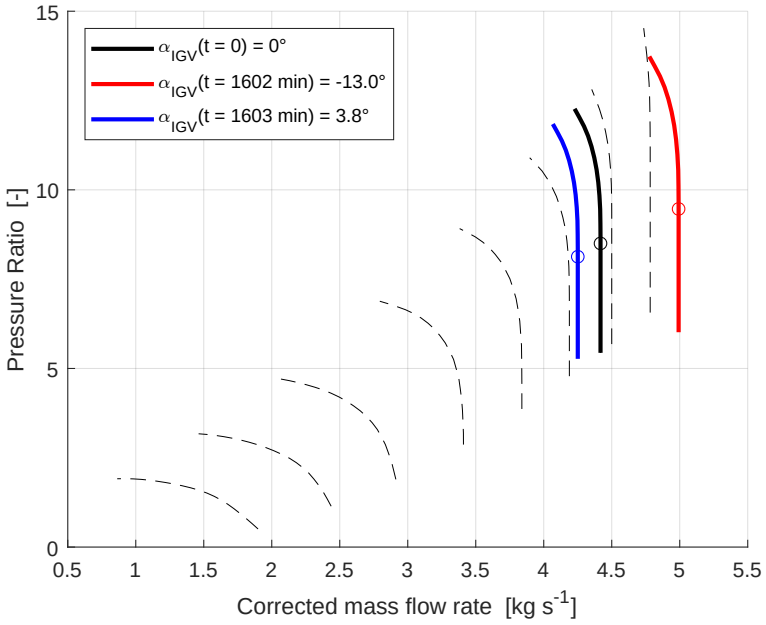

Figure 4: Shift of the speedline according to α_{IGV}.

step, and this is due to an increase in the compressor pressure ratio related to the regulation of α_{IGV}.

The discontinuities in the temperature trend come from the step regulation of the net power, as shown in Figure 3. The graph in Figure 5 also shows the trend of TIT over time. The TIT follows the trend of the last layers of the reservoir.

Figure 6 shows the thermodynamic cycle at both the beginning and the end of the discharge. Note that, at the end of discharge, both $\eta_{is,c}$ and *TIT* are lower compared to the design point.

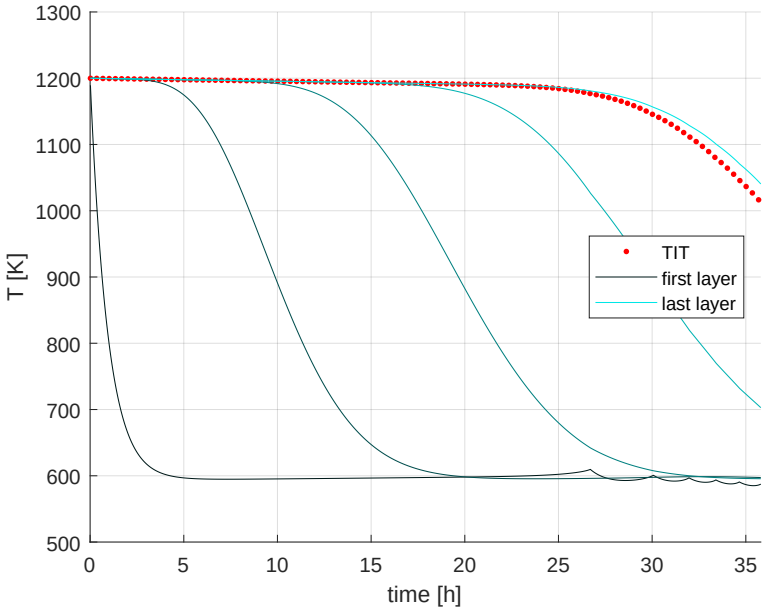

Figure 5: Temperature trend of some sample layers and TIT trend over time.

The choice of the number of layers for the discretisation of the packed bed influences the accuracy of describing the thermofluid dynamics of the reservoir [13]. However, the focus of this work is to study the performance of the whole system, rather than the thermal storage itself. Therefore, a sensitivity analysis is performed to evaluate the effect of the number of layers (*n*) on the accuracy of the model.

The turbine inlet temperature is selected as a key parameter as the driving variable in the calculation of the thermodynamic cycle. The analysis revealed that, varying *n* from 30 to 160 with a step of 30, the standard deviation in the TIT calculation at the end of discharge is approximately 0.02%. For this reason, a number of 60 layers is chosen as a good compromise between computational speed and accuracy.

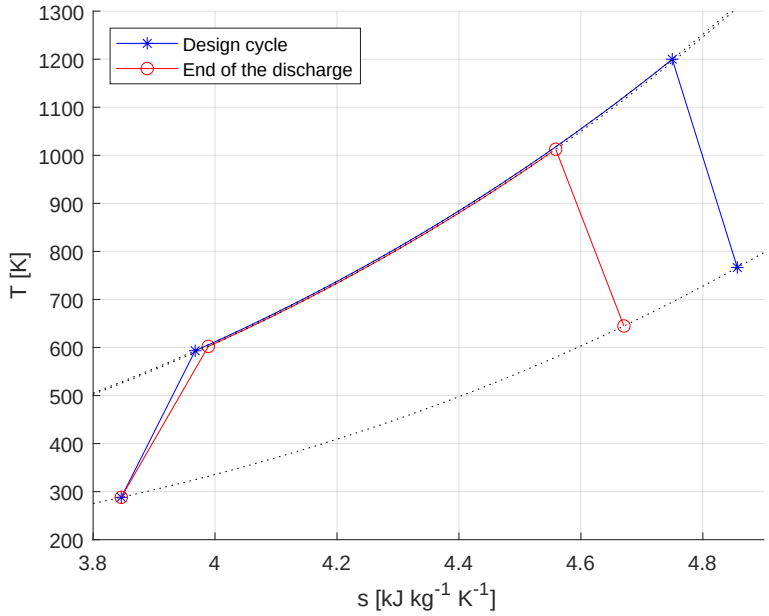

Figure 6: Thermodynamic cycle at the design point and at the end of the discharge.

After this preliminary investigation devoted to the definition of the technical minimum and the number of layers in which storage needs to be discretised, it is interesting to study the total discharge time and the discharge time at nameplate power by varying by the tank temperature, the design power and the power step size.

Figure 7 shows the influence of design parameters on the total discharge time and the discharge duration at the nameplate power.

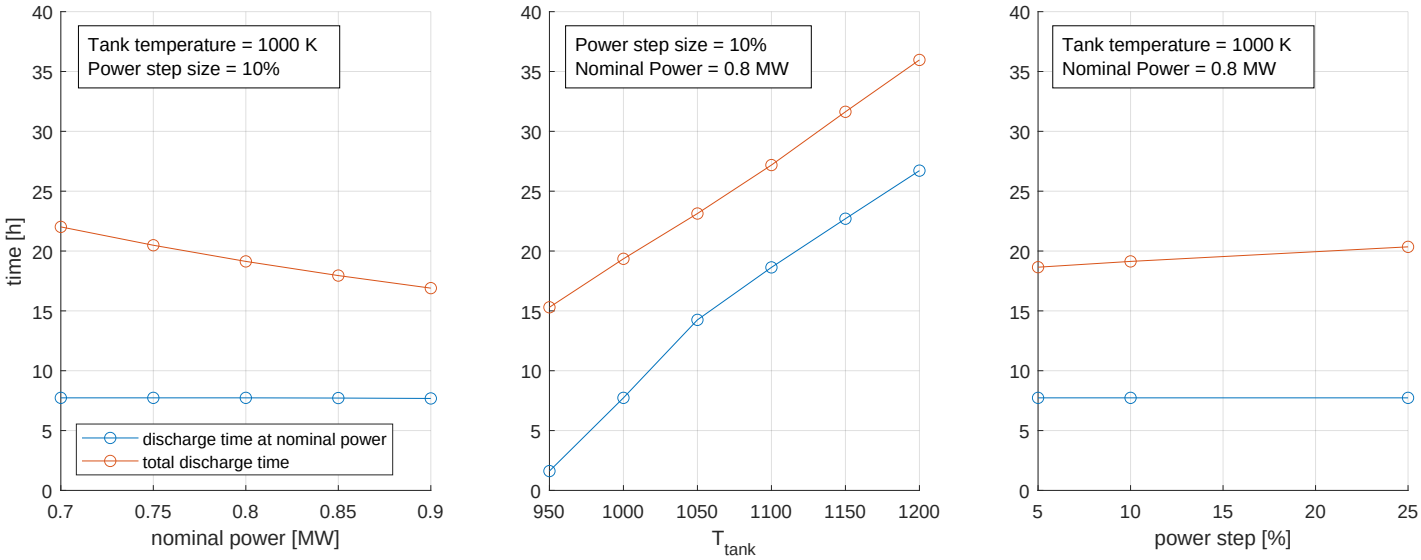

Figure 7: Influence of design parameters on the total discharge time and the discharge duration at nameplate power.

The discharge time at nameplate power is strongly influenced by the reservoir temperature: the higher the temperature, the longer the time for which the system can deliver the nameplate power.

The nameplate power and the power step size do not affect discharge duration. Furthermore, the total discharge time increases rapidly if the storage temperature increases, while it increases only slightly with the power step size. However, the total discharge time decreases if the nominal power is high.

It is also interesting to analyse the maximum thermal energy that can be stored in the tank. With the hypothesis of heating the tank from ambient temperature (293 K) to 1200 K, the maximum storable thermal energy is 201.6 MWh_{th}.

Taking into account the full discharge, the maximum exploitable energy can be calculated as:

$$E_{th,discharge} = M \cdot \frac{1}{n} \cdot \sum_{j=1:n} \left(\int c_p(T) \cdot dT \right) \tag{11}$$

where n is the number of layers, M is the mass of the solid and c_p is the specific heat of the solid.

Given the technical minimum fixed at 50%, the maximum exploitable thermal energy is 106.1 MWh_{th}, which results in 26.9 MWh_{el}.

Note that, for the hypothesis of the investigation performed, the charge phase is not modelled. Therefore, the Round-Trip Efficiency (RTE) cannot be defined on the basis of the selected starting state of charge.

Hovewer, considering the TES isothermal (not reachable condition) at a temperature of 1200 K, the efficiency of the discharge phase can be computed as

$$\eta_{discarge} = \frac{E_{el,discharge}}{E_{th,discharge}} \tag{12}$$

and resulted equal to 25.3%.

5. Conclusions

The off-design performance of an Integrated Electricity Storage System (I-ESS) has been analysed in this study. To this end, a proper off-design model of the plant has been built. The model takes into account the part-load behaviour of the turbomachines with a zero-dimensional approach using performance maps. Although it includes a dynamic description of the Thermal Energy Storage, the model of the system calculates pseudo-steady-state points. In this way, the behaviour of the plant during a complete discharge can be studied, starting from an isothermal reservoir. The results show that the temperature of the reservoir is the parameter that affects primarily the performance of the plant in the delivery mode.

With an increase in tank temperature, both the total discharge time and the nameplate power discharge time increase. In contrast, as the design power is increased, the total duration of the discharge decreases. In addition, the power step size has a smaller influence on these parameters.

The results also show that the number of layers for TES discretisation is not as relevant for the calculation of the performance of the whole system. Therefore, this parameter can be kept to the minimum possible to speed up the computation time without significantly affecting the model accuracy. The efficiency of the delivery phase, for the selected working conditions, is equal to 25.3%. Future developments will involve the implementation of off-design characteristics of the fan, electric heater, and heat exchanger in the charging model. In this way, the round-trip efficiency can be defined and computed as well as the thermodynamic and economic performance of the full operation of the system. After that, the dynamic behaviour can be analysed and tailor-made management strategies developed based on grid needs.

Nomenclature

Abbreviations

CAES Compressed Air Energy Storage

CB Carnot Battery

EH Electric Heater

ES Energy Storage

FB Flow Batteries

HX Heat Exchanger

I-ESS Integrated Electricity Storage System

LAES Liquid Air Energy Storage

PHS Pumped Hydro Storage

PTES Pumped Thermal Energy Storage

RES Renewable Energy Storage

TES Thermal Energy Storage

TIT Turbine Inlet Temperature

VIGVs Variable Inlet Guide Vanes

Constants and variables

cp specific heat, J/(kgK)

$\dot{m}$ mass flow rate, $\mathrm{kg\,s^{-1}}$

N rotational speed

n number of layers

pr pressure ratio

T temperature

α_{IGV} Variable Inlet Guide Vanes position

β auxiliary coordinate of turbomachinery performance maps

η_{is} isentropic efficiency

Subscripts and superscripts

c compressor

t turbine

el electrical

th thermal

References

[1] Andrea Vecchi et al. "Carnot Battery development: A review on system performance, applications and commercial state-of-the-art". In: *Journal of Energy Storage* 55 (Nov. 2022), p. 105782. ISSN: 2352152X. DOI: 10.1016/j.est.2022.105782.

[2] Alessandro Lampasi et al. "Review of Carnot Battery Technology Commercial Development". In: (2022). DOI: 10.3390/en15020647.

[3] Olivier Dumont et al. "Carnot battery technology: A state-of-the-art review". In: *Journal of Energy Storage* 32 (2020), p. 101756.

[4] Tristan Desrues et al. "A thermal energy storage process for large scale electric applications". In: *Applied Thermal Engineering* 30.5 (2010), pp. 425–432.

[5] Joshua D McTigue, Alexander J White, and Christos N Markides. "Parametric studies and optimisation of pumped thermal electricity storage". In: *Applied Energy* 137 (2015), pp. 800–811.

[6] Alberto Benato. "Performance and cost evaluation of an innovative Pumped Thermal Electricity Storage power system". In: *Energy* 138 (2017), pp. 419–436.

[7] Alberto Benato and Anna Stoppato. "Energy and cost analysis of an Air Cycle used as prime mover of a Thermal Electricity Storage". In: *Journal of Energy Storage* 17 (2018), pp. 29–46.

[8] Alberto Benato and Anna Stoppato. "Integrated thermal electricity storage system: Energetic and cost performance". In: *Energy Conversion and Management* 197 (2019), p. 111833.

[9] Alberto Benato, Francesco De Vanna, and Anna Stoppato. "Levelling the Photovoltaic Power Profile with the Integrated Energy Storage System". In: *Energies* 15.24 (2022), p. 9521.

[10] J Kurzke. *Gasturb 12: A program to calculate design and off-design performance of gas turbines. users manual*. 2012.

[11] Muhammad Baqir Hashmi, Tamiru Alemu Lemma, and Zainal Ambri Abdul Karim. "Investigation of the Combined Effect of Variable Inlet Guide Vane Drift, Fouling, and Inlet Air Cooling on Gas Turbine Performance". In: *Entropy* 21.12 (2019). ISSN: 1099-4300. DOI: 10.3390/e21121186.

[12] Alexej Paul et al. “High temperature sensible thermal energy storage as a crucial element of Carnot Batteries: Overall classification and technical review based on parameters and key figures”. In: *Journal of Energy Storage* 56 (Dec. 2022). ISSN: 2352152X. DOI: 10.1016/j.est.2022.106015.

[13] Alberto Benato et al. “TES-PD: A Fast and Reliable Numerical Model to Predict the Performance of Thermal Reservoir for Electricity Energy Storage Units”. In: *Fluids* 6.7 (2021), p. 256.

[14] AMY Razak. *Industrial gas turbines: performance and operability*. Elsevier, 2007.

[15] Michael JD Powell. *A Fortran subroutine for solving systems of nonlinear algebraic equations*. Tech. rep. Atomic Energy Research Establishment, Harwell, England (United Kingdom), 1968.

[16] Andrea Lazzaretto and Toffolo Andrea. “Analytical and Neural Network Models for Gas Turbine Design and Off-Design Simulation”. In: *International Journal of Thermodynamics* 4 (Dec. 2001). DOI: 10.5541/ijot.78.

ECOS 2023: The Energy Storage Capabilities Of Single And Mixture Sorbent Salts Impregnated Pumice And Anodic Aluminium Oxide Based Composite Materials

Behiye Yüksel[a], Esra Ayan[b] and Zafer Utlu[c]

[a] Halic University, Department of Mechanical Engineering, Istanbul, Turkey,behiyeyuksel@halic.edu.tr
[b] Istanbul University-Cerrahpasa, Department of Metallurgy and Materials Engineering, Istanbul, Turkey, ayanesra13@gmail.com,
[c] Halic University, Department of Mechanical Engineering, Istanbul, Turkey,zaferutlu@halic.edu.tr,

Abstract:

In recent years, when the energy demand has increased day by day, the continuity of energy has become an important issue as well as the need to meet the demand from nature-friendly technologies. Thermochemical Heat Storage (THS) systems are among the important approaches that help the continuous and efficient use of renewable energy resources with its high energy storage density and long storage times. Researches on composite structures consisting of sorbent salt and porous matrix couple among storage materials are noteworthy for the development of sorption materials and thus the heat storage system. Composite sorbents were prepared by impregnating sorbent salt ($CaCl_2$ and $MgCl_2$ etc.) as single and mixture into two different matrix materials, anodic Aluminium oxide (AAO) template and pumice (P), is carried out in this study. The cyclical heat storage behaviours of the obtained composite structures were investigated with the laboratory scale thermochemical heat exchanger prototype system. The aim of this study is that the effect of host matrices with different pore diameters one of whose is produced in the laboratory and other is natural on the thermochemical heat storage capability. Moreover, different sorbent salts which are impregnated into these pores on the heat storage capability is also compared with the help of prototype system.

Keywords:

Thermal Energy Storage (TES), AAO templates, Pumice, Composite Material, Salt-impregnation.

1. Introduction

The visible and tangible negative effects caused by the use of fossil fuels shows that we are facing a global climate crisis. Due to the intermittent nature of renewable energy sources, a great majority of the energy demand today is still met by fossil fuels [1]. While this situation reveals the importance of storage for the efficient use of the energy, it is also critical to improve these systems in order to meet the energy demand of the increasing population with environmentally friendly and sustainable technologies [2,3]. Thermal Energy Storage (TES), one of the energy storage approaches, has important application areas such as the efficient use of intermittent solar energy and the recovery of low-grade industrial waste heat released directly into the atmosphere [4,5]. There are three types of TES systems such as sensible, latent and thermochemical heat storage [3,6]. Thermochemical Heat Storage (THS) systems, in which heat is stored and released as a result of the reversible sorption-desorption process, are remarkable for their long storage times and high energy storage density [7,8]. In sorption heat storage systems, heat is stored as a result of physical changes in the storage medium. During the charging (desorption) process, hot dry air (eg, waste heat, heat emitted from solar collectors) is passed through the storage material to remove absorbed water. As a result of the endothermic reaction, heat is stored by the material as potential energy. During the discharge (sorption) process, water vapour absorption occurs by passing humid air through the storage material and the stored heat is released. As long as the storage material is not in contact with humid air, heat is stored with almost no loss [9,10]. For storage systems with low thermal losses and high energy storage capacity, mass and heat transfer are expected to be high as well as the material maintaining thermal, physical and cyclic stability [8]. Therefore, the development of storage mediums is very important for the improvement of these systems.

In recent years, composite materials obtained by impregnated sorbent salt into a porous host matrix are among the prominent sorption materials [6,11]. In the literature, many porous matrices with different pore diameters and surface areas are used as a structural support for sorbent salts such as zeolite [12], silica gel [13], activated carbon [14], attapulgite [15], wakkanai siliceous shale (WSS) [4], vermiculite [16], etc. The porous matrix helps to maintain the physical stability of the material during repetitive cycles while also improving mass and heat transfer [17]. In recent studies for the development of sorption materials, in addition to natural rocks, new generation porous materials such as MWCNT [18], MOF [19], AAO [20], silicone foam [21], concrete [22], which are synthesized in the laboratory, are also preferred as host matrix.

Sorbent salts, the main absorbing component that stores heat, are notable for their high energy storage densities [2]. The existence of problems such as deliquescence and agglomeration that make the use of sorbent salts difficult is stabilized by the porous host matrix [23]. In the literature, many sorbent salts such as $CaCl_2$, LiCl, $LiNO_3$, $MgCl_2$, $SrBr_2$, $SrCl_2$, LiBr, $MgSO_4$, K_2CO_3 are used for sorption heat storage with host matrix [2]. Also salt mixtures are impregnated into porous matrices in order to improve their water uptake capacity and operate at relatively low regeneration temperatures [6,15]. Different porous matrix/salt pairs are investigated to develop systems with high energy storage capacity and cyclic stability [24]. Nejhad et al. [22], the cyclic heat storage capacities of the composite sorbents they synthesized with 3 different porous matrices (aerated porous concrete, vermiculite, zeolite) were investigated with a laboratory scale fixed-bed open THS prototype system. Accordingly, energy storage densities of 196-175, 180-163, and 251-114 kWh/m^3 were obtained, respectively, for APC-$CaCl_2$, vermiculite-$CaCl_2$ and zeolite-$CaCl_2$ composites at low regeneration temperature (85-95 °C). Mehrebadi et al. [25] investigated the composite sorbents prepared with two porous (pumice, expanded clay) matrix and different sorbent salts ($Al_2(SO_4)_3$, $MgSO_4$, $CaCl_2$, $MgCl_2$, $SrCl_2$) using a laboratory scale filled bed reactor. According to the results, $SrCl_2$ has the highest energy storage density (29 kWh/m^3 for expanded clay and 7.3 kWh/m^3 for pumice) and the study points out that pumice has cyclic stability. Yilmaz et al. [26], used anodic Aluminium oxide (AAO) templates produced with two step anodization method in the laboratory as porous host matrix for four different sorbent salts and their mixtures. The energy storage densities obtained for AAO-LiCl and AAO-CaCl2 composites as a result of DSC analysis are 242.2 and 220.8 kJ/kg, respectively.

In this study, anodic aluminium oxide (AAO) templates and pumice (P) used as porous host matrix. Composite materials were prepared by impregnating mono and mixed sorbent salts ($CaCl_2$, $MgCl_2$) into host materials. AAO templates with pore size controlled by electrochemical process parameters were produced in the laboratory with a two-step anodization process. The aim of the study is to compare the behavior of sorbent salts impregnated into different host matrices. For this purpose, the cyclical energy storage density (E_d) of the obtained composite materials were investigated with the laboratory scale thermochemical heat exchanger prototype system.

2. Materials and Method

In this study, anodic Aluminium oxide produced by anodization from 99.99% pure aluminium and pumice, a natural rock, were used as host material in order to be able to absorbed sorbent salts. AAO templates were obtained by applying two-step anodization method to high purity (99.99%) aluminium plates. Aluminium plates were immersed in an isopropyl alcohol at 35-40 °C in an ultrasonic bath for 10 minutes prior to anodization and then they etched in an etching solution containing $CuSO_4$, H_3PO_4 and HNO_3 at 85 °C for 2 minutes. Following these processes, two-step anodization process was started. Aluminium plates were anodized in a 0.6 M oxalic acid solution at 10 °C at 40 V for 30 minutes during both the first and second step anodization process. AAO with regular pore structure were obtained at the end of second anodization step. AAO samples obtained via the two-step anodization method were immersed in 0.1 M NaOH solution for 15 minutes in order to enlarge the existing pore diameter prior to salt impregnation. Then the moisture in the pores was evaporated by keeping it in an oven at 110 °C for 24 hours. The similar procedure was also applied to pumice to be completely dehumidified and ready for salt impregnation. The dried AAO and pumice templates were filled with two mono salts and their mixtures.

In order to be able to obtain composite structure, matrix materials (AAO and Pumice) completely were immersed into saturated mono and mixed salts and they were hold at 10 Psi and 30 ^oC under vacuum for 48 h. This aimed to fill existing pores with salt solution via capillary action. Dry sample weights before and after salt impregnation are given in Table 1. The amount of impregnated salt in pumice was measured by taking the sample weight before and after the salt impregnation. The amount of salt absorbed per unit area for AAO samples was calculated empirically by dividing the amounts of salt impregnated into each sample by the total surface area as in our previous study [26].

Table 1. Dry sample weights before and after salt impregnation.

Impregnated salt and ratios	Sample weight before salt impregnation (g)	Sample weight after salt impregnation (g)
Matrix: AAO		
$CaCl_2$	0.157	0.278
$MgCl_2$	0.149	0.349
$CaCl_2$ + $MgCl_2$ (1:1)	0.133	0.219
Matrix: Pumice		
$CaCl_2$	16.12	42.29
$MgCl_2$	16.24	40.72
$CaCl_2$ + $MgCl_2$ (1:1)	17.01	43.03

2.1. Characterization

Microstructures of both AAO and pumice, acting as a matrix, before and after salt impregnation were investigated with Zeiss brand Sigma 300 model FESEM. Theoretical thermal energy storage capacities of the composites were characterized using a Differential Scanning Calorimetry (DSC). Analyses were performed with a TA Instruments Q2000 model DSC instrument in the temperature range of 30-140 °C, according to BS EN ISO 11357-4 standards. In addition, composite materials were characterized by a laboratory-scale prototype. Figure 1 shows the prototype system consisting of a humidifier, heater, cabinet and fan.

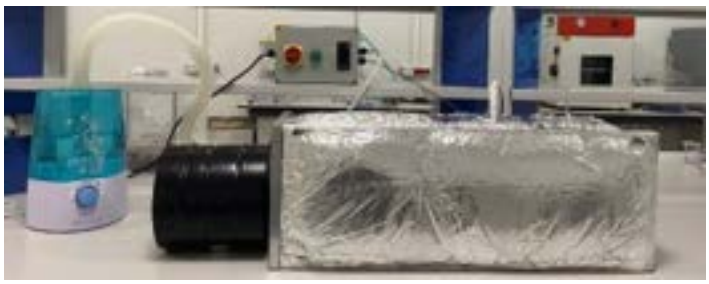

Figure 1. Thermochemical heat exchanger prototype.

In the prototype system, experiments were carried out as three consecutive discharge-charge cycles and the cyclic behaviour of composites were investigated. During discharge process, the air was humidified and blown through the cabin with help of a fan. The humid air was passed through across the composite material. Water vapour was absorbed by the composite and heat released during this time. During charging process, air was heated to 80-85 °C with the help of an electric heater and hot dry air passed across the composite material. Meanwhile, moisture inside the composite was removed and heat stored.

3. Results and Conclusions

In this study, the results show that the average pore diameter of AAO film was about 85±5 nm as shown in Figure 2(a). The pores were regular and high ordered. Figure 2(b) shows a cross-sectional view of the AAO template.

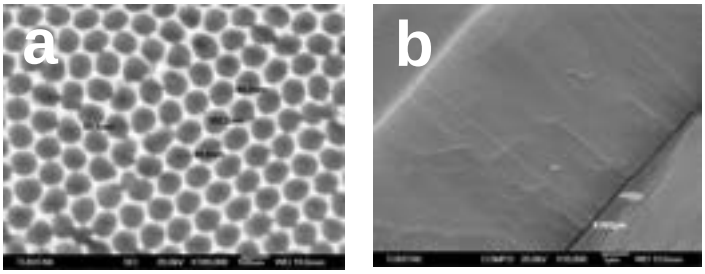

Figure 2. FESEM image from top: a) and cross-section b) of AAO template

The average thickness of the nanotubes is approximately 8µm. The increase of the lengths of the nanotubes depends on the increase of the anodization period. The lengths of the nanotubes are directly proportional to the duration of second step of the two step anodizing. The images of pumice, used as matrix material, before and after salt impregnation are given in figure 3.

Figure 3. Images of pumice: a) before salt impregnation, b) $CaCl_2$ impregnated, c) $MgCl_2$ impregnated and d) mixed sorbent salts impregnated.

Figure 4 shows the FE-SEM images obtained after salt impregnation of both matrix materials: (a) AAO-based composite structure following salt impregnation, (b) pumice before salt-impregnation, and (c) pumice-based composite structure following salt impregnation. SEM images show that the pores of both matrix materials could be filled with sorbent salts.

Energy storage density (Ed), is one of the important parameters for evaluating the suitability of any material for THS application. In this regard, after synthesizing composites structures of salt impregnated, Ed of these materials were evaluated through characterization methods. For the DSC analysis, synthesized materials were kept in a moist environment (RH=90%) over 48 hours to ensure that they are saturated with water. Later on the fully hydrated materials were placed within DSC device. For evaluating the Ed, total energy consumption for moisture desorption (until the material reaches anhydrous state) was calculated. Within the DSC studies, the specific heat capacity (Cp) is determined with the Equation (1). In the Equation ΔQ and ΔT represents the variation of heat supplied to the material and the variation of the applied desorption temperature with the time, while m shows the mass of the sample by integrating the area under the desorption heat–Cp curve.

$$Cp= \Delta Q/(m.\Delta T) \quad (1)$$

Theoretically, total energy consumption for moisture desorption in charging could be considered equal to the thermal energy generated in discharging process for the same amount of moisture adsorption. Consequently, energy density of the material could be obtained by calculating the ratio of desorption energy consumption to the weight of the sample [26]. As shown Table 2, the highest theoretical Ed value was obtained for $MgCl_2$ impregnated into both pumice and AAO. On the other hand, $CaCl_2$ has also the lowest E_d value for both host matrices.

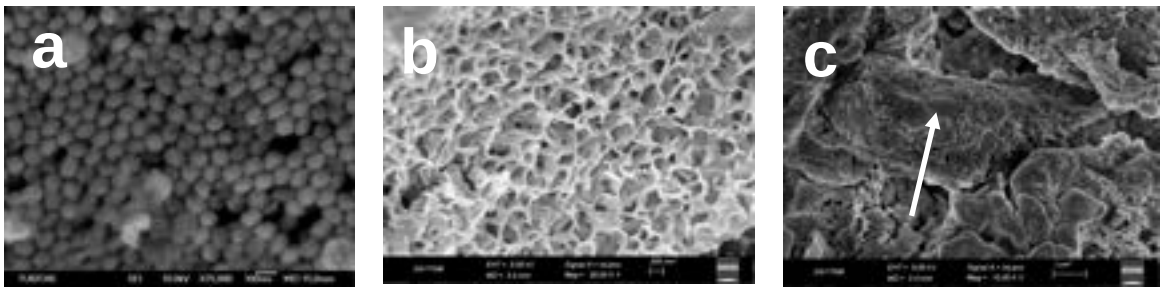

Figure 4. FESEM images of a) AAO after salt impregnation, b) pumice before salt impregnation and c) pumice after salt impregnation

Table 2. E_d values calculated as a result of DSC.

Samples	E_d (kJ/kg)
AAO-$CaCl_2$	161.68
AAO-$MgCl_2$	836.19
AAO-$CaCl_2$+ $MgCl_2$	795.12
P-$CaCl_2$	1255.83
P-$MgCl_2$	1700.39
P-$CaCl_2$+ $MgCl_2$	1657.41

The heat storage capacities of the composite structures, whose theoretical energy storage capabilities were determined with DSC, were also measured with the laboratory scale thermochemical heat exchanger prototype system. The experiments were carried out as three consecutive discharge-charge cycles for each composite and the cyclic heat storage capabilities of the composite sorbents were obtained. Figure 5 (a) and (b) shows the outlet air temperature (T) changes for AAO and pumice composite materials over three discharge cycles, respectively. The input air temperature was measured 18-20°C as it was affected by the fluctuating room temperature during the experiment. Due to the high absorption rate, temperature rise was observed at the beginning of each cycle in all composites.

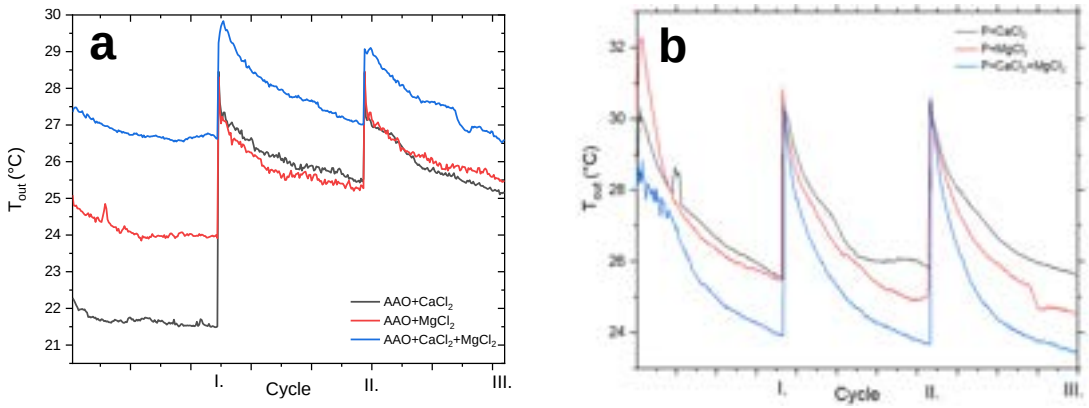

Figure 5. Output temperature changes of (a) AAO matrix composites, (b) pumice matrix composites

The heat output rate (out) values of all composite materials during the discharge process are shown in Figure 6. The heat output rate can be determined based on the enthalpy changes before and after the sorption material (Eq. 2), as well as the mass flow rate (discharge) in the discharge phase, the specific heat (Cp) at constant pressure and the difference between input and output temperatures of the system [22].

$$\dot{Q}_{\text{out}} = \dot{m}_{discharge} C_p (T_{\text{out}} - T_{in}) \qquad (2)$$

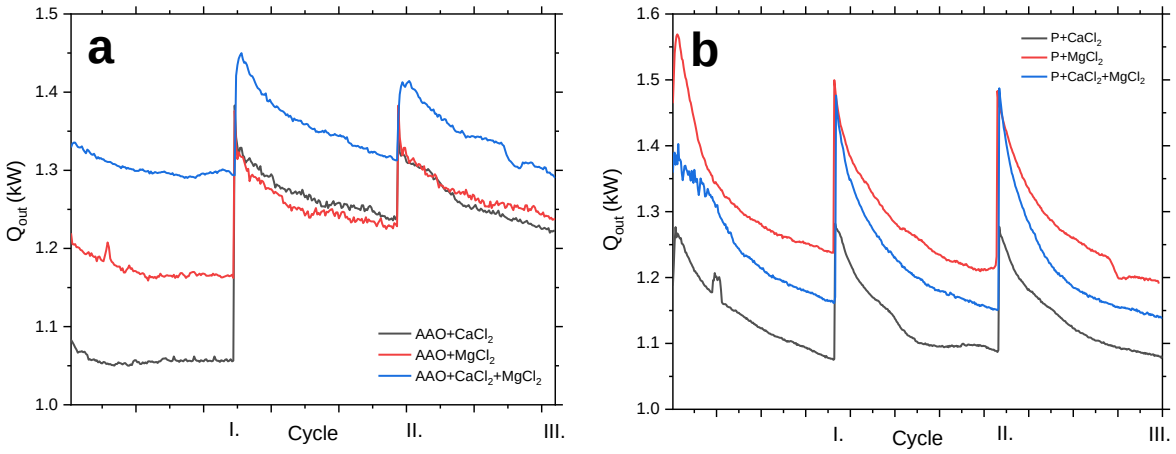

Figure 6. Heat output rate values of six composite materials over three discharge cycles: a) AAO matrix composites and b) pumice matrix composites .

It is seen that the average output heat flow rates for AA0-$MgCl_2$:$CaCl_2$ are 1.29, 1.37 and 1.35 kW for all three cycles, respectively. Just as at the output temperature, the heat flow rates for the mixed salt impregnated

sample exhibit also stable behaviour in all three cycles. On the other hand, while the heat flow rate for the AAO-$MgCl_2$ sample is average 1.18 kW in the first cycle, this value reaches the order of 1.28 and 1.29 kW in the second and third cycles, respectively. It is seen that these values for Pumice-$MgCl_2$:$CaCl_2$ are on average 1.25, 1.24 and 1.24 kW. Especially in the first cycle, the sample with the lowest heat flow rate was the AAO-$CaCl_2$ and pumice-$CaCl_2$ samples with 1.06 kW and 1.16 kW, respectively. On the other hand, the reason for the increase in the output heat flow rate of the AAO-$MgCl_2$ and AAO-$CaCl_2$ composites, especially in the 2nd and 3rd cycle, might have been due to the increase of ΔT in the repeated cycles.

The energy storage densities of the system were calculated by the ratio of the total energy output value to the volume of the composite material for the discharge phase to be obtained by integrating the equation (2) over the discharge period [22].The cyclic energy density (Ed) values of the discharge phases of the six composite materials are given in Table 3.

Table 3. *Cyclic energy density (E_d) values of six composite materials over three discharge cycles.*

Matrix	Impregnated salt	Cycle	E_d (kWh/m^3)	Matrix	Impregnated salt	Cycle	E_d (kWh/m^3)
AAO	$CaCl_2$	1	180	Pumice	$CaCl_2$	1	411
		2	92			2	328
		3	70			3	269
	$MgCl_2$	1	131		$MgCl_2$	1	658
		2	99			2	485
		3	88			3	518
	$CaCl_2$ + $MgCl_2$ (1:1)	1	160		$CaCl_2$ + $MgCl_2$ (1:1)	1	597
		2	144			2	469
		3	135			3	418

As can be seen, the highest energy density values were obtained in the mixed salt in AAO matrices and in $MgCl_2$ impregnated samples for pumice matrices throughout all cycles. Accordingly, while the highest energy density value was obtained for the AAO-$MgCl_2$:$CaCl_2$ composite in the first cycle, the highest value was obtained for the pumice-$MgCl_2$ composite in the similar cycle. Ed values of all composite samples obtained using the thermochemical heat exchanger prototype test setup are different from the values calculated as a result of DSC analysis. This result shows that, theoretically, the statement that the total energy absorbed by the material during desorption is equal to the energy it can produce during sorption is not entirely true.

Within this study, mono and mixed salt impregnated AAO and pumice based composite samples were synthesized and characterized for thermochemical heat storage applications. The results obtained are given below:

- In the prototype test setup, the highest Ed value was obtained in the pumice-$MgCl_2$ composite with 658 kWh/m^3.

- As a result of the measurements in the thermochemical heat exchanger prototype, AAO-$MgCl_2$:$CaCl_2$ composite had a high exit temperature in all three cycles and exhibited a high stable performance during repeated cycles compared to AAO-$CaCl_2$ and AAO-$MgCl_2$.

- Similar stable behaviour for all three cycles was also obtained in pumice-$MgCl_2$ composite.

- The fact that the Ed values obtained for AAO-$MgCl_2$:$CaCl_2$ in every three cycles are close to each other, unlike the AAO-$CaCl_{l2}$ and AAO-$MgCl_2$ composites, is an indication that the AAO-$MgCl_2$:$CaCl_2$ composite has cyclic stability, and this is promising for the efficient use of THS systems. Similarly, pumice-$MgCl_2$ is preferable in the efficient use of THS systems.

Acknowledgments

This study was supported by the Scientific and Technological Research Council of Turkey (TUBİTAK) (Project No: 119M073).

References

[1] Clark RJ, Mehrabadi A, Farid M. State of the art on salt hydrate thermochemical energy storage systems for use in building applications. J Energy Storage 2020;27:101145. https://doi.org/10.1016/j.est. 2019.101145.

[2] Lin J, Zhao Q, Huang H, Mao H, Liu Y, Xiao Y. Applications of low-temperature thermochemical energy storage systems for salt hydrates based on material classification: A review. Sol Energy 2021;214:149–78. https://doi.org/10.1016/j.solener.2020.11.055.

[3] Aydin D, Casey SP, Riffat S. The latest advancements on thermochemical heat storage systems. Renew Sustain Energy Rev 2015;41:356–67. https://doi.org/10.1016/J.RSER.2014.08.054.
[4] Liu H, Nagano K, Sugiyama D, Togawa J, Nakamura M. Honeycomb filters made from mesoporous composite material for an open sorption thermal energy storage system to store low-temperature industrial waste heat. Int J Heat Mass Transf 2013;65:471–80. https://doi.org/10.1016/J.IJHEATMASSTRANSFER .2013.06.021.
[5] Palomba V, Frazzica A. Recent advancements in sorption technology for solar thermal energy storage applications. Sol Energy 2019;192:69–105. https://doi.org/10.1016/j.solener.2018.06.102.
[6] Zhang Y, Wang R. Sorption thermal energy storage: Concept, process, applications and perspectives. Energy Storage Mater 2020;27:352–69. https://doi.org/10.1016/J.ENSM.2020.02.024.
[7] Tatsidjodoung P, Le Pierrès N, Luo L. A review of potential materials for thermal energy storage in building applications. Renew Sustain Energy Rev 2013;18:327–49. https://doi.org/10.1016/J.RSER.2012.10.025.
[8] N'Tsoukpoe KE, Liu H, Le Pierrès N, Luo L. A review on long-term sorption solar energy storage. Renew Sustain Energy Rev 2009;13:2385–96. https://doi.org/10.1016/J.RSER.2009.05.008.
[9] Vasta S, Brancato V, La Rosa D, Palomba V, Restuccia G, Sapienza A, et al. Adsorption heat storage: State-of-the-art and future perspectives. Nanomaterials 2018;8. https://doi.org/10.3390/NANO8070522.
[10] Li W, Klemeš JJ, Wang Q, Zeng M. Development and characteristics analysis of salt-hydrate based composite sorbent for low-grade thermochemical energy storage. Renew Energy 2020;157:920–40. https://doi.org/10.1016/j.renene.2020.05.062.
[11] Yu N, Wang RZ, Wang LW. Sorption thermal storage for solar energy. Prog Energy Combust Sci 2013;39:489–514. https://doi.org/10.1016/J.PECS.2013.05.004.
[12] Xu JX, Li TX, Chao JW, Yan TS, Wang RZ. High energy-density multi-form thermochemical energy storage based on multi-step sorption processes. Energy 2019;185:1131–42. https://doi.org/10.1016/j.energy. 2019.07.076.
[13] Yu N, Wang RZ, Lu ZS, Wang LW. Development and characterization of silica gel–LiCl composite sorbents for thermal energy storage. Chem Eng Sci 2014;111:73–84. https://doi.org/10.1016/J.CES.2014.02.012.
[14] Korhammer K, Druske MM, Fopah-Lele A, Rammelberg HU, Wegscheider N, Opel O, et al. Sorption and thermal characterization of composite materials based on chlorides for thermal energy storage. Appl Energy 2016;162:1462–72. https://doi.org/10.1016/J.APENERGY.2015.08.037.
[15] Posern K, Kaps C. Calorimetric studies of thermochemical heat storage materials based on mixtures of MgSO4 and MgCl2. Thermochim Acta 2010;502:73–6. https://doi.org/10.1016/j.tca.2010.02.009.
[16] Zhang Y, Wang R, Li T, Zhao Y. Thermochemical characterizations of novel vermiculite-LiCl composite sorbents for low-temperature heat storage. Energies 2016;9. https://doi.org/10.3390/en9100854.
[17] Zhang YN, Wang RZ, Zhao YJ, Li TX, Riffat SB, Wajid NM. Development and thermochemical characterizations of vermiculite/SrBr2 composite sorbents for low-temperature heat storage. Energy 2016;115:120–8. https://doi.org/10.1016/j.energy.2016.08.108.
[18] Grekova A, Gordeeva L, Aristov Y. Composite sorbents "li/Ca halogenides inside Multi-wall Carbon Nano-tubes" for Thermal Energy Storage. Sol Energy Mater Sol Cells 2016;155:176–83. https://doi.org/10.1016/j.solmat.2016.06.006.
[19] Touloumet Q, Silvester L, Bois L, Postole G, Auroux A. Water sorption and heat storage in CaCl2 impregnated aluminium fumarate MOFs. Sol Energy Mater Sol Cells 2021;231:111332. https://doi.org/10.1016/j.solmat.2021.111332.
[20] Chumnanwat S, Watanabe Y, Taniguchi N, Higashi H, Kodama A, Seto T, et al. Pore structure control of anodized alumina film and sorption properties of water vapor on CaCl2-Aluminium composites. Energy 2020;208:118370. https://doi.org/10.1016/j.energy.2020.118370.
[21] Calabrese L, Brancato V, Palomba V, Frazzica A, Cabeza LF. Innovative composite sorbent for thermal energy storage based on a SrBr2·6H2O filled silicone composite foam. J Energy Storage 2019;26:100954. https://doi.org/10.1016/j.est.2019.100954.
[22] Karim Nejhad M, Aydin D. Synthesize and hygro-thermal performance analysis of novel APC-CaCl2 composite sorbent for low-grade heat recovery, storage, and utilization. Energy Sources, Part A Recover Util Environ Eff 2021;43:3011–31. https://doi.org/10.1080/15567036.2019.1666187.
[23] Courbon E, D'Ans P, Permyakova A, Skrylnyk O, Steunou N, Degrez M, et al. Further improvement of the synthesis of silica gel and CaCl2 composites: Enhancement of energy storage density and stability over cycles for solar heat storage coupled with space heating applications. Sol Energy 2017;157:532–41. https://doi.org/10.1016/j.solener.2017.08.034.
[24] Xu ZY, Wang RZ. A sorption thermal storage system with large concentration glide. Energy 2017;141:380–8. https://doi.org/10.1016/j.energy.2017.09.088.
[25] Mehrabadi A, Farid M. New salt hydrate composite for low-grade thermal energy storage. Energy 2018;164:194–203. https://doi.org/10.1016/J.ENERGY.2018.08.192.
[26] Yilmaz B, Yüksel B, Orhan G, Aydin D, Utlu Z, Yilmaz B, et al. Synthesis and characterization of salt-

impregnated anodic Aluminium oxide composites for low-grade heat storage. Int J Miner Metall Mater 2020;27:112–8. https://doi.org/10.1007/S12613-019-1890-X.

[

PROCEEDINGS OF ECOS 2023 - THE 36TH INTERNATIONAL CONFERENCE ON
EFFICIENCY, **C**OST, **O**PTIMIZATION, **S**IMULATION AND ENVIRONMENTAL IMPACT OF ENERGY SYSTEMS
25-30 JUNE 2023, LAS PALMAS DE GRAN CANARIA, SPAIN

Modeling of a combined solar system including a thermal battery based on phase change material

Diane Le Roux[a], Sylvain Serra[b], Sabine Sochard[c], Zakaria Aketouane[d], Tessa Hubert[e], Ryad Bouzouidja[f], Alain Sempey[g] and Jean-Michel Reneaume[h]

[a] Universite de Pau et des Pays de l'Adour, E2S UPPA, LaTEP, Pau, France, diane.le-roux@univ-pau.fr, CA
[b] Universite de Pau et des Pays de l'Adour, E2S UPPA, LaTEP, Pau, France, sylvain.serra@univ-pau.fr
[c] Universite de Pau et des Pays de l'Adour, E2S UPPA, LaTEP, Pau, France, sabine.sochard@univ-pau.fr
[d] Nobatek/INEF 4, Anglet, France, zaketouane@nobatek.inef4.com
[e] Nobatek/INEF 4, Anglet, France, thubert@nobatek.inef4.com
[f] University of Bordeaux, CNRS UMR 5295, Arts et Metiers Institute of Technology, Bordeaux INP, INRAE, I2M Bordeaux, Talence, France, ryad.bouzouidja@u-bordeaux.fr
[g] University of Bordeaux, CNRS UMR 5295, Arts et Metiers Institute of Technology, Bordeaux INP, INRAE, I2M Bordeaux, Talence, France, alain.sempey@u-bordeaux.fr
[h] Universite de Pau et des Pays de l'Adour, E2S UPPA, LaTEP, Pau, France, jean-michel.reneaume@univ-pau.fr

Abstract:
Thermal energy storage (TES) is a key issue in efficient energy system applications, especially in the context of renewable energies. In this respect, phase change materials (PCM) have attracted interest as an active solution for efficient energy management, particularly in the building sector. This paper presents a modeling of a thermal battery based on PCM in the case of solar systems assisted by heat pump (SAHP). The storage tank allows to store the heat produced via unglazed solar panels (Batisol®) and represents the heat source of the heat pump. The heat pump can supply the heating and domestic hot water (DHW) needs of a building. The storage consists of a block of PCM contained between two plates of heat transfer fluid (HTF). A 2D model is used to describe the behaviour of the PCM and a 1D model is preferred for the HTF plates. The objective of the study is to dynamically simulate the thermal behaviour of this storage for different hot inlet temperature profiles: step, trapezoidal functions and profile of the temperature at the outlet of the thermal panels for a winter and summer period of 8 days. This 2D model would be useful to validate a simpler model for optimisation of the operational parameters of the system.

Keywords:
Thermal energy storage, Phase change material, Solar system assisted heat pump, Domestic hot water, Low-temperature heating.

1. Introduction

In order to limit temperature rise, it is important to reduce the environmental impact of energy production and consumption. According to the International Energy Agency [1], the building sector is considered to be one of the largest energy end-use sectors in the world. The growing demand for energy is increasing the pressure on the environment. One of the main challenges to reduce the environmental impact of buildings is therefore to replace fossil fuels with renewable resources. Thermal energy storage (TES) has been particularly studied in recent years as it is essential to compensate for the intermittency of renewable energies, by correcting the mismatch between energy supply and demand [2]. Moreover, TES are increasingly used to meet the heating and cooling needs of buildings. There are three types of TES: sensible, latent and thermochemical [2]. Phase Change Materials (PCM) are materials that can store large amounts of thermal energy in the form of latent heat of fusion when they change from a solid to a liquid state for example at a specific phase change temperature or temperature range if the PCM is not a pure compound. This phase transition process is reversible, allowing thermal energy to be stored and released at relatively constant temperatures. Compared to sensible heat storage materials, PCM offer several significant advantages, like a higher heat storage density at small temperature ranges [3]. PCM can store between 5 and 14 times more thermal energy per unit volume than sensible heat storage materials [4]. As a result, the use of PCM can help to reduce the size of heat storage systems, making them more suitable for residential applications. Thermochemical storage is more interesting in terms of storage density. However, this technology is less mature than that with PCM.

Solar systems assisted by heat pump (SAHP) can provide an efficient and environmentally friendly heating

and cooling solution for residential and commercial buildings. The role of a heat pump in the heating system is to increase the thermal energy from a lower temperature level to a higher temperature level [5]. Moreover, the use of PCM heat storage between the solar facade and the heat pump can improve the overall performance of the SAHP. Several studies have been conducted to assess the benefits of using PCM in SAHP [6–9]. Firstly, the solar energy stored in the PCM unit can be used as a heat source for the evaporator in the heat pump. As a result, the temperature of the evaporator is almost constant and the heat pump can operate under more stable conditions. This leads to a better Coefficient of Performance (COP) for the heat pump.

Depending on the type of application at the output of the heat pump (heating, cooling), the temperature levels are not the same and therefore the PCM used changes [6]. Four temperature ranges have been listed by Du *et al.* [6]: low (-20 to 5 °C), medium-low (5 to 40 °C), medium (40 to 80 °C) and high (80 to 200 °C) temperatures. For a heating or domestic hot water applications, the medium temperature level is considered since the buffer tank temperature setpoint is usually expected at 60 °C. Many studies have been carried out on such systems [6, 8–10]. However, as each storage is different (size, design and PCM used in particular), it is important to model its thermal behaviour correctly in order to explore the optimal operating parameters later.

The objective of this paper is to dynamically simulate a TES based on PCM integrated on SAHP. In a first part, the methodology and the case study will be presented. Then, several operating scenarios will be investigated in the results section. The profile of the hot temperature entering in the thermal battery will be a step, then a trapezoidal function, and finally this of the outler temperature of thermal panels in winter and summer periods using measured climatic conditions as boundaries. Finally, last part will conclude.

2. Material and Methods

This section is divided in three parts. Firstly, the global system is described, composed by solar thermal panels, PCM battery and heat pump. In next steps, the models of the different components of the system are defined. Dynamic models are based on the conservation of mass and energy equations.

2.1. Definition of the system

The studied system is composed of solar panels, a TES based on PCM, and a heat pump, as illustrated in Fig. 1. The system is divided in three circuits. The first, connecting the solar facade to the buffer tank, is made up of glycol. The second circuit, connecting the thermal battery to the heat pump, is composed of water. An air heater is integrated in parallel with the solar storage to supply heat to the heat pump when the temperature of the thermal battery is not high enough. The last circuit, also made of water, connects the PCM battery for heating and domestic hot water (DHW) to the heat pump.

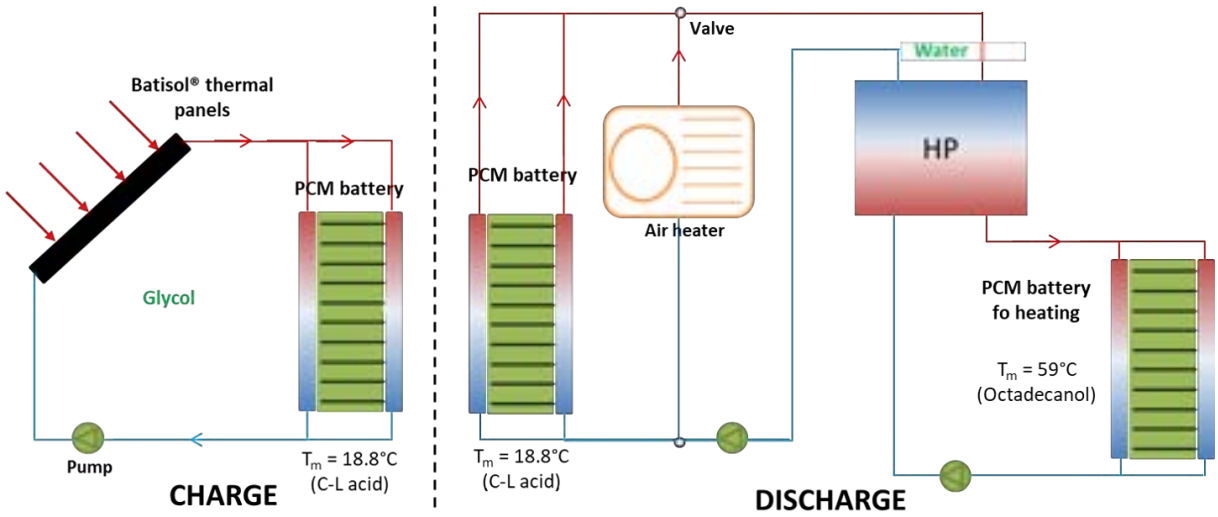

Figure 1: Global diagram of the solar assisted heat pump with thermal battery based on PCM.

The solar facade is composed of unglazed thermal panels (Batisol®) [11, 12], developed by Nobatek/INEF 4 [13]. The dimensions of the PCM-based storage are 0.4 m x 0.4 m x 0.4 m (Fig. 2a). The heat pump can produce both low temperature heating and DHW for a building application. The same thermal battery is used for the DHW and buffer tanks. Only the PCM changes between the two batteries, to match the desired temperature level. For the buffer tank, a mixture of 61.5% capric acid and 38.5% lauric acid (C-L acid) is used. Its melting temperature is 291.95 K. For the heating PCM battery, octadecanol is prefered. Indeed, its melting temperature is 332.46. The thermophysical properties of these materials are depicted in Table 1.

Table 1: Thermophysical properties of C-L acid [14] and octadecanol.

Name	Value for C-L acid	Value for octadecanol	Unit
T_m	291.95	332.46	K
L	$140.8 \cdot 10^3$	$208.45 \cdot 10^3$	J/kg
ρ_{PCM}	897.5	850	kg/m^3
$c_{p,l}$	1970	1750	$J/kg/K$
$c_{p,s}$	2240	2150	$J/kg/K$
λ_s	0.143	0.301	$W/m/K$
λ_l	0.139	0.205	$W/m/K$

2.2. Model of the Batisol® panels

The model of the thermal solar facade was described previously by Bouzouidja *et al.* [15]. From the time-varying input parameters, taken from a weather file, and the operating parameters, the temperature at the panel outlet is determined [15]:

$$T_{out,sol} = \frac{T_{in,sol} \cdot \dot{m} \cdot c_{p,H} + \alpha \cdot A_{sol} \cdot (0.5 \cdot T_{in,sol} - T_{ext}) + G_{sol} \cdot A_{sol} \cdot \gamma}{\dot{m} \cdot c_{p,H} - 0.5 \cdot \alpha \cdot A_{sol}} \tag{1}$$

Where $T_{in,sol}$ and T_{ext} are the temperatures at the entrance to the solar facade and outside (K), A_{sol} the surface of the solar facade (m^2), G_{sol} the solar flux (W/m^2), $\dot{m}$ the low rate of the Heat Transfer Fluid (HTF) circulating in the thermal panels (kg/s) and $c_{p,H}$ the specific heat capacity of the hot fluid (glycol) ($J/(kg \cdot K)$). The coefficients α and γ have been determined experimentally (γ = 0.63). The first one depends on the wind speed:

$$\alpha = -(7.84 + 3 \cdot v_{wind}) \tag{2}$$

2.3. Model of the thermal energy storage based on phase change material

In order to model the behaviour of latent heat storage, the following simplifying assumptions have been made:

- Natural convection is neglected. Only conduction is considered,
- No supercooling or superheating,
- Incompressible and Newtonian HTF,
- Kinetic and potential energy variations are neglected,
- Isothermal phase change (Octadecanol is a pure body so this assumption is correct. Since C-L acid is a mixture, the phase change temperature range is between 291.65 and 292.25 K [16]. As the melting temperature of this PCM is considered to be 291.95 K, the uncertainty of this assumption is +/- 2%),
- Density variation of PCM neglected during the phase change,
- Thermophysical properties are independent of temperature, but different for liquid and solid phases,
- The storage walls are assumed to be perfectly insulated (adiabatic boundary conditions) (Fig. 2b).

The shape of the thermal battery and its operation are described schematically in Fig. 2. The PCM is placed between two plates where the HTF circulates. Thus, a symmetry plane is visible in the middle of the battery. During the charging step, hot fluid is injected into the two plates. During the discharging step, cold fluid is injected. As a result, the charging and discharging steps are carried out separately. The plates where circulates the HTF are modelled in one dimension, a plug flow being assumed. The PCM part located between two plates is modelled in 2D because the heat diffusion operates in axial and longitudinal directions.

Fins are added to the plates to increase the contact area between the PCM and the HTF. To account for the fins, the effective conductivity of the PCM is expressed as:

$$\lambda_{eff} = a \cdot \lambda_{PCM} + (1 - a) \cdot \lambda_{fin} = a \cdot (\lambda_s + f_l \cdot (\lambda_l - \lambda_s)) + (1 - a) \cdot \lambda_{fin} \tag{3}$$

Where a is the proportion of PCM in the volume under consideration ($-$), λ_{PCM}, λ_s, λ_l et λ_{fin} are respectively the thermal conductivities of the PCM, the solid and liquid phases of the PCM and the fins ($W/m/K$), and f_l the liquid fraction of the PCM ($-$).

The enthalpy, the temperature and the liquid fraction of the PCM (according to x and y), and the temperature of the hot HTF (according to y) are determined with 4 to 11.

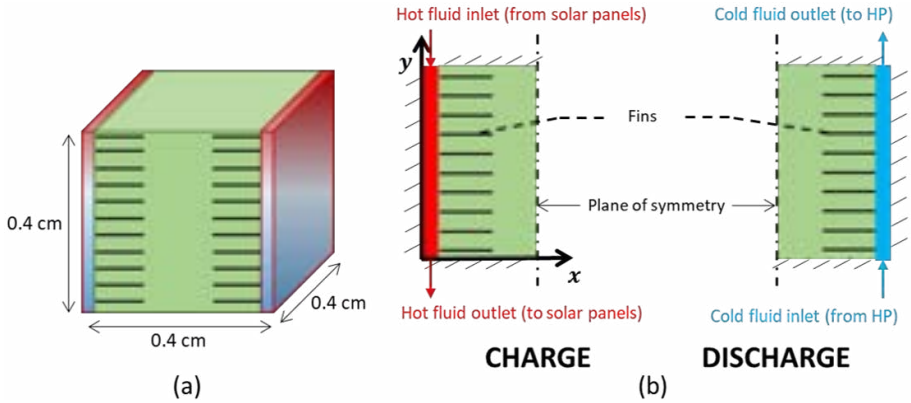

Figure 2: Diagram of the dimensions of the PCM-based thermal battery (a), and diagram of the PCM-based thermal battery with two plates for the charging and discharging steps (b).

- **Exchanges between the HTF (hot or cold) and the PCM:**

  For hot fluid:

$$\rho_H \cdot V \cdot c_{p,H} \frac{\partial T_H}{\partial t} - \dot{m}_H \cdot c_{p,H} \cdot \frac{\partial T_H}{\partial y} \cdot P = h_H \cdot A \cdot (T_H - T_{PCM}) + \lambda_H \cdot V \cdot \frac{\partial^2 T_H}{\partial y^2} \tag{4}$$

  For cold fluid:

$$\rho_C \cdot V \cdot c_{p,C} \frac{\partial T_C}{\partial t} + \dot{m}_C \cdot c_{p,C} \cdot \frac{\partial T_C}{\partial y} \cdot P = h_C \cdot A \cdot (T_C - T_{PCM}) + \lambda_C \cdot V \cdot \frac{\partial^2 T_C}{\partial y^2} \tag{5}$$

- **Exchanges in the PCM:**

$$\frac{\partial H_{PCM}}{\partial t} = \frac{\partial \lambda_{eff}}{\partial x} \cdot \frac{\partial T_{PCM}}{\partial x} + \frac{\partial \lambda_{eff}}{\partial y} \cdot \frac{\partial T_{PCM}}{\partial y} + \lambda_{eff} \cdot \frac{\partial^2 T_{PCM}}{\partial x^2} + \lambda_{eff} \cdot \frac{\partial^2 T_{PCM}}{\partial y^2} \tag{6}$$

$$H_{PCM}(T_{PCM}) = f_l \cdot H_l + (1 - f_l) \cdot H_s = \rho_{PCM} \cdot ((c_{p,s} + f_l \cdot (c_{p,l} - c_{p,s})) \cdot T_{PCM} + L \cdot f_l - f_l \cdot (c_{p,s} + f_l \cdot (c_{p,l} - c_{p,s})) \cdot T_m) \tag{7}$$

$$f_l = \begin{cases} 0 & for\ H_{PCM} < H_s \\ \frac{H_{PCM} - H_s}{H_l - H_s} & \\ 1 & for\ H_{PCM} > H_l \end{cases} \tag{8}$$

- **Boundary conditions for the PCM in contact with hot (during charging step) or cold (during discharging step) HTF:**

  For hot fluid (for x = 0 and 0.4 m):

$$h_H \cdot (T_H - T_{PCM}) = -\lambda_{eff} \frac{\partial T_{PCM}}{\partial x}\ for\ x = 0\ m \quad and \quad h_H \cdot (T_H - T_{PCM}) = \lambda_{eff} \frac{\partial T_{PCM}}{\partial x}\ for\ x = 0.4\ m \tag{9}$$

  For cold fluid (for x = 0 and 0.4 m):

$$h_C \cdot (T_C - T_{PCM}) = -\lambda_{eff} \frac{\partial T_{PCM}}{\partial x}\ for\ x = 0\ m \quad and \quad h_C \cdot (T_C - T_{PCM}) = \lambda_{eff} \frac{\partial T_{PCM}}{\partial x}\ for\ x = 0.4\ m \tag{10}$$

- **Boundary conditions for the PCM in contact with the outside (adiabatic conditions):**

$$\lambda_{eff} \frac{\partial T_{PCM}}{\partial y} = 0\ for\ y = 0\ and\ 0.4\ m \tag{11}$$

- **Initial conditions:** All temperatures are fixed at 283.15 K. The enthalpy of the PCM is determined by 7 at 283.15 K. The liquid fraction is considered equal to 0.

Where h_H and h_C are the convective exchange coefficients of the hot and cold fluid respectively ($W/m^2/K$), T_H, T_C, T_{PCM} and T_m are the hot and cold temperature, the temperature of the PCM and the melting temperature of the PCM, L the latent heat (J/kg), ρ_{MCP} the PCM density (kg/m^3), $c_{p,l}$ and $c_{p,s}$ are the specific heat capacity of the liquid and solid phases respectively ($J/kg/K$), P the exchange perimeter (m), A the exchange area (m^2) and V the volume of the representative element considered (m^3). The convective exchange coefficients are determined from the Nusselt number, assuming that the wall thickness of the plate is very thin and therefore negligible.

The boundary conditions of the thermal battery depend on the configuration studied. Four scenarios have been investigated. Firstly, the profile of hot temperature entering the thermal battery follows a step. In a second stage, it is a trapezoidal function. Finally, the battery based on PCM is connected to the Batisol® panels and two periods of 8 days are simulated: winter (from January 1 to 8) and summer (from July 1 to 8). In the latter two cases, the profile of the outlet temperature of the solar panels is used as input to the PCM:

$$T_H(x, y = 0.4, t) = T_{out,sol} \tag{12}$$

2.4. Resolution of the differential algebraic equations and software used

The software used to model the system is OpenModelica v1.18.0. The Modelica library (v3.2.3) is considered. The spatial discretisation is performed manually while the temporal discretisation is performed via the DASSL integrator available on OpenModelica. The tolerance used in the DASSL integrator is 10^{-6}. For the PCM-battery model, equations are discretised using an explicit second-order discretisation scheme with finite differences. For the boundary conditions (9 to 11), second-order decentred schemes are used.

3. Results and Discussion

This section is divided into three parts. The first one aims at studying the behaviour of PCM-based TES for a hot inlet temperature profile following a ramp (case 1). The second part investigates the behaviour of the system under trapezoidal loads (case 2). Finally, the battery is connected to the Batisol® solar facade and an 8-day simulation is performed for two periods of the year: from 1 to 8 January (winter, case 3) and from 1 to 8 July (summer, case 4). The hot HTF temperatures investigated at the buffer tank inlet are shown in Fig. 3. The colours red, green, blue and yellow refer to cases 1, 2, 3 and 4 respectively. For the next figures, the coordinates (x = y = 0 m) are placed at the bottom left of the PCM in Fig. 2.

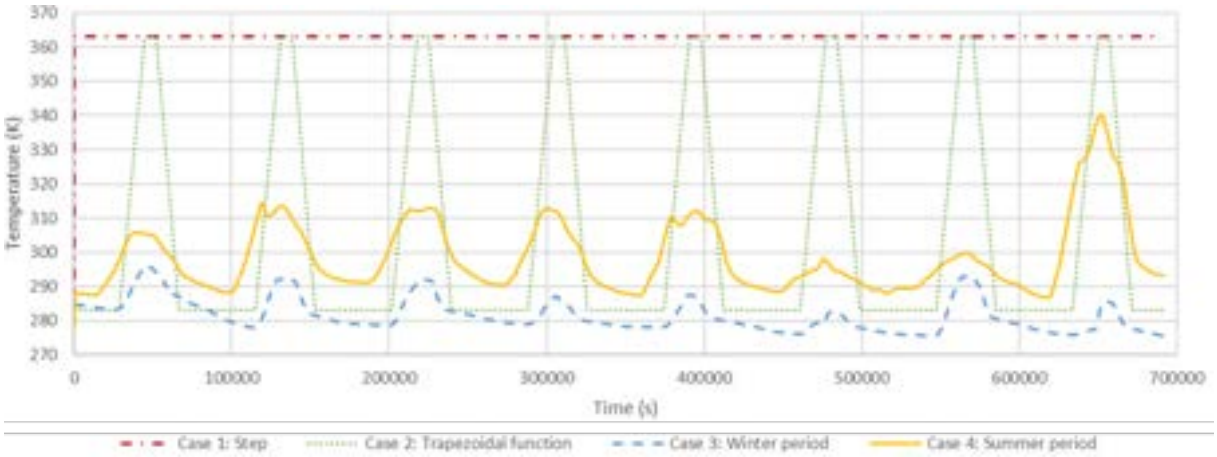

Figure 3: Four hot temperatures profiles considered at the input of the PCM-based TES battery.

The simulation times are relatively fast for simulating 8 days ($6.912 \cdot 10^{-5}$ s) on a standard laptop (processor: 12th Gen Intel®Core(TM) i7-12700H 2.69 GHz and RAM: 32 Go). They amount to 30 s and 2 min for cases 1 and 2 respectively. When the weather file is used and the Batisol® thermal panel model is added, the simulation times are slightly longer but remain below 5 min.

3.1. Profile of the hot inlet temperature following a step

For the case 1, the input temperature profile follows a ramp from 283.15 to 363.15 K in the first second of the simulation. The evolution of the liquid fraction and the temperature of the PCM in the tank are studied in Fig. 4 over time for the first slice of PCM in contact with the hot plate (for x = 0 m), according to the vertical. The colours purple, green and red refer to the high (y = 0.4 m), middle (y = 0.2 m) and low (y = 0 m) parts of the PCM respectively. Solid lines are used for the temperature and dashed lines are preferred for the liquid fraction. The same marking and colour code will be used in the following sections. Initially, the PCM is in the solid state

(f_l = 0) at 283.15 K. Its temperature increases until it reaches the melting temperature (291.95 K) at 18.2 s for y = 18 (in purple), the top of the PCM in contact with the hot plate. This temperature is reached at 20.8 s for the middle of the PCM (in green), and 23.2 s for the bottom of the PCM (in red). From these times onwards, the temperature of the PCM remains constant while the liquid fraction increases until it reaches unity, indicating that all the PCM has changed from the solid to the liquid state. This event occurs at 78.0, 82.1 and 87.5 s for the top, middle and bottom of the PCM respectively. From then on, the liquid fraction remains constant and the temperature of the PCM gradually increases, while approaching the temperature of the hot HTF.

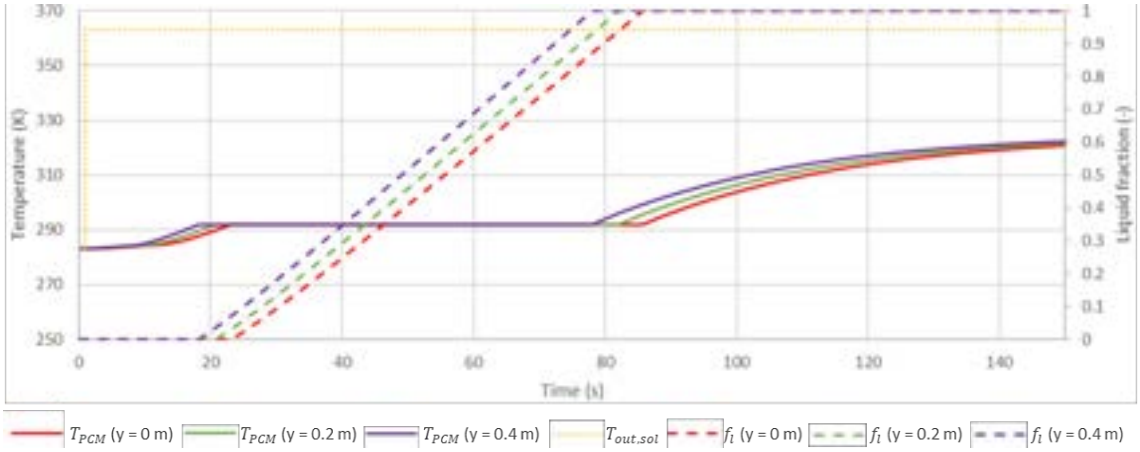

Figure 4: Case 1: Temperature and liquid fraction evolution for the first PCM layer in contact with the hot plate (x = 0 m) and for y = 0, 0.2 and 0.4 m.

The evolution of these two variables has also been studied for different values of x in Fig. 5. As the battery is symmetrical, only the coordinates at x = 0 (in red), 0.06 (in yellow) and 0.2 m (in green) are presented for the sake of clarity. In this case, the profiles are clearly different. The phase change from solid to liquid state is clearly visible for the first layer in contact with the hot plate. For x = 0.06 m, the temperature evolves linearly without reaching the melting temperature. As a result, the liquid fraction remains constant and equal to zero. For the PCM in the middle of the battery (x = 0.2 m), the temperature remains almost constant (283.15 K), indicating that the heat has not reached the core of the battery in 150 s.

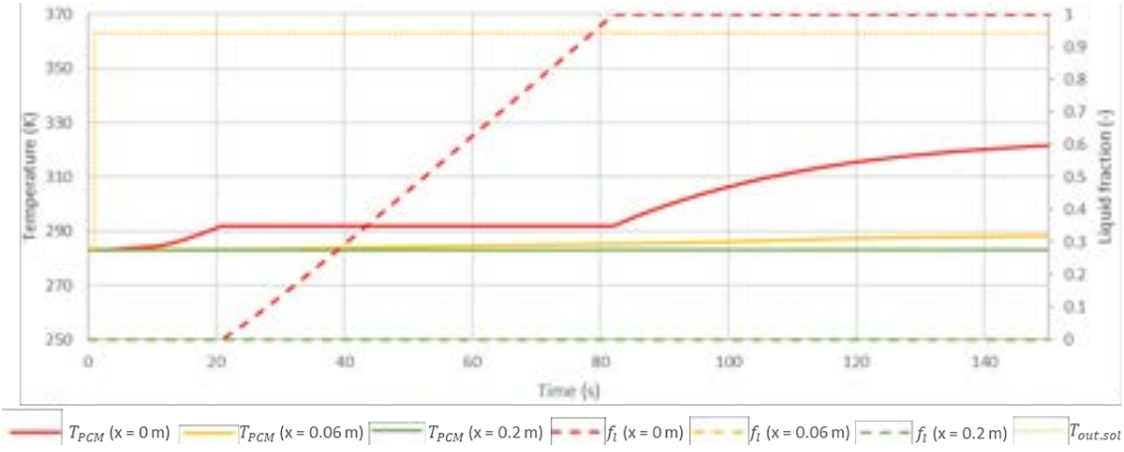

Figure 5: Case 1: Temperature and liquid fraction evolution in the longitudinal direction (for x = 0, 0.06 and 0.2 m) for the PCM layer in the middle (y = 0.2 m).

Figures 4 and 5 show the interest of considering a 2D model for PCM tank, according to longitudinal (x) and vertical (y) directions, since the temperatures in the PCM are different in both directions.

3.2. Profile of the hot inlet temperature following a trapezoidal function

Before studying the thermal behaviour of the storage connected to the solar facade, a trapezoidal function is used to simulate the evolution of the hot temperature at the battery inlet (Fig. 3). The period of this function is decomposed on 28800 s of width, 16200 s of rising , 7200 s of width, 14400 s of falling, for a total period of 86400 s. The temperature and liquid fraction are studied as before, for the first slice in contact with the hot

plate (for x = 0 m) (Fig. 6), and the slice in the middle of the PCM (for y = 0.2 m) (Fig. 7). The same evolution as for the ramping test is observed. In a first step, the temperature of the PCM increases until it reaches the melting temperature of the PCM (at 30634 s) (Fig. 6a). Then the liquid fraction increases until it reaches unity (Fig. 6b). At this point (31049 s), the temperature of the PCM increases again (Fig. 6a). The temperature of the PCM follows the temperature of the hot HTF at the battery inlet, with an average difference of less than 6%. In order to store as much heat as possible and not send it to the solar circuit, it can be interesting to stop the charging step when the temperature of the PCM becomes higher than that of the hot coolant. Figure 6 shows that this moment occurs at 52200 s.

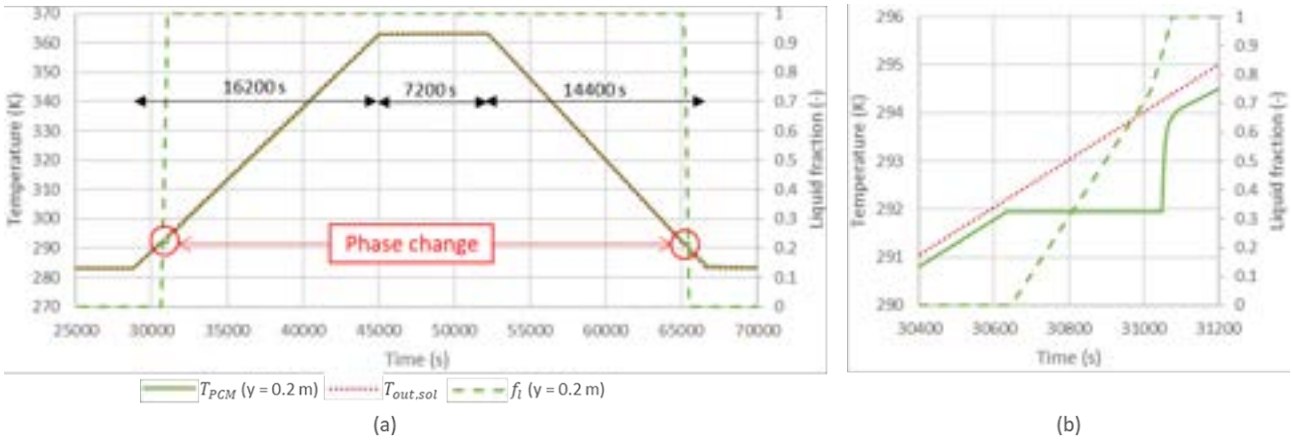

Figure 6: Case 2: Temperature and liquid fraction evolution for the first PCM layer in contact with the hot plate (x = 0 m) and for y = 0.2 m (a), focus on the phase change between 30634 and 31049 s (b).

Figure 7a shows the evolution of the temperature and liquid fraction of the PCM in the longitudinal direction (x = 0, 0.06 and 0.2 m) for the PCM layer at y = 0.2 m. The difference in temperature is clearly visible for the three curves. The further the PCM is from the hot plates, the lower its temperature and the longer the phase change takes. The heat propagation is thus clearly visible along the PCM. The core of the PCM (x = 0.2 m in green) takes the longest time to melt, but also to solidify as the hot inlet temperature decreases. The change from liquid to solid state is thus much longer (13 times longer) than for the PCM layers closer to the hot plate. For the yellow curve (x = 0.06 m), after the phase change, slight instabilities are visible in the PCM temperature. This must be due to the discretisation step and/or the discretisation scheme, whose order should be increased to be more accurate, and/or the DASSL integrator whose tolerance must be increased. The phase change step is significantly larger for x = 0.2 m. This is because the heat propagates from layer to layer. During the phase change of a PCM layer, all the energy required to achieve the phase change is absorbed. Therefore, for the liquid fraction of the layer x = 0.2 m to fluctuate, the liquid fractions of the previous layers must already have reached an equilibrium (solid or liquid state). This is illustrated in Fig. 7b, which shows a zoom of the transition from solid to liquid state (between 31000 and 35000 s) for the layers x = 0 (in red), 0.02 (in purple), 0.04 (in blue) and 0.06 m (in yellow). It can be seen that the liquid fraction of the next layer increases when the liquid fraction of the layer under consideration has reached 1. As a result, even if the melting temperature of the PCM has been reached for a PCM layer, it is necessary to wait until the change of state has taken place in the layers closer to the hot plates before the phase change begins in the PCM layer.

3.3. Profile of the hot inlet temperature following the outlet temperature of the Batisol® panels

When the PCM-based storage is connected to the Batisol® thermal panels, the temperature of the inlet hot HTF is calculated by 1. The surface area of the thermal panels is 25.5 m^2 (5 m wide by 5.1 m long). The surface area consists of 16 panels with 24 channels. Meteorological data from Cholet (next to Nantes) in 2021, in the northwest of France, are used. Figure 8 presents the evolution of the solar power and the outdoor temperature for the 2 periods (winter and summer) considered. The solar power amounts to 112 W/m^2 over the 8 winter days considered, whereas over the summer period considered this value is 2.5 times higher. The average outdoor temperature is 280 K and in summer 291.83 K. These two periods were chosen to represent different types of days, with more or less sunshine and wind, cold or hot outside temperatures (Fig. 8). In addition, 8-day periods were considered in order to determine the capacity of the battery to store heat during renewable energy intermittencies and day/night alternations.

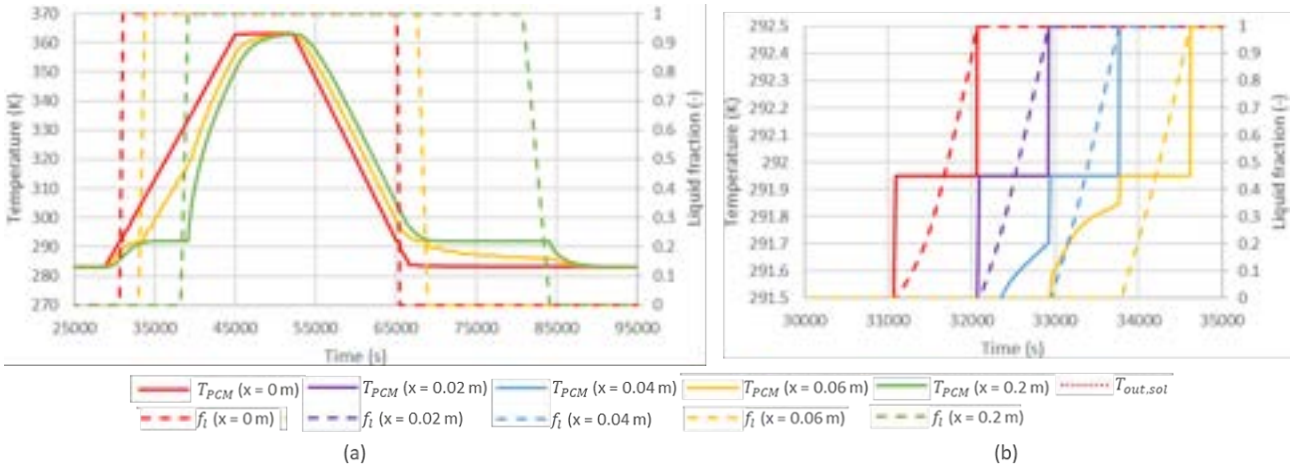

Figure 7: Case 2: Temperature and liquid fraction evolution in the longitudinal direction (for x = 0, 0.06 and 0.2 m) for the PCM layer in the middle (y = 0.2 m) (a), focus on the phase change of the first four PCM layer (from x = 0 to 0.06 m) (b).

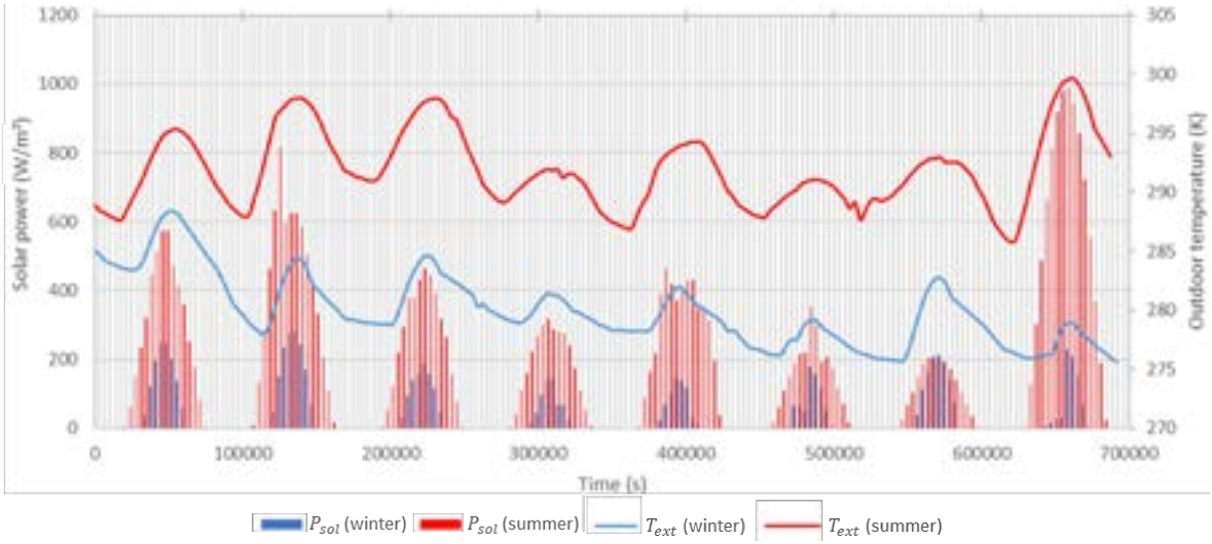

Figure 8: Cases 3 and 4: Evolution of solar power and outdoor temperature over the 8 days studied in winter and summer.

3.3.1. Winter period

The winter period chosen to simulate the behaviour of the PCM battery is from January 1 at 0am to January 8 at 23pm. In order to simplify the understanding of the graphs over longer periods (8 days), only the temperature and liquid fraction of the middle cell (y = 0.2 m) of the layer in contact with the hot plate (x = 0 m) are considered in Fig. 9. Over the 8 days simulated, the temperature at the exit of the solar facade is only higher than the melting temperature of the PCM on four days (Fig. 3). The PCM temperature exceeds the melting temperature only on January 1, 2, 3 and 7, as shown in Fig. 9. Indeed, the liquid fraction remains zero except between 11.15am and 4.5pm on January 1st, between 12.4pm and 16pm on January 2, between 14pm and 15.15pm on January 3, between and 13pm and 15.5pm on January 7. On other days, the PCM never reaches the melting temperature. Nevertheless, heat is stored in the solid state, as with sensible TES but with low efficiency. Fig. 9 shows that it is important to choose a material with a melting temperature that is not too high in order to take advantage of the phase change. If the melting temperature was 298.15 K (291.95 K for C-L acid), the PCM would not have changed state during the winter period under consideration. As a result, the use of PCM-based storage would not be interesting.

The temperature of the PCM in contact with the hot plate is almost as high as that of the hot HTF at the inlet, with an average difference of 0.3% over the 8 days. Figure 10a shows the evolution of the temperature and liquid fraction for the PCM layer at y = 0.2 m and for x = 0 (in red), 0.06 (in yellow) and 0.2 m (in green). As seen earlier, the temperatures are lower and lower from the outside of the PCM towards the inside. Indeed,

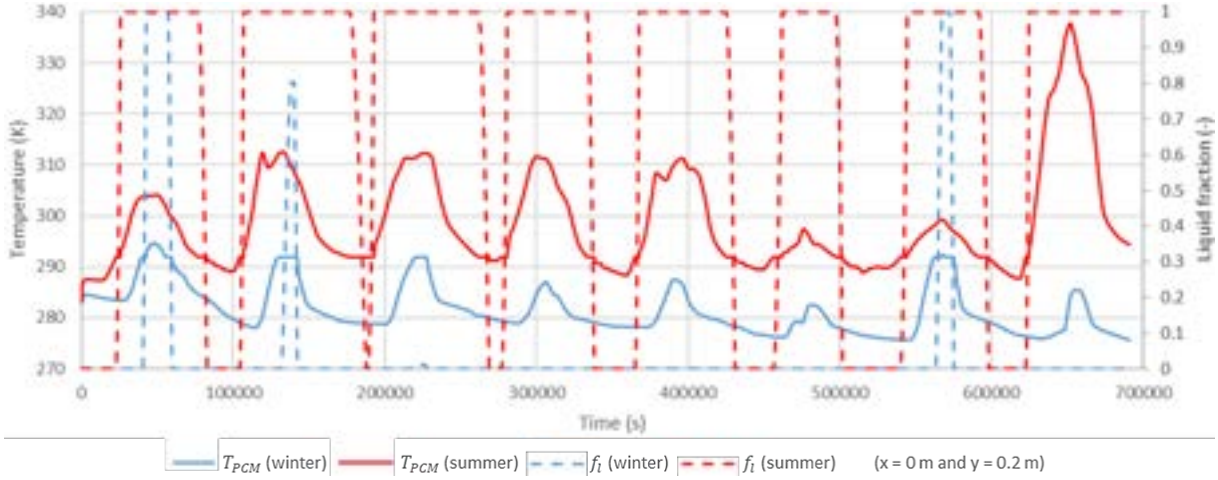

Figure 9: Cases 3 and 4: Temperature and liquid fraction evolution for the first PCM layer in contact with the hot plate (x = 0 m) and for y = 0.2 m.

the green curves show that the PCM has not changed state in the middle of the thermal battery. Furthermore, Fig. 10 shows the heat propagation along the PCM, with lower temperatures at the ends of the PCM, after the hot temperature at the inlet is decreased (after 60000 s). In general, the heat propagates well in the PCM, since the temperature differences between the different layers of PCM in the hot HTF are less than 0.8%. The instabilities visible at x = 0 and 0.06 m are due to the slight change in temperature at the outlet of the thermal panels (red dotted line in Fig. 10a), which of course depends on the weather conditions. These instabilities appear at the extremities of the PCM close to the hot plates (such as at x = 0 and 0.06 m) but not at the centre of the PCM (at x = 0.2 m). As seen previously, the liquid fraction of the x = 0.2 m layer remains zero while the melting temperature has been reached (291.95 K at 53100 s). This is due to the liquid fractions of the layers closer to the hot plate, which have not all reached unity. The output temperature of the solar panels decreases from 47483 s onwards, and consequently the energy supplied to the PCM. As a result, the middle layer (x = 0.2 m) has not received enough energy to make its phase change. Figure 10b is a zoom of the phase change (solid to liquid) in Fig. 10a. Before a layer changes phase, it is necessary that the liquid fraction of the previous layer has reached unity. Figure 10b shows this clearly, with the increase from 0 to 1 in the liquid fraction at x = 0 m (38900 to 40440 s), then that at x = 0.02 s (40440 to 42747 s), then that at x = 0.04 m (42747 to 44826 s) and finally that at x = 0.06 m (44826 to 47470 s).

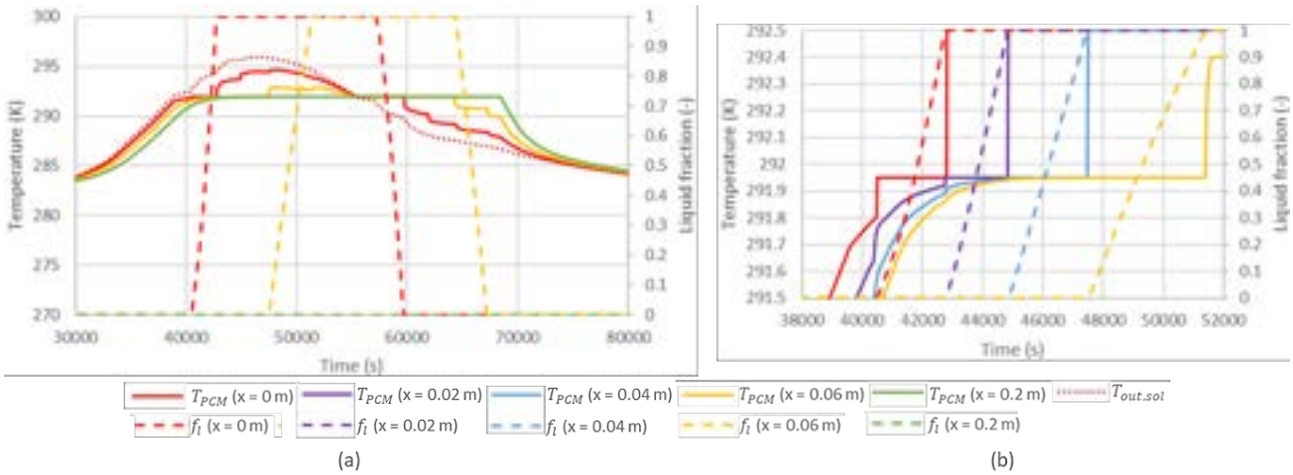

Figure 10: Case 3: Temperature and liquid fraction evolution in the longitudinal direction (for x = 0, 0.06 and 0.2 m) for the PCM layer in the middle (y = 0.2 m) (a), focus on the phase change of the first four PCM layer (from x = 0 to 0.06 m) (b).

3.3.2. Summer period

The summer period chosen to simulate the behaviour of the PCM battery is from July 1 at 0am to January 8 at 23pm. The temperature and liquid fraction at x = 0 m and y = 0.2 m are shown in the same figure as the winter period (Fig. 9). The temperature of the hot HTF at the storage inlet is significantly higher than during the winter

period (up to 340 K vs 296 K as illustrated in Fig. 3). The differences between the maximum temperatures expected by the hot fluid at the outlet of the thermal panels range from 2% (January 7 and July 7) to 16% (January 8 and July 8). On average the temperatures are 8% higher in summer. As a result, the behaviour of the PCM is also different between winter and summer periods, with phase changes occurring less often in winter. The advantage of using PCM in summer is therefore much greater, since it is possible to limit the size of the battery thanks to the change in the state of the material, unlike the use of sensible storage. Even on less sunny days such as July 6, when the temperature of the hot HTF does not exceed 297 K, there is enough heat to allow the PCM to change state. The PCM remains in a liquid state longer than in winter, between 7am and midnight on average over the 8 days considered.

As for the winter period, the difference between the temperature of the PCM in contact with the plate and that of the hot HTF is small (0.5% difference on average over the 8 days). Figure 11a shows the evolution of the temperature and liquid fraction for the PCM layer at y = 0.2 m and for x = 0. (in red), 0.06 (in yellow) and 0.2 m (in green). The temperature differences from the outside to the inside of the PCM are also clearly visible. From 16.4pm onwards, the temperature of the PCM in the core of the battery is higher than that of the PCM in contact with the hot plate. It would therefore be interesting to stop the charging step and start the discharging step by switching the hot (solar system) and cold (heat pump) inputs. The same instabilities as for winter period appear in Fig. 11a for the same reasons (small fluctuations of the temperature at the outlet of the thermal panels due to climatic conditions). The phase change zoom of the first four layers is illustrated in Fig. 11b (for x = 0 (in red), 0.02 (in purple), 0.04 (in blue) and 0.06 m (in yellow)).

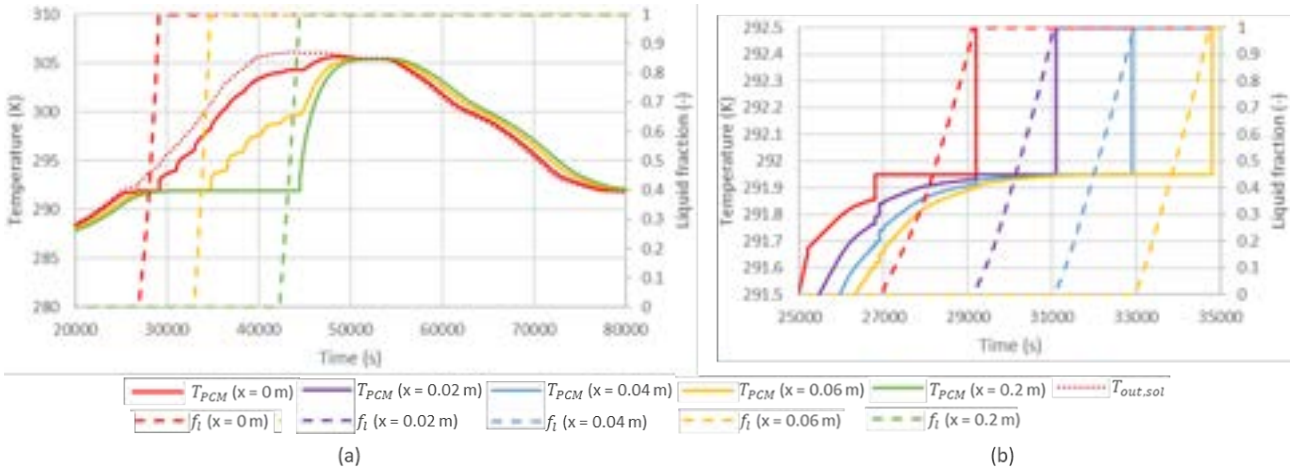

Figure 11: Case 4: Temperature and liquid fraction evolution in the longitudinal direction (for x = 0, 0.06 and 0.2 m) for the PCM layer in the middle (y = 0.2 m) (a), focus on the phase change of the first four PCM layers (from x = 0 to 0.06 m) (b).

The energy stored by the thermal battery for the two periods considered (winter and summer) is given in Table 2. During the winter period under consideration, the average stored energy is 164 Wh per day. In summer, this value is 6 times higher. The sunniest days (January 1st in winter and July 8 in summer) store 5 to 7.5 times more energy than the days less suitable for thermal collectors (January 6 and July 6). On average, the PCM battery can store 2.6 kWh/m^3 per day of energy in winter and 6.6 kWh/m^3 for January 1st. In summer this value reaches 15.1 kWh/m^3 per day on average and 29.3 kWh/m^3 for July 8. The benefit of PCM is clearly visible in summer, with almost 6 times more energy stored by the battery than in winter, partly due to the more frequent phase changes.

Table 2: Energy stored in the thermal battery per day (Wh).

Period	Minimal value	Maximal value	Mean
Winter	56 (January 6)	423 (January 1st)	164
Summer	385 (July 6)	1877 (July 8)	964

4. Conclusion

A dynamic model of a SAHP based on the use of thermal panels (Batisol®) and a latent heat storage was presented. This system aims to provide the heating and domestic hot water needs of a building. The TES is

composed of a PCM contained between two plates where HTF circulate. During the charging step, the hot HTF is fed by the thermal panels. During the discharging step, the direction of the fluid is reversed and the cold HTF is fed by the heat pump.

The thermal behaviour of the PCM tank is studied for four different profiles of the charging temperature: ramping, trapezoidal functions, temperature at the outlet of the thermal panels in winter (from January 1 to 8) and in summer (from July 1 to 8). The simulations carried out in OpenModelica showed the behaviour of the PCM during the phase change. The developed model showed the importance of choosing a PCM with a melting temperature range suitable for the studied application. In winter, only the sunniest days allows the PCM to melt while in summer the phase change occurs every day. On average, this thermal battery can store 6.6 and 15.1 kWh/m^3 per day of energy in winter and summer respectively.

The simulations showed that the 2D model of the system is necessary to take into account the horizontal and vertical temperature variations in the battery. This model will be further validated with experimental data. It will also allow the development and the validation of a simpler model. The final goal will be to optimise the SAHP system on its operational parameters with the simpler model.

Acknowledgments

This work was supported in the case of MCPBat project granted by the Region Nouvelle Aquitaine. Grant number 11385520-11389020 in the framework of the joint research team between the University of Pau and Pays de l'Ardour and Nobatek/INEF4.

Nomenclature

Letter symbols

- a proportion of PCM in the volume considered,
- A exchange surface, m^2
- c_p specific capacity, $J/(kgK)$
- f_l liquid fraction,
- G_{sol} solar flux, W/m^2
- h heat transfer coefficient, W/m^2K
- H enthalpy (including sensible and latent forms), J/m^3
- L latent heat, J/kg
- $\dot{m}$ mass flow rate, kg/s
- P exchange perimeter, m
- T temperature, K
- v_{wind} wind speed, m/s
- V exchange volume, m^3

Greek symbols

- λ thermal conductivity, $W/m/K$
- ρ density, kg/m^3

Subscripts and superscripts

- C Cold HTF
- eff Effective
- ext Exterior/Outdoor
- fin Fin
- H Hot HTF

in In

l Liquid phase

m Melting

out Out

PCM PCM

s Solid phase

sol Solar

References

[1] International Energy Agency. *Energy Efficiency: Buildings the global Exchange for Energy Efficiency Policies, Data and Analysis.* IEA Publications; 2021 Nov. Technical Report No.: Energy Efficiency 2021.

[2] Dincer I. *On thermal energy storage systems and applications in buildings*. Energy Build. 2002 May 1;34(4):377–88.

[3] Zalba B, Marin JM, Cabeza LF, Mehling H. *Review on thermal energy storage with phase change: materials, heat transfer analysis and applications*. Appl Therm Eng. 2003 Feb 1;23(3):251–83.

[4] Devaux P, Farid MM. *Benefits of PCM underfloor heating with PCM wallboards for space heating in winter*. Appl Energy. 2017 Apr 1;191:593–602.

[5] Stritih U. *An experimental study of enhanced heat transfer in rectangular PCM thermal storage*. Int J Heat Mass Transf. 2004 Jun 1;47(12):2841–7.

[6] Du K, Calautit J, Wang Z, Wu Y, Liu H. *A review of the applications of phase change materials in cooling, heating and power generation in different temperature ranges*. Appl Energy. 2018 Jun 15;220:242–73.

[7] Faraj K, Khaled M, Faraj J, Hachem F, Castelain C. *A review on phase change materials for thermal energy storage in buildings: Heating and hybrid applications*. J Energy Storage. 2021 Jan 1;33:101913.

[8] Seddegh S, Wang X, Henderson AD, Xing Z. *Solar domestic hot water systems using latent heat energy storage medium: A review*. Renew Sustain Energy Rev. 2015 Sep 1;49:517–33.

[9] Jin X, Zhang H, Huang G, Lai ACK. *Experimental investigation on the dynamic thermal performance of the parallel solar-assisted air-source heat pump latent heat thermal energy storage system*. Renew Energy. 2021 Dec 1;180:637–57.

[10] Zhou D, Zhao CY, Tian Y. *Review on thermal energy storage with phase change materials (PCMs) in building applications*. Appl Energy. 2012 Apr 1;92:593–605.

[11] Martinez RG, Goikolea BA, Paya IG, Bonnamy P, Raji S, Lopez J. *Performance assessment of an unglazed solar thermal collector for envelope retrofitting*. Energy Procedia. 2017 Jun 1;115:361–8.

[12] Bonnamy P, Raji S, Lopez J, Garay R. *Expérimentation et modélisation d'un collecteur solaire opaque pour préchauffage de l'eau*. In: Kjelstrup S., Hustad E., Gundersen T., Røsjorde A., Tsatsaronis G., editors. ECOS 2005: Proceedings of the 18th International Conference on Efficiency, Cost, Optimization, Simulation, and Environmental Impact of Energy Systems; 2016 Jun 20-25; Trondheim, Norway. Tapir Academic Press:777-84.

[13] Nobatek/INEF 4. *BATISOL: Capteurs solaires thermiques - solutions Nobatek/INEF 4* Available at: `https://www.nobatek.inef4.com/batisol/` [accessed 03.09.2023].

[14] Dimaano MNR, Watanabe T. *The capric–lauric acid and pentadecane combination as phase change material for cooling applications*. Appl Therm Eng. 2002 Mar 1;22(4):365–77.

[15] Bouzouidja R, Aketouane Z, Lhomer R, Varela B, Cruz JL, Serra S, Reneaume J.M., Sempey A. *Choice of the Suitable Melting Temperature of Phase Change Material: Application on Solar Assisted Heat Pump*. In: 2022 IEEE 10th International Conference on Smart Energy Grid Engineering (SEGE). 2022. p. 58–62.

[16] Kauranen P, Peippo K, Lund PD. *An organic PCM storage system with adjustable melting temperature*. Sol Energy. 1991 Jan 1;46(5):275–8.

Role of energy storage in residential energy demand decarbonization: system-level techno-economic comparison of low-carbon heating and cooling solutions

Marko Aunedi[a], Andreas V. Olympios[b], Antonio M. Pantaleo[c,d], Matthias Mersch[e] and Christos N. Markides[f]

[a] Imperial College London, UK, m.aunedi@imperial.ac.uk, CA
[b] Imperial College London, UK, a.olympios18@imperial.ac.uk
[c] Imperial College London, UK, a.pantaleo@imperial.ac.uk
[d] University of Bari, Italy, antonio.pantaleo@uniba.it
[e] Imperial College London, UK, m.mersch@imperial.ac.uk
[f] Imperial College London, UK, c.markides@imperial.ac.uk

Abstract:

This paper explores various combinations of electric heat pumps (EHPs), hydrogen boilers (HBs), electric boilers (EBs), hydrogen absorption heat pumps (AHPs) and energy storage technologies (electric and thermal) to assess their potential for matching heating and cooling demand at low cost and with low carbon footprint. Thermodynamic and component-costing models of various heating and cooling technologies are integrated into a whole-energy system cost optimisation model to determine cost-effective configurations of heating and cooling systems that minimise the overall investment and operation cost for both the system and the end-user. Case studies presented in the paper focus on two archetypal systems that differ in terms of heating and cooling demand and availability profiles of solar and wind generation. The proposed approach quantifies how the cost-efficient portfolios of low-carbon heating and cooling solutions are driven by the characteristics of the system such as share of variable renewables or heating and cooling demand. Modelling results suggest that capacity choices for heating and cooling technologies will vary significantly depending on system properties. More specifically, air-to-air EHPs, with their cost and efficiency advantages over air-to-water EHPs, could make a significant contribution to low-carbon heat supply as well as cooling, although their contribution may be constrained by the compatibility with existing heating systems. They are found to be a useful supplementary source of space heating that is able to displace between 20 and 33 GW_{th} of capacity of other heating technologies compared to the case where they do not contribute to space heating.

Keywords:

Heat decarbonisation; Cooling; Heat pumps; Energy storage; Hydrogen.

1. Introduction

An increasing number of countries and regions worldwide have committed to net-zero carbon emission targets, including the United Kingdom (UK) [1] and the European Union (EU) [2], who aim to reach net-zero by 2050. Reaching this target will require widespread decarbonisation across all sectors of the economy [3], including the residential energy sector, which accounts for over one-third of global carbon emissions [4].

A large portion of carbon emissions from the residential sector can be attributed to heating, which is predominantly supplied by natural gas boilers in many countries. In the UK for example, gas boilers account for more than 85 % of domestic heat supply [5]. The main low-carbon alternatives are electrically-driven vapour-compression heat pumps, which have seen a large market growth in recent years [6]. Electric heat pumps (EHPs) do however depend on a decarbonised electricity supply to realise their emission reduction potential [7]. Alternatives are hydrogen boilers (HBs) [8] or hydrogen-fired absorption heat pumps (AHPs) [9], which require a supply of low-carbon hydrogen, or solar-thermal heating systems, which typically require a backup heating system.

In addition to space heating and hot water, provision of space cooling is becoming increasingly relevant. It already constitutes a significant share of energy demand in warmer climates, with the demand also increasing in moderate climate countries, such as in central Europe, as the average temperatures increase and extreme heat waves become more frequent [10]. Over the last decade, energy demand for space cooling increased more than twice as fast as the overall energy demand in buildings. Higher temperatures caused by climate

change [11], coupled with increasing incomes and growing populations, are driving rapid growth in residential cooling, with the share of households with air conditioning increasing globally from 25% in 2010 to 35% in 2021 and estimated to increase further to 45% by 2030 [12]. As reported in [13], some 2 to 4 billion people could be exposed to heat stress due to lack of effective indoor cooling, giving rise to multiple risk factors for heat-related illnesses [14].

It is also recognised that access to effective cooling (and heating) does not need to come at the expense of the environment if it is pursued through clean technologies. Residential cooling can account for a large share of peak electricity demand in critical periods of the year [15], potentially causing outages or requiring costly upgrades to energy infrastructure. These could be mitigated by demand response strategies, integration of energy storage assets and other sector coupling based solutions. IEA's Net Zero Emissions by 2050 Scenario [16] sets three space cooling-related goals: (i) 20% of existing buildings and all new buildings net zero by 2030, (ii) cooling set-point moderated in the range of 24-25°C, and (iii) average efficiency of new cooling devices increased by at least 50% by 2030.

EHPs come in various types and with various heat-source and sink fluids [17]. Space cooling has been traditionally provided by conventional electrically driven air-conditioning units [18], which are mostly able to only pump heat in one direction (i.e., to be only used for cooling). However, air-conditioning units are fundamentally air-to-air (AA) EHPs, and recently, almost all new commercially available AA EHPs are designed to be reversible [19]. This means that they can be used to provide both space heating and cooling, depending on the given weather. Naturally, however, air-to-air heat pumps cannot provide hot water.

At the same time, space heating can also be provided by air-to-water (AW) EHPs, which use water as the heat sink fluid. In this case, the heat is transferred to air using radiators. The advantage of AW EHPs is that they can also provide domestic hot water (which is often required at a temperature close to that required by modern radiators) [20], but unlike AA EHPs, they cannot be used to provide space cooling directly (additional equipment like ducts would be required in that case).

Large-scale electrification of heating and cooling will significantly increase national electricity demands. Moreover, it will increase seasonal differences in load, as heating and cooling demands are primarily driven by the ambient temperature. Therefore, it is expected that, in cold countries, electricity load in winter will be significantly higher, especially during peak hours. Similarly, hot countries are expected to have high electricity loads in the summer. In the UK context, Quiggin and Buswell [21] predicted an increase in peak electricity demand of 55 GW as a result of heating electrification, while Hoseinpoori et al. [22] expect that the peak demand may increase by up to 170% by 2050. It has been shown that energy storage, both at household-level and whole-energy system level, alongside other means of flexibility can help reduce necessary investments in low-carbon power generation capacity and therefore deliver decarbonisation objectives at a lower cost [23].

At the household level, energy storage typically comes in the form of thermal energy storage via hot water tanks or other sensible heat options, or more advanced approaches via thermochemical storage, phase change materials, building thermal inertia or molecular storage, which offers potential for inter-seasonal storage with extremely low energy losses [24,25]. In the case of storage integration to EHP, such storage could be in the form of thermal energy (to achieve higher seasonal COP due to the night-day temperature lift fluctuations) or electric energy, enabling demand response capabilities and withdrawal of electricity during off peak periods. In both cases, the strategy is to decouple heat demand of the household and electricity demand of the heat pump, thus allowing households to shift their demand to off-peak hours to level the electricity demand profile [20]. At the whole-system level, a distinction is typically made between short-term and long-term energy storage. Short-term storage is valuable for quick load balancing and grid stability [26], while long-term storage can provide large quantities of dispatchable generation for multiple hours or even days. The conventional large-scale energy storage technology is pumped-hydro storage, but further development potential is limited. Instead, novel storage technologies such as compressed-air energy storage [27], hydrogen storage [28] or large-scale batteries [29] show promise for application in future decarbonised energy systems.

This paper aims to provide a quantitative framework for identifying cost-optimal portfolios of heating and cooling technologies, including electrically driven technologies (i.e., AW EHPs and reversible AA EHPs) and hydrogen-driven technologies (HBs and AHPs) that can provide heating and cooling. Cost-optimisation is carried out from the whole-system cost perspective, including investment and operation cost of energy production, storage and end-use technologies. Heating demand is hereby distinguished between space heating, space cooling and domestic hot water demand. One of the main novelties of this specific work is the fact that, for the first time, the two types of EHPs (AW and AA) are included in the energy system optimisation framework, allowing the investigation of energy-system implications, and discussing transition cost trade-offs between different technological options in the context of simultaneously decarbonising residential heating and cooling. Additionally, the impact of long-duration energy storage is also explored as a means to reduce the impact of heat electrification on the electricity system.

The methodology used to identify energy-system implications of different heating technologies and the description of the techno-economic models is provided in Section 2. Energy-system results are provided in Section 3 and Conclusions are provided in Section 4.

2. Method

This section presents the key features of the energy system model that is applied to identifying cost-efficient portfolios of low-carbon heating and cooling technologies. This is followed by the description of the techno-economic models of heating and cooling technologies that have been used in the energy system model. The section concludes with the summary of key assumptions and scenarios used in the analysis.

2.1. Energy system model with decarbonised heating and cooling

The model presented in this section represents an upgraded version of the energy system model presented in [30]. This model optimises the total investment and operation cost of a carbon-constrained energy system, including electricity and hydrogen production and storage technologies, as well as the key techno-economic features of end-use heating and cooling technologies. The objective of the model is to minimise the overall cost of delivering electricity, heat, and cooling to end-consumers. Some features of the model that are not central for this paper have been omitted from the formulation due to space constraints.

Key extensions to the energy system model, when compared to [30], include: a) explicit consideration of investment decisions into end-use technologies for cooling; b) adding AA EHP to the portfolio of end-use heating and cooling technologies that the model can invest in; and c) distinguishing between heat demand for space heating (SH) and for hot water (HW), as well as between heat outputs from various technology to supply these two heat demands.

2.1.1. Objective function

The model minimises the total system cost, which contains terms associated with: a) investment in electricity generation and storage and the associated operation cost (φ_{el}), b) investment in hydrogen production and storage with associated operation cost including, if relevant, hydrogen import cost ($\varphi_{\mathrm{H_2}}$), and c) investment cost in end-use technologies for low-carbon heating and cooling ($\varphi_{\mathrm{heat-cool}}$):

$$\min z = \varphi_{\mathrm{el}} + \varphi_{\mathrm{H_2}} + \varphi_{\mathrm{heat-cool}} \tag{1}$$

Terms representing the electricity sector and hydrogen sector costs are formulated in the same way as in [30]. The electricity cost includes investment cost of generation assets and battery energy storage systems (BESS) as well as generators' operating cost, while the hydrogen sector cost includes the investment and operation costs of electrolysers, methane reformers and hydrogen storage, as well as the cost of hydrogen imports. This ensures that the cost of supplying electricity and hydrogen to low-carbon heating and cooling systems are not fixed input parameters into the calculation, but rather endogenously integrated into the cost-minimisation model by explicitly representing all investment and operation cost categories associated with electricity and hydrogen supply.

The investment cost of end-use heating and cooling technologies $\varphi_{\mathrm{heat-cool}}$ includes the cost of investment into heating and cooling assets, which is the product of the capacity decision variable μ and per unit cost π for AW EHP, AA EHP, EB, HB, AHP and TES assets:

$$\varphi_{\mathrm{heat-cool}} = \pi^{\mathrm{AW}}\mu^{\mathrm{AW}} + \pi^{\mathrm{AA}}\mu^{\mathrm{AA}} + \pi^{\mathrm{EB}}\mu^{\mathrm{EB}} + \pi^{\mathrm{HB}}\mu^{\mathrm{HB}} + \pi^{\mathrm{AHP}}\mu^{\mathrm{AHP}} + \pi^{\mathrm{TES}}\mu^{\mathrm{TES}} \tag{2}$$

Note that the operating cost of low-carbon heating and cooling technologies is implicitly considered through electricity and hydrogen balance equations.

2.1.2. Energy balance constraints

The balance constraint for power supply and demand stipulates that in each time interval t the total electricity supply, which consists of the total electricity generation (p^{gen}) plus net electrical storage output ($p^{\mathrm{bs}}_{\mathrm{dch}} - p^{\mathrm{bs}}_{\mathrm{ch}}$), needs to match total demand across various categories, which include electrified heating (p^{AW}_t, p^{AA}_t and p^{EB}_t) but also other non-heat segments such as baseline system demand, appliance and EV demand (d^{el}_k), and electricity demand for operating methane reformers and electrolysers, which is expressed as the product of their hydrogen output ξ and specific electricity consumption L^{el}:

$$\sum_{g=1}^{G} p^{\mathrm{gen}}_{g,t} + \sum_{s=1}^{S}\left(p^{\mathrm{bs}}_{\mathrm{dch},s,t} - p^{\mathrm{bs}}_{\mathrm{ch},s,t}\right) = \sum_{k=1}^{K} d^{\mathrm{el}}_{k,t} + p^{\mathrm{AW}}_t + p^{\mathrm{AA}}_t + p^{\mathrm{EB}}_t + \sum_{r=1}^{R} L^{\mathrm{el}}_r \xi^{\mathrm{ref}}_{r,t} + \sum_{e=1}^{E} L^{\mathrm{el}}_e \xi^{\mathrm{elH2}}_{e,t} \tag{3}$$

Hydrogen balance constraint (4) ensures that the total hydrogen supply from electrolysers (ξ^{elH2}), reformers (ξ^{ref}) and imports (ξ^{imp}) matches the total demand for each t, including non-heat demand for hydrogen (Ξ^{ext}), demand from HBs and AHPs (ξ^{HB} and ξ^{AHP}), consumption of hydrogen power generators (ξ^{gen}) and net hydrogen storage operation ($\xi^{\mathrm{hs}}_{\mathrm{ch}} - \xi^{\mathrm{hs}}_{\mathrm{dch}}$):

$$\sum_{r=1}^{R} \xi^{\mathrm{ref}}_{r,t} + \sum_{e=1}^{E} \xi^{\mathrm{elH2}}_{e,t} + \sum_{i=1}^{I} \xi^{\mathrm{imp}}_{i,t} = \sum_{u=1}^{U}\left(\xi^{\mathrm{hs}}_{\mathrm{ch},u,t} - \xi^{\mathrm{hs}}_{\mathrm{dch},u,t}\right) + \xi^{\mathrm{HB}}_t + \xi^{\mathrm{AHP}}_t + \xi^{\mathrm{gen}}_t + \Xi^{\mathrm{ext}}_t \tag{4}$$

2.1.3. Energy production and storage constraints

The model also includes standard constraints for conventional and variable renewable generation, which are omitted here to avoid repetition. These constraints include limits on allowed new capacity of generation technologies, unit commitment and output constraints, operating cost constraints including no-load cost, variable cost and start-up cost, annual output limits and dynamic constraints (ramping, start-up, reserve, response and inertia). This part of model formulation is described in more detail in [35]. In a similar way, standard constraints on hydrogen production and storage are implemented as presented in [36].

2.1.4. Constraints on end-use heating and cooling technologies

End-use heat balance is represented separately for space heating and hot water (given that some technologies, such as AA EHP, can only provide one of those). The space heating constraint (5) ensures that the net space heating output of all technologies, expressed as the product of either hydrogen or electricity consumption and the relevant COP or efficiency coefficient η, or in case of TES as net discharging, meets the SH demand X^{sh}:

$$p_t^{\mathrm{AW,sh}}\eta_t^{\mathrm{AW}} + p_t^{\mathrm{AA,sh}}\eta_t^{\mathrm{AA,sh}} + p_t^{\mathrm{EB,sh}} + \xi_t^{\mathrm{HB,sh}}\eta^{\mathrm{HB}} + \xi_t^{\mathrm{AHP,sh}}\eta_t^{\mathrm{AHP}} + h_{\mathrm{dch},t}^{\mathrm{TES,sh}} - h_{\mathrm{ch},t}^{\mathrm{TES,sh}} = X_t^{\mathrm{sh}} \quad (5)$$

Expression (6) does the same for hot water demand X^{hw}; note that this constraint does not include any contribution from AA EHP, as it was assumed that they cannot be used to supply hot water.

$$p_t^{\mathrm{AW,hw}}\eta_t^{\mathrm{AW}} + p_t^{\mathrm{EB,hw}} + \xi_t^{\mathrm{HB,hw}}\eta^{\mathrm{HB}} + \xi_t^{\mathrm{AHP,hw}}\eta_t^{\mathrm{AHP}} + h_{\mathrm{dch},t}^{\mathrm{TES,hw}} - h_{\mathrm{ch},t}^{\mathrm{TES,hw}} = X_t^{\mathrm{hw}} \quad (6)$$

Finally, cooling demand balance is very straightforward as it assumes only AA EHPs can meet residential cooling demand X^{cl} (note that cooling COP for AA EHPs, $\eta^{\mathrm{AA,cl}}$, may be different from heating COP $\eta^{\mathrm{AA,sh}}$):

$$p_t^{\mathrm{AA,cl}}\eta_t^{\mathrm{AA,cl}} = X_t^{\mathrm{cl}} \quad (7)$$

Upper bounds on heating and cooling technology outputs limit their total output (which is the sum of space heating, hot water and cooling outputs, as applicable to different technologies) to the level of their installed heating capacity μ, which is ensured through constraints (8)-(10). Note that all heat technology capacities μ are expressed as heat output rates, except AA EHPs, where the capacity is expressed in terms of cooling output. Also note that the COP values for AA EHPs are differentiated between space heating and cooling, while for all other technologies the same COP applied for all types of heat output.

$$\left(p_t^{\mathrm{AW,sh}} + p_t^{\mathrm{AW,hw}}\right)\eta_t^{\mathrm{AW}} \le \mu^{\mathrm{AW}}, \qquad \frac{p_t^{\mathrm{AA,sh}}\eta_t^{\mathrm{AA,sh}}}{W_{\mathrm{HC}}^{\mathrm{AA}}} + p_t^{\mathrm{AA,cl}}\eta_t^{\mathrm{AA,cl}} \le \mu^{\mathrm{AA}}, \qquad p_t^{\mathrm{EB,sh}} + p_t^{\mathrm{EB,hw}} \le \mu^{\mathrm{EB}} \quad (8)$$

$$\left(\xi_t^{\mathrm{HB,sh}} + \xi_t^{\mathrm{HB,hw}}\right)\eta^{\mathrm{HB}} \le \mu^{\mathrm{HB}}, \qquad \left(\xi_t^{\mathrm{AHP,sh}} + \xi_t^{\mathrm{AHP,hw}}\right)\eta_t^{\mathrm{AHP}} \le \mu^{\mathrm{AHP}} \quad (9)$$

$$h_{\mathrm{dch},t}^{\mathrm{TES,sh}} + h_{\mathrm{dch},t}^{\mathrm{TES,hw}} \le \mu^{\mathrm{TES}}, \qquad h_{\mathrm{ch},t}^{\mathrm{TES,sh}} + h_{\mathrm{ch},t}^{\mathrm{TES,hw}} \le \mu^{\mathrm{TES}} \quad (10)$$

Coefficient $W_{\mathrm{HC}}^{\mathrm{AA}}$ in (8) denotes the ratio between heating and cooling capacity for AA EHPs, which in this study was assumed to be equal to 1.2.

Given that AA EHPs can provide space heating through hot air rather than hot water, it was assumed that they cannot produce excess heat output to be stored in TES, but rather to only meet a proportion of instantaneous heat demand. This is ensured through constraint (11):

$$p_t^{\mathrm{AA,sh}}\eta_t^{\mathrm{AA,sh}} \le X_t^{\mathrm{sh}} \quad (11)$$

TES balance and energy limit constraints are implemented using expressions (12) and (13), where q^{TES} is the State-of-Charge (SOC) of TES, τ is its duration, $\eta_{\mathrm{ch}}^{\mathrm{TES}}$ and $\eta_{\mathrm{dch}}^{\mathrm{TES}}$ are charging and discharging efficiencies, respectively, $\alpha_{\mathrm{loss}}^{\mathrm{TES}}$ is the hourly loss rate, and Δ is the duration of the unit time interval:

$$q_t^{\mathrm{TES}} = q_{t-1}^{\mathrm{TES}}\left(1 - \alpha_{\mathrm{loss}}^{\mathrm{TES}}\Delta\right) + \Delta\left[\eta_{\mathrm{ch}}^{\mathrm{TES}}\left(h_{\mathrm{ch},t}^{\mathrm{TES,sh}} + h_{\mathrm{ch},t}^{\mathrm{TES,hw}}\right) - \frac{1}{\eta_{\mathrm{dch}}^{\mathrm{TES}}}\left(h_{\mathrm{dch},t}^{\mathrm{TES,sh}} + h_{\mathrm{dch},t}^{\mathrm{TES,hw}}\right)\right] \quad (12)$$

$$q_t^{\mathrm{TES}} \le \mu^{\mathrm{TES}}\tau^{\mathrm{TES}} \quad (13)$$

2.1.5. System-wide constraints

Total carbon emissions in the energy system result from the operation of thermal generators and methane reformers. An annual system-wide carbon emission target is implemented as in [30], while the system reliability constraints are also included in the model as in [35].

2.2. Techno-economic models of end-use heating and cooling technologies

In this work, detailed techno-economic models of AW EHPs, AW AHPs, EBs and HBs previously developed by the authors in Refs [17] and [30] are used to estimate the cost of heating and cooling technologies as a function of size and their performance as a function of the outside temperature. In addition to these, comprehensive data has been now collected to also properly model AA EHPs. The characteristics of these technologies are integrated

within the energy system model so that key technology attributes are adequately represented, allowing for an informed comparison of heating and cooling options from an energy system perspective.

EHPs in households are mainly made of four components: a condenser, an expansion valve, an evaporator and an electricity-driven compressor. The process involves heat being absorbed from a certain heat source, transferred to a working fluid (often referred to as refrigerant) in the evaporator. This is followed by the compression of the vapour working fluid, the temperature and pressure of which are raised during this process until it is condensed. Heat is then transferred to a heat sink fluid, which is used to satisfy the heat demand. The working fluid is lastly passed through an expansion valve, a process which reduces its temperature and pressure, and the cycle is then repeated. AHPs, like EHPs, involve a condenser, an expansion valve and an evaporator. The only difference is that the electricity-driven compressor is replaced by an absorption cycle, meaning that the main source of energy in an AHP is heat.

For all technology models, steady-state operation of components and negligible heat and pressure losses in heat exchangers and pipes are assumed. Both performance and cost estimates are validated using data obtained from UK manufacturers in the case of EHPs, where for AHPs the performance was validated against relevant previous studies. A simplified thermodynamic model was used to estimate the performance of the HB, while an efficiency of 100% was assumed for the EB. Unlike in previous work [30], EHPs are now separated in AW EHPs, which can provide space heating and hot water (but not space cooling), and AA EHPs, which can provide space heating and space cooling (but not hot water). It should be mentioned that an AW EHP could also provide cooling assuming ductwork and other equipment is installed, but this option is not common in residential applications and is not considered in this study.

Heat pump performance is often measured by the coefficient of performance (COP), which is a measure of the ratio between heat output and energy input. For EHPs, energy input is in the form of electricity $\dot{W}_{\mathrm{in}}$, while for hydrogen-driven AHPs, it in the form of heat $\dot{Q}_{\mathrm{in}}$ coming from a hydrogen boiler. Similarly, boiler efficiency is the ratio of heat output to energy input, where the latter is in the form of electricity for EBs and hydrogen fuel $\dot{Q}_{\mathrm{fuel}}$ for HBs. Technology performance is described by Eqs. (14)-(17):

$$COP_{\mathrm{EHP}} = \frac{\dot{Q}_{\mathrm{EHP}}}{\dot{W}_{\mathrm{in}}} \tag{14}$$

$$COP_{\mathrm{AHP}} = \frac{\dot{Q}_{\mathrm{AHP}}}{\dot{Q}_{\mathrm{in}}} \tag{15}$$

$$\eta_{\mathrm{EB}} = \frac{\dot{Q}_{\mathrm{EB}}}{\dot{W}_{\mathrm{in}}} \tag{16}$$

$$\eta_{\mathrm{HB}} = \frac{\dot{Q}_{\mathrm{HB}}}{\dot{Q}_{\mathrm{fuel}}} \tag{17}$$

The specific price of heating and cooling technologies is shown as a function of heat output at nominal operating conditions in Figure 1. The prices for AW EHP, AHP, EB and HB are estimated using the validated component-costing models and manufacturer data as in Ref. [30]. For AA EHPs, data has been collected for more than 75 currently commercially available units and a best-fit line based on power regression is generated. Installation costs are not included in Figure 1, but are set to be equal to £2,200 for all investigated HPs and £1,400 for all investigated boilers. All prices include VAT (20%).

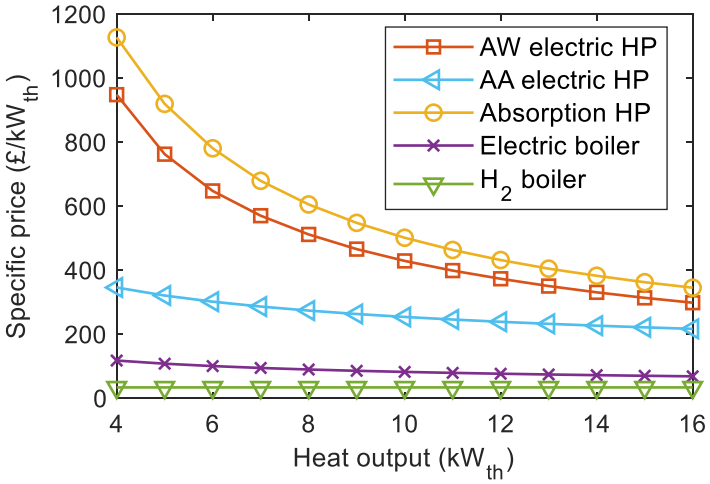

Figure 1. Specific price of heating and cooling technologies as a function of heat output at nominal operating conditions. Prices include VAT.

Heat pump COP is plotted as a function of outside air temperature for different HP types in Figure 2. For the AW EHP and AHP options, the hot-water delivery temperature is assumed to be equal to 55 °C, while the performance curves for heating and cooling of the AA EHP assume an indoor target air temperature of 21°C. The efficiencies of EB and HB are also shown for comparison purposes.

It is interesting to note the significantly lower cost and higher performance of AA EHPs when compared to AW EHPs. The cost difference is attributed to the need for additional components when installing AW EHPs, as well as the larger surface area required to transfer low-temperature heat to radiators and then to air. However, AA heat pumps have the disadvantage of requiring a separate system for hot water, while they may be often accompanied with noise and air-movement issues which may impact end-users and require careful consideration.

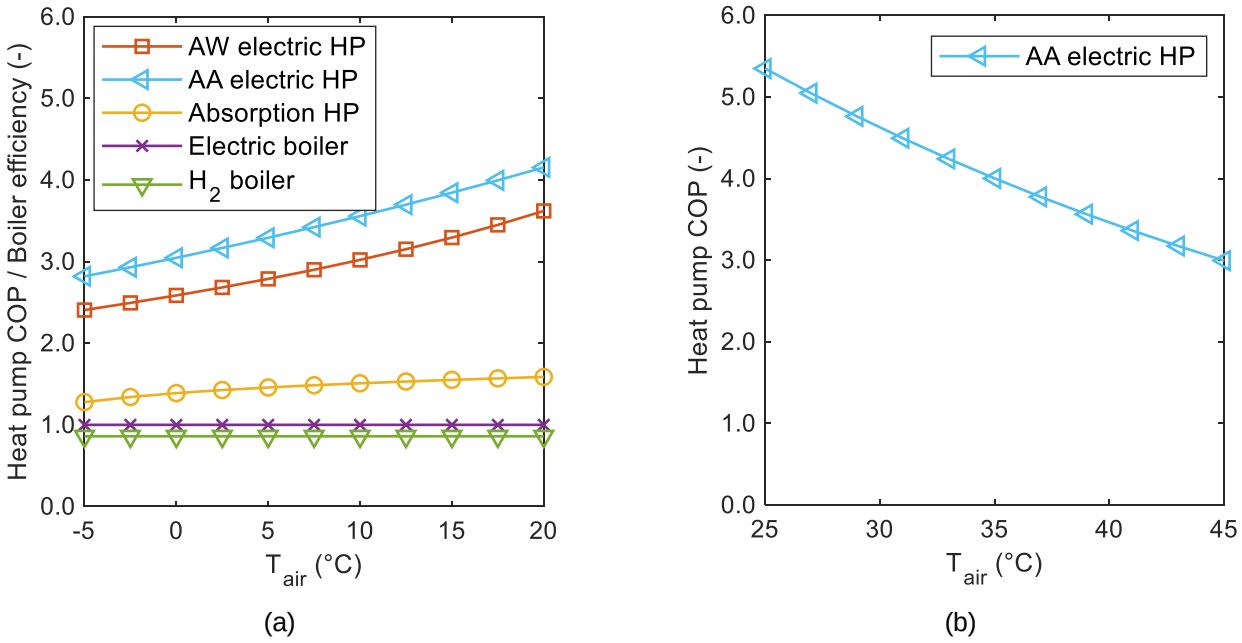

Figure 2. Heat pump COP or boiler efficiency as a function of outside air temperature for (a) heating; and (b) cooling. For heating using AW electric HP or absorption HP, a hot-water delivery temperature of 55 °C is assumed. For heating and cooling using AA electric HP, an indoor target air temperature of 21 °C is assumed.

2.3. Key assumptions and system scenarios

This section discusses the key features of energy system scenarios used in the study and assumptions on the demand for end-use heating and cooling.

2.3.1. Archetypal energy systems

One of the main objectives of the paper is to study the impact of system characteristics on cost-efficient portfolios of low-carbon heating and cooling technologies. To that end, two archetypal energy systems are assumed in the study, North and South, similarly to the approach in [30]. Size of both systems has been chosen to approximately correspond to the size of the UK electricity system, with an annual demand of 400 TWh_{el}. The two archetypal systems have the following key distinctive features:

1. North system represents a simplified version of the UK energy system, characterised by cooler climate conditions, which has a much higher residential heating demand (142 TWh_{th} for SH and 43 TWh_{th} for HW) than the South system (30 TWh_{th} for SH and 21 TWh_{th} for HW), which is broadly modelled to resemble a southern European country. Peak heat demand was also much higher in the North than in the South, as illustrated in the heat Load Duration Curves (LDCs) for the two systems in Figure 3. At the same time the energy demand for cooling energy was assumed to be about 10 times higher in the South (203 TWh_{th}) than in the North (19 TWh_{th}). LDCs for cooling demand are also shown in Figure 3.
2. Availability profiles for renewable generation are assumed to be different between the two systems, with the wind utilisation factor in the North significantly higher than in the South (58% vs. 35%), and the solar PV utilisation factor in the North much lower than in the South (11% vs. 24%). As a result, the nominal Levelised Cost of Electricity (LCOE) of wind and PV in the North was £43/MWh_{el} and £56/MWh_{el}, respectively, while in the South the same LCOEs were £39/MWh_{el} and £25/MWh_{el}.

In each case study the model cost-optimised the supply of low-carbon heating and cooling to 15.7 million residential customers by investing in end-use technologies including AW EHPs, AA EHPs, AHPs, EBs, HBs and TES. Any electricity or hydrogen demand for residential heating was subject to optimisation by the model, depending on investment choices for end-use technologies. Additionally, it was also assumed the system

needs to supply a hydrogen demand of 97.5 TWh annually to meet the hydrogen requirements outside the residential heating sector, such as in the industrial and transport sectors.

In all studies both systems are cost-optimised with the objective to achieve net zero carbon emissions. The model can meet this target by investing in a range of production technologies (both zero-carbon and positive-carbon) as well as in carbon offsets in the form of electricity generation using Bioenergy with Carbon Capture and Storage (BECCS). In all cases the energy system is modelled in hourly resolution as a single node system, i.e., ignoring the transmission, interconnection or distribution networks.

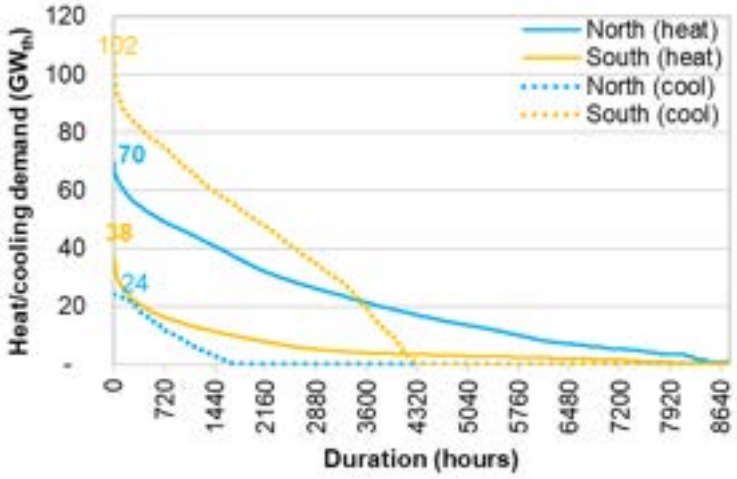

Figure 3. Load duration curves (LDCs) for hourly heat and cooling demand in North and South systems.

The assumed price of natural gas for power generation and H_2 production was £21.8/MWh, while hydrogen import was also assumed to be available (in addition to production) at the price of £100/MWh. District heat networks or industrial heat demand were not included in the scope of this analysis.

2.3.2. Space heating and hot water demand modelling

Household-level heating and cooling technologies are optimised for a typical UK household, which was identified by applying a k-means clustering method to the Cambridge Housing Model [31] data set, which contains detailed information on the UK building stock. The data set only provides annual values for space heating and domestic hot water demand, however, hourly demand values are required as model inputs. For space heating, the methodology of Watson et al. [32] is used to disaggregate the demand. The daily space heating demand is determined from a correlation with the daily mean ambient temperature. It is then distributed to the individual hours using the daily profile for the coldest range presented by Watson et al. [32], as it was deemed to be the most representative of pure space heating demand. For domestic hot water, the daily hot water flowrate profile of Herrando et al. [33] is applied. The flowrate is then converted into an energy demand by assuming a hot water delivery temperature of 55 °C and a monthly-varying cold water mains temperature according to [34].

UK-representative space heating and hot water demand profiles were used in the North archetypal system, as well as representative cooling demand profiles for the UK. In the South system, all heating demand was scaled down according to temperature fluctuations that are representative for Greece, while at the same time cooling demand was scaled upward in the same way. Daily average values for COP for various heating and cooling technologies for the North and South annual temperature profiles (obtained based on Figure 2) are shown in Figure 4. As expected, due to generally lower temperatures, the North system is characterised by higher COP values for cooling but lower COPs for heating. There is also a noticeable COP advantage when using AA EHPs to provide space heating rather than AW EHPs, although as discussed elsewhere in the paper using AA EHPs for space heating may not be practical, especially in colder climates.

The assumed costs of low-carbon heat options were based on the analysis presented in the previous section and on typical asset sizes, as follows (note that these figures include both the component costs from Figure 1 and the relevant installation cost):

- AA EHP: £578/kW_{th}
- AW EHP: £300/kW_{th}
- AHP: £638/kW_{th}
- EB: £139/kW_{th}
- HB: £98/kW_{th}
- TES: £75/kWh_{th}

In addition to the upfront investment cost, it was also assumed that all assets require an annual maintenance cost in the amount of £35/kW_{th}/yr for all HP and boiler technologies, and £20/kW_{th}/yr for TES. Asset lifetime

was assumed to be 20 years for AA EHPs, AW EHPs and AHPs and 15 years for EBs, HBs and TES. A 5% interest rate has been assumed for all heating technologies to convert overnight cost into annualised values required by the model. The assumed duration of TES (the ratio between energy capacity and heat charge and discharge rate) was 3 hours.

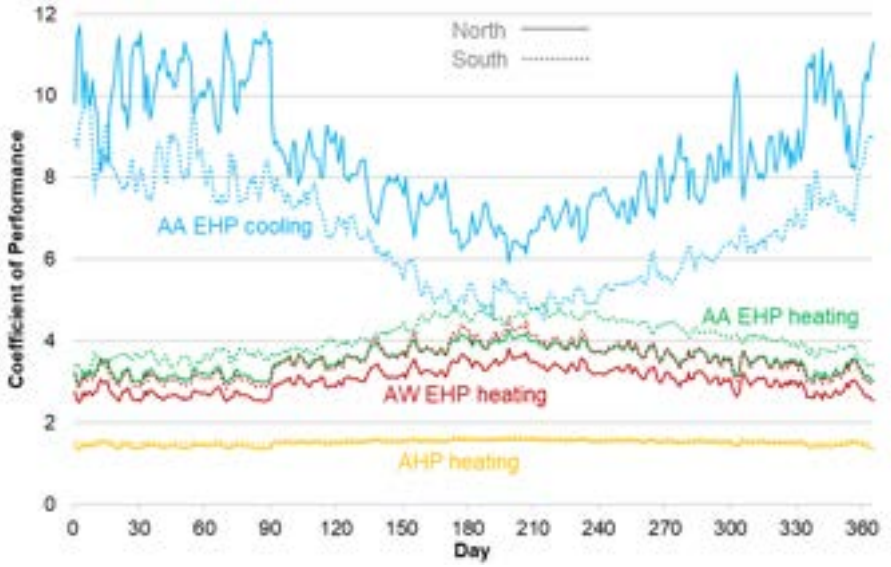

Figure 4. Values of Coefficient of Performance for various heating and cooling technologies in North and South systems.

2.3.3. Case studies

Main case studies run for both the North and South archetypal energy systems with a net-zero caron target include:

- Unlimited: no limits to provision of space heating (SH) from AA EHPs
- No SH from AA EHPs: no SH allowed from AA EHPs
- AA SH 30%: share of AA EHPs in SH limited to 30%
- AA SH 20%: share of AA EHPs in SH limited to 20%
- AA SH 10%: share of AA EHPs in SH limited to 10%

The main purpose of these studies is to explore the potential contribution of various heating technologies, and in particular AA EHPs, to space heating under different assumptions and constraints. The reason for this is that although AA EHPs could potentially offer a competitive alternative to AW EHPs with high COP values for heating, there are several practical barriers for their widespread deployment in countries such as the UK. These include space constraints, multiple room installations, difficult integration with existing heating systems and radiators etc. For that reason, AA EHPs are often seen as a possible top-up source of space heating rather than a bulk source of heat, and the range of case studies listed above is an attempt to explore how various levels of contribution of AA EHPs to space heating affect the overall portfolio of end-use heating technologies.

In addition to the case studies above, another set of modelling runs was carried out to study the impact of peakiness of heat demand, where the heat profiles used in this study were replaced with peakier heat demand profiles used in [30], in order to assess the impact of the shape of the heat profile on the cost-efficient portfolio of heating technologies. For illustration, heating profiles used in the main case studies had a peak per household of around 4.5 kW_{th}, which is lower than the peak of 7 kW_{th} that was used in the previous study. Case studies with higher peak heat demand were only carried out for the two extreme cases, i.e., “Unlimited” and “No SH from AA EHPs”.

The final set of studies assumed that the system also had an option to invest in very low-cost long-duration energy storage (LDES). The aim of these studies was to test whether installing LDES in the electricity system could help with managing the seasonality of heating and cooling demand. The LDES case studies were also run only for the “Unlimited” and “No SH from AA EHPs” scenarios. The cost of LDES in these studies was assumed at the level of 100% (£6.5/kWh) and 50% (£3.2/kWh) of the cheapest LDES option identified in [37], which was a 120-hour underground Compressed Air Energy Storage (CAES).

3. Results

This section discusses the results of various case studies aimed at establishing cost-efficient portfolios of low-carbon heating and cooling technologies across different system conditions and scenarios. More specifically, the case studies presented here focus on the following aspects:

- Impact of system geography, reflected in the volumes of heating and cooling demand and in the availability profiles of wind and solar PV generation;
- Impact of availability of AA EHPs for space heating;
- Impact of availability of low-cost long-duration electricity storage (LDES);
- Impact of heat demand profile, i.e., the level of peak demand for space heating.

Key modelling results presented in this section focus on the cost-optimal capacity mix of low-carbon heating and cooling technologies and the annual volumes of supplied heat and cooling from different technologies.

3.1. Cost-efficient portfolios of end-use heating and cooling technologies in baseline scenarios

Results for the cost-optimal compositions of heating and cooling portfolios across the main case studies for the North and South systems are shown in Figure 5. Not surprisingly, a significant volume of AA EHP capacity is added across all case studies as it represents the only option to supply cooling demand. This capacity is at least 24 GW_{th} in the North and 104 GW_{th} in the South system. In the "Unlimited" scenarios in the North the model adds even more AA EHPs than the minimum required for cooling, around 43 GW_{th}, as it represents a more cost-efficient option than installing AW EHPs. Such high capacity is sufficient to cover almost the entire space heat demand in the "Unlimited" scenarios for the North and South systems. Given that AA EHPs cannot provide hot water, a relatively small volume of AW EHPs and TES (as well as some HBs in the North) is installed to ensure that hot water demand is met.

In the other extreme, where AA EHPs are not used to provide any space heating, the heat demand is met through a mix of AW EHPs (49 GW_{th} in the North, 13 GW_{th} in the South), EBs (3 GW_{th} and 15 GW_{th}), HBs (10 GW_{th} and 5 GW_{th}) and TES (8 GW_{th} and 6 GW_{th}). Due to their higher investment cost, AW EHPs are installed to operate as baseload heat source, meeting most of the heat requirements, while boilers and TES are used as peak heat sources. AHPs are not chosen as part of the cost-optimal portfolio in any case studies due to their high assumed investment cost.

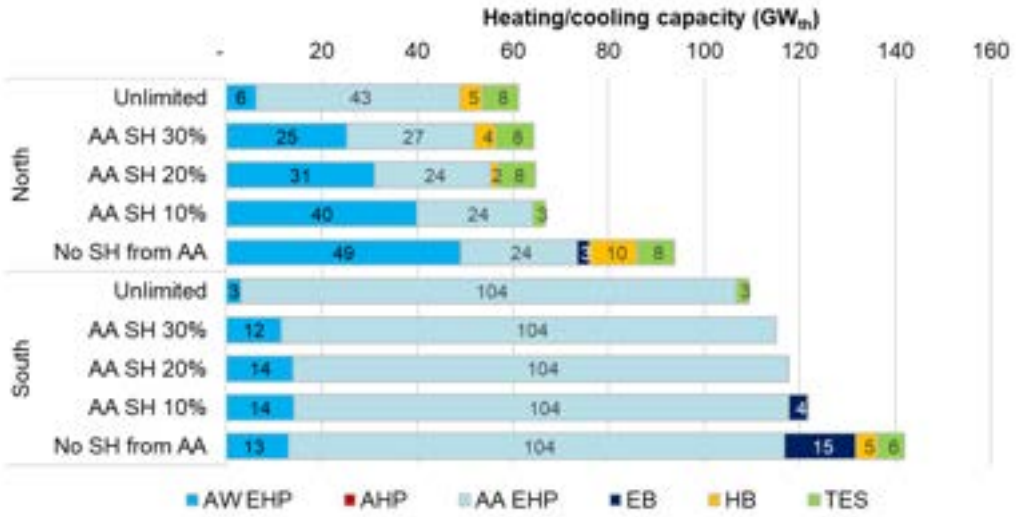

Figure 5. Cost-optimal capacities of low-carbon heating and cooling technologies for various scenarios in North and South systems.

In case studies where AA EHPs were allowed to contribute between 10% and 30% of the annual space heating demand, the model installed a significantly higher capacity of AW EHPs than in the "Unlimited" scenarios, but lower than in the opposite extreme without contribution of AA EHPs to SH, as it was now possible to use AA EHPs as a peaking technology instead of boilers or TES. In the North system, reducing the target contribution of AA EHPs to heat supply also reduced their capacity to 24 GW_{th}, the minimum needed to meet cooling load.

Finally, it needs to be noted that the case studies with low-cost LDES available for investment in the electricity system did not yield any change in system investment decisions including the investment in end-use heating and cooling technologies. In other words, even at a low cost the model did not decide to invest in LDES, resulting in the same investment decisions as in the case studies without LDES.

3.2. Share of various technologies in heating and cooling supply in baseline scenarios

Figure 6 shows the split of annual supply of space heating (SH), hot water (HW) and cooling between different technologies. Supply of cooling is very straightforward as it was assumed that only one technology (AA EHPs) can meet cooling demand.

In both North and South systems most of the HW demand is supplied using AW EHPs, which is the most efficient technology for converting electricity into heat for HW supply (note that AA EHPs were not assumed to be able to supply HW). In scenarios with no SH from AA EHPs there is some supply of HW from EBs and HBs, although their share in HW supply is well below 10%.

The mix of SH supply on the other hand varies significantly across different scenarios. In the "Unlimited" scenarios the contribution to of AA EHPs to space heating is between 93% (South) and 96% (North), while the remainder is supplied by AW EHPs. As the share of AA EHPs in SH supply is gradually constrained to 30%, 20%, 10% and 0% of total SH demand, the share of AW EHPs expectedly increases to make up for the shortfall, as does the installed AW EHP capacity (see Figure 5). When the share of AA EHPs in SH supply drops to zero, some of the SH is also supplied from boiler technologies (mostly from EBs), at the level of 2% in the North and 17% in the South. Higher share of EBs in heat supply in the South can be explained by the availability of low-cost electricity from solar PV in the South, allowing for inexpensive supply of electricity to EBs.

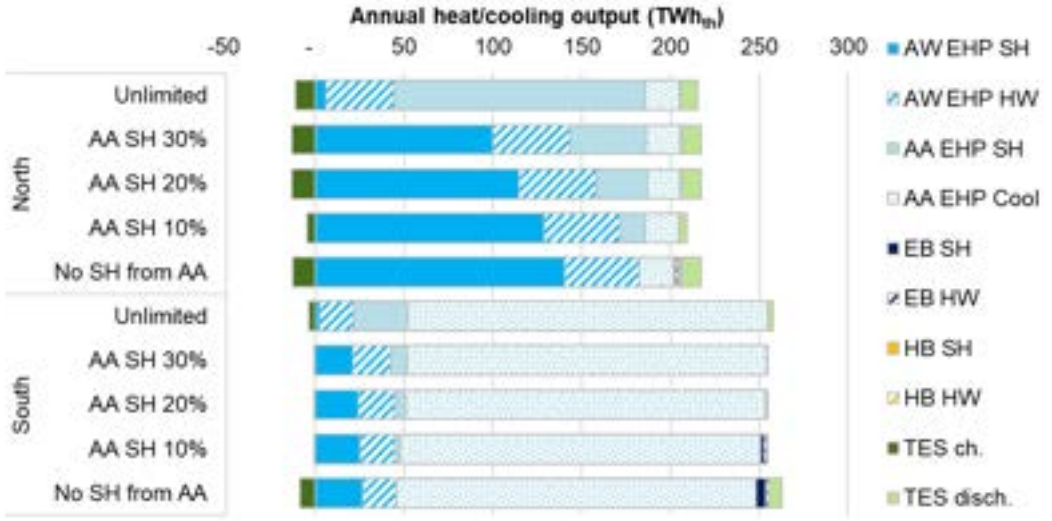

Figure 6. Annual output of low-carbon heating and cooling technologies for various scenarios in North and South systems.

In all North scenarios and the 0% scenario in the South there is also a visible contribution of TES to total SH and HW supply, at the level of up to 6% of total heat in the North and 14% in the South. Note, however, that due to cycle losses associated with charging and discharging TES, it effectively represents a net heat demand.

3.3. Impact of heat demand profiles

Sensitivity studies with higher peak heat demand resulted in cost-optimal portfolios of end-use technologies shown in Figure 7. Higher peak heat demand did not affect the technology portfolio in the "Unlimited" scenario in the South, while in the North the capacity of AA EHPs increases by 9 GW$_{th}$ as it is used to contribute to meeting the higher peaks in heating demand.

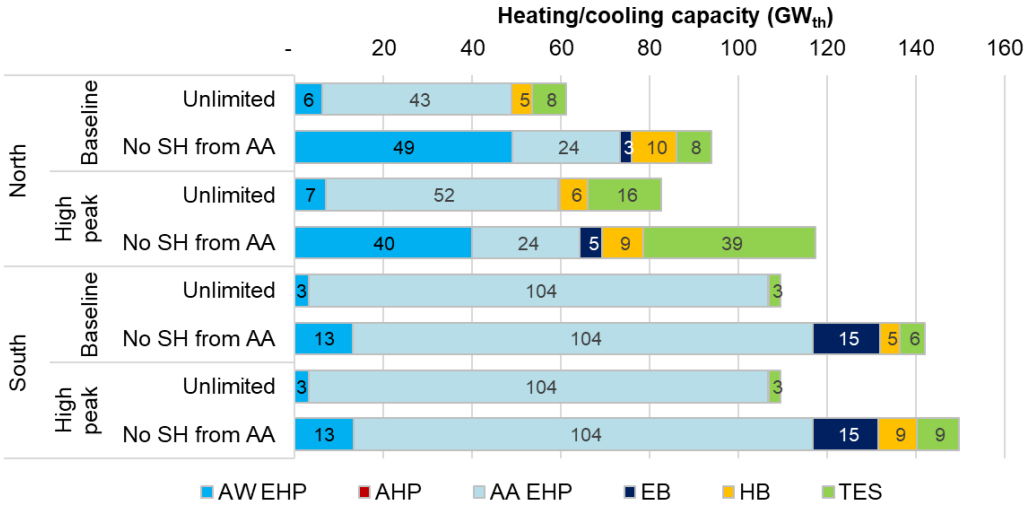

Figure 7. Cost-optimal capacities of low-carbon heating and cooling technologies for various peak heat demand scenarios in North and South systems.

In the scenarios with the AA EHP share in SH supply constrained to 0% there are more notable differences in the cost-optimal technology portfolios. In the South system, where the SH demand is several times lower than in the North, the main change is that the higher peak requires a slightly higher capacity of HBs (9 vs. 5 GW_{th}) and TES (9 vs. 6 GW_{th}) than in the baseline studies, while the capacities of other technologies remain the same.

In the North system, however, the SH peak demand is much higher and therefore the composition of end-use heating technologies changes to a much greater extent. Peakier demand makes AW EHPs slightly less economically attractive due to their cost structure (high investment cost but relatively low operation cost), so their capacity reduces from 49 to 40 GW_{th}. At the same time, higher peaks make technologies such as boilers (with lower investment cost but higher operating cost) more attractive, so their total capacity increases from 13 to 14 GW. Nevertheless, the greatest change is observed in the capacity of TES, which increases from 8 to 39 GW_{th}. This indicates that TES is the preferred end-use option to meet high peak demand through discharging heat, while being recharged during off-peak periods using the heat produced by AW EHPs.

4. Conclusion

This paper formulated an approach for making cost-optimal selection of low-carbon heating and cooling technologies from the system perspective, looking at two archetypal systems, North and South, with different heating and cooling demand characteristics as well as different availability profiles for variable renewables. The modelling included various boiler technologies, thermal energy storage and heat pumps, including a distinction between two types of EHPs (Air-to-Water and Air-to-Air), into the energy system optimisation framework.

Case studies presented in the paper show that a cost-optimal portfolio of end-use heating and cooling options will greatly depend on the characteristics of the system where they are deployed, both in terms of typical heating and cooling demand patterns, but also with respect to the availability of low-cost variable renewable generation. The results suggest that AA EHPs, with their cost and efficiency advantages over AW EHPs, could make a significant contribution to the future low-carbon heat supply in addition to cooling, although their share of heat supply may be constrained by several factors such as compatibility with incumbent heating systems or the need for multiple unit installations. Nevertheless, they could be used as an efficient top-up source of space heating in addition to AW EHPs, displacing some of the need for electric or hydrogen boilers, as well as thermal energy storage.

Note that the presented approach considers the aggregate heating/cooling sector, and therefore does not suggest an appropriate mix of technologies for an individual household. Given the variety of heat requirements across different customers and the diversity of heat demand, different households would install different portfolios of technologies depending on their specific circumstances, including their individual heat demand patterns, willingness to adopt new low-carbon technologies, and the household income profile. Future work in this area will focus on the effects of diversity and extreme weather on capacity requirements for low-carbon heating and cooling technologies, where higher peaks during extreme weather conditions may require more peaking capacity.

Acknowledgments

The research presented in this paper has been supported by the UK Engineering and Physical Sciences Research Council (EPSRC) [grant number EP/R045518/1] (IDLES Programme).

List of acronyms

AA EHP	Air-to-air electric heat pump	HB	Hydrogen boiler
AW EHP	Air-to-water electric heat pump	HP	Heat pump
AHP	Absorption heat pump	HW	Hot water
BECCS	Bioenergy with carbon capture and storage	IEA	International Energy Agency
BESS	Battery energy storage system	LCOE	Levelised Cost of electricity
CAES	Compressed air energy storage	LDC	Load duration curve
COP	Coefficient of performance	LDES	Long-duration energy storage
EB	Electric boiler	SH	Space heating
EHP	Electric heat pump	SOC	State of charge
EU	European Union	TES	Thermal energy storage
EV	Electric vehicle	UK	United Kingdom
HB	Hydrogen boiler		

References

1. Department for Business, Energy and Industrial Strategy (BEIS). Net Zero Strategy: Build Back Greener. 2021. https://www.gov.uk/government/publications/net-zero-strategy
2. European Commission, A European Green Deal. 2019. https://commission.europa.eu/strategy-and-policy/priorities-2019-2024/european-green-deal_en
3. Climate Change Committee, Sixth Carbon Budget. 2020. https://www.theccc.org.uk/publication/sixth-carbon-budget
4. International Energy Agency, Global status report for buildings and construction. 2019. https://www.worldgbc.org/news-media/2019-global-status-report-buildings-and-construction
5. Climate Change Committee, Heat in UK buildings today. 2016. https://www.theccc.org.uk/wp-content/uploads/2017/01/Annex-2-Heat-in-UK-Buildings-Today-Committee-on-Climate-Change-October-2016.pdf
6. Rosenow J., Gibb D., Nowak T., Lowes R., Heating up the global heat pump market. Nature Energy 2022;7:901-904. https://doi.org/10.1038/s41560-022-01104-8
7. Thomaßen, G., Kavvadias, K., Jiménez Navarro, J.P., The decarbonisation of the EU heating sector through electrification: A parametric analysis. Energy Policy 2021;148:111929.
8. Sunny, N., Mac Dowell, N., Shah, N., What is needed to deliver carbon-neutral heat using hydrogen and CCS? Energy and Environmental Science 2020;13:4204-4224. https://doi.org/10.1039/D0EE02016H
9. Critoph, R., Metcalf, S., UK Summary report on IEA heat pump technology collaboration programme (TCP) Annex 43: Thermally driven heat pumps, 2019. https://www.gov.uk/government/publications/fuel-driven-heat-pumps
10. Attia, S., Levinson, R., Ndongo, E., Holzer, P., Kazanci, O.B., Homaei, S., Zhang, C., Olesen, B.W., Qi, D., Hamdy, M., Heiselberg, P., Resilient cooling of buildings to protect against heat waves and power outages: Key concepts and definition. Energy and Buildings 2021;239:110869. https://doi.org/10.1016/j.enbuild.2021.110869
11. Intergovernmental Panel on Climate Change, Climate Change 2021 – The Physical Science Basis, 2021. https://www.ipcc.ch/report/ar6/wg1/downloads/report/IPCC_AR6_WGI_SPM_final.pdf
12. International Energy Agency, Space Cooling – Analysis, 2022. https://www.iea.org/reports/space-cooling
13. Mastrucci, A., Byers, E., Pachauri, S. and Rao, N.D., 2019. Improving the SDG energy poverty targets: Residential cooling needs in the Global South. Energy and Buildings, 186, pp. 405-415. https://doi.org/10.1016/j.enbuild.2019.01.015
14. Ebi, K.L., Capon, A., Berry, P., Broderick, C., de Dear, R., Havenith, G., Honda, Y., Kovats, R.S., Ma, W., Malik, A. and Morris, N.B., 2021. Hot weather and heat extremes: health risks. The Lancet, 398(10301), pp. 698-708. https://doi.org/10.1016/S0140-6736(21)01208-3
15. Waite, M., Cohen, E., Torbey, H., Piccirilli, M., Tian, Y. and Modi, V., 2017. Global trends in urban electricity demands for cooling and heating. Energy, 127, pp. 786-802. https://doi.org/10.1016/j.energy.2017.03.095
16. International Energy Agency, Net Zero by 2050: A Roadmap for the Global Energy Sector, 2021. https://www.iea.org/reports/net-zero-by-2050
17. Olympios A.V., Aunedi M., Mersch M., Krishnaswamy A., Stollery C., Pantaleo A.M., Sapin P., Strbac G., Markides C.N., Delivering net-zero carbon heat: Technoeconomic and whole-system comparisons of domestic electricity- and hydrogen-driven technologies in the UK. Energy Conversion and Management 2022;262:115649. https://doi.org/10.1016/j.enconman.2022.115649
18. Goetzler, W., Guernsey, M., Young, J., Fuhrman, J., Abdelaziz, O., The future of air conditioning for buildings. US Department of Energy, Navigant Consulting, Oak Ridge National Laboratory, 2016. https://www.energy.gov/sites/prod/files/2016/07/f33/The%20Future%20of%20AC%20Report%20-%20Full%20Report_0.pdf
19. International Energy Agency, Heat Pumps. 2022. https://www.iea.org/reports/heat-pumps
20. Olympios, A.V., Sapin, P., Freeman, J., Olkis, C., Markides, C.N., Operational optimisation of an air-source heat pump system with thermal energy storage for domestic applications. Energy Conversion and Management 2022;273:116426. https://doi.org/10.1016/j.enconman.2022.116426
21. Quiggin, D., Buswell, R., The implications of heat electrification on national electrical supply-demand balance under published 2050 energy scenarios, Energy 2016;98:253-270.
22. Hoseinpoori, P., Olympios, A.V., Markides, C.N., Woods, J., A whole-system approach for quantifying the value of smart electrification for decarbonising heating in buildings, Energy Conversion and Management 2022;268:115952. https://doi.org/10.1016/j.enconman.2022.115952
23. Strbac, G., Pudjianto, D., Aunedi, M., Djapic, P., et al., 2020. Role and value of flexibility in facilitating cost-effective energy system decarbonisation, Progress in Energy, 2.
24. Wang, Z., Roffey, A., Losantos, R., Lennartson, A., Jevric, M., Petersen, A.U., Quant, M., Dreos, A., Wen, X., Sampedro, D. and Börjesson, K., 2019. Macroscopic heat release in a molecular solar thermal energy storage system. Energy & Environmental Science, 12(1), pp.187-193. https://doi.org/10.1039/C8EE01011K

25. Shangguan, Z., Sun, W., Zhang, Z.Y., Fang, D., Wang, Z., Wu, S., Deng, C., Huang, X., He, Y., Wang, R. and Li, T., 2022. A rechargeable molecular solar thermal system below 0° C. Chemical science, 13(23), pp.6950-6958. https://doi.org/10.1039/D2SC01873J
26. Aunedi, M., Strbac, G., System benefits of residential heat storage for electrified heating sector in the United Kingdom. ISGT-Europe: 2022 IEEE PES Innovative Smart Grid Technologies Conference Europe; 2022 Oct 10-12, Novi Sad, Serbia.
27. Mersch, M., Sapin, P., Olympios, A.V., Ding, Y., Mac Dowell, N., Markides, C.N., 2022. Thermo-economic optimisation of grid-scale compressed-air energy storage systems with solid and liquid thermal storage. 17th Conference on sustainable development of energy, water and environment systems; 2022 Nov 6-10, Paphos, Cyprus.
28. Kharel, S., Shabani B., Hydrogen as a long-term large-scale energy storage solution to support renewables, Energies 2018;11(10):2825. https://doi.org/10.3390/en11102825
29. Zhu, Z., Jiang, T., Ali, M., Meng, Y., Jin, Y., Cui, Y., Chen, W. Rechargeable batteries for grid scale energy storage. Chemical Reviews 2022;122(22):16610-16751. https://doi.org/10.1021/acs.chemrev.2c00289
30. Aunedi, M., Olympios, A.V., Pantaleo, A.M., Markides, C.N., Strbac, G. System-driven design of hybrid electricity- and hydrogen-based systems for domestic heat decarbonisation. 17th Conference on Sustainable Development of Energy, Water and Environment Systems; 2022 Nov 6-10, Paphos, Cyprus.
31. Department for Business, Energy & Industrial Strategy (BEIS). Cambridge housing model and user guide. 2015. https://www.gov.uk/government/publications/cambridge-housing-model-and-user-guide
32. Watson, S. D., Lomas, K. J., and Buswell, R. A., Decarbonising domestic heating: What is the peak GB demand? Energy Policy 2019;126:533–544. https://doi.org/10.1016/j.enpol.2018.11.001
33. Herrando, M., Markides, C. N., and Hellgardt, K., A UK-based assessment of hybrid PV and solar-thermal systems for domestic heating and power: System performance. Applied Energy 2014;122:288–309. https://doi.org/10.1016/j.apenergy.2014.01.061
34. Davies, G., Maidment, G., Paurine, A., Rutter, P., Evans, T., Tozer, R., Large scale cooling systems using mains water. Refrigeration Science and Technology 2016;1076–1083. https://doi.org/10.18462/iir.gl.2016.1183
35. Pudjianto, D., Aunedi, M., Djapic, P., Strbac, G., Whole-systems assessment of the value of energy storage in low-carbon electricity systems. IEEE Transactions on Smart Grid 2014;5:1098-1109. https://doi.org/10.1109/TSG.2013.2282039
36. Fu, P., Pudjianto, D., Zhang, X., Strbac, G., Integration of hydrogen into multi-energy systems optimisation. Energies 2020;13:1606. https://doi.org/10.3390/en13071606
37. Olympios, A.V., McTigue, J.D., Farres-Antunez, P., Tafone, A., Romagnoli, A., Li, Y., Ding, Y., Steinmann, W.D., Wang, L., Chen, H. and Markides, C.N., 2021. Progress and prospects of thermo-mechanical energy storage—a critical review. Progress in Energy, 3(2), p.022001. https://doi.org/10.1088/2516-1083/abdbba

PROCEEDINGS OF ECOS 2023 - THE 36TH INTERNATIONAL CONFERENCE ON
EFFICIENCY, **C**OST, **O**PTIMIZATION, **S**IMULATION AND ENVIRONMENTAL IMPACT OF ENERGY SYSTEMS
25-30 JUNE 2023, LAS PALMAS DE GRAN CANARIA, SPAIN

Energy-power relations and Ragone plots for packed bed thermal energy storage

Inga Beyers[a], Astrid Bensmann[b] and Richard Hanke-Rauschenbach[d]

[a] Leibniz University Hannover, Institute of Electric Power Systems, Hannover, Germany, beyers@ifes.uni-hannover.de
[b] Leibniz University Hannover, Institute of Electric Power Systems, Hannover, Germany, astrid.bensmann@ifes.uni-hannover.de, CA
[c] Leibniz University Hannover, Institute of Electric Power Systems, Hannover, Germany, hanke-rauschenbach@ifes.uni-hannover.de

Abstract:
Packed beds are essential components for future utility-scale long duration energy storage, such as A-CAES and Carnot batteries, and are expected to operate under a large variety of operating conditions. The operating behaviour can be visualised compactly within Ragone plots, which show the extractable energy over a range of discharge powers. They can additionally demonstrate the effect of different operational limits. Ragone plots are a well-known framework within electrochemical energy storage, but have not been applied to packed bed thermal energy storage. In this work, Ragone plots of packed beds are developed, to quantify off-design behaviour and the energy-power trade-off. For this purpose, a one-dimensional, two-phase, transient, Schumann-style model for a non-pressurized packed bed is implemented in the modelling language Modelica. It is charged up to a nominal thermal energy of 100 MWh and subsequently discharged with two different discharge regimes, namely a constant mass flow discharge or a constant heat tranfer rate discharge. The shape of the obtained Ragone plots is characterised by limited self-discharge and little decline in available energy at high constant mass flow discharges. The enforcement of the mass flow limit and imperfect heat transfer dynamics lead to a residual thermal energy within the storage, which can be extracted at lower heat transfer rates. Analogies to electrochemical energy storage are drawn, where polarisation causes a conceptually similar residual energy.

Keywords:
Energy Storage, Packed Bed, Thermal Energy Storage, Ragone plots, Energy-Power relations

1. Introduction

In this paper, a packed bed thermal energy storage (TES) is studied and characterised within the Ragone plot framework and analogies between electrochemical energy storage are demonstrated. This is important since packed beds are considered strong contenders for TES components in future long-duration energy storage, such as Carnot batteries [1], compressed air energy storage (CAES) [2] and in the decarbonisation of industrial heat [3], due to their favourable characteristics. These characteristics include excellent heat transfer, low material costs, a low environmental impact, a high operational temperature range and high output temperature levels, due to thermal stratification. The study of packed beds has attracted considerable research attention, especially their modelling [4, 5], parametric optimisation [6] and performance aspects [7].

The Ragone plot shows the available energy as a function of discharge power and thus characterises the inherent energy-power trade-off of energy storage [8]. It is a very fundamental relation and can be construed as a “common language” of energy storage [9]. The characterisation of packed beds within this framework therefore enables the direct comparison with different energy storage technologies, across their respective fields.

The Ragone plot was first introduced by David Ragone in 1968 [10], and over the following years established itself a concept in the field of electrochemical energy storage, e.g. batteries and supercapacitors. They have recently also been applied in the field of TES (and associated technologies). Latent heat TES has been characterised with Ragone plots by [11–13]. Of these, Woods et. al. [12] presents a comprehensive Ragone plot analysis of different phase change materials. Here, the energy-power trade-off in a finite volume is shown, whereby heat transfer is improved at the cost of energy capacity. The publication lays the foundation for Ragone plot characterisation of TES as standalone components. The thermal energy is extracted at different constant heat transfer rates $\dot{q}$, as the thermal equivalent to electric power.

Christen [9] characterised pumped thermal energy storage (PTES) with both latent and sensible TES via Ragone plots. Here the TES is not characterised directly, but as a component within electric energy storage.

The analysis employs endoreversible thermodynamics [14] (perfect heat engine with irreversible heat transfer) to estimate the electric power delivered. Further, a lumped-model approach is used, which means there is no spatial temperature variation. This implies perfect mixing within the sensible TES, where the output temperature decays during the entire discharge process. In contrast, in a thermally stratified packed bed, a high, nearly constant output temperature can be held over the first part of a discharge until thermal front has migrated towards the outlet. A packed bed therefore lies somewhere between mixed sensible and latent TES in terms of maintaining high output temperatures, which is beneficial in a thermodynamic power cycle.

The contribution of this paper is to conduct the first analysis of packed beds within the Ragone plot framework, as this has not been attempted before. For this, a state-of-the-art packed bed model is used. Analogies between packed bed TES and electrochemical energy storage discharge modes are developed, to effectively translate the Ragone plot framework. An assessment of off-design performance of packed beds follows, both in the context of pure thermal energy storage and as a thermal reservoir for a power cycle. The remainder of the paper is structured as follows: Section 2 describes the methodology of the Ragone plot and the employed packed bed model. Section 3 shows the obtained results and highlights key findings. Section 4 summarises the results and derives the conclusion from the presented analysis.

2. Methodology

2.1. The Ragone plot framework and discharge regimes

A Ragone plot essentially is a collection of energy-power value pairs from full discharges of any kind of energy storage. These value pairs form a Ragone curve or energy-power (E-P) curve. Ragone curves are often presented as specific values, based on storage mass (gravimetric energy and power density) or on storage volume (volumetric energy and power density) However, absolute values are also used, depending on what makes most sense in the given context.

Christen and Carlen [8] have expressed the Ragone curve as stemming from constant-power (CP) discharges, where a constant power P can be applied to an fully charged energy storage for a finite time t_{end} until an internal operating limit terminates the discharge. This results in the following E-P relation:

$$E(P) = P \cdot t_{\text{end}}(P) \tag{1}$$

However, the electrochemical ES community routinely characterises batteries with constant-current (CC) discharges. This does not result in an unambiguous energy-power point, because the power varies in the course of this type of discharge. In these cases, the E-P value pair for a constant current I is obtained by averaging the power over the discharge time, resulting in

$$E(I) = P_{\text{ave}}(I) \cdot t_{\text{end}}(I) \tag{2}$$

These two fundamental discharge regimes found in batteries (CC/CP) have direct equivalents in packed bed TES, which are all shown together for illustration purposes in Fig. 1. All subfigures show the potential variable of the energy storage (voltage U for the lithium-ion battery and the specific enthalpy difference Δh of the fluid at inlet and outlet for the packed bed) and the flow variable (current I for the lithium-ion battery and mass flow rate $\dot{m}$ for the packed bed) over the course of the discharge time.

Fig. 1 a) and b) are the respective constant flow discharge regimes. In a CC-discharge of a lithium-ion-battery in a), the output voltage decays until the discharge is terminated by reaching the predefined operating limit U_{min}. The output power $P(t) = U(t) \cdot I$ also decays. Analogously, in Fig. 1 b) Δh decays during the constant mass flow discharge (referred to as “CF”-discharge hereafter), until termination at T_{min}. Here the potential variable and flow variable multiplied result in a decaying heat transfer rate $\dot{q}(t) = \Delta h(t) \cdot \dot{m}$ delivered to the application. The Ragone plot from a CF-discharge of a packed bed can thus be expressed as:

$$E(\dot{m}) = \dot{q}_{\text{ave}}(\dot{m}) \cdot t_{\text{end}}(\dot{m}) \tag{3}$$

To compensate the decaying voltage in lithium-ion batteries, the current can be increased during the discharge to deliver a constant power, see Fig. 1 c). The packed bed equivalent is increasing the mass flow to compensate the decaying Δh and deliver a constant heat transfer rate $\dot{q}$, referred to as a “CQ”-discharge hereafter. The CP and CQ discharge regimes have a higher control effort, but are necessary if load-following must be achieved [9]. Here, the discharge can be terminated by reaching a potential variable limit (i.e. U_{min} or T_{min}) or by reaching a flow variable limit, here I_{max} or $\dot{m}_{\text{max}}$. The Ragone plot derived from multiple CQ-discharges become simply:

$$E(\dot{q}) = \dot{q} \cdot t_{\text{end}}(\dot{q}) \tag{4}$$

It must be noted, that in [12], the constant heat transfer rate for the latent heat TES Ragone plots is realised by adjusting the inlet temperature instead of the mass flow. We consider an increase in mass flow better suited for

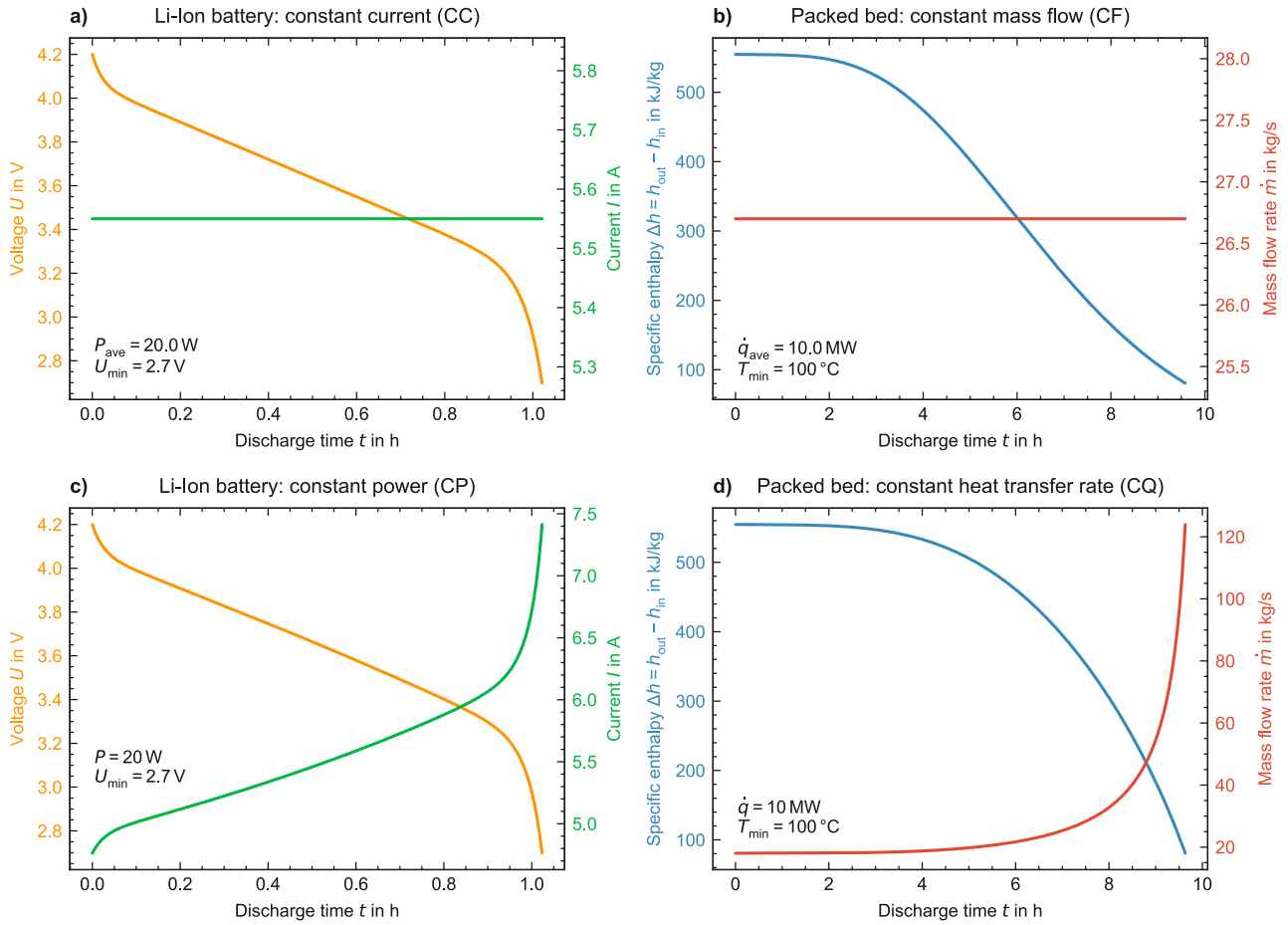

Figure 1: Equivalent discharge regimes for electrochemical ES, represented here by a lithium-ion battery, in a) and c) and packed bed TES in b) and d).

this analysis. The adjustment of the inlet temperature premises another heat source/sink apart from the TES itself, which is deemed impractical. In the course of this analysis, a representative packed bed will be studied under both CF and CQ discharge regimes.

2.2. Packed bed sizing

The packed bed is sized for a nominal energy capacity $E_{\text{nom}} = 100\,\text{MWh}$ in a top-down design approach, with inlet temperatures assumed at $T_{\text{in}} = T_{\text{max}}$ of 550 °C during charge and 20 °C = $T_{\text{amb}} = T_{\text{min}}$ for discharge. The packed bed is considered a non-pressurised rock-air system. The amount of rock mass m_s needed is calculated from [6] as follows:

$$E_{\text{nom}} = \frac{m_{\text{s}}}{\beta} \cdot c_{\text{p,s}} \cdot (T_{\text{max}} - T_{\text{min}}) \tag{5}$$

The packed bed is oversized by a factor $\beta = 1.5$ to prevent energy and exergy lost by exiting hot air, in accordance to results from Cardenas et. al. [6]. The basic geometry, namely radius r and height H is calculated via (6) and (7), for an aspect ratio of $\alpha = 0.7$ [6].

$$r = \left(\frac{m_{\text{s}}}{2\pi \cdot \alpha \cdot \rho_{\text{s}} \cdot (1 - \epsilon)} \right)^{1/3} \tag{6}$$

$$H = 2 \cdot r \cdot \alpha \tag{7}$$

The nominal discharge time is set at $t_{\text{nom}} = 10$ hours. From this, the nominal mass flow $\dot{m}_{\text{nom}}$ can be calculated via the following simplified relation:

$$\dot{m}_{\text{nom}} = \frac{E_{\text{nom}}}{t_{\text{nom}} \cdot \overline{c_{\text{p,f}}} \cdot \overline{\Delta T}} = \frac{E_{\text{nom}}}{t_{\text{nom}} \cdot \dfrac{c_{\text{p,f}}(T_{\text{max}}) + c_{\text{p,f}}(T_{\text{min}})}{2} \cdot \dfrac{(T_{\text{max}} - T_{\text{min}})}{2}} \tag{8}$$

The according specific mass flow G_{nom} is:

$$G_{\text{nom}} = \frac{\dot{m}_{\text{nom}}}{2\pi \cdot r^2} \tag{9}$$

The key design parameters of the packed bed are summarised in Table 1, where the values are colour-coded according to their degree of freedom in the design process. The design process chronology is from the top to bottom of the table.

Table 1: Overview over packed bed design parameters, colour-coded according to their degree of freedom in the design process. With = high degree of freedom, = limited degree of freedom and = resulting value.

Design parameter	Unit	Value	Source
E_{nom}	MWh	100	
T_{min}	°C	20	
T_{max}	°C	550	[4]
solid specific heat capacity $c_{\text{p,s}}$	J/kgK	960	[15]
solid density ρ_{s}	kg/m^3	2560	[15]
rock mass m_{s}	t	1061.3	
aspect ratio α	-	0.7	[6]
oversize factor β	-	1.5	[6]
porosity ϵ	-	0.40	[4]
rock diameter d	m	0.02	[4]
radius r	m	5.40	
height r	m	10.80	
cross section A	m^2	91.47	
t_{nom}	h	10	
nominal mass flow $\dot{m}_{\text{nom}}$	kg/s	36.33	
nominal specific mass flow G_{nom}	kg/sm^2	0.3972	

The wall is composed of three layers, adopted from [16]: an internal tube, an insulation layer and an outer steel vessel. Their respective parameters are listed in Table 2.

Table 2: Wall composition of packed bed

Design parameter	Unit	Tube	Insulation	Steel vessel
thickness r	m	$0.001 \cdot 2r$	$0.05 \cdot 2r$	$0.001 \cdot 2r$
thermal conductivity k	W/mK	0.12	0.15	20

2.3. Packed bed model description and validation

The Ragone plot analysis is conducted on the basis of a dynamic physical model of the packed bed, according to current standard modelling practise. The model is a transient, two-phase, Schumann-style model, widely used in the study of packed beds. The model is governed by mass conservation and by an separate energy balance for solid and fluid respectively, linked through the convective heat transfer between fluid and solid. The model further considers axial conduction through the solid and losses from fluid to ambient. The equations are taken from [4]. For the fluid phase this is:

$$\epsilon\, \rho_{\text{f}}\, c_{\text{p,f}}(T_{\text{f}})\, A\, \frac{\partial T_{\text{f}}}{\partial t} = h_{\text{V}}\, A\, (T_{\text{s}} - T_{\text{f}}) + c_{\text{p,f}}(T_{\text{f}})\, G\, A\, \frac{\partial T_{\text{f}}}{\partial x} + U_{\text{wall}}\, 2\, \pi\, r\, (T_{\text{amb}} - T_{\text{f}}) \tag{10}$$

with the volumetric heat transfer coefficient h_{V} from the correlation of Coutier and Faber [15] and the overall loss coefficient through the wall U_{wall}. U_{wall} is calculated as conduction through a multi-layered cylinder wall [19] with no thermal capacitance of the wall. The convection at the inner wall is from [20], while the convection at the outer wall is considered as free convection near a vertical surface [18]. For the solid phase the energy conservation equation is:

$$(1 - \epsilon)\, \rho_{\text{s}}\, c_{\text{p,s}}\, \frac{\partial T_{\text{s}}}{\partial t} = h_{\text{V}}\, (T_{\text{s}} - T_{\text{f}}) + k_{\text{bed}}\, \frac{\partial^2 T_{\text{s}}}{\partial x^2} \tag{11}$$

with the axial thermal conductivity of packed bed k_{bed}. This is evaluated according to the model of Zehner, Bauer and Schlünder [18]. The two-phase formulation is important to capture transient effects, i.e. when fluid

and solid are not in thermal equilibrium [17]. The energy E contained in the packed bed is determined via the temperature of the solid [4] and is given in (12). The pressure loss in the packed bed is calculated via the Ergun equation [18].

$$E = \int_0^H \rho_s \, c_{p,s} \, A \, (T_s(x) - T_{amb}) \, dx \tag{12}$$

2.3.1. Implementation

The numerical model is implemented in the acausal, multi-physics modelling language Modelica and solved within the open source modelling environment OpenModelica. As OpenModelica cannot solve partial differential equations (PDE), a finite volume discretisation is applied to (10) and (11) to form a set of coupled ordinary differential equations (ODE), where each control volume is governed by an ODE. The discretisation scheme and structure of the layer-based equations are adopted from [17]. The temperature-dependent thermodynamic properties of air are calculated at every point in time with the integrated "ReferenceAir" medium model contained in the Media library. This is a real gas model for dry air in the range of 130 K to 2000 K, based on Helmholtz equations of state.

2.3.2. Validation

The packed bed model is validated with the experimental data of Meier et. al. [21], further described by Hänchen et. al. [4], by scaling the model to the geometric dimensions specified. The result is shown in Fig. 2. The model shows good thermal agreement, but overestimates pressure losses by approx. 10 %, which is a known effect of the Ergun equation for randomly packed, spherical rock beds [22]. However, the equation is standard practise [18] and agreement is deemed satisfactory for the scope of this work.

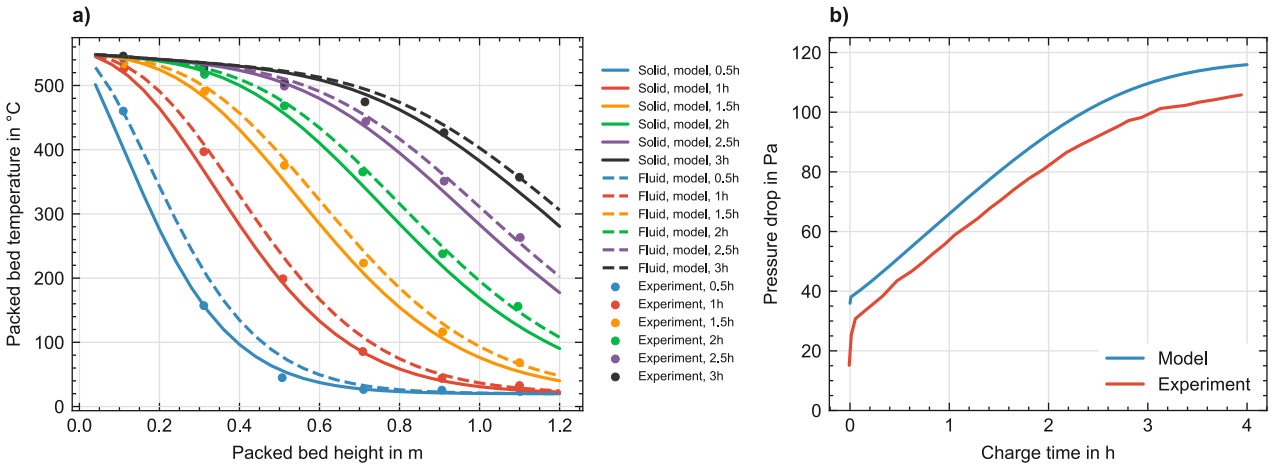

Figure 2: Validation of a) thermocline behaviour and b) pressure drop of the packed bed model with U_{wall} = 0.678 W/m²K at 523 K and a bypass flow of 15 % reported in [4]. Comparison with experimental data from [21]. The model is discretised into 30 layers.

2.4. Consideration of auxiliary components

In a non-pressurised packed bed, airflow is driven by an auxiliary fan/blower and the pressure drop Δp incurred through the bed must be compensated [6]. This must be considered in the Ragone plot analysis, because high mass flows result in higher pressure drops. Additionally, because the mass flow will be varied between discharges in the CF regime and during the course of a discharge in the CQ regime, a reasonable $\dot{m}_{max}$ must be determined. Whether the auxiliary is considered a fan or a blower depends on the pressure ratio, but the distinction is not clear-cut in literature [23]. For simplification purposes, we only refer to "fan" from this point onward.

The required auxiliary fan power is expressed as [24]:

$$P_{aux} = \frac{\dot{V} \cdot \Delta p}{\eta_{fan}} \tag{13}$$

with η_{fan} assumed at 80 % [24] for all operating points. This is a simplification, as the fan will operate in unsteady, off-design conditions. Even in a constant mass flow CF charge/discharge, the pressure loss to be compensated varies in the course of the charge/discharge, as the thermodynamic properties of the fluid inside

the packed bed change. This is also confirmed experimentally in Fig 2 b). The off-design behaviour of fans can be characterised with performance maps, which are usually determined experimentally and are specific to a fan type and geometry. However, with variable speed drives, satisfactory efficiencies can be achieved over a large range of mass flows, respective volume flows [24]. Therefore the consideration with a single efficiency is considerd sufficient and analysis with detailed performance maps is not deemed expedient.

Up to a pressure ratio of 1.3, air can be assumed as a incompressible medium [25], and therefore P_{aux} is calculated with the volume flow at inlet in 13. This is often viewed as the limit between fans and compressors [25]. This limit adopted here as the maximum allowable fan pressure ratio and higher pressure losses are a priori deemed impractical. From this condition, a maximum mass flow $\dot{m}_{max}$ can be iteratively determined from simulation runs, resulting in $\dot{m}_{max} = 158\,\mathrm{kg/s}$ or $4.3 \cdot \dot{m}_{nom}$. The maximum specific mass flow is thus $G_{max} = 1.727\,\mathrm{kg/sm^2}$.

3. Results and Discussion

3.1. Ragone plots from CF-discharge

In a first step, Ragone plots are developed from multiple constant mass flow (CF) discharges, as specified in Section 2.1. The packed bed is fully charged to nominal energy, then subsequently immediately discharged until the cut-off temperature is reached. This is repeated multiple times, starting from a mass flow of $0.1 \cdot \dot{m}_{nom}$ up to $\dot{m}_{max} = 4.3 \cdot \dot{m}_{nom}$. The result is shown in Fig. 3 a) for a cut-off temperature of $T_{min} = 20\,^{\circ}\mathrm{C}$ and in b) for $T_{min} = 100\,^{\circ}\mathrm{C}$.

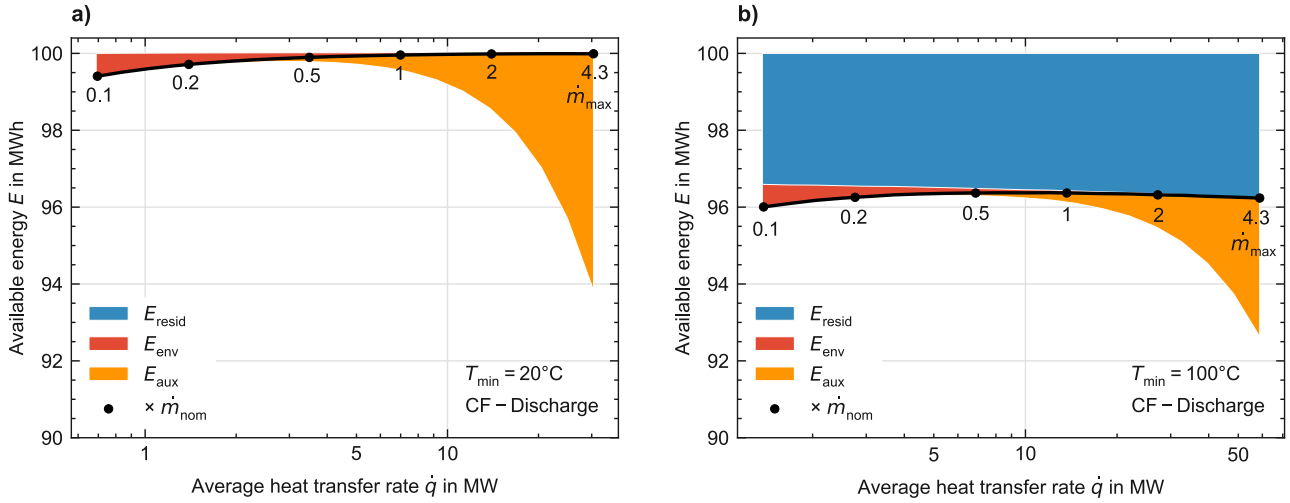

Figure 3: Ragone plots from multiple CF-discharges.

The Ragone curves (in black) show the available thermal energy over the average heat transfer rate. Certain mass flows are demarcated by dots; these are multiples of the nominal mass flow (conceptually similar to the C-rate in lithium-ion batteries). Classically, the Ragone curve is shown without any other descriptive elements. In this case, a novel visualisation is implemented to demonstrate how the Ragone curves are composed. The area above the curve (thermal energy that cannot be extracted) is color-coded, where red equals energy lost to environment and blue is residual energy in the storage. Further included is the electric energy required by the auxiliary fan to achieve the respective mass flows (yellow). This is not subtracted from the Ragone curve, because it does not lessen the available thermal energy, but is included for reference. It rises sharply for higher mass flows.

The Ragone curves confirm known packed-bed qualities. Thermal energy can be contained well, even for long discharge durations at low mass flows, signalled by low losses to the environment. Additionally, higher mass flows don't negatively impact available thermal energy to the extent that, e.g. high currents limit available energy in Li-Ion batteries. The forced convective heat transfer is still very good at high mass flows. Because of these characteristics, the shape of the Ragone curve in the CF-discharge regime is relatively flat. It is important to note that thermal front degradation does not show itself in Fig. 3, because the energy content remains the same and the bed is oversized to the extent that the thermal front degradation does not reach the outlet in the discharge durations considered.

The location of the Ragone curve on the E-Q plane is largely determined by the cut-off temperature. In Fig. 3 a), no thermal energy remains in the packed bed, whereas in Fig. 3 b) the higher cut-off temperature moves the entire Ragone curve downward, resulting in residual thermal energy. This is shown in Fig. 4, for multiple

different T_{min}. The residual energy and energy lost to the environment are not included here for visual clarity, only the auxiliary energy.

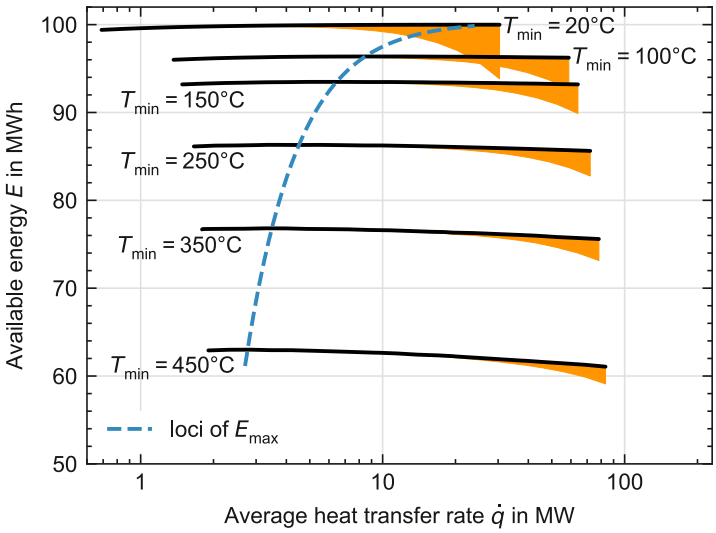

Figure 4: Ragone plots with varying cut-off temperature limits T_{min}.

One thing that becomes clear in Fig. 4, is that there is no single unique assignment between $\dot{q}_{ave}$ and $\dot{m}$. Depending on T_{min} and the resulting discharge end time, a specific $\dot{m}$ might result in different $\dot{q}_{ave}$. Secondly, one can observe a slight decrease in available energy at higher $\dot{q}_{ave}$. This can be attributed to an effect that is equivalent to polarisation in lithium-ion batteries. Polarisation is when charge transfer from and into the electrode cannot keep up with high current demands, resulting in overpotentials [26]. These lead to a premature termination of discharge and cause a residual energy that can only be extracted at lower currents. In the packed bed, imperfect heat transfer dynamics at high mass flow rates results in a temperature difference between fluid and solid. At the end of the discharge, the solid still has a higher temperature, but the fluid outlet temperature is lower and triggers the discharge cut-off. This effect is shown in Fig.5. It shows the temperature difference ΔT between solid and fluid, plotted over the specific mass flow G for several different lower cut-off temperatures.

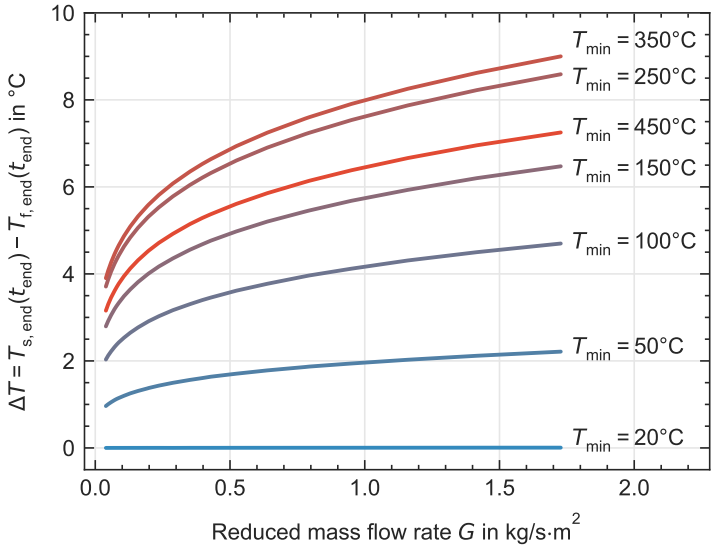

Figure 5: Temperature difference $\Delta T(t_{end})$ between solid and fluid at the end of discharge for different T_{min}.

From Fig.5 it can be seen that higher mass flows generally result in higher ΔT and thus higher "polarisation". But ΔT is also dependent on T_{min}. The temperature difference is highest within the thermocline, and stopping the discharge as the steepest point of the thermocline exits, results in highest ΔT (here at $T_{min} = 350\,°C$). This in turn leads to the highest amount of residual energy due to heat transfer limitations.

3.2. Ragone plots from CQ-discharge

In the second part of the analysis, Ragone plots constant heat transfer rate (CQ) discharges are developed, presented here in Fig. 6. As in Section 3.1., the packed bed is fully charged and immediately discharge until termination by either reaching the predefined maximum mass flow $\dot{m}_{\mathrm{max}}$ or the cut-off temperature T_{min}. This is repeated for multiple heat transfer rates, with the E-Q value pairs forming the Ragone curve. In 6 a), the

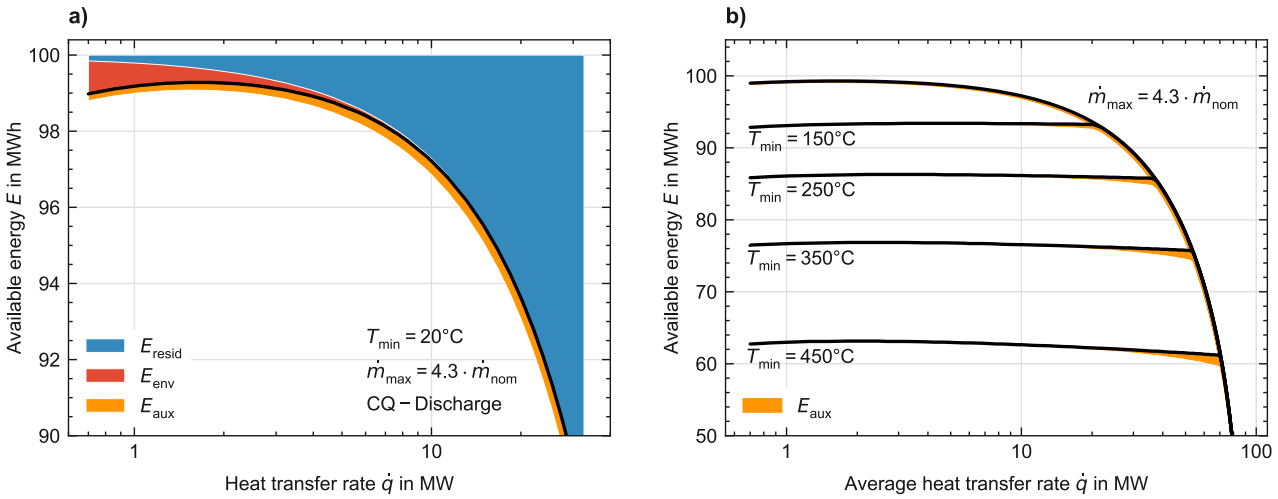

Figure 6: CQ-Ragone plots, curve composition in a) and variation of T_{min}.

Ragone plot for $T_{\mathrm{min}} = 20\,^{\circ}\mathrm{C}$ shows a very different curve, than its CF-counterpart in Fig. 3 a). Here, the minimum temperature cut-off does not come into play, because the Ragone curve (in black) is limited by the maximum mass flow $\dot{m}_{\mathrm{max}}$ in every discharge. As shown in Section 2.1., the mass flow is increases towards the end of the discharge, to compensate the decaying output. In this case, $\dot{m}_{\mathrm{max}}$ is always reached before $T_{\mathrm{min}} = 20\,^{\circ}\mathrm{C}$. This cut-off leaves a residual energy (blue) within the storage that can only be extracted at lower heat transfer rates, even in the case of $T_{\mathrm{min}} = 20\,^{\circ}\mathrm{C}$. The auxiliary energy needed is more evenly distributed, because the fan only operates at high mass flow rates at the end of the discharge.

Figure 6 b) shows the Ragone curves for different lower temperature limits T_{min}. Here, for higher T_{min} limits, the Ragone curves are each composed of two distinct sections, a relatively flat temperature-limited section and a mass-flow-limited section, where the available energy drops quickly. The mass flow limit forms an outer enveloping curve for all the Ragone curves.

It must be noted, that the available energy reaches a limit of 0 at $\dot{q}_{max}$. This is not shown in Fig. 6 b) as it is not considered an actual practical operating point and the axes are identical to the CF-discharge in Fig. 3 b) for comparison purposes. At this point $E \to 0$, $\dot{q}$ is only applied for infinitesimally short discharge duration, and the maximum mass flow limit $\dot{m}_{max}$ is immediately enforced.

3.3. Packed bed as a thermal reservoir for a power cycle

The Ragone plots presented in Section 3.2. and 3.1. show only available energy and do not differentiate between exergy and anergy. This energy-based analysis is valid, as packed beds can be utilised purely in a thermal energy storage context, e.g. in the recuperation of waste heat, that is used to preheat fluid streams at a later point. If desired, energy quality (i.e. exergy) demands can be encoded in these Ragone plots, by setting a certain T_{min}, but this is a quite roundabout way.

Alternatively, a simple way to evaluate the packed bed as a thermal reservoir for a power cycle is to apply a Carnot efficiency $\eta_{\mathrm{carnot}} = 1 - T_{\mathrm{out}}/T_{\mathrm{amb}}$ to the output, which has been employed by [9]. This is a theoretical analysis, as there is no consideration of control regimes or any other irreversibilities apart from those included in the packed bed model, but it is a quick and convenient manner in which to produce electric energy over power Ragone plots, based on a specific TES. Fig. 7 a) shows the result of such an analysis, where the output power P is kept constant, until the storage is unable to deliver it and the discharge is terminated. Unlike the analysis in Section 3.1. and 3.2., the maximum mass flow is set as $\dot{m}_{max} = 1.5\dot{m}_{nom}$ because the achievable mass flow variations are more limited in a power cycle.

Here, also $E(P_{\mathrm{max}}) \to 0$, which Christen [9] generally asserted for sensible heat storage. However, the shape of the Ragone curve is bulged outwards towards higher E and P values, instead of inwards like the mixed sensible TES [9]. The thermal stratification and good heat transfer of the packed bed enable a higher Carnot efficiency over a longer part of discharge. This Ragone plot can easily be compared to the E-P relation of other electric storage technologies, regardless of their functional principle. This is demonstrated in Fig. 7 b), where

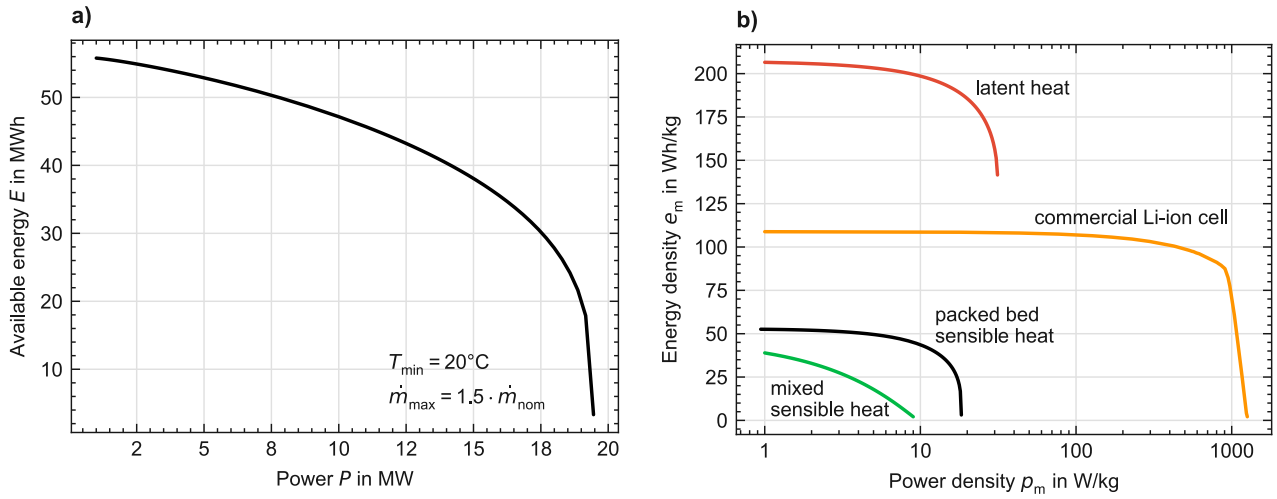

Figure 7: a) Ragone plot from CP-discharge of the 100 MWh packed bed via a Carnot engine. b) Gravimetric Ragone plot of the packed bed-based PTES and comparison to mixed sensible and latent heat PTES from [9], in addition to a commercial Li-ion battery cell.

the specific-value Ragone curves of perfectly mixed sensible and latent heat PTES from [9] are included for comparison purposes, in addition to a commercial Li-ion battery cell. It should be noted that the specific-value Ragone curve of a full Li-ion system with periphery would have lower specific values. The Ragone curve shape of the packed bed PTES underlines its characteristics, as it shares both the property of mixed sensible heat, where $E(P_{max}) \rightarrow 0$, but also the convex Ragone curve shape of latent heat. As a storage technology, packed bed-based PTES have relatively low gravimetric energy and power densities.

3.4. Comments on cyclic stability

Packed bed behaviour is known to reach quasi-stationary cyclic temperature profiles in charge-discharge cycles of constant duration [7]. This is achieved after a certain number of cycles (5-20 cycles is the range typically found in literature). In the packed bed analysed here, the cyclic stability is reached after ten cycles, as shown in Fig. 8. Packed bed analyses are often conducted on the basis of these quasi-stationary temperature pro-

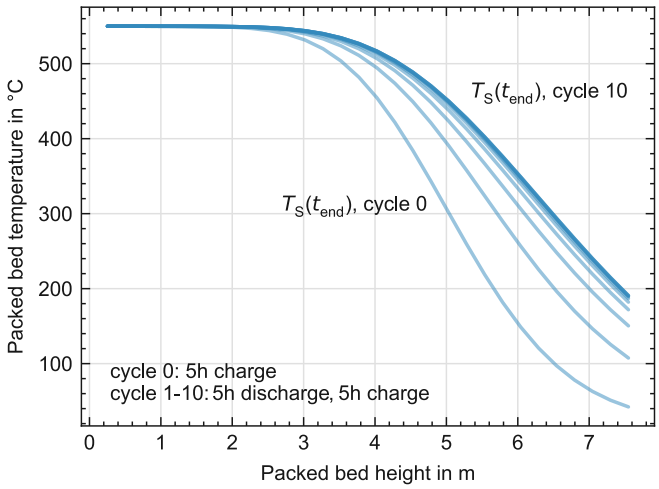

Figure 8: Cyclic stability in the packed bed temperature profile: Final temperature $T_s(t_{end})$ after charge.

files [4, 5, 7], however in case of Ragone plots, we have not integrated this into the analysis. Several issues arise when applying the cycle stability logic into the Ragone framework. Firstly, the stable temperature profile is different for every cycle length [7], introducing an additional level of variability. Secondly, the energy in the packed bed after reaching cyclic thermal stability will differ from the nominal energy. In Fig. 8 it is approx. 25 % higher than E_{nom}. Additionally, the losses incurred along the way by the multiple cycles cannot be cleanly integrated into a subsequent Ragone plot analysis. Cyclic analysis makes sense in a cyclical load regime, e.g. storage for concentrated solar power. However in a thermal load-following paradigm or variable discharge

waste heat output, cyclic operation will not be given in any case. And while the Ragone plot also does not cover all possible load scenarios, its benefit lies in the formulation of a consistent scenario [9] and the comparability to other storage technologies.

4. Conclusions

The presented analysis aimed to evaluate packed bed TES within the Ragone plot framework and draw analogies to the field of electrochemical energy storage. An exemplary 100 MW packed bed model was sized and simulated under different discharge regimes. The main conclusions are derived as follows:

- Two discharge regimes are identified for packed beds, namely CF (constant mass flow) and CQ (constant heat transfer rate), which have direct counterparts (CC and CP) in the field of electrochemical energy storage.
- The energy-power trade-off of packed beds, quantified here with Ragone plots, is low and the analysed packed bed shows good performance over a large range of discharge demands.
- Imperfect heat transfer dynamics cause a residual energy in packed beds, that is conceptually equivalent to polarisation in electrochemical energy storage.
- The Ragone plot framework is well-defined, simple-to-use scenario, that is well-suited for off-design characterisation of TES. This can be done both within the function as pure thermal energy storage and as a thermal reservoir for a power cycle. The obtained results can be compared directly and quantitatively with any other energy storage technology.

Acknowledgments

We thank Alexander Wernke and Fabian Geerling for helpful discussions.

References

[1] Liang T, Vecchi A, Knobloch K, Sciacovelli A, Engelbrecht K, Li Y, et al. *Key components for Carnot Battery: Technology review, technical barriers and selection criteria.* Renewable and Sustainable Energy Reviews. 2022 Jul;163:112478.

[2] Barbour E, Mignard D, Ding Y, Li Y. *Adiabatic Compressed Air Energy Storage with packed bed thermal energy storage.* Applied Energy. 2015 Oct 1;155:804–15.

[3] Manente G, Ding Y, Sciacovelli A. *structured procedure for the selection of thermal energy storage options for utilization and conversion of industrial waste heat.* Journal of Energy Storage. 2022 Jul 1;51:104411.

[4] Hänchen M, Brückner S, Steinfeld A. *High-temperature thermal storage using a packed bed of rocks – Heat transfer analysis and experimental validation.* Applied Thermal Engineering. 2011 Jul;31(10):1798–806.

[5] Mertens N, Alobaid F, Frigge L, Epple B. *Dynamic simulation of integrated rock-bed thermocline storage for concentrated solar power.* Solar Energy. 2014 Dec;110:830–42.

[6] Cárdenas B, Davenne TR, Rouse JP, Garvey SD. *Effect of design parameters on the exergy efficiency of a utility-scale packed bed.* Journal of Energy Storage. 2018 Aug;18:267–84.

[7] McTigue JD, Markides CN, White AJ. *Performance response of packed-bed thermal storage to cycle duration perturbations. Journal of Energy Storage.* 2018 Oct;19:379–92.

[8] Christen T, Carlen MW. *Theory of Ragone plots.* Journal of Power Sources. 2000 Dec;91(2):210–6.

[9] Christen T. *Ragone plots and discharge efficiency-power relations of electric and thermal energy storage devices.* Journal of Energy Storage. 2020 Feb;27:101084.

[10] Ragone DV. *Review of Battery Systems for Electrically Powered Vehicles.* Presented at the Mid-Year Meeting of the Society of Automotive Engineers 1968, p. 680453.

[11] Yazawa K, Shamberger PJ, Fisher TS. *Ragone Relations for Thermal Energy Storage Technologies.* Front Mech Eng. 2019 Jun 4;5:29.

[12] Woods J, Mahvi A, Goyal A, Kozubal E, Odukomaiya A, Jackson R. *Rate capability and Ragone plots for phase change thermal energy storage.* Nat Energy. 2021 Mar;6(3):295–302.

[13] Shanks M, Shoalmire CM, Deckard M, Gohil KN, Lewis H, Lin D, et al. *Design of spatial variability in thermal energy storage modules for enhanced power density.* Applied Energy. 2022 May;314:118966.

[14] Curzon FL, Ahlborn B. *Efficiency of a Carnot engine at maximum power output.* American Journal of Physics. 1975 Jan;43(1):22–4.

[15] Coutier JP, Farber EA. *Two applications of a numerical approach of heat transfer process within rock beds.* Solar Energy. 1982;29(6):451–62.

[16] Anderson R, Bates L, Johnson E, Morris JF. *Packed bed thermal energy storage: A simplified experimentally validated model.* Journal of Energy Storage. 2015 Dec;4:14–23.

[17] Opitz F. *Packed bed thermal energy storage model - Generalized approach and experimental validation.* Applied Thermal Engineering. 2014;8.

[18] VDI e. V. *VDI Heat Atlas.* Berlin, Heidelberg: Springer Berlin Heidelberg; 2010.

[19] Incropera FP. *Fundamentals of heat and mass transfer.* 6th ed. Hoboken, NJ: John Wiley; 2007. 997 p.

[20] Ismail KAR, Jr RS. *A parametric study on possible packed bed models for PCM and sensible heat storage.* Applied Thermal Engineering. 1999;32.

[21] Meier A, Winkler C, Wuil D. *Experiment for modeling high temperature rock bed storage.* Solar Energy Materials. 1991;24(255–264):10.

[22] Allen KG, von Backström TW, Kröger DG. *Rock bed pressure drop and heat transfer: Simple design correlations.* Solar Energy. 2015 May;115:525–36.

[23] W. Neise, U. Michel. *Aerodynamic noise of turbomachines.* German Aerospace Center (DLR) Institute of Propulsion Technology, Department of Engine Acoustics; 1994. Report No.: Report 22314-94/B5.

[24] Schönholtz F, Grundmann, Reinhard, Eidam, Herbert, Rahn, Bernd. *Elementary Fan Technology.* TLT Turbo-GmbH; 2013.

[25] Menny K. *Strömungsmaschinen: hydraulische und thermische Kraft- und Arbeitsmaschinen.* 5th edition, Wiesbaden: Teubner; 2011. 327 p.

[26] Bard AJ, Faulkner LR. *Electrochemical methods: fundamentals and applications.* 2nd ed. New York: Wiley; 2001. 833 p.

Integration of Salt Cavern Hydrogen Storage in a 100% Renewable Energy Supply Scenario

Francesco Piovesan[a,b], Ali Akbar Eftekhari[b]

[a] *University of Padova, Padova, Italy, francesco.piove@gmail.com*
[b] *Technical University of Denmark, Lyngby, Denmark, aliak@dtu.dk*

Abstract:
We address two critical environmental and technical problems for the integration of subsurface salt cavern hydrogen storage with 100% renewable electricity. First, the storage/production rate of hydrogen must match the unpredictable pattern of renewable electricity supply and (more predictable) demand for electricity by creating and strategically locating enough salt caverns. Secondly, creating and maintaining so many salt caverns requires large volumes of fresh/seawater. We develop two static and dynamic models for Denmark as a successful case of wind power development, considering the surplus energy and demand forecasts. The static model predicts the minimum amount of hydrogen needed for balancing the average annual supply and demand of electricity and fresh water necessary for the construction of required salt caverns. The model considers all the round-trip exergy losses of electricity-H2-electricity in the electrolyzers, fuel cells, compressors, and pipelines. The dynamic model considers the variable supply from wind farms and user demand over time; We also include the effect of the inertia of the electrolyzers, fuel cells, and compressors, and technical constraints, e.g. salt cavern pressure and pipeline flow capacity, to design sufficient storage sites that can dynamically balance the fluctuating supply of renewables and variable user demand. The static model predicts a realistic volume of salt caverns for storing the surplus green hydrogen; however, in the absence of small-scale storage solutions (batteries), we show that the number of required caverns and injection/production wells become unrealistically high, with high energy demand and cost for maintenance water treatment.

Keywords:
Salt Caverns, Energy Storage, Hydrogen Storage, Renewable Energy.

1. Introduction

The unprecedented consequences of climate change caused by greenhouse gases emissions and the geopolitical circumstances have increased investments on renewable energy production to limit the environmental impact while maintaining the energy security. The increasing penetration of intermittent renewable energy sources, i.e., wind and solar, in the energy production mix stresses the necessity of finding storage solutions to cope with their intrinsic intermittency and unpredictability. In a fully renewable scenario, it is necessary to evaluate which are the most convenient and relevant solutions for storage. Here, we address these concerns focusing on the salt cavern storage of green hydrogen integrated in the electricity supply of Denmark. Different solutions for energy storage exist (Figure 1), with different storage capacity and power rating (i.e. energy charge and discharge per unit time). Many of these technologies are already available commercially, while some others are in lower Technology Readiness Level (TRL).

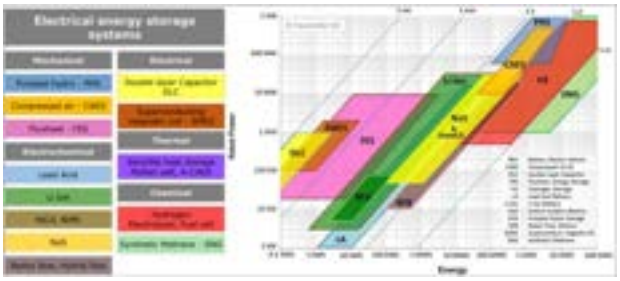

Figure 1: Classification of electrical energy storage systems according to energy form (a); Comparison of rated power, energy content and discharge time of different EES technologies (b), own representation based on (International Eletrotechnical Commission (IEC), 2011).

Electrochemical technologies cover the majority (over 85% as 2016 new installation data) of the new energy

storage solutions, with the Li-Ion technology being the predominant one. Research and development is focused on increasing the number of charge cycles (i.e. the number of times the battery can charge and discharge), reducing production costs and tackling the recycling problem. Different technologies are available, e.g., NaS (Sodium Sulphur), $NaNiCl_2$ (Sodium Nickel Chloride), Pb-Acid (Lead-Acid), Li-Ion (Lithium Ions), Ni-MH (Nickel metal hybrid), Ni-Cd (Nickel-Cadmium), and flow batteries, all with a general common issue of not presenting sufficiently high energy densities to be considered for large storage systems. Second type of technologies is Thermal Energy Storage (TES). All TES technologies are based on the usage of thermal energy as mechanism of storing energy [5]: **MSTES** (Molten Salt thermal energy storage) is the most used TES technology; it has good heat transfer properties and relatively low cost; drawback is the usage of corrosive salts and the necessity of maintaining a minimum temperature value to avoid the solidification of the salts. **PCM** (Latent-phase change material) is based on the latent heat stored by phase change material; as TCS this technology is still in a development stage. **TCS** (Thermochemical storage) where heat or cold is stored by means of different chemical reactants; as PCM, it is in a development stage. **SHS** (Sensible Heat storage) is another possibility to store energy through sensible heat storage; this storage can be done through the usage of solid materials (like sand, concrete or similar materials [4]) or liquid materials (most common used is water, fundamental in the solar thermal systems [11]). TES technologies are mainly in development stage so they do not represent at the moment a suitable solution for our purpose. The most exploited large-scale technologies for energy storage are based on storage of energy through gravity (for hydro) and pressure (for CAES) [4] [8]. These technologies allow high long-term energy storage capacities but present major drawbacks as high investment costs (for civil constructions), high environmental impact (especially hydro), not widely available conditions for their construction and high inertia of the system (charge-discharge process) compared to electrochemical or electrical storage technologies. Electrical storage technologies, like SMES (superconduction magnetic energy storage), Capacitors and Supercapacitors, allow high power densities and really fast charge/discharge times (as well as response times) but they have low energy density so they are not useful for large-scale energy storage purposes. Here, we focus on green hydrogen that has a higher energy density compared to TES and CAES, and can be stored in much larger scales in the safe subsurface salt caverns. The technology is mature, but the current research is generally focused on the capacity and safety of storage. Consequently, the production rate that is critical to the integration of hydrogen storage in the energy networks, has not received considerable attention specially on its technical aspects. We will, therefore, focus on the dynamic behaviour of salt cavern storage and production of hydrogen in the Danish future electricity network to further investigate the technical obstacles of integrating salt caverns in a realistic safe and resilient energy supply and demand scenario.

2. Materials and Methods

The base of this project is the analysis of salt caverns hydrogen storage solutions to permit the switch to a completely renewable energy-based society. To cover the entire energy demand curve with only resources like wind or solar it is necessary to consider a storage solution that is able to cope with the intermittency and unpredictability of the renewable supply. The analysed storage solution is artificial subsurface salt caverns: the calculations have started with an estimation of the amount of hydrogen that must be produced to cover the demand. Once completed, it has been possible to calculate the required salt caverns volume that had to be artificially created.
This type of static analysis has been carried out considering initially a simplified model. In this model a limited number of cities and storage locations has been considered and their positioning and connections have been manually evaluated. This method will be explained in the dedicated section 3.1.. The consequences of the functioning of the system in terms of behaviour over time, with a set of defined assumptions, will be instead analyzed in the second dedicated paragraph 3.3.. The case study related to Danish 2050's wind production and demand projections starts with the simplified model case.

3. Case Study

3.1. Simplified Model

In order to proceed in the study and evaluation of the simplified model it has been necessary to make few assumptions:

1. No limits on number and dimension of wind farms that can be installed in the North Sea: this hypothesis doesn't differ excessively from the actual conditions present in the North Sea.
2. Analysis starts from the demand and goes backwards, considering all the efficiencies of the components of the energy system, to the necessary production to cover it.
3. Electrolyzers are considered to be modular so the efficiency is evaluated as approximately independent from the size of the plant.

4. It is considered possible to place caverns for storage on the entire area of the simplified map (even though some more limited regions are considered to proceed with the modelling process).
5. All industries have been able to convert their production lines and processes to the usage of hydrogen instead of methane: this hypothesis is used to pursue the simplified analysis but the conversion of the industrial lines to hydrogen could be an issue that has to be addressed.
6. Injection and extraction points are considered placed in the center of the respective regions and it is supposed to have one cavern for each city of the model.

Before defining all the scenarios it is necessary to design a simplified map for the calculations (sm stands for simplified map), which is here reported (Figure 2).

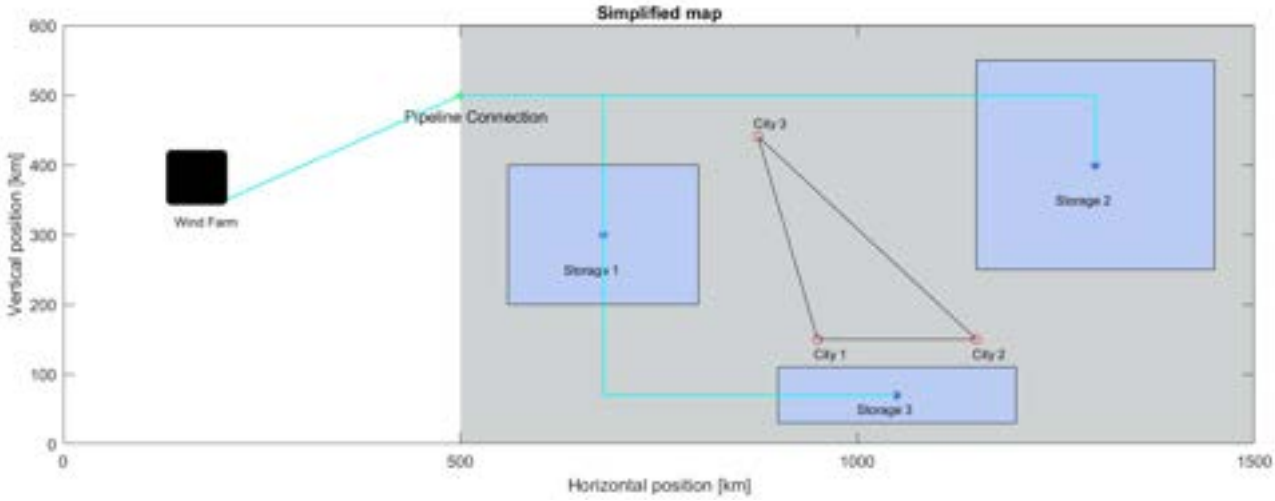

Figure 2: Map for the simplified model with pipeline connections

In this map three cities have been reported, considering a subdivision of the peak power requested into 50%, 30% and 20% respectively for cities 2, 3 and 1. The storage sites 1, 2 and 3 are respectively dedicated to cities 3, 2 and 1. Under the hypothesis of having in 30 years four times the wind power capacity and 1.5 times the power demand by users, through the Danish data of the last 10 years the future trends of production and consumption have been evaluated for each city (Figure 3) and overall (Figure 4).

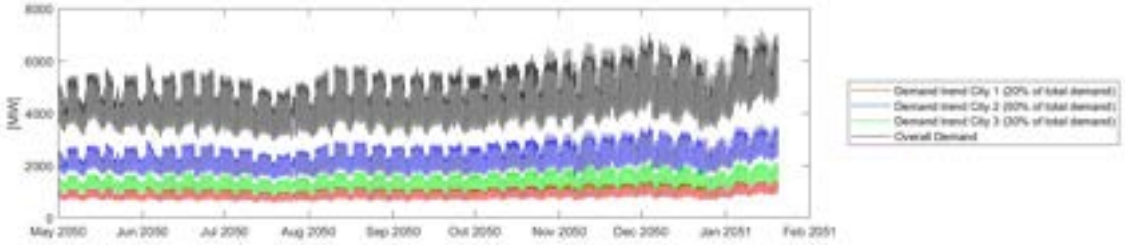

Figure 3: Projection of demand trend for each city and overall in 30 years based on Danish past electricity supply and demand data

We have assumed one offshore wind farm that covers all the electricity production. Moreover, we have defined a hydrogen island where we have the convergence of the power produced by the wind farm, the electrical transformers and the hydrogen production and storage. It is important to note two characteristics of this island:

- Average Sea Depth: North Sea has an average depth of 90 m with maximum depth of 700 m so it has been considered a value of 200 m for the analysis. [1]
- From the 20 GW 70% H_2 case (page 51 of [12]) we have obtained a set of reference dimensions for the artificial island.

With a temporal resolution of 1 hour, a 9-months time frame considered and an overall shortage (calculated as the difference between the overall demand and the wind farm production per each unit of time) in terms

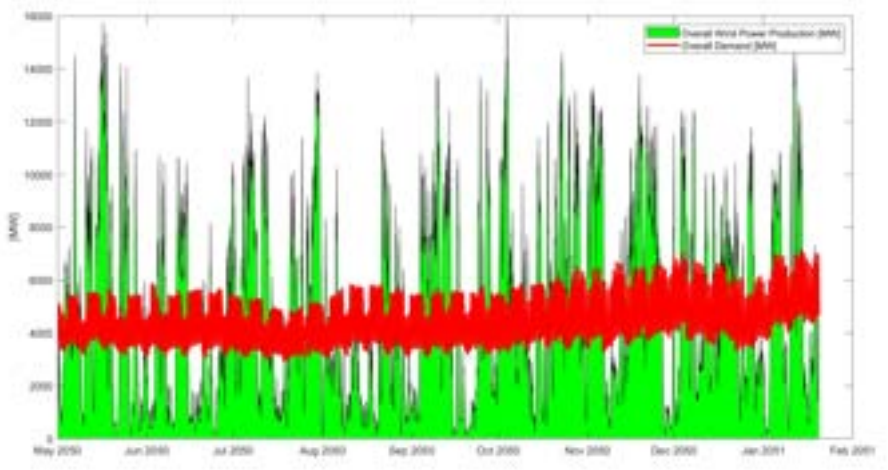

Figure 4: Projection of overall demand and wind production trend in 30 years based on Denmark's supply and demand data in 2020

of power it has been possible to integrate over time to obtain the energy shortage and divide per each city obtaining:

- $E_{shortage,city1} = 6.97 \times 10^4$ MWh
- $E_{shortage,city2} = 1.74 \times 10^5$ MWh
- $E_{shortage,city3} = 1.05 \times 10^5$ MWh

We then calculate the surplus that has to be extracted and stored to cover these shortages.

3.2. Analysis and Results

3.2.1. Fraction of surplus energy needed

With the efficiency ranges of fuel cells and electrolyzers (see Table 1 and Table 2), we calculate and obtain the energy required surplus to cover the average shortages, presented in this paragraph. The conversion efficiency to hydrogen and back to electricity are considered in our calculations.

Table 1: Overview of main electrolyzers technologies efficiencies [13]

Technologies	Minimum Efficiency [%]	Maximum Efficiency [%]
Alkaline	51	65.3
PEM	55.5	72.4

Table 2: Overview of main Fuel Cells technologies efficiencies [3]

Technologies	Electrolyte	$T_{operating,min}[K]$	$T_{operating,max}[K]$	$\eta_{electrical,min}[\%]$	$\eta_{electrical,max}[\%]$
AFC	Aq. KOH	333.15	393.15	60	60
DMFC	PEM	303.15	363.15	80	80
MCFC	Molten Li2CO3 and K2CO3	873.15	923.15	45	47
PAFC	Phosphoric Acid	433.15	473.15	40	40
PEMFC	PEM	333.15	363.15	53	58
SOFC	Yttrium stabilized zirconia	1073.15	1273.15	35	43

Considering these efficiencies permits to understand the amount of energy that has to be taken from the surplus to cover this shortage of electricity and quantify the energy losses. The quantities for all cities are reported in Table 3, while a bar chart has been used to evaluate the requirements for each city based on the electrolyzers-FC technologies considered (Figure 5). These values may change quite significantly with the chosen conversion technology, from average values in the order of $10^5 MWh$ for maximum efficiency factors to values in the order of $10^6 MWh$ for the minimum efficiency factors.

Table 3: Average energy [MWh] that has to be used from surplus to cover the shortage for all cities considering the minimum and maximum efficiencies for each fuel cell technology (columns) and electrolyzers (rows)

	AMC		DMFC		MCFC		PAFC		PEMFC		SOFC	
Alkaline	$1.14*10^6$	$8.90*10^4$	$8.55*10^4$	$6.68*10^4$	$1.52*10^6$	$1.13*10^6$	$1.71*10^6$	$1.34*10^6$	$1.29*10^6$	$9.21*10^4$	$1.95*10^6$	$1.24*10^6$
PEM	$1.05*10^6$	$8.03*10^4$	$7.85*10^4$	$6.02*10^4$	$1.40*10^6$	$1.03*10^6$	$1.57*10^6$	$1.20*10^6$	$1.19*10^6$	$8.30*10^4$	$1.80*10^6$	$1.12*10^6$

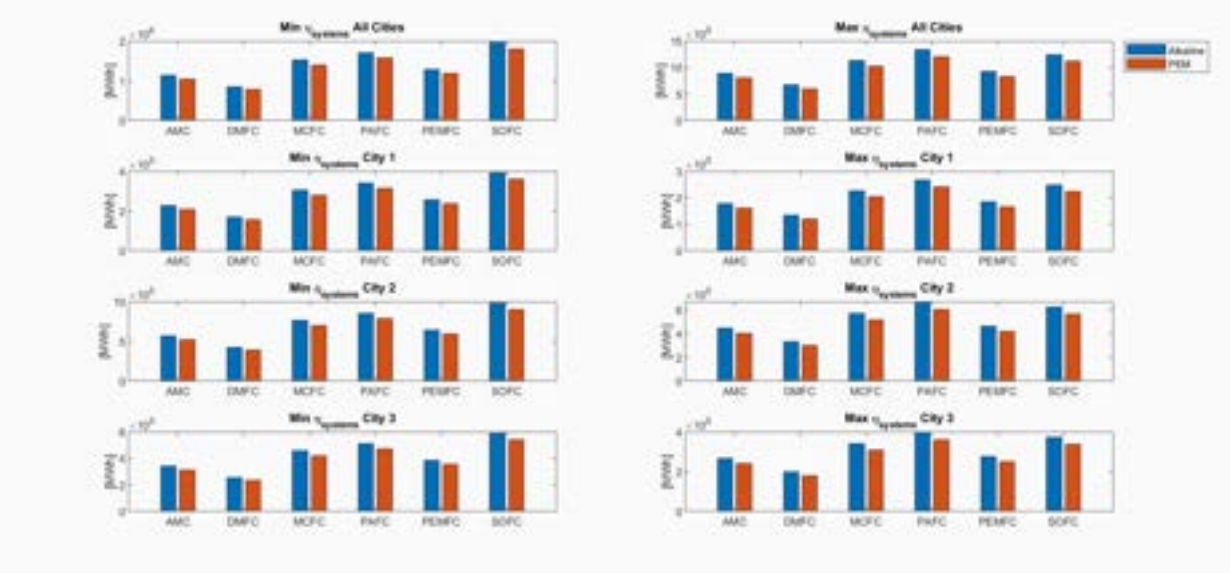

Figure 5: Visual representation of energy requirements from surplus considering minimum and maximum efficiencies of each system for all the cities and for each city taken singularly

After estimating the energy that has to be stored and the fraction of energy surplus that has to used to address the energy shortage, we define two scenarios. The first one is based on production of hydrogen in a dedicated offshore island and then sent to the coast to the storage sites. The second possibility is energy transmission through electrical cables, meaning that hydrogen storage and conversion is done offshore and the onshore storage is done with hydrogen produced locally.

3.2.2. Evaluated Scenarios: Hydrogen Island and local production

In this scenario it is considered that hydrogen is produced and transmitted to onshore storage sites through the usage of pipelines. In both this scenario and the following electrical one there is the presence of offshore storage site, used as first storage location. This storage site can be considered as a solution also to avoid the construction of onshore storage sites but the costs for the construction are higher offshore than onshore. Considering the presence of an offshore wind farm at a distance of 300 km from the coast in east direction, we evaluate: the production and storage of hydrogen offshore, the transmission of it through pipeline, and the conversion to electricity onshore through the usage of fuel cells. Previously (3.2.1.) the calculations of the energy shortages and the storage (energy and hydrogen) have been presented. Now we also include the energy required for the compression for storage, the compression for transmission and the volume of the necessary artificial salt caverns. The production of hydrogen is carried out in a designated artificial hydrogen island which should be placed at maximum 5 km from the wind farm. Moreover, its position has to be chosen considering aspects like the positioning of salt caverns and the pipeline design, as presented in Figure 2.

To evaluate the dimensions of the necessary salt caverns and, at the same time, the effect on hydrogen density and the geothermal gradient, we developed an iterative function. This permitted to calculate the dimensions (height and diameter), average temperature and average density starting from the the cavern roof depth, an initial estimate of the cavern bottom depth, storage pressure, mass of hydrogen to be stored, an equation of state for hydrogen density, and the height-diameter ratio of the cavern. The cavern roof depth and the pressure, considered to be the maximum pressure, have been taken from the set of values (cavern roof depth, maximum and minimum storage pressures) cited in [9]. The results for the first city, in terms of height and diameter of the caverns, are reported in Table 6.

In order to evaluate the amount of freshwater needed to build the salt cavern the construction process of the horizontal caverns HA-4 and HA-5 in Huai"an (China) has been taken as reference [6]. For these caverns the

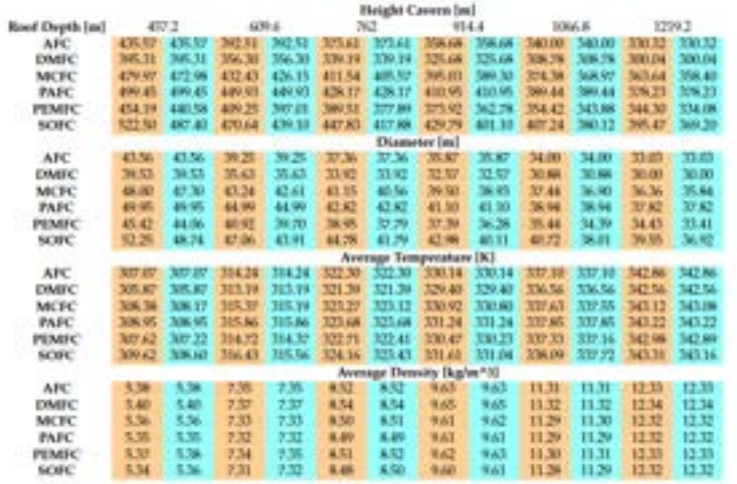

Figure 6: Results for city 1 in terms of Height and Diameter of caverns, average temperature and density of hydrogen; the orange colour refers to the minimum efficiency of FC technologies, the light blue refers to the maximum

characteristics are presented in the Table 4.

Table 4: HA-4 and HA-5 cavern and building process characteristics (Huai"an, China) [6]

Cavern	**HA-4**	**HA-5**
Volume Cavern [m^3]	52000	121000
Volume Freshwater Needed [m^3]	3329000	3690000
Volume Cavern/Volume Freshwater needed	64.02	30.50
Concentration Brine [kg_{salt}/m^3]	300	

From the volume ratio of cavern to freshwater needed for salt cavern construction, we calculated the volume of freshwater needed considering the minimum and the maximum values of this ratio and the minimum and maximum efficiencies of the FC technologies. The amount of freshwater needed in all cases (maximum and minimum efficiency for FC technologies, maximum and minimum volume ratio cavern - volume freshwater) is not negligible and has to be taken into account in terms of environmental impact and economic costs to treat and transport the salty brine after dissolving the subsurface salt. Lastly, it has been evaluated the pressure drops of the hydrogen pipelines necessary to cover the energy demand for each city. Based on a defined set of assumptions the pressure drops have been calculated and presented in Table 5. The values of the pressure

Table 5: Pressure drops in [*bar*] per each pipeline (column, first for city 1, second for city 2 and third for city 3), considering all the FC technologies (rows) with their minimum and maximum values of efficiencies

	Min η_{FC}			**Max** η_{FC}		
AFC	305.00	282.74	759.39	234.07	295.03	654.65
DMFC	375.93	442.55	903.41	361.74	381.08	890.32
MCFC	191.51	221.27	536.81	241.16	270.44	602.28
PAFC	156.04	245.86	549.90	156.04	233.57	445.16
PEMFC	255.35	282.74	680.83	198.60	295.03	615.37
SOFC	163.14	233.57	405.88	177.32	295.03	628.46

drops make necessary the presence of intermediate pumping stations to increase the pressure and guarantee the arrival of the hydrogen to the storage sites.
The second possible solution is the transmission of energy through the usage of electrical lines and having the production of hydrogen directly on the storage sites. In this scenario there is no hydrogen transmission through pipelines: hydrogen is produced on the hydrogen island and stored offshore in a dedicated site for the purpose of converting to electricity when the windmills are down. Hydrogen is also produced onshore with surplus of energy sent with electrical interconnection between the hydrogen island and the shore. The possible presence of offshore storage would permit to reduce the number of storage sites onshore and to increase the social acceptance of the hydrogen storage on the first place. As for the other scenario, the analysis has been carried out from the storage site while acknowledging that it is necessary to consider also the efficiency of electrical

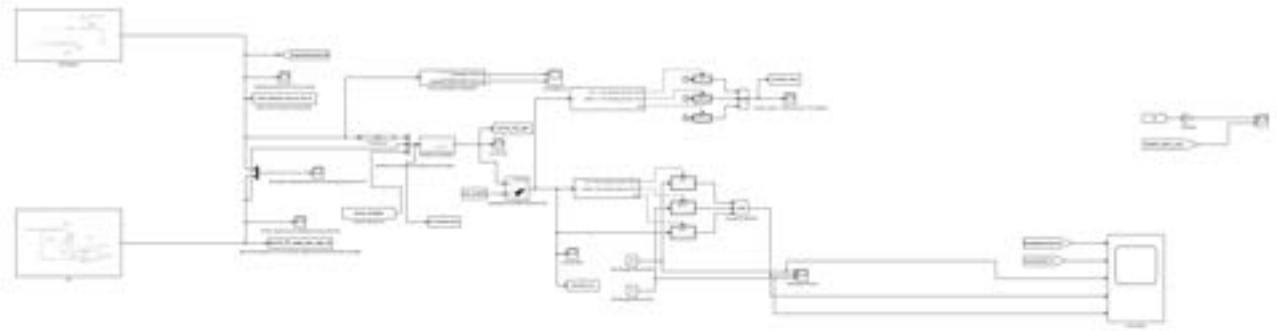

Figure 7: Simulink Dynamic Model

transmission from sites to cities.
The process for the calculation of the dimensions of the artificial caverns is the same as the previous scenario, the main difference is related to the addition of electrical components (with their efficiencies) between the hydrogen island and the onshore storage sites. The elements that have to be considered are inverters (DC-AC), transformers (AC-AC) and transmission lines (in DC or AC).

3.3. Dynamic Model

In section 3.1., the hydrogen storage requirements have been analyzed and calculated considering a static approach, serving two purposes: first, the overall shortage of energy caused by the mismatch of the wind production and the user demand curves. Secondly the percentage of the surplus needed to cover that shortage through the production and storage of hydrogen. The latter point has been carried out taking into account constant values of the efficiencies of the components of the system and ignoring the dynamic behaviour of the system. Here, we consider the functioning and the consequences of the behaviour of the system components over time, under a defined set of assumptions, that includes:

1. The system is considered to be isolated thus no interconnections with other countries or grids are considered.
2. We projected the increase of the wind power installed and the increase of user demand with an expected enhancement of 50% of the current demand and a nominal wind power installed equal to 5 times the currently installed power with respect to the data considered (2017-2019).
3. Dynamic behaviour for electrolyzers, fuel cells (start up and ramp up time) and compressors (time to reach predefined pressure specifications) are considered.
4. The model used for the description of the storage behaviour is 0-D (zero-dimensional or bulk model).

a Matlab script and a Simulink model have been developed to calculate the impact of inertia of system components and the constrained injected and extracted mass flow rates and fixed volumes of storage sites on the security of energy supply for a dynamic demand. We also use the script to estimate the required number of caverns for a balanced supply and demand of electricity in Denmark.

Figure 7 shows the Simulink model developed to solve this problem, implementing specific subsystems (with relative control systems) for fuel cells, electrolyzers and compressors necessary to manage the system and allowing it to be able to follow the demand and production trends (Figure 8). Here the electrolyzers system (with its control system) is briefly presented. For the fuel cell system the function principle is similar.

3.4. Electrolyzers system

Electrolyzers functioning (as molar flow rate of hydrogen produced [mol/s]) is related, following the Faraday's law (Equation 1), to the number of cells n_{cells}, to the current flowing through I_{Ez}, Faraday's parameter F, and Faraday's efficiency η_F (calculated with Equation 2). [10]

$$\dot{n_{H_2}} = \frac{n_c I_{Ez}}{2F}\eta_F \tag{1}$$

$$\eta_F = 96.5 \exp\left(\frac{0.09}{I_{Ez}} - \frac{75.5}{I_{Ez}^2}\right) \tag{2}$$

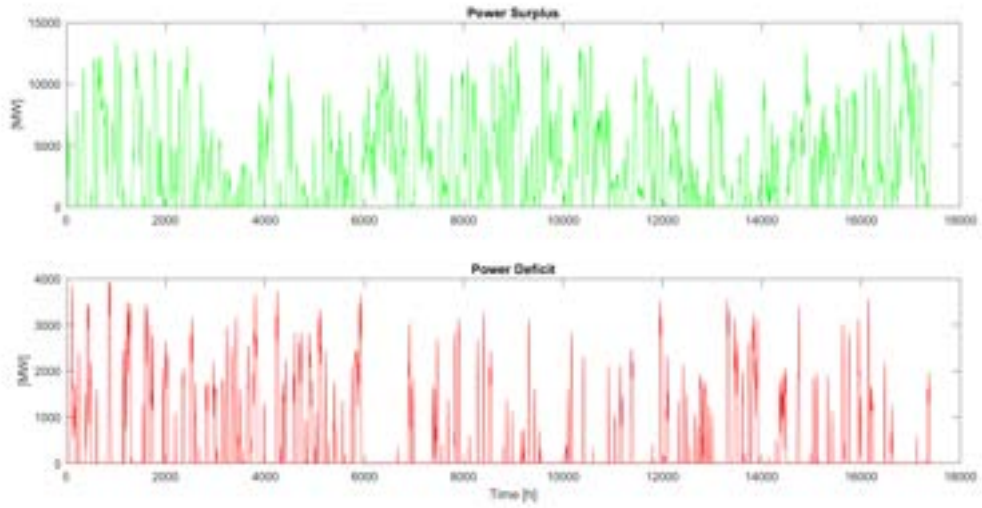

Figure 8: Power surplus and deficit of the system (expressed in [MW])

In the analysis, a simplified version of electrolizer efficiency is considered, that is independent of the above parameters and the outlet pressure. Instead, we consider the behaviour over time of the electrolyzers in terms of start-up time (supposing a hot start-up) and ramp-up time, which are respectively defined as the time interval between the electrical connection and the beginning of the hydrogen production and the time interval necessary to reach the nominal power output from the end of start-up process.
These two parameters have been considered as part of the main simulation and have been obtained from data of products available on the market, like the electrolyzer Plug EX-425D [2]. They have been fixed at these values (even though they have been modified to see their impact on the simulation):

- $\Delta t_{Start-Up} = 10s$
- $\Delta t_{Ramp-Up} = 30s$

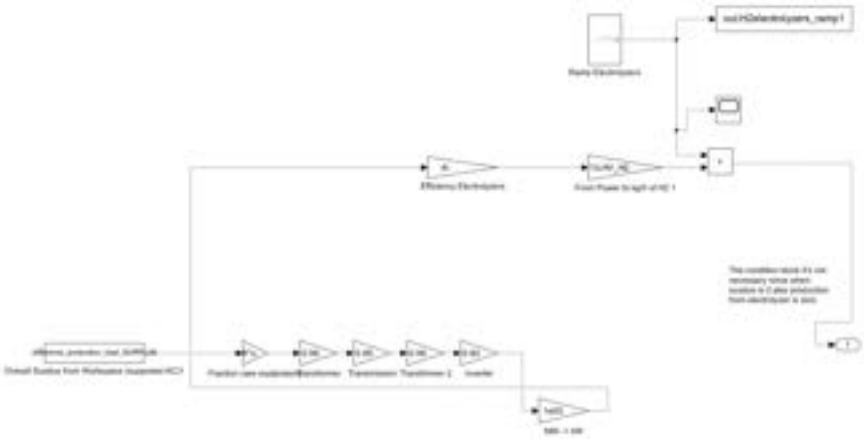

Figure 9: Simulink electrolyzer simplified model

These parameters have been added to Simulink as presented in Figure 9. It has been considered a constant value of efficiency and then converted the value of energy consumed by electrolyzers to the amount of hydrogen produced. Considering the start-up and ramp-up times, we obtain the produced hydrogen mass flow rate over time (Figure 10). This mass flow rate has been then used in the zero-dimensional storage model to evaluate the amount of hydrogen stored and withdrawn over time. It is important to highlight that not the entire overproduction is converted into hydrogen to reduce the number of electrolyzers required. For this purpose a value of 30% of the surplus production has been considered and also varied to evaluate the impact of this parameter on the system.

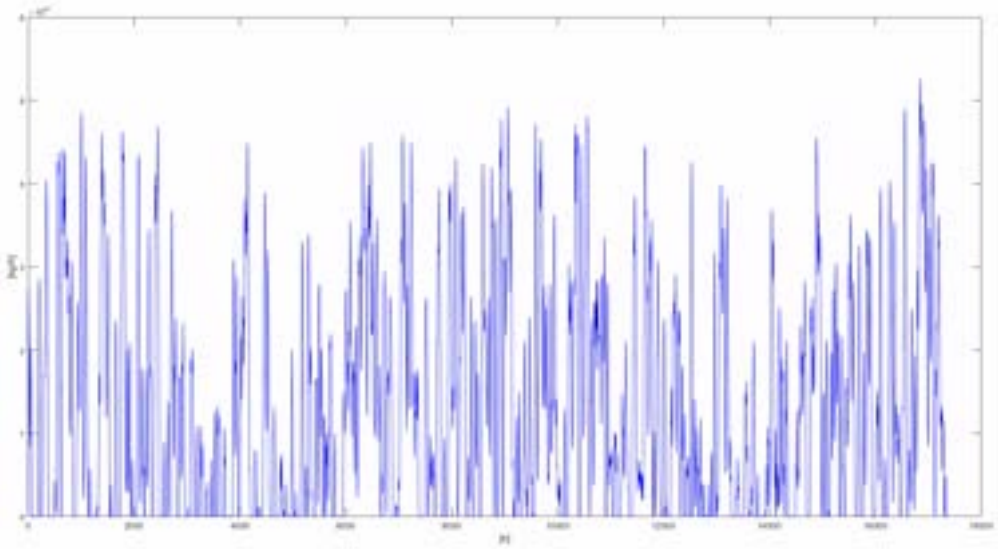

Figure 10: Electrolyzers hydrogen mass flow production rate (reference conditions)

3.5. Parameters of the simulation

The following parameters are the reference ones of the simulation :

- $fraction_{surplus}$ = 0.3 $\Rightarrow$ fraction of the wind surplus power that is used to power the electrolyzers;
- $percentage_{fillingstorage}$ = 0.8 $\Rightarrow$ initial percentage of storage filling;
- $T_{H_2} = 300K \Rightarrow$ fixed temperature for the analysis;
- $\Delta t_{Start-up,El} = 10s \Rightarrow$ start-up time for electrolyzers;
- $\Delta t_{Ramp-up,El} = 30s \Rightarrow$ ramp-up time for electrolyzers;
- $\Delta t_{Start-up,FC} = 10s \Rightarrow$ start-up time for FC;
- $\Delta t_{Ramp-up,FC} = 15min = 900s \Rightarrow$ ramp-up time for FC;
- $V_{simulation,firstattempt} = 6.49 \times 10^8 m^3 \Rightarrow$ first attempt value for simulation storage volume (placed equal to the volume of storage in first case of minimum efficiency in the static model multiplied by 10^3);
- $\Delta p_{\%,Max,FC} = 10\% \Rightarrow$ maximum percentage pressure drop admitted for storage-FC pipelines;
- $d_{pipe,FC} = 18cm = 0.18m \Rightarrow$ diameter extraction well and storage-FC pipeline connection (considered a typical value for natural gas underground storage wells diameter [7])
- $\Delta p_{\%,Max,El} = 5\% \Rightarrow$ maximum percentage pressure drop admitted for electrolyzers-storage pipelines;

the simulation has returned the results presented in Table 6:

Table 6: Simulation results with reference values of simulation parameters

	FC	Electrolyzers
λ	0.01	0.01
$v_{H_2}\,[m/s]$	59.5	49.3
Re_{H_2}	1.19×10^6	9.87×10^5
$\dot{m}_{H_2,SinglePipe}\,[kg/s]$	6.64	4.87
$\dot{m}_{H_2,SinglePipe}\,[kg/h]$	2.4×10^4	1.75×10^4
n_{wells}	18	3
$V_{Storage}[m^3]$	1×10^9	

These parameters have been iteratively modified to evaluate their impact on the simulation and possible solutions to the related issues.

4. Discussions of Results

4.1. Simplified Model

From the results of the simplified model we can clearly observe the impact of the chosen fuel cell - electrolyzers technologies on the required storage volume, even without considering the dynamic behaviour of unit operations. This choice directly affects, considering the range of efficiencies of the system, the amount of energy that has to be extracted (by electrolyzers) from the power surplus and the amount of energy that has to be actually stored in the form of hydrogen in the storage sites. This latter aspect is essential since it influences the dimensions of the underground artificial storage site in height and diameter, modifying the amount of freshwater (and, therefore, the environmental and economical impact) required for the construction process. These values can range, depending on roof depth, FC technology and cavern-freshwater volume ratio between $6.5 \times 10^6 - 7.2 \times 10^7 m^3$ for city 1, $1.6 \times 10^7 - 1.8 \times 10^8 m^3$ for city 2, and $9.7 \times 10^6 - 1.1 \times 10^8 m^3$ for city 3. These values are around 1% to 10% of annual Danish freshwater consumption.
Moreover, as it has been possible to highlight with the two scenarios, design choices in terms of storage placement and energy transmission can affect the cavern design and the system behaviour. System that can range from an offshore solution with main storage solution build under the seabed and electrical energy converted and transmitted from the hydrogen island to hydrogen production carried out in this dedicated artificial island, transmitted to land via pipelines and stored locally underground ready to be employed by the fuel cells system.

In the simplified model we ignored the inertia of the components of the system, e.g., fuel cells, electrolyzers, and compressors. Using the dynamic model, through running simulations for a 2 years time frame (with 1 hour resolution), we analysed the impact of the dynamic behaviour of each unit on the overall energy supply and demand. All these components have been implemented in a Simulink model, each one considering their fundamental working parameters and control systems. For the electrolyzers we included the start-up and ramp-up time intervals in the model and its blocks. Similarly it has been done for the fuel cells, applying the same parameters and blocks in the model. Concerning the compressor, based on its pressure-time dependency curve, a simplified control system has been implemented. Lastly, for the overall system, different control systems has been added. This Simulink model has been then exploited, as other functions that have been developed, inside a Matlab script with the aim of evaluating the storage volume, the number of electrolyzers and fuel cells wells and the mass flow rates through them respecting the pressure drop constraints and other model assumptions. This script has been iteratively modified changing the value of the main parameters of the system elements to visualize their impact on the overall system.

4.2. Dynamic Model

From the results of the dynamic model it is possible to analyse the sensitivity of the supply/demand system to the parameters that define the dynamic behaviour of its individual units. The first noticeable result is the storage volume difference between the static simplified model and the dynamic one: in the first case, the values obtained in the simulation are in the order of $10^6 m^3$, which can be covered by a few small to average-sized caverns (depending on the chosen FC-electrolyzers technologies considered and the characteristics of the cavern such as the roof depth). However, for the dynamic model we obtained required storage volumes in the order of $10^9 m^3$, e.g., around 1000 relatively large salt caverns. This 3 orders of magnitude difference between the two cases are related to physical constraints (mass flow rates of the pipelines and the following of the production and consumption curves), cavern pressure limits (i.e., $2.23 \times 10^6 - 7.09 \times 10^6 Pa$) and the start up times of the elements of the system (that do not allow the perfect following neither the production nor the consumption curves).
Moreover, choosing a fuel cell or electrolyzer technology with a high start-up time causes a system failure in following respectively the demand (in terms of shortage) and the production surplus curves (results not shown). This issue can be solved by developing or choosing components with lower start-up time or with predictive approaches to the system control, through which the components are activated earlier in time considering the predictions of production and demand. Components with high ramp-up times, instead, do not allow to fully exploit the potential of the power surplus (electrolyzers) or be able to supply the power needed by user in time: this problem may be solved with different approaches such as developing faster technologies, installing a higher number of these components to counterbalance the effect (but with additional investment costs and overdimensioning the system) or adding fast technologies (such as electrochemical storage) in parallel to mitigate this issue.
We also considered the fraction of surplus electricity to be converted into hydrogen and the initial storage filling percentage. The first aspect is important since considering higher fractions allows to increase the production of hydrogen thus being a possible mitigating solution for electrolyzers with high start-up and ramp-up time intervals. Higher fraction though results in higher number of components, higher mass flow rates and therefore an increase of the size of the system with consequent increase of complexity and costs. Moreover, it does not allow the electricity network to be integrated in a larger European network by exporting the surplus to other

countries or regions with a high demand. Lastly, the initial storage filling percentage, also known as the cussion gas, is significant in the starting of the system since low initial level do not allow to have a sufficient buffer to follow the user demand; for this reason it is necessary to consider the initial filling as part of the installation procedure.

5. Conclusions

The large-scale storage of hydrogen in salt caverns, although a mature technology and relatively safe to implement, presents some important issues that have to be resolved. Firstly, the volume necessary to support even a simple 3-cities system is extremely high; it is challenging to find energy and water resources for the construction of around 1000 caverns and to find environmentally friendly and less energy-intensive solution to clean up and dispose off the construction and maintenance brine. Secondly, a large volume of cushion gas is required to start up the caverns such that it can reach a minimum required pressure for producing hydrogen from the caverns. This requires a large amount of surplus energy that might not be available. Thirdly, the high start up time of the fuel cells makes the use of hydrogen as the only grid balancing solution almost impossible. It is therefore necessary to address the immediate shortages of electricity in the network by other solutions, e.g., the aforementioned parallel electrochemical battery systems, or use reliable predictive models to deal with the not perfect following of the surplus and shortage curve by the components of the system. Finally, we would like to encourage the researchers in the field of subsurface hydrogen storage to dedicate more time and resources to investigating the production rate of hydrogen from the storage sites such as salt caverns, aquifers, and depleted reservoirs. The safe storage, although a necessary condition, is not sufficient to integrate the subsurface hydrogen storage in the energy supply and demand.

References

[1] North sea: General introduction to the north sea and the north sea region. the european maritime spatial planning platform. https://web.archive.org/web/20221018095906/https://maritime-spatial-planning.ec.europa.eu/sea-basins/north-sea-0. last visited: 18/10/2022.

[2] Plug EX-425d electrolyzer datasheet (english), https://tinyurl.com/2cxkf9bh. last visited: 01/12/2022.

[3] K. Hall. 4.14 - future perspective on hydrogen and fuel cells. In Ali Sayigh, editor, *Comprehensive Renewable Energy*, pages 351–360. Elsevier.

[4] Fayaz Hussain, M. Zillur Rahman, Ashvini Nair Sivasengaran, and M. Hasanuzzaman. Chapter 6 - energy storage technologies. In MD. Hasanuzzaman and Nasrudin Abd Rahim, editors, *Energy for Sustainable Development*, pages 125–165. Academic Press.

[5] Abraham Alem Kebede, Theodoros Kalogiannis, Joeri Van Mierlo, and Maitane Berecibar. A comprehensive review of stationary energy storage devices for large scale renewable energy sources grid integration. 159:112213.

[6] Jinlong Li, Chunhe Yang, Xilin Shi, Wenjie Xu, Yinping Li, and Jaak J.K. Daemen. Construction modeling and shape prediction of horizontal salt caverns for gas/oil storage in bedded salt. 190:107058.

[7] Wenjing Li, Xiuxiu Miao, Jianfu Wang, and Xiaozhao Li. Study on thermodynamic behaviour of natural gas and thermo-mechanical response of salt caverns for underground gas storage. 262:125601.

[8] Xing Luo, Jihong Wang, Mark Dooner, and Jonathan Clarke. Overview of current development in electrical energy storage technologies and the application potential in power system operation. 137:511–536.

[9] D. D. Papadias and R. K. Ahluwalia. Bulk storage of hydrogen. 46(70):34527–34541.

[10] Raúl Sarrias-Mena, Luis M. Fernández-Ramírez, Carlos Andrés García-Vázquez, and Francisco Jurado. Electrolyzer models for hydrogen production from wind energy systems. 40(7):2927–2938.

[11] Y. Tian and C. Y. Zhao. A review of solar collectors and thermal energy storage in solar thermal applications. 104:538–553.

[12] DEME RUG TNO, NEC. 8a.-FINAL-NSE3_d3.8-final-report-on-the-techno-economic-environmental-and-legal-assessment-of-offshore-energy-islands.pdf.

[13] Jose M. Yusta and Guillermo Matute. Techno-economic analysis of hydrogen electrolysis systems. In *Comprehensive Renewable Energy*, pages 505–532. Elsevier.

PROCEEDINGS OF ECOS 2023 - THE 36TH INTERNATIONAL CONFERENCE ON
EFFICIENCY, **C**OST, **O**PTIMIZATION, **S**IMULATION AND ENVIRONMENTAL IMPACT OF ENERGY SYSTEMS
25-30 JUNE 2023, LAS PALMAS DE GRAN CANARIA, SPAIN

Potential evaluation of Carnot battery integrating waste heat recovery in industry

Olivier Thomé [a], Olivier Dumont [b] and Vincent Lemort [c]

[a] *Thermodynamics Laboratory, University of Liège, Belgium, o.thome@uliege.be, CA*
[b] *Thermodynamics Laboratory, University of Liège, Belgium, olivier.dumont@uliege.be*
[c] *Thermodynamics Laboratory, University of Liège, Belgium, vincent.lemort@uliege.be*

Abstract:
One of the keys to the current energy and ecological transition is the development of electrical energy storage. This demand has motivated the development of alternative technologies that overcome some of the shortcomings of the storage systems used until now. Among these, Carnot battery has experienced a rapid development in the last decade. Its principle is to store electrical energy in the form of heat and restore it with a heat engine. This technology has several advantages: a long life span, the possibility to increase easily its storage capacity, and the use of small environmental footprint materials. Current research tends to show the lack of competitiveness of classical Carnot batteries architectures compared to other technologies due to their relatively low roundtrip electric efficiency. It is therefore necessary to investigate the integration of heat streams in order to increase their attractiveness. A large part of the industrial energy consumption is used for thermal purpose. It is estimated that a large part of this energy is then lost as waste heat. The aim of this paper is to provide economic key performance indicators concerning the potential of a Carnot battery integrating waste heat recovery in a given industry. The key performance indicators provided are based on the temperature level of the waste heat, the energy rates consumed and dissipated by the industry, the type of primary energy used and the electricity pricing. This paper shows that electricity pricing is the key to this technology development. High price variability and negative purchase prices are factors leading to a potentially interesting profitability of this system. The primary energy ratio is the second most important parameter influencing the results. As an illustrative example: an industry with a recoverable waste heat at 100 °C, a gas consumption three times higher than the electricity consumption, and a ratio of the minimum (positive) purchase price of electricity to the maximum sale price equal to 50% can expect a maximum reduction in its electricity bill of 25%. This maximum reduction rises to 50% if the the gas consumption is seven times higher than electricity consumption or if the electricity price ratio is 27%.

Keywords:
Waste Heat Recovery, Carnot Battery, Key Performance Indicator, Industry, Mapping.

1. Introduction

1.1. Context

The main challenge to massively develop renewable energy is the electrical storage. Among the different possible technologies, the Carnot Battery (CB) is more and more developed. This concept uses a Heat Pump (HP) to convert excess renewable electricity into thermal energy . The thermal energy is stored until there is a peak of electrical consumption, a Heat Engine (HE) can re-convert this thermal energy into electricity. In its stand-alone layout, this technology presents a low roundtrip efficiency. However, its potential to integrate heat fluxes makes it profitable in various cases (Thermally Integrated Carnot Battery). In the most common configuration, the heat pump can work with a low temperature difference between the waste heat temperature and the thermal energy storage temperature. This leads to high Coefficient Of Performance (COP) and therefore high roundtrip efficiencies [1, 2]. Waste heat represent a huge waste, especially in the industry sector. 42% of the waste heat is lost at temperatures below 100 °C and 20% between 100 °C and 299 °C [3]. The integration of Carnot batteries in the industry is promising since it makes an efficient use of waste heat and it allows to store electricity (increase of renewable energy self-consumption).

1.2. State of the art

Few papers discuss the potential of Carnot batteries based on mappings. Some papers refer to specific case studies and are listed in [4]. The first attempt to characterize the performance of such a system in a wide range of operating conditions is performed in [5] through a constant efficiency model. In this paper, the roundtrip efficiency of a Thermally Integrated Carnot Battery is plotted for different waste heat temperatures and ambient temperatures. It allows to identify which cases are interesting (high waste heat temperature, low

glide of the sensible storage and low ambient temperatures). Also, it was shown that the efficiency is improved in zones where the compactness (and the use of the waste heat) of the system is low. This conclusion has been discussed in several papers [1, 4, 6]. [4] proposed an enlarged mapping with a larger range of working temperatures. A zone where the three Key Performance Indicators (waste heat use, roundtrip efficiency and compactness) are not competing has been found. To the best authors' knowledge, no literature focus on the waste heat constraints in the industrial sector which can significantly affect the Carnot battery potential.

1.3. Aim of this paper

The main question that an industry could ask about the installation of a Carnot battery to valorize its waste heat is the profitability. A precise calculation of the benefit can not be obtained without a detailed study of the case. The aim of this paper is to give the absolute maximum values that could be reached in terms of benefit of such a system for a given industry. The Key Performance Indicators (KPIs) provided are determined according to global parameters allowing to easily characterize an industry (primary energy ratio, electricity pricing and waste heat temperature mainly) without an in-depth study. The results provided are voluntarily very optimistic so that a mismatch between the industry's expectations and these results indicates a clear incompatibility. In this case, the installation of a Carnot battery integrating waste heat recovery is not justified and this possibility can be dismissed without further study. The case of favorable results for the industry studied will automatically lead to a further study of the solution integrating the time constraints that such a system implies to determine the real benefit that can be brought. The compatibility of the industry's expectations with the results of this study is therefore a necessary but not sufficient condition for the profitability of the system.

2. Methodology

2.1. Assumptions

2.1.1. Conservatism principle

Since the aim of this paper is to provide the necessary conditions for the further study of the potential integration of the system, it is important not to exclude any case. To this end, all the assumptions made in this study are deliberately very optimistic. In particular, the cycles studied as well as the exchangers are considered as perfect. Since this study ignores the temporality for the purpose of convenience, the coordination of the waste production with the electricity costs is considered ideal in order to favor advantageous results. The limitations in terms of electrical power exchanged with the grid is largely overestimated. No limitation are put on the thermal storage volume. Also, the investment cost of the system is neglected. This is a very conservative assumption since this cost is directly linked to the nominal power of the system and its storage volume. On the other hand, the evaluation of the benefits in terms of cost reduction of the electrical substation is not considered. In view of the previous hypothesis, it is considered that neglecting this element will not put in default the conservatism required in this study.

2.1.2. Restriction on industry studies

Since the problem is treated ignoring temporal constraints and for the clarity of the methodology, some limitations must be set on the industries studied. The studied industry is taken as a whole and a single CB is matched as appropriate as possible. This CB has only one storage whose nominal temperature is fixed and greater than the maximum waste heat temperature considered. This consideration implies that an additional cold storage is not considered. It is assumed for each process (or sub-process) a nominal waste temperature invariable over time. The ambient temperature is fixed at $20^\circ C$. The waste heat is entirely dedicated to the CB. No district heating or recovery of this heat to reintegrate it into the process is considered. The waste heat not used by the CB is lost. The waste heat rejected by the heat engine of the CB is also lost.

The availability of Renewable Energy Sources (RES) internal to the industry, whose production is not always self-consumed, is a special case that requires a specific methodology. This case is treated in Section 3.6..

2.1.3. Limit values of the studied system

Based on the literature and in order not to exclude any case according to the principle of conservatism, the following values are used as limit values of the studied system:

- The unavoidable irreversibilities of a real system lead to the consideration of an efficiency g with respect to the ideal cycles. This value is often estimated [5] between 0.4 and 0.5 so in this study, $g = 0.5$.
- According to [7], the waste heat of the industry not directly recovered on-site is below 200 °C excepted for the iron and steel industry (200-400 °C, 700-900 °C) and the glass industry (500-600 °C). Waste heat temperature $T_w \in [T_{amb}, 200]^\circ C$ is considered for this study. This choice is justified in Section 3.5..
- The highest temperature cycle (Brayton) that can be applied to a CB is in the order of 1200 °C [1, 2]. This value (used in (22)) is considered as the limit reached in the system.

2.2. Carnot battery description

The purpose of this section is to describe the Carnot battery as it is considered in the following development. The goal is to define the most generic architecture in order not to exclude any case and to make assumptions that allow to respect the conservatism principle announced in the previous section. Two approaches are considered in the description of the cycles used: a machine working with a Carnot cycle and one working with a Lorenz cycle. This allows to cover entirely the existing and future Carnot batteries.

2.2.1. Generic architecture

Figure 1 represents the architecture of a CB as general as possible when it integrates waste heat recovery. An amount of used waste heat $Q_{w,used}$ extracted from the available waste heat Q_w such that

$$Q_{w,used} = Q_w \frac{\Delta_{T_w}}{T_{w,in} - T_{amb}} \tag{1}$$

corresponds to a quantity of heat stored according to the COP of the heat pump considered:

$$Q_{sto} = Q_{w,used} \frac{1}{1 - \frac{1}{COP\ g}} \tag{2}$$

The electrical energy W_{HP} stored by the CB is determined by

$$W_{HP} = Q_{sto} - Q_{w,used} \tag{3}$$

The stratification of the storage and its thermal insulation are considered perfect so that the amount of thermal energy recovered from this storage is equal to the stored amount Q_{sto}. This thermal energy is used to feed the heat engine and to extract the electrical energy W_{HE} according to

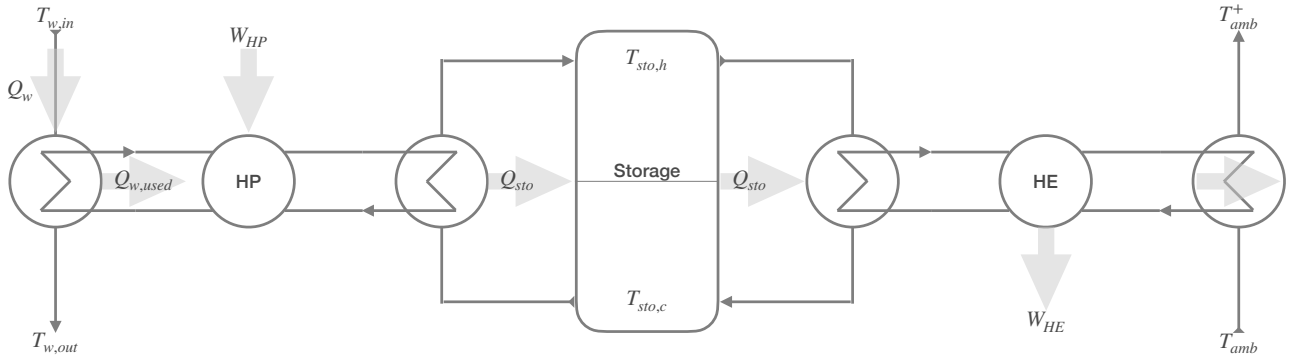

Figure 1: Generic architecture of a Carnot battery integrating waste het recovery

2.2.2. CB with Carnot cycles

Cycles based on Carnot HP and HE are mainly used in CBs. These ideal cycles are represented by their T-S diagram in Fig.2 and Fig.3 respectively. The performance of these cycles is determined by the system temperature levels also shown in the diagrams. For the HP, the COP is expressed by

$$COP_{Carnot} = \frac{T_{sto,h}}{T_{sto,h} - T_{w,out}} = \frac{T_{w,in} + lift_{HP}}{lift_{HP} + \Delta_{T_w}} \tag{5}$$

The COP can be maximized by minimizing Δ_{T_w}. However, according to (1), this will decrease $Q_{w,used}$ and thus the maximum stored energy. This value is therefore kept as a parameter in the study. Concerning the HE, its performance η is expressed by

$$\eta_{Carnot} = 1 - \frac{T^+_{amb}}{T_{sto,c}} = 1 - \frac{T^+_{amb}}{T_{w,in} + lift_{HP} - \Delta_{T_{sto}}} \tag{6}$$

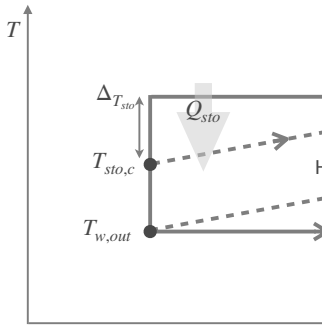

Figure 2: Ideal HP based by the characterizing temp sented in T-S diagram

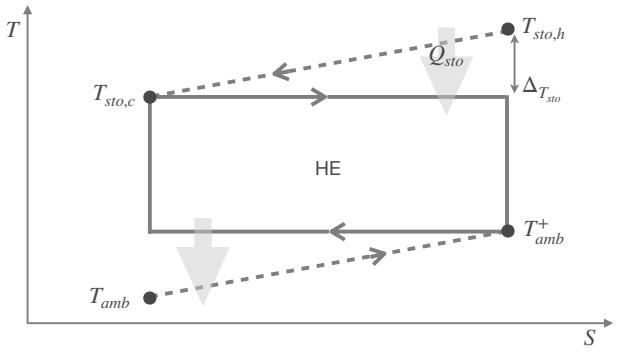

Figure 3: Ideal HE based on Carnot cycle limited by the characterizing temperatures of the CB represented in T-S diagram

2.2.3. CB with Lorenz cycles

Lorenz cycles [8] are based on heat exchanger at variable temperatures when Carnot cycles are isothermal. The implementation of these cycles requires zeotropic working fluids, super or trans-critical cycles, or a serial assembly of multiple HP and EH. This type of cycle is less implemented in CB than the Carnot cycle. However, with identical temperature glides, it theoretically gives better performance and several projects are currently developing this type of system. In order to remain conservative and to cover a maximum of possibilities, these two types of cycles will be used to obtain results according to the implementation of a CB working with Carnot or Lorenz cycles. Figures 4 and 5 represent the two Lorenz ideal cycles as well as the system temperatures in T-S diagrams. The COP and η are expressed by

$$COP_{Lorenz} = \frac{T_{sto,h} + T_{sto,c}}{T_{sto,h} + T_{sto,c} - T_{w,in} - T_{w,out}} = \frac{2T_{w,in} + 2lift_{HP} - \Delta_{T_{sto}}}{2lift_{HP} + \Delta_{T_w} - \Delta_{T_{sto}}} \tag{7}$$

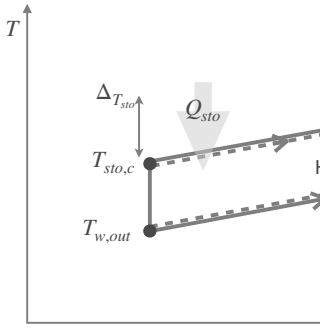

Figure 4: Ideal HP basec by the characterizing temp sented in T-S diagram

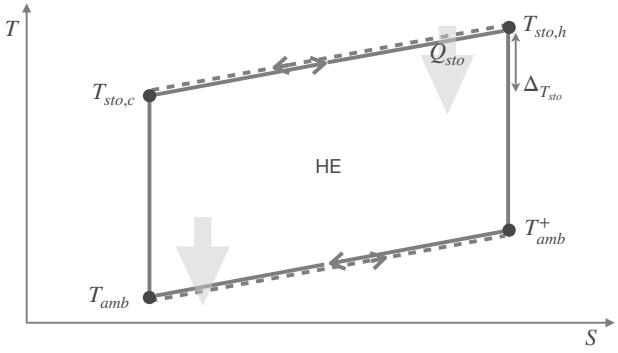

Figure 5: Ideal HE based on Lorenz cycle limited by the characterizing temperatures of the CB represented in T-S diagram

2.3. Industry description

The purpose of this section is to provide a generic description of energy flows in an industry so that it can be adapted to any industry. The characteristics of the industry allowing further development will also be identified.

2.3.1. Characteristic period

Temporal considerations of energy flows in industry would involve complex modeling to obtain results. Since the purpose of this study is to provide a first approach, these considerations are ignored. The different energy flows are integrated over a characteristic period $\Delta t(0 \rightarrow T_f)$.

This period is to be chosen on a case by case basis. Ideally, it should cover a duty cycle representative of the industry. This period also corresponds to a cycle on the storage, so it would seem judicious that it is of the

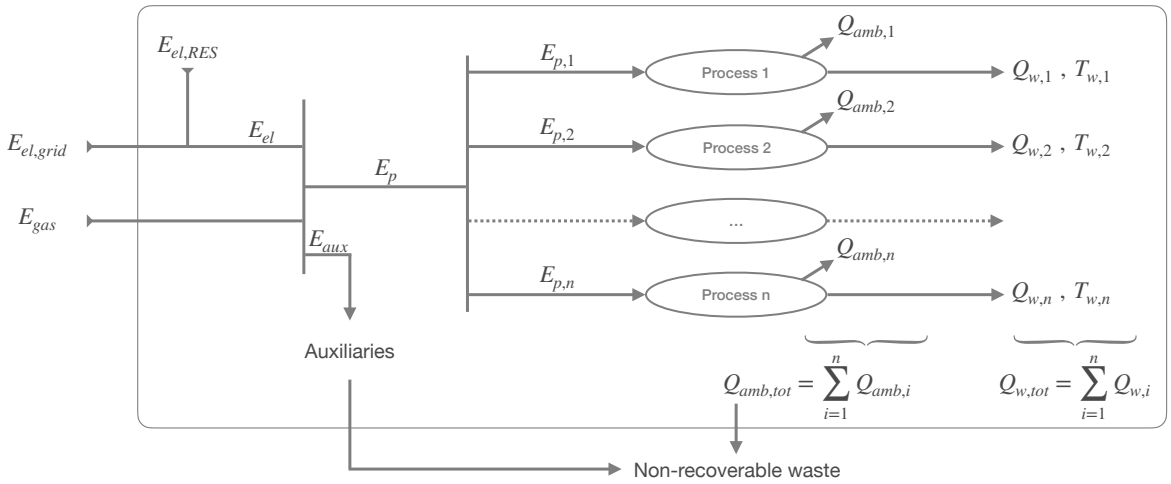

Figure 6: Generic representation of energy fluxes distribution in an industry integrated on the characteristic period Δt

2.3.3. Distribution of primary energy

A first useful characteristic of the industry is its primary energy allocation E_{gas}/E_{el}. In the case of fully self-consumed RES, E_{el} should be taken as the sum of RES electricity production and imported electricity $E_{el,grid}$ (Fig.6).

2.3.4. Waste heat temperatures

The processes are ranked from 1 to i such that $T_{w,1} > T_{w,2} > ... > T_{w,n}$. According to [7], this ranks in most cases the amount of waste heat such that $Q_{w,1} < Q_{w,2} < ... < Q_{w,n}$ but it is not a necessary condition.

2.3.5. Electricity pricing

Considering the variable cost C of electricity over the period Δt, different electricity pricing are identified:

- (A) $C_{buy} = C_{sell} = C \in \mathbb{R}_0^+ \ , \ \forall t \ \in [0, T_f]$
- (B) $C_{buy} = C_{sell} = C \in \mathbb{R}^+ \ , \ \forall t \ \in [0, T_f]$
- (C) $C_{buy} \in \mathbb{R}_0^+ \ , \ \forall t \ ; \ C_{sell} \in \mathbb{R}^+ \ , \ \forall t \ ; \ with \ C_{buy} \geq C_{sell} \ , \ \forall t \ \in [0, T_f]$
- (D) $C_{buy} \in \mathbb{R} \ , \ \forall t \ ; \ C_{sell} \in \mathbb{R}^+ \ , \ \forall t \ ; \ with \ C_{buy} < C_{sell} \ iff \ C_{sell} = 0 \ , \ \forall t \ \in [0, T_f]$

By these definitions: $(A) \subseteq (B) \subseteq (D)$ and $(A) \subseteq (C) \subseteq (D)$. An industry included in several electricity pricing as defined will be characterized by the most restrictive.

An electricity cost ratio C_{min}/C_{max} used as a parameter in the study is determined for each electricity pricing with for (A) and (B):

$$C_{min} = \min_{\forall t}(C) \text{ and } C_{max} = \max_{\forall t}(C) \tag{9}$$

By definition, the ratio is strictly greater than zero for (A) and equal to zero for (B). For (C) and (D), the ratio is determined with:

$$C_{min} = \min_{\forall t}(C_{buy}) \text{ and } C_{max} = \max_{\forall t}(C_{sell}) \tag{10}$$

By definition, the ratio is strictly greater than zero for (C) and less or equal to zero for (D).

This definition of the electricity cost ratio for (C) and (D) cannot be applied in the special case $\max_{\forall t}(C_{sell}) = 0$. It is therefore necessary to defined two sub-categories ((C*) and (D*)) of electricity pricing for which a special treatment is applied with a definition of the electricity cost ratio given by

$$\frac{C_{min}}{C_{max}} = \frac{\min_{\forall t}(C_{buy})}{\max_{\forall t}(C_{buy})} \tag{11}$$

Using strictly the limits of the electricity cost for determined C_{min} and C_{max} ensures conservatism. A more moderate choice of these values can lead to more restrictive results but closer to reality. These values are used to define the price for the entire selling and buying period. If the limits used represent only a very short period compared to Δt, the results will be so optimistic that they will no longer be useful. A good practice rule would be to choose a limit if it represents at least 5% of the period Δt.

2.4. Recoverable waste heat

The quantity of waste heat Q_w available for the HP is an important parameter to characterize the industry. With the usability factor u representing the proportion of primary energy converting in available waste heat, it is defined by

$$Q_w = u(E_{gas} + E_{el}) \tag{12}$$

In an ideal configuration, $u = 1$. This will never be the case in reality. u is bounded by a value $u_{s,max}$, with the subscript s refers to the selected $T_{w,s}$. It is defined by

$$u_{s,max} = (1 - \frac{E_{aux}}{E_{gas} + E_{el}}) \sum_{i=1}^{s} (\frac{E_{p,i}}{E_p}(1 - \frac{Q_{amb,i}}{E_{p,i}})) \tag{13}$$

The purpose of this section is to describe in more detail the expression of $u_{s,max}$.

2.4.1. Auxiliary consumptions

In the frequent case where all the incoming energy of the industry is not dedicated to the processes on which waste recovery is possible, it is necessary to deduct these auxiliary consumptions from the primary energy transformed into usable waste heat. This consumption is included in the factor $(1 - \frac{E_{aux}}{E_{gas}+E_{el}})$.

2.4.2. $T_{w,s}$ selection

Since it is assumed that there is only one CB and one storage, the temperature of the waste heat exploited $T_{w,s}$ must be unique and chosen between the $T_{w,i}$ temperatures. In the case $T_{w,s} > T_{w,n}$, part of the processes are excluded from the waste heat recovery system. This reduces the amount of energy exploitable by the factor $(\sum_{i=1}^{s} \frac{E_{p,i}}{E_p})$.

However, the choice of $T_{w,s}$ higher than $T_{w,n}$ has the advantage of increasing the performance of the system. At the time of the exploitation of the results, it is necessary to test various couples $[T_{w,s}; u_{s,max}]$ in order to select the optimum for the considered industry. The selected $T_{w,s}$ corresponds to the temperature $T_{w,in}$ of Section 2.2..

2.4.3. Processes ambient losses

In any process, not all of the primary energy $E_{p,i}$ used can be converted into usable waste heat. Unavoidable losses $Q_{amb,i}$ are rejected throughout the process ($Q_{w,i} = E_{p,i} - Q_{amb,i}$), which completes the previously developed factor:

$$\sum_{i=1}^{s} (\frac{E_{p,i}}{E_p}(1 - \frac{Q_{amb,i}}{E_{p,i}})) \tag{14}$$

In the case where $Q_{amb,i}$ is too difficult to evaluate for each process, a value $Q_{amb,tot}$ can be estimated for all the processes so that this factor is replaced by

$$(1 - \frac{Q_{amb,tot}}{E_p}) \sum_{i=1}^{s} \frac{E_{p,i}}{E_p} \tag{15}$$

2.4.4. Direct measurement of the available waste heat

The determination of the above factors can be complex. In some cases, it is easier to measure the quantity of waste heat directly after the processes. In this case, (13) becomes

$$u_{s,max} = \frac{\sum_{i=1}^{s} m_i c_{p,i} (T_{w,i} - T_{amb})}{E_{gas} + E_{el}} \tag{16}$$

with m_i the mass flow rate of the waste heat constituent for the process i integrated over Δt and the corresponding specific heat $c_{p,i}$. It is necessary to note that if waste heat constituents can condense in the considered temperatures, it is necessary to take into account the latent energy.

2.5. Calculation of the economic gains generated by the CB

Based on the assumptions, equations and values previously introduced, it is possible to calculate the maximum economic gain brought by the installation of a CB integrating waste heat recovery. The evaluation of this gain is directly linked to the considered electricity pricing and will be evaluated differently for each case. Since the aim is to determine the maximum profitability of the system, the waste heat will always be considered as available when the prices are the most favorable.

The purpose of these gain expressions is to highlight the terms characterizing an industry: C_{min}/C_{max}, u and E_{gas}/E_{el}. These latter two terms are expressed on the basis of (1-4,12) by W_{HP}/E_{el} and W_{HE}/E_{el} such as

$$\frac{W_{HP}}{E_{el}} = u(\frac{E_{gas}}{E_{el}} + 1) \frac{\Delta_{T_w}}{T_w - T_{amb}} \frac{1}{COPg - 1} \tag{17}$$

$$\frac{W_{HE}}{E_{el}} = u(\frac{E_{gas}}{E_{el}} + 1) \frac{\Delta_{T_w}}{T_w - T_{amb}} \frac{COP\eta g^2}{COPg - 1} \tag{18}$$

2.5.1. (A) and (C) electricity pricing

For electricity pricing (A) and (C), the maximum gain can be defined as the reduction in the electricity bill. The most favorable conditions are a purchase (W_{HP}) of electricity at C_{min} and a resale (W_{HE}) of electricity at C_{max}. To ensure maximum gain, the electricity consumed is hypothetically purchased at C_{min}.

$$gain_{(A,C)} = \frac{W_{HE} C_{max} - W_{HP} C_{min}}{E_{el} C_{min}} = \frac{W_{HE}}{E_{el}} (\frac{C_{min}}{C_{max}})^{-1} - \frac{W_{HP}}{E_{el}} \tag{19}$$

2.5.2. (B) and (D) electricity pricing

For electricity pricing (B) and (D), the previous gain formulation cannot be used since C_{min} is less than or equal to zero. The maximum payoff must therefore be evaluated as the maximum net profit generated by the installation of the system. Stored electricity is always bought and sold at the most favorable prices. The gain must be normalized in order to express a usable value in the results.

$$gain_{(B,D)} = W_{HE} C_{max} - W_{HP} C_{min} \quad \rightarrow \quad \frac{gain_{(B,D)}}{E_{el} C_{max}} = \frac{W_{HE}}{E_{el}} - \frac{W_{HP}}{E_{el}} \frac{C_{min}}{C_{max}} \tag{20}$$

2.5.3. (C*) and (D*) electricity pricing

For electricity pricing (C*) and (D*), it is never interesting to sell electricity back to the grid. Electricity restitution (W_{HE}) must only be used to cover the electricity consumption of the industry E_{el}. In the formula, the cost of electricity applied to W_{HE} must therefore be the same as applied to E_{el}. In order to express the maximum gain, C_{max} is used. This formula expresses the gain as the maximum reduction of the electricity bill.

$$gain_{(C^*,D^*)} = \frac{W_{HE} C_{max} - W_{HP} C_{min}}{E_{el} C_{max}} = \frac{W_{HE}}{E_{el}} - \frac{W_{HP}}{E_{el}} \frac{C_{min}}{C_{max}} \quad \text{with } W_{HE} \leq E_{el} \tag{21}$$

2.5.4. Choice of system parameters

In accordance with the principle of conservatism, for each point $[T_w, E_{gas}/E_{el}, C_{min}/C_{max}]$ the choice of the system parameters $(\Delta_{T_w}, \Delta_{T_{sto}}, lift_{HP})$ as described in the Section 2.2.1. is determined by the following optimization problem:

$$\begin{aligned} & \max(gain) \\ s.t. \quad & 0 \leq \tfrac{W_{HP}}{E_{el}} \leq 1 \quad , 0 \leq \Delta_{T_w} \leq T_w - T_{amb} \\ & 0 \leq \tfrac{W_{HE}}{E_{el}} \leq 2 \quad , 0 < \Delta_{T_{sto}} \leq T_{sto,h} - T_{amb} \\ & 0 \leq \tfrac{Q_{sto}}{E_{el}} \quad , 0 < lift_{HP} \leq 1473K - T_w \; [K] \end{aligned} \tag{22}$$

It is assumed that the consumption of electricity by the CB must be in the order of the industry's electricity consumption. The value of 1 is deliberately optimistic in order to remain conservative. Considering the electricity restituted by the CB distributed between the consumption of the industry and the grid, the value of 2 is chosen with the same considerations. For the electricity pricing (C*) and (D*), the constraint $W_{HE}/E_{el} \leq 1$ is added. In the case where Carnot cycles are considered, $\Delta_{T_{sto}} = 0$ (Section 2.2.2.).

3. Results and discussions

Results are determined with T_w=100 °C as an example and for discussions. Complementary results are shown in Appendix A, with waste heat temperatures covering the whole range considered.

Figures 7, 9 and 11 show the results for a CB based on Carnot cycles. Figures 8, 10 and 12 show the results for a CB based on Lorenz cycles. These results correspond to the gain as defined by (19), (20) and (21).

It is important to note that the results (Fig.11 and 12) for electricity pricing (B) and (D) express the maximum net benefit normalized by E_{el} and C_{max} and not the maximum reduction in electricity bill. The scale applied is therefore different.

All results are obtained with u = 1 and are expressed as a function of E_{el}. In order to apply u, it is necessary to multiply the results obtained by its value. In the case of a self-consumed RES electric production, the results must be expressed as a function of $E_{el,grid}$ and are therefore to be multiplied by $E_{el}/E_{el,grid} = 1+(E_{el,RES}/E_{el,grid})$.

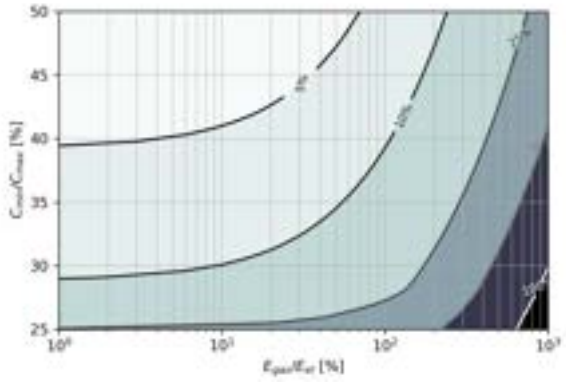

Figure 7: Maximum gain for electricity pricing (A) and (C) with CB based on Carnot cycles (T_w=100 °C)

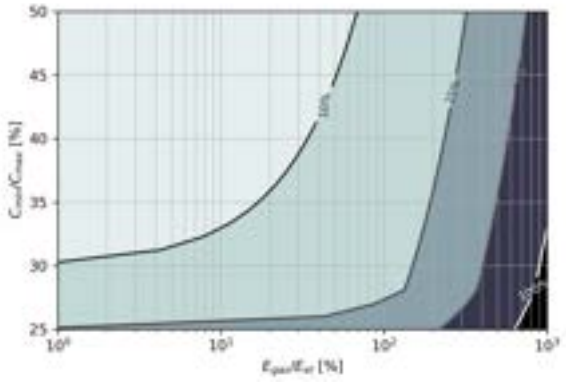

Figure 8: Maximum gain for electricity pricing (A) and (C) with CB based on Lorenz cycles (T_w=100 °C)

Based on the results obtained for 100 °C (representative of the other T_w trends), some preliminary observations are made. Calculations based on the Lorenz formulations always give similar or better results than those based on the Carnot formulations. A clear superiority of the Lorenz cycles is visible from an electricity cost ratio higher than 30%. However, the differences are small compared to the assumptions. It is necessary not to jump to conclusions. Moreover, in practice, the application of Lorenz cycles is more expensive and more complex to implement. [9]. It is interesting to note that the optimum glides $\Delta_{T_{sto}}$ for Lorenz cycles are close to the maximum of the allowed values, while they are at zero for Carnot cycles. This gives an important advantage to Lorenz cycles in real considerations. Increasing waste temperatures promotes good results. Also, the results improve with the increasing of gas proportion and/or the decreasing of electricity cost ratio.

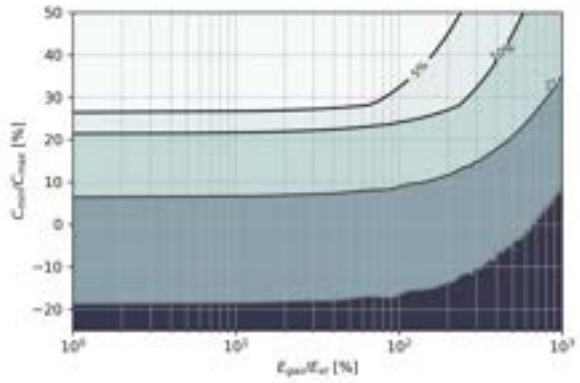

Figure 9: Maximum gain for electricity pricing (C*) and (D*) with CB based on Carnot cycles (T_w=100°C)

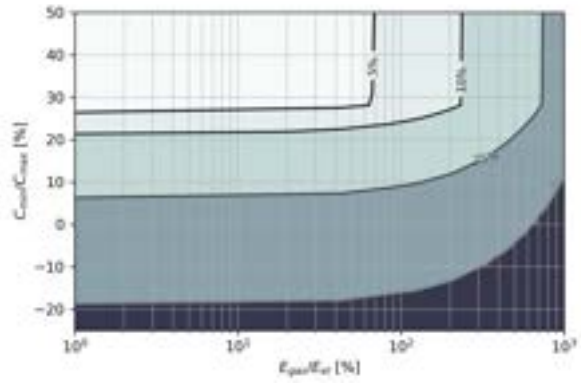

Figure 10: Maximum gain for electricity pricing (C*) and (D*) with CB based on Lorenz cycles (T_w=100°C)

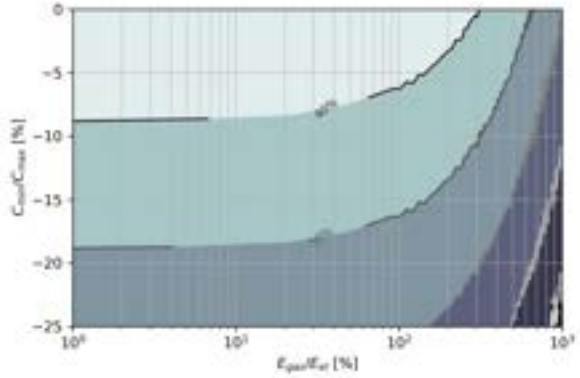

Figure 11: Maximum gain for electricity pricing (B) and (D) with CB based on Carnot cycles (T_w=100°C)

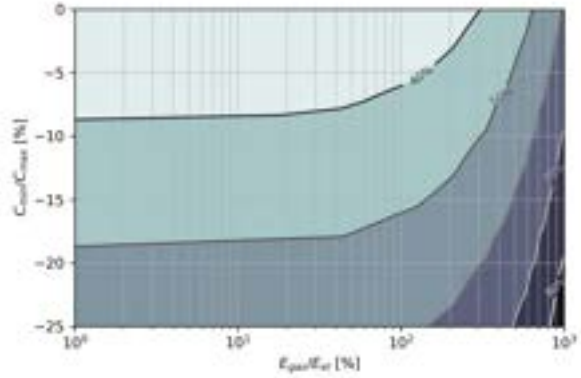

Figure 12: Maximum gain for electricity pricing (B) and (D) with CB based on Lorenz cycles (T_w=100°C)

3.1. Impact of the electricity pricing

For (A) and (C), a realistic case is an electricity cost ratios above 35%. In the case of E_{gas}/E_{el}=1, the gain is 10% for T_w=100°C. These results are weak compared to the hypotheses. Moreover, in some industries, the cost of electricity is still constant. The results for T_w at 50 and 200°C are respectively 5% and 25%. (C*) must tend towards (D*) to be in the same order, i.e. a purchase cost less than or equal to zero.

Cases (B) and (D) seem more interesting. In general, a purchase cost less than or equal to zero seems to be a necessary condition for profitability. Considering the investment of the system, the conservative assumptions and the fact that u = 1 for these results, a gain of 10% seems to be the minimum to find interest in the system. A more variable electricity pricing will therefore be the key to this technology.

3.2. Impact of the gas consumption

Increasing gas consumption increases gains. It is obvious that the objectives in terms of reducing emissions of greenhouse gases lead to avoid this solution. It is therefore an additional argument for an adapted electricity pricing.

In the case of a gas-intensive industry, the system can be interesting. First of all, it allows to reduce the electricity bill and to use the RES more advantageously. In a second time, its decarbonization will make the system less efficient. However, since this transformation of the industry will be done over the next 30 years and that the life cycle of a CB is of the same order, it is interesting to consider that the installation of the system will already put in place heat recovery devices that will be later used for other purposes.

3.3. Discussion on the restriction of the industries studied

The industry studied is considered to be entirely operated by a single CB and storage (Section 2.1.2.). It is possible to remove this assumption by dividing the processes by groups and linking each group to a CB and a storage (so different T_w). It is necessary to adapt the corresponding i indices in 13 and repeat the methodology

several times. The gains can then be summed up. This method, if not applied sparingly, has the disadvantage of further distorting the results of reality by neglecting the investment cost of several systems instead of one.

An ambient temperature different from 20 °C has a significant impact on the results (a lower T_{amb} improves the gains and vice versa). This is one of the reasons why the characteristic period must be chosen carefully. It is always possible to do once the methodology for a winter case and once the methodology for a summer case and then average the results. The results for different T_{amb} are available in the Appendix A.

Finally, [5] demonstrates that considering only batteries with hot storage remains conservative.

3.4. Waste heat used

From Fig.13 and Appendix A, it appears that the maximum recoverable waste heat fraction is below 50% in realistic cases for electricity pricing (A), (C) and (C*). For (B), (D) and (D*) this fraction can rise to between 60 and 70% for restricted areas of application. Thermal Integrated Carnot Battery is therefore not a dedicated waste heat recovery technology (it makes use of it but with constraints).

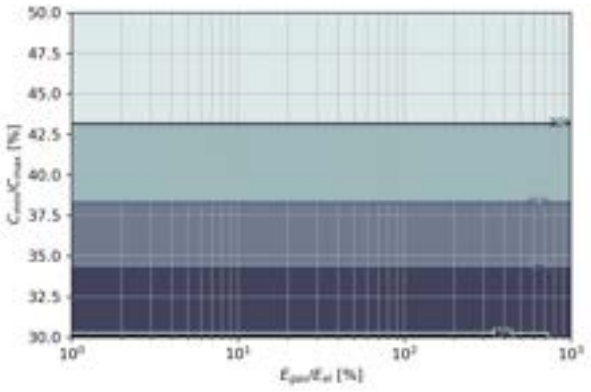

Figure 13: Waste heat used $Q_{w,used}/Q_w$ to obtain the maximum gain for electricity pricing (A) and (C) with CB based on Carnot cycles (T_w=100 °C)

3.5. Optimized use of Thermal Integrated Carnot Batteries

Another application for Thermal Integrated Carnot Battery is the integration of district heating. This solution has an interesting potential of profitability [10]. It could be possible to combine the two systems to increase the potential benefits. In this case, the methodology of this paper can no longer be used as is. It is possible to include the consumption of the district heating network in the ambient losses ($Q_{amb,i}$ for (14) or $Q_{amb,tot}$ for (15)) . In this case, the results give lower gains to which must be added the economic gains due to the district heating network.

The waste heat temperatures considered in this paper are based on a study [7] considering that higher temperatures waste heat are used to feed the lower temperature processes. In most sectors, waste heat above 200 °C is used for this purpose. The iron and steel industry and the glass industry are special cases. The waste heat temperatures, although very high, are not converted because the majority of the processes require an even higher temperature. The recovery of this waste is however not considered because its quality allows a much more interesting balance with other technologies [1]. Graphs in Appendix A show the limits of the considered system, for high temperatures, in terms of energy efficiency.

3.6. Non-self-consumed RES

The case of non-self-consumed RES are directly related to time constraints. Despite the assumptions made, it is not possible to express the gain for all electricity pricing:

- (D*) is used instead of (C*) with $\frac{C_{min}}{C_{max}} = 0$
- (D*) can be used as is
- (D) is used instead of (B) with $\frac{C_{min}}{C_{max}} = 0$
- (D) can be used as is

For the transformations in (B) and (D), a strong assumption must be made: non-self-consuming production occurs only when the network is saturated and imposes $C_{sell} = 0$. In all these cases, the term $E_{el,RES}$ of the correction $1 + (E_{el,RES}/E_{el,grid})$ factor must be evaluated as the sum of the RES production (self-consumed

or not). For (A) and (C), it is not possible to conclude. In any case, if the energy of the non-self-consumed RES is small compared to the self-consumed RES, these steps can be neglected given the advantageous assumptions on which the gain calculations are based.

4. Conclusions and perspectives

The objective of this paper was to determine Key Performance Indicators concerning the potential of Carnot battery integrating waste heat recovery in Industry. A generic definition of the Carnot Battery was determined according to Carnot and Lorenz. Industry was also described generically. The necessary assumptions were made to cover as wide a range as possible. The different parameters of the system were then determined. On the one hand for the industry with simple to define values: ratio of primary energy used, ratio of minimum and maximum electricity costs, temperatures of available waste heat, and electricity pricing type. On the other hand, the Carnot Battery parameters are optimized to give the most optimistic results. For each combination of industry parameters, a maximum gain is calculated, which is the main result of this work. Throughout, conservative assumptions are applied so that the results are as robust as possible.

Industries using at least as much electricity as gas and for which the ratio of the minimum (positive) purchase price to the maximum selling prices is over 50% cannot expect significant benefits from using Carnot batteries integrating waste heat recovery. Intermediate results are also defined and discussed leading to the following conclusions:

- Electricity pricing with high variability and negative purchase prices will be the key to this technology.
- The application of Lorenz cycles can theoretically significantly increase the benefits of the system compared to Carnot cycles in the least favorable cases.
- The system is more efficient for gas-intensive industries. It can be a gateway to low temperature waste heat recovery.
- The amount of waste heat recovered remains low in all cases. It is used for the benefit of the system, but Thermal Integrated Carnot Battery is not a dedicated waste heat recovery technology
- The introduction of other heat streams (District Heating) can contribute to the sustainability of the system.
- It is difficult to conclude in the case of a Renewable Energy Sources not entirely self-consumed without strong assumptions. Further study will often be required.

An interesting perspective will be to test several cases and to position them on the graphs. This will allow to determine more precisely which industries are unsuitable for the system and which ones would deserve a more advanced study. On the other hand, it would be interesting to realize a more complex model integrating temporal considerations, investment prices and a Carnot Battery defined according to considerations closer to reality. Describing this model on the basis of the same parameters as those of this paper will allow the second more advanced study. Finally, the confrontation of the results with other storage systems as well as with a model integrating more widely the use and the management of heat flows would be of great interest.

Appendix A Additional mappings

Although reduced to a minimum, the number of parameters in this study only allows to propose mapping for illustration purposes. In order to provide to the reader the specific KPIs adapted to his case of interest, all the results for the considered ranges can be found at: `https://hdl.handle.net/2268/302631`

Nomenclature

Latin letters

C	electricity cost, €/J
c_p	specific heat, J/kg.K
E	energy, J
g	ideal cycle efficiency, $-$
m	mass, kg
Q	thermal energy, J
S	entropy, J/K
t	time, s
T	temperature, K
u	usability factor, $-$
W	electrical energy, J

Greek symbols

η	efficiency

Abbreviations

CB Carnot battery

COP coefficient of performance

HE heat engine

HP heat pump

KPI key performance indicator

RES renewable energy source

Subscripts

amb ambient

aux auxiliary

c cold

el electric

h hot

in input

max maximum

min minimum

out output

p process

s selected

sto storage

tot total

w waste heat

References

[1] Dumont O., Frate F., Pillai A., Lecompte S., De Paepe M., Lemort V. *Carnot battery technology: A state-of-the-art review*. Journal of Energy Storage 2020; 32: 101756.

[2] Novotny V., Basta V., Smola P., Spale J. *Review of Carnot Battery Technology Commercial Development*. Energies 2022; 15: 647.

[3] Forman C., Kolawole Muritala I., Pardemann R., Meyer B. *Estimating the global waste heat potential*. Renewable and Sustainable Energy Reviews 2016; 57: 1568-1579.

[4] Laterre A., Dumont O., Lemort V., Contino F. *Systematic and multi-criteria optimisation of subcritical thermally integrated Carnot batteries (TI-PTES) in an extended integration domain*. ORC2023: Proceedings of the 7th International Seminar on ORC Power Systems; 2023 Sep 4-6; Seville; Spain.

[5] Dumont O., Lemort V. *Mapping of performance of pumped thermal energy storage (Carnot battery) using waste heat recovery*. Energy 2020; 211: 118963.

[6] Weitzer M., Müller D., Karl J. *Advanced organic Rankine cycles for thermally integrated Carnot batteries*. ORC2021: Proceedings of the 6th International Seminar on ORC Power Systems; 2021 Oct 11-13; Munich; Germany.

[7] Hammond G.P., Norman J.B. *Heat recovery opportunities in UK industry*. Applied Energy 2014; 116: 387–397.

[8] Reinholdt L., Kristófersson J., Zühlsdorf B., Elmegaard B., Jensen J., Ommen T., Jørgensen P.H. *Heat pump COP, part 1: Generalized method for screening of system integration potentials*. GL2018: Proceedings of the13th IIR-Gustav Lorentzen Conference on Natural Refrigerants; 2018 June 18-20; Valencia; Spain.

[9] Dumont O., Dickes R., De Rosa M., Douglas R., Lemort, V. *Technical and economic optimization of subcritical, wet expansion and transcritical Organic Rankine Cycle (ORC) systems coupled with a biogas power plant. Energy conversion and management*. Energy conversion and management 2018; 157: 294-306.

[10] Dumont O., Thomé O., Lemort V. *Techno-economic assessment of a Carnot battery based on a Rankine cycle with waste heat integration*. SDEWES 2022: Proceedings of the 5th South East European conference on Sustainable Development of Energy, Water and Environment Systems; 2022 May 22-26; Vlöre, Albania.

PROCEEDINGS OF ECOS 2023 - THE 36TH INTERNATIONAL CONFERENCE ON
EFFICIENCY, **C**OST, **O**PTIMIZATION, **S**IMULATION AND ENVIRONMENTAL IMPACT OF ENERGY SYSTEMS
25-30 JUNE 2023, LAS PALMAS DE GRAN CANARIA, SPAIN

Thermodynamic and economic analysis of a Carnot battery with a two-zone water tank as thermal energy storage

Josefine Koksharov[a], Jonas Klingelhöfer[a], Frank Dammel[a], Peter Stephan[a]

[a] *Institute for Technical Thermodynamics, Technical University of Darmstadt, Darmstadt, Germany, koksharov@ttd.tu-darmstadt.de, CA*

Abstract:

In the process of energy transition, the share of renewable energy sources is increasing. This leads to strong fluctuations in power generation. To balance supply and demand, energy storage is required. Carnot batteries could be a promising storage technology to solve this problem. These batteries convert electrical energy into thermal energy through an electrical resistance heater or a heat pump and stores this energy for a period of time. Later, the thermal energy is converted back into electrical energy through a heat engine.

A Carnot battery with a two-zone tank and water as a storage medium was investigated. This type of storage allows storage temperatures above 100 °C under atmospheric conditions. The system studied here applies a storage temperature of 115 °C. Charging is realized with a CO_2 heat pump, while discharging uses a heat engine with an organic fluid. This Carnot battery was implemented and simulated in EBSILON® *Professional*. The supplied electrical power was 18 MW and the maximum outlet temperature was 150 °C. Derived from the day-ahead market [1], a charging and discharging time of 4 h was applied. To identify the most promising concept for practical applications, the round trip efficiency, levelized cost of electricity (LCOE), and technology readiness level (TRL) of the different Carnot battery configurations were compared. In addition, a simplified sensitivity analysis was performed to assess the influence of the uncertainties of the economic parameters on the LCOE. Furthermore, the change in the LCOE with a variation in the charging and discharging duration was investigated.

The advantage of a CO_2 heat pump is that applications with high input power have already been implemented, which leads to an estimated TRL of at least 6. By contrast, heat pumps for temperatures above 100 °C utilizing screw or piston compressors are only available for lower power applications.

Keywords:

Carnot Battery, CO_2 Heat Pump, Organic Rankine Cycle, Water Storage Tank.

1. Introduction

Electricity generation from renewable energy is subject to fluctuations due to weather conditions. To ensure a secure power supply with an increasing share of renewable energy, energy storage systems are needed to temporarily store electrical energy, and thus compensate for fluctuations. Pumped thermal electricity storages, known as a Carnot battery (CB), is a promising technology in this respect. A CB is a system that converts electrical energy into thermal energy through an electrical resistance heater or a heat pump and stores this energy for a period of time. Later, the thermal energy is converted back into electrical energy through a heat engine. CBs have been studied in different configurations involving supercritical, transcritical, and subcritical processes [2]. Comprehensive overviews of CBs can be found in [2, 3]. For storing thermal energy, sensible, latent, or thermo-chemical energy storage systems are available. A sensible energy storage system consists of a single storage tank with a thermocline (stratified storage) or two tanks, where the storage medium is pumped from one tank into the other.

An overview of the research literature is given below. This study focuses on configurations in which CO_2 transcritical processes are used. Several authors dealing with CBs have considered transcritical processes predominantly using CO_2 [4–11] as a working fluid. Energy storage on the hot side is often realized in tanks with hot water [4,7,8,10]. This allows a temperature glide between the storage medium (water) and the working fluid. On the cold side, either an ice storage tank [4, 7] or the environment [10, 11] are considered as storage units.

Mercangöz et al. [9] described a transcritical charging and discharging process using CO_2 as a working fluid. The concept included two storage units, one of which stored thermal energy at higher temperatures in water

tanks at a maximum temperature of 123 °C and the other stored energy in an ice storage tank at a temperature of -5 °C. Because of the irreversibilities that occur in the process, the ice storage is supplemented by an additional circuit during the charging process to dissipate losses to the environment. With a nominal turbine power of 1 MW (η_{turbine} = 86 %, $\eta_{\text{compressor}}$ = 81.5 %, η_{expander} = 80 %, and η_{pump} = 80 %) for a pilot project and a nominal turbine power of 50 MW (η_{turbine} = 91 %, $\eta_{\text{compressor}}$ = 89 %, η_{expander} = 88 %, and η_{pump} = 86 %) for a commercial plant, round trip efficiencies of 51 % and 65 %, respectively, were achieved.

Morandin [4, 5], starting from the base case, optimized the transcritical CO_2 charging and discharging process. The base case included, on the hot side, a sensible energy storage system using water as a storage medium, with several tanks storing energy at different temperatures, and, on the cold side, an ice storage system consisting of two tanks. The ice storage tank contained a salt mixture to lower the freezing point to -21.2 °C. An air fan was also integrated into the charging and discharging process to release the resulting irreversibilities to the environment in the form of heat. By optimizing the base case with eight water tanks and a maximum discharge temperature of 177 °C, a round trip efficiency of 60 % was achieved. By adding an internal heat exchanger in the charging and discharging process to the base case configuration, the round trip efficiency was increased to 62 %. The expansion of the working fluid occurs in the two phase/wet steam area, which is associated with technological problems. To prevent these problems, a throttle can be used instead of the expander, which in turn leads to a drop in round trip efficiency.

Another study on CB was presented by Kim et al. [8], based on Morandin and Mercangöz [4, 9]. Nevertheless, in the study by Kim et al. [8] the concept involved isothermal compression/expansion using a liquid expander and a water injection to cool the working fluid during the charging process and to heat it during the discharging process, respectively. At a maximum pressure of 160 bar and a maximum charging temperature of 150 °C, and under high isentropic efficiencies ($\eta_{\text{compressor,charging}}$ = 90 %, $\eta_{\text{expander,charging}}$ = 85 %, $\eta_{\text{compressor,discharging}}$ = 0.85 %, $\eta_{\text{expander,discharging}}$ = 90%) an overall efficiency of 74.5 % was obtained.

Steinmann et al. [7] studied a CB that consisted of transcritical CO_2 cycles and two storage units at different temperatures. The first storage unit was a pressurized water storage tank with a temperature up to 160 °C. The other one was an ice storage unit with a temperature of 0 °C. With an isentropic compressor and turbine efficiency between 80 % and 90, % the round trip efficiency was about 45 %.

Baik et al. [10] investigated CBs with a transcritical CO_2 process involving two-tank liquid systems, each on the hot and cold side. The tanks on the cold side used the environment with a temperature of 20 °C as a heat source and heat sink, respectively. These storage tanks were operated with water. Compared to the concepts in [4, 5, 7], a throttle was integrated into the charging process instead of an expander. The maximum storage temperature was 120 °C and isentropic efficiencies of 85 % were assumed for the: compressor, turbine, and pump. The round trip efficiency was studied as a function of the lower storage temperature of the two-tank system on the hot side, which varied between 25 and 70 °C. Under these conditions, round trip efficiencies ranged from 14.7 % to 29.1 %, with the maximum reached at the lower storage temperature of 40 °C on the hot side.

Koen et al. [11] analyzed the transcritical process by testing different working fluids, such as CO_2, R1234yf, R1234ze(e), R1234ze(z), R152A, R161, R13I1, and ammonia, and different storage media such as water,Therminol D12, and Therminol 66. The concept included a compressor and an expander for both charging and discharging processes. A storage unit was implemented on the hot side, designed as a two-tank system. A low-temperature storage tank was dispensed, with and thus, a heat exchanger used the environment as the second storage unit. Under optimal operation conditions with polytropic component efficiencies of 90 %, round trip efficiencies between 50.5 % and 57.6 % were obtained. The best result was achieved using the working fluid R13I1 at a maximal storage temperature of 206 °C.

The described concepts generally use the round trip efficiency to evaluate their configurations. In this study, besides the round trip efficiency, the levelized cost of electricity (LCOE) and the technology readiness level (TRL) were determined to answer the following questions:

With which CBs could a system be realized in a timely manner?

Which efficiencies are achieved and what are the resulting LCOEs of the investigated CBs?

How does reducing the pinch point of the heat exchangers affect the round trip efficiency, purchased equipment cost, and LCOE?

The study focuses on various CB concepts based on the transcritical charging process with CO_2 as a working fluid. Using CO_2, an appropriate compressor at an outlet temperature greater than 100 °C, allows the implementation of a heat pump at a larger scale [12, 13]. So far, it is only possible to implement heat pumps in the kW range with positive displacement machines, using a high compressor discharge temperature [14]. A two-zone storage tank is used as a thermal energy storage (TES). This type of storage consists of an upper and a lower chamber, which are separated from each other by a partition wall. These chambers are filled with water

at different temperatures and are connected by pipes. The water in the upper chamber exerts pressure on the lower chamber. This allows the storage of water in the lower chamber in a pressureless state at temperatures $> 100\,^{\circ}\mathrm{C}$. Compared to pressure-loaded tanks with water, the two-zone storage tank is a safer and cheaper option [15]. In combination with the two-zone storage tank, the working fluid (CO_2) is suitable for the transcritical charging process. This mode of operation has the advantage that the CO_2 approximates the course of the temperature glide of the storage medium (water) in the two-zone storage tank. One way to discharge the TES is to use a heat engine, which is also operated with the same working fluid (CO_2) in transcritical mode. Alternatively, subcritical processes with different organic working fluids can be considered as these subcritical processes are already used in practice, (e.g., in geothermal plants) [16].

2. Design and Simulation of the Carnot Battery

The CB consists of a transcritical charging process and a sensible thermal energy storage (TES). The discharge of the TES is either transcritical or subcritical. The schemes of the charging and discharging subprocesses are shown in Fig. 1 a) and b), respectively. The subprocesses are described below.

Charging Process

Excess electrical energy is used to compress the working fluid to a supercritical pressure (HP1-HP2). After transferring the heat to the TES (HP2-HP3), the working fluid is further cooled in the regenerative heat exchanger (HP3-HP4) until the liquid state is reached. Then, the working fluid is first expanded in a liquid expander to a nearly saturated liquid (HP4-HP5) before it is further expanded in the throttle to the evaporating pressure (HP5-HP6). The working fluid evaporates in the heat exchanger (HP6-HP7) by the heat supply from a river and is further heated in the regenerative heat exchanger (HP7-HP1).

Discharging Process

The liquid working fluid is compressed in the pump to a high-pressure level (HE1-HE2). Heat is then transferred to the fluid in the heat exchanger (HE2-HE3), using the two-zone energy storage. In a transcritical process, the fluid is heated with a phase change during temperature decrease, whereas in a subcritical process, the fluid undergoes a phase change at a constant temperature and evaporation also takes place. Then, the working fluid is expanded in the turbine (HE3-HE4), which drives the generator. To close the cycle, the working fluid is condensed in the heat exchanger (HE4-HE1) by releasing the heat to a river and reaches the initial state (HE1).

For the discharging process, a heat engine in transcritical operation mode with the same working fluid (CO_2) as in the charging process was compared with heat engines in subcritical operation mode, using the following working fluids:

- R600a (isobutane), R134a, and R245fa as these fluids are already used in geothermal power plants [16].
- R1233zd(E), as this working fluid is already used in CB laboratory setups [17, 18].
- R1234yf, discussed as replacement fluid for R134a [19].
- R290 (propane), which is used in refrigeration and heat pump systems [20].

2.1. Modeling and Simulation

The modeling and steady-state calculation of the Carnot battery were performed in EBSILON® *Professional* [21]. For this purpose, the components (e.g., the turbine, heat exchanger, and others) are placed on the graphical surface and connected by lines. The line between the components corresponds to electrical, mechanical, or physical lines through which fluids flow. At a point of the physical line, a starting value and the fluid must be defined. With further measuring points, which are to be placed on the corresponding lines, further operating points in the system can be defined. The component 'controller' allows changing an actual value until the setpoint is reached. These controllers are used to determine the mass flow in the subprocesses. For implementing different working fluids, substance databases such as Refprop [22] are available.

The charging process is supplied with 18 MW of electrical power, which is needed to operate the compressor and the two pumps for pumping the river water and the hot water from the two-zone storage. According to [12], the upper pressure and temperature level in HP2 is a maximum of 140 bar and 150 °C, respectively. The maximum storage temperature in ST1 is 115 °C and is based on the already implemented two-zone storage [15]. The heat losses in the two-zone storage tank are neglected in this work. To evaporate the CO_2 in the heat exchanger from HP6-HP7, water is taken from the environment at 10 °C and 1 bar (state: w1), which is reduced by 5 K (state: w3).The temperature in HP6 is determined by specifying a terminal temperature difference or a pinch point in the heat exchanger. This, in turn, results in the evaporation pressure and thus the pressure HP6 and HP7. The same pinch point is specified in all heat exchangers. Pressure losses are also neglected in the process. Isentropic, mechanical, and electrical efficiencies of the components are specified

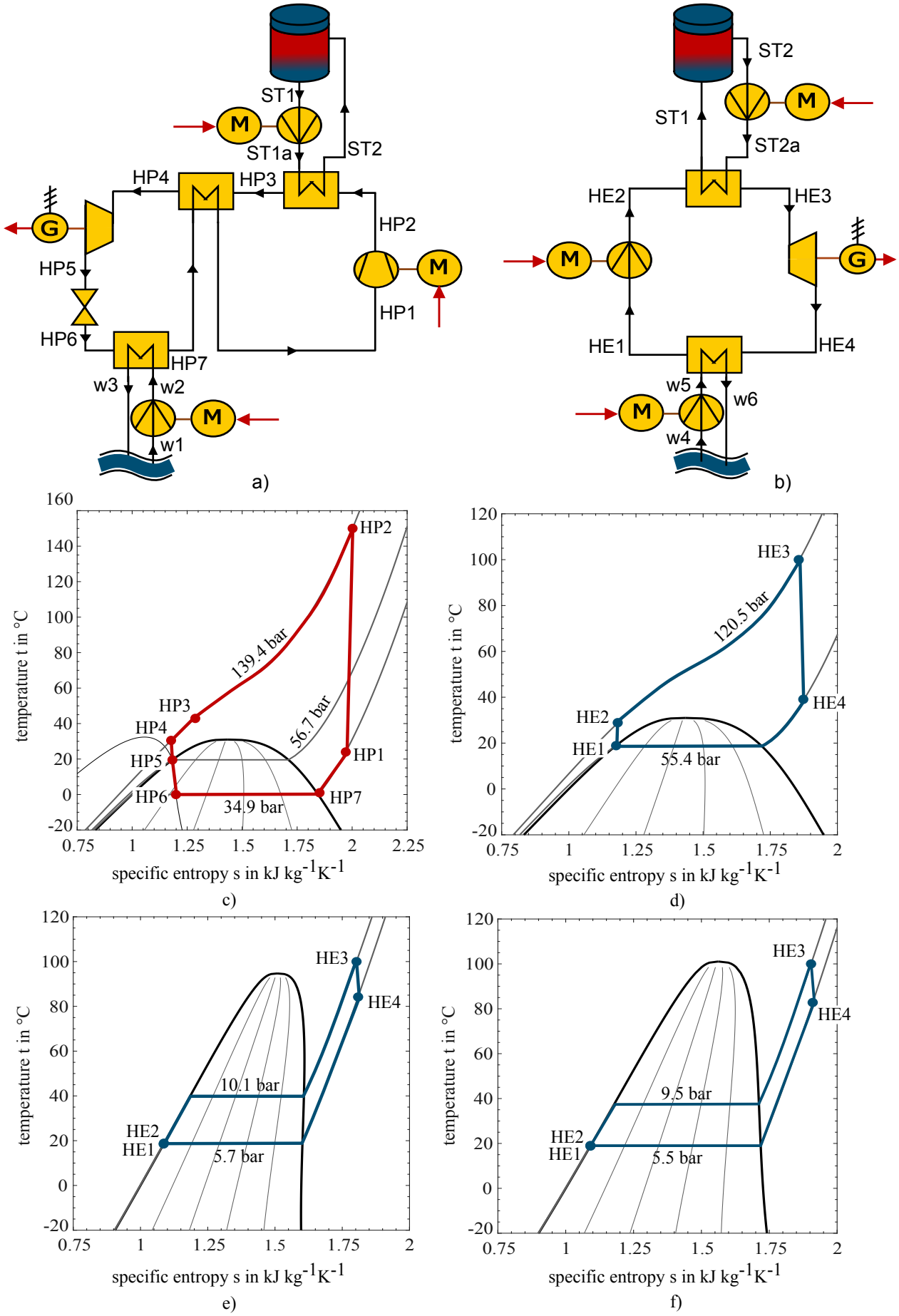

Figure 1: Scheme of the a) charging cycle and b) discharging cycle; t,s diagram of c) charging with CO_2; d) discharging with CO_2; e) discharging with R1234yf and f) discharging with R134a [22].

(see Table A.1). These values are the same for all concepts. As a condition, the lower storage temperature T_{ST1} is defined in such a way that the CO_2 is liquid in state HP4.

2.1.1. Results of the Simulations

Tables 1 and 2 present an overview of the simulation results for the different configurations when two different pinch points are specified. Under a pinch point of 5 K, the transcritical CO_2 discharge process (Configuration 1) achieves the highest round trip efficiency (21.9 %), whereas the other configurations with ORC fluids vary between 9.6 % and 13.7 %. In general, a decrease in pinch point leads to an increase in round trip efficiency. This may be because, the evaporation pressure in the discharge process can be increased and the condensation pressure in the discharge process can be decreased. The overall process of Configuration 1 thus increases in efficiency from 21.92 % to 33.48 %. A greater increase in round trip efficiencies is achieved with Configurations 2-6 (see Figure 2) compared with the pinch point of 5 K. The lower pinch point allows the lower storage temperature T_{ST1} to be increased, which has a positive effect on the heat engine. However, the lower storage temperature is limited upward, otherwise, the state of aggregation before the liquid expander in the heat pump is gaseous. Figure 2 shows the temperature curves of the fluids in the heat exchangers between HP2 and HP3 and between HE2 and HE3, assuming different pinch points. With a reduction of pinch point, the cost of the purchased equipment increases because of the need for a larger heat exchanger area. Considering the LCOE, the financial cost at the expense of efficiency is examined as well. In the following, the working fluids R1233zd(E) and R245fa are not considered for the economic analysis because of the low round trip efficiencies and the low pressure ratios obtained in the discharge process.

Table 1: Results of the simulation with a pinch point of 5 K in the heat exchangers. COP = 3.04, T_{ST1} = 35°C and T_{ST2} = 115°C.

Configuration	1	2	3	4	5	6	7
Discharging process							
Fluid	CO_2	R600a	*R*134*a*	*R*245*fa*	R290	R1234yf	R1233zd(E)
p_{ev} in [bar]	120.5	4.8	9.5	2.2	12.9	10.1	1.8
p_{con} in [bar]	55	2.9	5.5	1.2	8.1	5.7	1.1
η_{HE} in [%]	7.94	3.83	4.28	3.73	4.22	4.48	3.17
η_{rt} **in [%]**	21.92	11.64	13.01	11.35	12.84	13.63	9.65

Table 2: Results of the simulation with a pinch point of 1 K in the heat exchangers.

Configuration	1	2	3	4	5	6	7
Charging process							
Fluid	CO_2	CO_2	CO_2	CO_2	CO_2	CO_2	CO_2
COP in [-]	3.57	3.24	3.2	3.19	3.20	3.21	3.20
TES							
T_{ST1} in [°C]	30.9	41.1	42.4	42.3	42.4	41.8	42.4
Discharging process							
Fluid	CO_2	R600a	*R*134*a*	*R*245*fa*	R290	R1234yf	R1233zd(E)
p_{ev} in [bar]	140	7.9	17.3	4.2	21.8	18.4	3.3
p_{con} in [bar]	51	2.6	5.0	1.0	7.7	5.1	1
η_{HE} in [%]	9.39	8.45	9.40	8.69	9.41	9.47	7.83
η_{rt} **in [%]**	33.48	27.38	30.03	27.77	30.07	30.44	25.03

3. Economic Analysis

This subchapter describes the methods used for calculating the purchased equipment costs (PECs) as well as the levelized cost of electricity (LCOE).

3.1. Equipment Cost

In addition to its efficiency, the cost of a CB is also important. For a first estimation of component costs, the Turton method [23] was used. With this method, the PECs are calculated on the basis of cost functions, which result from predefined factors and characteristic size parameters, such as the power or heat exchanger area.The estimation of the PEC of the generators' was based on the six-tenths rule [24]. The reference values were obtained from the cost of the generator by Balli et al. [25]. The PEC of the throttle was negligible compared to the other components. A detailed description for estimating PEC is available at [26]. For calculating the PEC

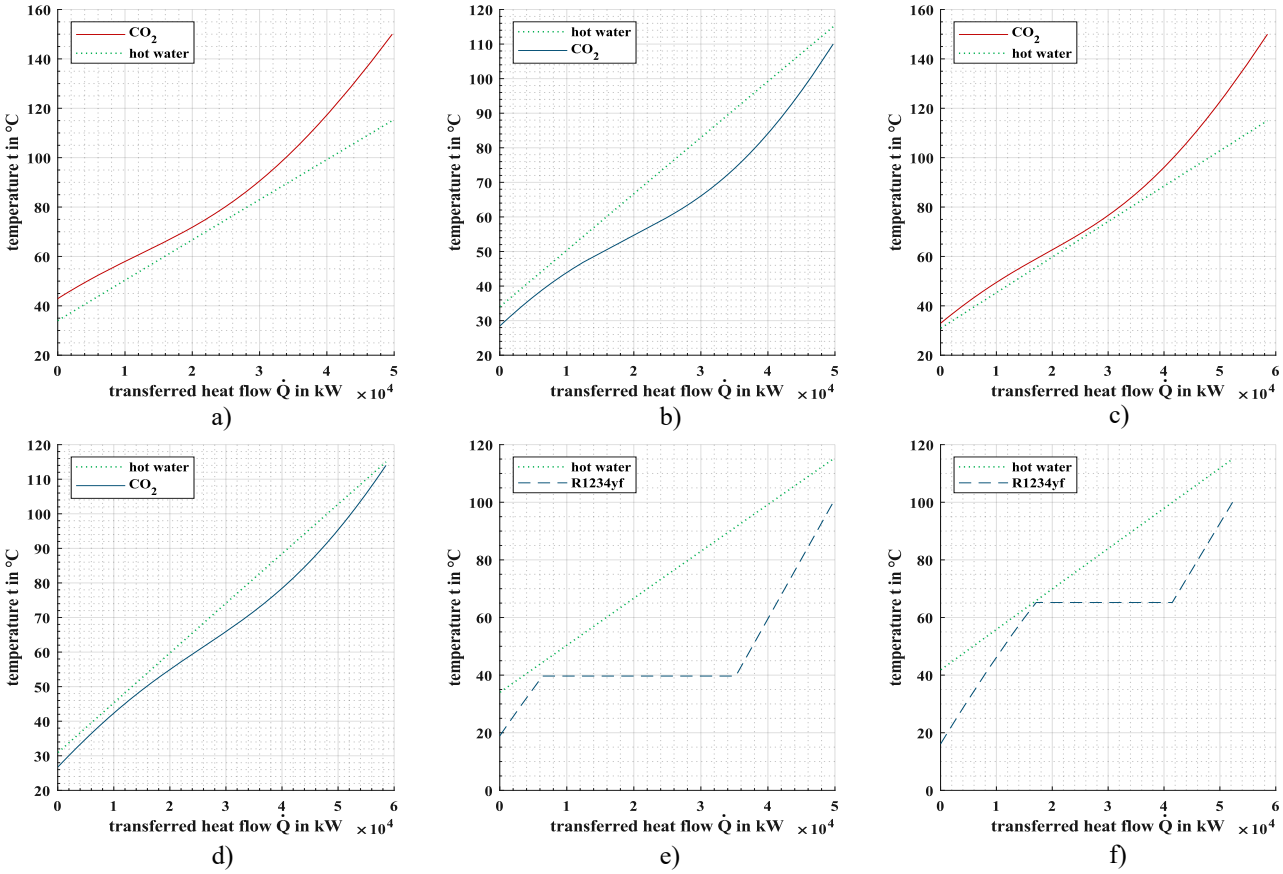

Figure 2: t,Q diagram of a) Configuration 1 in the heat exchanger (HP2-HP3) with pinch point= 5 K; b) Configuration 1 in the heat exchanger (HE2-HE3) with pinch point= 5 K; c) Configuration 1 in the heat exchanger (HP2-HP3) with pinch point= 1 K; d) Configuration 1 in the heat exchanger (HE2-HE3) with pinch point= 5 K; e) Configuration 6 in the heat exchanger (HE2-HE3) with pinch point= 5 K; f) Configuration 6 in the heat exchanger (HE2-HE3) with pinch point= 1 K for illustration of the curve between the fluids.

of the two-zone storage tank, an average value of 550 €/m^3 [15] was applied. The PECs are based on specific reference years. Hence, it is necessary to update costs by considering the price development, inflation, and other factors, with the aid of the cost index Chemical Engineering Plant Cost Index (CEPCI). For the selected reference year (2021), the CEPCI was 708 [27]. The official exchange rate of the European Commission [28] was applied for converting other currencies into euros.

3.2. Levelized Cost of Electricity

For comparing the CB configurations, LCOE was calculated according to [29]. The LCOE is composed of the economic expenditure of the system during its lifetime and the total amount of electricity generated. Taking into account the purchase cost of the supplied electrical energy $c_{\mathrm{el,in}}$, the LCOE can be calculated according to the following equation:

$$LCOE = \frac{I + \sum_{t=1}^{n} \frac{A_t}{(1+i)^t}}{\sum_{t=1}^{n} \frac{En_{t,\mathrm{el}}}{(1+i)^t}} + \frac{c_{\mathrm{el}}}{\eta_{\mathrm{rt}}}. \tag{1}$$

The time period is set to n = 25 years. The aim is to operate the CB 365 days a year with a uniform charging and dicharging time of $\Delta\tau$ = 4 h. This results in the annually produced amount of electricity $En_{t,\mathrm{el}}$ with $En_{t,\mathrm{el}} = 365 \cdot \Delta\tau \cdot P_{\mathrm{out}}$. The investment costs I include not only the PECs, but also take into account other costs (e.g., for pipes, measuring devices and installation) [30]. To determine the investment costs I, the total PECs are multiplied by the Lang factor (F_{Lang} = 4.74) [30]. The annual operation and maintenance costs A_t are determined using a constant factor F_{op} = 0.015. This factor (F_{op}) is multiplied by the total investment costs.The purchase cost $c_{\mathrm{el,in}}$ of the supplied electrical power during charging is determined using the day-ahead market for Germany and Austria of the European Energy Exchange. Application of the approach of Dietrich [31] to the reference year 2021 results in a purchase cost of $c_{\mathrm{el,in}}$ = 6.64 € cents/(kWh)$^{-1}$ [32]. The debt interest rate i is estimated from the program 'Renewable Energies Standard' [33] of the credit bank KfW. This program is

finances renewable energy systems such as battery storage and power-to-X systems and enables debt capital financing of 100 %. A debt interest rate of i = 3.49 % [34] was selected for the program at a maximum fixed interest period of 20 years. Because the period of time is 25 years in this study, we assumed that the interest rate remains fixed and does not change over the additional 5 years. No adjustments for inflation were made.

3.3. Results of the Economic Analysis

Table 3 gives an overview of the total PEC and LCOE of the different configurations for a uniform charging and discharging time of 4 h at a pinch point of 5 K in all heat exchangers. The total PEC of the subcritical processes of Configurations 1-3,5,6 averages $12.209 \cdot 10^6$ €. Configuration 1, based on the CO_2 HE, has PECs about 3 million euro higher than others. Despite, Configuration 1 has the lowest LCOE (123 €cents $(kWh)^{-1}$). The other configurations are in the range of 183-214 €cents $(kWh)^{-1}$ because of their poor round trip efficiency. With the decrease in pinch point, component costs for Configuration 1 increased by almost 57 %, whereas the other configurations became on average 20 % more expensive (see Table 4). A higher LCOE for Configuration 1 was obtained. This is mainly due to the increased costs for the heat exchangers, resulting from the reduced temperature differences within them in the heat engine, from the hot TES to the discharging process. For the other configurations, a reduction in pinch point had a positive effect on LCOE, which was reduced by 50 % on average. Tables 5 and 6 show that the LCOEs were further reduced with a uniform charging and discharging time of 5 and 6 h, respectively. The two-zone storage system should be larger, but this additional cost does not affect the total PEC or the LCOE as much. In addition, Fig. 3 compares the shares of the PECs of the different components for Configuration 1 (CO_2) and for Configuration 6 (R1234yf) with different pinch points. The subprocesses of charging, storage, and discharging are presented in different colors. For all variants, the compressor (including the motor) is the most cost-intensive component, but with a lower pinch point, the cost proportion of the heat exchangers increases. The distributions of the PECs of the other configurations are similar to Configuration 6.

Table 3: PEC and LCOE with a pinch point of 5 K in heat exchangers during uniform charging and discharging for 4 h.

Configuration	1	2	3	5	6
PEC [10^6 €]	15.387	12.152	12.213	12.236	12.233
LCOE [€cents $(kWh)^{-1}$]	123	214	192	195	183

Table 4: PEC and LCOE with a pinch point of 1 K in heat exchangers during uniform charging and discharging for 4 h.

Configuration	1	2	3	5	6
PEC [10^6 €]	24.118	14.670	14.683	14.712	14.751
LCOE [€cents $(kWh)^{-1}$]	128	105	96	96	95

Table 5: LCOE with a pinch point of 5 K in heat exchangers during uniform charging and discharging for 5 h with $c_{el,in}$ = 6.8 € cents $(kWh)^{-1}$

Configuration	1	2	3	5	6
PEC [10^6 €]	15.685	12.449	12.512	12.535	12.532
LCOE €cents $(kWh)^{-1}$	106	187	168	170	160

Table 6: LCOE with a pinch point of 5 K in heat exchangers during uniform charging and discharging for 6 h with $c_{el,in}$ = 7 € cents $(kWh)^{-1}$

Configuration	1	2	3	5	6
PEC [10^6 €]	15.984	12.747	12.810	12.833	12.830
LCOE [€cents $(kWh)^{-1}$]	95	169	152	154	145

3.4. Sensitivity Analysis of the LCOE

A sensitivity analysis was performed to identify the parameters with the most substantial effects on the LCOE. Table 7 lists the parameters and the corresponding results of the sensitivity analysis. The results of one configuration are shown in this work, because they are comparable to those of the other configurations. Only the absolute values differed among configurations. The fluctuation of the purchase costs exerted the greatest influence on the LCOE. The lower and upper limits of the purchase costs corresponded to 2020 and 2022, respectively. With a relative deviation of around 18.7 %, investment costs also have a major influence on the LCOE. Fluctuations between 6 and 10 percent occur with different period of time and debt interest rate. Due

to the large uncertainties in LCOE, these configurations are not suitable to evaluate economic viability. In this work, LCOE is applied to compare the different configurations.

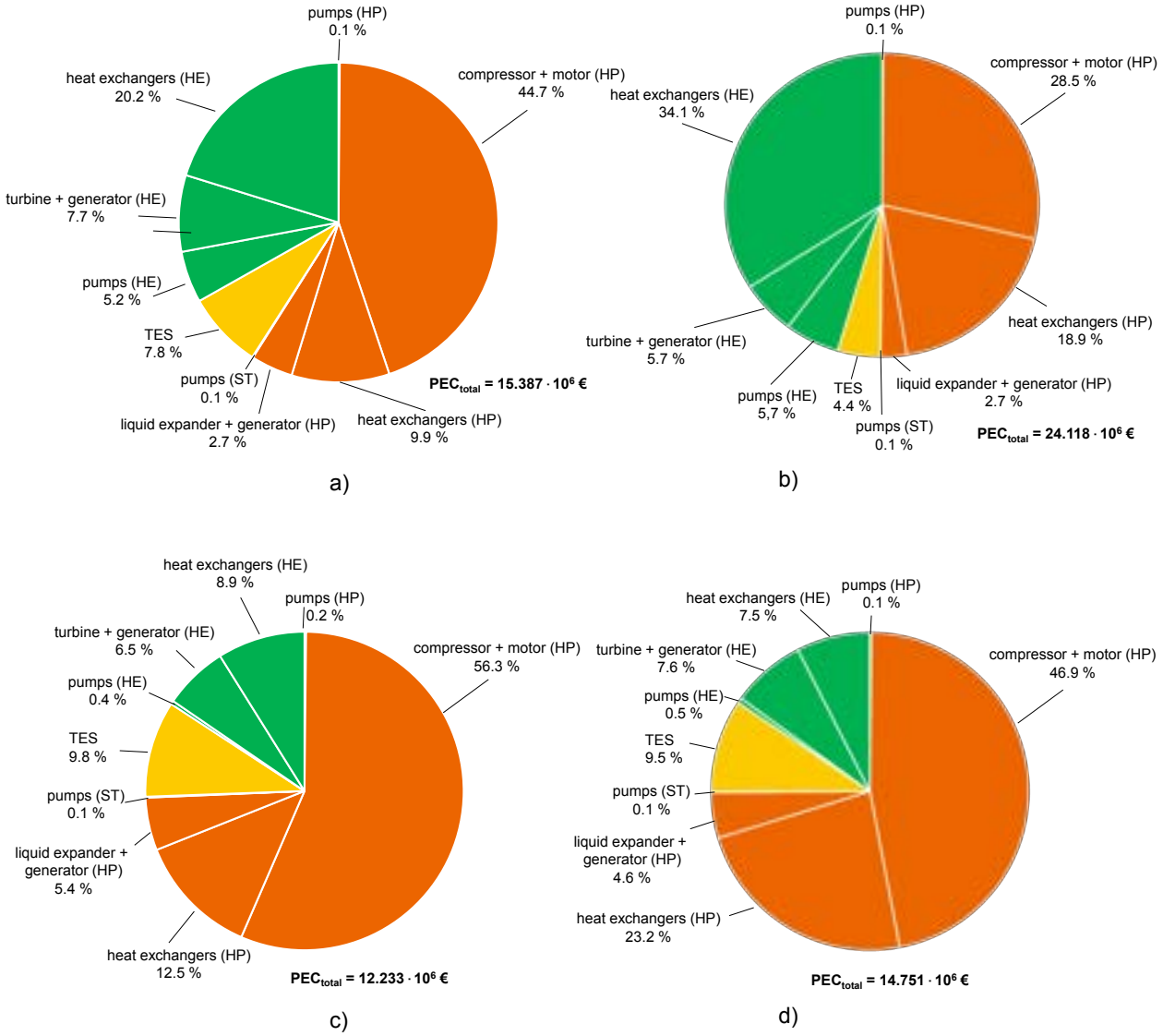

Figure 3: PEC distribution for configuration 1 a) with a pinch point of 5 K, b) with a pinch point of 1 K and for configuration 6 a) with a pinch point of 5 K and b) with a pinch point of 1 K.

Table 7: Sensitivity analysis of the LCOE for configuration 1 with a pinch point of 5 K

Parameter	**Value**	**Variation of LCOE**
Investment costs I	$0.7 \cdot I_{\text{base case}}$	-18.68 %
(base case: $72.935 \cdot 10^6$ €)	$1.3 \cdot I_{\text{base case}}$	+18.68 %
Factor for operational costs F_{op}	1 %	-5.14 %
(base case: 1.5 %)	2 %	+5.14 %
Period of time n	20 years	+9.95 %
(base case: 25 years)	30 years	-6.48 %
Debt interest rate i	2.39 % [34]	-7.20 %
(base case: 3.49%)	4.69 % [34]	+8.38 %
Purchase cost of electricity $c_{\text{el,in}}$	1.82 €cents $(\text{kWh})^{-1}$	-16.21 %
(base case: 6.64 €cents $(\text{kWh})^{-1}$)	16.31 €cents $(\text{kWh})^{-1}$	+32.54 %

4. Technology Readiness Level

The technology readiness level (TRL) scale of the European Commission [35] is a method used to assess the maturity and readiness of a technology or concept. The TRL scale ranges from 1 to 9, with 1 being the

Table 8: TRL scale [35]

Phase	TRL level	Condition
Research	1	Basic principles observed
	2	Technology concept formulated
	3	Experimental proof of concept
Development	4	Technology validated in lab
	5	Technology validated in relevant environment
	6	Technology pilot demonstrated in relevant environment
Deployment	7	System prototype demonstration in operational environment
	8	System complete and qualified
	9	Actual system proven in operational environment

lowest level of technological maturity and 9 being the highest. In the following section, the TRL is applied to the subprocesses.

4.1. Evaluation of the Subprocesses

CO_2 heat pump
CO_2 heat pumps using positive displacement machines and throttle for expanding CO_2 are already offered on the market. However, these are limited in their capacities [14]. A configuration similar to the concept in this study was developed and successfully implemented in the form of a test rig by MAN Energy Solutions [12, 13]. The necessary components are also offered by this company. Instead of a displacement machine a barrel compressor is used, enabling a higher capacity. As a result, the subprocess is classified as TRL6. Since there is not evidence yet of a prototype in a relevant operational environment, a TRL of 7 is not achieved.

Two-zone storage
This storage system is assigned a TRL of 8 because it is already being used in various facilities [15], but is not yet in mass production.

CO_2 heat engine
The CO_2 discharging process has been studied experimentally [36]. Therefore, a TRL of at least 3 is achieved. One manufacturer offers a commercial system [37] based on a supercritical process and with high temperature heat supply. In our study, a lower heat supply temperature of 115 °C is used. Consequently, the subprocess is assessed as TRL = 5, and still needs further testing and development under operational conditions to achieve a TRL of 6.

ORC with R600a
In Grünwald, Germany [16], an ORC process with isobutane as the working fluid is already used to generate electricity. An electrical output of 4.3 MW is achieved at a geothermal spring inlet temperature of 135 °C,. Consequently, the subprocess achieves a TRL of 8.

ORC with R134a
A geothermal power plant using the working fluid R134a is in operation. The power plant is able to generate 5.5 MW of electrical power using a geothermal spring with an inlet temperature of 118 °C [16]. Therefore, the HE is assigned a TRL of 8.

ORC with R290
Propane is widely used as a working fluid in refrigeration systems [20]. So far, only one research group [38] is known to use propane in their transcritical process for geothermal power generation. Hence, the subprocess results in a TRL of 5.

ORC with R1234yf
R1234yf was developed as a replacement for R134a. ORC with this working fluid has been investigated and verified through numerical simulations, achieving a TRL of 3. However, a prototype or experimental investigation has not yet been developed or conducted, which is necessary to achieve a TRL of 4 [19].

4.2. Evaluation of the Overall Process

The TRL of the overall processes is determined by the lowest TRL resulting from the subprocesses. Configurations 2 with R600a and 3 with R134a reach the highest TRL level with 6. The lowest TRL level is reached by configuration 6 with R1234yf.

5. Discussion

Under the assumption of a pinch point of 5 K, the investigated configurations achieved round trip efficiencies between 9 % and 22 % and LCOEs between 123 and 214 €cents $(kWh)^{-1}$, with Configuration 1 using CO_2 in

the heat engine process achieving the best results. Reducing the pinch point demonstrated that configurations using subcritical processes result in better round trip efficiencies and substantially lower LCOEs. Compared to Configuration 1 with CO_2 in the discharge process, increasing efficiency by 11.5 % results in a higher LCOE because in the greater heat transfer surface area between the hot water and CO_2 during the discharge. This results in high component costs. Configurations 2 and 3 with R600a and R134a, respectively, achieved the highest overall TRL and therefore enable prompt implementation. The ORC fluid R134 achieved better results compared to isobutane. However, because of its high global warming potential (GWP), this fluid may be excluded from ORC processes in the future by the European Union.

Although Configuration 1 with a pinch point of 5 K showed the highest round trip efficiency, the lowest LCOE, and an overall TRL of 5, this combination with the environment as a heat reservoir is unsuitable because if the ambient temperature increases, the evaporating pressure and temperature in the heat engine approach the critical point of CO_2, leading to technical problems. One possibility is the combination of an ice storage with an intermediate circuit. However, in this case, a heat exchanger must be integrated into the process to dissipate the heat generated by irreversibilities from the system to the environment. Nevertheless, indirect ice storage adds further costs and irreversibility.

CBs based on transcritical CO_2 cycles showed a substantially higher round trip efficiency in some studies [4, 7–9, 11]. The reason for this is primarily due to the utilization of different CBs. First, the CBs use a second storage tank at a low temperature, integrated directly into the subprocesses, either with ice slurry storage [9] or ice storage [7]. Because of the high pressure of the working fluid (CO_2), ice storage is not feasible [13]. Ice slurry storage tanks are uncommon [39], resulting in a lower TRL level. Higher round trip efficiencies also result for pressurized tanks with water at high storage temperatures, as shown in previous publication [4]. Moreover, multiple high-temperature storage tanks are employed to improve the temperature glide between CO_2 and the storage medium (water). This necessitates the use of multiple heat exchangers, which substantially increase the complexity of the system.

Furthermore, unlike the approach taken in this study, many publications do not account for losses in the motors and generators, and rely solely on machine for the expansion process during charging, which could make the system unfeasible from a technical point of view.

Another improvement in round trip efficiency is achieved through supercritical discharge processes and ORC fluids as working fluids [11]. However, this requires higher storage temperatures and the use of alternative storage media in case the storage medium exceeds 160 °C. Furthermore, an appropriate compressor that can achieve high temperatures is needed for the charging process. Consequently, a low TRL is expected.

Under simplified assumptions, such as the absence of storage heat and pressure losses, the actual forward and return efficiencies of the system are expected to be lower than those predicted by the configurations.

6. Conclusion and Outlook

In this study, CBs based on a transcritical CO_2 charging process with an electrical power input of 18 MW were numerically modeled and simulated stationarily, using the Ebsilon software. A two-zone storage tank with water as a storage medium at a maximum temperature of 115 °C was used. For the discharge, a transcritical CO_2 process and subcritical processes with different organic working fluids were investigated and compared to each other on the basis of round trip efficiency, LCOE, and TRL. With a pinch point of 5 K, Configuration 1 (transcritical CO_2 HE) resulted in the highest round trip efficiency and the lowest LCOE. Despite an overall TRL of 5, this configuration is unsuitable for implementation because the operating points of the evaporator in the HE approach the critical point as the ambient temperature increases, which could lead to technical problems. The other configurations resulted in very low round trip efficiencies, leading to a high LCOE. By reducing the pinch point in the heat exchangers, the efficiencies can be increased, which has a positive effect on the LCOE. Among the subcritical processes, the working fluid R1234yf (Configuration 6) could be an alternative. However, this variant was classified with the lowest TRL level. Similar round trip efficiencies and LCOE at a higher TRL level were achieved with the ORC fluid R134a (Configuration 3). However, the refrigerant R134a has a high global warming potential and is already banned in the automotive sector [40]. The same TRL level was achieved with R600a (Configuration 2), which has the highest LCOE due to its poorer round trip efficiency. The economic values were estimated under considerable uncertainties, as the sensitivity analysis on LCOE showed. Detailed information on component costs and a full financing calculation are required for an economic evaluation of the configurations, as well as the specifications of an accurate plant design, such as the isentropic efficiency of the turbine, compressor, and pumps. With a uniform charging and discharging time of 4 h, the LCOEs are very high, but can be reduced if the charging and discharging duration increases. Because Configuration 1 is excluded as a possible option in this study, replacing the environment as a storage unit with ice could be considered in further investigations to obtain an overview of the possible round trip efficiency, LCOE, and TRL compared to the configurations studied here.

Appendix A

Table A.1: Component parameters used in Ebsilon

Parameter	Symbol	Value	Unit
Isentropic efficiency compressor	$\eta_{is,compressor}$	85	%
Isentropic efficiency liquid expander	$\eta_{is,expander}$	85	%
Isentropic efficiency pumps	$\eta_{is,pump}$	80	%
Isentropic efficiency turbine	$\eta_{is,turbine}$	85	%
Mechanical efficiency compressor	$\eta_{mech,compressor}$	99	%
Mechanical efficiency liquid expander	$\eta_{mech,expander}$	99	%
Mechanical efficiency pumps	$\eta_{mech,pump}$	99	%
Mechanical efficiency turbine	$\eta_{mech,turbine}$	99	%
Mechanical efficiency motor	$\eta_{mech,motor}$	99	%
Electrical efficiency motor	$\eta_{el,motor}$	95	%
Electrical efficiency generator	$\eta_{el,generator}$	98	%

References

[1] European Power Exchange, *EPEX SPOT SE.* `https://www.epexspot.com` [accessed 12.03.2023]

[2] Liang, T., Vecchi, A., Knobloch, K., Sciacovelli, A., Engelbrecht, K., Li, Y., Ding, Y., *Key components for Carnot Battery: Technology review, technical barriers and selection criteria.* Renewable and Sustainable Energy Reviews 2022;163:112478.

[3] Zhao, Y., Song, J., Liu, M., Zhao, Y., Olympios, A. V., Sapin, P., Yan, J., Markides, C. N., *Thermo-economic assessments of pumped-thermal electricity storage systems employing sensible heat storage materials.* Renewable Energy 2022;186:431-456.

[4] Morandin, M., Marchal, F., Mercangöz, M., Buchter, F., *Conceptual design of a thermo-electrical energy storage system based on heat integration of thermodynamic cycles Part A: Methodology and base case.* Energy 2012;45(1):375-385.

[5] Morandin, M., Marchal, F., Mercangöz, M., Buchter, F., *Conceptual design of a thermo-electrical energy storage system based on heat integration of thermodynamic cycles Part B: Alternative system configurations.* Energy 2012;45(1):386-396.

[6] Morandin, M., Mercangöz, M., Hemrle, J., Marchal, F., Favrat, D., *Thermoeconomic design optimization of a thermo-electric energy storage system based on transcritical CO_2 cycles.* Energy 2013;58:571-587.

[7] Steinmann, W.D., Jockenhöfer, H., Bauer, D., *Thermodynamic Analysis of HighTemperature Carnot Battery Concepts.* Energy Technol. 2020;8(3):1900895.

[8] Kim, Y.-M., Shin, D.G., Lee, S.Y., Favrat, D., *Isothermal transcritical CO_2 cycles with TES (thermal energy storage) for electricity storage.* Energy 2012;49:484-501.

[9] Mercangöz, M., Hemrle, J., Kaufmann, L., ZGraggen, A., Ohler, C., *Electrothermal energy storage with transcritical CO_2 cycles.* Energy 2012;45(1):407-415.

[10] Baik, Y.J., Heo, J., Koo, J., Kim, M., *The effect of storage temperature on the performance of a thermo-electric energy storage using a transcritical CO_2 cycle.* Energy 2014;75:204-215.

[11] Koen, A., Farres Antunez, P., White, A., *A study of working fluids for transcritical pumped thermal energy storage cycles* In: 2019 Offshore Energy and Storage Summit (OSES), 2019 Jul 10-12, Brest, France. p.1-7.

[12] Hirsch T. *MAN Wärmepumpen-Wie wir die klimaneutrale Zukunft der Stadt Esbjerg gestalten.* 27. Dresdner Fernwärme-Kolloquium, 2022.

[13] Decorvet R.C., Jacquemoud E., *Industrial heat pumps - MAN Energy Solutions.* Research report, 2021. `https://www.man-es.com/campaigns/download-request` [accessed 03.02.2023]

[14] Cordin Arpagaus, Frdric Bless, Michael Uhlmann, Jürg Schiffmann, Stefan S. Bertsch, *High temperature heat pumps: Market overview, state of the art, research status, refrigerants, and application potentials.* Energy 2018;152:985-1010.

[15] Maximini M., *Flexibilisierung der Strom- und Wärmeerzeugung durch Wärmespeicher.* Available at: `https://enerko.de/wp-content/uploads/2019/11/191120-Flexibilisierung-der-Strom-und-Waermeerzeugung-durch-Waermespeicher-.pdf` [accessed 08.02.2023]

[16] Heberle F., Brüggemann D., Weiß A.P., Grundemann L., *Geothermische Kraftwerke in Deutschland: Individuelle Lösungen durch die geeignete Wahl des Arbeitsmediums.* In: BWK: Das Energie-Fachmagazin 2017;69(6):51-54.

[17] Dumont, O., Charalampidis, A., Lemort, V., *Experimental Investigation Of A Thermally Integrated Carnot Battery Using A Reversible Heat Pump/Organic Rankine Cycle.* In: Proceedings of the International Refrigeration and Air Conditioning Conference, 2021.

[18] Eppinger, B., Steger, D., Regensburger, C., Karl, J., Schlücker, E., Will, S., *Carnot battery: Simulation and design of a reversible heat pump-organic Rankine cycle pilot plant.* Applied Energy 2021;288:116650.

[19] Garca-Pabn J.J., Mndez-Mndez D., Belman-Flores J.M., Barroso-Maldonado J.M., Khosravi A. *A Review of Recent Research on the Use of R1234yf as an Environmentally Friendly Fluid in the Organic Rankine Cycle.* Sustainability. 2021; 13(11):5864.

[20] Redouane Ghoubali, Paul Byrne, Frdric Bazantay, *Refrigerant charge optimisation for propane heat pump water heaters*International Journal of Refrigeration 2017;76:230-244.

[21] Iqony Solutions GmbH, *EBSILON® Professional, Process Simulation Software*. Available at: `https://systemtechnologies.iqony.energy/de` [accessed 03.02.2023]

[22] Lemmon, E.W., Bell, I.H., Huber, M.L., McLinden, M.O. *NIST Standard Reference Database 23: Reference Fluid Thermodynamic and Transport Properties-REFPROP.* Version 9.1, National Institute of Standards and Technology, 2013.

[23] Turton R., Bailie R. C., Whiting W.B., Shaeiwitz J.A., Bhattacharyya D., *Analysis, synthesis, and design of chemical processes.* Pearson, Upper Saddle River, 4th edition, 2013.

[24] A. Bejan, G. Tsatsaronis, M. Moran, *Thermal Design and Optimization.* Wiley-Interscience publication, Wiley, 1996.

[25] Balli O., Aras H., Hepbasli A., *Exergoeconomic analysis of a combined heat and power (CHP) system*. International Journal of Energy Research 2008;32(4):273-289.

[26] Koksharov J., Teles de Oliveira H., Dammel F., Stephan P., *Evaluation of different pumped thermal energy storage systems*. In: Amano, Y., Sciubba, E., Elmegaard, B. (Editors). ECOS 2021: Proceedings of the 34th International Conference on Efficiency, Cost, Optimization, Simulation and Environmental Impact of Energy Systems; 2021 Jun 27 - Jul 2; Taormina, Italy. p. 679-690.

[27] Towering Skills, *Cost Indices,* Available at: `https://www.toweringskills.com/financial-analysis/cost-indices/` [accessed 23.02.2023].

[28] European Commission, *Exchange rate.* Available at: `https://www.ecb.europa.eu/stats/policy_and_exchange_rates/euro_reference_exchange_rates/html/eurofxref-graph-usd.de.html` [accessed 08.02.2023]

[29] Kost C.,Shammugam S.,Fluri V., Peper D., Memar A.D., Schlegl T., *Stromgestehungskosten Erneuerbare Energien*. Study, Jun 2021.

[30] Towler G.P., Sinnott R.K., *Chemical Engineering Design: Principles, Practice, and Economics of Plant and Process Design.* Butterworth-Heinemann, Boston, MA, 2nd edition, 2013.

[31] Dietrich A., *Assessment of Pumped Heat Electricity Storage Systems through Exergoeconomic Analyses [dissertation]* Darmstadt, Germany: TU Darmstadt; 2017.

[32] entsoe, *Transparency Platform.* Available at: `https://transparency.entsoe.eu` [accessed 23.02.2023].

[33] KfW, *KfW-Programm Erneuerbare Energien 'Standard'.* Available at: `https://www.kfw.de/inlandsfoerderung/Unternehmen/Wohnwirtschaft/F\unhbox\voidb@x\bgroup\accent127o\penalty\@M\hskip\z@skip\egrouprderprodukte/Erneuerbare-Energien-Standard-(270)` [accessed 23.02.2023].

[34] KfW, *Konditionenübersicht für Endkreditnehmer.* `https://www.kfw-formularsammlung.de/KonditionenanzeigerINet/KonditionenAnzeiger` [accessed 01.06.2021].

[35] De Rose A., Buna M., Strazza C., Olivieri N., Stevens T., Peeters L., Tawil-Jamault D., *Technology Readiness Level: Guidance Principles for Renewable Energy technologies.* Report, 2017.

[36] Lecompte S, Ntavou E, Tchanche B, Kosmadakis G, Pillai A, Manolakos D, De Paepe M. *Review of Experimental Research on Supercritical and Transcritical Thermodynamic Cycles Designed for Heat Recovery Application.* Applied Sciences. 2019;9(12):2571

[37] Echogen Power Systems, *EPS100 Heat Recovery Solution.* Available at: `https://www.echogen.com/_CE/pagecontent/Documents/EPS100_brochure_2017.pdf` [accessed 02.03.2023]

[38] Gardella L., Wiemer H.-J. *First experimental results of a supercritical Organic Rankine cycle using propane as working fluid.* Annual Report 2020 of the Institute for Thermal Energy Technology and Safety. Editor: W. Tromm, KIT Scientific Publishing, 2022.p.59-65.

[39] Dincer I., Erdemir D., *Heat Storage Systems for Buildings; Chapter 2 - Heat Storage Methods.* Elsevier, 2021.p. 3790.

[40] Macchi E., Astolfi M., *Organic Rankine Cycle (ORC) Power Systems, Technologies and Applications.* Woodhead Publishing, 2017.

Evaluation of dual side cooling system for prismatic batteries for vehicle application

Said Madaoui[a], Bartlomiej Guzowski[b], Roman Gozdur[c], Zlatina Dimitrova[d], Nicolas Audiot[e], Jocelyn Sabatier[f], Jean-Michel VINASSA[g] and Franck Guillemard[h]

[a] Stellantis,Paris, France, said.madaoui@stellantis.com
[b] Lodz university of technology,Lodz, Poland, bartlomiej.guzowski@p.lodz.pl, [c]
[c] Lodz university of technology,Lodz, Poland, roman.gozdur@p.lodz.pl
[,d] Stellantis,Paris, France, zlatina.dimitrova@stellantis.com
[,e] Stellantis,Paris, France, nicolas.audiot@stellantis.com
[f]Bordeaux university,Bordeaux, France, jocelyn.sabatier@u-bordeaux.fr
[,g]Bordeaux university,Bordeaux, France, jean-michel.vinassa@ims-bordeaux.fr,
[,h] Stellantis,Paris, France, franck.guillemard@stellantis.com

Abstract:

Today lithium-ion stands out among the various battery technologies in vehicle applications thanks to their good energy density, low self-discharge and the absence of the memory effect. Nevertheless, lithium-ion batteries pose many challenges such as driving range, lifespan, safety issues and also the charging time which is still significant

In order to reduce the charging time, it is necessary to inject a very high current into the battery which may drastically raise its temperature and thus reduce its lifespan. Today, in most cases, the battery pack of an electric vehicle is cooled through flat cooling plates, mounted either by the lateral or the bottom surfaces. These cooling plates can also be used to warm up the battery in cold weather. But during the fast charge, this configuration poses some problems and can be not efficient enough to cool or heat the batteries.

In this study, a battery module is thermally managed not only by the bottom cooling plate but also by a second cooling plate placed on the busbars. According to simulations and experimental tests regarding one case study, this configuration makes it possible to not only cool the module more quickly by reducing the thermal time constant by 47% but also reduces the battery maximum pick temperature reached with a conventional cooling system by 6°C. It stands out that the top cooling plate acts like a thermal bridge which unifies the temperature inside the battery module and thus support the equal ageing process of the batteries.

Keywords:

Electric vehicle, batteries, thermal management, cooling plate, thermal gradient, lifespan

1. Introduction

The battery pack is the only and main source of energy of an electric car, and to be able to replace an internal combustion engine vehicle, several technical challenges exist that engineers and specialists must face, in order to both increase the autonomy and lifespan while reducing the charging time. Lithium-ion batteries (LIBs) have gradually evolved from a variety of technologies due to their low self-discharge rate, high energy density and lack of memory effect, this type of batteries has revolutionized the energy storage technology and enabled the mobile revolution [1]. Li-ion batteries are available in different shapes and configurations, including cylindrical, prismatic and pouch cells. Temperature is one of the key limiting factors for battery pack performance and lifetime. Temperature heterogeneity inside LIBs causes different electrochemical reaction rates within the cells. This can lead to uneven current density distributions, local State of Charge (SoC) differences and local ageing differences, which may not only accelerate the global ageing, but also reduce the accessible energy of the battery. Temperature rise and spatial temperature gradient minimization inside the cell is among the main thermal challenges during fast charge [2]. Thermal Management Systems (TMS) are employed in majority of vehicles to counter these challenges [3]. A 5°C variation in temperature can reduce the battery pack's capacity by

1.5–2% [4], and its power capabilities by 10% [5]**.** To improve cooling capability of LIBs, various researchers have incorporated different cooling techniques. Nowadays, liquid cooling, air cooling and phase change material are widely adopted for battery thermal management. Depending on the technical requirements and cost, battery pack manufacturers can use one or several cooling methods. The TMS can be classified into active cooling and passive cooling.

Active cooling consumes extra energy for pumps and fans powering but still more efficient than passive cooling[6]. The active liquid cooling can also be classified into direct-contact and indirect contact. For indirect contact, the liquid is a combination of water and ethylene glycol to avoid liquid freezing at low temperatures inside the cooling plates, while for direct contact, the liquid must be dielectric to avoid any short-circuits. Recently, the direct-contact liquid cooling method has gained increased attention due to its high cooling efficiency [7]. The battery thermal management serves to monitor, control and maintain the optimum operating temperature conditions of a battery. The items that are considered in designing the cooling plate are: (a) the cooling plate should maintain the temperature of batteries at the manufacturer's recommended temperature during normal operation, (b) the cooling plate should dissipate maximum possible heat from the batteries in case of thermal runaway, (c) the coolant pressure drop inside the cooling plate should be minimized, and (d) the size and weight of the TMS should be minimized [8].

Although the above research has achieved remarkable results in battery thermal management, some challenging questions remain: (a) there is little previous literature on battery inner thermal gradient minimization based on both experimental tests and simulations, (b) so far, little work has investigated the benefits of cooling and heating the batteries by putting a cooling plate on top of the battery module, and its role in the battery thermal management.

The aim of this study is to better manage the battery temperature by reducing not only the pick maximum temperature but also the inner thermal gradient, by adding a cooling plate on top of the battery module. The objectives of the present work are as follow:

-perform different experimental tests on a battery module managed thermally in the first case by a bottom cooling plate and then by a top and bottom cooling plates
-compare the results of both technologies in term of thermal management
-build a model and do the calibration using the data acquired during the experimental tests
-use the model to investigate other scenarios in extreme conditions (current and temperature), and of course assess the role of top cooling plate in the battery temperature variation. The last sections conclude and give perspectives on the research topic

2. Electrothermal modelling of Li-ion batteries

2.1. Battery module model

The battery module consists of 12 prismatic cells connected with busbars to form a 3p4s battery module as represented in the Fig. 1(a). To model the battery module, a fine modeling of its constituents is necessary, by modeling the cells in Fig. 1(b) and also the busbars. Fig.1(c) shows the cover detached from the casing and also the Jelly roll (JR) which represents the heart of the cell and the main part of the battery.

In this section the proposed model is established. With the current, the initial temperature, and the environment temperature as inputs, the model can predict the internal temperature distribution and the state of charge of the battery. The battery module model consists of three sub models, a thermal model, an electrical model based on Electrical Circuit Network ECN and a heat generation model.

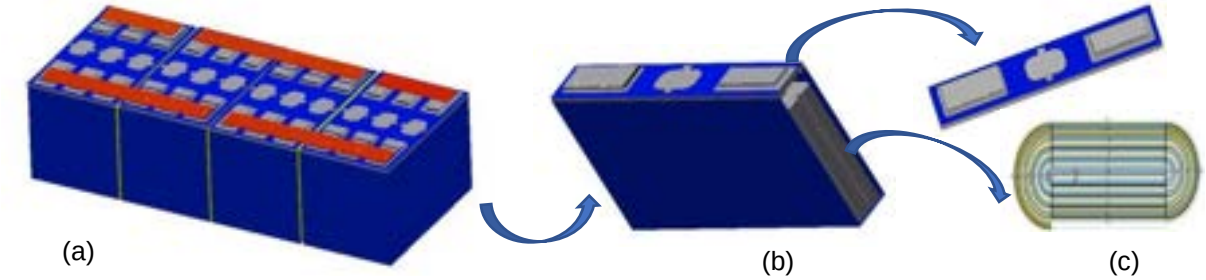

Figure. 1. Structure of the studied system: a) battery module, b) battery cell, c) Cover detached from the casing and JR inside the battery cell

One of the most critical steps for developing battery prognostics solutions is to establish a battery model which enables the auto-maker to simulate battery behavior and interpret battery issues in a form that can be understood by users and designers [9].
Different methods from the electrical, thermal, mechanical and electrochemistry perspectives have been used to establish different battery models, and the dynamic behaviors of the battery regarding different charging/discharging rates and temperatures have been investigated. Among the various battery models, electro-thermal modeling is commonly used to study the relationship between the current and the temperature of battery. The battery electro-thermal model couples the electrical and thermal models closely. The initial inputs of the electrical model are the discharge current, the SOC level and the temperature. The inputs of the electrical model generates heat for the thermal model, this last provides a temperature output signal. Then this temperature signal is fed back to the electrical model, since the new temperature affects the electrical parameters such as the internal resistance.

Generally, the heat generation of the battery Q_{gen} during charge and discharge contains two parts: reversible and irreversible heats, and it can be expressed by Eq. (1). The entropy change is responsible for the reversible heat Q_{rev} which can be expressed by Eq. (2), and the irreversible Q_{irr} heat the heat generated by ohmic resistance is expressed by Eq. (3)

$$Q_{gen} = Q_{irr} + Q_{rev} \tag{1}$$

$$Q_{rev} = I\, T_b \frac{dOCV}{d\, T_b} \tag{2}$$

$$Q_{irr} = I^2 R \tag{3}$$

In order to avoid the accumulation of heat at the level of the cell, this heat is often exchanged with the neighboring elements of the cell by conduction Q_{cond}, or dissipated by different TMS by convection Q_{dis}. The two modes of heat exchange are detailed in the two equations below Eq. (4) and Eq. (5) respectively

$$Q_{cond} = \frac{(T_{neigh} - T_B)}{R_{th}} \tag{4}$$

$$Q_{dis} = h_{conv}(\, T_{env} - T_B) \tag{5}$$

The battery temperature is affected by various heat transfer paths. To reduce the battery temperature, part of the heat generated has to be dissipated to the external environment in order to avoid the heat accumulation and thus reduce the temperature raise [10].

2.1.1. Battery cell model

The research object is a commercial 67 Ah prismatic battery cell. The battery cell specifications are tabulated in table 1.

Table 1. Specifications of the battery cell

Specification	$Value$
Cathode material	NMC
Anode material	Graphite
Nominal capacity	67Ah
Cut off voltages	2.8-4.2V
Dimensions	150mm 30mm 100mm
Thermal conductivities	40-2.5-40 W/m.K
Thermal capacity	1200 J/Kg.K

The battery cell is a complex system since it consists of several elements such as JRs, a casing, a cover and electrical insulating films. To finely model the cell, the JRs and the casing are modeled in order to be able to represent the thermal behavior of the battery by having a temperature response at each point of the cell whether at inside or outside. The JR and the casing modeling approaches are now described.

2.1.1.1 JR modeling

The challenge is to be able to visualize and quantify the temperature gradients within the cell, while having a model that can be simulated in seconds so that it can be embedded on an electric vehicle. Considering the complex geometry of the JR, it was necessary to design a mesh which makes it possible to represent all the heat exchanges in all directions inside the cell. To successfully reproduce the thermal behaviour of the JR, it is essential to provide a reliable mesh able to represent as good as possible the heat exchanges within the JR, and good assessment of the cell inner thermal gradient. The proposed model consists of meshing the JR in thickness as well as in height. The particularity of this mesh compared to what could be found in literature, is that it takes into account the orthoradial direction which shows that the heat can be exchanged between the meshes by going around the windings. The Fig. 2 shows the proposed mesh by considering the three directions, axial (according to the height of the JR), radial (normal to the winding), orthoradial (parallel to the winding).

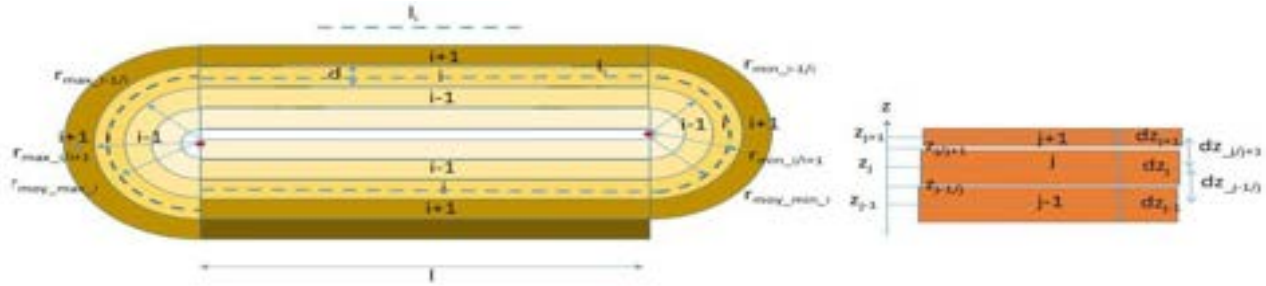

Figure. 2. The proposed mesh of the JR

The JR is obtained by wrapping the electrodes around a hollow space. Each turn is qualified as an elementary layer which is made of different sub layers. Each elementary sub layer has its own thermal conductivity and capacity, its own thickness as well as its own density. All these essential data for the thermal model are taken from literature in absence of having been able to obtain them from the supplier. The JR model is well detailed in [11] with all the equations that represent the physics at the JR level.

To summarize, the heat generated by a mesh i,j can be calculated according to the following equation:

$$\dot{Q}_{i,j} = R_{30s\,i,j} I^2{}_{i,j} + I_{i,j} T_{i,j} \frac{\partial OCV_{i,j}}{\partial T_{i,j}} \tag{6}$$

2.1.1.2 Casing modeling

To get a full model of the cell, the JR have to be linked to the other elements of the cell that surround it, starting with the casing which acts as a thermal bridge between the JR and the external environment. In order to visualize the thermal gradient on the casing, the latter is meshed in height, and each mesh j of the casing is connected with a mesh imax,j of the JR. Since the casing is made of aluminium, its specific characteristics are known.

2.1.1.3 Busbar modeling

The busbar modeling strategy consists of breaking down the busbar into meshes and assign to each mesh the following Fourier equation:

$$m_{BBi} C_{BB} \frac{dT_{BBi}}{dt} = Q_{generated} + Q_{dissipated} + Q_{exchanged\ by\ conduction} \tag{7}$$

where m_{BBi} is the mass of a mesh i,j of a busbar, C_{BB}, $Busbar$ specific heat capacity, and $Q_{generated}$ represents the heat generated mostly by Joule effect according to eq. (8) ,

$$Q_{generated} = \frac{\rho\, l_{BBi}}{S_{BB}} * I^2 \tag{8}$$

$Q_{dissipated}$, denotes the heat dissipated either by natural or forced convection, and $Q_{exchanged\ by\ conduction}$ represents the heat that could be exchanged between the busbar and the upper part of the tab and also with the neighbouring meshes of the busbar. The fig. 3 shows the meshed busbar. The heat exchange by radiation was neglected in this paper.

Figure. 3. The meshed busbar connecting six cells

2.1.1.4 Battery module model

Once the battery cell model is well obtained, it is duplicated 12 times to form the 3p4s module model, thus the module is made of 4 blocks of 3 cells each. The cells of the same block are coupled thermally through the busbars as well as through the meshes of their casings. Once the block is built, it is duplicated four times by assuming that the cells are identical, and they have all the same characteristics. Then the four blocks are coupled thermally together through busbars to form what we call a 3p4s battery module.

Figure 4(b) shows the temperature responses of the 12 cells for the current profile represented in the Fig. 4(a). This current profile was chosen to represent both charge and discharge scenarios, and also investigate the electrical resistance variation as function of SoC.

The hypothesis are not detailed for this part, because the goal is to show that the model allows to have the temperature responses of the twelve cells for a given current profile, the assumptions will be detailed in the part dedicated to (results and comparison).

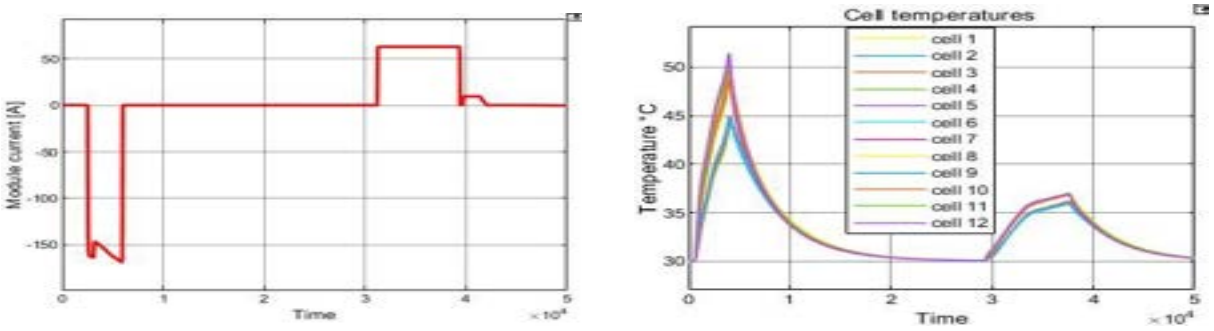

(a) (b)

Figure. 4. Simulation results after building the model: a) Input current, b) cells temperatures

2.2. Model calibration

Before starting the calibration of the module model, some assumptions have been considered.

2.2.1. Assumptions

The following assumptions have been made for model calibration

-the cells inside a module are all identical

-the presence of thermal spacers between the blocks means that the only thermal path between the block of cells becomes the busbars

-the electrical resistances between the busbars and the tabs are considered null.

-the temperatures of the air in the climatic chamber and of the liquid circulating inside the plates are constant throughout the test.

-the initial and boundary conditions of the model are supposed to be suitable to the experiment conditions

(a) (b) (c)

Figure.5. Battery module thermal management: a) module without any cooling plate, b) module with bottom cooling plate, c) module with top and bottom cooling plates

2.2.2. Battery module without any cooling plate

In order to calibrate the model detailed above, some electrothermal tests have been carried out on the 3p4s module. The first tests have been carried out on the module without any cooling plate as shown in the Fig. 5(a), and the goal is to reproduce correctly the thermal and electrical responses of the twelve cells. At first the battery module has been put in a climate chamber. So, the first parameter to be determined was the heat exchange coefficient h_{conv}. The second parameter was the contact electrical resistances between the electrical load and the battery module terminals. These contact electrical resistances can play a very important role in the thermal behavior of the batteries, especially when the contact is bad.

2.2.3. Battery module with a top and bottom cooling plate

The same electrothermal tests have been carried out, first on the battery module coupled to a bottom cooling plate (first case see the Fig. 5(b)) and then on the battery module coupled to the top and bottom cooling plates (second case as shown by the Fig. 5(c)).

Once the data acquisition is done through thermocouples, the goal was to assess the benefits of adding the cooling plates and then compare the technologies in term of efficiency in thermal management of the batteries. At the model level the only parameters that had to be determined in order to reproduce the thermal responses of the cells were: (a) the thermal resistances between the bottom cooling plate and the bottom surfaces of the cells for the first case and (b) the thermal resistance between the top cooling plate and the busbars for the second case.

3. Measurement setup and test procedures

A dedicated test stand has been developed to assess the efficiency of the cooling system extended with a cooling plate through the upper surface on which the connection electrodes are installed. All experimental tests were performed for the same battery module at the same, strictly controlled conditions. Each time, preconditioning procedure was preceded to reach the same initial state of charge and state of health of the tested battery module before tests. The test stand consists of the Li-Ion battery module, the thermal management system, charging/discharging system and a control and acquisition system.

3.1. Tested battery module

For the evaluation of the cooling improvements, the high-power battery module has been selected. The battery module was made of 12 Li-Ion prismatic cells connected in the 3s4p setup. Technical parameters of the cells were listed in subsection 2.1.

3.2. Thermal Management system and thermal test procedure

The thermal management system consists of two water cooling plates, water chiller and thermal chamber. As shown in Fig. 6, the battery module was placed in the thermal chamber. The bottom dedicated cooling plate was connected in parallel with top cooling plate and supplied from the chiller CW-6100AN. The inlet temperature of purified water was control by the chiller. Cooling plates were integrated with battery module through 3 mm thick thermal pad.

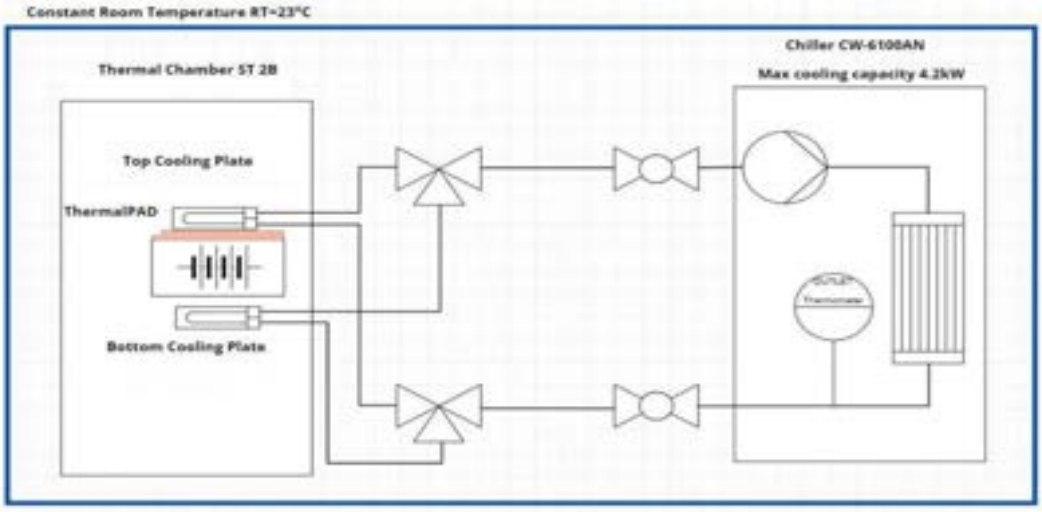

Figure. 6. The diagram of the thermal management system

4. Experimental results

4.1. Charging battery module

The thermal response of the battery module was measured during charge test, where coolant temperature was set at T_C = 20 ºC and ambient temperature was T_A = 25 ºC. The thermal response of battery module with only bottom cooling plate during the charge test is shown in Fig. 7. The temperature of a bottom cooling plate was measured by sensor labeled as T_{cp} which was placed between battery module and cooling plate. Temperature inside climate chamber was recorded by two sensors TA and TA1. Time constant for this process equals to τ = 5700s. Maximum temperatures were recorded on terminals of tested module. The temperature 49.6°C was recorded by sensor 37. The highest temperature recorded inside battery module exceeded 43°C (sensor 19, sensor 20, sensor 21) and it was recorded during highest charge current I_{CHA} = 190A. On the other hand, the lowest temperature was recorded on side walls of battery module, and it did not exceed 37°C (sensor 43, sensor 45, sensor 41 and sensor 40).

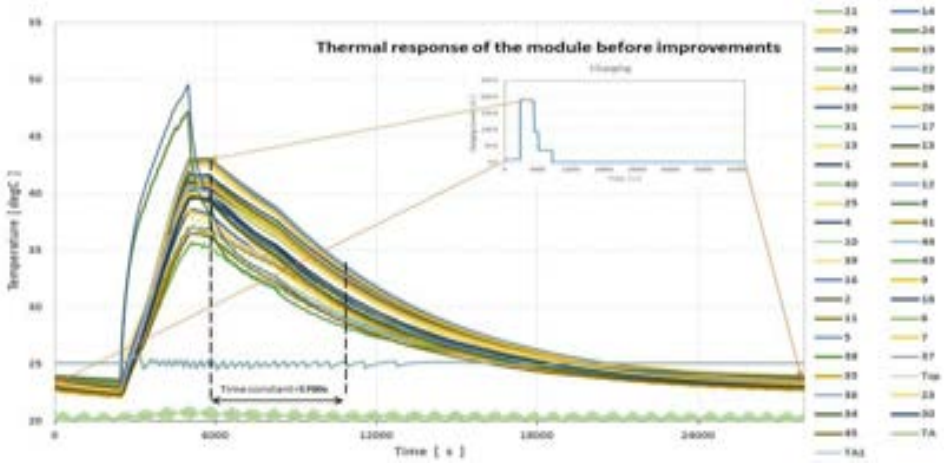

Figure. 7. Thermal response of battery module with bottom cooling plate during charge process, where T_A = 25 ºC, T_C =20 ºC

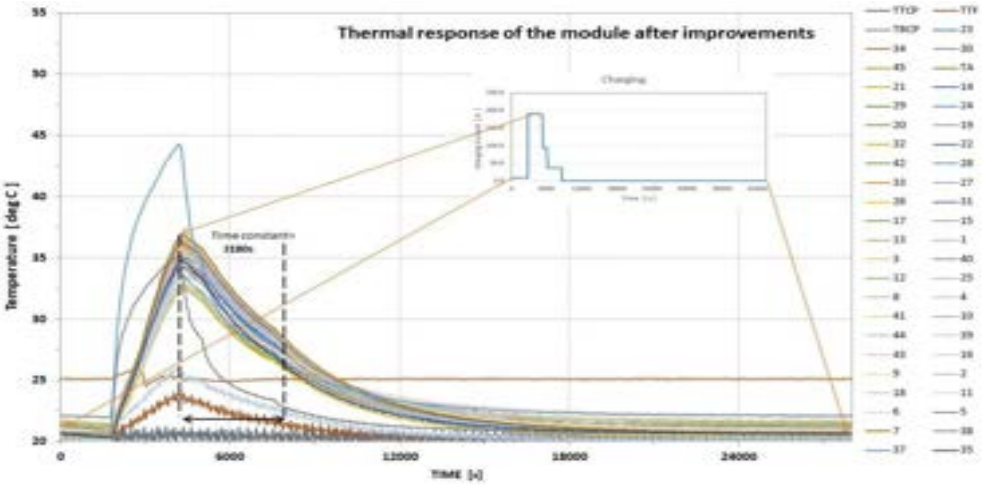

Figure. 8. Thermal response of battery module with top and bottom cooling plate during charge process, where T_A = 25 ºC, T_C =20 ºC

Additional top cooling plate caused drop of maximum temperature measured on terminals to 44°C (sensor 37) and 35°C (sensor 38) as shown in Fig. 8, and also the drop in the average temperature of battery module. Highest temperature recorded by sensors placed inside the battery module (e.g. sensor 19, sensor 20, sensor 21) was 37°C and it was lower by 6°C in comparison to the test with only one cooling plate. Temperature on the side walls of battery module did not exceed 33°C. Cooling time constant was decreased by 44% from τ = 5700s to τ = 3180s. Another advantage of adding the top cooling plate is clearly visible with a smaller temperature discrepancy inside the battery module from

7°C to 3.5°C. Therefore, the aging process of batteries inside the battery module can be easily controlled. Average relative improvement rate equals to 21%. The highest improvement (37%) was recorded for sensor 38 placed on one of terminals. Average relative improvement inside the battery module was around 19%.

The thermocouples described above are shown in the figure bellow.

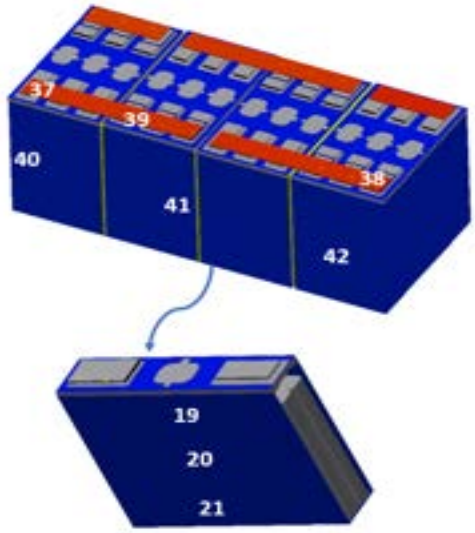

Sensor position		Sensor number
Module external busbar connection	Negative side	37
	Positive side	38
Module busbar cell connection	4th cell from module negative side	39
Module side plate	HV connector side (module negative side)	40
	HV connector side (module middle side)	41
	HV connector side (module positive side)	42
	Non-HV connector side (module negative side)	43
	Non-HV connector side(module middle side)	44
	Non-HV connector side (module positive side)	45

Sensor position		Sensor number
Cell casing greatest surface	Upper of surface	19
	Middle of surface	20
	Bottom of surface	21

Figure 9. Layout of the temperature sensors

4.2. Discharging battery module

After charging tests, the discharge test was conducted with T_A = 25°C and T_C = 30°C. In Fig. 10, thermal response of battery module with only bottom cooling plate during the investigation is given. The same test was conducted once again for battery module equipped with bottom and top cooling plates. Thermal behavior of the module is shown in Fig. 11. Differences in C-rate profile caused longer time constant for cooling process which was equaled to τ = 7260s. For this case study, the time constant was decreased by 55% in the tests with two cooling plates. Maximum temperatures before and after adding the top cooling plate (45°C and 43°C) were recorded on terminals of battery module. Maximum recorded temperature after improvement inside the battery module dropped by 2°C, but on the other hand the temperature inside the module was more uniform in a test with top and bottom cooling plates. At t = 6000 s, the temperature difference measured inside the battery module and on external walls dropped by half from 5°C to 2.5°C. It stands out that the average relative improvement rate was 31%.

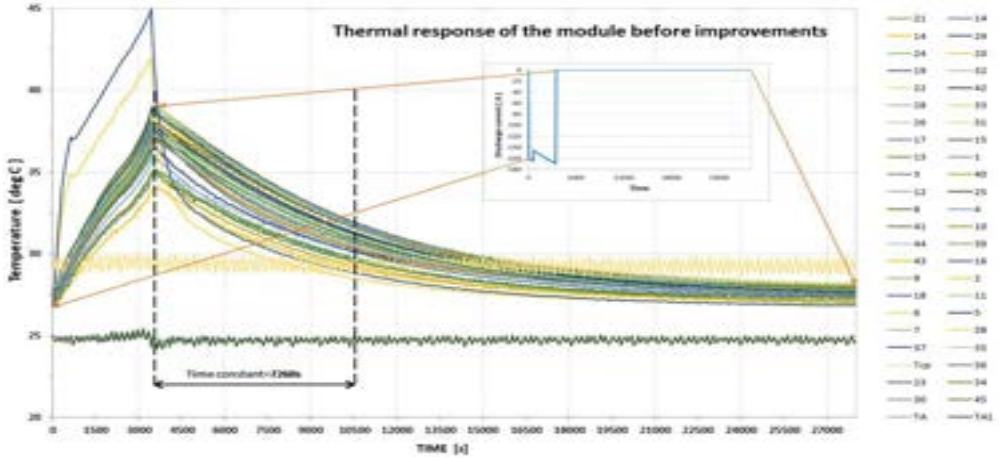

Figure. 10. Thermal response of battery module with bottom cooling plate during discharge process, where T_A = 25 ºC, T_C =30 ºC

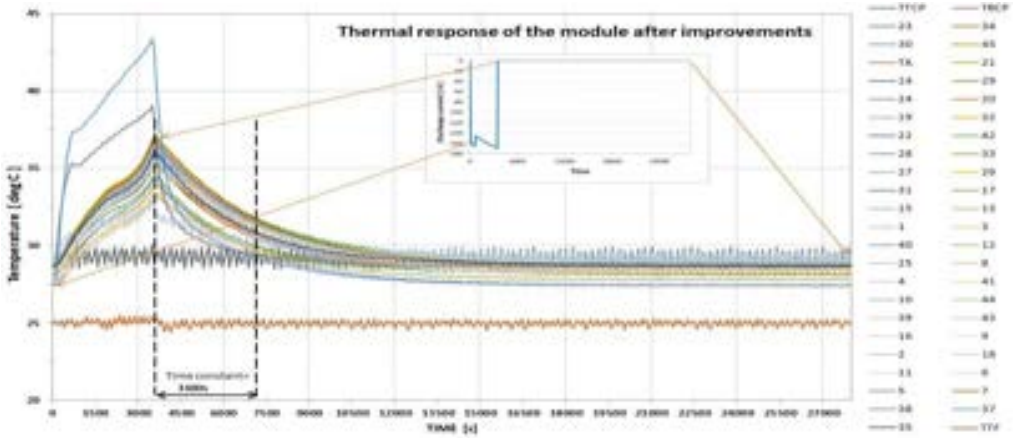

Figure. 11. Thermal response of battery module with top and bottom cooling plate during discharge process, where T_A = 25 ºC, T_C =30 ºC

5.Results comparison

Different electrothermal tests have been carried out to validate the battery module model. In this paper for the sake of brevity, only one test will be discussed.

In this test, the current profile used to validate the model is shown in Fig. 12(a). The advantage of this current profile is that it allows to scan the entire SoC range in order to check the lookup-tables of the electrical resistances of the batteries during charge and discharge as well as that of the OCV, this current profile also permits to assess the effect of the current amplitude on the thermal and electrical responses of the batteries.

The experimental test conditions have been taken into consideration and some simplifying assumptions and boundary conditions have been set in order to simulate the model and compare the obtained signals with those of the experiment:

-the module is cooled with the top and bottom cooling plates

-the air temperature is set at 25°C and coolant temperature at 20°C

-the initial temperature is set at 20.7°C

-one cell of the module is targeted to do the comparison between the model and the experiment, and the considered thermocouple is fixed at the center of the great surface of this battery

The Fig. 12(b) shows the temperature response of the model in red compared to the temperature given by the thermocouple in black.

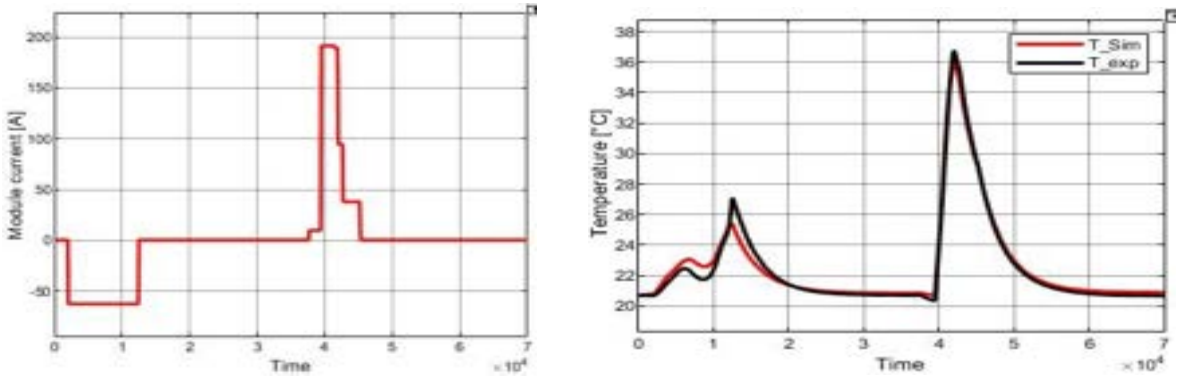

(a) (b)

Figure.12. Model validation results: a) Input current, b) cell temperature

In this section a comparison between the three configurations presented in the Fig. 5 has been done in order to assess the benefits of adding the cooling plates regarding the battery module thermal management. According to the Fig.13, the third configuration (module with top and bottom cooling plates) represented by the blue color is the most efficient in term of thermal management, and it's the

best way of extracting and dissipating the calories generated by the battery during charge and discharge. As a consequence, the maximum pick temperature is reduced compared to the configuration represented by the black curve where the module is cooled only by the bottom cooling plate. Also, one can note that the time constant is shortened which proves the efficiency of this configuration.

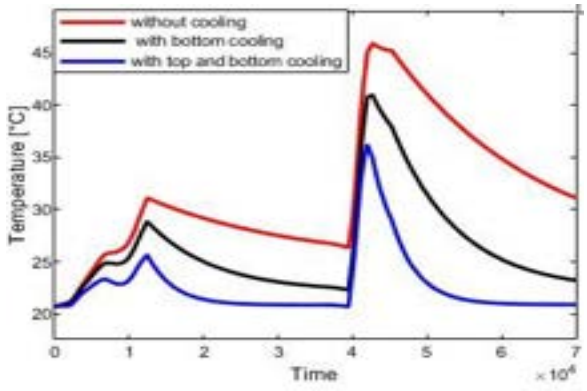

Figure. 13. Thermal management system performance

6.Conclusion

In this study, a methodology of battery module modelling is proposed, by taking into account the battery cells, the busbars and also the thermal spacers between the battery cells. A qualitative study is done on a battery module by investigating the benefit of adding the top cooling plate in the overall battery module thermal management. According to simulations and experiments regarding one case study, the configuration with top and bottom cooling plates makes it possible to not only cool the module more quickly by reducing the thermal time constant by 47% but also reduces the battery maximum pick temperature reached with a conventional cooling system by 6°C. Different electrothermal tests have been carried out to validate the battery module model with different scenarios in term of air/coolant temperatures and current profiles in (charge and discharge). It stands out that the model has a good reproducibility, and the error is always below the thermocouple's uncertainty. It stands out also that it gets easier and more efficient to extract calories from the batteries by adding the top cooling plate.

In this paper, only the prismatic cells are concerned, but the methodology can be applied on different battery types and for different battery module topologies.

Acknowledgments

This work took place in the framework of the OpenLab 'Electronic and Systems for Automotive' combining IMS Laboratory, Lodz Laboratory and Stellantis. This work was carried out under a CIFRE agreement and granted by the ANRT

Nomenclature

C_{BB} busbar specific heat, J/(kg K) h_{conv} convective heat transfer coefficient, W/(m^2 K)

I current flowing through the battery and busbar, A

I_{CHA} charge current, A

I_{DIS} discharge current, A

Q_{dis} heat dissipated by the battery, W

Q_{irr} irreversible heat, W

Q_{rev} reversible heat, W

l_{BBi} length of the busbar mesh, m

m_{BBi} busbar mesh mass, Kg

T_b battery temperature, K

T_{env} environment temperature, K

Q_{cond} heat exchanged with the battery by conduction, W

Q_{gen} heat generated by the battery, W

R_{th} thermal resistance, K/W

S_{BB} cross-sectional area of the busbar, m²

T_A ambient temperature, ºC

T_{BBi} temperature of the busbar mesh, K

T_C coolant temperature, ºC

T_{neigh}, neighbour elements of the cells, K

Greek symbols

ρ density, Kg/m^3

Subscripts and superscripts

JR jelly roll

$LiBs$ lithium-ion batteries

OCV open circuit voltage

SoC state of charge

TMS thermal management system

References

[1] F. Maisel, C. Neef, F. Marscheider-Weidemann, et N. F. Nissen, « A forecast on future raw material demand and recycling potential of lithium-ion batteries in electric vehicles », *Resour. Conserv. Recycl.*, vol. 192, p. 106920, mai 2023, doi: 10.1016/j.resconrec.2023.106920.

[2] M. Steinhardt, E. I. Gillich, M. Stiegler, et A. Jossen, « Thermal conductivity inside prismatic lithium-ion cells with dependencies on temperature and external compression pressure », *J. Energy Storage*, vol. 32, p. 101680, déc. 2020, doi: 10.1016/j.est.2020.101680.

[3] Y. Zhou, Z. Wang, Z. Xie, et Y. Wang, « Parametric Investigation on the Performance of a Battery Thermal Management System with Immersion Cooling », *Energies*, vol. 15, nº 7, p. 2554, mars 2022, doi: 10.3390/en15072554.

[4] I. A. Hunt, Y. Zhao, Y. Patel, et J. Offer, « Surface Cooling Causes Accelerated Degradation Compared to Tab Cooling for Lithium-Ion Pouch Cells », *J. Electrochem. Soc.*, vol. 163, nº 9, p. A1846-A1852, 2016, doi: 10.1149/2.0361609jes.

[5] X. Feng, C. Xu, X. He, L. Wang, G. Zhang, et M. Ouyang, « Mechanisms for the evolution of cell variations within a LiNixCoyMnzO2/graphite lithium-ion battery pack caused by temperature non-uniformity », *J. Clean. Prod.*, vol. 205, p. 447-462, déc. 2018, doi: 10.1016/j.jclepro.2018.09.003.

[6] T. Amalesh et N. Lakshmi Narasimhan, « Liquid cooling vs hybrid cooling for fast charging lithium-ion batteries: A comparative numerical study », *Appl. Therm. Eng.*, vol. 208, p. 118226, mai 2022, doi: 10.1016/j.applthermaleng.2022.118226.

[7] J. Liu, Y. Fan, et Q. Xie, « Feasibility study of a novel oil-immersed battery cooling system: Experiments and theoretical analysis », *Appl. Therm. Eng.*, vol. 208, p. 118251, mai 2022, doi: 10.1016/j.applthermaleng.2022.118251.

[8] A. H. Mohammed *et al.*, « Dual-purpose cooling plate for thermal management of prismatic lithium-ion batteries during normal operation and thermal runaway », *Appl. Therm. Eng.*, vol. 160, p. 114106, sept. 2019, doi: 10.1016/j.applthermaleng.2019.114106.

[9] S. M. Rezvanizaniani, Z. Liu, Y. Chen, et J. Lee, « Review and recent advances in battery health monitoring and prognostics technologies for electric vehicle (EV) safety and mobility », *J. Power Sources*, vol. 256, p. 110-124, juin 2014, doi: 10.1016/j.jpowsour.2014.01.085.

[10] R. Gozdur, B. Guzowski, Z. Dimitrova, A. Noury, G. Mitukiewicz, D. Batory. An energy balance evaluation in lithium-ion battery module under high temperature operation. *Energy Conv. and Manag*., vol. 227, p. 113565, Jan 2021, doi:10.1016/j.enconman.2020.

[11] S. Madaoui *et al.*, « A detailed Electro-thermal model of an NMC lithium-ion prismatic cell », *VTC2023Spring conference.*

Methodology for the sizing of a Carnot battery based on a Rankine cycle and application to a 10 kWe system for district heating application

Olivier Dumont[a], Chiara Poletto[b], Olivier Thomé[c] and Vincent Lemort[d]

[a] Uliège, Liège, Belgium, olivier.dumont@uliege.be
[b] Chiara Poletto, Bologna, Italy, chiara.poletto3@unibo.it
[c] Uliège, Liège, Belgium, olivier.thome@student.uliege.be
[d] Uliège, Liège, Belgium, vincent.lemort@uliege.be

Abstract:
The basic technological principle of a Carnot Battery is to transform electricity into heat, store the heat and transform the heat back into electricity and/or heat. This technology has been developed more and more in the last years. This study considers the integration of a 10 kW Carnot battery in a district heating in a building with photovoltaic panels. It allows to provide both thermal and electrical peaks shaving. Few prototypes exist up to now and a clear methodology to size a Carnot battery properly does not exist. This paper tries to draw guidelines based on a state of the art, simulation models and lessons learnt from experimental campaigns. The idea is to help engineers to develop Carnot battery which are cheap, robust and efficient.

Keywords:
Carnot battery, electrical energy storage, district heating, heat pump, Rankine cycle, Thermal Energy Storage.

1. Introduction

1.1. Context

The share of electricity production needs to increase sharply in the next decades to decrease the impact of humans on the environment. However, there is a significant mismatch between renewable energy production and consumption. This means that electrical energy storages will play a very important role in the future. A recent alternative technology has therefore been studied for several years: the Carnot battery [1-4].

1.2. Carnot battery

The principle of a Carnot battery is rather simple: a heating cycle converts electricity into thermal energy, to store it and to use a power cycle to convert it back to electrical energy when needed. Different configurations are possible to achieve a Carnot battery (CB): the considered technology in this paper is a heat pump (HP) combined with a Rankine cycle (RC) [1-4]. This technology is interesting because it relies on massively produced components (low-cost), it allows the integration of heat flux trough the low operating temperatures and one single machine can replace the combination of the HP et RC (reversible HP/RC) [5-8].

1.3 Thermal integration

Typically, the power-to-power ratio (P2P), defined as the electrical energy output (discharge) divided by the electrical energy input (charge) is below 60% for classical CB. This is the reason why it can be helpful to valorize heat fluxes in the system to improve its performance. There are two different options to integrate heat into a CB. On the one hand, the hot storage configuration uses a heating system (heat pump in this example) to increase the waste heat temperature. This allows the power cycle (RC in this example) to increase its performance by working with a higher temperature difference. On the other hand, the cold storage configuration stores thermal energy at temperatures lower than the ambient (through a vapor cycle in this example). Once again, it allows the power cycle to work efficiently with a higher temperature difference.

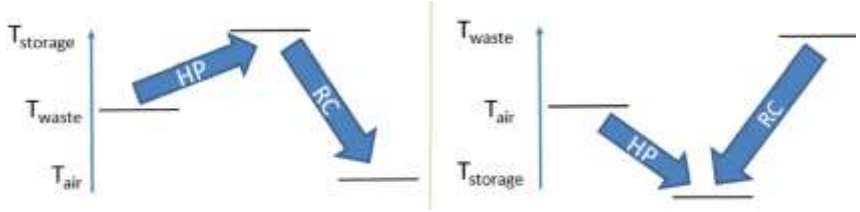

Figure. 1. Hot storage configuration versus cold storage configuration [4].

1.4 District heating

The coupling of a Carnot battery, using a hot water tank as thermal energy storage, with a district heating (DH) is promising. Figure 2 depicts an illustrative theoretical example of the system. First, it can shave the DH thermal consumption of the building (Fig. 2) through a direct use of the stored hot water. Secondly, the excess renewable production converts thermal energy from the DH in a hot water tank at higher temperature (Fig. 2). When the electrical power consumption of the building exceeds the renewable production, the CB (Rankine Cycle - RC) can convert the thermal energy into electricity to cover the electrical peak (Fig. 2).

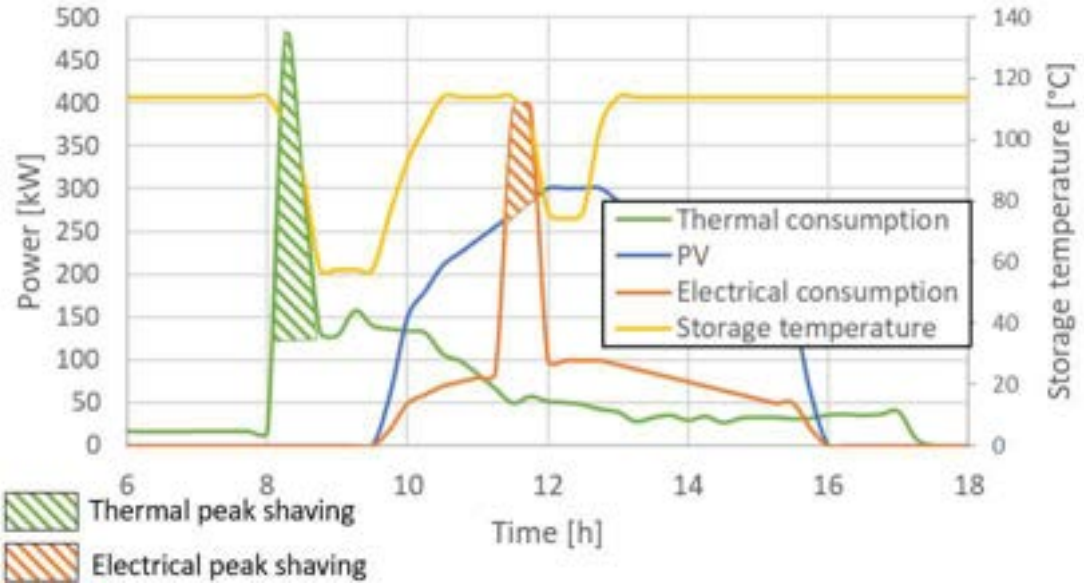

Figure. 2. Coupling of a Carnot battery using a hot water tank with a district heating

Few papers discuss the integration of such a CB with a DH. In 2019, some authors [9] show the interest of the system compared to electro-chemical batteries. To the author best knowledge, [10] is the only paper discussing the design of a CB using a reversible HP/RC system. The authors show the interest of having one single machine to decrease the investments (reversible volumetric machine and reversible heat exchangers). Several fluids have been considered and the optimal fluid is selected (R1233ZD) [11]. Also, the trade-off in the glide of the storage (difference between high and cold temperature) is highlighted: a high glide leads to low roundtrip efficiency while a low glide leads to a bulky hot water tank (and related high investments) [11].

1.5 Aim of the paper

This paper is only focusing on Rankine based Carnot batteries. After a short introduction, the methodology of optimal and robust sizing is exposed. The case study is described: the integration of a Carnot battery in a district heating system. Following this, the optimal design is presented. The objective is to propose a machine which is robust, optimized and cheap. Finally, a discussion analyses the results and provides guidelines for future machines.

2. Methodology

2.1. Case study

The case study is the thermodynamics laboratory of the ULiège (Belgium). Typical annual energy consumption from the DH is 344 MWh, the electrical production from PV is 568 kWh and the electrical consumption of the building is 105 MWh. The DH operates typically between 65°C and 75°C with morning peak up to 470 kW (15 mins – see Figure 2). According to Uliège data, the electrical consumption presents very high peaks (up to 200 kW) for short periods of time (few minutes), the electricity price is assumed to be 0.3 eur/kWh (buy) and 0.1 (sell) and the cost of the thermal heat from district heating is 0.07 eur/kWh.

2.2. Method

As this section will show, there is a large number of possible configurations to design a CB integrated in a given case study. For this reason, it is helpful to have guidelines to select which one should be the most profitable before performing detailed simulations. It is also possible to simulate all the configurations but this is time consuming and usually this step can be simplified thanks to some guidelines (Figure 3).

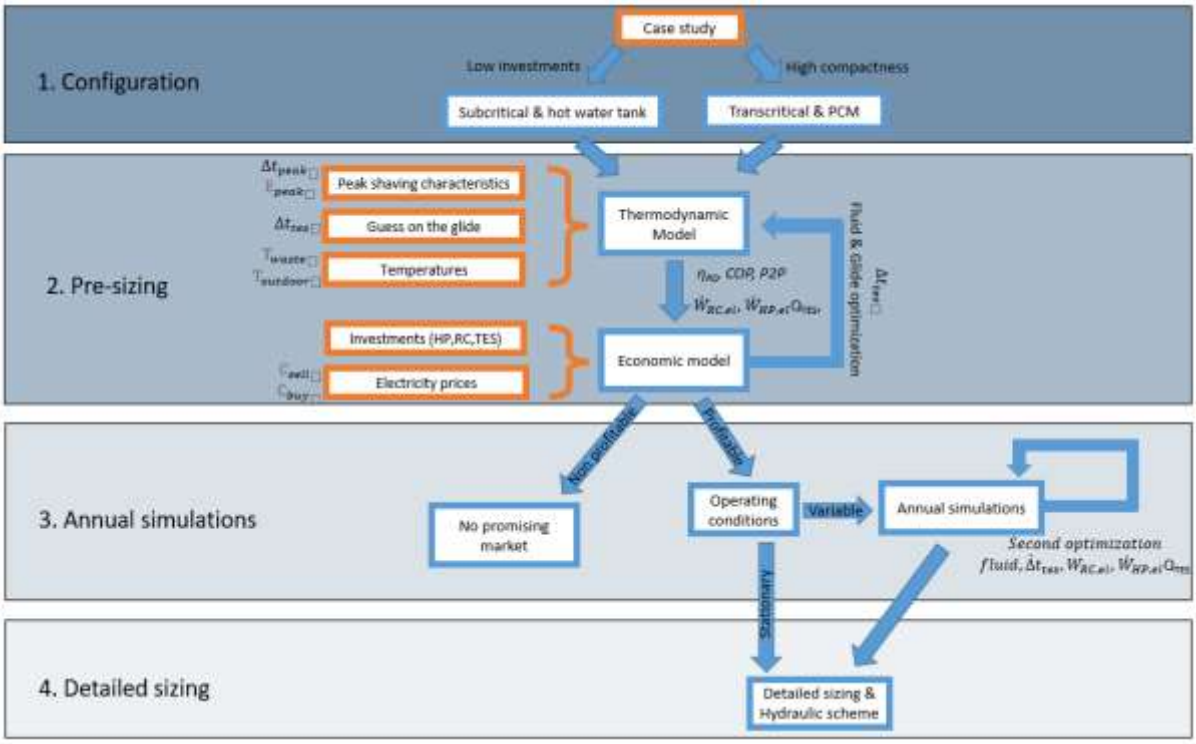

Figure. 3. Flowchart to perform the sizing of a Carnot battery based on a Rankine cycle.

2.2.1. Configuration: Selection of the configuration based on the case study

Depending on the system, constraints could be different from one application to the other.

Classically, the configuration for Rankine based Carnot battery uses a hot configuration (see section 1.3) with a subcritical thermodynamic cycle and a hot water tank. If the application presents temperature close to 0°C, then the cold configuration seems promising [10]. If no heat flux is integrated, if the heat flux allows a high temperature glide (>50 K) or if a high compactness is required, a transcritical cycle is more suitable. If an application requires a low glide, a rather low power density and a high energy density, PCM could be profitable.

Table 1. Selection of the configuration

Configuration	*Hot* Higher efficiency [11]	*Cold* Optimal for ice storage
Thermodynamic cycle	*Sub-critical* Cheap	*Transcritical* Optimal for high glides (>50 K)
Thermal energy storage	Hot water tank Low cost	PCM Optimal for low glides

2.2.2. Pre-sizing: Sizing based on the nominal conditions (temperature, power and capacity)

The main parameter to optimize is the glide of the thermal energy storage. The high thermal energy storage temperature should be optimized in order to obtain a compromise between high revenues (low glide – high power-to-power ratio) and low investments (high glide - compact storage). In the nominal point, the low temperature of the thermal energy storage should be slightly above the highest temperature of the thermal flux (waste heat or district heating) [10,11]. To start the design procedure, let's assume a guess glide (e.g. 25 K). This value will be optimized a posteriori.

Boundary conditions of the case study needs to be known (outdoor temperature, electricity price – buy (C_{buy}) and sell (C_{sell}), energy production from renewable, electrical consumption of the building and other thermal fluxes (E_{heat})). Also, the peak consumptions (thermal and/or electrical), which have to be shaved, should be identified in terms of power and duration. A decent approximation is to consider that the power of the RC $\left(\dot{W}_{RC,el}\right)$ should be able to cover the difference of power between the electrical peak consumption and the base load consumption. Another approximation that can be done at this step is to consider the same power for the HP and for the RC. This allows to get comparable discharge/charge durations. Based on the nominal conditions and the a priori chosen glide, it is possible to evaluate the efficiency of the Rankine cycle

and the COP of the HP. In some cases (high glides, low waste heat temperature) the COP can be very low and therefore an electrical resistance could be more profitable. Based on the RC efficiency and the COP of the HP, it is possible to identify the power-to-power ratio with a constant efficiency model [11]. An open source Matlab model using Coolprop with documentation is available [12]. The thermal energy storage should be able to store energy to cover the peak duration (Δt_{peak}). If the peak shaving is related to the thermal consumption, the capacity of the thermal energy storage (Q_{TES}) is straightforward. If the aim is to perform electrical peak shaving, the capacity of the storage can simply be computed as Eq. 1. At this step, it is important to check if the energy of the thermal flux (waste heat or district heating) is sufficient.

$$Q_{TES} = \frac{\Delta t_{peak} \dot{W}_{RC,el}}{\eta_{RC}} \quad (1)$$

This calculation allows to compute the HP power, the RC power and the storage capacity for a given glide. The yearly benefits (Eq. 2) are expressed as the gains from electricity production of the RC (E_{RC}) and from the eventual sub-sizing of the electrical or thermal and electrical substations ($fees_{red}$) minus the cost (electricity consumed by the HP (E_{HP}) and eventual cost of the thermal flux - E_{heat}).

$$Benef_{yearly} = E_{RC} + C_{buy} - E_{HP} - C_{sell} + fees_{red}(\dot{W}) - (E_{heat}.C_{heat}) \quad (2)$$

The investment can be estimated through literature for the RC [13], the HP [14] and the thermal energy storage [15]. Therefore, it is possible now to simulate a wide range of glide to optimize a chosen economic indicator (Pay-Back Period, Return On Investments…). At this point, if the system does not produce benefits, the integration of a Carnot battery for the application could be of lower interest (too low-price variability, too low temperature of waste heat…). Iterations on the TES glide and the working fluid [11] are necessary to obtain the final design.

2.2.3 Annual Simulations: perform yearly simulations /off design model/control

If the working conditions of the system are similar every day of the year, this step could be skipped. If not, yearly simulations should be performed for a more detailed performance evaluation. Optimally, a dynamic model should be developed. However, since this is time consuming, a steady-state model can be used in a first approach. An optimal control strategy is mandatory in order to optimize the performance and the profitability of the system. At this step, it is possible to optimize in a more accurate way the glide, the RC and HP powers and the storage capacity.

2.2.4 Detailed sizing

The power of both heat pump and RC, the glide and the capacity of the storage are defined. The selection and sizing of heat pump components are classical and manufacturers can provide accurate performance data. Generally thermostatic expansion valves are preferred because of their low cost but, in some cases, electronic expansion valves can be used (highly variable operating conditions). For the Rankine cycle, a reference book presents the process of sizing and selection for the components [17]. This paper will therefore not focus on these aspects which are already well documented. However, some specific comments can be highlighted for Carnot batteries.

If HP and RC conditions are similar, it is interesting to consider the mutualization of some components. Sometimes, only heat exchangers are shared between the HP and the RC [7,8,10] but it is also possible to use the same volumetric machine to act as a compressor and as an expander [16]. High efficiencies of the compressor and expander are crucial to obtain promising performance [6]. In this configuration it is important to control actively the circulating charge of working fluid in the system in order to obtain a high robustness and optimized performance [8]. Also, in the case of volumetric machines, the oil circulation must be ensured through a dedicated oil loop or through an optimal sizing of the piping in order to ensure sufficient speed of working fluid to entrain the oil [6]. Finally, it is possible to keep the working fluid flow direction identical in HP and RC (classical configuration) or to invert the direction of the working fluid (inverted configuration). Few comparisons exist between both systems and more information can be found in [6].

3. Results and discussion

The case study is described in section 2.1. The methodology from section 2.2 is applied to the case study to illustrate the design flowchart.

3.1. Configuration

The first step is to choose a given configuration. Because of the absence of compactness constraints, a classical sub-critical cycle with a hot water tank is chosen according to Table 1.

3.2. Pre-sizing

According to section 2.1, electrical peaks appear for a very short fraction of the time. However, thermal consumption peaks occur every morning during 15 mins. Therefore, the sizing of the machine is performed according to the thermal discharge mode. It would make less sense to size a Carnot battery to shave the electrical peak if it is only used less than 1% of the year.

From there, knowing the daily thermal consumption peak power (≈400 kW) and its duration, the capacity of the hot water tank is calculated (100 kWth). The temperature spread of the district heating is from 63°C to 77°C. Knowing this and temperature levels, the hot water tank volume can be deduced (6.1 m^3). The HP is sized in order to get a full refilling of the thermal energy storage in one hour and a half (this value comes from the PV profiles and electrical consumption of the building). Therefore, the condenser power of the HP is 80 kW. Based on the temperature levels and power aforementioned, the sizing model can be run [12]. Since the working conditions of HP and RC are similar, a reversible HP/RC system is considered. The given design values are summarized in Table 2.

Table 2. Sizing of the components

Mode	Charge - HP	Discharge - RC
Electrical power [kW]	10.7	5.6
Condenser power [kW]	82.5	94.6
Evaporator power [kW]	67.3	100
Cold temperature [°C]	62	20
Hot temperature [°C]	76	70
Scroll efficiency [%]	69.5	61.8
COP/eta [-]	7.69	5.5
Optimal volume ratio [-]	1.68	3.04
Evaporator pressure [bar]	3.34	4.05
Condenser pressure [bar]	6.02	1.18
Condenser flow (sf) [l/s]	1.4	2.6
Evaporator flow (sf) [l/s]	3.2	2.99
Working fluid mass flow rate [kg/s]	0.422	0.449
COP/eta with rv optim [-]	1%	11%

3.3. Annual simulations

Simulations of the systems have extensively been described in a former paper [18]. It confirms that the pre-sizing is economically interesting.

Results, presented in table 3, show the Carnot battery expected performance when working in each possible operating mode: the HP runs to charge the storage for about 1967 hours during a year of operation, producing about 97509 kWh of thermal energy at the expense of 19672 kWh of renewable electricity surplus, working with an average COP of almost 5; over an operating year, 65133 kWh of thermal energy is reconverted into 5331 kWh of electricity, by the Carnot battery working in RC mode for about 1296 hours, with an average efficiency of 7.92 %; eventually, for a total of 290 hours per year, the Carnot battery works in pure thermal discharge mode to cover the early morning thermal demand peaks (peak shaving), for a total amount of 18036 kWh of thermal energy.

The economic convenience of adding the Carnot battery to the integrated system is evaluated in terms of pay-back (PB) period, which is obtain dividing the Carnot battery investment cost by its annual economic benefit: the investment cost includes the HP/RC cost (a specific cost of 2000 €/kW has been considered [4]) and the TES cost [15]. The economic benefit represents the differential gain between two scenarios, namely with and without the Carnot battery intervention, that is the sum of positive and negative contributions (represented as revenues and expenses in figure 4): the positive ones are due to the DH substation downsizing (lower DH substation investment costs), the thermal demand covered by the Carnot battery instead of been provided by the DH, and the RC production both for selling and self-consumption; while the additional negative contributions include the reversible HP/RC and storage levelized investment costs, and the HP electricity consumption both from photovoltaic (PV) surplus and grid purchase. As a result, the PB period is assessed to be slightly more than 6 years, which is acceptable considering 30 years as typical lifetime period for these systems.

Table 3. Annual results

Mode	Charge - HP	Discharge - RC	Thermal discharge
Average COP/efficiency [-]	4.957	0.0792	-
Electrical energy [kWh]	19672	5331	-
Thermal energy [kWh]	97509	65133	18036
Running hours [h]	1967	1296	290
Pay-Back Period [years]		6.12	

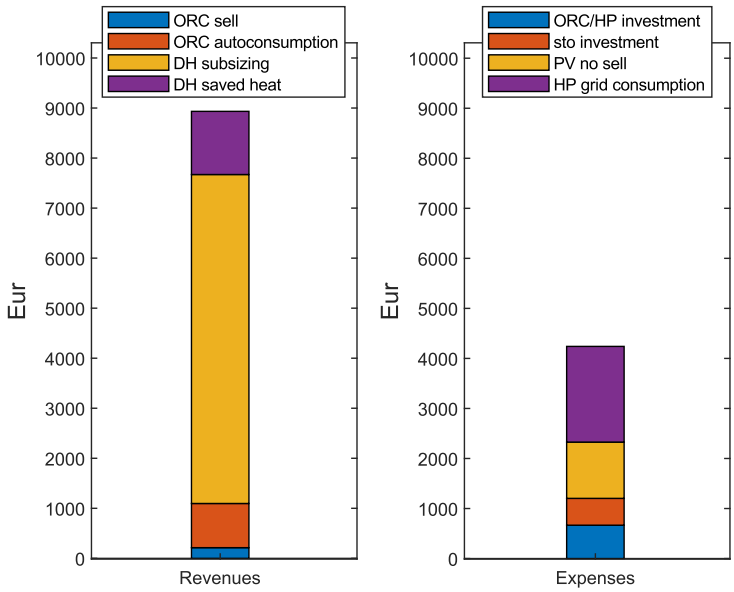

Figure. 4. Carnot Battery annual revenues and expenses

3.4. Detailed sizing in the case of the described case study

Unfortunately, it was not possible to find a suitable volumetric machine that can work properly in HP and RC mode. The proposed solution is to use three machines in parallel (table 4). Two scroll compressors ensure the compression for the HP (see Fig. 5) while three scrolls can be used for the RC (higher volumetric flow rate). The scrolls are run at constant speed. The glide of the RC is optimized to a value of 8 K for the RC. The last line of the table refers to the loss of efficiency related to the inadapted volume ratio of the volumetric machine compared to the optimal one. It would have been better to work with a machine able to vary its volume ratio actively to optimize the performance (no products were found in this operating conditions). A centrifugal pump is chosen because volumetric pumps are less robust and needs a higher degree of sub-cooling [6]. The heat exchangers are sized to reach a low pinch-point (2 K) since it significantly impacts the global performance. Also, the pressure drop on the refrigerant side is limited to 50 mbars. The expansion valve of the heat pump is electronically controlled. The liquid receiver volume is 10 liters, in order to adapt the charge depending on the operating mode.

Table 4. Description of the components

Component	Parameter	Value
Volumetric machines	Swept volume [cm3]	121
	Volume ratio	1.7
	Shaft speed [RPM]	6000
Pump	Volumetric flowrate [l/s]	0.5
	Shaft speed [RPM]	3000
LP heat exchanger	Area [m2]	15.2
	Number of plates [-]	120
HP heat exchanger	Area [m2]	17.8
	Number of plates [-]	140
Hot water tank	Volume [m3]	7
	Thermal isolation thickness (PU) [mm]	125

The layout of the system is presented in figure 5. The idea is to control the refrigerant charge through the valves. In HP mode, VLR and VEV are open while VPP is closed. In RC mode, VPP is open while VLR and VEV are closed. VEV can be opened for a short period in case there is not a sufficient charge in RC mode.

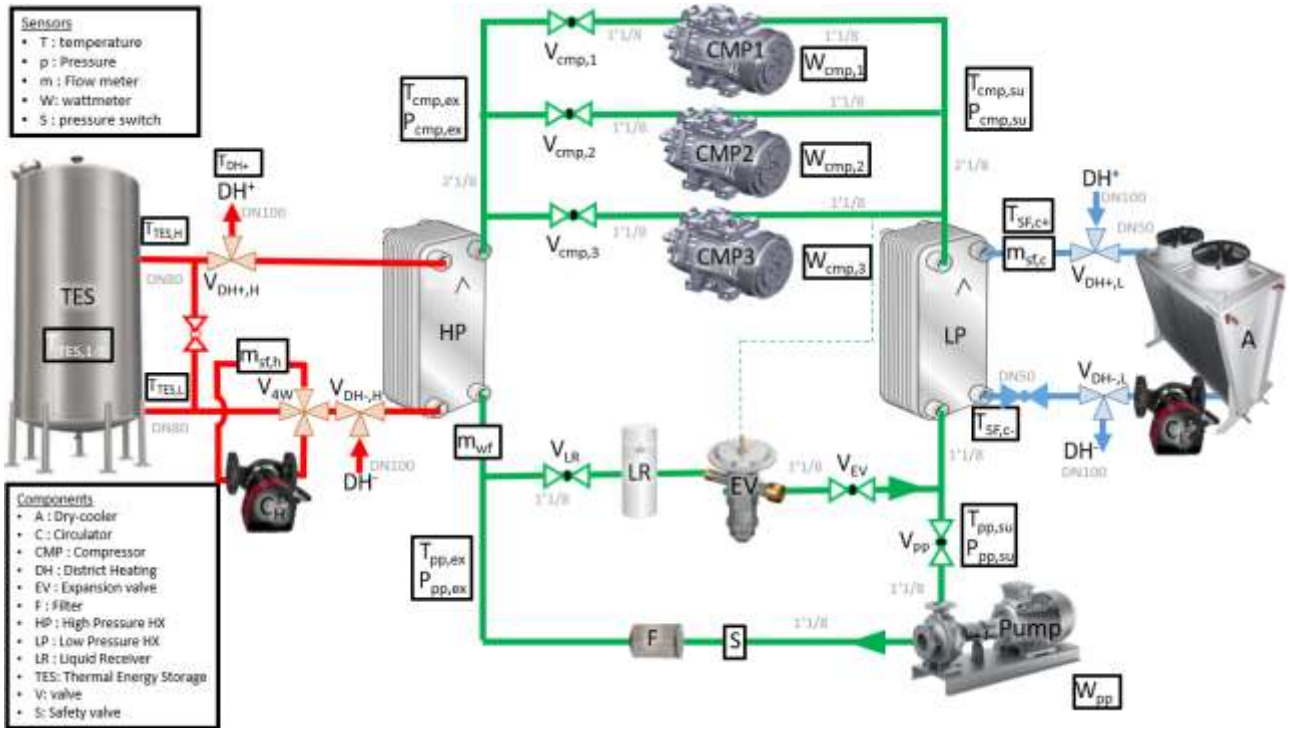

Figure. 5. Hydraulic scheme of the Carnot battery integration

In figure 5, DH- refers to the exhaust piping of the district heating (cold) while DH+ is the supply piping of the district heating (hot). In thermal discharge, the hot water circulator (CH) sends cold water from the district heating (DH-) to the hot water tank while hot water from the tank is sent to the hot part of the district heating (DH+). The other components are not used in this mode. In HP mode, the evaporator (LP heat exchanger) takes the heat from the dry-cooler or from the DH. Then, hot water is produced in the condenser (HP heat exchanger) and sent to the top of the hot water tank. In RC mode, the district heating is not used. The evaporator (HP heat exchanger) receives hot water from the top part of the thermal energy storage. The condenser dissipates its heat through the dry-cooler.

Conclusion

The design of a Carnot battery is a complex task (there are a lot of layouts, technologies and operating parameter to choose and optimize). This paper proposes a simplified approach to choose among the possible configurations and to size the components. The idea is, based on the state of the art and on experimental results, to ensure an optimal design with realistic hypothesis. An illustrative case is presented with a 10 kWe machine integrated to a district heating. The next step is to test the machine and to analyze the experimental results.

Nomenclature

A	*Dry-cooler*
C	*Cost [eur]*
E	*Energy [Wh]*
M	*Flowmeter*
P	*pressure [bar]*
Q	*thermal energy [Wh]*
T	*Temperature [°C]*
t	*time [s]*
$\dot{W}$	*Power [W]*

Acronyms

CB	*Carnot Battery*

CMP *Compressor*

DH *District Heating*

EV *Expansion valve*

HP *Heat Pump*

PB *Pay-back*

PCM *Phase Change Material*

P2P *power to power ratio*

PV *photovoltaic panel*

RC *Rankine Cycle*

TES *Thermal Energy Storage*

W *Powermeter*

Greek symbols

η *efficiency*

Subscripts and superscripts

el *Electrical*

HP *High pressure*

LP *Low pressure*

red *reduction*

References

[1] Benato A, Stoppato A. Pumped Thermal Electricity Storage: A technology overview. Therm Sci Eng Prog 2018a;6:301–15. https://doi.org/10.1016/j.tsep.2018.01.017.

[2] Review of Carnot Battery Technology Commercial Development, 2022. Novotny, V., Basta, V., Smola, P., Spale, J., *Energies* **2022**, *15*(2), 647; **https://doi.org/10.3390/en15020647**

[3] Frate Guido Francesco, Antonelli M, Desideri U. A novel Pumped Thermal Electricity Storage (PTES) system with thermal integration. Appl Therm Eng 2017;121:1051–8. https://doi.org/10.1016/j.applthermaleng.2017.04.127.

[4] Dumont, O., Frate, F., Pillai, A., Lcompte, S., De Paepe, M., Lemort, V. Carnot battery technology: A state-of-the-art review. Journal of Energy Storage, 2020, 32, 101756, https://doi.org/10.1016/j.est.2020.101756

[5] Dumont, O., Quoilin, S., Lemort, V., 2015. Experimental investigation of a reversible heat pump/organic Rankine cycle unit designed to be coupled with a passive house to get a Net Zero Energy Building, International Journal of Refrigeration, 54, 190-203, https://doi.org/10.1016/j.ijrefrig.2015.03.008.

[6] Dumont, O., 2017. Investigation of a heat pump reversible into an organic Rankine cycle and its application in the building sector, PhD Dissertation.

[7] Dumont, O., Charalampidis, A., Lemort, V., 2020. First Experimental Results of a Thermally Integrated Carnot Battery Using a Reversible Heat Pump / Organic Rankine Cycle 2nd international workshop on Carnot batteries http://hdl.handle.net/2268/250924

[8] Experimental investigation of a thermally integrated carnot battery using a reversible heat pump/ organic rankine cycle: influence of system charge on performance of the reversible scroll compressor/expander and global performance, 2022. Tassenoy, R., Dumont, O., Lemort, V., De Paepe, M., Lecompte, S., International Refrigeration and Air Conditioning Conference, Proceedings.

[9] CHESTER, 2019. https://www.chester-project.eu/, consulted on the 10/10/2019.

[10] Carnot battery: Simulation and design of a reversible heat pump-organic Rankine cycle pilot plant Bernd Eppinger a,1 , Daniel Steger b,1,* , Christoph Regensburger b , Jürgen Karl c , Eberhard Schlücker b , Stefan WillApplied Energy, Volume 288, 15 April 2021, 116650

[11] Dumont., O., Lemort, V., Mapping of performance of pumped thermal energy storage (Carnot battery) using waste heat recovery, Energy 211 (2020) 118963

[12] Dumont, O., https://github.com/oliviersIts/CB, consulted on the 11/10/2022.

[13] Lemmens, S., Cost Engineering Techniques and Their Applicability for Cost Estimation of Organic Rankine Cycle Systems', Energies, vol. 9, no. 7, p. 485, Jun. 2016, doi: 10.3390/en9070485.
[14] Croteau, R., Gosselin, L.,Correlations for cost of ground-source heat pumps and for the effect of temperature on their performance, International Journal of Energy Research, vol. 39, no. 3, pp. 433–438, 2015, doi: 10.1002/er.3243.
[15] Shamoushaki, M., Niknam, P.H., Talluri, L., 2021. Manfrida, G., Fiaschi, D., Development of Cost Correlations for the Economic Assessment of Power Plant Equipment, Energies, vol. 14, no. 9, p. 2665, May 2021, doi: 10.3390/en14092665.

[16] Dumont. O., Lemort., V., 2022. Pumped thermal energy storage based on ORC, Encyclopedia of energy storage, vol 2, 68-78.

[17] Macchi, E., Astolfi, M., 2017. Cover for Organic Rankine Cycle (ORC) Power Systems, Organic Rankine Cycle (ORC) Power Systems Technologies and Applications Book

[18] Torricelli, N., Branchini, L., De Pascale, A., Dumont, O., Lemort, V., 2022. OPTIMAL MANAGEMENT AND SIZING OF REVERSIBLE HEAT PUMP/ORC CARNOT BATTERIES, Turbo expo 2022.

Comparative analysis of sensible heat and latent heat packed bed cold energy storage for liquid air energy storage systems

Afshin Mashayekh[a], Jung Hwan Park[b], Nishith Babubhai Desai[c], Jeong Ik Lee[d], Fredrik Haglind[e]

[a] Technical University of Denmark, Department of Civil and Mechanical Engineering, 2800 Kongens Lyngby, Denmark, afmas@dtu.dk, CA
[b] Korea Advanced Institute of Science and Technology, Department of Nuclear and Quantum Engineering, Daejeon, South Korea, junghwanpark@kaist.ac.kr
[c] Technical University of Denmark, Department of Civil and Mechanical Engineering, 2800 Kongens Lyngby, Denmark, nbdes@dtu.dk
[d] Korea Advanced Institute of Science and Technology, Department of Nuclear and Quantum Engineering, Daejeon, South Korea, jeongiklee@kaist.ac.kr
[e] Technical University of Denmark, Department of Civil and Mechanical Engineering, 2800 Kongens Lyngby, Denmark, fhag@dtu.dk

Abstract:

A liquid air energy storage is a novel technology receiving substantial interest for balancing the supply and demand of energy because of its high energy density and not being geographically constrained. The main challenge of the liquid air energy storage system demonstrated so far is its low round-trip efficiency. Internal heat recovery, using hot and cold thermal energy storages, increases the round-trip efficiency of the liquid air energy storage. High temperature thermal energy storages are widely studied for different applications. However, the poor performance of the cold thermal energy storage is currently a bottleneck to achieve cost-effectiveness of the liquid air energy storage system. That is due to the very low temperatures and the large temperature span of the cold energy storage. In this paper, two types of cold thermal energy storages, a packed-bed sensible storage and a latent heat storage with cryogenic phase change materials, were applied to a stand-alone liquid air energy storage system. A one-dimensional transient numerical model was developed to analyse the storage systems. The round-trip efficiency, liquid air yield, and expansion work of the liquid air energy storage system were evaluated considering both storage options. The results indicate that the latent heat packed bed storage configuration has higher round-trip efficiency (41 %), liquid yield (58.1 %), and power output (42 MW) than those of the configurations with sensible heat storage. However, there are some sensible materials, like quartzite rocks that, with the same volume of the packed bed, perform as well as cryogenic phase change materials due to their high densities.

Keywords:

Cold thermal energy storage; Latent heat storage; Liquid air energy storage; Packed bed rock thermal energy storage; Phase change materials; Sensible heat storage.

1. Introduction

Large-scale energy storage systems are promising options to mitigate the variability of renewable energy sources and to balance the energy supply and demand [1,2]. Liquid air energy storage (LAES) is a novel technology that has recently gained increasing attention. The LAES system is not geographically restricted and requires much less storage volume than those of the more mature technologies – in the order of 700 times less than that of compressed air energy storage [3,4]. The LAES system comprises three processes: 1) charging process – excess electricity (e.g. from wind and/or solar energy) is used to drive a liquefaction process, 2) storing process – liquid air is stored in cryogenic tanks at nearly ambient pressure, and 3) discharging process – the liquid air is pressurized, regasified and expanded in turbines producing electricity. At present, the LAES technology is at an industrial demonstration level. The main challenge that the LAES system confronts is its low round-trip efficiency, the ratio of the electricity generated during the discharging process to the electricity consumed during the charging process, in comparison to other energy storage systems such as a compressed air energy storage [5]. The round-trip efficiency of the LAES system can be improved by introducing hot and cold thermal energy storages, which allow for the internal recuperation of

hot and cold fluid streams. However, the designs of the heat exchangers and thermal energy storages present some challenges – specifically with respect to the cold thermal energy storage system. So far, various studies have been conducted on High-Grade Cold Energy Storage (HGCS). Broadly speaking, HGCS can be divided into three types: storage using fluids (methanol and propane) [6], using packed beds (such as rock and pebbles) [7], and using phase change material (PCM) [8]. So far, various research studies on LAES systems have been done specifically focused on cold storage systems with different designs, and a majority of those consider packed bed rock storage systems.

Wang et al. [9] applied a dynamic model to analyse the performance of a standalone LAES system by using sensible heat packed bed rock storage for both the cold and hot energy storages, achieving a round-trip efficiency of 43 %. She et al. [4] studied an LAES system with a two fluids system for the cold energy storages and thermal oil for hot energy storage and attained a round-trip efficiency of 53 %. Ryu et al. [10] analysed a LAES system based on the Linde-Hampson refrigeration cycle using a combination of sensible and latent heat packed bed storage systems as the cold energy storage unit. A round-trip efficiency of 60.6 % was obtained. In this case the required temperature for liquefying air could be provided continually during the phase change of the PCM. Tafone et al. [11] investigated a cold thermal energy storage for the LAES system by using a cryogenic PCM. It was found that by using cryogenic PCM as the storage medium, the temperature at the outlet of the packed bed is limited by the melting point of PCM and therefore, the temperature of the heat transfer fluid at the inlet of cold box is lower than the case with sensible heat particles which reduces the compressor power requirement.

Bashiri Mousavi et al. [12] studied a packed bed with three layers of different PCM as a cold storage system of the LAES system and reached a round-trip efficiency of 42.5 % when the system has reached equilibrium. They designed the packed bed's tank with the PCM with lowest melting point located at the bottom of the tank and the PCM with highest melting point placed at the top of the tank. Sciacovelli et al. [13] used a modular packed bed system filled with quartzite rocks. They validated their numerical model with experimental of the LAES pilot plant available at the University of Birmingham, UK. They also investigated the effect of charging and discharging pressure on the round-trip efficiency of the LAES system. It was observed that there is an optimum value for charging pressure that results in the maximum round-trip efficiency (50 % under nominal conditions). Guo et al. [14] developed a dynamic model to analyse the packed bed as the cold energy storage in the LAES system. Granite was used as the storage material and the results suggested that because of both the intermittent period between charging and discharging cycles and the cold energy loss, the round-trip efficiency is 16.8% lower than that of the ideal system in quasi-steady state. Tafone et al. [15] developed a performance map for the LAES system. They investigated the effect of various parameters including turbomachinery isentropic efficiency, storage pressure of liquefied air in the tank, efficiency of hot and cold energy storage, charging and discharging pressure, and the ratio of recirculation mass flow rate. It was observed that increasing the liquid air tank pressure enhances the heat capacity of the recirculation fluid. In turn, this increases the efficiency of the cold box unit, and, as a result, the system's performance becomes independent of the charging pressure.

Wang et al. [16] applied a two tanks system with pressurized propane as the heat transfer fluid for cold energy storage in the LAES system and obtained an electrical round-trip efficiency of 50 % as well as a combined heat and electricity efficiency of up to 81%, using the excess heat available in the hot energy storage system as the heat source. Hüttermann and Span [17] studied nine different storage materials in a packed bed for the cold energy storage unit of the LAES system. The results demonstrated that the system with lead has the maximum efficiency of the packed bed cold storage among other materials due to its lower variation of specific heat capacity over the temperature span than that of the other storage particles. Peng et al. [18] developed a model to investigate the performance of an LAES with sensible heat packed bed (using rocks as the particles) as the cold energy storage. They found that the round-trip efficiency of LAES system is affected by the inlet temperature of cold box, charge and discharge pressure. A maximum round-trip efficiency of 62 % is reachable for optimal conditions for the LAES system.

Storage systems with two working fluids have the disadvantage of using working fluids that are usually flammable [9] and the necessity and using four tanks, increasing the complexity for industrial applications.[9] In this context, a packed bed energy storage system with sensible or latent heat particles is a promising technology for cold storage systems for industrial LAES systems. This technology can relatively easy be integrated into the LAES system and covers the entire temperature range of the cold storage in a single tank. In addition, because of large latent heat of PCMs, PCM based storage has a high energy density, which makes it suitable as a storage medium.

The objective of this paper is to identify the optimum storage medium for cold storage packed bed system in stand-alone LAES systems. Three different materials were investigated: quartz and silicon dioxide as sensible materials and an alcohol-based fluid as latent heat PCM. The materials are used in the form of particles placed in a tank. A thermodynamic model of the LAES system integrated with a 1-dimensional transient numerical model of the packed bed system was developed. The round-trip efficiency, liquid yield, and turbine output are compared for the three different cold thermal energy storage units for the LAES system. There is only a single previous study available in the open literature comparing sensible and latent

heat materials for packed bed cold storage for LAES applications [11]. However, in Ref. [11] different storage materials for the packed bed cold storage were evaluated solely in terms of storage performance. In contrast, the current paper presents, for the first time, an analysis of the effects of different storage materials for the packed bed cold storage on the LAES performance. Such analysis will be useful both for industry and academia for the future development of cold energy storage units for LAES systems.

In the following, section 2 discusses the methods. Section 3 presents and discusses the results obtained from numerical simulations, while section 4 summarizes the conclusions of the work.

2. Methods

2.1 System description

Figure 1 shows a schematic diagram of a liquid air energy storage system (LAES) with two tank hot and packed bed cold energy storages. The proposed system consists of a charging cycle and discharging cycle. The charging cycle consists of multi-stage compressors, air-oil heat exchangers with the thermal oil VP1, a cold-box, a cryo-turbine, a gas-liquid separator, and a liquid air tank. The discharging cycle consists of a cryo-pump, an evaporator, air-oil heat exchangers, and multi-stage turbines. In order to utilize the cold energy, a cold packed bed storage is located between the charging and discharging cycles. Packed bed storage improves the cycle efficiency by exchanging heat between the charging and discharging processes. When the electricity price is low, the air is compressed through multi-stage compressors. Initially, the cold packed bed storage transfers cold energy to the compressed air, causing the temperature of point A7 to decrease to a cryogenic temperature (A8) inside the cold box. After the cooling process, compressed air is expanded to ambient pressure through a cryo-turbine and separated into liquid (A_Liq) and gaseous forms (A10). At peak hours (during a discharge process), liquid air is evaporated while the cold energy is stored in the packed bed cold storage. Gaseous air is heated in the thermal oil heat exchangers and expanded through air turbines to generate electricity.

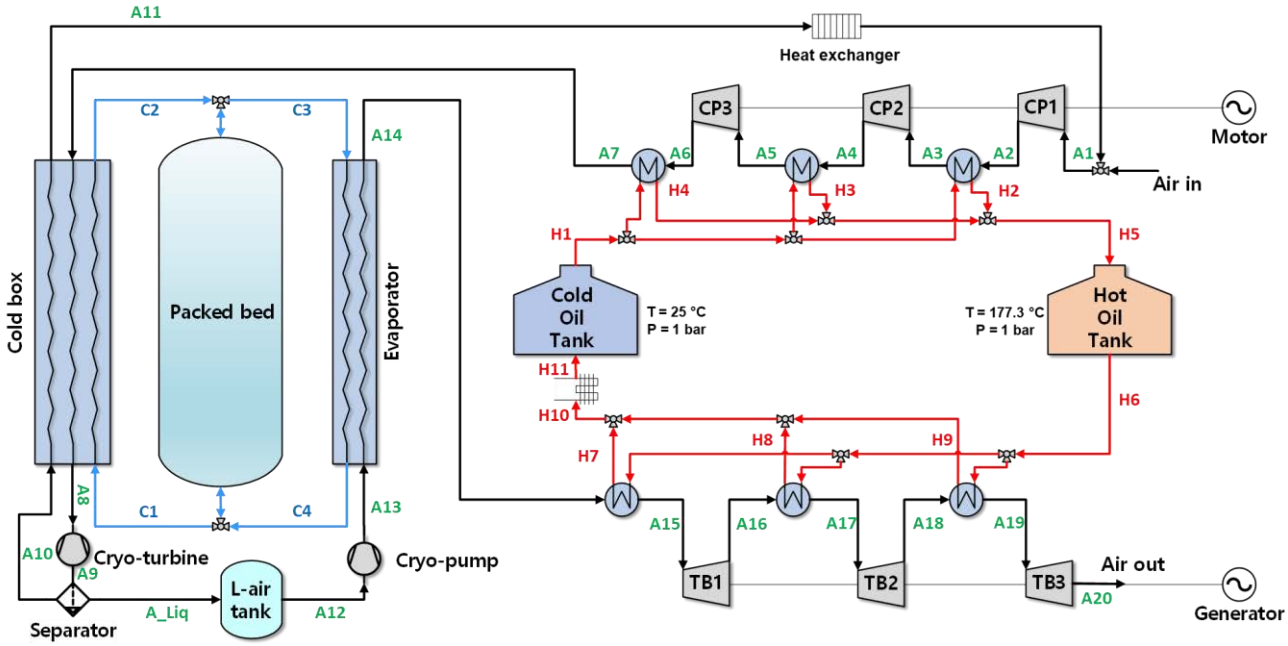

Figure. 1. *Schematic diagram of liquid air energy storage system with cold packed bed storage (CP and TB stand for compressor and turbine, respectively).*

The input parameters of the system are presented in Table 2. The design charging cycle power input (96 MWe), hot thermal energy storage capacity (800 MWh_{th}) and volume (9000 m^3), cold thermal energy storage systems' volume (15000 m^3), and charging time (8 hrs) were fixed for the analysis. The design discharging cycle power output is calculated based on the available liquid yield during charging cycle and discharge duration of 8 hrs. In order to achieve 96 MW of power input for the LAES charging cycle, 17 MPa was selected as the fitting charging pressure. It is worth to note that the LAES system is designed as a large-scale electricity storage system, which require a large volume of the packed bed storage for cold thermal energy as well as a large volume of tanks for the hot thermal energy.

Due to manufacturing constraints of packed bed systems, the diameter of the tank must not exceed 6 m, and the recommended H/D ratio for packed bed systems based on literature is 2 [19,20]. Based on these considerations, the packed bed's height and inner diameter were set to 12 m and 6 m, respectively. In order to achieve the total storage capacity needed for the system, a series of packed beds in a parallel

configuration was used. In total 44 packed bed tanks are needed, which means that the input of the packed bed system (C2 during LAES charging and C4 during LAES discharging) was divided among 44 packed bed tanks. Similarly, the outlet streams of the packed bed tanks were collected, leading to the desired outlet flow of the packed bed system (C1 during LAES charging and C3 during LAES discharging). In order to avoid the use of multiple cold energy storage tanks, it may be a possibility to use one or a few underground packed bed storage tanks [21], however, in this case the LAES system will not be geographically unconstrained, which is one of the major advantages of the LAES technology.

Table. 2. *Input parameters for the system modelling.*

Parameter	$Value$
Particle diameter	0.02 m
Ambient temperature	293 K
Ambient pressure	101 KPa
Charging pressure	17 MPa
Packed bed initial temperature	101.47 K
Pinch points:	
Air-Oil heat exchangers	5 K
Cold box	2 K
Evaporator	2 K
Turbomachinery isentropic efficiency [9]:	
Compressors	89 %
Cryo-turbines	90 %
Cryo-pump	80 %
Gas turbines	75 %

2.2 Component thermodynamic model

In order to simulate the proposed system, the mathematical modelling of the components is implemented into the MATLAB environment. The specific enthalpy change is modelled by the isentropic efficiency model. The compressor power input, $\dot{W}_C$, and the gas turbine power, $\dot{W}_T$, are calculated as follows:

$$\dot{W}_C = \dot{m}(h_{out} - h_{in}) = \dot{m}(h_{out.is} - h_{in})/\eta_{CP} \quad (1)$$

$$\dot{W}_T = \dot{m}(h_{in} - h_{out}) = \eta_{TB} \times \dot{m}(h_{in} - h_{out.is}) \quad (2)$$

where $\dot{m}$ is mass flow rate, h is specific enthalpy, and η is the isentropic efficiency of each component.

Heat exchangers are modelled with basic heat balance equations. The heat exchangers are assumed to be counter-flow heat exchangers and a pinch point limitation is applied.

$$\dot{Q}_{hot} = \dot{m}_{hot}(h_{H_{in}} - h_{H_{out}}) \quad (3)$$

$$h_{C_{out}} = h_{C_{in}} + \frac{\dot{Q}_{hot}}{\dot{m}_{cold}} \quad (4)$$

Pinch point: $min(T_{hot} - T_{cold}) = 5K$ (5)

where $\dot{Q}$ represents the heat transfer rate, h_H and h_C are specific enthalpy of the hot side and cold side, respectively. Subscripts in and out represent the inlet and outlet stream.

The multi-stream cold box is the most important component in the proposed system because the liquid air yield and round-trip efficiency are directly affected by its performance. Compressed air is cooled down to cryogenic temperature by compressed cold air from cold packed bed storage. For simplifying the multi-stream heat exchanger's calculation, it is assumed that there is no heat transfer between cold side fluids. Also, the outlet temperatures of the fluids on the cold side are imposed. The heat transfer rate of the hot side fluid and objective pinch point temperature are calculated as follows:

$$\dot{Q}_{hot} = \dot{m}_{hot}\left(h_{H_{in}} - h_{H_{out}}\right) = \dot{Q}_{pacekd\ bed} + \dot{Q}_{recycle} \quad (6)$$

Pinch point: $min\left(min\left(T_H - T_{packed\ bed}\right), min\left(T_H - T_{recycle\ air}\right)\right) = 5K$ (7)

where $\dot{Q}$ represents heat transfer rate, and T_{fluid} is the temperature of each fluid.

As the modelling is transient, and the mean liquid yield is calculated as follows:

$$Y = \frac{1}{t_{ch}} \int_0^{t_{ch}} y.\, dt \quad (8)$$

The round-trip efficiency is defined as the ratio of the total electricity generation in the discharging process to the power consumption in the charging process:

$$\eta_{RTE} = \frac{W_{discharging}}{W_{charging}} = \frac{\int_0^{t_{dis}} \dot{W}_T - \dot{W}_{CRP} dt}{\int_0^{t_{ch}} \dot{W}_C - \dot{W}_{CTB} dt} \quad (9)$$

where the subscripts CRP and CTB represents the cryo-pump and cryo-turbine, respectively.

2.3 Packed bed modelling

For calculating the heat transfer performance of packed bed storage, the energy balance equation is used. The energy equation for fluid and solid particles presents in Eq. (10) and Eq. (11), respectively. The packed bed storage is considered a 1D cylindrical tank and radial distribution of temperature based on Eq. (12) is considered inside the particles.

The following assumptions were made:

1. The distribution of velocity in the entire packed bed tank is constant and uniform. This assumption is valid for systems with $D/d_p > 30$ [22].
2. The heat transfer mechanism between the heat transfer fluid and particles are convection and conduction. Radiation is neglected.
3. The porosity is uniform along the packed bed tank.
4. The particles are of the same size and spherical shape.
5. The heat loss of the tank to the ambient is considered.

$$\varepsilon \rho_f c_{p.f} \left(\frac{\partial T_f}{\partial t} + u_f \frac{\partial T_f}{\partial z} \right) = \varepsilon k_f \frac{\partial^2 T_f}{\partial z^2} + \frac{6(1-\varepsilon)}{d_p} h_{fp} \left(T_s - T_f \right) + h_w \left(T_w - T_f \right) \quad (10)$$

$$(1-\varepsilon) \rho_s c_{p.s} \frac{\partial T_s}{\partial t} = (1-\varepsilon) k_s \frac{\partial^2 T_s}{\partial z^2} + \frac{6(1-\varepsilon)}{d_p} h_{fp} \left(T_f - T_s \right) \quad (11)$$

$$\rho_p c_{p.p} \frac{\partial T_p}{\partial t} = k_p \left(\frac{\partial^2 T_p}{\partial r^2} + \frac{1}{r} \frac{\partial T_p}{\partial r} \right) \quad (12)$$

where ε is the porosity of the packed bed, ρ is density, c_p is the specific heat of fluid, k is thermal conductivity, d_p is the particle diameter, h_{fp} is the heat transfer coefficient of fluid to solid, h_w is the heat transfer coefficient of heat loss to the ambient, and T is temperature. Subscripts f, p, and s are fluid, particle, and solid, respectively.

In order to model the thermophysical properties of the PCM, an effective heat capacity method is used [23]. The latent heat is represented as a sensible heat spread over a finite temperature difference. Thus, the specific heat of PCM is defined among three phases, namely solid, solid-liquid transition, and liquid phases:

$$c_{p.p} = \begin{cases} c_{p.s} & T_p < T_{m1} \\ \frac{c_{p.s} + c_{p.f}}{2} + \frac{L_H}{Tm2 - Tm1} & T_{m1} < T_p < T_{m2} \\ c_{p.f} & T_p > T_{m2} \end{cases} \quad (13)$$

$$k_{p.p} = \begin{cases} k_{p.s} & T_p < T_{m1} \\ \frac{k_{p.s} + k_{p.f}}{2} & T_{m1} < T_p < T_{m2} \\ k_{p.f} & T_p > T_{m2} \end{cases} \quad (14)$$

where T_{m1} and T_{m2} represent the solidification and melting temperatures of the PCM during the solid-liquid transition, and L_H is the latent heat. For updating the air properties which are temperature dependant, the REFPROP library [24] is used and applied to the model.

In order to solve the energy balance equation, boundary conditions and initial conditions are specified for the fluid and solid:

$$T_f(z=0) = T_{in}; \quad \frac{\partial T_f}{\partial z}(z=H) = 0 \quad (15)$$

$$T_s(z=0) = T_{in}; \frac{\partial T_s}{\partial z}(z=H) = 0 \quad (16)$$

$$T_f(t=0) = T_{in}; T_s(t=0) = T_o \quad (17)$$

$$\frac{\partial T_p}{\partial r}(r=0) = 0; \quad T_p\left(r = \frac{R}{2}\right) = T_s \quad (18)$$

where T_{in} is the packed bed inlet temperature, T_o is the initial temperature, and T_s is the solid temperature. Figure 2 depicts a schematic view of a packed bed filled with particles.

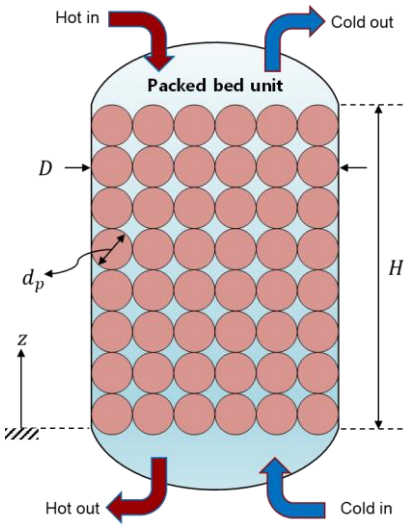

Figure. 2. *Schematic view of 1D packed bed with geometry indicators.*

In order to apply heat transfer between the fluid and solid, an empirical correlation is applied. For the Nusselt number, the following correlation is used [25]:

$$Nu = \frac{h_{fp} d_p}{k_f} = 2 + 1.1 Pr^{\frac{1}{3}} Re_p^{0.6};\ Pr = \frac{k_f c_{p,f}}{\mu_f};\ Re_p = \frac{\rho_f d_p \varepsilon u_f}{\mu_f} \tag{19}$$

For calculating the porosity of the bed, Eq. (20) is used. [25]

$$\varepsilon = 0.375 + 0.17 \frac{d_p}{D} + 0.39 \left(\frac{d_p}{D}\right)^2 \tag{20}$$

The heat loss to the ambient is calculated based on the overall heat transfer coefficient from the inner to the outer wall, see Eq. (21). The inner convection heat transfer coefficient is defined according to Beek [26], see Eq. (22).

$$\frac{1}{U_w} = \frac{1}{h_i} + \frac{D}{2} \sum_{j=1}^{m} \frac{1}{k_j} ln \left(\frac{d_{j+1}}{d_j}\right) \tag{21}$$

$$h_i = \frac{k_f}{d_p} \left[\left(0.203 Pr^{\frac{1}{3}} Re_p^{\frac{1}{3}}\right) + \left(0.220 Pr^{0.4} Re_p^{0.8}\right) \right] \tag{22}$$

where h_i is the inner convection heat transfer coefficient, Re is Reynolds number, and Pr is the Prandtl number.

The governing equations are solved by the MATLAB software [27] using finite difference method and the implicit method. The first-order upwind scheme is used to discretize the temporal and advective term, while the second-order central differencing is used to discretize the diffusion term. The overall calculation method is illustrated in Figure 3.

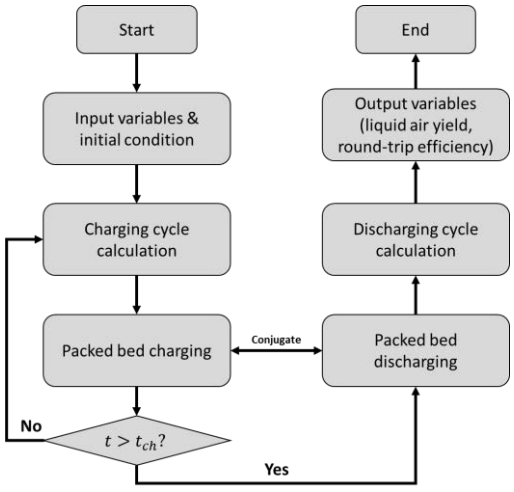

Figure. 3. *Overall calculation method of the LAES system.*

Table 2 represents the thermophysical properties of the quartz rocks [3] besides, the cryogenic PCM which is an alcohol-based fluid [11]. The thermophysical properties of silicon dioxide (SiO_2) are calculated based on correlations as a function of the particles' temperature proposed by Wang et al. [9] and Sciacovelli et al. [13].

Table. 2. *Thermophysical properties of particles [11,25].*

Properties	PCM	$Quartz$
Density, ρ	789.3 kg/m^3	2630 kg/m^3
Specific heat, C_p	1850 $J/kg\ K$, Solid	710 $J/kg\ K$
	1900 $J/kg\ K$, Liquid	
Thermal conductivity, k	0.22 $W/m\ K$, Solid	1.83 $W/m\ K$
	0.18 $W/m\ K$, Liquid	
Latent heat, L_H	86000 J/kg	-
Melting Point, T_m	155.15 K T_{m1}	-
	158.15 K, T_{m2}	

3. Results and discussion

In this section, first, the validation of the packed bed model is presented. Then the optimum value for discharging pressure is found based on a sensitivity analysis. Afterwards, the different particle materials are compared in terms of LAES round-trip efficiency, liquid air yield, and gas turbine power.

3.1 Model validation

The developed model for the packed bed is validated by comparing the results with experimental data from a study by Li et al. [28] who analysed a packed bed system with microencapsulation of molten salt as phase change material. The packed bed in their study had a height of 0.26 m and a diameter of 0.26 m. The particle diameter was 0.034 m. The authors considered both the axial and radial temperature distribution along the bed's tank by applying thermocouples at various locations of the tank. When validating results of the 1D model developed in this work, the mean value of the radial temperature distribution at each axial location of the experimental data is considered. Figure 4 presents a comparison of the model results with the experimental data showing PCM particle temperature profiles over time for different axial locations. It is found that the maximum mean absolute percentage error is smaller than 2 %, suggesting that the current model provides reasonable results.

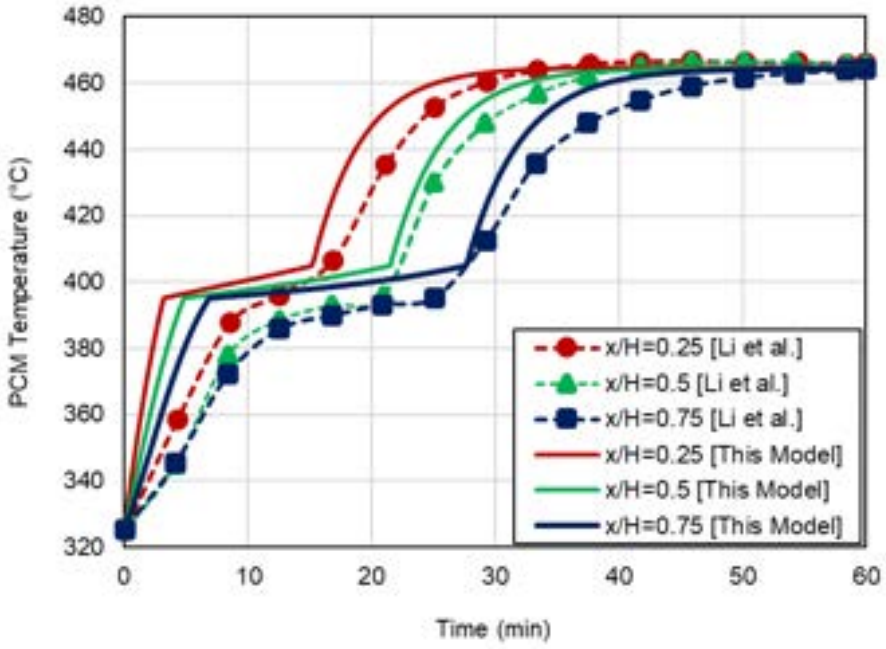

Figure. 4. *Validation of packed bed model.*

The validation of the LAES thermodynamic model is done by comparing the current model results with experimental results presented by Sciacovelli et al. [13], see Table 3. The experimental setup of the Sciacovelli et al. [13] research study only contains the LAES discharging cycle. The mass flow rate of air is

1.8 kg/s in that setup. The results presented in Table 3 indicate that the thermodynamic models developed in the current work provide reasonable results.

Table. 3. *The results of current model compared to the results from [13].*

Parameter	Results of the current model	Results of Ref. [13]	Deviation
Turbines' power	277.77 kW	277.85 kW	0.38 %
Cryo-pump's power	29.79 kW	30.01 kW	0.73 %

3.2 Optimal discharging pressure

Two important parameters of LAES systems that have a significant influence on their overall performance are the charging and discharging pressures. In this paper the charging pressure was defined and kept constant, while it is required to evaluate the optimum value of the discharging pressure. Figure 5 presents the LAES round-trip efficiency, cryo-pump power consumption, turbine power output, and net power output of the discharging cycle versus the discharging pressure varying from 10 MPa to 25 MPa. The results indicate that the round-trip efficiency increases with the increase of discharging pressure. However, the more dominant effect of the increase in discharging pressure is on the cryo-pump power consumption, which is increasing sharply with increasing discharging pressure. According to Figure 5, the additional gain in round-trip efficiency is small for discharging pressures exceeding 18 MPa. Thus, the discharging pressure is set to 20 MPa (purple band in Figure 5), resulting in a round-trip efficiency of 41 %, cryo-pump power consumption of 2.6 MW, turbine power output 42 MW, and hence a net power output of 39.4 MW.

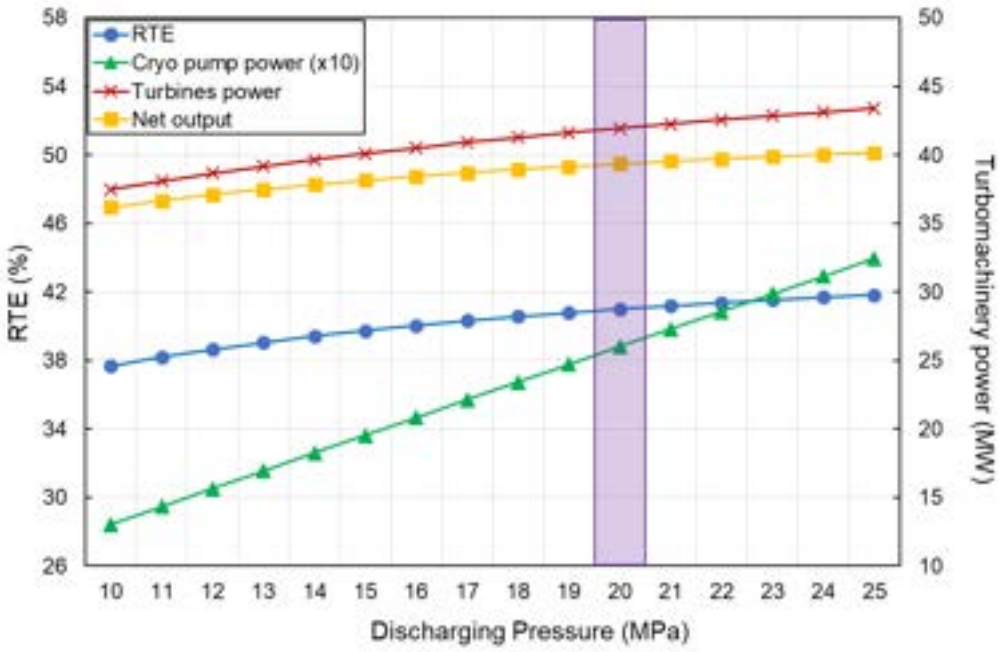

Figure. 5. *LAES round-trip efficiency, cryo-pump power consumption, turbine power output, and net power output of the discharging cycle versus the discharging pressure.*

3.3 Performance of LAES system with different particles in the packed bed

Figure 6 presents a comparison of the LAES round-trip efficiency, mean liquid air yield, and turbine power output for packed bed systems with the three different particles for the cold energy storage. The results suggest that the SiO2 particle results in the poorest performance, while the PCM and quartz particles attain very similar performances.

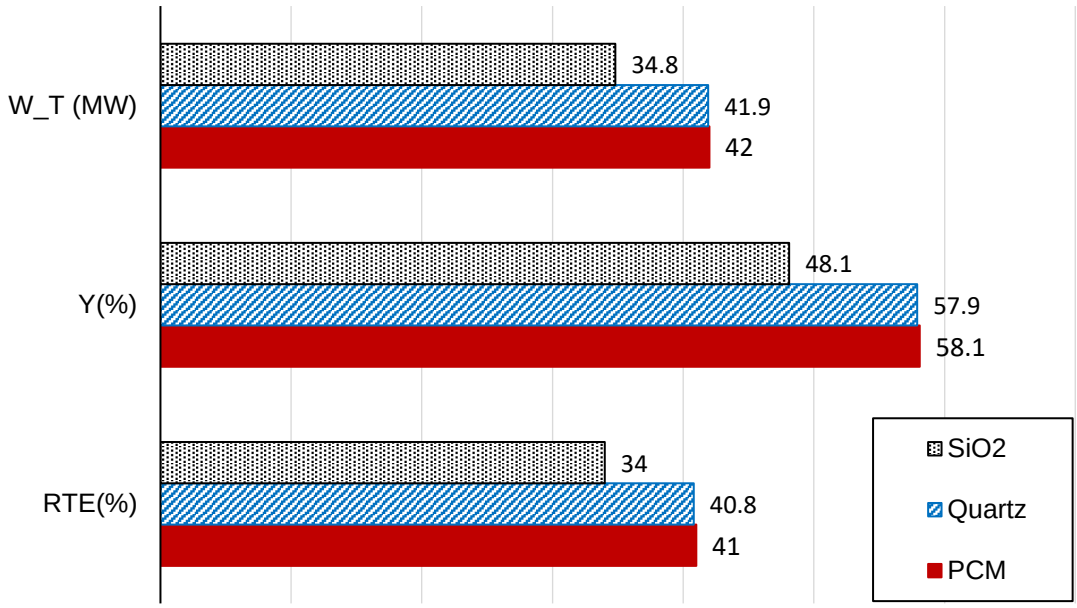

Figure. 6. *Round-trip efficiency (RTE), mean liquid air yield (Y), and output power of the turbines ($\dot{W}_T$) for the three different particle types.*

In order to understand the effects of the particle materials, Figure 7 presents the heat transfer fluid temperature at the outlet of the packed bed (point C1 in Figure 1) versus time for the three different particle materials. The outlet temperature of the air starts to increase after 66 minutes, 128 minutes and 161 minutes for the SiO2, PCM and quartz, respectively. The temperature of point C1 directly affects on the temperature of point A8, the parameter, which have a significant influence on the liquid air yield, the round-trip efficiency and the output power of the turbines. A lower temperature in point A8 results in a higher liquid air yield. The poor performance of SiO2 particles is because of the rapid increase in temperature of C1 (Figure 7), due to unfavourable thermophysical properties of SiO2 in terms of specific heat capacity and density in comparison with PCM and quartz. In contrast, the increase of air temperature over time for the cases of PCM and quartz is controlled in a better way and as a result, these two systems present better performance due to a lower temperature at the inlet of cold box. The phase change phenomenon of PCM is noticeable in the temperature range around the PCM melting point (155 K to 158 K), where the air temperature remains constant for the rest of the charging time. It can be observed that the outlet temperature (C1) does not exceed the melting point of PCM since there are still some particles in the solid state. The reason why the quartz particle achieves similar performance as that of the PCM, although it is not a phase change material, is that quartz particle keeps the air temperature equal to the packed bed's initial charging temperature for a longer time duration than does the PCM. This is because the density of quartz particles is more than 3 times higher than that of the PCM considered for the analysis. As the volume of the packed bed and the porosity are the same for all 3 particle materials, the higher particle density results in a higher particle mass. Therefore, the storage mass of the quartz system is more than 3 times than that of the PCM for the same volume of the packed bed system.

The behaviour of liquid yield over time for the three particle materials is presented in Figure 8. Similar to the temperature in point C1, the liquid yield is constant while the PCM changes phase, reaching a steady state of 0.467 after 354 min. The maximum value of the liquid yield (slightly above 0.7) is attained for the longest duration for the quartz particles because the temperature in point C1 is kept at the minimum value for the longest duration for this material. The liquid yield starts to decrease from the maximum value after 199 min, 160 min and 87 min for the quartz, PCM and SiO2, respectively.

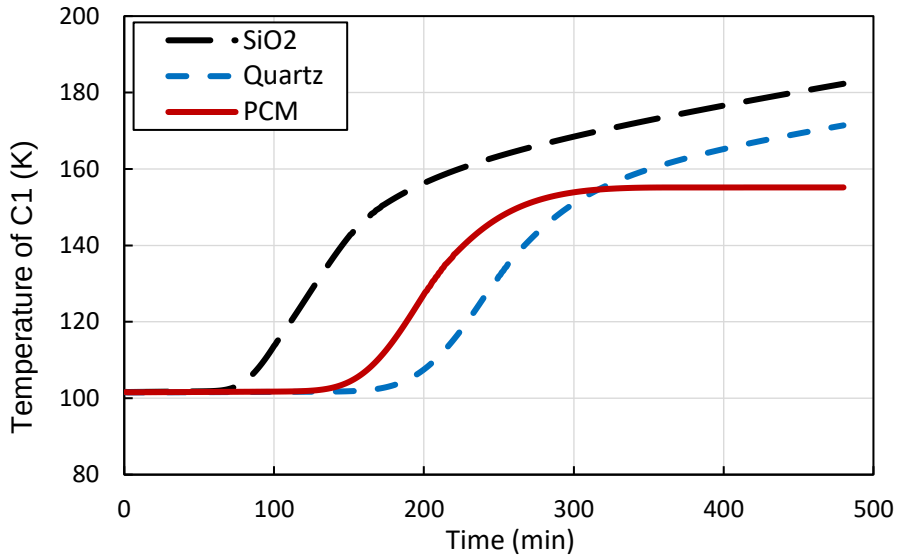

Figure. 7. *Air temperature at the outlet of packed bed versus charging time for the three different particles, SiO2, quartz and PCM.*

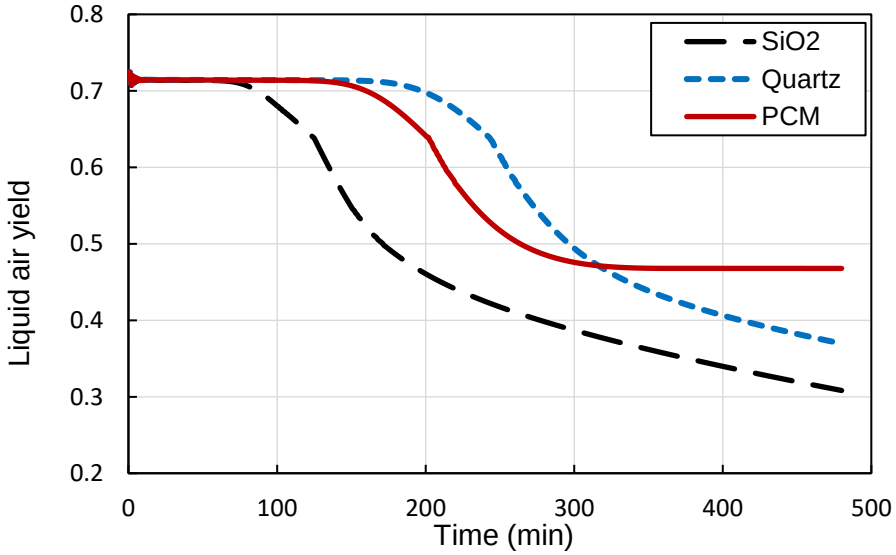

Figure. 8. *LAES liquid yield versus time for the three types of particles.*

4. Conclusions

In this paper a comparative analysis of sensible heat and latent heat packed bed cold energy storages for LAES systems was presented. The investigated particles are quartz and silicon dioxide representing sensible heat storage materials and an alcohol-based fluid representing a latent heat phase change material. A thermodynamic model of the LAES system integrated with a 1-dimensional transient numerical model of the packed bed system was developed. The particles were compared in terms of the LAES round-trip efficiency, mean liquid yield, and output power of the turbines. The results suggest that the optimum value for discharging pressure of the system is 20 MPa. Among the analysed particle materials, the PCM and quartz achieve the highest round-trip efficiency for the LAES system, 41 % and 40.8 %, respectively. The round-trip efficiency of the silicon dioxide is lower, 34 %, due to unfavourable thermophysical properties. The reason why the quartz particle achieves similar performance as that of the PCM, although it is not a phase change material, is that quartz particle keeps the air temperature at the cold storage outlet equal to the packed bed's initial charging temperature for a longer time duration than does the PCM. This is because the density of quartz particles is more than 3 times higher than that of the PCM considered for the analysis, resulting in a greater mass of the cold storage based on quartz. In general, the choice between PCM particles and quartz particles for a LAES cold storage system depends on factors such as the required energy density, the desired charging and discharging rates, the available space and weight limits, and the cost of the materials. These aspects will be investigated in future work.

Acknowledgment

The research presented in this paper was partly developed within the project “Sustainable large-scale energy storage in Egypt” (Project no. 21-M13-DTU), funded by the Ministry of Foreign Affairs of Denmark and administrated by Danida Fellowship Centre. In addition, the research was partly funded by a Korea Agency for Infrastructure Technology Advancement (KAIA) grant provided by the Ministry of Land, Infrastructure and Transport (Grant RS-2022-00143652). The financial support is gratefully acknowledged.

Nomenclature

C_p	Specific heat capacity, $J/kg.K$	$\dot{Q}$	Heat transfer rate, W
CRP	Cryogenic pump	r	Radial location inside each particle, m
CTB	Cryogenic turbine	R	Particles radius, m
D	Packed bed diameter, m	RTE	Round-trip efficiency
d_p	Particles diameter, m	t	Time, s
H	Packed bed height, m	T	Temperature, K
h	Specific enthalpy, J/kg	u_f	Velocity of air inside packed bed, m/s
h_{fp}	Convective heat transfer coefficient between air and particles, $W/m^2.K$	$\dot{W}$	Turbomachinery power, W
h_w	Convective heat transfer coefficient between packed bed and ambient, $W/m^2.K$	y	Liquid air yield
k	Thermal conductivity, $W/m.K$	Y	Mean liquid air yield
$\dot{m}$	Mass flow rate, kg/s	z	Axial location of packed bed tank, m
P	Pressure, Pa		

Greek symbols

ε	Porosity of packed bed	μ	Dynamic viscosity, $Pa.s$
η	Isentropic efficiency of turbomachinery	ρ	Density, kg/m^3

Subscripts and superscripts

amb	Ambient	p	Particle
C	Compressor	s	Solid particles inside packed bed
f	Fluid	T	Turbine

Reference

[1] Lin B, Wu W, Bai M, Xie C. Liquid air energy storage: Price arbitrage operations and sizing optimization in the GB real-time electricity market. Energy Econ 2019;78:647–55. https://doi.org/10.1016/J.ENECO.2018.11.035.

[2] Tafone A, Romagnoli A, Li Y, Borri E, Comodi G. Techno-economic Analysis of a Liquid Air Energy Storage (LAES) for Cooling Application in Hot Climates. Energy Procedia 2017;105:4450–7. https://doi.org/10.1016/J.EGYPRO.2017.03.944.

[3] Morgan R, Nelmes S, Gibson E, Brett G. An analysis of a large-scale liquid air energy storage system. Proceedings of Institution of Civil Engineers: Energy 2015;168:135–44. https://doi.org/10.1680/ener.14.00038.

[4] She X, Peng X, Nie B, Leng G, Zhang X, Weng L, et al. Enhancement of round trip efficiency of liquid air energy storage through effective utilization of heat of compression. Appl Energy 2017;206:1632–42. https://doi.org/10.1016/J.APENERGY.2017.09.102.

[5] Antonelli M, Barsali S, Desideri U, Giglioli R, Paganucci F, Pasini G. Liquid air energy storage: Potential and challenges of hybrid power plants. Appl Energy 2017;194:522–9. https://doi.org/10.1016/J.APENERGY.2016.11.091.

[6] Peng X, She X, Cong L, Zhang T, Li C, Li Y, et al. Thermodynamic study on the effect of cold and heat recovery on performance of liquid air energy storage. Appl Energy 2018;221:86–99. https://doi.org/10.1016/J.APENERGY.2018.03.151.

[7] Xu C, Li X, Wang Z, He Y, Bai F. Effects of solid particle properties on the thermal performance of a packed-bed molten-salt thermocline thermal storage system. Appl Therm Eng 2013;57:69–80. https://doi.org/10.1016/J.APPLTHERMALENG.2013.03.052.

[8] Borri E, Sze JY, Tafone A, Romagnoli A, Li Y, Comodi G. Experimental and numerical characterization of sub-zero phase change materials for cold thermal energy storage. Appl Energy 2020;275:115131. https://doi.org/10.1016/J.APENERGY.2020.115131.

[9] Wang C, Bian Y, You Z, Luo Y, Zhang X, Peng H, et al. Dynamic analysis of a novel standalone liquid air energy storage system for industrial applications. Energy Convers Manag 2021;245:114537. https://doi.org/10.1016/J.ENCONMAN.2021.114537.

[10] Ryu JY, Alford A, Lewis G, Ding Y, Li Y, Ahmad A, et al. A novel liquid air energy storage system using a combination of sensible and latent heat storage. Appl Therm Eng 2022;203. https://doi.org/10.1016/j.applthermaleng.2021.117890.

[11] Tafone A, Borri E, Cabeza LF, Romagnoli A. Innovative cryogenic Phase Change Material (PCM) based cold thermal energy storage for Liquid Air Energy Storage (LAES) – Numerical dynamic modelling and experimental study of a packed bed unit. Appl Energy 2021;301. https://doi.org/10.1016/j.apenergy.2021.117417.

[12] Bashiri Mousavi S, Ahmadi P, Hanafizadeh P, Khanmohammadi S. Dynamic simulation and techno-economic analysis of liquid air energy storage with cascade phase change materials as a cold storage system. J Energy Storage 2022;50:104179. https://doi.org/10.1016/J.EST.2022.104179.

[13] Sciacovelli A, Vecchi A, Ding Y. Liquid air energy storage (LAES) with packed bed cold thermal storage – From component to system level performance through dynamic modelling. Appl Energy 2017;190:84–98. https://doi.org/10.1016/j.apenergy.2016.12.118.

[14] Guo L, Ji W, Gao Z, Fan X, Wang J. Dynamic characteristics analysis of the cold energy transfer in the liquid air energy storage system based on different modes of packed bed. J Energy Storage 2021;40. https://doi.org/10.1016/j.est.2021.102712.

[15] Tafone A, Romagnoli A, Borri E, Comodi G. New parametric performance maps for a novel sizing and selection methodology of a Liquid Air Energy Storage system. Appl Energy 2019;250:1641–56. https://doi.org/10.1016/J.APENERGY.2019.04.171.

[16] Wang C, Cui Q, Dai Z, Zhang X, Xue L, You Z, et al. Performance analysis of liquid air energy storage with enhanced cold storage density for combined heating and power generation. J Energy Storage 2022;46. https://doi.org/10.1016/j.est.2021.103836.

[17] Hüttermann L, Span R. Investigation of storage materials for packed bed cold storages in liquid air energy storage (LAES) systems. Energy Procedia 2017;143:693–8. https://doi.org/10.1016/J.EGYPRO.2017.12.748.

[18] Peng H, Shan X, Yang Y, Ling X. A study on performance of a liquid air energy storage system with packed bed units. Appl Energy 2018;211:126–35. https://doi.org/10.1016/J.APENERGY.2017.11.045.

[19] Cascetta M, Cau G, Puddu P, Serra F. Numerical investigation of a packed bed thermal energy storage system with different heat transfer fluids. Energy Procedia, vol. 45, Elsevier Ltd; 2014, p. 598–607. https://doi.org/10.1016/j.egypro.2014.01.064.

[20] Ortega-Fernández I, Loroño I, Faik A, Uriz I, Rodríguez-Aseguinolaza J, D'Aguanno B. Parametric analysis of a packed bed thermal energy storage system. AIP Conf Proc, vol. 1850, American Institute of Physics Inc.; 2017. https://doi.org/10.1063/1.4984442.

[21] Knobloch K, Muhammad Y, Costa MS, Moscoso FM, Bahl C, Alm O, et al. A partially underground rock bed thermal energy storage with a novel air flow configuration. Appl Energy 2022;315:118931. https://doi.org/10.1016/J.APENERGY.2022.118931.

[22] Cohen Y, Metzner AB. Wall effects in laminar flow of fluids through packed beds. AIChE Journal 1981;27:705–15. https://doi.org/10.1002/aic.690270502.

[23] Ahmed N, Elfeky KE, Qaisrani MA, Wang QW. Numerical characterization of thermocline behaviour of combined sensible-latent heat storage tank using brick manganese rod structure impregnated with PCM capsules. Solar Energy 2019;180:243–56. https://doi.org/10.1016/j.solener.2019.01.001.

[24] Ewl, Ihb, MH, MML. REFPROP Documentation. 2018.

[25] Wakao N, Kaguei S, Funazkri T. Effect of fluid dispersion coefficients on particle-to-fluid heat transfer coefficients in packed beds: Correlation of nusselt numbers. Chem Eng Sci 1979;34:325–36. https://doi.org/10.1016/0009-2509(79)85064-2.

[26] Beek J. DESIGN OF PACKED CATALYTIC REACTORS. n.d.

[27] Mathworks®. MATLAB® 2022a.

[28] Li MJ, Jin B, Ma Z, Yuan F. Experimental and numerical study on the performance of a new high-temperature packed-bed thermal energy storage system with macroencapsulation of molten salt phase change material. Appl Energy 2018;221:1–15. https://doi.org/10.1016/j.apenergy.2018.03.156.

Low-temperature compressed air energy storage with reversibly operable turbo- and piston machines

Markus Hadam[a], Marcus Budt[b]

[a] Fraunhofer UMSICHT, Oberhausen, Germany, markus.hadam@umsicht.fraunhofer.de
[b] Fraunhofer UMSICHT, Oberhausen, Germany, marcus.budt@umsicht.fraunhofer.de

Abstract:

Adiabatic compressed air energy storage (A-CAES) is a promising storage technology to face the challenges of high shares of renewable energies in an energy system by storing electric energy for periods of several hours up to weeks. In order to reduce the investment costs and increase the flexibility of the storage system, the so called KompEx LTA-CAES® was developed by Fraunhofer UMSICHT. This new A-CAES concept is using a combination of reversibly operable turbo- and piston machines (KompEx machines). Doing so, these modules can achieve wide CAS pressure ranges (corresponding to high exergy densities) and thus can be combined with any compressed air storage volume. To realize efficient and stable operation despite a wide pressure range, a suitable control strategy of both KompEx machines is required. This paper investigates the introduced A-CAES system by a dynamic simulation, focusing on the interaction and synergy between the reversibly operable turbo- and piston machines. Results indicate that the roundtrip efficiency of this system is expected to be at the low end (55,5%) of literature values for A-CAES (52–66% for low-temperature A-CAES), which is relatively high compared to published A-CAES systems considering similar pressure ranges.

Keywords:

Compressed Air Energy Storage; Thermodynamics; Energy Storage; Dynamic Simulation

1. Introduction

A-CAES systems have the potential to play an important role in realizing a sustainable energy supply infrastructure based on renewable energy. The general interest in A-CAES is illustrated by many R&D activities all over the world in recent years. Nevertheless, the economically viable implementation of A-CAES plants is a great challenge under political and economic conditions in most countries at the present time – and probably also in near future.

This paper gives an overview of published thermodynamically investigated A-CAES concepts. Furthermore, a new low-temperature A-CAES concept developed by Fraunhofer UMSICHT called »KompEx LTA-CAES® modular« is presented (Section 3), which aims to overcome current barriers regarding the economic realization of A-CAES. Special features are the modular design and the use of reversibly operable turbo- and piston machines (KompEx machines).

2. State of the art

Although the individual components of many A-CAES concepts are commercially available, A-CAES systems are still almost exclusively in the R&D phase due to economic barriers. For this purpose, several demonstration plants have been built worldwide [1–4]. The first commercial adiabatic CAES plant was commissioned in Goderich (Ontario, USA) in 2019 [5], and others are currently under construction in China [6]. Nevertheless, A-CAES are still mainly studied on a theoretical level, which is illustrated by a large number of thermodynamic studies published in the last decades. This section briefly introduces the general function and typical classification of A-CAES systems and gives an overview of published layouts.

2.1. Functional principle of adiabatic CAES

The basic principle and the main components of adiabatic CAES are shown in Figure 1. During the charging process, ambient air is compressed by electrically driven compressors (C). The heated compressed air is cooled and stored in a compressed air storage volume (CAS), while the thermal energy is temporarily stored in a separate thermal energy storage (TES). During discharging, the stored compressed air is released from the CAS, heated via the TES and expanded in expanders (E) to generate electricity via generators.

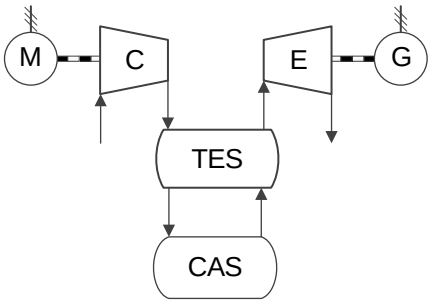

Figure 1. General block diagram of A-CAES (based on [7]).

The plant layout design, suitable technologies and the resulting operating behaviour of A-CAES systems are crucially dependent on the addressed storage temperature. Therefore, the following section gives an overview of general plant layouts and their special characteristics.

2.2. Classification of A-CAES

According to the importance of the process temperature, A-CAES can be divided into three different process types [8]:

- High temperature processes (HT) with temperatures above 400 °C
- Medium-temperature processes (MT) with temperatures between 200 °C and 400 °C
- Low-temperature processes (LT) with temperatures below 200 °C

The process temperature is essentially determined by the number of the used compression stages and heat management. In HT processes, ambient air is compressed via one or two stages, which leads to high process temperatures at corresponding final pressures. In LT processes, multi-staged compressors with intercooling are used, resulting in lower process temperatures. Higher process temperatures are leading to generally higher cycle efficiencies (Figure 2) but also to higher investment costs, since special thermally resilient components are required. Furthermore, the start-up times are limited to 10–15 minutes due to the high thermal stresses in the components [48]. A-CAES systems with lower process temperatures, in contrast, are technically easier to design (e. g. a simple storage medium such as water can be used), resulting in lower investment costs. Furthermore, lower thermal stresses are allowing faster start-up times (down to < 5 min.) and thus the participation in certain electricity markets like the ancillary service.
In contrast to a Carnot cycle process, the maximum process temperature has only a minor influence on the cycle efficiency of A-CAES systems (Figure *2*). The illustrated efficiency range (solid lines) is based on a simple equation introduced by Kreid [9], where fixed design values for relevant main components like efficiency of motor and generator, compressor and expander as well as pressure and thermal losses are taken into account. The efficiency range illustrated in Figure *2* is resulting by assuming a turbomachine efficiency between 70 and 85 %. The plotted data points are representing electrical cycle efficiencies of adiabatic plant layouts calculated in thermodynamical studies (Table A.1). The decreasing efficiency for lower storage temperatures is resulting from proportionally higher thermal losses at constant temperature gradients [10].

2.3. Key parameters of published A-CAES concepts

Published A-CAES concepts are varying widely regarding the design of compression/expansion stages, thermal storage and compressed air storage as well as implemented control strategies. To highlight the special features of the developed KompEx LTA-CAES®, the following section briefly provides an overview of typical plant layouts and key performance indicators of published A-CAES concepts.

Storage temperature and used thermal storage media

The storage temperature of the thermal energy storage of A-CAES plants is dependent on the final CAS pressure as well as on the design and heat management of the compression train. Depending on the process type, water, thermal oils or rockfills are most commonly used as thermal storage media (Table A.1).

Cycle efficiency

The plant efficiencies calculated in published A-CAES studies are showing a logarithmic dependency on the storage temperature (trend line in Figure *2*) and mostly a reasonable agreement with the predicted efficiency range according to Kreid [9]. The two upper outliers ([11, 12]) can be explained by the comparatively high design efficiencies of the compression and expansion machines of 88 to 92 % assumed in each of these papers. In comparison, the calculation of the upper cycle efficiency according to Kreid [9] is based on a maximum efficiency assumption of 85 %.

Several thermodynamic studies [13–19] are calculating A-CAES cycle efficiencies which are – in some cases significantly – below the cycle efficiency range according to Kreid [9] (Figure *2*). A closer look at the

corresponding plant layouts shows that in these the CAS volumes are operated within a relatively wide pressure range (Table A.1). As a result, the compressors are increasingly operated outside their optimum. Furthermore, the corresponding plant layouts are using throttle valves to ensure a constant inlet pressure in the expansion machines during the discharging process. This measure is leading to an optimum operation of the expanders at the cost of high losses of the usable potential energy stored in the CAS. These losses are rising with larger operating pressure differences of the CAS. The two negative effects described are leading to relatively low cycle efficiencies.

The developed KompEx LTA-CAES® addresses a relatively wide CAS pressure range but nevertheless reaches a comparatively higher electrical efficiency of 55.53 % (point 14 in Figure 2). This is obtained by the special constellation of the compressors/expanders and the implemented control strategy of the plant layout, which will be discussed later.

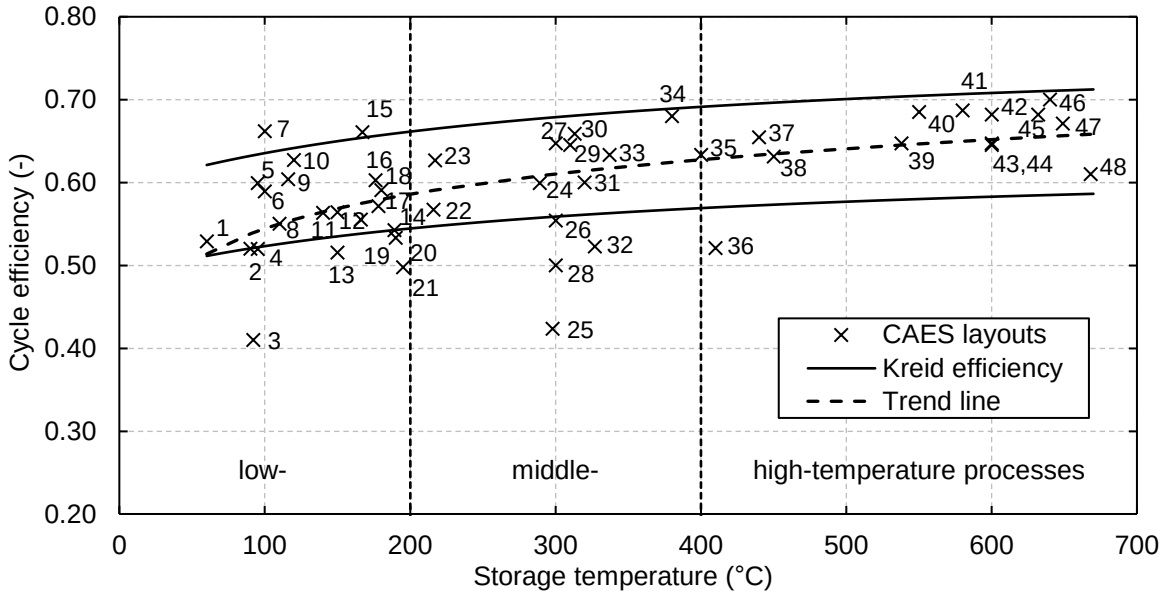

Figure 2. Predicted CAES cycle efficiencies according to [9] and calculated by published A-CAES studies depending on storage temperature (based on [8]); see Table A.1 for the literature allocation of the CAES layout data points.

Charging and discharging power

The designed installed charging/discharging capacity of investigated system layouts usually is depending on the addressed application. The focus of past studies is mostly on huge central applications. This usually includes storage systems that are used for the temporal shifting of large amounts of energy with high electrical power (> 20 MW_{el}, Table A.1). These systems usually operate at the medium and high-voltage level and can provide grid services such as minute reserves. In contrast, decentralized storage concepts are characterized by lower charging/discharging powers and energy storage volumes. They are usually located near the consumer and are suitable to compensate generation and consumption peaks or to backup island grids. Both centralized and decentralized storage applications are considered promising, especially when coupled with fluctuating renewable energies like wind turbines or photovoltaic plants. [20, 21]

CAS technology and exergy density

The amount of energy to be stored as well as geographical conditions have a decisive influence on the choice of a suitable CAS technology. In studies on centralized A-CAES concepts, underground salt caverns are generally used to store the compressed air (Table A.1), since they have low specific investment costs (€/m³) when storing large amounts of energy. The maximum pressure and the realizable pressure difference of salt caverns are strongly dependent on their geological characteristics. In corresponding studies, the salt caverns are commonly operated with pressure differences of less than 40 bar.

In the field of decentralized applications, storage capacities below 20 MW_{el} are usually required. Due to the strong geographical dependency and the high specific investment costs of salt caverns when storing smaller energy quantities, they are unsuitable in this case. Therefore, artificial CAS technologies with smaller storage volumes, e. g. in the form of steel tubes, steel cylinders or steel spheres are more appropriate in decentralized applications (Table A.1) [20]. In contrast to underground salt caverns, the maximum storage pressure and the realizable operating pressure difference for these CAS systems are much higher. Thus, significantly higher exergy densities can be achieved, which is of great importance for the economic operation of artificial CAS technologies as they have relatively high specific investment costs.

As an example: When charging the CAS isothermally at 15 °C, a pressure range of 80–100 bar results in an exergy density of about 2.5 kWh/m³, while a pressure range of 60–100 bar results in about 5 kWh/m³ [23].

3. KompEx LTA-CAES®

This section describes the new A-CAES concept which has been developed within the joint project »KompEx LTA-CAES® modular - Development of a modular low-temperature compressed air energy storage system with reversibly operable machines (KompEx)« funded by the German Federal Ministry for Economic Affairs and Climate Action [22]. The goal was to overcome existing barriers regarding the economic realization of adiabatic CAES based on four novel approaches. (1) A modular design to reduce unit costs through possible serial production. (2) Low storage temperatures to enable short start-up times and thus participation in profitable electricity markets. (3) To reduce investment costs, reversibly operable machine sets (KompEx machines) for compressed air are being developed. (4) By combining turbo- and piston machines, wide pressure ranges within the CAS can be realized, enabling an economical use of various CAS technologies, and thus reducing the geographical dependency from salt caverns.

3.1. Plant Layout

Figure 3 is showing the simplified block diagram of a KompEx module. Ambient air is compressed to a certain intermediate pressure via an intercooled multistage radial turbomachine ($TM_{1\text{-}n}$) driven by a motor-generator (MG). The Intercooling is carried out via plate heat exchangers ($HX_{1\text{-}n}$). The occurring thermal energy is stored by a two-tank liquid thermal energy storage – referred as low-pressure thermal energy storage ($LP\text{-}TES_{hot/cold}$) in the following. Depending on the current operating state (charging/discharging), the heat storage medium (water) is transported between the two tanks via a pump through the heat exchangers. The process section consisting of motor generator, radial turbomachine, heat exchanger and LP-TES is referred as low-pressure process (LP-process) in the following.

After the LP-process, high-pressure piston machines ($PM_{1\text{-}n}$) – each consisting of 2 individually operable cylinders – are compressing the low-pressure air to the pressure level of the CAS, which varies with the filling level. Each of the piston machines has its own motor-generator to switch single machines on and off during the charging or discharging process, which is important for the implemented process control strategy (Section 3.3). Due to the higher pressure ratios and thus higher outlet temperatures of the piston machines, the respective occurring thermal energy is stored via a high-pressure thermal energy storage (HP-TES) in the form of an indirect-flow concrete storage. Using two separated TES systems is resulting to a higher exergetic efficiency of the overall process. A trim cooler (TC) connected downstream of the HP-TES is ensuring low inlet temperatures to the CAS in order to reduce the required storage volume. The section consisting of piston machines including the motor-generators, HP-TES and trim cooler corresponds to the high-pressure process (HP-process) of the KompEx LTA-CAES®.

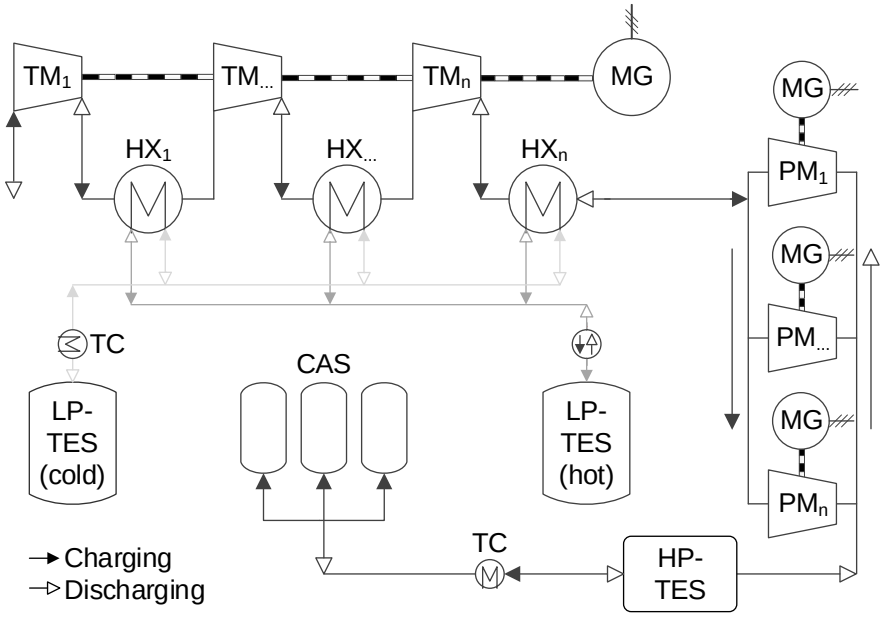

Figure 3. Simplified block diagram of the KompEx LTA-CAES® module [23].

During the discharging process, the compressed air is flowing through the same components in the reverse direction. The compressed air is heated via the respective TES system and then expanded in the KompEx machines to generate electricity in the motor-generators. By using the reversibly operable KompEx machines, a complete machinery train including expanders, heat exchangers and pipes can be omitted resulting in

reduced investment costs. Furthermore, the synergetic use of turbo- and piston machines enables an efficient operation of wide pressure ranges and thus the option of using artificial CAS technologies in addition to salt caverns. Finally, the described KompEx layout represents one module. In order to achieve higher storage capacities, several modules can be interconnected. This provides greater flexibility in terms of suitable storage applications and the potential to reduce costs by series production.

3.2. Design parameters

The design parameters of the investigated KompEx LTA-CAES® module were developed within the KompEx project (Table 1). The use of reversibly operable turbo- and piston machines in A-CAES systems leads to some special design constraints compared to concepts with separate compressors and expanders. Since the compression and expansion of the compressed air in the KompEx system are performed by the same machines, the respective design volume flows and thus the charging and discharging power are linked. This also applies to the design efficiency of the compression and expansion mode of the KompEx machines. Optimizing the KompEx machines for one of the two operating modes has a direct influence on the efficiency of the other one. Consequently, a compromise design of the KompEx machines is required. As a result, lower nominal efficiencies can be expected compared to separated state-of-the-art turbo- and piston machines. The listed nominal efficiencies (Table 1) of both machine types for each operation mode were calculated by detailed CFD simulations within the KompEx project [22]. Furthermore, the KompEx layout is specially designed for decentralized storage applications. Therefore, the CAS volume is operated within a wide pressure range to achieve high exergy densities and thus to reduce the investment costs of the CAS volume.

Table 1. Design parameters of the investigated KompEx LTA-CAES® module [23].

Design parameter	Value	Unit
Nominal electrical Power of charging	2	MW_{el}
Nominal electrical Power of discharging	1	MW_{el}
Pol. nominal efficiency in compression mode of TM	82	%
Is. nominal efficiency in expansion mode of TM	85	%
Pol. nominal efficiency in compression mode of PM	76	%
Is. nominal efficiency in expansion mode of PM	80	%
CAS volume	1.304	m^3
CAS pressure range	40–100	bar
Number of turbomachines	3	-
Number of piston machines	11	-

3.3. Control strategy

There are many different possible applications for energy storages. Examples include trading on spot markets, providing ancillary services, increasing power generation from fluctuating renewable energies and supplying electricity in off-grid regions. In some cases, a combination of different applications is also possible. Depending on the storage application, different regulatory and technical requirements must be fulfilled by the storage system. In particular, participation in ancillary services is associated with strong restrictions. The frequency restoration reserve relevant for CAES systems, for example, is requiring a constant power input and output over a defined period with a maximum deviation of 5 % [24, 25].

The KompEx LTA-CAES® is designed to cover a wide range of the mentioned applications. Therefore, a control strategy was implemented to provide constant charging and discharging power, which is necessary due to the strongly varying storage pressure. For this purpose, the turbomachine stages are designed with variable diffusor guide vanes, which enables a wide operating range of the entire turbomachinery train. In addition, single cylinders of the piston machines can be switched on and off during operation to adjust the pressure between turbo- and piston machines (Section 4.1). Furthermore, the valve on the pressure side of the piston machines can be adjusted during discharging process, which enables a less fluctuating controlling in contrast to the charging process.

3.4. Dynamic model

The investigation of the KompEx LTA-CAES® is carried out with a dynamic plant model developed in Modelica/Dymola considering real property data of humid air. The operation behaviour of the KompEx machines is modelled via black box models with implemented polynomial surface functions. In these, the efficiencies and pressure ratios of each compressor/expander stage are determined as a function of the volume flow and the respective actuating value (guide vane angle in the turbomachines; valve position in the piston machines). To consider thermal losses to the environment, the heat exchanger, ND-TES, HD-TES, CAS and piston machines are modelled diabatically. The dynamic behaviour of the heat exchangers and the HD-TES are considered by two-dimensional discretized models (finite volume method). Detailed information

regarding the dynamic model, the implemented KompEx surface functions and equations of each component can be found in [23]. The operating schedule of the simulated A-CAES is predefined via a time series in the form of the electrical charging and discharging power. The actual plant power is compared with the predefined power by means of a PID controller and adjusted accordingly via the control variables implemented in the turbo and piston machines.

4. Results and discussion

The introduced KompEx plant layout was investigated in detail regarding dynamic interactions, partial load and cycling behaviour as well as occurring exergetic losses. In this paper, the focus is only on the control strategy and interaction between the turbo- and piston machines. More detailed investigations can be found in [23].

4.1. Reference storage cycle

The dynamic curves of relevant process parameters presented in the following are based on the dynamic system simulation of a full storage cycle at nominal load operation and steady state. The system is considered to be steady state when the stored exergy in the CAS and TES after a full cycle is equal to that of the previous cycle within a deviation of ±1.0 %.

The charging and discharging process is taking about eight hours, the storage process is set up to four hours. During charging process the storage pressure in the CAS rises continuously to the maximum pressure of 100 bar, drops slightly during storage process due to thermal losses to the environment and decreases to the minimum storage pressure of 40 bar during discharging (Figure 4, diagram top left). The electrical power consumption and generation is kept practically constant (diagram top right) during the charging and discharging process via the mass flow rate (diagram bottom left), which is adjusted by the implemented control systems (diagram top right). This is necessary since the total pressure ratio and thus power of the turbo- and piston machines varies at constant mass flow rate. The exergetic charging and discharging efficiency is strongly dependent on the current operating point resp. storage pressure (diagram bottom right). This illustrates that a dynamic process simulation is crucial for a realistic representation and evaluation of the overall system. The characteristic behaviour of the illustrated process variables is primarily resulting from the interaction of the turbo- and piston machines and the implemented system control, which are described in detail in the following section.

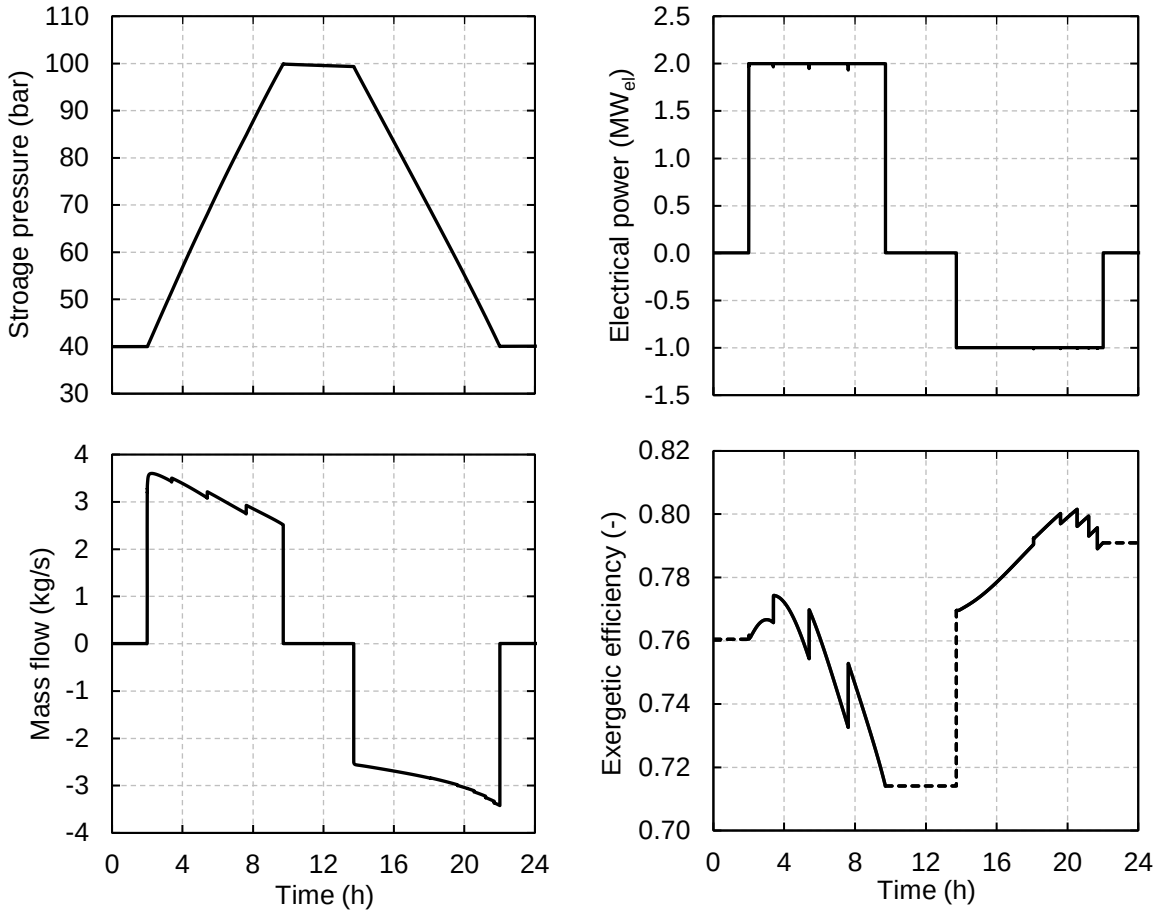

Figure 4. Storage pressure, electrical charging and discharging power, mass flow and charging and discharging efficiency of the reference storage cycle [23].

4.2. Interaction of the turbo- and piston machines

This section describes the control strategy and interaction of the turbo- and piston machines during a full charging process. The dynamic process behaviour of adiabatic CAES is essentially determined by the transient behaviour of the CAS. Therefore, the process parameters regarding the charging process are plotted as a function of the storage pressure (Figure 5). The pressure ratio (increasing from 3.58 to 8.88) and thus electrical power consumption of the piston machines is rising from 0.81 to 1.12 MW_{el} (diagram top left) due to the increasing storage pressure. This power increase is compensated by adjusting the mass flow via the variable guide vanes of the turbomachines reducing its power consumption (diagram top right).

The varying mass flow caused by the control system is resulting in a continuously varying operating point of the turbo- and piston machines, which is illustrated by the intermediate pressure (pressure between turbo- and piston machines) fluctuating during the charging process (Figure 5, diagram bottom left). The peaks observed in the shown diagrams are caused by the shutdown of single piston cylinders during the charging process, which is controlled by a discrete control loop. The reduction of the mass flow to provide a constant overall power consumption leads to an increased pressure ratio of the piston machines according to its implemented characteristic surface function. As a result, the pressure ratio of the three-stage turbomachine and thus the intermediate pressure decreases continuously. In order to ensure both machine types are operating efficiently and within their operation range, a piston cylinder is switched off at a specified minimum intermediate pressure of 11 bar (diagram bottom right). This causes an abrupt drop in the mass flow and thus in the electrical power consumption of the piston machinery train. The control system integrated in the turbomachinery train compensates this power drop by adjusting the guide vane angles of each stage resulting in an increased mass flow and power consumption. Due to the described abrupt interactions, both machine types are reaching a new operation point with a raised intermediate pressure. Further charging of the KompEx LTA-CAES® again causes the intermediate pressure to decrease until the next piston cylinder is switched off.

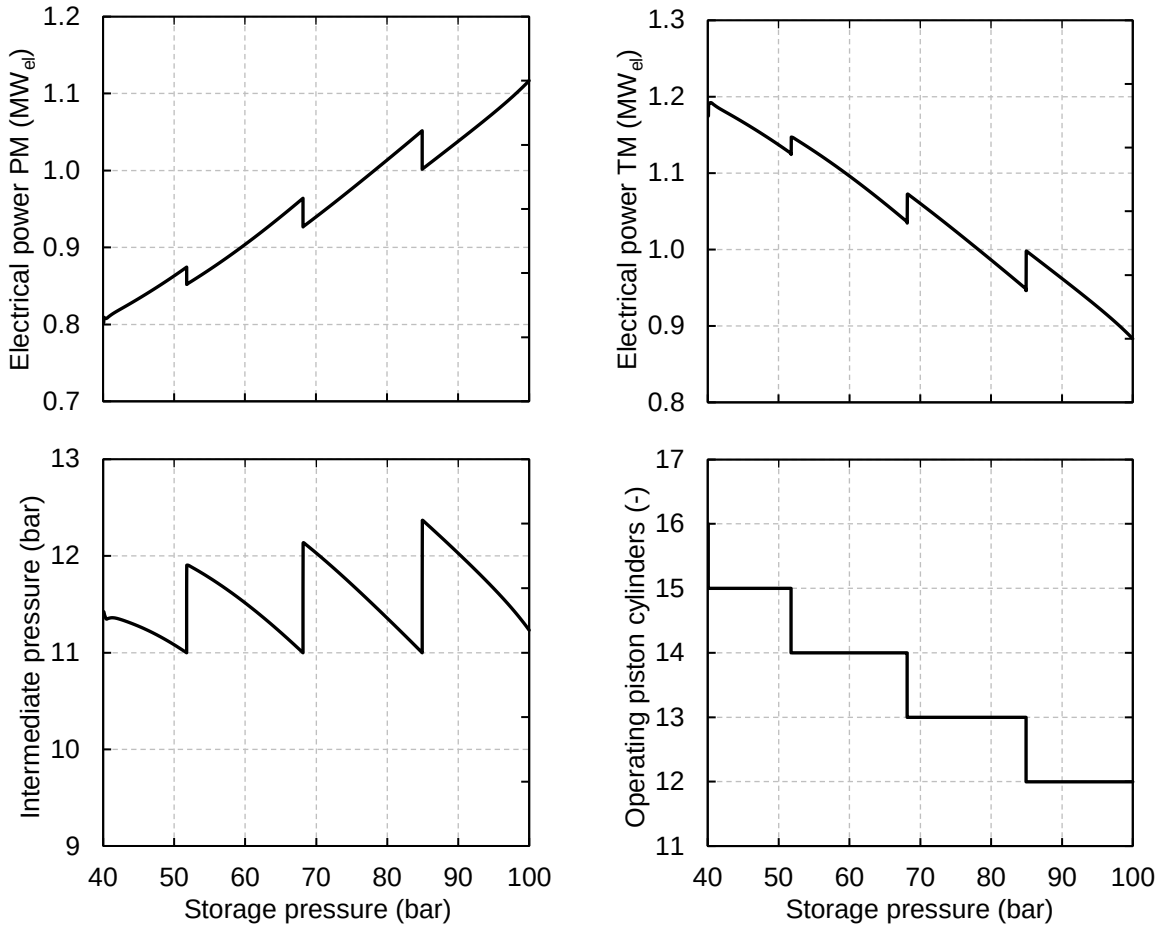

Figure 5. Electrical power of turbo- and piston machines, intermediate pressure and number of operating piston cylinders as function of the storage pressure for the reference storage cycle [23].

4.3. Part load behaviour

An important aspect that is often neglected in the literature investigating on A-CAES concepts using isochoric CAS is the influence of the varying CAS pressure range on the part load ability when a constant charging and discharging power shall be provided. To illustrate the described relationship, Figure 6 is showing a complete charging process (40 to 100 bar) with minimum and maximum power consumption of the KompEx system drawn in the efficiency map of the three-stage turbomachinery. Its operation limits are the limiting factor for the minimal operable power load of the overall system. The normalized efficiency and volume flow rate of 1.0 correspond to the respective design values.

During the charging process and thus rising storage pressure, the volume flow rate is reduced by the control system to realize a constant electrical power consumption of the overall system (Figure 4). Therefore, the volume flow rate must be reduced by up to 30 % via the outlet guide vanes of the turbomachine stages when charging with maximal power load. This implies that a great share of the part load ability of the turbomachinery – dependent on the operating CAS pressure difference – is consumed to provide a constant power consumption. Thus, the minimum electrical power consumption (62 % of nominal load) of the overall system is limited by the maximum applied storage pressure (100 bar in this case). Consequently, reducing the upper storage pressure leads to a better part load ability of the A-CAES system but also to a reduction of the exergy density.

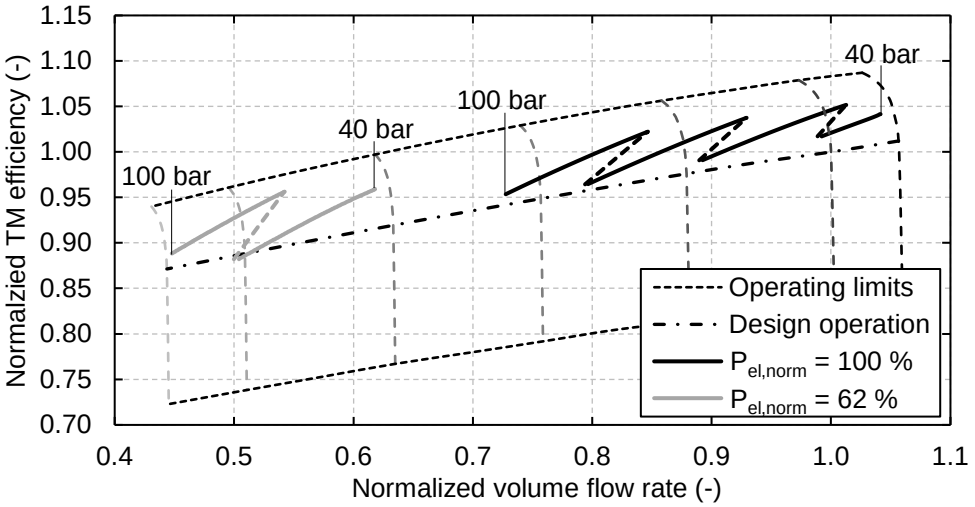

Figure 6. Efficiency map in the compression mode of the three-stage turbomachine and operating curve of the KompEx LTA-CAES® during charging process at minimum (62 % of nominal load) and maximum (100 % of nominal load) power consumption.

5. Conclusion

The introduced KompEx LTA-CAES® is able to efficiently realize wide CAS pressure ranges by the synergized use of turbo- and piston machines and appropriate control systems. Concretely, this is done by continuously varying the guide vanes of the turbomachines and a discrete control system to switch off single piston cylinders during the charging process. This offers an advantage compared to traditional A-CAES concepts using only turbomachines, especially when considering decentralized storage applications where artificial CAS technologies instead of salt caverns are usually suitable. For these applications, a high exergy density can have a decisive influence on the investment costs of the CAS volume and thus on the profitability of the overall system.

The strong fluctuations of process parameters during charging process (Figure 5) could be reduced by using piston cylinders with smaller swept volumes. Besides to the mass flow variation, the fluctuating intermediate pressure in particular is resulting to an operation of both machine types apart their design values. In order to realize a constant intermediate pressure and avoid discrete process fluctuations, a continuous control unit in the piston machinery train could be used, e. g. by implementing a variable speed control. This would lead to a more precise control and thus more efficient operation of the turbo and piston machines.

The operation behaviour of the reversibly operable turbo- and piston machines considered in this paper are derived from detailed CFD simulations within the KompEx project. In order to validate the respective data points, a test facility of the reversibly operable turbomachine is currently under construction.

Acknowledgments

The authors thank the German Federal Ministry for Economic Affairs and Climate Action for funding the project »KompEx LTA-CAES® modular« (FKZ 03ET6070A).

Appendix A

Table A.1. Overview of thermodynamically investigated A-CAES plant layouts sorted by increasing storage temperature.

Nr.	Literature[1]	$P_{el,in}$ MW_{el}	$P_{el,out}$ MW_{el}	$p_{CAS,min-max}$ bar	t_{TES} °C	η_{CAES} %AC-AC	TES-Medium	CAS[2]
1	[26]	N/A	0,7	8	60	52.90	Water	UW
2	[27]	8.1	8,6	75–125	90	52.00	Water	Artificial
3	[13]	N/A	0,5	17–80	92	41.00	Water	N/A
4	[28][1]	52.1	28.8	150	95	51.98	Water	Cavern
5	[29][1]	1.6	1.4	10–20	95	59.90	Water	N/A
6	[30][1]	0.4	2,0	46–66	100	58.90	Water	Cavern
7	[11][1]	27.1	19.2	42–70	100	66.17	Water	N/A
8	[31]	16.6	17.7	21–55	110	55.00	Water	Cavern
9	[32][1]	1.0	1.0	20–140	116	60.36	Water	Artificial
10	[33][1]	1.1	0.9	40–130	120	62.69	Oil	N/A
11	[28][1]	52.1	28.8	150	140	56.31	Water	Cavern
12	[7]	51.0	29	125–145	150	56.40	Water	Cavern
13	[34][1]	N/A	0.5	3–100	150	51.55	Water	Cavern
14	[23]	2.0	1.0	40–100	166	55.53	Water/ Concrete	Artificial
15	[12][1]	6.0	9.6	70–100	167	66.08	Water	N/A
16	[35][1]	17.7	5.3	25–64	176	60.27	N/A	N/A
17	[36][1]	83.3	96.0	40-60	178	57.14	Oil	N/A
18	[28][1]	52.1	28.8	150	180	59.07	Water	Cavern
19	[37][1]	26.0	14.4	120–155	189	54.25	Oil	Artificial
20	[38]	270.0	140.0	20–81	190	53.30	Water	Cavern
21	[15]	N/A	N/A	87–142	195	49.77	Oil	Cavern
22	[39]	85.5	131.5	140	216	56.70	Water	N/A
23	[40]	5.0	4.6	25–125	217	62.67	N/A	N/A
24	[41][1]	8.3	7.7	40–75	289	59.90	Rock	LRC
25	[19]	1.1	0.9	45–200	298	42.33	Oil	Artificial
26	[42]	60.0	110.0	70–100	300	55.40	Oil	Cavern
27	[43]	103.0	140.0	50–70	300	64.70	N/A	Cavern
28	[16]	60.0	161.0	43–70	300	50.00	Oil	Cavern
29	[44][1]	76.0	49.9	140	310	64.51	Water/PCM	Cavern
30	[45][1]	2.1	1.9	42–72	313	65.87	Oil	N/A
31	[46]	N/A	60.0	65–80	320	60.00	N/A	Cavern
32	[17]	N/A	N/A	20–70	327	52.25	Rock	N/A
33	[47]	60.0	40,7	72	337	63.31	N/A	LRC
34	[48]	70.0	40.0	40–65	380	68.00	Molten salt	Cavern
35	[49][1]	164.2	109.9	82.7	400	63.31	Oil	Cavern
36	[18]	0.1	0.0	4–20	410	52.07	Rock	N/A
37	[50][1]	0.5	N/A	20–80	440	65.43	Rock	Artificial
38	[51][1]	N/A	110.4	166	450	63.13	Oil	N/A
39	[49][1]	164.2	109.9	83	538	64.70	Oil	Cavern
40	[4]	N/A	N/A	28	550	68.50	Rock	LRC
41	[48]	70.0	40.0	40–65	580	68.70	Molten salt	Cavern
42	[52][1]	52.1	96.0	60–100	600	68.20	Rock	Cavern
43	[53][1]	N/A	N/A	10–100	600	64.51	N/A	N/A
44	[54][1]	104.2	96.0	46–66	600	64.70	Rock	Cavern

[1] The calculation of the cycle efficiency in thermodynamic studies is often not uniform. Many studies are only calculating the thermal efficiency resp. are neglecting mechanical and electrical losses. For a better comparability, the thermal efficiency in the marked sources is converted to the electrical cycle efficiency by assuming an electrical conversion efficiency of 0.96 for the charging and discharging process. In the respective sources, the charging and discharging power are also converted to electrical powers using the same factor.
[2] UW = underwater balloon, also called energy bag; Artificial: e. g. steel pipes or steel vessels; LRC = Lined Rock Cavern

Nr.	Literature[1]	$P_{el,in}$ MW_{el}	$P_{el,out}$ MW_{el}	$p_{CAS,min-max}$ bar	t_{TES} °C	η_{CAES} %AC-AC	TES-Medium	CAS[2]
45	[55][1]	104.2	211.2	46–72	632	68.20	Rock	Cavern
46	[56]	N/A	300.0	≤100	640	70.00	Rock	Cavern
47	[49][1]	164.2	109.9	82.7	649	67.09	Oil	Cavern
48	[57]	300.0	300.0	100–150	668	61.00	N/A	Cavern
49	[58]	N/A	100.0	120	N/A	56.60	Water	Artificial
50	[59]	80.0	100.0	40–80	N/A	54.50	Oil	N/A
51	[60]	0.8	0.6	42–85	N/A	55.50	Oil	N/A

References

[1] Hydrostor, Ed., “Hydrostor Activates World's First Utility-Scale Underwater Compressed Air Energy Storage System,” Press Release, 2015.

[2] S. Mei et al., “Design and engineering implementation of non-supplementary fired compressed air energy storage system: TICC-500,” Sci. China Technol. Sci., vol. 58, no. 4, pp. 600–611, 2015, doi: 10.1007/s11431-015-5789-0.

[3] J. Wang et al., “Overview of Compressed Air Energy Storage and Technology Development,” Energies, vol. 10, no. 7, p. 991, 2017, doi: 10.3390/en10070991.

[4] L. Geissbühler et al., “Pilot-scale demonstration of advanced adiabatic compressed air energy storage, Part 1: Plant description and tests with sensible thermal-energy storage,” Journal of Energy Storage, vol. 17, pp. 129–139, 2018, doi: 10.1016/j.est.2018.02.004.

[5] Hydrostor, “Projects,” 2021. Accessed: Aug. 24 2021. [Online]. Available: https://www.hydrostor.ca/projects/

[6] Z. Tong, Z. Cheng, and S. Tong, “A review on the development of compressed air energy storage in China: Technical and economic challenges to commercialization,” Renewable and Sustainable Energy Reviews, vol. 135, p. 110178, 2021, doi: 10.1016/j.rser.2020.110178.

[7] M. Budt, Thermodynamische Analyse adiabater Druckluftenergiespeicher unter Berücksichtigung feuchter Luft und Wassereinspritzung mittels dynamischer Simulation. Dissertation. Oberhausen: Karl Maria Laufen, 2016.

[8] M. Budt, D. Wolf, R. Span, and J. Yan, “A Review on Compressed Air Energy Storage: Basic principles, past milestones and recent developments,” Applied Energy, vol. 170, pp. 250–268, 2016, doi: 10.1016/j.apenergy.2016.02.108.

[9] D. K. Kreid, “Technical and Economic Feasibility Analysis of the No-Fuel Compressed Air Energy Storage Concept,” Pacific Northwest Laboratories, Richland, WA BNWL-2065 UC-94b, 1976.

[10] D. Wolf and M. Budt, “LTA-CAES – A low-temperature approach to Adiabatic Compressed Air Energy Storage,” Applied Energy, vol. 125, pp. 158–164, 2014, doi: 10.1016/j.apenergy.2014.03.013.

[11] C. Guo et al., “Comprehensive exergy analysis of the dynamic process of compressed air energy storage system with low-temperature thermal energy storage,” Applied Thermal Engineering, vol. 147, pp. 684–693, 2019, doi: 10.1016/j.applthermaleng.2018.10.115.

[12] H. Guo, Y. Xu, C. Guo, Y. Zhang, H. Hou, and H. Chen, “Off-design performance of CAES systems with low-temperature thermal storage under optimized operation strategy,” Journal of Energy Storage, vol. 24, p. 100787, 2019, doi: 10.1016/j.est.2019.100787.

[13] W. Zhang, X. XUE, F. Liu, and S. Mei, “Modelling and experimental validation of advanced adiabatic compressed air energy storage with off-design heat exchanger,” IET Renewable Power Generation, vol. 14, no. 3, pp. 389–398, 2020, doi: 10.1049/iet-rpg.2019.0652.

[14] Y. He, H. Chen, Y. Xu, and J. Deng, “Compression performance optimization considering variable charge pressure in an adiabatic compressed air energy storage system,” Energy, 2018, doi: 10.1016/j.energy.2018.09.168.

[15] M. Dooner and J. Wang, “Potential Exergy Storage Capacity of Salt Caverns in the Cheshire Basin Using Adiabatic Compressed Air Energy Storage,” Entropy, vol. 21, no. 11, p. 1065, 2019, doi: 10.3390/e21111065.

[16] L. Szablowski, P. Krawczyk, K. Badyda, S. Karellas, E. Kakaras, and W. Bujalski, “Energy and exergy analysis of adiabatic compressed air energy storage system,” Energy, vol. 138, pp. 12–18, 2017, doi: 10.1016/j.energy.2017.07.055.

[17] H. Peng, Y. Yang, R. Li, and X. Ling, “Thermodynamic analysis of an improved adiabatic compressed air energy storage system,” Applied Energy, vol. 183, pp. 1361–1373, 2016, doi: 10.1016/j.apenergy.2016.09.102.

[18] W. He et al., “Study of cycle-to-cycle dynamic characteristics of adiabatic Compressed Air Energy Storage using packed bed Thermal Energy Storage,” Energy, vol. 141, pp. 2120–2134, 2017, doi: 10.1016/j.energy.2017.11.016.

[19] S. Mucci, A. Bischi, S. Briola, and A. Baccioli, “Small-scale adiabatic compressed air energy storage: Control strategy analysis via dynamic modelling,” Energy Conversion and Management, vol. 243, p. 114358, 2021, doi: 10.1016/j.enconman.2021.114358.

[20] M. Sterner and I. Stadler, Eds., Energiespeicher - Bedarf, Technologien, Integration, 2nd ed. Berlin: Springer Vieweg, 2017. [Online]. Available: http://dx.doi.org/10.1007/978-3-662-48893-5

[21] J. Witte, Ed., Zentrale und dezentrale Elemente im Energiesystem: Der richtige Mix für eine stabile und nachhaltige Versorgung : Stellungnahme, 2020th ed. München, Halle (Saale), Mainz: acatech - Deutsche Akademie der Technikwissenschaften e. V; Deutsche Akademie der Naturforscher Leopoldina e.V. - Nationale Akademie der Wissenschaften; Union der deutschen Akademien der Wissenschaften e. V, 2020.

[22] M. Budt, M. Hadam, N. Kienzle, and E. Schischke, “Schlussbericht zum Verbundvorhaben KompEx LTA-CAES® modular: Entwicklung eines modularen Niedertemperatur-Druckluftenergiespeichers mit umkehrbar betreibbaren Maschinensätzen,” 2021.

[23] M. Hadam, “Thermodynamische Analyse eines modularen A-CAES mit umkehrbar betreibbaren Turbo- und Kolbenmaschinen,” Dissertation, Ruhr-Universität Bochum, Fakultät für Maschinenbau, Bochum, 2021.

[24] FNN, “TransmissionCode 2007: Anforderungen für die Umsetzung des SRL-Poolkonzepts zwischen ÜNB und Anbietern,” Anahng D2, Teil 2, Berlin, Nov. 2009.

[25] D. ÜNB, “Präqualifikationsverfahren für Regelreserveanbieter,” 2020.

[26] M. Ebrahimi, R. Carriveau, D. S.-K. Ting, and A. McGillis, “Conventional and advanced exergy analysis of a grid connected underwater compressed air energy storage facility,” Applied Energy, vol. 242, pp. 1198–1208, 2019, doi: 10.1016/j.apenergy.2019.03.135.

[27] F. Buffa, S. Kemble, G. Manfrida, and A. Milazzo, “Exergy and Exergoeconomic Model of a Ground-Based CAES Plant for Peak-Load Energy Production,” Energies, vol. 6, no. 3, pp. 1050–1067, 2013, doi: 10.3390/en6021050.

[28] C. Doetsch, M. Budt, D. Wolf, and A. Kanngießer, “Adiabates Niedertemperatur-Druckluftspeicherkraftwerk zur Unterstützung der Netzintegration von Windenergie,” Final report, Oberhausen, 2012.

[29] K. Yang, Y. Zhang, X. Li, and J. Xu, “Theoretical evaluation on the impact of heat exchanger in Advanced Adiabatic Compressed Air Energy Storage system,” Energy Conversion and Management, vol. 86, pp. 1031–1044, 2014, doi: 10.1016/j.enconman.2014.06.062.

[30] X. Luo et al., “Feasibility study of a simulation software tool development for dynamic modelling and transient control of adiabatic compressed air energy storage with its electrical power system applications,” Applied Energy, vol. 228, pp. 1198–1219, 2018, doi: 10.1016/j.apenergy.2018.06.068.

[31] X. Luo et al., “Modelling study, efficiency analysis and optimisation of large-scale Adiabatic Compressed Air Energy Storage systems with low-temperature thermal storage,” Applied Energy, vol. 162, pp. 589–600, 2016, doi: 10.1016/j.apenergy.2015.10.091.

[32] G. Grazzini and A. Milazzo, “A Thermodynamic Analysis of Multistage Adiabatic CAES,” Proc. IEEE, vol. 100, no. 2, pp. 461–472, 2012, doi: 10.1109/JPROC.2011.2163049.

[33] Y. He, MengWang, H. Chen, Y. Xu, and J. Deng, “Thermodynamic research on compressed air energy storage system with turbines under sliding pressure operation,” Energy, vol. 222, p. 119978, 2021, doi: 10.1016/j.energy.2021.119978.

[34] Y. He, H. Chen, Y. Xu, and J. Deng, “Compression performance optimization considering variable charge pressure in an adiabatic compressed air energy storage system,” Energy, vol. 165, pp. 349–359, 2018, doi: 10.1016/j.energy.2018.09.168.

[35] Z. Guo, G. Deng, Y. Fan, and G. Chen, “Performance optimization of adiabatic compressed air energy storage with ejector technology,” Applied Thermal Engineering, vol. 94, pp. 193–197, 2016, doi: 10.1016/j.applthermaleng.2015.10.047.

[36] Z. Han, S. Guo, S. Wang, and W. Li, “Thermodynamic analyses and multi-objective optimization of operation mode of advanced adiabatic compressed air energy storage system,” Energy Conversion and Management, vol. 174, pp. 45–53, 2018, doi: 10.1016/j.enconman.2018.08.030.

[37] T. Thomasson, “Dynamic Model Development of Adiabatic Compressed Air Energy Storage,” Master's Thesis, School of Energy Systems, Lappeenranta University of Technology, Jyväskylä, 2016.

[38] F. Uttke, “Modellierung eines adiabaten Druckluftspeichers in Modelica,” Masterarbeit, Institut für Energietechnik, Technische Universität Hamburg-Harburg, Hamburg, 2017.

[39] Y. Mazloum, H. Sayah, and M. Nemer, “Comparative Study of Various Constant-Pressure Compressed Air Energy Storage Systems Based on Energy and Exergy Analysis,” J. Energy Resour. Technol, vol. 143, no. 5, 2021, doi: 10.1115/1.4048506.

[40] A. Arabkoohsar, H. R. Rahrabi, A. S. Alsagri, and A. A. Alrobaian, “Impact of Off-design operation on the effectiveness of a low-temperature compressed air energy storage system,” Energy, vol. 197, p. 117176, 2020, doi: 10.1016/j.energy.2020.117176.

[41] J. Fan et al., “Thermodynamic and applicability analysis of a hybrid CAES system using abandoned coal mine in China,” Energy, vol. 157, pp. 31–44, 2018, doi: 10.1016/j.energy.2018.05.107.

[42] Helsingen, “Adiabatic compressed air energy storage,” Master's Thesis, Norwegian University of Science and Technology, Trondheim, 2015.

[43] Y. Huang et al., “Techno-economic Modelling of Large Scale Compressed Air Energy Storage Systems,” Energy Procedia, vol. 105, pp. 4034–4039, 2017, doi: 10.1016/j.egypro.2017.03.851.

[44] B. Ghorbani, M. Mehrpooya, and A. Ardehali, “Energy and exergy analysis of wind farm integrated with compressed air energy storage using multi-stage phase change material,” Journal of Cleaner Production, vol. 259, p. 120906, 2020, doi: 10.1016/j.jclepro.2020.120906.

[45] J.-L. Liu and J.-H. Wang, “A comparative research of two adiabatic compressed air energy storage systems,” Energy Conversion and Management, vol. 108, pp. 566–578, 2016, doi: 10.1016/j.enconman.2015.11.049.

[46] J. Bai et al., “Modelling and control of advanced adiabatic compressed air energy storage under power tracking mode considering off-design generating conditions,” Energy, vol. 218, p. 119525, 2021, doi: 10.1016/j.energy.2020.119525.

[47] S. Zhou, J. Zhang, W. Song, and Z. Feng, “Comparison Analysis of Different Compressed Air Energy Storage Systems,” Energy Procedia, vol. 152, pp. 162–167, 2018, doi: 10.1016/j.egypro.2018.09.075.

[48] D. Wolf, Methods for design and application of adiabatic compressed air energy: Storage based on dynamic modeling. Dissertation. Oberhausen: Karl Maria Laufen, 2011.

[49] V. de Biasi, “Fundamental analyses to optimize adiabatic CAES plant efficiencies,” Gas Turbine World, vol. 39, no. 5, Sep. 2009.

[50] E. Barbour, D. Mignard, Y. Ding, and Y. Li, “Adiabatic Compressed Air Energy Storage with packed bed thermal energy storage,” Applied Energy, vol. 155, pp. 804–815, 2015, doi: 10.1016/j.apenergy.2015.06.019.

[51] N. M. Jubeh and Y. S. Najjar, “Green solution for power generation by adoption of adiabatic CAES system,” Applied Thermal Engineering, vol. 44, pp. 85–89, 2012, doi: 10.1016/j.applthermaleng.2012.04.005.

[52] V. Tola, V. Meloni, F. Spadaccini, and G. Cau, “Performance assessment of Adiabatic Compressed Air Energy Storage (A-CAES) power plants integrated with packed-bed thermocline storage systems,” Energy Conversion and Management, vol. 151, pp. 343–356, 2017, doi: 10.1016/j.enconman.2017.08.051.

[53] H. Mozayeni, X. Wang, and M. Negnevitsky, “Exergy analysis of a one-stage adiabatic compressed air energy storage system,” Energy Procedia, vol. 160, pp. 260–267, 2019, doi: 10.1016/j.egypro.2019.02.145.

[54] H. Xue, “A comparative analysis and optimisation of thermo-mechanical energy storage technologies,” Apollo - University of Cambridge Repository, 2019.

[55] A. Sciacovelli et al., “Dynamic simulation of Adiabatic Compressed Air Energy Storage (A-CAES) plant with integrated thermal storage – Link between components performance and plant performance,” Applied Energy, vol. 185, pp. 16–28, 2017, doi: 10.1016/j.apenergy.2016.10.058.

[56] M. Bieber, R. Marquardt, and P. Moser, “The ADELE Project: Development of an Adiabatic CAES Plant Towards Marketability,” in 5th International Renewable Energy Storage Conference, Berlin, 2010.

[57] N. Hartmann, L. Eltrop, Bauer, N. Salzer, J, S. Schwarz, and M. Schmidt, “Stromspeicherpotentiale für Deutschland,” Universität Stuttgart, Stuttgart, Jul. 2012.

[58] Y. Mazloum, H. Sayah, and M. Nemer, “Exergy analysis and exergoeconomic optimization of a constant-pressure adiabatic compressed air energy storage system,” Journal of Energy Storage, vol. 14, pp. 192–202, 2017, doi: 10.1016/j.est.2017.10.006.

[59] Z. Han, Y. Sun, and P. Li, “Thermo-economic analysis and optimization of a combined cooling, heating and power system based on advanced adiabatic compressed air energy storage,” Energy Conversion and Management, vol. 212, p. 112811, 2020, doi: 10.1016/j.enconman.2020.112811.

[60] R. Jiang, Z. Cai, K. Peng, and M. Yang, “Thermo-economic analysis and multi-objective optimization of polygeneration system based on advanced adiabatic compressed air energy storage system,” Energy Conversion and Management, vol. 229, p. 113724, 2021, doi: 10.1016/j.enconman.2020.113724.

Potential for optimal operation of Industrial Heat Pumps with Thermal Energy Storage for emissions and cost reduction

Roger Padullés[a], Magnus Lyck Hansen[b], Martin Pihl Andersen[a], Benjamin Zühlsdorf[c], Jonas Kjær Jensen[a] and Brian Elmegaard[a]

[a] Department of Civil and Mechanical Engineering, Technical University of Denmark, Kgs. Lyngby, Denmark, rpiso@dtu.dk
[b] Viegand Maagøe, Copenhagen, Denmark, mlh@viegandmaagoe.dk,
[c] Danish Technological Institute, Aarhus, Denmark, bez@teknologisk.dk,

Abstract:

This paper presents an optimal control strategy for an industrial heat pump with thermal energy storage (TES) in a brewery. The objective of the study is to investigate the potential benefits of load shifting using the TES and the impact of the fluctuations of electricity price, solar radiation and carbon intensity of the grid on the system operating costs and CO_2 emissions. The study is conducted using a simulation model, and the results show that by utilizing the TES, the operating costs and CO_2 emissions of the heat pump can be reduced significantly. The optimal operation of the heat pump is found to be highly dependent on the electricity price and the efficiency of the heat pump. Furthermore, the study shows that cost-optimal operation leads to a reduction in CO_2 emissions and vice versa. The study highlights the potential benefits of implementing such an optimal control strategy in industrial settings, where energy demands are high and subject to electricity price fluctuations. However, accurately predicting parameters such as electricity price, solar radiation, and energy demand is crucial for the optimal control strategy to be effective. Implementing a predictive model that can accurately predict these parameters is necessary to exploit the potential of the optimal control strategy.

Keywords:

thermal energy storage, industrial heat pump, solar energy, heat recovery, energy efficiency, load shifting

1. Introduction

The transition from fossil fuels to renewable energy sources in the power sector presents a significant opportunity for the electrification of industry and the implementation of Power-to-Heat technologies, which would yield substantial environmental benefits. High Temperature Heat Pumps (HTHP) are capable of supplying heat up to 150 °C with high energy efficiency by upgrading industrial waste heat [1]. However, with the share of renewables in electricity production increasing, there is an emerging imbalance between energy production and consumption, necessitating new grid management approaches.

Thermal energy storage (TES) can play a vital role in enhancing grid flexibility by providing a means to balance the intermittent nature of renewable energy sources. TES systems enable excess thermal energy to be stored during times of high availability and used later during periods of low availability, such as during peak demand hours [2]. While TES have already been used for industrial waste heat recovery [3], the use of this technology may be key to help integrate HTHP and electrify industrial process heat.

While the combination of heat pumps and thermal energy storages to offer demand flexibility for domestic and district heating systems has been investigated in several papers [4]–[8], the industrial application is generally overlooked [9].

The objective of this study is to assess the capacity of an industrial heat pump system, when integrated with TES, to lower CO_2 emissions and operating expenses by optimizing its operating schedule. Additionally, this study examines the potential benefits of varying the system size, considering investment expenses, and conducts a sensitivity analysis of the parameters that mostly impact the results.

1.1 Case study

A brewery in Faxe, Denmark, previously described by Hansen et al.[10] is used as the case study throughout this work to evaluate the potential savings from the implementation of optimal heat pump operation. This industrial facility has an indirect heat recovery system that recovers heat from high-temperature processes and stores it in a 375 m^3 (V_{tank}) to later distribute it to various processes. The external heating is supplied by a

natural gas boiler through a pressurized hot water loop with a forward temperature of 145 °C. The cooling system currently rejects heat to the ambient through cooling towers. Additionally, the brewery installed a 12 MW ($P_{\mathrm{PV,nom}}$) photovoltaic (PV) park to reduce its electricity consumption.

As a measure to reduce the consumption of natural gas and contribute to its carbon neutrality goals, the facility will install a 1.2 MW ($Q_{\mathrm{HP,max}}$) heat pump to upgrade the heat from the condensers of the refrigeration system to deliver it to the heat recovery tank. This heat pump is the focus of this study. The heat source of the heat pump is stable throughout the year and the heat recovery tank offers an opportunity to optimize its operation.

A schematic representation of the system to be studied is given in Figure 1:

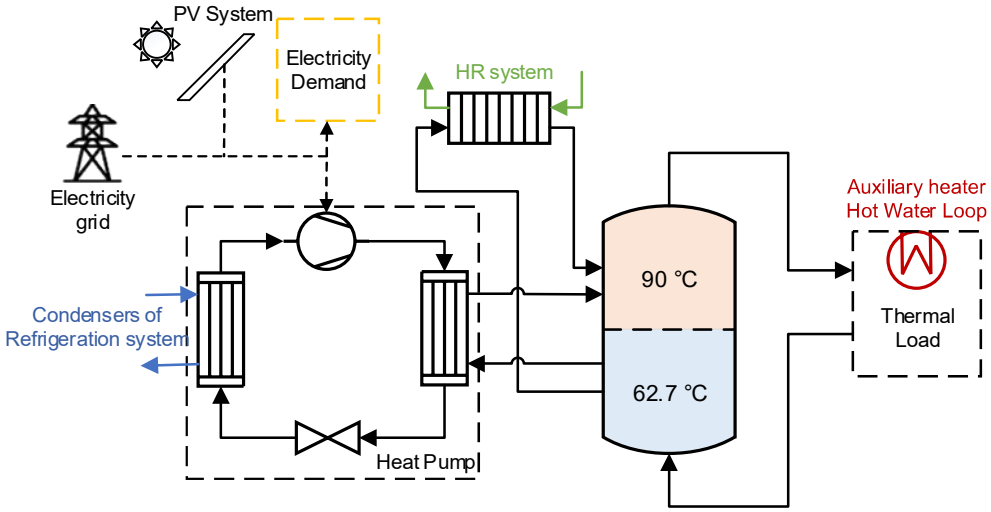

Figure 1:Schematic of the studied heat pump and TES system

Hourly data from the process demand ($Q_{\mathrm{Load},t}$), heat recovery system ($Q_{\mathrm{HR},t}$) and electricity consumption ($P_{\mathrm{load},t}$) is given by the brewery in order to calculate the potential savings from the optimal HP operation.

2. Methods

Hourly-based Time-series data of the electricity prices, carbon emission intensity and solar radiation, in combination with the thermal load, heat recovery and electricity consumption of the facility are used to optimize the operation of the heat pump delivering heat to the heat recovery tank. The optimization is performed in Python using Pyomo [11].

The study compares the CO_2-optimal and cost-optimal strategies with a base-case scenario that assumes no smart control. Additionally, an investigation is included to determine the optimal tank and heat pump size and to highlight the importance of thermal energy storage (TES) in the proper integration of the heat pump.

2.1. Preliminary calculations

In every case, the Coefficient of Performance (COP) of the heat pump is considered constant. It is calculated considering a fixed source temperature (T_{source}), which corresponds to the temperature of the condensers of the refrigeration system; fixed sink inlet ($T_{\mathrm{sink,in}}$) and outlet ($T_{\mathrm{sink,out}}$) temperatures corresponding to the temperatures in the tank; and a fixed Lorenz efficiency (η_{Lor}).

$$\mathrm{COP} = \eta_{\mathrm{Lor}} \cdot \frac{T_{\mathrm{sink,out}} - T_{\mathrm{sink,in}}}{T_{\mathrm{source}} \cdot \ln \frac{T_{\mathrm{sink,out}}}{T_{\mathrm{sink,in}}}} \quad (1)$$

The capacity of the tank ($E_{\mathrm{tank,max}}$) is also fixed for the entirety of the simulation. It is calculated as:

$$E_{\mathrm{tank,max}} = V_{\mathrm{tank}} \cdot \rho \cdot c_p \cdot \left(T_{\mathrm{sink,out}} - T_{\mathrm{sink,in}}\right) \quad (2)$$

The output from the PV system ($P_{\mathrm{PV},t}$) is calculated from the dataset representing a “Design Reference Year” on horizontal solar radiation ($G_{h,t}$) from the Danish Meteorological Institute [12] and the incidence angle (θ_t), dependant on the hour, day of the year, location, and tilt of the panels.

$$P_{\mathrm{PV},t} = P_{\mathrm{PV,nom}} \cdot \frac{G_{h,t}}{G_{\mathrm{STC}}} \cdot \cos(\theta_t) \quad (3)$$

2.2. Model description

The calculation of the annual cost and carbon emissions is based on the energy balance on the tank for every timestep (t) as well as the balance on the electricity used and the electricity generated from the PV panels.

In this study, the tank is considered a perfectly stratified tank, with two distinct temperature levels ($T_{\text{sink,in}}$ and $T_{\text{sink,out}}$) without mixing or ambient losses. The energy on the tank on the following timestep ($E_{\text{tank},t+1}$) is calculated using Eq. (4) from the current energy level ($E_{\text{tank},t}$), the heat recovered ($Q_{\text{HR},t}$), the energy output of the HP ($Q_{\text{HP,max}} \cdot x_t$) and the thermal demand ($Q_{\text{Load},t}$).

$$E_{\text{tank},t+1} = \begin{cases} 0 & if \quad E_{\text{tank},t} + Q_{\text{HR},t} + Q_{\text{HP,max}} \cdot x_t - Q_{\text{Load},t} < 0 \\ E_{\text{tank},t} + Q_{\text{HR},t} + Q_{\text{HP,max}} \cdot x_t - Q_{\text{Load},t} & if \quad 0 < E_{\text{tank},t} + Q_{\text{HR},t} + Q_{\text{HP,max}} \cdot x_t - Q_{\text{Load},t} < E_{\text{tank,max}} \\ E_{\text{tank,max}} & if \quad E_{\text{tank,max}} < E_{\text{tank},t} + Q_{\text{HR},t} + Q_{\text{HP,max}} \cdot x_t - Q_{\text{Load,t}} \end{cases} \tag{4}$$

Therefore, the energy from the heat recovery system to be curtailed ($Q_{\text{curt},t}$) and the energy that must be supplied to the load using the auxiliary boiler ($Q_{\text{boiler},t}$) are also calculated using Eq. (5) and Eq. (6):

$$Q_{\text{curt},t} = \begin{cases} 0 & if \quad E_{\text{tank},t} + Q_{\text{HR},t} + Q_{\text{HP,max}} \cdot x_t - Q_{\text{Load},t} < E_{\text{tank,max}} \\ E_{\text{tank,max}} - E_{\text{tank,t}} + Q_{\text{HR},t} + Q_{\text{HP,max}} \cdot x_t - Q_{\text{Load},t} & if \quad E_{\text{tank},t} + Q_{\text{HR},t} + Q_{\text{HP,max}} \cdot x_t - Q_{\text{Load},t} > E_{\text{tank,max}} \end{cases} \tag{5}$$

$$Q_{boiler,t} = \begin{cases} 0 & if \quad E_{\text{tank},t} + Q_{\text{HR},t} + Q_{\text{HP,max}} \cdot x_t > Q_{\text{Load},t} \\ Q_{\text{Load},t} - E_{\text{tank,t}} + Q_{\text{HR},t} + Q_{HP,\text{max}} \cdot x_t & if \quad E_{\text{tank},t} + Q_{\text{HR},t} + Q_{\text{HP,max}} \cdot x_t < Q_{\text{Load},t} \end{cases} \tag{6}$$

Finally, the operational costs and CO_2 emissions can be calculated. The price of electricity ($p_{\text{elec},t}$) and natural gas ($p_{\text{gas},t}$) in Denmark are found in Energinet [13] and the corresponding taxes as of 2021 are applied ($p_{\text{elec,taxes}}$). The data on the carbon intensity (CI_{elec}) is taken from ElectricityMaps database [14], and for the combustion of natural gas (CI_{gas}), a value of 200.8 g/kWh is considered [15].

The costs and emissions related to the combustion of natural gas are calculated using Eq. (7) and Eq. (8) respectively:

$$\text{Cost}_{\text{gas}} = \frac{1}{\eta_{\text{boiler}}} \cdot \sum_{t=0}^{t=n} Q_{\text{boiler},t} \cdot p_{\text{gas},t} \tag{7}$$

$$\text{CO}_{2\text{gas}} = \frac{\text{CI}_{\text{gas}}}{\eta_{\text{boiler}}} \cdot \sum_{t=0}^{t=n} Q_{\text{boiler},t} \tag{8}$$

For the electricity, the production from the PV panels is considered. The cost and emissions from the purchased electricity is calculated using Eq. (9) and Eq. (10) respectively:

$$Cost_{\text{elec}} = \sum_{t=0}^{t=n} \begin{cases} \left(p_{\text{elec},t} + p_{\text{elec,taxes}}\right) \cdot \left(\frac{Q_{\text{HP,max}} \cdot x_t}{COP} + P_{\text{load},t} - P_{PV,t}\right) & if \quad \frac{Q_{\text{HP,max}} \cdot x_t}{COP} + P_{\text{load},t} > P_{\text{PV},t} \\ p_{\text{elec},t} \cdot \left(\frac{Q_{HP,\text{max}} \cdot x_t}{COP} + P_{\text{load},t} - P_{PV,t}\right) & if \quad \frac{Q_{\text{HP,max}} \cdot x_t}{COP} + P_{\text{load},t} < P_{\text{PV},t} \end{cases} \tag{9}$$

$$CO_{2\text{elec}} = \sum_{t=0}^{t=n} \begin{cases} CI_{\text{elec},t} \cdot \left(\frac{Q_{\text{HP,max}} \cdot x_t}{COP} + P_{\text{load},t} - P_{\text{PV},t}\right) & if \quad \frac{Q_{\text{HP,max}} \cdot x_t}{COP} + P_{\text{load},t} > P_{\text{PV},t} \\ 0 & if \quad \frac{Q_{\text{HP,max}} \cdot x_t}{COP} + P_{\text{load},t} < P_{\text{PV},t} \end{cases} \tag{10}$$

2.3. Heat Pump operation

2.3.1. Base case operation

The basic control strategy of the heat pump does not consider fluctuations on electricity price or CO_2 emission intensity, nor the power produced by the PV system. In this case, the operation of the heat pump is solely regulated by the energy level stored in the tank.

When the state of charge of the tank ($E_{\text{tank},t}$ / $E_{\text{tank,max}}$) is below 50 %, the HP is working at its maximum capacity ($x_t = 1$). As the energy level in the tank approaches the 50 % threshold, the power output of the HP is proportionally reduced. In order to avoid curtailing energy from the HR system, the HP is deactivated ($x_t = 0$) when the tank level reaches 80 % of its maximum capacity. To avoid curtailment of energy from the heat recovery system, the HP is turned off when the level on the tank is at 80 % of its maximum capacity. This straightforward control strategy is intended to prevent energy wastage while maximizing the use of the heat pump. The control of the HP as function of the energy level on the tank can be shown in Figure 2:

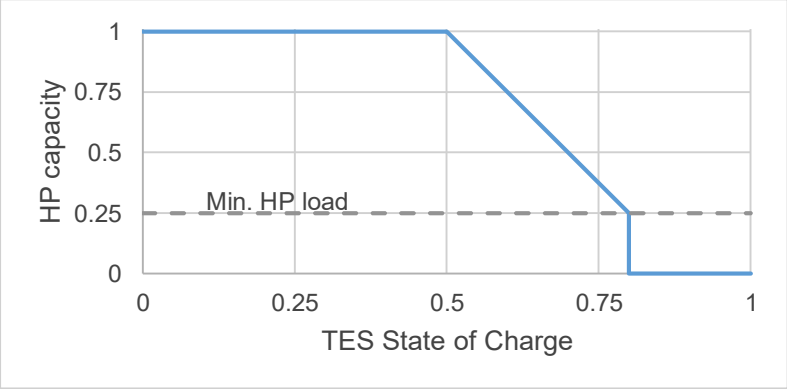

Figure 2: HP control strategy for the base case

2.3.2. CO_2 and cost-optimal heat pump operation

In contrast to the previous section, the CO_2 and the cost-optimal operation strategies consider the fluctuations on the electricity price or carbon intensity as well as the fluctuation of the power output of the PV panels. The model described previously is implemented in Pyomo, with the capacity of the HP at each timestep (x_t) as the optimization variable.

Two distinct optimizations are performed with two different objective functions: a cost-optimal operation ($\text{Cost}_{\text{gas}} + \text{Cost}_{\text{elec}}$) and a CO_2-optimal operation ($\text{CO}_{2_{\text{gas}}} + \text{CO}_{2_{\text{elec}}}$).

Additional constraints are included to limit the maximum ramp-up ($x_{\text{ramp-up}}$) and ramp-down ($x_{\text{ramp-down}}$) of the heat pump capacity between consecutive timesteps.

2.4. Uncertainty and sensitivity analysis

Throughout this analysis, certain parameter values have been assumed, and while some of these assumptions are reasonable, others, especially those related to the efficiency of the heat pump, are subject to significant uncertainty.

To investigate the robustness of the study's conclusions under different scenarios and to put the potential benefits of the optimal operation schedule into perspective relative to other sources of uncertainty, an uncertainty analysis is conducted. Table 1 shows the parameters that will be investigated.

Table 1: Parameters and uncertainties used in the analysis

Parameter	Mean value	Type of deviation	Deviation
T_{source}	15 °C	Uniform, absolute	3 K
$T_{\text{sink,in}}$	62.7 °C	Uniform, absolute	1 K
$T_{\text{sink,out}}$	90 °C	Uniform, absolute	1 K
η_{Lor}	50 %	Normal, absolute	5 %
η_{Boiler}	95 %	Normal, absolute	5 %
$x_{\text{min.load}}$	25 %	Uniform, absolute	5 %
$x_{\text{ramp-up}}$	90 %	Uniform, absolute	10 %
$x_{\text{ramp-down}}$	90 %	Uniform, absolute	10 %

The parameters related to the efficiency of the HP have high uncertainty. The value of 50 % is reasonable approach to the calculation of the efficiency of the HP and is taken from a recent market overview [1]. The other parameters including the ramp-up, ramp-down and minimum load are taken from the technology catalogue [16].

The values for the temperatures and the efficiency of the boiler are given by the brewery. For these parameters, less conservative approach to its uncertainty has been taken.

Among the possible techniques, the Monte Carlo analysis is chosen for the present study [17]. This method is chosen for its usefulness not only for uncertainty but for the sensitivity analysis by linear regression techniques. After defining the parameters and their uncertainties, a sampling number of *N*=2000 is defined, and a sampling matrix is generated by means of Latin hypercube sampling. Finally, *N* number of simulations are performed using this matrix, and the results are retrieved to analyse their uncertainties.

A sensitivity analysis is also performed for the economic savings and CO_2 reduction when using a cost-optimal operation schedule. For the sensitivity analysis on the model, the Standardized Regression Coefficient (SRC) method is used. The SRC method provides a measure of the sensitivity of the model output to each input parameter. It does this by quantifying the magnitude and direction of the effect of each input parameter on the output, while controlling for the effects of the other input parameters. This method quantifies the sensitivity of the results on input parameters by constructing a linear model based on the outputs from the Monte Carlo simulation [18].

2.5. Optimal heat pump and tank size

The optimized operation schedule of the HP may result in an improved business case for the HP and TES system. To explore this further, this work includes a small investigation on the investment costs of the system and compares the optimal sizing of the HP and TES to the base case operation.

The investment cost ($\mathrm{Cost}_{\mathrm{inv,tank}}$ and $\mathrm{Cost}_{\mathrm{inv,HP}}$) functions are found in the Technology Catalogue from the Danish Energy Agency [16]:

$$\mathrm{Cost}_{\mathrm{inv,tank}} = 7450 \cdot {V_{\mathrm{tank}}}^{0.53} \tag{11}$$

$$\mathrm{Cost}_{\mathrm{inv,HP}} = 0.73 \cdot Q_{\mathrm{HP,max}} \tag{12}$$

The investment cost is annualized by annualization factor considering a discount rate of *i*=5% and a lifetime of LT_{HP}=25 years and LT_{tank}=40 years.

$$\mathrm{Cost} = Cost_{\mathrm{inv}} \cdot i \frac{(1+i)^{\mathrm{LT}}}{(1+i)^{\mathrm{LT}} - 1} + \mathrm{Cost}_{op} \tag{13}$$

Note that, in this part of the analysis, an uncertainty analysis is not performed, as such an optimization would have been much more time-consuming and computationally demanding. The average values of the parameters presented in Table 1 are used.

3. Results

3.1. Energy use

The annual thermal energy demand of the facility is 16,815 MWh, with 8,587 MWh provided by the heat recovery system. The amount of heat delivered by the HP and the boiler, however, differ for every case. Table 2 shows the annual thermal energy use in the facility in all of the three cases:

Table 2: Results on heat use

	Base case operation	Cost-optimal operation	CO_2-optimal operation
Heat Pump	8,017.5 ± 0.2 MWh	8,166.4 ± 0.2 MWh	8,107 ± 4 MWh
Boiler	210.1 ± 0.2 MWh	61.3 ± 0.2 MWh	119 ± 4 MWh
Heat Recovery	8,587.3 MWh	8,587.3 MWh	8,587.3 MWh
Curtailment	0 MWh	0 MWh	0 MWh
Total load	16,815.0 MWh	16,815.0 MWh	16,815.0 MWh

In every case, the entirety of the energy from the HR system is utilized, and the curtailment of energy is avoided. From the three scenarios, the cost-optimal operation avoids utilizing the boiler as much as possible, even more than the CO_2-optimal operation. This implies that, with a sufficiently low HP efficiency and a very unfavourable electricity mix, the natural gas boiler is in fact avoiding CO_2 emissions. There is, however, a high degree of uncertainty in this aspect, and this strategy seems to be the most sensitive to the uncertainties of the inputs.

As for the electricity use, the electricity demand of the brewery before considering the HP is 28,063 MWh and the solar panels produce 8,074 MWh annually. Table 3 shows the main results on the electricity use on the three cases:

Table 3: Results on electricity use

	Base case operation	Cost-optimal operation	CO_2-optimal operation
Elec. Purchase	24,110 ± 12 MWh	24,120 ± 12 MWh	24,097 ± 10 MWh
Elec. Sold	1,283 ± 1 MWh	1,241 ± 1 MWh	1,241 ± 1 MWh
HP consumption	2,839 ± 13 MWh	2,891 ± 13 MWh	2,867 ± 12 MWh
PV production	8,074.4 MWh	8,074.4 MWh	8,074.4 MWh
Demand (without HP)	28,061.7 MWh	28,061.7 MWh	28,061.7 MWh

In both cost and CO_2 optimal operation schedules, the selling electricity from the PV power is avoided compared to the base case operation. The uncertainties in the results, especially in the electricity consumption of the HP, seem to be larger than the uncertainties presented in Table 2.

It is important to note that the electricity consumption of the heat pump, and therefore the focus of this optimization represents only between 9.1 and 9.3 % of the total electricity demand.

3.2. Potential for cost and CO_2 emission reduction

While the difference in annual energy consumption is not substantial, the cost and emissions reduction achieved through smart operation of the system is, given that the HP only represents a fraction of the energy consumption of the brewery, quite significant. Specifically, the total operation cost including natural gas and purchased electricity is 2,934,900 ± 1,500 € in the base case, but it is reduced to 2,901,700 ± 1,400 € and 2,918,800 ± 1,500 € in the cost- and CO_2-optimal cases, respectively. Additionally, the annual CO_2 emissions are 7,021 ± 3 kgCO_2eq. in the base case and are reduced to 6,964 ± 3 kgCO_2eq. and 6,922 ± 3 kgCO_2eq. in the cost- and CO_2-optimal cases, respectively.

The potential for reduction of costs and emissions is shown in Figure 3:

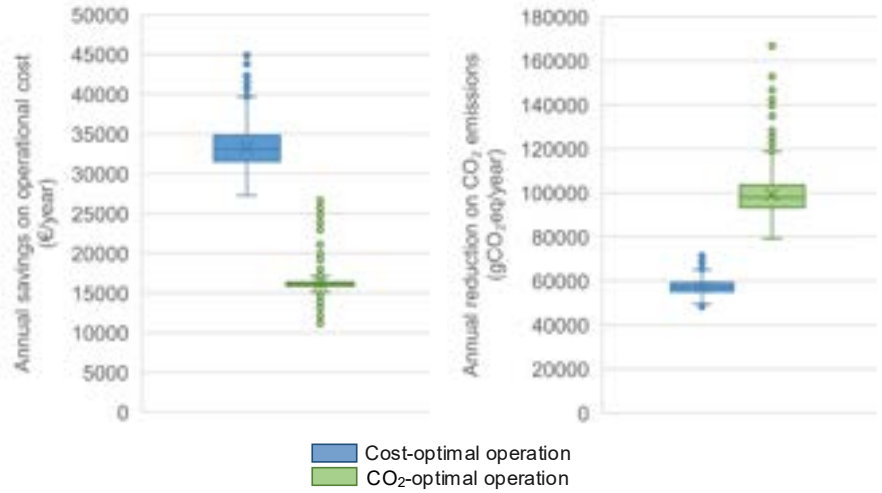

Figure 3: Potential for cost and emission reduction using a cost-optimal and CO_2-optimal HP operation

The average cost reduction is 33,286 ± 108 €/year and 16,148 ± 38 €/year for the cost- and CO_2-optimal operation, respectively. Similarly, the reduction in CO_2 emissions is 57.27 ± 0.13 kgCO_2eq. and 99.19 ± 0.38 kgCO_2eq. for cost- and CO_2-optimal operation, respectively. These results show that the cost-optimal smart operation of the heat pump not only would imply economic savings but also reduce CO_2 emissions and vice versa, as the CO_2-optimal operation would imply a reduction in the operational cost.

3.3. Sensitivity analysis

The sensitivity of the results shown in Figure 3 on the input parameters from Table 1 is measured using SCR method. The Standardized Regression Coefficients for each input with respect to each of the four model outputs are shown in Table 4:

Table 4: SRC of the input parameters for each of the outputs

	Cost reduction (Cost-optimal)	Cost reduction (CO_2-optimal)	Emissions reduction (Cost-optimal)	Emissions reduction (CO_2-optimal)
T_{source}	-0.126	-0.041	-0.106	-0.120
$T_{\text{sink,in}}$	-0.031	-0.070	-0.097	-0.041

$T_{\text{sink,out}}$	0.067	0.084	0.128	0.071
η_{Lor}	-0.947	-0.368	-0.798	-0.930
η_{Boiler}	0.217	-0.130	-0.564	-0.119
$x_{\text{min.load}}$	-0.140	-0.043	-0.117	-0.109
$x_{\text{ramp-up}}$	-0.001	0.002	-0.003	-0.007
$x_{\text{ramp-down}}$	-0.006	-0.005	-0.004	-0.013
R^2	0.981	0.165	0.985	0.900

The linear fit is good for the cost and emissions reduction on the cost-optimal operation case and for the reduction in emissions for the CO_2-optimal case, having a coefficient of determination (R^2) of 0.981, 0.985 and 0.900 respectively. On the other hand, a linear model cannot describe the variance of the reduction in cost on the CO_2-optimal case, with an R^2 that is 0.165, a value way below the acceptable threshold [19]. In this case, the SRC method does not capture all the interactions between the inputs and the non-linear behaviour of the system. Therefore, some sources of uncertainty may remain unaccounted for. It is possible that this uncertainty can be attributed to the non-linear relationship between the electricity price and the CO_2 intensity of the grid, which may not be fully captured by the linear model used in this study.

The Lorenz efficiency of the HP is in any case the main source of uncertainty. A negative, high SRC value indicates that an increase in the Lorenz efficiency will decrease the savings relative to the basic operation. This is an expected outcome, since the COP improvement will decrease the costs and CO_2 emissions, the absolute difference in the savings is diminished.

3.4. Optimal heat pump and tank size

The reduction of operational cost derived from the use of the TES for load-shifting affects the business case of the HP and the TES. The optimal size of the HP and TES system using an optimized operation schedule differs from the optimal size using the base case operation. Figure 4 shows the annualized costs (from Eq. 13) for different configurations of HP and TES for both the base-case and the cost-optimal operation:

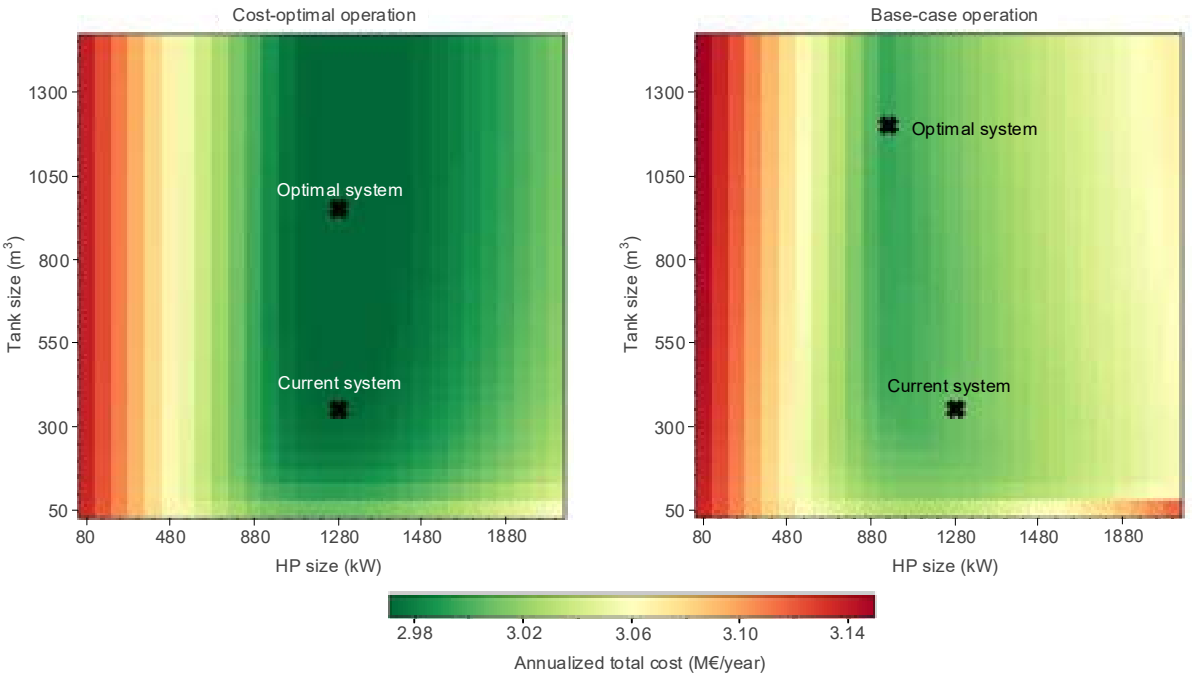

Figure 4: Annualized total costs of different HP and TES sizes using cost-optimal and base-case operation schedules

The optimal size of the system is a 960 kW HP with a 1,200 m^3 tank for the base case and a 1,280 kW HP with a 950 m^3 tank for the case with an optimized operation schedule.

As shown, the optimal size of the system is dependant on the operation strategy used. When the optimized operation is implemented, the HP size can be much larger, completely avoiding any combustion of natural gas

and being able to supply more heat during the hours with high solar output or low electricity prices. Additionally, the tank size much smaller, as its operation is optimized to take advantage of the entirety of its capacity.

Note that, due to space constraints, the current TES system installed in the brewery is largely undersized. With the current HP system projected, an additional 375 m^3 of storage capacity (doubling the size of the current tank) would reduce the annual operation costs of the facility by 8,300 € for the base case and 12,300 € for the cost-optimal case.

4. Discussion

The results show a big potential for savings with the smart operation of the Heat Pump. These reductions on cost and emission, however, do not necessarily come from a reduction on the energy use (as shown in Table 1 and Table 2) but from an optimal scheduling of the HP.

To visualize this effect, the consumption of electricity for three normal days of operation is shown in Figure 5 for the cost-optimal schedule. Note that, in this figure, the electricity has been normalized to the electricity demand of the brewery and does not represent absolute values.

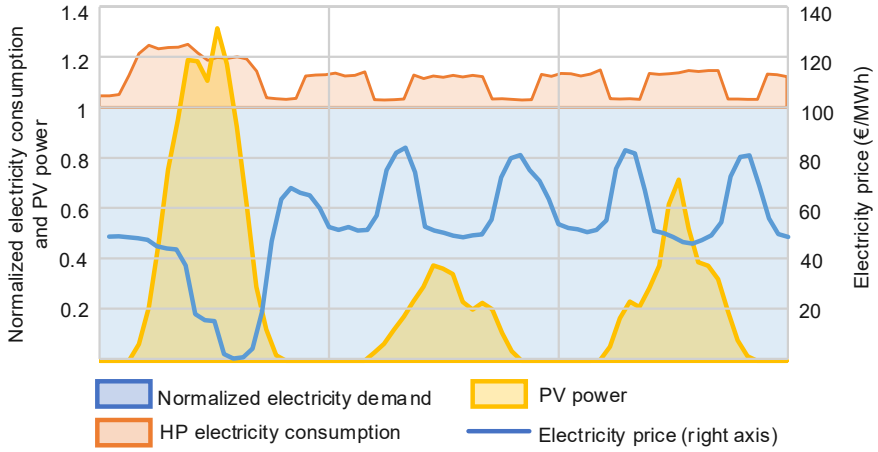

Figure 5: Normalized electricity consumption and electricity price for the Cost-optimal operation schedule for three days of operation

The electricity consumption of the HP represents, at most, less than 30 % of the rest of the brewery's electricity demand. This relatively small flexibility, however, is exploited in order to avoid an excess on the PV power production to be sold to the grid. It is also noticeable that, during the hours with peak electricity price (right axis in Figure 5), the HP is working at minimum load when possible.

A similar behaviour can be observed in the CO_2-optimal schedule. Figure 6 shows the electricity consumption in the CO_2-optimal case during the same three days of operation:

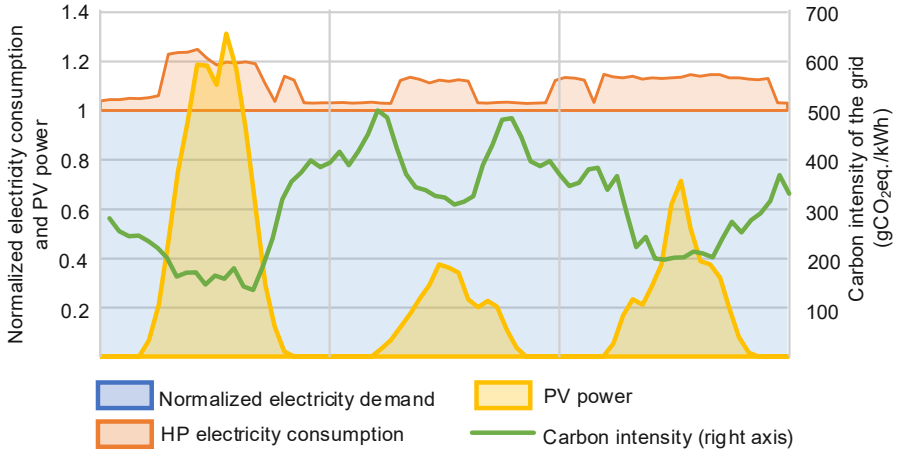

Figure 6: Normalized electricity consumption and carbon intensity of the grid for the CO_2-optimal operation schedule for three days of operation

In this case, the electricity from the PV park is used as much as possible, and the fluctuations in the carbon intensity of the grid also affect the operation of the HP. During high carbon intensity hours, the HP is working at minimum load.

The effects observed in Figure 5 and Figure 6 are, as shown in the results from Figure 3, not exclusive. The electricity cost is closely related to the electricity mix and therefore its carbon intensity. As the most carbon-intense are also the most expensive energy sources, the cost-optimal schedule is also reducing CO_2 emissions.

4.1. Heat pump operation

As shown in Figure 5 and Figure 6, both the fluctuations of the energy price or carbon intensity and the generation from the PV park increase the impact of the optimal HP operation. Figure 7 compares the operation of the HP in base case with the cost-optimal and CO_2-optimal operation for one day:

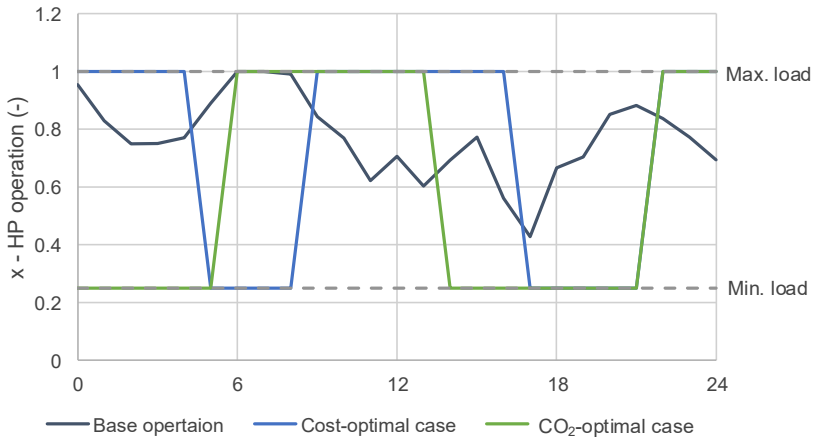

Figure 7: Heat pump operation for one day

In the optimal operation strategy, the HP operates almost independently of the energy level in the tank and instead follows a pattern that inversely corresponds to the electricity price. The HP operates intermittently between maximum and minimum loads, without operating at part-load. While this approach can improve the cost and emissions efficiency of the system, it may also cause more extreme and less smooth operation, potentially reducing the HP's lifetime and limiting its implementation [20]. Nevertheless, the maximum ramp-up and ramp-down speeds are already included in this work, with no significant impact observed.

The efficiency of the HP has the largest impact on results on absolute savings when comparing the optimal operation to the base case operation. While a heat pump with a given efficiency is a reasonable approximation for a preliminary study, a more detailed calculation of the COP and an actual dynamic HP model would be necessary to assess the potential savings in more detail.

4.2. Thermal energy storage operation

In the base case, the operation of the HP is determined by the energy level in the TES. It is designed to maintain an energy level that would avoid energy curtailment from the HR system and avoid emptying the tank as much as possible.

On the other hand, the optimized schedules take advantage of the flexibility given by the tank to optimize the schedule of the HP. In this case, the tank is charged and discharged more frequently, instead of being maintained at a certain energy level. An example of the TES operation is given in for the same day of operation in Figure 8:

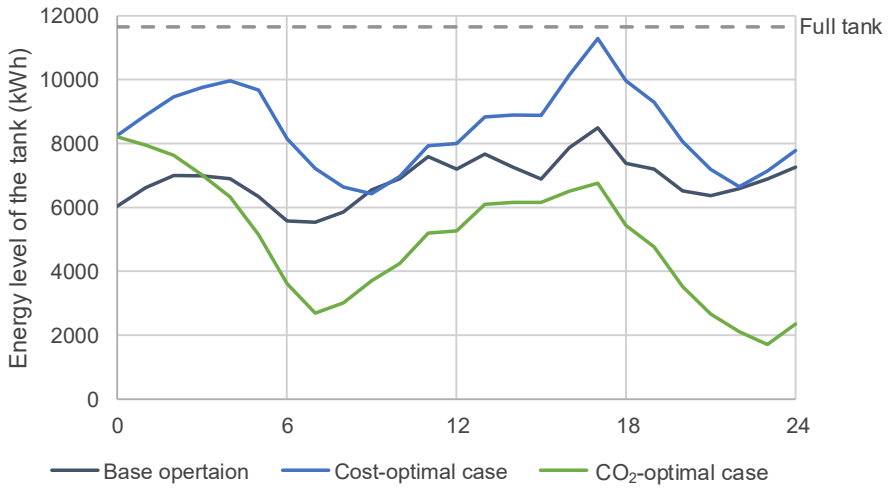

Figure 8:Thermal Energy Storage operation for one day

The model used in this research for the tank is very simple and does not take into account heat losses or mixing in the tank. Although assuming no mixing losses in the tank may seem unrealistic, it is reasonable only when the charging and discharging times are large. In the case of optimal operation, the heat pump (as shown in Figure 7), is working at its maximum or minimum load. Therefore, the tank is charged and discharged at faster speeds, which could lead to an increase in mixing losses of the tank [21].

The synergy of the TES and HP system is highlighted by the investment cost results. The existing tank in the facility was originally intended to be used for heat recovery. However, the investigation on investment costs shows that is largely undersized when it is used as a heat sink of the HP. A larger tank would allow the HP to deliver more heat to the load, and the use of natural gas could be avoided.

4.3. Directions for future research

While the sensitivity analysis demonstrated the significant impact of uncertainty on some parameters, particularly the efficiency of the HP, this study utilized fixed time datasets for the load, electricity consumption, PV power, heat recovery, and electricity price to evaluate the potential of the proposed smart operation. However, uncertainties associated with the accuracy of these parameter predictions must be taken into account when implementing this operational strategy.

To evaluate the actual system performance, it is necessary to incorporate a predictive model for these factors. Predictions on variables such as electricity price, solar radiation, or energy consumption within the brewery are typically only valid over a 24-hour time period. It would be interesting to investigate how such a predictive model would affect the results obtained in this study, thereby assessing the viability of implementing this approach in practice.

Furthermore, the heat pump and TES system considered in this study could be expanded to include more complex features, such as multiple heat sources or loads, and other possible energy storage systems (e.g., batteries) that could be used in conjunction with the TES. In addition, the use of a more detailed model for the heat pump, such as a dynamic model, would provide a more detailed assessment of the system's performance.

Finally, the investment cost analysis showed that a larger TES tank would be more cost-effective, which suggests that the sizing of the TES tank should be a consideration when designing a system of this kind. Further investigation into optimal tank sizing and operation could yield additional insights into system performance and cost-effectiveness.

Overall, this study provides a starting point for the development and implementation of smart energy management strategies and integration of HP with TES. However, additional research is needed to optimize and validate these strategies in practice.

5. Conclusion

The results of this study demonstrate the significant potential for reducing the cost of operation and CO_2 emissions of an industrial heat pump with thermal energy storage. By using an optimal control strategy that takes advantage of the thermal energy storage, load shifting can be achieved, which significantly improves the business case of the heat pump. The results show a significant correlation between the cost-optimal and CO_2-optimal operations of the HP. Optimal scheduling for cost reduction also leads to a reduction in CO_2 emissions

and vice versa. Therefore, regardless of the CO_2 emission policies or electricity purchase agreements, smart operation of the system is both economically and environmentally beneficial.

It is important, however, to carefully evaluate the performance of the system, especially the COP of the heat pump, in order to assess the potential savings. The smart operation of the HP should be investigated further, as its synergy with the TES could change the optimal system configuration and benefit the business case for the overall system.

While the potential of the optimal control strategy has been shown, implementing such a strategy in practice can be challenging. One challenge is making accurate predictions on parameters such as electricity price, solar radiation, and energy demand, especially in complicated industrial settings. The results of this study were based on fixed time datasets, and the actual performance of the system will depend on the accuracy of these predictions. Therefore, implementing a predictive model that can accurately predict these parameters is key to exploiting the potential of the optimal control strategy.

Another challenge is the impact of the optimal control strategy on the lifetime of the heat pump. The results of this study showed that the optimal control strategy resulted in less smooth, more extreme operation of the heat pump. While the maximum ramp-up and ramp-down speed was included in the analysis, the impact of this type of operation on the lifetime of the heat pump is still an open question.

Despite these challenges, the potential benefits of the optimal control strategy cannot be ignored. This study has shown that by using thermal energy storage and load shifting, significant cost and emission reductions can be achieved. These benefits are especially important for industries that have high energy demands and are subject to fluctuating electricity prices.

In summary, the potential of an optimal control strategy for an industrial heat pump with thermal energy storage has been shown to be a promising approach for reducing costs and emissions. However, implementing this strategy in practice requires accurate predictive models and careful consideration of the impact on the lifetime of the heat pump. Nonetheless, this study provides valuable insights into the potential benefits of this approach and sets the stage for further research in this area.

Nomenclature

COP	Coefficient of Performance (-)	Q	Heat (kWh)
CI	Carbon Intensity ($gCO_2eq./kWh$)	T	Temperature (°C)
c_p	Heat capacity (kWh/kg K)	V	Volume (m^3)
E	Energy (kWh)	x	Capacity factor (-)
G	Irradiance (W/m^2)	η	Efficiency (-)
LT	Lifetime of investment (years)	θ	Incidence angle (°)
P	Electrical power (kWh)	ρ	Density (kg/m^3)
p	Price (€/kWh)		

Acknowledgments

This research project was funded by The Energy Technology Development and Demonstration Programme (EUDP), under the project title: “SuPrHeat - Sustainable process heating with high-temperature heat pumps using NatRefs”.

We would like to express our sincere gratitude to Royal Unibrew (https://www.royalunibrew.com) for serving as a case study and providing us with the necessary data on the thermal energy demand, heat recovery, and electricity consumption used in this study. We would also like to thank Electricitymaps (https://www.electricitymaps.com) for providing us with the data on the carbon intensity of the electricity grid.

References

[1] C. Arpagaus, F. Bless, M. Uhlmann, J. Schiffmann, and S. S. Bertsch, “High temperature heat pumps: Market overview, state of the art, research status, refrigerants, and application potentials,” *Energy*, vol. 152, pp. 985–1010, Jun. 2018, doi: 10.1016/J.ENERGY.2018.03.166.

[2] I. Sarbu and C. Sebarchievici, “A Comprehensive Review of Thermal Energy Storage,” *Sustainability 2018, Vol. 10, Page 191*, vol. 10, no. 1, p. 191, Jan. 2018, doi: 10.3390/SU10010191.

[3] L. Miró, J. Gasia, and L. F. Cabeza, “Thermal energy storage (TES) for industrial waste heat (IWH) recovery: A review,” *Appl Energy*, vol. 179, pp. 284–301, Oct. 2016, doi: 10.1016/J.APENERGY.2016.06.147.

[4] S. Siddiqui, J. Macadam, and M. Barrett, “The operation of district heating with heat pumps and thermal energy storage in a zero-emission scenario,” *Energy Reports*, vol. 7, pp. 176–183, Oct. 2021, doi: 10.1016/J.EGYR.2021.08.157.

[5] A. Arteconi, N. J. Hewitt, and F. Polonara, “Domestic demand-side management (DSM): Role of heat pumps and thermal energy storage (TES) systems,” *Appl Therm Eng*, vol. 51, no. 1–2, pp. 155–165, Mar. 2013, doi: 10.1016/J.APPLTHERMALENG.2012.09.023.

[6] D. Fischer, T. R. Toral, K. B. Lindberg, B. Wille-Haussmann, and H. Madani, “Investigation of Thermal Storage Operation Strategies with Heat Pumps in German Multi Family Houses,” *Energy Procedia*, vol. 58, pp. 137–144, Jan. 2014, doi: 10.1016/J.EGYPRO.2014.10.420.

[7] K. Hedegaard and O. Balyk, “Energy system investment model incorporating heat pumps with thermal storage in buildings and buffer tanks,” *Energy*, vol. 63, pp. 356–365, Dec. 2013, doi: 10.1016/J.ENERGY.2013.09.061.

[8] T. S. Pedersen, P. Andersen, K. M. Nielsen, H. L. Starmose, and P. D. Pedersen, “Using heat pump energy storages in the power grid,” *Proceedings of the IEEE International Conference on Control Applications*, pp. 1106–1111, 2011, doi: 10.1109/CCA.2011.6044504.

[9] B. S. Sadjjadi, J. N. Gerdes, and A. Sauer, “Energy flexible heat pumps in industrial energy systems: A review,” *Energy Reports*, vol. 9, pp. 386–394, May 2023, doi: 10.1016/J.EGYR.2022.12.110.

[10] M. L. Hansen *et al.*, “Integration of high temperature heat pump for electrifying a brewery,” in *ECOS 2022 35th International Conference on Efficiency, Cost, Optimization, Simulation and Environmental Impact of Energy Systems*, Jul. 2022, pp. 1551–1565.

[11] M. L. Bynum *et al.*, *Pyomo–optimization modeling in python*, Third., vol. 67. Springer Science & Business Media, 2021.

[12] P. G. Wang, M. Scharling, K. B. Wittchen, and C. Kern-Hansen, “Dansk Design Reference Year Supplerende datasaet-Projektrapport til Energistyrelsen: Data til teknisk dimensionering for parametrene atmosfaeretryk, vindretning, skydaekke, vandtemperatur og jordtemperatur samt data til byggesagsbehandling,” 2001, Accessed: Mar. 07, 2023. [Online]. Available: www.dmi.dk/dmi/tr13-18

[13] “Energinet en,” *Energinet EN*. [Online]. Available: https://en.energinet.dk/

[14] “ElectricityMaps,” *Electricity Maps*. [Online]. Available: https://www.electricitymaps.com

[15] A. R. Darío Gómez *et al.*, “Chapter 2: Stationary Combustion 2006 IPCC Guidelines for National Greenhouse Gas Inventories 2.1 C H A P T E R 2 STATIONARY COMBUSTION Volume 2: Energy 2.2 2006 IPCC Guidelines for National Greenhouse Gas Inventories Contributing Author”.

[16] “Technology Data for Industrial Process Heat | Energistyrelsen.” https://ens.dk/en/our-services/projections-and-models/technology-data/technology-data-industrial-process-heat (accessed Mar. 08, 2023).

[17] N. Metropolis and S. Ulam, “The Monte Carlo Method,” *J Am Stat Assoc*, vol. 44, no. 247, pp. 335–341, 1949, doi: 10.1080/01621459.1949.10483310.

[18] A. Saltelli *et al.*, “Global sensitivity analysis: The primer,” *Global Sensitivity Analysis: The Primer*, pp. 1–292, Jan. 2008, doi: 10.1002/9780470725184.

[19] G. Sin, K. V. Gernaey, and A. E. Lantz, “Good Modeling Practice for PAT Applications: Propagation of Input Uncertainty and Sensitivity Analysis,” *Biotechnol Prog*, vol. 25, no. 4, pp. 1043–1053, Jul. 2009, doi: 10.1002/BTPR.166.

[20] J. J. Aguilera *et al.*, “Operational challenges in large-scale ammonia heat pump systems.” ECOS, pp. 1842–1853, 2021. Accessed: Mar. 11, 2023. [Online]. Available: https://orbit.dtu.dk/en/publications/operational-challenges-in-large-scale-ammonia-heat-pump-systems-2

[21] A. Karim, A. Burnett, and S. Fawzia, “Investigation of Stratified Thermal Storage Tank Performance for Heating and Cooling Applications,” *Energies 2018, Vol. 11, Page 1049*, vol. 11, no. 5, p. 1049, Apr. 2018, doi: 10.3390/EN11051049.

Methanol-based thermochemical storage for energy-saving district heating networks

D.A Rodríguez-Pastor[a], E. Carvajal[b], J.A Becerra[c], V.M Soltero[d] and R. Chacartegui[e]

[a] *University of Seville, Seville, Spain, drodriguez4@us.es*
[b] *University of Seville, Seville, Spain, ecarvajal@us.es*
[c] *University of Seville, Seville, Spain, jabv@us.es*
[d] *University of Seville, Seville, Spain, vmsoltero@us.es*
[d] *University of Seville, Seville, Spain, ricardoch@us.es*

Abstract:

With the increasing volatility in natural gas markets and the need for residential heat, research for alternative fuels is necessary for several regions. This paper presents a high-duration thermochemical energy storage system (TCES) based on methanol, evaluating its integration with district heating networks, offering a renewable solar-based storage solution and low-temperature heat generation from the exothermic discharge reaction heat. The system eliminates greenhouse gas emissions by using concentrated solar thermal energy to decompose methanol into synthesis gas. Applying the optimised operational thermodynamic parameters, it is possible to satisfy the thermal demand of 892 households in Spain through 12 MW of concentrated solar energy supported by 10 hours of energy storage. Storage efficiencies exceeding 30% and chemical conversion efficiencies exceeding 65% have been demonstrated, resulting in a combined efficiency of 55% for the heating network and methanol TCES. The results show a levelized cost of storage (LCOS) highly competitive with other storage systems (<100 €/MWh), given the simplicity and flexibility of the proposed system.

Keywords:

Thermochemical Energy Storage, Methanol, Concentrated Solar Power, District Heating

1. Introduction

Global energy consumption has increased significantly in recent decades [1]. IEA expects that the new renewable installed capacity in the next five years (>2300 GW) will be equivalent to that installed in the past 20 years [2]. Despite this effort to contribute to a clean and sustainable generation [3]–[5], many processes still require thermal power and an energy source constant over time.

The challenges posed by the COP21 objectives [6] regarding the control of the global average temperature increase assume the deployment of a storage capacity of 9000 GWh by 2050 [7]. Currently, sensible heat storage systems (SHS) and latent heat storage (LHTES) have gained commercial capacity [8]–[10], but still have high costs and unavoidable environmental losses. In this regard, thermochemical energy storage systems (TCES) are presented as an alternative. Thermal energy decomposes chemical bonds generating products that can release energy when integrated into a discharge cycle through an exothermic reaction [11]. The versatility and flexibility of the system, given various possible storage strategies, offer an additional solution to TES and phase-change material (PCM) systems [12].

District heating systems distribute heat from a central source, such as a power plant or industrial facility, to multiple buildings in a geographical area [13]. Energy storage can be used in district heating systems to enhance efficiency and reduce their environmental impact [14]. For instance, surplus heat generated by a power plant or industrial facility can be stored in a TES system [15]. This heat can then be used to meet the heating requirements of the buildings in the district during peak demand times, reducing the need to generate additional heat from fossil fuels [16], [17]. Furthermore, energy storage can be used in conjunction with renewable energy sources to provide a reliable heat source for district heating systems [18]–[20]. This can help reduce the dependence on fossil fuels and improve the overall sustainability of the district heating system [21]–[24]. Thermochemical energy storage (TCES) can be used in district heating systems to store and discharge heat from clean energy sources, such as solar or geothermal power [25]–[27]. In this application, methanol is heated to a relatively low temperature (<315 ºC) [28], leading to its decomposition into hydrogen (H_2) and carbon monoxide (CO). The heat produced by the synthesis reaction is then stored in a thermal energy storage system, such as a large tank of water or molten salt [29]. When the stored heat is needed, high-pressure hydrogen gas and carbon monoxide are recombined to produce methanol. This reaction releases heat, which can generate steam and power a turbine to produce electricity [30]–[32] or, as proposed in this work, to support permanent district heating operation. The TCES stores renewable energy and releases it when needed in the system, substituting the boilers. Liu and Yabe [30] proposed a system for transporting energy using methanol, which involves a two-stage process for synthesising methanol in a liquid phase. This

process includes the formation of intermediate products, such as methyl formate, achieving a transportation efficiency of 75% for a conversion ratio. In the study by Bai et al. [29], technical feasibility was evaluated for a 20 kW methanol-based thermal energy storage system consisting of a remodelled parabolic through the collector. A novel system proposed by Rodriguez-Pastor et al. [31] involved the conversion of methanol to methane TCES configuration, from its intermediate step to synthesis gas, obtaining an overall efficiency of 40%.

The advantage of using methanol TCES in district heating systems is that it allows surplus heat generated by renewable energy sources to be stored for later use [32], while methanol can be obtained from cheap and clean feedstocks, such as biomass [33]. Integration of district heating networks with storage further increases overall associated costs, but allows for a reduction in fuel consumption, typically natural gas with volatile prices. This can help to enhance the reliability and stability of the district heating system and reduce the need to generate heat from fossil fuels [34]. Therefore, thermochemical storage is a promising technology for storing and releasing heat from renewable energy sources [35], and its potential to improve the efficiency and sustainability of district heating systems is discussed in this work, by presenting a form of thermal energy generation, which is also storable and without greenhouse gas emissions. In addition, this paper demonstrates that its levelized cost of storage (LCOS) is highly competitive with other TCES systems, given the simplicity and flexibility of the proposed system.

2. System Description

The proposed system (**Figure 1**) makes use of methanol decomposition and synthesis reactions. Thermal integration for the endothermic reaction will be done with a central receiver system and a heliostat field. The liquid pumping of methanol at the inlet of the charge cycle will reduce the compressor power [31], bringing the liquid methanol to 10 bar at the reactor inlet.

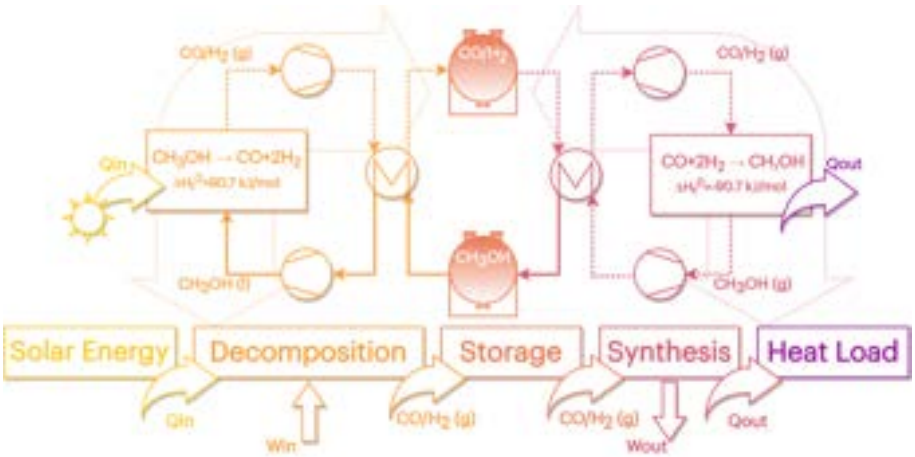

Figure 1. Conceptual process flow diagram of the proposed Methanol-based solar hybrid TCES system.

At the outlet of the charge phase, the synthesis gas (H_2/CO) is stored in tanks, to be discharged into the bottoming cycle, which will synthesise the syngas to methanol at 50 bar. The heat generated in this exothermic reaction will be recovered in a jacket exchanger for the generation of hot water for district heating. The full integration of both charging and discharging cycles is shown in **Figure 2**.

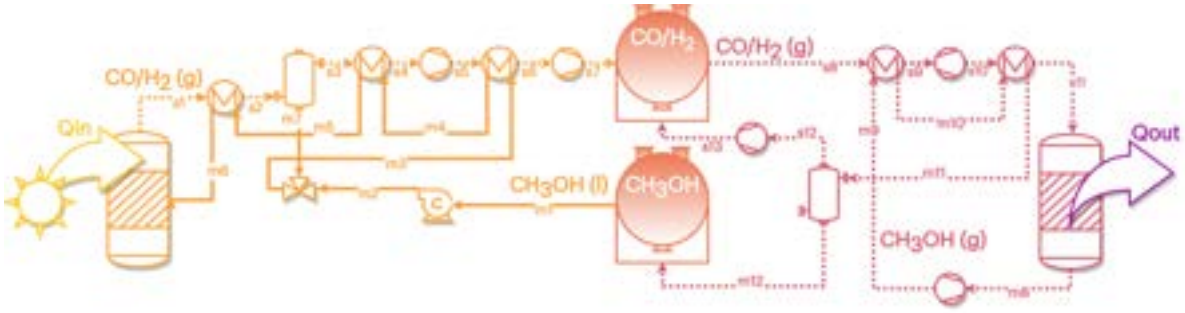

Figure 2. Process flow diagram of the Methanol-based solar hybrid TCES system. m: Methanol, s: Syngas, Qin: Required endothermic heat, Qout: Exothermic heat. Dotted lines: gas-state phase, solid line: liquid-state phase

Methanol-to-syngas conversion can occur in several ways: direct decomposition of methanol [36], steam reforming [37], partial oxidation [38] and auto-thermal reforming [39]. The direct decomposition reaction (Equation 1) is a simple reaction that occurs at temperatures below 350°C [40]. Full methanol conversion is obtained at higher temperatures as the inlet pressure increases.

$$CH_3OH \rightarrow CO + 2H_2 \qquad \Delta H_{298} = 90.7\ kJ/mol \tag{1}$$

Liquid methanol will be pumped into a network of heat exchangers (**Figure 3**), which will use the syngas generated at high pressure and temperature to preheat CH_3OH. Unreacted methanol is separated from a flash separator and recirculating this methanol back into the reactor to ensure complete conversion.

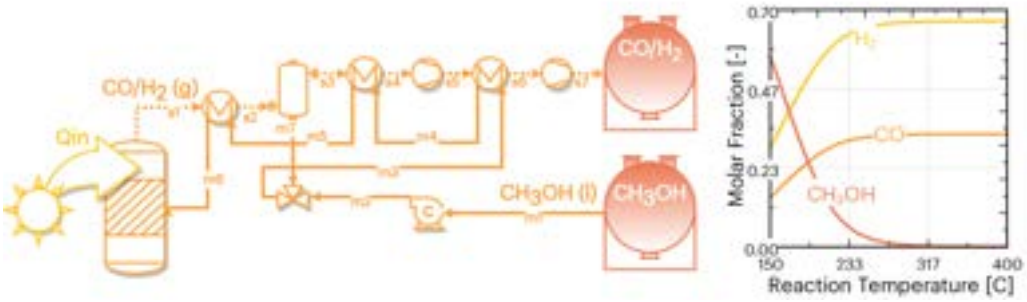

Figure 3. Process flow diagram of the direct solar decomposition of the methanol process (charge phase) and the associated conversion of the molar fraction as a function of reaction temperature. m: Methanol, s: Syngas, Qin: Required endothermic heat. Dotted lines: gas-state phase, solid line: liquid-state phase

The conversion of syngas to methanol releases thermochemical energy. Syngas is produced and stored at 100 bar and ambient temperature, avoiding thermal losses and providing long-term energy storage capability. This paper focuses on the analysis of the former, converting syngas to methanol in a closed-loop approach for TCES systems (Equation 2):

$$CO + 2H_2 \rightarrow CH_3OH \qquad \Delta H_{298} = -90.7\ kJ/mol \tag{2}$$

Syngas-to-methanol (**Figure 4**) is the main route of global methanol production [37]. The reaction occurs in a range of 15-150 bar, 180-300°C, and an H_2/CO ratio< 4.1 [26], [41], catalysed by a standard industrial catalyst ($Cu/ZnO/Al_2O_3$) [42]. This work assumes a quasi-isothermal tubular reactor at 50 bar. The heat released in the exothermic formation of methanol is provided to a heat transfer fluid (HTF) that circulates through a cooling jacket around the reactor [40].

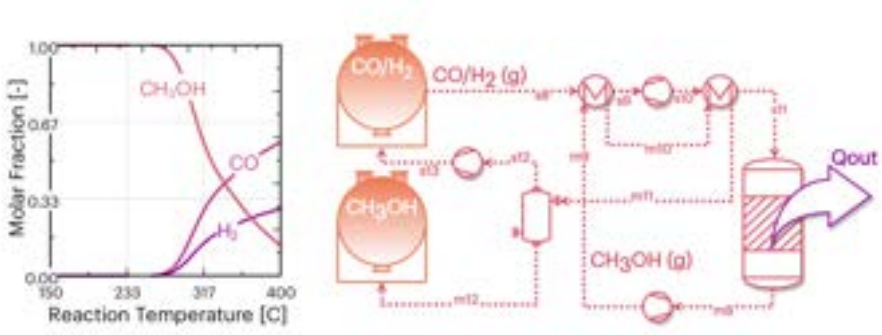

Figure 4. Process flow diagram of the methanol synthesis process (discharge phase) and associated molar fraction conversion as a function of reaction temperature. m: Methanol, s: Syngas, Qout: Exothermic heat. Dotted lines: gas-state phase, solid line: liquid-state phase

3. Simulation

The methanol TCES system has been simulated with the commercial software ASPEN HYSYS [45] using the Peng-Robinson thermodynamic package. The nominal input parameters of the system are shown in **Table 1**. The entire equipment required for the process is well-known in the industry and can be modelled using lumped

volume approaches, as discussed in [43]. However, more detailed kinetics and higher-resolution models maoffer even more precise results [44].

Table 1. Thermodynamic considerations assumed for the simulation of the methanol TCES system.

Variable	Value
Inlet CH_3OH molar flow of the charging process	100 mol/s
CH_3OH storage temperature/pressure	64.67 ºC / 1 bar
Heat Exchangers approach temperature	20 K
Isentropic efficiency of liquid methanol pump	65%
Isentropic efficiency of compressors	89%
Isentropic efficiency of turbines	92%
Endothermic reaction temperature/pressure	315 ºC / 10 bar
Exothermic reaction temperature/pressure	250 ºC / 50 bar
Syngas CO/H_2 storage pressure	100 bar
Discharge pressure	1 bar
Energy storage time	10 hours

Thermodynamic evaluation has been carried out based on the definition of the overall performance (η_{plant}) of the TCES system (Equation 3).

$$\eta_{plant} = \frac{\dot{Q}_{exo} + \dot{W}_T}{\dot{Q}_{CH_3OH} + \dot{Q}_{sol}} \cdot \psi = \frac{\dot{Q}_{exo} + \dot{W}_T}{HHV_{CH_3OH} \cdot \dot{m}_{CH_3OH} + \dot{W}_{PV} + \dot{Q}_{CSP}} \cdot \frac{h_{dis}}{h_{charge}} \quad (3)$$

The performance of the storage system ($\eta_{storage}$) considers the turbine energy outputs in the discharge phase, when considering the solar photovoltaic and thermal input (Equation 4).

$$\eta_{storage} = \frac{\dot{P}}{\dot{Q}_{sol}} \cdot \psi = \frac{\dot{W}_T}{\dot{W}_{PV} + \dot{Q}_{CSP}} \cdot \frac{h_{dis}}{h_{charge}} \quad (4)$$

Chemical conversion (η_{sol-ch}) is described by the solar-to-chemical efficiency, in terms of power (Equation 5).

$$\eta_{sol-ch} = \frac{X_{CH_3OH}\dot{m}_{CH_3OH}\Delta H_{CH_3OH}}{\dot{Q}_{CSP}} \quad (5)$$

Finally, the electrical recovery in the discharge phase turbines is quantified (Equation 6) with the solar-to-electrical efficiency ($\eta_{sol-elec}$) as a function of storage time.

$$\eta_{sol-elec} = \frac{\dot{P}}{\dot{W}_{PV} + \dot{Q}_{CSP}} \cdot \frac{h_{dis}}{h_{charge}} \quad (6)$$

Considering the nominal domestic hot water consumption of a person in the region of Spain, the number of single-family dwellings (4 persons) covered with exothermic heat will be given by Equation 7. The daily by domestic hot water consumption of a person in Spain is estimated to be 28 litres [45].

$$Dwellings = \frac{Q_{exo}/C_p\Delta T}{28} \cdot Persons \quad (7)$$

Where C_p is the specific heat of water (4.184 kJ/kg-K), ΔT is the temperature difference between the cold water return line and the hot water to meet the heat demand, assumed to be 50ºC [46].

Economic analysis depends on the development of component and product markets, which can affect the accuracy of the approximations used to estimate emerging technologies. The expressions presented in **Table 2** form the basis of the economic analysis.

Table 2. Mathematical expressions for estimating equipment costs.

Equipment	Expression	Reference
Compressors	$IC_C = 643.15 \cdot \dot{W}_C^{\,0.9142}$	[47]
Turbines	$IC_T = 4001.4 \cdot \dot{W}_T^{\,0.6897}$	[48]

Pump	$IC_P = 3531.4 \cdot \dot{W}_P^{0.71} \cdot \left[1 + \left(\frac{1-0.8}{1-\eta_{i,P}}\right)^3\right]$	[49]
Heat Exchangers	$C_{HE} = 2546.9 \cdot A_{HE}^{0.67} \cdot p_{HE}^{0.28} \cdot 10^{-6}$	[49]
Cooling Tower	$IC_{Cooling}^{tower} = 32.3 \cdot \dot{Q_{cool}}$	[50]
Endothermic Reactor	$IC_{Dr} = 13140 \cdot \dot{Q}_r^{0.67}$	[51]
Exothermic Reactor	$IC_{Mr} = 19594 \cdot \dot{Q}_r^{0.5}$	[51]
Tanks	$IC_{Tank} = 83 \cdot V$	[52]
Solar Photovoltaic Field	$IC_{PV} = 0.995 \cdot \dot{W}_{PV} \cdot 10^6$	[2]
CSP Tower	$IC_{tower}^{solar} = 57.07 \cdot \Phi_{Receiver}$	[53]

The levelized cost of storage (LCOS) indicator is proposed for the overall economic evaluation (Equation 7), considering a discount rate (r) of 5% and a useful life of the plant (n) of 20 years, and the exothermic reaction energy Q_{exo}.

$$LCOS = \frac{CAPEX + \sum_{i=1}^{n} \frac{OPEX_i}{(1+r)^i}}{\sum_{i=1}^{n} \frac{Q_{exo}}{(1+r)^i}} \quad (7)$$

$CAPEX$ being the initial investment cost of the plant, $OPEX_i$ the annual maintenance costs and Q_{exo} the annual energy produced in the exothermic phase of the synthesis reaction.

4. Results and Discussion

4.1. On-design results

The system design results are shown in **Table 3**. The overall efficiencies obtained for the plant η_{plant} are reduced (<15%) due to the consideration of the methanol input energy and the low exothermic heat of reaction. This fact significantly favours the load cycle since less thermal power is required for the decomposition of methanol to syngas, shown in the solar-to-chemical efficiency η_{sol-ch}, which reaches values above 65%.

Table 3. TCES system results on design for nominal operating parameters.

Parameter	Value
Solar-to-chemical efficiency (η_{sol-ch})	0.677
Solar-to-electrical efficiency ($\eta_{sol-elec}$)	0.071
Overall performance (η_{plant})	0.125
Storage performance ($\eta_{storage}$)	0.356
Required endothermic reaction heat [MW] ($\dot{Q}_{endo}$)	12.658
Exothermic reaction heat [MW] ($\dot{Q}_{exo}$)	-8.686
Dwellings covered	892
Covered annual heat demand [MWh]	53445
CAPEX [M€]	19.72
OPEX [M€]	0.936
LCOS [€/MWh]	85.61

On the other hand, the storage efficiency of the system $\eta_{storage}$ shows competitive values, exceeding 35%, given the recovery of the syngas decompression in the discharge cycle turbines and the reduced PV power output after thermal integration of the streams. With the 9 MW obtained at the output of the synthesis reactor, the demand for 892 single-family houses or the equivalent of a rural village can be covered. Thus, the initial investment of the plant is almost 20 M€, after considering an annual OPEX of almost one million euros in operating and maintenance costs of the plant. This value is lower in terms of fuel consumption compared to District Heating systems based on other fuels [34], although the cost assessment of the heat network has not been considered in this paper. The levelised cost value, LCOS, has been shown to be 60% lower than molten salt systems and competes with future predictions of hydrogen-based storage systems (90-160 €/MWh) [54].

Figure 5 shows the main thermal currents of the system, based on the above thermodynamic assumptions and considerations. Thus, a large amount of energy is returned to the methanol storage, given the low efficiency of the synthesis reactor. This high value is due to the high calorific value of methanol, which is not utilised given the low heat of the synthesis reaction. Heat exchanger losses are assumed to be 3%, and solar field losses are assumed to be 30%.

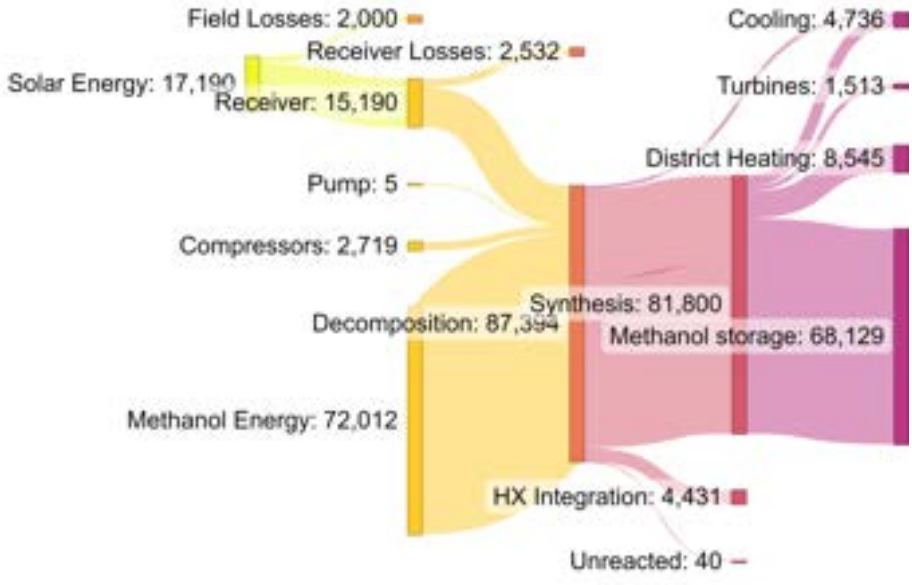

Figure 5. Sankey diagram for the nominal operating conditions of the methanol-TCES system.

Therefore, the solar photovoltaic field will feed 3 MW of compressor and pump consumption and 15 MW of receiver solar power will be required to extract 8.5 MW for the heat network. The efficiency in terms of solar power and DH power will be 47%, whereas the combined efficiency of cogeneration, considering the energy exported from the turbines, will be 55%, 40% lower than in internal combustion reciprocating engines [55].

4.2. Sensitivity analysis

The variation in thermal power from the solar receiver will be crucial in the sizing of the reactor and its auxiliary systems. **Figure 6** evaluates the variation in efficiency as a function of the endothermic temperature of direct CH_3OH decomposition. Chemical conversion efficiency reaches a maximum at intermediate reaction temperatures, although complete conversion cannot be ensured because of a higher molar enthalpy drop in the reactor and an increase in yield. However, maximum decomposition conversion is required for solar-to-electrical yields to ensure better utilisation in the gas turbines of the discharge cycle. This also applies to the overall plant performance, which will be higher as the methanol inlet pressure decreases, i.e., to ensure complete conversion to syngas.

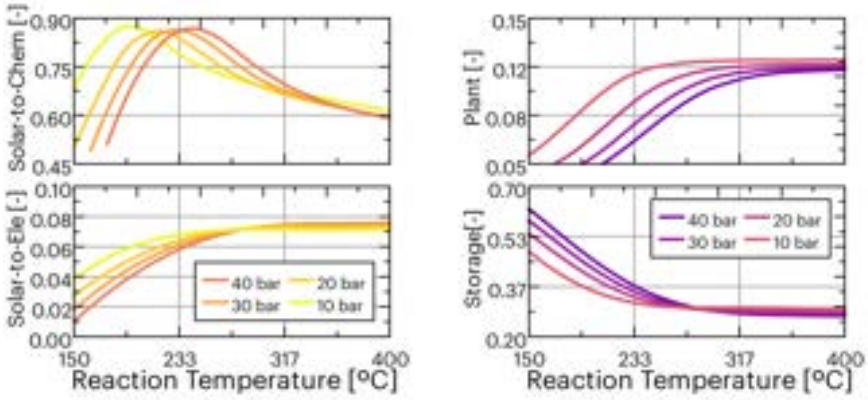

Figure 6. Solar-to-Chemical/Solar-to-Electrical yields on the left, and plant and storage yields (overall) as a function of direct methanol decomposition reaction temperature on the right.

This trend is also reflected when evaluating the performance of the heat network (**Figure 7b**), where higher reaction temperatures (right) will result in greater synthesis gas generation and consequently greater conversion in the exothermic reactor. The increase in covered households for a reaction temperature between 150-250ºC is 650 households, which then stabilises at the nominal value of close to 900 homes with the studied characteristics.

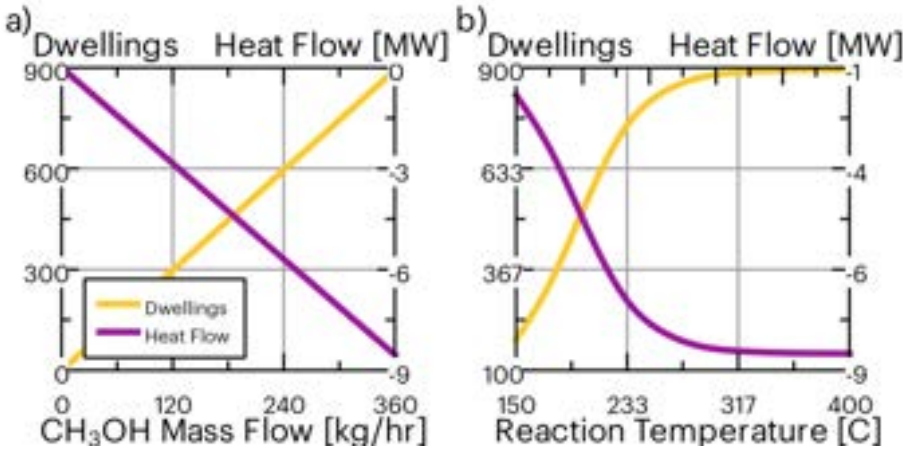

Figure 7. Number of dwellings covered (thermal demand) and exothermic power generated in the synthesis reaction as a function of a) methanol mass flow rate at the inlet of the charging process and b) reaction temperature of the direct decomposition of methanol.

The effect of the mass flow rate of methanol at the inlet is linear with respect to the exothermic power, where for every 120 kg/hr of methanol in the system, the demand of approximately 300 homes is covered (**Figure 7a**).

4.3. Economic Analysis

One of the most remarkable parameters of the proposed system is its low-levelized storage cost, optimised under nominal conditions to be minimal and achieve maximum overall yields. **Figure 8** shows the variation of the LCOS with respect to the operating conditions of the charging phase (**Figure 8a**) and the discharging phase (**Figure 8b**). Opposite trends are obtained, where higher decomposition reaction temperatures result in lower costs, given a higher thermal energy supply to the heat network.

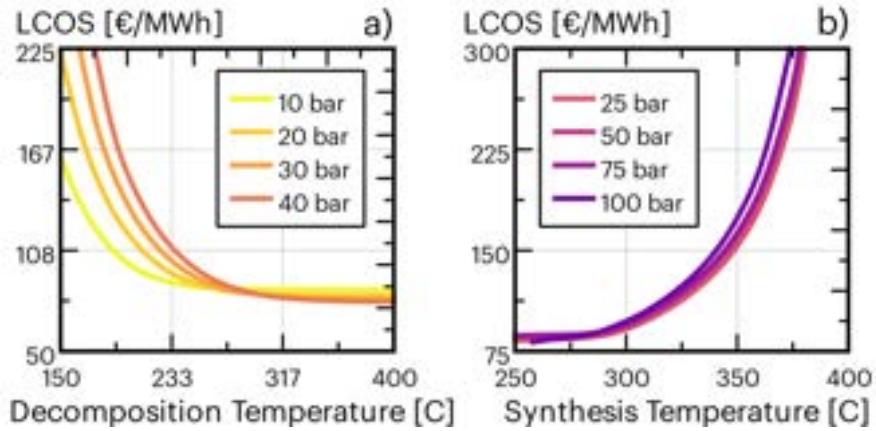

Figure 8. Levelised cost of storage as a function of a) direct methanol decomposition temperature and b) syngas to methanol synthesis temperature.

This LCOS is even lower for higher liquid methanol pressures due to lower compressor consumption. This trend is opposite in the case of the synthesis reaction, where higher temperatures result in lower conversion and lower exothermic energy, and higher pressures imply higher associated conversions but with less influence than in the case of the charging phase.

5. Conclusions

This paper proposes a high-duration thermochemical storage system based on methanol, which evaluates its integration with district heating networks, offering a renewable solar-based storage solution and low-temperature heat generation from the exothermic discharge reaction heat:

i) The system eliminates greenhouse gas emissions by using concentrated solar thermal energy to decompose methanol into synthesis gas.
ii) Given the low heat of the direct methanol decomposition reaction, chemical conversion efficiencies in the charging phase are greater than 65%.
iii) Storage efficiencies are greater than 35%, producing 8.5 MW of exothermic power from 15 MW of solar input that decomposes 100 mol/s of methanol.
iv) The proposed configuration serves 892 4-person single-family homes and can cover a rural town with green methanol.
v) Levelized storage costs are 60% lower than molten salt systems, as the system is simple and has a high associated energy density.
vi) An optimal decomposition temperature of 315°C/10 bar and 250°C/50 bar is demonstrated in the exothermic phase, striking a balance between demand coverage and the levelized cost of the system.

Acknowledgements

This work was partially funded by VS ENERGY TECH SL, a University of Seville spin-off company.

Nomenclature

c_{p} specific heat, J/(kg K)
$\dot{m}$ mass flow rate, kg/s
T temperature, °C
X molar fraction, [-]
Q heat energy, [kWh]
W power energy, [kWh]
$\dot{Q}$ heat power, [kW]
$\dot{W}$ power, [kW]

Greek symbols

η efficiency
ψ discharge/charge hours ratio

Subscripts and superscripts

CH_3OH methanol
exo exothermic
$endo$ endothermic
$sol-ch$ solar-to-chemical
$sol-ele$ solar-to-electrical

References

[1] A. Rehman, M. Irfan, S. Hena, and A. A. Chandio, “By applying an ARDL bounds testing approach and causality test to investigate the electricity consumption and production with economic growth: Empirical evidence from Pakistan,” *World Journal of Science, Technology and Sustainable Development*, vol. 17, no. 2, pp. 182–199, Apr. 2019, doi: 10.1108/WJSTSD-08-2019-0054.

[2] I. - International Energy Agency, “Renewables 2022,” 2022, Accessed: Feb. 26, 2023. [Online]. Available: www.iea.org

[3] H. Hashim and W. S. Ho, “Renewable energy policies and initiatives for a sustainable energy future in Malaysia,” *Renewable and Sustainable Energy Reviews*, vol. 15, no. 9, pp. 4780–4787, Dec. 2011, doi: 10.1016/J.RSER.2011.07.073.

[4] S. Chu and A. Majumdar, “Opportunities and challenges for a sustainable energy future,” *Nature 2012 488:7411*, vol. 488, no. 7411, pp. 294–303, Aug. 2012, doi: 10.1038/nature11475.

[5] D. A. Rodriguez-Pastor, A. F. Ildefonso-Sanchez, V. M. Soltero, M. E. Peralta, and R. Chacartegui, “A new predictive model for the design and evaluation of bifacial photovoltaic plants under the influence

of vegetation soils," *J Clean Prod*, vol. 385, p. 135701, Jan. 2023, doi: 10.1016/J.JCLEPRO.2022.135701.

[6] "COP 21 | UNFCCC." https://unfccc.int/process-and-meetings/conferences/past-conferences/paris-climate-change-conference-november-2015/cop-21 (accessed Sep. 15, 2022).

[7] IRENA, "Global Renewables Outlook: Energy transformation 2050," 2020. Accessed: Sep. 15, 2022. [Online]. Available: /publications/2020/Apr/Global-Renewables-Outlook-2020

[8] T. Kousksou, P. Bruel, A. Jamil, T. El Rhafiki, and Y. Zeraouli, "Energy storage: Applications and challenges," *Solar Energy Materials and Solar Cells*, vol. 120, no. PART A, pp. 59–80, Jan. 2014, doi: 10.1016/J.SOLMAT.2013.08.015.

[9] S. Koohi-Fayegh and M. A. Rosen, "A review of energy storage types, applications and recent developments," *J Energy Storage*, vol. 27, p. 101047, Feb. 2020, doi: 10.1016/J.EST.2019.101047.

[10] T. Bauer, N. Pfleger, N. Breidenbach, M. Eck, D. Laing, and S. Kaesche, "Material aspects of Solar Salt for sensible heat storage," *Appl Energy*, vol. 111, pp. 1114–1119, Nov. 2013, doi: 10.1016/J.APENERGY.2013.04.072.

[11] R. Chacartegui, A. Alovisio, C. Ortiz, J. M. Valverde, V. Verda, and J. A. Becerra, "Thermochemical energy storage of concentrated solar power by integration of the calcium looping process and a CO2 power cycle," *Appl Energy*, vol. 173, pp. 589–605, Jul. 2016, doi: 10.1016/J.APENERGY.2016.04.053.

[12] J. Lizana, R. Chacartegui, A. Barrios-Padura, and J. M. Valverde, "Advances in thermal energy storage materials and their applications towards zero energy buildings: A critical review," *Appl Energy*, vol. 203, pp. 219–239, Oct. 2017, doi: 10.1016/J.APENERGY.2017.06.008.

[13] B. Rezaie and M. A. Rosen, "District heating and cooling: Review of technology and potential enhancements," *Appl Energy*, vol. 93, pp. 2–10, May 2012, doi: 10.1016/J.APENERGY.2011.04.020.

[14] G. Elisa Politecnico di Torino, V. Vittorio Politecnico di Torino, E. Guelpa, and V. Verda, "Integrated optimal design and control of fourth generation district heating networks with thermal energy storage," *mdpi.com*, doi: 10.1016/j.apenergy.2019.113474.

[15] S. Cooper, G. Hammond, J. N.-J. of the E. Institute, and undefined 2016, "Potential for use of heat rejected from industry in district heating networks, GB perspective," *Elsevier*, Accessed: Dec. 08, 2022. [Online]. Available: https://www.sciencedirect.com/science/article/pii/S1743967114203588

[16] S. Moser, S. Puschnigg, V. R.- Energy, and undefined 2020, "Designing the Heat Merit Order to determine the value of industrial waste heat for district heating systems," *Elsevier*, Accessed: Dec. 08, 2022. [Online]. Available: https://www.sciencedirect.com/science/article/pii/S0360544220306861

[17] V. Verda, F. C.- Energy, and undefined 2011, "Primary energy savings through thermal storage in district heating networks," *Elsevier*, Accessed: Dec. 08, 2022. [Online]. Available: https://www.sciencedirect.com/science/article/pii/S0360544211002647

[18] I. Sarbu, M. Mirza, D. M.- Energies, and undefined 2022, "Integration of Renewable Energy Sources into Low-Temperature District Heating Systems: A Review," *mdpi.com*, 2022, doi: 10.3390/en15186523.

[19] M. A. Ancona *et al.*, "Comparative Analysis of Renewable Energy Community Designs for District Heating Networks: Case Study of Corticella (Italy)," *mdpi.com*, 2022, doi: 10.3390/en15145248.

[20] D. A. Rodriguez-Pastor, J. A. Becerra, and R. Chacartegui, "Adaptation of residential solar systems for domestic hot water (DHW) to hybrid organic Rankine Cycle (ORC) distributed generation," *Energy*, vol. 263, p. 125901, Jan. 2023, doi: 10.1016/J.ENERGY.2022.125901.

[21] K. Narula, J. Chambers, K. Streicher, M. P.- Energy, and undefined 2019, "Strategies for decarbonising the Swiss heating system," *Elsevier*, Accessed: Dec. 08, 2022. [Online]. Available: https://www.sciencedirect.com/science/article/pii/S0360544218324484

[22] A. Akhatova, L. Kranzl, F. Schipfer, C. H.- Energies, and undefined 2022, "Agent-Based Modelling of Urban District Energy System Decarbonisation—A Systematic Literature Review," *mdpi.com*, 2022, doi: 10.3390/en15020554.

[23] B. Morvaj, R. Evins, J. C.-A. Energy, and undefined 2017, "Decarbonizing the electricity grid: The impact on urban energy systems, distribution grids and district heating potential," *Elsevier*, Accessed: Dec. 08, 2022. [Online]. Available: https://www.sciencedirect.com/science/article/pii/S0306261917300661

[24] E. Mäki, L. Kannari, I. Hannula, J. S.-R. Energy, and undefined 2021, "Decarbonization of a district heating system with a combination of solar heat and bioenergy: A techno-economic case study in the Northern European context," *Elsevier*, Accessed: Dec. 08, 2022. [Online]. Available: https://www.sciencedirect.com/science/article/pii/S0960148121006364

[25] K. Räuchle, L. Plass, H. J. Wernicke, and M. Bertau, "Methanol for Renewable Energy Storage and Utilization," *Energy Technology*, vol. 4, no. 1, pp. 193–200, Jan. 2016, doi: 10.1002/ENTE.201500322.

[26] N. Monnerie, P. Gan, M. Roeb, C. S.-I. J. of Hydrogen, and undefined 2020, "Methanol production using hydrogen from concentrated solar energy," *Elsevier*, 2020, doi: 10.1016/j.ijhydene.2019.12.200.

[27] W. Li, Y. H.-A. Energy, and undefined 2017, "Efficient solar power generation combining photovoltaics and mid-/low-temperature methanol thermochemistry," *Elsevier*, Accessed: Sep. 15, 2022. [Online]. Available: https://www.sciencedirect.com/science/article/pii/S0306261917305913

[28] H. Hong, H. Jin, J. Ji, Z. Wang, R. C.-S. Energy, and undefined 2005, "Solar thermal power cycle with integration of methanol decomposition and middle-temperature solar thermal energy," *Elsevier*, Accessed: Sep. 15, 2022. [Online]. Available: https://www.sciencedirect.com/science/article/pii/S0038092X04001604

[29] Z. Bai, Q. Liu, J. Lei, H. J.-A. Energy, and undefined 2018, "Investigation on the mid-temperature solar thermochemical power generation system with methanol decomposition," *Elsevier*, Accessed: Sep. 15, 2022. [Online]. Available: https://www.sciencedirect.com/science/article/pii/S0306261918302265

[30] Q. Liu, A. Yabe, S. Kajiyama, and K. Fukuda, "A Review of Study on Thermal Energy Transport System by Synthesis and Decomposition Reactions of Methanol," *JSME International Journal Series B Fluids and Thermal Engineering*, vol. 45, no. 3, pp. 473–480, Aug. 2002, doi: 10.1299/JSMEB.45.473.

[31] D. A. Rodriguez-Pastor, R. Chacartegui, and J. A. Becerra, "Rutas de almacenamiento de energía basadas en Metanol," 2022, doi: 10.17616/R31NJNEG.

[32] A. Abedin, M. R.-T. open renewable energy journal, and undefined 2011, "A critical review of thermochemical energy storage systems," *benthamopen.com*, Accessed: Dec. 08, 2022. [Online]. Available: https://benthamopen.com/ABSTRACT/TOREJ-4-42

[33] Y. Liu *et al.*, "Comprehensive analysis of environmental impacts and energy consumption of biomass-to-methanol and coal-to-methanol via life cycle assessment," *Energy*, vol. 204, p. 117961, Aug. 2020, doi: 10.1016/J.ENERGY.2020.117961.

[34] V. M. Soltero, R. Chacartegui, C. Ortiz, and R. Velázquez, "Potential of biomass district heating systems in rural areas," *Energy*, vol. 156, pp. 132–143, Aug. 2018, doi: 10.1016/J.ENERGY.2018.05.051.

[35] T. Yan, R. Z. Wang, T. X. Li, L. W. Wang, and I. T. Fred, "A review of promising candidate reactions for chemical heat storage," *Renewable and Sustainable Energy Reviews*, vol. 43, pp. 13–31, Mar. 2015, doi: 10.1016/J.RSER.2014.11.015.

[36] Z. Bai, Q. Liu, L. Gong, and J. Lei, "Application of a mid-/low-temperature solar thermochemical technology in the distributed energy system with cooling, heating and power production," *Appl Energy*, vol. 253, p. 113491, Nov. 2019, doi: 10.1016/J.APENERGY.2019.113491.

[37] D. R. Palo, R. A. Dagle, and J. D. Holladay, "Methanol steam reforming for hydrogen production," *Chem Rev*, vol. 107, no. 10, pp. 3992–4021, Oct. 2007, doi: 10.1021/CR050198B.

[38] W. Chen, C. S.- Energy, and undefined 2016, "Partial oxidation of methanol over a Pt/Al2O3 catalyst enhanced by sprays," *Elsevier*, Accessed: Sep. 15, 2022. [Online]. Available: https://www.sciencedirect.com/science/article/pii/S0360544216302742

[39] W. Chen, B. L.-I. journal of hydrogen energy, and undefined 2013, "Hydrogen production and thermal behavior of methanol autothermal reforming and steam reforming triggered by microwave heating," *Elsevier*, Accessed: Sep. 15, 2022. [Online]. Available: https://www.sciencedirect.com/science/article/pii/S0360319913013438

[40] J. Brown, E. G.-C. Communications, and undefined 2004, "Hydrogen production from methanol decomposition over Pt/Al2O3 and ceria promoted Pt/Al2O3 catalysts," *Elsevier*, 2004, doi: 10.1016/j.catcom.2004.05.008.

[41] W. Li, Y. Ling, X. Liu, Y. H.-A. Energy, and undefined 2017, "Performance analysis of a photovoltaic-thermochemical hybrid system prototype," *Elsevier*, Accessed: Sep. 15, 2022. [Online]. Available: https://www.sciencedirect.com/science/article/pii/S0306261917305706

[42] G. L.-R. Energy and undefined 2020, "Analysis and optimization of a methanol reactor with the adsorption of carbon monoxide and water," *Elsevier*, Accessed: Sep. 15, 2022. [Online]. Available: https://www.sciencedirect.com/science/article/pii/S0960148119312716

[43] M. Formica, S. Frigo, and R. Gabbrielli, "Development of a new steady state zero-dimensional simulation model for woody biomass gasification in a full scale plant," *Energy Convers Manag*, vol. 120, pp. 358–369, Jul. 2016, doi: 10.1016/J.ENCONMAN.2016.05.009.

[44] N. Couto, V. Silva, E. Monteiro, P. S. D. Brito, and A. Rouboa, "Modeling of fluidized bed gasification: Assessment of zero-dimensional and CFD approaches," *Journal of Thermal Science*, vol. 24, no. 4, pp. 378–385, Jun. 2015, doi: 10.1007/S11630-015-0798-7/METRICS.

[45] M. of Development, "Código Técnico de la Edificación," *G. of S. Basic document HE - Energy savings*, 2019.

[46] N. Nord, E. K. Løve Nielsen, H. Kauko, and T. Tereshchenko, "Challenges and potentials for low-temperature district heating implementation in Norway," *Energy*, vol. 151, pp. 889–902, May 2018, doi: 10.1016/J.ENERGY.2018.03.094.

[47] M. Carlson, … B. M.-E., and undefined 2017, "Techno-economic comparison of solar-driven SCO2 Brayton cycles using component cost models baselined with vendor data and estimates," *asmedigitalcollection.asme.org*, Accessed: Sep. 29, 2022. [Online]. Available: https://asmedigitalcollection.asme.org/ES/proceedings-abstract/ES2017/57595/V001T05A009/230818

[48] M. Carlson, B. Middleton, and C. Ho, "Techno-Economic Comparison of Solar-Driven SCO2 Brayton Cycles Using Component Cost Models Baselined With Vendor Data and Estimates," Feb. 2017, p. V001T05A009. doi: 10.1115/ES2017-3590.

[49] S. Michalski, D. Hanak, V. M.-J. of C. Production, and undefined 2019, "Techno-economic feasibility assessment of calcium looping combustion using commercial technology appraisal tools," *Elsevier*, Accessed: Sep. 29, 2022. [Online]. Available: https://www.sciencedirect.com/science/article/pii/S0959652619304287

[50] S. Michalski, D. P. Hanak, and V. Manovic, "Techno-economic feasibility assessment of calcium looping combustion using commercial technology appraisal tools," *J Clean Prod*, vol. 219, pp. 540–551, May 2019, doi: 10.1016/J.JCLEPRO.2019.02.049.

[51] S. Michalski, D. P. Hanak, and V. Manovic, "Techno-economic feasibility assessment of calcium looping combustion using commercial technology appraisal tools," *J Clean Prod*, vol. 219, pp. 540–551, May 2019, doi: 10.1016/J.JCLEPRO.2019.02.049.

[52] A. Bayon, R. Bader, M. Jafarian, L. F.-H.- Energy, and undefined 2018, "Techno-economic assessment of solid–gas thermochemical energy storage systems for solar thermal power applications," *Elsevier*, Accessed: Sep. 29, 2022. [Online]. Available: https://www.sciencedirect.com/science/article/pii/S0360544217319424?casa_token=C6Us90EOssUAAAAA:Jx2xJ6e08S4dsUQqrrJeAdmxRn7KA5EhE8Ibb2fJh5aY8VnYp-sAQye9IKBBLk0tqJLiSqxT

[53] C. K. Ho, "A review of high-temperature particle receivers for concentrating solar power," *Appl Therm Eng*, vol. 109, pp. 958–969, Oct. 2016, doi: 10.1016/J.APPLTHERMALENG.2016.04.103.

[54] V. Jülch, "Comparison of electricity storage options using levelized cost of storage (LCOS) method," *Appl Energy*, vol. 183, pp. 1594–1606, Dec. 2016, doi: 10.1016/J.APENERGY.2016.08.165.

[55] U. Environmental Protection Agency, C. Heat, and P. Partnership, "Catalog of CHP Technologies, Full Report, September 2017," 2017.

Application of flat plate latent heat thermal energy storage for waste heat recovery and energy flexibility in maritime sector

Lorenzo Ciappi[a], Pouriya Niknam[b], Robin Fisher[c] and Adriano Sciacovelli[d]

[a] University of Birmingham, Birmingham, UK, l.ciappi@bham.ac.uk
[b] University of Birmingham, Birmingham, UK, p.niknam@bham.ac.uk,
[c] University of Birmingham, Birmingham, UK, r.fischer@bham.ac.uk
[d] University of Birmingham, Birmingham, UK, a.sciacovelli@bham.ac.uk, CA

Abstract:

Thermal energy storage (TES) fosters the use of renewable energy, improves the efficiency of existing processes and enhances the flexibility of energy availability. Extensively researched and applied in buildings, TES is still in the early stages of its evolution regarding other relevant applications for which decarbonisation of heat exchange is paramount. This is the case in the maritime sector. Therefore, this research proposes a novel modular latent heat thermal energy storage (LHTES) system functioning with a phase change material (PCM) as an energy storage medium for installation on ships. An analytical model was developed relying on a theoretical approach consolidated in the literature. Firstly, the model was validated through the comparison with a reference case. Then, it was utilised for evaluating the functioning of various configurations of a TES device operating on board a vessel. The performance of the proposed system was investigated during the charging and discharging phases considering operating conditions typical of cruising and cargo vessels. The effects of device length and height were assessed and the influence of these parameters on the amount of energy stored and energy storage density was determined. Overall, the paper provides an innovative application of TES technology and highlights the wider benefits of energy storage in the maritime sector.

Keywords:

Thermal energy storage; latent heat; maritime decarbonisation; waste heat recovery; PCM.

1. Introduction

The functioning of the vast majority of energy systems is currently based on transforming the energy of fuel into useful work for their scopes and waste heat released to the environment. This energy inefficiency is a paramount problem mainly for industrial thermal processes, heating systems and transportation. Heat wastage significantly affects marine applications, especially cruising and cargo vessels. Two-stroke internal combustion diesel engines represent the propulsion system of around 96% of modern civilian ships above 100 t of mass [1]. These engines have values of efficiency lower than 50% with the consequent wastage of at least half of fuel energy through cooling fluid streams and exhaust gases [2]. The thermal energy released is responsible for about 3% of total greenhouse gas emissions (GHG) worldwide and this level is expected to rise together with the global trade through shipping [3]. Since 2011, the International Maritime Organisation (IMO) is applying regulations for controlling air and water pollution with the aim of halving emissions by 2050 [4].

The reduction of GHG emissions can be successfully achieved by enhancing energy efficiency. Improvements to the existing engines and the use of other technologies on board were widely proposed for this purpose [5]. It is estimated that total engine efficiency could be boosted from 50% to 60% and fuel efficiency could be raised from 4% to 16% [1,2]. Regarding the energy source, alternative fuels to the traditional high sulphur fuel such as liquefied natural gas (LNG), hydrogen, ammonia and advanced bio-fuels can be utilised and auxiliary propulsion devices such as modern sails and renewable systems such as solar photovoltaic panels and solar hybrid devices can be placed on board. Concerning the direct limitation of carbon emissions, carbon capture and storage systems can be installed. Integrating these technologies with waste heat recovery (WHR) devices would foster the enhancement of vessel efficiency as at least half of fuel energy is lost by way of heat. Currently, the WHR systems used on vessels are waste heat boilers, steam turbine cycles or turbocharging devices. However, more sophisticated WHR solutions could be effectively installed on board for harnessing thermal energy from exhaust flue gases of diesel engines and their cooling fluids such as jacket water and lubricants.

The main technologies exploiting heat wastage are thermal energy storage (TES) systems, organic Rankine cycles, sorption desalination and refrigeration devices and isobaric expansion engines. They transform the thermal power losses of the engine into mechanical or electrical power (waste heat-to-power), cooling power (waste heat-to-cold), or they upgrade the excess thermal energy to generate added value for on-board demands such as steam or desalinated water.

The presented research regards the development of an analytical model for solving heat transfer in a TES device constituted by a flat plate heat exchanger functioning with air or water as a heat exchange fluid (HTF) and a phase change material (PCM) as an energy storage medium. The Methodology section defines the theoretical model developed and the finite element approximation strategy applied. The Results and discussion section first describes the process of the validation of the model through the comparison with consolidated literature data. Then, it shows the application of the model for evaluating the performance of five configurations of a TES device for the possible installation on board a vessel. Operating conditions typical of cruising and cargo vessels were considered.

2. Methodology

A theoretical model of a latent heat thermal energy storage (LHTES) system was developed for evaluating the behaviour of heat exchangers with multi-layer rectangular plates functioning with a heat transfer fluid to warm or cool a phase change material.

2.1. Modelling equations

The model of the multi-layer rectangular LHTES system relies on consolidated theoretical approaches present in the literature [6,7] and was successfully used for technical applications [8–10]. The methodology is based on three hypotheses regarding the heat transfer transformations.

- The axial conduction in the fluid is negligible during flow.
- The temperature gradients normal to the flow are negligible due to the sufficiently low Biot number.
- The heat losses outside of the domain are negligible.

The schematic of the model developed is illustrated in Figure 1. The heat transfer fluid with mass flow rate $\dot{m}_f$ and inlet temperature $T_{f,inl}$ crosses the device along the axial direction x passing through the cavities delimited by flat plates with PCM. The fluid can be a gas or a liquid. The phase change material is positioned between the flat plates of length L, total cross-sectional area A, and wetted perimeter P.

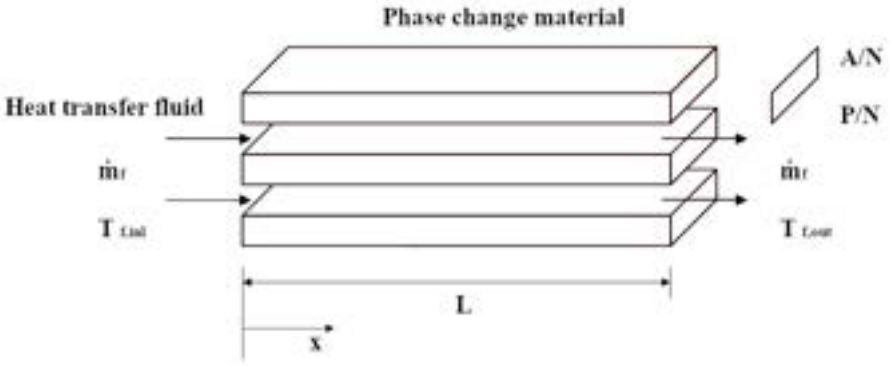

Figure 1. Scheme of a TES device with flat plate containers**.**

The set of equations imposing energy balance for the phase change material and the heat transfer fluid are stated in Eq. (1).

$$\begin{cases} \dfrac{\partial u}{\partial t} = \dfrac{k}{\rho}\dfrac{\partial^2 T}{\partial x^2} + \dfrac{UP}{\rho A}\left(T_f - T\right) \\ \dfrac{\partial T_f}{\partial t} = -\dfrac{\dot{m}_f}{\rho_f A_f}\dfrac{\partial T_f}{\partial x} + \dfrac{UP}{\rho_f A_f cp_f}\left(T - T_f\right) \end{cases} \quad (1)$$

where u, T, ρ and k are the specific internal energy, temperature, density, and thermal conductivity of PCM, T_f, ρ_f, c_{pf} and A_f are the temperature, density, specific heat and flow area of HTF, t is time and U is the overall heat transfer coefficient between the two materials.

The specific internal energy u depends on the temperatures of the HTF and PCM and the thermo-physical properties of the PCM based on Eq. (2).

$$\begin{cases} c_s(T - T_{ref}) & if\ T < T_m \\ c_s(T_m - T_{ref}) + \chi F & if\ T = T_m \\ c_s(T_m - T_{ref}) + F + c_l(T - T_m) & if\ T > T_m \end{cases} \quad (2)$$

where c_l and c_s are the values of the specific heat of the liquid and solid phases of the PCM, χ is its liquid mass fraction, T_m is its melting temperature, F is its latent heat of fusion and T_{ref} is the reference temperature corresponding to the null internal energy.

The general formulation of the energy balance of Eq. (1) can be simplified considering that the heat transfer due to axial conduction in the PCM during flow is negligible and assuming a low capacitance for the HTF. In these circumstances, the energy balance reduces to Eq. (3).

$$\begin{cases} \frac{\partial u}{\partial t} = \frac{UP}{\rho A}(T_f - T) \\ \frac{\partial T_f}{\partial x} = \frac{UP}{\dot{m}_f c p_f}(T - T_f) \end{cases} \quad (3)$$

The governing equations can be reformulated in a non-dimensional form in terms of the number of transfer units *NTU* as in Eq. (4) through the normalisation relying on the temperature difference between the PCM melting temperature and the reference temperature [6].

$$\begin{cases} \frac{\partial \bar{u}}{\partial \tau} = (\theta_f - \theta) \\ \frac{\partial \theta_f}{\partial \zeta} = NTU(\theta - \theta_f) \end{cases} \quad (4)$$

The normalisation procedure is based on the non-dimensional distance ζ defined as the ratio between the axial position x and plate length L and the equations from Eq. (5) to Eq. (9) that provide the non-dimensional temperature differences of the PCM and HTF θ and θ_f, the non-dimensional heat transfer coefficient $\bar{u}$ and the time τ.

$$\theta = \frac{T - T_{ref}}{T_m - T_{ref}} \quad (5)$$

$$\theta_f = \frac{T_f - T_{ref}}{T_m - T_{ref}} \quad (6)$$

$$\bar{u} = \frac{u}{c(T_m - T_{ref})} \quad (7)$$

$$\tau = \frac{tUPL}{\rho ALc} \quad (8)$$

$$NTU = \frac{UPL}{\dot{m}_f c_{pf}} \quad (9)$$

2.2. Finite difference approximation

The solution of the differential governing equations defined in the NTU formulation was achieved through the finite differencing technique [6]. This approach is based on the subdivision of the storage system into a set of *n* axial nodes as illustrated in Figure 2.

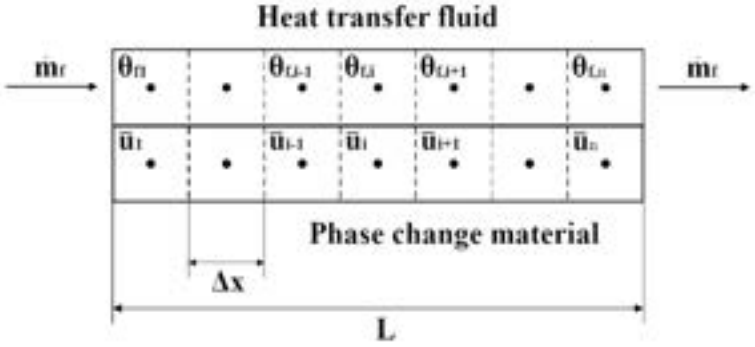

Figure 2. Scheme of the computational domain composed by a set of nodes**.**

At the beginning of each time step, the PCM internal energy, the HTF temperature at the axial nodes and the current inlet fluid temperature are known. Forward differencing techniques are then applied for updating these quantities. Therefore, the energy balance is expressed for each nodal position *i* from 1 to *n* through Eq. (10).

$$\begin{cases} \bar{u}_i' = \bar{u}_i + \Delta\tau\left(\theta_{f,i} - \theta_i\right) \\ \theta_{f,i+1}' = \theta_{f,i}' + \Delta\zeta NTU\left(\theta_i - \theta_{f,i}\right) \end{cases} \quad (10)$$

where the superscript refers to the variable at the new time step, $\Delta\tau$ is the non-dimensional time step and $\Delta\zeta$ is the non-dimensional nodal spacing.

The first formula of the set of Eq. (10) states that the change in PCM internal energy during the time step equals the heat transferred from the HTF to the PCM within this period. In analogy, the second equation indicates that the variation in HTF enthalpy from one node to the adjacent one equals the heat added by convection.

At each time step and for every node, Eq. (10) is applied for computing the non-dimensional values of the PCM internal energy $\bar{u}_i'$ and the HTF temperature at the end of the time step based on the known values of $\bar{u}_i$, θ_i and $\theta_{f,i}$ and the updated inlet flow temperature $\theta_{f,i}'$. At first, the updated HTF temperatures are determined and then the PCM internal energy of every corresponding node is defined.

The temperature and quality of all the PCM nodes are updated with Eq. (11) based on the liquid mass fraction provided by Eq. (12). The assumption of equivalent values of the specific heat of the liquid and solid phases of PCM is imposed.

$$\bar{u} = \theta + \frac{F}{c\left(T_m - T_{ref}\right)}\chi \quad (11)$$

$$\begin{cases} \chi = 0 & if\ \theta < 1 \\ 0 \le \chi \le 1 & if\ \theta = 1 \\ \chi = 1 & if\ \theta > 1 \end{cases} \quad (12)$$

The finite difference solution tends to the exact one by increasing the node number as a procedure for the discretisation of the computational domain is applied. It was shown in the literature that five nodes are sufficient for representing the TES device with a good approximation [6].

3. Results and discussion

The analytical model was validated through the comparison with a reference case selected in the literature regarding multi-layer thermal energy storage systems with PCM. Afterwards, the model was applied for evaluating the functioning of a TES device operating on board a vessel.

3.1. Model validation

A literature reference case was selected to validate the analytical model developed for assessing the process of heat transfer in TES devices operating with a phase change storage medium composed of cavities with parallel flow paths [9]. The schematic of the thermal energy system of the reference literature case is coherent with that of Figure 1 and its main geometric specifications are indicated in Table 1.

Table 1. Geometric parameters of the heat exchanger defined in the reference case [9].

Parameter	Symbol	Value	Unit
PCM layer number	N	3	-
Fluid channel number	N_f	2	-
PCM layer thickness	b	0.005	m
Fluid channel thickness	b_f	0.003	m

The complete definition of the model geometry requires the assumption of the dimensional value of the plate length and width. In the analyses conducted, equal dimensional values of 0.03, 0.04 and 0.05 m were imposed for these parameters. The wetted perimeter and cross-sectional area of the PCM layers were computed based on their width and thickness. The geometric parameters used in the calculations in addition to those defined in the reference case are defined in Table 2.

Table 2. Geometric parameters of the PCM layers assigned in the analyses.

Parameter	Symbol	Value	Unit
Plate length	L	0.03–0.05	m

Plate width	W	0.03–0.05	m
PCM perimeter	P	0.21–0.33	m
PCM area	A	4.50–7.50	cm^2

The heat transfer fluid crossing the cavities of the device is air and the storage medium is Glauber's salt (sodium sulphate decahydrate).

The physical properties and initial conditions of the PCM defined in the literature reference are listed in Table 3. In the reference case, the liquid state specific heat of the Glauber's salt is 3.26 kJ/kg/K. However, in the simplified model developed the specific heat of the liquid state is assumed equivalent to the value of the solid state, which is equal to 1.92 kJ/kg/K. The reference temperature for the simulations was set to 20°C.

Table 3. Physical properties and initial conditions of the Glauber's salt [9].

Parameter	Symbol	Value	Unit
Inlet temperature	T_{inl}	25	°C
Melting temperature	T_m	32	°C
Solid state density	ρ_s	1460	kg/m^3
Liquid state density	ρ_l	1330	kg/m^3
Solid state specific heat	c_s	1.92	kJ/kg/K
Specific latent heat of fusion	F	251	kJ/kg
Solid state thermal conductivity	k_s	0.514	W/m/K
Liquid state thermal conductivity	k_l	0.514	W/m/K

The temperature of the air at the domain inlet is 90°C and the initial temperature of the Glauber's salt is 25°C. Thus, the thermo-physical properties of air were evaluated at the average temperature of 57.5°C and the atmospheric pressure.

The characteristic length *l* of the flow cavities was calculated with Eq. (13). This parameter and the Nusselt number N_u of 8.235 defined in the reference case were utilised to determine the overall heat transfer coefficient *U* between the HTF and PCM through Eq. (14).

$$l = \frac{4A_f}{P_f} \tag{13}$$

$$U = \frac{N_u k_f}{l} \tag{14}$$

where P_f and A_f are the perimeter and area of the fluid channels regarding the PCM layer number and k_f is the air thermal conductivity.

The air velocity v_f was computed with Eq. (15) based on the Nusselt number, the Prandtl number P_r, the Reynolds number R_e, the dynamic viscosity μ and the density of the airflow and the characteristic length of the flow cavities.

$$v_f = \left(\frac{N_u}{0.664 P_r^{1/3}}\right)^2 \frac{\mu_f}{\rho_f l} \tag{15}$$

The time corresponding to the non-dimensional time t^* of 14 of the literature case was determined with Eq. (16) for comparing the results of the two models [9].

$$t = t^* \frac{\rho_s c_s b^2}{4k_s} \tag{16}$$

The values of the above parameters applied in the simulations are resumed in Table 4.

Table 4. Parameters and operating conditions used in the simulations of the reference case [9].

Parameter	Symbol	Value	Unit
Characteristic length	l	0.00545–0.00566	m
Nusselt number	N_u	8.235	-
Overall heat transfer coefficient	U	0.0426–0.0411	$kW/m^2/K$
Average air velocity	v_f	0.66–0.64	m/s
Air mass flow rate	$\dot{m}_f$	0.00013–0.00020	kg/s
Reference non-dimensional time	t^*	14	-

Reference time	t	477.2	s

The validation of the theoretical model was achieved through the comparison with the literature reference [9]. The results of the two models were confronted by analysing the predicted time series of the liquid mass fraction and temperature of the HTF and PCM. In Figure 3(a), the increase of the mass fraction of the liquid phase of the PCM is presented as a function of time. The convective heat transfer coefficient decreases as the plate size increases. The lower rate of heat exchange with growing dimensions determines a rise in the time required for reaching equilibrium. In the reference case, the complete melting of the PCM is obtained at time 477.2 s when the average liquid mass fraction equals the unit and the device is fully charged. For the simulation performed, the melting time is 1102, 1411 and 1710 s based on the increasing plate dimensions. The curves have a similar trend, indicating that the simplified analytical model proposed is capable of evaluating the melting process.
Figure 3(b) illustrates the liquid mass fraction computed at each domain node for the device with a length and a width equal to 0.04 m. The amount of time required for melting rises from the first to the last node due to the reduction of the temperature of the HTF across the flow cavities for the progressive reduction of the heat transfer rate.

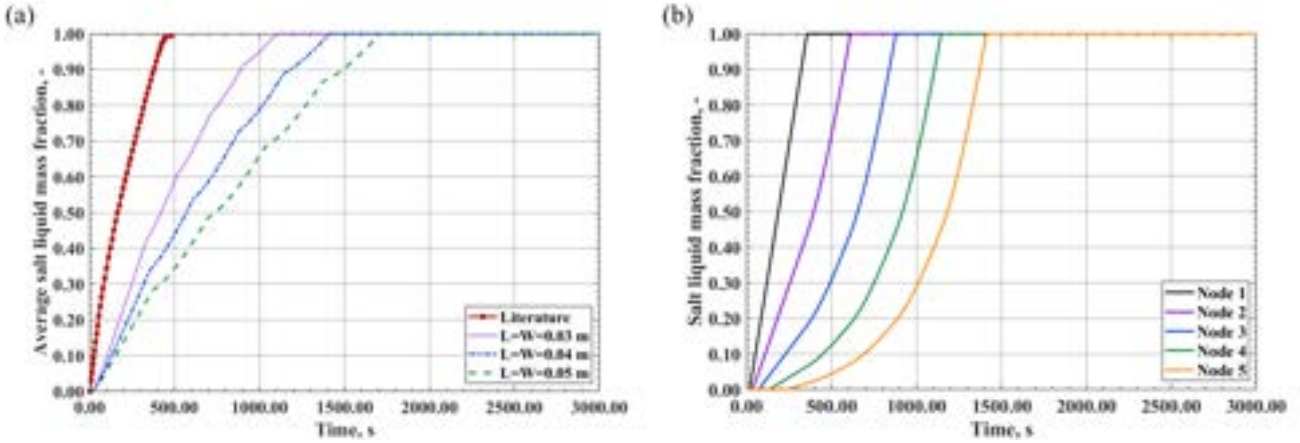

Figure 3. Time series of the liquid fraction of the Glauber's salt: (a) average values for the reference case and different plate dimensions, (b) values at the nodes for the device with the intermediate plate size.

Figure 4(a) depicts the increase in the average temperature of the Glauber's salt for the three configurations analysed. The rate of rise is greater reducing plate size for the higher heat transfer owing to the lower mass airflow rate. The average temperature of the PCM is 54.6°C corresponding to the instant of complete melting for the literature case. For the three configurations analysed, the values obtained for this parameter are 73.53, 75.43 and 76.58°C, respectively. The higher predictions are attributable to the specific heat of the liquid phase of the PCM that is assumed equivalent to that of the solid phase in the simplified model proposed.
In Figure 4(b), the temperature of Glauber's salt calculated at the five nodes is presented as a function of time during the charging process. The time required for heating up the PCM to the temperature of the HTF rises increasing the distance from the domain inlet as the rate of heat transfer decreases along the channel length.

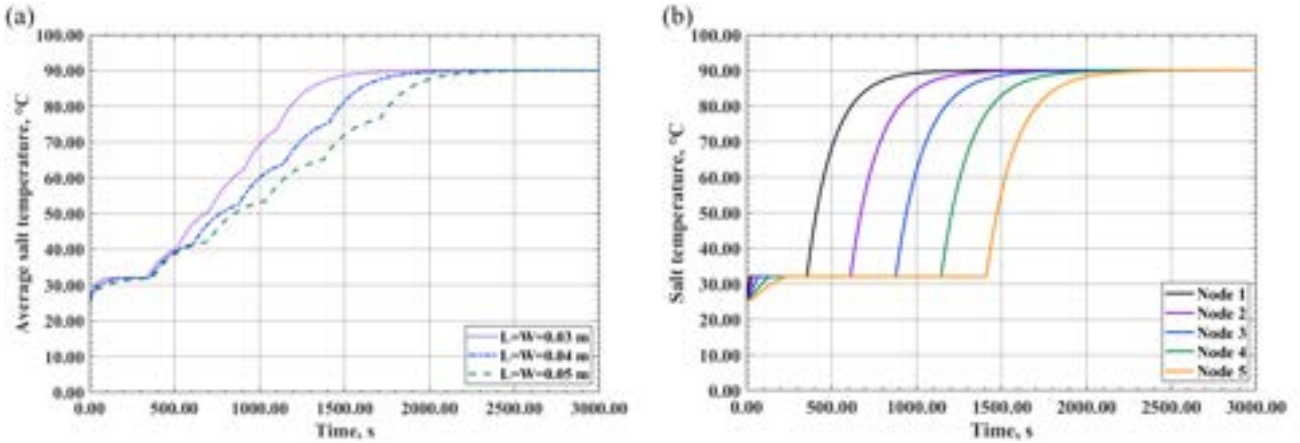

Figure 4. Time series of the temperature of the Glauber's salt: (a) average values for the reference case and different plate dimensions, (b) values at the nodes for the device with the intermediate plate size.

In Figure 5(a), the air temperature at the outlet of the TES device is shown as a function of time for the three configurations analysed. The temperature of the HTF increases with time as the PCM melts. When the PCM is completely melted, the temperature values are 60.55, 55.47 and 49.91°C, respectively. The temperature of the airflow exiting the device approaches the initial temperature of the PCM. The temperature difference reduces by increasing the plate size due to the enhancement of heat transfer.
Figure 5(b) presents the air temperature calculated at the five nodes of the computational domain. In particular, the temperature of node 1 is constant and equals the inlet temperature of 90°C of the charging fluid. The values of the other nodes rise up to 90°C requiring higher time as the distance from the domain inlet grows. The curves of the last three nodes indicate the presence of instabilities at the end of the melting transformation which could be minimised by increasing the number of axial nodes and reducing the time step size.

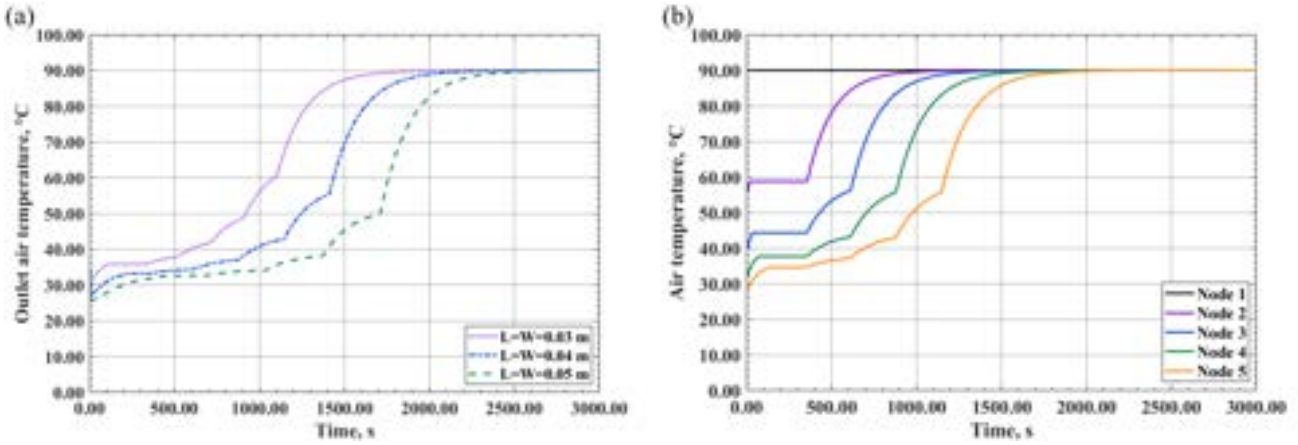

Figure 5. Time series of the air temperature: (a) values at the outlet for the reference case and different plate dimensions, (b) values at the nodes for the device with the intermediate plate size.

3.2. Case study

The TES device considered for the possible application on a vessel is a flat plate heat exchanger similar to the schematic illustrated in Figure 6. The plates are stacked parallel to each other and are bundled in a box where they are submerged in the phase change material. At each upper extremity of the device, a plenum manifold connects the pipe of the heat transfer fluid with all the plates.

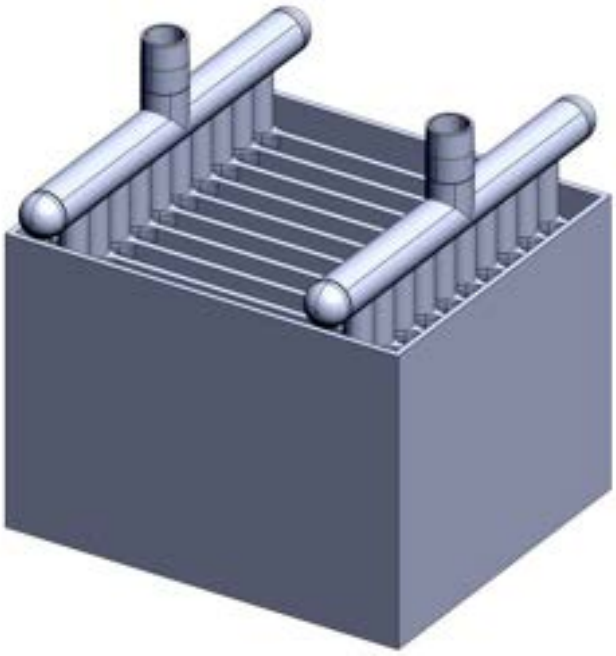

Figure 6. Schematic of the structure of the heat exchanger with the box, plates and pipes.

Five configurations of the TES devices for vessel application were investigated for evaluating the effects of plate dimensions on performance. A set of 10 plates with fixed values of thickness of the PCM layers and fluid channels was considered. The length and height of the device were varied to explore sizes comparable with traditional heat exchangers with submerged flat plates [11]. The length was assigned in the range from 0.8 to 1.2 m with intervals of 0.1 m and the height was set at 80% of the length. The geometric parameters defining the configuration of the case study are listed in Table 5.

Table 5. Geometric parameters of the TES device configurations considered for operating on a vessel.

Parameter	Symbol	Value	Unit
Plate length	L	0.80–1.20	m
Plate height	H	0.64–0.96	m
PCM layer thickness	b	0.030	m
Fluid channel thickness	b_f	0.018	m
PCM layer number	N	11	-
Fluid channel number	N_f	10	-
PCM perimeter	P	14.74–21.78	m
PCM area	A	0.2112–0.3168	m^2

The system uses water as heat transfer fluid and H105 as phase change material. This is an inorganic salt with the chemical formulation KNO_3 which is in the form of granules. This storage medium was selected as its melting temperature has a value close to the average of the charging and discharging temperatures of the water [12].

The physical properties and initial conditions of the PCM are provided in Table 6. The hypothesis of equal values of the specific heat of the solid and liquid phases was applied. The reference temperature of 20°C was considered in the calculations.

Table 6. Physical properties and initial conditions of the H105 [12].

Parameter	Symbol	Value	Unit
Inlet temperature	T_{inl}	90	°C
Melting temperature	T_m	104	°C
Solid state density	ρ_s	1700	kg/m^3
Solid state specific heat	c_s	1.50	kJ/kg/K
Specific latent heat of fusion	F	125	kJ/kg
Solid state thermal conductivity	k_s	0.500	W/m/K
Liquid state thermal conductivity	k_l	0.500	W/m/K

The water charges the device at 120°C and discharges it at 90°C in compliance with typical scenarios of heat wastage on vessels. A total mass flow rate of 1.50 kg/s was selected, resulting in a mass flow rate of 0.15 kg/s for each plate. The thermo-physical conditions of the water charging the device were evaluated at the average temperature of 105°C and the pressure of 3 atm.

The formulation of Eq. (13) was applied to determine the characteristic length *l* of the device. Since the mass flow rate of the device was imposed, the average velocity of the water flowing through the cavities was determined relying on the water density and the cross-sectional area of the cavity. Thus, the Nusselt number was calculated with Eq. (15) and then the overall heat transfer coefficient between the HTF and PCM was computed with Eq. (14). The parameters applied in the simulations and the duration of the analyses are listed in Table 7.

Table 7. Parameters and operating conditions used in the simulations of the case study.

Parameter	Symbol	Value	Unit
Water mass flow rate	$\dot{m}_f$	1.50	kg/s
Average water velocity	v_f	0.0136–0.0091	m/s
Characteristic length	l	0.03502–0.03534	m
Overall heat transfer coefficient	U	0.6298–0.5119	$kW/m^2/K$
Nusselt number	N_u	32.48–26.64	-
Time	t	6000	s

In Figure 7(a), the process of the phase change of the H105 is shown in terms of variation in time of the liquid mass fraction. Increasing the dimensions of the plates, the convective heat transfer coefficient reduces extending the time required for the charge. The duration of the melting process is 701, 819, 946, 1082 and 1226 s as the size increases. In analogy, the time for the solidification process is 797, 929, 1072, 1225 and 1386 s. Therefore, the charging phase is faster than the discharging phase. This is caused by the different contributions of heat transfer for conduction and natural convection in the melting and solidification processes.

Figure 7(b) indicates the variation in time of air temperature along the plate length at each domain node. The device with an intermediate size with a length of 1 m and a height of 0.8 m was considered for presenting the results. The time of melting and solidification increases from the first to the last node as the water temperature decreases flowing through the cavities. This determines a progressive reduction of heat transfer along plate length.

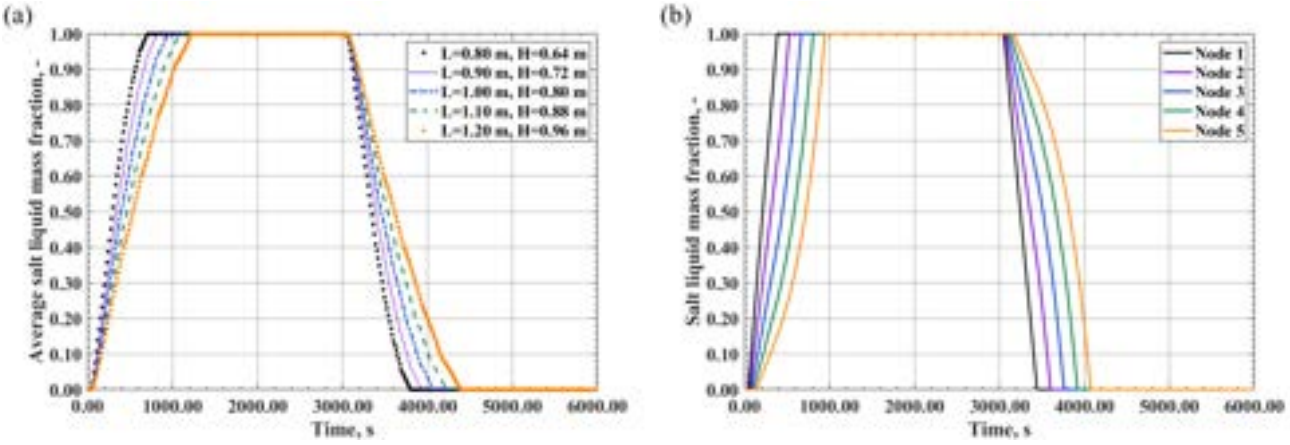

Figure 7. Time series of the liquid fraction of the H105 salt: (a) average values for the configurations investigated, (b) values at the domain nodes for the device with the intermediate size.

In Figure 8(a), the variation in the average temperature of the H105 salt during charging and discharging is depicted. The temperature gradients of both phase transformations are higher for the nodes close to the domain inlet for the reduction of the heat transfer in the direction of plate length. The discontinuities in the rate of rise of the temperature gradients of the salt are attributable to the presence of the interface between solid and liquid and to the duration of phase change along plate length, which is visible in Figure 8(b). The temperature gradients are higher during melting than solidification in accordance with the different duration of the two transformations. The average values of the temperature of the PCM at complete melting are equal to 115.90, 116.16, 116.35, 116.49 and 116.57°C for the various configurations. At complete solidification, the average temperatures correspond to 93.39, 93.25, 93.09, 92.97 and 92.95°C.

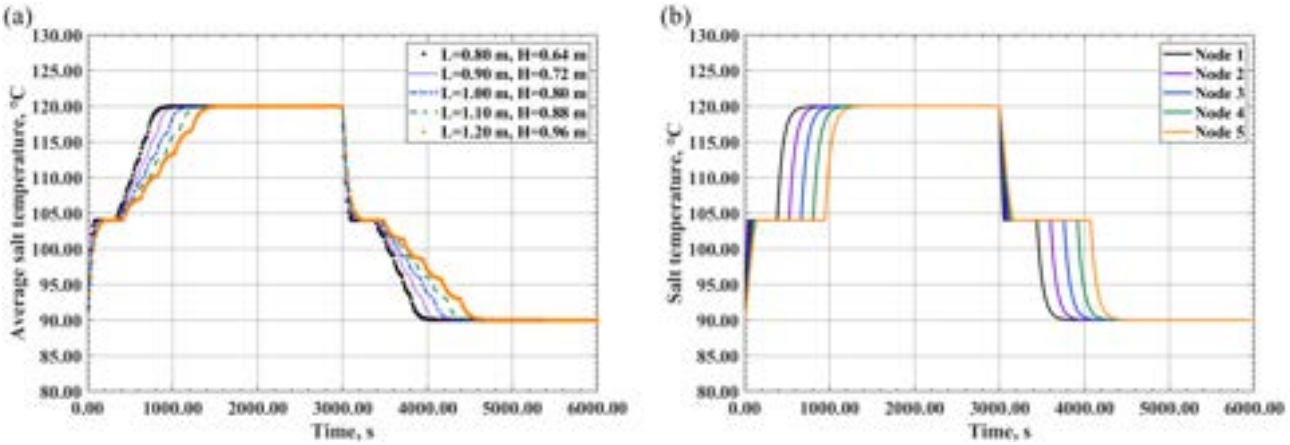

Figure 8. Time series of the temperature of the H105 salt: (a) average values for the configurations investigated, (b) values at the domain nodes for the device with the intermediate size.

The time series of the water temperature at the domain outlet is illustrated in Figure 9(a) for the five TES configurations. The HTF temperature rises during charging and decreases during discharging. The rate of rise is higher in the former process and it increases by reducing plate size due to the greater heat transfer.

The outlet water temperature in the charging phase is 115.45, 114.91, 114.31, 113.66 and 112.95°C based on the increasing device size, while it is 93.83, 94.33, 94.87, 95.45 and 96.09°C in the discharging phase. Figure 9(b) shows the water temperature computed at the five nodes along the domain. The temperature of the first node equals the values of the charging and discharging fluid during the relative phases. For the other nodes, the rate of variation increases moving from the inlet to the outlet.

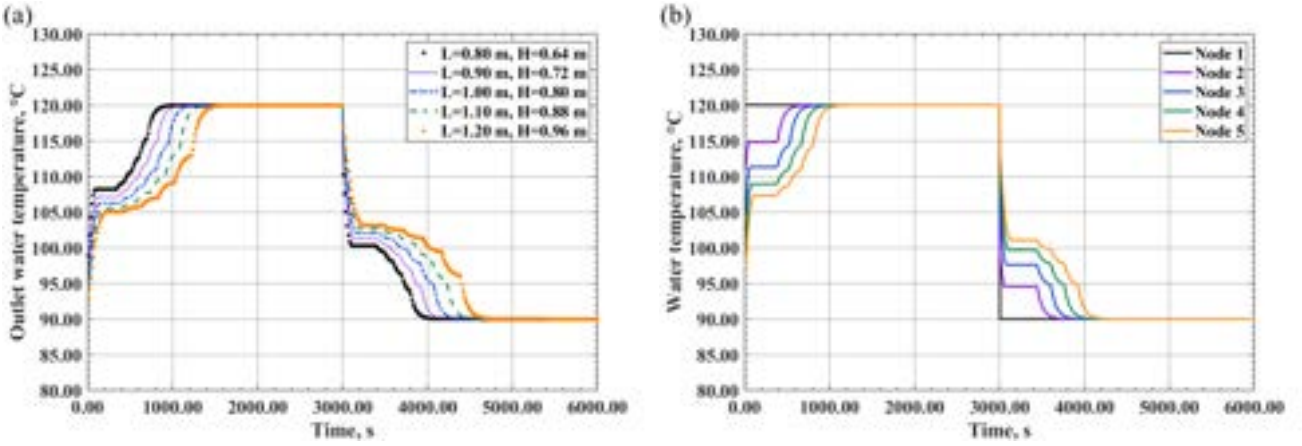

Figure 9. Time series of the water temperature: (a) values at the outlet for the configurations investigated, (b) values at the domain nodes for the device with the intermediate size.

The performance of the TES devices was evaluated in terms of volume and mass of the TES device, energy storage of the PCM and energy storage density, defined by the ratio between the first two parameters. The data achieved for the five configurations investigated are listed in Table 8. The selection of the best-suited configuration for the vessel application depends on the availability of thermal energy and the space and weight constraints on board vessels. The energy storage density slightly increases with device dimensions for the design space explored.

Table 8. Performance parameters of the TES devices analysed for the vessel application.

Parameter	Case 1	Case 2	Case 3	Case 4	Case 5	Unit
Volume	0.30	0.37	0.46	0.55	0.66	m^3
Mass	474	594	727	874	1034	kg
Energy storage	13.56	17.17	21.19	25.64	30.52	kWh
Energy storage density	45.57	45.85	46.07	46.26	46.41	kWh/m^3

4. Conclusions

A novel modular latent heat thermal energy storage (LHTES) system was proposed for the installation on cruising and cargo vessels. The main aim of the research is to increase the energy efficiency of ships for reducing the carbon emissions of the maritime sector. Moreover, these devices allow stabilising energy availability on board by smoothing the intermittency of thermal energy wastage. A theoretical methodology consolidated in the literature was applied to develop a fast and reliable analytical model capable of investigating a wide variety of geometric configurations and operating conditions. The code solves the heat exchange between the heat transfer fluid (HTF) and the phase change material (PCM) during the charging and discharging phases. It was found that the discharging time is longer than the charging time, which stems from the different contributions of conduction and natural convection heat transfer in melting and solidification. Operating conditions characteristic of cruising and cargo vessels were considered for evaluating the performance of a set of thermal energy storage (TES) device configurations. Geometric parameters suitable for their on-board application were selected to analyse a proper design space. The effects on the main performance indicators were assessed by varying the plate length between 0.80 and 1.20 m and the plate height from 0.64 to 0.96 m while keeping fixed the number of plates and the thickness of the HTF channels and PCM layers. The energy stored is between 13.56 and 30.52 kWh and the energy storage density ranges from 45.57 to 46.41 kWh/m^3.

Nomenclature

Roman symbols

A	area, m^2
b	thickness, m

Greek symbols

ζ	non-dimensional distance, -
θ	non-dimensional temperature difference, -

c	specific heat, J/kg/K
cp	constant pressure specific heat, J/kg/K
F	specific latent heat of fusion, kJ/kg
H	height, m
k	thermal conductivity, W/m/K
L	length, m
l	characteristic length, m
$\dot{m}$	mass flow rate, kg/s
N	plate number, -
NTU	number of transfer units, -
N_u	Nusselt number, -
n	node number, -
P	perimeter, m
P_r	Prandtl number, -
R_e	Reynolds number, -
T	temperature, °C
t	time, s
t^*	non-dimensional time, -
U	overall heat transfer coefficient, kW/m^2/K
u	specific internal energy, kJ/kg
$\bar{u}$	non-dimensional heat transfer coefficient, -
v	velocity, m/s
W	width, m
x	axial position, s
μ	dynamic viscosity, Pa·s
ρ	density, kg/m^3
τ	non-dimensional time, -
χ	liquid mass fraction, -

Subscripts and superscripts

f	fluid
i	node index
inl	inlet
l	liquid
m	melting
out	outlet
ref	reference
s	solid
$'$	new time step

Acronyms

GHG	greenhouse gas emissions
HTF	heat transfer fluid
IMO	International Maritime Organisation
LHTES	latent heat thermal energy storage
LNG	liquefied natural gas
PCM	phase change material
TES	thermal energy storage
WHR	waste heat recovery

References

[1] Singh D.V., Pedersen E., A review of waste heat recovery technologies for maritime applications. Energy Conversion and Management, 2016; 111: 315–28; doi.org:10.1016/j.enconman.2015.12.073.

[2] MAN Diesel & Turbo, Waste Heat Recovery System (WHRS) for Reduction of Fuel Consumption, Emissions and EEDI, 2014.

[3] United Nations, Developments in international seaborne trade, 2017; doi.org:10.18356/e9e3b605-en.

[4] Maritime Organisation International, Cutting GHG emissions from shipping – 10 years of mandatory rules, 2021; https://www.imo.org/en/MediaCentre/PressBriefings/pages/DecadeOfGHGAction.aspx [accessed 05.03.2023].

[5] Mallouppas G., Yfantis E.A., Decarbonization in Shipping industry: A review of research, technology development, and innovation proposals, Journal of Marine Science and Engineering, 2021; 9; doi.org:10.3390/jmse9040415.

[6] Morrison D.J., Performance of solar heating systems utilizing phase change energy storage, University of Wisconsin-Madison, 1976.

[7] Morrison D.J., Abdel-Khalik S.I., Effects of phase-change energy storage on the performance of air-based and liquid-based solar heating systems, Solar Energy, 1978; 20(1), 57–67; doi:10.1016/0038-092X(78)90141-X.

[8] Garg H.P., Mullick S.C., Bhargava, A.K., Solar Thermal Energy Storage. Springer Dordrecht, The Netherlands, 1985; doi:10.1007/978-94-009-5301-7.

[9] Majumdar P., Saidbakhsh A., A heat transfer model for phase change thermal energy storage, Heat Recovery Systems and CHP, 1990; 10(5–6); 457–468; doi: 10.1016/0890-4332(90)90196-Q.

[10] Duffie J.A., Beckman W.A., Solar Engineering of Thermal Processes (Fourth Edition), Wiley, 2013.

[11] Esteves L., Magalhães A., Ferreira V., Pinho C., Test of Two Phase Change Materials for Thermal Energy Storage: Determination of the Global Heat Transfer Coefficient, ChemEngineering, 2018; 2(1); 10; doi:10.3390/chemengineering2010010.

[12] Xu H., Yin Sze J., Romagnoli A., Py X., Selection of Phase Change Material for Thermal Energy Storage in Solar Air Conditioning Systems, Energy Procedia, 2017; 105; 4281–4288; doi: 10.1016/j.egypro.2017.03.898.

Modelling an ammonia cycle for thermochemical energy storage

A. García-Guzmán[a], D. A Rodríguez Pastor[b], J. A Becerra[c] and R.Chacartegui[d]

[a] *University of Seville, Seville, Spain, alejandrogarciaguzman10@gmail.com*
[b] *University of Seville, Seville, Spain, drodriguez4@us.es*
[c] *University of Seville, Seville, Spain, jabv@us.es*
[d] *University of Seville, Seville, Spain, ricardoch@us.es*

Abstract:
The penetration of renewable energies into the electricity system is making it increasingly cheaper, cleaner, and safer. It poses specific challenges, such as dispatchability periods and grid frequency stability.
Storage systems are needed to meet these challenges. Thermochemical reactions have great potential for energy transport and storage. Their integration into solar energy systems is of great interest due to the possibility of achieving high energy densities and seasonal storage. This work analyses the integration of a thermochemical storage system based on ammonia looping into a concentrating solar power (CSP). Energy storage is based on a charging phase, where heat is provided for ammonia decomposition and a discharging phase, where heat is recovered from ammonia synthesis. This work aims to evaluate the thermodynamic performance of a reference plant with a total capacity of 6.2 MW of CSP integrated into an ammonia loop power system. The performance and LCOS curves are discussed as a function of synthesis and decomposition temperatures.

Keywords:
TCES, Ammonia looping, CSP, Thermochemical energy storage

1. Introduction

Energy storage systems are used to ensure the availability of energy supply. Thermal energy storage (TES) and Thermochemical energy storage (TCES) systems are promising technologies for renewable energy storage [1]. In recent years, several thermal storage technologies for medium- and high-temperature CSP systems have been developed based on the use of materials in which energy is stored as sensible heat [1]–[5] or latent heat [6].The third form of storage is through thermochemical storage, in which the heat from the sun drives an endothermic reaction, which decomposes a compound into other species, storing the energy in chemical bonds. This has the advantage that it can be used for long-term energy storage. Different thermochemical energy storage approaches have promising results[7]–[9] based on the methanol decomposition into syngas [10] or iron carbonates [11].

They have an optimum operation at different temperature levels, offering solutions to efficiently convert, store and transport solar energy. They allow seasonal storage capacity allowing long mismatch between resource availability and discharge for covering demand. Depending on the involved reactions, they can have high energy densities [12]. The thermochemical energy storage system based on the ammonia looping is based on the decomposition and synthesis of the pair NH_3/H_2. It has an energy density of 131 MJ/m^3 with a turning temperature of 195 ºC [7] [11]. From the point of view of thermochemical storage, the reactions of synthesis and decomposition of ammonia are opposite reactions that share the absorption and desorption of dinitrogen stage.

Ammonia is a carbon-free hydrogen carrier with a reasonably good volumetric and gravimetric energy density compared to hydrogen. It has an energy density of 13.1 GJ/m, whereas hydrogen has an energy density of 3.5 GJ/m [13], and it is used as a feedstock and raw material to produce other chemicals [14].

The ammonia chemical industry has a high environmental impact and needs the integration of renewable energy to reduce it [15]. There are several possibilities for integrating renewables in the ammonia industry: using biomass gasification systems [16]–[18], solar energy [19], [20], and wind energy [21], [22]. Another option is to use biogas produced from the decomposition of organic material, such as agricultural waste or animal excrement [23], as a source of hydrogen.

Ammonia-based solar thermochemical storage systems can help ensure the stability of solar thermal power generation systems 24-h basis, offering a high potential for long-term energy storage. Besides, ammonia, the main raw material for fertiliser production, can be integrated into a thermochemical storage system. *Carden et al.* pioneered the idea of the ammonia-based energy storage system in 1974 [24]. Subsequent exergy analyses studies conducted concluded that the main irreversibility is the heat recovery process. The main losses are concentrated in the reaction, the heat transfer within the exothermic reactor and the losses of the exothermic reactor countercurrent heat exchanger[25]. In 2019, *Chen et al.* [26] studied the effects of dissociation reactor geometry by performing a 2-dimensional pseudo-homogeneous cylindrical 2-dimensional model of a dissociation reactor, concluding that converging conical reactors can achieve the highest conversions. *Lovegrove et al.* proposed an ammonia looping system which operates at a nominal power level of 1 kW_{chem} solar dissociation reactor kW_e [27], [28].

This work proposes a novel and flexible system in which the renewable energy produced by the sun can be stored for a long time. Subsequently, this stored energy is released in the form of heat. This can be used for power generation or to provide heat to a process. It is a carbon-free process where ammonia is produced based on renewables [29]–[31], thus reducing the consumption of fossil fuels. The efficient and simple form of the system results in a competitive levelised cost of storage.

2. System description

The system consists of a charging cycle, where the ammonia decomposition reaction is carried out, and a discharge cycle, where the ammonia synthesis reaction is carried out. The concentrating solar power and a heliostat field are integrated into the charge phase to generate syngas through endothermic decomposition. In the discharge phase, the syngas is released to the synthesis phase and is converted into ammonia, releasing heat to a power cycle.

In the charging phase, ammonia is stored at 30°C and 25 bar and released to a pump that raises the pressure to 100 bar. The ammonia is preheated with the outlet of the decomposition reactor. This ammonia feeds the endothermic reactor at 382.3 ºC and 100 bar. The outlet of the reactor contains syngas and unreacted ammonia at 500 ºC and 100 bar[13], [32]–[34]. This outlet stream is cooled with the ammonia inlet to the reactor to 94.31 ºC.

Figure 1. Conceptual process flow diagram of the ammonia cycle system

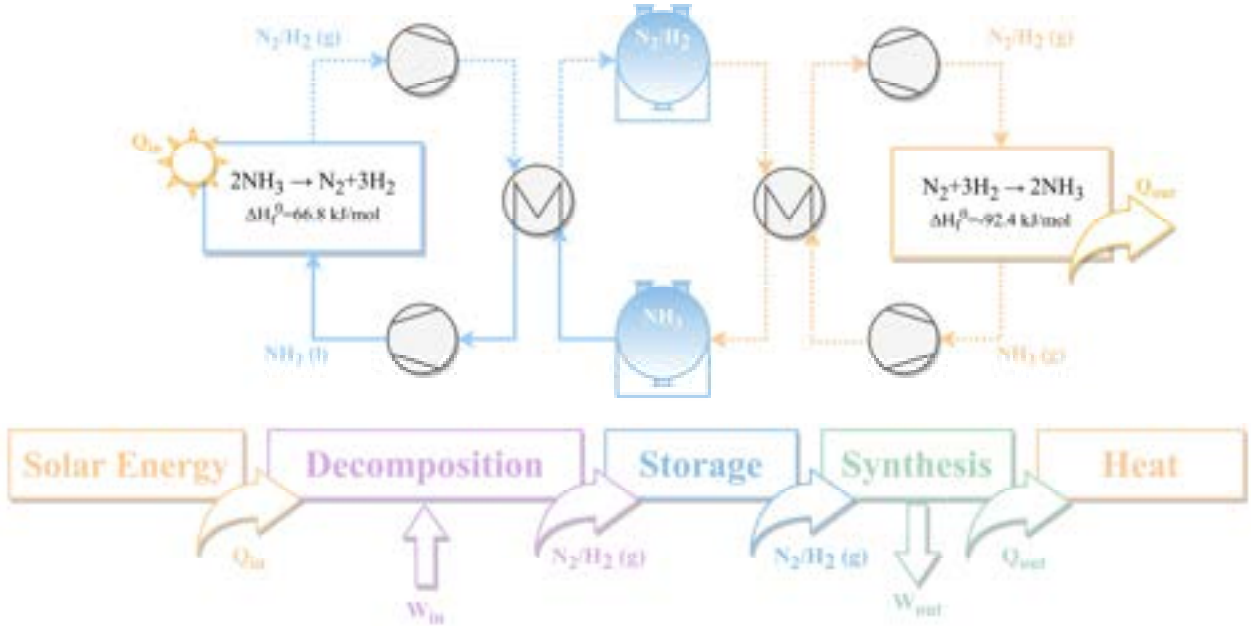

Figure 2. Process flow diagram of the ammonia cycle system

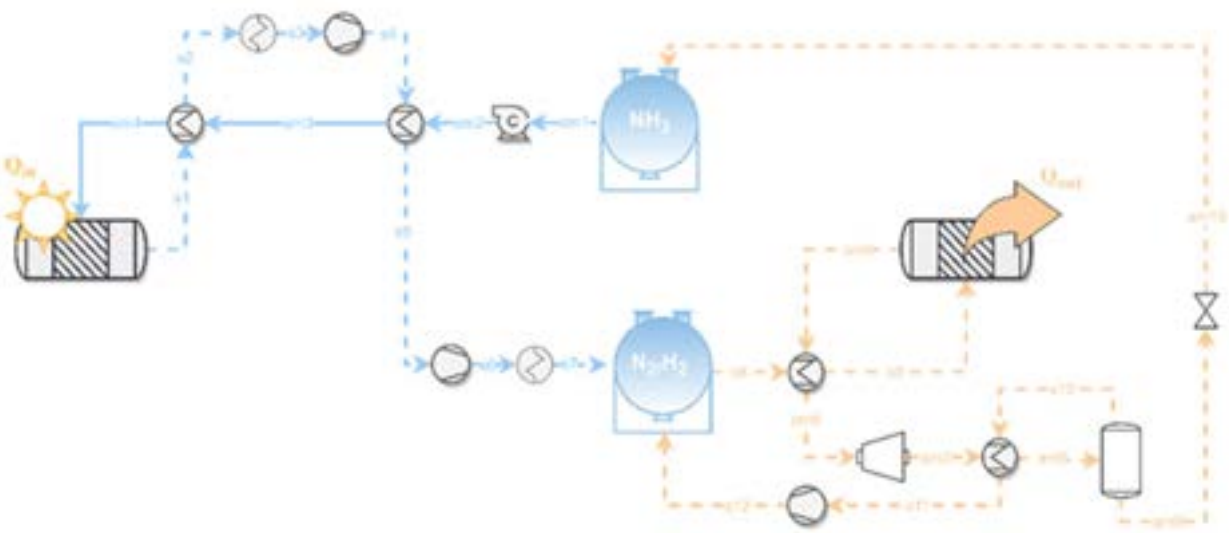

In the loading phase, ammonia is stored at 30°C and 25 bar and released to a pump that raises the pressure to 100 bar. The ammonia is preheated with the outlet of the decomposition reactor. This ammonia feeds the endothermic reactor at 382.3 ºC and 100 bar. The reactor outlet contains syngas and unreacted ammonia at 600 ºC and 100 bar. This outlet stream is cooled with the ammonia inlet to the reactor to 94.31 ºC and raises its pressure to 200 bar. Then, the syngas at 200 bar is stored [35].

Figure 3. Process flow diagram of the ammonia decomposition (charge phase)

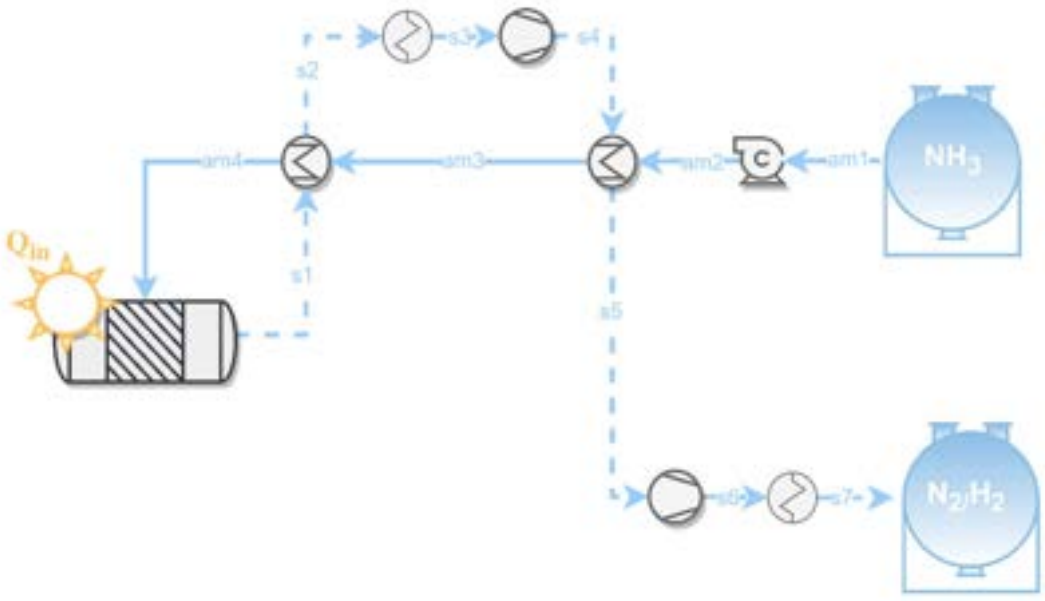

In the discharge phase, the synthesis gas is released from the tank, and this stream is cooled with the reactor outlet. The inlet stream to the synthesis reactor is at 189.4 °C and 200 bar [36] with a catalyst converter Ba/Ru/BN [35]. The reactor outlet stream is at 300 ºC and 200 bar [36]. It separates in a flash into ammonia and unreacted synthesis gas. At a steady state and with a sufficiently long residence time in the reactor, the syngas would tend to be zero in the synthesis reactor outlet stream.

Figure 4. Process flow diagram of the ammonia synthesis (discharge phase)

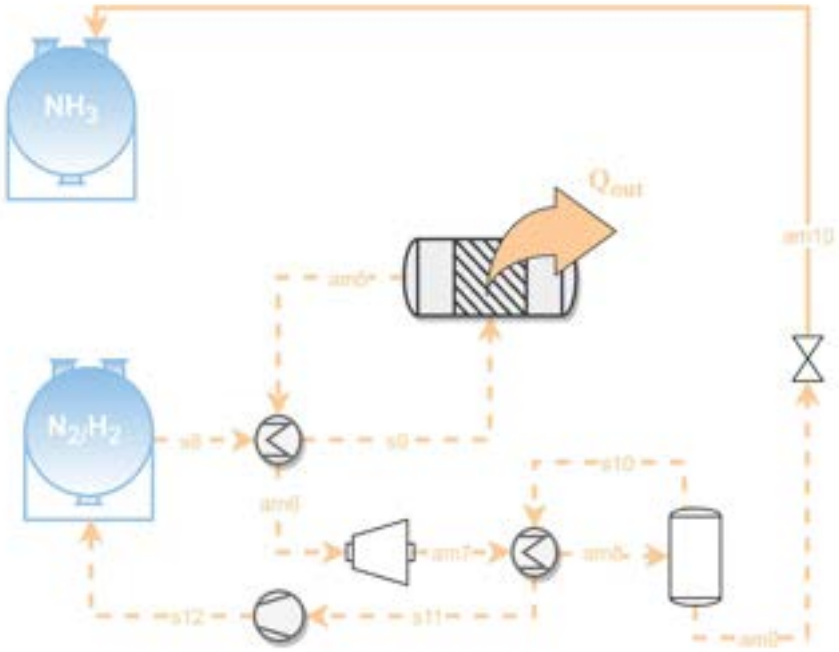

3. Simulation

In this section, simulations of the proposed system layout will be carried out. These simulations will be carried out in the Aspen Hysys commercial software.

A series of operating conditions were previously defined to simulate the model, both in the loading and discharging phases.

a. Steady-state model.
b. Sufficient residence time to achieve an overall conversion of 100%.
c. The minimum approach temperature for all heat exchangers is 20 ºC.
d. The efficiencies of the pumps, compressors and turbines are 80, 89, and 90%, respectively.
e. The global, solar-to-chemical and solar-to-electric efficiencies have been defined according to equations 1, 2 and 3.

Table 1. Main parameters of the plant

Parameter	Value	Unit
NH_3 storage temperature/pressure	30/25	ºC/bar
Syngas CO/H2 storage pressure	200	bar
Endothermic reaction temperature/pressure	500/100	ºC/bar
Exothermic reaction temperature/pressure	250/200	ºC/bar
Inlet NH_3 molar flow of the charging process	100	mol/s

The global performance of the plant is defined as follows.

$$\eta_{plant} = \frac{\dot{Q_{exo}} + \dot{W_T}}{HH\dot{V}_{NH_3}\dot{m_{NH_3}} + \dot{W_C} + \dot{Q_{CSP}}} * \frac{h_{discharge}}{h_{charge}} \text{ [1]}$$

The numerator represents the outputs, which are the energy extracted from the ammonia synthesis and the power generated by the expansion turbines, while the denominator represents the heat flow of the ammonia stream from the synthesis reactor outlet, the energy consumption by the compressors and the pump, and the heat supplied by the CSP. This is affected by a ratio of discharge hours to charge hours.

Also, equations [2] and [3] define a solar-chemical yield and a solar-electric yield. The former represents the thermal recovery of the dissociation reaction compared to the CSP power input, while the solar-electric yield represents the electrical energy recovery compared to the CSP power and the energy consumption of the compressors and pump. Both efficiencies are in terms of heat and electrical energy, respectively.

$$\eta_{sol-ch=} \frac{X_{NH_3} m_{NH_3} \Delta h_{NH_3}}{\dot{Q_{CSP}}} \text{ [2]}$$

$$\eta_{sol-elec} = \frac{\dot{W_T}}{\dot{W_C} + \dot{Q_{CSP}}} \text{ [3]}$$

3.1 Economic model

The technical-economic analysis was carried out by evaluating the CAPEX and OPEX and then evaluating the LCOS of the system.

The levelized cost of storage (LCOS) according to equation 4.

$$LCOS = \frac{CAPEX + \sum_{i=1}^{n} \frac{OPEX}{(1+r)^n}}{\sum_{i=1}^{n} \frac{Q_{exo}}{(1+r)^n}} \text{ [4]}$$

It is assumed a discount rate (r) of 3% and a useful life of the plant (n) of 20 years.

The CAPEX was evaluated using equipment costs. These equipment costs are calculated based on the correlations shown in **Table 2**. OPEX is assumed to be 20% of CAPEX.

Table 2. Correlations for estimating equipment costs.

Equipment	Scaling parameter	Expression	Reference
Pump	Brake power [kW] and isentropic efficiency	$IC_C = 6898 \cdot \dot{W}_{Compressor}^{0.7865}$	[37]
Compressor	Power [kW]	$IC_P = 750 \cdot (\dot{W}_p)^{0.71} \cdot \left[1 + \left(\frac{0.2}{1-\eta_{i,P}}\right)\right]$	[38]
Turbine	Power [kW]	$IC_T = 4001.4 \cdot \dot{W}_{Turbine}^{0.6897}$	[37]
Endotermic reactor	Power [kW]	$IC_{DR} = 193000 \cdot \dot{Q}_{endo}^{0.65}$	[39]

Exotermic reactor	Power [kW]	$IC_{SR} = 19594 \cdot \dot{Q}_{exo}^{0.5}$	[38]
Tank	Volume [m^3]	$C_{tank} = 83 \cdot V_{tank} \cdot 10^{-6}$	[40]
Heat exchangers	Exchanger Area [m^2] pressure [bar]	*Table*	[38]
Solar tower and receiver	$\Phi_{Receiver}\ [kW]$	$IC_{tower}^{solar} = 57.07 \cdot \Phi_{Receiver}$	[41]
Electric generator	Power [MW]	$IC_{EG} = 106 \cdot P_G^{0.95}$	[38]

4. Results

The results of the system at nominal conditions are shown in **Table 3**. The solar-to-chemical performance is high (>90 %) due to the high conversion achieved in the decomposition reactor regarding the power input by the sun. The global performance is low compared to other TCES, as expected by the temperature levels. However, it the LCOS is remarkable, which is fairly low compared to other technologies.

Table 3. Results at the operation point

Parameter	Value	Unit
Global performance	11.55	%
Solar to chemical performance	91.84	%
Solar to electrical performance	1.753	%
Exothermic reaction heat	-3.78	MW
Endothermic reaction heat	6.207	MW
CAPEX	3.964	M€
OPEX	0.793	M€
LCOS	63.98	€/MWh

It can be observed that the LCOS of the plant is 63.98 €/MWh, which is a competitive value, in comparison with other types of long-term thermochemical energy storage, such as H_2 and CH_4 storage with levelized cost of electricity of 260-430 €/MWh and 360-550 €/MWh, respectively. Table 4 shows the LCOS of the different technologies for long-term and short-term storage. [42]

Table 4. Comparison table of LCOS for the different technologies for long-term storage

Technology	Type of storage	LCOS [€/MWh]
PSH (Pumped Storage Hydroelectricity)	long-term	930-1850
dCAES (Diabatic Compressed Air Storage)	long-term	20
aCAES (Adiabatic Compressed Air Storage)	long-term	20-40
H_2 Storage	long-term	260-430
CH_4 storage	long-term	360-530
NH_3 storage	long-term	64

4.1. Sensitivity analysis

Different sensitivity analyses were performed as a function of endothermic temperature. **Figure 5** shows the effect of the molar fraction as a function of the decomposition temperature and synthesis temperature. As the decomposition temperature increases, the molar fraction of ammonia increases, whereas as the synthesis temperature increases, the conversion of ammonia to syngas decreases to a lesser extent than the decomposition reaction. These conversions justify performance trends.

Figure 5. Concentration profiles as a function of decomposition temperature (on the left) and synthesis temperature (on the right)

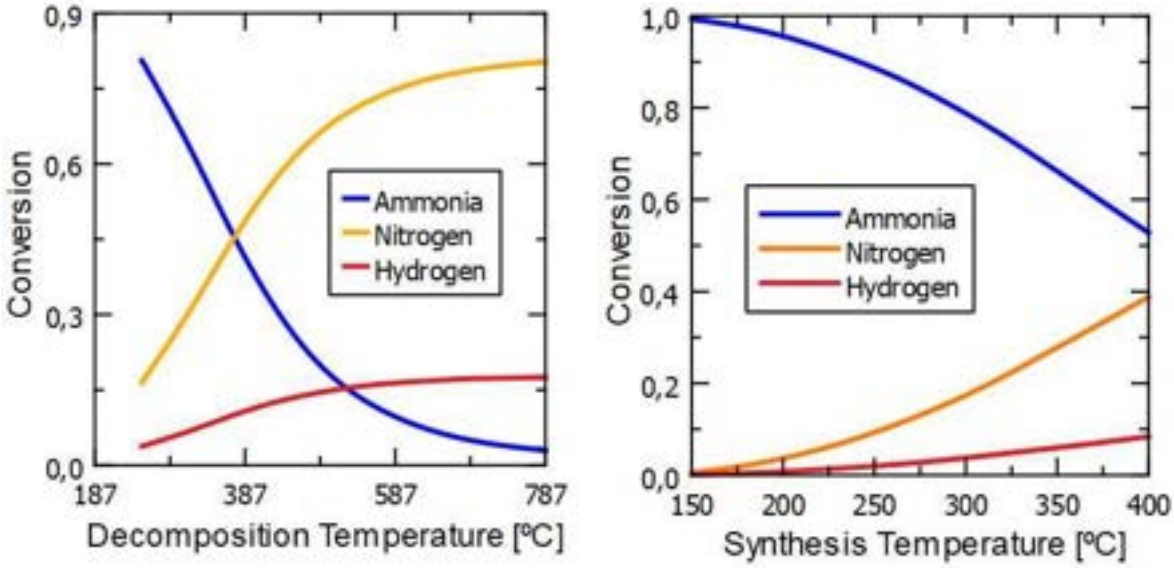

The next analysis is the global performance as a function of the decomposition and synthesis temperatures parametrised at four pressures. It has been shown that the higher the operating temperature, the higher the overall plant performance. Also, as operating pressures increase, lower overall plant performance. Increasing the endothermic temperature increases the conversion of ammonia to syngas, thus increasing the conversion in ammonia synthesis, releasing more heat of reaction, and increasing the yield. Likewise, the increase in pressure in the discharge phase increases the compression power, affecting the denominator and lowering the yield.

Figure 6 follows the same trend of the overall yield as a function of the decomposition temperature, but as the reaction temperature increases, the yield decreases. Increasing the reaction temperature the conversion decreases. Therefore, the heat flow of the reactor outlet stream is lower, affecting the numerator of the yield and decreasing it.

From these graphs, the optimum operating conditions that optimise the overall performance of the plant can be selected. The higher the decomposition temperature and the lower the synthesis temperature, the higher the overall plant performance.

Figure 6. Global performance as a function of decomposition temperature parametrised at four pressures (on the left) and parametrised at four synthesis temperatures.

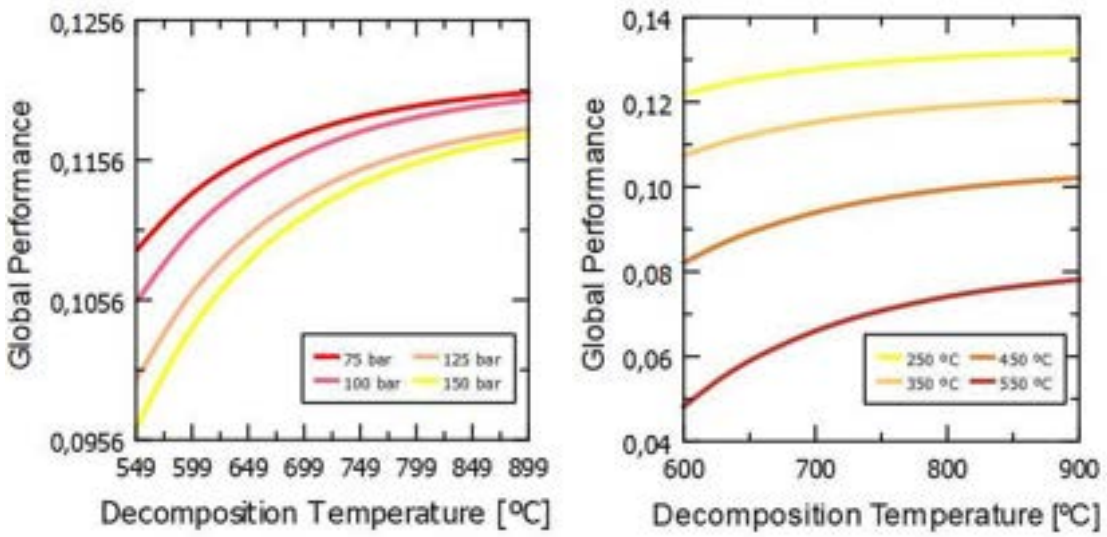

In figure 7 it is shown the exothermic heat release as a function of synthesis temperature parametrised at four decomposition temperatures. As a synthesis temperature increases, the exothermic heat released decreases. In the opposite trend, as the decomposition temperature increase, the heat releases increase. This fact is because as the decomposition temperature increases, the syngas produced is higher. Then, the conversion of syngas to ammonia in the synthesis reactor is greater, releasing more heat.

Figure 7. Exothermic heat release as a function of synthesis temperature parametrised at four decomposition temperatures.

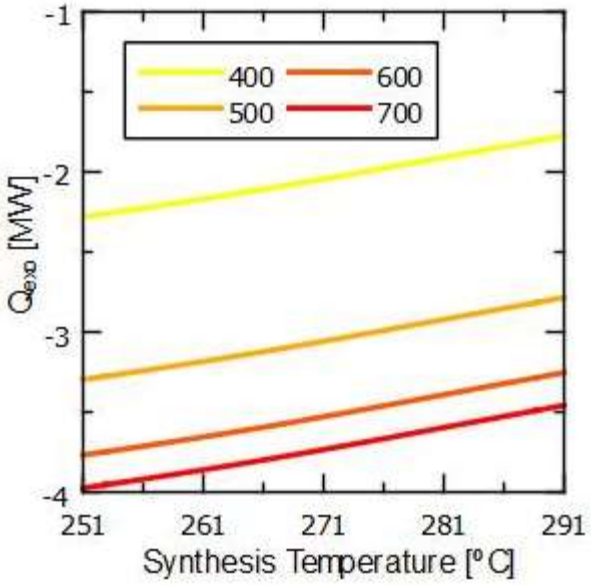

Figure 8 shows the levelized cost of storage as a function of the decomposition temperature and the synthesis temperature. As the decomposition temperature increases, the LCOS decreases. Likewise, as the synthesis temperature increases, the LCOS takes an opposite trend, decreasing.

Figure 8. LCOS as a function of decomposition temperature parametrised at four pressures (on the left) and synthesis temperature (on the right).

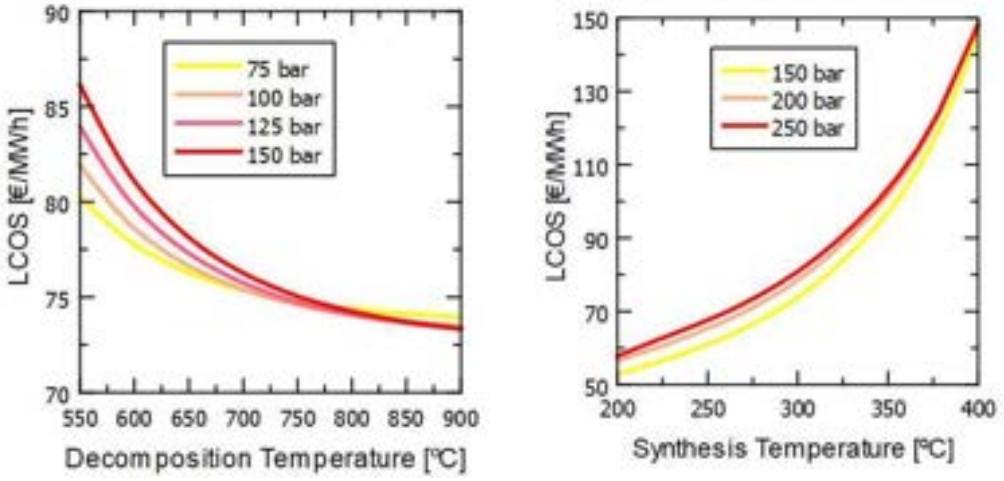

It is shown the higher the ammonia pressure at the reactor inlet, the higher the LCOS because the OPEX of the installation increases as the pressure drop in the pump increases. This trend is equal in the discharge phase.

When the decomposition temperature rises, the reaction is favoured and shifts to the right, producing more syngas. Then the heat released in the synthesis reactor will be higher. This increases the denominator of the LCOS by lowering it. As the synthesis temperature increases, the heat of reaction decreases, resulting in a rise in LCOS. The rise in the OPEX is reflected mainly in the pressure in both analyses. As the pressure increases, the LCOS increases.

5. Conclusions

A thermochemical storage system is proposed, based on the decomposition and synthesis of green ammonia, being a CO_2-free solution and a very dispatchable system in terms of energy production.

There are several advantages of the proposed system that can be mentioned.

i. The solar-to-chemical performance is high (92%) due to the high conversion of ammonia in the decomposition reaction. In contrast, the overall thermal efficiency of the system is 11.55%, which is low due to high compression consumption in relation to the exothermic energy generated in the synthesis reaction and the temperature levels.

ii. The system produces 3.78 MW of exothermic heat, with 6.2 MW of power input in the CSP, based on 100 mol/s of green ammonia.

iii. The system has a competitive LCOS value of 63.98 €/MWh for the design conditions. It is a competitive position concerning other long-term thermochemical systems storage, such as H_2 or CH_4 storage.

iv. The temperature/pressure torque for the load plus phase is 30ºC/25 bar, and for the discharge phase 250ºC/200 bar, making a compromise between overall plant performance and LCOS.

Acknowledgements

This work has been made possible thank to the project “Prueba de concepto en entorno relevante de nuevo diseño de calcinador solar de alta temperatura y elevada eficiencia”

Nomenclature

η efficiency, [-]

$\dot{Q}$ heat power, [kW]

$\dot{W}$ heat power, [kW]

X molar fraction [-]

$\dot{m}$ mass flow [kg/s]

Δh enthalpy difference, [kJ/kmol]

I_C Investment cost, [€]

References

[1] A. Gautam and R. P. Saini, “A review on sensible heat based packed bed solar thermal energy storage system for low temperature applications,” *Solar Energy*, vol. 207, pp. 937–956, Sep. 2020, doi: 10.1016/J.SOLENER.2020.07.027.

[2] G. Li, “Sensible heat thermal storage energy and exergy performance evaluations,” *Renewable and Sustainable Energy Reviews*, vol. 53, pp. 897–923, Jan. 2016, doi: 10.1016/J.RSER.2015.09.006.

[3] M. M. Sorour, “Performance of a small sensible heat energy storage unit,” *Energy Convers Manag*, vol. 28, no. 3, pp. 211–217, Jan. 1988, doi: 10.1016/0196-8904(88)90024-6.

[4] L. Seyitini, B. Belgasim, and C. C. Enweremadu, “Solid state sensible heat storage technology for industrial applications – A review,” *J Energy Storage*, vol. 62, p. 106919, Jun. 2023, doi: 10.1016/J.EST.2023.106919.

[5] L. Seyitini, B. Belgasim, and C. C. Enweremadu, “Solid state sensible heat storage technology for industrial applications – A review,” *J Energy Storage*, vol. 62, p. 106919, Jun. 2023, doi: 10.1016/J.EST.2023.106919.

[6] H. Jouhara, A. Żabnieńska-Góra, N. Khordehgah, D. Ahmad, and T. Lipinski, “Latent thermal energy storage technologies and applications: A review,” *International Journal of Thermofluids*, vol. 5–6, p. 100039, Aug. 2020, doi: 10.1016/J.IJFT.2020.100039.

[7] R. Chacartegui, A. Alovisio, C. Ortiz, J. M. Valverde, V. Verda, and J. A. Becerra, “Thermochemical energy storage of concentrated solar power by integration of the calcium looping process and a CO2 power cycle,” *Appl Energy*, vol. 173, pp. 589–605, Jul. 2016, doi: 10.1016/J.APENERGY.2016.04.053.

[8] A. Alovisio, R. Chacartegui, C. Ortiz, J. M. Valverde, and V. Verda, “Optimising the CSP-Calcium Looping integration for Thermochemical Energy Storage,” *Energy Convers Manag*, vol. 136, pp. 85–98, Mar. 2017, doi: 10.1016/J.ENCONMAN.2016.12.093.

[9] C. Ortiz, J. M. Valverde, R. Chacartegui, L. A. Perez-Maqueda, and P. Giménez, “The Calcium-Looping (CaCO3/CaO) process for thermochemical energy storage in Concentrating Solar Power plants,” *Renewable and Sustainable Energy Reviews*, vol. 113, p. 109252, Oct. 2019, doi: 10.1016/J.RSER.2019.109252.

[10] Z. Bai, Q. Liu, J. Lei, and H. Jin, “Investigation on the mid-temperature solar thermochemical power generation system with methanol decomposition,” *Appl Energy*, vol. 217, pp. 56–65, May 2018, doi: 10.1016/J.APENERGY.2018.02.101.

[11] S. Kuravi, J. Trahan, D. Y. Goswami, M. M. Rahman, and E. K. Stefanakos, “Thermal energy storage technologies and systems for concentrating solar power plants,” *Prog Energy Combust Sci*, vol. 39, no. 4, pp. 285–319, Aug. 2013, doi: 10.1016/J.PECS.2013.02.001.

[12] K. E. N’Tsoukpoe, H. Liu, N. Le Pierrès, and L. Luo, “A review on long-term sorption solar energy storage,” *Renewable and Sustainable Energy Reviews*, vol. 13, no. 9, pp. 2385–2396, Dec. 2009, doi: 10.1016/J.RSER.2009.05.008.

[13] S. Mukherjee, S. V. Devaguptapu, A. Sviripa, C. R. F. Lund, and G. Wu, “Low-temperature ammonia decomposition catalysts for hydrogen generation,” *Appl Catal B*, vol. 226, pp. 162–181, Jun. 2018, doi: 10.1016/J.APCATB.2017.12.039.

[14] A. Zarebska, D. Romero Nieto, K. v. Christensen, L. Fjerbæk Søtoft, and B. Norddahl, “Ammonium Fertilisers Production from Manure: A Critical Review,”

http://dx.doi.org/10.1080/10643389.2014.955630, vol. 45, no. 14, pp. 1469–1521, Jul. 2015, doi: 10.1080/10643389.2014.955630.

[15] M. J. Palys, H. Wang, Q. Zhang, and P. Daoutidis, "Renewable ammonia for sustainable energy and agriculture: vision and systems engineering opportunities," *Curr Opin Chem Eng*, vol. 31, p. 100667, Mar. 2021, doi: 10.1016/J.COCHE.2020.100667.

[16] C. Xu *et al.*, "Thermodynamic analysis of a novel biomass polygeneration system for ammonia synthesis and power generation using Allam power cycle," *Energy Convers Manag*, vol. 247, p. 114746, Nov. 2021, doi: 10.1016/J.ENCONMAN.2021.114746.

[17] R. Michalsky and P. H. Pfromm, "Thermodynamics of metal reactants for ammonia synthesis from steam, nitrogen and biomass at atmospheric pressure," *AIChE Journal*, vol. 58, no. 10, pp. 3203–3213, Oct. 2012, doi: 10.1002/AIC.13717.

[18] H. Ishaq and I. Dincer, "A novel biomass gasification based cascaded hydrogen and ammonia synthesis system using Stoichiometric and Gibbs reactors," *Biomass Bioenergy*, vol. 145, p. 105929, Feb. 2021, doi: 10.1016/J.BIOMBIOE.2020.105929.

[19] C. Zhang *et al.*, "Mimicking πbackdonation in Ce-MOFs for Solar-Driven Ammonia Synthesis," *ACS Appl Mater Interfaces*, vol. 11, no. 33, pp. 29917–29923, Aug. 2019, doi: 10.1021/ACSAMI.9B08682/SUPPL_FILE/AM9B08682_SI_001.PDF.

[20] H. Li, J. Shang, J. Shi, K. Zhao, and L. Zhang, "Facet-dependent solar ammonia synthesis of BiOCl nanosheets via a proton-assisted electron transfer pathway," *Nanoscale*, vol. 8, no. 4, pp. 1986–1993, Jan. 2016, doi: 10.1039/C5NR07380D.

[21] M. Malmali, M. Reese, A. v. McCormick, and E. L. Cussler, "Converting Wind Energy to Ammonia at Lower Pressure," *ACS Sustain Chem Eng*, vol. 6, no. 1, pp. 827–834, Jan. 2018, doi: 10.1021/ACSSUSCHEMENG.7B03159/ASSET/IMAGES/MEDIUM/SC-2017-03159W_0008.GIF.

[22] K. Verleysen, D. Coppitters, A. Parente, W. de Paepe, and F. Contino, "How can power-to-ammonia be robust? Optimisation of an ammonia synthesis plant powered by a wind turbine considering operational uncertainties," *Fuel*, vol. 266, p. 117049, Apr. 2020, doi: 10.1016/J.FUEL.2020.117049.

[23] X. M. Guo, E. Trably, E. Latrille, H. Carrre, and J. P. Steyer, "Hydrogen production from agricultural waste by dark fermentation: A review," *Int J Hydrogen Energy*, vol. 35, no. 19, pp. 10660–10673, Oct. 2010, doi: 10.1016/J.IJHYDENE.2010.03.008.

[24] P. O. Carden, "Energy corradiation using the reversible ammonia reaction," *Solar Energy*, vol. 19, no. 4, pp. 365–378, Jan. 1977, doi: 10.1016/0038-092X(77)90008-1.

[25] K. Lovegrove, A. Luzzi, M. McCann, and O. Freitag, "EXERGY ANALYSIS OF AMMONIA-BASED SOLAR THERMOCHEMICAL POWER SYSTEMS," *Solar Energy*, vol. 66, no. 2, pp. 103–115, Jun. 1999, doi: 10.1016/S0038-092X(98)00132-7.

[26] C. Chen, Y. Liu, H. Aryafar, T. Wen, and A. S. Lavine, "Performance of conical ammonia dissociation reactors for solar thermochemical energy storage," *Appl Energy*, vol. 255, p. 113785, Dec. 2019, doi: 10.1016/J.APENERGY.2019.113785.

[27] H. Kreetz and K. Lovegrove, "Theoretical analysis and experimental results of a 1 kWchem ammonia synthesis reactor for a solar thermochemical energy storage system," *Solar Energy*, vol. 67, no. 4–6, pp. 287–296, Jan. 1999, doi: 10.1016/S0038-092X(00)00064-5.

[28] K. Lovegrove, A. Luzzi, and H. Kreetz, "A solar-driven ammonia-based thermochemical energy storage system," *Solar Energy*, vol. 67, no. 4–6, pp. 309–316, Jan. 1999, doi: 10.1016/S0038-092X(00)00074-8.

[29] H. Zhang, L. Wang, J. Van herle, F. Maréchal, and U. Desideri, "Techno-economic comparison of green ammonia production processes," *Appl Energy*, vol. 259, Feb. 2020, doi: 10.1016/j.apenergy.2019.114135.

[30] N. Campion, H. Nami, P. R. Swisher, P. Vang Hendriksen, and M. Münster, "Techno-economic assessment of green ammonia production with different wind and solar potentials," *Renewable and Sustainable Energy Reviews*, vol. 173, Mar. 2023, doi: 10.1016/j.rser.2022.113057.

[31] M. D. Mukelabai, J. M. Gillard, and K. Patchigolla, "A novel integration of a green power-to-ammonia to power system: Reversible solid oxide fuel cell for hydrogen and power production coupled with an ammonia synthesis unit," *Int J Hydrogen Energy*, vol. 46, no. 35, pp. 18546–18556, May 2021, doi: 10.1016/J.IJHYDENE.2021.02.218.

[32] A. S. Chellappa, C. M. Fischer, and W. J. Thomson, "Ammonia decomposition kinetics over Ni-Pt/Al 2 O 3 for PEM fuel cell applications," 2002.

[33] G. Masci, C. Ortiz, R. Chacartegui, V. Verda, and J. M. Valverde, "The ammonia looping system for mid-temperature thermochemical energy storage," *Chem Eng Trans*, vol. 70, pp. 763–768, 2018, doi: 10.3303/CET1870128.

[34] Y. Ohtsuka, C. Xu, D. Kong, and N. Tsubouchi, “Decomposition of ammonia with iron and calcium catalysts supported on coal chars,” *Fuel*, vol. 83, no. 6, pp. 685–692, Apr. 2004, doi: 10.1016/J.FUEL.2003.05.002.

[35] J. Humphreys, R. Lan, and S. Tao, “Development and Recent Progress on Ammonia Synthesis Catalysts for Haber–Bosch Process,” *Advanced Energy and Sustainability Research*, vol. 2, no. 1, p. 2000043, Jan. 2021, doi: 10.1002/aesr.202000043.

[36] H. Zhang, L. Wang, J. Van herle, F. Maréchal, and U. Desideri, “Techno-economic comparison of green ammonia production processes,” *Appl Energy*, vol. 259, p. 114135, Feb. 2020, doi: 10.1016/J.APENERGY.2019.114135.

[37] M. D. Carlson, B. M. Middleton, and C. K. Ho, “PowerEnergy2017-3590 TECHNO-ECONOMIC COMPARISON OF SOLAR-DRIVEN SCO2 BRAYTON CYCLES USING COMPONENT COST MODELS BASELINED WITH VENDOR DATA AND ESTIMATES.”

[38] U. Tesio, E. Guelpa, and V. Verda, “Integration of thermochemical energy storage in concentrated solar power. Part 1: Energy and economic analysis/optimisation,” *Energy Conversion and Management: X*, vol. 6, p. 100039, Apr. 2020, doi: 10.1016/J.ECMX.2020.100039.

[39] E. De Lena *et al.*, “Techno-economic analysis of calcium looping processes for low CO2 emission cement plants,” *International Journal of Greenhouse Gas Control*, vol. 82, pp. 244–260, Mar. 2019, doi: 10.1016/J.IJGGC.2019.01.005.

[40] A. Bayon *et al.*, “Techno-economic assessment of solid–gas thermochemical energy storage systems for solar thermal power applications,” *Energy*, vol. 149, pp. 473–484, Apr. 2018, doi: 10.1016/J.ENERGY.2017.11.084.

[41] C. K. Ho, “A review of high-temperature particle receivers for concentrating solar power,” *Appl Therm Eng*, vol. 109, pp. 958–969, Oct. 2016, doi: 10.1016/J.APPLTHERMALENG.2016.04.103.

[42] V. Jülch, “Comparison of electricity storage options using levelized cost of storage (LCOS) method,” *Appl Energy*, vol. 183, pp. 1594–1606, Dec. 2016, doi: 10.1016/j.apenergy.2016.08.165.

Experimental analysis of the feasibility of using the ground as a temporary energy accumulator

Andrés Meana-Fernández[a], María José Suárez-López[b], Eduardo Blanco[c], Jesús-Ignacio Prieto[d] and David García[e]

[a,b,e] Thermal Machines and Engines Area, Department of Energy, University of Oviedo, Gijón, Spain, e-mail: [a]andresmf@uniovi.es (CA), [b]suarezlmaria@uniovi.es, [e]garciamdavid@uniovi.es
[c] Fluid Mechanics Area, Department of Energy, University of Oviedo, Gijón, Spain, e-mail: eblanco@uniovi.es
[d] Applied Physics Area, Department of Physics, University of Oviedo, Oviedo, Spain, e-mail: jprieto@uniovi.es

Abstract:

With significant percentages of worldwide energy consumption occurring in the building sector, it is intended to reduce energy consumption and, in turn, satisfy the demand with renewable energies. However, renewable energies suffer from high variability, so energy accumulation systems become relevant for adjusting the time gap between energy supply and demand. In recent years, air conditioning facilities with geothermal heat pumps have been on the rise, as they reach higher coefficients of performance (COP) than aerothermal heat pumps. In addition, they provide the opportunity to use the ground as a thermal reservoir. A first analysis of the feasibility of using the ground as a temporary energy accumulator has been performed in this work. To this end, tests have been carried out in an experimental facility with vertical buried pipes to evaluate the evolution of ground temperature after heat injection. Temperature probes were placed on the pipe surface and monitored at 5 different depths, with tests performed in three different months to observe seasonal effects. Dimensional analysis led to the identification of the influencing variables of the problem: depth, tube length, tube diameter, time and soil thermal diffusivity. An apparent thermal diffusivity was defined to characterize the soil from the thermal measurements. The results allowed identifying a subterranean water stream at a particular depth, as well as observing the effects of ambient conditions in the system. It was observed that the upper ground layers were heavily affected by ambient conditions, discouraging their use for thermal energy storage, whereas depths below the ground water table seemed suitable for storing heat efficiently. Differences were found between wet and dry soil, with wet soil better suited for the storage of higher energy amounts, but dry soil better suited for keeping the stored energy for longer periods without further isolation.

Keywords:

thermal energy storage; thermal reservoir; energy supply; temporary energy accumulator; experimental testing.

1. Introduction

Almost half of global energy use is employed for heat generation purposes, being the building sector one of the highest contributors to global emissions. In the current energy and environmental context, both the reduction of energy consumption and the use of renewable energy sources are critical issues. When renewable energy sources are used, the availability of energy often does not coincide with its need [1], so an accumulation system is interesting to absorb the gap between energy production and demand [2].

Among renewable energies, geothermal energy has been widely used from prehistoric times to the present day [3]. As the ground temperature keeps more constant along the year than the ambient temperature, it is very interesting for heating and cooling applications in buildings. This feature, combined with high COP heat pumps consists of a reliable solution itself. Furthermore, the geothermal facility can be used to store surplus production by other renewable sources, as it is the case of solar thermal projects [4,5]. Although ground has usually been used for long term accumulation purposes [6,7], Cruickshank and Baldwin [8] studied the diurnal performance, showing the interest in using the ground not only for long term accumulation purposes.

In the first decade of this century, five “Office Buildings Prototypes for Research and Demonstration” were constructed or retrofitted within the Singular Strategic Project ARFRISOL [9], showing the construction of more environmentally respectful buildings. As a complement to that project, the Gijón Solar Cooling Laboratory (GSCL) [10] was installed at the University of Oviedo. The GSCL is a modular plant that allows the testing of diverse equipment and technologies, including a geothermal installation with vertical buried pipes. With the fundings of the project RehabilitaGeoSol [11] the experimental equipment was completed, and the first test of the vertical pipes circuit has been obtained.

In this work, experimental results obtained during months of testing in the vertical buried pipes of the GSCL are analysed, and first impressions on the influence of the season on the thermal behaviour of the soil are discussed.

2. Materials and methods

2.1. Description of the vertical pipes circuit

The GSCL was designed and implemented for testing different technologies for solar cooling production in buildings. The laboratory is in the facilities that the University of Oviedo has in the Gijon Polytechnical Engineering School. The core of this facility is an absorption machine ClimateWell-CW10, connected to several heat sources and sinks. The absorption machine has two different barrels of lithium chloride and water, enabling the possibility of storing energy in one of the barrels while the other one is discharging. The heat dissipation from the absorption machine can be configured through different technologies: an air heat exchanger, an evaporative cooling tower, a water reservoir or different ground heat exchangers with horizontal or vertical buried pipes. Figure 1 shows the conceptual scheme of the vertical pipes circuit tested in this paper.

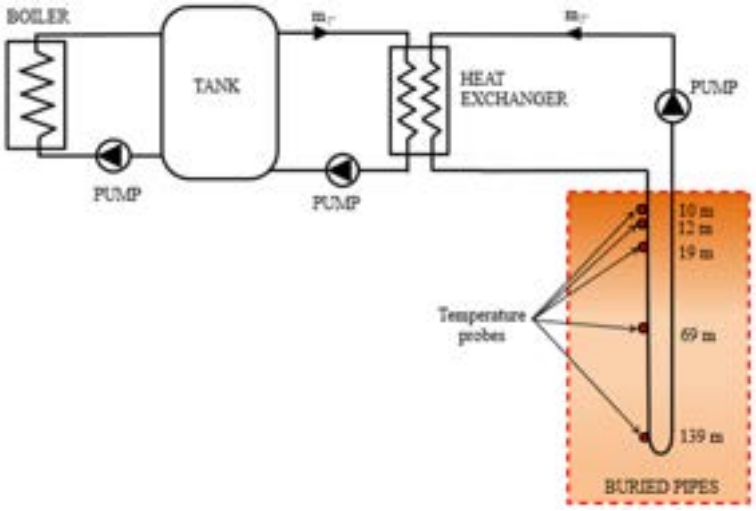

Figure 1. Conceptual scheme of the vertical pipes circuit.

The vertical pipes circuit consists of 2 U circuits of 32 mm diameter pipes, placed together into a 140 mm diameter hole filled with gravel, as can be seen in Figure 2. The pipes are buried down to 140 m depth, and 3-wires PT-100 probes are fitted to the outer surface of the pipes at five different depths (10 m, 12 m, 19 m, 69 m and 139 m), whereas flowrates were monitored with Kobold inductive flowmeters. PT-100 probes and flowmeters are connected to a Keithley 2700, multimeter equipped with a Keithley 7700 acquisition board and a GPIB/USB interface to be connected to a PC which records data every 5 minutes.

Figure 2. Detail of the pipes entering the ground.

2.2. Variables influencing in the problem

As a first approximation to the complexity of the problem, the temperature and physical properties of the terrain are assumed to be scalar functions with cylindrical symmetry. It is also assumed that the thermal conductivity of the terrain is isotropic. On the other hand, pending evaluation of the possible influence of environmental conditions by experimental results, the ground surface is assumed to be adiabatic.

At a point in the ground at distance r from the pipes and depth z from the surface, the temperature difference ΔT with respect to a point at the same depth and away from the influence of the pipes, depends on the physical properties of the ground, namely thermal conductivity k, specific heat capacity c and density ρ, the

diameter D and length L of the pipes, the temperature difference ΔT_0 at the beginning of the cooling, and the elapsed cooling time t. Therefore, a functional relationship of the following type can be written:

$$\Delta T = f(r, z, D, L, k, \rho, c, \Delta T_0, t) \quad (1)$$

The application of Buckingham's pi theorem to this equation, with the classical dimensional basis $\{L, M, T, \theta\}$ and using L, ρ, c and ΔT_0 as reference quantities, leads to the following functional relationship between dimensionless groups:

$$\frac{\Delta T}{\Delta T_0} = F\left(\frac{r}{L}, \frac{z}{L}, \frac{D}{L}, \Pi_k, \Pi_t\right) \quad (2)$$

where $\Pi_k = k/\left(\Delta T_0^{1/2} \rho\, L\, c^{3/2}\right)$ and $\Pi_t = \Delta T_0^{1/2} c^{1/2}\, t/L$.
Since the product of Π_k and Π_t is equal to the Fourier number $Fo = \alpha t/L^2$, equation (2) can be rewritten as follows:

$$\frac{\Delta T}{\Delta T_0} = F\left(\frac{r}{L}, \frac{z}{L}, \frac{D}{L}, Fo, \Pi_t\right) \quad (3)$$

The influence of Π_t is neither theoretically nor experimentally justified in the literature applicable to similar problems. In Appendix A it can be seen that spatially discriminated dimensional analysis predicts that such a monomial is spurious. Furthermore, variables r, D and L are constants in the case study, so the following functional relationship can be proposed as the basis of the experimental analysis:

$$\frac{\Delta T}{\Delta T_0} = F\left(\frac{z}{L}, Fo\right) \quad (4)$$

2.3. Data curation and postprocessing

The tests performed may be divided into two stages, as depicted in the example of Figure 3. In the first stage, heat was injected into the geothermal circuit below the ground until stationary conditions were obtained. After that, the heat supply was cut off and the evolution of the system was monitored. Specifically, the evolution of the temperature probes placed on the tube walls at 10, 12, 19, 69, and 139 m of depth was measured, and at first sight no influence of ambient temperature oscillations was found, even at the lower depth probes. The summary of the experimental tests performed is collected in Table 1. The tests were performed in May and September 2019 and February 2020, to observe seasonal effects in the behavior of the system.

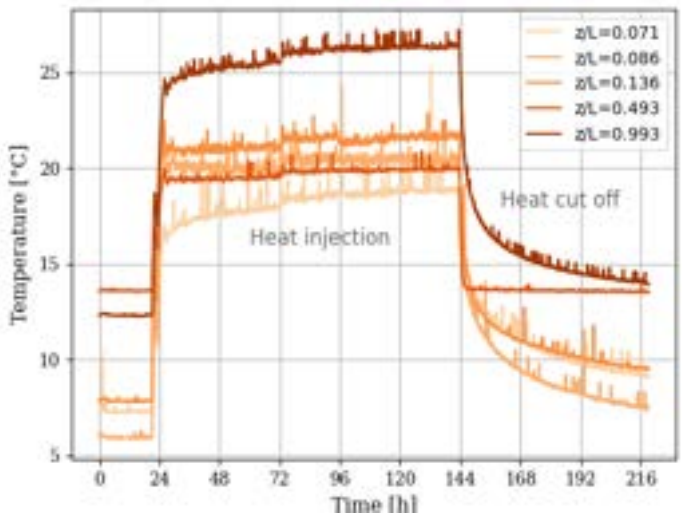

Figure 3. Loading curves performed in the experiments of May 2019.

Table 1. Summary of experimental tests

	February	May	September
Heat injection time	10,110 min	8,685 min	20,000 min
Heat injection flowrate	11.6 L/min	19.2 L/min	22.5 L/min
Average heat injection power	14 kW	17.5 kW	15.5 kW
Heat cut off monitoring time	21,690 min	4,515 min	19,315 min
Total experiment time	31,800 min	13,200 min	39,315 min

The measurements obtained were firstly filtered with a third order one-dimensional median filter [12] to eliminate possible outliers and obtain a clean signal for its subsequent analysis. An example is shown in Figure 4 for illustration.

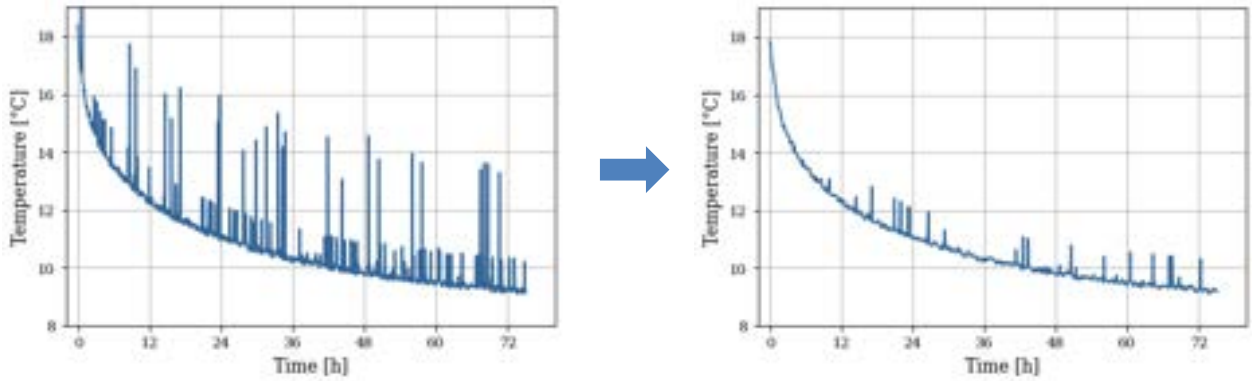

Figure 4. Postprocessing of measurements with 3rd order 1-D median filter

Then, the data were made dimensionless to compare measurements from different depths and periods. As the exact thermophysical properties of the soil are unknown, a constant apparent thermal diffusivity $\alpha_{ref} = 5.288 \cdot 10^{-7}$ m²/s was firstly used to make the data dimensionless. This value was estimated from the values obtained in the RehabilitaGeosol project [11] for the area of the experiments: a density of 3200 kg/m³, a specific heat of 1300 J/(kg·K), and a thermal conductivity of 2.2 W/(m·K). Thermal diffusivity was considered constant, and the underground soil isotropic.

It is possible, though, that each ground layer has different thermophysical properties. Therefore, with the aim of obtaining an estimative characterization of each ground layer, different apparent thermal diffusivities α_a were allowed for each ground depth (i.e., data series). The estimations of apparent thermal diffusivity α_a were obtained from the fitting of temperature measurements with respect to time. As a first approximation, in this work, an equation based on the proposed in [13] for transient heat conduction in semi-infinite solids was used, considering the soil as such:

$$\Delta T(t) = \Delta T_0 \, \mathrm{erf}\left(d/\sqrt{4\alpha_a t}\right) \quad (5)$$

Where T_0 is the initial temperature in K, T_∞ is the steady-state temperature in K, d is the distance between the tube center and the probe position, 0.07 m, α_a is the apparent thermal diffusivity of the soil in m²/s and t is the time in s. Typical values for soil thermal diffusivity are in the range of $5 \cdot 10^{-7}$ m²/s, [14,15,16] so values of α_a in the order of magnitude of 10^{-7} are expected.

2.4. Influence of ambient conditions

The soil is constituted by different minerals and rocks of different sizes, leaving gaps in between that may be filled with liquids and gases [17]. The estimation of soil thermophysical properties becomes a challenge due to this heterogeneous composition of the soil, which affects density, thermal conductivity, heat capacity and thus thermal diffusivity. When air is displaced by water from the gaps between solid fractions, the soil thermal conductivity is bound to increase. The increase of moisture also increases thermal conductivity due to the changes in the bond between water and soil, as well as the peculiar characteristics of water interfaces [18]. Volumetric heat capacity also increases with the addition of water. Once the thermal conductivity reaches a maximum value, the addition of more water continues increasing the soil heat capacity. As a consequence, thermal diffusivity exhibits an increasing trend for the addition of water at low moisture values, reaching a maximum for a particular moisture content, and then decreasing with further addition of water [19,20]. Apart from the composition, soil temperature affects its properties. Heat capacity and thermal conductivity are lower at lower temperatures, leading to variations in the thermal diffusivity of soil depending on the relative rate of change between these two variables.

In addition, it has been verified that ambient conditions influence the behavior of the upper ground layers and that both temperature and the amount of moisture influence soil properties [17], so meteorological data from the period in which the experiments were performed were collected from the Spanish State Agency for Meteorology [21] to provide a better insight into the results and their implications. Figure 5 shows the temperature and precipitation conditions at ground level from a month before starting the experiments until the experiments were finished. The exact dates in which the heat injection and cutoff processes for the experiment took place have been highlighted in the graphs. These data should help to generate the

landscape for understanding the initial conditions for the experiments and the evolution of the system throughout the heat injection and heat cutoff processes.

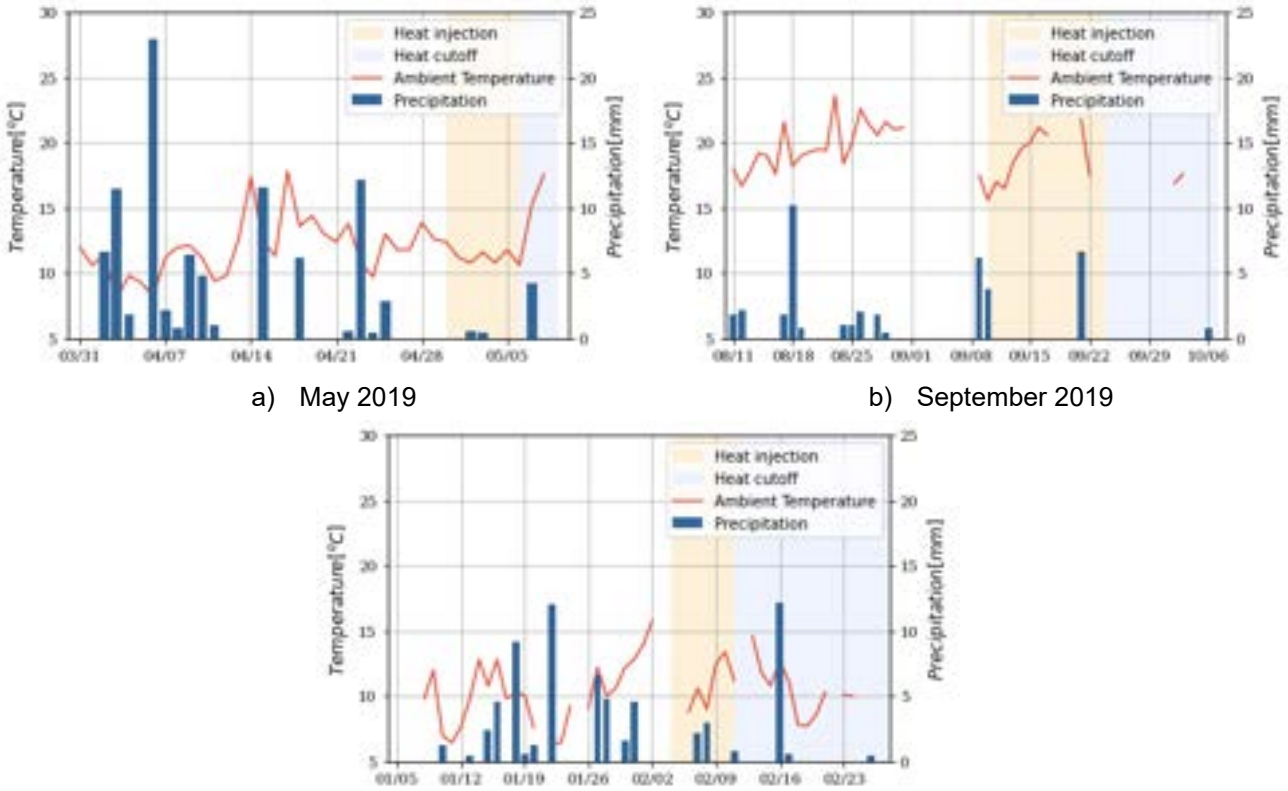

a) May 2019

b) September 2019

c) February 2020

Figure 5. Climate conditions above ground level at the experiment dates

Regarding the measurements from the meteorological station, it may be appreciated that there was a high period of rain before the experiments in May took place, with 91.9 mm, followed by February, with 49.2 mm and September, with 29.2 mm. Nevertheless, during the experiments, May had the driest conditions, 5.2 mm, followed by September, with 11.2 mm and February with 19.2 mm. Average temperatures are almost constant in the case of February, showing an increasing trend in May and a decreasing trend in September. Particularly, during the experiments, average ambient temperatures were 12.4 ºC in May, 18.4 ºC in September, and 10.7 ºC in February.

3. Results

3.1. Influence of depth

Figure 6 shows the evolution of dimensionless temperatures at all measured depths for the three seasons studied. It may be observed that there is an upper zone ($z/L \leq 0.086$), the temperature evolution is slower than in the lower zone ($z/L \leq 0.136$). This effect could be attributed to the fact that the water table where the experiments were performed is at 15 m underground ($z/L \leq 0.107$), so this depth could mark the fringe between both behavior types. A very different behavior may be appreciated for the temperatures at $z/L = 0.493$, which decrease abruptly as soon as heat injection is stopped. This behavior might be representative of a subterranean water stream, that draws heat at a higher rate than underground soil, as a result of the combination of conduction and also convection mechanisms. Comparing the three periods, the size of the gap between the upper and lower zones of the ground seems bigger in the case of May 2019. This could be attributed to the drier ambient conditions during the experiments, as the introduction of rainwater during the experiments in September and February may have helped to increase the slope of the cooling curves in these periods.

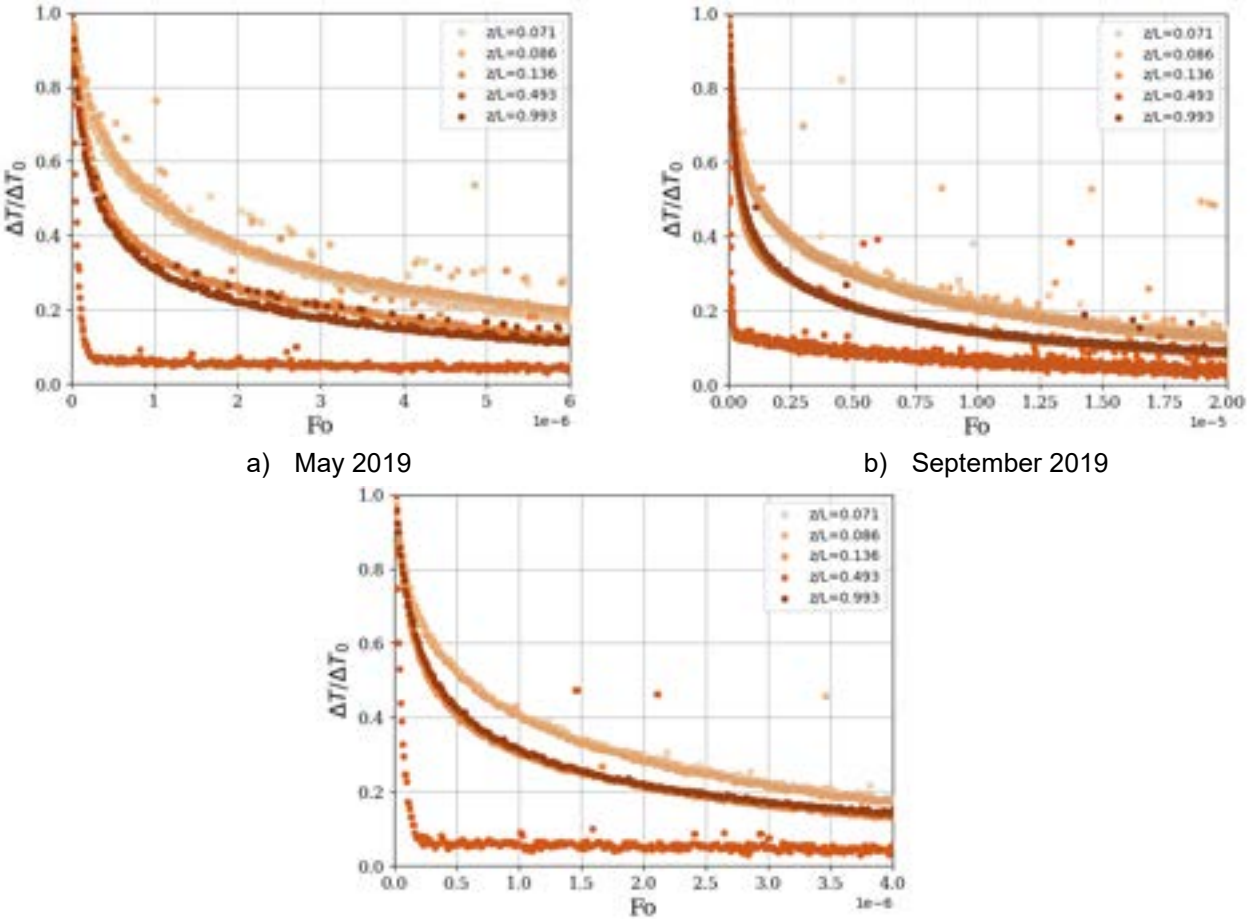

a) May 2019

b) September 2019

c) February 2020

Figure 6. Evolution of dimensionless temperatures in different seasons (same layer diffusivities)

When different apparent thermal diffusivities were allowed for each ground depth, an interesting result was obtained: all curves, apart from the one with the alleged underground stream, collapsed into one in the dimensionless representation, as shown in Figure 7. This might suggest that the heat transfer physical mechanism could be the same for the collapsing curves, considering the different initial conditions and soil thermophysical properties. The results also lead to think that the physical mechanism of heat transfer at the specific depth z/L = 0.493 could be different from the others, so the presence of a subterranean water stream drawing heat by convection seems more feasible. In addition, different behaviors for the whole system arise in different seasons. The values of the apparent thermal diffusivity obtained for each season and depth have been collected in Table 3.

Table 3. Apparent thermal diffusivities as a function of dimensionless depth and season

	May	September	February
z/L	$\alpha \times 10^7$ [m²/s]	$\alpha \times 10^7$ [m²/s]	$\alpha \times 10^7$ [m²/s]
0.071	1.75	1.10	2.69
0.086	1.52	1.10	2.83
0.136	3.54	2.45	4.95
0.493	64.97	25.53	69.15
0.993	5.52	1.74	8.50

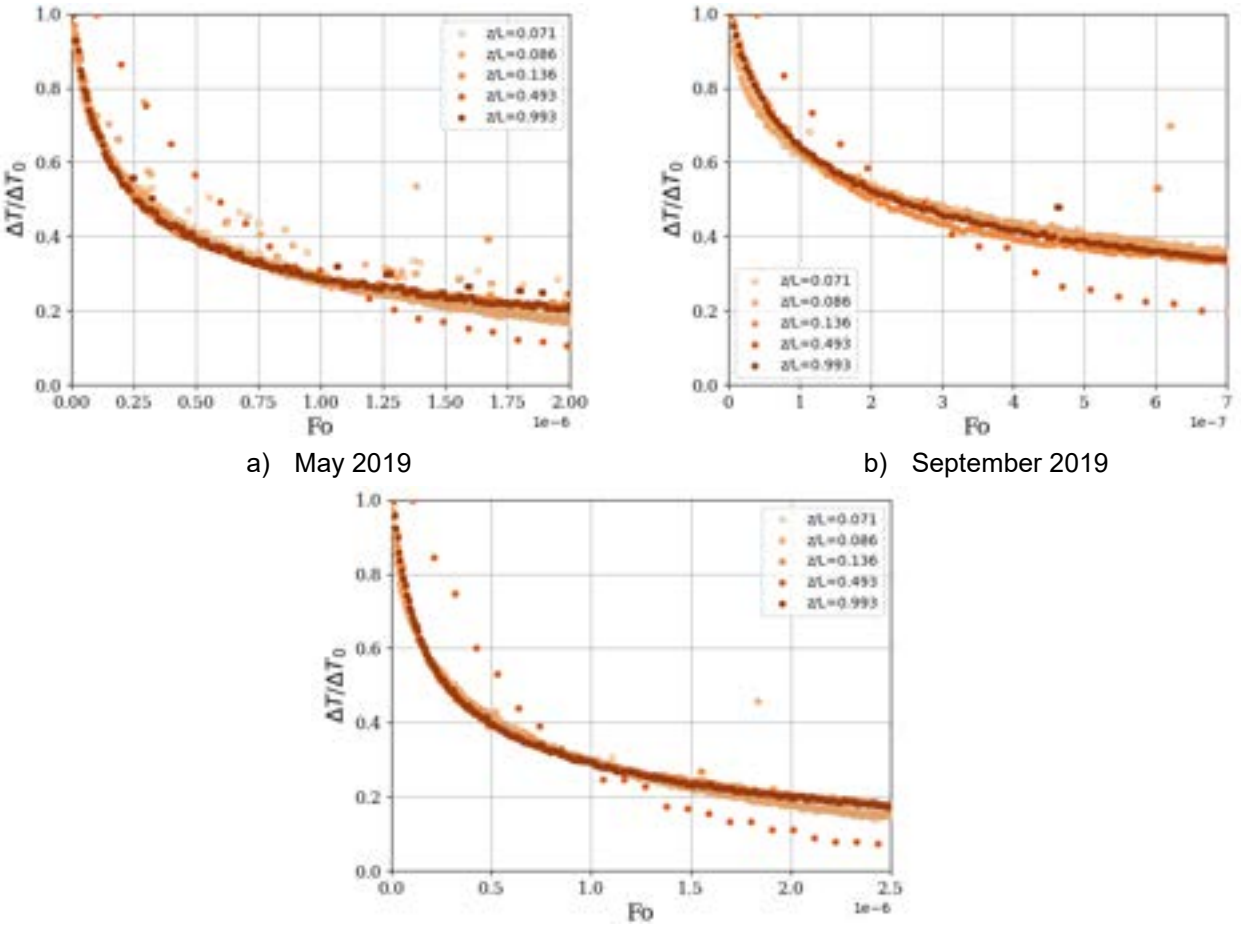

a) May 2019

b) September 2019

c) February 2020

Figure 7. Evolution of dimensionless temperatures in different seasons (different layer diffusivities)

Note that for z/L = 0.493, apparent thermal diffusivity is much higher than for water, air, and typical soil values; this could be a last hint that there might be an underground water stream carrying heat away from the ground by convection, also affecting heat conduction speeds in the nearest ground layers.

3.2. Influence of seasons

Due to the differences observed between different seasons, the results of the temperature evolution at different depths as a function of the season were studied, as shown in Figure 8. February was found to be the season in which temperatures were lower. This difference, which is more apparent in the upper layers of the ground, may be ascribed to the fact that the air in contact with the ground surface is colder in that month, as seen in the meteorological data. In addition, during winter season, the ground temperature profile is near its minimum values. On the other hand, higher target ground temperatures are found in May and September, because of higher ambient temperatures. In May, the ground is getting warmer each day, as spring advances towards the summer, whereas in September, before the summer ends, the ground is still relatively warm. In addition, as seen in the climate data presented in Figure 5, more rain intensity was found in February and May, leading to possibly more drenched ground layers in which water displaces air from the soil pores, resulting in potentially higher thermal diffusivities. From this analysis, it seems that the energy potentially stored at such small depths would be very influenced by ambient conditions and could be easily dissipated, so it would not be recommended to store energy above the water table of the ground, unless adequate isolation systems are provided.

At higher depths, nevertheless, there is almost no difference between the temperature evolution in February and May. It seems reasonable to think that the effect of ambient temperature and the humidity caused by the rain stops having an influence at such depths. The difference between the behavior at such depths in September with respect to the other months may be ascribed to the higher temperatures reached at steady conditions in the ground, but a probably more reasonable explanation could be the less amount of water carried by the underground stream that certainly circulates near z/L = 0.493. The amount of water carried by this stream depends ultimately on the amount of rain, which is definitely lower towards the end of summer (see Figure 5), reducing the capability of the stream to cool the ground by convection.

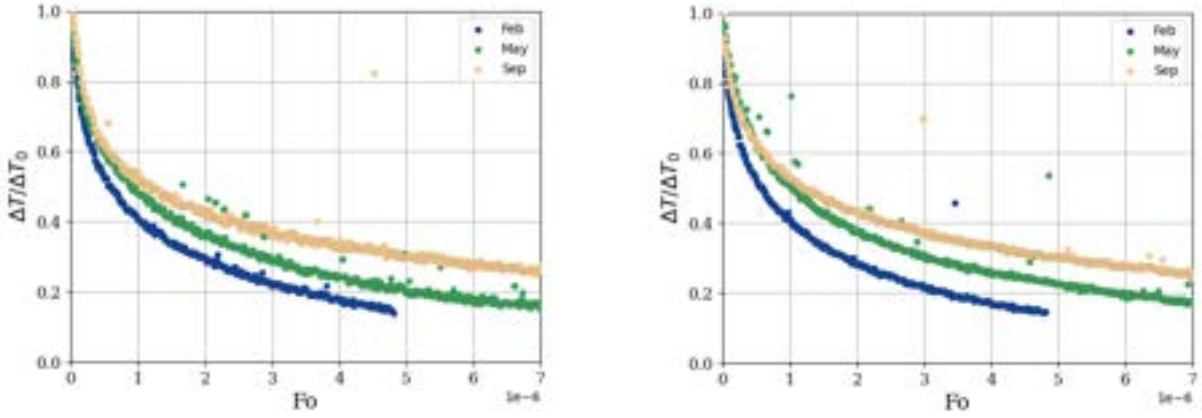

a) $z/L = 0.071$

b) $z/L = 0.086$

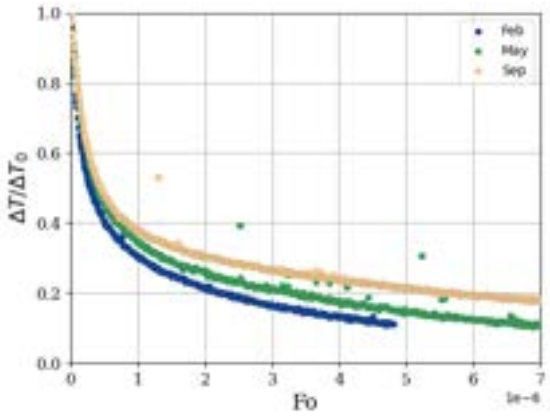

c) $z/L = 0.136$

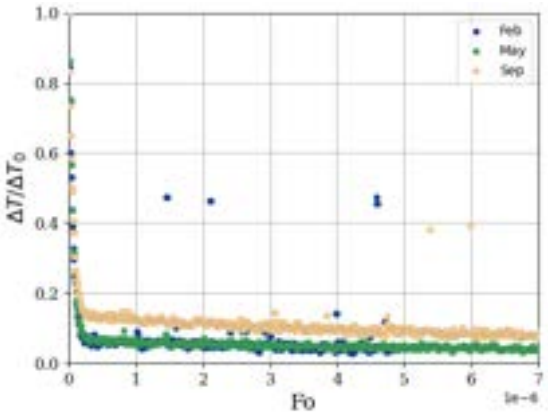

d) $z/L = 0.493$

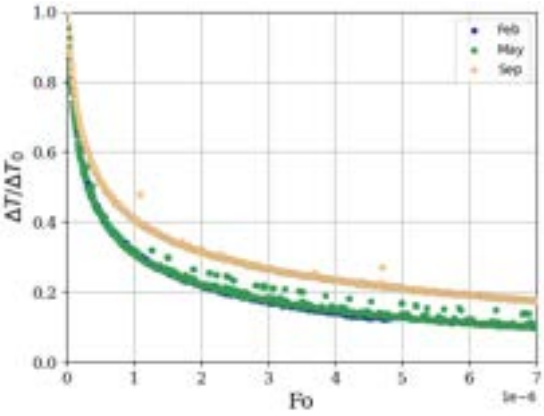

e) $z/L = 0.993$

Figure 8. Evolution of dimensionless temperatures in different seasons at different depths

To summarize, wet soil tends to have a higher apparent thermal diffusivity up to a certain amount of moisture, allowing for faster loading and unloading curves for energy storage. Dry soil, on the other hand, needs more time for storing and releasing heat. This may be appreciated in the heat injection times depicted in Figure 5 for the drier seasons, and the higher Fourier numbers necessary to bring the soil back to its original temperature presented in Figure 6, which were substantially higher in September, when the soil was drier. Depending on the application and the required heating power, wet soil might represent an advantage for storing a higher amount of thermal energy and delivering it at higher speeds, thanks to the higher thermal diffusivity and specific heat. Isolating materials might help to keep the heat stored for longer times if seasonal storage is planned. Nevertheless, if heat delivery speed is not a limiting factor, dry soil should be able to keep heat stored during longer times, preventing its diffusion throughout the ground, without additional works for isolation.

4. Conclusions

A preliminary analysis of the feasibility of using the ground as a temporary energy accumulator has been performed in this work. To this end, experimental tests have been carried out with vertical buried pipes in the

Gijón Solar Cooling Laboratory (GSCL) facility, monitoring the temperature evolution of probes placed at different depths. The methodology proposed in this work may be used to characterize the ground thermal behavior and its feasibility as a temporary energy accumulator. Particularly, the soil composition, soil moisture and the presence of underwater currents have been found as variables of interest influencing the possible design and operation of storage systems.

Experimental measurements were represented against the dimensionless depth and the Fourier number, finding that depth has a significant influence in the evolution of temperatures, with differences between the behavior at the upper and lower layers of the ground, probably as a consequence of the water table depth.

In the upper zone, temperature evolutions were relatively slower than in the lower zones. A very different behavior was observed at z/L = 0.493, where heat was dissipated at a much higher speed, hinting at a different physical heat transfer mechanism, such as a subterranean water stream dissipating heat by convection. The numerical results presented in this work must be interpreted in a qualitative way, allowing the comparison between different measurements, but they must not be considered as an exact characterization of the thermophysical properties of the soil.

Different behaviors for the whole system were found depending on the season. An explanation may be provided by the different thermal conductivity values of water and air, which fill ground pores. A relationship between the meteorological historical data for temperature and precipitation and the behavior of the upper layers of the ground might be inferred with colder air leading to colder target values for the temperature and higher rain levels related to higher soil thermal conductivity and diffusivity values. Ambient conditions seemed to influence the system behavior at low depths, discouraging their use as a heat reservoir. However, at higher depths, ambient conditions did not show such a high influence, with practically the same behavior in February and May. There were, indeed, differences with September, but they are likely more related to the effects of a lower water mass flow at higher temperatures in the subterranean stream than the seasonal change in the soil conditions. Hence, heat storage at higher depths may be more reliable. Regarding soil moisture, wet soil might represent an advantage for storing a higher amount of thermal energy and delivering it at higher speeds, thanks to the higher thermal diffusivity and specific heat. Nevertheless, if heat delivery speed is not a limiting factor, dry soil should be able to keep heat stored during longer times. Finally, considering the impracticability of a total characterization of the soil characteristics, including pore geometry, along all the ground to be used as storage, heat loading and cutoff curves as the ones presented in this work may prove useful to assess the feasibility of using the ground as a temporary energy accumulator.

Future works will focus on the development and application of accurate models for heat transfer in buried U-vertical pipes to improve the characterization of the thermophysical properties of the ground, the study of the heat injection stage, and the development of more experimental tests at other ambient conditions to try to obtain more generalizable results.

Acknowledgments

This research was funded by the National Research and Development Plan 2004–2007 (Ref. PS-120000-2005-1), co-financed by ERDF funds and supported by the Spanish Ministry of Science and Innovation. This research has also been developed in the framework of the REHABILITAGEOSOL (RTC-2016-5004-3) project. It is a multidisciplinary R&D program supported by the Spanish Ministry of Science and Innovation and co-financed by European Regional Development Funds (ERDF). The authors would like to thank the AEMET OpenData system from the Spanish State Agency for Meteorology (AEMET), for making available the meteorological data used in this work.

Appendix A

The classical method of dimensional analysis does not take into account the algebraic characteristics of the influencing variables in a physical problem. The first references to the idea of considering differences between spatial dimensions are attributed to Williams [22] and Huntley [23]. Later, Palacios [24] deals rigorously with this topic and lays the foundations of discriminated dimensional analysis (DDA). There are recent examples of the use of the DDA method for various applications [25,26]. Spatial discrimination increases the order of the dimensional basis so that, in general, spurious dimensionless groups that might occasionally be deduced from the classical method are eliminated.

Using the DDA method, only the scalar variables in equation (1) have equal dimensional exponents in each of the three spatial directions. The dimensional formula for the thermal conductivity is derived from Fourier's Law and the definition of the heat flux Q:

$$\vec{q} = -\bar{\bar{k}} \otimes \nabla T \quad \text{(A.1)}$$

$$Q = \int \vec{q} \cdot \overrightarrow{\mathrm{d}S} \quad \text{(A.2)}$$

Using cylindrical coordinates and the dimensional basis $\{L_r, L_\varphi, L_z, M, T, \theta\}$ (Figure A1), the following equations can be written:

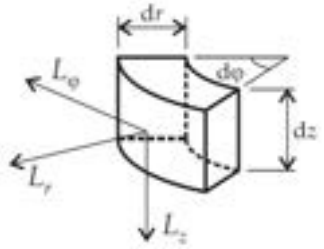

Figure A1. Spatial discrimination for Dimensional Analysis.

$$\vec{q} = \begin{bmatrix} k_{rr} & k_{r\varphi} & k_{rz} \\ k_{\varphi r} & k_{\varphi\varphi} & k_{\varphi z} \\ k_{zr} & k_{z\varphi} & k_{zz} \end{bmatrix} \begin{bmatrix} \partial T/\partial r \\ \partial T/(r\partial\varphi) \\ \partial T/\partial z \end{bmatrix} \quad \text{(A.3)}$$

$$\dot{q}_r = k_{rr}\,\partial T/\partial r + k_{rz}\,\partial T/\partial z \quad \text{(A.4)}$$

$$\dot{q}_z = k_{zr}\,\partial T/\partial r + k_{zz}\,\partial T/\partial z \quad \text{(A.5)}$$

where it has been assumed that the temperature has cylindrical symmetry, i.e.: $T = T(r,z) \leftrightarrow \partial T/\partial\varphi = 0$

Therefore, the following dimensional formulae for the components of the thermal conductivity tensor are derived:

$$[k_{rr}] = \frac{[\dot{q}_r]}{[\partial T/\partial r]} = \frac{\left(L_r^{2/3}L_\varphi^{2/3}L_z^{2/3}MT^{-2}\right)/(TL_\varphi L_z)}{L_r^{-1}\theta} = L_r^{5/3}L_\varphi^{-1/3}L_z^{-1/3}MT^{-3}\theta^{-1} \quad \text{(A.6)}$$

$$[k_{rz}] = \frac{[\dot{q}_r]}{[\partial T/\partial z]} = \frac{\left(L_r^{2/3}L_\varphi^{2/3}L_z^{2/3}MT^{-2}\right)/(TL_\varphi L_z)}{L_z^{-1}\theta} = L_r^{2/3}L_\varphi^{-1/3}L_z^{2/3}MT^{-3}\theta^{-1} \quad \text{(A.7)}$$

$$[k_{zr}] = \frac{[\dot{q}_z]}{[\partial T/\partial r]} = \frac{\left(L_r^{2/3}L_\varphi^{2/3}L_z^{2/3}MT^{-2}\right)/(TL_r L_\varphi)}{L_r^{-1}\theta} = L_r^{2/3}L_\varphi^{-1/3}L_z^{2/3}MT^{-3}\theta^{-1} = [k_{rz}] \quad \text{(A.8)}$$

$$[k_{zz}] = \frac{[\dot{q}_z]}{[\partial T/\partial z]} = \frac{\left(L_r^{2/3}L_\varphi^{2/3}L_z^{2/3}MT^{-2}\right)/(TL_r L_\varphi)}{L_z^{-1}\theta} = L_r^{-1/3}L_\varphi^{-1/3}L_z^{5/3}MT^{-3}\theta^{-1} \quad \text{(A.9)}$$

As a result, the following matrix of dimensional exponents is obtained:

	r	D	z	L	ρ	c	k_{rr}	k_{rz}	k_{zz}	ΔT_0	t	ΔT
L_r	1	1	0	0	-1	2/3	5/3	2/3	-1/3	0	0	0
L_φ	0	0	0	0	-1	2/3	-1/3	-1/3	-1/3	0	0	0
L_z	0	0	1	1	-1	2/3	-1/3	2/3	5/3	0	0	0
M	0	0	0	0	1	0	1	1	1	0	0	0
T	0	0	0	0	0	-2	-3	-3	-3	0	1	0
θ	0	0	0	0	0	-1	-1	-1	-1	1	0	1

As the rank of this matrix is 6, and taking D, L, ρ, c and ΔT_0 as reference variables, the following 6 dimensionless numbers are obtained:

$$\Pi_\theta = \frac{\Delta T}{\Delta T_0}; \qquad \Pi_r = \frac{r}{D}\ ; \qquad \Pi_z = \frac{z}{L}$$

$$\Pi_{k_{rr}} = \frac{k_{rr}t}{\rho c D^2} = \frac{\alpha_{rr}t}{D^2}; \qquad \Pi_{k_{rz}} = \frac{k_{rz}t}{\rho c L D} = \frac{\alpha_{rz}t}{LD}; \qquad \Pi_{k_{zz}} = \frac{k_{zz}t}{\rho c L^2} = \frac{\alpha_{zz}t}{L^2}$$

Thus, the following relationship can be written:

$$\frac{\Delta T}{\Delta T_0} = F\left(\frac{r}{D}, \frac{z}{L}, \frac{\alpha_{rr}t}{D^2}, \frac{\alpha_{rz}t}{LD}, \frac{\alpha_{zz}t}{L^2}\right) \quad \text{(A.10)}$$

Assuming isotropy, $\bar{\bar{\alpha}} = \alpha\bar{\bar{I}}$ would be satisfied, i.e. $\alpha_{ij} = \alpha(r,z)\cdot\delta_{ij}$, being δ_{ij} the components of Kronecker delta tensor, and the following numerical, but not dimensional, equalities are verified:

$$\alpha_{rr} = \alpha_{zz} = \alpha(r,z) \quad \text{(A.11)}$$

$$\alpha_{rz} = 0 \quad \text{(A.12)}$$

Then:

$$[\delta_{rr}] = \frac{[\alpha_{rr}]}{[\alpha]} = \frac{L_r^2 T^{-1}}{L_r^{2/3} L_\varphi^{2/3} L_z^{2/3} T^{-1}} = L_r^{4/3} L_\varphi^{-2/3} L_z^{-2/3} \quad \text{(A.13)}$$

$$[\delta_{zz}] = \frac{[\alpha_{zz}]}{[\alpha]} = \frac{L_z^2 T^{-1}}{L_r^{2/3} L_\varphi^{2/3} L_z^{2/3} T^{-1}} = L_r^{-2/3} L_\varphi^{-2/3} L_z^{4/3} \quad \text{(A.14)}$$

$$\Pi_{k_{rr}} = \frac{\alpha t}{D^2} \cdot \delta_{rr} = \frac{\alpha t}{L^2} \left(\frac{L}{D}\right)^2 \cdot \delta_{rr}; \qquad \Pi_{k_{rz}} = 0; \qquad \Pi_{k_{zz}} = \frac{\alpha t}{L^2} \cdot \delta_{zz}$$

$$\frac{\Delta T}{\Delta T_0} = F\left(\frac{r}{D}, \frac{z}{L}, \frac{\alpha t}{L^2}\left(\frac{L}{D}\right)^2 \cdot \delta_{rr}, \frac{\alpha t}{L^2} \cdot \delta_{zz}\right) \quad \text{(A.15)}$$

which can be rewritten as:

$$\frac{\Delta T}{\Delta T_0} = F\left(\frac{r}{D}, \frac{z}{L}, \frac{\delta_{rr}}{\delta_{zz}}\left(\frac{L}{D}\right)^2, \frac{\alpha t}{L^2} \cdot \delta_{zz}\right) \quad \text{(A.16)}$$

Experimental results can therefore be expressed in terms of $\alpha t/L^2$ and geometrical parameter ratios.

Nomenclature

COP Coefficient of performance

c specific heat capacity, J/(kg·K)

d distance from tube center to probes, m

D tube diameter, m

Fo Fourier number

k thermal conductivity, W/(m·K)

$\{L\}$ dimension of length

L tube length, m

$\{M\}$ dimension of mass

$\{T\}$ dimension of time

T temperature, ºC

T_0 initial probe temperature, ºC

T_∞ steady ground temperature, ºC

r radial distance to tube center, m

t time, s

z depth, m

Greek symbols

α thermal diffusivity, m²/s

α_a apparent thermal diffusivity, m²/s

α_r relative thermal diffusivity, m²/s

α_w water thermal diffusivity, m²/s

δ_{ij} component of Kronecker's delta tensor

ρ density, kg/m³

Π_x dimensional group associated to property x

$\{\theta\}$ dimension of temperature

Subscripts and superscripts

r radial coordinate

φ angular coordinate

z depth coordinate

References

[1] Alva, G., Lin, Y., Fang, G. An overview of thermal energy storage systems. Energy 2018; 144:341-378. DOI: 10.1016/j.energy.2017.12.037.

[2] Alkhalidi,A., Al Khatba, H., Khawaja, M.K. Utilization of Buildings' Foundations for a Seasonal Thermal Energy Storage Medium to Meet Space and Water Heat Demands. International Journal of Photoenergy 2021; 2021:6668079. DOI: 10.1155/2021/6668079.

[3] Barbier, E. Geothermal energy technology and current status: an overview. Renewable and Sustainable Energy Reviews, 6 (1-2), 3-65, 2002. doi.org/10.1016/S1364-0321(02)00002-3.

[4] Reed, A.L., Novelli, A.P., Doran, K.L., Ge, S., Lu, N., McCartney, J.S. Solar district heating with underground thermal energy storage: Pathways to commercial viability in North America. Renewable Energy 2018; 126:1-13. DOI: 10.1016/j.renene.2018.03.019.

[5] Mangold, D., Miedaner,O., Tziggili, E.P., Schmidt, T., Unterberger, M., Zeh,B. Technisch-wirtschaftliche Analyse und Weiterentwicklung der solaren Langzeit-Wärmespeicherung. Schlussbericht zum BMU-Forschungsvorhaben N, 329607, 2012.

[6] Beausoleil-Morrison, I., Kemery, B., Wills, A.D., Meister, C. Design and simulated performance of a solar-thermal system employing seasonal storage for providing the majority of space heating and domestic hot water heating needs to a single-family house in a cold climate. Solar Energy 2019; 191: 57-69. DOI: 10.1016/j.solener.2019.08.034.

[7] Lim, H.S., Ok, J.S., Park, J.S., Lee, S.J., Karng, S.W., Kang, Y.T. Efficiency improvement of energy storage and release by the inlet position control for seasonal thermal energy storage. International Journal of Heat and Mass Transfer 2020; 151:119435. DOI: 10.1016/j.ijheatmasstransfer.2020.119435.

[8] Cruickshank, C.A., Baldwin, C. Sensible thermal energy storage: diurnal and seasonal. In Letcher, T.M.; Ed. Storing Energy. Elsevier; 2016; 291-311. DOI: 10.1016/B978-0-12-803440-8.00015-4.

[9] Arquitectura Bioclimática y Frío Solar (ARFRISOL), Proyecto Singular Estratégico Ref. PS-120000-2005-1. Plan Nacional de Investigación y Desarrollo 2004-2007. Ministerio de Innovación y Ciencia.

[10] Suárez, M.J. Prieto, J.I. Blanco, E. García, D. Tests of an Absorption Cooling Machine at the Gijón Solar Cooling Laboratory. Energies, 13, 3962, 2020. doi:10.3390/en13153962.

[11] Eficiencia energética a través de la Rehabilitación, el Sol y la Geotermia en Asturias. (REHABILITAGEOSOL), RTC-2016-5004-3. Ministerio de Economía, Industria y Competitividad.

[12] Pratt, William K. Digital Image Processing. 4th Ed. Hoboken, NJ, USA: John Wiley & Sons; 2007

[13] Çengel, Y.A.; Ghajar, A.J. Heat and Mass Transfer – Fundamentals & Applications. 5th Ed. New York, USA: McGraw-Hill; 2015.

[14] Ándujar Márquez, J.M., Martínez Bohórquez, M.A., Gómez Melgar, S., Ground Thermal Diffusivity Calculation by Direct Soil Temperature Measurement. Application to very Low Enthalpy Geothermal Energy Systems. Sensors 2016; 16:306. DOI:10.3390/s16030306.

[15] Arkhangelskaya, T., Lukyashchenko, K., Estimating soil thermal diffusivity at different water contents from easily available data on soil texture, bulk density, and organic carbon content. Biosystems Engineering 2018; 168:83-95. DOI: 10.1016/j.biosystemseng.2017.06.011.

[16] Tong, B., Xu, H., Horton, R., Bian, L., Guo, J., Determination of Long-Term Soil Apparent Thermal Diffusivity Using Near-Surface Soil Temperature on the Tibetan Plateau. Remote Sensing 2022; 14:4238. DOI:10.3390/rs14174238

[17] Farouki, O.T. Thermal properties of soils. Hanover, NH, USA: Cold Regions Research and Engineering Lab; 1982.

[18] Dimo, V.N. Physical properties and elements of the heat regime of permafrost meadow-forest soils. Delhi: Indian National Scientific Documentation Centre, Cold Regions Research and Engineering Lab; 1969.

[19] Luikov, A.V. Heat and Mass Transfer in Capillary porous Bodies. New York, USA: Pergamon Press; 1966.

[20] De Vries, D.A. Heat transfer in soils. In De Vries, D.A. Afghan, N.A; Eds. Heat and Mass Transfer In the Biosphere. 1. Transfer Processes in Plant Environment. New York, USA: John Wiley & Sons, Inc., Halsted Press; 1974.

[21] Agencial Estatal de Meteorología de España. Datos abiertos. Available at:<https://www.aemet.es/es/datos_abiertos> [accessed 21/02/2023]

[22] Williams W. On the relation of the dimensions of physical quantities to directions in space. Phil. Mag. 1892;34:234−271. https://doi.org/10.1080/14786449208620315

[23] Huntley HE. Dimensional Analysis. London, UK: McDonald;1952.

[24] Palacios J. Dimensional Analysis. London, UK: McMillan;1964.

[25] Prieto JI, Fano J, Diaz R, Gonzalez MA. Application of discriminated dimensional analysis to the kinematic Stirling engine. Proc. Inst. Mech. Eng. C J. Mech. Eng. Sci. 1994; 208:347–353. https://doi.org/10.1243/PIME_PROC_1994_208_137_02

[26] Madrid CN, Alhama F. Discriminated dimensional analysis of the energy equation: Application to laminar forced convection along a flat plate. International Journal of Thermal Sciences 2005; 44:333–341. https://doi.org/10.1016/j.ijthermalsci.2004.11.008

Modelling and performance analysis of a Low Temperature A-CAES system coupled with renewable energy power plants

Francesca Carolina Marcello[a], Davide Micheletto[b], Daniele Cocco[b] and Vittorio Tola[b]

[a] Dept. of Mechanical, Chemical and Materials Engineering, University of Cagliari, Cagliari, Italy, francescac.marcello@unica.it
[b] Dept. of Mechanical, Chemical and Materials Engineering, University of Cagliari, Cagliari, Italy

Abstract:
The ever-increasing electricity production from non-programmable Renewable Energy Sources (RES) requires flexible and sustainable solutions for energy storage. In this paper, the design, and the performance of a Low Temperature Adiabatic Compressed Air Energy Storage (LTA-CAES) system are presented. The design of this system is optimised to better utilise the energy produced by either a photovoltaic (PV) power plant and an onshore wind farm in order to meet the energy demand of a small town of about 10,000 inhabitants, considered as the case study. To ensure efficient operation of the turbomachines, the mass flow rate during both the charge and discharge phases was fixed, allowing most of the compressors and turbines to operate at design conditions. Two packed-bed Thermal Energy Storage (TES) systems are used to store the thermal energy produced during the compression phase: the first exchanges heat directly with the compressed air, while the second uses Therminol-66 as a heat transfer fluid. A mathematical model of the LTA-CAES system was developed using MATLAB/Simulink to simulate its performance, considering the off-design behaviour of the turbomachines and the TES systems over a year. The results demonstrate that the LTA-CAES system increases the share of the yearly energy demand covered by renewable energy, from 41.8% to 60.7% when coupled with the PV plant, and from 48.0% to 56.5% when coupled with the wind farm.
Keywords:
Adiabatic Compressed Air Energy Storage (A-CAES); LTA-CAES; Energy Storage; Renewable Energy Sources; Thermal Energy Storage.

1. Introduction

The intermittent nature of Renewable Energy Sources (RES) results in significant fluctuations in energy production, often not aligned with the power demand of the end-users. Balancing the production and consumption of electrical energy is a highly debated issue, especially as RES penetration in the grid increases. To address this issue, various energy storage systems were developed, including chemical, electrochemical, mechanical, electrical and thermal storage systems [1]. Among the energy storage technologies characterised by medium-high storage capacities, Compressed Air Energy Storage (CAES) systems are one of the most promising options, with a lower cost per kWh than batteries [2], and comparable to pumping hydro systems. The system works by using a compressor to convert electrical energy into compressed air, which is stored in a reservoir. Later on, the process can be reversed by expanding the high pressure air through a turbine, generating electricity. However, one of the biggest challenges in the widespread adoption of CAES technology is the need for suitable reservoirs to store high-pressure air. For this reason, CAES plants are a promising option in regions with geological formations or disused mines. In particular, the island of Sardinia presents an ample availability of primary energy sources like solar and wind and numerous disused mines, potentially suitable for the storage of compressed air. Therefore, CAES plants are a very interesting option to repurpose a disused mine by storing the surplus energy generated by an RES plant and enhance the energy self-consumption of an end-user, such as small communities in the same area.

CAES configurations can be classified as Diabatic CAES (D-CAES), which is the first to be developed, Adiabatic CAES (A-CAES), and Isothermal CAES (I-CAES) [3]. In D-CAES systems, electrical energy is utilised by the compression train to compress the air, which is stored in a suitable reservoir. The compressed air is subsequently heated by using fossil fuels in a combustion chamber and expanded in the turbine train, generating electricity. In the I-CAES configuration, both the compression and expansion processes occur at approximately constant temperature, allowing an increase in the efficiency of the cycle. In the A-CAES configuration, a Thermal Energy Storage (TES) unit is utilised to store the thermal energy recovered by cooling the compressed air; the stored thermal energy is subsequently used to heat the air before expansion, thus

eliminating the need for the combustion section. As a result, an A-CAES plant is characterised by very low emissions, and it is well suited to be coupled with an RES power plant. Adiabatic CAES plants can operate at different TES temperatures and, in general, they can be divided into high-temperature (HTA-CAES) and low-temperature (LTA-CAES) systems. As described by Wolf and Budt [4], the round-trip efficiency tends to increase with the maximum temperature, but high-temperature systems are limited by the availability of suitable components. In fact, HTA-CAES systems operate at high temperature (around 600 °C) and high pressure (around 70 bar), leading to significant thermal and mechanical stress on the TES equipment, while LTA-CAES systems operate at lower temperatures (100 – 200 °C) and at atmospheric pressure. Due to limitations of the current centrifugal compressor technology, temperatures in the order of 600 °C cannot be achieved. As a result, the use of heat exchangers is necessary to maintain lower temperatures.

In the field of A-CAES systems, Grazzini and Milazzo [5] proposed one of the first models, characterised by a variable configuration system allowing for compressors and turbines to be arranged in different series and parallel configurations, to achieve the desired air pressure and charge time. A significant benefit of the system was the ability to use commercially available components. Hartmann et al. [6] investigated various configurations for A-CAES plants and concluded that the highest round-trip efficiencies are achieved with a two-stage compressor train and by reaching high temperatures in the thermal energy storage system, upwards of 600 °C. Wolf and Budt [4] designed an LTA-CAES system utilising multistage radial compressors and expanders with intermediate cooling, and storage temperatures ranging from 95 °C to 200 °C with a non-thermocline two-tank system. The system was estimated to reach a round-trip efficiency of 52 – 60%, with a start-up time of less than 5 minutes. Wang et al. [7] presented the results of the first experimental setup for an LTA-CAES, featuring a 5-stage compressor train and a 3-stage expansion train. Heat exchangers were utilised to transfer heat between air and water. The thermal energy generated during the charge phase was stored in two water tanks, while the air compressed at 9.34 MPa was stored in two steel tanks. The round-trip efficiency of the system was reported to be 22.6%. Budt et al. [3] devised a techno-economical model that utilises reversible turbo and piston machinery to reduce the capital cost of the LTA-CAES plant, resulting in enhanced competitiveness. They proposed a modular design, with a 2 MW_{el} compressor power input for each module. These modules can be coupled with any compressed air storage volume, whether natural (such as a cave) or artificial (such as tanks or pipes). In their study, Zhang et al. [8] examined an A-CAES system that employs a variable configuration in order to accommodate fluctuations in the production profile of a wind farm in China. The system consists of a 4-stage centrifugal compressor, a 4-stage radial expander and two pressure reservoirs (a low-pressure and a high-pressure one). The variable configuration enables the compressors and the expanders to operate under various modes, thus extending the operational range of the A-CAES. The authors reported that this system increases the wind power capacity factor from 26.29% to 71.02%. Arabkoohsar et al. [9] investigated the impact of part-load operation on the overall performance of an LTA-CAES, utilising real performance maps of all system components. For optimal efficiency, the energy storage system must operate close to design conditions. At nominal conditions, the round-trip efficiency can reach up to 68% at full load, while at 50% and 10% loads, the efficiency decreases to 52% and 28%, respectively.

The LTA-CAES configuration proposed in this work was developed with the aim of maximising the electrical energy utilisation between an RES power plant and a small town located in the south-west of Sardinia, a region with many decommissioned mining tunnels. The LTA-CAES was developed with the aim of utilising components already available on the market. To maximise the round-trip efficiency, the plant operation was studied by operating the turbomachines at mostly constant design conditions during both the charging and discharge phases. Moreover, differently from most LTA-CAES configurations, that typically incorporate a heat exchanger after each compressor to recover the thermal energy from the compressed air using a heat transfer fluid [10], this study proposes the use of two different TES units. In the first TES, the air stream directly exchanges heat with the storage material, thus eliminating the need for two heat exchangers, resulting in a more efficient heat transfer process. The second TES uses a thermal oil as a heat transfer fluid and therefore operates at low pressure. To study the operation of the LTA-CAES system integrated with RES power generation plants, a mathematical model was developed to simulate the performance of the system over an entire year. The model takes into account the off-design performance of the turbomachines, the TES units, and the heat exchangers. In this paper, the plant configuration, the mathematical models, the energy management strategy and the optimization method are described in detail. Moreover, the performance of the of the plant is then presented and discussed with reference to a case study.

2. Materials and methods

In this chapter, the configuration of the plant and the mathematical modelling of its components are presented. Moreover, the power demand and production profiles for the end-user and the RES power plants are discussed, with a description of the energy management strategy and of the optimization problem.

2.1. System description

The configuration of the LTA-CAES plant is presented in Fig 1. The power required by the end-user can be supplied either by the RES power plant, by the grid, or by the LTA-CAES plant itself. The plant operates in a

cyclical manner, with the excess energy produced by the RES plant used to compress the air, which is later used by the turbine when the end-user demand exceeds the RES production. When the LTA-CAES output power is higher than the end-user demand, part of the electrical energy is sent to the grid. The plant includes three main sections: the compression section, the expansion section, and the energy storage section. In the compression section, the air is compressed using four centrifugal compressors. The multistage low-pressure compressor (LPC) and the two multistage medium-pressure compressors (MPC1 and MPC2) are driven by the motor M1, while the single-stage centrifugal high-pressure compressor (HPC) is driven by the motor M2. Two intercoolers, IC1 and IC2, are located at the outlet side of MPC1 and MPC2 respectively, to cool the air by using thermal oil (Therminol-66) [13]. The energy storage section includes the TES system and the underground Compressed Air Storage (CAS) cavern. The TES system is based on two different thermocline packed-bed units, which are utilised to store the thermal energy recovered by cooling the compressed air. The TES1 unit exchanges heat directly with the air stream while the TES2 utilises the thermal oil as heat-transfer fluid (HTF). The heat transfer oil is stored at low temperature (25 °C) in a dedicated tank, and operates in a closed loop system, flowing through the heat exchangers on the compression and expansion sides during the charge and discharge phases, respectively. Both TES units are filled with gravel, selected for its low cost and widespread availability. At the outlet of the compression train, the high-pressure air is stored in an underground cavern obtained from a decommissioned coal mining tunnel. The expansion section of the plant includes three turbines. The high-pressure turbine (HPT), the medium-pressure turbine (MPT), and the low-pressure turbine (LPT) are connected to the generator G1. To maintain a constant mass flow rate during the discharge phase, the turbine inlet pressure is regulated using three valves, V1, V2, and V3. Two heat exchangers, HX1 and HX2, are utilised to heat the air before expansion. The aftercoolers AC1, AC2, AC3, AC4, and AC5 are used to regulate the temperature in some key sections of the plant and to ensure proper operation of the downstream components.

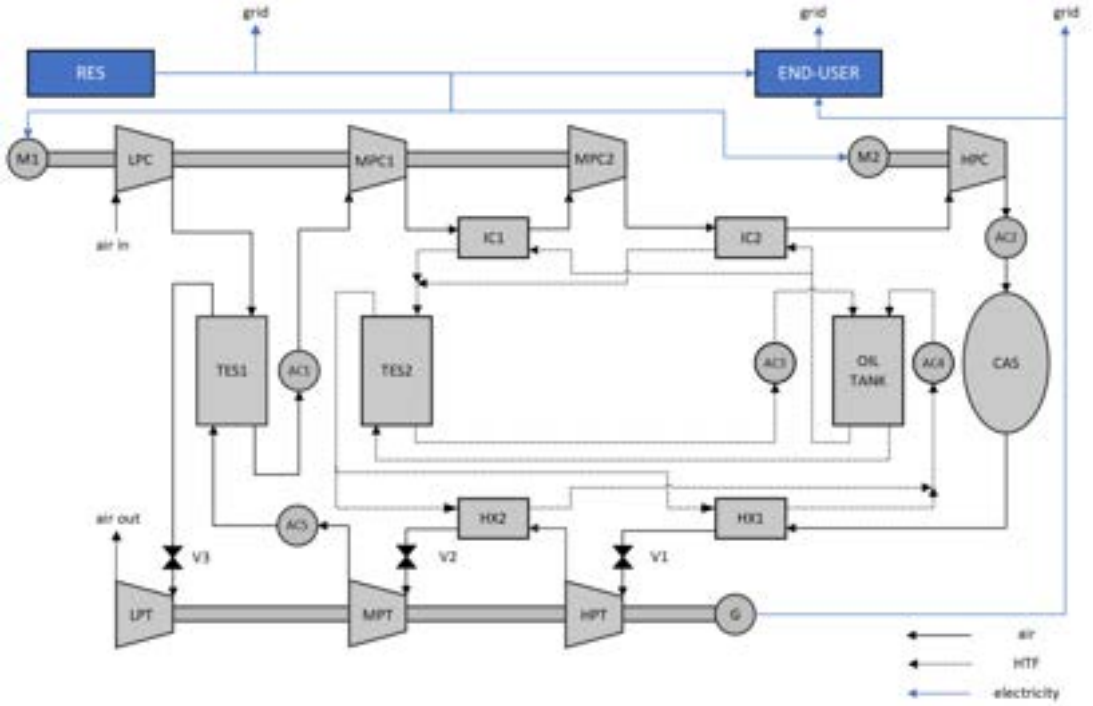

Figure. 1. Functional scheme of the LTA-CAES plant.

During the charge phase, the pressure inside the storage cavern increases, with a corresponding increase of the pressure ratio of the compression train, leading to off-design operating conditions. To mitigate this effect, the plant was designed to keep the air mass flow rate constant during the charge phase. Moreover, the LPC, MPC1, and MPC2 operate with a constant pressure ratio while the HPC regulates the pressure in the cavern by varying its rotational speed. For this reason, LPC, MPC1, and MPC2 are driven by the fixed-speed motor M1, while the HPC is driven by the motor M2 which can vary its rotational speed. The maximum pressure in the cavern is set to 100 bar, while the minimum pressure, which is strictly related to the minimum pressure ratio of the HPC, is set to 70 bar. During the discharge phase, the pressure at the inlet side of each turbine is regulated by a throttling valve.

2.2. Mathematical model

In the present section, the mathematical model used to simulate the LTA-CAES plant is presented. The mathematical models were developed on Matlab/SIMULINK by solving the mass and energy balances of all plant components and of the overall system for each time step (15 minutes, in this case) of the year.

2.2.1. Compressor model

The Casey and Robinson method [11] was utilised to estimate the design and off-design performance of the compressors. For each compressor, the number of stages is determined by equally dividing the enthalpy difference between the stages. With the Casey and Robinson method, the pressure ratio, the tip Mach number, the polytropic efficiency, and the non-dimensional factors were calculated for each stage of the compressor. The power required by each compressor, is calculated as:

$$P_c = \dot{m}_{air,ch} \frac{\gamma}{\gamma - 1} R_{air} T_{c,in} \left(\beta_c^{\frac{\gamma-1}{\gamma \eta_c}} - 1 \right) \quad (1)$$

Where $\dot{m}_{air,ch}$ is the mass flow rate of the compressor during the charge phase, γ is the specific heat ratio, R_{air} is the gas coefficient of air, $T_{c,in}$ is the temperature at the inlet side of the compressor, β_c is the pressure ratio of the compressor, and η_c is the polytropic efficiency of the compressor.

All compressors were designed imposing a maximum outlet temperature of 200 °C. The main performance parameters of the compressors are listed in Table 1.

Table 1. Main performance parameters of the compressors.

	LPC	MPC1	MPC2	HPC (design)
Pressure ratio	4.38	3.55	3.43	1.72
Number of stages	3	3	3	1
Inlet pressure [bar]	1.00	4.38	35.00	53.33
Outlet pressure [bar]	4.38	35.00	53.33	91.73
Inlet temperature [°C]	15	35	35	35
Outlet temperature [°C]	199.64	199.23	199.78	110.26
Polytropic efficiency	0.85	0.86	0.86	0.81

For the LPC, the inlet temperature is equal to the atmospheric temperature, set to 15 °C. For the other compressors, the two intercoolers are utilised to reduce the compressor inlet temperature to 35 °C. The HPC maps are shown in Fig 2, in terms of pressure ratio (a) and polytropic efficiency (b) as a function of the mass flow rate and the rotational speed. The blue circle indicates the design point, while the operational range of the compressor is highlighted by the double headed arrow. During the charge phase, the pressure ratio is controlled by varying the rotational speed. As shown by Fig 2, for a fixed mass flow rate, the compressor work point moves by changing the rotational speed between 70% and 110% of the design speed. The maps are generalized with the reference values, i.e., the design values. In Fig 2(b), can be observed that, at very low rotational speeds, the efficiency decreases rapidly. As a low-pressure ratio drastically reduces the efficiency, the minimum storage pressure was set to 70 bar.

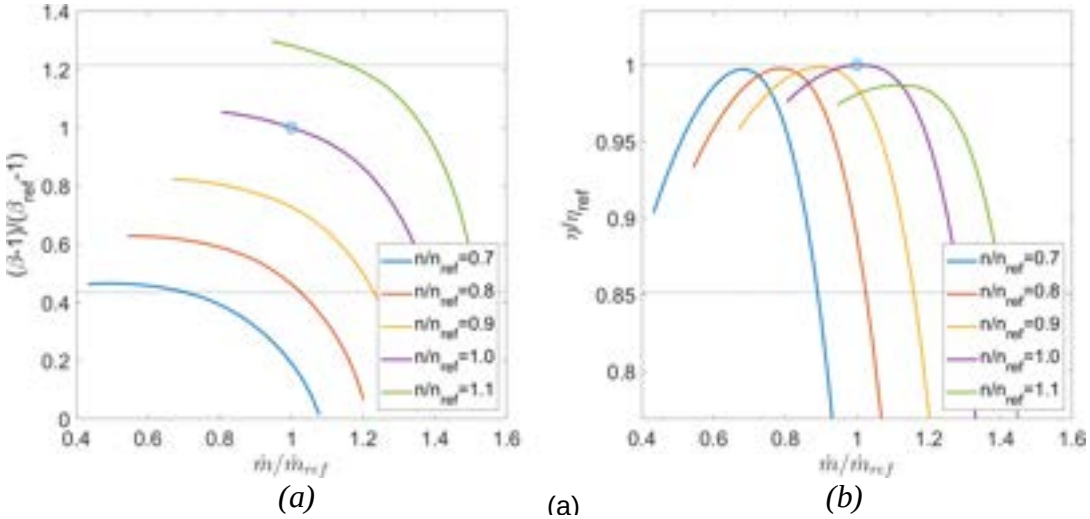

Figure. 2. High pressure compressor maps, with (a) generalised pressure ratio and (b) generalised efficiency as a function of the generalised mass flow rate for different rotational speeds.

2.2.2. Turbine model

The power produced by each turbine is calculated as:

$$P_t = \dot{m}_{air,dis} \frac{\gamma}{\gamma - 1} R_{air} T_{t,in} \left(1 - \beta_t^{\frac{\gamma-1}{\gamma} \eta_t} \right) \quad (2)$$

Where $\dot{m}_{air,dis}$ is the mass flow rate of the turbines, $T_{t,in}$ is the temperature at the inlet of the turbine, β_t is the turbine expansion ratio, and η_t is the polytropic efficiency of the turbine.

The design of the three turbines was based on [12], assuming a polytropic efficiency of 0.86 for each turbine. Throughout the discharge phase, as the pressure in the cavern decreases, a throttling valve located at the inlet side of each turbine regulates the pressure in order to maintain constancy in the mass flow rate and the reduced mass flow rate. The valves also account for the temperature variation caused by the thermocline profile of the TES units. Hence, the turbines operate in a choked flow condition throughout the entire discharge phase, achieving maximum efficiency.

The throttling valve model is based on the calculation of the reduced mass flow rate $\dot{m}_{rid}$, expressed as:

$$\dot{m}_{rid} = \dot{m}_{air,ch} \frac{\sqrt{T_{in}}}{p_{in}} \quad (3)$$

Where T_{in} and p_{in} are the inlet temperature and pressure.

2.2.3. Heat exchanger model

The following equations allow to calculate the thermal power and the heat transfer area of the heat exchangers:

$$\dot{Q} = \dot{m}_{air} c_{p,air} (T_{air,out} - T_{air,in}) \quad (4)$$

$$A = \frac{\dot{Q}}{U \, \Delta T_{ML}} \quad (5)$$

Where $\dot{Q}$ is the exchanged thermal power, $\dot{m}_{air}$ the mass flow rate of air, $T_{air,out}$ and $T_{air,in}$ are the outlet and inlet air temperature, respectively, A is the heat exchange area, U is the heat transfer coefficient, and ΔT_{ML} is the logarithmic temperature difference.

Two intercoolers recover the heat from the MPC1 and MPC2 allowing to store the produced thermal energy inside the TES2. Therminol-66 was selected as the heat transfer fluid because of its maximum temperature of 345 °C [13]. The intercoolers were designed to keep an outlet temperature of the hot fluid (air) at 35 °C assuring a steady inlet temperature for the compressors. Moreover, the approach temperature and the heat transfer coefficient were set to 10 °C, and $0.2 \frac{kW}{m^3 K}$, respectively [14].

The heat exchangers on the expansion side were designed to account for fluctuations in inlet pressure and temperature of the air during the discharge phase. This was achieved by using the same equations and parameters applied to the intercoolers and considering the lowest exchangeable thermal power $\dot{Q}$.

2.2.4. Thermal Energy Storage model

The volume of the TES tank is then calculated as:

$$V_{TES} = \frac{m_s}{\rho_b (1 - \epsilon)} \quad (6)$$

Where ρ_b is the density of the filler material, ϵ is the void fraction and m_s is the mass of the filler material, calculated based on the energy balance of the TES between the charge and discharge phases. A system of two equations, derived from the model developed in [15], is used to describe the operation of the two thermal energy storage (TES) units. The temperature of solid bed (T_b) and the heat transfer fluid (T_f), calculated in the direction of the air flow, are determined with the following equations (7) and (8):

$$\frac{\partial T_f}{\partial t} + \frac{G\gamma}{\rho_f \epsilon} \frac{\partial T_f}{\partial z} = \frac{h_v}{\rho_f c_{v,f} \epsilon} \left(T_b - T_f\right) + \frac{k_f}{\rho_f c_{v,f} \epsilon} \frac{\partial^2 T_f}{\partial z^2} \quad (7)$$

$$\frac{\partial T_b}{\partial t} = \frac{h_v}{\rho_b c_{v,b} (1 - \epsilon)} \left(T_f - T_b\right) \quad (8)$$

Where ρ_f is the density of the HTF, $c_{v,f}$ and $c_{v,b}$ are the volumetric specific heat of the HTF and the bed, respectively, h_v is the volumetric transmission of heat through convection, G is the mass velocity, and k_f is the thermal conductivity of the HTF.

The mathematical model, developed to simulate the behaviour of the two TES units, allows for calculation of the thermocline profile along the axial length of the tank, accounting for its variation during cyclical operation [16]. The mass flow rate of oil during both the charge and discharge phases was calculated based on the mass and energy balance equations.

2.2.5. Compressed Air Storage model

The compressed air storage (CAS) volume is calculated by solving the following system of equations:

$$\begin{cases} p_{min} V_{tot} = m_{min} R_{air} T_{st} \\ p_{max} V_{tot} = (m_{min} + \dot{m}_{air} t_{ch}) R_{air} T_{st} \end{cases} \quad (9)$$

Where p_{min} and p_{max} are the minimum and maximum air pressures, respectively, V_{tot} is the total storage volume, m_{min} is the mass of air in the cavern at minimum pressure, $\dot{m}_{air}$ is the mass flow rate of air, t_{ch} is the charge time, and T_{st} is the storage temperature inside the cavern.

An abandoned coal mine located in Sardinia was selected as the compressed air storage reservoir. The CAS, characterised by a depth of about 500 m and a diameter of 5 m, is assumed to be suitable for the high-pressure storage of air up to 100 bar [17]. Moreover, state-of-the-art lining of the internal volume was assumed, minimising air leakage [17]. The temperature inside the cave is set to 35 °C by the heat exchanger AC2 and was assumed to be constant during idling phases between charge and discharge phases.

In this study, a single pipe was used to transfer air from the turbomachines to the underground storage cavern and back, considering that the charging and discharge phases never occur simultaneously. The pipe is a welded steel tube, with a length of 500 m (equivalent to the distance from the surface level to the underground cavern) and an internal diameter of 0.3 m. For the sake of simplicity, the pressure losses (about 0.10-0.15 bar) were assumed to be negligible.

2.3. Power demand and production profiles

The LTA-CAES system was designed to better match the energy production of an RES power plant to the energy demand of an end-user. This section provides a comprehensive examination of the power demand profile of a small town, assumed as the end-user, and the energy generation from a wind farm and a photovoltaic plant. Subsequently, an optimisation problem is defined and solved to determine the optimal size of the LTA-CAES plant for maximum energy yield.

2.3.1. End-user electrical energy demand

The end-user in this study is assumed to be a small town with a population of about 10,000 inhabitants, for which the energy consumption data is available on a quarterly-hour base for a year. Residential, industrial, and commercial users contribute to the energy demand of the town together with the public lighting. Figure 3 displays (a) the typical load profile of the town for both a week and weekend day and (b) the overall monthly energy demand. The latter is a representative profile to be expected on a regular basis, used as reference to understand the energy consumption patterns. From Fig 3(a), it is evident that the load fluctuates rapidly throughout the day, reaching a maximum of 13.7 MW. Fig 3(b) highlights the seasonal nature of the energy demand, where energy consumption is generally higher in winter and lower in summer, except for July and August, because of the increase in energy consumption for cooling. The total annual energy demand is 64.67 GWh, with a mean monthly demand of about 5.39 GWh, as indicated by the horizontal line in Fig 3(b).

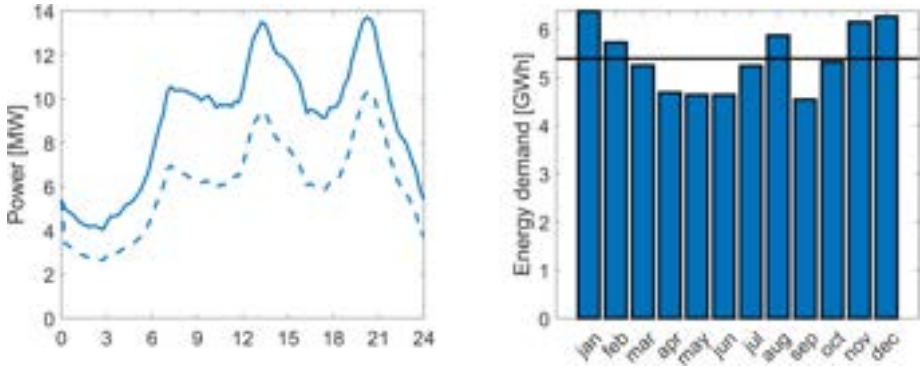

(a) *(b)*

Figure. 3. (a) Load profiles for a typical week (continuous line) and weekend (dashed line) day, (b) Monthly energy demand for the entire year and average annual energy consumption.

2.3.2. Wind power production

The wind power production profile was built according to data of a real wind farm located in Sardinia. The wind farm is composed of 15 Vestas V80 wind turbines with a nominal power of 2 MW each, with a cut-in speed of 4 m/s, a cut-off speed of 25 m/s and a rated wind speed of 16 m/s. The total yearly energy production is 64.70 GWh. Figure 4 shows (a) the wind speed distribution and the wind turbine nominal power profile and (b) the overall monthly energy production of the wind farm. According to the wind speed distribution depicted in Fig 4(a), the power production of the wind turbine tends to be low throughout the year, as most of the available wind speeds fall below the turbine's cut-in speed, or at levels resulting in low energy production. Figure 4(b) shows that the monthly energy production is generally higher during winter and lower during summer, with a trend similar to that of the end-user demand displayed in Fig 3(b).

2.3.3. Photovoltaic power production

The photovoltaic power plant is based on 62,272 monocrystalline Si modules, each rated at 650 W_p, with a conversion efficiency of 20.9% [18], for a total power of 40.5 MW. The plant was modelled using the System Advisor Model (SAM) [19] software and utilising data from the NREL database [20], recorded in 2019 for a site close to Nuraxi Figus (Sardinia, Italy). Considering the various efficiency losses, the yearly energy production of a 1 MW_p plant is approximately 1.6 GWh, with a capacity factor of about 18%. Figure 5 shows (a) the typical

daily power production profile during both a summer (continuous line) and a winter day (dashed line), and (b) the monthly energy production of the PV plant. As shown in Fig 5(a), the daily power production increases in the morning, reaching a maximum around 13:00, and decreases to zero in the evening. Figure 5b shows that the energy production is greater during the summer months, revealing a seasonal nature that is inverse to that of the end-user (displayed in Fig 3(b)). For this reason, a higher surplus energy is available for the LTA-CAES system during the summer months in comparison to winter months, as discussed in the following sections.

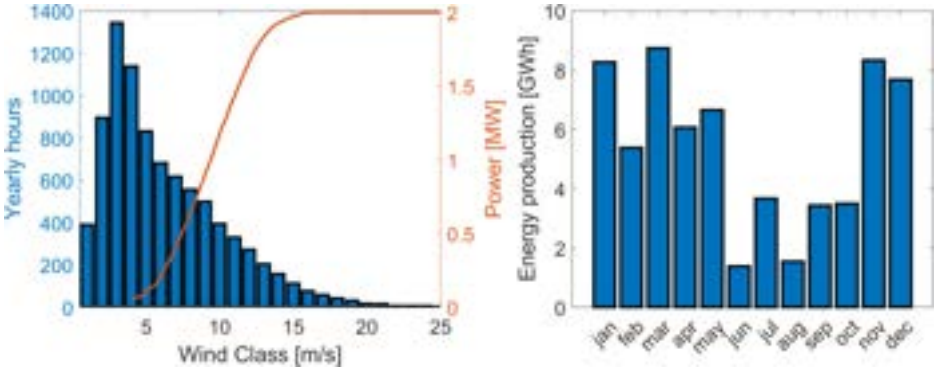

(a) *(b)*

Figure. 4. (a) Wind speed distribution and wind turbine nominal power curve, (b) Monthly energy production of the wind farm.

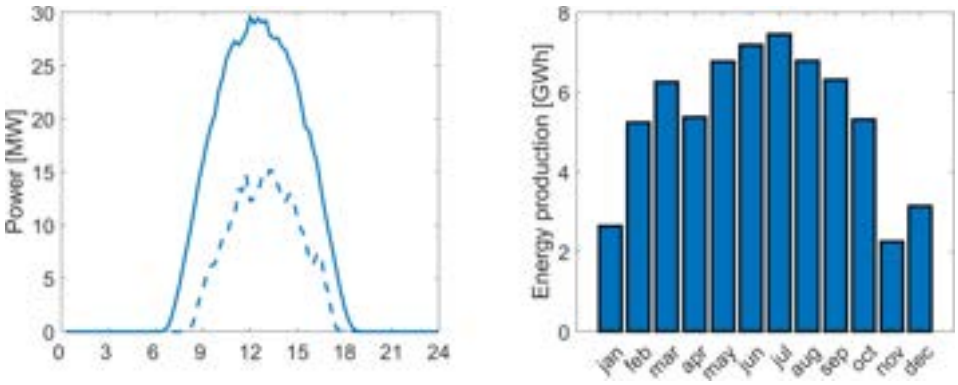

(a) *(b)*

Figure. 5. (a) Power production profile of the PV plant for a typical summer (continuous line) and winter (dashed line) day; (b) Monthly energy production of the PV plant during a year.

2.4. Energy management strategy

The aim of the LTA-CAES system studied is to optimise the usage of renewable energy sources for the end-users by directly connecting the RES power plant, either photovoltaic or wind, to the end-user. Surplus RES energy is used to charge the LTA-CAES plant if the RES output exceeds the end-user's demand, and the air storage is not full. If the excess RES production cannot be stored, it is sent to the grid. On the contrary, when the RES power output is less than the end-user's demand, the LTA-CAES plant operates in discharge mode. If the total power supplied by the RES and LTA-CAES plants is still lower than the overall demand, the remaining power is sourced from the grid. Several constraints were introduced to manage the energy flows. Firstly, a limit of the maximum charge or discharge time was set to 24 hours, in order to complete a full charge or discharge of the cavern in a day or less; the charging and discharging processes have minimum power requirements to start, depending on the power required by the compressors and by the grid, respectively; buying/selling electrical energy to/from the grid during these processes was not permitted. Consequently, the charging process can only start when the available RES power is sufficient to power the compression train, and the discharging process can only start when the end-user's load demand is greater than the RES power plant production.

Due to the fluctuating nature of power production and demand profiles, the charging and discharging processes may sometimes not be completed, and they can begin or end at various cavern pressure levels. Interruptions during the charging or discharging processes also affect the thermocline profile inside the TES tank. If the charging process is terminated before full capacity, the thermocline profile stops early, causing lower air temperatures and less power output during the subsequent discharge phase. Similarly, if the discharging process cannot be completed, the thermocline profile stops early, resulting in a high level of thermal energy retained in the TES. These two phenomena occur frequently during the cyclical operation of the LTA-CAES plant and reduce the performance of the TES system and of the entire plant.

2.5. Optimisation

The LTA-CAES plant is designed to optimise the use of the electrical energy generated by an RES power plant by maximising the share of renewable energy consumed by the end-user. The performance and size of the plant components were evaluated based on three key design variables: the air mass flow rate of the compressor train, the charge time, and the discharge time. These design variables influence the size of the compression and expansion trains, as well as the volume of the air storage reservoir and TES units. Furthermore, these variables affect the main energy flows, including the energy used for compression, the energy produced during expansion, the energy supplied to the end-user, and the energy dispatched to the grid [21]. The optimization problem was solved with the Genetic Algorithm (GA), included in the Matlab Optimization Toolbox [22]. The three design variables were calculated to maximize the total energy sent from the LTA-CAES to the end-user, considered as the objective function. The design variables were set as integers only, and the optimization was carried out with a stopping condition of 20 generations without improvement on the best fitness function value, with default settings.

3. Results and discussion

As mentioned, this study examines the performance of an LTA-CAES plant designed to better match the energy production of an RES power plant to the energy demand of an end-user. In particular, the LTA-CAES design variables have been evaluated for an RES power plant based either on a PV power plant or a wind farm. The results are presented in Table 2.

Table 2. Optimal design parameters for the analysed LTA-CAES plants.

	PV	Wind
Mass flow rate (kg/s)	24	16
Charge time (h)	10	24
Discharge time (h)	24	24

The results of the optimisation process are used to determine the size of the LTA-CAES plant. The size of the plant can be characterised by the input and output power of the plant, the volume of the TES units, and the length of the cavern (considering a diameter of 5 m). Table 3 shows the size of the main components of the plant. For the system coupled with the wind farm, the entire energy storage system (TES and cavern) is characterised by a larger volume, thus storing more energy. For the system coupled with the PV plant, the optimisation process results in a higher input power and lower output power compared to the system coupled with the wind farm. In the case of the PV, the surplus power is high, and the power demand is low, resulting in a high input power and low output power for the LTA-CAES plant.

Table 3. Main parameters for the LTA-CAES combined with a PV or wind power plant.

	Input power [MW]	Output power [MW]	TES1 volume [m^3]	TES2 volume [m^3]	Cavern length [m]
PV	14.9	4.2	1005	1683	1655
Wind	9.9	6.7	1683	2613	2647

The energy balances of the system were solved with a time step of 15 minutes for one year, considering the power output of the two RES plants and the power demand of the end-user. The performance of the compression and expansion trains of the LTA-CAES plant, throughout the full charge and discharge phases, is illustrated in Fig 6, where the reference power, denoted as P_{ref}, represents the nominal power of the turbomachine. This plot shows the generalised power (the ratio between the actual power and the reference power) as a function of the charge level of the storage volume. During the charge and discharge phases, variations in pressure within the cavern and temperature within the TES systems cause variations of the compression and expansion power. It can be observed that the power variation is limited: the compressors power curve shows a steady increase of about 8.4% throughout the charge phase, while the turbine power production remains mostly constant, decreasing only by 2.9% at the end of the discharge phase. The compressor profile increase is mainly due to the increase in the HPC compression power, as shown in Fig 6(a). The compression ratio increases from 1.31 to 1.87 during the charge phase, leading to a subsequent increase in the required compression power. The power curve shows a steady increase due to the relatively small variation in efficiency, ranging between 69% and 80%. Furthermore, most of the compression energy (88%) is required by the LPC, MPC1, and MPC2 that operate at design conditions, while the HPC is responsible for the remaining share of the total compression work. The power output of the turbines, shown in Fig 6(b), remains constant until it starts to drop towards the end of the discharge phase. This power reduction is caused by the temperature reduction at the outlet of the TES units. As the HPT and MPT operate at design condition, their polytropic efficiency remains constant. Similarly, the efficiency of the LPT is mostly constant since the variation in power of the turbines is low.

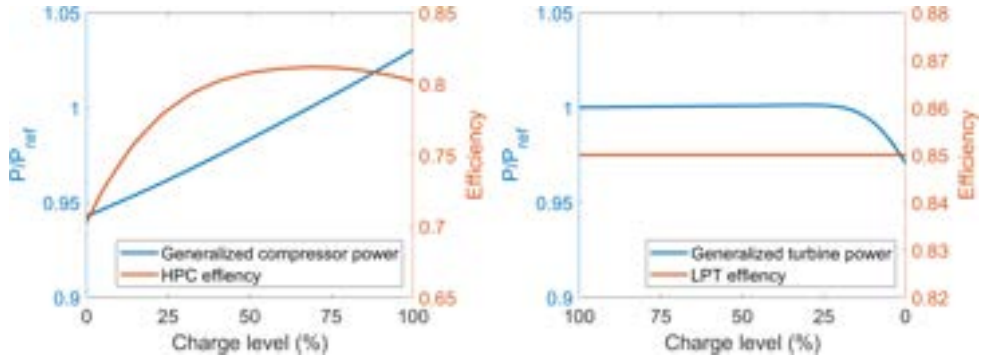

(a) *(b)*

Figure. *6.* (a) Generalised total compressor power and HPC efficiency during the charge phase and (b) Generalised total power production of the turbine train and LPT efficiency.

Figure 7 shows the key temperature profiles throughout a complete discharge phase and its evolution over fifty charge and discharge cycles. The temperature profile at the turbine inlet is shown in Fig 7(a) for the LPT, in Fig 7(b) for the MPT, and in Fig 7(c) for the HPT. The reduction in temperature towards the end of the discharge phase is responsible for the power reduction depicted in Fig 6(b). During the discharge phase of the first cycle, a substantial temperature decrease is observed. However, the minimum temperature gradually increases with each cycle, ultimately reaching a saturation state after about 50 cycles. Figures 7(b) and 7(c) additionally show the temperature difference between the inlet and the outlet (coincident with the turbine inlet) of the heat exchangers. By comparing the maximum temperature in Fig 7(a) with those of Fig 7(b) and 7(c), it is evident that the direct TES (TES1) results in improved energy utilisation. This is due to the fact that the indirect heat transfer section involves two temperature drops: one for the heat exchangers of the charge section (IC1 and IC2) and one for the heat exchangers of the discharge section (HX1 and HX2).

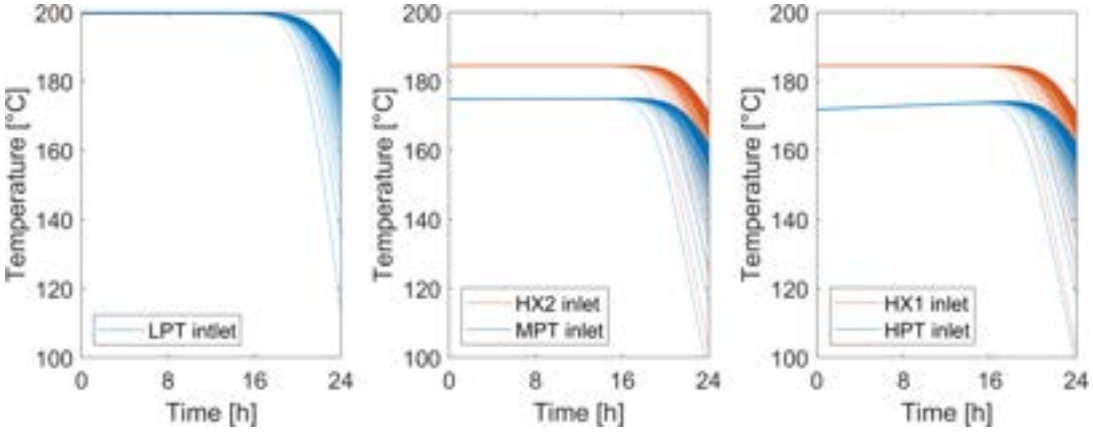

(a) *(b)* *(c)*

Figure. 7. Temperature profile during the discharge phase and its evolution over fifty full charge and discharge cycles at (a) the LPT inlet, (b) the MPT inlet (blue) and HX2 inlet (red), and (c) the HPT inlet (blue) and HX1 inlet (red).

Figure 8 represents the power production profile of the PV plant, the power demand profile of the end-user, and the input and output power profiles of the LTA-CAES plant, for both a typical high irradiance day (Fig 8(a)) and a low irradiance day (Fig 8(b)). During the daytime, when the PV power production (in blue) exceeds the demand (in orange) and is sufficient to drive the compressors, the excess energy is stored by the LTA-CAES (in yellow) for later use during the night (in purple), when the PV plant is not generating power. On a high irradiance day (typically during summer), the LTA-CAES plant can store enough energy during the day to meet the entire end-user demand during the night. In contrast, during a low irradiance day (typically during winter), the plant cannot fully satisfy the end-user demand.

Figure 9 displays the power production profile of the wind power plant, the power demand profile of the end-user, and the input and output power profiles of the LTA-CAES plant, for both a high wind speed day (Fig 9(a)) and low wind speed day (Fig 9(b)). Unlike the PV plant, the power production profile of the wind farm is highly variable, resulting in a less predictable behaviour of the LTA-CAES system. During a windy day (Fig 9(a)), the power generated by the wind power plant is sufficient to meet the end-user demand and fully charge the LTA-CAES system, which stores the excess energy for later use since the energy produced by the RES power plant is enough to cover the energy demand of the end-user. In contrast, during a low wind speed day (Fig 9(b)), the power production is lower, making it difficult for the LTA-CAES system to satisfy the end-user demand. The energy stored inside the CAES is enough to cover only a part of the demand of the end-user (in

purple). Unlike in the case of the PV plant, when the LTA-CAES is coupled with the wind power plant, the charge and discharge phase are not dependent on the time of day, since the wind power plant can generate energy throughout the day and night.

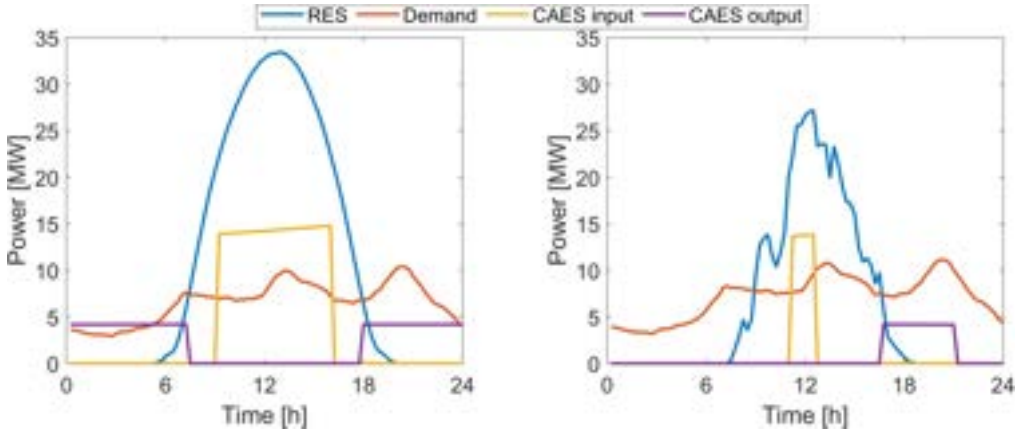

Figure. 8. Main power flows of the LTA-CAES plant for a high irradiance day (a) and a low irradiance day (b), when combined with a PV power plant.

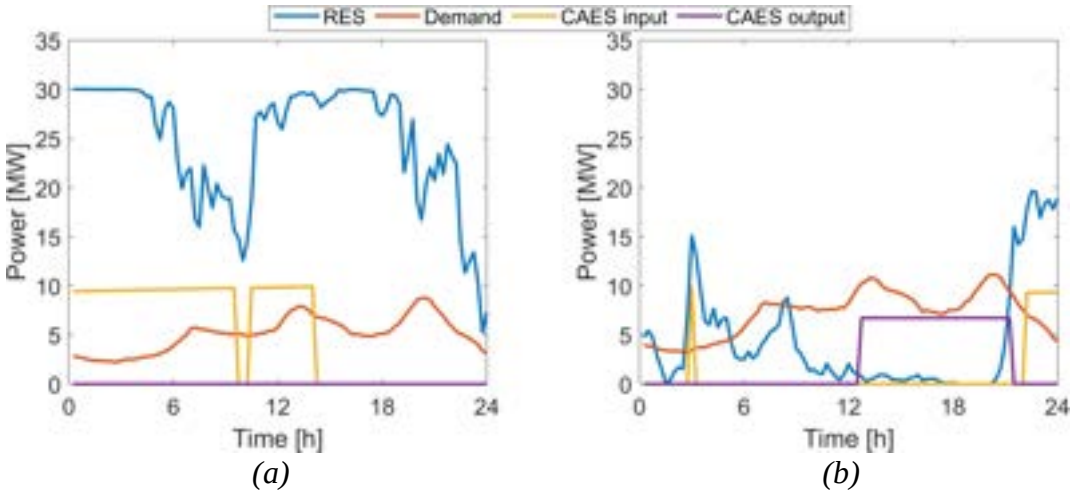

Figure. 9. Main power flows of the LTA-CAES plant for a high wind speed day (a) and a low wind speed day (b), when combined with a wind power plant.

Based on the power production and demand profiles, the mathematical simulation of the system allows evaluation of the operation of the LTA-CAES plant throughout the year. Figure 10, where the level of charge in the cavern is shown for the entire year, illustrates that the charging and discharging processes are frequently interrupted and rely heavily on power availability and demand throughout the day. As demonstrated in Fig 10(a), during the summer, the PV plant generates more energy than the end-user requires, resulting in surplus power that allows the LTA-CAES plant to charge more frequently. Conversely, during the winter, the PV plant's energy production is insufficient, and the LTA-CAES plant must compensate for the deficit. The trend is almost reversed for the wind plant in Fig 10(b), where production is greater during the winter.

Figure 11 shows the yearly energy balance of the system, where the yearly energy demand of the users amounts to 64.6 GWh. When coupled with the PV plant, the LTA-CAES system can supply a total of 39.2 GWh to the end-users (60.7% of the yearly energy demand). In particular, 41.8% of the total energy demand is directly provided by the PV plant and 18.9% by the LTA-CAES system, while the remaining 39.3% is covered by the grid. When coupled with the wind farm, the LTA-CAES is capable of supplying a total of 36.7 GWh of energy to the end-user (56.5% of the yearly energy demand). In this case, 48.0% of the energy demand is provided by the wind farm and the 8.4% by the LTA-CAES system, while the remaining 43.6% by the grid. The total energy produced by the LTA-CAES is 13.5 GWh and 8.0 GWh when coupled with the PV and the wind farm, respectively. The share of energy produced by the LTA-CAES and sent directly to the users is 90.6% and 68.2% for the plant coupled with the PV and the wind farm respectively, while the remaining produced energy is sent to the grid. The amount of energy produced and sent directly to the grid is higher for the system coupled with the wind farm, because the output power of the system is higher than the end-user power demand. The round-trip efficiency is about 67% for both plants. For the LTA-CAES coupled with the PV, the total charge time is equal to 1,388 h/year and the total discharge time is 3,328 h/year. For the LTA-CAES

coupled with the wind farm, the total charge and discharge time is 1,235 h/year. The total energy production of the LTA-CAES system coupled with the PV plant exceeds that of the system coupled with the wind farm by 8%. Hence, coupling the LTA-CAES system with the PV plant appears to be the optimal choice in terms of energy efficiency. Furthermore, the system coupled with the PV plant has a higher share of energy produced by the LTA-CAES and sent directly to the end-users compared to the system coupled with the wind farm. This suggests that the former configuration enables a greater degree of energy self-sufficiency for the end-user.

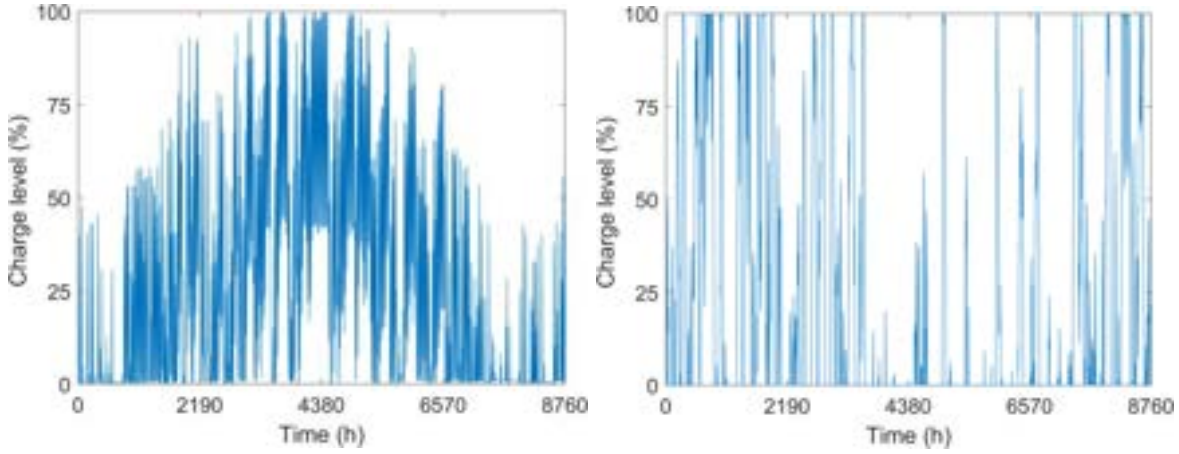

(a) *(b)*

Figure. 10. Yearly charge level of the cave coupling the CAES system with a) PV or b) wind farm.

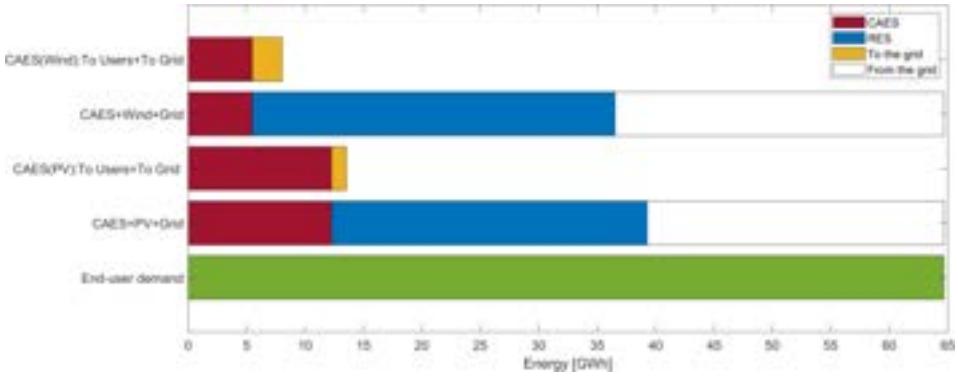

Figure. 11. Energy production from the LTA-CAES plant, coupled with a wind or a PV power plant, compared to the total annual energy demand of the end-user.

4. Conclusions

This paper proposed an LTA-CAES configuration for efficient utilisation of the electrical energy between an RES power plant and a small town in Sardinia. The plant configuration utilised readily available components in order to minimise costs and ensure efficient operation of the turbomachines during both charging and discharge phases. This was achieved by fixing the mass flow rate of air, allowing most of the compressors and turbines to operate at constant speed and at design conditions. The plant features two TES units to store the thermal energy while maintaining a low operative pressure inside the tanks. A dedicated circuit for the heat transfer oil is utilised in combination with heat exchangers to guarantee optimal working conditions for the turbomachines. To account for pressure and temperature variations during discharging, a throttling valve is located at the inlet side of each turbine. Mathematical models were developed to correctly size the plant and to simulate its operation under different conditions, accounting for off-design performance of the various components, i.e., the turbomachines, the TES units, and the heat exchangers.

Simulation results demonstrated the effectiveness of the proposed integrated LTA-CAES plant in managing energy production and consumption over the course of a year, when coupled with wind or photovoltaic power plants. With a wind power plant, a larger share of energy can be directly supplied to the end-user compared to the PV power plant. However, the LTA-CAES system coupled with the PV plant yields a higher total energy production. In fact, the results show that the LTA-CAES system increases the share of renewable energy supplied to the end-user from 41.8% to 60.7% when coupled with the PV plant, and from 48.0% to 56.5% when coupled with the wind farm.

Overall, the system was shown to be a viable low-emission energy management solution for a small community of about 10,000 people on the island of Sardinia. To increase the performance of the system, an integration of

the PV and wind power plants will help to determine the optimal RES plant configuration to be coupled with an LTA-CAES plant. Moreover, the development of a techno-economic analysis of the components of the plant will allow determination of the overall cost of the system.

Acknowledgements

This research was carried out as part of a project entitled “Advanced Energy Storage Systems for Sustainable Communities”, funded by the University of Cagliari with financial support from Fondazione di Sardegna, Year 2019 (CUP F72F20000340007).

Nomenclature

A heat exchangers area, m^2

c specific heat capacity, J/(kgK)

G mass velocity, kg/(m^2s)

h volumetric heat transfer coefficient, W/(m^3K)

k thermal conductivity, W/(mK)

m mass, kg

$\dot{m}$ mass flow rate, kg/s

n rotational speed, rpm

p pressure, bar

$\dot{Q}$ exchanged thermal power, W

R gas coefficient, J/(kg K)

t time, s

T temperature, K

U heat transfer coefficient, W/(m^3 K)

V storage volume, m^3

z axial position, m

Greek symbols

β pressure ratio

γ specific heat capacity ratio

ϵ bed void fraction

η polytropic efficiency

ρ density, kg/m^3

Subscripts and superscripts

b bed

c compressor

ch charge phase

dis discharge phase

f fluid

in inlet

max maximum

min minimum

ML medium logarithmic

out outlet

p pressure

ref reference

rid reduced

t turbine

v volume

References

[1] Ould Amrouche S, Rekioua D, Rekioua T, Bacha S. Overview of energy storage in renewable energy systems. Int J Hydrog Energy. 2016 Dec;41(45):20914–27.

[2] Kousksou T, Bruel P, Jamil A, El Rhafiki T, Zeraouli Y. Energy storage: Applications and challenges. Solar Energy Materials and Solar Cells. 2014 Jan;120:59–80.

[3] Budt M, Wolf D, Span R, Yan J. A review on compressed air energy storage: Basic principles, past milestones and recent developments. Appl Energy. 2016 May;170:250–68.

[4] Wolf D, Budt M. LTA-CAES – A low-temperature approach to Adiabatic Compressed Air Energy Storage. Appl Energy. 2014 Jul;125:158–64.

[5] Grazzini G, Milazzo A. Thermodynamic analysis of CAES/TES systems for renewable energy plants. Renew Energy. 2008 Sep;33(9):1998–2006.

[6] Hartmann N, Vöhringer O, Kruck C, Eltrop L. Simulation and analysis of different adiabatic Compressed Air Energy Storage plant configurations. Appl Energy. 2012 May;93:541–8.

[7] Wang S, Zhang X, Yang L, Zhou Y, Wang J. Experimental study of compressed air energy storage system with thermal energy storage. Energy. 2016 May;103:182–91.

[8] Zhang Y, Xu Y, Zhou X, Guo H, Zhang X, Chen H. Compressed air energy storage system with variable configuration for accommodating large-amplitude wind power fluctuation. Appl Energy. 2019 Apr;239:957–68.

[9] Arabkoohsar A, Rahrabi HR, Alsagri AS, Alrobaian AA. Impact of Off-design operation on the effectiveness of a low-temperature compressed air energy storage system. Energy. 2020 Apr 15;197.

[10] Tola V, Marcello FC, Cocco D, Cau G. Performance Assessment of Low-Temperature A-CAES (Adiabatic Compressed Air Energy Storage) Plants. Journal of Thermal Science. 2022 Sep 20;31(5):1279–92.

[11] Casey M, Robinson C. A Method to Estimate the Performance Map of a Centrifugal Compressor Stage. J Turbomach. 2012 Nov 8;135(2).

[12] Balje´ OE. A Study on Design Criteria and Matching of Turbomachines: Part A—Similarity Relations and Design Criteria of Turbines. Journal of Engineering for Power. 1962 Jan 1;84(1):83–102.

[13] Therminol-66 - Available online:<https://www.therminol.com/product/71093438> [accessed 14.3.2023].

[14] R. K. Sinnott. Chemical Engineering Design. Vol. 6. Pergamon Press; 1996.

[15] Cascetta M, Serra F, Cau G, Puddu P. Comparison between experimental and numerical results of a packed-bed thermal energy storage system in continuous operation. In: Energy Procedia. Elsevier Ltd; 2018. p. 234–41.

[16] Cascetta M, Cau G, Puddu P, Serra F. Numerical investigation of a packed bed thermal energy storage system with different heat transfer fluids. In: Energy Procedia. Elsevier Ltd; 2014. p. 598–607.

[17] Okuno T, Wakabayashi N, Niimi K, Kurihara Y, Iwano M. Advanced natural gas storage system and verification tests of lined rock cavern-ANGAS project in Japan. International Journal of the JCRM. 2009;5(2):95–102.

[18] Vertex DE21 - Available online:<https://www.trinasolar.com/it/product/VERTEX-DE21> [accessed 15.3.2023].

[19] System Advisor Model Version 2022.11.21 (SAM 2022.11.21). National Renewable Energy Laboratory. Golden, CO.

[20] NSRB. National Solar Radiation Database. – Available at:<https://nsrdb.nrel.gov/data-viewer> [accessed 15.3.2023].

[21] Cocco D, Licheri F, Micheletto D, Tola V. ACAES systems to enhance the self-consumption rate of renewable electricity in sustainable energy communities. J Phys Conf Ser. 2022 Dec 1;2385(1):012025.

[22] Optimization Toolbox version: 9.4 (R2022b), Natick, Massachusetts: The MathWorks Inc.; 2022.

Thermo-economic optimization of a Carnot Battery under transient conditions

Márcio Santos[a], Jorge André[b], Ricardo Mendes[c] and José B. Ribeiro[d]

[a] University of Coimbra, ADAI-LAETA, Coimbra, Portugal, marcio.santos@dem.uc.pt,
[b] University of Coimbra, ADAI-LAETA, Coimbra, Portugal, jorge.andre@dem.uc.pt,
[c] University of Coimbra, ADAI-LAETA, Coimbra, Portugal, ricardo.mendes@dem.uc.pt,
[d] University of Coimbra, ADAI-LAETA, Coimbra, Portugal, jose.baranda@dem.uc.pt

Abstract:

With the efforts to decarbonize the energy sector comes a growing demand of electricity, most of which is to be supplied by renewable generation in a carbon-neutral future. To balance the variability inherent to most renewable energy sources, some form of energy storage is required. In this work, a short review of current systems is made with a particular focus on Carnot Batteries, whose operating characteristics, long life and low environmental footprint make them competitive for daily energy storage. A transient model was developed to simulate the full operation of a Carnot Battery composed of a Vapour Compression Heat Pump and Organic Rankine Cycles in conjunction with sensible thermal storage. The key performance parameters were identified, and a Pareto optimization was carried out by balancing costs and performance across 25 configurations of storage temperature spread and heat exchanger pinch point. It was concluded that the wider storage spreads and higher pinch points lead to lower costs as they decrease the size of the water tank and the heat exchangers, and to lower efficiencies as unfavourable temperature gradients are created for the heat pump and heat engine. A Pareto front was identified, consisting of 10 configurations that were able to either optimize one criterion, or balance of two or more criteria, and conclusions were drawn as to the applicability of each configuration.

Keywords:

Carnot Battery, Thermal Energy Storage, Electric Energy Storage, Heat Pump, Organic Rankine Cycle

1. Introduction

According to the IPCC (Intergovernmental Panel for Climate Change), human-induced warming has already reached approximately 1ºC, in 2017. If all human emissions were to be immediately reduced to zero, it's estimated that the total rise in temperature in the time scale of a century would fall under 1.5ºC, in relation to pre-industrial levels. The Paris Agreement has set a goal to limit this global temperature rise to 2ºC, and preferably to keep it under 1.5ºC, as this would substantially reduce the effects of climate change in relation to a future in which no action is taken.

According to the RNC2050 (Roteiro para a Neutralidade Carbónica – Roadmap for Carbon Neutrality), a long-term plan for achieving net-zero emissions by 2050, the biggest drivers for decarbonization of the energy sector are the use of renewables, increased energy efficiency (which translates into reduced demand from sources), electrification, and new energy vectors such as hydrogen and other synthetic fuels. It states also that the inherent variability of most widespread renewable sources (namely wind and solar PV) creates problems of dispatchability and energy security. The document states that strong grid interconnection with the European Union, smart energy management, and increased usage of Energy Storage Systems (ESS) are key to solving these issues. This notion is supported by the scientific community, as current papers highlight the necessity for energy storage, often in conjunction with an interconnected and smart grid, to effectively manage the supply variability (on many time scales) resulting from large-scale renewable integration.

1.1. The Challenges of decarbonization in terms of energy storage

The need for inertia in our energy systems is clear – to mitigate variability in supply. However, while most issues caused by integration of Variable Renewable Energy (VRE) sources fall into this category, the features that characterize each problem vary in terms of power requirement, storage duration, discharge time, response time, and other technical characteristics.

The load Shifting and Seasonal Storage is the most important application of energy storage in the context of decarbonization. Because of the largely uncontrollable nature of VREs, supply of electric energy will rarely

match demand, so, in these cases, we often require storage systems to shift the supply to more favourable periods of time, to satisfy demand and prevent curtailing.

The needed storage duration will vary depending on the characteristics of the generation source, but it should fit roughly in the time scale of its natural variation; this can range from a few hours – the case for solar variation [1] – to days, weeks or even months – the typical long-term variation in wind speeds [2], [1].

Power requirements must also match the generation source, in the order of 10-100 MW for grid scale applications, with lower values for localized/consumer-scale situations. Maximum response times must be in the scale of minutes, and the capacity should be sufficient to absorb excess power and satisfy demand. For large scale applications with seasonal storage, it may reach values in the order of 100-1000 MWh [2]. At a very small-time scale, fluctuations in supply and demand can affect the properties of electric currents, such as voltage and frequency [2]. To maintain the power quality of the supplied energy, storage systems are often used. For these applications, storage duration and capacity may be limited, however, power and response time are critical parameters, as power (in the order of kW to several MW, depending on the scale of consumption) is to be processed almost instantaneously, in the order of milliseconds.

The Transmission and Distribution Management is extremely important. With increasing loads being placed on electric grids, bottlenecks may appear in periods of peak consumption. Alongside other measures, such as economic incentives for shifting consumption, storage systems may be used to absorb excess loads and delay costly investments into power grids. The storage duration required should fit the variations in demand (several hours). Power and capacity requirements depend on the scale of the application but are like those of grid-scale load-shifting. Response times of up to a few minutes should be sufficient.

Another major feature of ESS is the Backup Power. At the consumer scale, energy storage may be desired to maintain an uninterrupted power supply in case of an outage. In this case, power requirements should match the consumption load (from a few kW to tens of MW), and storage capacity and duration should match the expected outage period (usually up to a few hours, with enough capacity to satisfy power requirements over this period – up to the order of 10 MWh). Response time is a critical parameter as the grid power must be replaced immediately – a response in the order of milliseconds is ideal.

Lastly, to effectively replace fossil fuels in the transportation industry, the storage medium to be used must have high specific energies and energy densities, along with a quick response time. Power-To-Fuel technologies that produce fuels compatible with current fossil-based systems are a good solution for this sector [1].

1.2. Classification of Existing Technologies

Energy may be stored in various forms, the most common being chemical potential, magnetic fields, electric fields, pressurized gas, gravitational potential, thermal energy, and synthetic fuels, as showed in Table 1 [1], [2]. In the literature, the classification of storage systems varies slightly from author to author, as the mechanisms employed by storage systems, as well as the perspectives from which we classify them, are diverse.

Table 1. *Classifications of ESS*

Stored Energy	Storage Mechanism	Examples
Electric	Electric and magnetic fields	Supercapacitors, SMES
Electrochemical	Reversible chemical reactions	Conventional Batteries, Flow Batteries, High-Temperature Batteries, Metal-Air Batteries
Mechanical	Gas pressure, gravitational potential, kinetic energy	CAES, PHS, Flywheel
Thermal	Heat capacity of a material, latent heat of phase change, endothermal and exothermal reactions	TES (Sensible, Latent, Thermochemical)
Chemical	Production of synthetic fuels	P2G, P2L

Pumped Hydro Storage (PHS), exploits the change in elevation between reservoirs of water in order to store energy in the form of gravitational potential. In charge mode, water is moved to a high elevation, increasing its potential energy, and in discharge mode this energy is converted into kinetic energy as the water flows back to the lower reservoir, passing through a turbine which generates electricity. PHS has a good degree of maturity and commercial exploitation [1], [3], and is suitable for high power and high energy applications. It has low energy costs and a relatively high efficiency; however, it comes with the downsides of high environmental impact, and geographical restrictions. Additionally, this technology is becoming increasingly difficult to exploit, as in most developed countries the potential for new installations is nearly exhausted [3], [4].

Compressed Air Energy Storage (CAES) is a system which stores energy in the form of gas pressure. In the charging process, air is compressed and sent into an underground reservoir, and in the discharge process this pressurized air is expanded in a gas turbine to generate electricity. These systems benefit from a very low

environmental impact (if fossil fuel use is avoided), and excellent power and storage capacities. However, they suffer from geographical limitations, as they most often require an underground cavern for storage.

Electrochemical batteries store energy in the form of a reversible chemical reaction – in the discharge process, a redox reaction generates an electric current between the two electrodes. For charging, the reaction is reversed, absorbing electric current. Due to the speed of the reactions, the response time of these batteries is nearly instantaneous, making them adequate for applications requiring some agility, such as power quality and managing quick changes in renewable generation; however, this kind of battery generally suffers from environmental issues, high costs, and limited cycle life. In the realm of conventional batteries, the most commonly used are lead-acid, lithium-ion, nickel-cadmium and nickel-metal hydride. Other less common types of batteries are flow batteries and high-temperature batteries.

Other types include: Flywheel Energy Storage, that is one of the simplest forms of storage where storage takes the form of kinetic energy of a rotating mass; Supercapacitors that are an upgrade of regular capacitors, which store energy by accumulation of positive and negative charges on either side of a dielectric; and Superconducting Magnetic Energy Storage (SMES) systems that store energy in the form of a magnetic field, induced by a dynamic electric field passed through a coil.

Finally, Thermal Energy Storage systems store energy in the heat capacity of a solid or liquid material (Sensible Heat Storage), the latent heat of a phase change (Latent Heat Storage) or in a reversible thermochemical reaction (Thermochemical Storage). These systems can also vary by the method through which the storage medium is charged. Concentrated Solar Power (CSP) plants, if coupled with thermal storage, use solar radiation to heat a storage medium, which can then discharge to a heat engine for electricity production [13]. Another possibility is Wind-powered Thermal Energy System (WTES), in which wind power is converted directly to heat, which is stored in a TES and later used to power a heat engine [13]. The thermal storage may also be charged using electricity, in which case the whole system may be designated a Carnot Battery, and if a heat pump is used to charge the system it is designated a Pumped Thermal Electricity Storage (PTES), so long as the heat is used to produce electricity in the discharge phase. The Carnot Battery presents several advantages that make it competitive with other forms of ESS, mainly in terms of environmental impact, flexibility and efficiency, and so it will be the focus of this work.

2. Carnot Batteries

Carnot Batteries work by establishing a thermal gradient between a high temperature (HT) reservoir and a low temperature (LT) reservoir. Electric energy is used to charge the system by forcing heat flow against the natural gradient, thus storing thermal exergy. In the discharge phase, the heat flows from the hot environment to the cold one, and this flow is used to produce work in a heat engine. According to O. Dumont et al. [3], a Carnot Battery (CB) is defined as an EES technology where there is always an electric input, and an electric output. A thermal input may be used to improve the performance of the CB; however, its primary purpose remains the storage of electric energy. Similarly, the battery may output useful thermal energy, but the electric output must be comparable with the electric input. In practice, the reservoirs may be physical ones, such as water tanks or solid materials, or their role may be taken up by the environment (for example, the ambient air). Similarly, electric heat pumps or resistance heaters may be used for charging, and any heat engine (Rankine, Brayton, others) or even a thermoelectric generator may be used for discharging.

Carnot Batteries offer roundtrip efficiencies (ε_{rt}) in a wide range depending on their boundary conditions [3], [5–7], low energy costs [1][3], and high lifetimes [1][3]. These systems are mostly competitive for electricity storage on the scale of several hours, in situations that demand low Power/Capacity ratios, with values of 1 kW /4 kWh and lower. They have a very low environmental impact, and no dependence on geographical conditions [1], making them a suitable competitor to PHS and CAES, whose geographical constraints pose a considerable limit to their exploitability on a large scale. For local, small-scale implementations, Carnot Batteries may also present an adequate replacement for chemical batteries, which are often expensive and environmentally unsafe. Additionally, an important advantage of Carnot Batteries is the ability to integrate additional thermal reservoirs (such as industrial waste heat), which act as additional exergy sources [3]. This thermal integration increases the ε_{rt} of the system, potentially to values greater than unity (>100%), by decreasing the work input or increasing the work output. In Table 2 a brief summary is given of the technical characteristics of some different Carnot battery technologies.

Table 2. Technical summary of Carnot Battery technologies (adapted from [3]).

Cycle	Brayton Cycle	Electrical heater and Rankine Cycle	Heat Pump and Rankine Cycle
Power [MW]	Up to 100	Up to 100	Up to 10*
Energy [MWh]	Up to 400	Up to 400	Up to 40*
Temp [°C]	[-70:1000]	Up to 750	Up to 150
Compactness [kW/m^3]	25	~4	[0.05–1.72]

Compactness [kWh/m3]	200	~36	[0.2–207]
Self-discharge	medium	Very low	[30–73]
ε_{rt} [%]	[60-70]	[12-55]	[70-150]**
Price [$/kW]	[395-875]	~376	[272–468]
Price [$/kWh]	[55–198]	~94	[68–117]
Estimated TRL	5	9	7
Typical fluids	Argon, Air	Water	R1233zd(E), CO_2, NH_3, water

* Possible to extend by association in series ** Thermally integrated

If a heat pump is used to charge the thermal storage, the system is designated Pumped Thermal Electrical Storage. These systems may use Brayton heat pumps (HP) with Brayton heat engines (HE), Vapour Compression Heat Pumps (VCHP) in conjunction with Rankine Cycles (RC), or Brayton heat pumps with Rankine Cycles [4]. The presence of a heat pump for the charge cycle is advantageous if the Coefficient of Performance (COP) is higher than one, as the roundtrip efficiency of a PTES is generally the product of the COP with the HE efficiency (if thermal storage efficiency is not considered). The use of a heat pump brings advantages in terms of thermal integration, as it can increase the performance of the heat pump and/or the heat engine. This thermal integration allows an increase in efficiency without complex modifications to the thermodynamic cycles and makes the PTES more flexible, as it may now receive two inputs (electric and thermal) instead of just one – in this sense, Thermally Integrated PTES (TI-PTES) may be seen as a hybrid energy storage and waste heat power plant.

Brayton PTES is usually comprised of a Brayton heat pump, based on the inverse Brayton cycle, and a Brayton heat engine, typically working between two sensible reservoirs [3]. The typical layout contains two thermal reservoirs and four machines (two compressors and two expanders), however in a reversible system this number could reduce to two. In a Brayton cycle, the working gas is compressed, heated and expanded, and then cooled before the next compression. As the work produced by expansion is greater than the work used in compression, the expander drives the compressor with a net positive work output (as with any heat engine, the driving force is a temperature gradient between the two reservoirs) – this is the cycle followed in the discharge process. For charging, the inverse process occurs – the gas is heated and compressed, drawing heat from the LT reservoir, and then cooled, storing heat in the HT reservoir, followed by expansion [3].

HP/RC systems combine Vapour Compression Heat Pumps with Rankine Cycles, where the VCHP charges the reservoirs with thermal exergy, and the Rankine Cycle produces work by harnessing the temperature difference between HT and LT reservoirs. By comparison with Brayton systems, Rankine-based PTES offers the advantages of high energy density and low temperature operation – these features allow for more compact storage, lower self-discharge, and potentially more efficient integration of waste heat. One of the advantages of HP/ORC systems is the use of commercially available equipment (pumps, compressors, expanders, heat exchangers, valves), which facilitates their construction [3], [4], [8]. The schematic configuration for HP and ORC systems and the corresponding T-s diagrams are shown in Figure 1.

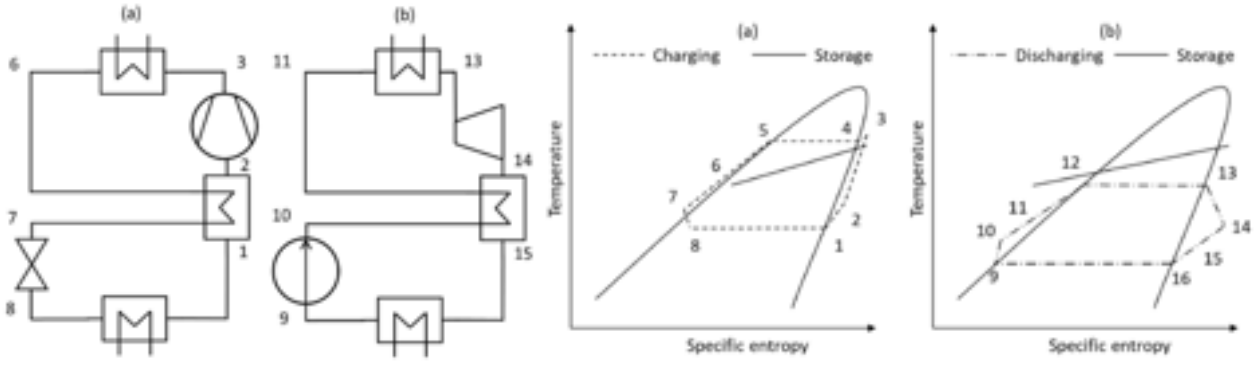

Figure. 1. Heat pump and ORC schematic diagrams (a) and T-s diagrams (b) [9]

3. Thermodynamic modelling

For the study of Carnot Battery systems, the HP/ORC architecture was chosen due to its simplicity and practical feasibility, as well as its low temperatures that facilitate thermal integration; this is also one of the most widely studied types of Carnot Battery, so reference values are readily available.

To study the performance of HP/ORC PTES, each thermodynamic cycle was modelled in MATLAB, with resort to the REFPROP database to calculate fluid properties. Following that, a transient model was developed to simulate the behaviour of a TES coupled to each cycle.

The effectiveness of the Carnot battery process is evaluated through the roundtrip efficiency. The value of this variable is affected by the behaviours of the two sub-cycles of vapor compression heat pump (COP) and the organic Rankine cycle (η), and is expressed by:

$$\varepsilon_{rt} = \mathrm{COP} \times \eta, \tag{1}$$

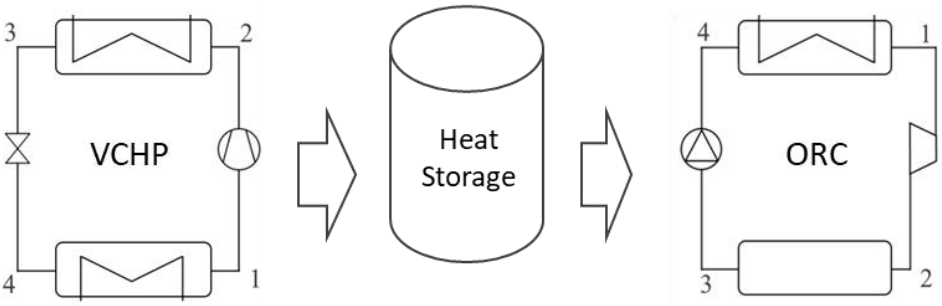

Figure. 2. Schematic representation of the Carnot battery with a simple VCHP, the sensible thermal energy storage and the simple ORC

3.1. Vapor Compression Heat Pump (VCHP)

The standard VCHP cycle is shown in Figure 3 In this cycle, almost all processes involve changes in enthalpy in which case, by definition, heat and/or mechanical work (associated with pressure and volume changes) are being exchanged, neglecting changes in kinetic and potential energy of the fluid.

From points 1 to 2, the enthalpy of the vapour is increased through compression, and the specific work performed on the system is equal to the enthalpy variation:

$$\dot{W}_c = \dot{m}_f(h_2 - h_1), \tag{2}$$

Between 2 and 3, the fluid cools and condenses in a condenser, releasing heat into the HT reservoir at the condensation temperature:

$$\dot{Q}_{cd} = \dot{m}_f(h_2 - h_3), \tag{3}$$

Between 3 and 4, the liquid is expanded into the two-phase region. If this happens in a throttling valve, the process is isenthalpic as heat exchanges can be neglected, and no work is performed on the surroundings. This process is highly irreversible, so it can never be isentropic.

$$h_3 = h_4, \tag{4}$$

Finally, the two-phase mixture receives energy in the evaporator and the fluid returns to a gas state, removing heat from the LT reservoir at the evaporation temperature:

$$\dot{Q}_{ev} = \dot{m}_f(h_1 - h_4), \tag{5}$$

The COP of the heat pump in heating mode is given by the ratio between the heat released from the condenser and the energy consumed in compression. This value is generally greater than unity.

$$COP = \frac{\dot{Q}_{cd}}{\dot{W}_c} \tag{6}$$

In reality, compression may be non-isentropic and there may be superheating of the vapour at point 1, as well as subcooling of the liquid at point 3, in which case the cycle is as shown in Figure 3.2. When the compression process is non-isentropic, which is the case with all real compression processes, the specific entropy of the fluid increases from 1 to 2 – this translates into higher compression work for the non-isentropic process. The isentropic efficiency of a compressor $\eta_{s,c}$ can thus be defined as the ratio between the specific work of the compressor in the isentropic scenario and that of the real scenario:

$$\eta_{s,c} = \frac{w_{c,s}}{w_c} = \frac{(h_{2,s} - h_1)}{(h_2 - h_1)} \tag{7}$$

3.2. Organic Rankine Cycle (ORC)

In the ORC, all processes involve enthalpy changes, as heat and/or mechanical work are exchanged at every step. Between 1 and 2, the vapour is expanded, generating mechanical work – the enthalpy variation is equal to the specific work produced by expansion:

$$\dot{W}_{exp} = \dot{m}_f(h_1 - h_2), \quad (8)$$

From 2 to 3, the working fluid is condensed, rejecting heat to the LT reservoir:

$$\dot{Q}_{cd} = \dot{m}_f(h_2 - h_3), \quad (9)$$

Subsequently, the liquid is pumped to the high-pressure level. The enthalpy variation is equal to the specific work performed by the pump; however, this value is very low as the entire process happens in the liquid phase.

$$\dot{W}_{pump} = \dot{m}_f(h_4 - h_3), \quad (10)$$

Finally, the pressurized liquid is heated and vaporized in the evaporator, drawing heat from the HT reservoir and returning to the state of point 1.

$$\dot{Q}_{ev} = \dot{m}_f(h_1 - h_4), \quad (11)$$

The efficiency of the ORC is given by the ratio between the net energy output, and the heat input at the evaporator:

$$\eta = \frac{\dot{W}_{exp} - \dot{W}_{pump}}{\dot{Q}_{ev}}, \quad (12)$$

As with the vapor compression cycle, the real Rankine cycle involves irreversibilities, some of the most significant being the non-isentropic behavior of the expander and the pump. The isentropic efficiencies of these machines are defined the same way as with the compressor – a ratio between an ideal and a non-ideal amount of work between two states:

$$\eta_{s,exp} = \frac{\dot{W}_{exp}}{\dot{W}_{exp,s}} = \frac{(h_1 - h_{2,s})}{(h_1 - h_{2,s})}, \quad (13)$$

$$\eta_{s,pump} = \frac{\dot{W}_{pump,s}}{\dot{W}_{pump}} = \frac{(h_{4,s} - h_3)}{(h_4 - h_3)}, \quad (14)$$

3.3. Storage Simulation

The TES may use a Sensible Heat Material (SHM), or a Phase Change Material (PCM). PCMs are more energy dense and work well with isothermal processes, however they're often costlier than SHMs [3]. For each case the choice of storage material should be based on several technical, economic, and environmental criteria, a process which is largely outside the scope of this work. Water was chosen as a SHM in the present case, as it presents a high specific heat capacity, low costs and no environmental concerns.

The thermal loss coefficient for the water tank is calculated by the inverse of the sum of a series of thermal resistances corresponding to the thermal barriers that were considered - conduction through a layer of steel and a layer of insulation material, and a convective resistance on the outside of the tank.

$$U_{storage} = \left(R_{cond,steel} + R_{cond,insulation} + R_{conv}\right)^{-1}, \quad (15)$$

The rate of heat loss from the storage to the environment $\dot{Q}$ is determined from the following equation:

$$\dot{Q} = U \cdot A \cdot \Delta T, \quad (16)$$

After the thermodynamic cycles have converged, the energy balance is calculated for the current time step (t) based in the heat transfer rates of charge, discharge and loss to the environment:

$$E_t = E_{t-1} - \left(\dot{Q}_{loss} \times \Delta t\right) + \left(\dot{Q}_{charge} \times \Delta t\right) - \left(\dot{Q}_{discharge} \times \Delta t\right), \quad (17)$$

The updated temperature of the water is obtained, using the equation

$$T_t = \frac{E_t}{m \cdot c_p}, \quad (17)$$

3.4. Dynamic MATLAB model

A dynamic model was developed in MATLAB software which considers the energy content in an insulated cylindrical tank at several points inside a specified time interval, applying an energy balance that considers charge power, discharge power, and losses to the environment.

The cycle begins by considering the first inputs provided by the user, then it proceeds to preliminary simulation of the VCHP and ORC. This determines reference values for mass flow and VCHP/ORC condenser and evaporator power, which are then used to design heat exchange areas for these components in the next step.

After this step, the thermal loss coefficient for the water tank is calculated, its value calculated by the inverse of the sum of a series of thermal resistances corresponding to the thermal barriers that were considered – conduction through a layer of steel and a layer of insulation material, and a convective resistance on the outside of the tank. After this, the iterative cycle begins, each iteration starts by simulating the HP and ORC cycles dynamically, varying the condenser and evaporator temperatures according to the storage tank temperature until the heat exchange rate matches the thermal power associated with phase change. The temperatures of the various points in the thermodynamic cycles, as well as the storage temperature, are constantly updated. The cycle stops when a stopping criterion (for example, a maximum/minimum temperature) is reached, or when it reaches the end of the specified time interval, and then final values are logged and plotted depending on the user's needs. The predefined time interval between two consecutive iterations is 30 seconds but it can be automatically for lower values if a higher resolution is needed, which depends mainly of the thermal energy storage capacity.

The capacity of the storage, nominal power of the compressor and expander, and components' efficiencies are defined inputs of the model as showed in Table 3. The algorithm needs to adjust these input parameters based on the output of the cycle, running the program several times until the desired results are achieved.

4. Results and discussion

4.1. Case study

Using the model presented in Section 3, the case of a solar PV power plant will be analysed. Excess power from the PV array is to be stored as thermal exergy in the water tank and used at night when the solar panels cannot provide any energy. As a means of thermal integration, a solar thermal system is used in conjunction with a secondary hot water tank to boost the temperature of the VCHP evaporator to 70°C. The VCHP compressor receives excess electric energy from the solar PV panels and uses it to upgrade the heat from the evaporator to the required temperature at the condenser. The hot water from the main water tank is then used as a heat source for the ORC, which produces electric energy in the expander as it discharges this heat to the environment. Figure 3 shows the layout of the proposed system.

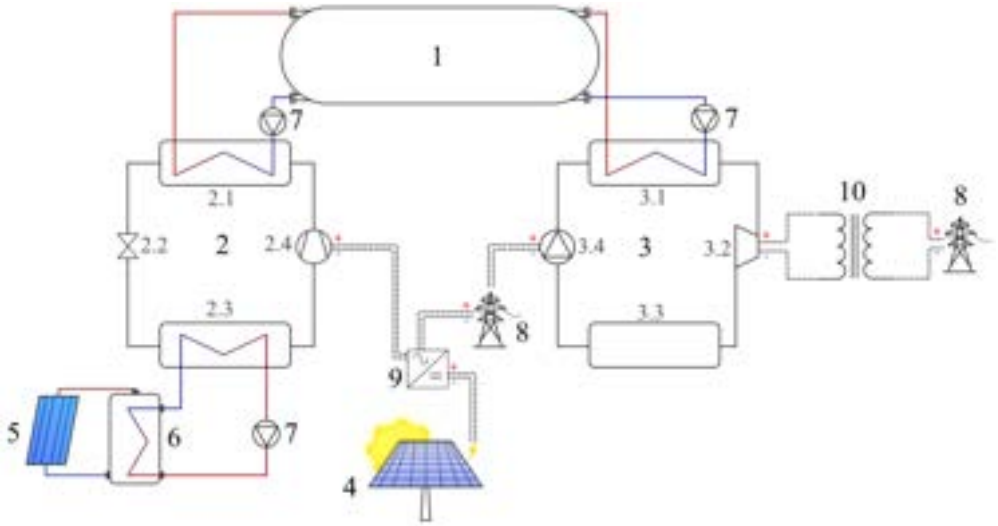

Figure. 3. Schematic representation of the proposed system (1 - Water Tank; 2 - Heat Pump; 2.1 - HP Condenser; 2.2 - HP throttling valve; 2.3 - HP Evaporator; 2.4 - HP Compressor; 3 - ORC; 3.1 - ORC Evaporator; 3.2 - ORC Expander; 3.3 - ORC Condenser; 3.4 - ORC Pump; 4 - PV Array; 5 - Solar thermal panel; 6 - Hot water tank; 7 - Pump; 8 - Power grid; 9 - DC/AC Converter; 10 - AC Transformer).

4.1. Modelling Validation

A first charge/standby/discharge cycle was performed to compare with other studies and obtain initial results and a primary validation, using the values in Table 3. For this first run, a full charge was simulated, followed by 4 hours of standby, and finally a complete discharge of the storage, returning to the initial temperature.

Table 3. *Validation Simulation Parameters.*

Water Tank		**ORC**	
Volume [m^3]	5	Condenser Temperature (design value) [ºC]	35

Aspect Ratio (Length/Diameter)	2	Evaporator Temperature (design value) [ºC]	60
Pressure (Absolute) [bar]	1	Expander Isentropic Efficiency	0.7
Steel Thickness [m]	0.01	Expander Power (design value) [W]	1000
Steel Thermal Conductivity [W/(m.K)]	50	Pump Isentropic Efficiency	0.8
Insulation Thickness [m]	0.05	Subcooling [ºC]	0
Insulation Thermal Conductivity [W/(m.K)]	0.05	Superheating [ºC]	0
VCHP		Evaporator Heat Transfer Coef. (U) [W/(m^2.K)]	1000
Condenser Temperature (design value) [ºC]	100	**Other**	
Evaporator Temperature (design value) [ºC]	60	Ambient Temperature [ºC]	25
Compressor Isentropic Efficiency	0.7	Time Step [s]	30
Compressor Power (design value) [W]	1000	Ambient Convection Coef. [W/(m^2.K)]	10
Subcooling [ºC]	0	Electric Generator Average Efficiency	0.95
Superheating [ºC]	0	Exchangers Pinch Point (design value) [ºC]	10
Condenser Heat Transfer Coef. (U) [ºC]	1000		
Condenser Temperature (design value) [ºC]	100		

The charge phase brought the storage up to a temperature of 90°C in about 17 hours and 46 minutes, with 123.6 kWh of thermal energy variation in the water. With a total electrical consumption of 13.54 kWh, this leads to a global COP of 9.13, factoring in thermal losses to the environment during the charge; if the losses are not considered, the COP is 10.41

The exact values change throughout the charge, as shown in Figure 4. The increase in compressor work and the decrease in condenser thermal power lead to a decrease in the COP as the temperature and pressure in the condenser increase. It can be observed that the VCHP has taken a relatively long time to charge the storage – the charging time mostly depends on the ratio between the total storage heat capacity and the charge power of the heat pump.

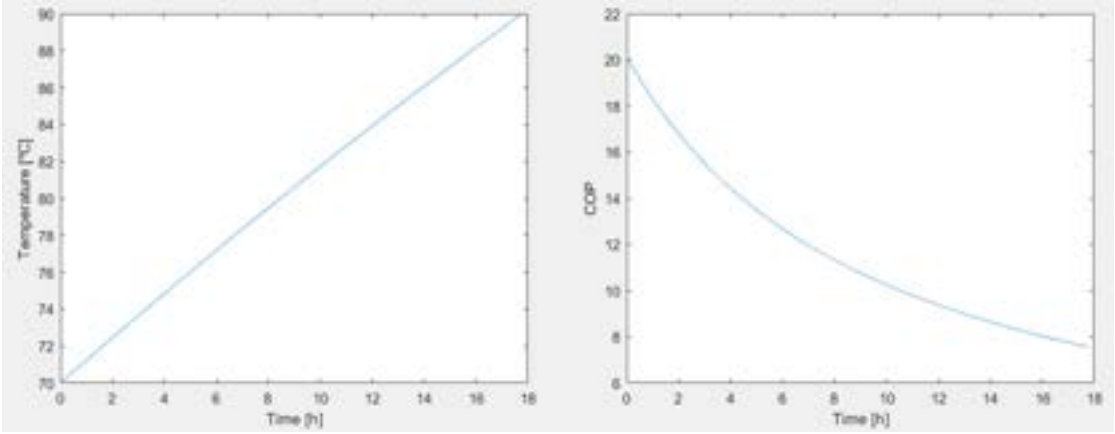

Figure. 4. Evolution of key parameters in the charge phase.

During the standby phase, the temperature of the storage tank decreased slightly due to losses to the environment, with a reduction from 90°C to 89.28°C. This decrease of 0.72°C corresponds to a loss of 4.53 kWh of thermal energy. Figure 5 shows the evolution of the temperature and the thermal loss power from the water tank over the 4-hour period.

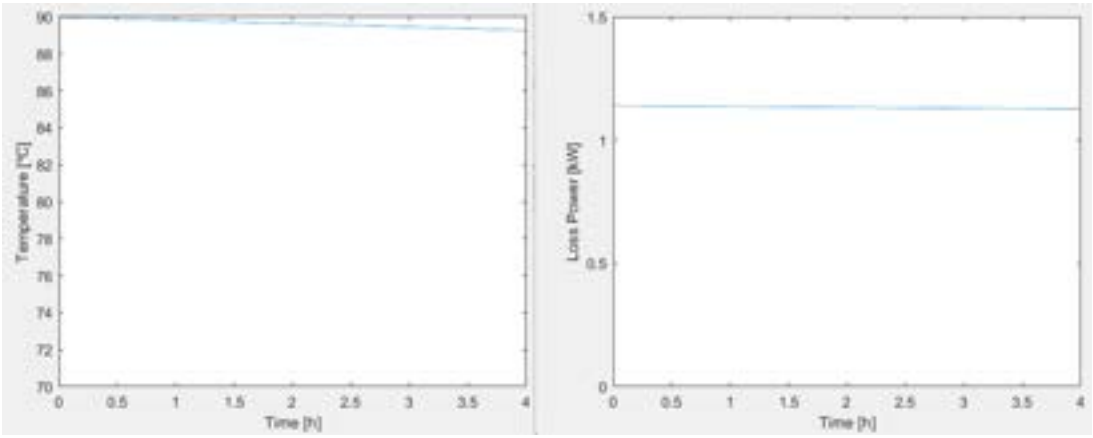

Figure. 5. Evolution of key parameters in the standby phase.

Finally, the discharge phase (Figure 6) brought the storage temperature back down to 70°C in about 10 hours and 27 minutes, with a thermal energy reduction of 119.06 kWh, and a net electrical generation of 8.08 kWh, leading to a global ORC efficiency of 6.8%; factoring out losses to the environment, the global ORC efficiency is 7.4%. With the decrease in evaporator temperature and pressure comes a decrease in evaporator thermal and pump power consumptions, and expander power generation, with an overall decrease in efficiency.

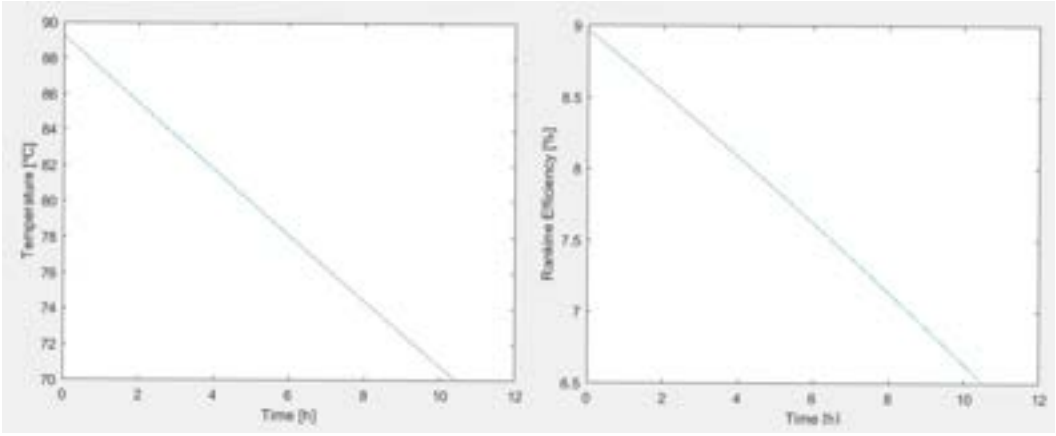

Figure. 6. Evolution of key parameters in the discharge phase.

Roundtrip efficiency is often estimated as the product of the COP with the Rankine efficiency, however this becomes inaccurate when thermal losses from the storage are considered. The use of a dynamic model allows the calculation of a precise value – in this first case, an ε_{rt} of 59.7% was obtained – a value consistent with those obtained in previous studies, and a satisfactory value for a non-optimized situation.

4.2. Optimization Method

The main driving parameters are: expander power, discharge time and charge time. The first two parameters determine an energy requirement, allowing the design of an adequate storage size. The heat pump can then be designed for a power that allows a full charge in 8 hours – roughly the time during which solar energy is available for the PV array.

In terms of optimization, the main objectives are the storage size/temperature variation and heat exchanger surface areas/pinch points. The optimization of these pairs of parameter involves a balance between cost and performance, as the best performance results from the largest surface areas and storage volumes, as these reduce the temperature differences, but they also lead to greater costs. To evaluate the effect of these parameters, a full discharge and a full charge were simulated for five nominal pinch point values (10K, 8K, 6K, 4K, 2K), and five storage temperature spreads at each pinch point (70°C – 75°C, 70°C – 80°C, 70°C – 85°C, 70°C – 90°C and 70°C – 95°C), resulting in a total of 25 charge simulations and 25 discharge simulations. For each case, the storage size was optimized for a 4-hour discharge with a nominal expander power of 20kW, and then a nominal compressor power was chosen to allow a full charge of the storage in 8 hours – these reference powers correspond to the maximum values that will be encountered throughout the simulation.

In terms of costs, the correlations in Table 4 adapted from Santos [10] were used to provide a rough estimate for capital costs in order to make the cost/performance optimization possible. The total cost of the system is given by the sum of the costs for each component.

Table 4. *Cost Correlations for components used in the Carnot Battery.*

Component	Cost Correlation [€]	Unit of Independent Variable
Storage Tank	$2000 + (625 \times Vol._{storage})$	m^3
Heat Exchangers	$150 \times Area$	m^2
ORC Expander	$1.5 \times (225 + (17000 \times \dot{V}_{in}))$	m^3/s
ORC Pump	$900 \times (\dot{W}_{pump}/300)$	W
VCHP Compressor	$225 + (17000 \times \dot{V}_{in})$	m^3/s
Control Electronics	4000	-

4.3. Results

As expected, lower pinch points lead to higher roundtrip efficiency for any storage spread, as this minimizes the temperature gradient of the VCHP and maximizes it for the ORC. A lower storage spread also improves efficiency, as it greatly increases the COP, with only a small decrease in ORC efficiency.

In terms of costs, while the lower pinch points and lower storage spreads lead to higher values (larger heat exchangers and storage tank), the effect of the storage spread seems far greater than that of the pinch point, so the best cost/efficiency ratios are mostly found with the lower pinch points and higher storage spreads – the highest value was obtained for the 10K pinch point and 70°C – 75°C storage spread, at 3979.70 [€/% roundtrip efficiency], with an ε_{rt} of 43.32%. By contrast, the best cost/efficiency ratio was obtained for the 2K pinch point and 70°C – 85°C storage spread, with a value of 586.73 [€/% roundtrip efficiency], and an ε_{rt} of 141.54%. For the 2K pinch point, all storage spreads above 70°C – 75°C return cost/efficiency values below 605 [€/% roundtrip efficiency], with roundtrip efficiencies between 173-105%. At this pinch point, the highest performance is reached with a 70°C – 75°C spread, at a cost/efficiency of 734.37 [€/% roundtrip efficiency], but with an ε_{rt} of 225.54%. In all cases for the 2K pinch point, the system becomes a hybrid between energy storage and a solar thermal power plant, as the efficiency exceeds 100%.

Figure 7 shows how the storage spread (70 – maximum temperature) and pinch point influence the cost/efficiency ratio. It can again be seen that most points along the 2K line are close to the optimal value.

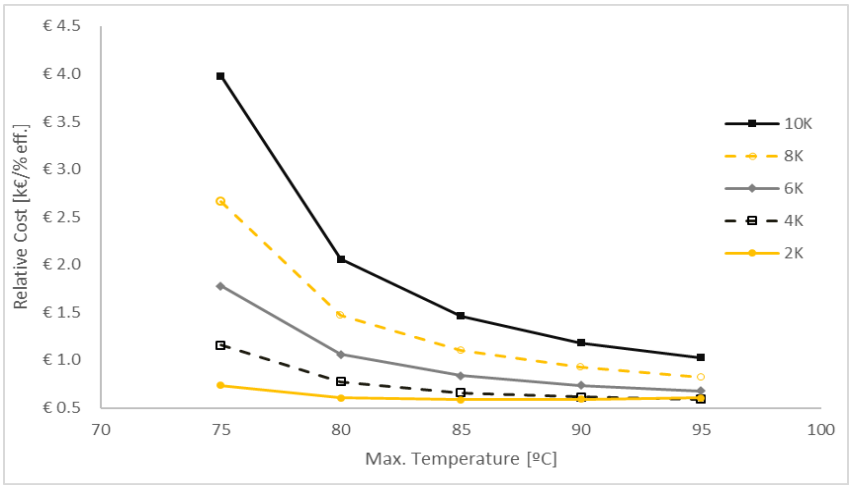

Figure. 7. Maximum storage temperature vs. relative cost for various pinch points.

Finally, payback time was analysed for the various configurations, as shown in Figure 8. The daily profit was calculated as the total electric energy of the discharge phase multiplied by a price of 0.20 €/kWh – a value assumed based on the costs of a few energy providers available in Portugal as well as reference values from the Energy Services Regulatory Authority (ERSE), for a contracted electric power up to 20.7 kVA. Furthermore, the system was assumed to generate this daily profit for 12 months of the year. In reality the performance would generally worsen in the winter months leading to lower profits. Even with enough solar thermal panels to offset unfavourable climate conditions, this fact could potentially affect the payback period in a real situation.

For all storage configurations, the shortest payback times are generally achieved with the 4K, 6K and 8K pinch points, and the shortest payback time between all the simulations is obtained with the 70°C – 95°C spread: approximately 9 years and 2 months. For a payback time of 4 years or lower, the average price of electricity would need to be at least 0.46 €/kWh.

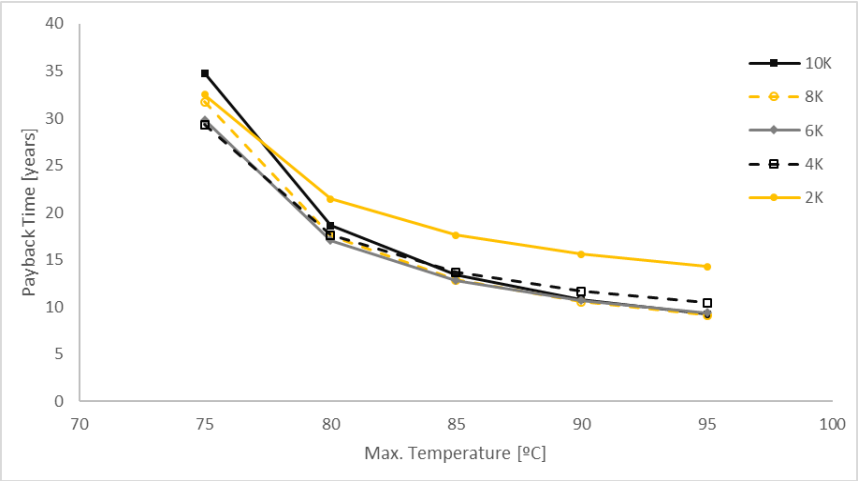

Figure. 8. Maximum storage temperature vs. payback time for various pinch points.

It can be concluded that a select few configurations optimize one parameter or another – the lowest pinch point (2K) and lowest storage spread (70°C – 75°C) optimize performance, the highest pinch point (10K) and the highest spread (70°C – 95°C) optimize costs, the 2K pinch point and 70°C – 85°C spread optimize the cost/performance ratio, and the 8K pinch point and 70°C – 95°C spread optimize the payback period. In this case, all of these solutions are ideal in one form or another – these configurations belong on the so-called Pareto Front (Figure 4.15), the set of all Pareto-optimal solutions. In other words, by moving between the points on this line it is impossible to improve any criterion without deteriorating another. This means that any point on this line represents a valid choice, and the selection should depend on the most relevant priority, or a balance of relevant priorities for a given implementation. For example, from a technological perspective, the best choice is the one with the highest efficiency. In terms of budget alone, the best choice has the lowest cost. For an efficient capital investment, one would select the machine with the best cost/performance ratio, and to minimize the risk of investment the machine with the lowest payback time should be chosen.

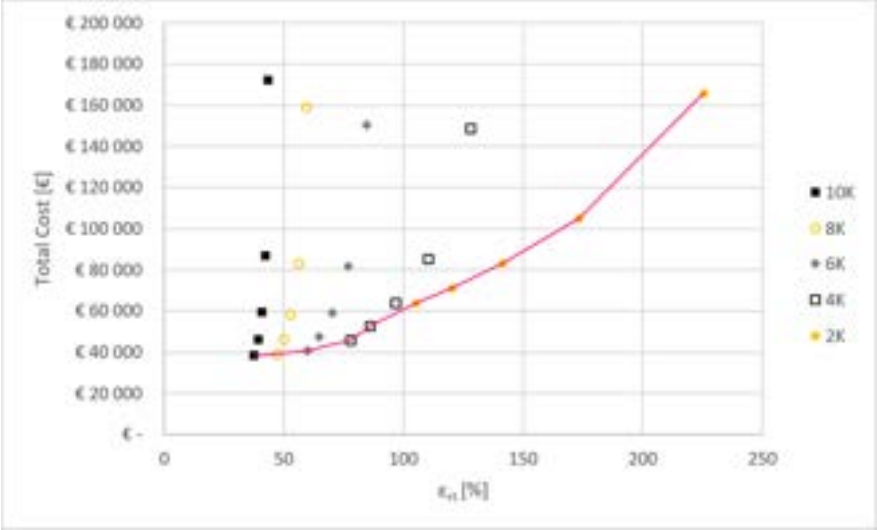

Figure. 9. Pareto Front for the tested configurations.

5. Conclusions

In this study, a case was made for the Carnot Battery as a suitable technology to replace current systems with relatively low Power/Capacity ratios, and a storage duration in the range of a few hours. A MATLAB script was developed which is capable of simulating the performance of a Carnot Battery composed of simple Vapour Compression Heat Pump and ORCs in dynamic charge/discharge conditions, as well as the thermal behaviour of a sensible storage in a standby situation. Despite the limited scope of the present study, the flexibility the developed model should allow its use in diverse situations with little to no modification, including off-design performance, thermal storage material selection, analysis of different thermal integration strategies, as well as more detailed techno-economic studies. Moreover, the model was used to study several configurations, taking into account the most critical parameters of the system, in an effort to discover an optimized arrangement; in the end, the optimal configuration depends on a balance of priorities – if performance is the only criterion, the

lowest pinch point (2K) and lowest storage spread (70°C – 75°C) should be selected despite the high costs; to minimize costs alone, one would select the highest pinch point (10K) and the highest spread (70°C – 95°C) in spite of the low efficiency, and for the best cost/performance ratio, the optimal choice would lie in between these two, with a 2K pinch point and a 70°C – 85°C spread. Additionally, for a minimized payback period the choice would be the 8K pinch point and a 70°C – 95°C spread. It was concluded that these four points belong on the Pareto front, in which all points represent either the optimization of one parameter, or a compromise between multiple parameters, and conclusions were drawn as to the applicability of each configuration.

Acknowledgments

This work is funded by National Funds through the FCT - Fundação para a Ciência e Tecnologia, I.P., under the scope of the project 2022.05282.PTDC.

Nomenclature

A	area, m^2
h	specific enthalpy, kJ/kg
$\dot{m}$	mass flow rate, kg/s
$\dot{Q}$	heat flux, W
R	thermal resistance,
T	temperature, °C
t	time step, s
U	heat transfer coefficient, W/(m^2.K)
$\dot{V}$	volume flow rate, m^3/s
vol	volume, m^3
$\dot{W}$	work, W

Greek symbols

η	efficiency
ε	effectiveness

Subscripts and superscripts

in	inlet
cd	condenser
c	compressor
cond	conduction
conv	convection
ev	evaporator
exp	expander
f	working fluid
loss	thermal loss
pump	flow pump
s	isentropic
rt	roundtrip

References

1. Jafari M, Botterud A, Sakti A. Decarbonizing power systems: A critical review of the role of energy storage. Renewable and Sustainable Energy Reviews. Elsevier Ltd; 2022.

2. Gallo AB, Simões-Moreira JR, Costa HKM, Santos MM, Moutinho dos Santos E. Energy storage in the energy transition context: A technology review. Renewable and Sustainable Energy Reviews. Elsevier Ltd; 2016. p. 800–22.

3. Dumont O, Frate GF, Pillai A, Lecompte S, De paepe M, Lemort V. Carnot battery technology: A state-of-the-art review. J Energy Storage. Elsevier Ltd; 2020;32.

4. Frate GF, Ferrari L, Desideri U. Rankine carnot batteries with the integration of thermal energy sources: A review. Energies (Basel). MDPI AG; 2020.

5. Weitzer M, Müller D, Steger D, Charalampidis A, Karellas S, Karl J. Organic flash cycles in Rankine-based Carnot batteries with large storage temperature spreads. Energy Convers Manag. Elsevier Ltd; 2022;255.

6. Dumont O, Lemort V. Mapping of performance of pumped thermal energy storage (Carnot battery) using waste heat recovery. Energy. Elsevier Ltd; 2020;211.

7. Steinmann WD, Bauer D, Jockenhöfer H, Johnson M. Pumped thermal energy storage (PTES) as smart sector-coupling technology for heat and electricity. Energy. Elsevier Ltd; 2019;183:185–90.

8. Eppinger B, Steger D, Regensburger C, Karl J, Schlücker E, Will S. Carnot battery: Simulation and design of a reversible heat pump-organic Rankine cycle pilot plant. Appl Energy. Elsevier Ltd; 2021;288.

9. Nadeem F, Hussain SMS, Tiwari PK, Goswami AK, Ustun TS. Comparative review of energy storage systems, their roles, and impacts on future power systems. IEEE Access. Institute of Electrical and Electronics Engineers Inc.; 2019. p. 4555–85.

10. Santos M. Modular architecture of steady-state simulation of Rankine based micro combined heat and power systems. 2020; Available from: http://hdl.handle.net/10316/95348

Green hydrogen and ammonia synthesis: a techno-economic feasibility analysis for different plant sizes (1 – 60 MW) and scenarios

Massimo Rivarolo[a], Daria Bellotti[b], Loredana Magistri[c]

[a] Thermochemical Power Group, DIME, University of Genova, Italy, massimo.rivarolo@unige.it
[b] Thermochemical Power Group, DIME, University of Genova, Italy, daria.bellotti@unige.it,
[c] Thermochemical Power Group, DIME, University of Genova, Italy, massardo@unige.it

Abstract:

As energy and environmental policies for 2030 and 2050 are encouraging several Countries to investigate the viability of alternative green fuels to replace fossil one and help decarbonizing energy sector, hydrogen and ammonia are two promising solutions.

Green hydrogen production is investigated considering both alkaline and PEM electrolysers commercial products, comparing the market solutions from the energetic standpoint considering three different plant sizes, representative of small (1 MW), medium (10 MW) and large (60 MW) scale applications. Hydrogen compression and storage in pressurized tanks is included in the analysis. Considering the drawbacks in hydrogen storage, a second plant lay-out is investigated considering an Air Separation Unit (ASU) and ammonia synthesis plant for the three different sizes. Ammonia is then stored in liquid form. For each solution, a techno-economic analysis is performed to evaluate: (i) CAPEX; (ii) OPEX; (iii) hydrogen and ammonia production costs. Authors evaluate the economic feasibility comparing final costs for green hydrogen and ammonia with market values, considering different scenarios and different green electrical energy prices. Finally, the authors investigate the influence of electrolysers' CAPEX decrease in a next future scenario (2030) on economic feasibility.

Keywords:

Hydrogen production; Energy; techno-economic analysis; green ammonia.

1. Introduction

To mitigate climate change in an effective and timely manner, rapid decarbonization of the global economy is needed. The transformation is already well advanced in the electrical energy sector in several industrialized countries, where competitive renewable energy technologies are increasingly replacing coal and gas-fired power plants [1]. Focusing on EU-27 Countries, total CO_2 emissions reduced from 4000 Mtons in 2005 to 3000 Mtons in 2020, with a strong increase in Renewable Energy Sources (RES) share on gross electrical (from 16.4% in 2005 to 37.4% in 2020), thermal (from 12.4% in 2005 to 23% in 2020) and transport consumptions (from 1.8% in 2005 to 10.3% in 2020) [2]. In the next years, according to the ambitious targets set for 2030, RES contribution is expected to further increase, helping the decarbonisation process.

In this context, the production [3][5] and transport [6][4] of hydrogen, ammonia [7][8][9] and other energy carriers [10][11] are receiving increasing attention, as they have the potential to replace coal, oil, and fossil gases as a global energy feedstock. Both hydrogen and ammonia do not contain carbon atoms, thus they do not impact in terms of CO_2 emissions, and they are considered very interesting alternatives to mitigate GHGs growth if they are produced starting from renewable electricity by the water electrolysis process. In this context, both Power to Hydrogen (P2H) and Power to Ammonia (P2A) are two of the most interesting emerging technologies having great potential as renewable energy storage for long periods, producing a chemical that can be considered as both an effective energy carrier and, in case of ammonia also an effective hydrogen carrier, and as alternative carbon free-fuel [10]. Both P2H and P2A have the potential to play an important role in the transition to a low-carbon economy [7]. They offer a way to store and use renewable energy, which can help to reduce greenhouse gas emissions and improve energy security. Furthermore, both technologies offer a pathway to decarbonize sectors such as transportation and industry, which have traditionally been difficult to decarbonize.

Despite the promising potential, there are still several technical and economic challenges that need to be addressed. For example, both processes are currently energy-intensive, and the production cost is still

relatively high compared to traditional methods. However, ongoing research and development in this area are expected to reduce costs and improve efficiency, making P2H and P2A increasingly viable options for a low-carbon future.

In this paper, in-depth research and evaluation of the market available technologies are reported. Moreover, the analysis and comparison of energy and economic feasibility for both hydrogen and ammonia production processes are carried out. The study is developed considering different plant sizes to evaluate the impact of the economy of scale. The fuel production cost for both the P2H and P2A is calculated for each plant size and considering different economic scenarios and different energy sources. The results are then compared with the market price of hydrogen and ammonia produced from fossil fuels.

2. Technologies

2.1. Electrolysers (hydrogen production)

Electrolysers are electrochemical devices that are used to split water molecules into hydrogen and oxygen using electricity. As fuel cells, electrolyzers are made by a certain number of electrolytic cells, each cell includes two electrodes and an electrolyte. More cells are connected in series to produce a stack to have the desired hydrogen production. Electrolysers' subsystems include equipment for cooling, hydrogen purification, DC/DC, and a supply system for demineralized water. Electrolysers are classified as Alkaline (AEC), Proton Exchange Membrane (PEMEC), and Solid Oxide Electrolysers (SOEC) [12]. The main features are reported in Table 1.

Table 1. Electrolysers' comparison

	AEC	**PEMEC**	**SOEC**
Electrolyte	Liquid (solution 20-30% KOH)	Solid (Polymeric membrane)	Solid (Ceramic)
Operating temp. [° C]	60 – 80	60 - 80	800 - 900
Efficiency [%]	70 - 75	70 - 75	85 - 90
Lifetime [hours]	100,000	80,000	< 20,000
Start-up time	Fast (minutes)	Very fast (seconds)	Slow (hours)
Current density [mA -cm^2]	0.2 – 0.4	1 – 2	0.5 – 1
Maturity	High (TRL9, Market solutions)	High (TRL9, Market solutions)	Medium (TRL7, Demonstration, early market)

While SOEC are still in development, AEC and PEMEC are experimenting a significant market diffusion in the last years, and commercial solutions are available from many producers also for significant sizes (multi-MW solutions). AEC are the most mature technology (developed in the last 50 years), they have lower costs than PEMEC and higher lifetime. However, compared to PEMEC, they have some drawbacks, as they have longer start-up time and dynamic response, which can represent a drawback in case of coupling with intermittent RES, such as wind and solar. Furthermore, PEMEC have higher compactness and allow for very high H_2 purity (99.99% vs 99.5% for AEC). Table 2 reports the main electrolysers' products, for sizes higher or equal to 1 MW, available on the market and their features in terms of technology, efficiency, and volume. It is worth observing that PEMEC performance are very similar to AEC and that both the technologies offer high power solutions in a wide range.

Table 2. Main AEC and PEM electrolysers' commercial products [13-18]

Type	**Producer and model**	**Delivery pressure**	**Power**	**H_2 production**	**Energy Cons.**	**Efficiency**	**Off design**
AEC	Mc Phy Mc Layzer 400-30	30 bar	1.8MW	400 Nm^3/h	4.5 kWh/Nm^3	78%	N/D
AEC	Mc Phy Mc Layzer 800-30	30 bar	3.6MW	800 Nm^3/h	4.5 kWh/Nm^3	78%	N/D
AEC	Nel Hydrogen A485	200 bar	1.6MW	390 Nm^3/h	4 kWh/Nm^3	88%	15-100%
AEC	Nel Hydrogen A1000	200 bar	3.1MW	785 Nm^3/h	4 kWh/Nm^3	88%	15-100%
AEC	Nel Hydrogen A3880	200 bar	12.4MW	3100 Nm^3/h	4 kWh/Nm^3	88%	15-100%
AEC	Sunfire Hylink	30 bar	10.5MW	2230 Nm^3/h	4.7 kWh/Nm^3	75%	25-100%
PEMEC	Nel Hydrogen MC500	30 bar	2.2MW	492 Nm^3/h	4.5 kWh/Nm^3	79%	10-100%
PEMEC	Nel Hydrogen M3000	30 bar	13.3MW	2952 Nm^3/h	4.5 kWh/Nm^3	79%	10-100%

PEMEC	Nel Hydrogen M5000	30 bar	22 MW	4920 Nm^3/h	4.5 kWh/Nm^3	79%	10-100%
PEMEC	Cummins Hy Lizer 1000	30 bar	4.6 MW	1000 Nm^3/h	4.6 kWh/Nm^3	77%	N/D
PEMEC	Cummins Hy Lizer 4000-30	30 bar	20MW	4300 Nm^3/h	4.6 kWh/Nm^3	77%	N/D
PEMEC	ITM POWER 3MEPCUBE	30 bar	2 MW	400 Nm^3/h	5 kWh/Nm^3	70%	N/D
PEMEC	ITM Power 2GEP Skid	30 bar	5MW	1002 Nm^3/h	5 kWh/Nm^3	70%	N/D
PEMEC	H-TEC Systems HCS	30 bar	10 MW	2100 Nm^3/h	4.8 kWh/Nm^3	74%	20-100%
PEMEC	Plug Power EX-4250D	40 bar	10 MW	2000 Nm^3/h	5 kWh/Nm^3	70%	N/D
PEMEC	H-TEC Systems ME450	30 bar	1 MW	210 Nm^3/h	4.8 kWh/Nm^3	74%	20-100%

Considering that PEMEC and AEC products available products on the market are similar from the efficiency, size, outlet pressure standpoints, PEMEC are chosen for the present study, considering that they guarantee higher purity and the have an advantage in terms of response, which make them more feasible for coupling with RES (i.e. wind energy) [5].

2.2. Air Separation Unit (ASU)

The required Nitrogen for the synthesis of Ammonia is usually obtained from the air (i.e. a mixture of N_2, O_2, and other gases) utilising an Air Separation Unit (ASU). The commercially available technologies for the nitrogen production are three: (i) Cryogenic Fractional Distillation; (ii) Pressure Swing Adsorption (PSA); (iii) membrane separation. All of them differs in operating principle, capacity, and energy consumption. The ASU is based on the Cryogenic Fractional Distillation approach starting from the liquefaction of the air and then the distillation and separation in its main components (O_2, N_2, Ar, etc). This process is usually employed for medium to large capacity plant (200 – 400,000 Nm^3/h of N_2), allows to obtain a very high purity level (up to 99.999%), the energy consumption ranges between 0.25 and 0.4 kWh/Nm^3 of N_2 and, considering the complexity of the process, the load range is quite limited (60%-100%). The PSA system is a discontinuous mechanical process based on the adsorption principle by means of vessels packed with Carbon Molecular Sieves that retains a specific molecule. The adsorption process depends on the operating pressure and the higher the pressure, the higher the N_2 purity at the outlet and the higher the energy consumption. Commercially, the PSA units operate at 6-8 bar, the N_2 purity can reach the 99.999% and the related energy consumption is up to 1.25 kWh/Nm^3 for very high purity nitrogen. Such a system is usually employed for medium-small applications (5-5000 Nm^3/h of N_2). As for the PSA, also the Membrane Separation is a pressure-driven process. The working principle is based on a selective gas permeation through a membrane substance that allows specific molecules to flow. The driving force is the difference in partial pressure between the two sides of the membrane. In the case of nitrogen production, when compressed air pass through the membrane's fibres, oxygen, water vapour, and carbon dioxide are selectively removed, creating a nitrogen-rich product stream. However, the purity grade that is achievable with membrane separation is usually in the range of 95%-99.5% resulting not suitable for ammonia synthesis via Haber-Bosch process. In the present work, considering the size and the purity required, the PSA technology is considered for the production of the nitrogen needed for the ammonia synthesis.

2.3. Haber-Bosch reactor

The SoA process for the synthesis of ammonia is known as Haber-Bosch process developed in the early 20th century. It is a thermochemical Fe-based catalytic process in which H_2 and N_2 (almost in stoichiometric ratio, 3:1) react at high pressure (140-250 bar) and temperature (300-500°C) according to the following reaction:

$$N_2 + 3H_2 \rightarrow 2NH_3 \qquad \Delta H_0 = -92\ kJ/mol$$

The ammonia synthesis reaction is exothermic and the number of moles decreases, thus it is favoured by low temperature and high pressure. Traditional process reach single-pass conversion around 15%-30% at typical working conditions (i.e 200 bar and 400-500°C, respectively). The overall conversion reach up to 95% with a recirculation factor around 7 to 10. The most used catalyst is Fe-based and therefore it is very susceptible to poisoning in presence of oxygen and water, and, for this reason, the required reacts purity is very high. In order to overcome the drawbacks of Fe-based catalysts and to reduce the operating conditions, new catalyst mostly based on ruthenium has been developed.

2.4. Hydrogen storage

Hydrogen storage represents one of the most critical aspects for the development of the hydrogen economy on global scale. In fact, despite its high energy content in mass terms (LHV 120 MJ/kg), hydrogen has a very

low density (0.09 kg/m^3 at ambient conditions), thus its energy content in volume terms is low (3.0 kWh/m^3). Today, there are three commercial solutions for hydrogen storage: (a) compressed gas; (b) liquid; (c) metal hydrides. Solution (a) is the most employed, as it presents high maturity for different scales [19]. Depending on the employed materials and to the final pressure storage, it is possible to identify four different tanks typologies for the storage. Type I consists in iron tanks (max pressure 200 bar), type II in aluminium tanks (max pressure 300 bar), type III in composite pressure vessel made of a metallic liner fully-wrapped with a fiber-resin composite (max pressure 700 bar) and Type IV in pressure vessel made of polymeric liner fully-wrapped with a fiber-resin composite (max pressure 700 bar). Type III and IV guarantee the best performance in terms of energy content (about 1300 kWh/m^3), thus they are considered in this study. In case of compressed gas storage, compression has to be considered. Since hydrogen is produced by electrolysers at 30 bar, the energy to bring it to 700 bar is estimated in 2.2 kWh/kg [20].

2.5. Ammonia storage

The ammonia presents physical characteristics very similar to the LPG and therefore they can share both the storage solutions and the infrastructure.

The ammonia can be stored in three main solutions: (i) fully-refrigerated tank; (ii) semi-refrigerated tank; (iii) pressurised tank. The first one is usually adopted in case of very high-capacity storage (10-50 ktons). In this case, the ammonia is stored at ambient pressure and saturation temperature (-33°C). The tank is equipped with a refrigeration circuit to maintain the design temperature and manage the blow-off. Such a solution is usually used as local storage at the production site or for the transportation into tanker ship, as well for the semi-refrigerated system. In this case, the ammonia is stored in liquid form at around -5°C - 0°C and saturation pressure (3-5 bar). The pressurised ammonia tank stores the ammonia as a liquified compressed gas at ambient pressure and related saturation pressure till a maximum of around 20bar. Inside this type of storage, both the liquid and vapour phase co-exist in equilibrium as function of the ambient temperature. This solution is mostly used for small-medium capacity, and for truck and rail transportation.

3. Case studies

In the present section, different case studies are analysed, considering:

- Small size case (1 MW electrolysers)
- Medium size case (10 MW electrolysers)
- Large size case (60 MW electrolysers)

For the three sizes, both green H_2 and NH_3 plant layouts are investigated. An energy and volume analysis is carried out, trying to minimize electrical energy consumption and occupied space for each configuration, considering the available products on the market. Figure 1 presents a simplified plant layout for green hydrogen production in a Power-to-Hydrogen (P2H) process. RES electrical energy gives power to electrolyser, splitting water in hydrogen and oxygen at a certain pressure (assumed 30 bar in this case). At the outlet, a compression system brings the hydrogen to the desired pressure level for the storage (from 200 to 700 bar, according to the scenario). The so produced H_2 has a very high purity and can be used in fuel cell electric vehicles, or for industrial/chemical applications. In P2A configuration, green hydrogen is compressed up to 200 bar and mixed with N_2, sequestered by ASU and then compressed; the reactants are sent to a Haber-Bosch synthesis loop and the so produced ammonia is stored in liquid form [21].

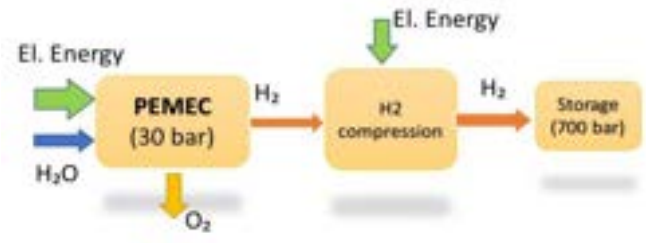

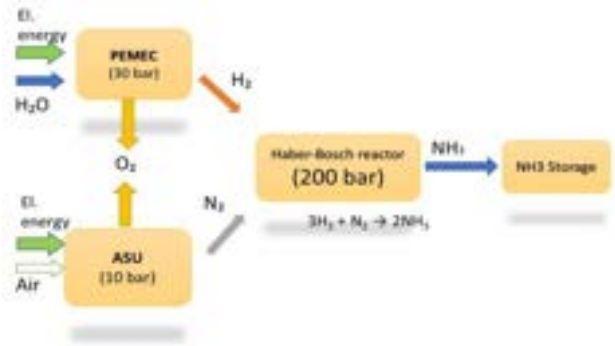

Figure. 1. Simplified plant layouts for P2H and P2A configurations

3.1. Small size (1 MW)

The 1 MW size is well-established in today's electrolyser market for both AEC and PEMEC technologies, as reported in Table 2. Considering PEMEC, the H-TEC PEM ME450 model is investigated as possible solution. Assuming the P2H plant operating for 4000 equivalent hours per year (considering average capacity factor for wind energy production, according to IRENA data), consumptions are nearly 700 ton/year of H_2O and 4165 MWh of electrical energy (4000 MWh for PEMEC, 165 MWh for H_2 compression up to 700 bar) for hydrogen production equal to 75 ton/year. The required space is about 87 m^2, including PEMEC (53 m^2) and storage (34 m^2).

In case of P2A configuration, operating for the same equivalent hours per year, water consumptions are the same, while electrical energy are slightly increased up to 4360 MWh (4000 MWh for PEMEC, 130 MWh for ASU, 230 MWh for nitrogen and hydrogen compression up to 200 bar for Haber-Bosch process), for ammonia synthesis equal to 425 ton/year. In this configuration, the required area results 87 m^2, including PEMEC (53 m^2), Haber-Bosch plant (26.5 m^2), ASU (1.4 m^2) and storage (6.1m^2).

3.2. Medium size (10 MW)

The medium size analysed in the present study is 10 MW, which is a capacity that is available for the single products for both PEMEC and AEC technologies (Table 2). However, considering that the minimum load is usually around 10-20%, this would imply a minimum available electrical energy from RES equal to 1-2 MW, which can decrease the operation time during the year. Thus, the combination of more commercial units in parallel is considered to guarantee higher plant flexibility. Considering PEMEC, two Cummins HyLYZER® 1000-30 (4.5 MW each) and one H-TEC PEM ME450 (1MW) models. Assuming the P2H plant operating for 4000 equivalent hours per year, consumptions are nearly 7000 ton/year of H_2O and 42470 MWh of electrical energy (40720 MWh for PEMEC, 1750 MWh for H_2 compression up to 700 bar) for hydrogen production equal to 795 ton/year. The required space is about 373 m^2, including PEMEC (113 m^2) and storage (260 m^2). It is worth noting that, in this case, the storage is the most influent voice in terms of area.

In case of P2A configuration, operating for the same equivalent hours per year, water consumptions are the same calculated for P2H 10 MW configuration. Electrical energy consumption slightly increases to 4360 MWh (40720 MWh for PEMEC, 1300 MWh for ASU, 2300 MWh for nitrogen and hydrogen compression up to 200 bar for Haber-Bosch process), for ammonia synthesis equal to 4250 ton/year. In this configuration, the required area results 242 m^2, including PEMEC (113 m^2), Haber-Bosch plant (56.6 m^2), ASU (11.4 m^2) and storage (61 m^2).

3.3. Large size (60 MW)

The large size analysed in the present study is 60 MW, corresponding to the size in the Tees Green Hydrogen project in UK for the production of green hydrogen using electrical energy generated by the Teesside offshore wind farm provided to local corporate customers to support decarbonisation [22]. Two options are investigated for the present case study: (a) 3 PEMEC units Cummins HyLYZER® 4000-30, 20 MW each; (b) 28 PEMEC units Cummins MC500, 2.2 MW each.

Assuming the P2H plant operating for 4000 equivalent hours per year, consumptions are nearly 38500 ton/year of H_2O and 247 GWh of electrical energy (237 GWh for PEMEC, 10 GWh for H_2 compression up to 700 bar) for hydrogen production equal to 4640 ton/year. In case of option (a), the required space is about 1842 m^2, including PEMEC (450 m^2) and storage (1392 m^2). Adopting solution (b), the required space results considerably higher (2232 m^2) due to the higher modules number.

In case of P2A configuration, operating for the same equivalent hours per year, water consumptions are the same calculated for P2H 60 MW configuration, while electrical energy consumption slightly increases to 4360 MWh (237 GWh for PEMEC, 5.2 GWh for ASU, 13.9 GWh for nitrogen and hydrogen compression up

to 200 bar for Haber-Bosch process), for ammonia synthesis equal to 25500 ton/year. In this configuration, the required area results 1060 m^2, including PEMEC (450 m^2), Haber-Bosch plant (225 m^2), ASU (10 m^2) and storage (375m^2).

4. Economic analysis

An economic analysis is then carried out to calculate the cost of green hydrogen and ammonia. The discussion continues by comparing the cost of producing hydrogen and ammonia obtained from green sources and the price on the market in the years 2021/2022. In addition, an analysis is performed on the possible incentives to be provided and the LCOE break-even in order to bridge the gap between the cost of fuels from fossil fuels and renewable energy sources.

To evaluate the economic viability [10], the Fuel Production Cost (FPC) is considered for both green hydrogen and ammonia, calculated as follows and expressed in €/kg:

$$FPC = (Annual\ Fixed\ Costs + Annual\ Variable\ Costs)/(Total\ Annual\ Production) \quad (1)$$

Where Annual Fixed Costs (AFC) are determined starting from the Total Capital Investment (TCI), considering the plant lifetime in years (n) and the WACC as rate (r):

$$AFC = TCI \cdot (r * (1+r)\text{^}n)/((1+r)\text{^}n\ -1) \quad (2)$$

Annual Variable Costs (AVC) include electrical energy cost and the OPEX of each plant component

$$AVC = \sum\_i \text{▒}\ 〖OPEX\_i〗\ + El.Energy\ cost \quad (3)$$

Economic analysis is performed considering the main assumptions reported below:

- Equivalent Operating Hours (EOH) for all the plant configurations are estimated in 4,000 h/year, considering that the renewable energy is produced by wind farms [23].
- Levelized Cost Of Electricity (LCOE) depends on the application scenario, assumed for the present analysis from IRENA 2021 report [23]. More in detail, for onshore wind farms LCOE is assumed 42 €/MWh for Europe, 31 €/MWh for USA, 28 €/MWh for China scenarios; for offshore wind farms LCOE is assumed 65 €/MWh for Europe, 78 €/MWh for USA, 79 €/MWh for China scenarios.
- Plant lifetime 20 years, corresponding to 80,000 equivalent operating hours, which is the guaranteed lifetime for electrolysers according to literature and producers [12][24].
- WACC 5%.

Capital Expenditure (CAPEX) for both alkaline and PEM electrolysers represents one of the most important voices for the economic feasibility, as electrolysers have a significant investment cost, as reported also in recent studies. Thus, a cost function is determined for both technologies based on recent data collected by IRENA in 2020 report as function of the installed power *P*, expressed in MW. The obtained cost functions are reported in Table 3. For the considered sizes, alkaline technology has a CAPEX of 1002 €/kW, 600 €/kW and 400 €/kW for 1 MW, 10 MW and 60 MW respectively, while PEMEC technology has higher CAPEX of 1155 €/kW, 742 €/kW and 526 €/kW for the same sizes [24].

The main assumptions for CAPEX and OPEX calculations are reported in Table 3.

Table 3. Main CAPEX and OPEC estimations for economic analysis [10][12][24]

Component	CAPEX	OPEX
PEMEC	$1155{\cdot}10^3 \cdot P^{0.808}$ [€]	4.5% CAPEX
AEC	$1002{\cdot}10^3 \cdot P^{0.778}$ [€]	4.5% CAPEX
H_2 compressors	16000 M_{H2} [€]	2% CAPEX
H_2 storage tanks	480 M_{H2} [€]	-
ASU	1450 M_{N2} [€]	2% CAPEX
Ammonia synthesis loop	50890 $M_{NH3}^{0.65}$ [€]	2% CAPEX

Ammonia storage	0.9 M_{NH3} [€]	-

4.1. Main techno-economic results

4.1.1. Annual costs breakdown

The first analysis is performed in order to evaluate the main costs distribution for both P2H and P2A configurations for 1 MW, 10 MW and 60 MW PEMEC sizes, respectively. For this first analysis, an average LCOE for electrical energy equal to 50 €/MWh is considered.

Figure 2 shows the cost breakdowns for green hydrogen production. Annual costs, including both CAPEX and OPEX contributions are about 0.48 M€/year for small size (1 MW), 4.00 M€ for medium size (10 MW) and 20.81 M€ for large size (60 MW). It is worth noting that the most relevant component is the cost of electrical energy for all the investigated sizes, followed by electrolysers' CAPEX and OPEX: these voices impact for 85-90% of total annual costs. Observing the three case studies, it is evident that, as the size increases, due to the decrease in the electrolysers CAPEX (sizing up), their incidence on the total percentage tends to diminish; in percentage terms, electrical energy cost influence increases more and more.

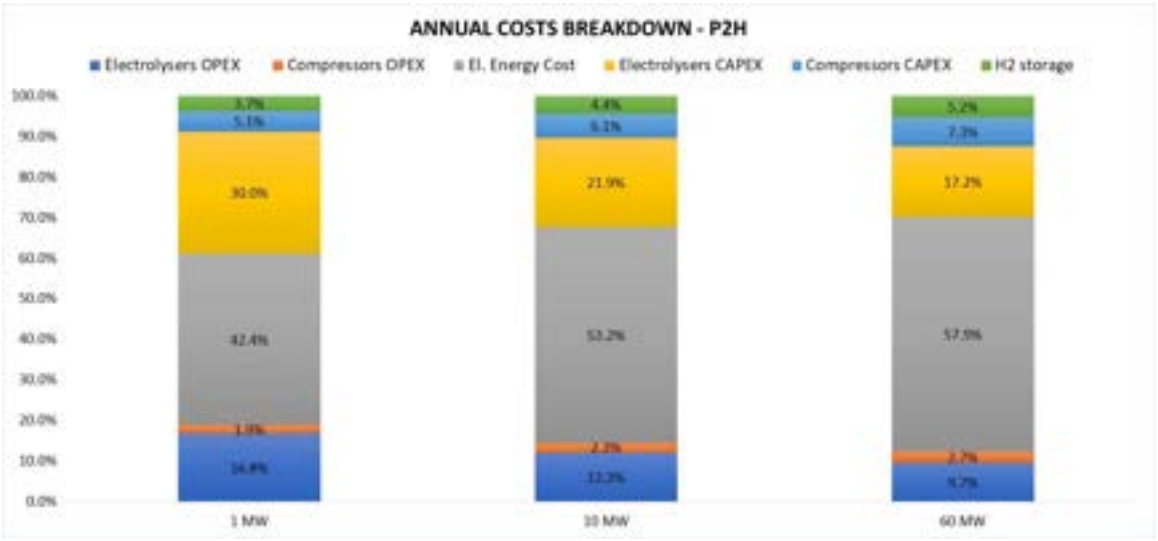

Figure. 2. Costs breakdown for P2H solutions

Figure 3 shows the main results for P2A configuration. Costs are slightly higher than in the P2H case: 0.56 M€/year for 1 MW size, 4.31 M€/year for 10 MW size and 21.12 M€/year for 60 MW size.

In the 1 MW case, most of the total annual cost (80%) is related to the electrolysers and the electrical energy costs. In the 10MW case, due to the sizing up of the electrolysers, the electricity cost, in percentage terms, becomes increasingly preponderant, around 53.5%. For the 60 MW size, as electrolysers and ammonia synthesis unit installed powers increase, their cost incidence decreases more and more, while electrical energy cost gains even more importance (61.7%).

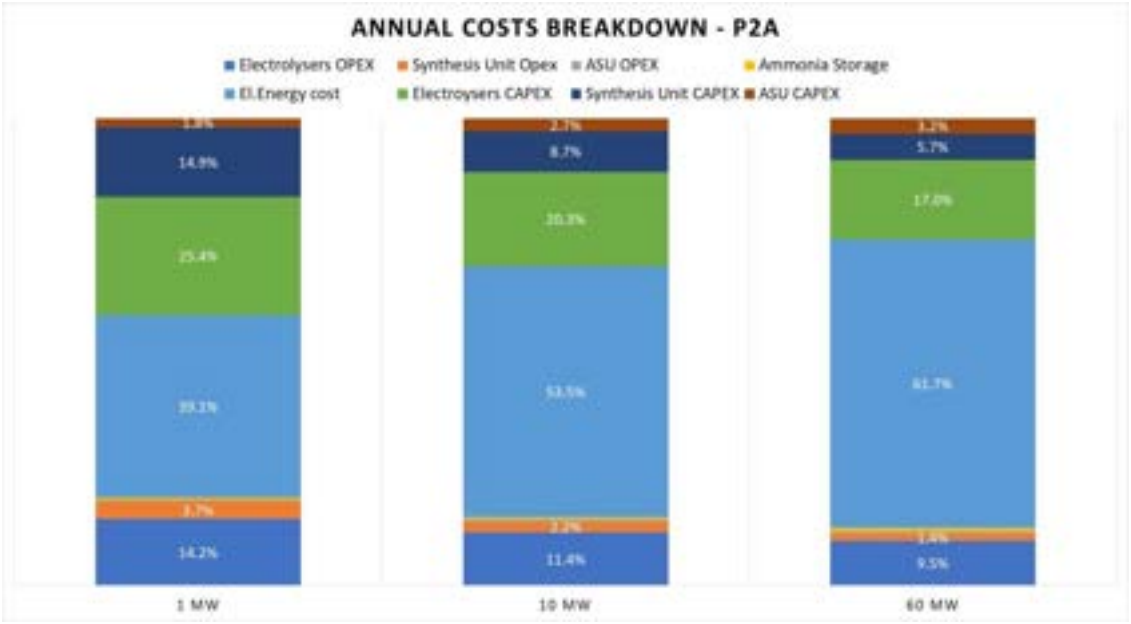

Figure. 3. Costs breakdown for P2A solutions

4.1.2. Results for different scenarios

In the previous analysis for costs breakdown, an average LCOE value of 50 €/MWh was assumed. In the present research the electrolysers are powered by renewable electricity generated by on shore/offshore wind turbine; thus, different LCOE values are investigated, according to the operating scenario. In this way, it is possible to investigate the influence of electrical energy cost. In this study, three geographic scenarios are considered: Europe, China and USA. LCOE values are obtained by 2021 data published by IRENA, reported in Table 4 [23]. Offshore wind plants are characterized by higher costs: in EU Countries the technology is well developed, thus costs are slightly lower for this kind of technology.

Table 4. LCOE estimations for economic analysis in different scenarios

	LCOE Wind on shore [€/MWh]	LCOE Wind offshore [€/MWh]
Europe	42	65
China	28	79
USA	31	78

For each scenario, the FPC for Hydrogen and ammonia are calculated. Figure 4 and Figure 5 show the main results. Production costs are positively affected by LCOE decrease and size increase (which lead to lower specific CAPEX for installed MW). As far as Hydrogen production is concerned, the lowest value is 3.1 €/kg (China, wind on shore, 60 MW) and the highest is 7.9 €/kg (USA, wind offshore, 1 MW). For P2A configuration, the FPC ranges between 0.6-1.2 €/kg for large size (60 MW) and 1.2-1.6 €/kg for small size (1 MW), depending on the cost of electricity.

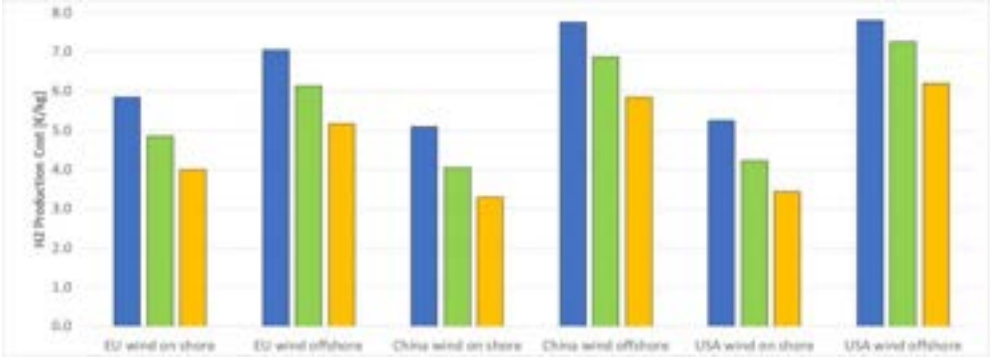

Figure. 4. Hydrogen production costs for different sizes in China, Europe, USA

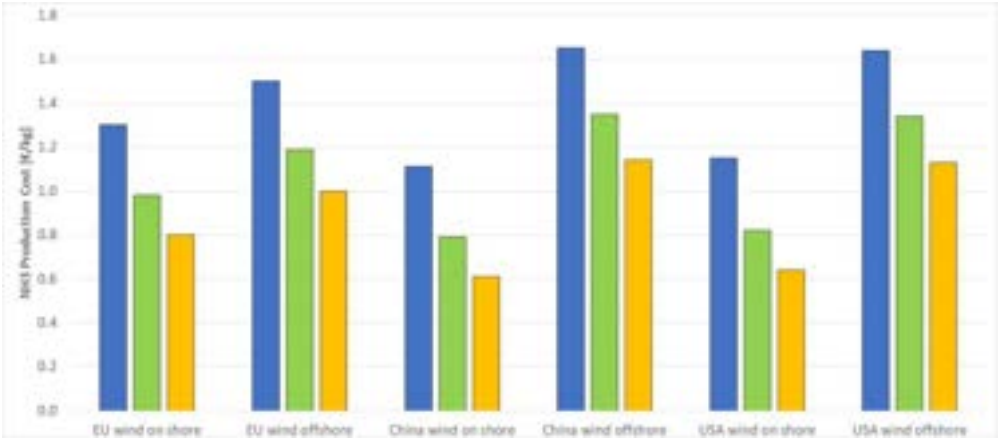

Figure. 5. Ammonia production costs for different sizes in China, Europe, USA

4.1.3. Comparison with actual H_2 and NH_3 market costs

In order to evaluate the economic feasibility of the proposed solutions, it is interesting to provide a comparison between the cost of green hydrogen/ammonia and their market prices in the last two years. Concerning Hydrogen, the most of it is produced by steam reforming of natural gas (grey hydrogen), thus its market price strongly depends on natural gas price [25]. Figure 6 compares the different H_2 production costs in the EU scenario with grey H_2 market price. While in a scenario with low-medium NG prices (until September 2021) green H_2 solutions are not economically feasible, the situation is different in a scenario characterised by high fossil fuels cost (2022). In this case, most of the green H_2 solutions, in particular the medium and large size ones become competitive from the economic standpoint.

Figure. 6. Comparison with market (grey) Hydrogen prices (2021-2022) in Europe

Figure 7 shows a similar trend for ammonia solutions, also in this case for EU scenario [26]. It is worth noting that green solutions are not affected by the fossil fuel market price variations.

Figure. 7. Comparison with market ammonia prices (2021-2022) in Europe

4.1.4. Next future scenario (2030)

In this section, the feasibility economic analysis is performed considering a next future European scenario (2030). To carry out the analysis, CAPEX reduction for PEM electrolysers is considered, starting from the study recently published by Gorre et al. [27]. In particular, according to new assumptions, specific CAPEX is 665 €/kW for 1 MW size, 470 €/kW for 10 MW size and 415 €/kW for 60 MW. LCOE from wind energy is assumed the same, considering that wind energy power plants are today a fully mature and developed technology, at least in the EU scenario. As Figure 8 shows, for on shore wind plants hydrogen costs range from 3.7 to 4.4 €/kg, with a significant reduction compared to actual costs shown in Figure 4 (from 4 to 5.8 €/kg); for offshore wind farms, H_2 costs range from 4.9 to 5.7 €/kg: also in this case, a significant reduction can be noted. The same trend is found for P2A configurations, with a minimum cost for 60 MW onshore (0.73 €/kg vs 0.8 €/kg in today scenario) and a maximum cost for 1 MW offshore (1.47 €/kg vs 1.50 €/kg in today scenario).

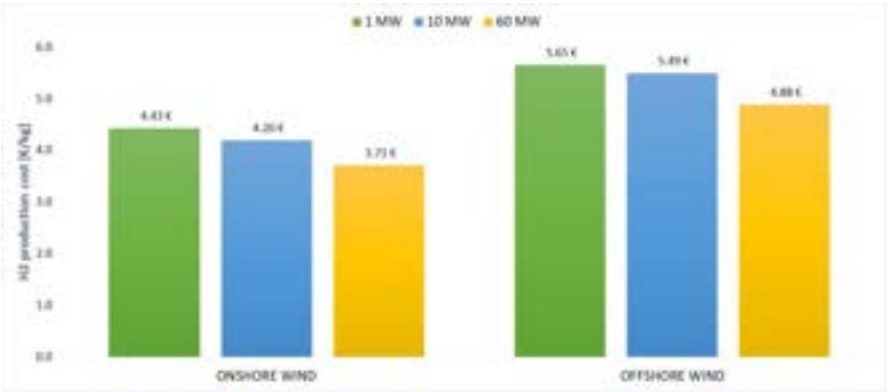

Figure. 8. Hydrogen production costs in Europe from RES (2030)

5. Conclusions

Green hydrogen and ammonia are considered among potential candidates to replace fossil fuels in the next future. However, hydrogen is still facing challenges for storage and transport. Green ammonia is another promising alternative.

The present study focused on different types of feasibility analyses:

- *Energy analysis*: for both green fuels, three different plant sizes are investigated, representative of small (1MW), medium (10 MW) and large (60 MW) electrical energy input. For the same size, electricity consumption varies within very limited ranges. The most impacting term is due to the PEM

electrolysers, which is common to both the configurations, while the impact of hydrogen compression (for P2H) and ASU/ammonia synthesis for (P2A) have a limited influence.

- *Volume analysis*: in the analysis of the overall dimensions, different results are obtained depending on the sizes. For 1 MW size, similar results are obtained for P2H and P2A configurations. In the case of medium and large sizes (10 and 60 MW), the impact of storage for P2H configuration becomes dramatic, thus this kind of solution seems not to be the best option. For large size, it is important to consider to couple different PEMEC modules, in order to guarantee also higher plant flexibility, in particular in presence of not constant/programmable RES electrical energy input.
- *Economic analysis*: the first analysis is performed to evaluate annual costs breakdown for all the sizes and the configurations investigated. The most relevant voices are electrical energy and PEMEC costs (together 75-85% of the total, depending on the configuration). Then, a scenario analysis is performed to investigate the influence of LCOE, considering both on shore and offshore wind farms, in EU, China and USA scenarios. Finally, production costs for hydrogen and ammonia are compared with market prices (2021-2022), finding out that small scale plants (1MW) are not economically feasible, if not encouraged by proper incentives. On the other hand, medium and large scale configurations (10MW and 60MW) are worthy solutions, in particular in a scenario (2022) characterized by higher natural gas cost and consequent larger production costs for grey hydrogen and ammonia.
- *Future scenarios*: in next future scenario (2030), it is realistic to assume a decrease in PEMEC market costs, which should lower green H_2 and NH_3 production costs. Furthermore, their lifetime may be extended, LCOE from offshore wind farms may be lower too and fees related to grey fuels production (or incentives to green fuels) may be included by some Countries: these latter factors may increase the economic feasibility of the solutions investigated in the present paper.

Acknowledgments

The Authors would like to acknowledge Simone Damanti, graduated student at University of Genoa, for his contribution to this research activity.

Nomenclature

AEC	Alkaline Electrolysers
AFC	Annual Fixed Costs
ASU	Air Separation Unit
FPC	Fuel Product Cost (€/kg)
IRENA	International Renewable Energy Agency
LCOE	Levelized Cost of Electricity (€/MWh)
LHV	Lower Heating Value (MJ/kg)
n	Plant lifetime (years)
PEMEC	Proton Exchange Membrane Electrolysers
P2A	Power to Ammonia
P2H	Power to Hydrogen
PSA	Pressure Swing Adsorption
RES	Renewable Energy Sources
SOEC	Solid Oxide Electrolysers
TCI	Total Capital Investment (M€)
WACC	Weighted Average Cost of Capital

References

[1] Dalala., Al-Omari M., Al-Addous M., Bdour M., Al-Khasawneh Y., Alkasrawi M., Increased renewable energy penetration in national electrical grids constraints and solutions, Energy 2022;246:123361.

[2] https://ec.europa.eu/eurostat/statistics-explained/index.php?title=Renewable_energy_statistics#Share_of_renewable_energy_more_than_doubled_between_2004_and_2021 [last accessed 16.2.2023]

[3] Ferrari M.L., Rivarolo M., Massardo A.F., Hydrogen production system from photovoltaic panels: experimental characterization and size optimization, Energy Conversion and Management 2016;116: 194-202.

[4] Kakoulaki G., Kougias I., Taylor N., Dolci F., Moja J., Jäger-Waldau A., Green hydrogen in Europe – A regional assessment: Substituting existing production with electrolysis powered by renewables, Energy Conversion and Management 2021;228:113649.

[5] Safari F., Dincer I., Assessment and optimization of an integrated wind power system for hydrogen and methane production, Energy Conversion and Management 2018; 177:693-703.

[6] Olabi A.G., Bahri A.S., Abdelghafar A.A., Baroutaji A., Sayed E.T., et al., Large-vscale hydrogen production and storage technologies: Current status and future directions, International Journal of Hydrogen Energy 2021;46(45):23498-23528.

[7] Zhang H., Wang L., Van Herle J., Maréchal F., Desideri U., Techno-economic comparison of green ammonia production processes, Applied Energy 259;2020:114135.

[8] del Pozo C.A., Cloete S., Techno-economic assessment of blue and green ammonia as energy carriers in a low-carbon future, Energy Conversion and Management 2022;255:115312.

[9] Ikäheimo J., Kiviluoma J., Weiss R., and Holttinen H., Power-to-ammonia in future north European 100% renewable power and heat system, International Journal of Hydrogen Energy 2018; 43(36):17295–17308.

[10] Bellotti D., Rivarolo M, Magistri L., A comparative techno-economic and sensitivity analysis of Power-to-X processes from different energy sources, Energy Conv and Management 2022;260:115565.

[11] Rivarolo M., Marmi S., Riveros-Godoy G., Magistri L. Development and assessment of a distribution network of hydro-methane, methanol, oxygen and carbon dioxide in Paraguay, Energy Conversion and Management 2014;77:680-689.

[12] Proost J., State-of-the art CAPEX data for water electrolysers, and their impact on renewable hydrogen price settings, Int. J. of Hydrogen Energy 2019;44(9):4406-4413.

[13] https://nelhydrogen.com/water-electrolysers-hydrogen-generators/ [accessed 16.1.2023].

[14] Hydrogen: the next generation – discover Cummins electrolyzer technologies - available at www.cummins.com [accessed 16.1.2023].

[15] https://mcphy.com/en/equipment-services/electrolyzers/ [accessed 16.1.2023]

[16] https://www.sunfire.de/en/hydrogen [accessed 16.1.2023]

[17] https://www.h-tec.com/en/products/detail/h-tec-pem-elektrolyseur-hcs/10-mw-hcs/ [accessed 16.1.2023]

[18] https://itm-power.com/how-it-works/pem [accessed 16.1.2023]

[19] Moradi R., Groth K.M., Hydrogen storage and delivery: Review of the state of the art technologies and risk and reliability analysis, Int. J. of Hydrogen Energy 2019;44(23):12254-12269.

[20] Tahan M.R., Recent advances in hydrogen compressors for use in large-scale renewable energy integration. International Journal of Hydrogen Energy 2022;47(83):35275–35292.

[21] Rivarolo M., Riveros-Godoy G., Magistri L., Massardo A.F., Clean Hydrogen and Ammonia Synthesis in Paraguay from the Itaipu 14 GW Hydroelectric Plant, ChemEngineering 2019;3(4):87.

[22] Kendall K., Green hydrogen in the UK: Progress and prospects, Clean Technologies 2022;4(2):345–355.

[23] Renewable power generation costs in 2021, International Renewable Energy Agency, Abu Dhabi, IRENA 2021.

[24] Green Hydrogen Cost Reduction: Scaling up Electrolysers to Meet the 1.5ºC Climate Goal, International Renewable Energy Agency, Abu Dhabi, IRENA 2020.

[25] https://businessanalytiq.com/procurementanalytics/index/natural-gas-price-index/[last access 16.2.2023]

[26] https://businessanalytiq.com/procurementanalytics/index/ammonia-price-index/ [last access 16.2.2023]

[27] Gorre J., Ortloff F., van Leeuwen C., Production costs for synthetic methane in 2030 and 2050 of an optimized power-to-gas plant with intermediate hydrogen storage, Applied Energy 2019;253:113594.

External control strategy for Seasonal Thermal Energy Storage

Jarosław Milewski, Olaf Dybinski, and Arkadiusz Szczesniak

Warsaw University of Technology, Warsaw, Poland, jaroslaw.milewski@pw.edu.pl

Abstract:

The paper presents the results of using an external control strategy to optimize seasonal thermal energy storage (STES). Literature studies have been carried out related to design and optimization of the STES. Two STES configurations were considered with adequate constraints. The objective function was defined as minimum operational costs of the entire system. A structural external strategy is proposed which optimizes all heat flows based on the simplex method (Solver(R)). Simulations of system operation were carried out with and without the proposed external strategy for randomly generated outside temperatures in a 5-year horizon.

Keywords:

STES; heat management; dynamic simulation; control strategy

1. Introduction

Rising fuel prices and increasing electricity consumption are driving research into more efficient electricity and heat generation sources [1]. Energy used for space and domestic water heating constitutes 1/3 of the total energy used in industrialized countries like Poland. Fossil fuel consumption and emissions may be reduced by using solar-based technologies. For electricity generation, solar energy may be used directly (PV panels) or indirectly utilizing biofuels [2–4] applying, for example, fuel cell technology which additionally features high efficiency due to the direct transformation of chemical energy into electricity [5–14]. However, the largest market for solar energy is now connected with the absorption of solar radiation into heat up media that are flowing through solar collectors.

Optimization of seasonal thermal energy storage dates to the times when these types of installations were being constructed. According to the design idea a seasonal heat accumulator does not operate separately and is an element of a power system composed of other devices that are typical for the system. The system comprises equipment like solar collectors, heat pumps, conventional gas or solid fuel boilers, pumps, etc. Sometimes, depending on technical conditions, the system may relate to an urban heating network. This creates additional possibilities for altering the amount of heat accumulated in the storage tank and makes the whole system more elastic. It should be noted that, particularly in the case of smaller installations, the urban heating network has an incomparably larger capability of storing heat when compared with the heat accumulator. Considering the set of parameters and external factors influencing the operation of devices and the whole system, a respective operation optimization algorithm for the system seems to be indispensable.

It should consider the specific features of all devices. In addition, it should be matched to the nominal design point of the system when applying it to an existing object or be given the flexibility to select individual devices (their size, operating parameters, etc.) if it is used at the design stage. During optimization particular attention should be focused on the accumulator itself and its interplay with other objects. Devices mentioned earlier that are part of the system, like solar collectors, heat pumps, boilers, etc., are generally commercially available and their operation characteristics and parameters are known. This does not however apply to the storage tank. There are several types of storage [15] that should be taken into consideration. Moreover, insulation plays a vital role here—its thickness, conductivity and above all resistance to ground humidity, which significantly increases the conductivity (this type of storage tank is usually partly or totally immersed in the ground). In the available literature there are few papers that include the optimization of system operation with a storage tank. There are however articles where a significant emphasis was put on optimization of the cooperation between an accumulator and an external network as well as with a co-generation plant, as in [16]. The authors use the commercial Excel (R) environment and the Monte Carlo method to select the optimal size of the accumulator. The analysis was made for three cases: for the cogeneration system electric power of 40 kW, 80 kW and 160 kW. Some authors present modelling methods and optimizing algorithms for storage equipped systems cooperating with a central air conditioning system in public utility buildings [17,18]. This case is somewhat different as cold instead of hot water is stored, but the idea remains substantially similar. The accumulator is charged during the night using cooling units (when electricity prices are lower) and discharged during the day,

when the cooling demand and electricity prices are higher. The authors analysed 5 operation scenarios for the system: cooling, storage charging, storage charging with operation of cooling units, discharging, discharging with operation of cooling units. It should be mentioned that the storage tank operates diurnally, and not seasonally. In other work [19] operation optimization of the accumulator is performed including economic conditions like variable electricity prices and climate changeability.

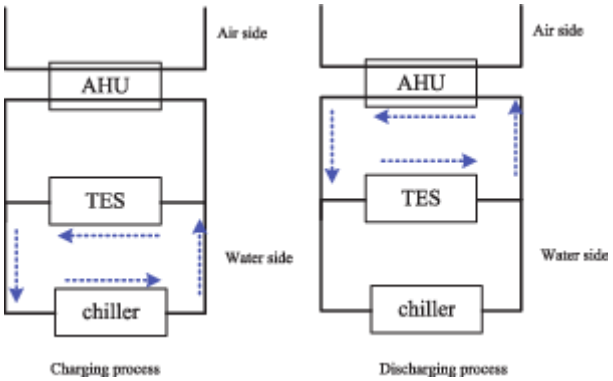

Figure 1: Diagram of charging and discharging processes for a thermal energy storage tank (TES) [18]

In fig. 1 a diagram of the charging and discharging process for a storage tank was presented according to [18]. In the paper, seasonal storage was analysed, where additional parameters considered during the modelling and optimization process were considered, e.g., variable ambient and ground temperatures.

Seasonal heat storage was analysed in the study [20], where the discussed installation was placed in a public utility building with a surface area of 3,700 m2. In contrast to the device investigated in this paper, a UTES (Underground Thermal Energy Storage) equipped with a heat pump was used.

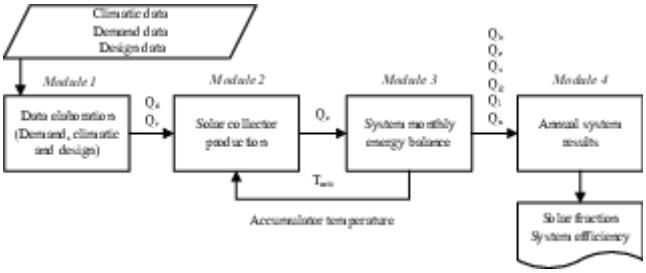

Figure 2: The block diagram used for calculations for the system analysed in [21]

In the paper [21] the authors proposed a simplified method for Central Solar Heating Plants with Seasonal Storage systems. The simplified method was graphically depicted in Fig. 2. Additionally a dynamic analysis of the system in TRNSYS [22] and an economic analysis were done by the authors.

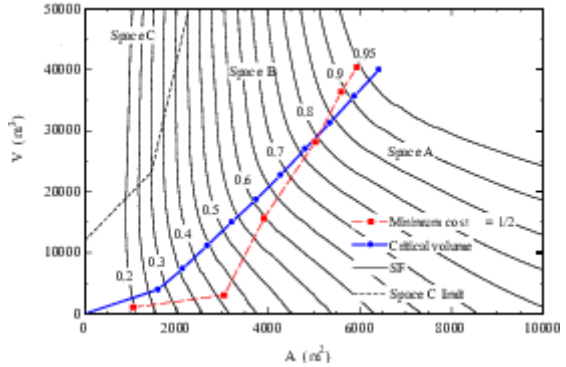

Figure 3: Solar collector area and volume of seasonal storage, isoquant lines of solar fraction [23]

In the same study, an authorial relationship diagram between the storage volume and the solar collector surface area was presented. In the diagram the Space C limit was presented that, according to the analysis made by the authors, is ineffective from the aspect of cooperation between the collectors and the storage tank. The authors also estimated that if the cost of the storage tank alone was decreased by about 50% and the investment costs that need to be borne for solar collectors and other, auxiliary devices, then the introduction

of a storage critical volume could become an attractive idea from the economic viewpoint (also shown in the graph).

Table 1: Comparison of methods for modelling seasonal thermal energy storage—yearly characteristics [23]

		Jan.	Feb.	Mar.	Apr.	May.	Jun.	Jul.	Aug.	Sep.	Oct.	Nov.	Dec.	Year
	Qr MWh	2759	3310	4400	4366	481	486	546	552	464	409	298	257	4978
Input Data	H MJ/(m2-day)	6.4	9.8	13.8	17.4	21.5	23.8	25.3	22.5	16.5	11.6	7.5	5.7	
	T °C amb	6.2	8.0	10.3	12.8	16.7	21.0	24.3	23.8	20.7	15.4	9.7	6.5	
	Qd MWh	1309	865	632	366	80	0	0	0	0	142	807	1287	5488
	Qc MWh	1650	2100	2889	2889	326	317	335	304	160	143	166	152	2856
TRNSYS [22]	Qg MWh	1130	659	347	162	0	0	0	0	0	0	0	389	2687
	SF %	14%	24%	45%	56%	100%	100%	100%	100%	100%	100%	100%	70%	51%
	Qc MWh	1820	2311	3166	3177	347	332	350	321	229	173	130	146	3075
Lunde [24]	Qg MWh	1132	638	320	53	0	0	0	0	0	0	0	359	2501
	Tacu °C	30	30	30	30	39.9	52.2	65.1	76.9	85.0	85.7	59.7	30.0	—
	SF %	14%	26%	49%	86%	100%	100%	100%	100%	100%	100%	100%	72%	54%
	Qc MWh	1750	2299	3133	3133	345	329	349	315	217	160	117	134	2996
BKM [25]	Qg MWh	985	647	375	89	0	0	0	0	0	0	0	517	2614
	Tacu °C	31.9	29.1	29.6	30.6	35.6	47.3	59.8	72.1	81.7	85.6	72.4	47.0	—
	SF %	25%	25%	41%	76%	100%	100%	100%	100%	100%	100%	100%	60%	52%
	Qc MWh	1620	2100	2799	2966	349	321	333	287	180	123	72	95	2708
GLS [26][27][28]	Qg MWh	1147	655	353	70	0	0	0	0	0	0	0	606	2830
	Tacu °C	29.8	29.7	29.5	29.4	43.4	54.2	69.3	80.5	87.2	82.8	55.3	30.0	—
	SF %	14%	23%	36%	71%	100%	100%	100%	100%	100%	100%	100%	59%	48%

In the study [23] a comparison was made of various modelling methods for systems comprising seasonal thermal energy storage. These methods were used in Engineering Equation Solver [29], which was also used to generate yearly operation characteristics for a system with storage. Except for the simplified method presented by the authors, two others were also analysed. One of them is a 1979 method proposed by Lunde [24,30], and the other from 1981 by Braun, Klein and Mitchell which they named BKF [16]. The list of modelling methods was presented in the Table 1. An integral element of this research was comparison of the results with simulations performed in the previously mentioned TRNSYS software (it is also mentioned in the table 1).

2. Base for calculations

2.1 Optimization method—Solver(R)

Optimization of the storage operation was performed using Solver(R) available in Excel(R)environment; detailed information on this topic may be found in [31]. When linear optimization is conducted using Solver

a numerical procedure is used called a simplex algorithm [32–35]. The simplex method, first proposed by George Dantzig in 1947, is the first algorithm of numerical optimization developed for the American army and widely used (in many variations) till the present day. The simplex method is basic and universal and enables one to solve all kinds of linear models. This is an analytical method allowing for computing models independent of their size. There are several versions of realizing the simplex algorithm, but, except for different ways of calculating and methods of improving the algorithm convergence, the idea remains unchanged. This method requires however that many calculations be made during the solving of the model and the calculation itself is iterative.

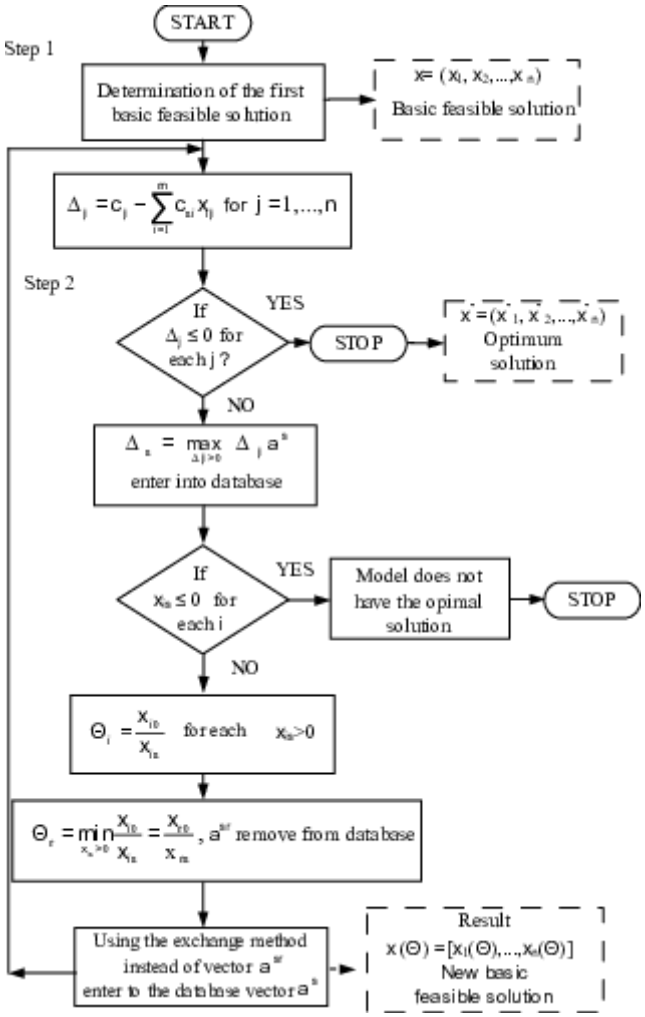

Figure 4: Block diagram of the simplex method (example for a model where the objective function is maximized) [36]

In the simplex algorithm, two basic stages may be distinguished. The first one consists of determination of the basic allowable solution. This may be achieved by introducing additional decision variables into the model. The second stage comprises correction of subsequently performed iterations of the basic allowable solution until an optimal solution is found if the solution exists. The correction of solutions is in fact tantamount to the generation of new basic allowable solutions and checking them from the angle of optimality. The value of the goal function for the subsequent solution (when the objective function is maximized) is often higher than the one before. It is possible that during computations the objective function value will be equal to the objective function value from the previous solution. It may not however be lower. There is a clear analogy in the case of minimizing the objective function. Calculations made with the simplex method have an iterative character. There are two criteria in the method, giving the possibility of terminating calculations and assessing whether the base solution is an optimal one or not; and if not, whether more solutions may be generated. The simplex algorithm is quite labour–intensive, particularly for large–scale models. Computer applications of the algorithm are used to solve such models. Many programs assisting mathematical calculations allow for the development of calculation procedures for the simplex method or are equipped with ready-made simplex modules, like Solver. The simplex method allows one to solve continuous models of linear programming. A block diagram of the method is presented in Fig. 4; in the next iteration of the simplex method the following cases are possible:

- $\Delta_j \leq 0$ for every j = 1, 2, ..., n is a basic, allowable solution,

- $x_{is} \leq 0$ for every $i = 1, 2, ..., n$ then the model does not have an optimal solution,
- there exists $\Delta_S > 0$ and there exists $x_{is} > 0$ then a new basic allowable solution may be obtained.

The simplex algorithms make it possible to go from one basic solution to subsequent ones, usually more correct due to the value of the objective function. Iterations are made if the optimal solution is obtained, if it exists. The quantity of iterations that need to be made when solving a model and achieving an optimal solution cannot be precisely specified. It is known that for a set of n decisive variables and m substantial limiting conditions, the number of base solutions is at a maximum:

$$\binom{n}{m} = \frac{n!}{m! \cdot (n-m)!}$$

The simplex method does not search all the base solutions, merely selected ones. The way of selection is directed. For most cases the algorithm is convergent within a finite number of iterations. From calculation experience it may be concluded that the number of iterations performed is embraced within the limits of the number of substantial limiting conditions to the triple of the number of conditions. Iteration number estimation commonly present in the literature is equal to $2 \cdot (n + m)$. All the data result mainly from computational experience and are solely estimated values.

It must be noted that the simplex method included in the Solver package is based on differential calculus, which has the effect that for significantly non–linear tasks, it does not give correct results. For this reason, the temperatures in the accumulator were set at 60°C before every optimization (mean value between the extreme values 40/80°C). In the future, methods based for example on artificial intelligence should be used [37–42].

2.2 The objective function

The operation criterion for the optimizer may be an economic function that will, for example, minimize the operating costs of STES operation. Therefore, the optimization goal will be to maximize the profit, which may be understood in different ways. A total profit/loss balance includes many various elements, including income or costs of a typical financial origin. Optimization does not influence these costs and it is not sensible to include them in the optimization process. Optimization influences operating costs. For this reason, the total operating cost in the analysed period will be the objective function, i.e., for periods n (from the beginning of calculations), n+1 till periods n+3 or n+6 respectively depending on the selected calculation mode. It may present mathematically as:

$$\mathrm{K_o} = \sum \mathrm{K^i_{Fuel}} + \Delta \mathrm{K_{HeatStorage}} - \sum \mathrm{K^i_{Penalty}} - \sum \mathrm{K^i_{Power}}$$

where: i —index of the following calculation steps; $\Delta K_{HeatStorage}$ —cost resulting, and amount of heat accumulated at the beginning and at the end of the analyzed time period (or from the price difference); K_{Fuel} —fuel cost in the subsequent calculation steps; $K_{Penalty}$ —penalty for heat not taken from the collectors; K_{Poweri} —cost of the consumed electricity.

Cost of fuel used for supplying other heat sources in consecutive settlement periods will be calculated as:

$$\mathrm{K^i_{Fuel}} = \mathrm{B^i_{NG}} \cdot \mathrm{k_{NG}}$$

where: B^i_{NG} —use of natural gas in respective calculation step; k_{NG} —unit price of the natural gas.

Cost of electricity supplied to auxiliary devices and the heat pump in consecutive settlement periods will be calculated as:

$$\mathrm{K^i_{Power}} = \frac{\mathrm{Q_{STES}}}{\mathrm{COP_{HP}}} \cdot \mathrm{k_{Power}}$$

where: Q_{STES} —heat taken from the accumulator; COP_{HP}—heat pump COP; k_{Power} —unit price of electricity.

Heat supplied to the buildings must maintain the right temperature level, which may not be achieved directly from the storage tank when its temperature drops below the returning water temperature.

Coefficient of Performance of the heat pump depends on the temperature difference between the upper and lower heat sources and its perfectness (with respect to the Carnot cycle); in the calculations the following relationship was assumed:

$$\mathrm{COP} = \eta_{\mathrm{HP}} \cdot \frac{\mathrm{t_{DH}} + 273.15}{\mathrm{t_{DH}} - \mathrm{t_{STES}}}$$

where: η_{HP} —heat pump perfectness; t_{DH} —temperature of water fed to the heating grid; t_{STES} —temperature in the storage tank.

The heat stream fed to the local heating grid was not optimized. It is not set and is independent of the control system operation. This value is not included in the objective function. The system incorporates a heat storage tank, therefore heat generation is not equal to the heat sale. Heat generation in the period for which forecasts were made may be different than the heat sold. As a result, it is necessary to consider the difference between

heat sale and heat generation. Heat prices are not variable in time, so only the total heat difference was included. It will be calculated as the difference between the heat kept in storage at the beginning of the analysed period and the heat at the end. Presented below is the relationship describing the cost resulting from the change:

$$\Delta K_{HeatStorage} = (Q_{Final} - Q_{Initial}) \cdot k_{HeatStorage}$$

where: $\Delta K_{HeatStorage}$ —cost of avoided heat sale that was accumulated in the storage tank during the analysed period; Q Begin —amount of heat accumulated at the beginning of the analysed period; Q Final —amount of heat accumulated at the end of the analysed period; $k_{HeatStorage}$ —unitary heat price of the heat accumulated in the storage tank. On the other hand, optimization with the condition that the amount of heat stored at the end must be equal to the heat stored at the beginning may be conducted.

In the period n or n and n+1 storage operation will be optimized by controlling its work so that it will be possible to realize the planned heat production and to recover all the heat generated in the solar collectors. Should the forecasts alter to the extent that it will not be able to balance the production, then the costs of heat generation from other sources or of heat lost that was generated by the collectors will be considered. The objective function contains a penalty element for unrecovered heat from the solar collectors and for over cooling of the storage tank in the following form:

$$Q^i_{Solar} > Q^i_{Plan} \text{ then } K^i_{Penalty} = K_{Overload} + k_{Overload} \cdot t \cdot Q^i_{Overload}$$

$$Q^i_{Overload} = Q^i_{Solar} - Q^i_{Plan}$$

$$Q^i_{Solar} = Q^i_{Plan} \text{ then } K^i_{Penalty} = 0$$

$$Q^i_{Solar} < Q^i_{Plan} \text{ then } K^i_{Penalty} = k_{Subcooling} \cdot t \cdot Q^i_{Subcooling}$$

$$Q^{\{i\}}_{\{Subcooling\}} = Q^{\{i\}}_{\{min\}} - Q^{\{i\}}_{\{Plan\}}$$

where: Q^i_{Solar} —heat recovered from the solar collectors in the i^{th} time interval for current heat forecast; Q^i_{Plan} —heat supplied to consumers in the i th time interval resulting from the forecast; $K^i_{Penalty}$ —penalty value; t — length of the time interval, month, week, day, hour; $k_{Overload}$ —coefficient of the penalty function for heat overproduction; $k_{Subcooling}$ —coefficient of the penalty function for heat underproduction (cost of heat supplied to the storage tank from auxiliary sources); Q^i_{min} —minimum of heat kept in storage; $Q^i_{Overload}$ —heat not recovered from the collectors in the i^{th} time interval.

Table 2: Objective function parameters for optimization processes

Parameter	Value*	Comment
kNG, EUR/GJ	12	cost of natural gas fed to the central heating boiler
kPower, EUR/GJ	44	cost of electricity supplied to the heat pump
kSubcooling, EUR/GJ	kNG	heat of additional heating of water in the boiler by a gas/coal boiler/heating grid or/and the heat pump
kOverload, EUR/GJ	6.0	cost of heat lost, full storage charging at positive balance of heat production from the collectors and heat demand

*at conversion rate EUR/PLN=4.2

Table 2 contains selected coefficients used in the developed objective function. The coefficients may vary depending on the season of the year and geographic location (country) as well as local conditions. The cost of natural gas supplied to the central heating boiler was calculated on the assumption that boiler efficiency was 80% and the gaseous fuel tariff was according to [43]: w-5 (gas) and E-1A (distribution) after PGNiG S.A. (in total 1.3678 PLN/Nm3); LCV was assumed to be 35 MJ/Nm3.

The cost of electricity supplied to the heat pump was assumed to be equal to the value mentioned in [44]— one–zone tariff C11 (“Simplest for your company”) after RWE Poland S.A. (0.6587 PLN/kWh). Heat lost in the case when the storage tank is fully charged and the collector heat production exceeds the amount of heat consumed was calculated for Hewalex KS2000 TP AC flat collectors [45]. The net price for this device is 151.04 EUR per m2 of working surface. It was assumed that the lifetime of solar collectors ranges from 15 to 25 years [46]. The cost of lost heat was calculated on the assumption that the collectors will work for 15 years (safer variant). All the above costs as well as other parameters and results presented in this work were determined using the currency conversion rate of PLN 4.2 = 1 EUR.

The presented methodology is also valid for other—not necessarily cost balance based—criteria. These could be the CO2 emission criterion [47,48], minimization of fossil fuel consumption or the idea of energy storage of external origin (e.g. at low electricity prices, which might even be negative as a Danish example showed).

2.3 Limitations

Optimization limitations

1. Water temperature in the storage tank: 40 .. 80C
2. Maximum storage charging/discharging rate, Δt_{STES}/month
3. Maximum heating power of the grid, Q_{DH}/month
4. Maximum heating power of the solar collectors, Q_{Solar}/month
5. Maximum heating power of the gas boilers, Q_{Boiler}/month

Except for limitations regarding the sole optimization process, the system model contained internal constraints not allowing the overheating or over-cooling of the storage tank, ti.e. it did not allow t_{values} outside of the range of 40 .. 80°C, however shut-off of those limitations was also possible.

2.4 Analysed case

To determine the possibility and test the proposed solutions a structure containing all typical devices cooperating with seasonal heat storage tanks was selected. Hence, the analysed system contained the following elements:

- flat solar collectors [45]
- heat pump of COP 3.5 [49]
- fossil fuel boilers (natural gas)

a: Variant I b: Variant II

Figure 5: Tentative depiction of both analysed variants

Two configuration cases for the whole system were considered:

1. Variant I, where the collector area was selected in such a way that their heat production corresponded to 100% of the heat demand in a yearly cycle—heat losses from storage were not covered by solar energy.
2. Variant II, where STES had to cover 100% of the heat demand and the solar collector area was chosen so that it also covered the heat losses from the accumulator.

Both cases differ in collector size and the heat capacity of the storage tank—see fig. 5.

3 Optimizing algorithm for the Seasonal Thermal Energy Storage system

3.1 Description of the main algorithm

A structural (hierarchical) optimizing algorithm is proposed for a Seasonal Thermal Energy Storage system. Based on the algorithm several layers cooperate with each other to obtain a solution of the previously defined problem.

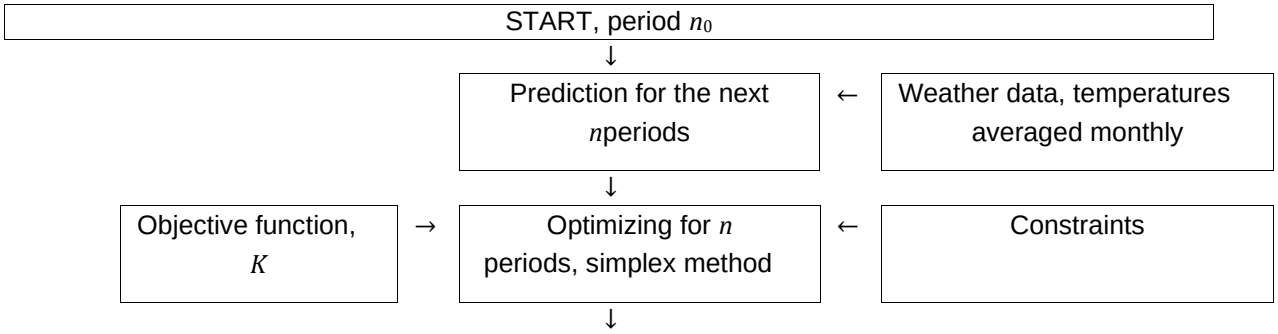

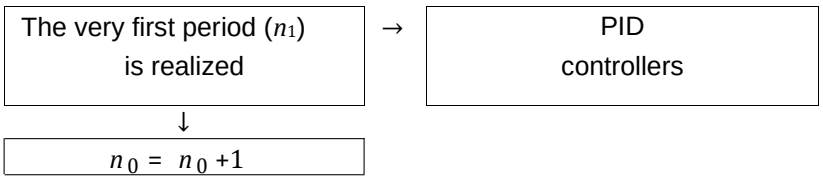

Figure 6: Optimizing algorithm for STES

Fig. 6 presents a block diagram of the proposed optimizing algorithm for STES. In the very first step, the prediction of heat consumption for the next n periods (e.g., 11 months) is made. The prediction may be based on forecast weather, temperatures, etc.; in the calculations randomly generated temperatures at the average level for Warsaw are used. Based on the forecast heat consumption and possible heat production/accumulation, the optimizing process is utilized for the chosen objective function while fulfilling the given limitations.

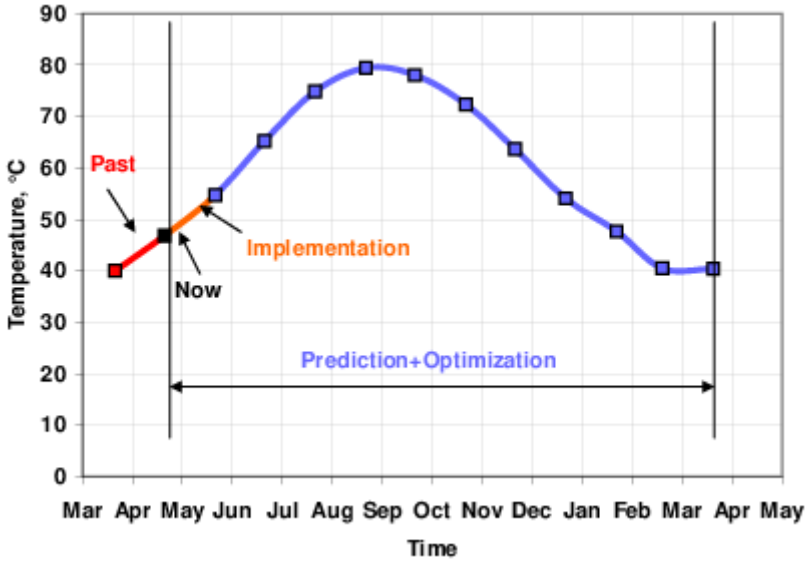

Figure 7: An example of utilization of the optimizing algorithm

Based on the obtained operational line for the next n periods (11 months), only the very first period is really done—see Fig. 7—and adequate PID controllers are set to fulfil the ending point. The rest of the operational line is deleted and no longer considered, but the whole process is repeated.

3.2 Choosing a design point of the system

The optimizing procedure regards the current period and next n periods (e.g., 11 months, so it is possible to use the algorithm to determine a design point for the whole system (solar collector area, water tank volume, etc.) based on the chosen/known heat consumption profile and averaged monthly weather data.

- In this case, the optimizing algorithm needs to be supplemented by two independent variables:
- solar collector area in relation to heated area, m2/m2
- water tank volume in relation to heated area, m3/m2

Table 3: Design point parameters chosen during the optimizing processes

Parameter	Case I	Case II
Heated area, m2	100	100
Solar collector area, m2	17	25
Tank volume, m3	70	102
Objective function value, EUR/a	113	52

By utilizing the optimizing algorithm, the design point parameter of the STES system was found as well as the temperature distribution during the year. (see Table 3).

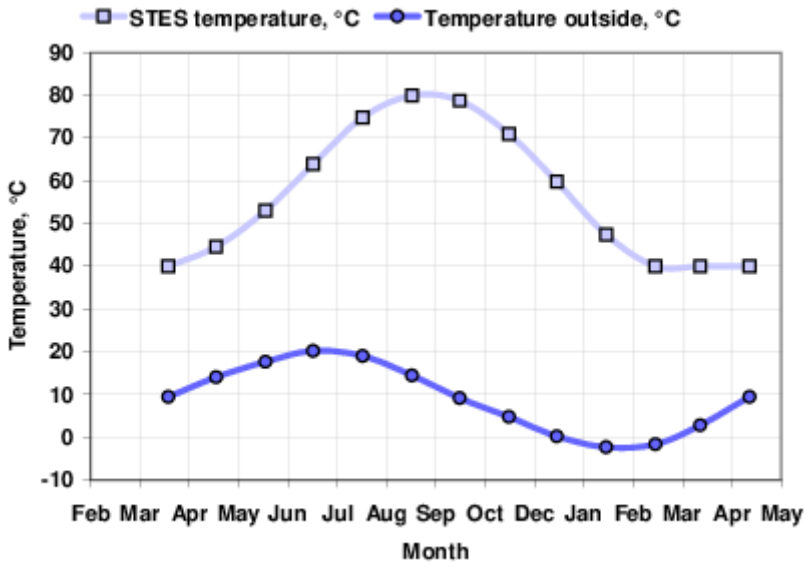

Figure 8: Monthly averaged temperatures distribution at the design point for Case I

Fig. 8 presents the temperature forecast at the design point, and related water temperatures in the tank.

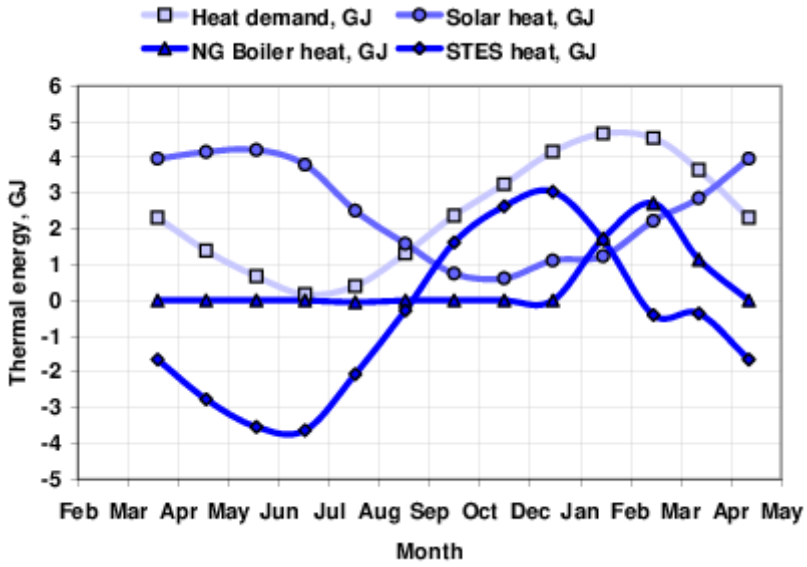

Figure 9: Heat generated by the system elements at the design point for Case I

Fig. 9 presents the amount of heat generated by the system elements in order to cover heat demand at the design point and chosen heat consumption profile. The negative values of heat fluxes denote that the charging process of the STES tank is in progress.

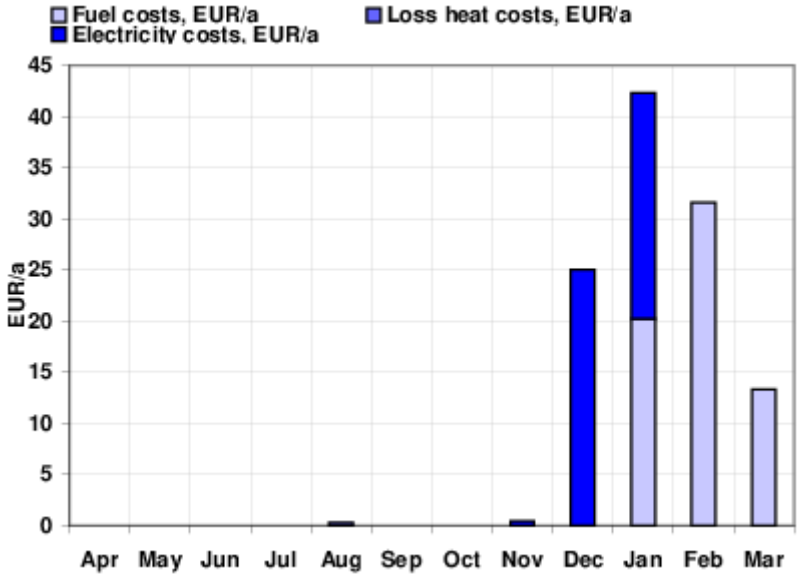

Figure 10: Objective function at the design point for Case I

At the design point for Case I, the value of the objective function is 113 EUR/a (for 100 m2); specific components of the function are presented in Fig. 15, the highest cost is electricity delivered to the heat pump in the periods when the water temperature in the tank falls below 60○C, the second highest cost is the fuel used in the boilers to cover heat demand when there is a fully discharged heat storage tank.

4 Conclusions

An external control strategy and optimizing algorithms are proposed for supporting the STES operation.

Table 4: Summary of all analyzed scenarios

Parameter	Case I limited	Case I optimized	Case II	Case II limited	Case II optimized
Averaged yearly costs, EUR/a	113	109	52	60	57
Water tank volume, m^3	70	70	102	102	102
Solar collector area, m^2	17	17	24	24	24
Minimum water temperature, °C	40	40	36	40	40
Maximum water temperature, °C	80	80	84	80	80
Maximum charging speed, GJ/month	3.8	3.9	5.3	5.3	5.3
Maximum discharging speed, GJ/month	3.3	3.3	3.4	3.4	3.0
Maximum heat produced by Natural Gas boiler, GJ/month	3.9	3.8	–	1.3	1.1
Maximum heat produced by solar collectors, GJ/month	4.2	4.2	5.8	5.8	5.8
Maximum heat demand, GJ/month	5.2	5.2	5.2	5.2	5.2

Table 4 presents a summary of all analyzed cases. The operating costs of systems with smaller sized devices (solar collectors by 41%, and water tank volume by 45%) are two times smaller than for the bigger sized system. Profits from utilization of the external control strategy are relatively small, on level 4...5%. Apart from economic profits, using the proposed external control strategy lowers the maximum heat produced by the natural gas boiler in the range 3...18%.

Use of the external control strategy does not provide spectacular profits, but theoretically a huge water tank can be run without any control system merely by applying a simple regulation system.

Acknowledgments

The research results presented in the paper were achieved within the project entitled “Development of the underwater autonomous transport system” (no. POIR.01.01.01-00-1514/19), co-financed by the Polish National Centre of Research and Development.

References

[1] Bartela L, Kotowicz J. Analysis of operation of the gas turbine in a poligeneration combined cycle. Arch Thermodyn 2013;34:137–59.

[2] Guerra C, Lanzini A, Leone P, Santarelli M, Beretta D. Experimental study of dry reforming of biogas in a tubular anode-supported solid oxide fuel cell. Int J Hydrogen Energy 2013;38:10559–66.

[3] Kupecki J, Jewulski J, Badyda K. Comparative study of biogas and DME fed micro-CHP system with solid oxide fuel cell. Appl Mech Mater 2013;267:53–6.

[4] Sánchez D, Monje B, Chacartegui R, Campanari S, Sanchez D, Monje B, et al. Potential of molten carbonate fuel cells to enhance the performance of CHP plants in sewage treatment facilities. Int J Hydrogen Energy 2013;38:394–405.

[5] Bakalis DP, Stamatis AG. Incorporating available micro gas turbines and fuel cell: Matching considerations and performance evaluation. Appl Energy 2013;103:607–17.

[6] Chacartegui R, Monje B, Sánchez D, Becerra JA, Campanari S. Molten carbonate fuel cell: Towards negative emissions in wastewater treatment CHP plants. Int J Greenh Gas Control 2013;19:453–61.

[7] Jannelli E, Minutillo M, Perna A. Analyzing microcogeneration systems based on LT-PEMFC and HT-PEMFC by energy balances. Appl Energy 2013;108:82–91.

[8] McLarty D, Brouwer J, Samuelsen S. Hybrid fuel cell gas turbine system design and optimization. J Fuel Cell Sci Technol 2013;10.

[9] Qian J, Tao Z, Xiao J, Jiang G, Liu W. Performance improvement of ceria-based solid oxide fuel cells with yttria-stabilized zirconia as an electronic blocking layer by pulsed laser deposition. Int J Hydrogen Energy 2013;38:2407–12.

[10] Sieniutycz S, Jezowski J. Energy Optimization in Process Systems and Fuel Cells. 2013.

[11] Wang S-B, Wu C-F, Liu S-F, Yuan P. Performance optimization and selection of operating parameters for a solid oxide fuel cell stack. J Fuel Cell Sci Technol 2013;10.

[12] Wang W, Li H, Wang X-F. Analyses of part-load control modes and their performance of a SOFC/MGT hybrid power system. Dalian Ligong Daxue Xuebao/Journal Dalian Univ Technol 2013;53:653–8.

[13] Hosseinzadeh E, Rokni M, Jabbari M, Mortensen H. Numerical analysis of transport phenomena for designing of ejector in PEM forklift system. Int J Hydrogen Energy 2014;39:6664–74.

[14] Ramandi MY, Dincer I, Berg P. A transient analysis of three-dimensional heat and mass transfer in a molten carbonate fuel cell at start-up. Int J Hydrogen Energy 2014;39:8034–47.

[15] Schmidt T, Mangold D, Muller-Steinhagen H. Seasonal thermal energy storage in Germany. ISES Sol. World Congr. 2003, 2003.

[16] Bella F Di, Chamarro A. Optimizing Thermal Energy Storage for Cogeneration Applications. Proc 2004 Am Soc Eng Educ Annu Conf \& Expo 2004;376.

[17] Khushairi M, Abdullah H, Hazran H. A Study on the Optimization of Control Strategy of a Thermal Energy Storage System for Building Air-Conditioning. Procedia Eng 2011;20:118–24.

[18] Sun Y, Wang S, Xiao F, Gao D. Peak load shifting control using different cold thermal energy storage facilities in commercial buildings: A review. Energy Convers Manag 2013;71:101–14. https://doi.org/http://dx.doi.org/10.1016/j.enconman.2013.03.026.

[19] DeForest N, Mendes G, Stadler M, Feng W, Lai J, Marnay C. Optimal deployment of thermal energy storage under diverse economic and climate conditions. Appl Energy 2014;119:488–96. https://doi.org/http://dx.doi.org/10.1016/j.apenergy.2014.01.047.

[20] Zhao J, Chen Y, Li X. Optimization for operating modes based on simulation of seasonal underground thermal energy storage. Front Energy Power Eng China 2008;2 (3):298–301.

[21] Guadalfajara M, Lozano MA, Serra LM. A simple method to calculate Central Solar Heating Plants with Seasonal Storage. Energy Procedia 2014;48:1096–109.

[22] TRNSYS 16. A Transient System Simulation tool. SEL, University of Wisconsin-Madison, 2004 n.d.

[23] Guadalfajara M, Lozano MA, Serra LM. Comparison of Simple Methods for the Design of Central Solar Heating Plants with Seasonal Storage. Energy Procedia 2014;48:1110–7. https://doi.org/http://dx.doi.org/10.1016/j.egypro.2014.02.125.

[24] Lunde PJ. Prediction of the performance of solar heating systems utilizing annual storage. Sol Energy

1979;22:69–75. https://doi.org/http://dx.doi.org/10.1016/0038-092X(79)90061-6.

[25] Braun JE, Klein SA, Mitchell JW. Seasonal storage of energy in solar heating. Sol Energy 1981;26:403–11. https://doi.org/http://dx.doi.org/10.1016/0038-092X(81)90219-X.

[26] Guadalfajara M. Evaluacion de centrales solares termicas para el sector residencial en Espana. Universidad de Zaragoza, 2013.

[27] Guadalfajara M, Lozano MA, Serra LM. Metodo simple de calculo de sistemas solares termicos centralizados con acumulacion estacional. 8 Congr. Nac. Ing. Termodin. Burgos, 2013.

[28] Guadalfajara M, Lozano MA, Serra LM. Criterios de diseno y optimizacion de sistemas solares centralizados con acumulacion estaciona. 8 Congr. Nac. Ing. Termodin. Burgos, 2013.

[29] EES, Engineering Equation Solver. F-Chart Software. http://www.fchart.com/ EES, February 2013 n.d.

[30] Lunde PJ. Prediction of the performance of solar heating systems over a range of storage capacities. Sol Energy 1979;23:115–21. https://doi.org/http://dx.doi.org/10.1016/0038-092X(79)90111-7.

[31] Zasady. No Title. Politechnika Warszawska Szkoła Nauk Technicznych i Społecznych w Płocku; n.d.

[32] Dantzig G. Linear Programming and Extensions. Princeton University Press; 1963.

[33] Grabowski W. Programowanie matematyczne. Państ. Wydaw. Ekonomiczne; 1980.

[34] Wagner H. Badania operacyjne. Zastosowania w zarządzaniu. PWE; 1985.

[35] Galas Z, Nykowski I. Programowanie liniowe Praca zbiorowa. PWN; 1986.

[36] Glinka M. Badania operacyjne (fragmenty wykładu), Wydział Transportu i Elektrotechniki Uniwersytetu Techniczno-Humanistycznego w Radomiu. n.d.

[37] Amirinejad M, Tavajohi-Hasankiadeh N, Madaeni SS, Navarra MA, Rafiee E, Scrosati B. Adaptive neuro-fuzzy inference system and artificial neural network modeling of proton exchange membrane fuel cells based on nanocomposite and recast Nafion membranes. Int J Energy Res 2013;37:347–57.

[38] Grondin D, Deseure J, Ozil P, Chabriat J-P, Grondin-Perez B, Brisse A. Solid oxide electrolysis cell 3D simulation using artificial neural network for cathodic process description. Chem Eng Res Des 2013;91:134–40.

[39] Hajimolana SA, Tonekabonimoghadam SM, Hussain MA, Chakrabarti MH, Jayakumar NS, Hashim MA. Thermal stress management of a solid oxide fuel cell using neural network predictive control. Energy 2013;62:320–9.

[40] Marra D, Sorrentino M, Pianese C, Iwanschitz B. A neural network estimator of Solid Oxide Fuel Cell performance for on-field diagnostics and prognostics applications. J Power Sources 2013;241:320–9. https://doi.org/10.1016/j.jpowsour.2013.04.114.

[41] Razbani O, Assadi M. Artificial neural network model of a short stack solid oxide fuel cell based on experimental data. J Power Sources 2014;246:581–6. https://doi.org/10.1016/j.jpowsour.2013.08.018.

[42] Zamaniyan A, Joda F, Behroozsarand A, Ebrahimi H. Application of artificial neural networks (ANN) for modeling of industrial hydrogen plant. Int J Hydrogen Energy 2013;38:6289–97.

[43] http://www.pgnig.pl/ n.d.

[44] http://www.rwe.pl n.d.

[45] http://www.hewalex.pl/ n.d.

[46] Fan J, Chen Z, Furbo S, Perers B, Karlsson B. Efficiency and lifetime of solar collectors for solar heating plants. ISES Sol. World Congr. 2009, Johannesburg, South Africa: 2009, p. 331–40.

[47] Budzianowski WM. Modelling of CO2 content in the atmosphere until 2300: Influence of energy intensity of gross domestic product and carbon intensity of energy. Int J Glob Warm 2013;5:1–17.

[48] Wee J-H. Carbon dioxide emission reduction using molten carbonate fuel cell systems. Renew Sustain Energy Rev 2014;32:178–91.

[49] Schmidt T. SUNSTORE 4---Minitoring results 2013 2014.

Concept of the non-equilibrium multi-dimensional model of the charging/discharging low-temperature thermochemical storage unit

Mateusz Młynarczyk[a], Piotr Łapka[b], Natalia Mikos-Nuszkiewicz[c] and Piotr Furmański[d]

[a] Faculty of Power and Aeronautical Engineering, Warsaw University of Technology, Warsaw, Poland, e-mail: mateusz.mlynarczyk2.stud@pw.edu.pl
[b] Faculty of Power and Aeronautical Engineering, Warsaw University of Technology, Warsaw, Poland, e-mail: piotr.lapka@pw.edu.pl
[c] Faculty of Power and Aeronautical Engineering, Warsaw University of Technology, Warsaw, Poland, e-mail: natalia.mikos.dokt@pw.edu.pl
[d] Faculty of Power and Aeronautical Engineering, Warsaw University of Technology, Warsaw, Poland, e-mail: piotr.furmanski@pw.edu.pl

Abstract:

Thermochemical energy storage is the least investigated thermal energy storage technology. Nowadays, research on this technology's development is very intensive, including high, medium, and low-temperature applications. However, for thermochemical energy storage technology to get market maturity, still many problems must be solved, and reliable design and optimization tools must be developed. The concept of such a tool, i.e., the multi-dimensional numerical model of the charging/discharging low-temperature thermochemical storage unit, is presented in this paper. The model considers hydration/dehydration reactions in the thermochemical medium working in the open system. It accounts for local hygric and thermal non-equilibrium at the macroscale by treating heat and moisture carrier fluid (moist air) and reactive porous bed separately. Therefore, two sets of governing equations have been derived, i.e., one dealing with moisture and heat transfer in the air flowing through the porous bed and the second one with phenomena occurring in the reactive porous bed. The model assumes regular regimes of heat conduction and moisture diffusion in the bed particles and a fast sorption/desorption rate in thermochemical materials. Moreover, it is assumed that the water removal from the bed particle surface controls the chemisorption process as being slower than reaction kinetics. The proposed model was simplified to heat storage using sorption/desorption phenomena and implemented in 2D axisymmetric space using commercial software. Such an approach allows for easy adjustment and modification of the reactor geometry in the design and optimization path. Then the model in simplified form was applied for the simulation of a sorption-based thermal energy storage unit. Parts of the charging and discharging phases were simulated. However, the long simulation time is the particular issue limiting the current broader testing and applications of the model.

Keywords:

Thermochemical energy storage; Hydration/dehydration; Numerical modeling; Non-equilibrium model; Sorption/desorption;

1. Introduction

To date, global energy consumption significantly relies on fossil fuels which are closely related to carbon dioxide (CO_2) emissions, contributing to climate change. Increasing global energy demands caused by rapid industrialization and population growth and, therefore, acceleration of fossil fuel depletion and the additional need for environmental protection attracts attention to the effective use of the other available energy sources, including renewable ones. These sources often deliver energy in times and locations different from its demand. This leads to an economically unjustified loss of useful energy.

The crucial role of energy storage systems is to reduce the time or rate of mismatch between energy supply coming from different sources and energy demand at a specific time and location. Among the energy storage systems, thermal energy storage (TES) is an important energy conservation technology to store heat and cold for later use [1]. Thermal energy can be stored as sensible heat, latent heat, and thermochemical energy or combinations of these methods [2]. Much research and development work has been carried out in the first two methods of the TES. The sensible heat storage associated with increased temperature of the storing material

is used in many domestic and industrial applications. The method requires a high heat capacity of the storing materials and very good thermal insulation of the storage system to reduce heat losses. These two features are the most significant drawbacks and limitations of sensible heat storage. The latent heat storage uses phase transformations associated with the absorption or release of heat during, e.g., melting/freezing. Therefore, it needs phase change materials (PCMs) of high latent heat and good thermal transport properties to effectively transfer heat to and from the storage. This storage technology has many lab-scale and market applications, including PCM in storage tanks [3] and in different elements of building envelopes [4-7]. However, the drawback of this storage technology, among others, is the low thermal conductivity of PCMs, which significantly limits the heat transfer rates during charging/discharging and heat storing at temperatures different than the temperature of the surroundings and related heat losses. Thermochemical energy storage (TChES) is one of the least investigated heat storage methods. However, it is the most promising and attractive technology because it offers the highest energy storage density of the three methods and allows for storing thermal energy at negligible heat loss for a long time by species separation [2]. Another difference between PCM-based storage and TChES in which gaseous product appears is that the former depends on temperature only, while the latter has an extra control parameter, namely the gas pressure, which follows from the equilibrium curve in the phase diagram of thermochemical material [8]. Recent developments in low/zero energy buildings promote the development of low-temperature TChES systems.

Mathematical models of TES units/systems using sorption and chemical reactions pose many difficulties in mathematical formulations and equations solutions. These processes are complicated and differ from the well-known and analyzed classical flow phenomena with heat transfer. In the TChES, it is required to simultaneously deal with the fluid flow and heat and mass transfer in the porous bed accompanied by sorption or chemical reactions, the dynamics of which also affect the system's operation [9]. Due to the large number of physical phenomena that need to be modeled and the need to combine equations that describe fluid flow, thermal, and chemical processes, modeling these phenomena was significantly simplified.

Several numerical approaches have been proposed to investigate the heat and mass transfer processes in the reactive packed bed and in the whole TChES units/systems. The most simplified are purely thermodynamic approaches based on energy and exergy methods to assess the closed or open-loop TChES systems/units [10, 11] or reaction cycles for the TChES systems/units [12]. The second group of the models is lumped-element or 0D models [13, 14], which provide general information on the TChES unit/systems operation. The next group is the 1D models, which can simulate the variation of the working medium and reactor parameters along the flow path [2, 9, 15, 16]. The most complex approaches are multi-dimensional (2 and 3D) models [17-21] capable of predicting fluid flow and thermal and chemical states at any time of the process and any point in the storage unit/system and, therefore, are applied for multi-criteria analyses of TChES units/systems.

Most of the TChES units/systems models assumed many simplifications. For example, local thermal equilibrium between working gas and the porous bed was applied [17-19, 21], the gas flow was modeled as isothermal [17-19], the flow of the gas in the porous bed was evaluated through Darcy law [17-19, 21], vapor transfer dynamics was omitted [17-21]. These simplifications are understandable and justified. The phenomena controlling the TChES process are very complex, and their modeling requires many assumptions to solve the problem. However, this paper will try to alleviate some of the mentioned assumptions by treating simplified or omitted phenomena more rigorously than in the previous works [17-21]. The proposed new 2D macroscale model, based on the previous 1D approach [9], considers low-temperature hydration/dehydration reactions in the TChES unit working in the open system. It assumes hygric and thermal non-equilibrium between the working medium (moist air) and the reactive porous bed and, in this way, accounts for the peculiarities and dynamics of heat and mass transfer processes in a porous bed. The model may be applied to simulate the chemical and physical sorption-based storage process.

2. Macroscopic mathematical model of TChES unit

This chapter contains a description of the complex TChES unit model. The model consists of the unsteady equations set describing the transport of momentum, mass, energy, and moisture in the gaseous phase and the transport of energy and moisture in the solid phase (porous bed). The first equation, i.e., the continuity equation for moist air in the storage, is written as follows:

$$\varepsilon_b \frac{\partial \rho_m}{\partial t} + \nabla \cdot (\rho_m \vec{u}) = 0, \tag{1}$$

where: ρ_m is the moist air density, ε_b is the reactive bed porosity, $\vec{u}$ is the velocity vector, and t is the time. The laminar flow was assumed to simplify the case. Therefore, the momentum equation is the following:

$$\frac{\partial \rho_m}{\partial t} + \nabla \cdot (\rho_m \vec{u}\vec{u}) = -\nabla p + \nabla \cdot \mu_m \left[(\nabla \vec{u} + \nabla \vec{u}^T) - \frac{2}{3} \nabla \cdot \vec{u} I \right] - \frac{\mu_m}{k} \vec{u} + C_2 \frac{1}{2} \rho_m |\vec{u}| \vec{u}. \tag{2}$$

In the equation above, p is the static pressure, I is the unit tensor, and μ_m is the moist air dynamic viscosity. The two last terms of Eq. (2) are source terms accounting for the porous zone region. The factor k is the permeability of the reactive bed, and coefficient C_2 is used to include inertial pressure losses. The moisture

must be properly managed in the reactive bed for proper storage work. During the charging cycle, dry air flowing through the bed should remove moisture from the system. In the discharging cycle, the moisture is supplied to the system as water vapor in the moist air. The following non-equilibrium equation describes the moisture transport in the air in a porous bed:

$$\varepsilon_b \frac{\partial \rho_g \omega}{\partial t} + \nabla \cdot \left(\rho_g \vec{u} \omega\right) = \nabla \cdot \left(D_{vb,eff} \nabla \omega\right) + A_b \alpha_{m,eff} \left(\rho_{v,e} - \rho_v\right), \tag{3}$$

where: ρ_g is the density of dry air, ω is the specific humidity (per mass of dry air), $D_{vb,eff}$ is effective vapor diffusivity in air, A_b is the specific surface area of the porous bed, $\alpha_{m,eff}$ is the effective mass transfer coefficient for water vapor, $\rho_{v,e}$ is equilibrium density of water vapor at the surface of bed particles, and ρ_v is the density of the water vapor in moist air. The non-equilibrium thermal model is applied to account for the porous zone's energy transport. The source term in the energy equation includes heat transport between the bed and gaseous phase and the energy transport caused by moisture exchange. Therefore, the energy equation for the moist air is written as:

$$\varepsilon_b \frac{\partial \rho_g \left(c_{v,g} + \omega c_{v,v}\right) T_f}{\partial t} + \nabla \cdot \left[\rho_g \vec{u} \left(c_{p,g} T_f + \omega c_{p,v} T_f + \frac{p}{\rho_g}\right)\right] = \nabla \cdot \left(\lambda_{m,eff} \nabla T_f\right) +$$

$$A_b \left[\alpha_{m,eff} c_{p,v} \left(\rho_{v,e} - \rho_v\right) + \alpha_{T,eff}\right] \left(T_s - T_f\right), \tag{4}$$

where: $c_{v,g}$ and $c_{p,g}$ are the specific heats of dry air at constant volume and pressure, respectively, $c_{v,v}$ and $c_{p,v}$ are the specific heats of vapor at constant volume and pressure, respectively, T_f is the temperature of moist air (working fluid), $\lambda_{m,eff}$ is the effective heat conductivity of moist air, $\alpha_{T,eff}$ is the effective heat transfer coefficient between gaseous phase and solid particles, and T_s is the temperature of the porous reactive bed. In the mass balance equation for the solid phase, the formation of new substances during the chemical reaction is taken into account. It is assumed that water in particles occurs only in the bound state of component A (hydrate). There is no diffusion between hydrated component A and dehydrated component B. Therefore, the mass balance equation can be written as:

$$\left(1 - \varepsilon_b\right) \frac{\partial \left(\rho_A + \rho_B\right)}{\partial t} = -A_b \alpha_{m,eff} \left(\rho_{v,e} - \rho_v\right), \tag{5}$$

where: ρ_A is component A's density and ρ_B is component B's density. The degree of transformation of species A into B varies with the location and time. The equation describing this parameter is the following:

$$\beta(\bar{x}, t) = \frac{C_{A0}(\bar{x}) - C_A(\bar{x}, t)}{C_{A0}}, \tag{6}$$

where: $\bar{x}$ is the position vector, C_{A0} is the initial molar concentration of component A, and C_A is the actual molar concentration of species A. The final expression describing the degree of transformation of species A into B is as follows:

$$\frac{\partial \beta}{\partial t} = \frac{A_b \alpha_{m,eff} \left(\rho_{v,e} - \rho_v\right)}{C_{A0} M_{AB} \left(1 - \varepsilon_b\right)}, \tag{7}$$

where M_{AB} is defined as:

$$M_{AB} = M_A - \frac{v_B}{v_A} M_B. \tag{8}$$

In the equation above, M_A is the molar mass of component A, M_B is the molar mass of component B, and v_A and v_B are stoichiometric coefficients. The energy equation for solid particles considers the heat and mass exchange with flowing air and energy released (or absorbed) during the chemical reaction. Therefore, this energy equation can be written using the formula:

$$\left(1 - \varepsilon_b\right) \left[\frac{v_B}{v_A} \frac{\partial H_B}{\partial T_s} + \left(1 - \beta\right) \frac{\partial H_{AB}}{\partial T_s}\right] = \nabla \cdot \left(\lambda_{s,eff} \nabla T_s\right) +$$

$$-A_b \left[\alpha_{m,eff} c_{p,v} \left(\rho_{v,e} - \rho_v\right) + \alpha_{T,eff}\right] \left(T_s - T_f\right) + \left(1 - \varepsilon_b\right) H_{AB}(T_s) \frac{\partial \beta}{\partial t}, \tag{9}$$

where H_{AB} is defined as:

$$H_{AB} = H_A - \frac{v_B}{v_A} H_B. \tag{10}$$

In Eq. (9) and (10), H_A is species A's molar enthalpy, H_B is species B's molar enthalpy, and $\lambda_{s,eff}$ is the effective heat conductivity of solid particles in the reactive bed. Equations (1)-(10) allow for calculating velocities, temperatures, and moisture molar concentration fields. Due to the high complexity of the proposed model, caused by the presence of chemical reaction in the bed and the coexistence of both species A and B, the above model was simplified and reformulated to account for a sorption/desorption-based heat storage, which mathematical description is much simpler, and in such form was implemented and tested. The model given by Eq. (1)-(10) will be implemented and tested in future work.

3. Model simplification to sorption/desorption-based heat storage

The proposed in section 2 TChES model was simplified, assuming that sorption/desorption phenomena are used to store heat instead of thermochemical reactions. The simplified mathematical model for sorption/desorption-based heat storage, presented below, replaces the mass balance equation, Eq. (5), with the equation describing water transport in the porous bed. It assumes that, during the sorption, the water vapor is adsorbed from moist air and bound with solid porous particles in liquid form. No other species are created in the bed because only physical adsorption occurs. Therefore, the density of the solid phase is constant, and the mass changes of particles arise only from the amount of adsorbed water. The following equation can describe the sorption phenomenon:

$$(1-\varepsilon_b)\rho_s \frac{\partial a_w}{\partial t} = (1-\varepsilon_b)\rho_s A_b \alpha_{m,eff}\left(a_{w,eq} - a_w\right), \tag{11}$$

where: ρ_s is the real density of solid particles, a_w is the mass of adsorbed water (per mass of adsorbent particles), and $a_{w,e}$ is the equilibrium amount of water. Both sides of Eq. (11) are multiplied by the mass of the adsorbent per volume to obtain the SI unit compatible with the moisture transport equation for moist air, i.e., kg H_2O m^{-3} s^{-1}. The source term of Eq. (3) also was changed because of replacing the driving force of water transfer. It is assumed that there will not be condensation, and water in the system occurs only in the form of water vapor in moist air and water adsorbed by porous particles. Therefore, Eq. (3) and (11) have the opposite source terms. The modified equation of moisture transport in the air is the following:

$$\varepsilon_b \frac{\partial \rho_g \omega}{\partial t} + \nabla \cdot \left(\rho_g \vec{u} \omega\right) = \nabla \cdot \left(D_{vb,eff} \nabla \omega\right) + (1-\varepsilon_b)\rho_s A_b \alpha_{m,eff}\left(a_w - a_{w,eq}\right). \tag{12}$$

In the energy equation for the moist air, Eq. (4), the only change will occur in the source term connected with energy transport as enthalpy of exchanged water. The modified equation can be written as:

$$\varepsilon_b \frac{\partial \rho_g \left(c_{v,g} + \omega c_{v,v}\right) T_f}{\partial t} + \nabla \cdot \left[\rho_g \vec{u} \left(c_{p,g} T_f + \omega c_{p,v} T_f + \frac{p}{\rho_g}\right)\right] = \nabla \cdot \left(\lambda_{m,eff} \nabla \mathrm{T}_f\right) +$$

$$A_b\left[(1-\varepsilon_b)\rho_s \alpha_{m,eff} c_{p,v}\left(a_w - a_{w,eq}\right) + \alpha_{T,eff}\right]\left(T_s - T_f\right). \tag{13}$$

The energy equation for the porous bed in the simplified model considers the specific heat of adsorbed water in porous particles and the heat of sorption. Therefore, the energy Eq. (9), is replaced by the following one:

$$\rho_s(1-\varepsilon_b) \frac{\partial \left(c_{p,s} + a_w c_{p,\mathrm{H2O}}\right) T_s}{\partial t} = \nabla \cdot \left(\lambda_{s,eff} \nabla \mathrm{T}_s\right) + (1-\varepsilon_b)\rho_s A_b \alpha_{m,eff}\left(a_{w,eq} - a_w\right) H_r +$$

$$-A_b\left[(1-\varepsilon_b)\rho_s \alpha_{m,eff} c_{p,v}\left(a_w - a_{w,e}\right) + \alpha_{T,eff}\right]\left(T_s - T_f\right), \tag{14}$$

where: $c_{p,s}$ is the specific heat of solid particles, $c_{p,\mathrm{H2O}}$ is the specific heat of liquid water, and H_r is the heat of sorption reaction (per mass of exchanged water). Flow equations, Eq. (1) and (2), remained the same in the simplified model.

4. Numerical implementation

4.1. Storage unit geometry and mesh

The sorption/desorption TES unit of cylindrical shape is investigated. During the modeling of the TES unit, the focus was not only on processes occurring in the porous medium but also on the part through which the air reached the reactive bed and flowed out of it. The 2D geometry of the modeled part of the TES unit consists of a circular inlet channel, a diverging nozzle, a cylindrical reactor with a porous material, a converging nozzle, and an outlet channel (see Figure 1). This geometry is axisymmetrical.

The axial symmetry of the geometry enabled a significant reduction in the number of mesh elements by treating the problem as a 2D axisymmetric. Consequently, only the upper part of the axial section needs to be prepared and meshed. A detailed view of the storage geometry with all dimensions is presented in Figure 2. The geometry of the TES unit was created using the ANSYS DesignModeler software.

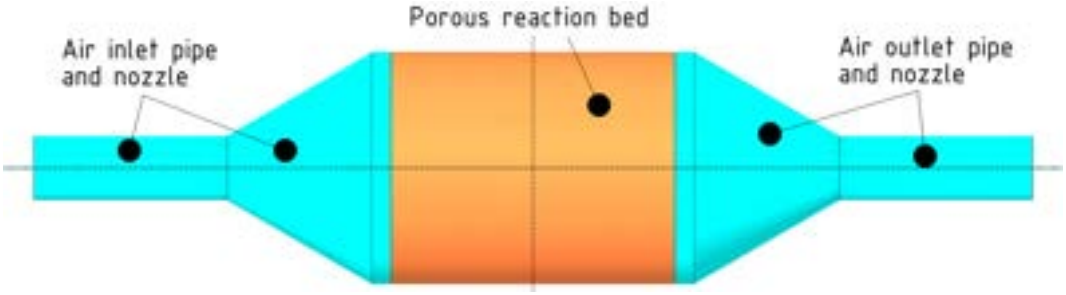

Figure. 1. The schematic view of investigated sorption/desorption TES unit.

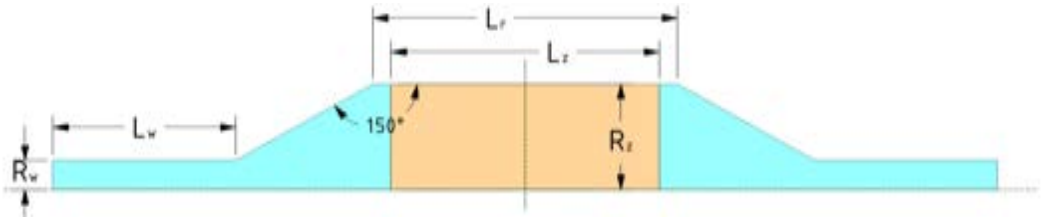

Figure. 2. The view of the upper axial section of the TES unit with all dimensions.

Table 1. Geometric dimensions of the investigated TES unit.

Geometrical parameters	Value
R_w (m)	0.05
R_z (m)	0.18
L_w (m)	0.30
L_r (m)	0.50
L_z (m)	0.44
Inlet/outlet surface (cm^2)	78.54
System volume (dm^3)	76.31
Reactive bed volume (dm^3)	44.79

Table 2. Mesh elements' quality properties.

Element property	Mesh 1 (15 680 elements)	Mesh 2 (273 570 elements)
Maximum aspect ratio	11.35	11.38
Minimum orthogonal quality	0.84	0.86
Maximum skewness	0.33	0.33

The TES unit's regular geometry allowed to generate meshes with 2D quadrangular elements. The meshes were created using the ANSYS Meshing software. Two computational grids, i.e., coarse and dense, were considered for testing the model's stability and solution sensitivity to the mesh size. The equations' convergence levels were also checked. Three factors were considered, i.e., aspect ratio, orthogonal quality, and skewness, to assess the quality of grid elements. As seen from the data presented in Table 2, the qualities of meshes are very good. During grids generations, refined meshes were created at the pipe and nozzle walls, thanks to which processes occurring in the boundary layers were simulated more accurately. For this reason, the aspect ratio level close to the walls was higher than in the rest of the domain. The reactive bed is the region with the best quality elements to decrease the meshing impact on equations convergence rates.

The coarse and dense meshes comprised 15 680 and 273 570 elements, respectively. But, this is not the final element numbers ANSYS Fluent used during the solution. Since a non-equilibrium approach was applied in solving the energy equation in the porous zone, ANSYS Fluent required a copy of the mesh in the porous region. The copied mesh consisted of the same number of elements as in the area of the porous medium, but these elements belonged to the solid material and used solid material properties during calculations. In this work, these were the properties of silica gel. The final sizes of meshes used for calculations were 21 344 and 346 170 elements. Because meshes in the porous media were copied, the elements' quality did not change.

4.2. Numerical implementation

The ANSYS Fluent 2022 R2 software was applied to solve the set of governing equations, Eq. (1), (2), and (11)-(14), utilizing parallel calculations. For the mesh with 21 344 elements, 4 computational nodes were used, and in the case of 346 170 mesh elements, 16 computational nodes were involved. Equations (1) and (2) were solved using a laminar flow model built-in within ANSYS Fluent software. The advanced customization interface, i.e., user-defined scalars (UDS), user-defined functions (UDF), and user-defined memory (UDM),

were applied to solve Eq. (11)-(14), along with all closing relationships presented in the next section. The model implementation using ANSYS Fluent software makes changing the geometry and computational mesh very easy, allowing for future optimization of the TES unit performance.

4.3. Closing relationships and input data

Several closing relationships and a set of input data are required to solve governing equations, Eq. (1), (2), and (11)-(14). These are the following. The density of the dry air in the system was calculated with the following incompressible ideal gas model:

$$\rho_g = \frac{p_{op}}{R_g T_f}, \tag{15}$$

where: p_{op} is the operating pressure assumed constant, and R_g is the individual gas constant of dry air. The density of the moist air changes with the amount of water vapor contained and is calculated using the relation:

$$\rho_m = \rho_g \frac{1+\omega}{1+\frac{R_v}{R_g}\omega}, \tag{16}$$

where: R_v is the individual gas constant of water vapor. The moist air's dynamic viscosity also varies with the contained water vapor as follows:

$$\mu_m = \mu_g + \left(\mu_v - \mu_g\right)\frac{\omega}{\frac{M_v}{M_g}+\omega}, \tag{17}$$

where: μ_g is the dynamic viscosity of the dry air, μ_v is the dynamic viscosity of water vapor, and M_g and M_v are molar masses of dry air and water vapor, respectively. The permeability of a porous medium composed of spherical particles can be calculated using a relationship that considers the grain diameter and the porosity of a given medium. The formula is the following:

$$k = \frac{d_p^2 \varepsilon_b^3}{150(1-\varepsilon_b)^2}, \tag{18}$$

where d_p is the diameter of the particle, i.e., silica gel granules. The coefficient of inertial resistance must be found to calculate the source term of the momentum equation in a porous medium. This coefficient can be calculated using the following formula:

$$C_2 = \frac{2C_F}{\sqrt{k}}, \tag{19}$$

where C_F is the dimensionless Forchheimer drag coefficient. This coefficient value can also be found based on the diameter of the silica gel granules and the porosity of the medium from the following equation:

$$C_F = \frac{1.75}{\sqrt{150}}\varepsilon_b^{-\frac{3}{2}}. \tag{20}$$

A model that considers the bed's porosity, tortuosity, and current air humidity is applied to find the effective diffusivity of moisture in the air in the reactive bed. The reference diffusivity was the one of water vapor in the atmospheric air, which depends only on the air temperature and is described by the following equation:

$$D_{v,a} = 2.6 \cdot 10^{-5}\left(\frac{T_f}{298}\right)^{\frac{3}{2}}. \tag{21}$$

Then the effective diffusivity of vapor in the air in the porous bed was calculated from the following relationship:

$$D_{vb,eff} = \frac{\rho_g D_{v,a}\varepsilon_b}{(1+\omega)\tau_b}, \tag{22}$$

where τ_b is the tortuosity of the bed. The effective thermal conductivity of the porous material was modeled with a simple equation in which the thermal conductivity between the bed's granules depends on the medium's porosity. The equation describing this conductivity can be written as follows:

$$\lambda_{s,eff} = (1-\varepsilon_b)\lambda_s, \tag{23}$$

where: λ_s is the real thermal conductivity of the solid material. The thermal conductivity of moist air was modeled similarly to the dynamic viscosity (see Eq. (17)) using the following equation:

$$\lambda_m = \lambda_g + \left(\lambda_v - \lambda_g\right)\frac{\omega}{\frac{M_v}{M_g}+\omega}, \tag{24}$$

where: λ_g is the thermal conductivity of the dry air, and λ_v is the thermal conductivity of water vapor. The effective thermal conductivity of moist air was modeled in a similar way to the effective conductivity of silica gel, and the equation that describes it is the following:

$$\lambda_{m,eff} = \varepsilon_b \lambda_m. \tag{25}$$

The specific surface area for a bed that consists entirely of spherical grains can be expressed as follows:

$$A_b = \frac{6(1-\varepsilon_b)}{d_p}. \tag{26}$$

The effective heat transfer coefficient was calculated assuming a regular regime and was based on dimensionless relations containing similarity numbers. The equation describing this coefficient can be written in the following form:

$$\alpha_{T,eff} = \frac{\alpha_T}{\sqrt{\mathrm{Bi}_T{}^2 + 1.437\mathrm{Bi}_T + 1}}, \tag{27}$$

where: α_T is the heat transfer coefficient, and Bi_T is the thermal Biot number. This Biot number can be calculated using the following formula:

$$\mathrm{Bi}_T = \frac{\alpha_T L_c}{\lambda_{p,ef}}, \tag{28}$$

where: L_c is the solid particle characteristic length, and $\lambda_{p,ef}$ is the effective thermal conductivity of the grains. The solid particle characteristic length can be found using the following relationship:

$$L_c = \frac{3d_p}{2\pi^2}. \tag{29}$$

The effective thermal conductivity of the grain is the average value between the minimum and maximum thermal conductivity in the porous particle expressed by the following formula:

$$\lambda_{p,ef} = \frac{1}{2}\left\{(1-\varepsilon_p)\lambda_s + \varepsilon_p\lambda_m + \left[\frac{(1-\varepsilon_p)}{\lambda_s} + \frac{\varepsilon_p}{\lambda_m}\right]^{-1}\right\}, \tag{30}$$

where ε_p is the porosity of a solid particle. The following Nusselt number correlation was employed to calculate the heat transfer coefficient:

$$\mathrm{Nu}_d = \frac{2.06}{\varepsilon_b}\mathrm{Re}_d^{0.425}\mathrm{Pr}^{\frac{1}{3}}, \tag{31}$$

where: Re_d is the Reynold number, and Pr is the Prandtl number. These dimensionless numbers can be calculated locally (for each mesh cell) with the following formulae:

$$\mathrm{Re}_d = \frac{\rho_m u d_p}{\mu_m}, \tag{32}$$

$$\mathrm{Pr} = \frac{\mu_m(c_{p,g} + \omega c_{p,v})}{\lambda_m}. \tag{33}$$

The Nusselt number allows finding the heat transfer coefficient using its following definition:

$$\alpha_T = \frac{\mathrm{Nu}_d \lambda_m}{d_p}. \tag{34}$$

The effective mass transfer coefficient was calculated using the heat and mass transfer analogy by applying the following formula:

$$\alpha_{m,eff} = \frac{\alpha_m}{\sqrt{\mathrm{Bi}_m{}^2 + 1.437\mathrm{Bi}_m + 1}}, \tag{35}$$

where: α_m is the coefficient mass transfer coefficient, and Bi_m is the mass Biot number found using the following relationship:

$$\mathrm{Bi}_m = \frac{\alpha_m L_c}{D_{vp,eff}}, \tag{36}$$

where: $D_{vp,eff}$ is the effective vapor diffusivity in the air filling the porous particle. This effective diffusivity is calculated with the formula:

$$D_{vp,eff} = \frac{D_{va,s}\varepsilon_p}{\tau_p}, \tag{37}$$

where: $D_{va,s}$ is the reference moisture diffusivity calculated by Eq. (21) with the silica gel temperature T_s instead of the moist air temperature, and τ_p is the tortuosity of the solid particle. Formulae similar to those used to determine the heat transfer coefficient were used to calculate the mass transfer coefficient. In these equations, the Sherwood number was used instead of the Nusselt number, and the Schmidt number instead of the Prandtl number. By applying the analogy between heat and mass transfer, the correlation given by Eq. (31) can be modified, obtaining the following one:

$$\mathrm{Sh}_d = \frac{2.06}{\varepsilon_b}\mathrm{Re}_d^{0.425}\mathrm{Sc}^{\frac{1}{3}}. \tag{38}$$

The Schmidt number can be found using the following relation:

$$\mathrm{Sc} = \frac{\mu_m}{\rho_m D_{va,s}}. \tag{39}$$

The Sherwood number allows finding the mass transfer coefficient using its following definition:

$$\alpha_m = \frac{\mathrm{Sh}_d D_{va,s}}{d_p}. \tag{40}$$

Table 3 Fixed physical properties of the model.

Property	Symbol	Value
Porosity of the bed (-)	ε_b	0.6
Porosity of the particle (-)	ε_p	0.6
Diameter of the particle (m)	d_p	0.004
Tortuosity of the bed (-)	τ_b	1000
Tortuosity of the particle (-)	τ_p	1000
Specific heat of dry air at constant volume (J kg^{-1} K^{-1})	$c_{v,g}$	719.53
Specific heat of dry air at constant pressure (J kg^{-1} K^{-1})	$c_{p,g}$	1006.43
Individual gas constant of dry air (J kg^{-1} K^{-1})	R_g	286.9
Thermal conductivity of dry air (W m^{-1} K^{-1})	λ_g	0.0242
Dynamic viscosity of dry air (Pa s)	μ_g	0.000017894
Specific heat of water vapor at constant volume (J kg^{-1} K^{-1})	$c_{v,v}$	1408.5
Specific heat of water vapor at constant pressure (J kg^{-1} K^{-1})	$c_{p,v}$	1870
Individual gas constant of water vapor (J kg^{-1} K^{-1})	R_v	461.5
Thermal conductivity of water vapor (W m^{-1} K^{-1})	λ_v	0.0182
Dynamic viscosity of water vapor (Pa s)	μ_v	0.000010057
Specific heat of liquid water (J kg^{-1} K^{-1})	$c_{p,\mathrm{H2O}}$	4186
Specific heat of solid particles J kg^{-1} K^{-1})	$c_{p,s}$	975
Density of solid particles (kg m^{-3})	ρ_s	2200
Maximum amount of water the silica gel can absorb (-)	$a0$	0.35
Characteristic activation energy (J mol^{-1})	βE	3780.8
Heat of sorption reaction (kJ kg^{-1})	H_r	2415
Correction parameter (-)	n	1.016
Operating pressure (Pa)	p_{op}	101325

The equilibrium moisture content in the solid was modeled based on the Dubinin-Astakhov equation and is expressed by the following formula:

$$a_{w,eq} = a_0 \exp\left[-\left(\frac{A_{ad}}{\beta E}\right)^n \right], \tag{41}$$

where: a_0 is the maximum amount of water the silica gel can absorb, A_{ad} is the adsorption potential coefficient, βE is the characteristic activation energy, and n is the equation parameter. The adsorption potential can be found with the following formula:

$$A_{ad} = BT_f ln\left(\frac{p_{sat}}{p_v}\right), \tag{42}$$

where: B is the universal gas constant, p_v is the pressure of water vapor, and p_{sat} is the saturation pressure of water vapor at temperature T_f calculated by the following expression:

$$p_{sat} = 3567 \exp\left[-5232\left(\frac{1}{T_f} - \frac{1}{300}\right)\right], \tag{43}$$

and the actual water vapor pressure in the moist air can be found by applying the following relationship:

$$p_v = \frac{\omega p}{\frac{M_v}{M_g} + \omega}. \tag{44}$$

Some of the physical properties of moist air (used as the working medium), silica gel (used as the thermochemical material filling the TES unit), and the structure of the porous bed were assumed to be fixed. These properties are listed in Table 3 with their respective descriptions and physical units. Table 4 summarises assumed initial and boundary conditions. Initial conditions were the same for the whole domain. All the walls of the TES units were assumed adiabatic.

Table 4 Initial and boundary conditions for charging and discharging.

Initial and boundary conditions	Symbol	Value (charging/discharging)
Initial velocity of the moist air in the unit (m s^{-1})	u	0 / 0
Initial gauge pressure of the moist air in the unit (Pa)	p	0 / 0
Initial specific humidity in the unit (-)	ω	0.025 / 0.00062
Initial mass of adsorbed water in the unit (-)	a_w	0.32 / 0.035
Initial temperature of moist air in the unit (K)	T_f	303 / 303
Initial temperature of solid particles in the unit (K)	T_s	303 / 303
Inlet velocity of moist air (m s^{-1})	u	2.5 / 2.5
Inlet temperature of moist air (K)	T_f	363 / 293
Inlet specific humidity (-)	ω	0.0095 / 0.0125

5. Results of the simulations

The model validation was not conducted at the current model development state, while model verification was limited to initial mesh size sensitivity analysis and assessing mass and heat conservation principles. But the experimental stand is under development, and the model will be validated in the future. The implemented model was used to simulate the charging and discharging of the sorption-based TES unit. Both simulations were run twice, using a smaller and larger computational grid. A small time step of 0.02 s was used for all tests to improve the equations' convergence rates. Preliminary simulation results were to verify that the implemented numerical model is stable and satisfies the basic mass and energy conservation principles. In addition, it was checked whether the size of the computational grid impacts the calculated characteristics of heat and mass transfer between the reactive bed and moist air. Due to the high complexity of the model, many coupling between equations and other parameters, and the resulting huge demand for computing power, the actual computation times were about a month for TES discharging and another month for charging. For this reason, simulations were stopped at the early stages of the process, and only several minutes of the charging and discharging process were simulated. The simulated charging times on the small and large grids are 2630 s (131 500 time steps) and 632.54 s (31 627 time steps), respectively. For discharge, the simulated times reached 2089.94 s (104 497 time steps) on the small grid and 821.4 s (41 070 time steps) on the large grid.

After the calculations, it was verified whether the implemented model obeyed the basic mass and heat conservation laws at each time step. To do so, the exact amount of masses and energies that were contained, entered, and left the system were recorded after each time step. The energy sources in the system were the entering air and the heat of the sorption reaction. Water was supplied to the system only through moist air. The overall energy balance in the system was calculated in each time step using the following formula:

$$(H_{in} - H_{out}) + H_r = \left(U_{gas}^{t} - U_{gas}^{t-1}\right) + (U_{sol}^{t} - U_{sol}^{t-1}), \tag{45}$$

where: H_{in} and H_{out} are entering and leaving air enthalpies, respectively, U_{gas} is the internal energy of air contained in the system, and U_{sol} is the internal energy of solid particles and bounded water. The superscript t means the value taken at the actual time step, while t-1 at the previous time step. Similarly, the water and moist air balances in the system can be written as:

$$\left(m_{w,in} - m_{w,out}\right) = \left(m_{w,gas}^{t} - m_{w,gas}^{t-1}\right) + \left(m_{w,sol}^{t} - m_{w,sol}^{t-1}\right), \tag{46}$$

$$\left(m_{a,in} - m_{a,out}\right) = (m_a^t - m_a^{t-1}), \tag{47}$$

where: $m_{w,in}$ and $m_{w,out}$ are the masses of water vapor entering and leaving the system, respectively, $m_{w,gas}$ is the mass of water vapor contained in the system, $m_{w,sol}$ is the mass of water contained in the silica gel bed, $m_{a,in}$ and $m_{a,out}$ are the masses of moist air entering and leaving the system, respectively, and m_a is the mass of moist air contained in the system. The right-hand sides of Eq. (45)-(47) have been moved to the left to simplify the balance evaluation. Thus, properly balanced quantities should take values close to zero.

Table 5 Balances of the energy, the mass of water, and the mass of moist air.

Average residues per time step	Value	Simulation time (s)	Number of grid elements
Average residue of energy during charging (J)	$1.0092 \cdot 10^{-3}$	632.54	21 344
	$4.2618 \cdot 10^{-3}$	632.54	346 170
	$4.0947 \cdot 10^{-5}$	2630	21 344
Average residue of water mass during charging (kg)	$5.0959 \cdot 10^{-12}$	632.54	21 344
	$-1.1001 \cdot 10^{-10}$	632.54	346 170
	$1.1861 \cdot 10^{-10}$	2630	21 344
Average residue of moist air mass during charging (kg)	$1.9798 \cdot 10^{-11}$	632.54	21 344
	$-2.3261 \cdot 10^{-9}$	632.54	346 170
	$3.4112 \cdot 10^{-12}$	2630	21 344
Average residue of energy during discharging (J)	$-7.0426 \cdot 10^{-4}$	821.4	21 344
	$-1.2043 \cdot 10^{-3}$	821.4	346 170
	$-1.7621 \cdot 10^{-4}$	2089.94	21 344
Average residue of water mass during discharging (kg)	$9.2381 \cdot 10^{-13}$	821.4	21 344
	$4.9613 \cdot 10^{-11}$	821.4	346 170
	$3.2810 \cdot 10^{-12}$	2089.94	21 344
Average residue of moist air mass during discharging (kg)	$-1.1574 \cdot 10^{-12}$	821.4	21 344
	$-3.2515 \cdot 10^{-11}$	821.4	346 170
	$5.6194 \cdot 10^{-12}$	2089.94	21 344

Table 6 Differences between results obtained applying a smaller and larger computational grid.

Simulation result	Value	Number of grid elements
Water adsorbed by silica gel during discharging (kg)	0.2261280	21 344
	0.2261438	346 170
Water desorbed by silica gel during charging (kg)	0.1712517	21 344
	0.1712699	346 170
Energy released during the adsorption reaction (J)	546099.10	21 344
	546123.98	346 170
Energy absorbed during the desorption reaction (J)	413572.40	21 344
	413616.44	346 170

The results in Table 5 confirm that the implemented model satisfies the mass and energy conservation principles. Although the residues of the energy equation seem quite large, and after multiplying the average per time step by the number of time steps, the result on the order of magnitude of 100 J was obtained. But this amount is a very small part of the energy released or absorbed during the sorption reaction. For example, the average energy residue per time step during charging was $4.2618 \cdot 10^{-3}$ J, and after 31 627 time steps amounted to 134.79 J. But solid particles absorbed 413 616 J of the heat during the desorption reaction. This means the error is insignificant and does not affect the simulation result.

Next, it was also checked whether the size of the computational grid impacted the simulation result, i.e., the initial mesh sensitivity analysis was performed. For this purpose, differences in the amount of water exchanged between the air and the porous bed as well as stored and released heat in sorption reactions, were checked. The operating period that was considered was 632.54 s of charging and 821.4 s of discharging. As can be seen in Table 6, the size of the computational grid has a very small effect on the simulated amounts of adsorbed and desorbed water as well as absorbed and released heat.

Exemplary simulation results are shown in Figures 3 and 4. However, only the initial charging and discharging phases were simulated due to the long computational times resulting from the model and its implementation complexity. Figure 3 shows how the moisture content of the silica gel granules changed as the TES unit was loaded. It can be seen that dehydration occurs best on the axis of the storage and near its outer wall. Figure 4 shows how the temperature of the moist air in the TES unit changes as it is unloaded. The silica gel granules adsorb water and, as a result, warm up and transfer heat to the flowing air. Here, too, it can be seen that the process is faster at the axis and near the wall of TES. Sorption and heat transfer processes occur fastest in axial and wall regions, most likely due to higher air velocity than in other storage zones. This higher velocity

results in a higher local Reynolds number making mass and heat transfer coefficients more intensive there. The air velocity distribution at the entrance to the porous bed results from the shape of the diffuser before the bed. The air with the highest momentum flows in the axis (the core of the flow), while at the outer walls, vortices are formed just in front of the bed in the central part of the diffuser, which improves mass and energy convection in the bed close to walls.

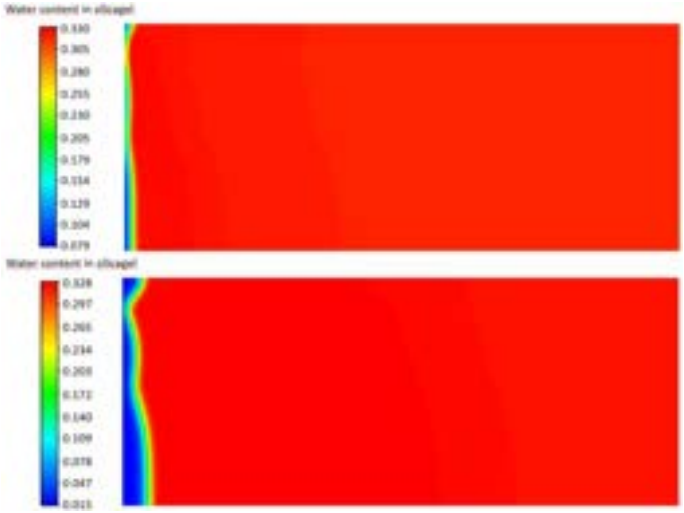

Figure. 3. The contour of water content a_w in silica gel during charging at 2 min (upper) and 10 min (lower) of simulation.

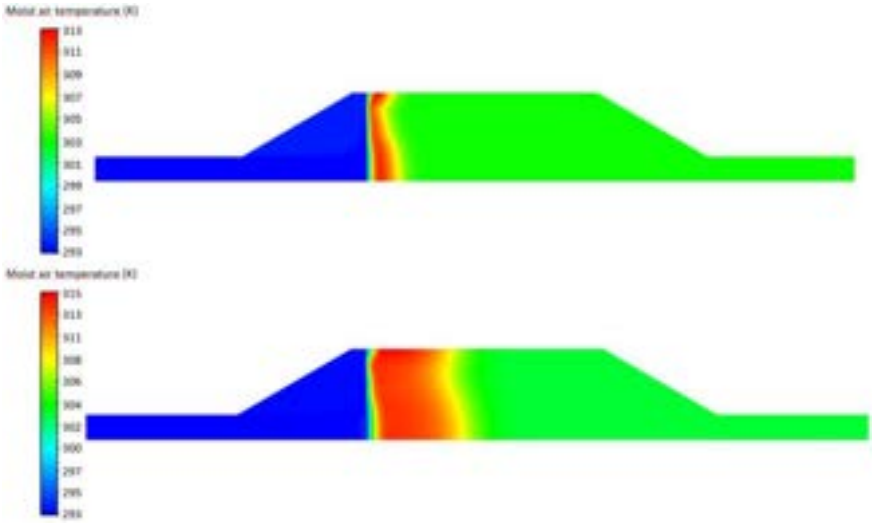

Figure. 4. The contour of moist air temperature during discharging at 2 min (upper) and 10 min (lower) of simulation.

6. Conclusions

The paper presents the concept of an advanced multi-dimensional TChES system model. The model simulates the charging/discharging of a low-temperature TChES unit that operates in an open system. The gaseous working medium (moist air) provides and removes heat and moisture from the unit. The porous thermochemical material stores the heat due to hydration/dehydration reversible reactions. The model's main feature is that it treats rigorous phenomena occurring in the TChES unit. It accounts for local hygric and thermal non-equilibrium by treating heat and moisture carrier fluid and reactive porous bed separately. Therefore, two sets of governing equations have been derived, i.e., one dealing with moisture transfer in the air flowing through the porous bed and the second one with phenomena occurring in the reactive porous bed. The model can simulate the chemical and physical sorption process occurring in the TES unit.

Currently, the proposed model has been simplified and modified to simulate the sorption/desorption TES unit. It was implemented in 2D axisymmetric space by applying commercial software ANSYS Fluent and its advanced customization options, i.e., UDS, UDF, and UDM. The model was tested regarding the initial mesh size sensitivity and obeying mass and energy conservation principles. The obtained results were physical. It turned out that the current model implementation is very computationally inefficient, i.e., the computational time is very long. Therefore, only several minutes of the discharging and charging processes were simulated.

These problems with long simulation times were probably related to many couplings between different equations and properties, which are not necessarily required and have not necessarily meaningful impacts on the model's accuracy. But they could significantly decrease the convergence rates. So further work will be devoted to optimizing model implementation and improving convergence rates by decoupling model equations and properties and testing different numerical techniques for solving governing equations.

Acknowledgments

This work was financially supported by the National Science Centre (Poland) within project no. 2020/37/B/ST8/04021.

References

[1] Dincer I., Rosen M.A., Thermal energy storage: Systems and applications. Chichester, UK: Wiley; 2010.

[2] Darkwa K., Ianakiev A., O'Callaghan P.W., Modelling and simulation of adsorption process in a fluidised bed thermochemical energy reactor. Appl Therm Eng 2006;26:838-45.

[3] Torres Ledesma J., Łapka P., Domański R., Casares F.S., Numerical simulation of the solar thermal energy storage system for domestic hot water supply located in south Spain. Therm Sci 2013;17:431-42.

[4] Jaworski M., Łapka P., Furmański P., Numerical modelling and experimental studies of thermal behaviour of building integrated thermal energy storage unit in a form of a ceiling panel. Appl Energ 2014;113:548-57.

[5] Dydek K., Furmański P., Łapka P., Influence of PCMs in thermal insulation on thermal behaviour of building envelopes. J Phys Conf Ser 2016;745:032138.

[6] Łapka P., Jaworski M., Efficiency optimisation of the thermal energy storage unit in the form of the ceiling panel for summer conditions. Int J Energ Res 2019;43:2151-61.

[7] Kubiś M., Łapka P., Cieślikiewicz Ł., Sahmenko G., Sinka M., Bajare D., Analysis of the thermal conductivity of a bio-based composite made of hemp shives and a magnesium binder. Energies 2022;15:5490.

[8] N'Tsoukpoe K.E., Schmidt T., Rammelberg H.U., Watts B.A., Ruck W.K.L., A systematic multi-step screening of numerous salt hydrates for low temperature thermochemical energy storage. Appl Energ 2014;124:1-16.

[9] Mikos-Nuszkiewicz N., Furmański P., Łapka P., A mathematical model of charging and discharging processes in a thermochemical energy storage reactor using the hydrated potassium carbonate as a thermochemical material. Energy 2023;262:125642.

[10] Abedin A.H., Rosen M.A., Assessment of a closed thermochemical energy storage using energy and exergy methods. Appl Energ 2012;93:18-23.

[11] Neveu P., Tescari S., Aussel D., Mazet N., Combined constructal and exergy optimisation of thermochemical reactors for high temperature heat storage. Energ Convers Manage 2013;71:186-98.

[12] Albrecht K.J., Jackson G.S., Braun R.J., Thermodynamically consistent modeling of redox-stable perovskite oxides for thermochemical energy conversion and storage. Appl Energ 2016;165:285-96.

[13] Flegkas S, Birkelbach F, Winter F, Freiberger N, Werner A, Fluidized bed reactors for solid-gas thermochemical energy storage concepts – Modelling and process limitations. Energy 2018;143:615-23.

[14] Benoit M., Mazet N., Mauran S., Stitou D., Xu J., Thermochemical process for seasonal storage of solar energy: Characterization and modeling of a high density reactive bed. Energy 2012;47:553-63.

[15] Shao H, Nagel T, Roßkopf C, Linder M, Wörner A, Kolditz O, Non-equilibrium thermo-chemical heat storage in porous media: Part 2 – A 1D computational model for a calcium hydroxide reaction system. Energy 2013;60:271-82.

[16] Wang M., Chen L., Zhou Y., Tao W.Q., Numerical simulation of the physical-chemical-thermal processes during hydration reaction of the calcium oxide/calcium hydroxide system in an indirect reactor. Transport Porous Med 2021;140:667-96.

[17] Michel B., Neveu P., Mazet N., Comparison of closed and open thermochemical processes, for long-term thermal energy storage applications. Energy 2014;72:702-16.

[18] Ranjha Q., Oztekin A., Numerical analyses of three-dimensional fixed reaction bed for thermochemical energy storage. Renew Energ 2017;111:825-35.

[19] Shi T., Xu H., Qi C., Lei B., Wu Y., Zhao C., Multi-physics modeling of thermochemical heat storage with enhance heat transfer. Appl Therm Eng 2021;198:117508.

[20] Li W., Klemeš J.J., Wang Q., Zeng M., Numerical analysis on the improved thermo-chemical behaviour of hierarchical energy materials as a cascaded thermal accumulator. Energy 2021;232:120937.

[21] Rui J., Luo Y., Wang M., Peng J., She X., Design and performance evaluation of an innovative salt hydrates-based reactor for thermochemical energy storage. J Energy Storage 2022;55:105799.

PROCEEDINGS OF ECOS 2023 - THE 36TH INTERNATIONAL CONFERENCE ON
EFFICIENCY, **C**OST, **O**PTIMIZATION, **S**IMULATION AND ENVIRONMENTAL IMPACT OF ENERGY SYSTEMS
25-30 JUNE 2023, LAS PALMAS DE GRAN CANARIA, SPAIN

Modeling of a combined solar system including a thermal battery based on phase change material

Diane Le Roux[a], Sylvain Serra[b], Sabine Sochard[c], Zakaria Aketouane[d], Tessa Hubert[e], Ryad Bouzouidja[f], Alain Sempey[g] and Jean-Michel Reneaume[h]

[a] Universite de Pau et des Pays de l'Adour, E2S UPPA, LaTEP, Pau, France, diane.le-roux@univ-pau.fr, CA
[b] Universite de Pau et des Pays de l'Adour, E2S UPPA, LaTEP, Pau, France, sylvain.serra@univ-pau.fr
[c] Universite de Pau et des Pays de l'Adour, E2S UPPA, LaTEP, Pau, France, sabine.sochard@univ-pau.fr
[d] Nobatek/INEF 4, Anglet, France, zaketouane@nobatek.inef4.com
[e] Nobatek/INEF 4, Anglet, France, thubert@nobatek.inef4.com
[f] University of Bordeaux, CNRS UMR 5295, Arts et Metiers Institute of Technology, Bordeaux INP, INRAE, I2M Bordeaux, Talence, France, ryad.bouzouidja@u-bordeaux.fr
[g] University of Bordeaux, CNRS UMR 5295, Arts et Metiers Institute of Technology, Bordeaux INP, INRAE, I2M Bordeaux, Talence, France, alain.sempey@u-bordeaux.fr
[h] Universite de Pau et des Pays de l'Adour, E2S UPPA, LaTEP, Pau, France, jean-michel.reneaume@univ-pau.fr

Abstract:
Thermal energy storage (TES) is a key issue in efficient energy system applications, especially in the context of renewable energies. In this respect, phase change materials (PCM) have attracted interest as an active solution for efficient energy management, particularly in the building sector. This paper presents a modeling of a thermal battery based on PCM in the case of solar systems assisted by heat pump (SAHP). The storage tank allows to store the heat produced via unglazed solar panels (Batisol®) and represents the heat source of the heat pump. The heat pump can supply the heating and domestic hot water (DHW) needs of a building. The storage consists of a block of PCM contained between two plates of heat transfer fluid (HTF). A 2D model is used to describe the behaviour of the PCM and a 1D model is preferred for the HTF plates. The objective of the study is to dynamically simulate the thermal behaviour of this storage for different hot inlet temperature profiles: step, trapezoidal functions and profile of the temperature at the outlet of the thermal panels for a winter and summer period of 8 days. This 2D model would be useful to validate a simpler model for optimisation of the operational parameters of the system.

Keywords:
Thermal energy storage, Phase change material, Solar system assisted heat pump, Domestic hot water, Low-temperature heating.

1. Introduction

In order to limit temperature rise, it is important to reduce the environmental impact of energy production and consumption. According to the International Energy Agency [1], the building sector is considered to be one of the largest energy end-use sectors in the world. The growing demand for energy is increasing the pressure on the environment. One of the main challenges to reduce the environmental impact of buildings is therefore to replace fossil fuels with renewable resources. Thermal energy storage (TES) has been particularly studied in recent years as it is essential to compensate for the intermittency of renewable energies, by correcting the mismatch between energy supply and demand [2]. Moreover, TES are increasingly used to meet the heating and cooling needs of buildings. There are three types of TES: sensible, latent and thermochemical [2]. Phase Change Materials (PCM) are materials that can store large amounts of thermal energy in the form of latent heat of fusion when they change from a solid to a liquid state for example at a specific phase change temperature or temperature range if the PCM is not a pure compound. This phase transition process is reversible, allowing thermal energy to be stored and released at relatively constant temperatures. Compared to sensible heat storage materials, PCM offer several significant advantages, like a higher heat storage density at small temperature ranges [3]. PCM can store between 5 and 14 times more thermal energy per unit volume than sensible heat storage materials [4]. As a result, the use of PCM can help to reduce the size of heat storage systems, making them more suitable for residential applications. Thermochemical storage is more interesting in terms of storage density. However, this technology is less mature than that with PCM.

Solar systems assisted by heat pump (SAHP) can provide an efficient and environmentally friendly heating

and cooling solution for residential and commercial buildings. The role of a heat pump in the heating system is to increase the thermal energy from a lower temperature level to a higher temperature level [5]. Moreover, the use of PCM heat storage between the solar facade and the heat pump can improve the overall performance of the SAHP. Several studies have been conducted to assess the benefits of using PCM in SAHP [6–9]. Firstly, the solar energy stored in the PCM unit can be used as a heat source for the evaporator in the heat pump. As a result, the temperature of the evaporator is almost constant and the heat pump can operate under more stable conditions. This leads to a better Coefficient of Performance (COP) for the heat pump.

Depending on the type of application at the output of the heat pump (heating, cooling), the temperature levels are not the same and therefore the PCM used changes [6]. Four temperature ranges have been listed by Du *et al.* [6]: low (-20 to 5 °C), medium-low (5 to 40 °C), medium (40 to 80 °C) and high (80 to 200 °C) temperatures. For a heating or domestic hot water applications, the medium temperature level is considered since the buffer tank temperature setpoint is usually expected at 60 °C. Many studies have been carried out on such systems [6, 8–10]. However, as each storage is different (size, design and PCM used in particular), it is important to model its thermal behaviour correctly in order to explore the optimal operating parameters later.

The objective of this paper is to dynamically simulate a TES based on PCM integrated on SAHP. In a first part, the methodology and the case study will be presented. Then, several operating scenarios will be investigated in the results section. The profile of the hot temperature entering in the thermal battery will be a step, then a trapezoidal function, and finally this of the outler temperature of thermal panels in winter and summer periods using measured climatic conditions as boundaries. Finally, last part will conclude.

2. Material and Methods

This section is divided in three parts. Firstly, the global system is described, composed by solar thermal panels, PCM battery and heat pump. In next steps, the models of the different components of the system are defined. Dynamic models are based on the conservation of mass and energy equations.

2.1. Definition of the system

The studied system is composed of solar panels, a TES based on PCM, and a heat pump, as illustrated in Fig. 1. The system is divided in three circuits. The first, connecting the solar facade to the buffer tank, is made up of glycol. The second circuit, connecting the thermal battery to the heat pump, is composed of water. An air heater is integrated in parallel with the solar storage to supply heat to the heat pump when the temperature of the thermal battery is not high enough. The last circuit, also made of water, connects the PCM battery for heating and domestic hot water (DHW) to the heat pump.

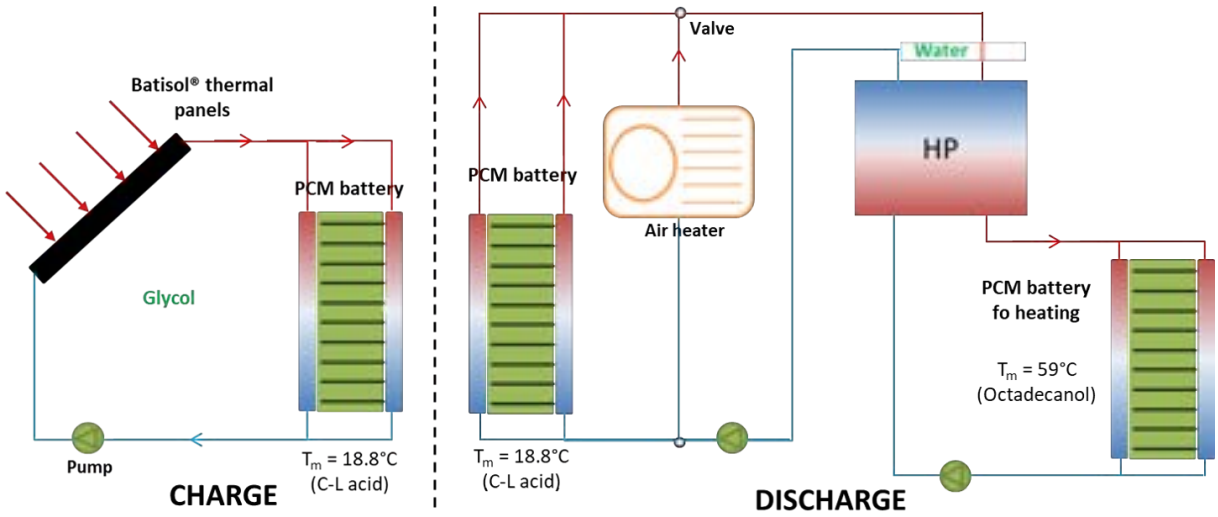

Figure 1: Global diagram of the solar assisted heat pump with thermal battery based on PCM.

The solar facade is composed of unglazed thermal panels (Batisol®) [11, 12], developed by Nobatek/INEF 4 [13]. The dimensions of the PCM-based storage are 0.4 m x 0.4 m x 0.4 m (Fig. 2a). The heat pump can produce both low temperature heating and DHW for a building application. The same thermal battery is used for the DHW and buffer tanks. Only the PCM changes between the two batteries, to match the desired temperature level. For the buffer tank, a mixture of 61.5% capric acid and 38.5% lauric acid (C-L acid) is used. Its melting temperature is 291.95 K. For the heating PCM battery, octadecanol is prefered. Indeed, its melting temperature is 332.46. The thermophysical properties of these materials are depicted in Table 1.

Table 1: Thermophysical properties of C-L acid [14] and octadecanol.

Name	Value for C-L acid	Value for octadecanol	Unit
T_m	291.95	332.46	K
L	$140.8 \cdot 10^3$	$208.45 \cdot 10^3$	J/kg
ρ_{PCM}	897.5	850	kg/m^3
$c_{p,l}$	1970	1750	$J/kg/K$
$c_{p,s}$	2240	2150	$J/kg/K$
λ_s	0.143	0.301	$W/m/K$
λ_l	0.139	0.205	$W/m/K$

2.2. Model of the Batisol® panels

The model of the thermal solar facade was described previously by Bouzouidja *et al.* [15]. From the time-varying input parameters, taken from a weather file, and the operating parameters, the temperature at the panel outlet is determined [15]:

$$T_{out,sol} = \frac{T_{in,sol} \cdot \dot{m} \cdot c_{p,H} + \alpha \cdot A_{sol} \cdot (0.5 \cdot T_{in,sol} - T_{ext}) + G_{sol} \cdot A_{sol} \cdot \gamma}{\dot{m} \cdot c_{p,H} - 0.5 \cdot \alpha \cdot A_{sol}} \tag{1}$$

Where $T_{in,sol}$ and T_{ext} are the temperatures at the entrance to the solar facade and outside (K), A_{sol} the surface of the solar facade (m^2), G_{sol} the solar flux (W/m^2), $\dot{m}$ the low rate of the Heat Transfer Fluid (HTF) circulating in the thermal panels (kg/s) and $c_{p,H}$ the specific heat capacity of the hot fluid (glycol) ($J/(kg \cdot K)$). The coefficients α and γ have been determined experimentally (γ = 0.63). The first one depends on the wind speed:

$$\alpha = -(7.84 + 3 \cdot v_{wind}) \tag{2}$$

2.3. Model of the thermal energy storage based on phase change material

In order to model the behaviour of latent heat storage, the following simplifying assumptions have been made:

- Natural convection is neglected. Only conduction is considered,
- No supercooling or superheating,
- Incompressible and Newtonian HTF,
- Kinetic and potential energy variations are neglected,
- Isothermal phase change (Octadecanol is a pure body so this assumption is correct. Since C-L acid is a mixture, the phase change temperature range is between 291.65 and 292.25 K [16]. As the melting temperature of this PCM is considered to be 291.95 K, the uncertainty of this assumption is +/- 2%),
- Density variation of PCM neglected during the phase change,
- Thermophysical properties are independent of temperature, but different for liquid and solid phases,
- The storage walls are assumed to be perfectly insulated (adiabatic boundary conditions) (Fig. 2b).

The shape of the thermal battery and its operation are described schematically in Fig. 2. The PCM is placed between two plates where the HTF circulates. Thus, a symmetry plane is visible in the middle of the battery. During the charging step, hot fluid is injected into the two plates. During the discharging step, cold fluid is injected. As a result, the charging and discharging steps are carried out separately. The plates where circulates the HTF are modelled in one dimension, a plug flow being assumed. The PCM part located between two plates is modelled in 2D because the heat diffusion operates in axial and longitudinal directions.

Fins are added to the plates to increase the contact area between the PCM and the HTF. To account for the fins, the effective conductivity of the PCM is expressed as:

$$\lambda_{eff} = a \cdot \lambda_{PCM} + (1 - a) \cdot \lambda_{fin} = a \cdot (\lambda_s + f_l \cdot (\lambda_l - \lambda_s)) + (1 - a) \cdot \lambda_{fin} \tag{3}$$

Where a is the proportion of PCM in the volume under consideration ($-$), λ_{PCM}, λ_s, λ_l et λ_{fin} are respectively the thermal conductivities of the PCM, the solid and liquid phases of the PCM and the fins ($W/m/K$), and f_l the liquid fraction of the PCM ($-$).

The enthalpy, the temperature and the liquid fraction of the PCM (according to x and y), and the temperature of the hot HTF (according to y) are determined with 4 to 11.

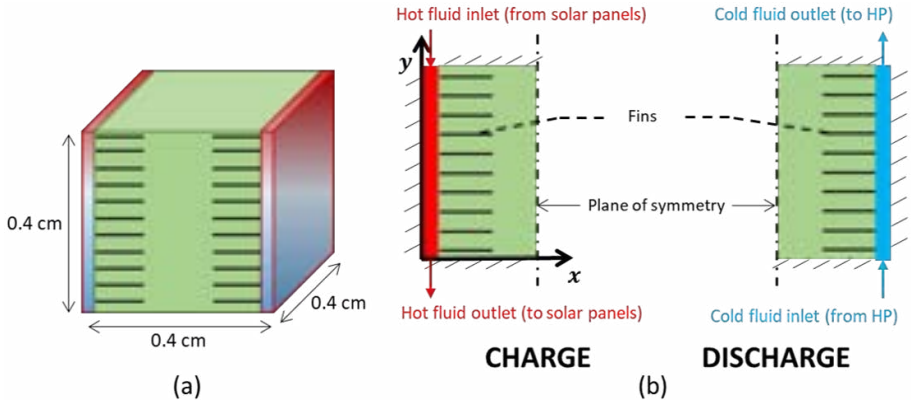

Figure 2: Diagram of the dimensions of the PCM-based thermal battery (a), and diagram of the PCM-based thermal battery with two plates for the charging and discharging steps (b).

- **Exchanges between the HTF (hot or cold) and the PCM:**

  For hot fluid:

$$\rho_H \cdot V \cdot c_{p,H} \frac{\partial T_H}{\partial t} - \dot{m}_H \cdot c_{p,H} \cdot \frac{\partial T_H}{\partial y} \cdot P = h_H \cdot A \cdot (T_H - T_{PCM}) + \lambda_H \cdot V \cdot \frac{\partial^2 T_H}{\partial y^2} \tag{4}$$

  For cold fluid:

$$\rho_C \cdot V \cdot c_{p,C} \frac{\partial T_C}{\partial t} + \dot{m}_C \cdot c_{p,C} \cdot \frac{\partial T_C}{\partial y} \cdot P = h_C \cdot A \cdot (T_C - T_{PCM}) + \lambda_C \cdot V \cdot \frac{\partial^2 T_C}{\partial y^2} \tag{5}$$

- **Exchanges in the PCM:**

$$\frac{\partial H_{PCM}}{\partial t} = \frac{\partial \lambda_{eff}}{\partial x} \cdot \frac{\partial T_{PCM}}{\partial x} + \frac{\partial \lambda_{eff}}{\partial y} \cdot \frac{\partial T_{PCM}}{\partial y} + \lambda_{eff} \cdot \frac{\partial^2 T_{PCM}}{\partial x^2} + \lambda_{eff} \cdot \frac{\partial^2 T_{PCM}}{\partial y^2} \tag{6}$$

$$H_{PCM}(T_{PCM}) = f_l \cdot H_l + (1 - f_l) \cdot H_s = \rho_{PCM} \cdot ((c_{p,s} + f_l \cdot (c_{p,l} - c_{p,s})) \cdot T_{PCM} + L \cdot f_l - f_l \cdot (c_{p,s} + f_l \cdot (c_{p,l} - c_{p,s})) \cdot T_m) \tag{7}$$

$$f_l = \begin{cases} 0 & for\ H_{PCM} < H_s \\ \frac{H_{PCM} - H_s}{H_l - H_s} & \\ 1 & for\ H_{PCM} > H_l \end{cases} \tag{8}$$

- **Boundary conditions for the PCM in contact with hot (during charging step) or cold (during discharging step) HTF:**

  For hot fluid (for x = 0 and 0.4 m):

$$h_H \cdot (T_H - T_{PCM}) = -\lambda_{eff} \frac{\partial T_{PCM}}{\partial x}\ for\ x = 0\ m \quad and \quad h_H \cdot (T_H - T_{PCM}) = \lambda_{eff} \frac{\partial T_{PCM}}{\partial x}\ for\ x = 0.4\ m \tag{9}$$

  For cold fluid (for x = 0 and 0.4 m):

$$h_C \cdot (T_C - T_{PCM}) = -\lambda_{eff} \frac{\partial T_{PCM}}{\partial x}\ for\ x = 0\ m \quad and \quad h_C \cdot (T_C - T_{PCM}) = \lambda_{eff} \frac{\partial T_{PCM}}{\partial x}\ for\ x = 0.4\ m \tag{10}$$

- **Boundary conditions for the PCM in contact with the outside (adiabatic conditions):**

$$\lambda_{eff} \frac{\partial T_{PCM}}{\partial y} = 0\ for\ y = 0\ and\ 0.4\ m \tag{11}$$

- **Initial conditions:** All temperatures are fixed at 283.15 K. The enthalpy of the PCM is determined by 7 at 283.15 K. The liquid fraction is considered equal to 0.

Where h_H and h_C are the convective exchange coefficients of the hot and cold fluid respectively ($W/m^2/K$), T_H, T_C, T_{PCM} and T_m are the hot and cold temperature, the temperature of the PCM and the melting temperature of the PCM, L the latent heat (J/kg), ρ_{MCP} the PCM density (kg/m^3), $c_{p,l}$ and $c_{p,s}$ are the specific heat capacity of the liquid and solid phases respectively ($J/kg/K$), P the exchange perimeter (m), A the exchange area (m^2) and V the volume of the representative element considered (m^3). The convective exchange coefficients are determined from the Nusselt number, assuming that the wall thickness of the plate is very thin and therefore negligible.

The boundary conditions of the thermal battery depend on the configuration studied. Four scenarios have been investigated. Firstly, the profile of hot temperature entering the thermal battery follows a step. In a second stage, it is a trapezoidal function. Finally, the battery based on PCM is connected to the Batisol® panels and two periods of 8 days are simulated: winter (from January 1 to 8) and summer (from July 1 to 8). In the latter two cases, the profile of the outlet temperature of the solar panels is used as input to the PCM:

$$T_H(x, y = 0.4, t) = T_{out,sol} \tag{12}$$

2.4. Resolution of the differential algebraic equations and software used

The software used to model the system is OpenModelica v1.18.0. The Modelica library (v3.2.3) is considered. The spatial discretisation is performed manually while the temporal discretisation is performed via the DASSL integrator available on OpenModelica. The tolerance used in the DASSL integrator is 10^{-6}. For the PCM-battery model, equations are discretised using an explicit second-order discretisation scheme with finite differences. For the boundary conditions (9 to 11), second-order decentred schemes are used.

3. Results and Discussion

This section is divided into three parts. The first one aims at studying the behaviour of PCM-based TES for a hot inlet temperature profile following a ramp (case 1). The second part investigates the behaviour of the system under trapezoidal loads (case 2). Finally, the battery is connected to the Batisol® solar facade and an 8-day simulation is performed for two periods of the year: from 1 to 8 January (winter, case 3) and from 1 to 8 July (summer, case 4). The hot HTF temperatures investigated at the buffer tank inlet are shown in Fig. 3. The colours red, green, blue and yellow refer to cases 1, 2, 3 and 4 respectively. For the next figures, the coordinates (x = y = 0 m) are placed at the bottom left of the PCM in Fig. 2.

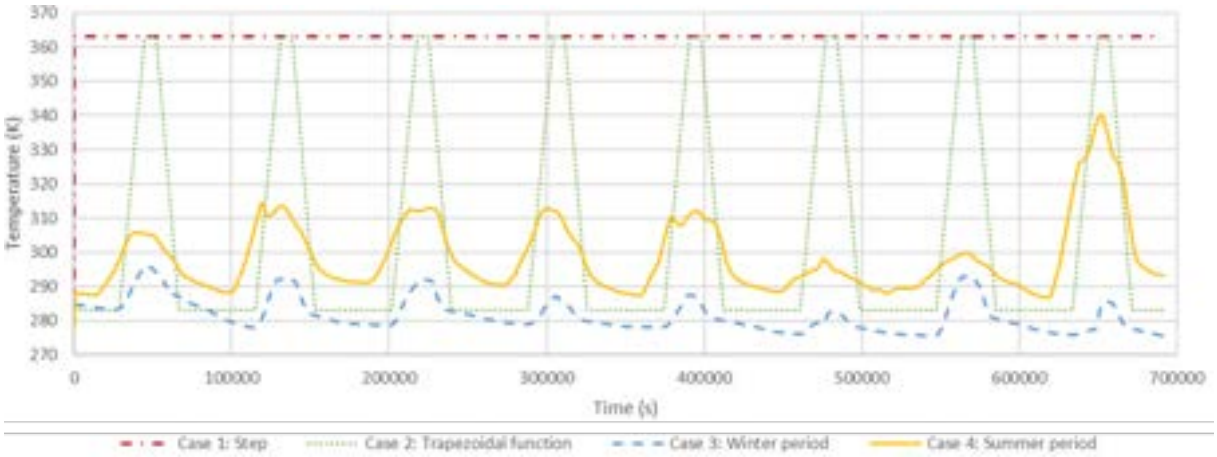

Figure 3: Four hot temperatures profiles considered at the input of the PCM-based TES battery.

The simulation times are relatively fast for simulating 8 days ($6.912 \cdot 10^{-5}$ s) on a standard laptop (processor: 12th Gen Intel®Core(TM) i7-12700H 2.69 GHz and RAM: 32 Go). They amount to 30 s and 2 min for cases 1 and 2 respectively. When the weather file is used and the Batisol® thermal panel model is added, the simulation times are slightly longer but remain below 5 min.

3.1. Profile of the hot inlet temperature following a step

For the case 1, the input temperature profile follows a ramp from 283.15 to 363.15 K in the first second of the simulation. The evolution of the liquid fraction and the temperature of the PCM in the tank are studied in Fig. 4 over time for the first slice of PCM in contact with the hot plate (for x = 0 m), according to the vertical. The colours purple, green and red refer to the high (y = 0.4 m), middle (y = 0.2 m) and low (y = 0 m) parts of the PCM respectively. Solid lines are used for the temperature and dashed lines are preferred for the liquid fraction. The same marking and colour code will be used in the following sections. Initially, the PCM is in the solid state

(f_l = 0) at 283.15 K. Its temperature increases until it reaches the melting temperature (291.95 K) at 18.2 s for y = 18 (in purple), the top of the PCM in contact with the hot plate. This temperature is reached at 20.8 s for the middle of the PCM (in green), and 23.2 s for the bottom of the PCM (in red). From these times onwards, the temperature of the PCM remains constant while the liquid fraction increases until it reaches unity, indicating that all the PCM has changed from the solid to the liquid state. This event occurs at 78.0, 82.1 and 87.5 s for the top, middle and bottom of the PCM respectively. From then on, the liquid fraction remains constant and the temperature of the PCM gradually increases, while approaching the temperature of the hot HTF.

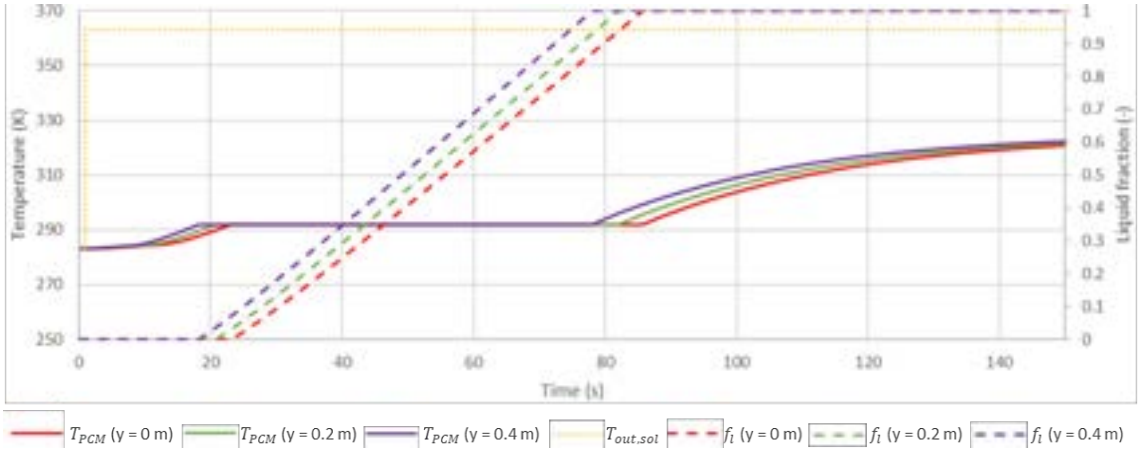

Figure 4: Case 1: Temperature and liquid fraction evolution for the first PCM layer in contact with the hot plate (x = 0 m) and for y = 0, 0.2 and 0.4 m.

The evolution of these two variables has also been studied for different values of x in Fig. 5. As the battery is symmetrical, only the coordinates at x = 0 (in red), 0.06 (in yellow) and 0.2 m (in green) are presented for the sake of clarity. In this case, the profiles are clearly different. The phase change from solid to liquid state is clearly visible for the first layer in contact with the hot plate. For x = 0.06 m, the temperature evolves linearly without reaching the melting temperature. As a result, the liquid fraction remains constant and equal to zero. For the PCM in the middle of the battery (x = 0.2 m), the temperature remains almost constant (283.15 K), indicating that the heat has not reached the core of the battery in 150 s.

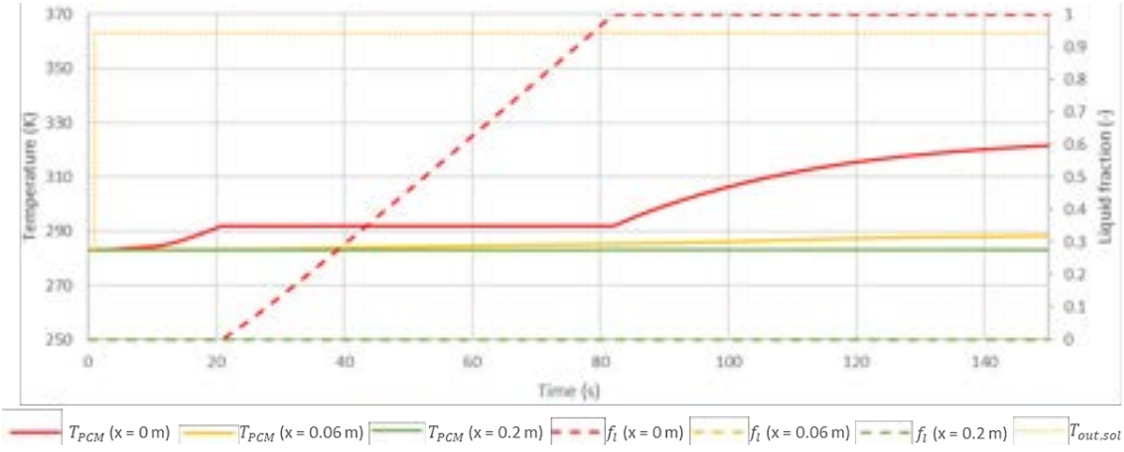

Figure 5: Case 1: Temperature and liquid fraction evolution in the longitudinal direction (for x = 0, 0.06 and 0.2 m) for the PCM layer in the middle (y = 0.2 m).

Figures 4 and 5 show the interest of considering a 2D model for PCM tank, according to longitudinal (x) and vertical (y) directions, since the temperatures in the PCM are different in both directions.

3.2. Profile of the hot inlet temperature following a trapezoidal function

Before studying the thermal behaviour of the storage connected to the solar facade, a trapezoidal function is used to simulate the evolution of the hot temperature at the battery inlet (Fig. 3). The period of this function is decomposed on 28800 s of width, 16200 s of rising , 7200 s of width, 14400 s of falling, for a total period of 86400 s. The temperature and liquid fraction are studied as before, for the first slice in contact with the hot

plate (for x = 0 m) (Fig. 6), and the slice in the middle of the PCM (for y = 0.2 m) (Fig. 7). The same evolution as for the ramping test is observed. In a first step, the temperature of the PCM increases until it reaches the melting temperature of the PCM (at 30634 s) (Fig. 6a). Then the liquid fraction increases until it reaches unity (Fig. 6b). At this point (31049 s), the temperature of the PCM increases again (Fig. 6a). The temperature of the PCM follows the temperature of the hot HTF at the battery inlet, with an average difference of less than 6%. In order to store as much heat as possible and not send it to the solar circuit, it can be interesting to stop the charging step when the temperature of the PCM becomes higher than that of the hot coolant. Figure 6 shows that this moment occurs at 52200 s.

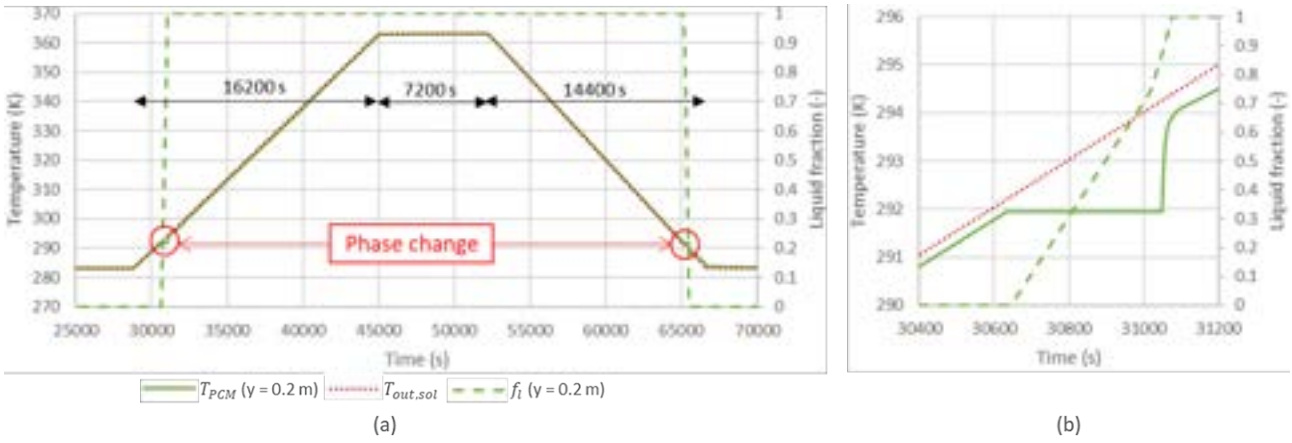

Figure 6: Case 2: Temperature and liquid fraction evolution for the first PCM layer in contact with the hot plate (x = 0 m) and for y = 0.2 m (a), focus on the phase change between 30634 and 31049 s (b).

Figure 7a shows the evolution of the temperature and liquid fraction of the PCM in the longitudinal direction (x = 0, 0.06 and 0.2 m) for the PCM layer at y = 0.2 m. The difference in temperature is clearly visible for the three curves. The further the PCM is from the hot plates, the lower its temperature and the longer the phase change takes. The heat propagation is thus clearly visible along the PCM. The core of the PCM (x = 0.2 m in green) takes the longest time to melt, but also to solidify as the hot inlet temperature decreases. The change from liquid to solid state is thus much longer (13 times longer) than for the PCM layers closer to the hot plate. For the yellow curve (x = 0.06 m), after the phase change, slight instabilities are visible in the PCM temperature. This must be due to the discretisation step and/or the discretisation scheme, whose order should be increased to be more accurate, and/or the DASSL integrator whose tolerance must be increased. The phase change step is significantly larger for x = 0.2 m. This is because the heat propagates from layer to layer. During the phase change of a PCM layer, all the energy required to achieve the phase change is absorbed. Therefore, for the liquid fraction of the layer x = 0.2 m to fluctuate, the liquid fractions of the previous layers must already have reached an equilibrium (solid or liquid state). This is illustrated in Fig. 7b, which shows a zoom of the transition from solid to liquid state (between 31000 and 35000 s) for the layers x = 0 (in red), 0.02 (in purple), 0.04 (in blue) and 0.06 m (in yellow). It can be seen that the liquid fraction of the next layer increases when the liquid fraction of the layer under consideration has reached 1. As a result, even if the melting temperature of the PCM has been reached for a PCM layer, it is necessary to wait until the change of state has taken place in the layers closer to the hot plates before the phase change begins in the PCM layer.

3.3. Profile of the hot inlet temperature following the outlet temperature of the Batisol® panels

When the PCM-based storage is connected to the Batisol® thermal panels, the temperature of the inlet hot HTF is calculated by 1. The surface area of the thermal panels is 25.5 m^2 (5 m wide by 5.1 m long). The surface area consists of 16 panels with 24 channels. Meteorological data from Cholet (next to Nantes) in 2021, in the northwest of France, are used. Figure 8 presents the evolution of the solar power and the outdoor temperature for the 2 periods (winter and summer) considered. The solar power amounts to 112 W/m^2 over the 8 winter days considered, whereas over the summer period considered this value is 2.5 times higher. The average outdoor temperature is 280 K and in summer 291.83 K. These two periods were chosen to represent different types of days, with more or less sunshine and wind, cold or hot outside temperatures (Fig. 8). In addition, 8-day periods were considered in order to determine the capacity of the battery to store heat during renewable energy intermittencies and day/night alternations.

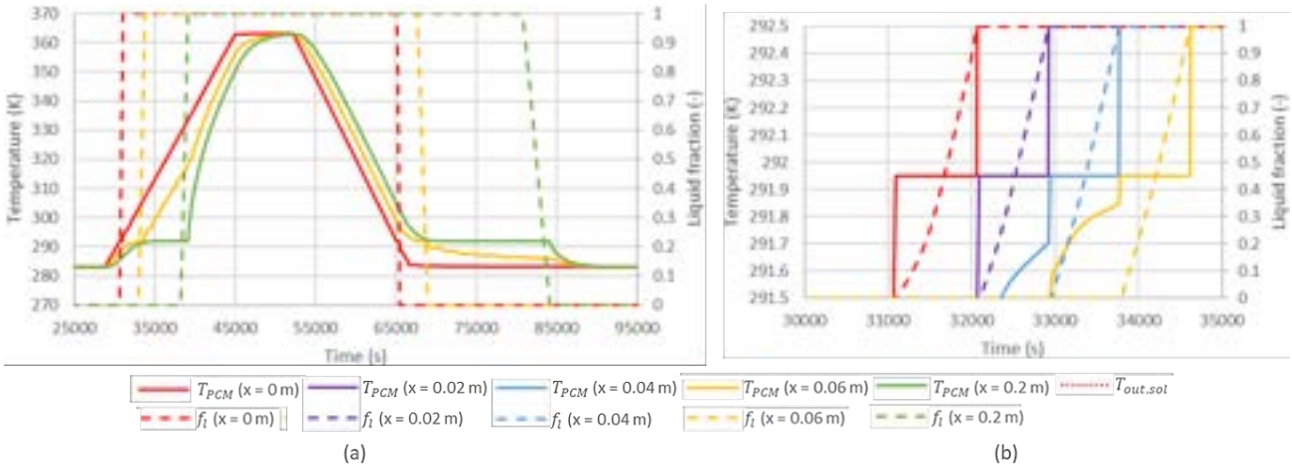

Figure 7: Case 2: Temperature and liquid fraction evolution in the longitudinal direction (for x = 0, 0.06 and 0.2 m) for the PCM layer in the middle (y = 0.2 m) (a), focus on the phase change of the first four PCM layer (from x = 0 to 0.06 m) (b).

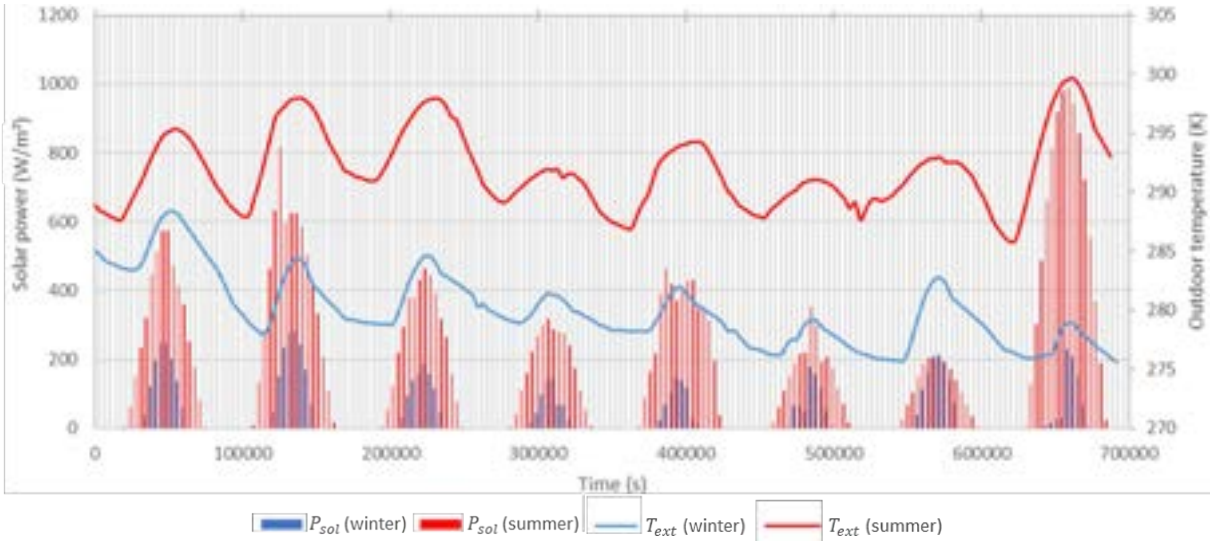

Figure 8: Cases 3 and 4: Evolution of solar power and outdoor temperature over the 8 days studied in winter and summer.

3.3.1. Winter period

The winter period chosen to simulate the behaviour of the PCM battery is from January 1 at 0am to January 8 at 23pm. In order to simplify the understanding of the graphs over longer periods (8 days), only the temperature and liquid fraction of the middle cell (y = 0.2 m) of the layer in contact with the hot plate (x = 0 m) are considered in Fig. 9. Over the 8 days simulated, the temperature at the exit of the solar facade is only higher than the melting temperature of the PCM on four days (Fig. 3). The PCM temperature exceeds the melting temperature only on January 1, 2, 3 and 7, as shown in Fig. 9. Indeed, the liquid fraction remains zero except between 11.15am and 4.5pm on January 1st, between 12.4pm and 16pm on January 2, between 14pm and 15.15pm on January 3, between and 13pm and 15.5pm on January 7. On other days, the PCM never reaches the melting temperature. Nevertheless, heat is stored in the solid state, as with sensible TES but with low efficiency. Fig. 9 shows that it is important to choose a material with a melting temperature that is not too high in order to take advantage of the phase change. If the melting temperature was 298.15 K (291.95 K for C-L acid), the PCM would not have changed state during the winter period under consideration. As a result, the use of PCM-based storage would not be interesting.

The temperature of the PCM in contact with the hot plate is almost as high as that of the hot HTF at the inlet, with an average difference of 0.3% over the 8 days. Figure 10a shows the evolution of the temperature and liquid fraction for the PCM layer at y = 0.2 m and for x = 0 (in red), 0.06 (in yellow) and 0.2 m (in green). As seen earlier, the temperatures are lower and lower from the outside of the PCM towards the inside. Indeed,

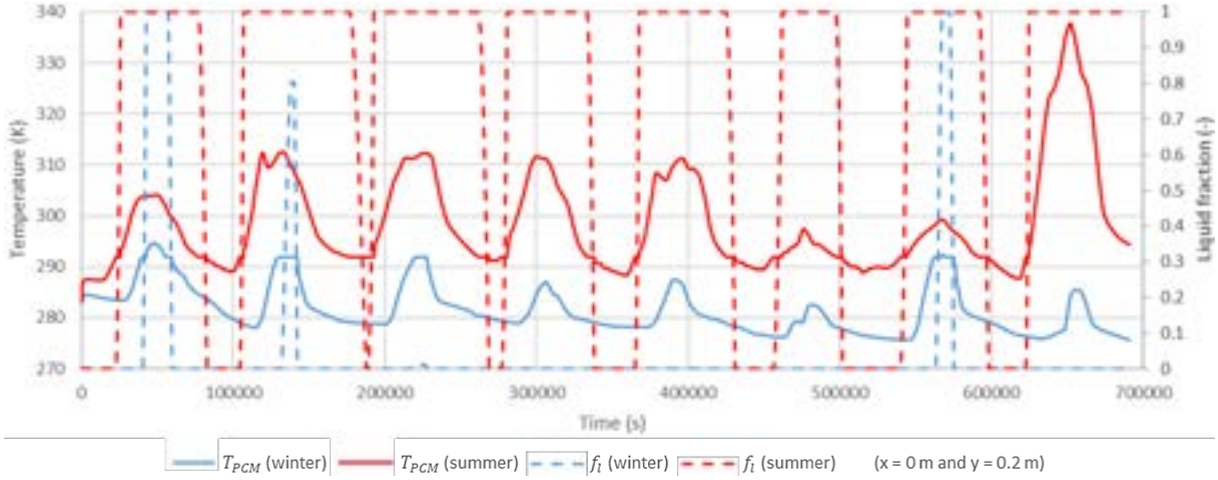

Figure 9: Cases 3 and 4: Temperature and liquid fraction evolution for the first PCM layer in contact with the hot plate (x = 0 m) and for y = 0.2 m.

the green curves show that the PCM has not changed state in the middle of the thermal battery. Furthermore, Fig. 10 shows the heat propagation along the PCM, with lower temperatures at the ends of the PCM, after the hot temperature at the inlet is decreased (after 60000 s). In general, the heat propagates well in the PCM, since the temperature differences between the different layers of PCM in the hot HTF are less than 0.8%. The instabilities visible at x = 0 and 0.06 m are due to the slight change in temperature at the outlet of the thermal panels (red dotted line in Fig. 10a), which of course depends on the weather conditions. These instabilities appear at the extremities of the PCM close to the hot plates (such as at x = 0 and 0.06 m) but not at the centre of the PCM (at x = 0.2 m). As seen previously, the liquid fraction of the x = 0.2 m layer remains zero while the melting temperature has been reached (291.95 K at 53100 s). This is due to the liquid fractions of the layers closer to the hot plate, which have not all reached unity. The output temperature of the solar panels decreases from 47483 s onwards, and consequently the energy supplied to the PCM. As a result, the middle layer (x = 0.2 m) has not received enough energy to make its phase change. Figure 10b is a zoom of the phase change (solid to liquid) in Fig. 10a. Before a layer changes phase, it is necessary that the liquid fraction of the previous layer has reached unity. Figure 10b shows this clearly, with the increase from 0 to 1 in the liquid fraction at x = 0 m (38900 to 40440 s), then that at x = 0.02 s (40440 to 42747 s), then that at x = 0.04 m (42747 to 44826 s) and finally that at x = 0.06 m (44826 to 47470 s).

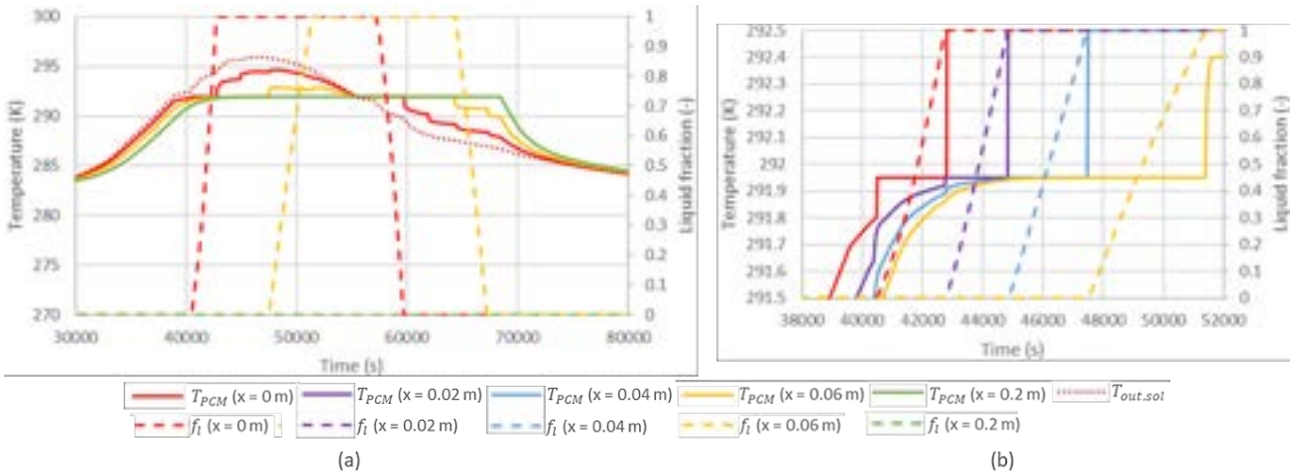

Figure 10: Case 3: Temperature and liquid fraction evolution in the longitudinal direction (for x = 0, 0.06 and 0.2 m) for the PCM layer in the middle (y = 0.2 m) (a), focus on the phase change of the first four PCM layer (from x = 0 to 0.06 m) (b).

3.3.2. Summer period

The summer period chosen to simulate the behaviour of the PCM battery is from July 1 at 0am to January 8 at 23pm. The temperature and liquid fraction at x = 0 m and y = 0.2 m are shown in the same figure as the winter period (Fig. 9). The temperature of the hot HTF at the storage inlet is significantly higher than during the winter

period (up to 340 K vs 296 K as illustrated in Fig. 3). The differences between the maximum temperatures expected by the hot fluid at the outlet of the thermal panels range from 2% (January 7 and July 7) to 16% (January 8 and July 8). On average the temperatures are 8% higher in summer. As a result, the behaviour of the PCM is also different between winter and summer periods, with phase changes occurring less often in winter. The advantage of using PCM in summer is therefore much greater, since it is possible to limit the size of the battery thanks to the change in the state of the material, unlike the use of sensible storage. Even on less sunny days such as July 6, when the temperature of the hot HTF does not exceed 297 K, there is enough heat to allow the PCM to change state. The PCM remains in a liquid state longer than in winter, between 7am and midnight on average over the 8 days considered.

As for the winter period, the difference between the temperature of the PCM in contact with the plate and that of the hot HTF is small (0.5% difference on average over the 8 days). Figure 11a shows the evolution of the temperature and liquid fraction for the PCM layer at y = 0.2 m and for x = 0. (in red), 0.06 (in yellow) and 0.2 m (in green). The temperature differences from the outside to the inside of the PCM are also clearly visible. From 16.4pm onwards, the temperature of the PCM in the core of the battery is higher than that of the PCM in contact with the hot plate. It would therefore be interesting to stop the charging step and start the discharging step by switching the hot (solar system) and cold (heat pump) inputs. The same instabilities as for winter period appear in Fig. 11a for the same reasons (small fluctuations of the temperature at the outlet of the thermal panels due to climatic conditions). The phase change zoom of the first four layers is illustrated in Fig. 11b (for x = 0 (in red), 0.02 (in purple), 0.04 (in blue) and 0.06 m (in yellow)).

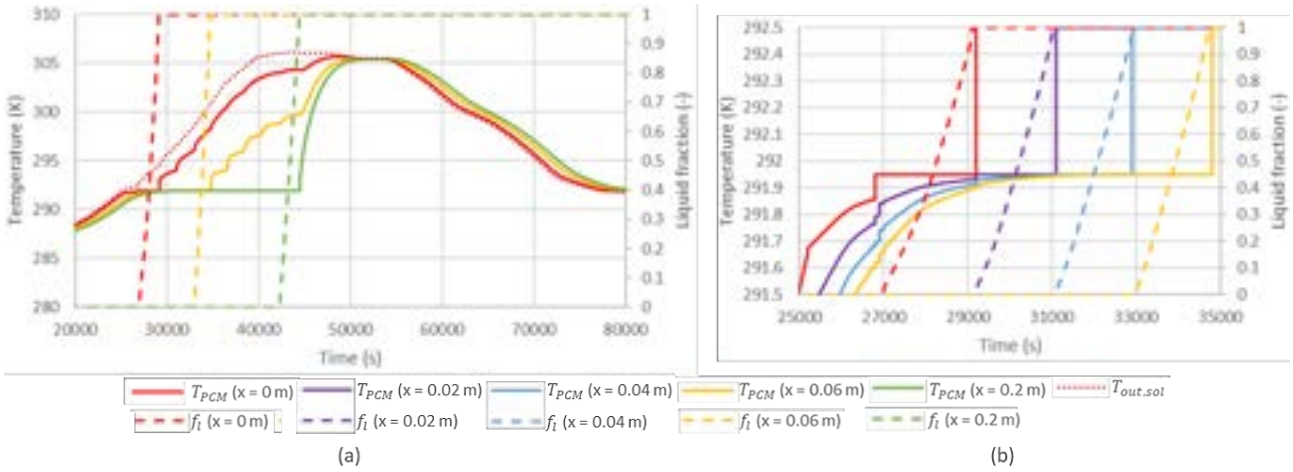

Figure 11: Case 4: Temperature and liquid fraction evolution in the longitudinal direction (for x = 0, 0.06 and 0.2 m) for the PCM layer in the middle (y = 0.2 m) (a), focus on the phase change of the first four PCM layers (from x = 0 to 0.06 m) (b).

The energy stored by the thermal battery for the two periods considered (winter and summer) is given in Table 2. During the winter period under consideration, the average stored energy is 164 Wh per day. In summer, this value is 6 times higher. The sunniest days (January 1st in winter and July 8 in summer) store 5 to 7.5 times more energy than the days less suitable for thermal collectors (January 6 and July 6). On average, the PCM battery can store 2.6 kWh/m^3 per day of energy in winter and 6.6 kWh/m^3 for January 1st. In summer this value reaches 15.1 kWh/m^3 per day on average and 29.3 kWh/m^3 for July 8. The benefit of PCM is clearly visible in summer, with almost 6 times more energy stored by the battery than in winter, partly due to the more frequent phase changes.

Table 2: Energy stored in the thermal battery per day (Wh).

Period	Minimal value	Maximal value	Mean
Winter	56 (January 6)	423 (January 1st)	164
Summer	385 (July 6)	1877 (July 8)	964

4. Conclusion

A dynamic model of a SAHP based on the use of thermal panels (Batisol®) and a latent heat storage was presented. This system aims to provide the heating and domestic hot water needs of a building. The TES is

composed of a PCM contained between two plates where HTF circulate. During the charging step, the hot HTF is fed by the thermal panels. During the discharging step, the direction of the fluid is reversed and the cold HTF is fed by the heat pump.

The thermal behaviour of the PCM tank is studied for four different profiles of the charging temperature: ramping, trapezoidal functions, temperature at the outlet of the thermal panels in winter (from January 1 to 8) and in summer (from July 1 to 8). The simulations carried out in OpenModelica showed the behaviour of the PCM during the phase change. The developed model showed the importance of choosing a PCM with a melting temperature range suitable for the studied application. In winter, only the sunniest days allows the PCM to melt while in summer the phase change occurs every day. On average, this thermal battery can store 6.6 and 15.1 kWh/m^3 per day of energy in winter and summer respectively.

The simulations showed that the 2D model of the system is necessary to take into account the horizontal and vertical temperature variations in the battery. This model will be further validated with experimental data. It will also allow the development and the validation of a simpler model. The final goal will be to optimise the SAHP system on its operational parameters with the simpler model.

Acknowledgments

This work was supported in the case of MCPBat project granted by the Region Nouvelle Aquitaine. Grant number 11385520-11389020 in the framework of the joint research team between the University of Pau and Pays de l'Ardour and Nobatek/INEF4.

Nomenclature

Letter symbols

- a proportion of PCM in the volume considered,
- A exchange surface, m^2
- c_p specific capacity, $J/(kgK)$
- f_l liquid fraction,
- G_{sol} solar flux, W/m^2
- h heat transfer coefficient, W/m^2K
- H enthalpy (including sensible and latent forms), J/m^3
- L latent heat, J/kg
- $\dot{m}$ mass flow rate, kg/s
- P exchange perimeter, m
- T temperature, K
- v_{wind} wind speed, m/s
- V exchange volume, m^3

Greek symbols

- λ thermal conductivity, $W/m/K$
- ρ density, kg/m^3

Subscripts and superscripts

- C Cold HTF
- eff Effective
- ext Exterior/Outdoor
- fin Fin
- H Hot HTF

in In

l Liquid phase

m Melting

out Out

PCM PCM

s Solid phase

sol Solar

References

[1] International Energy Agency. *Energy Efficiency: Buildings the global Exchange for Energy Efficiency Policies, Data and Analysis.* IEA Publications; 2021 Nov. Technical Report No.: Energy Efficiency 2021.

[2] Dincer I. *On thermal energy storage systems and applications in buildings*. Energy Build. 2002 May 1;34(4):377–88.

[3] Zalba B, Marin JM, Cabeza LF, Mehling H. *Review on thermal energy storage with phase change: materials, heat transfer analysis and applications*. Appl Therm Eng. 2003 Feb 1;23(3):251–83.

[4] Devaux P, Farid MM. *Benefits of PCM underfloor heating with PCM wallboards for space heating in winter*. Appl Energy. 2017 Apr 1;191:593–602.

[5] Stritih U. *An experimental study of enhanced heat transfer in rectangular PCM thermal storage*. Int J Heat Mass Transf. 2004 Jun 1;47(12):2841–7.

[6] Du K, Calautit J, Wang Z, Wu Y, Liu H. *A review of the applications of phase change materials in cooling, heating and power generation in different temperature ranges*. Appl Energy. 2018 Jun 15;220:242–73.

[7] Faraj K, Khaled M, Faraj J, Hachem F, Castelain C. *A review on phase change materials for thermal energy storage in buildings: Heating and hybrid applications*. J Energy Storage. 2021 Jan 1;33:101913.

[8] Seddegh S, Wang X, Henderson AD, Xing Z. *Solar domestic hot water systems using latent heat energy storage medium: A review*. Renew Sustain Energy Rev. 2015 Sep 1;49:517–33.

[9] Jin X, Zhang H, Huang G, Lai ACK. *Experimental investigation on the dynamic thermal performance of the parallel solar-assisted air-source heat pump latent heat thermal energy storage system*. Renew Energy. 2021 Dec 1;180:637–57.

[10] Zhou D, Zhao CY, Tian Y. *Review on thermal energy storage with phase change materials (PCMs) in building applications*. Appl Energy. 2012 Apr 1;92:593–605.

[11] Martinez RG, Goikolea BA, Paya IG, Bonnamy P, Raji S, Lopez J. *Performance assessment of an unglazed solar thermal collector for envelope retrofitting*. Energy Procedia. 2017 Jun 1;115:361–8.

[12] Bonnamy P, Raji S, Lopez J, Garay R. *Expérimentation et modélisation d'un collecteur solaire opaque pour préchauffage de l'eau*. In: Kjelstrup S., Hustad E., Gundersen T., Røsjorde A., Tsatsaronis G., editors. ECOS 2005: Proceedings of the 18th International Conference on Efficiency, Cost, Optimization, Simulation, and Environmental Impact of Energy Systems; 2016 Jun 20-25; Trondheim, Norway. Tapir Academic Press:777-84.

[13] Nobatek/INEF 4. *BATISOL: Capteurs solaires thermiques - solutions Nobatek/INEF 4* Available at: `https://www.nobatek.inef4.com/batisol/` [accessed 03.09.2023].

[14] Dimaano MNR, Watanabe T. *The capric–lauric acid and pentadecane combination as phase change material for cooling applications*. Appl Therm Eng. 2002 Mar 1;22(4):365–77.

[15] Bouzouidja R, Aketouane Z, Lhomer R, Varela B, Cruz JL, Serra S, Reneaume J.M., Sempey A. *Choice of the Suitable Melting Temperature of Phase Change Material: Application on Solar Assisted Heat Pump*. In: 2022 IEEE 10th International Conference on Smart Energy Grid Engineering (SEGE). 2022. p. 58–62.

[16] Kauranen P, Peippo K, Lund PD. *An organic PCM storage system with adjustable melting temperature*. Sol Energy. 1991 Jan 1;46(5):275–8.

Power vs. capacity performances of thermally integrated MH-PCM hydrogen storage solutions: current status and development perspectives

V. K. Krastev[a], L. Bartolucci[b], G. Bella[c], S. Cordiner[b], G. Falcucci[a] and V. Mulone[b]

[a] Enterprise Engineering Dept., University of Rome "Tor Vergata", Rome, Italy, krastev@dii.uniroma2.it
[b] Industrial Engineering Dept., University of Rome "Tor Vergata", Rome, Italy
[c] Engineering Dept., Niccolò Cusano University, Rome, Italy

Abstract:

The present work focuses on two particular performance indicators for hydrogen storage solutions based on the thermal integration of metal hydrides (MH) with phase-change materials (PCMs): i) the (specific) discharge power and ii) the system-level volumetric capacity. The paper first condenses available literature data from modelling and experimental activities, and then analyses a basic numerical benchmark of a low-temperature MH-PCM system.

Findings from the literature review show that, due to the interrelation between efficient thermal management and hydrogen desorption rate, the selected performance indicators are not independent one from another. It is also confirmed that simultaneously achieving high-power (flexibility) and specific capacity (compactness) is a challenging goal for such kind of hydrogen storage systems. The parametric analysis of the numerical benchmark system suggests that, for a given MH operating pressure-temperature envelope, special care should be given in the PCM accurate characterisation and selection, as well as in the quantification of the optimal trade-off between the PCM volume and desorption kinetics performance. Furthermore it is found that the geometrical distribution of the MH and PCM volumes have a larger than expected impact on the specific discharge power.

Keywords:

Hydrogen Storage; Metal Hydrides; Phase Change Materials; Power; Volumetric Capacity.

1. Introduction

In order to attain a net zero-carbon footprint, it is imperative to produce a substantial share of energy from sustainable sources (IPCC, 2022). Hydrogen is currently recognised as an essential element in facilitating the incorporation of large-scale renewable energy sources (Bartolucci et al., 2021). It also has the potential to become a primary energy carrier, being capable of transporting and distributing energy across various sectors and regions while also improving the energy system's resilience by serving as a buffer (Bartolucci et al., 2023; Kovač et al., 2021). To establish a commercially sustainable H2 economy, it is crucial to store, transport, and distribute H2 as needed for power and heat generation in various applications (Abohamzeh et al., 2021a). Recent research published through the H2 Technology Collaboration Program of the International Energy Agency has provided a positive outlook on the future prospects of H2-based energy storage. Several studies have explored the integration of renewable energy systems with H2 storage to achieve net-zero-emission energy systems and sustainable development goals (Petkov & Gabrielli, 2020). The increasing affordability of H2 utilization technologies, such as fuel cells, may replace battery storage through electrolysers/H2 storage due to their higher efficiency, reliability, and performance (Yue et al., 2021). To present, the cost of H2 systems is higher compared to battery systems, but recent research activities on the H2 value chain for various applications are anticipated to make them competitive by 2030 (Abbasi & Abbasi, 2011).

H2 storage techniques can be broadly categorised into two groups: physical storage and material storage. Physical storage relies on the principle of compression and liquefaction. In contrast, material storage encompasses several systems and provides various utilization methods based on service conditions. Currently, the accepted standard for H2 storage is in high-pressure gaseous form, with storage pressures of up to 700 bar in steel or carbon fibre reinforced polymeric vessels (Nazir et al., 2020). Compressed H2 (CH) technology offers the advantage of fast filling and release rates, as well as lower storage costs. However, CH has several well-known limitations, including reduced storage efficiency, limited volumetric storage capacity, and safety concerns. Compressing H2 from typical production conditions (20 bar) up to 700 bar results in a 9-

12% reduction in net energy stored (Nazir et al., 2020). If Type 4 vessels are considered, the effective volumetric storage capacity of CH at 700 bar is approximately 25 kg/m3. For stationary applications, it is preferable to storage pressures as low as 50 bar or less, for a better integration with renewable H2 generation and to operate under safer conditions. However, at 50 bar, the volumetric capacity of CH systems falls below 2 kg/m3, which would require very large vessels for long-term storage (Abohamzeh et al., 2021b; Maestre et al., 2021).

Metal hydrides (MH) are a promising alternative to replace compressed hydrogen (CH) for stationary applications due to their inherently higher volumetric storage capacity and moderate operating pressures and temperatures (Bellosta von Colbe et al., 2019; El Kharbachi et al., 2020). Mg-based and intermetallic hydrides are the focus of recent MH storage technology development (Ben Mâad et al., 2016; El Mghari et al., 2019, 2020; Garrier et al., 2013; Marty et al., 2013; Mellouli et al., 2015). Mg-based hydrides have attractive reversible gravimetric capacities, material safety, and low cost, but their high reaction enthalpy, high equilibrium temperature, and slow kinetics require catalyst particle additions (Pasquini et al., 2022). Intermetallic hydrides of the AB2 or AB5 types are preferred thanks to their ease of activation, good reversibility, and comparatively fast kinetics (Pasquini et al., 2022). Due to the highly exothermic/endothermic hydrogen absorption/desorption reactions, proper active or passive thermal management is necessary for high-power applications involving MH storage systems (Facci et al., 2021; Nguyen & Shabani, 2021). Active thermal control allows for effective performance tuning, but generates energy losses and may add significant mass and volume at system level (Motyka, 2014). Passive thermal control, specifically through the adoption of phase-change materials (PCMs), is a promising solution due to its energy efficiency gains and inherent simplicity (Nguyen & Shabani, 2021).

Darzi et al. (Rabienataj Darzi et al., 2016) examined how hydrogen is charged and discharged into and from a cylindrical metal hydride tank made of LaNi5, while also studying the heat transfer to a surrounding jacket filled with PCM. El Mghari et al. (El Mghari et al., 2020) analysed five different PCMs and emphasised that the ratio of the total heat of diffusion of the PCM to the total heat of reaction of the MH is a significant factor in achieving complete hydrogenation of the tank. Alqahtani et al. (Alqahtani, Mellouli, et al., 2020) used numerical methods to investigate the hydrogenation and dehydrogenation processes of an MH reactor surrounded by PCM. They doubled the number of interfaces between the MH reactor and PCM by encompassing the MH reactor with a cylindrical sandwich bed filled with PCM, resulting in an 81.5% and 73% improvement in the time required for hydrogenation and dehydrogenation processes, respectively, compared to a conventional MH-PCM system that includes only a single PCM tank (Alqahtani et al., 2020b). Ye et al. (Ye et al., 2020, 2021) proposed a novel MH-PCM unit where a PCM layer is sandwiched between two layers of MH, which exhibited average absorption and desorption rates about 4.5 and 2.4 times higher, respectively, than the traditional cylindrical configuration.

Several authors have examined the advantages of increasing the thermal conductivity of PCMs to improve the performance of hydrogen storage. To achieve this goal, various methods have been explored. For example, Nguyen et al. (Nguyen et al., 2022) investigated the application of an organic PCM for the thermal management of MH hydrogen storage and found that the use of embedded copper foam to enhance thermal conductivity is crucial for achieving an adequate power performance. Chibani et al. (Chibani et al., 2022) conducted numerical analysis to examine the impact of incorporating PCM into metal foam on the performance of hydrogen desorption from MH. Lewis and Chippar (Lewis & Chippar, 2021) studied the charging and discharging of hydrogen in a LaNi5-based reactor equipped with PCM and emphasised the influence of metal foam and its morphology on hydrogen storage and thermal performance, which can enhance hydriding/dehydriding reaction rates. Bourzgarrou et al. (Bouzgarrou et al., 2022) demonstrated that a well-designed U-type heat pipes insert in the metal and PCM media can significantly reduce loading time by up to 88%, depending on the melting temperature.

Although the majority of the papers discussed various methods to improve the power and capacity of MH tanks, they usually did not consider the overall H2 storage capacity at the system level, neither the power/capacity ratio. To address this gap, the authors conducted a thorough analysis of the relevant parameters for some of the studies mentioned above, selecting the ones where all the information required was directly or indirectly available. The purpose of this analysis was to illustrate the difficulty of simultaneously achieving a high discharge power/capacity ratio and a high system-level H2 volumetric storage capacity, as depicted in Figure 1. The current paper aims, therefore, in highlighting capacity and power enhancement factors through a representative MH-PCM computational framework, targeting at the optimisation of both performance indicators.

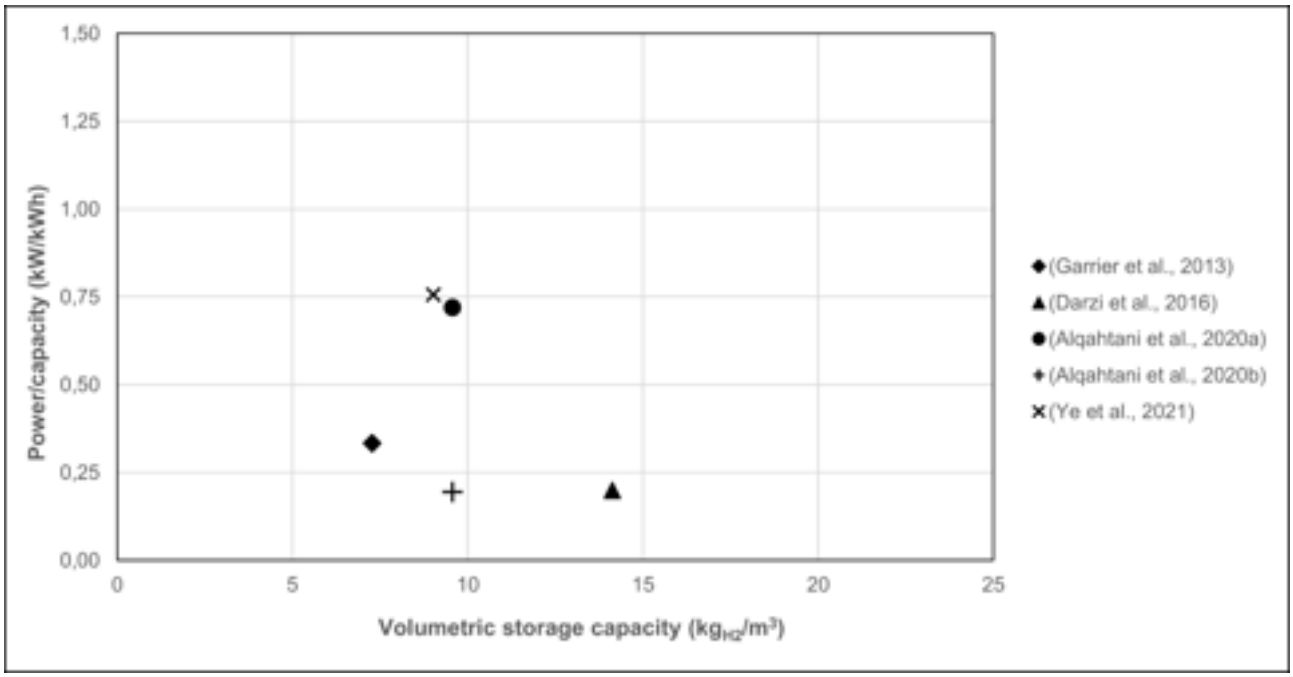

Figure 1. Specific discharge power vs. volumetric storage capacity of MH-PCM systems, literature review.

2. Numerical benchmark

2.1. Problem and setup description

A simple vertically oriented cylindrical MH reactor geometry, surrounded by a PCM-filled jacket, has been taken as a reference for the numerical analysis part of the present work (Figure 2). An analogous MH-PCM system has already been studied during hydrogen filling by two of the authors in a previous publication (Bartolucci & Krastev, 2022) , as well as by other researchers (Alqahtani, Bamasag, et al., 2020b) but none of them focusing on the specific discharge power vs. volumetric capacity performances. The selected MH is a low-temperature intermetallic $LaNi_5$-H_2 system, while the PCM is an inorganic $LiNO_3$-$3H_2O$ salt hydrate. The latter has been recognised in previous research works as one of the best performing PCMs for pairing with low-temperature MHs (Bartolucci & Krastev, 2022; El Mghari et al., 2020). The most relevant MH and PCM properties are listed in Tables 1 and 2. The baseline geometry is exactly equivalent to the one already investigated in (Bartolucci & Krastev, 2022), while it has been subsequently altered to optimise the PCM quantity and to test different slenderness factors H/D, with $D = 2R_i$ (see Table 3).

All the simulations here presented are based on the following main assumptions:

a. the MH-PCM reactors are represented as 2D axisymmetric geometries;
b. the MH bed volume is kept constant for all reactor geometries;
c. the external boundaries of the MH-PCM reactor (except for the hydrogen outlet boundary) are all adiabatic;
d. hydrogen is released from the MH bed at a known and constant pressure (atmospheric pressure);
e. gaseous hydrogen is assumed to follow the ideal gas law;
f. the MH bed is considered as an isotropic porous medium with uniform porosity and permeability;
g. local thermal equilibrium is assumed to hold within the $LaNi_5$-H_2 system;
h. buoyancy is not considered for the heat transfer and melting phenomena within the PCMs;
i. density of the PCM is considered constant and equal to the average between solid and liquid values;
j. other thermophysical properties of PCMs vary with temperature according to the available data, unless differently specified.

The MH-PCM system bed simulation framework has been implemented in ANSYS® Fluent (*ANSYS® Academic Research CFD, Release 2020 R2, Fluent User's Guide*, 2020), combining ad-hoc developed User

Defined Functions (UDFs) for hydrogen desorption with the enthalpy-porosity method (Voller & Prakash, 1987; Voller & Swaminathan, 1991) for phase transition. For a detailed explanation of model equations and of the UDF implementation procedure, the reader is redirected to (Bartolucci & Krastev, 2022). References for the phase transition modelling can be found also in (Krastev & Falcucci, 2021). All the numerical predictions reported here adopt a numerical time step equal to 0.1 s, with a physical simulated time of 10^4 s. All computational grids are made of quad-uniform elements with a 0.5 mm spacing. At the beginning of each simulation, the initial temperature of the system is set to 313 K and the pressure inside the MH tank is set at the equilibrium value for that temperature. Discharge pressure at the tank outlet is 1 bar.

Table 1. Main thermophysical and reaction properties of the $LaNi_5$-H_2 system.

Parameters	*Description*	*Values*
A_d	Plateau coefficient (desorption)	10.57
B_d	Plateau coefficient (desorption)	3704.6 K
C_d	Rate coefficient (desorption)	9.57 s^{-1}
$C_{p,g}$	Specific heat capacity (gas)	14890 J kg^{-1} K^{-1}
$C_{p,s}$	Specific heat capacity (solid)	419 J kg^{-1} K^{-1}
E_d	Activation energy (desorption)	16473 J mol^{-1}
ΔH_R	Enthalpy of reaction	30478 J mol^{-1}
K	Bed permeability	10^{-8} m^2
ε	Bed porosity	0.5
λ_g	Thermal conductivity (gas)	0.1815 W m^{-1} K^{-1}
λ_s	Thermal conductivity (solid)	2 W m^{-1} K^{-1}
μ_g	Dynamic viscosity (gas)	8.4 x 10^{-6} Pa s
ρ_{sat}	Saturated metal density	7259 kg m^3
ρ_{emp}	H_2-free metal density	7164 kg m^3
$w_{\%}$	Gravimetric capacity (bed only)	1.32 %
m_{LaNi5}	Metal mass	~ 0.422 kg
m_{H2}	H2 storage capacity	5.6 g

Table 2. Main thermophysical properties of the $LiNO_3$-H_2O PCM.

Parameters	*Description*	*Values*
$C_{pl,PCM}$	Specific heat capacity (liquid)	2770 J kg^{-1} K^{-1}
$C_{ps,PCM}$	Specific heat capacity (solid)	1730 J kg^{-1} K^{-1}
R_{CP}	Liquid-to-solid C_p ratio	1.6
L_f	Latent heat of fusion	296000 J kg^{-1}
T_m	Melting temperature	303 K
$\lambda_{l,PCM}$	Thermal conductivity (liquid)	0.58 W m^{-1} K^{-1}
$\lambda_{s,PCM}$	Thermal conductivity (solid)	1.32 W m^{-1} K^{-1}
R_λ	Liquid-to-solid λ ratio	0.44
μ_{PCM}	Dynamic viscosity (liquid)	0.0042 Pa s
$\rho_{l,PCM}$	Density (liquid)	1780 kg m^{-3}
$\rho_{s,PCM}$	Density (solid)	2140 kg m^{-3}

Table 3. Dimensional details of the considered jacket-type MH-PCM reactor geometries.

Parameters	*Description*	*Baseline (H/D = 2)*	*Optimised (H/D = 2)*	*Optimised (H/D = 1)*	*Optimised (H/D = 4)*
R_{H2}	H_2 outlet radius	0.5 cm	0.5 cm	0.5 cm	0.5 cm
R_i	Internal radius	2.1 cm	2.1 cm	2.65 cm	1.67 cm
R_e	External radius	3.45 cm	3.2 cm	4.05 cm	2.55 cm
H	Height	8.5 cm	8.5 cm	5.3 cm	13.4 cm
H/D	Slenderness	2	2	1	4
V_{MH}	MH volume (total)	118 cm^3	118 cm^3	118 cm^3	118 cm^3
V_{PCM}	PCM volume	200 cm^3	154 cm^3	154 cm^3	154 cm^3

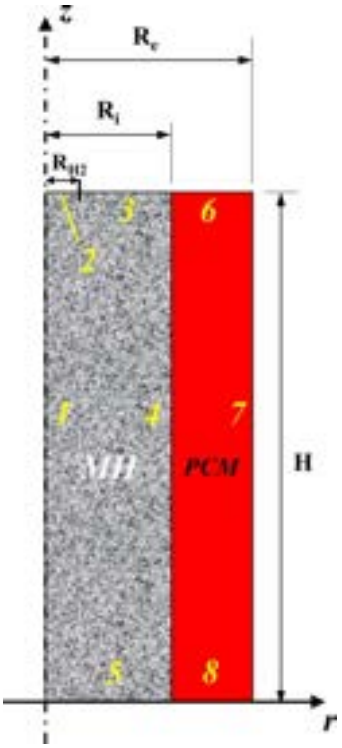

Figure 2. Schematic of the jacket-type MH-PCM cylindrical reactor.

2.2. Results

In this Section, numerical prediction results are shown in terms of the hydrogen discharge dynamics, PCM liquid fraction and temperature evolution in the MH and PCM tanks. Figures 3 and 4 compares the baseline and mass-optimised reactor configurations, where the same slenderness factor (H/D = 2) for the MH container is assumed for both. Note that the PCM mass optimisation was obtained through the following simple relationship between the total enthalpy of reaction of the desorbed H2 mass and the PCM latent heat of fusion:

$$m_{PCM} = \frac{m_{H2} \cdot \Delta H_R}{L_f} . \quad (1)$$

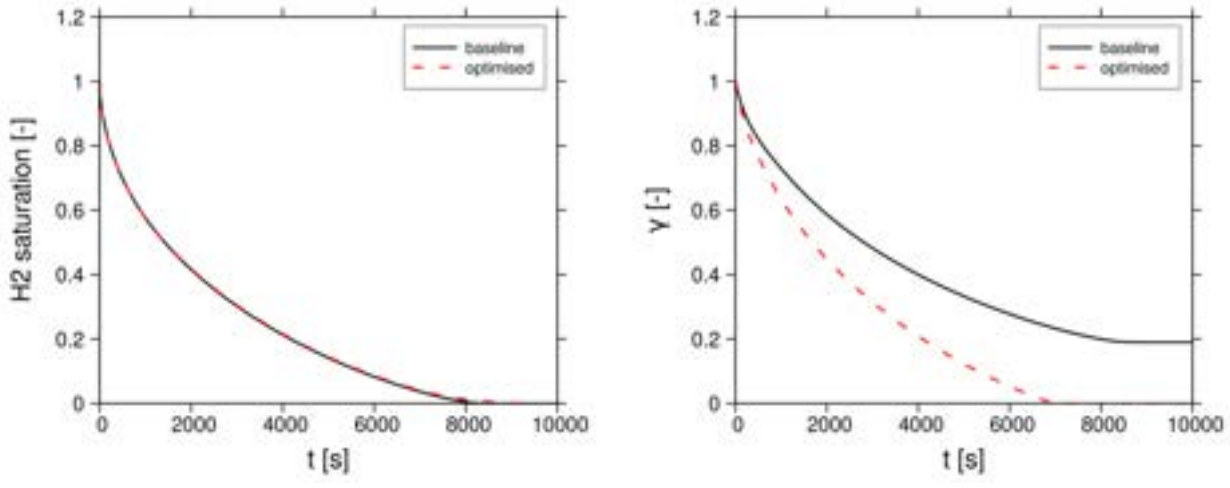

(a) (b)

Figure 3. Comparison between the baseline and mass-optimised MH reactor configurations, in terms of a) hydrogen discharge curve and b) PCM liquid fraction over time.

Figure 3a confirms that the baseline and mass-optimised configurations have essentially equivalent H2 discharge performances (both are able to discharge 95% of the absorbed H2 mass within 6800 s, with a 1.2 % deviation among the two), while Figure 3b evidences that around 20% of the PCM latent heat capacity is not exploited in the baseline case. Figures 4a and 4b show that, if the PCM has not undergone full phase transition, the MH-PCM system finds its thermal equilibrium close to the melting temperature. Conversely, if the PCM fully melts before all the H2 mass is completely desorbed, the system's equilibrium temperature is significantly lower (around 294 K vs. around 302 K) and closer to the MH equilibrium temperature at the discharge pressure (around 289 K for this case). The latter is beneficial for a subsequent H2 filling of the MH bed, as it would ensure larger temperature gradients between the MH and PCM containers during the initial phase of the exothermic H2 absorption process.

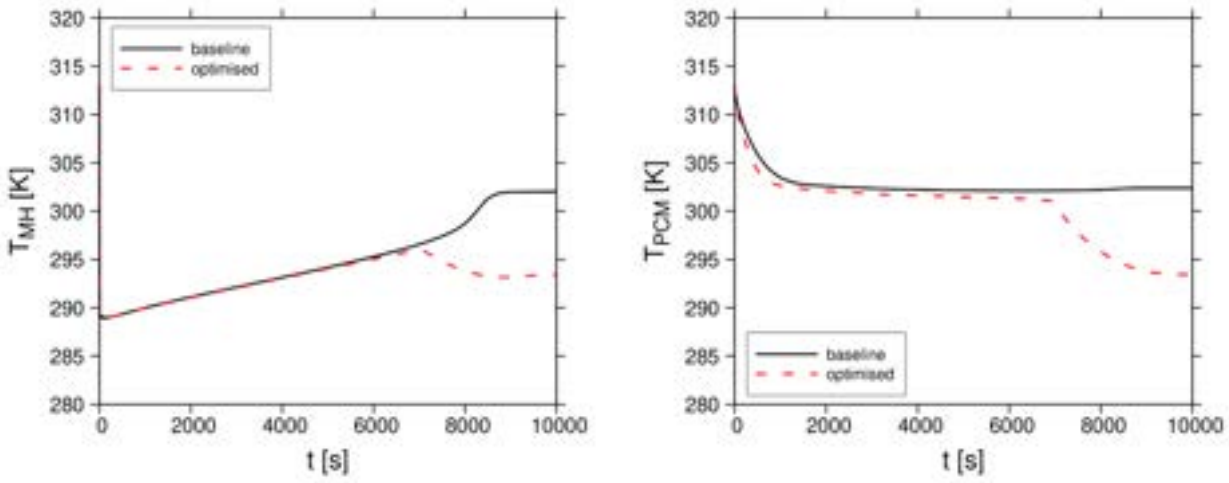

(a) (b)

Figure 4. Comparison between the baseline and mass-optimised MH reactor configurations, in terms of a) volume-averaged MH reactor temperature and b) volume-averaged PCM jacket temperature over time.

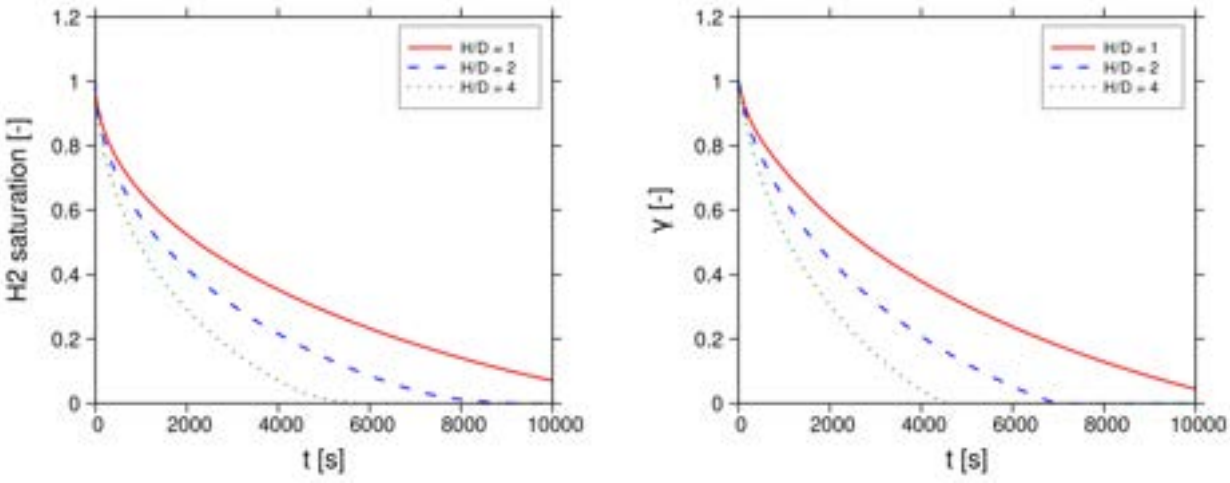

(a) (b)

Figure 5. Effects of the slenderness factor H/D on the hydrogen discharge performances: a) hydrogen discharge curve; b) PCM liquid fraction over time.

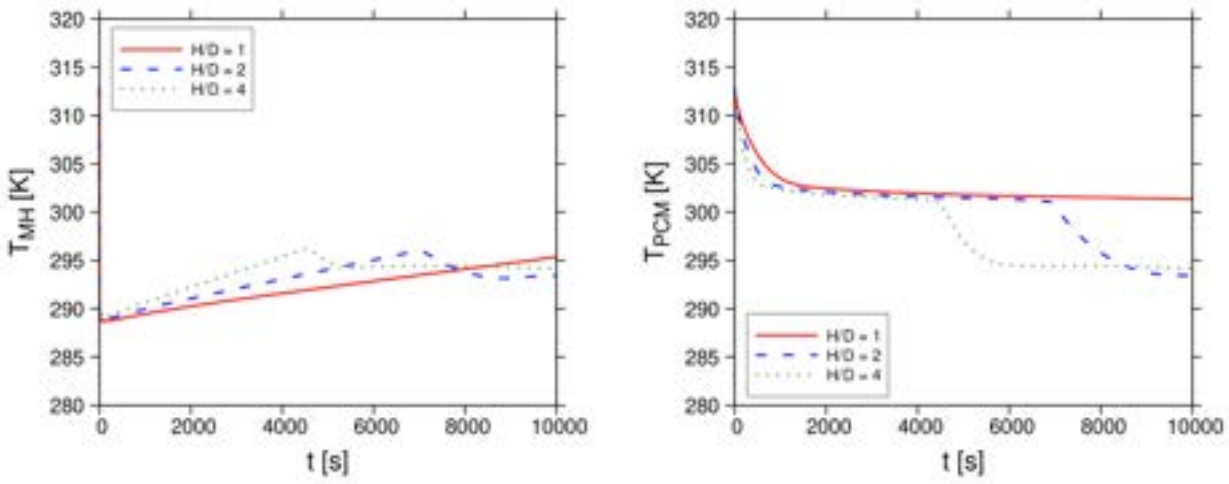

(a) (b)

Figure 6. Effects of the slenderness factor H/D on the temperature evolution: a) volume-averaged MH reactor temperature and b) volume-averaged PCM jacket temperature over time.

Figures 5 and 6 allow to evaluate the effect of the slenderness factor H/D on the MH-PCM system discharge dynamics, given the same MH and (optimal) PCM volumes. Raising H/D from 2 to 4 accelerates the hydrogen mass discharge by 37% and thus the average discharge power by 57%. On the opposite, the case with H/D = 1 has a 58% slower discharge dynamics compared to H/D = 2, with the 95% mass discharge actually occurring around 10700 s after the start of the simulation. These differences are most likely to be related to the changes in the radial-wise conductive thermal resistance, as the assumptions listed in Section 2.1 consistently suggests a quasi-1D conductive heat transfer regime in the radial direction, which is also well in line with findings from previous research on cylindrical MH-PCM systems (Bartolucci & Krastev, 2022).

A last series of computations has been performed on the H/D = 2 optimised geometry, changing some of the PCM properties within the simulations. Tests have been made with all constant properties and equal to the solid-liquid average, as well as with reversed Cp and λ liquid-to-solid ratios compared to the actual $LiNO_3$-$3H_2O$ material characteristics. Figure 7 condenses the results obtained, pointing out that: i) using constant and averaged properties introduces acceptable deviations from the actual material behavior (less than 10% deviation on the 95% discharge time); ii) the PCM Cp phase variations have little to no effect on the H2 discharge dynamics; iii) during H2 discharge, the PCM starts to immediately solidify at the PCM-MH heat transfer interface: the solid-phase radial thermal conductivity has, therefore, a dominant effect and when it falls below the MH effective radial conductivity (Reversed R_λ case) it might significantly slow down discharge dynamics.

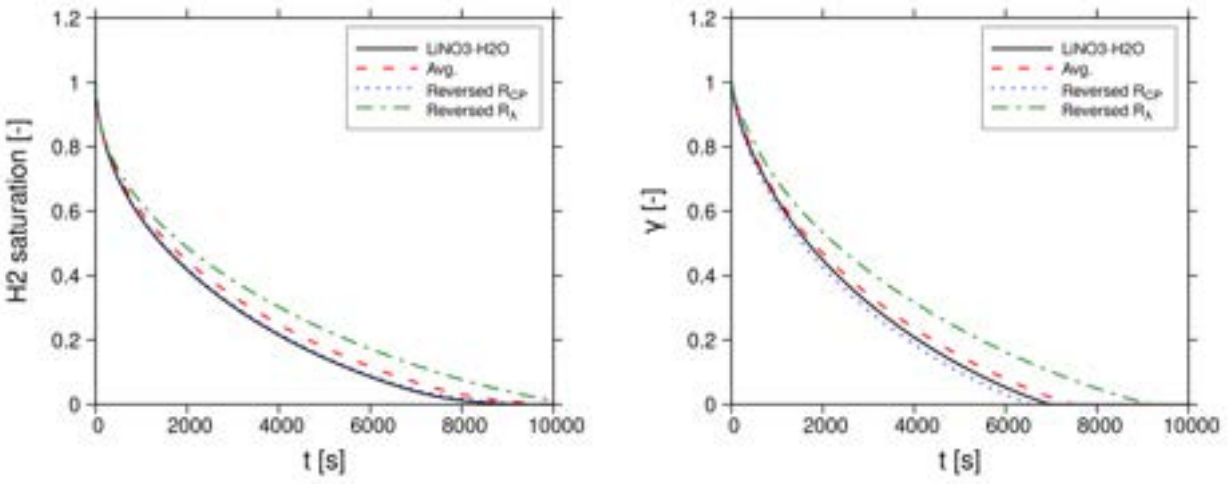

(a) (b)

Figure 7. Effects of changes in the PCM properties on the hydrogen discharge performances: a) hydrogen discharge curve; b) PCM liquid fraction over time.

Figure 8 resumes the major findings from the numerical simulations, within the context of the literature review already presented in the Introduction Section. Unsurprisingly, to reach system-level volumetric capacities above 15 kg_{H2}/m^3 it is essential to optimise the minimum required PCM mass and an effective first-level optimization can be made through simple latent heat-based principles. In that regard, selecting PCMs with high densities and latent heat of fusion, such as salt hydrates in the low-temperature PCM range, brings obvious additional benefits.

In terms of specific discharge power, an accurate geometrical optimization of the MH-PCM system, which must take into account the actually dominant heat transfer mechanisms, is crucial. Significant improvements can be potentially achieved even for very simple cylindrical layouts, with no complex conduction-enhancing solutions (e. g. metal fins or foams, blends with graphite fibres or other nano-particles). Still, theoretical and simulation based results has to be verified in realistic engineering environments, taking into account some complex material behaviour that might have been purposely omitted at modelling level: a typical example, related to the findings of the present work, is the well known tendency of salt hydrates to undesired vertical phase separation, which might be difficult to control or minimise in slender vertical containers.

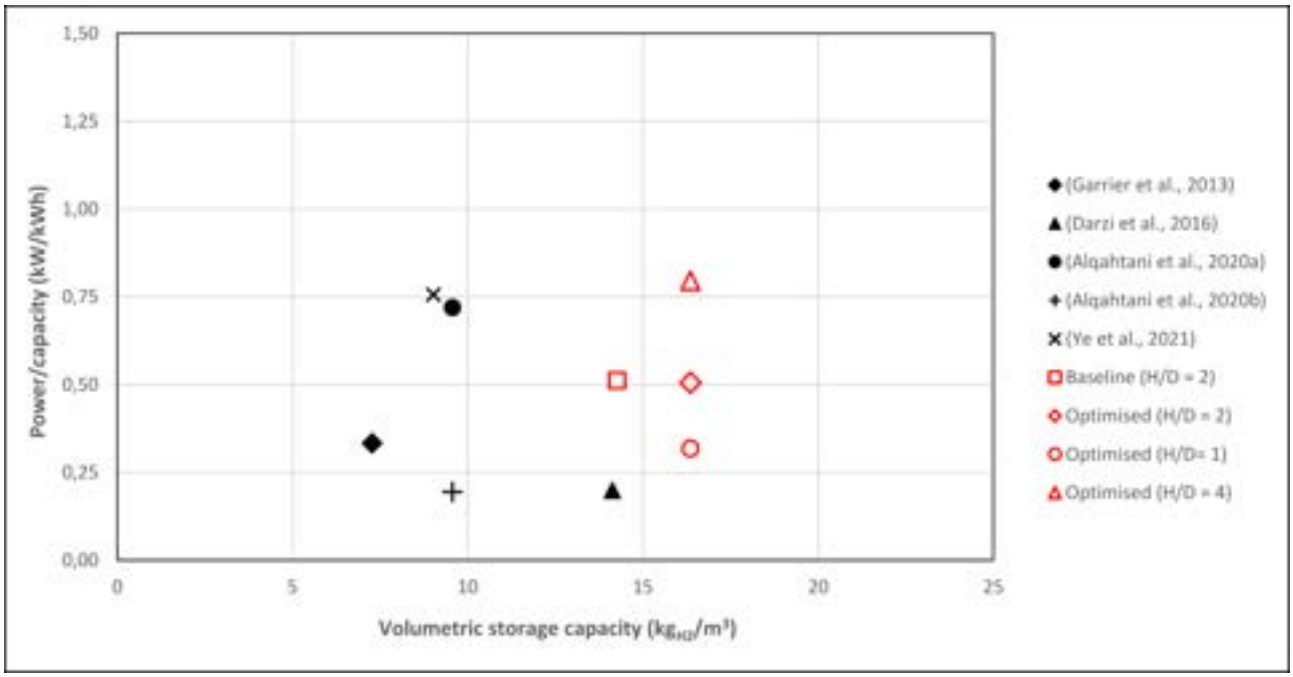

Figure 8. Specific discharge power vs. volumetric storage capacity of MH-PCM systems, literature review (black symbols) and results from the numerical benchmark analysed in the present work (red symbols).

4. Conclusions

From the literature analysis and numerical simulation results shown in this paper, the following conclusions can be drawn regarding MH-PCM system performances during hydrogen discharge:

- although it is often difficult to extract reliable performance indicators from the published works, the previously proposed systems cannot generally simultaneously achieve power/capacity ratios and system-level volumetric storage capacities above 0.75 kW/kWh and 15 kg_{H2}/m^3, respectively;
- the proposed numerical benchmark demonstrates that, in the case of jacket-like cylindrical MH-PCM configurations, these threshold can be exceeded through relatively simple optimization steps, like PCM mass optimization and system shape (slenderness factor H/D) optimization;
- mass optimization of the PCM is essentially linked to the latent heat of fusion, volume optimization comes as a consequence once the PCM density is also considered;

- for vertically-oriented jacket-like systems, higher slenderness factors significantly increase specific discharge power for a given volumetric capacity: is reported that moving from H/D = 1 to H/D = 4 produces a 150% power gain, peaking at a power/capacity ratio of 0.8 kW/kWh;
- the influence of the slenderness factor is explained by the quasi-1D nature of the heat transfer phenomena in this specific discharge case: heat transfer is dominated by conduction in the radial direction and, as such, it is accelerated by lowering the thermal resistance in that direction (smaller radial thicknesses);
- following the previous point, increasing the thermal conductivity in the radial direction both in the MH bed and PCM is also beneficial for a power increase; in that sense, on the PCM side the solid phase thermal conductivity plays the major role during hydrogen discharge (PCM solidification);

Future developments will include a further expanded literature research and the analysis of additional performance influence factors, such as the hydrogen discharge pressure, alternative MH-PCM system geometries, MH pressure-temperature-kinetics envelope.

Acknowledgments

The present research work has received financial support from the Italian Ministry of Universities and Research, Project of National Interest, PRIN 2020BFX8JY - HySuM. V. K. K. acknowledges financial support from the MEGACELL departmental research project, CUP n. E83C22006060005.

References

Abbasi, T., & Abbasi, S. A. (2011). “Renewable” hydrogen: Prospects and challenges. In *Renewable and Sustainable Energy Reviews* (Vol. 15, Issue 6, pp. 3034–3040). https://doi.org/10.1016/j.rser.2011.02.026

Abohamzeh, E., Salehi, F., Sheikholeslami, M., Abbassi, R., & Khan, F. (2021a). Review of hydrogen safety during storage, transmission, and applications processes. *Journal of Loss Prevention in the Process Industries*, *72*. https://doi.org/10.1016/j.jlp.2021.104569

Abohamzeh, E., Salehi, F., Sheikholeslami, M., Abbassi, R., & Khan, F. (2021b). Review of hydrogen safety during storage, transmission, and applications processes. *Journal of Loss Prevention in the Process Industries*, *72*. https://doi.org/10.1016/j.jlp.2021.104569

Alqahtani, T., Bamasag, A., Mellouli, S., Askri, F., & Phelan, P. E. (2020a). Cyclic behaviors of a novel design of a metal hydride reactor encircled by cascaded phase change materials. *International Journal of Hydrogen Energy*, *45*(56), 32285–32297. https://doi.org/10.1016/j.ijhydene.2020.08.280

Alqahtani, T., Bamasag, A., Mellouli, S., Askri, F., & Phelan, P. E. (2020b). Cyclic behaviors of a novel design of a metal hydride reactor encircled by cascaded phase change materials. *International Journal of Hydrogen Energy*, *45*(56), 32285–32297. https://doi.org/10.1016/j.ijhydene.2020.08.280

Alqahtani, T., Mellouli, S., Bamasag, A., Askri, F., & Phelan, P. E. (2020). Thermal performance analysis of a metal hydride reactor encircled by a phase change material sandwich bed. *International Journal of Hydrogen Energy*, *45*(43), 23076–23092. https://doi.org/10.1016/j.ijhydene.2020.06.126

ANSYS® Academic Research CFD, Release 2020 R2, Fluent User’s Guide. (2020). ANSYS Inc.

Bartolucci, L., Cordiner, S., Mulone, V., & Pasquale, S. (2021). Hydrogen based Multi Energy Systems: Assessment of the marginal utility of increasing hydrogen penetration on system performances. *International Journal of Hydrogen Energy*, *46*(78), 38588–38602. https://doi.org/10.1016/j.ijhydene.2021.09.108

Bartolucci, L., Cordiner, S., Mulone, V., Tatangelo, C., Antonelli, M., & Romagnuolo, S. (2023). Multi-hub hydrogen refueling station with on-site and centralized production. *International Journal of Hydrogen Energy*. https://doi.org/10.1016/j.ijhydene.2023.01.094

Bartolucci, L., & Krastev, V. K. (2022). On the Thermal Integration of Metal Hydrides with Phase Change Materials: Numerical Simulation Developments towards Advanced Designs. *SAE Technical Papers*. https://doi.org/10.4271/2022-24-0018

Bellosta von Colbe, J., Ares, J. R., Barale, J., Baricco, M., Buckley, C., Capurso, G., Gallandat, N., Grant, D. M., Guzik, M. N., Jacob, I., Jensen, E. H., Jensen, T., Jepsen, J., Klassen, T., Lototskyy, M. V., Manickam, K., Montone, A., Puszkiel, J., Sartori, S., … Dornheim, M. (2019). Application of hydrides in hydrogen

storage and compression: Achievements, outlook and perspectives. *International Journal of Hydrogen Energy*, *44*(15), 7780–7808. https://doi.org/10.1016/j.ijhydene.2019.01.104

Ben Mâad, H., Miled, A., Askri, F., & Ben Nasrallah, S. (2016). Numerical simulation of absorption-desorption cyclic processes for metal-hydrogen reactor with heat recovery using phase-change material. *Applied Thermal Engineering*, *96*, 267–276. https://doi.org/10.1016/j.applthermaleng.2015.11.093

Bouzgarrou, F., Mellouli, S., Alqahtani, T., & Algarni, S. (2022). Parametric study of a metal hydride reactor with phase change materials and heat pipes. *International Journal of Energy Research*, *46*(4), 4588–4598. https://doi.org/10.1002/er.7451

Chibani, A., Merouani, S., & Bougriou, C. (2022). The performance of hydrogen desorption from a metal hydride with heat supply by a phase change material incorporated in porous media (metal foam): Heat and mass transfer assessment. *Journal of Energy Storage*, *51*. https://doi.org/10.1016/j.est.2022.104449

El Kharbachi, A., Dematteis, E. M., Shinzato, K., Stevenson, S. C., Bannenberg, L. J., Heere, M., Zlotea, C., Szilágyi, P., Bonnet, J. P., Grochala, W., Gregory, D. H., Ichikawa, T., Baricco, M., & Hauback, B. C. (2020). Metal Hydrides and Related Materials. Energy Carriers for Novel Hydrogen and Electrochemical Storage. *Journal of Physical Chemistry C*, *124*(14), 7599–7607. https://doi.org/10.1021/acs.jpcc.0c01806

El Mghari, H., Huot, J., Tong, L., & Xiao, J. (2020). Selection of phase change materials, metal foams and geometries for improving metal hydride performance. *International Journal of Hydrogen Energy*, *45*(29), 14922–14939. https://doi.org/10.1016/j.ijhydene.2020.03.226

El Mghari, H., Huot, J., & Xiao, J. (2019). Analysis of hydrogen storage performance of metal hydride reactor with phase change materials. *International Journal of Hydrogen Energy*, *44*(54), 28893–28908. https://doi.org/10.1016/j.ijhydene.2019.09.090

Facci, A. L., Lauricella, M., Succi, S., Villani, V., & Falcucci, G. (2021). Optimized modeling and design of a pcm-enhanced h2 storage. *Energies*, *14*(6). https://doi.org/10.3390/en14061554

Garrier, S., Delhomme, B., De Rango, P., Marty, P., Fruchart, D., & Miraglia, S. (2013). A new MgH2 tank concept using a phase-change material to store the heat of reaction. *International Journal of Hydrogen Energy*, *38*(23), 9766–9771. https://doi.org/10.1016/j.ijhydene.2013.05.026

IPCC. (2022). Mitigation Pathways Compatible with 1.5°C in the Context of Sustainable Development. In *Global Warming of 1.5°C* (pp. 93–174). Cambridge University Press. https://doi.org/10.1017/9781009157940.004

Kovač, A., Paranos, M., & Marciuš, D. (2021). Hydrogen in energy transition: A review. *International Journal of Hydrogen Energy*, *46*(16), 10016–10035. https://doi.org/10.1016/j.ijhydene.2020.11.256

Krastev, V. K., & Falcucci, G. (2021). Comparison of enthalpy-porosity and lattice Boltzmann-phase field techniques for the simulation of the heat transfer and melting processes in LHTES devices. *E3S Web of Conferences*, *312*, 01002. https://doi.org/10.1051/e3sconf/202131201002

Lewis, S. D., & Chippar, P. (2021). Analysis of Heat and Mass Transfer During Charging and Discharging in a Metal Hydride - Phase Change Material Reactor. *Journal of Energy Storage*, *33*. https://doi.org/10.1016/j.est.2020.102108

Maestre, V. M., Ortiz, A., & Ortiz, I. (2021). Challenges and prospects of renewable hydrogen-based strategies for full decarbonization of stationary power applications. In *Renewable and Sustainable Energy Reviews* (Vol. 152). Elsevier Ltd. https://doi.org/10.1016/j.rser.2021.111628

Marty, P., De Rango, P., Delhomme, B., & Garrier, S. (2013). Various tools for optimizing large scale magnesium hydride storage. *Journal of Alloys and Compounds*, *580*(SUPPL1). https://doi.org/10.1016/j.jallcom.2013.02.169

Mellouli, S., Ben Khedher, N., Askri, F., Jemni, A., & Ben Nasrallah, S. (2015). Numerical analysis of metal hydride tank with phase change material. *Applied Thermal Engineering*, *90*, 674–682. https://doi.org/10.1016/j.applthermaleng.2015.07.022

Motyka, T. (2014). Hydrogen Storage Engineering Center of Excellence Metal Hydride Final Report. *SRNL-STI-2014-00226*.

Nazir, H., Muthuswamy, N., Louis, C., Jose, S., Prakash, J., Buan, M. E., Flox, C., Chavan, S., Shi, X., Kauranen, P., Kallio, T., Maia, G., Tammeveski, K., Lymperopoulos, N., Carcadea, E., Veziroglu, E., Iranzo, A., & Kannan, A. M. (2020). Is the H2 economy realizable in the foreseeable future? Part II: H2 storage, transportation, and distribution. In *International Journal of Hydrogen Energy* (Vol. 45, Issue 41, pp. 20693–20708). Elsevier Ltd. https://doi.org/10.1016/j.ijhydene.2020.05.241

Nguyen, H. Q., Mourshed, M., Paul, B., & Shabani, B. (2022). An experimental study of employing organic phase change material for thermal management of metal hydride hydrogen storage. *Journal of Energy Storage*, *55*. https://doi.org/10.1016/j.est.2022.105457

Nguyen, H. Q., & Shabani, B. (2021). Review of metal hydride hydrogen storage thermal management for use in the fuel cell systems. In *International Journal of Hydrogen Energy* (Vol. 46, Issue 62, pp. 31699–31726). Elsevier Ltd. https://doi.org/10.1016/j.ijhydene.2021.07.057

Pasquini, L., Sakaki, K., Akiba, E., Allendorf, M. D., Alvares, E., Ares, J. R., Babai, D., Baricco, M., Bellosta Von Colbe, J., Bereznitsky, M., Buckley, C. E., Cho, Y. W., Cuevas, F., De Rango, P., Dematteis, E. M., Denys, R. V., Dornheim, M., Fernández, J. F., Hariyadi, A., … Yartys, V. A. (2022). Magnesium- and intermetallic alloys-based hydrides for energy storage: Modelling, synthesis and properties. In *Progress in Energy* (Vol. 4, Issue 3). Institute of Physics. https://doi.org/10.1088/2516-1083/ac7190

Petkov, I., & Gabrielli, P. (2020). Power-to-hydrogen as seasonal energy storage: an uncertainty analysis for optimal design of low-carbon multi-energy systems. *Applied Energy*, *274*(April), 115197. https://doi.org/10.1016/j.apenergy.2020.115197

Rabienataj Darzi, A. A., Hassanzadeh Afrouzi, H., Moshfegh, A., & Farhadi, M. (2016). Absorption and desorption of hydrogen in long metal hydride tank equipped with phase change material jacket. *International Journal of Hydrogen Energy*, *41*(22), 9595–9610. https://doi.org/10.1016/j.ijhydene.2016.04.051

Voller, V. R., & Prakash, C. (1987). A fixed grid numerical modelling methodology for convection-diffusion mushy region phase-change problems. *Int. J. Heat Mass Transfer*, *30*(8), 1709–1719.

Voller, V. R., & Swaminathan, C. R. (1991). GENERAL SOURCE-BASED METHOD FOR SOLIDIFICATION PHASE CHANGE. *Numerical Heat Transfer, Part B*, *19*, 175–189.

Ye, Y., Ding, J., Wang, W., & Yan, J. (2021). The storage performance of metal hydride hydrogen storage tanks with reaction heat recovery by phase change materials. *Applied Energy*, *299*. https://doi.org/10.1016/j.apenergy.2021.117255

Ye, Y., Lu, J., Ding, J., Wang, W., & Yan, J. (2020). Numerical simulation on the storage performance of a phase change materials based metal hydride hydrogen storage tank. *Applied Energy*, *278*. https://doi.org/10.1016/j.apenergy.2020.115682

Yue, M., Lambert, H., Pahon, E., Roche, R., Jemei, S., & Hissel, D. (2021). Hydrogen energy systems: A critical review of technologies, applications, trends and challenges. In *Renewable and Sustainable Energy Reviews* (Vol. 146). Elsevier Ltd. https://doi.org/10.1016/j.rser.2021.111180

Performance comparison of cold thermal storage for gas turbine inlet cooling with traditional energy storage technologies in current electricity markets

Alberto Vannoni[a], and Alessandro Sorce[b]

[a] University of Genova, Genova, Italy, alberto.vannon@edu.unige.it, CA,
[b] University of Genova, Genova, Italy, alessandro.sorce@unige.it

Abstract:

In the current electricity grids, it is becoming pivotal to install a large amount of storage capacity in order to maximize the deployment of renewable energy sources, stabilize the grid, and mitigate electricity price volatility. Engineering research focused on improving storage technologies performance aiming to improve the round trip efficiency and increase the utilization opportunities. Besides storage implementation, power plant flexibility is pursued as well to support electricity grids in the transient stage towards a decarbonized energy mix. Recent studies have investigated the possibility of enhancing the flexibility of Combined Cycle Gas Turbine (CCGT) power plants by means of a heat pump and a cold thermal energy storage, this solution demonstrated a relevant potential, especially in those locations characterized by warm climates and volatile electricity markets. In such a situation is possible to fully exploit the cold thermal energy storage, decreasing the net power output, during storage charging in off-peak periods, and boosting it, through inlet cooling, during the most profitable periods. This paper performs a techno-economic comparison between cold thermal energy storage for gas turbines air inlet cooling and other established energy storage technologies (such as pumped hydro, batteries, compressed air, and pumper thermal storage) for time load shifting and energy arbitrage on the day ahead market. The analysis is based on Linear Programming (LP) and Mixed Integer Linear Programming (MILP) models for the optimization of the dispatch. The impact of market parameters on storage technologies performance is investigated and discussed, selecting the best option for each considered scenario.

Keywords:

Storage; Flexibility; CCGT; Heat Pump; Optimization; Electricity Market;

1. Introduction

The awareness about the ongoing climate change due to emissions of Green House Gasses (GHG) has led in the last decades almost every country to pledge drastic GHG emission cuts [1] and a complete transition to a decarbonized economy is commonly scheduled for the horizon of 2050 or 2070 [2]. The first step of the Energy Transition has been the massive installation of electricity generation capacity from Renewable Energy Sources (RES). Approximately 2 TW have been installed globally in the period 2010-20, and the overall share of electricity generation from RES reached 28%, overcoming 40% in many advanced economies even considering a significant contribution of hydropower [3]. Even a higher amount of RES capacity is forecast to be installed in the near future (between 2.4 and 3.7 TW by 2027 [4]); indeed, carbon intensity targets have been set more and more challenging and the demand for low-carbon electricity is expected to grow following the coupling of different energy sectors, such as Heating or Transportation [5].

Nevertheless, since the hydropower growth potential is limited, most RES capacity addiction depends on solar and wind sources, strongly characterized by discontinuity and stochasticity. Although forecasting of RES production in advance has improved significantly, especially thanks to artificial intelligence and data-driven modeling [6,7], the mismatch between demand and production remains a severe issue and a significant amount of green electricity is often curtailed because of an overgeneration or a lack of transportation capacity of electricity grids [8]. Curtailments are negligible for PV generation but are relevant for wind, Especially in countries characterized by high wind energy shares, i.e., above 30%, up to 10% of wind generation can be curtailed [9]. Within this context, energy storage became a pivotal technology that must be implemented massively at the grid scale to support the energy transition and maximize the dispatch of renewable energy [10]. To be impactful on energy system management, storage must present adequate both power and energy sizes, there is no unique definition of grid-scale storage size. However, in this paper, 1 MW discharge power for at least 1h is assumed as a threshold value. For such applications pumped hydro,

electrochemical batteries, compressed air, and pumped thermal energy storages are the most promising technologies, there many other solutions have been investigated, but currently present a too-low technology readiness level (TRL) on such a scale.

Besides bulk energy arbitrage, i.e., the action of buying cheap energy during off-peak price periods, storing it, and selling it during price-peaking periods, storage technologies can be employed to provide services to the grid. This paper focuses only on load time shifting by energy arbitrage as the most relevant use considering the energy involved and the pivotal importance to maximize the RES dispatch and reduce the carbon footprint of electricity generation.

Historically the first form of energy storage implemented on a large scale was pumped hydroelectric storage (PHS), it represents a variation of conventional reservoir hydroelectric power plants. Energy is stored in the form of potential energy of water that is pumped from a lower reservoir to an upper reservoir [11]. PHS is a consolidated technology, already implemented widely at the grid scale since the 1970s to absorb the excess base load production from coal and nuclear power plants [12]. PHS plants have been installed especially in those regions characterized by an existing hydroelectric potential, such as the Alps in Europe, and along both the East and West Coast in the US [13]. However, within a liberalized electricity market, oligopolistic ownership, especially if both PHS and conventional power plants are managed by the same operator, may lead to an under-exploitation of it, as in the case of Italy [14]. In fact, a strategic operation of PHS could reflect in social welfare losses [15]. From a technological perspective, PHS is characterized by a Round Trip Efficiency (RTE) typically ranging between 70% and 80% even if up to 87% have been claimed [11]. One of the major issues of PHS implementation concerns site identification that must satisfy criteria of technical and economic feasibility together with social acceptance. A systematic approach for new PHS site identification has been developed and applied by Connolly et al. [16]. An interesting variance application concerns seawater PHS whose main advantage is to be not subject to the constraint of water availability in the lower reservoir [17].

Battery Energy Storage (BES) are probably the technology expected to grow more in the next years. The International Energy Agency states that, according to the Net *zero emission by 2050* scenario, 680 GW of BES must be installed by 2030. 16 GW were already installed in 2021 [18]. Various BES types exist, the most interesting for large-scale applications include lithium-ion (Li-ion), sodium-sulfur (NaS), lead acid (Pb-acid), lead-carbon batteries, as well as zebra batteries (Na-$NiCl_2$), and flow batteries. Li-ion BESs represent almost the totality of installed grid-scale capacity (92% in the US [19]) mainly because of the round trip efficiency of up to 97% DC-DC [20,21], corresponding to 85-95% AC-AC [22]. NaS batteries are available since the early 2000s at MW scale [23] and are particularly appreciated for their achievable depth of discharge (up to 90%) [21], while the main drawback is the thermal management since they operate in the range of 300-350°C, causing up to 20% per day of parasitic losses during idle periods [24]; similar issues are presented by Zebra BES [23]. Lead-acid BESs are appreciated for their high recyclability [25] and reduced CAPEX even if characterized by a reduced lifespan [21]. Flow batteries use aqueous electrolytes with one or more dissolved active species; the electrolytes are stored in tanks, and, pumped through an electrochemical cell where energy conversion takes place, because of this architecture this kind of battery shows a unique capability to decouple energy and power [26], however, they are characterized by significantly higher energy density and lower efficiency. Vanadium redox flow batteries show the best values of RTE but are still limited to 75-85% [27]. A relevant issue of BES is the relevance of system degradation and aging: this strongly depends on usage mode and should be considered for optimal dispatch [28].

Compressed air Energy Storage (CAES), store energy as compressed air, for large applications typically underground reservoir are used. Even if porosity and permeability are mandatory requirements, geological constraints are not as strict as for PHS [29]. The clean medium, the moderate CAPEX for a unit of stored energy, and scalability are the most appreciated features. In contrast, low RTE, reduced depth of discharge, and a considerable response time are the main drawbacks [30]. RTE may be increased by advanced techniques for managing heat generated during the compression phase. According to these, CAPEX can be classified into Diabatic-CAES, more mature but less efficient, wasting compression heat and burning fuel, typically natural gas to preheat air before the expansion during the discharge phase, Adiabatic-CAES adopting a TES to store the compression heat and release it during the expansion without any fuel consumption, and Isothermal-CAES claiming RTE up to 70% but characterized by low TRL [31].

Pumped Thermal Energy Storage (PTES), also known as Carnot Batteries, is a type of energy storage system that uses thermal energy to store and release energy. PTES systems store energy by pumping a heat transfer fluid between two reservoirs at different temperatures. During the charging phase, power is used to drive a heat pump and transfer heat from the colder reservoir to the hotter one. To discharge the storage, the process is reversed, and the heat transfer fluid is pumped back from the hotter reservoir to the colder one, generating electricity in the process. PTES potential advantages for grid-scale applications include long cycle life, low life-cycle environmental impact, and appreciable energy density. However, the main drawback is a low RTE, which is typically in the range of 40-70% [32]. Additionally, PTES implies relevant specific CAPEX €/kW for the power and charging unit. PTES can be classified according to the discharging method, exploiting Brayton or Rankine cycles; the charging methods, mainly including reverse

thermodynamic cycles and or the use of electrical resistance; and type of Thermal Energy Storage (TES), sensible, latent, or chemical [33,34].

Besides these technologies, an interesting application was studied in recent years to couple a Combined Cycle Gas Turbine (CCGT) with an Inlet Conditioning Unit (ICU) consisting of a heat pump (HP) and a cold (5°C) TES, connected as in the scheme (Figure 1). The ICU could work i) continuously, employing the HP to conditionate the CCGT intake, ii) as equivalent energy storage indeed using cheap electricity to drive the HP and charge the cold TES and using it to cool down the CCGT intake and boost the power output during the price peak periods without additional auxiliary losses. Preliminary works assessed the impact of intake temperature on the CCGT performance to investigate the potentialities of an ICU integration [35]. Subsequently, by means of a Mixed Integer Linear Programming (MILP) approach, it was developed a methodology to optimize the scheduling of an integrated ICU-CCGT power plant on the day-ahead market only [36] or considering the potentialities from an ancillary services provision [37]. Finally, a comprehensive assessment was carried out considering different European and US market and climate scenarios [38]. Considering that an ICU can be installed retrofitting existing CCGT plants and that those plants currently represent the backbone of many electrical systems, installing an ICU is equivalent to an investment in energy storage technology since it may be employed for the purpose of energy arbitrage and increasing the ability of the plant to supply grid services.

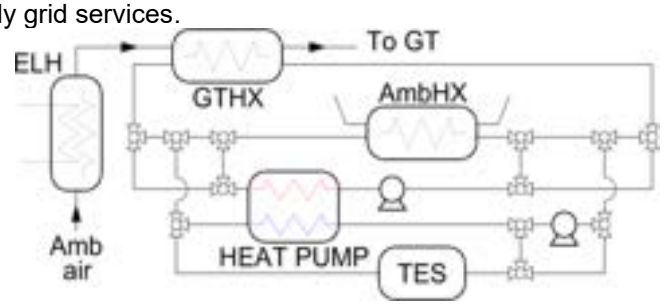

Figure. 1. Inlet Conditioning Unit (ICU) scheme

The present paper aims to carry out a marked-based economic comparison between grid-scale available storage technologies, including the ICU-CCGT integration. Even if the participation of storage in the flexibility markets is today an interesting perspective, such markets are strongly characterized by uncertainties and are hard to generalize among different country rules, therefore the proposed comparison only considers the possibility for storage to perform energy arbitrage on the day-ahead market. The novelty of the approach is to compare pure storage technologies against a flexible solution for refitting CCGT.

2. Methodology

A previous work identifies 9 market clusters in Europe and USA characterized by similar profit opportunities for ICU-CCGT integration [38]. In this paper, a techno-economic comparison between available grid-scale storages is carried out on the same markets (i.e., the centroids of previously identified clusters). The approach consists in determining the best scheduling of dispatch for each storage maximizing the Net Operational Profits (NetOP). Historical electricity price data have been used for this purpose [39,40]. Net Operational Profits are then used to compute techno-economic indicators: Pay Back Period (PBP) and Internal Rate of Return (IRR) are used for the economic assessment because of their independency of the storage size and the interest rate. Net Operational Profits, eq. (1), are defined as Revenues from selling electricity minus costs of charging and any cost associated with the degradation of the storage itself. Equations (2) define the PBP, and equation (3) the NPV such as the IRR is the value of i to which it follows NPV=0. Where N is the lifetime in years.

$$NetOP = \sum \left(Revenue - C_{charging} - C_{degr} \right) = \sum \left(OP - C_{degr} \right) \quad (1)$$

$$PBP = \frac{CAPEX}{OP} \quad (2)$$

$$NPV = -CAPEX + \sum_{n=1}^{N} \frac{OP_n}{(1+i)^n} \quad (3)$$

Storage operations are scheduled daily adopting an hourly resolution and an optimization horizon of 36h, as suggested by Vasylyev et al. [41]. According to this strategy price information beyond the daily horizon is provided to the optimizer. While the output concerning the first 24h is maintained, the scheduling from the 25th to the 36th will be overwritten by the following day optimization.

For the ICU-CCGT integration, the optimization of dispatch is carried out by means of the developed Mixed Integer Linear Programming (MILP) optimizer presented in detail by Mantilla et al. [36], and updated in the following works [37,38]. The objective function, equation (4) accounts for electricity price [39,40], gas cost (assumed as Henry Hub and TTF spot price for US and Europe respectively), CO_2 emission allowance cost [42], O&M cost, and cost associated with start-ups.

$$max \sum_{i=1}^{36} p_{el_i} \cdot (P_i^{out} - P_i^{HP} - Q_i^{elh}) - C_{gas_i} \cdot (Q_i^{fuel}) - C_{hs} V_{ji}^h - C_{ws} \cdot V_i^w - C_{CO2} \cdot e \cdot (Q_i^{fuel}) - O\&M_{var} \quad (4)$$

The first term in (4) represents the revenues from selling on the market the net power output, i.e., the algebraic sum of CCGT, HP, and electric heater power. The second term represents the cost of fuel, then two different start-ups are considered, hot (hs) and warm (ws), C is the cost associated with the start-up and V is a binary logic variable. The cost associated with CO_2 emission is computed as the unitary cost of allowance times the emission factor *e* times the fuel consumption. Finally, Operation and Maintenance costs are included.

For the other storage technologies, a linear Programming (LP) optimizer is proposed. The problem is formulated by equation (5). x represent the array of solutions, the first 37 elements are the solution itself, i.e., the State of Charge (SOC) before and after each of the 36 time intervals, elements from 38 to 73 represent the values of the first auxiliary variable (C_{degr}) dealing with the cost associate with degradation at each time step, finally, elements from 74 to 109 represent the second auxiliary variable (C_{ineff}) dealing with the cost of charge and discharge inefficiency at each time step.

$$\min_x f^T x \ \ s.t. \begin{cases} A \cdot \mathrm{x} \leq \mathrm{b} \\ A_{eq} \cdot \mathrm{x} = b_{eq} \\ lb \leq \mathrm{x} \leq \mathrm{u}b \end{cases} \quad (5)$$

$$x^T = \left(SOC_1 \quad \dots \quad SOC_{37} \quad , C_{degr_1} \quad \dots \quad C_{degr_{36}} \quad , C_{ineff_1} \quad \dots \quad C_{ineff_{36}}\right) \quad (6)$$

f is the array of coefficients of objective function expressing the linear dependence between the solution array x and objective, i.e., the sum of net operational profits over the optimization period.

The first 37 elements of f directly link the SOC and revenues from discharging and the cost due to charging, while the elements from 38 to 109 are equal to -1.

$$f^T = \left(\left(-p_{el_1}\right) \cdot \frac{E_{max}}{100} \quad \left(p_{el_1} - p_{el_2}\right) \cdot \frac{E_{max}}{100} \quad \dots \quad \left(p_{el_{36}}\right) \cdot \frac{E_{max}}{100} \quad , \quad -1 \quad \dots \quad -1 \, , \quad -1 \quad \dots \quad -1\right) \quad (7)$$

The linear constraints, expressed by the matrix A and array b, relate the auxiliaries variables C_{degr} and C_{ineff} to the difference of SOC within the relative time interval. More in detail 5 different types of constraints are imposed. The two first limits the maximum difference, respectively upward (equation(8)) and downward (equation (9)), the limit is imposed by the maximum admissible power (even expressed as C-rate for BESS) during charge and discharge. These constraints are expressed by means of the time constant τ, i.e., the minimum time [h] required by a complete charge or discharge, equal to the ratio between nominal capacity E_{max} and the maximum charging and discharging power.

$$SOC_i - SOC_{i-1} \leq \frac{100}{\tau_{ch}} \quad (8)$$

$$SOC_{i-1} - SOC_i \leq \frac{100}{\tau_{disch}} \quad (9)$$

Secondly, matrix A imposes the C_{degr} at each time interval. For some kinds of storage, such as BES, lifetime is determined by the maximum number of cycles. Consequently operating the storage has a cost since once the maximum number of equivalent cycles is reached the storage must be replaced paying again the CAPEX. Each equivalent cycle has, therefore, a cost equal to the ratio between CAPEX and the maximum number of equivalent cycles, equation(10), then the degradation cost at the time interval i depends on the fraction of equivalent cycle performed on that interval, equation (11).

$$C_{cycle} = \frac{CAPEX}{N_{cycle_{max}}} \quad (10)$$

$$C_{degr_i} \geq C_{cycle} \cdot \frac{|SOC_{i+1} - SOC_i|}{100} \quad (11)$$

Finally, the cost of charging and discharging efficiency is considered.

$$C_{inef_i} \geq \begin{cases} (SOC_{i+1} - SOC_i) \cdot p_{el_i} \cdot \frac{E_{max}}{100} \cdot \left(\frac{1}{\eta_{ch}} - 1\right), & (SOC_{i+1} - SOC_i) > 0 \\ (SOC_i - SOC_{i+1}) \cdot p_{el_i} \cdot \frac{E_{max}}{100} \cdot (\eta_{disch} - 1), & (SOC_{i+1} - SOC_i) < 0 \end{cases} \quad (12)$$

Furthermore, A_{eq} and b_{eq} impose the SOC at the initial time: for the first optimization, the minimum SOC allowed is used, while for the subsequent optimizations the SOC_{25} of the previous day is set. Lower bounds and upper bounds are imposed consistently as follows.

$$lb^T = (100 - DoD_{max} \quad \dots \quad 100 - DoD_{max} \, , \quad 0 \quad \dots \quad 0, \quad 0 \ \dots \ 0) \quad (13)$$

$$ub^T = (100 \quad \dots \quad 100, \quad inf \quad \dots \quad inf, \quad inf \quad \dots \quad inf) \quad (14)$$

3. Storage preliminary sizing

The ICU-CCGT integration design is a fairly complex process that must take into account the site market and meteorological specificity, even when focusing on just continuous cooling [43]. However, the size indicated by previous works (i.e., 10 MWh and 10 MW of Thermal Energy Storage and a 3.5 MW Heat Pump) as the preferable value was used to maintain comparable results. The corresponding CAPEX has been estimated at 6.3 M€ [36,44]. To proceed to a fair comparison between this solution and pure storage technologies a preliminary sizing of the latter is required.

Sizing is diriment because it directly impacts capital expenditure. The overall CAPEX depends on the storage size [MWh], the charging, and the discharging power [MW]. Table 1 reports assumed values for this paper from an existing literature survey. As a consequence, the specific CAPEX [€/kWh] depends on the storage duration τ_{disch} and the ratio between charging and discharging time constant, τ_{ratio}. Figure 2 shows the trend of specific CAPEX versus τ_{disch} considering τ_{ratio} between 1 and 6. However, BES CAPEX is typically expressed as an exclusive function of the storage capacity since capacity and power are strictly correlated and typically increased power does not imply extra costs, especially considering that if an hourly time interval is assumed, as in this paper, there is no advantage in adopting C-rate beyond 1 that are therefore not investigated. Thus BES curve in Figure 2 is flat.

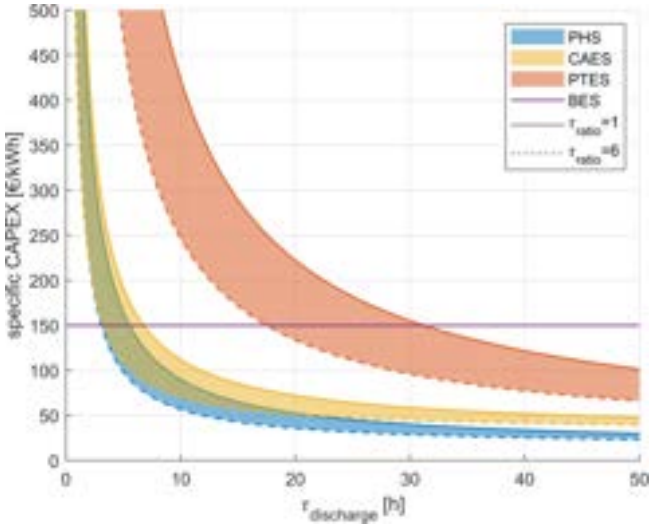

Figure. 2. Storage specific CAPEX versus duration of discharge

Figure 2 shows that BESs are the most economical storage for a short duration, generally, the other technologies CAPEX are very sensitive to the duration when it drops below 10h since the cost of power units becomes predominant. Increasing τ_{ratio} leads to savings in CAPEX decoupling charging and discharging power. Charging equipment cost weights more than the discharging one, so the impact of the τ_{ratio} is crucial in balancing the effect of reducing the CAPEX by decreasing the size of the charging equipment by a factor $1/\tau_{ratio}$, while increasing the operational charging time accordingly. This can be exploited if the duration of the off-peak price period is greater than the peak duration and if the off-peak price profile is constant, so $\tau_{ratio}>1$ is not directly reflected in an OP decrease. For a short duration, capital expenditure implied by CAES and PHS are comparable, nevertheless considering increased τ values the weight of storage cost itself is much more relevant if compared to the charging and discharging power units CAPEX, consequently in this case PHS is more advantageous because the cost per kWh is almost half of CAES.

Table 1. Technical and economic assumptions for each storage technology

	BESS	**PHS**	**CAES**	**PTES**
E_{max} [MWh]	1MWh	7 GWh	250 MWh	250 MWh
DoD_{max}	80%	90%	50%	100%
τ_{disc} [h]	1	2-24	2-24	2-24
$\tau_{ch\ min}$ / $\tau_{disch\ min}$	1	1-6	1-6	1-6
η_{ch}	92%	85%	75%	200%
η_{disch}	92%	88%	85%	30%
$CAPEX_{storage}$	150€/kWh	15€/kWh	32€/KWh	21€/KWh
$CAPEX_{ch}$	-	400€/kW	500€/kW	2125€/kW
$CAPEX_{disch}$	-	350€/kW	300€/kW	1900€/kW
Lifetime_max	25yr	80yr	35yr	35yr
$N_{cycle\ max}$	7500	-	-	-
ref	[28,45]	[46]	[46]	[47]

To preliminary size BES, PHS, CAES, and PTES, yearly optimizations are performed to quantify OP, PBP, and IRR. Different scenarios have been investigated, considering years from 2018 to 2022 and the 9 market zone identified as a relevant statistical sample for the ICU-CCGT integration [38]. The driving market factor for energy arbitrage is the price difference that can be exploited. Equation (15) expresses in a general form the minimum discharge price to be worth operating storage, it depends on the charging price, the efficiency of charging and discharging, and the degradation costs.

$$p_{el_{disch}} > \frac{C_{degr}}{\eta_{disch}} + \frac{p_{el_{ch}}}{\eta_{disch}\eta_{ch}} \tag{15}$$

Therefore to characterize each market scenario the average daily variability $\overline{\Delta p_{el_d}}$ is adopted highlighting the distance between the discharging price $p_{el_{disch}}$ and the charging price, $p_{el_{ch}}$, on a daily basis. Table 2 reports the values of $\overline{\Delta p_{el_d}}$ and the yearly average price, $\overline{p_{el_y}}$, for each year and zone. Optimizations have been performed considering data synthesized in Table 1 as input of the LP scheduler described in the Methodology section.

Table 2. Average daily electricity price spread and yearly price average [€/MWh] in the considered years and zones.

Bidding Zone	State/ Country	Ref. Location	2018		2019		2020		2021		2022	
			$\overline{\Delta p_{el_d}}$	$\overline{p_{el_y}}$	$\overline{\Delta p_{el_d}}$	$\overline{p_{el_y}}$	$\overline{\Delta p_{el_d}}$	$\overline{p_{el_y}}$	$\overline{\Delta p_{el_d}}$	$\overline{p_{el_y}}$	$\overline{\Delta p_{el_d}}$	$\overline{p_{el_y}}$
ARKANSAS_HUB	AR	Pine Bluff	21.64	25.03	15.67	21.27	13.83	17.72	24.29	31.05	44.87	56.81
AT	AT	Vienna	31.15	46.32	26.72	40.06	28.25	33.14	72.32	106.85	163.51	261.4
CENTRL	NY	Syracuse	48.87	50.38	33.52	40.00	14.74	17.40	49.60	57.42	107.56	123.35
LZ_CPS	TX	San Antonio	73.52	29.41	137.54	35.70	40.28	20.15	113.63	123.85	125.88	63.65
NEWHAMPSHIRE	NH	Manchester	29.92	37.32	20.95	28.13	19.29	22.01	29.57	39.09	59.98	81.56
NO3	NO	Trondheim	13.10	44.08	8.81	38.54	3.61	9.46	21.58	41.07	40.04	41.94
NORD	IT	Milan	31.28	60.71	28.05	51.25	26.06	37.79	59.40	125.2	161.52	307.81
SCE	CA	Los Angeles	60.13	37.28	49.52	33.13	69.16	31.13	65.64	43.60	99.56	82.07
SICI	IT	Palermo	56.99	69.49	71.75	62.77	48.87	46.21	73.15	129.02	172.8	295.07

Table 3 reports the Utilization Factor (UF) as the first output of storage dispatch optimizations, the reported τ_{disch} and τ_{ratio} are selected as the best in the following economic analysis for each storage technology. The UF is defined as the ratio between the discharged energy and the energy discharged if a cycle until the maximum allowed depth of discharge was performed daily.

$$UF = \frac{\sum_1^{n_{days}} E_{disch}}{E_{max} \cdot \frac{DoD_{max}}{100} \cdot n_{days}} \tag{16}$$

Table 3. UF [-] computed on a yearly basis for the best storage duration

Bidding Zone (State/Country)	BES τ_{disch}=1h τ_{ratio} =1					PHS τ_{disch}=12h τ_{ratio} =1					CAES τ_{disch}=12h τ_{ratio} =1					PTES τ_{disch}=2h τ_{ratio} =1				
	2018	2019	2020	2021	2022	2018	2019	2020	2021	2022	2018	2019	2020	2021	2022	2018	2019	2020	2021	2022
ARKANSAS_HUB (AR)	0.339	0.156	0.101	0.372	0.760	0.765	0.701	0.743	0.734	0.745	1.006	0.952	0.982	0.977	0.969	0.001	0	0.002	0.002	0
AT (AT)	0.55	0.449	0.461	1.127	1.686	0.730	0.716	0.749	0.734	0.717	1.091	1.070	1.134	1.107	1.055	0.101	0.096	0.126	0.076	0.042
CENTRL (NY)	0.871	0.656	0.105	0.862	1.275	0.788	0.743	0.554	0.755	0.749	1.066	1.012	0.781	1.025	1.019	0.016	0.001	0.004	0.001	0.003
LZ_CPS (TX)	0.741	0.722	0.536	0.805	1.145	0.820	0.817	0.815	0.828	0.85	1.057	1.064	1.035	1.084	1.131	0.042	0.094	0.021	0.044	0.079
NEWHAMPSHIRE (NH)	0.507	0.282	0.270	0.552	1.171	0.750	0.737	0.761	0.730	0.720	1.037	1.062	1.078	1.059	1.042	0.008	0.004	0.004	0.004	0.004
NO3 (NO)	0.125	0.038	0.008	0.253	0.387	0.355	0.301	0.455	0.476	0.546	0.450	0.356	0.566	0.605	0.696	0.020	0.011	0.01	0.03	0.066
NORD (IT)	0.599	0.545	0.493	0.912	1.557	0.575	0.666	0.692	0.597	0.611	0.846	0.973	1.034	0.879	0.902	0.001	0.007	0.021	0.007	0.008
SCE (CA)	1.064	1.088	0.962	1.037	1.207	0.866	0.867	0.865	0.855	0.842	1.239	1.256	1.231	1.210	1.159	0.097	0.151	0.211	0.159	0.164
SICI (IT)	1.266	1.401	1.122	1.239	1.636	0.788	0.827	0.828	0.686	0.639	1.196	1.263	1.268	1.028	0.959	0.031	0.111	0.057	0.043	0.074

Table 3 indicates that the highest UFs are reported by BES in 2022, under considerably favorable market conditions. This occurs especially in those bidding zones, typically as southern and central Europe, characterized by two distinct and prominent price peaks, in the morning and early evening, and presenting the opportunity to perform two cycles in a day. On the opposite side, other markets, e.g. Texas, even characterized by a relevant daily variability, typically show only one peak in a day, thus the second daily

discharge is very rare. Finally, markets characterized by flat electricity price and reduced variability, e.g., Norway, shows reduced potential for arbitrage for all the storage technologies.

If BES scored the UF highest values, CAES UF is considerably robust (around 1) even under less favorable market scenarios. However, CAES is characterized by a very low allowed DoD (50%), which means that, designing τ_{disch}=12h, just 6h are required to discharge until the maximum allowed depth. 12h and 10.8h are required by PTES and PHS respectively. The operativity of storage would depend only on the frequency with equation (15) is satisfied, consequently BES has a great advantage thanks to high efficiency, and low τ_{disch} and τ_{ch} but, differently than other technologies, it pays the impact of degradation costs, especially in low and moderately variable markets. If the amount of energy discharged is considered, PHS operates more than CAES because of the highest efficiency, while PTES is almost unutilized because of the too low efficiency and therefore excluded by the following analyses.

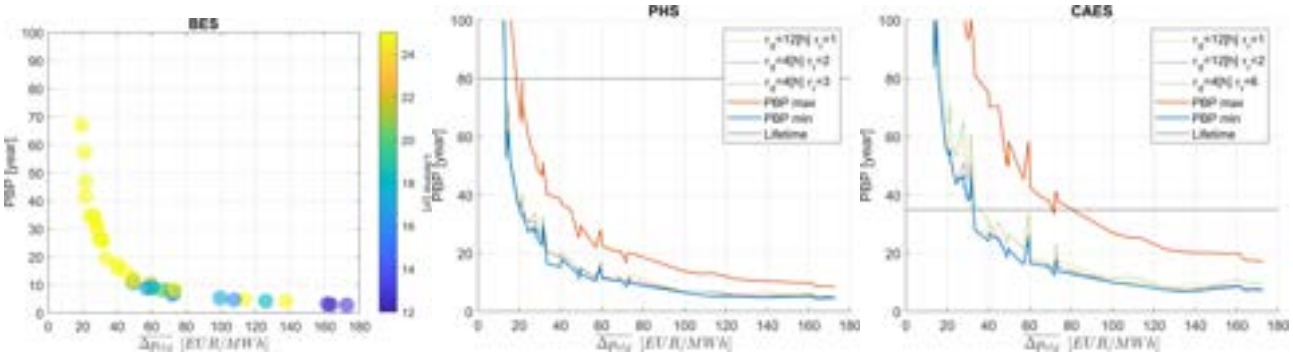

Figure. 3. BES, PHS, and CAES Pay Back Period (PBP) vs the average daily variability of electricity price

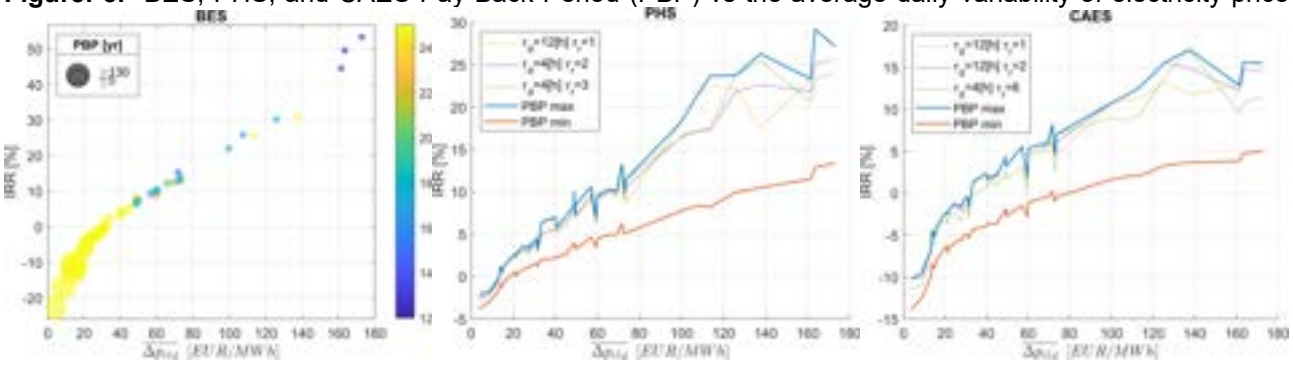

Figure. 4. BES, PHS, and CAES Internal Rate of Return (IRR) vs the average daily variability of electricity price

Figures 3 and 4 show the PBP and the IRR assessed by means of the annual cash flow, as an output of the yearly optimizations. Consequently, trends are drawn considering 45 values and the relative $\overline{\Delta p_{el_d}}$, from 5 years and 9 bidding zone reported in Table 2. Trends appear smooth enough to confirm the outcome of [38], identifying $\overline{\Delta p_{el_d}}$ as the best predictor for energy storage economic performance.

BESs present the lowest PBP; for $\overline{\Delta p_{el_d}}$ >50-55 €/MWh it drops below 10 years, however, the expected lifetime reduces as well because of the increased utilization. Besides the cycling aging of BES, calendar aging must be considered. According to the model presented by Stroe et al. [28], the maximum calendar life for an idling battery is about 25 years, this value is assumed as ceil even if the maximum number of cycles is not reached. Such an underutilization is typical of those markets with daily variability below 50€/MWh. The IRR increases with $\overline{\Delta p_{el_d}}$ and it is positive beyond 30€/MWh of daily variability.

For PHS and CAES the ranges of τ_{disc} and τ_{ratio} (i.e., the ratio between τ_{ch} and τ_{disc}) indicated in Table 1 are investigated. The blue and the red lines in Figures 3 and 4 represent the envelope of best and worst points respectively, moreover, three other lines are plotted for the three combinations of τ_{disc} and τ_{ratio} that more often result as the best possible. Both for PHS and CAES the best couple is τ_{disc}=12h and τ_{ratio}=1, while the second and the third rank differ for the two technologies showing that selecting τ_{ch} about 12-24h is preferable for CAES to limit CAPEX. PBP shows similar trends for CAES and PHS, even if under extremely favorable conditions (right side of charts) the PBP stabilizes at a slightly lower value for PHS (about 5 years, while 8 years are required to pay back the CAES) because of the lower specific CAPEX, as shown by Figure 1, and the higher efficiency. Moreover, it must be considered that the expected lifespan is significantly higher for PHS and this is reflected in the IRR which is positive even for reduced $\overline{\Delta p_{el_d}}$ (>10-15€/MWh).

For the purpose of the comparison between traditional storage technologies and the CCGT-ICU integration in Section 3, the best τ_{disc} and τ_{ratio} are selected.

4. ICU-CCGT comparison

The comparison is carried out on the three market zones that showed the highest potential for the integration of an ICU in an existing CCGT: SCE in California, northern Italy (NORD), and LZ_CPS in Texas[i] [38]. Respective reference locations for historical climate data are Los Angeles, Milan, and San Antonio. The previous section highlights how the bidding zone is not relevant for BES, PHS, and CAES but what is diriment is the exploitable variability in electricity price on a daily basis. Thus, for these technologies, is proposed an aggregated analysis, Figure 5 shows trend lines both for PBP and IRR built on rational 3rd-degree function fitting all 45 available values.

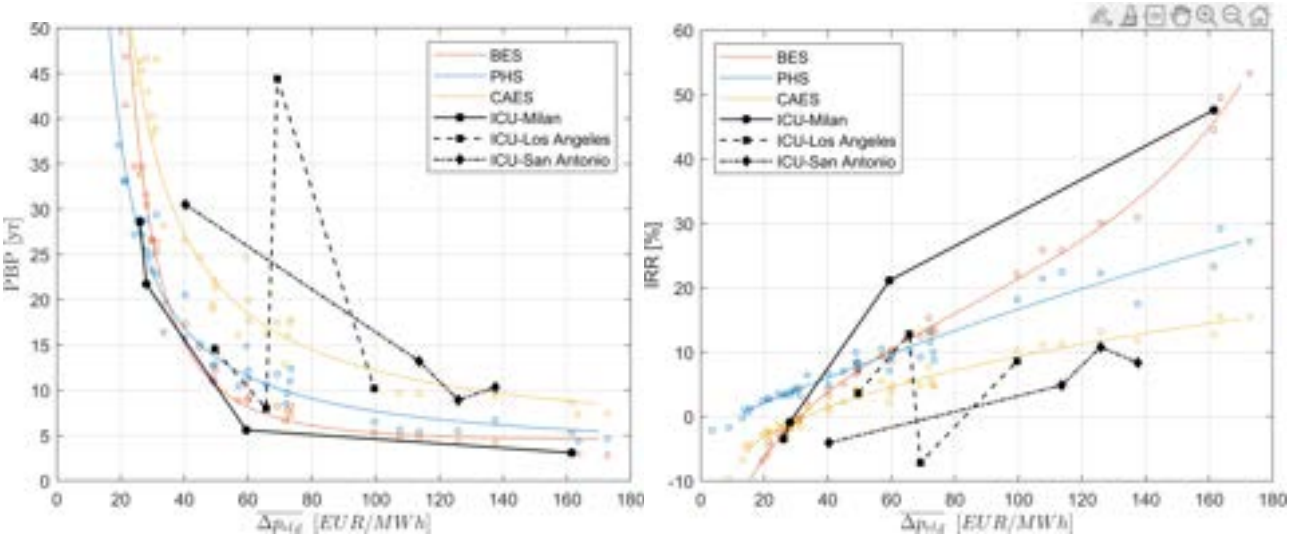

Figure. 5. PBP and IRR comparison for BES, PHS, CAES, and ICU-CCGT in three different locations

The analysis reported in a previous paper [38], was focused on one year and highlighted structural differences between market zone clusters considering both markets and climate parameters. On the other hand, this paper considers several years of operations highlighting that for systems with ICUs, an in-depth analysis is necessary and the expected economic outcome it is difficult to generalize because of the additional influence of ambient temperature and, secondly, of electricity price-gas price relationship, often synthesized by the Clean Spark Spread, the difference between the electricity price and the CCGT production cost, including CO_2, as defined in eq. (18). However, $\overline{\Delta p_{el_d}}$ confirms to be an effective indicator and the economic performance constantly improves as it increases. The only exception is represented by Los Angeles in 2020 due to the low Clean Spark Spread that year.

Even if in Texas and California higher $\overline{\Delta p_{el_d}}$ values are more common historically, for the same value the ICU-CCGT potential is higher in northern Italy. As Confirmed by Figure 6 and Table 4, in this location the potential for using directly the HP for heating and cooling the inlet air is higher (about 30% of operating hours for each of these operational modes), conversely, the TES is more exploited in California and Texas. In this last location is common to discharge the TES more than once a day and the inlet cooling by means of TES discharging is adopted for about 15% of operational modes. Despite the typical single peak price profile of this zone, this is possible because the value of energy discharged by the TES depends both on the electricity price and the potential CCGT power increase following the cooling depending on the ambient temperature. Thus, if the daily trends of ambient temperature and electricity price present two peaks characterized by sufficient prominence and temporal shifting, the resulting profits opportunities may result in a two peaks profile allowing a UF beyond 1.

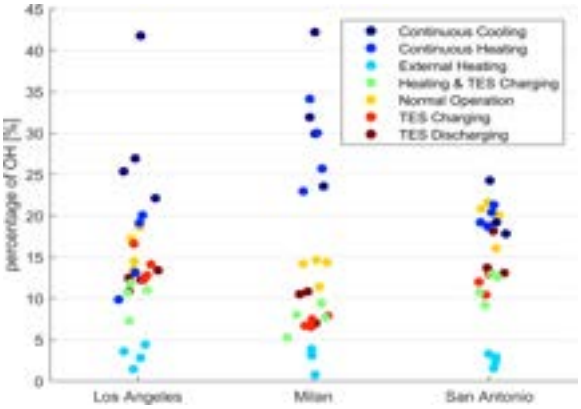

Table 4. Inlet Conditioning Unit TES UF [-]

	Bidding Zone (State/Country)		
	SCE (CA)	**NORD (IT)**	**LZ_CPS (TX)**
2019	0.706	0.372	1.01
2020	0.627	0.311	1.032
2021	1.056	0.783	1.548
2022	0.819	0.5991	1.139

Figure. 6. Operating mode as a percentage of overall operating hours

More in detail, from an economic perspective the main difference between the ICU-CCGT integration and the other storage technologies relies on the value at which the discharging power is awarded. The thermal energy discharged by the TES is reflected in an extra power output of the CCGT and a slight variation in efficiency since the fuel consumption increases as well, a detailed investigation of the dependence on the ambient temperature and the GT load is provided in [35]. Thus the economic value of the discharged energy is the power increment, due to inlet cooling by TES discharging, times the Clean Spark Spread (CSS), i.e., the profit margin of a CCGT power plant considering the fuel consumption and the cost of carbon dioxide allowance emissions, equation (18). Conversely, the cost of charging the TES is proportional to the ratio of electricity price on the HP COP. Analogously to equation (15), is possible to state the minimum condition to be worth operating the TES of an ICU. For the sake of simplicity, equation (17) neglects the variation in efficiency and thus in CSS following the TES discharge.

$$\Delta P \cdot CSS_{disch} = E_{disch} \cdot f(T_{amb}, Load_{GT}) \cdot CSS_{disch} \geq \frac{E_{disch} \cdot p_{el_{ch}}}{COP(T_{amb})} \tag{17}$$

$$CSS = p_{el} - C_{gas} \cdot \left(\frac{1}{\eta_{CCGT}} - C_{CO2} \cdot e \right) \tag{18}$$

Finally, Figure 7 confirms the pivotal importance of CSS reporting the boxplot distributions versus $\overline{\Delta p_{el_d}}$ for each year in the analyzed locations, in the hours in which the TES is discharged, CSS_{disch}. It is immediate to appreciate the strict correlation between the trend lines connected the CSS median values and the IRR or the opposite of PBP in Figure 5. CSS can be considered as a carrier signal, then on the right part of the chart trends diverge because the extra benefits on economic KPIs of increased $\overline{\Delta p_{el_d}}$.

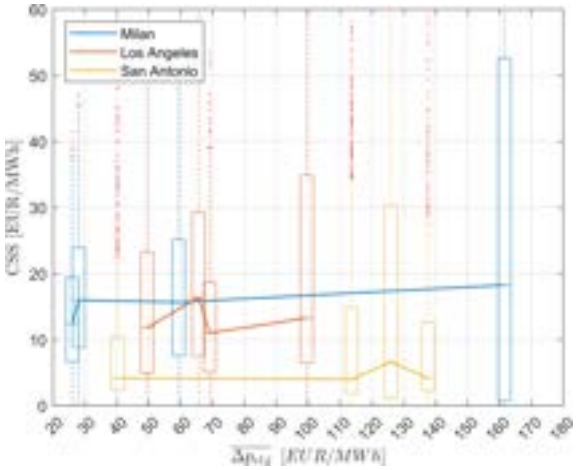

Figure. 7. Yearly Clean Spark Spread distribution versus the average daily variability

5. Conclusions

This paper performs a market analysis by means of Linear Programming and Mixed Integer Linear Programming optimizer of different storage technologies for energy arbitrage on the day-ahead market. Battery Energy Storage (BES), Pumped Hydro Storage (PHS), Compressed Air Energy Storage (CAES), and Pumped Thermal Energy Storage (PTES) are compared against the integration of a Combined Cycle Gas Turbine with an Inlet Conditioning Unit consisting of a Heat Pump and a cold Thermal Energy Storage (CCGT-ICU). Different scenarios have been analyzed considering historical data from different bidding zones and years.

First, it was observed how the operativity of energy storage depends on the conversion efficiency and any possible cost associated with the degradation of the storage itself, this is an important issue for batteries. It was observed that PTES presents a very low utilization factor, because of the low round trip efficiency profit opportunities from arbitrage with PTES are very rare and it is not possible to pay the investment back. PTES is then excluded by the following analysis.

A sizing procedure applied to PHS and CAES identifies both an optimal charging and discharging duration of about 12h, highlighting how limiting the charging power is an effective approach to reduce CAPEX and enhance economic KPIs. The daily electricity price variability is the driving factor for storage opportunities. Thanks to the absence of degradation costs and a good round trip efficiency, PHS performs better on markets characterized by moderate variability (<40-60 €/MWh), while batteries are the best solutions when the price is extremely variable (>60 €/MWh), in such a condition the high efficiency represents an advantage despite the cost associated to the storage degradations; performing even two cycles per day. CAES may find an application in low variable markets (<30-40 €/MWh), if there is no site availability for PHS. However in such conditions, the PBP is close to the expected lifespan, thus the viability of investment for CAES is still uncertain if only arbitrage profits are considered.

Introducing the ICU-CCGT integration in the comparison requires separately analyzing bidding zones because of the impact of local climate and the Clean Spark Spread (CSS). The proposed integration wins

the comparison against other storage technologies in northern Italy and demonstrates to be competitive in California while it shows lower performance in Texas. It was demonstrated that what drastically impacts this outcome is the CSS and the opportunities to use the ICU also for direct inlet cooling and heating.

It is possible to conclude that, as pure storage, the ICU integration presents low performance if compared to a system designed for this purpose. However, within the ICU investment, an HP is included that, if exploited in continuous heating and cooling mode, can increase the extra profits generated by the ICU retrofitting. Moreover, it must be considered that such an investment can avoid the closure or mothballing of the CCGT power plant, therefore keeping available to the Transmission System Operator a relevant capacity for supplying services to the grid, including the rotational inertia typical of turbomachinery-based power plants and essential for the purpose of frequency regulation.

Nomenclature

Acronyms

BES	Battery Energy Storage
CAPEX	Capital Expenditure
CAES	Compressed Air Energy Storage
CCGT	Combined Cycle Gas Turbine
GT	Gas Turbine
HP	Heat Pump
HX	Heat Exchanger
ICU	Inlet Conditioning Unit
LP	Linear Programming
MILP	Mixed Integer Linear Programming
OH	Operating Hours
PHS	Pumped Hydro Storage
PTES	Pumped Thermal Energy Storage
RES	Renewable Energy Sources
TES	Thermal Energy Storage

Variables

C	Cost, €, €/MWh, €/ton
COP	Coefficient of Performance, -
CSS	Clean Spark Spread, €/MWh
DoD	Depth of Discharge, %
e	Emission factor, ton/MWh
E	energy, MWh
i	Interest rate, -
IRR	Internal Rate of Return, %
O&M	Operating and Maintenance Costs, €/MWh
OP	Operational Profits, €
P	Power, MW
p	Price, €/MWh
PBP	Pay Back Period, yr
Q	Quantity, MWh
RTE	Round Trip Efficiency, %
SOC	State of Charge, %
T	Temperature, °C
UF	Utilization Factor, -
V	Start-up Binary Variable, logic
η	Efficiency, %
τ	Duration, h

Subscripts and superscripts

amb	Ambient
d	Daily
el	Electricity
ch	Charge
disch	Discharge
T	Transpose
inef	Inefficiency
degr	Degradation
w	Warm
h	Hot
s	Start-up

References

[1] Tavoni M, Kriegler E, Riahi K, Van Vuuren DP, Aboumahboub T, Bowen A, et al. Post-2020 climate agreements in the major economies assessed in the light of global models. Nat Clim Chang 2015;5:119–26. https://doi.org/10.1038/nclimate2475.

[2] Lang J, Hyslop C, Yeo XY, Black R, Chalkley P, Hale T, et al. Net Zero Tracker 2023.

[3] International Energy Agency. World Energy Outlook 2022. Paris: 2022.

[4] Yasmina Abdelilah, Heymi Bahar, Trevor Criswell, Piotr Bojek, François Briens. Renewables 2022: analysis and forecast to 2027. Paris: 2022.

[5] Ramsebner J, Haas R, Ajanovic A, Wietschel M. The sector coupling concept: A critical review. WIREs Energy Environ 2021;10:e396. https://doi.org/https://doi.org/10.1002/wene.396.

[6] Aslam S, Herodotou H, Mohsin SM, Javaid N, Ashraf N, Aslam S. A survey on deep learning methods for power load and renewable energy forecasting in smart microgrids. Renew Sustain Energy Rev 2021;144:110992. https://doi.org/https://doi.org/10.1016/j.rser.2021.110992.

[7] Corizzo R, Ceci M, Fanaee-T H, Gama J. Multi-aspect renewable energy forecasting. Inf Sci (Ny) 2021;546:701–22. https://doi.org/https://doi.org/10.1016/j.ins.2020.08.003.

[8] Ramesh AV, Li X. Reducing Congestion-Induced Renewable Curtailment with Corrective Network Reconfiguration in Day-Ahead Scheduling. 2020 IEEE Power Energy Soc. Gen. Meet., 2020, p. 1–5. https://doi.org/10.1109/PESGM41954.2020.9281399.

[9] Yasuda Y, Bird L, Carlini EM, Eriksen PB, Estanqueiro A, Flynn D, et al. C-E (curtailment – Energy share) map: An objective and quantitative measure to evaluate wind and solar curtailment. Renew Sustain Energy Rev 2022;160:112212. https://doi.org/https://doi.org/10.1016/j.rser.2022.112212.

[10] Bouakkaz A, Mena AJG, Haddad S, Ferrari ML. Efficient energy scheduling considering cost reduction and energy saving in hybrid energy system with energy storage. J Energy Storage 2021;33:101887. https://doi.org/https://doi.org/10.1016/j.est.2020.101887.

[11] Rehman S, Al-Hadhrami LM, Alam MM. Pumped hydro energy storage system: A technological review. Renew Sustain Energy Rev 2015;44:586–98. https://doi.org/https://doi.org/10.1016/j.rser.2014.12.040.

[12] Deane JP, Ó Gallachóir BP, McKeogh EJ. Techno-economic review of existing and new pumped hydro energy storage plant. Renew Sustain Energy Rev 2010;14:1293–302. https://doi.org/https://doi.org/10.1016/j.rser.2009.11.015.

[13] Guittet M, Capezzali M, Gaudard L, Romerio F, Vuille F, Avellan F. Study of the drivers and asset management of pumped-storage power plants historical and geographical perspective. Energy 2016;111:560–79. https://doi.org/https://doi.org/10.1016/j.energy.2016.04.052.

[14] Kougias I, Szabó S. Pumped hydroelectric storage utilization assessment: Forerunner of renewable energy integration or Trojan horse? Energy 2017;140:318–29. https://doi.org/https://doi.org/10.1016/j.energy.2017.08.106.

[15] Schill W-P, Kemfert C. Modeling Strategic Electricity Storage: The Case of Pumped Hydro Storage in Germany. Energy J (Cambridge, Mass) 2011;32:59–87. https://doi.org/10.5547/ISSN0195-6574-EJ-Vol32-No3-3.

[16] Connolly D, MacLaughlin S, Leahy M. Development of a computer program to locate potential sites for pumped hydroelectric energy storage. Energy 2010; 35:375–81. https://doi.org/https://doi.org/10.1016/j.energy.2009.10.004.

[17] McLean E, Kearney D. An Evaluation of Seawater Pumped Hydro Storage for Regulating the Export of Renewable Energy to the National Grid. Energy Procedia 2014;46:152–60. https://doi.org/https://doi.org/10.1016/j.egypro.2014.01.168.

[18] International Energy Agency. Grid-Scale Storage. Paris: 2022.

[19] U.S. Department of Energy. Battery Storage in the United States: An Update on Market Trends. 2021.

[20] Farhadi M, Mohammed O. Energy Storage Technologies for High-Power Applications. IEEE Trans Ind Appl 2016;52:1953–62. https://doi.org/10.1109/TIA.2015.2511096.

[21] Argyrou MC, Christodoulides P, Kalogirou SA. Energy storage for electricity generation and related processes: Technologies appraisal and grid scale applications. Renew Sustain Energy Rev 2018;94:804–21. https://doi.org/https://doi.org/10.1016/j.rser.2018.06.044.

[22] Rancilio G, Lucas A, Kotsakis E, Fulli G, Merlo M, Delfanti M, et al. Modeling a Large-Scale Battery Energy Storage System for Power Grid Application Analysis. Energies 2019;12. https://doi.org/10.3390/en12173312.

[23] Dunn B, Kamath H, Tarascon J-M. Electrical Energy Storage for the Grid: A Battery of Choices. Science (80-) 2011;334:928–35. https://doi.org/10.1126/science.1212741.

[24] Gallo AB, Simões-Moreira JR, Costa HKM, Santos MM, Moutinho dos Santos E. Energy storage in the energy transition context: A technology review. Renew Sustain Energy Rev 2016;65:800–22. https://doi.org/https://doi.org/10.1016/j.rser.2016.07.028.

[25] May GJ, Davidson A, Monahov B. Lead batteries for utility energy storage: A review. J Energy Storage 2018;15:145–57. https://doi.org/https://doi.org/10.1016/j.est.2017.11.008.

[26] Sánchez-Díez E, Ventosa E, Guarnieri M, Trovò A, Flox C, Marcilla R, et al. Redox flow batteries: Status and perspective towards sustainable stationary energy storage. J Power Sources 2021;481:228804. https://doi.org/https://doi.org/10.1016/j.jpowsour.2020.228804.

[27] Fan X, Liu B, Liu J, Ding J, Han X, Deng Y, et al. Battery Technologies for Grid-Level Large-Scale Electrical Energy Storage. Trans Tianjin Univ 2020;26:92–103. https://doi.org/10.1007/s12209-019-00231-w.

[28] Stroe DI, Knap V, Swierczynski M, Stroe AI, Teodorescu R. Operation of a grid-connected lithium-ion battery energy storage system for primary frequency regulation: A battery lifetime perspective. IEEE Trans Ind Appl 2017;53:430–8. https://doi.org/10.1109/TIA.2016.2616319.

[29] Houssainy S, Janbozorgi M, Kavehpour P. Thermodynamic performance and cost optimization of a novel hybrid thermal-compressed air energy storage system design. J Energy Storage 2018;18:206–17. https://doi.org/https://doi.org/10.1016/j.est.2018.05.004.

[30] Bazdar E, Sameti M, Nasiri F, Haghighat F. Compressed air energy storage in integrated energy systems: A review. Renew Sustain Energy Rev 2022;167:112701. https://doi.org/10.1016/j.rser.2022.112701.

[31] Aghahosseini A, Breyer C. Assessment of geological resource potential for compressed air energy storage in global electricity supply. Energy Convers Manag 2018;v. 169:161-173–2018 v.169. https://doi.org/10.1016/j.enconman.2018.05.058.

[32] Vecchi A, Knobloch K, Liang T, Kildahl H, Sciacovelli A, Engelbrecht K, et al. Carnot Battery development: A review on system performance, applications and commercial state-of-the-art. J Energy Storage 2022;55:105782. https://doi.org/https://doi.org/10.1016/j.est.2022.105782.

[33] Dumont O, Frate GF, Pillai A, Lecompte S, De paepe M, Lemort V. Carnot battery technology: A state-of-the-art review. J Energy Storage 2020;32:101756. https://doi.org/https://doi.org/10.1016/j.est.2020.101756.

[34] Novotny V, Basta V, Smola P, Spale J. Review of Carnot Battery Technology Commercial Development. Energies 2022;15. https://doi.org/10.3390/en15020647.

[35] Sorce A, Giugno A, Marino D, Piola S, Guedez R. Analysis of a Combined Cycle Exploiting Inlet Conditioning Technologies for Power Modulation. Proc. ASME Turbo Expo 2019 Turbomach. Tech. Conf. Expo. June 17-21 2019, Phoenix, Arizona, USA: 2019. https://doi.org/https://doi.org/10.1115/GT2019-91541.

[36] Mantilla W, Garcia J, Guédez R, Source A. Short-Term Optimization of a Combined Cycle Power Plant Integrated With an Inlet Conditioning Unit. J Eng Gas Turbines Power 2021;143. https://doi.org/10.1115/1.4050856.

[37] Vannoni A, García J, Guedez R, Sorce A. Ancillary Services Potential for Flexible Combined Cycles. ASME Turbo Expo 2021 Turbomach. Tech. Conf. Expo. June 7-11 2021, Virtual: 2021.

[38] Vannoni A, Garcia JA, Guedez R, Sorce A, Massardo AF. Combined Cycle, Heat Pump, and Thermal Storage Integration: Techno-Economic Sensitivity to Market and Climatic Conditions Based on a European and United States Assessment. ASME Pap. GT2022-82698, ASME Turbo Expo 2022, Rotterdam, The Netherlands.: 2022.

[39] LCG Consulting. Energy Online Data n.d. http://www.energyonline.com/Data (accessed March 13, 2023).

[40] ENTSO-E. ENTSO-E Transparency Platform n.d. https://transparency.entsoe.eu/transmission-domain/r2/dayAheadPrices/show (accessed March 13, 2023).

[41] Vasylyev A, Vannoni A, Sorce A. Best Practices For Electricity Generators And Energy Storage Optimal Dispatch Problems. ASME Turbo Expo 2023 Turbomach. Tech. Conf. Expo. Vol. 4 Control. Diagnostics, Instrumentation; Cycle Innov. Cycle Innov. Energy Storage; Educ. Electr. Power. June 26–30, 2023., Boston: 2023.

[42] The World Bank. State and Trends of Carbon Pricing 2017-2021. Washington DC: n.d.

[43] Giugno A, Sorce A, Cuneo A, Barberis S. Effects of market and climatic conditions over a gas turbine combined cycle integrated with a Heat Pump for inlet cooling. Appl Energy 2021;290:116724. https://doi.org/https://doi.org/10.1016/j.apenergy.2021.116724.

[44] Vannoni A, Sorce A, Traverso A, Massardo AF. Techno-Economic Analysis of Power-to-Heat Systems. E3S Web Conf 2021;03003. https://doi.org/https://doi.org/10.1051/e3sconf/202123803003.

[45] Mauler L, Duffner F, Zeier WG, Leker J. Battery cost forecasting: a review of methods and results with an outlook to 2050. Energy Environ Sci 2021;14:4712–39. https://doi.org/10.1039/D1EE01530C.

[46] Jülch V. Comparison of electricity storage options using levelized cost of storage (LCOS) method. Appl Energy 2016;183:1594–606. https://doi.org/https://doi.org/10.1016/j.apenergy.2016.08.165.

[47] Tassenoy R, Couvreur K, Beyne W, De Paepe M, Lecompte S. Techno-economic assessment of Carnot batteries for load-shifting of solar PV production of an office building. Renew Energy 2022;199:1133–44. https://doi.org/https://doi.org/10.1016/j.renene.2022.09.039.

[i] Days from February 13 and 19, 2021 have been excluded from the Texan analysis because of the exceptional energy crisis occurred during those days. Extremely high electricity prices occurred in that period cannot be considered as regular neither fully exploitable because of the generalized unavailability of many generators following the severe weather conditions.

Techno-Economic Analysis of Latent Heat Thermal Energy Storage Integrated Heat Pump for Indoor Heating

Lianying Shan[a], Andrew Martin[b], Justin NW Chiu[c]

[a] Department of Energy Technology, KTH Royal Institute of Technology, Brinellvägen 68, SE-10044 Stockholm, Sweden, lianying@kth.se, CA
[b] Department of Energy Technology, KTH Royal Institute of Technology, Brinellvägen 68, SE-10044 Stockholm, Sweden, andrew.martin@energy.kth.se
[c] Department of Energy Technology, KTH Royal Institute of Technology, Brinellvägen 68, SE-10044 Stockholm, Sweden, justin.chiu@energy.kth.se

Abstract:

Electricity prices have increased significantly in Europe and other regions due to the recent energy crisis. Latent heat thermal energy storage (LHTES) implemented in residential heating systems has attracted attention for its role in peak/load shifting to reduce heating costs. A new layout with LHTES integrated with a heat pump (HP) is proposed here to store low grade heat during off-peak demand periods, later used as heat source for the heat pump during peak demand periods. This novel layout is assessed for its heat capacity variation and levelized cost of energy (LCOE). The results show that increased amount of power input is required when a storage component is integrated into the heating system, while it can be compensated by shifting to off-peak electricity usage.

Keywords:

Phase Change Material; Thermal Energy Storage; Heat Pump; Techno-Economic Analysis

1. Introduction

The Paris Agreement targets reductions in greenhouse gas emissions and tacklinge climate change [1] where the largest source of greenhouse gas emissions is carbon emissions from energy use [2]. To comply with this agreement, Sweden has set a long-term goal of achieving zero net emissions of greenhouse gas by 2045 at the latest [3]. In 2020, the Sweden's final energy use in the residential and service sector was 140 TWh, of which district heating and electricity accounted for more than 80% [4]. As of December 2021, 2.6 million dwellings in Sweden were multi-family buildings, accounting for 52% of the total residential sector, and they were responsible for a third of total energy use [5,6]. Space heating in terms of energy use in buildings plays a pivotal role in decarbonisation [7–9]. The transition towards low carbon society requires novel energy technologies and solutions. Heat pumps with their high coefficient of performance (COP) have gained increasing attention for emission reduction, as they can reduce energy demand and increase the uptake of variable renewable energy in electricity grid [10–12].

Many research efforts have focused on improving heat pumps in space heating. Fraga et al. [13] compared heat pumps with different heat sources implemented in non-retrofitted, retrofitted and new multi-family buildings. Sun et al. [14] focused on the mixed-refrigerant recuperative heat pumps, suitable for large temperature lift in space heating, and introduced an assisted-cycle to improve the system performance. Dongellini et al. [15] studied the effects of control strategies of different air-to-water heat pumps on seasonal heating system. Blázquez et al. [16] analysed the suitability of air source heat pump and ground source heat pump in different climate conditions. Manuel et al. [17] also studied these two kinds of heat pumps and analysed the performance by reducing heating system circuit temperature.

Heat pumps consume a small amount of power to shift larger amount of heat from a heat source, but at the same time, they also become the major consumer of household electricity [18]. Due to the recent energy shortages and inflation [19], electricity prices have increased significantly. Figure 1 shows the hourly electricity trading price of SE3-Stockholm region in November 2022 (blue line) and its monthly average electricity trading price in November each year from 2018 to 2022 (orange bar). The electricity price is highly fluctuating during November 2022. Due to the impact of wind power generation, there are cases where the electricity prices is very low. While through the comparison of electricity prices in different years, it can be clearly seen that the overall electricity price has risen significantly. Thermal energy storage implemented in residential heating

systems has attracted attention for its role on peak load shifting to reduce heating costs [20,21]. The LHTES is favourable due to the high energy density, small volume change of phase change material (PCM) in melting and in solidification processes [22,23]. The heat transfer rate of PCM affects the thermal performance of LHTES. To counter the low conductivity of PCM, a number of heat transfer area enlargement techniques with spherical mini & micro encapsulations, metal fin extensions and matrix foam impregnations have shown good results [24–28]. The melting and solidification temperature should be carefully selected to match the operating temperature range. For space heating, paraffin and sodium acetate tri-hydrate based PCMs have been tested [9,29].

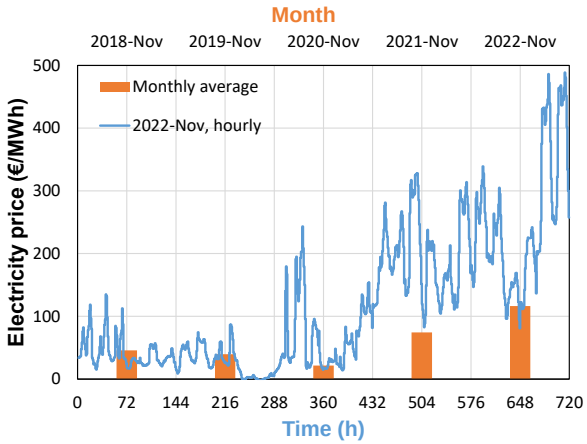

Figure 1. Electricity trading price in SE3-Stockholm region (exclude any fees, charges or taxes) [30].

Different layouts of integrated LHTES and HP systems have been studied for space heating. Yu et al.[5] presented an integrated heat pump & LHTES system and proposed a mathematical model including energy, environmental and economic analysis for four typical cities in China. The LHTES component was a bulk storage configuration, in which the refrigerant directly transfers heat to PCM during the charging process and the circulated water absorbed heat during the discharging process. The results showed that the integrated systems had a good application prospect. Xu et al. [20,32,33] conducted the experimental and numerical investigation on cylindrical macro-encapsulated PCM. Different integrated LHTES-HP layouts by introducing desuperheater, subcooler were displayed, and the assessment of their technical, economic and environmental performance showed that the heat performance and operational expense were improved. Olympios et al.[10] established a heat pump system powered via a solar PV system. The heat pump is coupled with two different PCM thermal storage components, one for domestic hot water and one for space heating. The system showed large potential of economical savings. Zhang et al. [34] proposed a CO_2 heat pump system integrated with ejector and LHTES system. The new system had better thermodynamic and economic performance than conventional CO_2 heat pumps. Despite these research efforts the integration of heat pumps in multi-family buildings still faces many barriers, such as high heating temperature requirement for non-retrofitted building, complicated access to geothermal sources and high capital costs [35,36]. Therefore, further studies are needed.

This paper proposes a novel layout of integrated LHTES and HP to cover the heating requirement of a typical multi-family building. LHTES component is connected to the return side of radiator to absorb low-grade heat during off-peak periods. The stored energy then transfer to the ambient air through a shell-and-tube heat exchanger during on-peak periods to improve the inlet temperature of evaporator. The performance of heat pump thus will be improved and the economic outcome will be better through the on-peak/off-peak price scheme.

2. Methodology

In this work, the techno-economic performance evaluation of integrated LHTES and heat pump system was conducted with MATLAB (R2022b) and COMSOL (6.0) as follows: (1) the heating demand and heat pump supply were matched based on a typical heat pump heating system; (2) a novel layout of LHTES and heat pump system was proposed; (3) a cylindrical LHTES component was designed with spherical encapsulated PCM; (4) the techno-economic performance of this integrated system was assessed.

2.1. Heat pump heating system

A typical heat pump heating system in serial configuration is shown in Figure 2. The air source heat pump (ASHP) is connected to a hydronic radiator, which is the most common combination for space heating due to its simple operation and low maintenance cost [37,38]. The evaporator absorbs heat from ambient air, and evaporates the refrigerant. After being compressed in the compressor, the high-temperature refrigerant transfers heat to water in the condenser. The end users are assimilated into one hydronic radiator as shown

in Figure 2. The heated water is pumped to demand-side radiator with the supply temperature (T_{su}) for the indoor space heating. The water is forwarded to condenser at the radiator return temperature (T_{re}). The supplementary electric heater is used to cover the heating gap between heat pump supply and user demand.

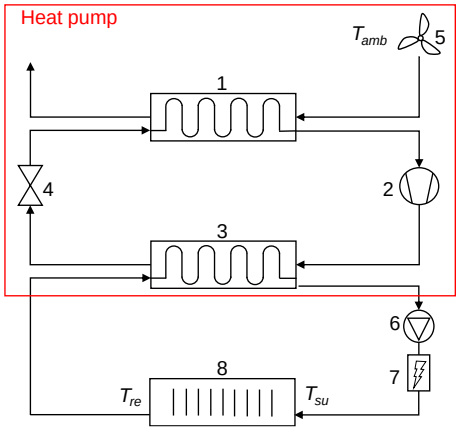

1. evaporator; 2. compressor; 3. condenser; 4. throttle valve; 5. fan; 6. pump; 7. supplementary electric heater; 8. hydronic radiator.

Figure 2. Typical heat pump heating system.

A Multi-family building with heated area of 1420 m^2 built before the 1960's [39] is considered. The calculation parameters of the retrofitted building are listed in Table 1. The total UA-value includes the heat transfer through building envelope and ventilation losses. The indoor comfort temperature was set at 20 °C during the heating season [40]. The heating demand is 51.8 kW at designed outdoor temperature (*DOT*) of -16 °C according to Eq. (1). The heating demand of the multi-family building at ambient temperature is calculated with Eq. (2).

$$q_{bd,DOT} = UA_{bd} \cdot (T_{ind} - DOT) \quad (1)$$

$$q_{bd} = UA_{bd} \cdot (T_{ind} - T_{amb}) \quad (2)$$

Table 1. Calculation parameters of the general retrofit multi-family building [39].

Parameters	Units	Value
UA-value by transmission (including roof, wall, floor, window, door and thermal bridge)	W/K	824
UA-value by ventilation	W/K	616
Total UA-value of building, UA_{bd}	W/K	1440

Based on logarithmic mean temperature difference (LMTD) method, the heating capacities of radiator at DOT and ambient temperature were given by Eq. (3)-Eq. (6). The radiator exponent (*n*) due to non-linear heat transfer [37] is 1.25 in this study.

$$q_{rad,DOT} = UA_{rad} \cdot LMTD^{n}_{rad,DOT} \quad (3)$$

$$LMTD_{rad,DOT} = (T_{su} - T_{re}) / \ln\left[(T_{su} - DOT)/(T_{re} - DOT)\right] \quad (4)$$

$$q_{rad} = UA_{rad} \cdot LMTD^{n}_{rad} \quad (5)$$

$$LMTD_{rad} = (T_{su} - T_{re}) / \ln\left[(T_{su} - T_{amb})/(T_{re} - T_{amb})\right] \quad (6)$$

The hydronic radiator heating system was designed with constant water flow rate ($\dot{V}_{rad}$). The supply temperature and return temperature are commonly 55 °C/45 °C ($T_{su,DOT}$ / $T_{re,DOT}$) at DOT [41]. The heating capacity of water through radiator can be calculated with thermodynamic parameters by Eq. (7) and Eq. (8).

$$q_{hs} = \dot{V}_{rad} \cdot \rho_w \cdot c_{p,w} \cdot (T_{su,DOT} - T_{re,DOT}) \quad (7)$$

$$q_{hs} = \dot{V}_{rad} \cdot \rho_w \cdot c_{p,w} \cdot (T_{su} - T_{re}) \quad (8)$$

Fehrm and Hallén proposed a curve-fitting model for the ambient air temperature [37]. The duration curve for Stockholm condition with annual average temperature of 8.2 °C [42] is presented in Figure 3. The hours through a year at a certain temperature (bin hours) is accounted for the discrete temperatures in Figure 3. November with monthly average ambient temperature of 3 °C (T_{amb}) [43] was selected for the assessment, which can cover around 50% hours when the heating seasons starts at the temperature below 10 °C.

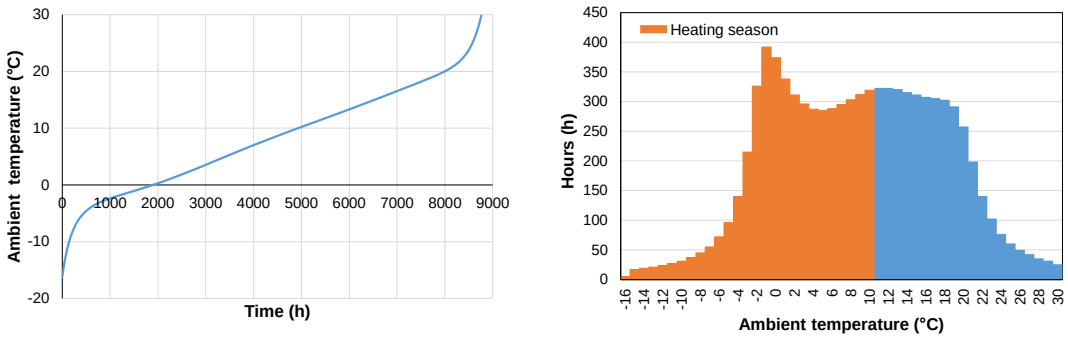

(a) *(b)*

Figure 3. Ambient temperature through a year and bin hours in Stockholm: (a) Duration temperature curve for Stockholm; (b) bin hours in Stockholm.

The heat pump system was assumed as quasi-steady state. Based on energy balance, the heating demand of building, heating capacity of radiator and heat capacity of water are equal [20,37]. The parameters of the heat pump heating system were calculated with Eq. (1)-Eq. (8). The results are exhibited in Table 2.

Table 2. Parameters of heat pump heating system.

Parameters	Units	Value
Heating demand, q_{bd}	kW	24.5
Volume flow rate, $\dot{V}_{rad}$	m³/h	4.52
Supply temperature, T_{su}	°C	38.8
Return temperature, T_{re}	°C	34.1

2.2. Integrated system

A novel layout of integrated system is proposed in this paper. LTHES with auxiliary heat exchanger and pump are introduced in a typical heat pump heating system acting as the heat source during off-peak hours. The schematic of the integrated system is shown in Figure 4.

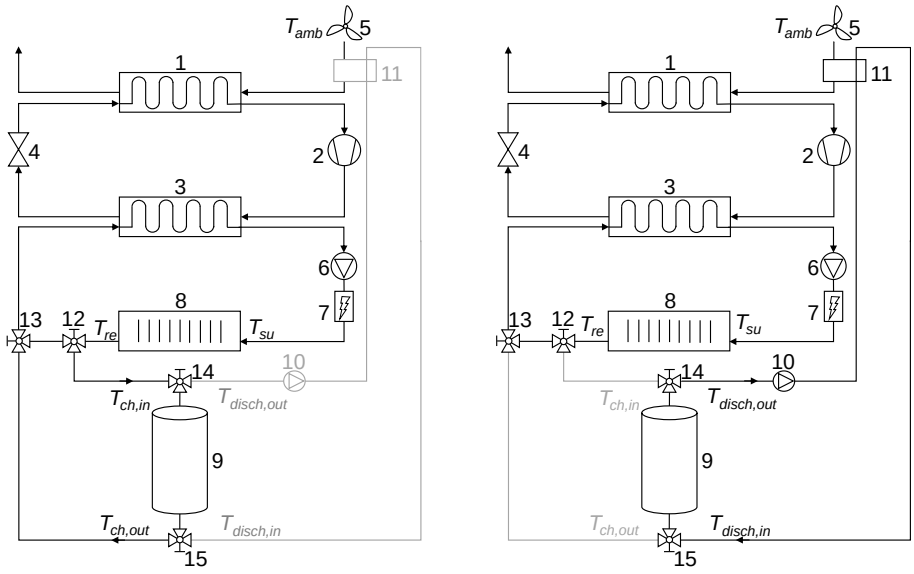

(a) *(b)*

1. evaporator; 2. compressor; 3. condenser; 4. throttle valve; 5. fan; 6. pump; 7. supplementary electric heater; 8. hydronic radiator; 9. latent heat thermal energy storage component; 10. pump; 11. heat exchanger; 12-15: three-way valve.

Figure 4. A LHTES component integrated HP system: (a) charging mode, (b) discharging mode.

The LHTES component is placed inside the building and connected to the return line of the radiator. The charging and discharging processes are controlled based on the off-peak and on-peak periods, as shown in Figure 5. The off-peak is from 00:00 to 7:00 (exclusive) and from 21:00 to 24:00 (exclusive). The on-peak is

from 16:00 to 20:00 (exclusive). When the electricity price is in the off-peak periods, the three ports of three-way valve 12 are all open and a proportion (pro) of the return water as heat transfer fluid (HTF) flows into the LHTES component from the top to charge the storage. The water after the heat release flows out from the bottom and merges into the remaining return water at the position of three-way valve 13. The flow then enters the condenser. When the LHTES is fully charged, the valve controlling the flow into the LHTES closes. When the electricity price is at the on-peak periods, the discharging process of LHTES starts, also using water as HTF. The HTF flows into the LHTES from the bottom and is heated by the PCM. After absorbing heat, HTF flows out from the top. In this study, a shell-and-tube heat exchanger with counter flow was selected. The ambient air used as the heat source to the heat pump discharges heat from HTF resulting in a rise in temperature, hence an increase in COP. After that, the cooled HTF flows back to the LHTES.

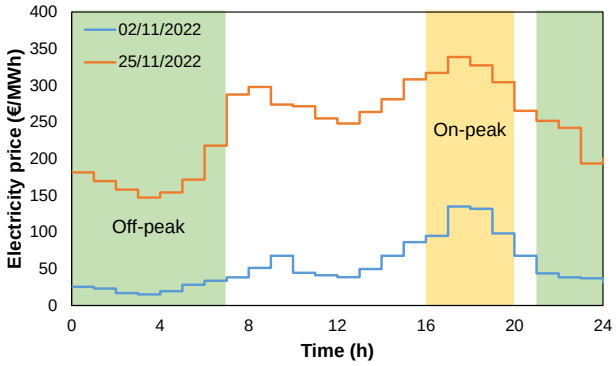

Figure 5. Off-peak and on-peak based on hourly electricity trading price.

2.3. LHTES component

Based on the optimal return temperature of the radiator, ATP 28 organic material was selected as the PCM. The thermophysical properties of ATP 28 are listed in Table 3.

Table 3. Thermophysical properties of PCM [44].

Parameters	Units	Value
Melting temperature	°C	27~29
Solidification temperature	°C	26~28
Latent heat (charging/discharging)	kJ/kg	220/225
Specific heat capacity	kJ/(kg·K)	2
Thermal conductivity	W/(m·K)	0.2
Liquid density (solid/liquid)	kg/m^3	864*/760

*calculated from the volume expansion

Height-to-diameter ratio (H/D) is a crucial parameter in designing a thermal energy storage tank. The increase of H/D can improve the charging and discharging efficiency and reduce the occupied area, while it also results in increased weight and cost of the tank, and in increased heat loss [45–47]. Considering the charging/discharging time and required heat capacity, the H/D was set as 1.7 with inner diameter of 0.6 m. A 2D axis-symmetrical model was built to simulate the thermal processes of LHTES, shown in Figure 6.

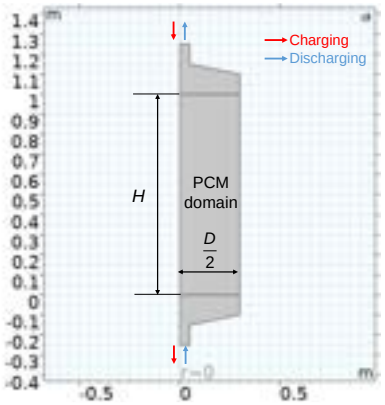

Figure 6. The 2D model of packed bed storage tank.

Spherical encapsulated PCMs, which are easier to maintain [48], were placed in the packed bed tank. The melting and solidification processes of the 2D model were simulated with the following simplifying assumptions:

(1) incompressible flow of water; (2) homogenous and isotropic PCM; (3) neglected density difference of PCM in phase and liquid phases; (4) heat loss coefficient (h_{loss}) of 5 W/(m^2·K) from outside shell to surrounding air [49]. The main parameters used in the simulation are displayed in Table 4. The thermophysical properties of Aluminum for outside shell and Water for HTF were taken from the Material Library in COMSOL [50]. The heat convective coefficient (h_{sf}) between water and PCM was calculated with Eq. (9) [51].

$$h_{sf} = \left[d_{pe} / \left(k_f \mathrm{Nu} \right) + d_{pe} / \left(10 k_s \right) \right]^{-1} \tag{9}$$

Table 4. Parameters of LHTES component.

Parameters	Units	Value	Reference
Height/diameter of PCM domain	m	1/0.3	
Porosity of PCM domain	-	0.4	
Diameter of PCM encapsulation	mm	50	
Quantity of PCM encapsulation	-	324	
PCM weight	kg	138	
Shell material	-	Aluminum	
Specific heat capacity of shell	kJ/(kg·K)	900	[50]
Thermal conductivity of shell	W/(m·K)	238	[50]
Shell density	kg/m^3	2700	[50]
Shell thickness	mm	3	
Shell weight	kg	20	

The charging and discharging thermal power of LHTES component was calculated from the temperature difference of HTF from inlet and outlet, as shown in Eq. (10) and Eq. (11). The stored or released thermal energy in the LHTES component were obtained with Eq. (12) and Eq. (13).

$$q_{ch} = \dot{m}_{ch} c_{pf} \left(T_{ch,in} - T_{ch,out} \right) \tag{10}$$

$$q_{disch} = \dot{m}_{disch} c_{pf} \left(T_{disch,out} - T_{disch,in} \right) \tag{11}$$

$$Q_{ch} = \int_0^t q_{ch} \mathrm{d}t \tag{12}$$

$$Q_{disch} = \int_0^t q_{disch} \mathrm{d}t \tag{13}$$

Firstly, the charging process were computed in COMSOL with different inflow rate proportion. Considering the melting and solidification temperatures, the initial temperature in this model was set as 24 °C, which is the end temperature of discharging process. Different meshing methods with mesh elements of 2244, 4134, 6747 were compared and the difference in the calculation results can be ignored. The curves of accumulated thermal energy during charging process with inflow rate proportion of 0.2, 0.3 and 0.5 are exhibited in Figure 7. In this study, the inflow rate was selected as 30% of radiator return water and the complete melting time was 4.4 hours.

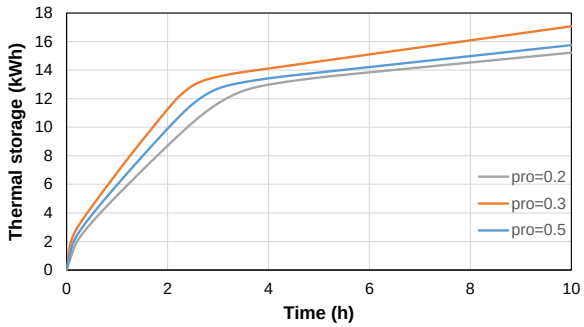

Figure 7. Accumulated thermal storage with different inflow rate.

The mass flow rate of discharging process was set as the same with charging process. The discharging process is related to the outside heat exchanger, which is explained in Section 2.4. With the cooling effect of the heat exchanger, the inlet temperature is variable during the charging process.

2.4. Heat exchanger

The shell-and-tube heat exchanger with one-pass shell was designed, totally 14 tubes with diameter of 0.04 m and height of 1 m. Water flows in the tubes, and air flows counter-currently between the shell and tubes. The material and thickness of shell and tubes are Aluminum and 3 mm, respectively. The heat transfer coefficient (U_{hex}) of the shell-and-tube heat exchanger was set as 500 W/(m^2·K) [52].

The heat capacity of heat exchanger is calculated with Eq. (14). According to ε-NTU method (effectiveness-number of transfer units) [53], the maximum heat transfer rate between water and air is given in Eq. (15), where $C_{\min}$ is the minimum of C_{disch} and C_{air}. The value of C_{air} was determined by comparison of commercial pumps. The thermal capacity ratio (Cr) and NTU is calculated with Eq. (16) and Eq. (17). For counter-current flow, the effectiveness is obtained with Eq. (18).

$$q_{hex} = C_{disch}(T_{disch,out} - T_{disch,in}) = C_{air}(T_{air,out} - T_{amb}) \quad (14)$$

$$q_{\max} = C_{\min}(T_{disch,out} - T_{amb}) \quad (15)$$

$$Cr = C_{\min} / C_{\max} \quad (16)$$

$$NTU = U_{hex} A / C_{\min} \quad (17)$$

$$\varepsilon = q_{actual} / q_{\max} = \left\lfloor 1 - e^{-NTU(1-Cr)} \right\rfloor / \left\lfloor 1 - Cr \cdot e^{-NTU(1-Cr)} \right\rfloor \quad (18)$$

Through the Eq. (14)-Eq. (18), $T_{disch,in}$ and $T_{air,out}$ can be obtained by overall analysis of the heat exchanger. It is assumed that the inlet temperature of LHTES is cooled down under the influence of average actual heat transfer rate.

2.5. Performance evaluation

The rated heat capacity of heat pump was designed to cover 60% of the required heat demand at DOT, which covers around 90% of the annual heating demand [41]. The COP of heat pump is the ratio of heat pump capacity to the compressor power input, as shown in Eq. (19). In this study, COP was assessed with the ambient temperature based on commercial heat pump data.

$$COP = q_{hp} / P_{comp} \quad (19)$$

The electrical appliances in this system includes a compressor, two pumps, a fan and a supplementary electrical heater. The extra power of electrical appliances is shown in Eq. (20).

$$\Delta P_{tot} = \Delta P_{comp} + \Delta P_{pump} + \Delta P_{fan} + \Delta P_{elect} \quad (20)$$

The levelized cost of energy is calculated with Eq. (18) [54].

$$LCOE = \left\{ \sum_{t=1}^{N} \left[(CAPEX_t + OPEX_t) / (1+i)^t \right] \right\} / \left\{ \sum_{t=1}^{N} \left[E_t / (1+i)^t \right] \right\} \quad (21)$$

The compressor, fan and pump 6 in Figure 4 are assumed to be the same in the typical system and in the integrated system due to their abilities to be adjusted within a certain operating range. The extra capital cost (CAPEX) in integrated system is LHTES component (PCM and tank), heat exchanger and pump 10, as exhibited in Table 5.

Table 5. Extra capital costs of integrated system.

Components	PCM	Tank of LHTES	Heat exchanger	Pump 10	Total
Price (€)	509	467	187	334	1498

3. Results and discussions

3.1. Techno-analysis

The total heat pump capacity of integrated LHTES and HP system and typical system is displayed in Figure 8 for November 2022. The heat pump capacity is fluctuating in the integrated system. The capacity above the typical system curve is due to the charging of the LHTES component during off-peak periods. More energy is required from heat pump side. The capacity below the typical system curve is the process by which LHTES releases heat to preheat inlet air as heat source of the heat pump. The warmer air into the evaporator with higher temperature contributes to COP increase, which leads to the decrease of heat pump electric power demand, reducing thus the electricity cost and allowing peak/load shifts alleviating thus the electricity grid supply.

During the on-peak periods in the integrated system, the warmer air temperature rises to 5.9 °C~8.9 °C, leading to the increase in COP between 3.74 and 3.91 compared to 3.56 for the typical system. The amount of the shifted electricity from on-peak to off-peak periods is 25.6 kWh.

3.2. Economic-analysis

The heating costs including electricity trading price, tax, transmission fee and value-added tax [20] are presented in Figure 9. As it can be seen in Figure 9 (b), the hourly heating costs of integrated system are lower than the typical system during on-peak periods, while the heating costs increase during the off-peak periods with higher heat pump electricity input for charging. The peak/load shifting scheme can potentially compensate for the increased heating costs. From the view of whole November, the monthly accumulated heating costs in the integrated system are 0.8% higher than in the typical system.

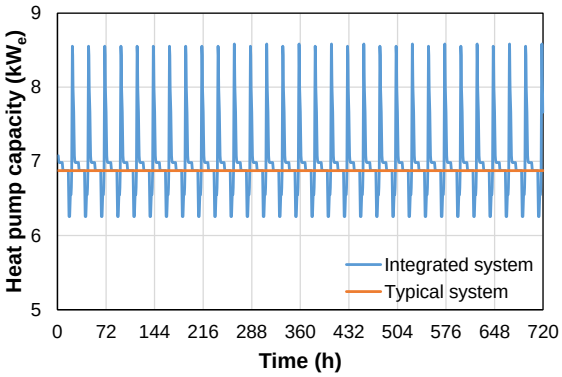

Figure 8. Total heat pump capacity.

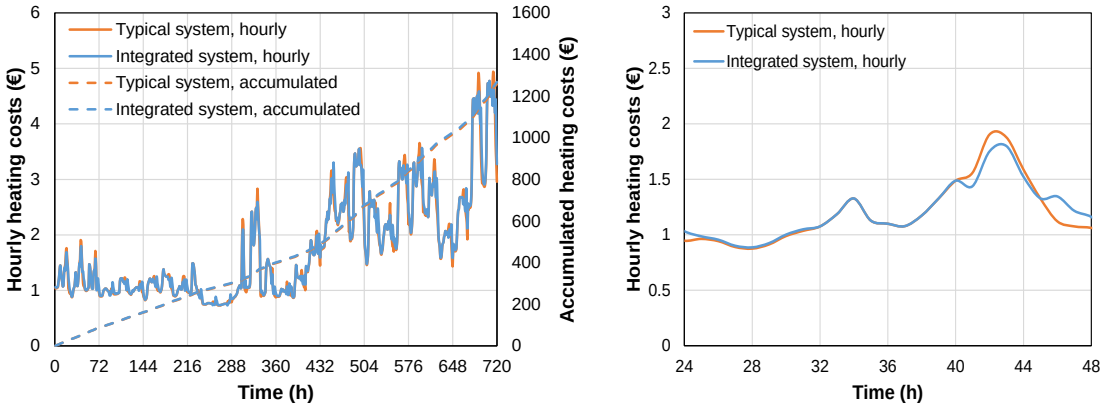

(a) *(b)*

Figure 9. Heating costs: (a) in November 2022; (b) on Nov 2, 2022.

In case the relationship between average electricity trading prices during on-peak and off-peak periods is $\overline{RP}_{onpeak} > 2.35 * \overline{PR}_{offpeak} + 85$ €/MWh in November 2022, the reduced heating cost will overweight the increased cost in integrated system and will breakeven the investment. In addition, the alleviated peak/load shifting allows the reduction of the power plants and electricity grid expansion costs.

Assuming the life periods of the integrated system is 15 years and the discount rate at 10%, with heating months from September to April in Stockholm, the LCOE leads to 0.072 €/kWh.

4. Conclusions

This paper proposed a novel layout of LHTES component integrated to the return line of radiator in a heat pump heating system. The heating demand of a typical multi-family building was calculated. A packed bed cylindrical LHTES component was simulated in an axisymmetric 2D model with spherical encapsulated PCM. The LHTES component was connected to a shell-and-tube heat exchanger as a heat source for the evaporator. The results show that the LHTES needs higher thermal power input in charging, while the heat pump capacity is intrinsically lower during on-peak periods. This study needs further studies including the other months of the year with detailed LHTES and heat exchanger design. The LCOE can be further reduced from optimal tank sizing, heat storage materials selection and enhanced heat exchanger design.

Acknowledgments

Lianying Shan would like to appreciate the China Scholarship Council (CSC) and the Karl Engver's foundation for PhD financing.

Appendix A

Nomenclature

A	area, m^2
c	specific heat capacity, J/(kg·K)

C	heat capacity rate, J/(K·s)
Cr	heat capacity ratio
$CAPEX$	capital expense, SEK
$OPEX$	operating expense, SEK
COP	coefficient of performance
E	annual generated energy
d	diameter of PCM encapsulation, m
DOT	designed outdoor temperature, K
h	heat convective coefficient, W/(m^2·K)
H / D	height to diameter ratio
k	thermal conductivity, W/(m·K)
$LMTD$	logarithmic mean temperature difference, K
$\dot{m}$	volume flow rate, kg/s
n	radiator exponent
N	year N
Nu	Nusselt number
P	power, W
$\overline{PR}_{onpeak}$	average electricity trading price during on-peak periods, €/MWh
$\overline{PR}_{offpeak}$	average electricity trading price during off-peak periods, €/MWh
pro	proportion of water from radiator return water into LHTES
q	thermal power, W
Q	thermal heat, J
r	discount rate
t	time/year
T	temperature, K
$\mathbf{u}$	velocity field
U	overall heat transfer coefficient, W/(m^2·K)
UA_{bd}	UA-value of building, W/K
UA_{rad}	UA-value of radiator, W/K^n
$\dot{V}$	volume flow rate, m^3/s
Δ	Difference between typical heat pump heating system and novel integrated system

Greek symbols

ε	porosity of packed bed
ε	effectiveness
κ	permeability of packed bed, m^2
μ	viscosity, Pa·s
ρ	density, kg/m^3

Subscripts and superscripts

$actual$	actual value
air	air
amb	ambient
bd	multi-family building
ch	charging process
$comp$	compressor
$elect$	supplementary electrical heater
$disch$	discharging process

fan	fan
hex	heat exchanger
hs	heating system
in	inlet
ind	indoor
$loss$	heat loss
$\min$	minmum
out	outlet
p	pressure
pe	encapsulation of phase change material
$pump$	pump
rad	radiator
re	radiator return side
s	solid matrix (phase change material)
$shell$	shell of the LHTES component
f	fluid (water)
su	radiator supply side
w	water

Abbreviations

HP	heat pump
HTF	heat transfer fluid
LHTES	latent heat thermal energy storage
LCOE	levelized cost of energy
NTU	number of transfer units
PCM	phase change material

References

[1] United Nations. Paris agreement. Paris: 2015.

[2] British Petroleum. Energy Outlook 2020. 2020.

[3] Ministry of the Environment, Government offices of Sweden. Sweden's long-term strategy for reducing greenhouse gas emissions. 2020.

[4] The Swedish Energy Agency. Energy in Sweden 2022 An overview. 2022.

[5] Statistics Sweden. Nearly 5.1 million dwellings in Sweden 2022. https://www.scb.se/en/finding-statistics/statistics-by-subject-area/housing-construction-and-building/housing-construction-and-conversion/dwelling-stock/pong/statistical-news/dwelling-stock-december-31-2021/.

[6] La Fleur L. Energy renovation of multi-family buildings in Sweden: An evaluation of life cycle costs, indoor environment and primary energy use, and a comparison with constructing a new building. Linköping University, 2019.

[7] Ürge-Vorsatz D, Cabeza LF, Serrano S, Barreneche C, Petrichenko K. Heating and cooling energy trends and drivers in buildings. Renew Sustain Energy Rev 2015;41:85–98. https://doi.org/10.1016/j.rser.2014.08.039.

[8] Yu M, Li S, Zhang X, Zhao Y. Techno-economic analysis of air source heat pump combined with latent thermal energy storage applied for space heating in China. Appl Therm Eng 2021;185:116434. https://doi.org/10.1016/j.applthermaleng.2020.116434.

[9] Xu T, Gunasekara SN, Chiu JN, Palm B, Sawalha S. Thermal behavior of a sodium acetate trihydrate-based PCM: T-history and full-scale tests. Appl Energy 2020;261:114432. https://doi.org/10.1016/j.apenergy.2019.114432.

[10] Olympios A V., Sapin P, Freeman J, Olkis C, Markides CN. Operational optimisation of an air-source heat pump system with thermal energy storage for domestic applications. Energy Convers Manag 2022;273:116426. https://doi.org/10.1016/j.enconman.2022.116426.

[11] Jin X, Zheng S, Huang G, CK Lai A. Energy and economic performance of the heat pump integrated with latent heat thermal energy storage for peak demand shifting. Appl Therm Eng 2023;218:119337.

https://doi.org/10.1016/j.applthermaleng.2022.119337.

[12] Nowak T. Heat Pumps: Integrating technologies to decarbonise heating and cooling. 2018.

[13] Fraga C, Hollmuller P, Schneider S, Lachal B. Heat pump systems for multifamily buildings: Potential and constraints of several heat sources for diverse building demands. Appl Energy 2018;225:1033–53. https://doi.org/10.1016/j.apenergy.2018.05.004.

[14] Sun S, Liu Z, Sun Y, Guo H, Gong M. Performance evaluation of a novel mixed-refrigerant recuperative heat pump with a large temperature lift for space heating. Appl Therm Eng 2023;221:119828. https://doi.org/10.1016/j.applthermaleng.2022.119828.

[15] Dongellini M, Abbenante M, Morini GL. A strategy for the optimal control logic of heat pump systems: impact on the energy consumptions of a residential building. 12th IEA Heat Pump Conf 2017 2017.

[16] Blázquez CS, Nieto IM, García JC, García PC, Martín AF, González-Aguilera D. Comparative Analysis of Ground Source and Air Source Heat Pump Systems under Different Conditions and Scenarios. Energies 2023;16:1289. https://doi.org/10.3390/en16031289.

[17] Lämmle M, Bongs C, Wapler J, Günther D, Hess S, Kropp M, et al. Performance of air and ground source heat pumps retrofitted to radiator heating systems and measures to reduce space heating temperatures in existing buildings. Energy 2022;242. https://doi.org/10.1016/j.energy.2021.122952.

[18] Park M, Eom YH, Kim MS. Predictive optimization of the air flow rate for a residential heat pump in seasonal performance conditions. Int J Refrig 2021;131:51–60. https://doi.org/10.1016/j.ijrefrig.2021.07.008.

[19] British Petroleum. Energy Outlook 2023. 2023.

[20] Xu T, Humire EN, Chiu JN, Sawalha S. Latent heat storage integration into heat pump based heating systems for energy-efficient load shifting. Energy Convers Manag 2021;236:114042. https://doi.org/10.1016/j.enconman.2021.114042.

[21] Ermel C, Bianchi MVA, Cardoso AP, Schneider PS. Thermal storage integrated into air-source heat pumps to leverage building electrification: A systematic literature review. Appl Therm Eng 2022;215:118975. https://doi.org/10.1016/j.applthermaleng.2022.118975.

[22] Alva G, Lin Y, Fang G. An overview of thermal energy storage systems. Energy 2018;144:341–78. https://doi.org/10.1016/j.energy.2017.12.037.

[23] Kapsalis V, Karamanis D. Solar thermal energy storage and heat pumps with phase change materials. Appl Therm Eng 2016;99:1212–24. https://doi.org/10.1016/j.applthermaleng.2016.01.071.

[24] Fan LW, Zhu ZQ, Xiao SL, Liu MJ, Lu H, Zeng Y, et al. An experimental and numerical investigation of constrained melting heat transfer of a phase change material in a circumferentially finned spherical capsule for thermal energy storage. Appl Therm Eng 2016;100:1063–75. https://doi.org/10.1016/j.applthermaleng.2016.02.125.

[25] Abdi A, Shahrooz M, Chiu JN, Martin V. Experimental investigation of solidification and melting in a vertically finned cavity. Appl Therm Eng 2021;198:117459. https://doi.org/10.1016/j.applthermaleng.2021.117459.

[26] Bédécarrats JP, Castaing-Lasvignottes J, Strub F, Dumas JP. Study of a phase change energy storage using spherical capsules. Part I: Experimental results. Energy Convers Manag 2009;50:2527–36. https://doi.org/10.1016/j.enconman.2009.06.004.

[27] Zauner C, Hengstberger F, Mörzinger B, Hofmann R, Walter H. Experimental characterization and simulation of a hybrid sensible-latent heat storage. Appl Energy 2017;189:506–19. https://doi.org/10.1016/j.apenergy.2016.12.079.

[28] Tian Y, Zhao CY. A numerical investigation of heat transfer in phase change materials (PCMs) embedded in porous metals. Energy 2011;36:5539–46. https://doi.org/10.1016/j.energy.2011.07.019.

[29] Pardiñas Á, Alonso MJ, Diz R, Kvalsvik KH, Fernández-Seara J. State-of-the-art for the use of phase-change materials in tanks coupled with heat pumps. Energy Build 2017;140:28–41. https://doi.org/10.1016/j.enbuild.2017.01.061.

[30] Nord Pool. Market Data n.d. https://www.nordpoolgroup.com/.

[31] Lin Y, Fan Y, Yu M, Jiang L, Zhang X. Performance investigation on an air source heat pump system with latent heat thermal energy storage. Energy 2022;239:121898. https://doi.org/10.1016/j.energy.2021.121898.

[32] Xu T, Chiu JN, Palm B, Sawalha S. Experimental investigation on cylindrically macro-encapsulated latent heat storage for space heating applications. Energy Convers Manag 2019;182:166–77. https://doi.org/10.1016/j.enconman.2018.12.056.

[33] Xu T, Humire EN, Chiu JNW, Sawalha S. Numerical thermal performance investigation of a latent heat storage prototype toward effective use in residential heating systems. Appl Energy 2020;278:115631.

https://doi.org/10.1016/j.apenergy.2020.115631.

[34] Zhang D, Fang C, Qin X, Li H, Liu H, Wu X. Performance study of transcritical CO2 heat pump integrated with ejector and latent thermal energy storage for space heating. Energy Convers Manag 2022;268:115979. https://doi.org/10.1016/j.enconman.2022.115979.

[35] Calame N, Freyre A, Rognon F, Callegari S, Rüetschi M. Air to water heat pumps for heating system retrofit in urban areas: Understanding the multi-faceted challenge. J Phys Conf Ser 2019;1343. https://doi.org/10.1088/1742-6596/1343/1/012079.

[36] IEA HPT. The next step in the green revolution: Heat pumps in multi-family buildings. Heat Pump Technol Mag n.d.;35:40–9.

[37] Karlsson F. Capacity Control of Residential Heat Pump Heating Systems. Chalmers University of Technology, 2007.

[38] Gaur AS, Fitiwi DZ, Curtis J. Heat pumps and our low-carbon future: A comprehensive review. Energy Res Soc Sci 2021;71:101764. https://doi.org/10.1016/j.erss.2020.101764.

[39] TABULA. TABULA WebTool n.d. https://webtool.building-typology.eu/#bm.

[40] Teli D, Psomas T, Langer S, Trüschel A, Dalenbäck JO. Drivers of winter indoor temperatures in Swedish dwellings: Investigating the tails of the distribution. Build Environ 2021;202. https://doi.org/10.1016/j.buildenv.2021.108018.

[41] Karlsson F, Axell M, Fahlen P. Heat Pump Systems in Sweden - Country Report for IEA HPP Annex 28. Borås, Sweden: SP Swedish National Testing and Research Institute; 2003.

[42] Statista. Annual average temperature in Stockholm from 2006 to 2021 n.d. https://www.statista.com/statistics/744463/annual-average-temperatures-in-stockholm/.

[43] Weather Spark. Climate and Average Weather Year Round in Stockholm n.d. https://weatherspark.com/y/84156/Average-Weather-in-Stockholm-Sweden-Year-Round.

[44] AXIOTHERM. Axiotherm PCM-ATP28 n.d. https://www.axiotherm.de/en/produkte/axiotherm-pcm/.

[45] Agboola OO, Akinnuli BO, Kareem B, Akintunde MA. Decision on the selection of the best height-diameter ratio for the optimal design of 13,000 m3 oil storage tank. Cogent Eng 2020;7:0–17. https://doi.org/10.1080/23311916.2020.1770913.

[46] Zhu C, Zhang J, Wang Y, Deng Z, Shi P, Wu J, et al. Study on Thermal Performance of Single-Tank Thermal Energy Storage System with Thermocline in Solar Thermal Utilization. Appl Sci 2022;12. https://doi.org/10.3390/app12083908.

[47] Labidi M, Eynard J, Faugeroux O, Grieu S, Labidi M, Eynard J, et al. Optimal design and management of thermal storage tanks for multi-energy district boilers To cite this version : HAL Id : hal-01118538 OPTIMAL DESIGN AND MANAGEMENT OF THERMAL STORAGE TANKS FOR MULTI-ENERGY DISTRICT BOILERS 2015.

[48] Xu T. Integrating Latent Heat Storage into Residential Heating Systems A study from material and component characterization to system analysis. KTH Royal Institute of Technology, 2021.

[49] Engineering E, Edition T. Mechanical Engineering. Explor. Eng. 3rd editio, Elsevier; 2013. https://doi.org/10.1016/C2011-0-04445-9.

[50] COMSOL. Material Library n.d.

[51] COMSOL. Heat Transfer Module User's Guide 2015:1–222.

[52] ENGINEERS EDGE. Overall Heat Transfer Coefficients in Heat Exchangers n.d. https://www.engineersedge.com/heat_transfer/overall_heat_transfer_coefficients_13827.htm.

[53] Shah RK, Sekuli DP. Selection of Heat Exchangers and Their Components. 2007. https://doi.org/10.1002/9780470172605.ch10.

[54] Aldersey-Williams J, Rubert T. Levelised cost of energy – A theoretical justification and critical assessment. Energy Policy 2019;124:169–79. https://doi.org/10.1016/j.enpol.2018.10.004.

Efficiency analysis in the chemical loop process of base metals.

I.Marques-Valderrama[a], J. A Becerra[b], C. Ortiz[c], D. A Rodríguez Pastor[d] and R.Chacartegui[e]

[a] University of Seville, Seville, Spain, imarques2@us.es
[b] University of Seville, Seville, Spain, jabv@us.es
[c] University of Seville, Seville, Spain, cortiz7@us.es
[d] University of Seville, Seville, Spain, drodriguez4@us.es
[e] University of Seville, Seville, Spain, ricardoch@us.es

Abstract:

This work proposes a thermochemical storage system for Iron, aluminium, and nickel oxidation/reduction reactions. The chemical looping process based on the analysed reaction pairs will involve high energy efficiencies, given their high energy density (40-80 MJ/l) and the contribution of reducing agents such as hydrogen and carbon monoxide. The mix of these reductor agents is considered according to the Baur-Glassner diagram. In the charging process, it will make use of renewable energy sources (CSP+PV) to carry out the decomposition process (570°C or lower, depending on the number of stages in the reduction in the iron case). In the discharge phase (800°C depending on the metal and the particle radius), the reduced metal passes through a combustion chamber where it is oxidised, generating thermal energy useful for other processes, and obtaining metal oxides that will serve to close the proposed cycle. The temperatures required in the charge/discharge processes by the different metals have been studied, including an analysis of the energy integration of the different equipment and heat for processes. The simulations were carried out in the commercial software EES to evaluate the more suitable metals to obtain the reductant. a Round Trip Efficiency study has been carried out to evaluate the different TCES configurations.

Keywords:

Thermochemical storage, Chemical looping, Hydrogen, Energy integration, Round Trip Efficiency.

1. Introduction

Reducing dependence on carbon sources meeting the growing energy demand of society [1], is together with climate change one of the main challenges facing the world today [2]. One of the current lines of greatest development is energy storage. Have systems that take advantage of the surplus energy production offered by other facilities to be used later.Developing low-carbon energy carriers has become crucial for reducing dependence on fossil fuels in energy production and distribution. This, together with other fundamental aspects of decarbonization and the use of renewables, leads to the search for cost-efficient energy storage systems. Energy storage is crucial for a market with a high presence of renewable generation. To increase the availability of renewable generation and increase the inertia of the grid. One of the main advantages of energy storage is the possibility of designing renewable facilities of greater capacity, improving their inertia in the electricity grid [3]. Parameters for the competitiveness of renewable energies.

Different types of energy can be stored depending on the systems to which they are linked [4] and the form in which the energy is stored/released: chemical, electrical, magnetic, electrochemical, mechanical, and thermal storage systems [5]. The use of these systems supports installations to produce electricity.Metal oxides can be integrated as energy storage systems [6]. These materials have been studied from the electrical point of view, to be used directly in batteries. Recently, they have been studied as regenerative fuel sources [7], in reactors with metals as a fuel source, taking advantage of the thermal energy generated in the oxidation process [8]. It arises because of the high energy density of these materials, which require a lower fuel volume, availability, and regenerative capacity. The iron powder has been tested in the MP100 reactor developed by the University of Eindhoven [9]. There are possibilities for considering the use of a series of metals for this application. Based on the development of these reactors, it is feasible to create a thermochemical storage system based on metals, obtaining thermal energy from their oxidation. Regeneration of the reduced metal from different metal oxides can be obtained in elements such as nickel [10] or iron [9] from reducing agents such as Hydrogen or Carbon Monoxide [11]. Having identified the possibility of integration of these systems,

this work analyses different configurations of thermochemical storage systems, analysing their potential as energy storage systems [11] and their potential to advance in this line.

2. State of the art

2.1. Energy storage based on metals

Metals have high energy densities when compared to other types of fuels. The graph below shows the gravimetric energy density [MJ/kg] versus the volumetric energy density [MJ/L] of a wide range of fuels used today.

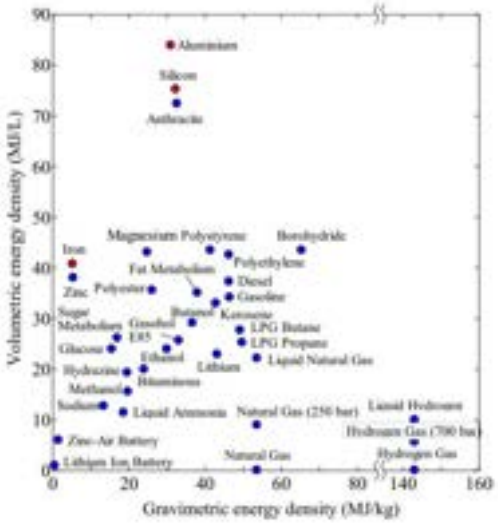

Figure. 1. Gravimetric energy density versus volumetric energy density of different fuels.[8]

Figure 1 shows a number of metals with high volumetric energy densities, like Iron, providing the opportunity of reducing the required volume for an energy design and smaller equipment if used in oxidation/combustion processes. Figure 1 shows the main metals studied. This study also will address the use of Nickel, that is not included in Figure 1 [8]. Their use in an energy storage system considers a closed chemical looping system, operating sequentially on loading and discharging stages, where the metal is oxidised and regenerated. The metals subjected to the oxidation/combustion process will form the discharge system. The metal oxides formed in the process will be stored in the loading system, from which the initial fuel will be regenerated from a reduction process [13]. Figure 2 shows a general operating scheme that has been proposed that will be used for assessing the use of different metals:

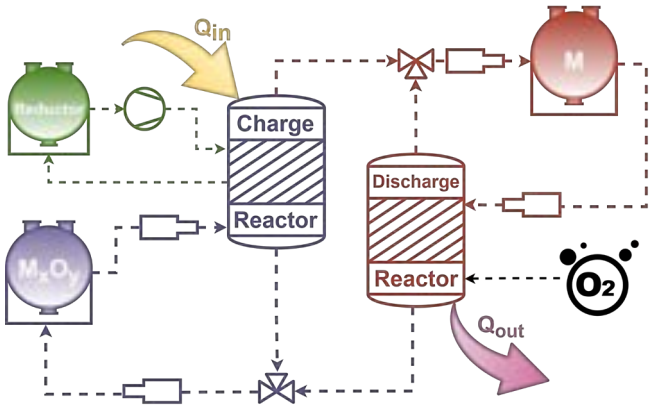

Figure. 2. General diagram of the storage system.

The cycle is divided into two main blocks/reactors:

- Charging system: Consists of two subsystems. The storage and management of metal oxide and the management of the reducer to reconvert the product of the discharge into fuel.
- Discharging system: Management of the storage and oxidation of the original fuel in the discharge reactor.

For the operation of the loading system, two possible reducers will be considered: carbon monoxide as a reductant as a product of synthesis gasification and hydrogen. This hydrogen can be produced within the gasification or by electrolysis powered by photovoltaic or wind energy. The selected metals to analyse the concept were Fe, Al, and Ni.

2.3. State diagrams

2.3. 1 Charging process

Departing with the charging process, integrating a metal oxide and a reducer generates a reduced metal. The reaction requires appropriate temperature and reaction conditions. In this work, Fe and Ni have been considered. To identify their behaviour and evolution under different conditions, their state diagrams graphs were modelled in the FactSage program for the following combinations of metals and reducers:

Table 1. Generated status diagrams.

Chart No.	Process	Elements evaluated
1	Reduction	$Fe – H_2 – H_2O$ $Fe – CO – CO_2$
2	Reduction	$Al – H_2 – H_2O$ $Al – CO – CO_2$
3	Reduction	$Ni – H_2 – H_2O$ $Ni – CO – CO_2$
4	Oxidation	$Fe – O_2$
5	Oxidation	$Al – O_2$
6	Oxidation	$Ni – O_2$

The elements were included using the FactPs and FToxid databases [12] These state diagrams provide guidelines about phase equilibria temperatures depending on the amount of oxidiser or reductant in the reactors. In this environment, metals, their oxides, oxygen, reducers, and their products are considered. These graphs provide the temperatures for reducing metal oxides as a function of the minimum metal fraction and the operating atmospheres of CO / CO_2 and H_2 / H_2O [13]. Different reduction processes of iron oxide are considered for the generation of DRI (Direct Reduced Iron) [14]. The Bauer-Glaessner diagram can be used to [10] compare the reducer's concentrations and process temperatures using Carbon Monoxide and Hydrogen [11]. The curves for the case of Aluminum and Nickel used in this study obtained using FactSage, are presented in Figure 3.

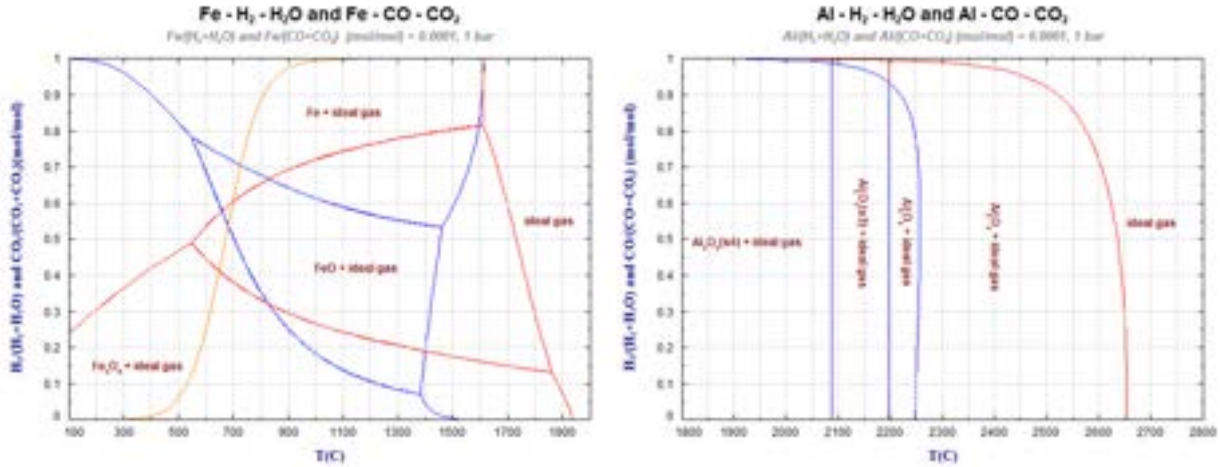

Figure. 3. Comparison of temperatures in the reduction of oxides of Iron and Aluminum.

2.2.3 Discharging process

The oxidation process is studied for the selected metals. The Figure 4 represents the equilibrium curves and metal concentration in all cases.

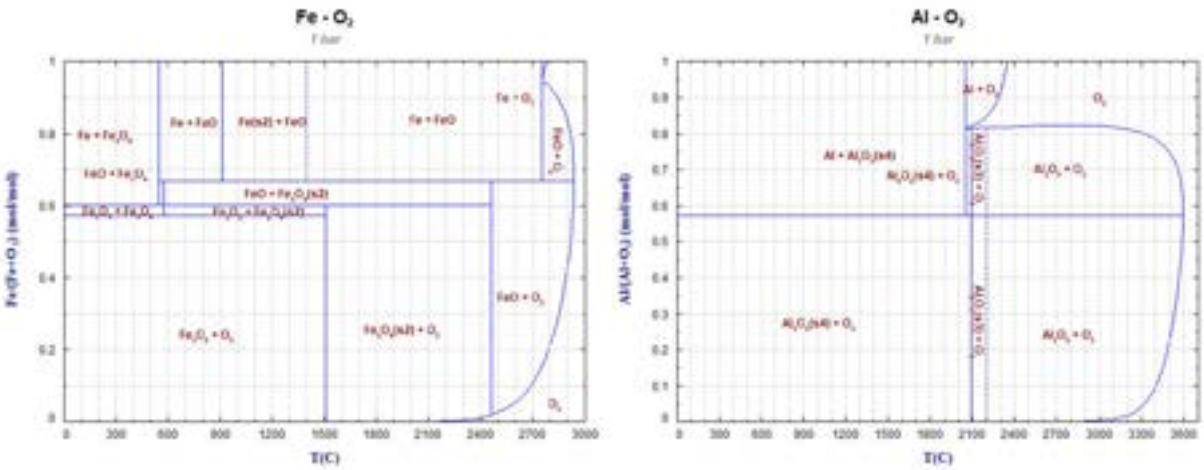

Figure. 4. Comparison of temperatures in the oxidation of Iron, Aluminum and Nickel.

The analysis of gigures 3 and 4 shows seen how in the case of Iron and Aluminum, different metal oxides can be obtained depending on the reaction temperature and the proportion of metal and oxidiser. On the other hand, it is also observed that in the reduction processes, depending on the metal chosen, a different amount of reducer is required if Hydrogen or Monoxide is chosen as a reducing agent.

2.3.4 Reducer mixtures

As can be seen in the case of Iron, reducer concentrations mark different equilibrium curves. For mixtures of CO and H_2, as in the case of syngases, the resulting equilibrium curve will be between the two represented in the diagram, in a phase diagram with intermediate states that depend on the concentration of the reducer mixture, Figure 5.

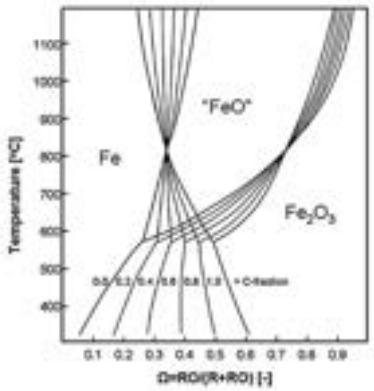

Figure. 5. Baur-Glaessner diagram for CO-H2 mixtures as reducing agent.[14]

It is observed how the equilibrium curves are distributed between the two extreme cases depending on the concentration of reducers in the mixture and the amount of monoxide present. Therefore, regarding the proposed charging system, cases have been studied in which only Hydrogen or Carbon Monoxide is available as a reducer agent. The reducer management schemes in both cases could be as presented in Figure 6:

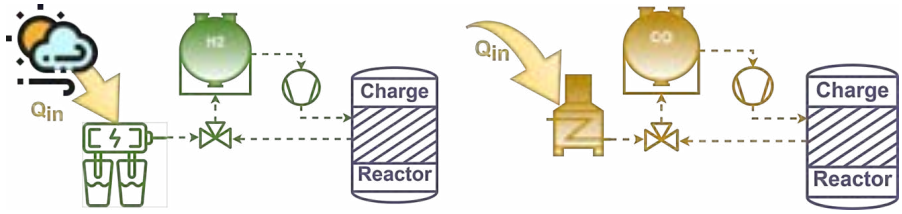

Figure. 6. Possible operating schemes for the reducing agent.

2.3.2 Activation energies

A relevant aspect is the activation energy of the reactions. It will penalise the available energy, both in the case of the charge and the discharge. The energy needed to activate the process will depend, among other factors, on the kinetics of each reaction. The dependencies of variables depend on each reaction. Accurate information can be obtained by measuring the concentrations through thermogravimetric analyses. Based on the experimental results of the specific results, methods such as Kissinger's are used [15] to determine the kinetic characteristics of the reaction. The activation energies of the following reactions are identified in the literature:

Table 2. Activation energies.

Reaction	Mechanism	Minimum [kJ/mol]	Maximum [kJ/mol]
$NiO(s) + H_2(g) \rightleftarrows Ni\,(s) + H_2O\,(g)$	Reduction	85 [16]	126 [16]
$Ni(s) + \frac{1}{2}\,O_2(g) \rightleftarrows NiO$	Oxidation	172,38 [17]	209,2 [17]
$3Fe(s) + 2O_2(g) \rightleftarrows Fe_3O_4(s)$ below 570°C	Oxidation	130 [18]	170 [18]
$3Fe_2O_3(s) + 4H_2(g) \rightleftarrows 2Fe_3O_4(s) + 4H_2O_{(g)}$	Reduction	89,1 [19]	282 [20]
$Fe_3O_4(s) + 4H_2(g) \rightleftarrows 3Fe(s) + 4H_2O_{(g)}$	Reduction	54,0 [19]	167 [21]
$2Fe(s) + \frac{3}{2}O_2(g) \rightleftarrows Fe_2O_3(s)$	Oxidation	110 [22]	
$Fe_3O_4(s) + H_2(g) \rightleftarrows 3FeO(s) + H_2O_{(g)}$	Reduction	47 [23]	
$FeO\,(s) + H_2(g) \rightleftarrows Fe\,(s) + H_2O_{(g)}$	Reduction	30 [23]	

To determine the power of the use of the metals selected for the described application, a theoretical Round-Trip Efficiency (RTE) [24] is defined [25]. It determines the energy recovery potential of the system at different operating temperatures, equation 1.

$$\eta_{RTE} = \frac{Q_{Av}}{Q_N} = \frac{\left|Q_{disc} + E_A^{Disch}\right|}{\left|Q_{ch} + E_A^{ch}\right|} \tag{1}$$

Where Q_{Av} refers to the energy per mole of fuel available in the discharge process. This is determined from the discharge energy per mole of fuel obtained, Q_{disc} minus the activation energy term needed to start the process E_A^{Disch}. The same reasoning is applied to the charging process, Q_N where Q_{ch} is the energy per mole of fuel necessary for the reduction of the metal oxides studied and refers to the term of activation energy necessary to start the charging process E_A^{ch}, Figure 7.

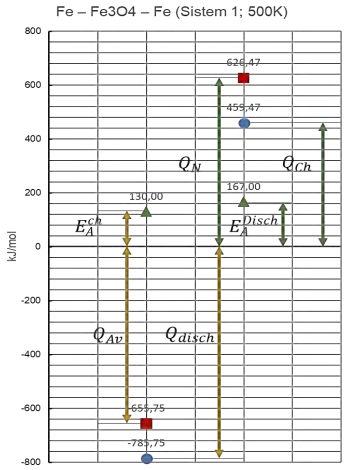

Figure. 7. Theoretical Round Trip Efficiency of Iron.

3. Results and discussion

3.1. Description of the system

Considering the layout in Figure 2, two sources have been taken to obtain the reducer. First, there is the possibility of using hydrogen from electrolysis. This process will be powered by a photovoltaic solar installation. On the other hand, the production of carbon monoxide through gasification from synthesis is proposed.

3.2. Calculation of properties

For the analysis of the different configurations, metals and potential metal oxides, a series of models have been implemented in OpenModelica [26], [27]. An OpenModelica library for the calculation of thermodynamic properties has been implemented based on Glenn coefficients[28], equations 2 to 4.

$$\frac{c_p^{\circ}(T)}{R} = a_1T^{-2} + a_2T^{-1} + a_3 + a_4T + a_5T^2 + a_6T^3 + a_7T^4 \tag{2}$$

$$\frac{h°(T)}{RT} = -a_1T^{-2} + a_2\frac{lnT}{T} + a_3 + a_4\frac{T}{2} + a_5\frac{T^2}{3} + a_6\frac{T^3}{4} + a_7\frac{T^4}{5} + b_1T^{-1} \tag{3}$$

$$\frac{s°(T)}{R} = -a_1\frac{T^{-2}}{2} - a_2T^{-1} + a_3 lnT + a_4T + a_5\frac{T^2}{2} + a_6\frac{T^3}{3} + a_7\frac{T^4}{2} + b_2 \quad (4)$$

Using the coefficients by intervals for each element/substance, the demands and energy released in the loading and unloading processes can be calculated [29]. The "Equilibrium" module included in FactSage has been used, as well as the [30] Chemical Equilibrium Applications (CEA), for the verification of the calculation of the properties[31], [28]. A second library was generated aimed at performing energy analysis of the charge/discharge processes where the enthalpies of the reaction and Gibbs free energy of all processes were calculated.

$$h_{reac} = \sum n_P \cdot \Delta h(T)_{,P} - \sum n_R \cdot \Delta h(T)_{,R} \quad (5)$$

$$g = \Delta h - T\Delta s \quad (6)$$

The reaction enthalpies were calculated based on the moles of metal in the reactors. In this way, the molar mass, the energy demand of the charging process, and the amount of energy of the discharge process produced per kilogram of metal can be calculated.

3.3. Discharging process

The processes modelled for the discharge of the thermochemical system are presented in Table 3

Table 3.- Discharge reactions considered.

$$2Fe(s) + O_2(g) \rightleftarrows 2FeO(s) \quad (6)$$

$$2Fe(s) + \frac{3}{2}O_2(g) \rightleftarrows Fe_2O_3(s) \quad (7)$$

$$3Fe(s) + 2O_2(g) \rightleftarrows Fe_3O_4(s) \quad (8)$$

$$2Al(s) + \frac{3}{2}O_2(g) \rightleftarrows Al_2O_3(s) \quad (9)$$

$$Ni(s) + \frac{1}{2}O_2(g) \rightleftarrows NiO \quad (10)$$

The models performed simultaneous calculations within a temperature range from 300K to 3600K. This range was selected based on the analysis of phase diagrams.

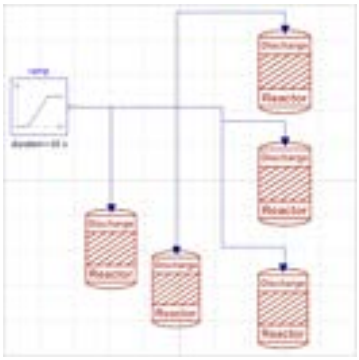

Figure 8.- OpenModelica graphical representation of reactor models.

Graph 4, 5 and 6 shows the enthalpy and Gibbs free energy curves for the different reactions resulting from the simulations.

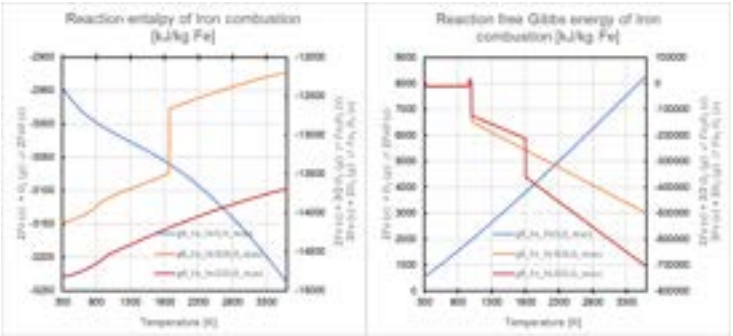

Graph1.- Enthalpy of reaction and Gibbs free energy for possible oxidation reactions of Iron.

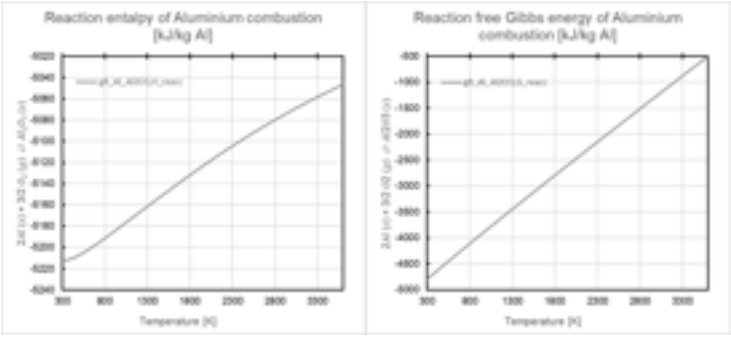

Graph2.- Enthalpy of reaction and Gibbs free energy for the oxidation of Aluminum.

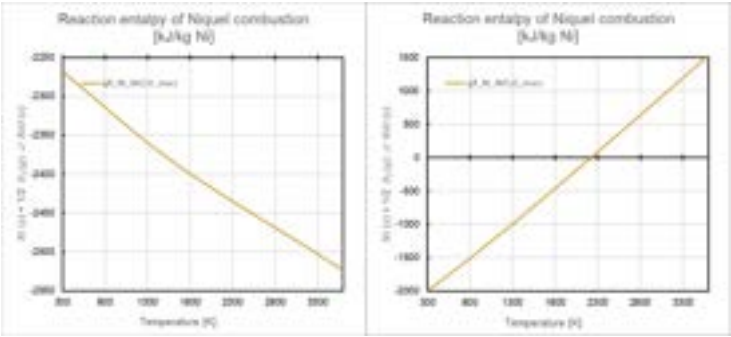

Graph3.- Enthalpy of reaction and Gibbs free energy for the oxidation of Nickel.

The variation of the power obtained per kilogram of fuel is observed in temperatures ranging from 300K to 3600K. They show the high energy potential of these metals as fuels in oxidising processes. On the other hand, within the oxidation reactions studied for the case of Iron, it is known according to literature that the majority product generated in the oxidation process can be Hematite or Magnetite depending on the conditions.

3.4. Charging processes

In the charging process the reactions evaluated are presented in Table 4:

Table 4.- Charge reactions considered.

$$3Fe_2O_3(s) + 4H_2(g) \rightleftarrows 2Fe_3O_4(s) + 4H_2O_{(g)}$$
$$Fe_3O_4(s) + H_2(g) \rightleftarrows 3FeO(s) + H_2O_{(g)} \quad (11)$$
$$FeO\ (s) + H_2(g) \rightleftarrows Fe\ (s) + H_2O_{(g)}$$

$$3Fe_2O_3(s) + CO(g) \rightleftarrows 2Fe_3O_4(s) + CO_2(g)$$
$$Fe_3O_4(s) + CO\ (g) \rightleftarrows 3FeO\ (s) + CO_2(g) \quad (12)$$
$$FeO\ (s) + CO\ (g) \rightleftarrows Fe\ (s) + CO_2(g)$$

$$Fe_3O_4(s) + 4H_2(g) \rightleftarrows 3Fe\ (s) + 4H_2O(g) \quad (13)$$
$$Fe_3O_4(s) + 4CO(g) \rightleftarrows 3Fe(s) + 4CO_2(g) \quad (14)$$
$$NiO(s) + H_2(g) \rightleftarrows Ni\ (s) + H_2O\ (g) \quad (15)$$
$$NiO(s) + CO(g) \rightleftarrows Ni\ (s) + CO_2\ (g) \quad (16)$$
$$Al_2O_3(s) + 3H_2(g) \rightleftarrows 2Al\ (s) + 3H_2O\ (g) \quad (17)$$
$$Al_2O_3(s) + 3CO(g) \rightleftarrows 2Al\ (s) + 3CO_2\ (g) \quad (18)$$

Two different paths have been identified for the reduction of Magnetite (Fe_3O_4),since if it is reduced to a temperature lower than 843K, the reduction occurs directly without passing through the state of Wüstite (FeO), as observed in Figure 3, It should also be noted within the initial scope of this study, Hydrogen, and Carbon Monoxide have been chosen as reductants, but the use of combinations of metals in the reduction process that requires a lower amount of energy in the process can be studied.

3.4.1. Reduction of F2O3 to Fe at temperatures above 843K

For temperatures above 570K the reduction of Hematite is done in three steps. First, it is reduced to Magnetite (Fe3O4). Subsequently, increasing the concentration of the reducer is passed from Magnetite to Wüstite (FeO). Finally, it is reduced to Iron. This 3-phase process has some interesting characteristics when compared

to the loading processes of systems with Nickel or Aluminum since, depending on the operating conditions, up to two exothermic phases can be achieved, corresponding to the reduction of Hematite and Wüstite.

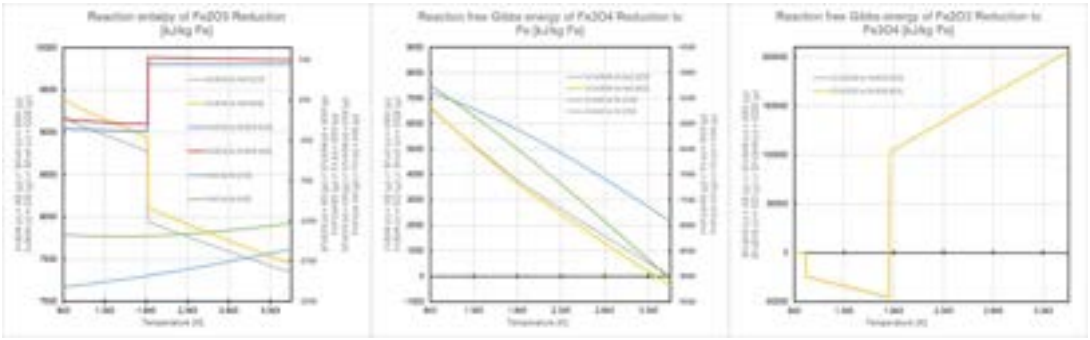

Graph4.- Enthalpy and Gibbs free energy for the reduction of Hematite to Iron at temperatures greater than 843K.

It is observed that, in the first step of the process, the reduction of Hematite to Magnetite is spontaneous between 843K and 1800K. From that temperature, the equilibrium between phases is not given[12]. On the other hand, in the overall balance of the reduction, having the same temperature for all phases, the following process demand is obtained depending on the operating temperature:

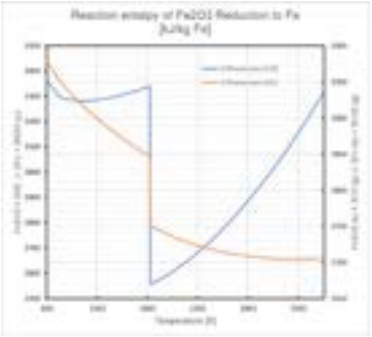

Graph5.- Total loading process in the reduction of Hematite at temperatures above 843K.

It is observed how this configuration offers a variety of configurations where lower demands can be obtained than those shown if adequate temperatures of reduction of Hematite and Wüstite are chosen. In the same way, this demand can be reduced according to the reducer chosen in each phase.

3.4.2. Reduction of F2O3 to Fe at temperatures below 843K

In this case, the reduction occurs directly from the Magnetite phase to Iron. Therefore, the charging system would have two phases. An initial phase in which the Hematite is reduced obtaining Magnetite, and a final phase in which the Magnetite is reduced directly to Iron. This system, as in the previous one, can be operated at different temperatures depending on the phase being studied, so the system can operate as follows:

- The first phase can occur at any temperature, provided that the product obtained is Magnetite.
- Once Magnetite is obtained as a product, it is passed to a temperature within the study range. Process heat will be obtained from the temperature reduction.
- When the temperature of the Magnetite is lower than the 843K that has been marked as a limit, the reduction to Iron is made.

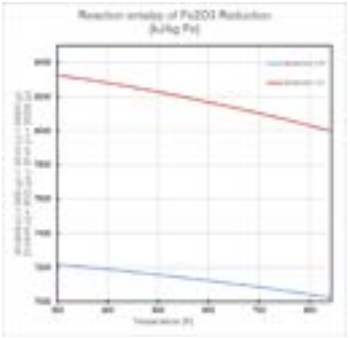

Graph 9.-6 Total loading process in the reduction of Hematite at temperatures below 843K.

3.4.2. Reduction from NiO to Ni

For this system of cages, the demand for the reduction process per kilogram of Nickel has been studied. In this case, as in the previous ones, the reduction has been compared using Hydrogen and Carbon Monoxide as reducers.

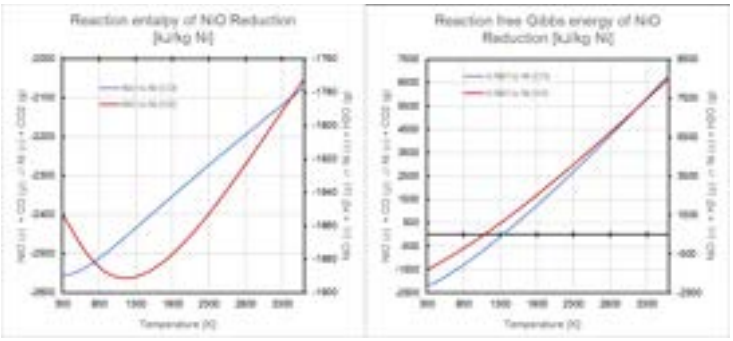

Graph7.- Enthalpy and Gibbs free energy in the reduction of NiO to Ni.

3.4.2. Reduction of Al2O3 to Al

In the charging system corresponding to obtaining reduced Aluminum, the same approach has been followed as in the case of nickel, making a temperature analysis with the two reducers chosen. Taking this into account, the demand for the reduction of 1kg of Aluminum would be as follows:

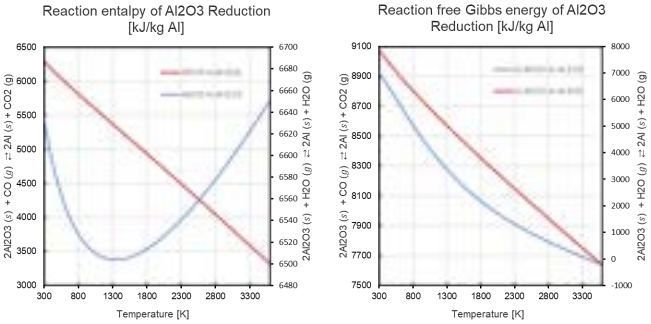

Graph8.- Enthalpy and Gibbs free energy in the reduction of Al2O3 to Al.

3.4. Energy Storage Layouts

The energy storage layouts and processes are presented following the layout presented in ***Figure 2,*** *with* different configurations depending on the metal used, and in the case of Iron, depending on the temperature of reduction of Magnetite Three different systems are proposed:

- System 1: In the case of working with Nickel or Aluminum.
- System 2: In the case of working with Iron and carrying out the reduction of Magnetite to a temperature below 873K. It will have two charge stages.
- System 3: For the case in which you work with Iron, the magnetite reduction process is carried out in 2 stages, forming Wüstite in phase 2.

The general operating schemes of the different configurations presented would be as follows:

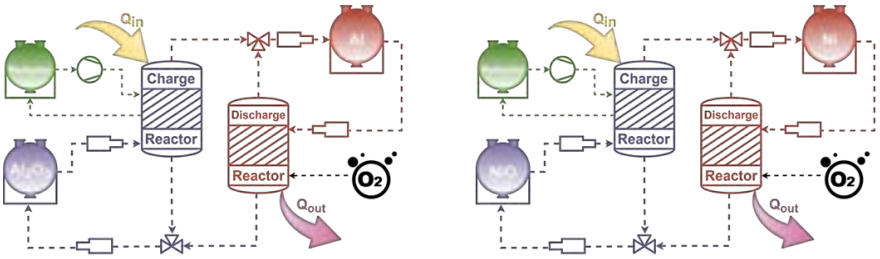

Figure 9.- Operating scheme type 1 charge / 1 discharge.

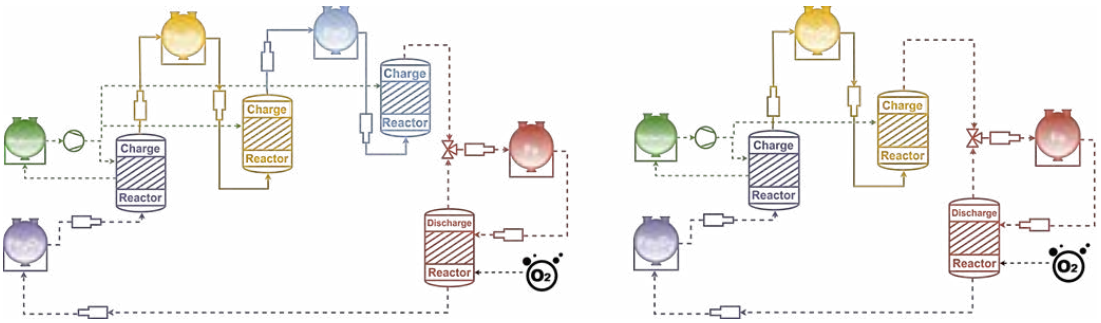

Figure 10.- Operating scheme type 1 charge / 2 discharges, and operating scheme (2 charges/ 1 discharge).

For the operating schemes in the case of Iron, the tanks defined as charge, in the case of the reduction of hematite will demand or offer energy to the system depending on the operating conditions that define the process.

3.5. Performance

This section makes ana preliminary study of the performance of the systems based on their Round-Trip Efficiencies. The same temperature has been considered for the charging and discharge processes, although any other could have been selected. The viability of the process and the RTE have a strong dependence on the reaction's evolution.

Table 5.-5 Results of RTE at different temperatures.

Temperature [K]	Metal	System	RTE	Notes
500	Fe	2	78,83%	Oxidation to Fe2O3, reduction by H2
800	Fe	3	78,92%	Oxidation to Fe2O3, reduction by H2
1100	Fe	3	87,89%	Oxidation to Fe2O3, reduction by H2

The description of the type of system in the table can be found in section 3.4.

Once the graphs relating to the selected metals have been presented, and an RTE has been proposed for iron-based systems (due to having a wider and more reliable amount of information in these reactions), it can be observed how for ranges between 500K and 1800K, the oxidation processes of the three metals studied have an energy potential that can range since 2.4 MJ/kg in the case of Nickel to 5 MJ/Kg in the case of Aluminum. These results have been obtained under the assumption of complete conversion. As presented in [7], it is also verified that the work of the discharge system in the range of the proposed temperatures is possible. On the charging process side, the amount of energy required and the possibility of performing the reduction depending on the mechanism employed. It is verified that there are cases in which the most favorable reducing agent (energetically) is carbon monoxide, where differences of up to 1MJ / Kg of reduced metal can be found compared to using hydrogen as a reducing agent. On the other hand, taking into account the state diagrams presented in Figure 3, it is observed that the reduction process is more favorable energetically at certain temperatures, being usually more favorable when increasing the temperature of the process. The energy required in the reduction processes as a function of temperature is different for the three metals due to the stability of the phases. In terms of activation energies necessary for the processes, several sources in the literature have been evaluated, and those for which more information was available under the conditions that have been studied have been chosen for the initial estimation of the RTE. It is observed how the importance of determining the conditions in which the charging process will take place is vital to minimize the activation energies. It was considered that taking into account the conditions under which the activation energies were determined, those used for the determination of the RTE would be the ones of greater value, even considering that, for the reactions studied, these values may be higher. Finally, it is observed that the values of RTE vary between 78% and 88%.

4. Conclusions

This work presents a preliminary analysis of metal-based energy storage systems. The energy potential of these types of reactions raises the modality of the proposed thermochemical storage system. The analysis in a wide range of temperatures shows how there are conditions for charge and discharge reactions, which make using metals as a thermochemical storage base possible. The systems were modelled in an OpenModelica library. It has been assembled where the entire modelling process has been carried out, from the properties of the materials to the study of the reactions. This library is designed to be able to make comparisons with laboratory tests and will serve as support for the study of this storage system.

The analyses show the feasibility and potential of the proposed energy storage layouts. Taking into account the range of working temperatures, it opens the possibility of integrating these facilities in processes with high thermal production, increasing the energy integration of existing facilities with the possibility of energy recovery. The analyses show how activation energies for the specific working conditions affect the round-trip efficiency values.

For this proposal of thermochemical energy storage based on the combustion of metals, the interest that the use of this type of materials as fuel can offer is observed. Among the points raised in this article, different lines of study are opened that will have this concept as a starting point. They include the study of the integration of green hydrogen production facilities from photovoltaic solar energy in this system, as well as carbon monoxide production plants and energy integration of the system depending on the chosen configuration.

Acknowledgments

This work has been partially developed within the project, New modular high-temperature thermo-chemical energy storage concept based on innovative processes (TED2021-131839B-C21) funded by the Recovery and Resilience Funds of the European Union and Spanish Ministry of Science and Innovation.

Nomenclature

Fe	Iron	
Fe_2O_3	Hematite	
Fe_3O_4	Magnetite	
FeO	Wüstite	
Al	Aluminium	
Al_2O_3	Aluminum Oxide	
Ni	Nickel	
NiO	Nickel (II) oxide	
CO	Carbon monoxide	
H_2	Hydrogen	
CO_2	Carbon Dioxide	
H_2O	Water	
c_p	Heat capacity	[kJ/(kg·K)]
h	Especific enthalpy	[kJ/kg (fuel)]
s	Especific entropy	[kJ/(mol·K)]
g	Gibbs free energy	[kJ/kg (fuel)]
RTE	Round Trip Efficiency	[-]

References

[1] "Estadísticas de consumo energético mundial | Enerdata." https://datos.enerdata.net/energia-total/datos-consumo-internacional.html (accessed Apr. 24, 2023).

[2] U. Nations, "Global Issues | Naciones Unidas", Accessed: Apr. 24, 2023. [Online]. Available: https://www.un.org/es/global-issues

[3] "e-REdING. Biblioteca de la Escuela Superior de Ingenieros de Sevilla." https://biblus.us.es/bibing/proyectos/abreproy/5641 (accessed Apr. 24, 2023).

[4] I. Hadjipaschalis, A. Poullikkas, and V. Efthimiou, "Overview of current and future energy storage technologies for electric power applications", doi: 10.1016/j.rser.2008.09.028.

[5] "Technologies | EASE: Why Energy Storage? | EASE." https://ease-storage.eu/energy-storage/technologies/ (accessed Apr. 24, 2023).

[6] Y. Wang *et al.*, "Application of MOFs-derived mixed metal oxides in energy storage," *Journal of Electroanalytical Chemistry*, vol. 878, p. 114576, Dec. 2020, doi: 10.1016/J.JELECHEM.2020.114576.

[7] "La primera cervecería en quemar hierro como energía verde es holandesa | IKERA." https://ikera.es/la-primera-cerveceria-en-quemar-hierro-como-energia-verde-es-holandesa/ (accessed Apr. 24, 2023).

[8] "J. Bergthorson, McGill University - Metal Fuels for Compact Zero-carbon Power - YouTube." https://www.youtube.com/watch?v=VjCGXxFHGcw (accessed May 31, 2022).

[9] “Mapping Temperature Characteristics of Iron Powder Combustion in the MP100 Setup — Eindhoven University of Technology research portal.” https://research.tue.nl/en/studentTheses/mapping-temperature-characteristics-of-iron-powder-combustion-in- (accessed Apr. 24, 2023).

[10] K. V Manukyan *et al.*, “Nickel Oxide Reduction by Hydrogen: Kinetics and Structural Transformations,” *J. Phys. Chem. C*, vol. 119, p. 42, 2015, doi: 10.1021/acs.jpcc.5b04313.

[11] A. Carlos, G. Tello, P. Jaime, L. Mateo, J. Ángel, and P. Llorente, “PURIFICACIÓN DE MEZCLAS H 2-CO 2 MEDIANTE EL PROCESO ‘STEAM-IRON’ CON ÓXIDOS DE HIERRO,” 2016.

[12] “Phase Diagram The Phase Diagram module 1.2”, Accessed: Mar. 25, 2023. [Online]. Available: www.factsage.com

[13] “Use el módulo de diagrama de fase Diagrama de fase de FactSage para dibujar el diagrama de equilibrio del sistema Fe-OC.” https://zhuanlan.zhihu.com/p/419199865 (accessed Mar. 25, 2023).

[14] L. Kolbeinsen, “Modelling of DRI processes with two simultaneously active reducing gases,” *Steel Res Int*, vol. 81, no. 10, pp. 819–828, Oct. 2010, doi: 10.1002/SRIN.201000144.

[15] S. Vyazovkin, “Kissinger Method in Kinetics of Materials: Things to Beware and Be Aware of,” *Molecules 2020, Vol. 25, Page 2813*, vol. 25, no. 12, p. 2813, Jun. 2020, doi: 10.3390/MOLECULES25122813.

[16] J. T. Richardson, R. Scates, and M. V Twigg, “X-ray diffraction study of nickel oxide reduction by hydrogen,” 2003, doi: 10.1016/S0926-860X(02)00669-5.

[17] J. P. Baur, R. W. Bartlett, J. N. Ong, and W. M. Fassell, “High-Pressure Oxidation of Metals, Nickel in Oxygen”.

[18] L. del Campo, R. B. Pérez-Sáez, and M. J. Tello, “Iron oxidation kinetics study by using infrared spectral emissivity measurements below 570 °C,” *Corros Sci*, vol. 50, no. 1, pp. 194–199, Jan. 2008, doi: 10.1016/J.CORSCI.2007.05.029.

[19] A. Pineau, N. Kanari, and I. Gaballah, “Kinetics of reduction of iron oxides by H2: Part I: Low temperature reduction of hematite,” *Thermochim Acta*, vol. 447, no. 1, pp. 89–100, Aug. 2006, doi: 10.1016/J.TCA.2005.10.004.

[20] C. Kuhn, A. Düll, P. Rohlfs, S. Tischer, M. Börnhorst, and O. Deutschmann, “Iron as recyclable energy carrier: Feasibility study and kinetic analysis of iron oxide reduction,” *Applications in Energy and Combustion Science*, vol. 12, p. 100096, Dec. 2022, doi: 10.1016/J.JAECS.2022.100096.

[21] A. Pineau, N. Kanari, and I. Gaballah, “Kinetics of reduction of iron oxides by H2: Part II. Low temperature reduction of magnetite,” *Thermochim Acta*, vol. 456, no. 2, pp. 75–88, May 2007, doi: 10.1016/J.TCA.2007.01.014.

[22] E. N. Lysenko, • A P Surzhikov, • S P Zhuravkov, V. A. Vlasov, • A V Pustovalov, and N. A. Yavorovsky, “The oxidation kinetics study of ultrafine iron powders by thermogravimetric analysis”, doi: 10.1007/s10973-013-3456-x.

[23] A. A. Barde, J. F. Klausner, and R. Mei, “Solid state reaction kinetics of iron oxide reduction using hydrogen as a reducing agent,” *Int J Hydrogen Energy*, vol. 41, no. 24, pp. 10103–10119, Jun. 2016, doi: 10.1016/J.IJHYDENE.2015.12.129.

[24] “IEEE Xplore Full-Text PDF:” https://ieeexplore.ieee.org/stamp/stamp.jsp?tp=&arnumber=8738863 (accessed Apr. 13, 2023).

[25] Y. Zhang and Z. Yang, “Comparative study on optimized round-trip efficiency of pumped thermal and pumped cryogenic electricity storages,” *Energy Convers Manag*, vol. 238, p. 114182, Jun. 2021, doi: 10.1016/J.ENCONMAN.2021.114182.

[26] “JModelica.org User Guide Version 2.4 JModelica.org User Guide: Version 2.4,” 2018.

[27] P. A. Fritzson, *Introduction to modeling and simulation of technical and physical systems with Modelica*. Wiley, 2011.

[28] B. J. Mcbride, M. J. Zehe, and S. Gordon, “NASA Glenn Coefficients for Calculating Thermodynamic Properties of Individual Species,” 2002, Accessed: Mar. 21, 2023. [Online]. Available: http://www.sti.nasa.gov

[29] B. J. Mcbride, S. Gordon, and A. Cleveland, “NASA Reference Computer Program for Calculating and Fitting Thermodynamic Functions,” 1271.

[30] “EquiSage”.

[31] M. J. Zehe, S. Gordon, and B. J. Mcbride, “CAP: A Computer Code for Generating Tabular Thermodynamic Functions from NASA Lewis Coefficients,” 2002, Accessed: Mar. 25, 2023. [Online]. Available: http://www.sti.nasa.gov

Analytical prediction of the phase change front movement to characterize tube in tube phase change material heat exchangers

Maité Goderis[a,b], Julie Van Zele[a], Kenny Couvreur[a,b], Wim Beyne[a,b] and Michel De Paepe[a,b]

[a] Department of Electromechanical, Systems and Metal Engineering – UGent, Ghent, Belgium, Maite.Goderis@UGent.be
[b] FlandersMake@UGent – Core lab EEDT-MP, Leuven, Belgium, www.flandersmake.be

Abstract

Tube in tube phase change material (PCM) heat exchangers have great potential as latent thermal energy storage (LTES) systems. However, sizing and designing these systems is still a challenge. Standard heat exchanger models cannot be applied due to the non-linear and transient heat transfer behavior of the PCM. Several alternative methods are suggested but these models are unable to predict the complete outlet state as a function of time. To fill this gap, an analytical model is derived to estimate the phase change front position as a function of time. It is proposed that the time the front needs to reach a certain vertical position is a linear function of the position. To validate the proposed analytical model, experiments are performed on a vertical tube in tube heat exchanger with varying inlet conditions. In the inner tube, water flows as heat transfer fluid (HTF). A paraffin is used as PCM in the outer tube. The phase change front position is evaluated at the outside of the tube. The movement of the phase change front is represented by plotting the vertical position of the front as a function of time. The position of the front is determined based on visual measurements using a camera placed next to the tube. By predicting the front position as a function of time, the performance of the heat exchanger can be determined. Different designs can be compared more easily, without needing to experimentally test or simulate, leading to a shorter and less expensive design phase for LTES systems, enhancing their large-scale roll-out.

Keywords:

Latent thermal energy storage; Phase change material; Tube in tube; Phase change front.

1. Introduction

Latent thermal energy storage (LTES) systems are regarded as an effective means of storing thermal energy, utilizing phase change materials (PCMs) that absorb or release energy during the phase change. The European Union (EU) has set ambitious goals concerning energy efficiency and reducing carbon emissions [1, 2]. To reach these goals, the EU has made energy storage systems one of its research goals [2]. Especially thermal energy storage systems are of paramount importance, as 50% of our energy use is thermal [3]. LTES systems offer an effective way to store thermal energy, which is beneficial in reducing energy consumption during peak demand periods and can help in the reduction of reliance on fossil fuels.

Different types of LTES systems exist. A distinction can be made between systems that use or do not use heat transfer fluids (HTFs) to exchange heat or cold [4]. In this paper, the focus is on LTES systems that use HTFs: LTES heat exchangers. Different geometries are possible but the shell and tube configuration is the most commonly used [5].

However, designing an effective LTES heat exchanger can be challenging. The key design problem requires determining the heat transfer rate from HTF to PCM (or from PCM to HTF) as a function of time and the outlet HTF temperature as a function of time, based on the system's geometrical and operational conditions [6]. When designing conventional heat exchangers, the effectiveness-number of transfer units (NTU) and logarithmic mean temperature difference (LMTD) methods can be used. The methods are developed for heat exchangers which reach a steady state, implying that the local state of the heat transfer fluid is no longer a function of time. However, LTES systems are transient in nature [4], consequently, these methods are not applicable to such systems.

Previous attempts have been made to develop analytical methods that are suitable for LTES heat exchanger design. Some of the methods that have been proposed are the average effectiveness method, which was

introduced by Tay et al. [6, 7], and the phase change time method proposed by Raud et al. [8]. However, these methods only allow an estimation of a specific aspect of the outlet state of an LTES heat exchanger. Another approach is the charging time energy fraction method (CTEFM) method developed by Beyne et al. [9], which allows the outlet HTF temperature to be estimated as a function of time. However, this method cannot be used as a design method, as fitting to experimental data is required. Alternatives such as purely experimental methods and Computational Fluid Dynamics (CFD) based design are often too expensive and time-consuming.

Despite the above-mentioned efforts, there is still a gap in LTES heat exchanger design methodology. Therefore, there is a need for further research to develop more accurate and cost-effective analytical methods that can be used to design LTES heat exchanger systems with high efficiency and performance, for specific applications.

Recently, Beyne et al. [10] developed an analytical solution to predict the performance of LTES heat exchangers based on the heat transfer model of a cross section. A model is used for the local heat transfer under constant boundary conditions, based on the solution to the Stefan problem. In the Stefan problem, sensible heat is neglected compared to the latent heat of the PCM and the phase change is assumed to occur isothermally. The phase change problem is considered purely conductive and the PCM properties are assumed independent of the temperature. Computation of the phase change front location as a function of time allows determining the phase change fraction as a function of time. This relates to the PCM internal energy per unit of heat transfer surface. Next, this solution is integrated to determine the overall phase change fraction of the complete LTES heat exchanger. In [10] this analytical solution is verified for a planar geometry by comparing it to a numerical simulation. The results had small average deviations for the phase change fraction and effectiveness. The total phase change time was very well predicted.

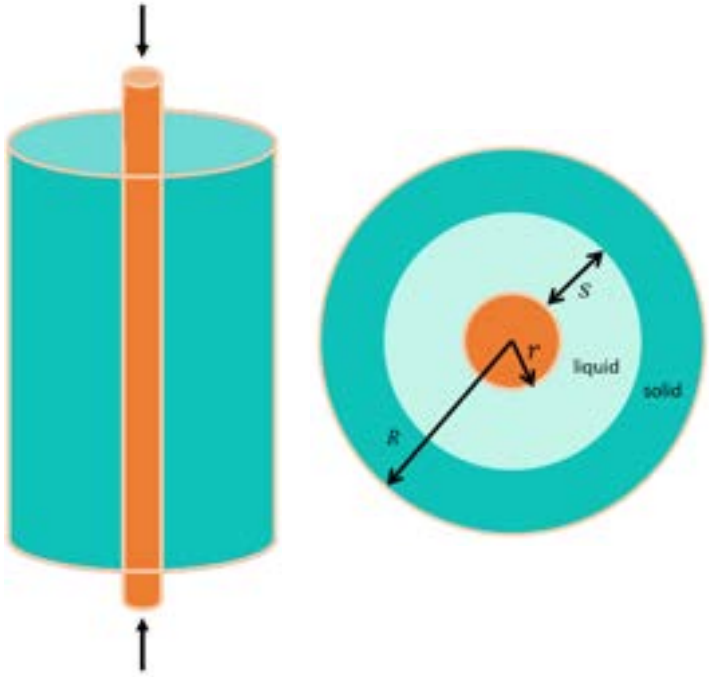

Figure 1. Schematic of tube in tube system during phase change.

In this paper, the proposed analytical method will be evaluated based on experimental data of a tube in tube LTES heat exchanger. The geometry is schematically shown in Figure 1. Similar to the planar geometry, analytical equations can be derived to predict the phase change front behavior as a function of time, now for a cylindrical geometry. The overall phase change fraction of a tube in tube heat exchanger can be determined based on the position of the phase change front in a cylindrical cross-section with constant boundaries, which relates to the PCM internal energy per unit of heat transfer surface. When this solution is integrated over the heat exchanger, the overall phase change fraction of the complete LTES system can be determined.

Beyne et al. [10] states that the phase change front moves linearly in time over the length of the tube. The time for the front to reach a certain vertical position $x = x_1$ is then given by Equation 1. The x-axis indicates the position of the phase change front at the outer diameter of the tube, as indicated in Figure 2.

$$t(x_1) = t_0 + \sigma . x_1 \qquad 1$$

t_0 is the time that is needed for the phase change front to reach the outer diameter of the PCM tube for the first time, thus at height $x = 0$. The slope σ can be estimated as in Equation 2. U_a is the latent heat of phase change of the PCM per length unit. $\dot{m}$ and c_p are respectively the mass flow rate and specific heat capacity of

the HTF, and ΔT_0 is the temperature difference between the HTF temperature at the inlet and the PCM phase change temperature.

$$\sigma = \frac{U_a}{\dot{m} c_p \Delta T_0} \quad (2)$$

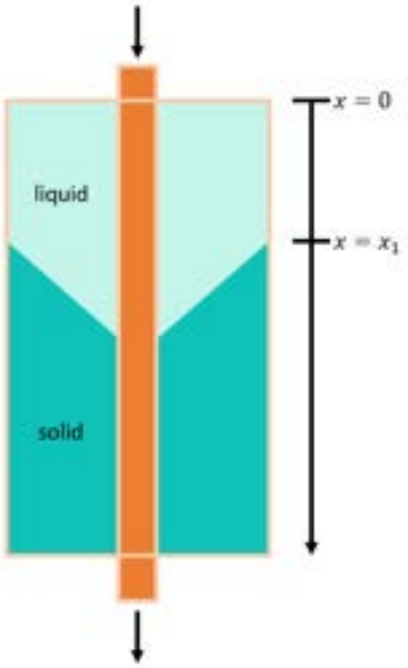

Figure 2. Section of tube in tube heat exchanger with phase change front schematically shown.

Mehling and Cabeza [11] provide a correlation for the radial movement of the phase change front in a one-dimensional cylindrical geometry. This correlation is based on the solution to the Stefan problem. Equation 3 denotes the time t that is needed for the phase change front to move a distance s away from the HTF tube with radius r. Equation 3 can be split up into two factors. The first factor relates the front position s to the phase change fraction, defined based on the latent heat of phase change the PCM h_{lat}, the density of the PCM ρ_{PCM}, the thermal conductivity k of the PCM and the temperature difference ΔT_0 between HTF temperature at the inlet and the phase change temperature of the PCM. The second factor f is a function of the ratio of the thermal conductivity k of the PCM to the convective heat transfer coefficient h of the HTF and the radial front position s. This factor describes the deviation of the solution compared to the solution of the Stefan problem, due to the boundary effects of the HTF. For the considered tube in tube heat exchanger, the second factor can be calculated as in Equation 4. It is assumed that the thickness of the HTF tube wall is much smaller than the outer HTF tube radius r and that the conductivity of the HTF wall is much larger than the conductivity of the PCM. These assumptions apply to the considered experimental setup (see Section 2). Equation 3 can be used to calculate t_0 in Equation 1, by defining $s = R - r$.

$$t(s) = \frac{h_{lat} \cdot \rho_{PCM} \cdot s^2}{2 \cdot k \cdot \Delta T_0} \cdot f\left(s, \frac{k}{h}\right) \quad (3)$$

$$f\left(s, \frac{k}{h}\right) = \left(1 + \frac{r}{s}\right)^2 \ln\left(1 + \frac{s}{r}\right) - \left(1 + \frac{2r}{s}\right)\left(\frac{1}{2} - \frac{k}{hr}\right) \quad (4)$$

A series of experiments on a tube in tube heat exchanger are conducted while the position of the phase change front is tracked over time. The observed results regarding the phase change front position are compared to the expected front position, based on the correlations from Beyne et al. [10] and Mehling and Cabeza [11], mentioned above. The accuracy of the proposed analytical model is investigated.

2. Setup description

The heat exchanger tested, is a tube in tube configuration with a length of one meter, which is oriented vertically to take advantage of the axisymmetry [12]. In this configuration, the heat transfer fluid (HTF) flows through the inner tube, while the PCM is located in the shell region. The direction of flow of the HTF can be changed using two three-way valves. During the melting process, the HTF flows from the top of the heat exchanger to the bottom. During the solidification process, it flows in the opposite direction to limit thermal stresses imposed by the PCM volume change.

The HTF flows through a copper tube with an outer diameter of 15 mm and a wall thickness of 2 mm. The copper tube is positioned concentrically within a transparent polycarbonate tube, which houses the PCM. The

shell has an outer diameter of 60 mm and a wall thickness of 3 mm. In the experiments, the paraffin RT35HC provided by Rubitherm [13] is used. This nontoxic PCM has a high thermal storage capacity and stable performance during the phase change cycles. An overview of the properties of RT35HC can be found in Table 1. A total of 1.497 kg of PCM is used during the experiments, which corresponds to a total latent heat capacity of about 380 kJ. Water is used as HTF.

Table 1: RT35HC properties [13].

Melting area	34-36	°C
Congealing area	36-34	°C
Specific heat capacity	2	kJ/kgK
Density solid (at 25°C)	0.88	kg/l
Density liquid (at 60°C)	0.77	kg/l
Heat conductivity	0.2	W/mK
Max. operating temperature	70	°C

Figure 3. Picture of the setup: insulation box.

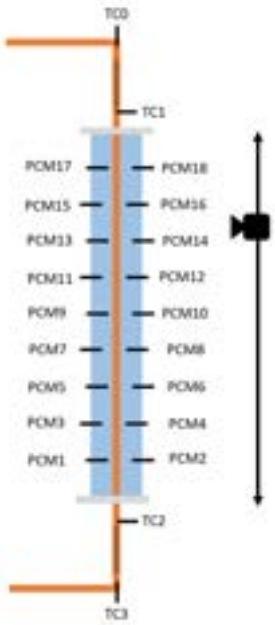

Figure 4. Schematic of the heat exchanger with camera slider, placed inside the insulation box.

A picture of the setup and a schematic of the heat exchanger be seen in respectively Figure 3 and Figure 4. Next to the tube, a camera on a linear slider is placed to allow observation of the location of the phase change front over the complete tube length. The whole of the heat exchanger and camera slider are placed in a big box filled with insulation granulates [14]. This way, thermal losses are limited in a uniform way. On the schematic, the thermocouples which are used to measure the temperature of the PCM and the HTF are indicated. The temperatures inside the PCM are measured with 18 1 mm K-type thermocouples, placed every 10 cm in the axial direction. At each height, a temperature measurement at both 0.5 and 1 cm from the outside shell wall is performed. These thermocouples are calibrated to an uncertainty of ± 0.15 °C and are acquired by a Keithley 2700 multiplexer with a sampling rate of 2.5 s. The temperatures at the HTF inlet and outlet of the heat exchanger are also measured. Mixers are inserted into the HTF tubes, ensuring the thermocouples measure the bulk HTF temperature. Before and after each mixer, a 1.5 mm K-type thermocouple was added. This way, both melting and solidification experiments can benefit from the effect of the mixers. These thermocouples are again calibrated with an uncertainty of ± 0.15 °C and are sampled with a sampling rate of 0.5 s, as the transient behavior needs to be captured. During melting, TC1 and TC3 will be used as respectively inlet and outlet of the HTF in the heat exchanger. While during solidification, this will be TC2 and TC0, as now the HTF flows from bottom to top.

In Figure 5 a picture taken during a melting experiment is shown. The figure includes a tape measure and a part of the transparent container, where the PCM can be seen. The transparent PCM is liquid, the white is solid.

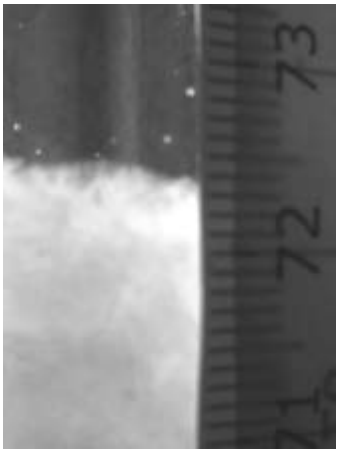

Figure 5. Picture of the phase change front during melting, taken with the camera installed next to the tube in tube heat exchanger (x = 72.4 cm).

In Table 2 an overview is given of the operational conditions of the considered melting experiments performed on the above-described setup. For each experiment, the HTF mass flow rate and two temperature differences are given. ΔT_0 quantifies the difference between the HTF inlet temperature and the phase change temperature (here assumed equal to 35 °C). ΔT_{init} is the difference between the phase change temperature and the initial temperature of the PCM. To define the initial PCM temperature, the mean of all PCM temperature measurements is used. The last column of the table gives the Reynolds number linked to the HTF.

Table 2. Overview of performed experiments.

experiment	$\dot{m}\ [kg/h]$	$\Delta T_0\ [°C]$	$\Delta T_{init}\ [°C]$	$Re\ [-]$
M1	68	26.5	8.0	4762
M2	80	25.6	14.5	5482
M3	20	22.5	17.0	1300
M4	156	19.5	10.0	9824

Only melting experiments are performed and no solidification data is taken into consideration in the context of this paper. The focus of this work is on melting experiments because during solidification tests, difficulties arise when visually observing the front. During solidification, conduction is the dominant heat transfer mode [15]. Therefore, the solidification front moves very radially from the inner shell diameter to the outside shell diameter. Because of this, it is very difficult to visually determine the moment when the front reaches the outside diameter. Similar difficulties were observed by Longeon et al. [12]. Lipnicki et al. [16] observed during their experiments that the solidification front almost has a constant radial thickness along the length of the heat exchanger, explaining the difficulties concerning determining the vertical front position at the outside of a PCM tube.

3. Results

3.1 Experimental results

As explained before, during each melting experiment, the location of the phase change front at the outer diameter of the heat exchanger is tracked over time. The position of the phase change front is normalized to the total height of the PCM ($L_{PCM} = 0.93m$), as in Equation 5. L_{PCM} is a bit smaller than 1m, as the tube is not completely filled with storage material to allow volume expansion during melting.

$$\xi = \frac{x}{L_{PCM}} \qquad 5$$

In Figure 6, the evolution of the position of the phase change front at the outer diameter of the PCM tube can be seen as a function of time, during melting experiment M1. The different melting regimes, as also observed in previous studies, can be recognised in the shape of the front-curve. In the initial phase, conduction is the

main heat transfer mode and the PCM closest to the tube will melt. As melting continues, heat transfer by convection will gain dominance and will fasten the heat transfer in the PCM. This can be seen by the steeper slope of the front-curve, meaning an increasing melting rate of the PCM when a significant part of the PCM has molten. Next, the heat transfer reaches a quasi-steady state regime with a constant heat transfer rate. The phase change front now moves linearly through the tube. Finally, when most of the PCM has molten, the shrinking solid phase starts while the heat transfer, and thus the speed with which the phase change front moves, decreases. These different melting regimes lead to the S-shape that can be recognised in the front-curve in Figure 6.

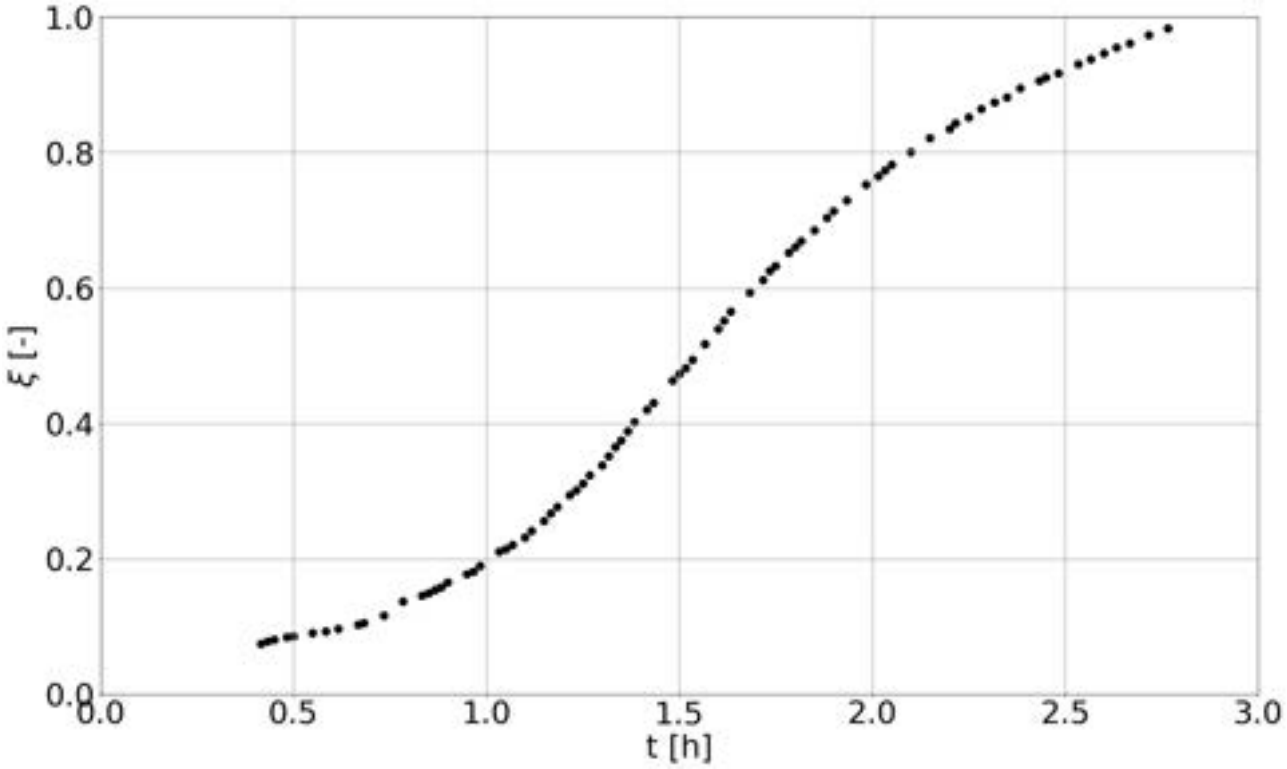

Figure 6. The evolution of the position of the phase change front at the outer radius of the PCM tube, as a function of time (melting test M1), based on the visual tracking of the phase change front position.

As mentioned above, a quasi steady-state melting regime is present during the melting process. During this phase, the melting front at the outside of the PCM tube moves linearly over time. The slope of this part of the front-curve is denoted by β for the remainder of this paper. β is only based on experimental data where ξ ranges from 0.25 to 0.65. In Figure 7 the visual, experimental data for all melting experiments is shown, and the linear approximation of the front movement during the quasi-steady melting regime is shown by the dotted black line. The linear approximation is of the shape as given in Equation 6. Some of the visual measurement points are omitted in Figure 7, to clarify the figure. The shape of the front-curve is however still obviously visible.

$$t(\xi) = \alpha + \beta \, . \, \xi \qquad 6$$

When comparing the different experimental results in Figure 7, the influence of the operational conditions can be seen. Especially increasing the temperature difference between HTF inlet temperature and the phase change temperature of the PCM, decreases the total melting time. These observations are in line with literature [17-20]. In literature is also seen that increasing the mass flow rate of the HTF, shortens the total melting time. However, when comparing experiments M1 and M2, a small increase in melting time is seen for the larger mass flow rate. Khan et al. [21] observed that for higher HTF inlet temperatures, the influence of varying the mass flow rate decreases. The shortened melting time for a larger mass flow rate can probably be explained by experimental uncertainties. The studies found in literature agreed with the observation that the heat transfer characteristics are more sensitive to a change in inlet temperature than a change in mass flow rate [22].

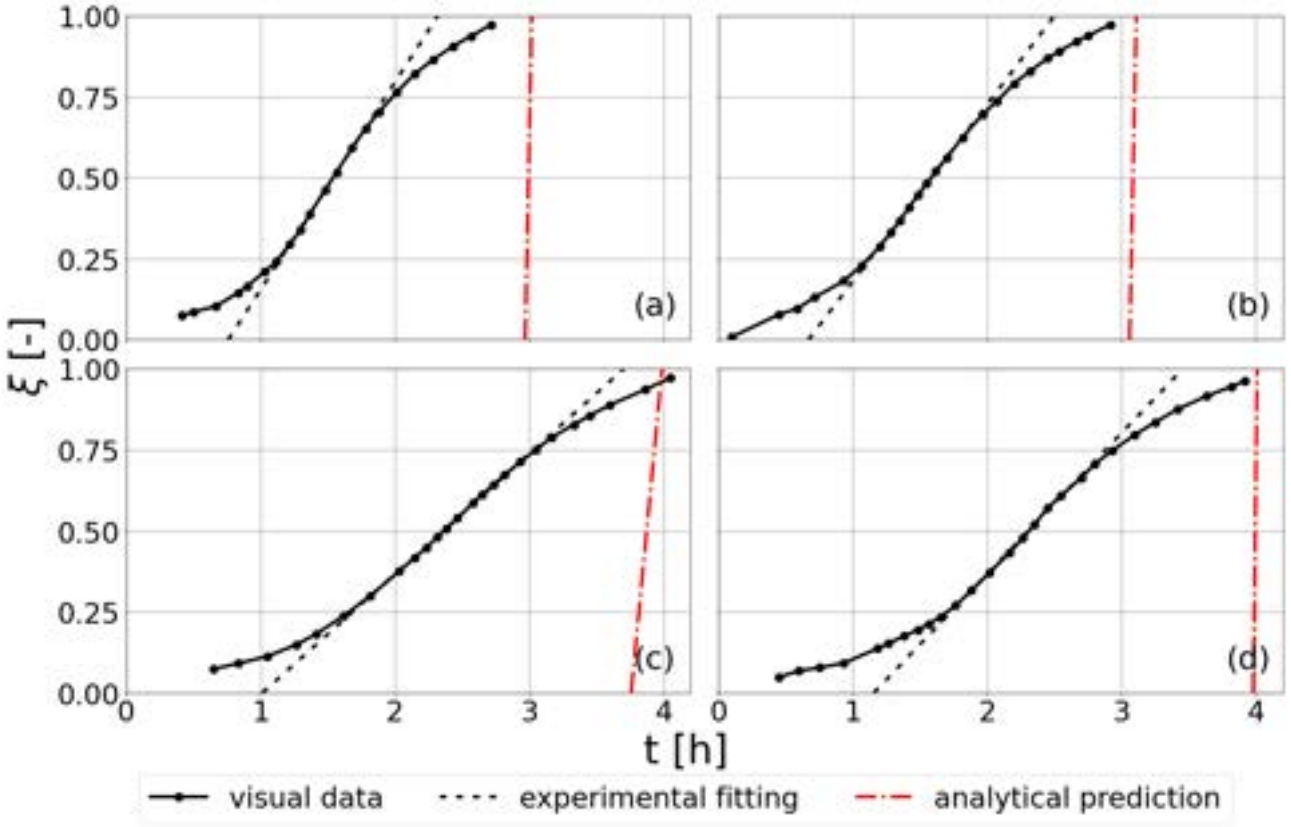

Figure 7. Experimental front data with fitted linear correlations based on β and σ for melting experiments (a) M1, (b) M2, (c) M3 and (d) M4.

3.2 Analytical correlations

As explained in Section 1, various studies propose that the phase change front moves linearly in time during melting experiments. In this Section, the analytical obtained intercept t_0 (Equation 3) is compared to the experimental α, and the analytical obtained slope σ (Equation 2) is compared to the experimental slope β, seen during the quasi-steady melting phase. Table 3 gives an overview of both intercepts and slopes for the considered operational conditions of the melting experiments of Table 2. The comparison between experimental and analytical results is visualized in Figure 7 where the black and red lines respectively represent the experimental and the analytical linear fit.

Table 3. Comparison of experimental and analytical slope.

experiment	$\boldsymbol{\alpha}$ $[\boldsymbol{h}]$	$\boldsymbol{t_0}[\boldsymbol{h}]$	$\boldsymbol{\beta}$ ***[h]***	$\boldsymbol{\sigma}$ ***[h]***
M1	1.560	2.97	0.760	0.05
M2	1.831	3.06	0.669	0.05
M3	2.689	3.76	1.015	0.23
M4	2.299	3.98	1.157	0.03

From Table 3 and Figure 4 it is clear that the proposed analytical correlations are not able to accurately predict the movement of the phase change front as a function of time of a tube in tube heat exchanger. The prediction for the total melting time is a quite an acceptable prediction. However, more experimental data is required to make any conclusions on this statement. Below some considerations are listed, explaining the deviations between experimental and analytical results.

First of all, measurement uncertainties on the measured experimental quantities must be taken into account. To calculate t_0 and σ the mean HTF inlet temperature and mean HTF mass flow rate are used. During the complete melting test, small deviations on these mean values are possible, however, these will not have a significant influence on the obtained results. The error on the visual measurements is difficult to determine but is limited to 2-3 mm. As the front position is measured every 3 minutes, this visual error will not influence the general trend of the front.

Thermal losses during the experiments could also influence the phase change front propagation. Due to the undertaken actions by installing the insulation box around the PCM heat exchanger, heat losses are limited as much as possible. Heat losses will decrease the melting rate and consequently, a faster front movement could be expected using the theoretical correlations, compared to the experimental data. However, it is improbable that the influence of the limited heat losses could be of the proportion that is seen when comparing β and σ.

Furthermore, in the derivation of the analytical correlations, only the latent heat of the PCM is considered. The sensible heat of the PCM also needs to be taken into account, as well as the heat transferred from the HTF to the container during the experiments. However, the latent heat is dominant as it is significantly larger than the other contributors to the internal energy of the system. For example for experiment M1, the latent heat of the PCM corresponds with 380 kJ, whereas the sum of the sensible PCM energy and the energy stored in the container is about 80 kJ. Including all the energy contributions would thus only have a limited influence on the value of σ.

The above-mentioned considerations concerning uncertainties in the experimental results or assumptions in determining the analytical correlations can explain a deviation between experimental and analytical results. However, the observed discrepancies cannot be explained. Therefore, a more fundamental look is taken into the analytical model, and the applicability of the model to the considered melting experiments is evaluated.

In the analytical derivation, pure conduction is assumed and the influence of natural convection is neglected, but during melting, natural convection is the dominant heat transfer mode [15]. It can thus be expected that the analytical solution will overestimate the duration of the melting process, due to the increased heat transfer during melting because of the influence of natural convection. However, the analytical prediction is a large underestimation of the experimental melting duration. A large deviation is seen between the theoretical and experimental obtained intercepts and slopes. From Table 3 and Figure 7, it is clear that the analytical slope σ is a large underestimation of the experimentally obtained β. It is predicted that the phase change front moves faster over the length of the tube, than what is visually observed.

The analytical model is based upon the assumption that the tube in tube heat exchanger can be modelled as distinct infinitesimal slices, stacked upon each other. The heat transfer behavior of the slices is assumed uncoupled. In reality, the phenomena in the different slices will be coupled, especially during melting due to vertical convection bubbles formed in the PCM. The experimental intercept α is expected to be smaller than the predicted t_0 based on purely, uncoupled conduction, due to the enhanced heat transfer because of the natural convection. This is as observed in Table 3 and Figure 7.

The analytical solution is obtained for a tube in tube heat exchanger with a temperature difference between the inlet and outlet of the heat transfer fluid. In the experiments, however, this temperature difference is rather limited. For example, for mass flow rates above $\pm 50 kg/h$ the temperature difference over the heat transfer is not measurable anymore. To validate the analytical solution, meaningful experimental data is required. To achieve this, the temperature over the heat transfer tube must be increased, by increasing the heat transfer rate between HTF and PCM. This can be done by for example adding fins to the HTF tube. However, preferably the analytical method is verified on a basic geometry. Another option to increase the heat transfer rate would be adding metal foam into the PCM to increase the effective conductivity of the storage material. Another approach could be to test a heat exchanger with an increased length. However, the height of the setup is limited due to practical limitations of the lab. In future studies, numerical simulations can be performed, eliminating the height limitations of the heat exchanger. Available experimental results can be used to fit the numerical method.

When analyzing the above-discussed results, the hypothesis arises that the analytical model can have better applicability for solidification experiments. During solidification, conduction is the dominant heat transfer mode, eliminating the deviation between experiments and model due to the influence of natural convection. Furthermore, when tracking the solidification front as a function of time, difficulties arise in determining the exact front position, because the phase change interface moves almost radially from the HTF wall to the outer PCM tube wall. The analytical model predicts such a front behavior: the predicted front moves in a couple of minutes over the complete length of the heat exchanger. In future work, solutions can be developed enabling tracking of the solidification front during experiments, or numerical simulations can be performed to validate this hypothesis.

4. Conclusions

Melting experiments are performed on a tube in tube LTES heat exchanger, with varying operational conditions. During these experiments, the location of the phase change front at the outer diameter of the PCM tube is tracked over time based on photographs. The distinct melting regimes described in literature can be seen in the obtained front movement-curve. The experimental results are compared to a predicted phase change front behavior, based on an analytical model developed by Beyne et al. [10]. It is seen that the analytical model overestimates the movement speed of the phase change front. However, a realistic estimation of the total melting time can be obtained with this model. In future work, numerical simulations are

recommended. Furthermore, tracking the phase change front during solidification experiments is required to validate the applicability of the analytical model for solidification.

Acknowledgment

The authors would like to express their gratitude and appreciation to the technical staff of Ghent University, especially Frederik Martens, Bart Van Daele, and Thomas Blancke for building and maintaining the setup used to obtain the discussed experimental data.

Nomenclature

c_p	specific heat capacity, J/kgK
h	convection coefficient, W/m²K
h_{lat}	latent heat of the PCM, J/kg
k	thermal conductivity, W/mK
L	length, m
m	mass, kg
$\dot{m}$	mass flow rate of HTF, kg/h
r	outer radius of HTF tube, m
R	inner radius of PCM tube, m
Re	Reynolds number, -
s	radial distance the phase change front has traveled, m
t	time, h
t_0	time the phase change front needs to reach the outer diameter of the PCM tube for the first time, h
U_a	latent heat of phase change of the PCM, per length unit, J/m
x	front position, m

Greek symbols

α	experimental intercept, h
β	experimental slope, h
ΔT_0	difference between HTF inlet temperature and PCM phase change temperature, °C
ΔT_{init}	difference between mean initial PCM temperature and PCM phase change temperature, °C
σ	analytical slope, h
ξ	dimensionless front position, -

Subscripts and superscripts

PCM	phase change material
HTF	heat transfer fluid

References

[1] "European Comission, official website." https://commission.europa.eu/index_en (accessed 17-10-2022.

[2] EUagenda. "A clean planet for all - a European long-term strategic vision for a properous, modern, competitive and climate neutral economy." https://eur-lex.europa.eu/legal-content/EN/TXT/?uri=CELEX%3A52018DC0773 (accessed 16-09-2022.

[3] IEA. "Heating - Fuels & Technologies." https://www.iea.org/fuels-and-technologies/heating (accessed 15-02-2023.

[4] A. Castell and C. Solé, "Design of latent heat storage systems using phase change materials (PCMs)," in *Advances in Thermal Energy Storage Systems*, 2015, pp. 285-305.

[5] G. S. Sodhi, V. Kumar, and P. Muthukumar, "Design assessment of a horizontal shell and tube latent heat storage system: Alternative to fin designs," *Journal of Energy Storage,* vol. 44, 2021, doi: 10.1016/j.est.2021.103282.

[6] N. H. S. Tay, M. Belusko, A. Castell, L. F. Cabeza, and F. Bruno, "An effectiveness-NTU technique for characterising a finned tubes PCM system using a CFD model," *Applied Energy,* vol. 131, pp. 377-385, 2014, doi: 10.1016/j.apenergy.2014.06.041.

[7] N. H. S. Tay, M. Belusko, and F. Bruno, "An effectiveness-NTU technique for characterising tube-in-tank phase change thermal energy storage systems," *Applied Energy,* vol. 91, no. 1, pp. 309-319, 2012, doi: 10.1016/j.apenergy.2011.09.039.

[8] R. Raud *et al.*, "Design optimization method for tube and fin latent heat thermal energy storage systems," *Energy,* vol. 134, pp. 585-594, 2017, doi: 10.1016/j.energy.2017.06.013.

[9] W. Beyne, K. Couvreur, I. T' Jollyn, R. Tassenoy, S. Lecompte, and M. De Paepe, "A charging time energy fraction method for evaluating the performance of a latent thermal energy storage heat exchanger," *Applied Thermal Engineering,* vol. 195, 2021, doi: 10.1016/j.applthermaleng.2021.117068.

[10] W. Beyne, R. Tassenoy, and M. De Paepe, "An approximate analytical solution for the movement of the phase change front in latent thermal energy storage heat exchangers," *Journal of Energy Storage,* vol. 57, 2023, doi: 10.1016/j.est.2022.106132.

[11] H. Mehling and F. L. Cabeza, *Introduction to heat and cold storage*. 2008.

[12] M. Longeon, A. Soupart, J.-F. Fourmigué, A. Bruch, and P. Marty, "Experimental and numerical study of annular PCM storage in the presence of natural convection," *Applied Energy,* vol. 112, pp. 175-184, 2013, doi: 10.1016/j.apenergy.2013.06.007.

[13] Rubitherm. "RT35HC." https://www.rubitherm.eu/media/products/datasheets/Techdata_-RT35HC_EN_09102020.PDF (accessed 13-03-2023.

[14] Deschacht. "Vermiculite." https://shop.deschacht.eu/nl-be/7921/vermiculite-g3-medium-9kg-100l (accessed 13-03-2023.

[15] M. Medrano, M. O. Yilmaz, M. Nogués, I. Martorell, J. Roca, and L. F. Cabeza, "Experimental evaluation of commercial heat exchangers for use as PCM thermal storage systems," *Applied Energy,* vol. 86, no. 10, pp. 2047-2055, 2009, doi: 10.1016/j.apenergy.2009.01.014.

[16] Z. Lipnicki and B. Weigand, "An experimental and theoretical study of solidification in a free-convection flow inside a vertical annular enclosure," *International Journal of Heat and Mass Transfer,* vol. 55, no. 4, pp. 655-664, 2012, doi: 10.1016/j.ijheatmasstransfer.2011.10.044.

[17] R. Karami and B. Kamkari, "Experimental investigation of the effect of perforated fins on thermal performance enhancement of vertical shell and tube latent heat energy storage systems," *Energy Conversion and Management,* vol. 210, 2020, doi: 10.1016/j.enconman.2020.112679.

[18] M. Esen, A. Durmus, and A. Durmus, "Geometric design of solar-aided latent heat store depending on various parameters and phase change materials," *Solar Energy,* vol. 62, no. 1, pp. 19-28, 1998, doi: 10.1016/S0038-092X(97)00104-7.

[19] M. K. Rathod and J. Banerjee, "Thermal performance enhancement of shell and tube Latent Heat Storage Unit using longitudinal fins," *Applied Thermal Engineering,* vol. 75, pp. 1084-1092, 2015, doi: 10.1016/j.applthermaleng.2014.10.074.

[20] A. Trp, K. Lenic, and B. Frankovic, "Analysis of the influence of operating conditions and geometric parameters on heat transfer in water-paraffin shell-and-tube latent thermal energy storage unit," *Applied Thermal Engineering,* vol. 26, no. 16, pp. 1830-1839, 2006, doi: 10.1016/j.applthermaleng.2006.02.004.

[21] Z. Khan and Z. A. Khan, "Experimental investigations of charging/melting cycles of paraffin in a novel shell and tube with longitudinal fins based heat storage design solution for domestic and industrial applications," *Applied Energy,* vol. 206, pp. 1158-1168, 2017, doi: 10.1016/j.apenergy.2017.10.043.

[22] L. Kalapala and J. K. Devanuri, "Influence of operational and design parameters on the performance of a PCM based heat exchanger for thermal energy storage – A review," *Journal of Energy Storage,* vol. 20, pp. 497-519, 2018, doi: 10.1016/j.est.2018.10.024.

Utilizing Historical Operating Data to increase Accuracy for Optimal Seasonal Storage Integration and Planning

Maximilian Sporleder[a,b], Michael Rath[a,c], Yuwei Xu[a], Mathias van Beek[d], and Mario Ragwitz[a,b]

[a] Fraunhofer Research Institution for Energy Infrastructures and Geothermal Systems (IEG), Cottbus, Germany, maximilian.sporleder@ieg.fraunhofer.de
[b] Brandenburg University of Technology Cottbus-Senftenberg (BTU CS), Cottbus, Germany
[c] Bochum University of Applied Sciences, Bochum, Germany, michael.Rath@hs-bochum.de
[d] Fraunhofer Institute for Environmental, Safety and Energy Technology (UMSICHT), Oberhausen, Germany, mathias.van.beek@umsicht.fraunhofer.de

Abstract:

Policies reasoned by global climate change and increasing commodity prices due to the international energy crisis force district heating providers to transform their assets. Pit thermal energy storage combined with solar energy can improve this transformation process. Optimal energy planning of district heating systems is often achieved by applying a linear programming model due to its fast computing. Unfortunately, depicting those systems in linear programming requires complexity reduction. We introduce a method capable of designing and operating the system with the complexity increase of considering the top and bottom temperatures of the pit thermal energy storage in linear programming.
Firstly, we extract and clean data from existing sites and simulations of seasonal storages. Secondly, we develop a polynomial regression model based on the extracted data to predict the top and bottom temperatures. Lastly, we develop a mixed-integer linear programming model using the predictions and compare it to existing sites. The model uses solar thermal energy, a pit thermal energy storage, and other units to meet the demand of a district heating system.
The polynomial regression results show an accuracy of up to 92 % with only a few features to base the prediction. The optimization model can design the storage and depict the correlation between decreasing specific costs and thermal losses due to an increasing volume. The control strategy of the heat pump requires further improvement.

Keywords:

MILP; Seasonal Storage; Optimization; District Heating; Design.

1. Introduction

The energy transition to a carbon-free system is one of the key challenges in the 21st century. Therefore, district heating systems (DHS) need renewable options and flexibility to reduce the impact of global warming. [1] predicts an expansion of DHS and emphasizes the importance of seasonal storages. Seasonal storages could enhance the integration of renewables like solar thermal energy and increase the system's flexibility. [2] identifies pit thermal energy storages (PTES) as economically feasible compared to other technologies. Combining different renewable technologies and seasonal storages supplying a DHS and the connected consumers is a tested concept in Denmark [3]. However, the planning process of a DHS with different technologies and different locations can be complex and overwhelming. In order to support decision-making processes for planers, we analyze historical and simulation data from seasonal storages. We develop a method to design a DHS with a PTES and other technologies inside a discretized thermal grid.

Figure 1 illustrates the concept of storing solar thermal energy in a PTES and unloading it through a heat pump into a district heating network. The goal is to design and operate energy converters and storages connected to the grid by modeling pipes, consumers, and production units. This approach tries to model a district heating network with all components and allows the integration of PTES in this system. The main research question is how a PTES integration into a DHS with different components can be optimized.

1.1. State-of-the-art

In recent years, several different strategies to model PTES and DHS, design and operate them, have been introduced (see Table 1). Most studies focus on a detailed depiction of the storage to calculate the operation and thermal losses due to charging, discharging, and environmental temperatures. A more in-depth review of those studies is given in the following paragraphs.

Appropriate simulation tools are helpful for the project's economic viability. TRNSYS is found to be the most widely used simulation tool for PTES simulations due to its component sets. [2] used TRNSYS to optimize the efficiency by using the data from a pilot solar heating system combining PTES. Results show that control strategies significantly improve heat collection performance and exergy efficiency, and stratification of seasonal storage impacts collection efficiency, especially at the end of the non-heating season [4]. EnergyPlus has some advantages in modeling heating systems on the demand side to satisfy various loads and is focused on building simulations [5]. FLUENT and COSMOL specialize in the PTES device temperature and velocity field analysis rather than system integration. SDH calculation tools is a bundle of tools developed by EU project SDHp2m [6]. It specializes in calculating solar district heating systems [7].

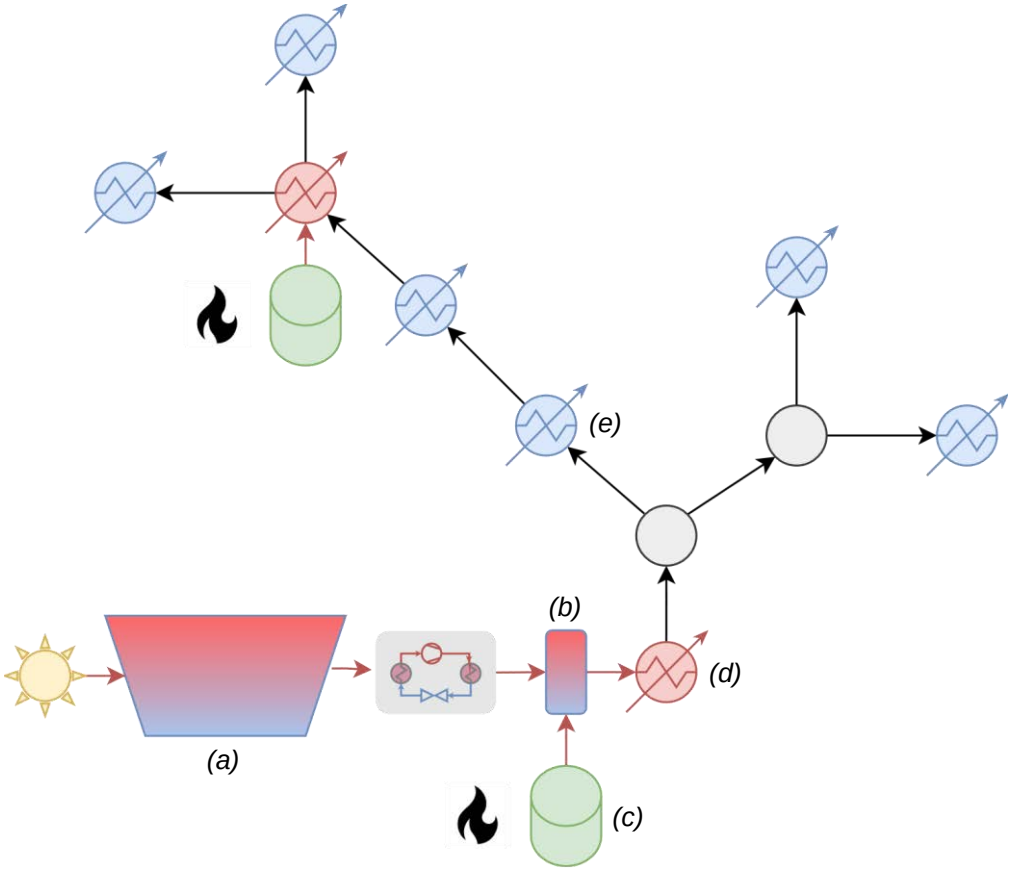

Figure 1: Fictional grid for this research with: a) PTES, solar thermal field, and heat pump as central units, b) buffer storage, and c) biomass boiler as a decentral unit; d) is referred to as a production unit; e) is referred to as consumer.

[8] considers using a biomass trigeneration system and an absorption heat pump to supplement the temperature gap and stabilize the water temperature in PTES at 85 to 90 °C. The model considers the overall efficiency of a power plant and maximizes the net present value to meet the district heating demand [8]. [9] uses TRNSYS to model the combined heating supply system to determine the performance of each plant and the ideal size. [10] studies the Dronninglund water pit thermal energy storage focusing on the balance model of energy and mass flow and providing the charging and discharging data for further research. In winter, the district heating supply temperature in Dronninglund is 75 °C; when the top temperature of the PTES is below the supply temperature, the heat pump works as a compensator. In Marstal, when the PTES top temperature drops below 70 °C, the PTES serves as the heat source for the heat pump to provide the gap between the district heating water temperature and the storage unit [11]. We apply the concept of Marstal using the PTES as a heat source for the heat pump.

The space for the PTES and solar panels affects the economics of the system. [12] compares the parameters of PV panels with thermal solar collectors. Using TRNSYS, three locations across Poland are examined, and the results show solar thermal collectors' advantages in area occupation and economics [12]. [12] uses an

electrode boiler to feed into the PTES. [13] calculates an energy system with additional units and suggests a ratio of the seasonal storage volume to the solar field area of 2 to 3 m. [14] compares distributed and centralized thermal solar collectors in Finland with 1231 MWh yearly heating demand and concludes that the centralized units have a significant advantage in the heat generation costs. The lower costs for central units are caused by decreasing specific investments with increasing dimensions [2].

Table 1. Typical energy system model comparison [15]

Energy system model	Min. Time step	Space range	Related function	Ref.
TRNSYS	Seconds	PTES/System	• Economic analysis [9] • Control strategy [16] • Validation [17] • Efficiency [18] • PTES structure optimization [19] • Model development [17]	[20]
COMSOL	Not available	PTES	• Validation [21] • PTES structure optimization [22] • Stratification model [21]	[23]
FLUENT	Not available	PTES	• PTES structure optimization [24] • Stratification model [25]	[26]
Mathematical model		PTES/System	• PTES structure optimization [27] • Validation [28] • Scenario analysis [28] • Stratification model [27]	
SDH calculation tools	Hourly	System	• Combined five mixed system • Economic analysis • Scenario analysis • Efficiency (sizing)	[7]
PyLESA	Hourly	System	• Economic analysis [29] • Control strategy [29] • Temperature dependence for heat pump models [29] • Stratification model [29]	[29]

The mentioned research gives and models the storage geometry and volume inside the simulation. We set the geometry as a variable and contribute to this extensive research with an approach in mixed-integer linear programming (MILP), including

- dynamic network behavior by depicting temperatures inside the grid,
- designing and controlling PTES in combination with other energy converters and storages located at different positions in the grid,
- introducing realistic PTES temperatures from simulations and measured data to obtain more realistic, dynamic coefficients of performance (COPs) (see Marstal concept),
- modeling and calculating the geometry of the PTES inside the optimization to account for thermal losses, space requirements, and specific investments.

The major problem of designing seasonal storage systems in energy system models based on MILP is the temperature modeling inside the storage – which would introduce nonlinearity – and the lack of information concerning the geometry. Our approach is based on the fact that already-designed systems have been operated for several years. [30] gathers data concerning the ratio between volume and surface, while the storages in Marstal and Dronninglund provide operational data. This information provides a generic approach supporting planners in the design phase of a carbon-neutral DHS.

The paper is structured in the method section, result section, discussion, and conclusion. In the method, we explain how we utilize the data from existing sites to model temperatures of PTES supplied by solar thermal energy. Additionally, we explain how we model the geometry of the PTES leading to specific investments, thermal losses, and space requirements. In the result section, we validate our approach by simulating the temperatures in the PTES and comparing the geometry and other parameters to existing sites. We continue by discussing our results and conclude with the most important findings.

2. Method

To find the optimal design for our energy system, we utilize MILP. MILP is a mathematical optimization technique for solving problems where some variables are constrained to be integers. It is used to model real-world problems where decisions are made based on discrete choices [31]. Our approach uses historical data from existing, and simulated PTES projects supplied by solar thermal fields and predicts temperature profiles for the location where the energy system model is applied. Figure 2 gives an overview of the methodology. We train a regression model based on the extracted data to predict the top and bottom temperature. With that temperature information, the MILP model optimizes the heat pump operation, and we also obtain the temperature losses at the surfaces. To create a dynamic PTES surface model, we used existing sites to build a piecewise function in the MILP model that takes the variable volume as an input and delivers the areas of the bottom, top, and sides as an output. The specific investments are modeled analogously. The MILP model includes energy balances around pipes, consumers, energy converters, and storages. The mass flow inside the pipes is estimated a priori, preventing nonlinearity.

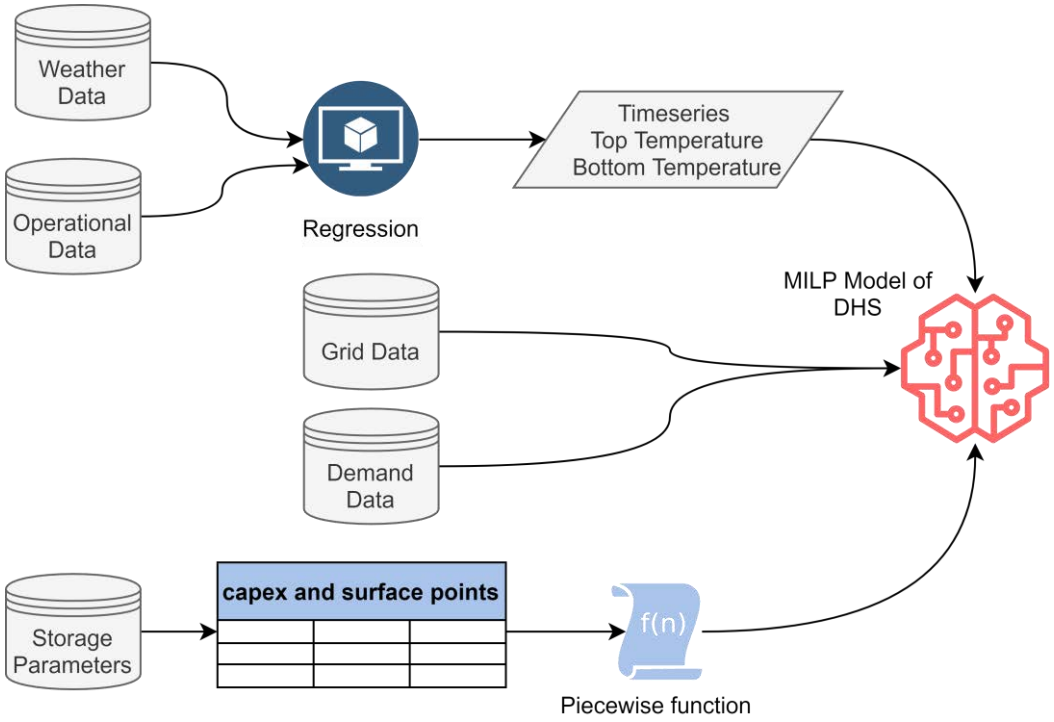

Figure 2: Illustrating the method dividing into the prediction of the temperatures, the piecewise functions for the capex and the surface areas of the storage depending on the volume, and the MILP model for the DHS.

2.1. Regression Model predicting PTES Top and Bottom Temperature

For our approach, we assume that the temperatures in the PTES behave similarly independent of the system due to the seasonal storing of solar thermal energy. To examine this assumption, four datasets were used in this research to predict the internal temperature of the PTES. We use the existing sites in Marstal and Dronninglund [3] and the simulation data from Wadelheim [32] and Florence [33]. The temperatures are extracted using the tool WebPlotDigitizer [34].

Many features can affect the temperature in the PTES. First of all, the environmental factors should be considered. The database of photovoltaic geographical information [35] provides the ambient temperature – two meters above the surface – and irradiance. [30] analyzes the slope and azimuth of solar thermal collectors' installation. Based on this work, the slope is set at 35 degrees, and the azimuth is chosen at 180 degrees. The soil temperature is relatively constant according to the monitoring results in [3]. So, the effect of the deep soil temperature on the tank's bottom temperature is neglected in our model. Additionally, the geometry – volume and surface area – of the PTES could affect the top temperature. However, this effect cannot be considered because the volume is a decision variable in the MILP model; therefore, the storage's geometry is unknown when we apply the regression model (see Figure 2). In conclusion, we use the features time, solar irradiance, and ambient temperature at the given location.

Before applying a polynimal regression [36], we resturcture the data input to improve the accuarcy. The feature time is separated into hour $t^{\text{hour}} \in [1,\ldots,24]$ and day $t^{\text{day}} \in [1,\ldots,365]$. The time is then split into sine and cosine such as $\sin/\cos\left(2\pi\frac{t^{\text{hour}}}{24}\right)$ and $\sin/\cos\left(2\pi\frac{t^{\text{day}}}{365}\right)$. The time is now categorized into four features.

Afterward, we apply the StandardScaler from scikit-learn [37] to all features. Then we use three data sets to train the model and one to test it. To evaluate the performance of the regression, mean squared error, root mean squared error (RMSE), mean average error (MAE), R-squared, explained variation, and accuracy are set as measurements.

2.2. The Energy System Model

A description of all used nomenclature can be found in the Nomenclature section after the conclusion. The energy system model is a MILP model minimizing the costs of the system represented by an objective function

$$\min\left(f^{\text{opex,var}}, g^{\text{opex,fix}}, h^{\text{capex}}\right). \quad (1)$$

$f^{\text{opex,var}}$ is the variable operational cost for energy converters combining costs for energy carriers, maintenance, and repair. $g^{\text{opex,fix}}$ are the fixed costs for storages or energy converters for the operation, maintenance, and repair, and h^{capex} are the investments. The economic calculation is based on [38]. The calculation is performed for one year in 3-hour timesteps. The model was solved with Gurobi [39].

The mass flow in the network is calculated a priori per day based on a fixed temperature delta of 30 K, meeting the demand of the highest peak in the grid of that day. Additionally, the velocity in the pipes is limited by a minimum pressure loss of 80 Pa/m and a maximum pressure loss of 300 Pa/m [40]. The energy balance for the pipes is formulated as

$$c_{\text{p}} m_a \frac{T_{a,t-1}^{\text{out}} - T_{a,t}^{\text{out}}}{\Delta t} + \dot{m}_{a,t} c_{\text{p}} \left(T_{a,t}^{\text{in}} - T_{a,t}^{\text{out}}\right) - U_a A_a^{\text{m}} \left(T_{a,t}^{\text{out}} - T_t^{\text{soil}}\right) = 0 \;\; for\; a \in Z^{\text{ff}}, Z^{\text{bf}}, t \in \tau, \quad (2)$$

where the first term represents the storage capacity of the pipe, the second term is the enthalpy rate entering and exing the pipe, and the last term is the loss of the pipe. The energy balance of the consumers is given by

$$\frac{\dot{Q}_{a,t}^{\text{con}}}{\mu^{\text{con}}} = \dot{m}_{a,t} c_{\text{p}} \left(T_{a,t}^{\text{in}} - T_{a,t}^{\text{out}}\right) \quad for\; t \in \tau, a \in Z^{\text{con}}, \quad (3)$$

and the energy balance of the production units is formulated analogously with

$$\dot{Q}_{a,t}^{\text{pro}} \mu_a^{\text{pro}} = \dot{m}_{a,t} c_{\text{p}} \left(T_{a,t}^{\text{out}} - T_{a,t}^{\text{in}}\right) \quad for\; t \in \tau, a \in Z^{\text{pro}}. \quad (4)$$

The temperatures in the grid are limited by the consumers, with $T_{a \in Z^{\text{con}},t}^{\text{in}} \geq T_{a \in Z^{\text{con}},t}^{\text{min}}$ and a technical limitation between 0 °C and 130 °C.

The heat flow at a production unit is the summation of all heat flows by storages and energy converters at that location a. Therefore, $\dot{Q}_{a,t}^{\text{pro}}$ is given by

$$\dot{Q}_{a,t}^{\text{pro}} = \sum_{k \in Z^{\text{conv}}(a)} \dot{Q}_{k,t}^{\text{conv}} + \sum_{k \in Z^{\text{stor}}(a)} \left(\dot{Q}_{k,t}^{\text{out,stor}} - \dot{Q}_{k,t}^{\text{in,stor}}\right) \quad for\; t \in \tau, a \in Z^{\text{pro}}, \quad (5)$$

$Z^{\text{conv/stor}}(a)$ is the set of energy converters and storages at that location. The solar thermal field is modeled with

$$\dot{Q}_{k=\text{solar},t}^{\text{conv}} = \mu_{k=\text{solar}} \gamma_t^{\text{rad}} A^{\text{collector}} \quad for\; t \in \tau, \quad (6)$$

where $A^{\text{collector}}$ is the variable dimensioned by the optimizer to calculate the area of the collectors. $\mu_{k=\text{solar}}$ is the efficiency of the solar field here assumed to be 0.5 [41]. The solar field charges the PTES, and a heat pump lifts the temperature of the PTES, if necessary, before injecting the heat into the grid. The energy balance of the PTES can be described as

$$E_{k=\text{PTES},t} = E_{k=\text{PTES},t} + \Delta t \left(\mu_{k=\text{PTES}} \dot{Q}_{k=\text{PTES},t}^{\text{in}} - \frac{\dot{Q}_{k=\text{PTES},t}^{\text{out}}}{\mu_{k=\text{PTES}}} - \dot{Q}_{k=\text{PTES},t}^{\text{loss}}\right) \quad for\; t \in \tau. \quad (7)$$

The energy balances for the buffer storages are modeled analogously. The PTES has a cyclic condition where $E_{k=\text{PTES},t=\text{start}} = E_{k=\text{PTES},t=\text{finish}}$. The PTES energy is limited by

$$E_{k=\text{PTES},t} \leq V_{k=\text{PTES}} \rho c_{\text{p}} \left(T_{k=\text{PTES}}^{\text{top,max}} - T_{k=\text{PTES}}^{\text{top,min}}\right) \quad for\; t \in \tau. \quad (8)$$

The heat flow when discharging the storage can only be directly injected into the grid if the supply temperature is lower than the temperature of the PTES at the top. This is given by

$$\dot{Q}_{k=\text{PTES},t}^{\text{out,stor}} = \begin{Bmatrix} \dot{Q}_{k=\text{PTES},t}^{\text{out,stor}}, & T_{k=\text{PTES,t}}^{\text{top}} \geq T_t^{\text{supply}} \\ \frac{COP_t}{COP_t - 1} \dot{Q}_{k=\text{PTES},t}^{\text{out,stor}}, & T_{k=\text{PTES,t}}^{\text{top}} < T_t^{\text{supply}} \end{Bmatrix} \quad for\; t \in \tau. \quad (9)$$

The COP is calculated a priori based on the predicted temperature profile of $T_{k=\text{PTES,t}}^{\text{top}}$. The heat losses $\dot{Q}_{k=\text{PTES},t}^{\text{loss}}$ correlate with the geometry of the storage and decrease with increasing volume. The heat losses $\dot{Q}_{k=\text{PTES},t}^{\text{loss}}$ are calculated identically to [42]. However, in this study, we do not know the size of the surface yet due to the unknown size of the storage. Therefore, we applied a piecewise function [43] calculating the sides, top, and bottom area of the PTES depending on the volume. We use existing sites to get grid points and summarize them in Table 2. We calculate the areas for each storage based on the geometry of an obelisk and assume that the bottom and top areas are quadratic. Furthermore, we assume a standard correlation between the top area side length and the bottom area side length of 78 to 48 due to the detailed information of Dronninglund from [42].

Table 2: PTES information about the geometry and specific investments used for the piecewise functions. [2, 30, 44]

Site	Volume [m^3]	Total surface [m^2]	Angle [°]	Height [m]	Calculated bottom area [m^2]	Calculated top area [m^2]	Calculated side area [m^2]	Specific investments [€/m^3]
Stuttgart	1050	835	45	5	118.4	312.65	403.95	
Ottrupgård	1500							150
Eggstein	4500	1924.9	30	9	182.9	482.97	1259.04	113.02
Sunstore 2 Marstal	10000							67
Dronninglund	60000	17076	26	16	2247.49	5934.78	8893.73	38
Toftlund	70000	19204	27	14.5	2826.33	7463.28	8914.4	
Sunstore 4 Marstal	75000	20298	32	16	3174.36	8382.31	8741.33	36
Gram	122000	28893	20	15	3957.6	10450.53	14484.87	34
Vojens	210000							24

3. Results

The result section divides into examining the results of the regression model to predict the top and bottom temperature of a PTES charged by a solar thermal field. Afterward, the MILP model uses this profile to design the PTES and other energy converters in a district heating network. The design is evaluated by comparing it to the existing sites of Marstal and Dronninglund. Additionally, we simulate the storage heat losses in Marstal with our predicted temperatures and compare the error. To evaluate the heat pump control, we perform two optimization runs: the first is with the predicted temperature profile, and the second is with averaged temperatures – not using the regression model in the pre-processing. We then re-simulate the actual temperatures in the storage and calculate the electrical demand for the heat pump in both optimization runs. For the re-simulation, we take the energy level $E_{k=\mathrm{PTES},t}$ and divide by the volume, the specific heat capacity, and the density resulting in the current temperature delta. This temperature delta is added to $T_{k=\mathrm{PTES}}^{\mathrm{top,min}}$ and the COP of the heat pump is recalculated.

3.1. Polynimal Regression Results

Table 3: Polynomial regrssion results for three sites as training and one site as testing.

Dataset		Polynomial Regression		
train	test	RMSE	MAE	Accuracy
Marstal, Dronninglund, Florence	Wadelheim	0.6336	0.5687	0.5986
Marstal, Florence, Wadelheim	Dronninglund	0.8395	0.6668	0.2953
Dronninglund, Florence, Wadelheim	Marstal	0.5964	0.4906	0.6443
Marstal, Dronninglund, Wadelheim	Florence	0.2896	0.2337	0.9161

Table 3 shows the results for using three data sets as training and one dataset as testing. The accuracies for Wadelheim and Marstal are around 60 % due to the daily fluctuations in the demand. The result for Florence is realtively high with an accuracy of 91.6 %. The prediction accuracy for Dronninglund as testing is relatively low, at 29.5 %. The deterministic solution of the polynomial regression is given by

$$T_t^{\mathrm{PTES,top}} = 4.0255 T_t^{\mathrm{ambient}} + 2.2715 \gamma_t^{\mathrm{rad}} + 0.2065 \sin\left(2\pi \frac{t^{\mathrm{hour}}}{24}\right) + 2.7253 * \cos\left(2\pi \frac{t^{\mathrm{hour}}}{24}\right) - 23.6073 * \sin\left(2\pi \frac{t^{\mathrm{day}}}{365}\right) - 9.9604 * \cos\left(2\pi \frac{t^{\mathrm{day}}}{365}\right) + 56.6761, \quad (10)$$

where the temperatures have the unit of °C and the irradiance W/m^2. Before Eq. 10 can be used, the StandardScaler (see method section) has to be applied to every feature.

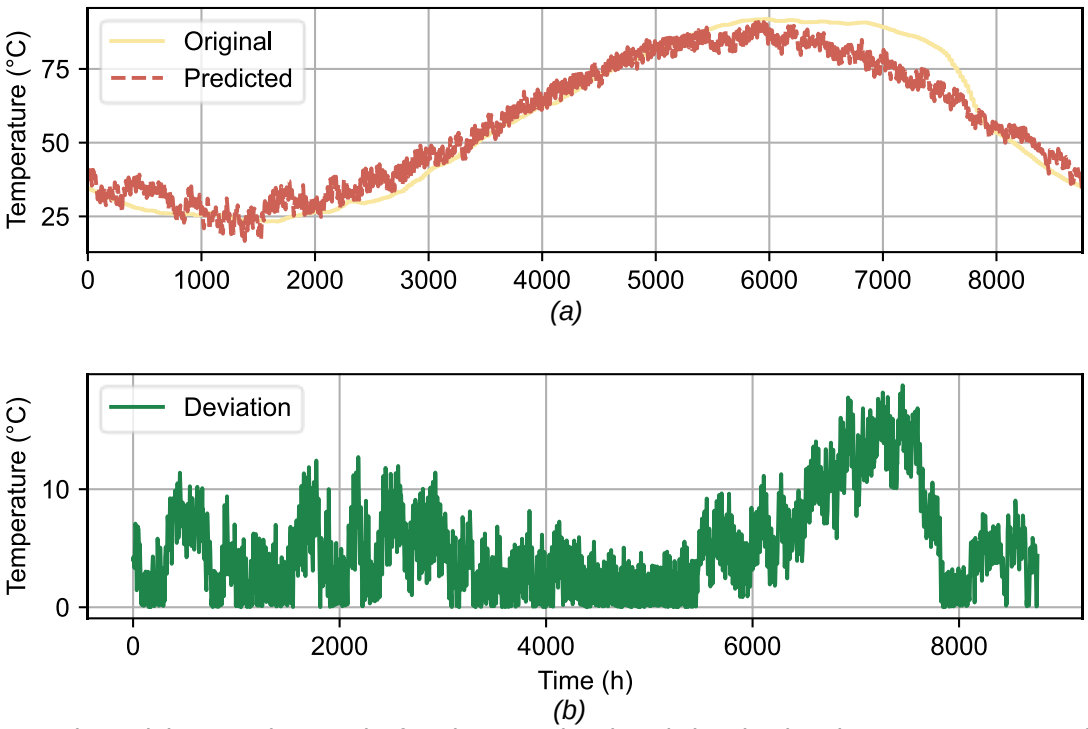

Figure 3: Polynomial regression results for Florence showing a) the simulated top temperature and the predicted top temperature and b) the deviation between the two temperature profiles. [33]

Figure 3 shows the simulated top temperature for the PTES in Florence [33] compared to the predicted temperature. A high correlation can be examined in Figure 3 a) between the two temperature profiles. However, the deviation has a maximum of 18 °C and an average of 5 °C. A deviation of 18 °C in the calculation for the COP of a 1 MW heat pump supplying 90 °C would result in an error of around 100 kW for the electrical input. This error indicates potential weaknesses in the modeling approach. To evaluate the effects on the geometry, we simulated the heat losses of the Marstal storage in 2014 based on the predicted top and bottom temperatures. The simulation results in a heat loss of 2391.85 MWh, causing an error of 17.7 % compared to the measured data [3].

3.2. Results for Designing the Energy System

The MILP model is applied to a fictional grid (see Figure 1). The design optimization of a central production unit results in a 250 kW central biomass boiler, a 12555 m^2 solar thermal field, a 26725 m^3 PTES, a 62 m^3 buffer storage, and a 958 kW heat pump. Furthermore, a decentral production unit consisting of a 50 kW biomass boiler is installed. The heat generation costs are 14.5 ct/kWh. The operation and investments of the system are displayed in Figure 4. The costs are based on the year 2020 using the Day-Ahead prices. The solar thermal field mainly loads the PTES in the summer. The heat pump also has the opportunity to charge the PTES. Due to the heat pump's partial load limit of 50 %, the biomass boilers cover peak loads. The buffer storage serves as a day-to-day flexibility supporting the heat pump operation. However, the heat flows of the buffer storage are not included in Figure 4, for clarity and due to the low impact on the energy system. The storage is mainly loaded in spring and summer, and the discharging starts mainly in October. In October, the temperatures in the storage are high enough to inject into the grid directly; therefore, the other units do not operate.

The temperature in the storage affects the electrical input for the heat pump, influencing the operational expenditures (opex). This effect is measured by resimulating the temperatures inside the storage and recalculating the COP. Based on the COP, the electrical power for the heat pump is recalculated. We also perform an optimization run without the predicted temperature profiles assuming a constant temperature inside the PTES. Using the constant temperature inside the PTES leads to a deviation of the electrical input for the heat pump of 45 %, while the predicted temperature profiles of the PTES cause an error of 29 %.

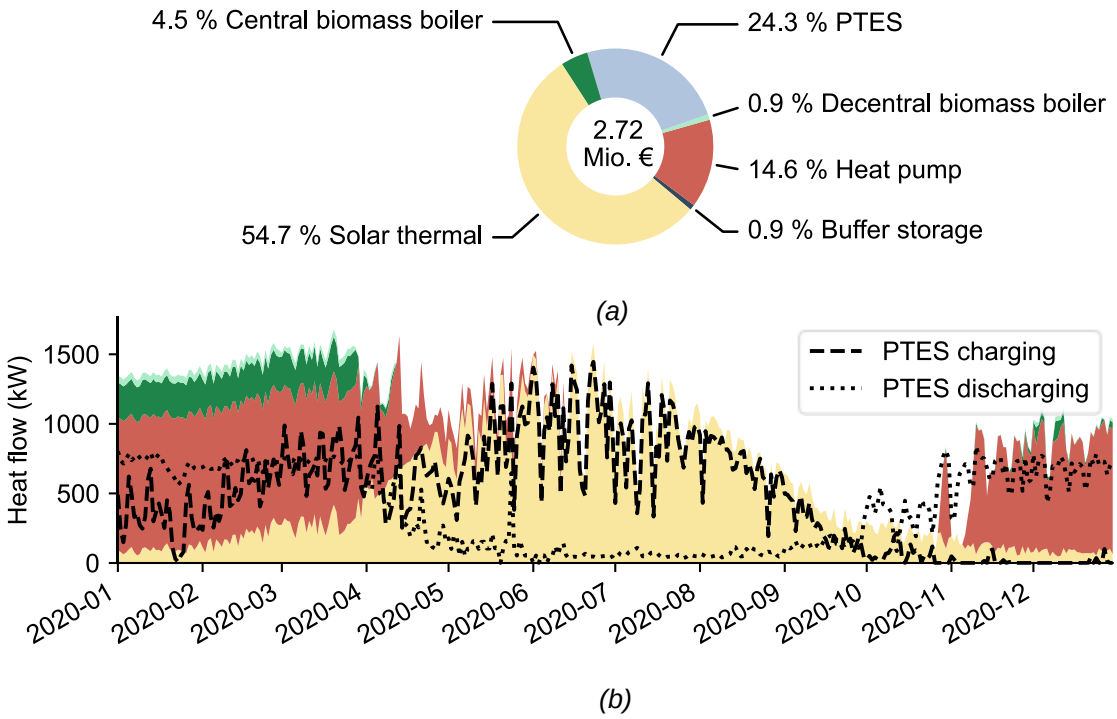

Figure 4: b) optimized operation of the energy system model and a) the investments in the energy system with the different shares for the energy converters and storages.

4. Discussion

The discussion divides into highlighting the benefits and drawbacks of the regression model and comparing the results of the energy system model with the existing sites in Marstal and Dronninglund.

4.1. Discussion of the Polynomial Regression Results

The difficulty of the regression model is the prediction of temperature profiles without knowing the demand or the volume of the PTES. Therefore, the model only has the time, the solar irradiance, and the ambient temperature as features. Using three storages as training data and Dronninglund as testing leads to a relatively low accuracy due to the considerable fluctuations in the temperature profile of Dronninglund. This clearly shows the disadvantages of the model because it cannot depict hourly or daily fluctuations. However, the prediction results improve up to 91 % for Florence. This improvement is due to the data being a simulation; therefore, no rapid changes are in the gradient. The regression model cannot replace a detailed storage simulation but can estimate the seasonal behavior at a given location for a pre-analysis.

4.1. Discussion of the Energy System Results

Utilizing the predicted temperature profiles in the energy system model leads to reasonable results, see Table 4. It should be noted that the energy system model is not applied to the demand structure in Marstal or Dronninglund due to the lack of data. Therefore, the results can only be compared relatively. The storage is about half the size compared to Marstal and Dronninglund; the same applies to the solar thermal field. The storage charging is 4362 MWh, while the storages in Marstal and Dronninglund are charged with 7813 MWh and 12760 MWh. The ratio volume to solar field is 2.13 m, while for Marstal and Dronninglund, it is 2.25 and 1.68 m. [13] suggests a ratio between 2 and 3 m, with 3 being relatively compared to our calculations and the existing sites. This comparison shows a correlation between the optimization results and the existing sites. Additionally, the results verify the approach of the piecewise functions to calculate the areas of the storage based on the volume due to the moderate deviation of 17.7 % compared to the measured data of Marstal in 2014.

A significant drawback is the deviation of the electrical input for the heat pump – 29 %. Utilizing the predicted temperature profiles increases the accuracy, but a deviation of 29 % is still not accurate. We also tested a binary-based model leaving the temperature calculation inside the optimization. We applied this model to the same use case and obtained a solution for a timestep of 24 h after 8 h computational time on a windows machine with 488 GB and an AMD EPYC 7542 32-Core Processor. Reducing the timestep length to 8 h led to computational times over 24 h. Therefore, we conclude that the model is not applicable. Feeding the optimization model with fixed temperature profiles already suggests a control strategy for the heat pump and

influences the results. The last option would be to assume a constant temperature inside the storage and calculate the COP based on a constant value. Based on this study, we suggest using a constant temperature inside the storage for the COP calculation and performing a more detailed simulation of the PTES with TRYNSYS or other simulation software mentioned in the state-of-the-art. This has the advantage that the energy system model already calculates the design of the PTES, and the simulation can focus on the control strategy. Assuming a constant temperature inside the PTES for the energy system model would allow loading the storage with other technologies. The regression model can only work if a seasonal behavior is present in the charging process; however, other technologies like air heat pumps would load the storage based on the electricity market.

Table 4: Comparison of results with the existing sites in Marstal and Dronninglund. [3]

Parameter	Marstal (2015)	Dronninglund (2015)	Energy System Results (2020)
Charging, MWh	7813	12760	4362
Discharging, MWh	5435	11983	3433
Thermal losses, MWh	2946	1275	853
Heat capacity, MWh	5430	5500	2086
T-max, °C	84	89	92
T-min, °C	20	10	23
Volume, m^3	75000	63000	26725
Solar gain, $kWh/m^2/a$	395	447	355
Solar field, m^2	33300	37573	12555
Ratio volume / solar field, m	2.25	1.68	2.13

5. Limitation of Results

The method is applied to a fictional grid with six consumers. The grid size does not represent the usual DHS, and larger grids would lead to higher computational times. However, the solver needed ca. 1 h, and the model is applied in the planning phase; therefore, the computational time can be slightly higher than in a control optimizations. Nevertheless, the method must be applied to larger grids to evaluate its performance.

6. Conclusion

In this study, a method is developed to design PTES supplied by solar thermal energy inside a DHS. Our approach utilizes historical data and identifies strong correlations between the modeling results and the existing sites. The results suggest a ratio of ca. 2 m for volume vs. solar field. For 1 GWh capacity of a PTES, an area of around 1500 m^2 combined with 37500 m^2 solar thermal collectors would be needed. Achieving a more accurate result, our model can be applied in the planning phase for a grid-based DHS supplying heat from and to different locations. The model can depict the decreasing specific investments and thermal losses due to an increasing volume. This behavior is achieved by a piecewise function taking the volume as input and the investments and geometry of the PTES as output.

The difficulty within the optimization is the control strategy of the heat pump, depending on the temperature inside the storage. We examined three possibilities:

1. Predicting the temperatures of the storage before the optimization and calculating the COP a priori
2. Assuming one constant temperature of the storage and calculating the COP a priori
3. Calculating the temperature and the COP during the optimization

The first option already induces a control strategy inside the optimization and causes an error of 29 % for the electrical input. The second option did not depict any temperature changes inside the storage and caused an error of 45 %. The third option was not applicable due to a high computational time. In conclusion, we suggest the second option, followed by a detailed simulation. This study showed the computational limits for a mathematical optimization in the design stage due to the fact that the dimension – the volume of the PTES – and operation – the temperature of the PTES – is a variable. In the future, new methods could be developed depicting volume and temperature as a variable and computing results in a practical manner.

Furthermore, it would be interesting to investigate different technologies supplying a PTES and compare it to solar thermal energy due to its high investments. For Power-to-Heat technologies, the investigation should optimize at the Day-Ahead market to react to price fluctuations. In addition, large grids should be examined due to the large space requirements for PTES charged by solar thermal energy.

Contributions and Acknowledgements

MS advised the research of the polynomial regression model, developed the energy system model, and wrote the manuscript. YX developed the polynomial regression model. MiR and MvB advised the development of the energy system model. MR acquired the finance for this research via the project ODH@Jülich.

Nomenclature

Letter symbols

A area, m^2

c_p specific heat capacity, kJ/(kg K)

COP coefficient of performance for heat pumps

DHS district heating system

E energy, kJ

$f^{\mathrm{opex,var}}$ variable opex of the components in the energy system, €

$g^{\mathrm{opex,fix}}$ fixed opex of the components in the energy system, €

h^{capex} capex of the components in the energy system, €

m mass, kg

$\dot{m}$ mass flow, kg/s

MAE mean average error

MILP mixed-integer linear programming

PTES pit thermal energy storage

$\dot{Q}$ heat flow, kW

RMSE root mean squared error

t time

Δt timestep length of the optimization, s

T temperature, K

U heat transfer coefficient, kW/(m^2 K)

Z set of arcs – pipes, consumers, producers

Greek symbols

τ set of timesteps

γ solar irradiance, kW/m^2

μ efficiency

Subscripts and superscripts

a pipe

capex capital expenditures

$\mathrm{collector}$ solar collectors

con consumer

conv energy converter

ff forward-flow

bf backward-flow

in entering a component

k energy converter or storage

m shell

min minimum

loss losses

$\mathrm{opex,var}$ variable operational expenditures

$\mathrm{opex,fix}$ fixed operational expenditures

out leaving a component

pro producer

rad irradiance

soil soil/ground

stor storage

supply for the supply / to the consumer

t timestep

top at the top level

References

[1] Paardekooper S, Lund RS, Mathiesen BV*, et al.* Heat Roadmap Europe 4: Quantifying the Impact of Low-Carbon Heating and Cooling Roadmaps: Aalborg University; 2018.

[2] Yang T, Liu W, Kramer GJ, Sun Q. Seasonal thermal energy storage: A techno-economic literature review. Renewable and Sustainable Energy Reviews 2021; 139: 110732.

[3] Schmidt T, Sorensen PA. Monitoring Results from Large Scale Heat storages for District Heating in Denmark. 14th International Conference on Energy Storage 2018.

[4] Li X, Wang Z, Li J*, et al.* Comparison of control strategies for a solar heating system with underground pit seasonal storage in the non-heating season. Journal of Energy Storage 2019; 26: 100963.

[5] Crawley DB, Lawrie LK, Winkelmann FC*, et al.* EnergyPlus: creating a new-generation building energy simulation program. Energy and Buildings 2001; 33(4): 319–31.

[6] Pauschinger. Solites Bericht.

[7] Lyden A. Modelling and design of local energy systems incorporating heat pumps, thermal storage, future tariffs, and model predictive control 2020.

[8] Dominković DF, Ćosić B, Bačelić Medić Z, Duić N. A hybrid optimization model of biomass trigeneration system combined with pit thermal energy storage. Energy Conversion and Management 2015; 104: 90–9.

[9] Reiter P, Poier H, Holter C. BIG Solar Graz: Solar District Heating in Graz – 500,000 m2 for 20% Solar Fraction. Energy Procedia 2016; 91: 578–84.

[10] Sifnaios I, Gauthier G, Trier D, Fan J, Jensen AR. Dronninglund water pit thermal energy storage dataset. Solar Energy 2023; 251: 68–76.

[11] Sifnaios I, Jensen AR, Furbo S, Fan J. Performance comparison of two water pit thermal energy storage (PTES) systems using energy, exergy, and stratification indicators. Journal of Energy Storage 2022; 52: 104947.

[12] Słomczyńska K, Mirek P, Panowski M. Solar Heating for Pit Thermal Energy Storage – Comparison of Solar Thermal and Photovoltaic Systems in TRNSYS 18. Adv. Sci. Technol. Res. J. 2022; 16(5): 40–51.

[13] Lindenberger D, Bruckner T, Groscurth H-M, Kümmel R. Optimization of solar district heating systems: seasonal storage, heat pumps, and cogeneration. Energy 2000; 25(7): 591–608.

[14] Rämä M, Mohammadi S. Comparison of distributed and centralised integration of solar heat in a district heating system. Energy 2017; 137: 649–60.

[15] Martins F, Patrão C, Moura P, Almeida AT de. A Review of Energy Modeling Tools for Energy Efficiency in Smart Cities. Smart Cities 2021; 4(4): 1420–36.

[16] Bai Y, Wang Z, Fan J*, et al.* Numerical and experimental study of an underground water pit for seasonal heat storage. Renewable Energy 2020; 150: 487–508.

[17] Pan X, Xiang Y, Gao M*, et al.* Long-term thermal performance analysis of a large-scale water pit thermal energy storage. Journal of Energy Storage 2022; 52: 105001.

[18] Xie Z, Xiang Y, Wang D*, et al.* Numerical investigations of long-term thermal performance of a large water pit heat storage. Solar Energy 2021; 224: 808–22.

[19] Gauthier G. Benchmarking, and improving models of subsurface heat storage dynamics: Comparison of Danish PTES and BTES installation measurements with their corresponding TRNSYS models 2020.

[20] Preuss J. 250520_Kurzbeschreibung_Trnsys-1.

[21] Dahash A, Michele Bianchi Janetti M, Ochs F. Numerical Analysis and Evaluation of Large-Scale Hot Water Tanks and Pits in District Heating Systems. In: Corrado V, Fabrizio E, Gasparella A, Patuzzi F, editors. Numerical Analysis and Evaluation of Large-Scale Hot Water Tanks and Pits in District Heating Systems; 2020. IBPSA; 1692–9.

[22] Detailed 3-D models of a large-scale underground thermal energy storage with consideration of groundwater conditions 2018.

[23] COMSOL. COMSOL Release Notes.

[24] Chang C, Nie B, Leng G*, et al.* Influences of the key characteristic parameters on the thermal performance of a water pit seasonal thermal storage. Energy Procedia 2017; 142: 495–500.

[25] Chang C, Leng G, Li C*, et al.* Investigation on transient cooling process in a water heat storage tank with inclined sidewalls. Energy Procedia 2017; 142: 142–7.

[26] Ansys. MASTER SOFTWARE LICENSE AGREEMENT.

[27] Bai Y, Yang M, Fan J*, et al.* Influence of geometry on the thermal performance of water pit seasonal heat storages for solar district heating. Build. Simul. 2021; 14(3): 579–99.

[28]Narula K, Oliveira Filho F de, Villasmil W, Patel MK. Simulation method for assessing hourly energy flows in district heating system with seasonal thermal energy storage. Renewable Energy 2020; 151: 1250–68.

[29]Lyden A, Flett G, Tuohy PG. PyLESA: A Python modelling tool for planning-level Local, integrated, and smart Energy Systems Analysis. SoftwareX 2021; 14: 100699.

[30]Xiang Y, Xie Z, Furbo S, Wang D, Gao M, Fan J. A comprehensive review on pit thermal energy storage: Technical elements, numerical approaches and recent applications. Journal of Energy Storage 2022; 55: 105716.

[31]Achterberg T, Bixby RE, Gu Z, Rothberg E, Weninger D. Presolve Reductions in Mixed Integer Programming. INFORMS Journal on Computing 2020; 32(2): 473–506.

[32]Anthrakidis A, Merten F, Buddeke M*, et al.* Die kommunale Effizienzrevolution für den Klimaschutz in den deutschen Städten – „KomRev“. Jülich: Solar-Institut Jülich der FH Aachen; 2017.

[33]Salvestroni M, Pierucci G, Fagioli F*, et al.* Design of a seasonal storage for a solar district heating in Florence. IOP Conference Series Materials Science and Engineering 2019; 556(1): 12026.

[34]Rohatgi A. Webplotdigitizer: Version 4.6; 2022. Available at: <https://automeris.io/WebPlotDigitizer>.

[35]Energy, DG Joint Research Centre /. JRC Photovoltaic Geographical Information System (PVGIS) - European Commission. Available at: <https://re.jrc.ec.europa.eu/pvg_tools/en/> [accessed 01.02.2023]

[36]Fabian Pedregosa, Gaël Varoquaux, Alexandre Gramfort*, et al.* Scikit-learn: Machine Learning in Python. Journal of Machine Learning Research 2011; 12(85): 2825–30.

[37]scikit-learn developers. StandardScaler. Available at: <https://scikit-learn.org/stable/modules/generated/sklearn.preprocessing.StandardScaler.html> [accessed 13.03.2023]

[38]VDI The Association of German Engineers. Economic efficiency of building installations - Fundamentals and economic calculation. Berlin: Beuth Publisher; 2012 2012 Sep 1. Available at: <https://www.vdi.de/richtlinien/details/vdi-2067-blatt-1-wirtschaftlichkeit-gebaeudetechnischer-anlagen-grundlagen-und-kostenberechnung-1#:~:text=Die%20Richtlinienreihe%20VDI%202067%20behandelt,Richtlinienreihe%20in%20mehrere%20Bl%C3%A4tter%20gegliedert.> [accessed 15.02.2023]

[39]Gurobi Optimization LL. Gurobi Optimizer Reference Manual. Available at: <https://www.gurobi.com> [accessed 07.03.2023]

[40]Verenum. Planungshandbuch Fernwärme. Version 1.1 vom 21. September 2017. Ittigen, Bern: EnergieSchweiz Bundesamt für Energie 2017 Sep 21.

[41]Sara Ortner, Martin Pehnt, Sebastian Blömer, Andreas Auberger, Jan Steinbach, Jana Deurer, Eftim Popovski, Oliver Lösch, Nora Langreder, Nils Thamling, Malek Sahnoun, Dominik Rau. Analyse des wirtschaftlichen Potenzials für eine effiziente Wärme- und Kälteversorgung: Beitrag zur Berichtspflicht EnEff-RL, Artikel 14 - Anhang VIII: Institut für Energie- und Umweltforschung Heidelberg gGmbH, Heidelberg; IREES GmbH, Karlsruhe; Prognos AG, Berlin.

[42]Sorknæs P. Simulation method for a pit seasonal thermal energy storage system with a heat pump in a district heating system. Energy 2018; 152: 533–8.

[43]Hart WE. Pyomo - optimization modeling in Python. 2cd ed. Cham, Switzerland: Springer Optimization and its Applications 2017.

[44]Danish Energy Agency. Technology Data for Energy storage. Copenhagen; 2018 [accessed 15.02.2023] Available at: <https://solarthermalworld.org/wp-content/uploads/2019/05/technology_data_catalogue_for_energy_storage.pdf?x32997>.

ULPGC
Universidad de
Las Palmas de
Gran Canaria

grres ULPGC
group for the research on renewable energy systems

M. Energy use in the industrial, residential, transportation, agricultural sectors. District heating/cooling

ECOS2023

PROCEEDINGS OF ECOS 2023 - THE 36TH INTERNATIONAL CONFERENCE ON
EFFICIENCY, **C**OST, **O**PTIMIZATION, **S**IMULATION AND ENVIRONMENTAL IMPACT OF ENERGY SYSTEMS
25-30 JUNE 2023, LAS PALMAS DE GRAN CANARIA, SPAIN

Flexibility from Industrial Demand-Side Management in a Net-Zero Sector-Coupled Energy System

Patricia Mayer[a], Mario Heer[a], David Yang Shu[a], Nik Zielonka[a], Ludger Leenders[a], Florian Baader[a], André Bardow[a]

[a] *Energy Process Systems Engineering, ETH Zurich, Zurich, Switzerland, abardow@ethz.ch*

Abstract:

Energy systems require flexibility to help with the penetration of variable renewable energy. A promising solution for flexibility provision is demand-side management (DSM) from industry. However, the extent of flexibility from industrial DSM depends on the characteristics of industrial processes. In this work, we investigate the potential of industrial DSM as a flexibility provider to a net-zero sector-coupled energy system. Specifically, we investigate the cost reductions and the change in deployment of other flexibility options due to industrial DSM. We examine three system configurations for the Swiss sector-coupled energy system, varying the attractiveness of alternative flexibility options. To consider the characteristics of industrial processes, we parameterize the study with three representative industrial process characteristics: load-shifting potential, storage capacity, and losses. Our results show that the value of flexibility from industrial DSM highly depends not only on the process characteristics, but also on the system's flexibility alternatives, particularly for flexibility over longer time horizons. Due to differences in flexibility alternatives, the maximum cost reductions from industrial DSM vary between 2% and 27%. Additionally, we find that the effects of the three investigated characteristics on cost reductions also depend on the interactions with the alternative flexibility options. Depending on the interactions, cost reductions may stagnate as flexibility from industrial DSM is enhanced. Our study shows that while industrial DSM can serve as a flexibility provider to a net-zero sector-coupled energy system, the value of industrial DSM highly depends on both the characteristics of industrial processes and the system's alternative flexibility options. Both aspects must be considered when evaluating the extent of flexibility from industrial DSM.

Keywords:

Demand-Side Management, Flexibility, Sector-Coupling, Energy System, Net-Zero, Industry, Switzerland

1. Introduction

Countries are increasingly setting net-zero emissions targets to address climate change [1]. To meet these targets, fossil fuels must be replaced by renewable energy sources in all energy-consuming sectors [2], and direct air carbon capture and storage (DACCS) must be implemented to abate residual emissions. As energy-consuming sectors transition away from fossil fuels, electrification becomes increasingly important as the medium for integrating renewables into other sectors. For example, the heating sector can be electrified by heat pumps and the mobility sector can be electrified by battery electric vehicles [3]. The resulting reliance of all energy sectors on the electricity sector leads to sector-coupling, where the electricity sector becomes the central pillar for the overall energy system. However, most renewable energy is intermittent, such that flexibility is needed for systems with a high share of variable renewable energy. Flexibility refers to an energy system's ability to cope with the variability and unpredictability that variable renewable energy introduces in different time scales, while reliably supplying all the demanded energy to end users [4]. Shaner et al. [5] show that the need for flexibility increases rapidly after 80% variable renewable energy share.

Flexibility can be provided from the supply side through storage, imports, and fossil-based electricity with carbon capture and storage (CCS). However, each of these options has limitations: storage technologies, such as batteries, are expensive and not suitable for long duration energy storage due to their self-discharge characteristic. [6–8]. Power-to-hydrogen is a storage technology that is stable over long time horizons, but has a low round-trip efficiency [8, 9]. Pumped hydro storage, while efficient, is subject to high capital costs, topographic limitations, and environmental concerns regarding surrounding areas [10]. Electricity imports are subject to availability abroad. Fossil fuel imports are also subject to availability abroad. Additionally, the required CCS is not widely accepted and can thus be difficult to scale due to both social and physical constraints [11].

Due to the limitations of supply-side flexibility, demand-side management (DSM) serves as a promising alternative. Demand-side management refers to the shifting of energy consumption patters to obtain a desired

energy consumption profile [12]. A good candidate for demand-side management is the industry sector due to its large energy demand, its potential for storing products over long time horizons, its already-existing metering infrastructure, and the avoidance of consumer behaviour change [13]. An example of industrial demand-side management is the shifting of production schedules to better-follow the availability of renewable electricity. For instance, an industrial process can over-produce during the daytime hours to take advantage of low prices caused by photovoltaic availability, store the overproduction, and under-produce during night-time hours such that the overall production stays the same. Promising example processes for industrial DSM are aluminum electrolysis, cement and raw mills, air separation, electric arc furnace and pulp production due to their high electricity demands and technical possibilities for load shifting [14].

The extent of flexibility from industrial DSM depends on several characteristics of industrial processes:

- **Load-shifting potential**: The percentage of the base industrial energetic demands that can be shifted to another time interval in response to volatility.
- **Storage capacity**: The amount of product that can be stored at a time.
- **DSM losses**: The losses associated with demand-side management, such as efficiency losses from off-design operation and product losses from storage.

These three characteristics influence the potential value from industrial DSM for the overall system. Promising industrial candidates can be identified by identifying promising combinations of these characteristics. Additionally, some of these characteristics can be influenced via financial incentives, e.g. the installation of larger storage capacities. Therefore, understanding the characteristics' effects on industrial DSM can help guide financial incentives.

Studies have shown how industrial DSM can affect the costs and environmental impacts for individual industrial sites [15–17]. Studies have also considered the contributions of industrial DSM from an overall system perspective [18, 19]. However, these studies have typically focused only on the electricity sector. For instance, Paulus et al. [18] analyzed the economic benefits of industrial DSM from energy-intensive industries to electricity markets. Papadaskalopoulos et al. [19] also studied the economic benefits of industrial DSM to the European power system by varying the load shifting potential. Thus far, to the best of our knowledge, no study has resolved the potential contributions of industrial DSM to a net-zero sector-coupled energy system.

In this study, we evaluate how varying degrees of industrial DSM affect the costs and the needs for other flexibility options of a net-zero energy system considering multiple sectors. Varying degrees of industrial DSM are modelled by varying the industrial process characteristics listed above. We aim to answer the following research questions:

1. What are the potential cost reductions of a net-zero sector-coupled energy system from industrial DSM?
2. How does industrial DSM interplay with other flexibility options?

To answer these research questions, we model the Swiss sector-coupled energy system using the linear optimization framework SecMOD [20]. We use a snapshot approach, constrain the system to net-zero emissions, and determine the system's cost-optimal investments and operation for varying degrees of industrial DSM. We do not consider costs associated with industrial DSM to determine an upper bound on the potential cost reductions. We consider three scenarios with varying assumptions regarding natural gas prices and use in power plants. By considering three scenarios, we can compare the contributions from industrial DSM across systems with varying flexibility alternatives. Of particular importance are the alternatives for long-duration flexibility, referring to durations longer than 12 hours. To represent industry, we create a generic, process-agnostic model comprised of the Swiss industry's electricity and heat requirements. This approach allows us to vary DSM characteristics without the need to model specific industries and processes. To model the varying degrees of industrial DSM, we perform a parameterized study by introducing parameters representative of industrial process characteristics. Our approach allows us to study the potential of industrial DSM as a flexibility provider to a net-zero sector-coupled energy system.

In Section 2., we briefly introduce the energy system model and discuss the modeling of industrial DSM in detail. Section 3., presents the results of the parameterized study. Finally, Section 4., summarizes the most important points of this study.

2. Modelling industrial DSM in Sector Coupled Energy Systems

As the focus of this study is industrial DSM, we only briefly summarize the Swiss energy system modelling in Section 2.1.. We describe the modelling of industry and the industrial DSM characteristics in more detail in Section 2.2.. Section 2.3. introduces the three scenarios.

2.1. Swiss Sector-coupled Energy system

The Swiss sector-coupled energy system is modelled with the open-source linear optimization framework SecMOD [20]. We consider the electricity, heat, and private mobility sectors within the energy system and focus on the year 2050 with an exogenous net-zero operational emissions constraint. Within the heat sector, we consider civil heating along with industrial heating at three temperature levels. Industry also has en electricity demand which we consider together with industrial heat demands (Section 2.2.). The optimization framework determines the cost-optimal investment and operation decisions to reach the net-zero emissions target, while ensuring that exogenous demands are met. Demands for civil electricity, civil heat, and private mobility are provided separately, while demands for industrial electricity and heat are provided in an aggregated fashion to represent Swiss industrial demands. Only operational emissions are considered for the net-zero target. The technology options included in the model of the sector-coupled energy system are shown in Table 1.

The energy system is modelled as a 1-node system. Hourly time series are provided and aggregated with a temporal resolution of 25 typical days. To allow for seasonal storage, the typical days are interlinked using the method developed by Kotzur et al. [21]. Note that Switzerland today has 8.8 TWh of seasonal storage from hydro reservoirs [22], comprising 14% of the overall electricity demand in 2019 [23].

Table 1: Technology options provided for modelling the Swiss sector-coupled energy system

Electricity	**Civil heat**	**Transportation**
photovoltaics onshore wind natural gas combined cycle* run-of-river large dam hydro geothermal biogas	thermal insulation electrode boiler heat pump natural gas boiler	battery electric vehicle
Low-temperature heat	**Medium-temperature heat**	**High-temperature heat**
electrode boiler heat pump	electrode boiler natural gas boiler	natural gas boiler
Storage technologies	**Negative emission technologies**	**Power-to-X**
Li-ion batteries pumped hydro storage	direct air capture	power-to-methane

**CCS_lowprice* and *CCS_highprice* scenarios

2.2. Implementation of Industrial Demand-side Management

In this section, we explain how industry is modelled within the energy system and how the industrial DSM characteristics were represented by three parameters. The hourly electricity and heat demands of Swiss industry are aggregated into a generic industrial process. This aggregated process produces 1 "good/hour", while consuming the hourly industrial energy demands for Switzerland. We use an industrial electricity demand of 6 TWh [24] and a heat demand of 20 TWh [25] in 2050. The heat demand is split into three temperature levels (Table 2) according to a report from the Swiss Federal Office of Energy [24]. The demands in Table 2 represent the base industrial energy demands, d^{base}_{energy}, from which the benefits of industrial DSM are explored. Industrial production is assumed constant throughout the year, such that an exogenous demand of 1 good/hour, or d^{base}_{goods}, is introduced. Thus, without industrial DSM, the hourly electricity and heat demands of Swiss industry must be supplied for every hour of the year. This assumption introduces a basis from which to measure the benefits from industrial DSM. However, the benefits may be greater or smaller depending on how the actual industrial energy demand profiles follow renewables availability.

Table 2: Base energy demands of Swiss industry, d^{base}_{energy}, for the production of 1 $\frac{good}{hour}$, or d^{base}_{goods}

Input/Output	Temperature Range	Value (MW)
electricity	–	685
low temperature heat	$< 200°C$	750
medium temperature heat	$200°C - 800°C$	907
high temperature heat	$> 800°C$	571

The contributions from industrial DSM are evaluated by performing a parameterized study on three parameters

representative of the industrial process characteristics introduced in Section 1. An industrial goods storage tank is introduced to serve as a buffer for industrial over and under-production (Figure 1). No investment or operating costs are associated with storage capacity to evaluate an upper bound on cost reductions from industrial DSM. The calculated cost reductions can then be compared to the real costs associated with the necessary storage capacities. The three modelled parameters are described below:

- **Load-shifting potential** (*iflex*): The load-shifting potential, referred to as *iflex*, represents to the fraction of the base load, d^{base}_{energy}, that can be shifted up or down at a given time step, t, similar to [19]. *Iflex* can take any value between 0 and 1, as shown in Equation (1).

$$0 \leq iflex \leq 1 \tag{1}$$

  An *iflex* value of 0 corresponds to no load-shifting potential and an *iflex* of 1 corresponds to the ability to shift 100% of the base load at a given time step, ranging from a complete shutdown to the doubling of base production.

- **Storage capacity** (t_{SC}): The storage capacity refers to the maximum amount of goods in the industrial storage tank, and limits the amount of goods can be stored at a time. We parameterize the storage capacity, SC, with the time interval t_{SC} over which the base demand of $1 good/hour$, or d^{base}_{goods}, can accumulate (Equation (2)).

$$SC = t_{SC} \cdot d^{base}_{goods} \qquad t_{SC} \in [12\ hours, 6\ months] \tag{2}$$

  For example, with a t_{SC} of $1 day$ the storage capacity is constrained to a day's worth of industrial demand. We range t_{SC} from 12 hours to 6 months in our parameterized study. Throughout this text, we refer to t_{SC} as the storage capacity.

- **DSM losses** (η): DSM losses refer to production lost as a result of industrial DSM. Losses can arise from off-design operation as well as storage leakage. To study the effect of DSM losses, we introduce the discharge efficiency, η, that represents the amount of goods that can be withdrawn from the storage of industrial goods per goods stored. A lower efficiency means that less goods can be withdrawn per goods stored and therefore more goods need to be produced to meet the overall demand. The discharge efficiency, η, can take any value from 0 to 1 as shown in Equation (3).

$$0 \leq \eta \leq 1 \tag{3}$$

  An η value of 0 corresponds to 100% product losses and an η value of 1 corresponding to no product losses. Note that while η only represents discharge efficiency associated with storage in our mathematical formulation, the wide η range investigated can be interpreted as also considering additional efficiency losses.

The relationship between the three parameters (*iflex*, t_{SC}, and η), the industrial production, and the storage can be seen schematically in Figure 1 as well as in Equations (4) to (8). Equation (4) constrains the production used at a given time step, $P(t)$, between the range defined by the *iflex* parameter.

$$d^{base}_{goods} \cdot (1 - iflex) \leq P(t) \leq d^{base}_{goods} \cdot (1 + iflex) \tag{4}$$

Equation (5) prevents the industry storage from acting as a source or sink for industrial products by setting the initial and final storage levels (SL) equal, similar to [15].

$$SL_{t=0} = SL_{t=T} \qquad T = 8760h \tag{5}$$

Equation (6) models the stored product. $in(t)$ refers to the product stored at time t and $out(t)$ refers to the product withdrawn.

$$SL(t+1) = SL(t) + in(t) - \frac{out(t)}{\eta} \tag{6}$$

Equation (7) shows how the demand of industrial goods is met at every time step with a combination of production, $P(t)$, and storage.

$$d^{base}_{goods} = P(t) - in(t) + out(t) \tag{7}$$

Finally, Equation (8) constrains the storage level with respect to the parameterized storage capacity, t_{SC}.

$$SL(t) \leq t_{SC} \cdot d^{base}_{goods} \tag{8}$$

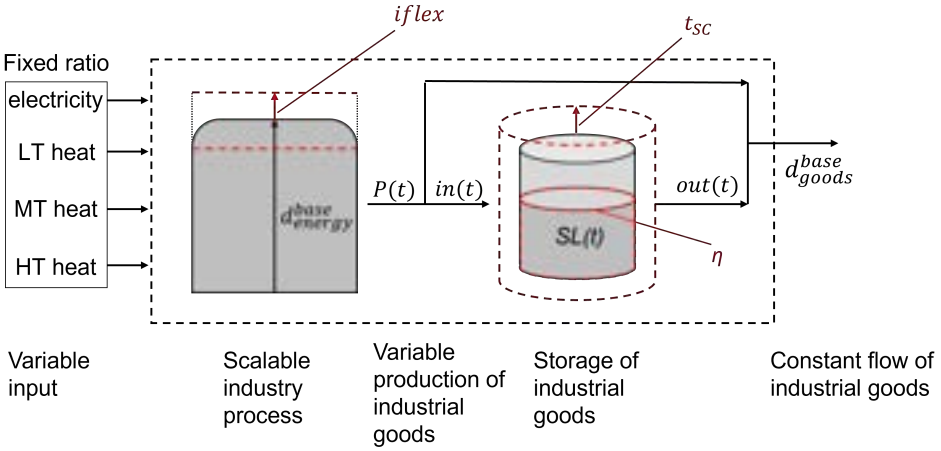

Figure 1: Schematic representation of the relationship between the industrial DSM parameters (*iflex*, t_{SC}, and η), industrial production, and storage of industrial goods. The three parameters are shown in red. *iflex* corresponds to load-shedding potential, t_{SC} correspods to the time interval over which the base industrial demand of $1 good/hour$, or d^{base}_{goods}, can accumulate. η corresponds to the storage discharge efficiency. LT, MT, and HT correspond to low, medium, and high temperature heat demands for Swiss industry. $P(t)$ is the production of industrial goods at time t. $in(t)$ and $out(t)$ are the product stored and withdrawn, respectively, and $SL(t)$ is the storage level.

2.3. Scenarios

Three scenarios represent different assumptions on natural gas prices and on the utilization of natural gas power plants as a flexibility option. The three scenarios, described below, allow us to compare the contributions from industrial DSM across systems with varying flexibility alternatives.

CCS_lowprice: This scenario includes the cheapest flexibility alternative to industrial DSM by allowing for electricity production from natural gas power plants with carbon capture and storage (CCS). It assumes a natural gas import price of 31€/MWh, representative of a stable historical average [26].

CCS_highprice: This scenario also allows for electricity production from natural gas power plants with carbon capture and storage (CCS) while assuming a high natural gas import price of 135 €/MWh, representative of the average for 2022 [26].

minCCS: This scenario includes the most expensive flexibility alternative to industrial DSM by only allowing for electricity production from renewable energy sources. This scenario represents an extreme case where both the use of CCS and fossil fuel imports are minimized. Natural gas can still be imported at a price of 31 €/MWh, but only for use in natural gas boilers for high and medium temperature heat. In this scenario, batteries become important as the flexibility alternative to industrial DSM.

3. Results and Discussion

The contributions from industrial DSM depend on both the industrial DSM characteristics, represented by the three parameters (*iflex*, t_{SC}, and η), and on the system characteristics, represented by the three scenarios. The most influential system characteristics are the alternative flexibility options, particularly over time horizons greater than 12 hours. Our results show that the system cost reductions from industrial DSM range from 1.7% to 27% due to the differing flexibility alternatives across scenarios. The flexibility alternatives also influence the relationships between the industrial DSM characteristics and the industrial DSM contributions.

In subsection 3.1. we discuss the effect of the load-shifting potential on the contributions from industrial DSM. In subsection 3.2., we discuss the effect of storage capacity, and in subsection 3.3. we discuss the effect of DSM

losses. We place particular emphasis on how the contributions vary depending on the system's alternative flexibility options.

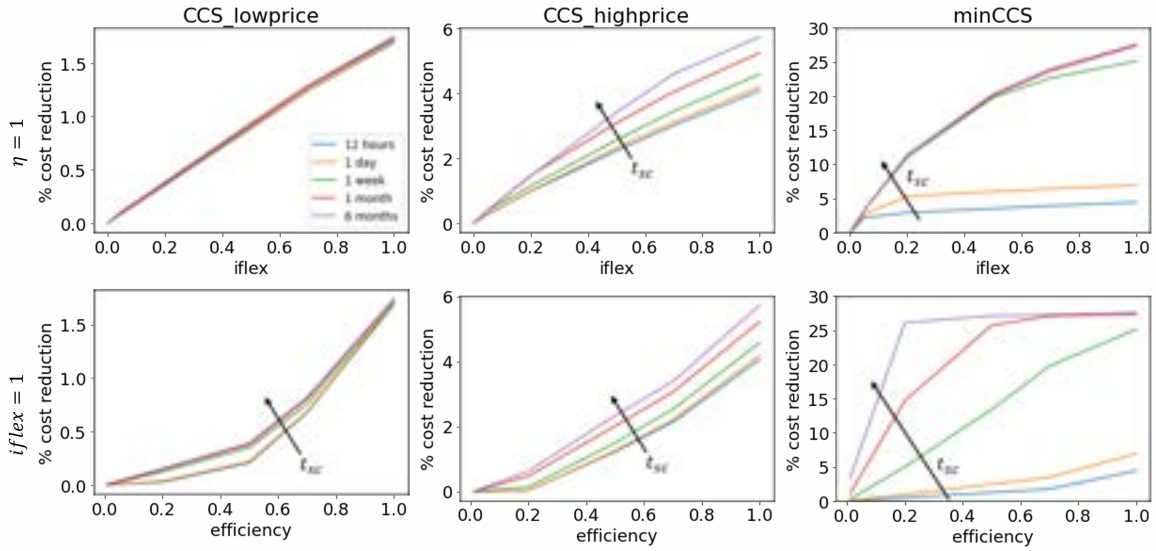

Figure 2: Top row: % cost reduction compared to a system with no industrial DSM as a function of load-shifting potential, *iflex*, for 100% discharge efficiency (η = 1). Bottom row: % cost reduction compared to a system with no industrial DSM as a function of discharge efficiency, η, for 100% load-shifting potential (*iflex* = 1). The columns correspond to scenarios and the colors correspond to storage capacities, t_{SC}. Arrows point in the direction of increasing storage capacity. The ranges for % cost reduction vary across scenarios.

3.1. Load-shifting Potential

Load-shifting potential can decrease the overall system costs for all scenarios (Figure 2). However, the magnitude of the maximum cost reduction differs significantly depending on the scenario: for the *CCS_lowprice* scenario, the maximum cost reduction is 1.7% whereas for the *minCCS* scenario, the maximum cost reduction is 27%. This magnitude difference is mainly driven by the attractiveness of industrial DSM as a flexibility provider over longer time horizons, as shown by the jump in cost reduction for the *minCCS* scenario between 1 day and 1 week storage capacities (Figure 2, top row, third column).

Additionally, the relationship between cost reduction and load-shifting potential differs across scenarios: the *CCS_lowprice* and *CCS_highprice* scenarios show a more linear relationship between cost reduction and *iflex* whereas the *minCCS* scenario shows a non-linear relationship (Figure 2, top row). The relationships are driven by the effect of increasing load-shifting potential on the implementation of the alternative flexibility options as explained in detail in the subsections below.

3.1.1. CCS_lowprice

In the *CCS_lowprice* scenario without industrial DSM, electricity from natural gas is used to balance both the intraday and the seasonal fluctuations in renewables availability. To help with the seasonal imbalance of PV availability, which peaks in the summer, direct air capture (DAC) with carbon capture and storage (CCS) is deployed flexibly, maximizing its CO_2 capture in the summer following PV availability (Figure 3, Reference). Once DAC capacity is installed, it can be deployed flexibly throughout the year while incurring no additional costs for the flexible operation. DAC capacity thus serves as a seasonal flexibility alternative to industrial DSM.

As load-shifting potential is introduced (assuming η = 1, t_{SC} = 12 *hours*), the electricity from natural gas needed to balance the intraday fluctuations reduces substantially due to the shifting of industrial production to daytime hours. Maximum load-shifting potential (*iflex* = 1) and a storage capacity of 12 hours (t_{SC} = 12 *hours*) reduces both natural gas imports and CO_2 stored by 19%. The cost reduction of 1.7% is mainly due to the decrease in natural gas imports. The imports decrease linearly for increasing load-shifting potential, driving the linear cost reduction observed in Figure 2.

Increasing storage capacity does not lead to significantly higher cost savings relative to the 1.7% observed for a 12 hour storage capacity. Increasing storage capacity leads to a flatter operation of DAC throughout the year (Figure 3, 6 months), decreasing DAC capital expenditures slighty. However, the decrease in capital expenditures is much smaller than the 1.7% cost reduction associated with intraday natural gas imports and

therefore increasing storage capacity does not greatly enhance the cost savings from industrial DSM in the CCS_lowprice scenario (Figure 2 top row, first column).

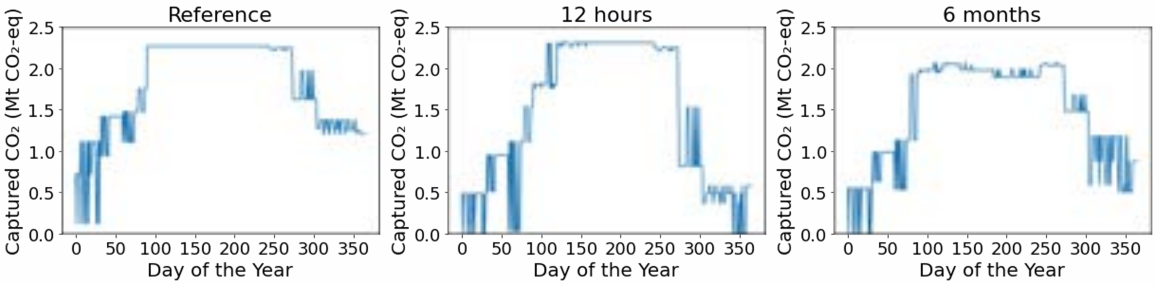

Figure 3: CCS_lowprice scenario: daily CO_2 captured across storage capacities. The Reference case corresponds to no industrial DSM. The 12 hour and 6 month storage capacity plots assume 100% load-shedding potential (*iflex* = 1) and 100% discharge efficiency (η = 1).

3.1.2. CCS_highprice

In the *CCS_highprice* scenario without industrial DSM, batteries are used in the winter to balance renewables fluctuations over several days. Additionally, electricity from natural gas is needed in the winter to supplement the lower renewables availability (Figure 4, Reference). As load-shifting potential is introduced (assuming η = 1, t_{SC} = 12 *hours*), the system no longer needs batteries to balance fluctuations over several days, but rather only to balance intraday fluctuations. Additionally, less electricity from natural gas is needed in the winter, reducing natural gas imports by to 25% (Figure 4, 12 hours). The reduction in battery capacity and in natural gas imports are the main drivers for cost reductions as industrial DSM is introduced. Because of the decreased need for natural gas combustion for electricity, less direct air capture is needed in the summer, thus freeing up some renewable electricity to produce methane for industrial heating. This effect further reduces the need for natural gas imports. As storage capacity increases, the long-duration flexibility offered by industrial DSM further decreases the amount of natural gas imports needed for electricity production in winter (Figure 4, 6 months). Thus, the maximum cost reduction for full load-shifting potential results from the long-duration flexibility offered by industrial DSM, displacing batteries at smaller storage capacities and electricity from natural gas at larger storage capacities.

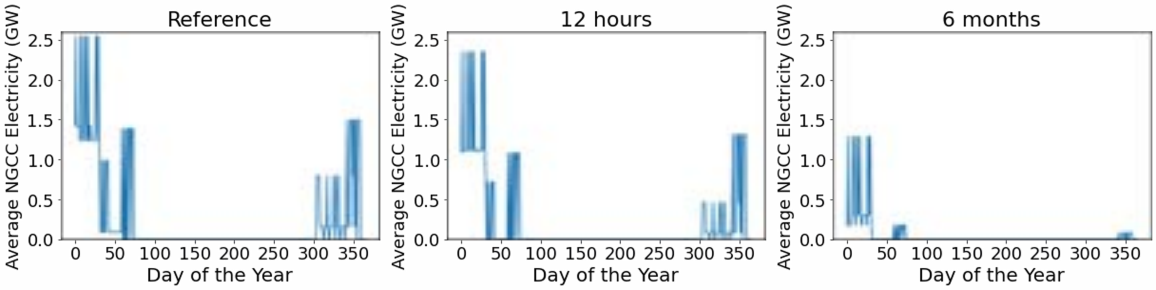

Figure 4: CCS_highprice scenario: average daily electricity production from natural gas combined cycle (NGCC) across storage capacities. The Reference case corresponds to no industrial DSM. The 12 hour and 6 month storage capacity plots assume 100% load-shedding potential (*iflex* = 1) and 100% discharge efficiency (η = 1).

3.1.3. minCCS

In the *minCCS* scenario without industrial DSM, battery storage is needed over several months to balance the fluctuations in renewables availability (Figure 5, Reference). Investment in Li-Ion battery capacity comprises 41% of the total system costs and is the largest cost contributor. As load-shifting potential is introduced (assuming η = 1, t_{SC} = 12 *hours*), the required battery capacity decreases, reducing costs by 4.4%. However, the reduction in installed battery capacity stagnates at low load-shifting potential (*iflex* = 0.05) (Figure 2): small load-shifting potential is sufficient to shave off peak battery capacity. Thus, for smaller storage capacities, a small amount of load-shifting potential yields most of the benefits from industrial DSM. As storage capacity increases, the battery capacities decrease significantly due to the long-duration flexibility that industrial DSM provides: a 6 month storage capacity reduces the battery capacity required for inter-day storage by 59% relative

to a 12 hour storage capacity (Figure 5, 6 months). The large reduction in battery capacity drives the highest cost reductions across all three scenarios of 27%. It must be noted that the *minCCS* scenario represents an extreme scenario with no imports of electricity or natural gas for electricity production. Thus, the magnitude of the cost reduction serves as an upper bound on reductions from industrial DSM.

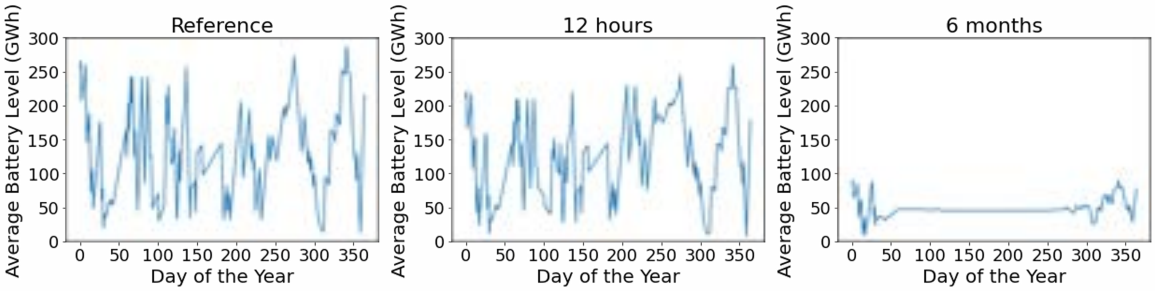

Figure 5: minCCS scenario: average daily battery storage level across storage capacities. The Reference case corresponds to no industrial DSM. The 12 hour and 6 month storage capacity plots assume 100% load-shedding potential (*iflex* = 1) and 100% discharge efficiency (η = 1).

3.2. Storage Capacity

The effect of storage capacity on the contributions from industrial DSM differs for each scenario and depends on whether industrial DSM provides a beneficial alternative for flexibility over longer time horizons. Storage capacity exhibits a saturation, above which contributions from industrial DSM stagnate. The saturation capacity is qualitatively determined based on the results and explained in the subsequent paragraphs.

In the *CCS_lowprice* scenario, storage capacity has little impact on the cost reductions associated with industrial DSM, as explained in section 3.1.1. The saturation capacity for the *CCS_lowprice* scenario can thus be observed at 12 hours. In the *CCS_highprice* scenario, natural gas imports exhibit a step decrease at a storage capacity of 1 month, indicating the displacement by industrial DSM for long-duration flexibility. The saturation capacity for the *CCS_highprice* scenario can thus be observed at 1 month. In the *minCCS* scenario, the installed battery capacity exhibits a step decrease at a storage capacity of 1 week. This phenomenon explains the jump in % cost reduction between 1 day and 1 week for the *minCCS* scenario shown in Figure 2. Storage capacities larger than 1 week do not lead to significant additional cost reductions for a system with 100% discharge efficiency. At lower discharge efficiencies, however, the effect of storage capacity can be more significant, as explained in section 3.3. and shown in Figure 2 (bottom row, third column).

All scenarios exhibit a maximum useful storage capacity determined by the duration, t_{SC}, at which industrial DSM displaces the long-duration flexibility alternatives. If industrial DSM contributes no long-duration flexibility benefits relative to the flexibility alternatives, then small storage capacities are sufficient to obtain the maximum cost reductions from industrial DSM.

3.3. DSM Losses

For all scenarios, efficiencies must be above a certain threshold to obtain benefits from industrial DSM. However, the threshold efficiency varies depending on the scenario, and can also be affected by the storage capacity. For the sake of comparison, we focus the following discussion on an *iflex* value of 1 and define a threshold efficiency as the efficiency at which 20% of the maximum cost reductions are reached (Figure 6, red lines).

In the *CCS_lowprice* and *CCS_highprice* scenarios, the threshold efficiency decreases by approximately 10% from a 12 hour to a 6 month storage capacity. However the threshold efficiencies differ. The *CCS_lowprice* scenario exhibits threshold efficiencies between 45% and 55% whereas the *CCS_highprice* scenario exhibits threshold efficiencies between 30% and 40%. In the worst case across both scenarios, corresponding to the *CCS_lowprice* scenario with a 12 hour storage capacity, cost reductions up to 20% can still be obtained with discharge efficiencies below 55%.

In the *minCCS* scenario, storage capacity has a more significant effect on the threshold efficiency (Figure 2, bottom row, third column). The threshold efficiency decreases from 37% to 3% from a 12 hour to a 6 month storage capacity (Figure 6, row 3). In the case of a 6 month storage capacity and low efficiencies around 3%, the system shifts its use of renewable electricity in the summer from synthetic methane production to additional industrial production. The system overproduces industrial goods throughout the summer, requiring large storage capacities. As a result of reducing synthetic methane production, more natural gas for heat

production is imported. However, importing additional natural gas is significantly cheaper than the battery capacities needed without industrial DSM, and thus large cost reductions are seen even at low efficiencies when storage capacities enabling seasonal storage are available. For smaller storage capacities, the significant overproduction during the summer is not possible and thus higher efficiencies are needed to yield comparable cost reductions to the 6 month storage capacity.

Our results show that industrial DSM can reduce costs even for efficiencies as low as 3%, depending on the costs of the system's flexibility alternatives. Therefore, even processes with high storage losses or low part-load efficiencies could reduce system costs through industrial DSM.

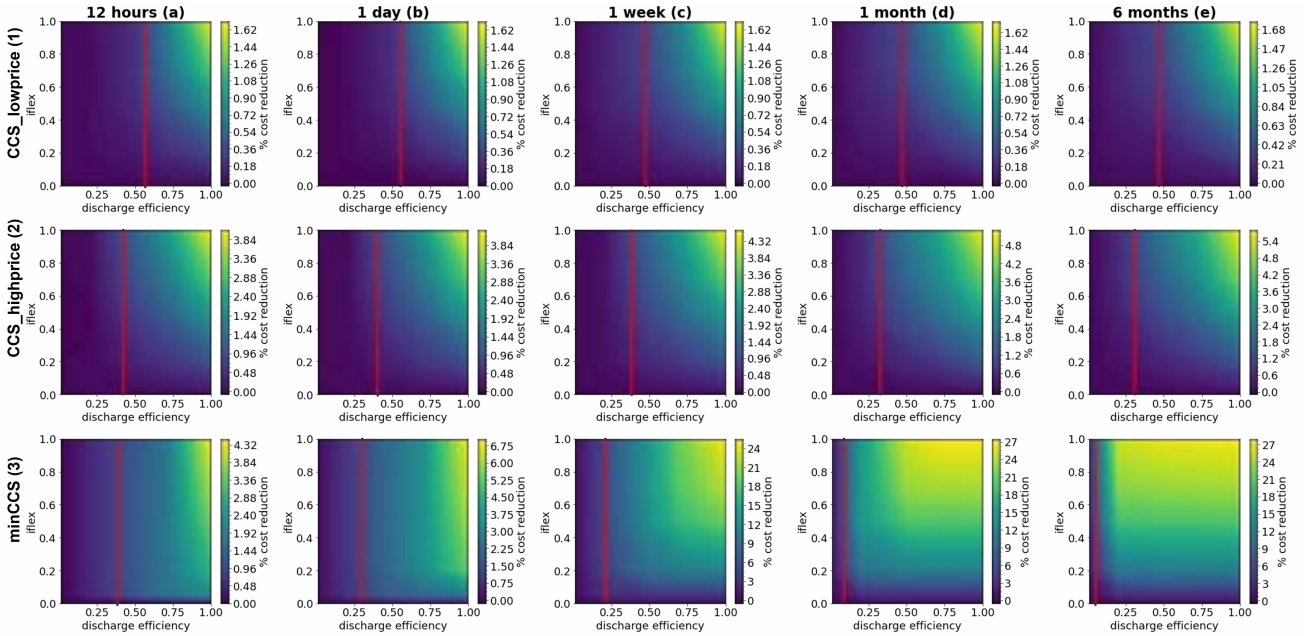

Figure 6: % cost reduction for the net-zero sector-coupled system for different values of iflex and discharge efficiency, η, vs. the reference case of zero iflex and η. Rows correspond to scenarios (numbers) and columns correspond to the storage capacity in terms of the storage capacity time interval, t_{SC}, over which the demand for goods, d_{goods}^{base}, is accumulated (lower case letters). Red lines indicate the efficiency corresponding to 20% of the maximum cost reduction, when considering *iflex* = 1.

4. Conclusions

In this study, we investigate the potential of industrial DSM as a flexibility provider to a net-zero sector-coupled energy system. Specifically, we investigate cost reductions and the change in deployment of other flexibility options due to industrial DSM. We focus on the Swiss sector-coupled energy system comprised of the electricity, heating, and private transportation sectors. To study the effects of industrial DSM, we carry out a parameterized study with three parameters representative of industrial DSM characteristics: load-shifting potential, storage capacity, and DSM losses. We consider three scenarios ranging from cheapest alternative flexibility to industrial DSM to most expensive.

We find that industrial DSM reduces costs for all three scenarios. However, the magnitude of the cost reduction depends on the system's alternative flexibility options, particularly for flexibility over time horizons longer than 12 hours. Thus, the value of industrial DSM must be evaluated within the context of the overall energy system. In a system with inexpensive natural gas imports and the ability to produce electricity from cheap natural gas with CCS (*CCS_lowprice* scenario), industrial DSM reduces costs by up to 1.7%. In a system with electricity only from renewable energy sources (*minCCS* scenario), the maximum cost savings from industrial DSM are 27%. The difference arises because in the *CCS_lowprice* scenario, direct air capture serves as an inexpensive alternative long-duration flexibility option whereas in the *minCCS* scenario, batteries serve as an expensive long-duration flexibility option. Therefore, potential cost reductions from industrial DSM for the *minCCS* scenario are much higher.

We also find that while cost reductions from industrial DSM depend on the industrial DSM characteristics, the influence of the characteristics on cost reductions depends on the interactions with the system's alternative flexibility options. For example, increasing load-shifting potential can have either a linear or a non-linear effect on cost reductions depending on the resulting deployment of the alternative flexibility options. Depending on

the relationship, small load-shifting potential may be sufficient to yield large cost reductions for the system. Storage capacity reaches a saturation capacity, above which contributions from industrial DSM stagnate. The saturation capacity depends on the long-duration flexibility benefits that industrial DSM provides. If industrial DSM provides little to no long-duration flexibility benefits, such as in the *CCS_lowprice* scenario, smaller storage capacities are sufficient to obtain most cost reductions from industrial DSM. Otherwise, contributions stagnate beyond the capacity at which industrial DSM displaces the alternative long-duration flexibility options. Regarding DSM losses, industrial DSM can reduce system costs despite high DSM losses depending on the costs of the alternative long-duration flexibility options. The *minCCS* scenario exhibits 20% of the maximum cost reductions from industrial DSM with only 3% efficiency due to the high costs of Li-ion batteries.

Based on our study, we conclude that while industrial DSM can serve as a flexibility provider to a net-zero sector-coupled energy system, the magnitude of the contributions highly depends on the flexibility alternatives for the system. Particularly, industrial DSM is most beneficial when industrial products can be stored seasonally and long-duration flexibility options are missing or expensive. Therefore, both the characteristics of industrial processes and the system's characteristics must be considered when evaluating flexibility provision from industrial DSM.

In this work, we aggregate all Swiss industry energy demands and assume that the energy demands can be shifted all together. As our results show potential, future research should focus on obtaining a more precise estimate of the potential flexibility provision from industrial DSM in Switzerland. We suggest differentiating between industries and introducing industry-specific, time-dependent energy demand profiles. The ranges of the considered industrial DSM parameters can also be adapted to better-fit the operation of the specific industries. Additionally, we suggest comparing the resulting system cost reductions from industrial DSM to the costs that industries would incur to implement DSM measures, such as investments in over-capacities and storage containers. This comparison would allow for a better estimate of the cost benefits from industrial DSM to the Swiss energy system.

Acknowledgements

P.M., F.B.,and A.B. acknowledge funding by the Swiss Federal Office of Energy's SWEET program as part of the project PATHFNDR.

References

[1] United Nations. *For a livable climate: Net-zero commitments must be backed by credible action* Available at: https://www.un.org/en/climatechange/net-zero-coalition [accessed 12.1.2023].

[2] Ramsebner J., Haas R., Ajanovic A., Wietschel M. *The sector coupling concept: A critical review*. WIREs Energy Environ. 2021;10(4):e396.

[3] Baumgärtner N., Deutz S., Reinert C., Nolzen N., Kuepper L.E., Hennen M., Hollermann D.E., Bardow A. *Life-Cycle Assessment of Sector-Coupled National Energy Systems: Environmental Impacts of Electricity, Heat, and Transportation in Germany Till 2050*. Front. Energy Res. 2021;9:621502.

[4] IRENA. *Power System Flexibility of the Energy Transition.* 2018, Available at: https://www.irena.org/-/media/Files/IRENA/Agency/Publication/2018/Nov/IRENA_Power_system_flexibility_1_2018.pdf [accessed 08.05.2023].

[5] Shaner M.R., Davis S.J., Lewis N.S., Caldeira, K. *Geophysical constraints on the reliability of solar and wind power in the United States*. Energy Environ. Sci. 2018;11(4):914–925.

[6] Sepulveda N.A., Jenkins J.D., Edington A., Mallapragada D.S., Lester R.K. *The design space for long-duration energy storage in decarbonized power systems*. Nat Energy. 2021;6(5):506–516.

[7] Albertus P., Manser J.S., Litzelman S. *Long-Duration Electricity Storage Applications, Economics, and Technologies*. Joule. 2020;4(1):21–32.

[8] Gabrielli P., Poluzzi A., Kramer G.J., Spiers C., Mazzotti M., Gazzani M. *Seasonal energy storage for zero-emissions multi-energy systems via underground hydrogen storage*. Renewable and Sustainable Energy Reviews. 2020;121:109629.

[9] Pellow M.A., Emmott C.J.M., Barnhart C.J., Benson, S.M. *Hydrogen or batteries for grid storage? A net energy analysis*. Energy Environ. Sci. 2015;8(7):1938–1952.

[10] Koohi-Fayegh S., Rosen M. A. *A review of energy storage types, applications and recent developments*. Journal of Energy Storage. 2020;27:101047.

[11] Budinis S., Krevor S., MacDowell N., Brandon N., Hawkes A. *An assessment of CCS costs, barriers and potential*. Energy Strategy Reviews 2018;22:61–81.

[12] Meyabadi A. F., Deihimi, M. H. *A review of demand-side management: Reconsidering theoretical framework*. Renewable and Sustainable Energy Reviews. 2017;80:367–379.

[13] Zhang Q., Grossmann I.E. *Enterprise-wide optimization for industrial demand side management: Fundamentals, advances, and perspectives*. Chemical Engineering Research and Design. 2016;116:114–131.

[14] Arnold K., Janssen T. *Demand side management in industry: necessary for a sustainable energy system or a backward step in terms of improving efficiency?*. Europ. Council for an Energy Efficient Economy. 2018.

[15] Schäfer P., Daun T.M., Mitsos A. *Do investments in flexibility enhance sustainability? A simulative study considering the German electricity sector*. AIChE J. 2020;66(11).

[16] Torabi R., Gomes A., Lobo D., Morgado-Dias F. *Modelling demand flexibility and energy storage to support increased penetration of renewable energy resources on Porto Santo*. Greenhouse Gas Sci Technol. 2020;10 (6):1118–1132.

[17] Klaucke F., Karsten T., Holtrup F., Esche E., Morosuk T., Tsatsaronis G., Repke J. *Demand Response Potenziale in der chemischen Industrie*. Chemie Ingenieur Technik. 2017;89 (9):1133–1141.

[18] Paulus M., Borggrefe F. *The potential of demand-side management in energy-intensive industries for electricity markets in Germany*. Applied Energy. 2011;88(2):432–441.

[19] Papadaskalopoulos D., Moreira R., Strbac G., Pudjianto D., Djapic P., Teng F., Papapetrou M. *Quantifying the Potential Economic Benefits of Flexible Industrial Demand in the European Power System*. IEEE Trans. Ind. Inf. 2018;14(11):5123–5132.

[20] Reinert C., Schellhas L., Mannhardt J., Shu D.Y., Kämper A., Baumgärtner N. et al. *SecMOD: An Open-Source Modular Framework Combining Multi-Sector System Optimization and Life-Cycle Assessment*. Front. Energy Res. 2022;10:Article 884525.

[21] Kotzur L., Markewitz P., Robinius M., Stolten D. *Time series aggregation for energy system design: Modeling seasonal storage*. Applied Energy. 2018;213:123–135.

[22] Swiss Federal Office of Energy (SFOE). *Schweizerische Elektrizitätsstatistik 2019*. 2020, Available at: https://www.bfe.admin.ch/bfe/de/home/versorgung/statistik-und-geodaten/energiestatistiken/elektrizitaetsstatistik.html [accessed 12.1.2023].

[23] Swissgrid AG. *Energy Statistic Switzerland 2019*. 2020, Available at: https://www.swissgrid.ch/en/home/operation/grid-data/generation.html [accessed 12.1.2023].

[24] Swiss Federal Office of Energy (SFOE), Prognos AG, TEP Energy GmbH, INFRAS AG. *Analyse des schweizerischen Energieverbrauchs 2000-2019 nach Verwendungszwecken*. 2020, Available at: https://www.bfe.admin.ch/bfe/en/home/supply/statistics-and-geodata/energy-statistics/analysis-of-energy-consumption-by-specific-use.html [accessed 12.1.2023].

[25] Marcucci A., Guidati G., Giardini D. *Swiss Energy Scope - ETH - Swiss Energy Scope with hourly resolution.*,tech. rep., ETH Zürich, Joint Activity Scenarios and Modelling (JASM), 2021, Available at:https://sccer-jasm.ch/JASMpapers/JASM_SES_ETH_documentation.pdf [accessed 12.1.2023].

[26] Trading Economics. *EU Natural Gas* Available at: https://tradingeconomics.com/commodity/eu-natural-gas [accessed 12.1.2023].

Efficient energy mapping for supporting green transition in industries

Nasrin Arjomand Kermani[a*], Martin Ryhl Kærn[b], Rikke Hovedskov Andersen[c], Jorrit Wronski[b], Fridolin Müller Holm[c], Brian Elmegaard[a]

[a] Department of Civil and Mechanical Engineering, Technical University of Denmark, Lyngby, Denmark, nasker@mek.dtu.dk, CA, brel@dtu.dk
[b]IPU, Virum, Denmark, mrk@ipu.dk, jowr@ipu.dk
[c]Viegand & Maagøe A/S, Copenhagen, Denmark, ran@viegandmaagoe.dk, fmh@viegandmaagoe.dk

Abstract:
The process industry is facing the green transition from conventional to renewable energy sources. Executing it in a cost-effective manner will require increased energy efficiency, electrification, and a clear overall strategy from the beginning. A prerequisite for a strong strategy is an energy mapping that describes the energy use within an industrial facility. However, creating such a mapping can be expensive and time-consuming.

The primary goal of the proposed process mapping methodology is to effectively obtain production and energy data from industrial plants in a short time. This can be analyzed to provide a generic, holistic, and flexible model. The model is a step towards creating a software tool that generates energy flow mappings for industrial end-users to make energy optimization decisions. In addition to documenting energy flows, the tool supports the continuous improvement of the energy mapping itself and the actual energy use.

The required data is collected by reviewing existing specifications of production facilities, complemented with interviews with personnel working on the production lines, as well as other on-site investigations. The information is then entered into the developed model, which produces energy flow mapping as output. The model' s output can then be used to gain an overview of the primary energy used and identify future opportunities for energy optimization, electrification, and decarbonization of industrial sites. An industry use case has successfully illustrated the performance of the model reaching 88% accuracy.

Keywords:
Energy mapping, Generic model, Support tool, Green transition, Decarbonization of industry

1. Introduction

The global challenge of achieving emission reductions and climate neutrality necessitates the prioritization of resources across various industries and sectors worldwide. In many countries, including Denmark, the manufacturing industry significantly contributes to energy use and greenhouse gas emissions. In Denmark specifically, the manufacturing industry accounts for 160 PJ or 21% of final energy use [1]. Consequently, optimizing energy use becomes crucial when it comes to industrial processes. However, energy mapping can be costly, as it requires a detailed understanding of the process at hand.

Recent studies indicate that the current trends and implementation of existing policies aimed at reducing primary energy use in Europe will not achieve a 20% improvement in energy efficiency [2]. Various barriers hinder the adoption of energy-efficient technologies and practices, as categorized by Sorrell et al. [3]] in a taxonomy that compiles important contributions from literature. These barriers are divided into economic, organizational, and behavioral aspects, with fifteen different barriers identified as significant in literature. The study highlights the high cost associated with gathering, analyzing, and applying information, as well as the lack of information leading to missed opportunities for cost-effective energy efficiency. Additionally, the

perceived cost of energy conservation has been recognized as a barrier to industrial energy efficiency investments in Greece [4].

Furthermore, Bunse et al. [5] conducted a review of methodologies for incorporating energy efficiency performance into production management and found that most industrial companies still lack effective methods to comprehensively and practically address energy efficiency. The authors attribute the gap between industrial needs and scientific literature to several reasons, including the complexity of production sites, which often operate multiple production processes to meet business needs, variability in energy intensity factors across different products, and isolated analysis of specific energy use without considering production operations. Consequently, there is potential for misleading conclusions when attempting to account for all variables associated with energy efficiency. Additionally, the authors note that analyzing thermal energy usage is more challenging in practice compared to analyzing electrical usage.

Currently, existing software designed for energy mapping focuses on the entire process operation, requiring a high level of detail and many input parameters. In many cases, these parameters are unknown, resulting in unnecessary efforts on details that may have little importance for actual energy optimization. Alternatively, using Excel software as a tool for energy mapping is challenged by the complexity of systems, causing the program to become too slow for practical use. Additionally, achieving accurate results with Excel requires decent experience in energy mapping and the calculation tool.

Energy mapping is currently mandated under the European Union's Energy Efficiency Directive (EED) [6]. It is the first step in performing mandatory energy audits every four years, to develop projects that increase energy efficiency. Complying with the DS/EN ISO 50001 "Energy Management Systems" also requires companies to perform an "Energy Review" with the same core ideas, establishing key performance indicators (KPIs) and identifying significant energy users (SEUs).

The primary goal of the project presented in this study is to develop a generic, holistic, and flexible process mapping methodology that efficiently obtains production and energy data from industrial plants within a short time frame. The aim is to describe at least 85% of thermal energy used at any industrial facility, using only a few days on-site with qualified staff and an additional day for preparations and fine-tuning. This approach enables the creation of energy mappings in a cost-effective and efficient manner, contributing significantly to the transition towards a greener process industry. By making energy audits cheaper and faster, the number of energy mappings created each year is expected to increase, thereby reducing energy use and quantifying optimization potential [7]. Moreover, studies [8,9] have demonstrated that energy efficiency measures can have a broader impact beyond energy savings, such as process, facility, and organizational levels. These measures can also lead to non-energy benefits, such as increased productivity, improved product quality, reduced costs of environmental compliance, decreased carbon and emission footprint, and lower waste disposal expenses, among others. Worrell et al. [10] have compiled a comprehensive list of non-energy benefits associated with energy efficiency technologies.

In addition, the model presented in this study is a step towards creating a software tool that generates energy flow mappings for industrial end-users, enabling decision-making with energy optimization in mind. The tool supports the continuous improvement of the energy mapping itself and actual energy use. It also serves as the foundation for continuous generation of energy savings, turning a single-shot approach to energy mapping into an ongoing cyclic process, aligning well with the current trend towards increasing energy efficiency targets.

Such a tool can provide sufficient data from numerous manufacturers required to train machine algorithms designed for energy management in different types of processing activities, introducing the digital twin concept for industrial energy systems, intelligent recommendations, and demand-side management in the future.

2. Method

2.1. Generic process mapping approach

The primary goal of the proposed process mapping methodology is to effectively obtain production and energy data from industrial plants in a short time. This data can then be analyzed to provide a generic, holistic, and adaptable model that covers the following perspectives.

- The model should be generic in nature, making it applicable to diverse production plants, ranging from small and medium-sized companies (which typically face obstacles towards energy-efficiency measures) to large-sized companies.
- It should pursue a holistic perspective on the relationship between manufacturing processes and energy usage, encompassing all relevant processes and energy flows.

- The model should be adaptable to changes in the production environment, such as equipment relocation or process improvement.
- It should provide a data set for multi-dimensional evaluation, including energy savings, electrification, and carbon neutrality strategies in all relevant fields of action. Additionally, it should support the continuous improvement of energy mapping.

The methodology consists of four main steps and several sub-steps, as illustrated in Figure 1, and described in the following text. These steps are generally applied to all production lines and can be scaled up and/or aggregated to the factory level. The outcome of the calculations and data validation also serves as the basis for iteratively improving the quality of the energy mapping. By gradually adding more sensor data and reducing uncertainties one node at a time, the user can maintain an overview of the overall plant operation while working with individual components.

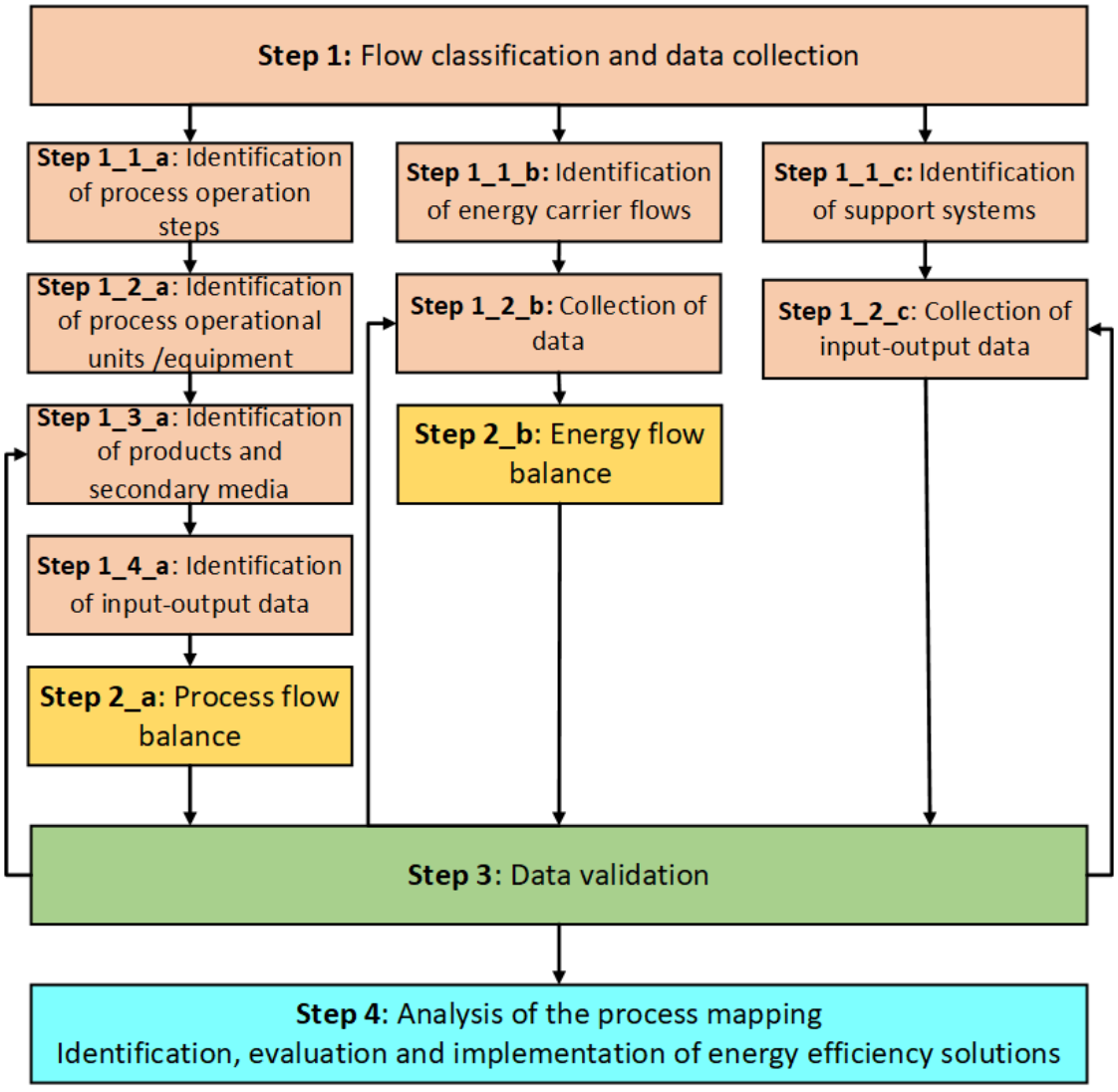

Figure. 1. The proposed methodology consists of 4 main steps and several sub-steps

Step 1: Flow classifications and data collection

Effective flow classifications and data collection are essential for developing a comprehensive understanding of energy use within production plants. This understanding will lead to the identification of areas of energy inefficiency and waste, facilitating the development of strategies for overall energy efficiency improvement in the future. Flow classifications involve categorizing energy usage based on its source, form, and utilization within a production process. This includes identifying the various inputs and outputs of energy within the facility, as well as how energy is transformed and used by different machines, equipment, and production lines. Data collection is the process of gathering and analyzing information on energy usage in a production environment, which can be done in various ways.

To further understand the amount of energy use in production plants, it is crucial to map out the flow of energy within an industrial facility, categorize energy usage, and analyze its correlation with production processes and outputs. Raw materials are consumed in production processes, which convert them into products, along with potential by-products that may or may not be desirable. These processes often require a significant amount of energy, which is partially utilized for value-added activities contributing to the final form and composition of products. However, the remaining energy is wasted in the form of heat losses and emissions. It is important to understand not only the operation of the equipment but also the actual energy requirement from the process. This is achieved by establishing a process flow balance, which involves tracing the flow of the product through process operations (POs) from start to finish and accounting for the mass and energy balance of each PO, as explained briefly in step 2. Energy mapping utilizes streams to track the conversion paths of different forms of primary inputs, such as chemical energy, electrical energy, and thermal energy.

The concept of flows allows for the design of a structure that can serve as the foundation for a software application. The data structure should be designed with various processes in mind and be tested with a variety of applications and industries. By applying these steps to a production environment, the relationship between process, equipment, and energy usage is highlighted, providing insights into how production activities function within an industrial facility and how energy and production are interconnected.

Production flow (sub-steps: 1_1_a -1_4_a)

Step 1_1_a: Identification of the process operational steps

The entire production line can be further divided into different process operational steps. Each process step can be defined and labeled according to production specifications or internal factory documents. Understanding the current production system and breaking it down into appropriate steps will provide a solid foundation for the energy mapping and future assessments. This involves identifying the individual process steps, their sequence, and the inputs and outputs for each step.

Step 1_2_a: Identification of the process operational units/equipment

Once an industrial process has been selected, the next step is to describe the existing process steps and their corresponding unit operations and equipment. This can be achieved by assuming that the product flow passes through several blocks, which can be arranged in parallel, series, or loops. Each block represents a unit operation with significant energy demand, such as pasteurization, boiling, evaporation, drying, and distillation, along with their respective subprocesses, if applicable. The equipment used for each process is then identified, along with the quantity of equipment per step. While a real production plant may consist of many process operation units and components, the focus should be on those with the highest energy demand. Table 1 presents list of process operational units and equipment that can be included in this part.

It is important to note that there may be many interconnections between the process step and process equipment, as well as primary and secondary production flows, but simplification is necessary to illustrate that each product will only follow one main path through the process.

To ensure consistency throughout the energy mapping process, the basic operational blocks developed in the previous step should be reused. This necessitates testing the proposed blocks and interconnections in various production plants and refining them to establish a robust foundation for future implementation in the software tool.

Table 1. List of process operational units and equipment that can be included

Process operational units and equipment				
Mechanical	**Thermal (indirect)**	**Thermal (direct)**	**Electric**	**Heat transfer**
- Collector - Mixing, stirring, suspension, sedimentation, wetting, absorption - Splitters - Separation of flows, filtration, extraction, centrifuge, decanters, press	- Evaporator - indirect drying - Boiling - Baking - Distillation - Reactor	- Drying - Stripping	- Compressor - Induction cooker	- Warm up - Cooling - Pasteurization - fermentation

Step 1_3_a: Identification of the products and secondary media

The amount and type of raw materials used in the production process, as well as the flow of products through the process, should be recorded annually and updated regularly. This information can be used to track changes in the amount and type of raw materials used in the production process, as well as changes in the flow of products through the process.

Apart from the main production flow, it is important to identify the secondary media used in each operational unit to heat up, cool down, pasteurize, or wash the main product flow. These secondary media could be anything used to transfer heat to or from the product flow, such as air, water, or steam, etc.

For example, in a drying operation, hot air might be blown into the dryer to heat up the product. In a pasteurization or washing operation, hot water might be sprayed into the unit to pasteurize the main product or to wash the equipment used in the production line. In some cases, steam might be injected directly into the product flow to increase the temperature of the product flow or change its consistency. In all these cases, the secondary media requires energy, which should be accounted for in the energy use of the operational unit process.

Additionally, this information can also be used to evaluate the effectiveness of different energy-saving strategies, such as optimizing the use of secondary media or using alternative methods to heat up, cool down, or pasteurize the product flow in the future**.**

Step 1_4_a: Collection of input-output data

In this step, all inlet and outlet data of the product and secondary flows in production lines are collected, along with their respective state conditions, such as temperature, pressure, mass flow rates, specific heat, and other relevant parameters.

If energy meters are installed at this step, the information can be gathered from the energy monitoring system. Otherwise, the required data is collected by reviewing existing production specifications complemented with interviews with personnel, such as production associates, supervisors, and managers, as well as other on-site investigations, information from control rooms, and manual calculation of the remaining required information.

Step 1_1_b: Identification of energy carrier flows through the facility

The main objective of this step is to identify the main energy supply systems, including electricity, heating and cooling utilities, and their corresponding purchasing, conversion, and transmission processes.

Energy carrier flows are the sources of energy that supply electricity, steam, or other forms of energy required for powering equipment, heating, and cooling in an industrial plant. These sources can either be purchased from outside (i.e., electricity from the grid or heat from district heating network) or generated on-site by converting primary energy sources, such as natural gas, oil, coal, biomass, or renewable sources, such as solar, wind, or geothermal energy.

To convert primary energy sources into usable energy, various types of equipment, such as boilers, cooling systems, heat pumps, turbines, generators, and motors, are used. These systems can transform energy from one form to another. Heating utility refers to systems or equipment that provide heat energy to a process or facility. The source of heat energy can be steam, hot water, thermal oil, or combustion gases from a furnace, boiler, or heat pump. On the other hand, cooling utility removes heat energy from a process or facility by consuming a certain amount of electricity, depending on the system's coefficient of performance (COP). Cooling utilities can be supplied through cooling towers, chillers, or refrigeration systems, and the source of cooling energy can be air, water, or other fluids. These heating and cooling utilities are commonly used in various industrial processes, such as chemical reactions, food processing, and manufacturing, where temperature control is critical. The temperature and flow rate of the heating and cooling utilities are usually monitored and controlled to ensure that process conditions are maintained within the desired range.

Energy transmission refers to the distribution of energy from the source to the end-use consumers, which can involve various transmission systems, such as pipelines for transporting natural gas or liquids, electrical grids for transmitting electricity, and piping systems for delivering steam, hot water or cooled fluid. The end-use consumers can be divided into different categories of production processes, support systems, space heating, or even direct delivery to a district heating network.

In addition to supplying energy, industrial plants can also implement various energy recovery and conservation measures to improve efficiency and reduce costs. Heat recovery systems can capture waste heat from one process and reuse it in another, reducing the need for additional energy input. Compressed air systems can

be optimized to reduce energy consumption, and motors and pumps can be upgraded to more energy-efficient models.

Step 1_2_b: Collection of data
Data collection for electricity consumption, heating, and cooling utilities in an industrial plant typically involves gathering information on various aspects, such as:

- Electricity consumption: This typically involves identifying the equipment with the highest electricity consumption, such as motors, pumps, fans, compressors, and conveyors. The common methods of collecting electricity consumption data can be smart meters, manual meters, and billing data.

- Heating and cooling utilities: This includes the amount of heat generated by the heating equipment (e.g., boilers, furnaces, heat exchangers), the type of fuel used (e.g., natural gas, oil, biomass), and the efficiency of the heating systems. It also includes the amount of cooling generated by the cooling equipment (e.g., chillers, cooling towers, heat exchangers), the type of refrigerant or cooling medium used (e.g., water, glycol), and the efficiency of the cooling system.

Excess heat recovery: Any excess heat that is recovered from process equipment or buildings and reused for other applications. This includes information on the heat recovery equipment (e.g., heat exchangers) and the amount of heat recovered.

The required data for the last parts can be collected through various means, such as using sensors and meters installed on the heating and cooling equipment and piping network to monitor temperature, pressure, flow rate, and energy use. Data can also be collected manually by taking measurements at specific intervals or by reviewing equipment logs and maintenance records or interviewing personnel.

Step 1_1_c: Identification of support systems
In an industrial plant, support systems are crucial for the efficient and safe operation of the facility. One important support system is cleaning in place (CIP), which allows for the cleaning of process equipment and piping without disassembly. Additionally, industrial plants may have other support systems in place, such as:

- Water treatment systems: Since industrial processes often require large amounts of water, water treatment systems may be necessary to ensure that the water is safe for use and meets the required quality standards.
- Waste treatment systems: Industrial processes can generate waste products that must be treated or disposed of properly to prevent environmental contamination.

Step 1_2_c: Collection of input-output data
To collect energy data for support systems in industrial plants, it is typically necessary to gather information on equipment specifications and energy requirements for running the systems that support the main production process. Energy meters can be installed on the equipment to measure usage, while energy bills and consumption records can be reviewed to track energy use. Here are some examples of energy data that may be collected for support systems:

- Electrical power consumption: Monitoring the power consumption of motors, pumps, and other electrical equipment used to support the manufacturing process can help determine the energy usage of support systems.
- Steam consumption: Measuring the amount of steam used to support the manufacturing process can help determine the energy usage of the steam system.
- Water consumption: Measuring the amount of water used to support the production process can help determine the energy usage of the water supply and treatment systems.

Step 2_a: Process flow balances

This step involves conducting energy and mass balances for each unit operation that comprises the industrial processes. Inlet and outlet process streams, along with their respective state conditions (such as temperature, pressure, mass flow, specific heat, etc.), which are collected in previous steps, are used to determine the energy and mass balances of the production throughout the facility based on the first law of thermodynamics.

By conducting the process flow balance, we can understand the energy requirements of the process. Each cooling and heating demand yields a specific energy demand that can be calculated. These demands will vary depending on the amount of product input into the model. All these individual demands are then summed up

to establish the process energy requirement, both in terms of heating and cooling. These energy demands can be reduced and optimized.

Step 2_b: Energy flow balance

An energy flow balance is carried out in addition to the process flow balance, to describe the energy flow through and the efficiency of the utility systems at the process site. It involves four overall sub-steps: “Purchase”, “Conversion”, “Distribution”, and “Energy Use”. The starting point of this balance “Purchase” is the energy bill, based on energy consumed as purchased fuels.

To illustrate, consider the example of a natural gas boiler producing steam for a process. In the “Purchase” sub-step, the purchased energy is examined from the company's bookkeeping to determine the gas input for the boilers. In the “Conversion” sub-step, all conversion losses related to producing steam from natural gas in the boiler are accounted for, including flue gas loss, radiation loss, blowdown, and deaerator. Additionally, conversion gains can be estimated, such as the introduction of valuable heat from waste heat through a heat pump.

The “Distribution” sub-step involves accounting for all distribution losses related to distributing the steam on the process facility, mainly consisting of heat loss from piping and condensate losses. Subtracting all losses from the known purchased amount yields the amount of steam consumed on site. Finally, the “Energy Use” step is the output of the energy flow balance. Figure 2 provides an example of energy supply and energy use and their interconnection, corresponding to four sub-steps of step 2_b.

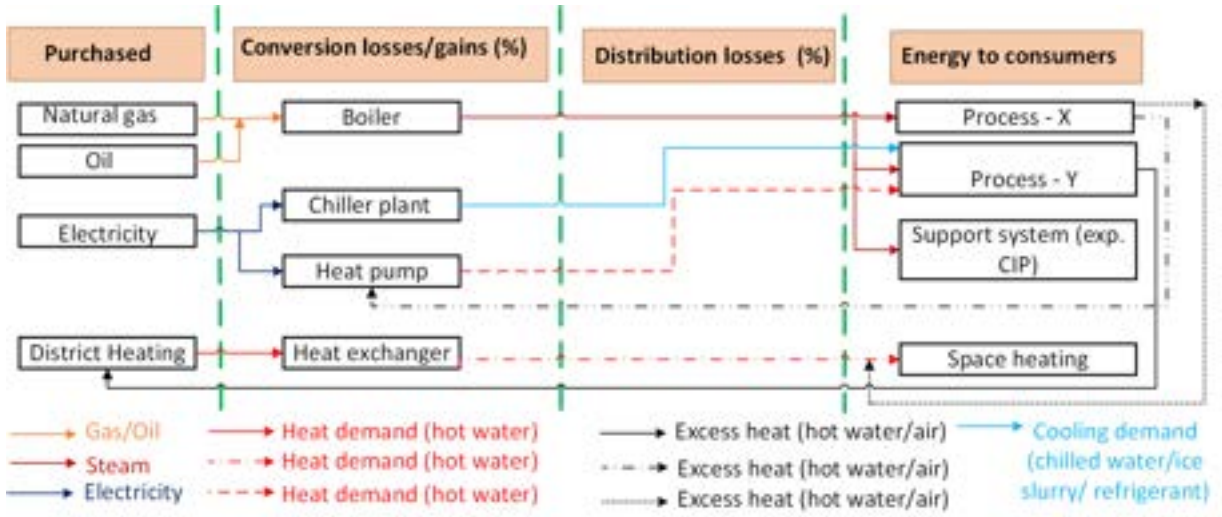

Figure. *2*. An example of energy supply and energy use and their interconnection, corresponding to the four sub-steps of step 2_b. Different arrows of the same color correspond to different temperature levels of similar media

Step 3: Data validation

In an ideal energy mapping scenario, the energy flow balance output (i.e., “Energy use” calculated in step 2-b) should equal the energy requirement calculated from the process flow balance (calculated in step 2-a). However, due to measurement uncertainties, poor data quality, and generalizations of complex processes, some deviation from this ideal situation can be expected. The accuracy of the energy mapping can then be determined as follows.

$$Accuracy = \frac{(Process\ energy\ requierment + Conversion\ losses + Conversion\ gains + Distribution\ losses)}{(Purchased\ energy + Conversion\ gains)} \quad (1)$$

Step 4: Analysis of the process map (including evaluation of energy efficiency solutions and implementation)

Once all the necessary data has been collected, the energy mapping analysis can be completed, and the outputs can be generated. The immediate outputs of a thorough energy mapping exercise include:

- Simple energy overview: This involves identifying trends, patterns, and areas of high energy demand within the production line. Such an analysis can help identify significant energy users (SEUs), equipment KPIs, and efficiencies that can be easily developed and maintained to comply with ISO certifications.
- Pinch analysis: This involves analyzing the energy use in the process in relation to the temperature requirements. The analysis determines the minimum possible demands for heating and cooling utilities. This information can be used for further process integration studies, the integration of heat pumps into the process, and the optimal selection of utilities.

2.2. Case study

The methodology was implemented for a case study to provide a preliminary assessment of its quality. The case study involved a production plant for fishmeal and fish oil. The site descriptions and outcomes of the implementation are detailed below. It should be noted that the proposed method was evaluated up to the end of step 3, while step 4 will be continued in future work.

The production site specializes in the manufacturing of fishmeal and fish oil, operating 24/7. The plant processes fish by-products, such as the remains of fish that are not used for human consumption, to create high-quality protein and oil products. The process begins with the delivery of raw materials to the plant, where they are sorted. The fish is then cooked and pressed to extract the liquid portion, which is separated into fish oil and water. The solid portion is dried and ground into fishmeal. The resulting products are packaged and shipped to customers worldwide. Fishmeal is a valuable source of protein and other nutrients used in animal feed, while fish oil is a rich source of omega-3 fatty acids, which are essential for human health and used in dietary supplements, pharmaceuticals, and other industrial applications.

3. Results

The first three steps of the proposed methodology have been implemented in a production line, and the required data has been collected and evaluated. The results provide a visual representation of the process and energy relationship for the presented production line and are briefly summarized below.

3.1. Case study

Figure 3 and 4 show the general overview of the process steps and process units (sub-step 1_1_a and 1_2_a of the proposed methodology). The process steps identified for the plants are the main production line to produce fish meal, oil cleanser, and deodorization. The identified process steps related to the main production line include process operational units, such as the cooker, presser, dryer, decanter, evaporator, and centrifuge. The oil cleanser and deodorization include process operational units, such as the centrifuge, filter, stripper, and scrub.

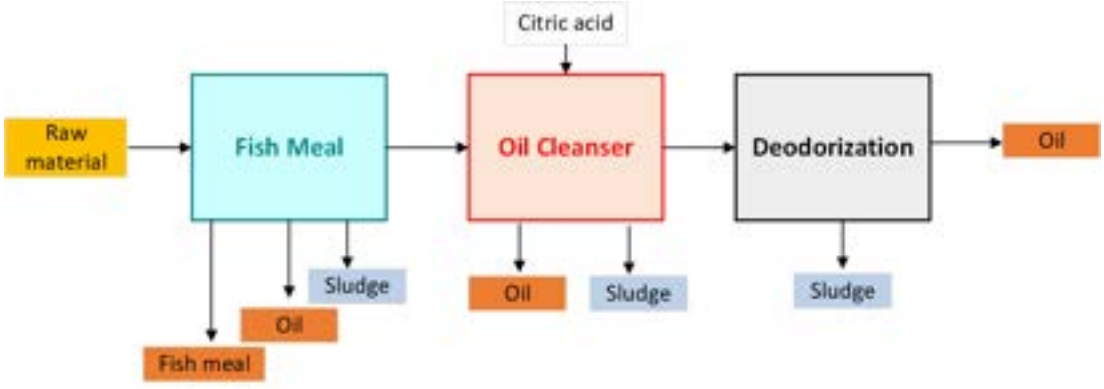

Figure. 3. The process operational steps for the presented case study, corresponding to step 1_1_a of the proposed methodology

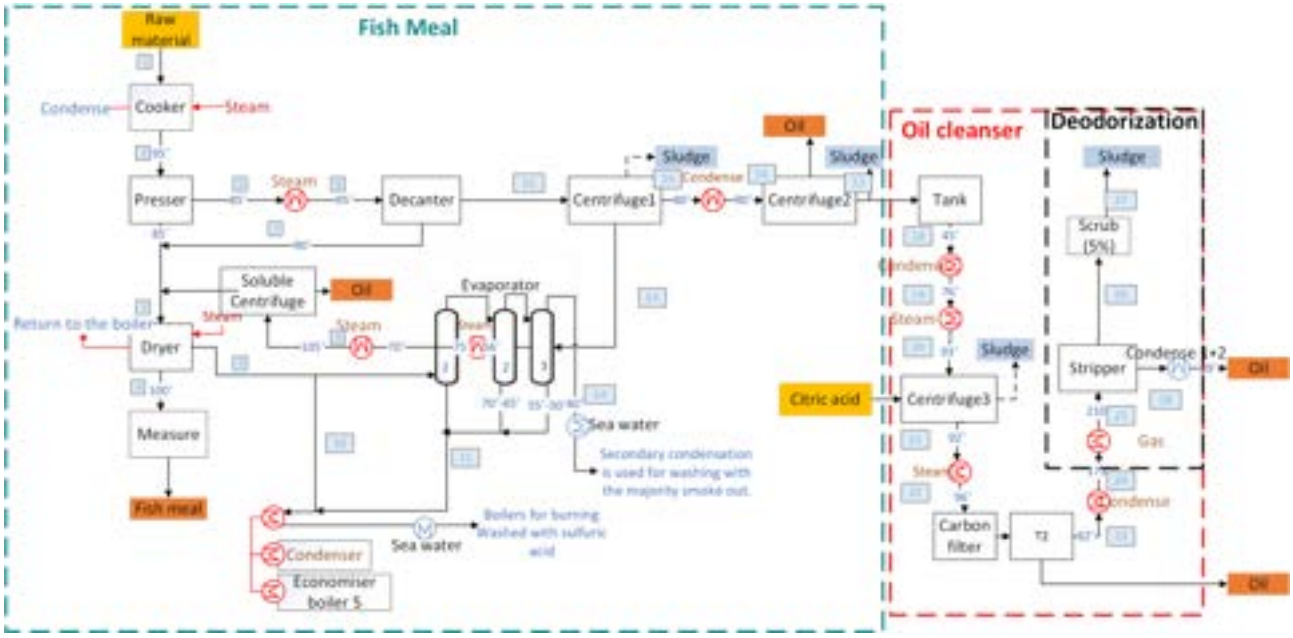

Figure. 4. The process operational units for the case study, corresponding to step 1_2_a of the proposed methodology.

Figure 5 presents the process flow balance (sub-step 2-a), considering the process step related to the main production line to produce fish meal and process operational units that influence the mass balances or final energy use. The required data, including temperature, mass flows, and recipes (fraction of water, fat, and solid), are introduced as input and output data of the main production flow.

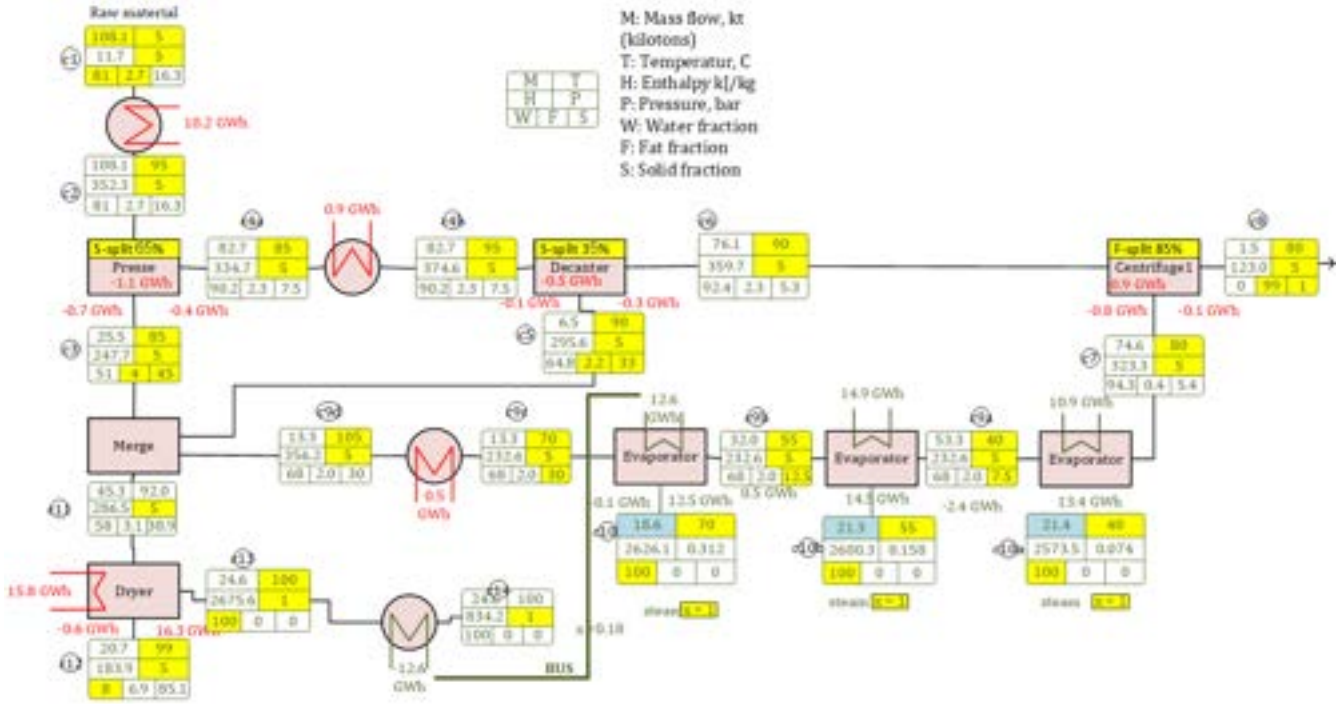

Figure. 5. The mass and energy balance for the case study, corresponding to step 2_a of the proposed methodology.

It should be mentioned that the mass and energy balance presented in Figure 5 belongs only to one type of material. However, in practice, the company has handled three different types of raw materials, equal to 108143, 919221, and 70293 tons/year, which requires a total of 73242561 kWh heating demand.

Figure 6 presents steps 1_1_b, 1_2_b, and 2_b including the identification of energy flows, data collection, and energy flow balances for the presented case study. The steam is generated by five steam boilers mainly

run on oil and natural gas. Table 2 presents the amount of energy calculated in the four sub-steps of step 2_b. It should be mentioned that since the production plant does not have a significant user of a support system such as CIP, steps 1_1_c and 1_2_c have been neglected.

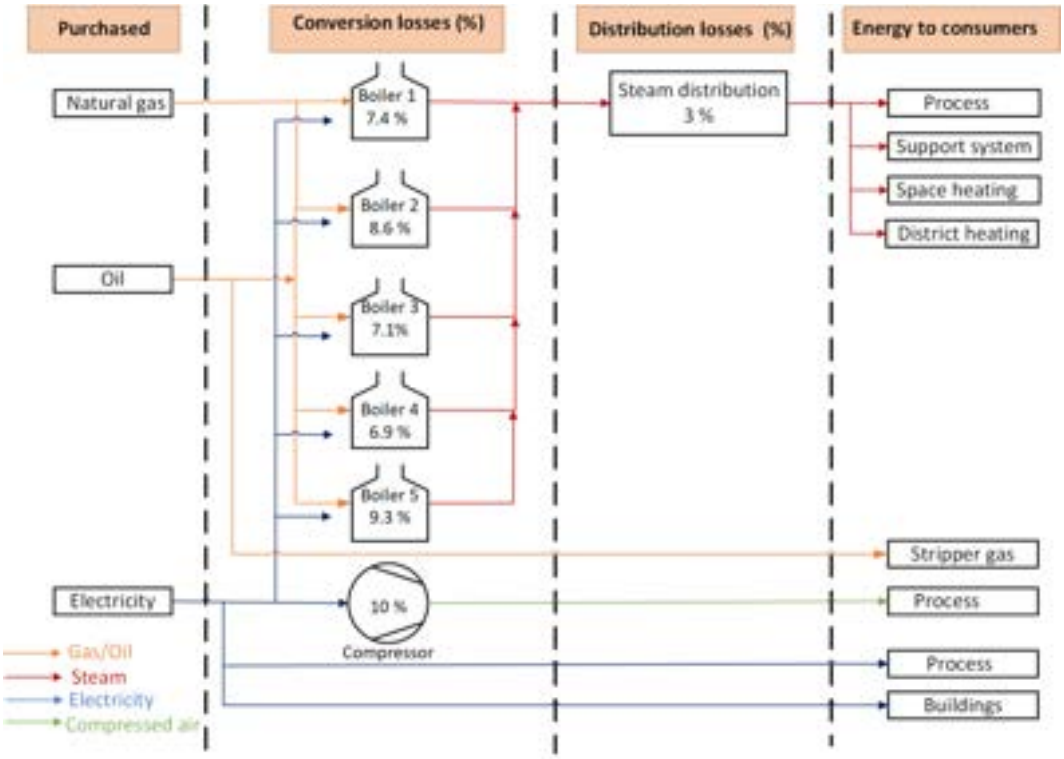

Figure. 6. The energy flows, data collection, and energy flow balances for the presented case study, corresponding to steps 1_1_b, 1_2_b, and 2_b of the proposed methodology

Table 2. The required amount of energy in *four overall sub-steps: "Purchase", "Conversion", "Distribution", and "Energy Use",*

		Heating utility			
		Purchase fuel	**Conversion losses**	**Distribution losses**	**Energy (steam) to end-use consumers**
Equipment	5 steam boilers Using natural gas and oil, with 0.92 - 0.94 % efficiency slightly differ for different boilers	Natural gas: 115184432 kWh Oil: 7619 kWh Total steam produced: 22993535 kWh	6-9 % ≃1701522 kWh for each boiler depending on efficiency Total steam: 105954221 kWh	3 % 3178626 kWh Total steam: 102775585 kWh	Production flow: 73.242.562 kWh (obtained from step 2_a) Space heating: 6.277.252 kWh Delivery to district heating 13.026.300 kWh

Finally, from step 3, Eq.1, an 88 % accuracy of the mapping can be obtained.

4. Discussion

The proposed methodology acknowledges the challenges that may arise when verifying step 3, particularly in diverse and complex production plants. It is crucial to ensure that the interconnections between production flow, secondary media, and utilities are accurately represented to obtain correct values for the process and

energy flow balance. To address this, further verification and validation of the methodology should be conducted across a range of production plants with varying complexities. This will help establish the methodology's robustness and reliability, allowing for adjustments and improvements as necessary.

A comprehensive guideline should also be developed to assist users, especially those in the manufacturing industry who may not be well-versed in energy mapping techniques. The guideline should provide clear instructions and explanations, enabling users to effectively follow and utilize the software developed based on the proposed methodology. To ensure the usability and practicality of the software, it is essential to involve a diverse group of participants in case studies representing different industries. This will enable real-world testing and feedback from consultants, engineers, and production managers who possess domain-specific knowledge and experience. Their involvement will help identify potential challenges, provide valuable insights, and ensure that the software meets the requirements and expectations of various industries. By conducting extensive testing and gathering feedback, the methodology and accompanying software can be refined and optimized to maximize their effectiveness and usability in different production environments.

Figure 7 illustrates a screenshot of the software that is currently under development. The software aims to represent the steps outlined in the methodology and provide a user-friendly interface for conducting energy mapping in production plants. Before the software is officially launched, it is essential to thoroughly test and evaluate its performance and functionality. This testing phase should involve different groups, as mentioned above. By involving these diverse groups, their valuable insights and feedback can be gathered to identify any potential issues, improve usability, and ensure that the software meets the specific needs and requirements of different production environments.

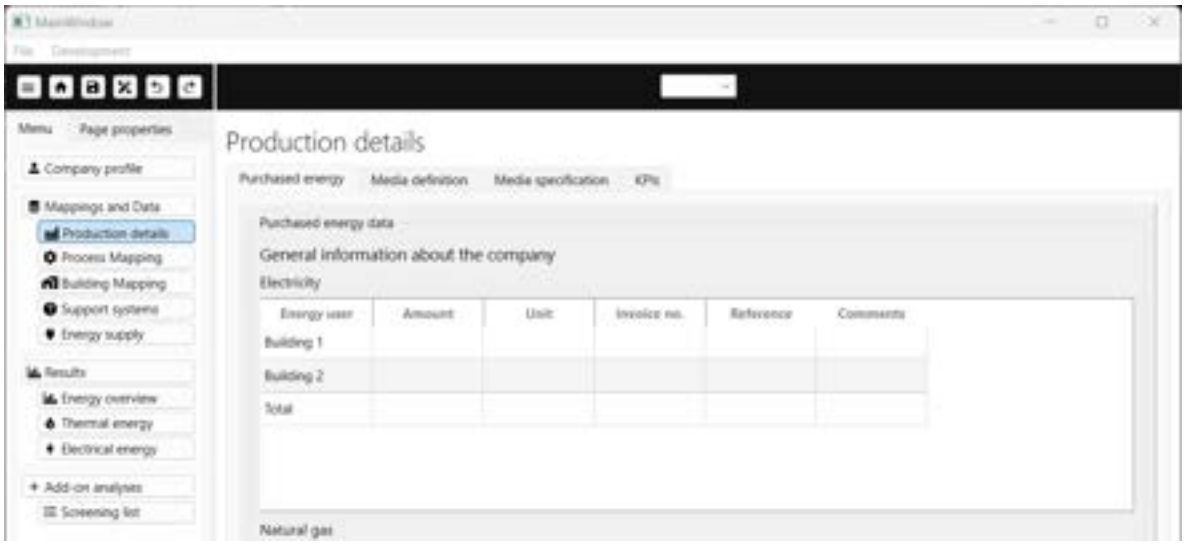

Figure. 7. Screen shot of the current software in the development phase

Conclusion

The paper presented a generic methodology to accelerate the energy mapping of production lines. The performance of individual process steps is modeled with a few inputs following the steps presented in the following methodology. Process operational units representing different operational steps are identified. A few readily available data are collected, while the rest are defined by exploiting engineering judgment, such as the experience of the involved industrial partners visiting the plant, and estimated default values. Being able to bypass blind spots with regards to sensor data allows us to continue the work without costly and time-consuming measurement campaigns. The procedures developed in the proposed methodology thus enable the user to complete an energy mapping that may have been much more difficult to carry out otherwise.

The methodology was implemented in a case study as an examples of Danish food industry. By implementing the methodology in a case study, it was demonstrated that the necessary data can be collected and evaluated effectively, representing 88% accuracy.

The results of the case study showcased the potential of the methodology in visualizing the process and energy relationships within production lines. This enables the identification of significant energy users, equipment key performance indicators (KPIs), and opportunities for improving energy efficiency.

Acknowledgments

The work was financially supported by EUDP, the research and development fund of the Danish Energy Association, under the project (64022-1073) “Efficient Energy Mapping and Analysis for Optimization and Green Transition of Industrial Processes”. The authors thanks FF Skagen A/S for their participation as a case study in the project.

References

[1] Energistyrelsen. Energistatistik 2020: Data, tabeller, statistikker og kort. 2019.
[2] Trianni A, Cagno E, Thollander P, Backlund S. Barriers to industrial energy efficiency in foundries: A European comparison. J Clean Prod 2013;40:161–76. doi:10.1016/j.jclepro.2012.08.040.
[3] Sorrell S, Mallett A, Nye S. Barriers to industrial energy efficiency: a literature review. United Nations Ind Dev Organ 2011;Working pa:98 pp.
[4] Sardianou E. Barriers to industrial energy efficiency investments in Greece. J Clean Prod 2008;16:1416–23. doi:10.1016/j.jclepro.2007.08.002.
[5] Bunse K, Vodicka M, Schönsleben P, Brülhart M, Ernst FO. Integrating energy efficiency performance in production management - Gap analysis between industrial needs and scientific literature. J Clean Prod 2011;19:667–79. doi:10.1016/j.jclepro.2010.11.011.
[6] European Comission; Guidance note on Directive 2012/27/EU on energy efficiency, Article 8: Energy audits and energy management systems. 2013.
[7] Kluczek A, Olszewski P. Energy audits in industrial processes. J Clean Prod 2016;142. doi:10.1016/j.jclepro.2016.10.123.
[8] Mikulčić H, Klemeš JJ, Vujanović M, Urbaniec K, Duić N. Reducing greenhouse gasses emissions by fostering the deployment of alternative raw materials and energy sources in the cleaner cement manufacturing process. J Clean Prod 2016;136:119–32. doi:10.1016/j.jclepro.2016.04.145.
[9] Pye M, McKane A. Making a stronger case for industrial energy efficiency by quantifying non-energy benefits. Resour Conserv Recycl 2000;28:171–83. doi:10.1016/S0921-3449(99)00042-7.
[10] Worrell E, Laitner JA, Ruth M, Finman H. Productivity benefits of industrial energy efficiency measures. Energy 2003;28:1081–98. doi:10.1016/S0360-5442(03)00091-4.

Simplified dispatching method for unlocking energy flexibilities of decentralized energy systems for the day-ahead and balancing power market

Joram Wasserfall[a], Mahmoud Ouso[a] and Stefan Kirschbaum[a]

[a] Society for the Advancement of Applied Computer Science (GFaI), Berlin, Germany, wasserfall@gfai.de

Abstract:

The expansion of renewable energies in the power supply and the shutdown of conventional power plants can only succeed with an advancing flexibilization of the energy system. Decentralized energy systems, such as the energy supply system of a chemical site, can contribute to this, by unlocking the still unused potential for flexibilization. In order to lower the barriers to market participation, user-friendly and simple methods for the economic evaluation of flexibility with regard to the day-ahead and balancing power market are necessary.
Accordingly, in this work a simplified dispatching method considering the day-ahead and the balancing power market in Germany for the mentioned distributed energy systems is developed using mixed-integer linear programming. Linear constraints commonly used in dispatching problems, such as energy balances, conversion efficiencies, and technical constraints, are coupled with new constraints representing the participation in the day-ahead and balancing power market. For the balancing power market the reserve of capacity and the balancing of energy with the uncertainty of calls are taken into account. As a result, the method can be used for day-ahead dispatching by considering the day-ahead energy market and the balancing power market simultaneously.
Because the developed simplified method has low computation times compared to stochastic optimization, for example, it can additionally be applied for hourly resolved annual input data. These evaluations can support strategic planning by determining the economic value of flexibility in the event of market participation. Thus, the results form a starting point for further decisions to unlock unused flexibility.

Keywords:

Electricity markets, Balancing power market, Decentralized energy systems, Energy system optimization.

1. Introduction

1.1 Multi market participation

The expansion of renewable energies in the power supply and the shutdown of conventional power plants can only succeed with an advancing flexibilization of the energy system. Decentralized, small energy systems, such as the energy supply system of a chemical site, can contribute to this, by identifying the existing flexibilities in a first step and offering them on the market in a second step. However, marketing these distributed energy systems goes along with challenges because the systems are complex and the different demands on the site can only be supplied through an integrated operation. In practice, the dispatching is realized in simple systems based on heuristic rules, such as the definition of a switch-on sequence, or in more complex systems based on experienced methods, such as mathematical optimization. Typically, the unit commitment of the decentralized energy systems, such as hybrid renewable systems [1] or combined cooling, heat, and power generation systems [2] is optimized for the participation on the day-ahead market. In most cases, due to the availability of robust and efficient solving methods, mixed-integer linear programming (MILP) formulations are used to minimize economic parameters, such as total operating cost [1–4]. The models, which are mainly based on energy balances, conversion efficiencies, and technical conditions, such as part load behaviour, can be applied to a wide range of large, real world optimization problems. Following this, dispatching can be managed for the day-ahead market of distributed energy systems with several technologies, including renewable energy systems, cogeneration systems, energy storages, or conventional generation [5–7].

The expansion of fluctuating renewable energy sources increases supply uncertainty in the power grid. As a result more short-term system balancing is needed [8,9]. Thus, the demand of flexibility on the short-term markets will also increase in the future. In this changing market environment, it may be economically worthwhile

for the decentralized energy systems to identify their flexible capacity and monetize it on either the balancing-power market or the continuous intraday market in addition to the aforementioned participation on the day-ahead market. However, simultaneous participation in different energy markets is a complex problem that leads to a sequential decision-making process. In Germany and similarly in other European power markets, for example, the balancing reserve capacity auction starts in the morning on the day before delivery. Shortly thereafter, trading on the day-ahead market closes, and the continuous trading on the intraday market starts finally. In this marketing procedure, flexibility that has been already traded on one market can no longer be offered on another market. The optimal behavior with coordinated bidding in the mentioned multiple markets is usually computed by multi-stage stochastic optimization problems [10–12]. In these approaches, uncertainties, such as the request of control energy or the acceptance of a bid in the balancing power market, can be handled. The literature of multi market participation can be classified based on the model complexity of the market on the one hand and on the nature of the portfolio of assets in form of the complexity of the energy system on the other hand. On the market side, the work from [13] considers the day-ahead and balancing power market using averaged prices of capacity and energy without optimizing price bids. Other works optimize only the bids of the capacity price [14] or only the bids of the energy price [15] for balancing power. An even more detailed modeling of the balancing power market taking into account the relevant market rules for capacity and work can be found in [16]. In addition to the aforementioned works with the coupled marketing on the day-ahead and balancing power market, there are more complex models with the additional consideration of the intraday market [12,17,18]. On the energy system side, the developed methods are applied on hydro power plants [19,20], a virtual power plant [21,22], a portfolio with biogas power plants and photovoltaic systems [17], combined heat and power plants [13,23], a cement mill [16], energy storages [24], or a distributed multi-energy system [12].

1.2 Contribution of this work

The presented multi market participation of a decentralized energy system is a cross-sectional topic from the field of energy system engineering with the unit commitment problem and the field of operations research with the optimal trading problem for multiple markets. The combination of these areas leads to the multi-stage stochastic optimization problems that are formulated for the energy system to participate in the multi-market setting. The detailed modeling of the day-ahead, intraday and balancing power market leads to a complex problem with a large scenario tree that is additionally linked to an often no less complicated energy system model. Thus, in case studies, the complexity is usually reduced to keep the problems manageable [17, 24]. However, the methods mentioned remain complicated to handle, for example, due to the modeling of scenario trees, discretization of bid prices or the use of possible reduction methods.

Accordingly, this paper presents an alternative deterministic method that simplifies the described complexity on the market side, taking into account the day-ahead and the balancing power market in Germany, resulting in the following advantages:

1) As complexity on the market side is reduced, complexity on the energy system side can be maintained, and common unit commitment models with constraints for start costs, load changes, or piecewise linear characteristics can be used. Thus, an easy integration into possibly existing dispatching procedures using existing MILP-models is possible.
2) Due to the low computation times, the developed method can be used not only for dispatching but also for strategic planning by using hourly resolved annual input data. In comparison, the temporal resolution of the mentioned case studies is, for example, a quarter-hourly resolution of 18 typical days [18] or an hourly resolution for four typical weeks [13]. However, based on such results, the economic value of the different flexibilities or units in the energy system in case of a market participation can be quickly determined. These evaluations are of interest to companies planning to enter a specific market. They form a starting point for further decisions to unlock the unused flexibility.

Another aspect that is relevant in the energy transition is the changing actor structure. As more and more small players, who do not have the capacity to apply multilevel stochastic programming methods, enter the market, the demand on user-friendly, simplified methods increases. For the small market players, such as the operators of decentralized energy systems, the market entry is accompanied by technical and economic risks, which are caused by the additional personnel and administrative effort on the one hand and by the changed operation modes of the units, which are adapted to the market, on the other hand. Based on the developed method, some of the risks can be minimized, because the behavior of the energy system during market participation is calculated while the economic value of the flexible capacities can be estimated.

2.Simplified dispatching method for the day-ahead and balancing power market

The proposed method allocates the flexible capacity of a distributed energy system to the balancing power and the day-ahead market. In a first chapter 2.1, the constraints for the German short term electricity and balancing power market are presented. In order to investigate the mechanisms of the balancing power market,

historical data is analysed in a subchapter. Based on this, subchapter 2.2 presents the developed methods with their respective modelling equations.

2.1 Short term electricity and balancing power market in Germany

Germany's electricity market design is similar to the EU's overall electricity market design, but with some specific characteristics and features. The design of the balancing power market in Germany has undergone some adjustments in recent years. To ensure consistent market constraints, we focus on the rules for the period 08/01/2019 to 07/31/2020 in this work.

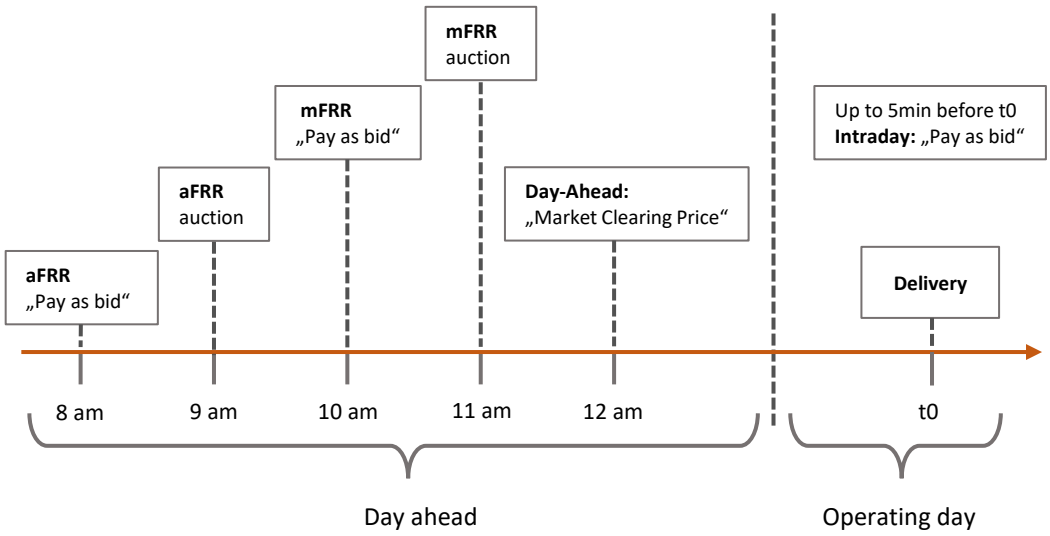

Figure 1: Germany's electricity market design with trading deadlines for the secondary (aFRR) and tertiary (mFRR) reserve of the balancing power market, followed by the day-ahead auction and the continuous intraday trading.

day-ahead market. In the balancing power market, balancing power is traded in the form of automatic frequency restoration reserve (aFRR) and frequency restoration reserve with manual activation (mFRR) in pay-as-bid procedures. For both products, suppliers can submit bids for 4-hour time slices for positive or negative control energy. In addition to the capacity quantity, the participants offer a price for the reserve of the capacity and an energy price for the actual request of balancing power. The tenders have to be submitted for aFRR by 9 a.m. The auction results are published at 10 a.m. This is followed by an equivalent procedure for the mFRR with the results being published at 11 a.m. The transmission system operator (TSO) realizes in a two-stage procedure the procurement of aFRR and mFRR. In the first stage, a merit order is used to select which suppliers are accepted. The decision is based on the capacity price bids and the total balancing power demand, which is determined by the TSO. In the second stage, a merit order for the operating day is formed from all the suppliers accepted in the first stage. The merit order is based on the energy price bids. If balancing power is needed, the suppliers with the lowest energy prices are called up first. In this paper, we focus on the aFRR market, which is the most important balancing power market in Germany with the highest demands [25].

On the day-ahead market, electricity is traded in hourly contracts for the following day. The market closes at 12 p.m., and results are published at 1 p.m. Trading on this market is subject to the market-clearing principle, where the last accepted bid sets the price for all transactions.

2.1.1 Historical data of the balancing power market

This Section analyzes the historical data of the balancing power market for the mentioned one-year period 08/01/2019 to 07/31/2020. The evaluations are based on raw data with a resolution of four seconds from the platform regelleistung.net [26]. In a first step, the request probabilities for positive and negative aFRR are calculated as a function of the energy price bids for the respective 4 h time slices of a day, as illustrated in Figure 2. Following the work of [27], the request probability results from the number of all 4-second blocks with request of aFRR for the respective energy price, divided by the total number of 4-second blocks. The results show a decrease of the request probability with increasing energy prices for positive and negative aFRR. For positive aFRR, the most frequent calls were made in the range below 40 EUR/MWh with a probability of about 50 %. In the energy price range from 40 EUR/MWh to 100 EUR/MWh, there is a large gradient where the number of requests strongly depends on the energy prices offered.

For the negative aFRR, electricity is supplied from the grid during the request, leading to profitable negative energy prices, as seen in Figure 2 (right). The request probabilities for negative aFRR are highest at energy prices below minus 20 EUR/MWh with 50%.

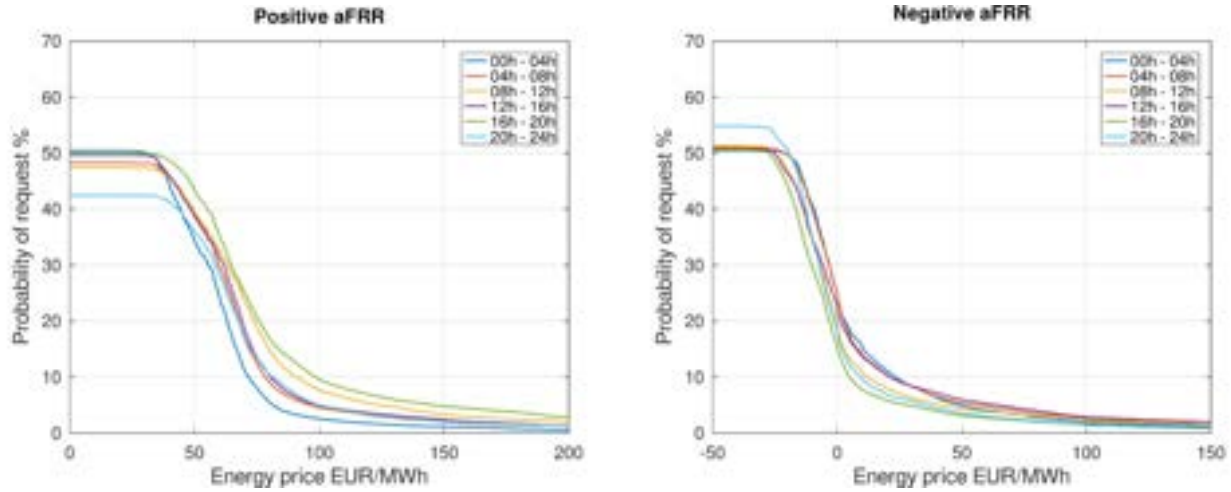

Figure 2: Probabilities of request as a function of energy price bids for positive aFRR (left) and negative aFRR (right) for the period 08/01/2019 to 07/31/2020.

Following the work of [27], the theoretical potential of the profits regarding the balancing power requests can be determined on the basis of the historical data, as shown in Figure 3 (left) for positive aFRR. This potential of profit can be calculated for different flexible capacities in form of different marginal costs. The marginal costs were assumed to be constant costs that are incurred when the balancing power is requested. These results give an insight into the relationship between the energy price bid, the energy system with the respective marginal costs, and the possible profits regarding the balancing requests. The balancing providers have to manage the trade-off between the bids for energy prices and the corresponding request probabilities: Low energy prices lead to high requests with low revenues per request, and high energy prices lead to low requests but with high revenues per request on the other side. As seen in Figure 3 (left), in theory there are optimal electricity bids that resolve the mentioned trade-off with maximum potential of profit. This maximum potential of profit decreases rapidly with increasing marginal costs, as illustrated in Figure 3 (right).

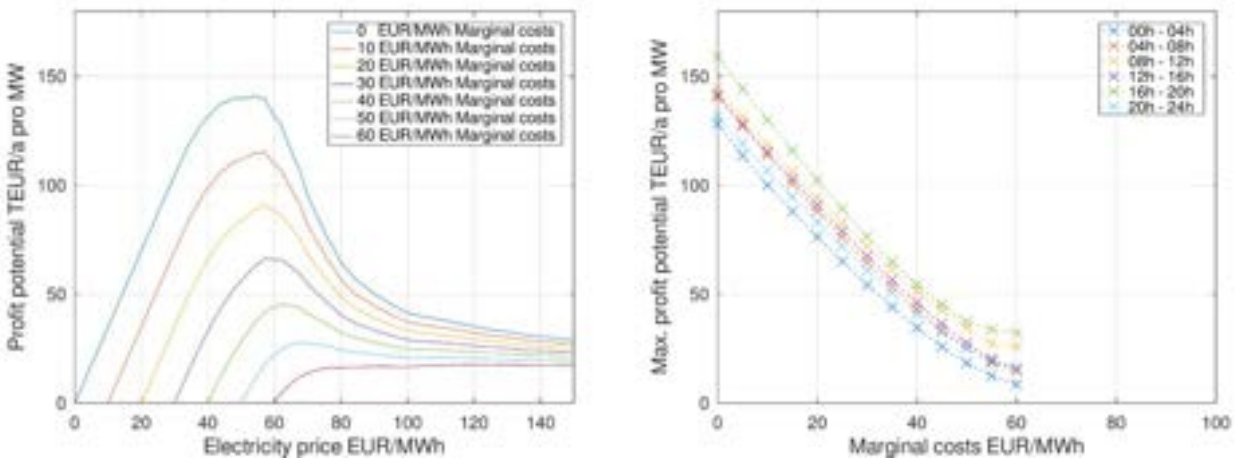

Figure 3: Potential of profit from positive aFRR requests for different marginal costs of electricity generation as a function of energy price bids (left) and the maximum potential of profit as a function of the marginal costs (right) the period 08/01/2019 to 07/31/2020.

2.2 Formulation of the developed dispatching methods

The developed methods optimize the participation of a distributed energy system in the balancing power and day-ahead market for the next day (*d-1*), as seen in Figure 1. In this paper, we focus on the market of aFRR, which is the most important balancing power market in Germany [25]. The coupled multi-market optimization can resolve the trade-off faced by flexibility providers in deciding which of the two markets to operate in. The methods are based on a mixed-integer linear programming (MILP) model of the energy system. This approach is commonly used for unit commitment by minimizing the operating costs of the system under linear constraints such as energy balances, efficiencies, and technical constraints for the day-ahead market [3,4].

In the following Section, the two developed methods *Perfect forecast* and *Virtual capacity price* are presented. The method *Perfect forecast* calculates an upper limit of the possible profits for a first estimation

of the market potential. The method *Virtual capacity price* uses a 2-stage modeling approach that represents the balancing power market in more detail. In the presentation of the methods, we focus on the formulation of the market constraints because modeling the energy system is implemented according to the aforementioned common formulations. Note that all MILP variables are formatted in bold style while normal font style is used for all coefficients.

One-stage algorithm: Perfect forecast

The basis of the *Perfect forecast* method is the assumption that the exact request of balancing power on the day of marketing *d-1* is known. The power reserve is modeled using integer variables for positive $\boldsymbol{BP_t^+}$ and negative $\boldsymbol{BP_t^-}$ balancing power for each time step $t \in T$. Each integer variable represents the acquisition in discrete 1 [MW] steps. The variables are coupled to represent the respective 4 h time slices of the aFRR product, as illustrated in Figure 4.

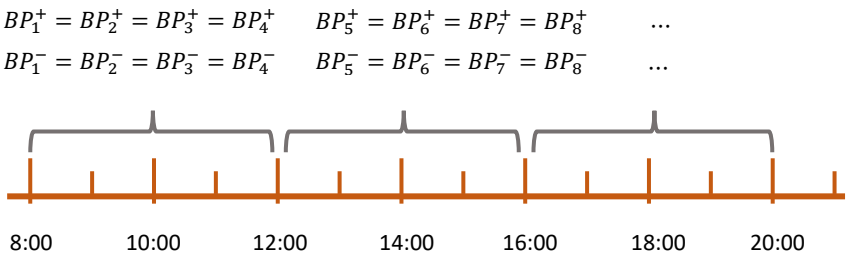

Figure 4: Modelling of positive and negative balancing power for the respective 4h time slices using integer variables, representing the acquisition in discrete 1 [MW] steps.

Based on the mentioned variables, a technical constraint with the blocking of the respective unit capacity for the balancing power market is modeled, using the electrical power $\boldsymbol{\dot{P}_{el,t}}$ with the associated minimum partial load $\dot{P}_{min}$ and nominal load $\dot{P}_{max}$ of the unit. The blocking is reduced to allow the request of balancing power with $\boldsymbol{\dot{P}_{req,t}}$.

$$\dot{P}_{min} + \boldsymbol{BP_t^-} \geq \boldsymbol{\dot{P}_{el,t}} + \boldsymbol{\dot{P}_{req,t}} \geq \dot{P}_{max} - \boldsymbol{BP_t^+}, \qquad \forall\, t \in T \tag{1}$$

Note that, in this formulation, it is assumed that the unit is not capable of fast start-ups and can offer balancing power only in the range between the minimum part load and the nominal load. The request of balancing power is calculated with the factors f_t^- and f_t^+. The factors represent a specific time series of requested balancing power for a given energy price pe and were created from historical data:

$$\boldsymbol{\dot{P}_{req,t}} = -\boldsymbol{BP_t^-} \cdot f_t^- + \boldsymbol{BP_t^+} \cdot f_t^+, \qquad \forall\, t \in T \tag{2}$$

The revenues on the balancing power market for the capacity reserve is formulated with the average, historical capacity prices for positive and negative pc_t^- balance of the pay-as-bid procedure. By using the average prices, it is assumed that with these average price bids, the surcharge for the balancing power offered in the pay-as-bid procedure is always accepted. The revenues acquired from requests are calculated using the energy prices pe^- and pe^t. Both revenues are added to the common target function of the operational cost *OPEX* of the energy system model.

$$\boldsymbol{OPEX_{BP,t}} = -\boldsymbol{BP_t^-}(f_t^- \cdot pe^- + pc_t^-) - \boldsymbol{BP_t^+}(f_t^+ \cdot pe^+ + pc_t^+), \qquad \forall\, t \in T \tag{3}$$

In summary, this formulation means that when deciding whether participation in the balancing power market is worthwhile, the optimization simultaneously takes into account the request of balancing power with the respective remuneration via the energy price. In this respect, the model can perfectly predict during optimization on *d-1* at which exact points in time balancing power will be requested.

The revenues from the day-ahead market participation equals the electricity fed into the grid $\boldsymbol{\dot{P}_{el,t}^{DA,fed-in}}$ and purchased from the grid $\boldsymbol{\dot{P}_{el,t}^{DA,pur}}$ multiplied with the day-ahead market price for selling $pe_t^{DA,sell}$ and buying $pe_t^{DA,buy}$.

$$\boldsymbol{OPEX_{DA,t}} = -\boldsymbol{\dot{P}_{el,t}^{DA,fed-in}} \cdot pe_t^{DA,sell} + \boldsymbol{\dot{P}_{el,t}^{DA,pur}} \cdot pe_t^{DA,buy}, \qquad \forall\, t \in T \tag{4}$$

Because the prices of the day-ahead market are well predictable on *d-1*, the method uses the exact historical data of the market clearing price.

Two-stage algorithm: Virtual capacity pricing

Compared to the *Perfect forecast* method, the *Virtual capacity pricing* algorithm takes uncertainties of the balancing power market into account. For this purpose, an averaged statement about the balancing power requests on the following day is made on *d-1*, based on historical request probabilities. In detail, the procedure is as follows:

Stage 1: In addition to the average capacity price pc_t^+ and pc_t^-, a virtual capacity price $pc_{\mathrm{virtual,t}}$ is integrated into the model.

$$\boldsymbol{OPEX_{BP,t}} = -\boldsymbol{BP_t^-}(f_t^- \cdot pe^- + pc_t^- + pc_{virtual,t}^-) - \boldsymbol{BP_t^+}(f_t^+ \cdot pe^+ + pc_t^+ + pc_{virtual,t}^+), \qquad \forall\, t \in T \qquad (5)$$

This virtual price is calculated with historical data and reflects the averaged revenues from a possible balancing power call on the operating day. Specific balancing power requests are not considered in this stage by setting the request factors· f_t^- and f_t^+ to zero in equation (2). In this stage, the optimization model can calculate the trade-off between the participation on the balancing power market with the possible reserve of power and the day-ahead market based on the resulting capacity price.

Stage 2: In this stage, the market participation from stage 1 is fixed. The virtual capacity price is removed and the historical requests are imposed with a fixed energy price. This stage calculates in detail how the power system behaves after the optimal marketing on *d-1* from stage 1 on the operating day while responding to the specific balancing power requests.

The challenge of the methodology is the calculation of the virtual capacity price, which has a large impact on the optimization results. Exact details of these difficulties are presented in the case study. All equations not mentioned in this method are formulated equal to the *Perfect forcast* method.

3. Case study for market participation of an ideal-typical utility infrastructure of a chemical site

3.1 Input parameters and solving method

The methods proposed are applied to an ideal-typical utility infrastructure (iCV) of a chemical site from [28]. The utility infrastructure supplies electricity and heat for the local chemical companies. The layout of the supply structure is shown in Figure 5. The heat demand consists of a medium-pressure (31 bar) and a low-pressure (6 bar) steam demand. The primary process unit is a gas turbine with 114 MW electrical power followed by a heat recovery steam generator with 150 MW thermal power. In addition to the heat recovery steam generator, two separate gas-fired steam generators and an electrode boiler can provide steam. The high-pressure steam can be expanded to 31 bar and 6 bar via a turbine system, generating additional electricity. The supply structure is generally operated on a heat-led basis to cover the 31 bar and 6 bar steam demand. Differences between electricity generation and electricity demand are balanced by the purchase of electricity from the grid.

Table 1: Data sources for the case study of the iCV model.

Parameter	Data source	Parameter	Data source
Electricity demand	Bauer et al. [28]	Capacity price balancing power market	Regelleistung.net [26]
Steam demand 31bar		Energy price balancing power market	
Steam demand 6bar			
Gas price	EPEX SPOT [29]	Day-ahead market price	Bundesnetzagentur SMARD.de [30]

The overall iCV energy system participates in the day-ahead market (DA) and the gas turbine additionally participates in the balancing power market (BP) for aFRR. The gas turbine in the iCV model generates electricity and steam and this coupled generation is tightly integrated in the overall energy system. Therefore, the entire iCV energy system must be considered to analyze the multi-market participation of the gas turbine.

Historical data from the period August 2019 to July 2020 are used to ensure consistent market constraints for the balancing power market. An overview of the data sources for the relevant input parameters is shown in Table 1. All optimization problems are calculated with Gurobi 9.5.0 on an Intel Core i5-8250U processor with 8GB RAM with hourly resolved annual input data. All solving parameters are set to default values with a relative gap of 1e-3. To handle the time-coupled constraints such as the coupling of time steps for the 4 h time slices of the balancing power market, a rolling horizon approach with a time horizon of 24 h was applied in all optimization runs [31].

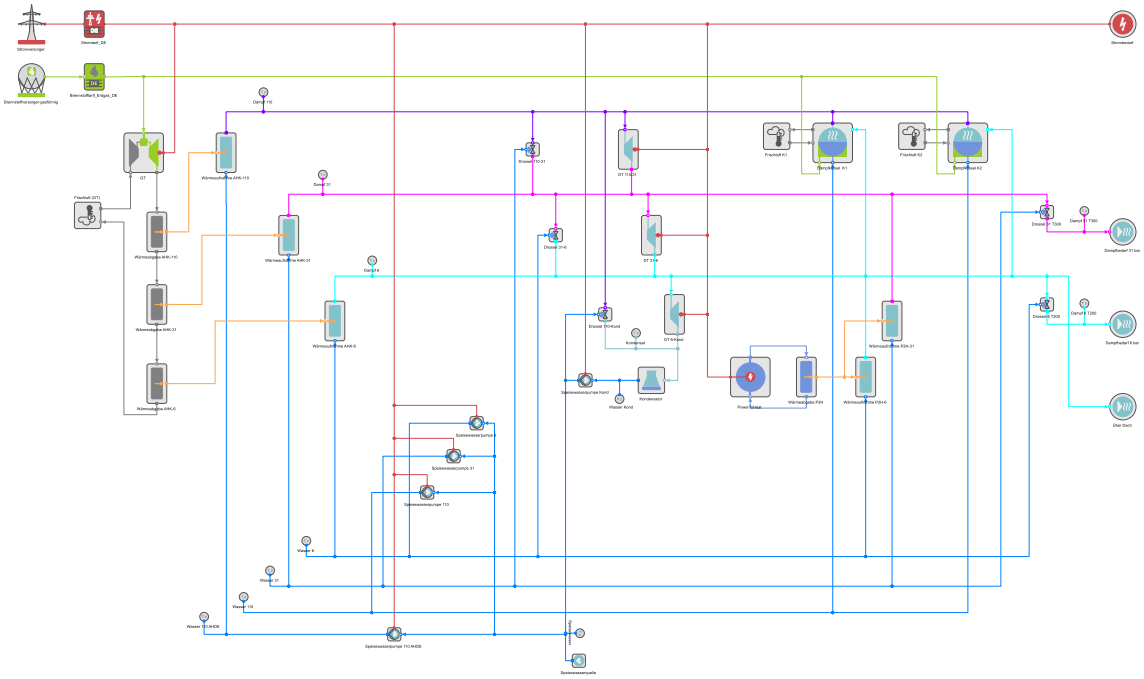

Figure 5: Layout of the ideal-typical utility infrastructure of a chemical site by [28] in the software TOP-Energy. A gas turbine with heat recovery steam generator, two gas-fired steam generators and a power-to-heat unit can produce steam, which is expanded to 31 bar and 6 bar by a turbine system to cover the heat demands.

3.2 Perfect forecast method

The operation of the gas turbine for the case of marketing on the day-ahead market is shown in Figure 6, as a function of the ratio of electricity price to clean gas price R. For low ratios of R with low electricity prices, electricity generation on site using the gas turbine is not worthwhile. For values of approximately R≥1.2, own generation is profitable with the operation at full load with 114 MW electrical power.

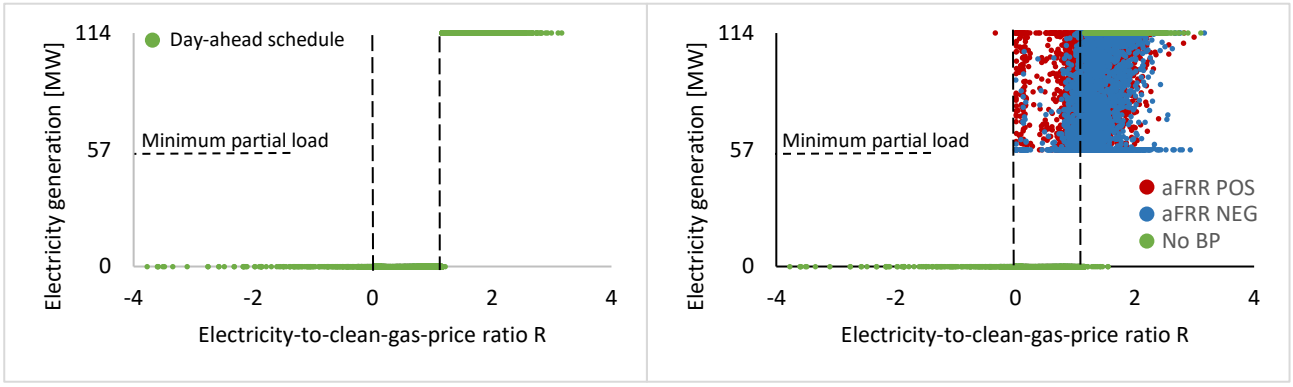

Figure 6: Electricity generation of the gas turbine for the case of marketing on the day-ahead market (left) and marketing on the day-ahead and balancing power market for aFRR using the *Perfect forecast* method (right) as a function of the electricity-to-clean-gas-price ratio R.

Compared to the pure day-ahead marketing, Figure 6 (right) shows the result of the coupled marketing on the day-ahead and balancing power market. The gas turbine is not capable of fast start-ups and can offer balancing power only in the range between the minimum part load and the nominal load with a maximum flexibility of 57 MW. In a range around the turnover point with R=1.2, the marketing of positive and negative aFRR is worthwhile. During the respective marketing of balancing power, the gas turbine operates flexible in the range above the minimum part load to control the balancing requests.

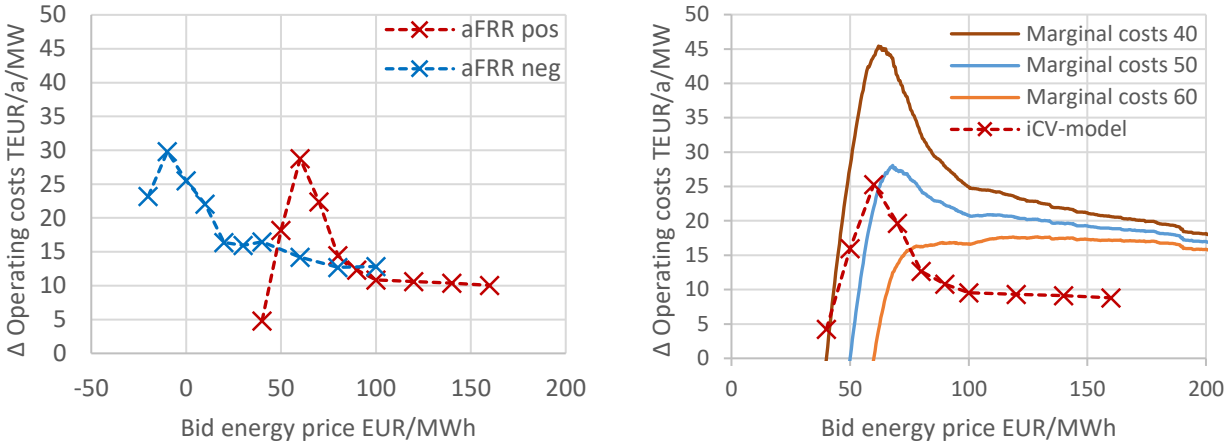

Figure 7: Delta of operational costs (DA – DA and BP marketing) per MW of gas turbine flexibility as function of the energy price bid for positive and negative aFRR (left) and the comparison to the theoretical potential of profit for positive aFRR for different marginal costs in EUR/MWh, as originally presented in Figure 3 (right).

The influence of revenues from the marketing of positive and negative aFRR on energy price bids is presented in Figure 7 (left). The revenues are illustrated as difference of operating costs between the scenario with day-ahead marketing and the scenario with day-ahead and balancing power marketing. Both curves show an optimum with maximum revenues at 60 EUR/MWh for positive aFRR and –10 EUR/MWh for negative aFRR. However, the optimal energy price bid depends on the marginal costs of the unit, as analyzed in Section 2.1.1. A comparison of the discussed theoretical profit to the results of the iCV-model for positive aFRR is shown in Figure 7 (left) for different marginal costs. The average marginal costs of the gas turbine can be estimated at 40 EUR/MWh for the iCV-model, taking into account the coupled generation of electricity and steam. The curve of the iCV-model corresponds qualitavely to the theoretical evaluation when the same marginal costs are assumed, with the same energy price bid at the optimum. This result shows that a reasonable energy price bid can be estimated using historical data and marginal costs of the unit participating in the market. Quantitatively, the revenues of the iCV-model are lower, because the model takes into account the entire energy system with more precise technical constraints, such as partial load behavior.

3.3 Virtual capacity pricing

In the 2-stage algorithm *Virtual capacity pricing*, a constant virtual price is added to the original capacity price time series in the first stage. The results of the algorithm depend on the level of this virtual price accordingly, as shown in Figure 8.

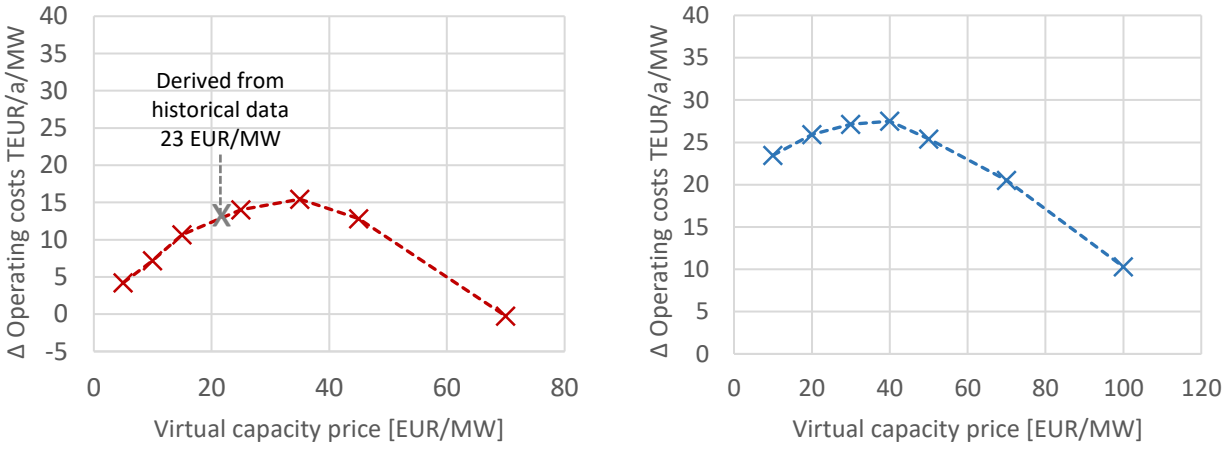

Figure 8: Delta of operational costs (DA – DA and BP marketing) per MW of gas turbine flexibility as function of the virtual capacity price for positive (left) and negative aFRR (right).

For both positive and negative aFRR, the revenues on the balancing power market are underestimated if a too small virtual capacity price is chosen. In these cases, only a few time slices are purchased on the balancing power market in the first stage of the algorithm, resulting in low total revenues in the second stage of the optimization. The choice of a too large virtual capacity price causes a possibly too strong marketing of

balancing power in the model. This also leads to a non-optimal operation in the second stage with lower total revenues. At the highest virtual power capacity for positive aFRR, economic losses even occur compared to the pure day-ahead marketing. The best results are achieved for positive aFRR at a virtual capacity price of 35 EUR/MW and for negative aFRR at a virtual capacity price of 40 EUR/MW.

The challenge of the methodology is to determine a suitable virtual capacity price without performing a parameter study as illustrated in Figure 8. For this purpose, a price can be calculated in advance from the theoretical profit potential of the balancing power market using historic data, as demonstrated in Figure 3. However, the marginal costs of the unit participating in the market must be estimated for this purpose. In the case study, the approximate marginal costs of the gas turbine are 40 EUR/MWh. In theory, such a unit can generate about 50 TEUR/MW per year with balancing requests following the evaluations in Figure 3. From this, an average virtual capacity price of 23 EUR/MW can be calculated. Although this value does not meet the optimum of 35 EUR/MW, it still provides a good estimation for setting a reasonable virtual capacity price.

3.4 Evaluation and comparison with simple trading strategies

A comparison of the developed methods *Perfect forecast* and *Virtual capacity price* is shown in Figure 9. In both methods, the total revenues on the balancing power market consist of a small share of revenues from the capacity reserve and a main share of revenues from balancing power requests. When deciding whether participation in the balancing power market is worthwhile or not, the *Perfect forecast* method can simultaneously take into account the balancing requests with the respective revenues. In doing so, the model can preferentially select profitable time slices with many request calls. Accordingly, the results for this methodology in Figure 9 show high revenues from balancing power requests compared to the *Virtual capacity price* method. The total number of purchased time slices on the balancing power market is similar for both methods. However, more negative time slices are marketed in the *Virtual capacity price* method compared to the *Perfect forecast* method, resulting in increased use of the gas turbine with higher fuel costs and lower electricity costs due to the higher on site electricity generation.

In summary, the results of the presented *Perfect forecast* method with the total revenues of 55 TEUR/MW provide a theoretical profit potential of the market. A more realistic view, in which no exact requests are predicted on *d-1*, is calculated by the *Virtual power price* method leading to lower total revenues of 33 TEUR/MW.

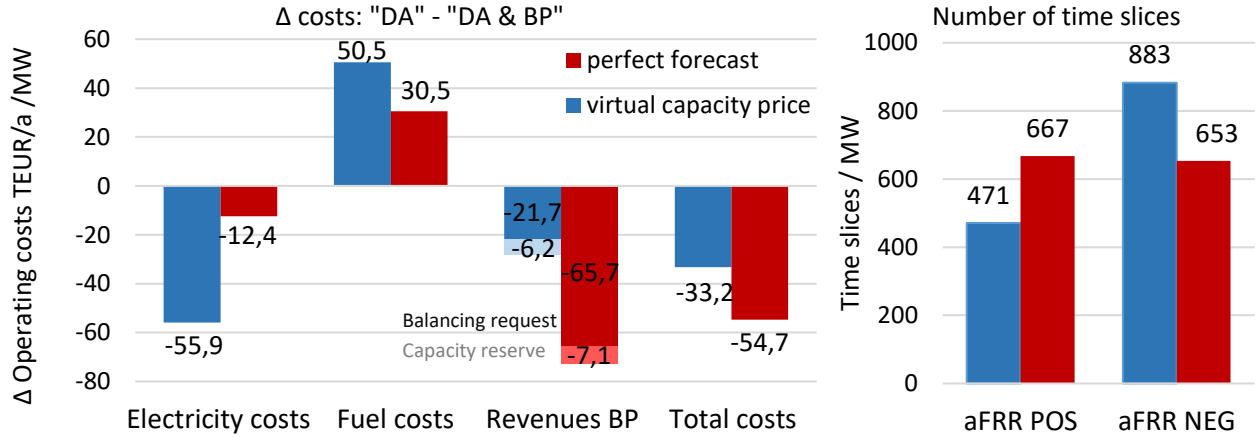

Figure 9: Delta of cost components (DA – DA and BP marketing) for electricity, fuel and balancing power (aFRR) per MW of gas turbine flexibility (left) and the number of aFRR time slices acquired (right).

In summary, the results of the presented *Perfect forecast* method with the total revenues of 55 TEUR/MW provide a theoretical profit potential of the market. A more realistic view, in which no exact requests are predicted on *d-1*, is calculated by the *Virtual power price* method leading to lower total revenues of 33 TEUR/MW.

The presented results are compared with different simple bidding strategies for the balancing power market in the following Section. These simple bidding strategies are based on the optimal gas turbine commitment for the scenario where the energy system participates only on the day-ahead market, as illustrated in Figure 6 (left). Accordingly, the following presented strategies 1a), 1b), 2a) and 2b) are derived from the optimal gas turbine schedule, as also shown in Figure 10.

1a) The day-ahead schedule is not adjusted and negative balancing power is marketed at the times when the gas turbine is running at full load. In this strategy, a maximum capacity price and a maximum energy price are bid. It is assumed that by bidding the high energy price, no balancing power is requested.

1b) As in 1a) but a bidding strategy with a medium capacity price and a medium energy price with consideration of balancing requests.

2a) The day-ahead schedule is adjusted. At the times when the gas turbine is off, the turbine is ramped up to market positive balancing power. At times when the gas turbine is on, negative balancing power is marketed. For positive and negative balancing power, an average capacity price and an average energy price are used, taking into account balancing power requests.

2b) The day-ahead schedule is adjusted. At the times when the gas turbine is on, the gas turbine is shut down to minimum partial load in order to offer positive balancing power. For the positive balancing power, an average capacity price and an average energy price are used, taking into account balancing power requests.

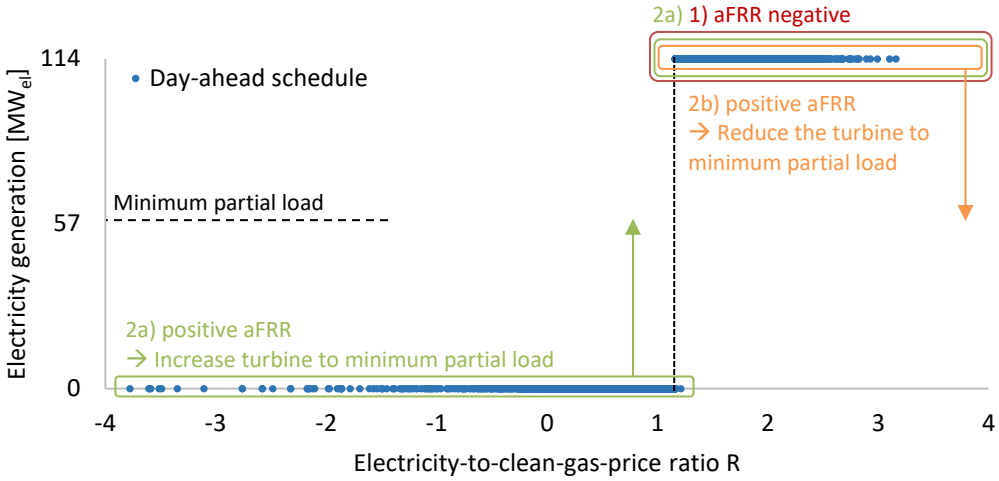

Figure 10: Simple bidding strategies 1), 2a) and 2b) for the balancing power market based on the optimal day-ahead schedule (without BP) of the gas turbine.

The overall results are shown in Figure 11 for the presented four bidding strategies (schedule adjusted) and the developed methods *Perfect forecast* and *Virtual capacity price* (Coupled optimization). The first three bidding strategies 1a), 1b) and 2a) show small revenues between 2.2 TEUR/MW to 5.5 TEUR/MW. In strategy 1a) the high energy price bid leads to the avoidance of balancing power requests. However, we have shown that balancing power requests are relevant for the generation of profits and, accordingly, higher revenues are found in strategy 1b), which considers requests. In bidding strategies 2a) and 2b) the day-ahead schedule is adjusted leading to strongly different revenues. In strategy 2a) very low revenues are generated, whereas strategy 2b) leads to significant profits with 18 TEUR/MW per year.

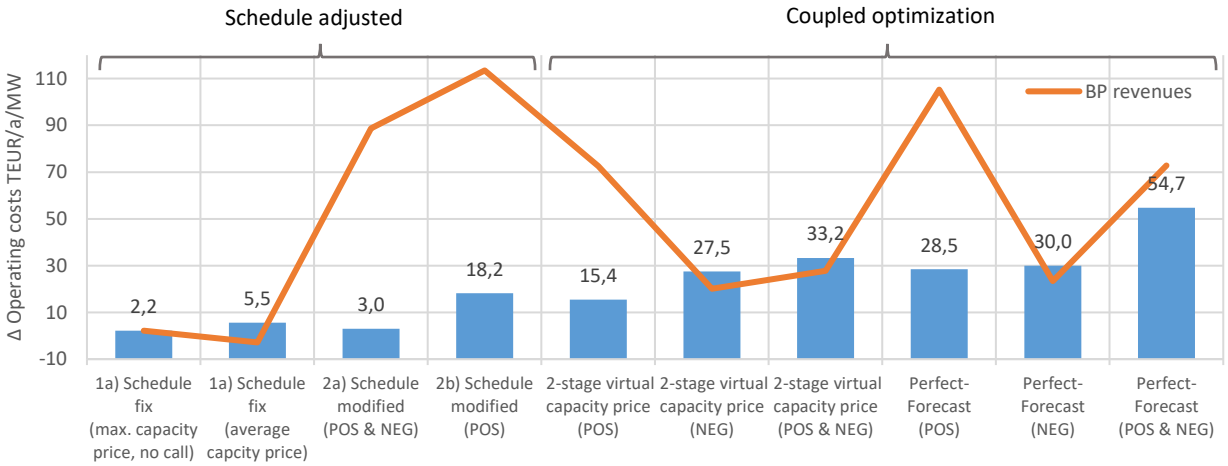

Figure 11: Delta of operational costs (DA – DA and BP marketing) per MW of gas turbine flexibility for the presented four simple bidding strategies (schedule adjusted) and the developed methods *Perfect forecast* and *Virtual power price* (Coupled optimization).

Basically, the simple bidding strategies for the balancing power market based on the day-ahead schedule can generate profits. However, this scheduling "by hand" is not ideal and the revenues are fluctuating and difficult to estimate. In comparison, marketing with the presented simplified optimization methods can generate higher revenues. The one-stage *Perfect forecast* method provides a theoretical potential of profit based on historical

data, resulting in the maximum revenues in Figure 11. The *Virtual capacity price* method takes into account the uncertainties of the requests in a simple way, providing a more realistic market potential with lower revenues.

4. Conclusion

The results of the case study demonstrate that the developed methods manage the coupled marketing of a distributed energy system on the day-ahead and balancing power market in a simplified way. For the methods, historical data can be used to determine reasonable values for energy price bids and virtual capacity prices by considering the marginal cost of the corresponding unit.

The disadvantages of the simplified methods are caused by the complexity reduction of the market side. In reality, market participation leads to a sequential decision-making process that is not modeled in detail. Accordingly, it is not possible to compute optimal bidding strategies taking into account uncertainties, as is the case by using common multi-level stochastic programming approaches.

However, the main advantage of the methods is the low complexity, compared to e.g. stochastic optimization, leading to a high user-friendliness with an easy integration into possibly existing dispatching procedures. The methods can additionally be used for strategic planning to quickly estimate the economic value for different flexibel capcities in the energy system in case of a market participation, as seen in the case study. These evaluations are of interest to companies planning to enter a specific market. In particular, as more and more small players enter the market in the context of the energy transition who do not have the capacity to apply multi-level stochastic programming methods, the demand for user-friendly, simplified methods is increasing. However, the developed methods must be extended in the future for the complete short-term electricity market. For this purpose, the opportunity of intraday trading must be taken into account at *d-1*.

Acknowledgments

This study is funded by the German Federal Ministry for Economic Affairs and Climate Action (ref. no.: 03EI1015B). The support is gratefully acknowledged.

Supported by:
Federal Ministry for Economic Affairs and Climate Action
on the basis of a decision by the German Bundestag

References

[1] Siddaiah R., Saini R.P., A review on planning, configurations, modeling and optimization techniques of hybrid renewable energy systems for off grid applications. Renewable and Sustainable Energy Reviews 2016;58:376–96.

[2] Al Moussawi H., Fardoun F., Louahlia-Gualous H., Review of tri-generation technologies: Design evaluation, optimization, decision-making, and selection approach. Energy Conversion and Management.

[3] Frangopoulos C.A., Recent developments and trends in optimization of energy systems. Energy 2018;164:1011–20.

[4] Montero L., Bello A., Reneses J., A Review on the Unit Commitment Problem: Approaches, Techniques, and Resolution Methods. Energies 2022;15(4):1296.

[5] Bischi A., Taccari L., Martelli E., Amaldi E., Manzolini G., Silva P. et al., A detailed MILP optimization model for combined cooling, heat and power system operation planning. Energy 2014;74:12–26.

[6] Wang H., Yin W., Abdollahi E., Lahdelma R., Jiao W., Modelling and optimization of CHP based district heating system with renewable energy production and energy storage. Applied Energy 2015;159:401–21.

[7] Voll P., Klaffke C., Hennen M., Kirschbaum S., Bardow A., Synthesis and Optimization of Distributed Energy Supply Systems using Automated Superstructure and Model Generation. In: Computer Aided Chemical Engineering: Elsevier; 2012, p. 1712–1716.

[8] Ocker F., Ehrhart K.-M., The “German Paradox” in the balancing power markets. Renewable and Sustainable Energy Reviews 2017;67:892–8.

[9] Kern T., Hinterstocker M., Roon S. von, The value of intraday electricity trading – Evaluating situation-dependent opportunity costs of flexible assets. FfE Munich 2019.

[10] Klæboe G., Fosso O.B., Optimal bidding in sequential physical markets—A literature review and framework discussion. In: 2013 IEEE Grenoble Conference; 2013, p. 1–6.

[11] Möst D., Keles D., A survey of stochastic modelling approaches for liberalised electricity markets. European Journal of Operational Research 2010;207(2):543–56.

[28]

[12] Nolzen N., Ganter A., Baumgärtner N., Leenders L., Bardow A., Where to Market Flexibility? Optimal Participation of Industrial Energy Systems in Balancing-Power, Day-Ahead, and Continuous Intraday Electricity Markets; 2022.
[13] Muche T., Höge C., Renner O., Pohl R., Profitability of participation in control reserve market for biomass-fueled combined heat and power plants. Renewable Energy 2016;90:62–76.
[14] Schäfer P., Westerholt H.G., Schweidtmann A.M., Ilieva S., Mitsos A., Model-based bidding strategies on the primary balancing market for energy-intense processes. Computers & Chemical Engineering 2019;120:4–14.
[15] Leenders L., Starosta A., Baumgärtner N., Bardow A., Integrated scheduling of batch production and utility systems for provision of control reserve. In: Proceedings of ECOS 2020: 33rd International Conference on Efficiency, Cost, Optimization, Simulation and Environmental Impact of Energy Systems: ECOS; 2020, p. 712–723.
[16] Bohlayer M., Fleschutz M., Braun M., Zöttl G., Energy-intense production-inventory planning with participation in sequential energy markets. Applied Energy 2020;258:113954.
[17] Kraft E., Russo M., Keles D., Bertsch V., Stochastic optimization of trading strategies in sequential electricity markets. European Journal of Operational Research 2022.
[18] Dowling A.W., Kumar R., Zavala V.M., A multi-scale optimization framework for electricity market participation. Applied Energy 2017;190:147–64.
[19] Fleten S.-E., Kristoffersen T.K., Stochastic programming for optimizing bidding strategies of a Nordic hydropower producer. European Journal of Operational Research 2007;181(2):916–28.
[20] Klæboe G., Braathen J., Eriksrud A.L., Fleten S.-E., Day-ahead market bidding taking the balancing power market into account. TOP 2022;30(3):683–703.
[21] Pandžić H., Morales J.M., Conejo A.J., Kuzle I., Offering model for a virtual power plant based on stochastic programming. Applied Energy 2013;105:282–92.
[22] Wozabal D., Rameseder G., Optimal bidding of a virtual power plant on the Spanish day-ahead and intraday market for electricity. European Journal of Operational Research 2020;280(2):639–55.
[23] Kumbartzky N., Schacht M., Schulz K., Werners B., Optimal operation of a CHP plant participating in the German electricity balancing and day-ahead spot market. European Journal of Operational Research 2017;261(1):390–404.
[24] Löhndorf N., Wozabal D., The Value of Coordination in Multimarket Bidding of Grid Energy Storage. Operations Research 2023;71(1):1–22.
[25] Next-Kraftwerk, Primärreserve & Primärregelleistung - Was ist das? [March 12, 2023]; Available from: https://www.next-kraftwerke.de/wissen/primaerreserve-primaerregelleistung.
[26] Regelleistung.net, aFRR Datencenter: Regelleistungsmarkt; Available from: https://www.regelleistung.net.
[27] Loesch M., Rominger J., Nainappagari S., Schmeck H., Optimizing Bidding Strategies for the German Secondary Control Reserve Market: The Impact of Energy Prices. In: 2018 15th International Conference on the European Energy Market (EEM): IEEE; 2018 - 2018, p. 1–5.
[28] Bauer T., Prenzel M., Klasing F., Franck R., Lützow J., Perrey K. et al., Ideal-Typical Utility Infrastructure at Chemical Sites - Definition, Operation and Defossilization. Chemie Ingenieur Technik 2022;94(6):840–51.
[29] EPEX SPOT, Market Data. [June 28, 2021]; Available from: https://www.epexspot.com/en/market-data.
[30] Bundesnetzagentur SMARD.de, SMARD - Strommarktdaten; Available from: https://www.smard.de.
[31] Marquant J.F., Evins R., Carmeliet J., Reducing Computation Time with a Rolling Horizon Approach Applied to a MILP Formulation of Multiple Urban Energy Hub System. Procedia Computer Science 2015;51:2137–46.

Analysis of building energy performance based on sensor data for building retrofitting

Noelia Vicente [a], Belén Zurro [b], Sara González [c], Imanol Ruiz [d], José María Sala [e], José Manuel González [f] and Ana Picallo [g]

[a] TECNALIA, Basque Research and Technology Alliance (BRTA), Derio, Spain, noelia.vicente@tecnalia.com, CA
[b] University of Burgos, Burgos, Spain, bzurro@ubu.es,
[c] University of Burgos, Burgos, Spain, sgmoreno@ubu.es,
[d] University of Basque Country, Vitoria-Gasteiz, Spain, imanolruizdevergara@gmail.com,
[e] University of Basque Country, Bilbao, Spain, josemariapedro.sala@ehu.eus,
[f] University of Burgos, Burgos, Spain, jmgonza@ubu.es,
[g] University of Basque Country, Bilbao, Spain, ana.picallo@ehu.eus

Abstract:

The current building stock is responsible for a large part of the final energy consumption in Europe and most of it presents the greatest potential for energy savings. One of the most important steps in the retrofitting process is to understand its pre-retrofitting stage energy performance, and the building energy simulation (BES) models can play a significant role in that sense. In this paper, a building case study has been monitored during a whole year. A methodology has been developed specifically for the pre-processing procedure of the building monitored data. Then, based on the available detailed building drawings, building operational data and the data sets obtained after data calibration, a first approach of a BES model is carried out. In addition, some window samples have been tested in the Laboratory of Building Quality Control of the Basque Government to measure their thermal transmittance. These samples will be introduced in the BES model in future works, to evaluate the reduction in heating demand after the windows replacement. A sensibility analysis of the recorded data justifies their good quality. In consequence, the accumulated heating energy supplied by the boiler reaches a value of 44.05 MWh in the monitored year and the total electric energy consumption is 16.71 MWh.

Keywords:

Building energy simulation model; data pre-processing; energy retrofitting; thermal transmittance calculation.

1. Introduction

This paper is developed under the scope of the AGORA project, founded by Next Generation EU. The project aims to bring to the market a holistic smart solution capable of promoting more sustainable energy and water consumption from producer to final consumer. The tool developed will be tested in some pilot buildings, such as the Faculty of Nursing and Health Science “Building 2” of the University of Burgos in Spain.

In recent years, building energy simulation (BES) is playing a significant role for designing and optimising buildings, but also for pre-rehabilitation procedures. A high level of accuracy in BES results can only be achieved through optimization of three factors as determined by Waltz [1]: (1) an intimate understanding of the simulation tool; (2) an intimate understanding of the building to be simulated and (3) a careful analysis and critique of output data. In their research, [2] presented a critical review of data-driven methods for BES modelling and their practical applications for improving building performance. The paper focuses on methods based on larger datasets and demonstrates that the insights obtained from big building data can be extremely helpful for enriching the existing knowledge repository regarding building energy modelling. However, [3] determined that due to the complexity of the built environment and the prevalence of large numbers of independent interacting variables, it is difficult to achieve an accurate representation of real-world building operation. The difference between measured and calculated energy consumption is known as the “energy performance gap” and reducing this gap is an important task to provide confidence in the models for evaluating energy efficiency. Therefore, calibrating the BES model by reducing discrepancies between model outputs with measured data is a key process to achieve more accurate and reliable results.

In their work [4] focus on reducing the technical issues which are one of the main causes of the energy performance gap, e.g., poorly adjusted thermal parameters in the envelope, inefficient boiler operation or lack of adjustment in parameters of heat pumps, baseboard radiators or air handling units, etc. As a result of the

calibration process, they obtained a whole building calibrated BES model that considers the building's envelope behaviour and incorporates into the simulation the detailed behaviour of its HVAC systems.

Other researchers like [5] proposed a systematic feature-selection procedure for developing the BES model which integrates a statistical analysis, apart from building physics and engineering experiences. This includes data pre-processing based on domain knowledge, implementation of filter methods to remove irrelevant and redundant data and feature grouping through wrapper method to search for the best feature set. In the building context, [6] points out that data pre-processing can be very challenging considering the relatively poor data quality and the intrinsic complexity of building operations. A review done by [7] considers existing case studies and methods for calibrating whole building energy models related to measured data. This research describes a systematic, evidence-based methodology to calibrate these models. In terms of data-driven methods, [8] presented a review of data-driven building energy consumption prediction studies with a particular focus on scopes of prediction, data properties and data pre-processing methods used, among others.

A new method was developed by [9] involving dynamic simulation and on-site measurements aiming to evaluate refurbishment solutions for a historical building. The authors demonstrate how a specific calibration of the dynamic model using only indoor temperature measurements can overcome the problem of in situ measurements of thermal parameters (U-values). In this field, there exist some standardized methods to determine the thermal resistance and thermal transmittance of different building components. Several research studies ([10], [11]) have been carried out to analyse and compare different approaches to thermal transmittance measurements, which pay particular attention to the hot box method.

2. Objectives

This paper analyses and models the energy performance of a real pilot building based on available sensor data. A specific data pre-processing approach is developed and applied to obtain clean and useful data to interpret and apply into a BES model by using the DesignBuilder software.

The case study is related to an academic in-use building located in Burgos, Spain, described in detail in section 4. The building was retrofitted some years ago and the effect of the windows replacement over the heating demand wants to be tested. In collaboration with the Laboratory of Building Quality Control (LBQC) of the Basque Government, some window samples have been characterized under standard rules. The obtained thermal transmittance of the windows is used to characterize the BES model.

According to [3], an accurate calibration process relies on the importance of occupant behaviour as well as the need for instrumentation to monitor its behaviour. For that reason, as the occupant behaviour is not been currently controlled in the pilot building, the calibration process will be addressed in future work. However, this article describes the first steps to achieve a calibrated BES model.

3. Methodology

The methodology described in this section is applied in the case study presented in Section 4, following the similar calibration procedures found in the literature and divided into two main actions:

- On the one hand, the monitored data of the building is acquired and subsequently processed to implement it into a BES model. Therefore, the building has been modelled using the DesignBuilder software to carry out an energy performance simulation.
- On the other hand, a set of window samples were tested in the laboratory and characterized through their performance in a guarded hot box. As a result, the real heat transmission coefficient (U-value) of these windows was accurately determined. The process and samples are described in detail in Section 3.3.

3.1. Monitoring system

An advanced monitoring system was installed in the case study building (see Section 4) whose data were available from the 1st of May 2021 to the 31st of May 2022 and have been registered on a sub-hourly basis. Unfortunately, and due to technical problems, not all monitored parameters have been recorded during some time periods, so some blackouts have been identified and discussed in more detail in Section 3.2. Monitored variables are classified into outdoor conditions, indoor conditions, and general consumptions (including lighting and heating consumptions).

- Outdoor conditions gather two measured parameters obtained from the weather station in the adjoining building: outdoor ambient temperature (ºC) and relative humidity (%). These variables are used to calibrate the climate data file for the BES model.
- Indoor conditions are composed of three parameters: indoor temperature (ºC), relative humidity (%) and CO_2 concentration (ppm). The monitoring system consists of THERMOKON WRF04-CO2-RH-LON sensors located in each room (see Figure 1). These parameters are used to compare BES results.
- Heating consumption is monitored by a KAMSTRUP MULTICAL 602, which is a thermal energy meter connected to a KAMSTRUP ULTRAFLOW 54 flowmeter monitoring the return water volumetric flow (m^3/h). The MULTICAL 602 also receives the monitored temperature of the delivery and return circulating water

(ºC) via two Pt500. The monitoring system calculates energy based on the EN 1434-1:2007 formula, in which the international temperature scale from 1990 (ITS-90) and the pressure definition of 16 bar is used. The energy calculation can in a simplified way be expressed as indicated in Eq. (1):

$$\mathrm{E_t}[Wh] = \mathrm{V_{wa}}[\mathrm{m^3}] \cdot k_{wa}\left[\frac{Wh}{m^3 \cdot K}\right] \cdot (\theta_{inlet}[K] - \theta_{outlet}[K]) \quad (1)$$

where k is the thermal coefficient of water which is a function of the properties of the energy-conveying liquid at the relevant temperatures and pressure. The calculated energy is registered in Wh units and expressed as accumulated energy. These parameters are used to compare BES results and to define heating schedules.

- Lighting consumptions are monitored with eight NICO 8101L clamp ammeters that monitor two electrical parameters: current (A) and accumulated electrical energy consumption (Wh). One of them is located in the boiler and the rest are in each room[1]. These parameters are also used to compare BES results, as well as to define lighting schedules.

Figure 1 depicts the sensors installed in the building.

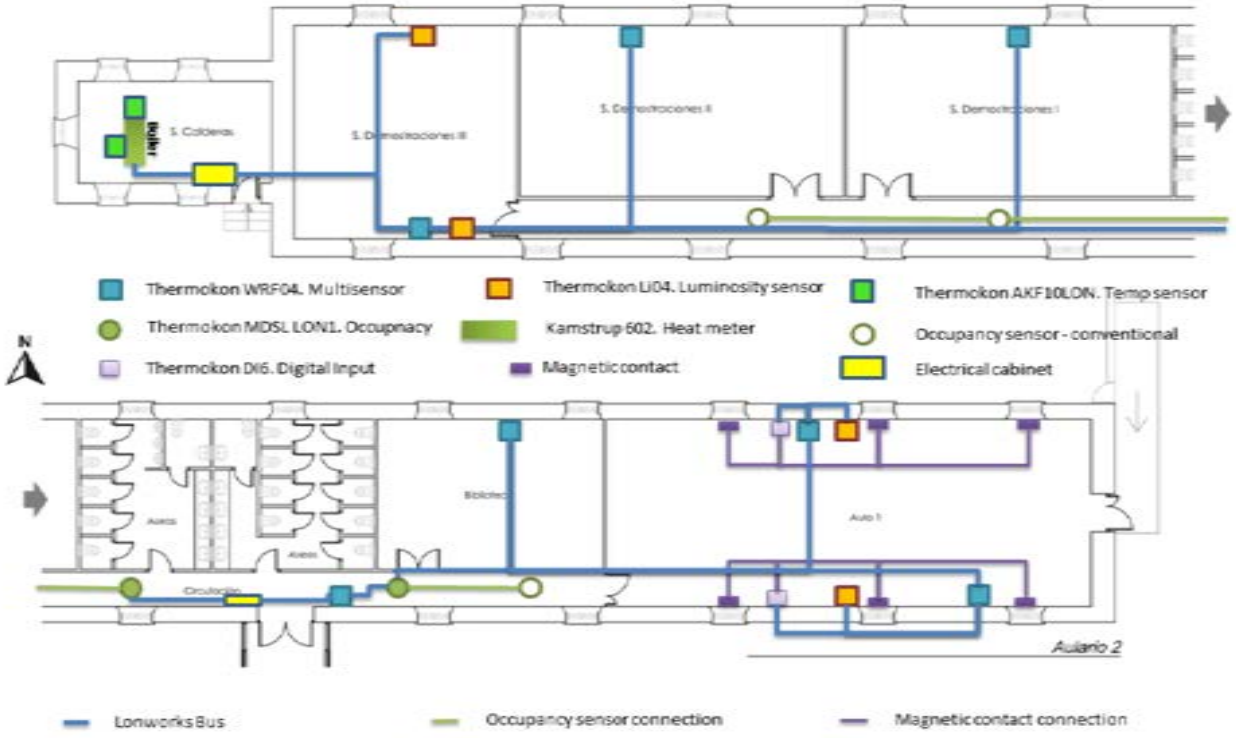

Figure 1. Distribution of monitoring devices within the building.

3.2. Data analysis

This section describes the initial data calibration procedure after collecting them.

3.2.1. Data pre-processing

Data pre-processing is an essential part of any data-driven BES model. This process, according to [12], aims to detect the outliers (i.e., any incorrect or outlier data) that may distort the results. As explained by [8], data pre-processing may include data cleaning, data integration and data transformation.

3.2.1.1. Data cleaning

Data cleaning is defined by [8] as the process of detecting and correcting the incomplete, incorrect, inaccurate, irrelevant and/or noisy parts of the data.

To begin with, a specific cleaning procedure was developed by using different filters on the raw data files. This step aims to correct the effect of outliers, e.g., taking away noisy data and detecting resets in the accumulated energy register.

For the particular case of the monitored energy, the heating energy from the boiler and the lighting energy at each time step has been calculated as expressed in Eq. (2):

[1] Note: data are not available for Demonstration Room III.

$$E_t[Wh] = \Delta E_{register}(t) - \Delta E_{register}(t-1) \quad (2)$$

Besides, for the particular case of outdoor conditions, the registered data were cumulated or averaged, respectively, in periods of 30 minutes, to make them coincident with the minimum simulation time interval allowed by DesignBuilder. After that, hourly, monthly and annual data were also obtained. Unfortunately, the monitored outdoor data was incomplete since the data for some periods were not available due to technical problems and were considered as blackouts. Nevertheless, the observed lack of data does not affect the results since they last few hours during the monitored year, and only on four occasions, the interruption period affects two or more consecutive days, as indicated in Figure 2. This process for the identification of blackouts has been repeated for each variable and then superimposed on the annual calendar, and as a result, it has been seen that the interruption periods coincide for all the variables recorded.

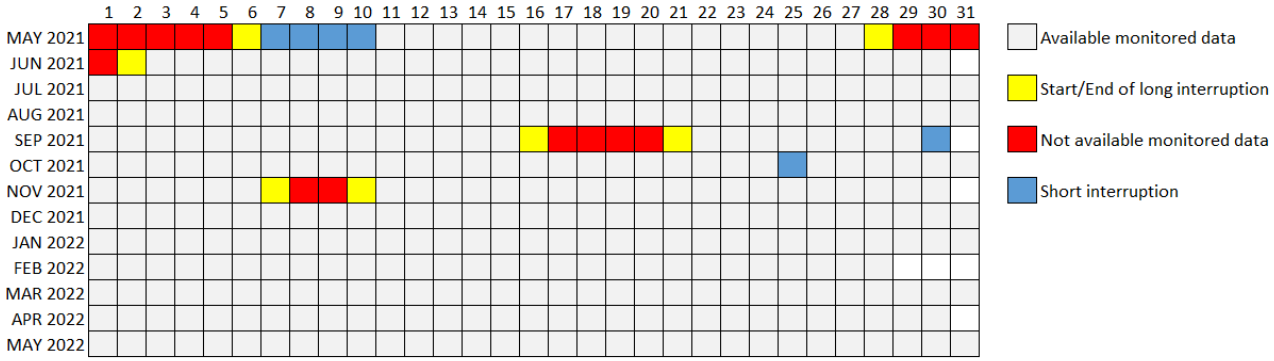

Figure 2. Identification of blackouts on the monitored data during one year.

The period of study covers a whole year from June 2021 to end of May 2022, in order to avoid blackouts detected in May of 2021.

3.2.1.2. Data integration

According to [8], data integration is the process of combining multiple data from different sources. Therefore, since the variables recorded by each sensor were stored in different monthly files, an essential task was to unify the data in an annual one.

In this work, the blackouts detected in the outdoor conditions file (see Figure 2) were substituted with hourly data taken from Meteostat. To verify the suitability of the Meteostat data, three days on which monitored data were available were randomly selected and compared with the Meteostat data from those days. The results obtained for temperature and relative humidity show minor differences, as shown in Figure 3, so the Meteostat data have been justified as suitable.

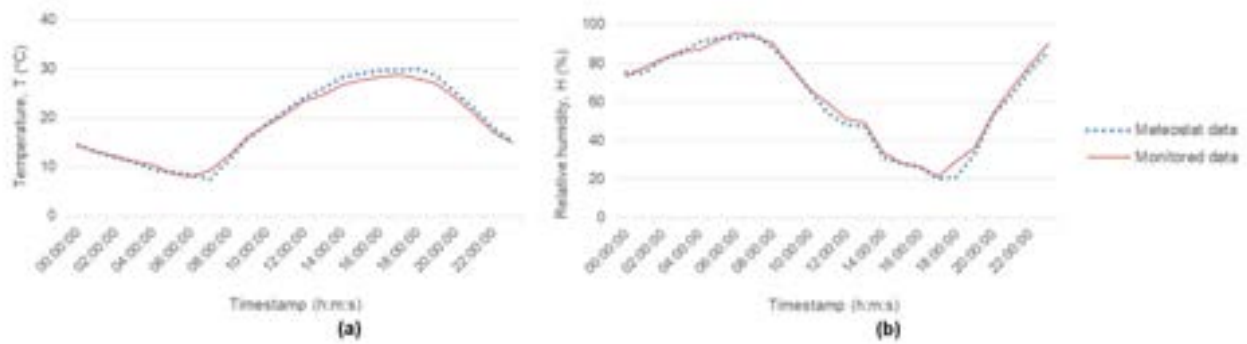

Figure 3. Comparison between meteorological data from Meteostat and monitoring data considering outdoor temperature (a) and relative humidity (b).

3.2.1.3. Data transformation

As mentioned by [8], data transformation is the process of transforming the data into the required format. Data transformation may include normalization, smoothing, aggregation/ disaggregation, and/or generalization of the data.

In this case, in order to compare the analysis with simulation results, data collected on a minute basis (apart from the previous outdoor conditions data) were averaged and/or cumulated in 30-minute intervals and then hourly data were obtained. However, inasmuch as the data were not homogenously registered (i.e. the time interval between timestamps was not constant) it required further treatment. Fortunately, it was identified that the time-step took values multiples of five in the vast majority of the cases, so, the original data series were converted into 5 minutes step values. For this purpose, the variables have been considered to remain constant between each timestamp. After that, a method based on an analogy with a linear equation has been applied

in order to obtain average values for sub-hourly, hourly, daily and monthly data series. All the intensive variables have been calculated as averages, but the energy-related parameters, which are the extensive ones, have been calculated as a sum of the values registered within each interval.

Once the database consists of hourly average series and blackouts are fulfilled, the files are prepared for implementation in future work. As an example, the specific case of the outdoor conditions file requires adapting the format to DesignBuilder software. This software operates with EnergyPlus Weather File (EPW) format and integrates a Climate Data File Processor allowing the user to convert an EPW file into another type. Therefore, in this case, the data file was converted into a CSV file, to substitute the “default input data” with the monitored registered data. Another option is to calculate the heating days (HD) during the simulation period according to monitored data and implement the annual values in DesignBuilder, without modifying the standard climate data file.

3.2.2. Data interpretation

After the data pre-processing, the obtained data needs to be interpreted. This process aims to extract useful information from the monitored variables such as operational schedules, occupation schedules and input parameters for modelling the BES model. The more reliable information is obtained, the more input data and model parameters will be available and the higher the accuracy of the calibration will be [13]. Once the data files are correctly organized, operational periods of the building during the year must be established. Then, a typical sub-operational period has been chosen for each season defined in the previous step. The results of the monitoring demonstrate that there are weekly patterns which are repeated during the academic course, so typical weeks were defined for each month to obtain operational schedules of the heating system and lighting system.

3.3. Thermal characterization of windows

As is already said, the Laboratory of Control Quality of Buildings (LCQB) of the Basque Government deals with, among others, the characterization of building components to research new construction solutions and enhance the thermal performance of the active and passive systems. Because of that, some windows were tested in order to further implement them in building refurbishment, as can be in the building of this case study.

One of the objectives of future work is to analyse the increase in the efficiency of the building after changing the windows, according to the simulation results. Therefore, in order to describe their thermal behaviour, the most important parameter is the thermal transmittance (U). In this work, the method described by UNE-EN ISO 12567-1 of the hot box method was implemented in the LCQB to characterize the thermal transmittance of the studied windows.

3.3.1. Guarded hot box Method

This test method is carried out under UNE-EN ISO 12567-1:2011 to determine the thermal transmittance of doors and windows. Based on the UNE standard, a sample solution is located between two different spaces called chambers (see Figure 4): the hot chamber where the measurement box is located, and the cold chamber, which is used to simulate the exterior conditions, as [11] explained in their work. Therefore, there is a heating system on the hot chamber and a cooling system on the cold one to create a temperature difference (normally 20ºC). Then, by measuring the temperature difference and the heat flow passing through the sample, the thermal resistance of the window can be calculated. Once there is a steady-state condition in both chambers, the heat flow inside the chamber equals the heat input required to keep the hot side at a constant temperature [11].

In this work, U-values from four different windows are measured thanks to the guarded hot box tests developed in the LQCB, where the temperature difference between the hot and cold chambers is 20ºC and the average temperature of the sample is 10ºC. Multiple sensors are located in the sample, the chamber and the sample holder (frame). The employed metering chamber has a section of 1.63 x 1.88 m^2 while the normalized size of the samples is 1.23 x 1.48 m^2, with a sample holder of 1.63 x 1.88 m^2 (see Figure 4).

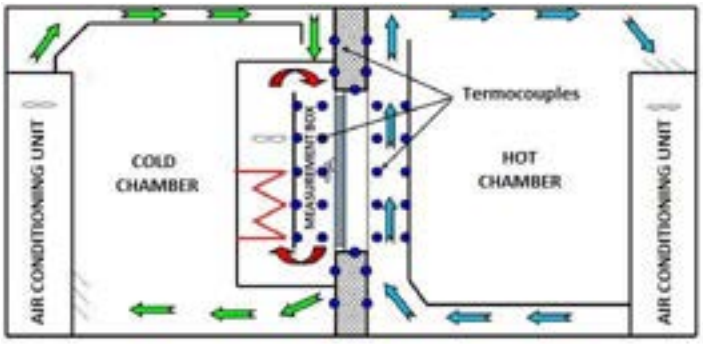

Figure 4. Chambers scheme of the guarded hot box employed for window testing. Source: Building Quality Control Laboratory of the Basque Country.

The measured thermal transmittance (U_m) of the window system is calculated according to the standard UNE-EN ISO 12537-1:2002 with Eq. (3).

$$U_m\left(\frac{W}{m^2 \cdot K}\right) = \frac{\frac{\Phi\,(W)}{A\,(m^2)}}{\theta_{ni} - \theta_{ne}(K)} \quad (3)$$

This measured U_m, must be corrected in order to obtain the normalized thermal transmittance U_w. Therefore, it is necessary to include the thermal resistances of inner and outer surfaces, see Figure 5 and Eq. (4). The normalized value of $R_{(s,t)st}$ takes a value of 0.17 (m^2·K)/W in Europe.

$$U_w\left(\frac{W}{m^2 \cdot K}\right) = \frac{1}{\frac{1}{U_m} - R_{s,t} + R_{(s,t)st}} \quad (4)$$

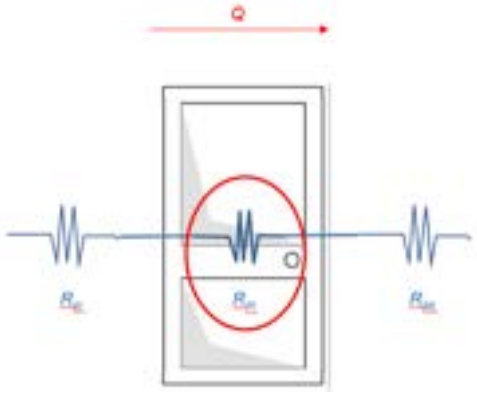

Figure 5. Thermal resistances characterization. Source: Building Quality Control Laboratory of the Basque Country.

3.3.2. Tested windows

Since the thermal properties of building envelope systems significantly alter the overall energy performance of buildings, so these properties must be accurately determined. In this case, the building façade was previously refurbished so special attention will be paid to the windows replacement. Additionally, four glazing systems have been selected from the experimental test. The normalized thermal transmittance (U_w) determined during those tests is shown in Table 1 for each glazing system illustrated in Figure 6.

Table 1. Features of the glazing systems with a dimension of 1.23 m x 1.48 m.

Window	Glazing composition	U_w, W/(m^2·K)	Profile	Shutter box
TW-0412-50	4+4 / CAM 16 argon / 3+3	1.38 ± 0.07	PVC	PVC isolated with EPS, e = 1.5 cm
TW-0412-48	4+4 / CAM 16 air / 6	1.55 ± 0.08	PVC with aluminium reinforcement	-
TW-0412-7	Fixed sash: 3+3 / CAM 10 air / 4+4 Tit-and-turn sash: 4+4 / CAM 12 air / 4	3,07 ± 0.16	Aluminium, e = 14 cm	PVC, 1.22 m x 0.185 m, e = 18.5 cm
TW-0412-21	Fixed sash and casement sash: 4+4 / CAM 15 air / 10	3.14 ± 0.16	Lacquered aluminium, e = 12.8 cm	-

Figure 6. Tested samples of (a) TW-01412-50, (b) TW-0412-48, (c) TW-0412-7 and (d) TW-0412-21.

3.4. Building energy simulation model

To initiate the calibration of the BES model, different data sources have been used such as monitoring, building and construction detail drawings and personal audits. As a result, operational periods and schedules have been obtained for their implementation in the BES model. This includes heating and lighting schedules, weather data and also tested thermal transmittance values. Natural ventilation has not been considered.

Thermal zones have been determined by considering use and conditioning characteristics, so in this case, each room is taken as an individual thermal zone.

The envelope features have been modelled accurately by considering U-values calculated theoretically during walk-through audits. In the case of windows, the U-value determined during the guarded hot box method has been used.

PV modules have been integrated into façades and roofs as shown in the building drawings and modelled with a constant 15% efficiency.

4. Case study

The proposed methodology is applied to a single-floor occupied building, in particular, Building 2 of the Faculty of Nursing and Health Science of the University of Burgos, located in the city of Burgos in Spain (characterized by a moderate continental climate). The building has an academic use, so the occupation is related to the academic schedule and calendar, but in reality, it varies greatly from the expected occupancy. This building is a former Military Hospital built in 1880 with a single rectangular floor of 545.49 m^2, composed of five classrooms and two bathrooms, connected by a longitudinal corridor (see Figure 7). Over the years, the building has faced different rehabilitations and after the last one, two façade solutions were installed above the original wall. Table 2, Table 3 and Table 4 show the main construction and thermal characteristics of the building envelope.

The ventilated façade is predominant above the others, only in the Boiler Room have remained the original walls of the building. The non-ventilated panels have a total width of 2.3 m and have been installed between windows. The South orientation contains integrated photovoltaic modules and some ventilated PV modules have been integrated into the westernmost part of the South façade.

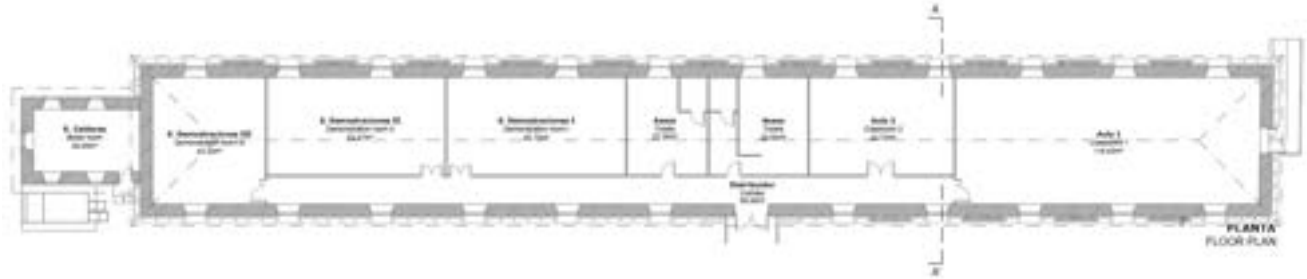

Figure 7. Indoor distribution of Building 2.

Table 2. Dimensions of building and envelope components.

Number of floors	1
Overhang height	5.15 to 5.31 m
Ridge height	7.70 m (approx.)
Constructed surface	545.49 m^2
Conditioned surface	431.39 m^2
Total façade surface	789.77 m^2; 752.22 m^2 (without openings)
East façade area	43.35 m^2; 40.55 m^2 (without openings)
West façade area	23.83 + 15.64 = 39.47 m^2; 38.81 m^2 (without openings)
South façade area	323.19 + 21.62 = 344.81 m^2; 295.27 + 18.59 = 313.86 m^2 (without openings)
North façade area	337.43 + 21.71 = 359.14 m^2; 311.61 + 20.39 = 332.00 m^2 (without openings)
Total openings surface	64.55 m^2
% openings east façade	2.80 m^2; 6,46%
% openings west façade	0.66 m^2; 1.67%
% openings south façade	30.95 m^2; 8.98%
% openings north façade	27.14 m^2; 7.56%
Roof area on the ground floor	623.51 m^2 (approx.)
Roof inclination	28º (approx.).

Table 3. Composition and thermal characteristics of the different layers of the opaque envelope.

Original wall	Masonry load-bearing wall, e = 62 cm
	Garnishing and plastering of gypsum, e = 1.5 cm
	U = 1.40 W/(m^2·K)
Ventilated façade (ULMA)	Mineral wool, e = 5 cm
	Air chamber, e = 15 cm
	Polymer concrete cladding, e = 3 cm
	U = 0.518 W/(m^2·K)
Separation between ULMA and STAM panels	Aluminium sheet, e = 0.2 cm
Non-ventilated façade (STAM)	Mineral wool, e = 15 cm
	EPS, e = 5 cm
	Polymer concrete panel, e = 3 cm
	U = 0.166 W/(m2·K) *
Metallic panel (SOLARWALL)	Mineral wool, e = 5 cm
	Air chamber, e = 15 cm
	Metallic cladding, e = 3 cm
	U = 0.42 W/(m2·K) *

*Estimated with DesignBuilder in function of selected material and thickness

Table 4. Composition and heat transmission coefficient value (U) of opaque envelope and openings.

Roof composition	Mixed trusses (metal and wood)
	Pine wood decking 800x150mm, e = 2.5 cm
	Ceramic flat tile of baked clay. Double side and upper lace
	U = 2.40 W/(m^2·K)
False ceiling	Mineral wool rigid panel, e = 8 cm
	Smooth laminated plasterboard (accessible roof) 60x60 cm, e = 1.5 cm
Slab composition	Metal beam, ceramic vault, compression layer + mesh
	U = 2.10 W/(m^2·K)
Non-slip laminate flooring	High density fibreboard, e = 1.25 cm
Window type	Wooden pre-frame 70 mm x 50 mm
	Mixed carpentry. PVC profiles and Wood finished.
	Exterior double low-e glass 4+12+6 mm
	Aluminium sheet in window perimeter trims and lower closure in ventilated façade, e = 0.2 cm
	U = 2.20 W/(m^2·K)

Regarding the thermal facilities, the building has two high-efficiency condensing gas boilers Remeha 65 PRO of 61 kW each, which supply heat through two independent circuits, both to Building 2 and to adjoining Building 3, in which another European project is being developed. The thermal demand only corresponds to the heating system, neither cooling nor DHW systems are operating in the building.

Referring to electricity generation, there are also photovoltaic panels as mentioned before. The PV installation is divided into three systems, independently connected to three inverters as indicated in Table 5. Besides, the lighting of the entire pavilion is composed of 2x32 W fluorescent lamps with a protection box at the entrance.

Table 5. Characterization of the PV system.

PV characteristics	Ventilated façade (ULMA)	Non-ventilated façade (STAM)	Roof (SOLARWALL)	Complete System
Power, kW_p	4.95	4.16	4.42	13.53
PV module model	VS21 C24 P99	SPS istem 260P plus	SPS istem 260P plus	-
Nº modules	50	16	17	83
Azimuth / Inclination	-26º / 90º	-26º / 90º	-26º / 28º	-
Occupied area, m^2	41.3	26.1	27.7	95.1
Inverter model	Sunny Boy 3.6	Sunny 3.6	Sunny Boy 4.0	-
Inverter Power, kW_{AC}	3.6	3.6	4.0	-

5. Results

In this section, the analysed data are interpreted and the preliminary BES model is depicted, which will be fully calibrated in future research. The results of the methodology described in Section 3 are presented below.

From the data analysis, hourly average data and monthly and annual averages were obtained. Besides, operational schedules for heating and lighting systems have also been obtained.

The monitoring of the heating system during June 2021 and May 2022 shows a standard distribution of the heating demand according to the Burgos climate zone. As observed in Figure 8, higher heating demands

correspond to the cold period from November to April and lower heating demands are required in September, October and May. Summer months from May to the last of August represent a non-heating period. The accumulated heating energy supplied by the boiler reaches a value of **44.05 MWh** in the monitored year, which means an average supply of **80.82 kWh/m^2·year**.

Due to the academic use of the building, the operational schedules of heating and lighting systems have a weekly basis and vary according to the academic timetable and calendar. Four typical weeks were selected, see Figure 9. The heating system operates in a defined time period from Monday to Friday, being off during weekends and holidays.

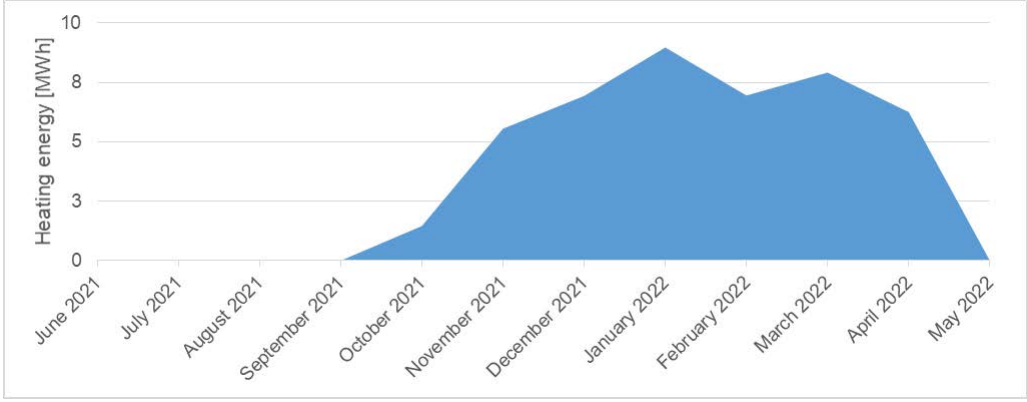

Figure 8. Annual distribution of heating energy attending to the measured data in the monitored period from June 2021 to May 2022.

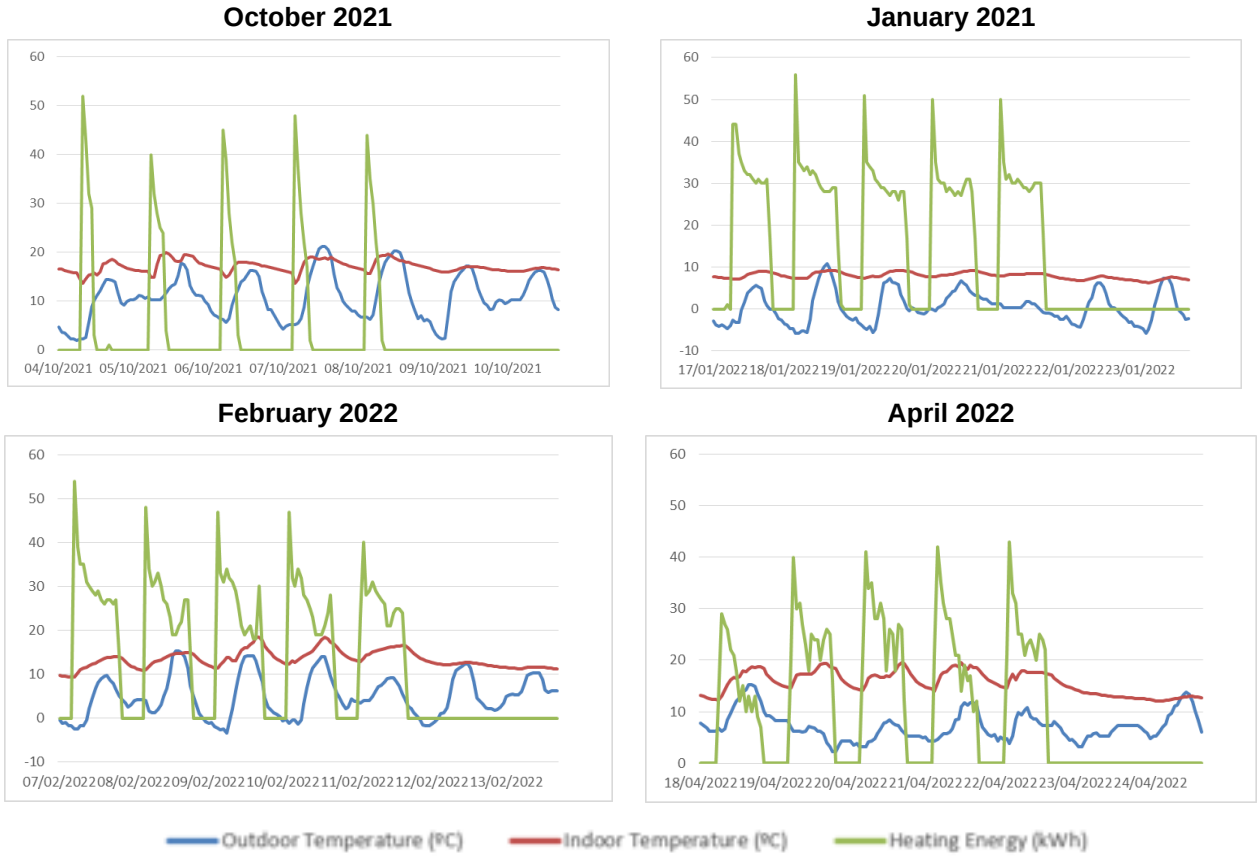

Figure 9. Typical week selected for calibrating the operational schedule of the heating system.

As appreciated in Figure 9, the highest recorded energy data correspond to the “start-up” of the heating systems during the morning and decrease during the day as external and internal gains increase. The boiler charge varies during the day according to the indoor conditions, see Figure 10.

In contrast to the heating system, there does not seem to be a clear operating pattern for the lighting system. This is due to a presence sensor in the building, as well as the variability in the occupancy period of the different classrooms. However, it has been identified that the auxiliary energy required by the building and its equipment is around 100 Wh with an electric current of 2 A. The total energy consumption measured in the building in the monitored period is **16.71 MWh** and an average of **30.66 kWh/m^2·year,** being gathered in Table 6 the data classified by zones.

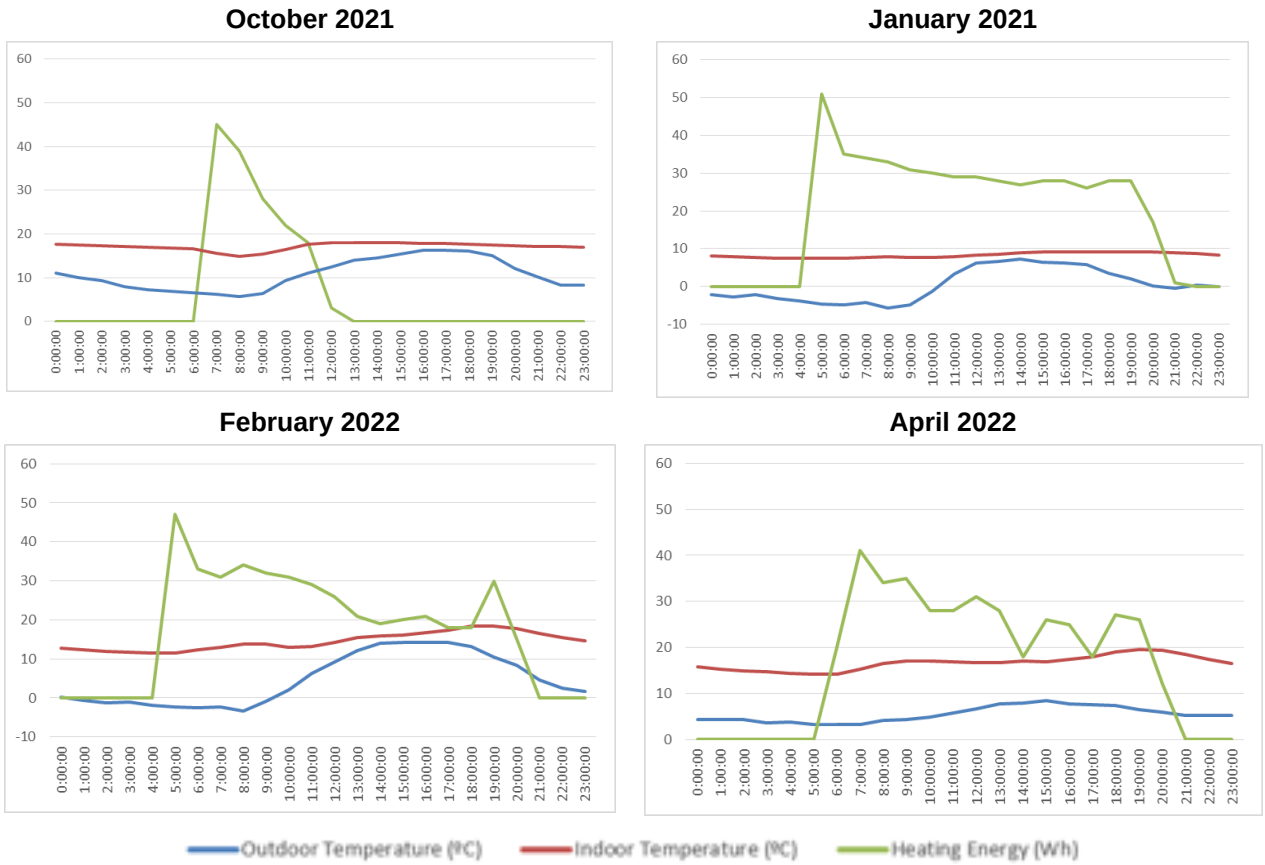

Figure 10. Typical days selected for calibrating the operational schedule of the heating system.

Table 6. Electrical energy consumption classified by zones in the period from June 2021 to May 2022.

Classroom 1	**Classroom 2**	**Toilets (right)**	**Toilets (left)**
2556.15 kWh/year	6762.37 kWh/year	3099.57 kWh/year	671.41 kWh/year
21.92 kWh/m^2·year	125.30 kWh/m^2·year	108.41 kWh/m^2·year	28.71 kWh/m^2·year
213.01 kWh/month	563.53 kWh/month	258.30 kWh/month	55.95 kWh/month
15.30%	**40.47%**	**18.55%**	4.02%
Demonstration room I	**Demonstration room II**	**Corridor**	**Boiler room**
926.11 kWh/year	125.59 kWh/year	1261.96 kWh/year	1307.05 kWh/year
17.56 kWh/m^2·year	2.39 kWh/m^2·year	22.16 kWh/m^2·year	30.17 kWh/m^2·year
77.18 kWh/month	10.47 kWh/month	105.16 kWh/month	108.92 kWh/month
5.54%	0.75%	7.55%	7.82%

From the data shown in Table 6, it can be interpreted that a large part of the teaching activity in the building takes place in Classroom 2 and that most of the occupants of the building are women since the women's toilet (right) has a higher annual electricity consumption. The building has been modelled in DesignBuilder according to constructive detail drawings and walk-through audits as shown in Figure 11.

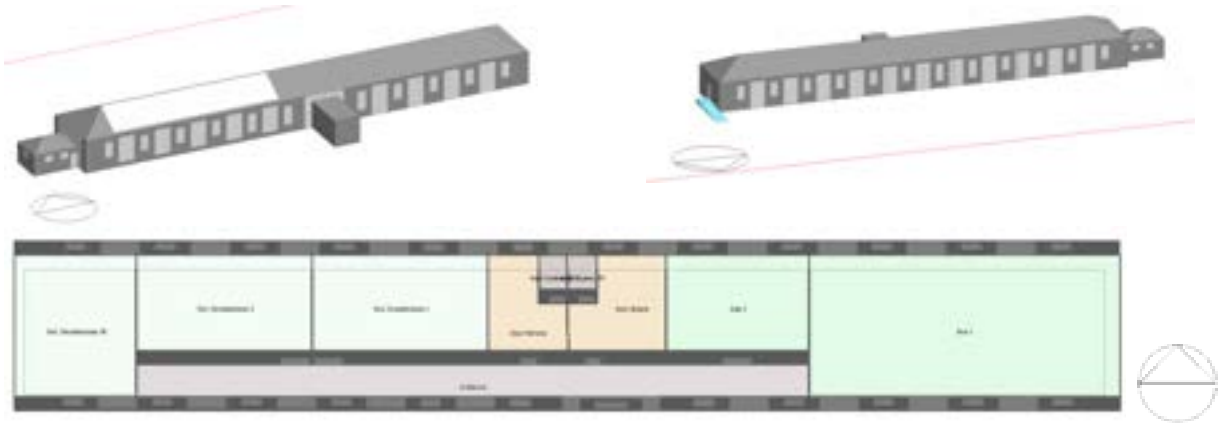

Figure 11. Visualization of building model created in DesignBuilder according to constructive details.

6. Conclusions and discussion of results

A data calibration process has been developed in this paper and deployed to implement it in a BES model calibration of Building 2 of the Faculty of Nursing and Health Science of the University of Burgos. It is necessary to define a specific methodology to accurately calibrate the monitored data. Including experimentally tested thermal transmittance values reduce uncertainties and, thus, also the energy performance gap of the BES model. In this study, the available monitoring data have been pre-processed and accurately prepared for implementing them into the BES model, so these data are used in the whole model calibration procedure. In this first part of the research, data have first been used to better understand the in-use operational schedule of the building. In addition, some of the monitored variables have been implemented as inputs to the model and others as outputs to verify the accuracy of the model calibration in future research.

The more complex step consists on the data pre-processing, including data cleaning and transformation, where a specific and accurate methodology was developed for the case study, in order to obtain averaged hourly data for the model calibration. In this sense, it must be highlighted that a whole year monitoring period has been used during this work, which means a more complex analysis process, but it also provides a more accurate BES calibrated model.

After the previous analysis, the BES model will be easily calibrated in further works. This calibrated BES model will encourage the estimation and prediction of reliable energy savings for different retrofitting scenarios of the building, such as this proposed for windows replacement. To fulfil the calibration of the model, occupancy schedules and density must be analysed from monitored data in order to implement reliable inputs in the BES model.

Acknowledgements

This work is part of the project CPP2021-008975, entitled “Advanced manaGement and cOntRol for buildings smArtness: Towards a more sustainable energy and water (AGORA)”, funded by MCIN/AEI/10.13039/501100011033 and by the European Union "NextGenerationEU"/PRTR."

To the University of Burgos (UBU) for providing the studied in-use building to the AGORA project and for providing the data collected by the monitoring systems.

To the Building Quality Control Laboratory of the Basque Government for conducting tests to measure the thermal transmittance of the windows studied.

Nomenclature

A	surface of window sample, m^2
e	thickness, cm
E	Energy, Wh
k	thermal coefficient, $Wh/(m^3 \cdot K)$
t	timestamp, h
$R_{s,t}$	sum of the tested thermal resistances of the outer and inner surfaces, $(m^2 \cdot K)/W$
$R_{(s,t)st}$	sum of the normalized thermal resistances of the outer and inner surfaces, $(m^2 \cdot K)/W$
T	Temperature, ºC
U	Thermal transmittance, $W/(m^2 \cdot K)$
V	Volume, m^3

Greek symbols

ΔE	Accumulated energy, Wh
Φ	Heat flux through the test tube, W
θ	Temperature, K

Subscripts and superscripts

inlet	delivery boiler circuit
m	measured
ne	cold side
ni	hot side
outlet	return boiler circuit
t	timestamp
w	window
wa	water

References

[1] Waltz, J. P. (1995). Practical experience in achieving high levels of accuracy in energy simulations of existing buildings. Strategic Planning for Energy and the Environment, 15(2). https://www.osti.gov/biblio/128815

[2] Fan, C., Yan, D., Xiao, F., Li, A., An, J., & Kang, X. (2021). Advanced data analytics for enhancing building performances: From data-driven to big data-driven approaches. Building Simulation, 14(1), 3–24. https://doi.org/10.1007/s12273-020-0723-1

[3] Coakley, D., Raftery, P., & Keane, M. (2014). A review of methods to match building energy simulation models to measured data. Renewable and Sustainable Energy Reviews, 37, 123–141. https://doi.org/10.1016/j.rser.2014.05.007

[4] Pachano, J. E., & Bandera, C. F. (2021). Multi-step building energy model calibration process based on measured data. Energy and Buildings, 252, 111380. https://doi.org/10.1016/j.enbuild.2021.111380

[5] Zhang, L., & Wen, J. (2019). A systematic feature selection procedure for short-term data-driven building energy forecasting model development. Energy and Buildings, 183, 428–442. https://doi.org/10.1016/j.enbuild.2018.11.010

[6] Fan, C., Chen, M., Wang, X., Wang, J., & Huang, B. (2021). A Review on Data Preprocessing Techniques Toward Efficient and Reliable Knowledge Discovery From Building Operational Data. Frontiers in Energy Research, 9. https://www.frontiersin.org/articles/10.3389/fenrg.2021.652801

[7] Raftery, P., Keane, M., & O'Donnell, J. (2011). Calibrating whole building energy models: An evidence-based methodology. Energy and Buildings, 43(9), 2356–2364. https://doi.org/10.1016/j.enbuild.2011.05.020

[8] Amasyali, K., & El-Gohary, N. M. (2018). A review of data-driven building energy consumption prediction studies. Renewable and Sustainable Energy Reviews, 81, 1192–1205. https://doi.org/10.1016/j.rser.2017.04.095

[9] Cornaro, C., Puggioni, V. A., & Strollo, R. M. (2016). Dynamic simulation and on-site measurements for energy retrofit of complex historic buildings: Villa Mondragone case study. Journal of Building Engineering, 6, 17–28. https://doi.org/10.1016/j.jobe.2016.02.001

[10] Asdrubali, F., & Baldinelli, G. (2011). Thermal transmittance measurements with the hot box method: Calibration, experimental procedures, and uncertainty analyses of three different approaches. Energy and Buildings, 43(7), 1618–1626. https://doi.org/10.1016/j.enbuild.2011.03.005

[11] Lu, X., & Memari, A. M. (2018, September). Comparative study of Hot Box Test Method using laboratory evaluation of thermal properties of a given building envelope system type. https://doi.org/10.1016/j.enbuild.2018.08.044

[12] Hellerstein, J. M. Quantitative Data Cleaning for Large Databases.

[13] Martín Escudero, K., Atxalandabaso, G., Ercoreca González, A., Uriarte, A., & Porta, M. (2021). Comparison between Energy Simulation and Monitoring Data in an Office Building. https://doi.org/10.3390/en15010239

Identification of typical district configurations: A two-step global sensitivity analysis framework

Arthur Chuat[a] (CA), Jonas Schnidrig[a,b], Cédric Terrier[a] and François Maréchal[a]

[a] Ecole Polytechnique Fédérale de Lausanne (EPFL), Sion, Switzerland, arthur.chuat@epfl.ch (CA)
[b] University of Applied Sciences Western Switzerland (HES-SO), Sion, Switzerland

Abstract:
The recent geopolitical conflicts in Europe highlighted the sensibility of the current energy system to the volatility of energy carrier prices. In the prospect of defining robust energy system configurations to ensure energy supply stability, it is necessary to understand which parameters modulate the system configuration. This paper presents a framework that identifies a panel of technological solutions at the district level. First, a global sensitivity analysis is performed on a mixed integer linear programming model which optimally size and operate the system. The sensitivity analysis determines the most influential parameters of the model and provides a representative sampling of the solution space. The latter is then clustered using a density-based algorithm to identify typical solutions. Finally, the framework is applied to a suburban and residential Swiss neighborhood. The main outcome of the research is the high sensitivity of the model to energy carrier prices. As a result, the sampling space separates itself into two system types. The ones based on a natural gas boiler, and the ones relying on a combination of electrical heater and heat pump. For both types, the electricity demand is either fulfilled by PV panels or by electricity imports.

Keywords:
Mixed Integer Linear Programming (MILP), global sensitivity analysis (GSA), clustering, district energy system (DES), solution space sampling

1. Introduction

1.1. Background

The energy transition presents itself as one of the main levers to mitigate global warming as the energy sector accounts for 73% of global emissions and is expected to increase over the coming decade [1]. Therefore, developing a sustainable system requires careful energy planning from policymakers. In this prospect, energy system models are essential tools for understanding and assessing the potential impact of new technologies or policies.
The built environment, which accounted for 36% of final energy consumption in 2020 [2], is viewed as a promising pathway to a sustainable energy mix. Moreover, distributed energy systems, such as those composed of interconnected energy hubs, have great potential when deployed at the district scale, increasing self-consumption, and mitigating grid congestion.

1.2. Literature review

1.2.1. Energy system modelling

Energy models play a crucial role in guiding decision-makers towards a fossil-free energy system. The decarbonization of the current system requires a profound restructuring and involves a deeper electrification [3]. Low-carbon technologies, such as solar and wind, are spreading rapidly and are expected to become the main source of electric power [4, 5]. However, those renewable energies are intermittent and decentralized, bringing new challenges such as redistribution of electricity, stabilization of the power grid, intra and inter-day storage [6]. The multiplication of energy vectors, i.e., electricity, heat, oil, waste, biomass, or even hydrogen, increases the complexity of the task to provide an optimal configuration and operation of the system. Consequently, the majority of models focus on one specific energy sector (electricity, heat, mobility, etc.) and do not account for cross-sectoral synergy [7]. Additionally, on a more general aspect, the scale of the system can vary from a single building to an entire country. Whether or not, energy subsystems are considered in the overall scale of the system, e.g., interconnected buildings to represent a district system or the regionalisation of a country-wide system.

Buildings archetypes have been widely used to define large-scale systems [8] as their emissions have doubled in the last 30 years [4]. Kotzur and al. [9] developed a bottom-up model based on residential building stock. They deployed an aggregation algorithm to define archetype buildings. Their configuration and operation, which includes the buildings' interaction, are then optimized to acquire cost-effective solutions. Stadler and al. [10] assessed the impact of model predictive control (MPC) on the Swiss building stock. Three typical buildings were defined, each having 9 variations based on their construction date. The deployment of MPC allowed the reduction of the operational expenditure (OPEX) as well as the increase of the self-consumption. This result emphasizes the importance of the interconnection and operation improvement of building energy system.

In this regard, the design and operation of interconnected distributed energy systems, such as buildings, have proven to be part of the solution to help improve sustainable development in many countries [11–14]. The distributed aspect of such systems comes from the interconnection of multiple energy sources. Those sources can be energy hubs linked by local multi-energy grids. As discussed in the review of district-scale energy systems by Allgerini and al. [15], there has been a significant improvement in the models and tools used to analyze such systems.

In their paper, Morvaj and al. [16] performed an optimization of an urban scale energy system composed of twelve buildings. For each building, an optimal design and operation have been identified and the district heating network associated was optimized to reduce greenhouse gas (GHG) emissions and the total expenditure (TOTEX). Maroufmashat and al. [17] highlighted the importance of considering multiple energy hubs in order to observe significant cost and GHG emissions reduction. Their case study showed that the implementation of distributed combined heat and power (CHP) units was limited while operating an electricity grid with low CO_2 emissions. Additionally, the operation of interconnected energy hubs can significantly increase the robustness of the power grid, e.g. mitigation of congestion and ensuring reliability.

1.2.2. Global Sensitivity Analysis

Most current models assume a perfect knowledge of the input parameters, which induces the absence of uncertainty in the model and characterizes them as deterministic [12]. However, there is some uncertainty in a number of areas, including current policy, renewable energy production, and economic trends. Therefore, specific models are developed to consider the uncertainty of input parameters: stochastic models. However, it might be complicated to transform a deterministic model into a stochastic one without major remodeling. An alternative is the application of sensitivity analysis (SA) to deterministic models as proposed in [18, 19].

The utilization of sensitivity analysis is an effective approach to evaluate the impact of input parameters on a model. There exist two main types of SA: local and global. The most common method is the local sensitivity analysis, which evaluates the sensitivity by computing partial derivatives and gradients. Even though its ease of implementation makes it popular, the sampling scheme does not scan the entire space of input parameters. This gap is filled by the global sensitivity analysis (GSA), which covers the sampling space by varying several parameters at once. In doing so, it can capture parameters interaction [20].

The review of the SA method for building energy systems performed by Tian and al. [21] emphasized the importance of choosing the right method. They concluded that the choice should be based on the following criteria: research purpose, computational cost of energy models, number of input variables, and familiarity with the methods. Another review was performed by Westermann and Evins [22], 57 studies on building design were analyzed, focusing on objective, sampling strategy, and surrogate model type. Among all studies only 16 included a SA of the model, their sampling strategies were primarily based on Latin hypercube sampling (LHS), and only 3 used an optimization model, highlighting the low implementation of SA in optimization models.

A two-stage GSA framework has been used in several studies [18, 19, 23]. Their goal is diverse, from assessing the uncertainty, and sensitivity of the system, or to explore the multidimensional design space, but the applied framework stays the same. First, a screening method filters out non-influential parameters to reduce the computational cost of further model evaluations. It is then combined with a Sobol sequence to obtain a proper sampling of the solution space for the final sensitivity analysis.

1.3. Gaps and contribution

As emphasized throughout subsection 1.2., the literature lacks an application of distributed energy systems as energy hub in large-scale energy system optimization. The role of districts as renewable energy hubs can be

central in the optimization of a carbon-neutral national energy system as the operation of energy fluxes can help considerably improve the thermo-efficiency of the system. In this prospect, the proposed configurations should represent at best the district's solution space. This paper attends to provide a framework to identify a set of optimal district configurations. The framework consists of a two-step GSA on a district-wide energy system model to explore its solution space. The latter will then be aggregated to identify typical configurations. The purpose of this paper is to contribute to the following research points:

- Identification of the most influential parameters.
- Exploration of the solution space.
- Identification of typical configurations.

2. Methodology

2.1. Global sensitivity analysis

2.1.1. Overview

In order to develop a panel of solutions for the district, it is necessary to explore the whole solution space of the model. The following methodology is inspired by the publication of Saltelli and al. [20] which assesses the state-of-the-art of GSA. A sensitivity analysis can be decomposed into four main steps:

1. Identification: k input parameters of the model are selected
2. Sampling: the input parameters space is discretized by N samples
3. Evaluation: the model outputs are computed for each sample
4. Comparison: some metrics are derived from the N outputs of the model for the k parameters

The methodology used consists of two separate SAs:

1. A screening method is performed to identify the most influential factor of the model, i.e. the parameters inducing the greatest variation of the objective function.
2. A variance-based method is used to efficiently explore the solution space of the model and quantify its sensitivity.

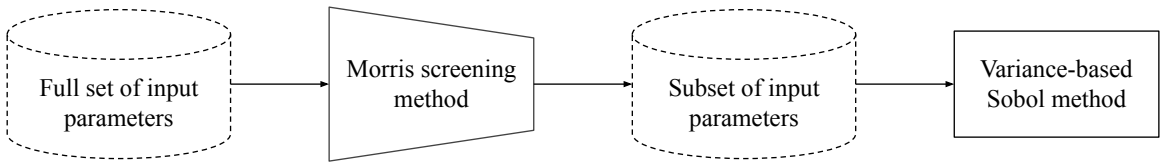

Figure 1: Scheme of the two-step GSA composed of first the Morris method as a screening and then the Sobol method is applied on the most influential parameters previously identified.

2.1.2. Morris screening

The screening method used is the Morris method, which allows to qualitatively compare the influence on the model output of a large number of parameters with a few evaluations [24]. The method discretizes the input parameters space, which is a k-dimensional hypercube, into a p-level grid, where k is the number of independent input parameters and p is a sampling parameter. Afterward, it performs a one-step-at-the-time method (OAT), i.e. it randomly modifies one input parameter by $\pm\Delta$ to generate r trajectories.
Finally, it evaluates the elementary effect of the i_{th} input parameter (EE_i) as a function of the model output $Y = f(X_1, ..., X_n)$, see Equation 1. The EE can be interpreted as a local partial derivative, thereby it represents the sensitivity of the model at a specific point w.r.t the input parameter:

$$EE_i = \frac{\partial Y}{\partial x_i} \simeq \frac{Y(X_1, X_2, \dots, X_{i-1}, X_i \pm \Delta, \dots X_k) - Y(X_1, X_2, \dots, X_k)}{\Delta} \tag{1}$$

Where Δ is defined as a function of p: $\Delta = \frac{p}{2(p-1)}$ and can be considered as the size of the discretization mesh. The total number of model evaluations amounts to $r(k+1)$, where r is suggested between 4-10 [20]. The choice of p and r has to be made jointly to ensure that the k dimensions and their interactions are correctly sampled, Saltelli proposed $p = 4$ and $r = 10$ [25] whereas Morris used $r = 4$ in [24], which seems to be the minimum usable value.

In its original work, Morris proposed the computation of the mean μ_i (Equation 2) and standard deviation σ_i (Equation 4) of the elementary effect distribution for each parameter i. However, by doing so, the positive and negative effects cancel each other out, which would falsely influence the results of the mean value. Thereby, the method has been improved by Campolongo and al. [26], by considering the absolute mean elementary effect μ_i^* (Equation 3).

$$\mu_i = \frac{1}{r} \sum_{j=1}^{r} EE_i^j \tag{2}$$

$$\mu_i^* = \frac{1}{r} \sum_{j=1}^{r} |EE_i^j| \tag{3}$$

$$\sigma_i^2 = \frac{1}{r-1} \sum_{j=1}^{r} \left(EE_i^j - \mu_i \right)^2 \tag{4}$$

Those indicators allow to compare the input parameters between each other. A small absolute mean value means a non-influential parameter. The standard deviation reflects the interaction between parameters: a high value means that the output is highly dependent on the sampling point, i.e. on the other input parameters values. Conversely, a low standard deviation indicates that the elementary effect is not subject to fluctuate with other factors variation.

The representation of the mean absolute value of the EEs and their standard deviation makes it easy to identify to which group the parameter belongs. As represented on Figure 2, one can see the different zones and the line ($x = y$) separating quadrant 1 that defines whether parameters interact together or not. The different zones can be defined as follows:

1. Non-influential parameters.
2. Influential, non-interacting parameters.
3. Influential, interacting parameters.
4. Influential parameters.

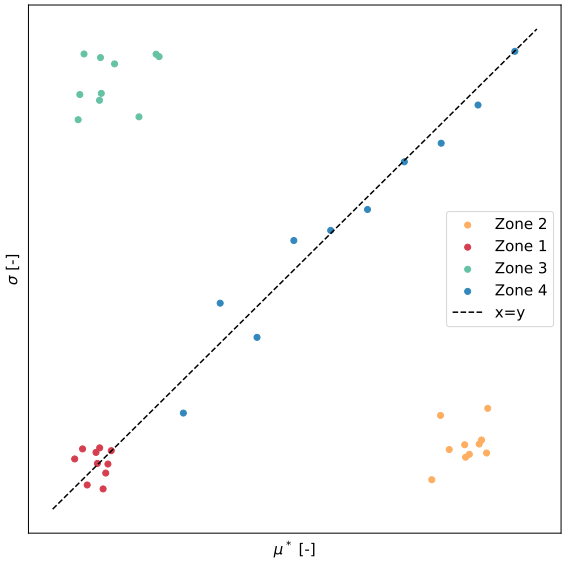

Figure 2: Identification of the typical zone on the $\mu^* - \sigma$ plane.

The comparison of μ and μ^* gives an extra insight in the monotony of the model. If the model output increases with an augmentation of the parameter, the EE will stay positive thus μ^* and μ will have a similar value. Whereas, if the EE changes sign regularly its cumulative will be lower, i.e. μ will be lower than μ^*.

2.1.3. Sobol sampling

The Sobol method is a variance-based sensitivity analysis named after the mathematician Ilya M. Sobol. The method is developed in [20, 27] and uses Sobol's recommendation on the sequencing of quasi-random numbers. However, Saltelli extended her work in [28] to reduce the error rate when computing sensitivity indices.

2.1.3.1 Sensitivity indices

The method evaluates two different sensitivity indices, the first one is the first-order sensitivity coefficient (Equation 5). It results from the ratio of the variance of the mean output, considering all parameters except the i-th, to the variance of the output. The secondary sensitivity coefficient is the total effect index, i.e. first and higher-order sensitivity coefficient (Equation 6).

Assuming: $Y = f(X_1, ..., X_n)$ is the model output, $\mathbf{X}_{\sim i}$ symbolizes all parameters but $\mathbf{X}_i$, $E_{\mathbf{X}_{\sim i}}(Y \mid X_i)$ is the mean of Y for every possible $\mathbf{X}_{\sim i}$ and finally the variance V_{X_i} is calculated for all values of X_i.

$$S_i = \frac{V_{X_i}\left(E_{\mathbf{X}_{\sim i}}(Y \mid X_i)\right)}{V(Y)} \tag{5}$$

$$S_{Ti} = \frac{E_{\mathbf{X}_{\sim i}}\left(V_{X_i}(Y \mid \mathbf{X}_{\sim i})\right)}{V(Y)} = 1 - \frac{V_{\mathbf{X}_{\sim i}}\left(E_{X_i}(Y \mid \mathbf{X}_{\sim i})\right)}{V(Y)} \tag{6}$$

The first-order coefficient only takes into account the effect of itself on the output value, but not the possible effect when considering higher-order interactions with other parameters. The total-order index evaluates the effect of a parameter considering all possible interactions with other parameters. Meaning that a parameter with a value of $S_T = 0$ can be considered as non-influential on the output Y. The total number of model evaluations is $N(k+2)$ with N being typically between 500 and 1000 and it is suggested to choose a power of two [20].

2.2. Clustering

2.2.1. Standardization and features selection

It is necessary to standardize the data when various features are used for clustering. Otherwise, the aggregation algorithm mainly takes into account the large numerical values. The chosen standardization technique is the *z-score*, see Equation 7. Each feature Y_i of the data set is standardized as follows:

$$Z_i = \frac{Y_i - \mu_i}{\sigma_i} \tag{7}$$

where μ_i is the mean and σ_i is the standard deviation of the feature Y_i. The features selected for the clustering, i.e. the district characteristics, are a mix of economic and technical attributes of the optimization result. The key performance indicators (KPI) chosen are capital and operational expenditure (CAPEX and OPEX). Installed capacity of energy conversion and storage units are included in the clustering as they are key properties of the district configuration. Regarding the exchange with the network, the total and peak energy supply and demand are considered for the natural gas (NG) and the electricity grid.

2.2.2. Aggregation techniques

Several aggregation techniques, such as K-means, DBSCAN, and HDBSCAN, performance are analyzed for this specific clustering. The K-means method is a clustering technique that minimizes the variance within clusters, which is a difficult problem to solve optimally. However, heuristic algorithms can be used to find a local optimum efficiently. To determine the appropriate number of clusters for K-means, two common techniques are the Silhouette score and the Elbow method. The Silhouette score evaluates how well each data point fits within its assigned cluster, based on the density of points within the cluster and the distance between clusters. The Elbow method involves observing the point of inflection on a plot of the sum of squared errors (SSE) as the number of clusters increases.

Another assessed method is the DBSCAN, which is based on the concept of core points. Points are defined as core points of one specific cluster when they can reach a minimum of *minPts* neighbours within a ϵ distance. Additionally, points within reach, but not satisfying the minimum neighbours criterion still belong to the cluster. However, points non-reachable from a core point are considered outliers. The choice of *minPts* and ϵ should be based on the data properties [29].

The HDBSCAN algorithm is an extension of the DBSCAN method with a hierarchical approach. The algorithm can be decomposed in a few steps to get a broad overview. First, the space is transformed based on its density. This allows to construct a minimum spanning tree used to build the cluster hierarchy. Then, the cluster tree is condensed to finally extract the clusters [30, 31].

To support the clustering task, a score is introduced to quantify the quality of the clusters. The chosen score is the density-based clustering validation (DBCV) index presented by Moulavi and al. [32]. It is based on a parameterless core distance defined by the density of objects and mutual reachability. The index ranges between -1 and 1, which represents a bad and a good score respectively.

2.3. Case study

The application of the presented framework is carried out on a suburban and residential district located in the climatic zone of Geneva, Switzerland. The energy system consists of 15 buildings, including 5 single-family houses and 10 apartment buildings [33], selected from a pool of 30 available options. Various characteristics of the buildings, such as type, year of construction, energy reference area, and height, are obtained from the cantonal and federal Official Building Registry [34,35], while the ground surface area is provided by the cantonal administration [35, 36]. The climate data, solar irradiation, and temperature are extracted from Meteonorm [37], and the characteristics of the building envelope are calculated following SIA norms 380/1 [38]. The physical information gathered on the buildings allows to define the electric and heat demands based on a 1R1C model detailed in [39]. The PV orientation is optimized based on roofs and façades information extracted from Swisstopo [40,41], while the grid specifications and electricity demand are furnished by Romande Énergie [42]. The time series are divided into 10 typical periods formed of 24 hours and 2 extreme periods of 1 hour each, resulting in a total of 242 different timesteps being considered. Various parameters are fixed during the problem definition, including unit parameters, district parameters, and energy carrier price. More information on these parameters can be found in [43].

3. Results and Discussions

3.1. Sensitivity analysis

The considered parameters for the screening step are energy conversion and storage units parameters as well as the energy carriers prices. A total of 60 parameters were considered. Following the sampling indications of Morris, 610 optimizations were required to compute the sensitivity metrics. As the result of each run is a complete system configuration and operation, a specific output value had to be identified to compare each optimization. The chosen indicator is the TOTEX, assuming an economically rational behaviour.
A good practice is to plot the absolute mean value (μ^*) and standard deviation (σ) of the EE distribution of each input parameter, Figure 3 shows such a plane for the six most influential parameters. Two parameters stand out from the rest: the supply cost of electricity and natural gas. The supply cost of electricity has a high influence on the TOTEX, high μ^*, however, its standard deviation is low, indicating that its EE is not correlated to the other input parameters. This low correlation comes from its key role in the district model. It serves to directly supply the electric demand when no installed units can fulfill it and it can also serve to supply the heat demand via HPs and electrical heaters. The retail price of NG is less influential as fewer units consider natural gas as a resource. However, it can be considered as an influential parameter as a small price of NG can help provide heat at a very low cost with a gas boiler. Note that the HP and boiler parameters are also influential with a low standard deviation, highlighting that the technologies installation is not correlated to the energy carriers prices.

Table 1 presents the Morris results of the aforementioned parameters. Comparing the absolute (μ^*) and non-absolute (μ) mean value of EE shows the monotonic correlation between TOTEX and input parameters values, e.g., an increase in electricity supply cost will always increase the TOTEX. Furthermore, the negative sign of the mean EE of the electricity feed-in tariff indicates that it contributes to the reduction of TOTEX.

Table 1: Sobol's indices, mean and absolute mean EE for retail and feed-in tariffs of energy carriers. The sensitivity of the parameters for the Morris and Sobol approaches all trend in the same direction.

	S_1	S_{Ti}	μ^*	μ
Electricity retail tariff	0.86	0.91	93k	93k
Natural gas retail tariff	0.09	0.14	33k	33k
Electricity feed-in tariff	1e-4	6e-4	0.9k	-0.9k

In order to reduce the computational time of the SA a selection of the input parameters was required. The decision to focus on the energy carrier prices was based on obtained results and similar conclusions presented in subsubsection 1.2.2..

The input parameter space is explored with 2560 samples following recommendations presented in subsubsection 1.2.2., $p = 4$, $r = 10$, and $N = 512$. The parameters variation range is $\pm 50\%$ for retail tariffs, as displayed in Figure 4, and $\pm 30\%$ for the feed-in tariff. The sensitivity indices of the Sobol can be observed in Table 1 alongside Morris μ^* values for comparison.
The Sobol results have a similar trend than the qualitative sensitivity indices from the Morris method. The electricity feed-in tariff is less influential regarding Sobol's results. Since the first-order Sobol effect and the total effect have a similar value, the interaction between energy carrier prices is mainly of additive nature, ie. S_1 and S_{Ti} are close. The retail tariff of electricity is much more influential than the NG tariff. One possible explanation is that, as mentioned before, there is a greater amount of technology using electricity compared to the NG. Therefore, a low electricity price can help to significantly reduce TOTEX, as both electricity and heat demand can be met using electricity.

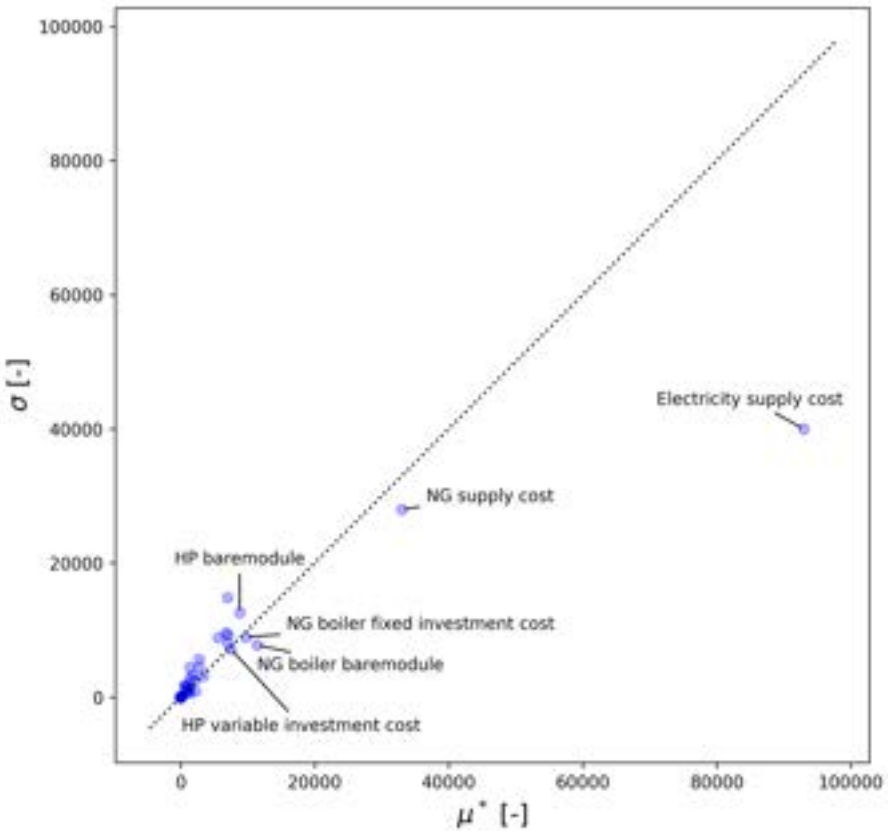

Figure 3: Morris analysis results on $\mu^* - \sigma$ plane.

3.2. Typical configurations identification

First, a Silhouette score is calculated for various numbers of clusters to identify a range of potential optimal values. The score decreases from 1 to 10 and then seems to stabilize, meaning that the optimal number of clusters is $k = 1$. Whereas, for the Elbow method the inflection occurs in the range of $k = 5 - 7$. Finally, the DBCV index is computed for the K-means clustering with k varying from 5 to 11 and the optimal number of clusters appears to be around $k = 10$ with a score of -0.54.

The DBSCAN algorithm recognizes a total of 28 clusters and obtains a DBCV index of -0.12, which is significantly better than the K-means DBCV indices. Regarding the HDBSCAN result, it obtains the best DBCV index with a value of 0.04. However, it identifies 73 clusters, which is far from the initial estimation of $k \simeq 10$.

Looking more precisely at the size distribution of the DBSCAN clusters, one can remark that beyond the tenth cluster, the size dropped abruptly. Indeed, the first ten clusters represent more than 90% of the data points, corresponding to the approximated required number of clusters. Regarding the HDBSCAN distribution, there was no sharp decrease in the cluster size. As a consequence, only data from the first ten DBSCAN clusters were considered for further calculations.

3.3. Presentation of the typical district configurations

3.3.1. Distribution of the configuration in the sampling space

Figure 4 represents with different colors the distribution of the clusters over the retail tariffs variation range. As observed in subsection 3.1., the output of the model, i.e. the district configuration, is strongly correlated to those tariffs. This relation can be observed in the figure below as the different configurations can be identified. Additionally, the sampling space naturally separates itself in half, the separation is highlighted by the amount of NG imports. Configurations 1 to 4 are based on NG and the configurations above, 5 to 10, on electricity. The NG configurations are located in the bottom right corner where the electricity tariff is high. Inversely, the electricity-based ones are in the top left region where the NG price is high. One can note that the space has fewer samples below the separation line, this is due to the data selection done in subsection 3.2..

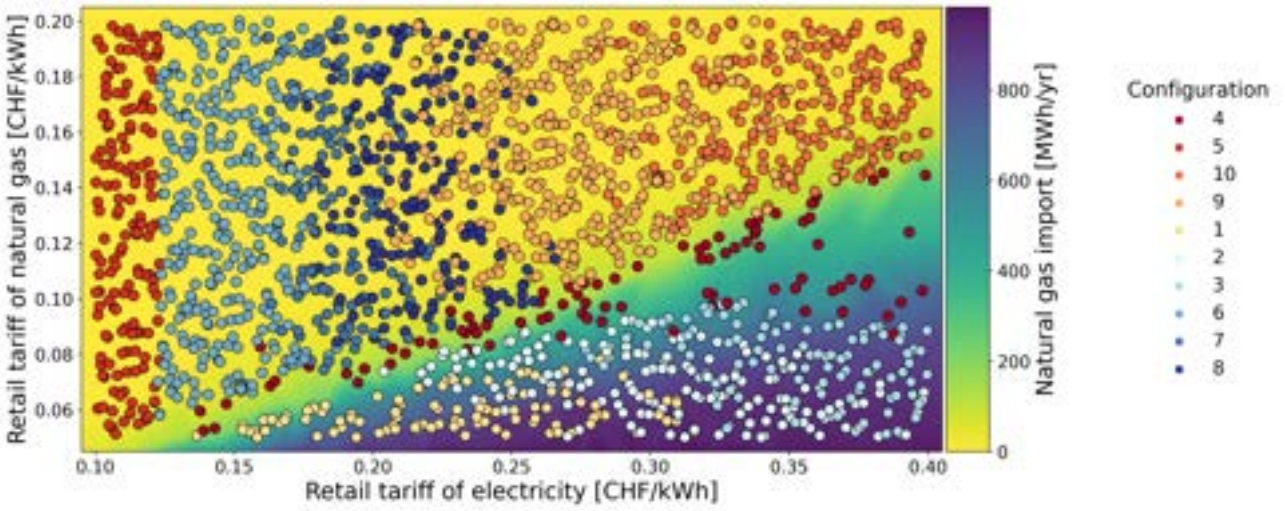

Figure 4: Typical configurations distribution in the retail tariffs space.

3.3.2. Installed units capacity

Figure 5 shows the installed units capacity for each configuration alongside their grid exchanges. The main variation between configurations is the total installed capacity, almost ranging from single to double. This discrepancy is due to the extreme period (high demands and rash environment) included in the model, as the demand is either fulfilled by imports or by an installed unit. The model installs a minimum heating capacity to supply heat in any condition. This minimum heating capacity appears in all configurations and is either composed of NG boiler or a combination of an electrical heater and HP. The additional capacity is formed by various PV capacity deployments.

Concerning the units' installed capacity, there is no positive correlation between HP and PV installation, as one would have expected from previous results discussed in subsubsection 1.2.1.. If no PV panels are installed, electricity imports increase considerably to supply the HP or the electrical heater. The HP installation triggers the deployment of water tanks to serve as a buffer. Large installation of boilers is accompanied by significant imports of NG since boilers are used as the main heat source when they are installed. The presence of HP and PV in most configurations underlines their high potential in district energy systems. Although, the electric grid is more strained with PV implementation as imports are reduced, but exports are increased, requiring a sufficient absorption capacity of the grid.

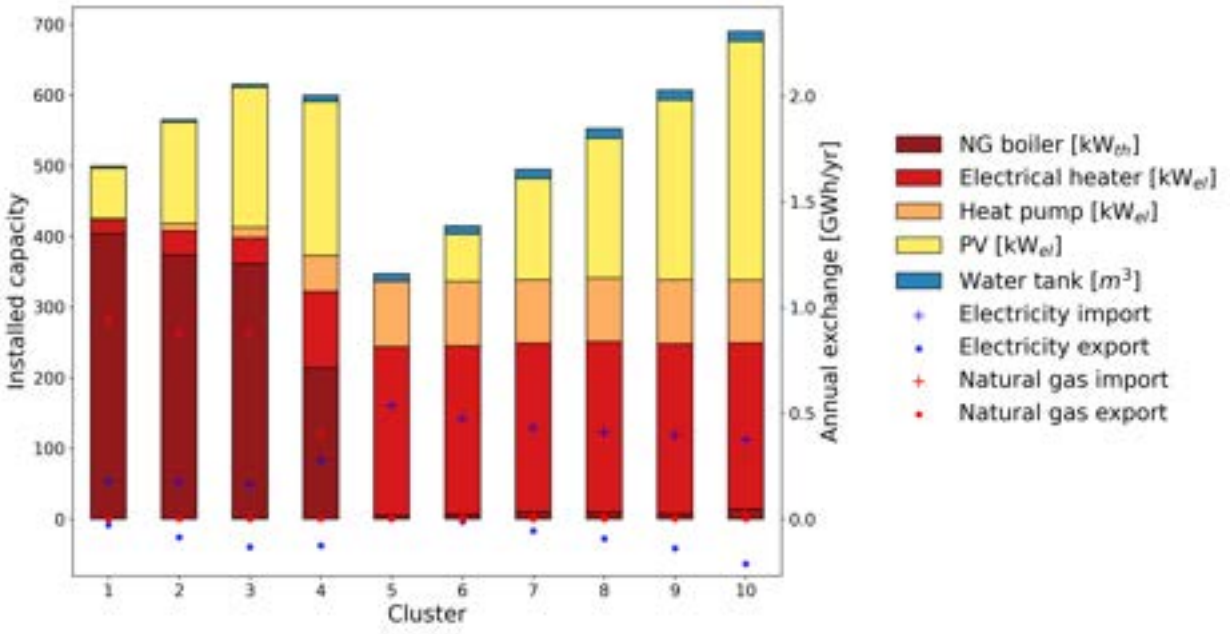

Figure 5: Identified configurations of the district and their grids exchanges.

3.3.3. Dimensionality reduction

Principal component analysis (PCA) is a dimensionality reduction technique used to facilitate the exploration of data sets. The algorithm identifies the eigenvectors of the covariance matrix. The dimensions are sorted from most to least explaining components. Usually, only the first two components are used to project the data points, as can be observed in Figure 6.

The first dimension explains 64.8% of the variance and the second 33.2%, thereby the plot illustrates 98% of the data set variance. The indicators can be regrouped into three main groups which align with the principal components, this is a direct result of having 98% of the variance explained with only 2 dimensions. The first component can be interpreted as the global warming potential (GWP) and the second as the TOTEX. The first deviates slightly from the x-axis, however, the second is perfectly aligned.

A group is positively correlated to the first dimension and contains the NG import, boiler installed capacity, and GWP. Their correlation is natural as the boiler is fueled by NG, which has a high CO_2 emission factor. Inversely, another group is negatively correlated to the first dimension. It contains the installed capacity of the heat pump and electric heater, which are low emissions technologies when coupled with a low-carbon electricity grid like the Swiss one. The electricity import is closely related to the group but helps reduce the TOTEX, negative correlation to the second dimension. This second dimension is highly correlated with the installed PV capacity, electricity export, and TOTEX. The relationship between PV capacity and electricity export stems from the high production potential of the technology in summer, which exceeds the demand. This results in a redistribution of the electricity surplus in the grid. This electricity export is sold at a low price, so the gain from the electricity buyback may not offset the operational cost of the microgrid and the PV installation cost. Note that the influence of the indicators is somewhat similar.

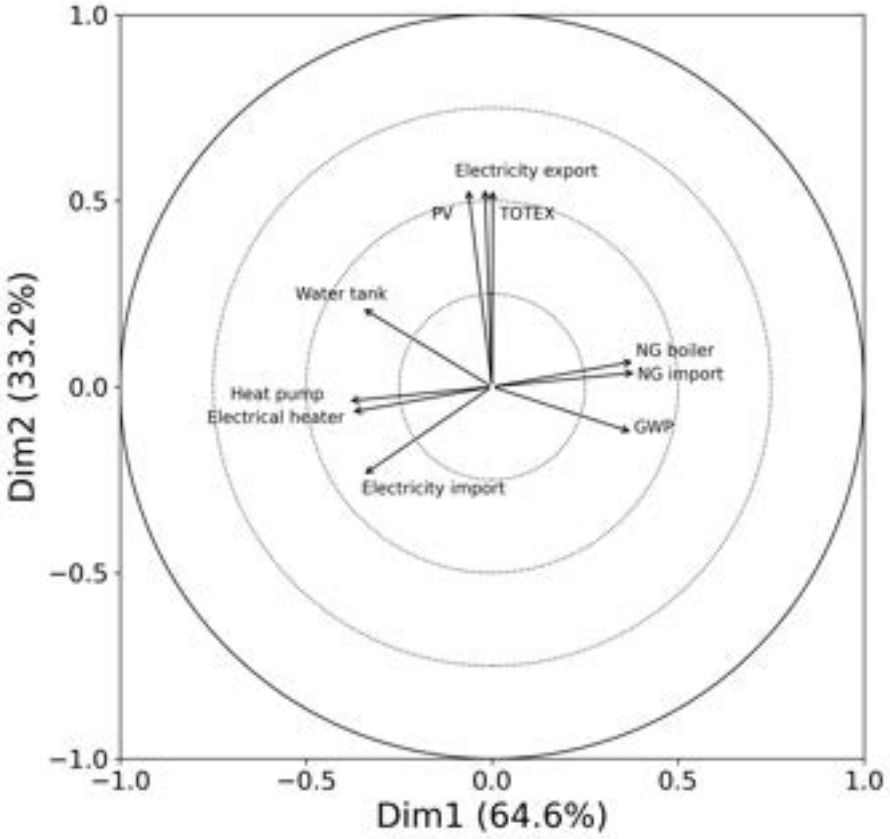

Figure 6: Variable correlation plot of the first two principal components. Indicators pointing in the same direction are correlated, those pointing in the opposite direction are inversely correlated, and those that are perpendicular are uncorrelated. The length of the arrow indicates the influence of the indicator.

4. Conclusion

The objective of this paper was to develop a framework able to identify typical district configurations. The methodology is composed of a two-fold GSA to efficiently sample the space of solutions, and a clustering step to determine typical technical solutions. The Morris method is used to screen input parameters and the sampling scheme is acquired using the Sobol method. The space of solutions obtained from the Sobol sequence was clustered using multiple algorithms. The range of optimal number of clusters was identified using two cluster validation indices and the Elbow method.

- The conclusion of the GSA emphasized the importance of the retail tariff of energy carriers in such systems.
- From 8 to 10 configurations were necessary to represent at best the solution space. The results from each technique were compared using the DBCV index. The tenth first clusters from the DBSCAN were selected as they represent 90% of the data and obtain one of the best score.
- The identified configurations can be separated into two types of systems, those based on NG and the others on electricity. Each type has a pretty basic configuration, i.e. the configurations based on NG install a boiler and the electric ones combine HP and electrical heater.
- In terms of electricity consumption, the import and export of electricity correlate negatively, respectively positively, with the installed photovoltaic capacity.

The presented results indicate that the presented framework allows to efficiently identify districts configurations. The next logical step would be to implement this framework to define a panel of configurations for district representatives of a large-scale energy system and study the impact of optimal built environment in the infrastructure.

5. Fundings

The research published in this report was carried out with the support of the Swiss Federal Office of Energy SFOE as part of the SWEET project acronym. The authors bear sole responsibility for the conclusions and the results of the presented publication.

References

[1] Hannah Ritchie, Max Roser, and Pablo Rosado. CO and greenhouse gas emissions.

[2] GlobalABC, IEA, and UNEP. GlobalABC roadmap for buildings and construction: Towards a zero-emission, efficient and resilient buildings and construction sector.

[3] Daniel M. Kammen and Deborah A. Sunter. City-integrated renewable energy for urban sustainability. 352(6288):922–928.

[4] P.R. Shukla, J. Skea, R. Slade, A. Al Khourdajie, R. van Diemen, D. \{McCollum\}, M. Pathak, S. Some, P. Vyas, R. Fradera, M. Belkacemi, A. Hasija, G. Lisboa, S. Luz, and J. Malley. Climate change 2022: Mitigation of climate change. contribution of working group III to the sixth assessment report of the intergovernmental panel on climate change.

[5] Hans-Kristian Ringkjøb, Peter M. Haugan, and Ida Marie Solbrekke. A review of modelling tools for energy and electricity systems with large shares of variable renewables. 96:440–459.

[6] Rahul Gupta, Fabrizio Sossan, and Mario Paolone. Countrywide PV hosting capacity and energy storage requirements for distribution networks: The case of switzerland. 281:116010.

[7] Gauthier Limpens, Stefano Moret, Hervé Jeanmart, and Francois Maréchal. EnergyScope TD: A novel open-source model for regional energy systems. 255:113729.

[8] Kody M. Powell, Akshay Sriprasad, Wesley J. Cole, and Thomas F. Edgar. Heating, cooling, and electrical load forecasting for a large-scale district energy system. 74:877–885.

[9] Leander Kotzur, Peter Markewitz, Martin Robinius, Gonçalo Cardoso, Peter Stenzel, Miguel Heleno, and Detlef Stolten. Bottom-up energy supply optimization of a national building stock. 209:109667.

[10] P. Stadler, Luc Girardin, and F. Maréchal. The swiss potential of model predictive control for building energy systems.

[11] M. Di Somma, B. Yan, N. Bianco, G. Graditi, P. B. Luh, L. Mongibello, and V. Naso. Operation optimization of a distributed energy system considering energy costs and exergy efficiency. 103:739–751.

[12] M. Di Somma, B. Yan, N. Bianco, G. Graditi, P. B. Luh, L. Mongibello, and V. Naso. Multi-objective design optimization of distributed energy systems through cost and exergy assessments. 204:1299–1316.

[13] Hongbo Ren, Weisheng Zhou, and Weijun Gao. Optimal option of distributed energy systems for building complexes in different climate zones in china. 91(1):156–165.

[14] David A. Copp, Tu A. Nguyen, Raymond H. Byrne, and Babu R. Chalamala. Optimal sizing of distributed energy resources for planning 100% renewable electric power systems. 239:122436.

[15] Jonas Allegrini, Kristina Orehounig, Georgios Mavromatidis, Florian Ruesch, Viktor Dorer, and Ralph Evins. A review of modelling approaches and tools for the simulation of district-scale energy systems. 52:1391–1404.

[16] Boran Morvaj, Ralph Evins, and Jan Carmeliet. Optimising urban energy systems: Simultaneous system sizing, operation and district heating network layout. 116:619–636.

[17] Azadeh Maroufmashat, Ali Elkamel, Michael Fowler, Sourena Sattari, Ramin Roshandel, Amir Hajimiragha, Sean Walker, and Evgueniy Entchev. Modeling and optimization of a network of energy hubs to improve economic and emission considerations. 93:2546–2558.

[18] Georgios Mavromatidis, Kristina Orehounig, and Jan Carmeliet. Uncertainty and global sensitivity analysis for the optimal design of distributed energy systems. 214:219–238.

[19] Tianjie Liu, Wenling Jiao, and Xinghao Tian. A framework for uncertainty and sensitivity analysis of district energy systems considering different parameter types. 7:6908–6920.

[20] Andrea Saltelli, Marco Ratto, Terry Andres, Francesca Campolongo, Jessica Cariboni, Debora Gatelli, Michaela Saisana, and Stefano Tarantola. *Global Sensitivity Analysis. The Primer*. Wiley. Edition: 1.

[21] Wei Tian. A review of sensitivity analysis methods in building energy analysis. 20:411–419.

[22] Paul Westermann and Ralph Evins. Surrogate modelling for sustainable building design – a review. 198:170–186.

[23] Torben Østergård, Rasmus L. Jensen, and Steffen E. Maagaard. Early building design: Informed decision-making by exploring multidimensional design space using sensitivity analysis. 142:8–22.

[24] Max D. Morris. Factorial sampling plans for preliminary computational experiments. 33(2):161–174. Publisher: Taylor & Francis _eprint: https://www.tandfonline.com/doi/pdf/10.1080/00401706.1991.10484804.

[25] Andrea Saltelli. Making best use of model evaluations to compute sensitivity indices. 145(2):280–297.

[26] J {and} Saltelli A Campolongo, F {and} Cariboni. Sensitivity analysis: the morris method versus the variance based measures.

[27] Will Usher, Jon Herman, Calvin Whealton, David Hadka, Xantares, Fernando Rios, Bernardoct, Chris Mutel, and Joeri Van Engelen. Salib/salib: Launch!

[28] Andrea Saltelli, Paola Annoni, Ivano Azzini, Francesca Campolongo, Marco Ratto, and Stefano Tarantola. Variance based sensitivity analysis of model output. design and estimator for the total sensitivity index. 181(2):259–270.

[29] Martin Ester, Hans-Peter Kriegel, Jörg Sander, and Xiaowei Xu. A density-based algorithm for discovering clusters in large spatial databases with noise. In *Proceedings of the Second International Conference on Knowledge Discovery and Data Mining*, KDD'96, pages 226–231. AAAI Press.

[30] Ricardo J. G. B. Campello, Davoud Moulavi, and Joerg Sander. Density-based clustering based on hierarchical density estimates. In Jian Pei, Vincent S. Tseng, Longbing Cao, Hiroshi Motoda, and Guandong Xu, editors, *Advances in Knowledge Discovery and Data Mining*, Lecture Notes in Computer Science, pages 160–172. Springer.

[31] Leland McInnes and John Healy. Accelerated hierarchical density based clustering. In *2017 IEEE International Conference on Data Mining Workshops (ICDMW)*, pages 33–42. ISSN: 2375-9259.

[32] Davoud Moulavi, Pablo A. Jaskowiak, Ricardo J. G. B. Campello, Arthur Zimek, and Jörg Sander. Density-based clustering validation. In *Proceedings of the 2014 SIAM International Conference on Data Mining*, pages 839–847. Society for Industrial and Applied Mathematics.

[33] Luise Middelhauve, Cedric Terrier, and Francois Marechal. Decomposition strategy for districts as renewable energy hubs. page 10.

[34] Federal Statistical Office. Géodonnées etat de vaud, registre cantonal des bâtiments (RCB).

[35] Federal Statistical Office. Federal register of buildings and dwellings.

[36] OpenStreetMap contributors. Planet dump.

[37] J. Remund et al. METEONORM - global meteorological database for engineers, planners and education.

[38] SIA. vernehmlassung sia 380/1 heizwärmebedarf.

[39] Luc Girardin. A GIS-based methodology for the evaluation of integrated energy systems in urban area.

[40] Federal Office of Topography. swissBUILDINGS3d 2.0.

[41] Swiss Federal Office of Energy Geoinformation. Switzerland in 3d.

[42] Administration cantonale vaudois. Distribution networks database.

[43] Middelhauve, Luise. On the role of districts as renewable energy hubs.

PROCEEDINGS OF ECOS 2023 - THE 36TH INTERNATIONAL CONFERENCE ON
EFFICIENCY, **C**OST, **O**PTIMIZATION, **S**IMULATION AND ENVIRONMENTAL IMPACT OF ENERGY SYSTEMS
25-30 JUNE 2023, LAS PALMAS DE GRAN CANARIA, SPAIN

Thermo-economic comparison of CO_2 and water as a heat carrier for long-distance heat transport from geothermal sources

Pietro Ungar[a], Christopher Schifflechner[b], Christoph Wieland[b,c], Hartmut Spliethoff[b] and Giampaolo Manfrida[d]

[a] University of Florence, Florence, Italy, pietro.ungar@unifi.it, CA
[b] Chair of Energy Systems, School of Engineering and Design, Technical University of Munich, Germany
[c] Chair of Energy Process Engineering and Energy Systems, University of Duisburg-Essen, Germany
[d] University of Florence, Florence, Italy

Abstract:
Deep geothermal energy has tremendous potential for decarbonizing the heating sector. However, one common obstacle can be the mismatch between geologically attractive regions in the countryside and urban areas with a high heat demand density, which are therefore attractive for district heating systems. In the last years, an increasing number of regions consider the transport of geothermal heat into urban clusters. One example of such a region is the South German Molasse Basin in Upper Bavaria. However, such heat transport pipelines come along with massive upfront investment costs due to the required large pipe diameter and insulation thickness. While the classic concept foresees the use of water as a heat carrier in such long-distance heat transportation pipelines, CO_2 can be an attractive alternative. This study investigates the thermo-economic performance of CO_2 as a heat transport carrier for a potential long-distance heat transmission pipeline with a length of 20 km, which could connect a planned geothermal project in the South of Munich with the existing district heating network of Munich. The results of the base case scenario demonstrate that for both heat carrier options water and CO_2 rather low LCOH for the transport of the heat can be achieved. The resulting additional LCOH by the long-distance heat transport of around 0.6 c€/kWh are rather small compared to the typical overall LCOH of geothermal district heating systems. Comparing the thermo-economic performance of water and CO_2 reveals rather similar achievable LCOH, with a slight advantage for the classical concept of using water. However, this changes if the installation of a high temperature heat pump (HTHP) is considered in order to increase the thermal capacity of the heat transport system. In the case of using CO_2, the additional temperature increase takes place directly within the CO_2 stream by just installing a compressor, while in the case of the water system, a complete HTHP system needs to be installed. In combination with a higher achievable COP, the CO_2 HTHP configurations results in lower overall LCOH compared to the water system.

Keywords:
District Heating Networks, Geothermal Energy, Heat Transfer, Economic Analysis, Carbon Dioxide

1. Introduction

Deep geothermal energy can play a significant role in the necessary transformation of the heating sector [1]. While there is an increasing number of geothermal projects worldwide [2], the vast majority of the worldwide potential is still untapped [3]. However, one major challenge for the utilization of geothermal energy is the common mismatch between urban areas with a high heat demand density and areas with favourable geological conditions for heat extraction. For example, promising geothermal resources in the countryside with temperatures between 80 - 110 °C can not be economically utilized without long-distance heat transport. While such resource temperatures are highly suitable for district heating supply, their temperature is too low for economic power generation by a binary cycle such as an Organic Rankine Cycle (ORC) [4].
Thus, since the local heat demand is too low in order to justify the high investment costs, without the ability to transport the heat over long distances, many promising geothermal resources would remain untapped. Molar-Cruz et al. [5] have recently studied the application potential of long-distance heat transport for geothermal energy in the Greater Area of Munich, Germany. The findings demonstrate that applying long-distance heat transportation systems can reduce the overall cost of heat supply by 15 % compared to a scenario without heat transport. Furthermore, despite the high investment costs of the transportation system, the resulting heat costs are still competitive with other heating technologies. Kavvadias and Quoilin [6] show that long-distance heat transport from conventional combined heat and power plants (CHP) can be economical and is already applied in several European countries. Furthermore, Moser and Puschnigg [7] investigated the concept of a supra-regional district heating network for a use-case area in Austria. Their results suggest that long-distance

heat transport networks between several different actors might become economical in a future non-fossil energy system and has a high potential to connect industrial waste heat and renewable energy heat sources. Thus, long-distance heat transport is a promising approach to boost the utilization of geothermal energy and the transformation of the heating sector in general.

However, due to high upfront investment and operational costs, an optimal design of the transportation system is pivotal. While the classical concept foresees the use of water as a heat carrier, CO_2 has gained increasing attention as an alternative heat carrier in both geothermal systems [8]–[10] and district heating networks (DHN) [11]. The concept of urban CO_2 district energy systems is mainly investigated for modern networks that provide both heating and cooling by heat pump systems being installed in each building. Thus, due to the low operating temperature of such systems and the corresponding CO_2 phase change, the costs of heat distribution can significantly be reduced [12].

Thus, while CO_2 is currently investigated as an energy carrier within DHN systems, its application potential for long-distance heat transport has not been evaluated in existing studies so far. The scope of this work is the evaluation of the thermo-economic potential of CO_2 as a heat carrier for a potential application case in the greater area of Munich. This area is a promising case study since the connection of the geothermal attractive region in the South of Munich with the existing DHN system of Munich is currently under discussion and within a preliminary planning phase [13]. This work investigates several technical options for the heat transport of CO_2 and compares the resulting thermo-economic performance with a conventional concept using water as a heat carrier.

2. Methodology

In the system under scrutiny, the heat is transported circulating fluid between the geothermal field and the DH (district heating) network as shown in Fig. 1.

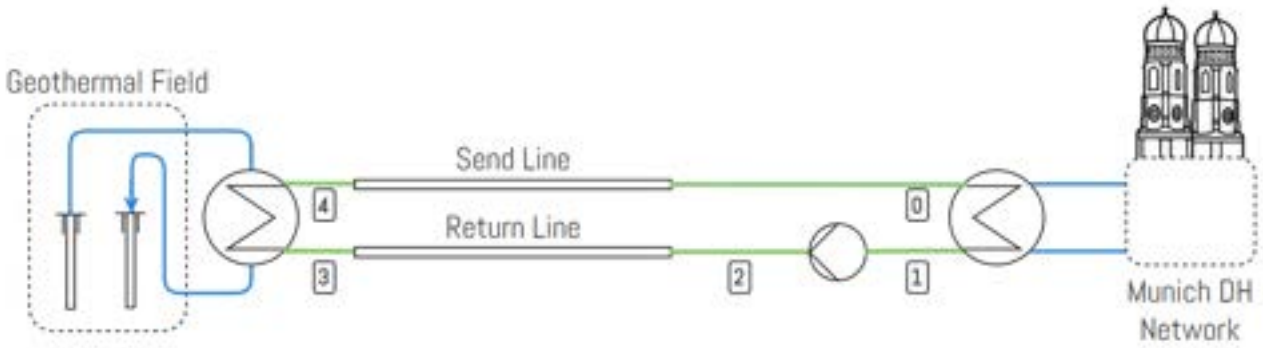

Figure 1: Base transport system scheme

2.1. Pipeline Model

The behavior of the system is highly dependent on the model of the pipelines connecting these two locations due to their length. To assess the condition of the fluid within the pipeline, pressure and enthalpy balances (1) were integrated over its length using the Runge-Kutta solver [14] implemented in Scipy [15].

$$\begin{cases} \frac{dp}{dx} = f \frac{1}{2\rho d} \left(\frac{4\dot{m}}{\pi d^2}\right)^2 \\ \frac{dh}{dx} = \frac{\Delta T}{r_{tot}\dot{m}} \end{cases} \tag{1}$$

The friction factor in (1) has been calculated using the Churchill correlation [16] while the linear thermal resistance in (1) has been defined as follows:

$$r_{tot} = r_{conv} + r_{ins},\ r_{conv} = \frac{1}{Nu\ \pi k_{fluid}},\ r_{ins} = \frac{\ln\left(1 + \frac{2s_{ins}}{d}\right)}{2\pi k_{ins}} \tag{2}$$

with:

$$Nu = 0.023 Re^{0.8} Pr^{0.3} \tag{3}$$

The formulation of the balance equations (1) implies that the kinetic and gravitational terms have been neglected in both the momentum and energy balances. The integration process used in the analysis provides a

high level of accuracy while still maintaining a reasonable computational time. However, especially for water-based systems, it is possible to achieve an acceptable level of accuracy by discretizing the duct into a few sections (less than 10).

2.2. System Model

Given the high investment costs and anticipated slow transients in the pipelines, the system is expected to operate in a steady state condition, providing a constant heat flux to the Munich area DH Network throughout its lifetime. Thus, the water flow rate in the DH is evaluated based on the system's heat transport capacity rather than on the heat demand from the grid. Various configurations of the heat transfer system were analyzed for both the water-based and CO_2-based cases, as illustrated in Fig. 2 and discussed in the following section.

2.2.1. Base Case

The most basic approach for long-distance heat transportation, as depicted in Fig. 2a, involves circulating the fluid via a pump placed after the DH network heat exchanger. The flow rate of the fluid is optimized to minimize the *LCOH* under specific design conditions. Additionally, for CO_2-based systems, the pipeline pressure is also optimized.

2.2.2. Heat Pump Case

The industrial requirement of fixed lowest temperature (65℃) in standard district heating networks can limit the amount of heat that can be transported for a given flow rate, as the temperature at the outlet of the DH heat exchanger cannot go below a certain value. To overcome this limitation, a heat pump can be installed after the DH heat exchanger outlet to further cool down the working fluid before redirecting it to the geothermal field, as shown in Fig. 2b.

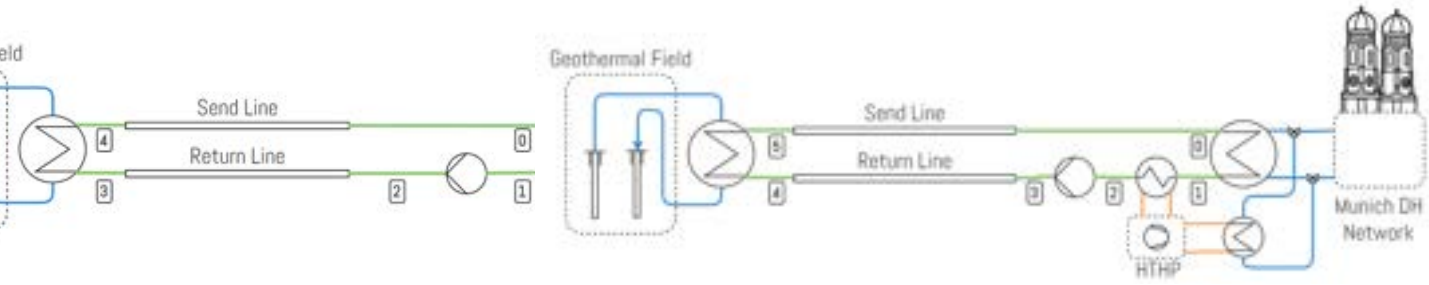

(a) Base Case **(b)** High Temperature Heat Pump (HTHP) Case

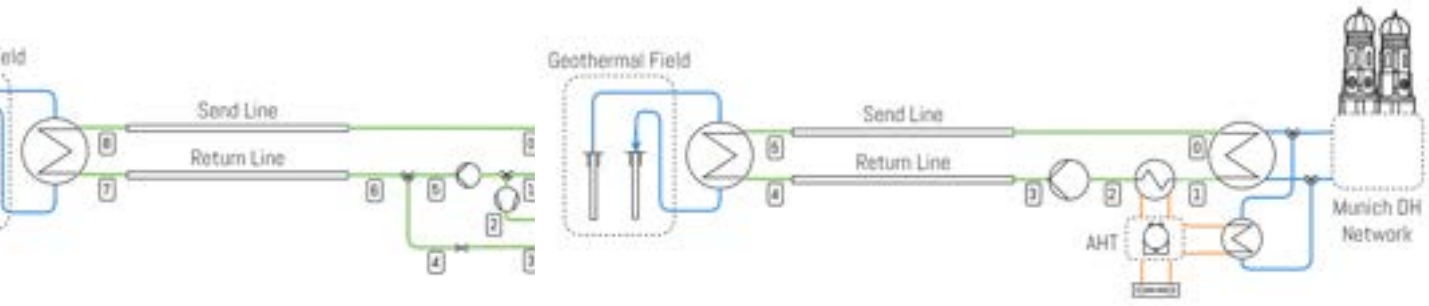

(c) Simplified Heat Pump for CO_2-based system **(d)** Absorption Heat Transformer (AHT) Case

Figure 2: Different configuration on the DH network side of the system

This configuration not only improves the heat transfer rate but also reduces the pumping power for CO_2-based systems as CO_2 becomes less compressible at lower temperatures. Alternatively, a compression set-up can replace the heat pump in CO_2-based systems as shown in Fig. 2c, which removes the inefficiencies associated with the heat pump evaporator.

The heat pump in Fig. 2b has been modeled with a fixed exergy efficiency of 0.4, according to experimental results from literature [17], to avoid the need for complete modeling. Knowing the exergy efficiency is possible to estimate the electrical power demand as:

$$\dot{W}_{heat\ pump} = \frac{1}{\eta_{exergy}} \left(1 - \frac{T_{low}}{T_{high}}\right) \dot{Q}_{heat\ pump} = \frac{1}{0.4} \left(1 - \frac{T_{low}}{T_{high}}\right) \dot{Q}_{heat\ pump} \tag{4}$$

T_{low} and T_{high} have been evaluated considering $\Delta T_{pinch\ point} = 5$℃ in the heat pump's heat exchangers.

2.2.3. Absorption Heat Transformer Case

Heat pumps can increase power extraction from the geothermal fluid, but at the expense of increased electricity consumption. To minimize the electricity consumption, heat transformers can be used instead of heat pumps. However, the heat transformer method requires the dissipation of some of the transported heat to allow for the remaining heat to reach the desired temperature, as depicted in Fig. 2d.

The heat transformer has been modelled as a black box considering a 50% exergy efficiency [18] in analysing the various configurations. The ratio between the transmitted power and the incoming one can then be determined modifying the equation for the exergy efficiency presented in [18]:

$$\frac{\dot{Q}_{out}}{\dot{Q}_{in}} = \frac{1}{\eta_{exergy}} \frac{1 - \frac{T_{amb}}{T_{in}}}{1 - \frac{T_{amb}}{T_{out}}} \tag{5}$$

2.2.4. Heat Pump Temperature Considerations

If the output temperature from the main DH heat exchanger exceeds the requirements of the DH network, the temperature at the outlet of the heat pump can be lowered resulting in a reduction of the compression power needed (Fig. 3 should clarify this point).

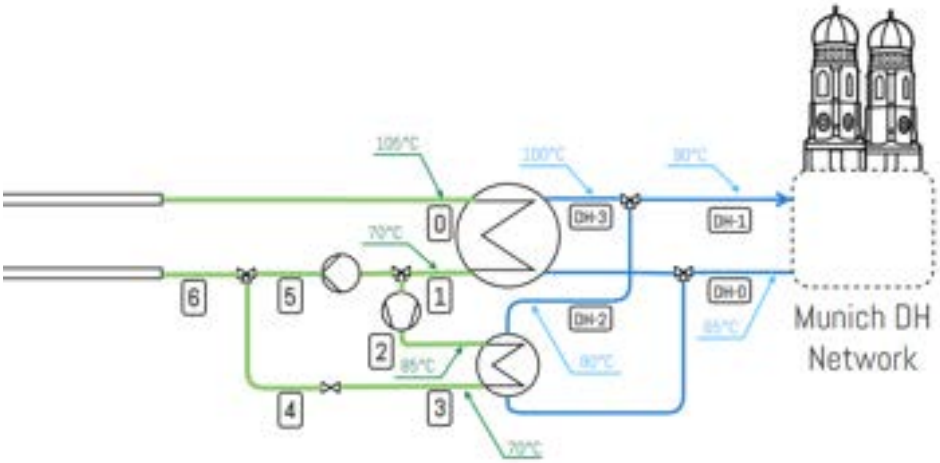

Figure 3: Example of how a lower output temperature can be set to the heat pump outlet: Temperatures of *points [DH-0]* and *[DH-1]* are fixed due to the grid design constraints (65℃ and 90℃ in this example). If temperature in *point [DH-2]* is higher than required, temperature in *point [DH-3]* can be lower to compensate

With reference to Fig. 3, temperature at *point [DH-3]* can be identified starting from an adimensional parameter defined as:

$$T_{ratio} = \frac{T_{DH3} - T_{DH0}}{T_{DH1} - T_{DH0}} \tag{6}$$

Notice that choosing T_{ratio} implies defining the ratio between the flow rate in *[DH-3]* and in *[DH-2]*:

$$\dot{m}_{DH_{ratio}} = \frac{\dot{m}_{DH3}}{\dot{m}_{DH2}} = \frac{h_{DH2} - h_{DH1}}{h_{DH1} - h_{DH3}} \approx \frac{T_{DH2} - T_{DH1}}{T_{DH1} - T_{DH3}} \tag{7}$$

Moreover, is interesting to notice that a heat pump scheme with $T_{ratio} = 0$ is equivalent to a base scheme (as defined in section 2.2.1.) in which the temperature in the DH network is controlled by letting some fluid by-pass the DH heat exchanger.

2.3. Economic Model

The levelized cost of heat (LCOH) has been evaluated to optimize the design parameter of the different schemes and to compare the different solutions. The LCOH is calculated as the minimum cost at which the heat must be sold in order to recover the investment after the lifetime of the plant, it can be derived by setting the NPV of the system to 0:

$$NPV = -C_{tot} + \sum_{t=1}^{L_e} CF_t \, (1 + i)^{-t} = 0 \tag{8}$$

Where the annual cash flow (CF_t) is:

$$CF_t = h_y \left(LCOH \dot{Q}_{DH} - \dot{W}_{pump} c_{el} \right) - C_{om} \tag{9}$$

The LCOH can then be calculated rearranging (8) and (9) assuming a constant annual cash flow:

$$LCOH = \frac{C_{tot}\beta + \dot{W}_{pump} c_{el}}{\dot{Q}_{DH}}, \quad \beta = \frac{1 + \alpha OM_{ratio}}{\alpha h_y}, \quad \alpha = \frac{1 - (1+i)^{-L_e}}{i} \tag{10}$$

The costs are evaluated using some specific correlations listed in Table 1.

Table 1: Cost correlation used in economic analysis

Component	Cost Correlation	Notes	Ref.
Overall Investment	$C_{tot} = 2C_{pipe} + \sum C_{HE} + \sum C_{other}$	*Result in [€], conversion €/$ applied if needed. Pump acquisition cost has been neglected. C_{other} represents the cost of additional components such as the heat pump or the CO_2 compressor*	-
Yearly Maintenance	$C_{om} = OM_{ratio} C_{tot}$	*5% OM_{ratio} considered*	-
Pipeline	$C_{pipe} = \left(0.6492\, d^{0.9779} + C_{ins}\right) L$	*Result in [$], pipe diameter in [m]*	[6]
Pipe Insulation	$C_{ins} = c_{ins}\left(\pi s_{ins}\left(d + s_{ins}\right)\right)$	*Result in [$/m], c_{ins} in [$/m^3]. It depends on the insulation material (see [6])*	[6]
Heat Exchangers	$C_{HE} = 49.45 UA_{HE}^{0.7544}$	*Result in [$], Correlation for CO_2, UA_{HE} in [W/K], it is the product of the HE area and heat transfer coefficient*	[19]
Heat Pump	$C_{heat\ pump} = 0.33667 \dot{W}_{heat\ pump}$	*Result in [M€], $\dot{W}_{heat\ pump}$ in [MW], Correlation for $\dot{W}_{heat\ pump}$ up to 10MW, Only the heat pump acquisition cost has been considered.*	[20]
Heat Transformer	$C_{heat\ transformer} = 375 \dot{Q}_{in}$	*Result in [€], $\dot{Q}_{in}$ in [kW], correlation valid for $\dot{Q}_{in} \approx$10MW, correlation for absorption heat pumps used following the approach of [21]. 375 is the mean of the range (300-450) presented in [22]*	[22].

2.3.1. Remarks on the LCOH calculation

Following the approach defined in [6], the LCOH calculated in 10 refers only to the process of transporting the heat. In order to identify the real cost of heat for DH users, heat production costs (well drilling, reservoir circulation pump, etc.) must be taken into account:

$$LCOH_{tot} = \frac{(C_{tot} + C_{prod})\beta + (\dot{W}_{pump} + \dot{W}_{pump_{prod}}) c_{el}}{\dot{Q}_{DH}} \tag{11}$$

In order to avoid the need for a complete economic evaluation of the production site, it is tempting to simplify the overall LCOH calculation considering a fixed price for the produced heat using values retrieved from literature:

$$LCOH_{tot} = \frac{C_{tot}\beta + \dot{W}_{pump} c_{el} + \dot{Q}_{geo} c_{heat_{prod}}}{\dot{Q}_{DH}} \tag{12}$$

It is important to consider that using equation (12) may lead to distorted results. The reason for this is that more complex system schemes, such as those described in sections 2.2.2. or 2.2.3., are chosen because they have a lower temperature in the return line and thus a higher heat extraction rate ($\dot{Q}geo$) *for the same number of wells and reservoir pumping power.* However, due to the fixed value for $c_{heat_{prod}}$ in equation (12), this behavior cannot be accurately modeled. To address this issue, the most straightforward solution is to evaluate the overall production cost of different systems using a fixed design extraction power:

$$LCOH_{tot} = \frac{C_{tot}\beta + \dot{W}_{pump} c_{el} + C_{heat_{prod}}}{\dot{Q}_{DH}}, \quad C_{heat_{prod}} = \dot{Q}_{geo_{DESIGN}} c_{heat_{prod}} \tag{13}$$

3. Results

This section presents the results for the four different investigated technological concepts visualized in Fig.2.

3.1. Base case

Fig.4a displays the achievable LCOH for both water and CO_2 considering different pipe diameters. The results indicate that both heat carriers have a certain optimal pipe diameter, which corresponds to the optimal trade-off between investment and operational costs. For CO_2, the optimal pipe diameter is at around 130 cm, while it is at around 85 cm for water. While the deviation between both heat carries is rather small (0.1 c€/kWh), no clear advantages for using CO_2 as heat carrier in this standard scenario can be seen. The figure also shows the effect of the minimum CO_2 density in the system, showing an optimum in the LCOH for $\rho_{min} = 500 kg/m^3$.

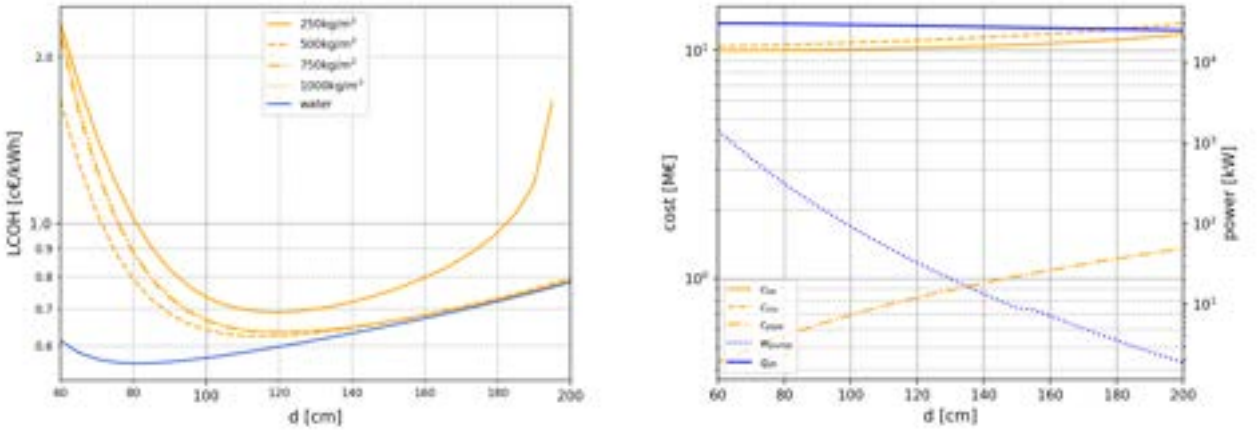

(a) LCOH with diameter

(b) Cost Composition for CO_2 with $\rho = 450[kg/m^3]$

Figure 4: Achievable LCOH for water and CO_2 considering different densities for the CO_2

The findings presented in Fig. 4a can be understood by analyzing the information provided in Figure 4b. Heat exchangers and pipeline installation are the biggest contributors to the capital investment, costing around 10 M€ and 1 M€, respectively. The cost of the heat exchangers can be explained considering that the system is required to transport a substantial amount of power with a limited temperature difference (ΔT) between the geothermal water (115℃) and the district heating network (90℃). As a result, the two heat exchangers can only have a limited logarithmic mean temperature difference (LMTD), 12.5℃ in the best case scenario, this increase the required UA and the heat exchanger cost. Increasing the pipeline diameter results in some additional heat loss to the environment because of the increase in surface area. These losses are negligible if compared with the overall power transported by the system, but make the UA requirements even more demanding.

3.2. HTHP case

Do to the high investment cost required for the acquisition of the heat exchangers the installation of an heat pump can be useful for increasing the available ΔT and allowing the installation of smaller heat exchangers.

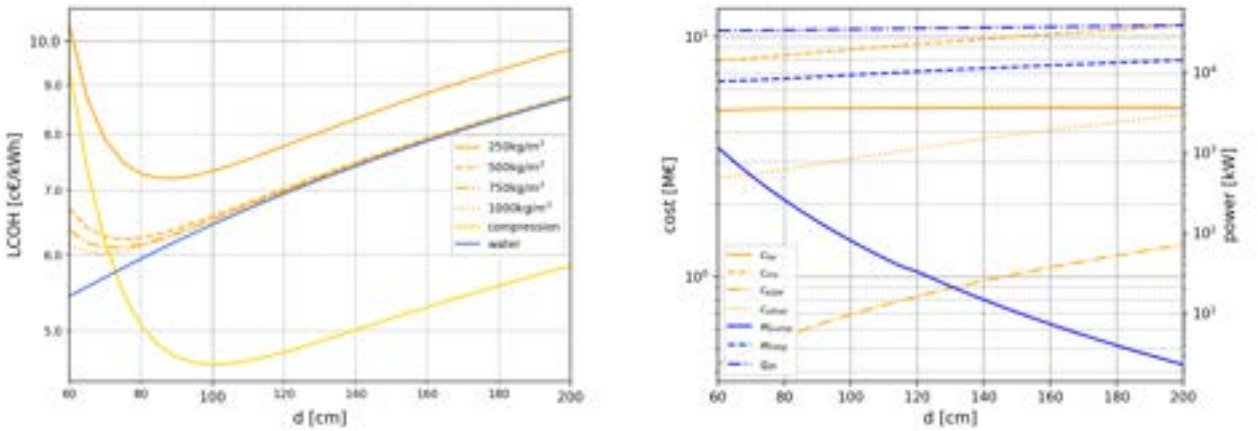

(a) LCOH with diameter

(b) Cost Composition for CO_2 with $\rho = 700[kg/m^3]$

Figure 5: Achievable LCOH for water and CO_2 for the HTHP (High Temperature Heat Pump) case

In Fig. 5, it is apparent that the LCOH has substantially increased when compared to the baseline scenario, despite a decrease in the cost of heat exchangers to 4M€. This is mainly due to the increased in electrical power consumption. The high cost of electricity (the average price for Bavaria in 2022 was 22.5 cents per kilowatt-hour [23], which is more than 30 times higher than the LCOH for the baseline scenario) makes it unprofitable to extract heat from the fluid using electrical power, even with a high COP. It is critical to note that this is true for the LCOH shown in Figure 5 which only considers the cost of the transport system, ignoring the cost of heat production, depending on the cost of heat production this effect can change dramatically.

Another interesting finding shown in Fig. 5 is that the CO_2 scheme the compression system replacing the heat pump (Fig. 2c) due to its simplicity and higher COP, is capable of performing better than the water-based system in the considered scenario. Especially against the background of high heat demand periods during the winter, the additional installation of a CO_2 compressor can be favourable from an operator's perspective, since it allows to supply of additional heat without the need for additional drilling.

3.3. AHT case

An absorption heat transformer can be considered as a solution of increasing the ΔT without using additional electrical power. In fact, as can be see from Fig. 6, the LCOH has decreased for both water and CO_2.

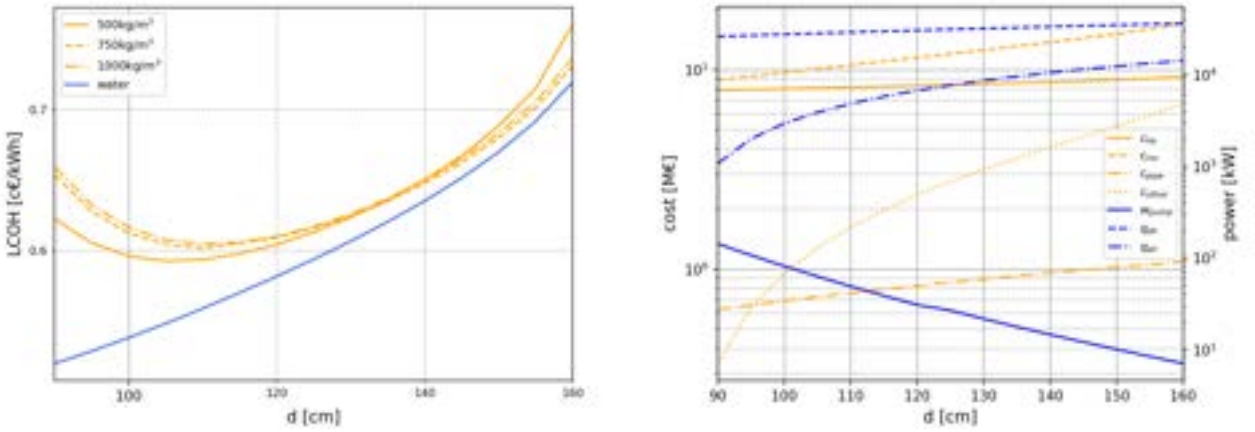

(a) LCOH with diameter **(b)** Cost Composition for CO_2 with $\rho = 450[kg/m^3]$

Figure 6: Achievable LCOH for water and CO_2 for the AHT (Absorption Heat Transformer) case

Fig. 6b, shows that the cost of the heat exchangers has decreased to 8M€. The power provided by the AHT in the optimal condition for CO_2 (d=110cm) if 4MW which is only about 10% of the overall heat transported by the network, this shows that the real advantage of installing an AHT it to increase the available ΔT in order to allow the installation of smaller heat exchangers.

4. Conclusion

The results of this work provide valuable insights into both the achievable LCOH of long-distance heat transport from geothermal sources in general and the thermo-economic comparison of water and CO_2 as potential heat carrier fluids. First, the results of the base case scenario (cf. Fig 4a) demonstrate that for both heat carrier options rather low LCOH for the transport of the heat can be achieved. The resulting additional LCHO by the long-distance heat transport of around 0.6 c€/kWh is rather small compared to the typical overall LCOH of geothermal district heating systems [24]. Considering that long-distance heat transport enables the utilization of geological attractive regions in the countryside with lower project-specific LCOH, installing the long-distance heat transport system might result in an overall lower LCOH of the whole geothermal heating system. Therefore, the findings of this work support the general conclusions by the work of Molar-Cruz et al. [5] on the theoretical advantages of geothermal heating systems with long-distance heat transport as well as the economic feasibility of the projects currently in the planning stage in the Greater Area of Munich, Germany [13].
Comparing the thermo-economic performance of water and CO_2 shows rather similar achievable LCOH, with a slight advantage for the classical concept of using water. While CO_2 reveals a lower pressure drop within the piping system, this advantage is overcompensated by the fact that the pressure increase for CO_2 is taking place at a lower density than for water, resulting in a higher power demand. Furthermore, considering the potential integration of an HTHP increases the LCOH significantly, mainly due to the currently rather high electricity prices. Nonetheless, the considered LCOH only address the installation and operation of the transportation system and the HTHP installation. However, installing an HTHP lowers also the LCOH of the geothermal project itself

(which are rather high especially caused by the drilling cost [25]) due to a higher utilization and it reduces the need for installing and/or integrating further alternative heat sources. Thus, while the installation of an HTHP might be useful from a thermo-economic perspective, it needs to be assessed in a broader system study considering also other available potential heat sources and technologies. Regarding the potential application of an HTHP into the long-distance heat transport system, the results of this work highlight the potential advantage of CO_2 as a heat carrier (cf. Fig. 5). In the case of using CO_2, the additional temperature increase takes place directly within the CO_2 stream by just installing a compressor, while in the case of the water system, a complete HTHP system needs to be installed. Thus, the usage of CO_2 allows significantly lower investment costs as well as higher COPs.
Concerning the thermo-economic comparison of water and CO_2 for the considered use case with a rather high required DH supply temperature, CO_2 results in comparable LCOH as water, but has no further positive impact on the economic performance despite in case of an additional HTHP system for increasing the thermodynamic capacity of the heat transport system. Furthermore, the future trends towards lower DH supply temperatures as well as the use of CO_2 as a heat carrier in geothermal systems (cf. [9] might result in a thermo-economic favourability of CO_2 as a heat carrier for long-distance heat transport and might be evaluated in future studies.

Acknowledgments

For the University of Florence contribution, this research received partial support from *Italian PNRR NEST Spoke 5 "Energy Conversion"*. On the other hand, regarding the contribution of the Technical University of Munich, funding from the *Bavarian State Ministry of Science and the Arts* in the framework of the Project *Geothermal-Alliance Bavaria* is gratefully acknowledged.

Nomenclature

Acronyms

AHT	Absorption Heat Transformer
CHP	Combined Heat and Power
COP	Coefficient Of Performance
DH	District Heating
HTHP	High Temperature Heat Pump
LCOH	Levelized Cost Of Heat, *c€/kWh*
LMTD	Logarithmic Mean Temperature Difference
NVP	Net Present Value, *€*

Economics

C	Absolute cost, *€*
c	Relative cost, *€/kW*
C_{om}	Operation and maintenance cost, *€/year*
C_{tot}	Overall investment cost of the system, *€*
CF_t	Yearly cash flow, *€/year*
h_y	Yearly operational time, *hours*
i	Interest rate
L_e	System operational life, *years*
OM_{ratio}	Ratio between C_{om} and C_{tot}

Geometrics

d	Pipeline diameter, *m*
s_{ins}	Pipeline insulation thickness, *m*

Thermodynamics

$\dot{m}$	Mass flow rate, *kg/s*
$\dot{Q}$	Heat flux, *kW*
$\dot{W}$	Mechanical power, *kW*
η_{exergy}	Exergy efficiency
k	thermal conductivity, *W/(m K)*
Nu	Nusselt number
Pr	Prandtl number
r_{tot}	Total thermal resistance, *K/W*
Re	Reynolds number

References

[1] D. Romanov and B. Leiss, "Geothermal energy at different depths for district heating and cooling of existing and future building stock," *Renewable and Sustainable Energy Reviews*, vol. 167, p. 112 727, 2022.

[2] J. W. Lund and A. N. Toth, "Direct utilization of geothermal energy 2020 worldwide review," *Geothermics*, vol. 90, p. 101 915, 2021, ISSN: 03756505. DOI: 10.1016/j.geothermics.2020.101915.

[3] J. Limberger, T. Boxem, M. Pluymaekers, *et al.*, "Geothermal energy in deep aquifers: A global assessment of the resource base for direct heat utilization," *Renewable and Sustainable Energy Reviews*, vol. 82, pp. 961–975, 2018, ISSN: 1364-0321. DOI: 10.1016/j.rser.2017.09.084.

[4] S. Eyerer, C. Schifflechner, S. Hofbauer, W. Bauer, C. Wieland, and H. Spliethoff, "Combined heat and power from hydrothermal geothermal resources in germany: An assessment of the potential," *renewable and sustainable energy reviews*, vol. 120, p. 109 661, 2020.

[5] A. Molar-Cruz, M. F. Keim, C. Schifflechner, *et al.*, "Techno-economic optimization of large-scale deep geothermal district heating systems with long-distance heat transport," *Energy Conversion and Management*, vol. 267, p. 115 906, 2022, ISSN: 0196-8904. DOI: 10.1016/j.enconman.2022.115906.

[6] K. C. Kavvadias and S. Quoilin, "Exploiting waste heat potential by long distance heat transmission: Design considerations and techno-economic assessment," *Applied Energy*, vol. 216, pp. 452–465, 2018, ISSN: 0306-2619. DOI: https://doi.org/10.1016/j.apenergy.2018.02.080.

[7] S. Moser and S. Puschnigg, "Supra-regional district heating networks: A missing infrastructure for a sustainable energy system," *Energies*, vol. 14, no. 12, p. 3380, 2021.

[8] C. Schifflechner, C. Wieland, and H. Spliethoff, "Co2 plume geothermal (cpg) systems for combined heat and power production: An evaluation of various plant configurations," *Journal of Thermal Science*, 2022, ISSN: 1003-2169. DOI: 10.1007/s11630-022-1694-6.

[9] M. Tagliaferri, P. Gładysz, P. Ungar, *et al.*, "Techno-economic assessment of the supercritical carbon dioxide enhanced geothermal systems," *Sustainability*, vol. 14, no. 24, p. 16 580, 2022.

[10] Y. Shi, X. Song, G. Wang, *et al.*, "Study on wellbore fluid flow and heat transfer of a multilateral-well co2 enhanced geothermal system," *Applied energy*, vol. 249, pp. 14–27, 2019.

[11] P. Ungar, L. Milli, G. Manfrida, D. Fiaschi, and L. Talluri, "Re-designing district heating networks through innovative co2 solutions," in *Journal of Physics: Conference Series*, IOP Publishing, vol. 2385, 2022, p. 012 125.

[12] R. Suciu, L. Girardin, and F. Maréchal, "Energy integration of co2 networks and power to gas for emerging energy autonomous cities in europe," *Energy*, vol. 157, pp. 830–842, 2018.

[13] J. Weber, H. Born, S. Pester, C. Schifflechner, and I. Moeck, "Geothermal energy use in germany, country update 2019-2021," in *Proceedings of the European Geothermal Congress 2022*, 2022.

[14] J. Dormand and P. Prince, "A family of embedded runge-kutta formulae," *Journal of Computational and Applied Mathematics*, vol. 6, no. 1, pp. 19–26, 1980, ISSN: 0377-0427. DOI: https://doi.org/10.1016/0771-050X(80)90013-3.

[15] P. Virtanen, R. Gommers, T. E. Oliphant, *et al.*, "SciPy 1.0: Fundamental Algorithms for Scientific Computing in Python," *Nature Methods*, vol. 17, pp. 261–272, 2020. DOI: 10.1038/s41592-019-0686-2.

[16] S. W. Churchill, "Friction-factor equatin spans over all fluid-flow regimes," *Chemical Engineering*, vol. 84, pp. 91–92, 1977.

[17] E. Bilgen and H. Takahashi, "Exergy analysis and experimental study of heat pump systems," *Exergy, An International Journal*, vol. 2, no. 4, pp. 259–265, 2002, ISSN: 1164-0235. DOI: https://doi.org/10.1016/S1164-0235(02)00083-3.

[18] I. N. Balderas-Sánchez, J. C. Jiménez-García, and W. Rivera, "Modeling of a double effect heat transformer operating with water/lithium bromide," *Processes*, vol. 7, no. 6, 2019, ISSN: 2227-9717. DOI: 10.3390/pr7060371. [Online]. Available: https://www.mdpi.com/2227-9717/7/6/371.

[19] N. Weiland, B. Lance, and S. Pidaparti, "Sco2 power cycle component cost correlations from doe data spanning multiple scales and applications," Jun. 2019. DOI: 10.1115/GT2019-90493.

[20] H. Pieper, T. Ommen, F. Buhler, B. L. Paaske, B. Elmegaard, and W. B. Markussen, "Allocation of investment costs for large-scale heat pumps supplying district heating," *Energy Procedia*, vol. 147, pp. 358–367, 2018, International Scientific Conference "Environmental and Climate Technologies", CONECT 2018, 16-18 May 2018, Riga, Latvia, ISSN: 1876-6102. DOI: https://doi.org/10.1016/j.egypro.2018.07.104. [Online]. Available: https://www.sciencedirect.com/science/article/pii/S1876610218302613.

[21] S. Smolen and M. Budnik-Rodz, "Technical and economic aspects of waste heat utilisation," *Thermal Science*, vol. 11, no. 3, pp. 165–172, 2007, Cited by: 6; All Open Access, Gold Open Access, Green Open Access. DOI: 10.2298/TSCI0703165S.

[22] A. Arnitz, R. Rieberer, and V. Wilk, "Industrial heat pumps, second phase, iea heat pump technology (hpt) programme annex 48, task 4: Training materials for industrial heat pumps," IEA Heat Pump Technology (HPT), 2019.

[23] Statista, *Strompreise für gewerbe- und industriekunden in deutschland in den jahren 2012 bis 2022*, 2022. [Online]. Available: https://de.statista.com/statistik/daten/studie/154902/umfrage/strompreise-fuer-industrie-und-gewerbe-seit-2006 (visited on 03/25/2023).

[24] E. D. Mattson and G. Neupane, “Lcoh estimated from existing geothermal district heating systems in the us,” Idaho National Lab.(INL), Idaho Falls, ID (United States), Tech. Rep., 2017.

[25] M. Shamoushaki, D. Fiaschi, G. Manfrida, P. H. Niknam, and L. Talluri, “Feasibility study and economic analysis of geothermal well drilling,” *International Journal of Environmental Studies*, vol. 78, no. 6, pp. 1022–1036, 2021.

PROCEEDINGS OF ECOS 2023 - THE 36TH INTERNATIONAL CONFERENCE ON
EFFICIENCY, **C**OST, **O**PTIMIZATION, **S**IMULATION AND ENVIRONMENTAL IMPACT OF ENERGY SYSTEMS
25-30 JUNE 2023, LAS PALMAS DE GRAN CANARIA, SPAIN

A MILP approach for demand management in renewable energy communities with residential end-users

Lazzeroni Paolo[a], Lorenti Gianmarco[b], Moraglio Francesco[c] and Repetto Maurizio[d]

[a] *Politecnico di Torino - Dipartimento Energia "*Galileo Ferraris*", Turin, Italy, paolo.lazzeroni@polito.it, CA*
[b] *Politecnico di Torino - Dipartimento Energia "*Galileo Ferraris*", Turin, Italy, gianmarco.lorenti@polito.it*
[c] *Politecnico di Torino - Dipartimento Energia "*Galileo Ferraris*", Turin, Italy, francesco.moraglio@polito.it*
[d] *Politecnico di Torino - Dipartimento Energia "*Galileo Ferraris*", Turin, Italy, maurizio.repetto@polito.it*

Abstract:

Nowadays, the energy sharing of RES production within Renewable Energy Communities (REC) is promoting the diffusion of a more decentralized energy system, where dispersed renewable generation can be locally self-consumed by REC members. The maximization of self-consumption through the matching between generation and demand is thus fundamental to ensure higher economic and environmental benefits for residential end-users joining REC configurations. However residential electricity demand and the corresponding load profile are generally influenced by end-users' behavior. In fact, even if most of the household appliances can be assumed as fixed loads, the usage of some appliances depends basically on the residents' habits. The engagement of customers in changing their energy consumption patterns is then challenging to promote flexibility in electricity demand to further increase the benefits of adopting and joining renewable energy communities. In this view, a MILP approach is proposed to model end-users' flexibility for investigating how the changing in consumption habits can potentially improve the energy sharing by maximizing the match between RES production and demand. User's discomfort is evaluated consequently as the distance between the desired or usual consumption pattern and the optimized one. An Italian multifamily residential building case study, where end-users adopt a collective self-consumption scheme, is considered to highlight energy and economic results assuming different level of end-users' flexibility. Finally, a comparison between the maximization of energy sharing and the minimization of discomfort rate is pointed out through weighted sum method to identify solutions with different relevance of the end-users' flexibility.

Keywords:

Demand Management, MILP, Energy Community, Residential buildings.

1. Introduction

Energy Communities (ECs) in Italy are a relatively new concept that has emerged as a response to the challenges posed by climate change and the need for a more sustainable energy future [1]. In fact, these communities aim to promote the use of clean and sustainable energy, reduce greenhouse gas emissions, and foster local economic development contrasting energy poverty [2]. For these reasons, in a EC, public and private entities as well as citizens and households jointly and collectively own and manage renewable energy resources (RES) to locally increase self-consumption [3]. Hence, ECs are based on the idea that energy production should be decentralized and democratized, with people taking an active role in shaping their energy future and in driving the energy transition towards a more sustainable energy system.

Since the main goal of an EC is to increase the match between the local RES based production with the local electricity demand, battery energy storage systems (BESSs) are assuming a relavant role. Storage systems are in fact assets for decoupling the timing of energy production from its consumption. Thus, the use of this system has the advantage of leaving the end-user free to keep its own consumption habits, while overproduction can be stored and released when needed. However, one of the possible critical aspect in adopting BESS is still its profitability without incentives [4–6].

A different and complementary approach can be instead considered by promoting the cooperation between people (e.g. households) and the energy system (i.e. the EC). In particular, to increase self-consumption and self-sufficiency, changes in consumption habits may be proposed to end-users to modify the timing at which these consumptions occur [7]. This lead to the adoption of demand management where, through a simulation approach, the optimal usage of some electric appliances in the households can be identified and suggested to end-users for adapting their habits to a more sustainable and profitable behaviour. Consequently, also the BESS sizing could benefits on the adoption of demand management due to lower expected RES overproduction.

In this view, the work presented by [8] gives a wider overview on the different approaches adopted to model the demand management in the residential sector. Some of them are based on linear programming (LP) and mixed integer linear programming (MILP) for deploying load-shifting and then minimize the energy bills for end-users. For instance, a MILP smart home energy management model has been presented in [9] to arrange the operation of the household appliances for minimazing costs by considering time-varying pricing model to control the system. In particular, electrically controllable appliances are shifted to reduce electricity bought from the grid by harnessing RES production and storage usage. Similarly, a home energy management strategy to minimize the customer's billing is presented in [10], where different components and appliances are modeled by MILP. Shiftable loads are modeled again as components with a fixed operational time window that can be arranged to reduce the electricity bought from the grid.

According to these examples, a MILP modeling approach is proposed in this work to exploit the benefits due to load shifting in residential sector, but considering the perspective of an energy community (see Figure 1). In this case, the self-consumption of RES-based production is maximized by suggesting different end-users' habits, so that the aggregated load demand can more efficiently match the RES production. Results are compared with ones achievable by using a different approach based on the integration of an energy storage system to figure out also potential interoperability with demand management. Additionally, end-users' discomfort is also modelled to take into account the end-users' acceptability of the demand management. In fact, costumers perception on flexibility tools is still controversial [11]. Then, multi-objective optimization is also proposed to investigate how different willingness to participate in demand management can influence the benefits.

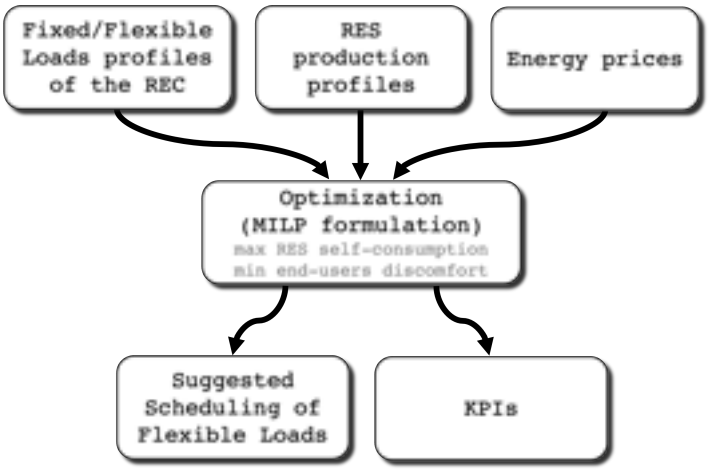

Figure 1: Scheme of the proposed MILP approach

2. Problem formulation

A Mixed Integer Linear Programming (MILP) formulation is proposed here to model the demand management of electric appliances used by residential end-users joining a collective self-consumption configuration. Consequently, equations and constraints representing this energy system are linear or alternatively should be linearized. In particular, two different kind of equations can be considered for describing the energy exchanges within an energy community, the interaction of the collective self-consumption with the grid and the management of the electricity demand: energy balance equations and constitutive equations representing the energy behaviours of the different assets. Binary (i.e., integer) variables are also introduced to describe the on/off status of the components and appliances and to consider their operational limits. A detailed description of this general approach can be found in [12].

The time horizon of the simulation is discretized by subdividing it in N_i intervals with length Δt equal to 5 minutes in this particular application for fully exploiting the potentiality of the demand management in residential end-users.

2.1. Modeling Demand Management

Demand management of the consumption aims at modify the end-users' habits in using electric appliances to meet specific goals of the energy community. As already pointed out, in this particular case, the objective is to increase the self-consumption of the RES production to maximize energy sharing and improve the economic benefits. Hence, end-users can actively participate by shifting the energy consumption for all those appliance that are programmable by definition as, for instance, washing machines and dishwashers [8]. These appliances, in fact, have a fixed duty-cycle whose start can be anticipated or deferred with respect to the end-users'

usual habits. As a consequence, assuming a daily time horizon discretized on N_i time intervals, the duty-cycle of an end-user's appliance can potentially be started at any time intervals.

This condition can be modelled by a squared matrix where each columns represents the load pattern (or load profile) of the *a*-th programmable appliance by assuming a different starting time interval for the duty-cycle. Practically, the first column is the usual load pattern, while the other columns are obtained by cyclic permutation of the first one, as follows:

$$\mathbf{P}_{j,a} = \begin{bmatrix} p_{j,a,1} & p_{j,a,N_i} & p_{j,a,N_i-1} & \cdots & p_{j,a,2} \\ p_{j,a.2} & p_{j,a,1} & p_{j,a,N_i} & \cdots & p_{j,a,3} \\ p_{j,a,3} & p_{j,a,2} & p_{j,a,1} & \cdots & p_{j,a,4} \\ \vdots & \vdots & \vdots & \ddots & \vdots \\ p_{j,a,N_i} & p_{j,a,N_i-1} & p_{j,a,N_i-2} & \cdots & p_{j,a,1} \end{bmatrix} \tag{1}$$

where $P_{j,a} \in \mathbb{R}^{N_i x N_i}$ and $p_{j,a,i}$ is the consumption of the *a*-th programmable appliances in a given *i*-th time interval for the *j*-th end-user. Clearly, an appliance can only adopt one load profile from the matrix *P*, while the other must be ignored. For this reason, N_i additional binary variables have to be introduced, one for each columns, so that:

$$\sum_{i=1}^{N_i} \delta_{j,a,i} = 1 \tag{2}$$

where $\delta_{j,a,i}$ is equal to 0 if the *i*-th consumption pattern (i.e. the *i*-th column) is not selected and equal to 1 if the corresponding *i*-th consumption pattern is chosen. Hence, equation 2 ensures that only a load profile can be selected, while the others are not considered. As a consequence, this representation introduces flexibility in the usage of electric appliances to be considered in the demand management purpose.

2.2. Energy storage

A battery electric storage system (BESS) is also considered as an essential element to further introduce flexibility in the management of an energy community [13]. Even if its integration can be complementary to the demand management, because of BESS basically introduce flexibility by potentially leaving consumption habits unchanged, its operation need to be modelled as well to exploit the interaction with demand management. The BESS formulation adopted here is based on the one already introduced in [14], where the BESS is studied considering passive sign convention. Under this assumption, the electric power input to the BESS has positive sign (during charge), viceversa the output one (during discharge) has negative sign. As a consequence, the State Of Charge (*SOC*) of the battery (i.e. its energy conten) in a given time interval is defined; as follows:

$$SOC(t_{i+1}) = \eta_{sd} SOC(t_i) + \left(\eta_c P_{b,c}(t_i) - \frac{P_{b,d}(t_i)}{\eta_d} \right) \Delta t \tag{3}$$

where η_{sd} is the self-discharge efficiency, η_c is the charge efficiency, η_d is the discharge efficiency and $P_{b,c}$ and $P_{b,d}$ are the battery power respectively during charge and discharge. However, electric power during charge and discharge are typically limited, so further constraints need to be introduced, as follows:

$$0 \leq P_{st,c} \leq \delta_c \frac{SOC_{max}}{T_c} \tag{4}$$

$$0 \leq P_{st,d} \leq \delta_d \frac{SOC_{max}}{T_d} \tag{5}$$

$$0 \leq \delta_c + \delta_d \leq 1 \tag{6}$$

where SOC_{max} is the storage capacity of the battery, T_c and T_d are the minimum charge and discharge time, while Equation 6 is a operational constraint where δ_c and δ_d are binary variables that compel charge and discharge powers to be different from zero only one at a time.

2.3. Energy balance of the community with demand management

As already depicted in Section 2.4., an energy community is a scheme where local RES production, energy storage systems and the end-users interact each other to increase local self-consumption. In this context, where residential end-users jointly acting as renewables self-consumers, if demand management is also introduced for some of the appliances, the energy consumption for each end-users can be divided in two different main categories: fixed load and a flexible one. The corresponding energy balance for the community can be then defined in each time interval, as follows:

$$P_{PV}(t_i) + P_p(t_i) + P_{b,d}(t_i) = P_s(t_i) + P_{b,c}(t_i) + \sum_{j=1}^{N_u} U_{fix,j}(t_i) + \sum_{j=1}^{N_u} \sum_{a=1}^{N_a} U_{flex,j,a}(t_i) \tag{7}$$

where P_{PV} is the RES production from PV, P_p is the electricity bought from the grid, $P_{b,d}$ is the electric power supplied by the battery, $P_{b,c}$ is the electric power consumed by the battery, $U_{fix,j}$ is the overall fixed load of the j-th end-whikle $U_{flex,j,a}$ is the flexible load of the a-th programmable appliance owned by the corresponding j-th end-user. Then, the left hand side of Equation 7 represents the *sources* for the energy community, while the right hand side identifies the *loads*, where P_s has the role of representing power injected and sold to the grid.

However, according to the modelling of demand management proposed in Section 2.1., each flexible load can be represented by N_i possible load patterns where only one of them is not actually zeroed. As a consequence, each flexible load introduced in Equation 7 can be also represented as follows:

$$\mathbf{U}_{flex,j,a} = \sum_{i=1}^{N_i} \delta_{j,a,i} \mathbf{p}_{j,a}^{(i)} \tag{8}$$

where $\mathbf{p}_{j,a}^{(i)}$ is the i-th column of the matrix $\mathbf{P}_{a,j}$, while $\mathbf{U}_{flex,j,a}$ is the vector describing the load profile for the a-th programmable appliance of the j-th end-user. Of course, Equation 2 ensures that only one load patterns will be selected during the search of the optimal solution.

Additionally, limitations owning to the contractually committed power have to be considered for each end-user. In fact, demand management shifts the flexible loads and consequently power demand can exceed the available power for a residential end-user which is usually equal to 3 kW in most of the Italian domestic costumers [15]. This can be avoided by introducing for each j-th end-user and in each i-th time interval a further constraints, as follows:

$$U_{fix,j}(t_i) + \sum_{a=1}^{N_a} U_{flex,j,a}(t_i) \leq P_c \tag{9}$$

where P_c is the contractually committed power for domestic costumers.

2.4. Objective functions

In this paper, according to the recent Italian rules [16], a multi-family building is considered where a PV plant is used to supply the energy demand of the residential end-users jointly acting as renewables self-consumers. In this context, the energy demand of the some electric appliances are supposed to be schedable to increase and maximize the self-consumption of the RES production. This goal is equivalent to reduce or minimize the electricity produced by the PV and injected into the grid, so the objective function is evaluated, as follows:

$$OF_1 = min \sum_{i=1}^{N_i} P_s(t_i) \Delta t \tag{10}$$

where P_s represents the electric power sold to the grid. However, the management of some of the electric appliances according to this policy, may be potentially in contrast with the users' habits. For this reason a measure of the end-users' discomfort in adopting demand management is also introduced. This is represented by a sort of weighted distance between the scheduled path demand of the shiftable loads (e.g. the one suggested by solving equation 10) and the end-user usual consumption habits. Consequently, an alternative objective function has been introduced to minimize this user's discomfort, as follows:

$$OF_2 = min \sum_{j=1}^{N_u} \sum_{a=1}^{N_a} \left[\sum_{i=1}^{N_i/2} i \cdot \delta_{j,a,i} + \sum_{(N_i/2)+1}^{N_i} (N_i - i + 2) \cdot \delta_{j,a,i} \right] \tag{11}$$

In this objective function, the coefficients i and $(N_i - i + 2)$ are introduced to weight differently each consumption patterns represented by a column of the matrix **P**. In particular, the consumption patterns far from the usual habit (i.e. the first column of **P**) are more penalised with respect to the closest one. In fact, for instance, if the 10th column was selected as consumption pattern, its weight (i.e. 10) would be higher than the one obtainable by the 3rd column (i.e. 3). In this way, the objective function naturally force the solution to be close to usual habits of the end-users. Additionally, weights are symmetric with respect to the center of the matrix, since each column of **P** is generated by a cyclic permutation of the usual consumption pattern of a given appliance. Hence, for example, the second and the last column of **P** have of course the same weight, because they represent two patterns symmetrically close to the end-user's habit.

Clearly, equation 11 states that minimum discomfort has to be reached (i.e., end-users do not change their consumption habits) and practically this in contrast to equation 10. For this reason, also a multi-objective approach have been also explored. In particular, since the formulation proposed here is MILP based, a weighted sum method [17] is adopted to combine the two objective functions, as follows:

$$MOF = min[\alpha OF_1^* + (1 - \alpha) OF_2^*] \tag{12}$$

where $0 \leq \alpha \leq 1$, while OF_1^* and OF_2^* are the normalized objective functions. Different weight α in Equation 12 givea the possibility to explore solutions where demand management is less compelling, consumption patterns are closer to end-users' habits and discomfort is reduced.

3. Key Performance Indicators

KPIs are used here to investigate the performances of the proposed demand management within an energy community on yearly basis, considering scenarios with different sizes of the active assets (i.e. PV and BESS). In particular, these reference scenarios are designed by supposing no demand management, because the considered use cases should investigate the role of the demand management in existing configuration of the collective self-consumption scheme. Three groups of KPIs were considered: energy, economic, environmental and discomfort.

3.1. Energy KPI

The energy impact of the demand management in a multi-family residential building has been evaluated considering two different indicators: the self-consumption (*SC*) and the self-sufficiency (*SS*). The *SC* identifies the self-consumed PV production compared to the yearly PV production, while the *SS* identifies the self-consumed PV production compared to the yearly electricity demand of the building, as follows [18]:

$$SC = \frac{E_{sh}}{E_{PV}} = \frac{\sum\limits_{year} P_{sh}(t_i) \cdot \Delta t}{\sum\limits_{year} P_{PV}(t_i) \cdot \Delta t} \tag{13}$$

$$SS = \frac{E_{sh}}{E_L} = \frac{\sum\limits_{year} P_{sh}(t_i) \cdot \Delta t}{\sum\limits_{year} U_e(t_i) \cdot \Delta t} \tag{14}$$

where U_e is the aggregated yearly electricity load profile including fix and flexible loads, while $P_{sh}(t_i)$ and E_{sh} represent the self-consumed PV production within the energy community also named shared energy and calculated, as follows:

$$P_{sh}(t_i) = min[(P_{PV}(t_i) + P_{b,d}(t_i)), (U_e(t_i) - P_{b,c}(t_i))] \tag{15}$$

3.2. Economic KPI

The economic impact of the demand management in an energy community has been evaluated only in terms of cost savings for the end-users. In fact, as already pointed out, demand management is supposed to be

adopted in existing scenarios of energy communities. Hence, economic feasibility and profitability of investing in the active assets of the community is not considered here, so economic indicators evaluating the return of investment are not included in this work.

In this light, the indicator named Percentage Cost Reduction (*PCR*) [19] is used to compare the yearly costs of the electricity bills YC_{dm} obtained by the energy community adopting demand management with the ones YC_{ref} where demand management is not adopted. Practically, *PCR* is calculated as follows:

$$PCR = \left[1 - \frac{YC_{dm}}{YC_{ref}}\right] 100. \tag{16}$$

Both yearly costs are calculated considering the per unit cost for the electricity bought from the grid E_L and the economic benefits and incentives offered to energy communities by the current Italian regulatory framework, as follows:

$$YC = E_L C_p - E_{PV} C_s - E_{sh} C_{sh}. \tag{17}$$

Specifically, the PV production injected into the grid E_{PV} is economically valued at the wholesale market price, while the shared energy E_{sh} benefits of an incentive. The former, considering 2019 as reference year, is assumed fixed at approximatively 50€/MWh [20], while the latter is equal to around 110€/MWh and the electricity retail price is assumed instead equal to 200€/MWh on average [19].

3.3. Environmental KPI

Environmental KPI measure instead how demand management influences the reduction in the primary energy consumption or, alternatively, in CO_2 emissions in an energy community. The carbon saving is in fact calculated by comparing the carbon emissions with and without demand management, as follows:

$$\Delta CO_2 = \left[1 - \frac{CO_{2,dm}}{CO_{2,ref}} \cdot 100\right] = \left[1 - \frac{E_{p,dm} \cdot EF_e}{E_{p,ref} \cdot EF_e}\right] \cdot 100 \tag{18}$$

where EF_e represents the national CO_2 emission factor for the electricity bought from the grid [21], while $E_{p,dm}$ and $E_{p,ref}$ are the yearly electricity demand of the building not fulfilled by RES production when DM is adopted and not implemented, respectively.

3.4. Discomfort KPI

Finally, also a further KPI is introduced to measure how demand management changes the usual habits of end-users and contemporarily create discomfort. This can be basically measured by comparing the suggested optimal path demand (gained by solving Equation 10) with the end-user's habits. Since each of the programmable appliances considered in this study have a specific duty-cycle, this comparison is equivalent to measure the distance between two duty-cycles with different starting time or, in other words, this distance is the difference of two starting time, as follows:

$$Dis = \sum_{d=1}^{N_d} \sum_{j=1}^{N_u} \sum_{a=1}^{N_a} \frac{1}{N_j} \mid t_{j,a}^{us} - t_{j,a}^{op} \mid \tag{19}$$

where $t_{j,a}^{us}$ and $t_{j,a}^{op}$ are the usual and optimal starting time of the duty-cycle for the j-th user and its programmable appliance a, while N_d is the number of the reference days adopted to represent a whole year. Clearly, $t_{j,a}^{op}$ is get from the solution obtained by solving Equation 10.

4. Case study description

A multifamily residential building of 40 apartments, located in the North-West part of Italy, was selected as reference use case in this study. In fact, this building typology is the most representative according to the current Italian building stock [19, 22]. The electricity demand of each apartment was estimated considering an open-source simulator developed by the CADEMA research group of the Politecnico di Torino [23]. The open-source simulator creates the daily load profiles of the main electric appliances for an aggregate of households. Then, different load profiles were generated for a whole day according to the season, the day of the week (i.e. weekdays and weekend days) and the energetic labels of the appliances with a time-resolution of 5 minutes.

In particular, the simulated load profile of each appliances are based on statistical data obtained from past load measurement campaign in National research project, so the generated patterns can be assumed as related

to end-users' habits. The appliances considered in the simulator are vacuum cleaner, dishwasher, washing machine, tumble drier, audio-video devices (tv, hifi stereo,...) and other electronic devices (laptop, personal computers) and lighting. Among the others, dishwashers and washing-machines were assumed as the ones suitable for the application of demand management due to their ability to be programmed [8]. Figure 2 shows on the left an example of the resulting aggregated electricity demand estimated for the residential building (including both fix and flexible loads of each end-users) with a focus (on the right) for a given end-users where fix demand (blue line) and the consumption of programmable appliances (red and yellow lines) are highlighted. Hence, loads that can be rescheduled have a duty cycle that can be anticipated or delayed with respect to the habits depicted in Figure 2 (right side).

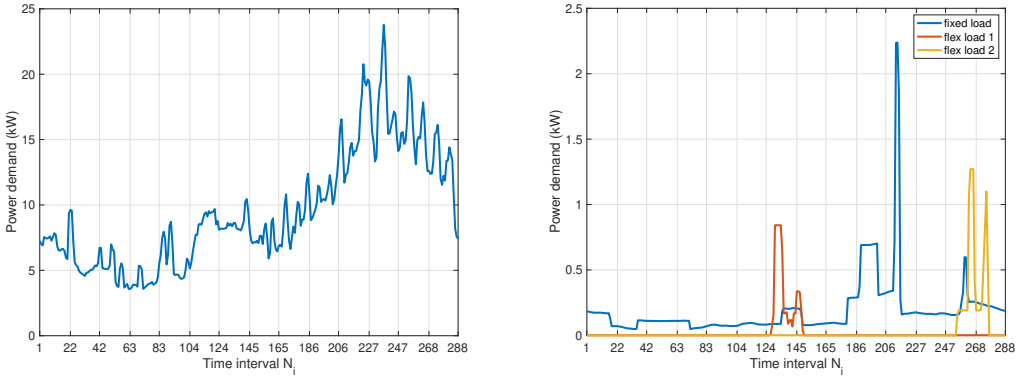

Figure 2: Load profiles of the case study: aggregated demand (left), consumption of a single end-user with fixed and flexible demand (right)

On the other hand, PV production was estimated by adopting the PVGIS database [24] to take into account the effect of the solar beam at the considered location of the case studies. Specifically, PV size was estimated a priori by adopting the sizing criteria proposed in [14] but assuming no demand management. In this light, the PV size is selected on energy basis according to the simultaneous maximization of the self-consumption (*SS*) and self-sufficiency (*SC*) for the energy community, so that the chosen PV size ensures the lowest distance with respect to the Utopia point in the $SC - SS$ plane. The maximum PV size was also limited to 70kW$_p$ due to the available roof surface of the residential building being studied [19]. Of course, since the open-source simulator is on a daily basis, also PV production was estimated on the same timeframe. However, to limit computational effort in simulating the proposed model, reference days were then identified to represent a whole year. In particular, two days (i.e., a weekday and a weekend day) for each seasons have been considered.

The resulting PV size were then considered to identify a reference configuration for the case study where the energy community exploits the RES production for increasing local self-consumption but without demand or BESS management. This reference scenario is firstly compared with one where the demand management is adopted to evaluate its impact without BESS. Later, other scenarios assuming the same PV size, but parametrically increasing BESS size without demand management, were compared to the reference configuration. In this way, demand management is also compared with a different approach based on the BESS management as described in Section 2.2..

5. Results

The assessment of demand management in an energy community with a collective self-consumption configuration is presented in this section. The use-case considered is a residential multi-family building with 40 flats located in the North-West of Italy [19]. According to the sizing approach proposed in Section 4. the installed PV capacity for maximizing both *SS* and *SC* is equal to 40 kW$_p$. Starting from this reference configuration (i.e., Scenario 0) without demand management (DM), the scenarios being studied are summarized in Table 1.

Table 1: PV and BESS size in different Scenarios

Scenario	0	1	2	3	4
PV	✓	✓	✓	✓	✓
BESS (kWh)	-	-	15	30	30
DM	-	✓	-	-	✓

In particular, Scenario 1 highlights the impact of the demand management, while Scenarios 2 and 3 points out the impact of BESS management with increasing BESS sizes. Scenario 4 has been further included to exploit also potential interaction between two different flexibility approach within the energy community. The main BESS characteristics considered in the simulations are also reported in Table 2. In this case, a round-trip efficiency of approximately 90% is assumed, the rated fully charging and discharging time are equal to 3 hours, while self-discharge effect is substantially neglected.

Table 2: BESS characteristics assumed in the simulations [5].

η_c	η_d	η_{sd}	T_c (h)	T_d (h)
0.95	0.95	1	3	3

Table 3 shows the KPIs obtained by the different Scenarios. It can be noticed that demand management in Scenario 1 has a positive impact from the economic, energy and environmental point of view. In fact, the shift of energy consumption for the programmable appliances can improve the match of the demand with the PV production. In other words, the aggregated demand of the flexible loads should mainly occur during PV production, as depicted in Figure 3, leading end-users to more virtuous behaviours for the energy community perspective. Consequently, self-consumption and self-sufficiency can be enhanced up to 12.7% and 5.7%, respectively, while energy cost and CO_2 emission can be reduced by 4.6% and 9.1%.

Clearly, the positive economic impact can also contribute in increasing cash-flows and, consequently, in making more profitable the PV investment for the community.

Table 3: KPIs obtained for different Scenarios

Scenario	0	1	2	3	4
SC (%)	83.2	95.9	91.7	96.3	99.4
SS (%)	37.2	42.9	41.0	43.0	44.4
PCR (%)	-	4.6	3.1	4.9	5.8
E_{sh} (MWh/y)	34.7	42.9	38.2	40.1	41.4
ΔCO_2 (%)	-	9.1	6.1	9.3	11.5
Dis	0	91.5	0	0	94.8

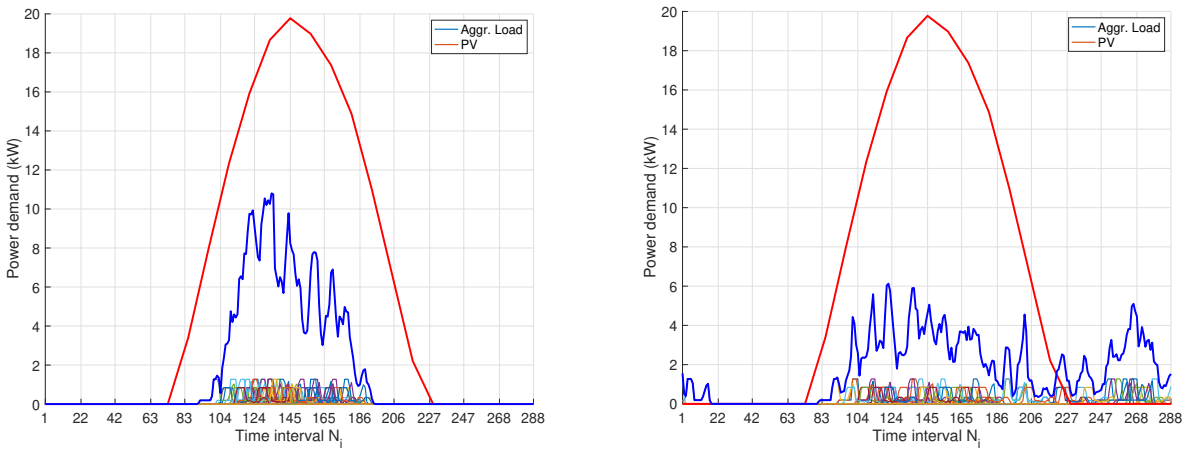

Figure 3: Aggregated load of all the programmable appliances in Scenario 1 with (left) and without (right) demand management during a spring day.

The resulting net load is then significantly close to zero during daytime, so that RES production is mainly self-consumed within the community and not injected into the grid as reported in Figure 4. Furthermore, demand management can also reduce the net load during the afternoon and evening hours, still due to load shifting effects. However, discomfort inevitably increases, since end-users' habits should be changed.

Similar benefits can be gained in Scenario 3 by optimally managing BESS to increase self-consumption, as noticed in Table 3 and Figure 4. In fact, even without demand management, the adoption of BESS with a rated capacity of 30 kWh can contribute to reach high levels of *SC* and *SS* close to 96% and 43% respectively, while cost and emission savings can be close to 4.9% and 9.3%. Nevertheless, this approach needs of the installation of a costly asset (i.e. electrochemical battery) while the end-users' behaviour is not involved at all. Additionally, BESS needs to be replaced once its cycle life is reached, making not yet totally profitable its usage in residential applications without the adoption of incentives [4, 25].

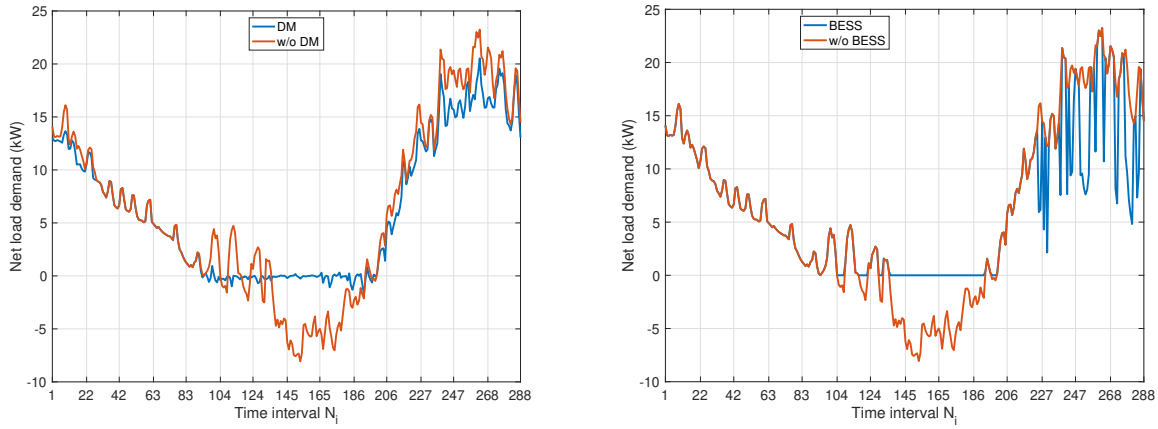

Figure 4: Net load of the energy community during a summer day for: Scenario 1 with (blue curve) and without (red curve) demand management on the left; Scenario 3 with (blue curve) and without (red curve) BESS management on the right.

However, when the interaction of the two different flexibility approaches is considered (i.e., Scenario 4), all the KPIs benefit of the demand management. In this case, a fully self-consumption of PV production is almost reached, while cost and emissions savings can be close to 6% and 11.5%, respectively. Specifically, the demand management allows a lower battery usage while ensuring a longer technical lifetime, postponing the need of investment for its replacement. Furthermore, demand management contributes in contrasting the injection of PV overproduction, as pointed out by the net load shown in Figure 5, while BESS benefits of a lower

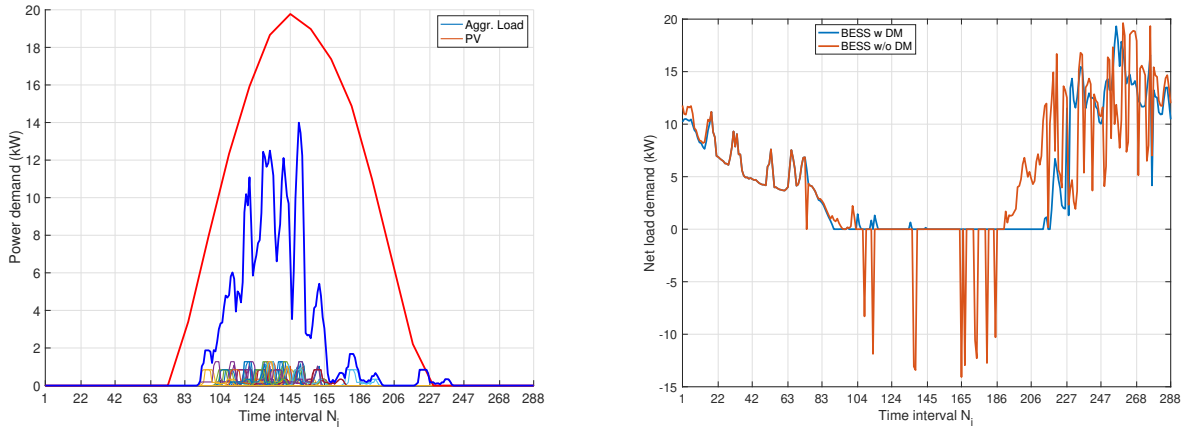

Figure 5: Scenario 4: aggregated load of the programmable appliances with and without demand management during a spring day; net load of the energy community during spring with and without demand management.

Finally, multi-objective simulations have been also explored to evaluate the impact of different end-users' availability in changing their habits for following or adopting demand management. As already observed, different end-users adaptability can be obtained by considering different weights α in Equation 12. In fact, a lower α represents a decreasing willingness to participate in demand management and vice versa. Table 4 shows the results of the multi-objective simulation for Scenario 1 considering different weights. As expected, the greater is α the better the economic, environmental and energy KPIs, while the higher the discomfort. Correspondingly,

the net load of Figure 6 has more negative values (i.e., reduced self-consumption) when OF_2 (i.e., the discomfort) is weighting more than the OF_1 (i.e., the self-sufficiency). These results suggest that some trade-off solutions can be achieved where end-users' acceptance or availability in following demand management is not fully agreed. Nevertheless, positive results can be still obtained and then end-users acceptability can be thus promoted to increase the willingness to participate in flexibility [7].

Table 4: KPIs obtained for Scenario 1 considering different weight in multi-objective simulation

α	0.75	0.5	0.25
SC (%)	95.8	92.4	88.6
SS (%)	42.8	41.3	39.6
PCR (%)	4.5	3.3	1.9
E_{sh} (MWh/y)	39.9	38.5	36.9
ΔCO_2 (%)	8.9	6.5	3.8
Dis	38.9	19.7	7.1

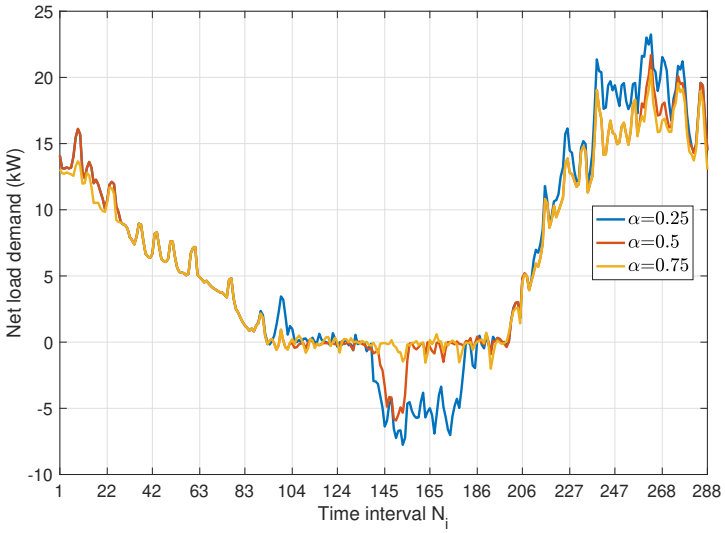

Figure 6: Scenario 1: aggregated load of the programmable appliances with and without demand management during a spring day; net load of the energy community during spring with and without demand management.

6. Conclusion

The energy communities represent a great opportunity to increase self-consumption of RES based production, fostering more sustainable energy ssystems with lower operational costs capable to contrast energy poverty. In this context, flexibility is assuming a relevant role for reaching these goals, because it can improve the match between consumption and production. Classically, storage systems are considered for decoupling the timing of energy production from the demand, so that overproduction can be stored and released when needed, leaving the costumers habits unchanged. In this work, instead, a complementary approach based on demand management was considered, by promoting changes in consumption habits that may be proposed to end-users. In particular, a Mixed Integer Linear Programming formulation is proposed here to model the demand management of electric appliances used by residential end-users joining an energy community under the Italian regulatory framework. An Italian residential multi-family building with PV is assumed for exploiting the economic and environmental benefits of the flexibility. Discomfort was also evaluated to highlights how demand management impacts the households habits.

The results figured out how demand management can effectively increase local self-consumption with a corresponding reduction in terms of energy costs and CO_2 emissions up to 4.6% and 9.1%, respectively. Similar results could be potentially obtained by using electric storage systems, but investment and operational cost increase as well, making stil less profitable this solution. Interoperability between battery and demand management can instead be supported, because storage units can be potentially undersized or alternatively less stressed, while energy, environmental and economic KPIs are improved. Of course, discomfort is being pe-

nalized, then multi-objective simulation has been also introduced to evaluate how KPIs are influenced by a different willingness to participate in demand management. Results show that potential trade-off solutions can be still found, even thought benefits are reduced. In this case, future work will be further developed to investigate how to economically enhance end-users availability according to their rate of flexibility.

References

[1] European Commission, "Energy communities." https://energy.ec.europa.eu/topics/markets-and-consumers/energy-communities_en.

[2] European Parliament, "Directive (eu) 2018/2001 of the european parliament and of the council of 11 december 2018 on the promotion of the use of energy from renewable sources." https://eur-lex.europa.eu/eli/dir/2018/2001/oj.

[3] M. Haji Bashi, L. De Tommasi, A. Le Cam, L. S. Relaño, P. Lyons, J. Mundó, I. Pandelieva-Dimova, H. Schapp, K. Loth-Babut, C. Egger, M. Camps, B. Cassidy, G. Angelov, and C. E. Stancioff, "A review and mapping exercise of energy community regulatory challenges in european member states based on a survey of collective energy actors," *Renewable and Sustainable Energy Reviews*, vol. 172, p. 113055, 2023.

[4] B. Zakeri, S. Cross, P. Dodds, and G. C. Gissey, "Policy options for enhancing economic profitability of residential solar photovoltaic with battery energy storage," *Applied Energy*, vol. 290, p. 116697, 2021.

[5] P. Lazzeroni, I. Mariuzzo, M. Quercio, and M. Repetto, "Economic, energy, and environmental analysis of pv with battery storage for italian households," *Electronics*, vol. 10, p. 146, 2021.

[6] Á. Manso-Burgos, D. Ribó-Pérez, T. Gómez-Navarro, and M. Alcázar-Ortega, "Local energy communities modelling and optimisation considering storage, demand configuration and sharing strategies: A case study in valencia (spain)," *Energy Reports*, vol. 8, pp. 10395–10408, 2022.

[7] J. Barnes, P. Hansen, T. Kamin, U. Golob, M. Musolino, and A. Nicita, "Energy communities as demand-side innovators? assessing the potential of european cases to reduce demand and foster flexibility," *Energy Research & Social Science*, vol. 93, p. 102848, 2022.

[8] S. Panda, S. Mohanty, P. K. Rout, B. K. Sahu, M. Bajaj, H. M. Zawbaa, and S. Kamel, "Residential demand side management model, optimization and future perspective: A review," *Energy Reports*, vol. 8, pp. 3727–3766, 2022.

[9] E. Shirazi and S. Jadid, "Cost reduction and peak shaving through domestic load shifting and ders," *Energy*, vol. 124, pp. 146–159, 2017.

[10] S. Golshannavaz, "Cooperation of electric vehicle and energy storage in reactive power t compensation: An optimal home energy management system considering pv presence," *Sustainable Cities and Society*, vol. 39, pp. 317–325, 2018.

[11] S. Hagejärd, G. Dokter, U. Rahe, and P. Femenías, ""it's never telling me that i'm good!" household experiences of testing a smart home energy management system with a personal threshold on energy use in sweden," *Energy Research & Social Science*, vol. 8, p. 103004, 2023.

[12] P. Lazzeroni, M. Repetto, and H. Gabbar, "21 - introduction to energy management in smart grids," in *Solving Urban Infrastructure Problems Using Smart City Technologies* (J. R. Vacca, ed.), pp. 447–473, Elsevier, 2021.

[13] F. Minuto, P. Lazzeroni, R. Borchiellini, S. Olivero, L. Bottaccioli, and A. Lanzini, "Modeling technology retrofit scenarios for the conversion of condominium into an energy community: An Italian case study," *Journal of Cleaner Production*, vol. 130, 2021.

[14] A. Cielo, P. Margiaria, P. Lazzeroni, I. Mariuzzo, and M. Repetto, "Renewable energy communities business models under the 2020 italian regulation," *Journal of Cleaner Production*, vol. 316, p. 128217, 2021.

[15] Italian Regulatory Authority for Energy, Networks and Environment, "Composizione percentuale del prezzo dell'energia elettrica per un consumatore domestico tipo." https://www.arera.it/it/dati/ees5.htm.

[16] Italian Regulatory Authority for Energy, Networks and Environment, "Definizione, ai sensi del decreto legislativo 199/21 e del decreto legislativo 210/21, della regolazione dell'autoconsumo diffuso. Approvazione del Testo Integrato Autoconsumo Diffuso." https://www.arera.it/it/docs/22/727-22.htm, 2023.

[17] C. A. Floudas, “Nonlinear and mixed-integer optimization: Fundamentals and applications.” Oxford University Press, 1995.

[18] IEA, “Photovoltaic Power Systems Programme - A methodology for the analysis of PV self-consumption policies.” https://iea-pvps.org/wp-content/uploads/2020/01/IEA-PVPS_-_A_methodology_for_the_Analysis_of_PV_Self-Consumption_Policies.pdf, 2016.

[19] A. Canova, P. Lazzeroni, G. Lorenti, F. Moraglio, A. Porcelli, and M. Repetto, “Decarbonizing residential energy consumption under the italian collective self-consumption regulation,” *Sustainable Cities and Society*, vol. 87, p. 104196, 2022.

[20] GME - Gestore dei Mercati Energetici. http://www.mercatoelettrico.org/It/Download/DownloadDati.aspx?Val=MGP_Prezzi.

[21] Istituto Superiore per la Protezione e la Ricerca Ambientale, “Fattori di emissione atmosferica di gas a effetto serra nel settore elettrico nazionale e nei principali Paesi Europei.” https://www.isprambiente.gov.it/it/pubblicazioni/rapporti/fattori-di-emissione-atmosferica-di-gas-a-effetto-serra-nel-settore-elettrico-nazionale-e-nei-principali-paesi-europei.-edizione-2020, 2021.

[22] I. Ballarini, V. Corrado, F. Madonna, S. Paduos, and F. Ravasio, “Energy refurbishment of the italian residential building stock: energy and cost analysis through the application of the building typology,” *Energy Policy*, vol. 105, pp. 148–160, 2017.

[23] CADEMA, “Household load profiler.” https://github.com/cadema-PoliTO/household_load_profile.

[24] Joint Research Center, “Photovoltaic geographical information system.” https://re.jrc.ec.europa.eu/pvg_tools/en/#PVP.

[25] O. Alavi, J. Despeghel, W. D. Ceuninck, M. Meuris, J. Driesen, and M. Daenen, “Economic study of battery profitability in residential solar panel systems: A case study of belgium,” in *2020 IEEE 14th International Conference on Compatibility, Power Electronics and Power Engineering (CPE-POWERENG)*, vol. 1, pp. 358–363, 2020.

PROCEEDINGS OF ECOS 2023 - THE 36TH INTERNATIONAL CONFERENCE ON
EFFICIENCY, **C**OST, **O**PTIMIZATION, **S**IMULATION AND ENVIRONMENTAL IMPACT OF ENERGY SYSTEMS
25-30 JUNE 2023, LAS PALMAS DE GRAN CANARIA, SPAIN

Innovative thermal management operating strategies for battery-electric heavy-duty trucks

Jan Friedrich Hellmuth[a], Michael Steeb[a], Markus Pollak[a], Florian Jäger[a], Wilhelm Tegethoff[a,b] and Jürgen Köhler[a]

[a] Technische Universtität Braunschweig, Germany, jan.hellmuth@tu-braunschweig.de
[b] TLK-Thermo GmbH, Braunschweig, Germany

Abstract:
Thermal management systems of electrified vehicles especially heavy-duty trucks face multiple competing goals such as minimum energy consumption, minimum battery degradation and highest passenger comfort. The design process of a suitable thermal management system addressing these goals requires a holistic approach including the various cross couplings occurring in real world operation. Therefore, a physics-based modular full-vehicle model is introduced. The model includes an electrified drive-train, passenger cabin and thermal management system. The mechanical and electrical drive-train components, including the battery, motor and power electronics are thermally connected with each other and the cabin using various cooling circuits. A reversible heat pump and several control units are used to adjust the specific thermal requirements leading to complex interconnections and cross couplings. We estimate the performance of a heavy-duty truck on typical long-distance trips including stops based on legal regulations used for fast charging and overnight charging. While charging overnight, conservation air conditioning of the cabin is performed as efficiently as possible. For this operation, we present different strategies for battery thermal conditioning. Operating strategies for the full vehicle, especially the thermal systems in a summer and a winter scenario are proposed. Simulations of a typical deployment scenario are performed to explore the effects of different operating and control strategies for thermal management. Our virtual deployment scenarios include easy to modify driving cycles, driving time regulations, charge stops and climatic boundary conditions. For evaluation purposes we present an energy-flow-diagram for the full vehicle. Based on the simulation results we recommend thermal system operating strategies in a full-vehicle context for heavy-duty truck long distance trips and charging.

Keywords:
battery, heating, cooling, electric trucks, R744 thermal management, driving range, battery degradation, fast charging.

1. Introduction

In order to fulfill Paris goals for reducing CO_2 emissions in the transport sector, electrically powered trucks are needed. Both, battery-electric or fuel-cell trucks show promise for flexible transport of goods [1]. Some recent investigations discuss opportunities and challenges for fuel-cell trucks [2, 3]. An overview of current long-haul heavy-duty fuel-cell trucks is given by Pardhi et al. [4]. While it is believed that both, battery-electric and fuel-cell technologies will be used to power future heavy-duty trucks [5]. In this research we only focus on battery-electric heavy-duty trucks.

The transformation from internal combustion engines to electrically powered vehicles has occurred rapidly for passenger cars, as observed in car registration statistics of different countries [6]. Although electrical powered trucks became available in recent years [5, 7], the adoption of heavy-duty vehicles has been slow compared to light-duty vehicles [8]. Several reasons for the slower transition can be identified. First, heavy-duty trucks are typically required to cover longer distances than light-duty vehicles, while carrying large amounts of cargo. Therefore, the battery systems suitable for a heavy-duty truck must be much larger compared to that of a light-duty vehicle. Second there is a lack of fast charging stations, especially *MW*-Chargers [9], for trucks along the main transport routes resulting in longer stop times compared to conventionally powered vehicles. Third, electric trucks are still much more expensive than conventional trucks [10] and their diesel engines are already optimized on efficiency [2].

Several investigations found in the literature motivate the current study. Verbruggen et al. [11] performed simulations for powertrain design of a battery-electric heavy-duty truck. Nykvist and Ollson [12] performed an analysis on the feasibility of battery electric heavy-duty trucks and in doing so considered fast-charging and range in their investigation. Several authors investigated thermal behavior of large battery packs suited for trucks, e.g. [13]. Furthermore, the influence of thermal encapsulation of truck batteries was investigated. Energy savings for overnight parking are highlighted [14].

Our study focuses on the choice of operating strategies for the thermal management system of the whole truck during driving and charging, which has not been addressed in the literature. To analyze the effects of different operating strategies on energy consumption, battery degradation and thermal comfort, we model the full vehicle in order to take into account cross couplings. As an extension to the previously published studies we propose to employ a detailed physics-based model to investigate battery-electric trucks. With our approach a detailed analysis of the entire vehicle and its subsystems is possible. Furthermore, we describe the degradation of the battery, which allows us to predict the overall lifetime of the truck. Our model also allows different vehicle configurations to be tested. Furthermore, sensitivity analysis for certain parameters can be performed and parameters can be optimized easily.

Our physics-based vehicle model (see figure 2.) accounts for all the main components of a battery-electric heavy-duty truck with a special focus on the details of the thermal systems. The truck uses a state-of-the art Li-Ion battery system designed for performing long-distance trips with full payload. Our system contains NMC-Pouch cells [12]. Other manufacturers plan to use LFP cells [15]. In the future, solid state batteries may also be used for heavy duty trucks [16]. Electric and mechanical components such as motors, power electronics and gears produce waste heat [17]. Our model accounts for this waste heat and also includes battery degradation, which increases significantly at operating temperatures that are either too high or too low [18, 19]. During fast-charging battery waste heat can be very high [20]. Additionally, there is a need for cabin air conditioning and a fresh air supply.

As a result of these points, there is a need for a multi-function thermal management system. Because a long driving range is a main requirement for heavy-duty trucks, the thermal management should be as efficient as possible [21]. Different operating strategies can be applied [22] to optimize energy consumption. Also, battery degradation in the context of a full truck and different environments and operating conditions can be investigated because of the implemented degradation model [18].

We employed test scenarios with challenging conditions for the analysis of the whole system of a battery-electric heavy-duty truck. Operating strategies are compared in terms of battery degradation and energy consumption. Long-distance trips are the most challenging deployment scenario for battery-electric vehicles [23] and therefore, we focus especially on these long-distance trips. There is a need for large battery capacities and rapid charging [5] to minimize break times. In a parameter study, the effects of different boundary conditions as well as operating strategies on the aforementioned energy consumption, battery degradation and thermal comfort are investigated. The boundary conditions include harsh climatic conditions such as very high or low temperatures that are challenging [14, 24], due to the increased energy demands for thermal management. Furthermore, the driving cycle could be challenging, especially for hilly terrain. Due to the large weight of a typical battery-electric truck, which can weigh as much as 42 metric tons [24], high rolling resistances and grade resistances occur. For downhill driving, significant recuperation is possible, which can reduce energy consumption but results in higher loads for the mechanic and electric components and more waste heat. Simulations of the battery-electric truck on different trips using different operating strategies are conducted and investigated. The effects of the different operating strategies on the behavior of the system are analyzed in detail.

2. Description of the Modular Full Vehicle Model

For our investigations we use a modular multi-scale vehicle model implemented in Modelica modelling language using models from the TIL suites [25]. Due to its modular structure, the model can be configured for different types of vehicles such as busses, heavy-duty trucks or passenger cars. An earlier version of the model was presented by Steeb et al. [26]. They combined the vehicle model with a high-dimensional battery model and investigated thermal hotspots in automotive batteries.

A block diagram of the vehicle model used in this study is shown in figure 1. The model in general can be structured into mechanical, electrical and thermal sub-models. Furthermore, the model includes boundary conditions and control units for several models.

The boundary conditions (described in details in section 3.) include climate data and a drive cycle. We set the ambient temperature,ambient humidity and solar radiation as climate conditions. These affect the driving resistance and, importantly, act as the boundary conditions for all thermal models, having particular influence on the cabin, cooling circuit, and the reversible heat pump (RHP).

The drive cycle provides time-based calculated data for the vehicle's velocity and slope. We took distance-based data and re-calculated those for use in a time-based calculation. The time-based format fits well into the overall solution process of the formulated system of equations. For example, time-based driver rest stops can be set easily. Also, for heavy-duty trucks, the payload can be varied, and a time-based format enables the payload to be modified during a multi-stage trip. Furthermore, the drive cycle can set a charging request if ignition is activated. A driver model compares target speed with actual speed. Target speed is set as a boundary condition by the drive cycle. The driver is designed as a controller calculating brake or acceleration

pedal position. Data for slope and payload are processed in the driving resistance.

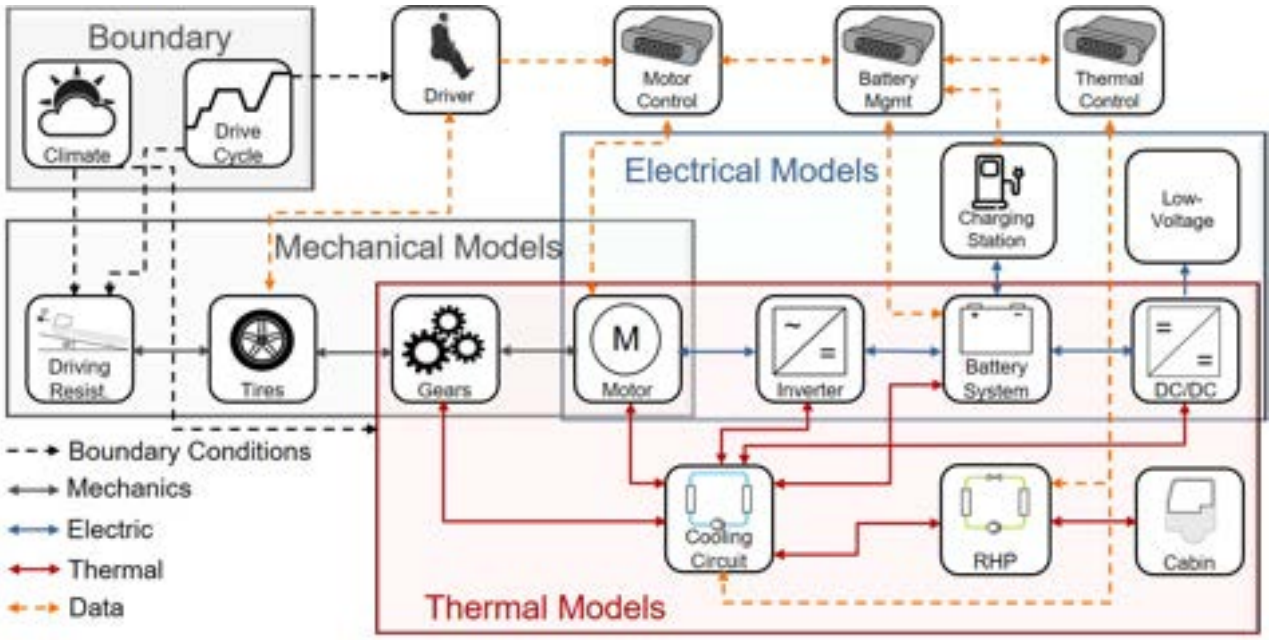

Figure 1: Model of a full vehicle including balance rooms for flow variables (mechanical and electrical power, heat), data connection , and boundary conditions, adapted from [26].

2.1. Models of Mechanical Drive-train and Force Components

The mechanic part includes models for driving resistance, tires, gears and an electric motor describing the driving dynamics of a configured vehicle. The driving resistance model includes replaceable parameter sets for drag coefficient c_w, frontal area A_{front}, weight $m_{vehicle}$ and rolling friction coefficient μ_{roll}. These values are summarized in Table 1. Traction force is calculated by summing roll, air, grade and acceleration resistance:

$$F_{Traction} = F_{Roll} + F_{Air} + F_{Grade} + F_{Acceleration} \tag{1}$$

Rolling resistance F_{Roll} and grade resistance F_{Grade} mainly depend on the vehicle mass $m_{vehicle}$ and rolling friction coefficient μ_{roll}. Air resistance F_{Air} is influenced by the frontal area A_{front} and drag coefficient c_w. The driving resistance model receives slope and the additional vehicle weight due to payload from the driving cycle model.

Table 1: Vehicle parameters used in all scenarios.

Vehicle total mass	Frontal area	Drag coefficient	Rolling friction coefficient
42 t	9.25 m^2	0.5	0.0055

The tires convert torque from gears into translational movements $F_{Traction}$ of the vehicle on the street (driving resistance model). The tire model also takes into account braking force and the tire inertia. Vehicle velocity and distance are calculated. Data are shared into a data-bus system. The gears model mechanically connects the tires and electrical motor. It operates at a constant efficiency and conserves inertia. Constant efficiency means that the incoming power is divided into a mechanical fraction, which is passed to the drive train, and heat. A thermal model is included in the gear model and accounts for waste heat rejected to the cooling circuit.

The electric motor is modeled with a fixed efficiency as well. The model includes replaceable data sets for motor characteristics such as torque data or inertia. The motor torque set-point is provided by the motor control unit. That translates the brake or acceleration pedal positions into motor torque. Constraints are taken into account including battery management data such as minimum recuperation temperature, maximum charging or discharging power, and motor limits. The motor provides mechanical power P_{mech} to the tires and calculates thermal losses P_{loss}.

2.2. Models of Electrical Components

The motor model acts as an interface to the mechanical and electrical models. The needed electric power P_{el} is calculated as the sum of P_{mech} and P_{loss}. While the motor operates at a constant voltage the electric

current depends on P_{el}. An inverter model provides electric power at a constant voltage level. It also operates at a constant efficiency. The inverter model is electrically connected to the battery system including a high voltage network. Furthermore, the DCDC-Converter enables a connection to a low voltage network. The low voltage network provides power for energy consumers such as ignition or infotainment. A charging station model is included. The charging can be activated by the station itself for time-based charging, or requested by the drive cycle. Charging power is controlled by the battery management. We implemented state-of-the-art charge maps that provide feasible charging powers depending on the actual battery temperature and its state of charge (SoC). Furthermore, a derating of charging power for high battery temperatures is applied.

The Li-Ion battery system is the key component of a battery-electric vehicle (BEV) and, therefore is modeled with many details [22, 26]. The battery system consists of a cooling plate, a thermal interface material and of a typical pouch cell with a nominal capacity C_N, as well as current arresters. On the battery system level, we model one representative battery cell and scale current, voltage and heat exchange up to system level. The battery system is designed for an on-board supply voltage of $800\,V$ and has a battery capacity of $725 kWh$. The representative single battery cell is modeled with a 2-dimensional (length and height) discretized model using thermally and electrically connected battery bundles. A battery bundle represents a single discretized part of a battery cell including the same behavior and equations for the adjusted cell volume, mass and capacity [27]. Each battery bundle includes an equivalent circuit model for electric modeling and calculating irreversible ($\dot{Q}_{irrev}$) and reversible ($\dot{Q}_{rev}$) heat production [28]:

$$\dot{Q}_{irrev} = R_i \cdot I^2 \tag{2}$$

$$\dot{Q}_{rev} = I \cdot T \cdot \frac{\partial U_{OCV}(T, SoC)}{\partial T} \tag{3}$$

The internal resistance $R_i(SoC, T)$ depends on temperature T and SoC. Irreversible heat production grows quadratic with higher currents, while the internal resistance typically decreases with higher temperatures. Reversible heat can be positive or negative. For high currents, its effect is small compared to $\dot{Q}_{irrev}$.

For State of Health (SoH) calculations, a semi-empirical battery degradation model based on the investigations of Wang et al. [18] was implemented. The SoH depends linearly on Ah-throughput $Ah_{Throughput}$, exponentially on the C-Rate, defined as $c\text{-}Rate = I/C_N$, and an Arrhenius-Term is used to describe the temperature dependence. Since the model is valid for a wide temperature and C-Rate range, it is capable of capturing the temperature and C-Rate coupling. Therefore, optimal thermal operating points for a given electric stress can be derived from the model. For moderate C-Rates, the optimum temperature of $25^\circ C$ results in the lowest degradation rate while higher and lower temperatures cause the degradation rate to increase rapidly. Other degradation dependencies like depth of discharge or SoC are neglected, which is a reasonable assumption due to the almost stationary use-case-scenarios of heavy-duty trucks. As outlined by [29], the chosen model seems to be the most suitable for the considered application. The model is valid for a wide temperature and C-Rate range. It is capable to describe the coupling of temperature and C-Rate. Optimal thermal operating points for given electric stress can be identified with an equation for ΔSoH depending on T, C-Rate and fitting parameters $a-e$:

$$\Delta SoH = (a \cdot T^2 + b \cdot T + c) \cdot \exp(d \cdot T + e) \cdot C-rate \cdot Ah_{Throughput} \tag{4}$$

2.3. Models of Thermal Components

As described previously, models of the gears, motor inverter and DCDC-Converter use thermal sub-models. The thermal sub-models contain the waste heat production as well as thermal capacitors and resistors describing the geometry and thermal behavior. Motor, gears and inverter thermally interact with the environment and the liquid cooling circuit. Similarly, battery cooling is connected to the cooling circuit. We use a cooling plate model for calculating convective and conductive heat transfer from liquid to the battery cells.

The cooling circuit model (see Figure 2; liquid) includes the interface to the ambient air that flows through the front-end heat exchanger of the truck. A fan is used to increase the air flow rate across this heat exchanger. Each of the two liquid loops are equipped with an air-liquid heat exchanger that is used for heat rejection to the ambient. A low temperature loop is designed for battery cooling. A high temperature liquid loop is used for cooling of motor, gears and inverter. Both cooling circuits use liquid pumps and for certain use cases, connections of the circuits are possible (e.g. battery heating).

Figure 2 depicts a piping and instrumentation diagram of the reversible heat pump with continuous lines marking the activated cooling mode. A third heat exchanger on the air path located in the front-end of the vehicle is used as an evaporator or gascooler/condenser in the reversible heat pump. It is designed as a two-stage R744-refrigeration cycle with switchable operation modes enabling heating or cooling of the battery and cabin. The refrigerant flows through the compressor and enters at a high pressure level in the *Gascooler*, which is bypassed on the air side. Next the refrigerant flows through the open *Valve 1*. Gascooling takes place in the

Front-End HX (heat exchanger) and the *Internal HX*. After that the refrigerant mass flow is divided to provide battery and cabin cooling. In the battery path refrigerant flows through *Valve 3* and is expanded in *Valve 4*. The R744 is evaporated in the *Battery HX* cooling the liquid coolant used for battery cooling. After that the refrigerant flows through *Valve 7* and *Valve 8*. For cabin cooling the refrigerant is expanded in *Valve 5* and flows through *Valve 6* and into the Evaporator, conditioning the fresh air for cabin cooling. Both refrigerant flows get mixed and enter the *Accumulator* and the the low pressure side of the *Internal HX*. Both, the RHP

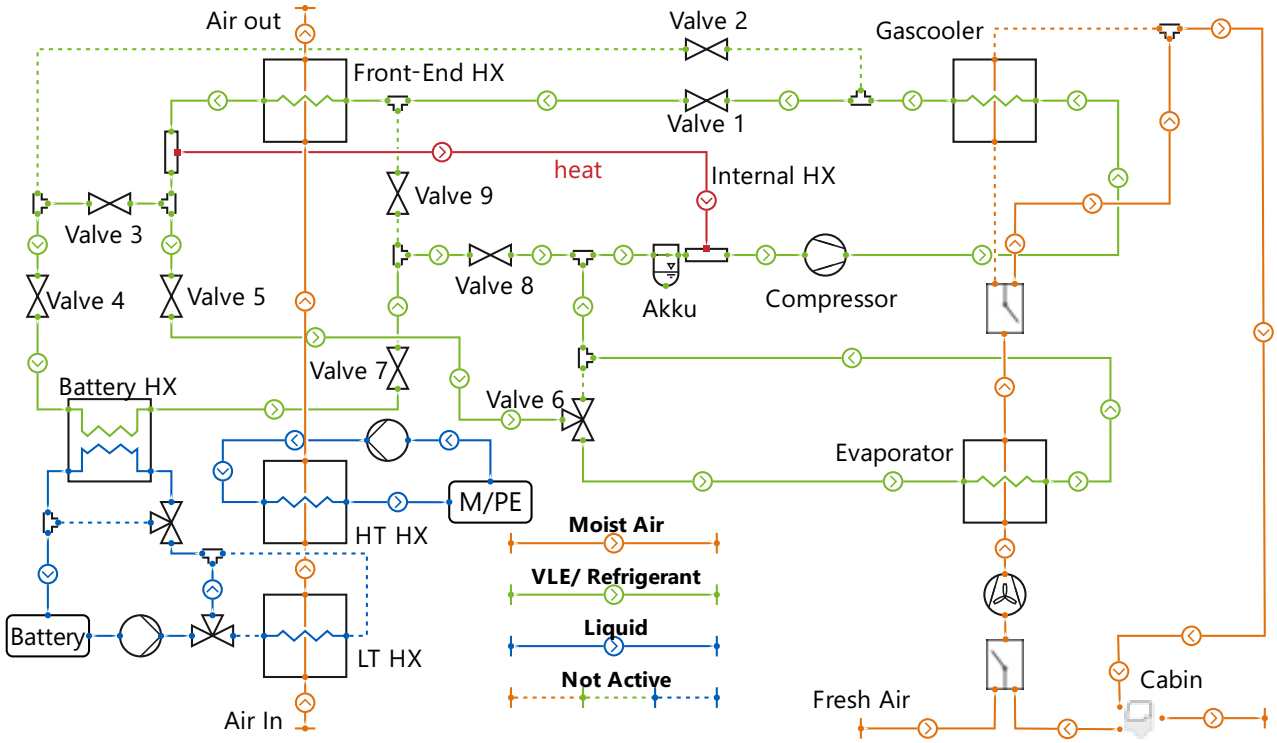

Figure 2: Piping and Instrumentation Diagram with TIL components of a reversible heat pump for cooling and heating of battery and cabin and the simplified cooling circuits including cooling of electric motor (M) and power electronics (PE). The case of the battery and cabin cooling is displayed.

and cooling circuit exchange data with a thermal control unit that specifies setpoint temperatures depending on the actual state of the vehicle and its subsystems. We use sets of PI-controllers for implementing different control strategies.

As described previously, the reversible heat pump is used for conditioning the vehicle cabin. The cabin interacts with the boundary conditions: Ambient temperature and humidity, solar radiation and driving speed. For simplicity, we always set $22°C$ as our target temperature for cabin air.

3. Deployment Scenarios and boundary conditions

We present two typical driving cycles each paired with two climatic conditions resulting in challenging deployment scenarios for a heavy-duty truck. These scenarios are used to investigate the effects of different operating strategies on the defined performance metrics. The applied operating strategies are discussed in the next section. The first drive cycle represents a typical long-distance day-trip for a truck in Germany and is depicted in Fig. 3. Starting in Hanover, the truck travels the 632 km distance to Munich in about 8 hours and 10 minutes excluding stops. The truck starts the drive cycle with half an hour of pre-conditioning followed directly by four and a half hours of mostly full-speed *Autobahn*-Driving. Due to regulations, a break of 45 minutes is required after that time. This break is also used for fast charging. Fast charging during the stop is required to cover the remaining driving distance for the day. For our analysis, the route is driven in a summer scenario with an outside temperature of $35°C$ and a high solar radiation affecting the truck's cabin.

Second, we investigate a two-day long distance trip. The two-day cycle is designed as a simplified driving cycle according to the maximum allowed driver's steering time in European Union regulations [31]. The whole trip runs for 1530 km on a flat terrain. Such a trip could be seen as a trans national European drive from Lithuania to Belgium. The velocity profile including pre-conditioning and rest (and charge) breaks can be seen in Figure 4. The tour starts with 3 hours of pre-conditioning, followed by two consecutive four and a half hour driving periods at $85\frac{km}{h}$ interrupted by a 45 minute resting and charging break. The night break is 11 hours and then

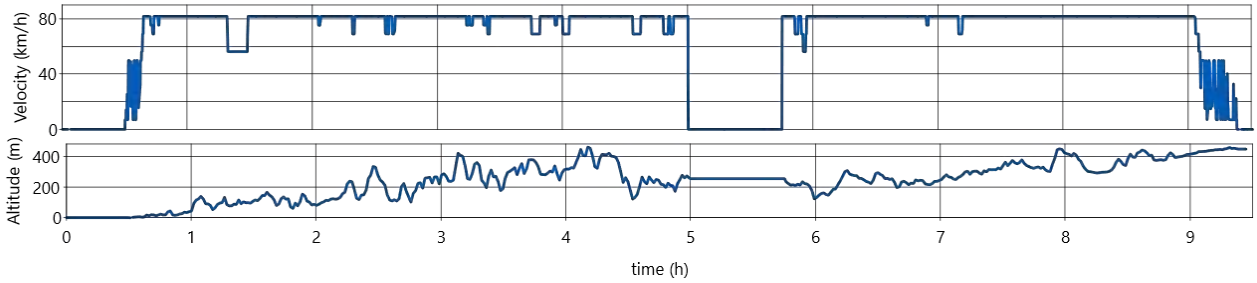

Figure 3: Hanover-Munich long-distance day-trip: Velocity and Altitude profile with rest and fast charging break, adapted from [30].

the same procedure will be driven the second day. During the short breaks fast charging will be performed. Slow charging is performed during the night break. During all charging breaks, cabin air conditioning must be provided.

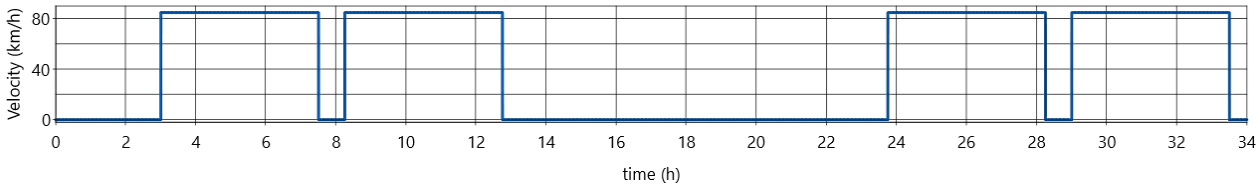

Figure 4: Velocity profile for a two-day long distance trip without altitude changes, including two fast charging brakes and one overnight brake.

4. Operating Strategies

An operating strategy is needed to handle competing goals pertaining to thermal management in the vehicle's operation. Those goals include:

- Minimum battery degradation
- Best thermal comfort for the driver
- Minimum energy consumption and maximum driving range

These goals are constrained by the following additional conditions: Safe operation of all vehicle components and systems, especially the battery and reaching suitable charging times. Most of these goals are in competition at various points of operation and must therefore be prioritized. Battery degradation can be reduced by maintaining optimum battery temperature and operating at low C-Rates. Maintaining suitable battery temperature, increasing energy consumption reduces driving range. If the reversible heat pump is working, a strategy for cooling or heating priority between the cabin and battery is necessary.

Two operation strategies for the summer scenario Hanover-Munich trip are suggested. One strategy prioritizes **minimum energy consumption**. The other strategy prioritizes **minimum battery degradation**. For safety reasons, thermal comfort of the driver is always prioritized and the best possible comfort is provided. For the **minimum battery degradation** strategy, the thermal system tries to cool the battery as much as possible to quickly reach and maintain the degradation-minimizing temperature. This is especially important during and after fast charging. For minimum energy consumption strategy, less intense battery cooling is performed at a more optimal operating point of the RHP and the target temperature for battery cooling is set higher than the degradation-minimizing temperature to save energy in thermal management.

Two operation strategies for fast charging during the two-day long-distance trip are suggested. We distinguish between a 45 minute daytime charging break that satisfies legal requirements, and lengthening the day-time charging breaks by 15 minutes resulting in a total of 30 minutes longer trip time. Minimum charging time competes with minimum battery degradation, which is expected to be higher when higher charging power is used.

In winter scenario we investigate the influence of battery pre-conditioning based on the two-day long distance trip. We compare different target temperatures for battery heating by the reversible heat pump during an hour of pre-conditioning before driving on a flat terrain for 9 hours including a fast-charging brake of 45 minutes.

The winter scenario also includes fast charging breaks but due to lower ambient temperatures battery cooling is easier. During overnight charging a constant heating and fresh air supply for cabin are required. For overnight charging, we study an eight hour night-time break for charging. The truck arrives with a nearly empty battery (SoC = 10%) and charges with a constant charging power (P_{charge} = 75 kW). We distinguish three thermal management operating strategies for RHP operation (see figure 2) during overnight charging. Our first strategy uses battery waste heat as the heat source for RHP, forming a water-air heat pump. Due to the relatively high temperature level and capacity of the battery a very high heating efficiency is expected. The second strategy utilises ambient air as heat source forming a typical air-air heat pump. Finally, the third strategy uses an electric heater. It is used as a benchmark for comparison of the electrical energy consumption and possible savings.

5. Results

To analyze cross couplings in the complex system that is the full truck model, we use a energy-flow diagram on the top level. Figure 5 shows the flow rates of the three main process variables: Mechanical and electrical power as well as heat flow rates. The diagram shows a summer case at an ambient temperature of 35°C and the Hanover-Munich route. The current and average consumption of electrical energy an other simulation parameters are depicted, cf. Fig 5. At the moment of the operational snapshot in Figure 5 the truck is climbing

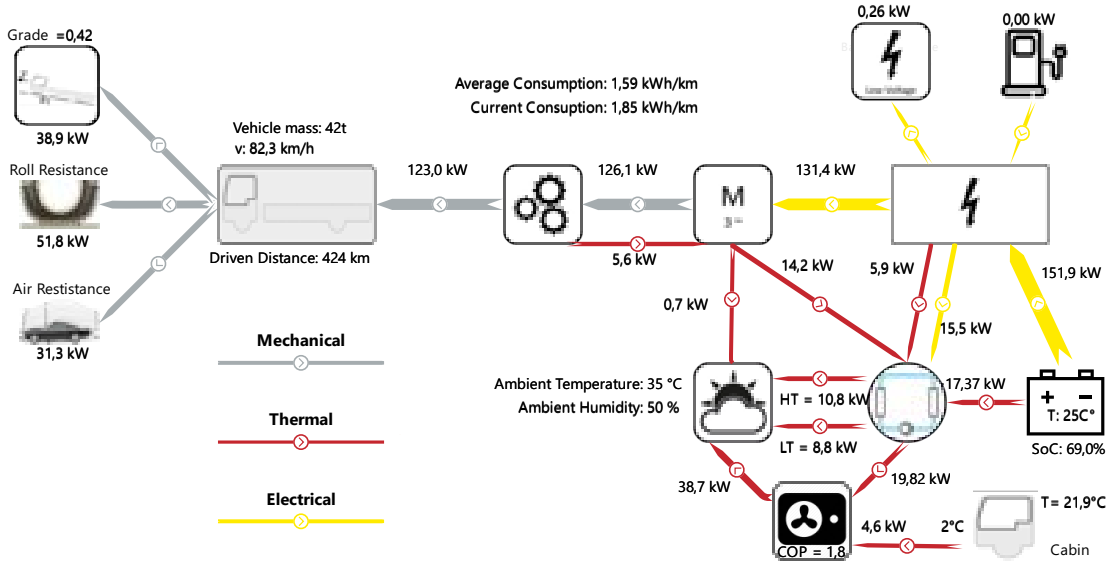

Figure 5: Energy flow diagram showing the mechanical, electrical and thermal power flows and additional information about the vehicle state an hour after fast charging in the Hanover-Munich cycle.

a slight grade. Efficiencies of sub models (e.g. gears) can be observed from the different powers displayed at each side of the component. Thermal and mechanical inertia of the components are included. The battery rejects 17.37 kW of heat to the cooling system. Heat is released to the cooling cycle and a small portion directly to the environment by the LT-Cooler and partly to RHP. Cabin cooling is also performed through RHP on a lower temperature level.

5.1. Model Plausibility Check

We checked the plausibility of our heavy-duty truck model by comparing it to test data available for the *Volvo FH Electric* [10], which is a battery-electric truck of the same class as the one that was modelled. The real world test of the Volvo truck resulted in an average energy consumption of 1.1 $\frac{kWh}{km}$ for a 338 km route with a diverse topography in Southern Germany [10]. We took the same route and chose a summer scenario with an ambient temperature of 28°C to investigate the modelled truck. Cabin cooling is performed to keep the cabin at 22°C. Our simulation resulted in an average energy consumption of 1.33 $\frac{kWh}{km}$. The 21% difference in the results can possibly be attributed to differences in the energy consumption for air conditioning, the truck's weight or slightly different roll and air resistances.

5.2. Influence of Thermal Management Operation Strategy for Summer Scenario

In Figure 6, the comparison of battery degradation, represented as the change in SoH and battery temperature for the Hanover-Munich trip in summer is shown for both operation strategies (see section 4.). The degradation is reduced by 40% when applying the **minimum battery degradation** operating strategy compared to the

minimum energy consumption strategy. On the other hand, at the beginning of fast charging at a time of 5 hours, 2.3% percent of SoC or 9 kWh of energy is saved for **minimum energy consumption** operating strategy.

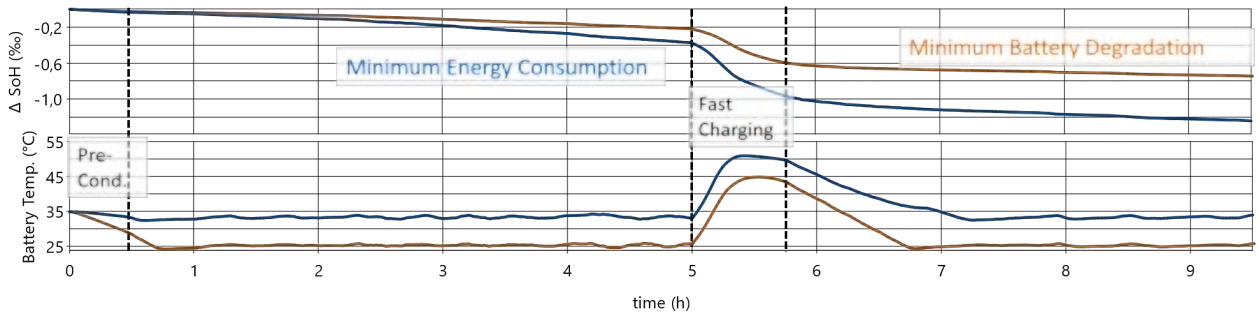

Figure 6: SoH degradation and battery temperature for a Hanover-Munich long distance day trip on challenging topology and two operation strategies: **minimum battery degradation** (orange) and **minimum energy consumption** (blue). Battery degradation is reduced by 40% using the **minimum battery degradation** operating strategy.

This investigation underlines the trade-off between energy consumption for thermal conditioning of batteries and battery degradation. Because only small energy savings are achieved with the **minimum energy consumption** strategy compared to the driving energy but large difference in battery degradation is observed using the **minimum battery degradation** strategy. Preference should be given to battery cooling to limit degradation.

5.3. Influence of Fast Charging Strategies on Long Distance Trips

We investigate the influence of fast charging on battery degradation incorporated in a long distance trip (see Figure 4.To do this we lenghtend the charging break from 45 minutes to 60 minutes and reduced the associated charging power by 25%. Figure 7 illustrates the differences in battery degradation for the two fast charging times over the whole two day trip.

First, this investigation shows the enormous influence of fast charging operation on battery life, which can be seen by comparing the blue and orange curves in Fig. 7. It can be seen that battery degradation during charging is significantly higher than while driving. This results from the larger currents that occur during fast charging compared to the discharging currents drawn from the battery while driving. Also the battery is facing those higher currents at higher temperature levels which is another crucial factor for the degradation.

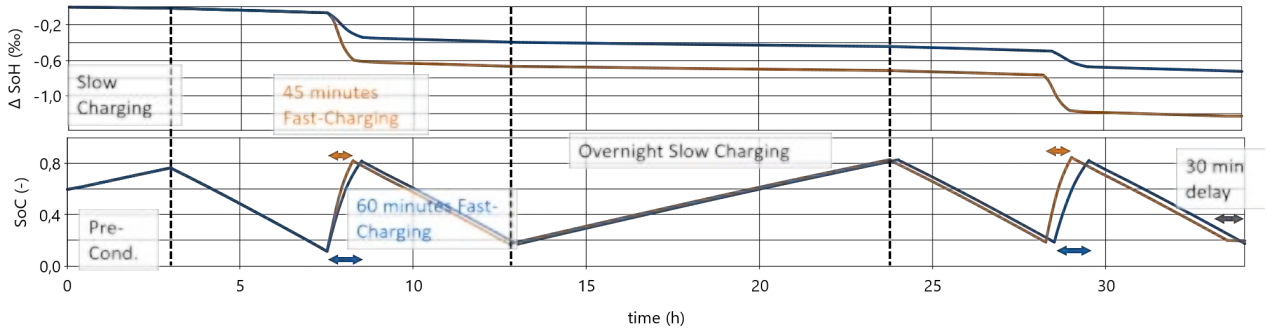

Figure 7: SoH degradation and SoC over a two-day long distance trip with two operating strategies for daily fast charging: 45 minute charging breaks (orange), extended 1 hour charging breaks (blue). Significant reductions (42%) in battery degradation are seen for longer charging breaks.

Second, Fig. 7 shows the effect of lengthening charging breaks by 15 minutes and at the same time reducing charging power on battery degradation. By extending the break time by 15 minutes, resulting in an additional 30 minutes beeing needed for the two-day trip, the battery degradation can be reduced by 42%. Further elaboration is recommended to analyze the economical trade-off between battery degradation and depreciation and delivery time. The preliminary discussed goals of fast charging time and battery degradation conflict strongly.

The results of this investigation enable us to approximate the total battery lifetime expectancy. Driving the two-

day long distance trip, the battery looses 0.07% of its state of health when taking 60 minute charging breaks. By extrapolating the result down to a SoH of 80%, a battery lifetime of 287 drive cycles or 437.000 *km* is approximated. Considering the result for the same drive cycle but using 45 minutes charging breaks a lifetime range of only 245.000 *km* can be achieved. This result confirms that battery change could be necessary during the lifetime of the truck, particularly if fast charging is performed regularly. A separate depreciation of the battery and other components is suggested, and battery degradation should be considered in logistics operation strategies.

5.4. Influence of Terrain on Battery Degradation

To asses the influence of terrain, we compare the Hanover-Munich trip (Fig. 6) to the long distance trip (Fig. 7) for total trip battery degradation. Although the long-distance trip is more than 2.42 times longer than the Hanover-Munich trip, the battery degradation is similar. This directly translates to a higher degradation per unit distance driven for the Hanover-Munich cycle. The effect can be explained by the challenging terrain of the Hanover-Munich cycle that results in much higher discharging C-Rates for hill climbing and recuperation when going downhill. When combined, these effects lead to a higher total number of battery charging and discharging cycles.

5.5. Influence of Battery Aging on Long-Distance Feasibility

To assess the impact of battery aging, we compare previous results for the Hanover-Munich trip for the summer scenario with the same conditions and an already degraded battery. Figure 8 shows a comparison of SoCs against the driving time for a new battery and a degraded battery with a SoH of 0.9. Due to the degradation, not only is the total battery capacity decreased, but the internal resistances are also increased, resulting in more irreversible heat production during charging and discharging. This puts an additional load on the cooling system. The truck reaches the fast charging stop with an SoC of 0.09 instead of 0.19 for a new battery. More intense fast charging needs to be performed, or the charging break needs to be extended, if the truck is required to cover the remaining drive cycle without another stop.

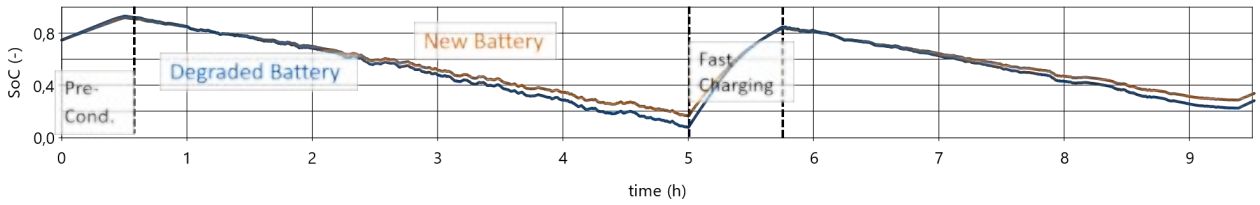

Figure 8: SoC over Hanover-Munich long distance day trip compared for new (orange) and degraded (SoH = 0.9, blue) battery. Less driving range and more intense fast charging result, for the degraded battery.

Our investigations indicate that the loss of battery capacity due to degradation should be taken into account when choosing an appropriate size of battery system for the given operational and range requirements of the vehicle. This again highlights the importance of appropriate thermal management operation strategies to reduce battery degradation.

5.6. Influence of Pre-Conditioning in Winter Scenario

For a one-day long distance trip we compare the influence of pre-heating in a winter scenario at $-5°C$ ambient temperature. After pre-conditioning the battery is heated using waste heat from the motor and electronics as well as its own produced heat.

From figure 9 it can be observed that in a winter scenario battery heating in the pre-conditioning phase can reduce battery degradation significantly. A battery heated to $10°C$ instead of $0°C$ through pre-conditioning reduces battery degradation caused in the first hours of the driving cycle by 33%. Pre-heating the battery up to $20°C$ (which takes more than one hour) does not reduce battery degradation much further. It is demonstrated that operating at low battery temperatures results in accelerated degradation. Battery heating before driving is strongly recommended in winter scenarios. A heat pump is suggested for this purpose to improve energy efficiency.

5.7. Overnight Charging in Winter Scenario

The energy consumption of the three different operation strategies for thermal management for an overnight cabin heating and simultaneous battery charging are displayed in table 2.

The results show, that a heat pump can reduce energy consumption for cabin heating significantly. For 8 hours of overnight cabin heating at an ambient temperature level of $-5°C$, 11.1 kWh of energy are saved using an air-air heat pump instead of an electric heater. Futher saving can be realized by employing the RHP

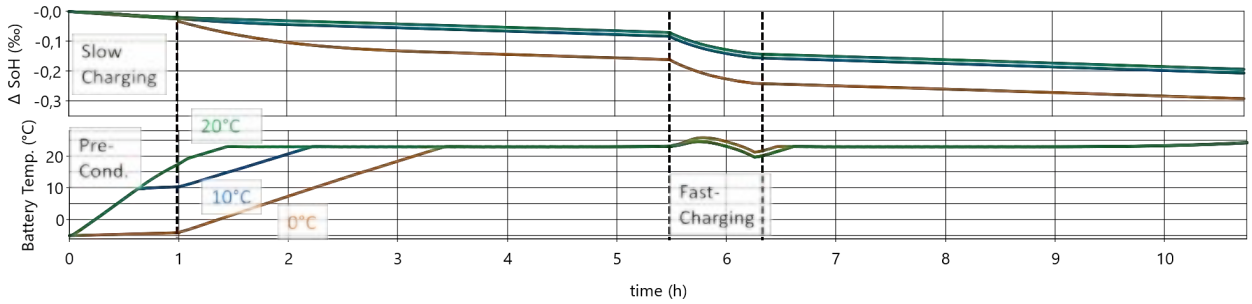

Figure 9: Influence of battery pre-conditioning (with RHP) before driving in a winter scenario with an ambient temperature of -5°*C*. Comparison on battery degradation and battery temperature. Target temperatures for battery heating while pre-conditioning is active: 0°*C* (orange), 10°*C* (blue), 20°*C* (green).

Table 2: Electric energy consumption of different cabin conservation air conditioning thermal management strategies (see section 4.) during overnight charging in winter scenarios.

Water-Air Heat Pump	Air-Air Heat Pump	Electric Heater
2 kWh	3.9 kWh	15 kWh

(see figure 2) as an water-air heat pump during overnight charging. The electrical energy consumption could be halved again for this operation strategy. When using the water-air heat pump only the *battery HX* and *gascooler* transfer heat. During overnight slow-charging the battery waste heat is efficiently used as RHP heat source. Depending on the chosen charging speed, the current SoC, the SoH of the battery and the ambient temperature the waste heat approximately covers the required heat for RHP. If the predicted demand of heat to keep the cabin temperatured exceeds the amount of available waste heat of the battery, that is produced while charging the battery, the battery could also be used as a thermal capacity. Therefore, battery operating temperature could be increased during the last hours of operation before overnight break in order to have a higher temperature level of the RHP heat source. After that battery temperature could slowly be decreased overnight using battery as heat source for RHP.

6. Conclusions and Outlook

In our study, we demonstrated that a physics-based full-vehicle model of a battery-electric truck is suitable to accurately predict the consumption of electrical energy in a benchmark scenario. Using the full-vehicle model, the effect of fast charging on the state-of-health of the battery was explored using real-world deployment scenarios. It was found that fast charging stops have an important impact on the achievable life time of a battery electric truck.

Our study also compared different operating strategies for summer and winter scenarios. Fast-charging breaks along with legally required minimum break time leads to accelerated battery degradation. A slight extension of charging times and associated lower charging currents lead to significantly less battery degradation and thus much less depreciation on the battery (truck). Prioritizing minimum battery degradation over minimum energy consumption as thermal management operating strategy leads to significant reduction in battery degradation.

Furthermore, our investigations showed how a challenging hilly terrain influences battery degradation due to high discharge currents while driving uphill and high charging currents for recuperating while driving downhill. In this context we exemplary contrasted the remaining capacity when reaching predefined charging stops of a pristine and a degraded battery to evaluate the long-distance feasibility over lifetime. The results showed that especially for long-haul trucks the battery size should be designed anticipating degradation due to aging. For the investigated winter scenario we showed the positive effect of pre-heating the battery before driving. Pre-heating lowers degradation significantly. For battery and cabin heating a heat pump is recommended due to energy efficiency. For overnight heating operation the heat pump is used as well. Battery waste heat while slow charging can be used as a heat source for an efficient heat pump.

Looking to the future, solid state batteries are a promising development in battery technology. It is predicted that they will require a higher temperature level for operation [16]. For long distances and driving times of heavy-duty trucks, as well as route planning and pre-conditioning times, solid-state batteries are especially suitable for trucks. Adjusted thermal management systems are needed with solid state batteries. There is a special need for heating technologies and battery pre-conditioning. Due to its modular structure, our model is well suited for such investigations in the future.

Acknowledgments

As this work was funded under grants AUTO-GEN (01IS20086B) and PHYMOS (19I20022I), the authors would like to thank the German Federal Ministry of Education and Research and the German Federal Ministry of Economic Affairs and Climate Action for their financial support.

References

[1] Camacho, María de las Nieves, D. Jurburg, and M. Tanco, "Hydrogen fuel cell heavy-duty trucks: Review of main research topics," International Journal of Hydrogen Energy, vol. 47, no. 68, pp. 29505–29525, 2022, https://doi.org/10.1016/j.ijhydene.2022.06.271.

[2] Wagenblast, M., Pollak, M., Trägner, J., Heinke, S., Tegethoff, W., Köhler, J., Swoboda, J.,*Design and Analysis of a Spray Cooling System for a Heavy-Duty Fuel Cell Truck*. SAE Technical Papers 2022 2022-01-5054 https://doi.org/10.4271/2022-01-5054

[3] Cullen, D. and Neyerlin, K.C. and Ahluwalia, R. and Mukundan, R. and More, K. L. and Borup, R. L. and Weber, A. and Myers, D. and Kusoglu, A.,*New roads and challenges for fuel cells in heavy-duty transportation*. Nature energy 2021;6:462–474.

[4] S. Pardhi, S. Chakraborty, D.-D. Tran, M. El Baghdadi, S. Wilkins, and O. Hegazy, "A Review of Fuel Cell Powertrains for Long-Haul Heavy-Duty Vehicles: Technology, Hydrogen, Energy and Thermal Management Solutions," Energies, vol. 15, no. 24, p. 9557, 2022, https://doi.org/10.3390/en15249557.

[5] NOW GmbH, Nationale Organisation Wasserstoff- und Brennstoffzellentechnologie, "Marktentwicklung klimafreundlicher Technologien im schweren Straßengüterverkehr: Auswertung der Cleanroom-Gespräche 2022 mit Nutzfahrzeugherstellern," 2023.

[6] IEA, Electric car registrations and sales share in selected countries, 2016-2021;Charts – Data & Statistics - IEA. [Online]. Available: https://www.iea.org/data-and-statistics/charts/electric-car-registrations-and-sales-share-in-selected-countries-2016-2021 (accessed: Feb. 24 2023).

[7] S. Bhardwaj and H. Mostofi, "Technical and Business Aspects of Battery Electric Trucks—A Systematic Review," Future Transportation, vol. 2, no. 2, pp. 382–401, 2022, https://doi.org/10.3390/futuretransp2020021.

[8] M. Muratori et al., "The rise of electric vehicles—2020 status and future expectations," Prog. Energy, vol. 3, no. 2, p. 22002, 2021, https://doi.org/10.1088/2516-1083/be0ad.

[9] W. Shoman, S. Yeh, F. Sprei, P. Plötz, and D. Speth, "Public charging requirements for battery electric long-haul trucks in Europe: A trip chain approach," 2023.

[10] Volvo FH Electric — Testbericht Trucker 2022-01. [Online]. Available: https://brochures.volvotrucks.com/de/volvo-trucks/testberichte/2022/volvo-fh-electric-testbericht-trucker-2022-01/?page=10 (accessed: Feb. 24 2023).

[11] F. Verbruggen, V. Rangarajan, and T. Hofman, "Powertrain design optimization for a battery electric heavy-duty truck," in 2019 American Control Conference (ACC), Philadelphia, PA, USA, 2019, pp. 1488–1493, https://doi.org/10.23919/ACC.2019.8814771.

[12] B. Nykvist and O. Olsson, "The feasibility of heavy battery electric trucks," Joule, vol. 5, no. 4, pp. 901–913, 2021, https://doi.org/10.1016/j.joule.2021.03.007.

[13] A. Ramesh Babu, J. Andric, B. Minovski, and S. Sebben, "System-Level Modeling and Thermal Simulations of Large Battery Packs for Electric Trucks," Energies, vol. 14, no. 16, p. 4796, 2021, https://doi.org/10.3390/en14164796.

[14] A. Ramesh Babu, B. Minovski, and S. Sebben, "Thermal encapsulation of large battery packs for electric vehicles operating in cold climate," Applied Thermal Engineering, vol. 212, p. 118548, 2022, https://doi.org/10.1016/j.applthermaleng.2022.118548.

[15] L. Leicht, "Mercedes E-Actros Long Haul," 18 Sep., 2022. https://www.auto-motor-und-sport.de/elektroauto/mercedes-e-actros-long-haul-elektro-lkw-fuer-den-fernverkehr/(accessed: Mar. 2 2023).

[16] R. Hughes and C. Vagg, “Assessing the Feasibility of a Cold Start Procedure for Solid State Batteries in Automotive Applications,” Batteries, vol. 8, no. 2, p. 13, 2022, https://doi.org/10.3390/batteries8020013.

[17] F. Liu, M. Li, B. Han, J. Guo, and Y. Xu, “Research on integrated thermal management system for electric vehicle,” Proceedings of the Institution of Mechanical Engineers, Part D: Journal of Automobile Engineering, 2022, https://doi.org/10.1177/09544070221114677.

[18] Wang, J. ; Purewal, J. ; Liu, P. ; Hicks-Garner, J. ; Soukazian, S.; Sherman, E. ; Sorenson, A. ; Vu, L. ; Tataria, H.; Verbrugge, M. W.: *Degradation of lithium ion batteries employing graphite negatives and nickel–cobalt–manganese oxide + spinel manganese oxide positives: Part 1, aging mechanisms and life estimation*. Journal of Power Sources 269 (2014), 937–948. https://doi.org/10.1016/j.jpowsour.2014.07.030.

[19] X. Zhang, Z. Li, L. Luo, Y. Fan, and Z. Du, “A review on thermal management of lithium-ion batteries for electric vehicles,” Energy, vol. 238, p. 121652, 2022, https://doi.org/10.1016/j.energy.2021.121652.

[20] A. K. Thakur et al., “Critical Review on Internal and External Battery Thermal Management Systems for Fast Charging Applications,” Advanced Energy Materials, p. 2202944, 2022, https://doi.org/10.1002/aenm.202202944.

[21] V. Mali, R. Saxena, K. Kumar, A. Kalam, and B. Tripathi, “Review on battery thermal management systems for energy-efficient electric vehicles,” Renewable and Sustainable Energy Reviews, vol. 151, p. 111611, 2021, https://doi:10.1016/j.rser.2021.111611..

[22] Hellmuth, J., Steeb, M., Tegethoff, W., Köhler, J.: Thermische Simulation im Gesamtfahrzeugkontext. Werkstoffsymposium 2022, Wolfsburg, 17.-18. Mai 2022.

[23] P. Chakraborty et al., “Addressing the range anxiety of battery electric vehicles with charging en route,” Sci Rep, vol. 12, no. 1, p. 5588, 2022, https://doi.org/10.1038/s41598-022-08942-2.

[24] Basma, Hussein, Rodríguez, Felipe, “Long-haul battery-electric trucks in Europe,” icct, The International Council Of Clean Transportation, Berlin, Feb. 2022.

[25] TLK-Thermo GmbH: TIL Suite Simulates thermal systems. https://www.tlk-thermo.com/index.php/en/software/til-suite [accessed 27.02.2023]

[26] Steeb, M.; Flieger, B.; Tegethoff, W.; Köhler, J.: *Avoiding Thermal Hotspots in Automotive Battery Systems using a Multiscale Full Vehicle Model*. 16th Symposium on Modeling and Experimental Validation of Electrochemical Energy Technologies, Braunschweig, 12.-13. March 2019.

[27] Veth, C.; Dragicevic, D.; Pfister, R.; Arakkan, S.; Merten, C. (2014b): 3D Electro-Thermal Model Approach for the Prediction of Internal State Values in Large-Format Lithium Ion Cells and Its Validation. In: J. Electrochem. Soc. 161 (14), A1943-A1952. https://doi.org/10.1149/2.1201412jes.

[28] D. Bernardi, E. Pawlikowski, and J. Newman, “A General Energy Balance for Battery Systems,” J. Electrochem. Soc., vol. 132, no. 1, pp. 5–12, 1985, https://doi.org/10.1149/1.2113792.

[29] X. Jia, C. Zhang, L. Wang, W. Zhang, and L. Zhang, “Modification of Cycle Life Model for Normal Aging Trajectory Prediction of Lithium-Ion Batteries at Different Temperatures and Discharge Current Rates,” World Electric Vehicle Journal, vol. 13, no. 4, p. 59, 2022, https://doi.org/10.3390/wevj13040059.

[30] Kaiser, C.: *Untersuchungen zur Effizienz- und Leistungssteigerung von Omnibusklimaanlagen*. Dissertation, Technische Universität Braunschweig, 2020 https://leopard.tu-braunschweig.de/receive/dbbs_mods_00068696?q=christian%20kaiser.

[31] Your Europe, EU rules for working in road transport - Your Europe. [Online]. Available: https://europa.eu/youreurope/citizens/work/work-abroad/rules-working-road-transport/index_en.htm (accessed: Feb. 22 2023).

Analysis of Sodium Water Reaction as heat source for district heating and cooling

Alberto Abánades Velasco[a], Ángel Jiménez Álvaro[b], and Juan Guerrero Padrón[c]

[a] *Universidad Politécnica de Madrid, Madrid, Spain, alberto.abanades@upm.es*
[b] *Universidad Politécnica de Madrid, Madrid, Spain, a.jimenez@upm.es*
[c] *IDACOVERTRUCK, Madrid, Spain, jguerrero@idacovertruck.com*

Abstract:
Finding new alternatives to current energy systems is a need to develop disruptive solutions. In this case, a complete new approach the Sodium as energy resource is described. Tradicionally, Sodium has been considered a risky element even if it were proposed as coolant in many applications, as nuclear or solar thermal plants. Such applications has been concerned by the explosive reaction of alkali as Na with water. In this communication, we analysed the altenative of profiting of such highly exothermic reaction for an energy use. Previuosly , we analised the utilization of sodium as propellant, and next steps presented in this paper shows the proposal of a sodium-water based heater to feed heating and cooling networks. A tentative configuration for the design of such heater, and the heat exchangers to adapt heated water temperatures will be presented. We present the conceptual design of a 13.5 MW district heating plant for a $\Delta T = 10^oC$ heating water from 60 to 70 ^{o}C, consuming 1 kg/s Sodium, reaching an efficiency of 95%, comparable with existing boilers..

Keywords:
Sodium-Water reaction, District Heating

1. Introduction

The energy sector is facing the need of a systemic transformation to reduce as much as possible the carbon dioxide content in the atmosphere, increasing the circularity of all the energy and industrial processes , as well as fulfilling the global energy demand. Current tendencies to improve the sustainaiblity of the energy system into the framework of the energy transition are based on the massive deployment of renewable primary energy sorces, the implementation of high capacity storage systems to manage intermitent generation of such sources. In addition, some authors consider nuclear energy [1] to support that high penetration of renewables to achieve zero-emissions targets. Additionally, even if fossil resources are expected to be axhausted at any time in the future, they would be able to contribute to decarbonise the energy system during such energy transition by the utilization of carbon captire and sequestration (CCS) technologies [2], as well as hydrocarbon pyrolysis [3].

Solutions for a decarbonised energy transition my be provided for electric and themal energy uses, either for industry or for heating/cooling application. Current solutions based on batteries, hydrogen or incremental developments of emerging, existing technologies, may have some limitations to provide a suitable scheme that would allow to comply with the maximun environmental targets. This could be specially critical for a complex system as it is the energy system itself, that should increase significatively its integration into circular processes coupling with other sectors. To increase the chance to achieve the required environmental targets seems necessay to analyze disruptive alternatives that can be added to the options that are currently available to increase the technological options to implement a sustainable energy system. Oxygen oxidation has generally been used as the fundamental form of enthalpy or chemical energy release, giving rise to combustion reactions. Another option is the use of water as an oxidizing element. One of the possibilities is the use of the sodium-water reaction, which responds to the exothermic balance expressed in 1:

$$Na + H_2O \longrightarrow NaOH + \frac{1}{2}H_2 \qquad \Delta H_0 = -141\frac{kJ}{mol_{Na}} = -6.13\frac{MJ}{kg_{Na}} \tag{1}$$

This reaction, when it occurs in excess of water, is followed by the dissolution of sodium hydroxide in water, which is also exothermic, and can offer, in the case of developing the reaction in a closed vessel, a practical heat generation of the order of 188 kJ/mol_{Na}(8.174MJ/kg_{Na}), The hydrogen produced recombines with oxygen that may be present in the reaction environment with an extra heat production, so that the total energy release

obtained in a total oxidation of Na to NaOH with water and oxygen and a subsequent dissolution of NaOH in water reaches 326.6 kJ/mol_{Na}(14.21MJ/kg_{Na}). In the case of developing an application that takes advantage of this energy, the final product would be a solution of solid hydroxide in water, which can be extracted in liquid form and continuously.

We have previously evaluated experimentally the sodium-water reaction in excess of water [5], qualifying its performance of sodium as candidate fuel for rocket propellant. Such works was one of the fist attempt to convert the inhetent risk associated to the use of sodium as coolant due to its high reactivity with water [6], to a potential valid decarbonised fuel. In this communication we analyse the application of such reaction to one of the most important sectors for the decarbonization of our Society. The residential sector accounts for a significant amount of CO_2 emissions due to the utilization of fossil fuels for climatization and heated water demand.

2. Sodium water reaction closed fuel cycle

The utilization of sodium as main fuel, combined with and oxydising agent as water, has as one of its primary source the common salt (NaCl). The extraction of sodium from sodium chloride, energy is needed according with the following electrochemical potential:

$$Na^+ + Cl^- \longrightarrow Na + \frac{1}{2}Cl_2 \qquad E_0 = -4,07V \tag{2}$$

The energy that is needed, for instance, in form of electricity may be calculated by electrolytic conversion with the following semi-reactions:

$$Cathode : Na^+ + e^- \longrightarrow Na \qquad E_0 = -2,71V \tag{3}$$

$$Anode : 2Cl^- \longrightarrow Cl_2 + 2e^- \qquad E_0 = -1.36V \tag{4}$$

The reaction enthalpy may be evaluated fromn the Gibbs energy of the reaction, which is calculated from the Faraday constant (F=96485 C/mol), and taking into account that one electron is needed for the formation of one Na molecule (23 g/mol) as:

$$\Delta G_0 = -n_e F E_0 = -96485 \cdot 4.07 \frac{J}{mol_{Na}} = 392.6 \frac{kJ}{mol_{Na}} = 17 \frac{MJ}{kg_{Na}} \tag{5}$$

The total enthalpy or enegy requirements for the dissociation of sodium clodride has to add the energy to heat it up to the fusion temperature and meld the compound, according to:

$$\Delta H = \Delta G_0 + C_{p,NaCl} \cdot (T_{f,NaCl} - T_a) + h_{fg,NaCl} = 17 + 1.9 + 0.32 \frac{MJ}{kg_{Na}} \approx 19.2 \frac{MJ}{kg_{Na}} \tag{6}$$

This number may be compared with the total amount of energy that is produced by the sodium water reaction (equation 1), what gives an overall potencial energy efficiency of the conversion of primary energy into heat of 73 % in the case of extracting Na from sodium chloride. Obviously, this figure is the maximum thermodynamic efficiency, that will be reduced by the losses of the electrochemical arrangement for Na synthesis, as well as the heat efficiency of the sodium-water reactor.

The utilization os NaCl as input raw material for the generation of the sodium reactant may be replaced by the recovery of sodium from the sodium hidroxide product of the raction. In this case, the redox reactions are:

$$Na^+ + OH^- \longrightarrow Na + \frac{1}{2}H_2O + \frac{1}{4}O_2 \qquad E_0 = -3,11V \tag{7}$$

In this case, the amount of electrons (n_e) involves in the redox semireaction is 4, leading to a minimum potential energy demand of 8.2 MJ/kg_{NaOH}, that is a net energy demand for the recovery of sodium of 14 MJ/kg_{Na}. The efficiency of the NaOH/Na cycling depends only on its irreversibilities and the efficiency of the electrochemical and heat management equipment.

The energy needed to run both sodium synthesis processes is intended to be provided by low-carbon electricity, as wind, solar FV or nuclear.

3. Sustainability of the Sodium Water Reaction

One of the most important aspects related to the utilization of any energy source is the evaliation of its sustainability, what includes concepts as environmental impact, resources availability and circularity. The evaluation of the alternative of the sodium-water reaction, as a possible alternative to combustion in the context of the decarbonization of the energy system, can be analyzed based on sustainability criteria, and the comprison with the use of fossil resources today and some other alternatives. Among these generic characteristics for the evaluation of an energy source are:

- Greenhouse gases emissions related to its use as energy source.
- Circularity potential.
- Abundance and availability of primary resources.
- Energy density.

3.1. Environmental impact and circularity

The decarbonization of the energy system requires the development and implementation use of technologies with zero or very low emissions of greenhouse gases, such as methane or carbon dioxide, and to a lesser extent, water vapor or other triatomic molecules. As described, the sodium-water reaction has as its final product sodium hydroxide (NaOH) dissolved in water. Being a set of reactions that are not related to carbon chemistry, there is no recombination with oxygen to form CO or CO_2. It can be said that it is a high exergy thermal power generation without greenhouse gas emissions, which is compatible with applications in which fossil fuels such as natural gas are difficult to replace.

Regarding the potential for circularization, the result of the reaction is a solution of Na(OH) with water, which can be reintroduced into the reactor, increasing the hydroxide concentration. From a certain concentration after some recirculation cycles, after making the last thermal exchange, if it is allowed to cool in a open deposit, the NaOH crystallizes and precipitates [9]. The maximun concentration that may be reached depends on the process temperature, as seen in the NaOH/water system shown in figure 1. For instance, if operating at 25 ºC, NaOH concentration should not exceed 50 %.

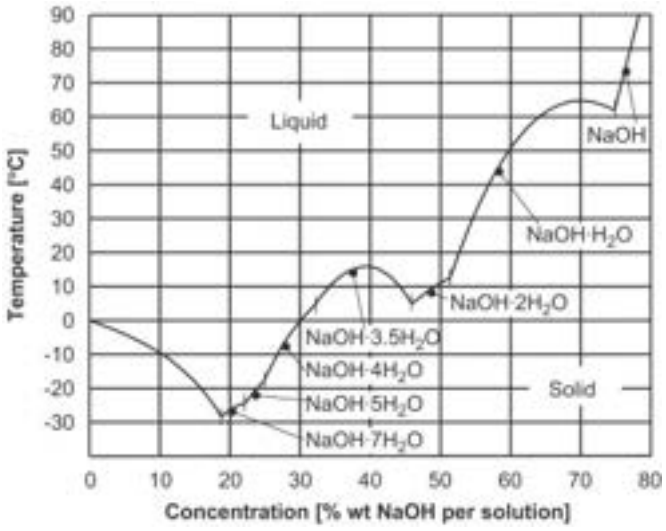

Figure 1: The NaOH–H2O system. Stability ranges of the different hydrates and the respective solidification lines [11]

3.2. Abundance of the primary source

Sodium is the sicth element in abundance accounting for 2.83 % of the Earth‘s crust [7]. That means that is far from being considered a risk from the geo-political point of view, being widely available. A list of the most abundant elements are listed in table 1. Sodiun is very reactive and it is not found as a single element. The most common sodium compound is sodium chloride. This very soluble salt has been leached into the oceans over the lifetime of the planet. Salt beds can be found where ancient seas have evaporated. It is also found in many minerals including cryolite, zeolite and sodalite.

The high availability of sodium compounds implies to fulfill one of the most important constraints for the sustainability of energy sources, that is the possibility to grant access to the resource to everyone.

Table 1: Element abundance on Earth [8]

Element	atomic number	% by weight
oxigen	8	46.60
silicon	14	27.72
aluminium	13	8.12
iron	25	5.00
calcium	20	3.63
sodium	11	2.83

3.3. Energy density

The development and application of the sodium water reaction convert sodium in an enegy vector, thjat could be compared with the rest of the vectors and storage techonology available. Suche comparison may be done in terms of energy density. The energy density of sodium has been evaluated as 14.2 MJ/kg_{Na} by mass or 13.8 GJ/m_3 by volumem in the case of adding the heat of the sodium-water reaction and the hydrogen oxidation, what is expected in excess of water. A comparison with other energy carriers is depicted in the table 2. All of the energy carriers that are considered now are based on liquid or gaseous substances. Sodium is a solid substance, what reduces energy lost during storage, enabling its use for long term storage.

From the point of view of the energy density, sodium is comparable in terms of volumetric capacity with other carriers as compressed natural gas, ammonia and liquid hydrogen. In any case, either compressed natural gas or different forms of hydrogen storage alternatives requires the implementation of criogenics or dedicated compression systems. Its performance is lower respect to liquid fuels, specially interms of energy per mass. Sodium as solid energy carrier is comparable with ammonia.

From this comparison, it can be assessed that sodium has energetic properties that are comparable with other energy vectors that are proposed as key for the implementation of a decarbonised energy system.

Table 2: Energy density of several energy carriers [10]

Carrier	Energy per mass (MJ/kg)	% Energy per volume (GJ/m^3)
Hydrogen (liquid)	143	10.1
Hydrogen compressed (700 bar)	143	5.6
Hydrogen at STP	143	0.0107
Natural gas (liquid)	53.6	22.2
Natural gas (250 bar)	53.6	9
Natural gas at STP	53.6	0.036
Methane at STP	55.6	0.0378
Gasoline	46.4	34.2
Diesel	45.4	34.6
Ammonia	18.6	11.5
Sodium	**14.2**	**13.8**

STP stands for Standard Temperature and Pressure (25 ºC, 1 bar)

4. Application to District Heating

I has been shown how the highly exothermic sodium-water reaction has certain potential to be integrated into the enegy system. Nevertheless, the reaction evolution should be controlled, as it has been done with combustion, to convert a reasonable reaction heat into a useful sevice. At this respect, district heating and cooling are one of the most important potential applications. Currently, the residential sector is the responsable of a very significant part of current CO_2 emissions in many countries, in many case above 50 % [4].

4.1. Process description

A full process that has been designed for the implementation of a district heating and cooling installation based on the sodium-water reaction is depicted in figure 2. The process is composed of the following functional circuits:

- Water feeding system (WFS).
- Sodium feeding system (SFS).

- Sodium-water reactor (SWR).
- Heat exchange to District Heating (HDH)
- Reactor outflow treatment system (ROTS).
- Air Purge System (APS).

The water feeding system (WFS) pumps water to the sodium water reactor. A pump controls the inflow of fresh running water to the process, that is mixed with pure water rejected by the osmotic separator of the reactor outflow treatment system (ROTS). The sodium feeding system (SFS) preheat sodium up to its liquid state (98 ºC) from the sodium inflow at room temperatura. It is composed by a preheater that melts sodium according to the inlet rate set up for the reactor. We have assumed in our design a sodium consumption of 1 kg/s as described in table 3. Such massflow is contolled by the reaction rate and volume of the sodium-water reactor (SWR). The basic parametes for the control of such reaction may be established by the experimental work already done for the characterization of the reaction in a fixed volume [5] and depicted in figure 3. Oor experimental work shows as the energy that is generated in the reactor is proportional to the amount of sodium that is present in the reaction chamber, with a low impact of the excess of water, or addicional material, as in this case is the remaining sodium hidroxide. As we intend to avoid water vaporization, the reactor should be pressurized.

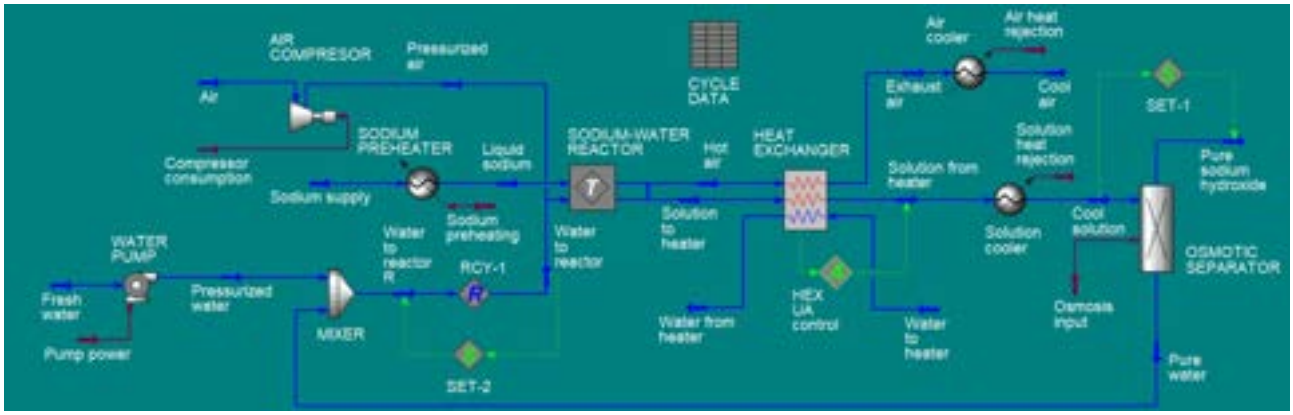

Figure 2: Process for the DHC application of the sodium-water reactor boiler including an osmotic separator for Na(OH)

The continuous reaction product stream passed to one leg of a heat exchanger of the HDH system to transfer the useful heat to the district heating loop. The service hear exchanger has an additional input from the air purge system (APS), which main purpose is to clean up the reactor stream from residual hydrogen that could remain in the reactor product stream. The air stream contributes to the total amount of heat transferred to the district loop, increasing efficiency.

The reactor outlet stream from the heat exchanger, composed by a sodium hydroxide solution in water is treated in the ROTS system to extract to extract pure Na (OH) and and water to be recirculated and mixed with running fresh water. The core of the reactor outflow treatment system is an osmotic separator that extract sodium hydroxide. Such separators are operating at low temperature [13] that is achieved by a cooler downstream the HDH. As an alternative, depending on the concentration of the solution, it can be solidified by lowering temperature. To improve the energy efficiency of the ROTS system, it i spossible to regenerate heat in the solution cooler exchanging energy between the pure water stream and the solution from the DHD. Such temperature reduction in the solution from water may happen with concentrations higher than 30 %. Such concentration may be achieved by the reduction of the pressure to enhance water vaporization of the mixture. For low concentration of Na(OH), the product stream can feed directly an electrolytis section to recover Na in case of the integration of a sodium recovery section. In that case, the facility will decouple electricity consumption from heat generation for the district heating, using sodium as storage.

4.2. Process data estimation

A conceptual analysis of the process that is proposed for the application of the sodium-water reaction to district heating (DH), that may be extended to dostrict cooling (DC) adapting the set-points of the control variables (mainly temperatures), has been modelled with UniSim R491 Suite [12]. From the previous discussion, we have analysed the substitution of the ROTS for a solution storage, that will increase the content of Na(OH) during operation. The simplified conceptuak process is depicted in fiigure 4 The size of the facility has been set to the processing of 1 kg/s of sodium, what is considered representative for a full scale district heating.

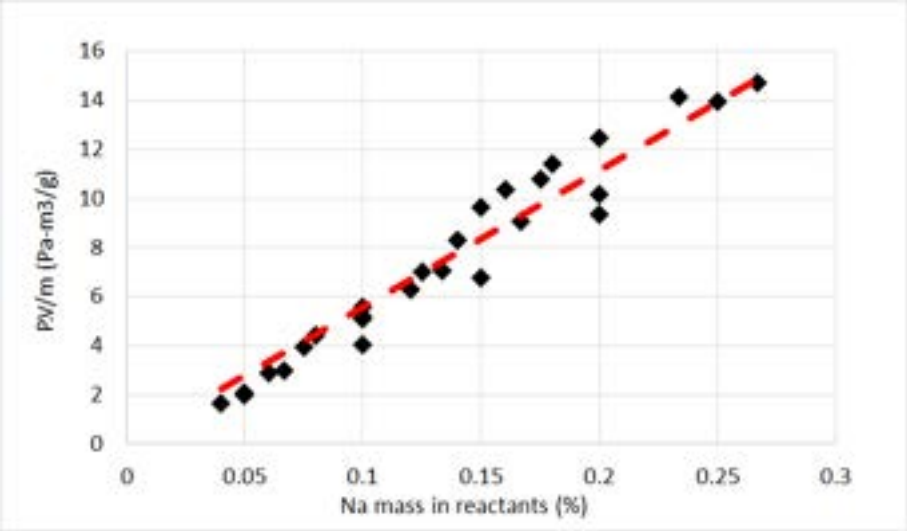

Figure 3: Normalised energy generation vs. Na in excess of water. [5]

Such sodium consumption corresponds to a heat plant of 13.5 MW. In this first analysys we have designed the service heat exchanger for district heating $\Delta T = 10^{o}C$ heating water from, 60 to 70 ^{o}C. In the case of the the application to district cooling, that may require higher temperatures, for instance, to drive absorption chillers, such service temperature may be upgraded by certain change in the set-points, as pressure and outlet temperature, of the reactor.

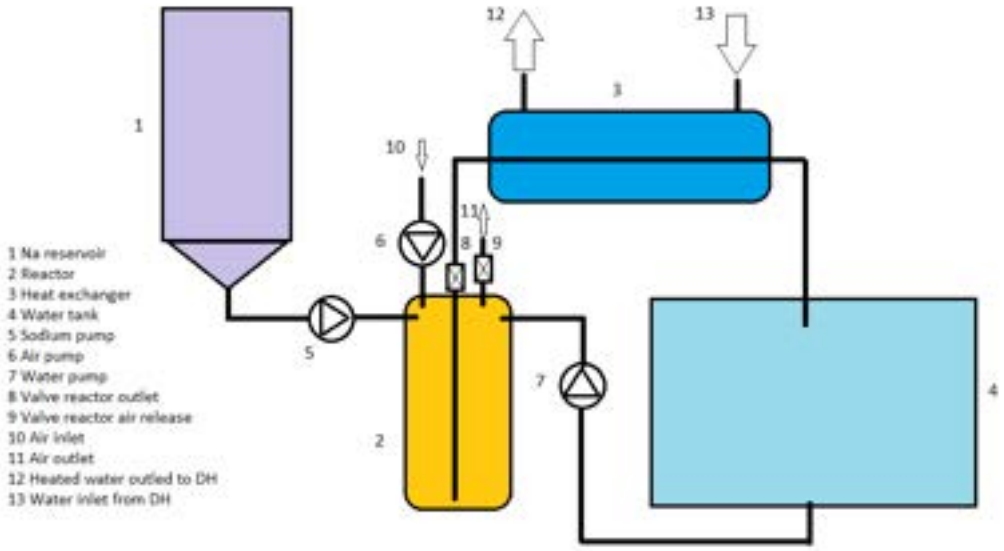

Figure 4: Conceptual design of a simplified process with Na(OH) solution recirculation

Pressure is one of the main parameters to avoid water vaporization from the reactor. The pressure into the reactor and the product and reactant loops will depend on the temperature that is intented to reach. In this case, we have fixed a pressure of 10 bar, providing a balanced between losses by water vaporization, compressor consumption and material requirements. For 10 bar, the outlet tempetature from the reactor has been set at 140 ºC, adjusting the reactants mass flow (water and sodium) to control the heat that is produced in the mixture. Water excess defined as the ratio of total water to the reactor respect to the stechiometric water of the reaction is 62. Water inyection allows the control of the temperature into the reactor preventing overheating.

The total efficiency of the facility is defined from the heat power to the district heating (Q_{DH}), the total heating value of the complete oxidation of sodium (including hydrogen combustion, HV_{tot}) and the auxiliary electric consumption (compressor, pumps,) (P_{aux}):

$$\eta = \frac{Q_{DH}}{HV_{tot} + P_{aux}} = \frac{14093kW}{14206kW + 551kW} = 0.95 \quad (8)$$

The mass balance of the facility is descibed in table 3, with the temperature and pressure of each main stream. The main process data for the facility are sumarised in table 4.

Table 3: Main process mass balance datasheet

Stream	massflow (kg/s)	T (^{o}C)	P (bar)
Fresh water	0,8	15	1
Pure water from ROTS	50.1	80	10
Aire	1. 513	15	1
Water to reactor	50.9	78.92	10
Sodium supply	1	15	10
Liquid sodium	1	98	10
Solution to heater	51.9	140	10
Pure Na(OH)	1.75	80	10
Water to DH	335.1	70	1

Table 4: Main process energy balance datasheet

Equipment	Power (kW)	Specific consumption (Wh/kg$_{watertoDH}$)
Auxiliaries	550.3	0.047
Water pump	0.95	$8.2 \cdot 10^{-4}$
Heaters	6035	0.52
Heat power to DH (Q_{DH})	13540	-
Thermal losses APS	245.3	0.02

5. Conclusions

There is a need for disrupting technologies that could deiversify the available tools to tackle the enormeous challenge of the global climatic crisis. There is a general consensus about the need to shift from a fossil-based society to a more sustainable system that could be more integrated into the natural mass and energy balance of the Earth, reducing as much as possible the impact of the current human activity. That transformation should find alternatives to carry out succesfully such deep systemic changes. Some technologies are on the table. In paricular renewable based primary sources as wind and solar are having every year a more important role. Nevertheless, additional technologies are needed to complement and be added to those sources to solve some of theur limitations as management capacity, inttermitency and storage.

The utilization of sodium as energy vector has been scarcely developed. In this communication we have described how sodium may be considered as an energy vector, with storage capacity and potential of application to end users. In this case, we introduce a district heating (that may be extended to cooling) facility that provides heated water with a reasonable efficiency (95 %), comparable with existing boilers, with storage capacity if a sodium electrolytic section is added. In that case, a circular operation Na-Na(OH) will have a potential efficiency very similar with other Power-to-Heat or Power-to-Power storage technologies, as thermal storage, Carnot batteries [15] and better than electrolitic hydrogen (electrolyser-fuel cell combination, Power-to-Heat) [14]. Heat pumps offers as well a good solution to impove efficiency of district heating solutions depending on the ΔT that they should provide, with Coefficients of Performance (COP) between 3 and 5, but must add as well Power-to-Power energy storage to integrate energy management cost.

The description of the facility includes a definition of the process with its functional blocks, as well as the mass and energy balance, to process 1 kg/s of sodium, estimating the water excess that should be needed to keep the temperature and pressure conditions to reasonable thermal losses and auxiliary energy consumption.

Further work will apply a complete parametric analysys of the facility design to optimize efficiency and describe more in detail the facility to operate to use surplus renewable electricity production for heating delivery, adding management and storage capacity to decarbonised electric grid, and coupling electric and thermal networks. A lot of work should be done to evaluate the application of this technology to low/medium temperature applications as district heating, as well as high temperature application including thermal conversion to power.

Acknowledgments

This work does not received any funding, but it has been developed thanks to the effort of staff involved in the PhD program of sustainable energy, nuclear and renewable of the UPM, for the PhD thesis of Juan Guerrero Padrón.

Nomenclature

n_e: Electrons involved in the redox reaction.

E_0: Standard electrochemical potential (V)

G_0: Gibbs energy in standard conditions (MJ/kg)

$h_{fg,NaCl}$: Latent heat of NaCl

Q_{DH}: Heat power to the district heating (kW)

HV_{SWR}: Heating value of the reaction (kW)

Q_{aux}: Auxiliary heating power in the process (kW)

P_{aux}: Electric power consumption in the process. (kW)

WFS: Water feed system

SFS: Sodium feed system

SWR: Sodium-water reactor

HDH: Heat exchange to District Heating System

ROTS: Reactor outflow treatment system

APS: Air Purge System

References

[1] Marques, A. C., Junqueira, T. M. *European energy transition: Decomposing the performance of nuclear power*. Energy 2022; 245: 123244

[2] Singh, S. P., Ku, A. Y., Macdowell, N., Cao, C. *Profitability and the use of flexible CO2 capture and storage (CCS) in the transition to decarbonized electricity systems* . International Journal of Greenhouse Gas Control 2022; 120: 103767

[3] Weger, L., Abánades, A., Butler, T. *Methane cracking as a bridge technology to the hydrogen economy*. International Journal of Hydrogen Energy 2017; 42: 720-731

[4] Liu, L., Qu, J., Maraseni, T. N.; Niu, Y., Zeng, J.; Zhang, L., Xu, L. *Household CO2 Emissions: Current Status and Future Perspectives* . International Journal of Environmental Research and Public Health 2020; 17

[5] Guerrero, J., Gil, I., Navlet, J. J., López-Paniagua, I., Abánades, A. *Experimental Evaluation of Sodium-Water Reaction (SWR) as Propellant* . Propellants, Explosives, Pyrotechnics 2019; 44: 379-382

[6] Takata, T., Yamaguchi, A. *Numerical Approach to the Safety Evaluation of sodium-water Reaction*. Journal of Nuclear Science and Technology 2003; 40: 708-718

[7] Li, F., Wei, Z., Manthiram, A., Feng, Y., Ma, J., Mai, L. *Sodium-based batteries: from critical materials to battery systems* .J. Mater. Chem. A 2019; 7: 9406-9431

[8] Terrestrial abundance of elements. *Distribution of elements in Earth's crust (by weight)* Available at: `https://www.daviddarling.info/encyclopedia/E/elterr.html` [accessed 22.2.2023].

[9] Alvin G. Stern, AG. *Scalable, Self-Contained Sodium Metal Production Plant for a Hydrogen Fuel Clean Energy Cycle.*. In: Chapter 8 IntechOpen, 2017

[10] Mazloomi, K., Gomes, C. *Hydrogen as an energy carrier: Prospects and challenges* . Renewable and Sustainable Energy Reviews 2012; 16: 3024-3033

[11] *Gmehlin handbook of inorganic chemistry. Na. Natrium. Sodium (System-No. 21) 8th ed., Vol. 4, and System-No. 21, 8th ed., Main volum*. Berlin: Springer; 1964.

[12] *UniSim Design simulator basics. Reference Design*. London (Ontario) Honeywell; 2020.

[13] Stei, S., Bruno, J.C., Alberto Coronas, A., Fresnedo San Roman, M., and Ortiz, I. *Separation of Ammonia/Water/Sodium Hydroxide Mixtures Using Reverse Osmosis Membranes for Low Temperature Driven Absorption Chillers*. Ind. Eng. Chem. Res. 2008,;47: 10020–10026.

[14] Behabtu, H. A., Messagie, M., Coosemans, T., Berecibar, M., Anlay Fante, K., Kebede, A. A., Mierlo, J. V. *A Review of Energy Storage Technologies' Application Potentials in Renewable Energy Sources Grid Integration* . Sustainability 2020; 12.

[15] Vecchi, A., Knobloch, K., Liang, T., Kildahl, H., Sciacovelli, A., Engelbrecht, K.; Li, Y. , Ding, Y. *Carnot Battery development: A review on system performance, applications and commercial state-of-the-art* . Journal of Energy Storage 2022; 55: 105782

Method for building's thermal flexibility in a multi energy vector district

Mathieu Brugeron[b], Mathieu Vallée[b], Antoine Leconte[a], Aurélie Foucquier[a], Adrien Brun[a]

[a] *Université Grenoble Alpes, CEA, Liten, INES, DTS, 73375 Le Bourget du Lac, France, firstname.lastname@cea.fr*

[b] *Université Grenoble Alpes, CEA, Liten, INES, DTCH, 73375 Le Bourget du Lac, France, firstname.lastname@cea.fr*

Abstract:

This article describes thermal flexibility of building methods at a district level considering different level of details of building models, illustrated by a case study in a newly built district in Grenoble. Heat represents a huge part of final consumption (81% for the residential sector, 60% for the industry), so district heat networks represents a major action lever towards energy transition. In previous work, a mix thermal and electric architecture has been designed and described at district level. This architecture has been upgraded to simulate the thermal building flexibility and integrate model-predictive controllers. Therefore, this upgrade considers a tool for co-simulation between an optimization problem modeler and several simulation models (an electric model and a set of models for the thermal simulation). On the optimization side, we considered one to eight buildings to be flexible in the district, and assess the impact of its flexibility on the system. A refinement of their flexibility potential is one difficult key aspect of this study, considering a complex multi-vector MILP model. The calibration process has been developed in order to identify the optimization model of this flexible equivalent building. On the simulation side, the simulation models are divided into: the production, the heat network, the heat distribution at building level and the building.

Keywords:

Thermal Flexibility, Multi-vector energy, district scale, Co-simulation, MPC.

1. Introduction

In a context of climate change, research in the efficient energy management field have greatly improved.

Complexity in the energy network have raised by including more and more renewable energies at a local scale [1], a deeper coupling between different energy vectors [2] and a multiplicity of storage system [3]. Aiming a reduction of the carbon emission, building, especially residential building, represent a massive impact as a third of the global energy consumption and a quarter of the carbon emissions [4]. To tackle this factual state according to the energy context, researchers are currently studying a new approach considering the building as a flexible element in energy systems.

2. State of the art

Considering its thermal inertia, building can be a flexibility tool in the same way as Electrical Vehicles in the control strategy at district scale. Its impact grew by considering coupling network such as thermal-electrical coupling. In order to integrate flexibility of buildings, solutions such as cosimulation ([5], [7], [8]) or aggregation ([6], [8], [11], [12]) have been explored. The main issue is the complexity of the model that can be:

- Physical model, with different levels of complexity ([5], [6], [7], [10], [11], [12])
- Data-based model driven from physical simulation ([8], [9])

Considering the aggregated approach, despite solid results and processes, it seems lacking some level of fineness in the study of flexibility of each building at district scale. On the cosimulation side, a classic control is applied which have proven its robustness but is not perfectly adapted to flexibility.

Thus, in this article, we propose to study the impact of thermal flexibility of building at district scale, with an individual approach for building simulation. We enhance a cosimulation process including Model Predictive Control (MPC) [13] in the loop in order to take benefit from the flexibility approach.

First, we present the main tool and method included in the cosimulation approach carried by the cosimulation engine PEGASE. Then, we present the theoretical aspects of the multi-vector cosimulation via the thermal models, the electrical models and the Mixed Integer Linear Programing (MILP) model used to determine the

optimised control strategy. Finally, we present a use case based on a real district Cambridge in which we study the impact of thermal flexibility from none to ten building.

3. Tools and methods

In this section, we present the methods and tools used in our work.

This work focuses on the management of district energy systems providing electricity and heat (Domestic Hot Water DHW and Space Heating SH) through a coupling between electric and heat network including renewable energy and storage.

3.1. Multi-Energy Networks Case Study

To illustrate our approach, we use a district-scale multi-energy network case study presented in previous works ([13], [14], [15]). This case study is inspired from the Cambridge district, based in Grenoble: it takes into account the electric, space heating (SH) and domestic hot water (DHW) needs of the buildings, and the objective is to satisfy them is an optimal way using a combination of renewable energy sources, storage and district heat network and the power distribution grid. Table 1 recalls some of the energy systems considered. A more detailed description of the case study can be found especially in [15].

Table 1. List of the energy system considered in this work.

Production	Storage	Loads
Photovoltaic panels	Battery	Electric loads from building
Cogeneration	Thermal Energy Storage	Heat loads
Heat pumps	Fuel cells	DHW consumption
Solar panels	Electric Vehicles	
Gas Boiler		

In the current work, we especially study the impact of thermal flexibility at building level on the energy management at district level.

3.2. Co-simulation and Model-Predictive Control Approach

In order to account for the dynamic behaviour and complex control of such a multi-energy coupled system, we use a co-simulation and model-predictive control (MPC) approach. More precisely, we use the PEGASE tool [15] to couple an optimisation model with several dynamic simulation models it controls. Thanks to the cosimulation process, a complex multi-vector system at district scale can be scattered into several subsystems, for which specific software are chosen.

Figure 2 shows the overall process and presents the main components involved:

- A model of the electric distribution network (“Electric Model”), including photovoltaic (PV) production and electricity storage
- Three thermal models, for the District Heating production systems (“DHN Model”, standing for District Heating Network model), for the buildings (“Building Model”) and for the internal heat distribution in the building (“HDC Model”, standing for Heat Distribution Circuit).
- An optimisation model, based on the Mixed Integer Linear Programming (MILP) formalism (“MILP Problem Solver”)

All dynamic simulation models are encapsulated using the standard Functional Mock-up Interface. To perform the MPC process, the MILP problem is solved recursively with a rolling horizon, using a commercially available MILP solver (see [15] for details).

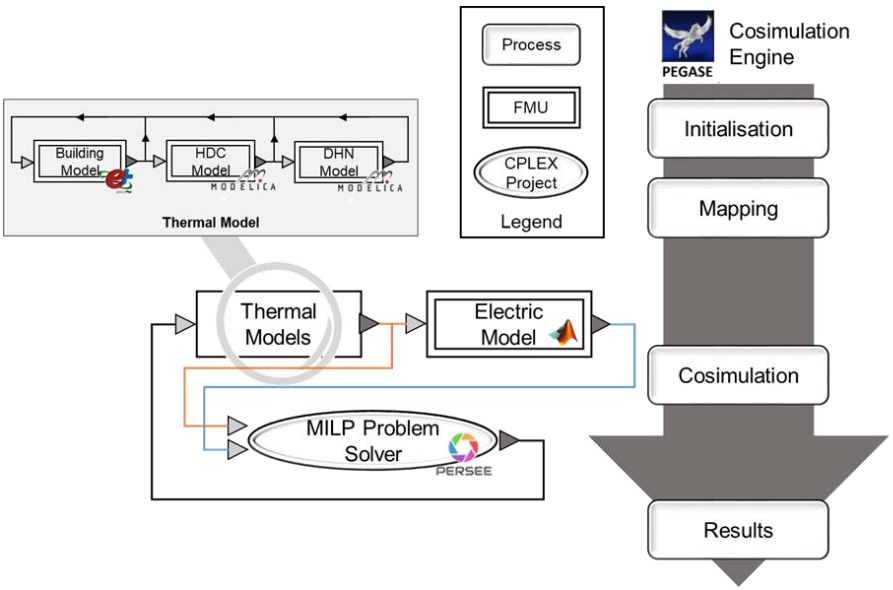

Figure 1. General principles of co-simulation driven multi-vector energy management. (Source: Authors)

3.3. Dynamic simulation models

This section describes more in details the dynamic simulation models used in the case study. It should be noted that these models are designed in a rather generic way, with parameters adapted to the case study. Also, the use of the co-simulation approach and FMI standard enables using the most adapted software to design each of them.

3.3.1. District-scale electric distribution network

This model is presented more in details in [14]. The electric network is scattered into subsystems such as:

- Building electric load using precalculated timeseries
- PV plants using solar irradiation and exterior temperature timeseries in order to provide their electricity production at each time step
- Electrical storage considering an electrochemical model and an inverter model
- Electrical grid consisting of a power balance of all components.

This model is implement using Matlab-Simulink [16] with a library of specific models dedicated to electric smart grid simulation.

3.3.2. District-scale heat production systems

Figure 2 from Rava et al. [14] describes the thermal model included into this work. This model is composed of four different type of energy systems:

- Controllable generators (P_i) such as cogeneration or heat pump
- Non-controllable generators (R_j) such as solar thermal field
- Storages (S_k) such as heat storage
- Load-tracking generator (LT) such as a gas boiler

In this model, the boundary conditions are the global heat set point imposed to generators by the controller (Q_{DHN}), and the inlet temperature (Tr_{DHN}) on the inlet side and the outlet temperature (Td_{DHN}). We consider a constant flow rate ($\dot{m}_{DHN}$)

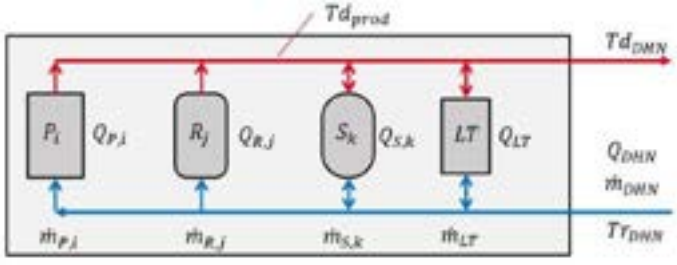

Figure 2. Schematic representation of the model of the thermal network production plant. (Source [14])

This model is implemented using Modelica [17], an object-oriented simulation tool that can simulate a various kind of thermo-dynamics simulation.

3.3.3. Buildings

Dynamic models are developed to represent several buildings of the district. Each building is considered as one thermal node. Given the footprint, the number of levels, the number of apartments and a global window area ratio of a building:

- The thermal zone is extruded from the footprint up to the total height of the building (3m by level)
- External surfaces are composed of layers with respect of typical thermal resistance values for French
- Building (typology LC24 in the PROFEEL project methodology)
    - Vertical surface : 5.3m².K/W;
    - Floor : 4.6m².K/W;
    - Ceiling : 6.5m².K/W;
- A global double glazing window is considered on each external surface with respect to the window ratio of the external surface;
- The 2012 French Thermal Regulation internal gains scenario, calculated according to the number of person in the building, is considered to reproduce the presence of inhabitants and their occupations;
- The air of the building is renewed considering air infiltration (1.2m3/h/m² @4Pa) and mechanical ventilation (0.3Vol/h).

Building simulations are carried out with the EnergyPlus software. EnergyPlus [17] is a validated and physicsbased Building Energy Simulation (BES) program used worldwide by researches, engineers and architects, and is developed by US Department of Energy. EnergyPlus building models are exported as FMUs using the energyplus-fmus export tool, considering the heat supplied by heat emitters as input, and the air, operative and ambient temperature as outputs.

3.3.4. Heat Distribution Circuit (HDC)

Since previous work [20] illustrated the impact of the thermal inertia of heat distribution circuits on flexible building control strategies, we included a detailed heat distribution circuit for each building in our simulation. Figure 3 represents the model of the secondary heat loop for each building.

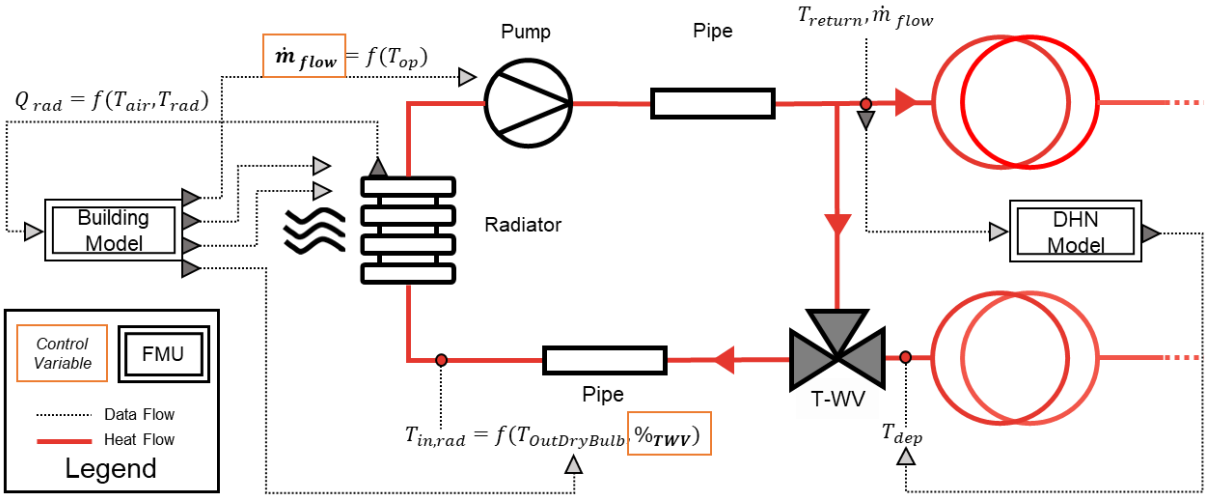

Figure 3. Schematic representation of the Heat Distribution Circuit model and its interaction with other models. (Source: Authors)

The model simulates the inertia of the distribution circuit and controls the building model temperature. It is composed of:

- A radiator providing heat to the thermal zone of the corresponding building (Q_{rad})
- A pump providing the proper flow rate (m_{flow}) to ensure the set point temperature
- A three-way valve (T_WV) used in order to control the input temperature of the radiator ($T_{in,rad}$) according to a heating law based on the outdoor temperature ($T_{OutDryBuld}$).
- Two pipes (after the valve and before the return loop) which simulate the inertia of the distribution circuit.

In addition, it takes into account the meta-control coming from the MILP model. Thus, a maximal value of heat is set to limit the heat provided to the building model according to the control strategy determine by the MILP model on the horizon.

3.4. Optimisation models for Model-Predictive Control

A Mixed Integer Linear Programming (MILP) model is used to compute an optimised strategy of control considering the overall multi-vector system. The MILP model is built using the in-house Persee software [20], which provides building blocks for multi-energy systems similarly to other tools, e.g. OmegAlpes [21].

3.4.1. MILP model for the Multi-energy networks

Figure 4 gives an overview of the MILP model of a multi-vector system based on previous work [15, 16].

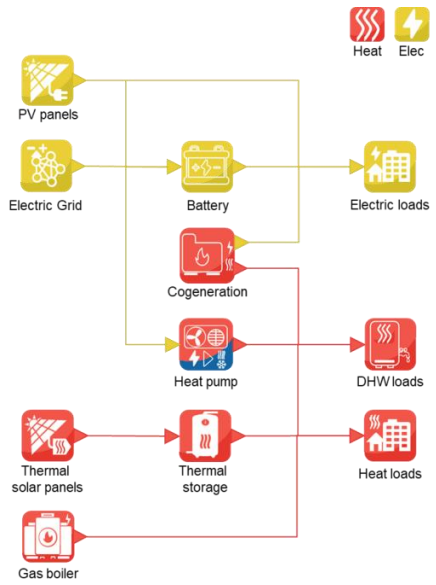

Figure 4. Design of an example of a complex multi-vector optimisation model at district scale. (Source: Authors)

The specificities of PERSEE enable the multi-vector modeling with complex system, including renewable energies. Using the model depicted by Figure 4 as an example, there are two energy vector:

- **Heat vector**
  - Production side
    - Thermal solar panels models: imposed thermal power injection into the system between min and max forecast time series
    - Gas boiler model: Thermal production from fuel gas into thermal
  - Storage side
    - Thermal storage: Storage model as a water tank considering energy power ○ Consumption side
    - Heat needs: imposed heat extraction from a pre-existing heat profile
    - DHW needs: imposed DHW extraction from a pre-existing DHW profile
- **Electric vector**
  - Production side
    - PV panels: imposed electrical power injection into the system, between min and max forecast time series
    - National electrical grid: computed flow injection or extraction to real or fictive grid
  - Storage side
    - Electro-chemical storage: batteries tank model with power map limitation
  - Consumption side
    - Electrical needs: imposed electric extraction from a pre-existing electric need profile
- **Coupling elements**
  - Heat pump: heat pump model consuming electricity to produce Heat and possible Cold
  - Cogeneration: thermal production from 3 input flows with optional electrical cogeneration

3.4.2. Flexible MILP model for flexible buildings

Figure 5 represents the building flexible MILP model implemented in PERSEE from previous work by Aoun et al. [22].

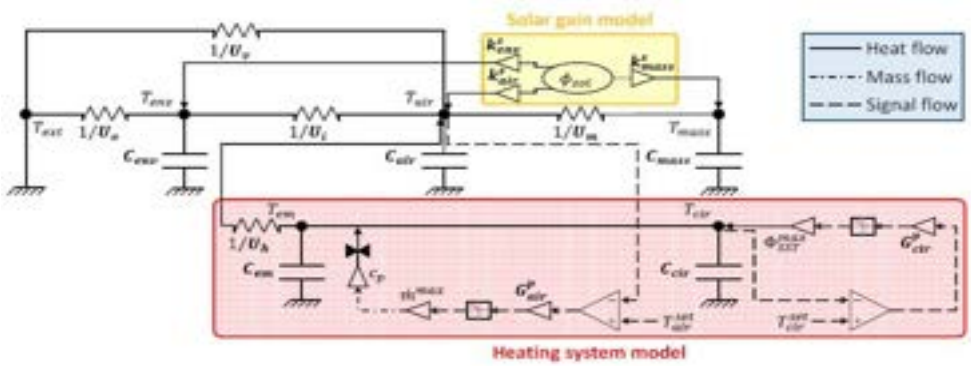

Figure 5. RC Model from which the building flexible MILP Model is inspired. (Source [24]) This model consists in the set of constraints and objective as follow (1):

$$min(dt^h.\sum_{t\in T}[c_T.\Phi_t + \Phi^{max}.c^{mean}.\Delta T_t + \lambda^{losses}.\Phi^{max}.c^{mean}.(T_t^{cir} - T_t^{air})])$$

$$\begin{cases} C^{air}.\frac{dT^{air}}{dt^s} = U_{air}^{ext}.(T_t^{ext} - T_t^{air}) + U_{air}^{env}.(T_t^{env} - T_t^{air}) + U_{air}^{mas}.(T_t^{mas} - T_t^{air}) + U_{air}^{em}.(T_t^{em} - T_t^{air}) + K_{air}.I_t^{sol} \\ C^{env}.\frac{dT^{env}}{dt^s} = U_{env}^{ext}.(T_t^{ext}(t) - T_t^{env}) + U_{air}^{env}.(T_t^{air} - T_t^{env}) + K_{env}.I_t^{sol} \\ C^{mas}.\frac{dT^{mas}}{dt^s} = U_{air}^{mass}.\left(T_t^{air} - T_t^{mas}(t)\right) + K_{mass}.I_t^{sol} \\ C^{em}.\frac{dT^{em}}{dt^s} = U_{air}^{em}.\left(T_t^{air} - T_t^{em}(t)\right) + \Psi_t \\ C^{cir}.\frac{dT^{cir}}{dt^s} = \eta^{cir}.\Phi_t - \Psi_t \\ \Psi_t \le m^{max}.cp.(T_t^{em}(t) - T_t^{cir}) \end{cases} \quad (1)$$

In this model, two distinct parts are considered:

- The building part where the air (T_{air} for the air temperature, C_{air} for the air capacity and K_{air} for the air solar gain factor), the building envelope (T_{env}, C_{env} and K_{env}), and the thermal mass of the building (T_{mas}, C_{mas} and K_{mas}) are modelled. The interactions between those thermal nodes and with the outdoor are taken into account with the thermal inductances (exterior/air (U_{air}^{ext}), envelope/air (U_{air}^{env}), mass/air (U_{air}^{mas})).
- The HDC part where the circuit (T_{cir} for the inlet circuit temperature, C_{cir} for the circuit capacity) and the emitter (T_{em} and C_{em}) are modelled, considering their interaction with the air via the emitter (U_{air}^{em}).

Φ_t represents the boundary condition with the heat transferred by the primary loop of the HDN and Ψ_t represents the heat transfer between the emitter and the circuit.

3.5. Calibration of the MILP model for Flexible buildings

Calibration of building model is a complex process. In this work, the MILP model needs to be calibrated to have similar thermal inertia as its EnergyPlus twin.

Figure 6 depicts the process of calibration applied on this study.

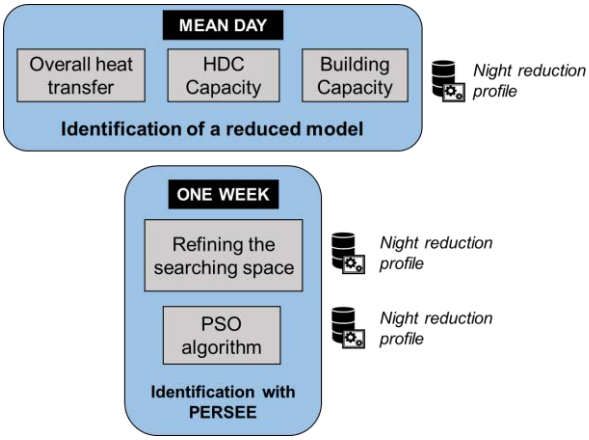

Figure 6. Process for calibration of optimization building model for flexibility (Source: Authors)

This calibration consists in two phases with two options for the second phase.

3.5.1. Phase one: initial parameters estimation

Figure 7 depicts the reduced model used in the phase one of calibration

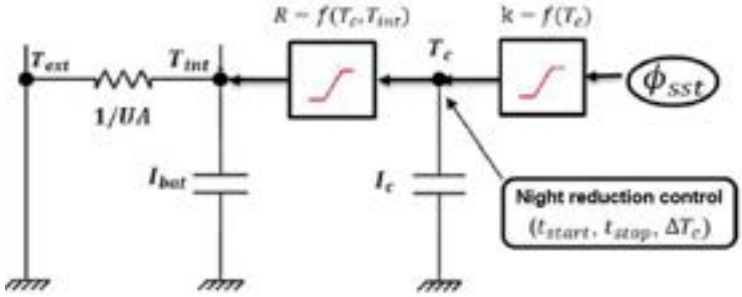

Figure 7. Reduced model used in the first phase of calibration process (Source: CEA)

This phase consists in the identification of the thermal parameter of the building considering this reduced model using a heat profile with night reduction as an input:

- The overall heat transfer coefficient of the building: determined in the night period following an empiric relation between this heat transfer coefficient and the difference between the indoor temperature and the outdoor temperature.

$$QHeat = UA.\,(Tindoor - Toutdoor) \tag{2}$$

- The total building capacity: determined using an empiric relation between the morning peak ($Q_{morning}$ when the setpoint passes from the night to the day mode) and the descending phase of the evening peak ($Q_{down,ve}$ when the setpoint temperature passes from the day to the night mode) and night and day setpoint temperatures (respectively T_{night} and T_{day}).

$$C_{building} = \frac{Q_{morning} - Q_{down,eve}}{T_{day} - T_{night}} \tag{3}$$

- The heat distribution circuit (HDC) capacity: determined by using an empiric linear relation with the descending phase of the evening peak.

$$C_{HDC} = \frac{Q_{down,eve}}{15} \tag{4}$$

- The solar coefficient aperture: determined by evaluating the total energy gain of the building during the solar period. Then, solar gain are obtained by subtracting the total energy the emitter heat and the internal gain from energy plus simulation.

$$K_{Building} = \frac{\mathrm{UA.(Tindoor - Toutdoor) - Q_{int} - Q_{heat}}}{\mathrm{Irr}} \tag{5}$$

The parameter of the reduced model are then used in order to give a first-phase value (FPV) for each parameter of the PERSEE building model. The table 2 details their relation:

Table 2. List of the energy system considered in this work.

Persee parameter	Relation with reduced model parameters
C^{air}, C^{env}, C^{mas}	$\frac{C_{building}}{3}$
C^{cir}, C^{em}	$\frac{C_{HDC}}{2}$
U_{air}^{ext}, U_{air}^{env}, U_{env}^{ext}, U_{air}^{mas}	$\eta_{Uxxx} * \mathrm{UA}$
K^{air}, K^{env}, K^{mas}	$\eta_K^{xxx} * \mathrm{K_{building}}$
U_{air}^{em}	$(\frac{\Phi_{heat}^{nom}}{\Delta T_{nom}})^{1.33}$ and $\Delta T_{nom} = \frac{\mathrm{T}_{out,nom}^{em} + \mathrm{T}_{out,nom}^{em}}{2} - T_{setpoint}^{air}$

η_{Uxxx} and η_K^{xxx} are extrapolating from the Building 2022 parameter in Table 2 of [24].

3.5.2. Phase two: refined parameter estimation

In order to refine the estimation of parameters, we use a Particle-Swarm Optimisation (PSO [23]) algorithm to identify the parameters using the MILP model for calibration. For a calibration assessment purpose, we choose a specific indicator, based on the root-mean-square error (RMSE) between observed and measured air temperature profiles and observed and measured heat profiles:

$$RMSE = \frac{rmse_{heat} + rmse_{temp}}{2}$$

$$rmse_{heat} = \frac{t_f}{\Delta t}\sqrt{\sum_{0}^{t_f} \frac{(\hat{\Phi}_{heat} - \Phi_{heat})^2}{max(\hat{\Phi}_{heat} - \Phi_{heat})}}$$

$$rmse_{temp} = \frac{t_f}{\Delta t}\sqrt{\sum_{0}^{t_f} \frac{(\hat{T}_{air} - T_{air})^2}{max(\hat{T}_{air} - T_{air})}}$$

The calibration with the MILP model in the loop consist in two steps. Figure 8 details the first step.

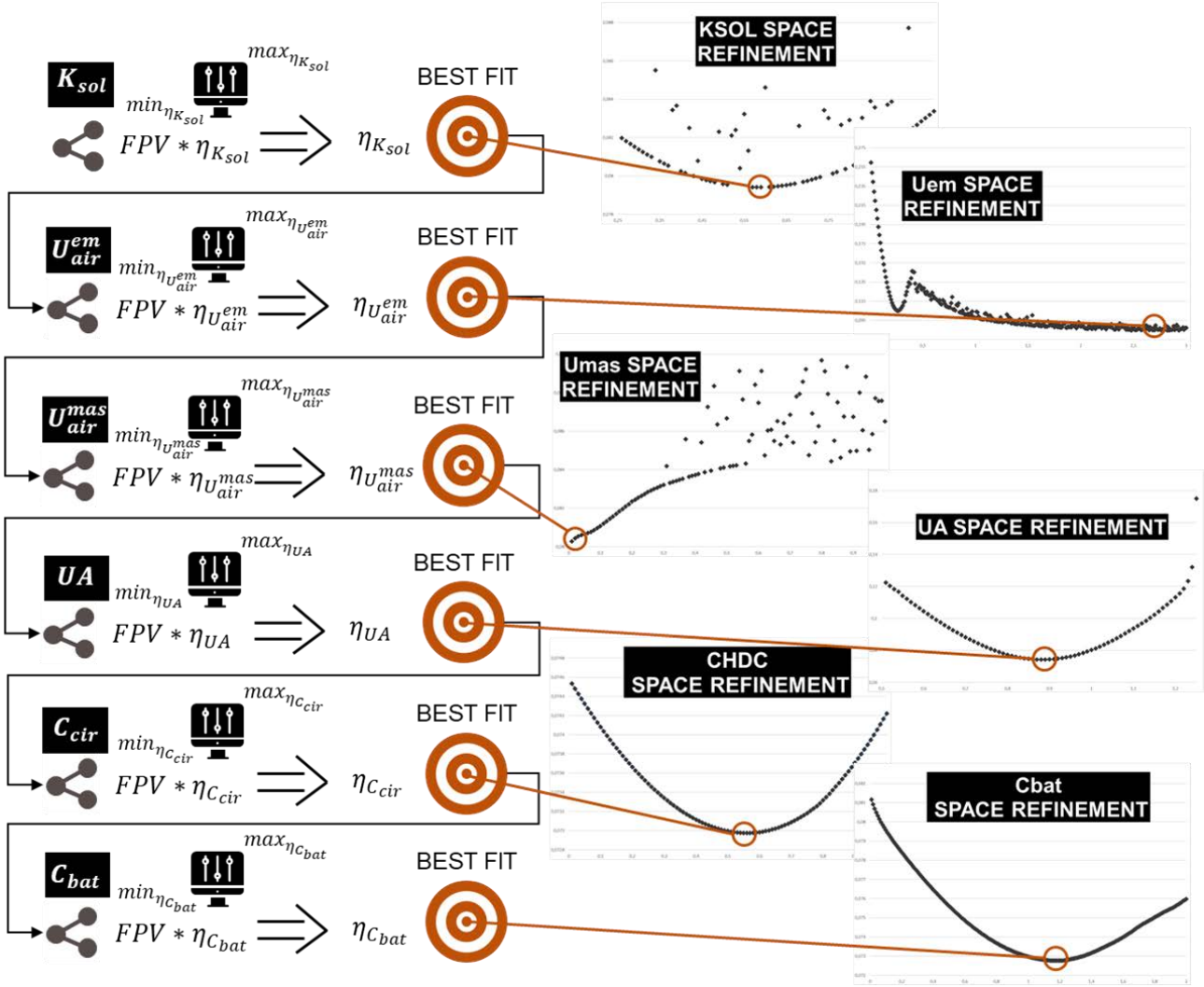

Figure 8. Heuristic method for refining the search step (Source: Authors)

At this stage, we aim to refine the search space for each parameter of the Persee model. The parameters are aggregated by their specificities as follow:

- Solar aperture coefficients (K^{air}, K^{env}, K^{mas}) are aggregated within K_{sol}
- U^{em}_{air} and U^{mas}_{air} are treated individually because of the specificity of their extrapolation.
- U^{ext}_{air}, U^{env}_{air}, U^{ext}_{env} are aggregated within UA
- C^{cir}, C^{em} are aggregated within C_{HDC}
- C^{air}, C^{env}, C^{mas} are aggregated within C_{bat}

Beforehand, the order of this heuristic algorithm has no importance, except for the solar aperture coefficient. Thus the error defers from the one from (6) by considering the RMS only during solar period. At each stage, the best-fit coefficient is selected from the assessment sample. This assessment sample is defined around the FPV. A discretization of the sample enables to assess 100 to 300 assessment in which we keep the value with the lowest RMSE. In the end, a new set of refined parameter is determined using their corresponding best-fit coefficient and their FPV.

4. Results

4.1. Simulation Hypothesis

- **Optimisation**: Considering the optimisation part, we consider a constraint in CO2 emission rate at district level of 20000kg and an economic objective function. The feed-in-tariffs of electricity consists in a conditioned one to day-and-night time slots.
- **MPC and cosimulation**: The horizon of the MPC, the time slots within the optimisation runs, is a 36 hours period. Both optimisation and simulation considers a 1 hour time step. Then, the co-simulation runs with a timeshift of 1 hours meaning that the control strategy is recalculated every timestep. The cosimulation runs during 60 days.
- **Thermal production**: On the thermal model part, the impact of the flexible building on its flowrate is neglected. We consider it as a constant value. The overall district heat production is adapted by considering the building flexible integrated in the district. The heat profile of each flexible building is subtracted from the district heat profile.
- **Building model**: At our current state of work, we consider a monozone building model and HDC model. Considering multi-zone building model in order to evaluate its effect on the calibration and flexibility is a perspective for further studies. 8 building on the 13 are modelled.
- **Calibration**: The full calibration process is set for five buildings; the first heuristic results are applied on others.

4.2. Calibration Results

For this case study, we applied the full calibration process presented in section 3.5. for the five main buildings. For the three last, the process end at the heuristic step of the second phase. In order to evaluate the calibration performances, the table 3 records the RMS for each building at each stage, in addition with a test of the performance of PSO algorithm using the unrefined search space. Considering the two PSO, we defined their search space giving the same minimal and maximal coefficient.

Table 3. Recording of RMS during the calibration process.

Buildings	RMSE with FPV	RMSE after refinement	RMSE with unrefined PSO	RMSE with refined PSO
CastelO	0.09359	0.06114	0.08039	0.06089
Panache	0.10103	0.07276	0.08729	0.07303
Python	0.07741	0.03935	0.06536	0.03924
Up	0.11137	0.09039	0.09707	0.0857
Zenae	0.09712	0.03566	0.07720	0.03453
Novae	0.05511	0.03210	-	-
Thales	0.07851	0.03514	-	-
Soleil	0.06842	0.06130	-	-

Figure 9 focuses on the two extreme buildings

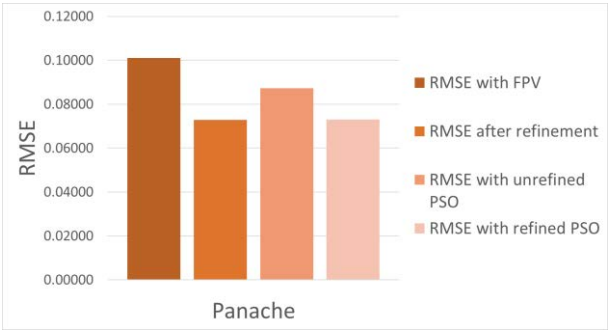

(a)

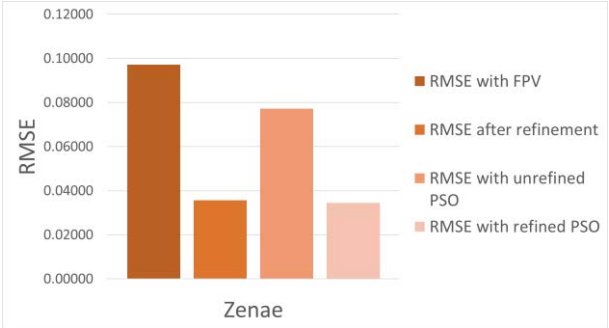

(b)

Figure 9. Focus on two buildings a) building obtaining the worst amelioration with refining b) building obtaining the best amelioration with refining (Source: Authors)

At this stage, the refining seems to have a positive effect on the global error, considering the chosen indicator. At best case, the amelioration is around 60% from the first phase calibration with a mean value of 38% with the heuristic algorithm and 40% with refined PSO. The worst case is interesting because the PSO algorithm have found a slightly less performant set of parameter than the heuristic algorithm. Moreover, the gain from PSO is a mean of two point compared to the heuristic. Two possibilities can explain this fact. Firstly, the heuristic algorithm differs from the PSO on the solar aperture assessment. Indeed, for the heuristic algorithm, we have chosen to evaluate only the solar timeslots as those coefficients have no effect without solar irradiation on the model. Secondly, we have neglected a proper study on the configuration of the PSO, which could lead to underestimated performances. Section 4. Presents areas of improvement considering the calibration phase.

4.3. Co-simulation results

The main difficulty for the MILP model is to determine the flexibility coefficient for each flexible building model. This coefficient is set first using a standalone optimisation on the horizon time. Figure 10 shows the result for the chosen flexibility coefficient.

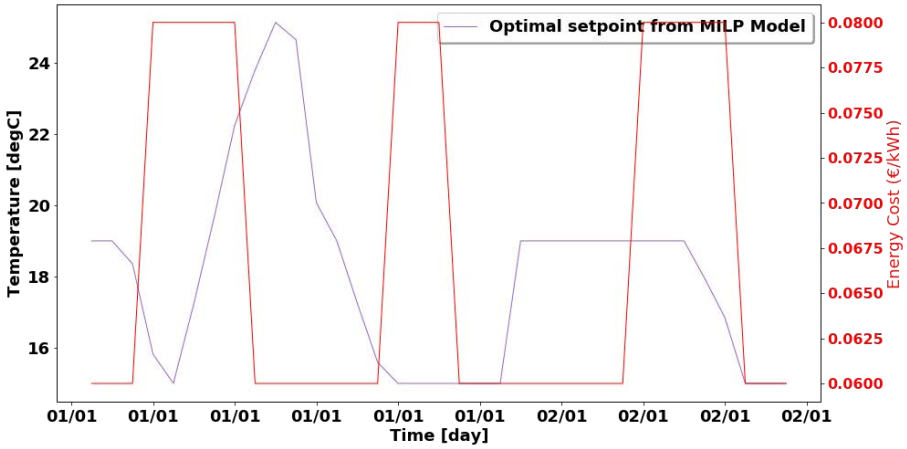

Figure 10. Optimal Air temperature from MILP Model on the horizon time (Source: Authors)

The multi-vector system is quite complex, leading to a difficulty to find a satisfying value for this coefficient. We applied this flexibility coefficient for the co-simulation. To give an idea of time solving for one building, a co-simulation with one building takes 8 minutes to run and 23 minutes with 8 buildings

Figure 11 shows the results concerning the co-simulation for one building.

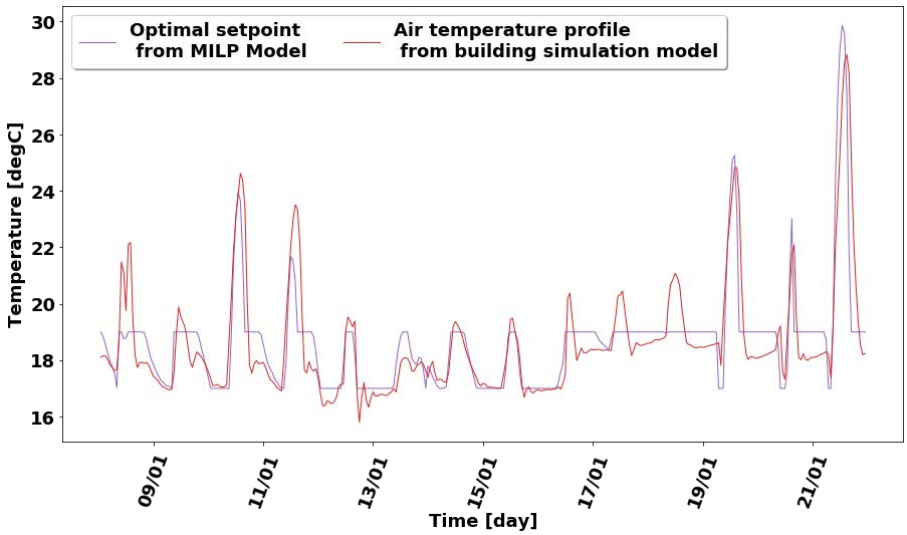

Figure 11. Set point temperature from MILP model profile and air temperature profile from building model (Source: Authors)

At this stage, we can obtain an effect on the temperature set point of EnergyPlus building model. However, those results aren't satisfying enough for one building and are the same kind for eight buildings. Further improvements would be necessary to obtain solid results at district scale.

5. Conclusion

This article presents a co-simulation procedure in order to process a flexibility assessment building by building. This co-simulation embeds an electric simulation model, a thermal model composed of a thermal production model, a heat distribution circuit model and a building model and a MILP model optimizer ensures MPC. The first aim is to calibrate the building models in order to implement them for co-simulation. A proper calibration procedure has been implemented with a satisfactory accuracy. Then we could test the co-simulation from one to eight buildings at district scale.

For future work, the calibration process could be improved by assess the configuration of the PSO algorithm on the one hand. On the other hand, the PSO process could be improved by splitting the search of solar aperture coefficients from the other parameters. In doing so, we could hope obtaining better results for calibration. Then, a better training phase could be implemented to refine the calibration process. On the co-simulation side, we would have to improve the flexibility coefficient study in order to find a procedure to set it. Another option that we would like to study is to reduce the time step from one hour to 10 minutes. Indeed, as we obtain decent computing time, this seems to be feasible. Reducing the time step of co-simulation could improve the sensitivity of the flexible building model and help to find a better flexibility coefficient.

6. References

[1] Sarbu I, Mirza M, Muntean D. 2022. Integration of Renewable Energy Sources into Low-Temperature District Heating Systems: A Review. Energies 15:6523.

[2] Onen PS, Mokryani G, Zubo RHA. 2022. Planning of Multi-Vector Energy Systems with High Penetration of Renewable Energy Source: A Comprehensive Review. Energies 15:5717.

[3] Chaudhary G, Lamb JJ, Burheim OS, Austbø B. 2021. Review of Energy Storage and Energy Management System Control Strategies in Microgrids. Energies 14:4929.

[4] M. González-Torres, L. Pérez-Lombard, Juan F. Coronel, Ismael R. Maestre, Da Yan, A review on buildings energy information: Trends, end-uses, fuels and drivers, Energy Reports, Volume 8, 2022, Pages 626-637

[5] Lavinia Marina Paola Ghilardi, Alessandro Francesco Castelli, Luca Moretti, Mirko Morini, Emanuele Martelli, Co-optimization of multi-energy system operation, district heating/cooling network and thermal comfort management for buildings, Applied Energy, Volume 302, 2021, 117480, ISSN 0306-2619

[6] J. Kozadajevs and D. Boreiko, "District Heating System Flexibility Studies Using Thermal Inertia of Buildings," 2020 IEEE 61th International Scientific Conference on Power and Electrical Engineering of Riga Technical University (RTUCON), Riga, Latvia, 2020, pp. 1-5

[7] Yang Li, Chunling Wang, Guoqing Li, Jinlong Wang, Dongbo Zhao, Chen Chen, Improving operational flexibility of integrated energy system with uncertain renewable generations considering thermal inertia of buildings, Energy Conversion and Management, Volume 207, 2020

[8] Q. Gao, M. Demoulin, H. Wang, S. Riaz and P. Mancarella, "Flexibility Characterisation from Thermal Inertia of Buildings at City Level: A Bottom-up Approach," 2020 55th International Universities Power

Engineering Conference (UPEC), Turin, Italy, 2020, pp. 1-6
[9] Vandermeulen, Annelies & Reynders, Glenn & van der Heijde, Bram & Vanhoudt, D. & Salenbien, Robbe & Saelens, Dirk & Helsen, L.. (2018). Sources of Energy Flexibility in District Heating Networks: Building Thermal Inertia Versus Thermal Energy Storage in the Network Pipes.
[10] Zhaoguang Pan, Qinglai Guo, Hongbin Sun, Feasible region method based integrated heat and electricity dispatch considering building thermal inertia, Applied Energy, Volume 192, 2017, Pages 395-407
[11] Optimal scheduling strategy of district integrated heat and power system with wind power and multiple energy stations considering thermal inertia of buildings under different heating regulation modes Dan Wang et al. Applied Energy 240 (2019) 341-358.
[12] Collaborative scheduling and flexibility assessment of integrated electricity and district heating systems utilizing thermal inertia of district heating network and aggregated buildings Xue Li et al. Applied Energy, 258 (2020)
[13] Pajot C, Artiges N, Delinchant B, Rouchier S, Wurtz F, Maréchal Y. 2019. An Approach to Study District Thermal Flexibility Using Generative Modeling from Existing Data. Energies 12:3632.
[14] Rava L., Wantier W., Vallée M., Alain R., Nicolas L., Assessment of Varying Coupling Levels between Electric & Thermal networks at District Level using Co-Simulation and Model-predictive Control. Smart Energy, Volume 6, 2022, 919-930.
[15] Fitó J., Vallée M., Ruby A., Cuisinier E., Robustness of district heating versus electricity-driven energy system at district level: A multi-objective optimization study, Smart Energy, Volume 6, 2022, 100073.
[16] Blochwitz, T., Otter, M., Åkesson, J. Arnold, M., Clauss, C., Elmqvist, H., Friedrich, M., Junghanns, A., Mauss, J., Neumerkel, D., Olsson, H., Viel, A. (2012). Functional Mockup Interface 2.0: The Standard for Tool independent Exchange of Simulation Models. Proceedings.
[17] Zhicheng X., Chuang Z., Bo Sun, SuZhen L., The electric-thermal coupling simulation and state estimation of lithium-ion battery, ournal of Energy Storage, Volume 58, 2023, 106431.
[18] Elmqvist, H., & Mattsson, S. E. (1998). An Overview of the Modeling Language Modelica. Paper presented at Eurosim'98 Simulation Congress, Helsinki, Finland.
[19] Crawley, D., Pedersen, C., Lawrie, L., Winkelmann, F. (2000). EnergyPlus: Energy Simulation Program. Ashrae Journal. 42. 49-56.
[20] Nadine Aoun, Roland Bavière, Mathieu Vallée, Antoine Aurousseau, Guillaume Sandou, Modelling and flexible predictive control of buildings space-heating demand in district heating systems, Energy, Volume 188, 2019, 116042.
[21] Cuisinier, E., Lemaire, P., Penz, B., Ruby, A., Bourasseau, C., (2021). New rolling horizon optimization approaches to balance short-term and long-term decisions: An application to energy planning. Energy.
[22] Hodencq S, Brugeron M, Fitó J, Morriet L, Delinchant B, Wurtz F. 2021. OMEGAlpes, an Open-Source Optimisation Model Generation Tool to Support Energy Stakeholders at District Scale. Energies 14:5928.
[23] Aoun, N., Bavière, R., Vallée, M., Sandou, Ge. (2019). Development and assessment of a reduced-order building model designed for model predictive control of space-heating demand in district heating systems.
[24] Gad, A. (2022). Particle Swarm Optimization Algorithm and Its Applications: A Systematic Review. Archives of Computational Methods in Engineering. 29.

PROCEEDINGS OF ECOS 2023 - THE 36TH INTERNATIONAL CONFERENCE ON
EFFICIENCY, **C**OST, **O**PTIMIZATION, **S**IMULATION AND ENVIRONMENTAL IMPACT OF ENERGY SYSTEMS
25-30 JUNE 2023, LAS PALMAS DE GRAN CANARIA, SPAIN

Hierarchical Distributed Model Predictive Control for Building Energy Systems

Maximilian Mork[a], André Xhonneux[b] and Dirk Müller[c,d]

[a] Forschungszentrum Jülich, Institute of Energy and Climate Research, Energy Systems Engineering (IEK-10), Jülich, Germany, m.mork@fz-juelich.de, CA
[b] Forschungszentrum Jülich, Institute of Energy and Climate Research, Energy Systems Engineering (IEK-10), Jülich, Germany, a.xhonneux@fz-juelich.de
[c] Forschungszentrum Jülich, Institute of Energy and Climate Research, Energy Systems Engineering (IEK-10), Jülich, Germany, di.mueller@fz-juelich.de
[d] RWTH Aachen University, E.ON Energy Research Center, Institute for Energy Efficient Buildings and Indoor Climate, Aachen, Germany, dmueller@eonerc.rwth-aachen.de

Abstract:
Buildings contribute to approximately 30 % of global energy consumption, which renders their energy-efficient control an effective measure to reduce overall energy consumption. This paper presents a hierarchical distributed Model Predictive Control (MPC) for building energy systems based on nonlinear Modelica controller models. It combines hierarchical and distributed optimization approaches to split the optimization complexity within the temporal and spatial dimension. The hierarchical optimization approach considers different dynamics in complex building energy systems and ensures both anticipation for systems with high inertia and reactivity with regard to errors in the forecasting of the disturbance quantities. The distributed optimization approach divides the centralized optimization problem into subproblems to improve the scalability and adaptability of the control framework. The subproblems are solved in a parallel and iterative manner and account for both thermal (heat transfer over zone boundaries) and hydraulic inter-zone coupling (induced by a central, shared Heating, Ventilation and Air Conditioning (HVAC) system). A particular focus of the control approach is placed on robustness with respect to errors in the forecasting of the disturbances that impact the building dynamics. The control performance of the proposed MPC framework is evaluated in a simulative case study of heating and shading control of a nonlinear six-room-building Modelica model, which is exposed to different forecast accuracies for the disturbances of occupancy, solar radiation and air exchange. The case study exhibits the benefits of the control framework in terms of energy consumption, thermal discomfort and computation time in comparison to a reference control concept of a non-hierarchical distributed MPC configuration.

Keywords:
Distributed MPC; Hierarchical MPC; HVAC; Model Predictive Control (MPC); Modelica.

1. Introduction

Approximately 30 % of global energy consumption and 27 % of CO_2 emissions are attributed to the building sector [1]. Heating, Ventilation and Air Conditioning (HVAC) systems contribute to a major extent to building energy consumption [2] and therefore, offer a large potential for an increase in energy efficiency and reduction of energy consumption on a global scale. Currently, conventional control strategies as Rule-Based Control (RBC) or Proportional-Integrative-Differential (PID) controllers are implemented in buildings due to their simplicity and low computational requirements [3]. They represent inflexible and reactive (non-predictive) control approaches that are unable to control inert systems with large time delays, to minimize energy consumption while operating between comfort bounds as well as to consider system or comfort constraints and future disturbances.

Model Predictive Control (MPC) constitutes a promising control approach that addresses the aforementioned challenges and exhibits various benefits and energy savings from 15 to 50 % [4] compared to the conventional control strategies. The central part of an MPC is a model of the building energy system based on which future system behavior is predicted and the building is controlled in an anticipatory manner minimizing a (multi-objective) cost function over a prediction horizon. The predictive characteristic of the control suits inert systems with time delays and integrates future disturbances, e.g., in the form of weather and occupancy forecasts. Apart from this, conflicting optimization goals such as the simultaneous minimization of discomfort and energy consumption as well as system and comfort constraints can be taken into account.

The model generation part is crucial for the implementation of an MPC as it consumes most of the project time and costs [5]. Due to the unique characteristics of every single building, a modeling language has to

be modular and flexible and support the user-friendly generation of (large-scale) building models. The modeling language Modelica [6] complies with these requirements as it supports open-source, equation-based, acausal and object-oriented modeling and is equipped with a user-friendly graphical interface for connecting and parametrizing components. Modelica allows for the collection of building component models in shareable libraries such as the Modelica IBPSA library [7] or extensions building upon this library.

If MPC is applied to large-scale multi-zone buildings, large and computationally complex optimization problems are created, which results in increased computation times. This can also lead to scalability issues when the optimization problems cannot be solved in a suitable time restricting the real-time capability of the control. Distributed MPC approaches tackle these challenges by splitting the central optimization problem into subproblems, which are solved in a distributed manner while accounting for the interactions between the subproblems [8].

On the other hand, buildings generally incorporate components and disturbances of different dynamics and time scales. For example, low-temperature heating and cooling systems based on Thermal Activated Building Systems (TABS) are characterized by a high thermal mass and large time constants requiring a long prediction horizon. They are often complemented by secondary, more reactive actuators such as radiators or convectors, where smaller prediction horizons and control periods are suitable. The simultaneous control of actuators of different time scales and preservation of both anticipation and reactivity poses an additional challenge for the application of MPC in buildings. An approach to tackle this challenge is hierarchical MPC, which splits the optimization problem into layers of different dynamics [8].

Compared to the total number of studies on building MPC, the review of literature for MPC in large-scale buildings exhibits only a relatively small share of distributed optimization approaches. This may be attributed to the nonlinear and nonconvex characteristics of building energy systems that complicate convergence of the distributed optimization approaches [4]. The most widely applied mathematical methods for distributed building MPC are the primal-dual active-set method [9], Benders decomposition [10], dual decomposition [11], information exchange [12], non-iterative look-up tables [13], Nash equilibrium [14, 15] or Alternating Direction Method of Multipliers (ADMM) [16–19]. Among these, Nash equilibrium constitutes an uncooperative, parallel and iterative distributed optimization approach, which builds upon information exchange between subsystems. After every iteration, each subsystem sends and receives updated trajectories for the coupling variables to/from interconnected subsystems and solves its subproblem again. The subsystems converge to a ”Nash equilibrium” if for all subsystems, the local optimization results deviate less than a predefined threshold between two consecutive iterations. Nash equilibrium is applied for considering thermal coupling based on exchanged local temperature trajectories [14] or for taking into account hydraulic control input coupling [15]. ADMM represents a distributed optimization approach with an iterative and cooperative structure, which is carried out mostly in parallel. It is based on the augmented Lagrangian, i.e., the Lagrangian formulation plus an additional quadratic penalty term for improved convergence and robustness compared to dual decomposition. ADMM makes use of two sets of variables, which allows separating the central cost function and coupled dynamics as well as splitting the problem into subproblems. The fulfillment of the coupling constraints between the different variable sets is steered via dual variables penalizing the deviations within the cost functions. ADMM is applied for considering thermal and hydraulic coupling [16], indoor air quality in rooms coupled by a central Air Handling Unit (AHU) [17], maximum constraints on shared resources (e.g., maximum capacity of an AHU) [18] and sharing problems (sum of local control variables is input to the global cost function) [19].

Hierarchical building MPC approaches are applied to split optimization problems into different layers with varying dynamics and time scales, which are controlled based on different prediction horizons and sampling periods. Abreu et al. [20] implement a hierarchical building MPC, which consists of a scheduling layer sending output trajectories and power profiles to the lower layer with a shorter prediction horizon and sampling period. The latter tracks the forwarded output trajectories while taking into account the constraining trajectory of the power profile. Fiorentini et al. [21] implement a hierarchical MPC for the operation of an HVAC system including an AHU coupled to a thermal storage. The upper layer with a longer prediction horizon and sampling period calculates an optimal sequence of discrete operating modes, which are executed by the lower level while tracking a reference temperature sent by the upper level. Long et al. [22] develop a distributed hierarchical MPC controlling a ventilated multi-zone building. An upper centralized layer calculates reference temperature trajectories for a lower layer consisting of several local controllers, which solve their local problems in an isolated, decentralized way based on local information and the upper temperature trajectories to be tracked.

In previous works, the concepts of hierarchical [23] and distributed [24] building MPC based on nonlinear Modelica models have been individually developed. The hierarchical MPC splits the optimization problem into two layers of different dynamics, which are equipped with different prediction horizons and sampling periods to guarantee both anticipation and reactivity. The distributed MPC splits the centralized optimization problem into subproblems and takes into account thermal and hydraulic coupling between building zones using an optimization approach based on Nash equilibrium and ADMM. In this work, the hierarchical and distributed

MPC approach are combined into one MPC framework and applied to a multi-zone building that incorporates actuators of different dynamics. The control quality and the reactivity of the MPC are evaluated for different scenarios of forecasting accuracy for the disturbance quantities. The forecast errors can be regarded as any deviation between the predicted and actual real-world behavior of the building, which are expected to appear in practical MPC implementations. By using the hierarchical distributed MPC approach, the complexity of the original optimization problem is split in both the temporal and spatial dimension. This alleviates modular, local high-accuracy modeling and at the same time, improves the scalability, real-time capability and adaptability of the control approach.

2. Methodology

2.1. Distributed MPC

The methodology for the distributed MPC has been elaborated in [24]. The approach considers both thermal and hydraulic coupling among different building zones and is executed in an iterative and parallel way. It is based on an uncooperative optimization approach for thermal coupling using Nash equilibrium and a cooperative approach for hydraulic coupling using ADMM. A central coordinator updates information and monitors the convergence process of the overall optimization.

The uncooperative Nash optimization regards the room temperatures of neighboring zones as known disturbances and thereby, can calculate the heating flows exchanged over the local zone boundaries. After every optimization iteration, the locally calculated trajectories for the local room temperatures are sent to the coordinator. The coordinator forwards the temperature trajectories to all neighboring zones that are thermally coupled to the corresponding zone and the local optimizations are executed again with updated trajectories for the neighboring room temperatures. The local subproblems converge to the ”Nash equilibrium” if, for all local subsystems, averaged over the MPC horizon, the absolute deviation of the local room temperature trajectories between two consecutive distributed iterations does not deviate more than a prefixed Nash threshold.

The hydraulic coupling comprises interactions between the zones induced by a shared, central HVAC system. In the case study in Section 3., the central HVAC system is constituted by a shared TABS in the form of Concrete Core Activation (CCA) in the floor. TABS builds upon the activation of the thermal mass of a building in the form of the concrete and offers passive storage capacities to shift the time between energy supply and demand. Due to the high inertia of the thermal mass, one TABS/CCA section generally supplies multiple building zones with similar thermal properties, demand or orientation [25], which introduces strong coupling between the rooms. Within the case study, the central CCA consists of six identically dimensioned subsections (one per room) and is controlled via one shared control input that regulates the supply water mass flow supplied to each subsection. The hydraulic coupling is taken into account using a consensus ADMM approach. The optimization problem is decomposed by introducing local copies of the global CCA control input for every subsystem, which are optimized separately. Linear and quadratic ADMM terms are added to the cost functions of both the local subsystems (1) and the coordinator (2) to coordinate the consistency between the local copies and the global CCA control input. The coordinator monitors the convergence of the ADMM applying both a primal and dual residual criterion according to [24, 26].

The communication structure of the overall distributed optimization approach is shown in Fig. 1. In every distributed optimization iteration, the local subproblems (1) are optimized in parallel and the resulting local trajectories for the CCA control input and room temperature are sent to the global coordinator. The global coordinator uses the updated information to optimize the global cost function calculating new trajectories for the global CCA control input (2). In the second step, the dual ADMM variables (Lagrangian multipliers) are updated coordinating the consistency between the global and local copies of the CCA control input (3). The coordinator checks the convergence status for both ADMM and Nash optimization according to the user-specified thresholds. Then it forwards the trajectories for the global CCA control input, dual variables, local room temperatures and the convergence status to the subproblems, which continue the local optimization procedures according to the convergence status. If the subproblems have converged, they send the local control inputs for all actuators to the global coordinator, which converts the local CCA control inputs into an averaged value and runs a simulation over a sampling period (right branch). If the subproblems have not converged and the maximum number of distributed iterations per MPC iteration is not exceeded, the subproblems are solved again based on the new information sent by the global coordinator (left branch).

2.2. Hierarchical MPC

The hierarchical MPC divides the optimized problem within the temporal dimension into two layers of different dynamics and time scales as proposed in [23]. For the upper, slow MPC layer, a longer prediction horizon and sampling period are chosen, whereas for the lower, fast layer, the horizon and sampling period are smaller. Thereby, the slow layer focuses on anticipation of the control, which is specifically suitable for inert systems with time delay (e.g., TABS or thermal storage). Due to the small sampling periods of the fast MPC layer,

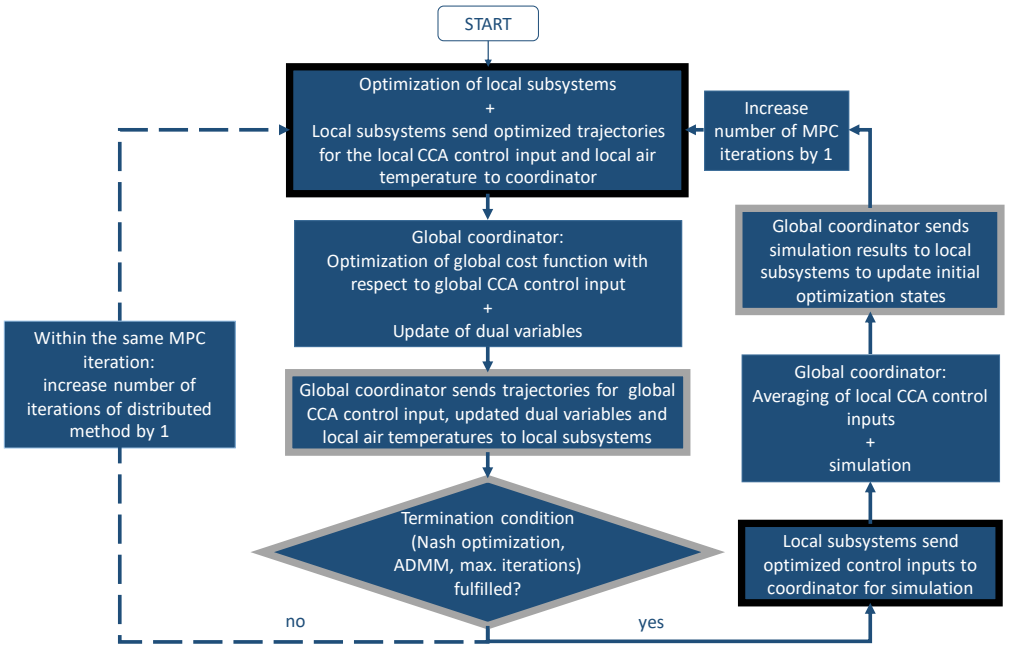

Figure 1: Overall communication structure of the distributed MPC (inputs to local MPC: gray frame, outputs of the local MPCs: black frame)

reactivity with regard to forecasting or unexpected influences can be ensured. The two layers communicate via state reference trajectories that are calculated by the slow layer and are sent to the fast layer to be tracked. Compared to a single MPC layer equipped with a long prediction horizon and small sampling period, the combination of the two layers increases the probability to preserve real-time capability.

2.3. Hierarchical Distributed MPC

The scheme of the aggregated hierarchical distributed MPC toolchain for the six-room-building use case is depicted in Fig. 2. Both the upper and lower hierarchical MPC layer are split into thermal zone subproblems in a distributed way (for each of the six rooms). Within each MPC layer, the subproblems are solved based on the distributed optimization approach based on Nash equilibrium and ADMM. An overall distributed MPC iteration is terminated if, in both the upper and lower MPC layer, the convergence criteria for the Nash equilibrium and ADMM are fulfilled or the maximum number of distributed iterations in one MPC iteration is exceeded. The cost functions of the subproblems in the lower layer contain quadratic tracking terms for the room temperature trajectories $T_{\mathrm{ref,i}}$ calculated by the room equivalent on the upper layer. The reference trajectories are recalculated in every distributed iteration of the upper MPC layer and the updated trajectories are forwarded to the lower layer. After convergence, the control inputs of the lower MPC layer are applied to the simulation model and based on the simulation results, the optimization states of the next optimization iteration are initialized both in the upper and lower MPC layer.

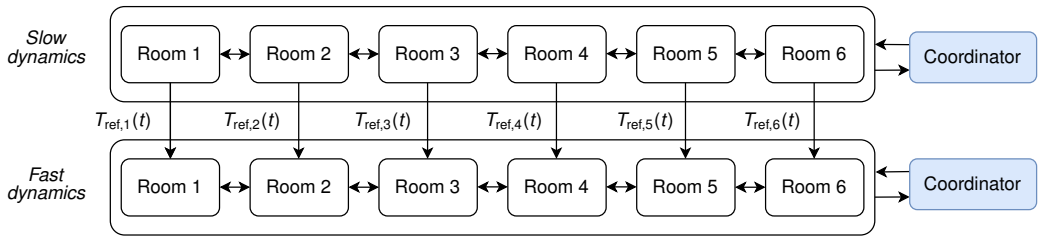

Figure 2: Communication structure of the hierarchical distributed MPC

3. Case study

In a simulative use case, the hierarchical distributed MPC is applied to the six-room-building shown in Fig. 3. The nonlinear model is generated based on the Modelica building simulation library AixLib [27] and comprises rooms that are thermally coupled via inner walls and data-driven models for air flow through doors [24]. All rooms are hydraulically coupled to a central, shared TABS implemented as CCA in the floor, which is operated via a central control input regulating the supply water mass flow. Each room is equipped with an identically

dimensioned CCA subsection, a convector, simplified pumps and an external window including external Venetian blinds for active solar shading [23]. Two pumps per room supply the CCA subsection and the hydraulically uncoupled convector with supply water mass flow rates calculated by the optimization (at fixed supply temperatures).

Control inputs of the subsystems are the local water mass flow rates to the convectors and the vertical position and inclination angle of the Venetian blinds. The shared control input of the central mass flow rate to the CCA applies to all subsystems. For occupant comfort, both thermal and visual comfort (minimum illuminance of 500 lux in occupied times) are considered. During the occupied periods (8 a.m.–12 p.m. and 1–6 p.m.), there is one person in rooms 3 and 5, two persons in rooms 1 and 6 and three persons in rooms 2 and 4. During unoccupied times the thermal comfort ranges are broadened according to a night set-back (occupied times: 293–295.5 K, unoccupied times: 292–296.5 K). Weather data is integrated based on an AixLib resource file of San Francisco, which represents a heating period. No model mismatch between the MPC controller and the simulation model is assumed to focus on the control performance of the hierarchical distributed MPC.

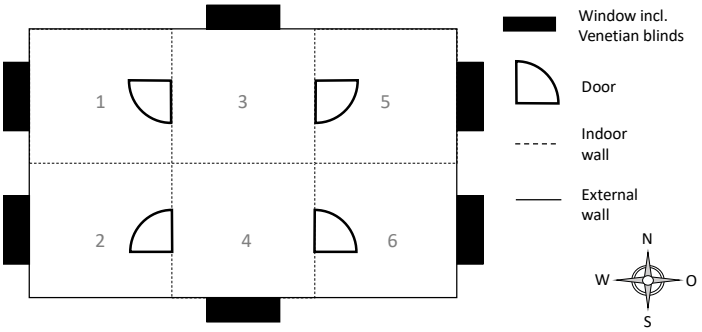

Figure 3: Building structure consisting of six thermal zones

For every subsystem $i \in \mathcal{N}$, the following local optimization problem is solved (for distributed iteration $k + 1$, the last term of the cost function including $T_{\text{ref,i}}$ is omitted for the upper hierarchical layer):

$$\begin{aligned}\{u_{\text{conv},i}, u_{\text{CCA,local},i}, u_{\text{al},i}, u_{\text{posShad},i}, u_{\text{inclAng},i}, \underline{\varepsilon}_i, \bar{\varepsilon}_i\}^{k+1} = \textit{argmin}_{u_{\text{conv},i}, u_{\text{CCA,local},i}, u_{\text{al},i}, u_{\text{posShad},i}, u_{\text{inclAng},i}, \underline{\varepsilon}_i, \bar{\varepsilon}_i} \\ \int_{t_0}^{t_f} [\alpha_{\text{conv}} \cdot u_{\text{conv},i} \cdot (T_{\text{supply,conv},i} - T_{\text{return,conv},i}) + \alpha_{\text{CCA}} \cdot u_{\text{CCA,local},i} \cdot (T_{\text{supply,CCA},i} - T_{\text{return,CCA},i}) + \\ \alpha_{\text{Light}} \cdot u_{\text{al},i} + \theta \cdot (\underline{\varepsilon}_i{}^2 + \bar{\varepsilon}_i^2) + \lambda^k_{\text{Dual,CCA},i} \cdot (u_{\text{CCA,local},i} - u^k_{\text{CCA,global}}) + \rho/2 \cdot (u_{\text{CCA,local},i} - u^k_{\text{CCA,global}})^2 + \\ \gamma \cdot (T_{\text{room,air,i}} - T_{\text{ref,i}})^2] \, dt \end{aligned} \quad (1)$$

The local cost functions (1) consist of the energy consumption of the convector, CCA and artificial lighting as well as discomfort (quadratic penalization of temperatures outside the comfort range through introduced slack variables $\underline{\varepsilon}_i$ and $\bar{\varepsilon}_i$). The terms are complemented by the linear and quadratic ADMM terms taking into account the consensus between the local and global CCA control variables (based on the Lagrangian multipliers $\lambda^k_{\text{Dual,CCA},i}$ and the ADMM penalty parameter ρ). The last term in the cost function applies only to subsystems in the lower hierarchical MPC layer and comprises the quadratic tracking of the reference temperature trajectories $T_{\text{ref,i}}$ sent by the room equivalent on the upper layer (weighted with γ).

$u_{\text{conv},i}$, $u_{\text{CCA,local},i}$, $u_{\text{al},i}$, $u_{\text{posShad},i}$ and $u_{\text{inclAng},i}$ correspond to the local control inputs of the convector and CCA supply water mass flows, artificial lighting, shading position and inclination angle of the Venetian blinds. $T_{\text{room,air},i}$ is the local room air temperature. $T_{\text{supply,conv},i}$, $T_{\text{return,conv},i}$, $T_{\text{supply,CCA},i}$ and $T_{\text{return,CCA},i}$ are the supply and return water temperatures of the convector and CCA. α_{conv} and α_{CCA} are energy weighting factors for the convector and CCA including the heat capacity of water, α_{Light} a weighting factor for the energy consumption of artificial lighting and θ a factor penalizing room temperatures outside the comfort range. The prediction horizon (t_0 - t_f) is 24 h for the upper MPC layer and 8 h for the lower layer, the sampling period is set to 15 min for the upper and to 5 min for the lower layer.

Based on the calculated trajectories for the local room-individual CCA control inputs $u^{k+1}_{\text{CCA,local},i}$ from (1), the global coordinator calculates the global CCA control input $u_{\text{CCA,global}}{}^{k+1}$ for iteration $k + 1$ (2). In the second step, the dual variables (Lagrangian multipliers) $\lambda^{k+1}_{\text{Dual,CCA},i}$ are updated for every zone (3).

$$u_{\text{CCA,global}}^{k+1} = argmin_{u_{\text{CCA,global}}} \int_{t_0}^{t_f} [\sum_{i \in \mathcal{N}} \lambda_{\text{Dual,CCA},i}^{k} \cdot (u_{\text{CCA,local},i}^{k+1} - u_{\text{CCA,global}}) + \rho/2 \cdot (u_{\text{CCA,local},i}^{k+1} - u_{\text{CCA,global}})^2] dt \quad (2)$$

$$\lambda_{\text{Dual,CCA},i}^{k+1} = \lambda_{\text{Dual,CCA},i}^{k} + \rho \cdot (u_{\text{CCA,local},i}^{k+1} - u_{\text{CCA,global}}^{k+1}) \quad (3)$$

The control quality of the implemented hierarchical distributed MPC is evaluated in terms of the following Key Performance Indicators (KPIs): energy consumption (for CCA, convector and artificial lighting; in MJ), thermal discomfort (quantification of room temperatures outside the comfort range; in Kh) as well as total computation time and computational time ratio. The computational time ratio represents the ratio of the total computation time to the simulated control time. A quotient smaller than 1 is equivalent to real-time capability of the control. The performance of the proposed hierarchical distributed MPC is compared to a non-hierarchical distributed equivalent consisting of only one MPC layer with a prediction horizon of 24 h and a sampling period of 15 min.

The control quality of the different control approaches is evaluated for different accuracy scenarios for the disturbance forecasts. In the first scenario, a perfect forecast for the disturbance quantities of occupancy, solar radiation (global horizontal, diffuse horizontal and direct normal) and air exchange rate is assumed. For the second and third scenario, forecast errors are artificially generated according to a normal (Gaussian) distribution, zero mean and varied standard deviations σ (based on the Python package *numpy*). A filter extracts negative values for radiation and occupancy. The occupancy value is rounded to an integer and during unoccupied times, no forecast errors are added to occupancy and solar radiation. The forecast error for occupancy represents a higher/lower number of occupants than forecasted, the error for solar radiation expresses the occurrence of unexpected clouds and the error for the air exchange constitutes higher or lower wind speeds than forecasted, which impact the air exchange of the building with ambient air. In the simulative case study, an old building structure with loose air tightness and high air infiltration with a base air exchange of 2.5 1/h is assumed to generate substantial heat demand and transfer the heat from solar and internal gains. The forecast errors can be considered representative of any deviation between the predicted and the real-world behavior of the buildings, such as errors in weather or occupancy forecasts, model errors or unexpected user influences (e.g., window/door opening or manual heating/shading). The standard deviations determining the dimension of the forecast errors are increased in intervals of 0.5 for occupancy, in intervals of 50 W/m^2 for solar radiation and in intervals of 0.1 1/h for the air exchange. The standard deviations are noted in the following manner: $\sigma = (\sigma_{\text{occupancy}}[-], \sigma_{\text{radiation}}[W/m^2], \sigma_{\text{air exchange}}[1/h])$. The optimizations are executed in JModelica.org 2.14 [28] (using linear HSL solver ma27 [29]) for gradient-based optimization of Modelica models with an interface to IPOPT 3.13.1 [30]. The simulation on the coupled building model has a horizon of 5 days. The optimizations are executed on an OpenStack instance with Ubuntu 18.04, 8 vCPUs and 32 GB RAM.

4. Results

Forecast scenario σ = (0,0,0)

For the perfect forecast scenario, the disturbances of outdoor temperature, solar radiation on each window facade and occupancy are depicted in Fig. 4. The results of the non-hierarchical and the hierarchical distributed MPC are shown in Fig. 5 and Fig. 6. The three last subplots "Actuator mass flow", "Shading position" and "Inclination angle" reveal a more dynamic operation of the control inputs for the hierarchical variant compared to its non-hierarchical equivalent, which is due to the higher temporal resolution and reactivity of the lower layer of the hierarchical MPC. At intervals of 5 min (compared to 15 min for the non-hierarchical variant), the hierarchical MPC receives updated measurements from the building and readjusts the control inputs. Since for the first scenario a perfect forecast is assumed, the local room temperatures in the "Local temperature" subplots resemble each other apart from individual violations at the beginning and end of the simulation horizon. The CCA covers the base load benefiting from a higher energy efficiency due to lower supply temperatures and is preheated to cover the heat demand at a later time, while the convectors are operated in a more reactive manner to cover peak loads. During the periods with heat gains from occupancy and solar radiation, the rooms are operated near the upper temperature bound to reduce heating and lighting energy by actively using the Venetian blinds to limit solar gains. During the non-occupancy periods, the temperatures are kept near the lower bound taking advantage of the night set-back to decrease heating energy consumption. The consumed energy is of a similar magnitude (681 MJ for the non-hierarchical and 683 MJ for the hierarchical variant). The hierarchical MPC can reduce thermal discomfort by 64 % (with 0.72 Kh compared to 1.99 Kh for the non-hierarchical MPC). As exhibited in the "CCA control input" subplot, the hierarchical variant regulates the CCA in a more dynamic manner, which results in the same Mean Average Error (MAE, 0.001 kg/s; averaged over all rooms) but a higher Root Mean Square Error (RMSE) for the ADMM consensus (0.003 kg/s compared to 0.002 kg/s). The computational time ratio of 0.191 for the hierarchical MPC (computation time of 82 359 s) is approximately 3 times higher than the one of 0.060 for the non-hierarchical MPC (computation time of 25 850 s), which is due to the execution of three lower MPC layer instances during one upper MPC layer MPC operation.

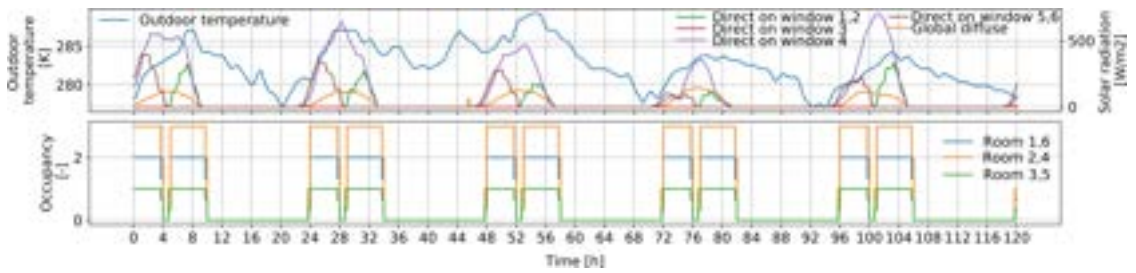

Figure 4: Disturbances for the standard deviations σ = (0,0,0) (perfect forecast)

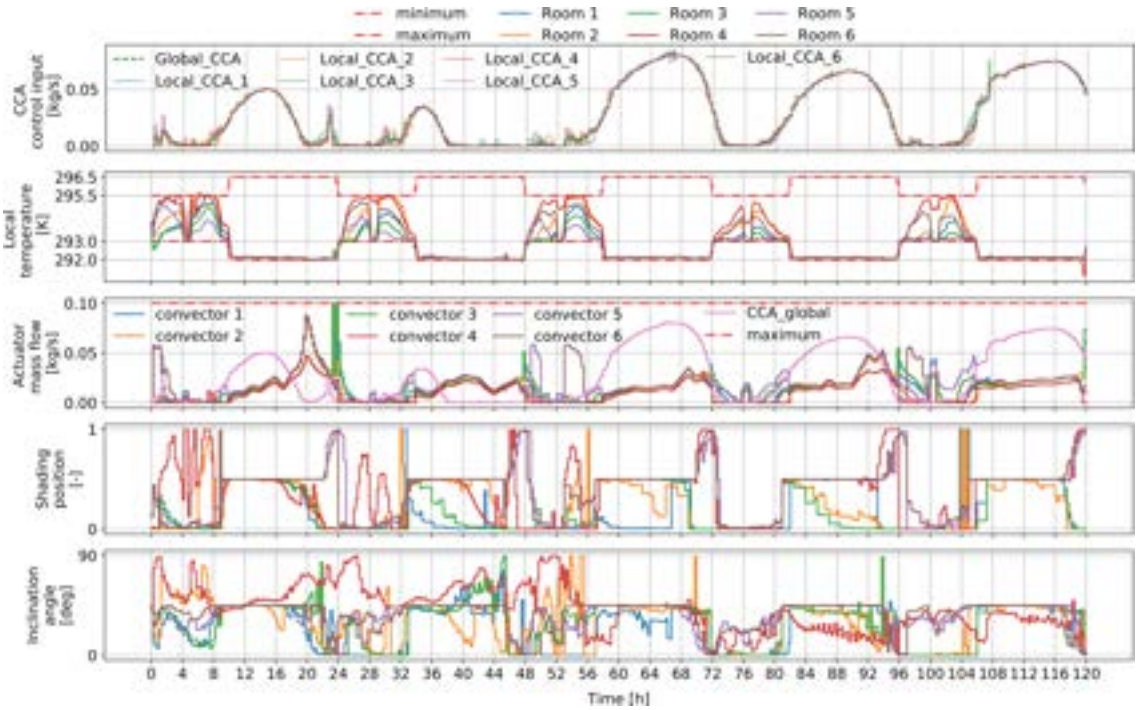

Figure 5: Non-hierarchical distributed MPC for the standard deviations σ = (0,0,0) (perfect forecast)

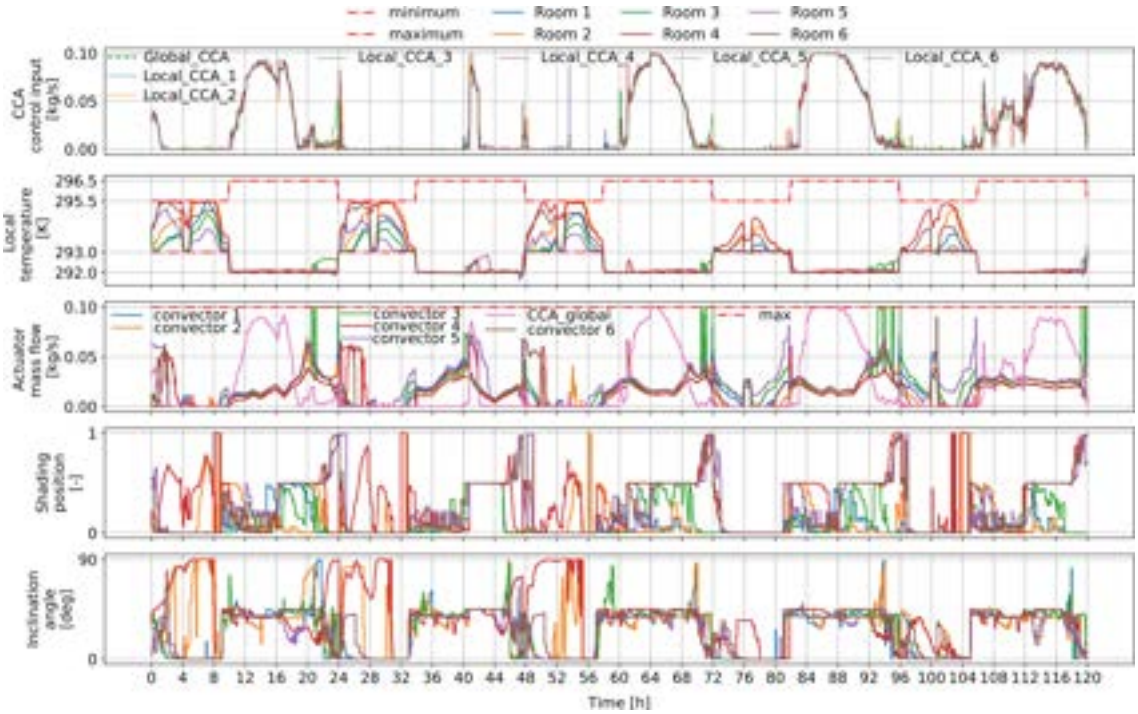

Figure 6: Hierarchical distributed MPC for the standard deviations σ = (0,0,0) (perfect forecast)

Forecast scenario σ = (0.5,50,0.1)

For the second scenario, the forecast errors are artificially generated based on normal distributions with fixed standard deviations for each disturbance quantity (0.5 for occupancy, 50 W/m^2 for the radiation quantities and 0.1 1/h for air exchange). The forecast errors are shown in Fig. 7 and range up to $\pm$1 for occupancy, $\pm$100 W/m^2 for the solar radiation quantities and $\pm$0.2 1/h for air exchange.

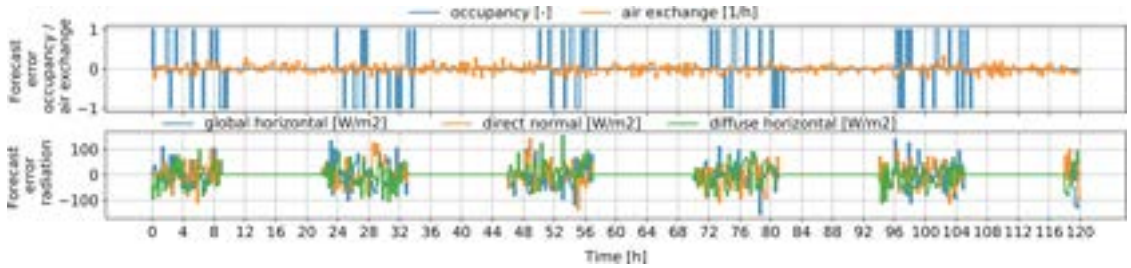

Figure 7: Forecast errors for the standard deviations σ = (0.5,50,0.1)

The simulation results for the non-hierarchical and the hierarchical distributed MPC are visualized in Fig. 8 and Fig. 9. As shown in the "Local temperature" subplots, the hierarchical MPC exhibits an increased reactivity to the occurring forecast errors and a higher capability of preserving thermal comfort and operating the room temperatures between the comfort bounds. For the non-hierarchical MPC, especially the lower comfort bounds are exceeded more frequently. This manifests itself during non-occupancy (e.g., during hours 38–46) and particularly during occupancy periods (e.g., during hours 48–58 and 72-84), when forecast errors are imposed on all disturbance quantities (see Fig. 7). The hierarchical MPC can reduce the thermal discomfort resulting from the operation of the non-hierarchical MPC (24.30 Kh) by 9.62 Kh (equivalent to a reduction of 39.6 %) resulting in a thermal discomfort of 14.68 Kh. The energy consumption for the hierarchical and non-hierarchical MPC are identical (679 MJ). The last three subplots of Fig. 8 and Fig. 9 reveal that the control inputs of the hierarchical MPC are operated in a more dynamic way to compensate for the forecast errors. The "CCA control input" subplots show a similar convergence for both MPC variants with few diverging outliers, which leads to an identical consensus MAE of 0.001 kg/s and an RMSE of 0.002 kg/s. The computation time for the hierarchical MPC (61 691 s) is approximately 3.4 times higher than the one for the non-hierarchical variant (18 173 s). The hierarchical MPC is seven times faster than real-time according to a computational time ratio of 0.14.

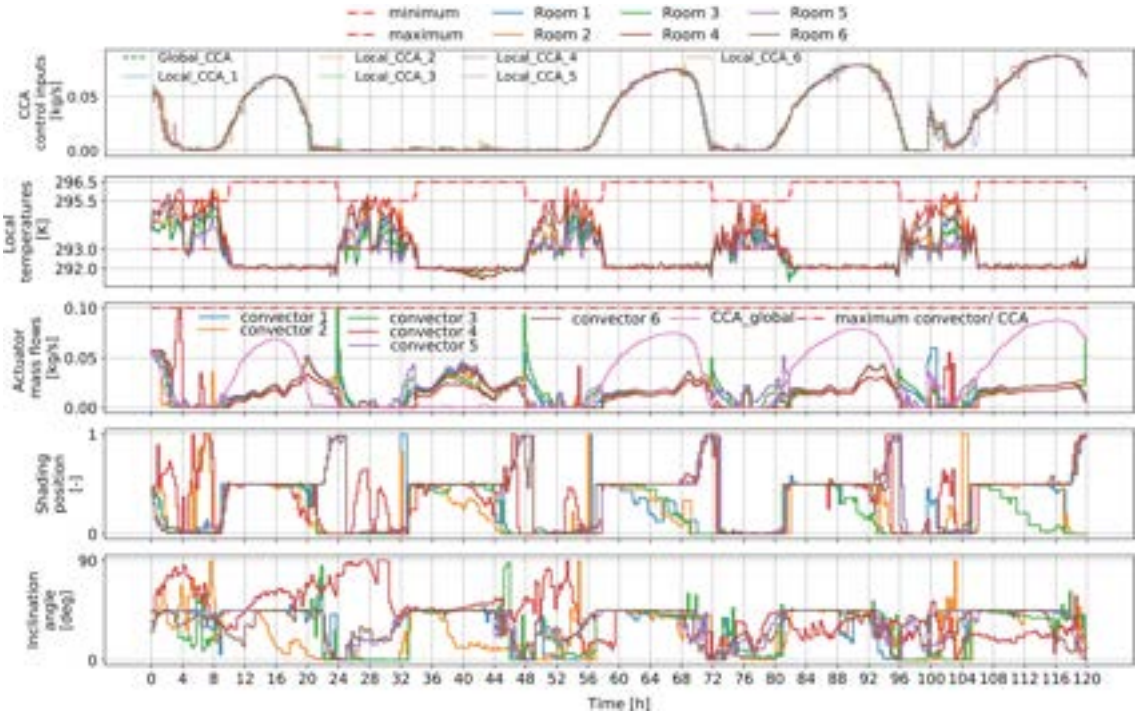

Figure 8: Non-hierarchical distributed MPC for the standard deviations σ = (0.5,50,0.1)

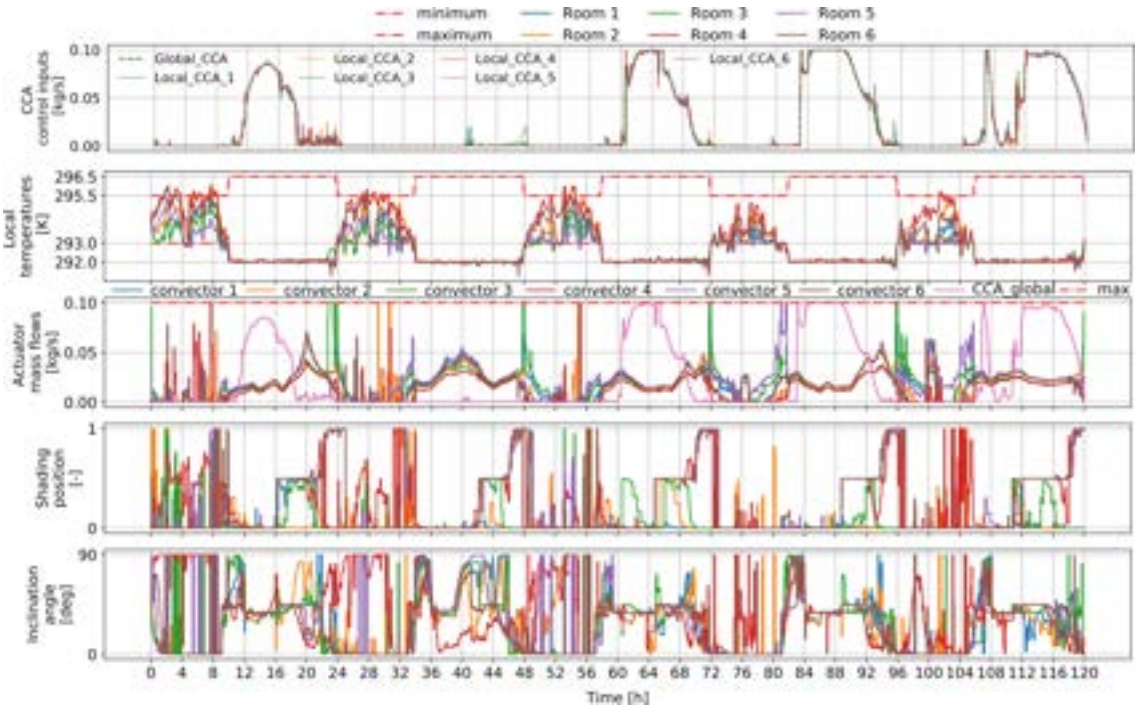

Figure 9: Hierarchical distributed MPC for the standard deviations σ = (0.5,50,0.1)

Forecast scenario σ = (1,100,0.2)

Figure 10 depicts the forecast errors for the σ = (1,100,0.2) scenario, which range up to $\pm$2 for occupancy, $\pm$200 W/m^2 for the solar radiation quantities and $\pm$0.4 1/h for air exchange. In Fig. 11 and Fig. 12, the performance of the non-hierarchical and hierarchical distributed MPC for this forecast scenario are shown. In analogy with the previous forecast scenario, the ”Local temperature” subplots manifest a substantially increased reactivity and ability of the hierarchical MPC to compensate for forecast errors. This shows itself by reducing the exceedance of both the lower (e.g., during hours 24–34, 34–48 and 72–82) and upper comfort bounds (e.g., during hours 100–106). The benefits of the hierarchical MPC are particularly revealed complying with the lower comfort bound, since in this case study, only heating actuators are included that are able to react to the forecast errors (apart from the predictive ”cooling” function of the solar shading). The exceedance of the comfort bounds, which is attributed to the deviation between predicted and real disturbance quantities, can be compensated in a shorter time by the hierarchical MPC benefiting from the small sampling period of the lower MPC layer. Thermal discomfort can be reduced from 43.25 Kh for the non-hierarchical to 30.91 Kh for the hierarchical MPC, which corresponds to a decrease of 28.5 % or an absolute reduction of 12.34 Kh. Again, the consumed energy is identical for both variants with 678 MJ.

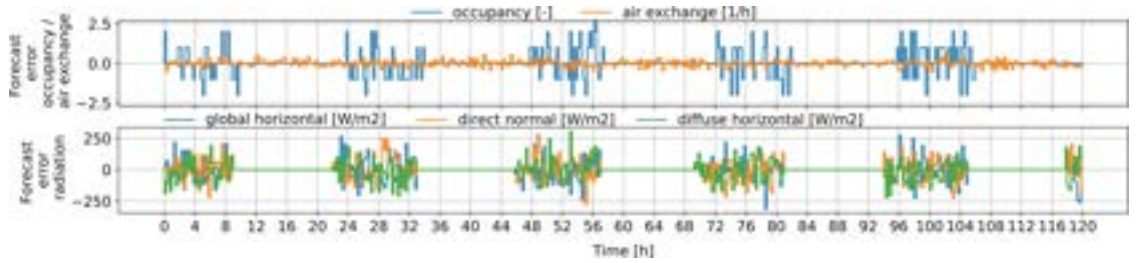

Figure 10: Forecast errors for the standard deviations σ = (1,100,0.2)

The subplots ”Actuator mass flow”, ”Shading position” and ”Inclination angle” exhibit the more dynamic operation of the control inputs. The potentially disturbing effect of frequent shading or wear and tear is not considered here. The focus is placed on the reactivity of the control and preservation of comfort. In future versions, constraining or penalizing the change in control inputs between two iterations could be added. The ”CCA control input” subplots show a comparable ADMM convergence for both MPC variants with an identical MAE of 0.001 kg/s and a consensus RMSE of 0.002 kg/s. The increased reactivity of the hierarchical MPC comes at the cost of three times larger computation times (computation time of 67 897 s for the hierarchical

and 20 245 s for the non-hierarchical MPC). With a computational time ratio of 0.16, the hierarchical MPC is six times faster than real-time.

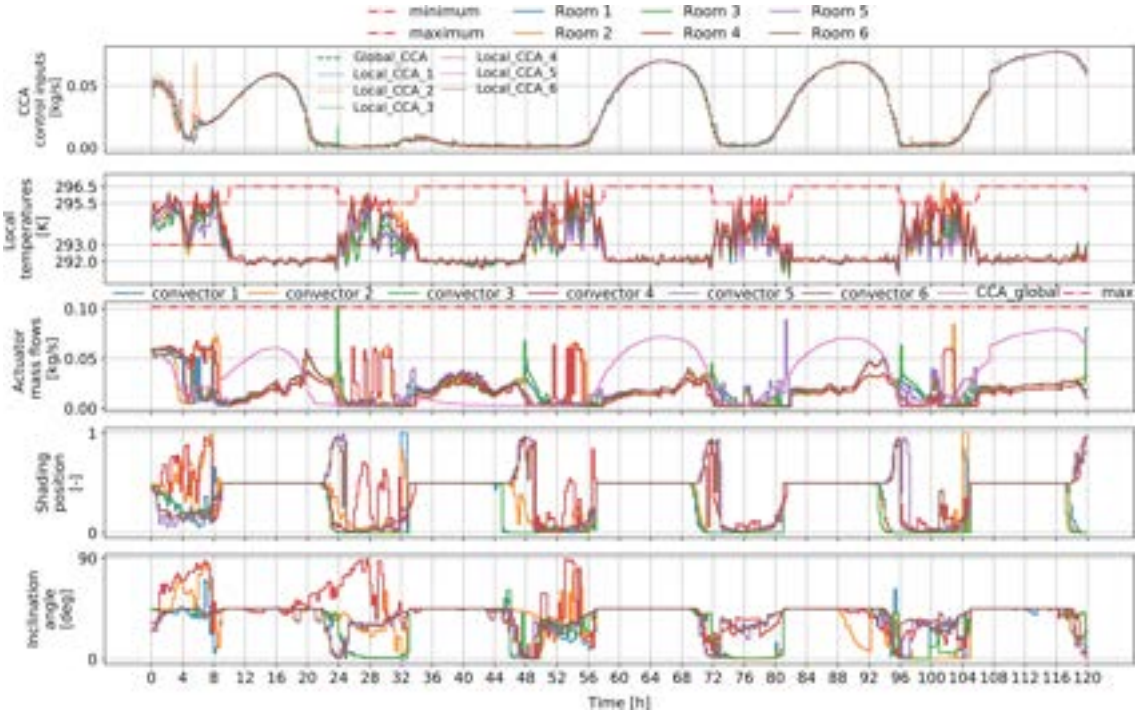

Figure 11: Non-hierarchical distributed MPC for the standard deviations σ = (1,100,0.2)

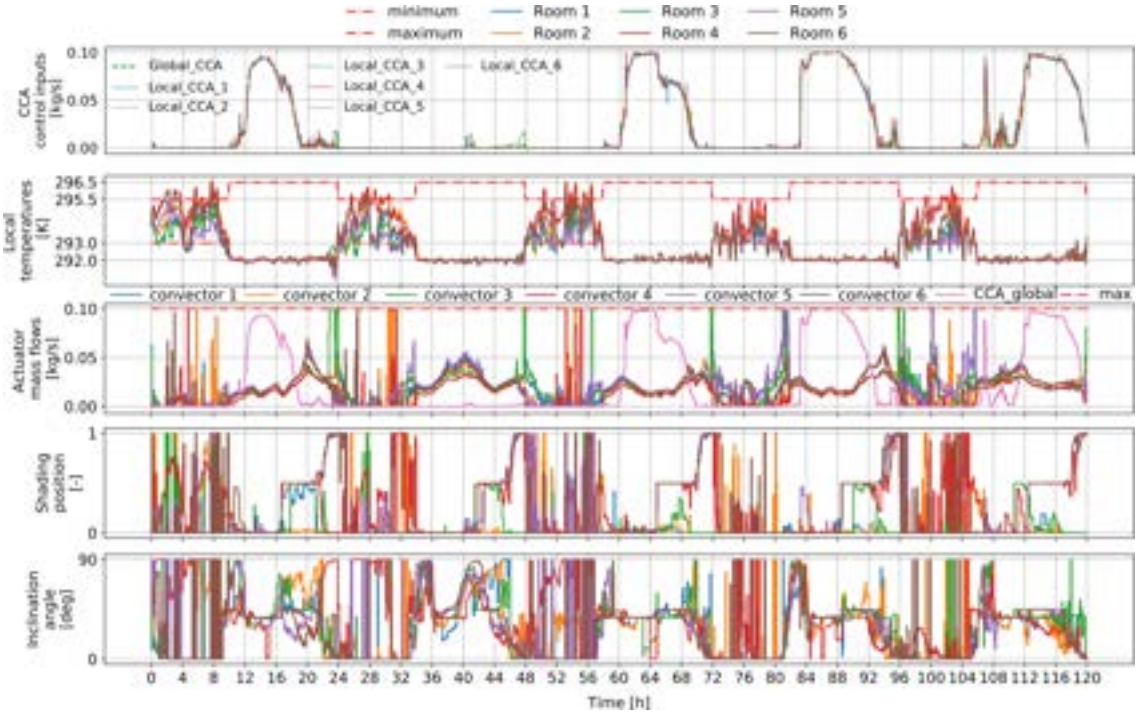

Figure 12: Hierarchical distributed MPC for the standard deviations σ = (1,100,0.2)

5. Conclusion

In this work, a hierarchical distributed MPC for building energy systems based on nonlinear Modelica controller models is presented. The MPC concept couples hierarchical and distributed optimization approaches to divide the optimization complexity within the temporal and spatial dimension and enable decoupled, modular modeling. The hierarchical optimization approach takes into account different dynamics in buildings and guarantees

both anticipation for components with high inertia and time delay as well as reactivity with respect to deviations between the predicted and the actual building behavior. The distributed optimization approach splits the optimization problem into subproblems to improve the scalability and real-time capability of the control while accounting for the coupling between the subproblems.

The flexibility and robustness of the proposed control approach are evaluated for different scenarios of the forecast accuracy for the disturbance quantities of occupancy, solar radiation and air exchange. The artificially generated forecast errors can be considered representative of any deviation between the predicted and real-world behavior of buildings. Applied to a six-room building Modelica model, the hierarchical distributed MPC demonstrates a considerably increased capability to keep the room temperatures within the comfort bounds and a relative discomfort reduction of 29 to 40 % for the scenarios with forecast errors in comparison to a non-hierarchical reference MPC. With an increase in forecast errors, the absolute thermal comfort that can be reduced by the hierarchical MPC increases. The increased reactivity comes at the cost of increased computation times. In the case study, the hierarchical distributed MPC manifests a good ADMM convergence and real-time capability by being six times faster than real-time.

In future work, the developed MPC framework will be practically applied to a multi-zone building including dynamic and inert (heating) actuators. Within the hierarchical MPC configuration, different model approximations/linearizations could be evaluated on the different layers focusing on specific components. Finally, integer optimization variables should be included for wider applicability in building control.

Acknowledgments

We gratefully acknowledge the financial support provided by the BMWK (Federal Ministry for Economic Affairs and Climate Action), promotional reference 03EGB0010A.

References

[1] United Nations Environment Programme. *2021 Global Status Report for Buildings and Construction: Towards a Zero-emission, Efficient and Resilient Buildings and Construction Sector*, 2021. URL `https://globalabc.org/resources/publications/2021-global-status-report-buildings-and-construction`.

[2] International Energy Agency. *Building Energy Performance Metrics- Supporting Energy Efficiency Progress in Major Economies*, 2015. URL `https://www.iea.org/reports/building-energy-performance-metrics`.

[3] Serale, G., Fiorentini, M., Capozzoli, A., Bernardini, D., Bemporad, A. *Model Predictive Control (MPC) for enhancing building and HVAC system energy efficiency: Problem formulation, applications and opportunities*. Energies, 11(3, 631), 2018. doi: 10.3390/en11030631.

[4] Drgoňa, J., Arroyo, J., Cupeiro Figueroa, I., Blum, D., Arendt, K., Kim, D., Ollé, E. P., Oravec, J., Wetter, M., Vrabie, D. L., Helsen, L. *All you need to know about model predictive control for buildings*. Annu. Rev. Control, 50:190–232, 2020. doi: 10.1016/j.arcontrol.2020.09.001.

[5] Cigler, J., Gyalistras, D., Siroky, J., Tiet, V.-N., Ferkl, L. *Beyond Theory: the Challenge of Implementing Model Predictive Control in Buildings*. In 11th REHVA world Congr. 8th Int. Conf. Energy Effic. Smart Heal. Build., pages 1008–1018, 2013.

[6] Mattsson, S. E., Elmqvist, H. *Modelica - An International Effort to Design the Next Generation Modeling Language*. IFAC Proc. Vol., 30(4):151–155, 1997. doi: 10.1016/s1474-6670(17)43628-7.

[7] Wetter, M., Van Treeck, C. *New Generation Computational Tools for Building and Community Energy Systems Annex 60 Final Report*. 2017. URL `http://www.iea-annex60.org/downloads/iea-ebc-annex60-final-report.pdf`.

[8] Scattolini, R. *Architectures for distributed and hierarchical Model Predictive Control – A review*. J. Process Control, 19(5):723–731, 2009. doi: 10.1016/j.jprocont.2009.02.003.

[9] Koehler, S., Danielson, C., Borrelli, F. *A primal-dual active-set method for distributed model predictive control*. Optim. Control Appl. Methods, 38(3):399–419, 2017. doi: 10.1002/oca.2262.

[10] Moroşan, P. D., Bourdais, R., Dumur, D., Buisson, J. *A distributed MPC strategy based on Benders' decomposition applied to multi-source multi-zone temperature regulation*. J. Process Control, 21(5):729–737, 2011. doi: 10.1016/j.jprocont.2010.12.002.

[11] Ma, Y., Anderson, G., Borrelli, F. *A distributed predictive control approach to building temperature regulation*. In Proc. 2011 Am. Control Conf., pages 2089–2094, San Francisco, CA, USA, 2011. IEEE. doi: 10.1109/acc.2011.5991549.

[12] Scherer, H. F., Pasamontes, M., Guzmán, J. L., Álvarez, J. D., Camponogara, E., Normey-Rico, J. E. *Efficient building energy management using distributed model predictive control*. J. Process Control, 24 (6):740–749, 2014. doi: 10.1016/j.jprocont.2013.09.024.

[13] Baranski, M., Fütterer, J., Müller, D. *Distributed exergy-based simulation-assisted control of HVAC supply chains*. Energy Build., 175:131–140, 2018. doi: 10.1016/j.enbuild.2018.07.006.

[14] Moroşan, P. D., Bourdais, R., Dumur, D., Buisson, J. *Distributed model predictive control for building temperature regulation*. In Proc. 2010 Am. Control Conf., pages 3174–3179, Baltimore, MD, USA, 2010. IEEE. doi: 10.1109/acc.2010.5530977.

[15] Li, Z., Zhang, J. *Study on the distributed model predictive control for multi-zone buildings in personalized heating*. Energy Build., 231:110627, 2021. doi: 10.1016/j.enbuild.2020.110627.

[16] Cai, J., Kim, D., Jaramillo, R., Braun, J. E., Hu, J. *A general multi-agent control approach for building energy system optimization*. Energy Build., 127:337–351, 2016. doi: 10.1016/j.enbuild.2016.05.040.

[17] Li, W., Wang, S. *A multi-agent based distributed approach for optimal control of multi-zone ventilation systems considering indoor air quality and energy use*. Appl. Energy, 275:115371, 2020. doi: 10.1016/j.apenergy.2020.115371.

[18] Hou, X., Xiao, Y., Cai, J., Hu, J., Braun, J. E. *Distributed model predictive control via Proximal Jacobian ADMM for building control applications*. In Proc. Am. Control Conf., pages 37–43, Seattle, WA, USA, 2017. IEEE. doi: 10.23919/ACC.2017.7962927.

[19] Lin, F., Adetola, V. *Flexibility characterization of multi-zone buildings via distributed optimization*. In 2018 Annu. Am. Control Conf., pages 5412–5417, Milwaukee, WI, USA, 2018. IEEE. doi: 10.23919/ACC.2018.8431400.

[20] Abreu, A., Bourdais, R., Guéguen, H. *Inter-Layer Interactions in Hierarchical MPC for Building Energy Management Systems*. IFAC-PapersOnLine, 50(1):12027–12032, 2017. doi: 10.1016/j.ifacol.2017.08.2136.

[21] Fiorentini, M., Cooper, P., Ma, Z., Robinson, D. A. *Hybrid Model Predictive Control of a Residential HVAC System with PVT Energy Generation and PCM Thermal Storage*. Energy Procedia, 83:21–30, 2015. doi: 10.1016/j.egypro.2015.12.192.

[22] Long, Y., Liu, S., Xie, L., K. H., J. *A hierarchical distributed MPC for HVAC systems*. In 2016 Am. Control Conf., pages 2385–2390, Boston, MA, USA, 2016. IEEE. doi: 10.1109/ACC.2016.7525274.

[23] Mork, M., Xhonneux, A., Müller, D. *Hierarchical Model Predictive Control for complex building energy systems*. Bauphysik, 42(6):306–314, 2020. doi: 10.1002/bapi.202000031.

[24] Mork, M., Xhonneux, A., Müller, D. *Nonlinear Distributed Model Predictive Control for multi-zone building energy systems*. Energy Build., 264:112066, 2022. doi: 10.1016/j.enbuild.2022.112066.

[25] Boydens, W., Helsen, L., Olesen, B. W., Laverge, J. *Renewable and Storage-integrated Systems to Supply Comfort in Buildings*. A & S/books on Architecture and Arts, 2021. doi: 10.5281/zenodo.5109932.

[26] Boyd, S., Parikh, N., Chu, E., Peleato, B., Eckstein, J. *Distributed optimization and statistical learning via the alternating direction method of multipliers*. Found. Trends Mach. Learn., 3(1):1–122, 2010. doi: 10.1561/2200000016.

[27] Müller, D., Lauster, M., Constantin, A., Fuchs, M., Remmen, P. *Aixlib - an Open-Source Modelica Library Within the IEA-EBC Annex 60 Framework*. In Proc. CESBP Cent. Eur. Symp. Build. Phys. BauSIM 2016, pages 3–9, Dresden, Germany, 2016.

[28] Åkesson, J., Årzén, K. E., Gäfvert, M., Bergdahl, T., Tummescheit, H. *Modeling and optimization with Optimica and JModelica.org-Languages and tools for solving large-scale dynamic optimization problems*. Comput. Chem. Eng., 34(11):1737–1749, 2010. doi: 10.1016/j.compchemeng.2009.11.011.

[29] *HSL. A collection of Fortran codes for large scale scientific computation.*, 2013. URL `http://www.hsl.rl.ac.uk/`.

[30] Wächter, A., Biegler, L. T. *On the implementation of an interior-point filter line-search algorithm for large-scale nonlinear programming*. Math. Program., 106(1):25–57, 2006. doi: 10.1007/s10107-004-0559-y.

Optimal integration of Power-to-Gas and district heating through waste heat recovery from electrofuel production

Agostino Gambarotta[a], Francesco Ghionda[a], Emanuela Marzi[a], Mirko Morini[a] and Costanza Saletti[a]

*[a] University of Parma, Parma, Italy, agostino.gambarotta@unipr.it; francesco.ghionda@studenti.unipr.it; emanuela.marzi@unipr.it,**CA**; mirko.morini@unipr.it; costanza.saletti@unipr.it*

Abstract:

The growing penetration of renewable energies, which have a fluctuating nature, requires the enhancement of energy system flexibility. This can be achieved through sector integration, which encompasses the conversion of energy into the most convenient vectors. In this regard, a promising option is represented by Power-to-Gas (PtG) technologies. They allow the direct conversion of surplus renewable electricity into fuels (e.g. green hydrogen or methane) and its long-term storage, operating as seasonal storage. The potential of PtG systems can be unlocked if the waste heat produced by exothermic components (e.g. electrolyzer and methanation reactor) is recovered and fed, for instance, into a district heating network (DHN) to be supplied to an end-user. However, since the operation of PtG systems may be discontinuous, a full integration of the fuel, electrical and heating sectors is possible only with advanced management and control tools. This work presents a control strategy based on Model Predictive Control, with the aim of operating the production of methane from a PtG system and the supply of waste heat to a DHN with minimal cost. The case study comprises an electrolyzer, a methanation reactor, storage tanks for hydrogen and methane, a boiler and a heat pump for upgrading the temperature level of the recovered heat. The controller feasibility is demonstrated through a Model-in-the-Loop simulation platform and its performances are compared to that obtained with a conventional controller. The novel controller enables a 54 % increase in operating margin and more than halves carbon dioxide emissions. A better exploitation of renewable energy is also obtained (+ 4.6 %), as well as an increase in the share of heat recovered from the PtG plant.

Keywords:

District Heating Network; Electrolyzer; Methanation; Model Predictive Control; Power-to-Gas; System Integration; Waste Heat Recovery.

1. Introduction

Due to the need to decarbonize the energy sector, a great effort is being made today to support the penetration of renewable energy sources (RES), and this is transforming the architecture of current energy systems. Indeed, the mismatch between energy production and demand creates challenges that add complexity and forces the integration of new technologies and solutions. This leads to a change in the conventional way of managing energy systems, and to the need to exploit the concept of Multi-Energy Systems (MES), which means to consider energy systems as a whole, and therefore to perform an overall optimization of energy exchanges, including sector integration.

Power-to-Gas (PtG) technologies are gaining importance in this context, enabling sector coupling through the production of synthetic fuels (i.e. electrofuels) from renewable electricity, as demonstrated by many ongoing research activities on this topic [1]. Electrofuels can be used as conventional fuels and even converted back into electricity when necessary: thus, they can serve as an energy storage solution avoiding renewable energy curtailments. As expected, the total efficiency of the process is low, but it can be increased by making profitable use of the waste heat. Indeed, being an exothermic process, when integrated into an energy system, a PtG plant can also provide additional heat to be used by the end-users. Böhm et al. [2] studied the potentials of coupling Power-to-Hydrogen with a District Heating Network (DHN), finding that there are several synergies and efficient interactions between them. While high-temperature electrolysis is comparable with industrial waste heat, low-temperature electrolysis is subject to infrastructure limitations: however, the modern low-temperature DHN represent an opportunity for its usage.

Due the complexity presented above, it is evident that when dealing with the problem of the future management of PtG systems integrated into MES, the control of such systems plays a key role. Indeed, how a PtG unit is integrated into the system and how it is operated, strongly influence its potential. Fischer et al. [3] found that Model Predictive Control (MPC) is a suitable control strategy for optimizing the operation of PtG technologies, mainly when such systems are integrated into complex MES. They successfully demonstrated the application

of an MPC for optimizing the operation of a PtG unit and on-site storage considering the limitations in energy networks and time variable electricity prices. Turk et al. [4] studied the application of an MPC for a system with PtG and gas storage for system flexibility, considering multiple uncertainties. The authors found that the MPC made it possible to reduce the wind curtailment and improve the economic performance of the system, compared with a traditional control strategy. They also investigated the impact of the MPC prediction horizon length on computational efficiency, finding that it should be selected based on the required computational efficiency and storage capacity of the system. Finally, Abdelghany et al. [5] investigated the implementation of a two-stage MPC for the integration of a PtG plant for hydrogen production from a wind farm, to be used for hydrogen-fueled road vehicles or for injection into the local grid. By using a two-stage predictive controller, they tackled different competing objectives and different time-scales, and optimally managed the interactions between the wind farm, end-user and power grid. As demonstrated by these studies, an intelligent control strategy is needed to successfully manage such systems. However, in the presented papers, the possibility of recovering the waste heat of the PtG plant was not considered.

Waste heat recovery was nonetheless studied by Huang et al. [6]. The authors analyzed the benefits of using a Mixed-Integer Linear Programming (MILP)-based economic MPC for the real time control of complex MES integrated with the production of hydrogen. They recovered the waste heat of a high temperature alkaline electrolyzer and used it directly in a DHN, achieving cost savings and a better exploitation of RES, compared to a conventional rule-based strategy.

Given the necessity to decarbonize current energy systems, a great effort is being made today in studying and applying novel control strategies and optimization tools in real systems for the integration of new technologies and for the exploitation of sector coupling. Nevertheless, being a complex problem, with many degrees of freedom, it is necessary to keep studying different applications and the benefits of the integration of PtG technologies in energy systems. In particular, considerable effort is still needed in the study of the smart management of PtG plants and of waste heat recovery from it, in order to exploit all the potentials of this technology.

The main contributions of this paper are the following:

- The development of a novel MPC controller with an integrated MILP algorithm for the optimal control of a PtG plant for the production of methane, coupled with a DHN for waste heat recovery.
- An innovative solution for recovering the waste heat from the PtG plant. A heat recovery circuit (HRC), which works at low temperatures, i.e. (40÷55) °C, is used to recover the waste heat of the PEM electrolyzer, the methanation reactor and the condenser, and then the low-temperature heat at 55 °C is upgraded by an industrial heat pump (HP) and is used in a DHN, as outlined in Figure 1.
- The quantification of the benefits of using the innovative control solution, compared to a conventional rule-based control strategy, by the implementation of both solutions in a Model-in-the-Loop (MiL) configuration.

2. Method

This section presents the methods exploited in this work: the concept of MPC, the optimization algorithm developed for its implementation and the detailed model used for the MiL application.

2.1. Model Predictive Control

The optimal control of a MES using smart control strategies is becoming more and more common and it is catching the attention of researchers and industries. Indeed, when using advanced control strategies, it is possible to perform the optimal management of complex systems, which follows the implemented objectives (such as cost or energy consumption minimization).

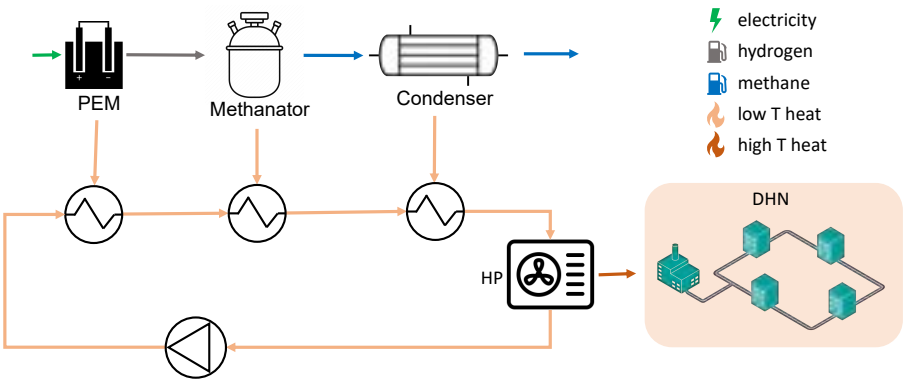

Figure 1: A schematic representation of the heat recovery from the Power-to-Gas plant.

MPC is a smart control strategy that has been demonstrated to be successful for many applications [7]. In this type of controllers, an optimization algorithm is embedded, which includes a simplified model of the system to control. At every time-step, the algorithm receives information on the actual behavior of the system, and calculates an optimal trajectory for the inputs over a future time-horizon, also known as prediction horizon, which is discretized into a certain number of time-steps. From this trajectory, only the first signal is implemented into the real system (e.g. as a set-point in low-level controllers), and after a time-step is passed, the system states are estimated and given again to the controller, together with the forecast of the disturbances, which repeats the calculation for a new prediction horizon.

With this control strategy, an optimal control of the system is allowed: the controller gives the optimal inputs to the system every time-step (e.g. 15 minutes), and there is an implicit feedback and feed-forward on the disturbances. Nevertheless, an adequate algorithm is needed to use this control strategy, which has to be fast and contain the model of the system to control. In this work, a MILP algorithm is used, which is described in detail in Paragraph 2.2.. The aforementioned advantages of using this technique, such as the consideration of the predicted disturbances, the possibility to handle constraints and the concomitant optimization, make MPC a suitable control technique for MES [6].

2.2. Optimization algorithm

As explained above, to develop an MPC controller, an optimization algorithm is required. It is embedded in the controller and calculates the optimal future trajectory for the control variables. Moreover, the algorithm needs to be fast, since it is run at every time-step, and needs to optimize the system over the entire prediction horizon. Among the existing optimization algorithms, the Mixed-Integer Linear Programming technique has revealed to be a successful optimization model for MES, if properly tailored to the case study. Indeed, this strategy makes it possible to optimize the systems with good accuracy and reasonable computational complexity. In addition, efficient commercial solvers are available for such problems, and the global optimality of the solution is guaranteed [8]. When using such approach, the equations that describe the physical behavior of the system must be linear, and therefore they need to be linearized. It is possible to model a general MES using the following components:

- **Conversion systems**: they represent all the plants involved, which transform the energy from one (or more) form to another one (or more), e.g. boilers, heat pumps, electrolyzers. To model them, the input-output relationship is linearized, and piecewise linearization can be used to consider variations in efficiency with the load [9, 10]. This formulation needs auxiliary variables and constraints, which are described in detail in [11]. Moreover, when necessary, the piecewise linearization has been performed on two variables (e.g. to model the compressor, the electrical energy used depends both on the gas mass flow rate and on the pressure ratio). While the piecewise linearization of one-degree of freedom performance curves is relatively straightforward, when the piecewise linearization is made on two variables, several piecewise linear approximation approaches exist. In this work, the triangle method was applied to those components that needed it [11]. In addition, for each plant, three operating modes can be modeled (ON, OFF and standby), and it is possible to set a start-up cost, as well as a minimum up-time (UT) and down-time (DT), and operating ramps, by adding additional equations and binary variables to the problem.
- **Energy storages**: they represent every component that can store energy, e.g. batteries, thermal energy storages, gas storage tanks. The equation that describes them relates the energy stored at the current time-step to the one stored at the previous time-step, by taking into account charge, discharge and self-discharge efficiencies.
- **Energy networks**: they are modeled as energy sinks/sources, to/from which the energy system can exchange energy by buying or selling it with certain costs, e.g. electricity grids, natural gas networks.
- **End-users and RES**: they are modeled as energy sinks/sources, with the needs to be fulfilled or the production rate given as disturbances to the algorithm.
- **Energy nodes**: they are not physical nodes, however, they are used to make sure the energy balance for each energy vector is fulfilled every time-step.

The optimization variables are all the power flows and the energy stored, and the algorithm calculates their optimal management for each time-step, in order to minimize the implemented objective function over the prediction horizon.

2.3. Simulation platform

As previously mentioned, the management presented was tested in a Model-in-the-Loop configuration. A detailed nonlinear model, which emulates the real system, was developed in the MATLAB®/Simulink® environment, and it was built by assembling the models of single energy system components. The application

consists of a wind farm, a PtG system for the production of synthetic methane and a DHN, which ensures heat supply to an end-user.

The Simulink® library used to model the DHN has already been presented in previous works [12], and it is composed of the pumping station blocks (expansion vessels and pumps), the heating network blocks (pipelines) and the thermal power unit blocks (boilers and heat exchangers). Nevertheless, for the present application, new components were developed, that constitute the PtG plant. The main components and how they were modeled is presented below.

Wind farm: this is an algebraic model which, starting from the undisturbed wind velocity module and direction $\mathbf{u}_{wind}$, and given the geometry of the wind turbines and their position in the wind farm, calculates the output electrical power production. It considers the wake effect by applying the Jensen wake model [13] and once the corrected wind velocity $\mathbf{u}_{wind_{corr}}$ for each turbine is determined, uses the power curve of the turbines to calculate the electricity generated: $P_{el} = f(\mathbf{u}_{wind_{corr}})$.

PEM electrolyzer: this is an algebraic model that, given the electrical power supplied and the operating mode returns the amount of hydrogen and the thermal power generated. It has three different operating modes: ON, OFF (i.e. no consumption, no production, cold start-up needed to switch on) and standby (i.e. no production, consumption of a certain amount of nominal electrical power, warm start-up needed to switch on). During the steady state operation, the relation for the efficiency of the electrolyzer is derived by interpolating operating data

$$\eta = \rho HHV \frac{aP_{el}^b + c}{P_{el}}, \tag{1}$$

and it is used to calculate the hydrogen flow rate produced as follows

$$\dot{V}_{H_2} = \frac{1}{\rho HHV} \eta P_{el}, \tag{2}$$

with ρ being the gas density, HHV its high heating value and P_{el} the input electrical power. The thermal power generated is calculated using the following equation

$$P_{th} = (1 - \eta) P_{el} - P_{loss}, \tag{3}$$

where P_{loss} represents the power loss and is calculated as $P_{loss} = \alpha P_{nom} + \beta P_{el} + \gamma P_{nom}$: the first term represents the losses due to the auxiliary systems, while the latter terms represent the linear model of the power losses in the conversion from AC to DC.

Methanation reactor: this is an algebraic model that correlates the input hydrogen flow to the output methane flow and thermal power generated. Similarly to the electrolyzer, it has three operating modes: ON, OFF and standby. In the steady state operation, the output flow is calculated using the yield of reaction y, which is estimated based on linear interpolation of experimental data as follows

$$y = a \frac{GHSV}{GHSV_{nom}} + b \tag{4}$$

where GHSV (gas hourly space velocity) is the rate between the total volumetric flow rate at inlet and the reactor's volume, and evaluates the load of the reactor.

Gas compressor: this is an algebraic model that, given the rotational speed, the input flow and the output desired pressure, calculates the output flow and the electrical power consumption. The block contains the performance maps of the turbocompressor for the calculation of the mass flow rate and of the polytropic efficiency, given the corrected rotational speed and the pressure ratio.

Gas storage: the proposed model represents a node in which the input flow is mixed with the gas inside the storage. It is a dynamic model that uses the energy balance and continuity equations for pressure and temperature calculation. In terms of causality, the incoming and outcoming flows are known, and the model calculates the pressure, temperature and composition of the gas contained in the storage. The energy stored is calculated using the gas HHV.

Gas pipeline: this is a dynamic model which, given the inlet pressure, temperature and composition, and the outlet pressure, calculates the output mass flow rate, temperature and composition of the gas. The mass flow rate is calculated as follows

$$\dot{m} = sign(\Delta p) \sqrt{\frac{|\Delta p| \rho A_{cs}}{\frac{\lambda L}{D_{in}} + Z}}, \tag{5}$$

where Δp is the pressure drop in the pipeline, A_{cs} the cross-section area of the pipeline, ρ the gas density, λ the friction factor, L the pipe length, D_{in} the inner diameter, and Z the total concentrated pressure drop. The governing equation for the temperature is the following

$$\frac{dT_{out}}{dt} = \frac{1}{\rho c_v V}\left(\dot{m}\left[(c_p T)_{in} - (c_p T)_{out}\right] - \dot{Q}_w\right), \tag{6}$$

where c_p is the gas specific heat at constant pressure, c_v the average gas specific heat at constant volume, V the volume of the pipeline and $\dot{Q}_w$ the heat exchanged through the wall.

Gas pressure reduction valve: this is an algebraic model that takes as inputs the income and outcome pressure, temperature and composition of the gas, and opening ratio of the valve φ , and returns the mass flow rate through the valve. The mass flow rate is calculated using the expansion factor Y, as

$$\dot{m} = N_x c_v Y \sqrt{\rho_{in} \Delta p}, \tag{7}$$

where N_x is a coefficient introduced to match the measurement units used.

Heat pump: this is an algebraic model in which the thermal power absorbed and that supplied by the heat pump are calculated based on the temperature of the cold and hot sources (T_c and T_h) and on the electrical power used P_{el}. The actual COP is calculated as follows

$$COP = \frac{COP_{nom}}{C_c(1-(1-C_c)}\frac{P_{el,nom}}{P_{el}}, \tag{8}$$

where C_c is a correction factor usually declared by the manufacturer, $COP_{nom} = \frac{COP_{max}}{\eta_{II}}$ and η_{II} is calculated with a lookup table with $\eta_{II} = f(T_c, T_h)$.

The inputs, outputs and states of the new components are reported in Table 1, while for the pumping station, heating network and thermal power unit blocks, the reader can refer to [12].

3. Application

This section describes the case study chosen and the main characteristics of the simulations. In addition, it presents how the control strategies have been implemented in the MiL application.

3.1. Case study description

The case study considered consists of a PtG plant for the production of synthetic methane, using the renewable electricity generated by a wind power plant. A simplified representation of the energy system is displayed in Figure 2.

The energy system is connected to the electrical grid and to the natural gas network, and it can exchange electricity and gas with them by buying and selling energy. The end-user has both electrical and thermal needs: the first are fulfilled by using the renewable electricity or by buying electricity from the power grid, while the latter are met with a gas-fueled boiler, and by recovering the waste heat from the PtG plant. Indeed, as mentioned above, two hot water circuits are employed: the HRC that works at low temperatures (40÷55) °C, in which three heat exchangers recover the waste heat from the PEM electrolyzer (available at a temperature of 55 °C), condenser (80 °C) and methanation reactor (290 °C), and the DHN which works at higher temperatures (60÷80) °C and is used for end-user heat supply (see Figure 1). An industrial heat pump (HP) connects the two circuits and upgrades the heat at 55 °C to the 80 °C needed for the DHN. The characteristics of the plants are shown in Table 2.

In Figure 2, all the energy flows involved are shown: the electricity produced by the wind farm can be used both for the fulfillment of the electrical needs, or by the PEM electrolyzer (PEM) that produces hydrogen,

Table 1: System components summary (Al = Algebraic, Dy = Dynamic).

Component	Model	Inputs	Outputs	States
Wind farm	Al	$\mathbf{u}_{wind}$	P_{el}	-
Electrolyzer	Al	P_{el}	$\dot{m}_{out}$, T_{out}, x_{out}, p_{out}	-
		Op mode	$\dot{m}_{H_2O}$, P_{th}, P_{loss}	
Methanation reactor	Al	$\dot{m}_{in}$, T_{in}, x_{in}	$\dot{m}_{out}$, T_{out}, x_{out}	-
		Op mode	P_{th}, P_{loss}	
Gas compressor	Al	N, p_{in}, p_{out}, T_{in}, x_{in}	$\dot{m}_{out}$, T_{out}, x_{out}, P_{el}	-
Gas storage	Dy	$\dot{m}_{in}$, T_{in}, x_{in}	p_{stor}, T_{stor}, x_{stor}	p_{stor}, T_{stor}, x_{stor}
Gas pipeline	Dy	p_{in}, T_{in}, x_{in}, p_{out}	$\dot{m}_{out}$, T_{out}, x_{out}	T_{pipe}
Valve	Al	p_{in}, T_{in}, x_{in}, p_{out}, φ	$\dot{m}_{out}$, T_{out}, x_{out}	-
Heat pump	Al	T_h, T_c, P_{el}	$P_{th_{out}}$, $P_{th_{in}}$	-

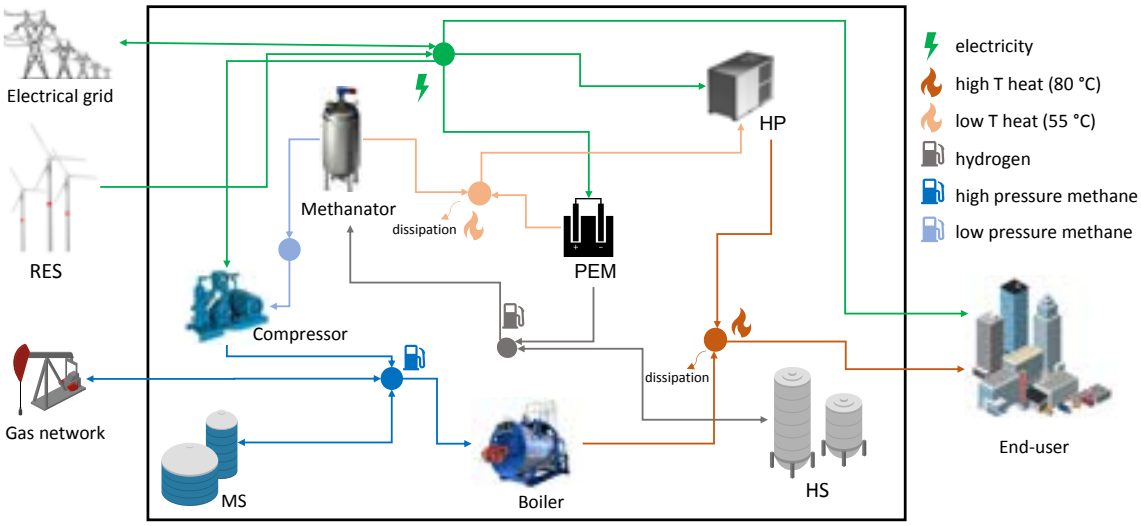

Figure 2: A schematic representation of the Multi-Energy System considered.

Table 2: Characteristics of the plants involved.

Technology	Parameter	Value	Technology	Parameter	Value
Wind farm	Number of turbines (-)	4	Boiler	Nominal inlet power (kW)	4000
	Nominal power (kW)	8000		Nominal efficiency (%)	92.4
Electrolyzer	Nominal inlet power (kW)	3750	Methanator	Nominal inlet power (kW)	2479
	Nominal operating temperature (°C)	55		Nominal operating temperature (°C)	290
	Nominal operating pressure (bar)	35		Nominal operating pressure (bar)	2.5
H_2 storage	Volume (m^3)	100	CH_4 storage	Volume (m^3)	100
	Maximum pressure (bar)	35		Maximum pressure (bar)	7.5
	Minimum pressure (bar)	2.5		Minimum pressure (bar)	3.5
Heat pump	Nominal inlet power (kW)	380			

and it is also consumed by the methane compressor and by the HP. The produced hydrogen can be stored in the hydrogen storage (HS) or used by the methanation reactor, which produces methane at low pressure (2.5 bar), which needs to be compressed before being used or stored in the methane storage (MS). After the compression, the methane can both be stored, sold, or used to feed the boiler, which produces the heat for end-user supply. In this work, the MPC controller is applied to a so-called system digital twin, which is a dynamic model, built by means of properly connecting the models of the single components involved which are developed in Simulink® and presented in Paragraph 2.3.. This allows the new control strategy to be tested, without affecting the operation of a real system. The controller is implemented as a supervisory controller, and gives the values of the manipulated variables calculated by the optimization algorithm as input set-points to low-level controllers (e.g. PID controllers) already implemented in the system.

3.2. Simulation setup

The main objective of this study is to compare the actual savings potential and the different management of the proposed MILP-based MPC with the use of a conventional rule-based control strategy. The following paragraphs present the two control strategies and describe how they are implemented.

3.2.1. MPC control

The schematic diagram of the MiL application of the MPC is shown in Figure 3: the MPC was set with a prediction horizon of two days and a time-step of one hour. At each time-step, the controller (i) gets the actual value of the system initialization variables, (ii) updates the forecast of the disturbances and the initial conditions and (iii) calls the optimization algorithm, which is run and returns the values of the optimal control variables as a result. The initialization and control variables, as well as the disturbances are described in Figure 3.

The objective function implemented is the maximization of the total operating margin of the system, which includes the costs of the electricity and natural gas bought and sold from/to the networks. The MILP algorithm described in Paragraph 2.2. was developed and adapted to the case study presented. The features of the linearization conducted to formulate the MILP algorithm are shown in Table 3, where it is specified whether or not the piecewise linearization has been conducted, its dimension, as well as the number of intervals employed. In addition, it is indicated if the UT, DT and operating ramps are modeled, as well as which operating modes are used.

The disturbances given to the MPC are the forecasts of end-user needs and the electrical power generated by the wind farm, and they are displayed in Figure 4 for the second simulated day. It is worth pointing out

that these forecasts are different from the disturbances applied to the Simulink® model, which represent the actual disturbances and are obtained by applying random deviations to the ideal disturbances given to the controller. In this way it is possible to evaluate how the predictive controller reacts to disturbances other than those expected, which usually happens in real applications.

3.2.2. Rule-based control

Depending on the definition of the conventional control strategy, the improvement due to management with the MPC control can vary, therefore a suitable and efficient rule-based control was developed. With this control strategy, the same set-points given by the MPC are calculated based on the logic displayed in Table 4.

It needs to be mentioned that the boiler set-point is not calculated with this control logic, and its input power is regulated through a PI controller, which keeps the supply temperature of the DHN equal to 80 °C. In addition, the actual amount of methane exchanged with the network is the set-point given for the methane sold minus the methane needed for the boiler.

3.3. Key Performance Indicators

To evaluate the results obtained, some Key Performance Indicators (KPIs) regarding the cumulative results of the second simulated day were analyzed. The KPIs identified are:

- Operating margin (EUR): the net revenue of the electricity and methane exchanged with the networks. Thus, it is the difference between the cost of the energy sold and the cost of the energy bought during the simulated period.
- CO_2 emissions ($kg_{CO_2,eq}$): the amount of carbon dioxide which is emitted due to the operation of the energy system. In particular, it considers the emissions related to the methane and electricity bought from the networks. Indeed, it was assumed that the electricity produced by the wind farm is associated with zero emissions, as well as the synthetic methane produced with the PtG plant. For the electrical grid, a coefficient of 224 gCO_2/kWh was considered [14], while for the gas 200.8 gCO_2/kWh [15].
- RES usage (%): the percentage of renewable electricity which is used by the system, and therefore not sold to the electrical grid.
- Gas production (kWh): the amount of methane produced by the Power-to-Gas system.
- Heat recovered share (%): the percentage of user thermal needs covered with the heat recovered from the PtG plant.

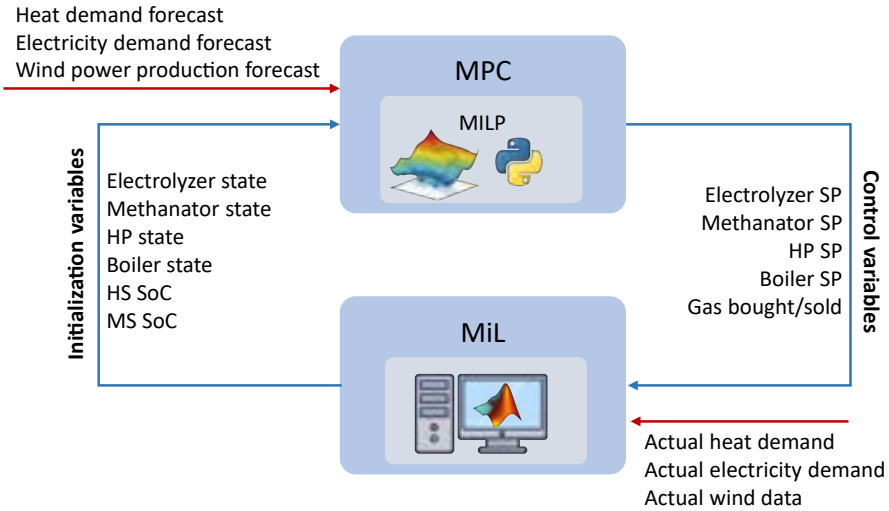

Figure 3: Model-in-the-Loop control with MPC (SP = set-point, SoC = State of Charge).

Table 3: Features of the model linearization for MILP formulation.

Component	Method	Intervals	Parameters	UT/DT	Ramps	Op. modes
Electrolyzer	piecewise 1D	1×3	$P_{out_{H_2}}, P_{out_{th}} = f(P_{in_{el}})$	no	no	ON/OFF/standby
Methanator	piecewise 1D	1×2	$P_{out_M}, P_{out_{th}} = f(P_{in_{H_2}})$	yes	yes	ON/OFF/standby
Gas compressor	piecewise 2D	2×2	$P_{in_{el}} = f(P_{in_{ng}}, E_{stor_{ng}})$	no	no	ON/OFF
Boiler	linear	1×1	$\eta_B = 92.2\,\%$	no	no	ON/OFF
Heat pump	linear	1×1	$COP = 5.42$	no	no	ON/OFF
H_2 storage	linear	1×1	$\eta_{ch} = \eta_d = 95\,\%$	-	-	-
Methane storage	linear	1×1	$\eta_{ch} = 95\,\%$, $\eta_d = 0.85\,\%$	-	-	-

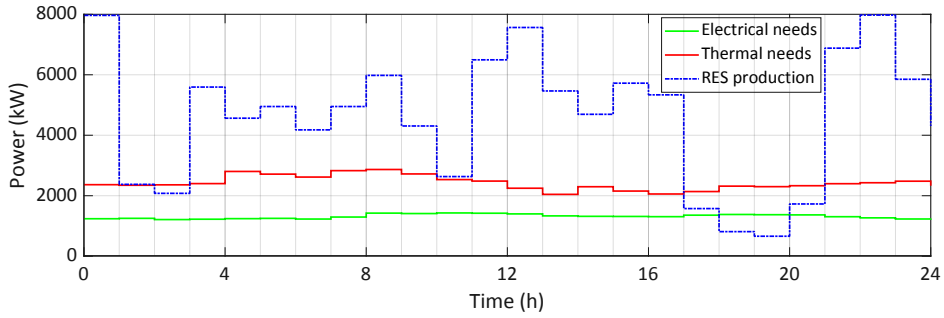

Figure 4: Forecasts of the disturbances given to the MPC controller for the second day.

Table 4: Rule-based control strategy definition.

Variable	Condition	Set-point value
Electrolyzer input power	$SoC_{HS} \leq 80\,\%$	$\min\{P_{nom}, (P_{wind} - P_{el_{user}})\}$
	otherwise	0
Methanator input power	$SoC_{HS} > 60\,\%$ & $SoC_{MS} \leq 95\,\%$	P_{nom}
	$SoC_{HS} > 60\,\%$ & $SoC_{MS} > 95\,\%$	$0.5\ P_{nom}$
	otherwise	0
Heat pump input power	methanator ON & $P_{th_{user}} > 0$	P_{nom}
	otherwise	0
Methane sold	$SoC_{MS} > 70\,\%$	1200 kW
	$30\,\% \leq SoC_{MS} \leq 70\,\%$	600 kW
	$SoC_{MS} < 30\,\%$	0 kW

4. Results and discussion

As previously explained, the aim of the simulations is to test the benefits of a novel controller based on MPC applied to a PtG plant coupled with a DHN. In order to do so, the novel control strategy was compared to a conventional rule-based one (see Paragraph 3.2.). The simulations were carried out over two days: nevertheless, the rule-based control strategy is used in both simulations on the first day, in order to have the same initial conditions for the second day, in which the two control strategies are compared. Therefore, the results are collected during the second day and only these results will be discussed.

Figure 5 shows how the electricity is managed with the two control strategies during the second day: it displays the energy balance among production, usage and exchange with the grid. It is possible to note that with the MPC strategy, less electricity is exchanged with the grid, and the renewable electricity is mainly used to work the electrolyzer and the HP for heat recovery. Indeed, this can be also seen in Figure 6: here, the total amount of energy exchanged with the networks during the entire day is displayed. With the rule-based control, a larger amount of electricity is sold to the grid, and at the same time a larger amount of methane needs to be bought from the gas network. Indeed, when the electrolyzer and methanation reactor are not operating, it is necessary to buy the gas needed to work the boiler, in order to fulfill the thermal needs of the user. This result shows that

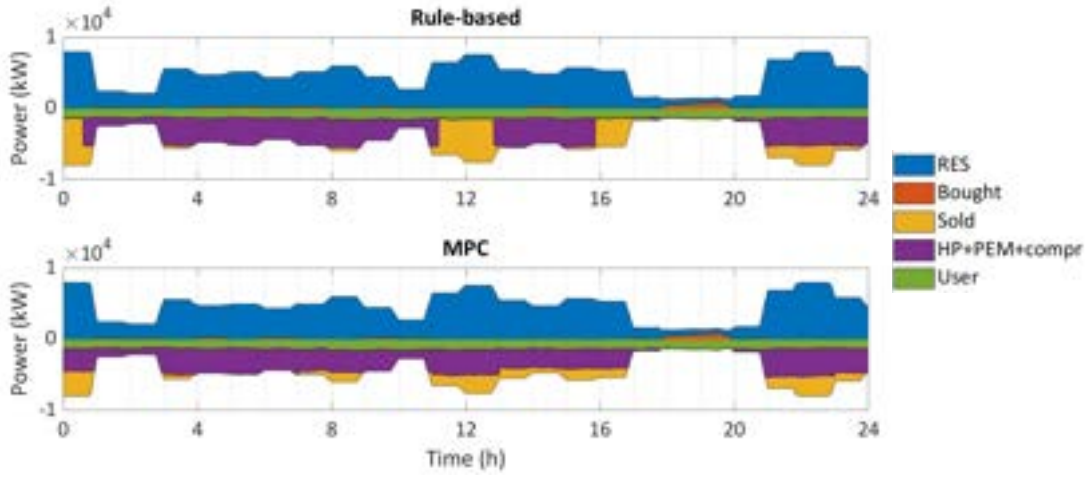

Figure 5: Energy balance at the electricity node (RES = wind power produced, Bought/Sold = exchanges with the power grid, HP = heat pump, PEM = PEM electrolyzer, compr = compressor, User = user needs).

it is better to exploit the self-produced energy as much as possible and to reduce the energy exchanges with the networks to a minimum to obtain a cheaper operation for the system. In addition, with such management, grid unbalances are prevented, as well as renewable energy curtailments.

In Figure 7, both the set-point and the actual input power to the methanation reactor are shown. The set-point is the actual set-point exiting the low-level proportional controller, and thus takes into consideration a correction based on the behavior of the hydrogen storage that corrects it in order not to exceed the storage limits. It can be seen that with the two control strategies the management is different. In fact, with the rule-based control, the set-point is kept constant most of the time at part load, while with the MPC a more precise set-point can be defined, which allows makes it possible to optimally manage the system and minimize the objective function.

Figure 8 shows the actual input power of the electrolyzer with the two approaches, and the State of Charge of the hydrogen storage. Indeed, these two dimensions are strongly related to each other. It can be noted that with the rule-based control strategy there are some periods in which the electrolyzer must be switched off since the hydrogen storage is too full. This does not happen with the MPC, which can optimally manage the electrolyzer and switch it off only when there is not enough RES production (see Figure 4).

In Table 5 the values obtained for the KPIs identified in Paragraph 3.3. are displayed. As expected, the operating margin of the system is higher when the MPC is used, since its maximization is the objective implemented in the optimization, and in one day it is possible to increase the operating margin by 54 % (around 475 EUR). In addition, with the MPC better results are obtained also for the CO_2 emissions, which are more than halved compared with the ones obtained using the rule-based control. Furthermore, when looking at the RES usage,

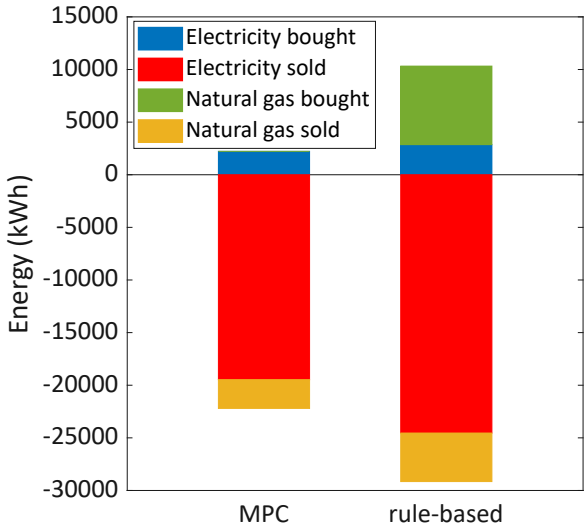

Figure 6: Bar plot with energy exchanged with the networks during the entire day.

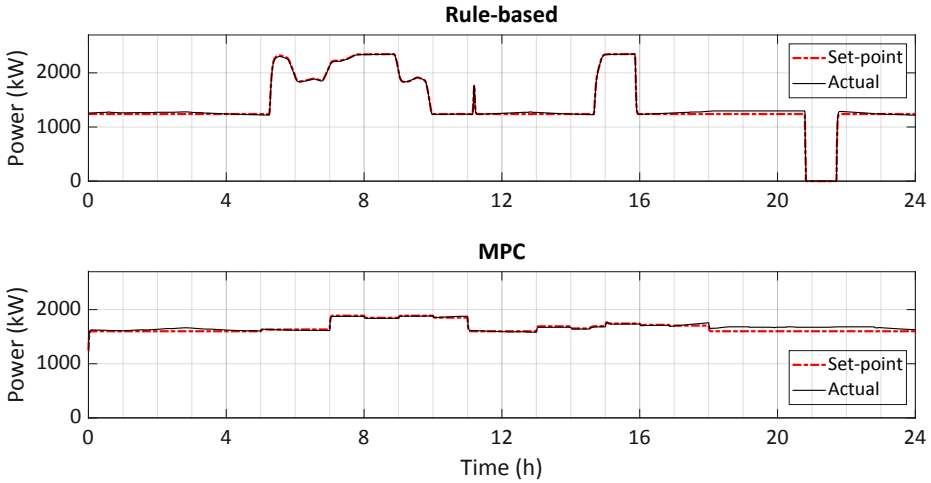

Figure 7: Input power set-point given to the methanation reactor with the two control strategies and actual input power.

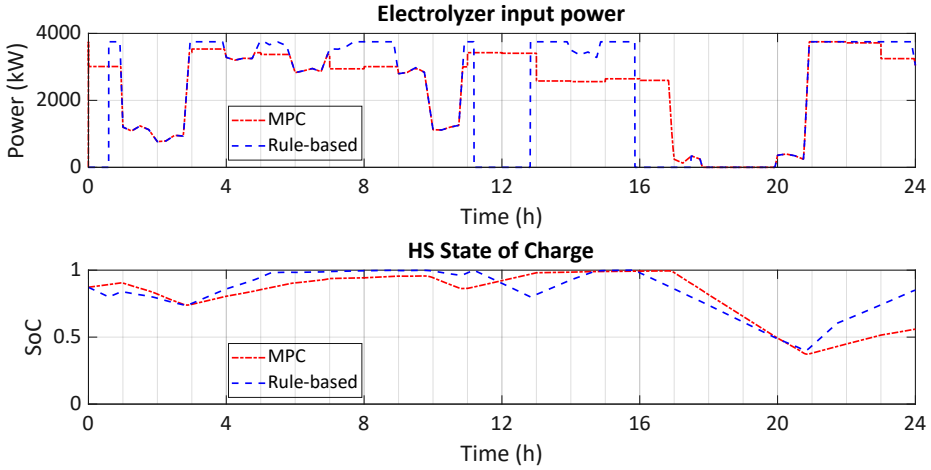

Figure 8: Actual input power of the electrolyzer and State of Charge of the hydrogen storage with the two control strategies.

Table 5: Values of the KPIs with the two control strategies.

Value	Rule-based control	MPC	Difference
Operating margin	874 EUR	1 349 EUR	**+ 475 EUR**
CO_2 emissions	2 139 $kg_{CO_2,eq}$	498 $kg_{CO_2,eq}$	**- 1 641** $kg_{CO_2,eq}$
RES usage	77.7 %	82.3 %	**+ 4.6 %**
Gas production	86 390 kWh	102 366 kWh	**+ 15 976 kWh**
Heat recovered share	42.0 %	44.8 %	**+ 2.8 %**

it is shown that with the MPC 4.6 % more renewable energy is exploited, and this leads also to a higher production of methane. Finally, the recovered heat is higher with the MPC: in particular with this strategy 44.8 % of the thermal demand is met by the recovered heat (2.8 % more than with the rule-based control).

It is worth noting that with the MPC better results are obtained for all the KPIs: this shows that maximizing the operating margin, the management of the system is more efficient under several aspects.

5. Conclusions

The energy transition is forcing the penetration of renewable energy sources and of new technologies into energy systems. Among them, Power-to-Gas solutions allow the production of synthetic fuels from renewable electricity, enable the storage of surplus electricity and permit sector integration. Due to these changes, energy systems are becoming increasingly complex and it is necessary to employ efficient and intelligent control strategies to manage them, in order to fully unlock the benefits of the novel solutions.

In this work, a controller based on Model Predictive Control was presented and it was applied to an integrated system with the production of methane from renewable electricity, with the objective of increasing the operating margin. Besides, a novel solution to recover the waste heat from Power-to-Gas exothermic components was proposed, which uses a heat pump to upgrade the heat available at low-temperature from the plant to the level of the supply temperature needed by a district heating network. The developed controller was tested in a Model-in-the-Loop configuration and compared to a traditional rule-based control strategy.

The results show that with the developed controller it is possible to have smarter energy management: indeed, the operation of the components and storage tanks is improved and the operating margin of the system is increased by 54 % in one day. In addition, with the novel controller 4.6 % more renewable electricity is exploited and the total emissions of carbon dioxide are strongly reduced, compared with the rule-based control.

Future studies will examine how the controller performs when adapted to different case studies and the use of different objective functions, which may include the minimization of energy consumption or carbon dioxide emissions. Furthermore, to fully understand the possible role of Power-to-Gas in the energy transition toward a sustainable energy framework, its potential as a long-term storage solution needs to be identified. To do that, the developed controller will be coupled with a supervisory controller, based on Model Predictive Control, which will provide it with further constraints regarding the correct long-term operation of the system. In this way, it would be possible to fully exploit the capabilities of Power-to-Gas as a seasonal storage solution.

Nomenclature

A_{cs}	Cross-section area of pipeline, m^2
C_c	Correction factor, $-$
c_p	Specific heat at constant pressure, $J/(kgK)$
c_v	Specific heat at constant volume, $J/(kgK)$
D_{in}	Inner diameter of pipeline, m
DT	Down-Time
DHN	District Heating Network
E	Energy, kWh
HHV	High Heating Value, kJ/kg
HRC	Heat Recovery Circuit
KPIs	Key Performance Indicators
L	Length of pipeline, m
λ	Friction factor, $-$
$\dot{m}$	Mass flow rate, kg/s
MES	Multi-Energy System
MiL	Model-in-the-Loop
MILP	Mixed-Integer Linear Programming
MPC	Model Predictive Control
N	Rotational speed, rpm
η	Efficiency, $-$
P	Power, kW
p	Pressure, Pa
PtG	Power-to-Gas
φ	Valve opening ratio,
$\dot{Q}_w$	Heat lost through wall, J/s
ρ	Density, kg/m^3
SoC	State of Charge
t	Time, h
T	Temperature, K
$\mathbf{u}$	Velocity, m/s
UT	Up-Time
V	Volume, m^3
$\dot{V}$	Volumetric flow rate, m^3/s
x	Mole fraction, $-$
y	Yield of reaction, $-$
Y	Valve expansion factor, $-$
Z	Total concentrated pressure drop through the pipeline, Pa

Subscripts and superscripts

c	cold
ch	charge
d	discharge
el	electrical

h hot

in input

nom nominal

out output

stor stored

th thermal

References

[1] Marzi, E., Morini, M., Gambarotta, A., *Analysis of the status of research and innovation actions on electrofuels under horizon 2020*. Energies 2022;15(2), 618.

[2] Böhm, H., Moser, S., Puschnigg, S., Zauner, A., *Power-to-hydrogen & district heating: Technology-based and infrastructure-oriented analysis of (future) sector coupling potentials*. International Journal of Hydrogen Energy 2021;46(63), 31938-31951.

[3] Fischer, D., Kaufmann, F., Hollinger, R., Voglstätter, C., *Real live demonstration of MPC for a power-to-gas plant*. Applied Energy 2018;228, 833-842.

[4] Turk, A., Wu, Q., Zhang, M., *Model predictive control based real-time scheduling for balancing multiple uncertainties in integrated energy system with power-to-x*. International Journal of Electrical Power & Energy Systems 2021;130, 107015.

[5] Abdelghany, M. B., Shehzad, M. F., Mariani, V., Liuzza, D., Glielmo, L., *Two-stage model predictive control for a hydrogen-based storage system paired to a wind farm towards green hydrogen production for fuel cell electric vehicles*. International Journal of Hydrogen Energy 2022;47(75), 32202-32222.

[6] Huang, C., Zong, Y., You, S., Træholt, C., *Economic model predictive control for multi-energy system considering hydrogen-thermal-electric dynamics and waste heat recovery of MW-level alkaline electrolyzer.* Energy Conversion and Management 2022;265, 115697.

[7] Blaud, P. C., Haurant, P., Claveau, F., Lacarrière, B., Chevrel, P., Mouraud, A., *Modelling and control of multi-energy systems through multi-prosumer node and economic model predictive control.* International Journal of Electrical Power and Energy Systems 2020;118, 105778.

[8] Urbanucci, L., *Limits and potentials of Mixed Integer Linear Programming methods for optimization of polygeneration energy systems*. ATI 2018: Proceedings of the 73rd Conference of the Italian Thermal Machines Engineering Association; 2018 Sept 12-14; Pisa, Italy. Energy Procedia, 148, 1199-1205.

[9] Maier, L., Schönegge, M., Henn, S., Hering, D., Müller, D., *Assessing mixed-integer-based heat pump modeling approaches for model predictive control applications in buildings.* Applied Energy 2022;326, 119894.

[10] Bischi, A., Taccari, L., Martelli, E., Amaldi, E., Manzolini, G., Silva, P., Campanari, S., Macchi, E. , *A detailed MILP optimization model for combined cooling, heat and power system operation planning*. Energy 2014;74, 12-26.

[11] D'Ambrosio, C., Lodi, A., Martello, S., *Piecewise linear approximation of functions of two variables in MILP models*. Operations Research Letters 2010;38(1), 39-46.

[12] De Lorenzi, A., Gambarotta, A., Morini, M., Rossi, M., Saletti, C., *Setup and testing of smart controllers for small-scale district heating networks: An integrated framework*. Energy 2020;205, 118054.

[13] Yang, K., Kwak, G., Cho, K., Huh, J., *Wind farm layout optimization for wake effect uniformity*. Energy 2019;183, 983-995.

[14] Statista 2023. *Carbon intensity of the power sector in Italy from 2000 to 2021* Available at: `https://www.statista.com/statistics/1290244/carbon-intensity-power-sector-italy/` [accessed 14.3.2023].

[15] volker-quaschning.de. *Specific carbon dioxide emissions of various fuels* Available at: `https://www.volker-quaschning.de/datserv/CO2-spez/index_e.php` [accessed 14.3.2023]

Large building stock energy simulation for the design of district heating networks : A case study on building retrofit policies

Mazarine Roquet[a] and Pierre Dewallef[b]

[a] University of Liège, Liège, Belgium, mazarine.roquet@uliege.be
[b] University of Liège, Liège, Belgium, p.dewallef@uliege.be

Abstract:

The Belgian building sector is responsible for a significant share of greenhouse gas emissions, partly because of the poor quality of its insulation and partly because fossil fuels are the main energy source for heating buildings. To decarbonize the heating of urban housing, district heating networks are good candidates. Indeed, district heating networks allow to improve load factor, to combine heat and power, to recover waste heat or to diversify the energy sources, including renewable sources (biomass, solar, geothermal, etc.). To design an efficient district heating network and take most of the improved load factor, a very precise knowledge of the heating needs of the buildings connected to the network is required. Thus, the first part of this work consists in creating robust, detailed, and automated physical models of the building stock, its equipment, and its use profiles to obtain detailed hourly load curve. The modelling tool used is the existing open-source Modelica library IDEAS, developed by the KU Leuven. The second part of the work includes the construction of a district heating network model and its regulation. This model is then coupled to the building simulation model. The combination of these two models allows to study the impact of a change in setpoint temperature in buildings or a massive insulation of the building stock on the buildings load curves and than on the regulation of the district heating network. The considered case study is a six buildings district of the University of Liège located on the Sart Tilman campus. The application of the building modelling methodology and energy saving policies to the test case shows that the approach considered is appropriate from a practical (easy scalable) and accuracy point of view and that energy saving measures cannot be taken without studying the consequences on the network operation.

Keywords:

District Heating Network, Building Simulation, Retrofit Policies, Large Building Stock

1. Introduction

The building sector is responsible of a significant part of the greenhouse gas emissions in Europe. According to [1], it is second largest contributor to greenhouse gas emissions in Belgium. This state of affair is mainly due to the use of fossil fuel combustion to heat the building and provide domestic hot water. The recourse to other primary energy sources is often expensive or not feasible when considering each building individually. District heating networks, on the other side, offer a different perspective by grouping the heat demands of different buildings on one single infrastructure thus providing economy of scales. District heating networks are also known to better exploit renewable energy resources such as biomass, solar or geothermal energy. Yet, developing and operating district heating networks is a challenging task as heat is difficult to transport efficiently and requires large investments.

Apart from the obvious economy of scales obtained from centralised rather than local heat production, an important advantage of district heating networks resides in the fact that all connected consumers will not need their peak consumption at the same time. Therefore, the rated power of the district heating network may be lower than the sum of the connected peak demand of the individual consumers. This improves the load factor and allows to leverage the high investment costs. Yet, taking advantage of the aggregation of loads requires a very accurate knowledge of the heating demands all throughout the year. To do so, monitoring data could be used to analyse the opportunity of district heating networks and optimise their structure and operation [2], however monitoring data for heating demands are very difficult to find and simulation is very often used instead to deduce heat demand curves.

A very large number of methodologies have been developed to obtain these demand curves from the building characteristics. They range from the very well known degree-days method [3] coupled to daily demand profiles [4] to the use of heating degree-hours and other methods such the one developed in the library *Demandlib* (see [5] for more details) that is based on air temperature and benchmark data. The very first scope of these

approaches is to simulate very large stock of buildings with synthetic information (the surface and the usage of the building) to determine an average heating demand curve directly from annual energy consumption data. These methods have the advantage of requiring very little data but do not take into account the individual properties of the buildings (e.g., orientation, occupant behaviour, ...) and also depend on a standard base temperature under which the building requires heating [6]. A slightly more advanced approach is considered by the library TEASER (see [7] for more details) where building archetypes, statistical data and national and international standards are used to simulate a large number of buildings from a minimum of information while maintaining the accuracy.

In this work, the aforementioned methods are not appropriate as the individual character of every buildings is overlooked, which prevents from properly predicting the peak loads and therefore to correctly evaluate the opportunity of lumping different loads altogether on one district heating system to improve the load factor. For example, while the tool TEASER enables the simulation of a large number of buildings in a dynamic and rapid manner, it is still built from archetypes. One of the goal of this contribution is to be able to model buildings taking into account their particular characteristics when they are available while considering standard configuration when they are not. It is especially the case for tertiary buildings whose structure changes widely from one building to the other and where different usages will generate totally different heat demand curve. The desired modelling must therefore be parametrised, based on observable characteristics, while remaining fast, robust and, hopefully, accurate. The first contribution of this work consists in defining a quick and accurate modelling methodology applicable to tertiary buildings. Moreover, the fact that the model is parametrised with observable characteristics (insulation thickness, orientation, window type, schedule of heating, regulation, ...) rather than on standards makes it possible to investigate specific energy saving measures in great details and to evaluate their influence on the operation of district heating networks.

The important outcome of the simulation are the peak demand (both in time and amplitude), the base demand and the total energy consumption per month and per year. As a result, it is possible to evaluate the impact of energy saving measures on the regulation and operation of the district heating network. On the one hand, a methodology to model the buildings is first established. Then, the district heating network is introduced and the basic assumptions are laid out. Two energy saving measures are considered herein namely, a change in user behaviour (i.e., a modification of the setpoint temperature in the buildings), and an additional thermal insulation.

In this contribution, the building stock model based on the library IDEAS [8] is used to build the simulation model which, in turn, is coupled to a district heating simulation model so as to underline the strong dependency between building renovation and/or regulation strategies and the operation/design of a district heating network. The outcome of a more accurate building simulation based on the actual and specific building architecture/use coupled to a model of the heat distribution is a more accurate evaluation of its thermal losses and pumping work therefore improving the evaluation of the heat transport efficiency. Both the building model and the district heating network model are thermal inertial models, taken into account the heat storage in the structure for the former and the dynamic behaviour of heat transport for the latter. More, these models are intended to compare the energy needs of the buildings and the district heating network for different energy policies and to study their impact on the network operation. Therefore, this article does not quantify the amount of primary energy required to operate the network or the associated emissions.

This contribution is primarily concerned on explaining the basic assumptions and philosophy of the building simulation model and then underlines its usage in the frame of district heating network operation. This is done by following an application framework from the campus of the University of Liège which is already equipped with a district heating network and where energy saving measures are currently discussed. For sake of simplicity, the test case is limited to a subset of 6 buildings among the 60 buildings located on the Campus. This application is insightful to understand the influence of building renovation and occupant behaviour on the future choice for the district heating network.

The methodology followed in this paper is described in Section 2.. Subsections 2.1. aims at describing the proposed building model, the one whose compatibility with the modelling of the tertiary sector must be studied. Subsection 2.2. describes the district heating network model and its assumptions. Then, Subsection 2.3. presents the reference test case studied as well as the variants considered as retrofit policies. The results of the simulations are then presented in Section 3.. This section is divided in different parts. First, the compatibility of the building model with the tertiary sector is assessed thanks to a validation through monitoring data. Then district heating simulation results for the variants are showed.

2. Methodology

The characteristics of a building simulation model is highly dependent upon its final use. Many building simulation models are intended to forecast the comfort conditions or for control of HVAC equipment and thus require a very detailed description of the building architectural structure. These models are usually accurate but require

an enormous amount of parameters not always available for existing buildings plus a significant amount of time to setup the model. These approaches are achievable when one is interested in one specific building but is not very accessible when hundreds of buildings or more have to be dealt with. Another important aspect resides in the connection of the building model to the district heating network that must be done in a standardised way whatever the complexity of the connected building, i.e., hourly heating and electrical demand.

2.1. Building simulation model

In order to benefit from previous research works in the modelling of district heating network (see [4]), the platform Dymola [9] has been first selected as a common platform. It has the advantage to support the open language Modelica and possesses numerous libraries for the building energy simulation. One specific library has been used as a building block for the building energy simulation, namely the library IDEAS (Integrated District Energy Assessment by Simulation) and developed by the KU Leuven (the interested reader is merely referred to [8] for a more complete information). It is a proven and robust library with a thorough manual available which provides rapid and safe implementation. It also provides, if necessary, a nice graphical user interface and does not require a very large number of parameters to be used. It is able to handle very simple buildings like houses and appartements but is also easily customisable to create complex building configurations like the ones considered hereafter.

For the buildings models, different assumptions are made. The building is divided into zones representing a set of rooms sharing the same temperature and ventilation requirements. This division into zones represents a simplification of the modelling as the thermal inertia of the internal walls is not taken into account when several rooms are lumped together. As an example, Fig. 1 exhibits the original available drawing of a building and the corresponding zones. A further simplification consists in reducing the shape of the buildings to rectangular zones so as to simplify the representation of complex buildings while keeping the exposed surfaces unchanged as well as their orientation. Each zone consists of a uniform air volume, a heating model, a ventilation model and the exterior surfaces (interior walls, exterior walls, windows, floors and ceilings). The model of a zone can be seen in Fig. 2.

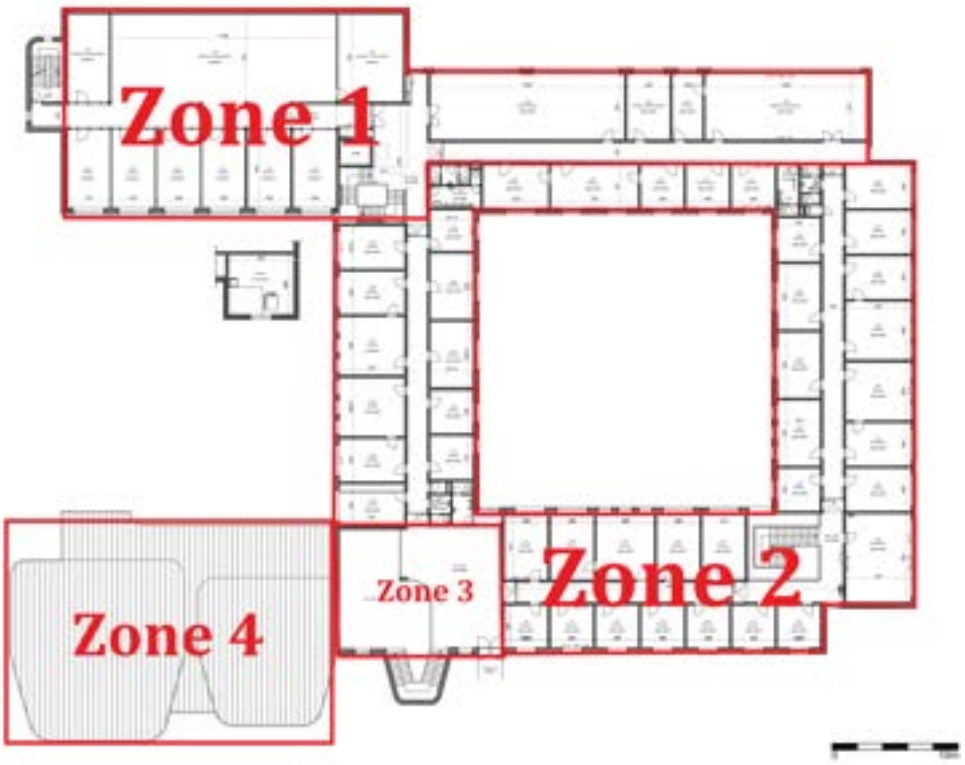

Figure 1: Building B37 first floor and its zones simplification.

The main air volume considers the large wavelength radiative heat exchanges and the radiative heat gain distribution, as well as the air infiltrations. It is very important to highlight the fact that the model computes the heat demand necessary to maintain the comfort conditions but does not assume any type of heating device used in the building and therefore imposes no restriction on level of temperature at which the heat should be delivered. This is done on purpose to focus on the energy demand as the building model is intended to be integrated to a district heating network for which different levels of temperatures can be considered. The

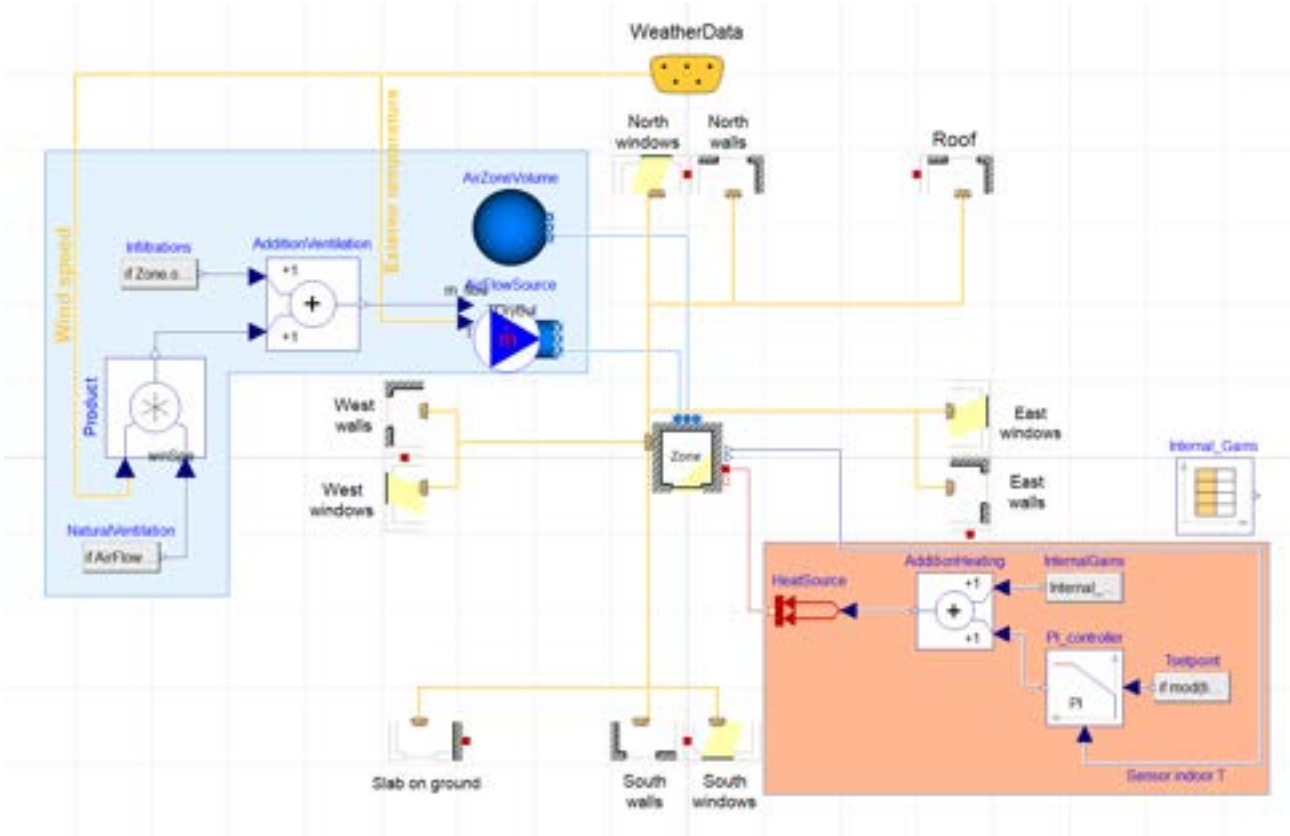

Figure 2: Dymola model for buildings zone model. The blue zone is the ventilation model, with infiltrations and natural ventilation based on wind speed. The red zone is the heating model which depends on the setpoint temperature, indoor temperature and internal gains. The weather data block contains the weather file. The walls, windows, roof and slab on ground models main parameters are the surface, the construction materials and the orientation.

necessary heating power to be extracted from the district heating network to maintain the indoor temperature is controlled by a PI controller comparing the measured temperature in the zone to the setpoint temperature.

The model for the ventilation is, for the time being kept at its simplest expression and considers only natural ventilation through window opening. When the indoor temperature rises above 23℃, the windows are open and the exchanged air flow rate is calculated based on the wind speed and the indoor and outdoor pressures. The heat transfers (by conduction, convection and radiation) between one zone and the adjacent ones or the exterior environment are considered in the exterior surfaces models. This model also takes into account internal free gains related to occupancy, lighting and appliances. A typical meteorological year weather file is linked to each building model in order to use external conditions such as temperature, solar radiation, humidity and wind speed.

The different data needed to make the building model described above are the main dimensions of the building required to estimate the heated volume and the exterior surface areas (solid and windowed), their orientation, the infiltration rate, the building materials, a local weather file and the usage of the building. By the *usage*, it is meant the control strategy, the occupancy level, the lighting and the appliances. This model is of course simplified but has the advantage of rapid development mainly because of the zone blocks that can be easily parameterised from accessible data. The most influencing parameters in terms of accuracy are the control strategy (schedule and setpoint), the occupancy, the building envelope and the air flow interactions (infiltrations and ventilation) (a more detailed explanation of these aspects can be found in [11]).

The construction of building models from the IDEAS library according to the proposed method has been developed on the basis of the test case of the International Energy Agency EBC Annex 60 [12]. To prove the easy scalability of the approach, an automated procedure to build the models for this test case has been realized. It allows an automatic model generation based on standard configurations customised according to the specific building location, orientation and size. This test case includes a set of 23 residential buildings, detached, semi-detached and terraced houses, and an office building. That approach proved to be satisfactory in terms of accuracy both individually and globally. In this contribution, an important question addresses the accuracy and feasibility of the approach on tertiary buildings where it is much more difficult to replicate

standard configurations.

2.2. District Heating Network Simulation

In this contribution a particular focus is put on the heat transport efficiency to satisfy the needs of the connected buildings. The basic brick of this network is the district heating piping made of one supply and one return pipe thermally insulated and buried into the ground. The model used for the pipes is the one collaboratively developed in the context of the Annex 60 Modelica Library and the IBPSA Project 1 Modelica Library [14]. This model is very simple to setup as it is based on a plug flow model (i.e., non-compressible fluid) to forecast the dynamic behaviour of the heat transport (i.e., the transport delays) and requires only the pipe length and diameter to be specified. The friction (i.e., pressure) and thermal losses are calculated to provide an accurate and complete picture of the transport losses. The general layout of the model is exhibited in Fig. 3 showing that all the buildings are connected by deriving a portion of the flow to supply heat to the substation. The only dynamic effect in the one-dimensional flow model is the thermal inertia. Both the mass and the momentum inertia are considered negligible on the time scale of one-hour which is the basic time step considered in this study.

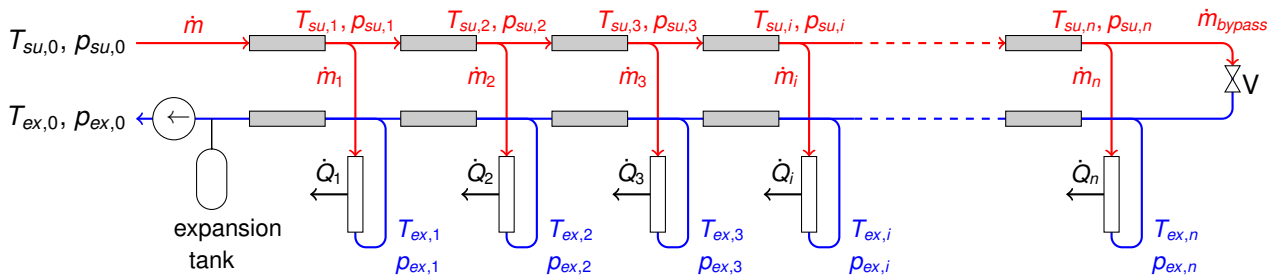

Figure 3: The model of district heating network where the pipes are in grey and the substation heat exchangers are in white. The supply flow is in red and the return flow is in blue.

The mass and momentum conservation involve:

$$\dot{m} = \sum_{i=1}^{i=n} \dot{m}_i + \dot{m}_{bypass} \text{ and } p_{su,i} - p_{ex,i} = K_{hex,i}\dot{m}_i^2, \tag{1}$$

together with pipe friction losses:

$$p_{su,i} - p_{su,i-1} = K_{su,i}\left(\dot{m} - \sum_{k=1}^{k=i-1} \dot{m}_i\right)^2 \text{ and } p_{ex,i-1} - p_{ex,i} = K_{ex,i}\left(\dot{m} - \sum_{k=1}^{k=i-1} \dot{m}_i\right)^2 \tag{2}$$

where $K_{hex,i}$, $K_{su,i}$ and $K_{ex,i}$ are constant characteristics of the heat exchanger and pipe configuration. The mass flow rate in the piping system is forced by a circulation pump with a characteristic:

$$p_{su,0} - p_{ex,0} = \frac{\Delta p_0}{N_{nom}^2} \cdot N^2 + c_2 \cdot \dot{m}^2, \text{ such that, } W_{pump} = \frac{\dot{m}}{\rho} \cdot (p_{su,0} - p_{ex,0}) \cdot \Delta t, \tag{3}$$

where Δp_0 is the no flow head at nominal rotational speed that is a function of the squared rotational speed, c_2 a constant specifying the nominal operating conditions and Δt is the considered time period. The rotational speed N is controlled by a PI controller between 20% and 100% of its nominal value so as to maintain the return temperature $T_{ex,0}$ at the setpoint value. For low flow conditions (i.e., that would correspond to $N < 20\%N_0$) the return temperature is allowed to fluctuate. An efficiency of 60% is considered to compute the electricity consumption of the pumps.

The only time dependency is due to the dynamic of the heat transport into the pipe introducing a delay between the entry temperature and the exhaust. Therefore, the pipe exhaust temperature $T_{su,i}(t)$ and the thermal losses $\dot{Q}_{loss,i}(t)$ depend on the past history of temperatures $\{T_{su,i-1}(0) \dots T_{su,i-1}(t)\}$ and mass flow rates $\{\dot{m}(0) \dots \dot{m}(t)\}$ and $\{\dot{m}_i(0) \dots \dot{m}_i(t)\}$. A similar reasoning holds for the return pipes. The detailed resolution algorithm used to determine the pipe exhaust temperature and thermal losses is beyond the scope of this contribution and the interested reader is merely referred to [14] for a more thorough information.

The supply temperature $T_{su,0}$ is ensured by a heat source (from the Modelica library *Buildings* [13]) representing the centralised heat generation. The return pipe temperature results from the heat extraction at each of the substation according to the building heat demand. Again for sake of simplicity, the heat transfer across

the substation is not fully modelled and the heat demand is directly extracted from the primary flow with a minimum bound on the exhaust temperature $T_{ex,i}$ in order to ensure it is always above the inner temperature of the building (plus the pinch point of the different heat exchangers) according to:

$$\dot{Q}_i = \min \left[\dot{m}_i \cdot c_p \cdot (T_{su,i} - T_{ex,i}) \; ; \; \dot{m}_i \cdot c_p \cdot (T_{su,i} - T_{ex,min}) \right] \tag{4}$$

where $T_{ex,min}$ is fixed according to the heat exchanger and substation configuration (here $T_{ex,min} = 35\,^{\circ}\text{C}$).

The different aforementioned equations are implemented in Modelica on the Dymola program with the hourly heat demand curves of the buildings as an input for the substation models. This implies that the indoor comfort conditions of the buildings are not evaluated inside the district heating network model. The goal of the network through the substation model is to satisfy the load as much as possible.

Finally, the network is equipped with a bypass circuit whose mass flow rate is controlled by a valve according to:

$$p_{su,n} - p_{ex,n} = K_{valve} \dot{m}_{bypass} \tag{5}$$

where again K_{valve} is constant characteristic. An expansion tank upstream of the pump is also installed to ensure a constant pressure $p_{ex,0}$ at the pump supply.

The independent variables are the supply temperature $T_{su,0}$, the return pressure $p_{ex,0}$, the setpoint for the return temperature $T_{ex,0}$ and the set of heat rates $\dot{Q}_i \; \forall i \in [1,6]$. With these boundary conditions and a suitable initial state of the system, the set of differential algebraic equations is solved by Dymola.

It is important to note that, according to equation 4, the required heat might not be available at the substation if the mass flow rate is not sufficient. If such conditions happen, there is no feedback on the building model to adapt the inner conditions accordingly to ensure the robustness of the resolution algorithm. Instead, an alarm is triggered that comfort conditions might not be met.

2.3. Case studies

2.3.1. Description

The objective of this test case is twofold. At first, it is intended to verify the accuracy of the model for tertiary buildings. The case of the university campus is particularly suited as lots of monitoring data are easily accessible for validation in terms in supply and exhaust temperature and mass flow rate. Secondly, the set of buildings is a good test to verify the integration of the building models into the district heating network in terms of robustness and accuracy. It is also a nice way to verify the scalability of the approach by replicating the procedure for the implementation of the model on existing buildings with very different characteristics.

The studied test case is the district heating network of the Polytech district on the Sart-Tilman campus of the University of Liège. This considered district is composed of 6 buildings: B28, B37, B47, B49, B52 and B65. They have various functions, such as classrooms, offices, laboratories, cafeteria, and a library. They, consequently, have different heating schedules or temperature settings. These buildings were also built in different time periods, between the 1970s and 2010s, and therefore have varying levels of insulation. The case studies only take into account the heating of the buildings and not the domestic hot water. The network is operated between 80 °C and 60 °C. The weather file used is a TMY file of the weather station of Uccle, the reference weather station in Belgium, with some modifications for the exterior temperature, to account for specific extreme conditions.

The reference case is based on the current use of the buildings and 6 buildings have been modelled and divided into zones based on the available existing drawings. The parameters specific to each building are collected namely, the heated volumes, the window areas, the wall orientations, the insulation materials, the heating schedules, the occupancy rates, the internal free gains and the setpoint temperature. For example, for the building B37, which is mainly an office and classroom building, the heating schedule is from 8 am to 5 pm, internal gains of a computer are considered by occupant, the temperature setpoint is 21 °C, etc.

The proposed model is particularly well suited for testing the influence of user behaviour as the inner setpoint temperature are easily accessible. Moreover, as the building model is essentially dynamic, transient effects due to thermal inertia are taken into account so that the effect of user behaviour on the heat demand can be expected to be accurately assessed.

Also changing thermal insulation and/or adding some insulation is straightforward and can be done by changing the value of different parameters, without having to rebuild the model from scratch. Quantifying load curve changes following a building modification is therefore quick and easy and can be done in less than 2 hours, computation time included. The time required depend on the number of zones and surfaces. The fewer zones and areas there are, the faster the modification, hence the interest in optimizing the zones and areas.

2.3.2. Change in user behaviour

The first modification to be considered is a change in user behaviour realised by modifying the inner setpoint temperature and to check the influence on the operation of the district heating network. For each building,

the setpoint temperature in each zone is lowered from 21 °C to 19 °C, while keeping all other parameters unchanged. This modification follows closely what happened during the energy crisis during the year 2022 and the results are great interest for the authorities of the university.

2.3.3. Insulation of the building stock

The second modification consists in increasing the thermal insulation of the building stock. Not all the buildings are equal with such a modification as some pretty old buildings will see their heat demand greatly influenced while more recent ones will not. Again, this case study reflects some of the actions taken by the authorities of the university to decrease on the long term the building energy consumption. The following rules are followed:

- For buildings with single glazing, replace the existing frames with new PVC and double glazing frames.
- For buildings already having double glazing, do not replace frames and glazing.
- For all buildings, add a 14 cm thick layer of glass wool insulation, in addition to any existing insulation.

Glass wool is an affordable and commonly used material. Its price ranges between 20 and 25 $€/m^2$ [1] and its thermal conductivity between 0.03 and 0.05 $W\,m^{-1}\,K^{-1}$ [15] which is superior to the insulation already installed on the buildings.

3. Results

3.1. Validation of the buildings models

Before proceeding to the different test cases, a validation phase is carried out to check whether or not the accuracy of the model is compatible with our application framework, namely the simulation of tertiary buildings. The simulation results of the 6 buildings of the Sart Tilman campus are compared to the available monitoring data in Table 1. Fig. 4 exhibits the heating demand curve of the B52 building offices during one winter day. It shows that the simulation results compare well to the monitoring results. The curves show the same pattern, with similar peak demands occurring at the same time of day. The root mean squared (RMS) error between the simulation results and the monitoring data is 85 kW. Accordingly, it can be concluded that the proposed methodology is applicable to tertiary building. In addition to the result accuracy, the modelling method allows the building models to be quickly setup (between half a day and two days depending on the number of zones in the building) and exhibits great robustness in terms of computation. Moreover, the standardisation of the approach enables different people to collaborate and associate their model as an input to the district heating network model.

Table 1: Buildings heating consumptions from monitoring data and simulation heating needs for the 3 scenarios [MWh]

	Monitoring data [MWh]	Reference scenario [MWh]	Scenario A [MWh]	Scenario B [MWh]
B28	642	544	482	299
B37	242	186	162	160
B47	Not available	66	59	44
B49	Not available	112	89	89
B52	1396	1219	1062	1129
B65	17	13	10	11
Total	/	2140	1864	1732

3.2. Impact on peak load and buildings annual energy consumption

As detailed in the previous section, two improvement scenarios are considered: the so-called *scenario A* where the setpoint is decreased to 19 °C and the *scenario B* consisting of an increased thermal insulation.

An interesting point of view is to compare the load curves of the different scenarios as exhibited in Fig. 5 and representing the cumulative number of hours during which a certain level of power is at least required. The intercept of the load curve with the y-axis (the heating power) is the peak load which is unchanged for scenario A with respect to the reference case while scenario B exhibits a decreased peak load from 3.9 MW to 3.5 MW (minus 10 %). The area under the load curve being the total energy consumed within a year, Fig. 5 shows that the reference case forecasts an annual energy demand of 2140 MWh which decreases to 1864 MWh and 1732 MWh respectively for the scenarios A and B respectively. The energy savings are therefore respectively 13% and 19% for each of the two variants.

[1] https://conseils-thermiques.org/contenu/laine-de-verre.php

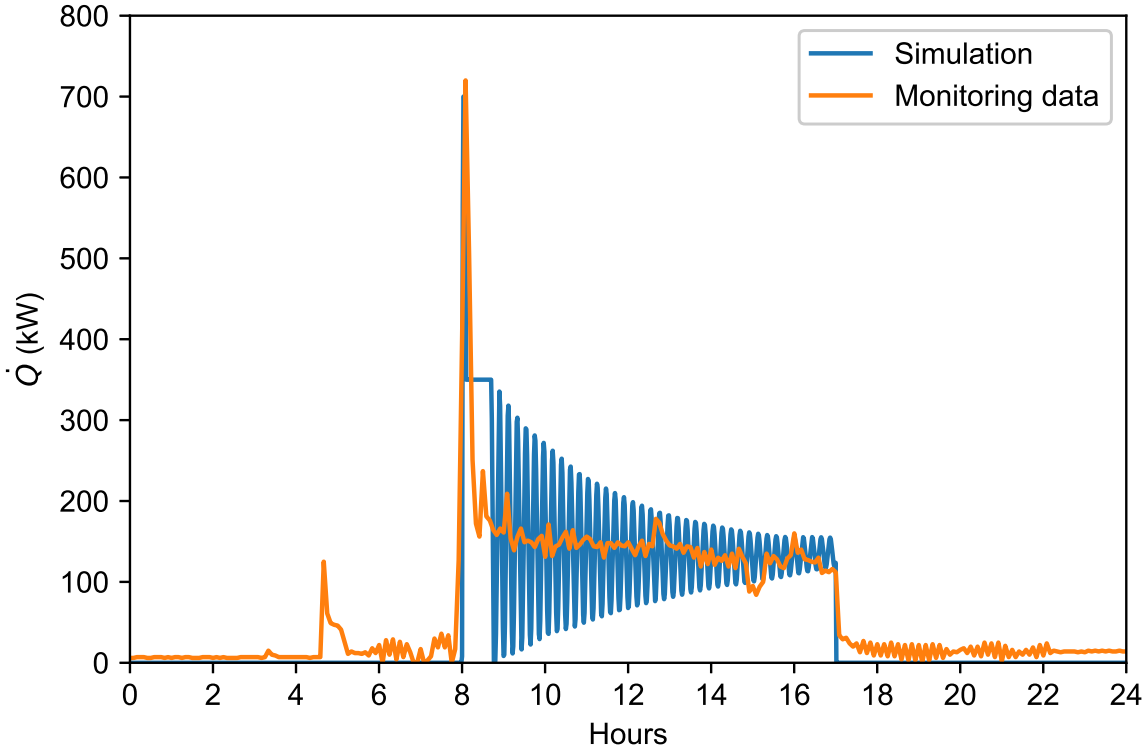

Figure 4: Heating demand profile of B52 offices over a winter day in 2022, simulation and monitoring results. RMS error over the year is 85 kW.

If one take a closer look at a smaller scale for the different buildings, it is is also insightful to see the discrepancies between the efficiency of one single measure on different buildings. Table 1 contains the simulated annual heating consumption for the three cases and the six buildings. It is interesting to see that already insulated buildings are less sensitive to energy saving measures. Indeed, for scenario B, with the added insulation layer, the average energy saving is around 23%. But by focusing on already insulated buildings, this economy is only of 12%, while it is of 33% for older buildings. For scenario A, the average energy savings are around 15%, and the results are quite similar for insulated and not insulated buildings. The conclusion is that a decrease of the setpoint temperature allows a uniform savings on the whole buildings, while the massive insulation of the building stock gives better energy savings on the least well insulated buildings.

3.3. Impact on electrical consumption of pumps and thermal losses

Heat transport efficiency is defined here as the ratio between the heat delivered to the building to the heat supplied to the district network and is a very important performance indicator, yet not the only one, as it characterises the rational energy use.

Table 2 summarizes the annual energy supplied to the district heating network, the annual heat losses and the annual pumping electricity consumption for the three considered cases. Reducing the setpoint temperature to 19 °C decreases energy consumption (minus 8.3%) while insulating the buildings results in an energy saving of 12.3%. In terms of electricity consumption from the pumps, the savings are 10.9% and 19.6% respectively for scenarios A and B.

This can readily be understood by a decrease of the mass flow rate for scenarios A and B which has a major effect on pumping consumption that is directly proportional to the mass flow rate while thermal losses are not significantly impacted as they are mainly driven by the pipe diameter and the supply and return temperatures that remained constant across the different test cases.

The heat losses represent 38.2% of the total injected energy into the district heating network for the 19 °C case. This figure goes to 40.0% for the scenario B, against 34.5% for the reference case. This shows that in the reference case, 65.5% of the energy consumed by the entire network is used for buildings heating while for the two scenarios this figure decreases to 61.8% and 60.0% of the total energy supply.

Heat transport efficiency might be a misleading figure as improving the energy efficiency of the buildings de-

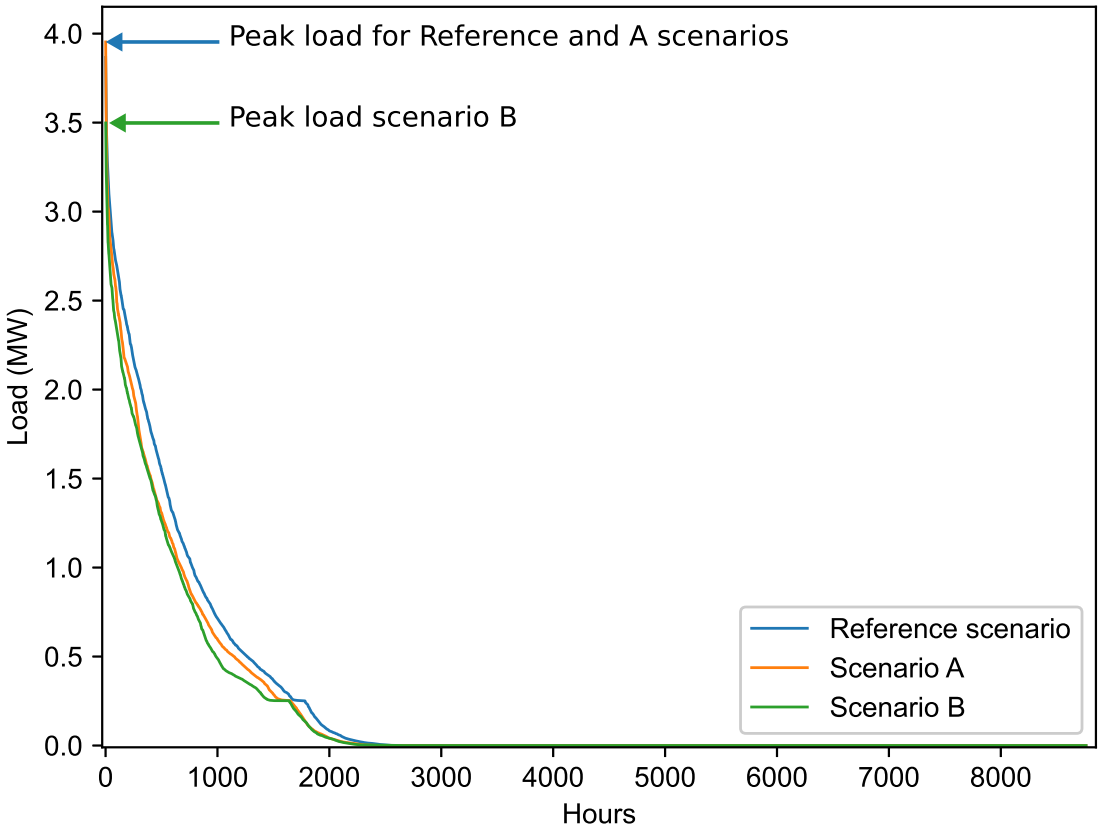

Figure 5: Overall load duration curves for the reference scenario and the two variants.

creases the energy efficiency of the network. Yet, one must bear in mind that the total energy input decreased but the transport losses are more difficult to decrease.

Moreover, the present analysis is purely made on an energy basis but the economic and/or environmental cost of heat and electricity should be taken into account. Nonetheless, these discussions also show that energy saving policies on building connected to district heating network cannot be done without studying the consequences on the operation of the network.

Table 2: DHN energy supply, heat losses and electrical pump consumption for the 3 cases (expressed in MWh)

	Reference scenario [MWh]	Scenario A [MWh]	Scenario B [MWh]
DHN energy supply	3292	3018	2886
DHN heat losses	1152	1154	1154
Electrical pump consumption	46	41	37

4. Conclusion

This work is primarily dedicated to the development of an integrated approach of building energy simulation for large building stock. This modelling approach allows a quick yet accurate simulation so as to obtain hourly buildings heat demand. The final objective is to connect these building models to a district heating network model. The knowledge of the load curves and peak demand (both in time and amplitude) has been shown to be essential. The main assumptions have been explained to introduce the building simulation model, based on the IDEAS Modelica library providing ease of use and robustness.

One important question also concerned the validity of the approach, already validated for residential building, for the tertiary buildings that are more heterogeneous in nature and use. The test case presented herein tends to demonstrate that the approach is purposeful both from a practical (it is easily scalable) and from an accuracy

point of view. The different models have been validated based on monitoring data showing that both the peak demand and the annual energy consumption represent faithfully the actual situation.

One important aspect characterising the present approach is that most of the methodologies for large scale building simulation are based on a top-down approaches starting from the annual energy consumption (based on benchmark) spread across the year on an hourly basis using pre-defined daily profiles and average daily or hourly temperature profiles. Contrarily, the presented method is a bottom-up approach based on the structure and use of the building able to predict both the peak demand and annual energy accurately thus providing a straightforward way to forecast the efficiency of energy saving measures.

In a second step, two energy saving scenarios are applied to evaluate their impact on the load curve and, in turn, on the operation of the district heating network. The considered energy saving measures are a modification of the setpoint temperature in the buildings and an increased insulation of the building envelope. The main conclusions drawn from the simulations is that when a district heating network is used it is very difficult to separate building energy saving measures from the network operation/design.

The presented model still requires some improvements mainly on the side of a better regulation by adapting more actively the supply temperature to the heat demand to decrease the thermal losses. The model of the substation also needs to be improved to avoid the recourse to a minimum exhaust temperature and model the heat exchanger efficiency to forecast the maximum heat demand supplied by the substation. However, the basic philosophy of the different developed models seems to be purposeful to consider very large district with thousands of buildings.

Nomenclature

$\dot{m}$	mass flow rate, kg/s
p	pressure, Pa
K	pressure drop coefficient, $kg^{-1}m^{-2}$
N	pump rotation speed, rpm
W	pump work, J
ρ	density, kg/m^3
$\dot{Q}$	power, W
$\dot{T}$	temperature, K
c_p	specific heat, J/(kgK)

Subscripts and superscripts

i	substation index
su	supply to the substation
ex	exhaust of the substation

References

[1] Singh M., Mahapatra S., Teller J., *An analysis on energy efficiency initiatives in the building stock of Liege, Belgium*. Energy Policy, http://dx.doi.org/10.1016/j.enpol.2013.07.138 (2013-09-04).

[2] Resimont T., Louveaux Q., Dewallef P., *Optimization Tool for the Strategic Outline and Sizing of District Heating Networks Using a Geographic Information System*. Energies 2021;14(17):5575.

[3] Kohler M., Blond N., Clappier A., *A city scale degree-day method to assess building space heating energy demands in Strasbourg Eurometropolis (France)*. Applied energy 2016;184:40-54.

[4] Sartor K., Quoilin S., Dewallef P., *Simulation and optimization of a CHP biomass plant and district heating network*. Applied energy 2014;130:474-483.

[5] open energy modelling framework *Demandlib* of the open energy modelling framework. Available at: `https://pypi.org/project/demandlib/` [accessed 17.03.2023].

[6] Littlewood J., Howlett R., Jain L., *Examining the Deviation in Energy Saving Estimations Due to the Use of the Degree Days Method*. In: Littlewood J., Howlett R., Jain L., editors. Smart Innovation, Systems and Technologies. Singapore: Springer Singapore Pte. 2021. Vol. 263. p. 1-10.

[7] Remmen P., Lauster M., Mans M., Fuchs M., Osterhage T., Müller D., *TEASER: an open tool for urban energy modelling of building stocks*. Journal of building performance simulation 2018;11(1):84-98.

[8] open-ideas IDEAS v3.0.0. Available at: `https://github.com/open-ideas/IDEAS` [accessed 25.09.2022].

[9] DassaultSystem Dymola. Available at: `https://www.3ds.com/products-services/catia/products/dymola/` [accessed 17.03.2023].

[10] Jorissen F., Reynders G., Baetens R., Picard D., Saelens D., Helsen L., *Implementation and verification of the IDEAS building energy simulation library*. Journal of Building Performance Simulation 2018;11(6):669-688.

[11] Goy S., Maréchal F., Finn D., *Data for urban scale building energy modelling: Assessing impacts and overcoming availability challenges*. Energies (Basel) 2020;13(6):4244.

[12] International Energy Agency, *New Generation Computational Tools for Building & Community Energy Systems: Annex 60 Final Report*. September 2017.

[13] Lawrence Berkeley National Laboratory Buildings v4.0.0. Available at: `https://github.com/lbl-srg/modelica-buildings/releases` [accessed 20.11.2022].

[14] van der Heijde B., Fuchs M., Ribas Tugores C., Schweiger G., Sartor K., Basciotti D., Müller D., Nytsch-Geusen C., Wetter M., Helsen L., *Dynamic equation-based thermo-hydraulic pipe model for district heating and cooling systems*. Energy Conversion and Management 2017;151:158-169.

[15] Kumar D., Alam M., Zou P., Sanjayan J., Memon R., *Comparative analysis of building insulation material properties and performance*. Renewable & sustainable energy reviews 20202;131:110038.

Optimization of the pipe diameters and the dynamic operation of a district heating network

Malik Hakim Elhafaia[a], Arley Nova-Rincon[b], Sabine Sochard[c], Sylvain Serra[d] and Jean-Michel Reneaume[e]

[a,b,c,d,e] Universite de Pau et des Pays de l'Adour, E2S UPPA, LaTEP, Pau, France
[a] malik-hakim.elhafaia@univ-pau.fr, CA, [b] arleynova@gmail.com, [c] sabine.sochard@univ-pau.fr,
[d] sylvain.serra@univ-pau.fr, [e] jean-michel.reneaume@univ-pau.fr

Abstract:

In the research field of district heating networks (DHNs), there is a need for more analysis on the economic optimization of the design and dynamic operation considering precise representations of the temperature and pressure drops in the pipes of the system. In this study, we develop a model tested in an academic case study of a DHN composed of a production unit, a distribution network, and twenty consumers. The dynamic behavior of the DHN is due to the variability of the heat demand and ambient temperature over a daily period. Inside the pipes, the temperature variation is described by a dynamic one-dimensional heat transfer equation while the pressure drops are computed using the Darcy-Weisbach equation. Energy and mass balances are applied in the interconnecting nodes of the system. In addition, the model includes design and operational constraints of the DHN. All these equations lead to a partial differential algebraic equation (PDAE) problem. Using the method of orthogonal collocation on finite elements (OCFE), the differential terms are discretized to obtain a set of algebraic equations. The resulting non-linear programming (NLP) problem is solved with an equation-oriented (simultaneous) approach using the solver CONOPT. The aim of the optimization is to find the best trade-off between the capital expenditures (CAPEX) of the pipes and the operational expenditures (OPEX) by considering the pipe diameters, temporal values of mass flows and spatio-temporal values of temperatures of each pipe as continuous optimization variables. The CAPEX include the cost of the pipes and the cost of deploying them in trenches. The OPEX include both production and pumping costs which are related to thermal losses and pressure drops, respectively. As the pumping cost is significantly lower than the heat production cost, the results showed that it is more economical to reduce the thermal losses than the pressure drops.

Keywords:
District Heating Network; Dynamic optimization; Non-Linear Programming; Orthogonal Collocation on Finite Elements.

1. Introduction

Heating and cooling demand accounts for around half of global final energy consumption. Nearly half of this energy is used in industrial processes, 46% is used in residential and commercial buildings mainly for space and water heating. Most of the energy used for heating and cooling continues to be produced from non-renewable sources. Consequently, heating and cooling is responsible for 40% of energy-related greenhouse gas emissions [1]. The development of district heating and cooling (DHC) systems is a good answer to face these energy and environmental issues. This technology has the advantage of accelerating energy transition by integrating an important part of renewable sources and waste heat. Due to their considerable investment and operational costs, currently in the energy field, one of the important challenges is the development of tools and methods for the optimization of DHC networks.

According to how the time dependency is taken into account in the model, it is possible to classify the works on the optimization of DHC into four main categories: steady-state, quasi-steady-state, dynamic multi-period, and dynamic. In the steady state models, the optimization is performed with no time dependency considering averaged values for the operating parameters like mass flows and temperatures in the system. In most of the cases, the optimization problem is of the mixed integer programming type [2–4]. In [2] and [3] mixed integer linear programming (MILP) approaches are used for the optimizations of the operational cost and the total annual cost, respectively. Linear equations for the computation of thermal losses and pressure drops in the pipes are defined. In [4], the authors chose a mixed integer non-linear programming (MINLP) approach where the global cost of a district heating network (DHN) is optimized over 30 years. The thermal losses and pressure drops were computed with more precise equations. For the 3 previous studies, the discrete variables represent the design choices (connection in the topology nodes and/or the choices of production technologies). On the

other hand, the continuous variables represent the operating parameters (production power, flows, temperatures, …). The authors of [5] opted for a non-linear programming (NLP) resolution where they used a numerical continuation strategy that gradually forces the design variables towards discrete choices. Steady-state models are interesting for long-term studies, but one of their main drawbacks is not considering a variable heat demand.

In what we classified as quasi-steady-state studies, it is possible to consider different values of the heat demand. The optimization is performed within a time interval which is subdivided into periods. For each period, the heat demand is averaged. The problem is a succession of steady-state problems. In this type of studies, Liu et al. [6] modeled an optimization of design parameters of a solar heating network. They took into account only discrete decision variables which were the network layout variables and pipe diameters. Sameti and Haghighat [7] studied the optimal design and operation of a DHN with a cogeneration unit. A MILP model was employed, and different buildings with different heat demands were considered. This kind of model is suitable for medium-term studies; however, it presents limits with dynamic aspects. As it does not include differential equations, for example, it is impossible to have the evolution of a thermal energy storage (TES) tank from one period to another.

In terms of time discretization, the studies we classify in the dynamic multi-period approach are quite similar to the previous category. The main difference is that they include at least one differential equation. In this category, Deng et al. [8] developed a MINLP model to perform what they called an optimal scheduling of a DHC. For each period, they define whether the technology is working or not, and the amount of power it produces (or charges/discharges in case of storage). Wirtz et al. [9] were also interested in the choice of technologies and the amount of produced and stored power of a DHC with multiple production technologies and TES. In addition, they optimized the temperature in the distribution network and the thermal losses. We have also Söderman [10] who optimized the topology and the operation to minimize the total annual cost of a district cooling network (DCN). He considered different consumers with different heat demands in each period. Another interesting study is the optimization of Khir and Haouari [11] of a DCN. They optimized chiller plant capacity, storage tank capacity, piping network size and layout, and produced and stored power during every period. In their operation, they ensure that supplied temperature corresponds to the desired one and that pressure drops are within the allowable limits. This type of works is suitable for medium-term studies with inclusion of dynamic aspects. In contrast, as they consider an important time step (≥ 1 hour), it is difficult to perform real-time control and/or to have precise evolutions of physical phenomena in the pipes.

What we chose to classify as dynamic approaches are the works that considered a small time step (<1 hour) and a short period of study (1-3 days generally). Two sub-categories can be distinguished, the studies that are for real-time optimization and the ones for dynamic offline optimization. In real-time models, Cox et al. [12] used a genetic algorithm to have the optimum control strategy of the operation of chillers and ice storage of a DCN. Lu et al. [13] developed a NLP optimization for the regulation of the operating parameters of a DHN. The limit with real-time models is that they require the calculation of the command in a short time. Therefore, they do not have precise thermo-hydraulic modeling of the pipes. This is where the interest of dynamic offline optimization (DOO) comes in with the possibility of having longer computation time; therefore, more accurate modeling of the pipes. In the DOO, Schweiger et al. [14] proposed a methodology to decompose a MINLP optimal control problem of a DHN into two sub-problems. A mixed problem to minimize the operational cost and a continuous one to minimize the production temperature. Nova Rincon et al. [15] studied another aspect of the optimal operation of a DCN. To avoid the technical issue of “Low ΔT syndrome” which reduces the efficiency of the system, they optimized the mass flows and temperatures in the distribution network to minimize the difference between the outlet temperature of consumers and a design outlet temperature. As they solve differential equations with a small time step, the DOO approaches have significant resolution times. To our knowledge, this is why we do not find studies that optimize at the same time the design and the dynamic operation of a DHC with accurate thermo-hydraulic modeling of the pipes. The originality of this work is that we conduct an optimization of the pipe diameters and the dynamic operation of a DHN with an economic objective function while having a precise modeling of the pipes.

In this study, we present a methodology for the optimal operation of an academic case study of a DHN comprised of twenty consumers over a daily study period. In addition to the optimization of mass flows and temperatures in the distribution network, the pipe diameters are also optimized. Considering a variable ambient temperature, a dynamic one-dimensional heat transfer equation is used to define the temperature evolution in the pipes. The Darcy-Weisbach equation is employed to compute the pressure drops in the distribution network. In the following parts, firstly we expose the case study. Secondly, we introduce the physical, the design and the operational constraints in addition to the objective function of the problem. Finally, we present the results and conclusions.

2. Case study

For this study, we used the same topology of the network presented in Figure 2 of [15] that serves 20 different consumers. In the outward path, there are 41 pipes, 21 main pipes ($0 - 20$) and 20 lateral pipes ($in_1 - in_{20}$). The lateral pipes are directly connected to the consumers through a sub-station unit where the thermal power

is transferred from the distribution network to the consumer's heating system. The return path is also comprised of 41 pipes that are parallel to the outward path ($0_r - 20_r$ and $out_1 - out_{20}$). The network is then constituted by 1 production unit, 20 substations and 82 pipes with a total length close to 19 km. In what follows, we use k as the index for all the pipes, p, p_r, in_p and out_p as the sub-indexes for main outward pipes, main return pipes, lateral pipes entering consumers and lateral pipes leaving consumers, respectively.

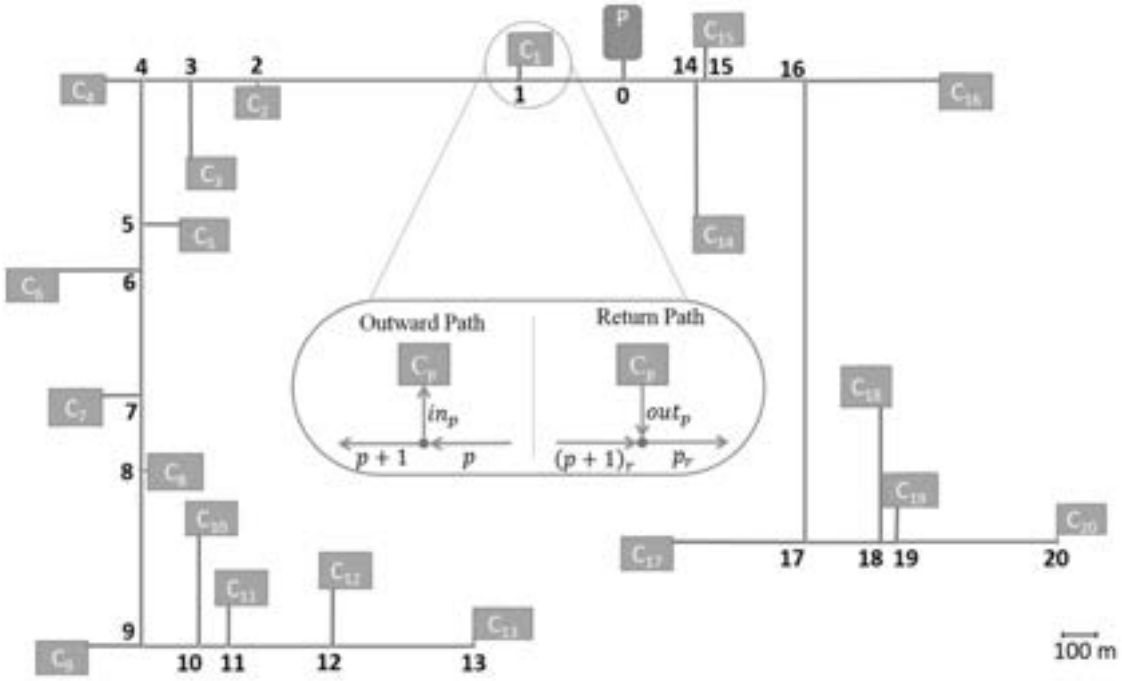

Figure 1. Representation of the network's configuration [15].

Concerning the heat demand, the same daily profiles used in district B of [16] are taking into account. Two types of profiles are considered, one for residential buildings, and one for commercial buildings. Table 1 shows the distribution of the type of buildings and their peak demand. The two profiles are represented as a function of the peak demand of each consumer as shown in Figure 2. To have a continuous representation of the two types of profile over time, a fit function was introduced for each profile. The two heat demand profiles of Figure 2 are defined by a sum of sinusoidal functions of the form:

$$Demand(t) = \sum_{i=1}^{8} \alpha_i \cdot \sin(\beta_i \cdot t + \gamma_i) \quad (1)$$

where α_i, β_i and γ_i are coefficients of the demand function.

Table 1. Type of consumers and their peak demands.

Consumer	Type	Peak demand	Consumer	Type	Peak demand
C_1	Commercial	1500	C_{11}	Commercial	720
C_2	Commercial	1260	C_{12}	Residential	180
C_3	Residential	360	C_{13}	Residential	450
C_4	Commercial	1440	C_{14}	Commercial	1500
C_5	Residential	210	C_{15}	Commercial	1050
C_6	Commercial	1020	C_{16}	Commercial	540
C_7	Residential	240	C_{17}	Commercial	990
C_8	Commercial	600	C_{18}	Commercial	1200
C_9	Commercial	990	C_{19}	Commercial	1170
C_{10}	Commercial	420	C_{20}	Commercial	1110

In Figure 3, the total heat demand of the network is represented. Its evolution is quite the same as the one of the commercial demand, because there are 15 commercial buildings in this case study and they have a higher peak demand than residential buildings. In the same figure, we also have the ambient temperature evolution which is one of a not very cold winter day.

3. System modeling

The model of the DHN is comprised of energy and mass conservation equations at each node and sub-station of the system. Inside every pipe, a heat transfer equation describes the temperature evolution. In this latter,

the mass flow is time dependent, while the temperature is time and space dependent. In addition, the Darcy-Weisbach equation describes the dynamic evolution of pressure drops in the pipes. In the following parts, we will detail the different equations of the system. These equations represent the physical, design and operational constraints of the optimization problem.

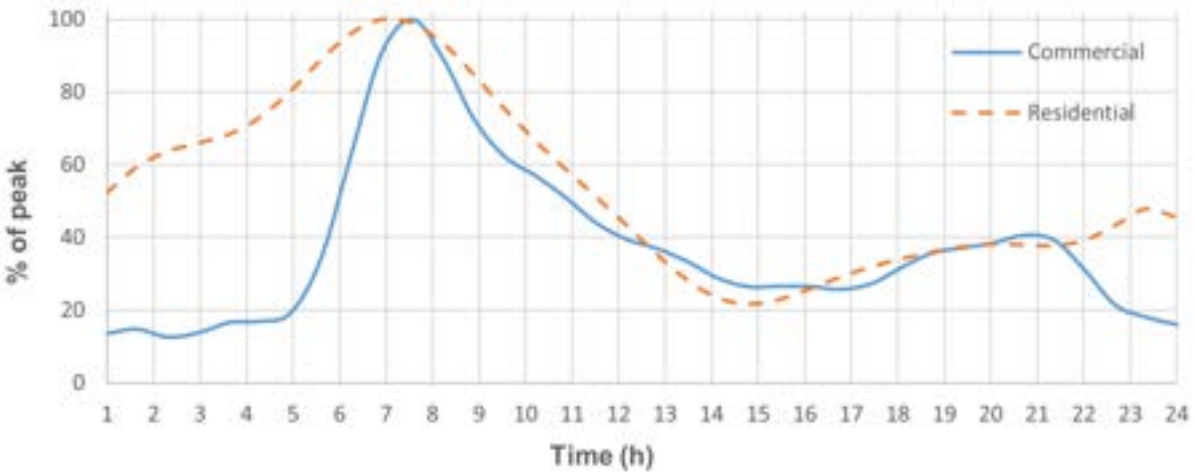

Figure 2. Heat demand profiles.

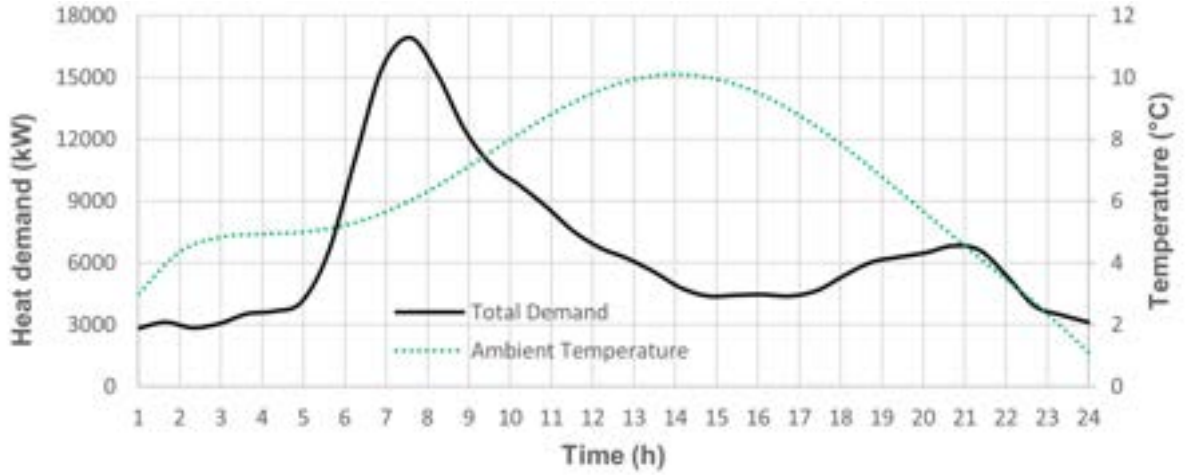

Figure 3. Total heat demand and ambient temperature profiles.

3.1. Production unit, nodes and sub-station

At the production level, we consider one fixed technology that delivers the hot water at a constant temperature:

$$T_{p=0}(t, x = 0) = constant \quad (2)$$

At every interconnecting node of the network, the mass balance is applied. For the outward path, we have:

$$\dot{m}_p(t) = \dot{m}_{p+1}(t) + \dot{m}_{in_p}(t) \quad p = 1 \dots 12, 14 \dots 19$$

$$\dot{m}_p(t) = \dot{m}_{in_p}(t) \quad p = 13, 20 \quad (3)$$

$$\dot{m}_0(t) = \dot{m}_1(t) + \dot{m}_{14}(t)$$

For the return path, we have:

$$\dot{m}_{p_r}(t) = \dot{m}_{(p+1)_r}(t) + \dot{m}_{out_p}(t) \quad p = 1 \dots 12, 14 \dots 19$$

$$\dot{m}_{p_r}(t) = \dot{m}_{out_p}(t) \quad p = 13, 20 \quad (3)$$

$$\dot{m}_{0_r}(t) = \dot{m}_{1_r}(t) + \dot{m}_{14_r}(t)$$

In the outward path, the nodes are splitters so the temperature entering the node is equal to the temperature leaving it:

$$T_p(t, x = L_p) = T_{p+1}(t, x = 0) = T_{in_p}(t, x = 0) \quad p = 1 \dots 12, 14 \dots 19$$

$$T_p(t, x = L_p) = T_{in_p}(t, x = 0) \quad p = 13, 20 \tag{4}$$

$$T_0(t, x = L_p) = T_1(t, x = 0,) = T_{14}(t, x = 0)$$

In the return path, the nodes are mixers. We apply an energy balance considering the equality between the inlet and outlet enthalpy flows. Assuming a constant specific heat capacity between the inlet and the outlet, the equation is:

$$\dot{m}_{p_r}(t) \cdot T_{p_r}(t, x = 0) = \dot{m}_{(p+1)_r}(t) \cdot T_{(p+1)_r}(t, x = L_{(p+1)_r}) + \dot{m}_{out_p}(t) T_{out_p}(t, x = L_{out_p}) \quad p = 1 \dots 12, 14 \dots 19$$

$$T_{p_r}(t, x = 0) = T_{out_p}\left(t, x = L_{out_p}\right) \quad p = 13, 20 \tag{5}$$

$$\dot{m}_{0_r}(t) \cdot T_{0_r}(t, x = 0) = \dot{m}_{1_r}(t) \cdot T_{1_r}(t, x = L_{1_r}) + \dot{m}_{14_r}(t) T_{14_r}(t, x = L_{14_r})$$

L, $\dot{m}(t)$ and $T(x, t)$ are the pipe length, mass flow and temperature of water in the pipes. x and t represent the time and distance dependencies.

The sub-station unit is also defined by mass and energy balance equations. The flow going from the outward path to the substation is equal to the flow going from the substation to the return path. Assuming a constant specific heat capacity, the energy balance is defined to have a difference in enthalpy flows between the inlet and the outlet equal to the demand. The conservation equations of the sub-station are:

$$\dot{m}_{in_p}(t) = \dot{m}_{out_p}(t) \quad p = 1 \dots 20 \tag{6}$$

$$Demand(t) = \dot{m}_{in_p}(t) \cdot \mathrm{c}_w \cdot \left[T_{in_p}(t, x = L_{in_p}) - T_{out_p}(t, x = 0)\right] \quad p = 1 \dots 20 \tag{7}$$

c_w is the specific heat capacity of water.

3.2. Thermal model of the pipe

As stated in [17], the choice of an adequate pipeline model that gives a good trade-off between accurate physics and computing costs is a key challenge for DHN optimization. As proposed in previous studies [14,18,19] we use a one-dimensional energy balance in the pipe which is described by the partial differential equation (PDE) written in Eq. (8). This heat transfer equation is submitted to the following assumptions:

- Plug flow
- Neglected axial conductive heat transfer in the fluid
- Material properties are constant and independent of temperature
- Thermal interaction between the supply and return pipes is not included
- Thermal inertia of the pipes, casing and insulation is neglected

$$\rho \cdot c_w \cdot A_k \cdot \frac{\partial T_k(t,x)}{\partial t} + \dot{m}_k(t) \cdot c_w \cdot \frac{\partial T_k(t,x)}{\partial t} = \frac{T_s(t) - T_k(t,x)}{R_k(t)} \tag{8}$$

$$k = \{0, \dots, 20, 0_r, \dots, 20_r, in_1, \dots, in_{20}, out_1, \dots, out_{20}\}$$

ρ and A are the water density and cross section area, respectively. $R(t)$ represents the total dynamic thermal resistance per unit length of pipe and $T_s(t)$ is the temperature of the soil surface.

The total thermal resistance over time $R(t)$ depends on the thermal conductivities of the pipe, insulation, casing and soil. $R(t)$ depends also on the internal convective heat transfer between the water and the inner wall of the pipe and is given by [18]:

$$R_k(t) = \frac{1}{2\pi r_{a_k} \bar{h}_k(t)} + \frac{\ln\left(\frac{r_b}{r_{ak}}\right)}{2\pi\lambda_{ab}} + \frac{\ln\left(\frac{r_c}{r_b}\right)}{2\pi\lambda_{bc}} + \frac{\ln\left(\frac{r_d}{r_c}\right)}{2\pi\lambda_{cd}} + \frac{1}{S_k \lambda_s} \tag{9}$$

where λ_{ab}, λ_{bc}, λ_{cd} and λ_s represent the thermal conductivities of the pipe, insulation, casing and soil, respectively, and r_a, r_b, r_c and r_d are the different radiuses from the inner wall of the pipe to the casing, as it is shown in Figure 4.

S is the conduction shape factor, for $d > 3r_d$, it can be approximated by [20]:

$$S_k = \frac{2 \cdot \pi \cdot L_k}{\ln\left(\frac{4 \cdot d}{2 \cdot r_d}\right)} \tag{10}$$

where d is the distance between the pipe axis and the soil surface.

$\bar{h}(t)$ is the convective heat transfer coefficient over time averaged for the entire length of the pipe, it is computed by:

$$\overline{h_k}(t) = \frac{\overline{Nu_k}(t) \cdot \lambda_w}{D_{a_k}} \tag{11}$$

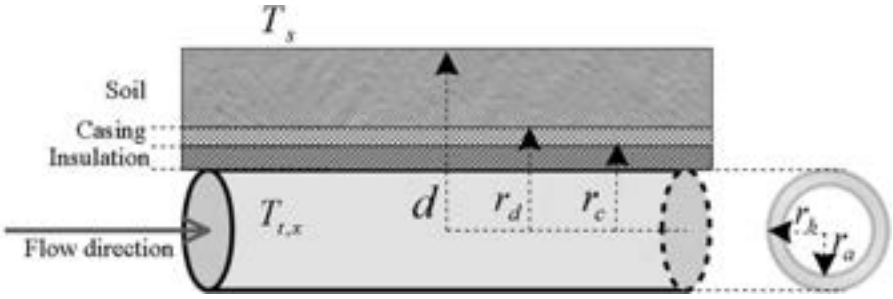

Figure 4. Representation of the buried pipe [15].

where D_a is the pipe internal diameter ($D_a = 2r_a$), $\overline{Nu}(t)$ is the Nusselt number over time averaged for the entire length of the pipe and λ_w is the thermal conductivity of water. Assuming that the system operates under a turbulent regime (Reynolds ≥ 9000), we use the correlation of Dittus-Boelter [21] to compute the Nusselt number in a circular tube:

$$\overline{Nu}_k(t) = 0.023 \cdot (Re_k(t))^{0.8} \cdot Pr^{0.4} \tag{12}$$

$Re(t)$ and Pr are the Reynolds number over time and the Prandtl number, respectively:

$$Re_k(t) = \frac{2 \cdot \rho \cdot v_k(t) \cdot D_{a_k}}{\mu} \tag{13}$$

$$Pr = \frac{\mu \cdot c_w}{\lambda_w} \tag{14}$$

$v(t)$ and μ are the flow velocity over time and dynamic viscosity of water, respectively.

3.3. Hydraulic model of the pipe

The work of the pumps in the distribution network is directly related to the pressure drops. For each pipe, to compute the linear pressure drops, the Darcy-Weisbach equation is used:

$$\Delta P_{linear_k}(t) = f_k(t) \cdot \frac{L_k}{D_{a_k}} \cdot \rho \cdot \frac{[v_k(t)]^2}{2} \quad k = \{0, \dots, 20, 0_r, \dots, 20_r, in_1, \dots, in_{20}, out_1, \dots, out_{20}\} \tag{15}$$

$f(t)$ represents the friction factor over time which depends on the flow regime and the rugosity of the pipe. For $4 \cdot 10^3 \leq Re \leq 10^8$ and a relative roughness ε/D smaller than 10^{-2}, it can be computed by the form of Colebrook-White equation proposed by Moody [22]:

$$f_k(t) = 0.0055 \left\{ 1 + \left[2 \cdot 10^4 \left(\frac{\varepsilon}{D_{a_k}} \right) + \frac{10^6}{Re_k(t)} \right]^{1/3} \right\} \tag{16}$$

We assume that we have smooth pipes, which means $\varepsilon/D_{a_k} = 0$. The singular pressure drops are assumed to be equal to 30% of the total pressure drops [4]. In each branch, the total pressure drop is equal to the sum of the linear and singular pressure drops. As we have parallel connections, we choose the longest path to compute the linear pressure drops. For the left branch (LB), the pressure drop is:

$$\Delta P_{Total_{LB}}(t) = \frac{1}{0.7} \sum_{k_{LB}} \Delta P_{linear_k}(t) \tag{17}$$

with: $k_{LB} = \{1, \dots, 13, 1_r, \dots, 13_r, in_{13}, out_{13}\}$

For the right branch (RB), the pressure drop is:

$$\Delta P_{Total_{RB}}(t) = \frac{1}{0.7} \sum_{k_{RB}} \Delta P_{linear_k}(t) \tag{18}$$

with: $k_{RB} = \{14, \dots, 20, 14_r, \dots, 20_r, in_{20}, out_{20}\}$

The fact that the LB is longer and serves more consumers than the RB, suggests that the $\Delta P_{Total_{LB}}(t)$ should be higher than the $\Delta P_{Total_{RB}}(t)$. We assume that at every time step, the pressure drop of the LB is higher than the one of the RB. We also neglect the singular pressure drops in the pipes 0 and 0_r. The electrical power required for the pump is:

$$Pw_{pump}(t) = \frac{\dot{m}_0(t)}{\eta\rho}\left[\Delta P_{linear_0}(t) + \Delta P_{linear_{0_r}}(t) + \Delta P_{Total_{LB}}(t)\right] \quad (19)$$

η is the pump efficiency, it represents the total efficiency of the pump which includes mechanical, transmission and motor efficiencies. η is assumed to be equal to 70%.

Depending on the inner diameter of the pipe, a maximum flow velocity is recommended, which limits the specific pressure drop over the pipe length. A threshold of maximum specific pressure drop of 100-150 Pa/m is common to avoid corrosion and increased pumping energy [23]. Using the recommended flow velocities for sizing pipes reported in [24], we imposed an inequality constraint on each pipe to don't exceed a maximum flow velocity per diameter:

$$v_k(t) \leq v_{max_k} \quad (20)$$

We consider that every consumer have to respect a contractual outlet temperature, for this purpose we defined this equality constraint:

$$T_{out_p}(t, x = 0) = constant \quad p = 1 \dots 20 \quad (21)$$

In order to have values that are available in reality, the diameters of the pipes are bounded to a maximum value of 0.57m that is based on the commercial availability of PVC pipes:

$$D_{a_k} \leq 0.57 \quad (22)$$

The set of Eq. (2) to (22) represent the equality and inequality constraints of the optimization problem, resulting in a partial differential algebraic equation (PDAE) system. The orthogonal collocation on finite elements (OCFE) method was used to discretize the PDE (8) in order to transform the PDAE system into a set of algebraic equations. The details of the implementation of the OCFE and the discretized mathematical model of the system are presented in the appendices A and B of [15], respectively.

4. Objective function

The objective function includes the operational expenditures (OPEX) of the system and the capital expenditures (CAPEX) of the pipes. The OPEX comprise both heat production and pumping costs. The heat production cost "$Cost_{prod}$" is obtained by multiplying the total thermal energy produced over the day by the unit cost of heat production:

$$Cost_{prod} = c_{hot} \cdot \int_1^{24} Pw_{hot}(t)\, dt \quad (23)$$

$$\text{with: } Pw_{hot}(t) = \dot{m}_0(t) \cdot c_w \cdot \left[T_0(t, 0) - T_{0_r}(t, L_{0_r})\right] \quad (24)$$

c_{hot} is the unit cost of heat production, its unity is (€/MWh), $\dot{m}_0(t)$ is the production mass flow (kg/s) and $T_0(t, 0)$ and $T_{0_r}(t, L_{0_r})$ are the production and return temperatures, respectively. The total thermal energy produced is computed by integrating with respect to time the thermal power $Pw_{hot}(t)$ which is equal to the difference between the enthalpy fluxes of production and return.

The pumping cost "$Cost_{pump}$" is the product of the total pumping energy over the day and the unit cost of electricity:

$$Cost_{pump} = c_{elec} \cdot \int_1^{24} Pw_{pump}(t)\, dt \quad (25)$$

c_{elec} represents the unit cost of electricity, its unity is (€/MWh). The pumping power of the network $Pw_{pump}(t)$ is integrated over the day to obtain the total pumping energy. As Gaussian quadrature methods are suited for the computation of integrals when the OCFE is used, for the resolution of the integrals presented in Eq. (23) and Eq. (25) the Gauss-Lobatto quadrature was employed.

The investment cost of the pipes "$Cost_{inves}$" which includes the cost of the pipes and the cost of deploying them in trenches is represented by a linear function as follows:

$$Cost_{inves} = \sum_k L_k \cdot (\alpha D_{a_k} + \beta) \quad (26)$$

Values of investment cost of different nominal diameter by unit length were given by a French company which operates DHN. Using these values, we create a linear regression to have a continuous representation of the cost depending on the diameter. Considering that the DHN of this case study has a lifetime of 30 years, we transform the coefficients of the linear regression (α and β) to have an investment cost for one day.

Using a Lagrange problem type formulation, the objective function is the sum of the three costs defined above:

$$\min_{\substack{D_{a_k} \\ \dot{m}_k(t) \\ T_k(x,t)}} \left(Cost_{prod} + Cost_{pump} + Cost_{inves}\right) \quad (27)$$

The optimization variables are the inner diameters of the pipes, the temporal values of mass flows, and spatio-temporal values of temperature in each pipe. This optimization aims to find the diameters that give the best trade-off between CAPEX and OPEX while finding the optimal operational values of mass flows and temperatures.

Since all the variables are continuous, Eq. from (2) to (26) and the objective function (27) constitute a dynamic NLP problem. The OCFE was employed on the PDE (8) to transform the problem into a set of algebraic equations. For the resolution, we used an equation-oriented (simultaneous) methodology, with the software GAMS for the modeling of the system, and the solver CONOPT for the solving.

As it is the case in most complex optimization problems, a resolution methodology was developed. The purpose of the methodology is to help the solver by creating a resolution process where we solve successive problems. We start from a simple problem and we get more complex until we finally solve the problem of this study. In the resolution process, we always use the last solution for the initial values of variables of the next problem.

5. Results and discussion

This optimization was done considering a production temperature of 92 °C and an outlet temperature of consumers equal to 72 °C. The unit cost of electricity was taken equal to 174 €/MWh. Concerning the unit cost of heat production, we considered the prices in France in 2022 for 3 different technologies: biomass boiler (50 €/MWh), gas boiler (150 €/MWh) and heat recovery (20 €/MWh). The thermo-physical properties of water are taken for the temperatures of 92 °C and 72 °C as it is shown in Table 2. In what follows, we will present some results obtained in the optimization of this case study.

Table 2. Thermophysical properties of water [20].

	ρ (kg/m^3)	c_w (kJ/(kg K))	$\mu \cdot 10^3$ (N s/m^2)	k (W/(m K))
Outward pipes (92 °C)	963.4	4.209	0.306	0.677
Return pipes (72 °C)	976.6	4.191	0.389	0.664

Figure 5 represents the daily evolutions of heat production and mass flow at the production level for the case of biomass boiler. We observe that the heat production has the same profile as the total demand with slightly higher values due to the thermal losses in the network. The thermal losses can also be observed in Figure 6 where the return temperature to the production is represented. The production mass flow of Figure 5 also has the same profile as the total demand. Since production temperature is constant and return temperature does not vary significantly, the mass flow follows the demand as it can be seen in Eq. (7). We obtain the same evolutions for the two other production technologies (gas boiler, heat recovery).

The pressure drops have daily profiles quite similar to the total demand due to the fact that they are proportional to the square of velocity (Figure 7). Inside the pipes, as there is a plug flow regime, the velocity and mass flow have the same profile. As expected, the pressure drop of the left branch is always higher than the one of the right branch which is explained by a more important demand on the left. In a real case, the DHN cannot operate under these pressure conditions. To guarantee a correct operation, it is necessary to have pressure control valves before mixing nodes that will maintain the same pressure drop in every parallel connection of pipes. Consequently, the pressure drop of the right branch will be equal to the one of the left.

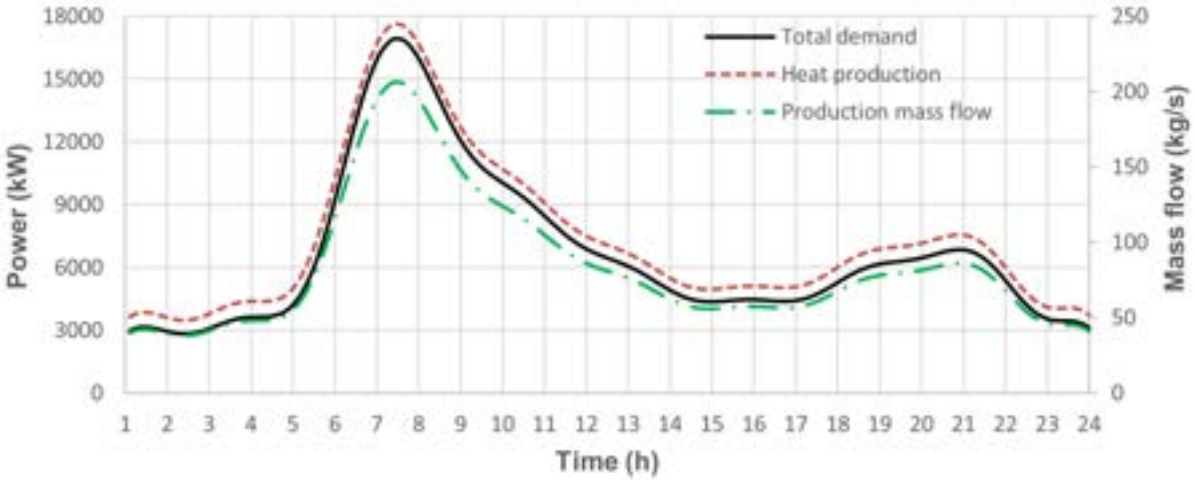

Figure 5. Heat production and production mass flow over time.

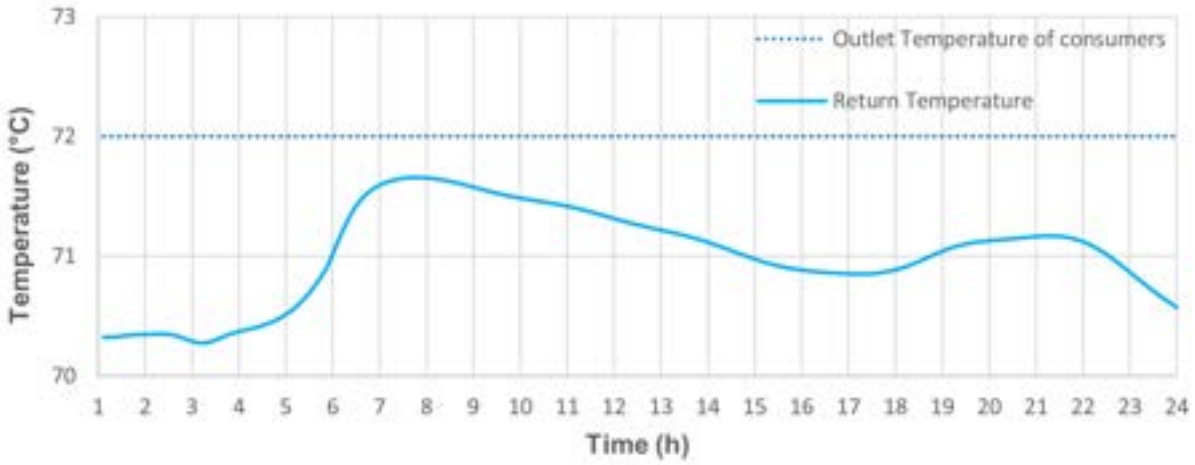

Figure 6. Outlet temperature of consumers and return temperature of the network over time.

In Table 3, we present the results of 3 optimizations where all the parameters are the same (c_{elec}, $Cost_{inves}$, $Demand(t)$, …) except for the unit cost of heat production (c_{hot}). Each unit cost represents a different production technology (gas, biomass and heat recovery). We observe that when c_{hot} increases, the heat produced energy decreases and the pumping energy increases. When the price of heat is more important, the solution tends to reduce the size of the diameters resulting in less investment for pipes, less thermal losses and more pressure drops as it can be observed in Figure 8.

Table 3. Optimization results for 3 different production technologies.

Type of production	Unit cost (€/MWh)	Total heat produced (MWh)	Total pumping energy (kWh)	Average diameter (mm)
Gas boiler	150	169.11	652.82	154.55
Biomass boiler	50	169.17	591.43	155.34
Heat recovery	20	169.20	567.35	155.86

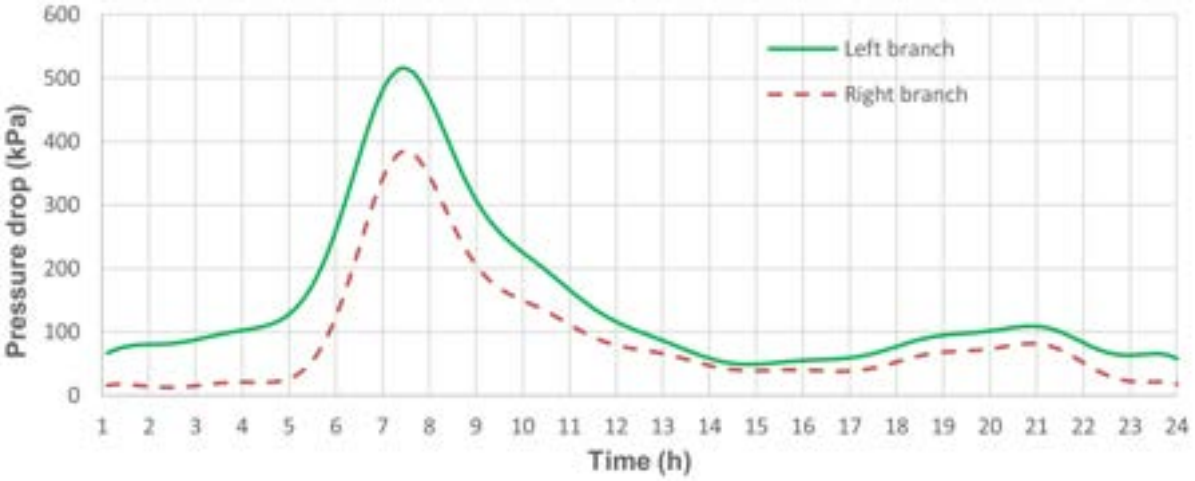

Figure 7. Pressure drops of the two branches of the network over time.

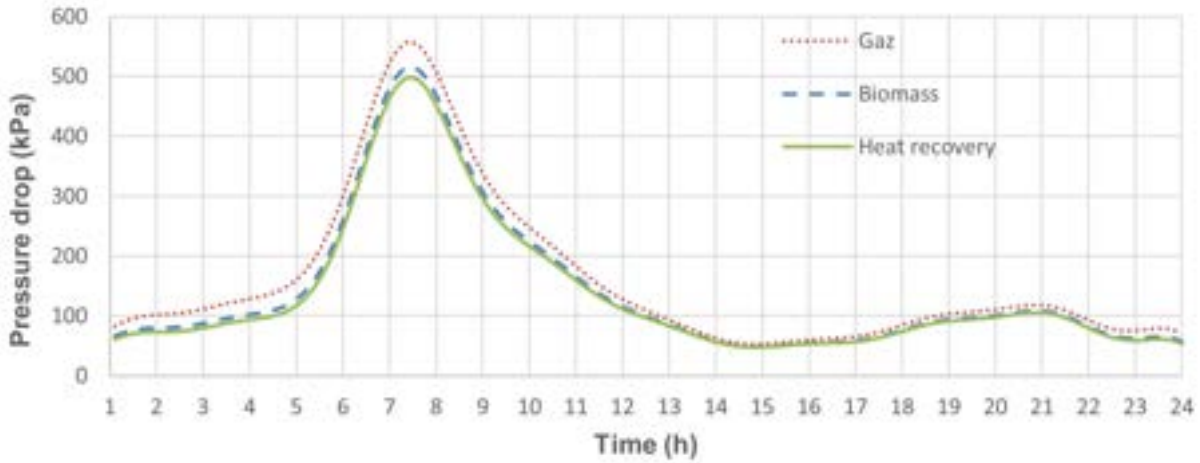

Figure 8. Pressure drop of the left branch of the network for 3 different production technologies.

6. Conclusions and perspectives

In this study, we developed a model for the optimization of the daily operation of a DHN. We optimized the pipe diameters in addition to the mass flows and temperatures in the distribution network. In the modeling of the pipes, the OCFE was used to discretize the heat transfer equation, and the Darcy-Weisbach equation described the pressure drops. The parametric study on the unit cost of heat production confirmed that it is better to have smaller diameters when the cost increases to reduce the thermal losses.

The results of this NLP optimization are a good starting point for a Mixed Integer Dynamic Optimization (MIDO). As we find only discrete values of diameters in the market, it is more interesting to solve a MIDO problem where the diameters will be discrete variables and mass flows and temperatures continuous ones. Moreover, to correctly design the pipes, it is necessary to take into account the operation of the DHN in the different seasons. An interesting study may be the consideration of different characteristic days (one for each season). Another interesting study is the consideration of more than one production unit and of a TES tank. The aim would be to optimize the management of all units while considering the same physical complexity in the pipes and the temperature distribution inside the TES. Currently, we are working on the development and the optimization of a model of this type.

Nomenclature

Abbreviations

CAPEX CAPital EXpenditures
DCN District Cooling Network
DHC District Heating and Cooling
DHN District Heating Network
DOO Dynamic Offline Optimization
MIDO Mixed Integer Dynamic Optimization
MILP Mixed Integer Linear Programming
MINLP Mixed Integer Non-Linear Programming
NLP Non-Linear Programming
OCFE Orthogonal Collocation on Finite Elements
OPEX OPerational EXpenditures
PDAE Partial Differential Algebraic Equation
PDE Partial Differential Equation
TES Thermal Energy Storage

Latin symbols

A cross section area of the pipe, m^2
c_w specific heat capacity of water, J/(kg K)
D pipe diameter, m
f friction factor
L pipe length, m

$\dot{m}$ mass flow in the pipe, kg/s

Pw_{hot} thermal power, W

Pw_{pump} electrical power of the pump, W

r radius, m

R total thermal resistance per unit length of pipe, (m K)/W

Re Reynolds number

t time variable, s

T temperature of the flow in the pipe, °C

v flow velocity, m/s

x space variable, m

Greek symbols

ρ water density, kg/m3

μ dynamic viscosity of water, Pa s

ΔP pressure drops, Pa

λ thermal conductivity, W/(m K)

η pump efficiency

Sets and indexes

a index for the inner diameter of the pipe

C_p set of consumers

k set of pipes

LB index of the left branch of the network

RB index of the right branch of the network

s index for the soil

w index for water

p sub-set for main forward pipes

p_r sub-set for main return pipes

in_p sub-set for pipes entering consumers

out_p sub-set for pipes leaving consumers

References

[1] "Renewable Energy Policies in a Time of Transition: Heating and Cooling – Analysis," *IEA*. https://www.iea.org/reports/renewable-energy-policies-in-a-time-of-transition-heating-and-cooling (accessed Mar. 14, 2023).

[2] M. Vesterlund, A. Toffolo, and J. Dahl, "Optimization of multi-source complex district heating network, a case study," *Energy*, vol. 126, pp. 53–63, May 2017, doi: 10.1016/j.energy.2017.03.018.

[3] R. E. Best, P. Rezazadeh Kalehbasti, and M. D. Lepech, "A novel approach to district heating and cooling network design based on life cycle cost optimization," *Energy*, vol. 194, p. 116837, Mar. 2020, doi: 10.1016/j.energy.2019.116837.

[4] T. Mertz, S. Serra, A. Henon, and J.-M. Reneaume, "A MINLP optimization of the configuration and the design of a district heating network: Academic study cases," *Energy*, vol. 117, pp. 450–464, Dec. 2016, doi: 10.1016/j.energy.2016.07.106.

[5] M. Blommaert, Y. Wack, and M. Baelmans, "An adjoint optimization approach for the topological design of large-scale district heating networks based on nonlinear models," *Applied Energy*, vol. 280, p. 116025, Dec. 2020, doi: 10.1016/j.apenergy.2020.116025.

[6] Y. Liu, H. Tang, Y. Chen, D. Wang, and C. Song, "Optimization of layout and diameter for distributed solar heating network with multi-source and multi-sink," *Energy*, vol. 258, p. 124788, Nov. 2022, doi: 10.1016/j.energy.2022.124788.

[7] M. Sameti and F. Haghighat, "Optimization of 4th generation distributed district heating system: Design and planning of combined heat and power," *Renewable Energy*, vol. 130, pp. 371–387, Jan. 2019, doi: 10.1016/j.renene.2018.06.068.

[8] N. Deng *et al.*, "A MINLP model of optimal scheduling for a district heating and cooling system: A case study of an energy station in Tianjin," *Energy*, vol. 141, pp. 1750–1763, Dec. 2017, doi: 10.1016/j.energy.2017.10.130.

[9] M. Wirtz, L. Neumaier, P. Remmen, and D. Müller, “Temperature control in 5th generation district heating and cooling networks: An MILP-based operation optimization,” *Applied Energy*, vol. 288, p. 116608, Apr. 2021, doi: 10.1016/j.apenergy.2021.116608.

[10] J. Söderman, “Optimisation of structure and operation of district cooling networks in urban regions,” *Applied Thermal Engineering*, vol. 27, no. 16, pp. 2665–2676, Nov. 2007, doi: 10.1016/j.applthermaleng.2007.05.004.

[11] R. Khir and M. Haouari, “Optimization models for a single-plant District Cooling System,” *European Journal of Operational Research*, vol. 247, no. 2, pp. 648–658, Dec. 2015, doi: 10.1016/j.ejor.2015.05.083.

[12] S. J. Cox, D. Kim, H. Cho, and P. Mago, “Real time optimal control of district cooling system with thermal energy storage using neural networks,” *Applied Energy*, vol. 238, pp. 466–480, Mar. 2019, doi: 10.1016/j.apenergy.2019.01.093.

[13] M. Lu *et al.*, “Operational optimization of district heating system based on an integrated model in TRNSYS,” *Energy and Buildings*, vol. 230, p. 110538, Jan. 2021, doi: 10.1016/j.enbuild.2020.110538.

[14] G. Schweiger, P.-O. Larsson, F. Magnusson, P. Lauenburg, and S. Velut, “District heating and cooling systems – Framework for Modelica-based simulation and dynamic optimization,” *Energy*, vol. 137, pp. 566–578, Oct. 2017, doi: 10.1016/j.energy.2017.05.115.

[15] A. Nova-Rincon, S. Sochard, S. Serra, and J.-M. Reneaume, “Dynamic simulation and optimal operation of district cooling networks via 2D orthogonal collocation,” *Energy Conversion and Management*, vol. 207, p. 112505, Mar. 2020, doi: 10.1016/j.enconman.2020.112505.

[16] I. Petkov and P. Gabrielli, “Power-to-hydrogen as seasonal energy storage: an uncertainty analysis for optimal design of low-carbon multi-energy systems,” *Applied Energy*, vol. 274, p. 115197, Sep. 2020, doi: 10.1016/j.apenergy.2020.115197.

[17] J. Maurer, O. M. Ratzel, A. J. Malan, and S. Hohmann, “Comparison of discrete dynamic pipeline models for operational optimization of District Heating Networks,” *Energy Reports*, vol. 7, pp. 244–253, Oct. 2021, doi: 10.1016/j.egyr.2021.08.150.

[18] J. Duquette, A. Rowe, and P. Wild, “Thermal performance of a steady state physical pipe model for simulating district heating grids with variable flow,” *Applied Energy*, vol. 178, pp. 383–393, Sep. 2016, doi: 10.1016/j.apenergy.2016.06.092.

[19] B. van der Heijde *et al.*, “Dynamic equation-based thermo-hydraulic pipe model for district heating and cooling systems,” *Energy Conversion and Management*, vol. 151, pp. 158–169, Nov. 2017, doi: 10.1016/j.enconman.2017.08.072.

[20] T. L. Bergman, F. P. Incropera, D. P. DeWitt, and A. S. Lavine, *Fundamentals of Heat and Mass Transfer*. John Wiley & Sons, 2011.

[21] R. H. S. Winterton, “Where did the Dittus and Boelter equation come from?,” *International Journal of Heat and Mass Transfer*, vol. 41, no. 4, pp. 809–810, Feb. 1998, doi: 10.1016/S0017-9310(97)00177-4.

[22] L. Zaghadnia, J. L. Robert, and B. Achour, “Explicit solutions for turbulent flow friction factor: A review, assessment and approaches classification,” *Ain Shams Engineering Journal*, vol. 10, no. 1, pp. 243–252, Mar. 2019, doi: 10.1016/j.asej.2018.10.007.

[23] I. Best, J. Orozaliev, and K. Vajen, “Impact of Different Design Guidelines on the Total Distribution Costs of 4th Generation District Heating Networks,” *Energy Procedia*, vol. 149, pp. 151–160, Sep. 2018, doi: 10.1016/j.egypro.2018.08.179.

[24] C. Branan, Ed., *Rules of thumb for chemical engineers: a manual of quick, accurate solutions to everyday process engineering problems*, 3rd ed. Amsterdam ; New York: Gulf Professional Pub, 2002.

Analysis of energy, economic and environmental performance of solar water heaters for domestic hot water supply in northern European climate

Anandhi Parthiban[a], Eoin Cotter[b], David McCloskey[c]

[a] School of Physics, Trinity College Dublin, Dublin 2, Ireland, parthiba@tcd.ie, CA
[b] School of Physics, Trinity College Dublin, Dublin 2, Ireland, cottereo@tcd.ie
[c] School of Physics, Trinity College Dublin, Dublin 2, Ireland, mccloskd@tcd.ie

Abstract:

A significant portion of energy expense of a residential household goes toward the provision of domestic hot water (DHW) ~19%. The use of solar thermal water heating provides a local way to offset this energy requirement with a renewable resource. Solar thermal water heating systems are commonly used in hot climates from Southern Europe to the Equator however in the past they were seen as not so economically viable in colder climates. The solar collector that is readily available on the market for DHW generation is the standard flat plate collector (SFPC), but they are not attractive for use in higher latitudes due to low operating temperature and high heat loss. Although convection suppression has been identified as a method to improve the performance of flat plate collector it has not yet achieved mainstream commercialisation. In this work we attempt to show that the conventional flat plate collector still has potential in higher latitude when modified to suppress convection heat loss. The modified FPC that is particularly of focus in this work is the one with honeycomb transparent insulation (MFPC). We compare the performance of SFPC and MFPC in colder climate considering different auxiliary heating options such as electricity, gas, and oil, at their recent energy prices. Using TRNSYS software, we modelled the annual energy generated by these collectors using a typical domestic load case and found that SFPC produced 1446.60 kWh/year while MFPC produced 1993.50 kWh/year. For a typical household with a daily hot water consumption of 200 L, SFPC requires 3858.69 kWh/year of auxiliary energy while MFPC requires 3458.24 kWh/year. The economic analysis shows that the MFPC with electrical heating is the highly viable option with a Net Present Value (NPV) of € 5078.95. The CO_2 emission reduction from the SFPC and MFPC with electrical auxiliary heating are 39.54 kgCO_2/year and 79.58 kgCO_2/year, respectively, compared to conventional electrical immersion heaters.

Keywords:

Solar water heater; Flat plate collector; Solar fraction; Evacuated tube collector; Economic analysis; Net Present Value.

1. Introduction

The global carbon dioxide emissions from space heating and water heating have hit a record high of 2500 Mt in 2021 [1]. Utilizing solar thermal technology for water heating offers a local solution to mitigate the CO_2 emissions linked to this process. Solar thermal water heating systems are commonly used to offset the energy requirement for domestic hot water (DHW) in hot climates from Southern Europe to the Equator, however in the past they were seen as not so economically viable in colder climates. The trend in northern Europe and UK is to promote heat pump technology for space heating and domestic hot water however this will add significant additional load to the electrical grid. Heat pumps are more suited to space heating than domestic hot water due to the higher tank temperature required and often an auxiliary heater such as an electrical immersion is required to meeting the DHW load requirements. As such and a local source of heat for Domestic Hot Water (DHW) would still be beneficial in colder climates to reduce electricity demand. Flat plate collectors (FPC) are well established and readily available Solar Water Heaters (SWH), but it suffers from poor performance in colder climates due to heat loss [2]. Numerous concepts have been employed in the past to mitigate heat loss from solar collectors, and one such concept is Evacuated Tube Collector (ETC), in which the gap between the absorber and the glass cover is evacuated to eliminate convection and conduction heat loss [3]. Although ETCs are more effective than traditional FPCs and attain significantly

higher collector temperatures, they tend to be costly to manufacture and install [4]. Solar thermal collectors incorporating transparent insulation offer a promising design to minimize heat loss while simultaneously reducing costs and weight. However, despite their potential benefits, these collectors have not yet achieved widespread commercialization due to challenges in manufacturing and the need to address issues related to stagnation temperature [5]. The inclusion of transparent insulation within the air gap between the absorber and the glass cover effectively reduces convection heat loss. This enhances the employability of FPCs, particularly in colder weather conditions.

Numerous works on the experimental and numerical analysis of SHW system can be found in literature and here we provide a review of selected works from the literature, highlighting their key findings and contributions. Ayompe and Duffy [6] conducted a year-round experimental analysis of a forced circulation SHW system installed in Dublin, Ireland which demonstrated that an FPC SHW system with a 4m^2 collector area can yield a solar fraction of up to 32.2% for an annual global insolation of 15,680.4 MJ. Hazami et al. [7] investigated the year-round performance of FPC and ETC SHW systems that were commercialized in Tunisia. Their findings showed that the ETC system generated 9% more energy than the FPC system. Specifically, the ETC system, with a collector area of 3.4 m^2, achieved a solar fraction of 84.4%. Tiwari et al. [8] utilized numerical simulations to assess the efficacy of FPC systems in Indian climatic conditions. Their study revealed that an FPC system with a collector area of 5 m^2 can meet 70% of the residential hot water demand. Kalogirou et al. [9] proposed a novel TRNSYS model component to evaluate the effectiveness of thermosiphon solar hot water (SHW) systems, which they simulated in three different European climates: Freiburg (47.9990° N), Naples (40.8518° N), and Larnaca (34.9182° N). The model was validated by comparing its results with experimental data. The research findings demonstrate that as the latitude decreases from Freiburg to Larnaca, the simple payback period (SPB) of the SHW systems also decreases. Zainine et al. [10] employed TRNSYS simulation to optimize the flow rate for a solar domestic hot water (SDHW) system installed in Tunisia. They estimated that the optimal flow rate for the primary and secondary circuits, for maximum annual yield, were 10 kg/h m^2 and 15 kg/h m^2, respectively. Additionally, their economic analysis demonstrated that SHW systems with gas auxiliary heating are more economically feasible than replacing conventional electric heaters. Bernardo et al. [11] conducted a study on the benefits of retrofitting existing domestic hot water systems with SWH. Their findings indicated that incorporating a smaller tank with an immersion heater in series with the solar storage tank could lead to optimal performance, with a solar fraction of up to 50%. The study also demonstrated that the TRNSYS simulation software is a reliable tool for determining the thermal performance of SHW systems.

Vig et al. [12] studied a variable flow vacuum tube solar thermal collector system. Their research demonstrated that the variable flow SHW system collected more energy compared to the constant flow one. Their effect was particularly significant when the radiation was low or when the temperature of water in the storage tank was high. Hayek et al. [13] conducted experimental investigations on two types of ETC collectors in the Eastern Mediterranean climate. Their findings demonstrated that the heat pipe-based ETC collector was 15-20% more efficient than the water-in-glass ETC collector. However, due to their high initial cost, these ETC collectors are not an economically feasible option. Maraj et al. [14] reported the yearly energy performance of a heat pipe ETC collector under Mediterranean climatic conditions. Their findings indicated that the annual collector efficiency of the ETC system was 62%, while for an FPC system, it was 49.4%. This result demonstrates that the thermal performance of the ETC system was superior to the FPC system. Al-Madhhachi et al. [15] conducted a study on the potential of SHW systems in two cities in Iraq. Their findings indicated that the SHW system has the potential to supply almost 60% of the hot water demand in winter. Kalogirou and Papamarcou [16] conducted experiments and numerical simulations on a thermosyphon SHW system based on FPC. The results showed that a FPC system with a total collector area of 2.7 m^2 can meet all the hot water demand of a household during summer. The Economic analysis showed that the system has a simple payback period of 8 years and a net present value (NPV) of 161 $C£_{2000}$. Hobbi and Siddiqui [17] performed a simulation-based optimization study for a forced circulation solar water heating system in Canada. Their results showed that the proposed design could meet 83-97% and 30-62% of hot water demand in summer and winter, respectively. Gao et al. [18] compared the performance of water-in-glass and U-pipe evacuated-tube solar collectors and optimised their flow rate for maximum energy production. The literature review shows that the TRNSYS simulation is a reliable tool for the determination of the yearly performance of the SHW systems [19]. Zhou et al. [5] conducted a numerical study to investigate the impact of operating conditions on the performance of FPC integrated with Transparent Insulation Material (TIM). The results highlighted that FPC with TIM proves to be highly efficient, particularly in colder ambient temperatures. Specifically, the efficiency of FPC with TIM was found to be 6.2% higher compared to traditional FPC collectors. Kizildag et al. [20] conducted a comparative analysis between FPC and modified FPC incorporated with TIM. The results indicated a remarkable difference in energy production, with the modified FPC outperforming the standard collectors by 2.5 times during winter and 1.4 times during spring. Kessentini et al. [21] conducted a comprehensive study on FPC integrated with TIM and an overheating protection system. Their research demonstrated that the FPC with TIM can achieve performance levels comparable to commercially available solar collectors, all while maintaining a low-cost advantage. Despite

the proven effectiveness of convection-suppressed flat plate technology utilizing transparent insulation in cold weather conditions, its widespread commercialization has not yet been realized. In this study, we aim to compare the performance of conventional flat plate technology with convection-suppressed flat plate technology in a European climate, considering current energy prices.

2. Modeling solar hot water heater system

2.1. System description

Flat plate collector refers to a particular geometry of solar collector employed for hot water generation. The FPC consists of an absorber plate that intercepts the incident light and generates thermal energy, which is transferred to water in the storage tank by the heat transfer fluid flowing through the cooling tubes attached to the absorber plate. To reduce the heat loss from the absorber, it is covered with a glass cover on top and thermal insulation at the sides and bottom. The glass cover on top reduces the convection heat loss and traps the long wave radiation emitted from the absorber plate thereby increasing the thermal energy available at the absorber. A solar selective coating is usually applied to the absorber plate which has strong absorption in the visible and near infra-red range and low emissivity in the infra-red range. The schematic of standard FPC and the modified FPC analysed in this work are given in Figure 1.

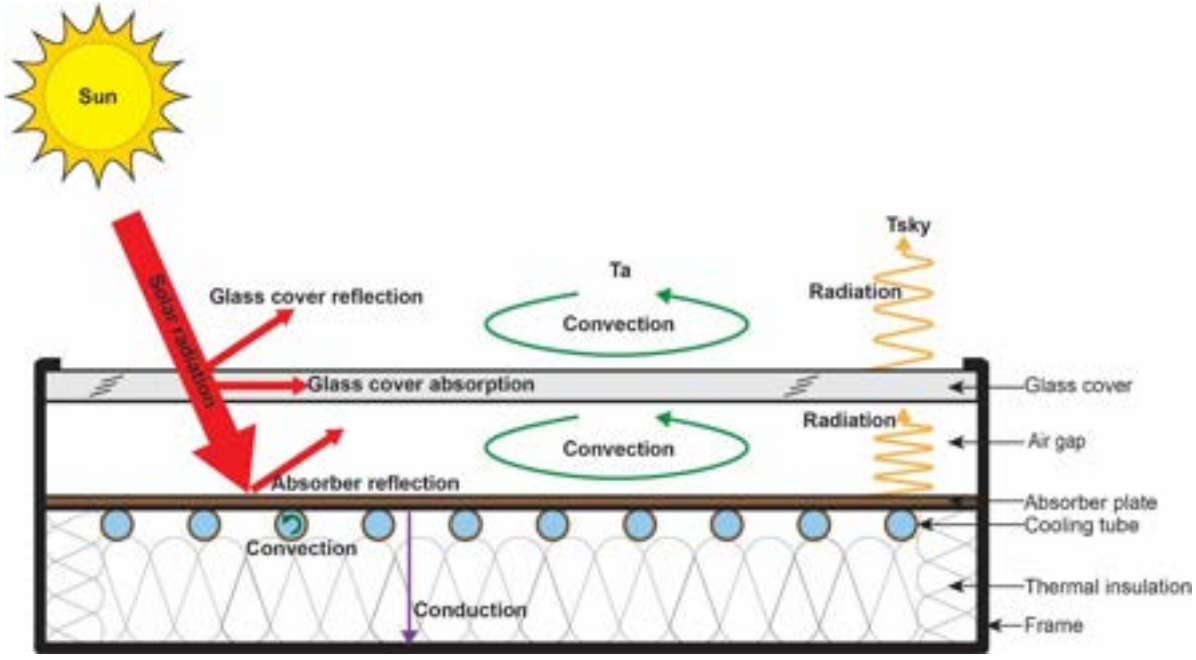

(a)

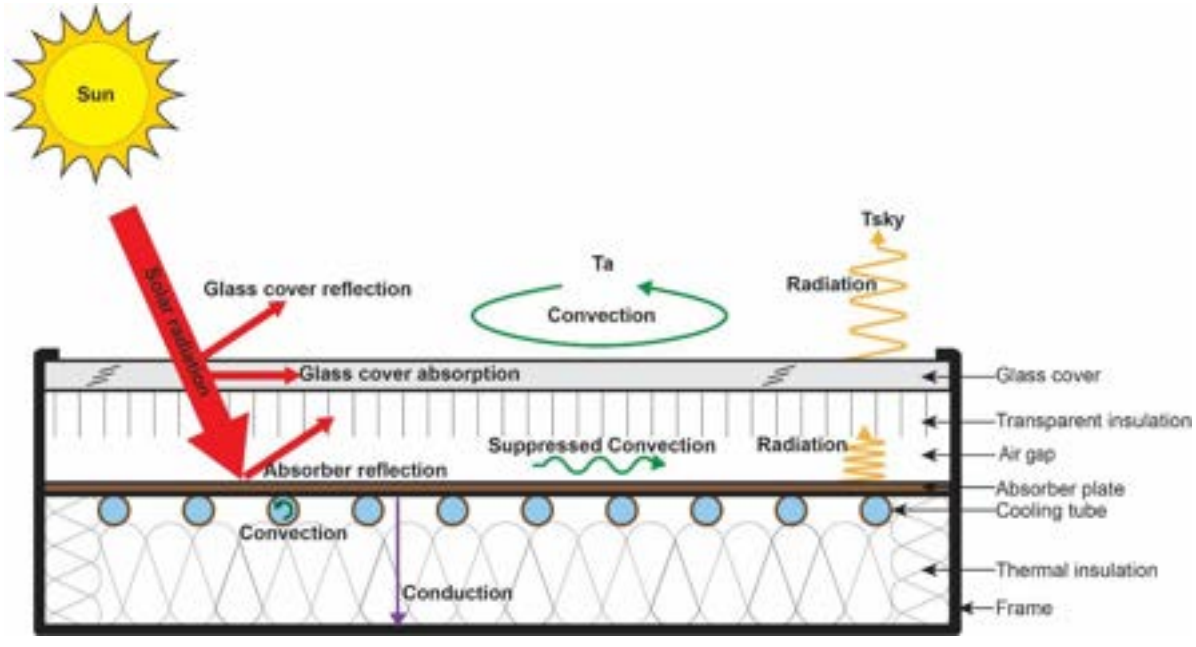

(b)

Figure. 1. Schematic of solar flat plate collector: a) SFPC, b) MFPC.

In the modified FPC design, a transparent insulation made of polycarbonate honeycomb is inserted in the airgap between the glass cover and the absorber plate with the aim to suppress the air circulation that is responsible for convection heat loss from the absorber plate. The performance of the solar thermal collector is described using a second order equation as a function of environmental and functional parameters and we use numerical simulation to determine the constants of the efficiency equation Eq. (1) [22].

$$\eta = a_0 - a_1 \frac{(T_m - T_a)}{G} - a_2 \frac{(T_m - T_a)^2}{G} \quad (1)$$

2.2. Numerical modeling for estimation of performance parameters

The steady state, two-dimensional thermal modeling of solar flat plate collector was done using the Multiphysics simulation software, COMSOL 6.1. For the numerical analysis, a portion of the FPC with one cooling tube was taken, this is supported by the assumption that the flow rate in each riser tube was the same. The specific collector being examined was the K420-EM2L, which was manufactured by KBB Kollektorbau GmbH and it has an aperture area of 1.97 m^2 [23]. Details of the computational domain and boundary conditions can be found in Figure 2. The thermophysical properties of the solid components that make up the FPC are constant and are listed in Table 1. It is assumed that the air flow between the absorber and the glass cover is laminar and incompressible. Therefore, the density of air is modeled as an incompressible ideal gas, using the Boussinesq approximation method [24]. The heat transfer and fluid flow problem were solved by solving the coupled continuity, momentum, and energy equations, with an additional transport equation for S2S radiation Eq. (2-4) [25].

Continuity equation, $\frac{\partial}{\partial x_j}(\rho u_j) = 0$ (2)

Momentum equation, $\frac{\partial}{\partial x_j}(\rho u_i u_j) = \frac{\partial}{\partial x_j}\left[\mu\left(\frac{\partial u_i}{\partial x_j} + \frac{\partial u_j}{\partial x_i}\right)\right] + \rho g_i \beta\,(T - T_\infty)$ (3)

Energy equation, $\frac{\partial}{\partial x_j}(\rho u_j C_p T) = \frac{\partial}{\partial x_j}\left[\lambda \frac{\partial T}{\partial x_j}\right] + \dot{Q}$ (4)

2.3. Boundary conditions and methodology

The solar radiation input to the collector is modelled by considering a volumetric heat source at the absorber and the glass cover Eq. (5,6) [27]. The laminar forced convection from the inside of the cooling tube is modeled with a convective heat transfer coefficient h_f calculated from the Nusselt number for the case with constant heat flux boundary condition (Nu_f=4.36), at mean water temperature $\left(T_m = \frac{T_{out} + T_{in}}{2}\right)$ [28]. The top and bottom surfaces of the collector are subjected to external natural convection due to ambient air in contact with the collector surface. There are two instances of radiation heat loss in the collector: one occurs externally from the glass cover to the sky, while the other occurs internally between the absorber and the glass cover [29]. Once the computational domain is assigned with material properties and boundary conditions, the necessary physics to solve laminar natural convection, heat transfer, and S2S radiation are added and coupled. The governing equations are solved using the stationary solver-multifrontal massively parallel sparse direct solver (MUMPS) with a relative tolerance of 0.001. The purpose of this simulation is to obtain the efficiency curve of the solar collector (η vs $\frac{T_m - T_a}{G}$), and therefore, a parametric study was done by varying the mean water temperature (285 K≤T_m≤350 K) keeping the insolation constant (G=800 W/m^2).

Heat generation in absorber, $\dot{Q}_{abs} = \frac{G\,\tau_g \alpha_p}{t_{abs}}$ (5)

Heat generation in glass cover, $\dot{Q}_g = \frac{G\,\alpha_g}{t_g}$ (6)

Table 1. Thermophysical properties of FPC collector [26].

Component	λ, (W/m-K)	ρ, (kg/m^3)	C_p, (J/kg-K)
Glass cover	1.38	2200	770
Absorber and cooling tube (Aluminium-D_o:12 mm, D_{in}:11 mm)	238	2700	900
Insulation	0.022	30	1000
Transparent insulation (Polycarbonate)	0.2	1200	1200

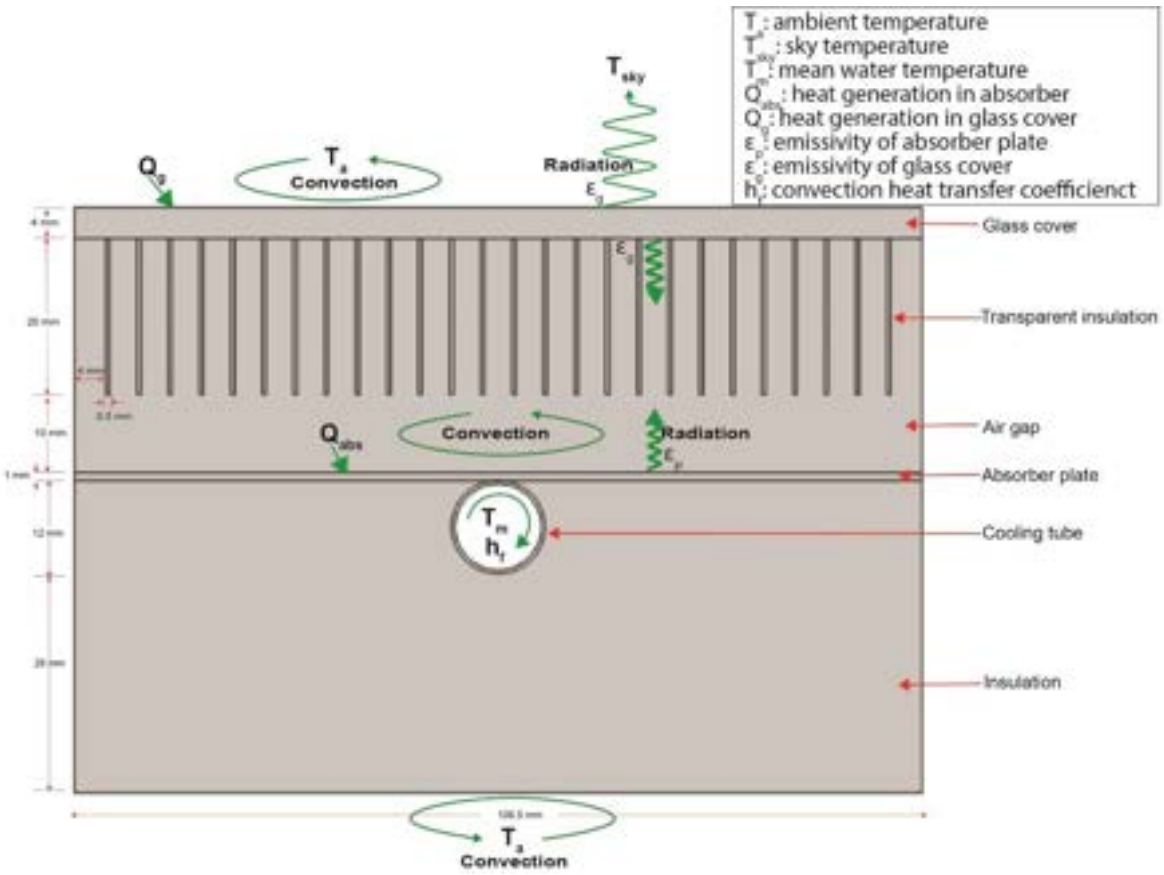

Figure. 2. Computational domain with boundary conditions.

2.4. Validation

The numerical model developed by Kim and Viskanta [30] for solving coupled laminar natural convection, surface radiation, and wall conduction in a differentially heated cavity is taken for validation. Figure 3 shows the plot of non-dimensional temperature $\left(\frac{T-T_c}{T_h-T_c}\right)$, obtained at the vertical wall; it can be seen that the proposed model agrees well with the existing model, with dimensionless temperature having a deviation between 0.25% and 7.61%.

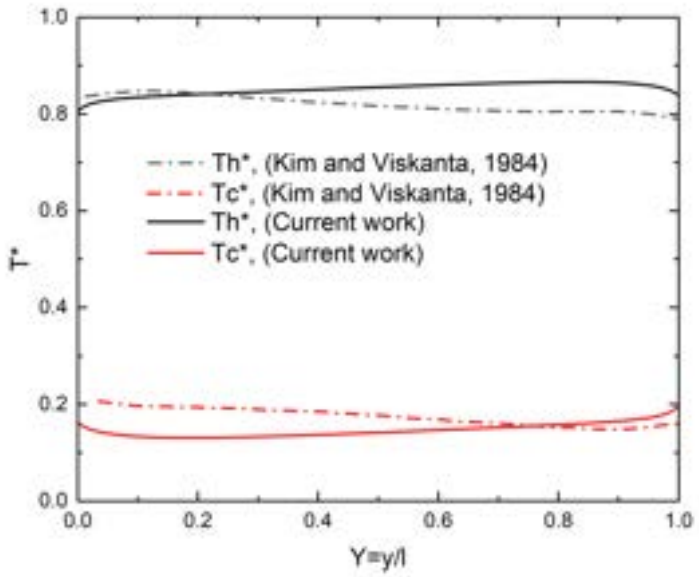

Figure. 3. Non-dimensional temperature obtained from the proposed model and the existing model.

2.5. TRNSYS simulation for the yearly energy produced

The useful thermal energy collected by the SFPC and MFPC over a year was obtained using the transient simulation software TRNSYS 18. In TRNSYS, models that represent the components of solar hot water system (Collector: Type 1b, Tank: Type 60d, Pump: Type 110) are connected similar to how they would be connected in real life. The forced circulation SHW system is implemented using a single tank model that has an internal heat exchanger coil connected to the solar collector. The hot water demand profile used is the EU reference tapping cycle 3 representing 200 L of hot water required in a day at 60 °C ($Q_{thermal}$ = 11.65 kWh/day) [31]. The storage tank has a built-in immersion heater (3kW) located at the middle of the tank and is turned ON in two batches, from 5 am to 7 am and 6 pm to 8 pm, whenever the tank top temperature falls below 55 °C. The overall heat loss coefficient of the tank is taken to be 1.6 W/m^{2}K [7]. The pump used is a constant flow rate pump and is controlled using an ON/OFF controller (Type: 2b). The controller sets the pump ON only when the difference in collector outlet water temperature and the tank bottom temperature exceeds 5°C, this is to ensure system operation at sufficient irradiance level. The FPC system modeling simulation diagram with interconnection of various components is given in Figure 4.

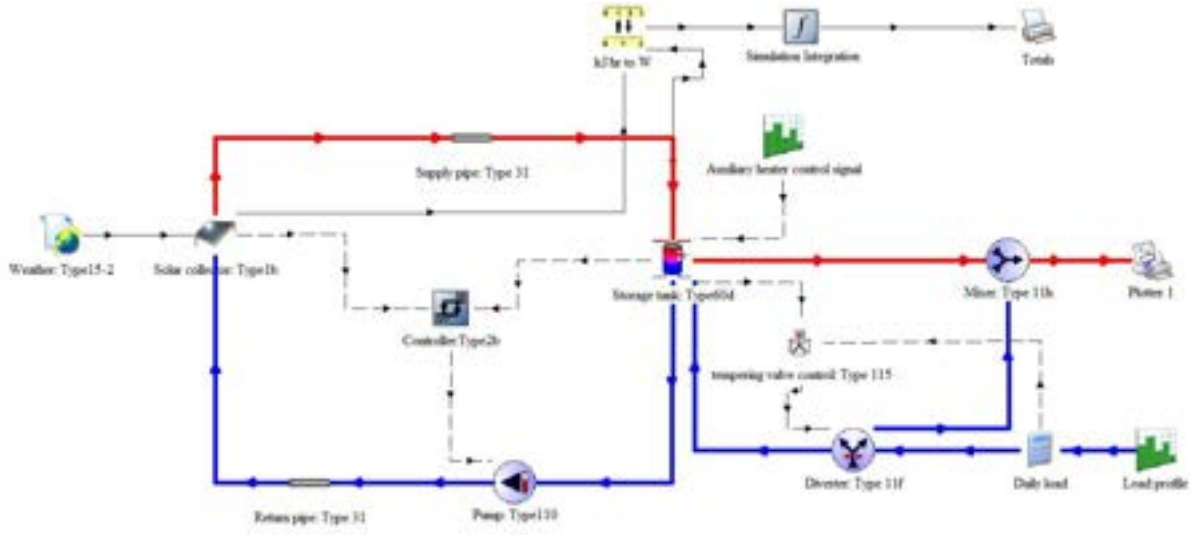

Figure. 4. TRNSYS simulation of SHW system modeling.

2.6. Economic and environment analysis

The economic evaluation parameters used in this study to show the benefit of installing a solar thermal hot water system are the net present value (NPV) and the simple payback period (SPB) Eq. (7,8) [29]. The NPV and SPB period are calculated for the two systems with different auxiliary fuels: electricity, oil, and gas at current energy price [32]. The economic analysis was done by assuming 8% annual discount rate and 20 years of useful life. The operation and maintenance cost were assumed to be 1% of the capital cost. The assumptions taken in the economic analysis of the solar hot water systems are listed in Table 2. The yearly CO_2 emission by the two solar hot water systems with different auxiliary fuel was calculated using Eq. (9). and are based on the country emission factor for CO_2 per unit of energy for particular fuel [33].

$$NPV = \sum_{j=1}^{N} Q_u \, C_{aux} \, \eta_{aux} \, \frac{(1+i)^{j-1}}{(1+d)^j} - \sum_{j=1}^{N} C_{o\&m} \frac{(1+i)^{j-1}}{(1+d)^j} - C_{capital} \quad (7)$$

$$SPB = \frac{C_{capital}}{Q_u \, C_{aux} \, \eta_{aux}} \quad (8)$$

$$Q_{CO2\ emission} = Q_{aux} \, S_{CO2} \quad (9)$$

Table 2. Economic analysis parameters [34,35].

Parameter	Value
Capital cost of FPC system	3500 €
Solar Water Heating Grant	1200 €
Inflation rate	3%
Cost of electricity	0.31 €/kWh
Cost of oil	0.14 €/kWh
Cost of gas	0.08 €/kWh
Efficiency of Electrical immersion heater	100%
Efficiency of oil boiler	65%
Efficiency of gas boiler	90%

3. Results and Discussion

3.1. FPC characteristics curve

The heat transfer and the fluid flow model are solved to determine the constants of the characteristic equation that describe the performance of solar thermal collector. Numerical simulations are done for the input conditions, such as incident radiation of 800 W/m^2, ambient temperature of 283 K, and collector tilt of 45°.The obtained efficiency curves along with their characteristic equation are given in Figure 5. The area under the efficiency curve reflects the useful energy gained, and it is evident that the MFPC collects more energy compared to the SFPC. The MFPC exhibits a 20% optical loss, whereas the SFPC has a 22% optical loss. The MFPC system's first and second order heat loss coefficients have been determined to be 1.7618 W/m^{2}K and 3.058$\times 10^{-3}$ W/m^{2}K^2, respectively. Meanwhile, the SFPC system has first and second order heat loss coefficients of 3.0632 W/m^{2}K and 7.7136$\times 10^{-3}$ W/m^{2}K^2, respectively.

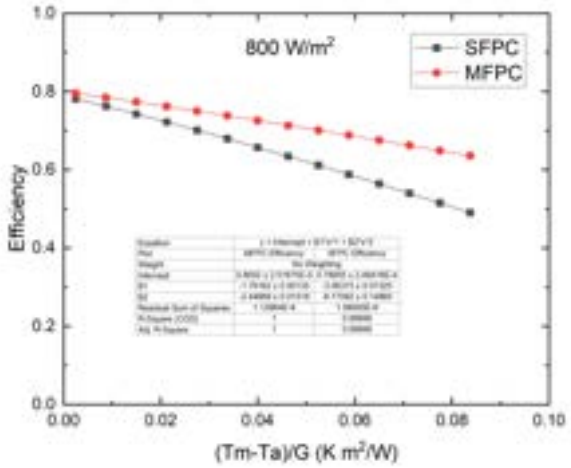

Figure. 5. TRNSYS simulation of SHW system modeling.

3.2. Yearly performance analysis

The yearly energy performance of the SFPC and MFPC SHW system was simulated in TRNSYS by using the performance parameters obtained from COMSOL simulations. The SHW system consisted of two FPC collectors connected in series each with absorber area 1.972 m^2. The collector tilt was taken to be 44°. The flow rate in the solar collector loop was maintained constant at 95 kg/h. The simulations were done for a year at 1 minute time step with meteorological data input relative to Dublin (53.3498° N, 6.2603° W). The SFPC and MFPC systems' yearly useful energy collected were 1446.60 kWh and 1993.50 kWh, respectively, as shown in Figure 6. The corresponding annual solar fractions of the SFPC and MFPC systems were 27.27% and 36.57%, respectively.

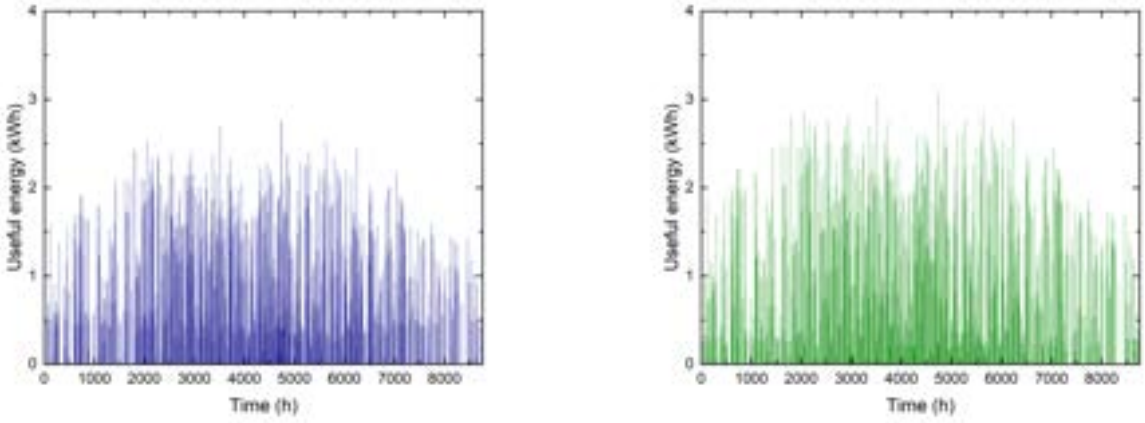

(a) SFPC (b) MFPC

Figure. 6. Useful energy generated by SFPC and MFPC for 4m^2 collector area installed in Dublin.

3.3. Economic feasibility and CO_2 emissions

The results of the NPV and SPB period calculations for both the SFPC and MFPC systems, using different types of fuel for auxiliary heating, are presented in Figures 7, respectively. The economic analysis reveals that FPC systems are financially viable only when electricity is used as the auxiliary fuel. After factoring in the solar grant, the NPV of the MFPC is notably high, amounting to € 5078.94. Additionally, the SFPC has a simple payback period of 5 years, whereas the MFPC has a comparatively shorter payback period of only 3.7 years when electricity is used as the auxiliary heating source. Table 3 shows the CO_2 emissions generated by the SFPC and MFPC systems when using different types of auxiliary fuel. It is evident that the CO_2 emissions are minimized when electricity is employed as the auxiliary heating source. The yearly CO_2 emissions from SFPC and MFPC SHW system with electricity as auxiliary heating is found to be 385.87 kg and 345.82 kg respectively. Using a conventional electrical immersion heater to generate hot water for a typical house result in an annual CO_2 emission of 425.22 $kgCO_2$. However, by implementing the proposed MFPC SHW system, this CO_2 emission could be significantly reduced to 345.82 $kgCO_2$/year.

Table 3. CO2 emission from SHW system [36].

Auxiliary fuel	$kgCO_2$/kWh	$kgCO_2$ emissions/year	
		SFPC	MFPC
Electricity	0.10	374.29	335.62
Gas	0.20	782.93	702.03
Oil	0.26	991.68	889.22

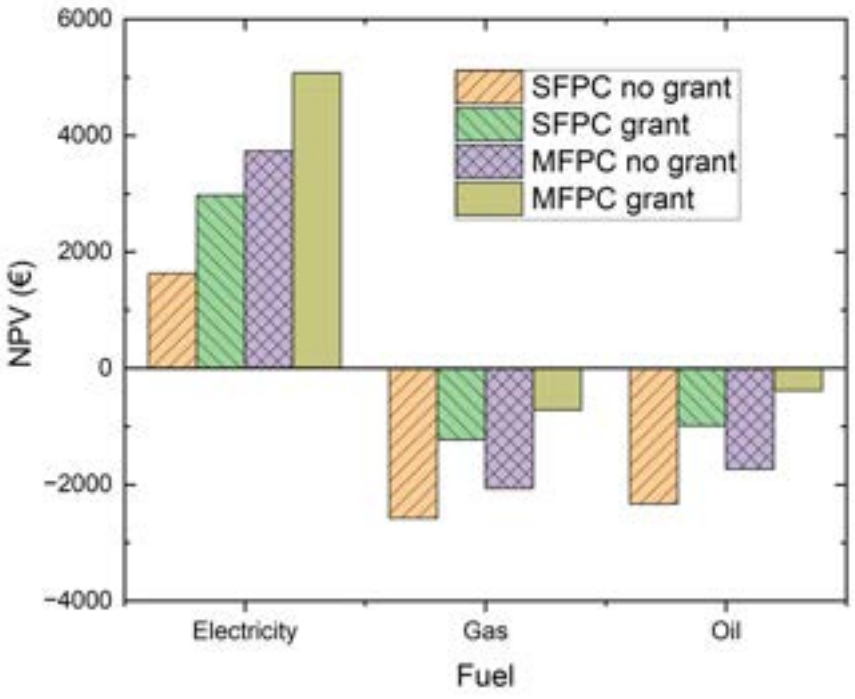

(a)

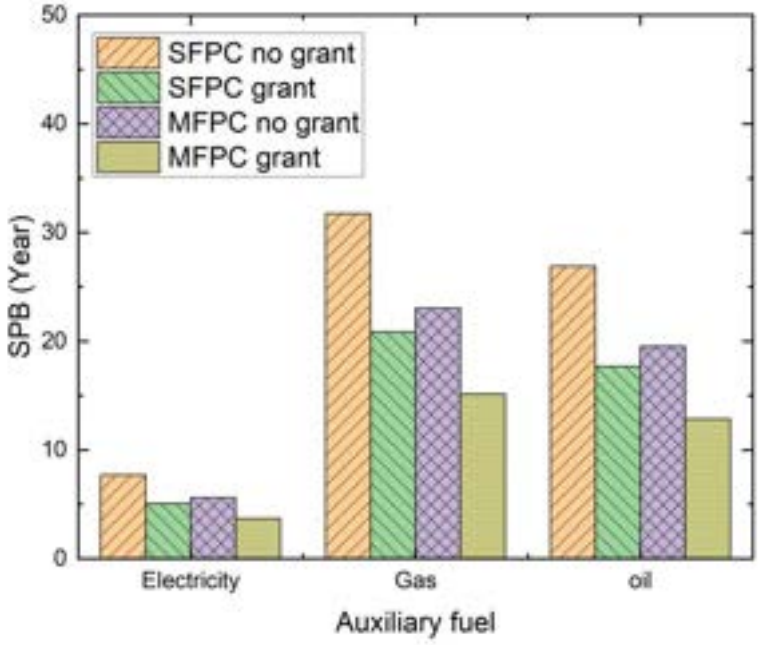

(b)

Figure. 7. Economic analysis: a) NPV and, b) SPB for the SHW system with different auxiliary heating.

4. Conclusions

A study was conducted to investigate the feasibility of implementing a SHW system in a northern European climate, taking into account the current energy costs for auxiliary heating. The study focused on two different FPC systems, each with a total aperture area of 4m^2. Numerical simulations were utilized to obtain the efficiency parameters of the systems based on a simplistic heat transfer and fluid flow model. These parameters were then utilized in TRNSYS simulations to determine the yearly thermal performance of each system. The energy collected by the two systems are found to be be 1446.60 kWh/year and 1993.50 kWh/year respectively. Results indicated that FPC systems are still a financially viable option for hot water generation, particularly when using electricity as the auxiliary heating source. The modified FPC system exhibited the best performance, with a high NPV of € 5078.94 and a short SPB period of 3.7 years. Moreover, by employing the MFPC system with electrical auxiliary heating, 79.58 kgCO_2 reduction in annual emissions is achievable when compared to conventional electrical immersion heaters. Future work is to optimize the collector size for different hot water consumption profile and also to explore the feasibility of using ETC collectors.

Acknowledgments

The financial support provided by Science Foundation Ireland under the project SOLARCOOL is acknowledged (grant no: 19/FIP/ZE/7484R). We would like to thank Cian Fogarty, a research assistant Nanothermal Research Group at Trinity College Dublin for the knowledge handed down on the modelling of collectors.

Nomenclature

a_0 intercept efficiency, %

a_1 efficiency slope, W/(m^2 K)

a_2 efficiency curvature, W/(m^2 K^2)

C cost, €

C_p specific heat, J/(kg K)

d market discount rate, %

G heat flux, W/m^2

g gravitational acceleration, m/s^2

h_f heat transfer coefficient, W/(m^2 K)

i inflation rate, %

N useful life

$\overline{Nu}$ average Nusselt number

$\dot{Q}$ volumetric heat generation, W/m^3

Q_u useful energy, Wh

S CO_2 emission coefficient, kgCO_2/(W h)

T temperature, K

t thickness, m

u velocity, m/s

x,y cartesian coordinate

Greek symbols

α absorptivity

β thermal expansion coefficient, K^{-1}

ε emissivity

η efficiency, %

λ thermal conductivity, W/(m K)

μ viscosity, kg/(m s)

ρ density, kg/m^3

τ transmissivity

Subscripts

a ambient

abs absorber

aux auxiliary fuel

c capital

g glass cover

in inlet

m average water

$o\&m$ operation and maintenance

out outlet

th thermal

u useful

References

[1] Heating - Fuels & Technologies – IEA – Available at:<https://www.iea.org/fuels-and-technologies/heating> [accessed 1.3.2023].

[2] Pandey KM, Chaurasiya R. A review on analysis and development of solar flat plate collector. Renewable and Sustainable Energy Reviews. 2017 Jan 1;67:641-50.

[3] Sokhansefat T, Kasaeian A, Rahmani K, Heidari AH, Aghakhani F, Mahian O. Thermoeconomic and environmental analysis of solar flat plate and evacuated tube collectors in cold climatic conditions. Renewable Energy. 2018 Jan 1;115:501-8.

[4] Hazami M, Naili N, Attar I, Farhat A. Solar water heating systems feasibility for domestic requests in Tunisia: Thermal potential and economic analysis. Energy conversion and management. 2013 Dec 1;76:599-608.

[5] Zhou L, Wang Y, Huang Q. Parametric analysis on the performance of flat plate collector with transparent insulation material. Energy. 2019;174:534–42. doi:10.1016/j.energy.2019.02.168

[6] Ayompe LM, Duffy A. Analysis of the thermal performance of a solar water heating system with flat plate collectors in a temperate climate. Applied thermal engineering. 2013 Sep 1;58(1-2):447-54.

[7] Hazami M, Kooli S, Naili N, Farhat A. Long-term performances prediction of an evacuated tube solar water heating system used for single-family households under typical Nord-African climate (Tunisia). Solar Energy. 2013 Aug 1;94:283-98.

[8] Tiwari AK, Gupta S, Joshi AK, Raval F, Sojitra M. TRNSYS simulation of flat plate solar collector based water heating system in Indian climatic condition. Materials Today: Proceedings. 2021 Jan 1;46:5360-5.

[9] Kalogirou SA, Agathokleous R, Barone G, Buonomano A, Forzano C, Palombo A. Development and validation of a new TRNSYS Type for thermosiphon flat-plate solar thermal collectors: energy and economic optimization for hot water production in different climates. Renewable energy. 2019 Jun 1;136:632-44.

[10] Zainine MA, Mezni T, Dakhlaoui MA, Guizani A. Energetic performance and economic analysis of a solar water heating system for different flow rates values: A case study. Solar Energy. 2017 May 1;147:164-80.

[11] Bernardo LR, Davidsson H, Karlsson B. Retrofitting domestic hot water heaters for solar water heating systems in single-family houses in a cold climate: A theoretical analysis. Energies. 2012 Oct 22;5(10):4110-31.

[12] Víg P, Seres I, Vladár P. Improving efficiency of domestic solar thermal systems by a flow control. Solar Energy. 2021 Dec 1;230:779-90.

[13] Hayek M, Assaf J, Lteif W. Experimental investigation of the performance of evacuated-tube solar collectors under eastern Mediterranean climatic conditions. Energy procedia. 2011 Jan 1;6:618-26.

[14] Maraj A, Londo A, Gebremedhin A, Firat C. Energy performance analysis of a forced circulation solar water heating system equipped with a heat pipe evacuated tube collector under the Mediterranean climate conditions. Renewable energy. 2019 Sep 1;140:874-83.

[15] Al-Madhhachi HS, Ajeena AM, Al-Bughaebi NA. Dynamic simulation and energy analysis of forced circulation solar thermal system in two various climate cities in Iraq. AIMS Energy. 2021 Jan 1;9(1):138-49.

[16] Kalogirou SA, Papamarcou C. Modelling of a thermosyphon solar water heating system and simple model validation. Renewable Energy. 2000 Nov 1;21(3-4):471-93.

[17] Hobbi A, Siddiqui K. Optimal design of a forced circulation solar water heating system for a residential unit in cold climate using TRNSYS. Solar energy. 2009 May 1;83(5):700-14.

[18] Gao Y, Zhang Q, Fan R, Lin X, Yu Y. Effects of thermal mass and flow rate on forced-circulation solar hot-water system: Comparison of water-in-glass and U-pipe evacuated-tube solar collectors. Solar Energy. 2013 Dec 1;98:290-301.

[19] Džiugaitė-Tumėnienė R, Streckienė G. Solar hot water heating system analysis using different software in single family house. InThe 9th International Conference “Environmental Engineering”, 22–23 May 2014, Vilnius, Lithuania 2014 May (p. 9).

[20] Kizildag D, Castro J, Kessentini H, Schillaci E, Rigola J. First Test field performance of highly efficient flat plate solar collectors with transparent insulation and low-cost overheating protection. Solar Energy. 2022;236:239–48. doi:10.1016/j.solener.2022.02.007

[21] Kessentini H, Castro J, Capdevila R, Oliva A. Development of flat plate collector with plastic transparent insulation and low-cost overheating protection system. Applied Energy. 2014;133:206–23. doi:10.1016/j.apenergy.2014.07.093

[22] Bouhal T, Agrouaz Y, Allouhi A, Kousksou T, Jamil A, El Rhafiki T, Zeraouli Y. Impact of load profile and collector technology on the fractional savings of solar domestic water heaters under various climatic conditions. International journal of hydrogen energy. 2017 May 4;42(18):13245-58.

[23] Biome solar industry- Available at:<http://www.biome-solar.com/medias/certification/performance%20test_K420-EM_english%20(2).pdf> [accessed 1.3.2023].

[24] Saravanan S, Sivaraj C. Combined thermal radiation and natural convection in a cavity containing a discrete heater: effects of nature of heating and heater aspect ratio. International Journal of Heat and Fluid Flow. 2017 Aug 1;66:70-82.

[25] Alvarado R, Xamán J, Hinojosa J, Álvarez G. Interaction between natural convection and surface thermal radiation in tilted slender cavities. International Journal of thermal sciences. 2008 Apr 1;47(4):355-68.

[26] Parthiban A, Mallick TK, Reddy KS. Integrated optical-thermal-electrical modeling of compound parabolic concentrator based photovoltaic-thermal system. Energy Conversion and Management. 2022 Jan 1;251:115009.

[27] Parthiban A, Reddy KS, Pesala B, Mallick TK. Effects of operational and environmental parameters on the performance of a solar photovoltaic-thermal collector. Energy Conversion and Management. 2020 Feb 1;205:112428.

[28] Incropera FP, DeWitt DP. Introduction to heat transfer. J. Wiley; 2002.

[29] Duffie JA, Beckman WA. Solar Energy Thermal Processes. New York etc.: Wiley; 1980.

[30] Kim DM, Viskanta R. Effect of wall conduction and radiation on natural convection in a rectangular cavity. Numerical Heat Transfer. 1984 Oct 1;7(4):449-70.

[31] European commission – Available at:<https://law.resource.org/pub/eu/mandates/m324.pdf> [accessed 1.3.2023].

[32] Fuel Cost Comparisons (seai.ie) – Available at:<https://www.seai.ie/publications/Domestic-Fuel-Cost-Comparison.pdf> [accessed 1.3.2023].

[33] Anoune K, Laknizi A, Bouya M, Astito A, Abdellah AB. Sizing a PV-Wind based hybrid system using deterministic approach. Energy conversion and management. 2018 Aug 1;169:137-48.

[34] How much do solar thermal panels cost in Ireland? (insulationcostsireland.com) – Available at:<https://insulationcostsireland.com/how-much-do-solar-thermal-panels-cost-in-ireland.html> [accessed 1.3.2023].

[35] Grant For Solar Water Heater | Home Energy Grants | SEAI Available at:<https://www.seai.ie/grants/home-energy-grants/solar-water-heating-grant/> [accessed 1.3.2023].

[36] Advice on installing solar water heating - Energy Saving Trust – Available at:< https://energysavingtrust.org.uk/advice/solar-water-heating/> [accessed 1.3.2023].

First step to define a predictive model of the behaviour of a building's thermal system to analyse the climate change influence

Irati Prol-Godoy[a], Ana Picallo Perez[b], Iñaki Inza[c], Roberto Santana[d], Jose María Sala Lizarraga[e] and Javier Rey Martínez[f]

[a] University of the Basque Country UPV/EHU, Vitoria-Gasteiz, Spain, irati.prol@ehu.eus
[b] University of the Basque Country UPV/EHU, Bilbao, Spain, ana.picallo@ehu.eus
[c] University of the Basque Country UPV/EHU, Donostia, Spain, inaki.inza@ehu.eus
[d] University of the Basque Country UPV/EHU, Donostia, Spain, roberto.santana@ehu.eus
[e] University of the Basque Country UPV/EHU, Bilbo, Spain, josemariapredo.sala@ehu.eus
[f] University of Valladolid, Valladolid, Spain, rey@eii.uva.es

Abstract:

Buildings account for 40% of the EU's final energy consumption and 36% of its energy-related GHG emissions. Therefore, to reduce the EU's GHG emissions it is needed to reduce the energy consumption and increase energy efficiency. For that, not only the design but also the maintenance of systems is essential to ensure the proper functioning and the energy efficiency. On the other hand, the environmental temperature is rising at a high rate because of the global warming. Therefore, this will undoubtedly influence on the energy efficiency of the buildings thermal systems. However, we can only estimate the effects from predictions based on previous data models.

In this work we develop a methodology in order to learn a predictive model of a simple thermal system of a building, consisting of a boiler and the distribution equipment that provides the dynamic DHW demand. The model is learn from databases obtained from a thermal system software to calculate the influence of climate change on the cost formation process. That is, we quantify the effects on costs due to outdoor temperature variation when the demand does not vary, based on thermoeconomic indices. The next step will be to incorporate heating demand that will also vary due to climate change.

The reference model of the thermal facility would serve to predict the behaviour when the climate changes, in order to implement it in maintenance tasks and thermoeconomic diagnosis for fault detection.

Keywords:

Predictive model; Thermal installation; Buildings; Climate-change.

1. Introduction

Buildings account for 40% of the EU's final energy consumption and 36% of its energy-related greenhouse gas (GHG) emissions. Therefore, reducing energy consumption and increasing energy efficiency are required to reduce the EU's GHG emissions [1].

On the other hand, due to climate change, environmental temperature is rising at a rapid pace. The global average temperature has risen by 0.76°C over the last 100 years [2] and, in addition, global average warming is estimated to be 2.2°C by 2100, 3.6°C by 2200 and 4.6°C by 2500, with all the consequences that this entails [3]. After all, buildings must generate thermal comfort and meet energy needs according to the variable external conditions and the profile of the users.

The research of predictive behavioural models to improve continuously the building installations and their maintenance is a key point to ensure the intelligent operation of equipment and to detect premature wear of engines. With predictive models learned from simulated thermal data, it is possible to set a competitive regime and timing of processes, to detect excess energy consumption, or to detect malfunctions.

For all these reasons, the key for a proper management and energy savings lies, among others, in predicting the operation of systems and the cost of the products required in the future, to (1) be able to take the necessary actions to adapt to new climatic conditions, and, to (2) slow down the increase in the Earth's surface temperatures, reducing GHG emissions. Thus, one of the keys to guarantee the proper functioning of thermal systems in buildings and to promote the energy efficiency are maintenance actions.

A survey of the state of the art of work applying thermoeconomics in combination with AI shows that there are some recent studies. The work in [4] creates a model that applies the principles of thermoeconomics to analyse

and optimize the performance of the Afyon geothermal power plant. This modelling approach is enhanced by using artificial neural networks to improve the plant's efficiency and cost-effectiveness. In Ref. [5] the thermoeconomics aspects of a system that combines geothermal and solar energy to produce both hydrogen and power are studied. This analysis involves using advanced techniques such as artificial neural networks and genetic algorithms to optimize the system's performance. In the work in [6] artificial intelligence and response surface methods are used in order to optimize the thermoeconomic performance of waste heat recovery system in a large internal combustion engine.

As shown in the literature, the studies are focused on the application of Thermoeconomics and Machine learning methods for optimising industrial systems. In this way, this study provides a methodology that combines both disciplines for maintenance work in building thermal systems.

Therefore, this paper presents a case study of a dynamic thermoeconomic analysis applied to a domestic hot water (DHW) installation and develops a methodology to create a model, which aims to predict the performance and the costs and consumption of thermal systems in buildings, for their maintenance. This model combines Thermoeconomics with data-driven Machine Learning (ML) methods. Data-driven methods extract patterns from historical process data [7], which are very useful for monitoring and model building thermal systems due to the large amount of data collected and the dynamic operation.

2. Materials and methods

This section explains the laboratory where the system has been designed, the thermoeconomics applied to the study as well as the thermoeconomics and TRNSYS software needed to carry out the case study.

2.1 Building Quality Control Laboratory of the Basque Government

The Building Quality Control Laboratory of the Basque Government (LCCE) is a laboratory prepared to carry out physical, mechanical and chemical tests on construction materials. It is divided into three areas: thermal, acoustic and materials. Thus, the thermal area has a flexible experimental plant designed to configure different installations depending on the required demand. For this purpose, the installation can be divided into different zones or islands, as can be seen in Figure 1: (1) low temperature zone, (2) high temperature zone and (3) solar collector zone. These three zones correspond to the different generation equipment. There are also (4) the distribution equipment zone, (5) the heating/DHW terminal zone and finally (6) the thermal storage zone.

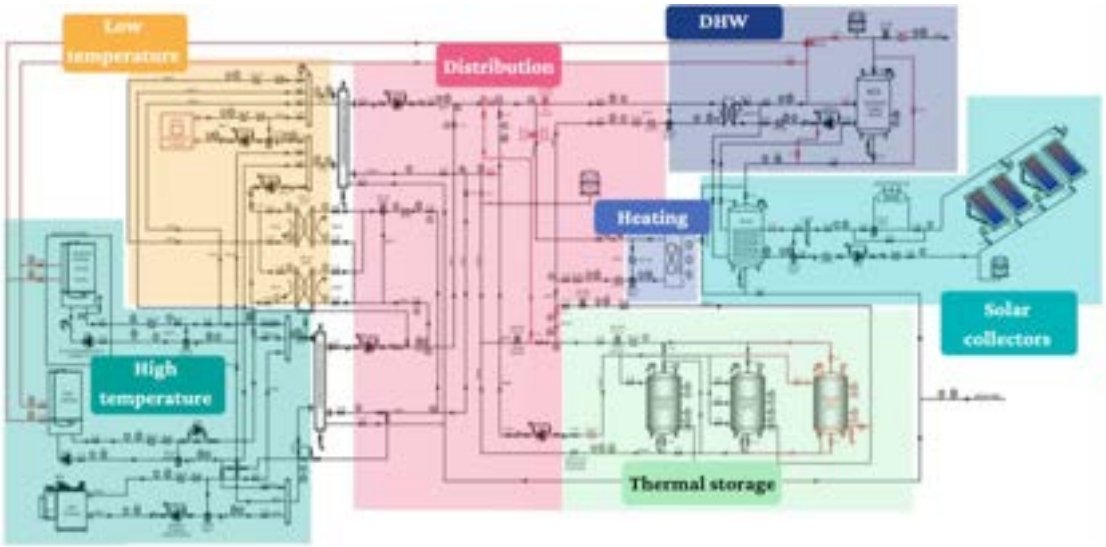

Figure 1. Experimental plant of the LCCE

The installation consists of more than 100 signals to control and monitor the variables to be evaluated. For this, 46 high precision Pt 100 class 1/10 temperature probes are used, 40 of them located in pipes and the rest in tanks, 11 SIEMENS FM electromagnetic flowmeters (MAG 3100 and 5100W sensors and MAG 6000 transmitters), 2 pressure switches, one in the general circuit and the other in the solar circuit. It also has ambient temperature, humidity and pressure sensors both inside and outside the laboratory. The boiler and the micro-cogeneration equipment have gas and electricity meters and the consumption of the heat pump is also monitored.

The entire control of the installation is managed by a Siemens IM 151-8 PN/DP CPU for ET200S and an expansion module, as well as the corresponding input and output cards for the signals, connected via Ethernet to a PC where the interface is available through which the operation is carried out and the data are collected.

2.2 TRNSYS

TRNSYS [8] is a flexible software environment for simulating the behaviour of transient thermal systems in buildings, composed of two parts:

- The first is an engine (called the kernel) that reads and processes the input file, iteratively solves the system, determines convergence and plots system variables. The core also provides utilities that determine thermophysical properties, invert matrices, perform linear regressions, interpolate external data files, etc.
- The second part consists of an extensive library of components, each of which models the performance of a part of the system. The standard library includes approximately 150 models ranging from pumps to multi-zone buildings, from wind turbines to electrolysers, from weather data processors to economics routines, and from basic HVAC equipment to the most advanced emerging technologies. The models are built in such a way that users can modify existing components or write their own, extending the capabilities of the environment.

Accordingly, TRNSYS version 18 has been used for this simulation.

2.3 THERMOECONOMICS

The Exergy Cost Theory is based on a series of Propositions, whose systematic application makes possible to unequivocally determine the value of the costs (in energy and monetary units) of each of the flows of the system under analysis [9].

The previous step for applying thermoeconomic analysis is to determine the *physical structure*, where all material and energy flows are represented. Furthermore, the approach of the structural theory of thermoeconomics goes beyond the physical structure of the system and defines its *productive structure* in a matrix form. In order to carry out a productive analysis, the flows are classified according to the function they perform in the equipment. This representation considers each equipment *i* as a black box with an input arrow, called fuel ($F_i\ [kWh]$), and an output arrow, product ($P_i\ [kWh]$). The F_i of a component *i* represents the resources (measured in exergy terms) needed to run the specific energy process and P_i contains the target of the process itself. Therefore, the difference between both terms represents the irreversibility of the process ($I_i = F_i - P_i$) and the ratio $\left(k_i = \frac{F_i}{P_i}\ \left[\frac{kWh}{kWh}\right]\right)$ reflects the unit exergy consumption of the component, which expresses the amount of fuel required to generate one unit of product. This coefficient is related to the other components through the specific $\mathbf{F}$ and $\mathbf{P}$ interrelationships, given by a matrix $\langle \mathbf{KP} \rangle$, which reflects the productive structure of the system. Likewise, a product of one component can be part of the fuel of another component, or also part of the final product, $\mathbf{P_s}$.

Consequently, the vector $\mathbf{P}$ and $\mathbf{F}$ containing the product and fuel of each team can respectively be calculated by means of the following equations [10]:

$$\mathbf{P} = \mathbf{P_s} + \langle \mathbf{KP} \rangle \cdot \mathbf{P} \tag{1}$$

$$\mathbf{F} = \mathbf{I} + \mathbf{P} = \mathbf{K_D} \cdot \mathbf{P} \tag{2}$$

where the final product vector is $\mathbf{P_s}$; $\mathbf{K_D}$ is a diagonal matrix containing the total unit exergy consumption of the components; $\mathbf{I}$ corresponds to the irreversibility vector, and the matrix $\langle \mathbf{KP} \rangle$ reflects, as mentioned before, the productive structure.

Similarly, the total fuel consumption of the system is calculated as follows:

$$F_T = I_T + P_T = \mathbf{k_e} \cdot \mathbf{P} \tag{3}$$

where I_T and P_T are the total irreseversibilities and the final product of the system respectively and $\mathbf{k_e}$ the consumption of external resources.

In relation to costs, the exergy cost $B_i^*\ [kWh]$ expresses the amount of resources used to obtain a specific flow B_i, and the unit exergy cost $k_i^*\ \left[\frac{kWh}{kWh}\right]$ expresses the ratio between the exergy cost and its exergy [11]:

$$k_i^* = \frac{B_i^*}{B_i} \tag{4}$$

Furthermore, k_i^* takes into account the resources needed to generate the flow *i* in the energy chain. It increases as the irreversibilities along the chain increase. The unit exergy costs of the equipment products $\left(\mathbf{k_P^*}\ \left[\frac{kWh}{kWh}\right]\right)$ are related to the unit exergy costs of the external resources $k_{e,i}^*$ of component *i* and to the marginal exergy consumption associated with the external resources $k_{e,i}$.

In addition, the exergoeconomic cost of *i* -flow c_i represents the economic resources required to obtain it. The economic costs of internal flows and final products depend on the thermodynamic efficiencies of the processes.

To calculate the exergoeconomic costs of fuels and products, fixed costs and variable costs have to be defined. Variable costs depend directly on the level of production, while fixed costs are the investment, maintenance and operating costs of the equipment, which are represented by the vector $\mathbf{Z}$ [€]. Because of space reasons, this paper defines only the variable costs for the exergoeconomic ones. Therefore, the exergoeconomic unit costs $c_{F,i},\ c_{P,i}\ \left[\frac{€}{kWh}\right]$ represent the unit cost of a given flow, either fuel or product.

To calculate the total cost of fuels and products, the unit exergoeconomic costs are multiplied by their exergy values:

$$C_{F,i} = c_{F,i} \cdot F_i \quad (5)$$

$$C_{P,i} = c_{P,i} \cdot P_i \quad (6)$$

2.4 THERMOECONOMICS SOFTWARE

In order to carry out this work, a software to control and diagnosis of thermal installations [12] has been used, which is based on Thermoeconomics. This software combines Matlab [13], where the calculations are performed, with Excel, where the data are recorded and the results are presented.

The software calculates the thermoeconomic costs of each of the flows of the installation, and detects the equipment with the highest irreversibilities, which are the ones that increase the cost the most along the energy chain. The costs are obtained from the productive structure that interconnects all the equipment according to (1) the distribution ratios b_{ij}, (2) the unit exergy consumption of each equipment k_i, and (3) the external resources $F_{e,i}$.

The software is able to make these calculations in a dynamic way, i.e. for a series of time stamps, so the results obtained are useful for future diagnosis analyses, given that when a parameter of an equipment varies, its unit exergy consumption varies; thus, the costs related to that component also change.

3. Case study

This work develops the previous steps to build a predictive model of a DHW installation based on the influence of climate change.

For this purpose, a simple DHW installation has been simulated in TRNSYS software emulating the installation designed in the LCCE´s experimental plant, since the final objective is to create the predictive model of real thermal facilities.

With the simulation data, thermoeconomic variables have been calculated for each instant of time, i.e. dynamic variables, such as the total cost of the installation product and, finally, the predictive model has been developed to predict the future values of these costs based on changes in the external temperature.

3.1 Design of the installation

As case study, the installation has been designed to produce DHW using a 24 kW gas boiler, as shown in Figure 2, for a residential building with 20 inhabitants in Vitoria-Gasteiz.

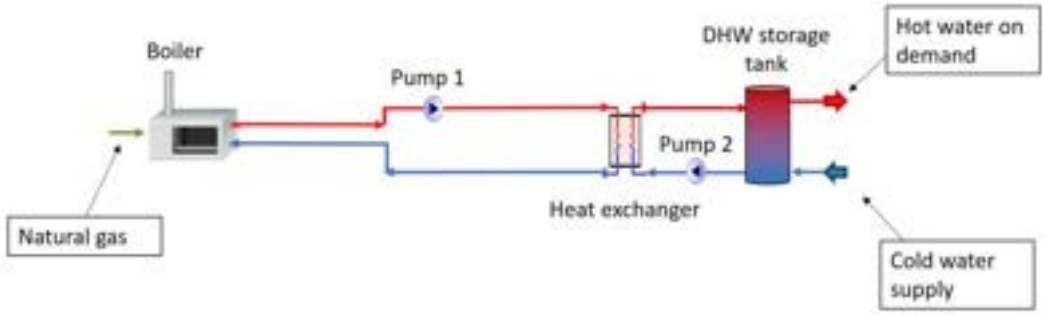

Figure 2. Installation diagram

The installation consists of:

- Generation: 24 [kW] gas boiler.
- Distribution: Hydraulic pumps, heat exchanger.
- Storage: DHW tank of 100 [l].

The parameters of the components are the ones of the LCCE´s experimental plant.

3.2 Physical configuration and productive structure

Once the installation has been designed, the physical configuration and the productive structure are determined to carry out a subsequent thermoeconomic analysis. To define the physical configuration, all material and energy flows are represented. Thus, as shown in Figure 3, 9 flows are defined:

- Energy consumption flow: 1.
- Mass flows: 2, 3, 4, 5, 8, 9.
- Virtual inertia flows: 6, 7, which represent the temperature charge and discharge of the tank.

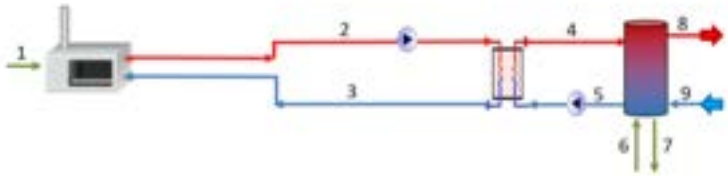

Figure 3. Physical configuration of the installation

In the productive structure, the components are defined as black boxes with interconnected input fuels and output products. In addition, virtual equipment (the green equipment in Figure 4) is added.

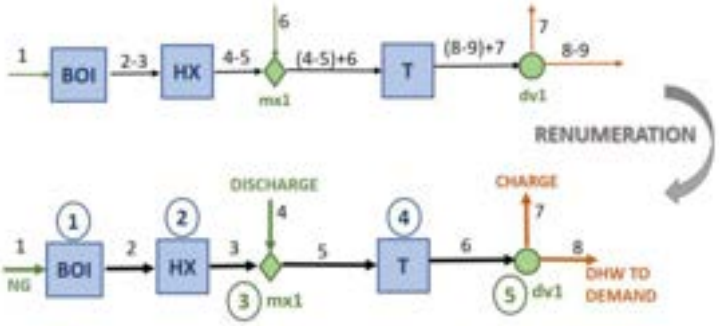

Figure 4. Productive structure of the installation

After renumbering the flows, for simplicity reasons, we have a total of 8 flows and 5 equipment: (1) BOI-boiler, (2) HX-heat-exchanger, (3) mx1-mixer 1, (4) T-tank and (5) dv1-diverter 1.

3.3 Modelling in TRNSYS

The designed installation has been modelled in TRNSYS software maintaining the parameters of the LCCE equipment (Figure 5).

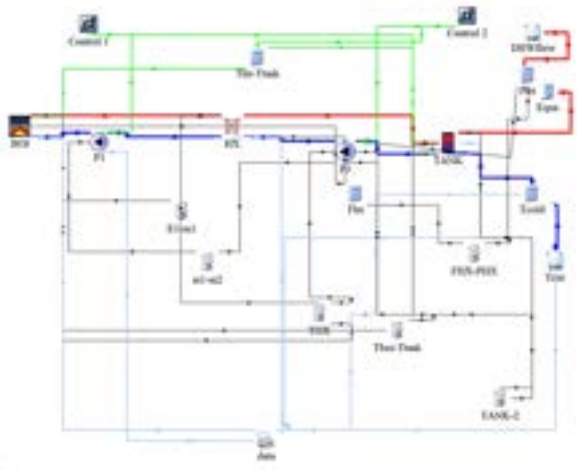

Figure 5. Simulation Studio interface in TRNSYS of the installation

3.3.1 Calculation of the DHW demand

The demand profile has been calculated according to the parameters set out in the HE4 of the CTE (Spanish Technical Code [14]) for a residential building with 20 inhabitants.

3.3.2 Implementation of the outdoor temperature

The main objective of this work is to predict the behaviour and the change in cost of the total product of the installation in future periods, when the outdoor temperature varies.

It is needed to take into account that, in order to achieve this, we have taken into account that the outdoor temperature and the cold water supply temperature are related. In this way, the temperature of the cold water supply entering the system can be calculated as a function of the outdoor temperature, which is used as a predictor variable we are going to use in the model.

Therefore, the average monthly values of the external temperatures in Vitoria-Gasteiz from the IDAE (Institute for Energy Diversification and Saving) [15] and the average monthly temperatures of the mains water in Vitoria-Gasteiz from the Spanish CTE were taken [14].

The relationship with the highest Pearson correlation (R) between these two variables is the linear one below with R=0.9795:

$$T_{cold\ water} = 0.6526 \cdot T_{ext} + 3.3462 \quad (7)$$

Thus, the cold water supply temperature is calculated for all outdoor temperatures according to the LCCE's outdoor temperature sensor.

3.3.3 Control configuration

The control has been configured as follows:

- The boiler starts when the domestic hot water storage tank is below 60.5ºC and stops when it exceeds 62ºC.
- The DHW production starts when the temperature at the primary inlet of the heat exchanger is 5ºC higher than the tank temperature and stops when it is less than 2ºC.

3.3.4 TRNSYS data

TRNSYS allows downloading an Excel file with the thermodynamic variables necessary for subsequent analysis. Specifically, each time-step it saves the following values:

- Temperatures of each flow and average temperatures of the hydraulic compensator and tank.
- Flow rates of each flow.
- Boiler fuel consumption.

The selected data coincide with the data that can be extracted from the LCCE installation and are sufficient to calculate the energy and exergy values for each flow of the productive structure as will be done later, during 168 [h] with 1-minute time-step.

3.4 Data analysis and pre-processing

From the extracted data, a "*raw database*" is obtained based on the dynamic data of temperatures, flow rates and consumption. They are used to calculate, once processed, the energies of each flow. These variables are the same as those that could be obtained from sensors installed in the LCCE.

First, in order to clean and pre-process raw data, the data are visualised to check for outliers that do not follow the normal pattern of the data series. In addition, some conditions are established to avoid intrinsic failures of TRNSYS when extracting the data.

With the pre-processed data, the corresponding energy flows in and out of each main equipment are calculated, based on the First Law of Thermodynamics, and the dynamic model is defined. Thus, an "*energy database*" is obtained that provides the global vision of the interconnections between the components.

3.5 Analysis of the active operating modes of the plant

The casuistry of the installation's behaviour is analysed on the basis of the productive structure, i.e. the active operating mode is identified at each moment, see Figure 6:

- 1st casuistry: Tank charge

The tank is below the temperature set in the control (60.5ºC), so there is a generation demand on the boiler that loads the tank.

- 2nd casuistry: Tank charge + demand

DHW demand exists and the tank is below the temperature set in the control (60.5ºC), so there are two products: tank charging and demand for DHW consumption.

- 3rd casuistry: Demand with tank discharge

DHW demand exists and the tank is above the temperature set in the control (62ºC), so the tank discharges.

- 4th casuistry: Demand without tank discharge

DHW demand exists and the tank is above the temperature set in the control (62ºC), but it does not discharge. This is physically impossible, as if there is a DHW demand, the tank must discharge, i.e. the temperature in the tank must be reduced. However, this casuistry does not cause any problem when carrying out the thermoeconomic analysis, as explained in the following section *3.6. Thermoeconomic analysis*.

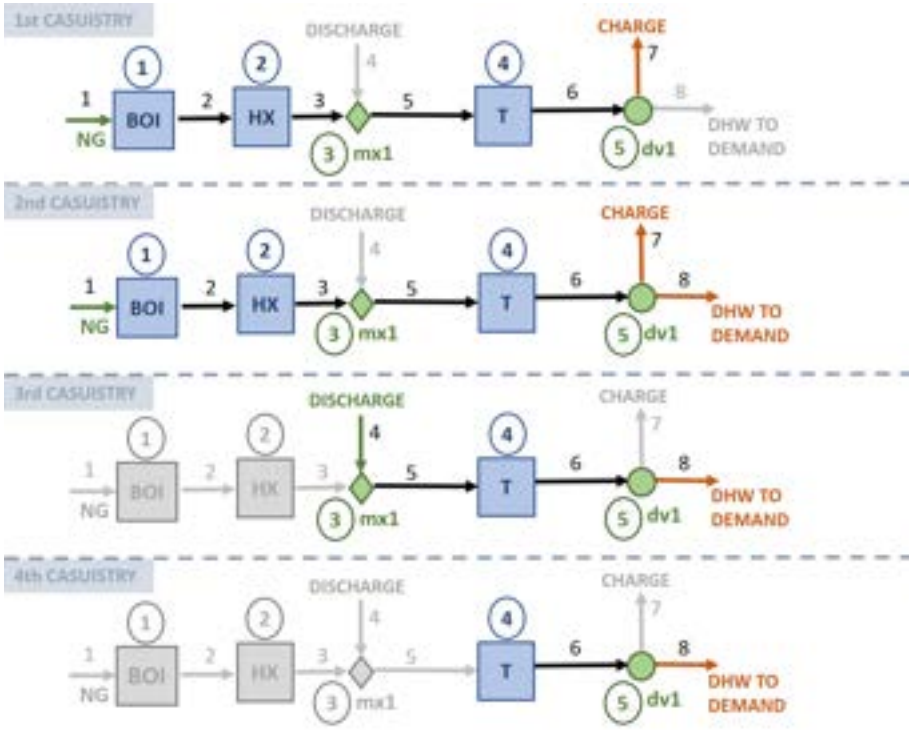

Figure 6. Casuistry of the behaviour of the installation

After analysing the operation modes, it is foreseen that in the 3rd casuistry, there is no natural gas consumption, as the boiler is off. Nevertheless, the discharge of the tank happens because in previous operation modes, gas is consumed to charge the tank. So, in order to consider the cost of charging-discharging the tank, a new methodology is developed to disregard this 3rd casuistry.

To understand the methodology, it is necessary to understand the tanks' energy-exchange formula:

$$\Delta E\ [kJ] = V_{tank}[l] \cdot \rho_w \left[\frac{kg}{l}\right] \cdot Cp_w \left[\frac{kJ}{kg \cdot K}\right] \cdot (T_{t-1} - T_t)[K] \quad (8)$$

To equal the ΔE value to 0, the tank temperature at the previous instant T_{t-1} needs to be equal to the tank temperature at the current instant, Tt.

Therefore, we only consider the Δt instants in which the tank temperature is equal to $T_t = T_{t-1} = 60.5$℃, as this is the lower temperature fixed in the control. Afterwards, we recalculate the corresponding Δt instants and energy flows in a "*new energy database*" consists of 215 lines of data, which is a 98% reduction of data lines compared to the previous data sheet extracted from TRNSYS. By means of this methodology not only the 3rd casuistry is disregarded, but also the computational burden for the thermoeconomic analysis is notably reduced.

3.6 Thermoeconomic analysis

In order to carry out the thermoeconomic analysis, the following steps are followed:

1. Calculation of the "*exergy database*": the exergy flows corresponding to all flows are calculated based on the First and Second Laws of Thermodynamics.
2. Definition of economic values: the price of natural gas is defined as the only external resource, without considering the net water price.
3. Calculation of the thermoeconomic values by means of the thermoeconomics software for the following results:
   - Unit energy consumption of the *n* equipment: k_n
   - Unit exergy costs of fuels and products: $k^*_{F_n}$, $k^*_{P_n}$
   - Unit exergoeconomic costs of fuels and products: c_{F_n}, c_{P_n}

With the unit exergoeconomic costs of the products, we calculate the total cost of the installation total product $C_{p_{DHW}}[€]$, which in this case is the DHW to demand.

3.7 Development of the predictive model

This study compares the $C_{p_{DHW}}[€]$ cost of the installation in a reference situation (calculated in this work) with the cost in a climate change condition (with an increase in the outdoor temperature). In this way, we calculate the change in the overall consumption of the system as well as the increase in the individual components Δk_n, that will indicate the effects generated by that change.

Therefore, it is needed to quantify how the outdoor temperature variable is related to the intermediate costs of the system. Therefore, the costs are modelled according to the following options:

1. Each variable to be predicted (the intermediate costs as a function of outdoor temperature) can be modelled independently, from known temperature data.
2. A stepwise process can be carried out in which, once variables are predicted, they are incorporated as predictors to infer the missing ones.
3. All variables can be predicted at once.

These three points can be implemented in two ways:

- Taking into account information from previous instants to predict the current instant. RNN (Recurrent Neural Networks) methods attempt to identify and exploit sequential information in the data. These methods retain in "memory" the information from consecutive components of the sequence. The logic is based on answering the question, "Can the information observed at the instants before the sequence be relevant to predict what happens at the current instant?" If the answer is “yes”, as is the case with time series, then the model tries to detect it and use it to predict variables.
- Considering each moment in time as an independent observation (i.e. ignoring time dependence). This can be applied if the observations of time instants are considered as independent observations; thus, any time dependence relationship between the samples is broken. In this case, other simpler models that do not take into account this temporal dependency, e.g. multi-layer perceptron, are an efficient modelling alternative.

Combining the data-driven application and thermoeconomic concepts, the effect of the change in cost due to a change in external temperature will be quantified.

4. Results and discussions

This section explains the obtained results.

4.1 Verification of the control

Figure 7 is used to check the control designed for the installation, where 2 days out of the 7 days of the test were depicted. These graphs also demonstrate the dynamism of the installation, with the following conclusions:

- On the one hand, Figure 7a shows that when the temperature difference between the primary heat exchanger inlet and the tank temperature is greater than 5ºC, DHW production starts and stops when it is below 2ºC.
- On the other hand, Figure 7b shows how the boiler starts up when the tank temperature is below 60.5ºC and stops when it is higher than 62ºC.

In other words, the control is correctly designed.

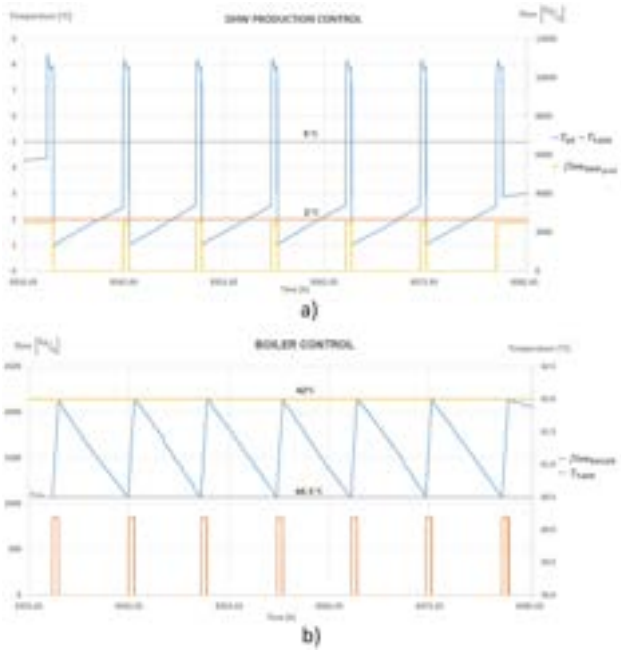

Figure 7. DHW production and boiler control verification graphs

4.2 Thermoeconomic results

Figure 8 shows the dynamic energy and exergy values of the fuel and boiler product.

- The exergy values for fuel are higher than the energy values because natural gas has a quality factor $QF_{NG} = 1.04 \left[\frac{kWh_{en}}{kWh_{ex}}\right]$
- However, exergy values of the product are lower than the energy values. This is because the exergy takes into account the quality of the energy flow, which in the case of the boiler is thermal energy. Average values show that the boiler has an energy efficiency of 89.26% compared to the exergy efficiency of 15.58%.

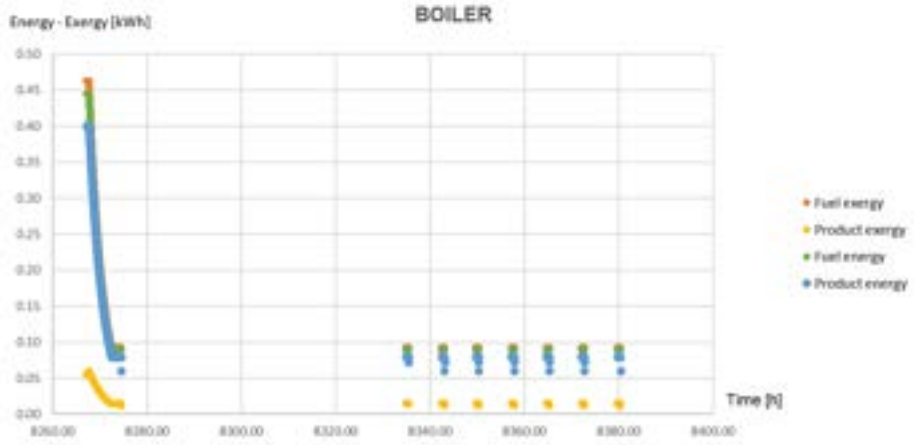

Figure 8. Energy and exergy values of fuel and boiler product

Despite having the dynamic values of the thermoeconomic results, due to space limitations, the following results show either the average values or the total sum of the values at each instant. Table 1 shows the total sums of fuels, products and equipment irreversibilities.

- On the one hand, as the energy chain progresses, the exergy values of the flows decrease. This is due to the accumulation of irreversibilities of the equipment.
- On the other hand, the equipment with the highest irreversibilities is the boiler, $I_{boiler} = 19.80\ [kWh_{ex}]$. This is due to the use of a fuel with a high exergy level (natural gas) to generate a product with a lower exergy level (hot water), in addition to the unavoidable exergy destruction intrinsic to the boiler.

Table 1. Fuel, product and irreversibilities of equipment

	EQUIPMENT	$F_{ex}\ [kWh_{ex}]$	$P_{ex}\ [kWh_{ex}]$	$I\ [kWh_{ex}]$
GENERATION	BOI	23.48	3.68	19.80
DISTRIBUTION	HX	3.68	2.16	1.52
PRODUCT	T	2.16	0.29	1.87

Table 2 shows the average values of the unit exergy consumptions of the equipment and the average values of the unit exergy costs of the fuels and products of each equipment.

- On the one hand, the unit exergy consumption of the equipment, $k_n \left[\frac{kWh_{ex}}{kWh_{ex}}\right]$, represents the amount of fuel required to produce one unit of product, showing that the equipment with the highest unit exergy consumption is the tank, $k_{TANK} = 8.87\ \frac{kWh_{ex}}{kWh_{ex}}$. This is due to the mixing of flows at very different temperatures.
- On the other hand, the unit exergy costs of the fuels $k^*_{F,i}$ of the generating equipment, (i.e. the boiler), $k^*_{F,BOILER}$ have the value of 1, since it is an external input flow. It is also observed that the ratio between the unit exergy costs of the fuels and the products of the equipment is proportional to the irreversibilities that occur.

Table 2. Unit exergy consumption of equipment and unit exergy costs of fuels and products

	EQUIPMENT	$k\ \left[\frac{kWh_{ex}}{kWh_{ex}}\right]$	$k^*_F\ \left[\frac{kWh_{ex}}{kWh_{ex}}\right]$	$k^*_P\ \left[\frac{kWh_{ex}}{kWh_{ex}}\right]$
GENERATION	BOI	6.41	1	6.41
DISTRIBUTION	HX	1.71	6.41	10.96
PRODUCT	T	8.87	10.96	96.12

Table 3 shows the average values of the exergoeconomic costs of the fuels and products of the system's equipment. For this analysis, only the exergoeconomic costs related to variable costs have been calculated, i.e. those that depend on the natural gas consumption.

- The exergoeconomic costs of fuels, c_F, take into account the irreversibilities accumulated up to that point in the energy chain; thus, moving down the energy chain, these costs increase.

- The exergoeconomic costs of the products, c_P, follow the same trend, as unit exergy costs, and increase when moving down the energy chain.

Table 3. Exergoeconomic costs of equipment fuels and products

	EQUIPMENT	$c_F \left[\frac{c€}{kWh_{ex}}\right]$	$c_P \left[\frac{c€}{kWh_{ex}}\right]$
GENERATION	BOI	5.07	32.52
DISTRIBUTION	HX	32.52	55.57
PRODUCT	T	55.57	487.43

The total cost of the DHW for the period studied is $C_P = 285.78 \ \frac{€}{7\ days}$.

4.3 Predictive model results

The Predictive model itself is not presented in this manuscript. Since we are now working in it, a coming work will contain the corresponding results

5. Conclusions

In this work a dynamic thermoeconomic analysis of a thermal installation of a building that produces DHW has been carried out and a methodology to predict the costs of the flows has been shown. This installation is designed based on the configuration of the LCCE's experimental plant and was simulated in the TRNSYS software.

During the thermoeconomic analysis, all the possible operating modes of the case study are analysed, with the following relevant conclusions:

- The equipment with the highest system irreversibilities is the boiler, $I_{boiler} = 19.80\ [kWh]$
- The equipment with the highest unit exergy consumption is the tank, $k_{TANK} = 8.87 \frac{kWh_{ex}}{kWh_{ex}}$.
- The total product cost of the installation is $C_{P,DHW} = 287.78 \left[\frac{€}{7\ days}\right]$

In addition, the first steps to develop an innovative methodology that combines Thermoeconomics and Machine Learning models is defined, in order to quantify the effects of climate change on the costs and consumption of thermal installations in buildings. This will help promoting maintenance work, which is essential for the proper functioning and for reducing GHGs.

5.1 Future lines

As said, we are working on this case study in order to develop the predictive model able to predict both the operation and the consumption and costs based on ML techniques.

Likewise, the fixed costs related to the operation, maintenance and amortisation costs of the installation will also be incorporated in the results.

The next step deals with the implementation in real systems.

In short, work will continue on a tool that combines Thermoeconomics and Machine Learning capable of predicting possible failures in thermal installations of buildings and optimising their operation.

6. Acknowledgments

The author would like to thank the *Misiones Euskampus 2.0* programme for the financial help received through Euskampus Fundazioa, as well as the Building Quality Control Laboratory of the Basque Government.

7. Nomenclature

Symbols

B: Exergy, kWh

c: Exergoeconomic unit cost, $\frac{€}{kWh}$

C: Total cost, €

c_P: Specific heat capacity, $\frac{J}{kg \cdot K}$

E: Energy, kWh

F: Fuel, kWh

$\mathbf{F}$: Fuel vector

I: Irreversibility, kWh

$\mathbf{I}$: Irreversibility vector

k: Unit exergy consumption, $\frac{kWh}{kWh}$

$\mathbf{k_e}$: External resources vector

$\mathbf{K_D}$: Diagonal matrix containing the unit exergy consumptions

$\langle \mathbf{KP} \rangle$: Productive structure matrix

P: Product, kWh

$\mathbf{P}$: Product vector

T: Temperature, K

V: Volume, m^3

$\mathbf{Z}$: Depreciation, maintenance and operation vector, €

Greek symbols

Δ: Difference

ρ: Density, $\frac{kg}{m^3}$

Subscripts

e: External resource

ext: External, outdoor

F: Fuel

i/j: Generic equipment

NG: Natural gas

P: Product

s: Final product

t: Time

w: Water

Superscripts

$*$ **:** Cost

8. References

[1] *Proposal for a Directive of the European Parliament and of the Council on the energy performance of buildings (in Spanish)*. Available: https://energia.gob.es/es-es/participacion/paginas/detalleparticipacionpublica.aspx?k=500.

[2] *Climate change* (in Spanish). Available: https://www.aragon.es/-/el-cambio-climatico.

[3] C. Lyon *et al*, "Climate change research and action must look beyond 2100," *Glob Change Biol,* vol. 28, *(2),* pp. 349, 2022. . DOI: 10.1111/gcb.15871.

[4] C. Yilmaz and I. Koyuncu, "Thermoeconomic modeling and artificial neural network optimization of Afyon geothermal power plant," *Renewable Energy,* vol. 163, pp. 1166-1181, 2021. Available: https://dx.doi.org/10.1016/j.renene.2020.09.024. DOI: 10.1016/j.renene.2020.09.024.

[5] C. Yilmaz and O. Sen, "Thermoeconomic analysis and artificial neural network based genetic algorithm optimization of geothermal and solar energy assisted hydrogen and power generation," *International Journal of Hydrogen Energy,* vol. 47, *(37),* pp. 16424-16439, 2022. Available: https://dx.doi.org/10.1016/j.ijhydene.2022.03.140. DOI: 10.1016/j.ijhydene.2022.03.140.

[6] L. R. de Araújo *et al*, "Response surface methods based in artificial intelligence for superstructure thermoeconomic optimization of waste heat recovery systems in a large internal combustion engine," *Energy Conversion and Management,* vol. 271, pp. 116275, 2022. Available: https://dx.doi.org/10.1016/j.enconman.2022.116275. DOI: 10.1016/j.enconman.2022.116275.

[7] Y. Wilhelm *et al*, "Overview on hybrid approaches to fault detection and diagnosis: Combining data-driven, physics-based and knowledge-based models," *Procedia CIRP,* vol. 99, pp. 278-283, 2021. Available: https://dx.doi.org/10.1016/j.procir.2021.03.041. DOI: 10.1016/j.procir.2021.03.041.

[8] *Welcome|TRNSYS: Transient System Simulation Tool*. Available: https://www.trnsys.com/.

[9] E.Querol *et al*, "Thermoeconomics and Energy Optimisation" (in Spanish), 2011.

[10] V. Verda, L. Serra and A. Valero, "Thermoeconomic Diagnosis: Zooming Strategy Applied to Highly Complex Energy Systems. Part 1: Detection and Localization of Anomalies. Part 1: The diagnosis procedure," *ASME J. Energy Resour. Technol,* vol. 127, *(1),* pp. 42, 2004. . DOI: 10.1115/1.1819314.

[11] A. Picallo-Perez *et al*, "A novel thermoeconomic analysis under dynamic operating conditions for space heating and cooling systems," *Energy (Oxford),* vol. 180, pp. 819-837, 2019. Available: https://dx.doi.org/10.1016/j.energy.2019.05.098. DOI: 10.1016/j.energy.2019.05.098.

[12] Picallo-Perez, A, Sala-Lizarraga, JM, Portillo-Valdes, L. Development of a tool based on thermoeconomics for control and diagnosis building thermal facilities. Energy (Oxford). 2022.

[13] Anonymous (). *MATLAB - MathWorks*. Available: https://www.mathworks.com/products/matlab.html.

[14] Anonymous "MINISTERIO DE TRANSPORTES, MOVILIDAD Y AGENDA URBANA Documento Básico HE Ahorro de energía,".

[15] Spanish government, "Energy Saving and Efficiency in Air Conditioning in Buildings - ENERGY EFFICIENCY AND SAVING - Technical guide Outdoor climatic conditions of project" (in Spanish).

Energy cost impact analysis on the total cost of the crop production for different operating conditions. A salad production case study

Alice Arcasi[a], Alfonso William Mauro[a*], Giovanni Napoli[a] and Antonio Marco Pantaleo[b]

[a] Department of Industrial Engineering, Federico II University of Naples, Naples, Italy,
[*]Corresponding author e-mail: wmauro@unina.it
[b] Department of Agro-Environmental Sciences, Aldo Moro University of Bari, Bari, Italy

Abstract:

Nowadays, with the constant global population growth, urbanization, pests use, climate change and resource degradation, the water-energy-food link is constantly stretched. In order to achieve water and food security, sustainable agriculture and energy production, the efforts of the next few years will be aimed to correctly balance these aspects. Therefore, it will be necessary both to improve the energy performance of traditional systems in the agricultural sector and at the same time to develop alternative and innovative ones. In this context, data from a local farm producing salad have been processed in order to relate the energy consumption of each processing phase to the produced kilogram of crop. In particular, thermal loads are attributed to the corresponding primary energy consumption. A thermo-economic analysis was carried out by considering different scenarios in terms of external ambient temperature and specific cost of electricity. Results show that the thermal load exchanged with the external ambient through the walls and the roof of the plant is about the 20% of the outgoing thermal load of the evaporator during the lighting hours whereas the thermal load of the auxiliaries (including the production lines) is about its 80%. Moreover, the variation of both the fourth range production lines operating time and the external daily temperature causes a variation in the total energy consumption related to the kilogram of processed product – up to 128%. Finally, several economic scenarios have been implemented in order to take into account the variation of the specific cost of electricity.

Keywords:

Thermo-economic analysis; Salad production.

1. Introduction

1.1. Context

Nowadays, with the constant global population growth, urbanization, pests use, climate change, resource degradation and scarcity, the water-energy-food link is constantly stretched and heavily tested. Particularly, serious and different problems affect the agricultural sector. First of all, the huge water usage accounts for 70% of the total global freshwater withdrawals [1] and it is expected that it will increase about 55% by 2050 [2]. In addition, energy consumption in the agricultural sector accounts for 3% in the European scenario and for 2% in the Italian one, respectively [3]. Moreover, the energy demand will increase about 3 times by 2050 worldwide [4]. On the other hand, it is estimated that the global population will reach 9.8 billion by 2050 and 11.2 billion by 2100 [5] in a non-uniform way worldwide. Additionally, the intense urbanization will affect more than 70% of world population. All these aspects will contribute to an intensification in the food production sector about the 60% by 2050 – it is worth noting that this sector accounts for 30% of the global energy consumption including also the cold chain and the transport sector. This scenario is exacerbated by the scarcity of arable land as well as the huge use of pesticides and chemical substances: in fact, about 1.9 Mtons of them have been employed in agricultural sector during 2019 in the EU context [6][7]. In order to achieve water and food security and at the same time sustainable agriculture and energy production, the efforts of the next few years will be aimed both to improve the energy performance of traditional systems of the agricultural sector (i.e. open fields and greenhouse systems) and at the same time to develop alternative and innovative ones by considering the ongoing energy transition – such as the indoor farming method.

As a matter of fact, several issues affect the traditional farming methods: their productivity is in fact strongly dependent on the exterior climate conditions, and they need an artificial lighting system and involve a high amount of water if greenhouse systems are installed in cold regions or hot/warm ones respectively, especially if compared to the ones of innovative and alternative agrifood systems such as vertical farms [8][9][10][11].

For the best of authors' knowledge, literature about the modelling of post cultivation phases of greenhouse systems is poor. Stanghellini et al [12] developed a model for the evaluation of evapotranspiration rate load of the plants by considering a greenhouse such it is considered one of the main energy load of those systems. The model includes the effect of the multilayers of the crop and the solar radiation is empirically evaluated as well as a careful calibration of the main parameters of interest is needed. Righini et al [13] developed and validated a greenhouse climate-crop yield model in order to correct manage those systems at high latitudes. Results show that the model is able to predict the air temperature with a very good agreement, with a relative root mean square error lower than 10%. A model for the energy optimization of greenhouses was developed by Weidner et al [14] for different climate zones in order to optimize the interior climate conditions and consequently productivity of the systems. From the abovementioned issues and lacks in literature, it is clear that in a context of energy transition regarding all the sectors and production processes, it is important to correctly model the post cultivation processes of traditional greenhouse systems in order to evaluate their energy consumption and relate it to the kilogram of processed product. The main purpose of this approach is to minimize their energy consumption as well as costs and at the same time maximize their productivity. In fact, from an economic and entrepreneurial point of view it is very useful to quantify both the rate of cost for electricity for the processed kilogram of product and the one for different scenarios by varying economic parameters (such as the specific cost of electricity) and those related to the performance of production lines, facilities and environmental conditions.

1.2. Objectives of the work

In this context the main goal of the manuscript is to model traditional agrifood system taking into account all the parameters of interest, such as external conditions, internal ones, crop type production, air conditioning and lighting systems and cost analysis. The modelling purpose is to relate the energy consumption of all the processing phases to the produced kilogram of product in order to maximize its productivity while minimizing its energy consumption and consequently its costs. In detail, data from a local farm producing salad have been processed and a thermo-economic analysis was carried out by considering different scenarios in terms of external ambient temperature and specific cost of electricity. Specifically, it is worth noting that the processing phases taken into account for the analysis are the post cultivation ones up to the final product picking for the shipping: consequently, both water and energy consumption concerning the raw materials cultivation phase are neglected.

2. Method

In order to relate the energy consumption of each processing phase (from post cultivation to final product) to the kilogram of final product intended for the market, it is fundamental to correctly evaluate all the energetic loads involved in the analysis. With this aim, in this section the implemented methodology is explained. The whole farm plant in which the entire production process takes place is reported in Figure 1 in which all the potentially thermal loads are considered.

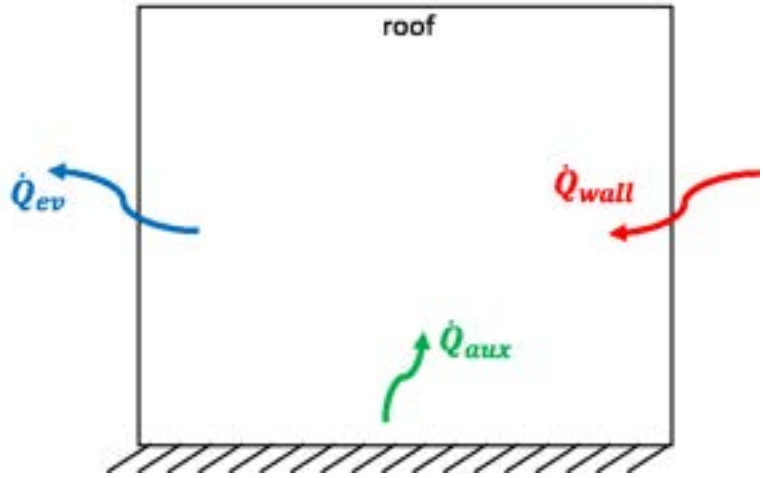

Figure 1 *- Plant schematization with the potentially energetic loads.*

In Figure 1 $\dot{Q}_{wall}$ is the thermal load exchanged with the external ambient through the walls and the roof of the plant, $\dot{Q}_{aux}$ is the thermal load caused by the auxiliaries (pumps, fans, lighting system, ecc) and the production lines; finally, $\dot{Q}_{ev}$ is the outgoing thermal load of the evaporator. It is clear that, from an energetic balance to the control volume reported in Figure 1, the sum of the thermal load exchanged with the external ambient

through the walls and the roof and the one caused by auxiliaries is counterbalanced by the outgoing thermal load of the evaporator:

$$\dot{Q}_{ev} = \dot{Q}_{tot} = \dot{Q}_{wall} + \dot{Q}_{aux} \tag{1}$$

In the energetic analysis the latent power due to the staff presence in the plant during the product's processing phases has been omitted as it is significantly lower compared to the previous ones as well as difficult to estimate. In order to evaluate the thermal load $\dot{Q}_{wall}$ through the walls and the roof of the plant it is useful to refer the analysis to the generic j-th cell in which a specific processing phase takes place as shown in **Figure 2** with both the plan and the section views reported:

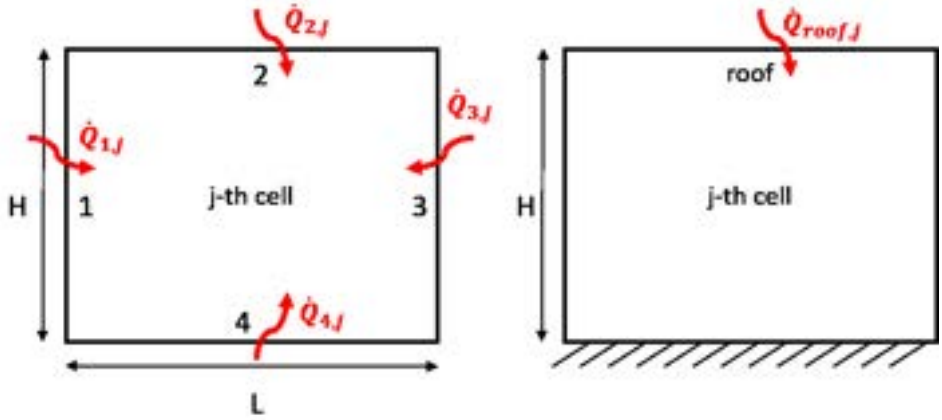

***Figure 2** - Plan and sectional view of the generic j-th cell with the indication of the thermal loads exchanged through the walls and the roof.*

The analysis was carried out by assuming that the internal temperature of the cell for the related processing phase is fixed to be T_j and by associating to each processing phase of the product a specific cell of the plant. Moreover, the whole plant is served by a refrigeration unit. The thermal load related to the j-th processing phase is defined as the sum of the thermal loads exchanged through the walls and the roof as reported in equation (1):

$$\dot{Q}_{cell,j} = \dot{Q}_{1,j} + \dot{Q}_{2,j} + \dot{Q}_{3,j} + \dot{Q}_{4,j} + \dot{Q}_{roof,j} \tag{2}$$

Thermal loads of the walls and the roof are evaluated taking into account the radiative, convective and conductive contributes to the heat transfer mechanism and they are reported in the follow equations:

$$\dot{Q}_{1,j} = \dot{Q}_{wall,1} = \dot{Q}_{c,int} \tag{3}$$

$$\dot{Q}_k = \dot{Q}_{c,int} \tag{4}$$

$$\dot{Q}_{rad} = GAa \cdot cos\vartheta \tag{5}$$

$$\dot{Q}_{c,ext} = h_{ext} A\left(T_{amb} - T_{wall,ext}\right) \tag{6}$$

$$\dot{Q}_{c,int} = h_{int} A\left(T_{wall,int} - T_j\right) \tag{7}$$

In the previous equations, A is the surface area, G is the solar radiation, ϑ is the angle of incidence of the solar radiation, h_{ext} is the external convective heat transfer coefficient, h_{int} is the internal convective heat transfer coefficient, $T_{wall,int}$ and $T_{wall,ext}$ are the internal and the external wall temperature respectively and a is the absorption coefficient. Therefore, the thermal load of the generic j-th cell $\dot{Q}_{cell,j}$ can be considered as the sum of the thermal power exchanged through the walls and the roof. Finally, the total thermal power of the considered plant $\dot{Q}_{wall}$ will be calculated as the sum of the thermal power of each cell. In detail, the total thermal power of the whole farm has been evaluated during the year by considering Naples' hourly temperature profile. Moreover, by knowing the quantity of product treated during the specific processing phase j-th (m_p^j) and its residence time inside the generic j-th cell $\left(\Delta\vartheta_j\right)$, the energy consumption of the j-th process will be evaluated and referred to the produced kilogram of raw material:

$$E_{raw\ mat.,j} = \left[\sum_{i=1}^{N_{step}} \left(\frac{\dot{Q}_{cell,j}(T_{amb,i}) + \dot{Q}_{aux,j}}{\dot{Q}_{tot}} \cdot \dot{L}_{comp,i} + \dot{L}_{aux,p,j,i}\right)\right] \Delta\vartheta_j \cdot \frac{1}{m_p^j} \quad (8)$$

In Equation (8) $\dot{Q}_{aux,j}$ is the thermal load caused by the auxiliaries (pumps, fans, lighting system, ecc) and the production lines during the j-th processing phase, $\dot{L}_{aux,p,i}$ is the mechanical power of auxiliaries (pumps, fans, lighting system, ecc) and the production lines of the considered processing phase whereas $\dot{L}_{comp,i}$ is the mechanical power of the compressor of the refrigeration unit serving the plant and $\dot{Q}_{tot}$ is the one defined in the previous Equation (1). Finally, N_{step} is the ratio between the time of the j-th process and the chosen time step. The energy consumption of the whole process for the considered raw material is the sum of the energy consumption of the j-th phases and, in order to evaluate the rate of cost for electricity – that will be defined as RCE – per kilogram of processed product, the total energy consumption of the M processes is then multiplied by the specific cost of electricity as reported in Equation (9):

$$RCE = \left(\sum_{j=1}^{M} E_{raw\ mat.,j}\right) \cdot specific\ cost\ of\ electricity \quad (9)$$

The considered case study is referred to the production of salad of a local farm and the analysis was carried out in order to include different scenarios in terms of external ambient temperature and specific cost of electricity by following the presented methodology.

3. Case study

For the present study data from a local farm near Naples have been processed in order to evaluate the rate of cost for electricity and relate it to the produced kilogram of product (salad). The identified processing phases are reported in Figure 3 in the relative flowchart:

Figure 3 *– Processing phases for the energy consumption analysis.*

In detail, the raw materials, previously grown in traditional greenhouse systems, arrive in the first cell (defined as cell 1); then the cooling process takes place and subsequently the raw materials are stored in the cell number 3. In the 4th cell both washing and drying processes occur and the semi-finished products are stored in the 5th cell from which they are bring to the cell number 6 for the subsequent phase of packaging. Finally, the products' weight control, labelling and palletizing occur in the 7th cell and then the final product is stored in the 8th cell from which it is picked for the shipping. In Table 1 the one-to-one correspondence between the specific processing phase and the nomenclature is reported:

Table 1 *- Nomenclature and relative area of the processing phases.*

Cell	*Processing phase*	$A\ [m^2]$
1	Raw materials receiving	1300
2	Vacuum cooling	310
3	Raw materials storage	2200
4	Product washing and drying	300
5	Storage of semi-finished products	450
6	Packaging of the products	750
7	Weight control, labelling and palletizing	1600
8	Storage and picking from the shipping cell	30

3.1. Operating conditions

Operating conditions of the farm in terms of quantity of product treated during the specific j-th processing phase m_p^j and its residence time inside the generic j-th cell $\Delta\vartheta_j$ as well as data about the refrigeration unit serving the whole plant and production lines with their on/off times have been processed and the rate of cost for electricity related to the processed kilogram of product was estimated. In detail, the analysis was carried out by considering several daily temperature profiles from January 9, 2023 to January 13, 2023. The thermal load $\dot{Q}_{wall}$ through the walls and the roof of the plant has been calculated by considering 0.1 as the absorption coefficient a and the value of the insulating material's thermal conductivity k has been fixed to $0.023\ W/mK$. As regard the thermal load caused by the auxiliaries $\dot{Q}_{aux}$, the first range production lines have been assumed all in operation from 4am to 8pm, whereas for the fourth range production lines data provided by the monitoring of the farm have been considered. Finally, data about the outgoing thermal load of the evaporator $\dot{Q}_{ev}$ during the second week of January 2023 have been taken into account from the monitoring of the local farm. Details about the operating conditions in which the analysis was carried out are reported in Table 2:

Table 2 *- Operating conditions for the thermo-economic analysis.*

Month	*Day*	$\dot{Q}_{wall}$	*First range production lines operating hours*	*Fourth range production lines operating hours*
January	9	$k = 0.023\ W/mK$ $a = 0.1$	16h	19h 30'
	10			16h
	11			17h
	12			16h 30'
	13			16h 30'

3.2. Thermal loads evaluation

In the operating conditions above described, all the thermal loads of interest – $\dot{Q}_{wall}$, $\dot{Q}_{aux}$ and $\dot{Q}_{ev}$ – have been calculated following the methodology presented in the previous section. Shown below the hourly dimensionless results of the thermal loads for the second week of January 2023, for the operating conditions reported in Table 2. It is worth noting that all the data shown in Figure 4(a)-(e) have been dimensionless with respect to the maximum value of the outgoing thermal load of the evaporator:

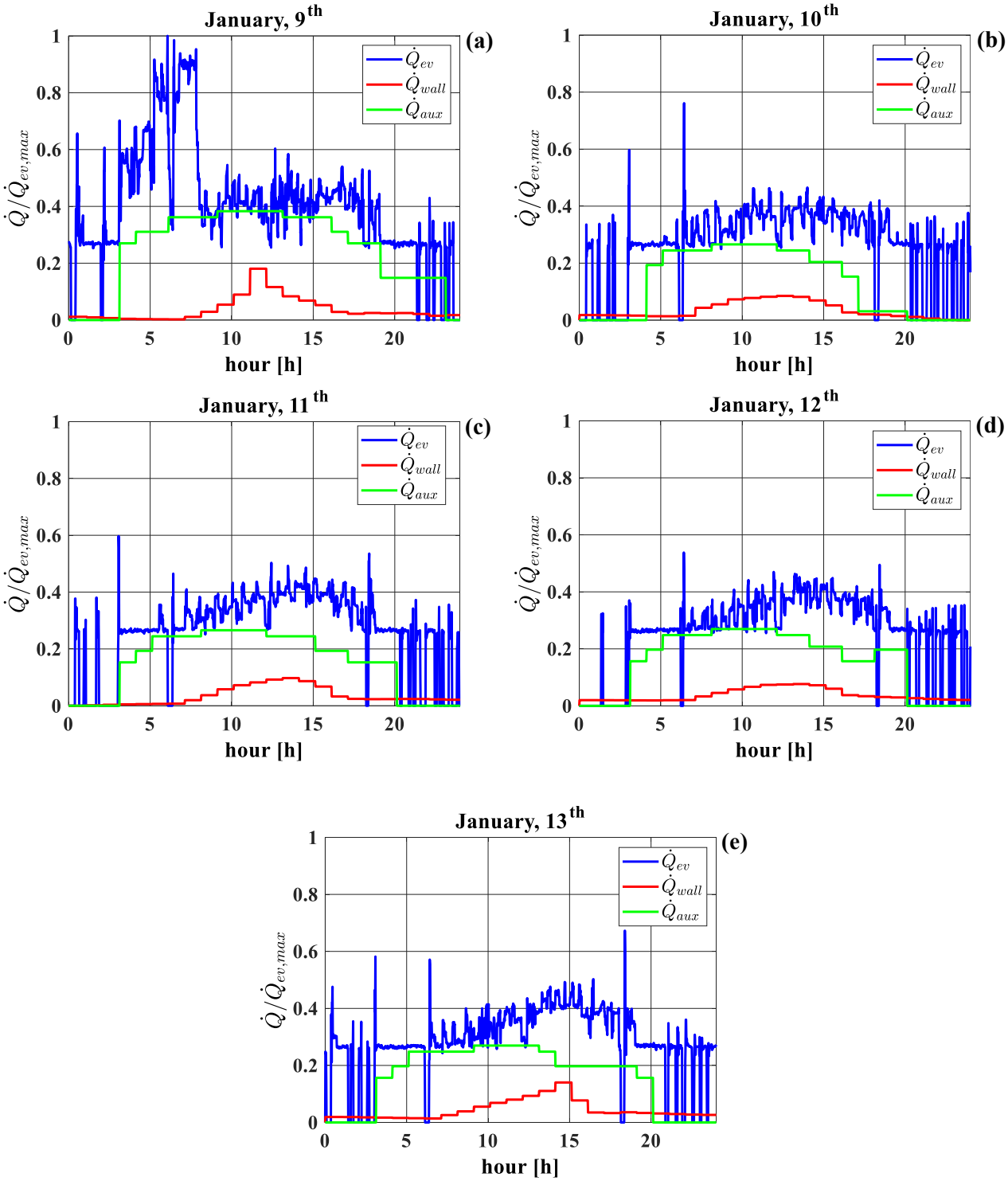

Figure 4 *- Hourly dimensionless thermal loads evaluation for the second week of January, 2023 in the operating conditions reported in Table 2. (a) January, 9th. (b) January, 10th. (c) January, 11th. (d) January, 12th. (e) January, 13th.*

It can be seen that the sum of the thermal load caused by the auxiliaries $\dot{Q}_{aux}$ and the one exchanged through the walls and the roof the plant $\dot{Q}_{wall}$ is continually counterbalanced by the outgoing thermal load of the evaporator. In detail, the thermal load exchanged with the external ambient through the walls and the roof of the plant is, at most, about the 20% of the outgoing thermal load of the evaporator during the lighting hours whereas the thermal load of the auxiliaries (pumps, fans, lighting system, ecc) and the production lines is about the 80% of it. This trend occurs for all the operating conditions considered and for all the days taken into account in the energetic analysis.

4. Results and discussion

4.1. Evaluation of the energy consumption related to the kilogram of product

Once the thermal loads of interest have been evaluated in the operating conditions reported in Table 2, the energy consumption related to the kilogram of processed product (salad) of each processing phase has been calculated by following Equation (8) for the second week of January. Data related to the quantity of product treated during the specific processing phase j-th (m_p^j) and its residence time inside the generic j-th cell $(\Delta\vartheta_j)$ have been taken into account from the monitoring of the local farm. Then, the total daily energy consumption related to the kilogram of processed product has been considered as the sum of the specific energy of each processing phase by following Equation (9). In Table 3 results in terms of total daily energy consumption related to the kilogram of processed product are reported:

Table 3 *- Daily energy consumption related to the kilogram of processed product during the second week of January.*

Month	*Day*	$\left(\sum_{j=1}^{M} E_{raw\ mat.,j}\right)\left[\frac{kWh}{kg}\right]$
January	9	4.46
	10	2.52
	11	2.37
	12	1.96
	13	2.36

It can be noted that the total energy consumption of January, 9th is significantly higher compared to the others daily total energy consumption: $+77\%$ and $+128\%$ compared to the ones of January, 10th and 12th, respectively. This trend is caused by the higher thermal load of the auxiliaries $\dot{Q}_{aux}$ during the operating hours of the farm due to the higher operating time of the fourth range production lines. It is worth noting that the energy consumption related to the kilogram of processed product shown in Table 3 is strongly dependent on the performance of the production lines, on their operating times and finally on the external conditions. Therefore values in Table 3 have not to be considered as reference ones, but they can allow to consider and compare different solutions and scenarios able to reduce the rate of cost for electricity for kilogram of processed product for the presented case study.

4.1. Economic analysis

Finally, once the thermodynamic analysis has been completed, an economic one was implemented by following Equation (9). In detail, the specific cost of electricity has been fixed to $0.22\ €/kWh$ [15] – the cost is referred to the average price during the whole year 2022 – and the daily rate of cost for electricity (RCE) related to the kilogram of processed product has been calculated for the second week of January, as shown in Figure 5.

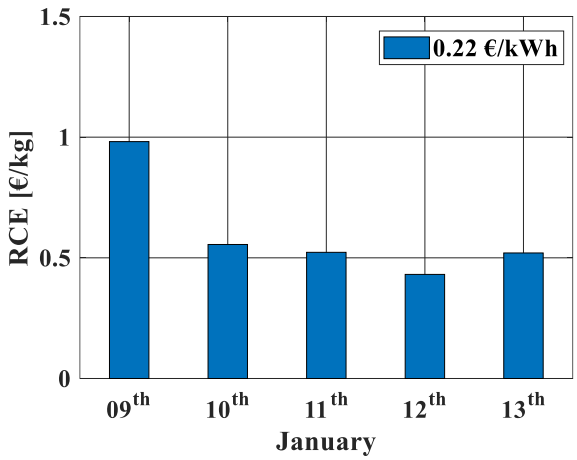

Figure 5 *- Daily rate of cost for electricity related to the kilogram of processed product for a specific cost of electricity of* $0.22\ €/kWh$ *for the second week of January.*

It can be noted that the daily RCE of January, 9th is significantly higher compared to the other ones, following the trend of the daily energy consumption shown in the previous sub-section (4.1): $+88\%$ and $+128\%$ compared to the ones of January 11th and 12th, respectively.

Finally, different economic scenarios have been considered by fixing the specific cost of electricity to $0.32\ €/kWh$ and $0.42\ €/kWh$, in order to take into account the variation of the specific cost of electricity. Results of the implemented scenarios are shown in Figure 6.

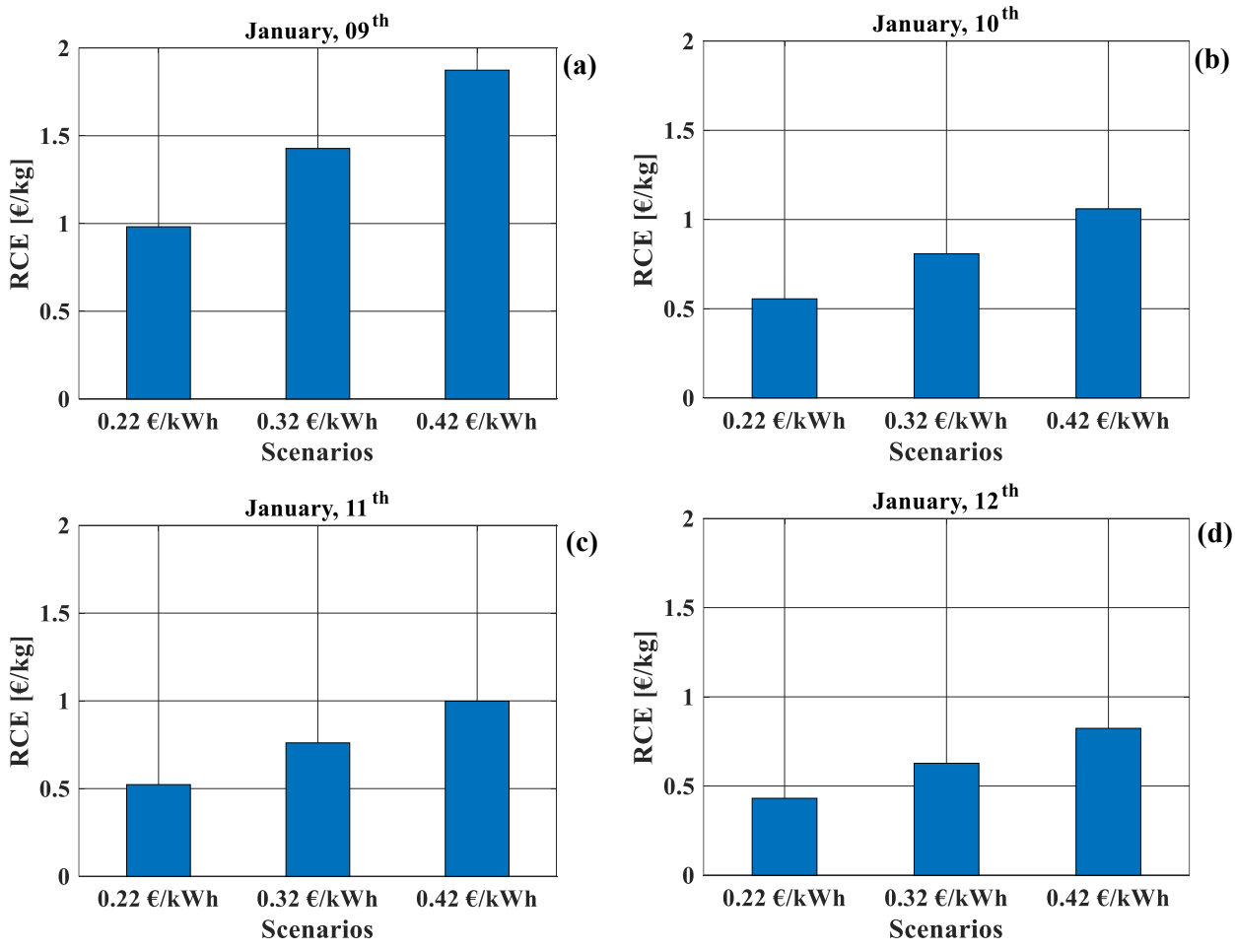

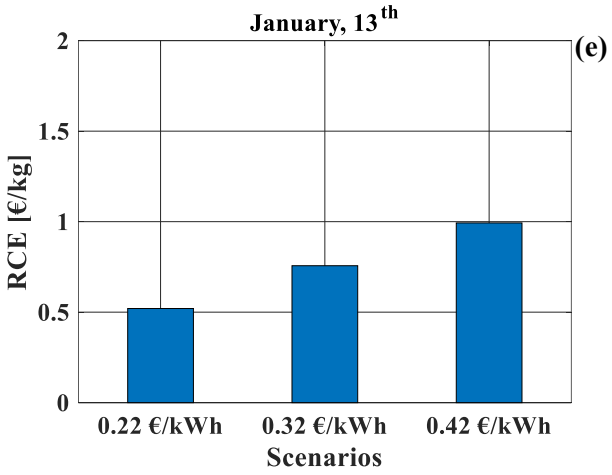

Figure 6 *– Daily rate of cost for electricity related to the kilogram of processed product for specific cost of electricity of* $0.22\ €/kWh$, $0.32\ €/kWh$ *and* $0.42\ €/kWh$. *(a) January, 9th. (b) January, 10th. (c) January, 11th. (d) January, 12th. (e) January, 13th.*

It can be noted that the increase in the specific cost of electricity involves an increase in the daily rate of cost for electricity per kilogram of processed product – $+92\%$ and $+94\%$ by passing from a specific cost of electricity of $0.22€/kWh$ to $0.42\ €/kWh$ by considering January 11th and 13th, respectively. The same trend is observed for all the operating conditions included in the analysis.

5. Conclusions

In this manuscript the modelling of a traditional agrifood system has been implemented taking into account all the parameters of interest, such as external conditions, internal ones, crop type production, air conditioning and lighting systems. In detail, data from a local farm producing salad have been processed in terms of quantity of product treated during the specific j-th processing phase m_p^j and its residence time inside the generic j-th cell $\Delta\vartheta_j$ as well as data about the refrigeration unit serving the whole plant and production lines with their on/off times. A thermo-economic analysis has been implemented by considering different operating conditions in terms of daily external temperature profile and specific cost of electricity. The main conclusions of the manuscript are reported as follow:

- For all the operating conditions considered and for all the days taken into account the thermal loads evaluation has highlighted that the thermal power exchanged with the external ambient through the walls and the roof of the plant is, at most, about the 20% of the outgoing thermal load of the evaporator during the lighting hours whereas the thermal load of the auxiliaries (including the production lines) is about the 80% of it.
- The total daily energy consumption related to the kilogram of processed product has been evaluated: for January 9th it is significantly higher compared to the others: $+77\%$ and $+128\%$ compared to the ones of January 10th and 12th, respectively.
- By considering the specific cost of electricity of January 2023 as $0.22\ €/kWh$, the daily rate of cost for electricity RCE has been evaluated. The same trend of the total daily energy consumption was found: in fact, the daily RCE of January 9th is significantly higher compared to the others, up to $+128\%$ with the one of January 12th.
- Finally, different economic scenarios in terms of specific cost of electricity have been included in the analysis. It was found that the increase in the specific cost of electricity involves an increase in the daily RCE, up to $+94\%$ for January 13th, by passing from specific cost of electricity of $0.32€/kWh$ to $0.42\ €/kWh$.

Nomenclature

a	absorption coefficient
A	surface area, m^2
G	solar radiation, W/m^2

h	heat transfer coefficient, W/(m^2 K)
H	height of the wall of the cell, m
k	thermal conductivity, W/(m K)
L	length of the wall of the cell, m
$\dot{L}$	mechanical power, kW
m	mass of processed product, kg
M	total processing phases
N	number of step integration
RCE	rate of cost for electricity, €/kg
T	temperature, K
$\dot{Q}$	thermal load, kW

Greek symbols

ϑ	angle of incidence of the solar radiation, rad
$\Delta\vartheta$	residence time of the mass during the processing phase

Subscripts and superscripts

amb	ambient
aux	auxiliaries
c	conductive
$cell$	cell
$comp$	compressor
ev	evaporator
ext	external
i	time step for the integration
int	internal
k	convective
j	specific processing phase
max	maximum
p	process
rad	radiant
$raw\ mat.$	raw material
$step$	step of integration
tot	total
$wall$	wall

References

[1] Fao. 2011. The state of the world's land and water resources for food and agriculture (SOLAW) – Managing systems at risk. Food and Agriculture, Organization of the United Nations, Rome and Earthscan, London.

[2] https://unesdoc.unesco.org/ark:/48223/pf0000225741_eng

[3] https://ec.europa.eu/eurostat/databrowser/view/NRG_BAL_S__custom_624870/default/table?lang=en

[4] Van Ruijven B J, De Cian E, Sue Wing I 2019 Nature Communication 10 2762

[5] United Nations, Department of Economic and Social Affairs, Population Division 2017 World Population Prospects: The 2017 Revision, Key Findings and Advance Tables. Working Paper No. ESA/P/WP/248.

[6] https://ec.europa.eu/eurostat/databrowser/view/AEI_FM_USEFERT/bookmark/table?lang=en&bookmarkId=4d3d0db8-76c1-4884-86e3-bdb23b1dae21.

[7] https://ec.europa.eu/eurostat/databrowser/view/AEI_FM_SALPEST09/bookmark/table?lang=en&bookmarkId=53792fd3-191d-4201-aab5-c01c67fd927c

[8] Graamans L, Baeza E, van den Dobbelsteen A, Tsafaras I, Plant factories versus greenhouses: Comparison of resource use efficiency, Agricultural Systems 160 31-43, 2018

[9] Ohyama K, Yamaguchi J, Enjoji A, Resource Utilization Efficiencies in a Closed System with Artificial Lighting during Continuous Lettuce Production, Agronomy 10 723, 2020

[10] Kozai T, Resource use efficiency of closed plant production system with artificial light: Concept, estimation and application to plant factory, Proc Jpn Acad Ser. B, 2013

[11] Harbrick K, Albright L D, Comparison of energy consumption: greenhouses and plant factories, Proc VIII Int. Symp. On Light Horticolture, 201

[12] Stanghellini C 1987 Institute of Agricultural Engineering

[13] Righini I, Vanthoor B, Verheul M J, Naseer M, Maessen H, Persson T, Stanghellini C, A greenhouse climate-yield model focussing on additional light, heat harvesting and its validation, Biosystems Engineering 194 (2020), 1-15

[14] Weidner T, Yang A, Hamm M W, Energy optimization of plant factories and greenhouses for different climate conditions, Energy Conversion and Management 243 (2021), 114336

[15] https://www.arera.it/it/dati/condec.htm

Simulation model for the evaluation of the effect of office dressing code on building space cooling demand

Francesco Calise[a], Francesco Liberato Cappiello[b], Luca Cimmino[c], Maria Vicidomini[d]

[a] Institution Department of Industrial Engineering, University of Naples Federico II P.le Tecchio 80125 (Italy), frcalise@unina.it
[b] Institution Department of Industrial Engineering, University of Naples Federico II P.le Tecchio 80125 (Italy), francescoliberato.cappiello@unina.it
[c] Institution Department of Industrial Engineering, University of Naples Federico II P.le Tecchio 80125 (Italy), luca.cimmino@unina.it
[d] Institution Department of Industrial Engineering, University of Naples Federico II P.le Tecchio 80125 (Italy), maria.vicidomini@unina.it, CA

Abstract:
The indoor air temperature in buildings is one of the main parameters determining both the indoor thermal comfort of inhabitants and the energy consumption of the Heating, Ventilation and Air Conditioning systems (HVAC). Clothing insulation of building residents is a key factor dramatically affecting people thermal comfort and HVAC energy demand. Indoor set point temperature, depends on clothing factor, relative humidity and mean radiant temperature. Although the clothing insulation values are selected according to well-known standards, clothing insulation depends on several factors: the metabolic heat production, activity and gender (females tend to be cooler than males in cool conditions). Therefore, users can adjust their clothing insulation according to the outdoor temperature change, suiting their own thermal comfort requirement. In this framework, a dynamic simulation model for the evaluation of the comfort conditions and the cooling energy consumption based on the variation in clothing insulation for office applications is developed in the present work. In order to calculate the space cooling demand, a suitable thermal zone was modelled by the TRNSYS Type 56 coupled to the Google SketchUp TRNSYS3d plug-in. The model was validated and applied to a suitable case study, an office room located at University of Federico II in Naples (Italy). Different sensitivity analyses were performed changing the clothing insulation and the office set-point temperature, to estimate both the comfort conditions and cooling energy demands. The model can be considered a flexible tool to suggest simple clothing adjustment behaviors which may represent a tradeoff among thermal comfort, energy saving and dressing code.

Keywords:
Dynamic simulations, Clothing insulation, Building energy saving, Thermal comfort

1. Introduction

In 2020, the global building sector accounted for 36% of energy consumption and 37% of CO_2 emissions, while the residential sector accounted for 22% of energy consumption and 17% of CO_2 emissions [1]. As a result, over the last two decades, a series of policies and regulations have been implemented in order to increase the energy efficiency and reduce carbon emissions. It is estimated that 80% of the current building stock will still be in use in 2050 and current renovations rates of 1% is too low to meet the Green Deal goals [1]. Advances in heating, ventilation, and air conditioning (HVAC) systems, energy-efficiency strategies for the building stock have been advocated to reduce energy consumption in the building sector and encouraging environmental friendly end-use behaviours [2]. These involve improved measures on the envelopes of buildings [3], such as employing innovative materials [4], advanced insulation and building structures [5], new construction and the renovation of existing buildings [6].

It is well known that, in both residential and non-residential buildings, different types of HVAC systems can be used to control the indoor air temperature, humidity and/or quality [7]. Such parameters significantly affect the indoor thermal comfort [8]. The building thermal comfort level is related to building energy consumption, therefore, a large amount of energy will be consumed while improving indoor thermal comfort [9]. Considering ongoing global warming issues and the increasing demand for cooling energy, it is also important for policy-makers and households to implement suitable strategies to reduce their cooling energy demand and resulting, consequently decreasing the related carbon emissions [10]. In this framework, energy refurbishment actions for the building envelope and HVAC systems are pivotal to reduce the building energy demand. Unfortunately, the majority of these actions are featured by high capital costs and long payback periods. However, significant energy savings can be also achieved simply modifying the users behaviour, avoiding any major refurbishment [11]. Tam et al. [12] argue that the actual occupant behaviour plays a crucial role to achieve an optimal building performance, from both energy and environmental points of view. They also suggest including occupant behaviour in the calculation procedure of the energy rating of existing buildings. A careless behaviour negatively affects the building energy demand, also affecting the thermal comfort. Energy dissipation is often due to a plurality of incorrect user habits. This is especially true in office buildings where occupants are not aware on the impact on the energy bills of their behaviours. Some previous works focused on the promotion of users behaviour change, by encouraging the adoption of positive energy management habits. These behavioural interventions include the use of interactive games to increase the user awareness regarding different energy-saving strategies [13], using monetary rewards to encourage energy conservation, introducing different forms of incentives to motivate the adoption of positive energy management habits [14].

In the framework of the user behaviour, the dress-code plays a pivotal role in the definition of the user thermal comfort [15], and therefore, of the thermal energy consumption. In many working environments (banks, universities, etc), the clothing insulation mirrors the “power” structure within the workplace, representing the symbol of credibility [16], and the dress code overrides the rational thermoregulatory behaviour. In fact, users are often expected to dress in a multi-layer wool suit, regardless of the hot outdoor climate. Corporate dress codes completely extinguish opportunities for clothing adaptation [17]. In these workspaces, the energy demand for space cooling is higher with respect to the case of more informal dressing codes. For example, a suit without the tie allows one to significantly improve the thermal comfort during the summer season. This results in a lower space cooling demand and environmental impact. Considering near-sedentary activities performed in office buildings, where the metabolic rate is approximately 1.2 met, the effect of changing clothing insulation on the optimum operative temperature is about 6 °C per clo (1 clo is equal to 0.155 m^2 K/W). Therefore, removing of a thin, long-sleeve sweater decreases clothing insulation by approximately 0.25 clo and would increase the optimum operative temperature by approximately 6 °C/clo × 0.25 clo = 1.5 °C [18]. The ASHRAE chart indicates that the clothing insulation should be reduced to 0.1-0.6 clo (ideally, 0.3) to maintain comfort at 25.6°C [19], and not at 21.5°C as in the case of 1 clo (to obtain for a standard office activity of 1.2 met, a relative humidity of 50%, an air velocity less than 0.1 m/s, and the air temperature equal to the mean radiant temperature, a Predict Mean Vote (PMV) equal to 0 and Predicted Percentage of Dissatisfied (PPD) equal to 5%). A change in clothing insulation by only 0.2 clo leads to a temperature change of about 1°C in a typical office building [20].

In civil building environments, many researchers have found that changing clothing to acclimate to different climate conditions has been an affordable and efficient method of achieving thermal comfort [21, 22]. Newsham [23] proposes a model to study the effect of different levels of clothing on thermal comfort and energy consumption. The model is applied to an office, located in Toronto, adopting high cooling set-point temperatures in summer and lower heating set-point temperatures in winter. The aim is to detect the clothing factor values suitable to guarantee a PPD index of around 5%. In case of a more flexible and adaptable clothing, the cooling set-point value of 25.55°C is detected. This decreases to 24.35°C for a value of 0.75 clo. However, both set-point temperatures are lower than the value of the dress factor corresponding to a classic formal dress (1 clo). It is worth noting that the space cooling energy demand significantly depends on the aforementioned set-point values, with an annual consumption of 218 kWh in the first case, 275 kWh in the second one, realizing an energy saving of 21%. Wu et al. [24] present a study dealing with an office building in Guangzhou, featured by a hot summer and a warm winter. To perform the study, once a week the office workers carried out a questionnaire regarding the thermal comfort, whereas physical environmental parameters were continuously recorded. For each season, different clothing factors were considered. They conclude that for the investigated weather zone, increasing the set-point temperature in office buildings from 26°C to 29°C would save about 60% cooling energy without thermal discomfort. Schiavon and Lee [25] developed two multivariable linear mixed models considering the clothing as a function of outdoor air temperature measured at 6 o'clock and of indoor operative temperature. These models allow more accurate thermal comfort calculation and HVAC sizing with respect to the common practice of keeping the clothing insulation equal to 0.5 clo in the summer and 1 clo in the winter. For example, the winter median clothing

insulation in Canada was 0.8 clo when the median winter outdoor air temperature measured at 6 o'clock was−7.5°C. Lakeridou et al. [26] suggest increasing the set-point temperature of the offices of the United Kingdom by 2°C with respect the current set-point values of 22 ± 2°C. They changedthe set-point temperature only for one floor of the building and measured the indoor air temperatures at various locations across the floors. The results of the statistical analysis for all 129 participants suggest that the increase led to the occupants feeling significantly warmer in comparison with the group at lower temperature settings. However, increasing the floor set-point of open-plan areas to 24°C appears not to cause substantial discomfort, even if the actual percentage dissatisfied (APD) in some offices was near its maximum acceptable value equal to 20%. De Dear [22] examines the influence of clothing for two different cases study located in Sydney (Australia), a suburban shopping mall and a call center. The company that operates the call center is based on a strict working dress code from Monday to Thursday, but employees were free to wear casual clothes on Fridays. The daily mean values for all workers of the clothing factors on Friday were significantly higher than values for other weekdays in winter and lower in summer. On Friday, in the Sydney office case study, workers showed their marked preference for clothing not imposed by codes of formality.

1.1. Aim of the work

Although this topic was widely studied in literature, a lack of knowledge regarding the analysis using dynamic simulations is detected. This kind of analysis allows one to control, for each time step of the simulations, the key variables affecting the thermal comfort, considering the users within a whole building-plant simulation system. Considering that the building is a complex system, the energy phenomena occurring are different and continuously correlated: these phenomena concern the features of the building envelope (walls, roofs, windows), the plants for the production of space heating and cooling, the intended use of the zones of the building (residential, offices, hotels), the presence of a large number of people or machines that produce heat. Avoiding experimental investigations, the dynamic simulation analyzes the energy performance of a building with precision and reliability, obtaining consistent estimates. For this reason, the present study is performed using the TRNSYS software, analyzing the actual influence of the relaxation of the dress code on the cooling energy demand and the thermal comfort of occupants. The developed model was applied to a typical office located in Naples (South of Italy) of the University Federico II. The proposal for an extreme relaxation of the dress code will give the opportunity to remove the jacket and tie from the classic formal dress. As a limit case study, the so-called "tropical" dress, consisting of a short-sleeved shirt and shorts, was also analyzed. Note that the hourly dynamic simulation allows one to evaluate the hours of discomfort of the users as a function of the cooling set-point temperature and clothing factor for any day of the summer season. The dynamic simulation model demonstrated its ability to accurately predict the thermal comfort perceptions. In addition, using the dynamic simulation tool, it is possible to properly design the HVAC systems capacity (oversized to respect specific and rigid thermal comfort conditions), and to determine their lower energy demand.

2. Method

In this section the method used to develop the calculations is presented. In particular, section 2.1 shows the model developed to perform the dynamic simulations and the economic, energy and economic analyses; section 2.2 reports the case study considered to run the simulations.

2.1. Model

The simulation model of the office is developed using the well-known tool TRNSYS. It includes a large library of components, which are able to accurately simulate the energy performance of the energy components included in the investigated system. The types included in TRNSYS environment are considered reliable and validated [27]. TRNSYS software is very reliable and accurate for the evaluation of building energy demand [28] and is considered by the scientific community as a benchmark tool to validate the in-house building simulation models [29-31].

Type 56 was selected to model the office. The validation of the whole Type 56 is presented in reference [32]. This component calculates the dynamic energy demand, by considering its 3D geometry (defined in the Google SketchUp TRNSYS3d plug-in [33], the effects of the environmental conditions (i.e. ambient temperature and humidity, solar radiation, etc.) the envelope thermophysical proprieties, as well as all the internal gains (people, lights, machineries), the ventilation and infiltration rate. The office geometry analyzed in this work is represented in

Figure ***1***. Details about the geometry are provided in the case study section. To simulate the external overhangs, the tool "Trnsys3d Shading Group" was used. In Type 56 a number of parameters can be set: material thermophysical properties of walls and layers, ventilation and infiltration profiles, heat gains, heating and cooling scheduling, etc. Note that the mathematical model of Type 56 allows one to evaluate the building user comfort according to the ASHRAE Standard 55-2013 [34]. It is also worth noting that Type 56, included in TRNSYS 18 release, includes a detailed model for the calculation of radiation in the building, taking into account a complex model for the calculation of view factors and considering the radiative properties of the surfaces as a function of the wavelength. As a consequence, the model returns the wall temperatures and the radiate flows emitted by the walls and transmitted by the glazing surfaces. Thus, the model can also calculate important comfort parameters such mean radiant temperature and operative temperature which directly affect the comfort indexes. The most relevant comfort parameters are calculated according to the Fanger theory [35]. In particular, according to the UNI EN ISO 7730 regulation [36], the calculated comfort indexes are Predicted Percentage of Dissatisfied (PPD) and Predicted Mean Vote (PMV). Therefore, the model allows one to detect the number of operating hours where the comfort parameters are outside the acceptability range (discomfort hours).

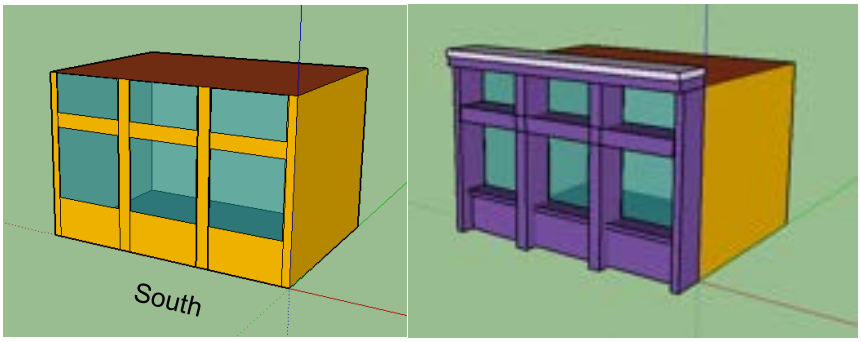

(a) *(b)*

Figure 1. Sketchup 3D model of the office, without (a) and with (b) external overhangs

Type 15 and 109 were used to simulate the weather conditions of the city where the selected office is located providing the hourly weather data files obtained by Meteonorm database. The cooling energy needed to cool the office at the desired set-point temperature is produced by a fan coil unit, simulated by the TRNSYS Type 600. The fan coil is supplied by chilled water by a suitable variable speed pump, simulated by Type 110. A suitable control strategy, managed by the proportional controller Type 1669, is implemented in the model to manage the water flow rate flowing through the pump. The controller manages the flow of water to be supplied to the fan coil according to the indoor air temperature of the office. When the indoor air temperature is higher than a fixed threshold value, the pump supplies the fan coil with the highest value of flow rate, which is proportionally reduced when the indoor air temperature decreases. The fan coil air flow is assumed to be constant, and it depends on the nominal cooling capacity of the fan coil.

2.2. Case study

The case study is a 22.3 m^2 office located at 10th floor of the building of University of Federico II, in Naples, South of Italy, see

Figure **2**. The office consists of one external vertical wall and three adjacent vertical walls, bordering other internal areas (offices and hallway). The building. On the external wall there are six double-glazed windows with aluminium frame and air gap.

(a) *(b)*

Figure 2. University of Federico II, Piazzale Tecchio, Naples, Italy (a), Investigated Office (b)

In particular, three windows (1.52m x 1.56m) are located on the lower side of the wall and three windows (skylights, 1.52m x 0.85m) are located on the upper side of the wall. The aluminium frame covers 35% of the whole glazed area for lower side windows and 40% of the whole glazed area for upper side windows. A venetian blind is also considered for all lower side windows, device that plays a fundamental role in calculating of the incoming solar radiation. To control the opening and closing of the shading device, a suitable control strategy of the solar radiation is implemented. In particular, if the total horizontal radiation is lower than a certain treshold, the shading device is completely opened. Conversely, the shading device is completely closed.

The building envelope was defined according to the period of construction of the building. The features of the typical buildings constructed during the years from 1955 and 1970 were assumed and reported in Table 1.

Table 1. Thermophysical proprieties of the office

Component	Thickness [mm]	U [W/m^{2}K]
Internal floor/ceiling	350	0.347
External wall	340	0.326
Outer pillar	470	1.899
Window glass (lower and upper wall)	4/16(air)/4	2.89

The heat gains due to the people, lighting systems and machineries were summarized in Table 2. The considered values were fixed according to the ASHRAE Handbook Fundamentals [37]. The infiltration rate was set equal to 0.6 1/h. The office is occupied by users from 9:00 am to 6:00 pm on weekdays. The closure of the office during the summer holidays was assumed from August 8th to 22nd. The cooling season was assumed from May 1st to September 30th. The cooling system operates only during the occupation hours.

A control strategy related to the switching on and off of the artificial lights was implemented. Easily, the lights are switched on when the total horizontal radiation is lower than a fixes value defined equal to 120 W/m^2.and switched off when it is higher than 200 W/m^2.

Table 2. Heat Gains

Mode	Total heat [W]	Radiative heat [W]	Convective heat [W]
	Two computers		
Continuous operating	65	6.5	58.5
Energy saving	25	2.5	22.5
	Four Monitors, 48 cm each one		
Continuous operating	80	8	72
Energy saving		0	
	Lights: 2 LED panels [60cmx60cm] 48W		
Switching on	31.2	8.4	22.8
	Two women	Activity: Light office work	
Total heat [W]	Sensible heat [W]	Latent heat [W]	Radiative Sensible heat [%]
115	70	45	60

For the comfort analysis of the office occupants, three different combinations of the main variables affecting on the thermal comfort condition were simulated.

In particular, the metabolic activity and air velocity values were set constant and equal respectively to 1.2 met (representative of the light metabolic activity for sedentary office work) and 0.1 m/s. Such values are consistent with the type of simulated indoor environment. As for the clothing factor, three different values were defined, each corresponding to a specific outfit. In particular, according to the EN ISO 7730:

- For the comfort condition C1, the value of 1 clo was associated, representative of the classic formal dress (trousers, long-sleeved shirt, jacket and tie);
- For the comfort condition C2, the value of 0.5 clo was associated, representative of a generic light summer clothing (light trousers and unbuttoned short-sleeved shirt);
- For the comfort condition C3, the value of 0.3 clo was associated, corresponding to a "tropical" outfit, consisting of shorts, a short-sleeved shirt, socks and sandals.

Concerning the energy, environmental and economic analysis, the following assumptions were considered. To convert the cooling energy demand of the office in electric energy, a constant coefficient of performance equal to 3 [38] and an electric efficiency of the national power plants equal to 0.46 [39], were assumed. The operating cost evaluation is carried out assuming a specific electric unit cost equal to 0.53 €/kWh_{el}. The total CO_2 emissions due to the electric energy demand were evaluated considering an equivalent emission factor equal to 0.48 $kgCO_2$/ kWh_{el} [40].

3. Results

In this section, the main results obtained by the dynamic simulations are discussed. The results are presented considering the hourly trends over a single day of the summer season as well as the energy trends obtained for each month of the summer season. The results obtaiened by a sensitivity analysis, performed by varying both the set-point temperature of the cooling plant as well as the clothing factor of the users are presented, considering their effect on the thermal comfort of the users itself. Note that for the comfort analysis, it was assumed that the user perceives a comfort condition according to the values assumed by PMV. If -1 <PMV<+1, the user perceives a comfort condition.

In

Figure ***3***, the hourly trends of the main physical parameters (relative humidity and radiant mean temperature) affecting the thermal comfort of the users (according to the UNI EN ISO 7730) are reported for a typical summer day. The air velocity was assumed constant at the value of 0.1 m/s, considering that in the investigated office no significant inflitration occurs. Note that both graphs of

Figure ***3*** report such trends for all the considered set-point temperatures of the cooling plant (from 24°C to 28°C).

For all the set-point temperatures similar trends of the mean radiant temperature can be observed. In particular, the mean radiant temperature decreases from 00:00 to 06:00 am following the trend of the outdoor air temperaure and it starts to increase from 06:00 and 09:00 am, when the sun rises and the solar radiation is directed on the external wall of the office. When the cooling plant is switched on (from 09:00 am to 6:00 pm), the radiant mean temperature decreases. The drop is more significant for the set-point temperature of 24°C Note that the office consists of one external wall and its windows all facing south. Therefore, although the indoor air temperature reaches the set-point value, the radiant mean temperatures increase reaching the maximum values at 12:30 pm, due to the high solar radiation incident on the office. For the set-point temperature of 28°C and 24°C, the radiant mean temperatures reach the values of 29°C and 26.5°C, respectively, although the cooling plant is switched on. The lowest peak values achieved at 06:00 pm occur at the closing time of the office and the switching off of the cooling plant. After that, the radiant mean temperature shows again an increase, due both to the solar heat which is absorbed during the day and released during the evening hours, and to the radiative and convective fluxes emitted by the computers which continue to be active in the energy saving mode. A slight reduction of radiant mean temperatures is verified during the late afternoon and evening hours when the solar radiation is zero and the outdoor air temperature starts to decrease. For all the set-point temperatures similar trends of the relative humidity can be observed. In particular, it is about lower than 70% during the office opening time, while it shows significant increases in the first and last hours of the day. Note that the cooling plant reduces the relative humidity of the investigated office but it is not designed to constantly control the relative humidity of the room. Therefore, for a typical sunny and humid day as the reported one, the relative humidity is high during the operation hours. However, the values fall within the range 30%-70%, suggested by the UNI EN ISO 7730.

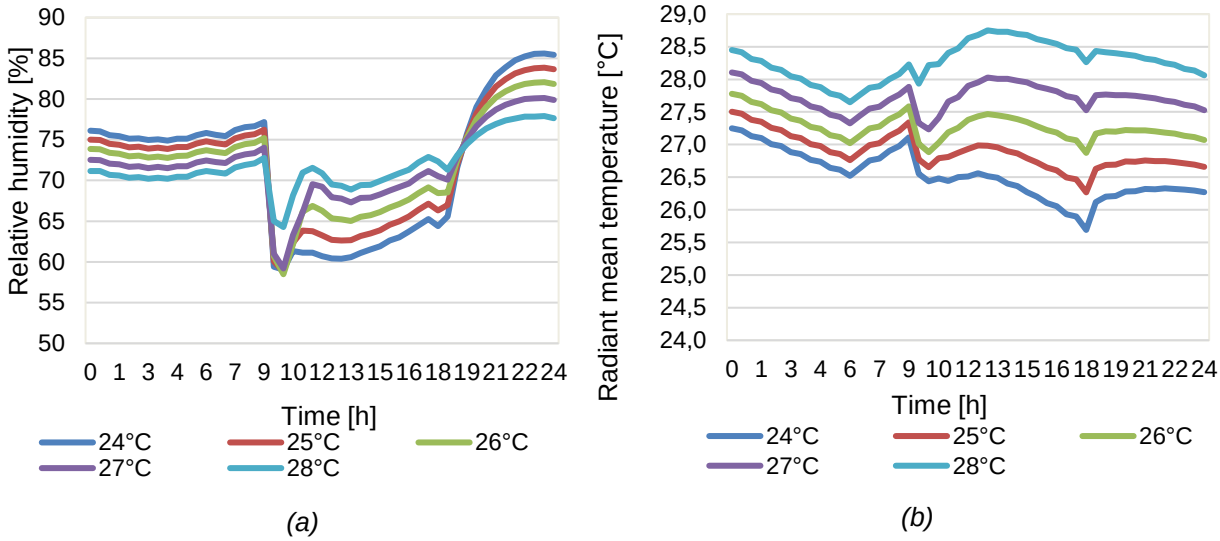

Figure 3. Hourly relative humidity (a) and radiant mean temperature (b)

In Figure 4, the monthly cooling energies from the cooling season (May-Sept) for all the investigated cooling set-point temperatures were reported. Considering the weather data of Naples, the hottest month is July. In this month the highest consumption for space cooling purpose is equal to 18 kWh/m^{2}month for the set-point temperature of 24°C. The lowest one is equal to 12 kWh/m^{2}month for the set-point temperature of 28°C, 33% lower than the previous case. Note that the low peak values occur in August are due to the two closing weeks of the university for the summer vacation.

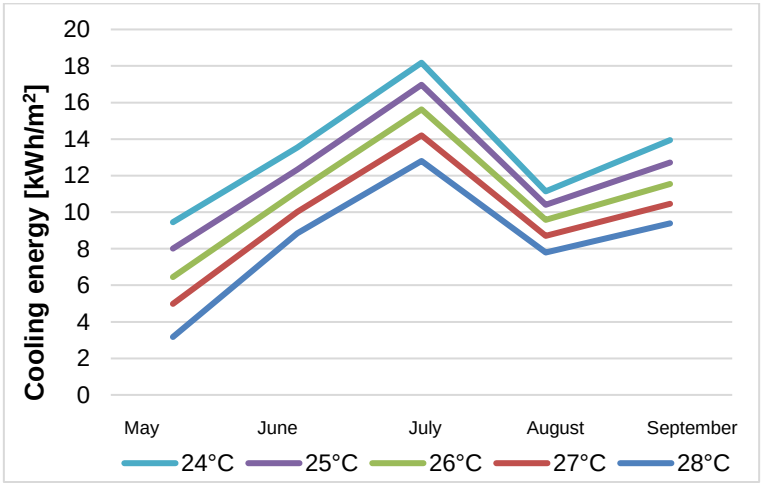

Figure 4. Monthly cooling energy vs cooling set-point temperatures

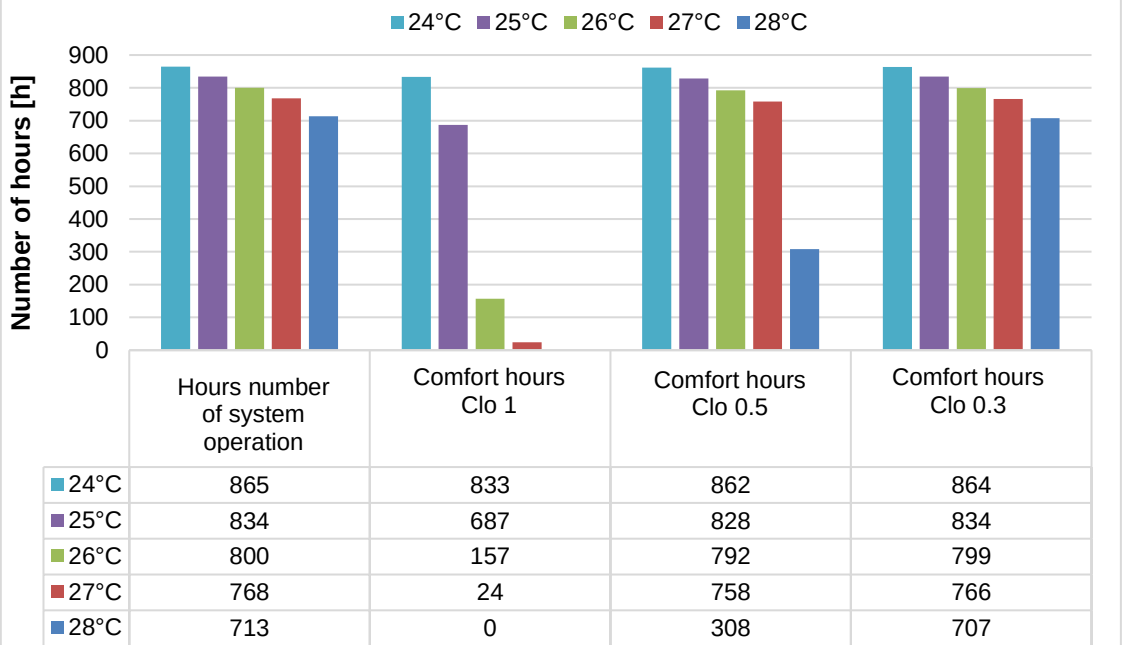

	Hours number of system operation	Comfort hours Clo 1	Comfort hours Clo 0.5	Comfort hours Clo 0.3
24°C	865	833	862	864
25°C	834	687	828	834
26°C	800	157	792	799
27°C	768	24	758	766
28°C	713	0	308	707

Figure 5. Comparison between hours of plant operation and hours of comfort

Figure 5 shows the comparison between the hours of plant operation and hours of comfort for the three considered scenarios of clothing factor, equal to 0.3 clo, 0.5 clo and 1 clo. As the set-point temperature value increases, the number of operating hours of the plant progressively decreases from 865 to 713. In the case of the classic formal dress, see CLO 1 scenario, the number of operating hours of the plant is high only at 24°C, whereas it is equal to 0 and 24 at 28°C and 27°C, respectively. With light summer dress, see CLO 2 scenario, the number of operating hours of the plant is high up to 27°C. With a tropical outfit, see CLO 3 scenario, also the cooling set-point temperature of 28°C becomes tolerable, considering that the number of operating hours of the plant is 707. The cooling set-point temperature of 28°C is not suitable for clothing factors equal to 1 and 0.5.

In Figure 6 the frequency distribution of PMV related to the number of plant operation for different cooling set-point temperatures were reported. Considering a clothing factor equal to 0.3 and a set-point temperature of 24°C, the PMVs are for about 850 hours lower than 0. For about 100 hours, a cooling perception, corresponding to -0.75<PMV<-1 was observed. Considering a clothing factor equal to 1, only a very low number of hours corresponds to PMVs higher than 1. For a set-point temperature of 25°C and a clothing factor of 1, for more than 150 hours, the obtained PMVs are higher than 1. For the same clothing factor, an increase of the set-point temperature of only 1°C determines a very significant increase of the discomfort hours, passing from about 150 to 650 hours. For a set-point temperature of 27°C and a clothing factor of 0.5, related to the summer light dress, almost all the PMVs are lower than 1 for all the operation hours. However, if the set-point temperature is raised to 28°C, for about 400 hours the PMVs are higher than 1. Conversely, if a summer light dress is adopted, i.e. a clothing factor equal to 0.3, all the PMVs are lower than 1 for all the operation hours. This means that the relaxation of the dress code is functional for the reduction of the cooling energy consumption, considering that the users will set a high cooling temperature due to the cooling perception due to the adoption of summer light dresses.

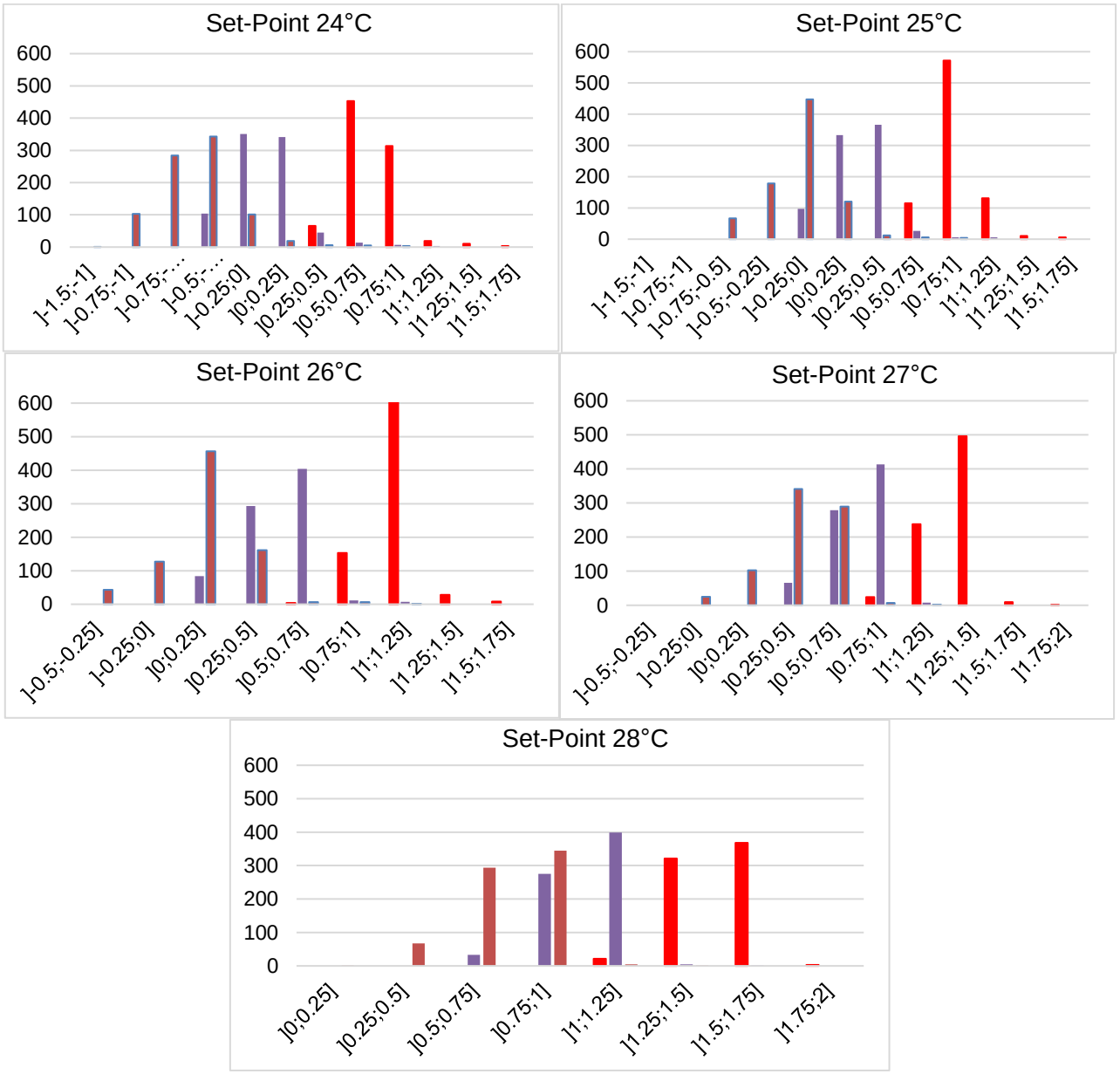

Figure 6. Frequency distribution of PMV indices for different cooling set-point temperatures

In Table 3, the results of the energy, economic and environmental analyses for all the set-point temperatures investigated, from 24°C to 28°C were reported. A set-point temperature of 24°C involves a cooling energy demand of 66 kWh/m^2 higher than the energy demand related to the set-point of 28°C, equal to 42 kWh/m^2 and higher than the demand related to the value of 26°C, equal to 54 kWh/m^2. The set-point temperature of 28°C and 27°C, determines primary energy savings over 32%, when compared with the set-point temperature of 24°C. The set-point temperature of 28°C corresponds to a reduction in the total CO_2 emissions of 108 kgCO_2/year when compared with the set-point temperature of 24°C. Concerning the operating cost for space cooling, for the set-point temperature of 24°C, the obtained value is 376 €/y, which reduces to 252 €/y for the set-point temperature of 28°C. Therefore, without any capital cost, this energy measure, simply wearing a tropical or light summers dresses, can be useful for reaching important energy, economic and environmental savings. Note that this energy measure was evaluated only considering one office of 22 m^2. Therefore, the results could be of course more advantageous and significative if the analysis will be extended to other offices of the university.

Table 3. Energy, economic and environmental analysis

Set-point temperature [°C]	Cooling energy [kWh/m^{2}y]	Primary energy [kWh/m^2 y]	Cost for space cooling [€/y]	Total CO_2 emissions [kgCO_2/y]	Increase of cooling energy [%]
24	66.24	67.60	376	332	57.80
25	60.41	62.34	347	306	43.92
26	54.35	56.81	316	297	29.47
27	48.36	51.24	285	252	15.21
28	41.98	45.32	252	224	-

4. Conclusion

This study evaluated the influence of classic formal dress-codes on the cooling energy demand and the perceived comfort, in office users during the summer season. A typical university office was selected to evaluate which effective consumption reduction could be obtained through a significant relaxation of the dress-code, when an increase of the air set-point temperature occurs. Several clothing factors were considered related to the classic, tropical and light summer clothing. The investigation was performed in TRNSYS environment by a dynamic simulation model evaluating both the common comfort indexes and the cooling energy demand of the office. The model was applied to a suitable case study, the office room located at the University of Naples Federico II, where authors of the presented study work. The results of the simulations showed that the clothing factor and the set-point temperature dramatically affect both energy consumption and the comfort indexes values. Furthermore, these results proved that the use of a more flexible dress-code, considering higher set-point temperatures, significant energy, economic and CO_2 emissions savings can be obtained. The increase of the summer air conditioning set-point temperature up to 28°C, is acceptable only for the dress code consisting of shorts and short-sleeved shirts. If this clothing is extreme and unacceptable for the type of office considered, a more formal dress-code, consisting of trousers, a short-sleeved shirt and closed shoes, can be adopted. However, in this case the increase in the air set-point temperature up to 27°C can be settled. If any relaxation of the dress-code can be accepted due to the fact that the classic formal dress is essential for the users, acceptable comfort index values can be obtained only if the air set-point temperature is decreased at least 24°C. This value not only is lower than the threshold set by the Italian normative (DL 1 March 2022, N. 17) regarding the summer air conditioning temperature, but also implies energy, economic and environmental impact increases. A set-point temperature of 24°C is the only value compatible with the classic dress, although this involves intolerable cooling energy demand. The set-point temperature of 27°C, compatible with light summer dress determines cooling energy savings over 37%. The set-point temperature of 28°C is compatible only with the tropical dress. and corresponds to a reduction in the consumption of cooling and primary energy by over 50%.

The analysis of the case study allowed, albeit on a small scale, to test the high potential of the increase of the cooling set-point temperature in the offices during the summer season, on the significant reductions in terms of energy, economic and environmental impacts. However, there are critical issues, which risk limiting the implementation of the initiative.

- Workers that may not feel adequate with a more flexible type of clothing and are still anchored to the choice of a formal outfit because it is coherent with the company policy.
- The difficulty of implementation within working contexts that require the interfacing with the public, considering the common idea that the dress worn reflects the degree of seriousness, reliability of employ, of professionalism and competence within a working context.

References

1. Buckley, N., et al., Using urban building energy modelling (UBEM) to support the new European Union's Green Deal: Case study of Dublin Ireland. Energy and Buildings, 2021. 247: p. 111115.
2. Malik, J., et al., Ten questions concerning agent-based modeling of occupant behavior for energy and environmental performance of buildings. Building and Environment, 2022. 217: p. 109016.
3. Dodoo, A., L. Gustavsson, and U.Y.A. Tettey, Cost-optimized energy-efficient building envelope measures for a multi-storey residential building in a cold climate. Energy Procedia, 2019. 158: p. 3760-3767.

4. Zhou, S. and A.G. Razaqpur, Efficient heating of buildings by passive solar energy utilizing an innovative dynamic building envelope incorporating phase change material. Renewable Energy, 2022. 197: p. 305-319.
5. Abden, M.J., et al., Combined use of phase change material and thermal insulation to improve energy efficiency of residential buildings. Journal of Energy Storage, 2022. 56: p. 105880.
6. Andersen, R., L.B. Jensen, and M. Ryberg, Using digitized public accessible building data to assess the renovation potential of existing building stock in a sustainable urban perspective. Sustainable Cities and Society, 2021. 75: p. 103303.
7. Calise, F., et al., Dynamic analysis of the heat theft issue for residential buildings. Energy and Buildings, 2023. 282: p. 112790.
8. Asif, A., et al., Investigating the gender differences in indoor thermal comfort perception for summer and winter seasons and comparison of comfort temperature prediction methods. Journal of Thermal Biology, 2022. 110: p. 103357.
9. Xiong, Y., J. Liu, and J. Kim, Understanding differences in thermal comfort between urban and rural residents in hot summer and cold winter climate. Building and Environment, 2019. 165: p. 106393.
10. Yu, L., et al., Do more efficient buildings lead to lower household energy consumption for cooling? Evidence from Guangzhou, China. Energy Policy, 2022. 168: p. 113119.
11. Huang, H., et al., Optimal plan for energy conservation and CO2 emissions reduction of public buildings considering users' behavior: Case of China. Energy, 2022. 261: p. 125037.
12. Tam, V.W.Y., L. Almeida, and K. Le Energy-Related Occupant Behaviour and Its Implications in Energy Use: A Chronological Review. Sustainability, 2018. 10.
13. Orland, B., et al., Saving energy in an office environment: A serious game intervention. Energy and Buildings, 2014. 74: p. 43-52.
14. Handgraaf, M.J.J., M.A. Van Lidth de Jeude, and K.C. Appelt, Public praise vs. private pay: Effects of rewards on energy conservation in the workplace. Ecological Economics, 2013. 86: p. 86-92.
15. Salata, F., et al., Dressed for the season: Clothing and outdoor thermal comfort in the Mediterranean population. Building and Environment, 2018. 146: p. 50-63.
16. Fountain, M., G. Brager, and R. de Dear, Expectations of indoor climate control. Energy and Buildings, 1996. 24(3): p. 179-182.
17. de Dear, R., G. Brager, and C. D, Developing an Adaptive Model of Thermal Comfort and Preference - Final Report on RP-884. Vol. 104. 1997.
18. ANSI ASHRAE 552010: thermal environmental conditions for human occupancy.
19. Rohles, F. and E. McCullough, Clothing as a Key to Energy Conservation. Industrial & Engineering Chemistry Product Research and Development, 1981. 20(1): p. 18-23.
20. Newsham, G. and D. Tiller, Field Study of Office Thermal Comfort Using Questionnaire Software. 1995.
21. Parsons, K.C., The effects of gender, acclimation state, the opportunity to adjust clothing and physical disability on requirements for thermal comfort. Energy and Buildings, 2002. 34(6): p. 593-599.
22. Bouden, C. and N. Ghrab, An adaptive thermal comfort model for the Tunisian context: a field study results. Energy and Buildings, 2005. 37(9): p. 952-963.
23. Newsham, G.R., Clothing as a thermal comfort moderator and the effect on energy consumption. Energy and Buildings, 1997. 26(3): p. 283-291.
24. Wu, T., B. Cao, and Y. Zhu, A field study on thermal comfort and air-conditioning energy use in an office building in Guangzhou. Energy and Buildings, 2018. 168: p. 428-437.
25. Schiavon, S. and K.H. Lee, Dynamic predictive clothing insulation models based on outdoor air and indoor operative temperatures. Building and Environment, 2013. 59: p. 250-260.
26. Lakeridou, M., et al., The potential of increasing cooling set-points in air-conditioned offices in the UK. Applied Energy, 2012. 94: p. 338-348.
27. Burke, M.J. and J.C. Stephens, Energy democracy: Goals and policy instruments for sociotechnical transitions. Energy Research & Social Science, 2017. 33: p. 35-48.
28. Calise, F., et al., Dynamic simulation, energy and economic comparison between BIPV and BIPVT collectors coupled with micro-wind turbines. Energy, 2020. 191: p. 116439.
29. Buonomano, A. and A. Palombo, Building energy performance analysis by an in-house developed dynamic simulation code: An investigation for different case studies. Applied Energy, 2014. 113: p. 788-807.
30. Buonomano, A., et al., Transient analysis, exergy and thermo-economic modelling of façade integrated photovoltaic/thermal solar collectors. Renewable Energy, 2019. 137: p. 109-126.
31. Calise, F., et al., Dynamic simulation and optimum operation strategy of a trigeneration system serving a hospital. American Journal of Engineering and Applied Sciences, 2016. 9(4): p. 854-867.

32. Voit, P., T. Lechner, and M.T. Schuler. Common EC validation procedure for dynamic building simulation programs - application with TRNSYS. in Conference of international simulation societies. 1994. Zürich.
33. Murray, M.C., et al. Live Energy Trnsys -Trnsys Simulation within Google Sketchup. in Eleventh International IBPSA Conference. 2009. Glasgow, Scotland July 27-30.
34. Ashrae, A.J.A.S.o.H., Refrigerating, and I.A. Air-Conditioning Engineers, Standard 55-2013: Thermal Environmental Conditions for Human Occupancy. 2013.
35. Vellei, M. and J. Le Dréau, A novel model for evaluating dynamic thermal comfort under demand response events. Building and Environment, 2019. 160: p. 106215.
36. http://www.enea.it/it. http://www.enea.it/it. 2019; Available from: http://www.enea.it/it.
37. https://www.unep.org/resources/report/2021-global-status-report-buildings-and-construction.
38. Calise, F., et al., Water-energy nexus: A thermoeconomic analysis of polygeneration systems for small Mediterranean islands. Energy Conversion and Management, 2020. 220: p. 113043.
39. Calise, F., et al., Dynamic modelling and thermoeconomic analysis of micro wind turbines and building integrated photovoltaic panels. Renewable Energy, 2020. 160: p. 633-652.
40. Calise, F., et al., Smart grid energy district based on the integration of electric vehicles and combined heat and power generation. Energy Conversion and Management, 2021. 234: p. 113932.

Optimal design of a renewable power-to-hydrogen system for the decarbonization of a semiconductor industry

Davide Trapani[a], Paolo Marocco[b], Marta Gandiglio[c] and Massimo Santarelli[d]

[a] Politecnico di Torino, Torino, Italy, davide.trapani@polito.it (CA)
[b] Politecnico di Torino, Torino, Italy, paolo.marocco@polito.it
[c] Politecnico di Torino, Torino, Italy, marta.gandiglio@polito.it
[d] Politecnico di Torino, Torino, Italy, massimo.santarelli@polito.it

Abstract:

Hard-to-abate industries require significant amounts of hydrogen, which is mainly used as feedstock, reducing agent and gas carrier. Currently, most of this demand is met by fossil-based hydrogen produced on-site or delivered by trailers. There is therefore huge potential to decarbonize these industries by replacing conventional grey hydrogen supply with sustainable power-to-hydrogen systems that exploit renewable energy to produce green hydrogen through electrolysis. In this work, a semiconductors production plant was considered as a case study. Hydrogen is used as gas carrier in epitaxial silicon growth and the demand is about 110 tons per year. The goal is to explore the cost-effectiveness of on-site green hydrogen production. The power-to-hydrogen system includes a photovoltaic plant, a PEM electrolyzer, a compressor, a hydrogen tank, a grey hydrogen back-up system and the electrical grid connection. The optimal system sizing was carried out by adopting the Particle Swarm Optimization (PSO) algorithm able to identify the configuration that minimizes the Levelized Cost of Hydrogen (LCOH) while ensuring the coverage of the hydrogen demand over the entire year. For a detailed techno-economic assessment, size-dependent cost functions were applied, and the lifetime of the electrochemical component was estimated based on its operating hours during the year.
Results show that the cost-optimal solution is the current scenario, where only grey hydrogen is employed (LCOH equal to 4 €/kg). Different decarbonization targets (i.e., grey hydrogen share constraint in the range 0-100%) were also investigated and the resulting LCOH ranges from 4 €/kg (full grey hydrogen scenario) to 10.85 €/kg (full green hydrogen scenario). The resulting Pareto front shows two distinct regions: the reduction of grey hydrogen share from 100% (current scenario) to 30% - corresponding to a decarbonization rate of 0% to 70% – follows a smooth trend with an LCOH increase from 4 to 6.2 €/kg (first region). Higher decarbonization rates (> 70%, second region) instead lead to a steeper increase in the LCOH, reaching 10.85 €/kg in the completely decarbonized scenario (0% grey hydrogen).

Keywords

Hydrogen, Electrolysis, Optimal sizing, Hard-to-abate, CO_2 savings

1. Introduction

Electronics manufacturing currently represents a niche industrial application of hydrogen. Specifically, high purity hydrogen (i.e., higher than 99.999%) is used as a gas carrier in the semiconductor industry for the epitaxial growth of the silicon wafers.

According to Rochlitz et al. [1], 16.5 million Nm^3 of hydrogen are consumed annually by the around 500 epitaxy reactors across Europe. This demand is largely met by fossil-based hydrogen (i.e., grey hydrogen) that is delivered – either compressed or liquid – by trailers to the industrial plants, or alternatively produced on-site through Steam Methane Reforming (SMR). Thus, renewable power-to-hydrogen (P-t-H) systems can represent a promising low-carbon strategy for the hydrogen supply of the semiconductor industries. In fact, using green hydrogen in hard-to-abate sectors can effectively reduce CO_2 emissions in a cost-effective way. Gärtner et al. [2] investigated the integration of a power-to-hydrogen system in a German glass industry and found out that CO_2 emissions can be reduced by up to 60% through the use of renewable hydrogen. Marocco et al. [3] investigated the role of hydrogen in decarbonizing the high-temperature heat production in the steel sector. Moreover, they highlighted that lower Levelized Cost of Hydrogen (LCOH) values can be achieved by exploiting cheaper electricity, such as that generated by on-site Renewable Energy Sources (RES). Röben et al. [4] assessed the techno-economic feasibility of reducing direct CO_2 emissions in copper production by

installing a power-to-hydrogen system. They confirmed that the electricity price is a crucial parameter to achieve a cost-efficient decarbonization. In addition, they pointed out that exploiting the by-product oxygen can boost the profitability of this solution. Gu et al. [5] carried out a techno-economic analysis of a green methanol production plant and the results emphasized the impact of the carbon price on reaching the breakeven with the conventional process. However, no studies that specifically assess the cost-effectiveness of exploiting green hydrogen in the silicon wafers manufacturing were found in the literature. Thus, the present work aims at filling this gap by proposing a detailed techno-economic optimization study for a power-to-hydrogen application in the semiconductor industry. The optimal sizing of the RES-based hydrogen production system was performed by adopting the Particle Swarm Optimization (PSO) algorithm and the effects of different decarbonization targets on the LCOH were investigated by applying the ε-constrain method. The PSO algorithm was chosen because its robustness and good convergence speed make it ideal for the design of energy systems [6].

The structure of this works is as follows: Section 2 describes the design methodology and reports the main techno-economic input data, Section 3 outlines the case study, Section 4 shows the results and Section 5 summarizes the conclusions.

2. Methodology

2.1. System layout

The renewable power-to-hydrogen system consists of the following components: the photovoltaic panels (PV), the electrolyzer (EL), the compressor (CP), the pressurized hydrogen tank (HT), the grey hydrogen back-up system (HBS) and the national electrical grid (GR). The schematic layout of the system is shown in Figure 1.

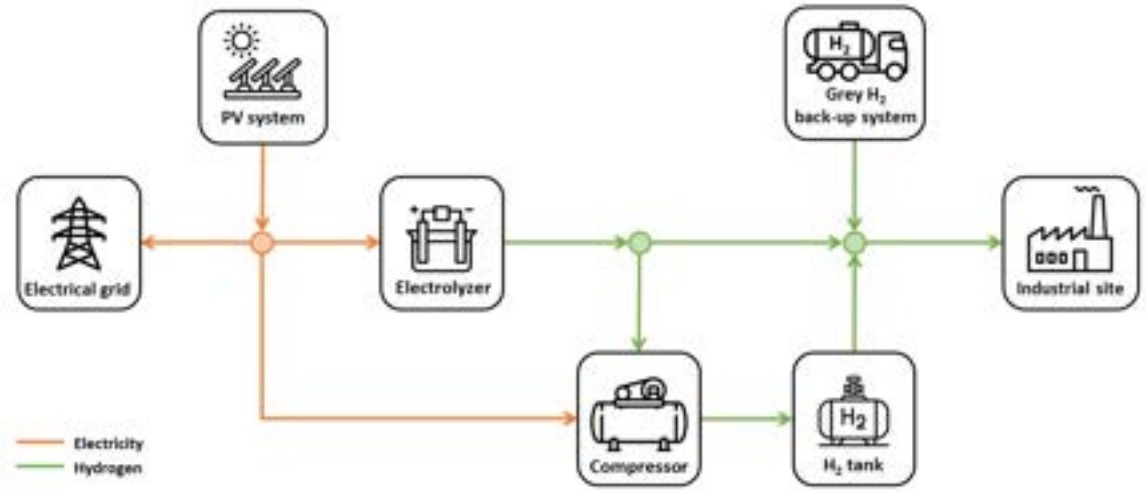

Figure 1. Schematic layout of the power-to-hydrogen system.

2.2. Modelling of the components

The modelling of the components of the power-to-hydrogen system is described below.

PV system

The PV power production was evaluated as follows [6]:

$$P_{PV}(t) = f_{PV} \cdot P_{PV,rated} \cdot \left(\frac{G_T(t)}{G_{STC}}\right) \cdot \left[1 + \alpha_P \cdot \left(T_c(t) - T_{c,STC}\right)\right] \quad (1)$$

where P_{PV} (in kW) is the output power of the PV system, $P_{PV,rated}$ (in kW) is the rated power of the PV system, G_T (in kW/m^2) is the incident solar radiation evaluated for the optimal configuration of tilt and azimuth angles, G_{STC} (in kW/m^2) is the solar irradiance at Standard Test Conditions (STC), T_c (in °C) is the actual PV cell temperature during operation, $T_{c,STC}$ (in °C) is the cell temperature at standard test conditions, α_P (in 1/K) is the temperature coefficient of power, and f_{PV} is the derating factor.

The meteorological data for the estimation of the PV power production were extracted from the Photovoltaic Geographical Information System (PVGIS) tool considering the dataset for the Typical Meteorological Year (TMY) [7].

Electrolyzer

The Proton Exchange Membrane (PEM) technology was considered for the electrolyzer since it offers faster dynamic response and wider operating range than the alkaline technology, which results in better

performances when coupled with variable RES. The nominal efficiency of the PEM electrolyzer was assumed equal to 55% and the operating pressure was set to 30 bar. Moreover, a specific modulation range (10-100% of the rated power) was imposed to ensure safe and efficient operation of the electrolyzer [6]:

$$P_{EL,min} \leq P_{EL}(t) \leq P_{EL,rated} \quad (2)$$

where P_{EL} (in kW) is the electrolyzer operating power, $P_{EL,min}$ (in kW) is the minimum electrolyzer operating power and $P_{EL,rated}$ (in kW) is the electrolyzer rated power.

Hydrogen tank

A pressurized storage tank is required to cope with the fluctuations in hydrogen production and demand throughout the year. A Type-I tank (i.e., made of seamless aluminium or steel) with a maximum storage pressure of 200 bar was chosen. In addition, the minimum pressure of the tank was set to 20 bar according to the specific requirements of the industrial process.

The Level of Hydrogen (LOH) in the tank, which is defined as the ratio between the amount of hydrogen stored in the tank and its maximum capacity, was evaluated as follows:

$$LOH(t) = LOH(t-1) + \frac{P_{EL}(t-1) \cdot \Delta t \cdot \eta_{EL}}{LHV_{H_2} \cdot Cap_{H_2}} - \frac{\dot{m}_{H_2}(t-1) \cdot \Delta t}{Cap_{H_2}} \quad (3)$$

where Δt is the time resolution (i.e., 1 hour in this study), η_{EL} is the efficiency of the electrolyzer, LHV_{H_2} (in kWh/kg) is the lower heating value of hydrogen, Cap_{H_2} (in kg) is the rated capacity of the hydrogen tank, and $\dot{m}_{H_2}$ (in kg/h) is the hydrogen flowrate sent to the industrial plant.

In order to guarantee the correct hydrogen supply to the industrial plant, at any time interval, the following constrain has to be met:

$$LOH_{min} \leq LOH(t) \leq LOH_{max} \quad (4)$$

The LOH_{min} can be evaluated as the ratio between the minimum and the maximum pressure storage, while LOH_{max} is set equal to 1.

Hydrogen compressor

A three-stage intercooled compressor was selected to increase the hydrogen pressure up to the storage tank value. The specific energy consumption to pressurize hydrogen from the operating condition of the electrolyzer (i.e., 30 bar) up to the maximum storage pressure (i.e., 200 bar) was assumed equal to 4 MJ/kg [8].

Grey hydrogen back-up system

A fossil-based back-up solution was also included in the system. Specifically, a tube trailer with pressurized grey hydrogen was considered.

2.3. Energy management strategy

In order to model the hourly operation of the power-to-hydrogen system over a reference year, an Energy Management Strategy (EMS) was implemented. The adopted control strategy sets the operating conditions of the system based on the hydrogen demand of the industrial plant and the availability of RES production.

The EMS starts with the evaluation of the hydrogen demand profile:

- If the hydrogen demand is higher than zero, the supply intervention has the following priority: first hydrogen from the electrolyzer (if electricity is available from RES), then green hydrogen from the pressurized storage tank and finally grey hydrogen from the fossil-based back-up system. Specifically, two sub-cases can occur:
    - In case of hydrogen demand higher than zero and sufficient electricity from the PV, the electrolyzer can be switched on and operated within its modulation range, while the excess power – if any – can be exported to the electrical grid. The electrolyzer production can be fed directly to the industrial plant or, if the hydrogen demand is exceeded, it can be compressed and stored.
    - In case of hydrogen demand higher than zero and power from the PV not available or not sufficient, the deficit must be covered first resorting to the green hydrogen storage and then to the grey hydrogen back-up system.
- If the hydrogen demand is zero, renewable electricity from the PV – if available – is converted into hydrogen, which is entirely stored. The excess power, if any, is then sold to the electrical grid.

2.4. Optimal design

The optimal design of the power-to-hydrogen system was performed by adopting the PSO algorithm and implementing a two-layer approach. According to this methodology, the sizing and dispatch problems are decoupled: in the outer loop a potential design solution (i.e., the sizes of the components) is iteratively generated by the PSO algorithm, while the operation of the power-to-hydrogen system is managed in the inner loop according to the rule-based EMS described in Section 2.2. The optimal design problem was formulated and solved in Matlab (r2022b) with a year-long time horizon and an hourly time-step resolution.

In the PSO algorithm, a population size of 100 was used and both the cognitive and social parameters were set to 1.9. The optimization procedure aims to identify the system configuration that minimizes the LCOH while satisfying the following constrains on the unmet hydrogen demand (UH_2) and the maximum share of grey hydrogen in the annual demand (GH_2):

$$UH_2 \leq UH_{2,target} \tag{5}$$

$$GH_2 \leq GH_{2,target} \tag{6}$$

Equation (5) represents the constraint on the system reliability and the target of unmet hydrogen demand ($UH_{2,target}$) was imposed to zero. Equation (6) defines the maximum share of grey hydrogen ($GH_{2,target}$) that can be used in the plant. The $GH_{2,target}$ term was varied between 100% and 0% to build up a Pareto front according to the ε-constrain method [6].

The LCOH (in €/kg), which represents the objective function to be minimized, is defined as follows:

$$LCOH = \frac{C_{NPC,tot}}{\sum_{n=1}^{N} \frac{M_{H_2}}{(1+d)^n}} \tag{7}$$

where $C_{NPC,tot}$ (in €) is the total Net Present Cost (NPC) of the system, M_{H_2} (in kg) is the annual hydrogen demand of the industrial site, d is the real interest rate (that includes both the nominal interest rate and the annual inflation rate) and N is the system lifetime (set equal to 20 years).

The NPC includes the capital expenditure, the operation and maintenance (O&M) costs and the replacement costs incurred over the whole lifetime of the system. The NPC was evaluated as (with i = PV, EL, HT, CP):

$$C_{NPC,tot} = \sum_i C_{inv,i} + \sum_{n=1}^{N} \left(\frac{\sum_i C_{O\&M,i,n} + \sum_i C_{rep,i,n} + C_{greyH_2,n} - C_{GR,sell,n}}{(1+d)^n} \right) \tag{8}$$

where $C_{inv,i}$ (in €) is the investment cost (i.e., CAPEX) of the i-th component incurred at the beginning of the project, $C_{O\&M,i,n}$ (in €) is the operation and maintenance cost of the i-th component during the n-th year, $C_{rep,i,n}$ (in €) is the replacement cost of the i-th component incurred at the n-th year (if required), $C_{greyH_2,n}$ (in €) is the annual cost due to the purchase of the fossil-based hydrogen and $C_{GR,sell,n}$ (in €) is the annual revenue for selling the surplus electricity to the grid.

The specific CAPEX of the PV system was assumed equal to 800 €/kW which is in line with the cost of the utility-scale projects in Europe [9].

The specific investment cost $c_{inv,EL}$ (in €/kW) of the PEM electrolyzer was estimated by using a modified power law that considers both the plant capacity and the maturity of the technology [10]:

$$c_{inv,EL} = \left(k_0 + \frac{k}{P_{EL,rated}} \cdot \left(P_{EL,rated}\right)^{\alpha} \right) \cdot \left(\frac{V}{V_0}\right)^{\beta} \tag{9}$$

where k_0 and k are the fitting parameters, $P_{EL,rated}$ (in kW) is the rated power of the electrolyzer, α is the scaling factor, β is the learning factor, V and V_0 are the plant installation year and the reference year, respectively. For a more detailed techno-economic assessment, the lifetime of the electrolyzer stack was evaluated based on the actual number of operating hours during the year.

The specific CAPEX of the pressurized tank was set at 500 €/kg, which is in good agreement with the costs of Type-I tanks with storage pressure below 250 bar [11]. The specific investment cost of the compressor was assumed equal to 1600 €/kW [8]. Finally, a cost of 4 €/kg was considered for the fossil-based back-up solution [1]. The main techno-economic input data are summarized in Table 1.

Table 1. Techno-economic input data.

Parameter	Value	Ref.
PV		
f_{PV}	86%	[6]
α_P	-0.003 1/K	[6]
CAPEX	800 €/kW	[9]
O&M (annual)	2% (of the CAPEX)	
Lifetime	20 yr	
Electrolyzer (PEM)		
Efficiency (η_{EL})	55%	[3]
Modulation range	10-100% (of the rated power)	[3]
Operating pressure	30 bar	[3]
Stack lifetime	40,000 h	[6]
Balance of plant lifetime	20 yr	[6]
α	0.622	[10]
β	-158.99	[10]
k_0	585.85	[10]
k	9458.2	[10]
V_0	2020	[10]
O&M (annual)	3% (of the CAPEX)	[6]
Stack replacement cost	26.7% (of the CAPEX)	[6]
Hydrogen tank		
Maximum pressure	200 bar	[3]
CAPEX	500 €/kg	[11]
O&M (annual)	2% (of the CAPEX)	[3]
Lifetime	20 yr	[3]
Hydrogen compressor		
Specific energy consumption	4 MJ/kgH_2	[8]
CAPEX	1600 €/kW	[8]
O&M (annual)	2% (of the CAPEX)	[3]
Lifetime	20 yr	[3]
Grey hydrogen		
Emission factor for SMR	9.5 kgCO_2/kgH_2	[12]
Cost	4 €/kg	[1]
Other assumptions		
Discount rate	4.9%	
Revenue for exported electricity	0.0363 €/kWh	
System lifetime	20 yr	

3. Case-study

A semiconductor production plant located in Southern Europe was considered as a case study. The real hourly demand profile over one reference year was used in this analysis. The plant operates continuously throughout the year with an average hydrogen demand of about 12.5 kg/h (which is in agreement with other literature

sources [1]) and a maximum consumption of around 15.5 kg/h. Further details on the demand profile are omitted for confidentiality reasons. The total annual hydrogen demand amounts to 110 tons and is currently met by a conventional fossil-based solution (i.e., grey hydrogen purchased externally and delivered by trailer).

4. Results and discussion

The optimal sizing was first performed without imposing any constraint on the $GH_{2,target}$ and the LCOH resulted in 4 €/kg, confirming that fossil-based hydrogen is currently the cheapest solution. However, adopting this strategy exhibits severe environmental drawbacks since the production of 110 tons of grey hydrogen generates 1045 tons of CO_2 emissions per year.

In order to assess the effect of the different decarbonization targets on the LCOH, the design of the energy system was then carried out by imposing a constraint on the annual grey hydrogen share, which was gradually reduced from 100% to 0%. The main sizing results and economic performance indicators are summarized in Table 2.

By reducing the amount of grey hydrogen that can be used by the industrial plant, the sizes of PV and electrolyzer increase significantly. Specifically, the rated capacities of PV and EL rise respectively from 0.68 MW and 0.27 MW (with 90% grey hydrogen share) to 11.96 MW and 3.3 MW (in the 100% RES-based configuration with 0% grey hydrogen share). Despite the considerable increase in the PV size (up to 11.96 MW), the corresponding footprint is consistent with the available space in the industrial site and the surrounding areas.

Furthermore, the results clearly show that the installation of a hydrogen storage (including hydrogen tank and compressor) is not economically convenient for scenarios with a grey hydrogen share higher than 70%. The size of the pressurized tank is relatively small (between 19 and 644 kg) when the grey hydrogen share is between 70% and 10%, and then sharply increases to 4930 kg when only green hydrogen is considered (0% grey hydrogen share).

Table 2. Main sizing results and economic performance indicators.

Grey H_2 share [%]	PV [MW]	EL [MW]	HT [kg]	CP [kW]	LCOH [€/kg]	CO_2 emissions [ton/y]
100%	0	0	0	0	4.00	1045
90%	0.68	0.27	0	0	4.46	940
80%	1.32	0.55	0	0	4.77	836
70%	1.98	0.83	19	7	5.07	731
60%	2.62	1.10	59	12	5.37	627
50%	3.23	1.39	101	22	5.66	522
40%	3.87	1.66	153	30	5.94	418
30%	4.62	1.94	201	35	6.23	313
20%	5.63	2.25	369	41	6.67	209
10%	7.29	2.75	644	50	7.50	104
0%	11.96	3.30	4930	60	10.85	0

As shown by the Pareto front in Figure 2, the cost of hydrogen ranges from 4 to 10.85 €/kg. Green hydrogen appears to be more expensive than fossil-based alternatives, but this solution can be beneficial from an environmental perspective since it allows the CO_2 emissions to be considerably reduced (up to 1045 ton/y of CO_2 emissions can be avoided).

It is worth noting that the LCOH increases evenly up to a grey hydrogen share of 30% – which corresponds to a decarbonization rate of 70% – with an LCOH of 6.2 €/kg (Figure 2). In this region, reducing the annual consumption of grey hydrogen by e.g., 50%, leads to a saving of 522 tons of CO_2 per year and an increase in the LCOH (compared to the 100% grey hydrogen scenario) of 41%. At higher decarbonization rates (> 70%), the Pareto front shows a steeper slope and increase in LCOH: the transition to a complete decarbonization of the energy system (0% grey hydrogen share) indeed leads to an increase in the LCOH of about 170%.

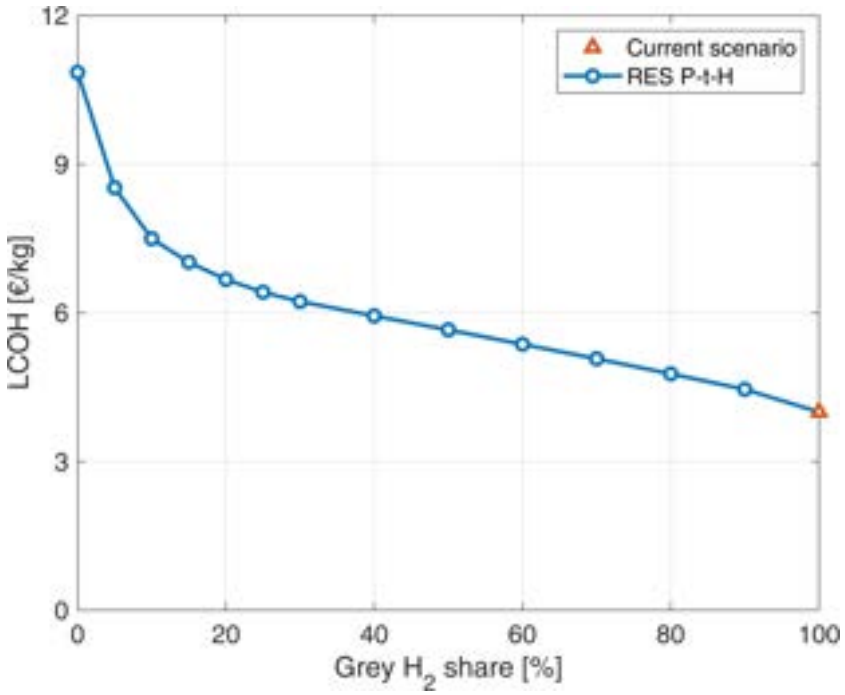

Figure 2. Pareto front between the levelized cost of hydrogen and the grey hydrogen share.

Figure 3 shows the breakdown of the NPC for different values of grey hydrogen share. For values above 50%, the purchase of fossil-based hydrogen represents the largest cost contribution (yellow area in Figure 3), while for the other scenarios the PV and EL costs have the largest impact. Moreover, it is evident that with the transition to lower values of grey hydrogen share, the revenues associated with the surplus electricity exported to the grid increase significantly ("Grid export" area in Figure 3) because of the sharp increase in the PV size. Finally, it is noteworthy that the storage system is an important cost contribution (20%) in the fully decarbonized scenario (0% grey hydrogen share), in which a large tank (4930 kg) is required to ensure a reliable supply of green hydrogen throughout the year.

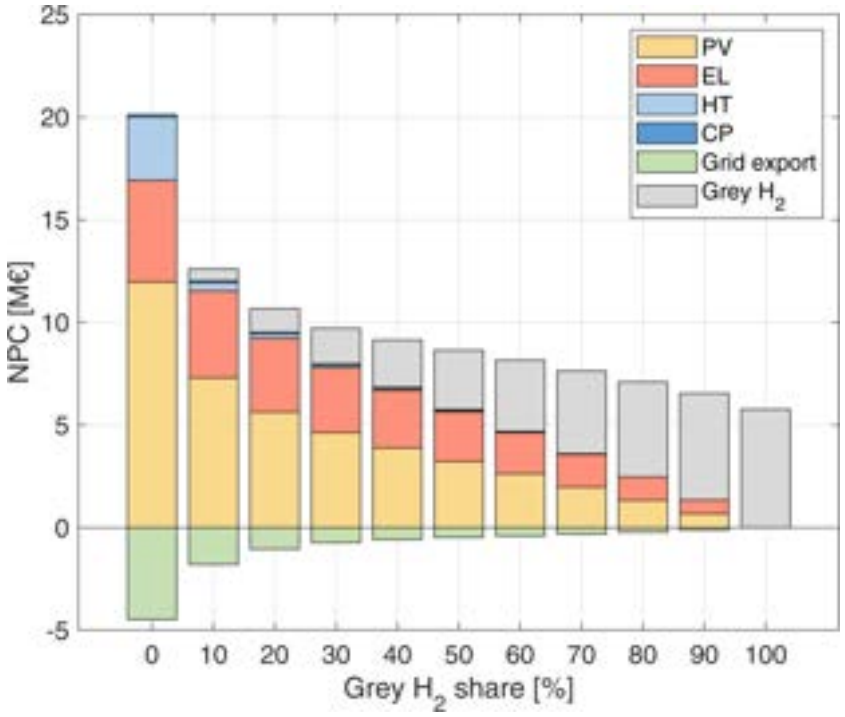

Figure 3. NPC breakdown for different annual grey hydrogen share.

5. Conclusions

This study aimed at assessing the techno-economic feasibility of decarbonizing a semiconductor industry by exploiting green hydrogen. The optimal sizing of the renewable power-to-hydrogen system was carried out by adopting the PSO algorithm in a two-layer optimization approach. Different decarbonization targets (i.e., 0% to 100%) were investigated and the LCOH resulted in the range between 4 and 10.85 €/kg. Producing green hydrogen proved to be more expensive than conventional fossil-based solutions but it can effectively reduce CO_2 emissions. The resulting LCOH-$GH_{2,target}$ Pareto front shows two distinct regions: the reduction of grey hydrogen share from 100% (current scenario) to 30% - corresponding to a decarbonization rate of 0% to 70% – follows a smooth trend with an LCOH increase from 4 to 6.2 €/kg (first region). Higher decarbonization rates (> 70%, second region) instead lead to a steeper increase in the LCOH, reaching 10.85 €/kg in the completely decarbonized scenario (0% grey hydrogen). In the scenarios with a grey hydrogen share above 50%, the purchase of grey hydrogen represents the main contribution of the NPC, while in the other scenarios PV and EL provide the largest shares. In the fully decarbonized configuration, the size of the storage system increases significantly, as it has to ensure the supply of green hydrogen throughout the entire year and reaches a share of 20% share of the overall NPC.

In conclusion, renewable power-to-hydrogen system does not represent the most cost-competitive solution, from an economic point of view, to provide hydrogen to the industrial plant. However, the profitability of the RES-based configuration can be significantly boosted when considering also the environmental benefits (i.e., CO_2 emission savings) generated by replacing the conventional grey hydrogen supply with the low carbon one. In addition, both the costs of photovoltaic and electrolyzer technologies are expected to decrease in the coming years, and this reduction could enhance the competitiveness of green hydrogen for industrial applications. In a future work, a sensitivity analysis on the main economic parameters will be carried out in order to identify the conditions in which green hydrogen can achieve the cost-parity with the current fossil-based supply.

Nomenclature

CAPEX	Capital Expenditures
CP	Compressor
EL	Electrolyzer
EMS	Energy Management Strategy
GR	Grid
HBS	Hydrogen Back-up System
HT	Hydrogen Tank
LCOH	Levelized Cost Of Hydrogen
LOH	Level of Hydrogen
NPC	Net Present Cost
O&M	Operation and Maintenance
PEM	Proton Exchange Membrane
PSO	Particle Swarm Optimization
P-t-H	Power-to-Hydrogen
PV	Photovoltaic
RES	Renewable Energy Sources
SMR	Steam Methane Reforming
TMY	Typical Meteorological Year

References

[1] L. Rochlitz *et al.*, “Second use or recycling of hydrogen waste gas from the semiconductor industry - Economic analysis and technical demonstration of possible pathways,” *Int J Hydrogen Energy*, vol. 44, no. 31, pp. 17168–17184, Jun. 2019, doi: 10.1016/j.ijhydene.2019.05.009.

[2] S. Gärtner *et al.*, “Simulation and techno-economic analysis of a power-to-hydrogen process for oxyfuel glass melting,” *Energies*, vol. 14, no. 24, Dec. 2021, doi: 10.3390/en14248603.

[3] P. Marocco, M. Gandiglio, D. Audisio, and M. Santarelli, “Assessment of the role of hydrogen to produce high-temperature heat in the steel industry,” *J Clean Prod*, vol. 388, Feb. 2023, doi: 10.1016/j.jclepro.2023.135969.

[4] F. T. C. Röben, N. Schöne, U. Bau, M. A. Reuter, M. Dahmen, and A. Bardow, “Decarbonizing copper production by power-to-hydrogen: A techno-economic analysis,” *J Clean Prod*, vol. 306, Jul. 2021, doi: 10.1016/j.jclepro.2021.127191.

[5] Y. Gu, D. Wang, Q. Chen, and Z. Tang, “Techno-economic analysis of green methanol plant with optimal design of renewable hydrogen production: A case study in China,” *Int J Hydrogen Energy*, vol. 47, no. 8, pp. 5085–5100, Jan. 2022, doi: 10.1016/j.ijhydene.2021.11.148.

[6] P. Marocco, D. Ferrero, A. Lanzini, and M. Santarelli, “The role of hydrogen in the optimal design of off-grid hybrid renewable energy systems,” *J Energy Storage*, vol. 46, Feb. 2022, doi: 10.1016/j.est.2021.103893.

[7] “Photovoltaic Geographical Information System.” https://joint-research-centre.ec.europa.eu/pvgis-online-tool_en (accessed Mar. 08, 2023).

[8] E. Crespi, P. Colbertaldo, G. Guandalini, and S. Campanari, “Design of hybrid power-to-power systems for continuous clean PV-based energy supply,” *Int J Hydrogen Energy*, vol. 46, no. 26, pp. 13691–13708, Apr. 2021, doi: 10.1016/j.ijhydene.2020.09.152.

[9] International Renewable Energy Agency (IRENA), *Renewable power generation costs in 2021*. Abu Dhabi, 2022. [Online]. Available: www.irena.org

[10] A. H. Reksten, M. S. Thomassen, S. Møller-Holst, and K. Sundseth, “Projecting the future cost of PEM and alkaline water electrolysers; a CAPEX model including electrolyser plant size and technology development,” *Int J Hydrogen Energy*, vol. 47, no. 90, pp. 38106–38113, Nov. 2022, doi: 10.1016/j.ijhydene.2022.08.306.

[11] “Technology Data-Energy storage.” [Online]. Available: http://www.ens.dk/teknologikatalog

[12] International Renewable Energy Agency (IRENA), “Hydrogen: a renewable energy perspective,” Abu Dhabi, 2019. [Online]. Available: www.irena.org

Innovative indicators for quantifying energy flexibility of district heating networks

Jaume Fitó[a], Julien Ramousse[a] and Frédéric Wurtz[b]

[a] Laboratoire Procédés Energie Bâtiment (LOCIE), CNRS UMR 5271 – Université Savoie Mont Blanc, Polytech Annecy-Chambéry, Campus Scientifique, Savoie Technolac, 73376 Le Bourget-Du-Lac Cedex, France, eng.fito@gmail.com (J.F.), julien.ramousse@univ-smb.fr (J.R.)
[b] Univ. Grenoble Alpes, CNRS, Grenoble INP, G2Elab, 38000 Grenoble, France, frederic.wurtz@g2elab.grenoble-inp.fr (F.W.)*

Abstract:

This article proposes a methodology to quantify the flexibility potential of a district heating network. By "flexibility potential" is meant here the degree of freedom in combining and controlling the energy units of a district heating network in order to meet a target demand. This potential has been modelled as the logarithm of the available combinations (or configurations), like the Shannon/Boltzmann entropy in statistical mechanics. The methodology produces a set of four entropy-inspired indicators. The first two, called "structural" and "operational" flexibility, are proportional to the number of available combinations of energy units and their input and output thermal powers, respectively. The other two indicators are the "effective" counterparts of structural and operational flexibility, and indicate the extent to which a given demand profile exploits the overall flexibility potential of a district heating network. The methodology takes into account the different sources of flexibility related to heat production, (de)storage, dissipation or diversion, as well as load adjustment techniques (demand management). Given its scaleless and dimensionless formulation, the methodology can be applied to energy systems of any size or energy type. The methodology is presented with the open-source tool used for the calculations and an illustrative example.

Keywords:

District heating, District heating networks, Energy flexibility, Operational flexibility, Thermodynamics, Entropy.

1. Introduction

The phenomenon of flexibility has been a source of many definitions and ambiguity in many fields of research. With respect to energy networks in the broadest sense, the International Energy Agency gave a first formal definition of "flexibility" in 2011: the ability of an energy system to react to temporal changes in energy production and demand [1].

The first active research on the subject of energy flexibility focused on power systems. The trigger for such issues was the decarbonization of these networks [2], which often leads to the inclusion of renewable sources in the energy mix [3], e.g., solar or wind power. Thus, possible sources of flexibility in electricity networks have been identified for a long time [4].

Although the question of flexibility in heat networks came later, several sources of flexibility have already been identified in the past, often with the intention of bringing flexibility to electricity networks [5]. The classical approach is to implement thermal energy storage, which can consist of centralized [6] or decentralized [7] collective physical storage units, or the use of the thermal inertia of the network itself [8], although the latter approach has its limitations in new generation (low temperature) networks [9]. Other approaches consist in controlling water flows [10] or their temperatures [7].

Thermal networks are generally considered as a way to increase the flexibility of electrical networks. For example, power-to-heat (P2H) systems increase flexibility because they allow excess electricity generated by PV panels to be converted into heat [11]. It is perhaps because of this "grid support" role that research on their intrinsic flexibility is less advanced. In addition, it is often evaluated indirectly, through a host of indicators that are related to flexibility: the ratio of renewables in the energy mix [12]; operational maps expressing the relationship between active and reactive power in an electrical network [13]; operational maps linking combined heat and power production in CHP units to the interface between electrical and thermal networks (see Fig. 5 in [9]); or the economic cost of improving flexibility, e.g., through better control devices [14].

While all the above approaches are useful and interesting, the authors of this paper believe that the field of heat networks lacks explicit and quantitative flexibility indicators. Similarly, the diversity of available energy units is an important source of flexibility, both for the design and the management of networks, yet it is not well known [15] and apparently lacks quantitative indicators. Finally, the authors also believe that efforts are needed to propose indicators that are decoupled from annual simulations and other indicators such as economic ones,

as these two factors prejudge the control strategy. Only when dedicated flexibility indicators with their own formulation and magnitude (or even units) are available, can network flexibility be accurately analyzed.

This article proposes an interpretation of flexibility inspired by the notion of entropy in statistical mechanics. That is, flexibility is understood as the logarithm of the possible combinations between the different energy units of a network. This notion is broken down into combinations of units (so-called "structural" flexibility) and combinations in the management of units (so-called "operational" flexibility). An explicit and non-dimensional indicator, proportional to the number of combinations, is proposed for each declination. The analysis allows to take into account controllable or non-controllable production units (renewables), thermal storage (physical unit or grid inertia), consumption or thermal dissipation, or demand-side management (DSM).

The paper is structured as follows: Section 2 describes in detail the method and the calculation of the indicators; Section 3 presents an illustrative case with its results and analysis; Section 4 discusses several aspects of the method that could be improved; and Section 5 summarizes the most relevant insights about the method and the illustrative case.

2. Materials and method

2.1. Hypotheses and data pre-treatment

This methodology is based on the first order thermodynamic analysis, and thus on the following assumptions and postulates:

- The system is in pseudo-permanent regime. Dynamic considerations are not taken into account. When the user declares a thermal unit, they must make sure that it can deliver heat at the exact moment required by the end-users. Any temporal mismatch due to ramp-up or ramp-down times, or inertia in general, must be ruled out before supplying a unit's thermal power range to the method. Taking into account temporal variability is a perspective for the authors, that will be treated in later researches.
- All units considered in the analysis are capable of producing heat at the temperature required by the demand profile. Issues related to temperature mismatch are not modelled. When the user declares a thermal unit, they must make sure that it can deliver heat at the temperature required by the end-users. Any decrease in temperature due to transport losses or heat exchange must be discounted from the unit's thermal output before supplying this information to the method.
- Spatial considerations are not taken into account. When the user declares a thermal unit with a power range, they must make sure it is the power range that the unit can deliver on the end-user side. Therefore, any heat losses due to transport must be discounted from a unit's power output before supplying this information to the method.
- Head loss along pipes is neglected.

The different sources of flexibility in a network are modelled as thermal power ranges. Table 1 shows how equivalence can be established for different flexibility sources.

Table 1. Equivalent thermal units considered by the method, with their interpretations and some examples.

Equivalent Thermal Unit	Interpretation	Example of a real unit
Adjustable production	A production unit whose thermal power output can be adjusted by its operator.	Biomass boiler
Non-adjustable production	A production unit whose thermal power output cannot be controlled by its operator.	Solar thermal collector field
Storage/de-storage	Any means of accumulating heat. It can be a physical unit or a management technique.	Thermal storage tank
Dissipation/Diversion	To displace heat outside of the system's boundaries.	Heat dissipation by aerothermal units. Heat exports to another aggregator.
Demand-Side Management	To act upon the demand profile in order to modify it for a better matching with the available thermal productions.	Using reward mechanisms in order to direct users' energy consumption to target periods of the day.

2.2. Underlying concept of the method

The indicators proposed in this article are inspired by the notion of entropy. In thermodynamics, if all possible configurations of a thermodynamic system have the same probability of existing, entropy is determined through Boltzmann's formula: $S = \ln(\Omega)$. The authors of this article took inspiration on that approach, and suggest the concept of 'combinatorial multiplicity' in order to analyze the flexibility of district heating networks.

Combinatorial multiplicity (Ω), an analogy to thermodynamic multiplicity, is understood as the number of possible ways to operate the units of energy in a district heating network given an external constraint. In this article, the external constraint is a thermal power demand.

The authors implemented this concept of flexibility through two approaches. One, called "structural flexibility", relates to the number of possible combinations of energy units that satisfy the demand. The other, called "operational flexibility", is related to the number of combinations of thermal energy outputs within the combined energy units. Figure 1 summarizes the two approaches visually, and the following subsection explains the calculation procedure in a formal and detailed manner.

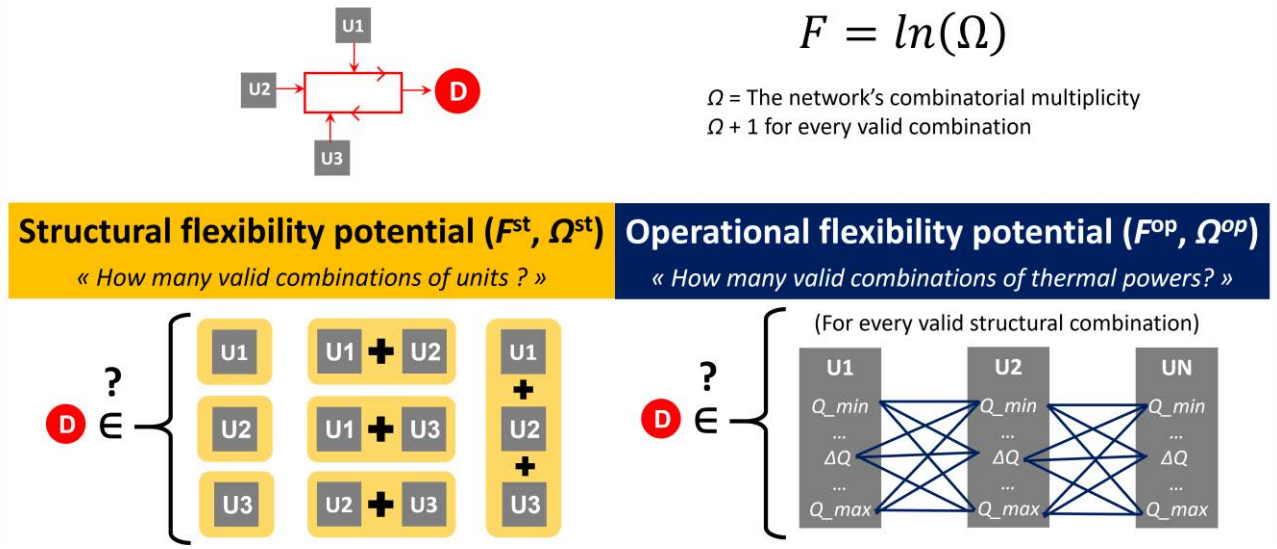

Figure 1. Flexibility potential assessment with a combinatorial approach inspired by the concept of entropy: structural flexibility (down, left) and operational flexibility (down, right).

2.2. Structural flexibility

Let us consider a heating network equipped with *N* equivalent units from the list provided in Table 1. The minimum and maximum heat outputs of the network are the sum of the minimum and maximum specific heat outputs of all units (1).

$$\dot{Q}_N^{\dagger} = \sum_{n=1}^{N} \dot{Q}_n^{\dagger} \qquad \langle \dagger = min, max \rangle \tag{1}$$

For the flexibility analysis, the global control step of the network has been defined as the greatest common divisor of the control steps of all units (2). This global control step, together with the global minimum and maximum power, determines the operating range of the network (3).

$$\Delta\dot{Q}_N = gcd\left(\Delta\dot{Q}_{j=1}, \dots, \Delta\dot{Q}_{j=J}\right) \tag{2}$$

$$Q_N \in \left[\dot{Q}_N^{min} : \Delta\dot{Q}_N : \dot{Q}_N^{max}\right] \tag{3}$$

The structural flexibility is evaluated over this operating range, power by power. All possible combinations of units are considered, from 1 to N selected units. For each combination of units, if the requested power is well within the combined operating range, the number of local configurations at that power (Ω_q^{st}) increases (4).

$$\forall\, Q \in Q_N \; and \; \forall\, st \in C^{st} \qquad if\; Q \in Q^{st} \implies \Omega_q^{st} = \Omega_q^{st} + 1 \tag{4}$$

The overall structural configuration number (Ωst) is the sum of all local structural configuration numbers over the operating range of the network (5). Because all combinations are assumed to be equiprobable, the structural flexibility is determined by a parallelism of the Boltzmann equation (6).

$$\Omega^{st} = \sum_q \Omega_q^{st} \tag{5}$$

$$F^{st} = ln(\Omega^{st}) \tag{6}$$

A value of $F^{st} = 0$ indicates a choke point, i.e., a thermal power demand that no structural combination of energy units can satisfy. An F^{st} of one indicates a structurally rigid point, i.e., only one structural combination can satisfy the demand. Note that a combination does not necessarily mean a single unit; it can be a combination of several units. An F^{st} greater than one means that the network is structurally flexible, i.e., several

combinations of units can meet the demand. The higher the F^{st} value, the more flexible the network is. These considerations apply to both local and global flexibilities.

2.3. Operational flexibility

Operational flexibility is concerned with the combinations of driving units, rather than the combinations of units. Indeed, often the same combination of units can be driven in different ways to satisfy the same demand. The number of operational configurations is determined in a similar way to the structural one, with one difference: each valid combination of thermal outputs counts (7).

$$\forall\, q \in Q_N \wedge \forall\, c^{st} \in C^{st} \qquad \forall\, q^{st} = q \implies \Omega_q^{op} = \Omega_q^{op} + 1 \tag{7}$$

A valid combination is one that satisfies the power demand even with overproduction, provided that the overproduction can be managed (i.e. stored or dissipated). It is important that there is no unmanaged overproduction. Operational flexibility is the logarithm of the number of operational configurations (8 and 9).

$$\Omega^{op} = \sum_q \Omega_q^{op} \tag{8}$$

$$F^{op} = ln(\Omega^{op}) \tag{9}$$

The structural and operational analyses, applied over the entire operating range of a network as defined by (4), lead to two distributions of flexibilities (structural and operational). Structural flexibility and operational flexibility provide non-redundant information with respect to each other. Structural flexibility does not take into account whether the units operate at their limits (upper or lower). Hence the need to define operational flexibility. Both give rise to different distributions of multiplicity, and their maximum will often be reached at different thermal powers. When combined, they make it easier to forecast choke points in the operation of a district heating system.

For clarity, a calculation example of both flexibilities is offered in Fig. 2. Let a district heating network feature three different thermal units. Each one has its own adjustable operating range. Then, the network is faced to a thermal power demand that falls within its production range. It is probable that the demand can be covered by combining the production units in different ways. Here, the term ‘combination’ is understood as ‘operating one or multiple thermal units simultaneously’. Following this logic, structural flexibility considers how many combinations of units can cover the demand *at least once*. Operational flexibility considers how many different ways of operating the units exist in order to cover a demand. In operational flexibility, every valid combination counts. In structural flexibility, every valid combination of units counts only once, independently of its number of valid operational combinations (see Fig. 2).

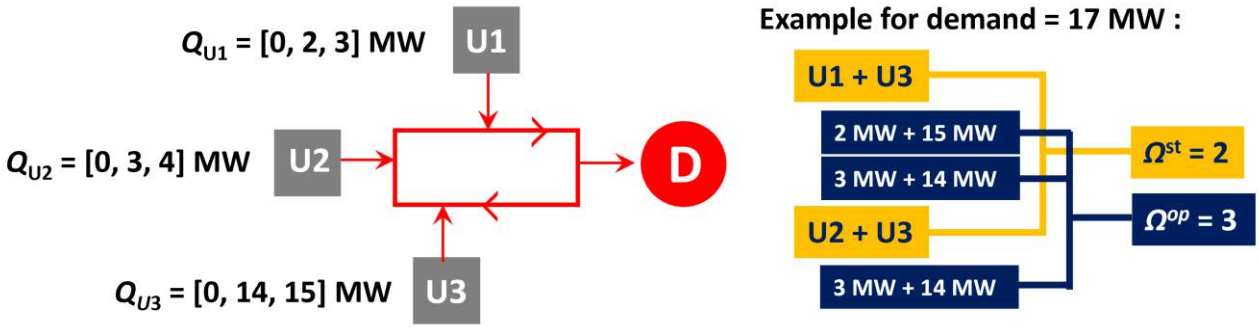

Figure 2. Calculation example of structural and operational multiplicities.

Let readers note that in order to count as a valid solution, a combination must satisfy the demand exactly. This logic applies in both structural and operational flexibility analyses. Therefore, in structural analysis, it is not sufficient that the demand be within a combination’s aggregated operating range. The structural combination must have at least one operating point where the thermal power output equals the demand exactly. This means that the discretization of thermal power ranges is an important point of the methodology. This aspect is discussed in section 4.

2.3. Dedicated open-source Python tool for the calculations

An open-source tool has been written in Python 3.9 for the implementation of the methodology and the calculation of the illustrative case presented in section 3. The tool allows to introduce a series of lists to declare the equivalent energy units in the system (adjustable production, non-adjustable production, storage, dissipation or DSM). Lists are used to declare unit names, operating ranges, and operating steps. Prohibited combinations of units may also be declared, in case the practical constraints of the case study do not allow the simultaneous operation of certain units. Then the tool starts with a routine to check the correctness of the input data (for example, that the operating steps are consistent with the operating ranges). After this check, a

dictionary of unit combinations is created and purged of all user-defined forbidden combinations. Then, the tool uses several "for" loops and "if" statements to analyze each combination and check if it complies with the energy balance and if it corresponds to a target demand value. If so, this combination is considered flexibility. The target value can be 1) either a user-defined request; 2) or each stage of operation of the neighborhood network as a whole, if the user requires a complete distribution of flexibility. After this process, the tool creates a dictionary of valid combinations and calculates flexibility indicators. After the whole process, the tool returns the numerical values of the flexibility for the network and plots the distributions of the structural and operational flexibilities (i.e., the figures presented in section 3). The tool is encoded in UTF-8 and requires the "itertools", "matplotlib" and "numpy" packages.

3. Results for an illustrative case

The previous section described innovative indicators of structural and operational flexibilities and how to evaluate them. This section shows how to apply the methodology and perform a detailed flexibility analysis of a heat network. For this purpose, a simple illustrative example has been developed to show all important information in the flexibility analyses. Readers are reminded that the actual output of this article is the methodology itself, not this illustrative example.

3.1. System description and input data

The illustrative example consists of a heat network with 6 units (Table 2). As a reminder, these are equivalent units, which can represent physical devices, a complete process/machine or an energy management technique.

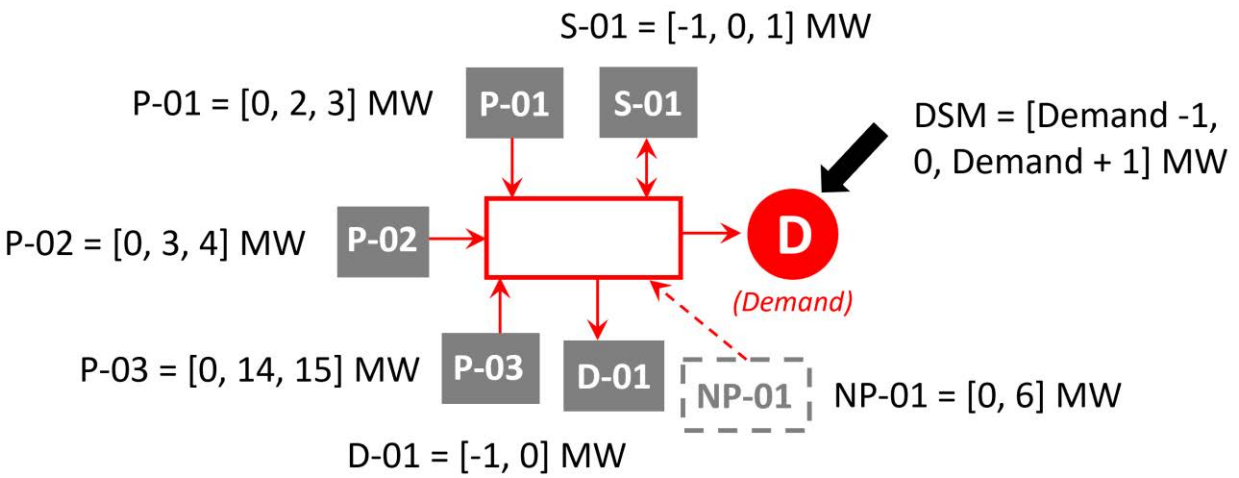

Figure 3. Schematical representation of the illustrative case.

Table 2. Equivalent thermal units considered in the illustrative case.

Unit name	Real unit	Equivalent thermal unit	Operating range
P-01	Biomass boiler	Adjustable production	[0, 2, 3] MW
P-02	Heat pump	Adjustable production	[0, 3, 4] MW
P-03	Heat import	Adjustable production	[0, 14, 15] MW
NP-01	Solar collector field	Non-adjustable production	[0, 6] MW
D-01	Aerothermal dissipation	Dissipation/Diversion	[-1, 0] MW
S-01	Thermocline storage unit	Storage/De-storage	[-1, 0, 1] MW
DSM	Tariff-incentivized modification of users' consumption patterns	Demand Side Management	[Demand -1, 0, Demand +1] MW

3.2. Analysis of structural and operational flexibility

Figures 4 and 5 show the so-called structural and operational flexibilities distributions, respectively. Both are to be represented on the aggregated power range of the network (x-axis). In this example, the lower bound (-3 MW) corresponds to 0 MW generated (P-01, P-02, P-03), 1 MW stored (S-01), 1 MW dissipated (D-01) and 1 MW shed (DSM). The upper bound (+24 MW) corresponds to 22 MW generated (P-01 = +3 MW, P-02 = +4 MW, P-03 = +15 MW), 1 MW de-stored (S-01) and 1 MW anticipated (DSM).

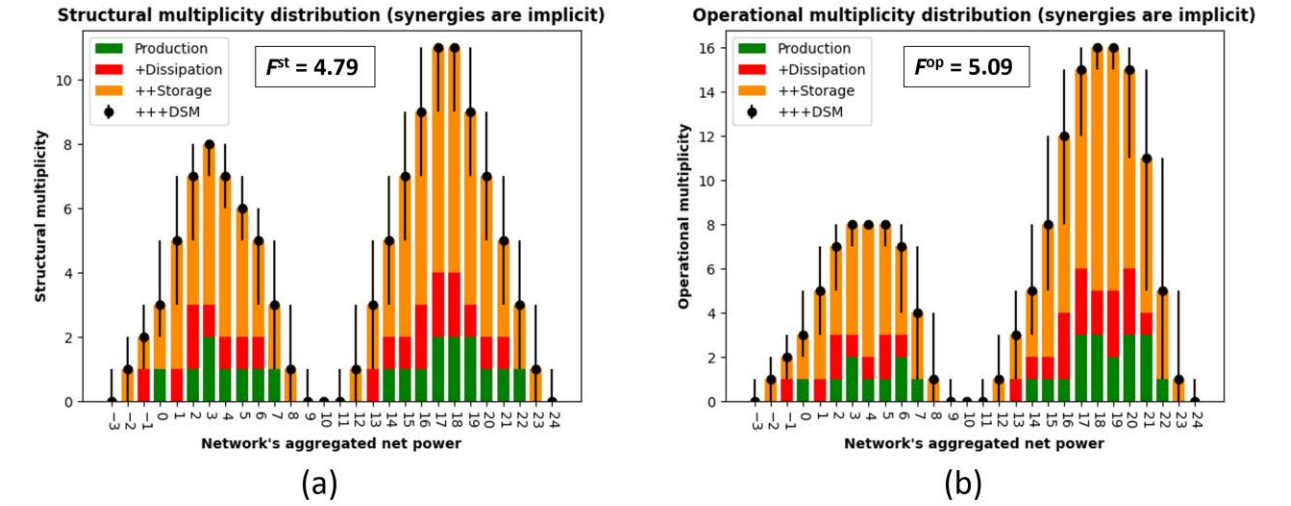

Figure 4. Flexibility distributions over full demand range: a) Structural flexibility, b) Operational flexibility.

The y-axis represents local flexibility at each power, determined by the methods described in Sections 2.2 (structural) and 2.3 (operational). The contribution of the generation units (green bars) is represented at the base of the distribution because it does not depend on the other unit types. Then, the dissipation units are represented in combination with the production (red bars), because they can only remove from the system heat already contributed by other units. The contribution of the storage units is shown in combination with the productions and dissipations (orange bars). It depends on a previous production (which could be partially dissipated), but also on the state of charge of the storage units. The asymmetric error bars represent the effects of the DSM techniques, once the other units are considered.

Thus, it turns out that the controllable generation units will determine the overall flexibility range to a large extent; the other units only expand the flexibility range implemented by the productions. Dissipation widens it only to the left, while (de-)storage widens it to the left and to the right. The DSM, rather than providing flexibility, shifts demand to other powers, which will be advantageous or not depending on the local flexibility of neighbouring powers.

In this illustrative case, the outputs allow two ranges of flexibility: [2 - 7] MW and [14 - 22] MW, which result from all possible combinations between P-01, P-02 and P-03. Then, adding dissipation widens them to 1 MW and 13 MW respectively, and allows to reach -1 MW if only dissipation is used. Storage extends the ranges further, to -2 MW or 12 MW under load, or to 8 MW or 23 MW under discharge. In addition, the storage load would have allowed -1 MW, 1 MW, and 13 MW even with no dissipation. And of course, dissipation and storage increase the local flexibility on the powers already covered by the productions. In fact, they include cumulative synergies. Quantifying and locating precisely the different synergies is an interesting perspective foreseen by the authors.

The potential effects of DSM (error bars on the y-axis) represent the largest possible change in F in the DSM range from a specific power. DSM can shift demand to powers where the local flexibility of the grid would be different. For example, the local structural flexibility at 4MW may switch between 1.79 and 2.08, as the DSM of +/- 1MW would shift demand to 5MW or 3MW respectively. Both the increase and decrease in flexibility are displayed, as the DSM is not always controllable. For example, time-shifted heating requirements often have to be made up later. The DSM can give flexibility to certain power demands that are not accessible by other units (-3 MW, 9 MW, 11 MW and 24 MW in this example). If a power unit is in a flexibility plateau (e.g., 10 MW), DSM will have no effect on its flexibility. DSM will not cause flexibility to rise above its overall maximum, nor will it cause it to fall below zero.

Any power that may fall to zero flexibility due to a poorly managed DSM is a potential choke point. Any power slice that has zero flexibility, but can be increased by DSM, is a bypassable choke point. Any slice of power with zero flexibility without a solution is a hard choke point.

The effects of non-drivable power generation (e.g., renewables) are displayed in Figures 3 and 4. A non-drivable generation of 6 MWth has been assumed. This could symbolize, for example, the installation of a solar thermal collector field with a peak generation of 6 MWth. The new flexibility distributions are given in Fig. 5.

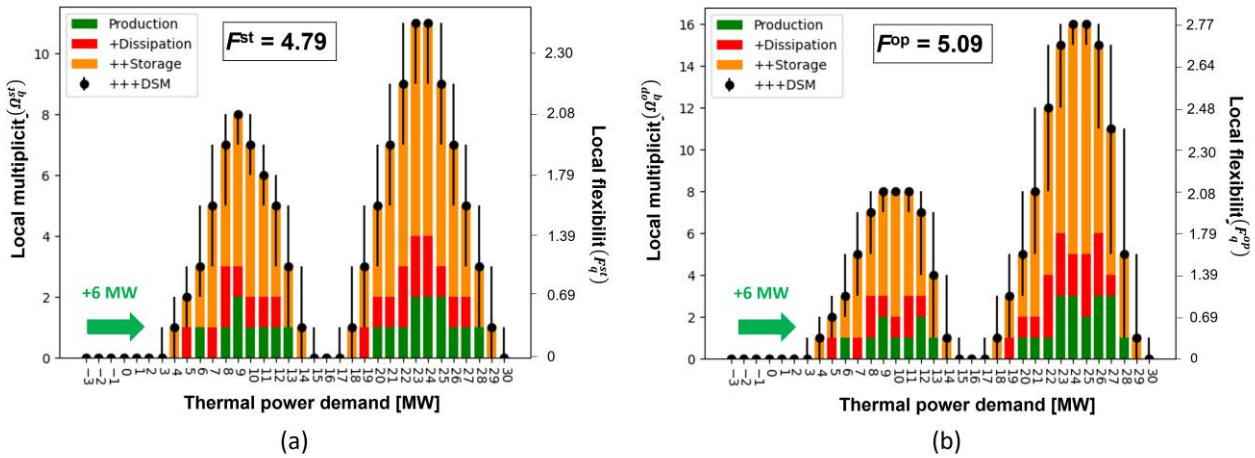

Figure 5. Flexibility distributions after consideration of renewables (non-adjustable production): a) Structural flexibility, b) Operational flexibility.

As a reminder: non-modulable generation is modeled as a heat input to the network that cannot be modulated in power. It must be either used, stored or dissipated. As a result, the two flexibility distributions are shifted to the right on the x-axis (see Figures 4a and 4b). While the old distributions went from -3 MW to 24 MW (Fig. 1), the new ones go from 3 MW to 30 MW. The old lower bound of -3 MW has been retained in the figure for illustrative purposes, but note that there is no flexibility before 3 MW.

Since non-adjustable heat generation is a "must" unit, there is no freedom to (not) select it. Therefore, this does not change the number of possible combinations. Note that there are still 32 combinations of units and 160 combinations of input/output heat outputs (see Appendix A), as in the previous scenario. The only change is that now all possible combinations include non-adjustable generation, and thus have +6 MW of heat output.

The effect of non-controllable productions may seem harmless, but it is not. When the district network is confronted to a demand profile, it will be forced to operate at certain regions of its flexibility distribution. The integration of new, non-adjustable thermal productions (like renewables) may completely unbalance the flexibility matching of the network. In other words, the effects of renewables on flexibility are difficult to forecast even if the network had been well-designed for a demand profile. The methodology presented in this paper (and its calculation tool) may be used for early detection of flexibility issues due to changes in the energy mix of a territory.

4. Discussion on the method

4.1. On the combinatorial approach

The main advantage of a combinatorial approach is that all possible configurations of the system are taken into account. This is the reason why the authors speak of "flexibility potential", instead of "flexibility". A dynamic simulation can only give a "circumstantial" idea of the flexibility of a network, because it prejudges the control strategy, and therefore may encounter difficulties not necessarily due to the configuration of the network at the base. On the other hand, the computation time is the weak point of a combinatorial approach, especially if the number of units is higher than 15.

4.2. On disregarding other performance criteria

This methodology and its indicators are free of preconceived ideas about optimal management or control strategies. Criteria such as energy efficiency, exergy efficiency, economic performance, environmental effects... are totally ignored. The methodology does not give less importance to a specific choice of technical units according to their abundant need of primary energy, or high implementation costs, or high CO2 emissions, or long start-up/shutdown times... In fact, none of these parameters are needed as input to the model. Any combination that satisfies the demand while respecting the energy balance is an equally valid solution.

Heat quality (temperature) considerations are also very limited. Any solution that meets the final heat demand at the requested temperature is valid, regardless of the upstream temperatures. For example, two generating units producing heat at 120°C and 50°C respectively, and both meeting heat requirements at 35°C, are also valid and important under this methodology. Although higher production temperature may indicate higher transmission losses or lower energy efficiencies in substations. In any case, the user must ensure that any generation, storage, dissipation or load control unit included in the analysis can satisfy the heat demands at the requested temperature.

The methodology does not rule out solutions that may seem counter-intuitive or unreasonable from the perspective of first-order thermodynamic analysis. This concerns in particular the overproduction of heat followed by the dissipation of the excess. For example, assume a generating unit and a dissipating unit with thermal power ranges Q_prod = [0, 1, 2, 3] MW and Q_diss = [-1, 0], respectively. If the demand is Q_dem = 2 MW, it is equally valid to produce Q_prod = 2 MW or to produce Q_prod = 3 MW and then to dissipate Q_diss = -1 MW. The methodology gives equal weight to both possibilities. Any arrangement of units that exactly matches the demand is considered flexibility.

All of these are deliberate choices by the authors, in order to create indicators that focus solely on combinatorial flexibility. There are also many methods and tools for multi-criteria analysis of heating networks, with a wide variety of criteria. As for counter-intuitive solutions, it is precisely the variety of criteria that justifies not discarding them. The optimality of a solution largely depends on the context and the decision criteria. Overproduction followed by partial dissipation may seem unreasonable, but it can allow the purchase of primary energy at better rates, for example. In this case, it can become economically optimal. If an exploitation decision is possible, it can become optimal under certain specific conditions and must therefore be taken into account.

4.3. On discretizing continuous ranges of thermal production

The discretization of continuous ranges of thermal power is probably the most debatable aspect of this methodology. Any thermodynamic system is indeed continuous, and trying to analyze it on finite increments may seem too reductionist an approach. The best answer of the authors to this remark at the moment is: control. District heating networks are equipped with demand-oriented energy systems and often subject to some type of control, often discrete. The thermal powers in this method should be considered as control steps.

4.4. On applying the method to other types of energy networks

The methodology, as presented in this article, is intended and more suitable for district heating networks with sources of flexibility from this list: thermal energy production (including partial load operation); storage and retrieval of thermal energy; dissipation (or diversion) of thermal energy; and any demand management techniques that impact thermal energy demand profiles. Only sources of flexibility that can be "translated" into thermal power can be modelled.

Nevertheless, with some data pre-treatment by the user, its applicability can be extended slightly. First, the methodology (and the corresponding Python tool) allows to the user to set the parameters. Thermal power was used in this article, but electrical power could be used to replicate the analysis for electrical networks. Since the methodology is based on balance sheets, the analysis remains consistent as long as the input data is consistent. The same could be done with district cooling networks, as long as their sources of flexibility can be routed as cooling powers. It could even be applied to gas networks, choosing mass flow rates as units.

Also, the methodology is not necessarily limited to the district level. As the notion of spatiality is not modelled, the methodology can be applied to micro-grids (mW) as well as very large-scale (GW) grids, provided that the sources of flexibility are modeled accordingly.

Furthermore, the sources of flexibility taken into account by the methodology are described in such a generic way that they can represent many types of real units/techniques. For example, a conversion unit can be modeled as equivalent production and dissipation units.

The authors are aware that the aforementioned adaptations, although feasible, represent a burden for the user. Their future work is to integrate as many of them as possible into the methodology (and by extension, into the open-source tool), as new features.

Using natural logarithms for quantifying these indicators becomes very useful when expanding/connecting networks. For example, let us assume that a district heating network is connected upstream with the electric grid via electrically-driven mechanical-compression heat pumps. When the heat pumps are implemented, the combinatorial multiplicity of the whole system is the product of the combinatorial multiplicities of the grid and the district heating network. At the same time, the authors would like the indicator of flexibility to be the sum of the flexibilities from the grid and the heating network. Using logarithms allows both addition properties.

5. Conclusions and perspectives

The district heating domain lacks explicit and quantitative indicators to describe the flexibility potential apart from other performance criteria. In this paper, the authors provide an answer to this deficiency through a combinatorial approach. It understands the flexibility potential as the degree of freedom in the selection and control (separately or simultaneously) of the energy units of a network in the face of various demands. The following findings and perspectives can be highlighted:

- The method can help in the energy planning of urban energy networks. Namely, it can help anticipate potential choke points, or the possible effects of renewable energy deployment on existing networks.
- It is planned to study the possibility of working with continuous distributions of flexibilities, rather than discrete ones.

- It is planned to study the applicability of the method to other energy networks, such as electricity networks, district cooling or gas networks. The dimensionless formulation of the method allows (in theory) to extend its application.
- It is planned to define additional indicators, for example an "effective" flexibility that would evaluate to what extent a given demand profile exploits the flexibility potential of the requested network.

The objective is to make the methodology as applicable as possible without putting the burden of data pre-treatment on the user.

Acknowledgments

The authors wish to express their gratitude to the Institut Carnot Energies du Futur for their support through the funding granted to the FlexENR project. The authors wish to express their gratitude to the Région Auvergne Rhône-Alpes for their support through the funding granted by the AXELERA program.

Appendix A

Table A.1 shows the detailed analysis of all possible combinations of units and their thermal powers for the illustrative case shown in Section 3 of the main part of the manuscript. DSM was not processed in the combinatorics because it is represented on the final distributions of flexibility.

Table A.1. Complete list of structural combinations, and their operating ranges, in the illustrative case.

	Combined units	Thermal power range of each unit involved [MW]
#1	No units	[0]
#2	['P-01']	[2.0, 3.0]
#3	['P-02']	[3.0, 4.0]
#4	['P-03']	[14.0, 15.0]
#5	['D-01']	[-1.0]
#6	['S-01']	[-1, 1]
#7	['P-01', 'P-02']	[[2.0, 3.0], [3.0, 4.0]]
#8	['P-01', 'P-03']	[[2.0, 3.0], [14.0, 15.0]]
#9	['P-01', 'D-01']	[[2.0, 3.0], [-1.0]]
#10	['P-01', 'S-01']	[[2.0, 3.0], [-1, 1]]
#11	['P-02', 'P-03']	[[3.0, 4.0], [14.0, 15.0]]
#12	['P-02', 'D-01']	[[3.0, 4.0], [-1.0]]
#13	['P-02', 'S-01']	[[3.0, 4.0], [-1, 1]]
#14	['P-03', 'D-01']	[[14.0, 15.0], [-1.0]]
#15	['P-03', 'S-01']	[[14.0, 15.0], [-1, 1]]
#16	['D-01', 'S-01']	[[-1.0], [-1, 1]]
#17	['P-01', 'P-02', 'P-03']	[[2.0, 3.0], [3.0, 4.0], [14.0, 15.0]]
#18	['P-01', 'P-02', 'D-01']	[[2.0, 3.0], [3.0, 4.0], [-1.0]]
#19	['P-01', 'P-02', 'S-01']	[[2.0, 3.0], [3.0, 4.0], [-1, 1]]
#20	['P-01', 'P-03', 'D-01']	[[2.0, 3.0], [14.0, 15.0], [-1.0]]
#21	['P-01', 'P-03', 'S-01']	[[2.0, 3.0], [14.0, 15.0], [-1, 1]]
#22	['P-01', 'D-01', 'S-01']	[[2.0, 3.0], [-1.0], [-1, 1]]
#23	['P-02', 'P-03', 'D-01']	[[3.0, 4.0], [14.0, 15.0], [-1.0]]
#24	['P-02', 'P-03', 'S-01']	[[3.0, 4.0], [14.0, 15.0], [-1, 1]]
#25	['P-02', 'D-01', 'S-01']	[[3.0, 4.0], [-1.0], [-1, 1]]
#26	['P-03', 'D-01', 'S-01']	[[14.0, 15.0], [-1.0], [-1, 1]]
#27	['P-01', 'P-02', 'P-03', 'D-01']	[[2.0, 3.0], [3.0, 4.0], [14.0, 15.0], [-1.0]]
#28	['P-01', 'P-02', 'P-03', 'S-01']	[[2.0, 3.0], [3.0, 4.0], [14.0, 15.0], [-1, 1]]
#29	['P-01', 'P-02', 'D-01', 'S-01']	[[2.0, 3.0], [3.0, 4.0], [-1.0], [-1, 1]]
#30	['P-01', 'P-03', 'D-01', 'S-01']	[[2.0, 3.0], [14.0, 15.0], [-1.0], [-1, 1]]
#31	['P-02', 'P-03', 'D-01', 'S-01']	[[3.0, 4.0], [14.0, 15.0], [-1.0], [-1, 1]]
#32	['P-01', 'P-02', 'P-03', 'D-01', 'S-01']}	[[2.0, 3.0], [3.0, 4.0], [14.0, 15.0], [-1.0], [-1, 1]]

Nomenclature

C Combinations

F Flexibility

gcd Greatest common divisor

N Total number of thermal management units in the district heating network being analysed

n n-th energy unit in the district heating network being analysed

Q Heat, or thermal power range (MW)

st Structural combination of units (i.e., simultaneous operation of several units)

T Temperature

Greek symbols

Δ step or increment

$\sum$ summation

Ω combinatorial multiplicity of the district heating network being analysed

Subscripts and superscripts

D thermal power demand range

d thermal power demand

j a particular combination (structural or operational) of thermal units in a district heating network

min minimal

max maximal

op operational

st structural

References

[1] H. Chandler, Harnessing variable renewables: A Guide to the Balancing Challenge. 2011. [Online]. www.oecd.org/publications/harnessing-variable-renewables-9789264111394-en.htm

[2] M. R. M. Cruz, D. Z. Fitiwi, S. F. Santos, and J. P. S. Catalão, “A comprehensive survey of flexibility options for supporting the low-carbon energy future,” Renew. Sustain. Energy Rev., 97 (2018), 338–353.

[3] C. Brunner, G. Deac, S. Braun, and C. Zöphel, “The future need for flexibility and the impact of fluctuating renewable power generation,” Renew. Energy, vol. 149, pp. 1314–1324, 2020.

[4] M. Z. Degefa, I. B. Sperstad, H. Sæle, Comprehensive classifications and characterizations of power system flexibility resources, Electr. Power Syst. Res., vol. 194 (2021), 107022.

[5] H. Golmohamadi, K. G. Larsen, P. G. Jensen, I. R. Hasrat, Integration of flexibility potentials of district heating systems into electricity markets: A review, Renew. Sustain. En. Rev., 159 (2020).

[6] J. Hennessy, H. Li, F. Wallin, and E. Thorin, “Flexibility in thermal grids: A review of short-term storage in district heating distribution networks,” Energy Proc., 158 (2019), 2430–2434.

[7] A. Hammer, C. Sejkora, and T. Kienberger, “Increasing district heating networks efficiency by means of temperature-flexible operation,” Sustain. Energy, Grids Networks, 16 (2018), 393–404.

[8] W. Wang et al., “Combined heat and power control considering thermal inertia of district heating network for flexible electric power regulation,” Energy, vol. 169, pp. 988–999, 2019.

[9] Y. Zhang, P. Johansson, A. Sasic Kalagasidis, Feasibilities of utilizing thermal inertia of district heating networks to improve system flexibility, Appl. Therm. Eng., 213 (2022), 118813.

[10] J. Vivian, D. Quaggiotto, and A. Zarrella, “Increasing the energy flexibility of existing district heating networks through flow rate variations,” Appl. Energy, 275 (2020), 115411.

[11] A. Gravelsins, I. Pakere, A. Tukulis, and D. Blumberga, Solar power in district heating. P2H flexibility concept, Energy, 181 (2019), 1023–1035.

[12] H. Schrammel, J. Kelz, W. Gruber-Glatzl, C. Halmdienst, J. Schröttner, I. Leusbrock, Increasing flexibility towards a virtual district heating network, Energy Reports, 7 (2021), 517–525.

[13] P. Li et al., “Operational flexibility of active distribution networks: Definition, quantified calculation and application,” Int. J. Electr. Power Energy Syst., 119 (2020), 105872.

[14] M. H. Abokersh et al., Flexible heat pump integration to improve sustainable transition toward 4th generation district heating, Energy. Conv. Manag., 225 (2020), 113379.

[15] Z. Ma, A. Knotzer, J. D. Billanes, and B. N. Jørgensen, “A literature review of energy flexibility in district heating with a survey of the stakeholders’ participation,” Renew. Sustain. Energy Rev., 123 (2020), 109750.

Qualitative comparison of on-site production of hydrogen and its synthesis products for steel processing industry

Gabriela Zabik[a], Felix Birkelbach[b], René Hofmann[c]

[a] TU Wien, Vienna, Austria, gabriela.zabik@tuwien.ac.at, CA,
[b] TU Wien, Vienna, Austria, felix.birkelbach@tuwien.ac.at,
[c] TU Wien, Vienna, Austria, rene.hofmann@tuwien.ac.at

Abstract:
Decarbonizing high temperature heat in industrial processes is challenging as there are only few alternative fuels to reach the necessary temperatures. In steel mills the material must be heated up to 1250 °C before hot rolling of steel. Currently, this energy-intensive step is done in steel reheating furnaces fueled with natural gas. Synthetic fuels such as green hydrogen, synthetic methane and green ammonia are possible alternatives for substituting the current polluting energy carrier and in many future climate strategies considered as a crucial component for achieving greenhouse gas neutrality. In this paper, we present options for on-site production of synthetic fuels for steel mills and discuss them by a qualitative approach. Specifically, we investigate hydrogen, synthetic methane and ammonia. We consider state of the art technologies and apply them to a real-world use case from the steel processing industry in Austria. We point out the benefits of on-site generation of synthetic fuels as opposed to external supply in the case of steel mills. Depending on technology, we discuss possibilities for heat integration, implementation of carbon dioxide looping and efficiencies of the systems. We highlight the significant increase in the demand for electrical energy. Further, we discuss challenges of combustion in relation to nitrogen emissions, combustion behavior and effects on steel quality. Our results show hydrogen to be advantageous in many aspects when considering a fuel switch in steel mills with on-site generation. But also we identify synthetic methane as an interesting option that should be further examined.

Keywords:
steel processing industry, on-site synthetic fuel production, hydrogen, synthetic methane, ammonia.

1. Introduction

The use of alternative fuels such as hydrogen, synthetic natural gas (SNG) and ammonia offers significant potential for decarbonizing industrial energy systems. These fuels can serve as an energy source for power plants or be utilized to produce heat directly for industrial processes. The first stage in generating synthetic fuels via the green route involves producing hydrogen from renewable electricity. The conversion of electricity into hydrogen is energy- and cost-intensive. Given that the demand for electricity in general will increase strongly in the future and given that the availability of renewable electricity is finite, it is crucial to carefully evaluate the most appropriate applications for these fuels. For high temperature processes exceeding 1200 °C, where electrification is not always a viable option, synthetic fuels can provide a suitable alternative and should be prioritized for these applications.

In Austria, the metal industry, particularly steel production, accounted for 61 % of the greenhouse gas emissions generated by the entire industrial sector [1]. Hot rolling of steel is one of the major energy consumers in the iron and steel production process chain, with energy consumption of around 1.5 to 3 gigajoules per ton of crude steel [2]. The main function of the hot rolling mill is to reheat steel blanks, called billets, above the recrystallization temperature and roll them thinner and longer through successive rolling stands. The billets are heated to about 1250 °C in industrial furnaces, mainly using natural gas as the primary energy source for heating [3]. The furnace for heating the billets is the major energy consumer in the rolling process and has a big impact on costs and emissions of the product. [2]

To date, only little literature is available concerning alternative fuels for steel reheating furnaces. Schmitz et al. [4] conducted a study on the reduction of CO_2 emissions from hydrogen-fired reheating furnaces, which considered the electricity generation mix. Their findings indicated a substantial potential for lower CO_2 emissions when compared to natural gas-fired furnaces. Similarly, Johansson [5] examined the economic feasibility of using bio-synthetic natural gas (bio-SNG) derived from biomass instead of LPG as a fuel source

for reheating furnaces. The results of this study indicated that the use of bio-SNG was not economically viable. Niska et al. [6] investigated solid biofuels from forest products and found problems arising from ash deposition.

Potentials and challenges of alternative fuels with on-site generation are not explored. To determine the feasibility of on-site synthetic fuel production for steel mills, an evaluation must consider not only quantitative results obtained from simulations, but also qualitative factors such as combustion, safety concerns, technical feasibility or heat integration. This study seeks to assess the most suitable technologies for different alternative fuel productions, specifically hydrogen, SNG and ammonia, based on the aforementioned factors, and to identify the factors that influence the suitability of each option. It highlights the potentials and challenges associated with on-site generation of synthetic fuels and demonstrates the circumstances under which on-site generation is viable.

2. Use Case

A company from the steel processing industry located in Styria, Austria, serves as a use case. The steel mill processes delivered steel billets through hot-rolling, heat-treatment and mechanical processing. The main product is peeled bar steel for the automotive industry. The billets are heated to a rolling temperature of about 1250 °C using a walking hearth furnace powered by natural gas. The furnace is heated by numerous top and side burners, which enable homogeneous heat transfer along the length and width of the furnace.

The steel mill typically operates for one or two eight-hour shifts during weekdays, Monday through Friday. During idle times, the walking hearth furnace is ramped down to a user-defined temperature. The energy demand for the steel reheating is about 360 kWh per tonne steel. Detailed process control data of the furnace are available. The steel mill is located in a residential area and due to the presence of an outdated electric arc furnace, the maximum power connection to the steel mill is 30 MW.

3. Concepts for on-site generation of synthetic fuels

In this section, we investigate various options for on-site generation of synthetic fuels such as hydrogen, SNG and ammonia, and provide an in-depth analysis of the associated technologies, storage methods, combustion processes, influence on steel quality, safety considerations, costs and efficiencies. By presenting a comprehensive overview of these important factors, we aim to explore the potentials and challenges of on-site generation of these alternative fuels for steel mills.

3.1. Option 1: Hydrogen

The production of green hydrogen involves the electrolysis of water to split it into hydrogen and oxygen gases. Renewable electricity is used to power the electrolysis unit. There are three main electrolysis technologies available: alkaline water electrolysis (AWE), polymer electrolyte membrane (PEM) electrolysis and solid oxide electrolyzer cell (SOEC). These technologies differ in various aspects, such as their dynamics, efficiency, temperature and pressure levels, technological advancements, and lifetime. AWE are the most advanced electrolysis technology, but they cannot respond well to load changes. Response to load changes are the main advantage of PEM. SOEC is a high temperature electrolysis which can be coupled with an excess heat source. This results in a high efficiency; however, SOEC technology is still in development stage. [8] [9]

Storage of hydrogen is crucial for on-site generation and mainly serves to decouple the operation of electrolysis and steel reheating. Storage of hydrogen presents challenging problems due to its light weight and gaseous nature. Several hydrogen storage options are available, including compressed gas storage, liquefaction, absorption (metal hydrides) and adsorption storage. Liquefaction of hydrogen demands a high amount of energy, approximately 30 to 40 percent of the energy content of hydrogen [9], and is mostly used for high-purity applications in the chemical industry and aerospace applications [10]. Absorption storage have low sorption and desorption kinetics and cannot be operated very dynamically. Adsorption storage operate at very low temperatures and require a lot of energy. [9] Therefore, compressed gas storage is considered the most suitable for our specific use case.

Compressed hydrogen storage systems can operate at pressures up to 700 bar, which requires the use of compressors to attain the required ultimate pressure. The process of compressing hydrogen also causes a significant amount of energy consumption, equivalent to 13-18 percent of the lower heating value of hydrogen. [9]. Furthermore, the negative Joule Thomson effect of hydrogen must be taken into account. During compression, hydrogen undergoes a cooling effect, which raises concerns regarding the potential for pressure vessel materials to be damaged if the temperature drops too low. Conversely, when hydrogen is relaxed, it undergoes a warming effect [11].

Figure 1 shows the layout of an on-site hydrogen generation system. The setup includes an electrolysis unit, a compressor, hydrogen and oxygen storage and a reheating furnace. The oxygen produced as a byproduct

during electrolysis is also stored and can be utilized for combustion. Moreover, the steel reheating furnace produces excess heat.

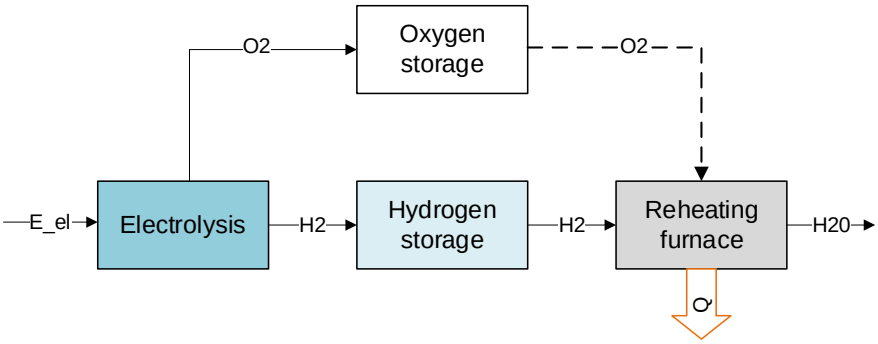

Figure 1. System hydrogen.

Hydrogen is well suited for generating high temperature heat due to a high flame temperature. However, there are significant differences between the combustion of hydrogen and natural gas. Due to its higher flame temperature, less fuel is required to generate the same amount of heat, resulting in less combustion air needed and lower convection within the combustion chamber. This must be considered in the process control when operating the furnace. [12]

Hydrogen can be burned with either air or oxygen. Combustion with air results in higher NOx emissions compared to natural gas combustion because the higher flame temperature (~2000 °C) produces more thermal NOx. Combustion with oxygen leads to lower energy input (approximately 30 %) and no NOx emissions; however, safety concerns regarding explosions and even lower convection due to the higher flame temperature (~2700 °C) make it challenging. Moreover, adaptation of the furnace is more expensive. [13] [12] [14]

Safe use and handling of hydrogen poses some unique challenges. Easy leaking, low ignition energy and possible damaging influence of equipment materials must be taken into account [10]. Scale formation on steel billets increases by 12 percent [15].

3.2. Option 2: Synthetic natural gas

Two main processes to produce synthetic natural gas (SNG) are catalytic methanation (CM) and biological methanation (BM). Methanation is a chemical reaction in which hydrogen and carbon dioxide and/or carbon monoxide, are converted into methane and steam with the aid of a catalyst or microorganisms. Catalytic methanation uses various metals as catalysts while biological methanation uses microorganisms as catalysts. Equation (1) shows the reaction equation for the synthesis of SNG:

$$CO_2 + 4\,H_2 \leftrightarrow CH_4 + 2\,H_2O \quad (1)$$

The CM unit typically operates within the temperature range of 300 to 550 °C and at a pressure of approximately 10 bar. The exothermic reaction involved in catalytic methanation generates a substantial amount of heat. The fixed-bed regenerator is the most commonly used reactor type for this process. In contrast, the biological methanation process operates at lower temperatures of 30 to 70 °C and at pressures ranging from 1 to 10 bar. Generally, larger reactor sizes are required to achieve high conversion efficiency. Both CM and BM units have good load response characteristics, although CM has a minimum load requirement of 40 percent and must maintain a standby temperature of 200 °C. The efficiency of the CM unit can be improved through heat integration. The catalyst used in CM is sensitive to impurities, whereas microorganisms utilized in BM are generally less sensitive. [16]

Figure 2 illustrates the arrangement of the system for SNG production. The SNG system consists of several components, including electrolysis, hydrogen and oxygen storage, methanation unit, and SNG storage. In addition, a carbon capture system is installed, which consists of an absorber and desorber. The CO2 separated from the flue gas is utilized for the methanation unit. Prior to absorption, the flue gas must undergo cooling through a heat exchanger, which generates excess heat. Oxygen can also be stored and utilized for combustion.

As previously mentioned, catalytic methanation produces excess heat, which can be employed for high-temperature electrolysis. The excess heat generated from the furnace can be utilized for the standby mode of the catalytic methanation unit or for high-temperature electrolysis utilizing SOECs. The excess heat produced during the operation mode of catalytic methanation can be also used for high-temperature electrolysis. Overall, the SNG system with carbon capture has the potential to utilize excess heat generated during various stages of the process to improve its overall efficiency. However, due to the two conversion steps involved, the process efficiency is lower, and additional space is required for the extra unit.

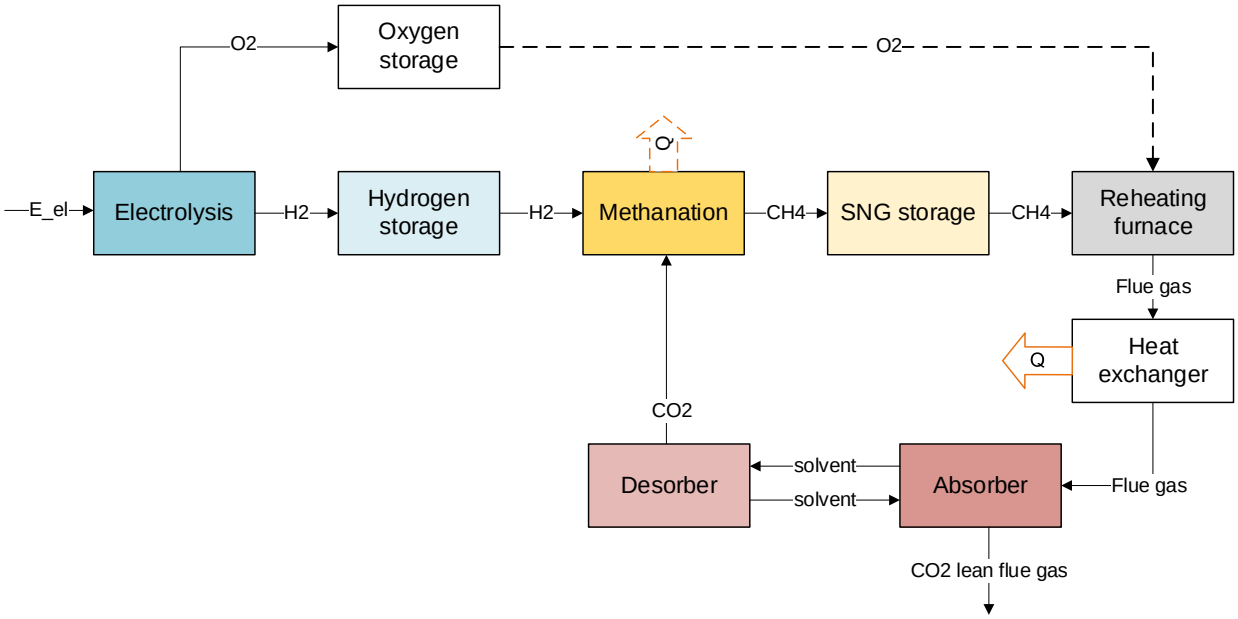

Figure 2. System SNG.

It is assumed that the combustion of SNG is similar to combustion of natural gas, and therefore no modifications to the furnace or process control are necessary.

SNG storage is less challenging than hydrogen storage due to the higher energy content per unit volume. Existing infrastructure for storage and pipeline transportation can be used for SNG. The pressures required for storage are significantly lower, resulting in negligible energy demands for storing SNG. Furthermore, lower storage pressures imply less strict safety requirements. The quality of steel and scale formation is not expected to differ significantly between natural gas and SNG.

3.3. Option 3: Ammonia

Ammonia today is mainly used for fertilizer, but is it an interesting option as an energy source for the future. Due to the high flame temperature, it is practicable to generate high temperature heat. Its main advantage is the easier storage of ammonia compared to hydrogen. For green ammonia, firstly hydrogen is produced through an electrolysis, additionally nitrogen is produced through an air separation unit and then hydrogen and nitrogen are processed into ammonia with the Haber Bosch process, according to Eq. (2): [17]

$$N_2 + 3\,H_2 \leftrightarrow 2\,NH_3 \tag{2}$$

More recently, ammonia is discussed as a fuel for generating heat for industrial applications. In the shipping sector it is seen as a promising alternative due to its stability and low transportation costs. However, ammonia combustion has disadvantages, including low burning velocity and high fuel nitrogen oxides production. To mitigate these issues, a blend of hydrogen or methane with ammonia can be used. Increased hydrogen proportion in the fuel mix leads to an increase in burning velocity, but also more NOx emissions. However, adding methane to the mix not only increases the burning velocity but also reduces the NOx emissions, making it a viable alternative.[18] [12]

Figure 3 shows the layout of the system ammonia. It consist of an electrolysis unit, hydrogen and oxygen storage, Air separation unit, Haber Bosch plant, ammonia storage and a reheating furnace. Excess heat is

generated by the Haber Bosch unit as well as by the reheating furnace. As combustion of ammonia with pure oxygen is not performed, the obtained oxygen is not used within the system.

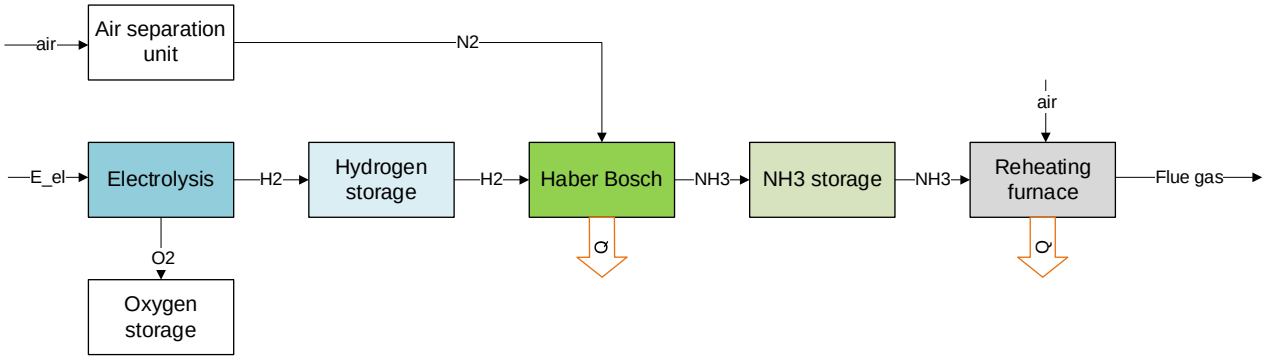

Figure 3. System Ammonia.

3.4. System specifications

While the focus of this paper is on qualitative comparison and analysis, basic evaluations of efficiencies, investment costs, and specific energy demand were also performed to provide a comprehensive overview of the subject and provide valuable insights. Consequently, Table 1 presents the summarized values for investment costs and efficiencies, which were utilized in further calculations.

Table 1. Investment costs and efficiencies of all components of the systems. [19]–[23]

Component	CAPEX	Efficiency, %
AWE	1400 €/kW_{el}	0.65
PEM	1800 €/kW_{el}	0.63
SOEC	2700 €/kW_{el}	0.81
Compressor + H2 storage	33 €/kWh_{H2}	0.85
Hydrogen burner	63.32 €/kW_{therm}	-
Catalytic methanation	750 €/kW_{SNG}	0.75*, 0.8**
Biological methanation	1050 €/kW_{SNG}	0.78*, 0.9**
SNG storage	33 €/kWh_{SNG}	1
CO2 storage	33 €/kWh	1
Carbon capture system	40 €/t_{CO2}	
Ammonia plant (ASU, Haber Bosch, NH3 storage)	850 €/t_{NH3}	0.85

*in relation to the calorific value, **conversion efficiency

For calculations of the investment costs, the approximate capacities of the plants were determined through a small optimization problem (MILP) using data from our use case. These capacity sizes are summarized in the Table 2 were used for further calculations. In the case of SNG and ammonia, the hydrogen storage serves as a buffer between electrolysis and methanation unit and is smaller than the storage of the hydrogen system.

Table 2. Capacities of the plants.

Plant	System hydrogen	System SNG	System ammonia
Electrolysis output	7 MW	8.75 MW	8.25 MW
Hydrogen storage size	35 MWh	10 MWh	10 MWh
Methanation output	-	7 MW	-
SNG storage size	-	35 MWh	-
Haber Bosch output	-	-	7 MW
NH3 storage size	-	-	35 MWh

4. Evaluation of concepts for alternative-fuel production

4.1. Qualitative discussion

There is no one-size-fits-it-all solution for substituting natural gas in steel mills. The suitability of the different alternative options depends on various factors. Important factors are space availability, location of the steel mill, environmental regulations, maximum power connection, integration of renewable energies, production schedule and energy demand for production. All these aspects will be discussed in the following.

The preconditions for on-site generation concepts include the sufficient space, a power connection capable of providing at least the same amount of power as the electrolysis unit, and the infrastructure to store hydrogen safely on premise. Additionally, integration with the company's renewable energy sources is advantageous.

For all alternative fuel options, out of the three electrolysis concepts, the Solid Oxide Electrolysis Cell (SOEC) exhibits the highest theoretical efficiency due to the availability of excess heat from the reheating furnace, which is at approximately 800°C without air preheating. However, the technology readiness level of SOEC remains below that of Proton Exchange Membrane (PEM) and Alkaline Water Electrolysis (AWE). Furthermore, SOEC typically operates at a constant level, so it depends on the scheduling of the rolling mill and energy prices. The suitability of PEM electrolysis depends on the operation of the electrolyzer, which may require dynamic operation due to fluctuating renewable energies, energy prices or irregular production schedules. AWE, even though the most advanced electrolysis technology, is likely unsuitable for this particular application due to a lower efficiency and static operation.

Hydrogen: When considering hydrogen as a fuel for steel reheating furnaces, on-site generation presents several advantages. First, it eliminates the challenges associated with hydrogen transport. Additionally, the production of oxygen as a byproduct of the electrolysis process prevents the need for costly external oxygen supply. Oxygen use enables more energy-efficient production and reduces the required capacities for electrolysis and hydrogen storage. However, utilizing oxygen for combustion requires more extensive modifications to the furnace compared to air combustion. Nevertheless, existing steel reheating furnaces can be retrofitted for the use of hydrogen. Further, additional adaptations for process control and investigations of scale formation and steel quality are required. Using hydrogen as a fuel in steel reheating furnaces does not produce CO_2 emissions, as long as electricity is obtained from renewable sources.

SNG: Due to the two conversion steps involved, the process efficiency is lower, and additional space is required for the extra methanation unit. Nevertheless, the easier handling of the fuel and its combustion behavior, which is very similar to natural gas, represent the main benefits of this approach. The SNG system does not necessitate any modifications to the furnace or process control, and the quality of the steel and scale formation remain the same.

The SNG system, coupled with carbon capture, has the potential to utilize excess heat generated during various process stages to improve its overall efficiency. To evaluate the performance of the SNG concept, simulations that take heat integration into account are necessary. The performance of the SNG system primarily depends on production capacity and schedule, which enables efficient heat integration. In addition, the oxygen produced by the electrolysis can be utilized for combustion, representing another advantage of the on-site generation concept. When comparing catalytic and biological methanation, the latter method has the advantage of being less sensitive to CO_2 source impurities; however, the reactor needs more space.

Ammonia: The use of ammonia combustion for industrial applications, including steel reheating furnaces, remains largely unexplored. Also, there is a lack of research investigating the effects of ammonia combustion on steel. The use of ammonia as a fuel presents significant challenges in relation to NOx emissions and burning velocity, making it a less viable option compared to hydrogen. Moreover, as the primary advantage of ammonia over hydrogen is its ease of transport, and small-scale Haber Bosch plants are not common, on-site generation may not be advantageous. Additionally, the generation of nitrogen from an additional air separation unit, and the oxygen obtained from electrolysis that is not used pose further disadvantages. While ammonia combustion remains an interesting option for industrial applications, extensive research and development is required before its widespread use. Generally, it may be better suited for external supply.

4.2. Quantitative results

In this section, results of some basic calculations are presented. Figure 4 shows the efficiencies of the systems with all possible combinations of technologies. It is evident that the hydrogen system achieves the highest efficiency. The SNG system shows the lowest efficiencies, with no significant difference between catalytic and biological methanation. The system ammonia lies in between.

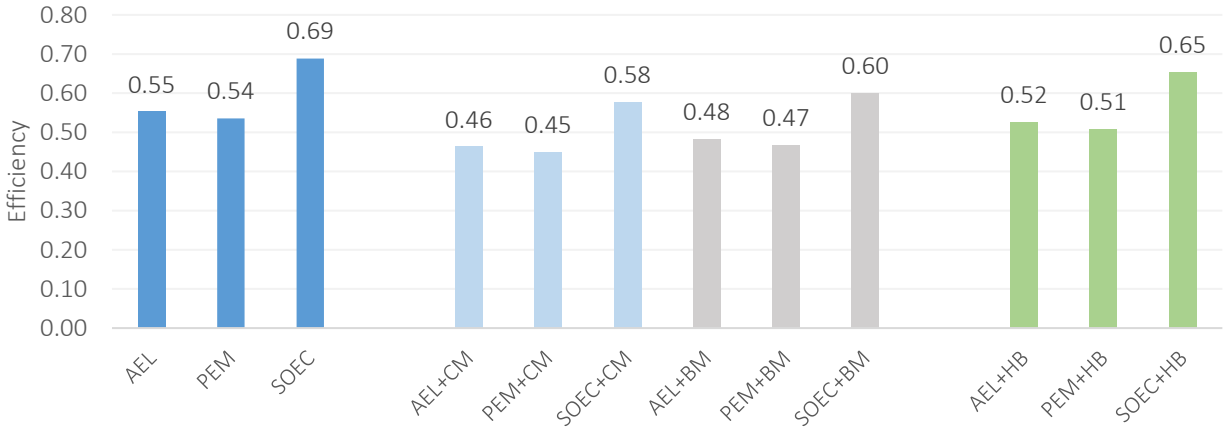

Figure 4. Efficiencies for the considered system configurations.

Figure 5 illustrates the total energy demand of the process chain for reheating of one tonne steel, for the different systems and depending on the combustion type (air/oxygen). Using oxygen for combustion can significantly lower the energy demand.

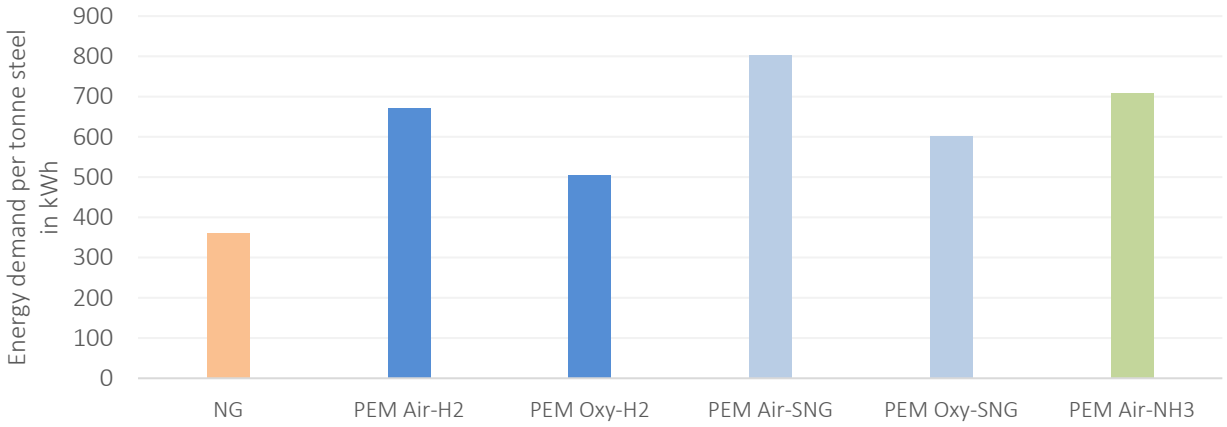

Figure 5. Energy demand per tonne steel reheated for air and oxygen combustion of different energy carriers.

Figure 6 gives an overview of investment costs for the different systems. The SNG system has the highest investment costs, primarily because of the additional costs for the carbon capture plant. Main investment costs in all systems are associated with the electrolysis unit, with SOEC being the most expensive one.

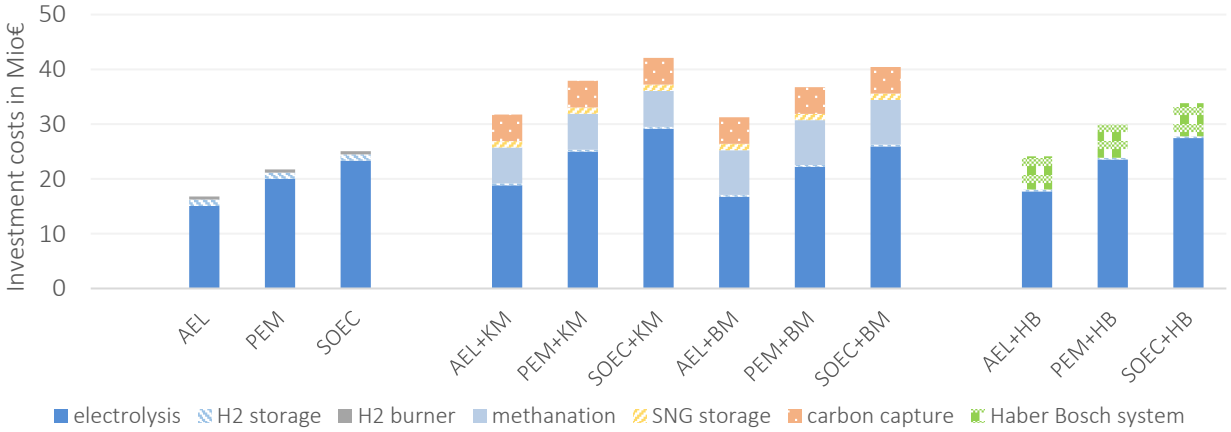

Figure 6. Investment costs for the considered system configuration.

5. Conclusion

In this paper, we presented concepts for on-site generation of hydrogen, synthetic natural gas (SNG) and ammonia, and conducted a qualitative comparison underpinned by basic estimates regarding investment costs and efficiencies. We discussed factors like combustion behaviour, heat integration, effects on steel quality. Our analysis revealed that on-site generation of hydrogen offers benefits related to transport, use of oxygen and low CO_2 emissions. For SNG, easy handling of the fuel and numerous possibilities of heat integration were identified as advantages. We found ammonia not to be suitable for an on-site generation concept. Also there are several challenges in combustion of ammonia, mainly related to low burning velocity and high NOx emissions. Overall, the production of synthetic fuels leads to a significant increase in electricity demand, requiring the company to have a sufficiently high power connection. If on-site generation will ever be economically viable will heavily depend of future natural gas prices and emission regulations.

Acknowledgments

The research presented is part of the research project LEOPOLD, funded by the Austrian research promotion agency (FFG) (Project number 35833857). The authors would like to thank all project partners for their contributions.

Nomenclature

Acronyms

AWE	Alkaline water electrolysis
BM	Biological methanation
CM	Catalytic methanation
HB	Haber Bosch process
NG	Natural gas
PEM	Proton exchange membrane
SOEC	Solid oxide electrolyzer cell
SNG	Synthetic natural gas

References

[1] umweltbundesamt, „Austria's national inventory report 2022". 2022.

[2] K. He und L. Wang, „A review of energy use and energy-efficient technologies for the iron and steel industry", *Renew. Sustain. Energy Rev.*, Bd. 70, S. 1022–1039, Apr. 2017, doi: 10.1016/j.rser.2016.12.007.

[3] The Energy and Resources Institute New Delhi, „Energy Efficient Technologies and Best Practices in Steel Rolling Industries". 2014.

[4] N. Schmitz, L. Sankowski, F. Kaiser, C. Schwotzer, T. Echterhof, und H. Pfeifer, „Towards CO2-neutral process heat generation for continuous reheating furnaces in steel hot rolling mills – A case study", *Energy*, Bd. 224, S. 120155, Juni 2021, doi: 10.1016/j.energy.2021.120155.

[5] M. T. Johansson, „Bio-synthetic natural gas as fuel in steel industry reheating furnaces – A case study of economic performance and effects on global CO2 emissions", *Energy*, Bd. 57, S. 699–708, Aug. 2013, doi: 10.1016/j.energy.2013.06.010.

[6] J. Niska, C.-E. Grip, und P. Mellin, „Investigating Potential Problems and Solutions of Renewable Fuel Use in Steel Reheating Furnaces", 2013.

[7] S. A. Grigoriev, V. N. Fateev, D. G. Bessarabov, und P. Millet, „Current status, research trends, and challenges in water electrolysis science and technology", *Int. J. Hydrog. Energy*, Bd. 45, Nr. 49, S. 26036–26058, Okt. 2020, doi: 10.1016/j.ijhydene.2020.03.109.

[8] E. Zoulias, E. Varkaraki, N. Lymberopoulos, C. Christodoulou, und G. Karagiorgis, „A Review on Water Electrolysis", *TCJST*, Bd. 4, S. 41–71, Jan. 2004.

[9] M. R. Usman, „Hydrogen storage methods: Review and current status", *Renew. Sustain. Energy Rev.*, Bd. 167, S. 112743, Okt. 2022, doi: 10.1016/j.rser.2022.112743.

[10] Y. S. H. Najjar, „Hydrogen safety: The road toward green technology", *Int. J. Hydrog. Energy*, Bd. 38, Nr. 25, S. 10716–10728, Aug. 2013, doi: 10.1016/j.ijhydene.2013.05.126.

[11] J.-Q. Li, Y. Chen, Y. B. Ma, J.-T. Kwon, H. Xu, und J.-C. Li, „A study on the Joule-Thomson effect of during filling hydrogen in high pressure tank", *Case Stud. Therm. Eng.*, Bd. 41, S. 102678, Jan. 2023, doi: 10.1016/j.csite.2022.102678.

[12] X. Xiyao, X. Sun, C. Wang, und Y. Hu, „Understanding the Hydrogen/Ammonia Combustion Behaviours under Air and Oxygen Environments in a Combustion Chamber", Volume 20: Sustainable Energy Solutions for a Post-COVID Recovery towards a Better Future: Part III, preprint, Feb. 2022. doi: 10.46855/energy-proceedings-9312.

[13] F. A. D. Oliveira, J. A. Carvalho, P. M. Sobrinho, und A. de Castro, „Analysis of oxy-fuel combustion as an alternative to combustion with air in metal reheating furnaces“, *Energy*, Bd. 78, S. 290–297, Dez. 2014, doi: 10.1016/j.energy.2014.10.010.
[14] S. H. Han, Y. S. Lee, J. R. Cho, und K. H. Lee, „Efficiency analysis of air-fuel and oxy-fuel combustion in a reheating furnace“, *Int. J. Heat Mass Transf.*, Bd. 121, S. 1364–1370, Juni 2018, doi: 10.1016/j.ijheatmasstransfer.2017.12.110.
[15] C. Uzor, „CHARACTERISTICS OF HYDROGEN FUEL COMBUSTION IN A REHEATING FURNACE“, thesis, Purdue University Graduate School, 2022. doi: 10.25394/PGS.21711737.v1.
[16] K. Baer, F. Mörs, M. Götz, und F. Graf, „Vergleich der biologischen und katalytischen Methanisierung für den Einsatz bei PtG-Konzepten“, *Gwf - GasErdgas*, Bd. 156, S. 466–473, Juli 2015.
[17] Seok Young Lee, In-Beum Lee, und Jun-Hyung Ryu, „A Preliminary Techno-Economic Analysis of Power to Ammnonia Processes Using Alkaline Electrolysis and Air Separation Unit“, gehalten auf der International Conference on Applied Energy, 2019. doi: 10.46855.
[18] W. S. Chai, Y. Bao, P. Jin, G. Tang, und L. Zhou, „A review on ammonia, ammonia-hydrogen and ammonia-methane fuels“, *Renew. Sustain. Energy Rev.*, Bd. 147, S. 111254, Sep. 2021, doi: 10.1016/j.rser.2021.111254.
[19] Katrin Salbrechter, Markus Lehner, und Sascha Grimm, „Standardisierte Biogasaufbereitung und Methanisierung“, gehalten auf der 12. Internationale Energiewirtschaftstagung an der TU Wien, 2021. [Online]. Verfügbar unter: https://scholar.googleusercontent.com/scholar?q=cache:q_vteC0RWWoJ:scholar.google.com/+Standardisierte+Biogasaufbereitung+und+Methanisierung&hl=de&as_sdt=0,5&as_ylo=2017
[20] J. Gorre, F. Ortloff, und C. van Leeuwen, „Production costs for synthetic methane in 2030 and 2050 of an optimized Power-to-Gas plant with intermediate hydrogen storage“, *Appl. Energy*, Bd. 253, S. 113594, Nov. 2019, doi: 10.1016/j.apenergy.2019.113594.
[21] Institute for Sustainable Process Technology, „Gigawatt green hydrogen plant“, Institute for Sustainable Process Technology, 2020.
[22] S. Stießel, „Entwicklung eines Referenzmodells zur multikriteriellen Bewertung von cross-industriellen Systemen“.
[23] P. Marocco, M. Gandiglio, D. Audisio, und M. Santarelli, „Assessment of the role of hydrogen to produce high-temperature heat in the steel industry“, *J. Clean. Prod.*, Bd. 388, S. 135969, Feb. 2023, doi: 10.1016/j.jclepro.2023.135969.

Energy and Exergy Analysis of a Biodiesel Plant

Flavia V. Barbosa[a], Paulo R. S. Mendes[b], Carlos Castro[c], Senhorinha F. C. F. Teixeira[d] and José C. F. Teixeira[e]

[a] MEtRICs R&D Center, University of Minho, School of Engineering, Guimarães, Portugal, flaviab@dem.uminho.pt
[b] MEtRICs R&D Center, University of Minho, School of Engineering, Guimarães, Portugal, a85297@alunos.uminho.pt
[c] MEtRICs R&D Center, University of Minho, School of Engineering, Guimarães, Portugal, ccastro@dem.uminho.pt
[d] ALGORITMI R&D Center, University of Minho, School of Engineering, Guimarães, Portugal, st@dps.uminho.pt
[e] MEtRICs R&D Center, University of Minho, School of Engineering, Guimarães, Portugal, jt@dem.uminho.pt

Abstract:

Despite the current push for full electrification of the transportation sector, the utilization of IC engines (either on their own or hybrid guise) will continue for the foreseeable future. This is even more evident in the freight industry and with construction equipment. Therefore, the use of alternative fuels is a vital stepping stone toward low-carbon transportation. Environmental regulations have been developing enormous interest in biodiesel as an alternating fuel, with the main objective of reducing emissions associated with the transportation sector. Biodiesel is a renewable fuel that is mainly produced from vegetable oils and animal fats. At an industrial scale, its production is an energy-intensive operation that contributes to the overall carbon footprint.
The present paper describes the energy and exergy analysis of an existing biodiesel plant. The facility applies used cooking oils and vegetable oils as raw materials and has an annual consumption of over 1,100 toe (as of 2021). The analysis identified the possibility of using biomass as a primary energy source for heat. Furthermore, the detailed analysis of the plant operation enables the identification of energy conservation measures that can reduce the electricity consumption and the pellet consumption by 29 tons a year.

Keywords:

Biodiesel; Energy; Exergy; Irreversibility; Thermodynamics.

1. Introduction

In recent decades, several concerns have arisen regarding the balance between energy consumption and sustainable, environmentally friendly, economically viable, and socially fair development. In this context, renewable energies started to play a leading role in order to reverse the worrying scenario of the possible depletion of fossil fuels (1). The energy consumption of society has contributed to the reduction of the existing reserves of coal, natural gas, and oil, and the ratio between consumption and production does not allow the continuous replenishment of these reserves, so depletion is inevitable (2). On the other hand, climate change is undoubtedly the greatest socio-environmental concern that the planet is facing today. Although burning fossil fuels is the main problem, it is also true that the increase in the volume of road traffic created by the world's dependence on transportation, particularly in large urban centers, has contributed on a large scale to the increase in pollutant emissions and energy consumption (3). In 2020, the total emissions of pollution gases emitted in Portugal (57.6 Mton CO_2) are estimated that 25% come from national transport, being the sector that consumed the largest amount of energy by year, around 32.6%, followed by industry (31.2%), domestic (19.5%), services (13.4%) and agriculture and fisheries (3.3%) (4).

To comply with the international goals to achieve carbon neutrality by 2050, renewable energy technologies have been at the top of the international discussion and several signs of progress have been conducted in this sector (5). However, no effective solution was implemented regarding the transportation sector and environmental regulations have been developing a huge interest in biodiesel as an alternating fuel, with the main objective of reducing hazardous emissions. In this context, it is believed that the replacement of fossil fuels by biofuels, such as biodiesel, can be a major contributor to the transportation sector (6). Currently, emphasis has been given to the study of bioethanol and biodiesel to replace gasoline and diesel respectively, since to use these biofuels it is not necessary to make major changes in road transportation (7). Biodiesel in particular is a biodegradable, non-toxic energy source synthesized from various raw materials, including man-made waste such as used oils and animal fats, which in contact with nature can cause major environmental

imbalances (8). According to the international energy agency (IEA) (7) biodiesel production has been gradually increasing, as shown in Figure 1 (a). Although insignificant, this increase tends to remain until 2025 with an estimated world production of 46 billion liters. Regarding the countries that lead the biodiesel production sector, data presented in Figure 1 (b) shows that in 2021, Indonesia was the world's largest producer of biodiesel with a total of 9.5 billion liters, followed by Brazil with 6.9 billion liters of biodiesel produced (6).

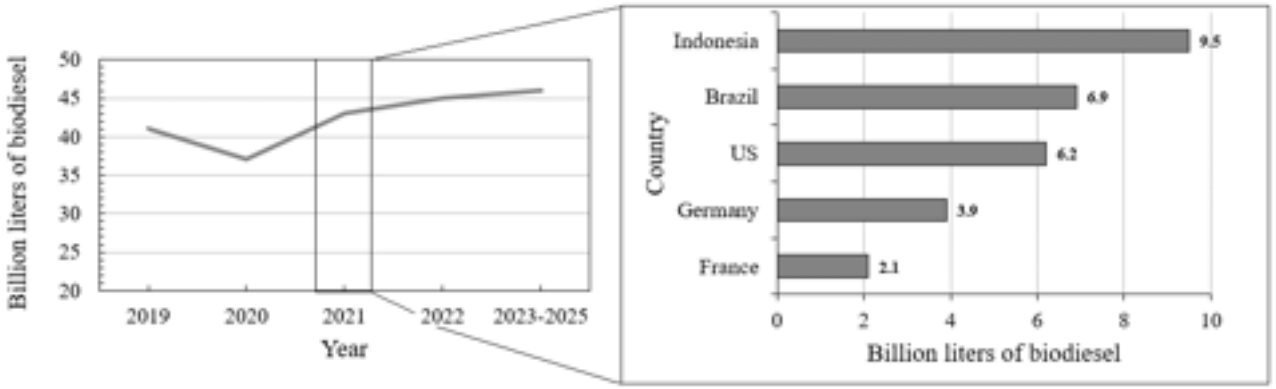

Figure 1. (a) World production of biodiesel; (b) Worldwide leading countries in biodiesel production in 2021.

Although biodiesel is pointed out as a solution for the transportation sector, the increased production worldwide has also led to an increase in the production of vegetable oils, as they are the main raw materials used for biodiesel production on an industrial scale. However, the high cost of biodiesel production, as a consequence of the high price of vegetable oils, is the biggest problem for its implementation and commercialization on a large scale, making biodiesel less economically competitive compared to diesel derived from petroleum [1]. To create alternatives, many methods have been explored to reduce this cost, one of which involves replacing vegetable oil with used cooking oils. Recycling frying oil as a biofuel not only removes a hazardous compound that is most of the time released to the environment but also allows the production of a renewable and less polluting source of energy (8,9).

From an industrial point of view, the biodiesel and conventional diesel production processes have almost equivalent efficiencies, with regard to the conversion of their raw materials into fuels (10). The opportunity to reduce the energy consumption in industrial plants, and therefore decrease the overall energy consumption of the process, allows for an intensification of the integration of biodiesel production on a large scale which could be very important for the dissemination of this fuel worldwide. In this context, this work focuses on an energy analysis carried out on a company in the biofuels sector in Portugal, more precisely, a company dedicated to the industrial production of biodiesel. Since the company is characterized by being an energy-intensive consumer, having consumed throughout 2021, 1120.46 toe, it is important to conduct an energy and exergy analysis of the plant in order to identify energy optimization solutions that can reduce the electrical and thermal energy consumption. Based on the identification of the processes involved in biodiesel production and the related products used for its production, the energy consumed and produced is estimated in this work. This allows to determine the efficiency of the process. However, energy analysis does not provide all the information needed to characterize the performance of the production process. Therefore, exergy analysis is useful to pinpoint the thermodynamic losses and inefficiencies (11). This study presents a methodology to determine energy and exergy efficiencies of biodiesel process production, which include both biodiesel and energy production. Moreover, solutions are presented to increase the energy performance of the biodiesel production process, highlighting the need to conduct a detailed thermodynamic analysis of biodiesel production plants to disseminate the use of this fuel in the transportation sector.

2. Theoretical Background

2.1. Biodiesel

Biodiesel is considered a biofuel, whose composition and properties comply with the European standard EN 14214 or the American standard ASTM D6751. It consists of a mixture of methyl esters of fatty acids formed by transesterification or esterification of vegetable oils (e.g. soybean, rapeseed, sunflower, and palm oils) or animal fats with methanol or ethanol, from various chemical or biological processes (12). From the chemical reaction between these raw materials, two products are obtained, an ester (biodiesel) and glycerol (also known as glycerin), which can be used, for example, by the pharmaceutical industry. The reaction is catalyzed by an acid or a base, depending on the characteristics of the oil and/or fat used. The reaction mechanism can be divided into three stages, where the triglyceride is sequentially converted to diglyceride, monoglyceride, and glycerol, in a sequence of three reversible reactions (12), as shown in Figure 2.

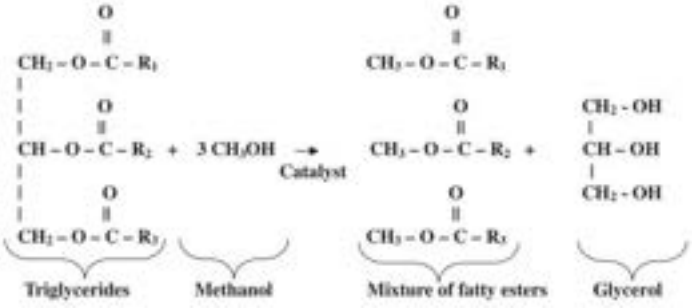

Figure 2. Methanolysis of triglyceride.

2.2. Mass and Energy Balance

The first law of thermodynamics is the main principle that governs the energy conservation principle of any system. The conservation of energy is closely linked to the mass conservation principle, stated by (13). In a steady state, the mass balance model of the biodiesel production process is expressed by Eq. (1).

$$\dot{m}_{in} = \dot{m}_{out} \tag{1}$$

Analogously, the energy balance results from the difference between the energy produced by a fuel and the energy required to obtain it (14), as expressed in Eq. (2) (15,16):

$$\dot{E}_{in} + \dot{Q} = \dot{E}_{out} \tag{2}$$

Except for the electrical energy, that was measured, the remaining forms of energy were calculated according to Eq. (3), as they do not contain any other form of energy other than the chemical energy of each compound.

$$\dot{E} = \dot{m}\, LHV \tag{3}$$

The heat supplied to the system comes from the burning of pellets, being $\dot{Q}$ expressed by Eq. (4).

$$\dot{Q} = \dot{m}\, LHV \tag{4}$$

2.3. Exergy Balance

While the majority of the chemical industry uses energy analysis to optimize their processes, this does not indicate that the energy is efficiently used (11). To determine if a process is thermodynamically efficient, entropy generation must be analyzed, the higher the entropy generation, the higher energy is degraded (17). This property can be estimated by exergy, which represents the useful amount of work that can be extracted from a system when taken into thermodynamic equilibrium with the environment. Exergy changes account for the irreversibility of a process that depends on entropy production. Consequently, this irreversibility can be obtained by the exergy analysis of the system. In this context, the exergy balance can be expressed in Eq. (5) (10).

$$\dot{\varepsilon}_{in} + \dot{\varepsilon}^{Q} = \dot{\varepsilon}_{out} + \dot{W} + \dot{I} \tag{5}$$

where subscripts *in* and *out* apply the same flows as the ones applied in the energy balance an $\dot{I}$ is the system's irreversibility.

The exergy of a system is composed of several elements, as presented in Eq. (6).

$$\dot{\varepsilon} = \dot{\varepsilon}^{ph} + \dot{\varepsilon}^{0} + \dot{\varepsilon}^{k} + \dot{\varepsilon}^{po} \tag{6}$$

where $\dot{\varepsilon}^{ph}$, $\dot{e}^{0}$ $\dot{\varepsilon}^{k}$ and $\dot{\varepsilon}^{po}$ are the physical, chemical, kinetic, and potential exergy, respectively.

In this study, only fluids with chemical energy (Eq. 7) are considered and all other forms of exergy are therefore neglected.

$$\dot{\varepsilon}^{0} = \dot{m}\, \varphi\, LHV \tag{7}$$

In Eq. (7), φ depends upon the chemical composition of the fuel, being considered approximately equal to 0.975 for liquids and gases and 1.07 for biomass (18,19).

2.4. Efficiency

In this study, two energy efficiencies are considered, the efficiency of the production of biodiesel, presented in Eq. (8), and the total energy efficiency of the process, expressed in Eq. (9).

$$\eta_{Bio} = \frac{\dot{E}_{Bio}}{(\dot{E}_{in} + \dot{P})} \quad (8)$$

$$\eta = \frac{\dot{E}_{Bio} + \dot{E}_{Gly}}{(\dot{E}_{in} + \dot{P})} \quad (9)$$

where $\dot{P}$ represents the pumping power. While the efficiency of biodiesel production, η_{Bio}, is obtained by the ratio between the biodiesel energy and the total energy consumed for its production, the efficiency of the process, η, takes into account the products that are collected from this process, biodiesel, and glycerine.

Regarding the exergetic efficiency, one can consider the rational efficiency for biodiesel production, expressed in Eq. (10), and the rational efficiency of the process, presented in Eq. (11).

$$\psi_{Bio} = \frac{\dot{\varepsilon}_{Bio}}{\dot{\varepsilon}_{in} + \dot{P}} \quad (10)$$

$$\psi = \frac{\dot{\varepsilon}_{Bio} + \dot{\varepsilon}_{Gly}}{(\dot{\varepsilon}_{in} + \dot{P})} \quad (11)$$

The rational efficiency of the production process is a measure of the process performance, being defined by the ratio between useful exergy output and the maximum input exergy. While ψ_{Bio} focuses on the biodiesel production process, ψ considers all the products obtained from this process.

3. Materials and Methods

3.1. Biodiesel Production Line

As previously mentioned, biodiesel is a product resulting from the transesterification of oils with an alcohol in the presence of an acid or alkaline catalyst. The biodiesel production process implemented in the industry where this study was conducted can be summarized in the flowchart shown in Figure 3.

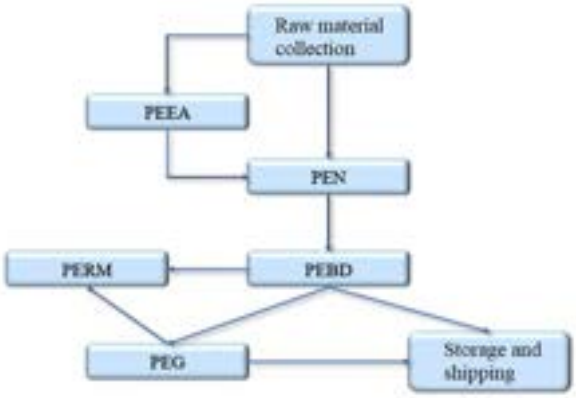

Figure 3. Biodiesel production process.

To ensure that the final product (biodiesel) meets the requirements, several process variables need to be controlled. The biodiesel to be shipped must have the parameters within the specifications, according to the European standard EN 14214. Some of the process parameters to be considered are the acid number (IA) and the percentage of free fatty acids (FFA) in the raw materials, residual raw materials (MPR), the degree of mixing between alcohol and triglycerides in the transesterification process as well as all operating temperatures and pressures.

The process begins with the collection of raw material that consists of waste oils. These oils are mainly wastes from the food industry (restaurants) or resulting from the oil refining industry. The incorporation of this type of waste as a raw material promotes industrial symbiosis and enhances the circular economy. The second stage begins with PEEA (Specific Acid Esterification Production Unit). The raw materials have characteristics that prevent them from being incorporated directly into PEBD (Specific Production of Biodiesel Unit), namely a high acidity index and high content of water, phosphorus, and other contamination. The high-acid MPR (IA > 10 mg/g and FFA > 5%) then need to go through an acid esterification process to be able to be incorporated into the PEN (Specific Neutralization Production Unit). The third phase consists of the pre-treatment of the low-acid MPR (IA < 10 mg/g and FFA < 5%) together with the MPR after the acid esterification process, which occurs in the PEN, to be ready to be incorporated into the PEBD. In the PEBD, biodiesel results from the transesterification of oils with methanol in the presence of a catalyst, sodium methylate. During this process, three reversible reactions take place. From the triglycerides (*TG*) of the oils, two intermediate components are formed, the diglycerides (*DG*) and the monoglycerides (*MG*). The reactions are as follows (12)-(14):

$$TG + CH_3OH \leftrightarrow DG + R_1COOCH_3 \quad (12)$$

$$DG + CH_3OH \leftrightarrow MG + R_2COOCH_3 \quad (13)$$

$$MG + CH_3OH \leftrightarrow GL + R_3COOCH_3 \quad (14)$$

where $R_{1,2,3}$ are organic radicals.

The global reaction, which characterizes the production of glycerol (*GL*) and biodiesel (R_3COOCH_3), is expressed by reaction (15).

$$TG + 3CH_3OH \leftrightarrow GL + 3R_3COOCH_3 \quad (15)$$

The crude glycerine produced in PEBD needs to be treated in order to be able to be exported. PEG is the glycerine treatment process that guarantees a minimum glycerol content of 75-80%. The methanol recovered from the PEBD and PEG (Specific Production of Glycerine Unit) processes needs to be purified (PERM - Specific Production of Methanol Rectification Unit) in order to be used again (> 98 %). Finally, both biodiesel and glycerine are stored in tanks to be later exported.

3.2. Specific Production of Biodiesel Unit

The biodiesel production unit is schematically represented in Figure 4. The process begins with the heating of neutral oils from the PEN (D-03) together with virgin vegetable oils from the D-05 by a plate heat exchanger and a tubular heat exchanger to a desired temperature. Then the raw material is mixed with methanol and sodium methylate, the catalyst. The mixture enters the R-3001 reactor (cavitation reactor) and the reaction takes place up to a percentage of methyl esters close to 85%. The products resulting from this reaction (biodiesel and glycerine) are sent to the D-06 decanter, where the glycerine is decanted and separated, going to the D-08. To simplify this operation, recirculation of the glycerine is conducted, i.e., part of the glycerine that leaves the D-06 goes back in to maintain the temperature and help with its separation (the greater the amount of glycerine, the greater the tendency for deposition). Biodiesel (light phase of D-06) is mixed again with the reagents and passes through the cavitation reactor R-3002 where the formation of esters is completed. The products go to the D-07 and the glycerine is decanted into the D-09 accumulator.

In the production of biodiesel, using an alkaline catalyst, some amount of soap is always produced. Thus, once the transesterification reaction is completed, the excess catalyst and soap tend to be concentrated in the glycerine phase. However, there is always some amount of these constituents that remain in the biodiesel stage. This fact can cause problems in the follow-up of the process: the soaps remain in the process and can cause the clogging of the resins. To solve the problem, when the mixture reaches the D-10 accumulator, phosphoric acid is added keeping the pH controlled (close to neutral). Acidification aims to create conditions less favorable to the formation of soaps and to end the transesterification reaction. This is followed by Flash 1 at approximately 75 ºC and a pressure of 130 mbar, the methanol in the biodiesel is dried to 5000 ppm. Methanol is recovered to D-11 while biodiesel goes to D-15. In the resin basins (R-3003 and R-3004) occurs the final adsorption of glycerine which has sodium, methanol, and some impurities. Biodiesel leaves the resins for Flash 2 where, under more severe conditions of pressure and temperature, methanol drops to values within the European standard, EN 14214, below 2000 ppm. After physical filtration, the biodiesel goes to D-01/D-02. Subsequently, an antioxidant is added to the biodiesel, and this is transferred to the shipping tanks.

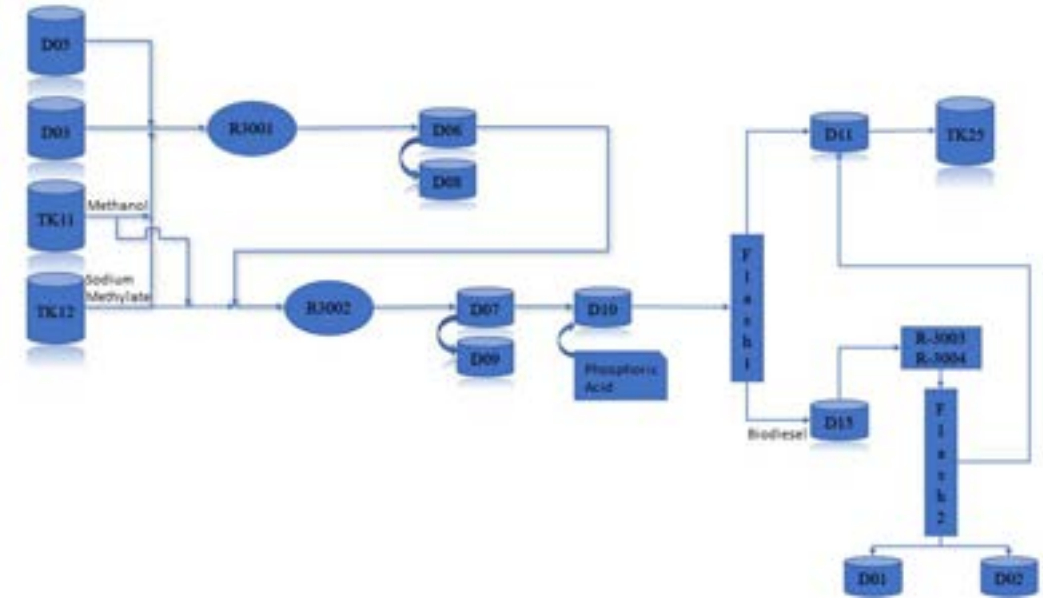

Figure 4. Scheme of the Specific Production of Biodiesel Unit.

4. Results and Discussion

4.1. Energy consumption and biodiesel production

Because of fluctuations in biodiesel production, energy consumption is not constant throughout the year. However, since biofuel production requires temperature control, the highest energy consumption is due to the heating and cooling operations. To better understand the energy needs in biodiesel production, it is essential to carry out an analysis of the history of energy consumption of the processes, which is divided into electricity consumption (electric motors for the pumps and chiller) and consumption of pellets (boiler). For this, the data referring to the year 2021 were used, as presented in Table 1.

Table 1. Typical energy consumption and biodiesel production in a year (2021).

Month	Pellets (ton)	Electricity (kWh)	Production of biodiesel (ton)
January	131.90	155,882.00	1,252.60
February	125.56	108,908.00	876.00
March	154.84	183,094.00	1,787.70
April	135.44	157,979.00	1,491.20
May	160.86	177,861.00	2,104.40
June	132.98	168,588.00	1,740.90
July	127.20	154,309.00	1,572.60
August	100.98	134,481.00	1,227.70
September	160.92	192,194.00	2,064.70
October	157.58	173,891.00	1,706.40
November	157.04	174,555.00	1,780.40
December	106.02	127,698.00	899.40
Total	**1,651.32**	**1,909,440.00**	**18,504.00**

To determine the energy consumption per ton of biodiesel produced, the consumption values are converted into toe to obtain a reference value in toe /ton of biodiesel, taking into account the thermodynamic and electrical conversion factors (1 toe = 41,868 MJ and 1 kWh = 215 $\times 10^{-6}$ toe) presented in Dispatch nº 17313/2008 (20). For calculation purposes, the lower heat value (LHV) of the pellets is considered equal to 18.0 MJ/kg. To determine the consumption of pellets in toe, Eq. (16) is used. On the other hand, the conversion of electrical energy consumption into toe is given by Eq. (17).

$$E_{\text{toe}} = \frac{m.\,\text{LHV}}{41.868} \tag{16}$$

$$E_{\text{toe}} = ec\,.\,215 \times 10^{-6} \tag{17}$$

where *m* is the mass in ton, the LHV is in MJ/kg and the *ec* corresponds to the electric consumption in kWh.

Regarding the energy consumption and using the values for 2021, it appears that the company is covered by the SGCIE (Portuguese Management System of Intensive Energy Consumption), since the total energy consumption exceeds 500 toe – 1120.46 toe (0.06 toe / ton biodiesel) – the company is considered an Intensive Energy Consumer (CIE).

Through the plot presented in Figure 5 (a), it is possible to observe the evolution of energy consumption throughout 2021. For the period under analysis, a significant variation in energy consumption over time is observed. Throughout January and February, the average flow rate of biodiesel produced was 2.7 tons/h, a value lower than the average flow rate seen in the rest of the year (3.5 tons/h). On the other hand, in February a stoppage of about 2 weeks due to a fire occurred. During the summer months, the company was once again stopped, for 3 weeks for the vacation period and in December the average flow rate of biodiesel produced was 2.4 ton/h due to a limitation in a pump. For these reasons, it is possible to perceive the existing variations in energy consumption and biodiesel production, Figure 5 (b), since energy consumption is directly related to biodiesel production. Moreover, an analysis was conducted to determine the major contributors to energy consumption. These contributors were divided into two groups, the boiler, which is responsible for heating the thermal oil that feeds the heat exchangers in the factory, and electrical equipment which includes all the electric motors that power the pumps, lighting, office equipment as well as other less relevant equipment. It should be noted that the Chiller is also included in electrical equipment, which further demonstrates that energy consumption related to utilities (production of heat and cold) is much higher than the energy consumption of

other equipment directly associated with the biodiesel production process. The plot depicted in Figure 6 (a) shows the difference between the weight of energy consumption between the boiler and the electric motors, being responsible for 63.4 % and 36.6 % of the consumption of the total energy consumed by the company, respectively. To provide more information regarding the energy consumption throughout 2021, the monthly specific energy consumption was plotted and presented in Figure 6 (b). The data show that although January, February, and December are the months with lower biodiesel production, 2.7 ton/h for the first two months and 2.4 ton/h for the last one, the specific energy consumption is much higher. On the other hand, this parameter in the coldest months (October to April) is higher than in the remaining months of the year due to the lower operating temperatures used in the production process, requiring a greater amount of thermal energy.

Figure 5. (a) Evolution of energy consumption throughout 2021; (b) Variation in biodiesel production throughout the year (2021).

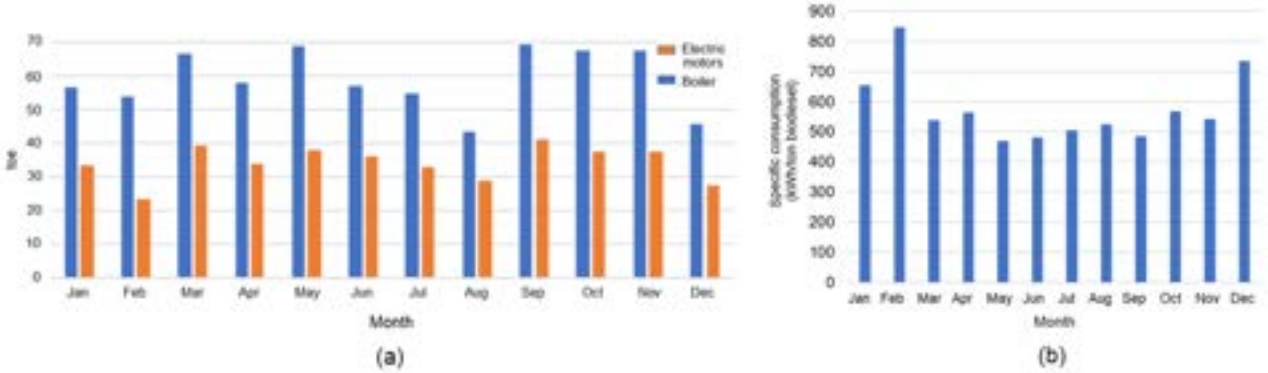

Figure 6. (a) Energy consumption by the boiler and electric motors; (b) Specific energy consumption.

4.2. Mass balance

As previously mentioned, the biodiesel is produced by a chemical reaction between triglycerides, which in this case are composed of virgin oils (VO) and used oils (UO), methanol (CH_3OH), and catalysts, in this case, the phosphoric acid (H_3PO_4) and the sodium methylate (CH_3NaO). In this unit, recovered biodiesel is also introduced into the process. From these inlet components, biodiesel, glycerine, and methanol are produced, as expressed in Figure 7.

Figure 7. Mass balance of the biodiesel production process.

Regarding the scheme presented in Figure 7, the mass balance of the PEBD unit can be written as follows:

$$\dot{m}_{in} = \dot{m}_{H3PO4} + \dot{m}_{UO} + \dot{m}_{VO} + \dot{m}_{CH3OH} + \dot{m}_{CH3NaO} + \dot{m}_{RecBio} \quad (18)$$

$$\dot{m}_{out} = \dot{m}_{bio} + \dot{m}_{gly} + \dot{m}_{CH3OH} \quad (19)$$

$$\dot{m}_{gly} = \dot{m}_{in} - (\dot{m}_{bio} + \dot{m}_{CH3OH}) \quad (20)$$

where $\dot{m}_{in}$ and $\dot{m}_{out}$ are the inlet and outlet mass flow rates, respectively. In this study, all the mass flow rates were measured, except for the case of the glycerine which was obtained by difference.

For the mass balance, in-site mass flow rate measurements were conducted in the PEBD Unit. The mass flow rate of each pump was recorded directly from the control room except for the following pumps: P-3005 and P-3007 in the Flash 31 and P-3010 Evaporator and P-3022 in the Flash 32 evaporator. To determine the mass flow of these 4 pumps it was necessary to take samples at strategic points, as presented in Figure 8. In Flash 31 (Evaporator Fe-31, Figure 8), 2 samples were collected: one before the evaporator (sample 1, Figure 8) and another later (sample 2, Figure 8). The analysis of these samples allowed to determine the methanol percentage in biodiesel upstream and downstream of the evaporator and, consequently, the evaporated methanol flow rate. This process was repeated for the Flash 32 evaporator.

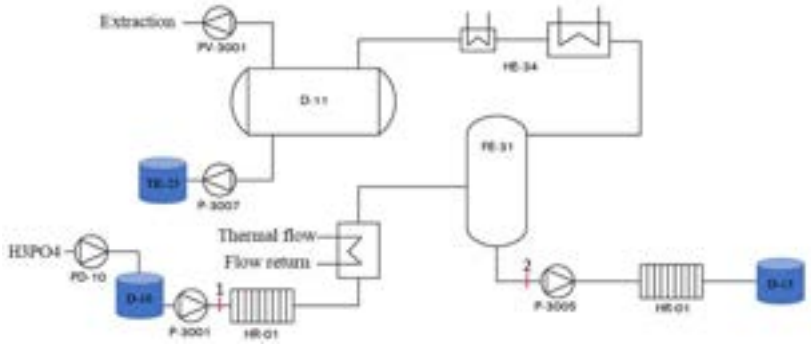

Figure 8. Schematic of sample collection in Flash 1.

According to the data presented in Table 1, it was possible to determine the working time of the PEBD for each month, based on the monthly production of biodiesel and the mass flow rate measured for each product that integrates the biodiesel production process is expressed in Table 2. The results are expressed in Figure 9 and represent the percentage of the products consumed (inlet) and produced (outlet) in 2021.

Table 2. Measured mass flow rates.

Process	Products	Mass flow rate (kg/h)
Output	Biodiesel	3404.32
	CH_3OH	195.68
	Glycerine	631.64
Input	H_3PO_4	3.15
	UO	2244.2
	VO	875
	CH_3OH	588
	CH_3NaO	140.49
	Rec. Biodiesel	380.8

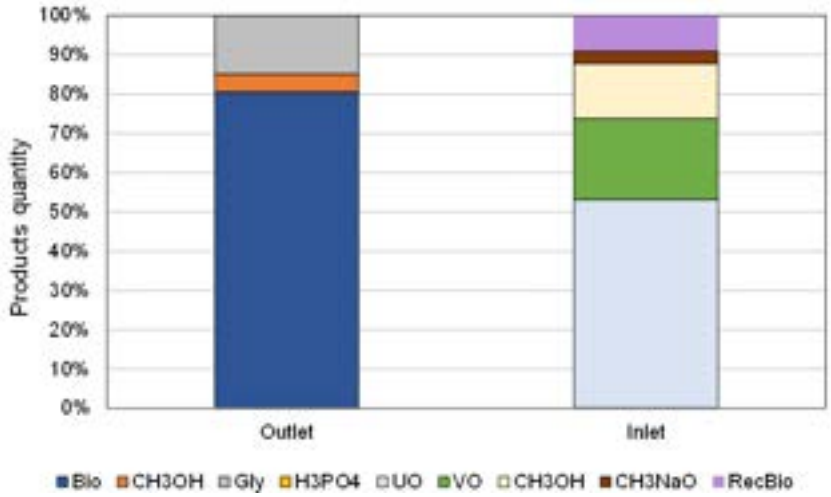

Figure 9. Products consumed (inlet) and produced (outlet) by the PEBD Unit in 2021.

As it can be observed in Figure 9, used cooking oils represent the major consumption (53 %), followed by virgin oils (21 %) and methanol (14 %). The recovered biodiesel introduced into the process is approximately

10 % while the catalysts are residual. Regarding the final products obtained from the PEBD Unit, the analysis shows that biodiesel represented 80 % of the products, followed by 15 % of glycerine and approximately 5 % of methanol.

4.3. Energy balance

The energy balance of the PEBD Unit is presented in Figure 10. As previously stated, the outflow energy from the production of the biodiesel process is equal to the energy inflow plus the thermal energy provided by the boiler. This initial energy is the sum of the energy provided by virgin oils (VO) and used oils (UO), methanol (CH_3OH), and catalysts - phosphoric acid (H_3PO_4) and the sodium methylate (CH_3NaO). Besides these products, the PEBD unit uses electrical energy (Elec.) that feeds the pumps and the chiller and biomass (Biom.) as the heat source that provides thermal energy to the entire process. From this process, biodiesel (Bio.), glycerine (Gly), and methanol (CH_3OH) are produced. Moreover, part of this energy is lost (Loss), which is obtained by the difference between the energy consumed and produced. The energy balance equations used are expressed in Eqs. (21)-(22). It should be noted that the calculations were conducted in function of mass instead of mass flow rate. Therefore, $\dot{E}$ in section 2.2 becomes E.

$$E_{in} = E_{H3PO4} + E_{CH3NaO} + E_{UO} + E_{VO} + E_{CH3OH} + E_{Bio.\ Rec} + E_{Elec.} + E_{Pellets.} \quad (21)$$

$$E_{out} = E_{Bio.} + E_{CH3OH} + E_{Gly.} \quad (22)$$

Regarding the energy of each product, E_{H3PO4}, E_{CH3NaO}, E_{UO}, E_{VO}, E_{CH3OH}, $E_{Gly.}$and $E_{Bio.}$, only the chemical energy is considered using the data obtained from the mass balance and the LHV of each compound. Based on the literature, the LHV used is as follows: $LHV_{H3PO4} = 23.5$ MJ/kg, $LHV_{CH3OH} = 19.9$ MJ/kg, $LHV_{UO} = 37.0$ MJ/kg, $LHV_{VO} = 37.0$ MJ/kg, $LHV_{Gly} = 19{,}0$ MJ/kg, $LHV_{Bio} = 19.0$ MJ/kg. No information was found regarding the sodium methylate LHV, therefore it was not considered in the energy balance. Regarding the thermal energy provided by the pellets, Pellets in Figure 10, it is obtained by multiplying the mass of pellets consumed by the PEBD unit by the biomass LHV which was considered equal to 18 MJ/kg.

To determine the pellet consumption of the PEBD, the heat exchanged between the thermal flow (thermal oil heated by the boiler) and the cold stream, which consists of used cooking oils, virgin oils, and biodiesel, in each three heat exchangers of this unit is calculated. From this analysis, it was found that the PEBD unit is responsible for 14 % of the total pellets consumption.

Regarding the consumption of electrical energy consumed by the pumps and the chiller, measurements were conducted. For the case of the power consumed by the pumps, the current and tension were measured, and the total power resulted from the sum of the power consumed by each pump, resulting in 18 % of the total electrical energy consumed. The chiller is used to produce cold water to condensate the methanol evaporated during the process of purification of biodiesel. To determine the power consumed by the chiller, the vapor-compression refrigeration cycle was analyzed. Temperatures involved in the heat exchanged between the cold source and the evaporator and between the hot source and the condenser were recorded. The refrigerant fluid used in this process is R410a. From these temperatures, the properties of the thermodynamic cycle were defined in terms of power consumption for each stage, resulting in a total of 684,050 kWh/year, which represents 36 % of the total electrical energy consumed.

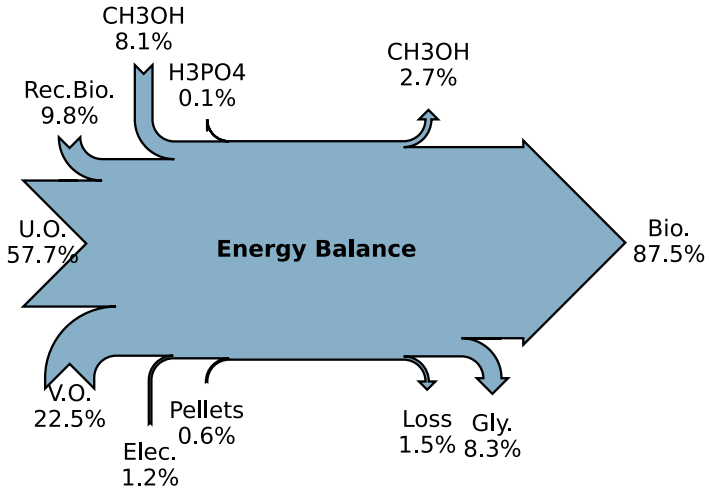

Figure 10. Energy balance of the PEBD Unit.

4.4. Exergy Analysis

The exergy balance is always performed along with the energy balance of the unit. However, energy analysis relates directly to the first law of thermodynamics, where exergy is always destroyed when a system involves an irreversible reaction (21). The irreversibility of the process was calculated using equation (5) by the difference between the exergy that enters the system and the exergy that leaves the system. The determination of the exergy flows was the same principle as the energy flows shown in Eq. (21) and Eq.(22). The electric exergy is the same as the electric energy, and the chemical exergy of the other streams was calculated using Eq. (7). The exergy balance of the PEBD was determined and is depicted in Figure 11.

The irreversibility of the process depends on the system's entropy variation. The literature shows that biodiesel production presents a higher exergy efficiency. This is mainly due to the reversibility of the transesterification reaction and the biodiesel's high chemical exergy in relation to the exergy consumed in the process (22,23). The boiler associated with the unit might be the equipment that most influence the irreversibility of the system. However, the total exergy of the pellets is insignificant compared to the total exergy of the input flows involved in the system (0.6 %) which explains the small difference between heat loss and irreversibility in the system.

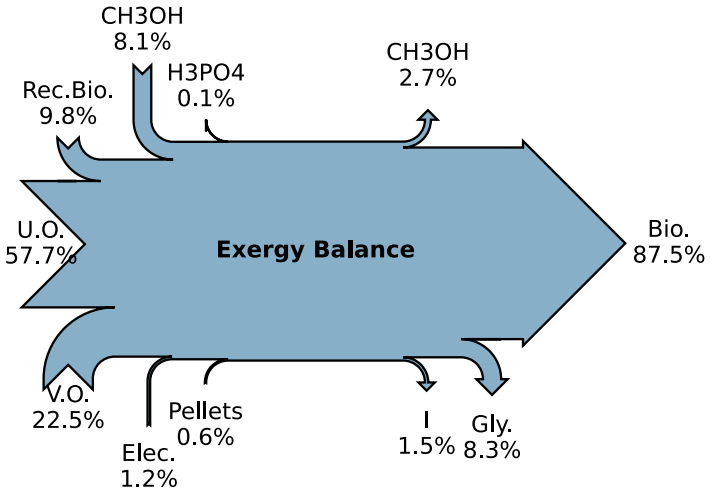

Figure 11. Exergy balance of the PEBD Unit.

4.5. Process enhancement

From the energy balance, it is clear that the PEBD unit is highly optimized in terms of heat consumption, representing around 14% of total pellet consumption this is mainly due to the use of heat exchangers at the beginning of each biodiesel purification stage, allowing the recovery of energy from the hot streams to preheat the cold streams. On the other hand, the use of low vacuum pressures in the evaporators allows operating conditions at lower temperatures, reducing the consumption of electrical energy. However, after a careful analysis of the PEBD unit, it was possible to find some solutions that improve the energetic process performance. Regarding the pellet consumption, it was found that the continuous operation of the heat exchanger HE-33 is redundant and unnecessary since it is expected to keep the operating temperature of Flash 1 near 77 ºC. With proper insulation, the heat exchanger HE-01 could be connected directly to the evaporator FE-31, since the heat lost from the biodiesel flowing through the pipe to the environment between the HR-01 and the HE -33 heat exchangers is of the same order of magnitude as the heat supplied by the HE-33. Thus, HE-33 can operate in a bypass mode during the first few hours of the unit starting time. With thermal equilibrium reached, it was found that deactivating the HE-33 exchanger would result in annual savings of more than 29.5 tonnes of pellets, which represents a decrease of approximately 2.2 % of the annual pellets consumption. Even though this value seems to be irrelevant, it corresponds to cost savings in the order of 7,000 €/year, taking into account the rising in prices observed for this fuel over the last months.

Regarding electricity consumption, an opportunity to improve the methanol recovery/condensation process was identified, by acting on the existing chiller. Measurements reveal a high water flow rate, compared to a low evaporated methanol flow rate, with a maximum ΔT between the inlet and outlet of the chiller of 1.6 ºC, showing that the water flow rate is oversized. Therefore, a need arises to calculate an optimized water flow rate for a minimum ΔT of 5 ºC in the evaporator, as well as an increase of 1 ºC at the cold water outlet, allowing the use of a lower refrigerant flow rate as well as the increase of temperature in the evaporator and, consequently, an increase in its pressure, reducing the compression work. Moreover, this optimized water flow rate allows to estimate the minimum cooling power needed by the process, allowing the selection of a new chiller. With this optimized equipment, a reduction of more than 70 % of the electrical power consumed by the chiller is possible.

Considering these optimized solutions, the energy and exergy efficiencies of the system were estimated and compared with the present scenario. To conduct this analysis, the equations presented in section 2.2 were used to plot the graphs presented in Figure 12. The results show that in the actual scenario, the energy and exergy efficiencies for biodiesel production are 87.6 % and 87.5 %, respectively. While for the process, which includes the production of both biodiesel and glycerine, the energy and exergy efficiencies are 96.0 % and 95.8 %, respectively. There is not much difference between both efficiencies as the thermal loss and the irreversibility of the system are identical. However, the difference is due to the irreversibility caused by the boiler.

Compared with the present scenario, the optimization proposed increases by almost 0.6 % in both energy and exergy efficiencies. It is not a significant increase as the energy saved is relatively low compared with the overall energy of the process. However, by observing Figure 13, it is possible to conclude that this optimization decreases around 117 toe the annual irreversibility. This may not have a major impact on the energy or exergy balances, however, it will be translated into a reduction in biodiesel production cost.

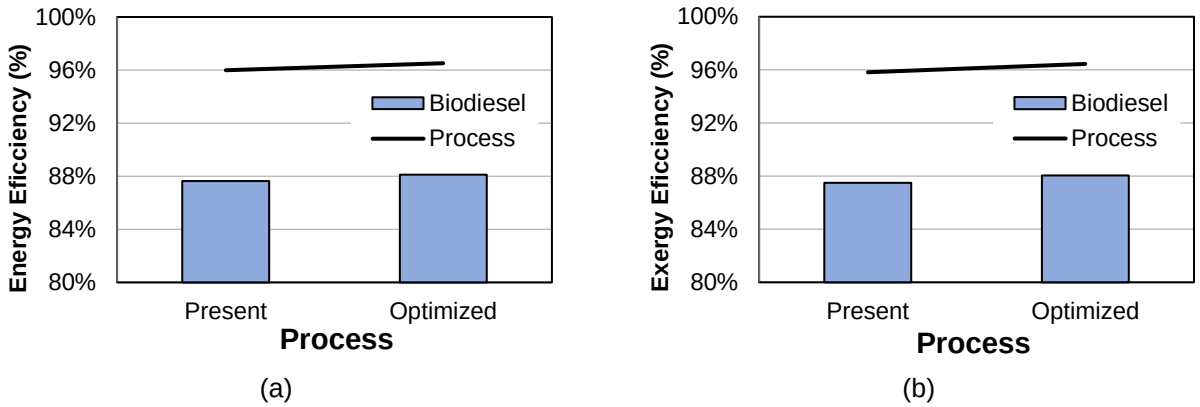

Figure 12. Energy (a) and Exergy (b) efficiency analysis for the present and optimized scenarios.

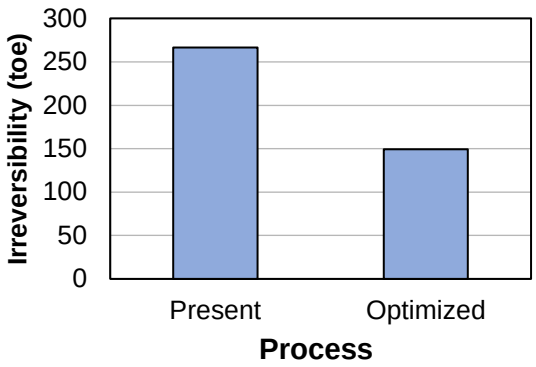

Figure 13. Influence of the optimization in the process irreversibility.

5. Conclusions

This study presents a detailed analysis of a biodiesel power plant. The different products used for biodiesel production are characterized and the different reaction processes are presented. Considering the complexity of analyzing the entire power plant, an energy and exergy analysis is conducted on the specific unit of biodiesel production or PBDE, as previously mentioned. To determine the mass balance, in-site measurements were conducted. From this analysis, a total of 18,504 tons of biodiesel are produced in 2021 as well as 3,433 tons of glycerine, which is sold for other industry sectors. These products represent a total of 87.6 % and 8.4 % of the total energy produced, the remaining percentage is methanol and energy loss. Regarding the sources of energy used for biodiesel production, electricity came from pumps and a chiller, while the thermal energy is provided by pellets burned in a boiler. The study conducted shows that the PEBD is responsible for a total consumption of electrical energy corresponding to 54 %, from which 36 % is consumed by the chiller, while this unit only consumes 14 % of the pellets. In terms of energy efficiency, the biodiesel production process is estimated to be equal to 88.1 %, while the process that includes both the production of biodiesel and glycerine represents an efficiency of 96.5 %. In terms of exergy, the results are slightly different from the energy analysis, being the difference mainly due to the irreversibility caused by the boiler. The entire process was analyzed and solutions were presented in order to enhance the process efficiency. This enhancement results in a slight

increase of both energy and exergy efficiencies of the process, approximately 0.6 %. Although this improvement seems to be reduced, it leads to non-negligible cost savings in the power plant.

Acknowledgments

This work was supported by FCT – Fundação para a Ciência e Tecnologia within the R&D Units Project Scope: UIDB/00319/2020 (ALGORITMI Center) and R&D Units Project Scope UIDP/04077/2020 (METRICS Center).

Nomenclature

E Energy, J
I Irreversibility, J
$\dot{m}$ mass flow rate, kg/s
$\dot{P}$ Pumping Power, W
Q heat, J
$\dot{W}$ Work, W

Greek symbols

ε exergy
η energy efficiency
φ chemical exergy conversion factor for fuels
ψ exergy efficiency

Subscripts and superscripts

in inflow
out outflow
0 Chemical
k kinetic
ph physical

References

1. IEA, IRENA, UNSD, Bank W, WHO. Tracking SDG 7: The Energy Progress Report 2021, World Bank, Washington DC [Internet]. Washington DC; 2021. Available from: www.worldbank.org
2. Administration USEI. Independent statistics & Analysis. Indep Stat Anal [Internet]. 2018;U.S. Depar(Washington, DC 20585). Available from: https://www.eia.gov/
3. European Environmental Agency. Air quality in Europe — 2018 report No 12/2018 [Internet]. Air quality in Europe -2018 Report. 2018. 1–64 p. Available from: papers2://publication/uuid/1D25F41B-C673-4FDA-AB71-CC5A2AD97FDD
4. Observatório da Energia, Direção Geral de Energia e Geologia (DGEG), Direção de Serviços de Planeamento Energético e Estatística, (ADENE) A para a E. Energia em Números [Internet]. 2022nd ed. Energia A-A para a, editor. Energia em Números Edição 2022. Lisbon; 2022. Available from: https://www.dgeg.gov.pt/media/zuffmfm4/dgeg-aen-2022e.pdf
5. Nadda R, Kumar A, Maithani R. Efficiency improvement of solar photovoltaic_solar air collectors by using impingement jets: A review. Renew Sustain Energy Rev. 2018;93:331–53.
6. Our World in data. Biofuel Production [Internet]. 2022 [cited 2022 Oct 22]. Available from: https://ourworldindata.org/grapher/biofuel-production
7. IEA. Global biofuel production in 2019 and forecast to 2025 [Internet]. 2022 [cited 2022 Oct 22]. Available from: https://www.iea.org/data-and-statistics/charts/global-biofuel-production-in-2019-and-forecast-to-2025
8. Lukic I, Skala D, Glišic S. Bioresource Technology Biodiesel synthesis at high pressure and temperature : Analysis of energy consumption on industrial scale. 2009;100:6347–54.
9. West AH, Posarac D, Ellis N. Assessment of four biodiesel production processes using HYSYS.Plant. Bioresour Technol. 2008;99(14):6587–601.
10. Sheehan J, Camobreco V, Duffield J, Graboski M, Shapouri H. An overview of biodiesel and petroleum diesel life cycles. USDepartment Agric US Dep Energy [Internet]. 1998;(May):1–60. Available from: http://www.nrel.gov/docs/legosti/fy98/24772.pdf
11. Amelio A, Van De Voorde T, Creemers C, Degrève J, Darvishmanesh S, Luis P, et al. Comparison between exergy and energy analysis for biodiesel production. Energy. 2016;98:135–45.
12. Amin A. Review of diesel production from renewable resources : Catalysis , process kinetics and technologies. Ain Shams Eng J [Internet]. 2019;10(4):821–39. Available from: https://doi.org/10.1016/j.asej.2019.08.001

13. Cengel Y, Turner R, Cimbala J. Fundamental of thermal fluid sciences. 2008. p. 1079.
14. Speight JG. Handbook of Gasification Technology. Handbook of Gasification Technology. 2020.
15. Basu P. Biomass Gasification, Pyrolysis and Torrefaction: Practical Design and Theory. Biomass Gasification, Pyrolysis and Torrefaction: Practical Design and Theory. 2013. 1–530 p.
16. Ahmed R, Sinnathambi CM, Eldmerdash U, Subbarao D. Thermodynamics analysis of refinery sludge gasification in adiabatic updraft gasifier. Sci World J. 2014;2014.
17. Bejan A. Fundamentals of exergy analysis, entropy generation minimization, and the generation of flow architecture. Int J Energy Res. 2002;26(7):0–43.
18. Michalakakis C, Fouillou J, Lupton RC, Gonzalez Hernandez A, Cullen JM. Calculating the chemical exergy of materials. J Ind Ecol. 2021;25(2):274–87.
19. Silva J, Teixeira SFCF, Preziati S, Teixeira JCF. ENERGY AND EXERGY ANALYSIS OF A BIOMASS POWER PLANT. In: Proceedings of the ASME 2016 International Mechanical Engineering Congress & Exposition IMECE2016 November 11-17, 2016, Phoenix, Arizona. 2016. p. 1–10.
20. Direção-Geral de Energia e Geologia. Despacho n.º 17313/2008 de 26 de junho. Diário da República. 2008;27912–3.
21. Dincer I, Abu-Rayash A. Sustainability modeling. Elsevier, editor. Energy Sustainability. Elsevier; 2020. 119–164 p.
22. Khoobbakht G, Kheiralipour K, Rasouli H, Rafiee M, Hadipour M, Karimi M. Experimental exergy analysis of transesterification in biodiesel production. Energy. 2020;196.
23. Velásquez HI, Benjumea P, Oliveira Jr. S de. Exergy Analysis Of Palm Oil Biodiesel Production By Base Catalyzed Methanolysis. 19th Int Congr Mech Eng [Internet]. 2007;(Bejan 2002):(em CD-ROM). Available from: https://www.abcm.org.br/anais/cobem/2007/pdf/COBEM2007-1557.pdf

Mild Hybrid Multi-Energy Systems: Waste Energy Recovery by Bottom ORC System

Roberto Capata

Sapienza, University of Roma

Abstract:

The goal of this paper is to evaluate, from a thermodynamic point of view first, and then constructive one, the possibility of inserting a waste heat recovery system in a hybrid vehicle in mild-hybrid configuration. The vehicle considered is a standard 1000 cc gasoline turbocharged ICE. The characteristic and proposed configuration of the vehicle allows to mechanically separate the existing turbo-compressor unit and to couple them with the respective electrical devices: electric motor and generator. This new architecture enables an electrical generation that can be used to recharge the installed battery package. Moreover, thanks to the new configuration of the turbine of the group, i.e. without the wastegate valve, the turbomachinery provides a high gas flow rate at high temperature (about 380 °C). These exhaust gases can be used for a bottom ORC group, with additional electricity generation. All these considerations permit to have an extra on-board recharge of the batteries, to consequently increase the electric range of the vehicle (a sort of range extender) and to install a battery group of limited size and power, with consequent advantages of payload and vehicle efficiency. Besides, it allows to achieve the well know and inflated aspects (from a citation point of view) of the emissions reduction.

Keywords:

Mild Hybrid Vehicle, Electric Generation, ORC plant, Compressor Turbine Condenser design

1. Introduction

The aim of the research is to verify the feasibility of an on-the-road prototype of a power train for a hybrid propulsion vehicle. In detail, the project consists in the study and implementation of an innovative complex energy plant for the ICE (900cc) of a city car [1-4]. The solution studied is to mechanically disconnect the compressor/turbine complex, supporting the C compressor with a dedicated electric motor and connecting the T turbine to a generator. Mechanical C/T decoupling allows both machines to be designed so that they operate close to the maximum efficiency point for the maximum part of the expected real operating range. Specifically, the turbine has a lower rotation speed than that of the original group and therefore is characterized by slightly larger dimensions. The advantage is that in current supercharger units the surplus at high revs is discharged through the waste-gate valve without expanding into the turbine. In the configuration proposed here, however, all the energy of the gases is used by the turbine to generate electrical power, that can be used where required. Finally, with a view to optimizing all energy flows, the turbine exhaust is used for a bottoming ORC group, for electricity generation. The surplus of energy thus obtained can be used to power the auxiliaries, reducing both fuel consumption and lengthening the time of use of the electrical part, via battery pack. The actions taken were [5]:

a) Study a suitable configuration of a new turbocharging unit (hereinafter, "TC") for the specific thermal engine chosen here (ICE 900 cc turbo ≈ 66 kW), separating the compressor and the turbine and realizing the two devices with ad hoc components;
b) Simulate the behavior of the new TC group over the entire operating range of the engine, possibly making appropriate changes to the configuration originally chosen;
c) Design and implement a prototype configuration of the new C/T group (integrating the part relating to the motorization/electric generation and test it in advance);
d) Simulate and design the submitted ORC group.

2. Compressor and Turbine design

Once the engine of the vehicle (999 cc) of the city car being searched was established, the existing group on the vehicle was identified, the operational map of which is shown in figure 2.

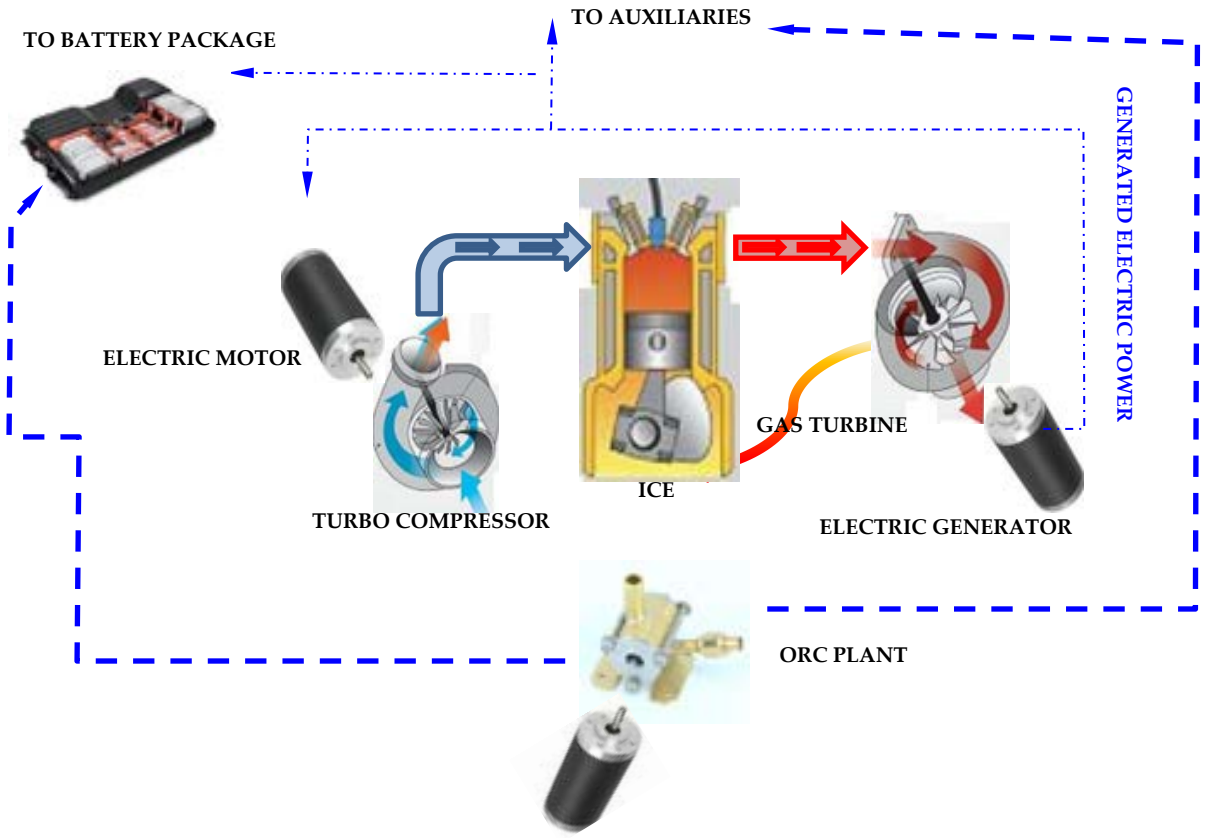

Figure 1. The electro-assisted configuration of the proposed turbocharging unit and the ORC group

Based on the n_s/d_s design theory [5-8], the geometric characteristics of the compressor shown in table 1 are obtained. Obviously, the dimensions and speeds are established here based on the values provided by the manufacturer of the installed compressor. The operating point was also fixed and derived since the maps of the business model [5,6]. The operating specifications are as follows:

$\beta = 1.5$
$\dot{m} = 0.02\text{-}0.06$ kg/s
n = 140000-210000 rpm

the range includes operation at the minimum and maximum speeds assumed by the ICE (2000-5000 rpm)

Table 1. Compressor data designed

m [kg/s]	0.02	**W_{EUL} [J/kg K]**	44652.74	ψ_2	1
β	1.4	**U_2 [m/s]**	211.3	ψ_1	0
c_p [J/kg K]	1004	**r_2 [m]**	0.014421	φ_1	0.3
T_1 [K]	293	**ΔT [K]**	22	φ_2	0.55
ω [rad/s]	14653	**ρ_1 [kg/m^3]**	1.20108	δ_p	0.98
ε	0.42	**Q_1 [m^3/s]**	0.016652	χ	0.65
p_1 [Pa]	101000	**r_{1e} [m]**	0.011005	R_ρ	0.5
T_2 [K]	337	**r_{1i} [m]**	0.007153	**$(1-\chi^2)$**	0.5775

From the analysis of the data it can be noticed the correspondence to the existing model, installed in the vehicle. The operation of the compressor at various speeds of the ICE engine was then evaluated and using the previous map it was possible to fill in the following table and the figure shows the trend of the power required by the compressor as the number of revolutions of the ICE changes.

Table 2. Compressor operation at different ICE speeds

rpm ICE	**$\dot{m}$ [kg/s]**	**rpm**	**β_c**	**T_{in} [K]**	**T_{out} [K]**	**P [W]**	**η**
2000	0.021	145000	1.42	298.4	344	920.71	0.68
3500	0.0408	180000	1.64	297.5	354	2474.39	0.8
5500	0.0619	210000	1.84	297.5	366.8	4444.96	0.82

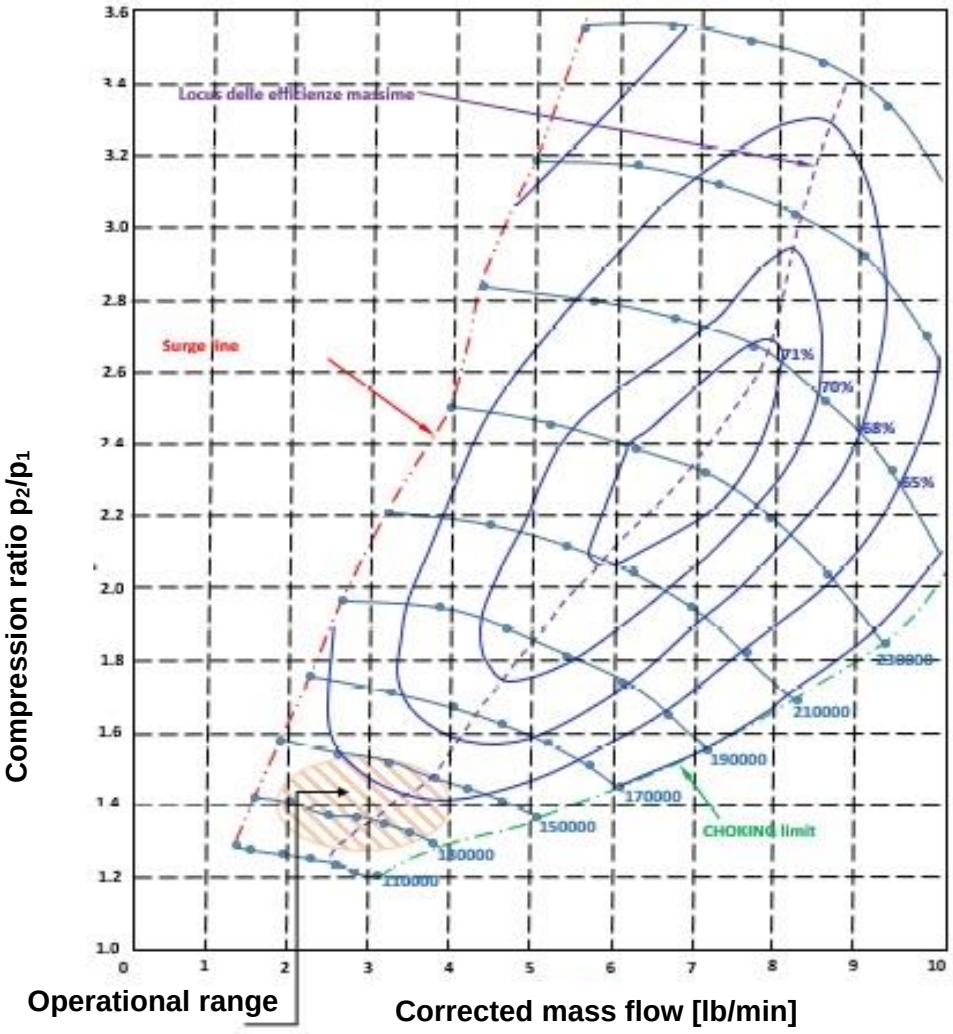

Figure 2. Compressor chart

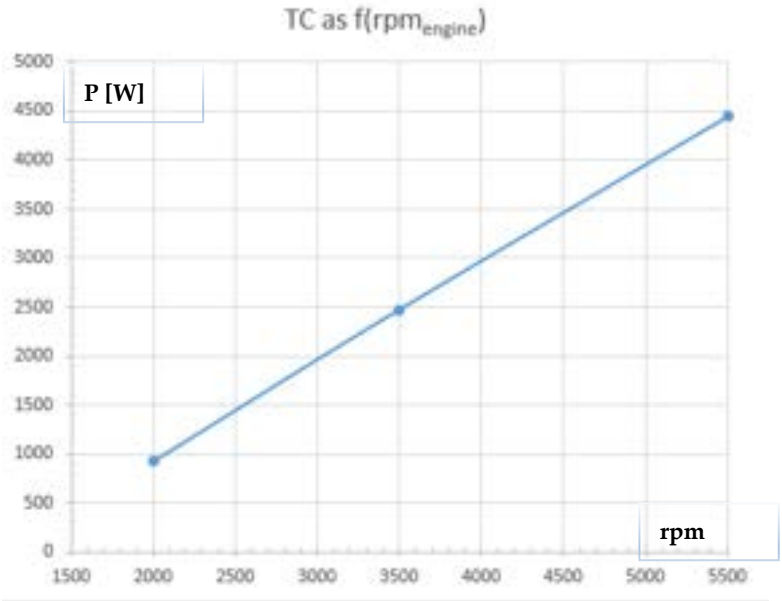

Figure 3. Compressor power required as a function of the ICE speed

Using the same procedure described above, the turbine was designed [9-15]. The main characteristics are shown in Table 3.

Table 3. Turbine data

m [kg/s]	0.021	**L_{EUL} [J/kg K]**	103194	ψ_2	0
β	1.4	**U_2 [m/s]**	321.2	ψ_1	1
c_p [J/kg K]	1397	**r_2 [m]**	0.051153	φ_1	0.3
T_1 [K]	980	**ΔT [K]**	34	φ_2	0.4
ω [rad/s]	6280	**ρ_2 [kg/m^3]**	0.387992	δ_p	0.98
ε	0.23	**Q_2 [m^3/s]**	0.05412	χ	0.65
p_2 [Pa]	101000	**r_{1e} [m]**	0.011159	R_ρ	0.5
T_2 [K]	907	**r_{1i} [m]**	0.007253	**$(1-\chi^2)$**	0.5775

From the analysis of the data, the correspondence to a turbine model available on the market is evident, whose operational map is represented in figure 4. The operation of the turbine at various ICE engine speeds was then evaluated using the map, so the turbine trend generation is reported in figure 5 and, as above, it is possible to fill the following table, in function of ICE speed.

Table 4. Turbine operation at different ICE speeds

rpm ICE	**$\dot{m}$ [kg/s]**	**rpm**	**β_c**	**T_{in} [K]**	**T_{out} [K]**	**P [W]**	**η**
2000	0.024	82170	1.2	954	922	780	0.87
3500	0.04	134483	1.6	1005	930	3510	0.86
5500	0.07	164002	2.00	1045	932	9500	0.81

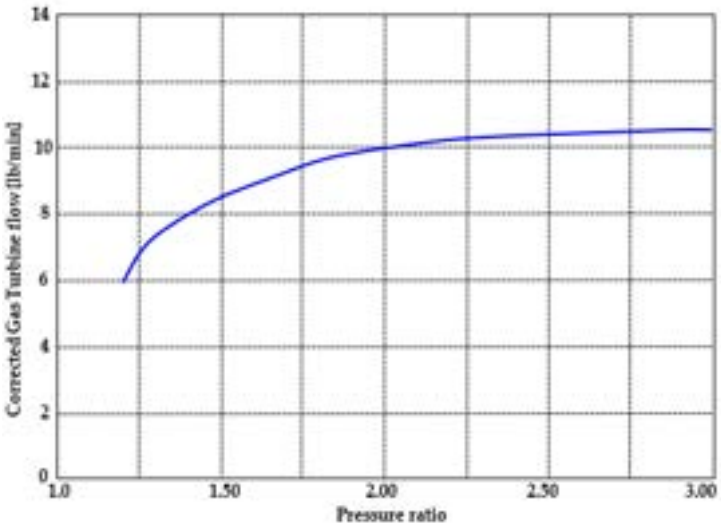

Figure 4. Turbine operational chart

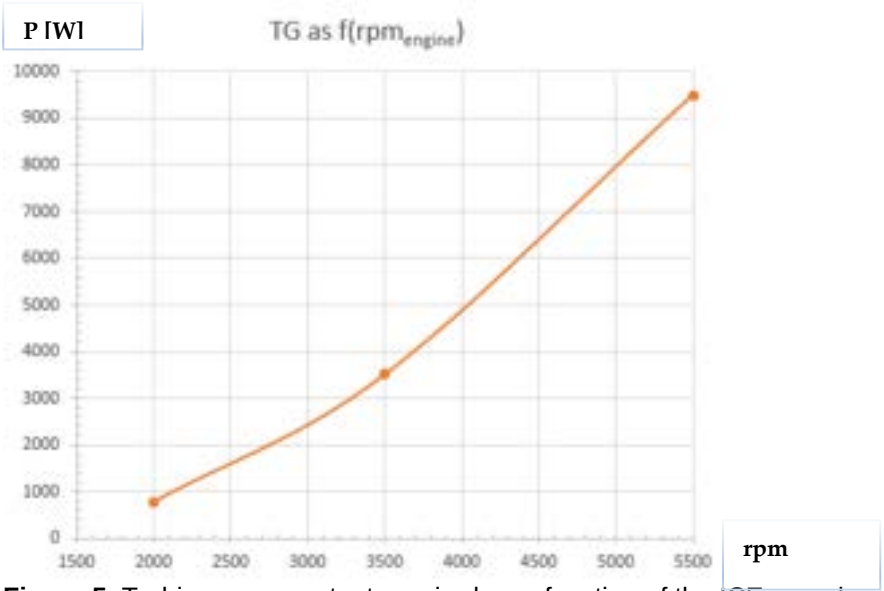

Figure 5. Turbine power output required as a function of the ICE speed

3. Energy Recovery and Vehicle Energy Balance

Thanks to the proposed design changes, the new electrically assisted turbocharger offers extra power at all engine speeds, except for about 2500 rpm and the power curve are shown in figure 6. It can be noted that the reported values include mechanical and electrical efficiency. For any type of mission (ETC, EUDC, WVU and NDC [17-21]), the engine energy balance is calculated by calculating the instantaneous power demand to the wheels, adding transmission losses, adding the compressor power and subtracting it from the turbine power and considering the battery charging efficiency. The effect of KERS has not been included in the simulations at this time. For almost the entire mission, the turbocharger unit can deliver extra net power. This power will be used mainly to recharge the battery pack and power the auxiliaries. When the power is negative (almost always on restart and during braking operations) the compressor will draw the required power from the on-board battery package. Since the vehicle is conceived as a *mild hybrid*, this battery pack is obviously much smaller than in a common HEV [22-29]. In longer missions, the instantaneous surplus generated by the turbocharger, minus the contributions sent to the auxiliaries, can lead to a condition in which the battery pack has a SOC close to 100% and cannot accept further charges. In these circumstances, the extra power could be used or sent to an auxiliary electric motor for additional propulsion.

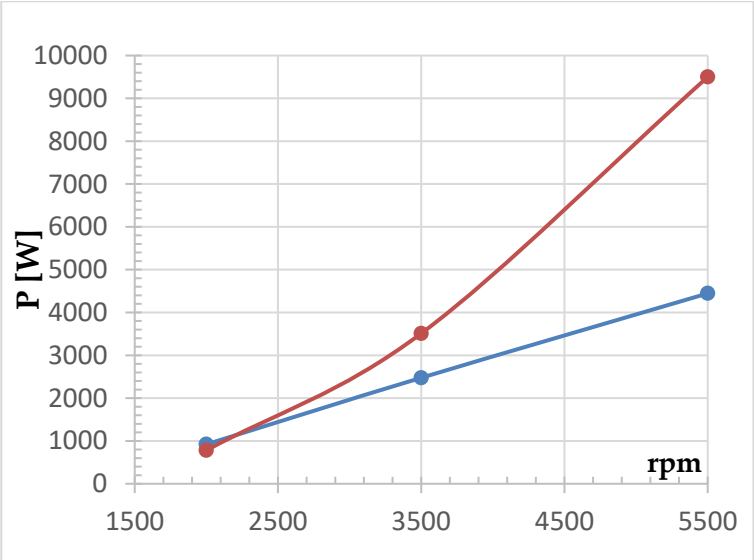

Figure 6. Power of the Turbine (orange curve) and the Compressor (blue) as a function of ICE rpm

The proposed solution, namely to physically decouple the compressor and turbine, using an electric motor for the first and producing electricity from the second via electric generator, showed that the total energy recovered on the simulated missions amounts to 1.01 kWh (compared to the 18 kWh of total energy required by the vehicle), which means that a net saving of about 5.6% can be achieved by the installation of this new turbocharger unit (figure 7).

4. The Bottoming ORC cycle

A further optimization of the considered system is to insert a bottoming ORC cycle. This possibility is thermodynamically feasible because the outlet temperature of the exhaust gases from the turbine, which must be remembered that it works without a wastegate valve, is about 800 K. The fluid used is an organic fluid R245fa. In the worst case, the exhaust gas flow rate is 0.024 kg/s. This temperature is high for a typical ORC application, especially for the required low power; this means that the energy content is too high and probably the use of Rankine Cycle instead an ORC would be more efficient, nevertheless for a compact application an organic fluid is more convenient, because the dimensions of the heat exchangers are smaller. Using commercial software, the thermodynamic simulation of the ORC cycle was performed. Among the various parameters to be set, the value of the maximum power that can be delivered, of about 2 kW, was chosen. Since the power is not high, it is not convenient to design a sophisticated cycle with preheaters or re-heaters commonly used in large-size plant. Thus, the cycle is very simple and only few components are required (Fig. 8) [30-35]:

1. Air Heat Recovery: it is a heat exchanger where the organic fluid warms up and changes its phase from liquid to vapor. This transformation is considered isobaric and, in the phase, changing is also isothermal.

2. Expander: it operates between the pressure imposed upstream and downstream by the heat recovery and the condenser.
3. Condenser: used to condensate the organic fluid with water. This transformation is considered isobaric and isothermal during the phase changing.
4. Pump: it increases the pressure of the organic fluid, now liquid, up to the pressure inside the Air Heat Recovery.
5. Flow Mixer: necessary to add the possible make up flow rate.

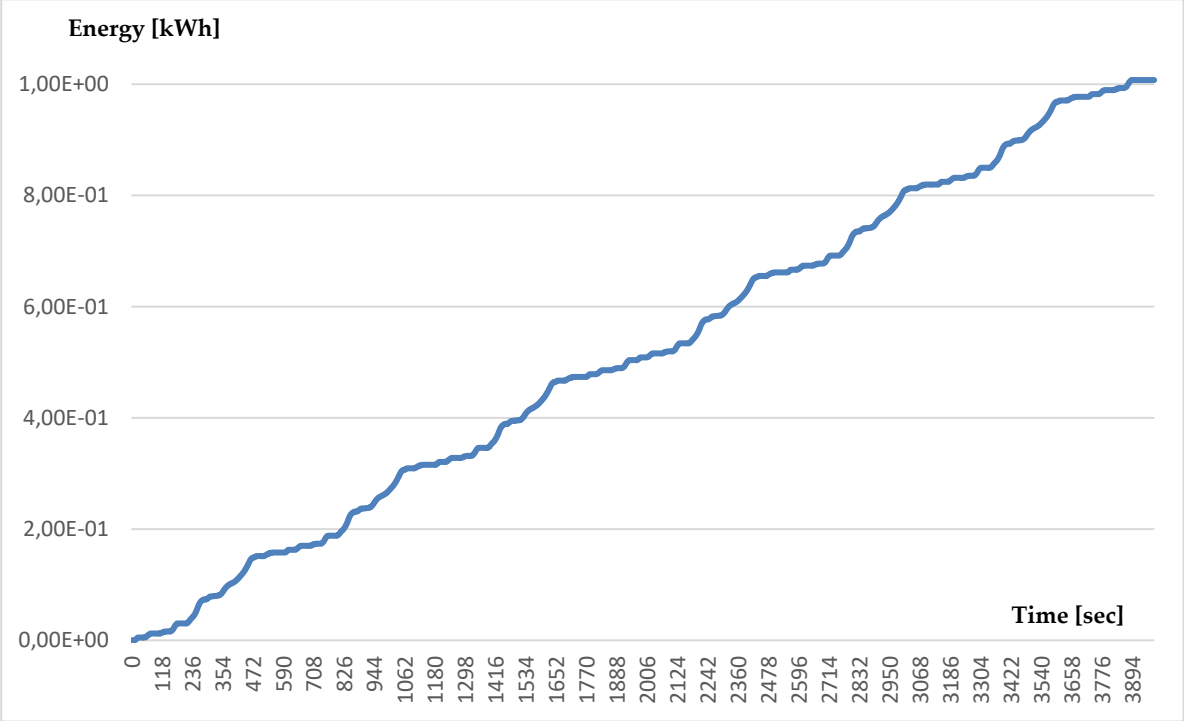

Figure 7. Net energy supplied by the GT group during the mission

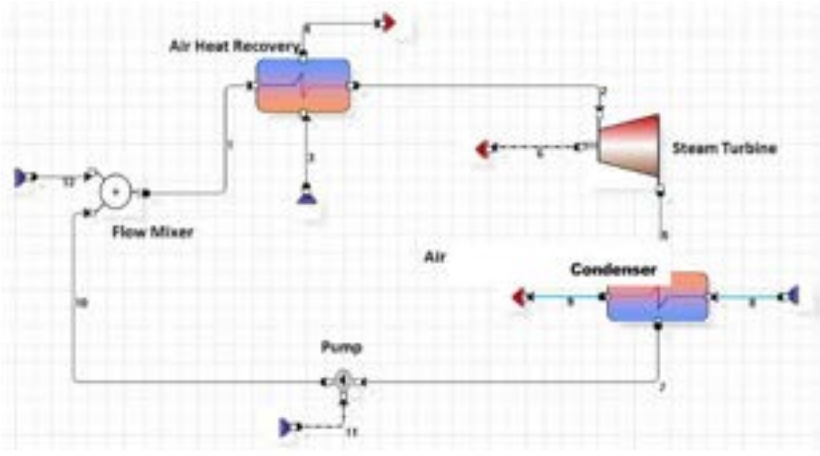

Figure 8. ORC cycle layout

From the statement of the problem, the input constrains are:

- The output power from the turbine (flow 6): 2 kW
- The available mass flow rate of the exhaust gas (flows 3): 0,024 m^3/s
- Temperature of the exhaust gas (flows 3): 723 K (conservative set)

The temperature of the inlet water is set to 293 K, hence, considering the finite dimensions of the condenser and its losses, the organic fluid should condense at 301 K, because it cannot reach lower temperature. Thanks to the thermodynamics properties, setting the condensation temperature means that the condensation pressure is fixed. From the thermodynamics tables for R245fa, this fluid condenses at 301 K with a pressure of 170 kPa. The expander efficiency has been underrated at 0.7 to be sure that the outlet power was at least 2 kW and the efficiency of the pump is fixed to 0,9. The results obtained by the process simulation indicates a mass flow rate for the organic fluid of 0.13 kg/s.
In summary, thermodynamic feasibility of whole system is confirmed. The current state of research focuses on the advisability of using a helical evaporator [36] for the ORC plant. For the study of the expander we will follow the procedure described in previous papers [31-37], trying to define the more efficient device. Only the condenser is under evaluation. First, the possibility of using the existing radiator of the car has been considered, but due to the limited overall available dimensions a compact capacitor [38-42] is being studied.

Table 5. R245fa operating specifications

Mass flow rate [kg/s]	0.13
Evaporator inlet temperature [K]	301
Evaporator outlet temperature [K]	383
Condenser inlet temperature [K]	370
Condenser outlet temperature [K]	301
Condenser inlet pressure [Pa]	170000
Water inlet temperature [K]	293
Water outlet temperature [K]	301
Pump required power [W]	100
Power output [W]	2000

4.1. Condenser design procedure

The chosen configuration (Figure 9) is the “circular tube fin”. It has several advantages such as reduced weight, better temperature control and easier transport. The type of tube is often chosen to reduce losses [28,29]. The inner diameter of the tube is 8 mm, the fin length is 3 mm, the tube thickness is 1 mm and the distance between two consecutive fins is 2 mm. The staggered arrangement is triangular, to avoid interference problems, and the distance between each arrangement center is 17 mm (the distance will be called p_t or p_l if it is from tube to tube or from tube to the outer shell). After the number of tubes is set, the width, thickness, and length are defined. At this point, we must distinguish what happens in the mono-phase or the two-phase condensation. The analysis will be conducted for both the working fluid (inside) and the water (outside).

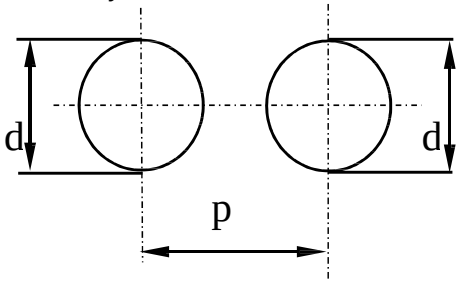

Figure 9. Reference scheme.

4.1.1 Monophasic Condensation

Working fluid side

The fluid characteristics (viscosity coefficient, thermal conductivity, etc.), were derived from the Coolprop library. First, the enthalpy difference is calculated to compute the thermal exchange. Then, the LMTD is derived with the HEM method. It is now necessary to compute the overall heat coefficient U to find the required exchange area. To compute the coefficient U we have to introduce the basic dimensionless numbers: Reynolds, Nusselt, Prandtl, and Froude. Once all quantities have been defined, the following procedure will be used.

1. The Prandtl number is calculated, and secondly, the calculation of the fluid velocity inside the pipes is evaluated, permitting the evaluation of the Reynolds number, which leads to the Nusselt numbers.

2. After computing the Nusselt numbers, it is then possible to estimate the "h_i" that is the heat transfer coefficient.
3. Finally, it is necessary to introduce the areas. When the numbers of tubes are known, where N_s is the number of pipes where the mass flow condensate, N_r is the numbers of transits of the same bundle of tubes, and the total number N_t, the geometrical properties can be calculated. The inner area of the pipes is:

$$A_i = \pi d_i \, L_1 \, N_t \quad (1)$$

and the minimum free flow area is:

$$A_{0,i} = \frac{1}{4}\pi \, d_i \, N_s \quad (2)$$

Cooling fluid side

As previously mentioned, the characteristics of the fluids are derived from the Cool- prop library. The main areas (external pipes side) are the A_p, the primary area, the fin area A_f and the heat transfer surface area A_0. The primary area is the difference between the pipe surface area and the area blocked by the fins. The A_0 is the total heat transfer area, computed by the sum of the primary area and the fin area. Another important parameter to determine is the minimum areas among the pipelines, where the water flows. If a triangular configuration is chosen [29], it is possible to consider that surface, as a flat surface.

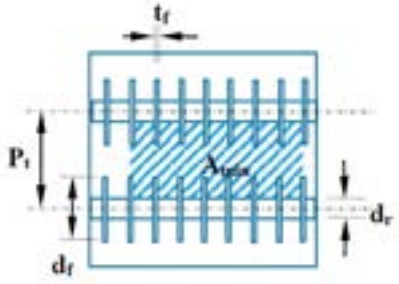

Figure 10. Minimum area description of the condenser.

4.2. Biphasic Condensation

As the condensation process proceeds along the pipes, the working fluid velocity decreases. At first, the condensation will occur on the wall of the pipes, then layer by layer, the liquid phase will increase. When the fluid is condensing, its thermodynamic characteristics change. The same procedure for the mono-phase has been adopted, introducing some necessary changes [40-44]. The evolution of the working fluid, from quality "0" to quality "1", has been divided into four-parts.

1. Part one, when the quality x is within 0 ÷ 0.75.
2. Part two, when x = 0.75 ÷ 0.5.
3. Part three, when x = 0.5 ÷ 0.25.
4. Part four, when x = 0.25 ÷ 0.

Similarly, for the cooling fluid side, there will be four corresponding stages. The four stages of the cooling water have been computed, if every property is changing linearly. From the working fluid side, the Martinelli parameter is introduced to compute the Nusselt number. The formulae used for the R245fa is:

$$Nu = 0.023 Re^{0.8} \, Pr^{0.3} \, g(Xtt) \quad (3)$$

4.2 Design results

The system geometry has been defined respecting the required constraints. A square configuration of the condenser has been chosen. The previous Figure 10 represents the simulated condenser. Streams numbers 1 and 2 are the inlet and outlet of the working fluid, and streams 4 and 5 are the inlet and outlet of the cooling fluid. Stream 3 is the refill of the fluid; in this case, it is not considered, but it is important to mention the fact that this opportunity exists. Table 6 reports the operating specifications of the main streams. After numerous iterations, the optimal solution has been found. The considered configuration is a compromise between a reasonable pressure drop and the smallest area. All data and a representation of the condenser are, respectively, reported in Table 7 and Figure 11

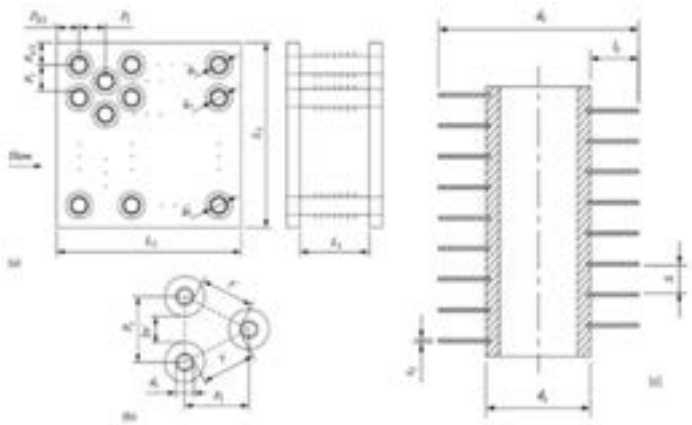

Figure 11. The condenser's chosen configuration. (a) actual disposition in the condenser assembling, (b) triangular configuration characteristics, (c) finned pipe representation.

Table 6. Condenser Streams**.**

Stream n° 1	
Temperature (K)	383
Pressure (kPa)	610
Stream n° 2	
Temperature (K)	346
Pressure (kPa)	606
Stream n° 3	
Temperature (K)	332
Pressure (kPa)	101.3
Stream n° 4	
Temperature (K)	301.2
Pressure (kPa)	170.3

Table 7. The condenser's main dimensions.

L_1	0.22
L_2	0.22
L_3	0.18
d_i	0.007
d_r	0.01
d_f	0.014
P_t	0.016
P_l	0.016
S (m)	0.002
t_f **(m)**	0.0003
N_r	16
N_S	14
N_{tot}	16 × 14 = 224

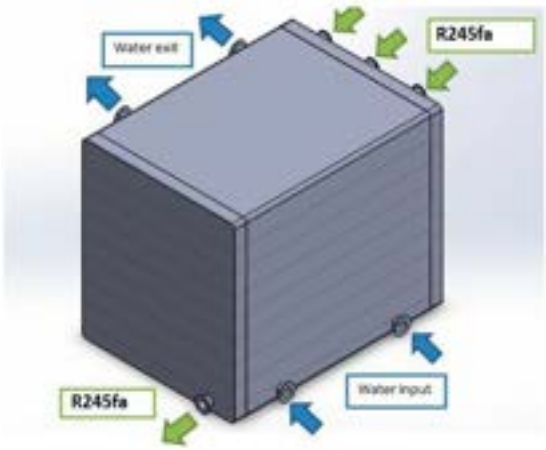

Figure 12. Condenser 3D assembled view.

Finally, the procedure adopted for the design is satisfactory. In fact, given that one of the constraints is the limited space inside the vehicle (the design philosophy is, remember, not to modify the vehicle and to use, when this is possible, all the existing devices and components), the exchanger obtained is small and can be easily inserted inside the vehicle, as will be described in the following paragraph.

5. The On-Board configuration of ORC cycle

An empirical method has been used to demonstrate that the proposed ORC system can be mounted on a vehicle. In the considered commercial vehicle, respecting the available spaces and volumes, the tank has been replaced and modified. For the positioning in the vehicle, since the HRSG has not been measured (at present), it has been assumed to be the same size as the condenser. It is known that the HRSG device is usually smaller than the condenser. Figures 13 represent the possible plant configuration in a commercial vehicle. It is important to remember that it is necessary to realize an auxiliary circuit forthe water cooling.

Figure 13. Proposed on-board ORC assembled plant configuration view.

Future Developments and Conclusions

The next steps in the realization of the vehicle and therefore for the completion of the project, the electrical part is now testing. The compressor side tests have almost been completed and have given satisfactory results and in line with what was assumed and chosen. On the turbine side, the test bench has been assembled, which involves the use of a rechargeable battery of about 17 kWh, and once the electrical connections have been completed, will be tested.

At the same time, the expander and evaporator for the ORC group will be designed, always trying to respect the overall constraints imposed by the chosen vehicle. As far as the expander is concerned, we will opt for a

compact solution and consequently the choice could fall on a dynamic expander or most likely on a rotary volumetric, screw type. For the evaporator, the opportunity to create a helical heat exchanger coaxial to the turbine exhaust pipe is being studied, to reduce the size as much as possible.
In conclusion, a very important and “innovative” aspect was the possibility of creating, as part of the electrification process of the power train for the mild hybrid, a “direct coupling” between the electric motor and compressor, and to optimize all waste energy fluxes of the vehicle. All these are thanks to the design of a new electric motor, operating at high rotational speeds, which are characteristics of turbomachinery. The redesigned turbine (now separated from the compressor) has confirmed to be less problematic than the compressor. The turbine can now use all the enthalpy drop of the ICE exhaust gases and operate at lower speeds. As a result, the connected electrical equipment is less complicated, compared to that designed and built for the compressor. The tests - cold site - validate the design choices and the further turbine ones - in case of positive results - confirm and "freeze" the electrical configuration. Then, thanks to the characteristic configuration of the turbine (no wastegate valve), the total exhaust gases can be used for generate additional energy by ORC plant. The bottoming ORC systems has to be completed, from a design point of view. Actually, the condenser realization is "on going". Once realized, a "substitute" circuit will be realized to simulate the operational conditions. The simultaneously design of expander and evaporator will conclude the design process. Last step will be to implement all devices and test the vehicle on the road.

Nomenclature

C	Compressor
EM	Electric Motor
EG	Electric Generator
ICE	Internal Combustion Engine
m	Mass flow rate [kg/s]
p	Pressure [bar]
P	Power [W], Pump, Pressure gauge
Q	Volumetric flow rate [m^3/s]
r	Radius [m], Resistance [Ω]
rpm	Revolutions per minute
R_ρ	Reaction degree
T	Temperature [K], Turbine
V	Velocity
Greek Symbol	
β	Compression ratio
χ	Hub to shroud ratio
δ	Blockage factor
ϵ	Diameter ratio
η	Efficiency
ϵ	Flow coefficient
ω	Rotational speed Density
p	[kg/m^3]
ψ	Load coefficient

References

[1] Yu H.; Song K.; Xie H. Research on Optimal Control of Air System of Diesel Engine with ETurbo Based on Model Prediction. *Chin. Intern. Combust. Engine Eng.* **2018**, *3*, 39–46.

[2] Song K.; Xie H.; Upadhyay D. An assessment of performance trade-offs in diesel engines equipped with regenerative electrically assisted turbochargers. *Int. J. Engine Res.* **2018**, 1–17.

[3] Dimitriou P.; Burke R.; Zhang Q.; Copeland C.; Stoffels H. Electric turbocharging for energy regeneration and increasedefficiency at real driving conditions. *Appl. Sci.* **2017**, *7*, 350.

[4] Capata R. Urban and extra-urban hybrid vehicles: A technological review. *Energies* 2018 (11), 2924; https:// doi.org/10.3390/en11112924

[5] Capata R., Sciubba E. Preliminary Analysis of a New Power Train Concept for a City Hybrid Vehicle. *Designs* 2021, 5(1), 19; https://doi.org/10.3390/designs5010019

[6] Capata R. Experimental Fitting of Redesign Electrified Turbocompressor of a Novel Mild Hybrid Power Train for a City Car. *Energies* 2021, 14(20), 6516; https://doi.org/10.3390/en14206516

[7] Shepherd J. Principles of Turbomachinery. J. Macmillan Pub. Co, NY 1956.

[8] Balje O. Turbomachines". Wiley & Sons, 1981.

[9] ATIP Scoop, Japan Office, "*Micro Gas Turbine Development*", Feb 2005.

[10] Capata R., Sciubba E. Experimental fitting of the re-scaled Balje maps for low-Reynolds radial turbomachinery. *Energies*, vol. Volume 8, p. 7986-8000, ISSN: 1996-1073, DOI: 10.3390/en8087986

[11] Ishihama Y., Sakai K., Matsuzuki T., Hikone. Structural Analysis of Rotating Parts Of An Ultra Micro Gas Turbine. *Proc. Int. Gas Turbine Congress 2003* Tokio, November 2-7, 2003.

[12] Gaydamaka I. V., Efimov A. V., Ivanov M. Ja., Ivanov O. I., Nigmatullin R. Z., Ogarko N. I. Some Aerodynamic Performances of Small Size Compressor and Turbine Stages. *Proc. Int. Gas Turbine Congress* 2003 Tokyo.

[13] Capata R. Turbocharged Decoupling and Turbine Electrification Design for Mild-Hybrid Vehicle. *IMECE2021-68935. Proc. IMECE2021 congress*, November 1-5-USA

[14]] Matsuura K., Kato C., Yoshiki H., Matsuo E., Ikeda H., Nishimura K., Sapkota R. Prototyping Of Small-Sized Two Dimensional Radial Turbines *Proc. Int. Gas Turbine Congress* 2003 Tokio, November 2-7, 2003.

[15] Iwai. Thermodynamic Table For Performance Calculations In Gas Turbine Engine *Proc. Int. Gas Turbine Congress 2003* Tokio, November 2-7, 2003

[16] Capata R. Experimental tests of the operating conditions of a micro gas turbine device. *Journal of Energy and Power Engineering*, vol. 9, p. 326-335, ISSN: 1934-8975, doi: 10.17265/1934-8975/2015.04.002, 2015.

[17] Capata R., Sciubba E. Study, Development and Prototyping of a Novel Mild Hybrid Power Train for a City Car: Design of the Turbocharger. *Appl. Sci*. 2021, 11(1), 234; https://doi.org/10.3390/app11010234

[18] Ahmed A.; Soffker D. Towards Optimal Power Management of Hybrid Electric Vehicles in Real-Time: A Review on Methods, Challenges, and State-Of-The- Art Solutions. *Energies* 2018, 11, 476.

[19] Capata R.; Sciubba, E. The low emission Turbogas hybrid vehicle concept-preliminary simulation and vehicle packaging. *J. Energy Resour. Technol*. 2013, 135, 13.

[20] Capata, R.; Sciubba, E. The Lethe (Low Emissions Turbo-Hybrid Engine) city car of the University of Roma 1: Final proposed configuration. *Energy* 2013, 58, 178–184.

[21] Wei, Z.; Xu, J.; Halim, D. HEV power management control strategy for urban driving. *Appl. Energy* 2017, 194, 705–714. R.

[22] Mocera, F.; Martini, V.; Somà, A. Comparative Analysis of Hybrid Electric Architectures for Specialized Agricultural Tractors. Energies 2022, 15, 1944. https://doi.org/10.3390/en15051944

[23] Martellucci, L.; Capata, R. High Performance Hybrid Vehicle Concept—Preliminary Study and Vehicle Packaging. Energies 2022, 15, 4025. https://doi.org/10.3390/ en15114025

[24] Ehsani, M.; Singh, K.V.; Bansal, H.O.; Mehrjardi, R.T. State of the Art and Trends in Electric and Hybrid Electric Vehicles. Proc. IEEE 2021, 109, 967–984.

[25] Hu, X.; Liu, T.; Qi, X.; Barth, M. Reinforcement Learning for Hybrid and Plug-In Hybrid Electric Vehicle Energy Management: Recent Advances and Prospects. IEEE Ind. Electron. Mag. 2019, 13, 16–25.

[26] Nguyễn, B.-H.; Trovão, J.P.F.; German, R.; Bouscayrol, A. Real-Time Energy Management of Parallel Hybrid Electric Vehicles Using Linear Quadratic Regulation. Energies 2020, 13, 5538.

[27] Liu, T.; Tan, W.; Tang, X.; Zhang, J.; Xing, Y.; Cao, D. Driving conditions-driven energy management strategies for hybrid electric vehicles: A review. Renew. Sustain. Energy Rev. 2021, 151, 111521.

[28] Guo, N.; Zhang, X.; Zou, Y.; Guo, L.; Du, G. Real-time predictive energy management of plug-in hybrid electric vehicles for coordination of fuel economy and battery degradation. Energy 2020, 214, 119070.

[29] Xia, G.; Cao, L.; Bi, G. A review on battery thermal management in electric vehicle application. J. Power Sources 2017, 367, 90–105.

[30] Leibowitz, H.; Smith, I.K.; Stosic, N. Cost-Effective Small Scale ORC Systems for Power Recovery from Low-Grade Heat Sources. In Proceedings of the ASME 2006 International Mechanical Engineering Congress and Exposition, Chicago, IL, USA, 5–10 November 2006.

[31] Tocci, L.; Pal, T.; Pesmazoglou, I.; Franchetti, B. Small Scale Organic Rankine Cycle (ORC): A Techno-Economic Review. Energies 2017, 10, 413.

[32] ORC System. Available online: https://www.turboden.com/products/2463/orc-system (accessed on 20 January 2023).

[33] Li, L.; Tao, L.; Li, Q.; Hu, Y. Experimentally economic analysis of ORC power plant with low-temperature waste heat recovery. Int. J. Low-Carbon Technol. 2021, 16, 35–44.

[34] Jafari, A.; Yang, C.; Chang, C. Optimization of heat exchanger size of a 10 kW organic Rankine cycle system. Energy Procedia 2017, 129, 851–858.

[35] Unamba, C.K.; White, M.; Sapin, P.; Freeman, J.; Lecompte, S.; Oyewunmia, O.A.; Markidesa, C.N. Experimental Investigation of the Operating Point of a 1-kW ORC System. Energy Procedia 2017, 129, 875–882.

[36] Landellea, A.; Tauveron, N.; Revellin, R.; Haberschill, P.; Colasson, S. Experimental Investigation of a Transcritical Organic Rankine Cycle with Scroll Expander for Low-Temperature Waste Heat Recovery. Energy Procedia 2017, 129, 810–817.

[37] Capata, F. Pantano. Expander design procedures and selection criterion for small rated Organic Rankine Cycle systems *Energy Science & Engineering*, Volume8, Issue10, October 2020. DOI:https://doi.org/10.1002/ese3.710

[38] Dumont O, Talluri L, Fiaschi D, Manfrida G, Lemort V. Comparison of a scroll, a screw, a Roots, a piston expander and a Tesla turbine for small-scale organic Rankine cycle. *5th International Seminar on ORC Power Systems*, September 9–11, 2019, Athens, Greece.

[39] Oudkerk JF, Dickes R, Dumont O, Lemort V. Experimental performance of a piston expander in small-scale organic Rankine cycle*. Proc of Int. Conf. on Compressors and their Systems*; 2015.

[40] Seher D, Lengenfelder T, Gerhardt J, Eisenmenger N, Hackner, M, Krinn I. Waste Heat Recovery for Commercial Vehicles with a Rankine Process. *Proceeding of the 21st Aachen Colloq*; 2012.

[41] Bonafoni G., Capata R. Proposed Design Procedure of a Helical Coil Heat Exchanger for an Orc Energy Recovery System for Vehicular Application. *Mechanics, Materials Science & Engineering Journal*, 10.13140/RG.2.1.2503.5282

[42] Capata R., Zangrillo E. Preliminary design of compact condenser in an organic rankine cycle system for the low grade waste heat recovery. *Energies* 2014, 7(12), 8008-8035; https://doi.org/10.3390/en7128008

[43] Capata R., Piras G. Condenser Design for On-Board ORC Recovery System. *Appl. Sci*. 2021, 11(14), 6356; https://doi.org/10.3390/app11146356

[44] Kuppan, T. *Heat Exchanger Design Handbook*, 2nd ed.; CRC Press: New York, NY, USA, 2013.

Holistic approach to improve cabin air quality in electric vehicles and energy savings

Matisse Lesage[a], David Chalet[b], Jérôme Migaud[c] and Christoph Krautner[d]

[a] Nantes Université, Ecole Centrale Nantes, CNRS, LHEEA, UmR 6598, Nantes, France, matisse.lesage@ec-nantes.fr, CA
[b] Nantes Université, Ecole Centrale Nantes, CNRS, LHEEA, UmR 6598, Nantes, France, david.chalet@ec-nantes.fr
[c] MANN+HUMMEL Filtration France, Laval, France, jerome.migaud@mann-hummel.com
[d] MANN+HUMMEL GmbH, Marklkofen, Germany, christoph.krautner@mann-hummel.com

Abstract:

In electric vehicles, the Heating, Ventilation and Air-Conditioning (HVAC) function is often performed by a heat pump. Heating and cooling the cabin air drains energy directly from the vehicle's battery. In addition, these vehicles may operate in environments with high level of air pollution. In the cabin, passengers are confined to a small space where particles and harmful gases can accumulate. In addition, the ventilation system must also handle the air which does not enter the cabin through blower operation. This "infiltration" is a function of the vehicle speed and allows pollution to enter the cabin without being filtered or thermally treated.
The objective of the study is to optimize the competing goals of the HVAC system: achieving the best air quality while maintaining good thermal comfort, at minimum energy costs.
A system simulation tool is calibrated to represent the heating and cooling of an electric car. With this model, the influence of key factors is evaluated. Depending on ambient conditions and other parameters (number of occupants, vehicle speed, etc.), the blower flow rate and recirculation ratio can be adjusted to reach the objectives. The management of the proportion of fresh and recirculated air allows to regulate the humidity and carbon dioxide levels. Optimum controls are proposed as good trade-offs to reduce the power consumption, while maintaining a safe and comfortable environment for occupants. Compared to the full fresh air mode, the driving range gains are estimated in cold (−15°C) and hot (30°C) scenarios at 9 and 26 km respectively.

Keywords:

Ventilation; Filtration; Heat pump; HVAC; Driving range.

1. Introduction

Heating and cooling of the vehicle cabin is an important feature, and its design can vary a lot based on the car model. It depends on cabin size, vehicle-mounted actuators, materials, and occupants (in terms of both perception and changes in thermal environment). In full electric vehicles, the motor efficiency leads to low heat losses. Contrary to thermal vehicles, this waste heat is not enough to heat the cabin. Previous research [1] shows that the HVAC system of electric vehicles can reduce the driving range by 35% to 50%, depending on weather conditions. There are other options to reduce the HVAC system's energy usage, for example by using reversible heat pumps. A key advantage of the heat pump is its ability to provide more heat output than its electrical consumption. This is made possible by its ability to absorb energy from the environment, even in cold or hot conditions. This solution is already implemented in Tesla vehicles, Renault ZOE, or also as an option in the Volkswagen ID series.

The heat pump is integrated to the HVAC module, with other main components as the blower and the recirculation flap. Figure 1 illustrates typical airflow within a passenger car. The air inlet is often found near the base of the windshield, where the blower forces the outside air into the cabin. The outlet is generally a decompression flap located in the car body near the rear trunk. As an alternative or complement to the fresh air intake, the vehicle also has a recirculation mode. Furthermore, there is the infiltration phenomena, which occurs due to the air entering the cabin through small openings in the (not airtight) car body and this is caused by the air resistance of the vehicle. This infiltrated air is not thermally treated by the HVAC system.

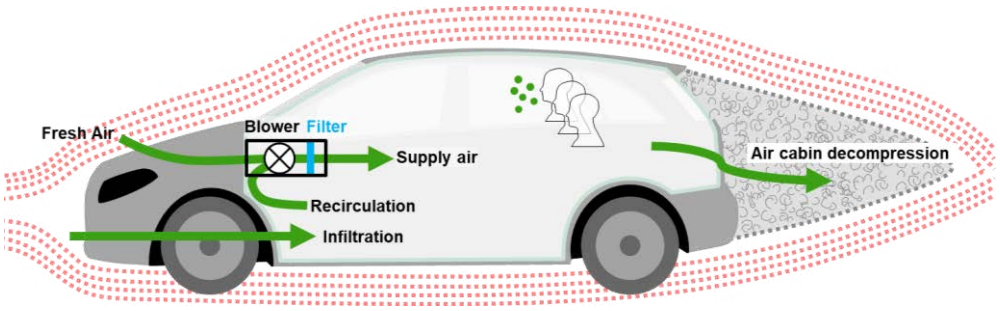

Figure 1. Overview of airflows inside a car cabin.

The global objective of the HVAC system is to provide a comfortable environment for the driver and the passengers. Thermal comfort can be characterized as a feeling of harmony with one's surroundings. Comfort in a closed environment is well documented, with many articles focused on the building sector. A passenger car cabin is significantly different because it has a small volume (generally less than 5 m^3) and can hold several passengers. In addition, driving a car requires a certain degree of attention. It is preferable to feel comfortable in order to prevent weariness, and thus a decline in driving ability. Fojtlín *et al* [2] links driver fatigue to different temperature settings. Heat stress has been found to negatively affect driver skill.

According to a standard [3], the human comfort depends on six parameters: human metabolism, clothing insulation, relative humidity, temperature, radiation, and air flow velocity. Thermal comfort, however, is a complicated idea that is challenging to guarantee and is not restricted to the aforementioned factors. This is because it's a mix of subjective, psychological and socio-cultural factors [4].

Assuming a comfortable temperature, the level of relative humidity for people should be between 30% and 70% (preferably in the range 40-60%) [5,6]. A low humidity level can irritate the eyes and throat and dry the mucous membranes and nasal passages. A high relative humidity can reduce the evaporative cooling of the body through sweating, causing a suffocating sensation. It also promotes the growth of fungi and leads to other moisture related problems. Experimental research [7] measures the comfort and fatigue of passengers in a cabin under different environmental settings and shows that an excess of water (humidity above 60%) increases the rate of fatigue related complaints, particularly on the eye dryness sensation and visual fatigue.

Moreover, air renewal, an essential component of comfort, has not yet been considered. The interior air must be changed frequently, to enable the removal of odours, contaminants, water vapour, and CO_2 (Carbon Dioxide) emitted by the materials and occupants. Monitoring the CO_2 concentration is one way to assess how well a ventilated space is perceived by humans. Carbon dioxide serves as a reliable indicator for biological effluents (i.e., odours) that are known to be unfavourable for comfort. Then, besides the comfort, the HVAC system plays an important role in keeping the driver at their full capacity. It is therefore important that temperature, humidity and CO_2 levels are regulated together in the vehicle's cabin.

The literature review reveals different solutions to either reduce the energy consumption, enhance the comfort, or improve the air quality in a vehicle cabin: air renewal [8], efficient filters [9], air purifier [10], catalytic conversion [11]. All the filtration and air treatment solutions mainly address the air quality issue, not the energy management nor the thermal comfort since CO_2 and humidity are not filtered. Some solutions are attractive for their field of application, but their use in a car cabin is often limited by a drawback on another aspect. For example, the use of recirculation mode to reduce the energy consumption should be used with caution because of the risk of high carbon dioxide levels. There are several good concepts, but with a single objective (limited scope). The literature review does not reveal any complete solution for air quality, energy savings and thermal comfort.

2. System modelling with holistic approach

To evaluate the HVAC system of an electric vehicle, a simulation tool is developed. It is a multi-physics model based on numerous individual elements: blower, filter, cabin, etc. All individual elements are connected to represent the complete system: the holistic approach focuses on a macro scale level. The model contains all necessary elements of the heating, ventilation and air-conditioning (HVAC) of a vehicle cabin, exposed to various external interactions. This model will be used to evaluate different strategies for the HVAC system.

2.1. 1D simulation tool

For the present work, a 1D simulation level is considered. It appears to be the most suitable tool to achieve a good trade-off between computational time and accuracy of results at a system level. Neither the time required to build such a model nor the chosen system approach is compatible with a 3D simulation tool. In addition, a bloc modelling with transfer function requires many calibration data without offering sufficient robustness in the results. With a 1D model, the geometry of components is simplified and only one spatial dimension is considered (commonly in the flow direction). It allows completing transient or stationary scenarios with a fast computational time.

GT-Suite, a software developed by Gamma Technologies is selected for this task. It is a well-known software for system modelling at a 0D/1D level in the automotive domain. At each time step, the solver integrates the conservation equations (mass, energy and momentum) in space and time.

The complete HVAC system is depicted in the model as shown in Figure 2. It can be divided in two main parts: the heat pump (left side of the figure) and the cabin air circuit (right).

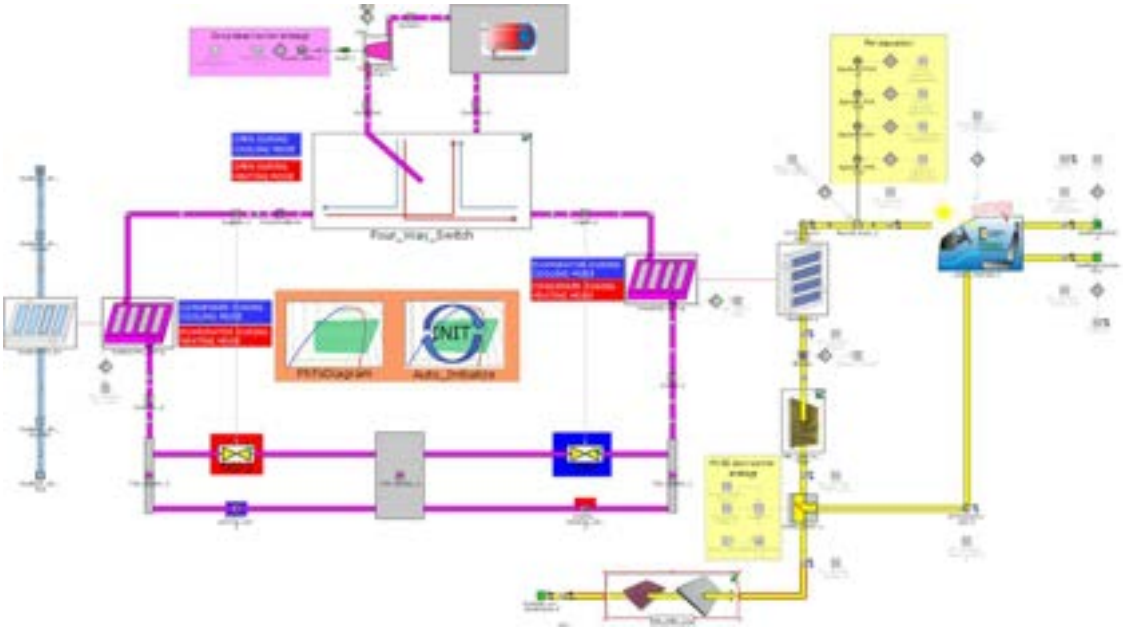

Figure 2. Overview of the complete simulation model in GT-Suite.

2.1.1. Heat pump model

This model is based on a Renault ZOE architecture, which remains a common structural design for electric vehicles. The elements of the heat pump circuit are a compressor, an accumulator, two heat exchangers, a four-way switch, two expansion valves and some piping elements. The refrigerant working fluid is R134a.

The cabin temperature is regulated by adjusting the compressor speed. This compressor is modelled from a GT-Suite template with a map-based approach relying on measured performance data. The refrigerant fluid is guided by the four-way switch from the compressor to the condenser.

In heating mode, the condenser is on the cabin side and the evaporator is on the outside air side. It is the opposite in cooling mode. The two heat exchangers are interacting with either the outside air circuit or the cabin air circuit. The outside air circuit is connected to ambient air conditions (pressure, temperature, humidity), with flow rate depending on vehicle speed (additional wind speed is assumed to be 0). For both heat exchangers, predictive correlations are used to compute Reynolds and Nusselt numbers during a simulation. The fluid phase changes are resolved in the exchangers with computation of the resulting variations in heat transfer coefficients.

The refrigerant fluid exits the condenser to enter the thermal expansion valve. It manages the flow rate of refrigerant released in the evaporator, thus controlling the superheat. Finally, the heat pump circuit is completed by a 1L accumulator upstream the compressor.

2.1.2. Air circuit model with mono-zone cabin

Like the heat pump circuit, the cabin air circuit is built with several components. The inlet of air from the outside is upstream the recirculation flap. This flap manages the amount of air coming either from the outside environment or back from the cabin. The next element after the recirculation flap is the blower and it drives the circulation of the airflow. Before entering the cabin module, the air is either heated or cooled in the heat exchanger connected to the heat pump circuit. From the cabin, the outlet is either the recirculation path or the outside environment.

Finally, an inlet is connected to the cabin element to represent the inlet of air directly from the outside into the cabin vehicle. This is called infiltration. This air, neither filtered nor set at proper temperature, can have great influence on the thermal balance (and air quality) in the cabin. The modelling and calibration of the infiltration flow rate is detailed in a previous study [12].

The cabin is a mono-zone volume based on the generic GT-Suite module to compute the thermal balance inside a medium size vehicle cabin. The mono-zone model implies that there is complete homogeneity inside the cabin. This approach against multiple volumes or CFD is motivated by fast computational time and less number of inputs required.

2.1.3. Humidity calculations and windshield condensation

Modifications are made in the model to consider further humidity calculations. It is a comfort parameter for occupants and a safety factor considering the condensation on front windshield and side windows. The objective is to have an accurate prediction of the humidity level and condensation risk in the cabin.

With that purpose, the standard GT-Suite windshield model is improved to include a variable heat transfer coefficient. A moving vehicle implies an air movement on the external surface of the front windshield, thus suggesting heat transfer by convection mode. The convective heat transfer coefficient can be calculated using the Nusselt number equation, as in Eq. (1), where L_c is the characteristic length of the windshield.

$$Nu = \frac{h.L_c}{\lambda}, \tag{1}$$

To simplify the model, no wind is considered. Hence, air velocity on windshield is equal to the vehicle speed. This improved convection heat transfer model allows a more accurate prediction of the windshield surface temperature, which plays an important part in the condensation risk assessment.

Assuming that all the water in the air above saturation condenses from gas into liquid, the condensation mass (mass of water per mass of dry air) can be computed with the mixing ratio as in Eq. (2).

$$\text{if } X_w > X_{ws} \text{ then } Cm\left(g_{water}/kg_{dry\ air}\right) = X_w - X_{ws}, \text{ with: } X_w\left(g_{water}/kg_{dry\ air}\right) = \frac{M(H_2O)}{M(air)}\frac{x_w}{1-x_w}$$

$$\text{and } X_{ws}\left(g_{water}/kg_{dry\ air}\right) = \frac{M(H_2O)}{M(air)}\frac{P_{ws}}{P_{tot}-P_{ws}} \tag{2}$$

Besides the calculation of the condensation mass, a complementary factor is created in order to have a second option to evaluate the creation of condensate. More precisely, it is made to estimate the risk of fog formation on the glass surfaces inside the vehicle's cabin. This factor, so called $Fog\ risk$, is based on the calculation of relative humidity on the glass surfaces, as in Eq. (3).

$$Fog\ risk = \frac{P_w}{P_{ws}}, \tag{3}$$

The partial pressure of water vapour (P_w) is obtained with Dalton's law ($P_w = P_{tot}.x_w$) where the mole fraction of water is taken from the mono-zone cabin air. The partial pressure of water vapour at saturation (P_{ws}) is calculated from the saturation tables, in which the temperature is taken at the wall of the involved surface (e.g., windshield temperature at cabin side). According to the definition of the factor:

- There should be condensation if $Fog\ risk$ is above 100%
- There should not be condensation if $Fog\ risk$ is below 100%

The fog risk factor gives additional information to the computation of condensation mass. On one hand if the condensation mass is zero, the fog risk factor gives an assessment to know the margin before condensation: the situation is more perilous with a 99% fog risk rather than a 1% risk. On the other hand, if the condensation mass is strictly positive, the fog risk factor gives knowledge about the closeness to regain a clean windshield: condensation with a 101% fog risk is easier to remove than condensation with a 150% fog risk.

The main limitation in the calculation of the condensation mass and the fog risk factor is the mono-zone approach. Indeed, the whole air volume inside the cabin is seen as one entity. There is no possibility to separate or orient the air flow driven by the blower. For instance, Figure 3 displays a photo of the windshield during an experiment made in the scope of this project. There is condensation on a major part of the windshield, besides a small area highlighted in the picture (zone A). This is explained by the air blown in this direction from the vent grid located at the bottom of the windshield. Locally, the humidity conditions do not trigger condensation while compared to the rest of the windshield. Such a phenomenon cannot be evaluated with the simulation model as is. So, the condensation mass and the fog risk factor only give a global evaluation.

Figure 3. Evidence of condensation on the windshield during an experiment.

2.1.4. Thermal model

There is a thermal interaction between the air flowing through the cabin, the internal elements and the outside environment factors (sun, wind). The modelling of the cabin involves many processes, showcased in Figure 4.

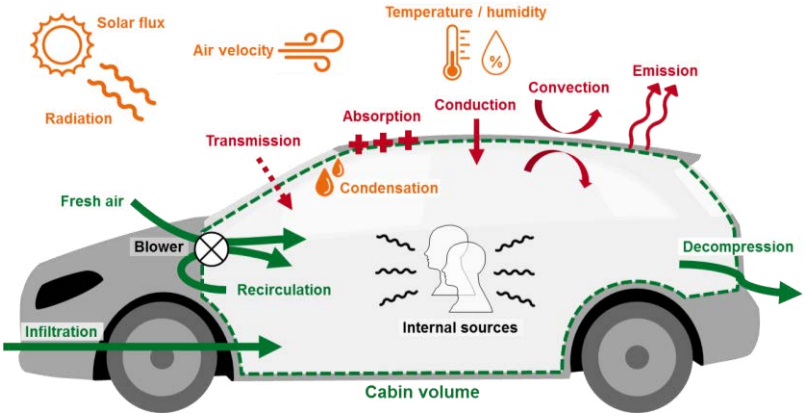

Figure 4. Model of the thermal behaviour of a car cabin.

The mono-zone modelling implies that the air temperature is homogeneous inside the whole cabin. The cabin characteristics are imported in the simulation code. A standard three-layer material is selected for doors, floor and roof: polyamide, polyurethane and stainless steel. Material properties like mass and geometry (thickness and surface area) are adjusted to match the characteristics of a Renault ZOE.

A solar view factor describes the portion of solar flux reaching each part of the cabin. The sun is considered to be at full height (90°C) for all simulations. Hence, the solar flux mostly affects the roof and the windshield while the side and rear parts of the car experience a lower impact. An absorptivity coefficient (0.4) and an emissivity coefficient (0.96) are introduced to represent the solar effect on the outside of roof and doors. Another set of coefficients is used for the glass windows (0.15 for absorptivity and 0.9 for emissivity), with the addition of a transmission coefficient (0.7).

The modelling of the cabin floor thermal interaction is obtained with convection at both sides: internal and external. Heat rate through the three-layer floor material is calculated with conduction. Similar modelling is also possible for the roof and side doors of the cabin, with the addition of the solar flux on the external side. This modelling is also the same for all glass surfaces (windows and windshield) but with a single layer instead of a three-layer material. The thermal effect on the internal lumped material of the cabin is governed by the solar flux coming through the glass surfaces. Finally, two heat sources are included in the cabin:

- 100W that represents the heat coming from the electrical motor and the dashboard auxiliaries
- 75W per person, which is the heat input from occupants [13,14]

2.1.5. Passenger model

In the model, the number of occupants is multiplied by the amount of heat, CO_2 and humidity emitted by an average adult. A CO_2 injector placed in the cabin volume simulates the exhalation flow rate from the occupants: CO_2 mass flow rate of 18.75 L/h. This value is an average for one human adult in normal seated activity level (e.g. office work, paper reading, driving…) [15]. The variability of CO_2 exhalation flow rate can be widely discussed as it is influenced by numerous factors, like age, metabolic rate, stress level, activity level, etc.

Breathing and sweating of the occupants is also a source of humidity. This is highly dependent on the ambient conditions (temperature and humidity) and human factors (clothing, activity level, metabolism, age, weight, etc.). Average values and models are found in the literature [16–18]. The main factors of influence that are relevant are the temperature and humidity. In the model, different cases are implemented depending on outside conditions: 30 g/h in cold condition (below 10°C), 50 to 65 g/h in standard condition (around 20°C and 50% of relative humidity) and 100 g/h in hot and humid condition (above 30°C and 65% of humidity). These values are fixed for the duration of a simulation, i.e., there is no dependence with cabin temperature. Lastly, the model considers that this H_2O source is emitted in pure vapour condition (and not liquid). It has a direct impact on the cabin humidity level, with consequences on the performance of the heat exchanger (e.g., condensation) connected to the heat pump circuit.

2.1.6. Ventilation strategies: opti-CO_2 and opti-H_2O

In the cabin air circuit, the ratio of fresh air against recirculated air is controlled by the recirculation flap. Control of the recirculation ratio is required to reduce the energy consumption, particularly in rough environments with extreme temperatures. It can be set at a predefined variable or constant value for a simulation scenario. For safety and health concerns, a full recirculation mode is not possible. Two additional modes are created in the

model: “opti-CO_2” and “opti-H_2O”. In both cases, the opening of the recirculation flap is controlled by a PID regulator. The idea is to find a trade-off between moderate energy consumption and safe air inside the cabin.

In the opti-CO_2 mode, the recirculation flap is regulated between its two extreme positions to achieve a target CO_2 concentration in the vehicle. As no regulation exists for vehicle in-cabin CO_2 level, a standard limit value between 1100 and 2000 ppm can be selected to keep passengers in a comfortable and safe space. According to an experimental study [19] this level is not associated to health risks, but is the baseline to first signs of cognitive dysfunctions (e.g. lack of concentration). The ASHRAE guideline [20] states that the comfort limit for air renewal in a closed space is strongly correlated to a CO_2 level below 1100 ppm. This limit can be discussed for a vehicle application, where the level and duration of exposure can be quite variable.

Similar to the opti-CO_2 mode, a control of the recirculation flap is implemented to limit the condensation issue. This opti-H_2O mode is based on the variable that monitors the risk of fogging on the front windshield. The target of the PID regulator is a fog risk of 95% (5% margin before condensation).

2.2. Calibration and validation with experimental data

If available, the input model data is filled to match the characteristics of a Renault ZOE (eco2 phase 1). It is a full electric car (88 ch), with five doors and a cabin volume of 2.5 m^3. In the scope of this project, different test campaigns (more than 20) are used to calibrate and validate the simulation model. Otherwise, the generic data provided by GT-Suite for similar sized-vehicle and components is used. This is as per the recommendation in the software manual and only considered if the input data is limited. Such data is mostly based on predictive correlations and literature models. Then, the calibration stage allows to adjust the parameters.

A small sample of the validation tests are described in this article, and a separate paper focuses on the infiltration topic [12]. The idea is to compare the experimental results with the simulation results. The test conditions are then reproduced in the simulation tool. Given the large number of experimental evidence, only a few examples are shown in this paper.

Figure 5 depicts the evolution of the CO_2 and humidity concentrations in the cabin over time. The test is done with a parked vehicle (0 km/h) for a duration of one hour. The blower flow rate and recirculation ratio are fixed respectively at 180 kg/h and 94%. This ventilation condition leads to a rise of the CO_2 and humidity concentrations in the cabin. Once again, the simulation tool gives similar results to the tests.

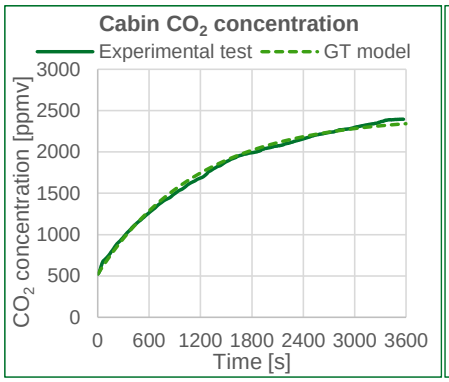

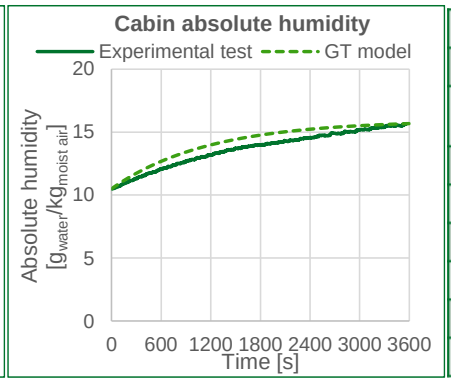

Vehicle speed	0 km/h
Cycle duration	3600s
Blower flow rate	position 4 out of 8 = 154 m^3/h (180 kg/h)
Recirculation ratio	94%
Amb. temperature	15°C
Ambient humidity	82%
Ambient CO2	445 ppmv
Occupants	1 (only the driver)
Water emission	50 g/h per person

Figure 5. Sample of the validation of the simulation tool with experimental results regarding cabin CO_2 concentration and absolute humidity.

These results are a part of larger experimental test campaigns, covering a diverse range of environmental conditions. It shows that the simulation tool can predict accurately the cabin state regarding temperature, CO_2 concentration and humidity level.

3. Results and discussion

3.1. Potential increase in driving range with the opti-CO_2 strategy

The traditional ventilation setting in a passenger car is the fresh air mode (0% recirculation). This configuration leads to a good amount of air renewal, but it is not optimised for the energy consumption of the HVAC system. In an electric vehicle, the heat pump energy required to heat or cool the cabin is drained directly from the battery, thus decreasing the driving range. Controlling the recirculation ratio is necessary to decrease the impact of the HVAC system, particularly in rough environments with extreme temperatures. For health and safety related concerns (CO_2 intoxication), a full recirculation mode is not possible. The idea of the opti-CO_2 mode is to find a trade-off between a moderate energy consumption and safe air inside the cabin.

Table 1 depicts the maximum recirculation ratio allowed to keep the cabin CO_2 concentration below the target. These values depend on the number of occupants (and their CO_2 emission), the blower flow rate, and the infiltration flow rate. If the CO_2 target is increased from 1100 to 2000 ppm, the recirculation ratio can be set to a higher value.

Table 1. Regulation of CO_2 concentration with a blower flow rate of 200 m3/h and assuming no infiltration.

	Stabilized volumetric recirculation ratio in opti-CO_2 mode	
Number of occupants	Target = 1100 ppm	Target = 2000 ppm
1	79%	90%
2	61%	83%
3	42%	75%
4	21%	65%
5	2%	57%

The power consumption for heating and cooling is calculated using the simulation tool. Three ambient scenarios are compared: summer, winter, and spring. The outside temperatures are 30°C, −15°C and 19°C, respectively with a solar flux of 750, 250 and 500 W/m^2. The heat pump targets a cabin temperature of 19°C in the case of winter and spring, and 25°C in the summer. The other simulation settings, along with the results regarding power consumption and driving range gain estimations are given in Figure 6. The range is roughly estimated using Eq. (4):

$$Range_{loss} = Range_{max} - \frac{Range_{max}}{1 + \frac{Spec_{range} * Power}{Speed}} \quad (4)$$

The maximum driving range is 300 km, with a specified range of 6.6 km/kWh and an average speed of 47 km/h as described in WLTC (Worldwide harmonized Light-duty vehicles Test Cycles). The “range gain” chart (Figure 6) is calculated by subtracting the $Range_{loss}$ of the given configuration to the common 0% recirculation case.

Eventually for the three scenarios, the best trade-off between energy consumption and safe air environment is achieved with the opti-CO_2 mode. Compared to the traditional “full fresh air” mode, the power gains of the heat pump in winter, spring and summer scenarios are respectively 14%, 19% and 38% (1100 ppm target). These gains are important because they can directly influence the driving range. In the 0% recirculation case, the range loss is estimated at 88, 26 and 85 km in the winter, spring and summer scenarios, respectively.

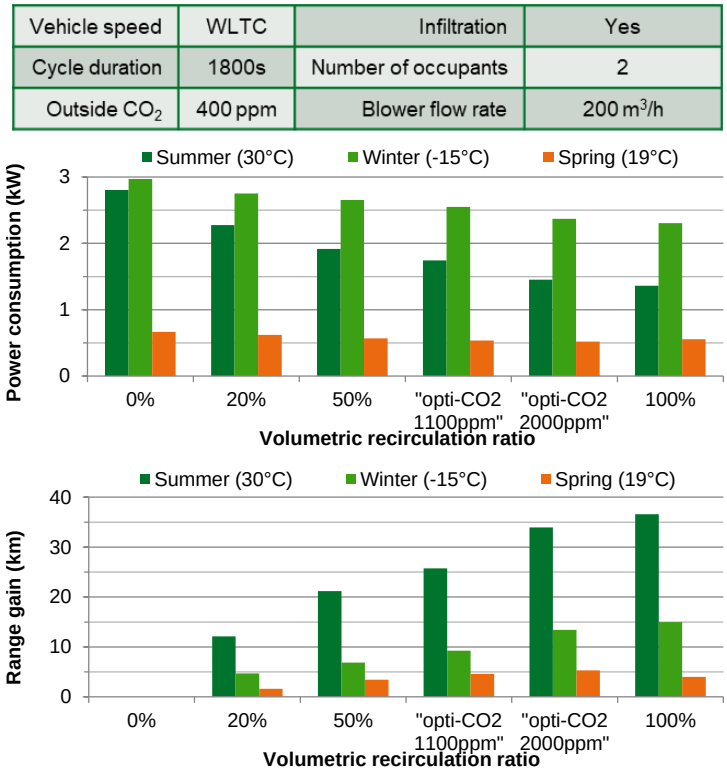

Figure 6. Power consumption (of compressor heat pump) needed for thermal comfort and impact on the driving range of an electrical vehicle.

With the opti-CO_2 mode at 1100 ppm, the driving range is increased by 9, 5 and 26 km compared to the full fresh air case. Increasing the opti-CO_2 target from 1100 to 2000 ppm gives an additional range gain in the three scenarios: 8, 4 and 1 kms. These benefits must be weighed against the potential health risks caused by slightly higher CO_2 exposure. The health aspect is not well documented, so it is difficult to give a precise health assessment in the range between 1100 to 2000 ppm. Besides, a different strategy could be applied to the HVAC system. In the simulation tool, the CO_2 target is continuously fixed over time. A new control strategy

could set the target at a higher value in steady state mode, but provide periods of fully fresh air. Nevertheless, the results presented in this section give an idea of the influence of the CO_2 target on increasing the driving range. The objective of the next subsection is to assess another risk inside the cabin: humidity accumulation.

3.2. Humidity level and evidence of fogging risk

The humidity level is evaluated with the simulation tool in simple scenarios. The objective is to establish the conditions under which condensation can occur on the glass surfaces inside the cabin. Different ambient temperatures are tested, from −10°C to +10°C, with a relative humidity of 85%. A moderate solar flux of 250 W/m^2 is also considered. The vehicle speed is set to 60 km/h for a duration of 10 minutes. A fixed speed is preferred rather than a realistic driving cycle to limit the variations due to infiltration. There are two occupants in the cabin. Each person emits water vapour at a 50 g/h rate. The blower flow rate is set to 200 m^3/h, which corresponds to a medium blower position in a Renault ZOE.

Different recirculation modes are compared, including the standard 0% and 100% fresh air modes. Depending on the vehicle speed, such ventilation settings can trigger infiltration. The infiltration flow rate is null in the fresh air mode, and at 20 m^3/h in recirculation mode. An additional recirculation mode is implemented in the simulation: opti-CO_2. The target of CO_2 concentration in the cabin is fixed at 2000 ppm. With two occupants, the recirculation mode is activated during 425s. This is the time required to increase the CO_2 concentration to 2000 ppm. Then, the fresh air ratio is fixed to 5%. The main simulation results of humidity and fogging with two occupants are given in Figure 7.

Vehicle speed	60 km/h	Infiltration	Yes	Ambient humidity	85%
Cycle duration	600s	Number of occupants	2	Solar flux	250 W/m^2
Blower flow rate	200 m^3/h	Water emission	50 g/h per person	Opti-CO_2 target	2000 ppm

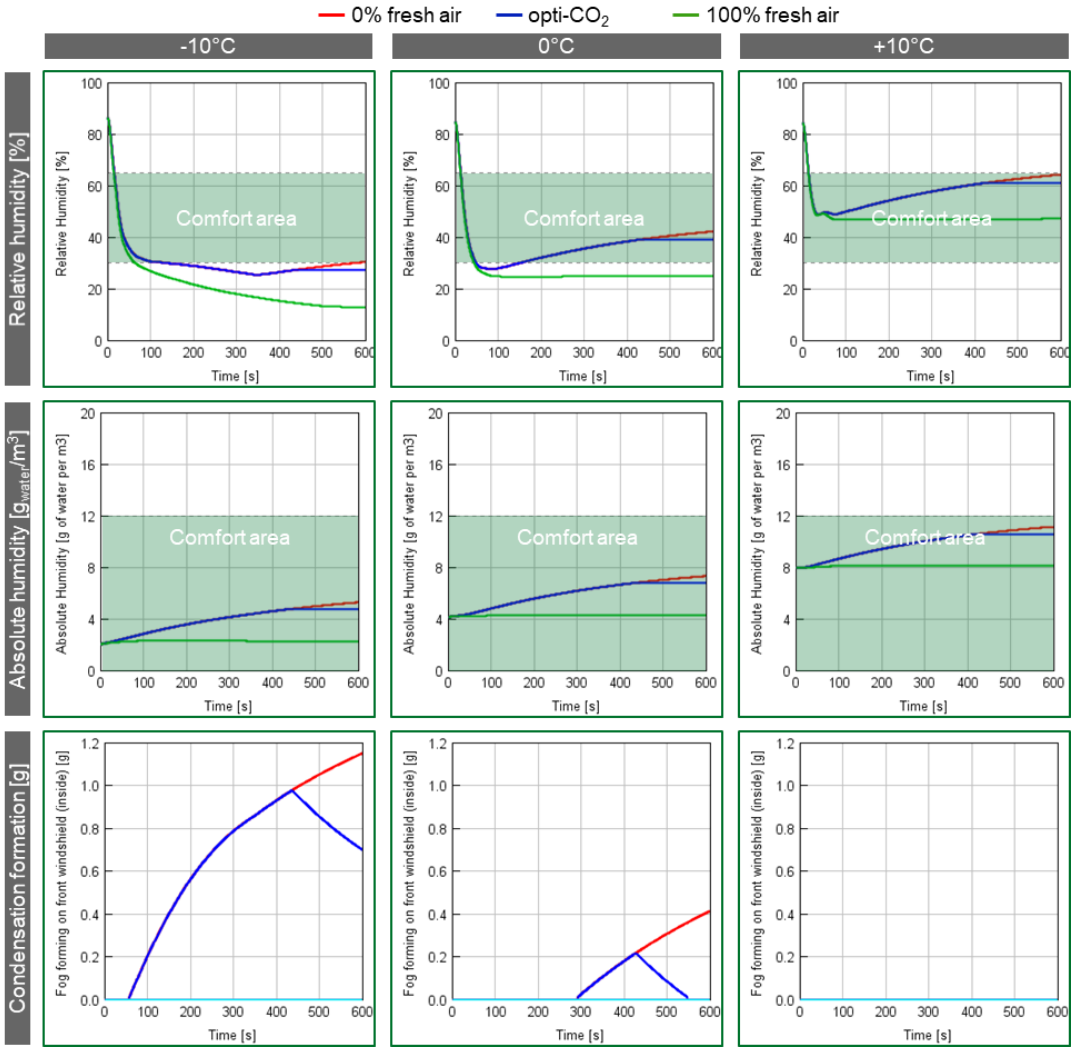

Figure 7. Cabin humidity level and fog formation in the front windshield for three ambient temperatures, and three recirculation modes.

The relative humidity in the cabin depends mainly on the outside temperature. In all cases, the relative humidity is dropping very quickly at the beginning of the cycle. In approximately one minute, the level drops from 85% to a value between 25% and 50%. At −10°C, the humidity ranges between 13% and 30% at the end of the simulation, which is just below the minimum requirement for comfort. At each step of increasing the temperature by 10°C, the relative humidity increases as well. At 0°C and 10°C, the comfort area is globally more achievable. The absolute humidity is kept below the comfort limit in all cases. Regardless of the temperature, humidity is increased by 17% when switching from the fresh air mode to the recirculation mode. It reaches 3.1 g_{water}/m^3 at the end of the simulation.

The amount of condensation on the windshield is also shown on Figure 7. It depends on the amount of water inside the cabin, and the wall temperature of the windshield on the cabin side. In fresh air mode, there is no condensation, regardless of the temperature. In recirculation mode, although there is less humidity at lower temperature, there is more condensation. It appears approximately one minute after the start at −10°C, and after five minutes at 0°C. During these iterations, the relative humidity decreases rapidly, but the absolute humidity increases. Once the absolute humidity reaches a sufficient level along the windshield temperature, there is condensation. At −10°C, it is up to 1.2 g at the end of the cycle, and 0.4 g at 0°C. However, at +10°C, there is no condensation.

The analysis of the amount of condensation in the opti-CO_2 configuration is very interesting. Until 425s, the condensation curve follows the 0% fresh air curve. This is because the vehicle is in recirculation mode to increase the CO_2 level. At 425s, the condensation amount is 1.0 g at −10°C, and 0.2 g at 0°C. At this time, the CO_2 concentration hits the target (2000 ppm). Then, the fresh air ratio is regulated at 5% to stabilise the CO_2 level. From 425s to 600s, the condensation amount decreases in opti-CO_2 mode. At −10°C, it is down to 0.7 g at the end of the cycle. At 0°C, there is no more condensation after 550s.

Inversely, in recirculation mode, there is still fog forming at the end of the cycle, the condensation amount is still increasing. Then, there is a large difference of condensation behaviour between the two configurations (opti-CO_2 mode vs. recirculation mode). However, the change in fresh air ratio is not much (5% vs. 0%). It means that a slight change of the recirculation flap position can lead to a large change in fogging.

A sensitivity analysis is made with the simulation tool. The responsiveness of the humidity level and the condensation amount against several parameters is summarised in Table 2.

Table 2. Influence of four parameters on the cabin humidity and amount of condensation.

If …… increases (↗),	then humidity level …….	and condensation ……
temperature	increases (↗)	decreases (↘)
fresh air ratio	decreases (↘)	decreases (↘)
blower flow rate	decreases (↘)	decreases (↘)
number of occupants	increases (↗)	increases (↗)

Globally, there is a higher relative and absolute humidity in the cabin as the temperature increases. However, the level of condensation on the front windshield is higher for lowest temperatures. At +10°C, there is no condensation. Besides, for all outside temperatures, the recirculation mode leads to a higher level of humidity and a higher level of condensation. The fresh air mode prevents the appearance of condensation on the front windshield, even at −10°C. Then, the blower flow rate has a limited influence on the humidity level and condensation. A minimum flow rate is required to limit condensation, but the gains at high blower flow rates are small. Finally, as the number of occupants increases, the source of humidity in the cabin increases as well. This leads to a much higher level of humidity in the cabin, and a higher risk of fog formation on the windshield.

3.3. Investigation of the opti-H_2O strategy

The opti-H_2O is applied to a set of simulations with the ambient temperature −10°C. The objective is to obtain the ideal recirculation ratio in each situation. Different parameters are varied to obtain a wide range of results. The blower flow rate is set between 100 and 350 m^3/h. The vehicle speed is fixed over time for each simulation, between 30 and 130 km/h. This allows the full spectrum of infiltration to be covered. Finally, the number of occupants is a major parameter for the humidity aspect. It is set between one and five. The other simulation parameters are fixed as described in Figure 8. In total, 180 simulations are performed: 6 vehicle speeds, 6 blower flow rates and 5 number of occupants. The cycle duration (2400s) is long enough to reach stabilisation in all cases. The recirculation ratio at the end of the simulation is presented in the five contour plots of Figure 8. Each map represents a single number of occupants, i.e., 36 simulations. The recirculation ratio at 2400s is given between 0 (full fresh air mode) and 1 (full recirculation mode). It should be noted that the fog risk might cross the 95% target during the transient stage of the cycle, thus condensation could appear.

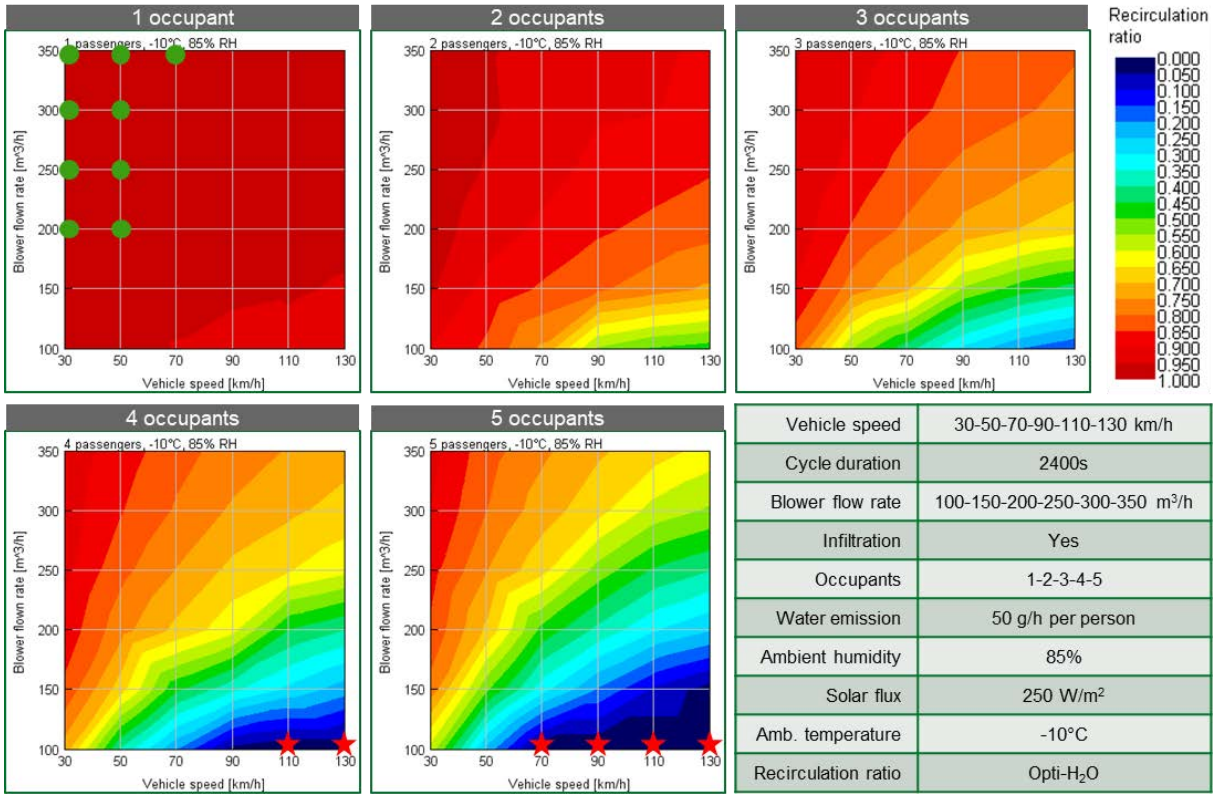

Vehicle speed	30-50-70-90-110-130 km/h
Cycle duration	2400s
Blower flow rate	100-150-200-250-300-350 m^3/h
Infiltration	Yes
Occupants	1-2-3-4-5
Water emission	50 g/h per person
Ambient humidity	85%
Solar flux	250 W/m^2
Amb. temperature	-10°C
Recirculation ratio	Opti-H_2O

Figure 8. Recirculation ratio in stabilised stage of opti-H_2O mode at −10°C, depending on vehicle speed (x axis), blower flow rate (y axis) and number of occupants (map).

In some cases (red stars), the 95% target cannot be reached even with 100% fresh air. The fog risk stays above 95% as there is too much humidity in the cabin. These cases are for a low blower flow rate combined with a high number of occupants and a high vehicle speed. These cases must be avoided to prevent continuous fog formation. In other cases (green dots), the 95% target cannot be reached event with 100% recirculation. These cases are not really an issue because the fog risk stays below 95%. It is possible to reach the minimum energy consumption without any risk of condensation. In the simulation, it occurs only with one occupant, at high blower flow rate and low vehicle speed.

The analysis of the results can be divided in three parts. Firstly, as the number of occupants increases, the humidity level in the cabin increases as well. A higher amount of fresh air is required to avoid condensation. With five occupants, at a medium speed (50 km/h) and medium blower flow rate (200 m^3/h), the recirculation ratio should be kept below 70%. With a single occupant in the cabin, whatever the ventilation settings, the recirculation ratio can be kept above 90% with a low risk of fog formation.

Secondly, as the blower flow rate increases, the recirculation ratio can be increased. Indeed, the idea is to keep a certain amount of fresh air that enters the vehicle. For a fixed amount of fresh air, the recirculation ratio can be increased if the total flow rate increases as well.

Finally, for a fixed blower flow rate, a higher vehicle speed tends to decrease the recirculation ratio. There are two impacts of a higher vehicle speed. On one hand, the infiltration flow rate increases. This brings more fresh air into the cabin, which helps for the condensation issue and also leads to a higher recirculation ratio. On the other hand, the windshield convection coefficient increases with speed. There is more heat exchange on the outside surface of the windshield, which leads to a colder temperature in the interior surface. At the end of the simulation, the interior windshield temperature is 6.6°C at 30 km/h, and −3.7°C at 130 km/h. A lower windshield temperature triggers the formation of condensation. This would lead to a lower recirculation ratio to avoid condensation. Due to the shape of the map, the impact of the convection coefficient is larger than the impact of infiltration: higher vehicle speed leads to lower recirculation ratio.

3.4. Air quality considerations

The air quality includes management of the CO_2 and H_2O species, but also the different pollutants in and out of the vehicle environment: volatile organic compounds (VOCs), fine and ultrafine particles (PM and UFP) or pollutant gases such as ammonia (NH_3). Alongside the regulation of temperature, CO_2 and humidity, the goal of the HVAC system is to provide a clean environment for the passengers. This function is performed by a filtration system, comprising of one or several filters. Then, the energy management strategy can influence the design of the filtration system. Depending on the pollution source (within the cabin or outside the car), the best position of the filter can be in the fresh air path or in the supply air path. In a small and closed volume, an

interior pollutant can rapidly degrade the health of the occupants. Similarly, an external pollutant may expose passengers to a health risk. In both cases, the ventilation strategy alone cannot provide a safe solution. As shown in Figure 9, both the recirculation and fresh air modes have some drawbacks. The use of filter appears as a more sustainable solution.

	100% Recirculation	Opti-mode	100% Fresh air
CO_2 concentration in the cabin	☹	Smart controlled recirculation ratio to find best trade-off depending on driving condition	☺
Protection against external pollutants	☺		☹
Protection against internal pollutants	☹		☺
Filter lifetime savings	☺		☹
Infiltration flow rate	☹		☺
Energy savings for thermal comfort	☺		☹
Condensation risk at low temperature	☹		☺
Humidity comfort	It depends on ambient conditions (temperature and relative humidity)		

Figure 9. Pros and cons of the different recirculation strategies.

Most vehicles have a single filter placed on the supply air path. This approach, which allows to get rid of a proper portion of the pollutants, can be improved by introducing additional and more efficient High Efficiency Particulate Air (HEPA) filters. This high-end media has >99% efficiency against fine particles. Thereby, it can decrease the level of particulate matter exposure for the passengers. With this technology, the lifetime of the filter must be evaluated to have a durable system. An aged filter has a high differential pressure that can decrease the blower performance. So, the ventilation system could include an air quality control strategy, alongside energy and humidity optimization strategies. A smart cabin air Filtration system (Smart CAF) has been evaluated in a study [21].

4. Conclusion

There is a difficult challenge with the ventilation system. In order to decrease the energy consumption to heat or cool the cabin, it is best to increase the recirculation ratio. However, it is not possible to have a prolonged full recirculation mode in the vehicle without having a high condensation risk and high concentration of CO_2. Both the opti-CO_2 and opti-H_2O modes intend to maximize the recirculation ratio up to a safe level. Consequently, it reduces the power consumption of the HVAC system. The gains in driving range compared to the common fresh air mode result to only a few kilometres. This is particularly appealing for electric vehicles in cold or hot regions. In the opti-CO_2 mode, the idea is also to provide good thermal comfort and keep the CO_2 concentration in the cabin at a safe level. In the opti-H_2O mode, the goal is to prevent the formation of condensation on the windshield. In a complete system, the opti-H_2O mode should probably be prioritised over the opti-CO_2 mode because it is a safety aspect for driving the vehicle.

These modes are only tested with the simulation tool and it has some limitations. The main one is that it is a mono-zone model. In most vehicles, it is possible to orient the blower flow rate in different directions, including toward the windshield. This can be a strategy to manage the level of humidity near the windshield.

Acknowledgments

The work in this article is done in a joint International Research Chair entitled “Filtration systems: fluid dynamics and energy consumption reduction” between MANN+HUMMEL and Ecole Centrale de Nantes. This research work is financially supported by the French Government and managed by the National Research Agency (ANR) with the Future Investments Program. The authors want to thank Antoine Bouedec for his contributions to the experiments.

Nomenclature

Cm Condensation mass (mass of water per mass of dry air), g/kg

h Convective heat transfer coefficient, W/m^2/K

Lc Characteristic length of the windshield, m

$M()$ Molecular weight of species (), kg/mol

Nu Nusselt number, -

p_{tot} Total pressure of air, Pa

p_{ws} Partial pressure of water vapour at saturation, Pa

x_w Mole fraction of water, -

X_w Mixing ratio (mass of water vapour per mass of dry air), g/kg

x_{ws} Mole fraction of water at saturation, -

X_{ws} Mixing ratio at saturation, g/kg

Greek symbols

λ Thermal conductivity, W/m/K

References

[1] Farrington R, Rugh J. Impact of Vehicle Air-Conditioning on Fuel Economy, Tailpipe Emissions, and Electric Vehicle Range. In Washington (DC), USA: National Renewable Energy Laboratory; 2000.

[2] Fojtlín M, Fišer J, Pokorný J, Povalač A, Urbanec T, Jícha M. An innovative HVAC control system: Implementation and testing in a vehicular cabin. Journal of Thermal Biology. 2017 Dec 1;70:64–8.

[3] ASHRAE Handbook - Fundamentals. SI Edition. ASHRAE (American Society of Heating, Refrigerating and Air-Conditioning Engineers); 2013. 1134 p.

[4] Schriver-Mazzuoli L. La pollution de l'air intérieur Sources, Effets sanitaires, Ventilation [Internet]. Dunod; 2009 [cited 2021 Jun 2]. 273 p. Available from: http://international.scholarvox.com/book/45006325

[5] Arundel AV, Sterling EM, Biggin JH. Indirect Health Effects of Relative Humidity in Indoor Environments. Environmental Health Perspectives. 1986;65:351–61.

[6] Matton TJP. Simulation and Analysis of Air Recirculation Control Strategies to Control Carbon Dioxide Build-up Inside a Vehicle Cabin [PhD thesis]. [Ontario, Canada]: University of Windsor; 2015.

[7] Tsutsumi H, Hoda Y, Tanabe S ichi, Arishiro A. Effect of Car Cabin Environment on Driver's Comfort and Fatigue. In: SAE Technical Paper [Internet]. Detroit, MI, USA: SAE Technical Paper; 2007 [cited 2020 Mar 6]. Available from: https://www.sae.org/content/2007-01-0444/

[8] Grady ML, Jung H, Kim Y chul, Park JK, Lee BC. Vehicle Cabin Air Quality with Fractional Air Recirculation. In: SAE Technical Paper [Internet]. Detroit, MI, USA: SAE Technical Paper; 2013 [cited 2020 Jan 24]. Available from: https://www.sae.org/content/2013-01-1494/

[9] Jung HS, Grady ML, Victoroff T, Miller AL. Simultaneously reducing CO 2 and particulate exposures via fractional recirculation of vehicle cabin air. Atmospheric Environment. 2017 Jul;160:77–88.

[10] Burtscher H, Loretz S, Keller A, Mayer A, Kasper M, Artley RJ, et al. Nanoparticle Filtration for Vehicle Cabins. In: SAE Technical Paper [Internet]. 2008 [cited 2020 Jan 24]. Available from: https://www.sae.org/content/2008-01-0827/

[11] Matte-Deschênes G. Modélisation de l'efficacité de capture de filtres particulaires pour moteur Diesel [MSc thesis]. [Montréal, Canada]: Ecole Polytechnique de Montréal; 2014.

[12] Lesage M, Chalet D, Migaud J. Experimental analysis and quantification of air infiltration into a passenger car cabin. Transportation Research Part D: Transport and Environment. 2021 Oct 1;99:103006.

[13] Li W, Sun J. Numerical simulation and analysis of transport air conditioning system integrated with passenger compartment. Applied Thermal Engineering. 2013 Jan;50(1):37–45.

[14] Marcos D, Pino FJ, Bordons C, Guerra JJ. The development and validation of a thermal model for the cabin of a vehicle. Applied Thermal Engineering. 2014 May;66(1–2):646–56.

[15] Yoon SH, Ahn HS, Choi YH. Numerical study to evaluate the characteristics Of HVAC-related Parameters to reduce CO2 concentrations in cars. International Journal of Automotive Technology. 2016 Dec;17(6):959–66.

[16] Gładyszewska-Fiedoruk K, Teleszewski TJ. Modeling of Humidity in Passenger Cars Equipped with Mechanical Ventilation. Energies. 2020 Jun 10;13(11):2987.

[17] Zemitis J, Borodinecs A, Frolova M. Measurements of moisture production caused by various sources. Energy and Buildings. 2016 Sep;127:884–91.

[18] Dullinger C, Struckl W, Kozek M. A modular thermal simulation tool for computing energy consumption of HVAC units in rail vehicles. Applied Thermal Engineering. 2015 Mar;78:616–29.

[19] Satish U, Mendell MJ, Shekhar K, Hotchi T, Sullivan D, Streufert S, et al. Is CO2 an Indoor Pollutant? Direct Effects of Low-to-Moderate CO2 Concentrations on Human Decision-Making Performance. Environmental Health Perspectives. 2012 Dec;120(12):1671–7.

[20] Petty S. Summary of ASHRAE's Position on Carbon Dioxide (CO2) Levels in Space. Energy & Environmental Solutions.

[21] Lesage M, Del Fabbro L, Migaud J, Chalet D, Le Nain, Eduin E, Ebnet D. Cabin air quality and energy savings in electric vehicles by using a smart filtration system. In: FILTECH [Internet]. Cologne, Germany; 2019 [cited 2020 Feb 24]. Available from: https://hal.archives-ouvertes.fr/hal-02330724

Energetic and economic analysis of novel concentrating solar air heater using linear Fresnel collector for industrial process heat

Antonio Famiglietti[a], Antonio Lecuona[b],

[a] Universidad Politécnica de Madrid, Escuela Técnica Superior de Ingenieros Industriales, Departamento de Ingeniería Energética, Madrid, Spain, antonio_famiglietti@live.it, CA
[b] Universidad Carlos III de Madrid, Departamento de Ingeniería Térmica y de Fluidos, Leganés, Spain, lecuona@ing uc3m.es,

Abstract:

Industrial processes share a relevant portion of global energy consumption. Heat can be provided by solar thermal technologies aimed at the sustainable industry. A large variety of high energy-demanding industrial processes need hot air in the medium temperature range, provided by natural gas combustion or by electricity. Hot air is used as a medium in a large variety of processes such as drying, curing, and thermal treatments of several products and materials. Non-concentrating flat plate type solar collectors can directly heat air up to 100 °C while higher temperatures can be achieved using linear concentrating technology. In this study an innovative system using linear Fresnel collectors directly provides hot air for the industry up to 350 °C, avoiding the need for liquid heat transfer fluids. Accordingly, the installation is simplified, and lower installation and maintenance requirements are expected compared to other solar technologies. The present studies provide an energetic and economic analysis of the concentrating solar air heater, considering a medium-scale benchmark as a reference case in Southern Europe locations. The results indicate that the solar technology here presented can be economically competitive with other solar thermal solutions, having a huge potential for fossil fuel source replacement in hot air based industrial processes.

Keywords:

Solar heat for industrial processes, linear Fresnel; solar air heater, thermo-economic analysis; solar drying

1. Introduction

Industry consumes more than one-third of global energy [1] and is responsible for a quarter of global emissions. The greater industrial energy demand is heat, followed by electricity, provided almost totally from fossil fuel sources. Industrial heat consumption is estimated at around 85 EJ at the global level and is almost completely provided from fossil fuel. The total heat demand for low and medium temperature applications (< 400°C) accounts for 44 EJ, required by a large variety of industrial processes in any industrial sector.

Aiming at decarbonization, solar thermal technologies are good candidates for replacing fossil fuel technologies in industrial heat production. Besides costs, space availability, and solar resource, the application of Solar Thermal (ST) technologies to industrial heat is limited by their operating temperature range. Flat Plate Collectors (FPC) and Evacuated Tube Collectors (ETC) are suitable for low-temperature heat requirements (< 150 °C). Linear concentrating solar collectors are capable to provide heat at higher temperatures and efficiency than non-concentrating solar collectors e.g. [2] and they are receiving increasing attention for application to industrial processes [3]. Both Parabolic Trough Collectors (PTC) and Linear Fresnel Collectors (LFC) can provide heat in the medium temperature range (150 - 400 °C).

Hot air is used as a medium (working fluid) in a large variety of processes such as drying, curing, and thermal treatments of several products and materials [4]. Hot process air can be obtained by heating ambient air “indirectly” through a heat exchanger which is fed by a proper heat transfer fluid HTF (thermal oil, steam, hot water). HTF is heated by a conventional heat supply. Another common option is to heat air “directly” through a burner so that heated air and exhaust gases are mixed and utilized in the thermal process.

Linear concentrating collectors such as Parabolic Trough Collectors PTC and Linear Fresnel Collector LFC are commonly equipped with a heat transfer fluid HTF. Such are pressurized water, thermal oil, or steam, to

carry heat from the receiver tube that absorbs the concentrated solar irradiance and conveys it to the industrial process where it is needed. A heat exchanger is required to deliver heat to the processes when the heating medium differs from the HTF.

Their application for hot air production has been rarely documented, e.g. [6] and [7]. They use an indirect scheme where an HTF/air heat exchanger HX is needed to heat the process air.

An innovative scheme was proposed by [8] aiming at direct heating air inside the evacuated tube-type receiver of a linear concentrating collector. The theoretical analysis carried out revealed the feasibility of direct heating air in PTCs or LFCs under the appropriate range of solar field configuration. The pumping power needed for blowing air through the standard evacuated receiver tube rapidly grows with the solar field scale. To overcome this limitation, they propose to couple the solar field with an automotive turbocharger in a specific Brayton cycle configuration. The turbocharger allows operating with higher air density without consuming external auxiliary energy for pumping and blowing. A further numerical study [9] confirmed the technical feasibility of the turbo-assisted concentrating solar air heater, in that case, using a linear Fresnel Collector. A prototype has been built and tested allowing the full characterization of the small-scale linear Fresnel solar field available, using only air as the heat transfer fluid [10]. It operated assisted by a commercial turbocharger for air pumping [11].

The present study provides an energetic and economic analysis of the turbo-assisted concentrating solar air heater (T-SAH) applied to a generic process air heating case study, considering a -medium-scale benchmark as a reference.

2. Turbo-assisted concentrating solar air heater

According to the methodology detailed in [12], a benchmark solar field configuration is set. It is based on a commercial linear Fresnel collector [13], Fig.1. The solar field consists of 32 modules with 26.4 m^2 of primary mirrors area, forming a total active area of 845 m^2. The gross area of each module is 36 m^2 which gives a gross area occupied by the installation of 1270 m^2, including minimum spacing.

The LFC is equipped with a standard evacuated receiver tube. An automotive turbocharger joins a compressor c and a turbine e in a compact device with a common shaft, Fig.1. The compressor increases the air pressure up to 2 to 3.5 bar, according to operating conditions, before solar heating. Air velocities and stagnation pressure drops are minimized due to the increased density. After heating up to 450 - 550 °C, air expands through the turbine, which recovers the compressing power. This way no external auxiliary power is needed for air blowing. An auxiliary compressor is used for control and during starting transients only, with negligible yearly energy consumption.

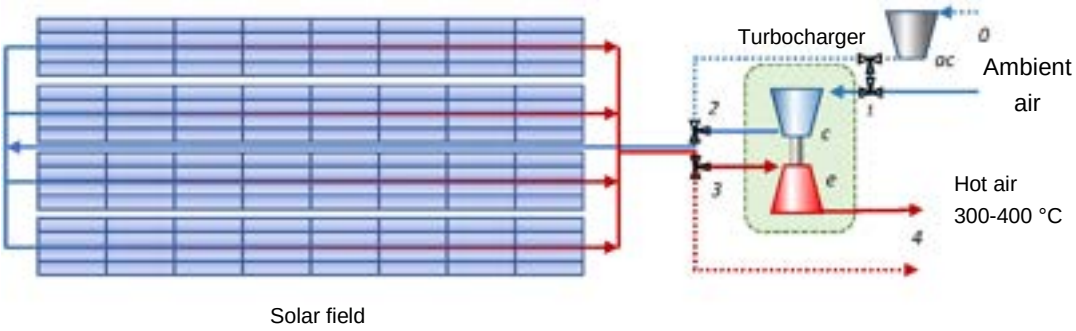

Figure. 1. Benchmark turbo-assisted concentrating solar air heater plant T-SAH.

Using a Typical Meteorological Year TMY, the delivered hot air stream and the thermal power delivered to the user are simulated for each hour of the year for a given location, resulting in a detailed yearly based assessment. The benchmark plant simulated is located in Madrid city, Spain.

Figure 2 shows the behavior of the system across a typical summer clear day through the main operating parameters involved. Fig.2 (a) reports the temperature profile during the day in the main points of the air circuit according to Fig. 1. It can be noticed as the delivered air temperature is relatively flat around T_4 =350 °C, thanks to the behavior of the turbocharger. The mass flow rate $\dot{m}_a$ varies according to the solar thermal power available. Pressurization imposed by the turbocharger reaches a pressure ratio of $\pi_c = \frac{p_2}{p_{amb}} = 3.5$ at midday,

which allows the minimization of pressure drops across the solar field and enables the turbine to drive the compressor without external aid (freewheeling). Accordingly, the required inlet turbine temperature goes up to 550 °C, while the receiver wall temperature T_w does not overcome its thermal limit ($T_{w,max} = 600$ °C). In spring and winter days both mass flow rate as well as operating temperature are lower, while the outlet air temperature is steadily above 300 °C.

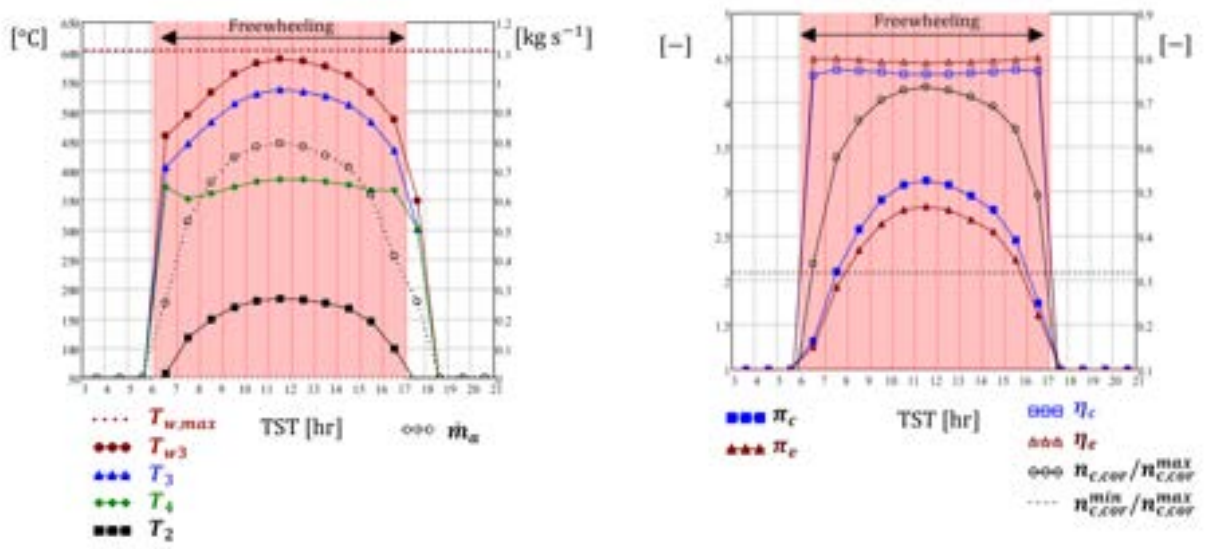

(a) (b)

Figure 2 Turbocharged Solar Air Heater T-SAH performances vs. true solar time TST during a clear summer day. Solar field orientation N-S. TST: true Solar Time; T, p: temperature and pressure according to Fig.1; $\boldsymbol{T_{w3}}$: receiver wall temperature at tube outlet, $\boldsymbol{T_{w,max}}$: maximum allowable receiver wall temperature; $\boldsymbol{n_{c,cor}}$: turbocompressor (corrected) rotational speed; $\boldsymbol{\eta_c}$: compressor efficiency; $\boldsymbol{\eta_e}$: turbine efficiency; $\boldsymbol{\pi_c}$: compressor pressure ratio; $\boldsymbol{\pi_e}$: turbine pressure ratio; $\boldsymbol{\dot{m}_a}$: mass flow rate; $\boldsymbol{\eta_{th}}$: thermal efficiency.

Extending the simulation to the whole Typical Meteorological Year (TMY) annual results can be obtained. Oriented in the North-South direction and located in Madrid, Spain (40° 24' 59'' N, 3° 42' 9'' W) the solar field provides an annual energy yield $Q_a = 500$ MW h year^{-1} of thermal energy as hot air between 300 °C and 400 °C, working 2880 h year^{-1}, Tab.1.

Table 1. Yearly energetic performances

$\boldsymbol{A_{tot}}$	m^2	845
$\boldsymbol{h_{ON}}$	h	2880
$\boldsymbol{Q_a}$	MW h y^{-1}	500
$\boldsymbol{Q_a/A_{tot}}$	kW h y^{-1}m^{-2}	592.1
$\boldsymbol{Q_{a,u}}$	MW h y^{-1}	491
$\boldsymbol{Q_d}$	MW h y^{-1}	1600
$\boldsymbol{SF_y}$	-	0.3

Although the previous results have general validity, in this analysis T-SAH delivers hot air to a specific thermal process, i.e. a medium-temperature drying process. The pre-existing conventional air heating device is assumed to be a natural gas burner, which is a common option in the industry. The burner sends to the process a mixture of combustion gases and air (referred to as hot air for simplicity) at the desired temperature, here assumed to be constant at 300 °C.

At least two options are viable for the integration of solar hot air into the existing air heating system: series and parallel integration with the natural gas burner, Fig.3. The integration concept chosen here is a parallel scheme

where T-SAH and the burner provide hot air for the process as in Fig.3(b). Whenever solar air flow is provided by the solar field it is totally sent to the process, having a priority over the burner airflow. The latter is adjusted by controlling the mass flow rate and temperature in order to meet the process requirements in terms of thermal power and air temperature. This way the solar air flow enables a reduction of burner thermal power, resulting in natural gas savings.

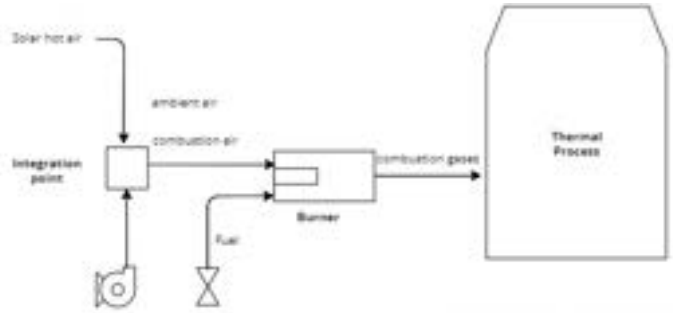

(a)

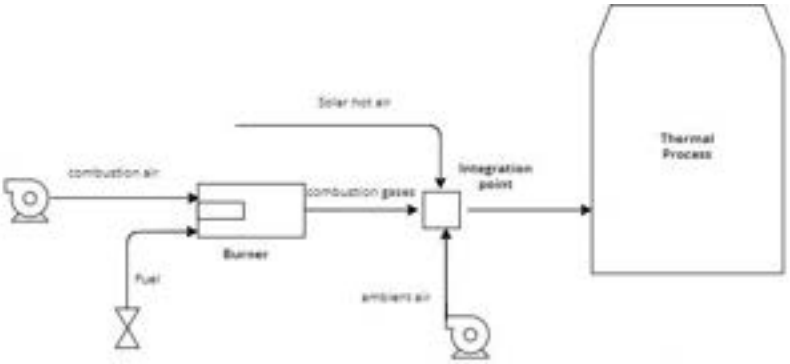

(b)

Figure. 3 Integration concept of T-SAH into air bases thermal process. i.e. drying: series integration (a); parallel integration (b).

The thermal load profile of the process depends on the specific factory, its requirements, and production schedule. Although any load profile is possible, some common patterns are recognized. A typical case is having a constant thermal load for continuous production. Another option is having a daily variation of thermal load according to the working hours of the factory. This can include or not the weekend among the working days. Here the thermal load $\dot{Q}_d$ is assumed to be 100% of the peak load $\dot{Q}_{d,pk} = 400\ \mathrm{kW}$, each day of the week including weekend days, from 7:00 a.m. to 6:00 p.m. During the rest of the hours thermal load is null.

The thermal load profile is shown in Fig.4 together with the solar production profile $\dot{Q}_a$ vs. the hours of the year for one week in summer Fig.4(a) and one week in winter Fig.4(b). The solar production interval and thermal load-interval are quite similar so that, even without thermal storage, the process can absorb almost all the solar thermal energy provided. The used thermal energy is in each hour $\dot{Q}_{a,u} = \min(\dot{Q}_d, \dot{Q}_a)$. On annual basis $\frac{Q_{a,u}}{Q_a} = 0.96$. The solar fraction SF is the ratio between the $\dot{Q}_{a,u}$ and $\dot{Q}_d$ in each time interval and indicates the amount of thermal load provided by solar. Fig. 4 reports on the second axis the SF for the selected weeks. It is clear that on summer days SF reaches up to 0.8, while it is much lower on typical winter days, $SF < 0.5$. On an annual basis, the solar fraction is $SF_y = 0.3$.

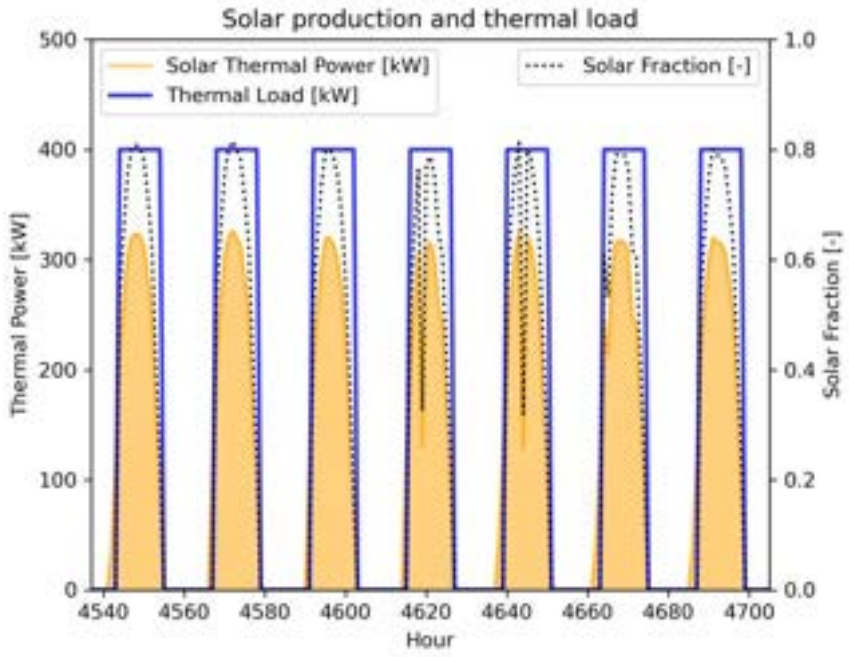

(a)

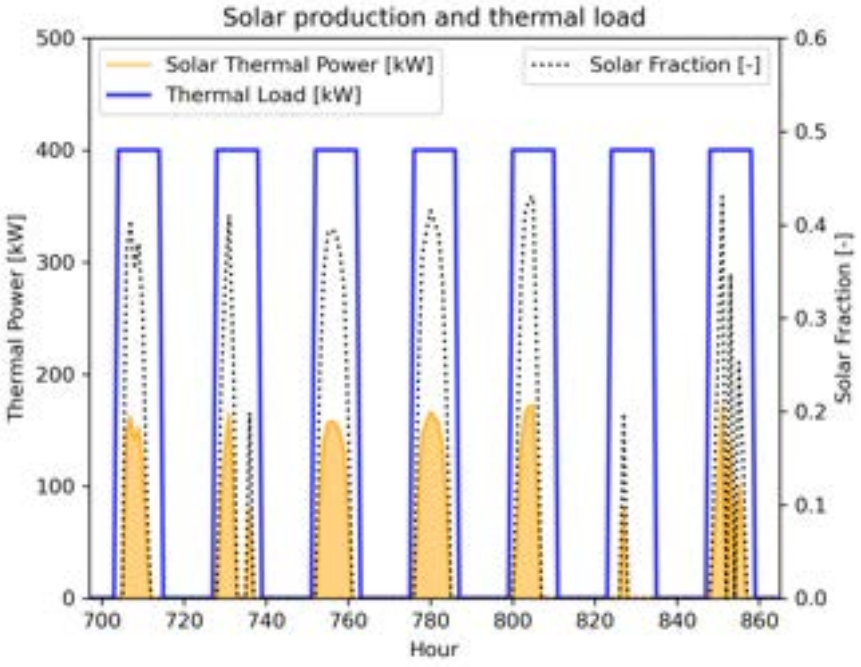

(b)

Figure 4. Solar production and thermal load weekly profiles: (a) typical summer week; (b) typical winter week.

3. Economy analysis

The economic analysis is carried out on the benchmark plant of Fig.1. Estimations of the installation costs CAPEX and operating cost OPEX are obtained on the grounds of the current stage of development of the technologies and products involved. Levelized cost of heat (LCOH) and discounted payback period (DPB) are used as the main economic parameters for the analysis.

Here it is assumed that solar-generated heat replaces the corresponding amount of convectional heat, generated by a natural gas burner.

The evaluation of conventional energy cost evaluation is non-trivial. Natural gas cost for industrial consumers varies by country, besides varying with the consumption volume of the factory and time. The price volatility has increased in Europe in recent months as a consequence of the geopolitical situation and supply uncertainties related to the major gas suppliers.

Eurostat [14] provides the natural gas price for "non-household" consumers across recent years in Europe. The "non-household" consumer definition includes industrial consumers and other large consumers with annual consumption above 1000 GJ (277 MWh), excluding powerplants and chemical process consumers. Non-household consumers are divided into six bands as reported in Tab.2.

As a general trend of the averaged value, since 2008 the price trend was increasing until 2013 reaching a peak at 42 €/MWh in the first half of 2013, then decreased down to 28 €/MWh in the first part of 2021. In 2021-2022 the prices have grown remarkably up to 65 €/MWh. Tab. 2 reports the recorded values for Spain and EU27 countries during the first semester of 2021 and 2022 when a large price variation occurred. These values are considered as a span for the price variation in the following economic study.

Table. 2. Non-household natural gas price including taxes by consumption bands, 2021-2022, €/MWh

		2021-S1		2022-S1	
Consumption band	Annual consumption	EU27	Spain	EU27	Spain
Band-I1	< 277 MWh	57.2	45.2	90.8	108.1
Band-I2	277 – 2 770 MWh	48.3	39.6	81.6	89
Band-I3	2 770 - 27 700 MWh	36.7	28.7	76.4	88.2
Band-I4	27 700 - 277 000 MWh	29.7	27.1	76.2	93.3
Band-I5	277 000 -1 108 000 MWh	27.7	28.1	87.7	92.1
Band-I6	> 1 108 000 MWh	26.6	26.1	97.7	89.2

3.1. LCOH

The LCOH is the cost of the generation of thermal energy (Heat), hence the minimum price at which it must be sold to recover the cost of installation (CAPEX) and the costs of operation and maintenance (OPEX, here named $C_{O\&M}$) during the lifetime of the plant. It is defined in an analogous way as the Levelized Cost of Energy $LCOE$ used for electricity production financial analysis. Here it is assumed that $LCOH$ is the cost of solar-generated heat, substituting the corresponding amount of convectional heat, generated by a conventional heating system.

According to IEA task 54, the $LCOH$ can be estimated as follows, considering constant annual discount rates r_{dis}:

$$LCOH = \frac{I_0 - S_0 + \sum_{n_y=1}^{N_y} \frac{C_{O\&M_{n_y}}(1-TR) - DEO_{n_y} TR}{(1+r_{dis})^{n_y}} - \frac{RV}{(1+r_{dis})^{N_y}}}{\sum_{n_y=1}^{N_y} \frac{E_{n_y}}{(1+r_{dis})^{n_y}}} \quad (1)$$

with I_0: initial investment and in due case discounted end-of-life replacements; S_0: subsidies on the installation; $C_{O\&M_{n_y}}$ yearly operation and maintenance cost, TR: corporate tax in %; DEO: asset depreciation; RV: residual value; E_{n_y}: Annual energy yield; N_y: Lifetime; r_{dis} discount rate % year-1.

The above expression results in the following simplified version when assuming $TR = 0$; $RV = 0$, and is used in this study.

$$LCOH = \frac{I_0 - S_0 + \sum_{n_y=1}^{N_y} \frac{C_{O\&M_{n_y}}}{(1+r_{dis})^{n_y}}}{\sum_{n_y=1}^{N_y} \frac{E_{n_y}}{(1+r_{dis})^{n_y}}} \quad (2)$$

Relevant parameters used are reported in Tab. 3. Initial investment $I_0 = C_{SF} + C_0$ has two main components.

The solar field $C_{SF} = A_{tot} C_{SFu}$ cost plays the major role compared to other costs C_0, including hydraulic and auxiliary equipment, control, and instrumentation. Solar field cost represents close to 90% of the initial investment. Although this is a common feature in solar installation, here is more evident since the auxiliary equipment is simplified thanks to the novel layout of direct air heating. The heat transfer fluid HTF and air/HTF heat exchanger are avoided with their related installation and maintenance costs.

Table 3. Financial parameters

Discount rate	r_{dis}	5%
Operation and Maintenance	$C_{O\&M}$	1% of initial investment I_0
Lifetime	N_y	25 years
Solar field cost per m²	C_{SFu}	380-580 €/m2
Other costs (hydraulic and auxiliary equipment, control and instrumentation…)	C_0	50 000 €

The LCOH is obtained as a function of unitary solar field cost C_{SFu}, for the benchmark case having an annual energy yield of $Q_{a,u} = 491$ MWh. It ranges between 61 €/MWh ($C_{SFu} = 380 \frac{€}{m^2}$) and 89 €/MWh ($C_{SFu} = 580 \frac{€}{m^2}$), with an average of 75 €/MWh ($C_{SFu} = 480 \frac{€}{m^2}$). The comparison with natural gas costs suggests as the adoption of T-SAH can be economically viable when natural gas cost stays above its average value.

Fig. 5 shows the obtained LCOH in comparison with the natural gas cost for different consumption bands as in Tab. 2. The LCOH is higher than the minimum natural gas price so economic convenience is not guaranteed. When the natural gas prices are higher (as in 2022) the solar heat can be competitive or even cheaper. Besides, the smaller consumers suffer higher prices which can facilitate the adoption of solar energy solutions, but they must be able to consume all the solar heat provided by a flexible heat demand or via storage, not considered in this analysis. Considering the subsidies on the initial investment LCOH decreases: 48 €/MWh with $C_{SFu} = 480 \frac{€}{m^2}$ and the percentage of subsidies on the initial investment of $s_0 = \frac{S_0}{I_0} = 40\%$.

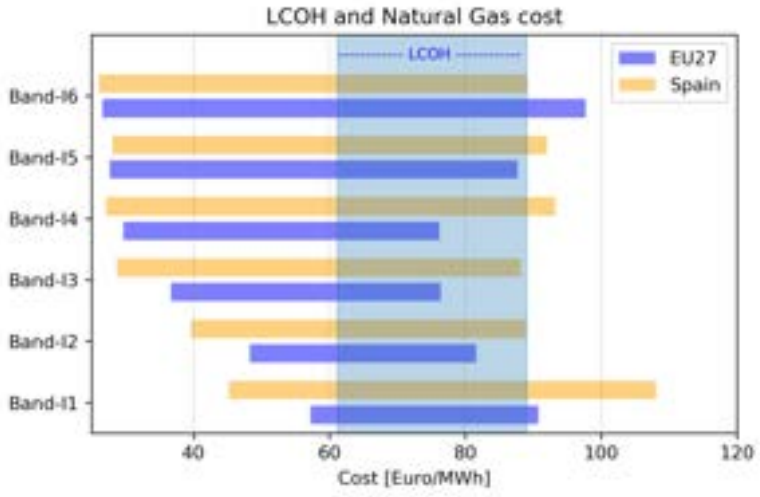

Figure 5. LCOH and natural gas cost span (2021-2022) in EU27 and Spain.

3.2. DPB

Discounted payback time DPB accounts for the time value of the money, hence it discounts the actual cash inflow for each year at the defined discount rate. Discounted Payback time DPB also depends on the cost of the conventional energy that is being replaced. A simplified equation is used for its evaluation are Eqs. (3) - (4). Yearly cash flow CF comes from natural gas costs avoided C_{NG} and operation and maintenance costs

$C_{O\&M}$. The conversion efficiency of natural gas burner is assumed unitary.

$$CF = \mathrm{Q_{a,u}} C_{\mathrm{NG}} - C_{O\&M} \tag{3}$$

$$DPB = \frac{\ln\left(\frac{CF}{CF - r_{dis}\,(I_0 - S_0)}\right)}{\ln(1 + r_{dis})} \tag{4}$$

Due to the variability of the conventional energy source price, it is convenient to show the DPB as a function of that price, as in Fig. 6. Three curves are shown representing the DPB assuming a solar field cost $C_{SFu} = 580\,\frac{€}{\mathrm{m^2}}$, $C_{SFu} = 480\,\frac{€}{\mathrm{m^2}}$, $C_{SFu} = 380\,\frac{€}{\mathrm{m^2}}$ and considering the subsidies $s_0 = \frac{S_0}{I_0} = 40\%$ of the capital costs. The DPB holds relatively high values, above 10 years in the actual range of natural gas prices. A decrease in LFC cost is required to lower the DPB either with subsidies or not. Considering an average natural gas price of 65 €/MWh, $DPB = 12$ years is obtained when the LFC cost drops to $C_{SFu} = 250\,\frac{€}{\mathrm{m^2}}$, without subsidies on the initial investment.

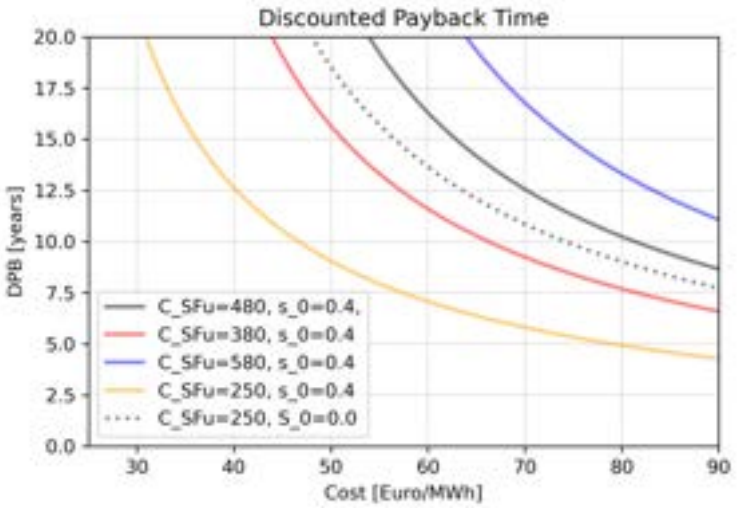

Figure 6. Discounted Payback Time *DPB* against the natural gas cost, for different unitary solar field costs and subsides percentage on the initial investment $s_0 = S_0/I_0$.

Conclusions

A novel layout for solar heat production for industrial processes has been studied from the economic perspective according to the energy yield utilization. The innovative concept uses concentrating linear Fresnel collectors to implement a solar air heater able to heat directly ambient air up to 300-400 °C for its usage in air-based thermal processes in the industry. An energetic analysis is carried out through numerical modeling of the solar heating system. A benchmark plant is configured and simulated across a typical meteorological year in Madrid city, Spain. The concentrating solar air heater is coupled with a thermal process, taking into account a parallel integration scheme and a given thermal load time profile. The simulation provides the annual performance of the solar facility in terms of energy provided and natural gas consumption avoided. An 845 m^2 solar field delivers to the process up to 500 MWh per year of thermal energy, corresponding to 30% of the consumption of the considered thermal process. The solar field allows for saving 52,000 Sm^3 of natural gas and 104 tons of CO_2 per year. The results indicate that the solar technology here presented can be competitive with other solar thermal solutions, having a huge potential for fossil fuel source replacement in hot air based industrial processes.

An economic analysis is carried out to evaluate the investment and operation costs of the solar system. The Levelized cost of Heat and Discounted Payback time indicates that the solution proposed can be competitive

with natural gas in the recent European price range, despite a reduction of solar field cost and sustained subsidies policy are required to improve economic feasibility.

Acknowledgments

This research was supported by the Industrial Ph.D. program of Comunidad de Madrid, Spain (BOCM Reference IND2017/ AMB7769) and “Ayudas Juan de la Cierva Formación de Ministerio de Ciencia e Innovación” funded by MCIN/AEI/10.13039/501100011033 and European Union “NextGenerationEU”/PRTR.

Nomenclature

Latin

A	Aperture surface area [m^2]
ac	Auxiliary compressor
CF	Cash flow
C_{NG}	Natural Gas cost
$C_{O\&M}$	Ôperation and Maintenance cost
C_{SFu}	Cost of solar field per m^2
C_0	Other costs
I_0	Initial Investment
$\dot{m}$	Air mass flow rate [kg s^{-1}]
n	Turbocharger rotating speed [rpm]
N_y	Lifetime [year]
p	Pressure [Pa]
$\dot{Q}$	Thermal power [W]
Q	Thermal energy [J]
r_{dis}	Discount rate
SF	Solar fraction
S_0	Subsidies
s_0	% of subsidies on I_0
T	Temperature [K, °C]
TST	True solar time [hr]

Greek

π	Pressure ratio [-]

Acronyms

HTF	Heat Transfer Fluid
DPB	Discounted payback
LCOH	Levelized cost of Heat
LFC	Linear Fresnel collector
PTC	Parabolic Trough Collector
SHIP	Solar Heat for Industrial Processes
T-SAH	Turbocharged Solar Air Heater

Subscripts

a	Air
amb	Ambient
a,u	Useful
c	Compression. Compressor
d	Demand, load
e	Expansion. Turbine
in	Inlet
ou	Outlet
tot	Total
w	Wall
0	Inlet from atmosphere
1	Compressor inlet
2	Compressor outlet
3	Turbine inlet
4	Turbine outlet

References

[1] “International Renewable Energy Agency (IRENA).” www.irena.org

[2] S. H. Farjana, N. Huda, M. A. P. Mahmud, and R. Saidur, “Solar process heat in industrial systems – A global review,” *Renewable and Sustainable Energy Reviews*, vol. 82, no. August 2017, pp. 2270–2286, 2018, doi: 10.1016/j.rser.2017.08.065.

[3] “SHIP Database.” http://ship-plants.info/

[4] A. K. Sharma, C. Sharma, S. C. Mullick, and T. C. Kandpal, “Solar industrial process heating: A review,” *Renewable and Sustainable Energy Reviews*, vol. 78, no. December 2016, pp. 124–137, 2017, doi: 10.1016/j.rser.2017.04.079.

[5] A. Saxena, Varun, and A. A. El-Sebaii, “A thermodynamic review of solar air heaters,” *Renewable and Sustainable Energy Reviews*, vol. 43, pp. 863–890, 2015, doi: 10.1016/j.rser.2014.11.059.

[6] S. Rehman, A. Ahmad, L. M. Alhems, and M. M. Rafique, “Experimental evaluation of solar thermal performance of linear Fresnel reflector,” *Journal of Mechanical Science and Technology*, vol. 33, no. 9, pp. 4555–4562, 2019, doi: 10.1007/s12206-019-0852-6.

[7] D. Pietruschka, I. Ben Hassine, M. Cotrado, R. Fedrizzi, and M. Cozzini, “Large Scale Solar Process Heat Systems -planning, Realization and System Operation,” *Energy Procedia*, vol. 91, pp. 638–649, 2016, doi: 10.1016/j.egypro.2016.06.223.

[8] A. Famiglietti, A. Lecuona-Neumann, J. Nogueira, and M. Rahjoo, “Direct solar production of medium temperature hot air for industrial applications in linear concentrating solar collectors using an open Brayton cycle . Viability analysis,” vol. 169, no. September 2019, 2020.

[9] A. Famiglietti, A. Lecuona, M. Ibarra, and J. Roa, “Turbo-assisted direct solar air heater for medium temperature industrial processes using Linear Fresnel Collectors. Assessment on daily and yearly basis,” *Energy*, vol. 223, 2021, doi: 10.1016/j.energy.2021.120011.

[10] A. Famiglietti and A. Lecuona, “Small-scale linear Fresnel collector using air as heat transfer fluid: Experimental characterization,” *Renewable Energy*, vol. 176, pp. 459–474, 2021, doi: 10.1016/j.renene.2021.05.048.

[11] A. Famiglietti and A. Lecuona, “Direct solar air heating inside small-scale linear Fresnel collector assisted by a turbocharger : Experimental characterization,” *Applied Thermal Engineering*, vol. 196, no. September, 2021, doi: 10.1016/j.applthermaleng.2021.117323.

[12] A. Famiglietti, A. Lecuona, M. Ibarra, and J. Roa, “Turbo-assisted direct solar air heater for medium temperature industrial processes using Linear Fresnel Collectors . Assessment on daily and yearly basis,” vol. 223, 2021.

[13] Solatom, “SOLAR STEAM FOR INDUSTRIAL PROCESSES.” http://www.solatom.com/

[14] “Eurostat.” https://ec.europa.eu/eurostat/

Towards a Low Carbon Future: Evaluating Scenarios for an Energy Community through a Multi-Objective Optimisation Approach

Ronelly J. De Souza[a,b], Emanuele Nadalon[a], Melchiorre Casisi[c], Mauro Reini[a], Luis M. Serra[b], Miguel A. Lozano[b]

[a] Department of Engineering and Architecture, University of Trieste, Trieste, Italy, ronellyjose.desouza@phd.units.it CA, emanuele.nadalon@dia.units.it, reini@units.it
[b] GITSE-I3A, Department of Mechanical Engineering, Universidad de Zaragoza, Zaragoza, Spain, serra@unizar.es, miguel.lozano@unizar.es
[c] Polytechnic Department of Engineering and Architecture, University of Udine, Udine, Italy, melchiorre.casisi@uniud.it

Abstract:

Several literature works have highlighted that the expansion of electrification across all sectors is a crucial factor in promoting the transition of energy systems towards carbon neutrality by mid-century. However, polygeneration systems through the appropriate integration of different renewable energy sources are expected to play an important role in such transition by effectively reducing the total primary energy demand, as explored in the present work for an energy community (EC) case study. Therefore, this paper presents the optimal synthesis, design, and operation of an EC system working under three different scenarios and evaluates the trade-offs between the total annual costs and greenhouse gas (GHG) emissions (evaluated as CO_2 equivalent emissions). The EC is a District Heating and Cooling Network (DHCN) composed of nine third sector buildings in the northeast of Italy. The DHCN superstructure includes several possible energy supply components for each EC member, a central unit, and heat and/or cooling connections between buildings. Moreover, peer-to-peer electricity sharing is allowed among EC members, through a local electricity grid, before buying/selling electricity from/to the main grid. The superstructure was optimised through a mixed integer linear programming (MILP) model considering a multi-objective optimisation for the total annual cost (for owning, operating, and maintaining the entire system) and the total annual CO_2eq emissions as the objective functions. The three scenarios through which the EC system is optimized and evaluated consider the type of consumed gas (natural gas or biomethane) and the electricity consumption configuration (on-grid or off-grid). Results have shown that the cost (per ton of CO_2eq) to reduce emissions is too high if the European Union's carbon market is considered. This was especially critic for the natural gas scenario, where the cost per ton of CO_2eq (between two optimal solutions) was about four times higher than its cost on carbon market.

Keywords:

Polygeneration systems; Renewable energy sources; Energy community; Carbon neutrality; Multi-objective optimisation.

1. Introduction

The 2021/2022 global energy crisis was essentially the consequence from two main worldwide problems regarding primary energy: supply and prices. According to a report by IEA [1], such problems were ignited by several factors, including the economic recovery that started to take place as the Covid-19 pandemic progressively weakened in 2021 and the beginning of Russia/Ukraine war in February 2022. The result was a brutal energy prices increase [2] in comparison with pre-pandemic levels, followed by a substantial coal consumption growth [3]. The European Union (EU), deeply affected by a plunge in Russian's gas supply, released a report [4] with a set of actions to avoid gas shortages in 2023 such as energy efficiency improvements of industries, and public and private buildings, deployment of renewables, and electrification of heat.

The aforementioned context has highlighted the ever importance of primary energy savings. Among the main solutions the scientific community has developed, energy communities have arisen as an advantageous way for energy savings in different types of buildings. In a recent work [5], our research group

studied the design and operation of an energy community (EC), comprising nine tertiary sector buildings, for a city in the northeast of Italy. Besides a reduction in total costs and CO_2eq emissions, the implementation of peer-to-peer electricity sharing within the EC demonstrated the possibility of saving primary energy (natural gas, in this case) since the cogenerated and shared electricity among the EC members allows a substantial reduction in the total amount of electricity imported from the main electric grid. It is possible to find in literature not only other works dealing with EC optimisation for tertiary sector buildings [6], but also studies focused essentially on the same kind of work but aiming residential, commercial, and industrial buildings [7-10].

In addition to primary energy savings, the report from EU [4] highlights also the importance of deploying renewables. This is a key concern for EU since it has fixed deadlines, through different pieces of legislation, to reach carbon neutrality by 2050. For instance, the EU 2030 target plan [11] aims a more ambitious and cost-effective direction to reach the carbon neutrality by 2050, without forgetting the encouragement for creating new green jobs and for stimulating international partners to also increase their carbon neutrality ambitious. As a part of the EU 2030 target plan, the so called “Fit for 55” package [12] proposes an ambitious target for decreasing the net greenhouse gas (GHG) emissions by at least 55% (of the 1990 net GHG emissions level) by 2030. According to the EU council [13], the package aims to create a balanced and coherent framework for attaining the EU's climate goals, while ensuring a just and equitable transition, promoting innovation and competitiveness of EU industry, and maintaining a level playing field with third country economic operators. Still according to them, to accomplish these goals, member states must implement concrete measures to decarbonize their economies, and the “Fit for 55” package provides legislative proposals and amendments to assist in achieving this objective.

Figure 1. Categories included in the “Fit for 55” package [12].

The “Fit for 55” package describes also, in detail, how the EU will translate its climate goals into legislation. Specific categories (Fig. 1) will give directives that include energy taxation, energy-efficient transition, reform to the EU emissions trading system, energy performance of buildings, and boost of renewable energy sources. For instance, the directive regarding energy-efficient transition [14] claims that energy saving is the most cost-effective solution for reaching the climate goals in the energy sector. Indeed, with such a solution it is possible to reduce lots of GHG emissions besides providing more affordable energy. In the same line, the directive for boosting renewable energy sources [15] says that moving towards such energy sources the GHG emissions will be substantially reduced while the human health and air quality will be improved. Different studies regarding improvement of energy communities have already analysed the agreement of their results with the “Fit for 55” package [16] or, at least mentioned their awareness and importance of such piece of legislation [17,18].

From the depicted literature review, one can verify the attention that the scientific community has given to enhancing energy communities’ performance. Moreover, it is also possible to verify the attention that the EU has given on the reduction of net GHG emissions by 2050. Such EC improvements aim not only to achieve lower costs and emissions but also lower levels of primary energy consumption (in line with the European Union report [4]). In agreement with these issues, this work aims to conduct an analysis of different scenarios in order to evaluate the performance of an EC (located in Pordenone, northeast of Italy) comprising nine buildings from the third sector and working with natural gas or biomethane, as one of the input energy vectors. For each one of these fuels, the EC behaviour will be assessed when it is connected or not to the electricity grid. The evaluation will be made through a multi-objective optimisation (total annual costs and CO_2eq emissions) using a mixed integer linear programming (MILP) model that evaluates the optimal solution regarding the synthesis, design, and operation of the specified superstructure for the EC. The

energy system structure for each building is optimised individually, in accordance with its energy demand. The district heating network (DHN) and the district cooling network (DCN) are also optimised, i.e., depending on the energy demand of each building and the distance between them, the pipelines network is also optimised in accordance with the energy system structure of each building. Besides heating and cooling, peer-to-peer electricity sharing is also allowed in the community, which gives the EC a lower dependency on the electric grid or even the possibility to be off-grid.

2. DHCN superstructure

The superstructure shown in Figure 2 is comprised of three main subdivisions. The first one is the Polygeneration Unit k, which is a set of equipment assigned to a specific user building (referred to as "User Building k"). The second subdivision is the central unit, an independent structure that provides heating and electricity to the energy community. The third subdivision is "User i", which represents the remaining buildings within the energy community. These three subdivisions are linked through the DHCN for thermal energy exchange and the distribution substation (DS), which serves as an electricity hub. The model optimizes the pipeline connections between buildings and central unit. Rather than being connected directly to the electricity grid, all buildings and the central unit are connected to the DS, which manages the flow of electricity for all three subdivisions. This means that based on an electricity balance, the DS can:

- distribute electricity to a building, if their Polygeneration Unit cannot meet their demand,
- receive electricity from a building, if it has an electricity surplus,
- purchase electricity from the grid, if the surplus from all buildings is insufficient, and
- sell electricity to the grid, if there is a surplus and all buildings demands have been met.

For a more detailed description about all internal energy flows among components, the reader may refer to our previous work [5].

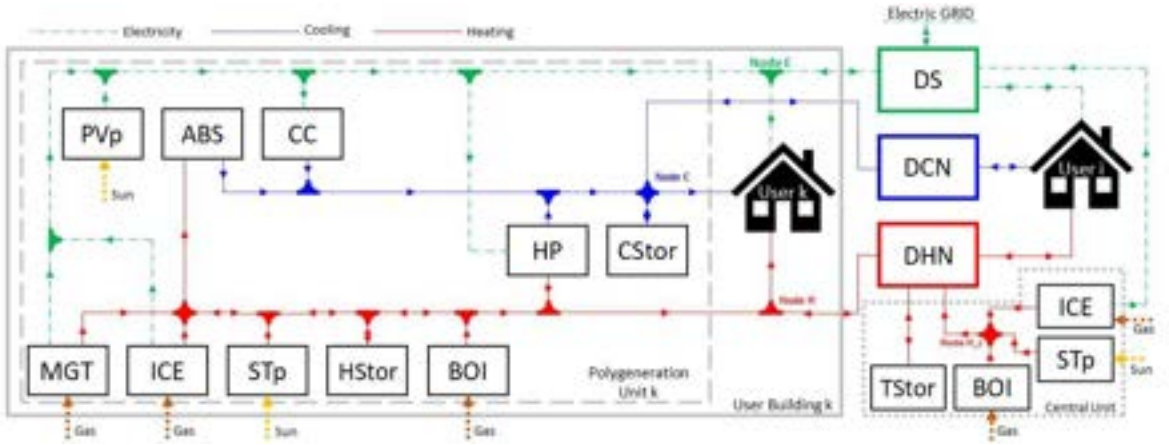

Figure 2. Superstructure of the energy community [5].

3. Model description

The optimal synthesis, design, and operation of the EC showed in Fig. 1 were defined using Mixed Integer Linear Programming (MILP) optimisation method, which involves decision variables, constraints, and objective functions. Decision variables can be binary or continuous and determine the selection, on/off status, and sizing of equipment. Constraints determine the model's limitations in terms of equipment size, performance, and energy balance, while objective functions aim to minimize predefined targets. A flow diagram of the inputs, outputs, and the core characteristics of the model can be found in Fig. 3.

The sizes of some devices, such as MGT, ICE, ABS, and HP, are predetermined, while others (BOI and CC) are left free to optimize their installation and sizes. ABS devices are only allowed to be fed by cogeneration systems and STp. The partial load performance of cogeneration systems is represented by linear relations obtained through a linear regression of their characteristic load curves. PVp and STp production data consider local hourly insolation obtained through a dedicated software [20], and the size of these solar technologies is limited to a maximum of 200 m^2 per building. The HP modelling is more complex than other devices, as the heating and cooling production cannot happen at the same time and considers both the heating and cooling demands of each EC building.

The DHCN pipelines layout and capacity are also optimised by considering the geographical location of the buildings and the distances between each other. Thermal losses are expressed by an equation that depends on the pipeline length and a coefficient of proportionality. A constraint does not allow the model to connect two users with two pipelines sending heating or cooling energy at the same time. The maximum heat flow

rate is constrained by the pipelines size, and the energy flow into each pipeline is bounded between a lower and upper limit. The optimisation of the DHCN is important to minimize thermal losses through pipelines and ensure efficient energy distribution.

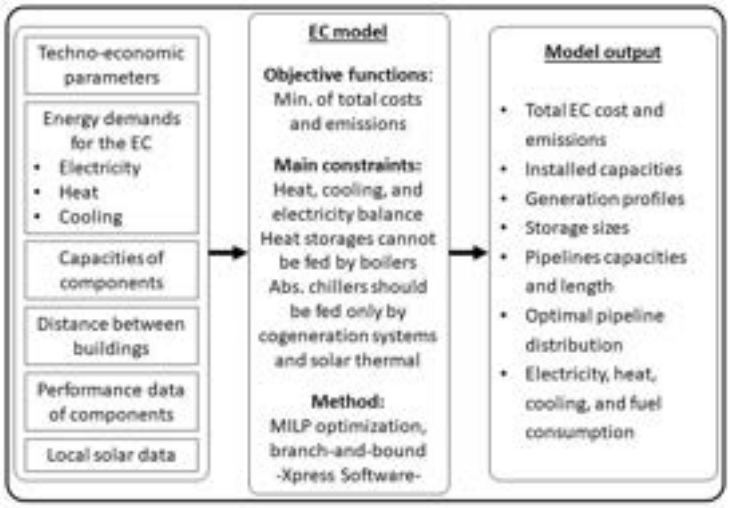

Figure 3. Flow diagram from main inputs to main outputs.

Thermal storages systems are implemented to overcome the intermittence and scarcity of sunlight during winter and, combined with cogeneration devices, to reduce the usage of backup boilers. In this way, fuel consumption and environmental impacts can be mitigated. The proposed thermal storage models provide a means of calculating the energy stored and the energy balance within them, considering thermal loss and energy input from the DHCN pipelines. These models describe the storage of thermal energy for the entire year, without time decomposition, and the connection between hours, days, weeks, and months for a whole year representation.

Energy balances are used to model the heating, cooling, and electricity constraints of the system, which are applied for the individual buildings, the central unit, and the distribution substation. The EC buildings require all three types of energy balances, which are applied at specific nodes for each type of energy. The central unit requires only the heating balance, as its electricity production is sent directly to the DS, which is responsible for managing the peer-to-peer electricity sharing among buildings.

The peer-to-peer electricity sharing methodology is implemented with the aim to reduce the amount of electricity exchanged with the electric grid, which can reduce overall costs and environmental impacts. The methodology involves the local production of electricity by each EC member and, in the case of surplus, send the overbalance to the DS to distribute it for other EC members or selling it to the electric grid. The proposed methodology has the potential to benefit EC members by reducing their reliance on the electric grid and promoting a more sustainable use of energy.

For this work, a multi-objective optimisation problem was defined to minimize the total annual cost and CO_2eq emissions. The total annual cost includes investment, maintenance, and operation costs, while the total annual CO_2eq emissions are related to the net electric energy received from the grid and the fuel consumption by boilers and cogeneration energy systems. The two objectives are conflicting, as adopting environmental efficient energy systems is costly and the solution that allows for minimum annual cost does not necessarily result in minimum total annual CO_2eq emissions. The ε-constrained method [21] is used to obtain the Pareto front solutions. The method involves identifying a set of intermediate emission levels and introducing each level as an additional constraint in further economic optimisation (it could be carried out in the other way around, i.e., performing an emissions optimisation while setting intermediate values for cost). The method allows decision-makers to explore the trade-offs between different solutions and identify the optimal trade-off between economic and environmental objectives.

For a more detailed description of the model, the reader may refer to our previous work [5].

4. Case study

The case study is an EC designed for the city of Pordenone, northeast of Italy, which provides heat, cooling, and electricity to nine different buildings: town hall, hospital, library, primary school, secondary school, retirement home, theatre, town hall archive, and a private swimming pool (Fig. 4). This study is based on a mathematical model that divides the year into 24 typical days (two typical days/month – working and non-working) of 24 hours each and calculates the optimal design and operation for the entire EC system based on the energy demand data of each building. The heterogeneous mix of buildings with different energy demands ensured that the results obtained were not biased towards a specific user profile. Furthermore, this mix of users is expected to be representative of many other small and medium-size towns in Europe.

As an example, Figure 5 illustrates the energy demand patterns of the hospital during winter and summer, based on two representative working days. During winter, the hospital exhibits a higher demand for electric energy during daylight hours, attributed to a higher occupancy factor. Additionally, there is a higher heating demand during morning and evening periods, and minimal cooling demand. Conversely, during summer, the hospital experiences a higher cooling demand, with the peak occurring around 2 p.m. The electric energy demand is similar to that of the winter season. Notably, comparing to the winter curve, the heat demand during summer is reduced by a factor between 2 and 3, as the hospital still have a high demand for sanitary water. It is noteworthy that the energy patterns of each building vary based on several factors, including occupancy factor, thermal insulation, and night lighting.

Selecting appropriate and proportionate equipment for the energy structure of the EC system is key to ensure its effective integration. The equipment should be capable of fulfilling the energy requirements of the buildings while maintaining compatibility with the system. The optimisation process involves considering two types of components, namely fixed and variable size, both of which are commercially available. The optimal size and configuration of the energy system can be achieved by determining the number of installed fixed size equipment and the size of variable size components including boilers, compression chillers, and thermal storages.

Figure 4. DHCN pipelines superstructure [5].

The interest rate is assumed to be 5%, while lifespan is determined to be 30 years for DHCN, 20 years for PV, ST panels, and TS, 15 years for ICE, MGT, ABS, and HP, and 10 years for BOI and CC. Operation costs are also considered, which include fuel and electricity costs. The price of natural gas, biomethane, purchased electricity, and sold electricity are introduced in the next section and specified for different scenarios. CO_2eq emissions related to electricity, natural gas, and biomethane consumption are taken from literature. Electricity carbon intensity was assumed to be 0.356 kgCO_2eq/kWh, natural gas carbon intensity 0.202 kgCO_2eq/kWh [5], while biomethane was assumed to produce zero net emissions [22] as the considered CO_2eq emissions for this work are only the ones related to the energy resources.

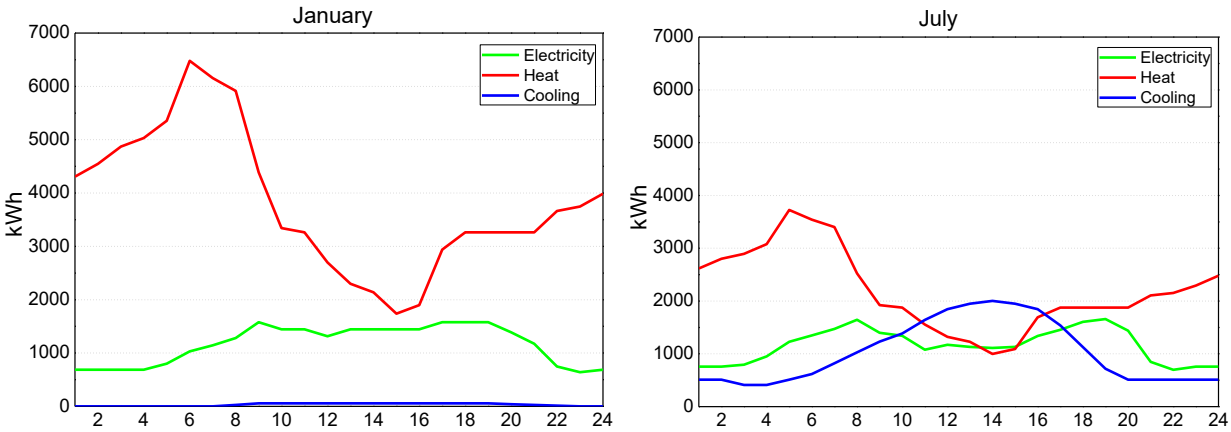

Figure 5. Hospital demands for working days of January and July.

5. Results and discussion

In order to have a reference case, a conventional solution (CS) scenario is designed, which reflects the current reality in most cases. In this scenario, electricity is obtained from the electric grid, while a local boiler (BOI) and a local compression chiller (CC) are used to meet heating and cooling demands, respectively. Heat and cooling storage systems were also taken into account to support the BOI and CC. In this case, there is no connection between the buildings, which means that there are neither DHCN pipelines linking them nor peer-to-peer electricity sharing. For a detailed CS schematic diagram, the reader may refer to reference [5]. In this scenario and for all the nine buildings combined, the total annual cost was 4370.7 k€/y

while the total annual emissions were 11,281.2 ton/y. These results are considered as the references to calculate the potential decrease in total costs and emissions.

For this work, a multi-objective optimisation of the EC was conducted considering the following scenarios:

- Scenario 1: Grid-connected - natural gas consumption
- Scenario 2: Grid-connected - biomethane consumption
- Scenario 3: Grid-isolated

In line with the “Fit for 55” package from the EU [12], these scenarios have, as the main objectives, the reduction of the total annual CO_2eq emissions from the CS scenario, while reducing also the total annual costs. The Grid-connected scenario means that the EC is allowed to buy electricity from the national grid at 170 €/MWh and to sell it, also to the national grid, at 100 €/MWh [5]. The difference between these two scenarios is that they are analysed also for two types of gas consumption: natural gas or biomethane. For this work, no proportion between them was considered for any of the scenarios. The purchase price for gas was dependent on the type of consumption: for CHP equipment or for boilers. For the scenario with natural gas consumption, the purchase price was 45 €/MWh (CHP) and 60 €/MWh (boilers) [5]. For the scenario with biomethane utilization, the purchase price was 52 €/MWh (CHP) and 70 €/MWh (boilers) [19].

5.1. Scenario 1: Grid-connected – natural gas consumption

Figure 6 shows the Pareto curve for scenario 1 and the comparison with the CS scenario. Tables 1, 2, and 3 present, respectively, the configurations for each building for points A, B, and C in the Pareto curve. Point A represents the optimal economic optimisation solution, point C represents the optimal emissions optimisation solution, while point B represents the optimisation solution which has the same emissions level as point C, but with 68.5% of the cost.

In the comparison between scenario 1 and CS scenario, one can observe that the lowest reduction in CO_2eq emissions was obtained for point A (optimal economic solution), which resulted in 34% less CO_2eq production. For the comparison between CS scenario and the optimal emissions solution (point C), the CO_2eq emission reduction was 51%. However, very similar level of reduction can be reached through the trade-off solution represented by point B, i.e., with a decrease of 31.5% on the total annual costs (which represents 1307.3 k€/y), the EC will still emit around half of the emissions resulted from the CS scenario. Such a fact can be explained by the amount of equipment installed by the solution in point C (Table 3). As the simulation, in this case, is not worried about costs, it will find a solution that has minimum emissions no matter how many components would have to be installed. One of the main characteristics of the model is that the economic sub-model is relatively more complex than the one for emissions. Therefore, when reducing emissions is the only target, the simulation will not do further calculations once it has found the optimal solution. Another plausible point of view for the results presented in Fig. 6 is a comparison between point A and B. The obtained results show that an increment in economic cost of 24.5% is capable of reducing the total CO_2eq emissions by 26%. Assuming point B as the best trade-off solution, the results regarding scenario 1 have demonstrated that the EC has the potential of cutting emissions by 51% (representing almost 5800 ton of CO_2eq/y) while reducing costs by 35% (representing savings around 1530 k€/y), when compared to CS scenario.

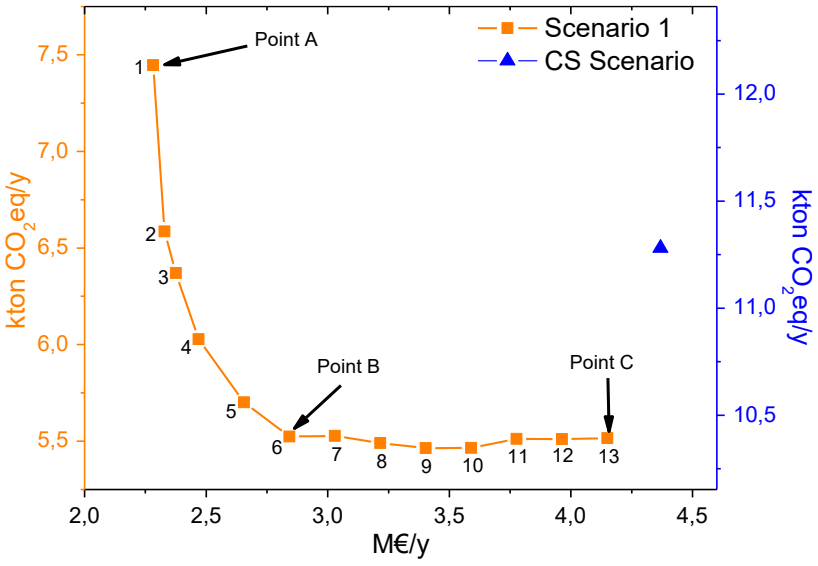

Figure 6. Pareto curve for scenario 1 and CS scenario data.

By analysing Tables 1 and 2 from the point of view of the communication between the EC and the national electric grid, it is possible to reveal some insights. The total electricity purchased by the EC was 1.18 MWh and 8168 MWh, while the total electricity sold by the EC was 3049.8 MWh and 819.1 MWh, for the optimal solutions from point A and B, respectively. Point A, which is the optimal economic solution, bought way less electricity and sold considerably more electricity compared to point B, i.e., the system of point A tried to compensate expenses related to investment, operation, and maintenance costs by selling more electricity. Moreover, the solution in point B installed 15% less engines (ICE), two thirds of heating storage (HST), one third of cooling storage (CST), and installed 43 times more solar thermal panels (ST), when compared to point A. Also, solution from point B installed around 50% more heat pumps (HP) and compression chillers (CC), which explains the higher level of electricity bought and the lower installed capacity of absorption chillers (ABS) (which is coherent with the lower installed capacities for ICE). In summary, point B saved emissions with respect to point A by consuming considerably less natural gas.

Table 1. Scenario 1: optimal economic solution (point A).

Building	ICE [kW]	MGT [kW]	BOI [kW]	ABS [kW]	HP [kW]	CC [kW]	PV [m^2]	ST [m^2]	HST [kWh]	CST [kWh]
1	70	0	0	0	70	65	0	0	1094	753
2	840	0	0	315	0	0	0	0	4000	2236
3	0	0	0	0	0	72	0	0	0	467
4	0	0	0	0	0	0	0	0	0	0
5	0	0	14	0	0	4	0	13	57	354
6	0	0	28	0	0	10	0	15	154	467
7	1200	0	0	525	420	68	0	0	4000	2185
8	420	0	0	0	0	0	0	0	115	0
9	280	0	0	0	0	0	0	0	1453	0

Table 2. Scenario 1: optimal trade-off solution (point B).

Building	ICE [kW]	MGT [kW]	BOI [kW]	ABS [kW]	HP [kW]	CC [kW]	PV [m^2]	ST [m^2]	HST [kWh]	CST [kWh]
1	0	0	0	70	0	0	0	200	568	183
2	420	0	0	105	0	0	0	200	1152	51
3	0	0	20	0	105	77	0	53	206	297
4	50	0	0	0	0	0	0	0	2	0
5	0	0	0	35	35	23	0	188	558	238
6	0	0	0	35	0	33	0	178	506	61
7	1200	0	60	105	630	208	0	200	3118	952
8	0	0	0	0	0	0	0	0	0	0
9	700	0	0	105	0	0	0	200	728	0

Table 3. Scenario 1: optimal emissions solution (point C).

Building	ICE [kW]	MGT [kW]	BOI [kW]	ABS [kW]	HP [kW]	CC [kW]	PV [m^2]	ST [m^2]	HST [kWh]	CST [kWh]
1	420	390	0	420	420	72	0	200	4000	4000
2	840	600	0	630	630	379	0	200	4000	4000
3	300	180	241	210	210	0	0	200	4000	4000
4	300	180	129	210	210	0	0	200	4000	4000
5	300	180	0	210	210	40	0	200	4000	4000
6	300	180	0	210	210	15	0	200	4000	4000
7	1200	1200	1626	630	630	77	0	200	4000	4000
8	420	390	0	420	420	0	0	200	4000	4000
9	840	600	0	630	630	0	0	200	4000	4000

5.2. Scenario 2: Grid-connected – biomethane consumption

In agreement with the EU 2030 target plan [11] for a more ambitious and cost-effective direction to reach the carbon neutrality by 2050, this section has been thought as a possible scenario to help EU achieving its environmental goals.

By picturing scenarios where the proportion of biomethane in the natural gas grid is increasingly higher, it is reasonable to infer that emissions in scenario 1 would be increasingly lower (biomethane has been considered a net-zero CO_2eq emitter [22]). From this point of view and considering the limit case of a natural

gas grid in which its methane content is completely replaced by biomethane, this work analysed the EC compared not only with the CS scenario, but also with scenario 1.

Figure 7 shows the Pareto curve for scenario 2, while Table 4 shows each building configurations for points D, in the Pareto curve, which represents the optimal economic solution. The first reasonable comparison is between points A and D (Figs. 6 and 7), which represent the optimal economic solutions for scenarios 1 and 2. The total annual costs for these solutions were, respectively, 2282.1 k€/y and 2587.8 k€/y, while the correspondent CO_2eq emissions were 7446.4 ton of CO_2eq/y and -457.1 ton of CO_2eq/y. Therefore, one can observe that an increase of 13.4% in the total annual costs (around 305.7 k€/y) allowed a reduction of 106% in the total annual CO_2eq emissions, which means that the emissions were cut off and then compensated by almost 460 ton of CO_2eq/y. This happened due to the CO_2eq emissions compensation when electricity is sold to the national electric grid. Although the total electricity sold in solution of point A was more than 2 times higher than that of point D, the fact that the biomethane emits way less CO_2eq than natural gas (net-zero for this work) has contributed for the dominance of the electricity compensation. By comparing Tables 1 and 4, it is possible to observe that, besides buying less electricity from the national grid, the solution of point D installed 10% less engines (ICE). To compensate the missing heat production, boilers (BOI) installed capacity for point D was more than five times higher with respect to point A. Also, solar thermal panels (ST) installed capacity for point D was more than three times higher than that of point A, which reflects the search of the model for more economical solutions.

Another reasonable comparison would be between points B and D (Figs. 6 and 7). As explained in section 5.1, point B represents the selected trade-off solution for scenario 1. The total annual cost for that solution was 2842.4 k€/y, while the total annual emissions 5523.5 ton of CO_2eq/y. In this case, there were reductions for both the costs (-9%) and emissions (-108%). Regarding emissions, the same thing happened as for the comparison between points A and D, i.e., emissions were cut off and compensated by the dominance of the electricity sold. As can be observed from Tables 2 and 4, the reduction on costs (around 255 k€/y) were due to a substantial reduction of installed CC and ST. They were reduced, respectively, by 13 and 15 times from solution in point B to the one in point D. As a way to compensate this reduction, it was installed three times more BOI, two times more ABS, and four times more cooling storage (CST).

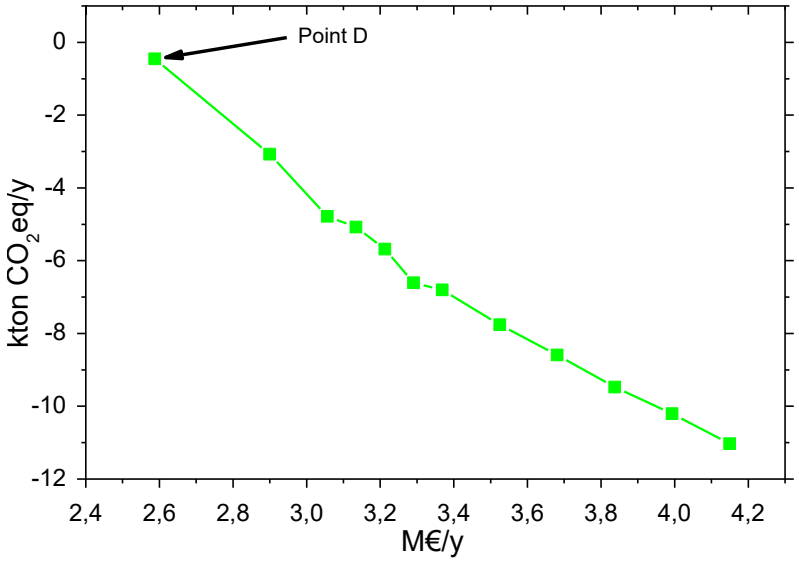

Figure 7. Pareto curve for scenario 2.

Table 4. Scenario 2: optimal emissions solution (point D).

Building	ICE [kW]	MGT [kW]	BOI [kW]	ABS [kW]	HP [kW]	CC [kW]	PV [m²]	ST [m²]	HST [kWh]	CST [kWh]
1	140	0	105	0	0	1	0	11	1579	826
2	840	0	0	420	0	0	0	0	4000	805
3	0	0	0	0	0	0	0	53	180	335
4	50	0	0	0	0	0	0	0	523	0
5	0	0	57	0	70	6	0	14	58	1200
6	0	0	62	0	0	0	0	13	58	1028
7	1200	0	0	525	630	15	0	0	4000	3007
8	0	0	10	0	70	0	0	0	0	0
9	280	0	0	0	0	0	0	0	1802	0

5.3. Scenario 3: grid-isolated

In the same direction of reducing CO_2eq emissions and primary energy consumption, another plausible scenario would be a completely isolated EC from the national electric grid. In this scenario, it was evaluated also the operation with natural gas or biomethane. The results demonstrated that a grid-isolated EC is not attractive from the economic and environmental viewpoints, either for natural gas or biomethane, which is in agreement, for instance, with references [23,24].

For the natural gas case, the optimal economic solution for an off-grid EC was 9.3% higher when compared to the optimal economic solution for grid-connected EC (point A, Fig. 6), which represents 212 k€/y. When the optimal CO_2eq emissions solution is analysed, the increase is even higher. The correspondent off-grid solution emits 21.2% more CO_2eq if compared to the equivalent solution for grid-connected (scenario 1). Besides, for this exact same comparison, the off-grid solution costs 2.2 times more.

In the case of biomethane, as expected, the emissions resulted zero. This is because the biomethane was considered net-zero CO_2eq emitter and there is no electricity bought from the main grid. When compared to the equivalent grid-connected solution (point D, Fig. 7), the grid-isolated one held a slight increase of 0.4% (which represents 12.6 k€/y) in the total annual costs. However, the grid-connected solution allows a CO_2eq compensation of almost 460 ton of CO_2eq/y. Moreover, considering the grid-connected (scenario 2), it could be possible to increase the CO_2eq compensation by around nine times by increasing the total annual costs by only 18%.

5.4. Brief comparison to carbon market and payback evaluation

As introduced in section 1, one of the foreseen directives from the “Fit for 55” package of the EU regards an update to the EU emissions trading system (ETS). According to the European Commission [25], international carbon markets have the potential to serve as a crucial factor in the cost-effective reduction of worldwide GHG emissions. This is demonstrated by the rising of emissions trading systems globally. In addition to the EU ETS, various national and sub-national emissions trading systems are currently in operation or being developed in several countries including Canada, China, Japan, New Zealand, South Korea, Switzerland, and the United States.

With lower environmental impacts and higher energy efficiencies, ECs have a substantial cost advantage if inserted in a carbon trading ecosystem [26]. Moreover, a personal carbon trading (PCT) scheme has been discussed in literature [27,28], as a promising and innovative policy tool to mitigate carbon emissions at the household and individual level, and to encourage the adoption of low-carbon lifestyles. In this sense, the present work analysed the cost of CO_2eq emissions reduction based on the data from Fig. 6. The reference cost was the one resulted from the optimal economic solution for scenario 1 (point A).

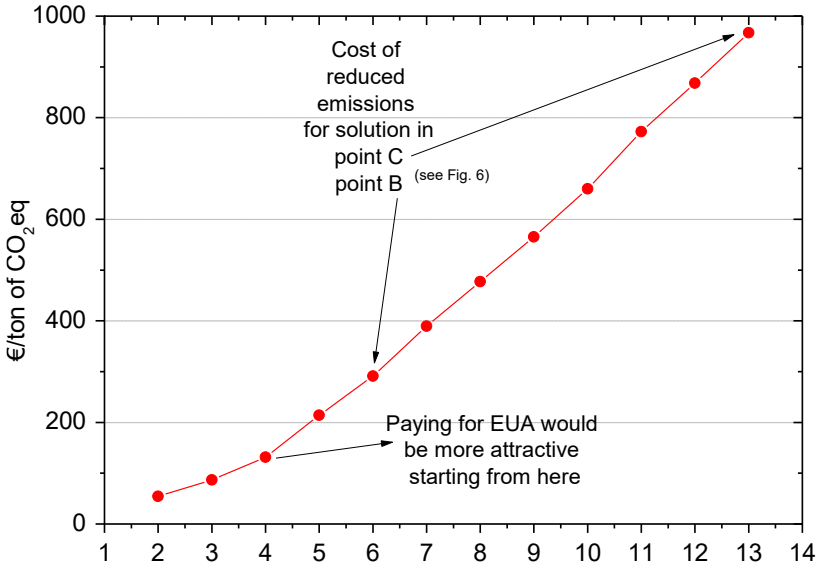

Figure 8. Cost of reduced CO_2eq emissions for each solution in the Pareto curve of scenario 1. Solutions 2 to 13 (see Fig. 6) are confronted to solution 1 (or point A) in order to compare results with the carbon market.

Figure 8 shows the cost of reducing CO_2eq emissions from solution number 1 (point A, Fig. 6) to each one of the other 12 solutions in the Pareto curve of scenario 1. Such cost raises from 54 (solution 2) to almost 970 €/ton of CO_2eq (solution 13). Considering an average European Emission Allowance (EUA) of 85 €/ton of CO_2eq [29] for the past year, the data suggests that, starting from the point indicated in Fig. 8, it would be economically more attractive to pay for the correspondent amount of EUA, rather than choose a solution for

the EC with a lower CO_2eq emissions level. In order to have an idea, if solution in point B would be chosen over that of point A (Fig. 6), the cost increase would be around 560 k€/y. On the other hand, if point A is chosen and the correspondent EUA is paid, the cost increase would be around 163 k€/y. Note that all the solutions of the Pareto fronts depicted in Figs. 6 and 7 present both lower economic cost and lower greenhouse gas emissions than the conventional solution (CS) and, therefore all of them represent an improvement.

Table 5 presents the payback (PB), cost reduction (CR), and CO_2eq emissions reduction (CO_2R) for the four main solutions analysed in sections 5.1 and 5.2. All solutions were confronted with the CS scenario data. Although point C (optimal emissions solution) owns one of the highest CO_2R, its cost decrease was the lowest one, while its payback was the highest one. By comparing points A and B from the CO_2R point of view, the latter would be the best one. However, by joining the perspectives of PB, CR, and carbon market, point A solution would be more attractive since it would have lower PB and lower overall costs (including the payment of EUA). In the perspective of a gas grid fed 100% by biomethane, point D would be attractive if the goal would be to cut off and compensate CO_2eq emissions.

Table 5. Evaluated solutions, payback (PB), cost reduction (CR), and CO_2eq emissions reduction (CO_2R) with respect to the CS scenario.

Solutions (points)	PB (y)	CR (%)	CO_2R (%)
A	1.5	– 48	– 34
B	1.8	– 35	– 51
C	4.7	– 5	– 51
D	1.8	– 41	– 104

6. Conclusions

In order to cover new climate change concerned policies, such as the “Fit for 55” package from EU, and reach a low-carbon future, solutions should be presented throughout different sectors. This is the case, for example, of the efficiency of energy systems and buildings. For that reason, this paper assessed the performance of different scenarios for an EC, through a multi-objective optimisation approach. The EC comprises nine third sector buildings located in Pordenone, northeast of Italy, and was modelled through a mixed integer linear programming (MILP) model. The evaluated scenarios were: 1) Grid-connected - natural gas consumption, 2) Grid-connected - biomethane consumption, and 3) Grid-isolated.

The results have shown that, as expected, all three scenarios present better trade-off solutions when compared to the CS scenario (reference case), i.e., lower total annual costs and CO_2eq emissions. However, each one of the three scenarios presented its particularities.

For scenario 1, which represents the current scenario of natural gas consumption, the selected trade-off solution according to the Pareto curve (Fig. 6) was the one of point B. This solution holds a total annual cost 31.5% (or 1307 k€/y) lower when compared to the optimal CO_2eq emission solution (point C, Fig. 6), but with approximately the same emissions level. When compared to the optimal economic solution (point A, Fig. 6), the total annual cost of the solution in point B is 24.5% (or 560 k€/y) higher, while its total annual CO_2eq emissions is 26% (or 1923 ton of CO_2eq/y) lower. Nevertheless, if the carbon market is considered, and with the current price for each ton of CO_2eq (March 2023), the solution in point B would no longer be economically attractive. Instead, the solution from point A along with the correspondent EUA payment would result an economic saving of around 70% with respect to the solution in point B. Besides, point A solution owns the lower payback among the analysed solutions.

Scenario 2 represents the limit case of a natural gas grid in which its methane content is completely replaced by biomethane (which was assumed a net-zero emitter for this work). When comparing the optimal economic solutions between scenarios 1 and 2, one can see that an increase of 13.4% in the total annual costs (or 306 k€/y) could allow a reduction of 106% in the total annual CO_2eq emissions, i.e., emissions would be cut off and, besides, a CO_2eq compensation of 460 ton per year would be obtained. Therefore, considering the possibility of moving from the optimal economic solution in scenario 1 (point A) to the optimal economic solution in scenario 2 (point D, Fig. 7), the cost per ton of reduced CO_2eq emissions would be economically more attractive when compared to the carbon market.

The third analysed scenario is the one where the EC (in both scenarios 1 and 2) would be completely isolated from the national electric grid. Results demonstrated that the off-grid EC version is not attractive from economic or emissions viewpoints. In scenario 1, the total annual cost and CO_2eq emissions of the EC would be, respectively, 9.3% and 21.2% higher. In scenario 2 the cost increase would be only 0.4%, however, the EC would not be able to compensate CO_2eq emissions by selling electricity to the grid.

Therefore, based on the obtained results, the implementation of an EC as the one analysed in this work would help not only to cope with new climate change policies (such as “Fit for 55”), but would be also economically more attractive than the current scenario.

Acknowledgements

This work was partially funded by the Spanish State Research Agency (research project PID2020-15500RB-I00), the Government of Aragon (Ref: T55-20R), and the European Regional Development Fund (ERDF). The first author would like to acknowledge the PhD scholarship from the Italian Ministry of University and Research as well as the Erasmus+ grant provided by University of Trieste.

References

[1] International Energy Agency (IEA). Evolution of key regional natural gas prices, June 2021-October 2022 – Available at: <https://www.iea.org/data-and-statistics/charts/evolution-of-key-regional-natural-gas-prices-june-2021-october-2022> [accessed 15.2.2023].

[2] International Energy Agency (IEA). Evolution of energy prices, Oct 2020-Jan 2022 – Available at: <https://www.iea.org/data-and-statistics/charts/evolution-of-energy-prices-oct-2020-jan-2022> [accessed 15.2.2023].

[3] International Energy Agency (IEA). Evolution of energy prices, 2020-2021 – Available at: <https://www.iea.org/data-and-statistics/charts/evolution-of-energy-prices-2020-2021> [accessed 17.2.2023].

[4] International Energy Agency (IEA). How to Avoid Gas Shortages in the European Union in 2023 – Available at: <https://www.iea.org/reports/how-to-avoid-gas-shortages-in-the-european-union-in-2023> [accessed 17.2.2023].

[5] De Souza R., Nadalon E., Casisi M., Reini M. Optimal Sharing Electricity and Thermal Energy Integration for an Energy Community in the Perspective of 100% RES Scenario. Sustainability 2022;14:10125. https://doi.org/10.3390/su141610125

[6] Casisi M., Buoro D., Pinamonti P., Reini M. A Comparison of Different District Integration for a Distributed Generation System for Heating and Cooling in an Urban Area. Appl. Sci. 2019;9(17):3521. https://doi.org/10.3390/app9173521

[7] Dorfner J., Hamacher T. Large-Scale District Heating Network Optimization. IEEE Trans. Smart Grid 2014;5:1884–1891. https://doi.org/10.1109/TSG.2013.2295856

[8] Buoro D., Casisi M., De Nardi A., Pinamonti P., Reini M. Multicriteria optimization of a distributed energy supply system for an industrial area. Energy 2013;58:128-137. https://doi.org/10.1016/j.energy.2012.12.003

[9] Buoro D., Pinamonti P., Reini M. Optimization of a Distributed Cogeneration System with solar district heating. Applied Energy 2014;124:298-308. https://doi.org/10.1016/j.apenergy.2014.02.062

[10] Casisi M., De Nardi A., Pinamonti P., Reini M. Effect of different economic support policies on the optimal synthesis and operation of a distributed energy supply system with renewable energy sources for an industrial area. Energy Conv. and Manag. 2015;95:131-139. https://doi.org/10.1016/j.enconman.2015.02.015

[11] European Commission. 2030 Climate Target Plan – Available at: <https://climate.ec.europa.eu/eu-action/european-green-deal/2030-climate-target-plan_en> [accessed 10.3.2023].

[12] European Council. Fit for 55 package – Available at:<https://www.consilium.europa.eu/en/policies/green-deal/fit-for-55-the-eu-plan-for-a-green-transition/#council> [accessed 13.3.2023].

[13] European Council. – Available at: <https://www.consilium.europa.eu/en/> [accessed 13.3.2023].

[14] European Council. Infographic - Fit for 55: how the EU will become more energy-efficient – Available at: <https://www.consilium.europa.eu/en/infographics/fit-for-55-how-the-eu-will-become-more-energy-efficient/> [accessed 14.3.2023].

[15] European Council. Infographic - Fit for 55: how the EU plans to boost renewable energy – Available at: <https://www.consilium.europa.eu/en/infographics/fit-for-55-how-the-eu-plans-to-boost-renewable-energy/> [accessed 14.3.2023].

[16] Masip X., Fuster-Palop E., Prades-Gil C., Viana-Fons J. D., Payá J., Navarro-Peris E. Case study of electric and DHW energy communities in a Mediterranean district. Renewable and Sustainable Energy Reviews 2023;178:113234. https://doi.org/10.1016/j.rser.2023.113234

[17] Roversi R., Boeri A., Pagliula S., Turci G. Energy Community in Action—Energy Citizenship Contract as Tool for Climate Neutrality. Smart Cities 2022;5:294-317. https://doi.org/10.3390/smartcities5010018

[18] Petrichenko L., Sauhats A., Diahovchenko I., Segeda I. Economic Viability of Energy Communities versus Distributed Prosumers. Sustainability 2022;14:4634. https://doi.org/10.3390/su14084634

[19] European Biogas Association. Market state and trends in renewable and low-carbon gases in Europe – Available at: <https://www.europeanbiogas.eu/market-state-and-trends-in-renewable-and-low-carbon-gases-in-europe/> [accessed 28.2.2023].

[20] System Advisor Model (SAM). – Available at: <https://sam.nrel.gov/weather-data.html> [accessed 05.2.2023].

[21] Takahama T., Sakai S., Iwane N., Solving Nonlinear Constrained Optimization Problems by the ε Constrained Differential Evolution. IEEE International Conference on Systems, Man and Cybernetics; 2006; Taipei, Taiwan. pp. 2322-2327. https://doi.org/10.1109/ICSMC.2006.385209

[22] Caposciutti G., Baccioli A., Ferrari L., Desideri U. Biogas from Anaerobic Digestion: Power Generation or Biomethane Production? Energies 2020;13:743. https://doi.org/10.3390/en13030743

[23] Pinto E.S., Serra L.M., Lázaro A. Design of affordable sustainable energy supply systems for residential buildings: A case study. Int J Energy Res. 2022;7556-7577. https://doi.org/10.1002/er.7660

[24] Pinto E.S., Serra L.M., Lázaro A. Energy communities approach applied to optimize polygeneration systems in residential buildings: Case study in Zaragoza, Spain. Sustainable Cities and Society 2022;82:103885. https://doi.org/10.1016/j.scs.2022.103885

[25] European Commision. International carbon market – Available at: <https://climate.ec.europa.eu/eu-action/eu-emissions-trading-system-eu-ets/international-carbon-market_en> [accessed 20.3.2023].

[26] Chen L., Xu Q., Yang Y., Gao H., Xiong W. Community Integrated Energy System Trading: A Comprehensive Review. Journal of Modern Power Systems and Clean Energy 2022;10(6):1445-1458. https://doi.org/10.35833/MPCE.2022.000044

[27] Fan J., Li J., Wu Y., Wang S., Zhao D. The effects of allowance price on energy demand under a personal carbon trading scheme. Applied Energy 2016;170:242-249. https://doi.org/10.1016/j.apenergy.2016.02.111

[28] Wu Y., Wu Z., Gu W., Xu Z., Zheng S., Sun Q. Decentralized Energy Market Integrating Carbon Allowance Trade and Uncertainty Balance in Energy Communities. Cornell University Press ArXiv; 2023. https://doi.org/10.48550/arXiv.2301.12129

[29] Trading Economics. – Available at: <https://tradingeconomics.com/> [accessed 21.3.2023].

Energy performance of loading and hauling operations in opencast mines

Lalit Kumar Sahoo*, Seema Ashishan Topno

CSIR-Central Institute of Mining & Fuel Research, Nagpur Research Centre, Nagpur, India, lalitsahoo@yahoo.co.in

Abstract:

Loading and hauling machines accounts for significant share of the total energy usage in large opencast mines. Major share of power is consumed in electric shovels used for loading operations and accounts for 32% of the total electricity usage in mine. Diesel is also used for operating hauling machines (dump trucks) in opencast mine and accounts for 56% of the total diesel consumption. In this paper, a methodology is proposed for calculating overall energy consumption in major energy intensive mining processes such as loading and hauling operations of the coal mine. Statistical approach has been used to estimate minimum SEC of a specific mine based on the annualized data. A linear regression method has been used to develop a mine specific model for estimating SEC by the correlation between SEC and composite production. A case study of an Indian opencast mine is presented to illustrate the results. Minimum SPC of electric shovels is calculated as 0.15 kWh/cum whereas the best operating SDC values of dump trucks operating in same mine is 0.47 l/cu.m. The overall SEC of loading and hauling operations calculated for the same opencast mine is 17.76 MJ/Cu.m and SEC of total operation in mine is 27.2 MJ/Cu.m. The best practices opencast mine without dragline from the literature is 26.3 MJ/cu.m.

Keywords:

Energy performance, Statistical approach, Loading, Hauling, Opencast mine, Specific energy consumption

.

1. Introduction

Dump trucks are used worldwide for handling of ore and waste in most of the opencast mines. It is considered as one of the versatile heavy earth moving equipment. The diesel consumption in dump trucks accounts for about 56 % of the total diesel consumption in opencast mine [1]. Dump trucks are used for material handling in opencast mines using shovel- truck combination. The transportation network of mine includes a fleet of dump trucks moving between crushers/dumping stations and shovels. The diesel consumption in dump trucks depends on the speed, material handling rate and distance between loading and unloading point. Benchmarking and optimization models are generally used for calculating minimum energy consumption. An energy benchmarking model is developed by Sardeshpande et al. for calculating minimum energy consumption in glass furnace [2]. Most of the exercises on optimization in transportation are based on linear programming approach for reducing cost. Energy efficiency of dump trucks operating in opencast mine has been rarely analyzed. The optimization of loading and transport system in opencast mine has been done to optimize number of trucks required serving at loading point, number of trips per hour and theoretical output of dump trucks [3]. Optimization of journey schedule of high capacity dump truck has been done by Vasil'ev et al. to reduce the travel time of dump truck [4]. Fuel consumption depends on the inherent resistances such as gradient resistance, drag force and rolling resistance. Fuel consumption rate is taken as objective function and solved by Langrage's multiplier method with constraint of total time. Solving the optimization problem shows that fuel consumption is minimum by keeping speed profile constant for level, ascending and descending gradient [5]. The results of study made Tolouei et al confirmed that fuel consumption increases as mass increases and is different for different combination of fuel and transmission type [6]. A benchmarking model was developed by Sahoo et.al. for optimization of specific fuel consumption for dump trucks [7]. Specific diesel consumption (SDC) can be used as energy performance indicators to assess and compare the energy performance of hauling operations in operating mine.

Electric shovels dominate the electrical energy consumption in opencast coal mine and consume 32% of the total electrical energy usage [8]. Energy efficiency indices have been used by researchers to assess energy efficiency in mining process. Specific power consumption (SPC) has been used previously to describe the

performance of digging equipment and operators. Energy benchmarking using statistical approach has been done for commercial building [9]. Past studies showed that operator's proficiency plays a significant role in the productivity of shovels [10-13]. Energy efficiency of loading and hauling operations depends on the equipment, operating conditions, mine planning and operator's performance [10]. Specific energy consumption (SEC) is used as energy benchmarking index and is measured as the energy consumed to the production output (MJ/t, kWh/t etc.). Oskouei et al. revealed that the operator's skill affect the energy efficiency of the mining machinery [11]. The study done by Karpuz et al. revealed that there is an increase in digging power consumption with the increase in the cutting depth and operator's performance [12]. The results of simulation experiments conducted by Awuah-Offei, K. et.al revealed that an operator operating near optimal levels with a 44 cu.m bucket capacity can save over $114,000/- in electricity costs for digging cycle alone as compared to an average operator [13].

From the literature review it is concluded that limited literature addresses benchmarking of specific energy consumption for loading and hauling operations in opencast mine using statistical approach. In this paper a methodology is developed for benchmarking of specific energy consumption for loading and hauling operation and validated with energy performance for best operating mine.

1.1. Mining process

Drilling and blasting is the first process of surface mining for fragmentation of overburden and coal seams. An efficient blasting result in lower cost of extraction as the particle size and density of material affects the energy consumption of an opencast mine. Excavators/Hydraulic backhoe, shovels are used for loading material in to dump trucks. Dump trucks are then used to transport coal and overburdens to the specified dumping stations. The fuel consumed in heavy earth moving machines operating in mines varies with mine topography, distance, material handled and the capacity utilization. Pie charts showing the fuel consumption and power consumption of Dipka opencast mine of South Eastern Coalfields Ltd (SECL) is shown in Fig.1a and Fig 1b. From the Fig. 1a, dump trucks consume about 56% of total diesel consumed in opencast mine.

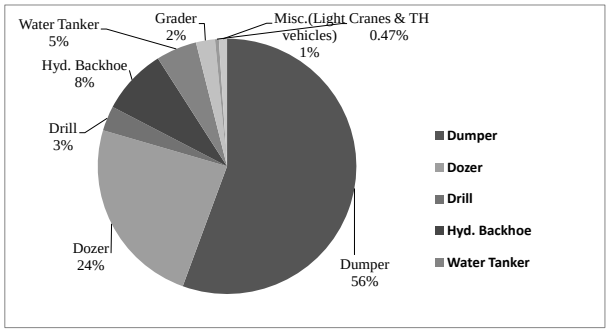

Fig 1a Diesel consumption profile in opencast mine of SECL

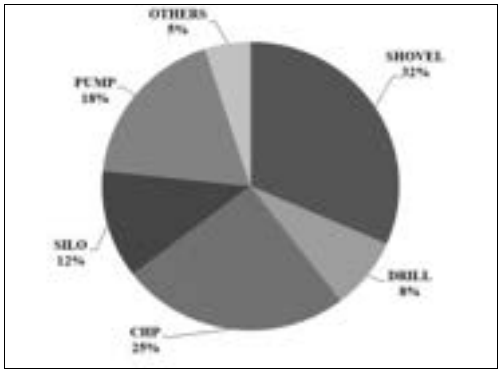

Fig 1b Power consumption in opencast mine of SECL

1.2. Objective

Diesel is used as fuel for operating heavy earth moving machines (HEMMs) such as dump trucks, dozers and drills etc. in an opencast mine. The diesel consumption in haul trucks used for hauling operation consume 32% of total energy consumed in an opencast coal mine and varies with mine topography, bulk density of coal and overburdens and operating practices of haul trucks. Similarly loading operation consume significant energy consumption. Electric shovel consumes 32% of total electrical energy consumption in opencast mine. Hence, these two operations such as loading and hauling consume significant energy in opencast mine. The objectives of the paper are given as follows.

1) Evaluate the energy performance of loading and hauling operations
2) Propose a method for energy benchmarking of shovels and sump trucks
3) Study the variation of SDC of hauling operations with composite production
4) Study the variation SPC of loading operation with composite production
5) Compare the benchmark SEC with best practices mines.

2. Methodology for Energy Benchmarking

2.1. Statistical Benchmarking

Statistical approach has been applied by many researchers for benchmarking energy consumption of commercial buildings, agriculture and industrial sectors. Benchmarking energy consumption in commercial building has been done by Chung et al. using a statistical approach [14]. Chauhan et al., and Omid et al. have also used statistical methods for benchmarking energy for agriculture [15,16]. Benchmarking energy efficiency for Dutch industries has been done by Phylipsen et al.[17]. These approaches are defined as statistical energy benchmarking. The loading and hauling machines in opencast coal mines can implement the idea of energy benchmarking. A study was conducted in a large opencast coal mine in India by author to apply statistical benchmarking methodology [18]. In present paper, the statistical approach has been applied for benchmarking energy consumption for two major operation:

- Loading operations using electric shovel
- Hauling operations using dump trucks

The statistical benchmarking can quickly estimate the minimum energy required per cubic meter of composite coal production in an opencast mine. The statistical benchmarking approach uses specific diesel consumption (SDC) as energy performance indicator for dump trucks, specific power consumption (SPC) for electric shovels and specific energy consumptionn(SEC) for overall energy consumption in loading and hauling operations in opencast mine. The SEC of the best performing year is considered as the energy benchmark target from the annualized data for the specific mine equipment. The monthly data is not appropriate due to seasonal variations of energy performance of mining equipment during rainy and off rainy season. In case of benchmarking mine quipment of different coal mines, multiple mine equipment of different capacities are compared to evaluate the minimum SEC. The specific energy consumption (SEC) of the mine is calculated from the aggregate energy consumption of both loading and hauling operations for electric shovels and dump trucks.

2.1. 1. Energy benchmarking for loading operations

Energy benchmarking of loading operations is the minimum SPC of electric shovels operating in the mine from best operating value. A benchmark SPC of the electric shovels is calculated by comparing progressive SPC based on the aggregated annualized data of power consumption and material handled. A mine specific model of benchmarking has been developed using linear regression analysis by correlating the SPC and composite production. The model helps in predicting the SPC of the mine equipment.

Electric shovels are used for loading materials in to the dump trucks in large opencast mines and consume significant quantity of electrical energy. Smaller opencast mines use diesel operated excavators for loading operations. Depending on the production requirement the machines are deployed by production supervisors. The SPC of electric operated shovel is obtained from the ratio of annualized energy consumed in shovel to the annual material handled and is given as:

$$SPC_j = \frac{\sum_{i=1}^{12} E_{c,ij}}{\sum_{i=1}^{12} Q_{t,ij}} \quad (1)$$

2.1. 2. Energy benchmarking for hauling operations

Specific diesel consumption (SDC) is an energy performance index to assess energy efficiency of heavy earth moving machines (HEMMs) operating in an opencast mine. Dump trucks consume major share of diesel consumption in mine. Therefore, SDC should be monitored regularly for targeting and minimizing diesel consumption in mine. The methodology for practical benchmarking approach for calculating SDC has been discussed in this section. The specific diesel consumption of single dump truck is defined as the ratio of diesel consumed during field trial period (t) to the material handled. The material handled is determined as the product of shovel bucket capacity, actual numbers of buckets filled, number of trips of truck and fill factor.

$$SDC_1 = \frac{m_f(t)}{C_b n_b(t) x_d(t) C_f} \quad (2)$$

Dump trucks are used for transportation of coal and OB from shovels to CHP or OB dumping stations in opencast mine and consume significant quantity of diesel for its operation. Dump trucks are generally accommodated in the workshop of the mine from where it goes to mine site for operation as per the planning and requirement of production supervisors. Diesel is filled once a day at diesel filling station located near the workshop. Diesel is issued to dump trucks of different capacity ($i = 1,2,3$) for example 240t, 120t, 100t trucks.

If 'Q' is material handled by different capacity dump trucks, the benchmark SDC (SDC_{BM}) of multiple dump trucks is obtained using following formula for rainy as well as off rainy season. Minimum SDC is considered as benchmark for same capacity dump trucks operating in same roots. For different roots, average value is taken.

$$SDC_{BM} = \frac{Min\sum_{i=1}^{n} SDC_i Q_i}{Q} \quad (3)$$

Where,

$$Q = \sum_{i=1}^{n} Q_i \quad (4)$$

Average SDC of dump trucks for of dump trucks for rainy/off rainy season is estimated as:

$$SDC_{Avg} = \frac{Avg\sum_{i=1}^{n} SDC_i Q_i}{Q} \quad (5)$$

Eq (3) to Eq (5) are used for calculating benchmark SDC.

3. Case study of large coal mines

A case study of Dipka opencast coal mine of M/s South Eastern Coalfields Ltd (SECL), Bilaspur has been presented for assessing the practical benchmark SDC [18]. Dipka opencast mine of M/s. SECL lies in the latitude 22^0 18'59" – $22^0$19'43" and longitude 82^0 30'47" - $82^0$33'34" and bears the toposheet No. 64J/11 in the *Survey of India* and is located in Korba district of Chattisgarh, India. The installed production capacity of the mine is 25 MTPA with average stripping ratio of the mine is 1 m^3/Te of coal. Diesel is used for operating different HEMMs including dump trucks. Dump trucks consume about 56% of the total diesel consumption. The minimum SDC of the mine from past 4 years data is 0.81 l/cu.m. whereas the benchmark of the mine by comparing with five operating mines of different production capacity is 0.66 l/cu.m. Dump trucks used in hauling operation consume major share of diesel consumption and therefore the benchmarking has been done to evaluate minimum SDC based on statistical approach using methodology given above in para 2.1.2.

Dump trucks of different capacity (240t, 120t, 100t) and model of BEML/Caterpillar/Terex are operating in mine for transporting overburden (OB) and coal from different levels of mine to coal storage/ OB dumping stations. BEML dump trucks uses Cummin's engine whereas Caterpillar has its engine of the own make. Engine performance is very important for fuel economy in mine. Selection of dumper with a fuel-efficient engine helps in reducing SDC of the dump trucks. The engine specifications of dump trucks are given in Table 1.

Table 1 Engine specification of dump trucks

PARAMETERS	CAT 793D (240t)	CAT777 (100t)	BH 100 (100t)	MK 30 /MT 3000 (120t)
Make	Caterpillar	Caterpillar	BEML/Cummins	Detroit diesel
No of cylinders	16	12	12	16
Bore & stroke	170mm x 215mm	145mm x162mm	140mm x165mm	130mm x 150 mm
Displacement	78 lits	32.1 lits	37.7 lits	32 lits
Gross power	1801 kW,2415 hp	765 kW,1025 hp	783 kW, 1050 hp	898 kW

Max torque	9553 N-m	5286 N-m	4629 N-m	-
Engine speed	1800 rpm	1750 rpm	2100 rpm	1900 rpm
Gear ratio	28.1:1	17.49:1	22.21:1	28.8:1
Payload	240 tons	100 tons	91.5 tons	108.8t
Volumetric capacity	96 m^3	41 m^3	41.5 m^3	49.4 m^3
Heaped capacity	129 m^3	60.1m^3	61 m^3	69.4 m^3

P & H electric shovels operating in Dipka opencast coal mine of M/s South Eastern Coalfields Ltd (SECL), Bilaspur, India has been presented in this paper for energy performance assessment using statistical approach. The annual electrical energy consumption of the mine is 49.3 GWh/y in 2014-15. The connected load of the electrical machinery in mine is 38.49 MW. The electric shovels (four numbers of 10 cu.m. and two numbers of 42 cu.m.) consume 32% of the total electrical energy. The power rating for hoist motors, crowd motor, swing motor and propel motors of electric shovel is 1887 kW, 547 kW, 746 kW and 716 kW respectively. The connected of electric shovel is 7235 kW (2 hoist motors, 1 crowd motor, 2 swing motors and 2 propel motors). The physical parameters of P & H electric shovel are given in Table 2. Five dump trucks were allocated to the shovel at the pit for hauling operation. The loading cycle of shovel include five different operations; digging, swinging, unloading, swing back and positioning/waiting time.

Table 2 Physical parameters of P & H electric shovel

Parameters/Model	Value	Unit
Model	4100C	
Nominal dipper capacity	45.9	cu.m.
Nominal Payload	81.6	t
Rated suspended load	154.2	t
Bucket fill factor	0.80	(assumed)

4. Results and Discussions

The variation of SDC with material handled for sample dump trucks during field measurement is shown in Fig.2a. From the analysis of results, SDC of dump trucks decreases with increase in material handling rate. The minimum SDC of 0.47 l/cu.m. is shown for maximum material handling rate of 348 cu.m./h for dump trucks with lead varies from 2.2 km to 2.97 km. The variation of SDC with monthly composite production shows non-linear trend and is shown in Fig 2b. Statistical approach of benchmarking considers minimum SDC of past 3 years progressive data to benchmark diesel consumption in mine. The analysis of annual progressive SDC showing monthly minimum and maximum value is shown in Table 3.

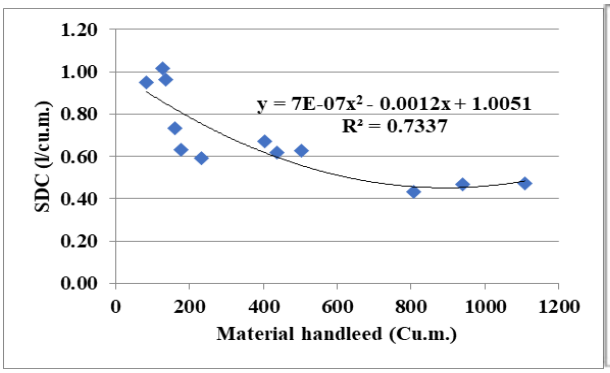

Fig 2a: Variation of SDC with total material handled

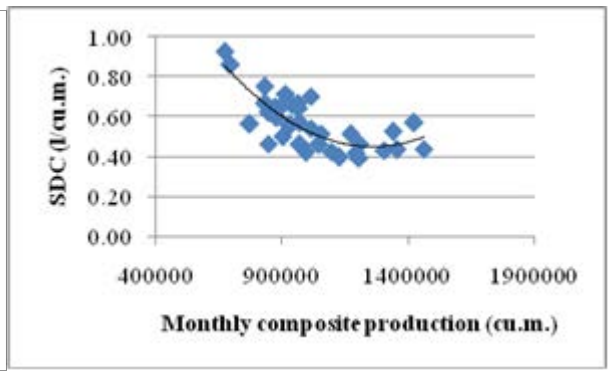

Fig.2b Variation of SDC of dump trucks with monthly material handled

Table 3 Analysis of progressive SDC of dump trucks for an opencast coal mine of SECL

Sample size:36 (monthly SDC); 03 (Annualized data of SDC)	SDC (l/cum)		
Year	Monthly Minimum	Monthly Maximum	Progressive
2012-13	0.60	0.93	0.69
2013-14	0.42	0.65	0.52
2014-15	0.39	0.66	0.47
Average	0.47	0.75	0.56

From statistical analysis, the minimum SDC of dump truck is 0.47 l/cu.m and average SDC is 0.56 l/cu.m. The progressive yearly variation of SDC is shown as Fig. 3a whereas the variation of SDC with material handled per hour is shown in Fig.3b from the actual measurement. The result of practical benchmarking is close to that by statistical approach. However, sometimes due to dynamic condition such as change of the haul road distance, material handles and operational practices statistical approach may not give accuracy in calculating the benchmark SDC. The disadvantage of statistical benchmarking is that it does not consider present operating conditions.

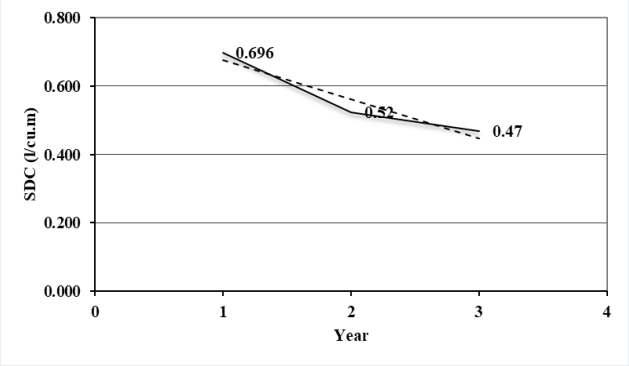

Fig 3a: Variation of progressive SDC

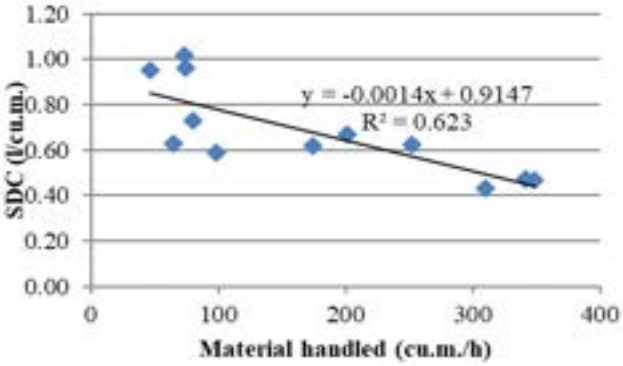

Fig.3b Variation of SDC of hauling with material handled

Statistical approach of benchmarking has also been applied for loading operation using electric shovel in large opencast mine. The annualized energy consumption and production data are used to calculate progressive SPC of the shovels operating in mine. Fig 4a shows the variation of SPC with composite production. The overall minimum SEC is then calculated to calculate benchmarking target for loading and hauling operation. Fig 4b shows the variation of overall SEC with composite production. Table 4 shows the minimum specific energy consumption of the loading and hauling operations. The minimum SEC is calculated as 17.76 MJ/cum in the year 2013-14.

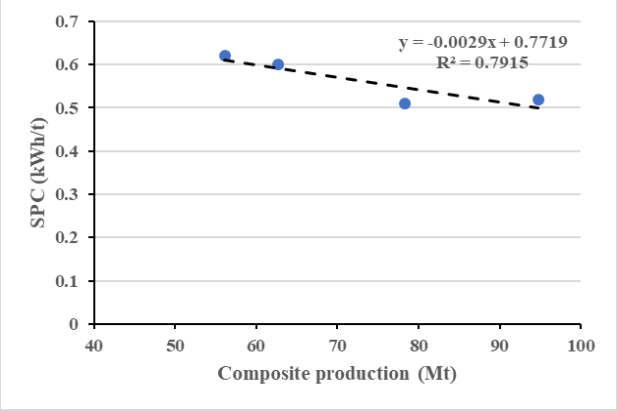

Fig 4a: Variation of progressive SPC with production

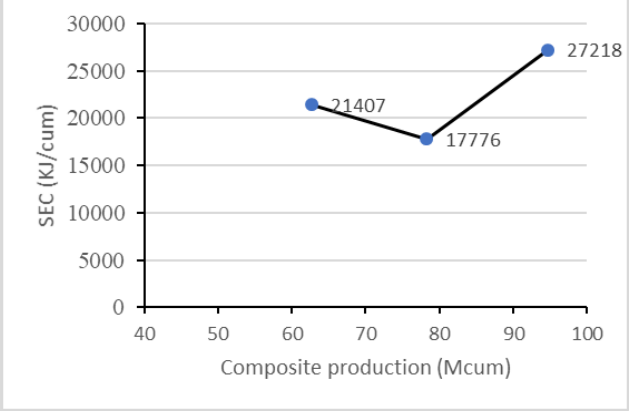

Fig.4b Variation of SEC of loading and hauling

Table 4 Analysis of progressive SDC and SPC of an opencast coal mine of SECL

	Energy performance values	
Mining operations		SEC (KJ/cum)
Hauling (SDC)	0.56	19756.8
Loading (SPC)	0.16	1651
SEC_{LH} (Year1)		21407.8
Hauling (SDC)	0.47	16228.8
Loading (SPC)	0.15	1548
SEC_{LH} (Year 2)		17776.8
Hauling (SDC)	0.7	24696
Loading (SPC)	0.44	2522
SEC_{LH} (Year 3)		27218

The result shows that both SDC and SPC decreases with increase in composite production in opencast mine whereas the overall energy consumption though increases with production, the minimum specific energy consumption target is assessed for lower production rate due variation in energy inputs and operating strategies for loading and hauling machines.

4.1. Best practices in opencast mines

The specific energy consumption of the best operating opencast coal mine for overburden handling taken from the literature is 26.9 MJ/cu.m.[12]. From the present benchmarking study the SDC of best operating coal mine with 92% overburden handling is 0.66 l/cu.m. for a large opencast mine and is equivalent to 25.4 MJ/cu.m. The present energy benchmark level of 25.4 MJ/cu.m. for Gevra opencast mine can be further minimized by improving operational practices and procurring new energy efficienct heavy earth moving machines like 240t dump trucks and optimising the number of dump trucks corresponding to the total numbers and capacity of electric shovels deployed in the coal mine. The benchmarking can be used for targeting and assessing the energy saving potential in opencast mining sector. A potential fuel saving of atleast 16 % is possible by comparing the minimum SEC with average SEC of the specific mine.

4.2. Energy saving potential

The fuel saving potential in the mine is estimated by comparing the minimum SEC and average SEC of the mine using Eq. (6) for bechmarking of a specific mine.

$$E_s = \frac{SEC_{avg} - SEC_{BM}}{SEC_{avg}} \quad (6)$$

The minimum SDC of 0.66 l/cu.m (25.4 MJ/cu.m) is obtained by comparing SDC of five opencast coal mines of different installed capacity. The capacity of the mines is variable and can be increased by increasing number of machines depending on the coal reserve of the mine. The diesel saving potential by comparing minimum SDC with average SDC is 16 %.

5. Conclusion

In the present paper, a statistical approach of benchmarking has been applied for calculating specific energy consumption (SEC) and is used as energy performance indicator for loading and hauling operations. The overall minimum SEC for loading and hauling operation is calculated as 17.7 MJ/cu.m.The benchmark SDC for of hauling operations is 0.47/cu.m whereas the benchmark SPC obtained for electric shovel is calculated as 0.15 kWh/cu.m. The mine specific model for benchmarking has been developed using linear regression method. There is a significant scope of diesel and power saving by use of this method in mine. A diesel saving potential of 16 % is estimated by comparing with benchmarking value and the overall saving potential of 19% is estimated on both loading and hauling operations in opencast coal mine. Though the result of

practical benchmarking is close to that by statistical approach, due to dynamic condition of mine operation such as haul road distance, material handling and operational practices statistical approach may not give accuracy in estimating the benchmark target. The disadvantage of statistical benchmarking is that it does not consider present operating conditions.

The statistical approach helps in quick estimation of benchmarking target for coal mines from the past data of diesel consumption, electrical energy consumption as well as composite production data of the mine. The benchmarking method can help in setting energy benchmarking target of the mine for continuous productivity improvement and energy saving in mine.

Acknowledgments

The authors are grateful to M/s South Eastern Coalfields Ltd, Bilaspur, for providing the data and extending cooperation.The authours acknowledge sincere thanks to Dr. Arvind Kumar Mishra, Director, CSIR-CIMFR for giving permission and support to publish the research work. The authours also thank Dr A.K.Singh, Dr A K Soni of CSIR –CIMFR for their help and support.

Nomenclature

C_b	Shovel bucket capacity, cum
C_f	Fill factor
E_c	Monthly energy consumption, kWh
SEC_{BM}	Benchmark specific energy consumption, KJ/kg
SEC_{LH}	Specific energy consumption, (Loading and Hauling), KJ/kg
SEC_{avg}	Average specific energy consumption, KJ/kg
SPC_{shovel}	Specific power consumption of shovel
$m_f(t)$	Mass of fuel consumption of dump truck, lit
n_b	number of buckets
$x_d(t)$	number of dump truck trips
$.Q$	Composite production, cu.m.
SDC_{BM}	Benchmark SDC for coal mine, l/cu.m.
SDC_{avg}	Average SDC of the coal mine, l/cu.m.
SDC_i	SDC of the coal mine for i^{th}mine, l/cu.m.
SDC_{min}	Minimum SDC of the coal mine, l/cu.m.
SDC	Specific diesel consumption, l/cu.m.

References

[1] Sahoo L. K., Topno S., Energy benchmarking of Indian opencast coal mines. Proceedings of ECOS 2018, , 2018, June 17-22, Guimaraes, Portugal

[2] Sardeshpande V., Gaitonde U. N. and Banerjee R., Model based energy benchmarking for glass furnace. Energy conversion and Management 2008,48:2718-2378.

[3] Vemba M.M.D.S ,The loading and transport system at SMC-Optimization, The Journal of South African Institute of Mining and Metallurgy 2004, 139-147.

[4] Vasil'ev M. V, Smirnov V. P., (1974) Optimization of the journey schedules of high capacity Quarry dump trucks , The Institute of mining , Ministry of Ferrous metallurgy of USSR,Sverdlovsk. translated from Fiziko-Tekhni-cheskie Problemy Razrabotki Poleznykh Iskopaemykh 1974 No.1, 63-69.

[5] Chang D.J ,Morlok E.K., Vehicle speed profiles to minimize work and fuel consumption , The Journal transportation engineering , 2005, 173-182.

[6] Tolouei.R.,Titcheridge H., (2009) Vehicle mass as a determinant of fuel consumption and secondary safety performance', Transport research Part D.

[7] Sahoo L. K, Bandyopadhyay S. and Banerjee R. Benchmarking energy consumption for dump trucks in mines.Applied Energy 2014;113:1382-1396.

[8] Topno S. A, Sahoo L K, Umre B. S. Energy efficiency assessment of electric shovel operating in opencast mine; Energy 2021,230:120703.

[9] Chung W., Hui Y. V. and Lam Y. M., Benchmarking the energy efficiency of commercial buildings. Applied Energy 2006; 83:1-14.

[10] Awuah-Offei K, Energy efficiency in mining: a review with emphasis on the role of operators in loading and hauling operations. Journal of cleaner production 2016. doi: 10.1016/j.jclepro.2016.01.035.

[11] Abdi Oskouei M, Awuah-Offei K.Statistical methods for evaluating the effect of operators on energy efficiency of mining machines. Mining Technology 2014; 123(4): 175–182.doi: 10.1179/1743286314Y.0000000067.

[12] Karpuz C, Ceylanoglu A, Pasamehmetoglu AG. An investigation on the influence of depth of cut and blasting on shovel digging performance. Int J Surface Mining 1992; 6(4): 161-167.

[13] Awuah-Offei K. Dynamic Modeling of Cable Shovel-Formation Interactions: For Efficient Oil Sands Excavation, LAP Lambert Academic Publishing 2009; 168 pp

[14] Chung W., Hui Y. V. and Lam Y. M., Benchmarking the energy efficiency of commercial buildings. Applied Energy 2006; 83:1-14.

[15] Chauhan N. S., Mohapatra P. K. J. and Pandey K. P., Improving energy productivity in paddy production through benchmarking: An application of data envelopment analysis. Energy Conversion and Management 2006, 47:1063-1085.

[16] Omid M., Ghojabeige F., Delshod M. and Ahmadi H., Energy use pattern and benchmarking of selected green houses in Iran using data envelopment analysis, Energy Conversion and Management 2011, 52(1):153-162.

[17] Phylipsen D., Blok K., Worrell E. and Beer D. J., Benchmarking the energy efficiency of the Dutch industry: an assessment of the expected effect on energy consumption CO_2 emissions. Energy policy 2002, 30:663-679.

[18] CIMFR studies conducted by authours at Dipka opencast mine of South Eastern Coalfields Ltd (SECL), Bilaspur of Coal India Ltd., 2015.

Techno-economic comparison of a solar absorption chiller and photovoltaic compression chiller

Juan José Roncal-Casano[a], Paolo Taddeo[b], Javier Rodriguez-Martín[c], Javier Muñoz-Antón[d] and Alberto Abánades Velasco[e]

[a] Universidad Politécnica de Madrid, Madrid, Spain, e-mail: juanjose.roncal@upm.es
[b] Institut de Recerca en Energia de Catalunya (IREC), Barcelona, Spain, e-mail: ptaddeo@irec.cat
[c] Universidad Politécnica de Madrid, Madrid, Spain, e-mail: javier.rodriguez.martin@upm.es
[d] Universidad Politécnica de Madrid, Madrid, Spain, e-mail: javier.munoz.anton@upm.es
[e] Universidad Politécnica de Madrid, Madrid, Spain, e-mail: alberto.abanades@upm.es

Abstract:

Cooling systems are becoming increasingly important around the world. While centralized heating systems have been around for decades, cooling systems tend to be something that is only kept for large buildings, and decentralized cooling has flourished and is becoming the first choice when it comes to comfort needs, disregarding the efficiency of larger systems.

In this work, TRNSYS was used taking advantage of the Wedistrict methodology to compare two different alternatives and analyze which technology fits better in a cold district solution. On one side, single-stage absorption chillers combined with solar thermal technologies (Fresnel) as its heat source, and on the other, compression chillers with high energy efficiency ratios combined with photovoltaic technologies were used.

The paper shows that the current technological state singles out the compression chiller as a more appropriate selection for variable demand systems, while leaving absorption chillers as a viable option for constant cooling demand systems where a high temperature heat source is available.

Keywords:

TRNSYS; District Cooling; Solar energy; Absorption chiller.

1. Introduction

The increasing temperatures throughout the world are leading to an expansion in cooling degree days (CDD), which leads to an increasing need for cooling systems worldwide. This trend is also visible in Europe, where the significance of CDD was previously overlooked while devising a cooling strategy. At present, CDD values are becoming difficult to ignore (Figure 1)[1].

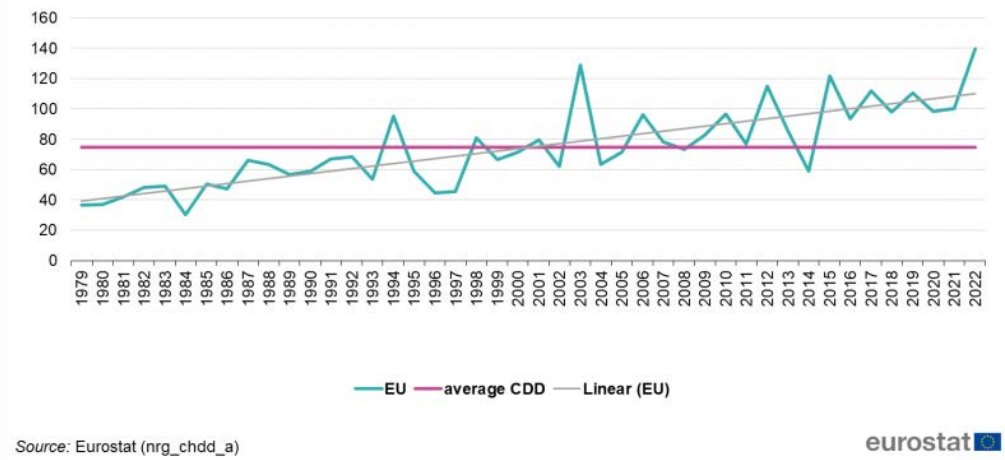

Figure 1. Cooling degree days statistics EU, 1979-2022.[1]

Two main cases have been analysed, the first one, photovoltaic panels have been used, and have been sized to be able to fully supply the compression chiller annually (Figure 2). In the other case, solar Fresnel panels have been sized to theoretically provide the energy needed for the conventional single stage absorption chiller, along with a natural gas boiler to ensure the correct inlet temperature for the chiller heat input (Figure 3).

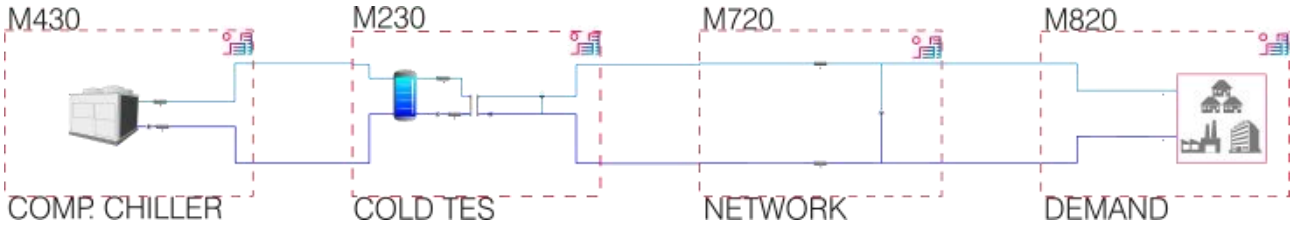

Figure 2. TRNSYS arrangement with tank.

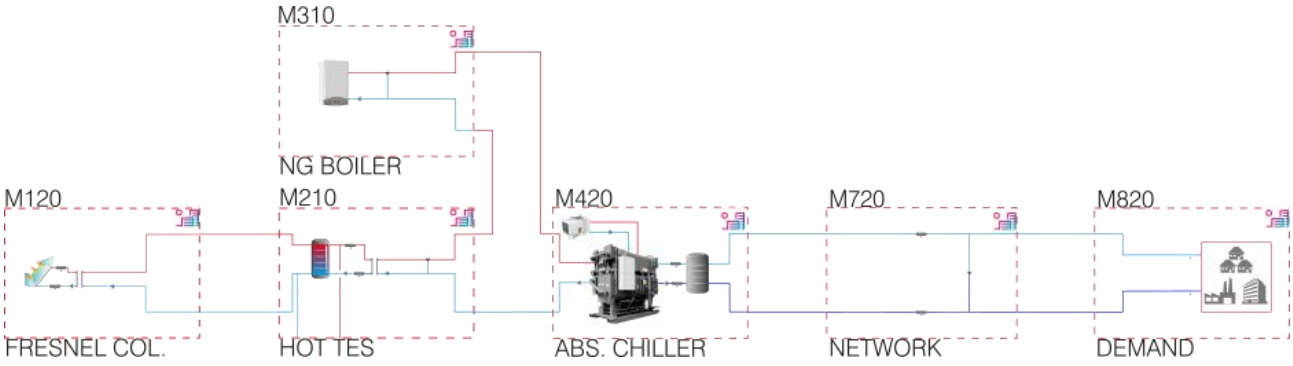

Figure 3. TRNSYS arrangement with absorption chiller with heat supply from solar energy plus boiler backup.

Different simulation approaches have been followed to arrive to correct plant sizes in order to compare technically and economically the results.

Both configurations have been simulated using TRSNYS (TRaNsient SYstems Simulation Program) following the modular methodology developed in the frame of the Wedistrict project [2]. Technical, environmental, and economic indicators have been calculated and analyzed [3].

2. Methodology

2.1. Software

TRSNYS (TRaNsient SYstems Simulation Program) software was applied in accordance with the modular methodology that was created specifically for the WEDISTRICT project.

This project studies the integration of innovative technologies for District Heating and Cooling (DHC) systems with an end goal of developing viable solutions for delivering fully renewable energy in climatization services [3].

The modular methodology is based in TRNSYS macros and decks. Macros are a series of TRNSYS types that are used together to reduce the number of connections to be done. The code to describe them has the letter "M" for "macro", followed by four numbers, the first three represent the code of the technology used, separated by the thousands in types of technologies (solar, storage, boilers, etc.), by the hundreds in different technologies between the same family, by the tenths in variations of the same technology. The unit is left in case the technology repeats itself in the same deck, due to the fact that TRNSYS, as many other software, does not allow variable name repetition.

WEDISTRICT macros have characteristics to improve the modularity and flexibility:

- Nomenclature: A standard nomenclature for macros, types, and variables
- Input and Output interfaces: Inputs and outputs variables are transmitted in and out of the macro by equation blocks. This method simplifies and reduces connections and allows replacing a macro by another more efficiently (Only a few connectors should be modified).
- Parametrization procedure: Parameters are variables that remain constant during the simulation time. A Python script has been developed to make this more fluent (from specific values calculate the majority of these parameters through correlations).
- Control strategy: Each macro has its own control strategy based on the technology represented. This method allows adding the same macro into different systems reducing the amount of control parameters to be set.
- Results: Each macro displays its own set of results and its internal calculations, such as energy and mass balance.

As an example, compression chiller macro has been taken (M4300). In this macro two different operation modes can be imposed, one in which the chiller works in series operation reaching an output temperature, and other, in which de chiller is controlled to work in parallel against a cold water storage to maintain a setpoint in the tank.

A simplified diagram is shown in Figure 4, along with its representation in TRNSYS. In the figure, heat flows are displayed in blue arrows (QCHI01 regarding the heat dissipated by the chiller, and QLsPI01 as the pipe losses), work flows are displayed in purple (WCHI01 as the power consumed by the electrical chiller and WPU01 for the pump), and mass flows with their corresponding temperatures are displayed in black arrows (MIn01/TIn01, MOu01/TOu01).

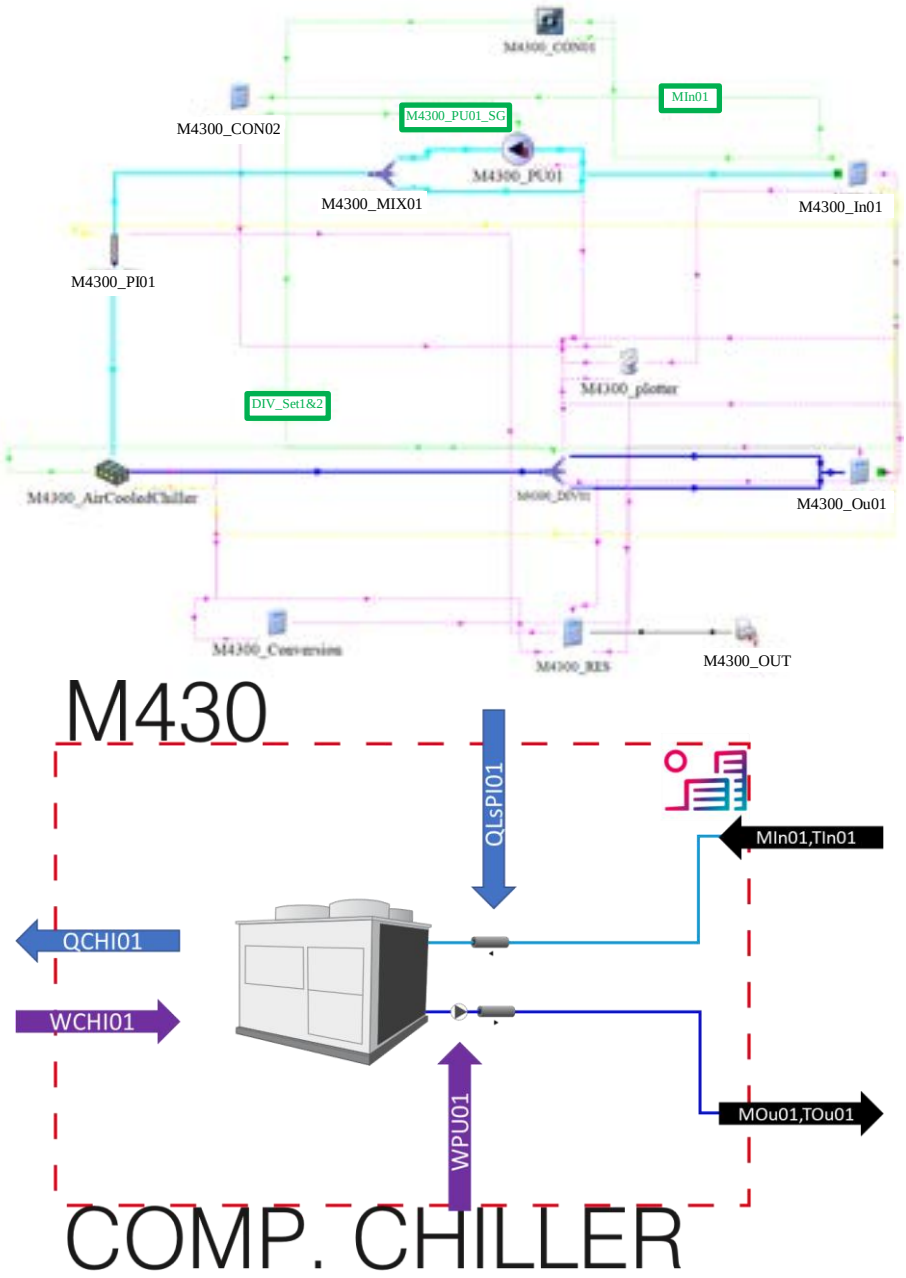

Figure 4. Compression chiller macro (M4300). Schematic diagram and TRNSYS translation.

This methodology is used to develop macros which allow a faster generation of decks to be run by TRNSYS. After running the simulations, all results are read and KPIs (Key Performance Indicators) calculated through the use of a Python script.

2.2. Location and Demand

This study has been carried out in Madrid where plenty of solar resource is available, and cooling demand is needed seasonally in summer.

Two demand profiles have been tested, a variable demand fixed by a yearly demand of approximately 733 MWh/y. And an experimental one, in which a constant value of 485 kW is considered.

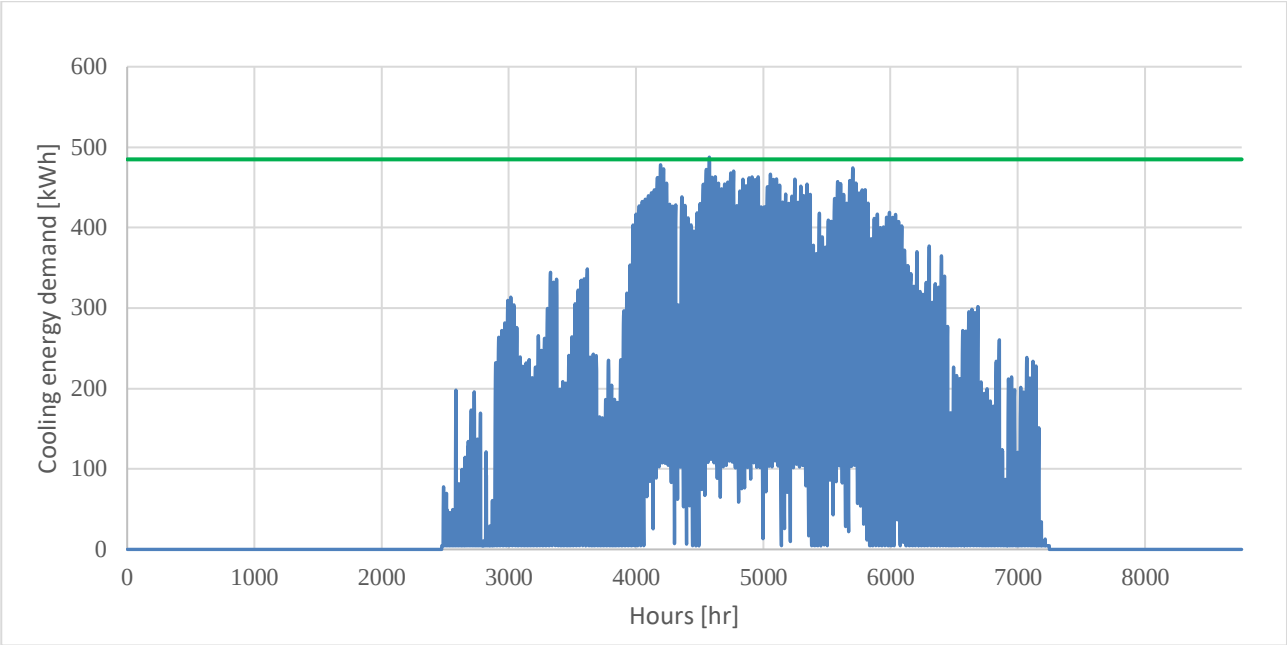

(a)

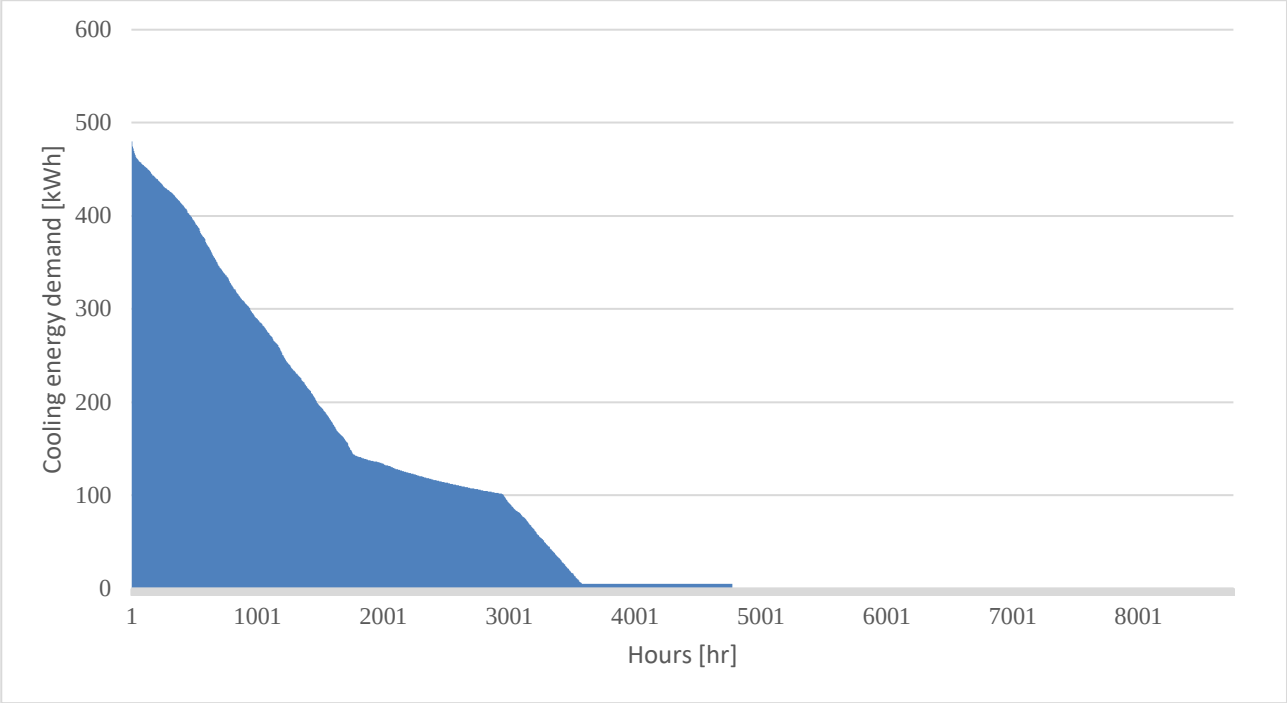

(b)

Figure 5. Hourly demand profile studied (a) and monotonic curve of thermal loads (b) [kWh].

The hourly demand distribution and the descending monotonic curve, which indicates the application of various thermal loads in the system, can be observed in Figure 5 (a and b). These graphical representations are valuable for determining the necessary capacity that must be implemented.

2.3. Technologies Considered

The discussion in this paper intends to compare two diverse options of cooling generation, in which one of the main aspects to be addressed is the coefficient of performance (COP). While absorption chillers are known not to have high COP values due to their theoretical limitations, their main advantage is that most of their energy consumption is thermal (which compared to electric energy tends to be cheaper). On the other hand, compression chillers are found, where all their energy consumption is electrical. In this regard, a single stage absorption chiller has been used for this analysis which reaches an assumed COP value of 0.75. While for the compressor chiller a value of 3 was assumed [4].

2.4. Prices Considered

For electricity prices, the EU statistical website was used as source, and the last value available for Spain was selected (0.2298 €/kWh from S1,2022, for big consumers > 15000kWh) [5].

As not many reliable sources of pricing for technologies are available online, three different were considered [6–8], and a final value of 196€/kW was selected for the compression chiller and a 288 €/kW for the absorption chiller.

Other than that, values for Fresnel collectors were set in 190 €/m^2 and thermal energy storage (TES) were set in 260 €/m^3.

2.5. KPIs Definition

All KPIs have been calculated according to the scientific article referenced written for the Wedistrict project [2,3].

Mostly values on Levelized Cost of Energy (LCoE) and CO_2 emissions have been reviewed for comparison.

2.5.1 LCoE

The Levelized cost of energy (LCOE) evaluates the average net present value of energy expenditures during a system's lifespan. It is an important instrument for comparing various power generation technology options, particularly in situations where significant initial investments are required but operating costs decrease over time. This situation frequently occurs in systems that rely heavily on renewable sources.

The levelized cost of energy (LCOE) methodology involves the discounting of future expenditures and earnings to their current value in a designated base year, thereby enabling the determination of unit costs for generating energy. These unit costs represent the ratio between discounted lifetime expenses and projected net present value (NPV) of total energy output. In effect, they correspond to an average price that consumers would need to pay in order to cover all associated costs while yielding a rate-of-return equivalent to that defined by the chosen discount rate.

CAPEX calculations are done through the software, the value from the total system cooling capacity is also taken from the simulation results for this calculation. The rest of economic values are added in postprocessing by the script, fixing these values by the user.

$$LCOE = \frac{CAPEX \cdot CRF + OPEX_f + OPEX_v}{Q_C}$$

$$CRF = \frac{\{i \cdot (1+i)^n\}}{\{[(1+i)^n] - 1\}}$$

- $LCOE$: Levelized cost of cooling energy [€/MWh].
- $CAPEX$: Capital expenditure for the equipment [€/MWh].
- $OPEX_f$: Fix operational costs for cooling [€/year].
- $OPEX_v$: Variable operational costs for cooling [€/year].
- CRF: Capital recovery factor
- i: interest rate.
- n: project lifetime and number of annuities received.
- Qc: Cooling energy supplied per year [MWh/year].

2.5.2 CO_2 emissions

The concept of equivalent emission coefficient pertains to the quantification of non-renewable fuel-derived greenhouse gas emissions within a district heating and cooling system. It is important to note that carbon emissions generated by biofuels are not considered, while accounting for the ones related to extraction, transformation, and transportation processes. The calculation is as follows:

$$k_{CO_2} = \frac{\sum_i E_i \cdot k_i}{Q_C}$$

Where:

- k_{CO2}: CO2 emission coefficient (kg/ MWh).
- E_i: energy supplied by energy carrier i per year [MWh/year].
- k_i: Emissions coefficient of energy carrier i [kg CO2/ MWh.
- Q_c: Cooling energy supplied per year [MWh/year].

For CO_2 emissions the following table has been taken as seen in the reference [3].

Table 1. Default primary energy factor and non-renewable emission coefficient from ISO-52000 table B-16).

Energy carrier Delivered from distant		Primary energy factor			Non-renewable CO_2 emission coefficient
		Non-renewable	Renewable	Total	g/ kWh
Fossil fuels	Solid	1.1	0	1.1	360
	Liquid	1.1	0	1.1	290
	Gaseous	1.1	0	1.1	220
Biofuels	Solid	0.2	1	1.2	40
	Liquid	0.5	1	1.5	70
	Gaseous	0.4	1	1.4	100
Electricity		2.3	0.2	2.5	420
Solar	PV-electricity	0	1	1	0
	Thermal	0	1	1	0
Exported					
Electricity	To the grid	2.3	0.2	2.5	420
	To non EPB uses	2.3	0.2	2.5	420

2.6. Cases Evaluated

A first effort has been aimed to establish what appears to be the preferred technology by the users. The definitions on LCoE and CO_2 emissions have been established for the compression chiller and studies have been held as to determine how much improvement does the system get from the use of PV solar panels to provide electricity for the system.

Then the same indicators were established for the absorption chiller case, reviewing how much power is required as heat input for the system and how different variations on the supply affect the system.

3. Results

3.1. Compression Chiller

First a calculation of the system with the compression chiller has been made.

Table 2. Results from compression chiller system

PV capacity [kW]	Battery autonomy [kWh]	TES capacity Chiller [m^3]	Comp. Chiller capacity [kW]	Deviation Cooling demand [%]	LCOE [€/MWh]	CO_2 emission coefficient [kg/MWh]
165.00	495.00	30.00	485.00	-4.05	59.97	40.14

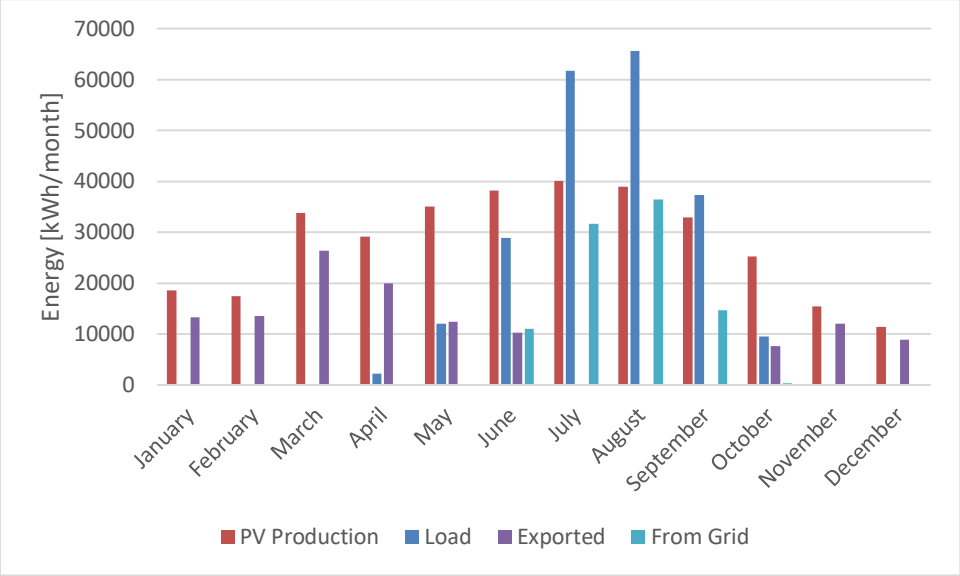

Figure 6. Photovoltaic production in analysed system and segregation [kWh/month].

From this first result we then took a step further to establish the same scenario without the PV panels, as to see the impact of these in the CO_2 emissions, and in the LCoE of the assumed network.

Table 3. Results from compression chiller system without PV panels.

TES capacity Chiller [m^3]	Comp. Chiller capacity [kW]	Deviation Cooling demand [%]	LCOE [€/MWh]	CO_2 emission coefficient [kg/MWh]
30.00	485.00	-4.05	87.98	129.84

These results show how LCoE values are improved by the installation of solar panels (31.8%), and how this investment reduces also the CO_2 emissions considerably (69.1%). This can be explained by the economic gain of exporting electricity throughout the year by the panels, and the reduction of the consumption from the grid, which has its assumed associated emissions (grid not completely green, Table 1).

3.2. Absorption Chiller

As for the compression chiller a first calculation has been made with the complete assumed system.

Table 4. Results from absorption chiller system.

Fresnel Collector area [m^2]	Hot TES capacity [m^3]	Boiler capacity [kW]	Abs Chiller capacity [kW]	Chiller Tank Vol [m^3]	Deviation Cooling demand [%]	LCOE [€/MWh]	CO_2 emission coefficient [kg/MWh]
1000.00	50.00	647.00	485.00	30.00	-5.94	205.67	604.75

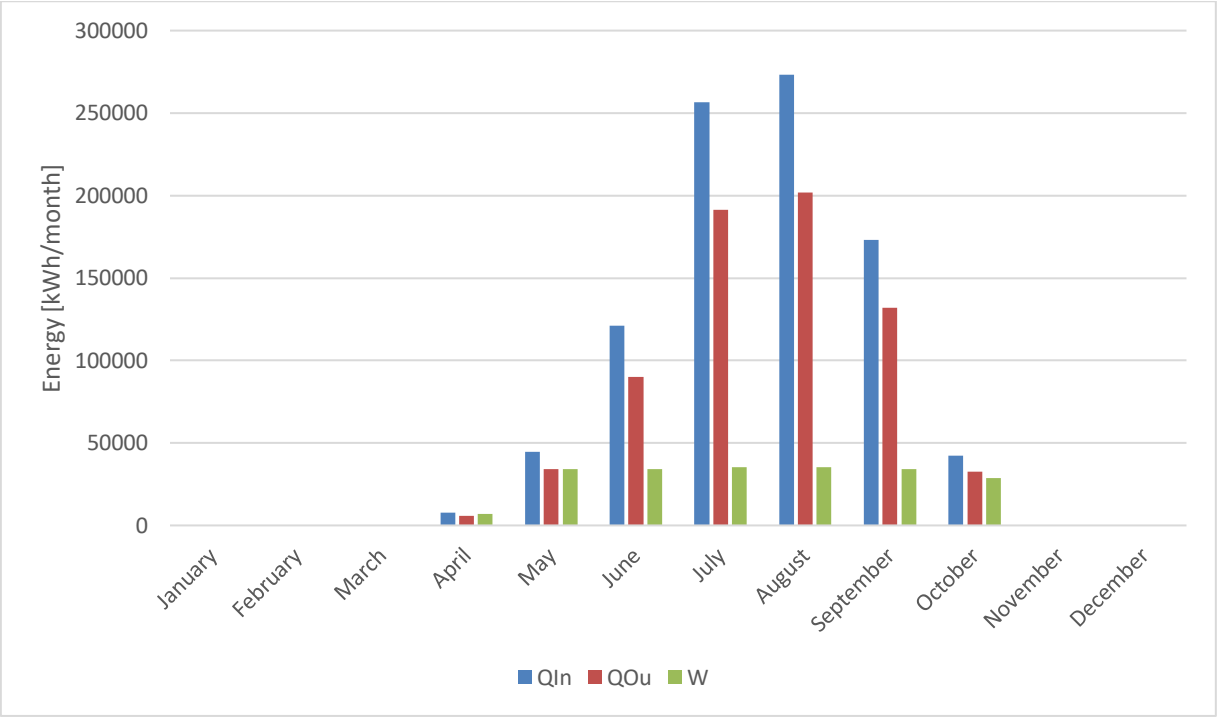

Figure 7. Absorption chiller energy flows [kWh/month].

From this first result we can see a gross difference from many different levels on the two principal KPIs compared:

To reduce the impact of the boiler production and its associated natural gas impact on the emissions we have assumed a scenario where this heat is provided by an existent net-zero emissions' source.

Table 5. Results from absorption chiller system reducing scope and emissions.

Fresnel Collector area [m^2]	Hot TES capacity [m^3]	Boiler capacity [kW]	Abs Chiller capacity [kW]	Chiller Tank Vol [m^3]	Deviation Cooling demand [%]	LCOE [€/MWh]	CO_2 emission coefficient [kg/MWh]
0.00	0.00	0.00	485.00	30	-5.94	122.51	181.00

The installation of the absorption chiller alone assumes a greater impact on the LCoE even without installing a full system to supply the heat. Given all these considerations further analysis seems inconsequential at this maturity stage of the technology.

The moment that this technology seems to flourish is when it works closer to its nominal operation point. It is interesting to compare the possibility of supplying a constant base value of cooling demand and see how this impacts the electrical consumption of both equipment.

3.3. Constant Case

A comparison of operations has been made for a constant demand equal to both equipment's nominal points. Considering that the energy supplied by the system to the absorption chiller still comes from an existent free net zero emissions source, while electrical consumptions have been taken into account.

Table 6. Results from absorption chiller with constant demand reducing scope and emissions.

Fresnel Collector area	Hot TES capacity [m^3]	Boiler capacity [kW]	Abs Chiller capacity [kW]	Chiller Tank Vol [m^3]	Deviation Cooling	LCOE [€/MWh]	CO_2 emission

[m^2]					demand [%]		coefficient [kg/MWh]
0.00	0.00	0.00	485.00	30	-11.17	35.49	57.03

Having considered nominal operation of the system and disregarded the price of installing solar Fresnel and the Boiler needed to supply the thermal demand (only considering electrical supply), absorption chiller shows a better cost and CO_2 emissions coefficient. But having made all these assumptions these results could be tied to too many considerations.

Table 7. Results from compression chiller constant demand, without PV panels.

TES capacity Chiller [m^3]	Comp. Chiller capacity [kW]	Deviation Cooling demand [%]	LCOE [€/MWh]	CO_2 emission coefficient [kg/MWh]
30.00	485.00	-4.05	86.70	129.84

On Table 7, it is visible that the electrical consumption of the chiller for this scenario yields a higher CO_2 emissions coefficient due to its electrical consumption throughout the year.

Table 8. Results from compression chiller constant demand, with PV panels.

PV capacity [kW]	Battery autonomy [kWh]	TES capacity Chiller [m^3]	Comp. Chiller capacity [kW]	Deviation Cooling demand [%]	LCOE [€/MWh]	CO_2 emission coefficient [kg/MWh]
165.00	495.00	30.00	485.00	-4.05	64.28	105.06

On Table 8, the improvement in LCoE found before due to the addition of PV panels in the variable case does not show the same impact, because panels do not generate the same amount of power throughout the year.

3.4. Discussion

From an economic standpoint, this system proves to be costlier for multiple reasons. Primarily, the implementation of absorption chillers is more financially burdensome when compared with compression chillers of equal capacity in terms of CAPEX (Figure 8). Additionally, since solar panels must be installed along with a natural gas boiler ensure diversity and generate heat input necessary for the absorption chiller's generator operation, these inputs punish severely, not only the LCoE due to these equipment CAPEX and operational expenditure (OPEX), but also, the CO2 emission coefficients linked to the production of said required heat input.

Although the absorption chiller operates efficiently during the peak months of July and August, utilizing only around 7% of its cooling capacity in electrical consumption, its lower coefficient of performance (0.75) compared to the compression counterpart (3) is significant enough to sway preference toward the compressor chiller option.

The aforementioned inclination is not upheld in situations where a consistent cooling necessity is obligatory for the system, as solar photovoltaic mechanisms do not yield an unchanging amount of electricity throughout every season (as shown in Figure 9). Therefore, absorption chillers show auspicious outcomes when considering that their energy supply originates from an already existent source.

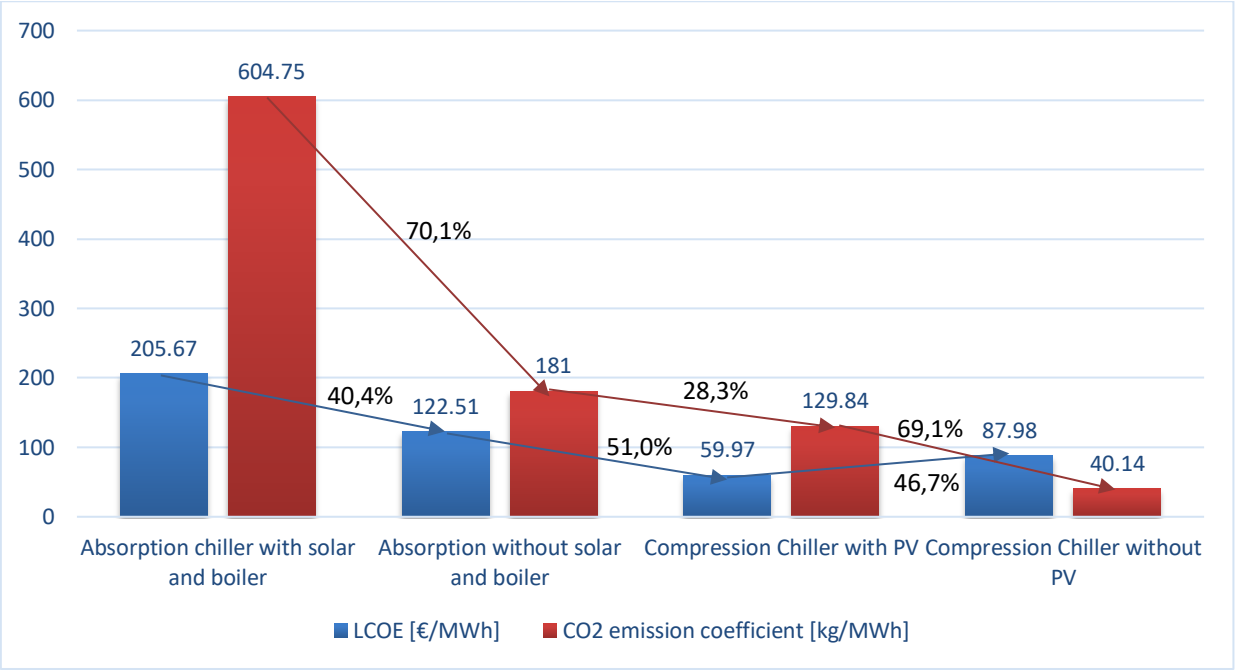

Figure 8. LCoE and CO2 emissions for variable demand cases and percentual evolution.

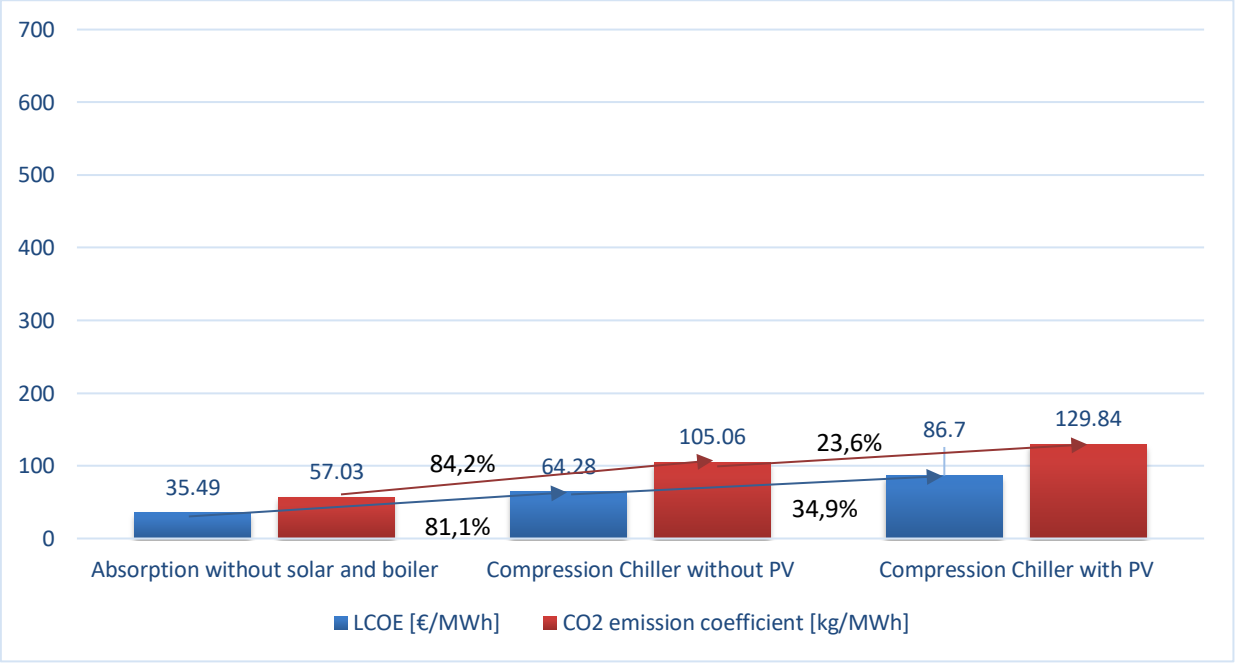

Figure 9. LCoE and CO2 emissions for constant demand cases and percentual evolution.

3. Conclusion

In terms of district cooling systems, the present circumstance limits options for technology selection. Presently, absorption chillers are viable if high-quality energy is anticipated to be wasted and their implementation can enhance system efficiency. However, when selecting a cooling system that will only supply a variable cooling demand, without any other interactions with other heating systems, the current technological state singles out the compression chiller as a more appropriate selection.

There is potential for utilizing the absorption chiller heat output as an energy source, considering that the outlet of the generator still can be rendered as a good energy source with temperatures around 85°C. This possibility presents itself as an intriguing subject of research from both financial and technical perspectives particularly when accounting for consistent cooling requirements such as those found in data centers.

Acknowledgments

The work on this communication has been generated in the framework of the W.E.DISTRICT project, received funding from the European Union's Horizon 2020 research and innovation program under grant agreement N°857801.

References

[1] Eurostat. Heating and cooling degree days - statistics n.d. https://ec.europa.eu/eurostat/statistics-explained/index.php?title=Heating_and_cooling_degree_days_-_statistics (accessed March 23, 2023).

[2] Wedistrict Project n.d. https://www.wedistrict.eu/ (accessed March 26, 2023).

[3] Ivančić A, Romaní J, Salom J, Cambronero MV. Performance assessment of district energy systems with common elements for heating and cooling. Energies (Basel) 2021;14. https://doi.org/10.3390/en14082334.

[4] Climaveneta. AIR SOURCE UNITS FOR 4-PIPE SYSTEMS, WITH SCREW COMPRESSORS AND FULL INVERTER TECHNOLOGY, FROM 341 TO 1125 kW n.d.

[5] Eurostat. Electricity Prices Households n.d.

[6] Florian Dittmann, Philippe Rivière, Pascal Stabat, (Centre for Energy efficient Systems (CES) MP– A. Space Cooling Technology in Europe. Technology Data and Demand Modelling. 2016.

[7] Shirazi A, Taylor RA, Morrison GL, White SD. A comprehensive, multi-objective optimization of solar-powered absorption chiller systems for air-conditioning applications. Energy Convers Manag 2017;132:281–306. https://doi.org/10.1016/j.enconman.2016.11.039.

[8] Arabkoohsar A, Sadi M. Technical comparison of different solar-powered absorption chiller designs for co-supply of heat and cold networks. Energy Convers Manag 2020;206:112343. https://doi.org/10.1016/J.ENCONMAN.2019.112343.

Innovative waste heat valorisation technologies for zero-carbon ships - a review

Robin Fisher[a], Pouriya Niknam[b], Lorenzo Ciappi[c] and Adriano Sciacovelli[d]

[a] University of Birmingham, Birmingham, UK, r.fisher@bham.ac.uk, CA,
[b] University of Birmingham, Birmingham, UK, p.niknam@bham.ac.uk,
[c] University of Birmingham, Birmingham, UK, l.ciappi@bham.ac.uk,
[d] University of Birmingham, Birmingham, UK, a.sciacovelli@bham.ac.uk CA

Abstract:

The growing intensity of international commerce and the high share of total global greenhouse gas emissions by the maritime sector have motivated the implementation of regulations by the International Maritime Organisation to curtail large vessel emissions. Waste heat recovery is an effective way to improve ship energy efficiency, lower the temperature and amount of waste heat rejection to the environment, and therefore curb green-house gas emissions. In this article, existing and developmental on-board waste heat recovery technologies for maritime applications are reviewed. Emphasis is placed on the integration and performance of these technologies within the broader on-board energy system. Performance indicators are drawn from existing systems, experimental prototypes, and simulations, to quantitatively compare the different technologies in terms of power capacity, efficiency / coefficient of performance, heat source temperatures and specific cost of installation.

Keywords:

Energy; ECOS Conference; Waste heat recovery; Sustainability.

1. Introduction

It is estimated that the totality of vessels above 100 tons are responsible for approximately 3% of global greenhouse gas emissions [1]. Furthermore, shipping for international trade is expected to grow further in the immediate future [2]. Consequently, the International Maritime Organisation has set the objective of halving naval-related emissions by 2050 [3]. Engine waste heat recovery (WHR) is a possible pathway to decarbonising marine shipping. In large-bore two-stroke diesel engines, which are the propulsion method of choice in 96% of ships above 100 tons [4], approximately 50% of the fuel input is lost as waste heat through exhaust gases, cooling fluids and radiation [5]. On this basis, developing on-board WHR is a viable strategy to improve ship energy efficiency and curb sector wide global greenhouse gas emissions.

Table 1 Summary of marine WHR technological reviews in the literature, and the technologies discussed in each review and the present review.

	Shu et al. [6]	Singh et al. [4]	Xu et al. [7]	Zhu et al. [8]	This review
Turbo-compound systems	x	x			x
Turbochargers	x	x			
Absorption Refrigeration	x		x		x
Adsorption Refrigeration	x		x		x
Thermoelectric Generation	x	x			x
Organic Rankine Cycle	x	x		x	x
Steam Rankine Cycle	x	x		x	x
Kalina Cycle		x		x	x
Thermal Energy Storage					x
Isobaric Expansion Engines					x

WHR has been demonstrated as viable by Baldi and Gabrielli [9] who showed that WHR systems with 2- to 5-year payback times, reducing fuel consumption by 4% to 16% respectively, are achievable. Marine WHR

technologies have previously been reviewed by Shu et al. [6], and by Singh and Pedersen [4]. However, these reviews are not recent (2013 and 2016, respectively), and are discrepant on the classification and selection of WHR technologies. Shu reviews exclusively turbine based WHR technologies, including power cycles, Rankine cycle and various forms of Turbocharging (**Table 1**). Turbocharging always features in large vessels, and should arguably be classified as relevant to the engine technology and operation rather than part of the WHR system [10]. Furthermore, other WHR technologies exist, such as refrigeration systems, which are discussed in Singh's review, or thermal energy storage or isobaric expansion technology which are novel and have never been reviewed as marine WHR technologies. Some reviews have been published which focus on specific applications of engine WHR. Palomba et al. [11] evaluated the feasibility of applying WHR for powering on-board refrigeration and cooling systems on fishing vessels with some suggestions for system configurations and integration, while Xu et al. [7] specifically reviewed the available technologies for on-board refrigeration which were broadly categorised into absorption, adsorption and hybrid refrigeration system, with a partial focus on components. Zhu et al. [8] specifically reviewed marine engine WHR with bottoming power cycles, which consist of traditional Steam Rankine Cycles, Organic Rankine Cycles (ORC), and Kalina cycles. A summary of existing literature reviews focused on on-board engine WHR, and the discussed technologies is shown in **Table 1**.

1.1 Motivations & specific aims

Modern ships are evolving, and are being considered more and more as multi-energy systems, i.e. systems in which different types of energy (thermal, cooling, power, propulsion) and utility (clean water, steam) demands are designed to interact optimally with one another [12]. In view of this development and in the light of the existing literature landscape surrounding WHR technologies, the specific aims of this article are to provide a systematic, holistic, and up to date review of the current and developmental WHR technologies for marine applications and specifically the recovery of engine waste heat. Taken into account are the working principle, the possible integration to the marine energy system, and, when available, techno-economic performance measured in terms of efficiency / coefficient of performance, power capacity and specific cost.

2. State of the art of on-board WHR technologies

2.1 Waste heat recovery heat exchangers

A conventional on-board WHR method direct recovery from exhaust gases through a WHR heat exchanger, and directly provide for one of the on-board thermal energy demands. With a WHR heat exchanger system, exhaust gases flow in the hot side, and exchange heat with water or air flowing in the cold side. According to Baldi et al. [13] and Jouhara et al. [14], 5 such technologies can be highlighted for marine energy systems:

- **Economisers**: finned tube heat exchanger designed for low to medium temperature waste heat, aimed at heating boiler feedwater in view of steam generation in a separate piece of machinery.
- **Waste heat boilers**: medium to high temperature exhaust gases pass through the tubes of this heat exchanger, exchanging heat with water flowing on the cold side with the aim to generate steam.
- **Recuperators**: medium to high temperature exhaust gases pass the through the tubes of this HX hot side and exchange heat with the inlet air circulating in adjacent channels to provide for various on-board thermal energy demands.
- **Regenerators**: a type of heat exchanger with some thermal capacity to temporarily store thermal energy, with both hot and cold fluid asynchronously using the same channels. During a so-called hot phase, exhaust gases flow through the channels of the regenerator, storing heat into the heat exchanger's packing, generally a ceramic or refractory material. Cold fluid (air) is then circulated through the heat exchanger channels in a so-called cold phase to recover the stored heat.
- **Heat recovery steam generators**: a multiple-pressure heat exchanger system designed to produce high quality steam from high temperature exhaust gas waste heat. Such a system typically features three pressure levels: economiser, evaporator, and superheater.

2.2 Turbocompounding

Turbocompounding consists in utilising heat in the exhaust gas stream to power a turbine system and generate electricity. Turbocompounding is different from turbocharging, the latter being a method for recovering exhaust waste heat to compress the engine intake air. Advances in turbocharging technology have resulted in a surplus amount of energy in the exhaust gas stream compared to the requirements for intake air compression [4], encouraging further use of the exhaust gas waste heat potential through turbomachinery. In the best-case scenarios both turbochargers and a turbocompounding WHR system can be installed together to reach high WHR. According to MAN, one of the main manufacturers of turbocompounding systems [5] there are three options for turbocompounding, ordered here by increasing efficiency and complexity **PTG**: power turbine generator unit. A so-called power turbine directly converts exhaust gas energy to electricity, recovering a potential η =3-5% of fuel energy according to MAN. **STG**: steam turbine generator unit. Exhaust gas energy

is used to generate steam in an exhaust gas fired boiler (EFB). The energy contained in the generated steam is then used to power a steam turbine. Such as system can achieve a potential 5-8% fuel energy recovery.

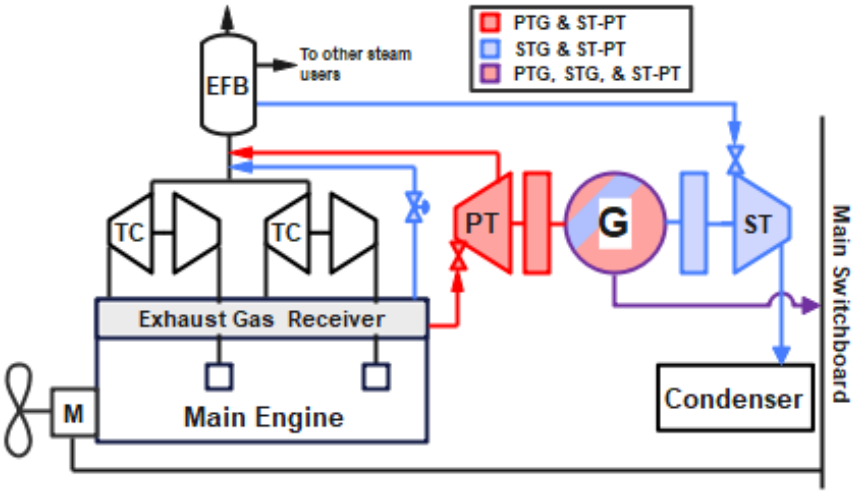

Figure 1 Schematic representation of turbocompounding WHR PTG system, STG system and combined ST-PT system.

ST-PT: combined steam and power turbine generator unit. Uses both preceding principles in a combined system with both turbines on the same shaft connected to the generator to potentially achieve 8-11% fuel recovery according to MAN, with a similar recovery ratio of approximately 10% for the Winterthur Gas & Diesel combined system [15]. These systems are shown schematically in **Figure 1**. In terms of maturity, turbocompounding is an established on-board WHR technology (technology readiness level~9) [13], favoured for its ease of installation and high retrofitting ability. To select the best turbocompounding system type, MAN recommend a PTG when the main engine power is below 15 MW, a STG for main engine powers between 15 MW and 25 MW, and the combined ST-PT for engine powers above 25 MW. **Table 2** shows typical specific installations costs and maintenance costs for the different types of turbocompounding systems. The data was synthesised by Olaniyi and Prause [16] from various turbocompounding WHR system manufacturers.

Table 2 Installation and maintenance costs for different types of turbocompounding WHR system, data originally collected in [16], costs actualized and converted from dollars to euros.

	Installation Costs [€/kW]	Maintenance Costs [€/year]
PTG	105	10,500
STG	320	21,000
PT-ST	420	32,000

2.3 Rankine cycles

Rankine cycles are a type of power cycle designed to convert thermal energy into useful mechanical power through an expander. The useful mechanical work is then converted to electricity via a generator. Thermal energy from the exhaust gases is used to evaporate a working fluid in the boiler (1 to 2). The working fluid vapour is expanded to the cycle's low pressure level in a turbine to produce useful work (2 to 3), then condensed (3 to 4), before being pumped to the cycle's higher pressure level (4 to 1) into the boiler, thus completing the cycle. The cycle presented in **Figure 2** shows a simple Rankine cycle layout using main engine exhaust gas as the heat source. Steam Rankine Cycles operate with water as the working fluid and thus require a high temperature heat source (T>200°C) [17], whereas Organic Rankine Cycles (ORC) use an organic working fluid with a lower boiling point to leverage lower temperature heat sources. Cycle performance is typically increased using modifications to the simple cycle such as regeneration, bleeding, and multiple loop cycles [18]. Regeneration involves a heat exchanger to extract residual thermal energy at the turbine outlet to pre-heat the working fluid between the pump and the boiler. Bleeding involves extracting part of the working fluid to preheat before boiler entry, and as a result a secondary lower pressure circuit which is expanded in a secondary turbine/expander. Multiple loop cycles involve two or more working fluids with different boiling points to leverage the multiple waste heat streams in marine energy systems. Most proposed systems for marine applications include one or several of these modifications. For example, Song et al. investigated the use of multiple waste heat streams as thermal energy source for a ~100 kW net power output ORC, with jacket cooling water for preheating and exhaust gas for the evaporation of the working fluid [19]. Lion et al. thermodynamically investigated a similar concept, except using hot scavenge air to preheat the working fluid and exhaust gas for evaporation [20]. Casisi et al. [21] modelled different ORC configurations for integration in marine energy systems: simple, regenerated and dual loop layouts. In these cases, the high temperature

cooling water circuit was used to preheat the working fluid. Rankine cycles have high technology readiness level ~ 8, with market ready systems being commercially available. Conventional ORC manufacturers are Ormat, Turboden and GE [22], with systems mainly targeted towards biomass, combined heat and power (CHP), geothermal and industrial WHR.

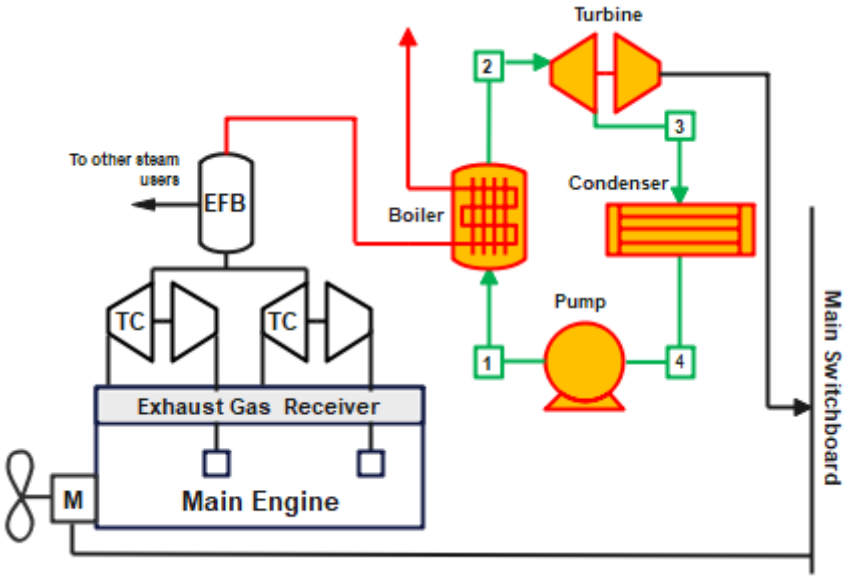

Figure 2 Schematic representation of a Rankine cycle WHR system using main engine exhaust gas as heat source.

Various manufacturers however offer ORC modules designed specifically for marine energy systems, such as Orcan-Energy's *Efficiency Pack* [23], Alfa Laval's *E-Power Pack* [24], or the Caltenix Mitsubishi partnership's *Hydrocurrent TM Organic Rankine Cycle Module 125EJW* [25]. The technical performance of some of these systems, both market ready and theoretical, is summarised in **Table 3**.

Table 3 Technical performance of marine ORCs (LT: low temperature, HT: high temperature)

Heat Source Temperature [°C]	Layout	Working Fluid(s)	Net Power Output [kW]	Efficiency	Ref
315	Basic	R123	625	16.38%	[26]
300 / 90	Dual Heat Sources	Cyclohexane	96	20.75%	[19]
300	Parallel ORCs	R245fa	101	10.20%	[19]
293.15	Regenerated	Benzene	396	22.00%	[27]
145	Regen.	Toluene	684	26.70%	[21]

Kalina cycles

Kalina cycles are a variation of the Rankine cycle, revolving around the evaporation of an ammonia-water mixture using the excess waste heat and operating an expander / generator train to generate electrical power [28]. The system was first introduced in 1983 as an alternative to ORCs, with higher efficiency and lower cost as the design objective. The crucial aspect of this cycle is that ammonia-water is a zeotropic mix, i.e., its boiling point changes with the respective mass fractions of the mix. Waste heat from the main engine exhaust gas is used to evaporate the ammonia-water zeotropic mix in the boiler. Working fluid vapour then flows through an expander connected to a generator, yielding electrical power transferred to the vessel main switchboard. Various process units internally improve cycle performance including heat recuperation and solution enrichment/separation processes. Detailed description of the working principle can be found in the original publication by Kalina et al. [28]. While the diagram in Error! Reference source not found. shows a single waste h eat source, exhaust gases, Kalina cycles are well suited to extract heat from multiple waste heat streams emanating from vessel diesel engine, such as preheating the zeotropic mixture with engine cooling circuits [29]. The performance and some main characteristics of various Kalina cycles for WHR are shown in **Table 4**. Data presented in this table were sourced mainly from theoretical literature studies, originally synthesised in [30]. The wide temperature range of heat sources from the WHR applications (98°C to 566°C), despite using the same working fluid (albeit in different mass fractions), and range of power outputs (21.7 kW to 8,600 kW), showcases the flexibility of the Kalina cycle in handling different waste heat sources. Efficiency of Kalina cycles tends to scale proportionally with plant size and is found in a similar range to Rankine cycles between 7.5% and 35%. The projected cost of Kalina cycles for various plant capacities is also shown in **Table 4**. The capital

cost for Kalina cycle systems above 1 MW can range from 1,000 to 1,500 €/kW, while for smaller systems, below 1 MW, significantly higher capital costs in the 2,000 – 3,000 €/kW range should be expected.

Table 4 Characteristics and techno-economic performance of WHR Kalina cycles, data originally synthesized in [30]**.**

Heat Source	Temperature [°C]	Power [kW]	Efficiency [%]	Cost [€/kW]	Ref
Coal combustion flue gas	150	320	12.3	2,000 – 3,000	[31]
Engine exhaust gases & cooling	524 / 86.8	21.7	25.6	-	[29]
Engine exhaust gases	346	1,615	19.7	-	[32]
Gas turbine exhaust gases	566	3,137	28.6	-	[33]
Gas turbine exhaust gases	522	86,136	35.6	1,157	[34]
Geothermal	-	1,850	-	1,150	[35]
Cement Plant	-	6,000	-	1,500	[36]

Thermoelectric generation

Thermoelectric generation (TEG) is a technology designed to directly generate electricity from a heat input using the Seebeck effect: a temperature gradient between two semi-conducting materials produces a voltage gradient proportional to the temperature different. TEG is particularly valued for its ability to continuously deliver electricity, its compacity and ruggedness in challenging environments: the first major field of application of TEG was the space industry. Today TEG is investigated for industrial WHR, including in marine energy systems [37]. TEG is at a technological readiness level where various commercial devices are available, their techno-economic performance being shown in **Figure 3**. The main drawbacks of TEG are low heat-to-electricity conversion efficiencies (below 5%) and low volumetric power output.

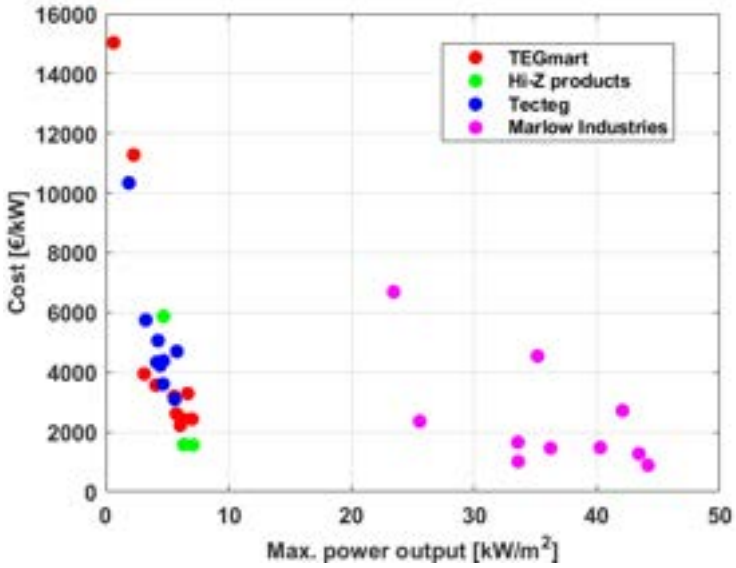

Figure 3 Commercial TEG modules techno-economic performance [38]–[41]**.**

Absorption refrigeration

The principle of absorption refrigeration revolves around leveraging the low boiling point of a refrigerant (typically ammonia). During this phase change the refrigerant will extract thermal energy from and cool down another fluid (typically water) yielding the intended refrigeration effect. A schematic representation of a simple single-stage absorption system is shown in the context of exhaust gas WHR in **Figure 4**. Cooling effect is produced in the evaporator where the ammonia evaporation process extracts thermal energy from a water flow which is sent to the vessel cooling load. Ammonia vapour then flows to the absorber to be absorbed to form a liquid solution, which is then pumped to a higher pressure towards the generator. The ammonia vapour is desorbed from the solution to a new vapour phase using water heated from main engine exhaust gases, and this vapour phase is then returned to liquid phase in the condenser, using sea water as cooling medium. The condensed ammonia phase then flows towards the evaporator, thus completing the cycle. Absorption refrigeration differs from conventional vapour compression systems for refrigeration, in that [42]:

- the vapour refrigerant is absorbed by a secondary substance to form a liquid solution before being pumped to a higher pressure. This process results in significantly less electrical work input compared to a vapour compression due to the much lower specific volume of liquid.

- the refrigerant is desorbed from the liquid solution using some thermal energy input before the condensation stage. Herein lies the main advantage of absorption refrigeration as it is a means to produce a cooling effect from a thermal energy source, thus making it highly relevant for marine energy systems with waste heat sources and potentially high cooling load.

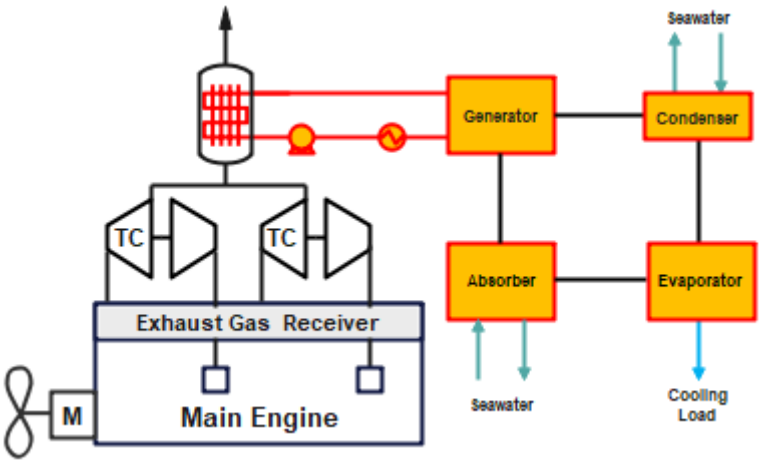

Figure 4 Schematic representation of an absorption refrigeration cycle WHR system using main engine exhaust gas as heat source.

While the system described is that of a single stage absorption refrigeration WHR system, various modifications and alternative layouts can help improve the performance. These alternative layouts include double stage, cascade and hybrid absorption / compression systems. The technical performance of various absorption cycles is shown in **Table 5**, while absorption refrigeration costs are shown in **Table 6**.

Table 5 Characteristics and performance of absorption cycles, data originally synthesised in [43]

Cycle	T_{evap} [°C]	COP	Working Fluid	Ref
Single-stage cascade	- 30 to 5	0.25 - 0.55	NH_3 - H_2O	[44]
Double-stage cascade	- 20 to 0	0.17 - 0.31	H_2O - LiBr // NH_3 - H_2O	[75]
Double stage	/	0.29	H_2O - NH_3	[47]
Absorption / Compression	- 10	1	NH_3 - H_2O	[80]

Table 6 Absorption refrigeration costing elements, data gathered from [50]

Design	Heat Source	Cooling Capacity (kW)	Installed Cost (€/kW)	Maintenance Costs (cts/kW/h)
Single Stage	Hot Water	175	1945	0.195
		1540	746	0.065
	LP Steam	4620	584	0.032
Two Stage	HP Steam	1155	973	0.097
		4620	713	0.032
	Exhaust Fired	1155	1070	0.097
		3500	648	0.032

Adsorption refrigeration

A cooling effect is generated with adsorption refrigeration by leveraging the boiling point of a refrigerant at low temperature to extract heat from another working fluid, a similar working principle to absorption refrigeration discussed previously. The principal difference is that the refrigerant vapour is then adsorbed onto the surface of a solid sorption material, rather than absorbed into a liquid solution. The adsorbed refrigerant is then separated from the condensed phase using a thermal energy input during a process called desorption. Typical adsorption materials (so-called adsorbents) include [51] silica gel and metal-organic frameworks.

Additionally, seawater can be used as the working fluid which can result in its desalination during the consecutive adsorption/desorption process; the relatively high boiling point of sea water (compared to traditional refrigerants such as ammonia) however limits the minimum temperature reached from the cooling process to that of chilled water (0°C to 5°C). A schematic representation of a two-bed adsorption refrigeration system with desalination function [52] is shown in **Figure 5**.

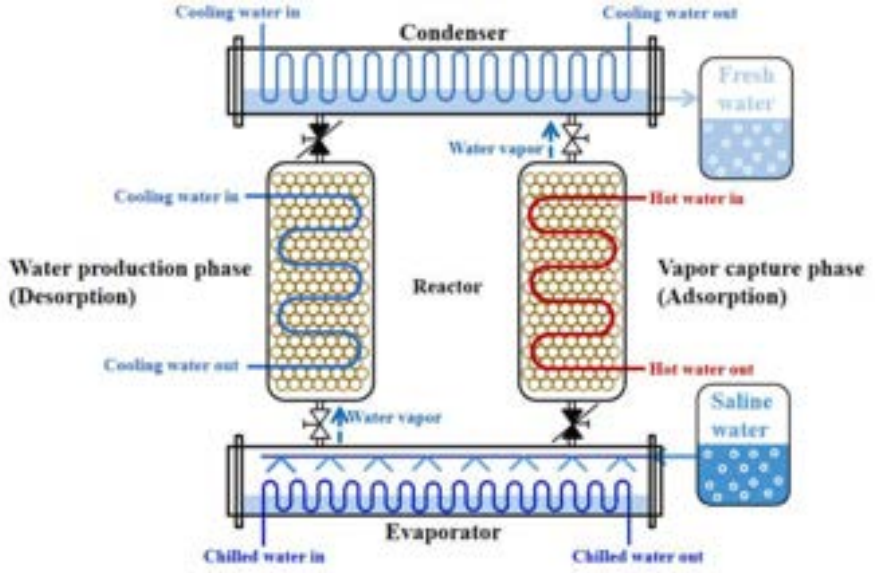

Figure 5 Schematic representation of two-bed adsorption refrigeration system [52]

Thus, this system can either be designed with a conventional refrigerant to generate sub-zero cooling, or with seawater as the refrigeration for chilling and desalination. The system shown in **Figure 5** is a two-bed system which is a rather simple configuration of this technology. Various modifications and more advanced configurations can be implemented to increase overall cooling power or rate of desalination. Three [53] and four [54] bed systems have been investigated, along with hybrid systems specifically designed for fishing vessel refrigeration [11] which combine adsorption refrigeration with conventional vapour compression systems. Adsorption refrigeration is a novel technology, thus techno-economic data is sparse. Costing elements for some adsorption chillers have been derived from analogous refrigeration technologies (absorption and vapour compression refrigeration) and are shown in **Table 7**. With the current state of the art, the maximum cooling power for adsorption chillers is around 100 kW.

Table 7 Cooling capacity and specific cost of various adsorption chillers.

Model	Cooling Power [kW]	Specific Cost [€/kW]	Ref
InvenSor LTC30 e plus	10 - 35	1,327	[55]
SorTech eCoo 2.0 Silica Gel IP20	16	1,188	[56]
Unnamed Silica gel / water adsorber	8	1,331	[57]

Isobaric Expansion Engines

Isobaric expansion engines (IEE) are a type of heat-to-mechanical power converter, based on a non-polytropic gas expansion process at theoretically constant pressure in a cylinder [58]. IEEs encompass various engine concepts such as Savery, Newcomen, and Watt pumps [59], Worthington direct-acting steam engines [60], and Bush thermo-compressors [61]. As seen from the provided examples, IEE is an old concept which has nonetheless received recent attention by technology makers due to the potential for useful work production from low temperature heat sources (as low as 40°C) and low temperature differences ($\Delta T = 30°C$), albeit with low efficiencies compared to other heat to work conversion technologies [62]. The latter of the two examples, Worthington and Bush-type engines have generated most of the recent interest; the Worthington engine is represented schematically in **Figure 6** in the context of WHR, where it is assumed that marine exhaust gases are used to generate steam (in the EFB) that undergoes the isobaric non-polytropic expansion process in the IEE. At the beginning the cycle, steam inlet valve **6** is manually opened, letting steam enter cylinder **1**, pushing piston **3** outwards and piston **4** inwards. During the entire stroke, steam enters at constant pressure with the inlet valve kept open, resulting in the so-called isobaric expansion. Cylinder **4** pushes the liquid out of cylinder **2** through the self-acting outlet valve **9**.

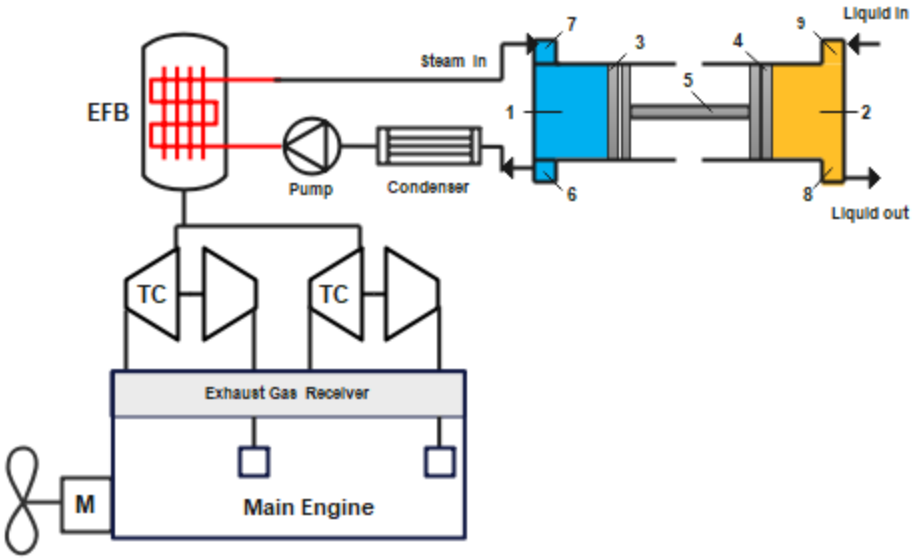

Figure 6 Schematic representation of the basic working principle of Worthington steam pump in the context of marine WHR.

When pistons **3** and **4** have fully displaced to the right-hand side, steam inlet valve **6** is closed, while liquid enters pumping cylinder **2** through the liquid inlet valve **8**, pushing piston **4** outwards and instigating the return motion of the engine stroke. Piston **3** displaces steam out of cylinder **1** through steam outlet valve **7** that is now opened until both pistons have fully moved to the left, thus completing the pumping cycle. It is assumed that the steam returning from the IEE is condensed (sea water used for cooling) and pumped back towards the EFB. The layout shown in **Figure 6** represents the simplest possible Worthington IEE. Extensive descriptions of more advanced IEE layouts can be found in [63]. For Worthington and Bush type IEEs, overall thermal efficiency can be found around 5%, for power deliveries below 1 kW, as shown in **Table 8**. The generated work can be used for a variety of on-board applications, such as powering pumps, compressors and other converters [58], or for water desalination [64]. However the simplest method may be to connect the IEE to a hydraulic circuit and generator [58].

Table 8 Performance characteristics of IEEs compared to thermal power pump (TPP). Data originally gathered in [62]**.**

	Cylinder Volume [L]	Cycle period [s]	Power [W]	Volumetric Power [W/L]	Efficiency [%]	Ref
TPP system	1.8	200	1	0.6	0.5	[65]
IEE-Bush	0.02	2.5	20	1200	6.4	[62]
IEE-Worthington	1	4	500	500	5.4	[62]

Thermal energy storage

Thermal energy storage (TES) is a technology designed to resolve the mismatch between heat availability and demand, particularly relevant for renewable thermal energy sources, namely solar, geothermal, and waste heat recovery. TES is classified into three distinct technologies [66], listed here in order of increasing complexity, cost, and energy storage density potential:

- Sensible TES (STES): heat is stored/released by increasing/decreasing the temperature of a solid or liquid [67]. STES materials include water, rocks, sand, molten salts, and metallic materials.
- Latent TES (LTES): heat is stored as the phase-change enthalpy of the melting/boiling process of a solid/liquid called phase change material (PCM). The reverse phase-change process is performed for discharge.
- Thermochemical energy storage (TCS): heat is stored/released as the reaction enthalpy of reversible exothermic/endothermic reactions. Typical thermochemical reactions for TCS include water sorption onto zeolite or other sorbents, hydration of inorganic salts, carbonation and oxide-reduction reactions.

The schematic representation of a thermal energy storage system integrated to a marine energy system is shown in **Figure 7**. TES is a passive WHR technology that doesn't directly convert waste heat to useful work but acts as a buffer to either store and release heat based on on-board demand or enable other WHR heat-to-X converters to operate with higher efficiency, such as power cycles.

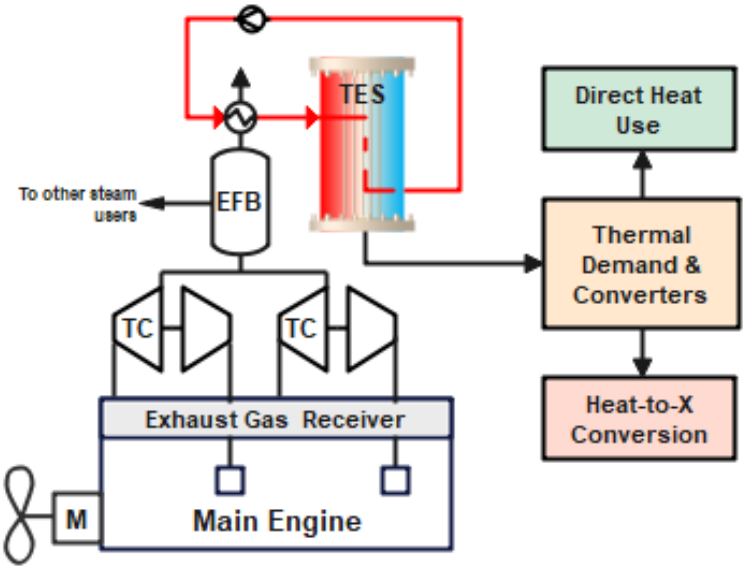

Figure 7 Schematic representation of the integration of TES to a marine energy system.

The system shown in the figure considers a single temperature level, with heat recovered from the exhaust gases. In real marine energy systems, TES has been envisioned for the storage of heat through a cascade of LTES systems with different PCMs each adapted to the temperature levels of the multiple onboard waste heat streams, potentially recovering 10% to 15% of fuel input as stored heat [68]; for the production of hot water on cruise ships to reduce by up to 80% fuel consumption in auxiliary boilers using a 1,000 m3 thermal oil-based STES [69]; for synergistically improving other WHR technologies, similarly to conventional WHR [70]. Excess heat stored in an LTES can be released at approx. 100°C to evaporate the working fluid in an on-board ORC [71]. An important design decision is how heat is transported to the TES and exchanged with the storage material. Typical techno-economic performance characteristics of various TES systems with these layouts are shown in Error! Not a valid bookmark self-reference.. STES generally displays low energy storage density (> 50 kWh/m^3), and TCS too low of a technological maturity, for realistic implementation in marine energy systems; thus, LTES can be considered as the most suitable TES sub-category for on-board WHR.

Table 9 Techno-economic performance of various TES systems, data originally synthesised in [72]**. ST: shell and tube, PB: packed bed, TT: tube-in-tank.**

Type	Material	Energy Storage Density [kWh/m^3]	Efficiency [%]	Volume [m^3]	Cost [€/kWh]	Ref
PB - LTES	$Li_2CO_3/K_2CO_3/Na_2CO_3$	66	80%	2	-	[73]
PB - LTES	$Li_2CO_3/K_2CO_3/Na_2CO_3$	115	61%	83,333	-	[74]
ST - LTES	Sodium Nitrate	-	-	77,161	65	[75]
ST - LTES	KOH	-	-	83,333	19	[76]
TT - LTES	Paraffin RT82	-	-	6	260	[77]
TT - LTES	Sodium acetate trihydrate	-	-	2,500	58	[78]

Conclusions

This article presented a systematic review of waste heat recovery technologies applicable to marine energy systems. The technologies were mainly characterised by their power capacity, efficiency / coefficient of performance, and specific investment cost. Furthermore, their applicability to marine energy systems for diesel engine WHR was discussed. It emerges from the review that:

- The turbine-driven heat-to-power technologies, i.e., turbocompounding systems and Rankine cycles, display the highest technological readiness level with market ready and proven systems, and highest potential power output each in the order of magnitude of at least 200 kW to 3 MW. These waste heat recovery technologies also have a high range of applicability since high electrical demand is likely regardless of vessel type and voyage.
- Kalina cycles typically show the same technical performance as Rankine cycles, but should still be considered as an unproven technology, with insufficient practical applications in conventional WHR let

alone marine waste heat recovery. Thermoelectric generation shows promising characteristics but low power outputs for individual modules severely limit economic viability.

- Through other technologies such as adsorption, absorption, and isobaric expansion engines, waste heat can be recovered and converted to other forms of useful work than electrical power. The suitability of the technology depends on the types of on-board energy demands which in turn depends on the vessel and voyage type. With their current technology readiness level however, only absorption refrigeration can deliver net power output in the same order of magnitude as the most powerful waste heat recovery technologies: 100 kW to 5 MW for absorption refrigeration, 8 kW to 35 kW for adsorption refrigeration, isobaric expansion engines are unproven beyond 1 kW.
- Thermal energy storage is in its own class of passive WHR technology, best used synergistically with other WHR technology to improve their performance by matching waste heat availability with on-board demands. Latent thermal energy storage is the best suited technology for on-board applications.

Acknowledgments

This work was supported by European Union's Horizon Europe under Grant Agreement 101056801 and by UK Research Innovation (UKRI). ZHENIT Project: Zero waste Heat vessel towards relevant ENergy savings also thanks to IT technologies.

Nomenclature

COP	Coefficient of Performance
IEE	Isobaric Expansion Engine
LTES	Latent Thermal Energy Storage
ORC	Organic Rankine Cycle
PB	Packed Bed
PCM	Phase Change Material
PTG	Power Turbine Generator
ST	Steam Turbine
STES	Sensible Thermal Energy Storage
STG	Steam Turbine Generator
ST-PT	Steam Turbine – Power Turbine
TCS	Thermochemical Energy Storage
TEG	Thermoelectric Generation
TES	Thermal Energy Storage
TT	Tube-in-Tank
WHR	Waste Heat Recovery

References

[1] P. Balcombe *et al.*, “How to decarbonise international shipping: Options for fuels, technologies and policies,” *Energy Convers. Manag.*, vol. 182, no. January, pp. 72–88, 2019, doi: 10.1016/j.enconman.2018.12.080.

[2] IMO *et al.*, “Third IMO Greenhouse Gas Study 2014,” *Int. Marit. Organ.*, p. 327, 2014, doi: 10.1007/s10584-013-0912-3.

[3] Maritime Organisation International, “Cutting GHG emissions from shipping - 10 years of mandatory rules,” *www.imo.org*, 2021. https://www.imo.org/en/MediaCentre/PressBriefings/pages/DecadeOfGHGAction.aspx (accessed Aug. 22, 2022).

[4] D. V. Singh and E. Pedersen, “A review of waste heat recovery technologies for maritime applications,” *Energy Convers. Manag.*, vol. 111, no. X, pp. 315–328, 2016, doi: 10.1016/j.enconman.2015.12.073.

[5] MAN Diesel & Turbo, “Waste Heat Recovery System (WHRS),” 2014.

[6] G. Shu, Y. Liang, H. Wei, H. Tian, J. Zhao, and L. Liu, “A review of waste heat recovery on two-stroke IC engine aboard ships,” *Renew. Sustain. Energy Rev.*, vol. 19, pp. 385–401, 2013, doi: 10.1016/j.rser.2012.11.034.

[7] X. Xu, Y. Li, S. Y. Yang, and G. Chen, “A review of fishing vessel refrigeration systems driven by exhaust heat from engines,” *Appl. Energy*, vol. 203, pp. 657–676, 2017, doi: 10.1016/j.apenergy.2017.06.019.

[8] S. Zhu, K. Zhang, and K. Deng, “A review of waste heat recovery from the marine engine with highly efficient bottoming power cycles,” *Renew. Sustain. Energy Rev.*, vol. 120, no. x, p. 109611, 2020, doi: 10.1016/j.rser.2019.109611.

[9] F. Baldi and C. Gabrielii, “A feasibility analysis of waste heat recovery systems for marine applications,” *Energy*, vol. 80, pp. 654–665, 2015, doi: 10.1016/j.energy.2014.12.020.

[10] M. Virtasalo and K. Vänskä, “Achieving improved fuel efficiency with waste heat recovery,” *Waste heat Recover. Syst.*, p. 6, 2013, [Online]. Available: https://library.e.abb.com/public/5f7cac28e876a9cbc1257a8a003cc6dc/ABB Generations_28 Achieving improved fuel efficiency with waste heat recovery.pdf

[11] V. Palomba, G. E. Dino, R. Ghirlando, C. Micallef, and A. Frazzica, “Decarbonising the shipping sector: A critical analysis on the application of waste heat for refrigeration in fishing vessels,” *Appl. Sci.*, vol. 9, no. 23, 2019, doi: 10.3390/app9235143.

[12] P. Mancarella, “MES (multi-energy systems): An overview of concepts and evaluation models,” *Energy*, vol. 65, pp. 1–17, 2014,

doi: 10.1016/j.energy.2013.10.041.

[13] F. Baldi, A. Coraddu, and M. E. Mondejar, *Sustainable Energy Systems on Ships: Novel Technologies for Low Carbon Shipping*. 2022. doi: 10.1108/s1574-8715(2013)0000012002.

[14] H. Jouhara, N. Khordehgah, S. Almahmoud, B. Delpech, A. Chauhan, and S. A. Tassou, "Waste heat recovery technologies and applications," *Therm. Sci. Eng. Prog.*, vol. 6, no. April, pp. 268–289, 2018, doi: 10.1016/j.tsep.2018.04.017.

[15] Winterthur Gas & Diesel, "Engine selection for very large container vessels," p. 18, 2016, [Online]. Available: https://www.wingd.com/en/documents/general/papers/engine-selection-for-very-large-container-vessels.pdf/

[16] E. O. Olaniyi and G. Prause, "Investment analysis of waste heat recovery system installations on ships' engines," *J. Mar. Sci. Eng.*, vol. 8, no. 10, pp. 1–21, 2020, doi: 10.3390/jmse8100811.

[17] A. Vecchi *et al.*, "Carnot Battery development: A review on system performance, applications and commercial state-of-the-art," *J. Energy Storage*, vol. 55, no. PD, p. 105782, 2022, doi: 10.1016/j.est.2022.105782.

[18] S. Lecompte, H. Huisseune, M. Van Den Broek, B. Vanslambrouck, and M. De Paepe, "Review of organic Rankine cycle (ORC) architectures for waste heat recovery," *Renew. Sustain. Energy Rev.*, vol. 47, pp. 448–461, 2015, doi: 10.1016/j.rser.2015.03.089.

[19] J. Song, Y. Song, and C. wei Gu, "Thermodynamic analysis and performance optimization of an Organic Rankine Cycle (ORC) waste heat recovery system for marine diesel engines," *Energy*, vol. 82, pp. 976–985, 2015, doi: 10.1016/j.energy.2015.01.108.

[20] S. Lion, R. Taccani, I. Vlaskos, P. Scrocco, X. Vouvakos, and L. Kaiktsis, "Thermodynamic analysis of waste heat recovery using Organic Rankine Cycle (ORC) for a two-stroke low speed marine Diesel engine in IMO Tier II and Tier III operation," *Energy*, vol. 183, no. x, pp. 48–60, 2019, doi: 10.1016/j.energy.2019.06.123.

[21] M. Casisi, P. Pinamonti, and M. Reini, "Increasing the energy efficiency of an internal combustion engine for ship propulsion with bottom ORCS," *Appl. Sci.*, vol. 10, no. 19, pp. 1–18, 2020, doi: 10.3390/app10196919.

[22] E. Macchi and M. Astolfi, *Organic Rankine Cycle (ORC) Power Systems: Technologies and Applications*. 2016.

[23] Orcan-Energy, "Efficiency Pack," *Orcan-Energy.com*, 2017. https://www.orcan-energy.com/en/applications-marine.html

[24] Alfa Laval, "Alfa Laval E-PowerPack," no. Cii, 2022.

[25] Mitsubishi Heavy Industries, "HydrocurrentTM Organic Rankine Cycle Module 125EJW - Compact and High-performance Waste Heat Recovery System Utilizing Low Temperature Heat Source," *Mitsubishi Heavy Ind. Tech. Rev.*, vol. 52, no. 4, pp. 53–55, 2015, [Online]. Available: https://www.mhi.co.jp/technology/review/pdf/e524/e524053.pdf

[26] G. Shu, P. Liu, H. Tian, X. Wang, and D. Jing, "Operational profile based thermal-economic analysis on an Organic Rankine cycle using for harvesting marine engine's exhaust waste heat," *Energy Convers. Manag.*, vol. 146, pp. 107–123, 2017, doi: 10.1016/j.enconman.2017.04.099.

[27] M. E. Mondejar, F. Ahlgren, M. Thern, and M. Genrup, "Quasi-steady state simulation of an organic Rankine cycle for waste heat recovery in a passenger vessel," *Appl. Energy*, vol. 185, pp. 1324–1335, 2017, doi: 10.1016/j.apenergy.2016.03.024.

[28] A. I. Kalina, "Combined cycle and waste heat recovery power systems based on a novel thermodynamic energy cycle utilizing low-temperature heat for power generation," *Proc. ASME Turbo Expo*, vol. 1983-Janua, 1983, doi: 10.1115/83JPGCGT3.

[29] F. Mohammadkhani, M. Yari, and F. Ranjbar, "A zero-dimensional model for simulation of a Diesel engine and exergoeconomic analysis of waste heat recovery from its exhaust and coolant employing a high-temperature Kalina cycle," *Energy Convers. Manag.*, vol. 198, no. May, p. 111782, 2019, doi: 10.1016/j.enconman.2019.111782.

[30] SoWHat, "D1.9 – TECHNO-ECONOMIC DATABASE OF INDUSTRIAL WH/C RECOVERY TECHNOLOGIES AND MODELLING ALGORITHMS," 2021.

[31] S. Ogriseck, "Integration of Kalina cycle in a combined heat and power plant, a case study," *Appl. Therm. Eng.*, vol. 29, no. 14–15, pp. 2843–2848, 2009, doi: 10.1016/j.applthermaleng.2009.02.006.

[32] P. Bombarda, C. M. Invernizzi, and C. Pietra, "Heat recovery from Diesel engines: A thermodynamic comparison between Kalina and ORC cycles," *Appl. Therm. Eng.*, vol. 30, no. 2–3, pp. 212–219, 2010, doi: 10.1016/j.applthermaleng.2009.08.006.

[33] A. I. Kalina and H. M. Leibowitz, "The design of a 3MW kalina cycle experimental plant," *Proc. ASME Turbo Expo*, vol. 3, 1988, doi: 10.1115/88-GT-140.

[34] A. I. Kalina, H. M. Leibowitz, D. W. Markus, and R. I. Pelletier, "Further technical aspects and economics of a utility-size Kalina bottoming cycle," *Proc. ASME Turbo Expo*, vol. 4, 1991, doi: 10.1115/91-gt-365.

[35] C. E. Campos Rodríguez *et al.*, "Exergetic and economic comparison of ORC and Kalina cycle for low temperature enhanced geothermal system in Brazil," *Appl. Therm. Eng.*, vol. 52, no. 1, pp. 109–119, 2013, doi: 10.1016/j.applthermaleng.2012.11.012.

[36] M. D. Mirolli, "The Kalina cycle for cement kiln waste heat recovery power plants," *2005 IEEE Cem. Ind. Tech. Conf. Rec.*, vol. 2005, pp. 330–336, 2005, doi: 10.1109/CITCON.2005.1516374.

[37] N. R. Kristiansen and H. K. Nielsen, "Potential for usage of thermoelectric generators on ships," *J. Electron. Mater.*, vol. 39, no. 9, pp. 1746–1749, 2010, doi: 10.1007/s11664-010-1189-1.

[38] TEGmart, "https://www.tegmart.com/," 2023. https://www.tegmart.com/ (accessed Jan. 09, 2023).

[39] Hi-Z, "Hi-Z," 2023. https://hi-z.com/products/ (accessed Jan. 09, 2023).

[40] Tecteg, "Tecteg," 2023. https://tecteg.com/ (accessed Jan. 09, 2023).

[41] II-VI, "II-VI," 2023. https://ii-vi.com/thermoelectrics/ (accessed Jan. 09, 2023).

[42] M. J. Moran, H. N. Shapiro, D. D. Boettner, and M. B. Bailey, *Fundamentals of Engineering Thermodynamics*. 2018. doi: 10.4324/9781315119717.

[43] W. Wu, B. Wang, W. Shi, and X. Li, "An overview of ammonia-based absorption chillers and heat pumps," *Renew. Sustain. Energy Rev.*, vol. 31, pp. 681–707, 2014, doi: 10.1016/j.rser.2013.12.021.

[44] R. M. Lazzarin, A. Gasparella, and G. A. Longo, "Ammonia-water absorption machines for refrigeration: Theoretical and real performances," *Int. J. Refrig.*, vol. 19, no. 4, pp. 239–246, 1996, doi: 10.1016/0140-7007(96)00016-3.

[45] S. C. Kaushik and R. Kumar, "Computer-Aided Conceptual Thermodynamic Design of a Two-Stage Dual Fluid Absorption Cycle for Solar Refrigeration," vol. 35, no. 5, pp. 401–407, 1985.

[46] Kaushik, S.C., Kumar, Rajesh, and S. Chandra, "Thermal Modelling and Parametric Study of Two Stage Absorption Refrigeration and Air-Conditioning Systems," *Energy Res.*, vol. 9, no. April 1984, 1985.

[47] M. Venegas, M. Izquierdo, M. De Vega, and A. Lecuona, “Thermodynamic study of multistage absorption cycles using low-temperature heat,” *Int. J. Energy Res.*, vol. 26, no. 8, pp. 775–791, 2002, doi: 10.1002/er.815.

[48] A. Ramesh kumar and M. Udayakumar, “Studies of compressor pressure ratio effect on GAXAC (generator-absorber-exchange absorption compression) cooler,” *Appl. Energy*, vol. 85, no. 12, pp. 1163–1172, 2008, doi: 10.1016/j.apenergy.2008.03.002.

[49] A. Ramesh Kumar and M. Udayakumar, “Simulation studies on GAX absorption compression cooler,” *Energy Convers. Manag.*, vol. 48, no. 9, pp. 2604–2610, 2007, doi: 10.1016/j.enconman.2007.03.013.

[50] United States Department of Energy, “Absorption Chillers for CHP Systems,” *Adv. Manuf. Off.*, pp. 3–6, 2017, [Online]. Available: https://www.energy.gov/sites/prod/files/2017/06/f35/CHP-Absorption Chiller-compliant.pdf%0Ahttps://energy.gov/sites/prod/files/2017/06/f35/CHP-Absorption Chiller-compliant.pdf

[51] J. G. Lee, K. J. Bae, and O. K. Kwon, “Performance investigation of a two-bed type adsorption chiller with various adsorbents,” *Energies*, vol. 13, no. 10, pp. 1–16, 2020, doi: 10.3390/en13102553.

[52] Y. Zhang, V. Palomba, and A. Frazzica, “Understanding the effect of materials, design criteria and operational parameters on the adsorption desalination performance – A review,” *Energy Convers. Manag.*, vol. 269, no. July, p. 116072, 2022, doi: 10.1016/j.enconman.2022.116072.

[53] K. Sztekler *et al.*, “Experimental study of three-bed adsorption chiller with desalination function,” *Energies*, vol. 13, no. 21, pp. 1–13, 2020, doi: 10.3390/en13215827.

[54] K. C. Ng, K. Thu, B. B. Saha, and A. Chakraborty, “Study on a waste heat-driven adsorption cooling cum desalination cycle,” *Int. J. Refrig.*, vol. 35, no. 3, pp. 685–693, 2012, doi: 10.1016/j.ijrefrig.2011.01.008.

[55] A. Wyrwa and Y. K. Chen, “Techno-Economic Analysis of Adsorption-Based DH Driven Cooling System,” *IOP Conf. Ser. Earth Environ. Sci.*, vol. 214, no. 1, 2019, doi: 10.1088/1755-1315/214/1/012128.

[56] J. McNally, “Techno-Economic Analysis of a Solar Adsorption Cooling System for Residential Applications in Canada,” 2020, doi: 10.22215/etd/2020-14434.

[57] A. M. Reda, A. H. H. Ali, M. G. Morsy, and I. S. Taha, “Design optimization of a residential scale solar driven adsorption cooling system in upper Egypt based,” *Energy Build.*, vol. 130, pp. 843–856, 2016, doi: 10.1016/j.enbuild.2016.09.011.

[58] M. Glushenkov, A. Kronberg, T. Knoke, and E. Y. Kenig, “Isobaric expansion engines: New opportunities in energy conversion for heat engines, pumps and compressors,” *Energies*, vol. 11, no. 1, Jan. 2018, doi: 10.3390/en11010154.

[59] B. J. G. Van der Kooij, *The Invention of the Steam Engine*. 2015.

[60] B. Nesbitt, *Handbook of Pumps and Pumping*, no. December. 2006. doi: 10.1016/B978-1-85617-476-3.X5000-8.

[61] V. Bush, “Apparatus for compressing gases,” 2,157,229, 1935

[62] M. Glushenkov and A. Kronberg, “Experimental study of an isobaric expansion engine-pump – Proof of concept,” *Appl. Therm. Eng.*, vol. 212, no. September 2021, p. 118521, 2022, doi: 10.1016/j.applthermaleng.2022.118521.

[63] S. Roosjen, M. Glushenkov, A. Kronberg, and S. Kersten, “Waste Heat Recovery Systems with Isobaric Expansion Technology Using Pure and Mixed Working Fluids,” no. July, pp. 1–14, 2022, doi: 10.20944/preprints202207.0002.v1.

[64] M. Glushenkov, A. Kronberg, T. Knoke, and E. Y. Kenig, “Heat Driven Pump for Reverse Osmosis Desalination,” *Encontech B. V.*, 2021. www.encontech.nl

[65] J. Nihill, A. Date, J. Velardo, and S. Jadkar, “Experimental investigation of the thermal power pump cycle – Proof of concept,” *Appl. Therm. Eng.*, vol. 134, no. December 2017, pp. 182–193, 2018, doi: 10.1016/j.applthermaleng.2018.01.106.

[66] L. F. Cabeza, A. de Gracia, G. Zsembinszki, and E. Borri, “Perspectives on thermal energy storage research,” *Energy*, vol. 231, p. 120943, 2021, doi: 10.1016/j.energy.2021.120943.

[67] G. Alva, Y. Lin, and G. Fang, “An overview of thermal energy storage systems,” *Energy*, vol. 144, pp. 341–378, 2018, doi: 10.1016/j.energy.2017.12.037.

[68] V. Pandiyarajan, M. Chinnappandian, V. Raghavan, and R. Velraj, “Second law analysis of a diesel engine waste heat recovery with a combined sensible and latent heat storage system,” *Energy Policy*, vol. 39, no. 10, pp. 6011–6020, 2011, doi: 10.1016/j.enpol.2011.06.065.

[69] F. Baldi, C. Gabrielii, F. Melino, and M. Bianchi, “A Preliminary Study on the Application of Thermal Storage to Merchant Ships,” *Energy Procedia*, vol. 75, pp. 2169–2174, 2015, doi: 10.1016/j.egypro.2015.07.364.

[70] G. Manente, Y. Ding, and A. Sciacovelli, “A structured procedure for the selection of thermal energy storage options for utilization and conversion of industrial waste heat,” *J. Energy Storage*, vol. 51, no. September 2021, p. 104411, 2022, doi: 10.1016/j.est.2022.104411.

[71] Zou Guangrong, “Ship energy efficiency technologies - now and the future,” 2017, [Online]. Available: http://www.vtt.fi/inf/pdf/technology/2017/T306.pdf

[72] SoWHat, “D1 . 6 – Report on H / C Recovery / Storage Technologies,” no. 847097, 2020.

[73] Y. Lin, G. Alva, and G. Fang, “Review on thermal performances and applications of thermal energy storage systems with inorganic phase change materials,” *Energy*, vol. 165, pp. 685–708, 2018, doi: 10.1016/j.energy.2018.09.128.

[74] N. Ahmed, K. E. Elfeky, L. Lu, and Q. W. Wang, “Thermal and economic evaluation of thermocline combined sensible-latent heat thermal energy storage system for medium temperature applications ☆,” *Energy Convers. Manag.*, vol. 189, no. March, pp. 14–23, 2019, doi: 10.1016/j.enconman.2019.03.040.

[75] M. Seitz, M. Johnson, and S. Hübner, “Economic impact of latent heat thermal energy storage systems within direct steam generating solar thermal power plants with parabolic troughs,” *Energy Convers. Manag.*, vol. 143, pp. 286–294, 2017, doi: 10.1016/j.enconman.2017.03.084.

[76] B. Xu, P. Li, and C. Chan, “Application of phase change materials for thermal energy storage in concentrated solar thermal power plants : A review to recent developments,” *Appl. Energy*, vol. 160, pp. 286–307, 2015, doi: 10.1016/j.apenergy.2015.09.016.

[77] K. Merlin, J. Soto, D. Delaunay, and L. Traonvouez, “Industrial waste heat recovery using an enhanced conductivity latent heat thermal energy storage,” *Appl. Energy*, vol. 183, pp. 491–503, 2016, doi: 10.1016/j.apenergy.2016.09.007.

[78] S. Guo *et al.*, “Mobilized thermal energy storage : Materials , containers and economic evaluation,” *Energy Convers. Manag.*, vol. 177, no. June, pp. 315–329, 2018, doi: 10.1016/j.enconman.2018.09.070.

Experimental and numerical study of geothermal rainwater tanks for buildings passive cooling

Lucas Striegel[a,c], Jean-Baptiste Bouvenot[a,c], Edouard Walther[a] and Hossein Nowamooz[b,c]

[a] National Institute of Applied Sciences (INSA); Department of HVAC (Heating, Ventilation, and Air Conditioning) and Energy Engineering, Strasbourg, France
lucas.striegel@insa-strasbourg.fr, CA
jean-baptiste.bouvenot@insa-strasbourg.fr
edouard.warther@insa-strasbourg.fr
[b] National Institute of Applied Sciences (INSA); Department of Civil Engineering, Strasbourg, France
hossein.nowamooz@insa-strasbourg.fr
[c] The Engineering science, computer science and imaging laboratory (ICube Laboratory), Illkirch, France

Abstract:

This communication presents the study of a new hybrid system consisting of a buried rainwater tank thermally activated through a water-to-water heat exchanger. This low-tech solution, little studied in the literature, performs the passive cooling of buildings and reduces domestic water network consumption (for non-potable uses). Firstly, experimental results obtained from two full-scale prototypes are presented. Then, numerical studies are discussed.

Keywords:

Building cooling; Geothermal energy; Measurement-simulation comparison; Rainwater collection; Thermal energy storage.

1. Introduction

With climate change, summer comfort and CO_2-emission reduction are two increasingly relevant topics. In this project, we are trying to develop a low-tech system allowing for the cooling of indoor spaces without using refrigerants or with a reduced energy expense.

The literature review shows a lack of detailed studies of such systems. The exploitation of experimental data of cold and hot water tanks connected to a thermo-active building system was treated by Kaltz [1], where the authors demonstrate that a 11 m^3 cistern could provide about 1000 kWh of cooling energy over a whole year. Simulation studies have been carried out by Upshaw [2] with the study of a non-buried rainwater storage tank. The approach considered the rainwater tank as a means of shifting the electrical peak load of an air conditioning unit. Sodah [3] simulates an open system with an aeration loop enhancing evaporative cooling but calculation is only monthly. While Gan [4], considered a tank with special design heat exchanger as a heat source for a heat pump (active system), which is also different from our approach. Marigo [5], also considered a ground coupled heat pump but the cold source is much closer to the rainwater tank we studied. The ground heat exchanger consists of helical shaped pipe in polyethylene immersed into a concrete-built water tank. The size of the tank and pipe are almost the same as our prototypes. To the best of our knowledge, the modelling of variable free-surface water storage and the related mass and heat transfers involved appears to be poorly documented.

To set up the model, the physical equations from both usual domestic water tanks and atmospheric reservoirs were combined, taking into account heat transfer between air and water. We hence aim here at establishing and validating an equation-based physical model, using the data of two full-scale prototypes in operation since July 2021.

In further works, the model will be coupled with a state-of-the-art building energy simulation tool in order to estimate the relevance of the system regarding summer comfort.

This work is organised as follows: first the principle of the system is explained, then the experimental setup and results are described and eventually a first version of numerical model and simulation is presented.

2. Main concept of the Rainergies system

The basis of the solution described consists in a new or existing buried rainwater tank, initially used for rainwater collection as non-potable domestic water and the relief of sewage networks. In France, the water resources management legislation locally enforces the water management at parcel level which could democratize the use of such rainwater tank. A helicoidal water-to-water heat exchanger (HX) is placed in the tank in order to take advantage of the heat storage capacity of water as a by-product. Thanks to an air-to-water heat exchanger connected to the ventilation supply duct, the tank delivers cooling energy to the building during summer [6].

In summary, the “Rainergies” system consist in following elements:

- A water tank for rain collection,
- A water/water coil heat exchanger immersed in the rainwater tank,
- A water/air heat exchanger placed after the supply air duct and connected to the immersed coil.

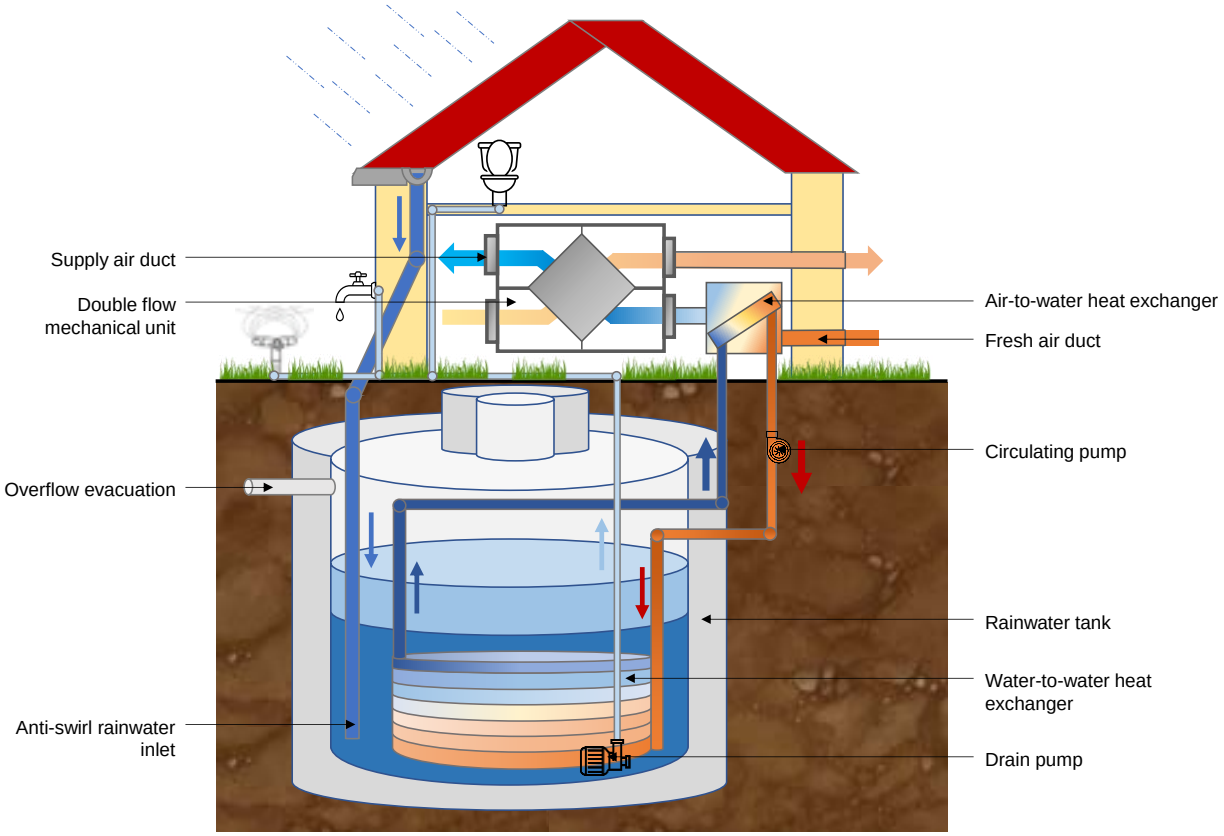

Figure. 1. Schematic diagram of the Rainergies principle (not at scale).

3. Experimental Study

3.1. Experimental set-up

Three Rainergies prototypes are installed in different locations in Alsace, France, in a semi-continental climate [7]. For the sake of conciseness, this article focuses on one prototype, located in Haguenau.

It consists of a 11 m^3 tank made of precast concrete with a coppered hundred-meter-long coiled heat exchanger. The surrounding ground is dry sand. A 1 kW cooling coil, placed before the double flow air handling unit, allows the heat transfer from the water loop to the supply air ventilation of a 150 m^2 family house which dates from the 1930’s but has been retrofitted lately to match current standards of the French building energy code.

Another prototype, also installed in a residential house, is very similar. The third system is located under a small office building with a larger tank of 25 m^3 and two immersed coils.

These prototypes will be the topic of a future communication, allowing to compare results with different setups (*e.g.* the position of the coil in the double flow mechanical ventilation) and ground properties (sandstone and groundwater flow).

3.2. Measurements

Presently, the Haguenau prototype is monitored with more than 25 sensors connected to dataloggers, with a minimum timestep of 10 min. The devices were installed in the summer 2021 and consolidated data is available since early 2022. The main measured data are:

- Water temperature stratification thanks to 5 fixed dataloggers evenly distributed over the height of the tank (0 m, 0.5 m, 1 m, 1.5 m, 2 m).
- Water level through total pressure of the bottom of the tank.
- Air temperature and humidity inside the tank.
- Temperatures at the air-to-water heat exchanger limits (both air and water).
- Meteorological data including rainfall, global solar radiation, air temperature and humidity.
- Temperature inside the buildings (at air vent and in the room)

3.3. Experimental Results

The results observed in winter operation mode and summer operation are encouraging.

During summer operation, as observed on Figure 2, the system can decrease the supply temperature of the ventilation by up to 13 °C, keeping indoor temperatures of the monitored houses under 27°C during the 2022 summer heatwave. The cooling energy between the 14th of May to 1st of September reached 455 kWh (considering an average ventilation flow rate). The average cooling power is 365 W but peaks of 1 kW were observed. Measurements show little variation of the air-to-water heat exchanger efficiency between [0.64 ; 0.88] with an average of 0.82 ± 0.16 which is consistent with the design value.

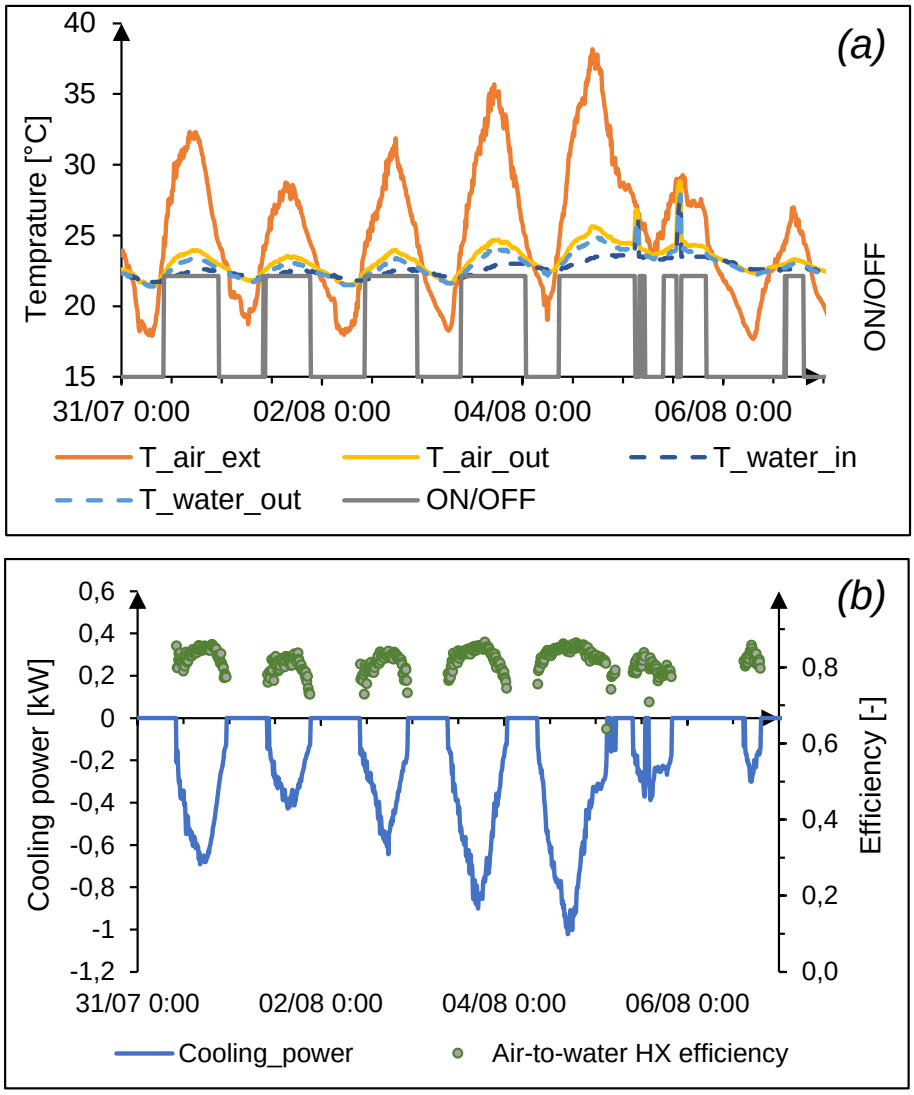

Figure. 2. Air-to-water heat exchanger, summer operation (a) and its cooling power produced and efficiency (b) (2022 – Week 31 – Haguenau).

In winter, it is also possible to use the energy in the tank for preheating before it passes through the double flow ventilation. This preheating is necessary to protect the ventilation elements from freezing in case negative outdoor temperatures. It is usually provided by an electrical heater. On the Haguenau prototype, this phenomenon was observed during 120 h over the winter period 2021-2022 (November 1st to March 15th), corresponding to ~ 39 kWh saved. The power supplied reaches 500W (average of 230W) and the air temperature was maintained above 0 °C despite outdoor dry bulb temperatures of - 6 °C (see Figure 3).

Thus, the system also allows for energy savings in winter (though in moderate quantities). Noticeably, winter operation allows to cool down the reservoir and its surrounding ground, which is beneficial for summer operation, as it participates to a seasonal energy storage.

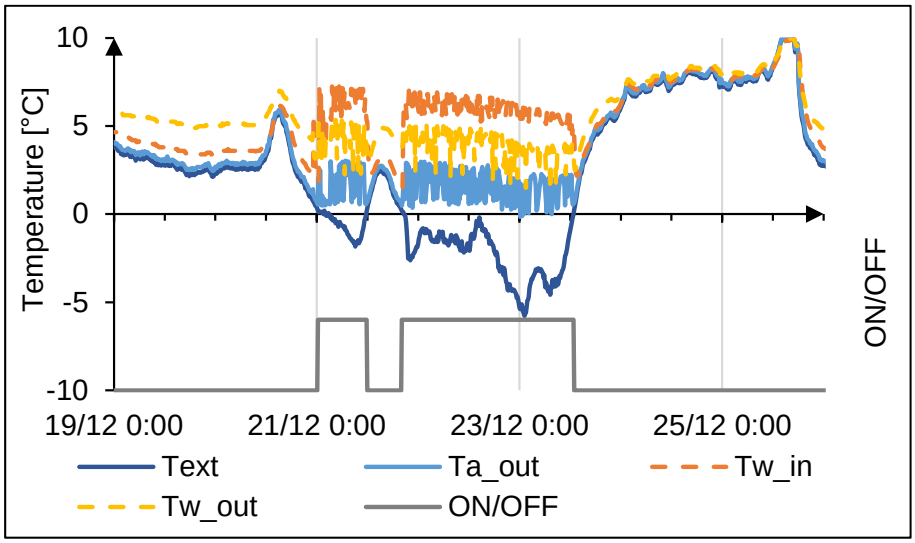

Figure. 3. Air-to-water heat exchanger, winter operation (2021 – Week 51 – Haguenau).

One of the difficulties of this project is to well assess the input parameters and their influence on the system behaviour. The experimental observation phase of the project can help to highlight and understand these events. For example, during rainfall the water temperature inside the tank is influenced by the quantity of rain but also its temperature (see Figure 3 – "T_Xm" meaning that the temperature sensor is at X m starting from the bottom of the tank) : during rainy events, for similar quantities water the temperature in the tank may drop significantly differently (up to 3 K). As this phenomenon is not observed after each rainfall, the hypothesis can be made that the temperature of the rain arriving in the tank is in cause. This parameter is difficult to evaluate, depending on pressure, air temperature but also probably of the roof surface temperature (harvesting surface) however recording the temperature inside the tank rainwater filter will allow in the future to validate the rain temperature model chosen.

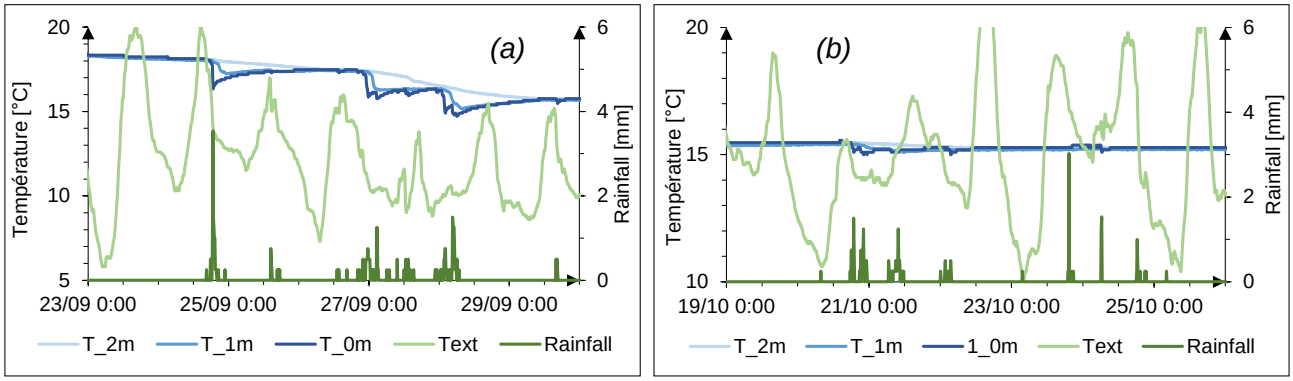

Figure. 4. Rainwater tank during rainy event with influence on the water temperature (a) and without influence (b) (2022 - Week 39 - Haguenau).

4. Numerical Modelling

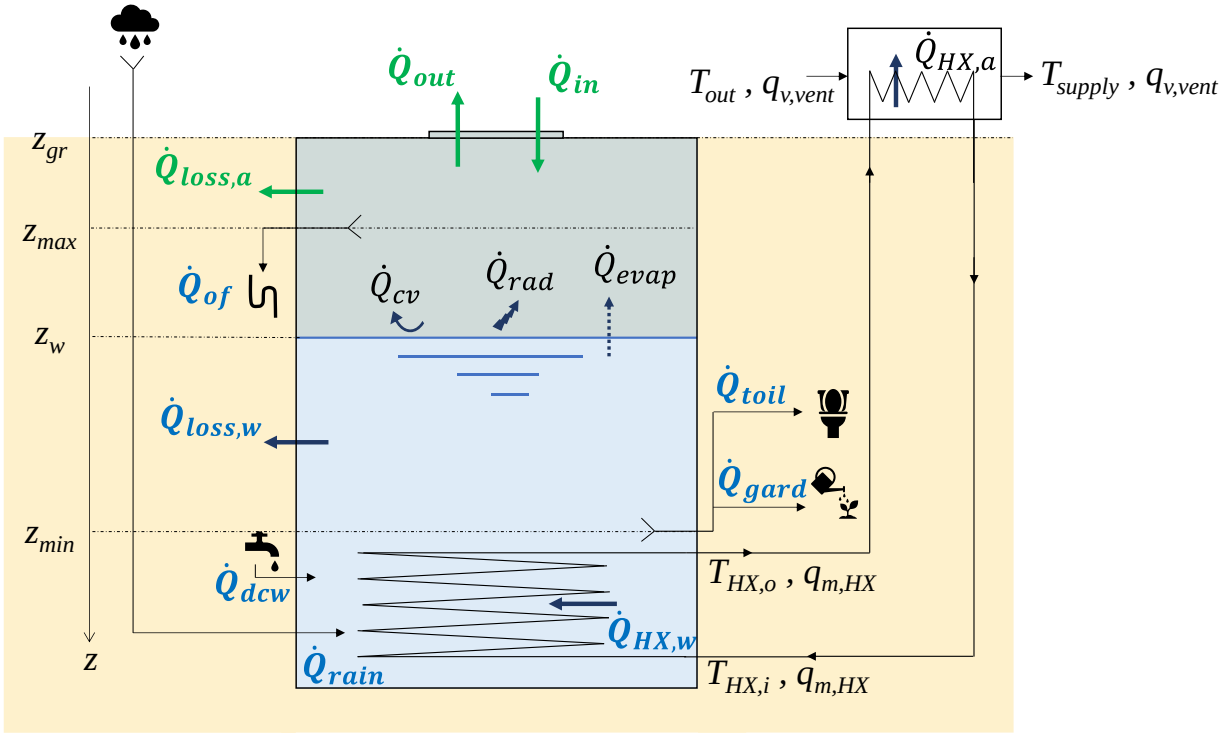

Figure. 5. System thermal balance.

4.1. Tank model

In first approach the tank is modelled with two temperature nodes, the ambient air temperature T_a (Eq. (2)) and the water temperature T_w (Eq. (1)), computed through the following thermal balances (a graphical representation of notations is given in Figure 5).

$$\rho_w c_{p_w} \frac{\mathrm{d}V_w T_w}{\mathrm{d}t} = -\dot{Q}_{loss,w} - \dot{Q}_{cv} - \dot{Q}_{rad} - \dot{Q}_{evap} + \dot{Q}_{HX,w} + \dot{Q}_{rain} + \dot{Q}_{dcw} + \dot{Q}_{toil} + \dot{Q}_{gard} + \dot{Q}_{of} \quad (1)$$

$$\rho_a c_{p_a} \frac{\mathrm{d}V_a T_a}{\mathrm{d}t} = -\dot{Q}_{loss,a} + \dot{Q}_{cv} - \dot{Q}_{out} + \dot{Q}_{in} \quad (2)$$

The different heat flows $\dot{Q}_X$ are detailed below, starting with the water node thermal balance.

- $\dot{Q}_{loss,w} = U_{w,gr} S_w \left(\overline{T_{w,gr}} - T_w\right)$ represents the convective and conductive losses from the water through the wall with $U_{w,gr}$ the heat transfer coefficient, taking into account the convection and conduction resistance, and $\overline{T_{w,gr}}$ the weighted mean temperature of the ground adjacent to water,.
- $\dot{Q}_{cv} = h_{c,\mathrm{a-w}} S_{w-a} (T_a - T_w)$ is the convective flux between the water and the air, with $h_{c,\mathrm{a-w}}$ the convection coefficient.
- $\dot{Q}_{rad} = h_{r,\mathrm{w-w}} S_{w-a} (\overline{T_{wall}} - T_w)$ stand for the radiative exchange between the surface water and the wall above it, with $h_{r,\mathrm{w-w}}$ the linearized radiative coefficient and $\overline{T_{wall}}$ the weighted mean temperature of the wall.
- $\dot{Q}_{evap} = q_{m,evap} L_v$ is the latent loss due to water evaporation, with L_v the vaporization latent heat and $q_{m,evap}$ the evaporation mass flow rate computed thanks to Hen's correlation [8].
- $\dot{Q}_{HX,w} = q_{m,HX} c_{\mathrm{p,gw}} \left(T_{HX,o} - T_{HX,i}\right)$ represents the heat flux extracted from the water-to-water heat exchanger.
- $\dot{Q}_{rain} = q_{m,rain} c_{p,w} T_{rain}$ is the heat flux due to precipitation and is treated as an advection flux. The same approach is used for the district cold water intakes, toilet flushing, gardening, or overflowing withdrawals represented by $\dot{Q}_{dcw}$, $\dot{Q}_{toil}$, $\dot{Q}_{gard}$, $\dot{Q}_{of}$ respectively.

The air node thermal balance is presented below.

- $\dot{Q}_{loss,a} = U_{a,gr} S_a (\overline{T_{a,gr}} - T_a)$ expresses also the convective and conductive losses through the wall but on the air side (similarly $U_{a,gr}$ stand for the heat transfer coefficient and $\overline{T_{a,gr}}$ the weighted mean temperature of the ground in contact with the air.
- $\dot{Q}_{out} = (q_{\mathrm{m,out}} + q_{m,leak}) T_a$ is an advection flux considering the air volume changes and the air leakage from the tank to the outside. $\dot{Q}_{in}$ is its counterpart but from the outside to the tank.

The inlet and outlet temperatures of the coil are computed through both equations of the air-to-water and water-to-water heat exchanger. As mentioned in the experimental results section, the air-to-water heat exchanger efficiency does not vary much, hence it is assumed constant which is also consistent with the forced convection that takes place in the exchanger. For the first simulations, the same hypothesis has been made for the water-to-water heat exchanger efficiency. The supply air temperature is determined by the equilibrium of the heat flow at the air-water heat exchanger.

4.2. Ground model

The ground is assumed to be homogeneous with constant properties not depending on the soil moisture. As the heat transfer is symmetrical according to the z axis, the 2D heat transfer equation in cylindrical coordinates was used:

$$\rho c_p \frac{\partial T}{\partial t} = \lambda \left(\frac{\partial^2 T}{\partial z^2} + \frac{\partial^2 T}{\partial r^2} + \frac{1}{r} \frac{\partial T}{\partial r} \right) \quad (3)$$

The numerical model for the heat equation is a discrete finite volume formulation of Equation (3). Depending on the volume location, thermal properties are adapted. A source term is added on the superficial node to consider the solar radiation. In this first model, the spatial discretisation is constant with 50 cm mesh, but it is intended that following models integrate a variable space discretisation with local refinements around the tank. The variation of ground moisture content is not modelled in this first model.

4.3. Solving Procedure

In order to solve simultaneously for the air, water and ground temperatures, the semi-implicit Crank-Nicolson numerical method was used as described by Walther [9]. It has the advantage of unconditional stability and is of second order in space and time.

5. Model validation

5.1. Simulation hypothesis

Input parameters, such as weather data or geometrical parameters, are extracted from measured prototype data. Glycol water mass flow and air ventilation flow are considered constant respectively at 0.14 $kg.s^{-1}$ according to the design value and 240 $m^3.h^{-1}$ according to one-off measurement values. Convection coefficients were assessed for steady state and kept constant throughout the simulation.

Marigo [5] using a previous study of Kusuda and Achenbach [10] explains that ground temperatures without thermal perturbations (*e.g.* geothermal probe or buried tank) depend on ground properties and outside air conditions (average annual air temperature and annual air temperature amplitude) :

$$T_{ground}(z,t) = T_m - A_T e^{-z\sqrt{\frac{\pi}{\alpha \tau_{year}}}} \cos\left(\frac{2\pi}{\tau_{year}} \left(t - t_0 - \frac{z}{2} \sqrt{\frac{\tau_{year}}{\alpha \pi}} \right) \right) \quad (4)$$

T_m is the annual average air temperature (°C), A_T is the annual amplitude of monthly average air temperature [°C], α is the ground thermal diffusivity ($m^2.s^{-1}$), τ_{year} is the annual periode (s) and t_0 is the date of the minimum surface temperature (s). Figure 6. shows the ground temperature variation as function of depth from the surface during the year, which is relatively stable at a 10 m depth. The ground temperature is therefore assumed constant at a depth of 10 meters below ground level (lower boundary condition). The soil temperature for $0 < z < 10$ m is initialised according to this model.

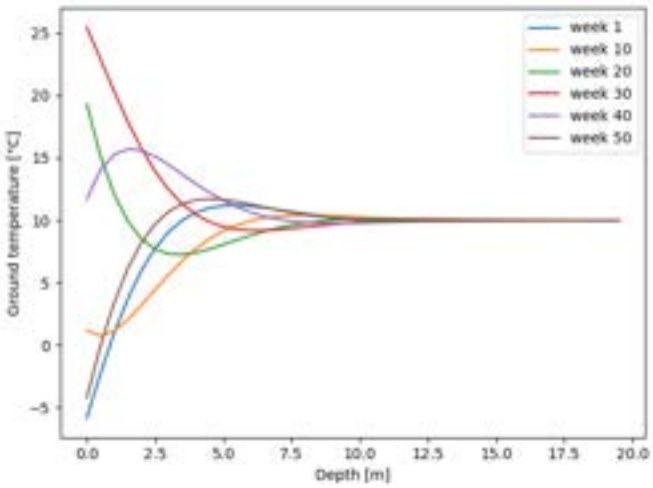

Figure. 6. Calculated ground temperature against depth for several week in Haguenau

The outdoor weather data are used as boundary condition for ground surface (temperature, wind and solar flux).

The input parameters are summarized below.

Table 1. Input parameters of the conducted simulation.

Parameter	value
Simulation parameters	
Timestep	600 s
Spatial step through z axis	0.5 m
Spatial step through radial axis	0.5m
Geometrical dimensions	
Tank diameter	2.5 m
Tank height	3 m
Roof surface	180 m²
Ground domain depth	10 m
Ground domain radius	10 m
Material properties	
Ground thermal conductivity	0.7 $W.m^{-1}.K^{-1}$
Ground heat capacity	850 $J.kg^{-1}.K^{-1}$
Ground density	1600 $kg.m^{-3}$
Heat transfer coefficients	
Water-to-water HX efficiency	0.7
Air-to-water HX efficiency	0.8
Water to tank wall convection coefficient	20 $W.m^{-2}.K^{-1}$
Air to tank wall convection coefficient	7 $W.m^{-2}.K^{-1}$
Air to water surface convection coefficient	6 $W.m^{-2}.K^{-1}$

5.2. Numerical results

The prototype setup was simulated over the summer period (from the 14/05/22 to the 31/08/22), using the boundary conditions described in previous section.

The simulation results obtained are presented on Figure 6, depicting the simulated versus measured water tank temperature (above) and the supply air temperature (below). This first model exhibits a correct behaviour in terms of dynamics of the phenomenon, although the magnitude of variations can possibly be fine-tuned.

Considering the simplifications made, the numerical results are very encouraging: the dynamics of water and air temperatures are respected and the simulated water-to-water heat exchanger inlet and outlet temperature and air supply temperature globally match the experimental data.

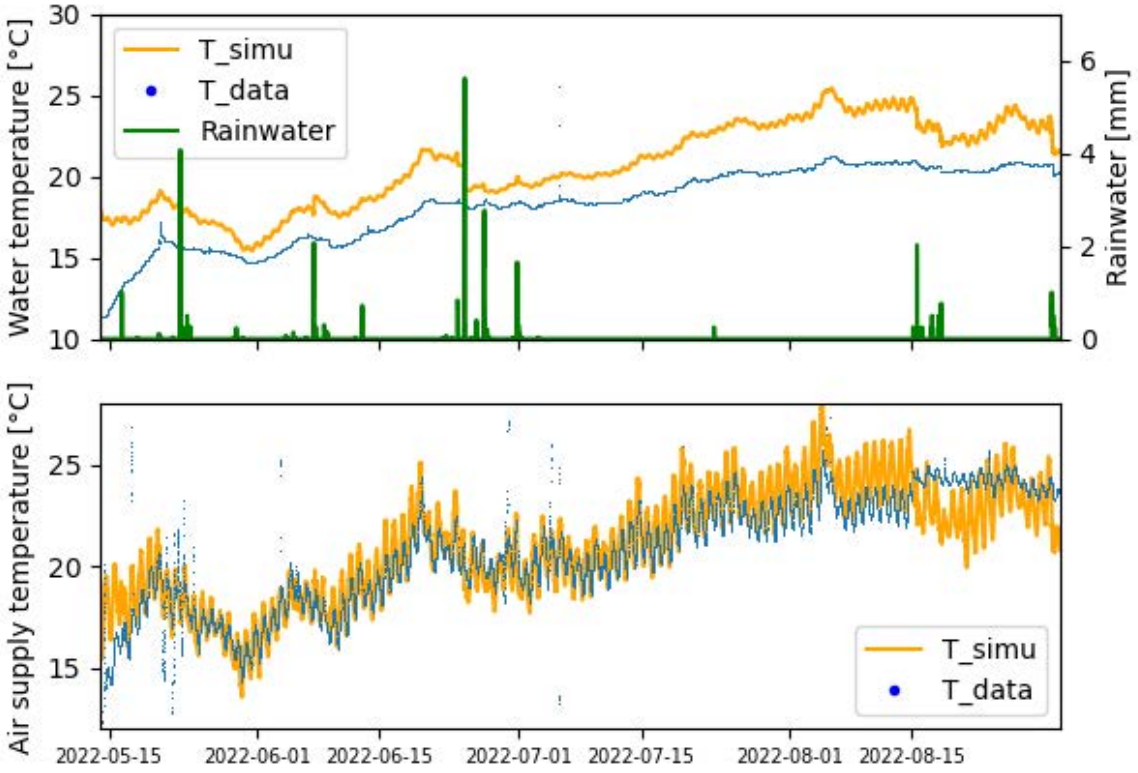

Figure. 7. Experimental and numerical data

Table 2. Root mean square error (RMSE) between numerical and experimental results

Analysed output	Root Mean Square Error (°C)
Air tank temperature	1.62
Water tank temperature	2.66
Inlet HX temperature	1.09
Outlet HX temperature	1.19
Supply temperature	1.22

In terms of RMSE, the preliminary simulation results obtained are as follow: the highest error is made on the tank temperature prediction (2.77 K) and errors of the order of 1.09 to 1.62 K are made on other temperatures.

In order to reduce the discrepancy between model and measurement, a sensitivity analysis of the model to its input parameters was undertaken.

5.3. Sensitivity analysis

In order to identify the influential parameters of the model, with the intention to obtain a better fit between model and measurements, a preliminary sensitivity analysis was conducted. We used Morris' [11] "one-at-a-time" sensitivity analysis method, taken up by Campolongo [12], which provides a ranking of parameters with an acceptable computational expense, given the involved simulation time (*id est* approximately 2 hours computation for 1 month simulated). The principle of Morris' method, nowadays widely used in the building simulation community, consists in computing the average elementary effect of the variation of one parameter at a time, usually for a dozen of repetitions. This was performed using the state-of-the-art SAlib python library.

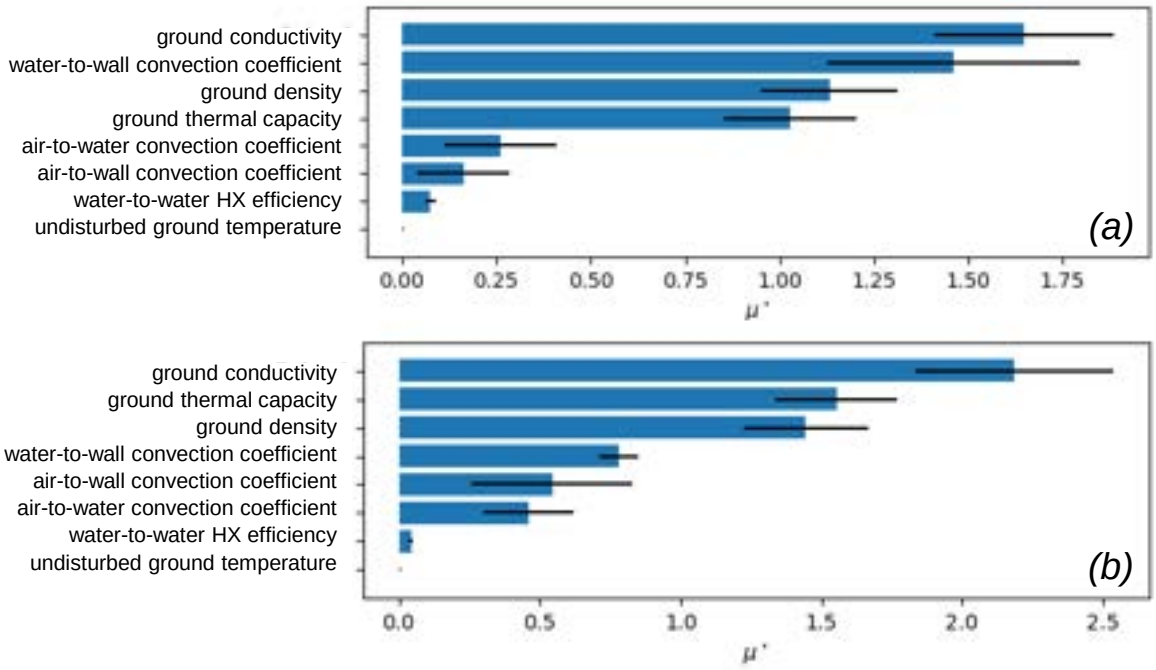

Figure. 8. Elementary effects of Morris's sensitivity analysis on the water tank temperature (a) and on the air tank temperature (b)

The investigation focusses on ground properties, thermal convection coefficients and the efficiency of the water-to-water heat exchanger.

The results obtained on the water tank temperature and air tank temperature are presented on Figure 7. Similar studies were also conducted on the inlet and outlet heat exchanger temperature and on the supply air temperature. The conductivity of ground, the thermal capacity of the ground and the density of ground are the three first influent parameters. The reservoir wall convective transfer coefficient of water is also influent on the water tank temperature.

The results show that following parameters are particularly influent on the outputs:

- All ground properties are significant on the water temperature output. Therefore, assessing those coefficients will be crucial for future work.
- The convection coefficient between wall and water, which calls for the numerical implementation of a temperature dependent correlation.

As a sequel, a parametric fit optimisation on the most influent parameters will be undertaken, with the aim of obtaining a better prediction of the measured temperatures.

6. Discussion

On the experimental side, the primary results exhibit good result with outside air temperature reduction of more than 10 K and cooling power reaching 1 kW. Noticeably, this system does not aim at replacing air conditioning, but it can reduce its use, especially in high-performance buildings. During winter, the prototype can pre-heat the air to protect the installation from frosting, saving the use of an electrical heater.

It is foreseen to conduct data acquisition within shorter timestep to try to better understand short-timed event such as rainfall and its impact on the rainwater tank temperature.

Regarding numerical aspects, ensuing the sensitivity analysis, a parameter fitting procedure will be lead in order to minimize the discrepancy between the model and measurements. Moreover, the models need improvement which have already been planned. The rainwater tank needs to integrate the water stratification and a better evaluation of air leakage which can strongly influence both air and water temperature. Thermal convection coefficients and water-to-water heat exchanger efficiency need also a finer calculation, *e.g.* depending on the air or water temperature instead of constant values. The time calculation will also be enhanced by changing the solving method and switching to a sparse linear algebra library. It will allow shorter time calculations and thus offer more options in terms of sensitivity analysis but also optimization.

7. Conclusion and perspectives

Coupling the model with a building energy simulation tool will allow in future works to optimize the controls and test the solution in different conditions (climate, …). It is also planned to explore the use of a dew point cooler that can provide extra cooling power by water evaporation into exhaust or supply air.

Moreover, with the rise of drought frequency, the applications of rainwater collection may widen, for example with the use of rainwater for laundry. This raises several new questions about the quality of the water stored in the tank. The water temperature increase may lead to microbiologic development, which can make the water unsuitable for certain uses (such as supply for washing machine). It is also possible for a biological film to develop on the heat exchanger leading to fouling and deterioration of its performance. This problem is not very common and deserves some investigation.

The applicability of such systems in real configurations, the performance prediction and the determination of design guidelines is obviously one of the objectives of the research conducted here, be it for commercial buildings or housing applications.

Acknowledgments

The authors would like to thank the ADEME (Agence de la transition écologique) and the Région Grand Est for the financial support. Many thanks to the Gasnier and Schneider families for their availability and letting us tinker their Rainergies systems.

Nomenclature

c_p	heat capacity, $J.kg^{-1}.K^{-1}$
D	diameter, m
h_c	convection coefficient, $W.m^{-2}.K^{-1}$
HX	heat exchanger
$\dot{Q}$	heat flux, W
q_m	mass flow, $kg.s^{-1}$
q_v	volume-flow, $m^3.h^{-1}$
RMSE	Root Mean Square Error
T	temperature, K
z	altitude, m

Greek symbols

α	thermal diffusivity, $m^2.s^{-1}$
λ	thermal conductivity, $W.m^{-1}.K^{-1}$
ρ	density, $kg.m^{-3}$
τ	oscillation period

Subscripts and superscripts

a	air
cv	convection
dcw	district cold water
evap	evaporation
gard	garden
gr	ground
HX,a	air to water heat exchanger
HX,w	water to water heat exchanger
HX,i	heat exchanger inlet
HX, o	heat exchanger outlet
in	to tank inside air
loss,a	wall in contact with the air
loss,w	wall in contact with the water
of	overflow
out	to outside
toil	toilet
rad	radiative

vent ventilation

w water

References

[1] D. E. Kalz, J. Wienold, M. Fischer, and D. Cali, Novel heating and cooling concept employing rainwater cisterns and thermo-active building systems for a residential building, Applied Energy, vol. 87, no 2, p. 650-660, Feb 2010.

[2] C. R. Upshaw, J. D. Rhodes, and M. E. Webber, Modeling electric load and water consumption impacts from an integrated thermal energy and rainwater storage system for residential buildings in Texas, Applied Energy, vol. 186, p. 492-508, Jan 2017.

[3] M. S. Sodha, R. L. Sawhney, and D. Buddhi, Use of evaporatively cooled underground water storage for convective cooling of buildings: An analytical study, Energy Conversion and Management, vol. 35, no 8, p. 683-688, Aug 1994.

[4] G. Gan, S. B. Riffat, and C. S. A. Chong, A novel rainwater–ground source heat pump – Measurement and simulation, Applied Thermal Engineering, vol. 27, no 2-3, p. 430-441, Feb 2007.

[5] Marco Marigo, Enrico Prataviera, Sara Bordignon, Michele Bottarelli, and Angelo Zarrella, Analysis of the thermal performance of a water storage cell with helical shaped pipe for ground source heat pumps, presented at Building Simulation 2021, Bruges, Belgium, Sept 2021, p. 8.

[6] J.-B. Bouvenot, Performance simulation of a hybrid geothermal rain water tank coupled to a building mechanical ventilation system, presented at Building Simulation 2021, Bruges, Belgium, Sept 2021.

[7] M.-O. SIU, Rainergy : Conception de prototypes de récupérateurs d'eau de pluie géothermiques, INSA Strasbourg, Strasbourg, Projet de fin d'études, 2021.

[8] H. Hens, Indoor climate and building envelope performance in indoor swimming pools, Energy efficiency and new approaches, Istanbul Technical University: 543-52, 2009

[9] E. Walther, Building Physics - Applications in Python. Paris: DIY Spring, 2021.

[10] T. Kusada and P.R. Achenbach, Earth temperature and thermal diffusivity at selected stations in the United States, ASHRAE Trans 71(1), p. 61-74, 1965.

[11] M. D. Morris, Factorial Sampling Plans for Preliminary Computational Experiments, Technometrics, vol. 33, no 2, p. 161-174, May 1991.

[12] F. Campolongo, J. Cariboni, and A. Saltelli, An effective screening design for sensitivity analysis of large models, Environmental Modelling & Software, vol. 22, no 10, p. 1509-1518, Oct 2007.

Energy Efficient Room Thermal Control Strategy with Consideration of Occupants' Thermal Comfortability

Yunfei Bai[a], Chenghao Li[b], Wei He[c], Jihong Wang[d]*

[a] School of Engineering, University of Warwick, Coventry, UK, yunfei.bai.1@warwick.ac.uk
[b] School of Engineering, University of Warwick, Coventry, UK, chenghao.li@warwick.ac.uk
[c] School of Engineering, King's College London, London, UK, wei.4.he@kcl.ac.uk
[d] School of Engineering, University of Warwick, Coventry, UK, jihong.wang@warwick.ac.uk
** Corresponding author*

Abstract:

In general, any changes to room temperature for energy savings should not impact the occupants' thermal comfortability. Therefore, the thermal control strategy should meet the occupants' thermal comfortability expectations while exploring the energy consumption reduction strategy. The paper presents our preliminary work in developing "people-centered" energy-saving methods. The work starts with building a CFD thermal dynamic model of the room by using an actual kitchen as the prototype. The model can simulate and derive the temperature at any position within the room space and capture its temperature dynamics. Then, a target-tracking people-centered control strategy is proposed. With the occupant's motion and position changes, the model can calculate the room temperature at the point where the occupant is located. The objective of the control is to ensure the occupant's thermal comfortability. The initial simulation study indicates that the target-tracking control strategy could potentially save 23.32% more energy and greatly enhance the occupant's thermal comfort compared to a fixed-position sensor-based control strategy.

Keywords:

Thermal Comfort Control; Energy Efficiency; CFD; Thermal Dynamic Model.

1. Introduction

The UK government has set an ambitious target to reduce emissions by 78% by 2035 compared to the 1990 level [1]. A more ambitious goal is to achieve zero carbon emissions by 2050 [2]. To achieve this target, significant efforts must be made for decarbonizing power generation, heating, and road transportation [3]. Power generation from renewable energy sources has proliferated in the past ten years [4]. However, emissions from heating are almost unchanged. Without decarbonising heating, Net Zero goal has no way to be achieved as heating contributes nearly half of the energy consumption in the UK, in which 57% is used to meet domestic space heating and hot water demands [5]. Electric heating using power from renewable energy sources can promote heating decarbonization and proper electric heating management may support flexible grid operation to allow increased integration of variable renewable energy [6]. Heating electrification in coordination with power generation from renewable energy is considered as feasible way of emission reduction [7].

It is well known that conversion from electricity to heat has an efficiency of 100%. However, the utilisation of the converted thermal energy may not have 100% efficiency while in a heating system. For space heating, temperature distribution and air velocity affect the occupant's thermal comfort level which will lead the variations to energy consumed. A good control strategy for an electric heating system should satisfy the occupants' thermal comfortability while minimising energy consumption.

The room thermal models with high fidelity are essential for thermal comfort control strategies [8]. Room thermal models can be divided into three categories: white, black, and grey box models [9]. The white box model is based on the derivation of physical equations and assigning values to parameters in the model based on empirical knowledge [10]. Jradi et al. [11] developed a dynamic energy performance model for four buildings in Aarhus, Denmark, considering realistically measured physical parameters of components such as roofs, exterior walls, windows, doors, and floors. The model guides the analysis and evaluation of energy retrofits in buildings. The black box model is a purely data-driven model that uses artificial neural networks (ANN) to model the mapping of input parameters to desired output parameters [12]. Attoue et al. [13] proposed an ANN-based indoor temperature prediction model that considers the effects of solar radiation,

historical indoor and outdoor temperatures, and indoor and outdoor humidity on indoor temperature. The grey-box model is a hybrid model that uses physical knowledge to build a mathematical model and uses ANN to mine the relationships between a large amount of actual residential thermal data to obtain the values of the parameters in the model [14]. Hu et al. [15] developed a self-learning grey box room thermal model which uses indoor air and outdoor air temperatures to pre-estimate and scale the model parameters. Case studies show that the model can accurately predict indoor air temperature variations.

However, in these models, the temperature distribution in a space is normally assumed to be uniform. In this way, it is common for occupants to experience differences in thermal comfort in different parts of the room, with some areas feeling hot and others cold, which will affect the occupants' thermal comfortability and may be accompanied by an increase in energy consumption. Focusing on this challenge, this paper explores energy efficiency control strategies for occupant comfort enhancement based on a thermal dynamic model of the room.

The main contributions of the paper present: i) a thermal dynamic model could predict the temperatures of any position point in a room space is built; ii) a target-tracking energy saving control strategy to enhance the occupants' thermal comfortability is proposed; iii) a simultaneously evolving dynamic thermal models and occupant thermal comfort-oriented control strategies is implemented based on a co-simulation multi-platform.

2. Description of a target-tracking thermal comfort control system

The target-tracking thermal comfort control system is shown in Figure 1. The aim of the control system developed to achieve energy efficiency while maintaining the occupant's thermal comfort. Three parts form the control system: room CFD thermal dynamic model, occupant location recognition, and control strategy. The parameters and location of the electric heater are fed to the CFD model to simulate heat dissipation and transfer in the room as a heat source. Then, the room temperature distribution will be calculated and updated via the CFD simulation during each simulation time step. By this way, the temperature at different mesh point locations in the room can be obtained. The occupant location recognition is performed by synthesizing the sensors' data so the temperature of the occupant's activity zone can be obtained. The control strategy will be formulated to regulate the heat dissipation power of the electric heater. The study is based on INVENTOR and COMSOL software to build room CFD thermal dynamic model and on COMSOL and SIMULINK software to develop and simulate control strategy. The occupant location recognition part is achieved by an occupant random path generation model based on MATLAB software.

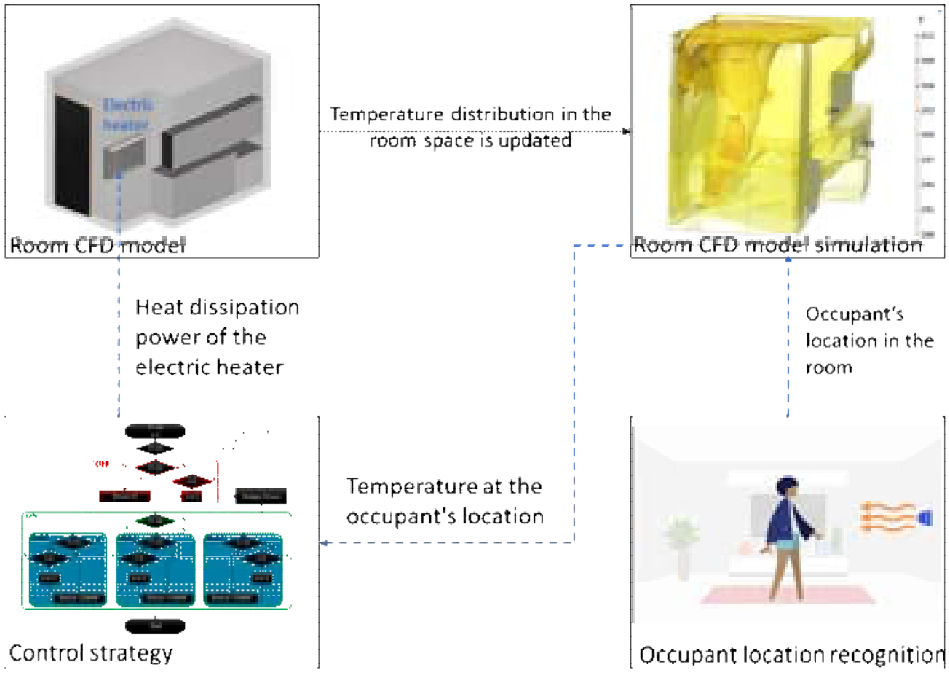

Figure. 1. Target-tracking thermal comfort control system illustration

3. Room CFD thermal dynamic model

Different from the current room thermal models assuming a uniform temperature distribution in the room space, the paper explores the room thermal dynamics and temperature distribution via a CFD simulation which will be performed with the information of room boundary conditions and the heat source (an electric heater in this study); the CFD model will be able to provide the temperature distribution for a different location in the room 3D space, and the resolution depends on the choices of mesh.

The CFD thermal dynamic model is built with the benefits of two software packages: INVENTOR and COMSOL. As shown in Figure 2(a), the laboratory kitchen is chosen as a base space for modelling. Use INVENTOR software to generate a 3D model of the room with consideration of the shapes and spaces of the interior furniture and appliances. The 3D room model is shown in Figure 2(b). The electric heater is the only heat source located in the room to heat up the space. The synchronization of this 3D room model in INVENTOR and COMSOL software is achieved via LiveLink for Inventor interface. In COMSOL, by assigning physical parameters to the components of the 3D room model and adding multi-physics field, the CFD model will obtain the temperature distribution inside the room space. Figure 2(c) shows the room CFD model mesh used in simulation.

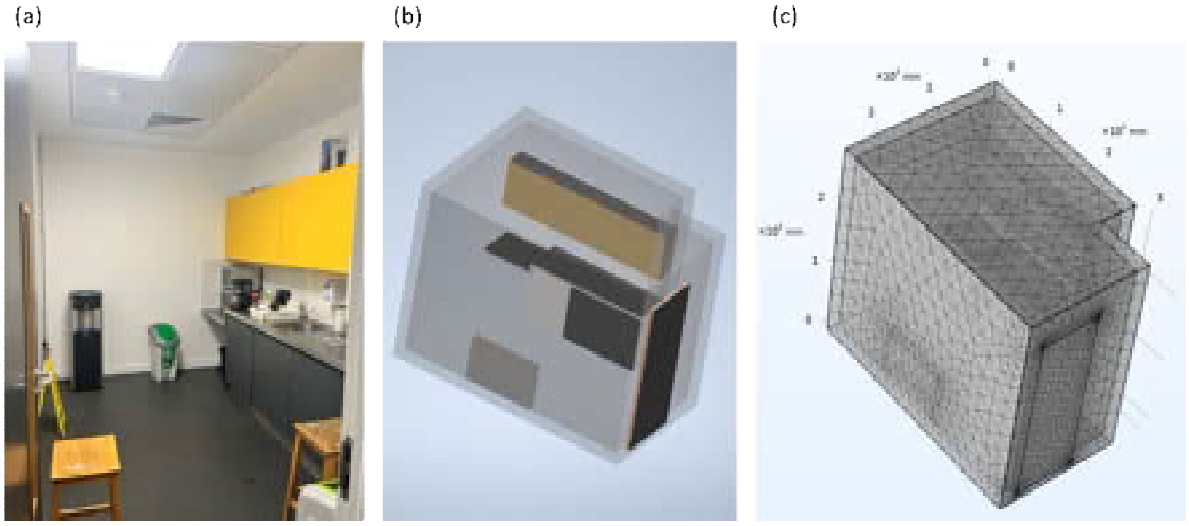

Figure. 2. a) The room, b) 3D model of the room, c) illustration of the room CFD dynamic thermal model mesh

In order to get the information about the temperature distribution inside the room space during the operation of an electric heater, multi-physics field simulations of coupled fluid flow and fluid-solid heat transfer are required in using COMSOL Multiphysics modelling. The laminar flow model is used to simulate the air flow in the room. The thermal model chooses using solid and fluid heat transfer physical fields. The total volume of the room is approximately 26.4 m^3. Physics-controlled mesh, shown in Figure 2(c), was generated automatically with element size set to coarse. The automatically generated mesh contains 127,313 domain elements, 15,887 boundary elements and 1,558 edge elements. Referring to the European National Building Code [16], heat transfer coefficients for the exterior wall and the door are selected to be 2.5 W/m^2K and 3 W/m^2K, respectively to represent the simulating scenario. The initial temperature is set as 10 ℃.

The input variable to this room CFD model is the thermal dissipation power of the electric heater. The state variable is the temperature distribution in the room space. By setting the thermal dissipation power of the electric heater, the temperature distribution in the room space will be updated at each simulation step.

4.Thermal comfort control strategies

A quantum series heater is investigated in this paper. This electric heater is an advanced product in the UK market. The heater used in this paper is model QM150RF, which has three electric heating modules, each operating at 1100 W and one fan, operating at 11W. The heater uses forced convection heat transfer to provide heat to the occupant. The electric heater is well insulated, the heat is released from underneath the heater, and a fan blows from underneath the heater to bring the heat into the room. In this study, the circuit of the electric heater has been modified so that it can now be heated at three levels of power: 1100 W, 2200 W, and 3300 W. The control strategy in this paper has been developed based on these three levels of power.

A commonly used temperature control strategy currently is thermostatic control. Based on the temperature data input from a fixed sensor to maintain the temperature near that sensor in a fixed interval, usually 21-25℃. Control strategies based on feedback from fixed temperature sensors are developed under the assumption that the temperature distribution within a room space is uniform. However, there is a large variation in the temperature distribution within the room space, which leads to erratic performance of control strategies based on fixed temperature sensor feedback. The CFD thermal dynamic model of the room developed in the third part of this paper can provide temperature variations at any location during the operation of the electric heater. LiveLink for Simulink interface enables the joint simulation of this CFD model in COMSOL and SIMULINK software. The development and simulation of the control strategy in this paper is based on the combined operation of SIMLINK and COMSOL software. The target-tracking thermal comfort control system proposed in this paper is shown in Figure 1. The heat dissipation power of the electric heater

is the control variable of the strategy and the temperature distribution in the room space is the state variable. The target-tracking thermal comfort control framework is present as follows:

$$\begin{cases} C(t) = f_{cs}(T(t)) \\ T(t) = S(t)|(x,y,z) \\ (x,y,z) = f_{olc}(t) \\ S(t+step) = f_{rtdm}\big(S(t), C(t)\big) \end{cases} \quad (1)$$

where, f_{cs} is the control strategy. $C(t)$ is the control variable at time t. $T(t)$ is the temperature at the occupant's location at time t; $S(t)$ is the state variable at time t, which is a function of the spatial coordinates. f_{olc} is the occupant location recognition model which is a time-dependent function. (x,y,z) is the occupant's spatial location. f_{rtdm} is the room CFD thermal dynamic model. $step$ is the simulation time step.

The control strategy is present in Figure 3. The control strategy development draws on the operating model of the actual electric heater. The operating states of an electric heater can be divided into two main categories, off and on. When the heater is on, it can be divided into three operating models, Mode 1 (power = 1100W), Mode 2 (power = 2200W), and Mode 3 (power = 3300W). The control strategy ensures that the temperature around the occupant is always between 21 and 25 ℃. Taking into account the time-dependent nature of heat diffusion and to avoid frequent start/stop of the electric heater, the control strategy is structured in a self-cycling manner for each mode.

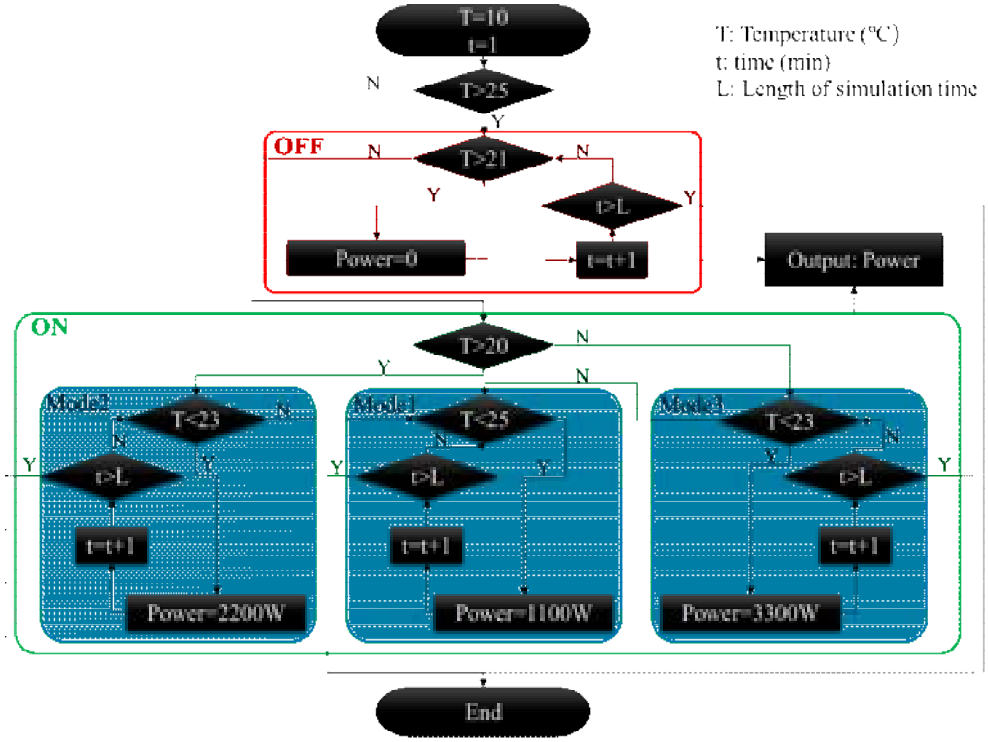

Figure. 3. Thermal comfort control strategy

In order to set the object of comparison, two fixed sensor-based control systems are designed for this study. These are, respectively, a control system based on a temperature sensor fixed to a doorway (TC@d), a control system based on a temperature sensor fixed near the heater (TC@h).

5. Results and discussions

This paper is based on a multi-software platform to complete the development and simulation of a CFD thermal dynamic model of the room and a target-tracking thermal comfort control strategy. The co-simulation flow is shown in Figure 4. During the co-simulation process, the synchronization the 3D room model on INVENTOR and COMSOL platforms via the LiveLink for Inventor interface. The interaction of the input and output data of the room CFD thermal dynamic model on the COMSOL and SIMULINK platforms is accomplished via the LiveLink for Simulink interface.

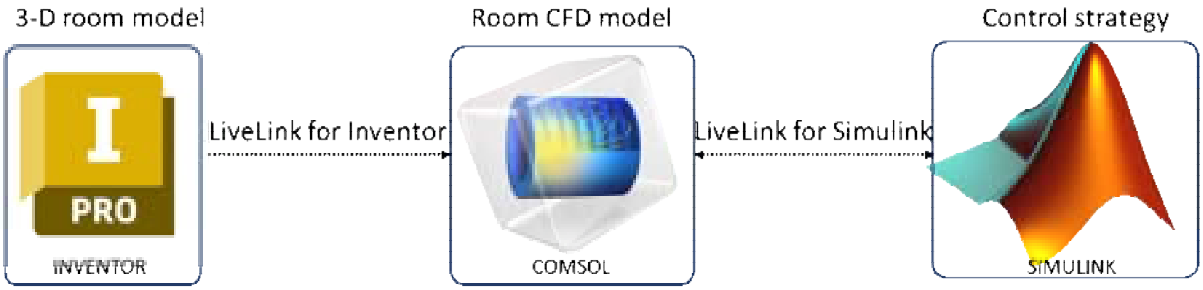

Figure. 4. Multi-platform co-simulation flow

This paper completes all simulations using a computer with an AMD Ryzen 5600H 3.30 GHz Processor, 16 GB of RAM, NVIDIA GeForce GTX 1650 GPU, and a 64-bit Windows operation system. Three temperature control strategies are simulated in this study, two based on fixed position sensor data feedback and the remaining on dynamic occupant activity trajectory temperature feedback. In the room CFD model, a plane one metre above the ground was set up as shown in Figure 5(a). Eight temperature probes were arranged on this plane, as shown in Figure 5(b). In this paper, the occupant's activity range in the room is divided into eight zones. The central temperature of the occupant's activity area is fed to the control strategy. The temperature at the occupant's activity area is always in a suitable range by selecting the appropriate control variables.

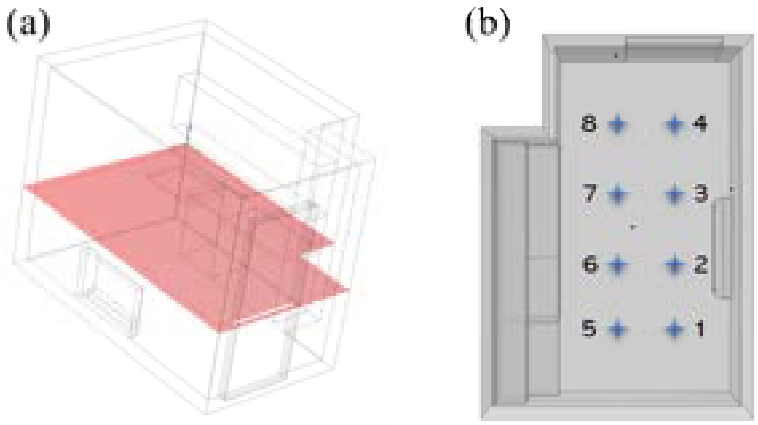

Figure. 5. Occupant activity zones: a) the plane, b) temperature probes

During the simulation, the occupant's activity trajectory needs to be given to verify the strategies' performance. After random sorting, one of the occupant's activity traces was obtained as: 6->3->7->8->5->1->2->4. It is assumed that the occupant spends a half hour in each zone. This paper adds two-time blocks of one hour each to this time location path. During these two-time blocks, the occupant leaves the room. Therefore, the final path obtained for the occupant's location over time is shown in Figure 6. This activity trajectory takes a total of 6 hours.

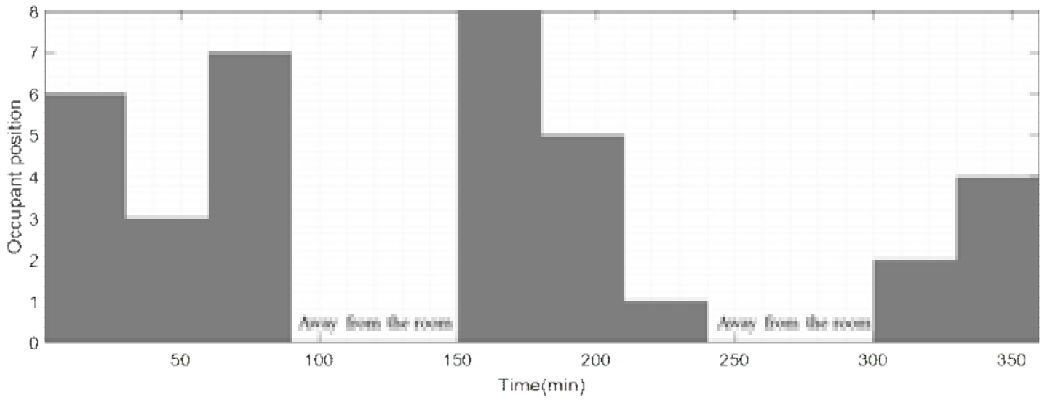

Figure. 6. Map of the location of occupant over time

A simulation analysis of three control strategies is carried out in this paper. These are, respectively, a thermal comfort control strategy for user target-tracking (TC@u), a thermal comfort control strategy based on a sensor fixed to a doorway (TC@d), a thermal comfort control strategy based on a sensor fixed near a heater (TC@h). Figure 7 shows the simulation results for the TC@u strategy. The position of the occupant

during each half hour and the temperature at that position before the occupant moves can be clearly obtained from the figure. The temperature at the occupant's location prior to movement is around 25 ℃. This shows that regardless of the temperature when the occupant enters this location, the TC@u strategy adjusts the temperature at the occupant's location to the set range, thus keeping the occupants thermally comfortable at all times.

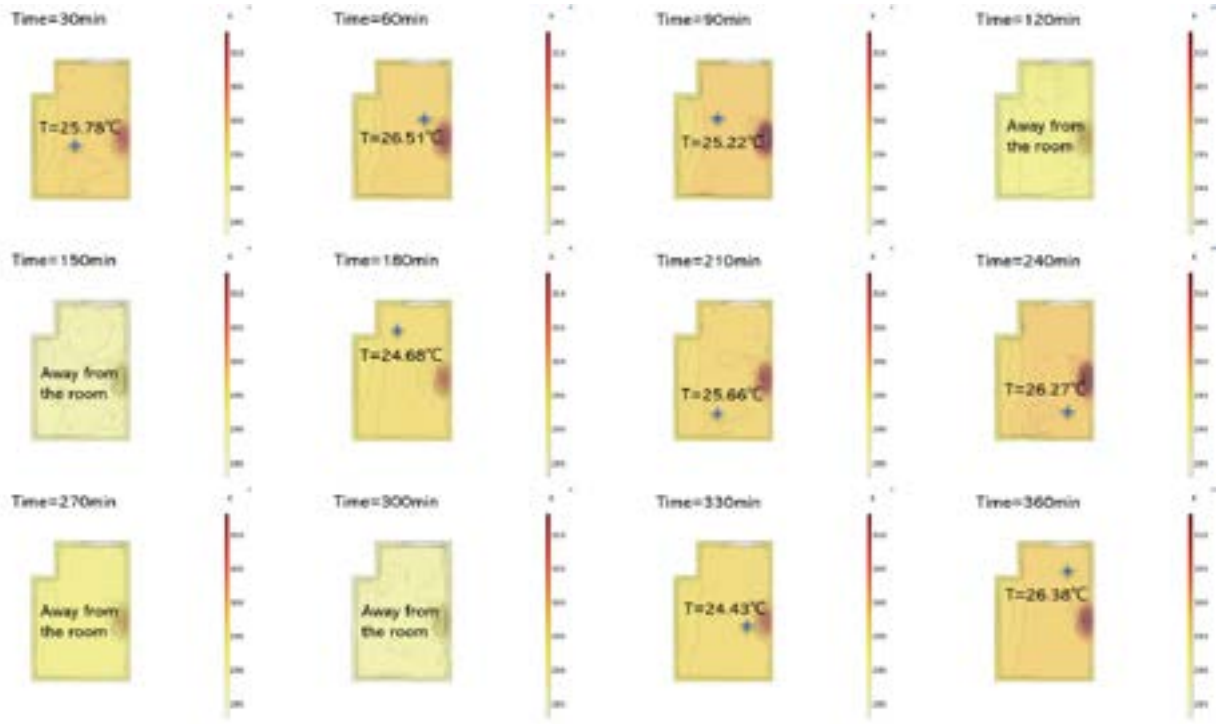

Figure. 7. The position of the occupant during each half hour and the temperature at that position before the position movement under TC@u strategy

Figure 8 shows the simulation results for the TC@h strategy. Prior to the move, the temperature at the occupant's location often exceeded 25 ℃, and even 30 ℃ in some locations. This shows that strategy TC@h does not guarantee the thermal comfortability of the occupants. Occupants tend to feel overheated.

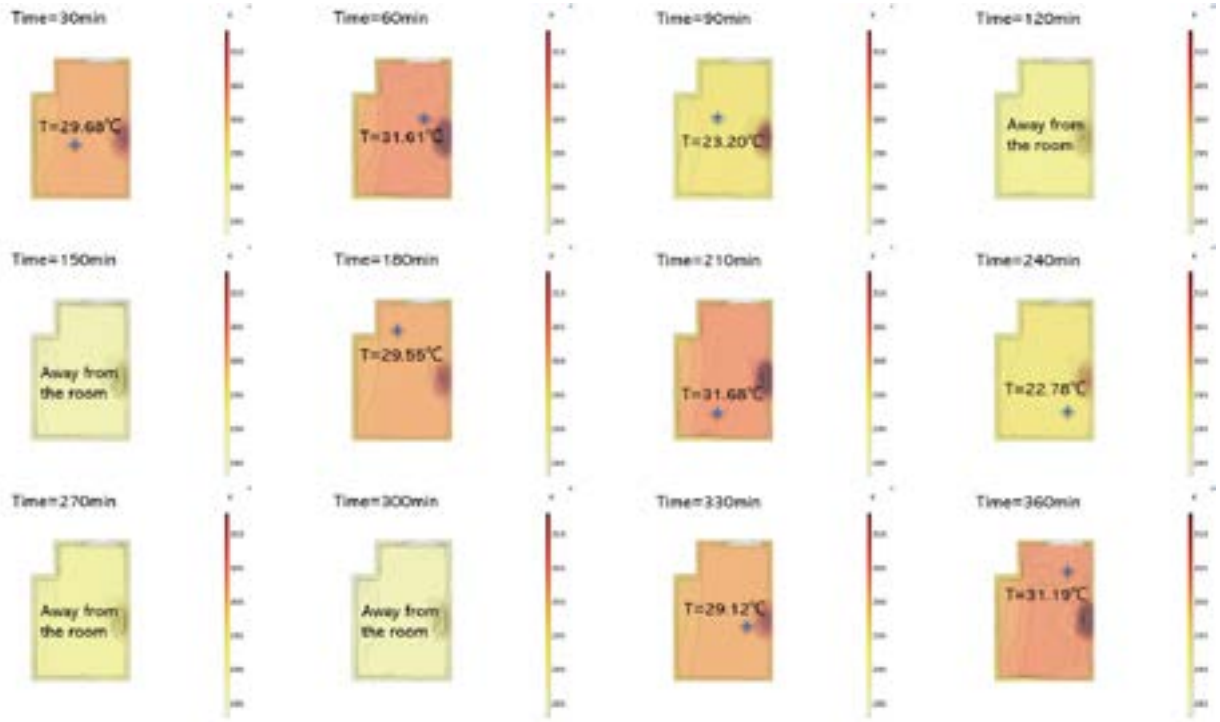

Figure. 8. The position of the occupant during each half hour and the temperature at that position before the position movement under TC@h strategy

The simulation result for the TC@d strategy is shown in Figure 9. Compared to TC@h strategy, the occupant's perception of the high temperature is much reduced in TC@d strategy. However, at 60min, 90min,

240min and 360min, the temperature around the occupant has reached 27 ℃, which has affected the occupant's thermal comfortability. Therefore, based on the simulation results in Figures 7, 8 and 9, TC@u strategy performs best in terms of occupant thermal comfortability.

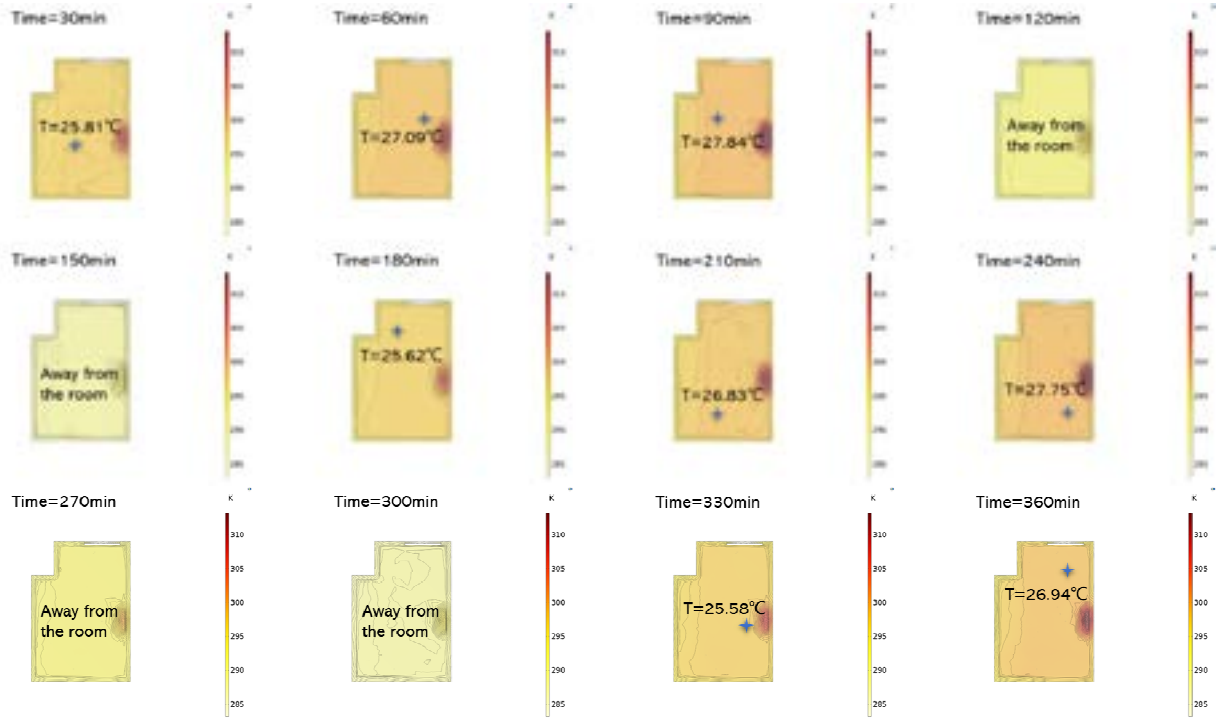

Figure. 9. The position of the occupant during each half hour and the temperature at that position before the position movement under TC@d strategy

Figure 10 shows the temperature variation for the three control strategies at the occupant's actual time location. Strategies TC@h and TC@d cause the occupant to be in the hot zone periodically, and the occupant tends to feel overheated. Strategy TC@u performs reasonably well, with the temperature at the occupant's activity trajectory remaining between 21-25 ℃ for most of the time. However, Strategy TC@u will occasionally experience high-temperature overshoot, as heat is a process quantity that will expand into the surrounding space over time. In subsequent studies, the control strategy needs to be tailored to address this high-temperature overshoot phenomenon.

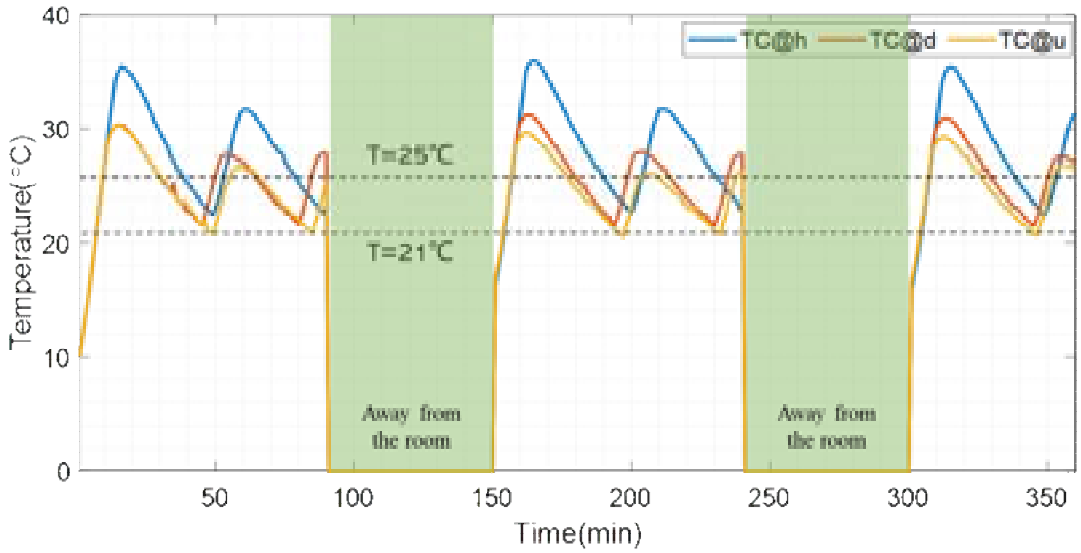

Figure. 10. Temperature at occupant activity trajectories with different temperature control strategies

In addition to comfortability, another indicator that occupants care about is the operating economy. The thermal energy consumption under the three temperature control strategies is shown in Figure 11. After six hours of operation, the energy consumptions under strategies TC@h, TC@d, and TC@u are 2.9887kWh, 2.5300kWh, and 2.2917kWh, respectively. Compared to strategies TC@h and TC@d, the economy of strategy TC@u is improved by 23.32% and 9.42%, respectively. Therefore, TC@u strategy ensures

occupants' thermal comfortability while reducing energy consumption. It is a promising strategy for energy-efficient temperature control.

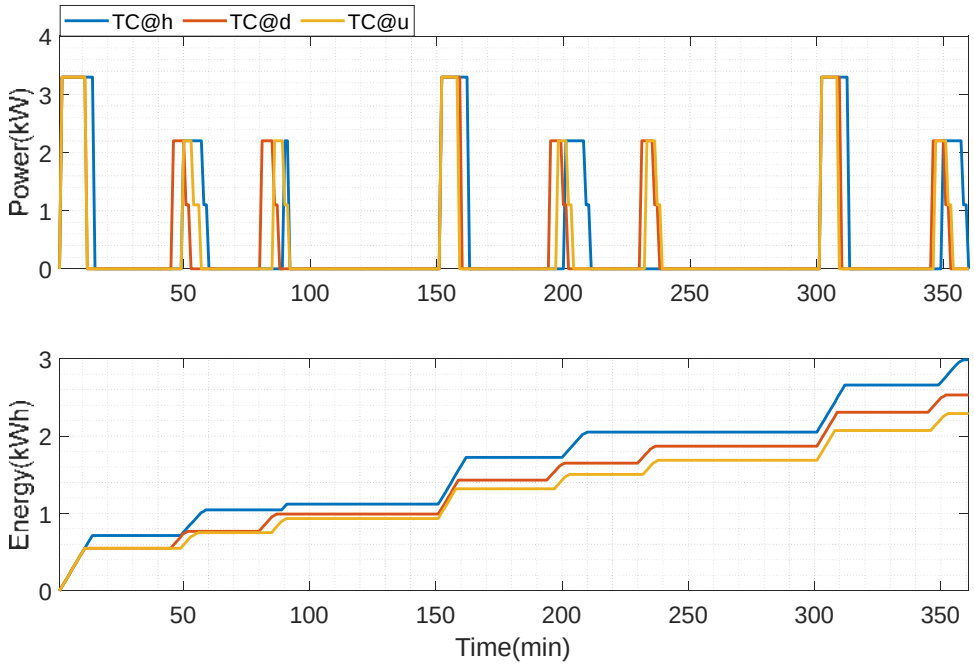

Figure. 11. Thermal energy consumption under different temperature control strategies

6. Conclusion

This paper built a room CFD thermal dynamic model based on the actual kitchen and an electric heater and then proposed a target-tracking thermal comfort control system based on this model. The strategy is developed and simulated through joint simulations on the COMSOL and SIMULINK platforms. The simulation results show that the strategy meets the thermal comfortability of the occupants while considering the economy.

Firstly, a 3D room model based on the INVENTOR platform was built based on the laboratory kitchen. The synchronization of this 3D room model on the INVENTOR and COMSOL platforms was implemented based on LiveLink for the Inventor interface.

Secondly, a room CFD model was created based on the COMSOL platform. The heat dissipation power of the electric heater is the input variable and the temperature distribution in the room space is the state variable. By setting the heat dissipation power of the heater to the model, the temperature distribution in the room space will be updated at each simulation time step.

Finally, a target-tracking thermal comfort control system is proposed and simulated by joint simulations with COMSOL and SIMULINK. The control system aims to achieve energy efficiency while maintaining thermal comfort. It mainly includes three parts: room CFD thermal dynamic model, occupant location recognition and control strategy. The simulation results show that this strategy both meets user comfort and operational economy compared with conventional control strategies.

Acknowledgments

The authors would like to thank the University of Warwick studentship combined with China Scholarship Council (202208060362) and the funding support from UK Engineering and Physical Science Research Council (EP/S032622/1).

Nomenclature

Symbols

$\mathrm{T(℃)}$	temperature.
$\mathrm{S(℃)}$	state variable, which is the temperature distribution in the room space.
$\mathrm{C(W)}$	control variable, which is the thermal dissipation power of the electric heater.
$\mathrm{f_{rtdm}}$	room thermal dynamic model.
f_{cs}	control strategy.
f_{olc}	occupant location recognition model.

$step$ simulation time step.

(x, y, z) occupant's spatial location.

Abbreviation

TC@u thermal comfort control strategy for user target-tracking.

TC@d thermal comfort control strategy based on a sensor fixed to a doorway.

TC@h thermal comfort control strategy based on a sensor fixed near a heater.

References

[1] GOV.UK. "UK enshrines new target in law to slash emissions by 78% by 2035." https://www.gov.uk/government/news/uk-enshrines-new-target-in-law-to-slash-emissions-by-78-by-2035 (accessed 13 June, 2022).

[2] GOV.UK. "UK's path to net zero set out in landmark strategy." https://www.gov.uk/government/news/uks-path-to-net-zero-set-out-in-landmark-strategy (accessed 9 July, 2022).

[3] P. Gudde, J. Oakes, P. Cochrane, N. Caldwell, and N. Bury, "The role of UK local government in delivering on net zero carbon commitments: You've declared a Climate Emergency, so what's the plan?," *Energy Policy,* vol. 154, p. 112245, 2021.

[4] I. Monasterolo and M. Raberto, "The impact of phasing out fossil fuel subsidies on the low-carbon transition," *Energy Policy,* vol. 124, pp. 355-370, 2019.

[5] R. Sikkema, S. Proskurina, M. Banja, and E. Vakkilainen, "How can solid biomass contribute to the EU's renewable energy targets in 2020, 2030 and what are the GHG drivers and safeguards in energy-and forestry sectors?," *Renewable Energy,* vol. 165, pp. 758-772, 2021.

[6] W.-P. Schill and A. Zerrahn, "Flexible electricity use for heating in markets with renewable energy," *Appl. Energy,* vol. 266, p. 114571, 2020.

[7] S. Bellocchi, M. Manno, M. Noussan, M. G. Prina, and M. Vellini, "Electrification of transport and residential heating sectors in support of renewable penetration: Scenarios for the Italian energy system," *Energy,* vol. 196, p. 117062, 2020.

[8] A. Baniasadi, D. Habibi, O. Bass, and M. A. Masoum, "Optimal real-time residential thermal energy management for peak-load shifting with experimental verification," *IEEE Trans. Smart Grid,* vol. 10, no. 5, pp. 5587-5599, 2018.

[9] K. Arendt, M. Jradi, H. R. Shaker, and C. Veje, "Comparative analysis of white-, gray-and black-box models for thermal simulation of indoor environment: Teaching building case study," in *Proceedings of the 2018 Building Performance Modeling Conference and SimBuild co-organized by ASHRAE and IBPSA-USA, Chicago, IL, USA*, 2018, pp. 26-28.

[10] M. Jradi, F. C. Sangogboye, C. G. Mattera, M. B. Kjærgaard, C. Veje, and B. N. Jørgensen, "A world class energy efficient university building by danish 2020 standards," *Energy Procedia,* vol. 132, pp. 21-26, 2017.

[11] M. Jradi, C. Veje, and B. N. Jørgensen, "A dynamic energy performance-driven approach for assessment of buildings energy Renovation—Danish case studies," *Energy Build.,* vol. 158, pp. 62-76, 2018.

[12] M. Macas *et al.*, "The role of data sample size and dimensionality in neural network based forecasting of building heating related variables," *Energy Build.,* vol. 111, pp. 299-310, 2016.

[13] N. Attoue, I. Shahrour, and R. Younes, "Smart building: Use of the artificial neural network approach for indoor temperature forecasting," *Energies,* vol. 11, no. 2, p. 395, 2018.

[14] P. Bacher and H. Madsen, "Identifying suitable models for the heat dynamics of buildings," *Energy Build.,* vol. 43, no. 7, pp. 1511-1522, 2011.

[15] M. Hu, F. Xiao, and L. Wang, "Investigation of demand response potentials of residential air conditioners in smart grids using grey-box room thermal model," *Appl. Energy,* vol. 207, pp. 324-335, 2017.

[16] M. Maaspuro, "Space heating and ventilation 3D-simulation for an office room," in *COMSOL Conference*, 2020.

Proceedings of ECOS 2023 - The 36th International Conference On
Efficiency, **C**ost, **O**ptimization, **S**imulation and Environmental Impact of Energy Systems
25-30 June, 2023, LAS PALMAS DE GRAN CANARIA, SPAIN

Looking beyond appliances: A study of the socio-economic determinants of electricity consumption in India

Afsal Najeeb[a], Anand B Rao[a], Satish B Agnihotri [a], Vinod Mishra[b] and Srinivas Sridharan[b]

[a] Indian Institute of Technology Bombay, Mumbai, India, afsal.najeeb @monash.edu, CA
[b] Indian Institute of Technology Bombay, Mumbai, India, a.b.rao@iitb.ac.in
[c]Indian Institute of Technology Bombay, Mumbai, India, sbagnihotri@gmail.com
[d]Monash University, Melbourne, Australia, vinod.mishra@monash.edu
[e]Monash University, Melbourne, Australia, Srinivas.sridharan@monash.edu

Abstract:
Techno economic worldview of electricity demand considers and studies appliance ownership and usage as the primary determinants of electricity demand. In emerging economies like India, electricity demand from the residential sector is influenced by a host of other parameters like ability to pay, availability of quality electricity, climate, cultural practices, and specificities of building envelope. The study tries to understand the socio-economic determinants of residential electricity consumption in India considering the state of Uttar Pradesh as a case study. Panel dataset for a five-year period covering 25,690 households have been used for the study. The results indicate that seasonality, availability of reliable electricity, caste, rural or urban nature of the region and gender of the household head were important determinants of electricity demand. A fixed effects model was used for the estimation and was able to explain 80% of the variation in the dataset. The results are significant in two ways. First, they indicate that electricity consumption has to be studied considering its socio-economic context and not from a techno economic standpoint. Secondly, the results indicate that there would be considerable merit in including socio economic variables in the modelling and forecasting of electricity demand, as opposed to the present methods that extensively rely on time series modelling of actual demand.

Keywords:
Residential electricity; Electricity modelling; Econometric modelling; Fixed effects; Energy policy

1. Introduction

Electricity is a critical enabler of quality living conditions. Rapid electrification across developing countries across the last four decades has seen the share of residential electricity consumption in developing countries increase to about 30% of the total electricity consumption [1]. Residential Electricity Consumption (REC) is an aggregated output of individual choices by a large number of actors. It is affected by demand side factors like changes in population, household size, demography, disposable incomes, consumer preferences, energy efficiency measures, technological progress, consumer time use patterns, emergence of new end uses etc. Supply side factors like quality, reliability and affordability of supply could also influence the net electricity consumption of a household. Technological progress and diffusion of new technologies are also an important factor that contributes to the dynamic nature of electricity demand. While lighting with incandescent lamps have been replaced almost entirely with more efficient Light Emitting Diode (LED) lamps, new uses like induction cooking and electric vehicle charging are coming up. As consumers become prosumers, reduced dependence on grid-based electricity could lead to new consumption behaviors. The rapid growth, diversity and dynamism necessitate appropriate methods to study the same.

As of 2021, residential electricity consumption accounts for about a quarter of India's total electricity consumption. The sector has registered significant growth since the 1980s when electricity access to households became a policy concern. The average residential electricity consumption has increased from 18

units (kWh) in 1950 to 1028 units (kWh) in 2020 [2]. It has also been one of the fastest growing sector in the last two decades as shown in Figure 1.2 [3]. The increase in residential electricity consumption in the last five years are most notable. The rise has been attributed to specific factors like increase in the number of households with electricity access, increase in household incomes and increased appliance penetration among others [4]. In 2001, only 55 % percent of the households in India were electrified. By 2021, 99.93% of the households were been electrified [5]. While the increase in consumption has not been uniform across geographies and consumer segments, residential electricity consumption is evolving as a significant dynamic component of the electricity mix. Estimates by International Energy Agency (IEA) indicate that increased appliance ownership and demand for space cooling could increase the residential electricity demand threefold by 2040, from 2021 levels [1].

The fast growing residential electricity sector is also diverse and dynamic. Residential electricity consumption varies widely across states, regions within states and across socio economic groups. In 2018, an average household in Delhi consumed around 270 units (kWh) of electricity per month while the value was much lower for cities like Mumbai (110 units) and Ahmadabad (160 units) [6]. A similar diversity can be observed among states as shown in Figure 1.3. Annual per capita electricity consumption varies from about 700 units in Delhi to less than 100 units in Assam [2]. Such differences across geographies could be due to climatic factors, demographic determinants, socio economic conditions, specific policies etc. [7]. Top-down estimation of electricity demand considering macro trends tend to overlook such differences.

Thus, in a comparative sense, the other sectors of electricity consumption viz. a viz. commercial, industrial, agricultural and traction are better understood due to higher levels of concentration, regulation and documentation. These sectors might have dedicated expertise in managing consumption, the direction of residential electricity is influenced by a very large number of individual strategies (or lack thereof) of consumers who try to maximize diverse personal gains. Policies and plans to manage the residential sector need robust inputs on the future direction the sector. It is also necessary to understand the pathways of increased electricity consumption; to know the sections of the society and economy that have been benefited by the same and those that have been left out. Modelling can be defined as the method of quantifying output parameter as a function of a given set of input parameters [8]. Models of residential electricity consumption are used to determine future supply requirements, effect of a policy, technology or appliance use on overall consumption, evaluate the effects of competing policy scenarios etc. Accurate information about the characteristics of residential electricity use is necessary to plan supply, expansion and efficient use of electricity. Modelling of residential electricity demand is also significant for demand management policies.

1.1 Motivation

The dominating approach to modelling REC has been through the lens of economic elasticities and appliance ownership. Price and income elasticities of populations and regions have been the dominating nature of discourse undertaken to understand REC. In other cases, REC has been viewed as a techno economic question and modelling efforts have focused exclusively on appliance ownership. Both approaches view electricity consumption in isolation, while this study argues that there would be merit in considering the other drivers of REC. Electricity consumption, though realized through the end uses of electricity by appliances, is also affected by other social, economic, climate related and building envelope related factors. They could even be over riding and explain the nature of REC. Income, Gross Domestic Product (GDP), appliance ownership and past patterns of consumption are the most commonly studied determinant factors of REC [9]–[12]. This study is motivated by the question “What other social, economic and other factors could possibly affect residential electricity consumption?”

Past studies have discussed this question in detail, even with contradicting conclusions. Studies like Pachauri (2004), Tuwaitha (2014) and Perera et al. 2021 present consensus that income is perhaps the most important determinant of household electricity consumption. But analysis by CEA (2019) points out that the elasticity might be decreasing [13]. Thus, answering the question “how much does a household consume and why” requires broad based understanding and careful analysis. There has been many studies about the determinants of residential electricity demand in developing countries. [12] presents a review of forty-two studies and discussed the socio economic, dwelling and appliance ownership related factors affecting residential electricity demand in North America and Europe. The study identified a total of sixty-two factors that could potentially affect electricity consumption in households.

1.2 Objective

From the discussion, it is clear that socio economic factors are an important attribute affecting the residential electricity consumption. This paper attempts to understand the nature of this structural determinants of electricity consumption. The objective of the study is to understand the significance of the socio economic, demographic, building environment related, appliance ownership related and climate related determinants of residential electricity consumption, considering the case of India. The question has been approached by constructing a fixed effects model of REC using household level survey data from the state of Uttar Pradesh in India.

2. Literature Review

The review of literature focussed on identifying the studies that have modelled the residential electricity consumption (REC) in India. Studies were identified using a systematic search on three databases viz. a viz. Google Scholar and Web of Science. The most significant studies that are closely aligned with the scope of the present study are discussed in this section.

A study conducted by Laurence Berkely National Laboratory (LBNL) at Berkley University tries to model India's future using a bottom-up modelling approach. The study focuses on modelling the potential for emission reductions in various sectors of the Indian economy including the residential sector. The study considers rural and urban areas separately. Within each, end uses like cooking, water heating, air conditioning, lighting and residual were considered. Further, use of different appliances for the same end use was also captured. While the methodology presents better granularity, it considers the energy use and not specifically electricity use [14].

A large number of forecasting studies are aimed at projecting a future level of consumption. Attention has not been provided to choose of factors that are to be considered in the modelling process (the independent variables) and their weightages. The study aims to fill this gap by understanding the relative importance of factors that determine the household electricity use. A recent study by Basumatary (2021). tried to determine the determinants of household electricity consumption with specific focus on the effects of financial incentives from the government on consumption [15]. The study considers 322 samples from four districts of Assam and concluded that socio economic variables of a household does not necessarily affect electricity consumption. The study suffers from the limitation of limited sample size restricted to a small geography and is focused specifically in the effect of government incentives, but uses novel variables like wattage of connected appliances, number of living rooms, material for construction etc. making the model more realistic [15].

A recent paper by Cazenave and Pachauri (2021) follows a simulation based approach to model household electricity demand using income, stock of appliances and future purchases of appliances. Micro data and representative national survey data is used to model the household electricity demand for four countries of the global south: Ghana, Guatemala, India and South Africa. The study finds that appliance penetration possibilities vary for all the countries spending on country, appliance type, climate and income but with high and stable demand of electricity for entertainment in all the four countries considered [9]. Tewathia (2014) tries to determine the factors that affect electricity consumption of households in Delhi using variables like location, household income, stock of appliances, family size, household size, household awareness and time spent outside. Seasonal variations are accounted for by creating three distinct dependent variables for each season. The study found out household income, temperature and appliance ownership to be significant factors influencing the electricity consumption [16].

Cialani and Mortazavi (2018) tries to estimate price and income elasticities and the effect of GDP and climate on household electricity consumption in Europe using data from the period 1995 – 2015 [17]. Dynamic partial adjustment models, Generalized Method of Moments and Maximum Likelihood approaches are used for the analysis. The study concludes that price elasticities in the short run are small while income elasticities are relatively large [17]. [18] estimates the determinants of electricity consumption in Jordan using data from 1986 to 2015. The study uses six variables viz a viz GDP, electricity prices, population, urbanization, structure of the economy and aggregate water consumption [18]. A study by Singh et al., (2018) uses survey data from 1140 households to characterize the effect of climate and ownership of appliances on household electricity demand. It considers factors like electricity price, dwelling area, number of inhabitants and ownership of ACs, refrigerators and geysers but does not include socio economic variables like income [19].

Pachauri and Muller (2008) try to understand the relative importance of changes in household size, population, increase in connectivity and consumption per connection in rural and urban regions of India from 1980-2005. The study presents a macro level analysis with the lowest geographic scale being the state [20]. Narayan et al., 2007 uses annual time series data of G7 countries from 1978 to 2003 to estimate long run and short run

price and income elasticities of household electricity demand. The study specifically focuses on these two aspects to understand if the elasticities present an opportunity to introduce emission linked taxation [21]. Filipini and Pachauri (2004) uses three seasonal linear econometric models to understand the effect of variables like electricity price in rupees, kerosene price in rupees, LPG price, household income, area of the dwelling, size of the household and average age of the household. This was a pioneering study that moved away from using national level macro indicators and used unit level from 35,000 households from round 50 for the year 1993-94 from the National Sample Survey conducted by Government of India. The results indicated that electricity demand with respect to income was fairly inelastic in all the three seasons but household size and average age of inhabitants influence electricity consumption significantly [22].

Pachauri (2004) estimated the energy requirements of a household considering a large set of explanatory variables and using a double log functional model. It considered region of the country, nature of dwelling, rural / urban, food habits of the inhabitants, literacy levels, monthly expenditure, area of the dwelling, household size, age of the household head and nature of employment to determine energy needs. Though the study estimated energy needs including food and travel, it used household level data making it a bottom up study [23]. NSSO household level panel data was used to conclude that total income or expenditure level of an individual household was the most significant determinant of energy demand. The study also comments on the effect of dwelling size and the age of household [23]. Reddy(2004) tries to understand the economic and social dimensions of electricity use. [24] uses survey data from 1983-2000 to understand the differences in electricity use based on employment, income and locality for rural and urban households. The paper presents only a descriptive analysis to bring out the disparity in electricity consumption between categories of employment [24].

From the analysis of literature, it becomes clear that there can be more contributions to the area of modelling residential electricity consumption in India with respect to the approach and data used. Studies that try to determine the determinants of residential electricity consumption are seen to have limited use of determinant variables. Most studies focus on income and price elasticities of electricity demand. Other explanatory variables used include climatic conditions, rural or urban nature etc. There are no studies where all or a large number of these variables have been comprehensively covered.

3. Data and Methods

3.1. Dataset and variables

The present study used panel data from the Consumer Pyramids Household Survey (CPHS) conducted by the Centre for Monitoring Indian Economy (CMIE) [25], [26]. The survey data for the state of Uttar Pradesh with 25,690 sample households included has been used. Longitudinal data from 2014 to 2021 has been used for the analysis. The dataset contains socio economic, demographic, electrical appliance ownership and asset ownership information about the households, available for each month. The data was modified to two variables viz. a viz. season and cooling degree days (CDD). The season variables denote the prevailing season and calculated CDD of the area corresponding to the month of the data collection. The urban and rural datasets have been separated for analysis. The monthly expenditure of the household on electricity has been considered as the dependant variable as it is a reasonable proxy for electricity consumption. The data on monthly electricity consumption was not available. The dependant variables fall into five categories; socio economic attributes of the household, household demography, electrical appliance ownership, building envelope and climate.

3.2. Method

The study used fixed effects model to estimate the determinants of residential electricity consumption. Literature reviews revealed an almost standardised use of the log-log functional form of model specification, especially in cases where expenditure variables were involved [16], [20], [27]. A general empirical specification of residential electricity consumption can be written as shown in Equation (1)

$$E = F(SE, DF, EL, CL, BE) \quad (1)$$

Where E is the monthly residential electricity consumption, SE denotes the set of socio-economic variables, DF denotes the demographic variables, EL denotes the electricity consumption and appliance ownership related factors, CL denotes the climatic factors and BE refers to the set of building envelope related factors.

The functional form chosen for the study follows a log linear form as suggested by many past studies [9], [16], [19], [20]. The respective variables are explained in Table 1. The function for electricity consumption of households can be represented as shown in Equation (2)

$$Log\ (EM) = \beta_0 + \beta_1 log\ (ME) + \beta_2\ CC + \beta_3\ LT + \beta_4\ RU + \beta_5\ AH + \beta_6\ SH + \beta_7\ PH + \beta_8\ TV + \beta_9\ RF + \beta_{10}\ CO + \beta_{11}\ AC + \beta_{12}\ SN + \beta_0 CD + \beta_{14}\ TW + \beta_{15}\ TR \quad (2)$$

Where ME is the monthly expenditure of the household across all categories, CC refers to the caste category of the household, LT refers to the status of literacy of the household head, RU refers to the rural or urban location of the household, AH refers to the age of the household head in years, SH refers to the size of the household (number of people regularly resident in the house), PH refers to the hours of power availability, TV refers to the number of television sets owned by the household, RF refers to the number of refrigerators owned by the household, CO refers to the number of air coolers, AC refers to the number of air conditioners, SN refers to the season corresponding to the particular data point, CDD refers to the cooling degree days (used as a measure of air conditioning demand) and TW and TR refers to the type of roof material and type of wall material of the household respectively.

Table 1: Description of explanatory variables

Dimension	Variable	Description
Socio Economic (SE)	Log (Me)	Log (Monthly expenditure of the household)
	CC	Caste Category
	LT	Literacy (Yes / No)
	RU	Region type (Urban / Rural)
Demographic Variables (DF)	AH	Age of household head
	SH	Size of the household
Electricity Consumption and Appliance Ownership (EL)	PH	Power availability (Hrs / day)
	TV	No. of Televisions
	RF	Number of refrigerators
	CO	Number of air coolers
	AC	Number of air conditioners
Climatic Factors (CL)	SN	Season
	CDD	Cooling Degree Days (CDD)
Building Envelope (BE)	TW	Type of roof
	TR	Type of wall

A fixed effects panel data model was used to estimate the coefficients. The fixed effects model takes into account the fact that individual units are repeatedly surveyed at a fixed frequency over a period of time and hence retail some intrinsic characteristics.

4. Results and Discussion

To determine the determinants of REC, a fixed effects panel data regression model was employed. The determinants of rural and urban areas were also analysed separately using the same method. The descriptive statistics of the determinant variables used for the study are provided in Table 2. The correlation between the determinant variables was ensured to be less than 0.7 to avoid auto correlation. The results of the fixed effect regression model are described in Table 3. The results indicate that the non appliance ownership parameters have a significant influence on REC. The results establish socio economic, climatic, building envelope related and demographic determinants of residential electricity consumption. We find that the socio-economic variables explain about 70% of the variation in REC. The results are significant as they expand the horizon of research on determinants of REC beyond the conventional factors like elasticity and appliance ownership.

4.1 Socio Economic Factors

The monthly expenditure of the household has a significant influence on the consumption of electricity. The elasticity is positive at 0.505 indicating that one unit increase in the expenditure level of the household would lead to about 0.50 units increase in their expenditure on electricity. Different studies like Pachauri (2004), Singh et al. (2018) and Tiwari (2008) have shown positive impact of expenditure on electricity consumption but with lower elasticities [19], [22], [28]. A number of studies have used income as an explanatory factor and calculated the income elasticity of REC. For the present study, the use of income data was limited by the quality of income data. Expenditure of the household is indicative of the income level of the household as well as its purchase choices. Thus, it is an important determinant of REC.

Caste has been identified as a social grouping that affects the access to quality services in India. The results indicate that the caste category of the household is a significant determinant of its access or use of electricity. The variable caste category used in the study classifies the households to five categories viz. a viz. Upper caste, Other Backward Castes, Scheduled Castes and Scheduled Tribes in addition to a fifth category of households that did not specify the caste or category to which they belong. The Upper Castes refer to a social group which have historically been owners of land and were endowed with political capital. The Other Backward Classes (OBCs) is a group of different castes and some minority religions which have historically been considered the middle classes. The scheduled castes, about 16% of the national population is a term used to collectively denotes groups belonging to the lowest rung of the caste hierarchy. The scheduled tribes constitute the tribal or indigenous communities. Caste represents historical and current disadvantages and can be considered a metric of inequality. While the upper castes include the traditional land owning and prosperous groups, the prosperity can be considered to decrease across the board from Upper Castes to Scheduled Tribes. Past studies like Bhattacharya & Saxena (2017) had studied the effect of caste, tribe and religion on energy access and found that such social structures remain significant despite years of affirmative action and the households belonging to scheduled tribe and scheduled caste communities had significantly poorer access to electricity and LPG for cooking. The results are in line with the findings as scheduled tribe households can be seen to have lower electricity consumption even after controlling for other exogenous factors. Households with a literate head of the household has been shown to have higher electricity consumption than others by many past studies. The results of the present study support this claim.

Table 2: Summary statistics of variables

Variable	N	Min	1st Quintile	Median	Mean	3rd Quintile	Max
Monthly Expense on Electricity	13,85,278	95	300	400	451	560	1,392
Total Monthly Expenditure	13,85,278	376	7,115	8,865	9,421	11,065	10,15,514
Age of household head	13,85,278	7	41	48	49	57	108
Power Availability (Hrs/Day)	13,85,278	1	16	19	19	22	24
No. of Televisions	13,85,278	0	1	1	1	1	3
Number of refrigerators	13,85,278	0	-	1	1	1	3
Number of air coolers	13,85,278	0	-	1	1	1	5
Number of air conditioners	13,85,278	0	-	-	0	-	3

4.2 Demographic Factors

The age of the household head can be seen to have a positive and significant but very small effect on residential electricity consumption. Similarly, size of the household has also been determined to be a significant variable. Smaller households can be seen to have positive impact on REC while households with higher number of members are seen to have a negative coefficient, which is counter intuitive and against the results of some past studies. The negative effect of higher household sizes on electricity consumption could be due to the socio-economic nature of the study area. In rural and urban areas, joint families with higher number of

household members could belong to the economically weaker sections and reside in small households or in slums. This could be a possible reason for the negative coefficients.

The results from the present study indicate that households in the urban areas have a higher electricity consumption than rural areas. Singh et al. (2018) has used household level survey data from about thousand households in different climatic zones of India to understand the different factors influencing residential electricity consumption. The study found a negative price elasticity of demand and weak influence of demographic factors. The study also showed that urban households belonged to a class of its own and had higher electricity consumption than rural households. Similar results were obtained by Basumatary (2021) and Pachauri (2021) [9], [15]. Thus, it can be concluded that households in the urban region have higher REC. The difference could be due to longer hours of electricity usage, larger number and diversity of appliances, better power quality, higher incomes or structural differences in lifestyle choices.

Table 3: Results of fixed effect regression

	Dependent variable:
	Log (Expense on electricity)
TOTAL_EXPENDITURE	0.505***
	(0.007)
CASTE_CATEGORY - Not Stated	-0.041
	(0.098)
CASTE_CATEGORY - OBC	0.065***
	(0.015)
CASTE_CATEGORY - SC	0.065***
	(0.015)
CASTE_CATEGORY - ST	0.300***
	(0.067)
CASTE_CATEGORY - Upper Caste	0.071***
	(0.014)
LITERACY - Y	0.125***
	(0.007)
AGE_YRS	0.002***
	(0.0002)
Sizeofhh < = 2 members	0.021
	(0.021)
Sizeofhh > = 7 members	-0.049***
	(0.012)
Sizeofhh 3-6 members	-0.041***
	(0.008)
REGION_TYPE URBAN	0.236***
	(0.007)
POWER_AVAILABILITY_IN_HOURS_PER_DAY	0.020***
	(0.001)
TELEVISIONS_OWNED	-0.066***
	(0.010)
REFRIGERATORS_OWNED	0.061***
	(0.006)
COOLERS_OWNED	0.027***
	(0.005)
AIR_CONDITIONERS_OWNED	0.031***
	(0.009)
Walls Mud / Thatch	-0.080***
	(0.021)
Walls Other	0.273
	(0.814)
Walls Sheet	-0.260***
	(0.053)
Walls Stone	-0.226
	(0.196)
Walls Wood	-0.404***
	(0.109)
Roof Sheets	-0.094***
	(0.023)
Roof Thatch	-0.060***

	(0.020)
Roof Tiles / Stone	-0.013
	(0.010)
cdd	-0.0002***
	(0.0001)
Season Summer	0.018***
	(0.005)
Season Winter	-0.105***
	(0.017)
Constant	-71.549***
	(1.558)
Observations	25,610
R^2	0.680
Adjusted R^2	0.679
F Statistic	565.682*** (df = 96; 25513)
Note:	*p**p***p<0.01

4.3 Electricity Consumption and Appliance Ownership (EL) Related Factors

Power availability is an important supply side constraint that has been found to have significant effects on REC. As indicated in Table, the average power availability in the study area was only 19 hours. This could be due to scheduled load shedding or unscheduled power outages. Power outages limit the ability of the consumer to use the appliances and hence reduce the REC. It has also been found to reduce the propensity of consumers to but appliances as indicated by Agarwal et. al [29]. Households might also engage in “electricity / energy stacking” whereby they use secondary sources of electricity to achieve higher level of services that are not provided by the primary service. For instance, households may employ a Solar Home System (SHS) or avail electricity from a mini grid to use electricity for the time when the central grid is unavailable or unreliable. In the case of India, change of policy direction along with increased expansion of electricity infrastructure has resulted in significant improvement in power availability. The results indicate that as the supply side constraint of power availability eases, it would act as a catalyst for increased electricity usage.

Appliance ownership has been identified by many past studies as the most significant factor in the bottom up modelling of REC [8], [12], [18], [20]. The results from the present study indicate that refrigerators have the highest positive influence on REC with a coefficient of 0.06. This could be attributed to the fact that refrigerators are a high wattage equipment that is used throughout the day as opposed to other appliances like air conditioners or televisions that are used for specific number of hours. Studies like Huang (2020) and Chunekar (2018) have noted that electricity use by refrigerators often go unnoticed and could contribute most significantly to energy savings through efficiency improvement [7], [30]. Among other appliances, air conditioners and air coolers have been found to have significant positive influence on REC. However, the results from the fixed effects model indicate that the number of televisions owned by a household can have a significant but negative effect on REC, which is counter intuitive and against the findings of previous studies like Agarwal (2019) [29]a. This needs further enquiry.

4.4 Climatic Factors

The Cooling Degree Days (CDD) is a measure of how hot the temperature of a particular region has been compared to a reasonable standard comfortable temperature. They essentially capture the need for air conditioning and hence, is an important determinant factor for estimating REC. The present study shows that the CDD has a significant but negative influence on REC with a very low coefficient. This could be due to two reasons. One, the study area has very low penetration of high wattage air conditioning equipment like air conditioners. Thus, cooling demand might not be converted to the end use of air conditioning, utilising electricity. Secondly, the critical threshold value of comfortable temperature to be used for the calculation of CDD for the region had been chosen as 22^0C in line with a previous study [31]. This could be an under estimation for a region with an average temperature of 35.61 ^{0}C in 2021 [32].

Similar, seasonality has been found to be an important determinant of REC. The study area has a hot humid summer and harsh winters. The results indicate that the summer months have higher consumption of electricity while compared to the rainy monsoon months (used as reference). This could be attributed to the increased use of fans or other room conditioning appliances. The winter months are associated with a significant but highly negative coefficient indicating reduced electricity consumption demand. The increased REC during summer months has been reported by previous studies like Singh et. al. (2018) and Tewathia (2014).

4.5 Building Envelope

Analysing the results about building environment, we find that concrete walls (which has been used as the reference category) can be seen to have the highest significant and positive effect on REC. Walls made of wood, stone and sheet have significant but negative influence on electricity consumption with coefficients of (-0.404, -0.226 and -0.260). Houses with walls made of mud or thatch are also found to have lower electricity consumption. A similar trend can be seen in the case of roofing material. Concrete roofs have been found to have the highest positive influence on REC while roofs made of thatch and sheets have significant negative influence on REC.

4.6 Limitations and scope for future research

While the present study is novel in the use of large scale, current and representative data, there could be several significant improvements. The anomalies found in the present results like the negative effect of television ownership opens up more room for research. The study has conclusively shown the relevance and significance of non technological factors in influencing REC. While the effects of factors like caste have been quantitively been estimated, there is considerable scope in understanding the exact pathways through which socio economic and demographic variables affect REC. For instance, questions like “why does households belonging to the scheduled tribes have a lower electricity consumption than other households?” could be explored. Further research would reveal if it is a problem of affordability, lack of access to appliances, poor quality of power supply or other institutional factors. Similarly, the age composition of the households have been found to have significant effects on REC. Huang (2021), Chen (2017), Huang (2020) and Jones et. al. (2015) has reported decreased REC in households with presence of elders. Further research could probe the actual pathways through which these effects happen.

4. Conclusion

The present study has tried to understand the non technological factors that act as determinants of residential electricity demand. While the overarching focus in researched literature was on modelling price elasticity, income elasticity and time variability of demand, the present study tries to account for socio economic, demographic, climatic and building envelope related factors in addition to electricity availability and appliance ownership. The study used panel data from household surveys in the state of Uttar Pradesh, India. The results indicate that many of these factors are significant. Monthly expenditure level of the household and caste category affect REC. Literacy and age of the household head have also been found to have significant effects on REC. Summer season is associated with higher REC while the effect of Cooling Degree Days (CDD) on REC requires further study. Households which use concrete for roofs and walls have been found to have higher levels of REC compared to those that use tiles, sheets and thatch. The present study validates the need to look beyond the narrow frame of appliance ownership to understand the driving factors behind REC.

References

[1] IEA, “India Energy Outlook 2021,” 2021. doi: 10.1787/ec2fd78d-en.

[2] Central Electricity Authority, “Central Electricity Authority General Review 2021,” 2021. [Online]. Available: https://cea.nic.in/general-review-report/?lang=en.

[3] Central Electricity Authority, “Growth of electricity sector in India from 1947 - 2021,” 2021. [Online]. Available: https://cea.nic.in/wp-content/uploads/pdm/2021/12/Growth_Book_2021.pdf.

[4] M. Aklin, N. Chindarkar, J. Urpelainen, A. Jain, and K. Ganesan, “The hedonic treadmill: Electricity access in India has increased, but so have expectations,” *Energy Policy*, vol. 156, no. May, pp. 1–9, 2021, doi: 10.1016/j.enpol.2021.112391.

[5] Rural Electrification Corporation (REC), “Saubhagya Portal,” *Website*, 2021. https://saubhagya.gov.in/ (accessed Jan. 26, 2021).

[6] A. Chunekar, S. Varshney, and S. Dixit, “Residential Electricity Consumption in India :,” p. 60, 2015, [Online]. Available: https://www.prayaspune.org/peg/trends-in-india-s-residential-electricity-consumption.

[7] A. Chunekar and A. Sreenivas, “Towards an understanding of residential electricity consumption in India,” *Build. Res. Inf.*, vol. 47, no. 1, pp. 1–16, 2019, doi: 10.1080/09613218.2018.1489476.

[8] L. G. Swan and V. I. Ugursal, "Modeling of end-use energy consumption in the residential sector: A review of modeling techniques," *Renew. Sustain. Energy Rev.*, vol. 13, no. 8, pp. 1819–1835, 2009, doi: 10.1016/j.rser.2008.09.033.

[9] M. Poblete-Cazenave and S. Pachauri, "A model of energy poverty and access: Estimating household electricity demand and appliance ownership," *Energy Econ.*, vol. 98, p. 105266, 2021, doi: https://doi.org/10.1016/j.eneco.2021.105266.

[10] B. Gao, X. Liu, and Z. Zhu, "A bottom-up model for household load profile based on the consumption behavior of residents," *Energies*, vol. 11, no. 8, 2018, doi: 10.3390/en11082112.

[11] S. Hafner, A. Anger-Kraavi, I. Monasterolo, and A. Jones, "Emergence of New Economics Energy Transition Models: A Review," *Ecol. Econ.*, vol. 177, no. June, p. 106779, 2020, doi: 10.1016/j.ecolecon.2020.106779.

[12] R. V. Jones, A. Fuertes, and K. J. Lomas, "The socio-economic, dwelling and appliance related factors affecting electricity consumption in domestic buildings," *Renew. Sustain. Energy Rev.*, vol. 43, pp. 901–917, 2015, doi: 10.1016/j.rser.2014.11.084.

[13] Central Electricity Authority, "Long Term Electricity Demand Forecasting," 2019. [Online]. Available: http://cea.nic.in/reports/others/planning/pslf/Long_Term_Electricity_Demand_Forecasting_Report.pdf.

[14] S. de la Rue du Can *et al.*, "Modeling India's energy future using a bottom-up approach," *Appl. Energy*, vol. 238, no. December 2018, pp. 1108–1125, 2019, doi: 10.1016/j.apenergy.2019.01.065.

[15] S. Basumatary, M. Devi, and K. Basumatary, "Determinants of household electricity demand in rural India: A case study of the impacts of government subsidies and surcharges," *Int. J. Energy Econ. Policy*, vol. 11, no. 6, pp. 243–249, 2021, doi: 10.32479/ijeep.11716.

[16] N. Tewathia, "Determinants of the household electricity consumption: A case study of Delhi," *Int. J. Energy Econ. Policy*, vol. 4, no. 3, pp. 337–348, 2014.

[17] C. Cialani and R. Mortazavi, "Household and industrial electricity demand in Europe," *Energy Policy*, vol. 122, no. April, pp. 592–600, 2018, doi: 10.1016/j.enpol.2018.07.060.

[18] S. K. Al-Bajjali and A. Y. Shamayleh, "Estimating the determinants of electricity consumption in Jordan," *Energy*, vol. 147, pp. 1311–1320, 2018, doi: 10.1016/j.energy.2018.01.010.

[19] J. Singh, S. S. Mantha, and V. M. Phalle, "Characterizing domestic electricity consumption in the Indian urban household sector," *Energy Build.*, vol. 170, pp. 74–82, 2018, doi: 10.1016/j.enbuild.2018.04.002.

[20] S. Pachauri and A. Muller, "A Regional Decomposition of Domestic Electricity Consumption in India: 1980 - 2005," *Annu. IAEE Conf.*, vol. 2, no. 1, pp. 2005–2007, 2008.

[21] P. K. Narayan, R. Smyth, and A. Prasad, "Electricity consumption in G7 countries: A panel cointegration analysis of residential demand elasticities," *Energy Policy*, vol. 35, no. 9, pp. 4485–4494, 2007, doi: 10.1016/j.enpol.2007.03.018.

[22] M. Filippini and S. Pachauri, "Elasticities of electricity demand in urban Indian households," *Energy Policy*, vol. 32, no. 3, pp. 429–436, 2004, doi: 10.1016/S0301-4215(02)00314-2.

[23] S. Pachauri, "An analysis of cross-sectional variations in total household energy requirements in India using micro survey data," *Energy Policy*, vol. 32, no. 15, pp. 1723–1735, 2004, doi: 10.1016/S0301-4215(03)00162-9.

[24] B. S. Reddy, "Economic Ans Social Dimensions Of Household Energy Use: A Case Study Of India," in *IV Biennial International Workshop "Advances in Eenrgy Studies,"* 2004, pp. 469–477.

[25] CMIE, "Consumer Pyramids Household Survey," *Online*, 2021. https://consumerpyramidsdx.cmie.com/ (accessed Feb. 01, 2021).

[26] Centre for Monitoring Indian Economy, "CMIE Consumer Pyramids dx," 2021. https://consumerpyramidsdx.cmie.com/ (accessed Apr. 26, 2022).

[27] W. H. Huang, "Sources of inequality in household electricity consumption: evidence from Taiwan," *Energy Sources, Part B Econ. Plan. Policy*, vol. 00, no. 00, pp. 1–22, 2021, doi: 10.1080/15567249.2021.1966133.

[28] P. Tiwari, "Architectural, Demographic, and Economic Causes of Electricity Consumption in Bombay," *J. Policy Model.*, vol. 22, no. 1, pp. 81–98, 2000, doi: 10.1016/s0161-8938(98)00003-9.

[29] S. Agarwal, N. Bali, and J. Urpelainen, "Rural Electrification in India: Customer behaviour and demand," 2019.

[30] Y. H. Huang, "Examining impact factors of residential electricity consumption in Taiwan using index decomposition analysis based on end-use level data," *Energy*, vol. 213, p. 119067, 2020, doi: 10.1016/j.energy.2020.119067.

[31] J. Migdalska, “Cooling Degree Day Analysis As a Climate Impact Indicator for Different Locations of Poland and India 1 Shanmuga Priya,” *Int. J. Adv. Sci. Eng. Technol.*, no. 4, p. 43, 2015, [Online]. Available: http://www.iraj.in/journal/journal_file/journal_pdf/6-222-145431937543-51.pdf.

[32] “Weather Atlas - Uttar Pradesh, India,” *Website*, 2023. https://www.weather-atlas.com/en/india/agra-climate (accessed Mar. 25, 2023).

Heating and cooling load analysis of a climate neutral proof of concept chicken farm

Xander van Heule[a,b], Jera Van Nieuwenhuyse[a,b], Willem Faes[a,b], Gerlinde De Vogeleer[c], and Steven Lecompte[a,b]

[a] Department of Electromechanical, Systems and Metal Engineering, Ghent University, Ghent, Belgium, Sint-Pietersnieuwstraat 41
[b] Flanders Make, Leuven, Belgium, FlandersMake@UGent.be,
[c] Institute for Agricultural and Fisheries Research (ILVO), Merelbeke, Belgium, Burg. Van Gansberghelaan 115

Abstract:

In this work, a proof of concept design for a poultry meat farm is studied. The design aims to be climate-neutral and energy-flexible by applying different technologies such as PV panels, PVT panels, BEO field, and high and low-temperature heat pumps. In order to size these systems, the farm's required heating, cooling power and (de)humidification rate has to be estimated, which is the focus of the current paper. For this purpose, a model was created in the Python environment. Based on the building's current design, expected weather conditions throughout a model year, and the required conditions for the chickens' well-being, the heating and cooling loads are calculated. The analysis does not yet take into account which technology is used to supply the heat as the sizing will be done based on the results of this analysis. In addition to the 'standard' climate requirements, some pens will be used to study the behaviour of the chickens during alterations in the temperature and humidity of the pen. These tests are predefined and the HVAC installation should be able to handle these test conditions as well. The results of the model can be used as a guideline to size the different HVAC systems. However, as the model is based on assumptions and simplifications, a sensitivity analysis was performed as well. This analysis shows that the conductive losses are small compared to ventilation and infiltration losses. The air changes per hour of the farm have a great impact on the total required heating and cooling power. Therefore, attention should be given to the air-tightness of the chicken pens to reduce the required installation size.

Keywords:

Energy-use; Poultry farm; Energy neutral; model.

1. Introduction

The sustainable development goals, adopted by the United Nations, are a set of 17 interconnected goals aimed at addressing global challenges such as poverty, hunger, inequality, and climate change. The second goal, "Zero Hunger," recognizes the need for sustainable agriculture to provide adequate food for a growing population while reducing the negative environmental impact of current agricultural practices.

Sustainable agriculture aims to achieve food security and enhance livelihoods while conserving natural resources and minimizing negative effects on the environment. To achieve this, it is essential to adopt low-carbon technologies in agriculture to reduce greenhouse gas emissions, improve resource-use efficiency, and promote biodiversity. Poultry farming, which is a vital component of the agricultural sector, has a significant role to play in achieving sustainable food production.

The ever-increasing demand for poultry products [1] due to the relatively low climate impact compared to other meat variants has put pressure on farmers to increase production. However, this increase in production must be achieved using renewable methods that minimize environmental impact. In this context, several studies [2-6] have been conducted to explore low-carbon technologies that can be implemented in the poultry farming industry to reduce greenhouse gas emissions and promote sustainable practices. However, not all technologies can be applied in all regions or for all power requirements.

Therefore, this study seeks to contribute to the development of sustainable poultry farming by focusing on a methodology to predict the required heating and cooling demand of a new poultry farm design. This methodology is essential to ensure that the heating and cooling systems used on the farm are appropriately sized, leading to energy efficiency and a reduction in greenhouse gas emissions. The findings of this study

can help farmers and policymakers make informed decisions about the design and implementation of sustainable heating and cooling systems in poultry farming which are currently not often used within this sector, ultimately contributing to achieving the second sustainable development goal of the United Nations.

Information on the dimensions and requirements for the poultry farm were provided by ILVO, a Flemish research centre [7]. This farm will be used to conduct detailed research with respect to a plethora of factors, ranging from feed composition, feed management, and animal well-being to emissions, impact of climate control, and energy flexibility of the stable depending on electrical grid conditions.

2. Modelling methodology

2.1. Standard boundary conditions

A new poultry farm has been designed to house up to 14,000 chickens. The goal is to construct this new farm in an energy-flexible and climate-neutral manner as a proof-of-concept. To achieve this, the required heating, cooling, humidification, dehumidification, and ventilation rate has to be estimated based on the required optimum conditions for the chickens and the outside weather conditions. The design temperatures and humidities are presented in Table 1 based on the age of the chickens within the pen expressed in days. On the days not mentioned in Table 1, the values are obtained by interpolating between the two adjacent values.

Table 1. Climate set point and minimum ventilation rate within the stable depending on the age of the chickens.

Chicken age (days)	Average weight (g)	Temperature (°C)	Relative humidity (%)	Minimum ventilation rate (m³/kg/h)
0	45	34	55	1.5
3	90	34	55	1.4
7	180	31	60	1.3
14	470	27	70	1.1
21	920	25	70	0.9
28	1480	22	70	0.8
35	2110	22	75	0.7
42	2770	21	75	0.7

Another important input characteristic to the developed model (see section 2.4) is the heat and humidity produced by the chickens themselves. The following equations, in function of the average chicken weight, are used for this:

$$Q_{chicken} = 10.62 \cdot m_{chicken}^{0.75}, \quad (1)$$

$$m_{vapour,chicken} = -17.7 \cdot m_{chicken}^{2} + 200 \cdot m_{chicken} + 22, \quad (2)$$

where $Q_{chicken}$ is the heat produced per chicken in watt, $m_{chicken}$ is the average mass of a chicken (at a certain age) in kilogram and $m_{vapour,chicken}$ is the amount of grams of water vapour produced by a chicken in a day.

The ventilation rate which can or should be applied in the farm has prescribed minimum and maximum values. The minimum ventilation rate depends on the chickens' weight and is also represented in Table 1. The maximum ventilation rate is 4 m³/kg chicken/h. This norm is quite high compared to other animals due to the high heat production of poultry. A second limitation to take into account is that the ventilation rate should always be sufficient to keep the carbon dioxide concentration beneath 3000 ppm. As the prescribed minimum ventilation rate already is always higher than the ventilation rate posed by this limitation, the carbon dioxide concentration is not taken further into account. The actual applied ventilation depends on the applied climate control. The climate control considered in this work is based on temperature solely and is illustrated in the next graph. It should be noted that this strategy holds when the outside temperature is lower than the temperature inside the pens. The target temperature (TT) inside the pen is allowed to vary between a certain range (defined by T0 and T1) without applying external measures. When the temperature drops below T0, which is already at a minimum ventilation rate, the heating system is turned on. When the temperature increases beyond T1, the temperature is controlled by increasing the ventilation rate. At a certain point (at T2), the temperature cannot be reduced enough by solely increasing ventilation flow rate. When the temperature exceeds T3, active cooling is applied to lower the temperature inside the pens.

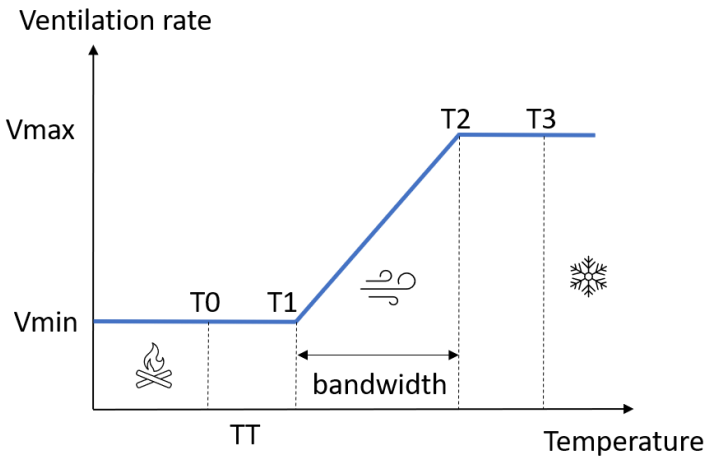

Figure 1.: Applied climate control in poultry farm.

2.2. Special boundary conditions for heat and cold stress tests

The temperatures and relative humidities from Table 1 represent the requirements for the chickens under 'standard' stable conditions. However, sometimes, extreme conditions have to be applied to the pens in order to create a 'stressful' environment for the chickens. This way, the researchers of ILVO can perform heat and cold stress tests and investigate the influence of these conditions on the chickens. The conditions for the heat stress tests are as follows (in function of the age of the chickens):

- Day 3-6: 24h at 40°C and RH 65%
- Day 7-25: 12h/day at 39.5°C and RH 65%
- From day 26: 8h/day at 36°C and RH 70%

The conditions for the cold stress tests are:

- Day 1-6: 24h at 24°C and RH 40-50%
- Day 7-13: 24h at 15°C and RH 40-50%
- Day 14: 24h at 13°C and RH 40-50%
- Day 15-26: 24h at 13°C and RH 50-55%

These conditions only have to be applied in 3 (adjacent) compartments of the 9 compartments, and have to be reached within 2 hours. Also, the return to standard conditions has to happen within 2 hours. 720 chickens are present in all 9 compartments. While 3 compartments are put under the stress test conditions, the other six compartments follow the standard conditions mentioned in section 2.1.

2.3. Layout of chicken farm

Table 2. Thermal resistances.

Type and location	Value [m²K/W]
Convection external side wall	0.02
Convection internal side wall	0.25
Convection floor	0.25
Convection ceiling	0.25
Conduction external wall between compartment and outside	7.77
Conduction internal wall between compartments	2.62
Conduction internal wall between compartment and air lock	2.52
Conduction internal wall between compartment and food compartment	2.52
Conduction internal wall between food compartments	2.43
Conduction external wall between food compartment and outside	1
Conduction ceiling	4
Conduction floor	4.17
Conduction roof	3.2

In addition to the required climate, the dimensions and layout of the modeled stable also have an important impact on the final results. The stable is divided into 9 compartments, which can each contain up to 1555 chickens. Three compartments make up one department, with each their own air conditioning unit. Next to these compartments, food compartments are located which separate the chicken compartments from the outer walls. Additionally, an attic is located above the chicken compartments. The design has predefined interior wall, exterior wall, floor, and ceiling construction materials and thicknesses which are used in the model to calculate conductive thermal resistances between two adjacent areas. The convective thermal resistances are calculated with constant convection coefficients, which are taken conservatively based on the default values of TRNSYS 16 TRNBuild [8]. The thermal resistances are listed in Table 2 and a sketch of the compartment layout is illustrated in Figure 2.

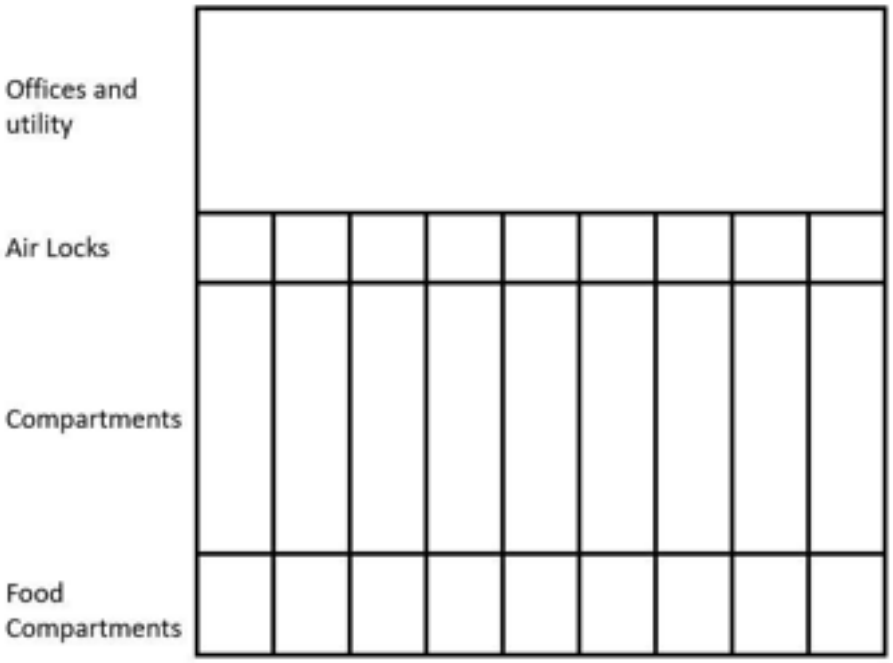

Figure 2. Sketch of the layout of the poultry farm consisting of nine air-locks, chicken compartments, and food compartments as well as a room for offices and utility.

2.4. Model strategy

For the modelling, which was done in Python 3.7 [9], the poultry farm was divided into 19 zones: 9 chicken compartments, 9 food compartments and the attic. For each zone, three balances were calculated: an energy balance, a mass balance (w.r.t. the air supply) and a moisture balance. In the zones containing chickens, the heat and vapour production by the chickens was taken into account, as well as the heat conduction to adjacent chicken zones, food compartment, attic, air-lock, ground and outdoors. In addition, direct solar gains due to six installed Solatubes [10] per chicken compartment, were also added. Lastly, the contribution of the heat and vapour transferred through ventilation and infiltration of air was included. For the food compartments, the conduction is similar to the chicken compartments. However, there are no internal (heat or vapour) gains, no ventilation and no Solatubes. When simulating the attic, only conduction to chicken compartments and the outdoor environment is taken into account.

For simplicity, the infiltration losses are taken into account by assuming a constant infiltration rate in the model. This is expressed by certain ‘air changes per hour (ACH)’. It is assumed the fresh air in the chicken compartments is coming from the food compartments. This same infiltration rate, in its turn, is coming through cracks and crevices from the outside environment. As a default, 1 ACH is taken, and the influence from this assumption is evaluated later on.

Two ventilation strategies are considered, which influence the energy balance. The first one dictates that the target temperature and humidity inside the chicken compartments are always maintained. In this strategy, the ventilation rate is put to the minimum value, and additional heating or cooling is applied to reach the target temperature. In the second strategy, the control depicted in Figure 1 is applied. Here, different temperatures than the target temperature are allowed (within a certain range) before heating or cooling is needed. This will have a significant impact on the required heating and cooling load. In the model, this problem is solved iteratively by searching for the temperature and ventilation rate combination where the required (sensible) load is minimal. As a default, the minimum ventilation strategy is applied. In section 3.4.2, the influence of applying the second strategy is discussed.

The heat losses to the air-lock are dependent on the temperature of the air-lock, which is unknown. Therefore, this temperature was assumed to be at the average temperature of the compartments and outdoors, with a minimum of 18°C. As the attic and food compartments do not have a target temperature, the temperature in these compartments is solved iteratively based on reaching an energy balance between the heat losses and the heat gains. In addition, a minimum temperature of 18°C is set in the food compartments.

3. Simulation results with fixed outdoor conditions

3.1. Steady-state cooling and heating loss calculations

In the calculations presented in this section, the outdoor temperature is fixed at certain values, varying from -10°C to 35°C. The outdoor relative humidity is fixed at 50%. The heating and cooling loads were calculated for different chicken occupations (both in age and number). 1555 chickens per compartment represents the maximum capacity of the farm, 720 chickens per compartment represents the standard occupation. Table 3 gives an overview of the sensible loads, expressed in kW, for the entire poultry farm. Positive values indicate heating, negative values indicate cooling. For standard occupation conditions, the maximum sensible heating load is thus 141 kW, the maximum cooling load is 157 kW.

Table 3. Heating and cooling loads (sensible) (in kW). RH (outside) = 50%.

		Number of chickens per compartment	
Outdoor temperature (°C)	Age (d)	720	1555
-10	0	107	113
	14	111	136
	28	120	168
	42	141	216
0	0	81	86
	14	75	88
	28	70	89
	42	74	101
10	0	55	58
	14	39	40
	28	19	16
	42	17	-30
20	0	30	31
	14	4	-8
	28	-31	-71
	42	-59	-128
30	0	7	7
	14	-29	-54
	28	-79	-149
	42	-124	-242
35	0	-5	-6
	14	-46	-77
	28	-104	-188
	42	-157	-299

The highest heating load corresponds to older chickens, however, this is strongly dependent on the outdoor conditions as well. In addition, the higher the number of chickens in a compartment, the higher the load. This finding is a result of the allowed ventilation rate and the chickens own heat production. The load for one department (so three compartments) is, by approximation, equal to 1/3rd of the total load. In reality, the demand of compartments located near the outdoor environment will be different to the ones more in the center, due to the heat losses to the environment.

3.2. Analysis of the energy balance

In this section, the results from section 3.1 are investigated in more detail by zooming in on the energy balance. In particular, identifying the dominant heat losses allows for reducing these by adjusting the farm design. The results presented in this section are based on the simulations for a stable with 720 chickens per compartment at an age of 42 days, as this age resulted in the highest cooling and heating loads according to section 3.1. The trends observed are however also applicable to the other occupation combinations. In Figure 3, the energy balance in winter (i.e. -10°C outside) for the entire stable is depicted, divided into energy input (left) and energy output (right). The input contains the heat production of the chickens, the heat gains because of the Solatubes and the required heating. The output contains the ventilation and infiltration losses (to the air-locks) and the conduction losses.

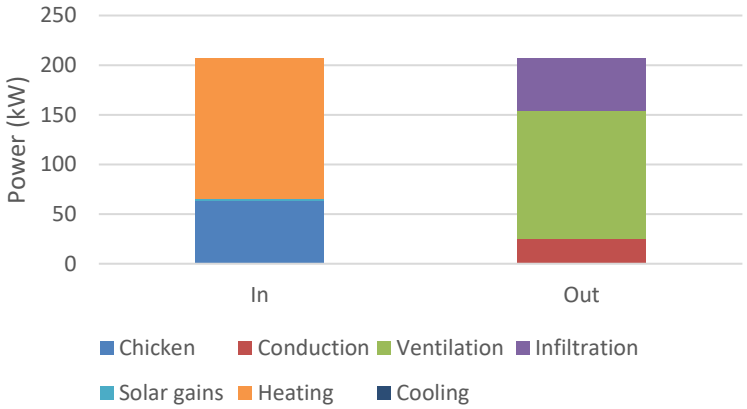

Figure 3. Energy balance (sensible) in winter (-10°C) for entire stable (720 chickens/compartment at 42 days old). RH (outside) = 50%.

Based on this figure, it can be concluded that the Solatubes mainly serve as light source, but do not really contribute to the heat balance. It should be noted that the impact of the incident solar radiation on the remainder of the roof and outer walls is not taken into account in the calculations, as the impact will be limited. The expectation is that when incorporating these, the conduction losses through the attic and outer walls will likely decrease, as they will be at a higher temperature than considered in the current simulations.

The conduction losses are also small compared to the ventilation and infiltration losses. The ventilation rate accounts for 62% of the total losses. This is the largest component for the oldest chickens, which is also likely the reason why the maxima occur for these ages as seen in Table 3. Therefore, if technically possible, the required heating load could be strongly reduced by incorporating an energy recuperation system on the ventilated air.

The conduction losses from Figure 3 are split up into each heat loss stream in Figure 4. The largest share of conduction losses is through the ground. This might be the result of some assumptions and simplifications that were made, as the ground is a difficult part to model due to the influence of floor heating and additional insulation. However, as the overall influence of conduction losses on the total heat balance is limited, it is expected that the applied model for the ground does not have a significant influence on the main results.

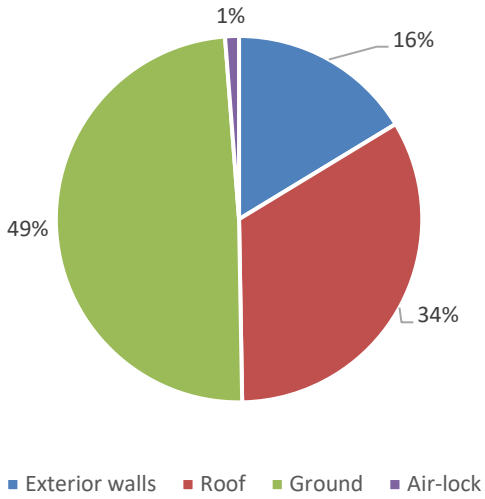

Figure 4. Distribution of conduction losses (sensible) in winter (-10°C) for entire stable (720 chickens/compartment at 42 days old). RH (outside) = 50%.

A similar analysis as described above was made for conditions during summer (i.e. 30°C outside). The results for the energy balance are given in Figure 5. The heat gains due to the Solatubes and the heat generation of the chickens are still the inputs. However, under these conditions, the ventilation, infiltration and conductive heat streams are also inputs as the outside temperature is higher than the target temperature. The largest share is the heat produced by the chickens themselves, ventilation is the second largest share. The only energy output is the cooling load.

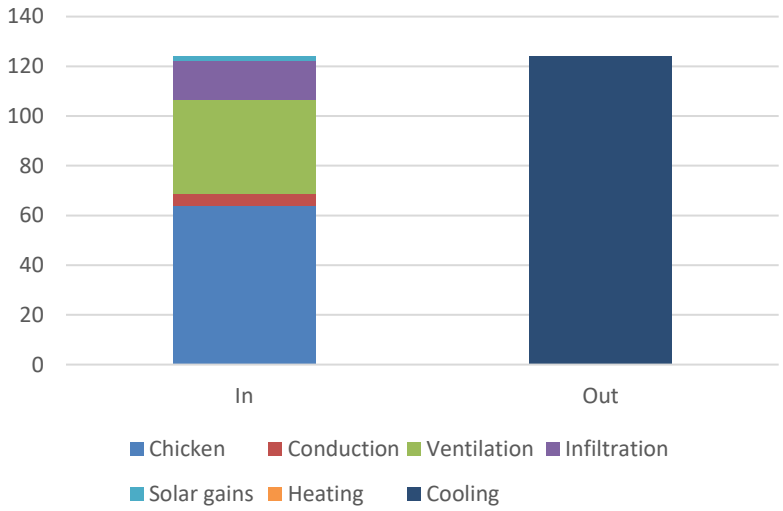

Figure 5. Energy balance (sensible) in summer (30°C) for entire stable (720 chickens/compartment at 42 days old). RH (outside) = 50%.

3.3. Required loads during stress testing

3.3.1. Heat stress tests

The heating loads for the three compartments put under the heat stress test conditions (as described in section 2.2) are illustrated in Figure 6. The heating loads are expressed in function of the age of the chickens and the outdoor temperature. The gap at day 25 is due to the change in setpoint condition as mentioned in section 2.2. As expected, the highest heating loads correspond to the lowest outdoor temperatures. For an outdoor temperature of 30°C or 35°C, no heating is required when the chickens are older (negative values in the graph). In these cases, there is cooling required, although reduced compared to the standard conditions. The maximum requirement for a heat stress test at 0°C outside temperature does not exceed the required heating power of one department at -10°C which is 47 kW. This is 1/3rd of 141 kW as can be seen in Table 3 for 720 chickens per compartment. So no additional capacity has to be installed.

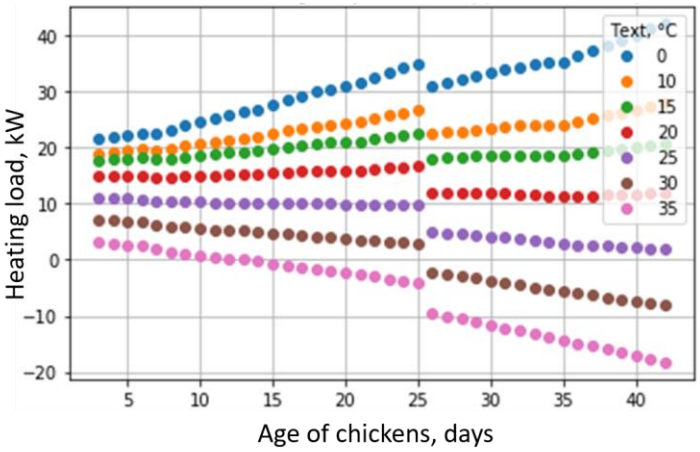

Figure 6. Heating load (sensible) for one department put under heat stress (720 chickens/compartment). RH (outside) = 50%.

3.3.2. Cold stress tests

The cooling loads for the three compartments during the cold stress tests are plotted in Figure 7, again in function of outdoor temperature and the age of the chickens. The gaps in this figure are once again a result of the change in setpoint condition as listed in section 2.2. The cooling load increases with an increase in outdoor temperature. At the lower outdoor temperatures, heating is required (indicated by the positive values) although reduced compared to the standard conditions. Once again, for the cold stress test conditions at an outside condition of 20°C, the required cooling power for one department is not exceeded for the standard conditions of one department at 35°C outside temperature.

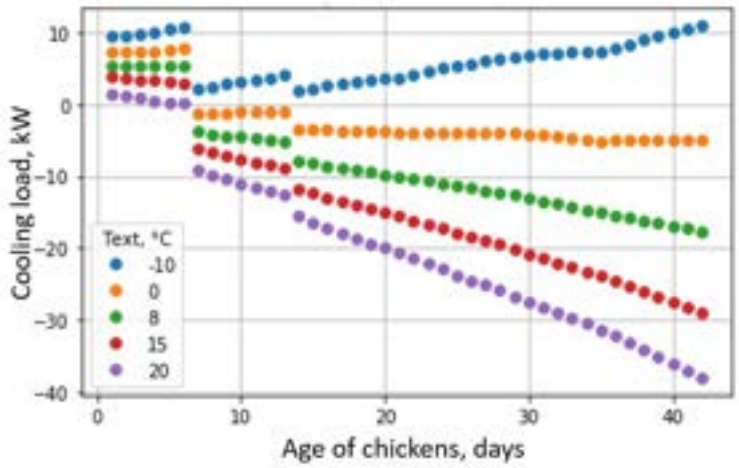

Figure 7. Cooling load (sensible) for one department put under cold stress (720 chickens/compartment). RH (outside) = 50%.

Combining the above mentioned results with the results presented in Table 3 (but rescaled to 6 compartments instead of 9) gives the total heating or cooling load of the entire farm during the periods with stress tests. It should be noted that these values are stationary loads, i.e. loads required to maintain the target temperature inside the compartments. However, in order to reach these temperatures within the required timeframe (2 hours), additional power is required, which can be based on dynamic calculations. As long as these tests occur at corresponding weather conditions, i.e. heat stress tests around summer time and cold stress tests around winter time, no additional power should have to be foreseen (compared to the values mentioned in Table 3) to be able to achieve the predefined conditions.

3.4. Sensitivity analysis of simulation parameters

In the calculations discussed above, several assumptions were made in the model. In this section, the influence of some of these assumptions on the results are investigated. A closer look will be taken at the air tightness of the farm and the applied ventilation strategy. The heating and cooling loads are recalculated with a different set of parameters, for the maximum and minimum loads during winter (-10°C outside) and summer (30°C outside) for 720 chickens per compartment.

3.4.1. Influence of air tightness

As already mentioned in section 2.4, a default value of 1 ACH was applied in the simulations. The next graph illustrates the influence on the results when the infiltration rate is either halved or doubled. The influence on the cooling load is rather limited compared to the influence on the heating load. This is also illustrated by the energy balances presented before (Figure 3 and Figure 5). During winter conditions, when heating is necessary, the infiltration rate has a large relative contribution in the energy balance. However, during summer conditions, when cooling is required, the infiltration rate has a less dominant contribution. Overall, a good air tightness is important as it drastically impacts the heating load.

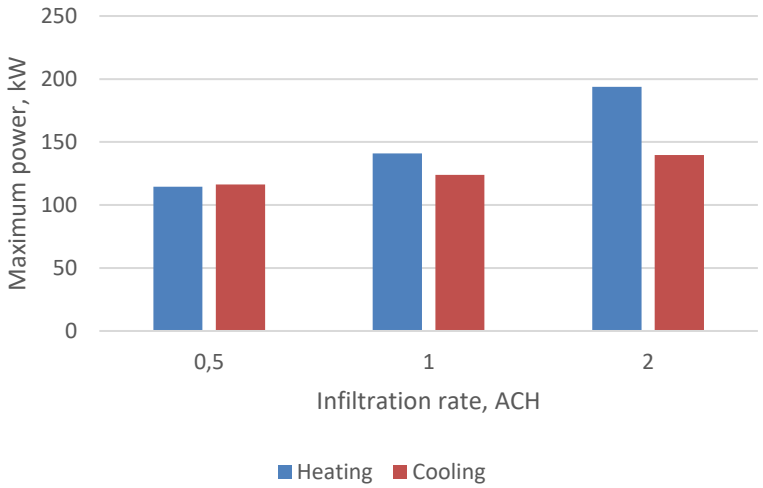

Figure 8. Influence of air tightness on (sensible) heating load (winter, -10°C) and cooling load (summer, 30°C) for the full stable (720 chickens/compartment at 42 days old). RH (outside) = 50%.

3.4.2. Influence of applied ventilation strategy

As a default, in the previous results, the minimum ventilation strategy was applied. In Figure 7, the influence of the choice of bandwidth in the strategy depicted in Figure 1 is investigated. In case cooling is required, first, 'free cooling' is used until the maximum ventilation flow rate is reached before active cooling is applied. The bandwidth "zero" means that the target temperature (TT) is always reached. For the "small" bandwidth, there is a 0.5°C tolerance on the target temperature (meaning T0 and T1 from Figure 1 are 0.5°C below and above TT, respectively). The bandwidth itself (difference between T1 and T2) is set to 2.5°C. This means that for this case, active cooling is started when the temperature is 3.5°C above the target temperature. The bandwidth "large" corresponds to a tolerance of 1°C on the target temperature and an actual bandwidth of 5°C, so active cooling will be started when the temperature is 7°C above the target temperature. From Figure 9, it can be seen that the influence of the ventilation strategy on the heating load is limited. This is because the tolerance on the temperature to apply heating is small in every case. For cooling, the tolerance is a lot higher. Only in a limited amount of cases, the outdoor temperatures will be 7°C higher than the target temperature, thus eliminating the need for additional cooling in a lot of scenarios.

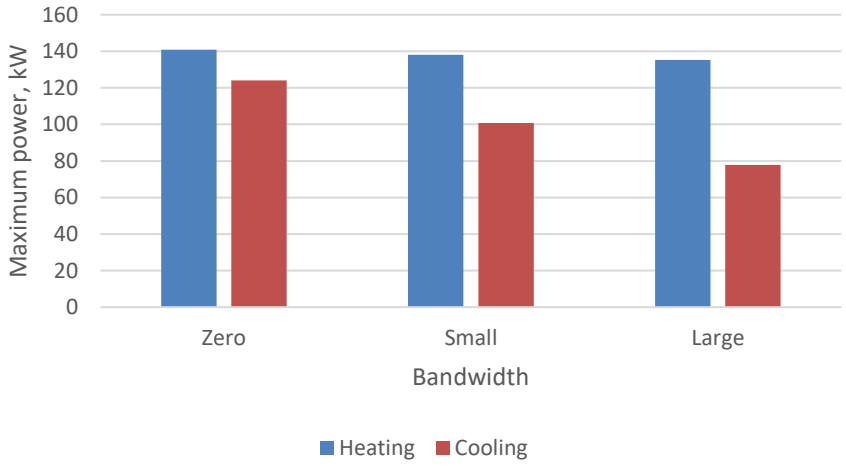

Figure 9. Influence of ventilation strategy on (sensible) heating load (winter, -10°C) and cooling load (summer, 30°C) for the full stable (720 chickens/compartment at 42 days old). RH (outside) = 50%.

3.5. Influence of outdoor relative humidity

The outdoor relative humidity has almost no impact on the sensible load but it does drastically change the total load through the latent heat requirements. Figure 10 shows the maximum humidifying and dehumidifying flow rate in function of the outdoor relative humidity. For humidification, this maximum occurs at the lowest outdoor temperature (-10 °C) and chickens of 14 days old. These values are almost constant as the saturated humidity ratio at this temperature is very low, resulting in only small changes of water content within the air flows. The maximum dehumidification flow rate occurs at the highest tested outdoor temperature (35 °C) and chickens of 42 days old. This value is more strongly dependent on the relative humidity as a similar change at this outdoor temperature represents a larger change in humidity ratio. At low relative humidities, dehumidifying is not necessary in any scenario. But at high relative humidities, the dehumidification has to balance the water vapour production from the chickens, infiltration flow rate, and ventilation flow rate, thus resulting in high required flow rates.

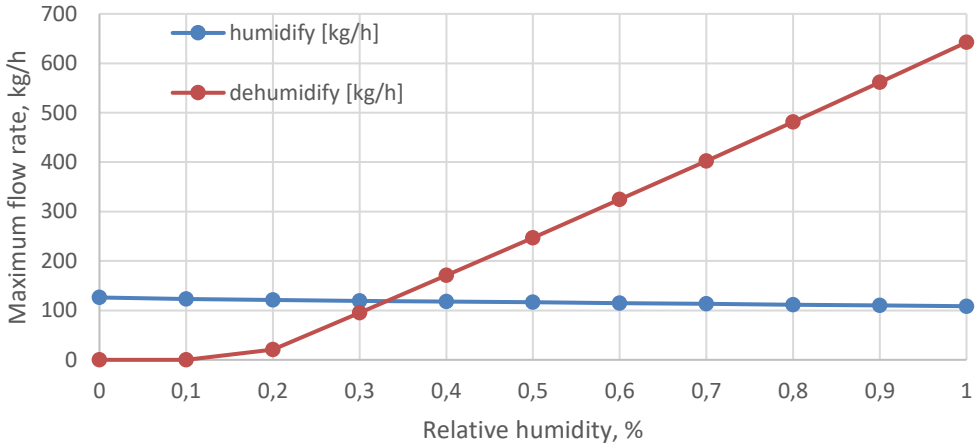

Figure 10. Influence of the outside relative humidity on the maximum required (de)humidifying flow rate for the full stable (720 chickens/compartment).

4. Simulation results over an entire year

Lastly, four simulations run over an entire year are compared based on representative weather data of the planned building location. The weather data is from a past year with measurements for every hour. The typical load for the planned farm is 720 chickens in each compartment, which grow over a period of 42 days. Before the next cycle of chickens occurs, an empty period of 10 days is required. A full cycle thus takes around 52 days. Four profiles are used to study the impact of when this 52 day cycle starts throughout the year. In the four different profiles the new chickens were introduced on days 1, 11, 26, and 40 of the year, where the rest of the occupancy is determined based on the 52 day cycle. The results of these simulations are presented in Table 4. There is some impact on the required heating and cooling depending on when the cycle is started. Some outliers are possible, as for example, the cooling demand for profile 2 is noticeably higher. The total cooling and heating loads presented in Table 4 also include the required cooling and heating to dehumidify, by cooling the air below the dew point and afterwards heating the air back to the required inlet temperature. The high cooling load in profile 2 is therefore also likely a result of the high dehumidification within this profile as a result of the unfortunate matching of this profile with a harsh weather period. It would thus be a good practice to try and match the 10 days empty period with harsh weather conditions if these are known sufficiently in advance.

Table 4. Simulations over a year for a representative weather year.

		Profile 1	Profile 2	Profile 3	Profile 4
Total heat load	MWh/y	521.1	519.2	523.5	515.4
Sensible heat load	MWh/y	286.8	284.4	288.3	285.2
Total cooling load	MWh/y	88.0	106.2	94.3	78.4
Sensible cooling load	MWh/y	29.0	35.0	34.7	26.5
Max total heat load	kW	191.0	174.0	180.9	184.7
Max sensible heat load	kW	126.7	101.1	105.5	119.7
Max total cooling load	kW	221.6	253.5	227.0	222.7
Max sensible cooling load	kW	92.4	97.6	115.9	97.0
Total humidification	kg/y	304,649	300,165	306,645	300,710
Total dehumidification	kg/y	57,540	69,647	59,092	49,346
Max humidification flow rate	kg/h	105.3	111.5	107.8	98.6
Max dehumidification flow rate	kg/h	149.8	171.1	139.0	158.3

5. Conclusion

In this paper, a model was developed to estimate the heating and cooling demand, irrespective of the HVAC system, for a proof-of-concept chicken farm that would house a maximum of 14,000 chickens. During standard chicken occupation with 720 chickens per compartment, for a total of 6,480 chickens, the stable would require a maximum of 140 kW of heating load and 157 kW of cooling load depending on the weather conditions. These maxima occur for the oldest chickens of 42 days old. The main conduction losses of the stable are primarily through the floor and secondly through the ceiling. However, the implementation of underfloor heating could have a drastic impact on floor conduction losses. In the overall balance, the conduction losses are neglectable in comparison to the ventilation and infiltration losses. The air tightness of the chicken pens, however, is an important factor in the required heating power and sufficient effort should be taken to lower the air changes per hour of the air-conditioned stables. This stable will also be used to test the impact of stressful temperatures and humidities on the chicken's behaviour. The HVAC unit should also be able to handle these conditions. As long as these tests align with the reigning weather conditions, such as heat stress tests in summer, then there should be no additional power required to achieve the wanted stress conditions. The results of this model will help in sizing the required HVAC installations of the proof-of-concept chicken farm, leading to increased energy efficiency and reduction in greenhouse gas emissions.

Acknowledgments

We would like to thank ILVO for asking the research question about the energy requirements of their new poultry farm design. Additionally, we want to thank the research foundation Flanders for their contribution through FWO grants 1SD9723N (Xander van Heule) and 1SA3722N (Jera Van Nieuwenhuyse).

Nomenclature

ACH air changes per hour, m^3/s

Q thermal power, W

m mass, kg

$\dot{m}$ mass flow rate, kg/s

RH relative humidity, %

T temperature, °C

TT target temperature, °C

V Ventilation rate, m^3/s

Subscripts and superscripts

a air

ext exterior

References

[1] MOTTET, A., & TEMPIO, G., Global poultry production: Current state and future outlook and challenges. *World's Poultry Science Journal 2017, 73*(2), 245-256. doi:10.1017/S0043933917000071

[2] Ernest F.B., Matthew A.B, Feasibility of solar technology (photovoltaic) adoption: A case study on Tennessee's poultry industry, Renewable Energy 2009, 34(3), 748-754

[3] I. Kilic, Analysis of the energy efficiency of poultry houses in the Bursa region of Turkey, Journal of Applied Animal Research 2016, 44:1, 165-172

[4] Muhammad A., Ijaz B., Nasrullah K., Mirza I.S., Muhammad Y., Mazhar A., Munawar I., Electricity generation from biogas of poultry waste: An assessment of potential and feasibility in Pakistan 2018, 81(1), 1241-1246

[5] Byrne J., Glover L., Hegedus S., VanWicklen G., The potential for solar electric applications for Delaware's poultry farms, University of Delaware, 2005, Final report, A renewable energy applications for Delaware yearly (READY) project

[6] Yuanlong C.., Elmer T., Tugba G., Yuehong S., Riffat S., A comprehensive review on renewable and sustainable heating systems for poultry farming, International Journal of Low-Carbon Technologies, 2019, 15(1), 121-142

[7] ILVO Vlaanderen. Instituut voor landbouw-, visserij- en voedingsonderzoek. url: https://ilvo.vlaanderen.be/nl

[8] TRNSYS 16 a TRaNsient System Simulation program, Multizone Building modeling with Type56 and TRNBuild, Volume 6, Available at: http://web.mit.edu/parmstr/Public/Documentation/06-MultizoneBuilding.pdf [accessed 28.02.2023]

[9] Van Rossum G., Python tutorial, Technical Report CS-R9526, Cebtrum voor Wiskunde en Informatica (CWI), Amsterdam, 1995

[10] Solatube, available at:< https://solatube.com/> [acceded 28.02.2023]

PROCEEDINGS OF ECOS 2023 - THE 36TH INTERNATIONAL CONFERENCE ON
EFFICIENCY, **C**OST, **O**PTIMIZATION, **S**IMULATION AND ENVIRONMENTAL IMPACT OF ENERGY SYSTEMS
25-30 JUNE, 2023, LAS PALMAS DE GRAN CANARIA, SPAIN

Efficient solving of time-coupled energy system MILP models using a problem specific LP relaxation

Stefan Kirschbaum[a], Marion Powilleit[b], Merlind Schotte[c] and Furkan Özbeg[d]

[a] Society for the Advancement of Applied Computer Science, Berlin, Germany, kirschbaum@gfai.de, CA
[b] Society for the Advancement of Applied Computer Science, Berlin, Germany, powilleit@gfai.de,
[c] Society for the Advancement of Applied Computer Science, Berlin, Germany, schotte@gfai.de
[d] Society for the Advancement of Applied Computer Science, Berlin, Germany, oezbeg@gfai.de

Abstract:

Energy system optimization models (ESOMs) often contain time coupling constraints, some of which couple short time frames as of daily storages or load changes of components, while other constraints couple longer periods like seasonal storages, peak load prices, or upper bounds to overall yearly CO_2 consumption.
Those ESOMs have binary constraints for minimal loads, efficiency curves, or discontinuous energy prices that are relevant for the short-term operation of the equipment. Calculation times for solving a whole year or longer as a coupled MILP problem are in many cases too high for practical applications that normally should not exceed one hour. Typical decomposition strategies to reduce calculation times are often designed for subclasses of energy system models and are not generally applicable. In order to have a generalized approach to solve these models efficiently, we investigate strategies that are based on a problem specific relaxation of integer constraints and downsampling of the input time series of the models.
A rolling horizon strategy is proposed that relaxes and downsamples the time steps from the end of the rolling horizon to the end of the year to consider the operation during the rest of the year. In order to reduce the error of the relaxation, binary constraints are reformulated to get the best LP approximation of the original MILP model. Using this rolling horizon strategy, models that are almost unsolvable as coupled MILP can be solved efficiently and very robustly and deliver a result that is feasible for the original problem and very close to the optimum of the original problem.

Keywords:

Energy system optimization; Time-coupling constraints; LP-relaxation; MILP; Downsampling.

1. Introduction to solving time-coupled energy system optimization

The optimization of the design and operation of energy supply systems plays an important role in the decarbonization of the industrial, commercial, and communal sector. Due to the vast number of new technologies and the interactions between different kinds of energy (sector coupling), designing and operating energy systems is a complex task which in most cases requires mathematical optimization models. Although some decisions can be made using simulation models, energy system optimization models (ESOM) are much more flexible and versatile to handle different kinds of decisions and target functions. Linear programming (LP) or mixed integer linear programming (MILP) has evolved as the state-of-the-art method to do these kinds of optimizations, although the problems themselves are often nonlinear. The complexity of these kinds of models is high if spatial, temporal, and/or technological dimension is high [1,2].

Many references in scientific literature deal with capacity planning of energy systems of countries [3,4] or even networks of more than one country [5,6]. Because electricity is very hard to store and has to be produced at the same time it is consumed, most of these models focus very much on electricity supply. In this paper, we focus on smaller sized energy systems, for example in industry, commercial buildings, or communal quarters. In contrast to countries or continents, those energy systems have an almost negligible spatial resolution. The technological options and temporal resolution on the other hand are often more versatile than in ESOMs for geographically large networks.

Optimizations are modeled as quasi-stationary states of operation for every piece of equipment and every point in time. Typical resolutions are hourly or quarter-hourly for a whole year or even longer. In cases where

the energy suppliers and demands are separated spatially and the energy distribution (grid) is also relevant, a spatial structure of the energy system can be taken into account as well.

In this paper, we focus on models that take hours to solve due to the coupling of time steps by storages or other effects. From a practical standpoint, these models are often considered unsolvable, as for some real-world applications it is not possible to wait for so long. The aim is to solve these models in less time by solving simplified models with results very close to the original model. Other scientific work often focuses on certain kinds of time-coupling variables or equations and propose very good solutions to solve these ESOMs very closely to the original full model. Many of these publications use the target function value of the replacement models as quality measure for the methodology. An overview of different approaches to tackle complexity in ESOMs is given in [1] and [7]. In this work, we want to evaluate the operation of the equipment as well, because for practitioners this is an important criterion to decide whether a solution makes sense.

1.1. Non-scientific requirements in energy system optimization

In this work, we focus on non-scientific use cases of energy system optimization. The GFaI develops a software toolkit called TOP-Energy for the optimization of industrial and communal energy systems [8,9]. The constraints to the methodology discussed here arise from customers and reflect practical considerations like economic constraints or usability constraints.

A very important boundary condition of solving time-coupled ESOMs in a consulting use case is the time to solve the model. Energy consulting projects often have a scope of one or two months and include data acquisition, modeling, scenario optimization, scenario comparison, and presentation of results. It is necessary to solve several models per day, so the time to solve one model should not exceed one hour.

Another important criterion is the comprehensibility of the results. Parameter variations should result in a reasonable change of the solution. This affects parameters like the gap of the MILP solver. Very high gaps can lead to solutions that are close to the optimal solution but are not explainable anymore. The operation of the energy system in the result should be reasonable. This is especially important for design optimization, in which errors in the target function may affect certain time points disproportionately and make them look wrong. This has happened in real world problems in the past and is a problem for the credibility of the ESOM itself.

Some applications exploit the convex nature of some constraints relative to the target function. Electric feed-in for example, usually does not need a constraint that forbids buying and selling electricity at the same time, as prices are usually pointing in the direction of minimizing feed-in. Practical applications nonetheless are very generic and can't exploit the seeming complexity of the constraint. Changing the target function from operating costs to CO_2 emissions for example changes the convexity, but is a very common feature in real-world models.

1.2. Idea of the paper

The idea of the paper is to propose a method that can handle all kinds of relevant time-coupling constraints in models of typical industrial or communal energy systems without exploitation of certain convex parts of the model or behavior of technical components. Some decomposition approaches only work for a subset of ESOMs. We are trying to use a very general approach that is based on a relaxation of binary variables and a downsampling of the time series rather than a decomposition. We do not want to use Benders or Dantzig-Wolfe decomposition because they rely on a very specific mathematical structure of the problem that cannot be guaranteed in every case. In order to get a reasonable mode of operation for every device in the final solution, the previously relaxed binary variables have to be set to 0 or 1 in a later stage of the optimization. By doing this, the solution presented to the user is feasible for the original problem.

We propose a multi-stage optimization approach, in which the first couple of stages determine the design variables and the peak power prices, and the last stage uses a rolling horizon with a relaxed look-ahead in order to calculate results that fulfill all constraints of the original problem. The complexity of the original problem is thus reduced by relaxation of binaries and downsampling of the input time series in a way, that the difference between the original and the downsampled time series is as small as possible.

In order to improve the quality of the relaxed solution, problem specific substitute formulations are used for specific binary variables. They are used to replace piecewise-linear functions and SOS1 formulations for feed-in prices in a way that the difference between the binary formulation and the LP formulation is as small as possible.

2. Structure of optimization problem

2.1. Mathematical structure of the design and operation optimization problem

The mathematical formulation of the optimization problem was stated similarly in many cited publications. We look for a generic formulation, which works for many energy conversion units (electricity, heat, cooling, steam, compressed air), many operational side conditions (minimum part load, minimum runtime, ramp-up behavior, maintenance), and many operating costs (costs per operating hour, costs per full load hour, costs per year).The mathematical formulation will only be given very briefly. In most cases, the total annualized costs (TAC) are

minimized, although in some cases minimizing CO_2 emissions is also relevant. So, inspired by [10] the target function is formulated like this:

$$\min_{\dot{V}_{n,t},\dot{V}_{e,t},\dot{V'}_{e,t},\delta_{n,t}} TAC = OPEX + CAPEX$$

$$= \sum_{t\in T}\left(\Delta t_t\left(\sum_{n\in C} f_{n,t}\left(\dot{V}_{n,t}\right) + \sum_{e\in E} c_{e,t}\dot{V}_{e,t} - r_{e,t}\dot{V'}_{e,t}\right)\right) + \sum_{e\in E}\hat{c}_{e,t}\dot{V}_{e,t}^{max} + a_{inv}\sum_{n\in C} f_n^{inv}\left(\dot{V}_n^N\right)$$

$$\sum_{n\in C^e}\dot{V}_{n,e,t} - \sum_{n\in C^e}\dot{V'}_{n,e,t} + \dot{V}_{e,t} - \dot{V'}_{e,t} - \dot{D}_{e,t} = 0 \quad \forall\, e\in E \,\wedge\, \forall\, t\in T \quad (1)\ \text{(energy balance)}$$

$$\dot{V}_{n,t} = f_n^{eff}\left(\dot{V'}_{n,t}\right) \quad \forall\, n\in C \,\wedge\, \forall\, t\in T \quad (2)\ \text{(energy conversion efficiency)}$$

$$\dot{V}_n^N \geq \dot{V}_{n,t} \quad \forall\, n\in C \,\wedge\, \forall\, t\in T \quad (3)\ \text{(nominal power per device)}$$

$$\dot{V}_{e,t}^{max} \geq \dot{V}_{e,t} \quad \forall\, e\in E \,\wedge\, \forall\, t\in T \quad (4)\ \text{(peak power grid connection)}$$

$$0 \leq \dot{V}_{n,t} \leq \delta_{n,t}\dot{V}_n^{max} \quad \forall\, n\in C \,\wedge\, \forall\, t\in T \quad (5)\ \text{(minimum part load)}$$

$$\Delta t_t\dot{V}_{n,e,t} \leq V_{n,e,t} \,\wedge\, \Delta t_t\dot{V'}_{n,e,t} \leq V_{n,e,t}^n - V_{n,e,t} \quad \forall\, n\in C_{st} \,\wedge\, \forall\, t\in T \quad (6)\ \text{(charging and discharging)}$$

$$\Delta t_t\left(\dot{V}_{n,e,t} - \dot{V'}_{n,e,t}\right) = V_{n,e,t} \quad \forall\, n\in C_{st} \,\wedge\, \forall\, t\in T \quad (7)\ \text{(filling level storage)}$$

$$\delta_{n,t}\in[0,1];\ \dot{V}_{n,e,t}\in\mathbb{R}^+;\ \dot{V'}_{n,e,t}\in\mathbb{R}^+;\ V_{n,e,t}\in\mathbb{R}^+;\ \left(\dot{V}_{e,t},\dot{V'}_{e,t}\right)\in SOS1$$

The operating expenditures consist of operating costs for running a certain piece of equipment $n \in C$ at a certain point of time $t \in T$. The operating costs are a function of the amount of energy $\dot{V}$ of a certain energy form $e \in E$ at that point in time. Additional costs for purchasing energy from the grid $c_{e,t}\dot{V}_{e,t}$ and revenues from selling energy to the grid $r_{e,t}\dot{V'}_{e,t}$ as well as peak power costs $\hat{c}_{e,t}\dot{V}_{e,t}^{max}$ are included in the OPEX. The capital expenditures (CAPEX) consist of the investment costs for a device n multiplied by the annuity factor a_{inv}. The investment costs are a function of the nominal power $\dot{V}_n^N$. The target function has to be minimized subject to other constraints, most importantly the energy balance. This implies that the demand of each energy form at a certain point in time $\dot{D}_{e,t}$ has to be met by the sum devices producing that energy form $\sum_{n\in C^e}\dot{V}_{n,e,t}$ plus the supply from the grid minus feed-in and the consumption of that energy form by other devices. The feed-in and grid supply are part of a special ordered set I (SOS1), so both cannot be non-zero at the same time. The energy supplied by a device is a function of other energy forms consumed. This function can be a constant efficiency of a piecewise-linear function. The minimum part load is modeled using a binary variable $\delta_{n,t}$ and a Big-M formulation using $\dot{V}_n^{max}$ as Big-M. Storage components (C_{st}) can only supply the amount of energy represented by their actual filling level $V_{n,e,t}$ and can only be charged up to the maximum filling level $V_{n,e,t}^n$.

2.2. Time-coupling constraints

Typical ESOMs for optimizing the design and operation of energy systems can have different kinds of time-coupling constraints, which can be divided into two different categories: On the one hand, there are couplings that introduce a variable as an upper limit for another variable for every single time step. This is the case for design variables, like the nominal power of devices that limit the power of a device for every single time step, and grid peak power variables that limit the power that can be taken from an energy supply grid for every single step in time. These coupling variables introduce complicating variables into the MILP. On the other hand, there are cumulating variables. Examples for these constraints are storage variables and upper limits to CO_2 emissions of an energy system. These variables introduce complicating constraints into the MILP.

One way to deal with these complicating constraints and variables in an MILP that otherwise has a block diagonal structure is Bender or Dantzig-Wolfe decomposition. Because we deal with all kinds of energy systems with very heterogeneous mathematical formulations and mixtures of complicating constraints and variables, these kinds of mathematical decompositions are not used in this work. There are some approaches to use Bender and Dantzig-Wolfe decomposition in literature ([11–13]), but they are tailored to a subset of use cases that are investigated in this work. Instead, the approach of this paper is a generic use of relaxations and downsampling to simplify the overall MILP model.

2.2.1. Upper limit (power price, capacity)

Complicating variables that represent an upper limit to another variable in every single time step occur, for example, in peak power pricing where a certain price has to be paid for the highest energy amount consumed from the electric grid per 15 minutes ((4) in Section 2.1). Another common example of variables representing an upper limit for every time step is the nominal power of a technical component in a design problem. The nominal power is an upper limit to the energy produced by that component per time step ((3) in Section 2.1).

2.2.2. Daily storage

Storages introduce complicating constraints into the ESOM. The state of charge of the storage couples two consecutive time steps and depends on the charged and discharged energy ((7) in Section 2.1).

Storages can be distinguished on the basis of their main application. Storages are economically most feasible, when they have many charging cycles throughout a year. Therefore, daily storages, which store electricity from photovoltaic, for example, are very common today. ESOMs containing these storages can be decomposed using typical days for calculating the storage operation ([14–19]). This kind of decomposition typically uses a cyclic constraint that couples the filling level of the first hour with the last hour of a typical day thus separating the solution of different typical days from each other.

2.2.3. Seasonal storage

Seasonal storages work exactly as daily storages, and the mathematical formulation of the overall problem looks exactly the same. However, the use case is different. Seasonal storages are designed to store energy for very long periods. They often have only one charging cycle throughout the year. A typical example is an ice storage that freezes water during the winter using the cold side of a heat pump. This ice can be used during the summer to cool buildings and thus be thawed again. Because we focus on models with a time frame of only one year, a cyclic constraint for seasonal storages has to be added to the mathematical formulation above, which couples the state of charge of the first time step with the last time step:

$$V_{n,e,0} = V_{n,e,max} \quad \forall\, n \in C_{st}$$

Due to the long-term storing of energy, decomposed typical days do not work for the design of these kinds of applications. There are approaches to couple typical days by a superimposed state of charge variable for every day of the year ([17,20,21]). These approaches do not perform very well for the design of seasonal storages because the order of the typical days has a very big influence on the design of the storage. Calculations with simplified energy system models resulted in deviations in the size of the storage between the full model and the decomposed model of over 85 %. Typical days are often determined using a clustering algorithm. Grouping of typical days by “charge-days” and “discharge-days” improves the design of the storage but still does not give reliable results.

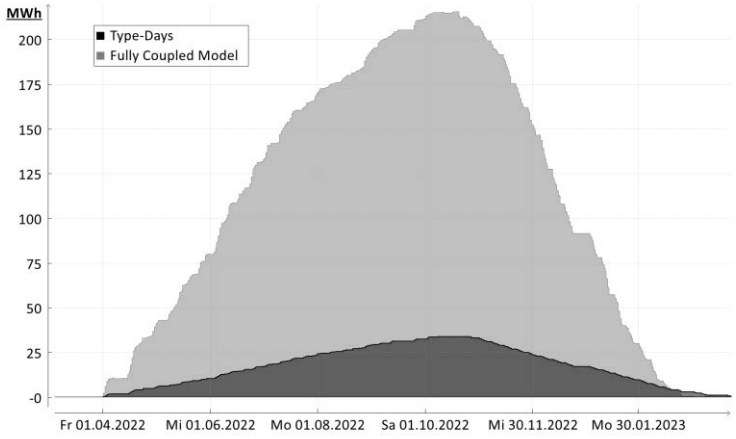

Figure. 1. *State of charge of a seasonal storage designed using typical days compared to the fully coupled original model.*

Figure. 1 shows the resulting state of charge using coupled typical days compared to the result of the original model. The underlying model consists of an oversized photovoltaic plant that produces electricity for hydrogen during the summer in order to produce electricity in a fuel cell during the winter season. The hydrogen is stored in a hydrogen storage of the size which is shown in the figure above. The fully coupled model results in a storage size of 215 MWh, whereas the decomposed model calculates a size of 33 MWh. The design of seasonal storages is one of the main reasons a method is developed that maintains the order of time steps in the reduced model in this paper.

2.2.4. Integral values

Another reason to have complicating constraints from cumulating variables in an ESOM are integral values. Typical examples are upper limits for CO_2 emissions of an energy system or performance indicators that should be met throughout the year. These constraints often come from corporate ecological goals or government regulations [22]. Equations of integral values are not included in Section 2.1. A typical formulation might look like this:

$$\sum_{e\in E}\sum_{t\in T}\theta_{e,t}\left(\dot{V}_{e,t}-\dot{V}'_{e,t}\right)\leq\theta_e^{max}\qquad\forall\, e\in E\qquad(8)\quad(CO_2\text{ emission limit})$$

$$\frac{\sum_{e\in n}\sum_{t\in T}\dot{V}_{e,t}}{\sum_{e\in n}\sum_{t\in T}\dot{V}'_{e,t}}\geq\hat{\eta}_c\qquad\forall\, n\in C\qquad(9)\quad(\text{Overall efficiency constraint})$$

In formulation (8), θ_e^{max} is an upper limit of an integral value: in this case, the CO_2 footprint of all energy forms bought from the grid minus the ones fed into the grid. In (9) the quotient of produced energy and consumed energy throughout the year of one component (overall efficiency) should be higher than a target efficiency $\hat{\eta}_c$. These formulations exist in cogeneration subsidies in Germany, for example.

2.3. Binary variables and their relaxations

The main idea of this paper is to use LP relaxations combined with the downsampling of time steps in order to reduce the complexity of the ESOM, while maintaining the chronological order of the time steps. Therefore, different typical applications of binary variables in ESOMs will be discussed in the following Section.

2.3.1. Part load characteristics and cost functions

Some variable relations in ESOMs are non-linear and have to be linearized in order to use them in MILP models. Typical examples are part load characteristics of technical equipment, which represent energy conversion efficiencies in part load ((2) in Section 2.1). Another common example are cost functions of technical components that usually have an economy of scale effect, which means the specific price of a technology is lower, when the plant size is bigger (f_n^{inv} in Section 2.1). The relation between variables is mostly described using piecewise linear functions (PWL) that are characterized by supporting points and interpolation in between those points. These PWLs can be modeled using special ordered sets (SOS) using the following formulation:

$$\sum_{i=1}^{n}\lambda_i x_i=x;\ \sum_{i=1}^{n}\lambda_i y_i=y\ ;\sum_{i=1}^{n}\lambda_i=1$$

$$\lambda_i\geq 0;\ \lambda_i\in \text{SOS2};\ i=1,\dots,n$$

in which the PWL is defined by the supporting points $(x_1,y_1),(x_2,y_2),\dots,(x_n,y_n)$. In a SOS constraint of type 2 (SOS2), not more than two variables are allowed to take a non-zero value, and these non-zero variables must be consecutive in the list. SOS constraints are often reformulated using binary variables.

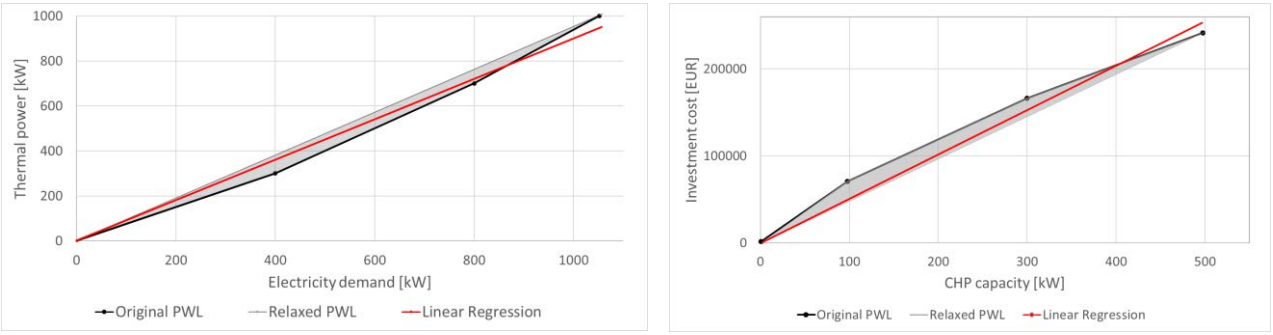

Figure. 2. *Typical structure of part load curves and investment cost function.*

The figure above shows two piecewise linear functions (black) and the space of possible solutions with relaxed binaries (grey). In this paper, we use a linear regression of the PWL function instead of an LP relaxation. This way, the deviation between the LP formulation and the PWL is smaller. The linear regression is also shown in Figure. 2 (red).

Typical part load curves have a convex structure due to inefficiencies in part load. Cost functions are usually concave due to economy of scale effects. However, in relation to the objective function, the PWLs are typically concave. In case of the part load curve, the objective function favors higher output power; in case of the cost function, the objective function favors lower investment costs. Therefore, binaries are needed for the formulation of the PWLs, and regression functions are used as replacement formulation in this work.

2.3.2. Semi-continuous variables for minimum part load and start/stop restrictions

Many energy conversion devices cannot be operated continuously between 0 % and 100 % of power output. In most cases, the part load behavior is continuous down to a point called minimum part load below which the device has to be turned off ((5) in Section 2.1). Therefore, the use of semi-continuous variables is very common in order to model this kind of behavior. Semi-continuous variables can either be 0 or in a range between a lower (ℓ) and an upper bound (u). They are reformulated using a binary variable (δ) by MILP solvers:

$$\ell \cdot \delta \leq x \leq u \cdot \delta$$
$$\delta \in \{0,1\}$$

Relaxing these kinds of variables leads to a continuous solution space between 0 and u for the variable x. So, in the LP relaxation, the minimum load of the component is not taken into account.

Because the binary variable δ is also the indicator for whether a component is on or off, this also cannot be distinguished in the LP relaxation leading to other constraints not being considered. Start and Stop constraints, for example, are often modeled in a way that a component cannot be switched on and off very frequently. If the on/off state cannot be determined anymore, start/stop constraints can also not be included.

2.3.3. Binary variables for buying and selling energy

Another typical application for special ordered sets represented by binaries are prices for buying electricity from the grid and the respective revenues for selling electricity to the grid. This can be represented by an SOS1 constraint, which means electricity can either be bought or sold, but not both at the same time. The amount of electricity bought and sold is represented by a variable that is part of an SOS1 in each case. So only one of them can be different from 0 at the same time step. These variables are then multiplied with the purchase or feed-in price and added to the target function.

In the LP relaxation, the variables in the SOS1 can both be different from 0 at the same time, which means buying and selling electricity at the same time step is allowed. As prices for buying electricity are usually much higher than the revenues for selling electricity to the grid, this is not a problem in most cases. Because the use cases discussed here are very heterogeneous, there might be situations where the price for buying electricity is very low. This can happen, when the selling price is determined by a subsidy (e.g., PV) and the buying price by a spot market (e.g., EPEX intraday). In these cases, the LP relaxation will buy cheap electricity from the grid and feed it back for a higher price, leading to an unbound MILP. This issue can be resolved by setting the same price for buying and selling electricity in the LP relaxation in these rare cases.

In cases in which the target function is not operating costs or annualized costs but rather CO_2 emissions or primary energy, simultaneous supply from the grid and feeding into the grid is possible. In these cases, the MILP will not become unbound, but the cost results of the model will be wrong.

2.3.4. Indicator constraints for if-then relations in control statements

Sometimes in ESOMs a constraint is only active if another condition is met. This can be modeled using indicator constraints, which themselves are represented using a binary variable with a Big-M formulation. An example is a heat pump that can only produce a certain amount of heat, when the heat source has a temperature above a certain value. The temperature of the heat source may be determined by another component (e.g., geothermal) that determines whether the source temperature can be reached. In this case, the heat pump can produce only a certain amount of heat, when the geothermal system is running. The on/off variable of the geothermal indicates the maximum power of the heat pump in this case. Using an LP relaxation of the original model, these indicator constraints cannot be modeled anymore, and the relation between the binary and the indicator constraint is lost.

3. Methodology

The methodology of this paper is based on a multi-stage approach using an LP relaxation and a downsampling in the first couple of stages to calculate the complicating variables and a rolling horizon approach in the last stage to calculate the complicating constraints and all other results. Using 5 different energy system models, times for solving LP relaxations were determined [23]. The measure to compare solving times are gurobi [24] work units, because they are independent of other processes running on the same machine and thus reproducible. A gurobi work unit is almost the same as a second on a single core processor. The measurements show a significant reduction in the LP relaxation. LP relaxations of MILP Models that do not solve in hours can be calculated in less than an hour.

The LP relaxations used in this paper are not only relaxations of the original model but in fact reformulations of characteristic curves and some energy prices in order to generate a formulation that is closer to the original model than the LP relaxation without using any binaries. These reformulations are described in Section 2.

An additional downsampling of the LP leads to another significant reduction of the solving time typically to less than a minute. We experimented with other time series reduction algorithms as described in [17]. Especially feature-based segmentation methods [25] that do not produce typical days but keep the order of the time steps intact were tested without significant improvements in the solution quality. Nevertheless, further investigations of these methods should be done in the future.

3.1. Substitute formulation of binary variables

In order to get as close as possible to the original unrelaxed formulation with the new LP formulation, some constraints can be reformulated in a way that does not require any binary variables. This has been done for piecewise linear functions using a linear regression with an axial intercept at 0/0. The advantages of this formulation were tested in [23]. It could be shown that a regression is faster. It is also more accurate in most

cases, but depending on the convexity of the PWL, it might also be worse than a relaxation. Nevertheless, we favor the regression because we do not want to exploit the convexity of PWL functions.

In the case of grid connections that have different purchase and feed-in prices, we use a different approach. In [23] we investigated different reformulations of the SOS1 constraint for feeding and purchasing electricity. Relaxing the SOS1 constraints led to high shifts in the target function value in time steps where the feed-in price is higher than the purchase price. Setting a medium price for buying and selling electricity would be a solution but also leads to high errors. So in this work, we propose for time steps in which electricity is bought and sold at the same time to add binary steps in later stages.

3.2. Fixing complicating variables (first stages)

Results of the LP relaxation are used to determine and fix complicating variables in the first stage of the optimization process. Because the LP relaxation violates a lot of binary constraints, the results of the complicating variables can be improved by re-adding some binary constraints that are violated in stage one back into the model. A solution of this partially relaxed model is stage two.

Further studies on two different ESOMs (see **Figure. 3** and **Figure. 5**) show the work units of models with different numbers of unrelaxed time steps (**Figure. 4** and **Figure. 6**). The figures show a significant increase in work units above 100 unrelaxed time steps. Another significant increase happens above 1000 unrelaxed time steps.

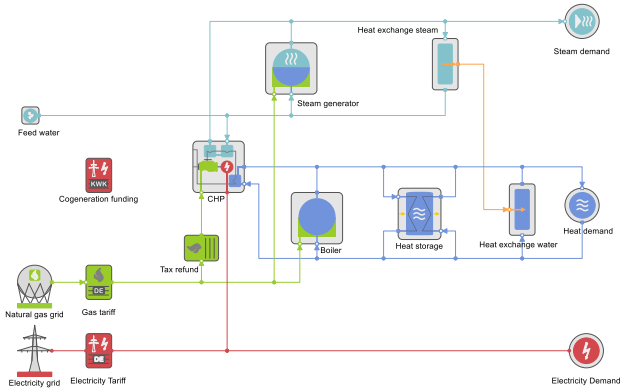

Figure. 3. *Heat and steam supply with efficiency constraint (Model A).*

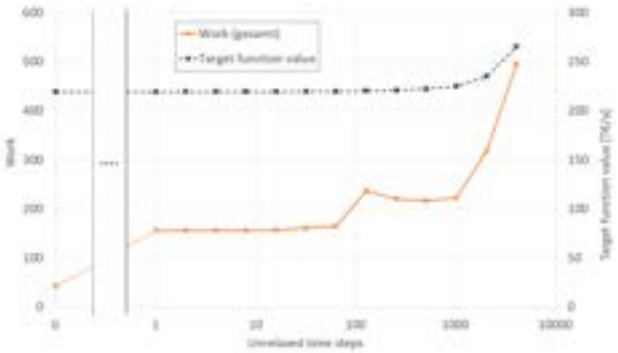

Figure. 4. *Work units and target function value over the number of unrelaxed steps (Model A).*

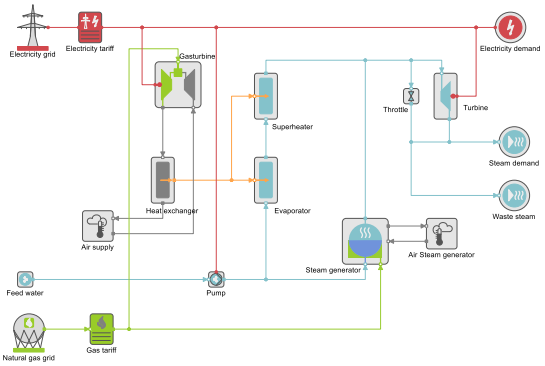

Figure. 5. *Steam supply with gas turbine and peak power price (Model B).*

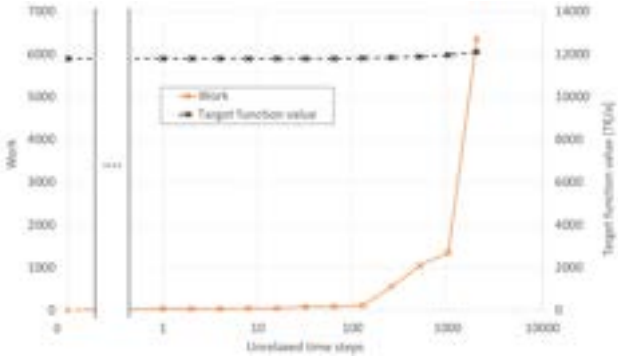

Figure. 6. *Work units and target function value over the number of unrelaxed steps (Model B).*

Model A consists of 259 continuous and 31 binary variables per time step of which presolve of gurobi removes about 90 %. Model B has 566 continuous and 70 binary variables per time step of which 96 % are removed during presolve.

The idea of the algorithm is to add binary variables back into the relaxed model and solve it until the violation of binary constraints is acceptable or calculation time are getting unacceptable. When this algorithm terminates, the complicating variables are fixed. These are nominal powers of technical components and peak power of the electric grid.

3.3. Calculating unrelaxed results using a rolling horizon

With the complicating variables fixed, the other results are calculated using a rolling horizon approach. The rolling horizon is designed in a way that results are calculated using unrelaxed time steps that are not

downsampled. The rest of the year is taken into account using a downsampled a relaxed time frame. This way, the development of complicating constraints by cumulating variables can be considered in the decision for the unrelaxed time frame. The advantage of this approach over a relaxed calculation is that the results do not violate any binary constraints and are not downsampled. The result is a solution of the original model, which is a requirement by most users. Analog to [26] the solution could be used to warm-start the original model. This has not been implemented in this work, but is subject to further investigation.

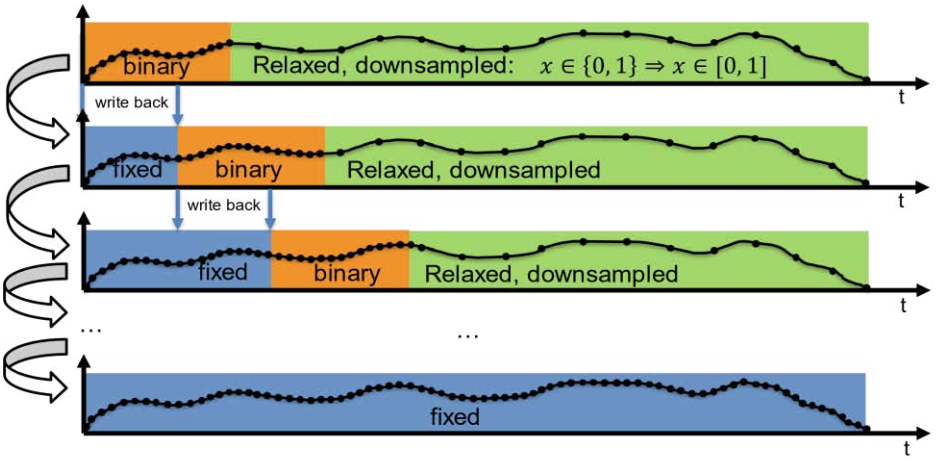

Figure. 7. *Illustration of binary rolling horizon, writing back, fixed past, and relaxed future.*

4. Runtime experiments

Whereas preliminary studies used many different models (Section 3.1) final experiments used a model with an oversized photovoltaic system and a power-to-gas unit to produce hydrogen out of a surplus of electricity. The hydrogen can later be used to produce electricity in a fuel cell. Both fuel cell and power-to-gas produce low temperature heat as a by-product. This heat can either be dumped in an emergency cooler or upgraded in a heat pump to high temperature heat. The high temperature heat from the heat pump is used to supply the high temperature heat demand. Heat that cannot be produced by the heat pump has to be generated using a common boiler. The ESOM was modeled using the modeling framework TOP-Energy. Most of the runtime measurements have been done using a python reimplementation of the same model. The model was chosen, because the full unrelaxed solution to a of gap 0.1 percent with 8760 time steps can be obtained in a reasonable time (about 30 minutes). Other example models did not solve in hours, which made it hard to do lots of evaluations with them. The prove of optimality for this model would take more than 24 h and has therefore not been carried out. A scheme of the ESOM is shown in Figure. 8.

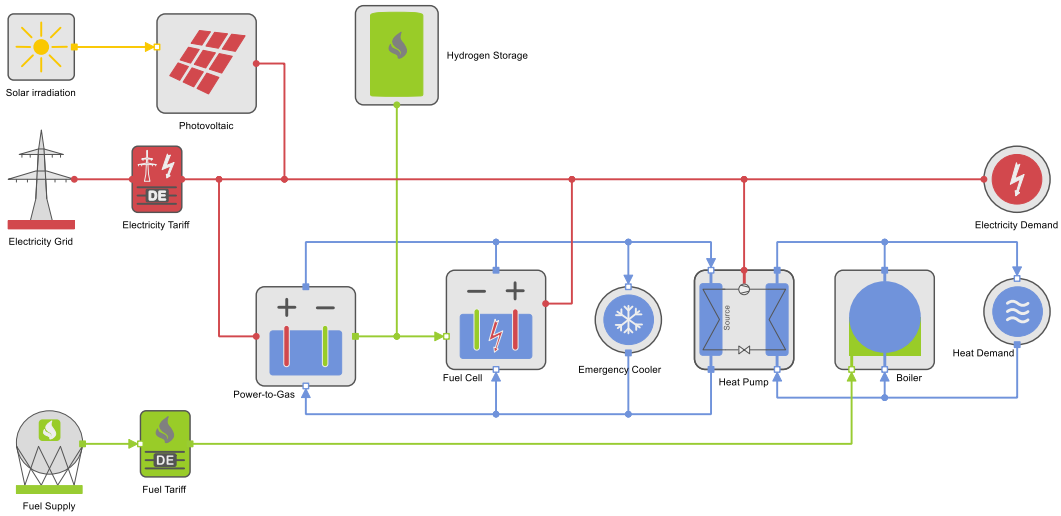

Figure. 8. *ESOM with photovoltaic and hydrogen storage for electricity and heat supply (Model C).*

The model contains two complicating constraints. One is the size of the hydrogen storage, and the other one is the peak power taken from the electric grid. The fuel cell has a minimum part load of 20 % and a nominal power of 600 kW. The heat pump has a characteristic curve that describes the part load behavior. The hydrogen storage has a characteristic curve that describes the investment cost function with an economy of

scale effect. Both characteristic curves have three supporting points which result in three variables in the SOS2 formulation.

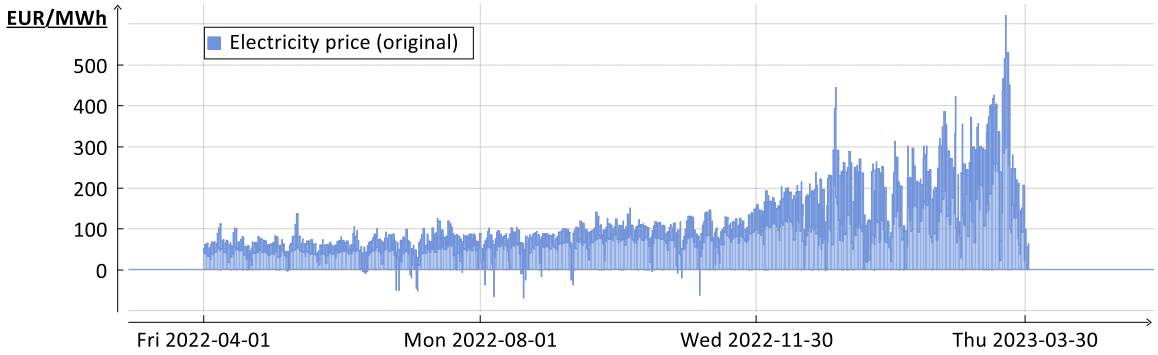

Figure. 9. *Electricity prices based on EPEX spot prices from 2021.*

The electricity price was taken from the EPEX day-ahead auction in Germany in 2021 [27] and moved 8 months back to cover the time frame of the model which is from April 2020 until the end of march 2021 (to get a better charging and discharging regime of the seasonal storage).

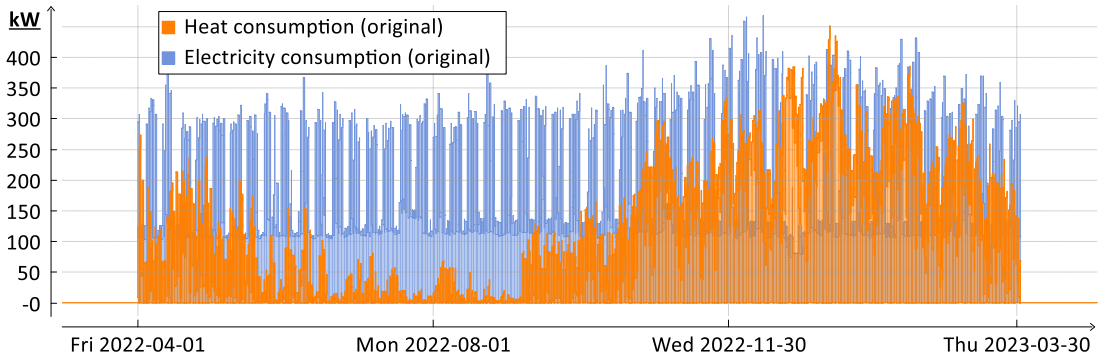

Figure. 10. *Heat and electricity demand.*

The electricity demand was measured at an office building and scaled up by a factor of 10. The heat demand was generated from a temperature profile of Berlin. The electricity production of the photovoltaic system is calculated using solar irradiation data of Berlin for a typical year. These data are provided by the German Meteorological Service DWD. A study from 2020 [28] states a price of 0.6 €/kWh for a very big cavern storage of 26 GWh. To make the storage economical for the sake of the study, these prices were further reduced. The specific costs of the hydrogen storage were set to 0.3 €/kWh for small storages (up to 300 MWh) and 0.255 €/kWh for bigger storages.

4.1. Runtime for stage one

The best available result for the complicating variables in stage 1 of model C was achieved by running the whole time frame (8760 steps) with binary variables and a gap of 0.1 %. This calculation took 1661 work units. Lower gap values took too long to calculate. This calculation results in 288 kW peak power for the grid connection and 569 MWh capacity of the hydrogen storage.

Table. 1. *Work units and errors of downsampled solutions in stage 1.*

Timesteps	Work units	Peak power	Error	Hydrogen storage	Error
1095	0.608	318 kW	10.4 %	554.92 MWh	2.5 %
1460	0.844	261 kW	9.4 %	475.36 MWh	16.5 %
2190	1.932	267 kW	7.3 %	492.49 MWh	13.5 %
4380	7.664	272 kW	5.6 %	494.53 MWh	13.1 %
8760	30.942	273 kW	5.2 %	490.47 MWh	13.8 %

The table above shows the work units of certain levels of downsampling and the respective results for hydrogen storage size and peak power. The downsampled models do not contain any binary variables. All binaries are replaced by substitute formulations or relaxed. While the peak power is getting better with a higher number of time steps, the storage size gets worse. This is not reproducible for different setups, so we assume it is a random behavior. The target function value of the overall problem is 211,126 Euro, so the error of the peak power as well as the error of the hydrogen storage size led to errors in the peak power price and the hydrogen storage price close to 0.1 % of the target function value in a solution with gap 0.1 %.

In this study, a downsampling rate of 4 was chosen for this example. Because the results from **Table. 1** are not known beforehand, we start the investigation with a downsampling to 4-hour intervals. This seems to be a reasonable resolution to account for fluctuating renewable energies, and it led to acceptable calculation times in the other models as well.

4.2. Adding binary steps in stage 2-5

In the next stages, the violation of binary constraints is fixed by adding binary steps to the relaxed model. The results of the stages are shown in the table below. Although the solution time other than the work units may depend on other tasks on the same processor, solution times are given next to work units for reference.

Table. 2. *Complicating variable results of the first 7 stages of optimization.*

Stage	Binary Steps	Work	Time	Peak Power	Error	Hydrogen Storage	Error
1	0	1.93	1.51 s	267 kW	7.3 %	492.49 MWh	13.5 %
2	137	5.12	4.37 s	265 kW	8.0 %	497.97 MWh	12.5 %
3	204	5.86	4.82 s	261 kW	9.4 %	511.89 MWh	10.0 %
4	220	4.13	3.90 s	259 kW	10.1 %	513.32 MWh	9.8 %
5	239	4.54	4.99 s	267 kW	7.3 %	518.92 MWh	8.8 %
6	250	3.66	4.22 s	267 kW	7.3 %	521.42 MWh	8.4 %
7	250			Stage 7 not carried out (no change)			
	Result 2-6:	25.26	23.80 s	267 kW	7.3 %	521.42 MWh	8.4 %

A peak power of 267 kW and a hydrogen storage size of 521,427 kWh is used for the last stage.

4.3. Rolling horizon stage

In the last stage, a rolling horizon of 84 time steps is used. Each frame is calculated using 96 unrelaxed time steps that are not downsampled and the rest of the year with a relaxed downsampling of 4. The first 84 time steps of each calculation are stored as results and fixed for the next frames. 103 calculations are needed to calculate the whole year. These 103 calculations take another 70 work units and 105 seconds. The sum of all stages took 95 work units and 129 seconds compared to 1661 work units and 1956 seconds for the full model.

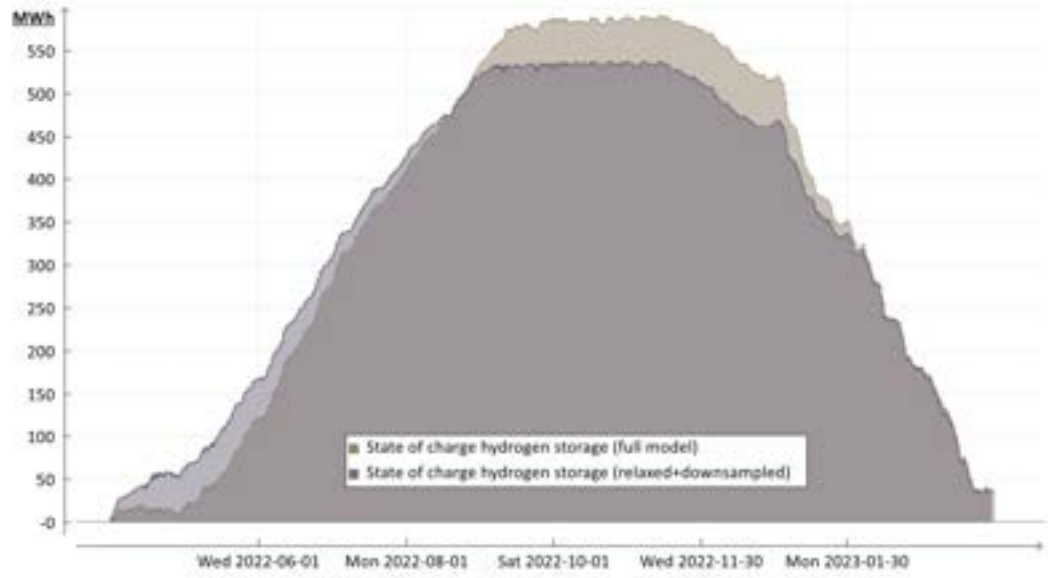

Figure. 11. *State of charge of the full model compared to the result acquired by the methodology.*

The patterns of charging and discharging the hydrogen storage are similar between the unrelaxed solution based on 8760 time steps and the relaxed and downsampled solution. The grid consumption of electricity (which is not shown here) is also very similar. For this example, the methodology delivers a reasonable result, which fulfils the requirements.

4.4 Sensitivity analysis

One requirement for the methodology was the traceability of results. Therefore, we carry out a sensitivity analysis for the original solution and the relaxed and downsampled solution to see whether the dependency on peak power pricing and hydrogen storage price are similar.

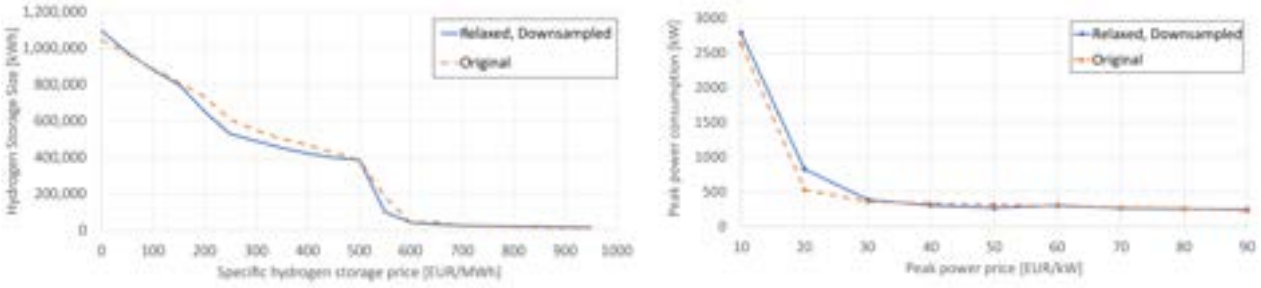

Figure. 12. *Dependency of prices and peak power (r) and storage size (l).*

The figure above shows the dependency of the consumed peak power on the peak power price and the dependency of the hydrogen storage size on the specific price of the hydrogen storage. The figure shows that the general behavior of the correlation is the same, and the methodology represents the values quite good.

5 Conclusions and future work

The examples above show that a relaxation of binary variables combined with a reformulation of some constraints together with a downsampling of time steps is capable of replacing the original more complex formulation and producing good results for design variables and peak power prices. In a multi-stage approach adding binary steps back into the problem in later stages and then calculating a feasible solution using a relaxed rolling horizon approach, reasonable results for problems with all kinds of time-coupling could be calculated.

The statements made here are tested against a small set of energy system models and should be investigated further. The fact that for some of the tested ESOMs the original solution is not known makes this evaluation a hard task.

In future work it should be tested whether the solution can be improved even further when the final solution of the rolling horizon approach (which is feasible for the original problem) is used to warm start the solution of the original problem. Having this lower bound of the original problem has proven to have big advantages [26].

Another way to improve the solution is to use a multivariate feature based segmentation [29] to reduce the number of time steps. This means removing steps from the input time series that change the time series as little as possible. An implementation based on the bottom-up approach from [25] was tried by the authors, but did not have a significant effect yet.

References

[1] Kotzur L, Nolting L, Hoffmann M, Groß T, Smolenko A, Priesmann J et al. A modeler's guide to handle complexity in energy systems optimization. Advances in Applied Energy 2021;4:100063.

[2] Scholz Y, Fuchs B, Borggrefe F, Cao K-K, Wetzel M, Krbek K von et al. Speeding up Energy System Models - a Best Practice Guide; 2020.

[3] Mehleri ED, Sarimveis H, Markatos NC, Papageorgiou LG. Optimal design and operation of distributed energy systems: Application to Greek residential sector. Renewable Energy 2013;51:331–42.

[4] Kydes AS. The Brookhaven Energy System Optimization Model: Its Variants and Uses. In: Ziemba WT, Schwartz SL, editors. Energy Policy Modeling: United States and Canadian Experiences: Volume II Integrative Energy Policy Models. Dordrecht: Springer Netherlands; 1980, p. 110–136.

[5] Leuthold FU, Weigt H, Hirschhausen C von. A Large-Scale Spatial Optimization Model of the European Electricity Market. Netw Spat Econ 2012;12(1):75–107.

[6] van der Voort E. The EFOM 12C energy supply model within the EC modelling system. Omega 1982;10(5):507–23.

[7] Cao K-K, Krbek K von, Wetzel M, Cebulla F, Schreck S. Classification and Evaluation of Concepts for Improving the Performance of Applied Energy System Optimization Models. Energies 2019;12(24):4656.

[8] Augenstein E, Herbergs S, Wrobel G. TOP-Energy - Ein Framework für Softwarelösungen in der Energietechnik. In: Oberweis A, Weinhardt C, Gimpel H, Koschmider A, Pankratius V, editors. eOrganisation Service-, Prozess-, Market-Engineering 8. Internationale Tagung Wirtschaftsinformatik: Universität Karlsruhe; 2007, p. 947–954.

[9] Kirschbaum S. Entwicklung eines Softwarepakets zur Simulation industrieller Produktionsprozesse unter energetischen Gesichtspunkten. Aachen; 2012.
[10] Baumgärtner. RiSES4 Rigorous Synthesis of Energy Supply Systems with Seasonal Storage by relaxation and time- series aggregation to typical periods 2019.
[11] Wirtz M, Heleno M, Moreira A, Schreiber T, Müller D. 5th generation district heating and cooling network planning: A Dantzig–Wolfe decomposition approach. Energy Conversion and Management 2023;276:116593.
[12] Binato S, Pereira MVF, Granville S. A new Benders decomposition approach to solve power transmission network design problems. IEEE Transactions on Power Systems 2001;16(2):235–40.
[13] Griset R, Bendotti P, Detienne B, Porcheron M, Şen H, Vanderbeck F. Combining Dantzig-Wolfe and Benders decompositions to solve a large-scale nuclear outage planning problem. European Journal of Operational Research 2022;298(3):1067–83.
[14] Bardow A, Bahl B, Hennen M, Hollermann DE, Chivite A, Wieland L et al. Ganzheitliche Optimierung von Energieversorgungssystemen in der Praxis sOptimo+. Aachen; 2018.
[15] Baumgärtner N, Bahl B, Hennen M, Bardow A. RiSES3: Rigorous Synthesis of Energy Supply and Storage Systems via time-series relaxation and aggregation. Computers & Chemical Engineering 2019;127:127–39.
[16] Bahl B, Söhler T, Hennen MR, Bardow A. Time-series aggregation to typical periods with bounded error in objective function for energy systems synthesis. In: [The 30th International Conference On Efficiency, Cost, Optimization, Simulation And Environmental Impact Of Energy Systems, ECOS 2017, 2017-07-02 - 2017-07-06, San Diego, CA, USA]: The 30th International Conference On Efficiency, Cost, Optimization, Simulation And Environmental Impact Of Energy Systems, San Diego, CA (USA), 2 Jul 2017 - 6 Jul 2017; 2017, p. 1–12.
[17] Hoffmann M, Kotzur L, Stolten D, Robinius M. A Review on Time Series Aggregation Methods for Energy System Models. Energies 2020;13:641.
[18] Kotzur L, Markewitz P, Robinius M, Stolten D. Impact of different time series aggregation methods on optimal energy system design. Renewable Energy 2018;117:474–87.
[19] Teichgraeber H, Brandt AR. Systematic Comparison of Aggregation Methods for Input Data Time Series Aggregation of Energy Systems Optimization Problems. In: Computer Aided Chemical Engineering: Elsevier; 2018, p. 955–960.
[20] Baumgärtner N, Shu D, Bahl B, Hennen M, Bardow A. From peak power prices to seasonal storage: Long-term operational optimization of energy systems by time-series decomposition. In: ; 2019, p. 703–708.
[21] Gabrielli P, Gazzani M, Martelli E, Mazzotti M. Optimal design of multi-energy systems with seasonal storage. Applied Energy 2018;219:408–24.
[22] Bundesamt für Wirtschaft und Ausfuhrkontrolle. Modul 2 - Prozesswärme aus erneuerbaren Energien: Anlage zum Merkblatt Bundesförderung für Energie- und Ressourceneffizienz in der Wirtschaft - Zuschuss 2021.
[23] Furkan Özbeg. Entwicklung einer problembezogenen Relaxierung zur effizienten Beschreibung von MILP-Modellen für Energiesysteme. Bachelorarbeit. Berlin; 2022.
[24] gurobi: gurobi Optimization LLC; Available from: www.gurobi.com.
[25] Miodrag Lovrić, Marina Milanović, Milan Stamenković. Algorithmic methods for segmentation of time series an overview. 1 2014;1(1):31–53.
[26] Kai Mainzer, Russell McKenna, Wolf Fichtner. Rolling Horizon Planning Methods in Long-Term Energy System Analysis MILP Models: Unpublished; 2015.
[27] Bundesnetzagentur | SMARD.de. SMARD | SMARD - Strommarktdaten, Stromhandel und Stromerzeugung in Deutschland. [March 12, 2023]; Available from: https://www.smard.de/home.
[28] Kreidelmeyer S, Dambeck H, Kirschner A, Wünsch M. Kosten und Transformationspfade für strombasierte Energieträger: Endbericht zum Projekt "Transformationspfade und regulatorischer Rahmen für synthentische Brennstoffe" 2020.
[29] Pang Y, Shi M, Zhang L, Sun W, Song X. A multivariate time series segmentation algorithm for analyzing the operating statuses of tunnel boring machines. Knowledge-Based Systems 2022;242:108362.

PROCEEDINGS OF ECOS 2023 - THE 36TH INTERNATIONAL CONFERENCE ON
EFFICIENCY, **C**OST, **O**PTIMIZATION, **S**IMULATION AND ENVIRONMENTAL IMPACT OF ENERGY SYSTEMS
25-30 JUNE 2023, LAS PALMAS DE GRAN CANARIA, SPAIN

Metaheuristic vs. mathematical optimization: A comparison of methods for the design optimization of residential building energy systems

Pierre Krisam[a], Lena Rosin[a], Sebastian Glombik[a] and Eva Schischke[a]

[a] *Fraunhofer Institute for Environmental, Safety, and Energy Technology, Oberhausen, Germany*

Abstract:
The energy system of residential buildings and their impact on the transition towards an emission-free energy supply has been a focus in a wide range of studies over recent years. For the design of energy systems, a variety of methods are used, most commonly heuristic, mathematical optimization and metaheuristic approaches. While the strengths and weaknesses of these methods are well known, knowledge about the discrepancy in results produced for the design of energy systems is limited. Moreover, metaheuristics have rarely been utilized in the field of household energy system planning. This leads to problems whenever findings from different studies are compared and raises the question about the optimal choice of methodology under given circumstances. To approach this question, we examine the energy system of a residential building with two different methods - a mathematical optimization and a metaheuristic optimization applied to the same MILP model. The energy system model considers a PV system, a heat pump, a heat and a battery storage system as well as a gas boiler. The layout and size of these components along with their operation are optimized. We compare the results regarding the difference in layout and size of individual components, investment costs, operational costs, CO_2 emissions and computational performance of the methods. In this case study, the mathematical optimization resulted in the best Pareto front. Using the metaheuristic approaches, it is possible to compute a Pareto front in a considerably shorter time. However, the quality of the Pareto front is significantly worse.

Keywords:
Design Optimization, Energy System Planning, Metaheuristic, Mathematical Optimization, MILP, Residential Building.

1. Introduction

The design and operational optimization of energy systems, considering renewable energies and the resulting temporal resolution, is a complex mathematical problem. The complexity of such optimization problems increases strongly with an increasing number of variables, local optima, and non-linearities, which also leads to increasing computational effort [1]. In general, global optimization algorithms can be divided into two methods: Deterministic methods also called mathematical optimization and probability-based methods referred to as metaheuristic optimization. In the past energy systems and especially unit commitment problems were mostly modeled as Linear Programming (LP) or Mixed Integer Linear Programming (MILP) optimization models [2] and solved using mathematical optimization techniques such as the branch and cut algorithm. Today, various metaheuristics are widely used to solve unit commitment problems [3] and are even predicted to become the standard for design optimization problems in the near future [4, 5].
While mathematical optimization is guaranteed to find the global optimum of a feasible problem, the complexity of global optimization problems can become so large that the global optimum cannot be found within a reasonable time. [6, 7] Metaheuristic methods, on the other hand, can solve complicated models in a shorter time frame, but do not guarantee the optimality of the results [8].
Since both solution techniques have their advantages, it is important to have a decision guide when to use which technique. Nevertheless, there is little research on how metaheuristics compare to other solution techniques such as mathematical optimization and heuristics in the field of energy system optimization. This paper aims to make a start in filling this research gap by comparing the performance of two popular metaheuristics, the Speed-constrained Multi-objective Particle Swarm Optimization (SMPSO) [9] and the Non-dominated Sorting Genetic Algorithm II (NSGA II) [10], with the performance of classical mathematical optimization on a MILP model for the design optimization of an energy system. The two selected metaheuristics are based on two different approaches.The NSGA-II is based on the principle of survival of the fittest, i.e. inheritance, mutation and selection of the best genes or, in this case, the decision variables. The SMPSO, on the other hand, is based on the flocking behavior of birds and schools of fish, and takes into account the speed of the neighbor

as well as a random change in the speed parameter.

There is a significant amount of papers comparing different metaheuristic algorithms [11, 12, 13, 14] but only a little research on how different solving techniques like metaheuristics, heuristics and classical mathematical optimization perform compared to each other, especially regarding the differences in results.
In Suh et al. [15] it is shown that metaheuristics outperform the heuristic layout of professionals by far in terms of finding the global optimum for this case study. Here, the layout refers to building decisions such as window area, insulation thickness and light bulbs.
In Silveira et al. [16] five different metaheuristics are compared to MILP, MINLP and MISOCP with classical optimization. As a case study, three different configurations of distribution systems are considered. The computational time of the metaheuristic optimization was significantly shorter than that of the mathematical optimization. For large problems, metaheuristics even found a better solution with regard to the objective function than classical mathematical optimization.
Stojiljković et al. [6] and Schmeling et al. [17] use a combined approach where the optimization problem is decomposed into two new problems. The main problem is the design optimization including synthesis, which is solved by a metaheuristic. The subproblem is the operational optimization, which is formulated as a MILP and solved by the brunch-and-cut method. The authors did not compare the results with solving the original problem using the branch-and-cut algorithm directly on the design optimization problem. However, it is noteworthy that the proposed approach has the potential for a comparison between metaheuristic algorithms and mathematical optimization, since the same constraints can be used to model the individual components of the power system.
In the following, we will compare the decomposed metaheuristic design optimization with a mathematical design optimization also referred to as structural optimization approach using MILP only.

The remaining sections of this paper are structured as follows: Section 2. provides an overview of the case study used to compare the methods. Section 3. introduces the unit commitment model used for design optimization and the corresponding metaheuristic approach. Section 4. presents and compares the results of the case study. Finally, section 5. discusses the results and draws relevant conclusions.

2. Case Study: Residential building energy system

Decarbonizing the building stock is a major challenge. As most of the existing building heat demand is met by fossil fuel-fired boilers, there is a high demand to find optimal solutions considering alternative technologies that reduce local emissions at minimal cost. Therefore, in this study, a residential building is chosen to test different approaches for designing energy systems as a problem with high practical relevance. A key strategy for decarbonizing building energy systems is to switch from combustion-based towards electricity-based heat supply combined with local electricity generation. Therefore, the design optimization of the energy system in this study considers a gas boiler, an electric heat pump for heat generation combined with heat storage. Local electricity can be provided by a photovoltaic system combined with battery storage. All components can be considered as options for the optimization algorithm. Thus, not all components have to be part of the final solution of the corresponding optimization problem. The full set of technology options and the possible energy flows in the system are given in Figure 1.

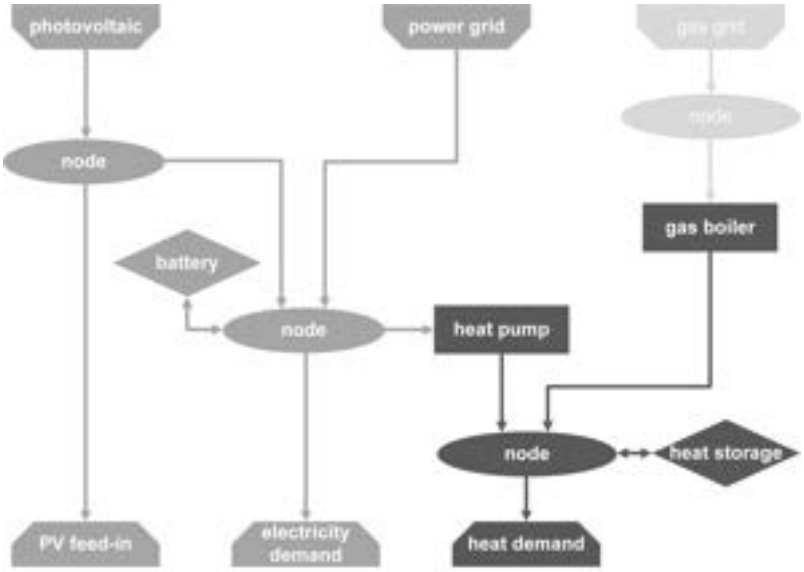

Figure 1: Schematic representation of the residential building energy system

The energy prices used in the model are form 2021. The emission data and the energy prices are listed in Table 1.

Table 1: Energy prices and CO_2 emissions

Data type	Costs	CO_2 Emissions
Electricity	0.337[€/kWh] [18, 19]	478 [g/kWh][20]
Gas	0.083 [€/kWh] [21, 22]	247 [g/kWh] [23]
PV feed-in tariff	0.073 [€/kWh] [24]	-

The investment costs for the various components are listed in Table 2.

Table 2: Investment costs of the components

Component	C_{var}	C_{fix}
Photovoltaics [25]	1260[€/kWp]	258 [€]
Heat pump [20]	426 [€/kW]	7072 [€]
Gasboiler[20]	445 [€/kW]	724 [€]
Heatstorage[26]	1000[€/kWh]	600 [€]
Battery (capacity)[27]	432 [€/kWh]	2130 [€]
Battery (inverter)[28]	150[€/kW]	-

The demands are modeled by using the open source tool *districtgenerator* [29] released by E.ON Energy Research Center, RWTH Aachen which is based on validated models from other research projects. It offers the possibility to define residential districts by specifying archetype buildings and generating building-specific energy demand profiles. The occupancy and corresponding electricity profiles are generated by a stochastic model based on [30]. The occupancy data is used to model the heating demand by modeling the domestic hot water consumption based on [31]. The space heating demand calculations are based on a 5R1C model according to EN ISO 13790 [32], where the corresponding building parameters are given by TABULA archetype buildings [33]. For this study a single building is defined. The *building type* is defined as a multi family house. The *construction year* is set to 1990 and the *retrofit state* according to TABULA [33] is a assumed to be in an usual refurbishment state. The *reference floor area* is defined as 778 m^2. The location is set to Potsdam (Germany) and the corresponding TRY dataset is used for the weather profiles.

3. Optimization models

In this section, the energy system model is described, starting with the unit commitment model for energy system operation, which forms the basis for both mathematical optimization and metaheuristic approaches. Next, the extensions to the unit commitment model necessary for design optimization are presented. Then, the modifications made to the unit commitment model in order to use the model with the metaheuristic algorithms are summarized. Finally, the metaheuristic method and the optimization setup are described.

3.1. Model for energy system operation

A mixed-integer linear unit commitment model is used as the base model for both the mathematical design optimization and the metaheuristic optimization. The model is implemented using the energy system optimization framework oemof. The household demand for electricity, heat, and hot water are modeled as sinks. The gas and electricity grids are represented as sources. The PV generation profile is simulated using a PVLib [34] model. For all other energy system components, we used the base class Transformer to write our own models. These models are briefly described below:

Let T be the set of all time steps that are considered in the optimization.

All components are limited by a maximum power rating $P_{el/th,max}$, either electric power or heat. Except for the heat pump and the gas boiler, all components are allowed to operate between 0 and this maximum power rating.

$$0 \leq P_{el/th}(t) \leq P_{el/th,max} \text{ for all } t \in T \tag{1}$$

For the heat pump and the gas boiler a minimum part load MPL is set as a percentage of the maximum power rating. To allow the output power to be zero, the binary variable Y_{op} is introduced.

$$Y_{op}(t) \cdot MPL \cdot P_{el/th,max} \leq P_{el/th}(t) \leq P_{el/th,max} \text{ for all } t \in T \tag{2}$$

The COP of the heat pump is modeled as ambient temperature dependent:

$$P_{th}(t) = P_{el}(t) \cdot cop(T(t)) \text{ for all } t \in T. \tag{3}$$

The efficiencies of the boiler and the battery storage are modeled as constant. The storage level is limited by a maximum storage capacity for both the battery and the thermal storage. The battery has no self-discharge, while the thermal storage has both temperature-dependent and level-dependent losses, which are calculated using the volume, the volumetric thermal transmittance and the density of the storage medium. The objective function of the model is to minimize the operating costs of the energy system, consisting of fuel and electricity costs for purchasing gas and electricity from the respective grid. Electricity produced by the PV system that is not consumed but fed back into the grid is compensated by the respective feed-in tariff. CO_2 emissions are calculated using constant emission factors assigned to the consumption of gas and electricity from the grid.

3.2. Design optimization model for the mathematical optimization

To transform the unit commitment model into a design optimization model constraints regarding the sizing of the components are added to the optimization problem. Additionally, the maximum power rating parameter $P_{el/th,max}$ of the unit commitment problem becomes a variable in the design optimization problem. To limit the solution space the maximum power rating is limited by P_{MAX}.

$$0 \leq P_{el/th,max} \leq P_{MAX} \tag{4}$$

In order to limit the solution space and thus the computation time, lower and upper bounds for the parameter P_{MAX} are introduced. The lower bound is set to zero and the upper bounds are determined by analyzing the energy demand, such as the maximum required heat output. For the PV system, the available roof area is used as the limit. When $P_{el/th,max}$ is zero the component is not built.
In both storage models, not only the capacity but also the maximum electrical/thermal power is optimized. For the battery, a power-to-energy ratio is implemented, to ensure a realistic battery layout. Furthermore, the total charged energy is limited according to cycle and calendar lifetimes.

$$\sum_{t \in T} P_{in}(t) \leq Capacity \cdot \frac{Lifetime_{cycle}}{Lifetime_{calender}} \tag{5}$$

We perform a multi-objective optimization with two objectives, the total annual cost of the system and the annual CO_2 emissions, to compute a Pareto front. For this purpose, the energy system is first optimized with respect to costs only. Here the objective function is the systems total annual costs (*TOTEX*).

$$TOTEX_{annual} = CAPEX_{annual} + OPEX_{annual}. \tag{6}$$

with $OPEX_{annual}$ the grid energy costs and maintenance costs for one year and $CAPEX_{annual}$ the investment costs annualized over the lifetime of the technology. Since the relation between the size of a component and its price is not linear, the *CAPEX* is calculated using a fixed C_{fix} and a variable C_{var} price component.

$$CAPEX = C_{fix} + P_{el/th,max} \cdot C_{var} \tag{7}$$

To build the Pareto front, an epsilon constraint is added to the optimization problem. This constraint limits the total annual CO_2 emissions of the system to x percent of the CO_2 emitted in the cost optimal case.

$$CO_{2_{total,annual}} \leq CO_{2_{total,annual,costoptimal}} \cdot \frac{x}{100} \tag{8}$$

In our case, x is decreased in steps of 2.5 starting at 100 (the cost optimal case) and stopping at 50 (a near CO_2 optimal case). No exclusively CO_2 optimization is carried out.

3.3. Metaheuristic optimization

The optimization problem has been decomposed into two subproblems, as proposed in [17]. The selection and sizing of the technologies here referred to as metaheuristic design optimization and the operational optimization of the resulting energy system (cf. Figure 2). The design optimization passes a set of variables to the operational optimization which returns the annual costs and emissions for each set of variables. Afterwards, the metaheuristic design optimization selects a new set of variables according to the KPIs, here CO_2 emissions and TOTEX, and passes it back to the operation optimization. The process ends when the termination criterion, here the computation time limit, is reached.

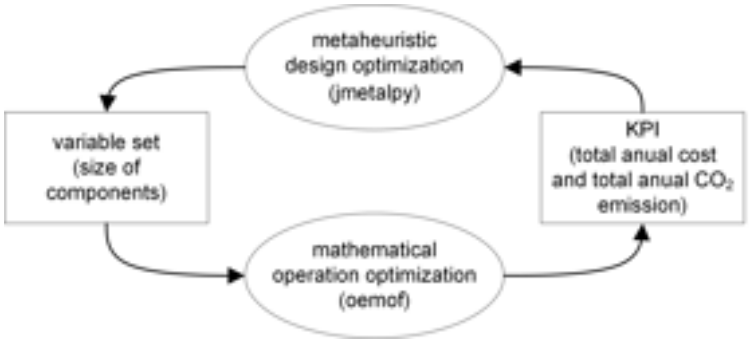

Figure 2: Two-level design optimization

The operation optimization is performed with the same unit commitment model described in 3.1.. The MILP is solved with Gurobi using a branch-and-cut algorithm. The emissions during the operation are limited by an emission factor to achieve comparable results to the MILP design optimization, which indirectly optimizes the operation to meet the global emission limit.
The main problem of design optimization is solved by a metaheuristic algorithm. The algorithm can determine the dimensions and capacity of the technologies and limit the emissions of the operation by an emission factor. The upper and lower bounds are set exactly as described in 3.2.
Analogous to mathematical optimization, two objective functions are used for metaheuristic optimization: The total annual costs and the total annual CO_2 emissions.
The metaheuristic optimization is done with the python package jmetalpy which uses the java-based framework jmetal.

3.4. Optimization Setup

In this section we give some insight into our setup and the software and settings we used. The calculations were performed on a computer with an Intel(R) Xeon(R) W-1390P @ 3.50Ghz and 128 GB RAM.
The design optimization MILP is solved with Gurobi Optimizer version 9.1.1 using up to 16 threads. A mipgap of 0.01 and a time limit of 6 hours per optimization is used. If the time limit is exceeded, the best solution and

the resulting mipgap are saved and the epsilon constraint method is continued.
The operation optimization MILP is solved with the same solver and solver settings except for the time limit, which is set to 5 minutes. The metaheuristic design optimization uses the default settings of the respective algorithms as presented in jmetalpy. In contrast to mathematical optimization, in metaheuristic optimization, it is not clear whether the global optimum has been found. Therefore, a termination criterion is needed. In order to be able to compare the results of the two methods, a time limit is set as the termination criterion. To make the results of the metaheuristic optimization reproducible, the same random seed is used for all algorithms and runs. All optimizations are computed for a whole year with a time resolution of one hour, i.e. 8760 time steps.

4. Results and Comparison

In this section, we analyze the results of the case study. We begin by examining the metadata of the algorithms used, followed by a comparison of the Pareto fronts. We then take a closer look at the actual energy systems built for the Pareto solutions.

Table 3 summarizes metadata such as the number of non-dominated solutions and the total computation time. A time limit of 20.15 hours and 5 hours was implemented for the metaheuristic methods, as well as a variation of the population or swarm size of 10 and 100. It can be seen that the termination criterion was not exactly met. Both NSGA-II and SMPSO exceeded the time limit. The population and swarm size appear to have a direct influence on the time limit violation. It seems that the termination criterion is applied only after the total generation has been computed. Mathematical optimization using the epsilon constraint produced 19 non-dominated solutions and two dominated solutions. The observed phenomenon is a direct consequence of the results reported in the recent research [35], which concluded that the epsilon constraint approach fails to accurately compute the true Pareto front. As a result, the use of lexicographic optimization is proposed to compute the true Pareto front. The metaheuristic methods found significantly more non-dominated solutions and total feasible solutions than mathematical optimization with the 20-hour time limit. Reducing the population/swarm size resulted in more optimizations and feasible solutions for both algorithms. For NSGA-II, the number of non-dominated solutions also increased significantly. For SMPSO, the number of non-dominated solutions decreased from 48 to 46.

Table 3: Meta data of the optimization

Method	MILP	NSGA-II	NSGA-II	NSGA-II	SMPSO	SMPSO	SMPSO
time limit [h]	N/A	20.15	5	20.15	20.15	5	20.15
total time [h]	20.15	21.40	5.40	20.19	21.66	5.55	20.18
population/swarm size [-]	N/A	100	100	10	100	100	10
generations [n]	N/A	12	3	140	10	3	121
total optimizations [n]	22	1200	300	1400	1000	300	1210
time limit reached [n]	0	11	5	1	11	5	10
infeasible [n]	1	259	91	226	279	94	470
feasible [n]	21	930	204	1173	710	201	730
non-dominated solutions [n]	19	38	14	85	48	22	46

Figure 3 shows the Pareto front of the different design optimization methods. The mathematical optimization Pareto front, hereafter referred to as the MILP Pareto front, is used as a reference in all subsequent figures. The computation time of the methods in this figure is about 20.15 hours (see Table 3) and the population and swarm size is set to 100. The solutions of the mathematical optimization for the case study lead to the best Pareto front in both dimensions. This implies that the Pareto front contains the most cost-optimal and CO_2 efficient Pareto points, in terms of all three algorithms. In this example, we observe that the SMPSO algorithm outperforms the NSGA-II algorithm in terms of finding the cost-optimal solution. However, we found that the NSGA-II algorithm was closer to the MILP front at the bending point of the Pareto curve. In other words, NSGA-II comes closer to the ideal point in Figure 3 than SMPSO. On the other hand, the emission-optimal point found by the SMPSO algorithm is more cost-optimal and has lower emissions than the one found by the NSGA-II algorithm. The emission-optimal solutions found by the metaheuristic methods are much more expensive than the emission-optimal solution of the MILP solution. In addition, the metaheuristic Pareto fronts continue to separate from the MILP Pareto front as emissions decrease.

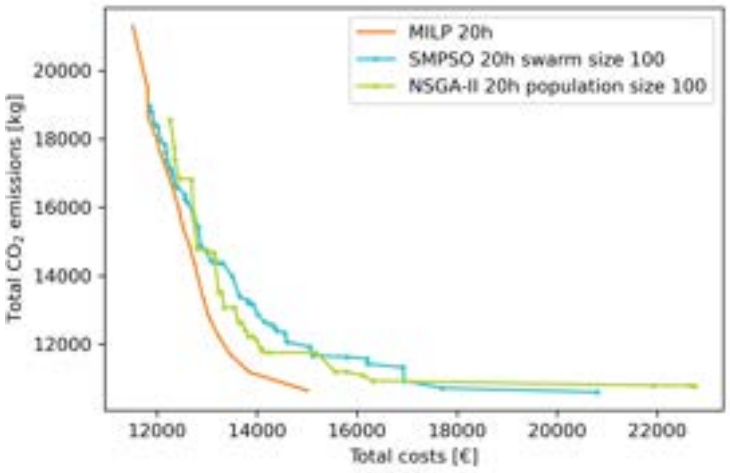

Figure 3: Pareto MILP, NSGA-II and SMPSO (20h time limit and population/swarm size of 100)

In Figure 4, the Pareto front of the MILP mathematical optimization from Figure 3 with a computation time of 20 hours is compared to the metaheuristic methods with a computation time of about 5 hours. The metaheuristic solutions are now much further away from the MILP Pareto front. For the same CO_2 emissions, the metaheuristics incur significantly higher total annual costs than the MILP Pareto solutions. This effect increases significantly with decreasing CO_2 emissions. The SMPSO, in contrast to the NSGA-II, found a point particularly close to the MILP Pareto front. Compared to the NSGA-II, the SMPSO found the solution with the lowest emissions and the solution with the lowest total annual cost.

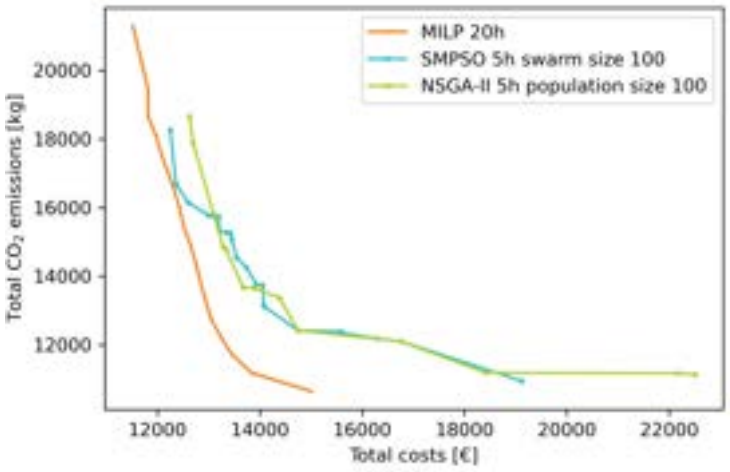

Figure 4: Pareto MILP, NSGA-II and SMPSO (5h time limit and and population/swarm size of 100)

In Figure 5 the population/swarm parameter was set to 10. The time limit here is 20.15 hours, as in Figure 3. The Pareto fronts of the NSGA-II and the SMPSO are close. The Pareto front of NSGA-II covers a smaller solution space than that of SMPSO. Compared to Figure 4, the Pareto front of the metaheuristics is much smoother. The NSGA-II and SMPSO perform slightly better with a swarm/population size of 10 in the emission optimal range. This could be due to the significantly higher number of generations. Compared to Figure 3, the algorithms perform better in some parts of the Pareto front and worse in others.

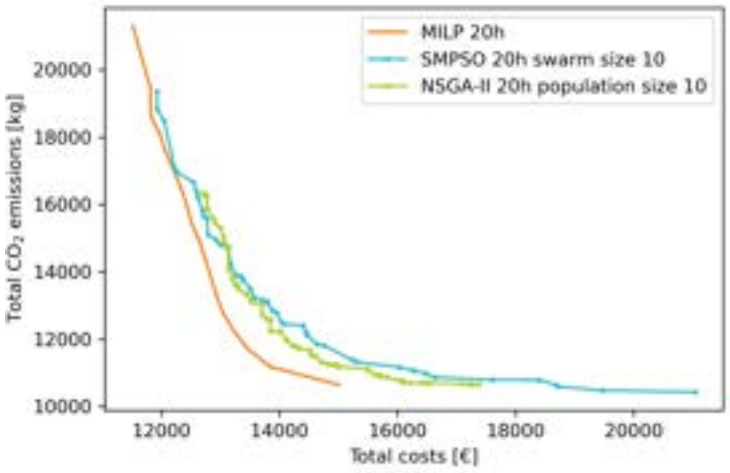

Figure 5: Pareto MILP, NSGA-II and SMPSO (20h time limit and population/swarm size of 10)

Closer examination of the energy systems built for the Pareto optimal solutions for the 20h mathematical optimization and the 20h metaheuristics with a population/swarm size of 100 reveals significant differences between the mathematical optimization and the metaheuristics. Figure 6 show the components and their sizes for all Pareto optimal results. The plots are sorted from cost optimality on the left to CO_2 optimality on the right .

Regarding the mathematical optimization, the capacity of the heat producers increases moderately across all solutions, as shown in 6a. It is noteworthy that only in the cost-optimal case no heat pump is built. For the next Pareto point, the gas boiler capacity decreases slightly and a heat pump is installed. Interestingly, the boiler and heat pump capacities remain almost constant for ten Pareto points until a tipping point is reached where no gas boiler is installed and the heat pump provides the whole heat demand.

Conversely, for both metaheuristics, a gas boiler is built for all Pareto optimal solutions.

For the NSGA-II algorithm, the gas boiler capacity initially decreases as emissions decrease, but then increases significantly for the last eight CO_2 optimal solutions, so that the gas boiler capacity for the cost-optimal and emission-optimal cases are nearly equal.

On the other hand, for the SMPSO algorithm, the gas boiler size remains nearly constant for the more cost-optimal Pareto points until a tipping point where only a very small gas boiler is built. But similar to the NSGA-II algorithm, the gas boiler size increases again for more emission-optimal solutions.

When analyzing the operation of the boiler over the course of a year for the SMPSO and NSGA-II algorithms for the emission-optimal solution, it can be observed that the boiler was rarely used, running only 54 hours and 249 hours, respectively, throughout the year. The installation of the boiler despite its limited use can be attributed to the absence of indirect emissions which are not included in this anaylsis. In fact, there are no "investment emissions" for the components. Similar to the mathematical optimization, figures 6b and 6c show that the heat pump size increases towards the CO_2 optimal solutions. However, in contrast to the mathematical optimization, the overall installed capacity of heat producers is higher for the metaheuristic algorithms.

Regarding the installed photovoltaic capacity, a constant growth along the Pareto front towards the CO_2 optimal solution is observed for both the mathematical optimization and the metaheuristics.

Despite an overall increase in storage capacity towards the CO_2 optimal solution for all three algorithms, significant differences in storage capacity are observed between the mathematical optimization and the metaheuristics.

The most notable difference is the approximately twofold increase in total storage capacity for the metaheuristics compared to the mathematical optimization. In the mathematical optimization, only the thermal storage is built in the cost-optimal case, and its size increases along the Pareto front until an additional battery is installed. At this juncture, the size of the heat storage drops before increasing again. Furthermore, the size of the battery increases steadily until the point where no gas boiler is installed. At this point, the size of the battery decreases to zero before increasing again toward the emission-optimal solution.

Similarly, both metaheuristics build thermal storage for all Pareto points. The NSGA II algorithm maintains a relatively constant heat storage capacity for most of the Pareto front. However, for more CO_2 optimal cases, the heat storage doubles in size. The battery size increases moderately toward the CO_2 optimal solution until a tipping point where the battery capacity increases dramatically to over 230 kWh.

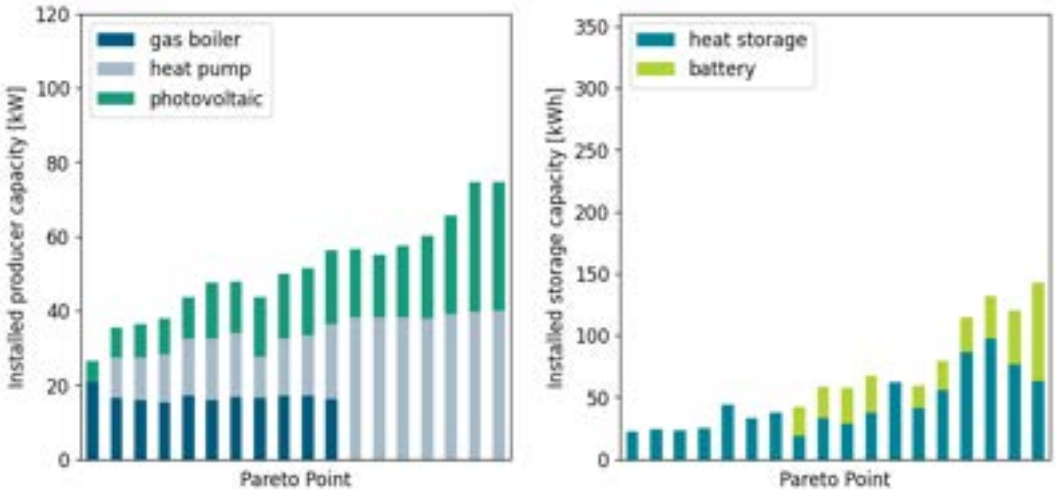

(a) mathematical optimization (MILP)

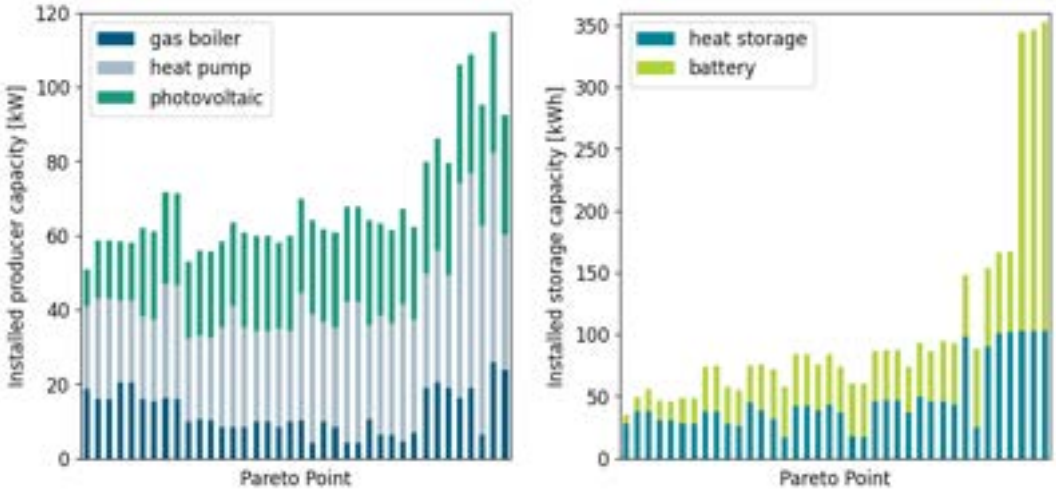

(b) metaheuristic optimization (NSGA-II)

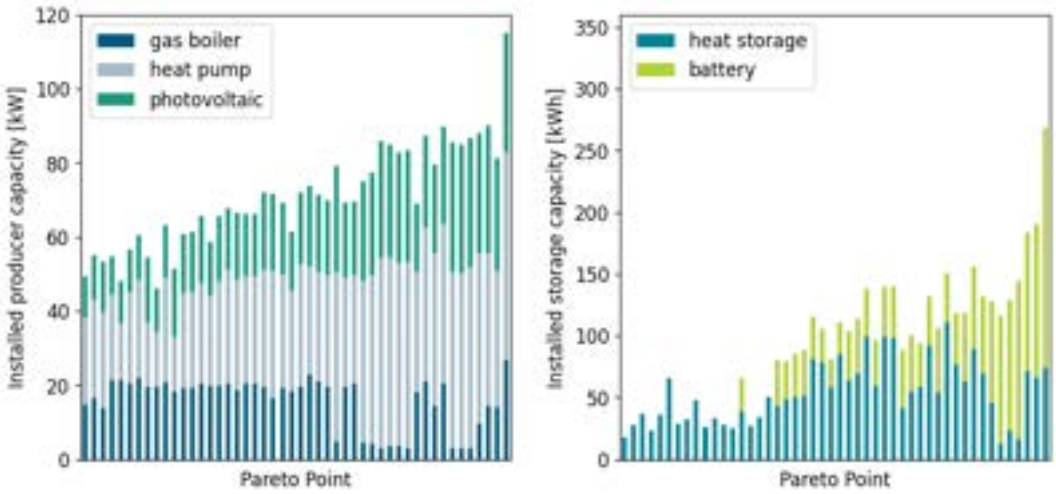

(c) metaheuristic optimization (SMPSO)

Figure 6: Energy systems from the pareto optimal results for different algorithms

In contrast to the NSGA-II algorithm, the heat storage capacity fluctuates significantly throughout the Pareto front of the SMPSO algorithm, peaking in the middle. In addition, the SMPSO algorithm does not install a battery until almost the middle of the Pareto front. Then the battery capacity increases steadily.

The higher costs associated with the emission-optimal solutions generated by the metaheuristics, as observed in Figures 3-5, can be attributed to the substantially higher storage and producer capacities employed by these algorithms. The reason for this could be that metaheuristics are severely penalized for choosing infeasible solutions or reaching the time limit in operations optimization. Therefore, the trained behavior of these metaheuristics is biased toward quickly producing feasible solutions, which results in larger capacities. This is probably the cause of the unexpected behavior of the metaheuristics in constructing a boiler for all solutions. This behavior can be reduced by allowing a higher time limit for operations optimization and more time overall for the computations, so that the metaheuristics can compute more generations.

Another notable characteristic of metaheuristics is the greater fluctuation in capacity sizing, as opposed to the smoother trend observed in mathematical optimization. This fluctuation can be explained by the random nature of the metaheuristics. This effect should be further investigated in future studies.

5. Conclusion

This paper compares two methods and their results for the design optimization of a residential building. A multiobjective mathematical design optimization approach and a two-stage metaheuristic design optimization approach using the metaheuristics SMPSO and NSGA-II were described, and the Pareto fronts and energy system designs of the Pareto solutions generated by each algorithm were analyzed.

In our case study, the mathematical optimization resulted in the best Pareto front. However, it should be noted that the calculation time was quite extensive at 20 hours. To reduce the computation time of the mathematical design optimization, a larger step size of the epsilon constraint could be applied. This would reduce the number of optimizations but at the same time the resolution of the Parteo front. Additionally, a lexicographic optimization approach can be used to compute the real Pareto front, which could lead to more accurate and efficient results and avoids caluating dominated solutions. Further research is needed to fully explore these possibilities and improve the efficiency of the optimization process.

Furthermore, our study has shown that the choice of parameters such as swarm/population size has a strong influence on the optimality of the results. Depending on the choice of metaheuristic parameters, either the NSGA-II or the SMPSO performed better. Therefore our optimization results do not allow a conclusion which of the two metaheuristic algorithms is better suited for the design optimization of residential buildings. In addition, it was shown that it is possible to compute a Pareto front with the metaheuristic approaches in shorter time frames, but this results in a significantly worse Pareto front compared to the MILP and 20 h metaheuristic solutions. For this reasons, further studies are necessary.

As mentioned above, the parameter settings of metaheuristic algorithms have a large influence on the quality of the results. For this reason, guidelines for the parameterization of metaheuristic design optimizations for energy systems would be beneficial. In order to ensure the comparability of the results of the different methods, a time limit was used as a stopping criterion in this study. However, when metaheruistic methods are used to obtain results in practice, a termination criterion is needed that allows a statement to be made about the quality of the solution or the convergence of the algorithm. Since one of the main advantages of metaheuristics is their computational efficiency compared to mathematical optimization, it would be worthwhile to investigate how solution-quality-oriented termination criteria such as the hypervolume could enhance performance. In addition, a warm start, i.e. the implementation of coherent start variables such as a standard desgin according to DIN norms, could make the solution process more efficient and robust. The factor that metaheuristics are not limited to MILP problems, like mathematical optimization, but can also be used with Non Linear Programming or simulation was not considered in this study. Hence it would be interesting to investigate a single-stage metaheuristic optimization instead of the two-stage approach used in this paper.

Lastly, additional case studies involving more complex energy systems and a wider range of scenarios are required to develop a reliable guideline for selecting an appropriate design optimization method.

Acknowledgments

This paper was written as part of the project ODH@Jülich, which was funded by the Federal Ministry of Education and Research (BMBF) and supported by the project BF-Quartier2020, funded by the Federal Ministry for Economic Affairs and Climate Protection. The paper also received financial support from the Friedrich Naumann Foundation for Freedom in the course of a scholarship for Lena Rosin.

References

[1] Leander Kotzur, Lars Nolting, Maximilian Hoffmann, Theresa Groß, Andreas Smolenko, Jan Priesmann, Henrik Büsing, Robin Beer, Felix Kullmann, Bismark Singh, Aaron Praktiknjo, Detlef Stolten, and Martin Robinius. A modeler's guide to handle complexity in energy systems optimization. *Advances in Applied Energy*, 4:100063, 2021. ISSN 26667924. doi: 10.1016/j.adapen.2021.100063.

[2] Elias Ridha, Lars Nolting, and Aaron Praktiknjo. Complexity profiles: A large-scale review of energy system models in terms of complexity. *Energy Strategy Reviews*, 30:100515, 2020. ISSN 2211467X. doi: 10.1016/j.esr.2020.100515.

[3] Yuan-Kang Wu, Hong-Yi Chang, and Shih Ming Chang. Analysis and comparison for the unit commitment problem in a large-scale power system by using three meta-heuristic algorithms. *Energy Procedia*, 141: 423–427, 2017. ISSN 18766102. doi: 10.1016/j.egypro.2017.11.054.

[4] Mehmet Polat Saka and Zong Woo Geem. Mathematical and metaheuristic applications in design optimization of steel frame structures: An extensive review. *Mathematical Problems in Engineering*, 2013: 1–33, 2013. ISSN 1024-123X. doi: 10.1155/2013/271031.

[5] Ali Tarraq, Faissal Elmariami, Aziz Belfqih, and Touria Haidi. Meta-heuristic optimization methods applied to renewable distributed generation planning: A review. *E3S Web of Conferences*, 234:00086, 2021. doi: 10.1051/e3sconf/202123400086.

[6] Mirko Stojiljković, Mladen Stojiljković, and Bratislav Blagojević. Multi-objective combinatorial optimization of trigeneration plants based on metaheuristics. *Energies*, 7(12):8554–8581, 2014. doi: 10.3390/en7128554.

[7] Gianfranco Chicco and Andrea Mazza. Metaheuristic optimization of power and energy systems: Underlying principles and main issues of the 'rush to heuristics'. *Energies*, 13(19):5097, 2020. doi: 10.3390/en13195097.

[8] Bryn et al. Pickering. Comparison of metaheuristic and linear programming models for the purpose of optimising building energy supply operation schedule.

[9] A. J. Nebro, J. J. Durillo, J. Garcia-Nieto, C. A. Coello Coello, F. Luna, and E. Alba. Smpso: A new pso-based metaheuristic for multi-objective optimization. In *2009 IEEE Symposium on Computational Intelligence in Milti-Criteria Decision-Making*, pages 66–73. IEEE, 2009. ISBN 978-1-4244-2764-2. doi: 10.1109/MCDM.2009.4938830.

[10] K. Deb, A. Pratap, S. Agarwal, and T. Meyarivan. A fast and elitist multiobjective genetic algorithm: Nsga-ii. *IEEE Transactions on Evolutionary Computation*, 6(2):182–197, 2002. ISSN 1089-778X. doi: 10.1109/4235.996017.

[11] Ioan Sarbu, Matei Mirza, and Emanuel Crasmareanu. A review of modelling and optimisation techniques for district heating systems. *International Journal of Energy Research*, 2019. ISSN 0363-907X. doi: 10.1002/er.4600.

[12] C. Schellenberg, J. Lohan, and L. Dimache. Comparison of metaheuristic optimisation methods for grid-edge technology that leverages heat pumps and thermal energy storage. *Renewable and Sustainable Energy Reviews*, 131:109966, 2020. ISSN 13640321. doi: 10.1016/j.rser.2020.109966.

[13] Ruifeng Shi, Can Cui, Kai Su, and Zaharn Zain. Comparison study of two meta-heuristic algorithms with their applications to distributed generation planning. *Energy Procedia*, 12:245–252, 2011. ISSN 18766102. doi: 10.1016/j.egypro.2011.10.034.

[14] *Proceedings of the WSEAS international conferences: Politehnica University of Timisoara, Romania, October 21 - 23, 2010 ; Applied Computing Conference 2010 (ACC '10) ; 6th WSEAS International Conference on Energy, Environment, Ecosystems and Sustainable Development (EEESD '10) ; 3rd WSEAS International Conference on Landscape Architecture (LA '10) ; 12th WSEAS International Conference on Mathematical Methods and Computational Techniques in Electrical Engineering (MMACTEE '10)*. Proceedings of the WSEAS international conferences. WSEAS Press, Athen, 2010. ISBN 9789604742394.

[15] Won-Jun Suh and Cheol-Soo Park. Heuristic vs. meta-heuristic optimal energy design for an office building. *Sustainability*, 9(4):508, 2017. doi: 10.3390/su9040508.

[16] Christoffer L. Bezão Silveira, Alejandra Tabares, Lucas Teles Faria, and John F. Franco. Mathematical optimization versus metaheuristic techniques: A performance comparison for reconfiguration of distribution systems. *Electric Power Systems Research*, 196:107272, 2021. ISSN 03787796. doi: 10.1016/j.epsr.2021.107272.

[17] Lucas Schmeling, Patrik Schönfeldt, Peter Klement, Steffen Wehkamp, Benedikt Hanke, and Carsten Agert. Development of a decision-making framework for distributed energy systems in a german district. *Energies*, 13(3):552, 2020. doi: 10.3390/en13030552.

[18] FfE. Deutsche strompreise an der börse epex spot in 2021 - ffe, 01.02.2023. URL https://www.ffe.de/veroeffentlichungen/deutsche-strompreise-an-der-boerse-epex-spot-in-2021/.

[19] Boston Consulting Group. Klimapfade 2.0 ein wirtschaftsprogramm für klima und zukunf: Ein wirtschaftsprogramm für klima und zukunft.

[20] KEA-BW Die Landesenergieargentur. Tabellen des technologie katalogs.

[21] Bdew. Bdew-gaspreisanalyse jahresbeginn 2023, 24.02.2023. URL https://www.bdew.de/service/daten-und-grafiken/bdew-gaspreisanalyse/.

[22] Investing.com. Dutch ttf natural gas futures historische preise, 24.02.2023. URL https://de.investing.com/commodities/dutch-ttf-gas-c1-futures-historical-data.

[23] Gemis 4.95, 2017. URL https://iinas.org/downloads/gemis-downloads/.

[24] BSW Solar. Feste einspeisevergütungen in cent/kwh gemäß bisherigem eeg 2021 und eeg 2017. URL https://www.solarwirtschaft.de/datawall/uploads/2021/02/EEG-Verguetungsuebersicht-Basis.pdf.

[25] Christoph Kost, Shivenes Shammugam, and Verena Fluri, Dominik Peper, Aschkan Davoodi Memar, Thomas Scheg´l. Stromgestehungskosten erneuerbare energien.

[26] Anna Kallert, Eric Lamvers, and Young Jae Yu. Thermische energiespeicher für quartiere: Überblick zurahmenbedingungen, marktsituation und technologieoptionen für planung, beratung und politische entscheidungen im gebäudesektor.

[27] PEC GmbH. Stromspeicher kosten – pec gmbh, 27.01.2023. URL https://pro-ec.de/photovoltaik/stromspeicher-kosten-preise-2023//.

[28] Carl Christian von Weizsäcker, Dietmar Lindenberger. *Interdisziplinäre Aspekte der Energiewirtschaft*. Springer, Wiesbaden, 2016. ISBN 978-3-658-12725-1.

[29] Github - rwth-ebc/districtgenerator: Tool for demand profile generation in districts, 16.02.2023. URL https://github.com/RWTH-EBC/districtgenerator.

[30] Ian Richardson, Murray Thomson, David Infield, and Conor Clifford. Domestic electricity use: A high-resolution energy demand model. *Energy and Buildings*, 42(10):1878–1887, 2010. ISSN 0378-7788. doi: 10.1016/j.enbuild.2010.05.023.

[31] Jan Schiefelbein, Jana Rudnick, Anna Scholl, Peter Remmen, Marcus Fuchs, and Dirk Müller. Automated urban energy system modeling and thermal building simulation based on openstreetmap data sets. *Building and Environment*, 149:630–639, 2019. ISSN 0360-1323. doi: 10.1016/j.buildenv.2018.12.025.

[32] DIN EN ISO 13790:2008. Din en iso 13790:2008 - energy performance of buildings: Calculation of energy use for space heating and cooling, 2008.

[33] Tobias Loga, Britta Stein, Nikolaus Diefenbach, and Rolf Born. *Deutsche Wohngebäudetypologie: Beispielhafte Maßnahmen zur Verbesserung der Energieeffizienz von typischen Wohngebäuden ; erarbeitet im Rahmen der EU-Projekte TABULA , EPISCOPE*. IWU, Darmstadt, 2., erw. aufl. edition, 2015. ISBN 9783941140479.

[34] William F. Holmgren, Clifford W. Hansen, and Mark A. Mikofski. pvlib python: a python package for modeling solar energy systems. *Journal of Open Source Software*, 3(29):884, 2018. doi: 10.21105/joss.00884.

[35] George Mavrotas. Effective implementation of the ϵ-constraint method in multi-objective mathematical programming problems. *Applied Mathematics and Computation*, 2009. doi: 10.1016/j.amc.2009.03.037.

A top-down approach based on simulations and optimisations to evaluate renovation of public buildings

Charlotte Marguerite[a], I-Gede Parwatha[b], Cécile Goffaux[c] and Anne Meessen[d]

[a] Cenaero, Gosselies, Belgium, charlotte.marguerite@cenaero.be, CA
[b] Cenaero, Gosselies, Belgium, igede.parwatha@cenaero.be
[c] Cenaero, Gosselies, Belgium, cecile.goffaux@cenaero.be
[d] Ville de Charleroi, Charleroi, Belgium, anne.meessen@charleroi.be

Abstract:

The renovation of buildings in urban areas has become an urgent need for public authorities to reduce energy consumption and comply with the Paris Agreement's objectives. The potential for energy consumption reduction through renovation is especially high in old European cities considering that in average 70% of the buildings were built before 1981. This paper presents the work realised within the Charl-e-district project, which addresses the renovation of public buildings through a new approach combining numerical simulations and optimisations. The objective is to develop a tool to help public authorities in decision-making regarding refurbishment of public buildings (measure, intensity, building selection, expected benefits). Firstly, a numerical building model is constructed using OpenStudio/EnergyPlus and calibrated using monitored data. Secondly, renovation scenarios are defined depending on the complexity and costs of implementation. A set of optimizations is then run to determine the values of parameters that will allow the maximum reduction in energy consumption. The novelty of this methodology is the top-down approach, indeed the sets of renovation measures to be investigated are known, the values of the parameters of interest are to be determined. The results are visualised in the METRON platform, with comprehensive modules and user-friendly dashboards that allow dynamic comparisons with monitored data and KPIs for renovation scenarios.

Keywords:

Building Energy Model; Optimisation; Renovation scenarios, Energy monitoring platform.

1. Introduction

The importance of the building stock in the global energy consumption is well-known internationally and the urge to reduce the energy consumption of buildings is commonly shared. To do so, several ways are available: build energy performant buildings, ensure an appropriate maintenance of buildings energy production and distribution systems and renovate existing buildings [1]. On the one hand considering that most of the buildings that will be in use by 2050 are already built and on the other hand considering that in old European cities in average 70% of the buildings were built before 1981 [2], the renovation of existing non-performant building is capital to reach the objectives of energy consumption reduction and CO2 emissions reductions in the building sector [3-5]. The Charl-e-district project consists in evaluating various renovation strategies of public buildings of the city of Charleroi, Belgium, to raise awareness of public authorities regarding their building assets and help in the decision-making process by providing insights regarding the potential and the impact of renovation measures (to improve their energy performance and indoor comfort, to reduce their carbon footprint and operation costs). This paper presents the work carried out within the framework of the Charl-e-district project for the evaluation of renovation scenarios of one public building.

As thermal renovation of buildings is not a new area of research, several methodologies and tools are available to evaluate the renovation potential of buildings. These tools are usually made for a quick estimation of renovation possibilities based on a few characteristics of the energy demand [6-8]. In such tools, the lack of details in the demand evaluation and building thermal characteristics lead to generic solutions. In [9] the authors developed a methodology based on Life Cycle Analysis to find optimal retrofitting solutions to introduce sustainability criteria in the evaluation and provide more insights. Several literature reviews on methodologies for building refurbishment have been carried out, considering different approaches

of classification. Today the common statement highlighted in all the literature reviews is the lack of a common evaluation framework, leading to the assessment of common renovation packages, but various results, interpretation, and considerations. In [10] the authors present a literature review of methodologies to evaluate renovation measures, categorized by building type and renovation packages, showing the difficulties in the decision-making process to pick the appropriate tool or evaluation method. In [11] the authors make a scientific and 'grey' literature review of challenges of the built environment and building renovations and conclude on the wide variety of tools, approaches and methodologies, but underline that there is no holistic or systematic approach to evaluate renovation potentials. Additionally, methodologies for assessment of building renovation measures are usually applied to residential buildings, and by consequence are not directly transferable to tertiary public buildings, because of their different energy behaviours (in terms of energy demand, building usage and potential for energy production). Based on these considerations, a new methodology using a detailed building numerical model and advanced optimisation methods, is developed for public buildings, providing very specific results to help the public authorities in developing their renovation plan at building scale. This methodology using a top-down approach, is developed and applied to a detailed multi-zone numerical building model after it is calibrated with real measured data. Packages of renovation measures are defined in 3 scenarios and the building model parameters related to the renovation measures are optimised with the objective to minimize the gas consumption. The results of the optimisations give the values of parameters of interest that will allow to reach the lowest gas consumption taking into account electricity consumption and thermal comfort constraints, to ensure the satisfaction of occupants needs. Through this top-down methodology, the renovation measures are sized to the studied building in terms of type and intensity of renovation.

2. Building case description

The building studied in this paper is a public school located in Charleroi, Belgium which host 1200 students. This building of 3 130m2 has 3 floors above ground and 2 underground floors. A gas boiler of 240kW supplies heat to the building, which has an annual consumption of approximately 560 633.76kWh of gas and 41 414.99kWh of electricity. As it is a public school and no domestic hot water (DHW) measured data are available, the DHW is not included in the study. The building was built in 1963 and no data were available regarding possible renovations.

3. Methodology for development and calibration of building model

The building iss modelled in two steps, first the 3D geometry along with the neighbouring shading surfaces are created from scratch in SketchUp, as illustrated in Figure 1, based on 2D architect plans and visual checks on the building. Then the building energy model is developed with 31 thermal zones, using the OpenStudio software, and thermal characteristics are added based on technical data, typical values, etc. The EnergyPlus calculation engine is used through the OpenStudio interface to simulate the energy behaviour of the building.

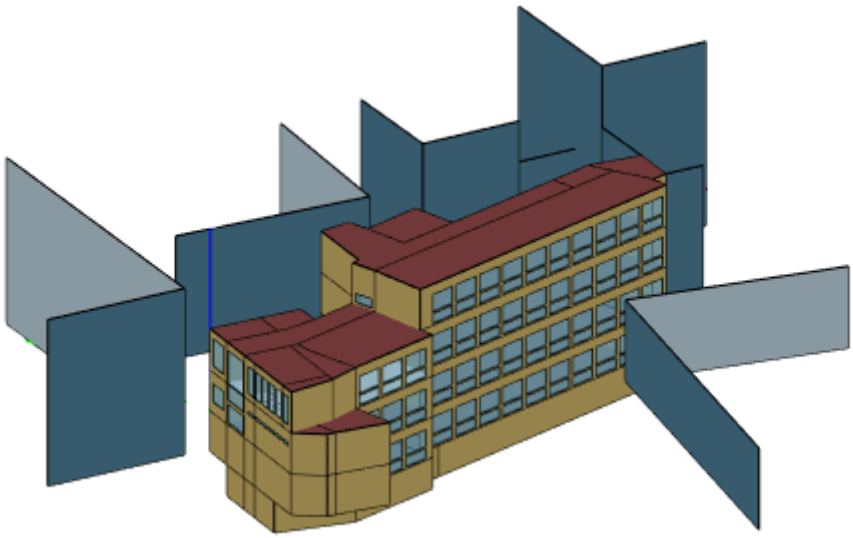

Figure. 1. 3D sketch of the studied building.

In this paper the objective of the study at building scale is to evaluate different renovation scenarios using dynamic Building Energy Simulation (BES). Therefore, the building model must be calibrated to provide relevant results. The building model is manually calibrated based on monitoring data, typically the gas

consumption measured by the gas meter and available through the METRON energy monitoring platform used by the city of Charleroi [12]. Based on previous experience [13] and literature review [14-16], key parameters are chosen, see Table 1, to be adjusted until the model is able to reproduce well enough the energy behaviour of the real building.

Table 1. Building's parameters to be adjusted to calibrate the model.

Type of parameter	Parameters
Building use	Building equipment schedule
	Building occupancy schedule
	Electrical loads
Heat production/distribution	Boiler capacity
	Boiler efficiency
	Heating setpoint temperature
	Pump motor efficiency
	Rated pump head
	Operating temperatures

The quality of the calibrated model is then evaluated by two statistical indices, often used as a pair to analyse the goodness-to-fit of Building Energy Model (BEM) i.e., NMBE (Normalized Mean Bias Error) and Cv(RMSE) (Coefficient of variation of the Root Mean Square Error). The definition of these statistical indices is given by the equations Eq. (1), Eq. (2) and Eq. (3). The NMBE measures the distance between simulated and monitored data, the closer it is to zero, the better the model represents the behaviour of the real building. For a monthly calibration of BEMs, the ASHRAE Guidelines 14-2002 [17] recommend: NMBE < 5% and Cv(RMSE) < 15%.

$$\mathrm{NMBE} = \frac{\frac{1}{N}\sum_i^N (S_i - M_i)}{\bar{M}} \quad (1)$$

$$\bar{M} = \frac{\sum_{i=1}^N M_i}{N} \quad (2)$$

Where:

- M_i is the measured value of i^{th} point
- S_i is simulated value corresponding to the ith point.
- N is the number of measured points

$$\mathrm{Cv}(RMSE) = \frac{1}{\bar{M}}\sqrt{\frac{\sum_i^N (S_i - M_i)^2}{\mathrm{N}}} \quad (3)$$

The results of the calibration evaluations are shown in Table 2, and the model results are illustrated in Figure 2 for the gas consumption and Figure 3 for the electricity consumption. Considering that the energy consumption presents both missing data and important variations from one year to the next one, especially during the covid years, several years of monthly gas and electricity consumption data are used to adjust the model parameters values and evaluate the precision of the model's responses (gas and electricity consumption). The so-called Reference year ("Ref" in this paper) is a virtual monthly profile generated based on the average monthly data available. Both indicators are calculated for 3 years and a reference year. Considering the values of NMBE and Cv(RMSE) correspond to the Guidelines criteria, (values highlighted in Table 2), the model is considered as calibrated.

Table 2. Values of NMBE et Cv(RMSE) indices after calibration using several years of monthly gas and electricity consumption data.

		2019	2020	2021	Ref
Elec	NMBE (%)	**6.77**	23.35	**-16.49**	**-2.41**
	RMSE	569.78	1062.40	810.32	334.40
	CV(RMSE)	16.51	30.78	23.48	**9.69**
Gas	NMBE (%)	**-0.56**	**11.10**	**-10.83**	**-3.71**
	RMSE	5822.09	12056.96	8164.90	3587.85
	CV(RMSE)	**12.46**	25.81	17.48	**7.68**

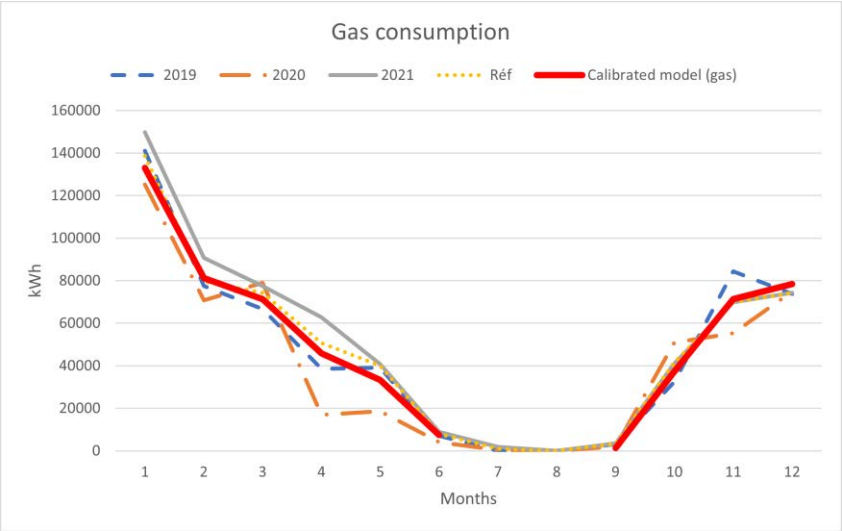

Figure. 2. Comparison between measured data and model results for gas consumption after calibration.

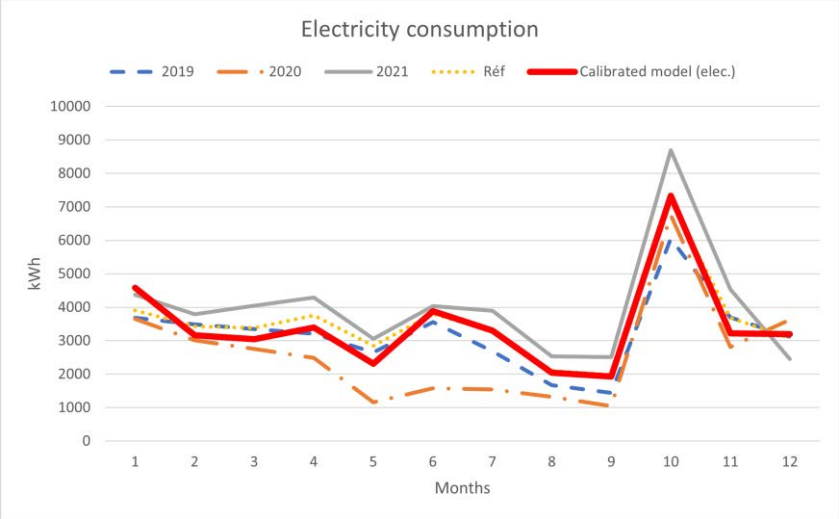

Figure. 3. Comparison between measured data and model results for electricity consumption after calibration.

3. Methodology for renovation scenarios study

The objective of the model calibration is to have a model detailed and reliable to perform renovation scenarios and evaluate the impact of the proposed renovation measures on the model responses (gas and electricity consumption). Different renovation measures are proposed within 3 scenarios, as presented in Table 3, depending on the complexity and costs of implementation. Indeed Scenario 1 (SC1) does not require any renovation works, only an improvement in the regulation of systems, while Scenario 2 (SC2) implies an adjustment of the regulation and deep renovation works, such as adding new material as insulation into walls, roofs and floors of the building. Scenario 3 (SC3) proposes to add the replacement of the gas boiler and pumps to all the previous measures. The model parameters corresponding to the renovation measures are identified with their variation ranges and a set of optimizations is run to optimise the values of these parameters and by doing so, allow the maximum reduction in energy consumption. In SC3, the measures of SC1 are applied except the “Improved boiler regulation measures”, because these regulations are linearly linked to the “Replacement of boiler” measures. To avoid losing in thermal comfort, the ranges of variation of the relative humidity and the temperature in the constraints used in the optimizations are the same as the initial ranges calculated as simulation results in the Base Scenario (Base SC).

Table 3. Description of renovations scenarios.

	Measures	Building parameters in EnergyPlus	Min value	Max value	ref value (Base SC)	Unit
SC1	Setpoint temperatures reduction	Setpoint temperatures	20	24	24	°C
	Improved boiler regulation	Boiler operating temperatures	85	120	110	°C
		Distribution system temperatures (at heat exchangers and radiants)	85	115	110	°C
SC2	SC1 Measures					
	Renovation of insulation	Wall Insulation : Thickness	0.0566	0.25	0.0566	m
		Wall Insulation : Conductivity	0.035	0.05	0.0432	W/(m.K)
		Roof Insulation : Thickness	0.05	0.3	0.05	m
		Roof Insulation : Conductivity	0.035	0.05	0.049	W/(m.K)
		Floor Insulation : Thickness	0.00001	0.3	0.00001	m
		Floor Insulation : Conductivity	0.022	0.04	0.035	W/(m.K)
	Replacement of windows	Thickness	0.003	0.24	0.003	m
		Conductivity	0.0195	0.672	0.0195	W/(m.K)
SC3	SC1 Measures SC2 Measures					
	Replacement of boiler	Nominal Thermal Efficiency	0.55	1	0.55	-
		Water Outlet Upper Temperature Limit	55	120	120	°C
	Replacement of pumps	Rated pump head	7000	17000	7000	Pa

The objective function for all the sets of optimisations is as in Eq. (4)

$$\mathrm{f} = \sum_{i=1}^{N} C_i^{gas} \quad (4)$$

Where C_i^{gas} is the gas consumption of *i*th day over a total number of N days. The constraints considered in all Scenarios are described in equations Eq. (5), Eq. (6) and Eq. (7). These constraints are related to electricity consumption (to avoid that the model compensates the reduction of heat gains by extra electricity consumption of appliances) and to thermal comfort of occupants (in terms of humidity and temperature).

$$C_{SC}^{Elec} \leq C_{Base\ SC}^{Elec} \times a \quad (5)$$

$$15\% < RH < 85\% \quad (6)$$

$$24 < T < 31 \quad (7)$$

Where $C_{Base\ SC}^{Elec}$ and C_{SC}^{Elec} are respectively the annual electricity consumption of the Base Scenario and the current Scenario, a is a coefficient equal to 1.015 (to simulate a slight increase of 1.5%) for Opti and 0.845 for Opti_2 et Opti_3 (to simulate a decrease of 15.5%). RH and T are the relative humidity and the temperature in each thermal zone at each time step. The different sets of optimisations and their related constraints are summarized in Table 4.

To optimise the parameters values in Scenario 3, only one set of optimisations that consider all constraints, is run. Indeed, Scenario 3 considers the same parameters as Scenario 2 plus extra parameters to be optimised. As the optimisation results of Scenario 2 show the importance of all the constraints (including the thermal comfort constraints) to optimise the parameters, it was chosen to run the optimisation for Scenario 3, using only one set of optimisations that consider all constraints.

The optimisations are performed using Cenaero's in-house multi-disciplinary optimization tool, Minamo, which uses a Surrogate Based Optimization (SBO) approach and relies on a genetic algorithm. A brief explanation is given in the following, but for further details about the Minamo tool and the use of SBO optimisation see [18]. The surrogate model used by Minamo for this study is the Tuned RBF model (Tuned Radial Basis Function), for more details about Minamo's surrogate models, see [19-20].

For each scenario, the first step while using the Minamo tool is to generate and evaluate a Design of Experiments (DoE). The DoE is a randomly generating set of points (each point (or individual) represents a set of optimization parameters or variables) sufficiently well distributed in the design space, illustrated by the blue circles on the Figure 4, Figure 5 and Figure7. Based on the evaluation of output results of the DoE, a surrogate model is built, it will allow to evaluate the objective function and constraints at low computational cost. Then the optimisations are run using the surrogate model to determine the optimum values of parameters that minimize the gas consumption (objective function).

Table 4. Constraints for the sets of optimisations of all Scenarios.

	Optimisation set 1		Optimisation set 2		Optimisation set 3	
	ID	Constraints	ID	Constraints	ID	Constraints
SC 1	Opti	$C_{SC}^{Elec} \leq C_{Base\ SC}^{Elec} \times 1.015$	Opti_2	$C_{SC}^{Elec} \leq C_{Base\ SC}^{Elec} \times 0.845$	Opti_cont.	$C_{SC}^{Elec} \leq C_{Base\ SC}^{Elec} \times 0.845$ $15\% < RH < 85\%$ $24 < T < 31$
SC 2	Opti	$C_{SC}^{Elec} \leq C_{Base\ SC}^{Elec} \times 1.015$	Opti_2	$C_{SC}^{Elec} \leq C_{Base\ SC}^{Elec} \times 0.845$	Opti_3	$C_{SC}^{Elec} \leq C_{Base\ SC}^{Elec} \times 0.845$ $15\% < RH < 85\%$ $24 < T < 31$
SC 3	-		-		Opti	$C_{SC}^{Elec} \leq C_{Base\ SC}^{Elec} \times 0.845$ $15\% < RH < 85\%$ $24 < T < 31$

3. Results analysis

Figure 4, Figure 5 and Figure 7 illustrate the set of values for the annual gas consumption after the DoE and different optimisations. Each dot of the graphs represents an experiment, in other words a set of parameters values from which the model responses are calculated. For each set of optimisations, various graphs are generated to interpretate the results, typically the responses and parameters vs the experiments. In the following, only the most relevant graphs are shown.

For Scenario 1, the first set of optimisations (Opti) gives better results than the later ones, in terms of annual gas consumption and at the same time these first optimisations respect the thermal comfort conditions (without imposing them as constraints). When the electricity constraint become stricter (Opti_2) and when comfort constraints are added (Opti_cont.), the gas consumption results from Opti to Opti_cont. increase of around 72% (from 325MWh to 560MWh). That is why the optimum parameters values belong to the first set of optimisations (Opti, orange dots on Figure 4). For Scenario 2, the first and second sets of optimisations give a lower gas consumption than the third set of optimisations, as illustrated by Figure 5, but for these two first sets the maximum comfort temperature constraint is not respected (between 40°C and 47°C) as illustrated by Figure 6, while for the third set of optimisations, the maximum temperature is between 30°C and 32.5°C, which is an acceptable range. For this scenario, the optimum parameters values belong to the Opti_3 set of optimisations. The DoE and optimisation results of Scenario 3 are illustrated by Figure 7. For this scenario, the results from the different runs of experiments converge rapidly to the optimum parameters values (the orange dots reach a value close to 100 000kWh from the 5th experiment).

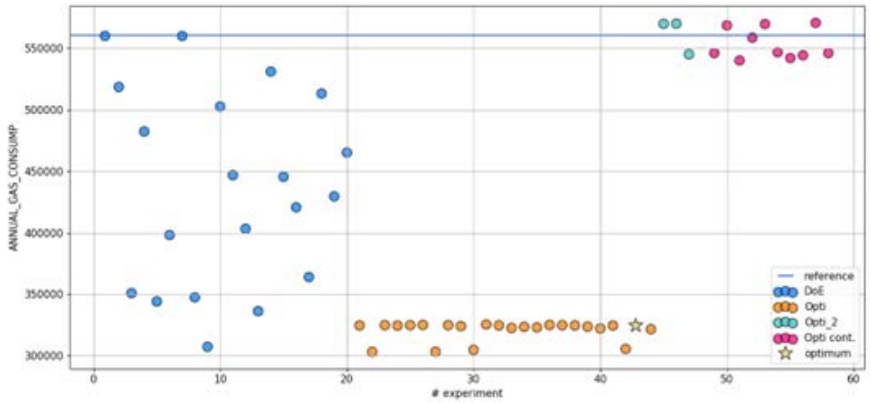

Figure. 4. DoE and optimisations results for Scenario 1.

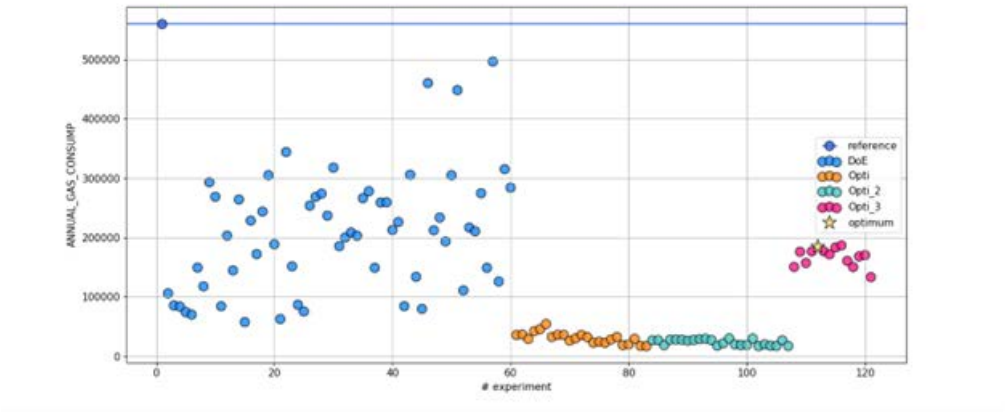

Figure. 5. DoE and optimisations results for Scenario 2.

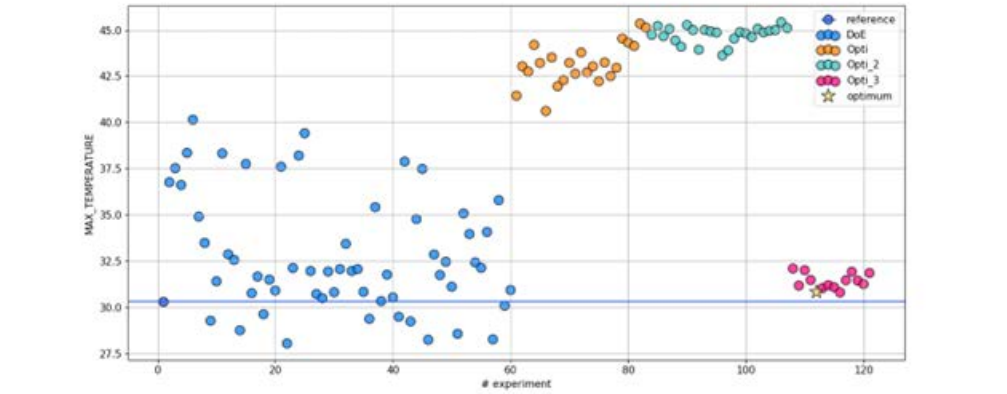

Figure. 6. Evolution of maximum temperature in the building for the DoE and different sets of optimisations for Scenario 2.

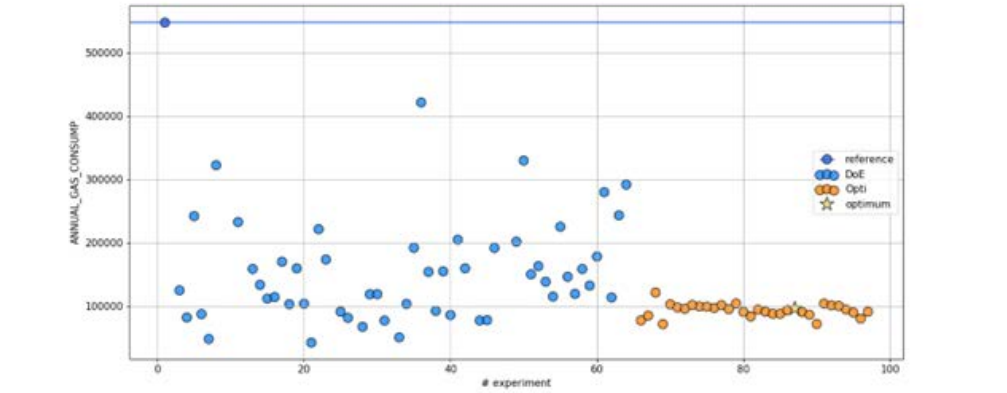

Figure. 7. DoE and optimisations results for Scenario 3.

The optimum values of the evaluated building parameters and the model responses are presented in Table 5 and illustrated by Figure 8. The optimum parameters values for SC1 indicate a reduction of all temperatures except the radiant temperature, while in the other scenarios all temperatures are reduced. For all scenarios, the optimum value of heating setpoint temperature is (or is close to) the lower boundary of the variation range of that parameter (20°C). A variance analysis (ANOVA), based on the decomposition of the variance of a function, [21-22], is carried out after the optimisations and shows that the setpoint temperature is by far (more than 50%) the most influencing parameter for the gas consumption. The results of this ANOVA are not shown in this paper because of the limited number of pages. The optimum values of thickness parameters for SC2 and SC3 are close to the upper boundaries of the variation ranges while the conductivity parameters are chosen by the optimizer around the mid-value of their variation ranges.

Table 5. Optimum values of parameters and model responses for all scenarios.

Parameters	Base SC	SC1	SC2	SC3
SETPOINT_REDUCTION	24	20	20.3	20
SETPOINT_SUPPLY_BOILER	110	104.2	102.7	-
SETPOINT_HX_RADIANTS	110	98.7	107.5	-
RADIANT_TEMPERATURE	110	115	107.5	-
WALL_INSULATION_THICKNESS (m)	0.0566	-	0.24	0.242
WALL_INSULATION_CONDUCTIVITY (W/mK)	0.0432	-	0.04	0.036
FLOOR_INSULATION_THICKNESS (m)	0.00001	-	0.217	0.3
FLOOR_INSULATION_CONDUCTIVITY (W/mK)	0.035	-	0.03	0.037
ROOF_INSULATION_THICKNESS (m)	0.05	-	0.216	0.197
ROOF_INSULATION_CONDUCTIVITY (W/mK)	0.049	-	0.043	0.037
DVITRAGE_INSULATION_THICKNESS (m)	0.003	-	0.1	0.089
DVITRAGE_INSULATION_CONDUCTIVITY (W/mK)	0.0195	-	0.497	0.437
BOILER_ETA	0.55	-		1
OUTLET_TEMP_LIMIT (°C)	120	-		90.7
SERVICE_PUMP_HEAD (Pa)	7000	-		7842.9
PLANT_PUMP_HEAD (Pa)	7000	-		7000
Responses				
ANNUAL_GAS_CONSUMP (kWh)	560.633	324.727	185.532	96.503
ANNUAL_ELEC_CONSUMP (kWh)	41.415	33.972	33.511	34.346
MINIMUM_HUMIDITY (%)	15.00	19.31	19.19	19.33
MAXIMUM_HUMIDITY (%)	85.00	84.40	79.62	79.62
MINIMUM_TEMPERATURE (°C)	24.00	20.00	20.26	20.00
MAXIMUM_TEMPERATURE (°C)	31.00	29.65	30.87	30.91

SC3 which proposes a replacement of the boiler, gives an optimum efficiency value of 1, which is relevant for the installation of a condensing boiler (this type of boilers generally presents efficiencies around 110%). The optimum values for rated pumps heads are surprisingly low considering the initial variation range, which would basically mean that there is no need to replace the pumps because the other measures are sufficient to decrease the total heat demand and the operating boiler temperatures, and consequently the gas consumption (objective function).

When analysing the simulation results for the optimum parameter values, one can clearly notice the decrease in gas consumption from one scenario to another. Indeed, in SC1 the annual gas consumption decreases of 42% compared to the Base SC, while this decrease is steeper in SC2 (-67%) and SC3 (-83%). As the electricity consumption is not part of the objective function for the optimisation, but part of a constraint, the reduction of electricity consumption is noticeable but not very different between the scenarios, it ranges between -17% for SC3 to -19% for SC2 compared to the Base SC. From SC1 to SC3, the maximum and minimum relative humidities are closer to the constraints limits, but tend to get respectively lower and higher than their maximum and minimum limits. The maximum and minimum temperatures are respectively around 4°C lower and 0.5°C lower than Base SC. The results from the simulations of the building model with the optimum values give maximum and minimum temperatures very close between all the scenarios (around 30°C and 20°C).

The results from the simulation runs with the optimum parameters values are pushed into the METRON energy platform database and visible through various comprehensive modules, named widgets, and user-friendly dashboards developed in the platform itself. The objective is to allow users, here public authorities, to visualize quickly the indicators calculated for each scenario and compare the KPIs of the different scenarios with monitored data, in order to understand better the current situation and the renovation potential and possibilities. The simplicity of the visualisation that allows dynamic comparisons together with the corresponding database if further analyses are required, give to this approach a powerful weight in decision-making processes. Examples of widgets are given by Figure 9 and Figure 10 to compare the scenarios in terms of monthly gas consumption, CO2 emission reductions and evolution of temperature throughout the year in one typical thermal zone (classroom) of the building. Other widgets are available on the platform, to visualise KPIs such as savings in gas consumption (economic indicator) or humidity heatmaps (thermal comfort indicator).

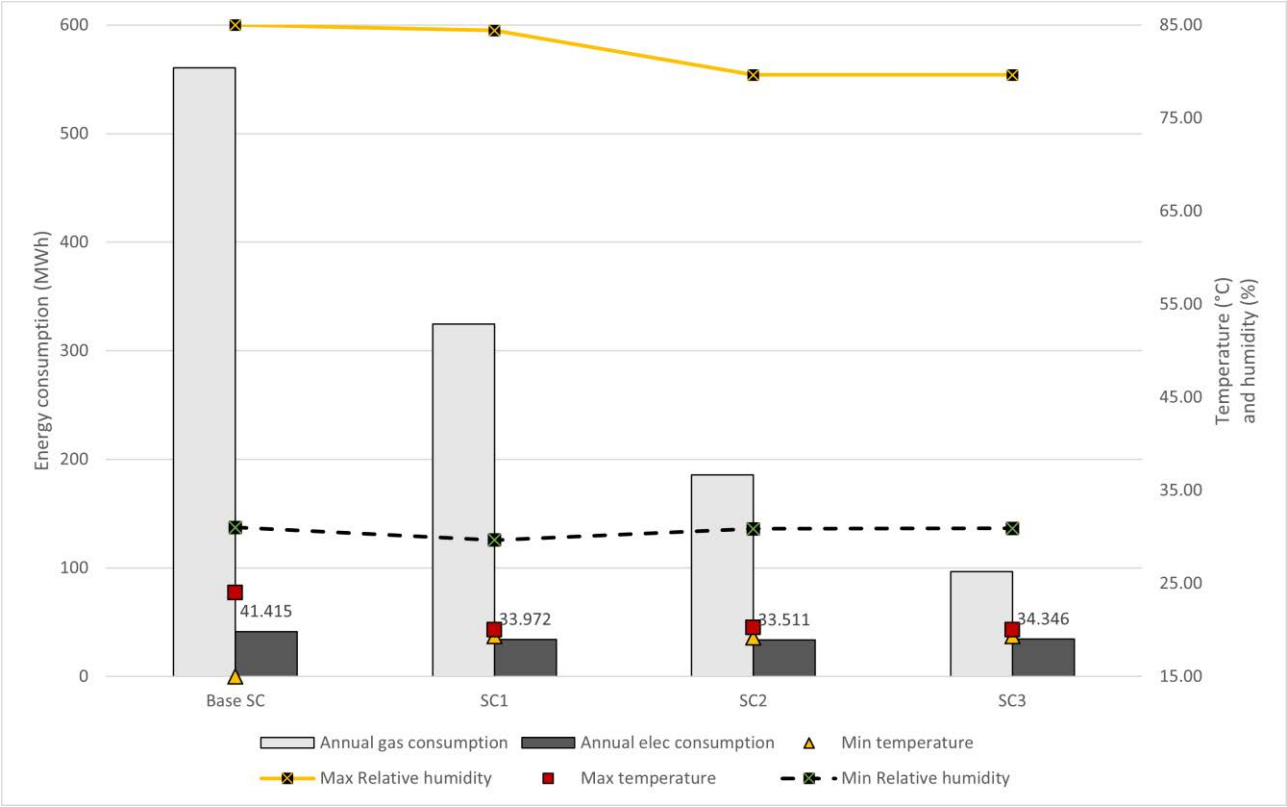

Figure. 8. Simulation results from optimum values of parameters for all Scenarios.

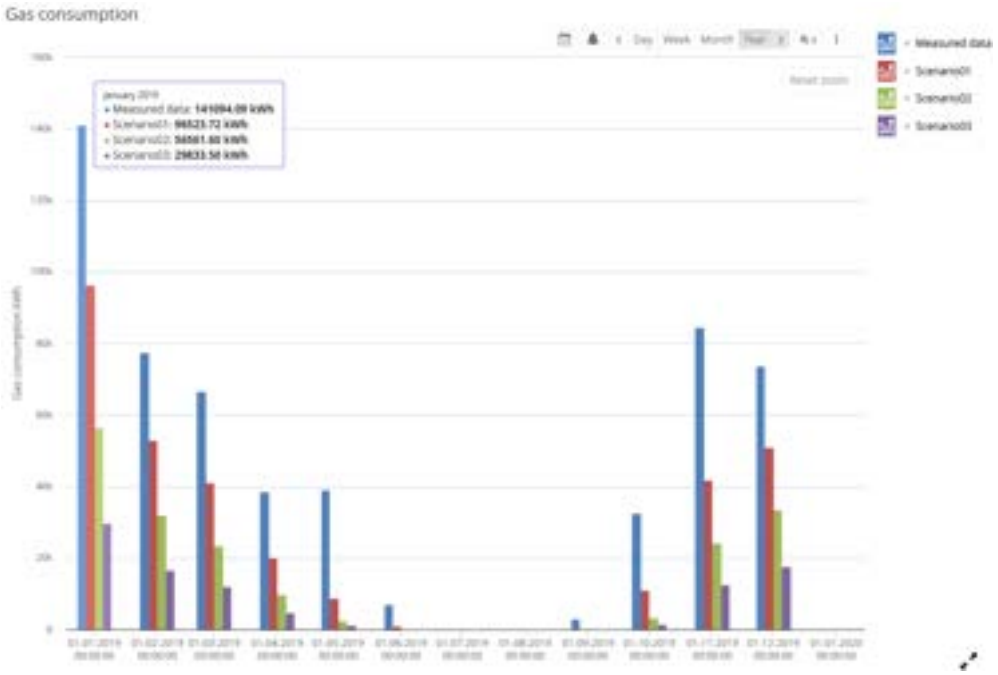

Figure. 9. Histogram widget in the METRON energy platform. Comparison of gas consumption between the measured data and the different results from optimum scenarios.

Figure. 10. Gauges widgets in the METRON energy platform. Comparison of CO2 emission reductions and temperature heatmaps in one typical thermal zone (classroom) between the different results from optimum scenarios.

3. Discussions and perspectives

To be useful and relevant, the results of the optimisations must be taken with hindsight. The optimum parameters are identified through advanced calculations and correspond to perfectly optimised systems. SC1 proposes the easiest measures to implement, because they do not require any work, only a new setup of the building setpoint temperature and a new setup of the regulation. Considering the uncertainties due to the assumptions made in the modelling (geometrical and technical assumptions) and the calibration steps (interpolation of measurements), one should expect some differences between the model results and the real gas consumption if the new setups are tested, however this scenario is in any case recommended for implementation insofar as it results in more than one third of gas consumption reduction compared to the Base SC. It is important to note that the renovation measures resulting from SC2 and SC3, correspond to deep renovation in real-life implementation (improvement of insulation, replacement of windows, boiler and pumps, etc.) and are implemented at building scale (all the walls are renovated, all the windows are replaced, etc.), which explains why the reduction of gas consumption decreases drastically for each scenario, to reach -83% with SC3 compared to the Base SC. In real-life implementation, such deep renovation is extremely costly and it is most probable that the renovation measures regarding the improvement of insulation would not be made for all building's walls, but only on the less exposed façades and the walls that present the most heat losses. For a more complete renovation study, it would be interesting to precise the renovation scenarios with measures that would consider partial building envelop renovation and evaluate the potential and interest of implementation of greener solutions, such as air-sourced heat pumps or the connection to the local district heating network. Further exploitation of results through economic analyses would also be an added value to help public authorities in the decision-making process.

4. Conclusions

This paper presents a new top-down approach to evaluate various renovation strategy, in terms of type and intensity of renovation measures, for a public building of the city of Charleroi, Belgium. In a first step, a numerical building model is developed and calibrated based on real gas consumption measurements, before being studied through 3 renovation scenarios for which the main parameters related to the renovation measures are optimised using a Surrogate Based Optimisation approach. The optimisations are carried out using Minamo, the Cenaero's in-house multi-disciplinary optimisation tool. The results of different optimisations of the parameters within the studied scenarios give combinations of values that ensure in general the same quality of thermal comfort (indoor temperature and humidity) and lead to similar results in terms of electricity consumption. The main difference in the scenarios results lies in the gas consumption reduction, which varies greatly from one scenario to another. Considering the investment costs and the complexity of implementation of the measures proposed in the scenarios (increasing from SC1 to SC3), the public authorities would have to consider other indicators such as investment costs, payback time, energy savings over time, urgency to reach objectives of CO2 emission reductions, etc. to choose a renovation strategy and how deep they want to implement the different measures.

A follow-up study is being carried out at district level, to evaluate the benefits of the connection of public buildings to the district heating network, with scenarios varying in terms of buildings number and renovation levels of connected buildings. The work detailed in this paper will serve as input to the district approach to facilitate the definition of building typologies and calibrate a district model using an Urban Building Energy Modelling (UBEM) tool. The objective is again to help the public authorities in decision-making regarding the

interests of renovation of public buildings together with / or the extension of the existing district heating network.

4. Acknowledgement

This work was carried out within the framework of the Charl-e-district project, co-financed by l'Agence du Numérique and the Wal-e-cities ERDF project.

4. References

[1] Macek D., Dobias J., Building renovation and maintenance in the public sector. Procedia Engineering 2014;85:368-376.

[2] Marini A., Passoni C., Riva P., Negro P., Romano E., Taucer F., Technology options for earthquake resistant, eco-efficient buildings. Europe: Research needs. Report EUR 26497 EN; 2014.

[3] United Nations Framework Convention on Climate Change. The Paris Agreements, 2015 – Available at: <https://unfccc.int/sites/default/files/resource/parisagreement_publication.pdf> [accessed 01.03.2023].

[4] Gupta J., A history of international climate change policy. WIREs Climate Change 2010;1:636-653.

[5] Buildings Performance Institute Europe (2021). Deep Renovation: Shifting from exception to standard practice in EU Policy – Available at: <https://www.bpie.eu/publication/deep-renovation-shifting-from-exception-to-standard-practice-in-eu-policy/> [accessed 01.03.2023].

[6] Mjörnell K., Boss A., Lindahl M., Molnar S., A Tool to Evaluate Different Renovation Alternatives with Regard to Sustainability. Sustainability 2014;6:4227-4245.

[7] Mata E., Sasic Kalagasidis A., Johnsson F., A modelling strategy for energy, carbon, and cost assessments of building stocks. Energy and Buildings 2013;56:100-108.

[8] Mequignon M., Adolphe L., Thellier F., Ait Haddou H., Impact of the lifespan of building external walls on greenhouse gas index. Building and Environment 2013;59:654-661.

[9] Pombo O., Rivela B., Neila J., The challenge of sustainable building renovation: assessment of current criteria and future outlook. Journal of Cleaner Production 2016;123(1):88-100.

[10] Yovko Ivanov A., Heiselberg P., Flourentzou F., Zbigniew Pomianowski M., Methodology for Evaluation and Development of Refurbishment Scenarios for Multi-Story Apartment Buildings, Applied to Two Buildings in Denmark and Switzerland. Buildings 2020;10(6): 102.

[11] Jimenez-Pulido C., Jimenez-Rivero A., Garcia Navarro J., Improved sustainability certification systems to respond to building renovation challenges based on a literature review. Journal of Building Engineering.Volume 2022;45.

[12] METRON Energy monitoring platform – Available at: <https://www.metron.energy/solution/energy-performance-monitoring/> [accessed 01.03.2023].

[13] Marguerite C., Lê V.L., Beauthier C., Fontaine de Ghélin O., Goffaux C., de Moffarts L., Calibration of a Multi-Residential Building Energy Model – Part I: Cluster-Based Sensitivity Analysis. In Proceedings of the Building Simulation 2021 Conference; 2021 Sept 1-3; Bruges, Belgium.

[14] Goldwasser D., Ball B., Farthing A., Frank S., Im P., Advances in calibration of building energy models to time series data. In Proceedings of the ASHRAE Building Performance Analysis Conference and SimBuild; 2018 Sept 26-28; Chicago, USA.

[15] Sun K., Hong T., Taylor-Lange S.C., Piette M.A., A Pattern-based automated approach to building energy model calibration. Applied Energy 2016;165:214-224.

[16] Wang, C., Tindemans, S., Miller, C., Agugiaro, G., & Stoter, J., Bayesian calibration at the urban scale: A case study on a large residential heating demand application in Amsterdam. Journal of Building Performance Simulation 2020;13(3):347-361.

[17] ASHRAE standards committee 2014–2015. Measurement of Energy, Demand, and water savings. ASHRAE Guidelines14-2014 – Available at: <https://upgreengrade.ir/admin_panel/assets/images/books/ASHRAE%20Guideline%2014-2014.pdf> [accessed 01.03.2023].

[18] Lê V.L., Marguerite C., Beauthier C., Fontaine de Ghélin O., Goffaux C., de Moffarts L., Calibration of a Multi-Residential Building Energy Model – Part II: Calibration Using Surrogate-Based Optimization. In Proceedings of the Building Simulation 2021 Conference; 2021 Sept 1-3; Bruges, Belgium.

[19] Sainvitu, C., Iliopoulou, V., Lepot I., Global optimization with expensive functions - sample turbomachinery design application. In: Diehl, M., et al., editors: Recent Advances in Optimization and its Applications in Engineering; 2010. Springer-Verlag, Heidelberg.

[20] Beaucaire, P., Beauthier, C., Sainvitu, C., Multi-point infill sampling strategies exploiting multiple surrogate models. In: Proceedings of the 2019 Genetic and Evolutionary Computation Conference Companion; 2019 July 13-17; Prague, Republic Czech, 1559–1567.

[21] Jacques, J., Pratique de l'analyse de sensibilité: comment évaluer l'impact des entrées aléatoires sur la sortie d'un modèle mathématique. Université de Lille; 2011.

[22] Saltelli, A., Ratto M., Andres T., Campolongo F., Cariboni J., Gatelli D., Saisanan M., Tarantola S., Global Sensitivity Analysis, The Primer. John Wiley & Sons, Ltd; 2008.

PROCEEDINGS OF ECOS 2023 - THE 36TH INTERNATIONAL CONFERENCE ON
EFFICIENCY, **C**OST, **O**PTIMIZATION, **S**IMULATION AND ENVIRONMENTAL IMPACT OF ENERGY SYSTEMS
25-30 JUNE 2023, LAS PALMAS DE GRAN CANARIA, SPAIN

A Nonlinear Optimization Method for Expansion Planning of District Heating Systems with Graph Preprocessing

Jerry Lambert[a] and Hartmut Spliethoff[b]

[a] *Technical University of Munich, Chair of Energy Systems Munich, Germany, jerry.lambert@tum.de, CA*
[b] *Technical University of Munich, Chair of Energy Systems Munich, Germany, spliethoff@tum.de*

Abstract:
This paper presents a method to find the optimal topology, pipe sizing, and operational parameters of a district heating system under consideration of one design point. The current high costs of district heating systems set limits regarding the minimum heat demand density required for economic network expansions. Optimized routing with ideal pipe sizing and optimal operating parameters offers a potential for cost reduction. With a lower network temperature, the consideration of nonlinear transport phenomena within the district heating network becomes increasingly important. Therefore, a new nonlinear optimization method is introduced, where graph preprocessing reduces the computational effort of the subsequent nonlinear optimization. A cost penalization method, using a smooth approximation of a Heaviside function is applied to pipe investment costs to account for discrete piping diameters. To guarantee fast convergence of the optimization algorithm, the Jacobian matrixes are calculated and the problem is solved with an interior point algorithm. As a proof of concept, the district heating system for a small fictional town with 42 consumers is optimized and analyzed. The whole nonlinear optimization is performed in 19.37 sec and in most cases discrete or near discrete diameters are achieved in a nonlinear continuous optimization.

Keywords:
Energy System, District Heating, Nonlinear Optimization, Topology Optimization.

1. Introduction

District heating systems can play a key role in a socially accepted, economic transformation towards a renewable energy system due to numerous advantages over a building-specific heat supply [1]. Currently, the high total costs of district heating systems usually require a high heat demand density for economic network expansions [2], as until recently there was very strong competition in the form of cheap individual heating from oil and gas. In addition, long amortization periods frequently prevent expansions from being economically feasible without subsidies. One possibility to reduce investment costs of district heating networks is a detailed nonlinear topology optimization, allowing optimized routing with ideal pipe sizing, as well as optimized operating parameters. Especially in less urbanized or rural areas, an untapped potential of environmentally friendly heat supply could be exploited [3]. In urban areas, [4] shows that an integration of industrial waste heat into district heating systems could further improve the potential of these systems. In the next section, different optimization techniques for district heating systems are explained in the following order: Mixed-integer linear programming (MILP), mixed-integer nonlinear programming (MINLP), heuristics, and adjoint-based optimization.

The discrete nature of network expansions and commercially available pipe diameters often leads to a mixed-integer programming formulation. [5] shows that most publications on district heating topology optimization are using MILP. In [6], mixed-integer linear programming is used to solve this structural optimization for a district cooling system. In [7], a similar MILP approach is used to perform a topology optimization of a single-commodity flow network. The optimization is reduced to a power flow in the network, neglecting e.g. mixing effects at junctions. Pressure dependencies are omitted. Different supply technologies, operational parameters and network topology are optimized in [8]. Heat losses are considered by calculating the enthalpy loss in a pipe with an average heat loss per unit length and pipe. Pressure losses in pipes were considered by linearizing the Haaland equation. Similar MILP formulations can be found in [9, 10]. In [11], a method is presented to create network topologies based on Geographic Information System data. In a second step, pressure losses are estimated in the network at the heat demand's peak load, and the pipe diameters are sized accordingly. [12] improved the method presented in [7] by calculating a maximal linear power flow with the help of a linearization based on a specific pressure loss and commercially available pipe diameters. [13] further improves on [12] by reducing the number of binary variables used in the optimization problem formulation. However, all these methods are not able to depict the nonlinear effects of district heating networks. Flow patterns in systems with

multiple spatial distributed producers, mixing temperatures at junctions or loops, can hardly be linearized while respecting the physical interrelations.

To combat these problems, mixed-integer nonlinear programming is used more frequently in recent publications. In [14], an MINLP is proposed to solve an operational-based optimal scheduling strategy to minimize the daily operational cost of an energy station with a heating and cooling demand, as well as storage. However, the distribution of the heat by a district heating network is neglected. The commercial MINLP solver DICOPT within GAMS is used in [15] to solve a nonlinear and discrete representation of a steady-state district heating system. In [16], the same method is used in a small-scale district heating system with 19 consumers. Moreover, the nonlinear effects of energy, as well as momentum conservation, are considered and solved with commercial solvers in [17, 18]. However, due to the nonlinear equations and the discrete nature of some variables, these methods are limited to a few consumers. [19] shows, solving the full MINLP leads to an exponential scaling of computational costs with network size during the discrete topology optimization.

Another method for solving district heating optimization problems is the use of heuristic optimization approaches. These procedures may provide a sufficiently good solution to an optimization problem while not always guaranteeing a local or global optimum. This becomes especially difficult with scaling dimensions of the problem. A commonly used heuristic approach are nature-inspired algorithms like the ant colony optimization or the genetic algorithm. In [20], the ant colony optimization was used to minimize fuel consumption while modelling a nonlinear gas flow. A parallel ant colony system algorithm is used in [21] to find a cost-optimal route between one producer and one consumer while neglecting the nonlinear effects of pressure or temperature dependencies, only considering investment costs of piping influenced by the surface condition. Similar in [22], the genetic algorithm is used to optimize a single long-distance heat transport system considering hydraulic and thermal nonlinear aspects. The genetic algorithm is used in [18] to optimize the district heating network topology and pipe diameters of a small network with ten heat consumers. Meanwhile, in [23], a hybrid strategy with a genetic algorithm and MILP is used to minimize the fuel costs of different heat producers. In [24], a methodology focusing on the optimal sizing of pipe diameters using a genetic algorithm to generate a set of Pareto-optimal sizing choices is presented.

The last presented optimization method is adjoint optimization. In [25], the adjoint method is used to optimize robust hydraulic district heating systems while neglecting thermal aspects within the network. Another adjoint method is presented in [26] that optimizes simultaneously the district heating topology and operational parameters of a district heating system. The method is further expanded in [27] and applied to a district of 160 consumers. The discrete optimization problem is transformed into a continuous optimization problem by using Heaviside functions. Moreover, constraint aggregation is used to increase the performance of the optimization procedure. In [28], the method of [27] is further developed by introducing a solid isotropic material with a penalization approach to reach discrete diameters.

2. Methodology

In this paper, the considered heat carrier medium is water at 60 °C. It is assumed to be liquid and therefore incompressible. Additionally, by assuming temperature changes smaller than $\Delta T = 40\,^{\circ}\mathrm{C}$, temperature dependencies of the fluid properties (e.g. density ρ, heat capacity c_p and dynamic viscosity μ) can be neglected. Moreover, this reduces the dependencies between the thermal and hydraulic parts of the optimization. During the nonlinear topology optimization of the district heating system, the following two main challenges occur:

- The formulation of equations in dependence of potential pipe connection (e.g. pressure or thermal losses in a pipe)
- The direction of the flow in pipes (e.g. mixing temperature in a node)

Therefore, a new preprocessing method is proposed to solve and improve the problems mentioned above. First, a linear thermal power flow optimization is performed on the district heating topology to determine flows through the network, eliminate unnecessary piping connections, and reduce the available choice of discrete piping diameters. Afterward, a detailed nonlinear optimization is performed on the preprocessed district heating system. In this optimization the nonlinear pressure and temperature drops as well as discrete diameters are determined, thus giving a far more realistic depiction of the network. First, in section 3. the graph representation of a district heating system is introduced. In section 4., the preprocessing method is explained, while the nonlinear optimization model is introduced in section 5.. Finally, in section 6. the results for a small district heating system of 42 consumers are shown and in section 7. a conclusion is drawn.

3. Representing a District Heating System as a Graph

To represent pipes, junctions, producers, or consumers mathematically a graph representation of a district heating system has to be introduced. The pipes of the district heating systems correspond to the arcs of the graph and the network's junctions to the nodes. The district heating network consists of a feed and return network which have arcs of opposite directions. This superstructure contains all possible connections and pathways from the heat source to the consumers. The set of all nodes N can be subdivided into three diffident subsets:

$$N_{int} \cup N_p \cup N_c = N \tag{1}$$

In Equation 1, *int* refers to all nodes without a consumer or a producer. The subscript p describes all nodes with a connection to at least one producer and the subscript c all nodes with a connection to at least one consumer. Similarly, A_{int} represents the geometrical pipe connection between two different internal nodes. A_p and A_c denote the state transition between the district heating system and a producer or a consumer. The set A representing all arcs of the network is given by:

$$A_{int} \cup A_p \cup A_c = A \tag{2}$$

A certain node of the network will be referred to as n, whereas a directed arc going from node i to node j as $ij \in A$.

4. Linear District Heating Model

In order to linearize the maximal power flow in a district heating pipe with length l, the maximal mass flow m with the corresponding velocities v of each considered piping diameter d has to be determined. First, the Bernoulli equation with a head loss Δh_f is used to calculate the pressure loss between two nodes i and j with equal height connected by a pipe:

$$\frac{p_i}{\rho} + \frac{v_i^2}{2} = \frac{p_j}{\rho} + \frac{v_j^2}{2} + \Delta h_f \tag{3}$$

The head loss Δh_f is calculated according to Darcy-Weisbach:

$$\Delta h_f = f_{ij} \cdot \frac{l_{ij}}{d_{ij}} \cdot \frac{v_{ij}^2}{2} \tag{4}$$

The Reynolds number Re is calculated as:

$$Re_{ij} = \frac{\rho \cdot v_{ij} \cdot d_{ij}}{\mu} \tag{5}$$

For Reynolds numbers $Re < 2320$ the friction factor f_{ij} is calculated by:

$$f_{ij} = \frac{64}{Re_{ij}} \tag{6}$$

The friction factor f_{ij} for $Re \geq 2320$ is given by the Haaland equation with the pipe roughness ε: [29]

$$f_{ij} = \left[-1.8 \cdot \log\left(\left(\frac{\varepsilon}{3.7 \cdot d_{ij}} \right)^{1.11} + \frac{6.9}{Re_{ij}} \right) \right]^{-2} \tag{7}$$

According to [30], the specific pressure drop per meter pipe length should range from 70 Pa/m to 350 Pa/m. In this study, a maximum specific pressure drop Δp_{max} of 250 Pa/m is assumed for the optimization. An iterative calculation is used to determine the maximal velocity in a pipe with a given inner diameter. Starting at an initial velocity of 0.01 m/s, the following equation is iterated until the relative difference of v between two consecutive steps is smaller than 10^{-6}:

$$v_{i+1} = \sqrt{\frac{2 \cdot \Delta p_{max} \cdot d}{f \cdot \rho}} \tag{8}$$

Finally, the maximal thermal power flow $\dot{Q}_{max}$ is calculated with the corresponding inner diameter and the feed and return line temperature. Next, the thermal aspect of an insulated pipe buried underground is considered. Therefore, the temperature difference Θ between the water temperature in the pipe T and the outside temperature T_∞ is introduced. In this study, T_∞ is set to 0 °C. The exit temperature Θ_{ij} of a pipe segment ij due to heat loss to its environment with an entry temperature Θ_i of the corresponding node is given by:

$$\Theta_{ij} = \Theta_i \cdot \exp\left(\frac{-l_{ij}}{c_p \cdot \dot{m}_{ij} \cdot R_{ij}}\right) \tag{9}$$

The combined thermal resistance of pipe and soil per unit length is calculated with the ratio r between outer and inner diameter: [27]

$$R_{ij} = \frac{\ln 4h/rd_{ij}}{2\pi\lambda_g} + \frac{\ln r}{2\pi\lambda_{insul}} \tag{10}$$

The ratio r in Equation 10 is determined with the actual inner diameter and the insulation thickness 1 based on [31]. After the hydraulic and thermal calculations, a linear regression of the investment costs and the thermal losses per trench length, using SciPy [32], is performed and shown in Figure 1. The total investment costs for piping are adapted from [2]. In this study, pipes ranging from DN20 to DN400 are considered.

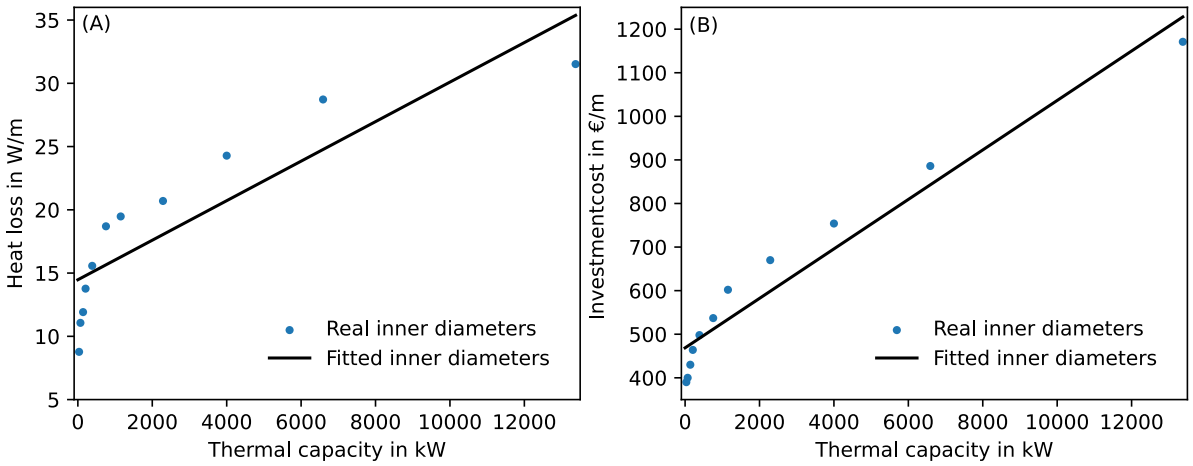

Figure 1: Optimization parameters of the district heating pipelines; (A) Thermal losses of the district heating pipes per trench length. (B) Costs of the district heating pipes per trench length.

.

Based on [7, 12], a mixed-integer linear programming model is introduced to calculate the optimal power flow through the district heating network, determine flow directions, and omit unnecessary connections. Therefore, a bi-directional pipe model is built. The thermal power input and output of every pipe are modelled according to the directed graph of the network. In order to allow flows in the opposite direction, every potential pipe ij is also modelled in the direction ji. The use of a pipe in a unique direction is assured by the objective function (see Equation 16). For simplicity, only the equations for pipes in the direction ij are provided. The heat outflow $\dot{Q}_{out}$ of each pipe results from the inflow $\dot{Q}_{in}$ minus the thermal loss $\dot{Q}_{loss}$:

$$\dot{Q}_{ij,in} - \dot{Q}_{ij,out} - \dot{Q}_{ij,loss} = 0 \tag{11}$$

$$\dot{Q}_{ij,in} \leq \dot{Q}_{max,cons} \cdot \lambda_{ij} \tag{12}$$

$$\dot{Q}_{ij,in} \leq \dot{Q}_{max} \tag{13}$$

In Equation 12, the binary variable λ_{ij} shows the usage of a potential pipe. Moreover, $\dot{Q}_{max,cons}$ can be seen as a Big-M-constraint, enforcing zero thermal flow if the direction ij of the pipe is not used. Meanwhile, in

Equation 13 the actual maximal thermal capacity $\dot{Q}_{max}$ is determined. This value is independent of the flow direction (*ij* or *ji*). The thermal losses are determined by the linear regression factor a_{therm} and b_{therm}:

$$\dot{Q}_{ij,loss} = \left(a_{therm} \cdot \dot{Q}_{ij,in} + b_{therm} \cdot \lambda ij\right) \cdot l_{ij} \tag{14}$$

Each connection of a consumer to the district heating grid is modelled unidirectional, and thus no heat feed-in from a consumer is possible. Moreover, energy conservation is assumed in every node under consideration of the consumer's heat demand and the heat source's feed-in:

$$\sum_{ij \in A_i} \dot{Q}_{ij} - \sum_{ji \in A_i} \dot{Q}_{ji} - \sum_{c \in A_c} \dot{Q}_c + \sum_{p \in A_p} \dot{Q}_p = 0 \tag{15}$$

Finally, the objective function aims to minimize the total investment costs of the district heating network under a set of given consumers which need to be connected to the grid. As every consumer's connection to the grid is mandatory, the investment costs in the objective function are not distributed over the depreciation period and no operational costs are considered. The investment costs are determined by the linear regression factors a_{cost} and b_{cost} from Figure 1:

$$min\left\{ \sum_{A_i} \left(a_{cost} \cdot \dot{Q}_{max} + b_{cost} \cdot (\lambda_{ij} + \lambda_{ji})\right) \cdot l_{ij} \right\} \tag{16}$$

The corresponding pipe diameter to the maximal heat flow $\dot{Q}_{max}$ can be calculated with fsolve from [32] with Equation 8. The initially assumed flow direction in the graph can be corrected according to λ_{ij} and λ_{ji}:

- $\lambda_{ij} = 0$ and $\lambda_{ji} = 0$: The pipe is not used and can be deleted from the graph.
- $\lambda_{ij} = 1$ and $\lambda_{ji} = 0$: The assumed flow direction in the graph is correct.
- $\lambda_{ij} = 0$ and $\lambda_{ji} = 1$: The flow direction in the graph is the opposite of the assumed one and needs to be corrected.

The linear diameter *d* and the corrected graph can be used to facilitate and speed up the nonlinear topology optimization, described in section 5.. Here, based on the linear diameter, determined by the preprocessing method, the choice of the available diameter is limited to the next and the following larger one.

5. Nonlinear District Heating Model

To account for more complex influences, such as mixing temperatures or pressure drops, a nonlinear transport model has to be developed. First, a nonlinear model for district heating pipes is presented. Subsequently, nonlinear models for consumers and heat sources are introduced. Finally, the objective functions and the pipe discretization method used are shown.

5.1. Transport Model

Similar to section 4., the pressure loss through any given pipe in the network has to be determined. By using the Haaland equation (see Equation 7) during the pressure loss calculations, the flow in the pipes is assumed to be turbulent. This flow regime is desired in a district heating network, to ensure a well-defined and continuous flow through the pipes. When Equation 3-5 are combined and the velocities converted to mass flows ($m_{ij} = (v_{ij} \cdot \pi \cdot d_{ij}^2)/(4 \cdot \rho)$), the pressure loss can be calculated as:

$$p_i - p_j = \frac{8 \cdot f_{ij}}{\pi^2 \cdot \rho} \cdot \frac{l_{ij}}{d_{ij}^5} \cdot \dot{m}_{ij}^2 \tag{17}$$

Analogical to section 4., a maximal specific pressure drop Δp_{max} in a pipe *ij* is imposed:

$$p_i - p_j \leq l_{ij} \cdot \Delta p_{max} \tag{18}$$

In each node *i* mass conservation must be fulfilled:

$$\sum_{ij \in A_i} \dot{m}_{ij} - \sum_{ji \in A_i} \dot{m}_{ji} - \sum_{c \in A_c} \dot{m}_c + \sum_{p \in A_p} \dot{m}_p = 0 \tag{19}$$

Moreover, inside a node of the district heating system, perfect mixing of the incoming fluids is assumed. All outgoing flows depart from the node with the corresponding node temperature Θ_n and energy is conserved in every node of the system:

$$\sum_{in \in A} \left(\dot{m}_{in} \cdot \Theta_{ij} \right) - \sum_{nj \in A} \left(\dot{m}_{nj} \cdot \Theta_n \right) = 0 \tag{20}$$

Heat losses are calculated analogously to section 4.. Only in Equation 10 a fixed ratio $d_{o,ij} = r \cdot d_{ij}$ between the outer and inner diameter of a pipe is assumed. In this study, r is set to 4.

5.2. Producer Model

At the producer, a fixed exit temperature of 90 °C is imposed as a boundary condition for the district heating system. In addition, a reference pressure is defined in one of the producer's return nodes to define the pressure throughout the network. As only pressure differences influence the mass flow solution, the solution is independent of the chosen reference. In Equation 21-22 *flh* refers to full load hours of the district heating network. In this study, the district heating network is assumed to have 2500 full load hours [33]. To consider pumping costs C_{pump} during the optimization, the electric power consumption of the pump is modelled with a constant efficiency η_{pump} and the specific electric power costs c_{el}:

$$C_{pump} = \frac{\dot{m}_p}{\rho} \cdot \frac{1}{\eta_{pump}} \cdot (p_i - p_j) \cdot flh \cdot c_{el} \tag{21}$$

Moreover, the optimization has to be able to benchmark different heat producers against each other. Therefore, the fuel costs C_{fuel} at each producer with the specific fuel costs c_{fuel} are considered:

$$C_{fuel} = \dot{m}_p \cdot c_{p,water} \cdot (\Theta_p - \Theta_i) \cdot flh \cdot c_{fuel} \tag{22}$$

5.3. Consumer Model

In the nonlinear optimization, every consumer is modelled with an individual substation. Each substation is composed of a heat exchanger and a throttle. This throttling configuration, shown in Figure 2, allows a variable mass flow in the district heating's and the consumer's circuit to control the heat transferred to the consumer, as well as low return flow temperatures with low flow velocities during partial load [31].

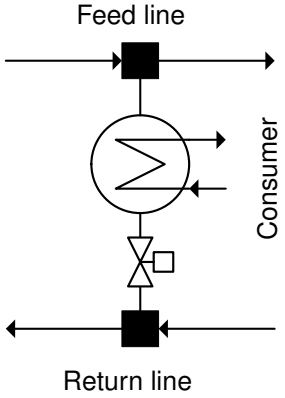

Figure 2: Configuration of a consumer substation in the district heating system.

The pressure drop over a consumer c which connects node f in the feed line and node r in the return line is assumed to be of the following form:

$$p_f - p_r - p_{throttle} = \Delta p_{des} \tag{23}$$

In this study, the design pressure drop Δp_{des} over each substation is set to 0.5 bar. To increase the numerical stability of the optimization, the heat demand of every consumer connected to the grid must be satisfied within a range of 95 % to 110 %:

$$0.95 \cdot \dot{Q}_c \leq c_{p,water} \cdot \dot{m}_c \cdot (\Theta_f - \Theta_c) \leq 1.10 \cdot \dot{Q}_c \tag{24}$$

Here, the minimal cooling temperature Θ_c at the exit of each substation is set to 55 °C.

5.4. Pipe Discretization

Thus far, the presented algorithm still allows continuous diameters. In order to perform a more realistic topology optimization, the algorithm should be able to do discrete choices in a continuous optimization. Therefore, based on [27], a numerical continuation strategy that gradually forces the continuous diameter variables into discrete diameter choices is introduced. A smoothed projection of the diameters onto the discrete diameter set is gradually enforced and intermediate diameters are more and more penalized through the piping cost relation (see subsection 5.5.). For the projection of the diameters on the discrete diameter set, a smooth approximation of a Heaviside function is used: [27]

$$P(x, \sigma, \chi) = \frac{tanh(\chi \cdot \sigma) + tanh(\chi \cdot (x - \sigma))}{tanh(\chi \cdot \sigma) + tanh(\chi \cdot (1 - \sigma))} \tag{25}$$

In Equation 25 the continuous decision variable $x \in [0, 1]$ is gradually projected onto a binary decision variable $\tilde{x} \in \{0, 1\}$. The variable $\chi \in]0, \infty[$ controls the steepness of the Heaviside approximation, while $\sigma \in [0, 1]$ determines the threshold above which the variable x is projected onto the upper limit [27]. To account for the gradient-based optimization and to improve the stability of the optimization, the projection P is interpolated with a linear function, controlled by the factor ν: [27]

$$-10^{-3} \leq \nu \cdot \left(d_1 + (d_2 - d_1) \cdot P\left(\frac{d - d_1}{d_2 - d_1}, 0.01, \chi \right) \right) + (1 - \nu) \cdot d \leq 10^{-3} \tag{26}$$

In Figure 3 different parameterizations for χ and ν of Equation 26 are shown with $d_1 = 0.1603\,\text{m}$ and $d_2 = 0.2101\,\text{m}$.

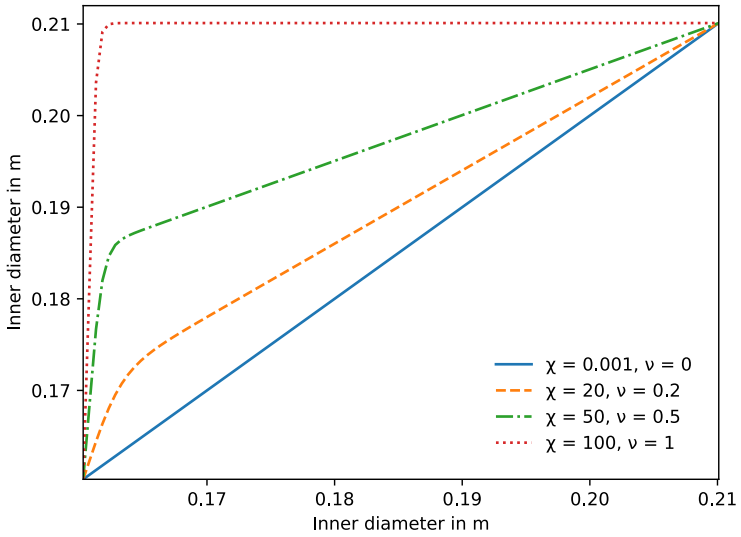

Figure 3: Function for pipe discretization for different values of χ and ν with $d_1 = 0.1603\,\text{m}$ and $d_2 = 0.2101\,\text{m}$

.

5.5. Objective Function

Similar to the pipe discretization method, the smooth approximation of a Heaviside function (see Equation 25) is used to penalize intermediate piping diameters during the optimization. To improve stability and to account for the gradient-based optimization, the projection is also interpolated with a linear function, controlled by the parameter ν. The investment costs for district heating pipes in the feed and return line C_{pipe}, connecting node i and j, are given by:

$$C_{pipe} = \left[\nu \cdot \left(c_1 + (c_2 - c_1) \cdot P\left(\frac{d - d_1}{d_2 - d_1}, 0.5, \chi \right) \right) + (1 - \nu) \cdot \left(c_1 + (c_2 - c_1) \cdot \frac{d - d_1}{d_2 - d_1} \right) \right] \cdot l_{ij} \cdot 2 \cdot A \tag{27}$$

In Equation 27, investment costs are distributed over the depreciation period n, using the annuity method. Without discounting, the annuity A is calculated with an interest rate i:

$$A = \frac{(1 + i)^n \cdot i}{(1 + i)^n - 1} \tag{28}$$

After [34], the depreciation period is set to 20 years and the interest rate i to 0.08. The objective function is formed by combining Equation 21, 22, and 27 and thus minimizing investment and operational costs. In Figure 4, different parameterizations of χ and ν for the investment costs of pipes are shown.

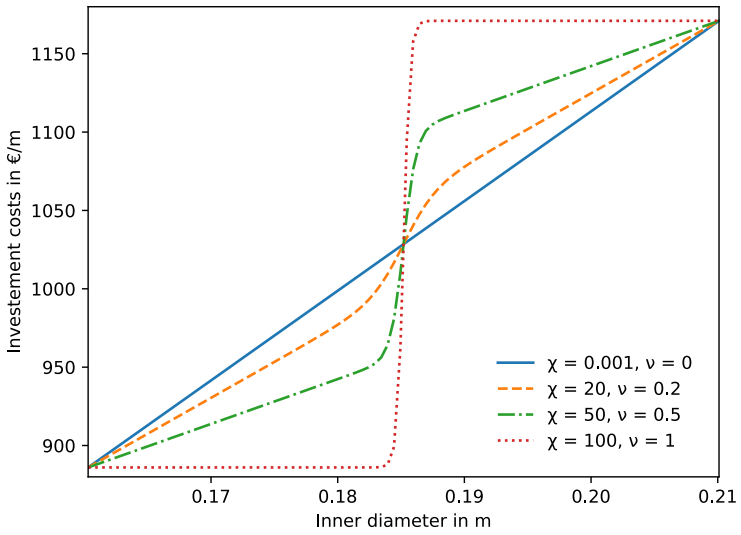

Figure 4: Heavyside projection of pipe investment cost for $d_1 = 0.1603\,\text{m}$ and $d_2 = 0.2101\,\text{m}$ with different values of χ and ν.

6. Example

The linear optimization is solved with Cplex 12.10.0 [35] using Pyomo [36, 37]. The nonlinear optimization is formulated with pyoptsparse [38] and solved with the interior point optimizer Ipopt [39]. An exemplary district heating system with 42 consumers is used to demonstrate the presented method. As every connection of a consumer to the grid is mandatory, independent of its economic efficiency, the preprocessing algorithm can only find the most favorable pathway to connect all consumers and delete dispensable pipes in the graph. The original network consists of 72 pipes. After the linear optimization, this is reduced to 69 pipes and 5 flow directions have been corrected, as shown in Figure 5. Here, the orange point represents the producer, grey nodes junctions, and blue nodes consumer in the district heating system. During preprocessing, the linear diameters, with their corresponding mass flows are determined and handed to the nonlinear optimization to be discretized. Due to the formulation of Equation 26, slight deviations from discrete diameters are allowed, but occur only in rare cases, as shown in Figure 6.

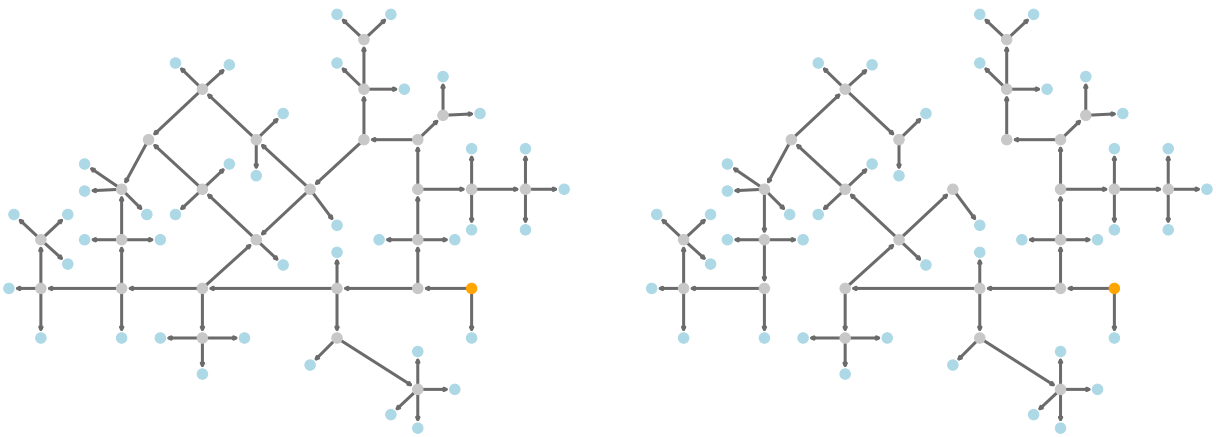

(a) Original

(b) Preprocessed

Figure 5: Representation of the original and preprocessed network.

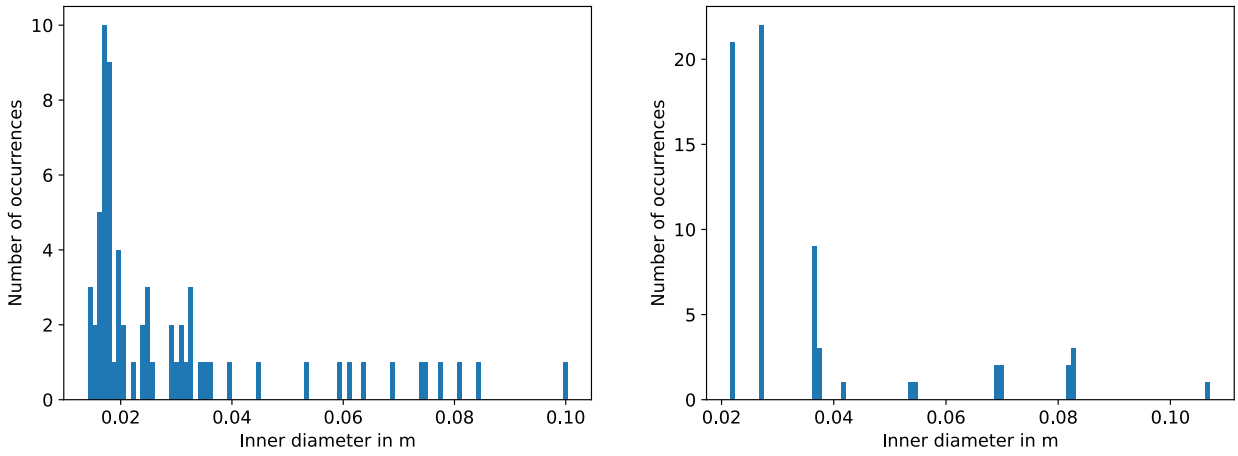

(a) Linear diameters

(b) Discrete diameters

Figure 6: Distribution of the inner diameters before and after the nonlinear optimization with 100 bins between DN20 and DN200.

The nonlinear optimization is iteratively performed while increasing in each iteration the value of ξ and ν. Over ten iterations, ξ is evenly spaced out from 0.001 to 100 and ν from 0 to 1. The whole nonlinear optimization is performed in 19.37 sec. Linear diameters below DN20 are assigned either to DN20 or DN25, as shown in Figure 6. For some connections to smaller consumers, DN25 is oversized, as the optimizer tries to find a viable solution under consideration of all thermohydraulic equations and Equation 26. If an oversized solution, respecting the constraints is found, it can be difficult for the optimizer to revert to the smaller diameter, as the differences in operational and investment costs for two subsequent diameters are rather small. The resulting pressure profile of the district heating network can be seen in Figure 7. The highest cumulative pressure losses can be observed at the most remote consumer, defining the pressure level at the heat source. By comparing Figure 7a and 7b, a maximal pressure difference, larger than the assumed constant pressure drop over a consumer's substation, can be seen. In the modelled throttle, a pressure offset occurs between the feed and the return network, which raises the pressure level in the feed network artificially. As the pressure level does not affect the sizing of the pipes but only the pressure differences and as the pumping costs are rather small compared to the investment costs of the district heating system, this offset is not reduced during the optimization.

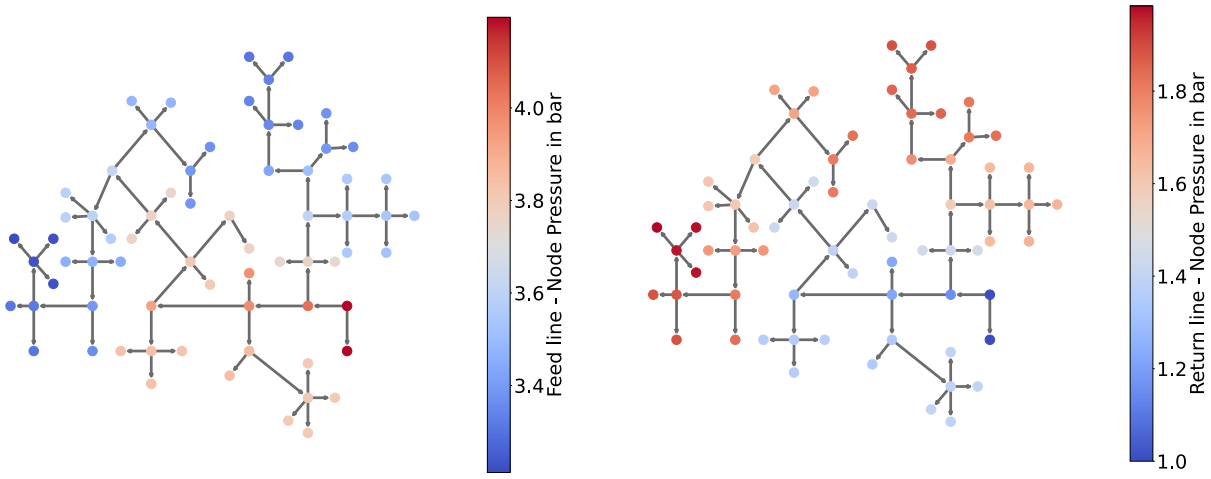

(a) Feed network

(b) Return network

Figure 7: Resulting pressure profile in the feed and return network.

Figure 8 shows the resulting temperature profile after the nonlinear optimization. As shown in Figure 8b the consumer always tries to maximize the energy available to them in order to satisfy their demands and are

cooling the fluid down to 55 °C. The desired heat demand is met with 95 % of the desired heat, thus minimizing the operational costs. Overall a total efficiency for the heat distribution of 98.01 % is reached.

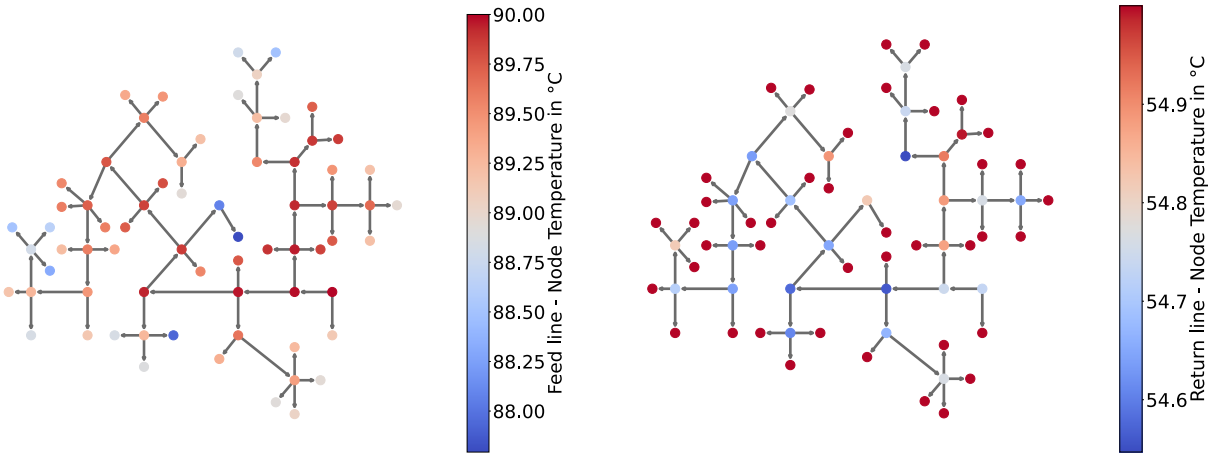

(a) Feed Network

(b) Return Network

Figure 8: Resulting temperature profile in the feed and return network.

7. Conclusion and Outlook

A two-step methodology for the optimization of a district heating network, based on a thermohydraulic model, is derived and successfully implemented as an optimization problem. This method allows a fast nonlinear optimization of a district heating system. The method presented in this paper allowed the optimization of a small exemplary district heating system. Given a set of possible pipeline configurations to connect all the consumers to the grid regardless of its economic viability, the simulation was able to derive an optimal network design. The determined network configuration aimed at minimization of investment and operational costs.

In further works, the method should be applied to larger districts to prove the scalability of the method. Moreover, the discrete pipe sizing method should be improved to eliminate all non-discrete diameters in the final results of the optimization. The optimization should also be developed to account for the profitability of the considered district heating network. Therefore, the preprocessing method could be extended to determine the profitability of a potential connection of a consumer to the grid. Moreover, the nonlinear depiction of the district heating grid could be further improved. In this study, a constant ratio between inner and outer diameter is assumed. In real pipes, this ratio decreases with increasing inner diameter. Gradient-based nonlinear optimization converges always into a local optimum, a global optimum is not guaranteed. Therefore, it should be investigated how different possible local minima can be compared to one another and how the optimization can efficiently choose between the different local minima that occurred during the optimization. At last, the influence of the preprocessing method on the final results should be investigated.

Funding

This work was supported by the ”Bayerische Forschungsstiftung” in the framework of the project ”Sektorkopplung und Microgrids” (STROM) [project no.: AZ-1473-20]. The financial support is gratefully acknowledged.

References

[1] S. Werner, “International review of district heating and cooling,” *Energy*, vol. 137, pp. 617–631, 2017. doi: 10.1016/j.energy.2017.04.045

[2] T. Nussbaumer and S. Thalmann, “Influence of system design on heat distribution costs in district heating,” *Energy*, vol. 101, pp. 496–505, 2016. doi: 10.1016/j.energy.2016.02.062

[3] A. Jentsch, K. Bohn, A. Pohlig, C. Dötsch, S. Richter, and M. Manderfeld, “Handbuch zur Entscheidungsunterstützung. Fernwärme in der Fläche: Leitungsgebundene Wärmeversorgung im ländlichen Raum.”

[4] U. Persson, B. Möller, and S. Werner, “Heat Roadmap Europe: Identifying strategic heat synergy regions,” *Energy Policy*, vol. 74, pp. 663–681, 2014. doi: 10.1016/j.enpol.2014.07.015

[5] M. Sporleder, M. Rath, and M. Ragwitz, “Design optimization of district heating systems: A review,” *Frontiers in Energy Research*, vol. 10, 2022. doi: 10.3389/fenrg.2022.971912

[6] J. Söderman, “Optimisation of structure and operation of district cooling networks in urban regions,” *Applied Thermal Engineering*, vol. 27, no. 16, pp. 2665–2676, 2007. doi: 10.1016/j.applthermaleng.2007.05.004

[7] J. Dorfner and T. Hamacher, “Large-Scale District Heating Network Optimization,” *IEEE Transactions on Smart Grid*, vol. 5, no. 4, pp. 1884–1891, 2014. doi: 10.1109/TSG.2013.2295856

[8] C. Haikarainen, F. Pettersson, and H. Saxén, “A model for structural and operational optimization of distributed energy systems,” *Applied Thermal Engineering*, vol. 70, no. 1, pp. 211–218, 2014. doi: 10.1016/j.applthermaleng.2014.04.049

[9] B. Morvaj, R. Evins, and J. Carmeliet, “Optimising urban energy systems: Simultaneous system sizing, operation and district heating network layout,” *Energy*, vol. 116, pp. 619–636, 2016. doi: 10.1016/j.energy.2016.09.139

[10] C. Bordin, A. Gordini, and D. Vigo, “An optimization approach for district heating strategic network design,” *European Journal of Operational Research*, vol. 252, no. 1, pp. 296–307, 2016. doi: 10.1016/j.ejor.2015.12.049

[11] Marcus Fuchs and Dirk Müller, “Automated Design and Model Generation for a District Heating Network from OpenStreetMap Data,” 2017.

[12] T. Résimont, Q. Louveaux, and P. Dewallef, “Optimization Tool for the Strategic Outline and Sizing of District Heating Networks Using a Geographic Information System,” *Energies*, vol. 14, no. 17, p. 5575, 2021. doi: 10.3390/en14175575

[13] J. Röder, B. Meyer, U. Krien, J. Zimmermann, T. Stührmann, and E. Zondervan, “Optimal Design of District Heating Networks with Distributed Thermal Energy Storages – Method and Case Study: 5-22 Pages / International Journal of Sustainable Energy Planning and Management, Vol. 31 (2021),” 2021. doi: 10.5278/IJSEPM.6248

[14] N. Deng, R. Cai, Y. Gao, Z. Zhou, G. He, D. Liu, and A. Zhang, “A MINLP model of optimal scheduling for a district heating and cooling system: A case study of an energy station in Tianjin,” *Energy*, vol. 141, pp. 1750–1763, 2017. doi: 10.1016/j.energy.2017.10.130

[15] T. Mertz, S. Serra, A. Henon, and J.-M. Reneaume, “A MINLP optimization of the configuration and the design of a district heating network: Academic study cases,” *Energy*, vol. 117, pp. 450–464, 2016. doi: 10.1016/j.energy.2016.07.106

[16] T. Mertz, S. Serra, A. Henon, and J. M. Reneaume, “A MINLP optimization of the configuration and the design of a district heating network: study case on an existing site,” *Energy Procedia*, vol. 116, pp. 236–248, 2017. doi: 10.1016/j.egypro.2017.05.071

[17] F. Marty, S. Serra, S. Sochard, and J.-M. Reneaume, “Simultaneous optimization of the district heating network topology and the Organic Rankine Cycle sizing of a geothermal plant,” *Energy*, vol. 159, pp. 1060–1074, 2018. doi: 10.1016/j.energy.2018.05.110

[18] H. Li and S. Svendsen, “District Heating Network Design and Configuration Optimization with Genetic Algorithm,” *Journal of Sustainable Development of Energy, Water and Environment Systems*, vol. 1, no. 4, pp. 291–303, 2013. doi: 10.13044/j.sdewes.2013.01.0022

[19] Y. Wack, S. Serra, M. Baelmans, J.-M. Reneaume, and M. Blommaert, “Non-linear Topology Optimization of District Heating Networks: A benchmark of Mixed-Integer and Adjoint Approaches.” [Online]. Available: http://arxiv.org/pdf/2302.14555v1

[20] A. Chebouba, F. Yalaoui, L. Amodeo, A. Smati, and A. Tairi, “New Method to Minimize Fuel Consumption of Gas Pipeline Using Ant Colony Optimization Algorithms,” in *2006 International Conference on Service Systems and Service Management*. IEEE, 10/25/2006 - 10/27/2006. doi: 10.1109/ICSSSM.2006.320759. ISBN 1-4244-0451-7 pp. 947–952.

[21] Y. Zhang, G. Zhang, H. Zhao, Y. Cao, Q. Liu, Z. Shen, and A. Li, “A Convenient Tool for District Heating Route Optimization Based on Parallel Ant Colony System Algorithm and 3D WebGIS,” *ISPRS International Journal of Geo-Information*, vol. 8, no. 5, p. 225, 2019. doi: 10.3390/ijgi8050225

[22] P. Hirsch, M. Grochowski, and K. Duzinkiewicz, “Decision support system for design of long distance heat transportation system,” *Energy and Buildings*, vol. 173, pp. 378–388, 2018. doi: 10.1016/j.enbuild.2018.05.010

[23] M. Vesterlund, A. Toffolo, and J. Dahl, “Optimization of multi-source complex district heating network, a case study,” *Energy*, vol. 126, pp. 53–63, 2017. doi: 10.1016/j.energy.2017.03.018

[24] Y. Merlet, R. Baviere, and N. Vasset, “Formulation and assessment of multi-objective optimal sizing of district heating network,” *Energy*, vol. 252, p. 123997, 2022. doi: 10.1016/j.energy.2022.123997

[25] A. Pizzolato, A. Sciacovelli, and V. Verda, “Topology Optimization of Robust District Heating Networks,” *Journal of Energy Resources Technology*, vol. 140, no. 2, 2018. doi: 10.1115/1.4038312

[26] M. Blommaert, R. Salenbien, and M. Baelmans, “AN ADJOINT APPROACH TO THERMAL NETWORK TOPOLOGY OPTIMIZATION,” in *International Heat Transfer Conference 16*. Connecticut: Begellhouse, 8/10/2018 - 8/15/2018. doi: 10.1615/IHTC16.cms.024074 pp. 2081–2089.

[27] M. Blommaert, Y. Wack, and M. Baelmans, “An adjoint optimization approach for the topological design of large-scale district heating networks based on nonlinear models,” *Applied Energy*, vol. 280, p. 116025, 2020. doi: 10.1016/j.apenergy.2020.116025

[28] Y. Wack, M. Baelmans, R. Salenbien, and M. Blommaert, “Economic Topology Optimization of District Heating Networks using a Pipe Penalization Approach,” *Energy*, vol. 264, no. 1, p. 126161, 2023. doi: 10.1016/j.energy.2022.126161. [Online]. Available: http://arxiv.org/pdf/2205.12019v2

[29] S. E. Haaland, “Simple and Explicit Formulas for the Friction Factor in Turbulent Pipe Flow,” *Journal of Fluids Engineering*, vol. 105, no. 1, pp. 89–90, 1983. doi: 10.1115/1.3240948

[30] I. Best, J. Orozaliev, and K. Vajen, “Impact of Different Design Guidelines on the Total Distribution Costs of 4th Generation District Heating Networks,” *Energy Procedia*, vol. 149, pp. 151–160, 2018. doi: 10.1016/j.egypro.2018.08.179

[31] *Planungshandbuch Fernwärme*, Version 1.1 vom 21. september 2017 ed. Ittigen and Bern: EnergieSchweiz Bundesamt für Energie, 21. September 2017. ISBN 3-908705-30-4

[32] P. Virtanen, R. Gommers, T. E. Oliphant, M. Haberland, T. Reddy, D. Cournapeau, E. Burovski, P. Peterson, W. Weckesser, J. Bright, S. J. van der Walt, M. Brett, J. Wilson, K. J. Millman, N. Mayorov, A. R. J. Nelson, E. Jones, R. Kern, E. Larson, C. J. Carey, Polat, VanderPlas, Jake, D. Laxalde, J. Perktold, R. Cimrman, I. Henriksen, E. A. Quintero, C. R. Harris, A. M. Archibald, A. H. Ribeiro, F. Pedregosa, P. van Mulbregt, and SciPy 1.0 Contributors, “SciPy 1.0: Fundamental Algorithms for Scientific Computing in Python,” *Nature Methods*, vol. 17, pp. 261–272, 2020. doi: 10.1038/s41592-019-0686-2

[33] European Commission. Directorate General for Energy., TU Wien., Tilia GmbH., Institute for Resource Efficiency and Energy Strategies GmbH., Fraunhofer ISI., and Öko Institut., *District heating and cooling in the European Union: overview of markets and regulatory frameworks under the revised Renewable Energy Directive*. Publications Office, 2022.

[34] AGFW, “FW 704 - Wirtschaftlichkeit nach §§ 20 und 24 KWKG - Pauschalierte Kennwerte,” 07.03.2023. [Online]. Available: https://www.fw704.de/hauptmenue/kennwerte/pauschalierte-kennwerte

[35] Cplex, “ILOG CPLEX Optimization Studio,” 2023. [Online]. Available: https://www.ibm.com/de-de/products/ilog-cplex-optimization-studio

[36] M. L. Bynum, G. A. Hackebeil, W. E. Hart, C. D. Laird, B. L. Nicholson, J. D. Siirola, J.-P. Watson, and D. L. Woodruff, *Pyomo — Optimization Modeling in Python*, 3rd ed., ser. Springer eBook Collection. Cham: Springer International Publishing and Imprint Springer, 2021, vol. 67. ISBN 9783030689285

[37] W. E. Hart, J.-P. Watson, and D. L. Woodruff, “Pyomo: modeling and solving mathematical programs in Python,” *Mathematical Programming Computation*, vol. 3, no. 3, pp. 219–260, 2011. doi: 10.1007/s12532-011-0026-8

[38] N. Wu, G. Kenway, C. Mader, J. Jasa, and J. Martins, “pyOptSparse: A Python framework for large-scale constrained nonlinear optimization of sparse systems,” *Journal of Open Source Software*, vol. 5, no. 54, p. 2564, 2020. doi: 10.21105/joss.02564

[39] A. Wächter and L. T. Biegler, “On the implementation of an interior-point filter line-search algorithm for large-scale nonlinear programming,” *Mathematical Programming*, vol. 106, no. 1, pp. 25–57, 2006. doi: 10.1007/s10107-004-0559-y

AIDRES: A database for the decarbonisation of the heavy industry in Europe

Luc Girardin[a], Juan David Correa-Laguna[b], Joris Valee[b], Shivom Sharma[a], Daniel Florez-Orrego[a], Meire Ribeiro-Domingos[a], Rafael Castro-Amoedo[a], Yi Zhao[a], Julia Granacher[a], Marie Jones[a], Francisco Mendez Alva[e], Wim Clymans[c], Ivan Kantor[d], Frank Meinke-Hubeny[b] and François Maréchal[a]

[a] École Polytechnique Fédérale de Lausanne, Industrial Process and Energy Systems Engineering (IPESE-EPFL), Sion, Switzerland, luc.girardin@epfl.ch
[b] VITO-Energyville, Mol, Belgium, joris.valee@vito.be
[c] VITO NV, Unit SEB - Smart Energy & Built Environment, Mol, Belgium, wim.clymans@vito.be
[d] Concordia University, Chemical and Materials Engineering, St. Catherine W., Canada, ivan.kantor@concordia.ca
[e] Ghent University. Faculty of Engineering and Architecture, Gent, Belgium, Francisco.MendezAlva@UGent.be

Abstract:
The AIDRES database aims to support the long-term objective of a fully integrated industrial strategy in the EU-27, providing a service to the European Commission and a catalogue for industries to understand the effectiveness, efficiency and cost of potential innovation pathways for achieving carbon neutral processes in the steel, chemical, cement, glass, fertilizers and refineries sectors by 2050. The approach considers the geographical distribution of the annual production of key products quantified at EU-NUTS3 regional level. Process integration techniques are used to generate and evaluate the reference and future optimal production routes, providing a quantitative, technical and multi-criteria estimate of energy demand in Europe's major industrial sectors. Decarbonisation of the production considers routes achieving (i) substitution of less energy intensive products, (ii) electrification of the production, (iii) use of oxy-combustion, (iv) carbon capture transport and storage, (v) use of alternative fuels and (vi) biomass. This results in a per-ton-of-product database containing energy demand, direct emissions at the plant, amount of captured CO_2 and the associated investment and operation costs. Scenarios 2018-2050 for the energy prices, indirect upstream emissions, CO_2 allowance and production shift are considered to foreseen the operation expenditure and total emissions. Finally, the per-ton database is scaled-up at the NUTS3 level by the regional production capacity. The application of the database is demonstrated at the EU level for the analysis of the present and future evolution of selected heavy industrial sectors, reaching a direct emission reduction between 90-95% compared with 2015-2019 average.

Keywords:
industrial processes, heavy industry, decarbonisation, renewable energies, process integration, database.

1. Introduction

The European Green Deal [7] and aims to transform the EU into a modern, resource efficient and competitive economy while making Europe the first climate neutral continent with a 2050 climate neutrality target. To reach this ambitious goal, an economical and societal transformation process is required. Europe's energy intensive industries (EIIs), especially the sectors steel, chemical, cement, glass, fertiliser and refineries, are today an integral part, if not the foundation, of the European economy and have therefore a leading role to play in this transition. To make this transition successful, unprecedented levels of industrial investments are required while the market actors face at the same time increasing global competition.

Previous studies for a carbon neutral industrial strategy [30] and [8] were developed in close collaboration with industrial representatives to define a realistic solution space for this ambitious transition. Valuable insights are provided in these studies, identifying and quantifying in an aggregated format the steps to the envisioned 90-95% emissions reductions by 2050 for EIIs, compared to 1990 levels.

Building from many collaborative experiences with private industries, industrially representative process models have been developed in the H2020 project EPOS[23] to build, so-called blueprints. Validated by industrial sector associations, industrial blueprints provide details of energy and material requirements of the processes, using average or obfuscated values to avoid disclosure of confidential data. Described in greater detail in [4] and [18], this approach allows for data and knowledge to be shared outside of an organization without

disclosing sensitive information.

The AIDRES project is providing the next level of necessary data to develop a sharper picture of potential pathways for industries at their respective sites or industrial clusters in Europe. This study is focused on the analysis of decarbonisation options such as further energy efficiency measures, further process integration, electrification of heat for processes, electrification of processes, production and use of hydrogen, use of biomasse, electricity from carbon neutral sources, Carbon Capture and Utilization (CCU) and Carbon Capture, transport and Storage (CCS) among others.

2. Approach

2.1. Blueprint model integration

Blueprints include details of heat, electricity and material flows as well as the annual investment and operation cost required for process operation. Process integration technique [17] is used to determine the optimal size of each process in typical production route, taking into account the internal use of heat/cold streams while balancing the overall material and energy resource, product and waste flows.

For production routes integrating carbon capture, transport and storage (CCS), the captured emissions (Em^{CCS}) given by (1) are equal to a fraction (η^{CCS}), typically 90%, of the non biogenic and biogenic emissions. Uncaptured direct emissions (2) from biogenic resources are not accounted ($\eta^{CSS} = 0$) but when carbon capture, transport and storage (CCS) is integrated ($\eta^{CCS} > 0$), biogenic direct emissions removed from the atmosphere are accounted negatively. The profits from trading negative emissions are therefore included in the OPEX.

$$Em^{CCS} = \eta^{CCS} \cdot (Em^{direct,non\ bio} + Em^{direct,bio}) \qquad [t_{CO_2}/y] \qquad (1)$$

$$Em^{direct} = (1 - \eta^{CCS}) \cdot Em^{direct,non\ bio} - \eta^{CCS} \cdot Em^{direct,bio} \qquad [t_{CO_2}/y] \qquad (2)$$

2.2. Per ton of product results

Pertinent production routes are selected form the result of a parametric optimisation [32] using various energy prices and emissions and different weight for the terms of the objective function (sum of operation cost, investment cost and impact/emissions). In general, the selection criteria is minimising the direct emission at the plant, however in some cases, the criteria is reflecting the plant's design in the EU context (e.g. steam network design for fertilizer plant). The resulting mass/energy flows, capital cost and direct emissions at the plant are expressed per ton of product.

2.3. AIDRES EU Mix production routes

The concept of EU mix routes is introduced to account for the uncertainty which emerges from the unknown of future production methods for each individual industrial site (NUTS3). Rather than applying one single production route across the European Union industrial production sites, the AIDRES EU mix routes can be considered as a balanced hypothetical alternative to represent values of energy and feedstock input and CO_2 emissions, without merit to actual industrial transition plans. The AIDRES EU Mix 2030 and 2050 production routes (3) are build up by weighting single production routes per ton results (r_i) according to the emission reduction targets. The integration of the mix to the mapped production sites at NUTS3 level are to be compared and understood at European level.

$$mix = \sum_{i \in routes} w_i \cdot r_i \text{ with } \sum_{i \in routes} w_i = 1 \text{ and } w_i \leq 1 \qquad [t/t] \text{ or } [€/t] \qquad (3)$$

The AIDRES mix are done in a way to meet the MIX EU Reference Scenario emission reduction targets in 2030 and 2050, as defined by the European Commission in 2021 [6] in line with the Fit for 55 and the EU Green deal roadmap [7].

2.4. Scenarios integration

To evaluate the impact of the different production routes, nine typical cost and emissions scenarios 2018-2030-2050, given in Table 1, have been considered. The criteria and values were selected based on EU reference scenarios, to create a diversity of different outcomes. The amount of scenarios was restricted to eigth plus a reference scenario to keep the number of modeled solutions under control. The values can be seen as boundaries and sensitivity with different values can easily be done afterwards without having to re-run the AIDRES model. The AIDRES model does not take limitations of resource availability into account and does not consider competition for the resource, such as biomass [22], between and with other sectors (e.g. food). The scenarios are aligned with the EC Fit for 55 [9]. In the AIDRES database, there is a record available for all AIDRES production routes on NUTS3 and this for every scenario.

Table 1: AIDRES reference scenario 2018 and future EU scenarios at horizons 2030 and 2050.

			CO_2	Electricity		Hydrogen		Natural gas
	Horizon	Scenarios	[€/kg$_{CO_2}$]	[€/kWh]	[kg$_{CO_2}$/kWh]	[€/kg]	[kg$_{CO_2}$/kg]	[€/kWh]
0	2018	Reference	0.025	0.125	0.231	1.8	8.2	0.024
1	2030	low H_2 price	0.150	0.071	0.120	3.0	0.0	0.025
2	2030	low H_2 & high NG price	0.150	0.071	0.120	3.0	0.0	0.050
3	2030	high H_2 price	0.150	0.071	0.120	5.0	0.0	0.025
4	2030	high H_2 & high NG price	0.150	0.071	0.120	5.0	0.0	0.050
5	2050	low H_2 price	0.350	0.071	0.000	1.5	0.0	0.035
6	2050	low H_2 & high NG	0.350	0.071	0.000	1.5	0.0	0.050
7	2050	high H_2 price	0.350	0.071	0.000	2.5	0.0	0.035
8	2050	high H_2 & high NG price	0.350	0.071	0.000	2.5	0.0	0.050

2.5. Regional integration

The single and mixed production scenarios per ton of product results (r_i [t/t] or [€/t]) are scaled-up at regional level (4) considering the annual production ($p_{NUTS3,i}$ $[t/y]$) in each NUTS3 region.

$$R_{NUTS3,i} = \sum r_i \cdot \left(p_{NUTS3,i}\right) \qquad \text{[t/y] or [€/y]} \qquad (4)$$

The aggregated annual production of the EIIs at EU level is given in Table 2.

Table 2: NUTS3 annual production aggregated at EU level for the AIDRES industrial sectors in [t/y].

Sector	Product [t/y]	2018	2030	2050
Cement	Cement	173'836	173'836	173'836
Chemical	Polyethylene	31'584	31'584	31'584
	poly-ethyl-acetate	25'920	25'920	25'920
	Olefins	36'956	36'956	36'956
Fertiliser	Ammonia	10'928	10'928	10'928
Glass	Container glass	32'256	32'256	32'256
	Fibte Glass	2'100	2'100	2'100
	Flat glass	10'072	10'072	10'072
Refineries	Light-liquid-fuel	360'543	306'268	104'674
Steel	primary	93'144	93'144	93'144
	secondary	65'709	65'709	65'709

3. Industrial production route

3.1. Cement sector

The cement sector (raw mill, kiln, calcination, product mill) has been structured with production routes using dry kiln and coal and alernative route using calcination process to produce Limestone Calcined Clay Cement (LC3).

Six types of cement have been modeled however, no distinction is made in the EU-NUTS3 level and we have therefore considered Portland cement II (BV325R with a clinker-to-cement ratio of 70%) as the reference and Calcined clay product (LC3) as a future alternative (best case). Portland cement I (cI425R) is a conservative type of cement with a clinker-to-cement ratio of 95% and has one of the highest CO_2 emissions (worst case).

In cement manufacturing, about 60% CO_2 comes from calcination process, and remaining 40% comes from fuel consumption.

The conventional route uses dry kiln, cement, coal(54%), alternative fuels mixture(30%) and biomass waste (BMW) to produce Portland cement type II with 70% clinker-to-cement ratio. The flue gases from a conventional cement plant contains 20-25% CO_2. Beside Monoethanolamine (MEA) Capture technology, Calcium looping seems to emerge as the most promising carbon capture technology in the sector.

Alternative production routes (a) replace coal by alternative fuel mixture (AFM) and biomass waste (BMW), (b) integrate monoethanolamine amine (MEA) or calcium looping (CaL) carbon capture, (c) use oxy-combustion with carbon capture and (d) use calcination process to produce Limestone Calcined Clay Cement (LC3), a new type of cement with a lower CO_2 footprint based on calcined clay. Through research and testing, LC3 aims at becoming a standard and mainstream general-use product in the global cement market [24].

Different calcination modes exist, e.g. Rotary kiln (soak calcination) and Flash gas suspension calciner. The latter is chosen for this model, as its product presents clinker subsitution rate of 30-40% (due to significantly higher reactivity of the calcined clay with cement), whereas the soak calcination product can only substitute 15-25%. Other advantages are no grinding requirement required after the calciner, and reduced CAPEX by 75% compared to the rotary kiln option. The calcination step involves mainly 2 reactions : drying of the clay (at around 100°C), and metakaolin reaction between 400 and 600°C, producing water (gaseous) as by-product.

3.2. Chemical sector

The chemical sector in Europe is highly complex, encompassing bulk chemical manufacturing, especially chemicals for the pharmaceutical industry and plastics production. This work considers the production of three main products: poly-ethyl-acetate, polyethylene and olefins. Olefins includes ethylene, propylene and other olefins products. Ethylene is an intermediate in the production of poly-ethyl-acetate and polyethylene. The production of methanol from biomass and coelectrolysis is considered as well for the production of olefins.

Three different routes are considered for the production of olefins: (a) naphtha for the reference route and methanol synthetized either from (b) renewable green biomass gasification or (c) from the co-electrolysis of carbon dioxide and water.

The reference case for the chemical sector uses light naphtha (LN) to produce Poly-ethyl-acetate (PE), Etylene and Propylene. The alternative route (LN+EL) uses an electrical furnace to provide heat for naphta cracking, thus avoiding direct emissions from combustion.

Methanol is either imported from the market (grey methanol from steam reforming process) or produced from biomass ((BM)MeOH) or coelectrolysis ((COEL)MeOH) using CO_2 from the market. One burner is included for offgas from methanol synthesis and upgrading. Crude methanol is directly fed to a methanol-to-olefin reactor with oxygen [14]. Four products are then recovered: ethylene, butene, propylene and other olefins [31]. The model was designed for a production of 600 ktonnes of ethylene per year.

Polyethylene (PE) production is modelled using four main units: preheating of the reactants (ethylene, hydrogen used as chain-transfer agent and nitrogen) to 70°C; polymerization of ethylene in a slurry; recycle of unreacted liquid and gas reagents to finishing step; and quenching with water followed by extrusion [10, 16, 20]. The model was designed for a production of 25'000 kilos of polyethylene per hour.

Ethyl-acetate is produced via the esterification of carboxylic acids [26]. A process whereby ethylene is reacted with acetic acid at 170°C to produce 15 tonnes per hour of ethyl acetate is simulated. Following reaction, the hot gases are cooled down to room temperature before being send to the separation section which consists of two flash drum in series to extract the unreacted ethylene from the hot gases and recycle it to the preheating unit. The acid is then recovered from the products and recycled. The product is purified and latter polished to remove light and medium hydrocarbons. The light hydrocarbons are stripped of acetaldehyde and recycled whereas both the high and medium hydrocarbons are disregarded following heat exchange with other cooled process streams. Finally, ethanol and water are recovered from the water rich stream exiting purification and recycled. All process conditions are based on the Blueprint model developed by [3]. The polymerization reaction requires cooling water and the injection of cold feedstock into the reactor to control temperatures between 150 and 200°C at pressures from 13 to 83 bar.

3.3. Fertilizer sector

The fertiliser sector has been structured in four routes for the production of ammonia, ammonia plus urea and ammonia plus urea plus nitric acid. The production routes use either natural gas with and without carbon capture, biomass or electricity.

The reference production route is a conventional natural gas-based ammonia production plants which is equipped with efficient energy integration networks able to recover the waste heat available throughout the chemical system [12]. Alternative routes use biomass gasification or nitrogen and hydrogen (H2)NH3 for replacing methane in the integrated ammonia production plant [11]. Hydrogen is either produced at the plan using Alkaline electrolyser (AEL) or imported from the market. In both cases, mechanical vapor recompression (MVR) can be integrated to recycle waste heat, thus lowering the natural gas demand and direct emissions.

Hydrogen is either coming from the market (grey and green hydrogen, Table 1 or alternatively produced on-site by alkaline electrolysis (AEL).

Ammonia process emissions is a particular case where CO_2 used for urea, which is captured by necessity from the SMR syngas, is accounted as direct emission at the plant and not as captured CO_2 (CSS). The

CO_2 in surplus from the gas purification unit is send to the market (beverages, plastics, slaughterhouses) and accounted as direct emission. The routes integrating diethanolamine carbon capture of CO_2 from the gas purification unit are labelled with (DEA), while the routes with CCS on the furnace using monoethanolamine carbon capture are labelled with (MEA).

Accounting and mitigation of the green house gas emission effect of NO_2 for the nitric acid production routes is out of the scope of the AIDRES project.

3.4. Glass sector

The glass sector has been structured in production routes using either natural gas, hydrogen or electric furnace with or without carbon capture technology. Hydrogen can be produced on site by an Alkaline electrolyzer (AEL) or purchased on the market.

Fibre glass consists out of roughly 10% of the total whereas majority of the glass products are container or hollow (60%) and flat glass (30%).

The high temperature requirement of the process is limiting the available options. Natural gas (NG) or Hydrogen (H_2) can be used to satisfy the heating demand. Electric melting furnaces are also been considered with an efficiency of 85% and a cost based on equipment recently installed.

3.5. Refineries sector

The Refineries sector (Distillation, Cracking, Isomerisation, Reforming Desulfurisation and Fischer-Tropsch process) has been structured in seven routes. The refinery and Fischer-Tropsch process are used with either Natural gas or Hydrogen furnace. Carbon capture (MEA) is considered only in conjunction with the use of a Natural gas furnace. The targeted product of both routes is a light liquid fuel (LHV = 42.87 MJ/kg). To produce 1 ton of light liquid fuel (LLF), 1.56 ton of crude oil is needed, which represents an LHV equivalent of 1.038 $ton_{eq_{LLF}}$ of Fischer-Tropsch fuel and 0.464 $ton_{eq_{LLF}}$ of methanol.

The reference refineries (REF) uses crude oil to produce, without carbon capture, light liquid fuel (LHV = 42.87 MJ/kg) including isomerate, heavy reformate, gasoline and gasoil (diesel) [1, 2, 15, 28].

Two routes (Biomass gasification and co-electrolysis) are producing syngas from biomass or co-electrolysis of CO_2 and water. The extra Carbon dioxide is separated from the syngas with a carbon capture unit [25, 33]. The purified syngas is further transformed into liquid fuel with two different production routes:
- methanol synthesis;
- Fischer-Tropsch (FT) process producing FT crude (C12, C18, C20).

Hydrogen from the market, steam Methane Reforming (SMR) [27] and Alkaine Electrolysis [19] (AEL) are competing options for the supply of hydrogen to the system. Hydrogen can indeed be used to avoid the water gas shift reaction in the gasifier [13].

3.6. Steel sector

The steel sector (iron making, steel making and shaping) has been structured in production routes for primary steel and one route using recycled scraps and electric arc furnace (EAF) to produce secondary steel. Steel from primary and secondary production routes have different quality that serves different purpose. The denomination does not refer to a distinction in value.

Special types of steel and stainless steel were not further disaggregated in the model. Special types of steel are produced under request and it is an alloy of iron and several other materials (such as nickel and chromium). Therefore, the desegregation was done based on the production route: primary steel (BF-BOF) and secondary steel (EAF). This approach is aligned with EUROFER [5] and World Steel reports [29] to facilitate comparison and reduce the number of products to be covered. For instance, EUROFER includes a report differentiating the production route, as it is done in AIDRED, and another report by steel quality. Both cases add up to the same annual production. Finally, the production of special steel was assumed to be included in the production of steel with EAF.

The reference case uses a blast furnace (BF) and a Basic oxygen furnace (BOF) to produce primary steel.

Alternative routes make use of (i) top gas Recycling blast furnace (TGRBF) or (ii) waste plastic injection BF to replace the BF. TGRBF is a promising technology to significantly reduce the CO_2 emission by recycling CO and H_2 from the top gas leaving the blast furnace (BF). CO and H_2 content of top gas has a potential to act as reducing gas elements, and hence their recirculation to the BF is considered as an effective alternative to improve the BF performance, enhance utilization of Carbon and hydrogen, and reduce CO_2 emission.

Other alternative for primary steel production routes are (iii) replacing the BF-BOF by an electric arc furnace (EAF) or (iv) by shaft furnaces using different fuels to feed an EAF with direct reduced iron (DRI-EAF). The use of molten oxyde electrolyser (v) is a route with low technology readiness level (TRL). Finally (vi) monoethanolamine carbon capture (MEA) can be used on the fumes of the different furnaces.

The consumption of coal of blast furnaces is much higher than the consumption of coke since the coke oven

plant is assumed to be within the boundaries of the sector. Nevertheless, the total energy intensity remains within the order of magnitude common for the BF-BOF (18-20 GJ/t).

Both alternatives, H_2 without and with electrolyzer on-site (AEL) are computed and available for comparison in all scenarios.

4. Results

A subset of the full AIDRES database, giving the specific energy flows, investment costs, emissions and captured CO_2 per ton of product for the routes of the AIDRES EU-mix 2018-2050, is reported in Table 3 of appendix A. The AIDRES EU-mix, shown in Figure 1 comply with the emission reduction targets for 2030 and 2050 based on the MIX EU Reference Scenario [6] in line with Fit for 55 and the EU Green deal [7]. The corresponding energy demand, aggregated at the EU level are reported in Figure 2. The map of Figure 3 shows the energy and direct emissions reduction, aggregated at country scale, for the AIDRES EU-mix at horizon 2050.

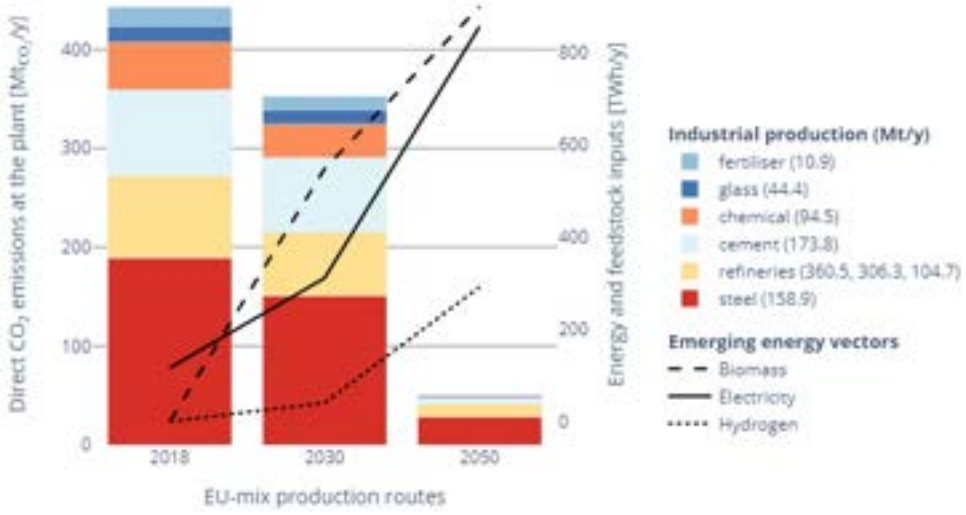

Figure 1: EU-27 EIIs direct emission at the plant [Mt_{CO_2}/y] and emerging energy vectors [TWh/y] AIDRES EU mix production routes meeting EU reference MIX scenario derived emission reduction targets.

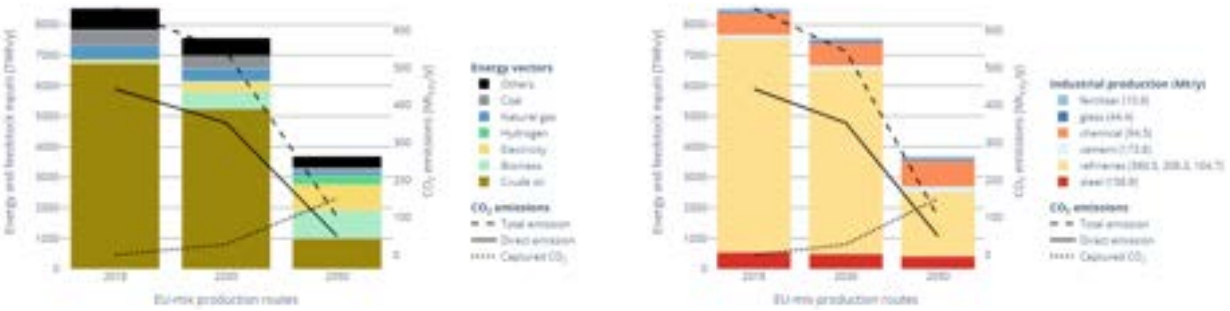

(a) Energy and feedstock inputs by vectors.

(b) Energy and feedstock inputs by sectors.

Figure 2: EU-27 EIIs energy and feedstock inputs flows [TWh/y], direct and total 2018 emissions [Mt_{CO_2}/y] for AIDRES EU mix production routes meeting EU reference MIX scenario derived emission reduction targets.

5. Conclusion

This paper presents a publicly available database for the decarbonisation of the heavy industry in Europe in line with other databases of energy intensive industries, such as EU ETS. The concept of AIDRES EU mix routes has been introduced to account for the uncertainty which emerges from the unknown of future production methods for each individual industrial site (NUTS3).

According to the AIDRES EU-EIIs decarbonisation pathway, the overall energy and feedstock inputs are expected to decrease by 57% by 2050, mainly due to the reduced refinery output, while the renewable electricity

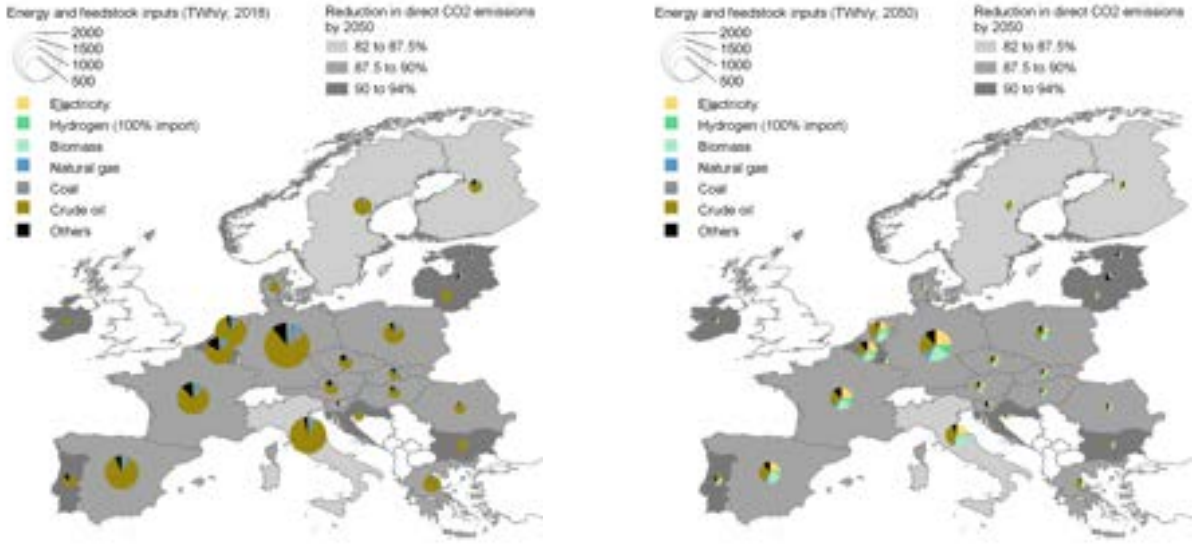

(a) AIDRES reference 2018.

(b) AIDRES EU-mix 2050.

Figure 3: Map of the energy and feedstock inputs flows [Twh/y] for the AIDRES EU-mix 2018 and 2050 with direct CO_2 emissions reduction [%] by 2050. Scales of Luxembourg, Estonia, Latvia and Slovenia x 3.

demand will see a sharp increase by a factor of three by 2030. Biomass could play a crucial role in the chemical and refinery sectors in the future, while methanol will replace naphtha as a vital feedstock for the chemical sector. The usage of green hydrogen is moreover expected to become essential in the steel, fertilizer, and chemical sectors. The cement industry will have to rely on a mixture of biomass waste and alternative fuels, combined with carbon capture technologies such as oxy-fuel combustion and calcium looping. Although there will be a strong decline in coal and natural gas usage, they can still have a role in some sectors combined with carbon capture technologies.

However, the AIDRES EU mix routes are not the only pathways toward the decarbonisation of the heavy industry in Europe. A virtual unlimited number of different combinations of different production routes, across the EU and at specific NUTS3 locations, can indeed be simulated using the publicly available AIDRES database.

The AIDRES database has already been applied to develop regional and sectoral approaches to identify potential industrial symbiosis initiatives, highlighting the optimization potential of symbiotic profiles and recommending the inclusion of additional sectors such as paper and power plants [21]. The proposed format can be used in future studies and model applications by EU institutions, such as the Directorate-General for Energy (DG ENER) and the Joint Research Centre (JRC).

Acknowledgments

This project is carried out with the financial support of the European Commission – Directorate General for Energy. Moreover, the authors would like to thank Arcelor Mittal, the Belgian Federation for Chemistry and Life Sciences (essenscia), CEMBUREAU, CEMEX, Dechema, European Chemical Industry Council (Cefic), European Steel Technology Platform (ESTEP), Federation of the Belgian Cement Industry (FEBELCEM), INEOS, Institut du verre, Glass for Europe, Vrije Universiteit Brussel (VUB), EU Joint Research Center (JRC) and Yara International for their participation in the AIDRES project.

References

[1] Pascal Barthe et al. *Best Available Techniques (BAT) Reference Document for the Refining of Mineral Oil and Gas Industrial Emissions : Industrial Emissions Directive 2010/75/EU (Integrated Pollution Prevention and Control)*. Joint Research Centre and Institute for Prospective Technological Studies, 2015. DOI: doi/10.2791/010758.

[2] Sabine Brueske et al. "U.S. Manufacturing Energy Use and Greenhouse Gas Emissions Analysis". In: (Nov. 2012). DOI: 10.2172/1055125. URL: https://www.osti.gov/biblio/1055125.

[3] Hélène Cervo. "Development of a Methodology Enabling the Identification of Industrial Symbiosis Opportunities and Their Assessment in the Petrochemical Industry". PhD thesis. 2020. URL: http://www.theses.fr/2020AIXM0135/document.

[4] Hélène Cervo et al. “Blueprint: A Methodology Facilitating Data Exchanges to Enhance the Detection of Industrial Symbiosis Opportunities – Application to a Refinery”. In: *Chemical Engineering Science* 211 (Jan. 2020), p. 115254. ISSN: 00092509. DOI: 10.1016/j.ces.2019.115254. URL: https://linkinghub.elsevier.com/retrieve/pii/S0009250919307444 (visited on 02/01/2023).

[5] EUROFER. *European Steel in Figures 2021*. 2021. URL: https://www.eurofer.eu/assets/publications/brochures-booklets-and-factsheets/european-steel-in-figures-2021/European-Steel-in-Figures-2021.pdf.

[6] European Commission. *2030 Climate Target Plan - Stepping up Europe's 2030 Climate Ambition Investing in a Climate-Neutral Future for the Benefit of Our People*. SWD(2020) 176 final. Brussels, Sept. 17, 2020. URL: https://climate.ec.europa.eu/eu-action/european-green-deal/2030-climate-target-plan_en#documents.

[7] European Commission. *Communication From The Commission To The European Parliament, The European Council, The Council, The European Economic And Social Committee And The Committee Of The Regions - The European Green Deal*. COM(2019) 640 final. Brussels, Nov. 12, 2019. URL: https://eur-lex.europa.eu/legal-content/EN/TXT/?uri=COM:2019:640:FIN.

[8] European Commission and Directorate-General for Internal Market, Industry, Entrepreneurship and SMEs. *Masterplan for a Competitive Transformation of EU Energy-Intensive Industries Enabling a Climate-Neutral, Circular Economy by 2050*. Publications Office, 2019. DOI: doi/10.2873/854920. URL: https://op.europa.eu/s/yis0.

[9] European council. Fit for 55. 2022. URL: https://www.consilium.europa.eu/en/policies/green-deal/fit-for-55-the-eu-plan-for-a-green-transition/ (visited on 03/20/2023).

[10] Heino Falcke et al. *Best Available Techniques (BAT) Reference Document for the Production of Large Volume Organic Chemicals.* EUR 28882 EN. Luxembourg: Publications Office of the European Union, 2017. ISBN: 978-92-79-76589-6. URL: https://data.europa.eu/doi/10.2760/77304.

[11] Daniel Flórez-Orrego, François Maréchal, and Silvio de Oliveira Junior. “Comparative Exergy and Economic Assessment of Fossil and Biomass-Based Routes for Ammonia Production”. In: *Energy Conversion and Management* 194 (Aug. 2019), pp. 22–36. ISSN: 01968904. DOI: 10.1016/j.enconman.2019.04.072. URL: https://linkinghub.elsevier.com/retrieve/pii/S0196890419305060 (visited on 01/05/2023).

[12] Daniel Flórez-Orrego et al. “Combined Exergy Analysis, Energy Integration and Optimization of Syngas and Ammonia Production Plants: A Cogeneration and Syngas Purification Perspective”. In: *Journal of Cleaner Production* 244 (Jan. 2020), p. 118647. ISSN: 09596526. DOI: 10.1016/j.jclepro.2019.118647. URL: https://linkinghub.elsevier.com/retrieve/pii/S0959652619335176 (visited on 01/05/2023).

[13] Julia Granacher et al. “A Study on Synergies of Combined Pulp and Fuel Production”. In: vol. 34. Proceedings of ECOS 2021. 2021, p. 11. URL: http://infoscience.epfl.ch/record/289996.

[14] Ilkka Hannula and Vesa Arpiainen. “Light Olefins and Transport Fuels from Biomass Residues via Synthetic Methanol: Performance and Cost Analysis”. In: *Biomass Conversion and Biorefinery* 5.1 (Mar. 1, 2015), pp. 63–74. ISSN: 2190-6823. DOI: 10.1007/s13399-014-0123-9. URL: https://doi.org/10.1007/s13399-014-0123-9 (visited on 10/19/2022).

[15] IPIECA. “Petroleum Refinery Waste Management and Minimization”. In: (Sept. 2014), p. 56.

[16] Dusan Jeremic. “Polyethylene”. In: *Ullmann's Encyclopedia of Industrial Chemistry*. John Wiley & Sons, Ltd, 2014, pp. 1–42. ISBN: 978-3-527-30673-2. DOI: 10.1002/14356007.a21_487.pub3. URL: https://onlinelibrary.wiley.com/doi/abs/10.1002/14356007.a21_487.pub3 (visited on 11/23/2021).

[17] Ivan Kantor, Nasibeh Pouransari, and François Maréchal. “A Perspective on Process Integration”. In: *Resource Efficiency of Processing Plants*. John Wiley & Sons, Ltd, 2018, pp. 403–440. ISBN: 978-3-527-80415-3. DOI: 10.1002/9783527804153.ch16. eprint: https://onlinelibrary.wiley.com/doi/pdf/10.1002/9783527804153.ch16. URL: https://onlinelibrary.wiley.com/doi/abs/10.1002/9783527804153.ch16.

[18] Ivan Daniel Kantor et al. “Thermal Profile Construction for Energy-Intensive Industrial Sectors”. In: *Proceedings of the 31st International Conference on Efficiency, Cost, Optimization, Simulation and Environmental Impact of Energy Systems*. 2018, p. 13. URL: https://core.ac.uk/download/pdf/211985119.pdf.

[19] Gauthier Limpens et al. “EnergyScope TD: A Novel Open-Source Model for Regional Energy Systems”. In: *Applied Energy* 255 (2019), p. 113729. ISSN: 0306-2619. DOI: 10.1016/j.apenergy.2019.113729. URL: https://www.sciencedirect.com/science/article/pii/S0306261919314163.

[20] Norma Maraschin. “Polyethylene, Low Density”. In: *Kirk-Othmer Encyclopedia of Chemical Technology*. John Wiley & Sons, Ltd, 2005. ISBN: 978-0-471-23896-6. DOI: 10.1002/0471238961.12152316050219.a01.pub2. URL: https://onlinelibrary.wiley.com/doi/abs/10.1002/0471238961.12152316050219.a01.pub2 (visited on 11/23/2021).

[21] Mendez Alva, Francisco. “Industrial Symbiosis Enabling Resource Circularity and Climate Neutrality in the Process Industry”. PhD thesis. Ghent University. Faculty of Engineering and Architecture / Ghent University, 2022, pp. XII, 156. ISBN: 9789463556682.

[22] Calliope Panoutsou and Kyriakos Maniatis. *Sustainable Biomass Availability in the EU, to 2050*. Imperial College London, Aug. 2021. URL: https://www.concawe.eu/wp-content/uploads/Sustainable-Biomass-Availability-in-the-EU-Part-I-and-II-final-version.pdf (visited on 09/15/2021).

[23] EPOS Partners. *Enhanced Energy and Resource Efficiency and Performance in Process Industry Operations via Onsite and Cross-Sectorial Symbiosis*. 2022. URL: https://www.aspire2050.eu/epos.

[24] Radhakrishna G. Pillai et al. “Service Life and Life Cycle Assessment of Reinforced Concrete Systems with Limestone Calcined Clay Cement (LC3)”. In: *Cement and Concrete Research* 118 (Apr. 2019), pp. 111–119. ISSN: 00088846. DOI: 10.1016/j.cemconres.2018.11.019. URL: https://linkinghub.elsevier.com/retrieve/pii/S0008884618303417 (visited on 01/05/2023).

[25] Marta G. Plaza, Sergio Martínez, and Fernando Rubiera. “CO2 Capture, Use, and Storage in the Cement Industry: State of the Art and Expectations”. In: *Energies* 13.21 (21 Jan. 2020), p. 5692. DOI: 10.3390/en13215692. URL: https://www.mdpi.com/1996-1073/13/21/5692 (visited on 07/19/2021).

[26] Wilhelm Riemenschneider and Hermann M. Bolt. “Esters, Organic”. In: *Ullmann’s Encyclopedia of Industrial Chemistry*. John Wiley & Sons, Ltd, 2005. ISBN: 978-3-527-30673-2. DOI: 10.1002/14356007.a09_565.pub2. URL: https://onlinelibrary.wiley.com/doi/abs/10.1002/14356007.a09_565.pub2 (visited on 11/23/2021).

[27] Yaser Khojasteh Salkuyeh, Bradley A. Saville, and Heather L. MacLean. “Techno-Economic Analysis and Life Cycle Assessment of Hydrogen Production from Natural Gas Using Current and Emerging Technologies”. In: *International Journal of Hydrogen Energy* 42.30 (2017), pp. 18894–18909. ISSN: 0360-3199. DOI: 10.1016/j.ijhydene.2017.05.219. URL: https://www.sciencedirect.com/science/article/pii/S0360319917322036.

[28] Michael Wang, Hanjie Lee, and John Molburg. “Allocation of Energy Use in Petroleum Refineries to Petroleum Products: Implications for Life-Cyde Energy Use and Emission Inventory of Petroleum Transportation Fuels”. In: *The International Journal of Life Cycle Assessment* 9.1 (Jan. 2004), pp. 34–44. ISSN: 0948-3349, 1614-7502. DOI: 10.1007/BF02978534. URL: http://link.springer.com/10.1007/BF02978534 (visited on 04/25/2022).

[29] World Steel Association. *World Steel in Figures 2021*. 2021. URL: https://worldsteel.org/wp-content/uploads/2021-World-Steel-in-Figures.pdf.

[30] Tomas Gilberte Wyns et al. *Industrial Transformation 2050 - towards an Industrial Strategy for a Climate Neutral Europe*. Apr. 25, 2019.

[31] Yangyang Xiang et al. “Exergetic Evaluation of Renewable Light Olefins Production from Biomass via Synthetic Methanol”. In: *Applied Energy* 157 (Nov. 1, 2015), pp. 499–507. ISSN: 0306-2619. DOI: 10.1016/j.apenergy.2015.05.039. URL: https://www.sciencedirect.com/science/article/pii/S0306261915006492 (visited on 09/09/2021).

[32] Min-Jung Yoo et al. “OsmoseLua – An Integrated Approach to Energy Systems Integration with LCIA and GIS”. In: *Computer Aided Chemical Engineering*. Vol. 37. Elsevier, 2015, pp. 587–592. ISBN: 978-0-444-63429-0. DOI: 10.1016/B978-0-444-63578-5.50093-1. URL: https://linkinghub.elsevier.com/retrieve/pii/B9780444635785500931 (visited on 01/12/2023).

[33] Wenbin Zhang et al. “Parametric Study on the Regeneration Heat Requirement of an Amine-Based Solid Adsorbent Process for Post-Combustion Carbon Capture”. In: *Applied Energy* 168 (Apr. 2016), pp. 394–405. ISSN: 03062619. DOI: 10.1016/j.apenergy.2016.01.049. URL: https://linkinghub.elsevier.com/retrieve/pii/S0306261916300290 (visited on 08/18/2022).

Appendix A Per ton results of the AIDRES single and EU-mix production routes.

Table 3: Per ton of product energy flows [GJ/t], investment costs [€/t], direct emissions and captured CO_2 [t_{CO_2}/t] for AIDRES single and EU mix [%] production routes.

Products	Production routes	Electricity [GJ/t]	AFM [GJ/t]	Biomass [GJ/t]	Biomass waste [GJ/t]	Coal [GJ/t]	Coke [GJ/t]	Crude oil [GJ/t]	Hydrogen [GJ/t]	Methanol [GJ/t]	Naphtha [GJ/t]	Natural gas [GJ/t]	Plastic mix [GJ/t]	Capex [EUR/t]	Direct emission [tCO2/t]	Captured CO2 [tCO2/t]	Direct em. reduction [%]	Mix 2018 [%]	Mix 2030 [%]	Mix 2050 [%]
Cement reference	**AIDRES EU-mix-2018**	**0.29**	**0.74**		**0.44**	**1.15**								**3**	**0.498**			**100.0**		
Portland cement II	CEM2-(Coal)	0.29				2.13								3	0.524		-5.2	54.0	47.1	5.1
	CEM2-(Coal)CaL	0.47				2.13								21	0.086	0.438	82.7		0.5	3.5
	CEM2-(Coal)Oxy-CaL	0.57				2.15								15	0.083	0.533	83.3		0.5	3.5
	CEM2-(AFM)	0.29	2.46											3	0.535		-7.4	30.0	26.2	2.9
	CEM2-(AFM)MEA	0.60	3.86											5	0.129	0.516	74.1		1.5	10.7
	CEM2-(AFM)CaL	0.47	2.46											22	0.088	0.448	82.3		1.5	10.7
	CEM2-(AFM)Oxy-CaL	0.51	2.46											15	0.075	0.457	84.9		1.5	10.7
	CEM2-(BMW)	0.29			2.77									3	0.342		31.4	16.0	14.0	1.5
	CEM2-(BMW)MEA	0.69			4.47									5	-0.308	0.650	161.8		1.6	11.6
	CEM2-(BMW)CaL	0.51			2.77									25	-0.188	0.530	137.7		1.6	11.6
	CEM2-(BMW)Oxy-MEA	0.65			3.16									4	0.020	0.706	96.0		1.6	11.6
	CEM2-(BMW)Oxy-CaL	0.58			2.77									16	0.014	0.665	97.2		1.6	11.6
Limestone calcined clay	LC3-(Coal)CaL	0.44				1.81								17	0.065	0.334	87.0		0.1	0.5
	LC3-(NG)MEA	0.50										2.99		4	0.082	0.329	83.5		0.1	0.5
	LC3-(NG)CaL	0.42										1.84		15	0.057	0.291	88.6		0.1	0.5
	LC3-(NG)Oxy-CaL	0.57										1.85		12	0.066	0.442	86.8		0.1	0.5
	LC3-(AFM)MEA	0.54	3.12											4	0.098	0.391	80.3		0.1	0.5
	LC3-(AFM)CaL	0.44	2.13											17	0.067	0.344	86.6		0.1	0.5
	LC3-(AFM)Oxy-MEA	0.52	2.46											4	0.068	0.367	86.4		0.1	0.5
	LC3-(AFM)Oxy-CaL	0.47	2.13											12	0.056	0.352	88.8		0.1	0.5
	LC3-(BMW)Oxy-MEA	0.57			2.56									4	0.010	0.545	98.0		0.1	0.5
	LC3-(BMW)Oxy-CaL	0.53			2.40									12	0.004	0.532	99.2		0.1	0.5
	AIDRES EU-mix-2030	0.32	0.78		0.61	1.03						0.00		4	0.433	0.071	13.2		100.0	
	AIDRES EU-mix-2050	0.54	1.06		1.59	0.27						0.03		12	0.034	0.501	93.2			100.0
Polyethylene	**(NG)PE**	**0.49**							**0.01**			**0.29**		**37**	**0.016**			**100.0**	**69.4**	
	(NG)PE-MEA	0.50							0.01			0.30		37	0.002	0.015	87.5		9.6	31.3
	(H2)PE	0.49							0.31					37			100.0		10.5	34.4
	(EL)PE	0.75							0.01					37			100.0		10.5	34.4
	AIDRES EU-mix-2018	0.49							0.01			0.29		37	0.016			100.0		
	AIDRES EU-mix-2030	0.52							0.04			0.23		37	0.011	0.001	29.4		100.0	
	AIDRES EU-mix-2050	0.58							0.11			0.10		37	0.001	0.005	96.1			100.0
Poly-ethyl-acetate	**(NG)PEA**	**1.30**										**8.16**		**112**	**0.459**			**100.0**	**69.4**	
	(NG)PEA-MEA	1.57										8.76		120	0.049	0.443	89.3		11.2	36.6
	(H2)PEA	1.30							8.64					115			100.0		9.7	31.7
	(EL)PEA	8.54												111			100.0		9.7	31.7
	AIDRES EU-mix-2030	2.03							0.84			6.65		113	0.324	0.050	29.4		100.0	
	AIDRES EU-mix-2050	3.69							2.74			3.21		116	0.018	0.162	96.1			100.0

Table 3: Per ton of product energy flows [GJ/t], investment costs [€/t], direct emissions and captured CO_2 [t_{CO_2}/t] for AIDRES single and EU mix [%] production routes.

Products	Production routes	Electricity [GJ/t]	AFM [GJ/t]	Biomass [GJ/t]	Biomass waste [GJ/t]	Coal [GJ/t]	Coke [GJ/t]	Crude oil [GJ/t]	Hydrogen [GJ/t]	Methanol [GJ/t]	Naphtha [GJ/t]	Natural gas [GJ/t]	Plastic mix [GJ/t]	Capex [EUR/t]	Direct emission [tCO2/t]	Captured CO2 [tCO2/t]	Direct em. reduction [%]	Mix 2018 [%]	Mix 2030 [%]	Mix 2050 [%]
Olefins	**(LN)O**	**1.06**									**60.52**			**55**	**0.967**			**100.0**	**69.4**	
	(LN)O-MEA	2.68									60.52	2.61		88	0.111	1.002	88.5		2.5	8.1
	(LN+EL)O	37.50									60.52			55			100.0		1.8	5.9
	(MeOH)O-MEA	0.74								49.01				17	0.015	0.132	98.4		9.5	31.1
	((BM)MeOH)O	5.62		96.08										246			100.0		3.6	11.9
	((BM+H2)MeOH)O	5.51		93.02					17.93					117			100.0		3.6	11.9
	((COEL)MeOH)O-MEA	68.66												881	0.059	0.528	93.9		9.5	31.1
	AIDRES EU-mix-2030	8.50		6.86					0.65	4.67	44.59	0.07		140	0.681	0.088	29.6		100.0	
	AIDRES EU-mix-2050	25.35		22.41					2.13	15.25	8.52	0.21		333	0.032	0.287	96.7			100.0
Ammonia	(NG)NH3	2.08										28.33		127	1.742			100.0	70.0	2.0
	(NG)NH3-DEA	2.08										28.33		127	0.322	1.420	81.5		1.8	5.8
	(NG)NH3-MEA-DEA	2.16										29.69		255	0.040	1.779	97.7		1.8	5.8
	(NG)NH3-MVR-DEA	2.14										26.19		104	0.202	1.420	88.4		1.8	5.8
	(NG)NH3-MVR-MEA-DEA	2.58										26.19		162	0.020	1.602	98.9		1.8	5.8
	(BM)NH3	4.46		40.52										170			100.0		1.5	5.0
	(H2)NH3	3.40							23.06					577			100.0		21.4	70.0
	AIDRES EU-mix-2030	2.41		0.62					4.94			21.77		227	1.229	0.110	29.4		100.0	
	AIDRES EU-mix-2050	3.16		2.03					16.14			6.91		452	0.068	0.358	96.1			100.0
Nitric-acid	**(NG)HNO3**											**6.50**		**30**	**0.409**			**100.0**	**76.6**	**23.7**
	(NG)HNO3-DEA											6.50		30		0.409	100.0		3.4	11.0
	(BM)HNO3			11.66										30			100.0		4.6	15.0
	(BM)HNO3-DEA			11.66										30	-0.736	0.736	280.0		3.4	11.0
	(H2)HNO3								6.64					30			100.0		12.0	39.3
	AIDRES EU-mix-2030			0.93					0.80			5.20		30	0.289	0.039	29.4		100.0	
	AIDRES EU-mix-2050			3.03					2.61			2.26		30	0.016	0.126	96.1			100.0
Urea	**(NG)Urea**	**0.82**										**14.88**		**33**	**0.186**			**100.0**	**69.3**	
	(NG)Urea-MEA	0.90										14.86		66	0.082	0.103	55.9		2.7	8.9
	(BM)Urea	1.74		22.99										11			100.0		14.0	45.6
	(H2)Urea	2.00							13.09					11			100.0		14.0	45.6
	AIDRES EU-mix-2030	1.12		3.21					1.83			10.72		28	0.131	0.003	29.5		100.0	
	AIDRES EU-mix-2050	1.78		10.48					5.96			1.32		16	0.007	0.009	96.1			100.0
Container glass	**(NG)**	**1.07**							**0.04**			**4.73**		**53**	**0.338**			**100.0**	**85.9**	
	(NG)-CC	1.13							0.04			4.73		55	0.011	0.097	96.7		3.5	24.5
	(H2)	1.07							5.04					55	0.073		78.4		1.9	13.3
	(H2)-CC	1.08							5.04					55	0.002	0.021	99.4		3.5	24.5
	(EL)	5.09							0.04					50	0.073		78.4		1.9	13.3
	(EL)-CC	5.10							0.04					51	0.002	0.021	99.4		3.5	24.5
	AIDRES EU-mix-2030	1.29							0.31			4.23		53	0.294	0.005	13.2		100.0	
	AIDRES EU-mix-2050	2.61							1.93			1.16		53	0.023	0.034	93.2			100.0

Table 3: Per ton of product energy flows [GJ/t], investment costs [€/t], direct emissions and captured CO_2 [t_{CO_2}/t] for AIDRES single and EU mix [%] production routes.

Products	Production routes	Electricity [GJ/t]	AFM [GJ/t]	Biomass [GJ/t]	Biomass waste [GJ/t]	Coal [GJ/t]	Coke [GJ/t]	Crude oil [GJ/t]	Hydrogen [GJ/t]	Methanol [GJ/t]	Naphtha [GJ/t]	Natural gas [GJ/t]	Plastic mix [GJ/t]	Capex [EUR/t]	Direct emission [tCO2/t]	Captured CO2 [tCO2/t]	Direct em. reduction [%]	Mix 2018 [%]	Mix 2030 [%]	Mix 2050 [%]
Fibre glass	**(NG)**	**2.16**							**0.04**			**7.24**		**80**	**0.634**			**100.0**	**85.9**	
	(NG)-CC	2.27							0.04			7.24		84	0.020	0.183	96.8		4.0	28.4
	(H2)	2.16							7.17					77	0.227		64.2		2.1	14.8
	(H2)-CC	2.20							7.17					79	0.007	0.066	98.9		4.0	28.4
	(EL)-CC	7.93							0.04					72	0.007	0.066	98.9		4.0	28.4
	AIDRES EU-mix-2030	2.40							0.48			6.51		80	0.551	0.013	13.2		100.0	
	AIDRES EU-mix-2050	3.84							3.12			2.06		78	0.043	0.089	93.2			100.0
Flat glass	**(NG)**	**0.80**							**0.04**			**5.43**		**61**	**0.487**			**100.0**	**85.9**	
	(NG)-CC	0.89							0.04			5.43		64	0.016	0.140	96.7		4.1	28.7
	(H2)	0.80							5.78					63	0.182		62.6		1.0	6.9
	(H2)-CC	0.83							5.78					64	0.006	0.052	98.8		4.1	28.7
	(EL)	5.41							0.04					58	0.182		62.6		1.0	6.9
	(EL)-CC	5.44							0.04					59	0.006	0.052	98.8		4.1	28.7
	AIDRES EU-mix-2030	1.04							0.33			4.88		61	0.423	0.010	13.2		100.0	
	AIDRES EU-mix-2050	2.49							2.09			1.56		62	0.033	0.070	93.2			100.0
Light liquid fuel	**REF-SMR**	**0.14**						**67.23**				**2.51**		**44**	**0.231**			**100.0**	**88.4**	**37.7**
	REF(H2)	0.14						67.23	0.51			1.73		44	0.189		18.2		3.4	14.0
	(BM)FT	3.06		85.27										193			100.0		3.3	13.5
	(BM)MeOH	4.34		84.08										201			100.0		3.3	13.5
	(COEL)FT-MEA	59.06												755	0.060	0.542	74.0		0.8	10.7
	(COEL)MeOH-MEA	59.43												755	0.038	0.346	83.5		0.8	10.7
	AIDRES EU-mix-2030	1.31		5.60				61.72	0.02			2.28		65	0.211	0.007	8.5		100.0	
	AIDRES EU-mix-2050	13.76		22.83				34.71	0.07			1.19		238	0.124	0.095	46.4			100.0
Primary steel	**BF-BOF**	**0.66**				**17.71**	**1.13**							**33**	**2.002**			**100.0**	**71.6**	
	BF-BOF-MEA	1.50				17.71	1.13					0.58		64	0.790	1.369	60.5		2.4	9.4
	WPI-BOF-MEA	1.71				15.95	1.13					0.23	1.89	62	0.781	1.333	61.0		2.4	9.4
	(NG)DRI-EAF	2.06				0.40						7.45		32	0.651		67.5		16.9	
	(NG)DRI-EAF-MEA	2.42				0.40						7.45		46	0.065	0.586	96.8		4.2	16.9
	(H2)DRI-EAF	2.06				0.40			11.40					32	0.193		90.4		2.5	58.9
	MOE	14.34												74			100.0			5.3
	AIDRES EU-mix-2030	1.06				13.56	0.86		0.29			1.60	0.04	35	1.588	0.089	20.7		100.0	
	AIDRES EU-mix-2050	2.69				3.48	0.21		6.71			1.34	0.18	42	0.273	0.354	86.4			100.0
Secondary steel	**Scraps EAF**	**1.50**				**0.30**						**0.19**		**18**	**0.040**			**100.0**	**100.0**	**100.0**

AIDRES reference 2018 in bold.

AFM: Alternative fuel mixture, **BM**: Biomass, **BMW**: Biomass Waste, **BOF**: Basic oxygen furnace (BOF), **CaL**: Calcium looping carbon capture, **CEM2**: Portland cement II - clinker-to-cement ratio of 70%, **COEL**: Co-electrolysis process for syngas production, **DEA**: Diethanolamine carbon capture, **DRI**: Direct Reduced Iron electric arc furnace, **EAF**: Electric Arc Furnace, **EIIs**: Europe's energy intensive industries, **EL**: Electrical furnace, **FT**: Fischer-Tropsch process, **HNO3**: Nitric acid production, **LC3**: Limestone Calcined Clay Cement - clinker-to-cement ratio of 50%, **LN**: Naphtha ctacking, **MEA**/**CC**: Monoethanolamine carbon capture, **MeOH**: Methanol, **MOE**: Molten oxide electrolyser, **MVR**: Mechanical vapor recompression, **NG**: Natural gas, **NG+H2**: Natural gas and hydrogen mix shaft furnace, **NH3**: Ammonia production, **NUTS**: Nomenclature of Territorial Units for Statistics, **O**: Olefins production, **Oxy**: Oxycombustion, **PE**: Polyethylene production, **PEA**: Poly-ethyl-acetate production, **REF**: Conventionnal crude oil refinning, **Scraps EAF**: EAF Scraps handling (recycling/secondary route), **WPI**: Waste plastic injection blast furnace.

Optimization-based energy system planning under long-term uncertainty: Rapid Monte Carlo analysis using linear regression

Hagen Seele[a,b], Jan Tautorus[a,c], Christiane Reinert[a,d], Niklas von der Aßen[a,e]

[a] Institute of Technical Thermodynamics, RWTH Aachen University, 52062 Aachen, Germany
[b] hagen.seele@ltt.rwth-aachen.de
[c] jan.tautorus@rwth-aachen.de
[d] christiane.reinert@ltt.rwth-aachen.de
[e] niklas.vonderassen@ltt.rwth-aachen.de, CA

Abstract:

Decision-making for distributed energy systems (DES) is subject to significant uncertainties. Therefore, assuming perfect foresight for long-term system planning might result in suboptimal decisions. Long time horizons result in a variety of possible scenarios. One way of considering uncertainty in DES design is Monte Carlo analysis (MCA). However, MCA suffers from the computational burden of repeatedly evaluating energy system models. Furthermore, MCA is sensitive to distribution assumptions of uncertain parameters. In this work, we combine linear regression and systematic uncertainty modeling in MCA to consider uncertainty effectively.

We propose a method for comparing different DES designs regarding total annualized cost (TAC) while reflecting uncertain parameters. We model uncertainties by introducing a small number of representative factors that scale reference parameters. We distinguish between constant and long-term uncertainties increasing over time. We use mixed-integer linear programs (MILPs) to minimize yearly costs of DES. We solve the burdensome MILPs only for Latin Hypercube samples to parameterize linear surrogate models. We use the obtained linear surrogate models during MCA to accelerate the computation of the TAC.

We apply our method to a case study adapted from the literature to compare promising DES designs while considering multiple sources of uncertainty. We compute the TAC of the DES designs for thousands of long-term scenarios and identify the design, which results most frequently in the lowest costs. We show that using linear regression can reduce the computational time by more than 99 %, while maintaining a high accuracy measured by the goodness of fit of the linear regression.

Keywords:

Distributed energy systems; Long-term scenarios; MILP; Multiple uncertainties; Surrogate modeling.

1. Introduction

Designing industrial energy systems given a multi-year planning horizon is challenging yet crucial for achieving a sustainable energy supply [1]. Energy systems are commonly designed to minimize total annualized cost (TAC), the global warming impact, or both. Long planning horizons suffer from a lack of good forecasts and also involve inherent uncertainties, which are recommended to be considered [1,2]. Optimization-based techniques for identifying the optimal energy system configuration under uncertainty include robust optimization, stochastic optimization, or chance-constrained optimization [3,4]. Here, the consideration of uncertainties lead to complex optimization problems that are challenging to solve resulting in a tradeoff between solution quality and computational tractability [3]. The presence of multiple uncertain factors, e.g., arising from the long-term evolution of energy prices and demand, adds further complexity in identifying the best suited design [3]. Energy system optimization under uncertainty can also be addressed using Monte Carlo analysis (MCA), where computation time is independent of the number of uncertain parameters for a single scenario [4,5]. However, MCA typically requires evaluating hundreds of scenarios while the computational time still increases linearly with the number of scenarios and thus can become prohibitively high, particularly when complex models are involved [5]. A promising approach is to use approximation methods involving sampling techniques like Latin hypercube sampling, which can facilitate the consideration of a wide range of scenarios [6,7]. Furthermore, MCA can be quite sensitive to probability distributions for uncertain parameters [5]. Even

though only a few parameters might be influential, the specification of uncertainties is challenging and should be done systematically [2]. Overall, the issue of efficiently incorporating multiple sources of uncertainties into the energy system design process for industrial systems with a multi-year planning horizon is challenging and needs to be addressed.

In this work, we propose a method that helps to make informed decisions regarding the selection of the optimal distributed energy system (DES) design from a set of promising designs considering long time horizons and multiple sources of uncertainty. This so-called Rapid Monte Carlo analysis (RMCA) incorporates uncertainty and surrogate modeling. The economic metric TAC is used to rank the designs. As a first step, we define the procedure of calculating TAC. Determining TAC for a design involves estimating operational expenditures by solving operational optimizations and using investment cost correlations. Accordingly, the metric depends on a variety of uncertain parameters that may influence the results. To model uncertainties, the full set of uncertain parameters is reduced to a few representative factors. Each factor is classified and parameterized to define the probability distributions of the long planning horizon. Next, computationally burdensome relationships between these representative factors and the TAC are replaced by linear surrogate models. The uncertainty and surrogate models allow a large number of long-term scenarios to be considered. Finally, a statistical analysis of the TAC of the DES designs is conducted to serve as a foundation for selecting a final design.

The paper is structured as follows. Section 2 presents the proposed method in detail by first providing an overview, then presenting the uncertainty parameterization and modeling as well as the linear surrogate model generation, and finally the RMCA. Section 3 applies the method to a case study adapted from the literature and discusses the results. Finally, in Section 4 conclusions are drawn.

2. Rapid Monte Carlo analysis via uncertainty and surrogate modeling

2.1. Method overview

We propose a method to analyze a set of promising DES design alternatives to identify the best design given a multi-year planning horizon and multiple sources of uncertainty. To rate a system's performance, we use the total annualized cost (TAC) as assessment metric. The given design alternatives can be, for example, user-defined or the result of an optimization-based design method. Figure 1 shows the four main steps of using our method.

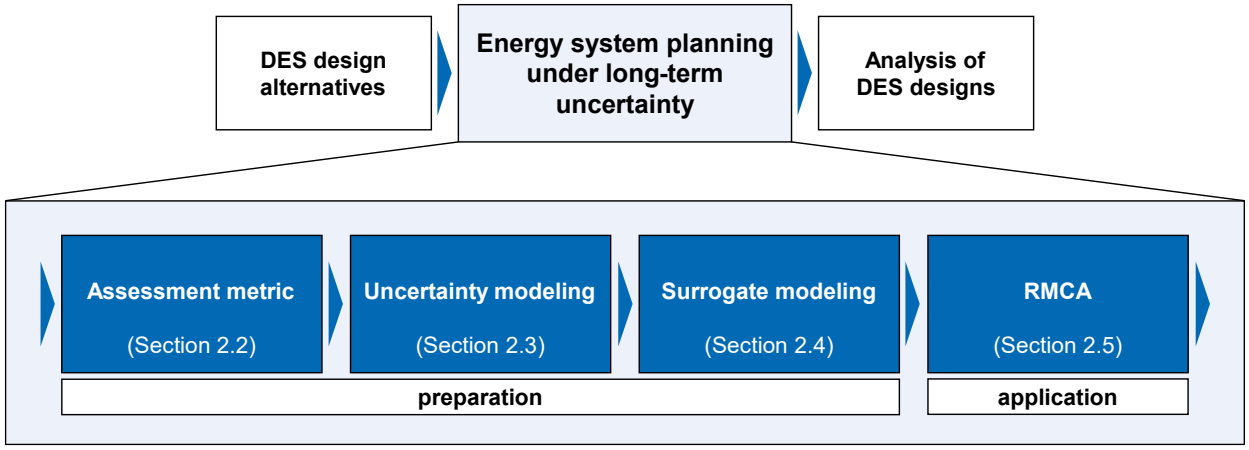

Figure 1. Energy system planning under long-term uncertainty: Steps for preparing and applying the proposed rapid Monte Carlo analysis (RMCA) via uncertainty and surrogate modeling for analyzing promising distributed energy system (DES) design alternatives to identify the best system according to an assessment metric.

Section 2.2 discusses the calculation of the assessment metric TAC and the involved optimization models. TAC depends not only on parameters such as investment costs but also on the operational expenditure (OPEX) including energy costs occurring within the multi-year planning horizon. Here, we consider the OPEX for each year of the planning horizon individually rather than resorting to only one year that is assumed to be representative for the whole horizon. We formulate mixed-integer linear programs (MILPs) for each DES design to determine the energy costs of each year. Each MILP depends on a large number of parameters (e.g., component efficiencies, heating demand for each hour of the year). As a result, the assessment metric depends on many potentially uncertain parameters.

In Section 2.3 we show, how we address uncertainties. We first identify a small number of representative factors that scale reference parameters to define the parameters of the assessment metric. We model the time-dependent development of these representative factors using probability distributions. After modeling uncertainties, probability distributions for all parameters of the TAC are defined. A direct calculation of the TAC

involves solving a MILP for each year of the multi-year planning horizon. Thus, calculating the TAC directly is computationally burdensome. Instead of solving multiple MILPs to obtain the energy costs for each year, we employ linear surrogate models.

Section 2.4 shows how we first generate Latin hypercube samples (LHS) of representative factor combinations to obtain the energy costs of representative years. We then use each combination to parameterize and solve MILPs. Afterwards, we use the LHS to parameterize linear surrogate models. These linear surrogate models allow approximating the energy costs of a single year given the representative factors specifying the respective year. The surrogate model generation is conducted for each DES design. As a result, we can approximate the TAC for long-term scenarios without solving additional MILPs. After following these three preparation steps, the RMCA is carried out.

In Section 2.5, we present the steps of conducting our RMCA. It relies on the probability distributions determined for uncertainty modeling and approximates the TAC using the generated surrogate models for evaluating the long-term scenarios. The RMCA provides decision support by evaluating a large number of multi-year scenarios and conducting a subsequent statistical analysis.

2.2. Assessment metric and energy system modeling

We evaluate DES design alternatives using the TAC as a metric where we consider the OPEX of each year individually, rather than using one representative year. The DES to be evaluated involve different technologies for converting and storing energy. The TAC of an energy system e is calculated as follows:

$$TAC_e = \frac{1}{PVF} * \left(I_{0,e} + \sum_{a=1}^{T} \frac{OPEX_{e,a}}{(1+i)^a} \right) \tag{1}$$

with the net present value factor PVF, the investment costs $I_{0,e}$ of the energy system e, the operational expenditures $OPEX_{e,a}$ of energy system e occurring in year $a \in \{1, \dots, T\}$, the time horizon length of T years, and the interest rate i. We determine the net present value factor as follows [8]:

$$PVF = \frac{(1+i)^T - 1}{(1+i)^T i} \tag{2}$$

We estimate the investment costs $I_{0,e}$ using cost correlations (e.g., cf. [9]). The OPEX $OPEX_{e,a}$ encompasses energy costs $OPEX_{e,a}^{\mathrm{e}}$ as well as maintenance costs $OPEX_{e,a}^{\mathrm{m}}$:

$$OPEX_{e,a} = OPEX_{e,a}^{\mathrm{e}} + OPEX_{e,a}^{\mathrm{m}} \tag{3}$$

The maintenance costs $OPEX_{e,a}^{\mathrm{m}}$ of energy system e are determined in accordance to [9]. To compute the energy costs $OPEX_{e,a}^{\mathrm{e}}$ of energy system e in year a, we utilize MILPs to determine the cost-optimal energy system operation to fulfil the energy demand. The objective function of each MILP is defined as the sum of costs for purchasing energy carriers in year a. Here, we assume that the costs of each year can be computed independently and obtain the energy costs $OPEX_{e,a}^{\mathrm{e}}$ by solving the respective MILP. We model the energy systems using quasi-stationary component models as used by [9] and consider part-load behavior as in [10]. As a result, the MILPs comprise equations for the objective function, energy balances, the conversion units, and the energy storage. The models for the operational optimization of energy systems encompass a variety of parameters (e.g., hourly-resolved heating demands, components' efficiencies). TAC_e of each energy system e can be determined if the parameters are known; however, some parameters like energy prices can be subject to uncertainty.

2.3. Uncertainty parameterization and long-term uncertainty modeling

The assessment metric usually depends on a large number of parameters which are potentially uncertain. We reduce the number of potentially uncertain parameters by first screening and then grouping them. Specifically, we first identify the parameters that can be assumed as constant. Afterward, we group the remaining parameters and assign each group to a representative factor that captures the shared variability. This screening and grouping, to which we refer to as uncertainty parameterization, results in a low number of representative factors. For each representative factor, we then conduct the long-term uncertainty modeling by choosing one of three uncertainty types and defining a permitted range for each representative factor. Thereafter, the uncertainty modeling is complete. The proposed procedure guides the uncertainty modeling steps (i.e., how uncertainty is modeled) and leaves case specific decisions to the user (e.g., which sources of uncertainty should be considered).

We start the uncertainty parameterization with a preliminary screening by first listing all parameters of the assessment metric. Next, parameters with known values, with negligible influence on the assessment metric, or with negligible uncertainty are set as constant. At this point, the risk of excluding influential parameters should be considered carefully and expert knowledge about characterizing uncertainty can be incorporated. For parameters assumed to be uncertain, we determine reference parameters. Following that, the uncertain parameters that are expected to be correlated (e.g., all hourly demands of one year) are grouped and assigned

to the representative factor of that group. As soon as all parameters of the assessment metric are either set as constant or assigned to a representative factor, the uncertainty parameterization is complete.

For the long-term uncertainty modeling, we distinguish three types of long-term uncertainty. The three types are adapted from [2]. Figure 2 illustrates the three types of uncertain parameter developments.

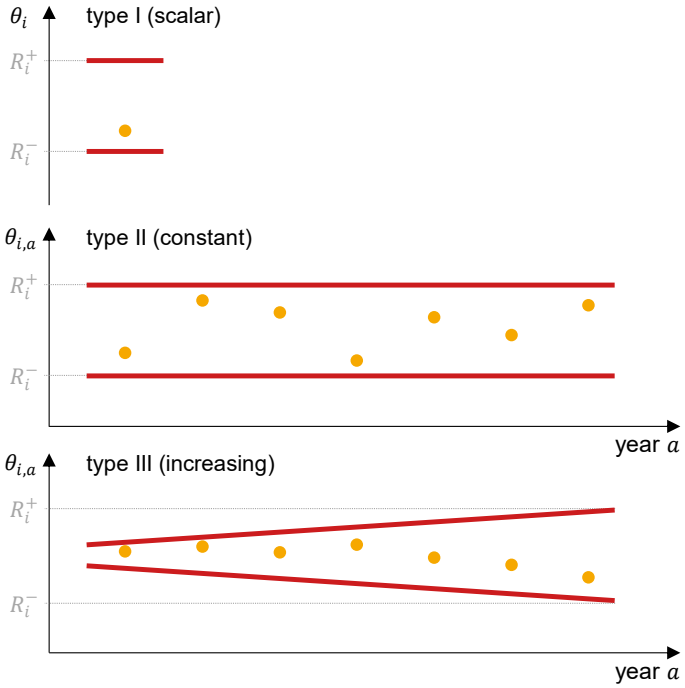

Figure 2. Three types of long-term uncertainty. Type I: Random scalar (e.g., investment costs, life expectancy of equipment). Type II: Constant long-term uncertainty (e.g., energy prices). Type III: Increasing long-term uncertainty (e.g., energy demand). The exemplary realizations (orange dots) of the representative factors (θ_i, $\theta_{i,a}$) lay within the permitted range which is defined by its bounds (R_i^+, R_i^-).

For each representative factor $i \in I = I^{\mathrm{I}} \cup I^{\mathrm{II}} \cup I^{\mathrm{III}}$, first, an appropriate long-term uncertainty type needs to be chosen. Second, a range of permitted scaling factor values needs to be selected. To parameterize the permitted range, an upper bound R_i^+ and a lower bound R_i^- need to be selected. These bounds can, for example, be derived from historical data or forecasts.

We derive the probability distributions of the representative factors as follows. We use normal (Gaussian) distributions, which are one of the most frequently used distributions [11], to model the uncertain parameters. The expected value μ_i of the normal distribution is assumed for all representative factors $i \in I$ as

$$\mu_i = \frac{R_i^+ + R_i^-}{2} \qquad \forall i \in I \tag{4}$$

The standard deviation σ_i is determined such that the permitted range matches the two-sigma interval:

$$\sigma_i = \frac{R_i^+ - R_i^-}{4} \qquad \forall i \in I \tag{5}$$

For type I factors $i \in I^{\mathrm{I}}$, we define the normal random variable $\tilde{\theta}_i$ that serves as an auxiliary variable:

$$\tilde{\theta}_i \sim N(\mu_i, \sigma_i^2) \qquad \forall i \in I^{\mathrm{I}} \tag{6}$$

Analogously, for type II factors $i \in I^{\mathrm{II}}$, we define for each year a an auxiliary variable $\tilde{\theta}_{i,a}$:

$$\tilde{\theta}_{i,a} \sim N(\mu_i, \sigma_i^2) \qquad \forall a \in \{1, \dots, T\}, i \in I^{\mathrm{II}} \tag{7}$$

We project these auxiliary variables to values within the permitted range. Thus, we obtain the probability distributions for the representative factors $\theta_{i,a}$ as follows:

$$\theta_{i,a} = \begin{cases} R_i^+ & \tilde{\theta}_{i,a} > R_i^+ \\ R_i^- & \tilde{\theta}_{i,a} < R_i^- \\ \tilde{\theta}_{i,a} & \text{otherwise} \end{cases} \qquad \forall a \in \{1, \dots, T\}, i \in I^{\mathrm{II}} \tag{8}$$

An analogous formulation for $\theta_i \in I^I$ (i.e., one where the index a is dropped) is used for type I parameters. The increasing uncertainty of type III factors $i \in I^{\mathrm{III}}$ is modeled using

$$\tilde{\theta}_{i,a} = \theta_{i,a-1} + \Delta_{i,a} \qquad \forall a \in \{1, \dots, T\}, i \in I^{\mathrm{III}} \tag{9}$$

with $\theta_{i,0} = \mu_i \ \forall i \in I^{III}$ and the random variable $\Delta_{i,a} \sim N(0, \sigma_{\Delta,i}^2) \ \forall a \in \{1, \dots, T\}, i \in I^{III}$ which corresponds to the difference of consecutive factor values. We determine the standard deviation $\sigma_{\Delta,i}$ as follows. If random variables are uncorrelated, the variance of their sum equals the sum of their variances [11]. To approximate the variance σ_i^2 for the final parameter $\theta_{i,T}$, we set the variance of each step to $1/T$-th of the final, desired variance. Thus, we determine the respective standard deviations using $\sigma_{\Delta,i} = \sigma_i/\sqrt{T} \ \forall i \in I^{III}$. After assigning each uncertain factor to an uncertainty type and parameterizing it, long-term scenarios can be generated, and the respective TAC can be computed.

2.4. Surrogate modeling via Latin hypercube sampling and linear regression

We use linear surrogate models to speed up the calculation of the assessment metric by replacing computational burdensome operations with linear approximations. For determining the TAC of a DES design, the energy costs need to be calculated for each year of the multi-year time horizon of length T. As a result, T optimization problems need to be solved for each long-term scenario. After introducing the representative factors in Section 2.3, which includes setting parameters to constant values and determining reference parameters, each optimization problem is fully defined by a small set of parameters:

$$OPEX_{e,a}^{e} = OPEX_{e}^{e}\left(\{\theta_i\}_{i \in I^{I}}, \{\theta_{i,a}\}_{i \in I^{II} \cup I^{III}}\right) \tag{10}$$

For each DES design, we obtain a linear surrogate model by first solving the respective MILP for a representative set of sampling points. We select these sampling points using Latin hypercube sampling and solve the MILPs for N^{LHS} combinations of representative factors. Afterwards, we use ordinary least squares [12] to parameterize the linear surrogate models which have the following form:

$$OPEX_{e,a}^{e} \approx \widehat{OPEX}_{e,a}^{e} = b_{e,0} + \sum_{i \in I^{I}} b_{e,i}\theta_i + \sum_{i \in I^{II} \cup I^{III}} b_{e,i}\theta_{i,a} \tag{11}$$

where $\widehat{OPEX}_{e,a}^{e}$ is the linear approximation of the energy costs $OPEX_{e,a}^{e}$ of DES design e in year a and $b_{e,i}$ is a surrogate model parameter. We assess the quality of fit using the coefficient of determination R^2 defined as [13]:

$$R^2 = 1 - \frac{\sum_{j=1}^{N^{LHS}} \left(X_j - Y_j\right)^2}{\sum_{j=1}^{N^{LHS}} \left(\bar{Y} - Y_j\right)^2} \quad \text{with} \quad \bar{Y} = \frac{\sum_{j=1}^{N^{LHS}} Y_j}{N^{LHS}} \tag{12}$$

where Y_j is the value of the observed data (i.e., the result of an optimization), X_j is the value predicted by a linear surrogate model, $\bar{Y}$ is the mean of the observed data, and N^{LHS} corresponds to the number of Latin hypercube samples. The coefficient of determination can take values $R^2 \leq 1$ and positive values of R^2 can be linked to the percentage of correctness of a regression [13]. However, a high value of R^2 cannot guarantee whether the linear surrogate model is an appropriate approximation. After having generated linear surrogate models, we approximate the TAC as follows:

$$TAC_e \approx \widehat{TAC}_e = \frac{1}{PVF} * \left(I_{0,e} + \sum_{a=1}^{T} \frac{\widehat{OPEX}_{e,a}^{e} + OPEX_{e,a}^{m}}{(1+i)^a}\right) \tag{13}$$

2.5. Rapid Monte Carlo analysis

Our rapid Monte Carlo analysis (RMCA) allows to analyze and compare promising DES design alternatives with a reduced computation burden considering multiple sources of uncertainty and long planning horizons. The RMCA is enabled by defining an assessment metric (Section 2.2), conducting uncertainty parameterization as well as long-term uncertainty modeling (Section 2.3), and generating surrogate models (Section 2.4). Our RMCA involves the typical steps of a MCA [5]. First, probability distributions are defined. Second, random values, i.e., long-term scenarios, are sampled. We use long-term uncertainty models to generate multi-year scenarios defined by a set of representative factors. Third, the samples are evaluated using approximations for the TAC. By using linear surrogate models, the computational burden of approximating the TAC can be neglected. After generating and evaluating a sufficiently large number of long-term scenarios, we conduct a statistical analysis to identify the best DES design alternative.

3. Case study and results

3.1. Distributed energy system design alternatives for a research campus

We apply our method in a case study adopted from the literature. In our case study, we seek to find the best DES design from a set of promising candidates to fulfill energy demands, i.e., the heating and electricity demands given in [9].

Figure 3 shows three user-defined DES design alternatives (i.e., ES1, ES2, ES3) which are to be analyzed. The designs are similar to the those obtained using an energy system design optimization in [9]. All designs include two boilers and a thermal energy storage. ES1 includes a combined heat and power (CHP) unit and a heat pump (HP), ES2 has two CHP units but no HP, and ES3 has two HPs instead.

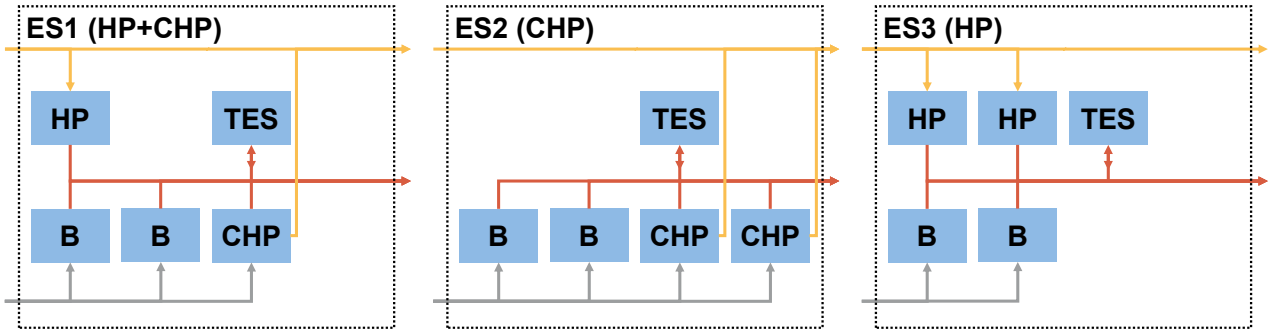

Figure 3. Promising distributed energy system design alternatives $e \in \{ES1, ES2, ES3\}$. The three designs encompass boilers (B), heat pumps (HP), combined heat and power (CHP) units, and thermal energy storages (TES) to fulfill an electricity as well as a heating demand. The systems are connected to an electricity and a natural gas grid.

Technical specifications of the conversion units are shown in Table 1. The part-load segment parameters ($\lambda_{k,\min}^{\text{in/out}}$; $\lambda_{k,\max}^{\text{in/out}} = 1$) are derived using correlations given in [9]. The thermal energy storage has for all cases a capacity of $Q^{\max} = 1000\,\text{kWh}$, charging efficiencies of $\eta^{\text{in}} = \eta^{\text{out}} = 0.95$, and a heat loss time constant of $\tau^{\text{loss}} = 200\,\text{h}$.

Table 1. Nominal power, nominal efficiency, and part-load segment parameters of the installed boilers (B), combined heat and power (CHP) units, and heat pumps (HP).

	Nominal power	Nominal efficiency	$\lambda_{k,\min}^{\text{in}}$	$\lambda_{k,\min}^{\text{out}}$
Boiler	$\dot{Q}_{\text{B}}^{\text{th}} = 530\,\text{kW}$	$\eta_{\text{B}}^{\text{th}} = 80.0\%$	0.173	0.200
CHP unit (electric)	$P_{\text{CHP}}^{\text{el}} = 380\,\text{kW}$	$\eta_{\text{CHP}}^{\text{el}} = 38.9\%$	0.582	0.500
CHP unit (thermal)	$\dot{Q}_{\text{CHP}}^{\text{th}} = 470\,\text{kW}$	$\eta_{\text{CHP}}^{\text{th}} = 48.1\%$	0.582	0.622
Heat pump	$\dot{Q}_{\text{HP}}^{\text{th}} = 200\,\text{kW}$	$COP = 2.998$	0.200	0.200

The investment costs and annual maintenance costs of each DES design alternative are determined using the cost correlations given in [9] and are shown in Table 2.

Table 2. Investment costs and annual maintenance costs of each DES design alternative.

	ES1 (HP+CHP)	ES2 (CHP)	ES3 (HP)
Investment costs $I_{0,e}$, €	383,901	551,542	216,260
Maintenance costs $OPEX_{e,a}^{\text{m}}$, €	24,331	46,089	2,574

Given the DES design alternatives, we conduct the first of the three preparation steps shown in Fig. 1: We define for each DES design an assessment metric according to Eq. (1) for a planning horizon length of $T = 10$ years. This step includes the formulation of MILPs to determine annual energy costs.

3.2. Uncertainty and surrogate modeling

Next, we present the preparation of the uncertainty and surrogate models for each DES design alternative. We start modeling uncertainty by listing all parameters influencing the assessment metric. As the designs include different components, the assessment metrics of the design alternatives depend on different sets of model parameters. Next, we identify the uncertain parameters. As the price of energy carriers can have a relevant impact in energy planning models [2], we model the gas price and the electricity price as time-dependent, uncertain parameters. Furthermore, we assume that also the heating demand and the electricity demand are relevant uncertain parameters. All other model parameters are set to appropriate constant values. Hence, due to the hourly resolution of the optimization models, a total number of $4 \cdot 8760$ parameters per year remain uncertain. We introduce three representative factors, i.e., one factor for scaling electricity prices ($\theta_{\text{c-el},a}$), one factor for scaling gas prices ($\theta_{\text{c-gas},a}$), and one factor for scaling electricity and heating demands ($\theta_{\text{d},a}$). We assign each of the $4 \cdot 8760$ uncertain parameters to one representative factor for scaling reference parameters (cf. Table 3). The representative factors serve as a low-dimensional representation of the uncertain parameters reducing the number of uncertain parameters to three per year.

Table 3. Representative factors and long-term uncertainty modeling. For all representative factors, the associated uncertain parameters of the assessment metric, the type of uncertainty, and the bounds (R_i^+, R_i^-) of the permitted range are given.

Representative factor	Associated parameters	Type of uncertainty	R_i^-	R_i^+
$\theta_{\mathrm{c-el},a}$	Hourly resolved electricity price	II (constant)	0.44	1.57
$\theta_{\mathrm{c-gas},a}$	Hourly resolved gas price	II (constant)	0.26	1.74
$\theta_{\mathrm{d},a}$	Hourly resolved electricity and heat demand	III (increasing)	0.60	1.40

We classify the representative factor $\theta_{\mathrm{d},a}$ as type III uncertainty as demand uncertainties typically increase over time. Furthermore, we assume that the demand might increase or decrease by up to 40 % over the time horizon of 10 years. This assumption results in an upper bound of $R_{\mathrm{d}}^+ = 1.4$ and a lower bound of $R_{\mathrm{d}}^- = 0.6$. We use the heating and electricity demand from [9] for defining the corresponding reference parameters. As done in [2], we assume that the accuracy of short and long-term energy price predictions is equal. Thus, we classify $\theta_{\mathrm{c-el},a}$ and $\theta_{\mathrm{c-gas},a}$ as type II uncertainties. For modeling the long-term uncertainty of the energy prices, we assume a low-price and a high-price scenario considering historical prices (cf. [14]). In the low-price scenario, we assume an average electricity price of $7.5\ \mathrm{ct/kWh}$ and a gas price of $2.5\ \mathrm{ct/kWh}$. In the high-price scenario, we assume an electricity price of $26.67\ \mathrm{ct/kWh}$ and a gas price of $17.44\ \mathrm{ct/kWh}$. We assume that within one year the energy prices remain constant. We choose the upper bound $R_{\mathrm{c-el}}^+$ such that the reference price parameters scaled with $R_{\mathrm{c-el}}^+$ result in the high-price scenario. We determine the lower bound $R_{\mathrm{c-el}}^-$ and the range of the representative factor $\theta_{\mathrm{c-gas},a}$ analogously. After defining a low-dimensional parameterization and modeling long-term uncertainty, we generate the surrogate models.

The linear surrogate models for approximating the energy costs of one year of operation are generated by first solving the respective MILPs for $N^{\mathrm{LHS}} = 25$ Latin hypercube samples and then applying linear regression to obtain the parameters of the linear surrogate models. We use Pyomo 6.4 [15,16] for modeling and Gurobi 10.0 [17] as a solver. Table 4 shows the linear surrogate model parameters for each of the DES design as well as the quality of fit given by the R^2-value.

Table 4. Linear surrogate models for approximating the annual energy costs of the energy systems. The linear surrogate models are defined by its parameters $b_{e,i}$. The coefficient of determination R^2 aids assessing the model quality.

e	$b_{e,0}$, €	$b_{e,c-\mathrm{el}}$, €	$b_{e,c-\mathrm{gas}}$, €	$b_{e,\mathrm{d}}$, €	R^2
ES1	-520,442	239,815	219,318	537,369	0.9429
ES2	-475,527	224,834	296,459	524,416	0.9617
ES3	-556,080	396,682	56,741	594,618	0.9746

Figure 4 shows by comparing observed and approximated energy costs that energy costs are predicted reasonably well by the linear surrogate models for each LHS and DES design.

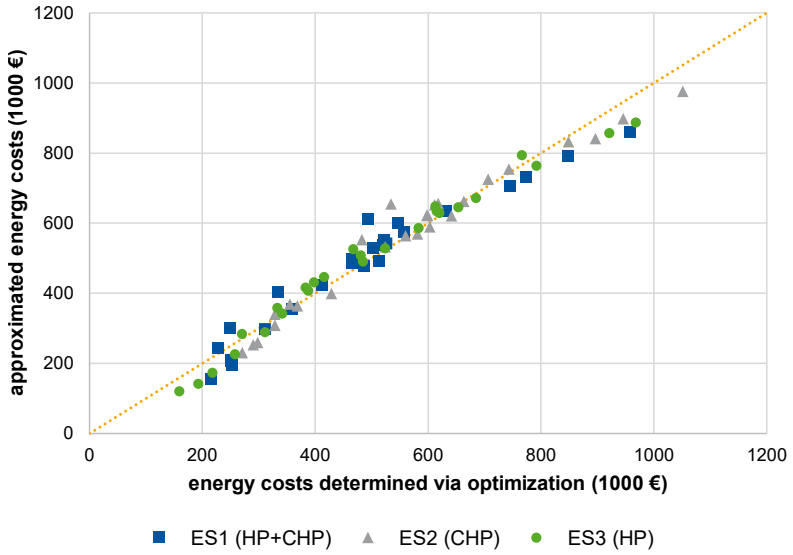

Figure 4. Scatter plot for assessing the accuracy of the three linear surrogate models based on the Latin hypercube samples. Small vertical deviations from the dotted line indicate a high approximation accuracy.

3.3. Rapid Monte Carlo analysis

The RMCA is applied employing the uncertainty and surrogate models. Our analysis is presented in three parts. First, we present the generated scenarios, which consist of $N = 5000$ long-term scenarios illustrated in Fig. 5. Next, we provide a statistical analysis from three views to evaluate the scenarios. Finally, we consider the computational burden associated with the RMCA.

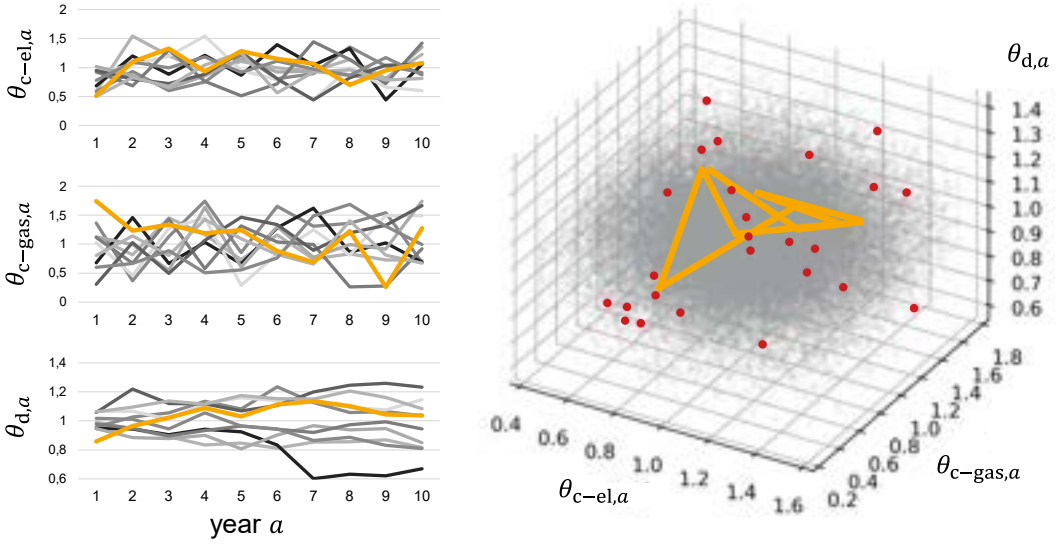

(a) (b)

Figure 5. Long-term scenarios ($N = 5000$) and Latin hypercube samples ($N^{\mathrm{LHS}} = 25$). a) The subset of ten long-term scenarios showing different trajectories of the representative factors ($\theta_{\mathrm{c-el},a}$, $\theta_{\mathrm{c-gas},a}$, $\theta_{\mathrm{d},a}$). b) The parameter space is spanned by the representative factors and is densely covered by the 50,000 years contained within the long-term scenarios (small gray dots). One long-term scenario and the Latin hypercube samples are illustrated in orange and by the red dots, respectively.

We evaluate the long-term scenarios using the linear surrogate models and thus avoid solving many optimization problems with similar parameterizations. We analyze the TAC obtained for the long-term scenarios and DES design alternatives from three views. First, we analyze the distributions of the TAC for each design.

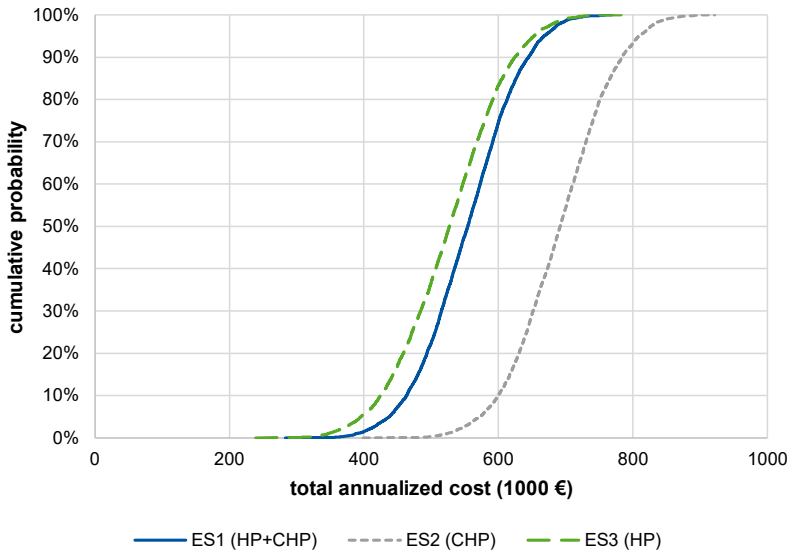

Figure 6. Cumulative probability plot for determining the probability of the total annualized cost (TAC) being lower or equal to the given TAC when choosing the respective design.

Figure 6 reveals the bandwidth of expected TAC. This view indicates that ES2 is likely to result in the highest TAC and that furthermore ES1 and ES3 lead to similar TAC. However, this visualization does not include information about the difference in TAC for specific long-term scenarios.

By comparing the TAC of the DES design alternatives in each scenario, we determine the frequency of having the lowest TAC for each design. We find that ES3 results in 87.7 % of the scenarios in the lowest TAC. In the remaining scenarios, ES1 results in the lowest TAC. However, this second view does not convey information about the differences in TAC, i.e., how high the regret is when another design would have been a better choice.

Third, we examine the differences in TAC. We normalize the differences using the expected TAC of ES3. We find that the maximal regret associated with choosing ES1, ES2, and ES3 is 19.4 %, 51.4 %, and 11.4 %, respectively. In this context, regret is defined as the difference between the TAC of the selected design and the TAC of the best design. Furthermore, we find that the average regret associated with choosing ES1, ES2, and ES3 is 5.5 %, 31.7 %, and 0.3 %, respectively. Thus, we recommend ES3 as it most likely results in the lowest TAC whereas choosing ES2 should be avoided. Overall, the different views of the statistical analysis provide insights about the probability distributions of the assessment metric. Furthermore, analyzing the differences in TAC can reveal which design should be preferred or avoided.

The computational performance of the RMCA is addressed next. Here, we use the number of MILPs to be solved as a proxy for the computational burden. We compare the RMCA to a MCA that does not employ surrogate models. When not using surrogate models, we need to solve one MILP for obtaining the energy costs for each year, scenario, and design. As a result, the computational burden increases linearly with the number of long-term scenarios. Given three DES design alternatives and a time horizon of ten years, each scenario requires solving 30 MILPs. Solving the MILPs of this work typically requires a few minutes. As MCA applied for energy system design might require hundreds of scenarios to be considered [4,5], not using surrogate models results in a significant computational burden.

Using the RMCA also requires solving MILPs. Before we can evaluate the first scenario using RMCA, we need to create the surrogate models first. We solve 75 MILPs for the three linear surrogate models in total. In comparison to solving MILPs, the computational burden of determining the parameters of the linear surrogate models and evaluating them is negligible. As a result, the RMCA is faster if three or more long-term scenarios are considered. For the considered 5,000 scenarios, the computational time is reduced by more than 99 %.

4. Conclusion

Designing distributed energy systems (DES) under uncertainty is a challenging task. One approach to address uncertainty is to use Monte Carlo analysis (MCA). However, the high computational burden associated with MCA for DES design and long planning horizons limits its application. Furthermore, MCA requires reasonable assumptions about probability distributions. To address the challenge of designing DES under uncertainty considering multi-year planning horizons, we propose a rapid Monte Carlo analysis (RMCA) approach enabled by long-term uncertainty modeling and surrogate modeling for optimization-based energy system planning under long-term uncertainty. Our method provides decision support when a set of promising DES designs is given.

To enable RMCA, three preparation steps are conducted. Firstly, an assessment metric is defined and mixed-integer linear programs (MILPs) for the operational optimization of each DES design are formulated. Secondly, a low-dimensional representation of uncertainty and a long-term uncertainty model are systematically derived. Thirdly, surrogate models are created after solving the respective MILP for representative Latin hypercube samples. The RMCA starts by generating a large number of scenarios by sampling the long-term uncertainty models. The scenarios are evaluated using the surrogate models. Subsequently, a statistical analysis reveals the expected distribution of the total annualized cost (TAC) for each design, the likelihood of a specific design resulting in the lowest TAC, and the regret of choosing one design over another.

We apply our method to a case study adapted from the literature to assess three promising DES designs for a time horizon of ten years. We formulate MILPs for the operational optimization of each DES design and represent uncertain parameters using three representative factors per year. We create accurate linear surrogate models with a coefficient of determination $R^2 \geq 0.94$ for all designs. In the RMCA, 5,000 scenarios are considered and the best design which most likely results in the lowest costs is identified. The RMCA approach is compared to a MCA that does not rely on surrogate models and thus does not require solving MILPs for representative samples but lacks the benefit of the low effort of evaluating a surrogate model. Using the surrogate models results in a speedup if three or more long-term scenarios are considered. When considering 5,000 scenarios, the computational time is reduced for the specific case study by more than 99 %.

The presented approach can be applied to a wide range of energy systems. Besides, created surrogate models could also be used in companioning sensitivity analyses, which would also benefit from the substantially reduced computational burden. The benefit of a sensitivity analysis is that it does not require information about probability distributions. For DES designs of higher complexity, nonlinear surrogate models might be required to reach a high quality of fit, increasing the effort of creating the surrogate models.

In summary, the RMCA approach enabled by uncertainty and surrogate modeling provides an efficient way of considering multiple sources of uncertainty and long planning horizons. The adaptability and the reusability of its components, i.e., of the energy system, the uncertainty, and the surrogate modeling, potentially enable wide applicability of the proposed approach for energy system design under uncertainty.

Acknowledgments

This study is funded by the German Federal Ministry of Economic Affairs and Energy (ref. no.: 03EN2031A). The support is gratefully acknowledged.

Nomenclature

COP	coefficient of performance, -
i	interest rate, -
$I_{0,e}$	investment costs of energy system e, €
N	number of long-term scenarios, -
N^{LHS}	number of Latin hypercube samples, -
$OPEX_{e,a}$	operational expenditure of energy system e in year a, €
$OPEX^{\mathrm{m}}_{e,a}$	maintenance costs of energy system e in year a, €
$OPEX^{\mathrm{e}}_{e,a}$ / $\widetilde{OPEX}^{\mathrm{e}}_{e,a}$	energy costs of energy system e in year a (observed/approximated), €
PVF	net present value factor, -
$\dot{Q}^{\mathrm{th}}_k$ / P^{el}_k	nominal thermal/electrical capacity of unit k, kW
$Q^{\max}$	capacity of thermal storage, kWh
R^2	coefficient of determination, -
R^+_i / R^-_i	upper/lower bound of the permitted range of representative factor i, -
T	time horizon length, -
TAC_e / $\widetilde{TAC}_e$	total annualized cost of energy system e (observed/approximated), €
η^{th}_k / η^{el}_k	nominal thermal/electrical efficiency of unit k, -
$\eta^{\mathrm{in/out}}$ / τ^{loss}	efficiency/heat loss time constant of thermal storage, -
θ_i / $\theta_{i,a}$	representative factor i in year a, -
$\tilde{\theta}_i$ / $\tilde{\theta}_{i,a}$ / $\Delta_{i,a}$	auxiliary variable for representative factor i in year a, -
$\lambda^{\mathrm{in/out}}_{k,\mathrm{min/max}}$	part-load efficiency parameter of unit k, -
μ_i	expected value of auxiliary variable for representative factor i, -
σ_i / $\sigma_{\Delta,i}$	standard deviation of auxiliary variable for representative factor i, -

References

[1] Mavromatidis G, Petkov I. MANGO: A novel optimization model for the long-term, multi-stage planning of decentralized multi-energy systems. Applied Energy 2021;288:116585. https://doi.org/10.1016/j.apenergy.2021.116585.

[2] Moret S, Codina Gironès V, Bierlaire M, Maréchal F. Characterization of input uncertainties in strategic energy planning models. Applied Energy 2017;202:597–617. https://doi.org/10.1016/j.apenergy.2017.05.106.

[3] Roald LA, Pozo D, Papavasiliou A, Molzahn DK, Kazempour J, Conejo A. Power systems optimization under uncertainty: A review of methods and applications. Electric Power Systems Research 2023;214:108725. https://doi.org/10.1016/j.epsr.2022.108725.

[4] Fodstad M, Crespo del Granado P, Hellemo L, Knudsen BR, Pisciella P, Silvast A, et al. Next frontiers in energy system modelling: A review on challenges and the state of the art. Renewable and Sustainable Energy Reviews 2022;160:112246. https://doi.org/10.1016/j.rser.2022.112246.

[5] Yue X, Pye S, DeCarolis J, Li FGN, Rogan F, Gallachóir BÓ. A review of approaches to uncertainty assessment in energy system optimization models. Energy Strategy Reviews 2018;21:204–17. https://doi.org/10.1016/j.esr.2018.06.003.

[6] Nolting L, Spiegel T, Reich M, Adam M, Praktiknjo A. Can energy system modeling benefit from artificial neural networks? Application of two-stage metamodels to reduce computation of security of supply assessments. Computers & Industrial Engineering 2020;142:106334. https://doi.org/10.1016/j.cie.2020.106334.

[7] Köhnen CS, Priesmann J, Nolting L, Kotzur L, Robinius M, Praktiknjo A. The potential of deep learning to reduce complexity in energy system modeling. Intl J of Energy Research 2022;46:4550–71. https://doi.org/10.1002/er.7448.

[8] Ross SA, Westerfield R, Jaffe JF. Corporate finance. Eleventh Edition. New York, NY: Published by McGraw-Hill Education; 2016.

[9] Sass S, Faulwasser T, Hollermann DE, Kappatou CD, Sauer D, Schütz T, et al. Model compendium, data, and optimization benchmarks for sector-coupled energy systems. Computers & Chemical Engineering 2020;135:106760. https://doi.org/10.1016/j.compchemeng.2020.106760.

[10] Voll P, Klaffke C, Hennen M, Bardow A. Automated superstructure-based synthesis and optimization of distributed energy supply systems. Energy 2013;50:374–88. https://doi.org/10.1016/j.energy.2012.10.045.

[11] Papoulis A, Pillai SU. Probability, random variables, and stochastic processes. 4th ed. Boston: McGraw-Hill; 2002.

[12] Seabold S, Perktold J. statsmodels: Econometric and statistical modeling with python. 9th Python in Science Conference 2010.

[13] Chicco D, Warrens MJ, Jurman G. The coefficient of determination R-squared is more informative than SMAPE, MAE, MAPE, MSE and RMSE in regression analysis evaluation. PeerJ Computer Science 2021;7:e623. https://doi.org/10.7717/peerj-cs.623.

[14] BDEW. Strompreisanalyse, Februar 2023. Haushalte und Industrie 2023. https://www.bdew.de/media/documents/230215_BDEW-Strompreisanalyse_Februar_2023_15.02.2023.pdf (accessed February 24, 2023).

[15] Bynum ML, Hackebeil GA, Hart WE, Laird CD, Nicholson BL, Siirola JD, et al. Pyomo — Optimization Modeling in Python. vol. 67. Cham: Springer International Publishing; 2021. https://doi.org/10.1007/978-3-030-68928-5.

[16] Hart WE, Watson J-P, Woodruff DL. Pyomo: modeling and solving mathematical programs in Python. Math Prog Comp 2011;3:219–60. https://doi.org/10.1007/s12532-011-0026-8.

[17] Gurobi Optimization, LLC. Gurobi Optimizer Reference Manual 2023.

ULPGC
Universidad de
Las Palmas de
Gran Canaria

grres ULPGC
group for the research on renewable energy systems

N. Environmental impact of energy systems. Sustainability, resilience, & circular economy. CO_2 and GHG mitigation

ECOS2023

Coupling system dynamics model and multi-criteria analysis for a sustainability assessment of a district heating system's development

Janis Edmunds Daugavietis, Jelena Ziemele*

Institute of Microbiology and Biotechnology, University of Latvia, Jelgavas Street 1, Riga LV-1004, Latvia

**Presenter and corresponding author: jelena.ziemele@lu.lv, +371 29120969*

Abstract:

The study provides the hybrid model that couples system dynamics (SD) modelling and multi-criteria analysis. The SD model allows obtaining energy, economic, environmental indicators of a DH company and evaluating its dynamics in a time horizon until 2050. Considered decarbonization scenarios include the transition of the DH system towards a 4th generation DH (4GDH) system adhering to 4 strategies: the DH system uses at least (a) 50% RES; (b) 50 % waste heat, (c) 75 % cogenerated heat or (d) 50 % of combined aforementioned energy and heat. In addition, the development scenarios include various energy efficiency improvement measures on the consumer side and in the heating networks. The sustainability of each scenario was assessed with multi-criteria analysis methods - TOPSIS. The hybrid model provides a ranking of the selected transition pathways according to their sustainability score and benchmarks results of developed scenarios against a carbon neutral DH system. This model serves as a guidance to DH system developers and decision makers. The case of Riga is presented in the study.

Keywords:

4th generation district heating, Decarbonisation, District heating system, Multi-criteria Decision Analysis, sustainability assessment, TOPSIS

1. Introduction

The district heating sector is responsible for a large share of greenhouse gas emissions. The environmental impact along with economic and technical limitations is increasingly looked as a key factor in decision making in development of DH systems [1]. These different parameters impact the current operation of these systems and will influence them in the future because of new legislation, market trends and changing public outlook.

Dynamic energy system models are used as a decision support tool that can characterize existing and future DH systems because they are designed to simulate the behaviour of energy systems over time, considering the interactions between heat production, distribution and utilization [2]. Different development scenarios therefore can be modelled to find the technological mix fit for a sustainable DH system. Decarbonization, transition to renewable energy sources can be set as an optimizable goal for the system in year 2050 together with the expected economic considerations.

This modelling approach produces a set of possible development scenarios that each have a unique combination and degree of developed technologies. The assessment of these scenarios is essential for decision-making process and different methodologies exist for this purpose. Maigret et al. modelled the development of a carbon intensive industry and compared the possible development scenarios by their Pareto fronts [3]. Finke and Bertsch developed a method for multi-objective optimisation of energy systems and a framework for finding Pareto-optimal solutions and trade-offs between objectives [4]. While these methods can provide insights into the energy systems' technological limits and possible development scenarios, they still require a final judgment of the decision-maker. Yuan et al. coupled smart energy system simulation with multi-objective optimization tool MOPSO and multi-criteria analysis (MCA) method TOPSIS for an optimal heating strategy selection moving towards 100% renewable energy use [5]. The use of MCA methods can alleviate the burden of decision-makers as those can consider different viewpoints and conflicting objectives. That makes them ideal for DH system assessment where often clashing economic, technical, environmental and social aspects play a significant role.

MCA methods are used in the field of renewable energy policy planning include AHP, TOPSIS, WSM, ELECTRE, PROMETHEE and VIKOR [6]. In a previous study it was assessed that TOPSIS method is a

suitable MCA method for sustainability analysis of DH systems due to its relative simplicity and similar results to other methods [7].

The aim of the study is therefore to evaluate the performance of waste heat (WH), high-efficiency combined heat and power (CHP) and RES technology in the DH system by moving towards carbon neutrality in various development scenarios. Based on an algorithm that combines the SD model with the TOPSIS method, the economic, environmental and energy parameters of the DH system development scenarios were evaluated for creating decarbonization strategy of a city DH system.

2. Methods

The algorithm of the study is presented in Figure 1. A system dynamics model of a DH system is taken as a base for further optimization and development planning.

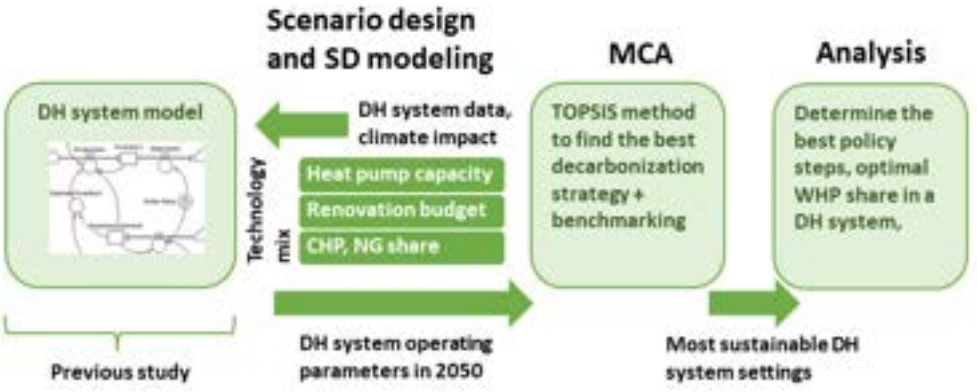

Figure 1. Algorithm of the study

Technological, climate and policy scenarios are designed based on literature review. Simulations with these scenarios and optimizable technological parameters are performed. The next step is MCA where the DH system operating parameters are assessed by the TOPSIS method to find the most sustainable technology mix within each scenario. The last step is analysis of MCA results and policy and development proposals.

2.1. DH model description for case study of DH system

In a previous study, a s SD model corresponding to the urban DH system was developed [2] and improved [1].The SD model includes all stages of DH - heat production, transmission and consumption. The model is based on the installed capacity of various technologies. Energy sources include fossil fuels (natural gas) and renewable energy sources, such as wood chips, as well as potentially developed technologies - heat recovery from treated wastewater, industrial processes, solar collectors. The DH technology block consists of eight different technologies. Heat consumption tends to decrease because of improved energy efficiency of buildings - its demand therefore can decrease by renovating buildings while also increasing due to building of new ones that correspond to the nearly zero energy standard. In addition, the possible impact of global warming on the thermal energy demand of buildings and the resulting changes in the installed capacity of DH systems with or without renovation of existing apartment buildings are evaluated to move to a sustainable 4GDH system in the long term. Table 1 shows the priority technologies in four developed scenarios clusters.

Table 1. Selection of priority technologies in various DH system development scenarios.*

Technologies	RES-NG scenarios	RES scenarios (50% renewable energy)	CHP scenarios (75% CHP& CHP priority)	WH scenarios (50% WH& WH priority)
CHP biomass	✓	✓	✓	
CHP NG	✓		✓	
HOB biomass	✓	✓		
HOB NG	✓			
Solar collectors		✓		
Large scale heat pumps		✓		✓
Heat exchangers & heat pumps		✓		✓
Wastewater heat pumps		✓		✓

* ✓ - priority technologies

The Directive on energy efficiency (2018) promotes development of technologies that allow achieving the highest cumulative end-use energy savings and lowest primary energy consumption [8]. Three scenario clusters were selected for the study considering the definition of an efficient district heating and cooling system set by the Directive 2012/27/EU: one ensures 50% of RES by using biomass as the energy source (RES); second, where 75% of heat is produced by CHPs (CHP); third that provides the use of WH in DH system. Fourth scenario cluster was considered where the DH company continued to produce part of the heat by NG (RES/NG).

2.2. Assumption and constrains of selected scenarios

The DH system of Riga city was chosen as a case study area. The initial installed capacity of the produced heat and assumptions of each development scenario is provided in Table 2.

Table 2. Current heat supply and assumption of capacity to be installed.

Scenarios	Technologies, MW							
	Boiler NG	Boiler biomass	CHP by NG	CHP by biomass	Solar collectors	Large scale HP	Industrial waste heat HP	Wastewater absorption HP (AHP)
Existing installed capacity	300*	68	47	22	0	0	18	0
RES-NG	No limit	250	No limit	No limit	19	20	14/0**	4
RES	Ban on new installations from 2025 [9]	No limit	No limit	No limit	19	20	14/0**	4
CHP	Ban on new installations from 2025 [9]	CHP priority	No limit	No limit	19	20	14/0**	4
WH	Ban on new installations from 2025 [9]	No limit	No limit	No limit	19	30	14/14**	8

*capacity of HOB by NG excluding reserve; **potential of recovered WH in DH company/ potential of recovered WH from industry

The capacity of solar collectors, large scale HP and WH shown in Table 2 are based on the technological limitations that exist in the case study area. It was assumed that solar collectors could only be installed on land belonging to the DH company (i.e. next to an existing heat source). Thus, the installed number of collectors was limited to 1,700 (approx. 21,000 m2), which corresponds to 19 MW (640 h per year). NG boilers are planned to be replaced by a large-scale HP in one of the existing heat sources, which is located on the riverbank. The use of industrial WH is currently related to the operation of condensing economizers. In all development scenarios, it is planned to expand the integration of industrial WH into DH system. The use of heat recovery from treated wastewater in Riga is limited due to the heat demands of the adjacent heating zone. It is possible to use a maximum heat capacity of 8 MW, which is much lower than the total heat potential of the treated wastewater. More details about investment and fixed O&M costs applied in the SD model can be find in previous article by Ziemele&Dace [1].

For all four scenario-clusters we applied one scenario without impact of global warming and three global warming scenarios, which include different level of representative concentration pathways (RCP) – RCP2.6 (low), RCP4.5 (medium) and RCP8.5 (high) (see Table 3). According to the selected climate change scenarios the outdoor temperature during the heating season is estimated to increase from the current +1.1 °C to 3.0, 3.4 and 4.0 °C in scenarios RCP2.6, RCP4.5 and RCP8.5, respectively. Additionally, the impact of building renovation on heat demand was evaluated. There are considered three level of renovation. The budget for building reconstruction in the selected DH area was 5.8 million EUR per year for first level, which roughly corresponds to the current financing. The depth of renovation was adopted according to national legislation, i.e. 60 kWh/m2 for heating existing apartment buildings (corresponding to class B) and 40 kWh/m^2 for heating new buildings (corresponding to class A) [10]. In addition, a scenario in which the energy efficiency policy will be implemented with acceleration and the available funding will be quadrupled is being considered.

Table 3. Description of scenarios

Nr.	Scenarios	Conditions		
		Renovation of multi-apartment buildings	Global warming	Investment
1.	RES/0/RCP0	-	-	0
2.	RES/0/RCP2.6	-	✓	0
3.	RES/0/RCP4.5	-	✓	0
4.	RES/0/RCP8.5	-	✓	0
5.	RES-NG/1/RCP0	✓	-	1
6.	RES-NG/1/RCP2.6	✓	✓	1
7.	RES-NG/1/RCP4.5	✓	✓	1
8.	RES-NG/1/RCP8.5	✓	✓	1
9.	RES-NG/2/RCP0	✓	-	2
10.	RES-NG/2/RCP2.6	✓	✓	2
11.	RES-NG/2/RCP4.5	✓	✓	2
12.	RES-NG/2/RCP8.5	✓	✓	2
13.	RES/1/RCP0	✓	-	1
14.	RES/1/RCP2.6	✓	✓	1
15.	RES/1/RCP4.5	✓	✓	1
16.	RES/1/RCP8.5	✓	✓	1
17.	RES/2/RCP0	✓	-	2
18.	RES/2/RCP2.6	✓	✓	2
19.	RES/2/RCP4.5	✓	✓	2
20.	RES/2/RCP8.5	✓	✓	2
21.	CHP/1/RCP0	✓	-	1
22.	CHP/1/RCP2.6	✓	✓	1
23.	CHP/1/RCP 4.5	✓	✓	1
24.	CHP/1/RCP 8.5	✓	✓	1
25.	CHP/2/RCP0	✓	-	2
26.	CHP/2/RCP2.6	✓	✓	2
27.	CHP/2/RCP 4.5	✓	✓	2
28.	CHP/2/RCP 8.5	✓	✓	2
29.	WH/1/RCP0	✓	-	1
30.	WH/1/RCP2.6	✓	✓	1
31.	WH/1/RCP 4.5	✓	✓	1
32.	WH/1/RCP 8.5	✓	✓	1
33.	WH/2/RCP0	✓	-	2
34.	WH/2/RCP2.6	✓	✓	2
35.	WH/2/RCP 4.5	✓	✓	2
36.	WH/2/RCP 8.5	✓	✓	2

As a result, 36 DH's system development scenario simulation in the SD model allows obtaining input parameters to create an initial matrix for multi-criteria analysis.

2.3. Coupling system dynamics (SD) modelling and multi-criteria analysis (MCA) for DH sustainability assessment

In the framework of this study, energy, environmental and economic parameters were chosen, which fully describe the DH system transition towards decarbonization and allow to identify the most sustainable paths for the transition towards 4GDH considering various conflicting goals. Table 4 summarizes the eight identified criteria that used in the research.

Table 4. Selected criteria of multi-criteria analysis.

Type of criterion	Name of criterion	Criterion designation, unit	Criterion designation in MCA
Energy	Primary energy factor	PEF	X1
	Specific heat consumption for heating in buildings	E_{buil}, kWh/m^2 per year	X2
Environment	Avoided CO_2 emissions from DH system	SA_{CO2}, t CO_2 per year	X3
	Radiation forcing	Rad	X4

Type of criterion	Name of criterion	Criterion designation, unit	Criterion designation in MCA
	Share of renewable energy sources	Sh_{res}, %	X5
	Share of recovered heat from waste heat	Sh_{rec}, %	X6
Economy	Avoided CO_2 emissions costs	AC_{CO2}, EUR/ t CO_2	X7
	Heat tariff	T_{tot}, EUR/MWh	X8

The PEF was calculated in accordance with the ISO 5200-1:2007 [11] using the primary resource factors given in Table 2:

$$PEF = (\sum_z F_z \cdot f_{nren,j} + \sum_z F_z \cdot f_{ren,z})/Q_{con} \quad (1)$$

where F_z is the energy source (fuel, electricity) consumption in the DH system, MWh per year; $f_{nren,z}$ is the primary resource factor of non-renewable energy of z^{th} sources; $f_{ren,z}$ is the primary resource factor of renewable energy of zth resources. The study uses the primary resource factors according to ISO 52000-1:2017 [11].

The calculation of CO2 emissions was done according to national legislation [12] that based on Emission factors from the IPCC methodology [13] and is part of the SD model. The avoided CO2 emissions (SA_{CO2}, %) are calculated as follows:

$$SA_{CO2} = A_{CO2_{init}} - A_{CO2_{fin}} \quad (2)$$

$$A_{CO2} = \sum_z F_z \cdot e_z \quad (3)$$

where $A_{CO2_{init}}$ is the initial amount of CO_2 emissions, t_{CO2}/yr; $A_{CO2_{fin}}$ is the amount of CO_2 emissions in end of period, t_{CO2}/yr; $\cdot e_z$ is the CO_2 emission factor for z^{th} resources.

Heat tariff in each scenario (T, EUR/MWh) is calculated using the following equation:

$$T = \sum_z T_{prod,z} \cdot \varphi_z + T_{tr} + T_s \quad (4)$$

where $T_{prod,z}$ – production tariff for j technology, EUR/MWh; φ_z – the share of z technology; T_{tr} – transmission tariff, EUR/MWh; T_s – sales tariff, EUR/MWh.

Investment and O&M costs for the technologies used in this study were assumed according to data reported in previous studies by the authors. [1]. For instance, investments for constructing wood chips CHP are 3000/2500 kEUR/MW_e for 2020/2050 years, but for wood chips boiler - 350/300 kEUR/MW_{th} for 2020/2050 years [14].

The values of these criteria for each scenario were used to create a decision matrix (Equation (Eq.5) and were normalized according to the linear 'Max' method (Eq.6 and 7).

$$\begin{array}{c} \\ A_1 \\ A_2 \\ \vdots \\ A_{11} \\ \vdots \\ A_{36} \end{array} \begin{array}{c} \begin{array}{cccccccc} X_1 & X_2 & X_3 & X_4 & X_5 & X_6 & X_7 & X_8 \end{array} \\ \begin{bmatrix} x_{11} & x_{12} & x_{13} & x_{14} & x_{15} & x_{16} & x_{17} & x_{18} \\ x_{21} & x_{22} & x_{23} & x_{24} & x_{25} & x_{26} & x_{27} & x_{28} \\ \vdots & \vdots & \vdots & \vdots & \vdots & \vdots & \vdots & \vdots \\ x_{111} & x_{112} & x_{113} & x_{114} & x_{115} & x_{116} & x_{117} & x_{118} \\ \vdots & \vdots & \vdots & \vdots & \vdots & \vdots & \vdots & \vdots \\ x_{361} & x_{362} & x_{363} & x_{364} & x_{365} & x_{366} & x_{367} & x_{368} \end{bmatrix} \end{array} \quad (5)$$

$$r_{ij} = \frac{maxX_{ij} - X_{ij}}{maxX_{ij} - minX_{ij}} \quad (6)$$

$$r_{ij} = \frac{X_{ij} - minx_{ij}}{maxX_{ij} - minX_{ij}} \quad (7)$$

where r_{ij} – normalized value of criterion x_{ij}; $maxX_{ij}$ – maximal value of the criterion; $minX_{ij}$ – minimal value of the criterion; X_{ij} – criterion value; I – number of alternatives; j – number of criteria.

The set of weights was calculated taking into account the dispersion of the input data and using the entropy method [15]:

$$p_{ij} = \frac{r_{ij}}{\sum_{i=1}^{m} r_{ij}} \; i = 1, \dots, m; \qquad j = 1, \dots, n \tag{8}$$

$$E_j = -\frac{\left(\sum_{i=1}^{m} p_{ij} \ln(p_{ij})\right)}{\ln(m)} \qquad j = 1, \dots, n \tag{9}$$

$$w_j = \frac{1 - E_j}{\sum_{i=1}^{n}(1 - E_j)} \quad j = 1, \dots, n \tag{10}$$

where r_{ij} – normalized value of criterion x_{ij}; E_j – information Entropy method; w_j – Entropy method weight.

The scenario ranking was done by the TOPSIS method. It is a MCA method that finds the ranks scenarios by calculating their closeness to an imaginary positive ideal scenario. It is done by weighting the input matrix (Eq.11), finding the positive and negative ideal scenarios (Eq.12 and 13) and the closeness of each scenario to the ideal scenario (Eq.14).

$$v_{ij} = w_j r_{ij} \tag{11}$$

where r_{ij} - normalized value of criterion x_{ij}, w_j – weight of criterion j, v_{ij}- the weighted normalized value of criterion x_{ij}.

$$S_i^+ = [\sum_{j=1}^{n} (v_{ij} - v_j^+)\,]^{1/2} \tag{12}$$

$$S_i^- = [\sum_{j=1}^{n} (v_{ij} - v_j^-)\,]^{1/2} \tag{13}$$

(S_i^+) – positive ideal scenario, (S_i^-) – negative ideal scenario, v_{ij} – weighted normalized value of alternative i with respect to criterion j; v_j^+ – maximal normalized value with respect to criterion j; v_j^- – minimal normalized value with respect to criterion j.

$$C_i^* = \frac{S_i^+}{S_i^+ + S_i^-} \tag{14}$$

where C_i^* – closeness to the ideal scenario.

2.4. Analysis

The results of the MCA can be expressed as a ranking of the technology combinations from best to worst for each of the climate scenarios. At first, the effect of different weights is evaluated. The best method for weight determination is then chosen. The most sustainable technology mixes for each of the climate scenarios are compared by determining trade-offs between the economic, technical and environmental parameters. The further choice of the development strategy of the DH company is made based on the policy makers' opinion of preference regarding the design of the DH company and its development strategy and based on balancing the components of the energy trilemma: economic feasibility, environmental sustainability, and security of energy supply.

3. Results and discussion

3.1. Results of MCA

The multi-criteria analysis includes 36 different scenarios for the development of the DH system, which differ in the amount of renovation of buildings, the mix and share of heat energy production technologies and outdoor air temperature during the heating season due to climate change (see assumption in table 2 and 3). The initial matrix of criteria of the multi-criteria analysis presented in Table 5.

Table 5. Multi-criteria analysis decision matrix.

Scenarios	Parameters							
	X1	X2	X3	X4	X5	X6	X7	X8
Weight	12.6%	14.1%	14.0%	12.1%	12.7%	7.8%	14.5%	12.2%
Optimal value	min	min	max	min	max	max	min	min
RES/0/RCP0	1.150	96.4	102 664	0.00	89.12	3.59	92.81	73.97

Scenarios	Parameters							
	X1	X2	X3	X4	X5	X6	X7	X8
RES/0/RCP2.6*	**1.145**	**83.2**	**106 709**	**2.60**	**88.60**	**3.76**	**77.76**	**73.82**
RES/0/RCP4.5	1.143	79.2	107 937	4.50	88.44	3.82	73.53	73.77
RES/0/RCP8.5	1.140	72.0	110 169	8.50	88.12	3.92	66.22	73.69
RES-NG/1/RCP0	1.146	93.1	77 517	0.00	73.03	3.61	114.71	79.06
RES-NG/1/RCP2.6	**1.142**	**81.0**	**83 663**	**2.60**	**72.73**	**3.78**	**99.05**	**79.10**
RES-NG/1/RCP4.5	1.141	77.4	85 515	4.50	72.64	3.83	94.66	79.11
RES-NG/1/RCP8.5	1.138	70.8	88 858	8.50	72.46	3.93	87.12	79.13
RES-NG/2/RCP0	1.143	83.3	82 371	0.00	72.80	3.74	102.26	79.09
RES-NG/2/RCP2.6	**1.140**	**74.6**	**86 826**	**2.60**	**72.55**	**3.88**	**91.51**	**79.12**
RES-NG/2/RCP4.5	1.138	72.0	88 167	4.50	72.47	3.93	88.44	79.13
RES-NG/2/RCP8.5	1.136	67.3	90 579	8.50	72.32	4.01	83.12	79.15
RES/1/RCP0	1.149	93.1	103 628	0.00	89.00	3.63	89.05	68.30
RES/1/RCP2.6	**1.144**	**81.0**	**107 330**	**2.60**	**88.50**	**3.79**	**75.45**	**67.91**
RES/1/RCP4.5	1.142	77.4	108 453	4.50	88.34	3.85	71.59	67.78
RES/1/RCP8.5	1.139	70.8	110 491	8.50	88.04	3.94	64.93	67.55
RES/2/RCP0	1.145	83.3	106 563	0.00	88.62	3.75	78.30	68.00
RES/2/RCP2.6	**1.141**	**74.6**	**109 222**	**2.60**	**88.19**	**3.90**	**68.70**	**67.66**
RES/2/RCP4.5	1.140	72.0	110 027	4.50	88.05	3.94	65.94	67.55
RES/2/RCP8.5	1.137	67.3	111 482	8.50	87.80	4.02	61.13	67.36
CHP/1/RCP0	1.160	93.1	102 832	0.00	88.66	3.54	104.67	70.56
CHP/1/RCP2.6	**1.154**	**81.0**	**109 744**	**2.60**	**90.24**	**3.74**	**84.20**	**68.56**
CHP/1/RCP 4.5	1.152	77.4	111 758	4.50	90.72	3.81	78.78	67.93
CHP/1/RCP 8.5	1.148	70.8	115 303	8.50	91.62	3.92	69.80	66.79
CHP/2/RCP0	1.155	83.3	108 377	0.00	89.94	3.69	88.18	68.97
CHP/2/RCP2.6	**1.150**	**74.6**	**113 323**	**2.60**	**91.17**	**3.87**	**74.66**	**67.35**
CHP/2/RCP 4.5	1.148	72.0	114 773	4.50	91.55	3.92	70.97	66.85
CHP/2/RCP 8.5	1.146	67.3	117 336	8.50	92.24	4.02	64.73	65.94
WH/1/RCP0	1.110	93.1	122 879	0.00	100.00	6.84	89.83	60.32
WH/1/RCP2.6	**1.103**	**81.0**	**125 800**	**2.60**	**100.00**	**7.13**	**77.23**	**60.32**
WH/1/RCP 4.5	1.101	77.4	126 675	4.50	100.00	7.23	73.63	60.32
WH/1/RCP 8.5	1.097	70.8	128 246	8.50	100.00	7.40	67.39	60.32
WH/2/RCP0	1.105	83.3	125 180	0.00	100.00	7.06	79.93	59.78
WH/2/RCP2.6	**1.099**	**74.6**	**127 311**	**2.60**	**100.00**	**7.32**	**71.02**	**59.16**
WH/2/RCP 4.5	1.098	72.0	127 949	4.50	100.00	7.40	68.45	58.96
WH/2/RCP 8.5	1.094	67.3	129 093	8.50	100.00	7.54	63.95	58.60

*scenarios with global warming RCP2.6 marked in bold

To achieve the highest degree of decarbonization, each criterion ought to be either minimized or maximized (table 5 – optimal value), thus creating a multi-objective optimization task.

Considering that the common trends of clusters of different global warming scenarios (RCP2.6, RCP4.5 and RCP8.5) are similar, scenarios with the level of representative concentration pathways RCP2.6 are analysed below. The sustainability of a DH system is determined by the optimal values of eight criteria, which tend towards the maximum (avoided CO_2 emissions from DH system, share of renewable energy sources, share of recovered heat from waste heat) or minimum values (primary energy factor, specific heat consumption for heating in buildings, radiation forcing, avoided CO2 emissions costs, heat tariff). The table 5 shows that more optimal criteria values are provided by the scenarios in which the waste heat is integrated into the DH system. Determining the sustainability of other scenarios is not straightforward, because, for example, scenario CHP/1/RCP2.6 compared to scenario RES/1/RCP2.6 achieves the biggest share of RES and most avoided CO2 emissions, but the heat tariff and avoided CO2 emissions costs are higher. The TOPSIS multi-criteria analysis method was used for sustainability evaluation of different scenarios the TOPSIS method was used.

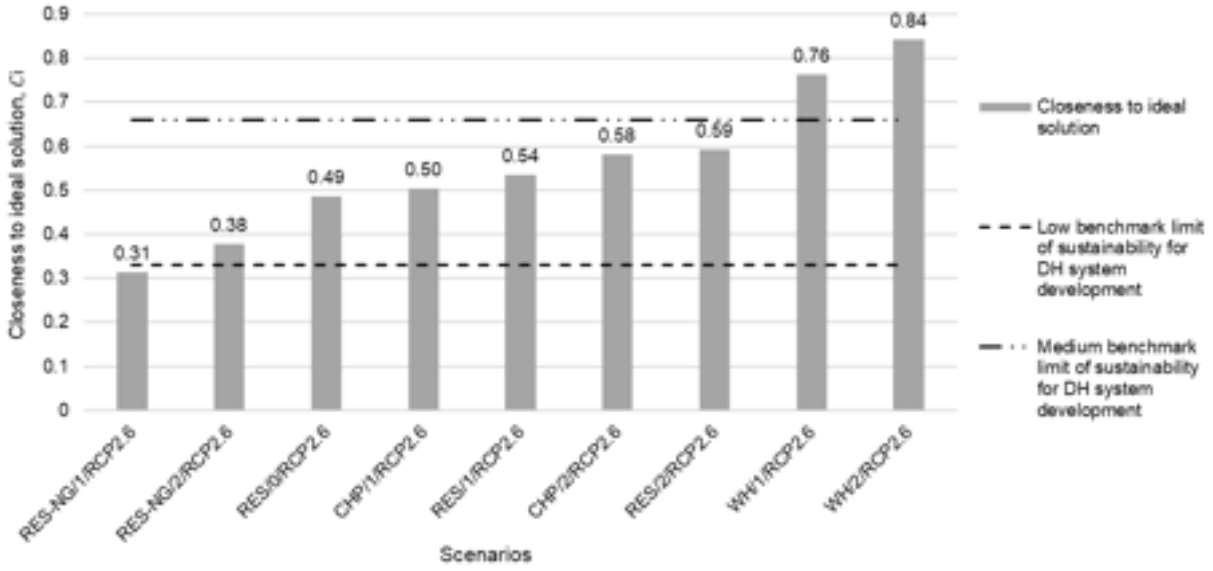

Figure 2. Results of sustainability assessment of DH development scenarios.

Figure 2 depicts the results of the multi-criteria analysis, which shows the ranking of all scenarios from the least sustainable to the most sustainable by expressing the closeness to the most ideal (sustainable) scenario.

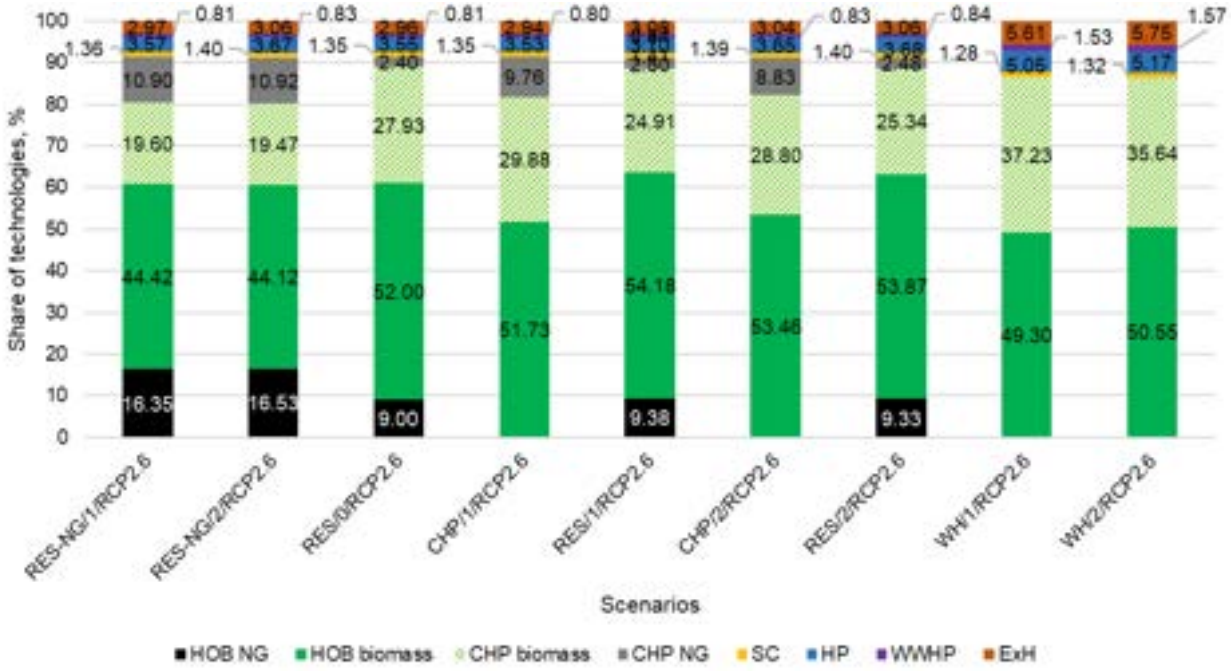

Figure 3. Share of technologies in different development scenarios in 2050.

The graph also includes low and average benchmark limits of sustainability for DH system development. The decarbonized scenarios, which characterize the sustainability vision, are defined by the penetration of several sustainable technologies in the DH system. Therefore, one of the main criteria determining the placement of the DH system's development scenario in the limits of the low, medium, or high level of sustainability is the mix of technologies used in heat energy production.

Figure 3 depicts share of technologies in all researched development scenarios. The scenarios in which the DH company continues to use natural gas in boilers and cogeneration plants show less sustainable results of performance. For example, scenarios RES-NG/1/RCP2.6 and RES-NG/2/RCP2.6 show the lowest sustainability level of the DH system performance (closeness to ideal solution - 0.31 and 0.38 for scenario RES-NG/1/RCP2.6 and RES-NG/2/RCP2.6, respectively), because in these scenarios the share of natural gas technologies is the highest and achieve approximately 27%. As described above, the highest level of sustainability is shown by scenarios (WH/1/RCP2.6 and WH/2/RCP2.6) that use RES for heat production, but also envisage the integration of waste heat into the DH system. Parameters of the closeness to ideal solution are 0.76 and 0.84 for these scenarios respectively. Six scenarios are within medium sustainability. Competing among these scenarios are scenarios that envisage CHP technology as a priority (CHP/1/RCP2.6 and

CHP/2/RCP2.6) and scenarios in which the RES is used in biomass chips (RES/1/RCP2.6 and RES/2/RCP2.6). Even though the CHP/1/RCP2.6 and CHP/2/RCP2.6 scenarios have higher avoided CO_2 emissions (109,744 tCO_2/year and 113,323 tCO_2/year) compared to RES/1/RCP2.6 and RES/2/RCP2.6 scenarios (107,330 tCO_2/year and 109,222 tCO_2/year), the latter generally show the best sustainability (closeness to ideal solution - 0.54 and 0,59 opposite 0.5 and 0.58), because the heat tariff and the cost of avoided CO_2 emissions are the lowest in them. Higher costs in scenarios that prioritize CHP technology are determined by the relative cost of these technologies compared to boilers (see chapter 2.3).

3.2. Results of decarbonization assessment of DH development

The choice of heat production technologies and related fuels determines the amount of CO2 emissions that will be emitted and the costs of these technologies. As a result, the costs of avoided emissions are calculated, which are then compared with CO_2 emission quotas.

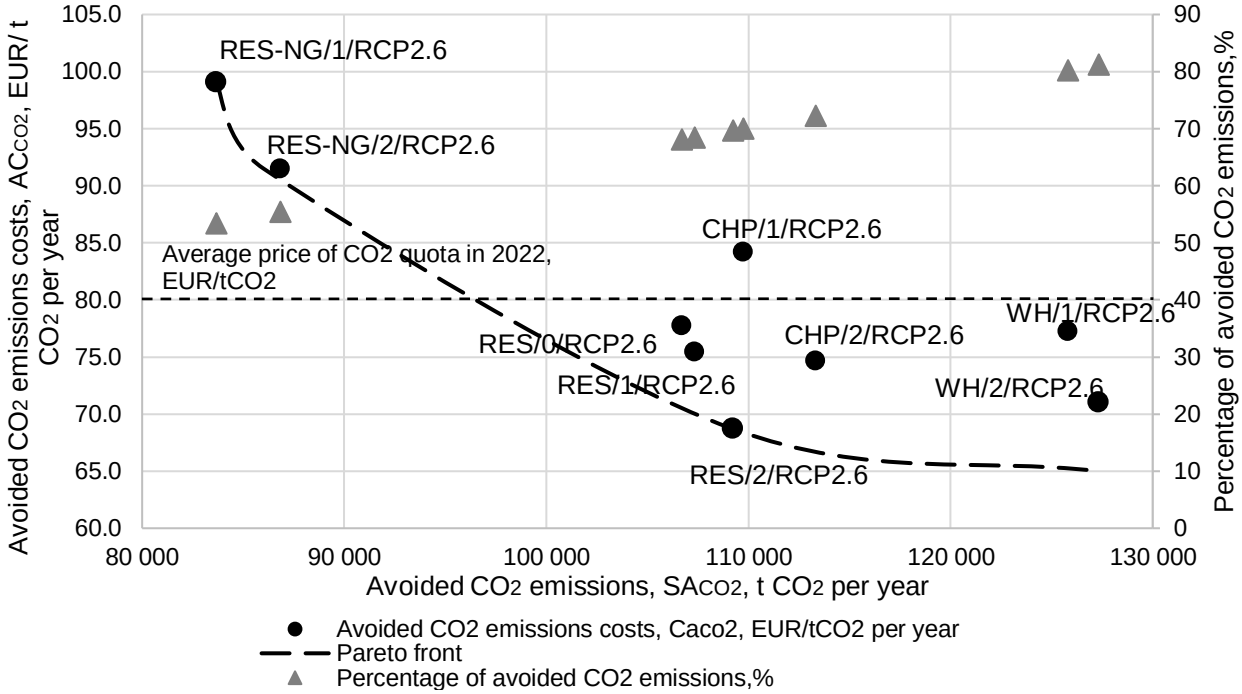

Figure 4. The corelation between the avoided CO_2 emissions costs and the amount of avoided CO_2 emissions.

Figure 4 shows the corelation between the avoided CO_2 emissions costs (economy criteria) and the amount of avoided CO_2 emissions (environmental criteria) and is based on one-objective optimization, where the economic objective function includes both the amount of avoided emissions and also indirectly used heat production technologies, that are strongly connected with the energy parameters of heat production. As a result, we can conclude that acquired dependence characterizes both environmental and economy criteria and indirectly also energy. A Pareto front limits the potentially possible solutions of DH development scenarios, in which we will be able to achieve the maximum amount of avoided CO_2 emissions by lowest their cost. Despite the fact that both scenarios including waste heat integration into the DH system have the highest closeness to the ideal solution, they ensure the highest amount of avoided CO_2 emissions (125,800 tCO_2/year and 127,311 tCO2/year for scenarios WH/1/RCP2.6 and WH/2/RCP2.6 respectively). The costs of avoided CO_2 emissions are not the lowest because the implementation of scenarios with waste heat need installation of heat pump technologies with relatively higher investment comparison to biomass boilers. Nevertheless, both scenarios (WH/1/RCP2.6 and WH/2/RCP2.6) allow to achieve the highest CO_2 emissions reduction and, as a result, a higher level of DH system decarbonization – 80.3% and 81.2%. The lowest costs of avoided CO2 emissions are in scenarios RES/1/RCP2.6 and RES/2/RCP2.6. These are 75.45 and 68.70 EUR/tCO_2 per year in scenarios respectively. The DH system decarbonization level in these scenarios is lower and achieve just 68.5 and 69.7 for these scenarios. The indicators of the worst-case scenarios coincide with the results of the multi-criteria analysis and provide only 53.4% and 55.4% reduction of CO_2 emissions (RES-NG/1/RCP2.6 and RES-NG/2/RCP2.6). The price level of quotas of CO_2 emissions in 2022 was 80.6 EUR/tCO_2 [16]. This price could be an additional argument for decision makers by choosing the implementation of a specific scenario.

4. Conclusions

The paper presents an evaluation of the DH systems' transition towards carbon neutrality by the implementation of WH and by using AHP, high-efficiency CHP and RES technology in various development scenarios. Based on an algorithm that combines the SD model with the TOPSIS method, the economic,

environmental and energy criteria were considered, and development scenarios were evaluated to find the best decarbonization strategy for the DH system of Riga.

The application of MCA allows to determine the closeness of each specific DH system development scenario to the ideal solution considering eight energy (Primary energy factor, specific heat consumption for heating), environmental (avoided CO_2 emissions from DH system, radiation forcing, share of renewable energy sources, share of recovered heat from waste heat), and economy (avoided CO2 emissions costs and heat tariff) parameters. The result of the multi-criteria analysis is a list of scenarios sorted in one of three sustainability classes: high, medium, or low.

The highest level of sustainability is shown by scenarios WH/1/RCP2.6 and WH/2/RCP2.6 that use 100% RES for heat production including approximately 7% of waste heat integration into the DH system. Parameters of the closeness to ideal solution are 0.76 and 0.84 for these scenarios respectively. These scenarios allow to achieve the highest CO_2 emission reduction by 80.3% and 81.2% (WH/1/RCP2.6 and WH/2/RCP2.6 respectively).

The correlation between the avoided CO_2 emissions costs and the amount of avoided CO_2 emissions is presented and provides one-objective optimization. A Pareto front depicts the potentially possible solutions of the DH development scenarios, in which the maximum amount of avoided CO_2 emissions can be achieved with the lowest cost. The lowest costs of avoided CO_2 emissions can be achieved in scenarios RES/1/RCP2.6 and RES/2/RCP2.6, there are 75.45 and 68.70 EUR/tCO_2 per year, for abovementioned scenarios respectively.

The hybrid model provided in this paper couples SD modelling and multi-criteria analysis and allows, on the one hand, the ranking of the selected transition scenarios according to their sustainability score and, on the other hand, to benchmark the results of developed scenarios against a carbon neutral DH system. In the future, decision makers can evaluate strengths and weaknesses in each case of specific scenarios.

Acknowledgments

This research has been supported by the European Regional Development Fund within the projects “Decision Support Tool for Decarbonisation Assessment of District Heating Systems (START)”, No. 1.1.1.2/VIAA/4/20/604”

References

[1] Ziemele J., Dace E., An analytical framework for assessing the integration of the waste heat into a district heating system: Case of the city of Riga. Energy 2022;10.1016/J.ENERGY.2022.124285.

[2] Ziemele J., Gravelsins A., Blumberga A., Vigants G., Blumberga D., System dynamics model analysis of pathway to 4th generation district heating in Latvia. Energy 2016;10.1016/J.ENERGY.2015.11.073.

[3] J. de Maigret *et al.*, A multi-objective optimization approach in defining the decarbonization strategy of a refinery. Smart Energy 2022;10.1016/J.SEGY.2022.100076.

[4] Finke J., Bertsch V., Implementing a highly adaptable method for the multi-objective optimisation of energy systems. Appl Energy 2023;10.1016/J.APENERGY.2022.120521.

[5] Yuan M., Thellufsen J. Z., Sorknæs P., Lund H., Liang Y., District heating in 100% renewable energy systems: Combining industrial excess heat and heat pumps. Energy Convers Manag 2021;10.1016/J.ENCONMAN.2021.114527.

[6] Bohra S. S., Anvari-Moghaddam A., A comprehensive review on applications of multicriteria decision-making methods in power and energy systems. Int J Energy Res 2022;10.1002/ER.7517.

[7] Daugavietis J. E., Soloha R., Dace E., Ziemele J., A Comparison of Multi-Criteria Decision Analysis Methods for Sustainability Assessment of District Heating Systems. Energies 2022;10.3390/EN15072411.

[8] DIRECTIVE (EU) 2018/2002 OF THE EUROPEAN PARLIAMENT AND OF THE COUNCIL - of 11 December 2018 - amending Directive 2012/27/ EU on energy efficiency.

[9] International Energy Agency 2021, Net zero by 2050: a roadmap for the global energy sector - A special report by the International Energy Agency. 2021.

[10] Regulations on the Latvian building code LBN 003-19 ‘Building climatology’. Available at:<https://likumi.lv/ta/id/309453-noteikumi-par-latvijas-buvnormativu-lbn-003-19-buvklimatologija> [accessed 13.03.2023].

[11] International Organization for Standardization, ISO 52000-1:2017. Energy performance of buildings — Overarching EPB assessment — Part 1: General framework and procedures’ , 2017.

[12] Regulations of the Cabinet of Ministers No. 222., Building energy efficiency calculation methods and building energy certification rules. Available at: <https://likumi.lv/ta/id/322436-eku-energoefektivitates-aprekina-metodes-un-eku-energosertifikacijas-noteikumi> [accessed 13.03.2023]

[13] IPCC Updates Methodology for Greenhouse Gas Inventories. 2019. Available at: https://www.ipcc.ch/2019/05/13/ipcc-2019-refinement/ [accessed 13.03.2023].

[14] Danish Energy Agency, Technology Data for Generation of Electricity and District Heating. Available at:<*https://ens.dk/en/our-services/projections-and-models/technology-data/technology-data-generation-electricity-and*.> [accessed 13.03.2023].

[15] Zardari N. H., Ahmed K., Shirazi S. M., Yusop bin Z., Weighting Methods and their Effects on Multi-Criteria Decision Making Model Outcomes in Water Resources Management. SpringerBriefs in Water Science and Technology. Springer Cham. 2014. p. 166.

[16] European Union Emission Trading System (EU-ETS) carbon pricing in 2022. Available at:<https://www.statista.com/statistics/1322214/carbon-prices-european-union-emission-trading-scheme/#:~:text=EU%2DETS%20futures%20pricing%20in%20the%20European%20Union%202022&text=The%20price%20of%20emissions%20allowances> [accessed 13.03.2023].

Integration of Life Cycle Impact Assessment in Energy System Modelling

Jonas Schnidrig [a,b] (CA), Justine Brun [b], François Maréchal [b] and Manuele Margni [a]

[a] University of Applied Sciences Western Switzerland (HES-SO), Sion, Switzerland, jonas.schnidrig@hevs.ch
[b] Ecole Polytechnique Fédérale de Lausanne, Sion, Switzerland

Abstract:
The Paris agreement is the first-ever universally accepted and legally binding agreement on global climate change. It is a bridge between today's and climate-neutrality policies and strategies before the end of the century. However, government and private companies still struggle to develop cost-effective carbon-neutral strategies. Energy system modeling has proved essential in creating strategies to generate carbon-neutral scenarios under minimal costs.
However, cost minimization does not necessarily lead to publicly acceptable solutions nor generate configurations that minimize environmental impacts.
Here we show a methodology to integrate LCIA indicators in an energy system model, assessing the impact of energy system configurations on economic and environmental aspects.
Here we show a methodology to integrate life cycle assessment metrics in an energy system model to account for (i) emissions and impacts beyond the operation of the energy system itself and (ii) identify configurations optimizing both economic and environmental aspects. The model is applied to the case study of Switzerland and shows that with little modifications to the energy system configuration, carbon neutrality can be reached under the cost minimization objective while identifying trade-offs with other environmental issues.
This work allows the generation of MOO of energy systems, minimizing burden shifting of environmental impacts and generating robust solutions for the energy transition, increasing social acceptance towards the biggest challenge of the 21st century.

Keywords:
Energy System, LCA, LCIA, Multiobjective optimization, Renewable Energy

1. Introduction

1.1. Background

With the increasing strength and frequency of climate change events, the urgency to mitigate climate change impact is ever so important as today.
The IPCC reports highlighting the importance of the international coalition to reduce GHG from human activities to limit global warming to 1.5 - 2°C, compared to pre-industrial levels.
As a response, the Paris Agreement, resulting from the COP21 in 2015, required all signers to submit ever more ambitious NDC every five years, listing mid and long-term emissions reduction objectives.
Companies, such as [1] and IRENA, evaluate whether NDCs are on track with the 1.5 - 2°C scenarios and advise countries for improvement.
Interest in energy system modeling has increased due to growing concern for sustainable development and the transition towards renewable energies.
LCA, which studies other environmental impacts, such as ozone layer depletion or particulate matter formation, has also grown exponentially in the past two decades [2].
When planning for a low-carbon energy system, one has to consider other impacts of AoP to monitor potential environmental burden shifting. Thus, this project's methodology aims to integrate LCA and LCIA within Energy System Modelling to monitor and optimize climate change impacts, human health, and ecosystem quality.

1.2. Literature review

In addition to the economic optimization classically used in energy system designs and operations, the focus on Life Cycle Analysis calculation is rapidly gaining momentum. While LCA is mainly applied to small-scale technologies [3–5], more complex systems such as processes [6], plants [7] and buildings [8] were analyzed in recent years. This evolution depicts a will to shift from small-scale towards bigger-scale energy systems. Small-scale systems are optimized on multi-objective functions (OF), integrating economic and environmental impacts. On the contrary, more extensive systems assess LCA indicators, using either post-calculation or solely focusing on the Climate Change indicator, which represents emissions of GHG emissions.

Therefore, energy system modeling at regional and national levels is currently based on economic optimization, while LCA indicators take a secondary place. [9] assessed the impact of a biomass-based energy system in Europe while optimizing the economic OF and monitoring LCA indicators with post-calculation on the energy system structure. [10] analyzed the electricity demands of the German energy system, focusing on the MOO of economic and Climate Change OFs.
A global energy system model has been developed by [11], generating robust solutions by optimizing the Swiss energy system on economic and environmental aspects by integrating the climate change indicator. [12] went one step further by not only assessing the climate change indicator but integrating the carbon mass flow conservation to the model by Moret.

While LCA optimization is a hot topic in current research, none of the previously cited literature integrates at the same time (i) the generation of a national model with all global energy demands, (ii) the direct optimization of multiple AoP within one model, (iii) and uncertainty.

1.3. Objectives and contribution

This project is based on ES using MILP to define a Swiss energy model through point-average consumption assumption [13]. It is also based on integrating LCA endpoint indicators for environmental impact optimization over three different AoP to compare resulting energy systems with purely economic optimization [14]. The goal is to analyze Switzerland's potential to decarbonize its energy system by 2050 while accounting for other environmental impacts and avoiding shifting the environmental burden.

Several research questions have been identified to tackle this project, which can be divided into three central problems.

- Single-objective optimization of LCA impacts in energy systems modeling
- MOO of LCA impacts in energy systems modeling
- Application of regional LCA modeling to the Swiss energy system

These questions will be treated by answering the following questions:

- How to characterize technologies in LCA?
- How to integrate LCIA in energy systems modeling?
- How to monitor LCA indicators in energy systems modeling and assess the resulting system's performance?
- Does a low-carbon Swiss energy system lead to environmental impact shifting?
- What is the effect of MOO on the energy systems configuration?

2. Methodology

2.1. Modelling Framework

Integrating LCIA in energy system modeling has been accomplished by Brun et al. [14], adapting the existing MILP EnergyScope framework developed by Moret et al. [11], Li et al. [12] and Schnidrig et al. [13]. *EnergyScope* models a global multi-energy model at a monthly averaged basis under the constraint of mass and energy conservation between demands and resources. The demands are categorized into four sectors (households, services, industry, and transportation) and three energy demand types: (i) electricity at four voltage levels, (ii) heat distinguished between process heat, space, and water heating, and (iii) mobility split in passenger and freight mobility. The resources are either available within the studied region or imported from outside. ES is written as MILP Problem in AMPL and optimizes the configurations, which are determined through the key decision variables $\mathbf{F}$ and $\mathbf{F_t}$, modeling the installation size and the temporal use of the technologies.

2.1.1. Economic objective

The primal OF of EnergyScope has been previously the total cost $\mathbf{C_{tot}}$ (Eq. 1). The total cost is calculated as the sum of the technologies' ($tec \in \mathcal{TEC}$) annualized investment $\mathbf{C_{inv}}$ and maintenance $\mathbf{C_{maint}}$ (Eq. 3) cost affected by $\mathbf{F}$, and the temporary variable as of the resources ($res \in \mathcal{RES}$) operation cost $\mathbf{C_{op}}$ (Eq. 4).

$$\mathbf{C_{tot}} = \sum_{tec}(\mathbf{C_{inv}}(tec) \cdot \tau(tec) + \mathbf{C_{maint}}(tec)) + \sum_{res} \mathbf{C_{op}}(res) \tag{1}$$

$$\mathbf{C_{inv}}(tec) = c_{inv}(tec) \cdot (\mathbf{F}(tec) - f_{ext}(tec)) \tag{2}$$

$$\mathbf{C_{maint}}(tec) = c_{maint}(tec) \cdot \mathbf{F}(tec) \tag{3}$$

$$\mathbf{C_{op}}(res) = \sum_{t} c_{op}(res) \cdot \mathbf{F_t}(res, t) \cdot t_{op}(t) \tag{4}$$

$$\forall \quad res \in \mathcal{RES},\ tec \in \mathcal{TEC},\ t \in \mathcal{PERIODS},$$

2.1.2. Carbon emissions objective

Li et al. [12] integrated the carbon balance and thus the resulting net emissions secondary objective, measured by the CO_2 equivalent **Emissions**. These emissions are modeled by considering technology-specific layers containing CO_2. The different CO_2 layers are categorized into five classes $c \in \mathcal{C} - \mathcal{LAYERS}$ (captured, sequestrated, stored, emitted to atmosphere). The technology conversion factor η [tCO_2/GWh] is valid for all periods t (Eq. 5) and is either positive or negative, allowing to model net emission limits ϵ (Eq. 6).

$$\mathbf{Emission}(t) = \sum_{tec} \mathbf{F_t}(tec) \cdot t_{op}(t) \cdot \eta(i, c) \quad \forall \quad tec \in \mathcal{TEC}, t \in \mathcal{PERIODS},\ c \in \mathcal{C} - \mathcal{LAYERS} \tag{5}$$

$$\sum_{t} \mathbf{Emission}(t) \leq \epsilon \quad \forall \quad tec \in \mathcal{TEC}, t \in \mathcal{PERIODS} \tag{6}$$

2.1.3. LCIA objectives

The environmental OF variable $\mathbf{LCIA_{tot}(i)}$ is constructed by combining the total cost composition, splitting in a constant (investment) and variable (operation) part and the technology-specific impact of the carbon flow model, where the impact of resources is integrated into the use of technologies: For each indicator i (Eq. 7 & table 3), $\mathbf{LCIA_{tot}(i)}$ is defined as the construction of the technology related to the installation size $\mathbf{F}$ (Eq. 8), and the operation of the technology proportional to its use $\mathbf{F_t}$ (Eq. 9). Finally, the construction impact is divided by the technologies' lifetime n.

$$\mathbf{LCIA_{tot}}(i) = \sum_{tec}(\mathbf{LCIA_{constr}}(i, tec) \cdot \frac{1}{\boldsymbol{n}(i)} + \mathbf{LCIA_{op}}(i, tec)) \tag{7}$$

$$\mathbf{LCIA_{constr}}(i, tec) = lcia_{constr}(i, tec) \cdot \mathbf{F}(tec) \tag{8}$$

$$\mathbf{LCIA_{op}}(i, tec) = lcia_{op}(i, tec) \cdot \sum_{t} \mathbf{F_t}(res, t) \cdot t_{op}(t) \tag{9}$$

$$\forall \quad i \in \mathcal{IND},\ tec \in \mathcal{TEC},\ t \in \mathcal{PERIODS},$$

2.2. Life Cycle Impact Assessment

LCA aims to evaluate the environmental impacts of a product throughout its life cycle. The approach usually considered is the cradle-to-grave, which starts with the extraction of raw materials and ends in the disposal of the product through recycling, landfill, or incineration. The fur stages of LCA consist of [15] (i) Definition of goal and scope phase, (ii) item Life cycle inventory (LCI) phase, (iii) Life cycle impact assessment (LCIA) phase, and (iv) Interpretation phase

2.2.1. Definition of goal and scope

Each technology is characterized separately to integrate an LCIA into the energy system model correctly. Every technology is defined by two products, one related to its construction and one for its operation, modeling the cradle-to-grave approach. Their functional units depend on the end-use categories the technology belongs to, where their units are reported in table 1.

2.2.2. Life cycle inventory

The LCI was computed using a matrix approach instead of a sequential one. The matrix method easily integrates feedback loops in product systems and avoids the explicit computation of scaling factors when the final demand vector f is known (Table 2).
The technology matrix A defines the exchanges between products. Its columns represent products, processes,

Table 1: Functional unit of the ES technologies' operation and construction products, depending on the end use category it belongs to.

End use categories	Unit of the technologies	
	Operation	**Construction**
Electricity	GWh	GW
Heat (low and high temperature)	GWh	GW
Mobility freight	Mtkm	$\frac{\text{Mtkm}}{h}$
Mobility passenger	Mpkm	$\frac{\text{Mpkm}}{h}$

or services, with each row representing its respective input or output. A is square, and its columns are linearly independent; thus, it is invertible. The matrix F defines the elementary flows for each process related to direct emissions. Both matrices are defined inside the Ecoinvent database [16]. The final demand f was defined as an all-ones vector; thus, the LCI represents each specific technology's total emissions per functional unit (table 1). The scaling factor vector s and the life cycle inventory vector g are defined as follows:

$$s = A^{-1} \cdot f \tag{10}$$

$$g = \text{LCI} = F \cdot s = F \cdot \left(A^{-1} \cdot f\right) \tag{11}$$

Table 2: Notation used in the life cycle inventory phase of the LCA

Notation	Name
A	Leontief technology matrix
F	Matrix of elementary flows
f	Final demand
s	Scaling factor
g	Life cycle inventory

2.2.3. Life cycle impact assessment

Seventeen mid-point indicators are categorized as endpoint levels into three main AoP for the LCIA: HH, EQ, and CC. Twenty-three endpoint indicators were considered in the matrix IW^+, based on the impact assessment method IMPACT world+ [17] (table 3). IW+ is multiplied by the LCI g to get the impact result matrix R:

$$R = \text{IW}^+ \cdot g \tag{12}$$

2.2.4. Technology characterization

EnergyScope was run on a national scale on economic optimization to identify which technologies to characterize in LCIA, allowing to make a trade-off between characterization time and methodology development.
Data collection was then performed, mainly with the Ecoinvent 3.8 database. The tools used to create the Leontief matrix A and the elementary flow matrix F directly from the database were given by [18]. The initial Leontief matrix directly resulting from the ecoinvent database was modified as follows :

$$A_{ES}^{nxn} = \mathbf{I}^{nxn} - A_{ecoinvent}^{nxn} \tag{13}$$

n represents the total number of products in the database, and $\mathbf{I}^{nxn}$ is an identity matrix of size n to align with the convention used in ES. Namely, negative values represent input flows or products, and positive values represent output flows or products, with an all-one diagonal to yield an invertible matrix.
In EnergyScope, conversion technologies are characterized by their construction and operation impacts. A similar decomposition of impacts was used for the LCIA. First, the products representing a technology's construction and operation were identified using data collection. In LCA, the impact of a technology's operation intrinsically considers the impact of its construction. Hence, to avoid the impacts of double counting, the construction of a technology needed to be discarded from matrix A. Then, new columns and rows are added to the matrix A to create a new matrix A', illustrated in figure 1. The size of the new technology matrix and the number of operation products will increase A' characterized by n' for a final dimension of $A'^{(n+n')x(n+n')}$.

New columns are added to the emission flows matrix $F^{(fxn)}$, where f is the number of emissions flows in the database for matrix multiplication compatibility. The new columns correspond to the emission flows related to P'_{op}, which are the same as the flows of the original product P_{op}, creating the new matrix $F'^{(fx(n+n'))}$.

Table 3: Table summarizing mid- and endpoint indicators, with the respective ones used for their integration in ES and the AoP they belong to according to IMPACT World +.
The unit of the endpoint indicators is expressed in $kgCO_2$-eq for Climate Change (CC). The impact of Ecosystem Quality (EQ) is given in PDF·m^2·year, representing the Potentially Disappeared Fraction of species on a one m^2 surface during a year. Finally, the impact on Human Health (HH) is expressed in DALY, the Disability Adjusted Life-Years, representing the loss of the equivalent of one year in perfect health.

Midpoint level indicator	Endpoint level indicator	Abbreviation	AoP
Climate change	Climate change, short term	CCST	CC
Freshwater acidification	Freshwater acidification	FWA	EQ
Freshwater ecotoxicity	Freshwater ecotoxicity, short term	FWEXS	EQ
Freshwater eutrophication	Freshwater eutrophication	FWEU	EQ
Human toxicity cancer	Human toxicity cancer, long term	HTXCL	HH
	Human toxicity cancer, short term	HTXCS	HH
Human toxicity non-cancer	Human toxicity non-cancer, long term	HTXNCL	HH
	Human toxicity non-cancer, short term	HTXNCS	HH
Ionizing radiation	Ionizing radiation, ecosystem quality	IREQ	EQ
	Ionizing radiation, human health	IRHH	HH
Land occupation	Land occupation, biodiversity	LOBDV	EQ
Land transformation	Land transformation, biodiversity	LTBDV	EQ
Marine acidification	Marine acidification, long term	MAL	EQ
	Marine acidification, short term	MAS	EQ
Marine eutrophication	Marine eutrophication	MEU	EQ
Ozone layer depletion	Ozone layer depletion	OLD	HH
Particulate matter formation	Particulate matter formation	PMF	HH
Photochemical oxidant formation	Photochemical oxidant formation	PCOX	HH
Terrestrial acidification	Terrestrial acidification	TRA	EQ
Thermally polluted water	Thermally polluted water	TPW	EQ
Water availability	Water availability, freshwater ecosystem	WAVFWES	EQ
	Water availability, human health	WAVHH	HH
	Water availability, terrestrial ecosystem	WAVTES	EQ

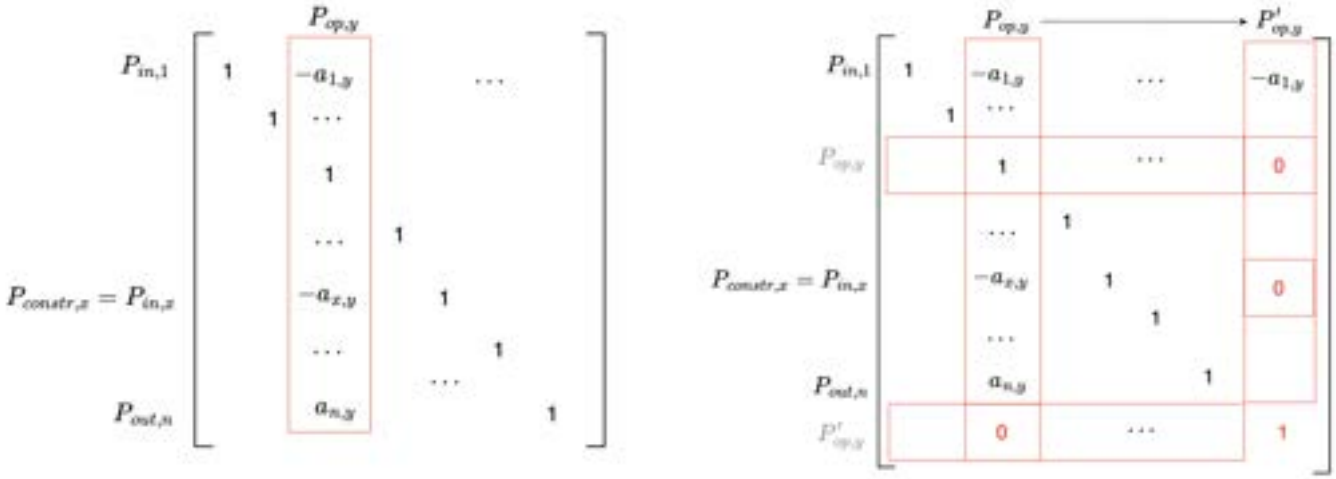

Figure 1: On the left-hand side : Initial technology matrix A^{nxn}. On the right-hand side: New technology matrix $A'^{(n+n')x(n+n')}$. n represents the total number of products in the database, and n' represents the number of conversion technologies characterized.
Example for a single technology: P_{op} represents the ecoinvent product for operating a certain technology. P_{constr} is the ecoinvent product related to the construction of the same technology. The matrix A' contains an additional column and row, with P'_{op} representing the operation of the technology while disregarding its construction, allowing later to compute the isolated impact of the operation

To assess the impact on the selected region, provincial data was selected. The following best resolution was used when unavailable: national, continental, or global. This methodology was applied to the technologies installed on economic optimization.

2.2.5. LCIA Integration in Energy System Modelling

After adding the technologies' operation products, they discarded their relations with their respective construction products (defined as P'_{op}) in the technology matrix A. Their respective LCI was computed by multiplying the new elementary flow matrix F' by the new technology matrix A'.

The subsequent step of the LCIA was to convert the emissions to their functional units (table 1.)
Most construction technologies are characterized by "units." Therefore, to convert the input-output and emissions flow to the ES functional unit, the capacity was defined as :

$$\text{Capacity} = \frac{GW^1}{\text{unit} \cdot \mathbf{c}_{p(i)} \cdot time_{tot} \cdot n_i} \tag{14}$$

[1] : [GW[] is only for electricity and heat, but [Mtkm] for freight mobility and [Mpkm] for passenger mobility.

Each technology LCI was multiplied by the impact matrix $IW+$, as in equation 12. This resulted in the impact matrix R as defined for the construction and operation per technology and region.

2.2.6. Assumptions

Regarding mobility, ecoinvent car products are defined per km. For unit conversion, 1.6 people per car are estimated for Switzerland, according to [19].

Technology maintenance and transportation impact are mainly accounted for within the operation. However, it is not always explicitly detailed. Therefore, the choice was not to isolate the technologies' maintenance and transport impacts but to keep them as part of the operational impact.

2.3. MOO

MOO (MOO) is a field of multi-criteria decision-making that deals with mathematical optimization problems in which multiple OFs must be optimized simultaneously. MOO has proven to be a valuable tool in energy planning, where the decision-maker has to select between two or more competing objectives. For example, EnergyScope traditionally optimized one OF only [11, 12, 20] or proceeded to bi-objective optimization with environomic Pareto curves generation in specific cases [19]. MOO consists of finding a single solution that fulfills the arbitrary preferences of the human decision-maker, locating a sample collection of Pareto optimum solutions, and quantifying the trade-offs involved in achieving various goals.

This work has realized the MOO by integrating the LCIA OFs $l \in \mathcal{LCIA} - \mathcal{I} \subset \mathcal{OF}$ as constraints under the economic optimization (Eq. 15), defining the technology size $\mathbf{F}$ and use $\mathbf{F_t}$. The weighting (Eq. 16) allows processing through the multidimensional Pareto-Curve in between the extreme points identified at mono-objective optimization, where $\omega(j) = 1$ and $\omega(i) = 0$, $\forall i \in \mathcal{OF} \setminus \{j\}$.

$$\min_{\mathbf{F},\mathbf{F_t}} \mathbf{C_{tot}} \tag{15}$$

$$\text{s.t.} \quad \mathbf{f_{obj}}(i) \leq \omega(i) \cdot f^{\max}_{obj}(l) + (1 - \omega(i)) \cdot f^{\min}_{obj}(l) \tag{16}$$
$$\forall \quad i \in \mathcal{OF} = \mathcal{COST} \cup \mathcal{LCIA}$$

To account for the solution space of the MOO, a Monte-Carlo approach [21] on the weights ω is applied. The decision variables define the modeled solution space under varying weighting parameters $\omega(i)$ (Eq. 17). The probability of appearance of $\omega(i)$ follows a uniform distribution U(0, 1) (Eq. 18).

$$\mathbf{F}(i), \mathbf{F_t}(i) : \quad f((\mathbf{F}(i), \mathbf{F_t}(i)), \omega(i)) \tag{17}$$
$$\text{s.t.} \quad \omega(i) = P(\tilde{\omega}, \text{U}(0, 1)) \tag{18}$$

3. Results

3.1. Case study

The methodology above is applied to the case study of Switzerland, aiming at following the energy strategy *Energieperspektiven 2050+* (EP50+) [22]. EP50+ analyzes the development of an energy system compatible with the long-term climate goal of net zero greenhouse gas emissions in 2050 while ensuring a secure energy supply without nuclear power. While EP50+ defined several variants of this scenario, differing in terms of a different mix of technologies and a different speed of expansion of renewable energies in the power sector, we consider within this study only the demands estimation, the potentials of energy vectors, and the constraints of carbon-neutrality and no nuclear power.

Demands

EP50+ decomposed the final energy demand evolution by sector in 5 years interval [22]. Taking the energy demand of 2019 [23] being split into the energy categories, allows us to extrapolate the specific energy demand by category to the sectoral energy demand estimation for 2050 (Tab. 4).

Table 4: Annual final energy demand per sector and energy type 2050.

		Households	**Services**	**Industry**	**Mobility**
Electricity LV	[GWh]	9818	9154	0	0
Electricity MV	[GWh]	0	1407	3173	0
Electricity HV	[GWh]	0	0	5350	0
Electricity EHV	[GWh]	0	0	0	0
Heat HT	[GWh]	0	183	5855	0
Heat LT SH	[GWh]	31849	6994	1965	0
Heat LT HW	[GWh]	6322	1605	393	0
Freight	[Mtkm]	0	0	0	21106
Passenger	[Mpkm]	0	0	0	74590

Potentials

We model an independent energy system, limiting the imports of any energetic vector to zero to achieve the goal of security of supply. Therefore all primary energy needs to originate from the studied region, defined by the potentials (Tab. 5). Furthermore, contrary to EP50+, we model the technical potential of the resources, as economic potential is subject to arbitrary and uncertain estimation of future renewable energy markets.

Table 5: Annual resources and renewable energy technologies potential.
The values in brackets for the hydropower technologies correspond to the potential with reinforcement.

Resources	**Waste Fossil**	**Waste Biomass**	**Wood**	**Wet biomass**	**Hydro Storage**
[GWh]	10833	8917	15278	12472	8900
Technologies	**Geothermal**	**Hydro Dam**	**Hydro River**	**PV**	**Wind**
[GW]	4.8	8.08 (8.52)	3.8 (4.65)	67	20
[GWh]	42.08	17.48	19.726	66.4	40.3

3.2. Mono-Objective Optimization

In the first step, every single OF is optimized individually, allowing to determine the maximum value $f_{obj}^{\min}$ and $f_{obj}^{\max}$ necessary for the normalization in the MOO. The tracking of the OF values on individual optimization is represented in Figure 2. For each optimization, the other OF values are at their maximum value, indicating significant differences in configurations and operations.

By digging into the energy system configurations of the respective individual optimizations via the cost composition (Figure 3), only the cost minimization is distinguished in a major way from the other configurations. The LCIA indicators minimization leads to higher investment costs at an almost equal level, similar to the observation in Figure 2). From the point of view of investments, the main difference is the deployment of massive quantities of PV, reaching the potential of PV (50 GW) in addition to geothermal electricity generation, while the wind share is reduced.

The discrepancy between wind and PV leads to a higher dephasing between the generation of electricity in Summer and consumption and winter, which affects the necessity of installing seasonal storage in the form of

Figure 2: OFs values comparison for mono-objective optimizations. Each sub-figure corresponds to an individual optimization. The height of the segments corresponds to the OF's relative variation to the 2020 reference scenarios OFs values [%].

natural gas between 7800 GWh-12 450 GWh. Hydro Dams are used in pumping and storing at their respective maximum capacity of 8900 GWh, leading to a combined maximum seasonal storage potential of up to 21 350 GWh.
The switching towards methane storage furthermore affects the service sector; on one side, while biomass still is converted in gaseous energy carriers, the excess electricity is converted into hydrogen via fuel cell technologies, such as SOEC, PEM, or Alkaline Electrolysis for a cumulative electrolysis capacity of 0.6 GW - 2.8 GW.
The additional gas production is transported in the existing methane infrastructure, while only minor investments in the construction of local Hydrogen infrastructure have to be made (0.8 GW-1.4 GW). Therefore, minimizing LCA indicators tends to limit the reinforcement of energy transportation infrastructure to a minimum.

The LCA indicators can be split into indirect (construction) and direct (operation) emissions (Figure 4), where we can identify the highest contributor sectors to the respective OFs. While cost minimization leads to a highly operation-intensive energy system environmental impact, the LCIA OF configurations have a lower impact on the operation side of the technologies and minimize the technologies' constructions individually while reaching the maximum value in the other indicators construction.
The sectors of mobility, hydropower, and electricity generation dominate the LCA indicators. The mobility sector mainly affects the operation, as technologies using methane release CO_2 in operation, which is not captured

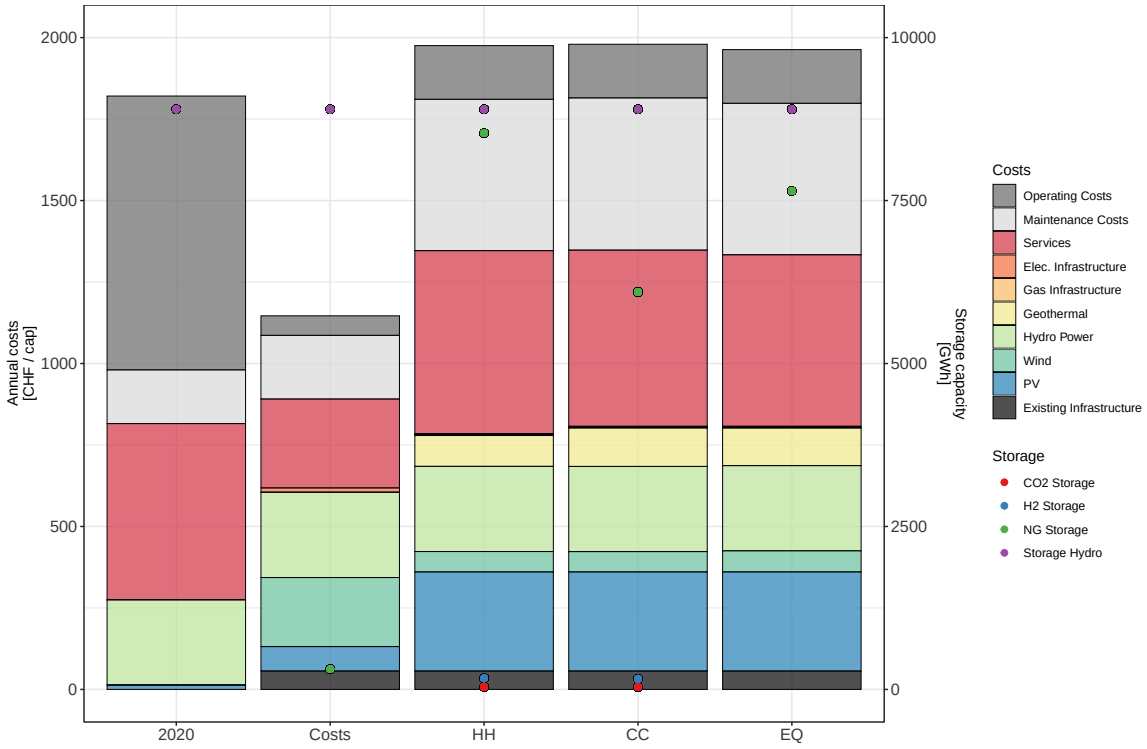

Figure 3: Total costs energy systems composition for mono-objective optimizations. The secondary axis displays the installed storage capacity. Case study Switzerland 2050 independent and CO_2-neutral, without nuclear power.

yet. Methane-powered vehicles are used for road freight transport in the cost minimization, while lower shares of methane-powered fuel cell vehicles in public transport are used in the LCA minimizations.
The hydro dam construction impact significantly impacts the EQ indicator while minimizing CC due to deploying new hydro dams. Differences in the operation between the optimizations can be explained by a different operation strategy of the hydro dams in the cost minimization scenario.
The electricity generation impact is visible on the construction side, where the impacts are shifted to minimize the respective indicator in the optimization. In this category, the concurrence between the installation of new hydro dams for CC minimization, installation of Hydrothermal gasification CHP in the HH minimization, and combined cycle gas turbines for the EQ minimization is visible, as the respective technologies have a minor impact on the specific indicator and similar impacts in the other ones.

3.3. MOO

Running the multi-objective optimization (Equation 17) 500 times results in 500 different configurations. The comparison between those configurations has been made by generating the Pearson correlation coefficient matrix of the technologies and the OFs. Figure 5 represents the main renewable energy resources installation capacities. In the upper half, clear correlations between technologies and between OFs are visible. The biggest correlation is between the OF cost and PV $r = 0.94$, indicating that further installing PV leads to higher total costs, or vice-versa; the more money is available, the more PV is installed. A high negative correlation is visible between geothermal power and wind ($r = -1$), as geothermal power is only installed as a backup to the missing wind. Lower correlations are visible between PV and EQ ($r = -0.61$) and between PV and HH ($r = -0.53$). This negative correlation can be interpreted as the lower the indicator; the more PV must be installed.
Meaningful correlations $r \geq 0.5$ between OFs can only be observed between costs and EQ ($r = -0.56$) and HH ($r = -0.55$), respectively, showing a negative correlation between the environmental indicators and the costs. The weak correlation between costs and climate change can be explained by the analyzed case study, modeling a carbon-neutral energy system, where CO_2 emissions highly contribute to the CC indicator.

The lower half represents the scatter plot of the different solutions. Observing the Pareto-front between the environmental indicators is possible when taking the total cost column. The points outside the Pareto-front are due to low weighting on the cost indicator. The strong correlation between cost and PV can be observed, as the points almost perfectly line up on $E^{PV}[\text{GW}] = \frac{20}{3}[\frac{\text{GW}}{\text{GCHF}}] \cdot C^{tot}[\text{GCHF}] - 91.7[\text{GW}]$ between 15 GW-35 GW.

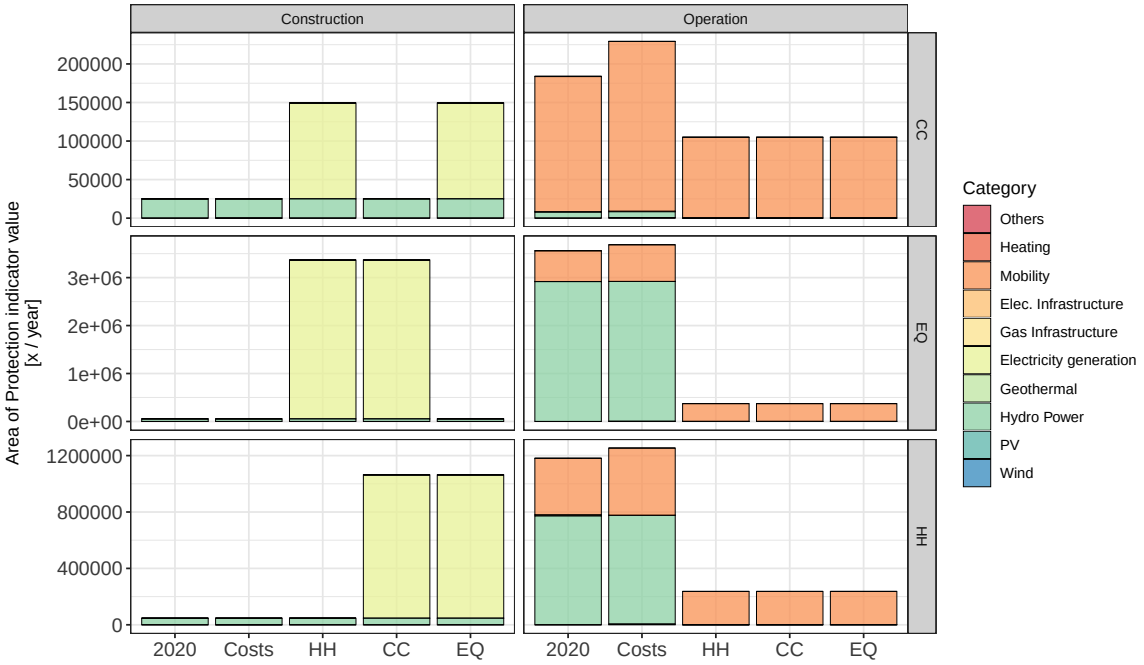

Figure 4: LCIA impacts composition for mono-objective optimizations. The secondary axis displays the installed storage capacity. Case study Switzerland 2050 independent and CO_2-neutral, without nuclear power.

Observing the other scatter point patterns in the LCA indicator columns allows us to identify the reason for the low correlation: The point distributions fill out the observed area in a well-distributed pattern, generated by the Monte Carlo method (Eq. 18).
Comparing the effect of the primary renewable resources, we can observe that PV is generating a Pareto-curve for all OFs; generating an upper border for PV, which is validated with the positive correlation, a lower horizontal border with CC and concave lower borders for the EQ and HH indicators.
Wind (20 GW) and geothermal (0 GW) are almost constant throughout the scenarios, except for only three outliers can be identified, installing 16 GW (-4 GW) of wind, which is compensated by 0.8 GW of geothermal power. This low variation also explains the low correlation validity ρ between those two technologies and the other indicators.

4. Conclusion

This work generated an LCIA database of technologies within a global energy system by characterizing over 200 technologies. This database allowed us to assess the impact of the energy system on environmental indicators by integrating their impact directly into the optimization rather than post-calculating it. The integration was achieved by splitting the LCIA impact into direct (operation) and indirect (construction) emissions related to the installation and use of the technologies within the global energy system MILP model EnergyScope.

The results have been generated by applying the framework to the case study of a CO_2 neutral and energy-independent Swiss energy system 2050. The individual optimizations show different configurations, where the economic and environmental burden is shifted to the other indicators depending on the objective. Independent of the scenario, the deployment of high shares of renewable energy in the form of PV, wind, hydropower, and biomass gasification is observed. The scenarios are distinguishing, in the end, uses sector, where different mobility types for long-distance public and freight mobility are selected: While cost-optimization prefers to reinforce the electric distribution grid, environmental aspects limit the reinforcement to a maximization of the use of existing infrastructure, leading to the gasification of the mobility sector.

The correlations between the main renewable technologies and the OFs are strongly dominated by economic optimization, drawing Pareto-fronts. The quantity of PV installed depends on the weight put on the environmental indicators, where the economic optimum is located at 16 GW. In contrast, more substantial weights on the LCA indicators lead to more deployed PV and higher costs. Wind and Geothermal energy stay constant, with some outlier exceptions ($< 0.6\%$), which needs further investigation with more runs. While low correla-

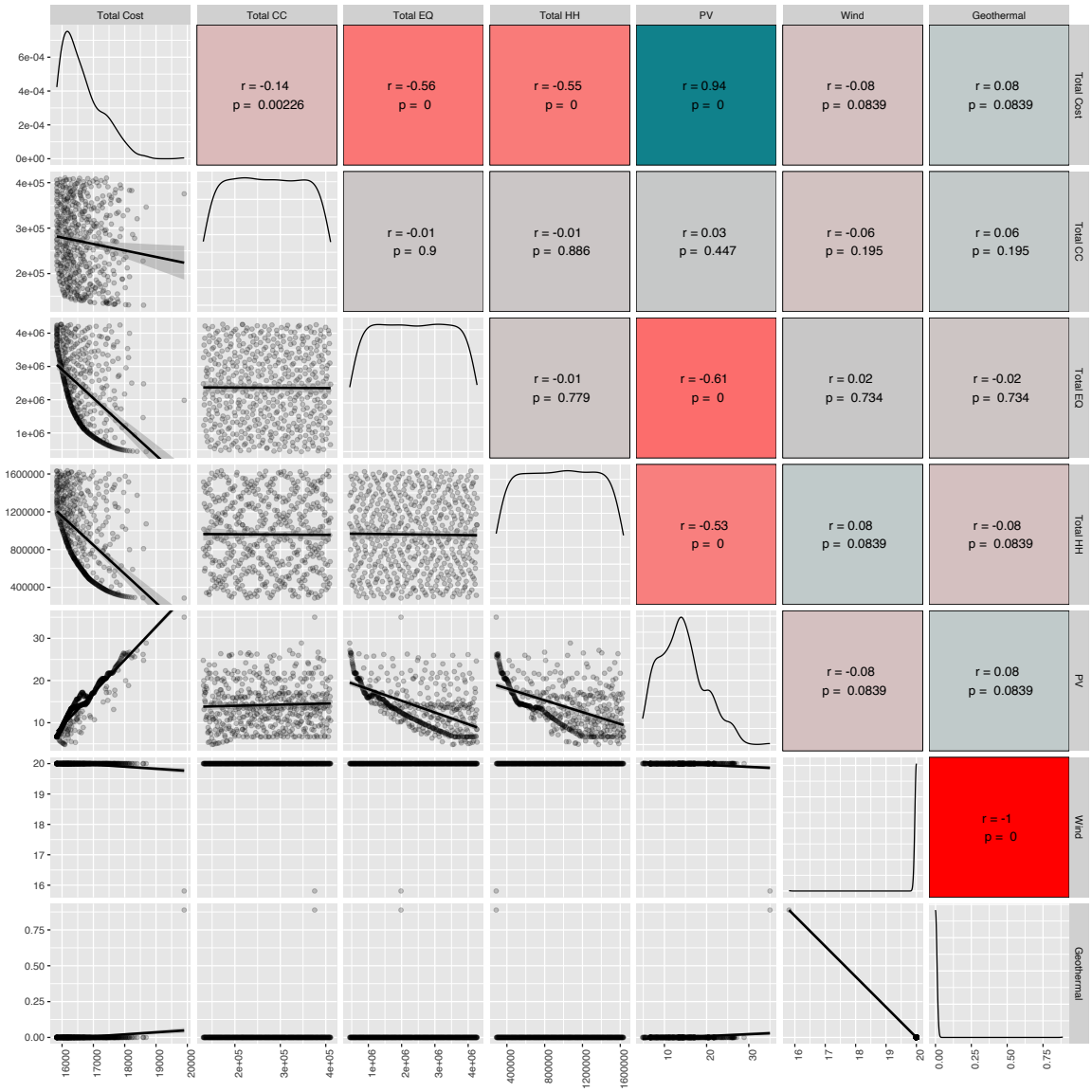

Figure 5: Pearson correlation coefficient matrix. The upper triangle depicts the correlation factor *r* with the color gradient and the significance *p* with the transparency. The diagonal depicts the distribution of the appearance of the individual variables. The lower triangle represents the observation distribution with the corresponding trend line and confidence interval.

tions between the LCA indicators are observed, the negative correlation between environmental impact and additional costs could be assessed, except for the climate change indicator, which is intrinsically integrated into the case study for carbon neutrality, where the carbon emissions are highly affecting the CC indicator.

While already general conclusions on the effect of economic and environmental indicators through the deployment of renewable technologies have been drawn, further work needs to be done in (i) separating the effect of double-counting in impact analysis by assessing the impact of midpoints, including resource depletion, endpoints and areas of protection, (ii) validating the multi-objective approach on economic optimization under parametrized environmental variables to generate the LCA-indicators Pareto-fronts, (iii) identifying the most-optimal solutions by applying multi-criteria decision methods, (iv) dig deeper in correlations between all technologies and the different indicators, and (v) identify typical energy system configurations by applying suitable clustering methods.
Further improving the methodology is necessary to (vi) remove the double-counting of energy system internal flows throughout scopes II and III. While, for example, electricity has been removed from the operational phase of using a heat pump, the construction phase still uses electricity based on the current energy system. The identification of those flows will allow the definition of a prospective LCA database coupled with the energy system.

Based on this paper's database and modeling framework, points (i)-(v) are subject to a future publication in preparation. Point (vi) is subject to a research project over several years in collaboration with CIRAIG.

Acknowledgments

The authors acknowledge the financial support from Innosuisse – Swiss Innovation Agency, for the innovation project "FLAGSHIP PFFS-21-03" within the scope of the flagship initiative.

References

[1] Climate Action Tracker, 2021.

[2] J. B. Guinée, R. Heijungs, G. Huppes, A. Zamagni, P. Masoni, R. Buonamici, T. Ekvall, and T. Rydberg, "Life Cycle Assessment: Past, Present, and Future," *Environmental Science & Technology*, vol. 45, pp. 90–96, Jan. 2011.

[3] A. Laurent, N. Espinosa, and M. Z. Hauschild, "LCA of Energy Systems," in *Life Cycle Assessment: Theory and Practice* (M. Z. Hauschild, R. K. Rosenbaum, and S. I. Olsen, eds.), pp. 633–668, Springer International Publishing, 2018.

[4] A. Petrillo, F. De Felice, E. Jannelli, C. Autorino, M. Minutillo, and A. L. Lavadera, "Life cycle assessment (LCA) and life cycle cost (LCC) analysis model for a stand-alone hybrid renewable energy system," *Renewable Energy*, vol. 95, pp. 337–355, 2016.

[5] A. Valente, D. Iribarren, and J. Dufour, "Life cycle assessment of hydrogen energy systems: A review of methodological choices," *The International Journal of Life Cycle Assessment*, vol. 22, no. 3, pp. 346–363, 2017.

[6] C. Pieragostini, M. C. Mussati, and P. Aguirre, "On process optimization considering LCA methodology," *Journal of Environmental Management*, vol. 96, no. 1, pp. 43–54, 2012.

[7] R. Wang, X. Wen, X. Wang, Y. Fu, and Y. Zhang, "Low carbon optimal operation of integrated energy system based on carbon capture technology, LCA carbon emissions and ladder-type carbon trading," *Applied Energy*, vol. 311, p. 118664, 2022.

[8] M. J. Mayer, A. Szilágyi, and G. Gróf, "Environmental and economic multi-objective optimization of a household level hybrid renewable energy system by genetic algorithm," *Applied Energy*, vol. 269, p. 115058, 2020.

[9] D. Tonini and T. Astrup, "LCA of biomass-based energy systems: A case study for Denmark," *Applied Energy*, vol. 99, pp. 234–246, 2012.

[10] S. Rauner and M. Budzinski, "Holistic energy system modeling combining multi-objective optimization and life cycle assessment," *Environmental Research Letters*, vol. 12, no. 12, p. 124005, 2017.

[11] S. Moret, *Strategic energy planning under uncertainty*. PhD thesis, EPFL, 2017.

[12] X. Li, T. Damartzis, Z. Stadler, S. Moret, B. Meier, M. Friedl, and F. Maréchal, "Decarbonization in Complex Energy Systems: A Study on the Feasibility of Carbon Neutrality for Switzerland in 2050," *Frontiers in Energy Research*, vol. 8, p. 549615, Nov. 2020.

[13] J. Schnidrig, X. Li, and François Maréchal, "Assessment of the role of infrastructure in high share renewable energy systems," in *Proceedings of ECOS 2022*, (Copenhagen, Denmark), p. 11, Jan. 2022.

[14] J. Brun, J. Schnidrig, M. Margni, and F. Maréchal, "Reducing Greenhouse Gas emissions is not the only solution," Master Thesis 1, IPESE, EPFL, Sion, Aug. 2022.

[15] International Organization for Standardization (ISO), "ISO 14040 : Environmental management— Life cycle assessment — Principles and framework," 2006.

[16] G. Wernet *et al.*, "The ecoinvent database version 3 (part I): overview and methodology," *The International Journal of Life Cycle Assessment*, vol. 21, pp. 1218–1230, Sept. 2016.

[17] C. Bulle, M. Margni, L. Patouillard, A.-M. Boulay, G. Bourgault, V. De Bruille, V. Cao, M. Hauschild, A. Henderson, S. Humbert, S. Kashef-Haghighi, A. Kounina, A. Laurent, A. Levasseur, G. Liard, R. K. Rosenbaum, P.-O. Roy, S. Shaked, P. Fantke, and O. Jolliet, "IMPACT World+: a globally regionalized life cycle impact assessment method," *The International Journal of Life Cycle Assessment*, vol. 24, pp. 1653–1674, Sept. 2019.

[18] G. Majeau-Bettez, “Ecospold2Matrix,” June 2022. original-date: 2014-11-12T18:15:21Z.

[19] J. Schnidrig, T.-V. Nguyen, X. Li, and F. Maréchal, “A modelling framework for assessing the impact of green mobility technologies on energy systems,” in *Proceedings of ECOS 2021*, (Taormina, ITALY), p. 13, ECOS 2021 Local Organizing Committee, 2021.

[20] G. Limpens, S. Moret, H. Jeanmart, and F. Maréchal, “EnergyScope TD: A novel open-source model for regional energy systems,” *Applied Energy*, vol. 255, p. 113729, Dec. 2019.

[21] N. Metropolis and S. Ulam, “The Monte Carlo Method,” *Journal of the American Statistical Association*, vol. 44, no. 247, pp. 335–341, 1949. Publisher: [American Statistical Association, Taylor & Francis, Ltd.].

[22] A. Kemmler, A. Kirchner, and S. Kreidelmeyer, “Energieperspektiven 2050+, technischer bericht,” gesamtdokumentation der arbeiten, BFE, 2021.

[23] G. Leuchthaler-Felber, “Schweizerische gesamtenergiestatistik 2019,” Tech. Rep. 2020/19, BFE, 2020.

Glossary

AoP	Area of Protection
CC	Climate change
EP50+	Energieperspektiven 2050+ [22]
EQ	Ecosystem quality
ES	EnergyScope
GHG	Greenhouse gas emissions
GWP	Global Warming Potential
HH	Human Health
IRENA	International Renewable Energy Agency
LCA	Life cycle analysis
LCI	Life cycle inventory
LCIA	Life cycle impact assessment
MILP	Mixed Integer Linear Programming
MOO	MOO
NDC	Nationally Determined Contributions
OF	OF
PV	Photovoltaic
WAVH	Water availability impact on human health

Thermoeconomic Modeling as a Tool for Internalizing Carbon Credits into Thermal System Analysis

I.C. Belisario[a], P.R. Faria[b,c], R.G. Santos[a,b], M.A. Barone[b] and J.J. Santos[b]

[a] Federal Institute of Espírito Santo (IFES), Vitória, Brazil, igor.belisario@ifes.edu.br, ***CA***
[b] Federal University of Espírito Santo (UFES), Vitória, Brazil, rodrigo.guedes@ifes.edu.br, mabacz@gmail.com, jose.j.santos@ufes.br
[c] Federal Institute of Espírito Santo (IFES), Cariacica, Brazil, pedro.faria@ifes.edu.br

Abstract:

According to the Intergovernmental Panel on Climate Change (IPCC), greenhouse gas emissions (GHG) have increased since 1990. Electricity and heat generation, along with transportation, accounted for more than two-thirds of emissions in 2018. As CO_2 represents the largest percentage of GHG, the term carbon has come to be adopted as a synonym for these gases in climate debates. In order to control emissions, the carbon market helps industries/sectors that are not able to meet the emission reduction goals to buy credit from the ones that have reduced their levels below the required. Thermoeconomics plays a fundamental role in the analysis of thermal systems. Therefore, this study aims to detail how thermoeconomic modeling can be used to include expenses or revenues related to the carbon market through an example in a gas turbine cogeneration system. In addition, it highlights that this modeling can be used in the internalization of other expenses such as environmental control devices, licenses, and permits. Results show that the environmental device is capable of internalizing carbon credits and systematically distributing them to the cost of final products.

Keywords:

Thermoeconomic modeling; Carbon credit; Carbon market; Environmental cost.

1. Introduction

According to the Intergovernmental Panel on Climate Change (IPCC) [1], greenhouse gas emissions (GHG) have increased since 1990. The combination of electricity and heat generation (cogeneration), along with transportation, accounted for more than two-thirds of emissions in 2018 [2]. As CO_2 represents the largest percentage of GHG, which can cause global warming, the term carbon has come to be adopted as a synonym for these gases in climate debates.

In order to control emissions, the carbon market provides industries/sectors that are not able to meet the emission reduction goals the possibility to buy credit from the ones that have reduced their levels below the required. One carbon credit corresponds, by convention, to one ton of carbon dioxide. Therefore, it can be considered an asset (financially and environmentally), representing the reduction or removal of one ton of CO_2 equivalent, which has been recognized and issued as a credit in the carbon market, regardless of whether it is voluntary or regulated [3].

This market is already regulated in some countries, such as in the European Union, which has well-defined credit values [4]. Nonetheless, in many others, such as Brazil, this market is still voluntary. Recently, the Brazilian government issued a decree [3] to regulate this market and institute the National System of Greenhouse Gas Emissions Reduction (SINARE); however, there are still no deadlines for implementation. According to the World Bank's 2022 report [5] and IPCC 2023 [6], the carbon market (associated with environmental preservation measures) is expanding worldwide, but still below the necessary levels to mitigate environmental problems and meet the environmental agenda signed in the Paris Agreement against the threats of climate change.

Thermoeconomics combines thermodynamic and economic concepts to provide pieces of information that are unavailable in conventional energetic and economic analyses. The information provided is fundamental in the design and operation of thermal systems [7]. The original objective of thermoeconomics was to mathematically combine the Second Law of Thermodynamics with economics. However, these analyses must also incorporate environmental issues [8]. In thermoeconomics, exergy is the most appropriate thermodynamic magnitude to use, because it takes into account aspects of the Second Law of Thermodynamics considering the quality of energy, locating and quantifying the irreversibilities of the

process [7]. The exergy is also the most appropriate connection between the Second Law and the environmental impact because it measures a system's state deviation in relation to the environment [9].

Multiproduct thermal system analyses such as cogeneration, in which two products (useful heat and power) are generated collectively from a single combustible, require rational criteria for distributing the cost of the combustible to the various final products. In these circumstances, thermoeconomics allows rational allocation (through physical criteria) of monetary, exergetic, and environmental costs for the final products. Therefore, it is possible to compare exergetic/monetary [10–14] and/or environmental [15–18] costs of each product with the production cost of each one in separate systems.

Thermoeconomic methodologies have already been used to include environmental aspects, such as specific CO_2 emissions. However, they were not used in the internalization of monetary costs associated with environmental issues, such as carbon credits. Therefore, the novel concept introduced in this study is to exemplify how to perform this internalization thermoeconomically.

Furthermore, it is observed that thermoeconomics has a fundamental role in energy conversion systems analyses. The main goal of this study is to detail how thermoeconomic modeling can be used as a tool to include the expenses or revenues relative to the carbon market in thermal systems analyses and allocate them to internal and final products of the system. The conventional modeling used to calculate the monetary costs of internal flows and final products can be adapted to address these environmental costs. This adaptation is detailed in matrix notation, through a case study of a gas turbine cogeneration system. It also shows how this inclusion can influence the monetary costs of the system's final products. In addition, it highlights that this modeling can also be used to internalize other costs such as environmental control devices, environmental licenses, and permits.

It is important to emphasize that the methodology used herein to exemplify and detail this internalization of environmental costs, which is the case of carbon credits, defines a device to represent the environment in the thermoeconomic diagrams and thus allocates environmental costs exactly on the environmental device. This study uses the H&S Model as the method; however, any other exergy-based thermoeconomic methodology that defines this device in a consistent way to represent the environment can be used to conduct the analysis in a similar way.

2. Thermoeconomic modeling

In addition to the conventional modeling used to determine the monetary and exergetic unit costs of the system's internal flows and final products, this section shows how the modeling is generally adapted to allocate specific pollutant emissions and further details how carbon credits can be included in thermoeconomic modeling.

2.1. Conventional Modeling

Equations (1) and (2) are used to determine the monetary (c) and exergetic (k^*) unit costs, respectively, of the internal flows and the systems' final products. The allocation of specific (λ) pollutant emissions, such as CO_2, NOx, and SOx can be performed through Eq. (3). In these equations, the subscripts "*out*" and "*in*" are associated with the outputs and inputs of flows, respectively. Y represents the generic thermodynamic magnitude which can be evaluated by power, heat, exergy flows, or its components. E_F is the exergy of the external combustible. c_F and k_F^* represent its monetary and exergetic unit cost, respectively. λ_F is the amount of emission generated due to the combustion of one unit of exergy from the external fuel. Z, conventionally, is the external hourly cost of the subsystem due to capital and equipment operation and maintenance.

$$\sum(c_{out}.Y_{out}) - \sum(c_{in}.Y_{in}) = Z + c_F.E_F \quad (1)$$

$$\sum(k^*_{out}.Y_{out}) - \sum(k^*_{in}.Y_{in}) = k^*_F.E_F \quad (2)$$

$$\sum(\lambda_{out}.Y_{out}) - \sum(\lambda_{in}.Y_{in}) = \lambda_F.E_F \quad (3)$$

Equation (2) is obtained through Eq. (1). In this case, the Z term should be zero and the exergy unit cost of the external fuel (k_F^*) is generally considered to be equal to its exergy; therefore, the exergy unit cost is equal to 1 kW/kW [7].

The monetary and exergetic unit costs can be interpreted as an economic and thermodynamic efficiency measure of a flow production process, respectively [7]. On the other hand, the balance represented by Eq. (3) can be interpreted as an environmental efficiency measure production process of this flow [16].

In all cases, Eqs. (1) - (3), auxiliary equations are generally necessary to complete the modeling equations system. These equations are defined according to the applied thermoeconomic diagram. In the case of productive diagrams, the equality criterion [19] is used. Following this criterion, all products of a subsystem have the same unit cost because they were generated in the same productive process under the same irreversibilities.

2.2. Inclusion of monetary costs of environmental charges

Equation (3) is used to allocate specific emissions to the internal flows and the thermal systems' final products, and, therefore, it is an analysis that considers environmental aspects in thermoeconomic modeling. However, it does not take into account monetary costs associated with environmental issues, such as carbon credits and environmental treatment/control equipment.

The Z term (Equation 1) is a key point in the allocation of environmental costs. In a conventional monetary cost evaluation, it represents the subsystem's external hourly rate due to the capital, operation, and maintenance. Nevertheless, it can also be used for the allocation of environmental costs through a device that represents the environment in the thermoeconomic diagrams. An energy conversion system can be defined as a set of components that interact with each other and with the environment through a set of flows of matter, work, or heat [20]; therefore, the environment is part of the system. Thus, it can be represented by an environmental device in thermoeconomic diagrams according to some models.

Equation (4) shows how a conventional thermoeconomic model of monetary unit cost (Equation 1) can be adapted to decompose the term (Z) in hourly costs due to environmental charges (Z_{env}) and capital, operation, and maintenance costs (O&M).

$$Z = Z_{cap} + Z_{O\&M} + \boldsymbol{Z_{env}} \tag{4}$$

The environmental device has no acquisition cost, but it is through it that environmental charges can be internalized and redistributed to the other equipment and the final products. For instance, when installing waste control devices in a plant, such as an electrostatic precipitator for ash disposal in flue gas or a bag filter for air pollution control, one can attribute the costs associated with its capital and O&M to the environmental device or any other equipment, that has the function of mitigating environmental impacts by decreasing the amount of GHGs emitted into the atmosphere.

The same can be done for devices used in the capture and storage of carbon, environmental permits, licensing costs, fines for emitting pollutants, and any other abatement cost (cost of resources employed in the treatment or proper waste disposal). Thus, allocating the environmental charges exactly on the device in the diagram defined to represent the environment. Since the term Z is always associated with some equipment, an adequate option is to associate environmental cost with the device that represents the environment in the diagrams.

2.2.1. Inclusion of carbon credits

In addition to the monetary costs mentioned in the previous section, this paper suggests that through the environmental device, it is also possible to take into account the pricing of carbon and internalize the expenses or revenues generated by carbon credits. In this case, the Z_{env} term can be positive or negative. Negative in case of a revenue generated due to the reduction or removal of emissions (which can generate a credit to be sold) and positive in case of an additional cost of buying carbon credits by a plant that failed to meet the emission reduction targets and had to buy credits from those that reduced theirs below the stipulated levels. The full detail of the thermoeconomic modeling taking this carbon market into account is presented in section 3.

3. Case study – gas turbine cogeneration system

The thermal system chosen to exemplify how thermoeconomic modeling can be used as a tool for internalizing carbon credits is a cogeneration system with a simple gas turbine as shown in Fig. 1. This system is composed by an air compressor (AC), combustion chamber (CC), gas turbine (GT), and recovery boiler (RB). Part of the power generated by the turbine is used to drive the compressor (W_{AC}). Two final products, net power (W_N) and useful heat (Q_U), are generated from a fuel (Q_F).

The parameters of the main flows of the physical structure (obtained with the Engineering Equation Solver - EES software [21]) can be found in Table 1. Table 2 indicates the quantities of the main productive flows. The reference conditions are defined by $T_0 = 25$ °C and $P_0 = 1.0132$ bar, and under these conditions the CO_2 mass flow from the exhaust gases is $\dot{m}_{CO_2} = 2228$ kg/h considering natural gas as fuel. More information of this system is available in [22]. The monetary unit cost of fuel (natural gas) is 24.04 $/MWh, according to the average value for the year 2022 in the international market [23].

Table 3 shows the external monetary flows due to the equipment of the cycle. These values were obtained from [22] and updated through the Chemical Engineering Cost Index (CEPCI) until the year 2022 [24]. The cost of the carbon credit used was 85 $/ton, which represents the average for the year 2022, according to [4].

The thermoeconomic modeling can be performed through different types of diagrams: physical, productive, and comprehensive. Since modeling with the physical diagram is not enough to identify the waste cost formation process [22], most methodologies use the productive diagram.

The description of the cost formation process of thermal systems based on productive flows is an original feature of the functional methodologies: Thermoeconomic Functional Analysis (TFA) [19] and Engineering Functional Analysis (EFA) [8]. However, other thermoeconomic methodologies, such as the H&S Model [22] used in this paper, have also adopted this feature.

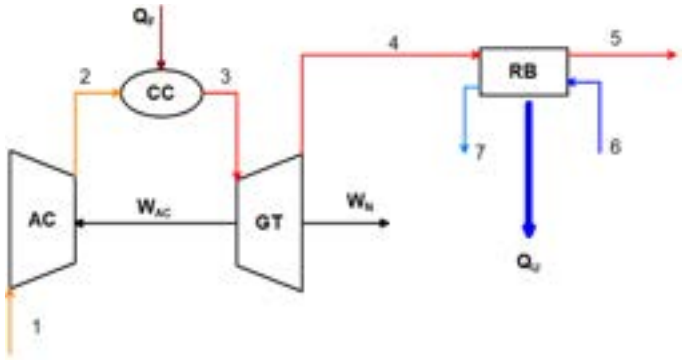

Figure 1. The physical structure: cogeneration system.

Table 1. Main physical flow parameters of the system.

Physical flow		ṁ [kg/s]	T [°C]	P [bar]
n. º	Description			
1	Air	14.72	25.00	1.0132
2	Air	14.72	230.20	5.1040
3	Gases	14.94	850.00	4.8480
4	Gases	14.94	537.30	1.0207
5	Gases	14.94	151.10	1.0132
6	Water	2.487	60.00	20.400
7	Steam	2.487	212.4	20.000

Table 2. Quantities of some productive flows (exergetic basis).

Equipment	Flow	Quantity [kW]
Air compressor (AC)	W_{AC}	3113.03
Combustion chamber (CC)	Q_F	11630.96
Gas turbine (GT)	W_{GT}	5546.50
	W_N	2433.47
Recovery boiler (RB)	Q_U	2246.32

Table 3. Equipment external monetary cost.

Equipment	Z [$/h]
Air compressor (AC)	25.33
Combustion chamber (CC)	9.04
Gas turbine (GT)	34.37
Recovery boiler (RB)	21.71

3.1. Thermoeconomic models

Thermoeconomic modeling can be carried out with the well-known E Model that uses total exergy flows to define the physical and/or productive flows of the diagrams. However, in some cases, it becomes necessary to disaggregate the exergy into components, such as to isolate dissipative equipment and carry out an adequate allocation of the waste cost in thermal systems. One such exergy disaggregation model is the H&S Model [22] which describes the behavior of thermodynamic cycles in the h-s plane considering the enthalpy

and entropy variation of the working fluid, as suggested by [25]. This is a model for disaggregating the physical exergy into its enthalpic(E^H) and entropic (E^S) parts, according to Eq. (5). The total exergy (E^{TOTAL}) can be defined by Eq. (6) as the sum of the physical (E^{PH}) and chemical (E^{CH}) components, disregarding nuclear, magnetic, electrical, surface tension, kinetic and potential effects [26].

$$E^{PH} = E^H - E^S \tag{5}$$

$$E^{TOTAL} = E^H - E^S + E^{CH} \tag{6}$$

The H&S Model defines the environmental device (ENV) in the productive diagram that interacts with the other plant subsystems. In this methodology, this device plays a fundamental role in the analysis of thermal systems, especially in the treatment of waste and the internalization of environmental costs. Both the physical (represented by $E^H_{5:1}$) and chemical ($E^{CH}_{3:2}$) components of the waste are dissipated in (ENV), see Fig. 4, and this is where the system receives air from the compressor inlet. The chemical component is generated in the CC due to the combustion reaction in which the air and fuel mixture is transformed into combustion gases. The E Model does not define a device to represent the environment in the diagram.

In addition, the environmental device (used in the H&S Model) is also responsible for closing the cycle (Figure 2); thus, redistributing the waste costs to the other plant components and consequently to the final products.

Figure 2 represents the cogeneration cycle in the h-s diagram and the numbering in this diagram represents the processes performed by the following components:

- 1-2: compressor (1-2s would be isentropic compression);
- 2-3: combustion chamber;
- 3-4: gas turbine (3-4s: isentropic expansion)
- 4-5: recovery boiler.

At the exit of the recovery boiler (point 5), the exhaust gases have exergy (therefore, they are waste). Although this equipment (RB) slightly reduces the entropy of the working fluid, the cycle is not fully closed. In the case of a Rankine cycle, for example, the condenser completely closes the cycle by reducing the entropy of the turbine's output steam to that of the saturated liquid at the pump entrance.

The device representing the environment in the diagram (ENV) performs process 5-1 and completely closes the loop. In this device, flow 5 represents the exhaust gases and flow 1 is the air drawn in by the compressor.

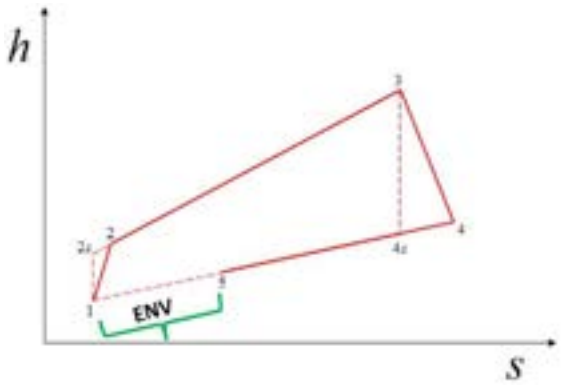

Figure 2. The environment device in open cycles.

3.1.1. Productive diagram

Figures 3 and 4 represent productive diagrams of the gas turbine cogeneration system according to E and H&S Models. In E Model, the flows represent exergy variations between two physical states (*i* and *j*) according to Eq. (7). In the H&S Model, the productive flows represent variations of the enthalpic, entropic and chemical components of the exergy between *i* and *j* according to Eqs. (8) - (10), respectively.

$$E_{i:j} = E_i - E_j \tag{7}$$

$$E^H_{i:j} = E^H_i - E^H_j \tag{8}$$

$$E^S_{i:j} = E^S_i - E^S_j \tag{9}$$

$$E^{CH}_{i:j} = E^{CH}_i - E^{CH}_j \tag{10}$$

In Figs 3 and 4 the system components are represented by rectangles that are real units (or subsystems); the rhombuses and circles are fictitious units called junctions (J) and bifurcations (B), respectively, which are used to interconnect the subsystems.

The fuel and product definitions follow the SPECO approach [27] as follows: if the variation of specific exergy (or of its components with a positive contribution to the exergy definition) is positive throughout the process, this variation plus the exergy of flows of energy generated in the component define the product. On the other hand, if the variation of the specific exergy (or of its components with a positive contribution to the exergy) is negative throughout the process, this variation is added to the exergy of the energy flows supplied to the component in the input definition. The opposite happens with the components with a negative contribution in the exergy definition, such as the entropic component in the H&S Model. In this case, the H&S Model defines the productive flows of the entropic ($E^{H}_{5:1}$) and chemical ($E^{CH}_{3:2}$) components as input from the environment, and the entropic ($E^{S}_{5:1}$) component as a product, see Fig. 4.

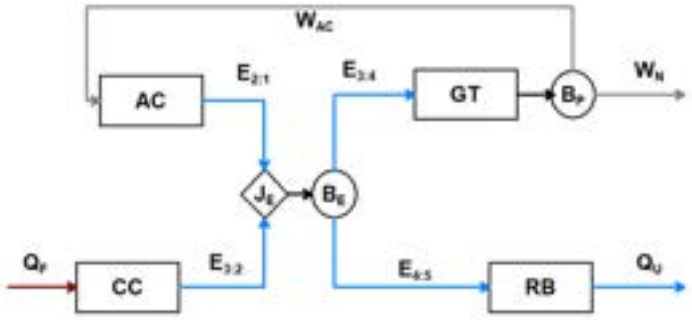

Figure 3. Productive diagram - E Model.

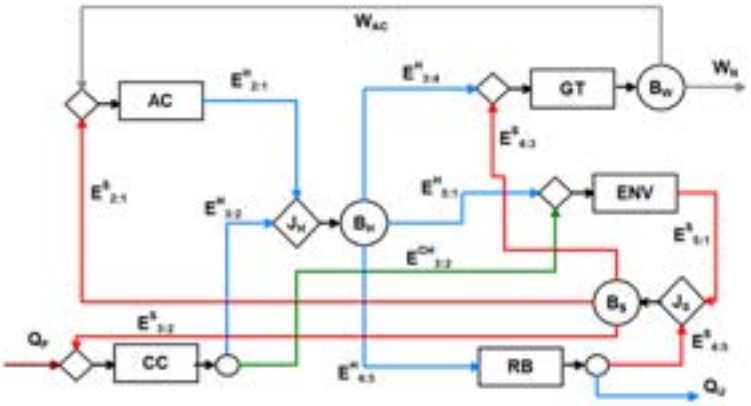

Figure 4. Productive diagram - H&S Model.

3.1.2. Monetary cost balance

Figure 5 shows the monetary cost balance for the H&S Model, expanded in matrix form, which is obtained by applying the cost balance from Eq. (1) to each of the 5 subsystems (AC, CC, GT, RB, and ENV) and at enthalpic (J_H-B_H) and entropic (J_S-B_S) junctions-bifurcations of the productive diagram (Figure 4).

$$\begin{bmatrix} E^{H}_{2:1} & 0 & -W_{AC} & 0 & 0 & 0 & -E^{S}_{2:1} \\ 0 & E^{N}_{3:2}+E^{CH}_{3:2} & 0 & 0 & 0 & 0 & -E^{S}_{3:2} \\ 0 & 0 & W_{AC}+W_{N} & 0 & 0 & -E^{N}_{3:4} & -E^{S}_{4:3} \\ 0 & 0 & 0 & E^{S}_{4:5}+Q_{U} & 0 & -E^{N}_{4:5} & 0 \\ 0 & -E^{CH}_{3:2} & 0 & 0 & E^{S}_{5:1} & -E^{N}_{5:1} & 0 \\ -E^{H}_{2:1} & -E^{H}_{3:2} & 0 & 0 & 0 & E^{H}_{3:4}+E^{H}_{4:5}+E^{H}_{5:1} & 0 \\ 0 & 0 & 0 & -E^{S}_{4:5} & -E^{S}_{5:1} & 0 & E^{S}_{2:1}+E^{S}_{3:2}+E^{S}_{4:3} \end{bmatrix} \cdot \begin{bmatrix} c_{AC} \\ c_{CC} \\ c_{GT} \\ c_{RB} \\ c_{ENV} \\ c_{JB-H} \\ c_{JB-S} \end{bmatrix} = \begin{bmatrix} Z_{AC} \\ c_{F}.Q_{F}+Z_{CC} \\ Z_{GT} \\ Z_{RB} \\ Z_{ENV} \\ 0 \\ 0 \end{bmatrix}$$

Internal valuation | Cost | External valuation

Figure 5. Monetary cost balance in matrix form.

It is visible that the internal valuation matrix is composed of flows of the exergy components, power, and useful heat. It represents the process from the distribution of external resources to the formation of the final

products' cost. The cost matrix (or vector) is the modeling's unknown factor and is composed of the monetary unit cost of the flows generated in each of the subsystems. For instance, c_{AC} is the monetary unit cost of the compressor (AC) product, i.e., the flow $E^{H}_{2:1}$.

Due to the use of the equality criterion, some flows have the same unit cost. Examples are: $E^{H}_{3:2}$ and $E^{CH}_{3:2}$; $E^{S}_{4:5}$ and Q_U; W_{AC} and W_N. In addition to those, all entropic component flows which leave J_H-B_H have the same unit cost as all entropic component flows leaving J_S-B_S.

The external valuation matrix contains the exergy of the fuel and its respective unit cost, plus the external hourly cost of each subsystem due to capital, and equipment O&M (Z). Because they are dummy components, the junction-bifurcations have zero Z-cost, as shown in the external valuation matrix in Fig 5.

The Z term, along with the device representing the environment in the diagrams, are key pieces in internalizing environmental costs in thermoeconomics. Figure 6 details this device and its input and output flows that are part of the monetary cost balance. The environmental device itself has no costs for acquisition, operation, and maintenance because it is a representation of the atmospheric environment itself. Nevertheless, in the case of the installation of some environmental treatment component (filter, electrostatic precipitator, among others) that generally is not represented in the physical diagram of the thermal system, the cost of this component can be internalized in the environmental device through the first two terms on the right-hand side of Eq. (4), and thus be redistributed to the entire system.

As for the cost of fines, environmental licenses, and permits, they should be internalized by Z_{env}, as well as the carbon pricing values. Nevertheless, the latter depends on whether it is revenue or expense in the carbon market.

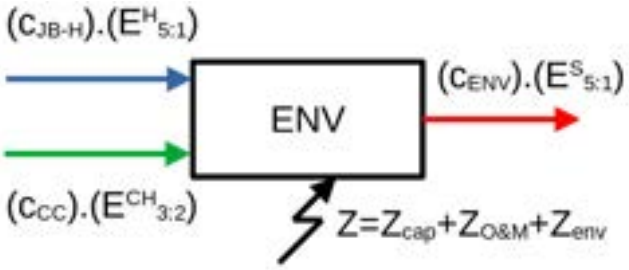

Figure 6. Cost balance in the environmental device.

In the case of revenue, which can occur due to a reduction in emissions below the stipulated which generates a saleable credit, the term Z_{env} enters negative on the balance sheet. Since the environmental device closes the loop and redistributes the costs to the other equipment and final products in the plant, this credit reduces the other monetary costs and can influence the plant's production decisions.

On the other hand, an expense related to carbon credits, such as the need to buy credits since the company was not able to reduce emissions as stipulated, makes the term Z_{env} positive and similarly ends up increasing the costs of other internal flows and final products of the plant.

In summary, the equation shown in Fig. 6 is highlighted in the text as Eq. (11) and its analysis can be done as follows:

- The environmental device (ENV) has no hourly cost due to capital and O&M, but in the case of using environmental treatment equipment (which is generally not represented in the physical structure of the system), these terms can be considered within Z_{ENV};
- The environmental costs of licenses and permits are internalized through the environmental device term Z_{env};
- The costs associated with the carbon market are also internalized through the term Z_{env}. In the case of revenue, this term is negative and in the case of expenditure, it is positive.

In all three cases, as device ENV closes the loop (Figure 2), the costs are systematically redistributed to the other subsystems and consequently to the final products of the plant in the case of the H&S Model (Figure 4).

$$Z_{ENV} = Z_{cap} + Z_{O\&M} + Z_{env} \tag{11}$$

3.1.3. Results

Figure 7 represents a generic cogeneration (combined heat and power – CHP) system in which out of one fuel (Q_F), two products (W_N and Q_U) are generated, as is the case with the gas turbine system in Fig. 1. By applying the cost balance of Eq. (1) to this generic system, one obtains Eq. (12), in which c_{W_N} and c_{Q_U} are the monetary unit costs of the final products. Note that Eq. (12) is the equation of a straight line of the type $y = A.x + B$, and can be written according to Eq. (13).

$$c_{W_N} = -\frac{Q_U}{W_N} c_{Q_U} + \frac{c_F . Q_F + Z}{W_N} \quad (12)$$

$$c_{W_N} = -A . c_{Q_U} + B \quad (13)$$

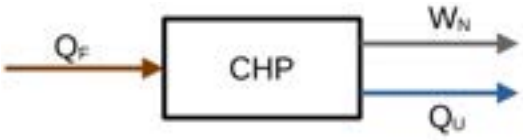

Figure 7. Accounting flows in cogeneration.

Regardless of the applied thermoeconomic methodology, the solution to Eq. (12) will be an ordered pair of the monetary unit cost of the net power (c_{W_N}) and of the useful heat (c_{Q_U}). Some studies [13,28–30] have already compared several methodologies in problems of this type and confirmed that these ordered pairs belong to the same straight solution when the system has its operational conditions defined, such as the net power/useful heat ratio and the global exergetic efficiency.

Figure 8 represents possibilities for this straight solution generically. In all the possibilities, the higher the unit cost of power, the lower the unit cost of heat, and vice versa.

Considering the central straight line (solid blue line) as the specific condition for a cogeneration system, changes in the thermodynamic model move the straight line to new positions parallel to the initial one [28,31], as shown by the dashed lines in Fig. 8.

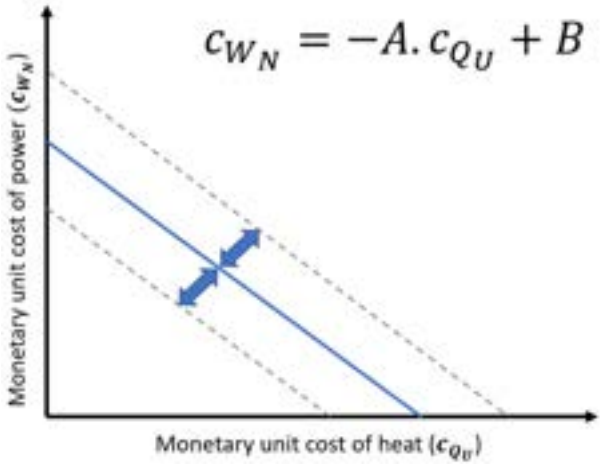

Figure 8. Unit cost solution line.

Figure 9 shows the monetary unit cost of the final products (ordered pair) of the cogeneration system for some situations. The values were obtained through the cost balance of Eq. 1 when applied to the diagrams of Figs 3 and 4 for E and H&S Models, respectively. For this second model, the balance is detailed (matrix form) in Fig. 5 to highlight the Z_{ENV}.

The points that belong to the central line, identified as the base case in the caption of Fig. 9, represent the case in which no carbon credit values are being internalized.

Note that the increase in emissions represents a reduction in the efficiency of the process and a consequent increase in production costs. Thus, the straight solution moves away from the origin and the costs of the final products increase. On the other hand, the reduction of emissions approximates the solution line to the origin, reducing the costs of the final products as a result of an improvement in the process's efficiency.

In order to analyze the expenses and revenues of the carbon market, some hypotheses were considered and realized. Starting from the base case, and considering that the increase in CO_2 emissions means that the system is emitting above the established, carbon credits must be purchased and thus an expense is generated for the plant. In the case of reduction/removal of emissions, the system generates a credit that could be sold and thus generate revenue. In the case of the H&S Model, the value of carbon credits is internalized in the environment device with ($Z_{env} > 0$) in the case of expenses and ($Z_{env} < 0$) for revenue. In E Model, internalization is done via CC with ($Z_{carbon\ credit} > 0$) in the case of expenses and ($Z_{carbon\ credit} < 0$) for revenue.

Hypotheses of increase (10% to 50%) and reduction (-10% to -50%) of emissions in relation to the base case were simulated. Table 4 shows the monetary unit costs of the final products ($k^*_{Q_U}$ and $k^*_{W_N}$) for all these

situations, in addition to the amount of carbon credits that these variations in emissions could generate and the costs (revenue and expense) associated.

When analyzing (c_{Q_U}) and (c_{W_N}), it is verified that in E Model the costs of the final products vary approximately 5% and 25% for the cases of increase/reduction of 10% and 50% in the emissions compared to the base case. In the case of the H&S Model, for these same situations, the variations in the costs of the final products are approximately 5% and 26%. The variations in the costs obtained are due to the different criteria of each model, such as the internalization of carbon credits in the CC and the environmental device.

When analyzing the carbon credits for the simulated situations, it is observed that a 10% variation in emissions generates 5.3 credits/day which corresponds to an expense/revenue of $455/day. In the most extreme case of variation (50%) in emissions, expenditure/revenue can reach $2276/day. The use of value generated by the purchase or sale of the carbon credit can be used as an indicator for the decision-making of companies concerning the installation of environmental equipment or the purchase of carbon credits.

Remembering that this work aims to demonstrate the thermoeconomic methodology to be used for the inclusion of carbon pricing in cogeneration systems and not in the behavior of the system that generates an increase or reduction/removal in emissions, nor in the definition of the emissions parameters that will regulate the carbon market.

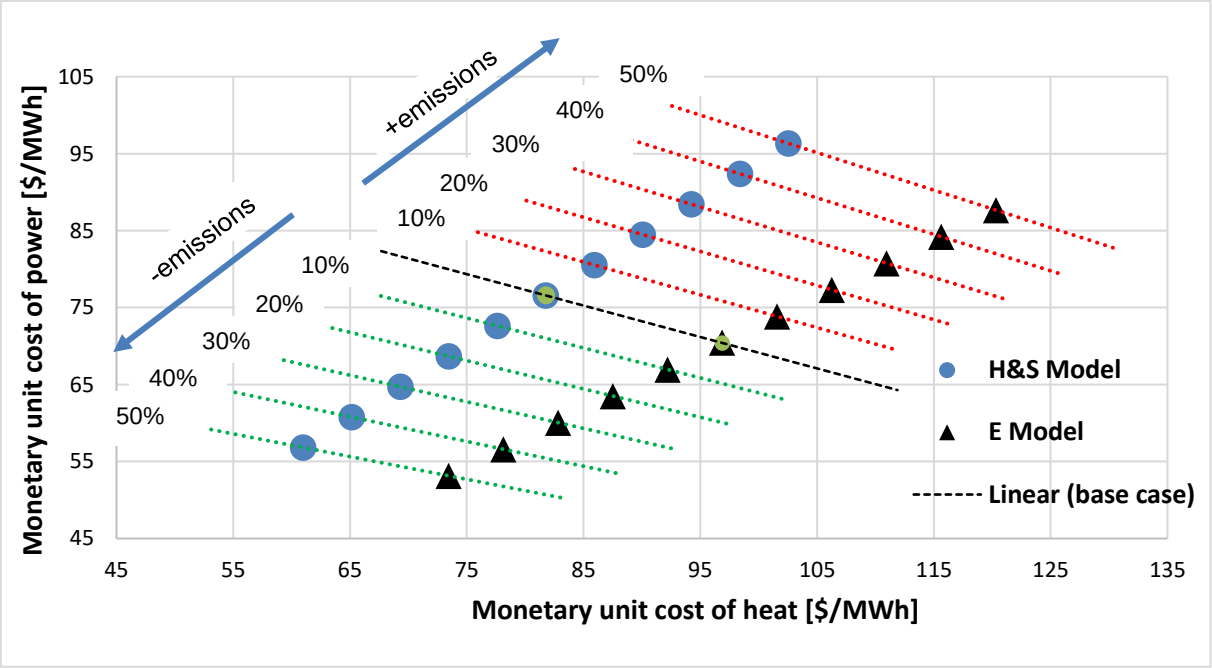

Figure 9. Monetary unit cost variation due to emissions.

Table 4. Monetary unit cost [$/MWh] and carbon credit for the simulated situations.

Emissions	E Model		H&S Model		Carbon credit/day	$/day
	(c_{Q_U})	(c_{W_N})	(c_{Q_U})	(c_{W_N})		
+50%	120.33	87.66	102.57	96.32	26.7	-2273
+40%	115.64	84.21	98.41	92.37	21.4	-1818
+30%	110.95	80.76	94.26	88.42	16.0	-1364
+20%	106.26	77.31	90.10	84.47	10.7	-909
+10%	101.57	73.86	85.95	80.52	5.3	-455
Base case	**96.88**	**70.41**	**81.79**	**76.57**	**0**	**0**
-10%	92.19	66.96	77.64	72.62	5.3	455
-20%	87.51	63.51	73.48	68.67	10.7	909
-30%	82.82	60.06	69.33	64.72	16.0	1364
-40%	78.14	56.6	65.17	60.77	21.4	1818
-50%	73.45	53.15	61.02	56.82	26.7	2273

Analyzing the inclusion of environmental costs, such as carbon pricing, one observes in Eq. (12) that the Z term, and consequently the Z_{env}, change the B coefficient of the straight line equation (Equation 13), and, therefore, would also shift the initial straight line (base case) to parallel lines compared to the initial condition. In the case of revenue ($Z_{env} < 0$), the straight line approaches the origin by decreasing product costs since revenue was generated from the sale of carbon credits. For expenses ($Z_{env} > 0$), the straight line moves away from the origin since it is necessary to buy carbon credits, that is, there is an increase in production costs. It is worth noting that the straight line moves to different but parallel positions. In any case, since coefficient A is not changed, the slope remains the same. Furthermore, by defining the system conditions and including the environmental cost, different thermoeconomic methodologies that consider the environmental device define ordered pairs of power and heat cost belonging to the same straight line solution.

4. Conclusions

This study described and detailed a thermoeconomic methodology to internalize monetary environmental costs in thermal system analyses through an example of a cogeneration system with a gas turbine.

The costs focused on the paper are the pricing of carbon emissions. However, the internalization of other environmental costs, such as the licenses, permits, and acquisition of environmental treatment/control equipment were also considered.

The cogeneration system was chosen because it is one of the main emitters of greenhouse gasses according to data from the International Energy Agency (IEA).

Models E and H&S were used. However, the focus is on H&S because it is a methodology that defines the device to represent the environment in the diagrams. This device is responsible for dissipating the cycle waste and has a key role in the internalization of environmental costs and in the systematized redistribution of costs for the remaining components and final products of the system. Nevertheless, any other thermoeconomic methodology, based on exergy, which coherently defines this environmental device, could be used following the same methods. Moreover, this model was proposed to take into account the treatment of waste (exhaust gases in the case of this work) and its costs, which are directly associated with pollutant emissions and, consequently, with the carbon market.

Since energy conversion systems generate environmental damage, their full analysis must take into account technical, economic, and environmental aspects to meet the environmental agenda signed in the Paris Agreement.

The current study presented the H&S Model as a feasible tool to reach this purpose by detailing how the carbon market can be taken into account and the pricing of carbon and other environmental costs internalized into the analysis. Besides detailing the calculation methodology, it also showed the behavior of the results of the cogeneration systems' final products' monetary costs. Incorporating costs associated with climate change into economic decision-making through carbon pricing can help encourage changes in production, consumption, and investment patterns. Thus, assisting in the energy transition process toward the planet's decarbonization.

This study concludes that the proposed methodology is coherent from the theoretical perspective of thermodynamics and thermoeconomics and can be used to allocate carbon credits to the internal and final products of thermal systems.

Acknowledgments

This study was supported by the Ufes Writing Center (Caesa), with its translation/revision services, offered free of charge. J.J. Santos thanks the “Fundação de Amparo a Pesquisa e Inovação do Espírito Santo – FAPES, T.O: 222/2023” and “Conselho Nacional de Desenvolvimento Científico e Tecnológico – CNPq, Process: 315990/2021-0”. The authors would like to thank IFES, PPGEM-UFES and CAPES for the funding.

Nomenclature

AC	Air compressor
c	monetary unit cost [$/MWh]
CC	Combustion chamber
CEPCI	Chemical Engineering Cost Index
CHP	Combined heat and power
E	Exergy Flow [kW]
ENV	environmental device
GHG	Greenhouse gas
GT	Gas turbine

IPCC Intergovernmental Panel on Climate Change
JB Junction-bifurcation
k^* Exergetic unit cost [kW/kW]
Q Heat (exergy) [kW]
RB Recovery boiler
W Power [kW]
Y Generic thermodynamic magnitude [kW]
Z Hourly equipment cost [$/h]

Greek symbols

λ specific CO_2 emission [g/MWh]

Subscripts and superscripts

0 Reference conditions
CH Chemical exergy [kW]
Env environmental
F Fuel
H Enthalpic flow [kW]
i;j Indexes for productive components
in Inlet
N Net
out Outlet
PH Physical exergy [kW]
S Entropic flow [kW]
U Useful heat

References

[1] IPCC. Mitigation of Climate Change. 2022.

[2] IEA. CO2 Emissions from Fuel Combustion: Overview-International Energy Agency. Paris: 2020.

[3] BRASIL. DECRETO Nº 11.075: Estabelece os procedimentos para a elaboração dos Planos Setoriais de Mitigação das Mudanças Climáticas, institui o Sistema Nacional de Redução de Emissões de Gases de Efeito Estufa e altera o Decreto nº 11.003, de 21 de março de 2022. Available: http://www.planalto.gov.br/ccivil_03/_ato2019-2022/2022/decreto/D11075.htm. (accessed: 5 out. 2022).

[4] SendeCO2. Precio Emisiones de CO2 2022. https://www.sendeco2.com/es/ (accessed March 18, 2023).

[5] The World Bank. State and Trends of Carbon Pricing 2022. Washington, DC: 2022.

[6] IPCC. AR6 Synthesis Report Climate Change 2023. 2023. Available: https://www.iea.org/reports/co2-emissions-in-2022. (accessed: 9 may 2023).

[7] Valero A, Serra L, Uche J. Fundamentals of Exergy Cost Accounting and Thermoeconomics. Part I: Theory. J Energy Resour Technol 2006;128:1–8. https://doi.org/10.1115/1.2134732.

[8] von Spakovsky MR. Application of engineering functional analysis to the analysis and optimization of the CGAM problem. Energy 1994;19:343–64. https://doi.org/10.1016/0360-5442(94)90115-5.

[9] Dincer İ, Rosen MA. Exergy: Energy, Environment, and Sustainable Development. 1st ed. Elsevier Science; 2007.

[10] Faria PR, dos Santos RG, Santos JJ, Barone MA, Miotto BM. On the Allocation of Residues Cost using Conventional and Comprehensive Thermoeconomic Diagrams. International Journal of Thermodynamics 2021;24:134–49. https://doi.org/10.5541/ijot.878173.

[11] Barone MA, Santos RG dos, Faria PR, Lorenzoni RA, Lourenço AB, Santos JJCS. On the Arbitrariness and Complexity in Thermoeconomics due to Waste Cost and Supplementary Firing Treatment. Engineered Science 2022;17:328–42. https://doi.org/10.30919/es8e624.

[12] Faria PR, dos Santos RG, Santos JJCS, Barone MA, Miotto BMF. On the Allocation of Residues Cost in Thermoeconomics using a Comprehensive Diagram. ECOS 2020 proceedings of the 33rd International Conference on Efficiency, Cost, Optimization, Simulation and Environmental Impact of Energy Systems, Osaka, Japan: 2020, p. 2444–56.

[13] Cerqueira SAAG, Nebra SA. Cost attribution methodologies in cogeneration systems. Energy Convers Manag 1999;40:1587–97. https://doi.org/10.1016/S0196-8904(99)00054-0.

[14] Modesto M, Nebra SA. Analysis of a repowering proposal to the power generation system of a steel mill plant through the exergetic cost method. Energy 2006;31:3261–77. https://doi.org/10.1016/j.energy.2006.03.032.

[15] Santos RG, Faria PR, Santos JJCS, da Silva JAM. Thermoeconomic modeling for CO2 allocation in steam and gas turbine cogeneration systems. Proceedings of Ecos 2015 - The 28th International Conference on Efficiency, Cost, Optimization, Simulation and Environmental Impact of Energy Systems, Pau - France: 2015.

[16] Faria PR, Barone MA, Santos RG, Santos JJCS. The environment as a thermoeconomic diagram device for the systematic and automatic waste and environmental cost internalization in thermal systems. Renewable and Sustainable Energy Reviews 2023;171:113011. https://doi.org/10.1016/j.rser.2022.113011.

[17] Faria PR, Torres C, Santos JJ, Valero A. On the thermoeconomic modelling of thermal waste cost allocation and diagnosis of malfunctions for environmental aspects assessment. ECOS 2022 - Proceedings of the 35th International Conference on Efficiency, Cost, Optimization, Simulation and Environmental Impact of Energy Systems, Copenhagen (Denmark): 2022, p. 1271–82.

[18] Fortes AFC, Carvalho M, da Silva JAM. Environmental impact and cost allocations for a dual product heat pump. Energy Convers Manag 2018;173:763–72. https://doi.org/10.1016/j.enconman.2018.07.100.

[19] Frangopoulos CA. Application of the thermoeconomic functional approach to the CGAM problem. Energy 1994;19:323–42. https://doi.org/10.1016/0360-5442(94)90114-7.

[20] Torres C, Valero A, Rangel V, Zaleta A. On the cost formation process of the residues. Energy 2008;33:144–52. https://doi.org/10.1016/j.energy.2007.06.007.

[21] F-Chart Software. Engineering Equation Solver - EES 2017. <http://www.fchart.com>

[22] Santos JJCS. Aplicação da Neguentropia na Modelagem Termoeconômica de Sistemas [in Portuguese]. PhD Thesis. Federal University of Itajubá - Brazil, 2009.

[23] Trading Economics. https://pt.tradingeconomics.com/commodity/natural-gas 2023. https://pt.tradingeconomics.com/commodity/natural-gas (accessed March 19, 2023).

[24] Chemical Engineering. CEPCI 2023. https://www.chemengonline.com/category/business-economics/ (accessed March 19, 2023).

[25] Valero A, Royo J, Lozano MA. The Characteristic Equation and Second Law Efficiency of Thermal Energy Systems. International Conference Second Law Analysis of Energy Systems: Towards the 21st Century, E. Sciubba, M.J. Moran. Roma “La Sapienza”; 1995, p. 99–112.

[26] de Oliveira Junior S. Exergy: Production, Cost and Renewability. London: Springer London; 2013. https://doi.org/10.1007/978-1-4471-4165-5.

[27] Lazzaretto A, Tsatsaronis G. SPECO: A systematic and general methodology for calculating efficiencies and costs in thermal systems. Energy 2006;31:1257–89. https://doi.org/10.1016/j.energy.2005.03.011.

[28] Santos RG, Faria PR, Santos JJCS, Da Silva JAM, Donatelli JLM. The Effect of the Thermodynamic Models on the Thermoeconomic Results for Cost Allocation in a Gas Turbine Cogeneration System. Revista de Engenharia Térmica 2015;14:47. https://doi.org/10.5380/reterm.v14i2.62133.

[29] Santos RG, Lourenço A, Faria PR, Barone MA, Santos JJ. A Comparative Study of a New Exergy Disaggregation Approach with Conventional Thermoeconomic Methodologies for Cost Allocation in an Organic Rankine Cycle Powered Vapor Compression Refrigeration System. ECOS 2022 - Proceedings of the 35th International Conference on Efficiency, Cost, Optimization, Simulation and Environmental Impact of Energy Systems, Copenhagen (DK): 2022, p. 1057–68.

[30] Bhering Trindade A, Luiza Grillo Renó M, José Rúa Orozco D, Martín Martinez Reyes A, Aparecido Vitoriano Julio A, Carlos Escobar Palacio J. Comparative analysis of different cost allocation methodologies in LCA for cogeneration systems. Energy Convers Manag 2021;241:114230. https://doi.org/10.1016/j.enconman.2021.114230.

[31] Araújo LR de, Morawski AP, Barone MA, Donatelli JLM, Santos JJCS. On the effects of thermodynamic assumptions and thermoeconomic approaches for optimization and cost allocation in a gas turbine cogeneration system. Journal of the Brazilian Society of Mechanical Sciences and Engineering 2020;42:323–41. https://doi.org/10.1007/s40430-020-02402-6.

Multi-criteria optimisation to align environmental impacts of industrial heat production with environmentally sustainable thresholds: case of the paper industry

Yoann JOVET[a*], Frédéric LEFEVRE[a], Alexis LAURENT[b] and Marc CLAUSSE[a]

[a] Univ Lyon, INSA Lyon, CNRS, CETHIL, UMR5008, 69621 Villeurbanne, France.

yoann.jovet@insa-lyon.fr, CA

[b] Section for Quantitative Sustainability Assessment, Department of Environmental and Resource Engineering, Technical University of Denmark (DTU), 2800 Kgs. Lyngby, Denmark.

Abstract

Human activities are currently at an unsustainable level and a significant reduction in greenhouse gas emissions is essential to limit global warming. Industry, which accounts for a large share of these emissions, has an important role to play, particularly in its energy consumption for heat production. One of the issues of this transformation is to assess, among all the possible energy solutions, those that are most likely to achieve the objective of reducing emissions of greenhouse gases without incidentally increasing other environmental impacts. The study proposes a method for classifying non-dominated solutions found using an optimisation model based on life cycle analysis (LCA), energy and economic indicators. This is complemented by integrating constraints represented by sustainability limits, i.e. an acceptable level of impact defined by planetary boundaries. A case study of a paper industry process in Italy is presented to highlight the capability of the method. For this example, the ranking shows that - with the current LCA weighting factors - waste heat recovered using a heat pump powered by electricity has the highest ranking. However, a scoring for which exceeding sustainable levels is penalized gives a higher ranking to solutions composed of a mix of several energy sources. Moreover, if one focuses only on the global warming indicator, the most effective solutions far exceed sustainable levels for other indicators. It is therefore necessary to adopt a comprehensive environmental approach to avoid shifting environmental burdens to other impact categories. On the other hand, no solution compatible with all sustainable levels has been found. It is therefore necessary to go further by proposing a global approach detailing the level of impact that each sector can have while ensuring an overall sustainable level.

Key words

Optimisation, Industrial energy process, Planetary boundaries, Sustainability, Environmental assessment

Nomenclature

C	Corrective factor		R1	Ranking method 1	
C’	Weighting score		R2	Ranking method 2	
C*	Corrected weighting factor		R3	Ranking method 3	
D	Process demand	(MW)	S	Energy stored	(MWh)
ε	Final energy losses	(%)	S_{eff}	System efficiency	
E_{in}	Final energy consumption	(MWh)	Sr	Sustainability ratio	
E_{out}	Process enery demand	(MWh)	T	Process temperature	(K)
I	Impact intensity	(kgCO2eq/FU)	Ws	Weighting score	
P	Heat generation	(MW)			

Acronym

CCS	Carbon Capture & Storage

Subscripts

j	Heat production technology

LCA	Life Cycle Assessment	rec	Recovered from waste heat
MHP	Mechanical Heat Pump	sto	Storage
GHG	GreenHouse Gas	sustainable	Environmentally sustainable thresholds
i	Impact category	up	Upgraded to be used by process

1. Introduction

It is unequivocal that human influence has warmed the atmosphere, ocean and land since pre-industrial times, which *is a consequence of more than a century of net greenhouse gas (GHG) emissions from unsustainable energy use, land-use and land use change, lifestyle and patterns of consumption and production* [1], [2]. There are now a large number of climate scenarios that attempt to estimate the consequences of human activities on future global mean surface temperature (GMST), which are compiled in the last intergovernmental panel on climate change (IPCC) assessment report [3]. The higher the increase in GMST, the larger the irreversible changes in natural cycles and the consequences on livelihoods of people, which is why it is essential to hold this temperature increase well below 2 °C above pre-industrial levels. The latest Intergovernmental Science-Policy Platform on Biodiversity and Ecosystem Services report [4] shows that global warming is not the only concern at the moment, and that other issues (land use, direct exploitation, pollution etc.) are at unsustainable levels leading to a huge decrease in biodiversity. This conclusion is also highlighted by the Stockholm Resilience Center in their proposed definition of planetary boundaries [5].

Many global warming mitigation options are already technically and economically viable or are going to become so in the near future [2]. Nevertheless, they can have other environmental impacts, which are necessary to evaluate. Therefore, an increasing number of studies, often called the 4E study, combined energy, exergy, economic and environmental approaches to reach this goal. For example, Chen et al. [6] proposed a comprehensive 4E approach applied to cascading systems, which has been shown to be beneficial in reducing greenhouse gas emissions. Yu et al. [7] go further in the environmental assessment by conducting a full life cycle analyses (LCA) to evaluate the most significant environmental impacts. Although these studies quantify the environmental impacts of a technical solution and the elements that significantly contribute to it, they do not relate them to sustainable thresholds, i.e. the maximum level of impact generated by the process that can be achieved without causing significant adverse effects on the environment, society or the ability of future generations to meet their own needs. Indeed, Bjørn et al. [8] have pointed out that one solution that is better than another from an environmental point of view is not necessarily an acceptable solution in the face of global limits..

In this study, we propose a 4E assessment framework including the sustainable levels defined by Vargas et al [9] to analyse the issue of sustainable heat production in industry. Starting with an industrial need defined by dynamic heat requirements at a certain temperature level, a set of mature solutions are compared to analyse the best compromise according to different energy, environmental and economic constraints. The main purpose of this article being to present the method, a simple case study is used for this purpose. It takes as example the paper production, which is a continuous industrial process, located in Italy, being able to benefit from a continuous flow of waste heat at a temperature lower than the process temperature. A period of one year is considered.

2. Methods and Material

2.1. Overall methodology

This study deals with the heat production for an industrial process at a defined temperature T, for a variable hourly demand. The objective is to define the best way to meet the dynamic heat demand by using combinations of different possible technologies like electric, gas and biomass boilers or heat pumps fed with waste heat or thermal storage. All the energy sources used to cover this need (including those used to generate grid electricity, with or without carbon capture and storage) have different environmental impacts and different costs that can vary at each time step. The aim is to analyse what is the best possible solution to produce this industrial heat according to environmental and economic criteria. The analysis being multicriteria, it is possible to find a set of possible solutions answering the optimization problem. The general assessment framework used to calculate and rank the optimal solutions is presented in Fig. 1.

From environmental, technological, energy, process-related and economic input data, it is possible to feed the economic, energy (yearly performance simulation) and environmental (LCA) models used in the optimization algorithm. The latter produces a set of non-dominated solutions capable of meeting the needs of the process. Note that for the sake of brevity, this article focuses only on the environmental impact presentation. The set of non-dominated produced solutions, also called Pareto front, is such that

there is no one solution that exhibits a best performance in all dimensions. Eventually, these solutions are ranked based on considerations related to global limits and economy. The different steps of this general assessment framework are detailed in the following sections.

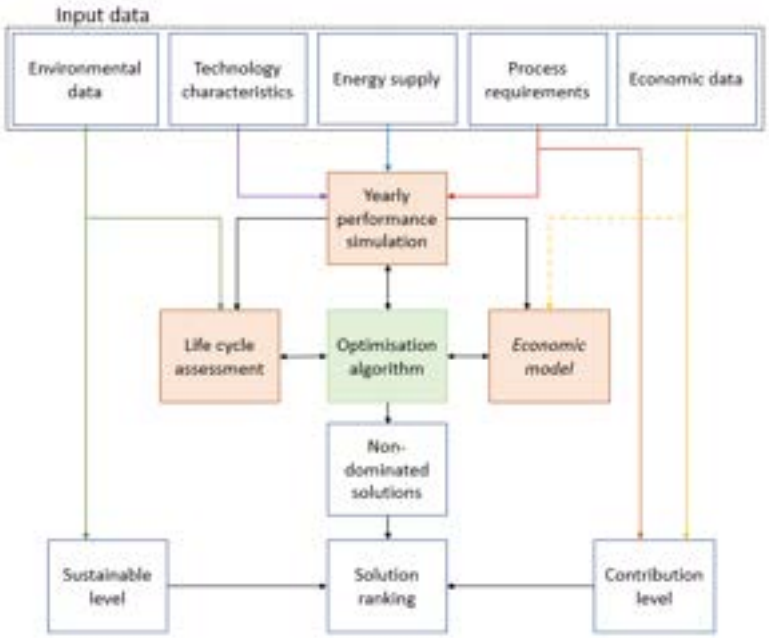

Fig. 1 - Assessment framework; dotted arrows and the block in italics are not presented in this study.

2.2. Input data

2.2.1. Environmental data

The environmental data are derived from Ecoinvent 3.7.1 LCI database [10]. This assessment considers the marginal process for all environmental data, which is defined by Hauschild et al. [11] as the transformation on the economy caused by the introduction of a new product system, i.e. the product system's consequence. For the proposed application, namely the heat production in industry sector, which represents a significant share of the energy market, the change of energy system will lead to a change in electricity production to satisfy this new demand. Considering marginal process requires to assess the environmental impacts caused by the change in energy supply over the average values.

2.2.2. Efficiency of the technologies

The efficiencies of the technologies considered in the study are summarised in Table 1. They include the heat loss to the environment due to the generation of heat and consider a reduction of the efficiency when the system operates in partial load. In addition to these efficiencies, a ramp-up power is considered for biomass production with a limited ramp-up equal to 4.2% per hour of the maximum available power as defined by Veyron et al.[12]. For the Mechanical Heat Pump (MHP), the power is limited according to the available waste heat at the considered time step. In this study, the source of waste heat is external to the process and corresponds to a contribution equivalent to 80% of the process requirement.

A thermal storage facility is also modelled to allow a phase shift between production and use. There are currently many options for thermal energy storage as reviewed by Sarbu et al [15]. As this work focuses on industrial applications, only short-term storage (water tank) is considered as a first step. Storage losses are estimated at 5% of the stored energy for a charge cycle of 8 hours and a discharge cycle of 16 hours [16]. Considering the charging and discharging times, the hourly storage efficiency is equal to $\varepsilon_{sto} = 0.996$.

Table 1 – Final energy consumption $E_{in,T}$, Process energy demand $E_{out,T}$ at temperature T, for the four technologies considered in the study. $S_{eff,T}$ is the system efficiency for a process temperature T in °C, with T_{up} the process temperature level and T_{rec} the waste heat temperature level, ε is the share of final

energy losses by the system in % which represents the heat losses to the environment of the heat generation technology as proposed by Bülher et al. [13].

Technologies	Final energy consumption $E_{in,T}(t) = \frac{E_{out,T}(t)}{S_{eff,T}(t).(1-\varepsilon)}$	Partial load efficiency
Electric boiler	$S_{eff,T}(t) = 1$ $\varepsilon = 0.00096(T + 273.15) - 0.115$	No partial load efficiency losses
Natural gas boiler	$S_{eff,T}(t) = 1$ $\varepsilon = 0.001154(T + 273.15) - 0.138$	No partial load efficiency losses
Biomass boiler	$S_{eff,T}(t)$ depends on the partial load $\varepsilon = 0.001154(T + 273.15) - 0.138$	Regression from [12] At 100% design load: $S_{eff,T}$ = 86.5% At 50% design load: $S_{eff,T}$ = 83.0%
MHP	$S_{eff,T}(t) = 1.91(T_{up}-T_{rec}+0.0884)^{0.89094}(T_{up}+0.0442)^{0.67895}$ $\varepsilon = 0.00096(T + 273.15) - 0.115$	Linear regression from [14] At 100% design load: $S_{eff,T}$ = COP At 50% design load: $S_{eff,T}$ = 0.985COP

2.2.3.Energy supply

The electricity production considered in this study is scenario BL2050 for Italy from the heat road map Europe [17]. Italy is a relevant study case to assess the impact of Carbon Capture & Storage (CCS) option because of its large share of thermal generation of electricity. The new installed electricity production relative to the current electricity mix is described in Table 2.

Table 2 – New installed electricity production sources in scenario BL2050 for Italy

Dammed hydro	Geothermal	Offshore wind	Onshore wind	Solar	River hydro	CHP Biomass	Condensing powerplants	Nuclear
5.7%	3.8%	0%	20.9%	23.9%	0%	2.1%	43.6%	0%

The proportion of CCS in the power generation mix as well as for on-site industrial CCS is derived from the scenario AIM/CGE 2.2 publish by Riahi et al. [18] from IPCC AR6 [3]. The data are presented in Table 3.

Table 3 – Average CCS share in electricity production and industrial heat production system

	2015-2040	2040-2065	2065-2090
Electricity production	8%	32%	71%
On-site industrial CCS	0%	2%	39%

The CCS captured efficiency, which is defined as the share of CO_2 not rejected by the CCS, is set at 88% according to García-Freites et al. [19]. The environmental impact of CCS is based on the LCA carried out by Bisinella et al. [20]. The efficiency penalty of CCS, which is the relative change on energy output, is set at 15% for gas [21] and 22.6% for BECSS and oxy-fuel [22]. For the gas boiler, a feed with 100% of conventional gas is assumed (no shale gas).

2.2.4.Process requirements

The consumption profile of the study is based on average data from a continuous paper production process [23]. The typical week is shown in Fig. 2 and is repeated throughout the year. The process temperature requirement is set at 130°C and the waste heat temperature is recovered at 80°C. The continuous heat requirement profile of the paper industry has the advantage of presenting a minimum of operating constraints for the heat production technologies. A batch profile would have higher constraints such as the ramp-up time of a biomass boiler or lower efficiencies at partial load. The same

method can of course be applied to more complex profiles, but the lack of space does not allow to deal with them in this article.

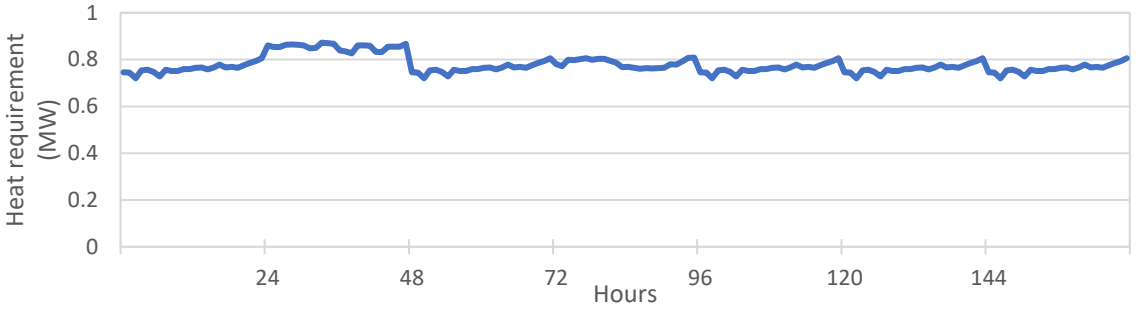

Fig. 2 - Weekly heat requirement profile for paper production process at a temperature level of 130°C

2.3. Yearly performance simulation

The energy model creates solutions that verify all the operating conditions of the technologies to meet the process demand. These solutions give for each time step the heat produced by each of the technologies:

$$\sum_{j=1}^{n} P_j(t) = D(t) + \frac{\mathrm{S(t)} - \mathrm{S(t-1)} - \mathrm{S(t)} * (1 - \varepsilon_{sto})}{\Delta t} \quad (1)$$

Where P_j is the heat production from source j in MW, D the process demand in MW, S is the amount of energy in thermal storage at time step t in MWh and Δt the time step. The size of the heat production facilities for CAPEX and LCA calculations is based on the maximum demand required for each technology over the year, no safety factor being considered.

2.4. LCA model

The LCA focuses on the generation and supply of heat to the industrial sector in Italy. The functional unit is therefore defined as the production of heat at 130°C to meet the industrial demand presented in part 2.2.4 over one year in Italy for both 2015-2040 and 2065-2090 periods. Background data specified in Sections 2.2-2.3 are used for the life cycle inventory modelling. The Life Cycle Impact Assessment method used is EF 3.0 [16] and the weighting scores (Ws) proposed by this method are presented in Table **4** as well as the 16 environmental indicators used in this study. The weighting scores are not used in the optimization algorithm but are considered to rank the obtained solutions in the final step of the assessment framework. Furthermore, as explained in section 2.2.1, this study considers consequential modeling.

Table 4 - Weighting score from LCIA EF 3.0

	Climate change	Ozone depletion	Ionising radiation	Photochemical ozone formation	Particulate matter	Human toxicity, non-cancer	Human toxicity, cancer	Acidification	Eutrophication, freshwater	Eutrophication, marine	Eutrophication, terrestrial	Ecotoxicity, freshwater	Land use	Water use	Resource use, fossils	Resource use, minerals and metals
Weighting EF 3.0 (Ws)	21%	6%	5%	5%	9%	2%	2%	6%	3%	3%	4%	2%	8%	9%	8%	8%

2.5. Optimisation algorithm

The non-dominated solutions are calculated using the genetic optimisation algorithm package from Matlab [24]. The genetic method works by combining initial solutions and adding mutations to test the solution space as efficiently as possible. This method is well suited to our case as the solutions with one single energy source can be combined to make any possible solution. The initial solutions are therefore easy to generate. The number of obtained solutions depends on the size of the studied population; in this study a population of 100 is considered which generates a number of 35 final non-dominated solutions. This method has been widely studied in the literature [25], [26] and is already applied for energy optimization [27], [28], although reproducibility may be a minor issue.

2.6. Ranking of the non-dominated solutions

2.6.1. Sustainable & contribution levels

The environmental sustainability limitfor each environmental impact category is derived from Vargas et al. [9], except for marine eutrophication which is based on Willett et al. [29] and climate change which is based on the scenario AIM/CGE 2.2 published by Riahi et al. [18] and used in IPCC AR6 as one of the reference scenario to limit warming to 2°C without overshoot [3].

In order to assess the sustainability of non-dominant solutions, it is necessary to evaluate the share of the considered industrial process in relation to all human activities, and this for all environmental impacts. The aim is to define the safe operating space for the process, that can be described as the maximum acceptable impact that a process can have to remain below sustainable thresholds [30]. Several methods can be used for that purpose. The allocation principle that is used in this study is derived from the economic value added of the process as described in Jovet et al. [31]. To evaluate the deviation of each impact category of a non-dominated solution with respect to the sustainable level, the sustainability ratio defined by equation (2) is used.

$$Sr_{\mathrm{i}}(x) = \frac{\mathrm{I}_i(\mathrm{x})}{\mathrm{I}_{i,sustainable}} \tag{2}$$

where $Sr_{\mathrm{i}}(x)$ is the sustainability ratio of solution x for impact category i, $\mathrm{I}_i(\mathrm{x})$ the impact of category i and $\mathrm{I}_{i,sustainable}$ the sustainable level for the impact category i for the considered industrial process, which is derived from the share of the process in relation to its value added as described in Jovet et al. [31]. Another criterion was introduced in [31] to assess the sustainability of an industrial process: the contribution level $C_i(x)$. This criterion compares the ratio of the impact I_i to the total impact $I_{i\ tot}$ of the category i to the share of the economic value added of the process $EVA_{process}$ to the total economic added value EVA_{tot}:

$$C_i(\mathrm{x}) = \frac{I_i(x)}{I_{i\,tot}} \cdot \frac{EVA_{tot}}{EVA_{process}} \tag{3}$$

This criterion puts the importance of the sustainability ratio into perspective. Indeed, if the sustainability ratio is above 1 (i.e. non-sustainable), but the contribution level is below 1 (i.e. less than the average for human activity), reducing the environmental impact of this process may not have a major impact on the global sustainability but remains a needed target. On the contrary, reducing the environmental impact of a process having a high contribution level can have a significant effect on the impact category even if the impact level of this process is below the threshold. As an example, Fig. 3 shows the sustainability ratio versus the contribution level for three different impact categories A, B and C. Impact category B has a high sustainability ratio but a small contribution level, while impact category C behaves in the opposite way. This work considers the contribution of impact categories B and C to be equivalent in their ability to achieve or maintain a sustainable level for their respective category. For this reason, we propose to use a corrective contribution level C* in this paper to consider the importance of a sector in the total contribution and not only the sustainable level. This corrective factor is based on the orthogonal projection of the impact category coordinate on the linear function y = x.

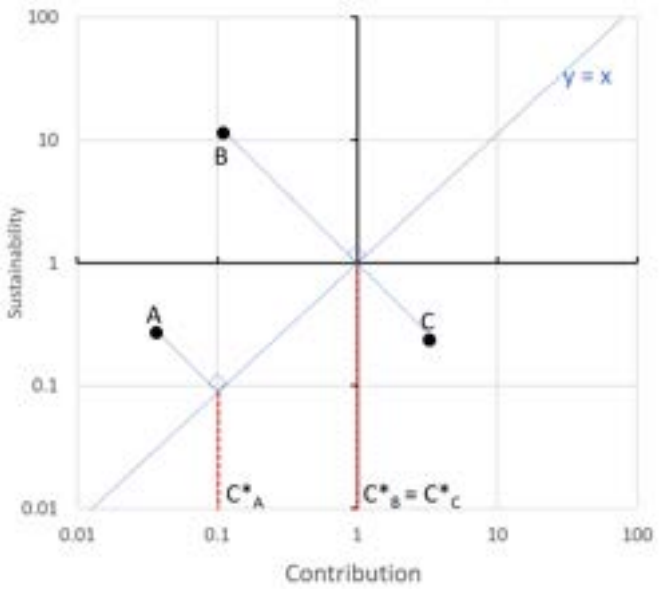

Fig. 3 – Contribution level corrected for each impact categories (A, B and C in this example) based on their sustainability level and contribution.

2.6.2. Classification

The classification of non-dominated solutions is realised using three different methods, (i) ranking 1 (R1) based on weighting the different impact categories with the EF 3.0 impact weighting scores Ws_i (

Table 4), (ii) ranking 2 (R2) by adjusting the previous score with the C* factor, (iii) ranking 3 (R3) using the C* factor to calculate a penalty score C' which becomes more penalizing the more the sustainability threshold is exceeded, according to equation (4).

$$\begin{cases} C'_i(x) = e^{C^*_i(x)-1} & \text{if } C^*_i < 0 \\ C'_i(x) = C^*_i(x)^2 & \text{if } C^*_i > 0 \end{cases} \quad (4)$$

The final score for each non-dominated solution and the three different ranking methods is obtained using equation (5).

$$\begin{cases} R1 = \sum_i Ws_i . Sr_i(x) \\ R2 = \dfrac{\sum_i Ws_i . |C^*_i(x)| . Sr_i(x)}{\sum_i |C^*_i(x)|} \\ R3 = \dfrac{\sum_i Ws_i . C'_i(x) . Sr_i(x)}{\sum_i C'_i(x)} \end{cases} \quad (5)$$

3. Results & Discussion

The results of non-dominated solutions before ranking are presented in Fig. 4 for 2015 - 2040 and 2065 - 2090 periods for the impact categories that are not always sustainable. The following impact categories are always sustainable for the considered industrial sector whatever the technological solution studied and are not presented in Fig. 4: ozone depletion, Ionising radiation, photochemical ozone formation, human toxicity, cancer, acidification, marine eutrophication, terrestrial and water use. In this figure, each line represents the ratio between the impact of the process and the sustainable level of one heat production solution across all environmental impacts. Each value at the left of the blue line can be considered as sustainable while the value at the right is not. The changes between the 2015-2040 and 2065-2090 periods come from the development of CCS technology and the evolution of the sustainable climate change thresholds (which uses a budgeting approach). For the period 2065-2090, which presents greater uncertainties, it cannot be excluded that the current challenges will evolve according to the choices made by then. It is already possible to do some projection for climate change based on the willingness to limit the temperature increase. On the other hand, this approach helps to evaluate which impact categories could be an issue if the process were to continue as it does today.

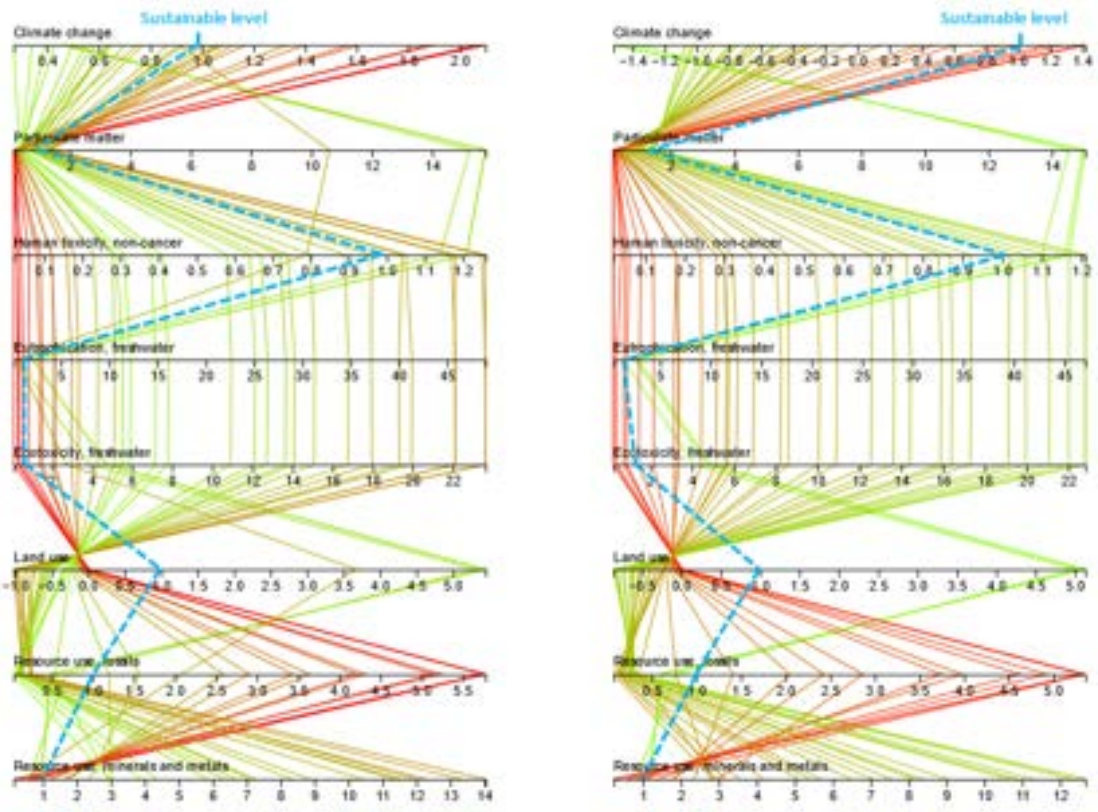

(a) (b)

Fig. 4- Sustainability ratios of non-dominated solutions for periods (a) 2015-2040 and (b) 2065-2090 for impact categories exceeding the sustainable threshold value. The blue dotted line shows the sustainability limit corresponding to all values below 1. Each line is one of the 35 non-dominated solutions. The colour code varies from green to red, from the lowest to the highest value of climate change indicators to present the trades-off.

The first observation is that none of the 35 non-dominated heat production systems respects all the sustainable thresholds for both periods of time, i.e. all impact indicators lower or equal to 1 for a same heat production solution. The dispersion of the non-dominated solutions on the climate change indicator shows a result well above the sustainable level on indicators such as toxicity with a result up to 20 times the limit, freshwater eutrophication with a factor up to 50 or mineral resource use with a factor up to 13. The largest exceedances of sustainable levels are seen for solutions that meet the sustainable level for the climate change indicator. In contrast, the solutions that exceed the limit for climate change are below the sustainable levels for the other indicators, except for the fossil fuel consumption and freshwater eutrophication indicators.

Using the ranking method R1, the MHP technology performs the best achieving a ranking of 1 and 2 for both periods as presented in Fig. 5. As the environmental constraint increases over the period 2065-2090, it can be seen that the biomass solution ranks 7 to 10 times behind the MHP. The R1 score is very stable for all solutions combining MHP and gas boiler despite a high weight for climate change with over 20% of the ranking based on this indicator. Electrical boilers are heavily impacted by their lower electricity to heat conversion factor compared to MHP that results on a ranking of these solutions among the least efficient. It can be noted that the storage solution does not provide any gain with a ranking that decreases with the increase in storage use. This is due to different factors such as the low share of intermittent energy, which results to a low variation of the environmental impact of the electricity between the different time steps, but also due to the lack of process intermittency which is not sufficient to compensate for storage losses. However, this conclusion is specific to the profiles of electricity consumption and production chosen in this example. For electricity mixes with greater variations in environmental impact between time steps, non-dominated solutions will be more time-dependent and therefore storage will have a more important role.

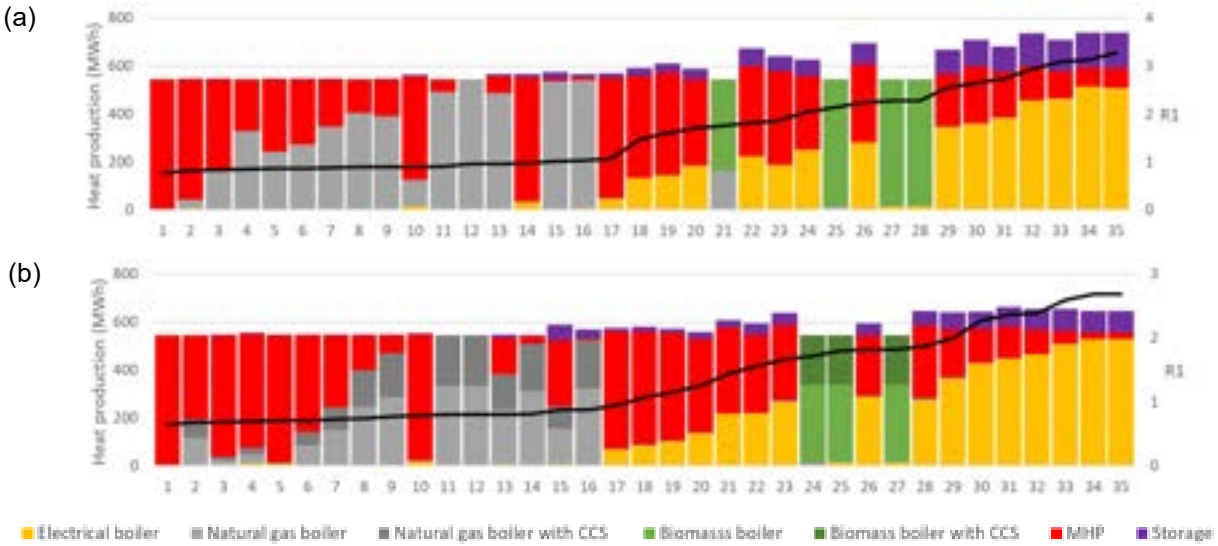

Fig. 5 – Non-dominated solutions ranked with method R1 using EF 3.0 ponderation factor for (a) years 2015-2040, (b) years 2065-2090. The score R1 is displayed with the black line.

The use of the R2 and R3 ranking methods, for which the higher the threshold exceedance, the higher the penalty, leads to significant changes compared to the R1 approach as presented in Fig. 6. The greater the penalty for exceeding global limits, the greater the share of gas combined with CCS development in the optimal solutions. Indeed, gas performs well in indicators for which electricity does not, and vice versa, which results to impacts closer to sustainable levels with fewer high-performing impact categories but simultaneously fewer categories far above the thresholds. Biomass boiler also benefits from these two-ranking methods but in a more limited way. On the other hand, the more we penalise exceeding the limits, the more the best ranked solutions exceed the threshold for the climate change indicator. For the period 2015-2040, among the 10 best solutions, only 2 meet the threshold for climate change whereas there were 4 with the R1 ranking method. The presence of CCS combined with the improvement of the carbon content of electricity increases this number to 7 solutions respecting the sustainable level for climate change over the period 2065-2090 while the R1 classification method is 9.

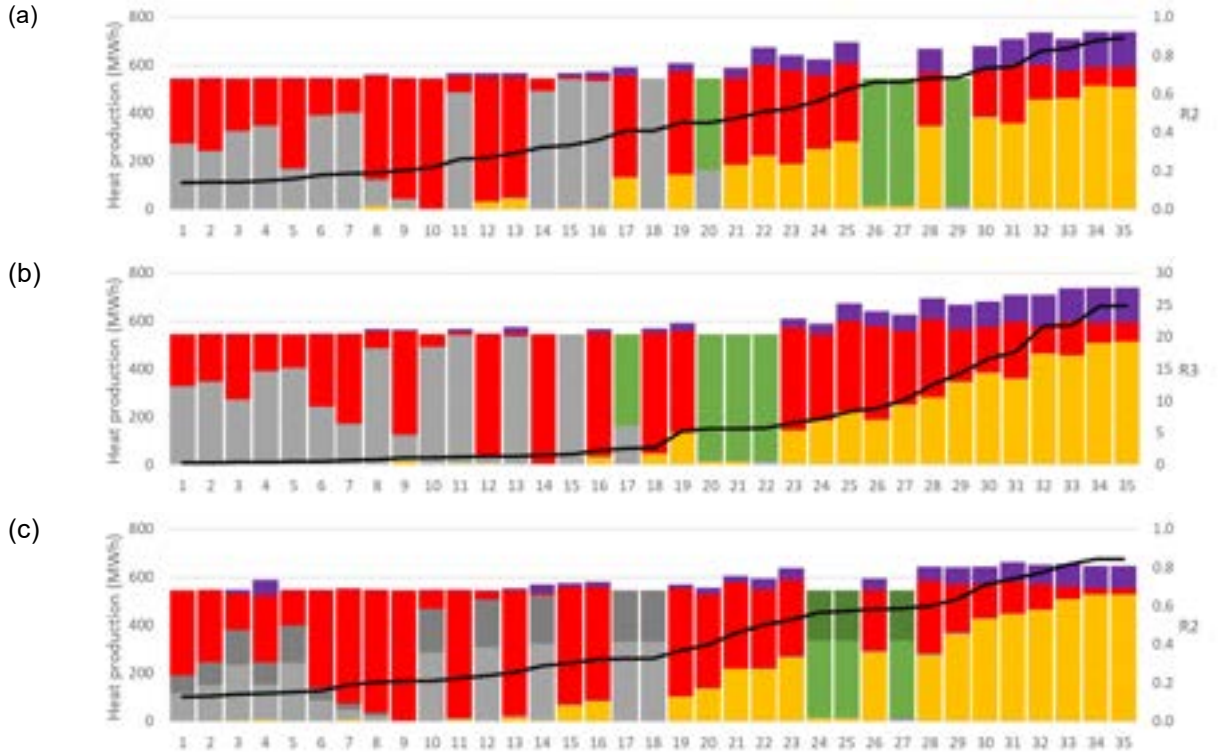

(d)

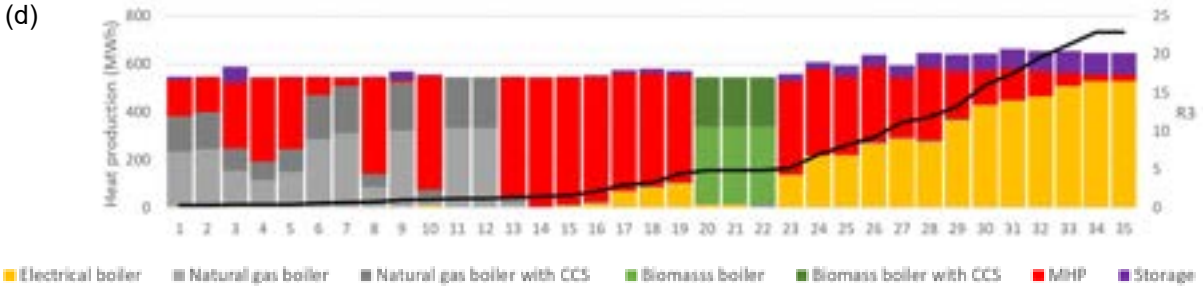

Fig. 6 – Non-dominated solutions ranked with method (a) R2 for the years 2015-2040, (b) R3 for the years 2015-2040, (c) R2 for the years 2065-2090, (d) R3 for the years 2065-2090. The score R2 and R3 are displayed with the black line.

Based on the results, it is possible to imagine two types of approaches to bring the industrial activity back to sustainable levels. The first approach requires each process to respect the global limits by defining a safe operating space for each process. This approach corresponds to the development of solutions where exceeding sustainable levels is strongly penalised, i.e. ranking method R3. The second approach requires each process to implement the best possible solution and therefore to adapt the process safe operating space for each impact category based and their ability to perform. However, this requires a comprehensive review of all human activities to ensure that the entire range of human activities is able to meet the thresholds of sustainability. The first method is simpler to implement because it is only necessary to allocate a share of the impacts to each process, whereas for the second method it is necessary to have a breakdown by impact category for each process. On the other hand, the first method will tend to ask for solutions as close as possible of the sustainable threshold (i.e. never the best but never the worst), which results in a multiplication of energy sources, and therefore in a multiplication of system for the industries to deal with, which increases the level of complexity on site.

However, if the transformation of industrial heat production means is oriented towards achieving the climate change objective, some impact categories are likely to exceed the sustainable limits. Fig. 7 shows that the best solutions with ranking method R3 are above the sustainable threshold for climate change for the period 2015-2040. The best solution for climate change indicator is ranked only 14th with the R3 method in 2015-2040 and 20th in 2065-2090, while the best solution with method R1 is also the best for the climate change indicator. However, high performing solutions on climate change exceed the sustainable levels on some other criteria, which explains their ranking with the R3 method, as can be seen in Fig. 7. Therefore, it is not possible to reach the sustainable level with the technology proposed and the safe operating space available for the process based on added value. This means that the safe operating space allocated to the process will not be sufficient to enable it to stay below the threshold. There are two ways to have sufficient safe operating space for the process:

(i) If the process needs to continue at the current level (e.g. for a vital process), other processes need to decrease in order for it to leave enough operating space.

(ii) this process must decrease

This will result in a modification of certain sectors of activity by reducing the operating space of some sectors that will be considered less essential or sufficiently efficient to leave enough safe operating space to sectors considered as essential. A reflection on this allocation is therefore essential to define the place of each sector in a sustainable world according to numerous technical parameters but also around political or sociological themes.

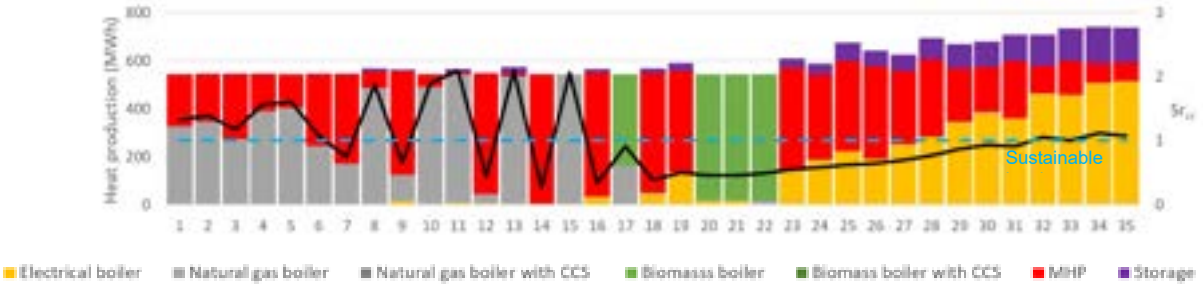

Fig. 7 – Non-dominated solutions ranked with method R3 for the years 2015-2040. The sustainable ratio for climate change is display in black and the sustainable level in blue.

4. Conclusions & Recommendations

In this paper, a method has been developed to optimize, from an energy, economic and environmental point of view, the combination of energy systems to be used to produce heat for a dynamic industrial process. The energy mix uses combinations of different possible technologies such as electric, gas and biomass boilers or heat pumps powered by waste heat or thermal storage. An optimisation model, based on LCA criteria, enables to obtain a number of non-dominated solutions. Even if some solutions enable to reduce some impact categories, no solution was found to reach sustainable levels for all impact categories. Thus, the best performing solutions on the climate change indicator also exceed the sustainable level for several other environmental impact indicators such as land use, toxicity, eutrophication or resource use fossil. By ranking the non-dominated solutions, using different weighting criteria, it can be seen that the more one penalizes the exceeding of sustainable levels for each impact category, the more mixed solutions are present and in particular the combination of MHP and gas boiler.

The results show that none of the studied solutions can reach a sustainable level regardless of the technology used and this, despite the use of resolution algorithms to highlight the best performing solution. This assessment shows that it is necessary to have a reflection on the share that each process can represent in human activities. It is possible to envisage this redistribution in two ways, (i) by requiring an identical effort from all sectors to reach the targeted level or (ii) by determining, according to the needs and potential of each sector, its maximum acceptable contribution for each impact category. The latter method requires in-depth knowledge of the potential of each sector, which could be determined using the optimization model presented in this paper but on a larger scale. For both approaches, it is essential to think holistically so that all human activities are taken into account and not to look at each sector individually to conclude about sustainability.

References

[1] Masson-Delmotte, V., P. Zhai, A. Pirani, S.L. Connors, C. Péan, S. Berger, N. Caud, Y. Chen, L. Goldfarb, M.I. Gomis, M. Huang, K. Leitzell, E. Lonnoy, J.B.R. Matthews, T.K. Maycock, T. Waterfield, O. Yelekçi, R. Yu, and B. Zhou (eds.), « IPCC, 2021: Summary for Policymakers. In: Climate Change 2021: The Physical Science Basis. Contribution of Working Group I to the Sixth Assessment Report of the Intergovernmental Panel on Climate Change », doi: 10.1017/9781009157896.001.

[2] P.R. Shukla, J. Skea, R. Slade, A. Al Khourdajie, R. van Diemen, D. McCollum, M. Pathak, S. Some, P. Vyas, R. Fradera, M. Belkacemi, A. Hasija, G. Lisboa, S. Luz, J. Malley, (eds.), « IPCC, 2022: Summary for Policymakers. In: Climate Change 2022: Mitigation of Climate Change. Contribution of Working Group III to the Sixth Assessment Report of the Intergovernmental Panel on Climate Change », doi: 10.1017/9781009157926.001.

[3] P.R. Shukla, J. Skea, R. Slade, A. Al Khourdajie, R. van Diemen, D. McCollum, M. Pathak, S. Some, P. Vyas, R. Fradera, M. Belkacemi, A. Hasija, G. Lisboa, S. Luz, J. Malley, (eds.), « AR6 Climate Change 2022: Mitigation of Climate Change — IPCC ». Consulté le: 11 octobre 2022. [En ligne]. Disponible sur: https://www.ipcc.ch/report/sixth-assessment-report-working-group-3/

[4] IPBES, « Global assessment report on biodiversity and ecosystem services of the Intergovernmental Science-Policy Platform on Biodiversity and Ecosystem Services », Zenodo, mai 2019. doi: 10.5281/ZENODO.3831673.

[5] J. Rockström *et al.*, « Planetary Boundaries: Exploring the Safe Operating Space for Humanity », *E&S*, vol. 14, nº 2, p. art32, 2009, doi: 10.5751/ES-03180-140232.

[6] W. D. Chen et K. J. Chua, « Energy, exergy, economic, and environment (4E) assessment of a temperature cascading multigeneration system under experimental off-design conditions », *Energy Conversion and Management*, vol. 253, p. 115177, févr. 2022, doi: 10.1016/j.enconman.2021.115177.

[7] M. Yu, X. Liu, Z. Liu, et S. Yang, « Energy, exergy, economic and environmental (4E) analysis of a novel power/refrigeration cascade system to recover low-grade waste heat at 90–150 °C », *Journal of Cleaner Production*, vol. 363, p. 132353, août 2022, doi: 10.1016/j.jclepro.2022.132353.

[8] A. Bjørn, « Better, but good enough? », PhD Thesis.

[9] M. Vargas-Gonzalez *et al.*, « Operational Life Cycle Impact Assessment weighting factors based on Planetary Boundaries: Applied to cosmetic products », *Ecological Indicators*, vol. 107, p. 105498, déc. 2019, doi: 10.1016/j.ecolind.2019.105498.

[10] G. Wernet, C. Bauer, B. Steubing, J. Reinhard, E. Moreno-Ruiz, et B. Weidema, « The ecoinvent database version 3 (part I): overview and methodology », *Int J Life Cycle Assess*, vol. 21, nº 9, p. 1218-1230, sept. 2016, doi: 10.1007/s11367-016-1087-8.

[11] M. Z. Hauschild, R. K. Rosenbaum, et S. I. Olsen, Éd., *Life Cycle Assessment*. Cham: Springer International Publishing, 2018. doi: 10.1007/978-3-319-56475-3.

[12] M. Veyron, A. Voirand, N. Mion, C. Maragna, D. Mugnier, et M. Clausse, « Dynamic exergy and economic assessment of the implementation of seasonal underground thermal energy storage in existing solar district heating », *Energy*, vol. 261, p. 124917, déc. 2022, doi: 10.1016/j.energy.2022.124917.

[13] F. Bühler, « Energy efficiency in the industry: a study of the methods, potentials and interactions with the energy system », DTU Mechanical Engineering : DCAMM, Lyngby, 2018. [En ligne]. Disponible sur: https://orbit.dtu.dk/en/publications/energy-efficiency-in-the-industry-a-study-of-the-methods-potentia
[14] H. Pieper, I. Krupenski, W. Brix Markussen, T. Ommen, A. Siirde, et A. Volkova, « Method of linear approximation of COP for heat pumps and chillers based on thermodynamic modelling and off-design operation », *Energy*, vol. 230, p. 120743, sept. 2021, doi: 10.1016/j.energy.2021.120743.
[15] I. Sarbu et C. Sebarchievici, « A Comprehensive Review of Thermal Energy Storage », *Sustainability*, vol. 10, nº 1, p. 191, janv. 2018, doi: 10.3390/su10010191.
[16] B. Koçak, A. I. Fernandez, et H. Paksoy, « Review on sensible thermal energy storage for industrial solar applications and sustainability aspects », *Solar Energy*, vol. 209, p. 135-169, oct. 2020, doi: 10.1016/j.solener.2020.08.081.
[17] Susana Paardekooper, Rasmus Søgaard Lund, Brian Vad Mathiesen, Miguel Chang, Uni Reinert Petersen, Lars Grundahl, Andrei David, Jonas Dahlbæk, Ioannis Aristeidis Kapetanakis, Henrik Lund, Nis Bertelsen, Kenneth Hansen, David William Drysdale, Urban Persson, « Heat Roadmap Italy: Quantifying the Impact of Low-Carbon Heating and Cooling Roadmaps ». [En ligne]. Disponible sur: https://heatroadmap.eu/roadmaps/
[18] K. Riahi *et al.*, « Cost and attainability of meeting stringent climate targets without overshoot », *Nat. Clim. Chang.*, vol. 11, nº 12, p. 1063-1069, déc. 2021, doi: 10.1038/s41558-021-01215-2.
[19] S. García-Freites, C. Gough, et M. Röder, « The greenhouse gas removal potential of bioenergy with carbon capture and storage (BECCS) to support the UK's net-zero emission target », *Biomass and Bioenergy*, vol. 151, p. 106164, août 2021, doi: 10.1016/j.biombioe.2021.106164.
[20] V. Bisinella, T. Hulgaard, C. Riber, A. Damgaard, et T. H. Christensen, « Environmental assessment of carbon capture and storage (CCS) as a post-treatment technology in waste incineration », *Waste Management*, vol. 128, p. 99-113, juin 2021, doi: 10.1016/j.wasman.2021.04.046.
[21] S. Budinis, S. Krevor, N. M. Dowell, N. Brandon, et A. Hawkes, « An assessment of CCS costs, barriers and potential », *Energy Strategy Reviews*, vol. 22, p. 61-81, nov. 2018, doi: 10.1016/j.esr.2018.08.003.
[22] A. Babin, C. Vaneeckhaute, et M. C. Iliuta, « Potential and challenges of bioenergy with carbon capture and storage as a carbon-negative energy source: A review », *Biomass and Bioenergy*, vol. 146, p. 105968, mars 2021, doi: 10.1016/j.biombioe.2021.105968.
[23] L. Ramirez Camargo, « Hourly electricity load profiles of paper producing and food processing industries ». Mendeley, 19 mars 2021. doi: 10.17632/TTX9CHKDCG.1.
[24] « MATLAB Optimization Toolbox ». The MathWorks, Natick, MA, USA.
[25] A. Neumann, A. Hajji, M. Rekik, et R. Pellerin, « A Didactic Review On Genetic Algorithms For Industrial Planning And Scheduling Problems* », *IFAC-PapersOnLine*, vol. 55, nº 10, p. 2593-2598, 2022, doi: 10.1016/j.ifacol.2022.10.100.
[26] A. K. Kesarwani, M. Yadav, D. Singh, et G. D. Gautam, « A review on the recent applications of particle swarm optimization & genetic algorithm during antenna design », *Materials Today: Proceedings*, vol. 56, p. 3823-3825, 2022, doi: 10.1016/j.matpr.2022.02.200.
[27] R. C. Peralta, A. Forghani, et H. Fayad, « Multiobjective genetic algorithm conjunctive use optimization for production, cost, and energy with dynamic return flow », *Journal of Hydrology*, vol. 511, p. 776-785, avr. 2014, doi: 10.1016/j.jhydrol.2014.01.044.
[28] S. Elsoragaby *et al.*, « Applying multi-objective genetic algorithm (MOGA) to optimize the energy inputs and greenhouse gas emissions (GHG) in wetland rice production », *Energy Reports*, vol. 6, p. 2988-2998, nov. 2020, doi: 10.1016/j.egyr.2020.10.010.
[29] W. Willett *et al.*, « Food in the Anthropocene: the EAT–Lancet Commission on healthy diets from sustainable food systems », *The Lancet*, vol. 393, nº 10170, p. 447-492, févr. 2019, doi: 10.1016/S0140-6736(18)31788-4.
[30] A. W. Hjalsted, A. Laurent, M. M. Andersen, K. H. Olsen, M. Ryberg, et M. Hauschild, « Sharing the safe operating space: Exploring ethical allocation principles to operationalize the planetary boundaries and assess absolute sustainability at individual and industrial sector levels », *Journal of Industrial Ecology*, vol. 25, nº 1, p. 6-19, févr. 2021, doi: 10.1111/jiec.13050.
[31] Y. Jovet, A. Laurent, N. A. Kermani, F. Lefevre, B. Elmegaard, et M. Clausse, « Environmental assessment of electrification of food industry for Denmark and France », présenté à ECOS 2022 35th International Conference on Efficiency, Cost, Optimization, Simulation and Environmental Impact of Energy Systems, juill. 2022. Consulté le: 2 novembre 2022. [En ligne]. Disponible sur: https://hal-insa-lyon.archives-ouvertes.fr/hal-03715592

Comparative study of oxygen separation using cryogenic and membrane techniques for nCO2PP

Maja Kaszuba, Paweł Ziółkowski, Dariusz Mikielewicz

Gdańsk University of Technology, Faculty of Mechanical Engineering and Ship Technology, Poland,
maja.kaszuba@pg.edu.pl CA, pawel.ziolkowski1@pg.edu.pl, dariusz.mikielewicz@pg.edu.pl,

Abstract:

Due to the intense use of coal and gas while producing electricity, carbon capture and storage technologies need to be developed. One of the perspectives is oxyfuel combustion. It is the easiest method in the light of subsequent capture and storage of carbon dioxide. Due to the lack of nitrogen in the substrate, there are no nitrogen oxides in flue gases. The main drawback of that method is the very high energy consumption of the oxygen production technology. These days well-known technologies are cryogenic distillation and pressure swing adsorption. There are also novel oxygen production techniques such as chemical looping air separation and membrane processes. In the paper, a comparison between cryogenic air distillation and membrane separation is taken into consideration. Energy consumption of the cryogenic air distillation is on average 250 kWh/ ton O_2. On the other hand, there is an oxygen transport membrane but this approach requires a heat source because the process takes place at very high temperatures. Produced oxygen is required for the concept of the negative CO_2 gas power plant (nCO2PP). The power cycle uses oxygen and sewage sludge gasification gas for the combustion process. The two mentioned earlier oxygen production installations were modelled and confronted with the needs of the nCO2PP. Obtained cumulative efficiencies of the nCO2PP cycles were 21.26% and 23.48% for the power cycle integrated with a cryogenic air separation station (depending on oxygen purity), and 24.89% and 24.59% for the cycle combined with oxygen transport membrane (depending on the membrane area). The power cycle consists of a gasifier, air separation unit, compressors, turbines, wet combustion chamber, spray ejector condenser, and a CCS installation. The nCO2PP cycle is equivalent to the Bioenergy with Carbon Capture and Storage idea, because of the use of sewage sludge as fuel and CO_2 capture.

Keywords:

Thermodynamic analysis; Oxy-combustion; Energy penalty; CCS; cryogenic ASU; oxygen transport membrane.

1. Introduction

The oxy-fuel combustion is supposed to be one of the remedies for global warming, next to pre-combustion and post-combustion technologies [1]. The use of oxygen as an oxidizer prevents the generation of nitrogen oxides and provides only water vapor and carbon dioxide in exhaust gases. It should be highlighted, that oxy-combustion is one of the Carbon Capture and Storage (CCS) technologies and it is said to be the most promising one for the power cycles fuelled with fossil fuels [2]. The oxygen is 21% of the atmospheric air, and its amount delivered to the combustion chamber is based on the combustion stoichiometry, which is approximately 18 – 20 tons of O2/ day for 1 MW of electric installed power [3], [4]. If the biggest Polish power plant “Bełchatów” would work with oxy-combustion technology it would require as much as 92 thousand to 102 thousand tons of O2 per day depending on the power output.

The presented paper refers to oxygen production for the needs of the “Negative CO_2 emission gas power plant” (nCO2PP) [5], which is a kind of bioenergy with carbon capture and storage (BECCS) power cycle. The nCO2PP is a cycle, which utilizes sewage sludge as fuel and works with the oxy-combustion process. In this work, cryogenic air distillation and oxygen transport membrane (OTM) were taken into consideration.

Cryogenic air separation is the most popular and developed way to produce oxygen for the needs of oxyfuel combustion [6-8]. This way of oxygen production also provides other gases, like nitrogen, argon, krypton, and xenon [9]. The technology of very low temperatures is used to generate methane and helium from natural gas or in hydrogen production from coke oven gas [6]. It is based on the use of boiling points of air components to separate them. The air must be cooled first and then transported to rectification columns where is separated [10].

The second oxygen production method is the one using an oxygen transport membrane. The separation process is able to be carried out because of the electrochemical mechanisms and diffusion [11]. There are two

types of designs of oxygen production with the OTM method that can be highlighted, namely the three-end and four-end ones. The first one is about creating a vacuum on the permeate side of the membrane. The four-end is about introducing recirculated exhaust gases in counter-current on the permeate side of the membrane in case to provide the driving force [11, 12]. Oxygen transport membranes are made of two main groups of materials, that is perovskite and fluorite [13]. The third technology of oxygen production is pressure swing adsorption [14, 15], but it is not considered in this work.

The aim of this paper is to compare two technologies of oxygen production (based on air separation) for the requirements of the nCO2PP and check their impact on cycle efficiency. In this case, two models of oxygen production stations have been examined and integrated with the nCO2PP model. All analyses have been carried out using the Ebsilon software [16].

2. The power cycle

2.1. Negative emission CO_2 gas power plant

The oxy-combustion technology is said to be the best solution to capture and store carbon dioxide from power plants [17]. Over the years many power cycle installations with oxy-combustion technology have been proposed [18-20]. The negative carbon dioxide emission gas power plant means that the electricity is produced with negative carbon dioxide emission in the total balance of emissions. Emission is negative because the power plant uses sewage sludge as fuel and an oxy-fuel method to capture CO_2. If only one of the mentioned approaches was used, only a zero-emission power cycle would be an outcome. The scheme of the nCO2PP is shown in Figure. 1.

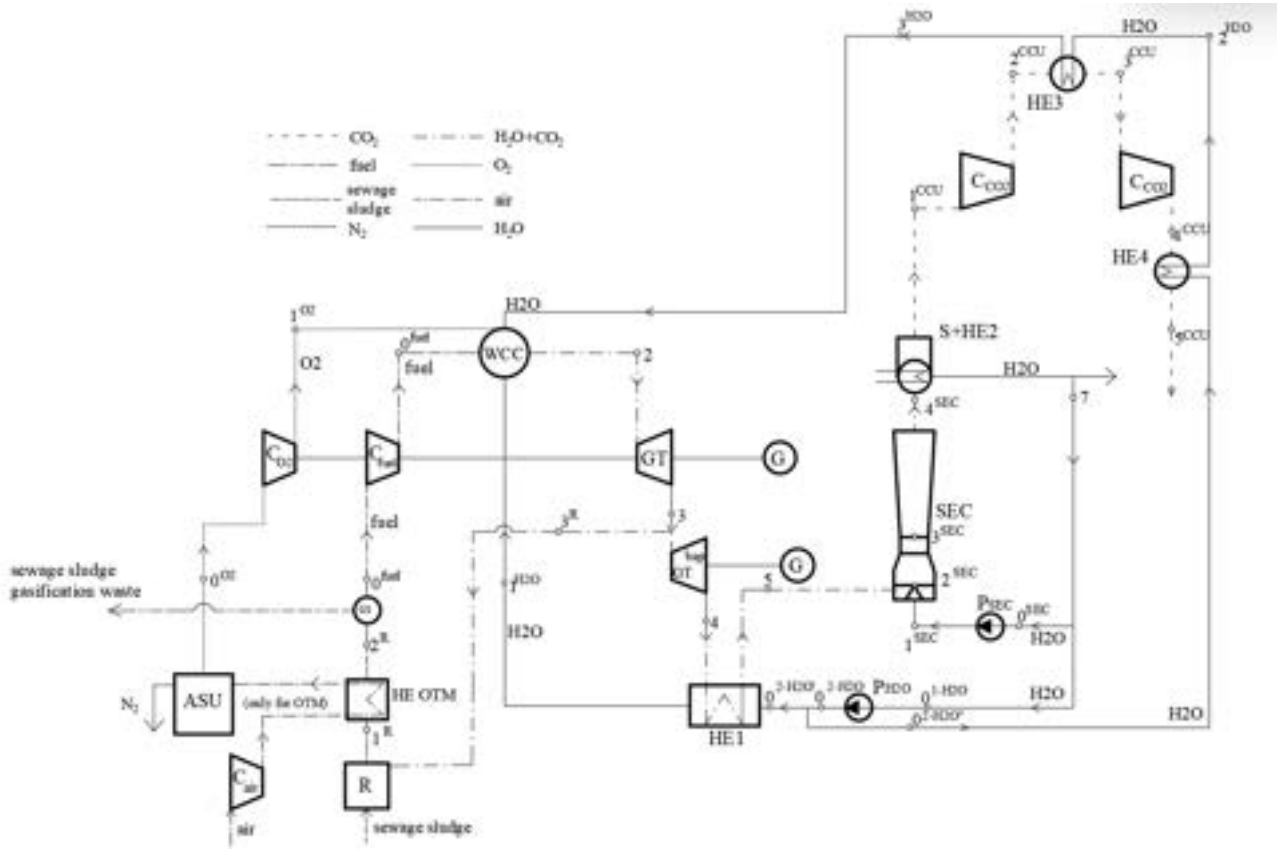

Figure. 1. The negative emission CO2 gas power plant (nCO2PP) integrated with gasification and oxygen transport membrane type of ASU, where: C_{air} – air compressor, C_{O2} – oxygen compressor, C_{fuel} – fuel compressor, WCC – wet combustion chamber, GT – gas turbine, GT^{bap} – low-pressure turbine, HE1 – heat exchanger 1, SEC – spray-ejector condenser, G – generator, P_{H2O} – water pump, P_{SEC} – SEC pump, S+HE2 – separator connected with heat exchanger 2, C_{CO2} – CO_2 compressor, HE3 – heat exchanger 3, HE4 – heat exchanger 4, HE OTM –heat exchanger for OTM separation, GS – gas scrubber, R – gasifier, ASU – air separation unit.

The nCO2PP cycle consists of an air separation unit (ASU), gasifier (R), carbon capture and storage installation (CCS), and the main part of the installation. The system is equipped with two compressors. The first one transports oxygen (C_{O2}), whereas the second one is for fuel transport (C_{fuel}). The cycle also consists of the high-pressure gas-steam turbine (GT – expansion from 10.5 bar to 1 bar), low–pressure turbine (GT^{bap} – expansion from 1 bar to 0.078 bar), wet combustion chamber (WCC – with temperature 1100℃), and generator (G). The main heat exchanger (HE1) heats the water supplied to the WCC with exhaust gases. The spray–ejector condenser (SEC) is a crucial device in the process of condensation of steam from a mixture of

CO_2+H_2O. A CCS installation consists of two compressors (C_{CO2}), two heat exchangers (HE3, HE4), and a heat exchanger connected with a water separator (S+HE2). The water pump (P_{H2O}) increases the pressure of water to a value of 10.5 bar, which is supplied to the WCC [5].

The initial nodes in the cycle can be established when fuel and oxygen compressors (C_{fuel}, C_{O2}) start transporting fluids to the combustion chamber (WCC). In WCC the combustion process takes place which creates a mixture of CO_2 and H_2O. Fuel and oxygen are necessary substrates, however, due to the high temperature of the processes there is injected water as a cooling medium to attain a temperature around 1100℃. Injection of the cooling medium is obligatory, because of the high temperature of stochiometric combustion, which can increase even to 3000 K as the effect of the oxy-combustion process. Additionally, the extra mass flow of water (nodal points 2^{H2O}, 3^{H2O}) contributes to the increase of the cycle efficiency, which is dependent on amount of regenerated heat. After the process in the WCC exhaust expands in the turbines (GT, GT^{bap}). Afterward, exhaust gases are used to heat water which is transported to the WCC in the regenerative heat exchanger (HE1). A part of the exhaust stream is directed to the gasification reactor (R) (or gasifier) and it is used in the gasification process. The spray-ejector condenser (SEC) intakes flue gases from the heat exchanger (HE1). Provided is also water, which is a motive fluid in the SEC with the pump (P_{SEC}). The presence of motive water, which breaks up into droplets and a mixture of steam and carbon dioxide enables the condensation process to take place. A mixture of water and carbon dioxide leaving the SEC goes to the separator connected with the heat exchanger (S+HE2). In the separator, water is isolated and directed to pumps (P_{SEC}, P_{H2O}). Subsequently, it is used as the motive fluid in SEC or as a coolant in the combustion chamber. The carbon dioxide is directed to the compressor (C_{CO2}), and then to the heat exchanger (HE3). It ought to be mentioned that in the air separation process with a membrane, the compressed air takes heat from fuel at the additional heat exchanger (HE OTM) downstream of the outlet of the gasifier. It is profitable because the oxygen production process with OTM needs to be carried out at a very high temperature, and fuel transported to the combustion chamber needs to be cooled before the fuel compressor (C_{fuel}).

2.2. Air separation units

As it was mentioned, two ways of oxygen production from the air were taken into consideration: cryogenic air distillation and oxygen transport membrane. Diagrams of them are shown in Figure. 2. For modelling using the Ebsilon software the cryogenic air separation unit is developed of an air compressor C_{air}, a pre-cooler PC, and two rectification columns RCI and RCII. In the separation process, the air is compressed to 5.8 bar, cooled in the pre-cooler, transported into the columns, and then separated into oxygen (O2), high-purity nitrogen (hN2), and low-purity nitrogen (lN2).

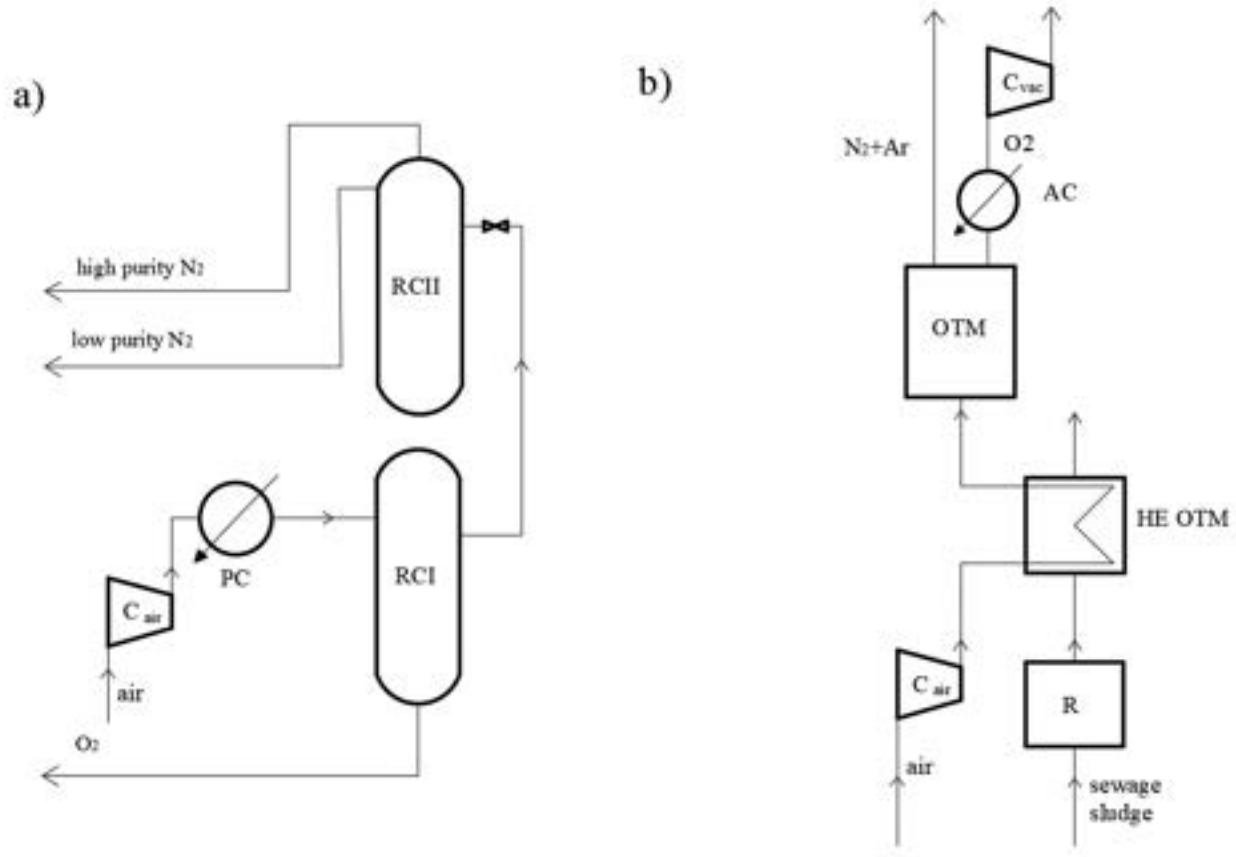

Figure. 2. Diagrams of oxygen production stations a) cryogenic b) oxygen transport membrane, where:

C_{air} – air compressor, PC – pre-cooler, RCI – column I, RCII – column II, R – gasifier, OTM – oxygen transport membrane, HE OTM – heat exchanger, AC – after-cooler, C_{vac} – vacuum pump.

The membrane separation unit consists of an air compressor C_{air}, a heat exchanger HE OTM, an after-cooler AC, a vacuum pump C_{vac}, and a membrane OTM. In this process, the proper oxygen partial pressure ratio at both sides of the membrane is set. These ratio values are 1.034 and 1.330 (depending on the membrane area), then heated to 740 ℃ in the HE OTM, separated in the membrane, and then cooled in AC before transporting to the oxygen compressor and the combustion chamber.

The main difference between the OTM method and the cryogenic ASU is that in the cryogenic separation air is cooled down in the pre-cooler after compression, whereas with the OTM, the air after compression must be heated to the correct temperature values for the electrochemical reaction to take place.

3. Methodology

The analyses have been carried out in the Ebsilon software, which uses mass and energy balance equations. Additionally, real gas correction equations such as the Peng-Robinson or the Redlich-Kwong equation can be set. The software predefined models are clearly expressed by thermodynamic tables for steam.

3.1. Efficiency calculation

The gross efficiency and the net efficiency have been calculated according to Eq. (1) and (2)

$$\eta_g = \frac{N_t}{\dot{Q}_{CC}} \tag{1}$$

where $N_t$is a combined power of turbines in kW and $\dot{Q}_{CC}$ is a chemical energy rate of combustion in kW.

$$\eta_{net} = \frac{N_t - N_{CP}}{\dot{Q}_{CC}} \tag{2}$$

Where $N_{CP}$is power needed for cycle own needs in kW and can by expressed by Eq. (3).

$$N_{CP} = N_{ASU} + N_{C_{fuel}} + N_{C_{O2}} + N_{P_{H2O}} + N_{P_{SEC}} + N_{C_{CCS}} \tag{3}$$

Where N_{ASU} is power for oxygen production, $N_{C_{fuel}}$ is power for fuel compressor, $N_{C_{O2}}$ is power for oxygen compressor, $N_{P_{H2O}}$is power for water pump, $N_{P_{SEC}}$ is power for SEC and $N_{C_{CCS}}$ is power for CCS compressors needs. All mentioned terms are expressed in kW.

Additionally, cumulative cycle efficiency which is a product of the net efficiency of the power cycle (η_{net}) and gasification process efficiency (η_{R_H}), has been calculated. The gasification process inside the gasifier was not calculated in this work but its efficiency has been taken from other work regarding nCO2PP [21]. The cumulative efficiency is presented in Eq. (4):

$$\eta_{cum} = \eta_{R_H} \cdot \eta_{net} \tag{4}$$

where gasification process efficiency (η_{R_H}) according to the literature [21] is equal to η_{R_H} =86.52% for the nCO2PP cycle.

3.2. Oxygen transport mechanism in the membrane

Oxygen permeation in the membrane is dependent on mass diffusion and electrochemical factors. Oxygen flux through the membrane can be formulated with the Wagner equation, which is presented in Eq. (5) [11]

$$j_{O2} = C_{wagner} \cdot \frac{T_m}{d_m} \cdot e^{\left(\frac{-K_{wagner}}{T_m}\right)} \cdot \ln \frac{P_{O2feed}}{P_{O2perm}} \tag{5}$$

Where j_{O2} is oxygen permeation rate in mol/(m²*s), T_m process temperature in K, d_m is membrane thickness in m, P_{O2feed} is pressure at the feed steam side in bar, P_{O2perm} is pressure at the permeate side in bar, C_{wagner} is a constant dependent on material in mol/(m*s*K), and K_{wagner} is a constant expressed in K.

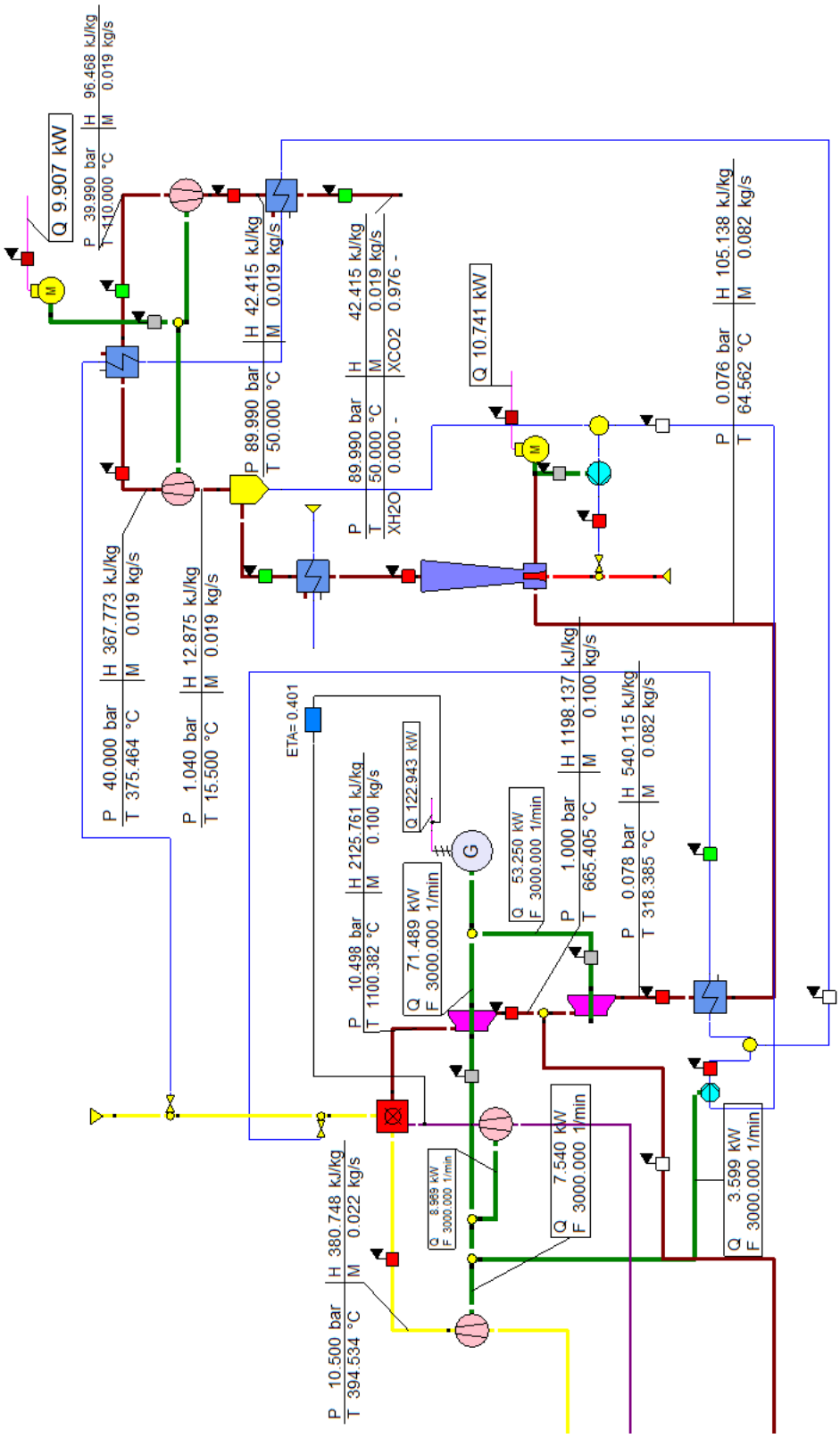

Figure. 3. The setup of the nCO2PP model in the Ebsilon software for the cryogenic case (without the ASU model) [22]

Coefficients K_{wagner} and C_{wagner} are dependent on the membrane material and they values are determined experimentally but in this case values from the literature were taken [11, 12].

The presented formula is an Arrhenius approach to Wagner equation, which assumes ionic conductivity is more important in the permeation process in the membrane than the electron based conductivity [11].

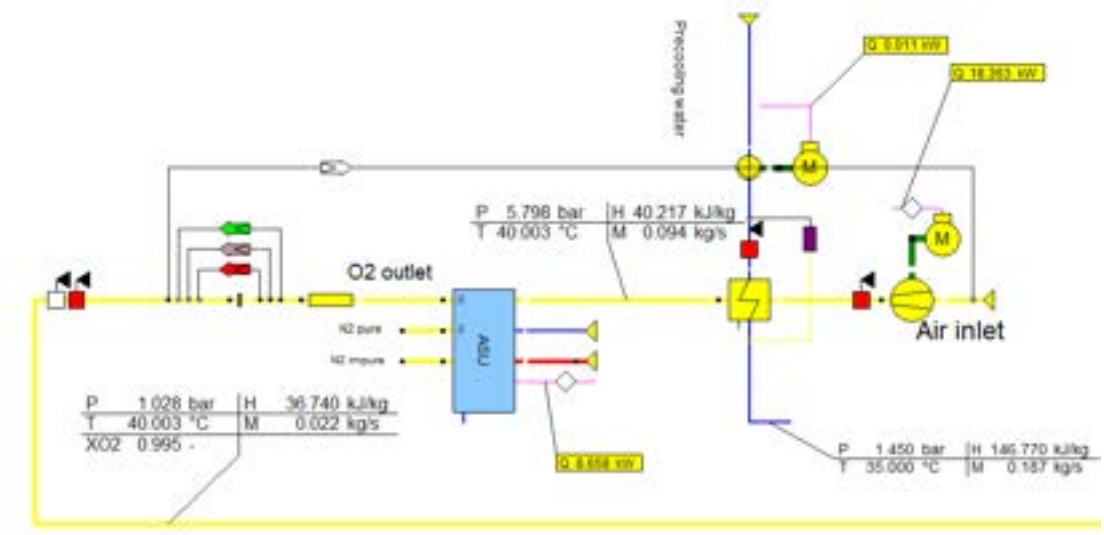

Figure. 4. The setup of the cryogenic ASU model in the Ebsilon software for 99.5% oxygen purity

3.3. Energy penalty and emissivity

For both oxygen production techniques, an important parameter is the energy penalty of oxygen production, which is expressed by the Eq. (6):

$$e_{pen} = \frac{N_{ASU}}{\dot{m}_{O2} * 3600} \tag{6}$$

where N_{ASU} is power for the needs of oxygen production expressed in kW and $\dot{m}_{O2}$ is the produced oxygen mass flow expressed in kg/s.

As the considered cycle name says, an essential factor is the emission potential (Eq. (7)) of the whole system, which can be defined with Eq. (7) [23, 24]:

$$eCO_2 = R\frac{\dot{m}_{4-CO_2}}{N_t - N_{cp}}3600 \tag{7}$$

where $\dot{m}_{4-CO2}$ is mass flow rate of carbon dioxide at the outlet of the CCS, R is a factor describing energy source as renewable energy (R for sewage sludge is 90% according to the Polish law [25]). Emission potential eCO_2 is expressed in $kgCO_2/(MWh)$.

The emission calculations should be carried out properly and carefully if the power cycle is integrated with the carbon capture and storage unit. If an energy source is only partly considered as a renewable source of energy, emissions should be multiplied by the factor that accounts for it. In this case, the relative emissions of carbon dioxide were multiplied by η_{net}. The relative emission is presented by Eq. (8).

$$\eta_{net} \cdot e_{CO_2} = \frac{N_t - N_{cp}}{LHV_{gas} \cdot \dot{m}_{0-fuel}} R\frac{\dot{m}_{4-CO2}}{N_t - N_{cp}}3600 = R\frac{\dot{m}_{4-CO2}}{\dot{Q}_{CC}}3600 \tag{8}$$

Avoided eCO_2 for the negative emission power plant is a sum of emissions without CO_2 capture and the value of negative emissions obtained because of the application of renewable energy source [24].

4. Assumptions

For the purpose of calculations, several assumptions were made. The nCO2PP cycle uses sewage sludge as feedstock for gasification and fuel production. The combustion process is carried out with oxygen as the oxidizer. On top of the mentioned earlier, the following assumptions have been made in calculations:

- mixture of fuel and oxidant is stoichiometric,
- mass flow rate of exhaust gases is constant, and its value is 0.1 kg/s,

- temperature in the combustion chamber is constant and its value is 1100 °C,
- pressure in the combustion chamber is constant and its value is 10.5 bar,
- pressure after turbines GT and GT^{bap} are respectively 1 bar and 0.078 bar.

Calculations were carried out for two oxygen production stations. For cryogenic installation, two analyses dependent on oxygen purity were made, namely one for 99.5% (extremely high with higher energy penalty) purity and the second for 96% purity (accepted value for many technical processes). The air at the inlet to the cryogenic unit was compressed to 5.8 bar. For OTM solution also two analyses were made with constant oxygen purity at the level of 99.5%. However, one for 96 cm^2 membrane area and the second for 12 cm^2. Oxygen flux through the membrane is dependent on several features. The first one is a membrane thickness, which was set as 1 mm as in the literature [26]. The process temperature was set as 740℃, because of possibility of heating up in the heat exchanger after gasification process. Values of the mentioned coefficients $\mathrm{K_{wagner}}$ and $\mathrm{C_{wagner}}$ were taken from literature respectively as 6201 K and 1.004*10^{-6} mol/(m×s×K) [11, 12]. Syngas from sewage sludge gasification has the following composition: 13.31% CO, 5.12% H_2, 11.46% CH_4, 59.29% CO_2, 8.03% C_3H_8, and its LHV is 17.44 MJ/kg.

Other assumptions are included in Table 1.

Table 1. Assumptions for the thermodynamic cycle negative CO_2 gas power plant (nCO2PP) integrated with gasification and ASU

Parameter	Symbol	Unit	Value
Initial fuel temperature	t_{fuel}	ºC	50
Initial oxygen temperature	t_{O2}	ºC	15
Syngas fuel pressure before C_{fuel} compressor	p_{0-fuel}	bar	1
Oxygen pressure before C_{O2} compressor	p_{0-O2}	bar	1
Regenerative water pressure to WCC	p_{1-H2O}	bar	254.95
Exhaust vapor quality after HE1	x_5	-	0.999
Exhaust temperature after HE1, before SEC	t_5	ºC	62.77
CO_2 pressure after compressor C_{CCU1}	p_{2-CCU}	bar	40
CO_2 pressure after compressor C_{CCU2}	p_{4-CCU}	bar	90
H_2O temperature after HE4	t_{2-H_2O}	ºC	91.67
CO_2 temperature after HE3	t_{3-CCU}	ºC	110
Water vapor from Separator in 1^{CCU} mixed with CO_2 vapor	-	%	100% humid
Pressure after GT^{bap}	p_4	bar	0.078
Temperature after SEC	t_6	ºC	18.03
Turbine GT, internal efficiency (η_i)	η_{iGT}	-	0.89
Turbine GT^{bap}, η_i	$\eta_{iGT-bap}$	-	0.89
Fuel compressor C_{fuel}, η_i	$\eta_{iC-fuel}$	-	0.89
Oxygen compressor C_{O2}, η_i	η_{iC-O2}	-	0.87
Water pump P_{H2O}, η_i	η_{iP-H2O}	-	0.43
Water pump P_{SEC}, η_i	η_{iP-SEC}	-	0.80
CO_2 compressor $C_{CO2\text{-}1}$, η_i	$\eta_{iC-CO2-1}$	-	0.85
CO_2 compressor $C_{CO2\text{-}2}$, η_i	$\eta_{iC-CO2-2}$	-	0.85
Mechanical efficiency for all devices	η_m	-	0.99
Gasification process efficiency	η_{R_H}	-	0.8652

5. Results

In the course of calculations four scenarios were considered, i.e.:

- cryogenic air separation with 99.5% oxygen purity,
- cryogenic air separation with 96% oxygen purity,
- oxygen transport membrane separation with 96 cm^2 membrane area,
- oxygen transport membrane with 12 cm^2 membrane area.

In all cases exhaust mass flow after the combustion chamber was 100 g/s, and the temperature in the combustion chamber was 1100℃. Also in all cases pressure in the combustion chamber was 10.5 bar. Start values of fluids (air at the inlet of the air compressor and fuel at the inlet to gasifier) were set as 1 bar pressure and 15℃ temperature. Between two turbines GT and GT^{bap} is a bleed stream for transporting part of the exhaust to the gasifier, and its pressure is 1 bar. All the results are shown in Table 2. In the first two columns on the left side are the results for nCO2pp with different oxygen purities produced in cryogenic air separation

unit. In the second two columns are presented results for nCO2pp with oxygen transport membrane with two different membrane areas. In Table 3 results of respective emissions are provided.

Table 2. Results of power output and efficiency of the analyses for all cases

			nCO2pp with cryogenic ASU		nCO2pp with OTM	
			oxygen purity 99.5%	oxygen purity 96%	membrane area 96 cm^2	membrane area 12 cm^2
Mass flow at the outlet of the WCC	m_2	g/s	100.00	100.00	100.00	100.00
Exhaust temperature at the outlet of the WCC	t_2	℃	1100.00	1100.00	1100.00	1100.00
Oxygen purity		%	99.50	96.00	99.50	99.5
Turbine bleed pressure		bar	1.00	1.00	1.00	1.00
Turbine power output	N_t	kW	143.05	143.68	144.54	144.61
Power for ASU/OTM needs	N_{ASU}	kW	27.03	18.97	14.00	14.81
Power for own needs	N_{CP}	kW	67.79	60.62	56.66	58.17
Fuel heat	*LHV*	kW	306.27	306.08	305.44	304.17
Gross efficiency	η_g	%	46.71	46.94	47.32	47.54
Nett efficiency	η_{net}	%	24.57	27.14	28.77	28.42
Cumulative efficiency	η_{cum}	%	21.26	23.48	24.89	24.59
Energy penalty	e_{pen}	kWh/kgO_2	0.346	0.242	0.179	0.190

Table 3. Results of emissions for all analyzed cases

			nCO2pp with cryogenic ASU		nCO2pp with OTM	
			oxygen purity 99.5%	oxygen purity 96%	membrane area 115.11 m^2	membrane area 300 m^2
Emission of CO_2	eCO_2	kgCO_2/MWh	-861.05	-741.15	-700.51	-712.20
Relative emissivity of CO_2	$\eta_{net} \cdot e_{CO_2}$	kgCO_2/MWh	-211.58	-201.12	-201.54	-202.39
Avoided CO_2 emission	Avoid CO_2	kgCO_2/MWh	1817.77	1564.65	1478.85	1503.52

6. Discussion

It was not obvious, which approach to oxygen production will be more appropriate for the negative CO_2 emission gas power plant. Both cryogenic distillation and oxygen transport membrane technologies are regarded as energy-consuming. In previous research, only cryogenic air separation was taken into consideration [22]. The nCO2pp power cycle has a characteristic gasifier that produces fuel at 967℃ [21]. This fact was a strong reason to investigate the oxygen transport membrane which needs a heat source.

Calculations indicate that net efficiencies of the nCO2PP for the cryogenic ASU for 99.5% and 96% oxygen purities are 24.57% and 27.14%. Taking into account a gasifier efficiency which was 86.52%, cumulative efficiencies values for the cycle with cryogenic ASU are 21.26% and 23.48% for higher oxygen purity and lower oxygen purity, respectively. It was similar to the cycle integrated with OTM. The nCO2PP reached higher efficiency when the OTM area was larger. For 96 cm^2 membrane area net efficiency and cumulative efficiency were 28.77% and 24.89%. For nearly six times smaller membrane area of 12 cm^2, these efficiencies were 28.42% and 24.59%. It is worth mentioning that by comparing cryogenic ASU (99.5% oxygen purity) and membranes, efficiency savings can be obtained. For 96 cm^2 of membrane area, it is 4.2%, and for 12 cm^2 is 3.85%. In [12] Portillo got 5% efficiency saving comparing these two technologies. Undeniably is the fact, that OTM ASU is thermally integrated with the nCO2PP, and the membrane does not require a heat source from the outside. All heat for air heating is taken from the gasification process, so it is internal cycle heat. It is very possible that the OTM solution would not be effective if there was a need to supply the heat source from the outside.

According to the results, the power demand for cryogenic ASU is 18.89% and 13.20% of the cycle generated power, respectively for 99.6% oxygen purity and 96% oxygen purity. According to the literature, cryogenic ASU should be responsible for 6-7% power loss for industrial solutions [27]. For lower stream rates, the energy requirement of the ASU becomes significantly higher, especially for demonstration and laboratory solutions. Therefore, this study considers a different solution, namely OTM. On the other hand, oxygen transport membrane unit power requirements are 9.69% and 10.24% of the generated power, respectively for 96 cm^2 membrane area and 12 cm^2 membrane area. It is very visible that power requirements for OTM are strongly dependent on the membrane area. It is similar to membrane thickness, air temperature, and membrane material [11, 12, 26].

An important thing is also the power needed to produce oxygen unit. To ensure a stoichiometric combustion process, to the combustion chamber 0.0217 kg/s oxygen mass flow was transported in all four cases. Obtained power consumption values for cryogenic ASU are 0.346 kWh/kgO_2 and 0.242 kWh/kgO_2 for 99.5% oxygen purity and 96% oxygen purity. It can be said those values are possible, especially in the light of the statement by Aneke [28] who says that for 99.9% oxygen purity the power consumption is 0.357 kWh/kgO_2, Tafone in [29] for 99.5% in his research assumes 0.370 kWh/kgO_2, and Fu C. in [4] says that for 95% purity the power consumption is 0.229 kWh/kgO_2. For OTM oxygen production 0.179 kWh/kgO_2 and 0.190 kWh/kgO_2 power consumption for 96 cm^2 and 12 cm^2 membrane area were obtained. Perhaps in this work, the membrane area doesn't occur to be a significant factor but if a bigger power cycle were considered, it would might be a very important thing for examination. According to every special case, it might be more effective to buy a smaller membrane but use more power during operation, or to buy a bigger membrane but use less power. Nevertheless, some researches show [30] that an infinite increase of the membrane area has rather a small effect on power saving.

Emissivity results are interesting. According to the results, cases with theoretically lower efficiency (cryogenic ASU with 99.5% oxygen purity and OTM with 12 cm^2 membrane area) reached a larger value of negative CO_2 emission. These two scenarios also obtained higher values of avoided CO_2 emission. It is because these two solutions have higher values of power for their own needs, which is important according to Eq. (7). Negative emission occurs due to the use of renewable energy source as fuel and using CCS installation. If there was only one of these two solutions, the power plant would be zero emissive.

7. Conclusions

The main novelty of the present work was the thermodynamic analysis of the nCO2PP cycle integrated with gasification and an OTM-type oxygen separation station. As the objective of the paper was to find an appropriate way of oxygen production technology for the negative CO_2 emission gas power plant (nCO2PP) it proved to be an uneasy task. Firstly, cryogenic air distillation was regarded to be a superior technology as it is recommended in most of the literature. However, the efficiency reductions obtained indicate that for such low flows of oxygen produced (as assumed in calculations), it makes more sense to buy it from industrial producers.

According to the obtained results, the oxygen transport membrane has better perspectives for the nCO2PP, especially because of a large amount of heat from the sewage sludge gasification process. To be sure of that, more factors such as membrane material, area, process temperature, and pressure difference at both sides of the membrane should be widely considered by CFD calculation. However, this is beyond the scope of this paper.

Acknowledgments

The research leading to these results has received funding from the Norway Grants 2014-2021 via the National Centre for Research and Development. This research has been prepared within the frame of the project: "Negative CO2 emission gas power plant" - NOR/POLNORCCS/NEGATIVE-CO2-PP/0009/2019-00 which is co-financed by programme "Applied research" under the Norwegian Financial Mechanisms 2014-2021 POLNOR CCS 2019 - Development of CO2 capture solutions integrated in power and industry processes.

Presented research regarding oxygen transport membrane is a result of a project and it was financed from RADIUM LERANING THROUGH RESEARCH PROGRAMS.

Nomenclature

C_{wagner} constant dependent on the material, mol/(m×s×K)

d_m membrane thickness, mm

eCO_2 emissivity, kgCO_2/MWh

e_{pen} energy penalty, mWh/kgO_2

j_{O2} oxygen permetaion rate mol/(m^2×s)

K_{wagner} constant dependent on the material, K

LVH lower heating value, MJ/kg

m mas flow, kg/s

N_{ASU} power for air separation needs, kW

$N_{C_{CCS}}$ power for CCS compressors needs, kW

N_{CP} power for own needs, kW

$N_{C_{fuel}}$ power for fuel compressor needs, kW,

$N_{C_{O2}}$ power for oxygen compressor needs, kW,

$N_{P_{H2O}}$ power for water pump needs, kW,

$N_{P_{SEC}}$ power for SEC pump needs, kW,

N_t combined turbines power, kW

P_{O2feed} pressure at the membrane feed stream side, bar

P_{O2perm} pressure at the membrane permeate stream side, bar

R factor describing energy source as renewable, -

t temperature, ℃

T_m process temperature, K

$\dot{Q}_{CC}$ chemical rate of combustion, kW

Abbreviations

AC after-cooler

ASU air separation unit

BCCS bioenergy with carbon capture and storage

C compressor

CCS carbon capture and storage

G generator

GS gas scrubber

GT gas turbine

HE heat exchanger

nCO2PP negative CO_2 emission gas power plant

OTM oxygen transport membrane

P pump

PC pre-cooler

R gasifier

RC rectification column

SEC spray ejector condenser

WCC wet combustion chamber

Greek Symbols

η_{cum} cumulative efficiency, %

η_g gross efficiency of the cycle, %

η_{net} net efficiency of the cycle, %

η_{R_H} gasifier efficiency, %

References

[1] Serrano J.R., Arnau F.J., García-Cuevas L.M., Gutiérrez F.A., Thermo-economic analysis of an oxygen production plant powered by an innovative energy recovery system. Energy,2022, vol. 255.

[2] Ye H., Zheng J., Li Y., Feasibility analysis and simulation of argon recovery in low oxygen-purity cryogenic air separation process with low energy consumption. Cryogenics, 2019, vol. 97.

[3] Nowak W., Chorowski M., Czakiert T., Spalanie tlenowe dla kotłów pyłowych i fluidalnych zintegrowanych z wychwytem CO_2. Produkcja tlenu na potrzeby spalania tlenowego. Częstochowa, Polska: Wydawnictwo Politechniki Częstochowskiej; 2014.

[4] Fu C., Gundersen T., Using exergy analysis to reduce power consumption in air separation units for oxy-combustion processes. Energy, 2012, vol. 44, no.1.

[5] Negative CO_2 emission gas power plant (nCO2PP) (https://nco2pp.mech.pg.gda.pl/pl)

[6] Chorowski M., Kriogenika. Podstawy i zastosowania. Gdańsk, Polska: IPPU MASTA; 2007.

[7] García-Luna S., Ortiz C., Carro A., Chacartegui R., Pérez-Maqueda L.A, Oxygen production routes assessment for oxy-fuel combustion. Energy, 2022, vol. 254.

[8] Darde A., Prabhakar R., Trainier J., Perrin N., Air separation and flue gas compression and purification units for oxy-coal combustion systems. Energy Procedia, 2009, vol.1.

[9] Kerry F., Industrial gas handbook: gas separation and purification. New York, USA: Taylor & Francis Group, LLC, 2006.

[10] Fu Q., Kasha Y., Chunfeng S., Liu Y., Ishizuka M., Tsutsumi A., A cryogenic air separation process based on self-heat recuperation for oxy-combustion plants. Applied Energy, 2015.

[11] Portillo E., Alonso-Fariñas E, Vega F., Cano M., Navarrete B., Alternatives for oxygen-selective membrane systems and their integration into the oxy-fuel combustion process: A review. Separation and Purification Technology, 2019, vol. 229.

[12] Portillo E., Gallego Fernández L.M., Vega F., Alonso-Fariñas B., Navarrete B., Oxygen transport membrane unit applied to oxy-combustion coal power plants: A thermodynamic assessment. Journal of Environmental Chemical Engineering, 2021, vol. 9, no. 4.

[13] Kotowicz J., Job M., Brzęczek M., Thermodynamic analysis and optimization of an oxy-combustion combined cycle power plant based on a membrane reactor equipped with high-temperature ion transport membrane ITM. Energy, 2020 vol.15.

[14] Rizk J., Nemer M., Clodic D., A real column design exergy optimization of a cryogenic air separation unit. Energy, 2012, vol. 37.

[15] Banaszkiewicz T., Chorowski M., Gizicki W., Comparative analysis of oxygen production for oxy-combustion application. Energy Procedia, 2015, vol. 51.

[16] Steag Energy Services Ebsilon®Professional

[17] Burdyny T., Struchtrup H, Hybrid membrane/cryogenic separation of oxygen from air for use in the oxy-fuel process. Energy, 2010, vol. 35, no. 5.

[18] Yantovski E., Zvagolsky K. N., Gavrilenko V. A.: The cooperate - demo power cycle. Energy Conversion and Management, 1995, vol. 36.

[19] Yantovski E.: Zero Emission Fuel-Fired Power Plants Concept. Energy Conversion and Management, 1996, vol. 37.

[20] Sanz W., Hustad C-W., Jericha H.: First generation Graz cycle power plant for near-term development. Proceedings of ASME Turbo Expo 2011.

[21] Ziółkowski P., Stasiak K, Amiri M., Mikielewicz D., Negative carbon dioxide gas power plant integrated with gasification of sewage sludge. Energy, 2023, vol. 262.

[22] Kaszuba M., Ziółkowski P., Mikielewicz D., Thermodynamical analysis of integration of a negative emission power plant cycle with oxygen generation station. 7th International Conference on Contemporary Problems of Thermal Engineering, 2022.

[23] Ziółkowski P. et al., Thermodynamic analysis of negative CO2 emission power plant using Aspen Plus, Aspen Hysys, and Ebsilon software. Energies, 2021, vol. 14, no. 19.

[24] Madejski P., Chmiel K., Subramanian N., Kuś T., Methoda and Techniques for CO_2 Capture: Review of Potential Solutions and Applications in Modern Energy Technologies. Energies, 2022, vo. 15.

[25] DZIENNIK USTAW RZECZYPOSPOLITEJ POLSKIEJ (Rozporządzenie Ministra Środowiska z dnia 8 czerwca 2016 r. w sprawie warunków technicznych kwalifikowania części energii odzyskanej z termicznego przekształcania odpadów).

[26] Chen W., van der Ham L., Nijmeijer A., Winnubst L, Membrane-integrated oxy-fuel combustion of coal: Process design and simulation. Journal of Membrane Science, 2015, vol. 492.

[27] Fu C., Gundersen T., Recuperative vapor recompression heat pumps in cryogenic air separation processes. Energy, 2013, vol. 59.

[28] Aneke M., and Wang M., Potential for improving the energy efficiency of cryogenic air separation unit (ASU) using binary heat recovery cycles. Applied Thermal Engineering, 2015, vol. 81.

[29] Tafone A., Dal Magro F., Romagnoli A., Integrating an oxygen enriched waste to energy plant with cryogenic engines and Air Separation Unit: Technical, economic and environmental analysis. Applied Energy,2018, vol. 231.

[30] Gutiérrez F.A., García-Cuevas L.M., Sanz W., Comparison of cryogenic and membrane oxygen production implemented in the Graz cycle. Energy Conversion and Management, 2022, vol. 271.

Use of residual energy from underground infrastructures: Madrid – Sevilla metro station.

Susana Sánchez-Orgaz[a], Javier Muñoz Antón[b], Marina Tadeo Cañete[c] and Javier Rodríguez Martín[d]

*a UPM, Madrid, Spain, susana.sanchez.orgaz@upm.es, **CA***
b UPM, Madrid, Spain, javier.munoz.anton@upm.es,
c UPM, Madrid, Spain, m.tadeo@alumnos.upm.es,
d UPM, Madrid, Spain, javier.rodriguez.martin@upm.es

Abstract:

Cities have great potential to implement innovative solutions and improve energy efficiency and the use of non-conventional energy sources, laying the foundations for a new, more sustainable urban model. With this vision and the aim of finding solutions to this challenge, Madrid Subterra emerges. This work is within the project of this association created with the aim of promoting the exploration and exploitation of the potential of clean and renewable energy of the urban subsoil of Madrid. This study analyses the energy use of the Seville Metro station for the thermal supply of the Building of the Ministry of Environment of the Community of Madrid. The main goal is to extract the waste heat generated in the metro tunnels due to the traction and braking of machines, auxiliary facilities, or transit of people on the platforms and use it to produce domestic hot water (DHW) using a heat pump to supply the referred building. This concept could reduce the temperature in Metro facilities and save energy. From the tunnel the ventilation flow and temperatures data, the performance of the system has been estimated using the CoolPack program. The results obtained show that this system could supply domestic hot water for 7640 people per month with a COP of 2.663 and SCOP of 1.975.

Keywords:

Circular Economy; Energy Saving; Sustainability; Thermal supply; Waste Heat;

1. Introduction

Cities today and focusing on the specific case of the city of Madrid, has a great potential for waste heat that is generated in tunnels and platforms. This waste heat could be studied, extracted and implemented innovative solutions for improving energy efficiency and using non-conventional energy sources. This potential can be boosted to further reduce CO_2 emissions and make cities more sustainable. For all the above, the Madrid Subterra Association arises, created with the aim of promoting the exploration and exploitation of the clean and renewable energy potential of Madrid's urban land, allowing to transform the current vicious circle of waste, and overheating into a virtuous circle of energy efficiency.

Heat pumps are considered one of the most efficient heating and cooling systems and, according to Directive 28/2009/EC, the aerothermal, geothermal or hydrothermal energy captured by these appliances is considered energy from renewable sources. For these reasons, they will play a key role in reducing greenhouse gas emissions [1].

Aerothermal energy encompasses all the systems that allow energy to be extracted from the air. The most used technology for the use of aerothermal energy is the air-water heat pump that is developed in this work and that allows heating or cooling the water of a building, Figure 1.

Heat pumps consume up to 70% less energy than a traditional heating system. The consumption will depend on the type of heat pump we have, in the case of the aerothermal heat pump, the consumption would be 1 kW electric and would allow to deliver up to 4 kW of heating.
The International Energy Agency, in its 2016 report on Energy Efficiency, considered the heat pump as the Best Available Technology (BAT) for space heating. In addition, Greenpeace in 2011 chose the heat pump as the best heating system when it comes to energy efficiency.
The objective of this work is to take advantage of clean and renewable energy from the subsoil in Metro de Madrid's infrastructures. It is intended to extract the waste heat generated in the metro tunnels due to the traction and braking of machines, auxiliary facilities, or transit of people on the platforms and use it to produce domestic heat water (DHW) of a building in the Community of Madrid, thus assuming savings in kWh.

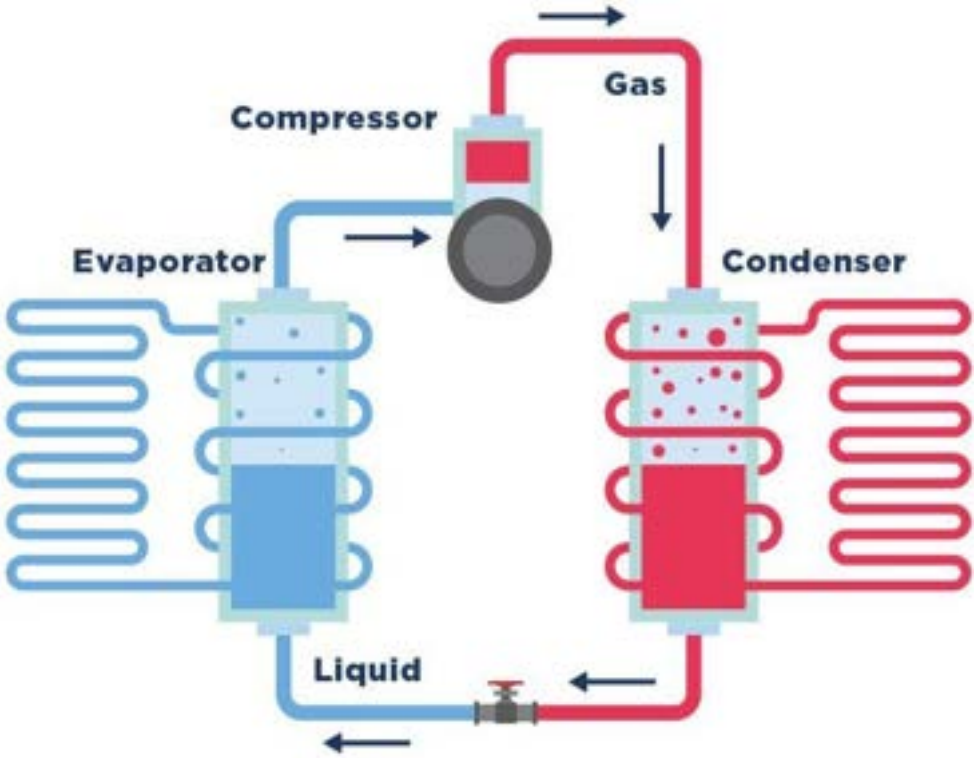

Figure 1. Heat Pump. Source https://www.bordgaisenergy.ie/home/heat-pump-guide

The study of the thermal use of air will be carried, out in the Seville metro station and in the Building of the Ministry of Environment of the Community of Madrid, Figure 2.

Figure 2. Location of Metro Sevilla and the building of the Ministry of Environment

Sevilla Metro station is a station on line 2 of the Madrid Metro located under Calle Alcala, at the junction with Calle de Sevilla, which gives its name to the station. It is a very small station of approximately 1000 m^2, with "light" trains of 4 cars, with platforms of 60 m and with low influx according to the data provided with Metro Madrid.

The objective of the work is, therefore, to have an estimate of the liters of domestic heat water that could be obtained from the flow of air extracted by means of the fans of the extraction well. In addition, the number of people inside the Building of the Ministry of Environment that could be supplied with that volume of water will be estimated.

2. Methodology

The methodology followed in this study consists of three steps:

- **Step 1:** The simulations provided by Metro de Madrid corresponding to the Seville station allow us to know and analyze the air temperatures and the ventilation flows of the tunnel and determine the design conditions.
- **Step 2:** The aerothermal heat pump is designed and sized. The result of this step is the fundamental parameters of the heat pump.
- **Step 3:** The installation performance is estimated using the CoolPack program [2] from the results obtained in the previous steps.

The centralized DHW installation object of this study has been designed according to the Technical Guide of Central Sanitary Hot Water of the IDEA [3]. This document establishes certain design criteria, especially highlighting the importance of control over Legionella. The hygienic-sanitary measures that must be adopted in those facilities in which Legionella is capable of proliferating and spreading are described on the Royal Decree 487/2022, of June 21 [4].

2.1. Analysis of the data provided by Metro Madrid.

For the calculation of the use of heat from the Seville Metro station, the simulations provided by Metro Madrid have been analyzed. In them, there is on the one hand the thermal evolution in a winter, half-time and summer day for four fundamental domains: station (platform level), vestibules and the two adjacent tunnel sections. On the other hand, there is the flow of air, which is massively directed to the shafts of the tunnels, and especially to the tunnel of Banco de España, (Tunnel 1) since it has forced ventilation. The place chosen to put the pump and carry out the study is Tunnel 1 due to its greater air extraction flow, Figure 3.

The following points have been considered for the study and diagnosis:

- It has been decided to work according to the key variables of the problem: the ventilation flow and temperatures. An average temperature will be taken for winter, halftime and summer, Table 1.
- Operating hours of the fans, in winter they would work 10 hours a day, in halftime 13 and in summer they would be on for 15 hours extracting the air flow, according to the data provided by Metro Madrid.

Table 1. Average data of the selected temperature Metro Madrid.

Parameters	Values
Average winter temperature	12.9 ^oC
Average halftime temperature	17.6 ^oC
Average summer temperature	20.9 ^oC

With these data, we proceed to define the design of the components of the heat pump that would be installed in Tunnel 1 and the selection of the parameters of the simple thermodynamic cycle with which it would work.

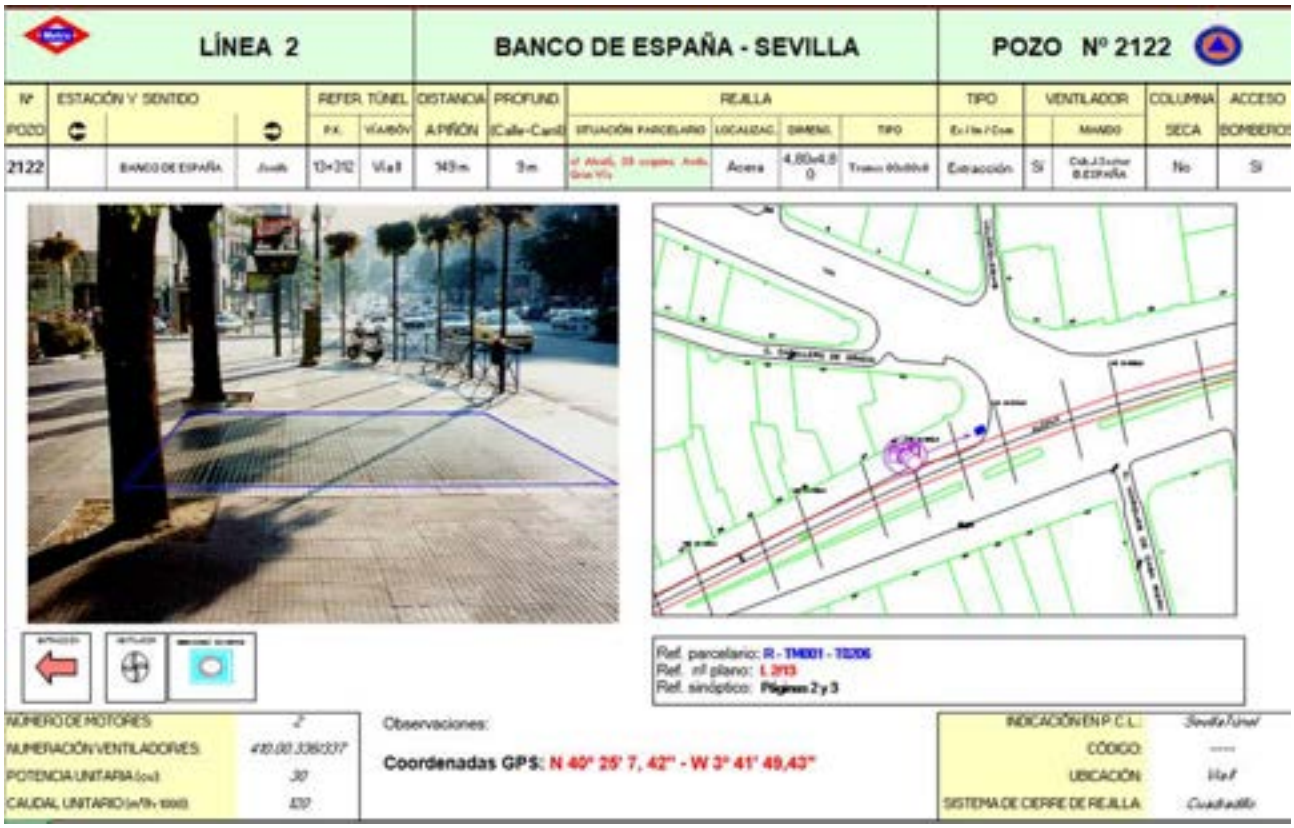

Figure 3. Photo of the place where the Heat Pump will be located.

2.2. Design and size of the aerothermal heat pump.

The proposed installation will comprise a simple heat pump system that consists of four primary components: a compressor, two heat exchangers (condenser and evaporator), and an expansion valve, as depicted in Figure 1. The initial calculation parameters selected for the analysis are specified in Table 2.

Table 2. Parameters for calculating.

Parameters	Data
Domestic hot water temperature	55ºC [3]
Condensation temperature	60ºC
Subcooling temperature	10K
Useful superheat temperature	7K
Exhaust air flow	30 m^3/s (Tunnel 1)
Seasonal temperature data	Table 1

2.2.1. Evaporator.

The evaporator serves as a heat exchanger, facilitating the phase change of the refrigerant from liquid to vapor while absorbing heat. In order to determine the power associated with the evaporator, Eq. (1) is employed, considering the parameters outlined in Table 3 in order to evaluate the energy balance between evaporator refrigerant and air to subtract heat.

$$Q(kW) = \dot{v}_{air}\left(\frac{m^3}{s}\right) \cdot \rho\left(\frac{kg}{m^3}\right) \cdot C_p\left(\frac{kJ}{kgK}\right) \cdot \Delta T = \dot{m}_{\text{refrigerant}} \cdot \Delta \text{h} \quad (1)$$

Table 3. Parameters for calculating the power of the evaporator.

Parameters	Data
Air flow ($\dot{v}_{air}$)	30 m^3/s
Air density (ρ)	1.2 kg/m^3
Specific heat of air (C_p)	1.007 kJ/kg K
Temperature difference at evaporator inlet and outlet (ΔT)	Variable in the study

Upon analysis of the evaporator power results presented in Table 4, it was observed that the extracted power remained independent of variations in the air inlet temperature. It should be noted that the calculation of efficiency is contingent upon the time of year for which it is being computed.

Table 4. Evaporator powers (Q_{evap}), according to thermal jump.

ΔT (K)	Q_{evap}(kW)
2	72.5
4	145.0
6	217.5
8	**290.0**

In order to determine the efficiency of the evaporator, the NTU (Number of Transfer Units) Effectiveness Method [5] is employed, Eq. (2). Number of Transfer Units (NTU) is a dimensionless parameter used in heat exchanger analysis to determine the efficiency of heat transfer. It is defined as the product of the overall heat transfer coefficient and the effective heat exchanger length, divided by the heat capacity rate.

$$\in = 1 - e^{NTU} \tag{2}$$

The analysis entails experimentation with varied evaporator temperatures (T_{evap}) during three seasonal periods, namely winter, mid-season, and summer. Ultimately, the case with the highest evaporator power Table 4 is chosen. The results, including T_{ms} (the temperature at the outlet of the evaporator), LMTD (logarithmic mean temperature difference), and UA (heat transfer coefficient per unit area) are documented in Table 5 and referred in [5] and [6].

Table 5. Data selected for the highest evaporator power in each seasonal period.

Period seasonal	T_{evap} (ºC)	ΔT (K)	T_{ms} (ºC)	Q_{evap} (kW)	LMTD	UA (kW/K)	NTU	**Efficiency**
Winter	4	8	4.9	290.0	3.4	83.1	2.3	89.9
Mid-season	4	8	9.6	290.0	10.2	28.4	0.8	54.3
Summer	4	8	12.9	290.0	12.4	23.3	0.6	47.4

2.2.2. Condenser.

The next point is to set the condensation temperature. As previously defined, the purpose of the work is to be able to supply DHW, therefore the temperature is 60 ºC which will be the same as the condenser temperature ($T_{cond.}$), the domestic heat water temperatures T_s = 55 ºC [3], the cold-water temperature (T_{water}), whose average values are detailed in Table 6 and the Eq. (3) and Eq. (4), we are defined the analysis of the condenser at each time of the year Table 7.

Table 6. Temperature of the cold-water network of Madrid.

Seasonal period	Cold water temperature of the Madrid network (ºC)
Winter	7
Halftime	13
Summer	10.8

$$Qcond = UA \cdot LMTD \tag{3}$$

$$LMTD = \frac{T_s - T_{water}}{ln\left(\frac{T_{cond} - T_{water}}{T_{cond} - T_s}\right)} \tag{4}$$

Table 7. Analysis of the condenser according to the seasonal period.

Seasonal period	T_s (º C)	T_{water} (º C)	T_{cond} (º C)	LMTD	UA (kW/K)	Q_{cond} (kW)
Winter	55	7	60	20.1	83.1	1667.2
Halftime	55	13	60	18.7	23.2	435.7
Summer	55	10.8	60	19.3	28.4	548.0

2.2.3. Compressor.

Its function is to increase the pressure (and temperature) of the refrigerant. The refrigerant must be entirely in a gaseous state, if there was refrigerant in a liquid state, it would lead to serious damage to the compressor. Gas compression losses and charge losses in refrigerant circulation shall be considered. Will be used for the calculation of the thermodynamic cycle performance the CoolPack Software [2]. This program uses by default an isentropic yield of 0.7 and a loss factor of 10%.

2.2.4. Expansion Valve.

The coolant passes through expansion valve, decreasing its pressure and increasing its volume abruptly at the outlet. Some of the liquid coolant evaporates with the pressure reduction. The amount of refrigerant gas produced shall be kept to a minimum to increase the performance of the evaporator.

2.3. Study of the system efficiency.

Determination of fundamental parameters of this type of systems to realistically study how efficient the aerothermal system is:

- ✓ **COP** (electricity consumption required to meet heat demand)
- ✓ **sCOP** (Seasonal Coefficient of Performance).

2.3.1. Determination of the COPs

This parameter is essential when analyzing the operation of a heat pump. To improve the COP of the pumps, it is important that the condensation temperature is as low as possible, and that the evaporation temperature is as high as possible.

The **operating or performance coefficient (COP)** is an expression of the efficiency of a heat pump. In this case, it is a relationship between the heat transferred and the electrical energy consumed mainly by the compressor, Eq. (5).

$$COP = \frac{Q}{W_{comp}} \tag{5}$$

The study of the electricity consumption required to meet the heat demand is carried out with the CoolPack program that allows you to enter the parameters with which you are going to work:

- evaporation temperature, condensation temperature, subcooling, useful reheating, compressor performance, air flow and type of refrigerant. The values of these parameters are reflected in the Table 8.

Table 8. Heat pump cycle parameters.

Parameters	Values
Evaporation temperature	4 ºC
Condensation temperature	60 ºC
Compressor efficiency	0.7
Evaporation capacity	290.016 kW
Subcooling	10 K
Useful reheating	7 K
Useless overheating	1 K
Refrigerant (the program defaults)	R290

This analysis is fundamental since this value supposes a first filter for the viability of the supposed heat pump. For proper efficiency and functionality, a heat pump must reach a COP of between 2 and 6, depending on the difference between the temperatures of both sources (indoor or outdoor). In this work, a value of **COP= 2.663** is obtained, Figure 4.

In addition, with the COP you can make a comparison between the price of fuel (natural heat source) and the electricity price (cost of operation with heat pump) that we see below:

- COP < 2.5 the variable thermal cost with boilers is lower than with heat pump.
- COP=2.5 the thermal variable cost is identical in both cases.
- COP > 2.5 the variable thermal cost with boilers is higher than with heat pumps.

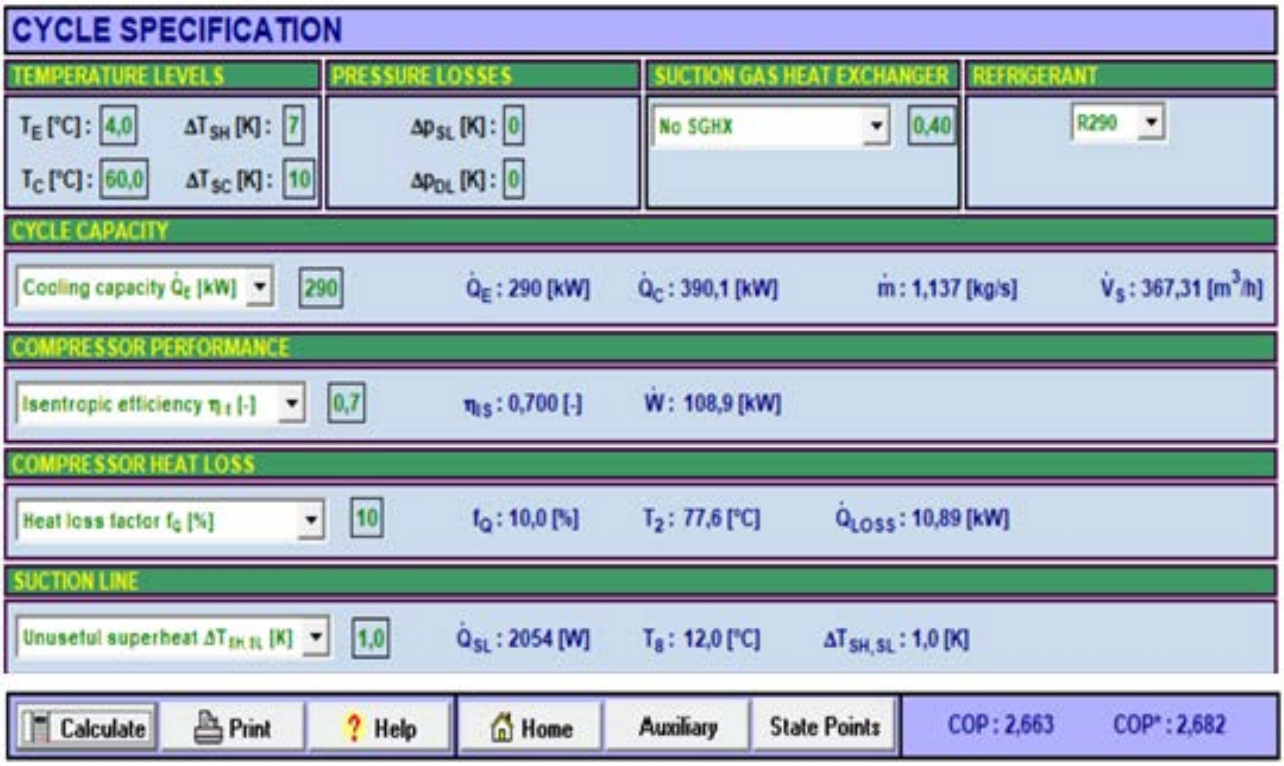

Figure 4. Obtaining COP with the CoolPack program.

There is a very important point in heat pumps, and it is the issue of the refrigerant used. In the previous analysis, the R290 is used, which defaults to the CoolPack program. To get an idea of how important the refrigerant is, is represented in the following, how the COP change depending on the refrigerant used, Figure 5.

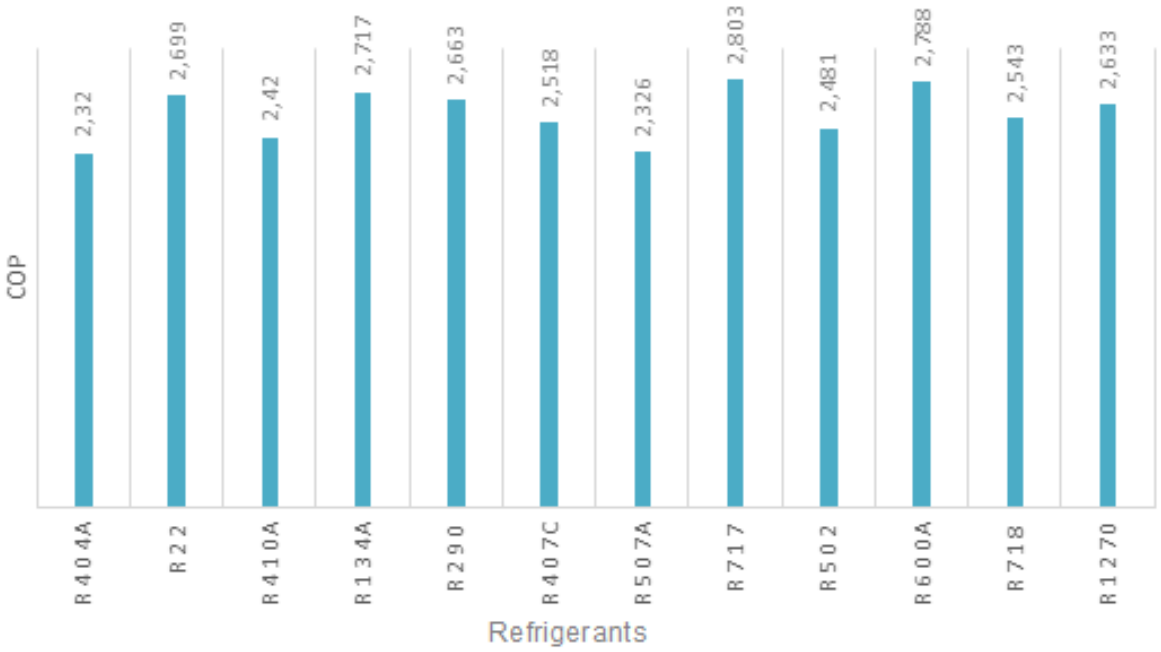

Figure 5. COP results with different refrigerants.

Based on this analysis we could conclude that the best refrigerant would be R717, but differences are quite small with R600A, R134a, R22, R1270, model uncertainties can group these refrigerants with the same possibilities to be the better one. However, other factors must be considered when choosing the refrigerant, such as safety, environment, corrosion resistance and at the same time good thermodynamic properties [7].

2.3.2. Determination of sCOP

After obtaining the potential COP values for a heat pump, an additional parameter that holds greater significance is introduced when evaluating the installation's performance. This parameter is known as the Seasonal Coefficient of Performance (sCOP). The main difference between the COP and the sCOP is that the latter refers to the seasonal term, i.e. a certain period of time, while the former refers to a specific operation conditions.

For the estimation of sCOP values, the procedure explained in the IDEA [8] document "Average seasonal performance of heat pumps" is followed.

The average seasonal performance of an equipment or system (SPF) shall be calculated by multiplying its rated performance (COP) by a factor called the representative weighting factor (FP), Table 9, and by a correction factor (FC), Table 10, for the different technologies and applications of electrically driven heat pumps. The weighting factor considers the different climatic zones of Spain marked by the CTE [9] and has been calculated using an exclusively technical methodology, using objective values and existing recognized documents. The correction factor considers the difference between the distribution or use temperature and the temperature for which the COP have been obtained in the test.

Table 9. Weighting factor (FP) [8]

Heat pump energy source	A	B	C	D	E
Aerothermal energy. Centralized teams	0.87	0.80	0.80	0.75	0.75
Aerothermal energy. Individual teams type Split.	0.66	0.68	0.68	0.64	0.64
Hydrothermal Energy	0.99	0.96	0.92	0.86	0.80
Closed-loop geothermal energy. Horizontal heat exchangers	1.05	1.01	0.97	0.90	0.85
Closed-loop geothermal energy. Vertical heat exchangers	1.24	1.23	1.18	1.11	1.03
Open Circuit Geothermal Energy	1.31	1.30	1.23	1.17	1.09

Madrid is a zone of climatic severity D as can be seen in Figure 6. The type of heat pump used throughout the document is aerothermal, therefore, the weighting factor (FP) that corresponds to it is FP **= 0.75.**

Figure 6. Climate zones in Spain

For the choice of the correction factor (FC) the one that agrees with the COP at 60ºC is chosen, this being the ideal condensation temperature to supply domestic hot water to the building of the Ministry of the Environment. According to Table 10 we are left with the correction factor being **FC=1.**

Table 10. FC correction factor

Condensation temperature (ºC)	FC (COP a 35 ºC)	FC (COP a 40 ºC)	FC (COP a 45 ºC)	FC (COP a 50 ºC)	FC (COP a 55 ºC)	FC (COP a 60 ºC)
35	1.00	------	------	-------	------	------
40	0.87	1.00	------	------	------	------
45	0.77	0.89	1.00	------	------	------
50	0.68	0.78	0.88	1.00	------	------
55	0.61	0.70	0.79	0.90	1.00	------
60	0.55	0.63	0.71	0.81	0.90	1.00

With the data explained above and the Eq. (6) a **sCOP = 1.975** is obtained.

$$\boldsymbol{sCOP} = COP\,nominal \cdot FP \cdot FC \tag{6}$$

The use of standard methodology to evaluate sCOP is clear, and it is quite useful. In this case, common methodology is not correct at all, because temperature in tunnels suffer different variations that in the environment air, so these coefficients are underestimating the real value of sCOP considering the comparison between air tunnels temperature variation and environmental air temperature variation. Further analysis with implemented temporal series will include this calculation of sCOP.

3. Amount of domestic heat water produced

With the data provided by Metro Madrid and the results calculated to compose the heat pump, the hot water flow is determined with the following Eq. (7),

$$Qcond = \dot{m}_{water}\left(\frac{kg}{s}\right) \cdot C_p\left(\frac{kJ}{kg*K}\right) \cdot (T_s - T_e) \tag{7}$$

The power of the condenser (Q_{cond}) estimated to calculate the production of domestic hot water is considered since the heating of the water occurs in this component. The formula uses a C_{pwater} = 4.196 kJ / kg K, the density of water ρ_{water} = 999.91 kg / m^3, the outlet temperature of domestic heat water T_s = 60ºC and the inlet temperature that coincides with that of the cold water of the Madrid network that will depend on the time of year collected in Table 6. Thus, the flow of domestic heat water produced during the months of the year would be represented in the following graph, Figure 7.

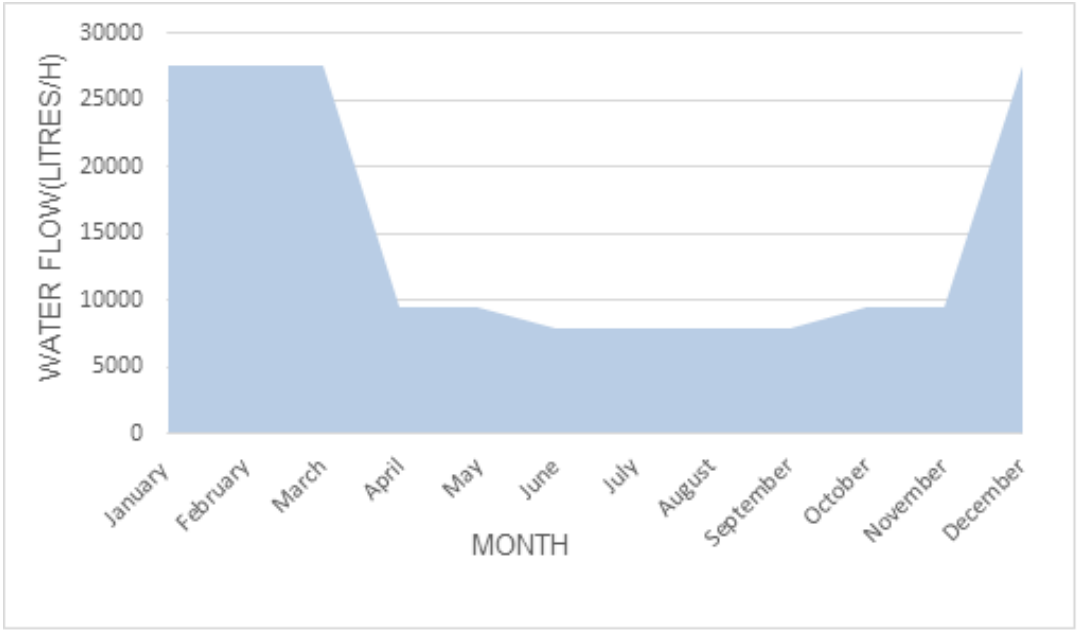

Figure 7. DHW flow during the year per operating hour

Upon analysis of the current air extraction rate from Tunnel 1 (108000 m^3/h), it was determined that an average flow rate of 15007 liters/hour of fan operation can be produced. It should be noted that higher flows will be obtained during the winter season due to the greater power in the condenser resulting from much lower average air intake temperatures. Additionally, the hours of fan operation coincide with those of the heat pump to be installed in Tunnel 1. As such, the monthly amount of domestic hot water that can be obtained is also presented in Figure 8.

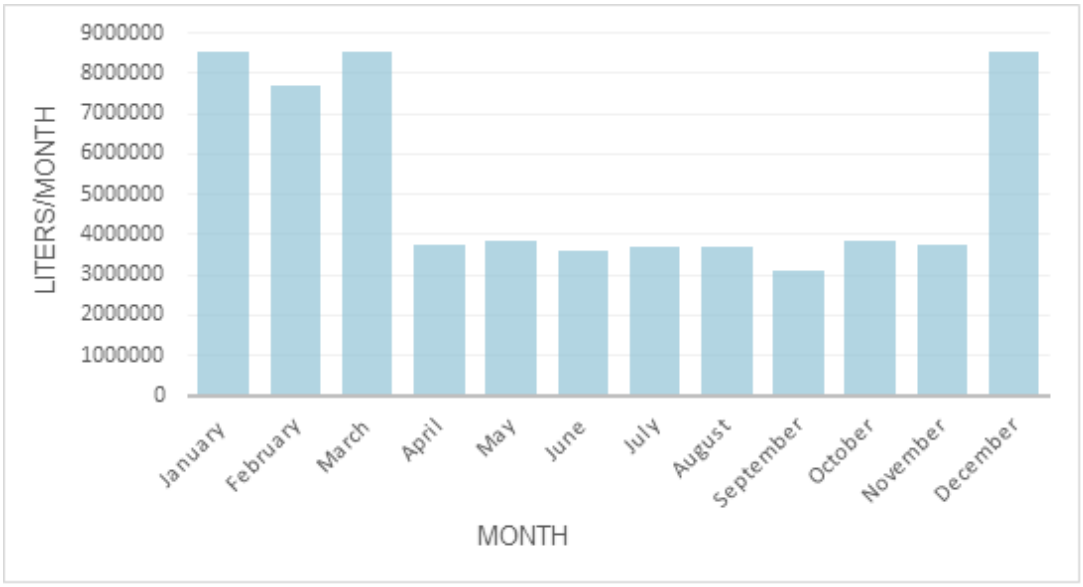

Figure 8. Flow rate in liters of DHW per month

Finally, if it is considered that in a public building such as the Building of the Ministry of Environment a person can consume 22.5 liters per day [9], an estimate can be made of the number of people that could cover the demand for DHW per month, Table 11.

Table 11. People who can be supplied with DHW from the extracted air flow.

Month	Q_{cond} (KW)	T_e (ºC)	$\dot{v}_{water}$(m³/s)	$\dot{v}_{water}$(l/h)	Hours of operation	l/day	People
January	1667	8	0.00764	27510	310	275096	12227
February	1667	8	0.00764	27510	280	275096	12227
March	1667	8	0.00764	27510	310	275096	12227
April	548	11	0.00265	9557	390	124243	5522
May	548	11	0.00265	9557	403	124243	5522
June	436	13	0.00221	7955	450	119325	5303
July	436	13	0.00221	7955	465	119325	5303
August	436	13	0.00221	7955	465	119325	5303
September	436	13	0.00221	7955	390	103415	4596
October	548	11	0.00265	9557	403	128384	5706
November	548	11	0.00265	9557	390	124243	5522
December	1667	8	0.00764	27510	310	275096	12227

4. Conclusions and future works

Once the methodology for the study of the use of waste heat from the Bank of Spain Tunnel of the Seville Metro station has been established, it can be concluded that the

1. Heat pump would produce an average flow of 15007 liters / hour during the hours in which they are operating throughout the day. In addition, the extraction of the air flow from Tunnel 1 could supply an average of 7640 people per month.
2. With respect to the heat pump placed at the outlet of the air extraction well, it is obtained that using the refrigerant R290, an evaporation temperature of 4ºC and a condensation temperature according to that required for DHW (60ºC) a COP = 2.663 is reached, a positive value (> 2.5) when measuring the viability of the system for correct efficiency and functionality that would mean savings in euros compared to gas, but which remains below the minimum COP necessary (6.08 for DHW at 60ºC) to be considered renewable.
3. The results of the Seasonal Coefficient of Performance are less encouraging since a value of 1.975 will be obtained, which is below the minimum 2.5 to be considered renewable according to the IDAE report. Anyway, IDAE sCOP methodology calculation procedure underestimate real value, as working conditions for Metro are better than the ones expected for the common use of this systems.[8]
4. This concept helps to reduce the temperature in Metro facilities, that is a problem for the infrastructure as an all-year net heat source.

However, the main essence of this project is the dissemination and awareness of the possibility of installing aerothermal systems capable of taking advantage of the residual heat of the subsoil of Madrid to achieve an energy use since a virtuous circle of heat recovery that would otherwise be wasted in the environment will be implemented regardless of whether it is renewable.

The methodology developed will allow, using more precise data and details on the installation of the Building of the Ministry of the Environment, the dimensioning of the installation necessary to take advantage of the heat of the metro or numerous other equally unknown infrastructures with enormous potential to exploit.
In conclusion, the results show that heat pumps are presented as indispensable allies of the energy efficiency of buildings in cities as it is the only proven and available system capable of producing great savings and reducing CO_2 emissions in indoor air conditioning.

Future works include the more precision evaluation of the annual production with temporal series of temperature and comparison with the alternative of a common aerothermal facility working with environmental air, as in summer the overground higher temperature gives better performance to the production of hot water.

Acknowledgments

Authors thanks to A*ula-Empresa Madrid Subterra* – Escuela Técnica Superior de Ingenieros Industriales de Madrid for promote and support this work.

References

[1] Madonna F., Bazzocchi F., Annual performances of reversible air-to-water heat pumps in small residential buildings, Energy and Buildings 2013; 65:299-309, https://doi.org/10.1016/j.enbuild.2013.06.016. (https://www.sciencedirect.com/science/article/pii/S037877881300354X)

[2] CoolPack, https://www.ipu.dk/products/coolpack/, IPU, Technology Driven Business Innovation, [accessed 15.3.2023]

[3] Documents_08_Guide_technica_hot_water_sanitary_central_906c75b2.pdf. Available in: https://www.idae.es/uploads/documentos/documentos_08_Guia_tecnica_agua_caliente_sanitaria_central_906c75b2.pdf. [accessed 15.3.2023]

[4] Royal Decree 487/2022, of June 21, which establishes the health requirements for the prevention and control of legionellosis. BOE-A-2022-10297 Real Decreto 487/2022, de 21 de junio, por el que se establecen los requisitos sanitarios para la prevención y el control de la legionelosis. [accessed 15.3.2023]

[5] Tadeo-Cañete M., Energy use of the Seville metro station for thermal supply of the building of the Ministry of Environment of the Community of Madrid, September 2022, ETSII-UPM, final degree project.

[6] Bergman, T. L., and Frank P. Incropera. Fundamentals of Heat and Mass Transfer. Seventh edition. Hoboken, NJ: Wiley, 2011.

[7] Royal Decree 552/2019, of 27 September, approving the Safety Regulation for refrigeration installations and their complementary technical instructions.

[8] Average seasonal performance of heat pumps for heat production in buildings (energia.gob.es)

[9] Technical Building Code, "Royal Decree 314/2006, of March 17, which approves the Technical Building Code.

Implementation of Chemical Looping Combustion technology with Waste-Derived Fuels: Process analysis and comparison with other prominent CO_2 capture technologies

Stella Theodoraki[1], Dimosthenis Plakias[1], Konstantinos Atsonios[1,*], Panagiotis Grammelis[1], Sotirios Karellas[2]

[1] Centre for Research & Technology Hellas /Chemical Process and Energy Resources Institute (CERTH/CPERI), 6th km. Charilaou-Thermis, GR 570 01 Thermi, Greece, st.theodoraki@certh.gr, plakias@certh.gr, atsonios@certh.gr (CA), grammelis@certh.gr
[2] Laboratory of Steam Boilers and Thermal Plants, National Technical University of Athens, Heroon Polytechniou 9, 15780, Athens, Greece, sotokar@mail.ntua.gr

Abstract

Solid wastes management constitutes an unavoidable issue in modern overconsuming societies, but apart from that, it is also an energy source. Combustion of waste, like other carbonaceous fuels, emits carbon dioxide, which needs to be mitigated in order to achieve the Paris Agreement targets, concerning the limitation of carbon dioxide emissions in the atmosphere. The CCS implementation at waste to energy (WtE) plants is an attractive strategy to achieve this. Chemical Looping Combustion (CLC) is considered as a very promising combustion for power plants to produce efficiently thermal energy, given that it includes an inherent CO_2 capture, avoiding in this way the cost or energy penalties that accompany other existing CO_2 capture technologies. In this study, the integrated model of a CLC unit fuelled with waste derived fuel for power production with the simultaneous CO_2 capture in an effective way is presented. Several aspects that affect the overall plant efficiency such as the heat recovery configuration, the steam pressure level and the fuel type are assessed. Moreover, the CLC is benchmarked with other two competitive CO_2 capture technologies, amine scrubbing and calcium looping.

Keywords: Chemical looping combustion; waste to energy plants; CO_2 capture; process modelling; Calcium looping; amine scrubbing

Introduction

Chemical Looping Combustion (CLC) is an emerging technology for waste incineration, with an inherent CO_2 capture. It is characterized by low energy penalty and high CO_2 capture efficiency. The basic idea behind the Chemical Looping Combustion technology lies in the recirculation of an oxygen-carrier material between two interconnected fluidized bed reactors, reacting with atmospheric air in the one reactor (Air Reactor) and with the feedstock in the other (Fuel Reactor). The oxygen-carrier material, usually in the form of a metal-oxide [1], has the ability to transfer oxygen from the atmospheric air to the fuel, therefore avoiding the formation of nitrogen oxides (NO_x) and leading to the production of almost pure CO_2 and H_2O in the Fuel Reactor. After condensation of the Fuel Reactor flue gas, vapour is removed and hence CO_2 can be captured and transported or further utilised. The Air Reactor flue gas consists mostly of N_2 and O_2 that did not react with the oxygen-carrier. What is more, apart from the fuel, a gas stream enters the Fuel Reactor needed for its fluidization, which is usually either steam or recirculated CO_2. Chemical Looping Combustion is a rather new and up-and-coming technology, so there is not so much experience yet with using waste as fuel. However, since waste incineration has been conducted already in fluidized beds in Waste-to-Energy plants, the transition to CLC is not expected to pose such a big challenge. The process flowsheet diagram of a simplified CLC system is depicted in Figure 1.

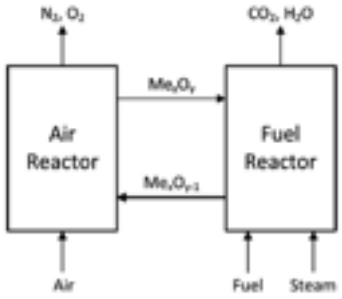

Figure 1: Schematic diagram of the Chemical Looping Combustion process (source: [2])

Regarding the post-combustion techniques for CO_2 capture, chemical absorption in an aqueous MEA solution is widely considered as the most mature available technology. In this process, CO_2 reacts with the solvent in an absorber column, forming chemical dissolved compounds. Subsequently, the solvent is regenerated in a stripper column due to the reversal of the chemical reactions at higher temperatures [3]. The necessary heat duty for the MEA regeneration is delivered by steam extraction of the initial power plant's Rankine cycle.

Calcium looping (CaL) is a promising post-combustion technology. This process relies on two reversible chemical reactions: carbonation and calcination. The first one occurs in a carbonator reactor, where CO_2 is captured by reacting with solid lime (CaO) and limestone ($CaCO_3$) is formed. Afterwards, the sorbent is regenerated in the calciner and CO_2 is released and purified in a PCU [4]. As the calcination is an endothermic reaction, fuel (RDF) combustion is necessary to maintain a constant temperature whereas pure O_2 is used as oxidizing agent in order to achieve high CO_2 concentrations in the calciner flue gas.

Several studies and projects can be found in the literature that are dedicated in the implementation of CO2 capture technologies in Waste-to-Energy plants. In [5], Fortum Oslo Varme AS used Shell's proprietary amine-based solvent DC-103 (previously untested in WtE flue gases) as a CO_2 capture technology in a WtE plant in Oslo and achieved high carbon-capture efficiency (around 90-95%) while also diminishing its amine emissions (fewer than 0.4ppm) and operating successfully for over 5000 hours. In Saga city, Japan, Toshiba has constructed a CCU facility, using an alkaline aqueous amine to capture CO_2 from a WtE plant situated nearby, accomplishing capturing up to 10 tons of CO_2 every day and further utilising it to cultivate crops and algae [6], [7]. Martin Haaf et al. in [8] presented the results of a $1MW_{th}$ CaL pilot plant, using SRF as fuel in the calciner, which captured carbon dioxide from the flue gases, provided by the combustion of pulverized coal or natural gas. In [9], the implementation of a CaL unit with a WtE plant was studied, with SRF, natural gas, and coal being tried out as the additional fuel. Their study showed that the use of SRF achieved the lowest net electrical efficiency out of them all. In [10], a process simulation was carried out for a $60MW_{th}$ CLC plant, fired by SRF, which achieved a very high carbon capture efficiency of 97% and had an oxygen demand of 17%, in order for the flue gas to be fully converted in the post-oxidation chamber. What is more, Yaqub et al., in [11] conducted experiments with plastic and paper waste in a batch fluidized-bed reactor, which showed that the paper waste had a higher fractional conversion of CO to CO_2, due to its augmented volatile content.

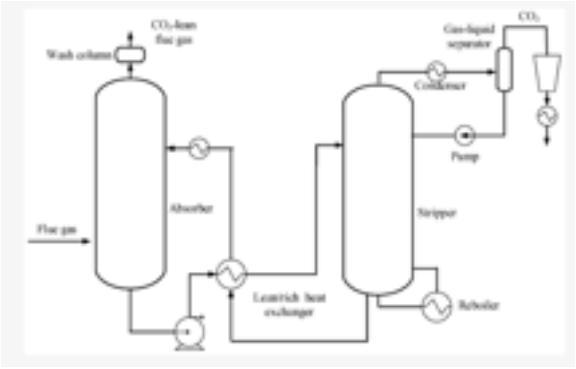

Figure 2: Amine Scrubbing process

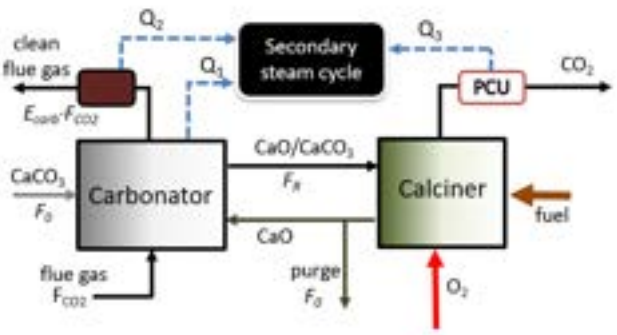

Figure 3: Calcium Looping process

This study analyses the implementation of the CLC technology with waste-derived fuels. The main purpose of this paper is to indicate which of the three abovementioned carbon capture technologies is more energy effective, taking into account in each case the net electricity production derived from the RDF combustion.

2. Model description

2.1 Chemical Looping Combustion

The process simulations for all technologies are performed with ASPENPlus^{TM}. The properties of the RDF fuel used in all cases are summarized in Table 1.

Table 1. Fuel properties

C (% d.b.)	H (% d.b.)	O (% d.b.)	N (% d.b.)	S (% d.b.)	Cl (% d.b.)	Ash (% d.b.)	Moisture (w/w %)	*LHV* (kJ/kg w/w)
40.03	4.1	24.9	0.47	0.19	0.51	29.8	27.8	9598.9

In CLC with solid waste, after the feedstock enters the Fuel Reactor, devolatilization and gasification of char take place, the products of which react with the oxygen-carrier. The reduced particles of the oxygen carrier (here ilmenite) are then transported to the Air Reactor to be oxidised, carrying some unconverted char particles with them. That char, if it reaches the Air Reactor, is oxidised by the air and transformed into CO_2, which will later on be emitted in the atmosphere. Both reactors are modelled as an RSTOIC in the ASPEN flowsheet. The reactions taking place in the AR are the (R1) and (R2), while the reactions (R3) until (R8) are the ones occurring in the FR:

$$C + O_2 \rightarrow CO_2 \quad \text{(R1)}$$

$$4FeTiO_3 + O_2 \rightarrow 2Fe_2O_3 + 4TiO_2 \quad \text{(R2)}$$

$$Char\ (mainly\ C) + H_2O \rightarrow CO + H_2 \quad \text{(R3)}$$

$$Char\ (mainly\ C) + CO_2 \rightarrow 2CO \quad \text{(R4)}$$

$$CO + H_2O \rightarrow CO_2 + H_2 \quad \text{(R5)}$$

$$CH_4 + Fe_2O_3 + 2TiO_2 \rightarrow CO + 2H_2 + 2FeTiO_3 \quad \text{(R6)}$$

$$CO + Fe_2O_3 + 2TiO_2 \rightarrow CO_2 + 2FeTiO_3 \quad \text{(R7)}$$

$$H_2 + Fe_2O_3 + 2TiO_2 \rightarrow H_2O + 2FeTiO_3 \quad \text{(R8)}$$

The rates of the reactions taking place in the FR were defined through ‘Design Specs’, so that the final composition of the FR exhaust gases would be in accordance with the composition of the

corresponding gases from an application of a CLC plant with biomass (see Table 2). Given that there aren't many literature sources regarding CLC operation with SRF, and that SRF has a large biogenic fraction, the admission was made that these two fuels should have a similar performance. Regarding the impurities such as SO_2, NO and HCl that form in CLC applications with SRF, these were produced in a separate RSTOIC in the ASPEN flowsheet, preceding the FR, the reaction rates of which were based on data from different literatures sources. It should be stated that in reality, all these reactions take place in one reactor (the FR). In the AR, both the char and the oxygen-carrier were considered to convert fully to their products in the reactions (R1) and (R2) respectively.

In order to reduce the amount of these CO_2 emissions, a Carbon Stripper is used, separating the char particles from the oxygen-carrier and returning them back to the Fuel Reactor to be gasified. Unconverted gases in the FR flue gas can be fully oxidised to CO_2 and H_2O in a Post-Oxidation Chamber (POC), using a pure stream of O_2. The thermal energy of the flue gases exiting the two reactors is used for the production of electricity in an adjoining Rankine Cycle and the preheating of air and steam needed in the AR and the FR respectively. For the superheating of steam, the heat of the AR flue gas is used, given that it is a stream clean from impurities, hence overcoming the problem of possible corrosion faced in most Waste-to-Energy plants, which limits the superheated steam temperature to 400°C. Therefore, the steam in this model was able to be superheated to a temperature of around 520°C and expanded in 3 stages in steam turbines [1]. The FR flue gas, being rich in CO_2, after being cooled down to just before its dew point in the Rankine Cycle, is purified and gradually compressed and condensed to reach the appropriate conditions for CO_2 capture and delivery [12]. On the other hand, the AR flue gas, after being cooled down to around 80°C, consisting mainly of N_2, O_2 and CO_2, is released in the atmosphere, therefore constituting the only CO_2 emissions of the CLC system.

Regarding the CO_2 emissions of the plant, the carbon capture efficiency was introduced, calculated as the amount of carbonaceous gases (measured in kmol/s) in the off-gas that is captured to the amount of the total carbonaceous gases both captured and emitted to the atmosphere.

$$\eta_{CC} = \frac{(F_{CO2} + F_{CO} + F_{CH4})_{FR\ flue\ gas}}{(F_{CO2} + F_{CO} + F_{CH4})_{FR\ flue\ gas} + (F_{CO2})_{AR\ flue\ gas}} \quad (1)$$

Table 2: Main characteristics of the CLC case

Temperature in FR / AR (°C)	950 / 1000
Feedstock mass flow (kg/sec)	5.21
Oxygen-carrier mass flow (kg/sec)	250
FR flue gas mass flow (kg/sec)	8.29
AR flue gas mass flow (kg/sec)	11.22
Supercritical steam conditions (°C / bar)	520 / 80
Total feedwater mass flow (kg/sec)	12.17
O_2 needed in POC (kg/sec)	1.22
AR outlet flue gas composition (%vol)	97% N_2, 2% CO_2, 1% O_2
FR outlet flue gas composition (%vol)	28% CO_2, 4% CO, 56% H_2O, 8% H_2, 3% CH_4, 1% impurities (SO_2, NO, HCl, N_2)
FR outlet flue gas composition range requirements (%vol d.b.) [13]	65-70% CO_2, 10-12% CO, 11-18% H_2, 5-8% CH_4

2.2 Reference Case

As for the reference case, a typical Waste-to-Energy plant is considered. This plant consists of a typical WtE supercritical boiler that produces steam at 400 °C in order to avoid corrosion problems [9], two reheaters and three steam turbines at escalated pressures. The feedwater preheating is performed using part of the thermal content of the flue gas. The main characteristics for the reference plant are summarized in Table {3}:

Table 3: Main characteristics of the reference case

Boiler efficiency (%)	93.6	HP/IP/LP Turbine isentropic efficiency (%)	92/94/88
Turbine inlet HP/IP/LP pressure (bar)	40/17.5/6.3	Superheated steam temperature/pressure (°C/bar)	400/40
Condenser pressure (bar)	0.077	Feedwater temperature (°C)	143.6
Flue gas outlet temperature (°C)	330		

2.3 Chemical Absorption with MEA

In MEA scrubbing, flue gas is in countercurrent flow with an aqueous MEA solution in an equilibrium absorption column that operates in atmospheric pressure. CO_2 separation from the flue gas is conducted via the following exothermic reactions [3]:

$$MEAH^+ + H_2O \leftrightarrow MEA + H_30^+ \quad (R9)$$

$$HCO_3^- + H_2O \leftrightarrow CO_3^{2-} + H_30^+ \quad (R10)$$

$$CO_2 + 2H_2O \leftrightarrow HCO_3^- + H_30^+ \quad (R11)$$

$$MEACOO^- + H_2O \leftrightarrow MEA + HCO_3^- \quad (R12)$$

$$2H_2O \leftrightarrow OH^- + H_3O^+ \quad (R13)$$

Subsequently, the abovementioned reactions are reversed and the solvent is regenerated in a stripper column. The necessary heat for solvent regeneration is given from low pressure steam (3.09 bar), which is extracted from the second turbine of the reference plant. The whole process is simulated and ELECNRTL is being used as property method. Variables like reboiler temperature (has to be lower than 120 °C in order to avoid thermal degradation), amine loading, etc. are presented in Table 4:

Table 4: MEA scrubbing key parameters

MEA scrubbing	
Lean solvent w/w	30 %
Lean solvent temperature	40 °C
Lean solvent loading	0.2
Rich solvent loading	0.49
L/G ratio	3.11 kg/kg
Specific heat duty	3.74 MJ_{th}/kg_{CO2}
Absorption capacity	349.3 g_{CO2}/kg_{MEA}
Auxiliary power demand	0.37 MJe/ kg_{CO2}
Reboiler temperature	118 °C
Steam temperature/pressure	133.5 °C/ 3.09 bar

2.4 Calcium Looping

In this study, chemical equilibrium between the inlet CO_2 (F_{CO2}) and the average fraction of the available CaO is assumed in order to form $CaCO_3$ ($X_{max} \cdot F_R$). This assumption is valid and widely found at literature [14], as the high operating temperature and fluidization phenomena of both carbonator and calciner lead to equilibrium conditions. Therefore, Gibbs free energy minimization is applied for the simulation of carbonator and calciner. As for the X_{max} parameter, it practically represents the fraction of the sorbent that is available to react and is a function of the make up limestone stream (F_0) and the solid recirculation ratio (F_R). It can be estimated by the following semi-empirical correlation [15]:

$$X_{ave} = \frac{f_m(1-f_w)F_0}{F_o + F_R(1-f_m)} + f_w \quad (2)$$

where f_m, f_w are constants based on each sorbent characteristics. The carbon capture efficiency in the carbonator is calculated via the following equation:

$$E_{carb} = \frac{F_{CO2,carb,in} - F_{CO2,carb,out}}{F_{CO2,carb,in}} \quad (3)$$

where $F_{CO2,carb,in}$ is the inlet CO_2 flow in carbonator and $F_{CO2,carb,out}$ the outlet CO_2 flow of the carbonator. Regarding the CO_2 capture efficiency of the whole Calcium Looping process, the following equation is applied:

$$E_{tot} = \frac{F_{CO2,calc,out}}{F_{CO2,carb,in} + F_0 + F_{CO2,RDF}} \quad (4)$$

where $F_{CO2,carb,in}$ is the inlet CO_2 flow in the carbonator and $F_{CO2,RDF}$ is the CO_2 flow due to the RDF combustion in the calciner.

The hot streams released from the carbonator and calciner can be further exploited in a secondary Rankine steam cycle for steam production, whereas the heat released from the exothermic reactions of the carbonator is being used for water evaporation. Apart from sorbent regeneration, RDF combustion takes place inside the calciner. Therefore, desulfurization and dechlorination of the RDF's combustion flue gas have been taken into account via the formation of $CaSO_4$ and $CaCl_2$. Concerning the secondary steam cycle, the efficiency is calculated with the following equation:

$$eff = \frac{Net\ power\ output}{mcp\Delta T_{flue\ gases} + Q_{carb}} \quad (5)$$

Table 5: Calcium Looping key parameters

F_R/F_{CO2}	7.5
X_{max}	0.25
T_{carb}	650 °C
T_{calc}	900 °C
E_{carb}	89.77 %
Raw supplementary fuel consumption	39.76 % of total fuel
$O_2/CO_{2\ cap}$	0.436 kg/kg
ASU specific power consumption	220 kWh/tn O_2
Air to fuel ratio	1.2
Secondary steam cycle's efficiency	32.89 %

3. Methodology

The fuel input was set as such, so that the total thermal input of the feedstock would be 50MW on an LHV basis. The net electric efficiency of the whole plant was calculated according to the following definition:

$$\eta_{net} = \frac{P_{gross\ electric} - P_{consumptions}}{Q_{thermal\ fuel}} \quad (6)$$

,where the consumptions mostly refer to the work of pumps or compressors needed and the gross electric is the power produced by the steam turbines.

In addition to the aforementioned efficiencies, the CO_2 emissions intensity was also calculated as the amount of carbon dioxide released in the atmosphere (measured in kg) divided by the amount of net total electricity produced by the plant:

$$CO_2\ intensity = \frac{m_{CO2,emitted}}{P_{net\ total}} \left(\frac{kg_{CO2}}{KWh_{el,net}}\right) \quad (7)$$

Furthermore, the specific fuel consumption was determined as the total amount of the input fuel to the net total electricity output of the whole plant:

$$\frac{m_{fuel}}{P_{net\ total}} \left(\frac{kg_{fuel}}{KWh_{el,net}}\right) \quad (8)$$

Lastly, for the cases of MEA scrubbing and CaL, where a reference plant already exists, SPECCA (Specific Energy Consumption for CO_2 Avoided) coefficient is introduced and expresses the additional fuel that is required to be consumed in order to avoid the emission of 1kg of CO_2:

$$SPECCA = 3600 * \frac{\frac{1}{n} - \frac{1}{n_{ref}}}{E_{ref} - E} \left(\frac{MJ}{kg_{CO2emitted}}\right) \quad (9)$$

4. Results and Discussion

Simulations of the reference Waste-to-Energy plant have shown that a net electrical efficiency can be achieved of around 27% on a LHV basis. Figures 4, 5, 6 depict the energy flow through a Sankey diagram in each scenario for amine scrubbing, Calcium Looping and Chemical Looping Combustion respectively.

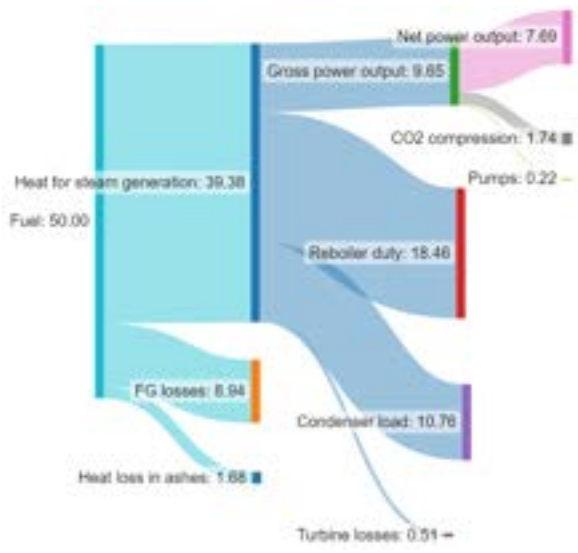

Figure 4: Sankey diagram for MEA scrubbing

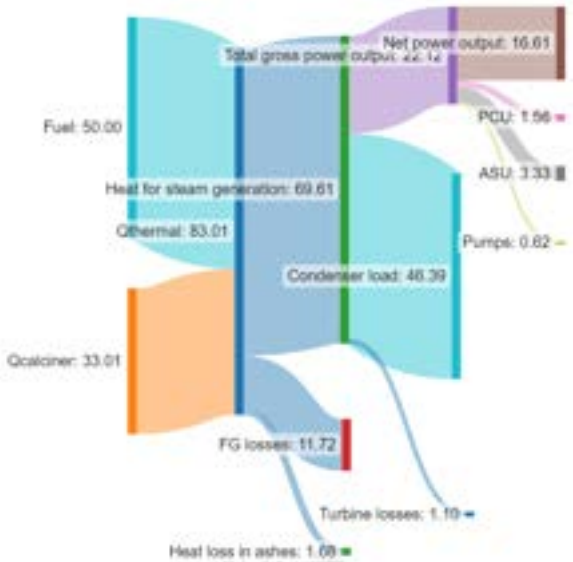

Figure 5: Sankey diagram for CaL

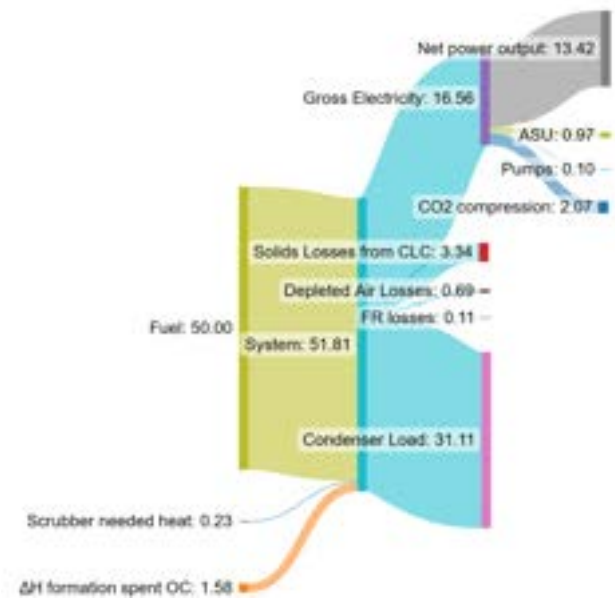

Figure 6: Sankey diagram of CLC plant

In the CLC case, around 51.5MW_{th} is inserted in the system, of which 50MW_{th} derive from the fuel thermal input, 220kW_{th} is needed for the Scrubber's operation and 1.6MW_{th} come from the difference of the enthalpy flows between the make-up material and the spent oxygen carrier. 31MW_{th} of that input is lost as waste heat in the condensers, 16.5MW_e of electricity is produced through the steam turbines and 4MW_{th} are heat losses in the atmosphere (in the form of the hot depleted air exiting the AR, the ash and spent OC exiting the FR and FR heat losses). Out of the 16.5MW_e of electricity produced, 2MW_e of electricity is consumed for the gradual compression of the CO2 stream, 100kW_e is consumed for the pumps operation and considering the use of an ASU for the oxygen production needed in the POC (requires 220kWh/tn_{O2}) [16], which consumes about 970kW_e, the remaining 13.4MW_e penetrate the grid. The overall net electric efficiency of the plant ended up being 26.84%.

Regarding the MEA scrubbing case, 50 MW_{th} of fuel is consumed. From this thermal input 39.38 MW_{th} is used for steam generation, while the rest thermal energy is considered to be waste heat. The gross electrical output of the initial plant steam cycle is approximately 9.65MW_e, but taking into account the electric consumption of pumps and the CO_2 compression unit, the net electrical output of turbines is estimated at 7.7MW_e. Hence, the net electrical efficiency of the whole process is about 15.4%. The rest of the useful heat to the Rankine cycle is used for solvent regeneration (18.46MW_{th}), as condenser load (10.76MW_{th}) and about 0.51MW_{th} are turbine losses.

As for the Calcium Looping process, the total thermal input is 83.01MW_{th}, of which 50MW_{th} is used as heat source for the steam cycle of the reference plant and 33.01MW_{th} in the calciner for the Ca sorbents regeneration. The useful heat for steam generation in both steam cycles (Rankine cycle of initial plant and secondary Rankine cycle of CaL process) is estimated at 69.61MW_{th}, while heat losses is 13.4MW_{th}. The gross electrical output of the whole process is 22.12MW_e. However, the electrical consumptions in PCU and ASU lead to a net power output of 16.61MW_e and a net electrical efficiency equal to 20%. The rest of the useful heat is consumed in the condensers of the two cycles (46.39MW_{th}) and turbine losses (1.10MW_{th}).

Table 6: Comparison of main indexes

	Reference WtE plant (no CO_2 capture)	**MEA scrubbing**	**Calcium Looping**	**Chemical Looping Combustion**
Capture efficiency (%)	-	90	93.41	94.64
Net electric efficiency (%)	27.13	15.38	20.00	26.84

Specific fuel consumption (kg_{fuel}/MWh_{el})	1382	2438	1874	1397
CO_2 emission intensity ($kg_{CO2emitted}/MWh_{el\_net}$)	1449.63	254.76	151.45	79.31
Energy penalty (%)	-	-11.75	-7.13	-0.29
SPECCA ($MJ/kg_{CO2emitted}$)	-	8.48	2.63	Not defined

Based on the data shown on Table 6, CLC technology can achieve a higher net electric efficiency than the other two methods, slightly lower than that of the reference plant. All three methods perform at a high capture efficiency, with no significant difference between them. Regarding the specific fuel consumption and the CO_2 emission intensity, MEA scrubbing has the lowest net efficiency of the three technologies, with CaL coming in second and CLC achieving the best performance. The energy penalty was calculated as the difference between the efficiency of each CO_2 capture technology and the efficiency of the reference plant. The SPECCA index cannot be defined for the Chemical Looping Combustion technology, given that it is not an equipment that can be implemented on an existing Waste-to-Energy plant. However, out of the two other methods, CaL achieved the lowest SPECCA index.

5. Conclusions

This study presented the comparison of three different CO_2 capture technologies implemented on Waste-to-Energy plants. In the case of MEA scrubbing, the net electric efficiency was calculated to be around 15%, mainly due to the significant amount of steam that is extracted from the power plant in order to regenerate the aqueous MEA solvent. Calcium Looping achieved a better efficiency, around 20%, with a rather low SPECCA of only 2.63MJ/ $kg_{CO2emitted}$ and seems to be less energy consuming than MEA scrubbing. Chemical Looping Combustion achieved the highest net electric efficiency out of the three technologies, while also being the least intense in terms of CO_2 emissions to the atmosphere. In CLC's case, a significant amount of heat was lost due to the thermal losses of the solids exiting the Fuel Reactor. Overall, all three technologies managed to reduce severely the CO_2 emission intensity of the reference plant, raising however the specific fuel consumption and decreasing, depending on the technology, the net efficiency. In conclusion, Chemical Looping Combustion is the least energy consuming and most effective technology and therefore is highly suggested as a CO_2 capture technology in case of a new power plant construction.

Acknowledgements

This project has been subsidized through ACT (EC Project no. 691712) by the German Federal Ministry of Economic Affairs and Energy (grant no. 03EE5096), the Research Council of Norway (grant no. 329886), the Greek General Secretariat for Research and Technology (grant no. T12EPA5-00023), and the Scientific and Technological Research Council of Turkey (grant no. 221N265).

Nomenclature

AR Air Reactor

ASU Air Separation Unit

CaL Calcium Looping

CLC Chemical Looping Combustion

E_{carb} carbonation efficiency, -

E_{tot} total carbon capture efficiency, -

eff efficiency of secondary steam cycle, -

F_0 looping ratio, kmol/kmol

F_R make-up ratio, kmol/kmol

FR Fuel Reactor

m mass flow rate, kg/s

n molar flow rate, kmol/s

Q heat stream, kW

P power, kW

POC Post-Oxidation Chamber

OC Oxygen Carrier

T temperature, ^{o}C

X average conversion of solids in the carbonator/calciner, -

Greek symbols

η efficiency

Subscripts and superscripts

ave maximum average

calc calcination

carb carbonation

th thermal

tot total

References

[1] J. Ströhle, "Chemical Looping Combustion of Waste—Opportunities and Challenges," *Energy & Fuels*, Feb. 2023, doi: 10.1021/acs.energyfuels.2c04297.

[2] J. Ströhle, M. Orth, and B. Epple, "Design and operation of a 1MWth chemical looping plant," *Appl Energy*, vol. 113, pp. 1490–1495, 2014, doi: 10.1016/j.apenergy.2013.09.008.

[3] A. Plakia, G. Pappa, and E. Voutsas, "Modeling of CO2 solubility in aqueous alkanolamine solutions with an extended UMR-PRU model," *Fluid Phase Equilib*, vol. 478, pp. 134–144, Dec. 2018, doi: 10.1016/j.fluid.2018.09.013.

[4] M. Haaf, J. Peters, J. Hilz, A. Unger, J. Ströhle, and B. Epple, "Combustion of solid recovered fuels within the calcium looping process – Experimental demonstration at 1 MWth scale," *Exp Therm Fluid Sci*, vol. 113, May 2020, doi: 10.1016/j.expthermflusci.2019.110023.

[5] J. Fagerlund *et al.*, "Performance of an amine-based CO2 capture pilot plant at the Klemetsrud waste incinerator in Oslo, Norway," *International Journal of Greenhouse Gas Control*, vol. 106, Mar. 2021, doi: 10.1016/j.ijggc.2020.103242.

[6] P. Wienchol, A. Szlęk, and M. Ditaranto, "Waste-to-energy technology integrated with carbon capture – Challenges and opportunities," *Energy*, vol. 198, May 2020, doi: 10.1016/j.energy.2020.117352.

[7] M. Bui *et al.*, "Carbon capture and storage (CCS): The way forward," *Energy and Environmental Science*, vol. 11, no. 5. Royal Society of Chemistry, pp. 1062–1176, May 01, 2018. doi: 10.1039/c7ee02342a.

[8] M. Haaf, J. Hilz, J. Peters, A. Unger, J. Ströhle, and B. Epple, "Operation of a 1 MWth calcium looping pilot plant firing waste-derived fuels in the calciner," *Powder Technol*, vol. 372, pp. 267–274, Jul. 2020, doi: 10.1016/j.powtec.2020.05.074.

[9] M. Haaf, R. Anantharaman, S. Roussanaly, J. Ströhle, and B. Epple, "CO2 capture from waste-to-energy plants: Techno-economic assessment of novel integration concepts of calcium looping technology," *Resour Conserv Recycl*, vol. 162, Nov. 2020, doi: 10.1016/j.resconrec.2020.104973.

[10] P. Mohn, C. Hofmann, F. Alobaid, J. Ströhle, and B. Epple, "Application of Chemical Looping Combustion on Waste-to-Energy: A Techno-Economic Assessment." [Online]. Available: https://ssrn.com/abstract=4276192

[11] Z. T. Yaqub, B. O. Oboirien, M. Hedberg, and H. Leion, “Experimental Evaluation Using Plastic Waste, Paper Waste, and Coal as Fuel in a Chemical Looping Combustion Batch Reactor,” *Chem Eng Technol*, vol. 44, no. 6, pp. 1075–1083, Jun. 2021, doi: 10.1002/ceat.202000501.

[12] E. Sanchez Fernandez *et al.*, “EUROPEAN COMMISSION DG RESEARCH SEVENTH FRAMEWORK PROGRAMME THEME 5-Energy FP7-ENERGY.2007.5.1.1: Enabling advanced pre-combustion capture techniques and plants CESAR CO 2 Enhanced Separation and Recovery Deliverable No. CESAR D2.4.1 Deliverable Title Common Framework Definition Document Dissemination level,” 2009.

[13] L. Zhou, K. Deshpande, X. Zhang, and R. K. Agarwal, “Process simulation of Chemical Looping Combustion using ASPEN plus for a mixture of biomass and coal with various oxygen carriers,” *Energy*, vol. 195, Mar. 2020, doi: 10.1016/j.energy.2020.116955.

[14] I. Vorrias, K. Atsonios, A. Nikolopoulos, N. Nikolopoulos, P. Grammelis, and E. Kakaras, “Calcium looping for CO2 capture from a lignite fired power plant,” *Fuel*, vol. 113, pp. 826–836, 2013, doi: 10.1016/j.fuel.2012.12.087.

[15] J. C. Abanades, E. J. Anthony, J. Wang, and J. E. Oakey, “Fluidized bed combustion systems integrating CO2 capture with CaO,” *Environ Sci Technol*, vol. 39, no. 8, pp. 2861–2866, Apr. 2005, doi: 10.1021/es0496221.

[16] K. Atsonios, P. Grammelis, S. K. Antiohos, N. Nikolopoulos, and E. Kakaras, “Integration of calcium looping technology in existing cement plant for CO2 capture: Process modeling and technical considerations,” *Fuel*, vol. 153, pp. 210–223, Aug. 2015, doi: 10.1016/j.fuel.2015.02.084.

CO_2 marine transportation: an energy & techno-economic analysis

Eduardo Pérez-Bódalo[a,b], Rafael D'Amore Domenech[a,b], Teresa J. Leo[a,b]

[a] Departamento de Arquitectura, Construcción y Sistemas Oceánicos y Navales, ETSI Navales, Universidad Politécnica de Madrid, Av. de la Memoria 4, Madrid 28040, Spain
[b] Grupo de Investigación UPM Pilas de Combustible, Tecnología del Hidrógeno y Motores Alternativos (PICOHIMA), ETSI Navales, Universidad Politécnica de Madrid, Avenida de la Memoria 4, Madrid, 28040, Spain

Abstract:
Anthropogenic carbon dioxide (CO_2) emissions have raised the global average temperature in 1.0 °C with respect to pre-industrial levels and this increase is likely to reach 1.5 °C before 2050, according to Intergovernmental Panel on Climate Change (IPCC, 2021).
To limit the temperature rise, most envisioned policies regarding CO_2 emissions rely on carbon capture, use and storage (CCUS), being essential to keep its concentration in the atmosphere below 450 ppm by 2100. IPCC forecasts 12 Gt/y of CO_2 removal in 2050 but the current capacity is 40 Mt/y. CCUS play a vital role in decarbonization, and it may be impossible to get emissions to net-zero fast enough without them.
For the marine industry, CCUS facilitate both CO_2 capture and transport. Ships fitted with this technology can capture carbon from burning fossil fuels. Among the newbuilding ships in 2021, 88% of them were fuelled with fossil fuels and according to ABS, in 2050 still 40% of them will be in this situation. Therefore, CO_2 capture onboard is necessary. Ships can also transport captured CO_2 to facilities for its use and/or storage.

This article investigates the value of ships as CO_2 carriers, focusing on the transport conditions of CO_2. An energy and techno-economic analysis is performed, considering several combinations of pressure and temperature. From an exclusive transport perspective, results show that lower pressures of CO_2 are likely to be more economic. From the pre-processing point of view, results suggest that higher pressures of CO_2 will imply energy savings and potentially cost savings. From the whole logistic chain perspective, the trade-off pressure is still unknown. More research is advised.

Keywords:
Carbon dioxide, shipping, CCUS, decarbonization, Sustainable Development Goals, Climate Change, Circular economy

1. Introduction

Carbon dioxide (CO_2) is an essential gas for the presence of life on our planet. It is also the main "greenhouse gas" (GHG). These gases absorb and emit infrared radiation that reaches Earth from the Sun, heating the planet's surface as well as the lower layers of the atmosphere.

It is present in the Earth's atmosphere naturally, historically, in concentrations of approximately 300 parts per million (ppm) or 0.03%. During the ice ages, the levels were around 200 ppm and during the interglacial periods, slightly less than 300 ppm. the concentration of other GHGs has increased very significantly in the Earth's atmosphere in recent decades. Scientists attribute most of this increase in CO_2 concentration to human sources.

Human activities are estimated to have caused approximately 1.0°C of global warming above pre-industrial levels, with a likely range of 0.8°C to 1.2°C. Global warming is likely to reach 1.5°C between 2030 and 2052 if it continues to increase at the current rate, according to the Intergovernmental Panel on Climate Change (IPCC).

Most of net CO_2 emission models developed by the IPCC [1] require significant use of CCUS. According to the IPCC, carbon capture, utilization and storage (CCUS) is essential to maintain the concentration of CO_2 in the atmosphere below 450 ppm in the year 2100.

According to the International Energy Agency (IEA) [2], currently CCUS facilities around the world have the capacity to annually capture more than 40 $MtCO_2$. However, the mean of IPCC global net CO_2 emissions scenarios predicts 12 $GtCO_2$/yr sequestration from the energy sector in 2050. Therefore, CCUS technologies

play a vital role in decarbonization and it may be impossible to reduce net emissions down to zero fast enough without them.

It shall be noted that CO_2 is a commodity but still without a market. Moreover, according to IEA [3], CO_2 utilisation is a complement but it is not an alternative to CO_2 storage. Mac Dowell et al. [4] estimated that the contribution of carbon capture and utilisation (CCU) to the global CO_2 emissions reduction would be negligible (0.2 $GtCO_2$/year in 2050) and it could not compete with carbon capture and storage (CCS) as it has a much higher CO_2 capture potential, which was estimated at 7.8 Gt CO_2/year in 2050 [5]. In the IEA Net Zero Scenario [6], over 85% of BECC (Bio-energy with Carbon capture) and DAC (Direct Air Capture) CO_2 is permanently stored, and under 15% is used as feedstock.

Roussanaly et al. [7] stated that CO_2 shipping can be expected to play an important role in early CCS development, for "small" capacities, and/or long distance transport. According to the Global Global CCS Institute [8], CCUS technology facilitates both CO_2 capture and transport for the marine industry. First, ships fitted with carbon capture technologies can catch carbon emissions released from burning fossil fuels onboard. This is done via the use of scrubbers, which already clean emissions from exhaust gas and can be adapted to capture CO_2. This would enable shipowners to remove significant quantities of CO_2 from the exhaust. Second, ships can transport captured CO_2 to its drop-off point or offshore. Technology providers have developed safe solutions for storing CO_2 during transport at the right temperature and pressure, similar to those for ammonia and liquid petroleum gas (LPG). As stated by Xing et al. [9], shipowners can choose among materials for CO_2 storage tanks and optimize onboard space with either a single large tank or several smaller tanks. CCS technologies in maritime applications are still at an early stage, and their future prospects depend on reasonable technological innovation in combination with policy support.

Transport is that stage of carbon value chain that links sources and storage sites. Alongside pipelines, CO_2 shipping can enable flexible and scalable CCS infrastructure that can adapt to future capture projects and storage sites. Ships are also preferable for small or short lifetime CO_2 sources that cannot justify a dedicated pipeline.

Gas transported at pressure close to atmospheric ones occupies such a large volume that very large facilities are needed. Gas occupies less volume if it is compressed, and compressed gas is transported by pipeline. Volume can be further reduced by liquefaction, solidification or hydration [10].

At atmospheric pressure, CO_2 is as gas phase or as solid phase depending on the temperature. Lowering the temperature at atmospheric pressure cannot by itself liquefy CO_2, only make so-called 'dry-ice'. Liquid CO_2 can only exist at a combination of low temperature and pressure well above atmospheric [11].

CO_2 can be liquified at various pressures between the triple point (5.18 bar, −56.6°C) and critical point (83.8 bar, 31.1°C). When pressured above its critical temperature and pressure, the CO_2 can be compressed to reach supercritical form that has a higher density and can avoid two-phase flow [12].

Currently there are three ways of transporting CO_2 to onshore reception facilities and or offshore underground storages [6]:

- Gaseous transportation: CO_2 is compressed up to 35 bar and transported by pipeline, with intermediate boosters.
- Liquid transportation: CO_2 is compressed and transported by ship or pipeline.
- Supercritical transportation: CO_2 is compressed up to 250 bar and transported by pipeline.

CO_2 transport by ships is based on the shipping experience in the food and beverage industries and it a mature technology (TRL 9) as it has been practised for over 30 years at small-scale, with only 3 Mt CO_2/year. According to Hong [5], CO_2 shipping is now considered for large-scale transport of CO_2 because it may be more economical when CO_2 needs to be transported on a large-scale over large distances or overseas than constructing new long-distance pipelines or repurposing gas pipelines at existing loading facilities and unloading platform.

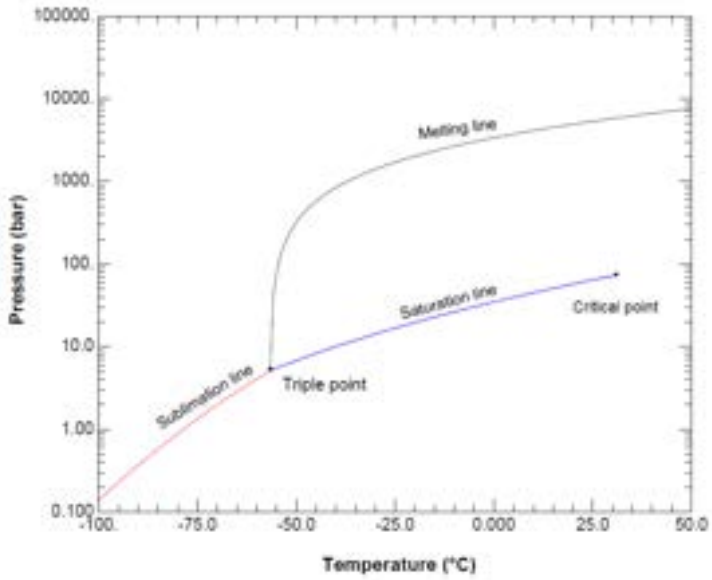

Figure. 1. CO_2 pressure-temperature diagram [13].

Liquefied CO_2 is the most obvious choice for ship transport, but even ships carrying compressed, gas phase CO_2 have been suggested. Transporting compressed CO_2 can be compared to transport of CO_2 in pipelines. Transport conditions will therefore be similar to that of pipelines, but with more flexibility and ease of inspection than pipelines. The temperature should be about 25°C and the pressure above 75 bar. The concept of compressed CO_2 on ships has been developed by ship companies, but remains untested and no international regulations exist for such transport of CO_2 [14].

Most literature recommends conditions near the triple point for shipping of liquefied CO_2, for the benefit of lower storage costs and enhanced density. However, other research suggests a higher liquefaction pressure for higher energy efficiency. Thus, there is no set optimal liquefaction pressure for all conditions; it should instead be determined from individual needs and the wider chain and project variables [12].

The code which applies to new gas carriers (built after 1986) is the International Code for the Construction and Equipment of Ships Carrying Liquefied Gases in Bulk. In brief, this Code is known as the IGC Code. The IGC Code, under amendments to Safety of Life at Sea Convention (SOLAS), is mandatory for all new ships since 1986 [15]. Kokubun et al. [16] stated that the physical properties of CO_2, specifically the vapor liquid equilibrium properties of CO_2, are such that the design of a storage tank for the containment of liquid carbon dioxide is very similar to existing designs for intermediate pressure liquefied petroleum gas (LPG) containment systems. The design methodology for LPG cargo tanks is well understood and is regulated by international standards (specifically the IGC code) and those of Classification Societies, such as Det Norske Veritas (DNV), Bureau Veritas (BV) and Lloyd's Register (LR).

As mentioned above, there is not enough number of CO_2 carriers for a realistic comparison. For this reason, it is assumed that similar ships can be a good starting point for energy and techno-economic comparison. The most similar ship to CO_2 carriers are LPG ships (pressurized or semi-pressurized) for liquid transportation and compressed natural gas (CNG) ships for gas transportation. However, there is only one existing CNG ship in the world fleet and compressed CO_2 transportation has not been developed yet as a practical solution.

The object of this article is to perform a comparison of transport conditions of liquid CO_2 by ship, considering several pressures of CO_2 (defined in Table 2), a common ship model and two different cargo tanks configuration, as defined in Section 2. The following CO_2 conditions have been considered:

Table 1. Thermophysical properties of CO_2 for pressures from 6 to 45 bar [17].

Case No.	Pressure, bar	Temperature, ºC	Density, kg/m^3
#1	6	-53.12	1166.00
#2	10	-40.12	1116.90
#3	15	-28.52	1069.50
#4	20	-19.50	1029.40
#5	25	-12.01	993.20
#6	30	-55.52	959.25
#7	35	0.16	926.47
#8	40	5.30	894.05
#9	45	9.98	861.27

2. Methods

Focusing on the maritime transport part of the CCUS chain, and in order to investigate the value of ships as CO_2 carriers, some Key Performance Indicators (KPI) are presented and discussed, considering a specific ship as a comparison element.

2.1 Ship definition

First of all, a ship has been identified and chosen as a model to compare transport cases defined in Section 1. Based on the information provided yearly by the Royal Institution of Naval Architects (RINA) in its publication "Significant Ships" [18], a LPG carried named "Alkaid" (named "Sibur Voronezh" until 2022) has been selected as a reference ship to compare the different transport conditions of CO_2 from a common base.

This ship was designed to carry liquefied gases such as propane, butylene, propylene, anhydrous ammonia, butadiene and vinyl chloride monomer (VCM). The cargo space is divided into four cargo holds to accommodate four independent self-supporting cargo tanks built to International Maritime Organization (IMO) type C standard of bi-lobe shape with a centre longitudinal bulkhead; along with one cylindrical type deck tank. The vapour pressure range of the cargoes carried is up to 5.3 bar, the minimum cargo temperature is -40 ºC and the maximum specific gravity 0.972. The main technical particulars and ship drawings are presented in Table 2 and Fig 2.

Table 2. Technical particulars and characteristics of LPG carrier "Alkaid" [18], [19].

IMO number	9655509
Length (overall) (m)	159.97
Length (between perpendiculars) (m)	152.20
Breadth (moulded) (m)	25.60
Depth (moulded) (m)	16.40
Draught (scantling) (m)	10.90
Deadweight (design) (t)	13 650
Deadweight (scantling) (t)	22 700
Cargo capacity (m^3)	20 800
EEDI [$gCO_2/(t \cdot nm)$]	10.7

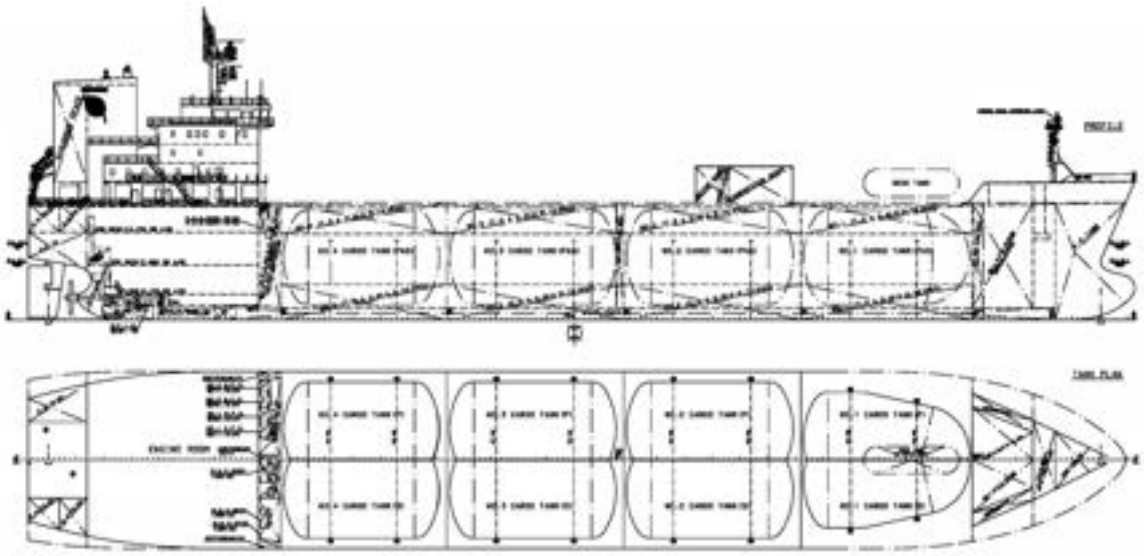

Figure. 2. "Alkaid" side and top views [18].

The dimensions of the cargo holds and LPG tanks (No.2-4) are shown in Fig 3. For calculation purposes, it is assumed that the fore tank (No. 1) has the same shape and volume as cargo tanks 2-4.

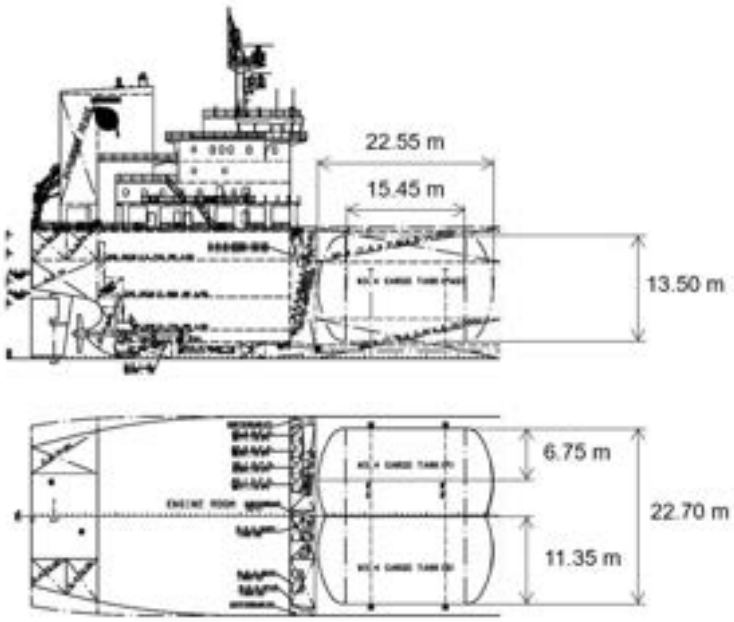

Figure. 3. Cargo hold and bi-lobe tank main dimensions [18].

As a general constraint for the different proposed arrangements, the following control volume has been defined, considering the maximum dimensions of the bi-lobe tank, as shown in Fig 3 and detailed in Table 3. In order to establish a common basis for comparison, the new redesigned tanks can occupy the complete control volume, despite its shape (bi-lobe, cylindrical) or its position (vertical, horizontal), thickness included.

Table 3. Dimensions of cargo hold control volume.

Dimension	Value
Length (m)	22.5
Breadth (m)	22.7
Height (m)	13.5

Redesigned bi-lobular tanks are arranged as in the existing ship. As the design pressures considered are higher than the LPG storage pressure (5.3 bar), the thickness growth will reduce the net volume of the cargo. The key parameter of the new configuration of the bi-lobular tanks for CO_2 storage is summarized in Table 4.

Table 4. Configuration and dimensions of bi-lobular tanks.

Characteristic	Value
Number of tanks per cargo hold	1
Total number of tanks	4
Length (thickness included) (m)	22.5
Breadth (thickness included) (m)	22.7
Height (thickness included) (m)	13.5
Main axis direction	Horizontal

Another proposed configuration is to store CO_2 in cylindrical tanks of smaller diameter, within the same control volume. New calculated cylindrical tanks can be transported vertically or horizontally. There are several variables (diameter, number of tanks per cargo hold, etc.) so the different potential configurations shall be considered carefully. Considering the boiloff management, and free-surface area to prevent sloshing and stability issues, a vertical arrangement seems preferable. In addition, a minimum clearance between cylindrical tanks must be considered for isolation, supporting structures, etc. Table 5 displays the key assumptions of the vertical cylinders. A 6x6 tank grid per hold has been deemed a good tradeoff considering a small free-surface area, while keeping the number of the ancillary components (pumps, valves, manifolds etc.) of all the tanks within reasonable levels.

Table 5. Configuration and dimensions of vertical cylindrical vessels.

Characteristic	Value
Number of vessels per cargo hold	36 (6x6)
Total number of tanks	144
Length (m)	13.5
Diameter (thickness included) (m)	3.5
Main axis direction	Vertical

Both CO_2 type of tanks proposed are based on ships in operation or projects under development, such as Samsung Heavy Industries (bi-lobular tanks) or KNCC (cylindrical tanks), both Approved in Principle by DNV in 2022 [20], [21].
According to American Bureau of Shipping (ABS) [22], both bi-lobe and cylindrical tanks are "pressure vessels", which are designed and built to meet the requirements of recognized pressure vessel standards such as the American Society of Mechanical Engineers (ASME) Boiler and Pressure Vessel Code (BPVC), as well as additional classification society requirements and statutory regulations.
The nominal body and head wall thicknesses are calculated based on ASME VIII Div. 1 UG-27 (Thickness of shell under internal pressure) and UG-32 (Formed heads and Sections, pressure on concave side). The main inputs and assumptions are listed below:

- For thickness calculations, the bi-lobe tank thickness has been calculated considering a cylinder with a radius of 6.75 m, in order to avoid complex strength calculations.
- The welded joint efficiency factor to be used is 0.875.
- The allowance for corrosion is 1 mm.
- The material selected for both types of tanks is American Society for Testing and Materials (ASTM) A537 Class 2 (quenched and tempered), a higher yield and tensile strength carbon steel used in the fabrication of pressurised vessels and steel boilers and a lowest usual service temperature −60 ºC.

Table 6. Mechanical properties of carbon steel ASTM A537 class 2 [23].

Material	Thickness, mm	Yield strength, MPa	Tensile strength, MPa
ASTM A537 class 2	< 65	415	550
	> 65 < 100	380	515
	> 100	315	485

2.2. Key Performance Indicators (KPI) definition

The following Key Performance Indicators (KPI) are analysed and discussed, considering the transport pressures described in Section 1.

- Preconditioning of CO_2 (liquefaction):
  - Thermomechanical Exergy
- Transport of CO_2:
  - Mass of CO_2
  - Ratio mass of CO_2 vs. tank structure
  - Ratio volume of cargo vs. cargo hold
  - Energy Efficiency Design Index

The first KPI is the *thermomechanical exergy* of the preconditioning phase of the CO_2. In this case it represents the minimum work required to change a substance from the restricted dead state to a particular state using the ambient as the only heat source [24]. This KPI is defined by Eq. 1, where U is internal energy, V volume and S entropy of a closed system that is in nonequilibrium with the environment, T_0 is the reference temperature of the surroundings environment (so called "restricted dead state"), and index 0 refers to the values of the parameters when the system is in thermomechanical equilibrium with the environment. The restricted dead state conditions are described in Table 7.

$$Ex = (E - U_0) + p_0(V - V_0) - T_0(S - S_0) \quad (1)$$

Table 7. Restricted dead state conditions.

Property	Value
Pressure (kPa)	100
Temperature (K)	288.15

The mass of CO_2 transported is calculated considering the two tank types defined in Section 2. The thickness of shell and head are calculated and the gross and net volume and mass of the CO_2 and tank are obtained, considering the size limitations. Mass and volume ratios are then calculated based on this. It is assumed that the balance of mass of LPG cargo and tanks of "Alkaid" shall remain invariant. Hence, if the mass of CO_2 and tanks is bigger than "Alkaid" cargo mass (to be called "Maximum CO_2"), the exceeding mass is considered as a cargo loss and will be deducted from the CO_2 mass.

$$Mass\ LPG + Mass\ LPG\ tanks = Mass\ CO_2 + Mass\ CO_2\ tanks \quad (2)$$

The last KPI considered is the Energy Efficiency Design Index (EEDI). It provides a specific figure for an individual ship design, expressed in grams of CO_2 per ship's capacity-mile and is calculated by a formula based on the technical design parameters for a given ship. EEDI was made mandatory by the IMO [25] for new ships and the Ship Energy Efficiency Management Plan (SEEMP) for all ships at Marine Environment Protection Committee No. 62 with the adoption of amendments to International Convention for the Prevention of Pollution from Ships (MARPOL) Annex VI.

The EEDI is calculated based on a complex formula, taking the ship's emissions, capacity, and speed into account. The lower a ship's EEDI, the more energy-efficient it is and the lower its negative impact on the environment. IMO regulations stipulate that ships must meet a minimum energy efficiency requirement, so their EEDI must not exceed a given limit.

$$EEDI = \frac{grams\ of\ emmited\ CO_2}{tonne\ of\ cargo \cdot nautical\ mile} = \frac{Power \times Fuel\ consumption \times CO_2\ emission\ factor}{Capacity \times Ship\ speed} \quad (3)$$

Aiming to compare EEDI of "Alkaid" with the calculated CO_2 cases, it is assumed that all factors of the equation remain equal except the cargo mass (capacity) so the following relation applies:

$$(EEDI \times Capacity)_{ALKAID} = (EEDI \times Capacity)_{CASE} \quad (4)$$

$$EEDI_{CASE} = \frac{EEDI_{ALKAID} \times Capacity_{ALKAID}}{Capacity_{CASE}} \quad (5)$$

According to the IMO, the EEDI reference line for gas carriers is calculated as follows [26]:

$$EEDI = 1120 \times DWT^{-0.456} \quad (6)$$

For gas carriers with 10000 DWT (deadweight) and above, the reduction factors are 20% in phase 2 (January 2020 to December 2024) and 30% in phase 3 (starting January 2025).

3. Results & Discussion

Figures 4 to 9 show the results of the analysis, giving the overview, and the results in detail.

In Fig 4 it is shown the specific exergy (kJ/kg) for the different cases studied, despite its packing conditions. Considering the dead state defined in Section 2, it is observed that the exergy is greater for low temperatures and low pressures than for higher temperatures and pressures. This means that the higher the pressure, the less energy is expected to be required to drive CO_2 from a restricted dead state to the saturated liquid state corresponding to the pressure. For example, the exergy of case #9 (45 bar, 10ºC) is 6.4% lower than case #1 (6 bar, -53ºC). Only from the exergetic point of view, liquefaction up to the highest range of pressures considered in this study is more convenient than low pressures close to the triple point. This metric reflects that the processes required to produce liquid CO_2 at 45 bar will foreseeably require less energy than the lower pressure alternatives. Energy savings at this stage are key considering they will have an associated cost that will impact for the whole lifetime of the logistic chain, which could easily span for 30 years.

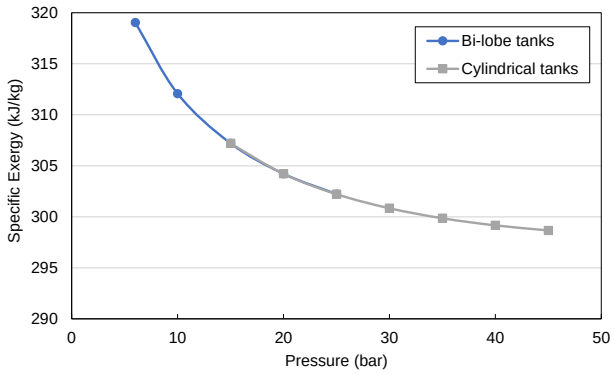

Figure. 4. Specific Exergy of CO_2 as a function of CO_2 pressure.

Regarding mass of cargo and tank structure, its different values are shown in Fig 5 for bi-lobe tanks (CO_2 cargo, tank structure and excess of CO_2) and Fig 6 for cylindrical tanks (CO_2 cargo, tank structure and lost mass/excess of CO_2). The maximum amount of CO_2 that can be stored in a bi-lobe and cylindrical tanks is shown in dark blue colour, called "maximum CO_2". However, as introduced in Section 2 and in order to do a consistent comparison, the balance of mass shall remain invariant with respect to the reference LPG ship. Therefore, the excess of mass compared with the LPG ship is identified and discounted, presented in blue colour, so called simply "CO_2".

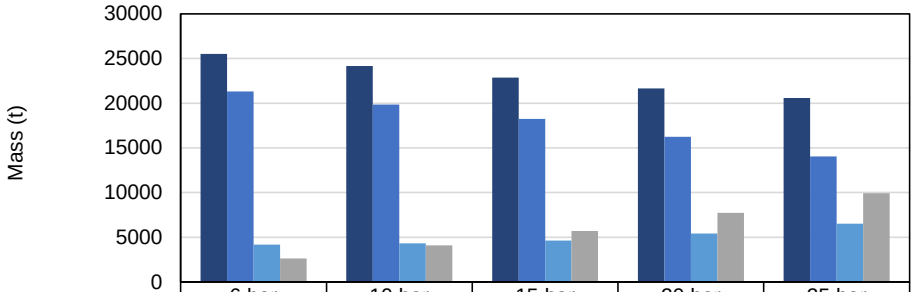

	6 bar	10 bar	15 bar	20 bar	25 bar
Maximum CO2 (t)	25512	24164	22867	21664	20572
CO2 (t)	21318	19848	18241	16234	14040
Excess of CO2 (t)	4194	4316	4626	5429	6532
Steel (t)	2639	4109	5716	7723	9917

Figure. 5. Mass of CO_2, tank structure and excess of CO_2 for bi-lobe tanks.

Opposite to the situation with bi-lobe tanks and due to the lower storage volume utilization, additional ballast must be supplied to the vertical cylinder arrangement at pressures under 35 bar to keep the balance of mass invariant. The additional ballast coincides with the loss of of CO_2 mass in Fig. 6.

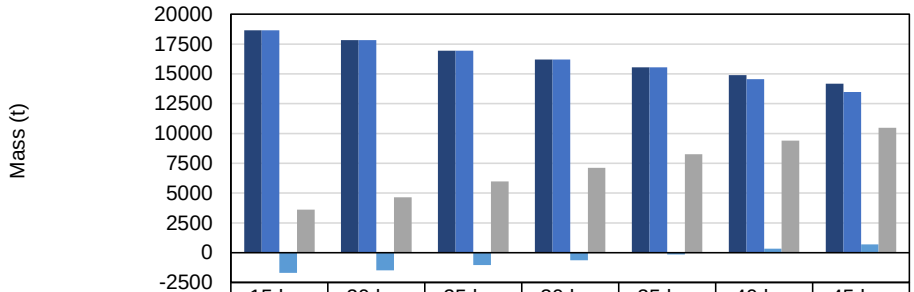

	15 bar	20 bar	25 bar	30 bar	35 bar	40 bar	45 bar
Maximum CO2 (t)	18656	17829	16955	16206	15545	14897	14175
CO2 (t)	18656	17829	16955	16206	15545	14559	13489
Loss/Excess of CO2 (t)	-1691	-1485	-1031	-642	-154	338	686
Steel (t)	3610	4643	5971	7109	8258	9397	10468

Figure. 6. Mass of CO_2, tank structure and lost mass or excess of CO_2 for cylindrical tanks.

With regard to the mass of transported CO_2 the best solution is to transport CO_2 at 6 bar in bi-lobe tanks as they are able to transport 21318 t while complying with the balance of mass constraint.

As shown in Fig 7, exclusively considering the amount of CO_2 transported, from pressures of 10-15 bar it is better to use cylindrical tanks as the CO_2 stored decreases rapidly from that operating pressure in bi-lobe tanks. It shall be noted that an optimized calculation of the bi-lobe tank structural strength may end up with a higher transition pressure, closer to the 15-20 bar range. Considering only the storage pressure, low pressures are more interesting, as the amount of CO_2 is higher. For example, the difference between transporting CO_2 at 10 and 45 bar is 47.1% and 70.5% (maximum CO_2).

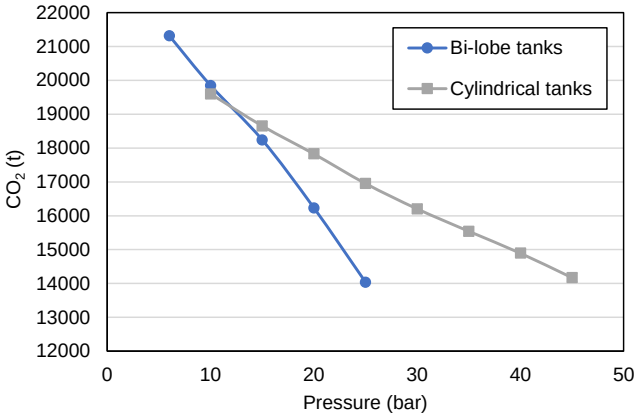

Figure. 7. Mass of CO_2.

Two ratios have been calculated: mass of CO_2 versus tank structure and volume of tank versus cargo hold, both shown in Fig 8. Both KPI serve as a measure of efficiency in the mass and volume dimensions. In both cases, the higher the ratio, the better. A low mass ratio implies that more mass of steel of the structure is being transported with respect with the CO_2. Analogously, a low volume ratio, implies that there is more empty space with regard to used space. As expected, the volume of cylindrical tanks makes much less use of available cargo hold space than bi-lobe tanks. However, bi-lobe tanks only take advantage of this for low pressures, as the mass of the structure increases rapidly. Note that for a storage pressure of 25 bar, the mass ratio of the bi-lobe tank considered is only 1.42. Under this KPIs, transporting CO_2 at low pressures, will probably result in a lower ship acquisition cost per unit mass of transported CO_2, as the mass of steel has a great influence on the final cost of a ship. The low ratios that this method yield, very likely imply that the base LPG ship main dimensions are not optimal for the transport of CO_2, thus a change of geometry in actual CO_2 could be expected Fig 2 and Fig 3 if an Ad hoc bulk CO_2 carrier was designed.

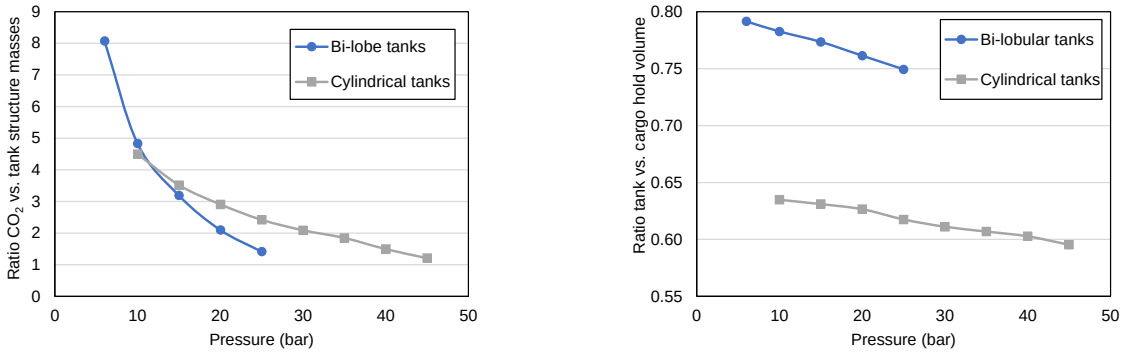

Figure. 8. Ratio of CO_2 vs. tank structure mass (left) and ratio of tank vs. cargo hold volume (right).

The last KPI is EEDI, presented in Fig 9, considering the mass of CO_2 for both type of tanks and the assumptions described in Section 2. As the storage pressure increases, so does EEDI value. In this case, the lower the value, the more efficient will be the ship. This KPI suggests that the ship with 6 bar and bi-lobe configuration will use less fuel per unit distance and unit mass of transported CO_2, probably meaning that the Voyage Cost of the low-pressure ship will be lower.

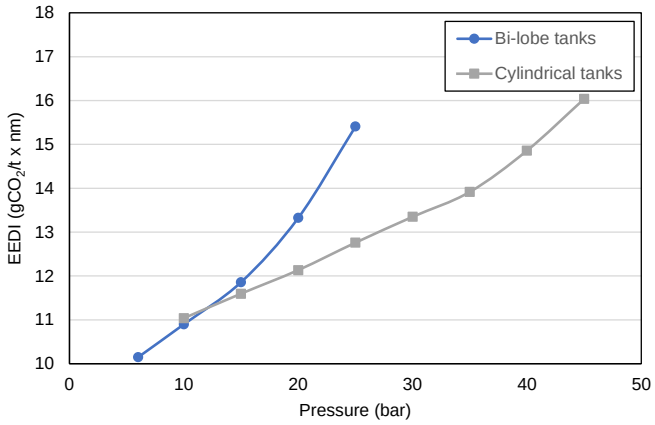

Figure. 9. EEDI of the ships proposed.

4. Conclusions

The results obtained in the different analyzes carried out establish unaligned conclusions. On one hand, from the exergetic point of view, liquefying the CO_2 to the highest range of pressures considered in this study is more efficient than lower pressures, closer to the triple point. Nevertheless, once thermoeconomy is included in the analysis, results could be different. On the other hand, lower CO_2 pressures allow more mass to be transported, and will probably result in reduced voyage costs, and the reduced steel mass in the ship's construction will probably mean cheaper acquisition costs. Considering that the whole logistic chain of CO_2 include the preprocessing costs, transport costs and post processing costs, it is not clear what the optimal transport pressure will be. Varying the pressure of the CO_2 cargo will have opposed effects in different elements of the logistic chain. Therefore, more research will have to be conducted to unveil the trade-off pressure, and the parameters that define it, considering the whole CCUS chain.

Attention should be paid to the tank design, as there is a transition pressure where bi-lobe tanks are no longer a smart option due to its mass and cylindrical tanks would be better even considering its worse volumetric efficiency. Attention should be paid to transporting CO_2 at low pressures close to the triple point, as in that region there is a higher risk of undesired CO_2 solidification, which can potentially clog pipes or damage pumps.

Acknowledgments

The authors acknowledge the Spanish Ministry of Science and Innovation through the State Agency for Research and European Regional Development Funds through the Research Project PID2021-124263OB-I00 funded by MCIN/AEI/10.13039/501100011033 and by "ERDF a way of making Europe".

Appendix A

Detail results of the calculations performed for this article are available on request.

Nomenclature

Symbols

Ex	exergy
E	energy
U	internal energy
p	pressure
V	volume
T	temperature
S	entropy

Subscripts and superscripts

0	restricted dead state

References

[1] IPCC, *Climate Change 2021 - The Physical Science Basis - Summary for Policymakers*. 2021.

[2] International Energy Agency, «Putting CO2 to Use», *Energy Rep.*, n.º September, p. 86, 2019.

[3] International Energy Agency, «CCUS in clean energy transitions». 2020.

[4] N. Mac Dowell, P. S. Fennell, N. Shah, y G. C. Maitland, «The role of CO2 capture and utilization in mitigating climate change», *Nat. Clim. Chang. 2017 74*, vol. 7, n.º 4, pp. 243-249, abr. 2017, doi: 10.1038/nclimate3231.

[5] W. Y. Hong, «A techno-economic review on carbon capture, utilisation and storage systems for achieving a net-zero CO2 emissions future», *Carbon Capture Sci. Technol.*, vol. 3, p. 100044, jun. 2022, doi: 10.1016/J.CCST.2022.100044.

[6] International Energy Agency, «World Energy Outlook 2022», 2022.

[7] S. Roussanaly, H. Deng, y G. Skaugen, «Toward the identification of optimal conditions for transport of CO 2 by ship».

[8] Global CCS Institute, «State of the Art State of the Art : CCS technologies 2022», *Glob. CCS Inst.*, vol. 1, p. 81, 2022.

[9] H. Xing, S. Spence, y H. Chen, «A comprehensive review on countermeasures for CO2 emissions from ships», *Renew. Sustain. Energy Rev.*, vol. 134, n.º April, p. 110222, dic. 2020, doi: 10.1016/j.rser.2020.110222.

[10] B. Metz, O. Davidson, H. De Coninck, M. Loos, y L. Meyer, «Carbon dioxide capture and storage», 2005. doi: 10.1016/bs.ache.2021.10.005.

[11] International Energy Agency, «SHIP TRANSPORT OF CO2», 2004.

[12] ABS, «CARBON CAPTURE, UTILIZATION AND STORAGE AUGUST 2021», 2021.

[13] E. W. Lemmon, M. L. Huber, y M. O. McLinden, «NIST Standard Reference Database 23: Reference Fluid Thermodynamic and Transport Properties (REFPROP), Version 9.0», *Physical and Chemical Properties …*. 2010, doi: citeulike-article-id:11896451.

[14] R. Skagestad, A. Anundskås, A. Mathisen, y H. A. Haugen, «CCS knowledge gaps Recommendations for R &D and innovation in the Nordic countries», 2015.

[15] Society for International Gas Tanker and Terminal Operators Ltd, «Liquefied Gas Handling Principles On Ship and in Terminals», *Witherby Co Ltd 32-36 Aylesbury Str. London*, p. 308, 2000.

[16] N. Kokubun, K. Ko, y M. Ozaki, «Cargo Conditions of CO2 in Shuttle Transport by Ship», *Energy Procedia*, vol. 37, pp. 3160-3167, ene. 2013, doi: 10.1016/J.EGYPRO.2013.06.202.

[17] National Institute of Standards and Technology, «Thermophysical Properties of Fluid Systems». .

[18] The Royal Institute of Naval Architects, *Significant Ships of 2013*. 2013.

[19] European Maritime Safety Agency, «CO2 Emission Report».

[20] DNV, «DNV awards AiP to SHI for innovative liquified CO2 carrier design», 2022.

[21] DNV, «DNV awards KNCC AiP for high pressure LCO2 transport concept», 2022.

[22] American Bureau of Shipping, «Guidance Notes on Strength Assessment of Independent Type C Tanks 2022», n.º January, 2022.

[23] ASTM, «ASTM A537/A537M-20 Standard Specification for Pressure Vessel Plates, Heat-Treated, Carbon-Manganese-Silicon Steel», 2020. .

[24] A. Bejan, *Advanced engineering thermodynamics*, 2 ed. New York: New York John Wiley & Sons, 1997.

[25] IMO, «Energy Efficiency Measures».

[26] IMO, «Module 2: Ship Energy Efficiency Regulations and Related Guidelines».

Dynamic Life Cycle Sustainability Assessment of Mini-grids: A Proof-of-Concept

Omkar Buwa[a], Jayendran Venkateswaran[b], and Anand B.Rao[c]

[a] CTARA, Indian Institute of Technology Bombay, Mumbai, India, onbphd@gmail.com, CA
[b] IEOR, Indian Institute of Technology Bombay, Mumbai, India, jayendran@iitb.ac.in,
[c] CTARA, Indian Institute of Technology Bombay, Mumbai, India, a.b.rao@iitb.ac.in

Abstract:

As per the 'World Energy Outlook 2022' projections, 660 million people worldwide (mostly from rural areas) would be without electricity access in 2030. There are three main approaches to rural electrification - centralised grid extension, mini-grids, and solar home systems (SHS) including pico-solar. Mini-grids are considered a promising solution in rural areas with higher reliability (as compared to the central grid) and higher capacity to meet demand (as compared to the SHS). However, there have been failures of several mini-grid projects worldwide. There are various challenges faced by mini-grids – technical, social, economic, and strategic. The past efforts to assess mini-grid sustainability have used static approaches. Consideration of dynamic variations in the mini-grids over the life cycle for sustainability assessment is an emerging research area and is being explored in this paper. An attempt has been made to show how the dynamics and the interdependency of different aspects related to the mini-grids can be considered for life cycle sustainability assessment. Complex environments, local operations, many interacting variables, and feedback processes characterise mini-grids. 'System dynamics' is a systems method suitable to describe behaviours of such systems and tackle relevant problems. A system dynamics approach has been used in assessing an Indian mini-grid for a systemic understanding of its life cycle. The analysis reveals the impact of different variables on the mini-grid's life cycle. Developed stock-flow (SF) diagram is useful for analysing different scenarios (e.g. arrival of centralised grid) and policies (e.g. tariff variations). This proof-of-concept (PoC) may help to develop a comprehensive framework for the dynamic life cycle sustainability assessment (D-LCSA) of mini-grids.

Keywords:

Mini-grids; System dynamics; Life cycle sustainability assessment; Proof-of-concept.

1. Introduction

1.1. Global electricity access

Electricity access has been a requisite part of any global development process. In the Sustainable development goals (SDGs) set by United Nations [1], SDG 7 is — Ensure access to affordable, reliable, sustainable, and modern energy for all. Particularly, SDG 7.1 aims at 'universal access to modern energy'. Modern energy access also includes other types of energy carriers like cooking fuels and transportation fuels. But due to its strong linkage with the development, 'electricity access' is an area of interest for researchers, policymakers, and executors.

In India, on 30th April 1945, Mahatma Gandhiji wrote a letter to Cambridge return economist Shri.Amiya Nath Bose and expressed his concern about the electricity access to every home in India. He asked "Have you worked out the problem of electricity for every home? What is the cost?" [2]. In later years, various schemes for the extension of the electricity network in India, as well as at the global level improved electricity access but the challenges like network expansion, and poor financial returns on investment, remain for remote areas. Due to rapid urbanisation, more focus was on urban electrification and a majority of the rural population remained without any electricity access during the development stages.

As per the 'World Energy Outlook 2022' [3] projections, 660 million people worldwide would be without electricity access in 2030. The report [4] published to track the progress of SDG 7 mentions that rural electricity access is more deficient than in urban areas. In 2020, out of the world's population without electricity access, 80% of people lived in rural areas. Also at the current pace, the 2030 target for rural electrification will fall short. Figure 1 highlights the need for more focus on rural electrification in the next few years.

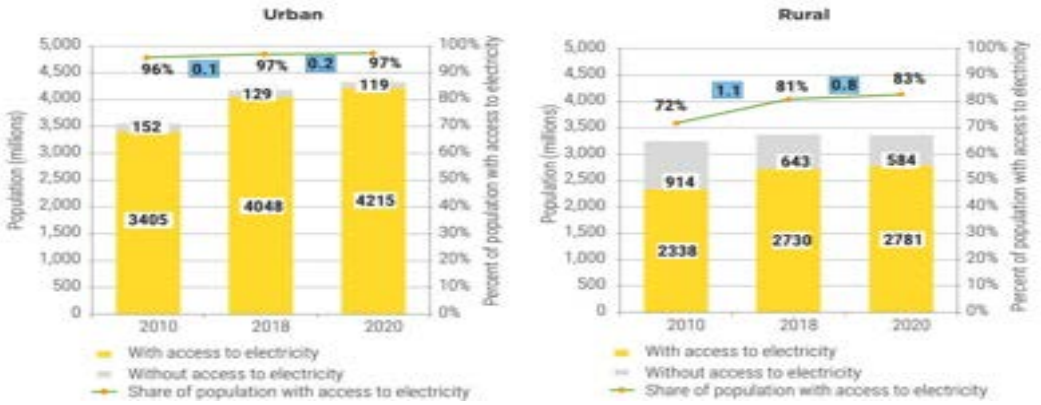

Figure. 1. Electricity access in urban and rural regions at the global level [4].

1.2. Approaches to rural electrification

Electricity access can be provided through three possible schemes/modes: - centralised electricity grid, mini-grids (or micro-grids), and solar home systems (SHS) including pico-solar. Off-grid electricity can be generated with more resources like diesel and biogas, but their share compared to solar electricity generation is much less. Moreover, the government schemes are more tilted towards “solar” due to the ease of installation, operation, and maintenance.

Centralised electricity supply is the conventional type of electricity supply scheme. This supply type is also called grid extension. The electricity is generated using various resources, such as fossil fuels (coal or NG-based plants), nuclear energy, and renewables e.g. water (hydropower plants), wind, or solar energy in centralised power plants. The same is transferred through the transmission and distribution network monitored by the national and state-level utilities. This is called the vertical structure of electricity supply. Until the technological advances started taking place in the renewable energy sector with the choice of decentralized electricity generation, the centralised supply scheme was the only option for providing electricity access.

The monopoly of the centralised supply scheme ended due to various reasons like increased competition in the electricity industry, entry of private players, technology development in renewable electricity generation, etc. There are various environmental, economic, technical, political, and social reasons for developing small-scale generation near the loads. This small-scale generation is called a decentralised electricity supply scheme. The systems can run in isolation (off-grid mode) or connected to the grid (grid-connected/online mode). The generation technology is either renewable (e.g. solar, wind) or non-renewable (diesel generator), or a combination of multiple technologies (hybrid mini-grids).

As discussed in [5], an SHS is usually defined as a solar PV-based generator rated 11 Wp to more than 100 Wp with suitable battery storage. The maximum PV module rating in an SHS kit is expected not to exceed 350 Wp as per the current standards. Products with rated PV power lesser than 11Wp are pico-solar.

Due to the various challenges like cost recovery and supply reliability for the central grid extension and the limitations of SHS and pico-solar ratings to fulfill the electricity demands, the rural areas find mini-grids as a promising solution. ‘Ease of electrification vs. Power level’ of various electrification modes is shown in Figure 2.

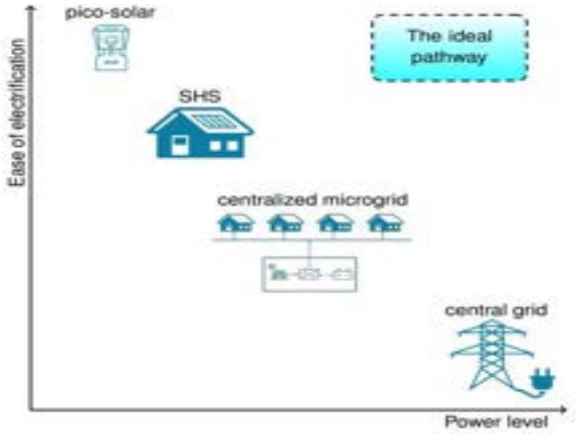

Figure. 2. Modes of electrification and comparison of ease of electrification vs. power level [5].

Delivery of electricity connections under the IEA Net Zero Emissions by 2050 Scenario, by technology, is shown in Figure 3.

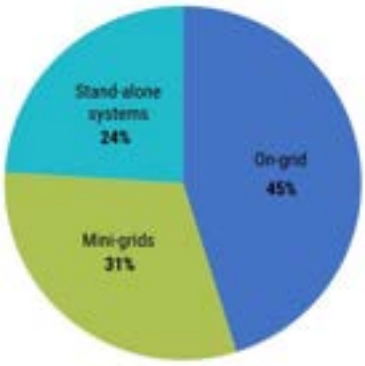

Figure. 3. Delivery of electricity connections by 2050 Scenario, by technology [4].

1.3. Mini-grids

1.3.1. Introduction

Mini-grids are off-grid systems but have provisions to connect with the grid and operate in parallel. They are local electric power networks with distributed generators, loads, and energy storage technologies. The term “mini-grid" is merged with “microgrid" in the literature though they have different generating capacities and a mini-grid has a higher capacity than a microgrid. A renewable energy-based mini-grid is defined in [6] as a system that uses a renewable energy-based generator (with a capacity of 10 kW or more) to supply electricity to a specific set of consumers (e.g. households and/or commercial, industrial, and/or institutional organizations) through a power distribution network. In this paper, the term “mini-grid" is used for off-grid AC electrical systems with solar PV as a source. Solar PV technology is more focused because of the maximum share as a mini-grid source as shown in Figure 4. A typical mini-grid consists of energy generation technology, battery energy storage, a power electronics converter, a power distribution system, and an energy management system (for metering and control purposes).

1.3.2. Global status and mini-grid scenarios

Plethora of literature discussing the technical aspects of mini-grids, their importance, and the challenges in mini-grids have been published. Their status in the global south and India are discussed in the reports [6,7] recently published by The Centre for Science and Environment (CSE). The status of the ten countries having best practices in mini-grid installations and the barriers to mini-grid installations and sustainable operations in India are explained in detail. There are 5,544 mini-grids deployed worldwide out of which 60 percent are present in Asia and 39 percent in Sub-Saharan Africa. India has 1,792 mini-grid installations, the highest in Asia. The status of mini-grid installations at the global level by technology and region is shown in Figure 4.

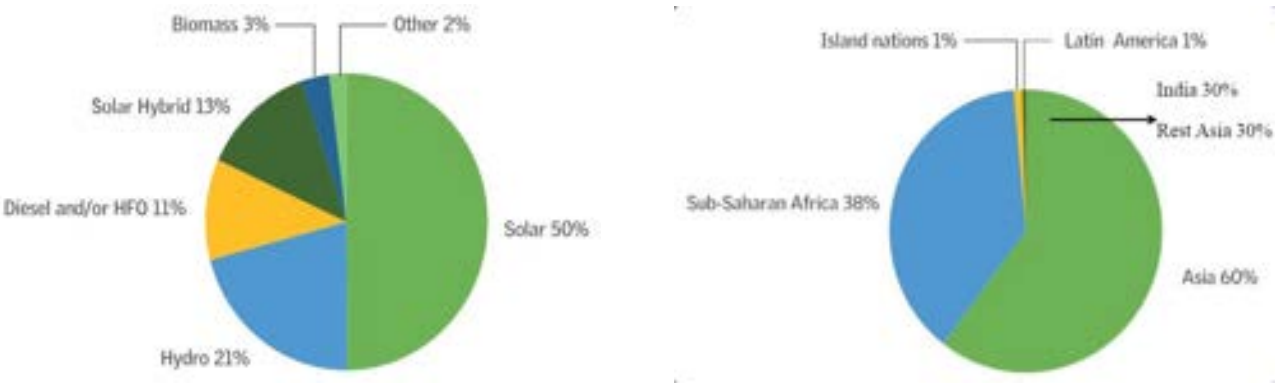

(a) (b)

Figure. 4. The global status of mini-grid installations: a) technology-wise, b) region-wise [6].

Mini-grid case studies discussed in [6] may be classified as off-grid (e.g. Raimongol Kumirmari Island and Madavchandra Satjelia Island in Sundarbans, West Bengal), mini-grids with grid extension but poor grid services (Jargatoli and Basua Gumla, Jharkhand and Chanpatia in West Champaran of Bihar), mini-grid not operational due to grid arrival (Darewadi, Maharashtra and Dharnai, Bihar), grid-connected mini-grid (Odanthurai, Tamilnadu) and mini-grids with SHS (Chopan, Maharashtra).

1.3.3. Need for sustainability assessment of mini-grids

Life cycle sustainability assessment (LCSA) is a combination of three approaches of sustainability assessment- environmental life cycle assessment (E-LCA), life cycle costing (LCC), and social life cycle assessment (S-LCA). This is also called the triple bottom approach. Some more dimensions such as 'technical' or 'institutional' are also considered in the LCSA. A sustainability assessment of mini-grids is needed for various reasons. The literature having the notion of mini-grid sustainability is evolving since 2009. Mini-grids play a vital role in rural electricity access and their unsustainability will impact the sustainable development goal achievement.

Turkson et al. [8] infer that several global and national level policies and practices are envisioned to ensure sustainable energy generation. Boche et al. [9] discuss various barriers like lack of business consideration, the gap in strategic planning approach, and the neglect of social issues. It is also mentioned that overall microgrid sustainability consideration is still deficient at the global level.

The need for sustainability assessment is also understood from the field experiences of mini-grid projects. A mini-grid case study at a village called Darewadi from Khed Taluka (District Pune, Maharashtra, India) is discussed in [6]. This mini-grid was in operation since 2012. In 2019, the battery replacement was carried out. The centralised grid reached the village in 2021 but reliability and quality of supply are poor. Mini-grid could have been used in grid-connected mode but tariff regulations for the interconnection were absent. This case study highlights the failure of mini-grid projects after certain years of operation. The Dharnai mini-grid in Bihar state and the Barapitha mini-grid in Odissa state faced similar issues.

The rest of the paper is organised as follows. Section 2 describes the review of the sustainability assessment of mini-grids and highlights the research gaps. Section 3 introduces dynamics and systemic approaches in mini-grids. In section 4, the conceptual framework and proof-of-concept model are discussed. Section 5 simulates the model with the mini-grid case study in Maharashtra state. The results of the simulations are discussed in section 6.

2. Sustainability assessments of mini-grids

The literature was reviewed for "energy sustainability" and "electricity sustainability". The literature for "mini grid sustainability" was shortlisted from the above two sub-areas. A literature database platform "Scopus" was used for the literature review. The use of suitable keywords and the operators like "AND" and "OR" helped to review the literature systematically. Research gaps in the area of mini-grid sustainability are summarised in Table 1.

Table 1. Literature and research gaps.

Author/s	Research Gap
Turkson et al. [8]---------	Sustainability as a systems problem, Practical implications of the different sustainability dimensions, Systems thinking for explaining dynamic interactions and the long-term effects of different dimensions in detail. "Dynamic life cycle sustainability assessment" as the state-of-the-art method supports static analysis.
Boche et al. [9]----------	Analysis of interdependence issues, Development of sustainability diagnosis tools, and systemic modeling of microgrids with short, medium, and long-term dynamics for causal linkages amongst various issues
Haase et al. [10]----------	Inclusions of more social indicators, the derivation of indicators, the consideration of methodical and input data uncertainties
Khatami ---------- and Goharian [11]	An all-inclusive approach toward energy sustainability and a better framework for defining sustainability giving equal weightage to all dimensions and spatial considerations
Brent and Roger [12]---	An understanding related to the complexity of the socio-institutional systems
Ilskog [13]----------	An interdisciplinary approach to sustainability evaluation.
Lassio et al. [14]----------	More emphasis on the social dimension of sustainability is recommended.
Viegas et al.[15] ---------	Project and location-specific sustainability assessment methods for integrative and at the same time customized assessment

Author/s	Research Gap
Corona and San Miguel [16] ---------	The use of a dynamic approach for sustainability assessment temporal and spatial variation in the criteria (indicators).
Poudel et al. [17]---------	Internal and external factors influencing the sustainability of mini-grids, and linkages between the project attributes and sustainability dimensions
Katre et al. [18]----------	Time-based sustainability studies capturing temporal variations.
Chatterjee et al. [19] ----	Microgrid definition, typology identification, standards revision, electrification planning, energy utilisation and planning, resiliency, system dynamics, and technology adoption and policy recommendations.

'Use of system thinking and system dynamics in sustainability assessment of mini-grids' is research gap as inferred by many authors. This paper explores the consideration of dynamics in the mini-grid life cycle for sustainability assessment. The next section discusses how the concept of dynamics is linked to mini-grids.

3. Dynamics in mini-grids

3.1. System thinking approach in mini-grids

Hartvigsson in his Ph.D. dissertation [20] discusses the systems thinking approach and its linkages with mini-grids. System thinking is a method for understanding interaction amongst variables and the resulting behaviour of the system. This is useful when systems are complex and influence the users at different levels. Systemic studies help to change the system structures which are the cause of certain behaviours. System thinking is divided into "soft" and "hard" system thinking. The "hard" approach is used in well-defined problems while the "soft" approach is useful when problems are "fuzzy", "messy" or "ill-defined". Mini-grids being complex and messy systems, the system thinking approach is useful for analysing mini-grids' behaviour. Some mini-grid problems can be engineered while others being societal are difficult to define. Thus mini-grids can be analysed with both "soft" and "hard" system thinking.

System dynamics (SD) is a dynamic thinking tool for qualitative (soft) and quantitative (hard) analysis which helps to understand the behaviour of the system over time. SD analysis consists of plotting behaviour over time (BOT) graph, development of causal loop diagram (CLD), and stock-flow (SF) analysis. Another characteristic of SD applicability is many feedback processes and interdependency among variables. The important literature in the area of SD applications to mini-grids is discussed in the next subsection.

3.2. System dynamics and mini-grids

SD conceptual modeling to tackle complexity in mini-grids is proposed in [21]. Variables and causal relations are either assumed or identified from literature and field visits. The paper develops CLDs for mini-grids but there is no discussion on part how they can be further used for the sustainability assessment of the mini-grids. Also, conceptual models like CLDs are often vague and ambiguous. Re-evaluation is needed by building SF diagrams. SF diagrams are useful for quantitative analysis and consideration of various scenarios. Riva et al. [22] develop CLDs for analysis of the impact of electricity access on rural-socio-economic development. Electricity- demand nexus with income generating activities (IGAs), local market production, households' economic availability, local health and population, education, habits, and social network is developed. This is a conceptual model development similar to the work published in [21]. Hence SF diagrams (simulation models) are required to validate the model. The authors also raise the need for reliable data collection from the field. Gonzalez et al. [23] construct CLDs using driving factors of social acceptance of renewable energy systems (RES). CLDs help to understand the multiple interactions of RES projects with rural communities. The sustainable livelihoods framework, created by the British Department for International Development (DFID) is used with system thinking qualitatively to understand RES acceptance. Though barriers to RES acceptance are discussed, their sensitivity to the project is not analysed through the SF diagram quantitatively.

Mini-grids behavior may be understood when their life cycle sustainability is analysed with system dynamics using simulations. To the best of the authors' knowledge, the research area is not much explored. The main contribution of this paper is proposing a PoC model for the "dynamic life cycle sustainability assessment (D-LCSA) of mini-grids".

4. Materials and methods

In section 4.1, a conceptual framework depicting the system boundaries and various sustainability dimensions is discussed and a visual summary is provided in Figure 5. Then, section 4.2 illustrates a PoC model built according to the conceptual framework and focuses on system dynamic analysis. The PoC model is implemented in section 5 as a case study. The PoC addresses dynamics in mini-grids by connecting LCSA, mini-grids, and SD.

4.1. Conceptual framework for D-LCSA of mini-grids

Decision-making in sustainability assessment has the least or no influence on background processes while foreground processes are under the control of the decision-makers. In this paper, the sustainability assessment of operating mini-grids is considered. Hence the phases considered in the foreground system are the “use phase” and the “end of life phase”. This is called as “Gate to Grave” approach in LCSA. The mini-grid system has physical exchanges (vertical arrows) for all phases in the form of input and output flows. These exchanges may be “elementary flows” (e.g. raw resources, emissions of pollutants and other materials into the environment, waste generated during the maintenance or at the end of the life cycle). The functional unit for LCSA is considered as 1 Unit (1 kWh) of electricity generated. A conceptual framework is shown in Figure 5.

For life cycle impact assessment, the conceptual framework considers the following two groups of variables: (i) variables in the mini-grid system (e.g. electricity generated, expenditure on maintenance, distribution losses) (ii) influencing variables in the socio-economic system (e.g. population, per capita income). These variables can be realised by different indicators like technical, economic, social, environmental, and institutional.

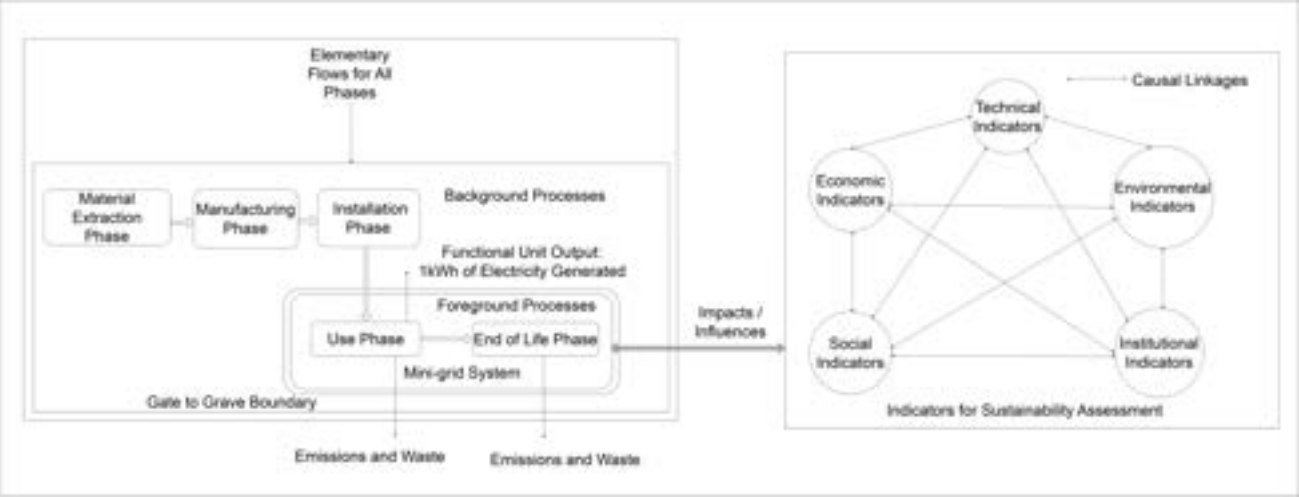

Figure. 5. Conceptual framework.

4.2. Proof-of- concept model for D-LCSA of mini-grids

Proof-of-concept model is developed to simulate “the dynamic impact assessment of mini-grid systems on livelihood and vice versa.” Figure 6 represents the steps and all the elements considered in the model. Indicators used for LCSA of mini-grids are finalised by literature review and field visits for systemic understanding. The indicators are classified as technical, economic, social, environmental, and institutional. Cause-effect relationships amongst the indicators can be represented by CLD. Once the indicators are finalised, the next important step in the model is to develop the SF diagram. SF diagram requires two inputs: i) mathematical relationships amongst variables and ii) variables' values and changes with time. For the second input, a detailed questionnaire and interactions with the stakeholders are required. This activity will help with the local characterisation of mini-grid sustainability. Consideration of mini-grid location-specific data helps to model the local impacts and their consequences on the mini-grid system.

SF diagrams can be used to simulate the behavior of mini-grids. To compare the results from the analysis, it is required to decide the criteria for mini-grid sustainability. Literature review and initial fieldwork may help in deciding criteria. These criteria may be different for different stakeholders and thus need multi-criteria analysis. Inference on mini-grid sustainability can be drawn by comparing the simulation results with defined criteria. Scenario and policy analysis may help to minimize the sustainability gap. The next section discusses the development of the CLD and SF diagram for an Indian mini-grid case study.

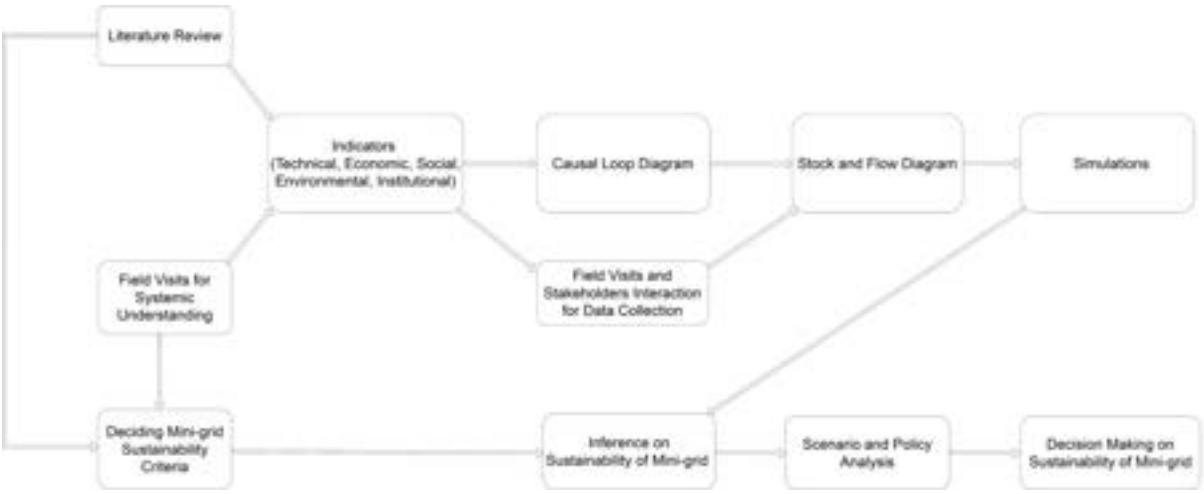

Figure. 6. Proof-of-concept model.

5. Case study

This section aims to develop CLD and SF diagram to assess mini-grid sustainability. The application of the PoC model is currently limited by the data availability for all the variables (indicators). In this paper, the development of CLDs and simulations of the behavior of a few indicators with SF diagrams are explored. Simulations show the variations in the mini-grid behavior with changes in the indicator values (assumed or collected during the field visit for systemic understanding). Comprehensive D-LCSA using all steps in the PoC model is envisaged after the survey questionnaire preparation and data collection from the field. CLD for a case study of a mini-grid at a place called "Makhla" is developed referring to [20-23] and modified as per interactions with stakeholders conducted for systemic understanding.

Makhla (Tembhurni Dhana) is a village in Chikhaldara taluka, Amravati district of Maharashtra state. The village is 104 km away from the district head quarter and is located in the Melghat tiger reserve forest. Electricity was not available in the village till October 2021 and the nearest centralised grid is 10 km away (Semadoh). 154 predominantly tribal families are residing in the village. Maharashtra Energy Development Agency (MEDA), a Government of Maharashtra institution has installed 37.8 kWp off-grid mini-grid in the village. Mini-grid was commissioned on 22nd October 2021. The basic energy requirement of the village is estimated at 200kWh/day. Energy storage of 110 kWh is supplied by 'amperehour solar technology Pvt. Ltd - energy storage solutions Company in Pune, Maharashtra, India. CLD for the Makhla mini-grid is shown in Figure 7.

In the developed CLD, the variables not bounded in any shape are referred from the literature. The variables in the solid box are the authors' contributions and in highlighted box are outcome of field interactions. In CLD, '+' sign represents the change in the variable in the same direction as the first. '-'sign represents the opposite change. Loops classified as reinforcing loops (R) and balancing loops (B) are marked in the CLD and listed in Table 2. Reinforcing loops create exponential growth while balancing loops create stability.

Table 2. Different loops in Makhla CLD.

Loop No.	Loop	Type
1	Mini-grid Income--Timely Repair and Maintenance--Battery Energy Storage Rating--Reliability of Electricity--Electricity Usage--Mini-grid Income	Reinforcing (R1)
2	Mini-grid Income--Timely Repair and Maintenance--Battery Energy Storage Rating--Reliability of Electricity--Social and cultural events--Conflicts between community and VEC--Mini-grid Income	Reinforcing (R2)
3	Mini-grid Income--Timely Repair and Maintenance--Battery Energy Storage Rating--Reliability of Electricity--Social and cultural events--Electricity Usage--Mini-grid Income	Reinforcing (R3)
4	Mini-grid Income--Timely Repair and Maintenance--Battery Energy Storage Rating--Reliability of Electricity--Electricity Usage--Cooking time--Health improvements--Satisfaction--Conflicts between community and VEC--Mini-grid Income	Reinforcing (R4)

Loop No.	Loop	Type
5	Mini-grid Income--Timely Repair and Maintenance--Battery Energy Storage Rating--Reliability of Electricity—Electricity Usage--Safety from wild animals--Health improvements--Satisfaction--Conflicts between community and VEC--Mini-grid Income	Reinforcing (R5)
6	Electricity Usage--Working hours--Number of IGAs--Business Income--Investment in IGAs--Local economic opportunities--Local Employment--Per capita income-- New Appliances Purchase--Demand for electricity--Battery Energy Storage Rating--Reliability of Electricity--Electricity Usage	Reinforcing (R6)
7	Electricity Usage--Study time for students, Education level--Per capita income-- New Appliances Purchase--Demand for electricity--Battery Energy Storage Rating--Reliability of Electricity--Electricity Usage	Reinforcing (R7)
8	Battery Energy Storage Rating--Reliability of Electricity--Repairs and Maintenance Needed--Repair and Maintenance--Battery Energy Storage Rating	Balancing (B1)

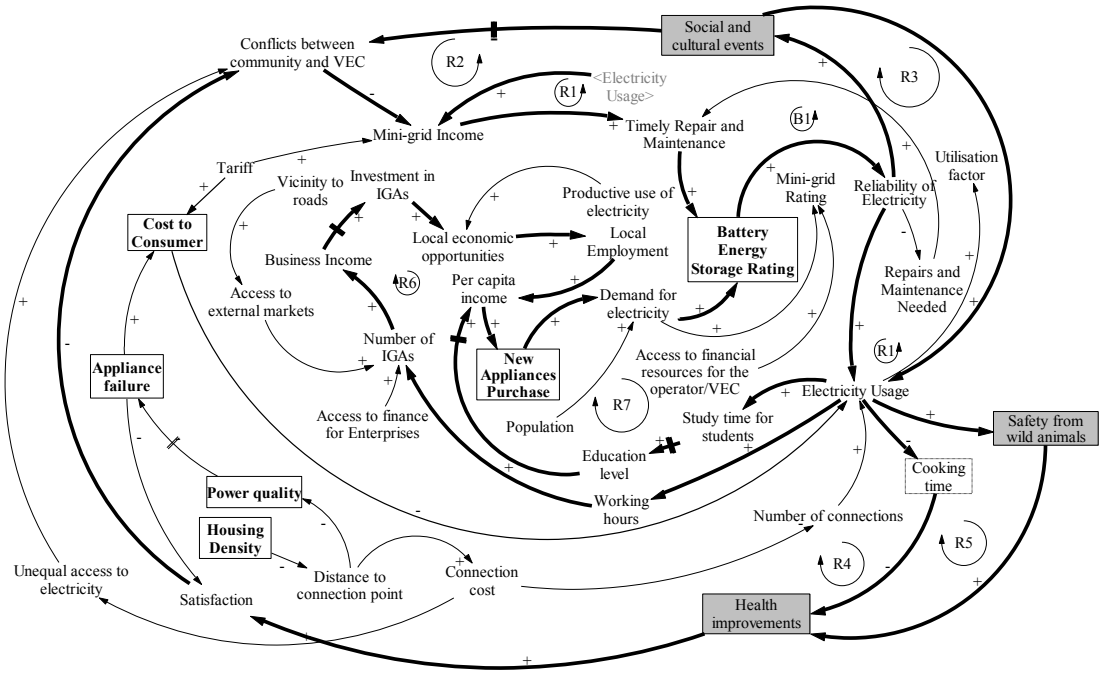

Figure. 7. CLD for Makhla mini-grid.

Mini-grid dynamics can be simulated using SF diagrams where stocks represent the accumulations in the system while flows represent the dynamics by defining how the stocks change with time. For SF analysis of the mini-grids, the identified stocks are mini-grid net income, battery capacity, electricity demand, electricity usage, and population. SF diagram for the Makhla mini-grid is shown in Figure 8. All variables from CLD, specifically qualitative ones are not included in the SF diagram as the aim is to show how quantitative analysis can be realised. Quantifying the qualitative variables is one of the challenges in the D-LCSA.

6. Results and discussions

In this section reinforcing loop R1 in Table 2 is simulated using Vensim software and results are explained in detail. Loop R1 consists of the variables: - “Mini-grid Income”, “Timely Repair and Maintenance”, “Battery Capacity”(Battery Energy Storage Rating), “Reliability of Electricity”, and “Electricity Usage”. “Mini-grid Income” is linked to “Timely Repair and Maintenance” by expressing later as the average delay in the process through a look-up table. The repair and maintenance are delayed due to lesser income which impacts the battery capacity. The relevant degrading factor is assumed. To calculate the “Reliability of Electricity”, it is necessary to understand the shortage of both battery energy and the power rating of the mini-grid system. For simplicity, faults or equipment failures are not considered. The “Reliability of Electricity” is linked to “Electricity Usage” through the sensitivity factor. Electricity usage will impact the mini-grid income and hence the loop is completed. The simulation results are shown in Figure 9 to Figure 12.

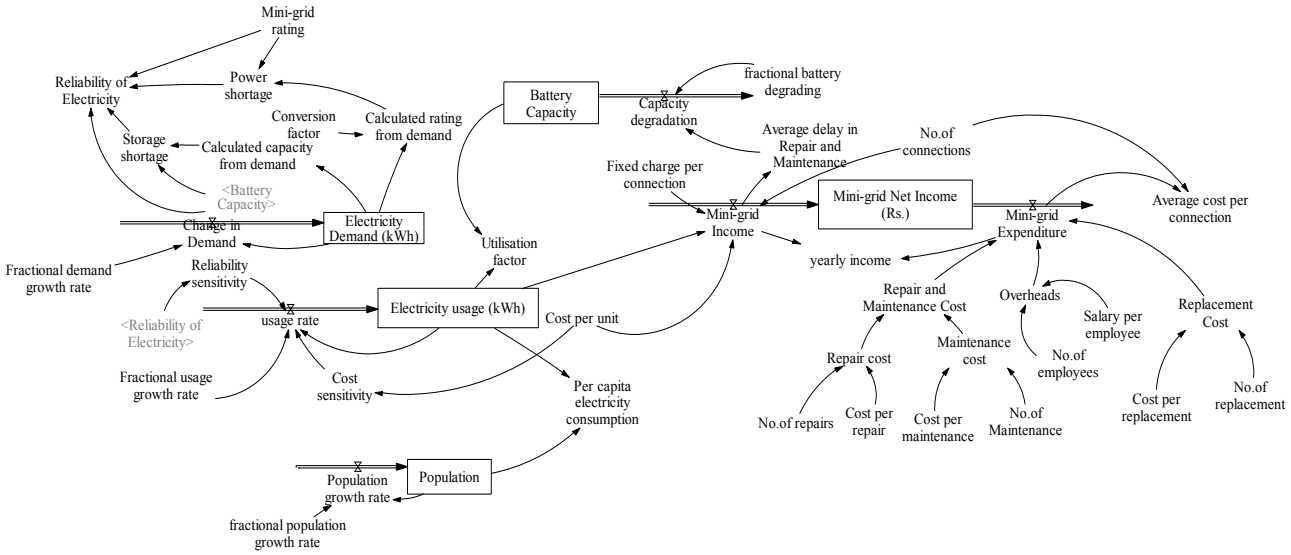

Figure. 8. SF diagram for Makhla mini-grid.

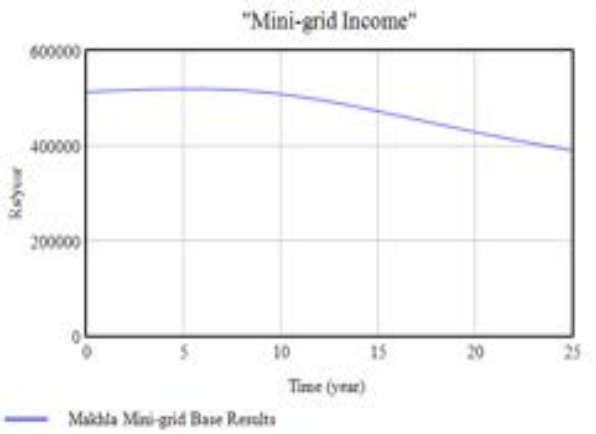

Figure. 9. Mini-grid Income.

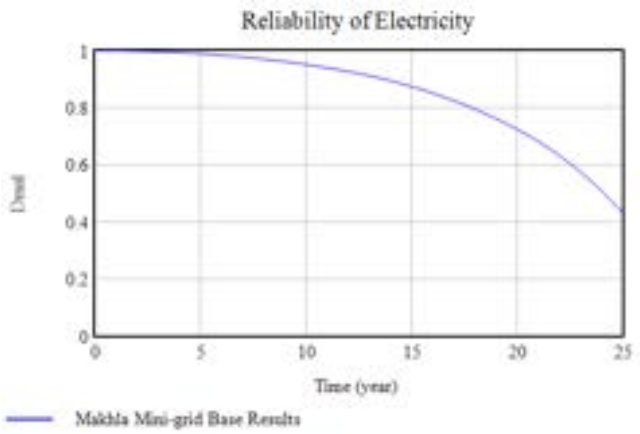

Figure. 10. Reliability of Electricity.

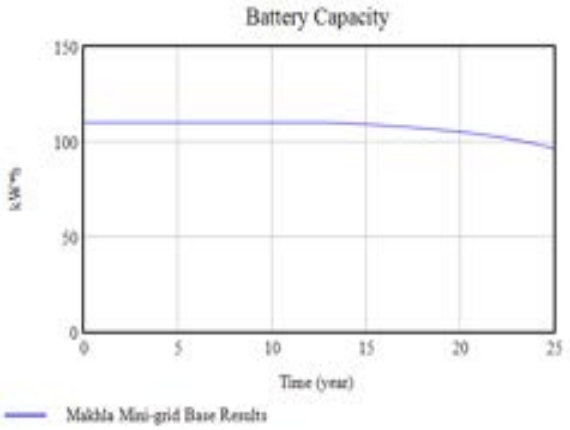

Figure. 11. Battery Capacity.

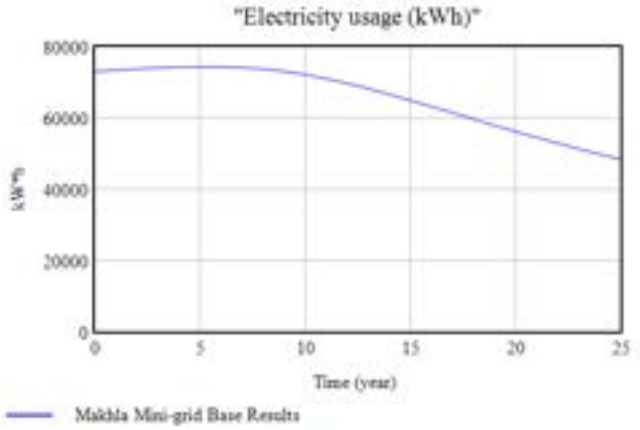

Figure. 12. Electricity Usage.

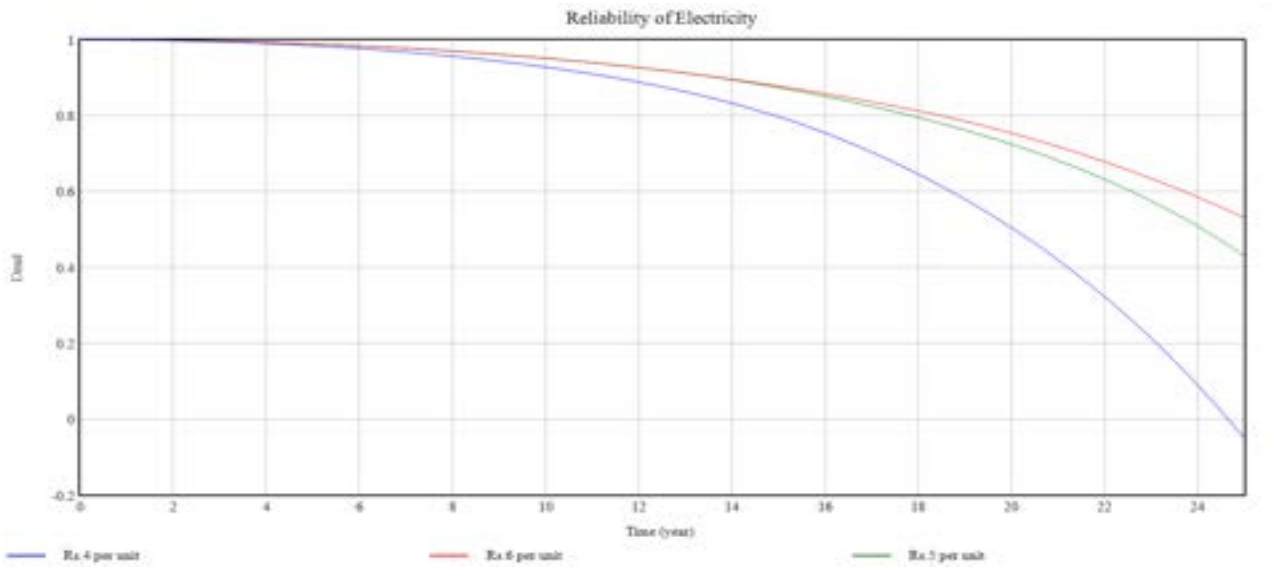

Figure. 13. Variations of Reliability of Electricity with Cost per Unit.

SF diagrams can be used for scenario analysis. The variation in the cost per unit (tariff) and its impact on reliability is shown in Figure 13. The existing tariff of Rs.5 per unit is first increased to Rs.6 per unit and then decreased to Rs.4 per unit for scenario analysis. Lower tariff results in higher usage decreasing reliability. Higher tariff reduces electricity usage and hence the reliability is higher. Similarly, the policies can also be analysed with the help of the SF diagram.

The inference for mini-grid sustainability can be drawn by comparing the simulation results with defined mini-grid sustainability criteria. The changes in the values of related variables may reduce or increase the gap in expected sustainability results. These analyses can be used as levers in decision-making related to mini-grid operations as shown in Figure 6. During the field visits, mini-grid systems are observed to follow some common patterns and face some common challenges irrespective of the location. These patterns may be modelled to generalise the performance of the mini-grid systems having similarities.

Conclusions

The framework presented in this paper attempts to conceptually identify limitations or scope of improvement in the LCSA of mini-grids. A proof-of-concept model was developed linking to dynamic causal relationships between technical, social, economic, environmental, and institutional variables to address life cycle changes in mini-grids. The important steps in models like the development of CLD, SF diagram, and simulation of the same are illustrated with a case study of a mini-grid in India. The results highlight the advantages of adding SD analysis into LCSA. The proposed model expands state-of-the-art impact assessment by incorporating dynamics. The results represent the behavior of the mini-grid systems by considering the complexity and non-linearity in the modeling. Developing the case study has highlighted the need for data monitoring for mini-grid systems. The accuracy of output depends on the availability of localised data. Future work could build on the research by use of the proposed model for comprehensive D-LCSA and developing a digital dashboard useful for all the stakeholders. Further applications of the D-LCSA model to case studies of various mini-grid scenarios may validate the proposed PoC model. “Defining mini-grid sustainability” is necessary to set the benchmark useful for sustainability analysis. The common and recurring patterns in the scenarios that shape the mini-grid behavior may be identified. Participatory SD not considered in the PoC can be explored for the formation of CLDs and quantify the feedback between different variables.

Acknowledgments

The authors would like to thank the officials of MEDA, Amravati Division of Maharashtra state (India) for the introduction to the installed mini-grids, the support extended during the field visits, and the participation in the stakeholders’ interactions.

References

[1] UN General Assembly, Transforming our world : the 2030 Agenda for Sustainable Development, 21 October 2015, A/RES/70/1, available at: https://www.refworld.org/docid/57b6e3e44.html [accessed 25.12.2022]

[2] Palit D., & Bandyopadhyay K. R., Rural electricity access in South Asia: Is grid extension the remedy? A critical review. Renewable and Sustainable Energy Reviews 2016;60:1505-1515.

[3] IEA, World Energy Outlook 2022, IEA, Paris https://www.iea.org/reports/world-energy-outlook-2022, License: CC BY 4.0 (report); CC BY NC SA 4.0 [accessed 28.12.2022]

[4] IRENA, UNSD, World Bank, WHO. 2022. Tracking SDG 7: The Energy Progress Report. World Bank, Washington DC. © World Bank. License: Creative Commons Attribution—NonCommercial 3.0 IGO (CC BY-NC 3.0 IGO) [accessed 28.02.2023]

[5] Narayan N., Solar home systems for improving electricity access: An off-grid solar perspective towards achieving universal electrification. [dissertation]. Delft, Netherlands: Delft University of Technology; 2019.

[6] Das Binit et al, CSE, 2022, Mini-Grids: A Just and Clean Energy Transition, Volume 1 https://www.cseindia.org/vol-2-mini-grids-a-just-and-clean-energy-transition-11276 [accessed 09.01.2023]

[7] Das Binit et al, CSE, 2022, Mini-Grids: A Just and Clean Energy Transition, Volume 2 https://www.cseindia.org/vol-2-mini-grids-a-just-and-clean-energy-transition-11277 [accessed 09.01.2023]

[8] Turkson C., Acquaye A., Liu W., Papadopoulos T., Sustainability assessment of energy production: a critical review of methods, measures and issues. Journal of environmental management 2020;264: 110464.

[9] Boche A., Foucher C., Villa, L. F. L. Understanding Microgrid Sustainability: A Systemic and Comprehensive Review. Energies 2022;15(8):2906.

[10] Haase M., Wulf C., Baumann M., Rösch C., Weil M., Zapp P., Naegler T. Prospective assessment of energy technologies: a comprehensive approach for sustainability assessment. Energy, Sustainability and Society 2022;12(1):1-41.

[11] Khatami F., Goharian, E. Beyond Profitable Shifts to Green Energies, towards Energy Sustainability. Sustainability 2022;14(8):4506.

[12] Brent A. C., Rogers, D. E., Renewable rural electrification: Sustainability assessment of mini-hybrid off-grid technological systems in the African context. Renewable Energy 2010;35(1):257-265.

[13] Ilskog E., Indicators for assessment of rural electrification—An approach for the comparison of apples and pears. Energy policy 2008;36(7):2665-2673.

[14] Lassio J. G., Magrini A., Branco D. C., Life cycle-based sustainability indicators for electricity generation: A systematic review and a proposal for assessments in Brazil. Journal of Cleaner Production 2021;311: 127568.

[15] Viegas Filipe E., Otsuki K., Monstadt J. Translating the sustainable development goals in national development planning: the case of Mozambique's energy for all programme. Sustainability Science 2021;16(6):1797-1809.

[16] Corona B., San Miguel G., Life cycle sustainability analysis applied to an innovative configuration of concentrated solar power. The International Journal of Life Cycle Assessment 2019;24(8):1444-1460.

[17] Poudel B., Maley J., Parton K., Morrison, M., Factors influencing the sustainability of micro-hydro schemes in Nepal. Renewable and Sustainable Energy Reviews 2021;151:111544.

[18] Katre A., Tozzi A., Bhattacharyya, S. Sustainability of community-owned mini-grids: evidence from India. Energy, Sustainability and Society 2019;9(1):1-17.

[19] Chatterjee A., Burmester D., Brent A., Rayudu R., Research insights and knowledge headways for developing remote, off-grid microgrids in developing countries. Energies 2019;12(10):2008.

[20] Hartvigsson E., To be or not to be: on system dynamics and the viability of mini-grids in rural electrification [dissertation]. Gothenberg, Sweden:Chalmers University of Technology;2018.

[21] Hartvigsson E., Ahlgren E., Molander S., Tackling complexity and problem formulation in rural electrification through conceptual modelling in system dynamics. Systems Research and Behavioural Science 2020;37(1):141-153.

[22] Riva F., Ahlborg H., Hartvigsson E., Pachauri S., Colombo, E., Electricity access and rural development: Review of complex socio-economic dynamics and causal diagrams for more appropriate energy modelling. Energy for sustainable development 2018;43:203-223.

[23] González A. M., Sandoval H., Acosta, P., Henao, F. On the acceptance and sustainability of renewable energy projects—A systems thinking perspective. Sustainability 2016;8(11):1171.

Sustainability Assessment of Typical Energy Storage Technologies for Peak Shaving Scenarios Based on the Full Life Cycle

Nana Chen[a], Xiaoqu Han[a], Yanxin Li[a], Xiaofan Huang[b], Jiarui Li[b], and Junjie Yan[a]

[a] State Key Laboratory of Multiphase Flow in Power Engineering, Xi'an Jiaotong University, Xi'an, China, hanxiaoqu@mail.xjtu.edu.cn, CA
[b] Huadian Electric Power Research Institute Co., Ltd., Beijing, China, xiaofan-huang@chder.com

Abstract:

With more renewable energy sources (RES) which are inherent intermittent and unpredictable connecting with power grid, various stability problems occur, among which the peak load regulation is the most prominent. Energy storage systems (ESSs) are essential for buffering the electricity grid. Selecting the most suitable energy storage technology among various alternatives is of great importance. In this work, the sustainability of typical energy storage technologies was studied with respect to four aspects for peak shaving scenarios, including technical (i.e. maturity, energy density, round-trip efficiency, duration ranges, life cycles, lifetime and position flexibility), economic (levelized cost of energy, net present value), environmental (i.e. global warming, damage to human health, damage to ecosystems, damage to resource availability) and social (public acceptance) based on the full life cycle. This study evaluated the soft criteria including maturity, position flexibility and public acceptance by Analytic hierarchy process (AHP). Life cycle assessment (LCA) and life cycle cost (LCC) methods were combined to study the life-cycle environmental and economic performance. Technique for order preference by similarity to an ideal solution (TOPSIS) was applied for determining the sustainability prioritization of energy storage technologies. The sensitivity analysis was carried out to investigate the effects of control and economic input parameters on environmental performance and economic performance. In addition, the effects of criteria weights, electricity sources and number of daily cycles were conducted on sustainability ranking of ESSs. The results showed Lithium iron phosphate battery (LIPB) and pumped hydro storage (PHS) had good sustainability performance, which could be the most suitable energy storage technologies for peak shaving scenarios.

Keywords:

Energy storage; Life Cycle Assessment; Life Cycle Cost; Peak shaving; Sustainability prioritization.

1. Introduction

More renewable energy sources (RES) have connected with power grid, but RES is inherent intermittent and unpredictable, which result in various stability problems in which the peak load regulation is the most prominent. Energy storage systems (ESSs) are essential for buffering the electricity grid [1]. There are various ESSs which have different properties and performances. Selecting the most suitable energy storage technology for specific scenario when facing various conflicting criteria is of great importance for the decision-makers [2].

A few studies are available that evaluate the performance of different ESSs in the specific application by multi-criteria decision making approach [1-8]. Vo T.T.Q et al. [1], Ren J.Z et al. [2] and Raza S.S. et al. [3] evaluated the energy storage technologies considering the economic, technical and environmental impacts. Walker S.B.et al.[4] and Petrillo A.et al.[5] assessed the Power-to-Gas technologies and a compressed air energy storage system respectively in technological, economic and social aspects. The performance of 27 energy storage alternatives which were classified into fast response and long-term clusters were assessed by Rostami F. et al. [6] considering the economic, environmental and social indicators using data envelopment analysis. Baumann M. et al. [7] and Cellura S. et al. [8] combined the environmental and economic assessments for batteries and flywheel energy storage, respectively. Davies D.M. et al. [9] assessed the batteries by combining economic and technological evaluation. However, the considered evaluation criteria are not comprehensive in these above studies, the disregarded aspects often also have a certain impact on the sustainability performance.

There are some literatures assessing the sustainability performance of ESSs in terms of comprehensive aspects including environmental, economic, technical and social categories [10-17]. Ilbahar E. et al. [10] proposed a methodology to evaluate the hydrogen energy storage systems. Baumann M. et al. [11] evaluated the overall performance of batteries for four grid services. Seven energy storage technologies including lead-acid batteries, Li-ion batteries, super capacitors, hydrogen storage, compressed air energy

storage, pumped hydro, and thermal energy storage for ten scenarios were evaluated by Albawab M. et al. [12]. Balezentis T.et al. [13] presented a novel multi-criteria utility analysis approach for ranking hydrogen storage, HPS, CAES, Li-Ion batteries, lead acid batteries, flow batteries, and molten salt energy storage. Lin R.J. et al. [14] studied the overall performance of energy storge technologies by innovative indices of sustainability efficiency and super-efficiency. Evaluation of PHS, CAES and NaS for integration with wind power in the Pacific Northwest region of the US was conducted by Turgrul U.D. et al. [15]. The sustainability prioritization of four alternatives including pumped hydro, compressed air, lithium-ion, and flywheel were assessed by Ren J.Z.et al. [16]. Acar C. et al. [17] analysed the sustainability performance of energy storage systems including Pumped hydro, conventional batteries, high−temperature batteries, flow batteries, and hydrogen for residential applications. In these literatures, the considered index are often hard criteria which have exact data and the assessments often rely on existing literatures without considering the varying of the input parameters such as round-trip efficiency, electricity sources in different scenarios.

In addition, the available literatures generally study the economic performance in terms of energy cost and power cost [13,17] or capital and operating cost [12,14-16] and study the environmental performance in terms of CO_2 which are both obtained from the previous literatures or the engineering reports. Mostafa M.H. et al. [18], Hunter C.A. et al. [19] and Chen X.J. [20] point out that levelized cost of energy, payback period and internal rate of return should be used to evaluate the life cycle economic performance of ESSs. Researchers [21-26] often conduct life cycle environmental assessments of different ESS to choose the best environment-friendly alternatives from the aspects of cumulative energy demand, global warming potential, ozone layer depletion potential, marine aquatic ecotoxicity potential, acidification potential, damage to human health, damage to ecosystems and damage to resource availability et al. Moreover, few literatures such as [11] analyze the sustainability of ESSs from the perspective of life-cycle aspect. In consequence, there is a lack of comprehensive assessment of different ESSs that consider not only the life-cycle costing but also quantifying the soft index from the aspects of technical, economic, environmental and social performances.

This study aims at tackling these gaps by providing a comprehensive sustainability assessment of different ESSs. The studied ESSs are pumped hydro storage (PHS), compressed air energy storage (CAES), lithium iron phosphate battery (LIPB) and vanadium redox flow battery (VRFB) which are applicable for the peak shaving scenarios. The soft criteria of technical and social categories are quantified by Analytic hierarchy process (AHP), and life-cycle assessment (LCA) and life-cycle cost (LCC) are adopted to evaluate the environmental and economic performance parameters based on the full life cycle of ESSs.

2. Methodology

2.1. Assessment framework

The sustainability assessment which can incorporate both hard and soft criteria was conducted with respect to technical, economic, environmental and social categories for peak shaving scenarios based on the full life cycle, in order to select the most suitable energy storage option, assessment framework of this study is shown in Figure 1. The technical category included round-trip efficiency, energy density, duration range, life cycles, lifetime, maturity and position flexibility. The environmental category included global warming (GWP), damage to human health (DHH), damage to ecosystem (DE) and damage to resource availability (DRA). The economic category was mainly levelized cost of energy (LCOE) and net present value (NPV). The social category mainly considered public acceptance.

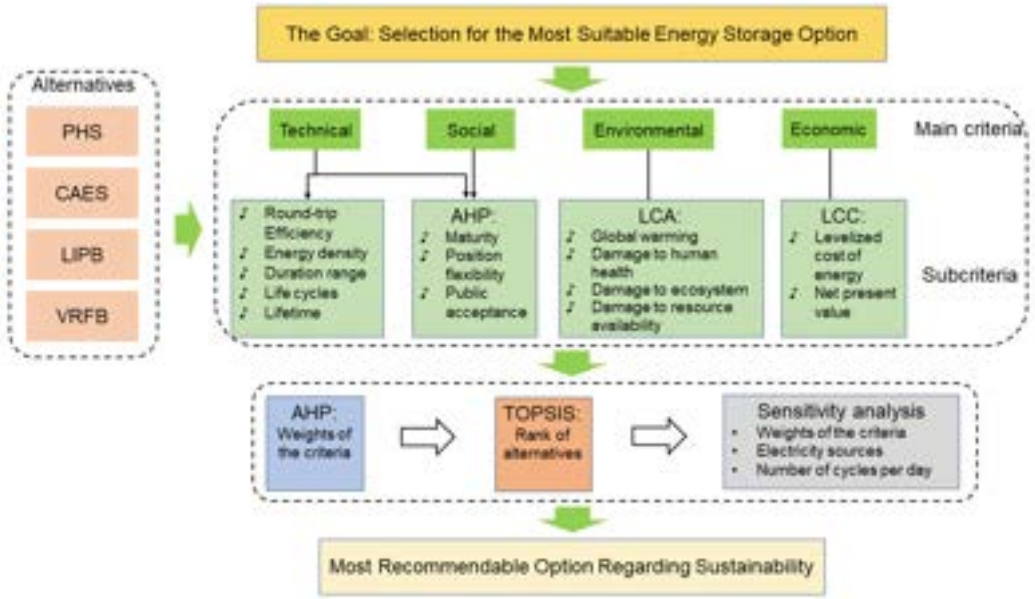

Figure. 1. Overview of the assessment framework.

AHP was applied to evaluate the soft criteria including maturity, position flexibility and public acceptance, it was also employed to determine weights of main criteria and subcriteria in each category. Environmental and economic performance were quantified by Life cycle assessment (LCA) and life cycle cost (LCC) methods, and they have the same system boundary including the raw materials extraction and processing, manufacturing, usage and disposal or recycling stage of ESSs. Technique for order preference by similarity to an ideal solution (TOPSIS) which can rank the alternatives was applied for sustainability prioritization of energy storage technologies. The effects of criteria weights, electricity sources and number of daily cycles on environmental performance, economic performance and sustainability order were conducted in the sensitivity analysis.

The technical and social performance assessment is based on the technology data about ESSs from literature, survey and interviews, and calculated by AHP method and interval approach for uncertainties [2]. Environmental performance assessment is calculated by Recipe endpoint approach in Simapro software whose life cycle inventory data (LCA input) is from literature and engineering reports. Economic performance assessment is conducted by the LCC model which is established by the author in which the life cycle cost inventory is from literature, survey and engineering reports.

2.2. Quantifying the soft criteria and determining the criteria weights

Maturity, position flexibility and public acceptance are important for the alternatives to evaluate the sustainability performance, but they are soft criteria whose data cannot be obtained directly, it is hard to be compared between different alternatives in the TOPSIS process [2], so it is essential to quantify the soft criteria.

AHP method was generally employed to determine the weights of considered four categories as well as that of the subcriteria in each category [13], it could also be used to assess the relative performance of the energy storage alternatives with respect to soft criteria. Table 1 shows the linguistic terms and their corresponding numbers for the pair-wise comparison in the analysis.

Table 1. Linguistic terms and corresponding numbers for the pair-wise comparison.

Numbers	Linguistic terms	Numbers	Linguistic terms
1	Equally important	7	Strongly more important
3	Slightly more important	9	Absolutely more important
5	More important	2,4,6,8	Intermediate values between the two adjacent judgments

2.3. Life cycle cost

Two economic indicators are conducted to compare the economic performance of different energy storage alternatives, namely levelized cost of energy (LCOE) and net present value (NPV) which are important index that be studied by many researchers [18-20]. Figure 2 shows the life-cycle cost of ESSs, it is worth mentioning that costs associated with the environmental impacts were not considered for avoiding the duplication among LCA and LCC indicators. The LCOE and NPV were calculated as equations (1) and (2).

$$LCOE = C_{investment} + \frac{\sum_{t=1}^{T} \frac{(C_{o\&m} + C_c + C_{rc} + C_{dr}) \cdot (1+r_{if})^{t-1}}{(1+r_d)^t}}{\sum_{t=1}^{T} \frac{E_t}{(1+r_d)^t}} \quad (1)$$

$$NPV = -p \cdot C_{investment} + \sum_{t=1}^{T} \frac{(C_{prof} - C_{loan} - C_{o\&m} - C_{rc} - C_{dr}) \cdot (1+r_{if})^{t-1}}{(1+r_d)^t} \quad (2)$$

Where $C_{investment}$ represents the investment cost, $C_{o\&m}$ is the sum of fixed and variable operation and maintenance cost, C_c is the charging electricity cost, C_{rc} is the replacement cost, the replacement time of ESSs is related to the maximum number of cycles, C_{dr} is the disposal and recycling cost, T is lifetime of the power station, r_d is the discount rate which is set as 5.49%[27], r_{if} is the inflation rate which is set as 2%[27], E_t represents the annual power generation, p is the proportion of initial investment which is set as 30%[20], C_{prof} is the annual profit considering the peak valley price difference of power grid, C_{loan} is the annual repayment of debt. E_t and C_{prof} are calculated as equations (3) and (4).

$$E_t = Q_E \times (1 - \eta_{self}) \times SOC \times \theta_{DOD} \times \eta_{dis} \times N_y \quad (3)$$

$$C_{prof} = E_t \cdot (p_s - p_p / \eta) \quad (4)$$

Where Q_E is the designed capacity of ESSs, η_{self} is the self-discharge efficiency, SOC represents the average proportion of capacity over ESSs' lifetime considering the decay rate, θ_{DOD} is the discharge depth, η_{dis} is the discharge efficiency, and N_y is the average number of cycles per year, p_s and p_p are the electricity prices for sale and purchase, η is the round-trip efficiency.

The lifetime of energy storage power station is considered as 20 years, which is inconsistent with the life of ESS, so it may face the problem of replacement of battery and equipment during the operation of power station. The replacement time is related to the number of cycles, number of daily cycles and the calendar life of ESS, the market price change of energy storage components (especially the battery cell) is also considered at the replacement time. Replacement cost C_{rc} is calculated as equation (5).

$$C_{rc} = c_{rc} \cdot (1 - r_b)^{t_r} \cdot Q_E \quad (5)$$

Where r_b represents the cost reduction rate of energy storage components, which is 7.78% for LIPB [20], c_{rc} is the unit replacement cost, t_r is the replacement time.

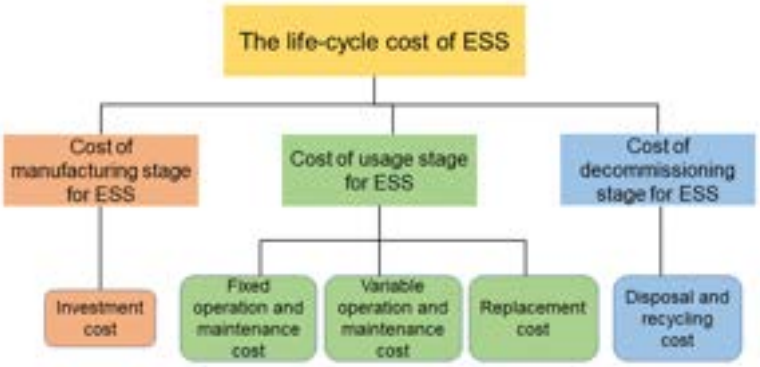

Figure. 2. The main elements of life-cycle cost of energy storage systems.

3. Results and discussions

3.1. Weights

As mentioned above, weights of considered indicators were calculated by AHP method. For the main criteria weights, environmental criteria were assumed to be the most important, followed by economic, technical and social criteria [11, 15], the maturity and position flexibility were the most important, which are followed by round-trip efficiency, duration ranges, life cycles, lifetime and energy density for the technical subcriteria, GWP and DHH were the most important, followed by DE and DRA for environmental subcriteria, the results were shown in Figure 3. The weights of environmental, economic, technical and social indicators were 0.46, 0.28,0.16 and 0.10, respectively. The maturity and position flexibility had the biggest weights which were 0.27, GWP and DHH had the biggest weights which were 0.35.

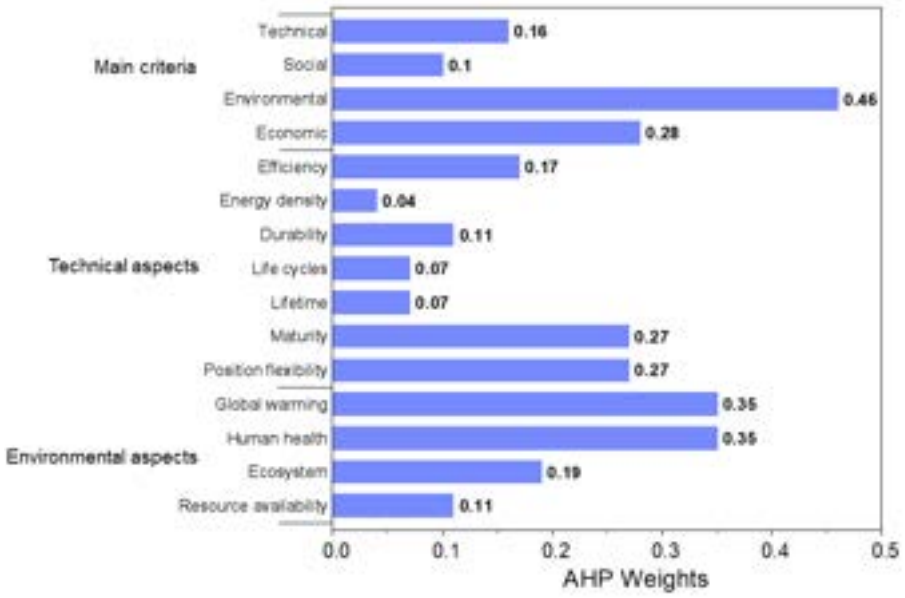

Figure. 3. The weights of the evaluated criteria.

3.2. Environmental aspects

A cradle-to-grave LCA model [21-25] was adopted for evaluating the environmental impacts of typical energy storage technologies, ReCiPe method was applied for the assessment which provides midpoint as well as endpoint indicators by using SimaPro 9.2 software. With the proposal of carbon peak and carbon neutral goal, researchers pay more attention to the contribution of ESSs to this goal, thus GWP was selected as a

separate index. The functional unit was set to one megawatt-hour of electricity delivery over the entire lifetime. The life cycle inventory (LCI) was mainly based on specific engineering reports. The environmental results of LIPB and VRFB were partly based on the previous work [26].

Figure 4 shows the environmental performance of ESSs, including the impacts of GWP, DHH, DE and DRA. Median results are provided including positive and negative whiskers for the 25% and 75% quartiles in Figure 4(a), and the author mainly analysed the median results in the work. What needs to point out is the electricity mix used in the usage process of baseline scenario throughout this work was the Chinese electricity mix in 2020.

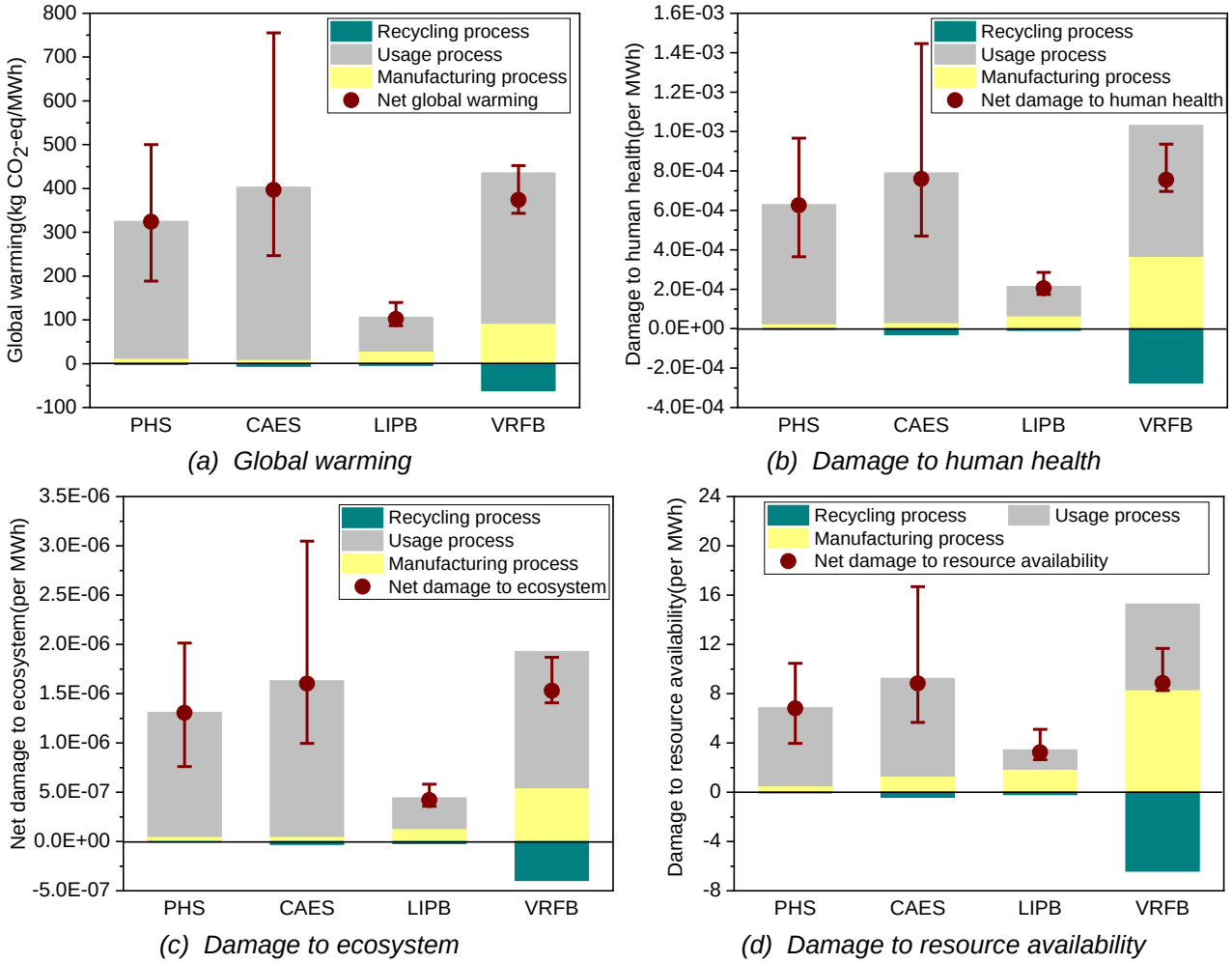

Figure. 4. The environmental performance of energy storage systems in the life cycle. The indicated whiskers in (a) represent 25% and 75% quartiles.

It can be observed that net GWP of PHS, CAES, LIPB and VRFB were 188.4-324.1-500.1, 246.6-397.0-755.4,86.9-102.3-139.8,343.5-374.1-452.4 kgCO_2-eq/MWh. LIPB had the best global warming performance, followed by PHS, VRFB and CAES. In general, the basically same trend was observed for the other three environmental impacts which was not demonstrated here. For the life cycle of ESSs, the usage process had the most impacts of GWP, DHH, DE and DRA, and the proportion of four environmental impacts of LIPB was 75.7%,73.0%,73.7% and 48.5%, respectively. The recycling process had the negative environmental impacts for the recycled materials were beneficial for the environment. Compared with PHS, CAES and LIPB, the recycling process of VRFB provided the greatest environmental benefits.

3.3. Economic performance

Levelized cost of energy (LCOE) and net present value (NPV) for PHS, CAES, LIPB and VRFB were displayed in Figure 5 in which median results are provided including positive and negative whiskers for the 25% and 75% quartiles. It should be noted that LIPB needed to be replaced once.

Figure 5(a) showed LCOE of PHS, CAES, LIPB and VRFB were 1.40-1.54-1.71,1.46-1.59-1.91,1.65-1.77-1.95 and 2.04-2.06-2.36 ¥/kWh, respectively. The performance of LCOE from the best to the worst was PHS, CAES, LIPB and VRFB, the rank results were consistent with the literature [11,18-20]. Take LIPB for example, the proportion of initial investment cost was 50.2%, the charging electricity cost was 30.2%, the O&M cost was 12.1% and the replacement cost was 7.5%. It can be found that initial investment cost and

charging electricity cost contributed most to LCOE. Figure 5(b) showed NPV of PHS, CAES, LIPB and VRFB were 43.1-58.1-70.6,29.5-55.6-67.0,10.1-29.8-43.0 and -31.9-1.1-2.5 million ￥, respectively. The NPV performance of PHS was best and that of VRFB was worst which was same to the LCOE results. LIPB had the least charging electricity cost for LCOE and the biggest profit for NPV, followed by PHS, VRFB and CAES, it was mainly related to the round-trip efficiency which were 95%, 75%,73% and 70% for LIPB, PHS, VRFB and CAES, respectively.

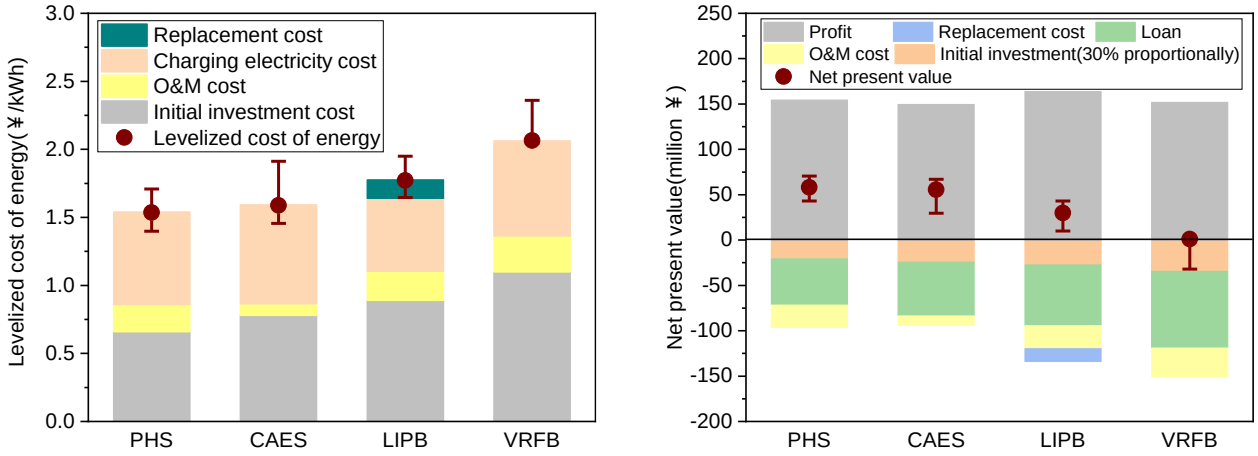

(a) Levelized cost of energy *(b) Net present value*

Figure. 5. The economic performance of ESSs. The indicated whiskers represent 25% and 75% quartiles.

3.4. Technology and social aspects

The results of quantified soft criteria with respect to maturity are presented in Table 2. The maturity of PHS, CAES, LIPB and VRFB were mature, developed/commercial, demonstration and demonstration, while the corresponding scores were 0.45, 0.26, 0.14 and 0.14, respectively. For the performance of position flexibility, PHS and CAES had strict restrictions, LIPB and VRFB had no special restrictions, so the scores were 0.13, 0.13, 0.38 and 0.38. For the performance of public acceptance, PHS has been accepted, CAES was developing, LIPB and VRFB depended on the station scale, so the public acceptance scores were 0.45,0.26,0.14,0.14. It can be found that the better the performance, the higher the score.

Table 2. The relative performances of ESSs with respect to maturity.

Maturity		PHS	CAES	LIPB	VRFB
PHS	Mature	1	2	3	3
CAES	Developed/ Commercial	1/2	1	2	2
LIPB	Demonstration	1/3	1/2	1	1
VRFB	Demonstration	1/3	1/2	1	1
Relative performances		0.45	0.26	0.14	0.14

In addition to the above soft criteria, the other technical indicators of ESSs were basically not definite values, but were in the range, it was also impossible to be compared directly in the TOPSIS process. Therefore, the interval approach for uncertainties proposed by Ren [2] was used to evaluate the technical performance of ESSs, the results were shown in Figure 6. Round-trip efficiency of PHS, CAES, LIPB and VRFB were 65%-85%, 54%-80%, 93.5%-96% and 70%-75%, while the corresponding scores were 1.77, 1.15, 3.5 and 1.58, respectively. Lifetime of PHS, CAES, LIPB and VRFB were 30-60 years, 20-40 years, 7.5-20 years and 10-20 years, while the corresponding scores were 3.3, 2.7, 0.94 and 1.06, respectively. It can be observed that best performance with higher scores of round-trip efficiency, life cycles, lifetime, duration range and energy density were for LIPB, PHS, PHS, CAES and LIPB.

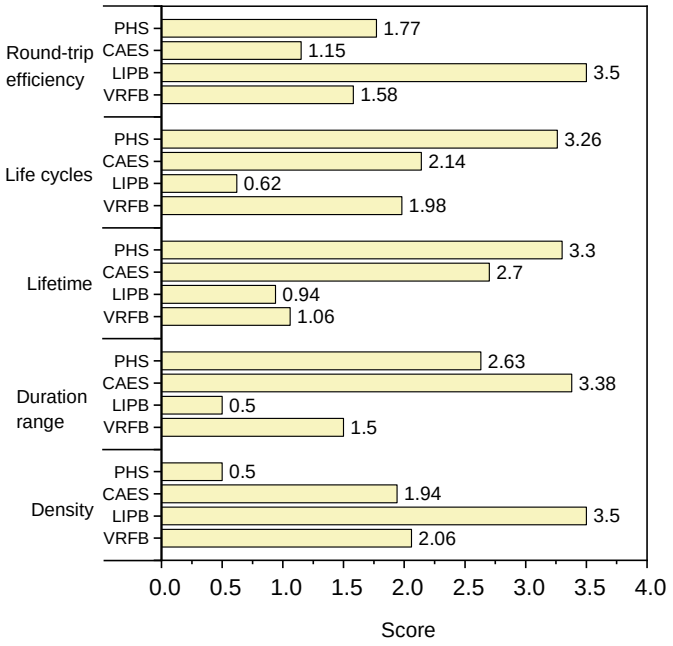

Figure. 6. The technical performance of ESSs.

3.5. Indicative scores and rankings

The considered technical, economic, environmental and social criteria have the inconsistent character, so the results can't be directly comparable, thus a single score was calculated by TOPSIS for multi-criteria decision analysis for sustainability assessment of typical ESSs. The rankings and sustainability scores of ESSs are shown in Figure 7. For environmental aspects, the performance which ranked from 1 to 4 was LIPB, PHS, VRFB and CAES. For economic aspects, the performance of PHS, CAES, LIPB and VRFB ranked from 1 to 4. And PHS performed best, CAES performed worst for technology aspects. The sustainability performance of PHS, CAES, LIPB and VRFB were 0.50, 0.30, 0.64 and 0.13. It was found that LIPB was best for sustainability performance, and VRFB was worst.

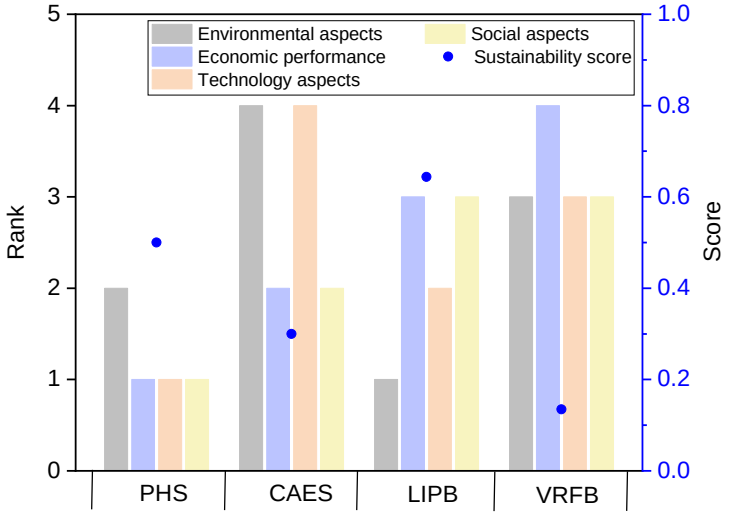

Figure. 7. The ranking and sustainability score of ESSs.

3.6. Sensitivity analysis

3.6.1. Sensitivity analysis of environmental impacts

Sensitivity analysis of electricity sources, discharge depth, round-trip efficiency and number of daily cycles on environmental impacts were conducted. Sensitivity analysis result of GWP was displayed here, the variation trend of DHH, DE and DRA were the same with that of GWP. Figure 8 shows the effect of changing the electricity sources on GWP including solar photovoltaic (PV) and wind, it is quite evident that PV and wind scenarios drastically reduced the environmental impacts compared with the grid mix scenario. The GWP for PV and wind scenario was reduced to as little as less than 31.8% and 26.5% of the impacts of grid mix scenario, respectively. Moreover, the relative ranking of the four ESSs changed and CAES became more

competitive in the wind scenario. Figure 8(b) shows the variation of GWP impacts of ESSs with the variation of the GHG emissions of the electricity sources. The GHG emissions of grid mix, PV and wind are 806, 79 and 23 kg CO2-eq/MWh, respectively. Considering the grid mix as the reference scenario, a decrease of one percentage of electricity sources' GHG emissions will lead to a corresponding decrease in GWP impacts of 0.97%,0.99%,0.76%,0.92% for PHS, CAES, LIPB and VRFB, respectively.

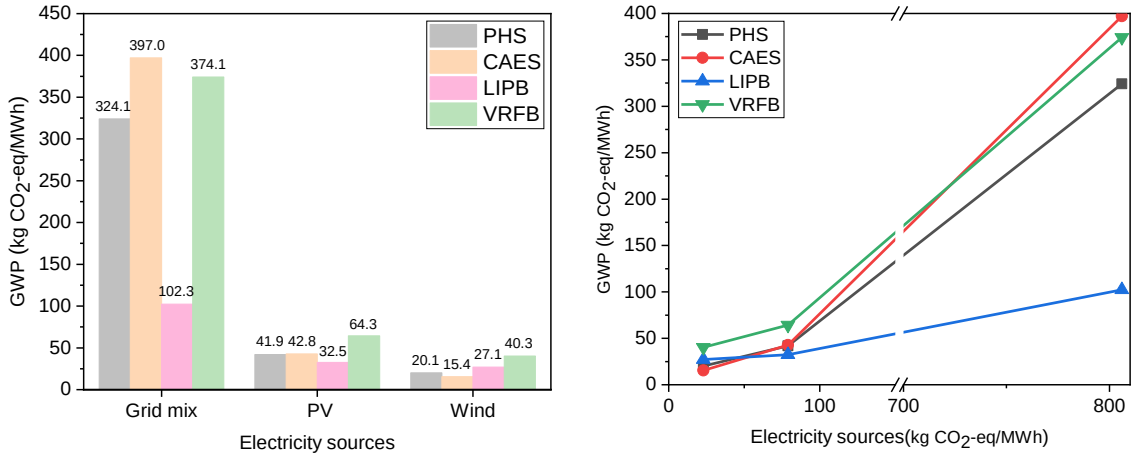

(a) *(b)*

Figure. 8. GWP impact of changing the electricity sources.

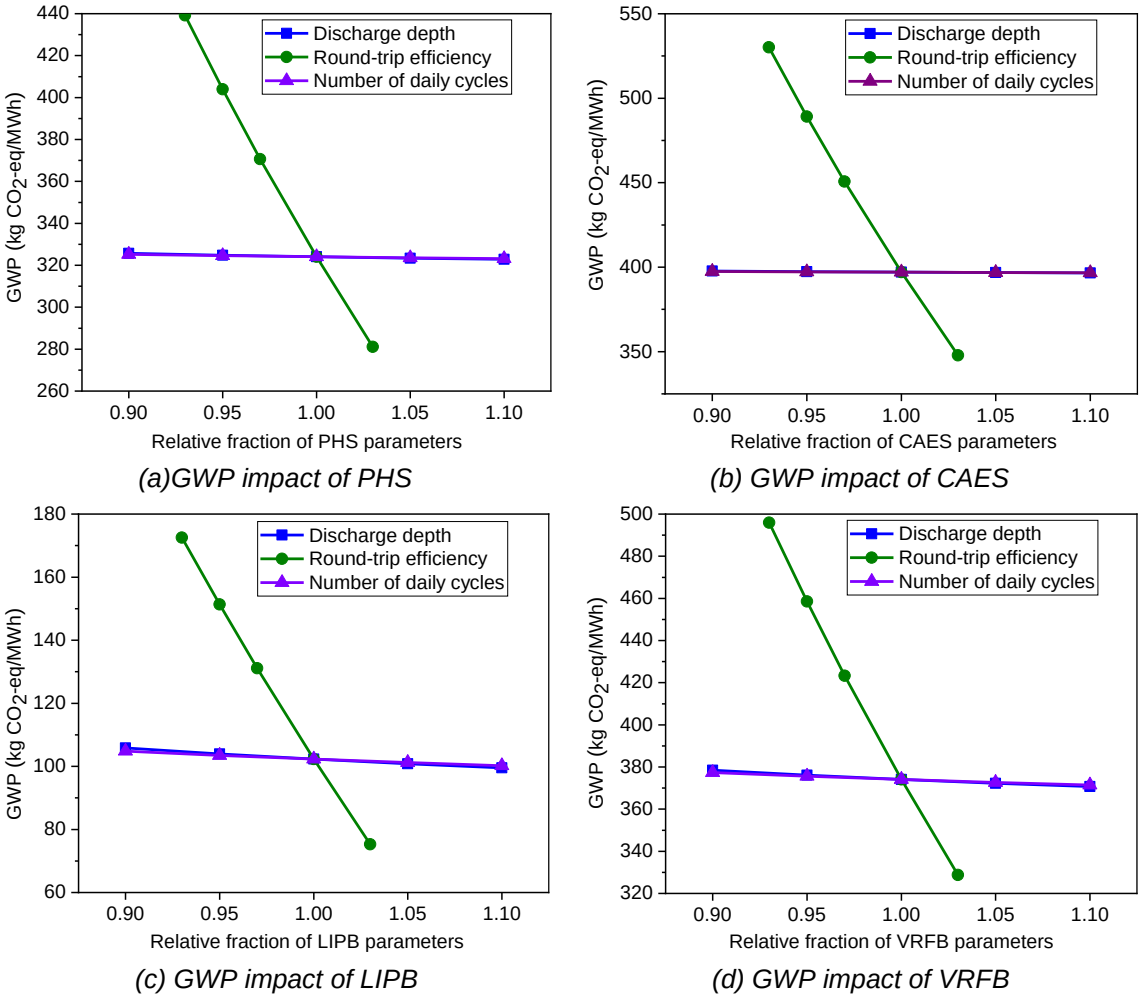

(a)GWP impact of PHS *(b) GWP impact of CAES*

(c) GWP impact of LIPB *(d) GWP impact of VRFB*

Figure. 9. Sensitivity analysis results of changing the discharge depth, round-trip efficiency and number of daily cycles on GWP impact.

The variation of GWP impact when the discharge depth, round-trip efficiency and number of daily cycles vary from the 0.90 to 1.10 times of reference value are shown in Figure 9. The reference round-trip efficiency values were 75%, 70%,95% and 73% for PHS, CAES, LIPB and VRFB, respectively. It can be found that an

increase of one percentage of round-trip efficiency will lead to a corresponding decrease in GWP impacts of 4.8%,4.5%,9.4%,4.4% for PHS, CAES, LIPB and VRFB, respectively. And the reference discharge depth and number of daily cycles values were 80% and 300 cycles per day for four ESSs, the variation of GWP impact was not changed evidently when the two input parameters varied. Therefore, electricity sources and round-trip efficiency had important impacts on the environmental performance of ESSs.

3.6.2. Sensitivity analysis of economic impacts

The effects of control and economic parameters on LCOE were conducted which is shown in Figure 10. In terms of control parameters, discharge depth, round-trip efficiency and number of daily cycles were selected for analysis, and the economic parameters of unit capacity cost and charging electricity price were analysed. LCOE increased with the increasing of economic parameters and the decreasing of control parameters. For LCOE of LIPB, an increase of one percentage of unit capacity cost and charging electricity price will lead to a corresponding increase of 58.1% and 28.3%. In addition, an increase of one percentage of discharge depth, round-trip efficiency and number of daily cycles will lead to a decrease of 72.1%, 29.3% and 67.3%, respectively. It is illustrated that the control parameters had more influence to LCOE than economic parameters, and LCOE was more sensitive to the discharge depth which was consistent with the literature [20].

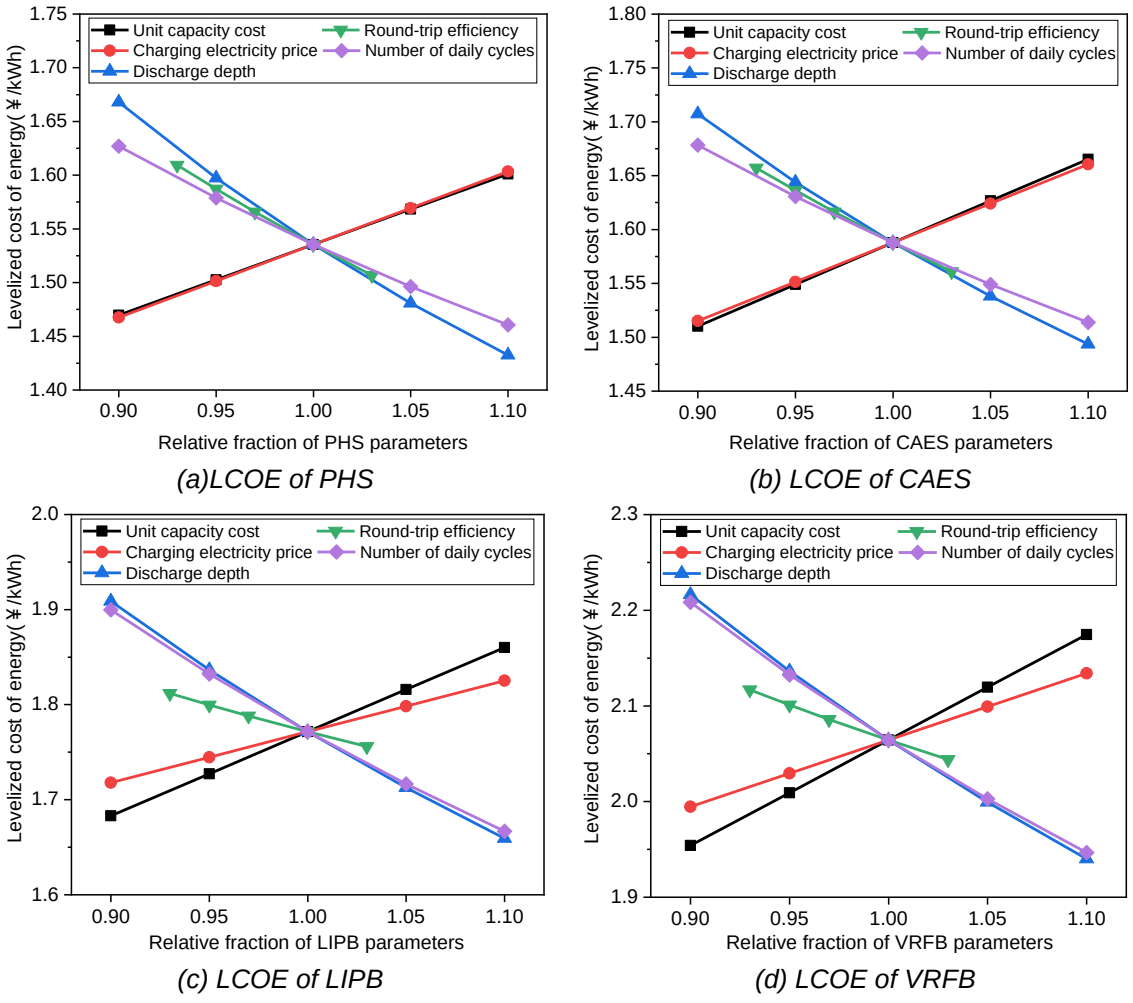

(a)LCOE of PHS *(b) LCOE of CAES*

(c) LCOE of LIPB *(d) LCOE of VRFB*

Figure. 10. Sensitivity analysis results of control and economic parameters on LCOE.

3.6.3. Sensitivity analysis of rankings

Sensitivity analysis was carried out to investigate the effects of electricity sources, number of daily cycles and criteria weights on sustainability score and rankings.

The variation of sustainability score of ESSs under different electricity sources is displayed in Figure 11, it can be noticed that the sustainability score and ranking varied while the electricity sources varied from grid mix to renewable energy (wind and solar PV), PHS changed its ranking from two to one and changed the score from 0.50 to 0.82 and 0.74, respectively. Figure 12 shows the sensitivity analysis under different number of daily cycles, the ranking did not change in a qualitative manner yet the sustainability score of ESSs changed, as the number of daily cycles increased, the superiority of LIPB was improved.

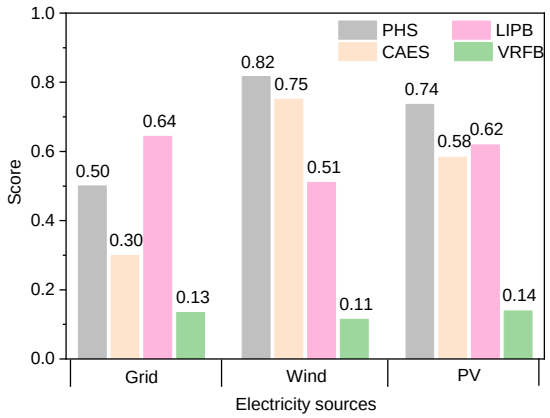

Figure. 11. Sensitivity analysis under different electricity sources.

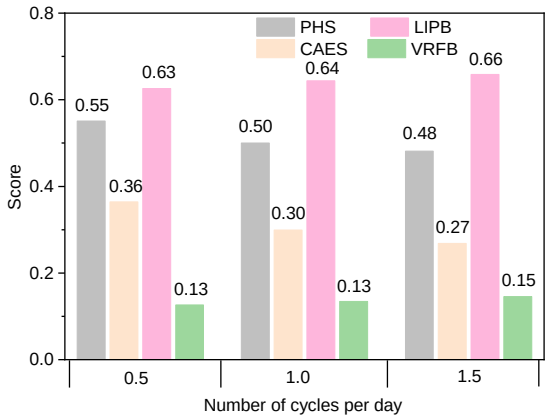

Figure. 12. Sensitivity analysis under different number of daily cycles.

Criteria weights were altered from 0 to 1 by increasing its value 0.1 at a time as shown in Figure 13. When the weight of one criterion was changed, the weights of the remaining three main criteria were kept the same proportionally. As can be noticed from all parts of Figure 13, the ranking varied noteworthily with varying weights of main criteria. For example, LIPB changed its ranking from three to one when environmental weight was given higher weights. As a whole, PHS and LIPB were the most sustainable energy storage option.

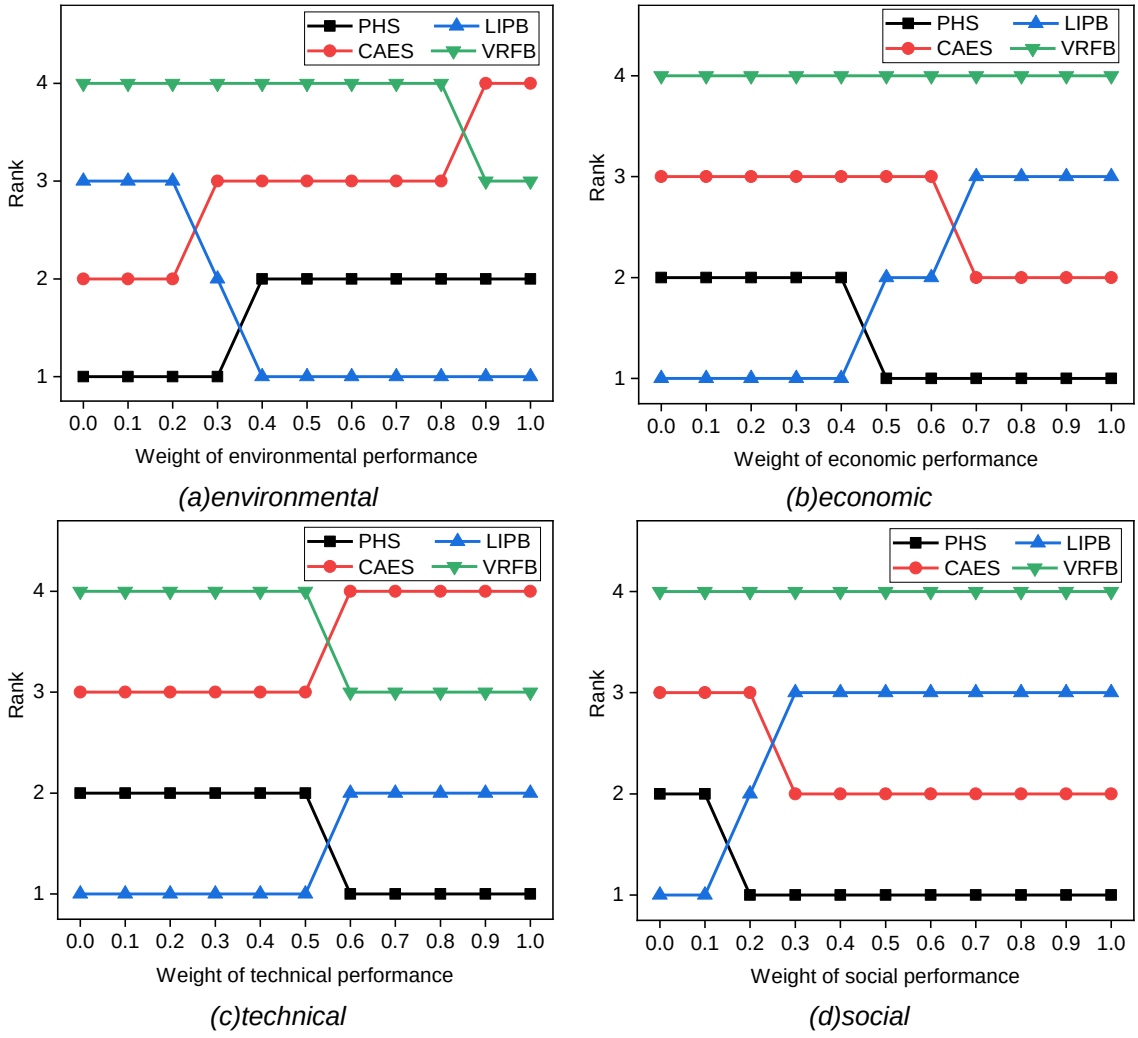

Figure. 13. Sensitivity analysis of varying the main criteria weights.

4. Conclusions

This study provides a sustainability assessment of typical energy storage systems for quantifying the considered environmental, economic, technical and social criteria for peak shaving scenarios, the studied alternatives include pumped hydro(PHS), compressed air energy storage(CAES), lithium-ion phosphate battery(LIPB) and vanadium redox flow battery(VRFB). A combination of life cycle assessment, life cycle cost, quantifying the soft criteria and TOPSIS methodology were applied based on the full life. The conclusions were:

(1) For PHS, CAES, LIPB and VRFB, environmental indicator of GWP for were 324.1, 397.0,102.3,374.1 $kgCO_2$-eq/MWh, economic indicator of LCOE were 1.54, 1.59, 1.77 and 2.06 ¥/kWh, NPV were 58.1, 55.6, 29.8 and 1.1 million ￥, the sustainability performance score were 0.50, 0.30, 0.64 and 0.13.

(2) The sensitivity results point out discharge depth are the main drivers of life cycle cost (LCC), while for the environmental performance, the electricity sources and round-trip efficiency are of paramount importance. The sustainability rank of ESSs depends on the weight of main criteria and electricity sources, PHS and LIPB are the most sustainable alternatives in the sensitivity analysis.

Acknowledgments

This work was supported by the Natural Science Basic Research Plan in Shaanxi Province of China (No.2023-JC-YB-444), the Fundamental Research Funds for the Central Universities [No.xtr012019001], and the Innovative Scientific Program of CNNC.

Nomenclature

Abbreviations:

AHP	analytic hierarchy process
CAES	compressed air energy storage
DE	damage to ecosystem
ESSs	energy storage systems
DHH	damage to human health
DRA	damage to resource availability
GWP	global warming potential
LCA	life cycle assessment
LCC	life cycle cost
LCOE	levelized cost of energy
LIPB	lithium iron phosphate battery
PHS	pumped hydro storage
RES	Renewable energy sources
TOPSIS	technique for order preference by similarity to an ideal solution
VRFB	vanadium redox flow battery

Greek symbols

C_c	charging electricity cost
C_{dr}	disposal and recycling cost
$C_{investment}$	investment cost
C_{loan}	annual repayment of debt
$C_{o\&m}$	operation and maintenance cost
C_{prof}	annual profit
C_{rc}	replacement cost
E_t	annual power generation
N_y	average number of cycles per year
Q_E	designed capacity of ESSs
SOC	average proportion of capacity
T	lifetime of the power station
p	proportion of initial investment
p_p	the electricity prices for purchase
p_s	the electricity prices for sale
r_d	discount rate
r_{if}	Inflation rate
η	round-trip efficiency
η_{dis}	discharge efficiency
θ_{DOD}	discharge depth

References

[1] Vo T.T.Q., Xia A., Rogan F., et al., Sustainability assessment of large-scale storage technologies for surplus electricity using group multi-criteria decision analysis. Clean Technol Envir 2017; 19(3): 689-703.

[2] Ren J.Z., Ren X.S., Sustainability ranking of energy storage technologies under uncertainties. J Clean Prod 2018; 170: 1387-98.

[3] Raza S.S., Janajreh I., Ghenai C., Sustainability index approach as a selection criteria for energy storage system of an intermittent renewable energy source. Appl Energ 2014;136: 909-20.

[4] Walker S.B., Mukherjee U., Fowler M., et al., Benchmarking and selection of Power-to-Gas utilizing electrolytic hydrogen as an energy storage alternative. Int J Hydrogen Energ 2016; 41(19): 7717-31.

[5] Petrillo A., De F.F., Jannelli E., et al., Life cycle assessment (LCA) and life cycle cost (LCC) analysis model for a stand-alone hybrid renewable energy system. Renew Energ 2016; 95: 337-55.

[6] Rostami F., Kis Z., Koppelaar R., et al., Comparative sustainability study of energy storage technologies using data envelopment analysis. Energy Storage Mater 2022; 48: 412-38.

[7] Baumann M., Peters J.F., Weil M., et al., CO2 footprint and life cycle costs of electrochemical energy storage for stationary grid applications. Energy Technol-ger 2017; 5(7): 1071-83.

[8] Cellura S., Mazza A., Bompard E.F., et al., Sustainability assessment of flywheel energy storage for grid applications. UPEC2022：57th International universities power engineering conference - big data and smart grids; 2022 Aug 30-Sep 02; Istanbul, Turkey.

[9] Davies D.M., Verde M.G., Mnyshenko O., et al., Combined economic and technological evaluation of battery energy storage for grid applications. Nat. Energy 2019; 4(1): 42-50.

[10] Ilbahar E., Colak M., Karasan A., et al., A combined methodology based on Z-fuzzy numbers for sustainability assessment of hydrogen energy storage systems. Int J Hydrogen Energ 2022; 47(34): 15528-46.

[11] Baumann M., Peters J., Weil M., Exploratory multicriteria decision analysis of utility‐scale battery storage technologies for multiple grid services based on life-cycle approaches. Energy Technol-ger 2020; 8(11):1901019.

[12] Albawab M., Ghenai C., Bettayeb M., et al., Sustainability performance index for ranking energy storage technologies using multi-criteria decision-making model and hybrid computational method. J Energy Storage 2020; 32: 101820.

[13] Balezentis T., Streimikiene D., Siksnelyte B.I., Energy storage selection for sustainable energy development: The multi-criteria utility analysis based on the ideal solutions and integer geometric programming for coordination degree. Environ Impact Asses 2021; 91: 106675.

[14] Lin R.J., Yi M., Lee C.R.M., et al., Comparative sustainability efficiency measurement of energy storages under uncertainty-An innovative framework based on interval SBM model. J Energy Storage 2021; 40: 102808.

[15] Turgrul U.D., Xin L., Jisun K., et al., Evaluation of energy storage technologies for integration with renewable electricity: Quantifying expert opinions. Environ Innov Soc Tr 2012; 3: 29-49.

[16] Ren J.Z., Sustainability prioritization of energy storage technologies for promoting the development of renewable energy A novel intuitionistic fuzzy combinative distance-based assessment approach. Renew Energ 2018; 121: 666-76.

[17] Acar C., Beskese A., Temur G.T., A novel multicriteria sustainability investigation of energy storage systems. Int J Energ Res 2019; 43(12): 6419-41.

[18] Mostafa M.H., Aleem S.H.E.A., Ali S.G., et al., Techno-economic assessment of energy storage systems using annualized life cycle cost of storage (LCCOS) and levelized cost of energy (LCOE) metrics. J Energy Storage 2020; 29: 101345.

[19] Hunter C.A., Penev M.M., Reznicek E.P., et al, Techno-economic analysis of long-duration energy storage and flexible power generation technologies to support high-variable renewable energy grids. Joule 2021; 5(8): 2077-101.

[20] Chen X.J., Huang L.S., Liu J.B., et al., Peak shaving benefit assessment considering the joint operation of nuclear and battery energy storage power stations Hainan case study. Energy 2022; 239: 121897.

[21] Hiremath M., Derendorf K., Vogt T., Comparative life cycle assessment of battery storage systems for stationary applications. Environ Sci Technol 2015; 49(8): 4825-33.

[22] Maryam A., Jeremiah X.J., Gregory A.K., Parameters driving environmental performance of energy storage systems across grid applications. J Energy Storage 2017; 12: 11-28.

[23] Chowdhury J.I., Balta-Ozkan N., Goglio P., et al., Techno-environmental analysis of battery storage for grid level energy services. Renew Sust Energ Rev 2020; 131: 110018.

[24] AlShafi M., Bicer Y., Life cycle assessment of compressed air, vanadium redox flow battery, and molten salt systems for renewable energy storage. Energy Rep 2021; 7: 7090-105.

[25] Lima L.D., Quartier M., Buchmayr A., et al., Life cycle assessment of lithium-ion batteries and vanadium redox flow batteries-based renewable energy storage systems. Sustain Energy Techn 2021;46: 101286.

[26] Han X.Q., Li Y.X., Nie L., et al., Comparative life cycle greenhouse gas emissions assessment of battery energy storage technologies for grid applications. J Clean Prod 2023; 392: 136251.

[27] Ruiz R.V., Ramirez F.J., Escribano A.H., et al., A techno-economic analysis of a real wind farm repowering experience: The Malpica case. Energ Convers Manage 2018; 172: 182-199.

Evaluating the value of photovoltaics in decarbonization scenarios: evidence from the Lombardy Region

Francesco Mezzera[a], Giuseppe Muliere[b], Marianna Pozzi[c], Fabrizio Fattori[d], Lorenzo Aurelio Cassetti[e] and Mario Motta[f]

[a] Department of Energy, Politecnico di Milano, Via Lambruschini, 4a – 20156 Milan, Italy, francesco.mezzera@polimi.it CA
[b] Department of Energy, Politecnico di Milano, Via Lambruschini, 4a – 20156 Milan, Italy, giuseppe.muliere@polimi.it
[c] Department of Energy, Politecnico di Milano, Via Lambruschini, 4a – 20156 Milan, Italy, marianna.pozzi@polimi.it
[d] Department of Theoretical and Applied Sciences, University of Insubria, Via J.H. Dunant, 3, 21100 Varese, Italy, fabrizio.fattori@uninsubria.it
[e] Department of Energy, Politecnico di Milano, Via Lambruschini, 4a – 20156 Milan, Italy, lorenzoaurelio.cassetti@polimi.it
[f] Department of Energy, Politecnico di Milano, Via Lambruschini, 4a – 20156 Milan, Italy, mario.motta@polimi.it

Abstract:
The review of national and international energy strategies forced by recent disruptive events emphasized the importance of developing tailored planning to pursue the increased decarbonization goals. Within this context, the presented article first describes the development of a bottom-up optimization tool tailored for the Lombardy region, in Italy. Then it evaluates different technology mixes to identify the optimal configuration to reach local decarbonization targets at minimum costs. The model has a solid spatial resolution and a wide range of technological options, and it is set to analyse the local energy system at the target year (2030). The work evaluates the response of the system to different decarbonization goals and is carried out by comparing the cost of an avoided ton of CO_2. A $CO_{2\text{-equivalent}}$ emission limit in line with the EU Fit-For-55 package returns a feasible solution with conventional technology options, such as thermal insulation, electrification, energy efficiency and a partial substitution of natural gas with biomethane. Electrification is strongly bound to the expansion of photovoltaics since the additional potential of other sources is negligible. However, at higher decarbonization targets, the cost of avoided CO_2 rises at unsustainable values. Analysis on resources' availability, utility scale photovoltaic power plants and on commodity prices investigate the possibility to overcome this limit and the main results emphasize their strong impact on final energy configuration mix. They suggest the need to promote new photovoltaic installation and increasing the photovoltaic availability by 1,5 GW (+12%) could reduce the cost of avoided CO_2 of about 16%.

Keywords:
Energy system modelling; oemof; bottom-up model; renewable sources availability; high spatial resolution.

1. Introduction

In recent months and years disruptive events have strongly driven the review of national and international energy strategies, to better suit decarbonization pathway with a focus on energy security. In the European Union (EU), more challenging targets are going to be set, by strengthening the importance of differentiating energy supplies. Existing National Energy and Climate Plans are going to be updated with new targets for 2030 set by the "Fit for 55" (FF55) [1] and the "REPowerEU" [2] packages, currently under discussion by EU authorities. In particular the FF55 sets the goal of a reduction of 55% of greenhouse gas (GHG) emissions compared to 1990 levels [3]. It introduces specific targets for each end-use sector: e.g., the upgrade of the European Emission Trading System (EU ETS), with the reduction of total emission allowances (-61%) compared to 2005 [1].
All these targets must be received by national and sub-national authorities, through the development of local plans. In Italy, also each Region (i.e., the highest sub-national administrative level), has the authority to implement specific policies regarding energy and climate themes, in compliance however with national standards.

Within the mentioned context, energy system modelling plays an important role. It can help policymakers to study the decarbonization process of energy systems and to identify minimum cost pathways. Several optimization framework's approaches exist. Fodstad et al. [4] provide a review of the state of the art, with a list of several studies which compare different frameworks and identify possible future developments. They recognize the importance to evaluate interdependencies among energy carriers, focusing on the integration of new energy carriers (e.g., hydrogen) or infrastructures (e.g., carbon capture and storage), to better describe interconnections within the system (e.g., sector coupling). They underline the required trade-off between spatial and time resolution, due to the computational issue related to the high level of detail for both.

1.1. Aim of the paper and outline

Through the development of an optimization tool tailored for the Lombardy region, in Northern Italy, the local energy system is evaluated at a target year (2030), in which the decarbonization targets are reached at the least cost. Within this context, the aim of the study is to evaluate the role of renewable energy sources (e.g., photovoltaic) and energy carriers (e.g., biomethane) and their impact in the GHG emissions reduction process. Multiple configurations of the system are then analyzed, by varying resources availability and prices of commodities. Lastly the work focuses on how system costs are influenced by the variation of boundary conditions (e.g., GHG emission target).
In the remainder of the paper, Section 2 presents the structure of the tool used for the analysis, the setup and the main assumptions of the analyzed case study. The construction of baseline case and sensitivity analyses are reported in Section 3, followed by main results in Section 4, while main outcomes and further developments are summarized in the conclusion (Section 5).

2. Methodology

In this Section the structure of the model is first presented, followed by the main assumptions and the setup of the case study.

2.1. Mathematical model structure

The possibility to evaluate interdependencies among energy carriers (e.g., through a multi-node representation), coupled to its open-source behaviour, led the choice of oemof framework [5], an open-source energy system modelling framework written in Python that can create and solve optimization problems, for the presented work.
To build the structure of an energy system, oemof framework uses different logical components: (i) buses, (ii) transformers, (iii) sources and sinks and (iv) storages. Buses represent energy carriers and commodities, such as electricity, heat or fossil fuels. Transformers represent processes or technologies which consume and/or produce one or more commodities. For example, a transformer may represent a gas power plant, which receives natural gas as input energy carrier and produces electricity as main output. Sources and sinks are two subcategories of transformers, respectively used to represent the production/introduction of a commodity in the energy system (e.g., the import of natural gas) and the final demand of an energy carrier (e.g., the heat demand in the civil sector). The storage component enables the system to decouple demand and supply of a specific energy carrier (e.g., electrochemical batteries). Lastly, the exchanges of a commodity between buses and transformers are named flows.
The objective function to be minimized, which represents the system total cost, is expressed, in a simplified way, as follows in Eq. (1):

$$\text{system total cost} = \sum_{h} \left[\sum_{c} \left(flow_{c,h} \cdot varcost_{c} \right) + \sum_{t} \left(capacity_{t} \cdot invcost_{t} \right) \right] \quad (1)$$

$flow_{c,h}$ is the flow of the commodity c at time-step h,

$capacity_t$ is the capacity of the technology/transformer t related to the investment,

$varcost_c$ is the variable cost of the commodity c,

$invcost_t$ is the investment cost of the technology t.

The constraints of the considered optimization problem guarantee the balance of energy carriers and the satisfaction of demand. Ad-hoc bounds that could be added to the problem might be GHG emission limits or availability of resources. The decision variables of the optimization problem represent the new installed capacity (investments) and the energy and/or mass flows within the energy system.
A point of strength of the framework is the modularity of its components, that can be replicated as many times as needed, in series or in parallel, to build the energy system, as will be presented in the following section.

2.2. Energy system structure and assumptions

The spatial resolution of the tool starts from the aggregation of those local administrative division with similar socioeconomic and environmental characteristics, and results in 17 local areas within the region.

Each area presents differences on the environment (e.g., climatic conditions, morphology and use of the land) and on the economics (e.g., gross domestic production, index per capita, average yearly income). For each area, final demands for end-use sectors, resources' availability and technological options were defined starting from a high spatial resolution and a modular scheme of the energy system was then built. In Figure 1 a simplified graphical representation is shown. Note that the energy efficiency option is modelled as a source of heat in order to quantify heat demand that can be avoided with that solution.

The resulting structure is quite complex, being characterized by more than 6500 exchanges (i.e., flows) between processes and technologies. The complexity of the energy system determines an important computational effort.

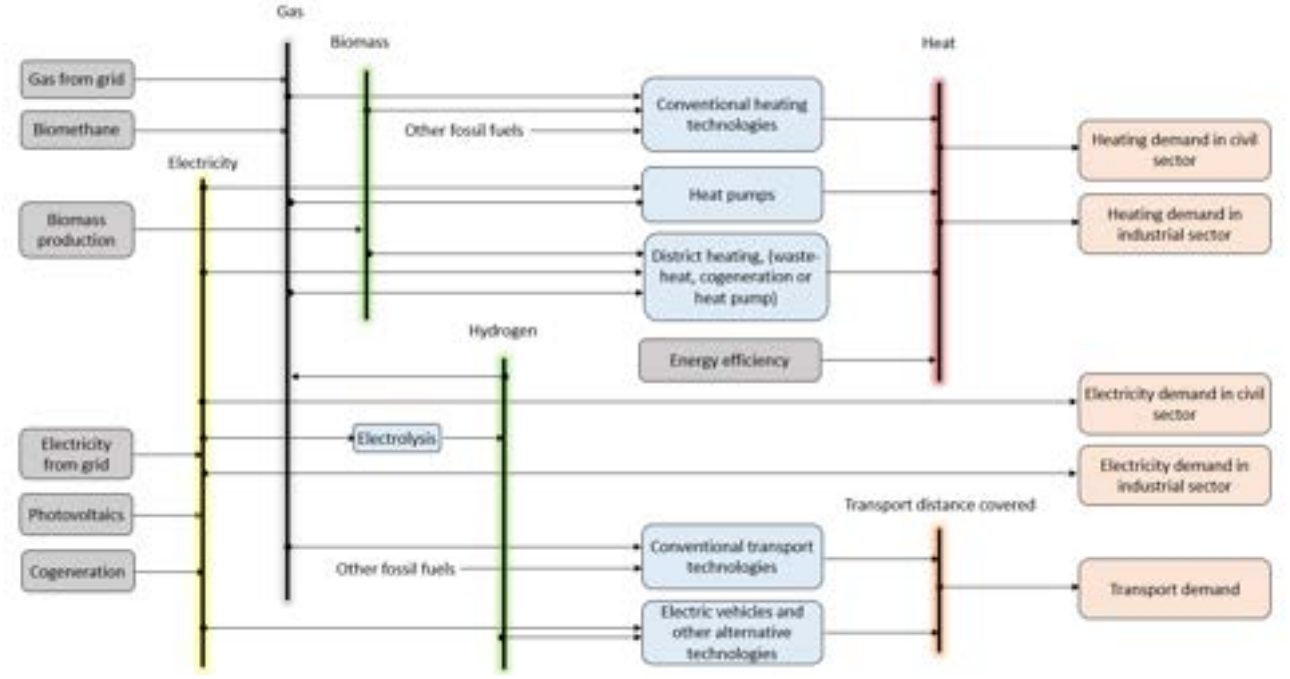

Figure. 1. Simplified scheme of the energy system for each area (commodities and processes are aggregated for sake of representation), represented through buses (vertical lines), sources (grey boxes, mainly on the left side), transformers (light-blue boxes, mainly in the central area) and sinks (pink boxes, mainly on the right); for sake of representation, other fossil fuels supply chain are not shown, as well as hydrogen blending process with natural gas.

Each technology or process is characterized by the following input parameters: (i) capital, variable and fixed costs; (ii) efficiencies, (iii) residual installed capacities in the years, (iv) availability or penetration limit of technologies.

Regarding the commodities and the energy carriers, the model considers: (i) natural gas, (ii) diesel, (iii) liquid petroleum gas for heating and (iv) for transport sector, (v) gasoline, (vi) electricity, (vii) solid biomass, (viii) biomethane, (ix) biodiesel, (x) hydrogen, and (xi) heat.

The end-use sectors are analyzed with different level of detail, strongly due to the availability of input data. The **civil sector** is the one with the highest technological detail, being investigated both the heating and cooling demand and the power demand. For each of the 17 areas, five types of building are identified, each one with its specific characteristics, to provide a realistic picture of the sector: (i) detached houses, (ii) apartment blocks for residential sector with an independent or (iii) a centralized heating system and (iv) tertiary buildings with independent or (v) centralized heating systems. For each one, the model provides different technological solutions to satisfy thermal needs, mainly: boilers, heat pumps, district heating from different sources (i.e., waste-heat from industry, natural gas or biomass fuelled dedicated plants, large size electric heat pumps). Also power self-generation by photovoltaics (PV) is considered in the civil sector. Different combinations of the PV technology (i.e., alone or coupled with an electrochemical storage) and final users (i.e., single users or energy communities) are considered.

Regarding the transport sector three main classes are considered: (i) light mobility, namely cars, with higher level of detail; (ii) light duty commercial vehicles, with an intermediate level of detail and (iii) other transport, which includes heavy road transport, naval and train, with a more aggregated description. For light mobility several technology options are compared: conventional propulsion systems based on internal combustion engines are in competition with plug-in hybrid electric vehicles or pure battery electric ones.

The industry sector has very heterogeneous characteristics, about processes, technologies and energy carriers, which make it difficult to provide a detailed picture. The power and thermal final demands are investigated as aggregated. The supply options for the former are represented by electricity coming from the power grid or from self-generation through dedicated PV. Electricity can be used also to provide heating services, through industrial high temperature electric heat pumps or by synthetizing hydrogen through water electrolysis process.

Being out of the scope of the presented analysis, the conventional power generation of Lombardy (mostly made up of hydro and thermal power plants) is not explicitly depicted, but it is represented as a generic power grid, with an electricity source as component. Emphasis is indeed given to non-sectorial renewable energy sources, meaning those sources that are not exclusively dedicated to a single end-use sector. The first example is represented by PV at utility scale on dedicated surfaces and floating on quarry lakes. For biogas and biomethane, the study considers only the potential related to livestock residues and biodegradable municipal wastes. Ligneous biomass is considered in two different ways: sustainable local biomass and generic imported biomass.

With the resulting model, tailored analyses on resources' availability and on final demands of different energy carriers are then possible, by enabling policymakers to define ad-hoc policies, well suited for the local areas and in this way to adopt and apply on the territory national/international decarbonization strategies.

3. Input data

In this section the definition of a baseline configuration is presented in parallel with the construction of alternative options as sensitivity analysis. The optimal configuration of the system is defined throughout a range of emission reduction targets. This allows to test the optimal configuration in the neighbourhood of the decarbonization targets proposed by EU FF55 package (i.e., -44% vs. 2005, with total allowed emission equal to 43,5 Mt).
A 2030 baseline case is defined starting from a GHG emission-unconstrained energy system, a configuration to evaluate a pure economic optimization, to the minimum emission target allowed by given boundary conditions (e.g., resources' availability). In Table 1 the main input parameters are presented.

Table 1. Main input data for the baseline case (on the left) and for the sensitivity analyses (on the right); note that for each sensitivity analysis only the modified parameters with respect to baseline case are reported [source: elaborations from the authors].

			Baseline case	Modified parameters compared to baseline configuration		
			Medium commodity price	Low commodity price	High commodity price	Very high commodity price
Natural gas		[€/MWh]	95	60	137	179
Electricity	Cost for end-users	[€/MWh]	280	160	460	640
	Price sold to the market	[€/MWh]	140	30	250	386
			Minimum PV utility scale availability	Medium PV availability	High PV availability	Maximum PV availability
Installation capacity potential	PV total	[GW_e]	11,79	13,3	14,8	16,3
	of which PV utility scale	[GW_e]	*1,64*	*3,14*	*4,64*	*6,14*
			Maximum biomethane availability	Medium biomethane availability	Low biomethane availability	Minimum biomethane availability
Biomethane annual availability		[TWh]	11,5	9,7	7,8	6

PV total includes rooftop installation potential in civil sector, industry and utility scale plants (ground and rooftop based).

In baseline case for PV utility scale only unused lands and coverage of quarry lakes are considered [source: elaboration of the authors on RSE [6]]; in sensitivity analysis, the potential of PV rooftop installation on public parking is added. Commodity prices are estimated from historical data (from 2013 to the first half of 2022); the configuration with very high commodity price considers the most recent period (first half of 2022); electricity values represent cost for end-users (first row), and the price of quantities sold to the power market (second row) [source: Italian Authority for the regulation of the energy, grid and the environment ARERA [7]]

For each configuration, the energy system is analyzed at different limits of emissions, each of which is independent from the others. The tool allows to identify the optimal distribution of cost effort (namely the required investments to reduce GHG emissions) between sectors. It returns an optimal configuration mix under specific assumptions, which are strongly related to the estimated evolution of parameters. Each sensitivity analysis presented below focuses on a specific topic. The structure and the assumptions of the energy system are the same of the baseline case, except for the boundary condition that is object of the analysis.

A first sensitivity study is driven on prices of electricity from power grid and natural gas. A second level of sensitivity concerns the availability of resources. Being wind power generation out of the scope (i.e., no potential is identified within the region) and being the installation of distributed PV plants difficult to be controlled by regional authorities, PV utility scale plants is selected. In the baseline case, a potential of 1,64 GW of new installation capacity is estimated for the utility scale PV, by considering available unused lands destined to regeneration and a potential surface coverage of quarry lakes. In the sensitivity analysis the role of potential PV installations on covertures of large size public parking is considered. Through the information provided by OpenStreetMap [8] and QGIS platform [9], open-source geographic database and geospatial data visualization tools, the available surface suitable for rooftop PV installations is estimated. Only parking spaces with a minimum surface area are considered and with assumptions on the eligible surface area to PV installation (e.g., lanes to manoeuvre might not be covered by rooftops) and on the share of total parking suitable for photovoltaics installation (e.g., in short-term large rooftop PV installation is more likely to occur on larger surface areas), a PV utility scale additional potential of about 4,5 GW_e is obtained.

Finally, some considerations can be made on biomethane. Being gas still an important energy carrier in base-case scenario (for example in civil sector, with a significant role in supplying heating systems), the switch from fossil-based gas to bio-based one is strongly promoted. Biomethane from biodegradable municipal waste and especially from livestock residues might be more difficult to be developed. A sensitivity analysis has then been conducted to evaluate lower potential, with a reduction of almost 48% in the worst case.

4. Results

This section returns and compare the main results, with an overview of the energy system first, and then by deepening the system total cost. In particular it presents the main comparison between present time, baseline case and the tested sensitivity analyses. Figure 2 shows the final consumptions, comparing the FF55 emission limit configuration (i.e., 43,5 Mt $CO_{2\text{-eq}}$) in 2030 vs. present time. The chart returns for every tested scenario an overall reduction in final consumption. Energy efficiency and the switch to less emitting technologies are the main drivers to pursue decarbonization targets.

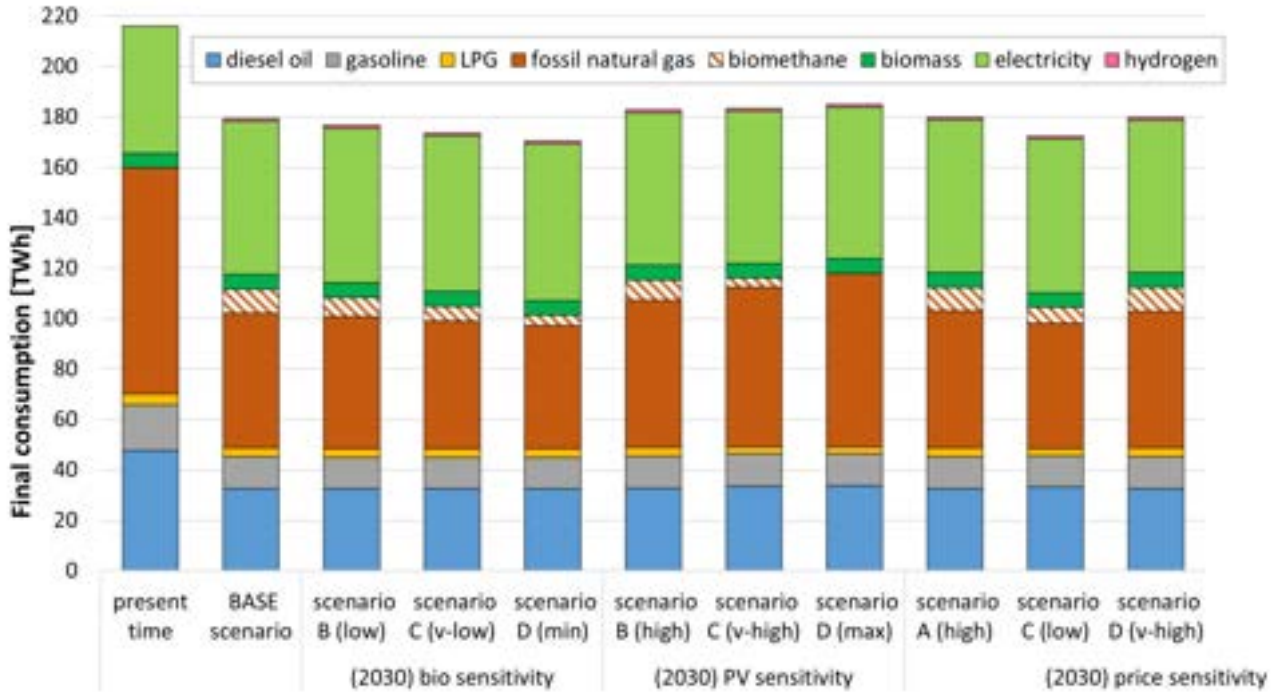

Figure. 2. Final consumption by energy carriers in different scenarios; v-low = very low; v-high = very high [source: elaborations from the authors].

For the baseline configuration a cumulative consumptions reduction of about 17% compared to present time can be observed. The most important contraction occurs in fossil natural gas consumption (-40%), thanks to the introduction of biomethane and to the electrification of different end-use sectors (+20%), such as space heating in the civil sector. The latter is interested by a strong consumption reduction through extended building refurbishments (up to 2% of the buildings/year, i.e., the maximum allowed), coupled with a strong electrification of the heat sector and the construction of district heating networks. Gas boilers keep playing an important role, with however a remarkable substitution with newer systems. The overall effect is a GHG emissions reduction of about 50% in civil sector, vs. 2005 levels. Regarding transport sector, there is a lower reduction in final consumptions (about 10%) between present time and 2030, mainly through the electrification of light road transport and the introduction of less carbon intensive solutions. The resulting configuration mix returns a reduction of about 35% of $CO_{2\text{-eq}}$ emissions in the sector vs. 2005 levels. Industry consumptions are reduced of about 18%, mainly thanks to the switch from gas to electricity.

By focusing on the sensitivity on RES availability, in case of biomethane reduction, an overall reduction of final consumption is observed compared to baseline one. Being PV installations, electrification option and building refurbishment in civil sector all completely exploited, more efficient options, such as electric heat pumps in DH networks or vehicles substitute conventional less efficient options (e.g., gas CHPs, fossil fuel-based vehicles). When the focus is on PV availability, the scenarios analyze the case of gradually additional PV capacity potential, by introducing new installation on rooftops of public parking. Electricity from PV can be self-consumed, shared between groups of local end-users (i.e., energy communities) or sold to the market. In every scenario the PV overall power generation is always at its maximum (about 11 TWh), although with different distributions in end-use sectors. Differences occur in installation of PV utility scale plants. As expected, in PV sensitivity scenarios, the increasing PV utility capacity potential is effectively installed, reaching a total PV electricity production nearly 15,8 TWh in maximum case. The last sensitivity analysis focuses on the price of gas and electricity. In the scenario with low prices the main output is an overall final consumption reduction. The lower cost of gas enables a more widespread use of conventional gas boilers in civil sector (both old and new models) at the expense of electrification and gas CHPs in DH networks. In the scenarios with high and very high commodity prices energy efficiency gains importance (e.g., gas heat pumps in substitution of conventional gas boilers).

To complete the description of the energy system, it might be useful to focus on the cost of the avoided GHG emissions, expressed in €/t_{CO2} avoided. This cost is defined as the ratio between the difference of the system total cost and the difference of total GHG emissions. The former is obtained as the sum of the total cost of annualized investment plus the operation cost of the target year. In Figure 3 the different trends of the cost of avoided GHG emissions are presented, both for biomethane availability (blue lines) and for photovoltaics one (green lines).

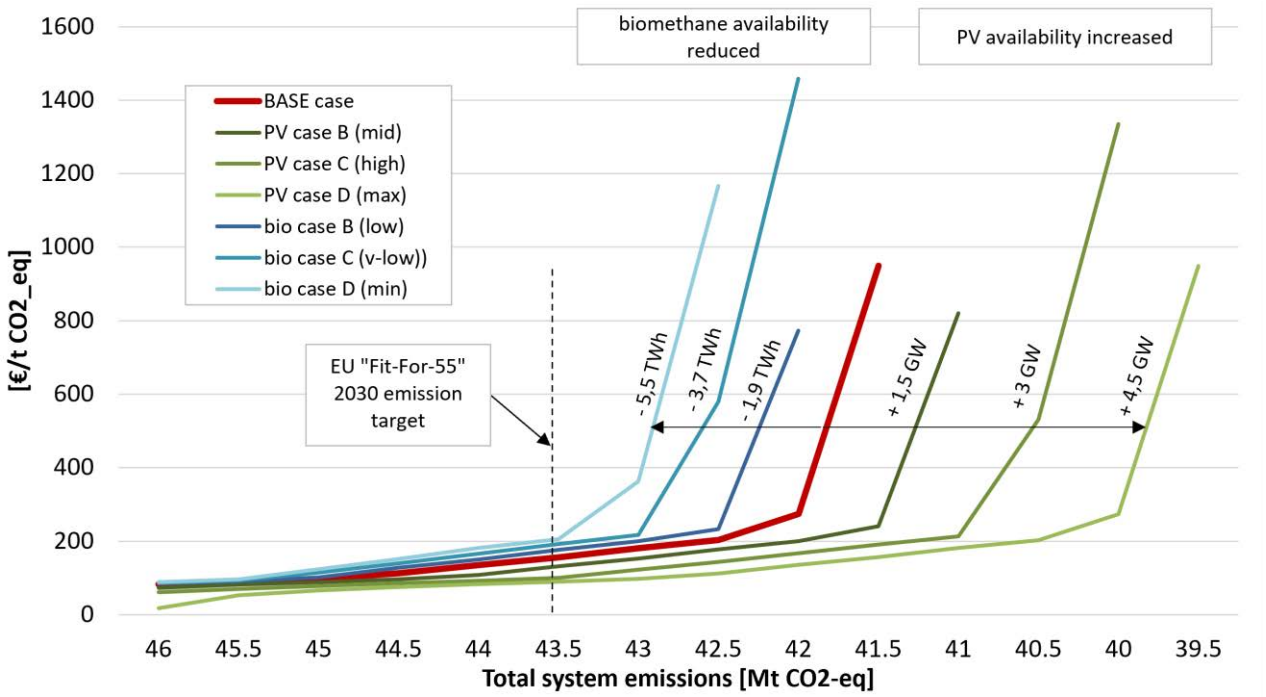

Figure. 3. Comparison of costs for avoided $CO_{2\text{-eq}}$ emissions between 2030 baseline scenario (red line, in the middle) and sensitivity on biomethane availability (blue lines, on the left) and PV availability (green lines, on the right); on X-axis the system total $CO_{2\text{-eq}}$ emission levels are reported, in line with Fit-for-55 package (with the target of 43,5 Mt); v-low = very low [source: elaborations from the authors].

Starting from PV, the graph shows that, at increasing installed PV capacity, it is possible to reach lower total system emission levels. The system's total cost of avoided GHG emissions can be kept at reasonable values in more challenging configurations. Similar trends can be observed in the sensitivity analysis of biomethane availability. The analysis investigates the effect of a less developed biomethane supply-chain. By reducing its availability in the energy system, the minimum emission limit (i.e., the physical limit for the configuration, given its boundary conditions) of the system shifts at higher levels. For both PV and biomethane case, the graph seems to identify a cost range (around 200-270 €/$t_{CO2\text{-eq avoided}}$) above which getting an additional reduction of the system's emission unit becomes economically not viable. In both sensitivity analyses, at the target of 43,5 $Mt_{CO2\text{-eq}}$, differences between costs are still quite limited, meaning that the configuration is not close to the technical limit (at given boundary conditions), except for case of minimum biomethane availability.

Last sensitivity analysis concerns the different prices of commodities. As expected, the variation of commodity costs has an immediate effect on the overall system total cost at every tested GHG system emission level. The differences between scenarios widen as the emission limit is reduced. At the target of 43,5 Mt of $CO_{2\text{-eq}}$ high and very high cost scenarios show an increase of about 97% and 199% compared to base-case levels (around 190 €/$t_{CO2\text{-eq avoided}}$), while a reduction of about 32% in minimum cost configuration can be observed.

5. Conclusion

The presented work aimed to study a possible optimal energy mix for the Lombardy region at the target year 2030 and to evaluate the weight of specific input parameters (e.g., resources' availability, commodity prices) on its composition. In a scenario in line with EU Fit-for-55 package, useful consideration emerged for local policymakers. The process of decarbonization takes place through a combination of electrification of final consumption and improvements thanks to energy efficiency. PV and building refurbishment options are exploited in every tested scenario at their maximum. The GHG emission reduction evolution is mainly driven by civil sector and transport one (-50% for the former, -35% for the latter compared to 2005 levels). Sensitivity analyses were conducted to evaluate the role of (i) commodity prices, (ii) PV potential installation capacity and (iii) biomethane availability.

Regarding the cost of electricity from the power grid and of natural gas, in high-cost scenarios energy efficiency gains importance and enables the introduction of technology options that would otherwise remain excluded by the market (e.g., gas heat pumps in civil sector). Sensitivity analyses on biomethane and PV utility scale seem to suggest the existence of a range of system's total cost of avoided GHG emissions around 210-270 €/tCO2-eq avoided, above which the further emission reduction would become economically unviable (at given boundary conditions). The increase (or the decrease) of RES availability shifts at lower (or higher) minimum GHG emission levels the energy configuration mix.

The main advantages of the developed tool are its replicability and its suitability to evaluate different energy systems, with a free level of customization on technological and spatial level. Further development might couple the results of the tool with frameworks with higher time-resolution, for example to better evaluate infra-day or day/night fluctuations both in demand and supply.

Nomenclature

CHP Combined Heat and Power plant
DH District Heating
ETS Emission Trading System
EU European Union
FF55 Fit-For-55 package
GHG Greenhouse gas
PV Photovoltaics

References

[1] General Secretariat of the Council, Fit for 55, 2022. [Online]. Available: https://www.consilium.europa.eu/en/policies/green-deal/fit-for-55-the-eu-plan-for-a-green-transition/ [accessed 16.09.2022].

[2] Directorate-General for Communication, REPowerEU: affordable, secure and sustainable energy for Europe, 2022. [Online]. Available: https://ec.europa.eu/info/strategy/priorities-2019-2024/european-green-deal/repowereu-affordable-secure-and-sustainable-energy-europe_en [accessed 16.09.2022].

[3] General Secretariat of the Council, European Green Deal, 2022. [Online]. Available: https://www.consilium.europa.eu/en/policies/green-deal/ [accessed 21.09.2022].

[4] M. Fodstad, P. Crespo del Granado, L. Hellemo, B. Rugstad Knudsen, P. Pisciella, A. Silvast, C. Bordin, S. Schmidt, J. Straus, Next frontiers in energy system modelling: A review on challenges and the state of the art, Renewable and Sustainable Energy Reviews, Volume 160, 2022, 112246, ISSN 1364-0321, https://doi.org/10.1016/j.rser.2022.112246.

[5] Open energy modelling framework website, [Online]. Available: https://oemof.org/ [accessed 16.09.2022].

[6] E. Garofalo, D. Airoldi, D. Acquati and M. Aiello, FV nel territorio lombardo - Potenziale di sviluppo del FV galleggiante e su tetto, RSE Ricerca sul Sistema Energetico, 2021.

[7] Autorità di Regolazione per Energia Reti e Ambiente, ARERA, Dati statistici. [Online]. Available: https://www.arera.it/it/dati/elenco_dati.htm [accessed 29.09.2022].

[8] OpenStreetMap. [Online]. Available: https://www.openstreetmap.org/about [accessed 26.09.2022].

[9] QGIS - A Free and Open Source Geographic Information System. [Online]. Available: https://www.qgis.org/en/site/ [accessed 26.09.2022].

CO_2 capture from flue gases: a possibility to reduce the CO_2 footprint in offshore oil installations

Murilo José Castro[a], Waldyr Luiz Ribeiro Gallo[b]

[a] University of Campinas, Campinas, Brazil, murilosilveiracastro@gmail.com
[b] University of Campinas, Campinas, Brazil, gallo@fem.unicamp.br ***(CA)***

Abstract:

The production of oil and gas in offshore units (FPSO) requires that all utilities (electricity, mechanical drive, hot fluids for heating and cooling water) must be available in the amount necessary at each operating condition. Lack or surplus of utilities are not allowed. Every production equipment is always sized for the highest demand condition, and then it operates at partial loads most of the time. The entire production of electricity, mechanical power and heating fluids depends on the fuel available in the FPSO – the natural gas produced with oil. Therefore, a typical FPSO has a strong carbon footprint associated with burning fuel. Carbon sequestration in an FPSO is facilitated by the possibility of re-injecting CO_2 into the reservoir, contributing to oil recovery. This work analyzes two possibilities for reducing the carbon footprint in a typical Brazilian FPSO: a) the use of a combined cycle for electrical generation, reducing fuel consumption and consequently the carbon footprint and b) the association of an amine absorption system to capture CO_2 from gas turbine exhaust gases. The analysis is performed for different oil and gas production conditions, and all systems are analyzed operating at partial loads. The combined cycle alone is capable of reducing CO_2 emissions by up to 20%. The CO_2 capture system, together with the combined cycle, achieves impressive results, with a reduction in CO_2 emissions of around 50% during the entire life of the platform. Problems of space and weight of the equipment are also discussed in the work.

Keywords:

Offshore oil and gas production; FPSO; Carbon capture and storage - CCS; Exergy, CO_2 footprint reduction.

1. Introduction

Due to environmental concerns, there is a need to decrease the carbon footprint in every energy-intensive industrial operations. In many cases, the use of renewable energy is possible. However, the production of oil and gas in offshore units (FPSO) far from coast and in deep waters requires utilities such as electric power, mechanical power and hot fluids for heating processes that depend on the use of fossil fuels, especially natural gas. If the fuel is fossil, the CO2 emissions can be reduce by two strategies: increasing the power efficiency in the processes, and/or by carbon sequestration. The electric power and process heat needs in a FPSO are huge. It is usual to adopt waste heat recovery from exhaust gases to supply hot fluid utilities - that is, cogeneration.

The prime movers to electric generators usually are gas turbines. To increase the low efficiency of gas turbines it is common the adoption of combined cycles. This is largely adopted in electric power generation onshore and is a mature technology. However, the available space and allowed weight in a FPSO is a challenge to adopt this technology. Nord et al [1] presented studies for the installation of combined cycle in offshore oil platforms in the North Sea. Again, Nord et al [2] made an optimization of the combined cycle under restrictions of power and weight for offshore oil production. Vidoza et al [3] explored the concept of “Power Island” to produce electricity to various FPSO’s simultaneously, using different combinations of combined cycle groups in a dedicated platform (the “power island”). All results described above showed the direct link of the fuel consumption (efficiency of the system) and the reduction in CO_2 emissions.

The other way to reduce CO_2 emissions is the Carbon Capture and Storage (CCS). The IPCC presented a special report [4] dealing with this option and discussing the technologies to obtain this desired effect, as an option in the portfolio of mitigation actions to stabilize GHG concentrations in the atmosphere. CCS presents two challenges: the transportation from the carbon capture location to the final destination, and the geological stability of the storage location. Offshore oil fields can be interesting to store CO_2, since the injection of CO2 is one of the EOR (enhanced oil recovery) technologies, and the geological structures associated to oil fields

are stable. Risks and costs associated with CO_2 transportation are avoided if the capture is made in the FPSO. Some studies [5-6] present strategies to capture CO_2 in offshore oil production.

Leung et al [7] presented a review on the different technologies and paths to CCS. For post-combustion separation, the CO_2 concentration in the gas mixture is a strong factor to induce the choice of a suitable separation process. Songolzadeh et al [8] indicate that cryogenic distillation and membrane processes are efficient for gas streams with high CO_2 concentration. However, absorption processes may be the best choice for CO2 separation in flue gases, since the gas stream have high temperature, low pressure and low CO2 concentrations.

Petrakopoulou [9] analyzed eight power plant concepts using CO2 capture technologies, both before and after the combustion, which are assessed based on efficiency, economic feasibility and environmental footprint. In the same direction, Madejski et al [10] discusses the CCS technologies and points to the oxyfuel combustion method as a promising solution due to its smaller energy penalty. However, this is not yet a proven technology.

The use of CCS from flue gases for diesel powered ships was proposed by Long et al [11]. An absorption process was optimized and the CO_2 sequestered must be stored in the ship in liquid phase until its final destination. The energy in the flue gases is used to drive the absorption process. Einbu at al [12] presented a similar study, but destined for future liquid CO_2 ships (transport phase of CCS).

The combination of combined cycle with CCS is being studied as a solution to reduce the carbon footprint in offshore oil and gas production. Øi et al [13] presented a study to optimize costs and weight for an absorption process in offshore operations. They suggest the dimensions for the system, as well as the design capture efficiency, fixed in 87%. Nord et al [14] also presented a study for a specific oil field in the North Sea. They defined a design capture efficiency of 90%, using MEA absorption process. Dimensions and weight of the system are also presented.

New separation methods are being proposed. The study of Hammera et al [15] describes the use of supersonic separation process to reduce the carbon footprint from gas turbines. A supersonic nozzle causes an expansion of the gases, and the temperature falls below the solidification point of CO_2, which is then separated from the gaseous stream. However, this method is not yet proven and requires the compression of exhaust gases, which is an energy penalty for the process. Liu et al [16] discusses the chemical absorption technology using rotating packed bed (RPB) instead of vertical static tower. This technology is also called “supergravity” separation, since the mass and energy transfers in the absorption phase are increased as compared with the conventional effect of gravity in the absorption tower.

Sukor et al [17] presents a study dealing with CO_2 separation from the natural gas in a Malaysian gas field, reducing the CO_2 content in the natural gas to acceptable levels. It is important to say that the current Brazilian Pre-Salt FPSO’s already processes natural gas currents and injects the CO2 rich current in the oil field. The world’s first project to implement offshore CO2-EOR was launched in 2011(in the so-called Lula-pilot oil field) and a second one in 2013 (Lula-NE oil field).

Although various studies presented results for combined cycle and CCS in offshore oil production, they are centered in the design and optimization of these systems. The design conditions must deal with the maximum electric power and maximum process heat. For absorption systems (CCS), with the maximum gas flow. However, most part of the time the FPSO operates at partial loads. Ortiz et al [6] presented a study dealing with partial load for the system, following the oil and gas production curve along the time, for a Brazilian oil field.

In this paper, the work of Ortiz et al [6] is revisited, with important changes in the FPSO configuration. One gas turbine acting as a mechanical prime mover is eliminated from the system, increasing the electrical power need, reducing CO_2 emission and liberating space for the steam turbine. This allows for a better combined cycle efficiency. A MEA absorption system can also be incorporated. Part of the steam generated in the HRSG is used as energy source for the separation process. The CO_2 stream coming from exhaust gases is injected in the oil field with the CO_2 stream coming from natural gas separation. This work presents the performance of the system in partial loads, according to the oil and gas production curve. It is important to note that the system to inject CO_2 in the oil field is standard for Pre-Salt FPSO’s. The changes made in the FPSO processes and the analyzed system are described in the Section 3.

2. The FPSO characterization and production curve

The FPSO design adopted for Pre-Salt oil fields is almost standardized. The maximum capacity is 150,000 bpd of crude oil separation. The associated gas is treated until a maximum capacity of 6 MMm^3/day. The FPSO has a capacity to store 1.67 MMb - near 10 days of production. A tanker ship is sent to FPSO each week to bring the oil to onshore refineries. In some cases, the natural gas, after a rough treatment, is delivered to shore by gas ducts.

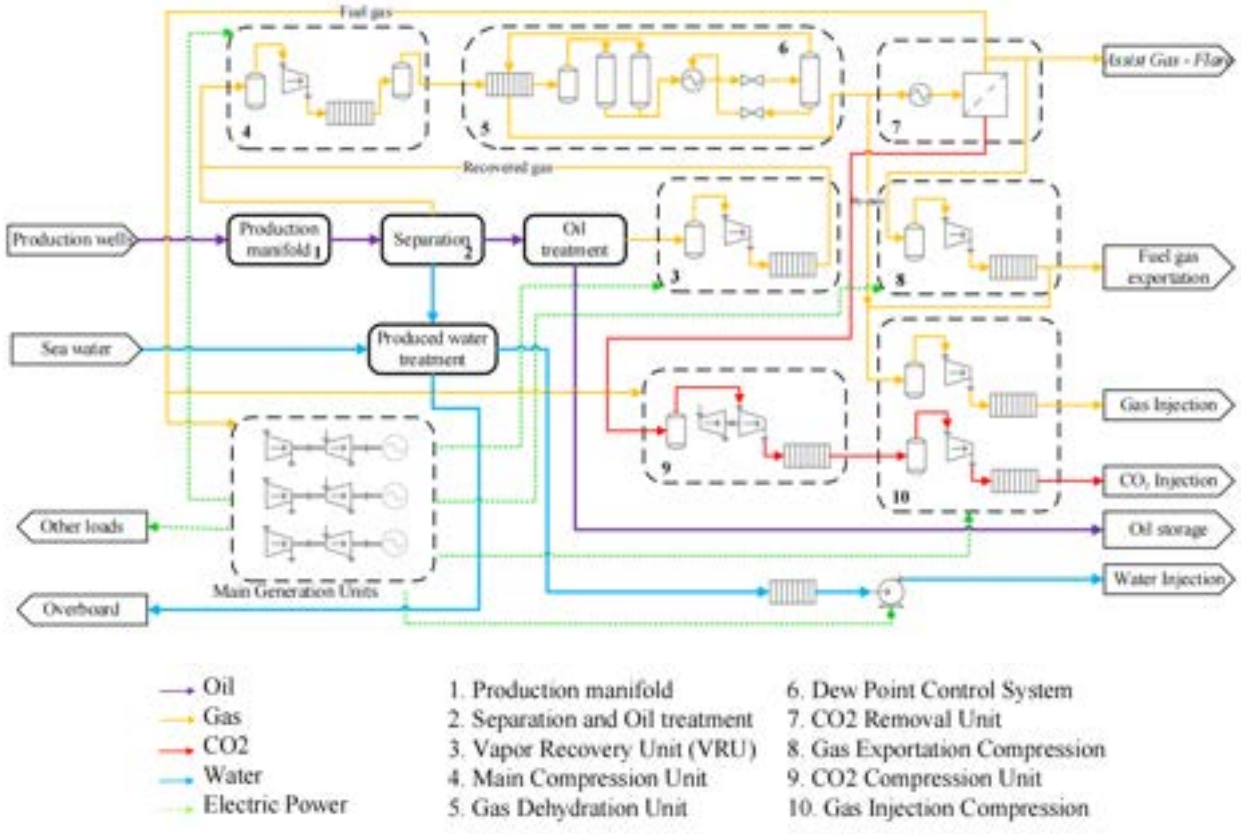

Figure 1. Topside processes in a typical Pre-Salt FPSO. Source: Ortiz et al. [18]

Due to the characteristics of the natural gas obtained, a membrane separation system is adopted to remove excess CO_2 from the natural gas, and the CO_2 rich stream is injected in the oil field. There is also compression systems to deliver the gas to the shore by gas ducts, and to inject natural gas or CO_2 rich streams in the oil field. Figure 1 shows schematically the FPSO topside processes. The electric power generation adopts three gas turbines, and another gas turbine acts as a mechanical driver for the CO_2 stream compression (subsystem 9 in the Fig.1). The exhaust gases from gas turbines generates pressurized hot water in closed circuit, which is the heat utility in the separation process. It is important to say that the FPSO already presents CO_2 capture (from natural gas). The compression equipment is present and CO_2 injection in the oil field is already made.

The oil and gas production of a FPSO is not constant. A typical production curve is presented in the Fig.2. The lifetime of an oil field is in the order of 25 years, and the FPSO is designed to stay anchored all this time. The topside processes are also designed for the entire production period. Therefore, the subsystems in the topside operate almost all the time in partial load, since they were designed for the critical condition for each one.

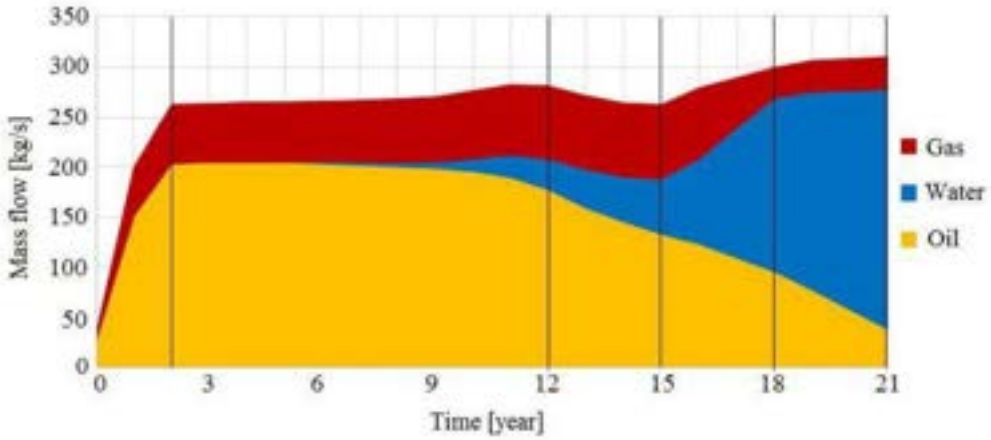

Figure 2. Typical crude oil production curve. Source: Ortiz et al [6]

Table 1. Operating points of the FPSO analyzed in this work. Source: Ortiz et al. [6]

Operating point	Oil production year	Electricity demand [kW]	Platform electric load [77MW max.]	Hot water demand [kg/s]
1	Year 2	72120	93,7	431.1
2	Year 12	73140	95,0	413.7
3	Year 15	70650	91,8	390.2
4	Year 18	48960	63,6	307.2
5	Year 21	46020	59,8	268.7

Table 1 indicates some important points in the oil production curve. The first condition is when the maximum oil and gas production is reached, in the second year of operation. Point 2 presents the maximum liquid capacity. Point 3 indicates a decreasing oil production in the year 15. Point 4 is related to the 50% BWS (basic sediment and water) and point 5 to the condition of maximum BSW. The values were obtained from a comprehensive FPSO operation simulation for each operation point presented in [6].

3. Alternatives to reduce CO_2 footprint from exhaust gases

This paper proposes modifications in the FPSO subsystems to reduce the CO_2 footprint: a) eliminating the mechanical drive gas turbine, substituting it by electric motors; b) introducing a HRSG before the hot water heaters; c) to adopt a steam turbine working in combined cycle; and d) introducing a MEA absorption system to capture CO_2 from flue gases. Captured CO_2 is sent to the already present CO_2 injection system.

The elimination of the mechanical drive gas turbine liberates space to the steam turbine installation and increases the electricity demand. However, the combined cycle can generate this additional demand with greater efficiency. The combined cycle is not designed to maximum power production, since there is no demand for extra power, and the hot water needs must be preserved. Part of the steam is diverted to water heaters, complementing the hot water heaters driven by exhaust gases coming from HRSG. When a CO_2 absorption system is added, more steam is diverted from steam turbine to drive this process. Figure 3 shows the proposed modifications.

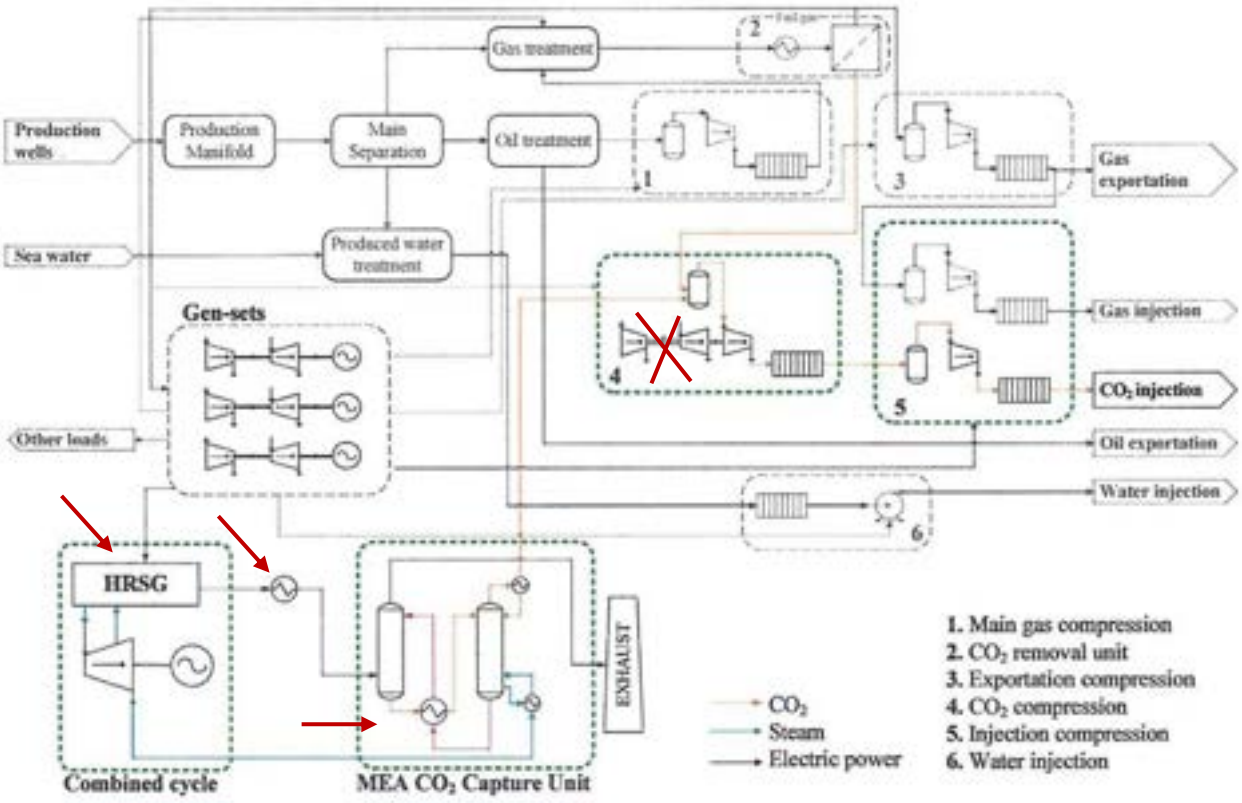

Figure 3. Proposed modifications in the FPSO topside processes. Source: Ortiz [6] modified.

4. Methodology of analysis

The methodology used was based on the mass and energy balances for each equipment or FPSO subsystem and for the process as a whole.

All equipment operate in partial loads, as mentioned before. So, for pumps and gas compressors, the performance curves were parameterized as a function of its load whenever available. Typical adimensional curves were adopted when true performance curves were not known.

Power from gas turbines were modeled first in Thermoflex® software to determine the fuel consumption, exhaust gas temperature and compositions, and energy efficiency as a function of load. This is possible since this software package has the gas turbines performance in the databank (GE-LM2500 for power generation, GE-LM2000 for mechanical drive). An adequate steam turbine was chosen to the steam cycle. Its isentropic efficiency was parameterized as a function of steam mass flow.

The whole processing and utilities subsystems were modeled in Aspen Hysys® software for complete properties and performance calculation. The HRSG and all other heat transfer equipment were modeled adopting the (ε - NTU) method for conditions off-design.

The CCS technology to reduce the CO_2 emissions from flue gases was simulated with Monoethanolamine (MEA) package, with a capture efficiency of 85%. The chemical absorption unit was modeled using the thermodynamic package Acid Gas module in Aspen Hysys software. This subsystem was installed downstream of the cogeneration heat exchangers for hot water. A compression stage for the separated CO_2, which raises the pressure from the atmospheric level to 4 bar, was also introduced since this is the suction pressure of the associated CO_2 booster compressor.

The total CO_2 emissions from flue gases were determined for five FPSO operating points and for three configurations: a) base case - the FPSO as it is today; b) removing the mechanical drive gas turbine and adopting a combined cycle; and c) the combined cycle with CCS as described above. In this way, it was possible to compare the base case with the effect of a combined cycle, and the effect of a combined cycle with CCS on the CO2 emissions.

4.1. Steam cycle characteristics

The combined cycle is composed by the three gas turbines adopted to generate electric power (GE-LM2500), each with its own HRSG and a single steam turbine. The vertical HRSG has one pressure level for steam generation, due to weight and area restrictions. Table 2 presents the design values for the HRSG. After passing the HRSG the flue gases passes through the hot water heaters. The steam turbine is an extraction-condensation with controlled extraction at 4 bar and condensation at 0.07 bar.

Table 2. HRSG design characteristics

Steam pressure [bar]	38.5
Steam temperature [ºC]	480
Pinch point temperature difference [ºC]	25
Approach temperature [ºC]	5
Pressure loss gas side [kPa]	3.5

4.2. Absorption system characteristics

The modeled absorption system is presented in the Fig.4. This is a typical MEA absorption system. In the model developed, some simplifications were assumed: the water wash in the absorber and the reclaimer part in the bottom of the stripper were eliminated. The solvent was assumed to stay inside the system, and do not need substitution. As mentioned before, the CO_2 flow exiting the absorption module are at atmospheric pressure and needs to be compressed to 4 bar. This compressor is not present in the Fig.4, but its power needs were considered in the complete simulation.

The design point for the CO_2 absorption system resulted in a preliminary size as given in the Table 3. It is important to mention that the absorber and the stripper columns are vertical, and the floor area is calculated. The columns are of the type with plates and barriers. Other geometries can be attempted to reduce weight and size.

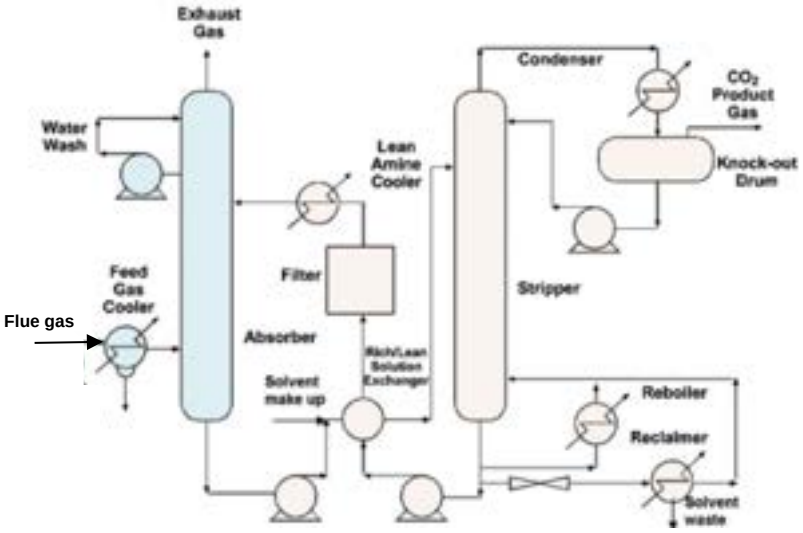

Figure 4. MEA absorption process characteristics. Source: IPCC [2005]

Table 3. Preliminary design for the MEA absorption system.

Dimensions	Absorption tower	Stripper tower
Diameter [m]	6.0	3.1
Height [m]	29.0	7.3
Number of plates	24	11
Plate spacing [m]	1.2	0.9
Barrier height [m]	0.18	0.14
Floor area [m²]	28.3	7.3

Øi et al [13] suggested conditions for an offshore application with 87 % capture efficiency, with 13 m absorber packing height (plus distribution and collecting height) and 15°C minimum approach temperature due to a decrease in equipment cost, size and weight. Nord [14] presents a design with a diameter of 13.6 m and packing height of 18.6 m for the absorber (plus distribution and collecting height). For the stripper, 3 m diameter and 7 m packing height.

4.3. Definition of efficiency calculation

In the next section are presented the obtained values for different efficiencies types. This section presents the definition adopted for each one of them.

Equation (1) presents the definition of electric power generation efficiency:

$$\eta_{\text{elect}} = \frac{\dot{W}_{\text{elect}}}{\dot{m}_{\text{fuel}} \text{LHV}} \tag{1}$$

The cogeneration system can be evaluated by a first-Law efficiency, taking into account each useful energy flow produced in each configuration as presented in the Eq. (2). In the base case, for example, there is mechanical power produced, but no reboiler heat. In the CC and CC+CCS configurations, there is no mechanical power produced. It is important to observe that the hot water heat is the same for each FPSO operating point, for every configuration.

$$\eta_{\text{cogen}} = \frac{\dot{W}_{\text{elect}} + \dot{W}_{\text{mech}} + \dot{Q}_{\text{hot water}} + \dot{Q}_{\text{reboiler}}}{\dot{m}_{\text{fuel}} \text{ LHV}} \tag{2}$$

The definition for the second Law efficiency is shown in the Eq. (3) and is similar to the first-Law, but dealing with exergy flows, instead of energy flows:

$$\varepsilon_{\text{cogen}} = \frac{\dot{W}_{\text{elect}} + \dot{W}_{\text{mech}} + \dot{B}_{\text{hot water}} + \dot{B}_{\text{reboiler}}}{\dot{m}_{\text{fuel}} \, b_{\text{fuel}}^{\text{ch}}} \tag{3}$$

The same observations made for the first Law efficiency applies in Eq. (3).

5. Results and discussion

The results obtained for each FPSO configuration are discussed in this section. Comparisons among the configuration are also presented.

5.1. The base case results - current FPSO configuration

The results for the base case are presented in the Table 4. The conditions 1 to 5 are those already defined in the Table 1. All electrical and mechanical power, as well as the hot water generation are those strictly necessary to the FPSO operation. The CO_2 compressor (CO_2 from natural gas processing) uses a gas turbine as prime mover. The total CO_2 emission from all exhaust gases is the main parameter for comparison purposes.

Table 4. FPSO power generation and CO_2 emission in the base case configuration.

Parameters	***FPSO operation condition***				
	1	**2**	**3**	**4**	**5**
Number of gas turbines (GT) for electricity power	3	3	3	2	2
GT Electrical power produced [MW]	72.12	73.14	70.65	48.96	46.02
GT - electrical power - load [%]	93.7	95.0	91.8	95.4	89.6
Electric power efficiency (LHV based) [%]	36.82	35.77	35.51	36.06	35.56
Number of gas turbines for mechanical power	1	1	1	1	1
GT mechanical power - for CO_2 compressor [MW]	12.21	15.15	14.22	7.00	6.87
GT mech. power load [%]	76.3	94.7	88.9	46.6	42.9
Total fuel consumption - all GT [kg/s]	5.03	5.50	5.41	3.43	3.30
Total CO_2 emission - all GT [Mt/year]	0.432	0.471	0.462	0.293	0.280

The electric power produced for each operation condition are the same as present in the Table 1 and were obtained from a detailed mass and energy balance for the topside processes and general electric loads (illumination, air conditioning, etc.). To compress the CO_2-rich stream separated from the natural gas, a dedicated gas turbine is employed and the mechanical power needed can be seen in the Table 4. The total fuel consumption is the sum of the needs of electric power gas turbines and the needs for the mechanical drive turbine. The total CO_2 emission is calculated from the total fuel consumption.

5.2. Combined cycle configuration results

The first approach to reduce the CO_2 footprint from the prime movers is the elimination of the mechanical power gas turbine, substituted by a steam turbine operating in Combined Cycle configuration with the gas turbines. Oil and gas production are maintained at operation conditions 1 to 5, as in the base case. The hot water need for heating purposes is also verified.

Figure 5 shows the temperature profiles for exhaust gases and the steam generator for operational condition 3, which produces the maximum amount of steam. It must be observed that the combined cycle was not optimized to maximize power, because the exhaust gas (still very hot) must provide the energy to produce the process hot water.

Table 5 shows the results for the combined cycle configuration. The elimination of the mechanical power gas turbine increased the electricity needs, but the combined cycle presents higher efficiency for power generation. The net effect is a reduction in the total CO_2 emission. In the operation conditions 4 and 5, the electric power is substantially reduced and one gas turbine must be deactivated. This reduces the steam mass flow for the combined cycle. The steam needs to water heaters contributes to reduce the power from the steam turbine, and the reduction in the CO_2 emissions are low.

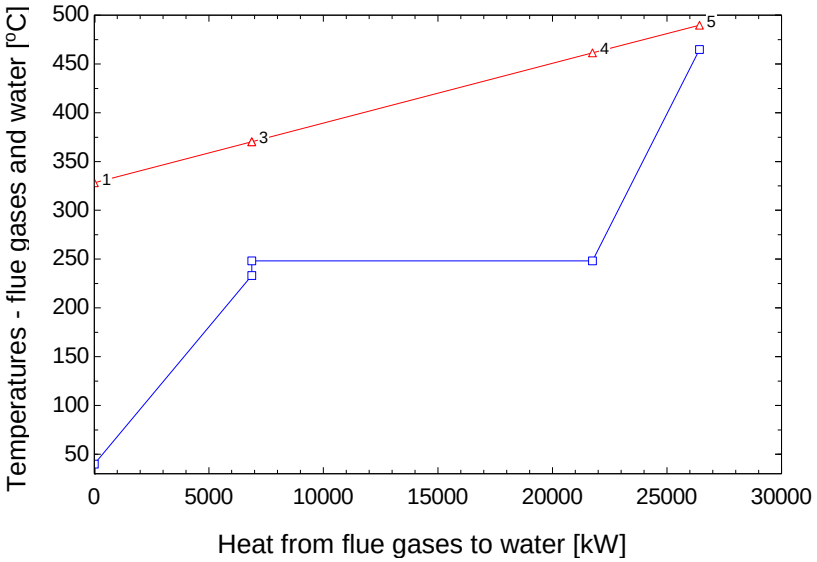

Figure 5. Temperature profiles in the HRSG. Operational condition 3

Table 5. FPSO power generation and CO_2 emission in the Combined Cycle configuration.

Parameters	FPSO operation condition				
	1	2	3	4	5
Number of gas turbines (GT) for electricity power	3	3	3	2	2
GT Electrical power produced [MW]	68.47	72.32	69.70	49.85	45.79
GT - electrical power - load [%]	84.15	89.00	85.70	92.08	84.41
Steam turbine [MW]	15.87	17.05	17.27	6.17	7.15
Electric power efficiency (LHV based) [%]	45.82	46.54	46.62	42.61	43.04
Total fuel consumption - all GT [kg/s]	4.04	4.23	4.12	2.90	2.73
Electric power for CO_2 compression [MW]	12.21	15.15	14.22	7.00	6.87
Total CO_2 emission - all GT [Mt/year]	0.347	0.362	0.352	0.248	0.231

5.3. Combined cycle with exhaust gas CCS

To reduce even more the exhaust gases CO_2 footprint, a third configuration was analyzed: a Combined Cycle with CCS. In this configuration, there is a carbon capture from the exhaust gases by a MEA system, with efficiency in the range 0.75 to 0.80.

The CO_2 separated from the exhaust gases and the CO_2 stream coming from the natural gas treatment are both re-injected in the oil field, after mixing and compression to adequate pressure. Table 6 presents the results.

Although the electricity production efficiency is reduced, the total CO_2 emission drops sharply, due to the sequestration of the CO_2 from exhaust gases. The electric power need for CO_2 compressors increases, due to the increased mass flow in the CO_2 compressors. To operate the separation, there is also a thermal energy utilization in the reboiler of the stripper, to liberate the CO_2 from the rich amine solution.

It is interesting to note that the steam turbine power must be derated when compared with the Combined Cycle configuration, since part of the steam flow must be diverted to supply the heat for the sequestration process. Øi et al [13] estimates the heat consumption to be approximately 5.5 MJ/kg CO2 removed. Nord et al [14] evaluated the specific reboiler duty for the process to be 3.6 MJ/kg CO2. Obtained values in this work are of the same order of magnitude.

Table 6. FPSO power generation and CO_2 emission in the Combined Cycle with carbon capture and sequestration (CCS) configuration.

Parameters	FPSO operation condition				
	1	2	3	4	5
Number of gas turbines (GT) for electricity power	3	3	3	2	2
GT Electrical power produced [MW]	79.65	80.68	79.56	52.72	48.75
GT - electrical power - load [%]	98.21	99.50	98.10	97.50	90.00
Steam turbine [MW]	9.13	11.26	10.16	3.88	5.07
Electric power efficiency (LHV based) [%]	42.80	43.86	43.30	41.37	41.54
Total fuel consumption - all GT [kg/s]	4.55	4.61	4.58	3.02	2.86
Electric power for CO_2 compression [MW]	16.05	17.86	18.35	7.36	7.30
Thermal energy in the CCS / CO_2 captured [MJ/kg]	4.198	3.917	4.155	3.918	3.891
Total CO_2 emission - all GT [Mt/year]	0.185	0.216	0.183	0.209	0.184
Total CO_2 captured by CCS system [Mt/year]	0.206	0.179	0.208	0.049	0.059
CCS system CO_2 capture efficiency [%]	77.59	73.12	76.08	79.21	76.88

5.4. Configurations comparisons

Figure 6 shows the electric power generation efficiency for each configuration, for the different operation conditions of the FPSO. The reduction of the efficiency observed for the CC+CCS configuration is due to the power derating of the steam turbine. The values obtained to CC and CC+CCS are far below traditional combined cycles designed to exclusive power generation because part of the exhaust gas energy must be allocated to generate hot water for FPSO processes, which is a priority.

The Figure 7 presents the first and second-Law efficiencies for each configuration and as a function of the year of FPSO operational phase for the cogeneration system. As usual, first-Law efficiencies are higher than second-Law ones when the driving force is a fuel. Apart from this, the exergy of a heat flow is smaller than the energy flow. It is interesting to note that the higher efficiencies occur for the CC configuration. When a CCS system is adopted, there is a need of extra power to compress the separated CO_2, and the cogeneration efficiency decreases.

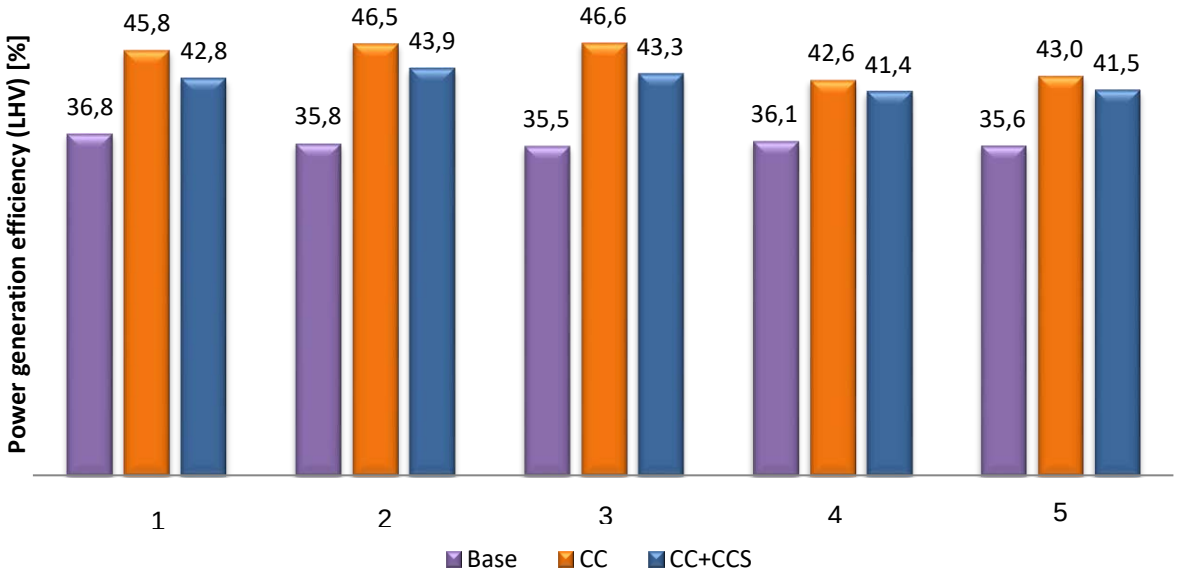

Figure 6. Electric power generation efficiency (LHV based) for different FPSO operation conditions.

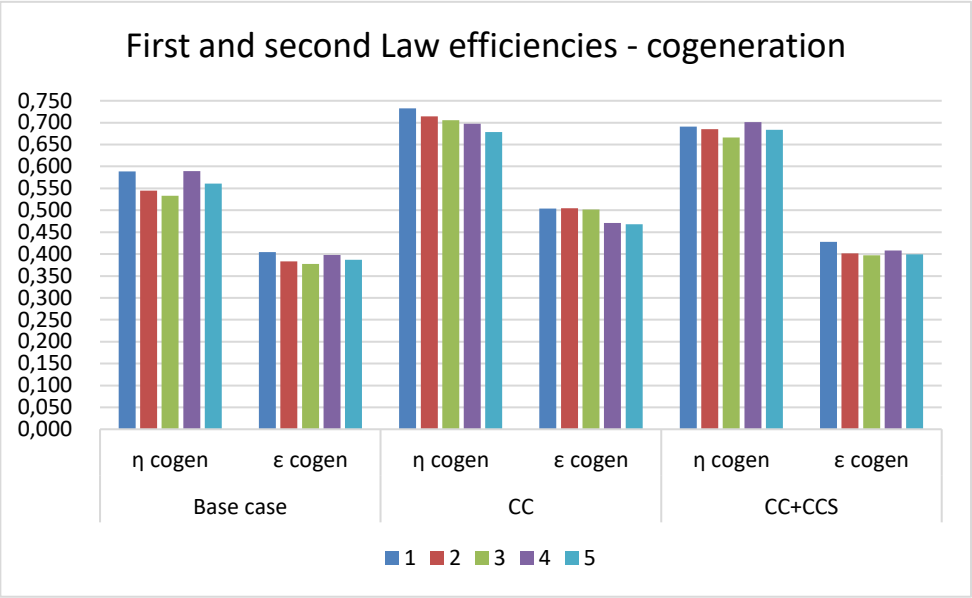

Figure 7. Efficiencies for the three configurations.

The reduction in the CO_2 emissions can be seen in the Fig.8. The reduction in the emissions are greater for the conditions which uses three gas turbines. With only two gas turbines operating, the derating of the steam turbine is high due to less available steam flow and hot water needs, and the benefits are not so evident. Fortunately, condition 4 occurs after 18 years of operation of the FPSO and condition 5 occurs after 21 years, near the end of the oil field lifespan.

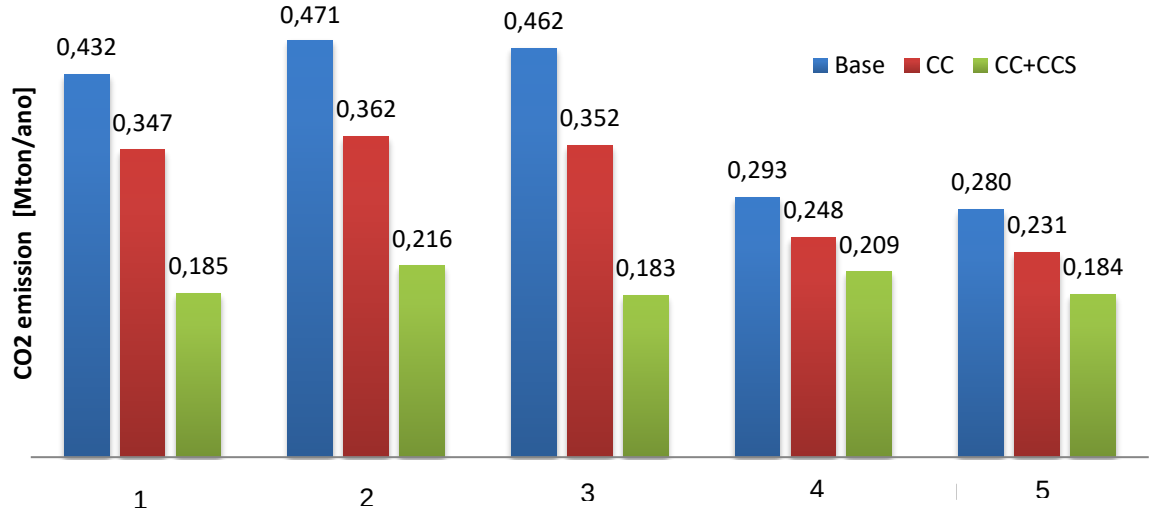

Figure 8. CO_2 emissions for different FPSO operating conditions

To make a comprehensive view of the CO_2 footprint reduction, Table 7 presents the CO_2 emission reduction as a percentage of the base case. The last column is the weighted average reduction for the analyzed period, considering the 21 years. Is to be noted that till the operation year 18, the reduction in the CO_2 emission is higher than 20% for the Combined Cycle configuration (CC) and higher than 50% for the Combined Cycle with CCS configuration (CC+CCS).

Table 7. CO_2 emission percentual reduction compared to Base Case

Configurations	FPSO operation condition					
	1	2	3	4	5	Average
CC to Base case	19,6%	23,1%	23,8%	15,3%	17,3%	21,6%
CC+CCS to Base case	57,2%	54,1%	60,5%	28,6%	34,3%	50,1%

Both alternative configurations presents interesting results. With the Combined Cycle configuration, the CO_2 footprint from exhaust gases is reduced by 20%, while the Combined Cycle with CCS reduced the CO2 emission by 50%. Only near the end of the FPSO lifetime the reduction is smaller, due the fact that only two gas turbines are operating and the hot water for FPSO processes does not reduces proportionally.

6. Concluding remarks

The results obtained in this work are of a prospective nature for new FPSO's, showing the order of magnitude of attainable CO2 footprint reductions. The proposed changes are not feasible for the operating FPSO.

The combined cycle configuration was not optimized for maximum power production, since electric power surplus is not allowed. In the same sense, the combined cycle is not optimized for maximum efficiency, since a compact system with a weight as low as possible is desirable. Apart from this, the need of hot water as an utility to the processes in the FPSO also puts a limitation to the maximum efficiency. Even with these limitations, a combined cycle proved to obtain 20% reductions in the CO_2 emissions.

The configuration with a combined cycle with Carbon Capture and Storage from flue gases can obtain near 50% CO_2 emissions reduction - an impressive figure. The proposed absorption system is a proven technology. The evaluation of the rotating packing bed (RPB) technology, instead of the usual gravitational packing bed, must offer a better weight and space solution for absorption systems. Other technologies, especially in the family of oxi-fuel combustion, may present even better results, provided they become mature.

Whatever the solution chosen, the topside processes in the new FPSO designs must be optimized for weight and size to accommodate the new subsystems.

Nomenclature

Variables

$\dot{B}$	Exergy flow [kW]
b	Specific exergy [kJ/kg]
$\dot{m}$	Mass flow [kg/s]
$\dot{Q}$	Heat flow [kW]
$\dot{W}$	Power [kW]
LHV	Lower heating value [kJ/kg]
η	First-Law efficiency
ε	Second-Law efficiency

Acronyms and abbreviations

BSW	Basic sediment and water
bpd	Barrels per day
CC	Combined-cycle configuration
CC+CCS	CC with Carbon Capture and Sequestration
EOR	Enhanced oil recovery technology
FPSO	Floating production storage and offloading facility
HRSG	Heat Recovery Steam Generator
MMb	Millions of barrels
ε - NTU	Method to evaluate partial load in heat exchangers

Subscripts

elect	Electric
mech	Mechanical
hot water	Hot water for processes
reboiler	Steam to drive the stripper
fuel	Natural gas used as fuel
cogen	Cogeneration system

Superscripts

ch	Chemical

References

[1] Nord, L.O.; Bolland, O. Steam bottoming cycles offshore - Challenges and possibilities. Journal of Power Technologies, v. 92, n. 3, p. 201–207, 2012.

[2] Nord, L. O.; Martelli, E.; Bolland, O. Weight and power optimization of steam bottoming cycle for offshore oil and gas installations. Energy, v. 76, p. 891–898, nov. 2014.

[3] Vidoza, J.A.; Andreasen, J.G. Haglind, F.; Reis, M.M.L.; Gallo, W.L.R. Design and optimization of power hubs for Brazilian off-shore oil production units. Energy, V176, 2019, p.656-666.

[4] IPCC, 2005: IPCC Special Report on Carbon Dioxide Capture and Storage. Prepared by Working Group II of the Intergovernmental Panel on Climate Change [Metz, B., O. Davidson, H. C. de Coninck, M. Loos, and L. A. Meyer (eds.)]. Cambridge University Press, Cambridge, United Kingdom and New York, NY, USA, 442 pp.

[5] ØI, Lars Erik. Aspen HYSYS Simulation of CO_2 Removal by Amine Absorption from a Gas Based Power Plant. Proceedings of the Scandinavian Conference on Simulation and Modeling, 48th, 2007, Gøteborg, Norway, 2007. p. 1 - 9.

[6] Ortiz, H.Y.; Castro, M.J.S.; Gallo, W.L.R.;Dias, R.; Gallego, A.D. Part-load exergy assessment of steam bottoming cycle and carbon capture systems: integration with oil and gas platforms. Proceedings of the 30thInternational Conference on Efficiency, Cost, Optimization, simulation and Environmental Impact of Energy Systems - ECOS 2017. San Diego, USA, July 2-6, 2017.

[7] Leung, D.; Caramanna, G.; Maroto-Valer, M. M. An overview of current status of carbon dioxide capture and storage technologies. Renewable and Sustainable Energy Reviews, v. 39, p. 426-443, aug. 2014.

[8] Songolzadeh, M.; Soleimani, M; Ravanchi, M.T.; Songolzadeh, R. Carbon dioxide separation from flue gases: A technological review emphasizing reduction in Greenhouse Gas emissions. Hindawi Publishing Corporation - Scientific World Journal, Article ID 828131, 2014.

[9] Petrakopoulou, F. Comparative evaluation of power plants with CO_2 capture: Thermodynamic, economic and environmental performance. [PhD Thesis]. Technische Universität Berlin, 2010.

[10] Madejski, P.; Chmiel; K.; Subramanian, N.; Kus, T. Methods and techniques for CO2 capture: Review of potential solutions and applications in modern energy technologies. Energies 2022, 15, 887.

[11] Long, N.V.D.; Lee, D.Y.; Kwag, C.; Lee, Y.M.; Lee, S.W.; Hessel, V.; Lee, M. Improvement of marine carbon capture onboard diesel fueled ships. Chemical Engineering & Processing: Process Intensification 168, 2021.

[12] Einbu A.; Pettersen T.; Morud J.; Tobiesen A.; Jayarathna, C.K.; Skagestad R.; Nysæther, G. Energy assessments of onboard CO2 capture from ship engines by MEA-based post combustion capture system with flue gas heat integration. International Journal of Greenhouse Gas Control, 113, 2022 103526.

[13] Øi, L.E.; Fazli, F.; Thapa, R. Offshore CO2 Capture from gas turbine with low investment optimized using Aspen HYSYS. Proceedings of the 63rd International Conference of Scandinavian Simulation Society - SIMS 63. Trondheim, Norway, September 20-21, 2022.

[14] Nord, L.O.; Anantharaman, R.; Chikukwac, A.; Mejdell, T. CCS on offshore oil and gas installation: Design of post-combustion capture system and steam cycle. Energy Procedia 114 (2017) 6650 – 6659.

[15] Hammera, M.; Wahla, P.E.; Anantharamana, R.; Berstada, D.; Yngve, K.; Lervåg, K.Y. CO2 capture from off-shore gas turbines using supersonic gas separation. Energy Procedia, 63, 2014, 243 – 252.

[16] Liu, P.; Wang, X.; Chen, W.; Hu, R.; Li, X. The Progress of Offshore CO2 Capture and Storage. Proceedings of the 4th International Conference on Green Energy and Sustainable Development - GESD 2021 .Nov 13-14, Shenyang, China.

[17] Sukor, N.R.; Shamsuddin, A.H.; Mahlia, T.M.I; Isa, M.F.M. Techno-economic analysis of CO2 capture technologies in offshore natural gas field: Implications to Carbon Capture and Storage in Malaysia. Processes 2020, 8, 350.

[18] Ortiz, H.Y.; Gallo, W.L.R.; Acevedo, V.L. Assessment of carbon capture and combined cycle integration with a maritime CO_2 injection compression system. Proceedings of the Rio Oil and Gas Expo and Conference 2016. IBP2162_16, Rio de Janeiro, October 24-27th, 2016.

A new approach for the hourly calculation of CO_2 emission factors of the thermal energy production in District Heating Systems

Chiara Monzani[a], Giulia Montanari[b], Alberto Poggio[c] and Giulio Abdin Cerino[d]

[a] Politecnico di Torino, Turin, Italy, chiara.monzani@polito.it
[b] Politecnico di Torino, Turin, Italy, giulia.montanari@polito.it,
[c] Politecnico di Torino, Turin, Italy, alberto.poggio@polito.it,
[d] Politecnico di Torino, Turin, Italy, giulio.cerino@polito.it

Abstract:

Reducing the environmental impact of anthropic activities is critical and requires a proper analysis of CO_2 emissions. This study focuses on the thermal energy sector's emissions carbon footprint, which is essential for many public and private institutions. The current practice of using average national and annual emission factors (EFs) may lead to inaccurate results on specific local entities, particularly in the case of combined heat and power production. This study aims to refine the EF calculation considering a combined cycle cogeneration plant and an hourly time step for the analysis. The case study chosen is the district heating system (DHS) cogeneration plants of Turin, one of the largest DHSs in Europe. The defined thermal EF is applied to the user case study of Politecnico di Torino supplied by the DHS. The study focuses on the thermal energy needs of the university campus on an hourly and seasonal scale. The results reveal that the emission factor of a DHS calculated with this methodology is different from the one calculated with other methodologies or using national EFs, better representing the real situation. Since the load profile of a university facility represents tertiary sector energy activities, the methodology used in this study is easily replicable in different contexts. This study emphasizes the importance of accurately estimating CO_2 emissions, which is fundamental in reducing the anthropic environmental impact.

Keywords:

Emission factors, sustainable university, decarbonization, district heating system, combined cycle.

2. Introduction

Anthropic activities have a significant environmental impact and reducing carbon dioxide (CO_2) emissions is essential for mitigating climate change. In recent times, there has been an increasingly crucial need for institutions to address their emissions. In this regard, universities play a pivotal role, by reducing their carbon footprint they can contribute to their own sustainability and promote environmental awareness in other sectors. Quantifying carbon emissions is essential to measure progress towards decarbonization goals and one effective way to track progress is using ranking systems such as Green Metric [1]. Many non-governmental actors have joined the Race to Zero campaign, promoted by the United Nations, which encourages the achievement of decarbonization targets aiming to strive for carbon neutrality by the mid-century [2]. The energy sector is the most impactful sector in terms of carbon footprint and emissions [3]; in the European Union (EU), buildings are responsible for approximately 40% of total energy demand and produce 36% of greenhouse gas emissions [4]. Heating, ventilation, and air conditioning play an important role in overall energy demand in Europe, making it crucial to accurately measure and define their emissions [4]. The European heating and cooling sector are characterized by varying building types and relies primarily on decentralized production units within buildings. Natural gas is the predominant fuel, meeting 42% of the heating demand. Additionally, District Heating Systems (DHSs) supply 12% of the building sector's demand for space heating and domestic hot water [5]. Due to the strong electrification trend in the heating sector, recent studies have focused on a more accurate estimation of CO_2 emissions of electricity system. Specifically, emission factors (EFs) have been evaluated on an hourly basis, focusing on technologies such as heat pumps [6]. In parallel, similar studies have investigated the variability of EFs at the national level in electricity production. From this latter study, it appears that European Directives fix values of CO_2 EFs, neglecting their intrinsic temporal variability due to the mix of primary energy sources used in electricity generation hour by hour. The use of a fixed value for these parameters could lead to inaccurate or erroneous results in various processes [7]. Similar to electricity grids, DHSs are characterized by various types of centralized thermal power generation systems, resulting in comparable complexities in defining EFs as with electricity. However, there is a gap in the literature concerning the hourly variability of DHS emission factors.

Additionally, current methodologies used to calculate emissions associated with DHSs do not take into consideration the high efficiency of technologies such as Combine Cycle Plants (CHP). Therefore, the goal of our study is to investigate the temporal variability of emissions produced by thermal energy consumption when a utility is supplied by CHP DHS. The new methodology presented is compered to different method currently in use. Specifically, we apply the methodologies presented to the case of the city of Turin's DHS, which is the most district-heated city in Italy and one of the main ones in Europe. The hourly EF developed with this methodology is then applied to the hourly thermal energy demand profile of the Politecnico di Torino providing an example of replicable application on tertiary sector users. As university facilities are representative of the energy consumption patterns of the tertiary sector, the methodology used in this study can be replicated in other contexts. By demonstrating how the environmental impact of energy consumption can be significantly affected by both the energy mix and the time of energy supply, we contribute to a better understanding of the challenges and opportunities for reducing carbon emissions associated with energy use in university facilities.

3. Methodology

3.1. Current methodologies for calculating CO_2 emissions for cogeneration plants

3.1.1. Allocation of CO_2 emissions in case of cogeneration heat and power combined cycle

Allocating CO_2 emissions in plants that generate both thermal and electrical energy is a complex issue. These plants produce heat as a by-product of electricity production, which adds complexity for a correct allocation of emissions. In Europe, DHS heavily rely on fossil fuel-based Combined Heat and Power plants (CHP), with cogeneration accounting for over 70% of the heat generated by EU member states [8]. Given the importance of cogeneration for district heating (DH), it is crucial to develop a methodology that can accurately account for the resulting CO_2 emissions.

Typically, DHS that supply large urban areas, are characterized by Combined Cycle CHP plants (CC). This type of plant combines two production phases, one based on gas and the other on steam. The high-temperature exhaust gases from the Gas Turbine (GT) are used to produce steam in a Heat Recovery Steam Generator (HRSG), which is then fed into a Steam Turbine (ST) to generate additional electrical power. CCs are typically used both in industrial settings that require the production of steam, superheated or hot water, and for DHS. They come in various sizes, ranging from 50 to 400 MWe, and offer electric efficiencies of approximately 45-58%. DHSs, which utilize combined cycle power plants, typically generate 80-90% of their annual heat energy production through cogeneration [9]. These plants produce thermal energy throughout the heating season but require additional support from backup generators during the coldest months and during peak demand hours. Thermal storage systems, which use hot water tanks to store excess heat generated during low-demand periods, are typically utilized in DH networks to manage the demand and supply of heat efficiently. During peak hours, the stored heat is released to ensure a consistent flow of heat to customers. Furthermore, these thermal storage systems can be charged using renewable sources if available, or by cogeneration plants. This approach not only reduces energy waste and improves the overall efficiency of the system, but also promotes the utilization of renewable energy sources in DH networks.

A simplified diagram illustrating the relationship between fuel input and the resulting output of electricity and heat for a typical DHS with a CC unit is shown in Figure 1. The nomenclature used in the figure is used in the following sections to explain the various methodologies available in the literature for calculating the DHS emission factor. The energy balance shown in the figure is annual.

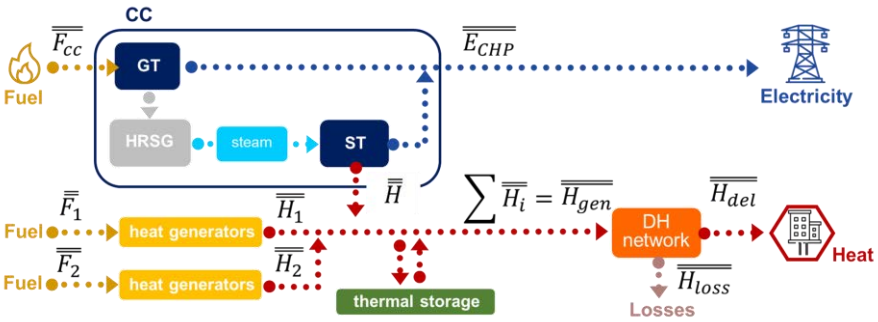

Figure 1. District heating system, CHP general scheme and relative nomenclature

3.1.2. Eurostat, Ispra and IPCC methodology (Method E)

The IPCC's Working Group 3, in Annex 2 Metrics and Methodology [10], defines carbon dioxide emission factors for electricity and heat based on the ratio between CO_2 emissions due to fuel inputs of power plants

and the delivered electricity and heat. The CO_2 emission factors of each fuel type, as defined in IPCC (2006) [11], are multiplied by the fuel inputs. The calculation of CO_2 emission factors for electricity and heat is conducted at the country level. Also the 2020 annual report on emission factors drafted by Ispra[1] and Snpa[2] [12] and Eurostat 2016 annual questionnaire report [13] present the same methodology for allocating the fuel between the electricity and heat generation components.

This methodology can be expressed in the following way:

$$\overline{f_{DHS,HE}} = \frac{\overline{\overline{F_i}}}{\overline{\overline{H_{del}}} + \overline{\overline{E_{CHP}}}} * f_{i,F} \qquad \left[\frac{kg_{CO_2}}{kWh}\right] \qquad (1)$$

According to the 2020 Ispra annual report, this formula is recommended only when national administrations have not adopted a more precise methodology for reporting combined heat and power (CHP) on a unit basis. Using this methodology, that we will call method E, the resulting EF is 0.30 kg_{CO2}/kWh.

3.1.3. UNI EN 15316-4-5:2018 methodology (Method U)

A different methodology for multi-output DHS is detailed in the regulatory document UNI EN 15316-4-5:2018. This approach has been utilized in various publications [14] and has been adopted as a standard methodology for creating CO_2 emission inventories for Italian universities, members of the Italian sustainable development network (RUS[3]). The formula for this methodology is the following:

$$\overline{f_{DHS,H_{del}}} = \frac{(\sum_i \overline{\overline{F_i}} f_{i,F} - \overline{\overline{E_{CHP}}} f_{el})}{\overline{\overline{H_{del}}}} \qquad \left[\frac{kg_{CO_2}}{kWh}\right] \qquad (2)$$

The issue with this approach arises in situations where the production of electrical energy from cogeneration systems is very high, resulting in a negative value of the derived emission factor. In case of negative values, the regulatory document recommends considering these cases as zero-emitting, underestimating the actual emissions from thermal energy consumption.

3.2. Introducing a new methodology for determining emission factors

The emission factors determined by current methodologies don't reflect the actual value that should be utilized in a real DHS supplied by CC CHP. Hence, it is necessary to develop a different approach that combines both hourly and simplified annual analyses for calculating CO_2 emissions in DHS.

3.2.1. Combined cycle cogeneration heat and power plants for district heating systems

As explained in section 3.1.1, in CC systems it is possible to recover heat for industrial purposes or DHS use from the steam cycle. Steam can be supplied by extracting pass-out steam at an intermediate point in the turbine. The rest of the steam continues to the exhaust, thereby generating further power, and exits the process at a lower pressure. Therefore, whenever there is a thermal demand and the plant operates in cogeneration mode, steam extraction results in less electricity production. A typical operating diagram for each plant is shown in Figure 2.

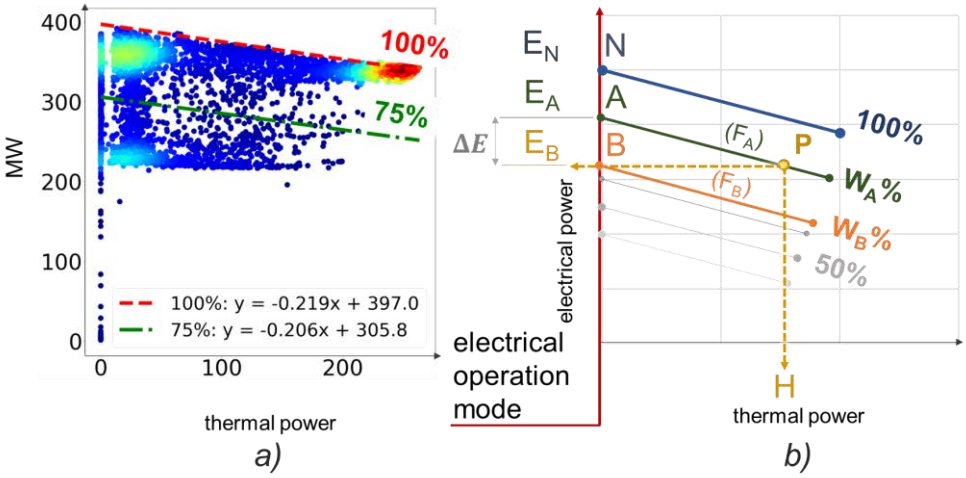

Figure 2. CHP operating diagram partial load. a) real operating diagram: hourly energy production (equation of regression lines *[15, 16]*); b) working point P

[1] Istituto Superiore per la Protezione e la Ricerca Ambientale.
[2] Sistema Nazionale per la Protezione dell'Ambiente.
[3] Rete delle Università per lo Sviluppo Sostenibile.

The y-axis shows the electrical power generated at various nominal loads, while the x-axis represents the corresponding heat output. The point N represents the working condition at nominal load in *electrical operation mode*. Thermal power is not generated, and electrical power corresponds to the nominal value. By working on the 100% load operating characteristic, the heat output increases, and the *cogeneration condition* is reached. Each load has a characteristic regression line whose points are characterized by the same fuel inlet power (F). Figure 2a shows the real hourly operation in one year of operation of a CC. A generic working point P in cogeneration condition at load W_A% is considered. The point is characterized by a thermal power H and an electrical power E_B. At the same fuel input power F_A and considering the electrical operation mode, a higher electrical power equal to E_A would be obtained. The production of thermal energy causes a reduction in the amount of electricity produced.

$$\Delta E = \mathrm{E}_A - \mathrm{E}_B \qquad [MW] \qquad (3)$$

The ratio of the two output energies K is the *cogeneration gain*, expressed in the equation (2). K is inversely proportional to the slope of the loads regression lines and it is approximately constant as leads changes. ΔE can consequently be expressed as in equation (5).

$$K = \frac{H}{\Delta E} = cost \qquad [MW] \qquad (4)$$

$$\Delta E = \frac{H}{K} \qquad [MW] \qquad (5)$$

By analyzing the hourly operating experimental data of a few combined-cycle plants, it was possible to outline a general trend in energy performance in *electric operation mode*. Isolating the hourly data in which the CC operated in electrical mode and excluding the transient operating values, the real operating data were averaged to obtain the percentage trend shown in Figure 3.

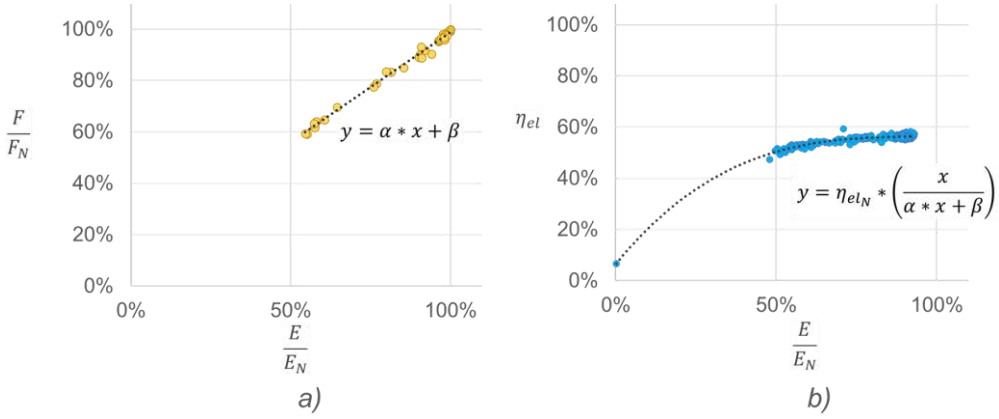

Figure 3. Electrical operation mode working performances of a generic CC unit. a) fuel inlet power; b) CC electrical efficiency.

Figure 3a shows the linear dependence of the fuel inlet power with respect to the load of the generated electrical power (equation (6)). The characteristic equation of CC electrical efficiency with respect to the electrical load variation is obtained. As shown in figure (b) the points of real operation validate the trend.

$$\frac{F}{F_N} = \alpha \frac{E}{E_N} + \beta \qquad [MW] \qquad (6)$$

3.2.2. Combined Cycle emission factor

To determine the *hourly emission factor* of a generic CC supplying a DHS, we consider a generic operating point *P* (Figure *2*b). As explained in the previous section, the generation of thermal energy results in a lower amount of electrical power generated ΔE for the same amount of fuel used. It is possible to allocate ΔE with the additional fuel inlet power ΔF consumed in cogeneration condition. The same electric power E_B could in fact be obtained by working at a lower load W_B% with less fuel input power F_B. From equation (6)(6)**Errore. L'origine riferimento non è stata trovata.** F_A and F_B are defined:

$$F_P = F_A = F_N \left(\frac{\alpha E_A}{E_N} + \beta\right) \qquad [MW]$$

$$F_B = F_N \left(\frac{\alpha E_B}{E_N} + \beta\right) \qquad [MW]$$

The nominal condition N in electrical operation mode at 100% load is characterized by electrical efficiency:

$$\eta_{el,N} = E_N / F_N$$

Therefore ΔF is defined:

$$\Delta F = F_A - F_B = \alpha \frac{\Delta E}{E_N} * F_N = \frac{\alpha}{K} \frac{H}{\eta_{el,N}} \qquad [MW] \qquad (7)$$

The additional amount of inlet power required must be multiplied by the fuel EF and normalized to the heat output:

$$f_{CC,H} = \frac{\Delta \mathrm{F} * f_{NG}}{\mathrm{H}} = \frac{\alpha}{\mathrm{K}} * \frac{1}{\eta_{el,N}} * f_{NG} \qquad \left[\frac{kg_{CO_2}}{kWh}\right] \qquad (8)$$

The remaining amount of fuel inlet power F_B is attributed to CO_2 emission on hourly electrical energy generated. It would, in fact, have been equally produced in the case of electric power generation in the electrical operation mode. In this case in contrast to the thermal EF, the hourly electric emission factor is not constant. It varies following the same trend as the electrical efficiency shown in Figure 3b.

3.2.3. District heating system emission factor

DHSs have different layout configurations based on the served volumetrics and climatic zone. These configurations can vary based on the type of generator employed, the characteristic size of each generator, and the number of generators installed. The various generation groups produce thermal energy with different strategies based on thermal demand and economic and environmental dispatching considerations. Therefore, the CO_2 emissions associated with the use of heat from a DHS depend not only on the type of generators involved in the annual production but also on the way they produce thermal energy hourly and during different seasons. To correctly assess the DHS thermal EF, it is, therefore, necessary to define the amount of thermal energy produced for each generation unit hour by hour. The DHS thermal emission factor is the weighted average of each characteristic EF of the fuel and generator used multiplied by the thermal energy delivered. To express the emission factor $f_{i,H}$ with respect to the energy produced by the generator instead of that of the input fuel F_i as used in methods E and U, we define the relationship between the characteristic EF of the fuel and the efficiency of the generator.

$$f_{i,H} = \frac{f_{i,F}}{\eta_i} \qquad \left[\frac{kg_{CO_2}}{kWh}\right] \qquad (9)$$

For DHS in which a part of thermal energy is generated by a natural gas CC unit in combination with other types of heat generators, CC thermal emission factor is defined in equation (8). The energy delivered by the storage system is associated with the EF of the generator that predominantly charges the storage. Methods E and U calculate the DHS emission factor with respect to the energy supplied to the users H_{del}. Therefore, the heat loss factor $p\%$ on the distribution network is defined:

$$p\% = 1 - \frac{H_{del}}{H} \qquad [\%]$$

The DHS emission factor expressed as the ratio between the tonnes emitted and the energy delivered to the user can be defined as:

$$f_{DHS,H_{del}} = \frac{H * f_{CC,H} + \sum H_i * f_{i,H}}{H_{del}} = \frac{H * f_{CC,H} + \sum H_i * f_{i,H}}{H_{gen}(1 - p\%)} = f_{DHS,H_{gen}} * \frac{1}{1 - p\%} \qquad \left[\frac{kg_{CO_2}}{kWh}\right] \qquad (10)$$

The definition of heat delivered to the user excluding network losses requires specific discussion. Network losses are typically defined as a percentage of the total energy delivered annually. The incidence of losses on an hourly basis cannot be considered constant. In the summer period when the thermal demand is low, the energy that is produced is mainly dispersed to keep the entire network at temperature. Therefore, network losses are very significant, and the EF reaches values much greater than 1.

The emission factor can be expressed as the sum of the emission factor of losses and the emission factor of thermal energy consumptions.

$$f_{DHS,H_{del}} = f_{DHS,H_{gen}} * \frac{p\%}{1 - p\%} + f_{DHS,H_{gen}} = f_{DHS,losses} + f_{DHS,cons} \qquad \left[kg_{CO_2} kWh\right] \qquad (11)$$

3.2.4. SEA Method

The application of hourly emission factor outlined in equation (11), can be difficult for a typical user connected to the DHS. In fact, the method assumes knowledge of DHS's hourly generators production, DHS hourly network losses, and hourly heat demand profile. The hourly load profile of the building may be known or calculable from consumption data with daily or monthly steps. On the other hand, system operating data

may not be public and available. A *simplified method* (SEA[4] method) for calculating emissions is therefore proposed. Equation (12) can be adopted by replacing the hourly energy with the energy delivered annually by each heat generator. The first term of the emission factor relating to network losses is an annual average value. For this reason, in the case of users characterized by winter heat load profile, the value of emitted tons of CO_2 may not be representative. Therefore, it is appropriate to simplify the expression (equation (13)).

$$\overline{f_{DHS,H_{del}}} = \frac{\overline{\overline{H}} * f_{CC,H} + \sum \overline{\overline{H_i}} * f_{i,H}}{\overline{\overline{H_{gen}}}(1 - \overline{\overline{p\%}})} = \overline{f_{DHS,H_{gen}}} * \frac{\overline{\overline{p\%}}}{1 - \overline{\overline{p\%}}} + \overline{f_{DHS,H_{gen}}} \qquad \left[\frac{kg_{CO_2}}{kWh}\right] \qquad (12)$$

$$\overline{f_{DHS,H_{del}}} = \overline{f_{DHS,H_{gen}}} * \left(\frac{1}{1 - \overline{\overline{p\%}}}\right) \qquad \left[\frac{kg_{CO_2}}{kWh}\right] \qquad (13)$$

3.3. Thermal energy demand profile evaluation

To calculate the hourly CO_2 emissions resulting from the Thermal Energy Consumption (TEC) of a tertiary user connected to a DHS, the first step is to gather data on the actual hourly energy consumption of the buildings. If energy demand profile is not available, it is still possible to estimate the energy consumption using specific values that consider external average temperature. A replicable methodology for the creation of a profile for other buildings with a similar occupancy profile is proposed.

3.3.1. Daily thermal energy consumption patterns and relation with external temperature

To investigate the thermal energy demand profile, the first step is to select the buildings to be included in the analysis and gather relevant energy-related data, such as energy consumption, variation in heated volumes, and average external temperature. By obtaining hourly data, it becomes possible to observe variations in consumption over time of day, external temperature, and day of the week. To facilitate year-to-year comparisons, we used the academic year (e.g., October to September) rather than the solar year. This enables the analysis of consumption trends during the same heating season, thereby minimizing potential errors arising from changes in heated volume across different years.

In the present case study, hourly data were collected from October 2021 to September 2022 for the demand side (University energy consumption), and from October 2010 to September 2011 for the production side (DHS data). Hourly consumption data of the university user are recorded in the heat exchange substation of the DHS serving the city and the analyzed user. In recent years, obtaining hourly energy consumption data from buildings has become increasingly accessible, although it is more challenging to obtain such data for the 2010-2011 heating season. With the improvement of data analysis services, it will be easier to perform hourly considerations in the future. In this case, however, we were forced to use the 2010-2011 period as a reference and consequently recalculate the hourly consumption. To do this, we used Energy Signature (ES) and load profile variation. As the variation in heated volumes between these two periods was negligible, this parameter was considered constant.

The analysis has allowed the identification of similar consumption pattern for the working midweek days: Tuesday, Wednesday, and Thursday. Monday consumption is higher due to its early heating starting time, Friday and Saturday have a lower thermal consumption because of a lower occupancy ratio. The midweek days were therefore used as Reference Days (RD) to create a daily ES that more accurately represents the buildings' behaviour of these days.

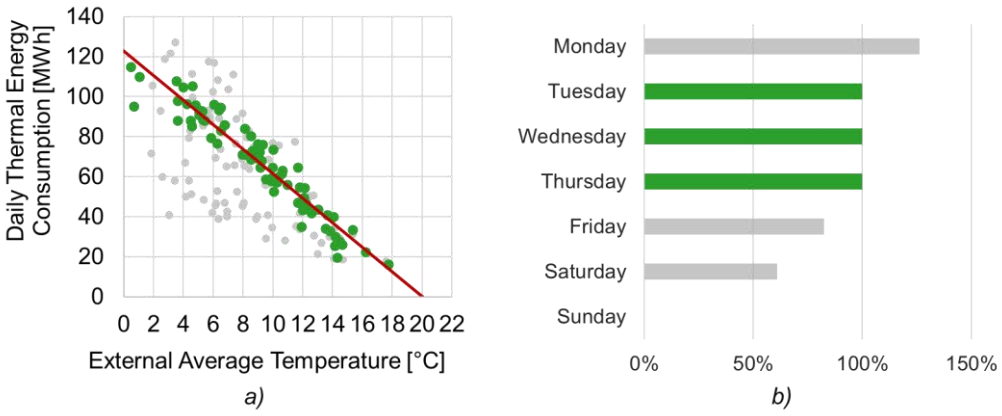

Figure 4. a) Daily Energy Signature, relationship between thermal energy consumption and external average temperature b) Ratio between TEC of a specific day of the week and average TEC of RD

[4] Sistemi per l'Energia e l'Ambiente.

To create a more representative linear regression model from the ES, some data was excluded: National holidays; days right after a day of building closure; and Mondays, Fridays, Saturdays, and Sundays. Daily average external temperature of 2010-2011 was then used in the equation of the ES trend-line. This output enabled the estimation of the daily TEC for all days with behaviour similar to RD.

To allocate the correct daily TEC for each day of the week, the ratio between the TEC of other days in the week and the average TEC of the RD was calculated for each week of the heating season. By taking the trimmed mean of these ratios, more realistic percentages were obtained as shown in Figure 1.b. The following specific considerations were made for the specific case study.

- On Monday, energy consumption is higher than the RD (126%) due to an early start time for heating after Sunday closure.
- On Friday, the occupancy rate of the facility decreases in the late afternoon and shutdown hour is later, leading to lower consumption than the RD (83%).
- On Saturday, the facility is only open in the morning, and its energy consumption is lower (61%).
- On Sunday, the facility is closed, with zero energy consumption.

To obtain the actual daily consumption, the values obtained from the linear regression model were multiplied by the ratios shown in Figure 4.b depending on the actual days of the week in 2010.

$$H_{s_{daily}} = \sum_{0}^{23} H_{hh} \qquad [kWh] \qquad (14)$$

This methodology enabled the calculation of daily heat consumption, denoted as $H_{s_{daily}}$, for the heating season 2010-2011. With these daily data, an hourly consumption profile was created using the methodology described in the following chapter.

3.3.2. A replicable methodology for identifying typical hourly heat demand profiles

A Python-based calculation method was created and developed to define the hourly TEC of a typical user. The model was built using daily energy consumption data obtained as explained in the previous chapter. The aim was to create hourly profiles depending on the days of the week and the months of the year. To express the hourly load, the ratio of hourly consumption to the total daily TEC was calculated (15).

$$L_{hh} = \frac{H_{\mathrm{hh}}}{\sum_{0}^{23} H_{hh}} \qquad [-] \qquad (15)$$

The hourly load was averaged for each month and day of the week. Afterwards, a matrix was extracted that contained the hourly percentage heat load values characteristic of the day of the week and month.

The Python model requires as input the daily energy consumption data, which can be obtained from the provider or using the energy signature and daily average external temperature of the same period for which CO_2 emissions are being calculated. Based on the required year, a usage schedule is developed, which can be modified in case of scheduled closures on non-holiday days.

The energy consumption value is then distributed over hourly values based on the percentage hourly load characteristic of the month and day being analyzed, resulting in the user's daily hourly consumption for the entire thermal season. By utilizing this calculation method, a typical hourly load profile can be obtained, which can be replicated for tertiary utilities that have similar heat management systems.

4. Results

4.1. Case study description

4.1.1. Thermal energy profile in the main campus buildings of Politecnico di Torino

The case study selected to develop and apply the new methodology of CO_2 emissions calculation from a user perspective is the Politecnico di Torino. Specifically, the analysis focuses on the hourly thermal energy consumption of the university's most energy-intensive DH substation. The reference period chosen is the academic year 2010-2011 as hourly data from DHS side was available for that period. Since hourly data of DHS substation was available from 2021 to 2023, the methodology described in section 2.3 was applied using data from October 2021 to September 2022. To ensure a representative heating season, data from the period of extended Covid-19 restrictions was excluded.

By applying the previously described methodology, a typical thermal consumption profile was generated for the reference heating season and hourly TEC data was extracted. The annual consumption of the reference buildings was 11.1 GWh. The aim of the chapter 3.2 is to calculate the resulting CO_2 emission using both hourly and yearly calculation.

The analysis enabled to show that start-up and shut-down times vary based on the month and outdoor temperatures, as well as the day of the week. An earlier start-up time of approximately one hour is observed on Mondays to warm up structures that have cooled down during Sunday, resulting in higher total energy consumption than on other days. Conversely, Friday sees an earlier shut-down time than other days by

approximately one hour. Heating on Saturdays ceases around 1 pm, and no heating is required on Sundays due to the facility being closed.

4.1.2. Turin district heating system

Knowing the hourly thermal load profile of the consumer, to define CO_2 emissions, it is necessary to define what is happening at the energy generation level. Therefore, the DHS in Turin is analyzed from the energy point of view. The data used in this study are divided into two sets. The first set includes information on the production of electric and thermal energy, natural gas consumption, water temperature, and water flow rate inputs into the distribution network for all the generation groups of the Torino DHS from 2001 to 2011. The second set of data covers the period from 2010 to 2015 and is focused exclusively on the combined cycle power plants. Data cover hourly thermal and electric energy production, natural gas consumption, and carbon dioxide and pollutant emissions. The EF is being calculated for the 2010-2011 heating season because data are complete and comparable from both datasets. The DHS is supplied by three plants located in three different areas of the city. In the main plant, two combined cycles (CCs) and three Integration and Backup Boilers (IBBs) are installed. The other two plants consist of IBBs and a storage system (STO). The installed capacities are summarised in Table 1.

Table 1. Turin DHS thermal power installed (2010-2011)

type of generator	number, -	thermal power, MW	electrical power, MW	storage capacity, m^3
CC	2	520	760	-
IBB	9	651	-	-
STO	1	-	-	2'500

To analyse the operation of the two combined cycles, thermal power and electrical power are represented as a set of two-dimensional coordinates x and y (Figure 5). The CC energy output for each hour of operation is represented by a point. Using the *gaussian_kde* class of the *scipy.stats* module in Python, it is possible to estimate the probability density of the two-dimensional data represented by x and y. The mathematical model used by the KDE is based on the convolution of a core function with the input data. In this case, the KDE uses a Gaussian kernel to evaluate the probability density of the data, producing a continuous function that describes the probability distribution of the two-dimensional data. For both CCs (Figure 5 a and b), the point density is highest in the operation region of in cogeneration condition at full load. This is followed in order of frequency by the region in electrical operation mode typical in summer period when users' thermal demand is lowest. A threshold operating zone of 230 MWe can be identified from the graph for both combined cycles. The output points are positioned along the regression lines representing operation from electrical to cogeneration operation at variable loads. As described in section 3.2.1, the slope of regression lines at variable loads are considered approximately constant. A change in slope is not significant to the emissions factor calculation. The slope is inversely proportional to K (equation (4)) and in Figure 5 a and b are equal to 4.5 and 4.3 respectively.

To simplify the simulation of plant operation, the outputs of the two CCs have been summed up (Figure 5c). The average cogeneration gain K_{ave} has been calculated and is equal to 4.4. In Figure 5c, the point density is higher when only one CC operates in electrical mode (summer periods) and when both CCs operate in full cogeneration condition (winter periods).

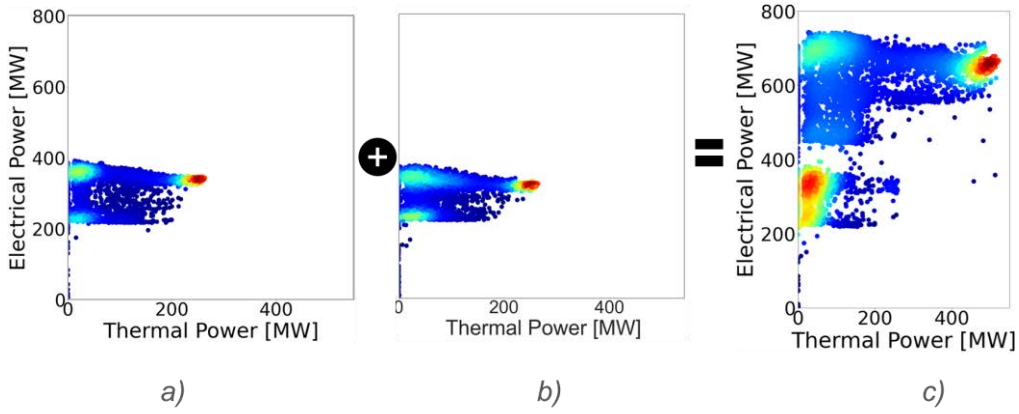

Figure 5. CC hourly energy output. a) CC_1; b) CC_2; c) $CC_1 + CC_2$

CCs produce 85% of the annual thermal energy, the remaining amount is produced by IBBs 13% and STO 2%.

4.2. CO_2 emissions in universities

4.2.1. Turin district heating emission factor

Starting from the overall operating data of the two CCs, the regression line shown in Figure 3a is derived. The characteristic coefficient α of the combined cycle is 0.902. The EF of the combined cycle (equation (8)) is 0.074 kg_{CO_2}/kWh. As shown in Table 1, the Turin DHS is connected with thermal storages. An analysis of the operation of the generation components hour by hour shows that the charging of the storage tanks occurs during night periods and during daytime periods when the thermal demand is lower. During such periods, the only operating generators are the CC units. For this reason, the storage unit also has an EF of 0.074 kg_{CO_2}/kWh.

By analysing the hourly operation of the heat generators of the DHS in Turin and applying equation (9), the hourly emission factor $f_{DHS,cons}$ is obtained. Figure 6a shows the hour-by-hour emission factors for the months of December, January, and February. Three different trends are identified. The points with a constant EF of 0.074 kgCO2/kWh are associated to *operating configuration 1*. It corresponds to the hours in which the thermal energy is exclusively produced by CCs and CCs with STO. As the thermal demand increases, the heat production is integrated by IBBs. The EF increases as the contribution of IBBs becomes more and more relevant. Thermal energy production from CCs, STO, and IBBs is represented by *operating configuration 2*. The 2010-2011 winter season was characterized by a few operation hours in which the thermal demand was satisfied by a single combined cycle CC at which the heat produced from IBBs was integrated. This operating configuration is represented by the *operating configuration 3*. The EF reaches the highest values. The average hourly emission factor $f_{DHS,cons}$ for each month is represented in the graph in Figure 6b.

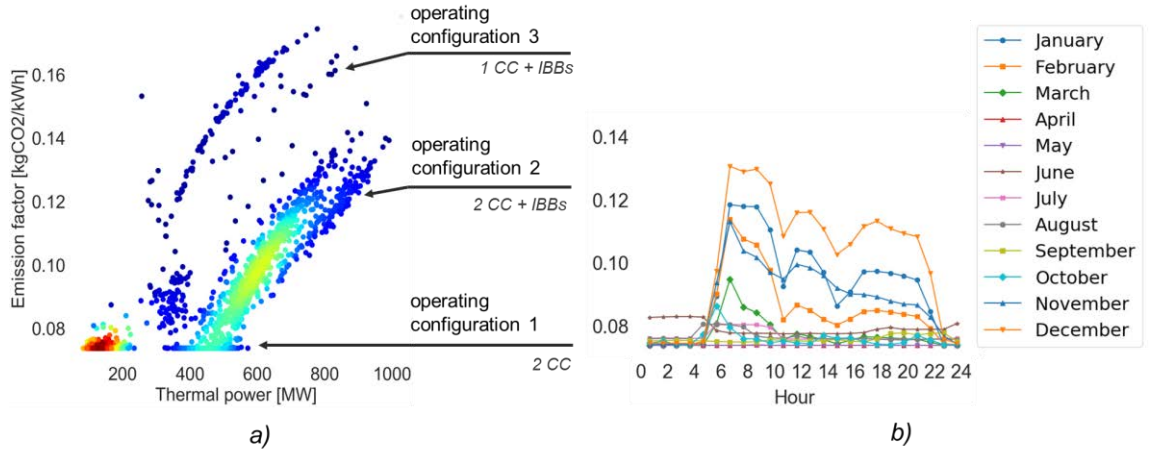

Figure 6. hourly EF (consumption factor). a) EF with respect to thermal energy generated in winter period; b) average EF with respect to time of day in the different months of the year

While in the summer months the emission factor $f_{DHS,cons}$ is lower, this is not true for the emission term related to network losses $f_{DHS,losses}$. Network losses contribution is lowest in the daytime hours of the heating season; it is most relevant in the night-time period, and it is highest in the summer period when the energy delivered is minimal and equal only to that required for domestic hot water production.

4.2.2. Annual emission factors methodologies comparison

To define the annual EF of the Turin DHS in the 2010-2011 thermal season, the annual energy performance is calculated. The total energy produced is 1'760 GWh_t, of which 8% is loss to the distribution network.

Table 2 shows the annual thermal emission factors calculated using the three methodologies presented in the previous sections. *SEA method* allocates the emission factor into two contributions: one related to heat losses in the distribution network, and the other related to actual thermal energy consumption. The EF obtained using this method is significantly lower than those obtained using the other two methods. *Method E* outputs an emission factor that is approximately three times higher than the one obtained using the SEA method proposed, and even higher than the EF of natural gas (0.202 kg_{CO_2}/kWh [17]). This implies that users who satisfy their thermal energy needs using DHS emit more tons of CO_2 than those who use a single natural gas boiler considering the same thermal energy consumption. Finally, *method U* considers electrical energy generated in cogeneration and produced as a substitute for fossil-fuelled non-cogeneration national thermoelectric plants. The electrical emission factor applied is the Italian gross thermoelectric production (fossil fuels only) as of the year 2010 and is equal to 0.565 kg_{CO_2}/kWh [12]. Method U generates a negative DHS thermal emission factor. The EF must be replaced by zero value. This implies that the production of thermal energy from DHS results in an inappropriate cutback of CO_2.

Table 2. annual emission factor comparison

		Losses factor, kg_{CO_2}/kWh	Consumption factor, kg_{CO_2}/kWh	*Total factor* , kg_{CO_2}/kWh
Method E	(eq. (1))	–	–	0.302
Method U	(eq.(2))	–	–	– 0.421 (0)
SEA method	*(eq.* (11))	0.009	0.093	0.102

4.2.3. Application of methodologies to case study and corresponding CO_2 emissions

The emission factors calculated (Table 2) are applied to the consumption of the 2010-2011 heating season of Politecnico di Torino. In the 2010-2011 heating season, the annual thermal energy consumption calculated for the user case study is 11.1 GWh_t.

Table 3. Politecnico di Torino CO2 emission. 2010-2011 heating season

	Thermal losses, CO_2 t	Thermal consumption, CO_2 t	**Total, CO_2 t**
Method E	–	–	**3'350**
Method U	–	–	**0**
SEA Method	96	1'035	**1'131**
Hourly approach	42	1'087	**1'129**

Annual CO_2 emission values are compared with the hourly calculation by applying the *hourly approach.* By applying the SEA method emission factor, the total annual emission value is characterized by a percentage error of less than 1% compared with the value calculated by applying the *hourly approach.* The allocation between emissions from thermal energy consumption and heat losses on the distribution network varies. As anticipated in section 3.2.4, the emission value associated to network thermal losses in the SEA method considers annual percentage losses (8%). The incidence of losses on total emissions is therefore lower for users characterized by an exclusive winter period heat load profile like in Politecnico di Torino case study.

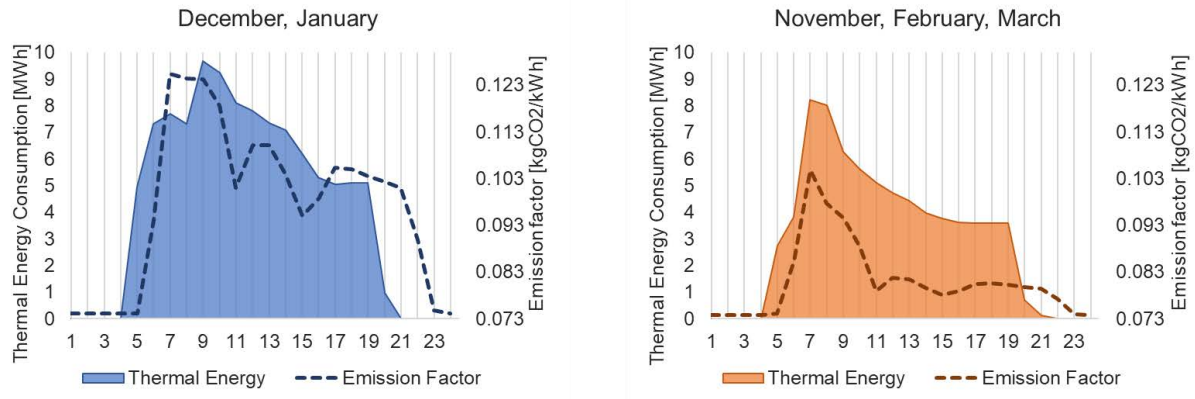

Figure 7. Hourly variation of average daily thermal energy consumption of RD (left axis) and variation of DHS emission factor (right axis).

Figure 9 illustrates the average profile of a typical daily thermal energy consumption at Politecnico di Torino, along with the EF trend shown in dashed lines. The hourly emission factor fluctuations depend on the usage patterns of other DHS users, and therefore the need for backup boilers. These graphs display a similar trend, with a noticeable deviation towards the morning hours. It may be inferred that the Politecnico di Torino begins heating operations earlier and terminates the early in contrast to the average schedule of users.

5. Discussion

This paper presents a new methodology for calculating the hourly variation of CO_2 emissions of DHS, specifically in the case of combined cycle cogeneration plants. A new methodology that enables the calculation of emission factors on an hourly basis and as well as a simplified annual method (SEA method) is presented and compered to existing methodologies. The methodologies described are applied to a representative case study of a tertiary DHS user. The case study selected is Politecnico di Torino. The total CO_2 emissions calculated using the three different methodologies showed a wide variability in the results. In particular, the two methodologies currently in use present two very contrasting results varying from values above that of natural gas to zero values. The need to find an alternative method is therefore confirmed. The emission value obtained with the more accurate hourly analysis is close to the annual value and the error il negligible. The application of the hourly methodology requires knowing the hourly operating data of the generation plants and the hourly heat load of the user. If the user's hourly consumption data is not available, a methodology applicable to tertiary users is proposed to evaluate the user thermal needs. Therefore, SEA method can be used to calculate the total emissions of a structure if thermal energy consumption data has a

yearly approximation or if it is not possible to access the hourly generation data of the DHS. SEA method is a good solution in defining total annual emissions, but as compared to the hourly approach it does not allow for a correct allocation of emissions between emissions due to thermal network losses and effective consumption, therefore one unresolved issue is the allocation of distribution thermal losses. At a regulatory level, it is unclear to whom to attribute the value of losses and in what period (annually or in the period of use only). Furthermore, since it can be challenging to ask local entities to conduct deep and complex analyses to determine their CO_2 emissions, it would be beneficial to require DH companies to include this information on bills. These future developments will help to improve the accuracy of CO_2 emissions calculations for users connected to DHS.

The hourly analysis has also highlighted opportunities for improvement in reducing CO_2 emissions. Knowing the hourly variation in emission factor due to the use of different generators, different energy consumption behavior could be motivated to reduce their emissions. For example, users may choose to adjust their energy demand during hours of less use, or install energy storage systems, to store energy when emissions are low and use it when emissions are high. These approaches could contribute to reducing the overall CO_2 emissions during the transition phase towards a complete decarbonization of energy sources. These analyses will become obsolete when DHS will become completely fossil fuel free.

The integration of hourly analysis of both electrical and thermal energy will become increasingly significant as renewable energy sources continue to grow in importance. Future developments should address this challenge by combining the hourly emission factors for both thermal and electric energy sources. This will enable the development of smarter storage and distribution systems for both thermal energy and electricity, ultimately leading to more sustainable and efficient energy use.

Nomenclature

CC CHP Combined Cycle

CHP Combined Heat and Power Plant

DHS District Heating Systems

E electrical power, MW

E_{CHP} ($\overline{\overline{E_{CHP}}}$) electrical power (energy) produced in CHP and delivered, MW $(kWh/year)$

EF emission factor

ES energy Signature

F fuel inlet power, MW

F_i ($\overline{\overline{F_i}}$) fuel inlet power (energy) used for each energy source *i,* MW $(kWh/year)$

F_{CC} ($\overline{\overline{F_{CC}}}$) natural gas fuel inlet power (energy) of Combined Cycle Plant*,* MW $(kWh/year)$

$f_{i,F}$ energy source *i* EF referring to fuel inlet energy, kg_{CO_2}/kWh

$f_{i,H}$ energy source *i* EF referring to thermal energy produced, kg_{CO_2}/kWh

f_{NG} natural gas EF, kg_{CO_2}/kWh

f_{el} electrical energy EF, kg_{CO_2}/kWh

$f_{CC,H}$ CC CO_2 EF referring to thermal energy produced, kg_{CO_2}/kWh

$\overline{f_{DHS,HE}}$ annual DHS CO_2 EF referring to total utilised energy, kg_{CO_2}/kWh

$f_{DHS,H_{del}}$($\overline{\overline{f_{DHS,H_{del}}}}$) hourly (annual) DHS CO_2 EF referring to utilised thermal energy, kg_{CO_2}/kWh

$f_{DHS,H_{gen}}$($\overline{\overline{f_{DHS,H_{gen}}}}$) hourly (annual) DHS CO_2 EF referring to thermal energy produced, kg_{CO_2}/kWh

$f_{DHS,losses}$ hourly DHS CO_2 EF of losses, kg_{CO_2}/kWh

$f_{DHS,cons}$ hourly DHS CO_2 EF of user's thermal consumption, kg_{CO_2}/kWh

H ($\overline{\overline{H}}$) thermal power (energy) produced by Combined Cycle Plant, MW $(kWh/year)$

H_i ($\overline{\overline{H_i}}$) thermal power (energy) produced by generator i, MW $(kWh/year)$

H_{gen} ($\overline{\overline{H_{gen}}}$) total thermal power produced, MW $(kWh/year)$

H_{losses}($\overline{\overline{H_{losses}}}$) losses thermal power (energy) in the distribution network, MW $(kWh/year)$

H_{del} ($\overline{\overline{H_{del}}}$) thermal power (energy) delivered to the user, MW $(kWh/year)$

$H_{s_{daily}}$ user's daily thermal energy consumption, kWh

IBB integration and Back-up Boiler

L_{hh} hour load

$p\%$ ($\overline{\overline{p\%}}$) hourly (annual) percentage thermal distribution losses, %

RD reference days

STO storage system

TEC thermal Energy Consumption

K cogeneration gain

References

[1] UI Green Metric, "World University Rankings," [Online]. Available: https://greenmetric.ui.ac.id/. [Accessed march 2023].

[2] United Nation Climate Change, "Race To Zero Campaign," [Online]. Available: https://unfccc.int/climate-action/race-to-zero-campaign. [Accessed march 2023].

[3] European Environmental Agency, "Annual European Union greenhouse gas inventory 1990–2019 and inventory report 2021.," 2021.

[4] European Commission, "European Green Deal: Commission proposes to boost renovation and decarbonisation of buildings," 15 December 2021. [Online]. Available: https://ec.europa.eu/commission/presscorner/detail/en/ip_21_6683. [Accessed march 2023].

[5] S. Paardekooper, R. Søgaard Lund, B. Vad Mathiesen and M. Chang, "Heat Roadmap Europe 4: Quantifying the Impact of Low-Carbon Heating and Cooling Roadmaps," 2018.

[6] P. Valdiserri, V. Ballerini and E. Ross, "Interpolating functions for CO2 emission factors in dynamic simulations: The special case of a heat pump," *Sustainable Energy Technologies and Assessments,* vol. 53, no. 102725, 2022.

[7] E. Marrasso, C. Roselli and M. Sasso, "Electric efficiency indicators and carbon dioxide emission factors for power generation by fossil and renewable energy sources on hourly basis," *Energy Conversion and Management,* vol. 196, pp. 1369-1384, 2019.

[8] Mathiesen , Bertelsen, Schneider, García, Paardekoopee, Thellufsen and Djørup, "Towards a decarbonised heating and cooling sector in Europe. Unlocking the potential of energy efficiency and district energy," Aalborg Universitet, 2019.

[9] AIRU, Il riscaldamento urbano. Annuario 2004 - 2022.

[10] W. G. I. IPCC, "Climate Change 2014: Mitigation of Climate Change. Contribution of Working Group III to the Fifth Assessment Report," 2014.

[11] J. Houghton, L. Meira Filho, B. Lim, K. Treanton and et.all, "IPCC Guidelines for National Greenhouse Gas Inventories," 2006.

[12] ISPRA, "Fattori di emissione atmosferica di gas a effetto serra nel settore elettrico nazionale e nei principali Paesi Europei," 2020.

[13] EUROSTAT, "Electricity and heat annual questionnaire 2015 and historical revisions," 2016.

[14] M. Noussan, "Performance indicators of District Heating Systems in Italy – Insights from a," *Applied Thermal Engineering,* 2018.

[15] IREN Energia, "Moncalieri Plant 2nd GT," 2013.

[16] IREN Energia, "Moncalieri Plant 3nd GT," 2013.

[17] ISPRA, Indicatori di efficienza e decarbonizzazione del sistema energetico nazionale e del settore elettrico. Rapporto 343/2021, 2021.

[18] H. Lund, S. Werner, R. Wiltshire, S. Svendsen, J. E. Thorsen, F. Hvelplund and B. V. Mathiesen, "4th Generation District Heating (4GDH): Integrating smart thermal grids into future sustainable energy systems," *Energy,* vol. 68, pp. 1 - 11, 2014.

[19] F. Reda, S. Ruggero, K. Auvinen and A. Temmes, "Towards low-carbon district heating: Investigating the socio-technical challenges of the urban energy transition," *Smart Energy,* vol. 4, no. 100054, 2021.

[20] U. E. 15316-4-5, *Prestazione energetica degli edifici - Metodo per il calcolo delle richieste di energia e delle efficienze del sistema - Parte 4-5: Teleriscaldamento e teleraffrescamento, Moduli M3-8-5, M4-8-5, M8-8-5, M11-8-5,* 2018.

ECOS 2023: How far should the UK go with negative emission technologies?

Semra Bakkaloglu[1,2], Matthias Mersch[3], Nixon Sunny[2], Christos Markides[3], Nilay Shah[2], Adam Hawkes[1,2]

[1] Sustainable Gas Institute, Imperial College, London, SW7 1NA, UK
[2] Department of Chemical Engineering, Imperial College London, London, SW7 2AZ, UK
[3]Clean Energy Processes (CEP) Laboratory, Department of Chemical Engineering, Imperial College London, London, SW7 2AZ, UK

Abstract

Negative Emissions Technologies (NETs), such as Bioenergy with Carbon Capture and Storage (BECCS) and Direct Air Carbon Capture and Storage (DACCS), are potentially valuable to offset carbon emissions and therefore commonly deployed in global climate change mitigation scenarios. However, they are controversial and sometimes seen as a means of delaying or avoiding emissions reduction efforts. Nonetheless, the UK has set an ambitious target of engineering 57 Mt CO_2 per year of removals by 2050 to achieve net zero emissions[1]. This study uses the UK TIMES, technology-rich bottom-up energy system model to investigate the nationwide deployment of NETs in the energy system, while varying model parameters to provide an overview of decarbonisation in line with the UK's net zero ambitions. We investigated DACCS and BECCS NETs technologies with regards to technological uncertainties and sensitivities. We revised the TIMES model structure for NETs implementation to ensure proper integration with industry. Our analysis estimates that the UK can remove 78.5 Mt CO_2 by 2050 under the balanced Net Zero Scenario. However, by integrating an updated characterisation of removal technologies, and enabling tighter integration of DACCS into industrial clusters, we can achieve a removal capacity of up to 209 Mt CO_2 by 2050 based on our preliminary results. Additionally, a 50% reduction in DACCS cost could further increase the removal capacity to 218 Mt CO_2. This study provides valuable insights for policymakers and stakeholders in the UK and beyond, highlighting how NETs can be integrated in industrial strategy.

Keywords: DACCS, BECCS, NETs, Energy System modelling, UK-TIMES, Net-Zero

1. Introduction

The increasing concentrations of greenhouse gases (GHG) in the atmosphere due to human activities have led to the unprecedented challenge of climate change. While mitigation efforts such as reducing emissions are crucial, they alone are not enough to limit the rise in global temperatures to well below 2°C, as carbon dioxide removal scenarios are highly incorporated into modelling scenarios [2]. Negative emission technologies (NETs) have thus emerged as a potential solution to extract and store carbon dioxide from the atmosphere. Two promising NETs are Direct Air Carbon Capture and Storage (DACCS) and Bioenergy with Carbon Capture and Storage (BECCS), which are a common feature of global climate change mitigation scenarios [1]

DACCS technologies remove carbon dioxide (CO_2) directly from the air using a chemical that selectively captures CO_2 molecules. Once the chemical is saturated with CO_2, the captured CO_2 is released and collected for processing. This process allows for CO_2 to be removed from the atmosphere and stored. DACCS can remove CO_2 directly from the atmosphere, regardless of the source of the emissions. This means that it can be used to remove CO_2 that has already been emitted, as well as to remove future emissions from sources that are difficult to decarbonise, such as aviation and shipping. DACCS technologies can be broadly classified into two categories: liquid absorbent (such as potassium hydroxide) and solid sorbents (such as amine-based solid sorbents). Liquid absorbent systems are

associated with high capital investment costs (CAPEX) and energy prices as they are operated at high temperatures, while solid sorbent DACCS is more sensitive to the adsorbent material costs and its performance with high CAPEX as well [3].

BECCS technologies, on the other hand, remove CO_2 from the atmosphere by using biomass production to generate energy and then capturing and storing the CO_2 emissions that are produced during the process. The CO_2 emissions produced during energy generation are offset by the CO_2 absorbed by the biomass during growth, and the captured CO_2 is stored underground, effectively removing it from the atmosphere, which can potentially provide negative emissions. BECCS technologies involve capturing CO_2 emissions from bioenergy facilities such as power plants, using carbon capture and storage (CCS) technology. The captured CO_2 is then stored underground. There are various types of BECCS systems that exist or are under development, including:

- Post-combustion capture: This technology involves capturing CO_2 emissions from the exhaust gas of a bioenergy facility after the combustion process.
- Pre-combustion capture: This technology involves converting biomass into a gas (syngas) before combustion. The CO_2 is then captured from the syngas before combustion.
- Oxy-fuel combustion: This technology involves burning biomass with oxygen instead of air. The resulting flue gas is mostly CO_2, which is then captured and stored.
- Chemical looping combustion: This technology involves using a metal oxide to react with biomass, producing a gas that is mostly CO_2. The metal oxide is then regenerated using air, producing a concentrated stream of CO_2 that can be captured and stored.

The total capacities of NETs deployed in Integrated assessment models (IAMs) show considerable variation. For example, International Energy Agency's (IEA) Net Zero scenario estimate that BECCS and DACCs can globally remove 1.9 gigatons of CO_2 globally by 2050 [4]. The National Academies of Science report [5] estimates that NETs could potentially remove around 10-20 Gt of CO_2 per year by 2050, which is equivalent to around one-third of current global emissions [6]. According to the Sixth Carbon Budget report of Climate Change Committee (CCC), DACCS and BECCS deployed in the UK can remove 57 Mt CO_2 emissions per year in 2050 in the balanced net-zero scenario [1] (Figure 1).

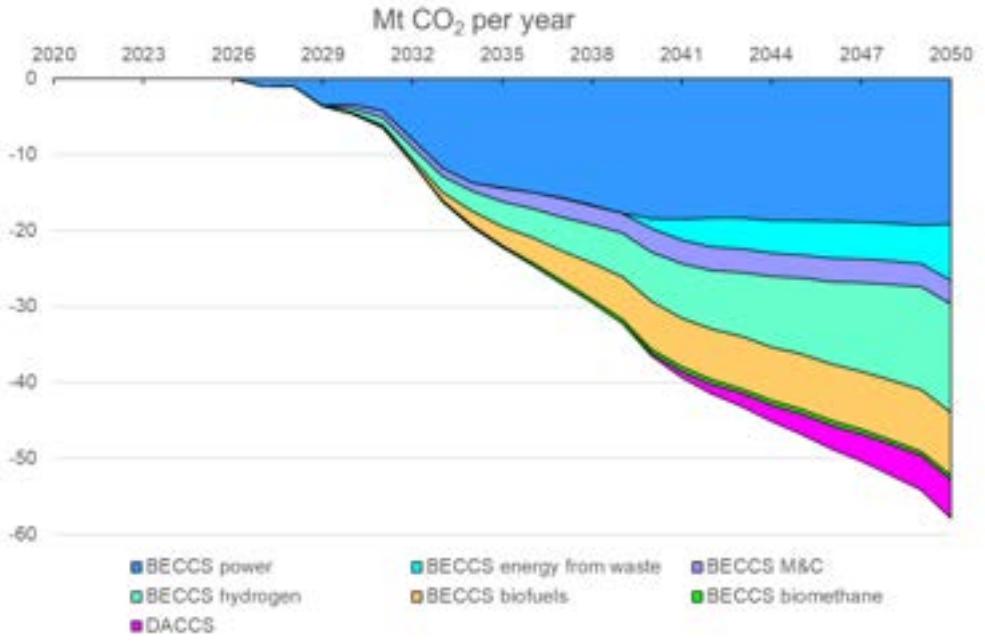

Figure 1. NETs deployment in the UK [7]

In recent years, there has been growing interest in integrating these NETs into industrial clusters in the UK. Industrial clusters are geographic regions of interconnected companies that accrue agglomeration effects from producing goods and services. By integrating NETs into these clusters, it is possible to reduce emissions from multiple sources while also generating economic benefits. Further benefits from co-locating NETs in industrial clusters include the potential availability of CCS infrastructure, potential integration of waste heat, a potentially easier permitting process, and higher

social acceptance. The UK has set ambitious targets for the deployment DACCS and BECCS in its industrial clusters as part of its efforts to reach net-zero emissions by 2050.

The UK has set a target that DACCS capture up to 5Mt of CO_2 per year by 2050, and BECCS remove 22 Mt CO_2 per year by 2035 and 53 Mt CO_2 per year by 2050[1]. The government has also set a target to deploy at least two industrial-scale DACCS facility by 2025 and to scale up deployment to reach 3 million tonnes of CO_2 captured per year by 2030 and world's first zero cluster by 2050[8]. To support the deployment of these technologies, the government has launched a £1 billion Net Zero Innovation Portfolio to fund the development and demonstration of innovative low-carbon technologies, including DACCS and BECCS[9]. The government has also launched a consultation on the design of a UK Emissions Trading System and the potential inclusion of carbon removal credits, generated from NETs, which will provide a financial incentive for industries to reduce their greenhouse gas emissions and encourage the deployment of low-carbon technologies such as DACCS and BECCS.

The future energy system scenarios addressing the transition towards a Net-Zero have been carried out for UK by using the UK-TIMES model. This model is widely used for creating energy system decarbonisation pathways [10-13]. UK-TIMES covers the full energy system and is applied in this study to explore the role of DACCS and BECCS in achieving the UK's net-zero goal, particularly in offsetting industrial cluster emissions. Removal technologies are interesting not only because they appear to be crucial to the achievement of global Paris Agreement mitigation targets in IPCC scenarios, but also at a national level because they may create emissions space for some hard-to-abate industries to survive in a country, with important ramifications for "just" transitions and promoting "place-based" transitions. However, there are still challenges to overcome, including the high cost of these technologies and the need for supportive policies and regulations to encourage their deployment at scale. This paper explores the potential of DACCS and BECCS integrated into industrial clusters in the UK and assesses their potential to contribute to negative emissions targets.

2. Methodology

2.1. DACCS

DACCS technologies pulls air from the surrounding environment and passes it through a pre-filter to remove any particles or contaminants. The air is then passed through a sorbent material, which selectively captures carbon dioxide (CO_2). The sorbent material can be a solid or liquid, depending on the specific DACS system design. Once the sorbent material is saturated with CO_2, it is heated to release the captured CO_2. This process is known as desorption or regeneration, pressure-swing or moisture swing system can also be utilised. The CO_2 is released as a concentrated stream that can be captured and compressed for storage. The captured CO_2 is compressed and transported to a storage site. The CO_2 can be stored in geological formations, such as depleted oil and gas reservoirs or deep saline aquifers, where it is securely stored underground to prevent it from entering the atmosphere.

There are four different DACCS systems defined in the default UK-TIMES model. We introduced an additional four DACCS systems with updated CAPEX and OPEX cost values (see Table 1). Technologies #1,2,3 and 7 already exist in the UK-TIMES model. We changed the commodities for technology #8 to connect with industrial waste heat, to represent industrial cluster integration. The existing data was adopted from a NAS study [5]. Additionally, we introduced new technologies #4,5,6 and 7 [3]. The capacity growth of all DACCS technologies is limited to 10% per year with a five-year seed value of 1 Mt CO_2 captured and stored.

Table 1. Techno-economical characteristics of selected DACCS technologies

#	DACCS Technologies	CAPEX [£/tCO_2], 2020	OPEX [£/tCO_2], 2020	Heat Req. [GJ/tCO_2]	Electricity Req. [GJ/tCO_2]	Lifetime [yr]
1	DACCS-Liquid solvent electric CCS[5]	630.7	25.8	10.68	1.2	30
2	DACCS-Liquid solvent electric NGA CCS[5]	630.7	25.8	10.68	1.20	30
3	DACCS-Liquid solvent electric hydrogen CCS[5]	630.7	25.8	10.68	1.20	30
4	DACCS-Solid sorbent electric CCS[3]	737.9	17.5	3.94	0.84	25

5	DACCS-Solid sorbent electric NGA CCS[3]	737.9	17.5	3.94	0.84	25
6	DACCS-Solid sorbent electric hydrogen CCS[3]	737.9	17.5	3.94	0.84	25
7	DACCS- Solid sorbent waste heat CCS[5]	714.4	10.8	3.94	0.84	30
8	DACCS- Solid sorbent waste heat CCS w/IND[5]	1,093.2	16.5	3.94	0.84	30

Notes: CAPEX: capital investment cost; CCS: carbon capture and storage; OPEX: operational and maintenance cost; Req.: requirement.

These CAPEX and OPEX values of DACCS are attributed to the year 2020. We have assumed a 50% reduction in CAPEX and OPEX by 2050 based on Fasihi et al [14]. As the liquid solvent requires high temperature (900°C) for the regeneration in the calciner, we did allow the integration of industrial waste heat (around 150°C) [15] with this technology.

2.2. BECCS

There are different types of BECCS systems, which vary based on the type of biomass feedstock, the conversion technology, and the carbon capture and storage (CCS) method used. Some of the different types of BECCS systems include:

1. Direct combustion BECCS: This involves the direct combustion of biomass to generate electricity or heat, with the resulting CO_2 emissions captured and stored using CCS technology.
2. Co-firing BECCS: In this system, biomass is co-fired with fossil fuels in power plants to reduce greenhouse gas emissions. The CO_2 emissions from the combustion process are captured and stored using CCS technology.
3. Gasification BECCS: This involves the gasification of biomass to produce a syngas, which is then combusted to generate electricity, heat or hydrogen. The resulting CO_2 emissions are captured and stored using CCS technology.
4. Anaerobic digestion BECCS: This system involves the anaerobic digestion of organic matter to produce biogas, which can then be used to generate electricity, heat or hydrogen. The CO_2 emissions from the combustion process are captured and stored using CCS technology.
5. Pyrolysis BECCS: In this system, biomass is heated in the absence of oxygen to produce a bio-oil and a solid char to produce hydrogen. The bio-oil can be used as a fuel, while the char can be used as a soil amendment. The resulting CO_2 emissions from the combustion of the bio-oil are captured and stored using CCS technology.

Each of these BECCS systems has its own advantages and limitations, depending on factors such as feedstock availability, energy efficiency, and cost-effectiveness. The UK-TIMES model utilises five different BECCS technologies (Table 5). The technologies with techno-economic properties are given in Table 2. The capacity growth of biomass technologies limited to 10% per year with maximum 20% of biomass import growth.

Table 2. Techno-economical characteristics of selected BECCS technologies

#	Technology name	CAPEX [£/kWh]	Var. OPEX [£/kWh]	Fix. OPEX [£/kWh]	EFF [%]	Lifetime year
1	Hydrogen Biomass gasification with CCS	0.254	-	0.018	46	30
2	Hydrogen Biooil SMR with CCS	0.151	-	0.010	54	30
3	Hydrogen Waste gasification with CCS	0.321	-	0.020	41	30
4	Biomass combustion with CCS	0.321	0.003	0.015	31	25
5	Biomass combustion with CCS-retrofit	0.208	0.004	0.009	89	25

Notes: CAPEX: capital investment cost for 2020; EFF: efficiency; Var: variable; Fix: fix; OPEX: operational and maintenance cost; Req.: requirement, AD: anaerobic digestion, SMR: steam methane reforming. The variable and fix operational and maintenance cost are for the year 2020.

2.3. TIMES model generator

The Integrated MARKAL-EFOM System (TIMES) model generator is maintained by International Energy Agency (IEA)- the Energy Technology Systems Analysis Programme (ETSAP) [16] to conduct in-depth energy and environmental analysis [17]. It is used for the analyse the possible future energy system scenarios [18]. The TIMES model is a bottom-up approach that uses a single or multi-regional model with a technology-rich database to analyse and plan energy systems at the national, regional, or city level. It is a techno-economic, partial equilibrium model-generator that assumes perfectly competitive markets and perfect foresight. Its source code, written in GAMS, is available for free download upon signing an ETSAP Letter of Agreement. In this study, we use the UK-TIMES which is built using the VEDA system (developed by UCL Energy Institute [19]) and it is now being utilised by His Majesty's Government departments to inform their climate policy analysis, including the 6th Carbon Budget [1].

The UK-TIMES model is a representation of the technology and fuel options available for various energy-consuming sectors when working towards the goal of decarbonisation. The decisions about these options are determined by what is the most cost-effective while taking into account various constraints that reflect the characteristics of the system. The model considers various factors, including the need to balance the supply and demand of energy over different periods of time, restrictions on the rate of technology deployment, and the availability of resources. One major advantage of this approach is that it trades off action between sectors, and captures interactions between sectors, allowing for more informed policy decision making. The UK-TIMES is structured in eight sectors, divided into three supply side and five demand sectors. The supply side consists of resources and trade, processing and infrastructure, as well as electricity generation transmission and distribution. The demand sectors include residential, services, industry, transport and agriculture. All sectors are calibrated based on the energy balance of the UK in the base year of 2010, and takes into account the existing portfolio of energy technologies in the Reference Energy System (RES). The UK-TIMES has flexible time periods and provides results for five-year periods until 2060. It consists of a total of 16 time-slices, with each of the four seasons being represented by a typical day divided into four time-slices.

The model aims to minimise the total system costs (least-cost solution), which includes investment cost, fixed and variable operation and maintenance cost, import cost, and export revenues for all modelled processes. The capacity of a particular technology remains until the end of its technical lifetime, and its salvage value is subtracted from the objective function if its economic lifetime goes beyond the modelling horizon. The inputs used to develop the UK-TIMES include exogenous service demand curves, supply curves, policies, and techno-economic parameters for each technology. Supply curves show the quantities of primary energy resources or imported commodities available at a specific cost. Techno-economic parameters are assigned to available and future technologies, including transformation and demand technologies. Technical parameters include efficiency and availability factor, while economic parameters include investment costs and interest rates. Policies may include the effects of legislation such as taxes and subsidies on specific technologies or fuels.

The outputs of TIMES models are region-specific and time-specific optimal investments, operations, and import/export levels. The model output includes not only the optimal solution but also costs, environmental indicators, marginal prices of commodities, and energy flows. UK-TIMES models both energy- and non-energy-related CO_2, CH_4, N_2O and HFC emissions, although non-CO_2 GHGs have not been explicitly considered in this study. Overall, the UK-TIMES VEDA model is a comprehensive tool for exploring different pathways to integrate DACCS and BESS into the UK's industrial clusters, providing insights into the costs, feasibility, and trade-offs associated with different options. In this study we have three main scenarios:

1. The default model runs: exploring the update of NETs without updates on technology characterisation.
    - We run the model with existing DACCS and BECCS technologies, including their techno-economic characteristics as described in sections 2.1 and 2.2.
2. The model runs where solid sorbent DACCS is integrated into industrial clusters.
    - We introduced four additional DACCS and integrated solid sorbent DACCS into industrial clusters, considering the low heat demand from industry/
3. The cost sensitivity of NETs deployment

- We changed the CAPEX of DACCS by ±50% to evaluate the cost sensitivity of DACCCS employment as well as NETs.

3. Results and discussion

3.1. Default results from the UK- TIMES model

Results show that 78.5 Mt CO_2 can be captured by DACCS and BECCS in the UK by 2050 under the balanced Net Zero Scenario (see Figure 2). The default DACCS (liquid solvent powered by electricity, electricity and gas, hydrogen; solid sorbent powered by waste heat from electricity generation without integration into industrial clusters) and BECCS (biomass incinerated gasification combined cycle (IGCC); hydrogen generation from biooil gasification with CCS; biomass gasification with CCS; waste gasification with CCS; electricity generation from biomass combustion with CCS) technologies are used to produce these results. In 2050, the most important technologies are:(1) hydrogen generation from biomass gasification with CCS, (2) solid sorbent DACCS, (3) hydrogen generation from waste gasification with CCS, and (4) biomass combustion with CCS for electricity generation following. The liquid solvent powered by electricity DACCS contributes the least to NETS.

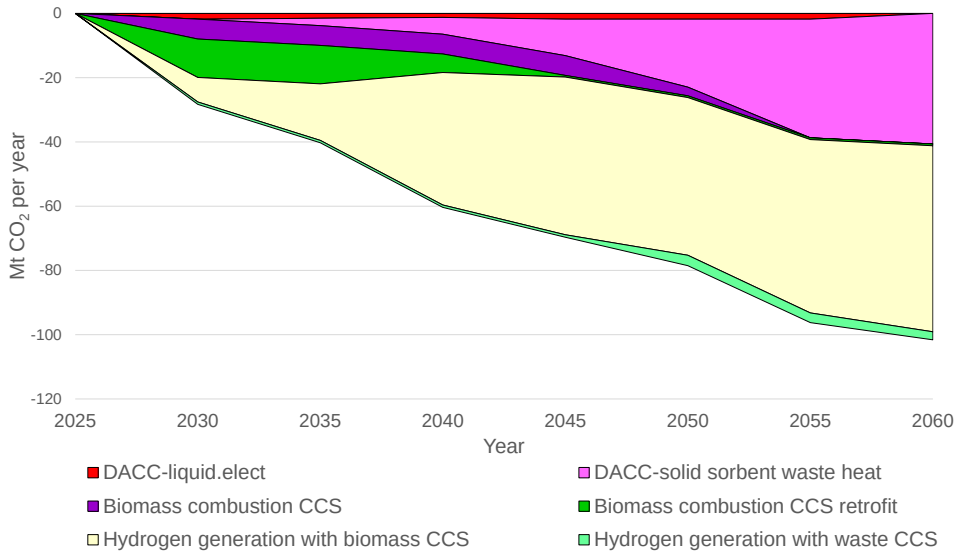

Figure 2. *NETs results from existing UK-TIMES model for Net Zero Balanced scenario*

According to the Net Zero balanced scenario, total positive CO_2 emissions would be 65 Mt CO_2 if DACCS, BECCS and natural negative emissions as well as industrial emissions sequestration are not taken into account (see Figure 3 for a breakdown of emissions by sector). It is evident that the positive emissions remain within the system, and it is not feasible to achieve the net-zero goal without the deployment of NETs, especially hard-to-abate sectors such as heavy industry, transportation, aviation and shipping. These sectors typically emit a large amount of greenhouse gases and require innovative and effective solutions to reduce their emissions and transition to a low-carbon economy.

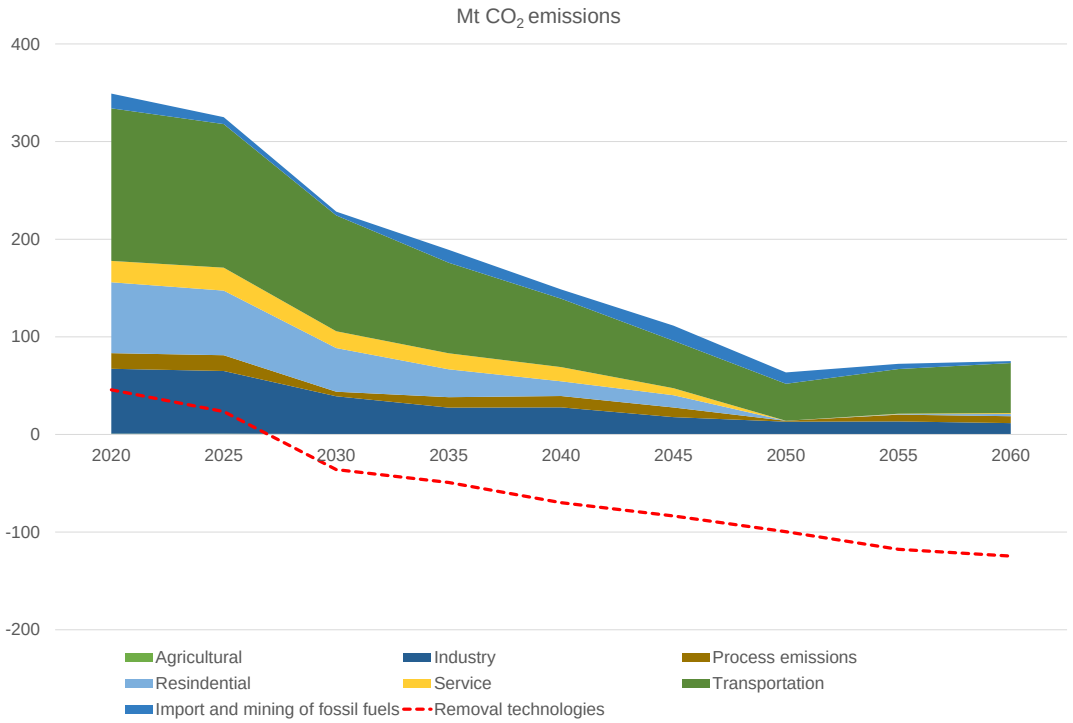

Figure 3. *Total CO_2 emissions from different sector in the UK.*

3.2. DACCS technologies integration into industrial clusters

According to Figure 2, the two leading DACCS technologies are solid sorbent waste heat DACCS and liquid solvent DACCS powered by electricity (as shown in Figures 2 and 3a) in the Net-Zero Balanced scenario. The UK-TIMES has not chosen other liquid solvent DACCS technologies powered by natural gas & electricity and hydrogen due to least-cost solution. In addition, we have included three other solid sorbent DACCS technologies, namely solid sorbent DACCS powered by electricity, natural gas & electricity, and hydrogen. Furthermore, we have explored the option of solid sorbent DACCS powered by low heat from industrial clusters, including the chemicals, food and drink, non-metallic minerals sectors, and other industrial low heat, in addition to waste heat from electricity generation processes.

We have found that DACCS can capture 22.9 Mt CO_2 by 2050 and up to 40.7 Mt CO_2 by 2060, mainly through the use of solid sorbent technology (as shown in Figure 4a), in the case where this DACCS is not integrated with industrial waste heat. There are 2 TWh (for 2050) to 19 TWh (for 2040) of low-grade heat available from industry that can be utilised in the DACCS system. By integrating solid sorbent DACCS with this available low temperature heat from industrial clusters, DACCS potential increases up to 180 Mt CO_2 by 2050 (Figure 4b) based on our preliminary results. Hence, the integration of DACCS technologies into industrial clusters can provide a fourfold increase in CO_2 removal in a net-zero scenario.

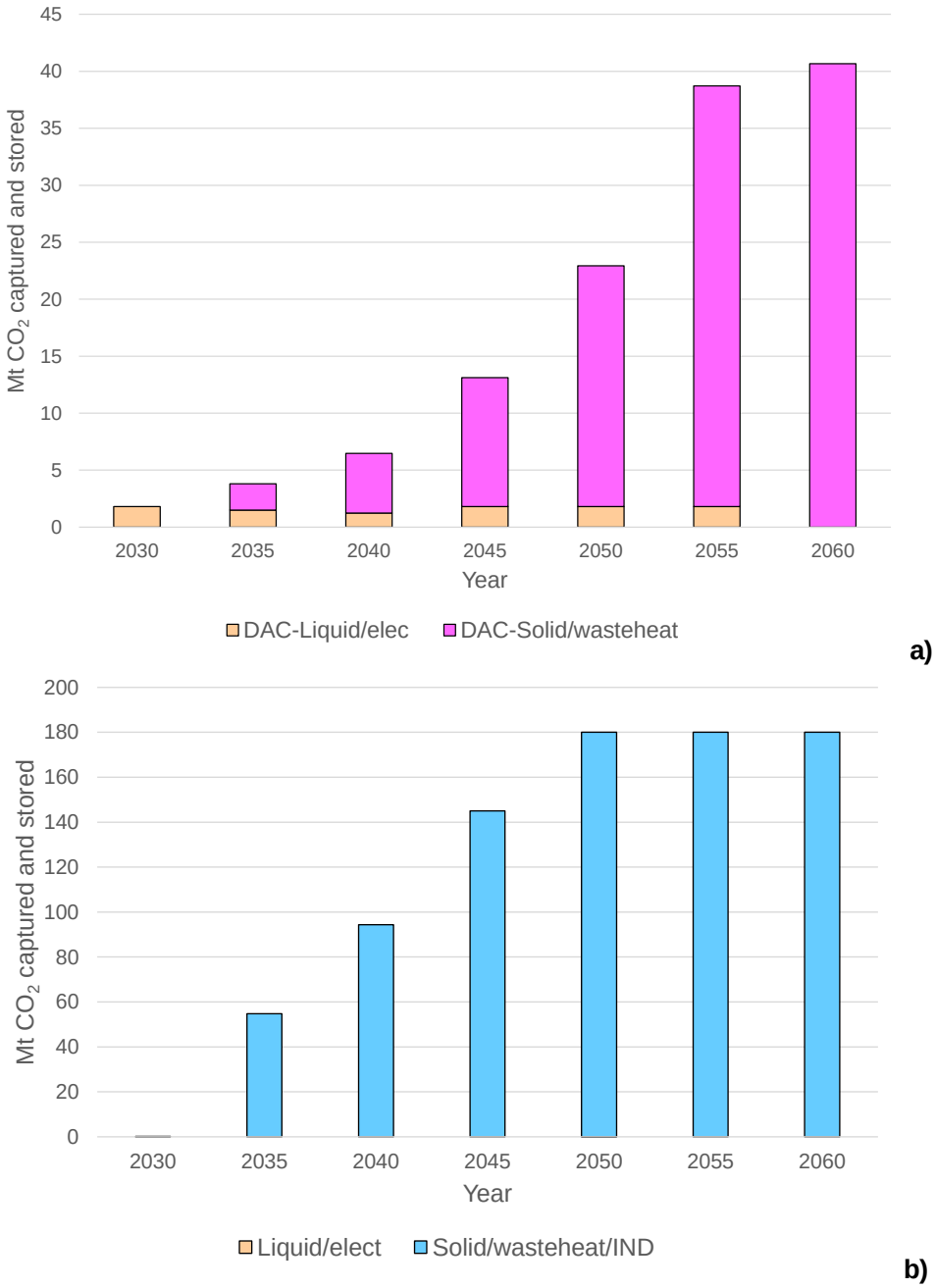

Figure 4. *DACCS technologies changes over time.* ***a)*** *Default results from Net-Zero Central scenario without industrial integration* ***b)*** *DACCS solid sorbent was integrated with industrial low heat. The same cost values are applied in both scenarios.*

It is important to note that increasing the deployment of DACCS will result in an increase in total positive CO_2 emissions (increase to around 178 Mt CO_2 in 2050) almost all sectors, primarily from the industrial, transport and process sectors due to the space created by NETs (see Figure A1 in the appendix). However, even though positive emissions will increase by 2.8 times, the integration of solid sorbent DACCS into the industry will provide a fourfold increase in CO_2 removal amount.

3.3. CAPEX cost impact on NETS

We have also explored the impact of capital cost (CAPEX) on the deployment of DACCS, given the uncertainty in the cost of DACCS in both the short and long term [3]. We varied the CAPEX by ±50% to estimate the amount of CO_2 that can be captured economically (as shown in Figure 5). When we increased the CAPEX, liquid solvent DACCS became less favourable, as CAPEX makes up a larger

share of the total cost compared to solid sorbent DACCS technologies. As we decreased the CAPEX, liquid solvent DACCS was still utilised but to a lesser extent than solid sorbent which is integrated to industrial low heat. Although the model includes DACCS options with and without industrial integration (as listed in Table 1), solid sorbent DACCS with integration of waste heat from industrial clusters is the dominant technology. When we decreased the CAPEX, we could increase the amount of captured and stored CO_2 up to 180.4 Mt by 2050. A 50% decrease in CAPEX resulted in a 7% increase in the capacity for CO_2 removal, whereas a 50% increase in CAPEX decreased the CO_2 removal capacity by 21%.

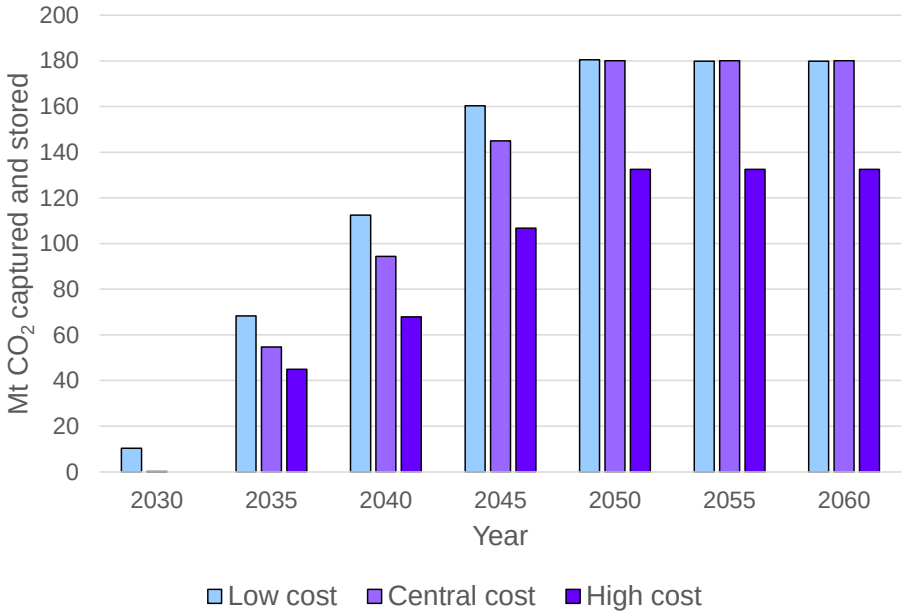

Figure 5. *The impacts of DACCC capital costs on DACCS capacity. The low cost and central scenarios utilise solid sorbent DACC with industrial waste heat integration and liquid solvent electricity powered DACCS. The high-cost scenario only considers the solid sorbent DACCS with industrial cluster integration.*

We have also assessed the overall NETs removal amount based on the range of DACCS CAPEX. A 50% decrease in DACCS CAPEX increases the total NETs removal capacity up to 219 Mt CO_2 by 2055 and 218 Mt CO_2 by 2050 (as shown in Figure 6). This removal capacity is expected to further increase as the BECCS CAPEX also decreases.

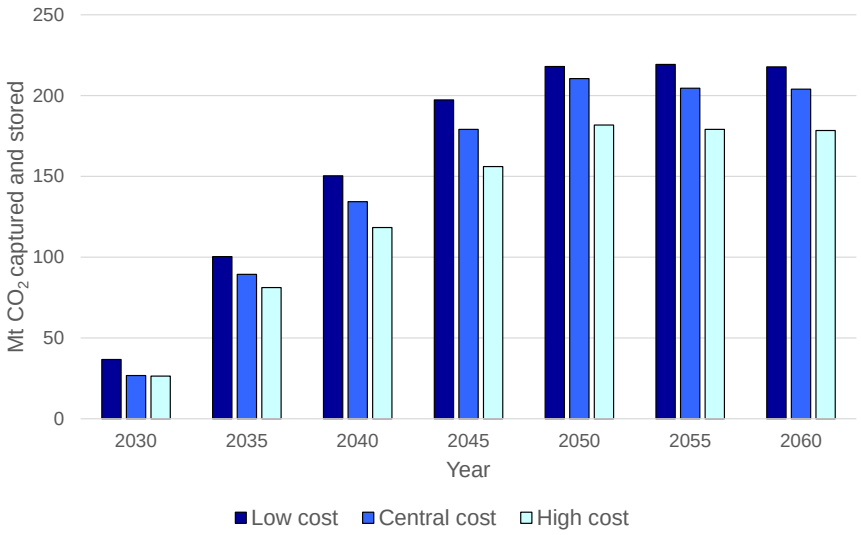

Figure 6. *The impact on DACCS's CAPEX on overall NETs deployment*

4. Conclusion

This study demonstrates the potential of Negative Emissions Technologies (NETs) to help achieve the United Kingdom's net zero ambition by 2050, with a particular focus on Direct Air Carbon Capture and Storage (DACCS) and Bioenergy with Carbon Capture and Storage (BECCS). By integrating additional NETs into industrial clusters and reducing costs, it is possible to significantly increase CO_2 removal amount from the atmosphere. Our findings indicate that solid sorbent DACCS powered by waste heat, ideally industrial low-temperature heat, is the leading DACCS technology. We also discovered that by integrating the solid sorbent DACCS into industrial low heat and reducing the CAPEX of DACCS by 50%, NETs can remove up to 219 Mt CO_2. We anticipate that lowering the CAPEX of BECCS will further increase this removal capacity. Our study underscores the importance of investing in and expanding NETs to combat climate change and achieve a sustainable future. These insights are of great value to policymakers and stakeholders in the UK and beyond.

5. Acknowledgements

This work was supported by the UK Engineering and Physical Research Council (EPSRC) through the Integrated Development of Low-Carbon Energy Systems (IDLES) programme [grant number EP/R045518/1].

6. Appendixes

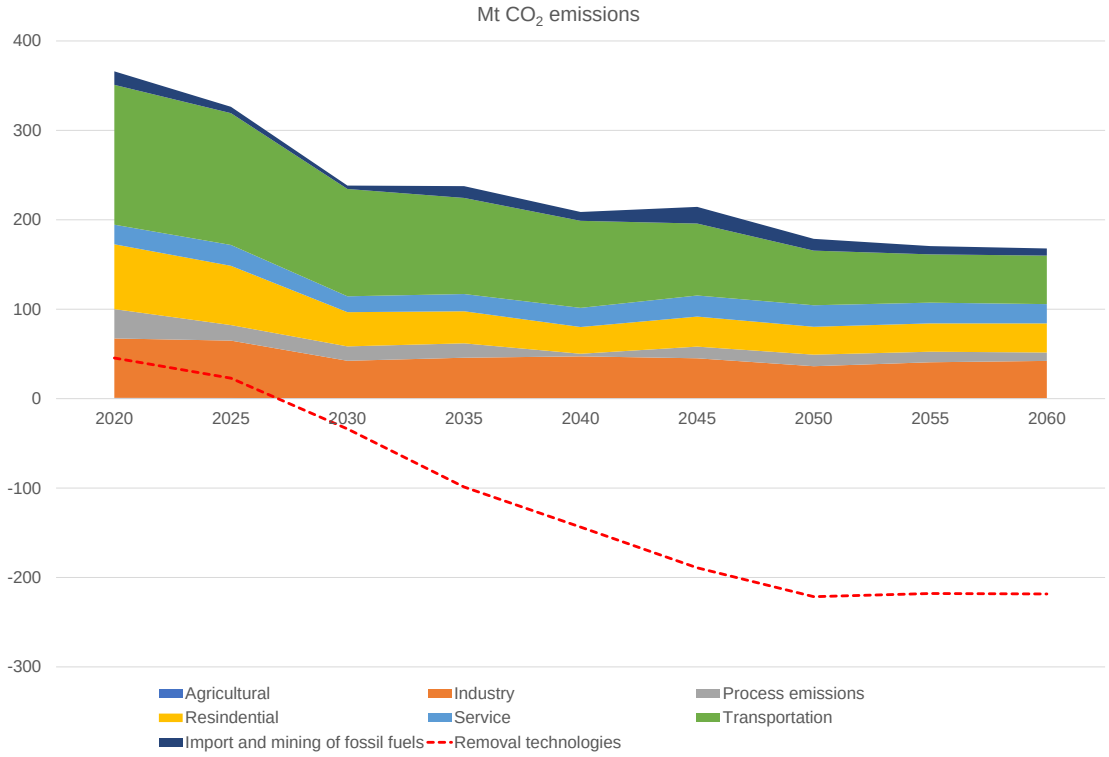

Figure A1. *Total positive CO_2 emissions when DACCS is integrated into industrial clusters.*

7. Nomenclatures

BECCS: Bioenergy carbon capture and storage
BEIS: Department of Business, Energy and Industrial Strategy
CAPEX: Capital investment cost
CCC: Climate Change Committe
CCS: Carbon capture and storage
DACCS: Direct air carbon cpture and storage
ETSAP: Energy Technology Systems Analysis Programme

GHG: Greenhouse gas
IEA: International Energy Agency
IND: Industry
MARKAL-EFOM: MARKet Allocation - Energy Flow Optimization Model
NETs: Negative Emission Technologies
OPEX: Operational and maintenance cost
RES: Reference energy system
TIMES: The Integrated MARKAL-EFOM System
UK: United Kingdom
VAR: variable

8. References

[1] CCC, The Sixth Carbon Budget - the UK's path to Net Zero. 2020.

[2] Paris, A., United Nations Framework Convention on Climate Change, Paris Agreement. 2015.

[3] Element Energy, Global Assessment of Direct Air Capture Costs. 2021.

[4] IEA, Net zero by 2050 - A road map for the global energy sector, IEA, Editor. 2021.

[5] National Academies of Sciences, E., and Medicine,, Negative Emissions Technologies and Reliable Sequestration: A Research Agenda. 2019: Washington, DC.

[6] Our World in Data. Annual greenhouse gas emissions: how much do we emit each year? 2019 [cited 2023 March 8]; Available at: https://ourworldindata.org/greenhouse-gas-emissions.

[7] CCC, Policies for the Sixth Carbon Budget and Net Zero. 2020.

[8] HM Goverment, Industrial Decarbonisation Strategy. 2021.

[9] HM Goverment, Greenhouse Gas Removals - Call for Evidence. 2021.

[10] Nerini, F.F., I. Keppo, and N. Strachan, Myopic decision making in energy system decarbonisation pathways. A UK case study. Energy strategy reviews, 2017. **17**: p. 19-26.

[11] Li, P.-H., I. Keppo, and N. Strachan, Incorporating homeowners' preferences of heating technologies in the UK TIMES model. Energy, 2018. **148**: p. 716-727.

[12] Pye, S., et al., Achieving net-zero emissions through the reframing of UK national targets in the post-Paris Agreement era. Nature energy, 2017. **2**(3): p. 1-7.

[13] Sun, W., G.P. Harrison, and P.E. Dodds, A multi-model method to assess the value of power-to-gas using excess renewable. International Journal of Hydrogen Energy, 2022. **47**(15): p. 9103-9114.

[14] Fasihi, M., O. Efimova, and C. Breyer, Techno-economic assessment of CO2 direct air capture plants. Journal of cleaner production, 2019. **224**: p. 957-980.

[15] Element Energy, E.I.C., The potential for recovering and using surplus heat from industry. 2014.

[16] ETSAP. 2023; Available at: http://www.iea-etsap.org/.

[17] Loulou, R., G. Goldstein, and K. Noble, Documentation for the MARKAL Family of Models, ETSAP. The MARKAL Family of Models, 2004.

[18] Loulou, R., et al., Documentation for the times model, part i: Energy technology systems analysis programme. International Energy Agency Paris, 2005.

[19] Daly, H.E. and B. Fais, UK TIMES model overview. UCL Energy Institute, London, UK, 2014.

ECOS 2023: Environmental life cycle assessment of a hydropower plant in Bolivia

Angelica Magne[a], Pablo Jimenez[b], Evelyn Cardozo[a]

[a] Centro Universitario de Investigaciones en Energías (CUIE), Facultad de Ciencias y Tecnología, Universidad Mayor de San Simón, Cochabamba, Bolivia, [b] Institude of Mechanics, Materiales and Civil Engineering, Université Catholique de Loubain, Belgium
angelica.magne@fcyt.umss.edu.bo, pablo.jimenez@uclouvain.be
evelyncardozo.r@fcyt.umss.edu.bo

Abstract:

Hydropower technologies are usually related to low-carbon emissions; however, detail discussion of a different number of environmental concerns is not properly done at the moment especially considering the lifetime phases. There is also a lack of evaluations when comparing with conventional technologies and when comparing with traditional Environmental Impact Assessments (EIA). In this context, this paper explored the environmental impacts using the LCA methodology of a hydropower plant to identify which lifetime phases damage more in health, ecosystems and resource areas of protection. A comparison between the impacts with the grid conventional electricity generation and a comparison with the results of the conventional EIA method are also presented. A database of a cascade hydropower in the tropical region is built using as a case study, the Bolivian project named “Ivirizu” with 290.21 MW of power capacity. Reservoir hydropower plant, campsite and road are analyzed. Data collection considered materials transportation, grave production, construction, maintenance, operation and disposal step. Data was obtained directly from the Governmental energy corporations and Ecoinvent database. Biogenic emissions were determined using the model proposed by Hertwich, 2013. ReCiPe 2016 method was employed to calculate the mid-point and end-points environmental impacts. The construction phase was found to impact most. This phase impacts on the resources depletion by 98.16%. This due to diesel is mainly required during the construction phase. This phase also impacts in 71.17% in human health mainly. The operation has 34.31% of contribution of impacts in ecosystems. This is due to high levels of water consumption during electric generation. The damage on resources is reduced in 63.32 % while hydropower lifetime is increased up to 150 years. Hydropower electricity has more than 79.00% less impacts compared with grid electricity. LCA results could contribute significantly in traditional EIA by providing quantitative information.

Keywords:

Hydropower; LCA; Reservoir; Run of River; Renewable Energy

1. Introduction

According to International Renewable Energy Agency (IRENA), the electricity generated by renewables was 7468 TWh in the world in 2020, where hydroelectricity represented almost 60.00% of the total [1]. Hydropower is growing up in the last years and some countries like Brazil rely almost entirely on this. However, other countries have not investment in this kind of infrastructure to generate electricity [2]. Global hydropower installed capacity increases in 1.90% in 2021 in comparison to 2020; however, an increase of more than 2% is expected to contribute to the reduction of climate change impacts [3].

Bolivia is a country located in the middle of South America where the base for the electricity generation are thermoelectric centrals. Due to the installation, operation and construction time is lower than for hydropower plants. The natural gas is also subsidized (Cost around 1,3 US$/MPC) representing a problem for the national economy and rapid depletion of gas reservoirs [4]. Bolivia has an Energy Development Plan (PDE) where they proposed the implementation of different alternatives like wind, photovoltaic, and hydropower centrals to cover the energy demand in all the country [5]. According an evaluation made by OLADE, the estimated hydropower potential is 39857 MW, but just the 1.2% was exploited in the country [6]. The majority of this potential are located in Pando, Beni, Tarija, La Paz and part of Cochabamba [7]. The overall effective power capacity at the beginning of 2023 in the country was 3626.27 MW, where 20.24% comes from hydroelectric, 68.17% from thermoelectric, 3.62% from eolic, 1.15% from solar and 3.38% from biomass [8]. Bolivia planned 28 hydroelectric projects, one of them is Ivirizu, located in the tropical region of Cochabamba with 290.21 MW of installed power capacity. This is a hydropower unit in cascade, shaped for two hydropower plants Sehuencas (198.66 MW) and Juntas (91.55MW) [9,10].

Hydroelectric projects bring negative and positive environmental impacts which depends of different variables like, the type of hydroelectric, the materials used during construction among others included the possible socioeconomic local impacts [4].Usually, a hydropower plant is considered a low-carbon option. This represents an attractive option to different governments to cover the electricity demand if they have the potential hydric resources [2]. However, hydropower plants produce greenhouse gases (GHGs) and different emissions to air, water and soil due to different materials, energy, and equipment are employed during the construction and operation stages [11]. Many studies have been focused only on the evaluation of environmental impacts during the electricity generation (i.e. operation phase), in the different types of hydropower plants (reservoir, run of river, and pumped) employing a life cycle assessment; however, the different phases during the lifetime of the plant and a comparison with traditional environmental impact assessment has been rarely done [12].

The life cycle assessment (LCA) is an analytical method to identify the resources flows and different environmental impacts associated with the products and services during their entire lifetime[12,13]. This methodology considers products and technologies from a “cradle to grave”. It can contemplate the raw materials extraction, processing, manufacturing, and use to final disposal [15]. This methodology is one of the most actual tools to carry out environmental impact evaluation and analysis for many process, system and products. This also can help to take decision in organization, industries and governments [16]. It is standardized by ISO 14040 [16–18]

Actually, few LCA studies evaluate hydropower plants focused in a reservoir [11]. In South America most of the analysis are located in Brazil focused on large hydropower plants [18,19]. This current study considers LCA methodology and RECIPE 2016 method applied in Ivirizu project which is a cascade hydropower plant that combines a reservoir and run of river plants. This is located in a tropical region in Bolivia. The main objective to determinate the environmental impacts during 1 KWh electric energy generation and create a detailed life cycle inventory (LCI) with the aim of having the real conditions, inputs and outputs flows. A comparison between the impacts with the grid conventional electricity generation and a comparison with the results of the conventional Environmental Impact Assessment method are also presented.

2. Materials and method

2.1. System description

Ivirizu hydropower project is located in the tropical region of Cochabamba, inside the limits of National Park Carrasco, in Bolivia. The power capacity installed is 290.21 MW. This plant is a cascade model. It is shaped for two plants, Sehuencas (reservoir plant) and Juntas (run of river plant). Figure 1 shows where the different parts of Ivirizu project are planned. The main purpose of this project is to generate electricity and it is still in the construction phase.

Sehuencas is the first plant, it is a reservoir plant with a dam to form a reservoir with a volume of 29.48 Hm^3. The water is transported 5.98 km through a concrete-lined tunnel and reaches a balance chimney with a height of 95.45 m, which balances the air pressure between the plant and the atmosphere. This is connected to a penstock with a length of 1.51 km that leads to the power house, where three hydro turbines, generators, and machines are located. The electricity generated is then transported to a substation. The second run of river plant, Juntas, is located 10 km from Sehuencas and it has an intake structure located in the Ivirizu river. It features elements such as a gravity diversion weir, right bank intake and drain, sediment traps with a flow of 6 m^3/s, a flow regulation float with a capacity of 40000 m^3, and a tunnel intake. To this intake structure also is transported the turbines water from Sehuencas through a discharge canal. The water flow is transported inside a tunnel that it is armored in the final part and then connected to a balance chimney and penstock, which transport the water flow to the power house where two Francis turbines are located. Both power plants have a substation where the electric generation tension of 11.50 kV is increased to the transport tension of 230 kV before being transported to Mizque substation and then to the International System Transmission [9]. The technical details of the Ivirizu hydropower plant are listed in Table 1.

Table 1. Description of Ivirizu Hydropower plant

Characteristics	UN	Sehuencas	Juntas
Installed Capacity	MW	198.66	91.55
Type of Plant		Reservoir	Run-of-river
Turbines	UN	3	2
Type of turbine		Pelton	Francis
Annual Power Production	GWh	805.29	355.6
Design flow rate	m^3/s	26.50	32.50
Heigh	m.a.s.l	1340	1009
Water head	m	843	326

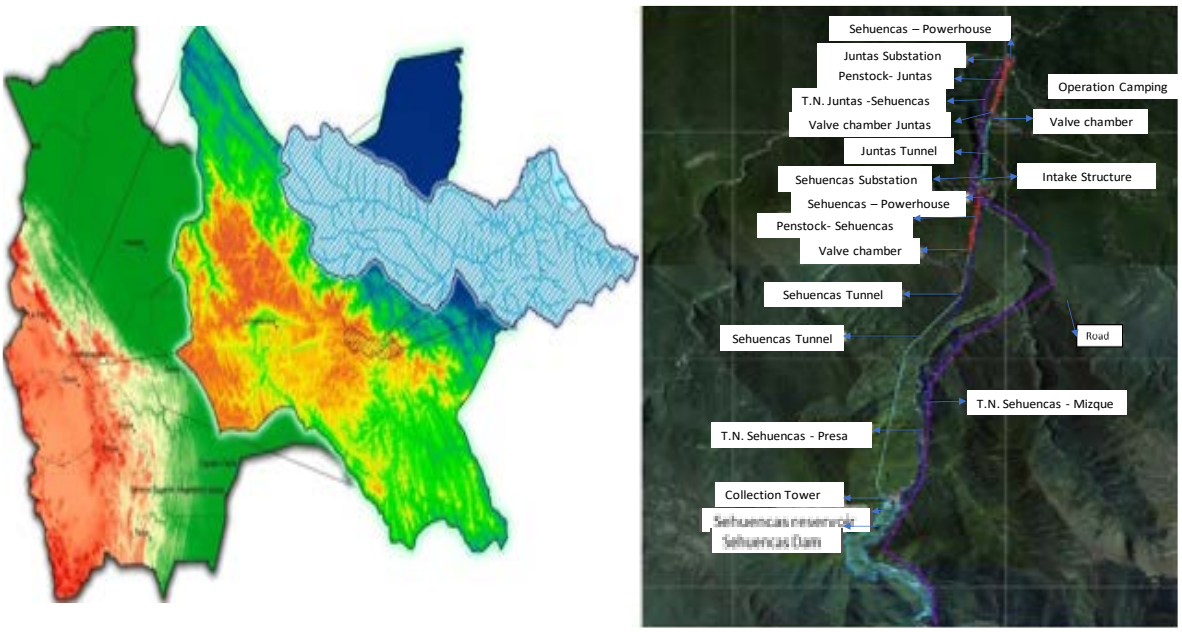

Figure. 1. Geographical location of Ivirizu hydropower plant in Bolivia [9]

2.2. Goal and scope definition

The primary objective of the study was to assess the environmental impacts associated with the generation of 1 KWh of electric energy in a hydropower plant located in Bolivia, using a cradle-to-grave approach and Life Cycle Assessment (LCA) methodology in accordance with ISO 14040 guidelines [18]. This research also aims to create a comprehensive life cycle inventory data, considering all the materials, equipment, transportation, and energy used throughout the entire life cycle. The emissions generated because of decomposition of biomass in the flooded area were also analyzed. All these factors were calculated based on 1 KWh generated defined as the functional unit.

2.3. System boundaries

The overall system boundary is presented in Figure 2. The system boundary includes five phases: construction (buildings, camp, equipment installation, gravel and sad extraction, roads and transmission network), operation, maintenance, transportation and disposal step. The preconstruction activities like deforestation for infrastructure development, materials, energy use from land preparation, materials extraction were part of the construction phase. Operation covers energy and materials require in this step, the emission caused for the biomass decomposition was also determined. The maintenance phase covered the materials throughout the lifespan of the hydroelectric plant. The lifespan of this plant is 50 years according to ENDE Corporation [9]. For the disposal phase was just considered the transport of recyclable materials, equipment and waste to a treatment place.

2.4. Life cycle Inventory Analysis (LCI)

The life cycle inventory (LCI) collect physical information of input and output flows such resources, materials, semi-products, products and the output of emissions [20]. Two kind of data are usually considered; one is the information obtained from the companies that design the plants. The second one is data acquired from different international database and adapted to study case like Ecoinvent [13]. In this study, the inventory considers both type of data and it is described for the five steps to generate 1 KWh of electric energy. Assumptions and limitations are described for each step and all data is presented in Table 2.

Construction: This phase includes the building work, equipment installation, road and camping building. Land preparation using explosives, raw material extraction in the place were considered in this stage. The building work contemplated the dam, penstock, powerhouse, balance chimney, substation, transmission network, waterway canal, etc. of both plants that make up Ivirizu. A diesel generator was considered to provide the required electricity for the equipment used in the construction zones. Ecoinvent data was considered for the diesel generator inventory. Different equipment and components used such generators, turbines, bridge crane, dampers, valves, etc. were discomposed in materials such steel. The description of each building works, materials, electromechanical and hydromechanical equipment were obtained from the final design study of Ivirizu, proportioned for ENDE Corporation.

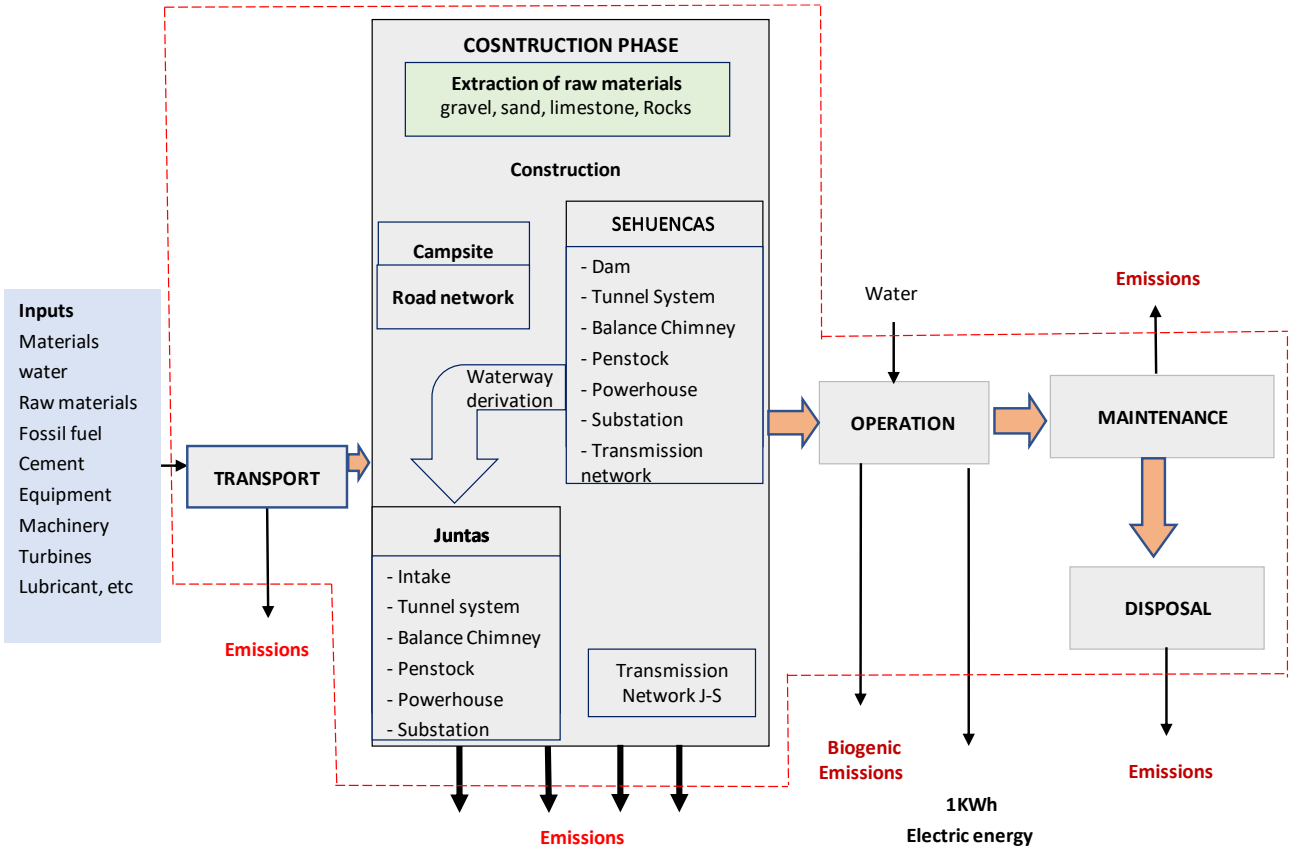

Figure. 2. System boundaries

Operation: This step requires just water flows for electricity generation; the value was achieved from the final design of Ivirizu project proportioned by ENDE corporation. The biogenic emission that are generate due to the degradation of biogenic carbon in reservoirs was included. This is produced by oxidation of organic carbon from biomass, organic carbon matter in soil, or sediments [21]. These were estimated using the methodology presented by Hertwich [21] in the Eq. (1), this model calculates biogenic carbon dioxide and methane emission per 1 kWh.

$$log\ E = const + B_{Land\ use} \times log(Land\ use) + B_{Age} \times Age + B_{NPP} \times log\ (NPP) \quad (1)$$

Where E represents the emission estimated (CO_2 or CH_4), land use is referring to reservoir flooded area, age is the reservoir lifetime, NPP is the net primary production. Const, $B_{Land\ use}$, B_{Age}, and B_{NPP} are constants for CO_2 an CH_4 described in [21]. The age is 50 years, and land use is 8.67E-4 m^2 calculated for 1 kWh. Both data were obtained from Ivirizu final project. NPP is 40000 gC/m2y, employed by Villarroel et.al map [22]

Maintenance: The lubricant oil necessary to perform a good operation for the equipment was considered. The replacement of turbines or generators was not included. The life time for this equipment were assumed to be the same as the hydropower plant. The lubricant data for this step was used from Ecoinvent.

Disposal: This step refers to the recollection of waste mineral oil and the transport to a treatment place, which is considered in this case to be Cochabamba city. After the lifetime of hydropower plant, the infrastructure is assumed to be abandoned but after the siltation of the lake and the dams. The adit systems will not be transported or demolished. The disposal of gravel, cement and reinforced steel were assumed from Ecoinvent data.

Transportation: This includes the transport of different materials used during the construction, maintenance, disposal and the transport of equipment to the plant site considered a freight lorry. The international transportation was not considered because this information is not available and therefore all the materials were assumed that were located in Cochabamba city, at the distance of 140 km. The transport process was employed from Ecoinvent database.

2.4. Life cycle Impact assessment (LCIA)

In this step the purpose was to quantify the environmental impacts of all inventory data recovering in the LCI [16] using the RECIPE 2016 method that evaluates 18 midpoints and 3 endpoint levels [23]. Characterization factors at the midpoint level are located somewhere along the cause-impact pathway, usually at the point after which the environmental mechanism is identical for each environmental flow assigned to that impact category.

The endpoint level reflect damage at one of three areas of protection which are human health, ecosystem quality and resource scarcity [24]. The computation of the environmental impacts was done in the SimaPro Version 9.4.0.2 software [25].

Table 2. LCI data for Ivirizu hydropower plant on 1 kWh of electricity for 50 years lifetime

Variable	Unit	Sehuencas	Juntas	Ivirizu	Total per 1 KWh
Construction					
Volume occupied, reservoir	m3	2.95E+05		2.95E+05	5.08E-04
Land use	m2	4.90E+06	1.8E+06	5.41E+06	9.32E-05
Explosive	kg	2.83E+04	1.25E+04	4.09E+04	7.04E-07
Water	kg	1.97E+08	8.70E+07	2.84E+08	4.89E-03
Sand	kg	3.06E+08	1.36E+08	4.42E+08	7.62E-03
Grave	kg	4.89E+08	2.17E+08	7.07E+08	1.22E-02
Stone	kg	2.60E+07	1.16E+07	3.76E+07	6.47E-04
Cement	kg	1.78E+08	7.97E+07	2.57E+08	4.44E-03
Reinforcing Steel	kg	1.53E+07	6.83E+06	2.21E+07	3.81E-04
Steel low alloyed	kg	8.07E+05	3.61E+05	1.17E+06	2.01E-05
Steel - equipment	kg	4.86E+05	4.36E+04	5.30E+05	9.13E-06
Diesel	kg	3.37E+07	1.49E+07	4.86E+07	8.37E-04
Lubricant	kg	1.25E+05	5.51E+04	1.80E+05	3.10E-06
Emissions					
Particulates, < 2.5 um	kg	5.92E+04	2.62E+04	8.54E+04	1.47E-06
Particulates, > 10 um	kg	6.85E+05	3.03E+05	9.88E+05	1.70E-05
Particulates, 2.5 -10um	kg	2.60E+05	1.15E+05	3.75E+05	6.46E-06
Water	m3	1.66E+05	7.35E+04	2.40E+05	4.13E-06
Emissions to Water	m3	1.67E+05	7.39E+04	2.41E+05	4.16E-06
Carbon Dioxide	kg	1.05E+08	4.64E+07	1.51E+08	2.61E-03
Carbon monoxide	kg	9.02E+05	3.98E+05	1.30E+06	2.24E-05
Nitrogen oxides	kg	1.90E+06	8.38E+05	2.73E+06	4.71E-05
Operation					
Water flow	m3	1.93E+10	2.27E+10	4.21E+10	7.21E-01
Emisions					
Carbon dioxide, biogenic	kg	4.35E+08		4.35E+08	7.49E-03
Methane, biogenic	kg	2.38E+05		2.38E+05	4.10E-06
Water/m3	m3	1.18E+09		1.18E+09	2.03E-02
Emissions to water	m3	1.82E+10	2.277E+10	4.09E+10	7.04E-01
Maintenance					
Lubricant	kg	3.04E+05	1.34E+05	4.39E+05	7.56E-06
Disposal					
Waste reinforced concrete	kg	2.60E+09	1.15E+09	3.74E+09	6.45E-02
Waste mineral oil	kg	5.15E+05	2.27E+05	7.42E+05	1.28E-05
Transportation					
Truck transport	Tkm	1.25E+09	5.50E+08	1.80E+09	3.10E-02
Diesel	Kg	8.92E+05	3.94E+05	1.29E+06	2.21E-05
Emissions					
Carbon dioxide, fossil	kg	7.79E+07	3.44E+07	1.12E+08	1.93E-03
Carbon monoxide, fossil	kg	1.20E+05	5.30E+04	1.73E+05	2.98E-06
Nitrogen oxides	kg	6.33E+05	2.79E+05	9.12E+05	1.57E-05
Sulfur dioxide	kg	3.98E+02	1.75E+02	5.73E+02	9.87E-09

3. Results and discussion

3.1. Life Cycle Interpretation

This is the last stage of LCA, where results are summarized and discussed according to ISO 14043 [26].

- Midpoints impacts

The average midpoint impact contribution of life cycle phases of Ivirizu hydropower plant is presented in Figure 3. The construction was the mayor contributor on seventeen environmental impacts with more than 98% in each one. This was due to the use of different materials required like diesel for electric generation, for the machinery used and for the raw material extraction.

The operation step had 99.73% of contribution in the water consumption equivalent to 2.03 E-02 m^3 per 1 KWh. The construction step just increased the water consumption in 5.42E-05 m^3 per 1 KWh. The construction phase contributed with 98.00% to the global warming and the operation phase with 0.97%. Those are due to the diesel used for machinery and for the electricity generation in the construction step and the biogenic emission during the operation step. The value of CO_2 in the global warming midpoint impact is similar to other hydroelectric plants quantification [27]

The mayor impacts in the maintenance phase were the Ionizing radiation and Fossil resource scarcity due to amount of the lubricant use in different equipment. For the transportation step, the mayor impact was the terrestrial ecotoxicity because of diesel employed during material transportation. The disposal was the step with the minor impact contribution, because it is just the recollection of materials to a treatment place.

Comparing the results with other authors in [11,28,13,29] construction phase was the mayor contributor to the environmental impacts and the second one was the operation even considering than in those studies the lifetime was among 50 to 100 years. Ecoinvent database for all hydropower plants assume 150 years of lifetime. Therefore, a sensitivity analysis for different lifetime years is presented below.

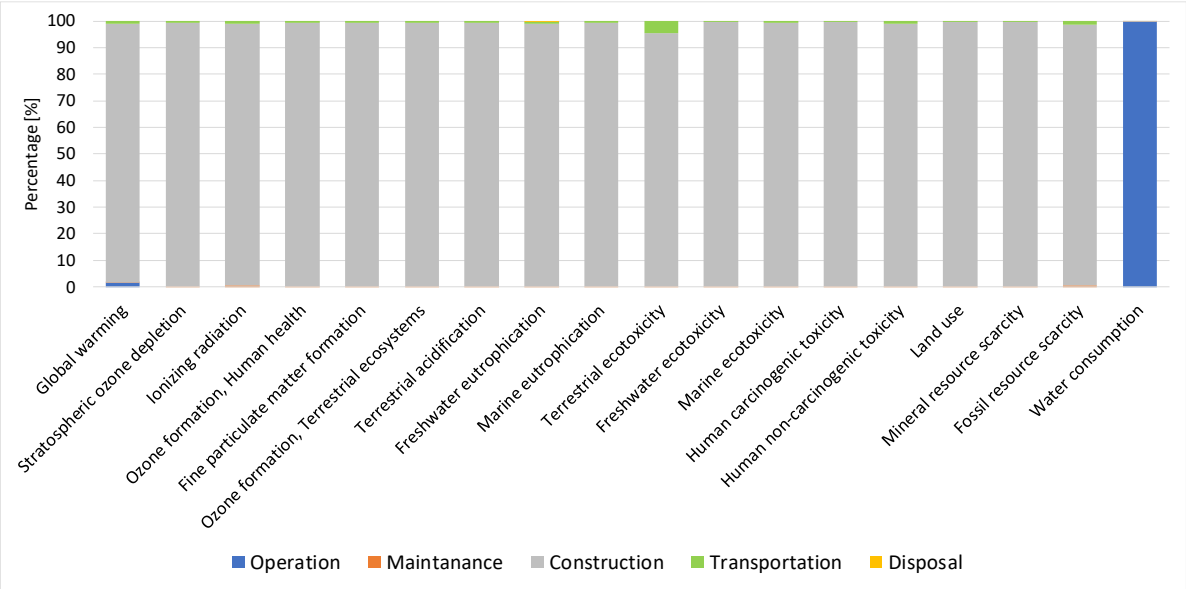

Figure. 3. Midpoints impacts results of 1 kWh hydropower electricity in Ivirizu

- Endpoint impacts

The endpoint results are presented in the Figure 4. The construction and operation phases had mayor damage in human health with 71.17% and 28.28%, respectively. The first one increased de problems in respiratory diseases and different kind of cancer with 2.81E-08 DALY due to the type of materials employed. The operation increased human health damage in 1.11E-08 DALY due to the biogenic emissions which change the water characteristics.

The damage in the ecosystems was 65.10% for the construction phase and 34.31 % for operation phase, this last was equal to 3.13E-11 species.yr induce for the water use and biogenic emission origins damage the freshwater, terrestrial and marine species during the electricity generation.

The construction phase had the mayor contribution in damage to resources availability with 98.16%. This increases the cost in mineral extraction, oil, gas, coal and energy in 8.52E-04 USD2 013 due to this phase uses many and different materials including the raw materials extraction.

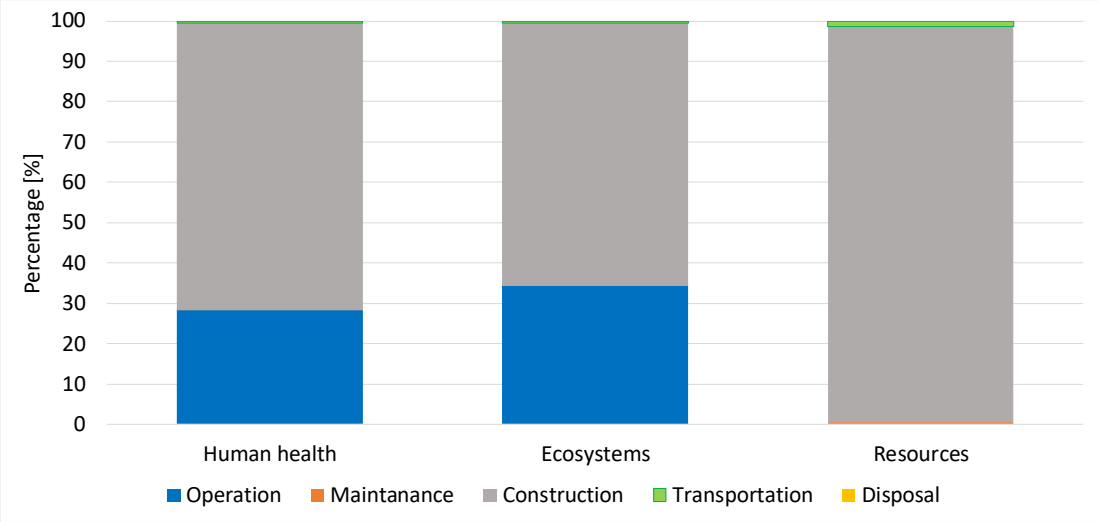

Figure. 4. Endpoints impacts results of 1 kWh in Ivirizu

- Construction

The results presented before shows that the construction phase had mayor impacts during the electricity generation. Due to the large amount and type of materials used and building process. Figure 5 presents the midpoints impacts for construction steps and materials. The mayor impacts were produced for diesel employed to generate electricity to satisfy the demand during the construction phase where Stratospheric ozone depletion had 1.51E+02 kgCFC11eq, Ozone formation Human health had 2.46E+06kgNOx eq and Ozone Formation Terrestrial ecosystems had 2.48E+06 kgNOxeq. The first two increases the damage to human health and the last one increases the damage in ecosystems in 36.57% and 37.74 %, respectively. But, the mayor effect was presented in the damage to resources which increases the cost in 43.15% during the 50 years because of minerals and fossil scarcity.

Water consumption impact increased more due to grave use; this was because the raw materials extraction was considered to be in the same place.

The impacts due to fabrication had more impact in the land use with a 7.31E+7 m^2a crop eq, this is due to activities the construction area.

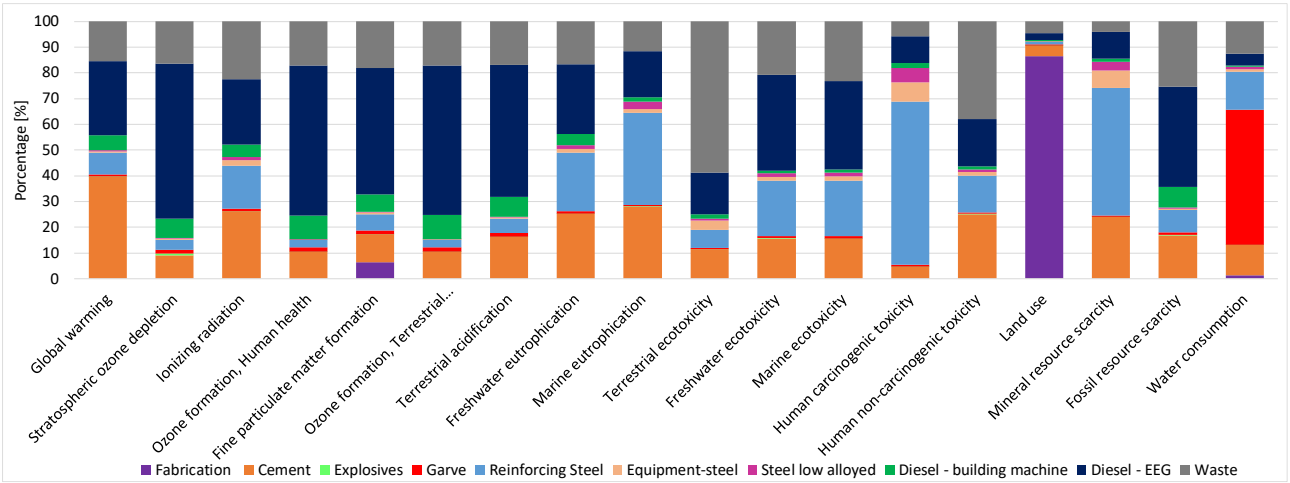

Figure. 5. Midpoints impacts results for Ivirizu hydropower plant construction

3.2. Sensitivity analysis

- Hydropower Lifetime

According the final design of Ivirizu project, the lifetime is 50 years. This value in Ecoinvent database for different hydropower is 150 years and other studies consider 100 years. It depends of each hydropower plant information. Therefore, the endpoint impacts for different lifetimes were evaluated. The results presented in Figure 6 show the decrease of environmental impacts with a mayor lifetime. The mayor reduction in comparison with the 50 years lifetime was for the damage to resources in 37.30%, 49.74% and 66.32 % in comparison to the lifetimes of 80, 100 and 150 years, respectively. For damage to human health and ecosystems, the decrease for the lifetime of 150 years is 55.59% and 54.23%, respectively. These results

show that environmental impacts for the electricity generation in the hydropower plants can be reduced when the lifetime is increased due to the impacts are distributed during these years.

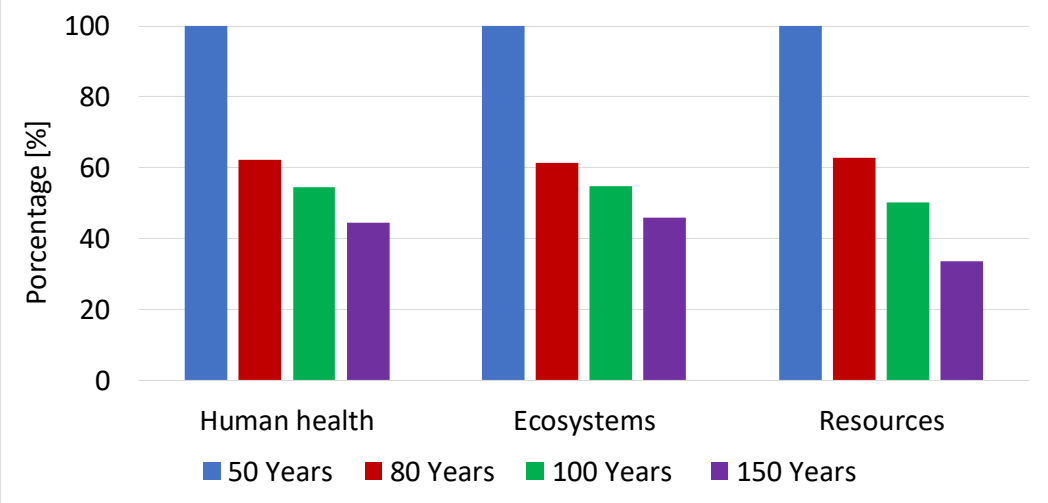

Figure. 6. Endpoint impacts 50, 80,100 and 150 years of lifetime

3.3. Comparison between hydroelectricity Vs Grid electricity generation

The electricity generated in Ivirizu during the operation phase is compared with the conventional grid electricity options in this section. Ecoinvent database for a conventional natural gas and an oil-based power plants were used. The results presented in Figure 7 shows the environmental impacts for 1 KWh. In most of the midpoint impacts, natural gas and oil power plants were higher than the hydropower plant but the water consumption. This is due to water was the principal flow inside the hydropower plant for the electricity generation.

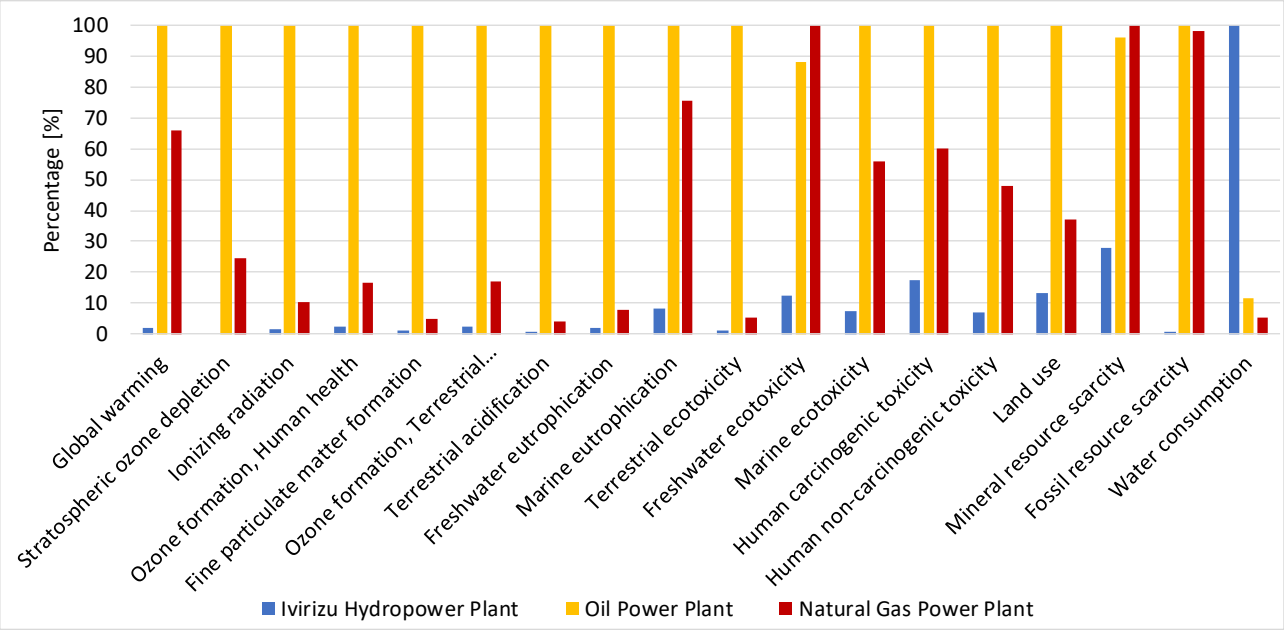

Figure. 7. Comparation between Hydroelectricity vs grid electricity generation

3.4. LCA vs EIA

The results of the traditional environmental impact assessment (EIA) of Ivirizu and the LCA performed in this study were analyzed in this section. The EIA of Ivirizu hydropower plant project includes the identification and assessment of the foreseeable effects on the socio-environmental aspects inventoried in the baseline, taking the area of influence as a reference [30]. Table 3 presents the results of the EIA where the environmental importance is describing according to the following scale:

- Less than 25 are **irrelevant or compatible** with the environment.
- Between 25 and 50 are **moderate** impacts.
- Between 50 and 75 are **severe**.

- More than 75 are **critical.**

According the results show in Table 3, the EIA considers four steps: 1) construction, 2) operation and maintenance, 3) abandon and 4) induced future. Where the construction and abandon step have several impacts in terrestrial flora, fauna, and ecosystems. LCA considers also the same steps except the induced future.

Table 3. Ivirizu Environmental Impact Assessment (EIA)

Environment	Attributes	Construction	Operation and maintenance	Abandon	Induced Future
PHYSICAL	Particulate Matter	32	22	32	24
	Combustion gases	26	20	26	24
	Noise	25	38	25	24
	Erosion	36	24		
	Instability of slopes	32			
	Soil contamination	37	32	37	
	Compaction	34	24	34	23
	Change in morphology	23	24		
	Sedimentation	23	24		
	Flow rate variation	30	39	30	
	Surface water quality	32		32	
BIOLOGICAL	Loss of vegetation cover	35			
	Aquatic flora	36	36	36	
	Terrestrial flora	66		48	20
	Birds	26	25		
	Terrestrial fauna	58	28	58	20
	Aquatic fauna	48	46	48	20
	Ecosystems and landscape	66	32	42	
SOCIO-ECONOMIC	Affectation of public and private properties	18			
	Health and safety (population)	33	20	24	
	Industrial Safety and Occupational Health	33	30	33	22
	Current land use	47			
	Job creation	32		32	25
	Tourism and recreation potential	19			28
	Archeology and cultural heritage	32	21	32	
	Improvement of the local economy	26	24		

Table 4 presents an identification of the major impacts using both methodologies. By applying EIA, several impacts on terrestrial flora, fauna and ecosystem in the construction step were identified to impact with more than 50 points. Those were related to have more impact on the biological environment. While by applying a LCA, the mayor damage was on human health; where 51.42% was due to contribution of global warming and 31.64% was due to contribution of fine particulate matter formation. But, when comparing the results of both methodologies, the particulate matter formation had a moderate punctuation in the EIA, this impact, according to the quantitative data provided by the LCA, should have a severe punctuation because in one of the mayor contributors. The damage on the resources due to fuel scarcity that can increase the cost in 98.12 % of the fuels and it is significant but this aspect is not evaluated in the EIA. The damage on ecosystems were 55.34% for global warming that affect the terrestrial ecosystem. This impact had also a severe punctuation in the EIA. The operation and maintenance step according to the EIA had severe impacts in aquatic fauna. While for LCA shows a mayor damage on ecosystems due to water consumption and global warming impacts. Those are related with EIA because of the impact on the water have effects on the aquatic fauna. The Abandon step according EIA have severe impacts on terrestrial fauna but according to the LCA, this step contributes less to the impacts and trigger more impact in the damage to resources. In this step, LCA analysis is considered as the recollection of materials to the treatment place and EIA considers the demolition of the central.

EIA considers social and economic variables like neighborhood disturbances or economic benefits which are very important for the public acceptability of projects [31]. But, it is limited for the objectives or the study. Global impacts are not considered during the evaluation while LCA considers that [32] EIA also presents qualitative results that depends on the judgment of an expertise while LCA not [31] Both methodologies can be complementary tools [32,33] and provide more information for decision making.

Table 4. EIA and LCA results comparison

Phases	EIA Identification of main local pressures/concerns (qualitative):	LCA Quantification of the impacts
Construction	Terrestrial quality Impacts on flora, fauna, ecosystems and landscape	- Climate change - Fine particulate matter formation - Fossil resource scarcity
Operation and maintenance	Impact Aquatic fauna	- Water consumption - Global warming - Fossil resource scarcity
Abandon	Terrestrial fauna	- Global warming - Fossil resource scarcity - Fine particulate matter formation

4. Conclusion

The LCA presented in this study, demonstrated that the construction phase of a hydropower plant has the largest impact in most of the mid-point environmental indicators. The contribution to global warming was, for this phase, of around 98% while for the operation phase was 0.97%. Fine particulate matter formation, water consumption and global warming are the main impact categories contributing the largest to human health damage. The last two of the midpoint indicators mentioned are also the mayor providers in the damage on ecosystems. Fossil resource scarcity is the mayor contributor in the damage on resources due to the large amount of diesel requirements in the construction step. The environmental impacts of the hydropower plant case decreases with a mayor lifetime. The damage on resources decreases of about 66.32 % when considering a lifetime of 150 years compared with 50 years showing that for this stage the impacts are distributed along the lifetime. The damage in human health and ecosystems reduce in 55.59% and 54.23%, respectively, for the same comparison of lifetime years. The impacts when comparing a hydropower plant with conventional fossil fuels plants are decreased in all the categories but the water consumption due being used for the electricity generation. The use of LCA as a complementary tool for traditional environmental assessment could provide quantitative relevant data.

Acknowledgments

This project is part of Integrated Monitoring of Biodiversity and the Impact of Hydroelectric Megaprojects (MIBIO) program, Project UNIBONN-UCB-UMSS. The authors thank ENDE corporation for sharing the EIA, project description and data for Ivirizu Hydroelectric power plant.

References

[1] RENA, “Renewable energy statistics 2022,” 2022. Available at: <www.irena.org> [accessed 15.12.2022].

[2] D. Verán-Leigh and I. Vázquez-Rowe, “Life cycle assessment of run-of-river hydropower plants in the Peruvian Andes: a policy support perspective,” International Journal of Life Cycle Assessment 2019;24: 1376–1395.

[3] International Hydropower Association, “2022 Hydropower Status Report,” 2022.

[4] A. N. Torrico Carmona, D. F. Sempértegui-Tapia, and R. Orellana Lafuente, “Análisis y propuesta para la Implementación y/o Complementación de Centrales Hidroeléctricas Reversibles en Bolivia,” Revista Investigación & Desarrollo 2022; 22.

[5] Ministerio de Hidrocarburos y Energía, “Plan eléctrico del Estado Plurinacional de Bolivia 2025,” 2014.

[6] S. Nin Zabala, “Mirada al 2050 de Bolivia con 100% de oferta hidroeléctrica hacia la integración eléctrica sudamericana,” Ciencia Latina Revista Científica Multidisciplinar 2022; 6: 2288–2301.

[7] M. Fernadez and A. Martínez, “Análisis preliminar de proyectos hidroeléctricos en Bolivia, sus impactos ambientales y la complementariedad energética.,” 2020.

[8] Comité Nacional de Despacho de Carga (CNDC), “Capacidad efectiva (January, 2023),” Capacidad efectiva (January, 2023), Jan. 16, 2023. Availableat:<https://www.cndc.bo/agentes/generacion.php> [accessed 15.01. 2023].

[9] ENDE, “Proyecto hidroeléctrico Ivirizu - Estudio de diseño final,” 2015.

[10] ENDE, “Proyecto Hidroeléctrico IVIRIZU,” 2015. Available at: <https://www.evh.bo/index.php/portfolio/17-proyecto-ivirizu> [accessed 15.01.2023].

[11] B. Chhun, S. Bonnet, and S. H. Gheewala, “Life cycle assessment of the Kamchay hydropower plant in Cambodia,” By Journal of Sustainable Energy and Environment Journal of Sustainable Energy & Environment 2021;12: 23–33.

[12] D. Verán and I. Vázquez, “Life cycle assessment of run-of-river hydropower plants in the Peruvian Andes: a policy support perspective,” International Journal of Life Cycle Assessment 2016; 24 (8)1376–1395.

[13] M. Pang, L. Zhang, C. Wang, and G. Liu, “Environmental life cycle assessment of a small hydropower plant in China,” International Journal of Life Cycle Assessment 2015; 20 (6)796–806.

[14] L. A. Martínez-Vallejo, H. G. Cortés-Mora, J. A. Méndez-Alcázar, and J. I. Peña-Reyes, “Un enfoque desde la sustentabilidad: análisis de ciclo de vida como herramienta para la toma de decisiones en el desarrollo de proyectos hidroeléctricos en Colombia,” Gestión y Ambiente 2022; 24(Supl2):224–237.

[15] A. Kadiyala, R. Kommalapati, and Z. Huque, “Evaluation of the life cycle greenhouse gas emissions from hydroelectricity generation systems,” Sustainability (Switzerland) 2016;8(6)

[16] International Organization for Standardization, ISO 14040-Environmental management - Life Cycle Assessment - Principles and Framework 2006; 3

[17] A. Kylili, E. Christoforou, and P. A. Fokaides, “Environmental evaluation of biomass pelleting using life cycle assessment,” Biomass Bioenergy 2016;84:107–117.

[18] A. Magne and E. Cardozo, “Analysis of environmental impacts due to the generation of electricity using sugar cane bagasse pellets in rural areas of Bolivia,” ECOS 2019: Proceedings of the 32nd International Conference on Efficiency, Cost, Optimization, Simulation and Environmental Impact of Energy Systems; 2019 Jun 23-28; Poland

[19] F. de M. Ribeiro and G. A. da Silva, “Life-cycle inventory for hydroelectric generation: a Brazilian case study,” J Clean Prod 2010; 18(1):44–54

[20] M. Z. Hauschild, “Introduction to LCA methodology,” in Life Cycle Assessment: Theory and Practice, Springer International Publishing, 2017:59–66.

[21] E. G. Hertwich, “Addressing biogenic greenhouse gas emissions from hydropower in LCA,” Environ Sci Technol 2013;47(17):9604–9611.

[22] D. Villarroel et al., “Estimation and modeling of the spatial distribution of aerial plant biomass for Bolivia,” Ecología en Bolivia 2021; 57(1):5–18.

[23] National Institute for Public Health and Enviroment, “ReCiPe 2016 v1.1 A harmonized life cycle impact assessment method at midpoint and endpoint level Report I: Characterization,” 2017.

[24] M. A. J. Huijbregts et al., “ReCiPe2016: a harmonised life cycle impact assessment method at midpoint and endpoint level,” Springer Verlag, Feb. 2017.

[25] PRè-Product Ecology Consultants, “SimaPro,” 2022. Available at: <https://simapro.com/about/> [accessed 07.11.2022].

[26] A. Laurent et al., “Methodological review and detailed guidance for the life cycle interpretation phase,” J Ind Ecol 2020; 24(5): 986–1003

[27] V. Motuzienė, K. Čiuprinskas, A. Rogoža, and V. Lapinskienė, “A Review of the Life Cycle Analysis Results for Different Energy Conversion Technologies,” Energies (Basel) 2022;15(22):22-8488

[28] Alejandro Lazo and David Urbina, “Análisis de ciclo de vida y energético de las centrales hidroeléctricas Agoyán y Paute Molino,” Escuela Polit´rnica Nacional, Ecuador, 2015.

[29] W. Suwanit and S. H. Gheewala, “Life cycle assessment of mini-hydropower plants in Thailand,” International Journal of Life Cycle Assessment 2011;16(9): 849–858.

[30] ENDE, “Estudio de Evaluación de Impacto Ambiental - IVIRIZU,” Bolivia, 2015.

[31] P. Larrey-Lassalle et al., “An innovative implementation of LCA within the EIA procedure: Lessons learned from two Wastewater Treatment Plant case studies,” Environ Impact Assess Rev 2017;63(63): 95–106.

[32] B. Morero, M. B. Rodriguez, and E. A. Campanella, “Environmental impact assessment as a complement of life cycle assessment. Case study: Upgrading of biogas,” Bioresour Techno 2015;190: 402–407.

[33] M. Janssen et al., “Development of a macro life cycle assessment method View project Mistra REES-resource-effective and efficient solutions based on circular economy thinking View project Using Life Cycle Assessment (LCA) as a Tool to Enhance Environmental Impact Assessments (EIA),” 2005.

A tool for the development of competencies in sustainability and carbon footprint reduction in schools.

I.Marques-Valderrama[a], R.Chacartegui[b], J. A Becerra[c], Yolanda Lechón Pérez[d], Antonio José Serrano Jiménez[e], Susana Marta López Almeida[f] and Carmen Díaz López[g]

[a] University of Seville, Seville, Spain, imarques2@us.es
[b] University of Seville, Seville, Spain, ricardoch@us.es
[c] University of Seville, Seville, Spain, jabv@us.es
[d] CIEMAT, Madrid, Spain, yolanda.lechon@ciemat.es
[e]University of Granada, Granada, Spain, serranojimenez@ugr.es
[f]Instituto Superior Tecnico, Lisbon, Portugal, smarta@ctn.tecnico.ulisboa.pt
[g]University of Seville, Seville, Spain, cdiazl@us.es

Abstract:

This work presents a tool for developing competencies in sustainability, focusing on evaluating the environmental impact and carbon footprint in schools. The tool is based on sustainability indicators and follows a methodology derived from the ClimAct and ECF4CLIM projects. It is conceived as a support for the users and the schools to identify and evaluate the relative impact of different actions and measures, to engage them in a sustainable pathway to low-carbon schools supporting their decision-making at the different levels of users. The areas are transport, waste, green procurement, green spaces, energy, water, and indoor air quality. The tool aims to support users and schools in identifying and evaluating the impact of various actions and measures, facilitating decision-making for a sustainable and low-carbon school environment. To quantify sustainability performance, Key Performance Indicators (KPIs) have been established for each area. The results from schools that tested the tool revealed low scores in green procurement (0.59/5) and water (2.03/5), while achieving higher scores in green spaces (3.46/5) and indoor air quality (3.92/5). These findings highlight the areas where improvement is needed and provide a basis for targeted interventions. Developed on the PowerApps platform, supported by Microsoft, the tool allows access to users of different ages and knowledge levels. It has been successfully tested in six schools in Andalusia, Spain, obtaining relevant results in the seven sustainable areas defined. Based on the results, this tool will be used within co-creation and co-implementation processes for more sustainable schools and competencies acquisition by the participants.

Keywords:

Methodology; Sustainability; Carbon footprint; low-carbon schools; KPI; PowerApps

1. Introduction

Innovation in sustainable education is a critical issue to consider for the formation of present and future generations. Developing tools that facilitate acquiring sustainable skills is fundamental to achieving these objectives. The development and promotion of sustainability education have become one of the key challenges to be addressed within European society, especially in the wake of the Paris Agreement [1], which recurrently calls for a society that lives and works in a sustainable way. The measures and policies were developed to enhance society's development to promote a low-carbon economy. To this end, programs have been developed ranging from the countries involved in the agreement to measures that affect the entire European community. The incentivization of programs that allow society to develop sustainably is a priority to achieve the objectives set out in the Paris Agreement. Programs such as Horizon 2020, promoted by the European Union [2], have encouraged the promotion of activities that favor sustainable development, seeking to strengthen the relationship between science and society by encouraging, among other things, the participation of civil society [3].

Considering the importance of developing sustainability competencies, the value of education as a fundamental tool to achieve the proposed objectives is emphasized. Developing sustainability competencies

in schools is one of the main ways to promote a low-carbon society. Considering that, in areas such as southern European Mediterranean countries, more than half of the buildings used for school use predate 1990 [4], and taking into account the social situation surrounding schools, there are opportunities to design strategies to trigger action in schools. In order to assess the adequacy of knowledge and skills transfer to schools, it is necessary to design indicators through which sustainability parameters can be determined [5]. To this end, within the framework explained above, projects such as ClimAct [5] have been developed, where a methodology has been implemented for the development of sustainability competencies that have been evaluated by measuring a series of indicators, applied in different schools in Spain, Portugal, France, and Gibraltar. The application of a methodology for monitoring and ensuring adequate knowledge acquisition and monitoring progress through indicators is a key tool for developing sustainability competencies in educational communities [6].

Taking into account the need to apply methodologies in schools to create a sustainable society, and taking advantage of the impetus offered by European projects such as ECF4CLIM - A European Competence Framework for a Low Carbon Economy and Sustainability Through Education, the use of computer applications was proposed with the aim of facilitating the transmission of knowledge and the application of methodologies to support sustainability, which is capable of providing support and content at all possible educational levels, from the beginning of the educational process to the higher stages [7]. The use of platforms developed by Microsoft for the development of multi-platform applications makes it possible to create tools that meet the proposed needs [8]. Combining the determination of performance indicators as well as the use of these results as support material for education, a tool has been designed within the PowerApps environment from Microsoft [9]. The purpose of the application developed is to allow the centres to self-audit their sustainability level and opportunities for improving it within their circumstances. The goal of this work it's to develop and validate a tool for improving the competences in sustainablity in schools, reducing at the same time the carbon fotprint due to the institution diary activity, using for this purpose, a testing process executed in six andalusian schools. The application is conceived to be used at all educational levels with different access levels. The tool allows for assessing the impact of the different actions. Combining the use of the methodology and the creation of the platform developed, we bring to schools a novel tool for identifying and developing sustainable competencies in students, supported by a friendly interface. As a consequence, the co-creation and co-implementation by the students, teachers and managers are expected to allow the acquisition of individual and global competencies in sustainability during the process. [6] The structure of the paper is the following. First, the methodology for sustainability skills acquisition is described. Then the structure of the tools is presented. Follows the application case to 7 seven schools in Andalusia. Finally, the main results of the application case and discussion are presented.

2. Methodology

The tool covers a wide range of sustainability aspects divided into seven areas. KPI behaviour indicators are defined for each area based on the specific school data (such as, for example, the number of students or area covered). These areas are [6]: *Transport, Energy, Water, Garbage, Indoor Air Quality (IAQ), Green Spaces and Green Supply.* The KPIs values provide a quantitative evaluation of different sustainability branches related to the school. It allows the analysis of discussion about the potential actions for improving them, if possible, and their implications. The methodology looks for analysis and debate about the sustainability areas to be improved and the evaluation and proposal of specific actions. The KPIs quantify the impact and provide a reference for assessing the departing point and evolution and the situation compared with other schools to identify the real range of the indicators and their adjustment. Once a roadmap with specific measures is defined, the centres will apply the appropriate actions. After their implementation, the results of the indicators will be reviewed again, being able to identify changes. Throughout this process, all the participants will develop sustainability skills. In addition to skills in sustainability, skills will be developed and acquired around the realisation of small-scale projects, which will allow for marking the objectives of the measure and identifying necessary resources.

2.1. ECF4CLIM Sustainability indicators

Behavioural indicators (KPIs) as support for decision-making is a common practice that aims to carry out actions more efficiently or sustainably. The study carried out and modelled in the PowerApps application is based on sustainability indicators whose concept was defined within the ClimAct project [5]. In total, 27 scores were defined, evaluating aspects related to 7 areas of sustainability. The areas of sustainability for this project are Water, Energy, Transport, Green Procurement, Green Areas, Garbage, and Indoor Air Quality. 34 KPIs distributed in the aforementioned sustainability areas were defined to calculate the scores. Table ***2*** breaks down the definition of the indicators used. Their calculation provides a normalised score in the range between 0 and 5.

2.2. Development of sustainability competencies

A five-step methodology has been developed to acquire capacities in sustainability by the educational community effectively. Sustainability indicators support the process, providing quantitative values for assessing the impact of the different steps and to guide the participants. For the correct execution of the steps, different groups of students will work as a team, carry out the audits, propose and implement measures, evaluate the departing and final situations, and evaluate the impact of the actions. The steps for the application of the methodology are as follows:

1. Determination of the initial situation: The methodology starts with evaluating the departing situation through auditing the centre based on the defined sustainability areas. Templates and forms are provided to guide the data collection process, providing an explanation of the different aspects related to the data collected. Different working groups will focus on specific areas collaborating to cover the whole set.
2. Evaluation of the initial situation: Audit results are analysed and evaluated by the groups, either jointly or separately, identifying those aspects in which the school has the potential to improve. The working groups validate the results and discuss the improvement capacity in relation to the current situation of the school.
3. Co-design of measures to improve sustainability: After completing previous steps 1 and 2, the working groups interact with the rest of the scholar community (students, teachers, administrative) to generate a list of possible measures to implement in the centre. From that list, measures are proposed and selected. The working group develops a specific implementation project for each action, defining the activities, schedule, milestones, resources and expected impacts. The selection includes the evaluation of their feasibility by the management of the centre.
4. Co-implementation of approved measures: The working groups execute the selected projects. Tasks are distributed as a function of the educational level of the participants with external support.
5. Determination of the impact of the measures implemented: The impact of the implemented measure is evaluated. In this phase, the cycle will be closed, returning to the initial phase through the completion of the audit.

The implementation of the methodology promotes the acquisition of competencies in sustainability by the students and staff participating. They evaluate, measure, analyse, discuss, propose and execute different aspects of sustainability in the centre. It generates individual and collective competencies in each stage.

3.3 Key Performance Indicators

The impact of the measures through the analyses is identified using indicators to take decisions. The Sustainability Key Performance Indicators used are defined in the table shown below:

Table 1. Definition of KPIs used.

Sustainable area	Environmental pillars	Key Performance Indicators
Transport	Car park	KPI-T1. No. of parking spaces for electric cars at school or periphery per student (up to a 100m radius)
Transport	Car park	KPI-T2. No. of parking spaces for bicycles at school or periphery per student (up to a 100m radius)
Transport	Public transport network	KPI-T3. No. of public transports passing daily per hour (1000 m radius)
Transport	CO2 emissions	KPI-T4. Annual CO2 Emissions per student (kgCO2/student)
Green procurement	Equipment efficiency	KPI-GP1. No. of equipment A+ or higher EU Energy Label per total no. of equipment
Green procurement	Paper usage	KPI-GP2. Annual paper usage in school per student (kg/student)
Green procurement	Paper usage	KPI-GP3. Recycled paper usage in school (kg recycled /kg consumed)
Green procurement	Training in green procurement	KPI-GP4. No. of staff with training in green procurement per total no. of staff
Green procurement	Organic food	KPI-GP6. Food with biological certificate (kg food with biological certificate/kg total food)
Green procurement	Suppliers	KPI-GP7. Local suppliers (No. local suppliers /total suppliers)
Green spaces	Green areas	KPI-GS1. Number of trees per non-covered area (m2)
Green spaces	Green areas	KPI-GS2. Number of trees per student (student1)
Green spaces	Green areas	KPI-GS3. Green area per non-covered area (%)
Green spaces	Green areas	KPI-GS4. Green area per student (m2/ student1)

Green spaces	CO2 sequestration	KPI-GS5. Annual CO 2 sank per non-covered area (kgCO 2/m2)
Green spaces	Use of chemicals	KPI-GS6. Total kg of chemicals used for green area maintenance (kg/m2)
Green spaces	CO2 emissions in maintenance	KPI-GS7. Annual CO 2 emissions for the space maintenance of non-covered area (kgCO 2/year.m2))
Energy	Energy consumption	KPI-E1. Annual final energy consumption per area (kWh/m2)
Energy	Energy consumption	KPI-E2. Annual final energy consumption per student (kWh/student)
Energy	Use of renewable energy	KPI-E3. Renewable energy production (%)
Energy	Energy cost	KPI-E4. Annual energy cost per m 2 (€/m2)
Energy	Energy cost	KPI-E5. Annual energy cost per student (€/student)
Energy	CO2 emissions	KPI-E6. Annual carbon footprint per student (kgCO2/student)
Water	Water consumption	KPI-H2O1. Water consumption (m3/m2)
Water		KPI-H2O2. Water consumption (m3/student)
Water	Water cost	KPI-H2O3. Water cost (€/m2)
Water		KPI-H2O4. Water cost (€/student)
Waste	Waste produced	KPI-W1. Volume of waste produced (non-recyclables and reusables (m3/student)
Waste	Waste recycled	KPI-W2. Volume of waste recycled (m3/student)
Waste	Waste reused	KPI-W3. Volume of waste reused (m3/student)

The combination of each indicator in each sustainable area, gives a result between 0 and 5. A tool for their evaluation, analyses and discussion has been developed to support the process [5]. Main characteristics are described in the next section.

3. Sustainability KPIs Tool

This section describes the tool developed to support the methdology in the schools.

3.1. Platform description

The tool has been developed based on the combination of two Microsoft solutions, PowerApps and Power Automate[10], tools designed to support the creation of applications. Both applications were framed in an environment created in Azure [11], where user management and license assignment were carried out [12]. On the other hand, database management was carried out for the calculations of indicators and monitoring of the studies from the SharePoint platform [13]. The interaction within the platform is described in the scheme of Figure 1:

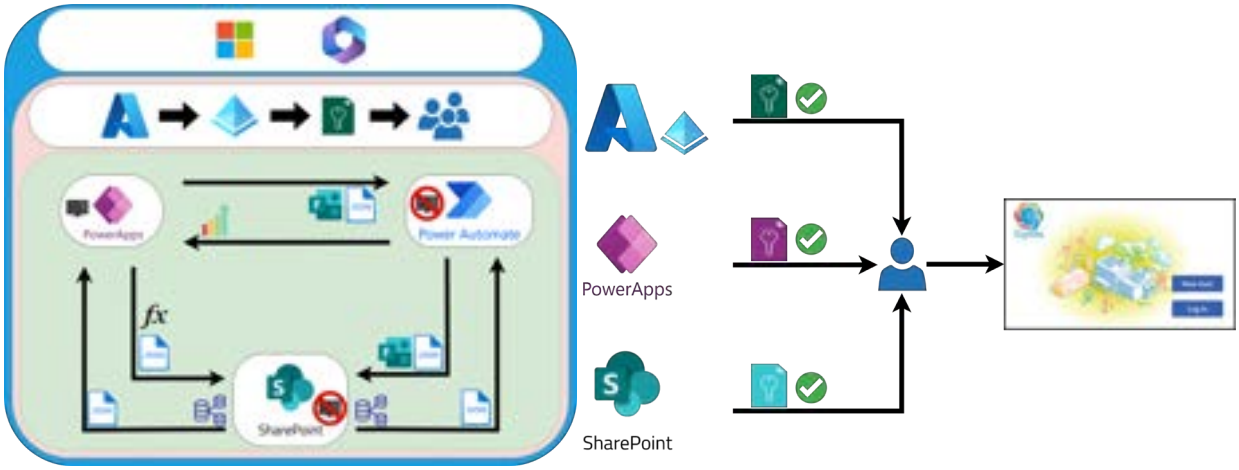

Figure 1.- Application situation diagram.

The use of Azure allowed the management of users, licenses and permissions. Different access levels are provided as function of the user's profile. From the user's point of view, authentication is done with the Microsoft user [14], which contains all the requirements that are requested for access.

3.2 Sustainability areas

For each of the seven sustainability areas, the application works independently. Their specific information is introduced into the study gradually. The data submenus include the possibility to edit or delete the information

entered. School's codes are used to define common characteristics for different studies or users(i.e. buildings parameters). Data introduction and navegation process are explained in the next schema:

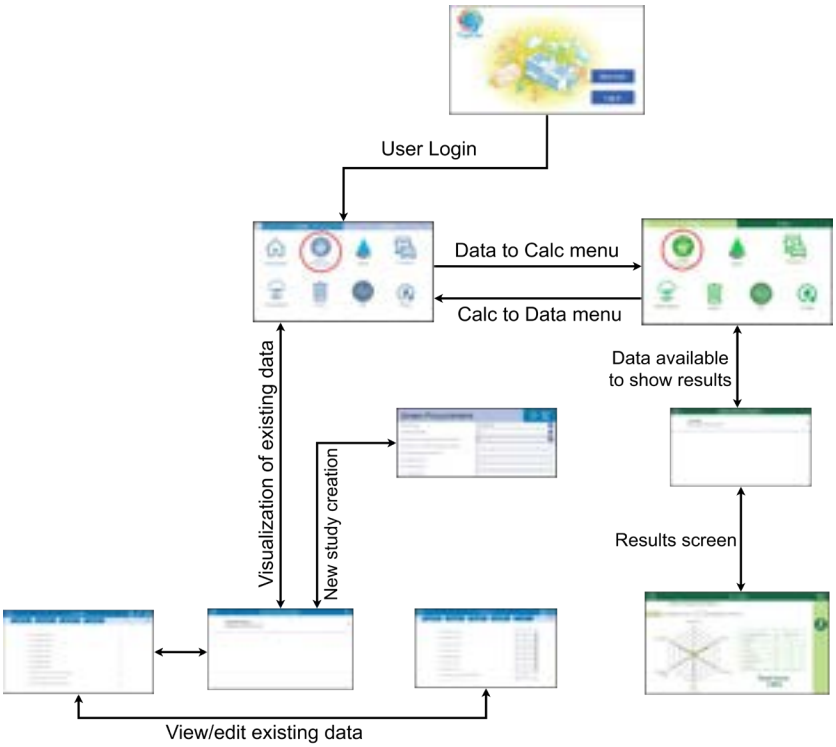

Figure. 2. Navigation scheme of the application.

The application is divided between the data collection part and the sample of results through colours (Blue – data menu; Green – calculations menu). The operation of the application is the same in all areas of sustainability. After login into the application, school study cases are available. The Data menu, blue theme, shows the data introduction menus for the sustainability area to study. For the chosen sustainability area there is a gallery with the created studies (if there are any). New studies are created by pressing the "+" button at the top right of the screen. Existing ones can be viewed/edited by selecting them.

The calculation menu (green theme), where the user, after creating a case in the data section, can represent the results of the sustainability indicators on a radar graph [15]. The application calculates the sustainability indicators based on the existing studies in the databases, allowing the creation of global studies and comparisons. Results are displayed in graphical and numerical form.

3.3.1. Display of scores

The general structure for visualising results is based on radar graphs representing the scores on the indicators related to the sustainability area studied, figure X:

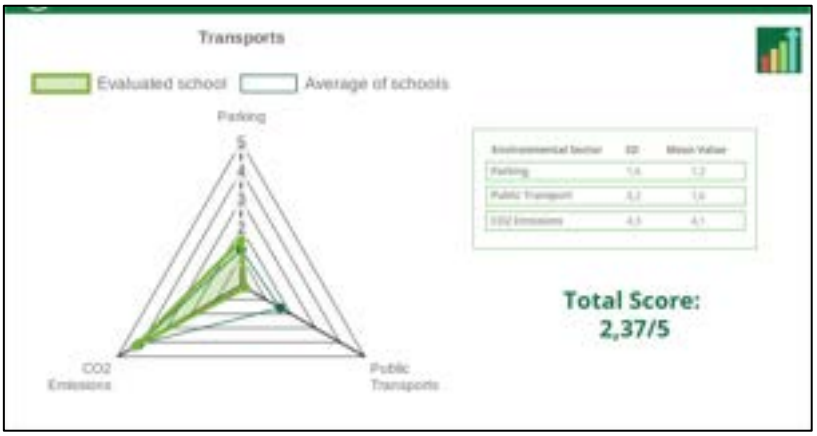

Figure. 3. Example of visualisation of results in the application.

4. Example of real application of the tool in schools

The objective of the application is to support schools in using the methodology for the acquisition of competencies. The application is being launched to the schools involved in the ECF4CLIM project, where the methodology will be implemented and assessed.

4.1 Youth with researchers pilot experience

The tool was tested in a pilot experience in 6 educational centres in Seville, Córdoba and Malaga (Spain). The context has been taken as the realisation of the 8th congress of the Youth with Researchers program convened by diferent organisations such as CSIC, SADC or US [16]. In this activity, 25 students from different centres interacted with University researchers during four seasons, developing research projects in four different groups related to different sustainability areas and applying the tool to different centres. The purpose was double, to identify the perception of the students about the tool, receiving their feedback, and to evaluate its adequateness to the methodology. The projects were:

1. Sustainable mobility in schools. Education, evaluation and proposals.
2. Zero Waste Life. Towards a future in harmony with our planet.
3. Air quality and renewable systems at school.
4. Do we improve our yard? Bioclimatic strategies and environmental education applied in schoolyards.

During the work sessions, students and teachers were guided in using the tool to support the analysis and discussion about measures that improve the sustainable behaviour of the educational community, covering with their activity the first three phases of methodology. The distribution of the participants in the activity are presetned in the next table.

Table 2. Schools participating in the JCI 2023 project.

School Name	Location	Type of school	Nº of students involved in theproject
School 1	Tomares, Seville	Secondary and High School	8
School 2	Camas, Seville	Secondary and High School	2
School 3	Camas, Seville	Secondary and High School	6
School 4	Montequinto, Seville	Secondary and High School	4
School 5	Ronda, Malaga	Secondary and High School	1
School 6	Córdoba	Secondary and High School	4

4.2 Results of the use of tool

After the audit work carried out by the JCI project students, the students determined those aspects in each center in which they obtained a lower score. Based on this result, they proposed sustainability measures, which, in some cases, have begun to be implemented in the centre. During the four sessions developed in the Youth with Researchers program, the students have been able to handle the tool, from which they detected possible ways of improvement in the centre. They were able to propose projects to increase sustainability skills in certain aspects of the centres involved. The developed application was used for all centres in the seven areas of sustainability. Below are the results obtained for the IES Ítaca school as an example of the activity carried out.

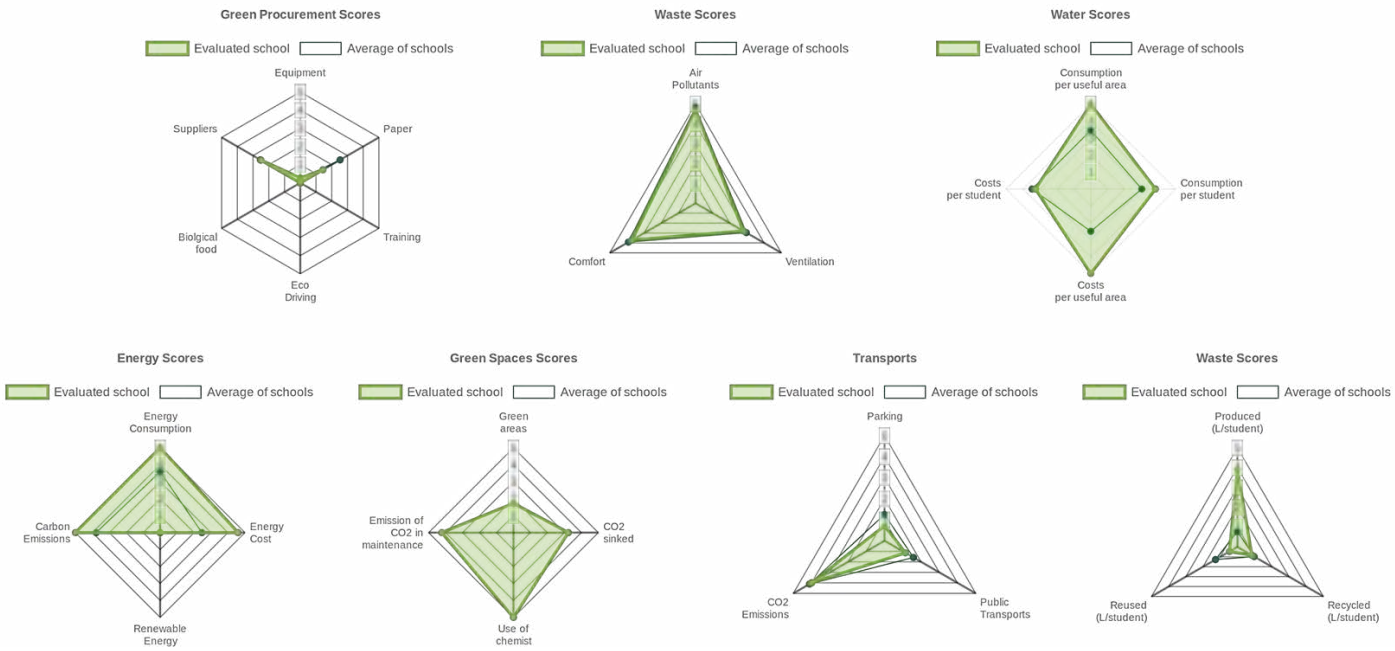

Figure. 4. Audit results for School1.

The students used the graphs of the different schools to discuss and obtain conclusions. First, they were able to interpret what information in the study had greater or lesser validity depending on the characteristics of the school. On the other hand, in areas such as Transport and garbage, students understood that there were sectors in which they could apply improvements. It was also detected that the use of the application in the specific area of garbage was not as expected since the students did not correctly understand the operation of this area of sustainability. Finally, the students who were working on the application could not have enough information concerning the generation of renewable energy in the centres, so they did not add that type of information to the study. However, in the case of School 1, they do have a photovoltaic installation in the school. Below is a graph summarising the results obtained in all centres by sustainability area.

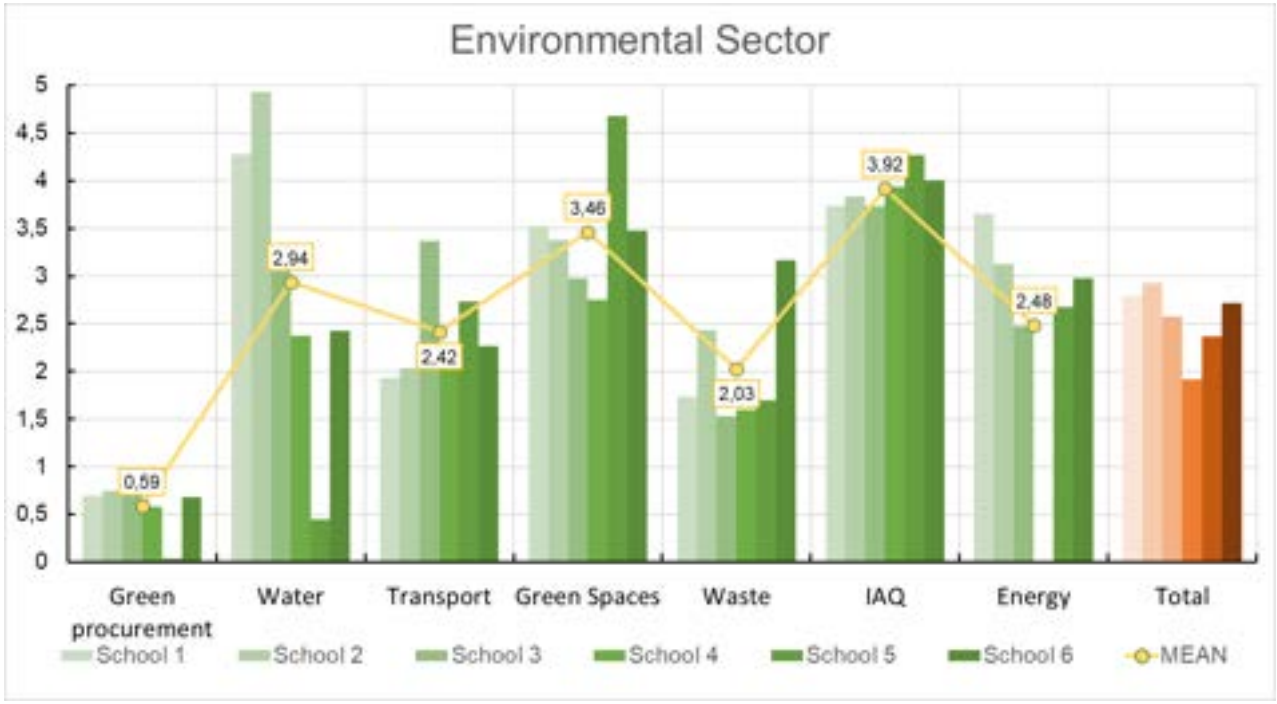

Figure. 5. Global results obtained in the centres by sustainability area.

The graph shows for each centre the overall score that summarises the 34 KPIs and the 27 scores in the 7 areas of sustainability measurable in the application. From this graph, it is possible to determine the collective and specific behaviours of the educational centres studied. In the representation of the results, the centres are sorted by colours, as shown on the labels at the bottom of the graph. On the other hand, the means of the results have been represented together with the value of said result for all the centres studied, as well as the total score of each centre. Next, characteristics related to the origin of the data or the value that the students have provided through the work with the tool will be analyzed, so that, next, considerations made in each area of sustainability will be exposed.

4.2.1. Indoor Air Quality

First, the performance in relation to Indoor Air Quality in the classrooms where the students worked was similar, considering that the measurements focused on determining CO2 concentration and temperature. In the schools 1 and 5, data on the concentration of different particles were available, thanks to previous measurements that were made through the ClimAct project, so these were added to the tool.

4.2.2. Waste

On the other hand, there were centers where it was understood that the information related to the garbage section was not introduced as expected, since inconsistencies were detected in the results. The approach of this area of sustainability assumes that the amount of waste recycled and reused will always be less than or equal to that produced according to the case. This fact was not correctly interpreted by all the students who used the tool, although in the follow-up sessions where the application was used, the results were discussed taking into account this fact. In centers such as IES Ithaca, there is a garbage management system through which they were able to evaluate this area of sustainability.

Figure. 6. Separation of garbage inside the IES ITACA center.

The image shown corresponds to one of the corridors of the school, where there are differentiated bins to carry out the correct separation of garbage. In addition, as transmitted by teachers and students, the same separation system is carried out inside the classrooms, so that students could make measurements based on the information they took from their own waste management system.

4.2.3. Transport

For this area of sustainability, a series of activities were carried out that served the students, among other things, to raise awareness about the CO2 emissions that are undertaken by the simple fact of traveling to school. The access routes to the centers were also studied, as well as the availability of parking in the vicinity of the school. On the other hand, based on the results obtained, the students were able to discuss the transport network available in each case to access the school.

Among the activities carried out in this area of sustainability, a survey was carried out that was introduced in the application, where each student could answer questions about the transport method used to access the

school, as well as behavioral issues related to this topic. The survey was shared with the students of the study schools to increase the data sample as much as possible, with the aim of characterizing the general behavior of the students in each school.

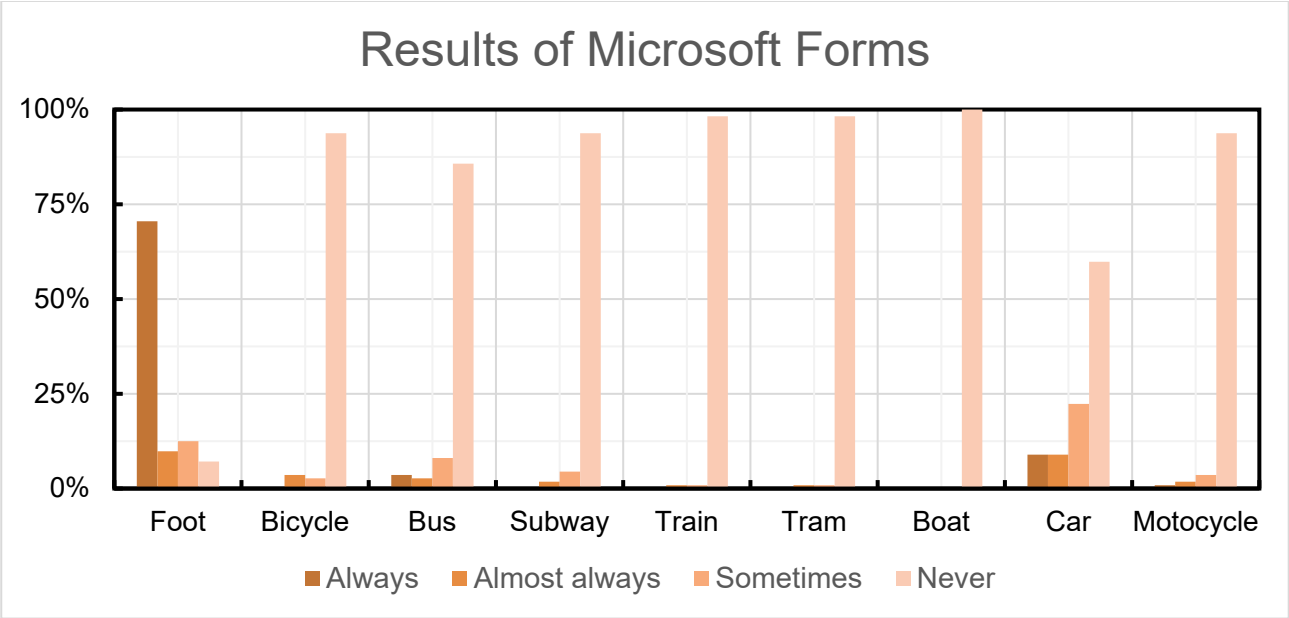

Figure. 7. Results of the user behavior survey launched through Microsoft Forms.

On the other hand, some notions related to the management of Google Earth and Google My Maps were taught with the aim that students could determine the position of the public network within a radius of 100m, 500m and 1000m. From the maps generated, they were able to determine the number of bus, train and metro stations among others, as well as the determination of the number of parking spaces at different distances from the school.

4.2.4. Water

For this area of sustainability, the students relied on the data available in the IES Ítaca and IES Martín Rivero centers in relation to the prices paid for consumption for the determination of their expenses, based on the consumption data they were able to obtain.

4.2.5. Energy

Within the development that the students made of the tool for this area of sustainability, they did not consider the part of the study dedicated to generation due to renewable facilities, although there are centers that do have a photovoltaic installation, as is the case of the IES Ítaca mentioned above.

4.2.6. Green Spaces

To answer the questions posed in the study of green spaces, students had to perform tasks related to tree counting or determining the dominant species. Because they were unable to obtain information about the use of chemicals for maintenance, they did not answer those questions. That is why in the grade entitled "Use of Chemist" all schools obtained a score of 5, although the students debated about the subject, being aware that this result had no validity. For the determination of the dominant tree species in the school, the students made use of the Google Lens tool, through which they could determine the scientific name, which they then selected in the application. Finally, the determination of the score related to "Green Spaces" was obtained from the work done in determining the different types of surface that each school has.

4.2.7. Green Procurement

Finally, for the sustainability area of green procurement, students focused their studies on questions related to suppliers, paper management and the energy level of equipment. The questions of the remaining three tags remained unanswered, so, in these specific cases, unlike what happened in Green Spaces, scores of 0 were obtained. Ittook into account, among other issues, that the centers do not have a dining room, so obtaining a result of 0 in "Biological food" did not imply the proposal of any improvement by the students.

4.3 Discussion of results obtained

The purpose of the students in relation to the use of the tool, was to be able to detect aspects from which to propose measures to support the sustainability of the center, while developing the common project for the JCI contest. After using the tool, and discussing the usefulness and validity of the results in a working session, those aspects in the areas of sustainability that needed a measurement proposal were chosen. For this, all the results obtained in the 6 centers were considered, reasoning the considerations made previously.

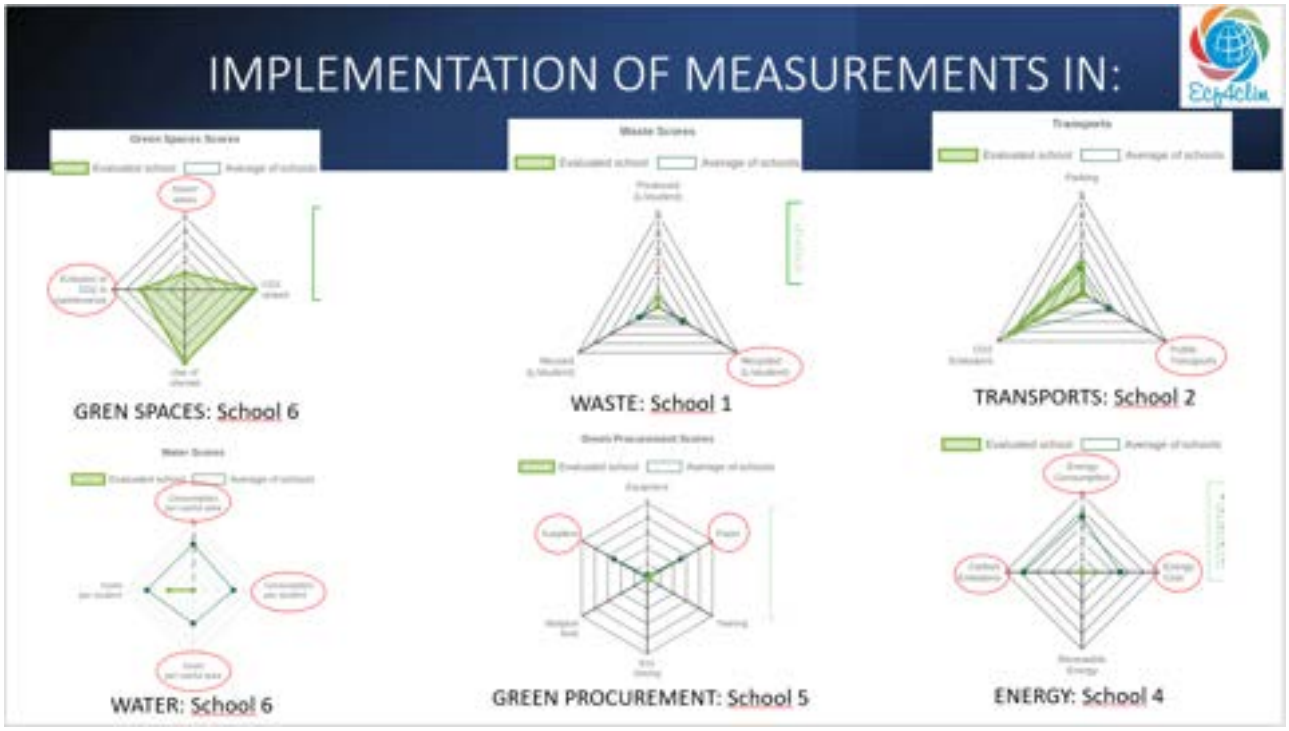

Figure. 8. Sectors in the different areas of sustainability in which to propose measures.

Making a summary of the process explained to obtain these results, the students audited their centres, entered the data in the application, and then compared the results obtained in the different centres. Once this task was performed, those centres in which the score was markedly different from the average were identified. Students noticed that, in certain respects, schools did not behave appropriately regarding sustainability. They also knew how to correctly interpret the results obtained since they understood that obtaining a low score in a specific indicator did not indicate a lack of sustainability skills or carrying out poor behaviour. Within the results obtained, they made an extraction of the graphs in which it was detected that the performance was not adequate. Based on the results obtained, improvement measures were proposed in the centres for which these scores had been detected.

5. Conclusions

Developing solutions that facilitate the development of sustainability skills in schools facilitates the learning-by-doing process that should be carried out by the schools involved in the ECF4CLIM project. This paper shows the tool developed to support the analysis and discussion of sustainability-related actions in schools. It guides and simplifies the process of collecting and analysis of information, providing information in a visual and simple way. On the other hand, through the use of the tool in the JCI program for two months, errors in programming have been detected, and learning has been carried out to identify those points of the tool that have been more complicated to understand. The feedback offered by both the students participating in the project, as well as the professors and the support research staff, has been decisive in identifying ways for improvement. In relation to the learning method, the students have followed a process in which they have been developing skills that have helped them to develop four projects that will be exhibited in the 8th congress of Youth with Researchers, where the tool has been a transversal aspect in work developed. Within the stages defined in the method, the students have managed to complete the first two phases satisfactorily.

Acknowledgments

This work has been developed within the project A European Competence Framework for a Low Carbon Economy and Sustainability Through Education - ECF4CLIM, grant agreement number 101036505, within the H2020 European research framework and within Young with Researchers-PIISA 2022-2023.

Nomenclature

ECF4CLIM – European Competence Framework for a Low Carbon Economy and Sustainability Through Education

JCI – Youth with Researchers

MS – Microsoft

M365E5 – License E5 Microsoft 365

KPI – Key Performance Indicator

AAD – Azure Active Directory

CSIC – Consejo Superior de Investigaciones Científicas (Spanish National Research Council)

SADC – Sociedad Andaluza para la Divulgación de la Ciencia (Andalusian Society for the Dissemination of Science)

US – University of Seville

References

[1] Unfccc, “Paris Agreement Spanish”.

[2] “Programa Marco Horizonte 2020 | Programme | H2020 | CORDIS | European Commission.” https://cordis.europa.eu/programme/id/H2020-EC/es (accessed Apr. 14, 2023).

[3] “THE EUROPEAN INSTITUTE OF INNOVATION AND TECHNOLOGY (EIT) | Programme | H2020 | CORDIS | European Commission.” https://cordis.europa.eu/programme/id/H2020-EU.7. (accessed Apr. 14, 2023).

[4] C. Díaz-López, A. Serrano-Jiménez, R. Chacartegui, J. A. Becerra-Villanueva, M. Molina-Huelva, and Á. Barrios-Padura, “Sensitivity analysis of trends in environmental education in schools and its implications in the built environment,” *Environ Dev*, vol. 45, p. 100795, Mar. 2023, doi: 10.1016/J.ENVDEV.2022.100795.

[5] J. Lizana *et al.*, “A methodology to empower citizens towards a low-carbon economy. The potential of schools and sustainability indicators,” *J Environ Manage*, vol. 284, Apr. 2021, doi: 10.1016/j.jenvman.2021.112043.

[6] “The Pathway towards Low Carbon Schools Criteria, Targets and Solutions.”

[7] M. Ampartzaki, M. Kalogiannakis, and S. Papadakis, “Deepening Our Knowledge about Sustainability Education in the Early Years: Lessons from a Water Project,” *Education Sciences 2021, Vol. 11, Page 251*, vol. 11, no. 6, p. 251, May 2021, doi: 10.3390/EDUCSCI11060251.

[8] T. Fin and D. E. Grado, “Desarrollo y despliegue de un sistema escalable y extensible con otros sistemas basado en Microsoft Azure y Dynamics CRM 365 Online potenciado con Power Apps,” 2020, Accessed: Apr. 17, 2023. [Online]. Available: https://uvadoc.uva.es/handle/10324/44424

[9] “Add an embedded canvas app on a model-driven form - Power Apps | Microsoft Learn.” https://learn.microsoft.com/en-us/power-apps/maker/model-driven-apps/embedded-canvas-app-add-classic-designer (accessed Apr. 17, 2023).

[10] “Microsoft Power Apps y Microsoft Power Automate.” https://www.microsoft.com/es-es/microsoft-365/business/microsoft-powerapps (accessed Mar. 28, 2023).

[11] “Colaboración B2B para organizaciones híbridas - Microsoft Entra | Microsoft Learn.” https://learn.microsoft.com/es-es/azure/active-directory/external-identities/hybrid-organizations (accessed Apr. 18, 2023).

[12] “Asignación o eliminación de licencias - Microsoft Entra | Microsoft Learn.” https://learn.microsoft.com/es-es/azure/active-directory/fundamentals/license-users-groups (accessed Apr. 18, 2023).

[13] “Conectarse a SharePoint desde una aplicación de lienzo - Power Apps | Microsoft Learn.” https://learn.microsoft.com/es-es/power-apps/maker/canvas-apps/connections/connection-sharepoint-online (accessed Apr. 18, 2023).

[14] “Función User en Power Apps - Power Platform | Microsoft Learn.” https://learn.microsoft.com/es-es/power-platform/power-fx/reference/function-user (accessed Apr. 18, 2023).

[15] “API parameters | QuickChart.” https://quickchart.io/documentation/usage/parameters/ (accessed Apr. 18, 2023).

[16] “Jóvenes con investigadores | Investigación en secundaria y bachillerato.” https://jovenesconinvestigadores.wordpress.com/ (accessed Apr. 17, 2023).

A comparative study of standard carbon capture process and Advanced Flash Stripper configuration using MEA

Ruitao Sun[a], Peng Huang[b], Jie Li[c], Li Sun[d]

[a] Centre for Process Integration, Department of Chemical Engineering, University of Manchester, Manchester, M13 9PL, UK, ruitao.sun@postgrad.manchester.ac.uk
[b] Department of Materials, Henry Royce Institute, The University of Manchester, Manchester, M13 9PL, United Kingdom, peng.huang@manchester.ac.uk
[c] Centre for Process Integration, Department of Chemical Engineering, The University of Manchester, Manchester, M13 9PL, UK, jie.li-2@manchester.ac.uk, CA
[d] School of Computing, Engineering and Physical Sciences, The University of the West of Scotland, Scotland, PA1 2BE, UK, li.sun@uws.ac.uk, CA

Abstract:

The advanced flash stripper (AFS) is proven to have benefits in capital investment and energy saving for carbon capture plants using piperazine, whilst monoethanolamine is still the most used amine in the existing commercial carbon capture plants. The production and use of energy and material consumed during CO_2 absorption and regeneration generate CO_2. In this research, the 130-tonne daily CO_2 capture plants with conventional configuration and AFS configuration are simulated in Aspen Plus. Their total annualized costs are estimated to be 3.33 million USD and 2.87 million USD, respectively. The life cycle assessment is conducted to evaluate the environmental impacts from the cradle and grave of energy and materials consumed during carbon capture, showing 58% equivalent CO_2 in flue gas is generated.

Keywords:

Carbon capture; Monoethanolamine; Advanced flash stripper; Techno-economic analysis; Life cycle assessment.

1. Introduction

Monoethanolamine (MEA) is the widely used amine solvent in commercial post-combustion carbon capture due to its high reaction rate with CO_2, high carbon capture capacity and low cost [1]. Current study related to the amine-based carbon capture process concentrates on the improvement of energy efficiency. The Separation Research Programme (SRP) proposed a novel stripper configuration called Advanced Flash Stripper (AFS) [2] allowing further heat recovery and lower capital investment of the stripper, as the heat duty used to release by a condenser is now partially recovered by a cold bypass stream, and an in-situ reboiler is replaced with a cheaper steam heater. This configuration has been employed in the carbon capture process using 5 m or 8 m piperazine (PZ) [2]. However, the significantly high price of PZ may not be a threat to the position of MEA in the existing commercialized carbon capture plants. Also, the simple but ingenious configuration modification is promising to retrofit the existing plants with low capital investments. Moreover, the CO_2 from flue gas is captured and regenerated in environmental concern, whilst energy and amine solvent is consumed in amine-based carbon capture processes, which may be accompanied by CO_2 emissions again. The impacts of cradle and grave of materials and energy are often ignored in previous work. Therefore, this work aims to investigate the techno-economic and environmental feasibility of AFS configuration in an MEA-based carbon capture process. A rate-based model will be built to validate the plant data from [3] as a base case. The AFS configuration will then be employed. The techno-economic analysis and life cycle assessment will be used to evaluate the equivalent energy for CO2 recovery, total annualized cost as well as environmental impacts.

2. Process description

2.1. Conventional configuration

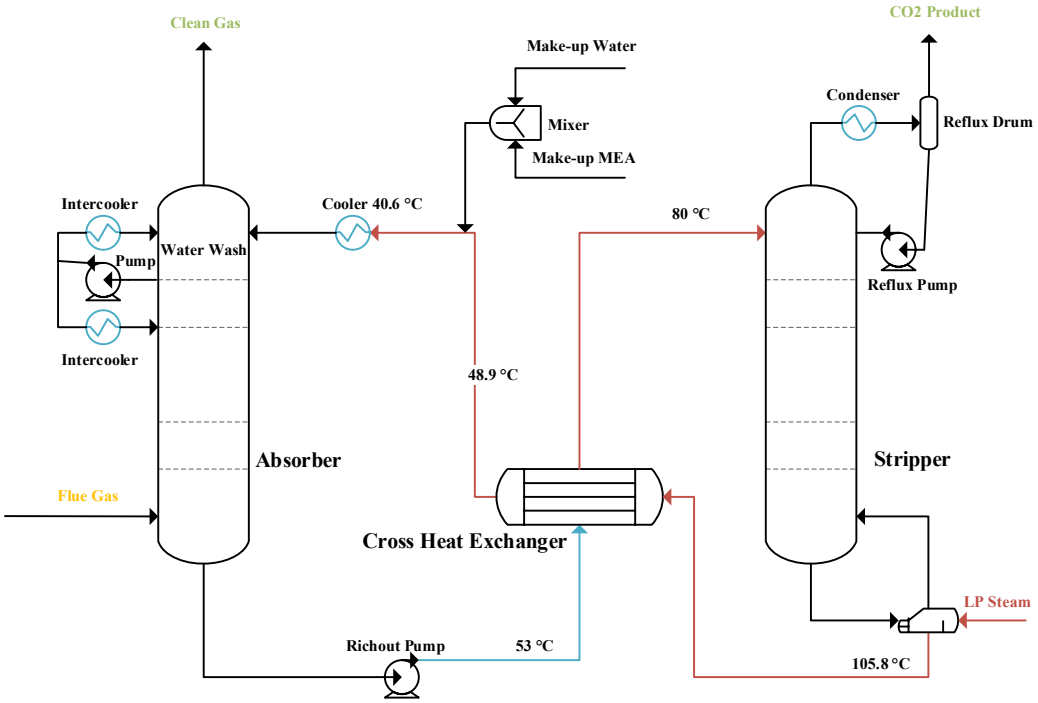

Figure 1. Simplified flowsheet of the carbon capture plant using MEA.

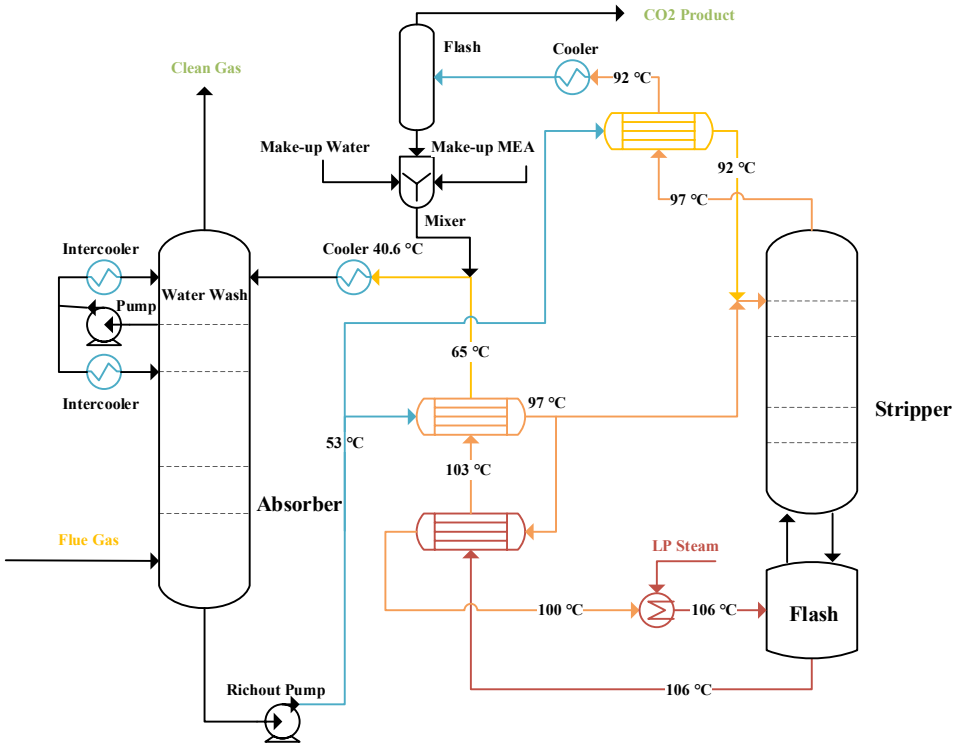

Figure 2. AFS configuration of carbon capture plant using MEA.

This simplified conventional configuration shown in Figure 1 is based on an existing carbon capture plant removing 130 tonnes of CO_2 per day [3]. After exhausted, desulphurized and cooled to 40 ºC, the flue gas (12 vol% CO_2) enters the bottom of the absorber packed with Polypropylene Ring, captured by the amine countercurrent (16%-17 wt% MEA). Around 80% of the liquid in the connection of the wash

section and absorption section is pumped back to the top of the absorber so that the amine loss of MEA can be alleviated. And the liquid is cooled to 40 ºC for the improvement of absorption performance and mitigation of MEA volatility. The clean gas is vented with nearly all nitrogen, oxygen and water. The rich solvent with high CO_2 loading is then heated to 80 ºC and pumped to the top of the stripper for CO_2 and amine regeneration. The 26-tray stripper is equipped with a condenser and reboiler. Approximately 14% of the bottom liquid is boiled up in the kettle reboiler and comes back to the stripper for further regeneration. The thermal energy of lean amine regenerated is recovered by a cross heat exchanger. After releasing the heat to the rich amine exiting from the absorber, the regenerated lean amine is then cooled and returned to the top of the absorber, before being mixed with amine and water makeup.

2.2. Advanced flash stripper configuration

The configuration of the carbon capture plant with an advanced flash stripper is presented in Figure 2. Unlike a conventional configuration where the thermal energy of distillate in the stripper is wasted, the in-situ condenser is replaced with an external cross heat exchanger to recover part of the heat. Moreover, two stream splitters are used to adjust the flowrate of rich solvent, which allows managing the feasibility of heat exchange (assume the minimum temperature approach is 5 ºC). Consequently, cold rich bypass and warm rich bypass are mixed and fed to the top of the stripper, contacting the gaseous countercurrent from a flash tank where part of hot rich solvent is vaporized and CO_2 is released to the bottom of the stripper. The regenerated lean solvent exits as the liquid product from the bottom of the flash tank. Its heat is recovered by a hot cross heat exchanger and a warm cross heat exchanger.

3. Methodology

The rate-based carbon capture process using MEA as an absorption solvent is developed in Aspen Plus V12.1. The property method employs an electrolyte NRTL model with the Redlich-Kwong equation of state [4]. For the rate-based setup, the Onda model is applied to calculate the mass transfer coefficient and interfacial area [5]. The heat transfer coefficient is then obtained from the mass transfer coefficient using the Chilton and Colburn analogy [6]. And the liquid holdup at each packing stage is estimated by the correlation of Stichlmair [7]. The chemistry of MEA absorbing CO_2 is described by a set of equilibrium reactions listed below in eqs. 1-5. The built-in power law expression is used to represent the kinetic reactions for controlling the performance of CO_2 absorption and regeneration. The corresponding kinetic parameters are provided in Table 1.

$$2H_2O \leftrightarrow H_3O^+ + OH^- \quad (1)$$
$$CO_2 + 2H_2O \leftrightarrow HCO_3^- + H_3O^+ \quad (2)$$
$$HCO_3^- + H_2O \leftrightarrow CO_3^{2-} + H_3O^+ \quad (3)$$
$$MEA^+ + H_2O \leftrightarrow MEA + H_3O^+ \quad (4)$$
$$MEA + HCO_3^- \leftrightarrow MEACOO^- + H_2O \quad (5)$$
$$CO_2 + OH^- \rightarrow HCO_3^- \quad (6)$$
$$HCO_3^- \rightarrow CO_2 + OH^- \quad (7)$$
$$MEA + CO_2 + H_2O \rightarrow MEACOO^- + H_3O^+ \quad (8)$$
$$MEACOO^- + H_3O^+ \rightarrow MEA + CO_2 + H_2O \quad (9)$$

Table 1. Kinetic parameter for build-in power law expression (eqs. 6-9)

Reaction No.	k_{abs}	$E_{abs}\ (cal/mol)$	k_{reg}	$E_{reg}\ (cal/mol)$
6	1.33e+17	1.32e+4	1.33e+17	1.32e+4
7	6.63e+16	2.57e+4	6.63e+16	2.57e+4
8	3.02e+14	9.86e+3	3.02e+14	9.86e+3
9	5.52e+23	1.65e+4	6.50e+17	2.28e+4

The cost estimation of the carbon capture process with two configurations is completed by Aspen Process Economic Analyzer (APEA). Instead of using installation factors to evaluate costs, APEA is able to manage that by required materials and labour. Furthermore, the combination of mathematical models and expert systems contributes to a more detailed economic measurement [8]. The parameters for calculating the costs are presented in Table 2. The annual cost is calculated by the summation of operating cost and annualized capital cost [9], which is represented by eqs. 10-11 below.

$$ACCR = \frac{DR \times (DR+1)^n}{(DR+1)^n - 1} \quad (10)$$

$$TAC = ACCR \times CAPEX + OPEX \quad (11)$$

Where ACCR is the annualized capital cost ratio; DR is the discount rate, assumed to be 10%; n is the estimated period; TAC, CAPEX and OPEX represent the total annualized cost, capital cost and operating cost, respectively.

Table 2. Parameters for cost estimation

Parameters	Price
Carbon fee/carbon tax ($/kg)	0.051
Make-up water ($/cum)	3
Make-up MEA ($/ton)	1200
Electricity ($/kJ)	1.60e-5
LP steam ($/kJ)	1.90e-6
Cooling water ($/kJ)	2.12e-7

The life cycle assessment is employed to identify improvement potential for environmental performance. The principles, frameworks, requirements and guidelines can be found in ISO 14040 and ISO 14044. An “operational guide to the ISO standards” was published by the Centre of Environmental Science of Leiden University (CML) in 2001, summarizing a list of impact categories and characterization methods and factors for corresponding substances. Guinee et al. explained these categories [10]. In this work, the ReCiPe method [11] is chosen to evaluate the environmental impact of material and energy consumption for equivalent CO_2 regeneration in two carbon capture processes. All impact indicators are obtained by commercial LCA software SimaPro, and the most 7 influential impact indicators are presented in Table 3. The “global warming potential” refers to the global temperature increment resulting from greenhouse gas emissions, which is measured by the kilogram of carbon dioxide equivalent. The exposure to “ionizing radiation” is detrimental to human health, which is estimated by the equivalent kilobecquerels of Cobalt-60 to air. The “land use” is a composite indicator measuring the use and occupation of land for agriculture, housing, mining, or other purposes, so the unit is square meter in the total period. The essential idea behind “fossil resource scarcity” is that the depletion of fossil fuels forces the extraction of other resources in the future, which is estimated in kilogram of equivalent oil. The following indicators are measured in kilogram of 1,4-dichlorobenzene emitted. Particularly, “terrestrial ecotoxicity” indicates the impact of toxic substances on terrestrial ecosystems (i.e., individual species and the functioning of the ecosystem). The “human carcinogenic toxicity” and “human non-carcinogenic toxicity” reveals the potential health damage leading to cancers and other diseases, respectively.

Table 3. Impact indicators for life cycle assessment

Abbreviation	Indicator	Unit
GWP	Global warming potential	kg CO_2 eq
IR	Ionizing radiation	kBq Co^{-60} eq
TEC	Terrestrial ecotoxicity	kg 1,4-DCB
HCT	Human carcinogenic toxicity	kg 1,4-DCB
HNCT	Human non-carcinogenic toxicity	kg 1,4-DCB
LU	Land use	m^2a crop eq
FRS	Fossil resource scarcity	kg oil eq

4. Results and discussion

The feasibility of the rate-based carbon capture model is validated by the plant data from [3]. The comparison between plant data and modelling results in terms of CO_2 loading, temperature, recovered CO_2 amount, steam usage and clean gas composition, is listed in Table 4. The modelling results show a great agreement with plant data. It is worth noting that the O_2 content takes account for a larger proportion with about 40% deviation. This may result from the oxidative degradation of MEA in reality, which is not considered in the model. Nevertheless, this model is still feasible to predict the absorber and stripper performance.

Table 4. Comparison between plant data and modelling results

	Plant	Model	RD (%)
Lean Loading (mole of CO2/mole of amine)	0.11	0.114	3.77
Rich Loading (mole of CO2/mole of amine)	0.411	0.425	3.33
Rich Amine Discharge temperature from absorber bottom (ºC)	57.22	53.479	6.54
Clean Gas Temperature (ºC)	40	40.57	1.43
CO2 Production (tonne/day)	125.2	127.225	1.62
Steam flowrate to reboiler (kg/hr)	17460	17466	0.03
Clean Gas Composition (mol%)			
CO2	0.223	0.228	2.24
O2	5.762	8.046	39.63
N2	87.315	85.005	2.65
H2O	6.672	6.591	1.22

*RD is the relative deviation.

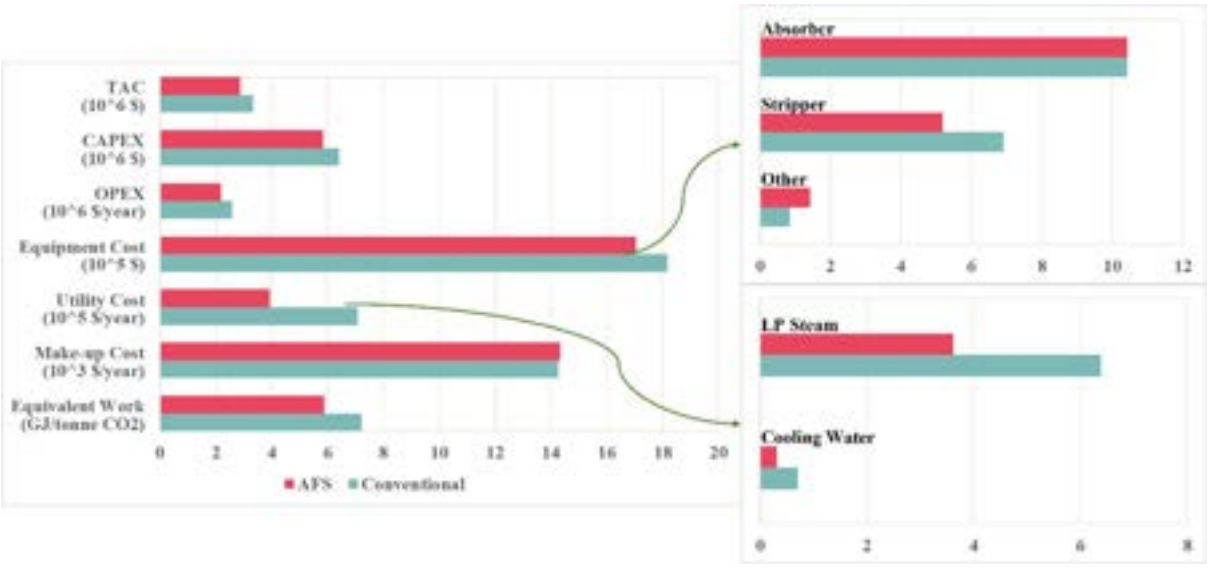

Figure 2. The comparison of conventional process and AFS process related to costs and equivalent work.

The comparison between conventional and AFS configurations is presented in Figure 2 in terms of costs and equivalent energy requirements for CO_2 recovery. The total annualized costs of conventional configuration and AFS configuration are 3.33 million USD and 2.87 million USD, respectively. It is shown that the capital investment costs around 6 million USD, and the annual operating expenditure is 2 million USD. Compared to the conventional configuration, using the AFS configuration will save about 8.94% and 15.1%, receptively for capital cost and operating cost. Although over 24% saving from eliminating the condenser and reboiler of the stripper in AFS configuration is reduced by the additional costs from two cross heat exchangers and one advanced flash drum, making the equipment cost reduction only 6.23%, the energy saving is tremendous due to the significant heat recovery realized by AFS configuration. The LP steam cost, contributing to 90% of the total utility cost, is reduced by 43.24%, and the demand for cooling water is reduced to over half, leading to a 44.55% reduction in utility cost. The same absorber condition and regenerative temperature result in nearly equal thermal degradation, showing great agreement with the negligible difference in make-up cost. As a kettle reboiler is replaced with a steam heater in AFS configuration, the heat duty is significantly reduced, and then the amount of regenerated CO_2 becomes less. Evaluating the energy usage by equivalent work per tonne of CO_2 regenerated is a relatively fair way. The existing carbon capture plant using standard MEA-absorption configuration consumes 7.22 GJ/tonne CO_2, whilst the AFS configuration is able to consume 5.89 GJ/tonne CO_2, saving 18.49% energy usage.

Table 5. Detailed characterization results of two carbon capture configurations

		Electricity	MEA makeup	Water makeup
Fossil resource scarcity	Conventional	30621.65	36.85	0.12
	AFS	24960.77	56.72	0.07
Land use	Conventional	39021.16	4.36	0.03
	AFS	31807.50	6.70	0.02
Human non-carcinogenic toxicity	Conventional	46117.39	43.68	0.52
	AFS	37591.88	67.22	0.32
Human carcinogenic toxicity	Conventional	3396.49	3.78	0.06
	AFS	2768.60	5.82	0.04
Terrestrial ecotoxicity	Conventional	60160.37	50.70	1.38
	AFS	49038.80	78.02	0.85
Ionizing radiation	Conventional	54628.20	7.32	0.04
	AFS	44529.34	11.26	0.02
Global warming potential	Conventional	86344.88	71.27	0.41
	AFS	70382.70	109.70	0.25

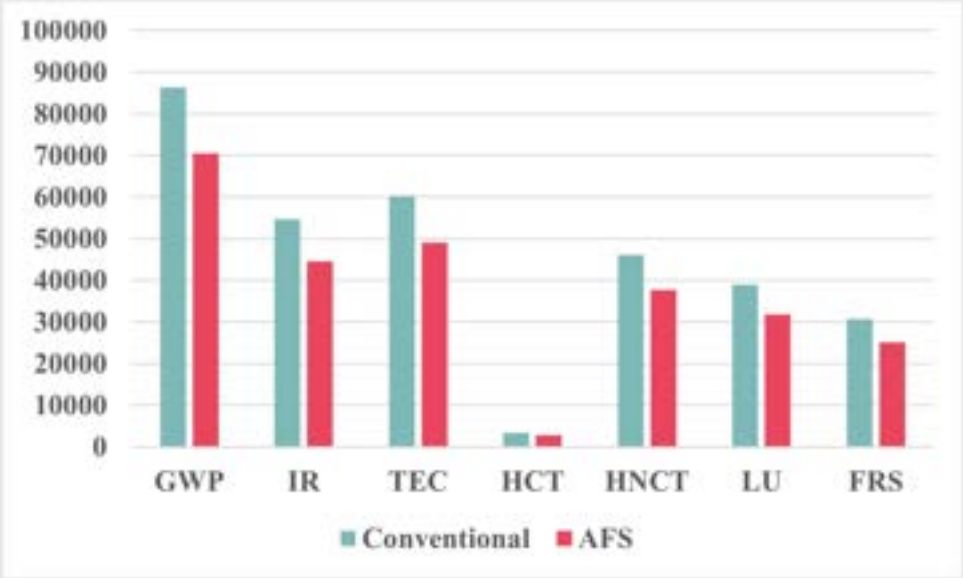

Figure 3. Characterization results of two carbon capture configurations using ReCiPe 2016.

The life cycle assessment measures the environment impacts of material and energy consumption in the carbon capture process quantitively: approximately 78000 kg CO_2, 50000 kBq Co-60, 55000 kg 1,4-DCb, 3000 kg 1,4-DCB, 42000 kg 1,4-DCB, 35000 m^2a cropland and 28000 kg oil. Furthermore, electricity contributes to around 99% of all impact indicators. The general pattern of impact indicators presented in Figure 3 shows that the AFS configuration contributes less to environmental and healthy damage, compared to the conventional configuration. This can be attributable to the significant reduction of energy usage in the carbon capture process using AFS configuration, according to Table 5 electricity (energy consumption is converted to equivalent electricity use) makes the main contribution to environmental influence. The most significant indicator is the global warming potential and the least influential indicator is human carcinogenic toxicity. This is because the cradle to grave of electricity generated by fossil fuels leads to a tremendous amount of greenhouse gas emissions whilst a relatively tiny amount of substance resulting in cancer potential to human health. As the aim of the carbon capture process is to capture CO_2 for sequestration or utilization, and the energy consumption itself leads to 78 tonnes of equivalent CO_2 (responsible for 58% of the flue gas in this work), the emphasis on the improvement of energy saving in carbon capture processes is not only reasonably in economic, but in climate change concern. Measured by the same units, the amount of toxic substances detrimental to

terrestrial individuals and the functioning of the ecosystem is relatively higher than that of toxic substances leading to non-carcinogenic diseases for humans. This is due to a larger scope of the terrestrial system including the living place of the human. Table 5 gives more details related to the impact contribution of electricity, MEA makeup and water makeup. In addition to the aforementioned role of electricity, it is interesting to see some clues from chemical processes and properties: MEA is produced by ammonia which is mainly produced via the energy-intensive Haber-Bosch process, leading to the scarcity of fossil resources and greenhouse gas emissions. Also, the toxic property of MEA corresponds to the detrimental impacts on human health and the terrestrial ecosystem associated with its individuals. Therefore, life cycle assessment gives a new perspective to see the improvement potential in the carbon capture process environmentally.

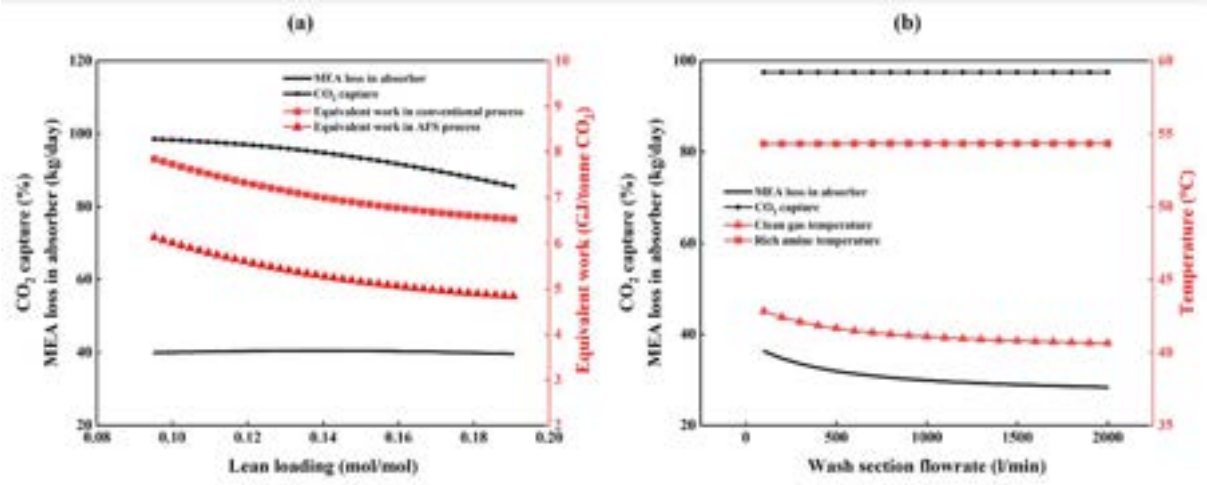

Figure 4. The effects of (a) CO2 loading and (b) water wash amount on CO2 removal, solvent loss and equivalent work.

The sensitivity analysis is conducted to investigate the effects of lean loading and wash section flowrate on absorption performance and energy usage. In Figure 3(a), no effect on amine loss is observed as the CO_2 loading in a lean solvent increases. The significantly decreased curves of equivalent work for CO_2 regeneration in both configurations show great benefits in energy saving. Specifically, with the increment of lean loading from 0.09 to 0.19, the equivalent work in conventional and AFS carbon capture processes reduces by 16.8% and 20.1%, respectively. Albeit the energy benefits, the capability of removing CO_2 is weakened to only 85%. The trade-off of energy saving and carbon penalty is therefore formed when the carbon tax is considered. The MEA loss in clean gas discharged to the atmosphere contributes to potential health and environmental consequences. In addition, the main degraded product of MEA is ammonia, which is soluble in water and detrimental to human health and the environment [12]. Therefore, the wash section is essential in carbon capture processes using MEA. In Figure 3(b), as the flowrate of the wash stream increases from 100 to 2000 litres per minute, the MEA loss decreases by 22%. Moreover, the outlet temperature of the overhead vapour is decreased from 42.8 ºC to 40.6 ºC. However, the wash section flowrate contributes little influence on the removal of CO_2 and the bottom temperature. The off-gas temperature can be a general reference to know the extent of amine loss.

Conclusion

Started with the rate-based simulation to study the operating performance of carbon capture processes with two configurations, the capital costs and operating costs were estimated, followed by the life cycle assessment. Finally, sensitivity analysis was conducted to locate key parameters. The conclusions are as follows:

1. The total annualized costs of the 130-tonne daily carbon capture plant were 3.33 million USD and 2.87 million USD, respectively for the conventional configuration and AFS configuration.
2. Energy consumption contributed to the main environmental impacts, and the cradle and grave of energy and materials consumed in the carbon capture process made approximately half of

the CO_2 capture in vain. Therefore, improving energy efficiency or using renewable energy could be environmentally beneficial.

3. The increment of lean loading reduced energy consumption for CO_2 regeneration but weakened the capability of CO_2 removal. The wash section was able to reduce amine loss significantly.

Reference

[1] N.Borhani T, Wang M. Role of solvents in CO2 capture processes: The review of selection and design methods. Renew Sustain Energy Rev. 2019 Oct 1;114:109299.

[2] Lin YJ, Chen E, Rochelle GT. Pilot plant test of the advanced flash stripper for CO2 capture. Faraday Discuss. 2016 Oct 17;192(0):37–58.

[3] Optimization of an Existing 130 Tonne Per Day CO2 Capture Plant from a Flue Gas Slipstream of a Coal Power Plant | Elsevier Enhanced Reader [Internet]. [cited 2022 Oct 31]. Available from: https://reader.elsevier.com/reader/sd/pii/S1876610213002695?token=C8AEFC00EEFAAB1D6AA89904433049EFB62C87118EC5757A4378ADED0CEB124EA2A2440C92584A7C3E9088CA6D08D0AB&originRegion=eu-west-1&originCreation=20221031192857

[4] Redlich Otto, Kwong JNS. On the Thermodynamics of Solutions. V. An Equation of State. Fugacities of Gaseous Solutions. Chem Rev. 1949 Feb 1;44(1):233–44.

[5] Onda K, Takeuchi H, Okumoto Y. MASS TRANSFER COEFFICIENTS BETWEEN GAS AND LIQUID PHASES IN PACKED COLUMNS. J Chem Eng Jpn. 1968;1(1):56–62.

[6] Mass Transfer (Absorption) Coefficients Prediction from Data on Heat Transfer and Fluid Friction | Industrial & Engineering Chemistry [Internet]. [cited 2023 Mar 6]. Available from: https://pubs-acs-org.manchester.idm.oclc.org/doi/abs/10.1021/ie50299a012

[7] Stichlmair J, Bravo JL, Fair JR. General model for prediction of pressure drop and capacity of countercurrent gas/liquid packed columns. Gas Sep Purif. 1989 Mar;3(1):19–28.

[8] Towler G, Sinnott R. Capital cost estimating. In: Chemical Engineering Design [Internet]. Elsevier; 2022 [cited 2022 Sep 20]. p. 239–78. Available from: https://linkinghub.elsevier.com/retrieve/pii/B9780128211793000078

[9] Wang W, Ma Y, Maroufmashat A, Zhang N, Li J, Xiao X. Optimal design of large-scale solar-aided hydrogen production process via machine learning based optimisation framework. Appl Energy. 2022 Jan 1;305:117751.

[10] Curran MA, editor. Life cycle assessment handbook: a guide for environmentally sustainable products. Hoboken, N.J: Wiley/Scrivener; 2012. 611 p.

[11] Huijbregts MAJ, Steinmann ZJN, Elshout PMF, Stam G, Verones F, Vieira M, et al. ReCiPe2016: a harmonised life cycle impact assessment method at midpoint and endpoint level. Int J Life Cycle Assess. 2017 Feb 1;22(2):138–47.

[12] Mertens J, Lepaumier H, Desagher D, Thielens ML. Understanding ethanolamine (MEA) and ammonia emissions from amine based post combustion carbon capture: Lessons learned from field tests. Int J Greenh Gas Control. 2013 Mar;13:72–7.

PROCEEDINGS OF ECOS 2023 - THE 36TH INTERNATIONAL CONFERENCE ON
EFFICIENCY, **C**OST, **O**PTIMIZATION, **S**IMULATION AND ENVIRONMENTAL IMPACT OF ENERGY SYSTEMS
25-30 JUNE, 2023, LAS PALMAS DE GRAN CANARIA, SPAIN

Possible circular use of CO_2 waste streams from geothermal power plants

A. Manfredi[a], G. Manfrida[b], V. Veltroni[c], C. Zuffi[d]

[a] University of Padua, Padua, Italy, alessia.manfredi.1@phd.unipd.it
[b,c,d] University of Florence, Florence, Italy, [b]giampaolo.manfrida@unifi.it,
[c]valentina.veltroni1@stud.unifi.it, [d] claudio.zuffi@unifi.it

Abstract:

Geothermal fluid is usually characterized by the presence of water and minor percentages of non-condensable gases (NCG), including CO_2. Relevant CO_2 streams are currently released from the cooling towers of geothermal power plants operating in Tuscany. These emissions are largely of natural origin. The output streams of NCG are treated for removal of contaminants (Hg and H_2S) and consist in nearly-pure CO_2: that is the reason why it is worth to investigate about its potential circular use. Specifically, the possibility of transport and use as a long-distance heating or cooling fluid stream for local communities is investigated; integration with hydrogen production is also considered, with production of methanol to be used as synfuel or energy storage. Hydrogen can be harvested from several sources: a) from the captured H_2S stream b) from industrial facilities already existing along the transport path c) from integrating an electrolyser in the power plant premises thereby providing load flexibility (currently not present in geothermal power plants). The study is tailored on the local geographical, productive structure and population situation. The remaining part of the CO_2 stream is delivered to the sea where it can be finally destinated to transportation (pipeline or ship) and sequestration. The results are encouraging in inspiring a potentially new sustainable economy structure.

Keywords:

Circular use; CO_2 stream; Geothermal power plant; Hydrogen; Methanol.

1. Introduction

A crucial environmental issue related to electricity generation using geothermal fluids is the emission of non-condensable gases. Vent stacks in geothermal plants emit carbon dioxide (CO_2) and methane (CH_4), raising serious concerns in terms of greenhouse gases. The amount of these emissions is quite small compared to carbon and fossil fuel plants, indicating that the contribution of these sources is practically negligible. Geothermal power plants (GPPs) also emit a higher amount of hydrogen sulphide (H_2S), as it is a main constituent of geothermal fluids. H_2S in air, water, soils, and vegetation is a vital environmental concern for geothermal fields [1].

Due to resource depletion, fossil fuels are not capable of compensating for the growing energy need. In addition, easily extractable fossil fuel is facing an increase in their prices. It is worth mentioning that greenhouse gases (mainly CO_2) have accumulated in the atmosphere by burning fossil fuels. Therefore, clean and sustainable energy has become relevant, with intensified research to make it more affordable and productive.

Currently, H_2 (hydrogen) and CH_3OH (methanol) are in the picture to fulfil the role of storable energy carriers [2]. Electricity surplus can be used to produce H_2 from the water via electrolysis, or further react H_2 with CO_2 obtained from the GPPs to synthesize CH_3OH (Power-to-Gas). This would mitigate greenhouse gas emissions and meet renewable energy directives. Methanol is a liquid that may give some advantages (e.g. it can be stored at ambient temperature and atmospheric pressure). Besides blending with gasoline in cars, an application that can be started directly as methanol is compatible with the current fuel infrastructure or using it as fuel in fuel cells, methanol can also be used as feedstock in the chemical industry.

This innovative renewable method for methanol synthesis may be applied in Tuscany, the Italian region with the highest use of renewable sources, thanks to the concentration of geothermal-electrical generation. Geothermal energy covers, in fact, about 33% of the electricity needs in Tuscany with a global nominal capacity of 914.5 MW and meets the electricity demand of about 2 million households [1].

From Tuscan geothermal plants, CO_2 can be easily stored and used for the synthesis of methanol. In addition, methanol can be produced more sustainably by synthesizing it from H_2 recovered from industries in the region as well as from H_2S reduction. The decomposition of hydrogen sulphide (H_2S) with simultaneous hydrogen (H_2) generation offers a sustainable energy production option and an environmental pollution abatement

strategy. Another way to use this carbon dioxide in order to provide additional services to the population is to exploit it for the production and distribution of heat and cold.

All in all, it is important to investigate both the potential exploitation of carbon dioxide emitted by GPPs and its mitigating implications using the Tuscany region as a case. In fact, this study tries to apply the possible circular uses of carbon dioxide just mentioned. Therefore, this document is part of the ecological transition trying to identify new forms of economy, a productive and industrial induced that can be strengthened and that is identified with the Tuscan territory.

2. Overall system configuration

The general configuration of the system includes a water electrolysis section, a unit for the direct splitting of hydrogen sulphide into hydrogen and sulphur, a methanol synthesis section (MSS), and the CO_2 district heating and cooling. Water electrolysis is performed with the commercially mature technology of alkaline electrolysers. The system operates in the charge phase when electricity in excess is stored as chemical power into hydrogen. Figure 1 shows a simplified functional scheme of the general configuration of the overall system.

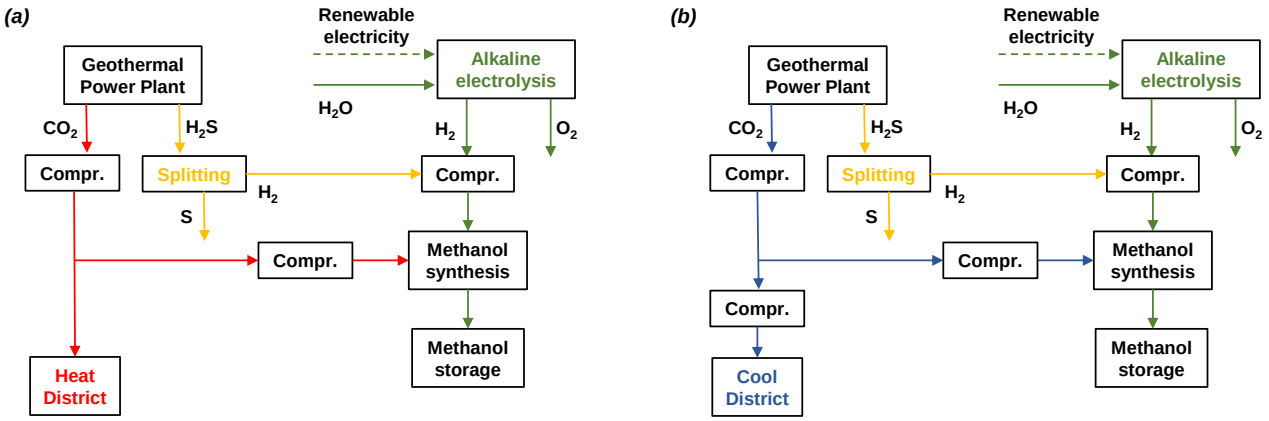

Figure 1. *Scheme of the overall system: a) winter operation, b) summer operation.*

Water and renewable electricity feed the electrolyser to produce hydrogen. Hydrogen sulphide from gaseous emissions in an AMIS system is separated into pure hydrogen and sulphur through the plasma catalytic reactor (PCR). Hydrogen and CO_2 are compressed at the operating pressure of the methanol synthesis reactor in two compressor trains. In the MSS, CO_2 hydrogenation to methanol is performed over a commercial catalyst ($Cu/ZnO/Al_2O_3$) and methanol is separated and purified in a distillation column. The non-synthesized CO_2 arrives in Livorno through a double pipeline: one transports liquid phase in summer operation, and the other, gaseous phase in winter operation. Along the way, the production and distribution of heat and cold is promoted.

3. CO_2 network

Carbon dioxide is practically the only gas that remains after the non-condensable gases have been cleaned with the mercury and hydrogen sulphide abatement system (AMIS®). In this study, one of the two 60 MWe Valle Secolo power plants was considered. The resulting CO_2 flow rate is 3.0 kg/s; with an operational period of 8760 hours/year, the total CO_2 emissions are 95371 t/year [3].

Two extreme seasonal functions were analysed, namely winter and summer operation, for each of which there is a dedicated pipeline. All CO_2 is first compressed up to 4 MPa and cooled to 40°C, in order to enter the steam pipe, which represents winter operation. Part of the stream is sent to the methanol production system. Then in order to enter the liquid pipeline, it is further compressed and cooled to reach winter operating conditions of 10MPa and 20°C. Indeed, the non-synthesized CO_2 will be transported from the GPP to the coast promoting along the way service uses: production and distribution of heat and cold.

Determining the pipeline route and length is the first thing to consider in the design of pipelines. The pipeline route will determine the total length of the pipeline and the bends on it. Even the pipeline pressure drop is dependent among other factors on the length of the pipeline.

The final terminal is identified in the SNAM refinery in Livorno, where there may be other possibilities for CO_2 transformation, or alternatively liquefaction and delivery in port areas for the purpose of confinement (for example, in deep water or underwater saline aquifers). Figure 2 shows the location and extent of the CO_2 pipelines, as well as the inhabited areas crossed. The road network was considered a general scheme for arranging CO_2 pipes. Existing brine ducts between the Saline di Volterra and Rosignano Solvay (dotted in green) have also been highlighted. The route starts from the Vallesecolo plant and passes through the Saline di Volterra, Cecina, Rosignano Solvay, and finally Livorno. It is proposed to implement another MSS along the route near Solvay Chimica S.p.A., located in Rosignano Solvay, where hydrogen is expected to be recovered.

In tracing the route, a possible development of district heating/cooling was considered, when passing through residential and commercial districts. Therefore, a doublet liquid/gas pipeline is proposed, with each pipe sized to transport the non-synthesized CO_2 flow rate. Friction and heat transfer correlations, implemented in the Engineering Equation Solver (EES) software, were used to model the CO_2 transport process.

Figure 2. *CO_2 pipeline and main residential area crossed.*

3.1. Optimization of the CO_2 pipeline system

The flow rate data determine the fluid volume transportation from source to sink and, consequently, the adequate pipeline diameter for transportation. A pipeline diameter too small for the flow rate would cause high velocity of the fluid with attendant high losses in pressure and erosion of the pipe wall. Very large pipeline diameters would reduce pressure losses, have low velocities, and low or non-existent noise and erosion, but result more expensive. The optimum economic pipe diameter was estimated using the following formula [4]:

$$D_{i,opt} = 0.363 m_v^{0.45} \rho^{0.13} \mu_c^{0.025}, \quad (1)$$

where $D_{i,opt}$ is the optimum inner diameter of the pipe, m_v is CO_2 volumetric flow rate in the pipeline, m^3/s; ρ denotes CO_2 density at average temperature through the pipeline, kg/m^3; and μ_c is average CO_2 viscosity.

Applying the above assumptions to Eq. (1) gives an optimum inner diameter of 0.15 m at a CO_2 flow rate of 2.86 kg/s with inlet conditions of 4 MPa and 40°C (vapour pipe); and an optimum inner diameter of 0.08 m at the same flow rate with inlet conditions of 10 MPa and 20°C (liquid pipe). These diameter values ensure that the losses are not too high even when the fluid is returned after the user in conditions of volume different from those designed for injection into the plant.

3.1.1. Pressure drop along the pipeline

An increase in pressure drop means higher operating costs and possibility the need to introduce recompression stations. Hence, it is necessary to estimate the pressure drop along the pipeline: the pressure drop is dependent on the flow rate as well as on the different geometric characteristics of the pipeline such as diameter, length, elevation changes, etc.

Since the CO_2 density is sensitive to pressure and temperature changes, the pressure drop along the pipeline will reduce the CO_2 density and increase the velocity, which will, in turn, increase the pressure drop.

In the simulation, the inlet conditions for CO_2 are fixed; it is transported to the point of arrival considering, as pressure drops, those distributed and those related to the contribution of the difference in height.

3.1.2. Effect of ambient temperature

Optimization of CO_2 transport via pipeline must account for the effect of ambient temperature because of heat transfer along the pipeline between the CO_2 in the pipe and the surroundings. For environmental conditions, atmospheric pressure and a temperature of 10°C and 27°C for winter and summer operations respectively were considered. The pipes are assumed to be carbon steel [5] and placed above the ground. The insulation is made of polyurethane foam (conductivity 0.027 W/mK) with a thickness of 25 mm. To evaluate the heat exchanger between CO_2 and the environment the following phenomena are considered.

Forced convection is present between CO_2 and the internal duct surface, and natural convection between the insulation external metallic surface and the environment (with air temperatures varying from summer to winter operation). Conduction is present in the duct thickness and in the insulation (including the outlet covering).

3.2. Operating conditions of pipes

Two methods were used for CO_2 transport and exploitation, each working under certain operating conditions. The superstructure of the system is represented in Fig 3.

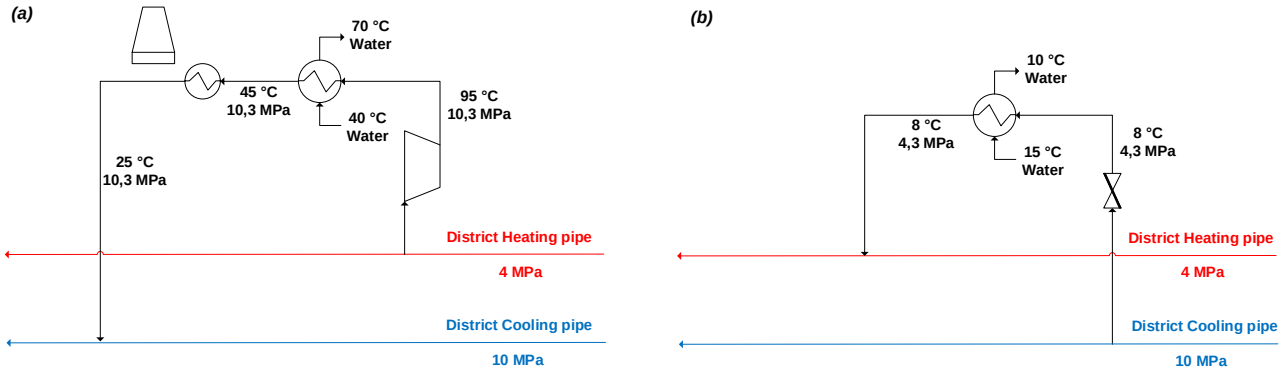

Figure 3. *General scheme: a) Heating mode, (b) Cooling mode.*

In winter operation CO_2 is drawn from the vapour phase pipeline. By setting through a valve the delivery pressure at subcritical values (p_c = 7.38 MPa), the fluid reaches the user at conditions similar to those at the condenser of a closed cycle heat pump. The condenser heat recovery is exploited to heat water for household or commercial building heating. The layout corresponds to a trans-critical heat pump operating directly with CO_2: typical pressures of these applications are 9-10 MPa at the condenser and 3.5-4.5 MPa at the evaporator. The trans-critical CO_2 heat pump solution is attractive because it is possible to operate with common radiator temperatures; also, the heat transfer match with the resource is good (30°C temperature glide on the cold utility side; 50°C on the resource (CO_2) side). The CO_2 leaving the heat recovery exchanger is still in vapour phase, therefore it is necessary to further cool it at least down to 25 °C to bring it to liquid conditions (recovery of the CO_2 stream in the liquid transport pipe, at supercritical pressure). The liquid CO_2 stream will not thus undergo phase changes along the way but will remain liquid despite the pressure drops along the pipeline

For the steam pipe, the inlet temperature is set at 40 °C to avoid two-phase formation due to the lowering of the temperature (T_s = 5 °C at 4 MPa). The pressure value of 4 MPa was selected considering the operation conditions of the heat pump. At higher pressures the saturation temperatures, T_s, are higher and thermal dispersion could determine a temperature below the saturation value (at 5 MPa T_s = 14.5 °C and at 6 MPa T_s = 22 °C) leading to the formation of liquid droplets along the pipe.

The same assumptions were made for summer operation: CO_2 is delivered to the user (needing cooling) in the liquid phase. The liquid pipeline is operated at high pressure in summer (10 MPa); a partial flowrate is laminated to low pressure and brought to the right saturation temperature for cooling (at 4.3 MPa T_s = 8 °C). The pressure of 10 MPa ensures that pressure drops do not lead to steam formation along the pipeline, with an inlet temperature of 20 °C. Expansion of the fluid to 4.3 MPa allows to cool a water stream from 15 to 10°C, which is used for cooling the rooms. After use as a coolant, the CO_2 stream can be recovered without pumps in the vapour phase pipe which is operated at 4 MPa.

4. Thermal energy needs

The main urban centres crossed along the pipeline were analysed to consider them as possible users for heating and cooling. Among the main ones, we find Cecina, Rosignano Solvay, and the final terminal located in Livorno. Referring to these towns, the winter and summer thermal loads have been estimated precisely to consider them as possible users. A shopping centre was also included - the only one that is present on the path to Livorno: is the Acquerta shopping centre, located near Cecina. Considering the available flow rate, we will discuss as an example the shopping centre of Acquerta and the thermal needs of part of the neighbouring residential area of San Pietro in Palazzi, which were evaluated as users.

The CO_2 infrastructure was considered to be possibly connected to representative buildings located in the San Pietro in Palazzi area, to study their different operating modes and performances. The Acquerta shopping centre and the San Pietro in Palazzi area are presently heated by natural gas, with an efficiency assumed as 0.9. For the energy performance index for cooling, no efficiency was considered because it is not supplied in terms of primary energy. In fact, that parameter does not take into account the efficiency of the installation providing the service and is therefore not primary energy.

From the climate conditions and the characteristics of the typical dwelling in this zone, heating (primary energy) and cooling demands throughout the year can be obtained. The characteristics of the representative buildings can be seen in Table 1. The Heating Degree Days (HDD) values are obtained using a base temperature of 20°C. For the calculation of the Cooling Degree Days (CDD), a base temperature of 24°C is assumed. It has to be mentioned that in Italy and unlike for heating, no national standard defines how to compute CDD.

Table 1. *Representative block of flats characteristics.*

San Pietro in Palazzi population	3141
Surface per dwelling [m^2]	100
Number of inhabitants per dwelling	3
Number of dwellings	1047
Heating efficiency with natural gas	0.9
Volume Acquerta S.C. [m^3]	48000

The area here studied falls within climate zone D, so heating systems can be operated from November until April 15 for 12 hours a day, or 1992 hours a year. 610 hours of annual cooling operation were assumed (no legislation limits exist in Italy for this), i.e. about 5 hours per day for four months, while for the shopping centre, 1342 hours per year were assumed, i.e. 11 hours per day for four months. For the two and a half months in which there is no need for thermal energy, it is assumed that the transport of CO_2 takes place with the methanol synthesis along the path.

5. Hydrogen recovery and production

A notable opportunity for circular economy based on CO_2 recovery is the production of synfuels using hydrogen. Here, the production of methanol through hydrogen reaction is considered attractive, as it produces a liquid synthetic fuel already used in the formulation of vehicle fuels. The hydrogen required for this reaction is partly recovered from geothermal and industrial activities, and partly produced. A recovery option is indeed possible at the GPP: considering the entire 120 MW plant operated by ENEL GP in Vallesecolo, it was assumed to produce hydrogen from the hydrogen sulphide present in the geothermal fluid. At the plant premises, it was hypothesized to produce hydrogen through electrolysers when substantial input to the grid from photovoltaics was present: this makes the GPP effectively operate as a substitute storage capacity, as the plant would be operated full load at night (when no PV input is available), and effectively decrease its nominal power feeding a large electrolyser at daytime. The most important industrial recovery option for H_2 takes place at Rosignano Solvay, where in the Solvay Chimica S.p.A. alkali plant hydrogen is a by-product in the soda-chlorine process. This section assesses the potential for recovering and producing hydrogen.

5.1. Plasma catalytic reactor section

The hydrogen sulphide emissions of both groups of Valle Secolo (120MW) are here considered as possible circular economy resources for the production of H_2 and S. The production of H_2S from the plant – currently captured by the AMIS plant - was taken from public monitoring reports [3], a value of 199 kg/h. The power plant emission treatment abatement system was ideally modified by adding a PCR (Fig 4) [6]. The stream to be processed is from the extraction compressor of non-condensable gas, which is currently being sent to the AMIS treatment (with oxidation and alkaline scrubbing for removal of sulphur species), finally delivering a nearly-pure CO_2 stream at the cooling towers (where dispersion profits from the highly buoyant plume).

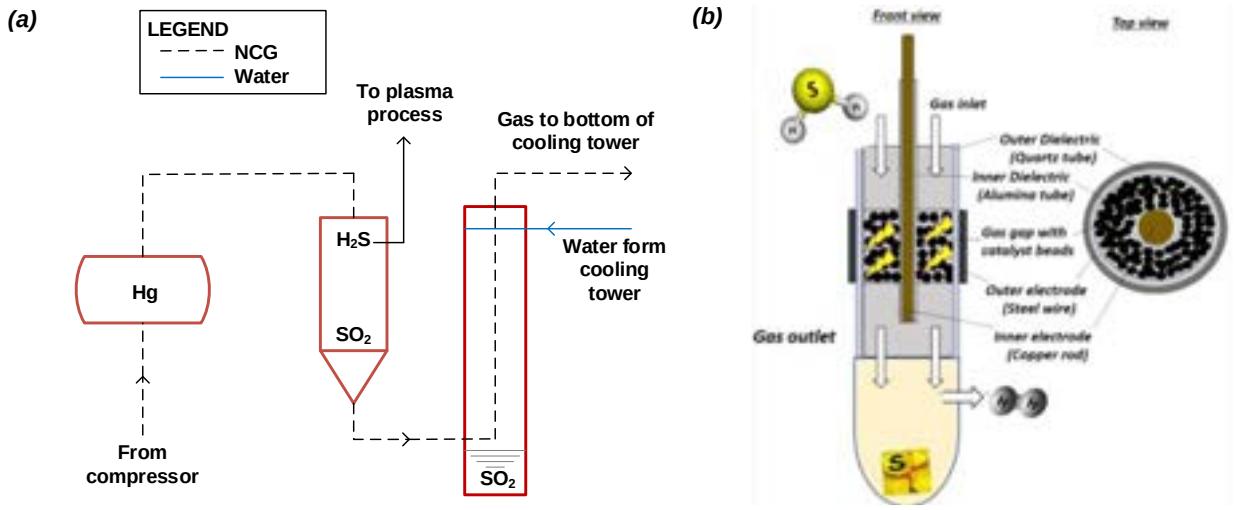

Figure 4. *Schematic illustration of the: a) modified AMIS system (modified from [7]), b) PCR [8].*

The electrified PCR is an innovative technology for H_2 production for waste streams or H_2S: compared to other technologies, it allows to achieve a good conversion at low temperatures (100-200°C). In addition, the purity of hydrogen is very high (99%) [6].

The plasma-assisted catalytic H_2S decomposition is performed at atmospheric pressure in a non-thermal dielectric barrier discharge (DBD) plasma reactor consisting of one or two coaxial dielectric tubes (quartz, alumina). The DBD plasma is created between two electrodes surrounded by the dielectric material (direct electric heating of the catalyst located between the two electrodes). The main electrode is connected to the high voltage supplied by an AC generator [8]. From stoichiometry ($H_2S \rightarrow H_2+S$), the amount of H_2 obtainable from hydrogen sulphide is 11.78 kg/h with a specific electricity consumption of 1.2 kWh/Nm^3 of H_2 [6]. The estimated production of H_2 is 103.2 t/year, so the energy demand would be 1378 MWh/year.

5.2. Alkaline water electrolysis section

Alkaline water electrolysis (AEL) is a low-temperature process to produce hydrogen in a commercially mature technology, namely the alkaline electrolyser. This type of electrolyser is here considered in place of the PEM technology, as large-scale units are needed. Water electrolysis is carried out in a liquid alkaline electrolyte solution of a base (KOH or NaOH), where hydroxide ions OH^- cross a diaphragm separating the electrodes. Typically, AELs operate between 60 and 90°C, while the operating pressure spans from ambient pressure up to 3.5 MPa [9]. In the present case, we assumed to perform the AEL at 3 MPa and 85°C, with a power consumption of 3.6 MW for a hydrogen flow rate of 72 kg/h, leading to a specific energy consumption of approximately 50 kWh/kgH_2 (4.5 kWh/Nm^3H_2), which is consistent with values reported in the literature [10].

Inside the reactor, water electrolysis is accomplished with the following reaction (R1):

$$H_2O \rightarrow H_2 + 0.5O_2, \quad \text{(R1)}$$

which is given by the combination of the cathode reaction (Eq. R2) and anode reaction (Eq. R3, R4):

$$H_2O + 2e^- \rightarrow H_2 + O^{2-}, \quad \text{(R2)}$$

$$O^{2-} \rightarrow 0.5O_2 + 2e^-, \quad \text{(R3)}$$

$$O + O \rightarrow O_2. \quad \text{(R4)}$$

In this case, three electrolysers are used along the CO_2 pipeline path, requiring on the whole an electricity consumption of 31536 MWh/year. It is assumed that electrolysers are powered by renewable energy, thereby enabling the possibility of producing at the end of the process green synfuel: this corresponds to the category of Power-to-X technologies. The electrolysers are assumed to be operational an average of 8 hours per day, thereby using with profit the photovoltaic energy available in Italy (2920 h/year equivalent operational time per year). In this way, it is estimated that it would be possible to produce 215 kg/h of hydrogen (630 t/year).

5.3. Hydrogen from the soda-chlorine process

Some of the hydrogen needed can be harvested from the soda-chlorine process at the Rosignano Solvay plant. Hydrogen is here a co-product of the electrolysis of brine (approximately 28 kg of H_2 per ton of chlorine). This high-quality hydrogen (purity > 99.9%) is currently used on-site (mainly as a fuel in co-firing steam boilers) or is sold to a distributor.

The alkaline electrolyser works following a membrane cell technology [11]. The basic principle in the electrolysis of a sodium chloride solution is the following:

- at the anode, chloride ions are oxidised and chlorine (Cl_2) is formed;
- at the cathode, water decomposes to form hydrogen (H_2) and hydroxide ions (OH^-).

The anode reaction is:

$$2\,Cl^- \rightarrow Cl_2 + 2e^-. \quad \text{(R5)}$$

The cathode reaction is:

$$2Na^+ + 2e^- + 2H_2O \rightarrow 2NaOH + H_2. \quad \text{(R6)}$$

The overall reaction is:

$$2NaCl + 2H_2O \rightarrow 2NaOH + H_2 + Cl_2. \quad \text{(R7)}$$

The products of the electrolysis are 1070–1128 kg of NaOH (100 wt-%) and approximately 28 kg of H_2 per ton of Cl_2 produced. The plant operates in a continuous cycle for 24 hours/day, for a nominal 350 days/year. The theoretical capacity of the plant is about 14.5 tons/hour of Cl_2, which correspond to about 125 kton/year of chlorine gas [12]. Considering the molar mass of chlorine gas equal to 70.906 kg/kmol, stoichiometry shows

that the amount of hydrogen resulting is 3.463 kton/year or 412.2 kg/h. The calculated consumption of electrical energy is equal to about 2600 kWh/t Cl_2 [11], or 6,23 kWh/Nm^3 of H_2.

6. Methanol synthesis section

The MSS allows the production of liquid fuel, which is used to store energy. The main blocks are the adiabatic reactor, where the catalytic CO_2 hydrogenation process is carried out, and the distillation column, where the purification process is carried out. Methanol is produced through the three main reactions of the CO_2 hydrogenation process: CO is given by the water gas shift reaction (R8) and converted into methanol by the CO hydrogenation reaction (R9), while methanol is also produced through the CO_2 hydrogenation reaction (R10).

$$CO_2 + H_2 \leftrightarrow CO + H_2O, \quad \text{(R8)}$$

$$CO + 2H_2 \leftrightarrow CH_3OH, \quad \text{(R9)}$$

$$CO_2 + 3H_2 \leftrightarrow CH_3OH + H_2O. \quad \text{(R10)}$$

At equilibrium conditions only two of these three reactions are sufficient to describe the composition [13]. Only Eqs. (R8) and (R10) were thus considered in the developed model.

The production of methanol was set considering the hydrogen production and recovery. It is supposed to locate two methanol production systems along the pipeline path, one near the GPP to exploit the hydrogen produced by electrolysers and that recovered from hydrogen sulphide (MSS1), the other plant is instead near Solvay Chimica S.p.A. (MSS2). Assuming the stoichiometric molar ratio of reactants (reaction (R10)), Table 2 was been obtained.

Table 2. *Stoichiometric reactants and products flow rates for MSS reactors [kg/h].*

Flow rate Species	MSS1	MSS2
H_2	83.68	412.2
CO_2	609.04	3000
CH_3OH	443.43	2184

The methanol production system is supposed to operate 8760 hours per year and the production was based on the study of [14]; the simulation was performed in the UNISIM DESIGN (Honeywell) modelling environment.

The methanol synthesis reactor operates at 6.5 MPa requiring the hydrogen and CO_2 to be compressed. CO_2 is compressed only when it is taken from the vapour pipeline at 4 MPa from the vapour pipe. Since MSS1 always takes carbon dioxide in the vapour phase, in this study we consider that CO_2 is taken from the vapour pipe for both MSS. A future investigation should concern the case of CO_2 withdrawal from the liquid pipe; when it is taken from the liquid tube at 10 MPa it must be laminated and then heated to have only steam entering the reactor. The number of compressor stages for the H_2 stream depends on the source. The hydrogen obtained from the reduction of hydrogen sulphide is compressed to the operating electrolysis pressure, and then joins the flow of hydrogen produced by the alkaline electrolyser.

Figure 5 shows a simplified functional scheme of the methanol synthesis and purification section. The compressed H_2 (2) and CO_2 (5) are mixed with the re-circulated gases (23) and preheated (HX1) to 210 ◦C prior to entering the synthesis reactor (R1). Within the adiabatic reactor, the exothermal CO_2 hydrogenation reaction increases the temperature up to about 280 °C and 231 °C for MSS1 and MSS2 respectively. The reactor outlet is mainly composed of hydrogen (about 85% by vol in MSS1 and 97% by vol in MSS2), whereas the methanol content is 4.1% by volume in MSS1 and 1.5% by volume in MSS2. To boost the production of methanol, two flash processes are performed (F1 and F2) and the un-reacted incondensable gases (18 and 21) are re-circulated back to the reactor. The first flash occurs at 6.5 MPa, after reducing the temperature to 50 °C in two heat exchangers (HX1 and HX2), that supply heat to other points in the process, and a cooler (C1). Here the gases are separated to liquid raw methanol and non-reacted gases. The non-reacted gases (18) are recycled to the reactor after purging 1% in order to prevent the accumulation of by-products and inert gases in the system. The second flash process takes place reducing the pressure and temperature of the liquid stream to about 0.12 MPa and 22 °C. Here raw methanol is expanded to further remove the non-reacted gases, especially CO_2, and by-products in order to ease the distillation process. The resulting liquid product (12), namely crude methanol, is mainly composed of methanol and water (both about 50% by vol in both systems) with a small content of CO_2. To boost the methanol purity, the separation of water and methanol takes place in a distillation column (D1). From the bottom of the distillation column, water (15) is recuperated in the liquid phase and can be recycled back to the electrolysers. The distillate at the top of the column (14) is

pure methanol; the CO_2 in the residue (16) is recycled to the inlet and mixed along with fresh CO_2 (3). Methanol is then sent to the storage tank. The resulting methanol has a purity greater than 99.85% in both systems and is therefore compliant with the IMPCA specification [15]. Table 3 reports the main MSS operating parameters.

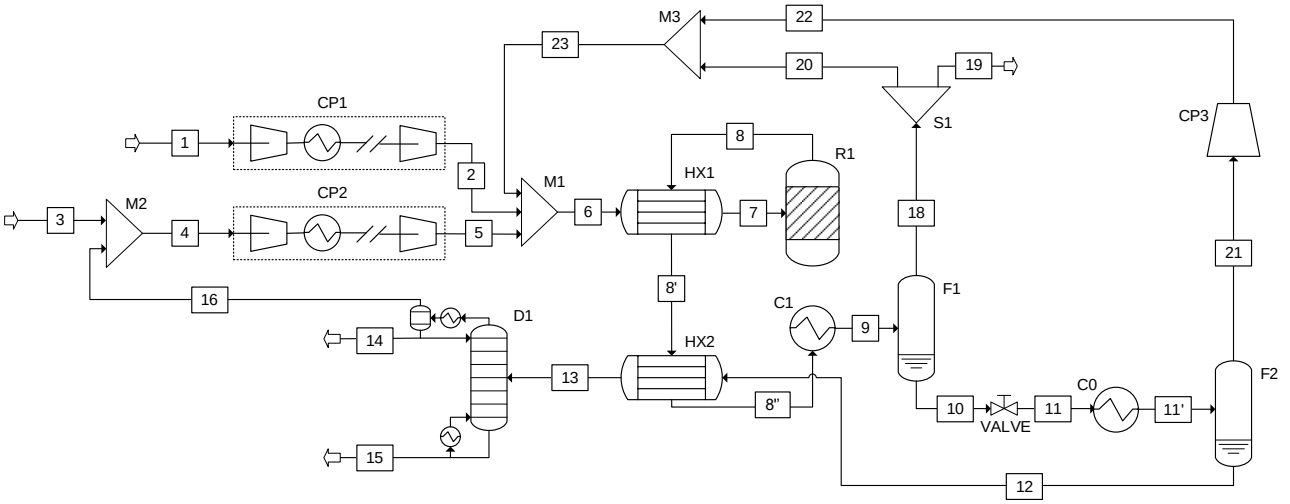

Figure 5. *Simplified functional scheme of the MSS, modified from [14] (C=Cooler; CP=Compressor; D=Distillation column; F=Flash; HX=Heat exchanger; M=Mixer; R=Reactor; S=Splitter).*

Table 3. *MSS main operating parameters.*

Parameter	Value
Reactor type	Adiabatic
Reactor pressure [bar]	65
Reactor inlet temperature [°C]	210
F1 pressure [bar]	65
F1 temperature [°C]	50
F2 pressure [bar]	1.2
F2 temperature [°C]	22
Methanol storage pressure [bar]	1
Methanol storage temperature [°C]	25

Since the reactor products are characterized by a high temperature, they can be employed to provide heat to some processes within the system, reducing the thermal energy that otherwise would be provided by an external source. Thermal energy is required by the following processes:

- the preheating of the reactants (6) from 80 to 210 °C;
- the heating of crude methanol (12) up to the inlet temperature of the distillation column (80°C).

Firstly, the reactor products are cooled (HX1) from 280 °C (8) to 144 °C (8') in MSS1 (from 231 °C to 84 °C in MSS2). Finally, the reactor products (8') are cooled (HX2) to about 132 °C in MSS1 and 80°C in MSS2, with the preheating of the crude methanol (12). To reach the first flash condition (50 °C), heat should be further removed from the reactor products in cooler C1. If a cooler heat recovery in the distillation column were also considered, the thermal self-sustainability of the section could be achieved.

7. Results and discussion

Drawing on the methodology presented in the previous section, the thermal energy demand and the district heating and cooling performance are discussed in detail as a first step. Then, the results of the two methanol production plants are shown. Finally, the energy requirements of the system and the emissions avoided are assessed.

7.1. Energy demand

Heating Degree Days (HDD) and Cooling Degree Days (CDD) patterns are presented in Fig 6 (a). The maximum daily values for HDD and CDD are 13.82 °C and 2.73 °C respectively. Moreover, the annual accumulated HDD is 1602°C and for CDD is 48°C.

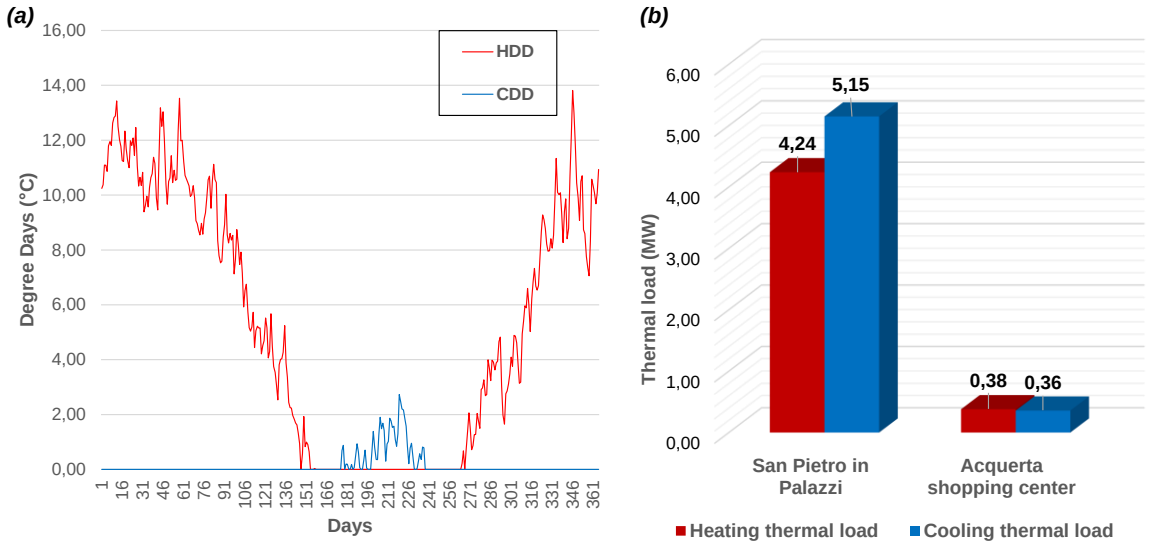

Figure 6. *a) Annual evolution of heating and cooling degree days in the selected location, b) Energy demand for the area studied.*

Figure 6 (b) illustrates the thermal needs of the Acquerta shopping centre - the main user to be satisfied - as well as those of the San Pietro in Palazzi community. The total thermal energy required annually by the shopping centre is 0.74 MW. 51.5% of which is for heating and 48.5% for cooling.

7.2. Heating and Cooling district

The CO_2 leaving the AMIS is brought to the desired conditions for the entrance to the steam pipe through three inter-refrigerated compressors up to 4 MPa and subsequent cooling up to 40 °C. A portion of the flow rate is sent to the methanol production system: the remaining CO_2 flow rate to be transported is 2.86 kg/s. The flow rate that must instead be introduced on the liquid side undergoes a further compression up to 10 MPa and subsequently, an absorption cooling (it is proposed the use of geothermal water for CO_2 cooling) is used to bring its delivery temperature to 20 °C.

The initial three compressors are about 300 kW each, the fourth – operational for the final liquid flow delivery rate - needs about 173 kW; the flow rate of water required (sets a maximum outlet temperature of 95 °C) for the two inter-refrigerations is a total of about 2 kg/s, that for cooling the steam up to 40 °C is 1.2 kg/s, while the thermal power that must be dissipated with the absorption cycle is 851 kW.

During winter operation, given the potential of the available CO_2 flow rate, it is possible to satisfy a 430kW thermal user. In this condition, therefore, the system is able to meet the heating needs of the Acquerta shopping centre, with the possibility of distributing about 50kW of heat to San Pietro in Palazzi buildings.

Figure 7 shows the representation of the system just described on the T-s diagram. The subcritical vapour at 4 MPa is compressed to 10.3 MPa (1-2 process) and then is cooled in the trans-critical heat pump to 45°C by rejecting heat to an external fluid (2-3 process, useful heating effect). Carbon dioxide at high pressure is further cooled to 25°C in the air heat exchanger (3-4 process).

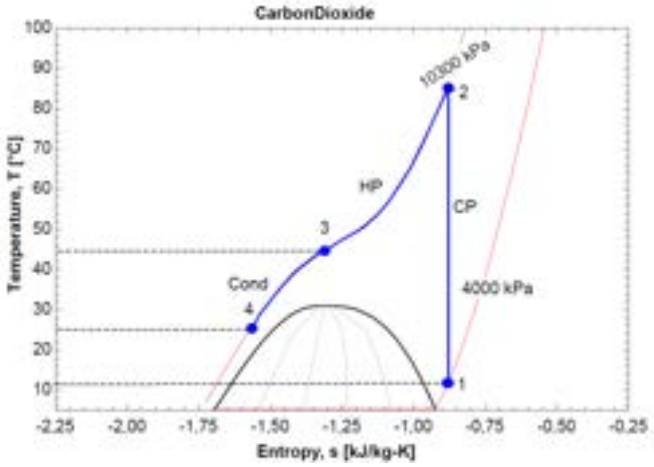

Figure 7. *Representation of winter operation on the T-s diagram (CP=Compressor, HP=trans-critical Heat Pump, Cond=Condenser).*

The conditions of the CO_2 entering the heat pump, which represents the user, depend on the losses that occurred upstream. In particular, the pressure remains at 4 MPa, but the temperature drops along the pipeline to an estimated value of 10.5 °C, despite the insulation of the pipeline. The power required by the compressor to compress CO_2 to 10.3MPa is 147.3 kW. The calculated COP of the heat pump is about 3. The thermal power required to cool down the CO_2 stream in the air exchanger to bring it back to the liquid state is 229.8kW. Figure 8 (a) illustrates the heat transfer profiles of the first heat exchanger, showing a good coupling between the resource and the user (a result of the selection of a trans-critical Heat Pump). Figure 8 (b) shows the heat transfer profile of the air exchanger that produces the liquid CO_2 recovery stream.

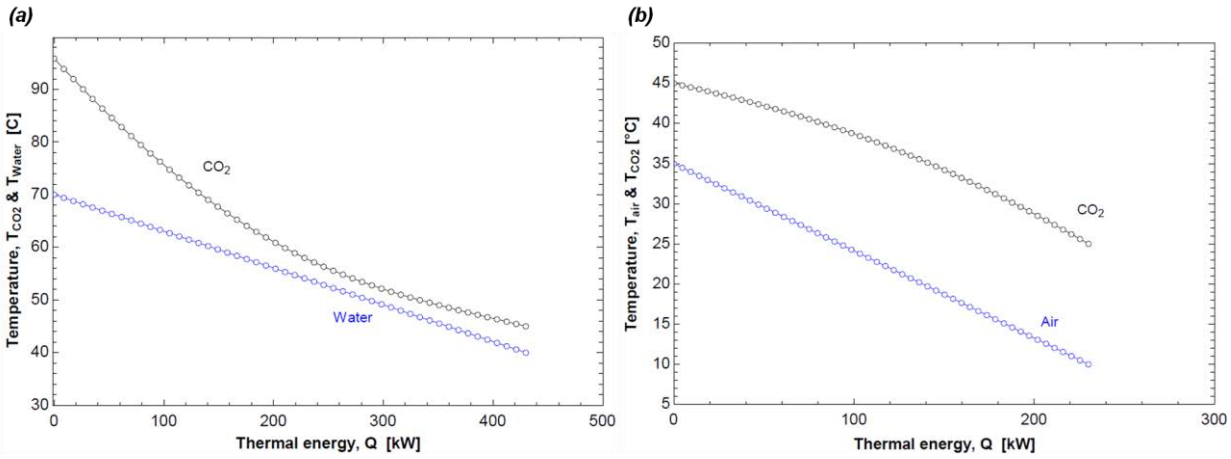

Figure 8. *Heat exchange profiles of a) the transcritical heat pump, and b) the air exchanger.*

During summer operation, given the potential of the available CO_2 flow rate, it is possible to satisfy a 480kW cooling load. In this condition, therefore, the system meets the cooling needs of the Acquerta shopping centre, with the possibility of distributing about 122kW of cold to the San Pietro in Palazzi households. The difference between summer and winter is dictated by the fact that in summer for cooling the load is greater for the individual user, especially considering the shopping centre.

7.3. Methanol Synthesis Systems

For the MSS1 system, hydrogen from H_2S is compressed to 3MPa in order to combine the hydrogen stream produced by the electrolysers. Then the hydrogen flow is further compressed up to 6.5 MPa, the working pressure of the MSS. The power consumed is equal to 81.72 kW. Since de compression power required by the CO_2 is equal to 9.4 kW, the total power absorbed by all compressors in the MSS1 is about 93 kW.

Also for the MSS2 system, located at the Solvay Chimica S.p.A. premises, hydrogen must be compressed to 6.5 MPa. In this case, the power consumed is equal to 329.6 kW. As previously specified, it is supposed to take CO_2 from the vapour phase pipe (4 MPa); therefore, it must also be compressed. The total compressor power for the MSS2 is about 193.3 kW. For both MSS systems, the overall power requirement of the compressors is mainly due to hydrogen compression.

As described previously, several heating and cooling processes take place in different sections of the system, requiring an accurate analysis to identify a correct coupling between the different flows to enhance the system's performance. An internal heat recovery was performed to reduce the external requirements of thermal energy (Fig 5). In Table 4 the heating and cooling processes within the MSS are summarised.

Table 4. *Main heat transfers in the MSS1 and MSS2.*

Heat requirement	Process	Fluid	Thermal power [kW]	
			MSS1	MSS2
Heating	HX1	Reactor inlet	440	8100
	HX2	Methanol and water	46.65	211.5
Cooling	C1	Reactor product	559.6	2368
	C0	F1 liquid product	22.10	107.9

As shown in Table 4, since the MSS does not need external heat input (HX1 and HX2), the main thermal energy load can be identified in the cooling process of the synthesis reactor products (C1) that need to be cooled to about 50°C to separate methanol and water from incondensable gases.

436.55 kg/h of methanol are obtained for the MSS1 system and 2078.6 kg/h of methanol for the MSS2 system, which correspond to 98% and 95% of stoichiometric methanol, respectively. Considering an operation of 8760 h/y, the annual methanol production of the plants is equal to 22 kton. Bearing in mind that the annual carbon

dioxide emissions of the Valle Secolo plant are about 95 kton/year, the two MSS allow using of about 33% of these emissions.

7.4. Mass and energy balance

Table 5 collects the results from the mass balance of the system, showing that the yield is 0.7kg of methanol per kg of CO_2 supplied. The production of oxygen is 0.47kg per kg of CO_2 supplied. A further development of the MSS could be the combustion of the purge stream 19 (Fig 5) and thus the production of electrical energy. The results from the energy balance of the system are gathered in Table 6, which shows that water electrolysis corresponds to 87.6% of the net electricity consumed by the entire process.

Table 5. *Mass balance (not including the remaining CO_2 transported to the final terminal).*

Compound	In (t/h)	Out (t/h)
CO_2	3.61	0.0121[a]
CO	0	0.0036[a]
H_2	0	0.1278[a]
H_2O	1.928	1.45
Methanol	0	2.52
O_2	0	1.71[b]

[a] Contained in stream 19 (purge)

[b] Oxygen generated by water electrolysis

Table 6. *Energy balance.*

Unit	Operation	Amount [MW_{el}]	Amount/tMeOh [kJ/ton MeOh]
Water electrolysis	Power to AEL	10.8	0.604
H_2S reduction	Power to PCR	0.157	0.003
CO_2 preparation	CO_2 Compression	1.09	0.02
Methanol synthesis and purification	Compressors	0.29	0.005
Total net electricity consumption		12.332	0.633

7.5. CO_2 emissions avoided

The assessment of avoided CO_2 emissions is done by investigating the difference between two scenarios: the conventional and the innovative. In the conventional scenario, emissions are due to conventional methanol production: most of the commercial methanol produced today comes from fossil fuels, typically using steam reforming from the natural gas feedstock. CO_2 emissions from conventional methanol generation are assumed equal to 0.555 kg CO_2/kg methanol [16]. In the innovative scenario, the emissions are only those of the scheme to produce methanol with the H_2+CO_2 reactor, i.e. 0.005 tons CO_2/t of methanol. It should be emphasized that the energy sources necessary for the processes described must be assumed consistently with the purpose of this investigation, therefore the use of electricity from renewables is necessary.

The total CO_2 emissions of both MSS are 105.7 tons/year, considering 8760 operating hours, and with a production of 22 kton/year of methanol; with the conventional system, on the other hand, 12kton/year of CO_2 would be emitted considering the same methanol production and the same operating hours.

The emissions avoided for utilities were calculated for heating from the values of the energy performance index already calculated in primary energy and assuming the use of natural gas with emissions of 199 g CO_2/kWh [17]. For the production of cold, the use of electricity for the supply of the refrigeration cycle with a COP 3 with emissions of 355 g CO_2/kWh for electricity was assumed [18]. Therefore, this results in a reduction in emissions related to the heating and cooling services provided of about to 237 tons of carbon dioxide per year.

8. Conclusion

This work tackles the problem of the greenhouse effect, which is a global problem, and something important on a regional scale. The Tuscany region has almost 1000MW of geothermal energy installed, the only region in Italy with a long tradition on this. Geothermal energy has raised problems, but it has also brought a lot of wealth: at present, geothermal is supplying the largest share (over 78%) of renewable energy in the Tuscany region [19]. The energy transition towards carbon waste-free urban districts relies on local renewable energy assets. As part of the ecological transition, some things will have to change, and this document investigates the possible circular uses of geothermal carbon dioxide, which represents a waste in electricity production, but also a fraction that would still have been released naturally from underground [20]. The scenario investigated in this study lies in some fundamental pillars:

- hydrogen recovery along the way: 103.2 tons/year of hydrogen from the reduction of hydrogen sulphide and 3463 tons/year from Solvay S.p.A.
- production of green hydrogen by electrolysers powered with renewable energy: 630 tons/year of green hydrogen are produced;
- implementation of Power-to-X technology: 22033 tons/year of methanol are produced by converting about 32 kton/year of carbon dioxide (about 33% of the Valle Secolo total emissions);
- promote the co-generation and distribution of heat and cold for users: 869 MWh/year of thermal load for heating and 543 MWh/year of cooling demand are satisfied. In this way, 100% of the thermal and cooling requirements of Acquerta S.C. and 1.2% and 2% of that of San Pietro in Palazzi are fulfilled during winter and summer operations, respectively.

The circular use of CO_2 also makes it possible to reduce emissions due to heating and cooling operated in an unconventional way: about 240 t/year of CO_2 would be saved. There is also a saving of emissions in the methanol cycle because if the same amount of methanol had to be produced through fossil fuels, about 12 kton/year of CO_2 would be emitted. Hypotheses of sequestration of CO_2 not converted along the route could also be evaluated, as well as bottling, liquefaction and shipment from the port of Livorno. A further future study will concern the economic feasibility of the system.

In conclusion, this work focused on the Tuscany region represents a screening of interesting possibilities for sustainable development.

Acknowledgments

This research partial support from Italian PNRR NEST Spoke 5 “Energy Conversion”.

Nomenclature

Abbreviations

AEL Alkaline water Electrolysis

AMIS Abatement of Mercury and Hydrogen Sulfide, in the Italian language

CDD Cooling Degree Days

DBD Dielectric Barrier Discharge

GPP Geothermal Power Plants

HDD Heating Degree Days

MSS Methanol Synthesis Section

NCG Non-Condensable Gases

PCR Plasma Catalytic Reactor

PV Photovoltaic

List of Symbols

D Diameter, m

m_v Volumetric flow rate, m^3/s

p Pressure, MPa

T Temperature, °C

Greek symbols

μ Viscosity, Pa.s

ρ Density, kg/m^3

Subscripts

c critical

i,opt optimum inner

s saturation

References

[1] Somma R., Granieri D., Troise C., Terranova C., De Natale G., Pedone M. Modelling of hydrogen sulphide dispersion from the geothermal power plants of Tuscany (Italy). Sci. Total Environ. 2017;583:408-20.

[2] Olah G. A. Beyond Oil and Gas: The Methanol Economy. Angew. Chem., Int. Edit. 2005;44:2636-2639.

[3] ARPAT. Monitoraggio delle aree geotermiche toscane. Controllo alle emissioni delle centrali geotermoelettriche. 2014.

[4] Zhang Z., Wang G., Massarotto P., Rudolph V. Optimization of pipeline transport for CO_2 sequestration. Energ. Convers. Manage. 2006;47:702-15.

[5] Serpa J., Morbee J., Tzimas E. Technical and Economic Characteristics of a CO_2 Transmission Pipeline Infrastructure. JRC 2011.

[6] Zaman J., Chakma A. Production of hydrogen and sulfur from hydrogen sulfide. Fuel Process. Technol. 1995;41(2):159-198.

[7] Baldacci A., Mannari M., Sansone F. Greening of Geothermal Power: An Innovative Technology for Abatement of Hydrogen Sulphide and Mercury Emission. Proceedings World Geothermal Congress, Turkey, 2005.

[8] Mikhail M., De Costa P., Amouroux J., Cavadias S., Tatoulina M., Gàlvez M.E., Ognier S. Tailoring physicochemical and electrical properties of Ni/CeZrOx doped catalysts for high efficiency of plasma catalytic CO_2. Appl. Catal. B Environ. 2021;294:120233.

[9] Zeng K., Zhang D. Recent progress in alkaline water electrolysis for hydrogen production and applications. Prog. Energy Combust. Sci. 2010;36:307-26.

[10] Gallandat N., Romanowicz K., Zuttel A. An analytical model for the electrolyser performance derived from materials parameters. J. Power Energy Eng. 2017;5:34-49.

[11] Brinkmann T., Santoia G.G., Schorcht F. Best Available Techniques (BAT) - Reference Document for the Production of Chlor-alkali. JRC91156, 2014.

[12] Solvay Chimica S.p.A. Sintesi non tecnica. 2007.

[13] Graaf G.H., Winkelman J. Chemical Equilibria in Methanol Synthesis Including the Water-Gas Shift Reaction: A Critical Reassessment. Ind. Eng. Chem. Res. 2016;55:5854-64.

[14] Lonis F., Tola V., Cau G. Assessment of integrated energy systems for the production and use of renewable methanol by water electrolysis and CO_2 hydrogenation. Fuel 2021;285:119160.

[15] IMPCA. Methanol Reference Specification. Brüssel 2015.

[16] Ravikumar D., Keoleian G., Miller S. The environmental opportunity cost of using renewable energy for carbon capture and utilization for methanol production. Appl. Energy 2020;279:115770.

[17] Pylsy P., Lylykangas K., Kurnitski J. Buildings' energy efficiency measures effect on CO_2 emissions in combined heating, cooling and electricity production. Renew. Sustain. Energy Rev. 2020;139:110299.

[18] ISPRA. Italian Emission Inventory 1990-2018. 2020.

[19] TERNA group. L'elettricità nelle regioni. 2021. [Online]. Available: https://download.terna.it/terna/8%20-%20REGIONI_8dae445e263948d.pdf. [Accessed 2023].

[20] Sbrana A., Lenzi A., Paci M., Gambini R., Sbrana M., Ciani V., Marianelli P. Analysis of Natural and Power Plant CO_2 Emissions in the Mount Amiata (Italy) Volcanic-Geothermal Area Reveals Sustainable Electricity Production at Zero Emissions," Energies 2021;14:4692.

Life Cycle Assessment and Scenario Analyses of an operating geothermal Heat Project in the Southern German Molasse Basin

Hannah Uhrmann[a], Florian Heberle[b] and Dieter Brüggemann[c]

[a] University of Bayreuth, Bayreuth, Germany, hannah.uhrmann@uni-bayreuth.de
[b] University of Bayreuth, Bayreuth, Germany, florian.heberle@uni-bayreuth.de
[c] University of Bayreuth, Bayreuth, Germany, brueggemann@uni-bayreuth.de

Abstract:

In order to mitigate climate change, the expansion of renewable sources especially in the fossil-dominated heating sector is necessary. Geothermal sources represent a promising low-carbon alternative for heat supply. In this study, a Life Cycle Assessment of an operating deep geothermal heat plant in the Southern German Molasse Basin is conducted according to ISO 14040 and 14044. The plant utilizes a hydro-geothermal source and consists of a total of two production wells and one injection well with thermal water temperatures of up to 107 °C and an output of 16.7 MW. For peak load and redundancy, three oil boilers with a total capacity of 17 MW are installed. The heat plant is connected to a 48.5 km district heating network for the supply of 1800 customers. As functional unit 1 kWh net heat at the customer is chosen. For the impact categories Global Warming Potential (GWP), fossil resource scarcity and terrestrial ecotoxicity are considered. The environmental impact amounts to 78.5 g CO_2-eq./kWh, 29.2 g oil-eq./kWh and 399.0 g 1,4-DCB/kWh, respectively. In addition to the main results, selected scenarios have been analyzed with regard to the potential of switching the electricity mix and the peak load coverage between oil, natural gas and biomethane. The results show that switching to a renewable electricity mix leads to the biggest reduction with 57.8 % for the GWP.

Keywords:

Geothermal heat plant, district heating, Life Cycle Assessment; peak load coverage, electricity mix, Sustainability

1. Introduction

In order to meet the objective of the IPCC and limit the anthropogenic impact on the environment, it is essential to decarbonize the heating sector. In Germany, especially, the share of renewable sources for heat is considerably low with only 16.5 % [1]. Geothermal energy has great potential and could substitute up to 40 % (7 655 MW) of the heat demand in the state of Bavaria [2]. Therefore, the technology has gained political interest also due to the independence of fossil fuel supply.

However, even with this technology, which is characterized by the costly deep drilling, the question of how well it is compatible with the climate is open. The Technical Expert Group on Sustainable Finance has set a threshold of 100 g CO_2-eq./kWh that makes a technology compatible with the Paris climate agreement [3]. Additionally, this threshold decreases every 5 years until net zero in 2050. This ensures the necessity to identify strategies for the reduction of Global warming potential (GWP).

In this study, a LCA is conducted analyzing the categories GWP, fossil resource scarcity (FRS) and terrestrial ecotoxicity (TE) for a currently operating geothermal heat plant in the Southern German Molasse Basin in the greater Munich area. Additionally, the influence of auxiliary energy is investigated and the potential of reducing the environmental impact is analyzed through scenario analyses regarding electricity mix and peak load coverage.

2. Goal and Scope

The LCA in this study is conducted according to ISO 14044 and 14040 [4,5] which include the four phases: definition of goal and scope, inventory analysis, impact assessment and interpretation. These phases are explained in detail in the next sections.

2.1. Objective

The objective of this study is to conduct an LCA of a currently operating geothermal heat plant and its district heating network (DHN) in the Southern German Molasse Basin which includes the impact categories GWP; FRS and TE. Furthermore, the use of auxiliary energy is analyzed by conducting scenarios regarding the electricity mix and the peak load coverage. For the applied electricity mix the location based German electricity mix is compared to two renewable mixes (see Table 6). With the peak load coverage, the fuels light fuel oil, natural gas and biomethane are weighted up.

For the LCA, all energy and material flows for the life cycle stages construction, operation and decommission are considered. Thus, a cradle to grave approach is applied. To ensure comparability with other LCAs, a lifetime of 30 years is chosen, as is suggested by [6]. According to [7] and [8] DHNs exceed the life time of the heat plant with respectively minimally 40 and 50 a. Therefore, it is assumed that the DHN either will be used for another heat plant right away or remains unchanged in the ground until a new use. Either way there is no decommissioning scenario attributed to the life-cycle of the geothermal plant.

For operators of geothermal heat plants and decision makers the results can be of interest for developing strategies for the reduction of the environmental footprint along with planning future plants.

2.2. Functional unit

In order to present the result in a comparable way, all energy and material flows are related to one variable according to [4]. In this study, 1 kWh of net energy at the consumer has been selected for this purpose. This means that both DHN losses and the generation of auxiliary energy for peak load coverage and redundancy by oil boilers were considered.

2.3. Geothermal heat plant

In this section, the analyzed geothermal heat plant is presented. It is located in the Southern German Molasse Basin which is characterized by a porous water-bearing carbonate rock layer at a depth of 2000 to 3000 m in the greater Munich area, sloping down to the south [2]. Therefore, the plant relies on hydrothermal energy. It went into operation in 2005. The 104 °C hot water is drawn from two production wells and after the heat transfer at the heat exchangers it is fed back into one injection well. The heat exchangers are connected to the district heating network (DHN) as well as light fuel oil fuelled boilers which cover peak load and redundancy in case of maintenance or component failure. Through the DHN the heat plant supplies heat to 1800 customers. Relevant parameters can be found in Table 1.

Table 1. General Parameters of the geothermal heat plant [9]

Parameter	Value
Maximal geothermal energy	16.7 MW
Maximal energy by peak load and redundancy boilers	17 MW
Average operating hours full load	4234 h
Proportion of heat from geothermal energy	95 %
Proportion of heat from peak load and redundancy boilers	5 %
Production well 1 measured depth	4666 m
Production well 2 measured depth	4120 m
Injection well measured depth	3984 m
DHN	
DHN total length	48.5 km
DHN users	1800
Total installed load (2021)	29.75 MW

2.4. Data source and methodology

In this section, the important matter of data quality is addressed which needs to be included in any report for a LCA according to [4]. As far as possible for this study, primary data provided by the plant operator was used. If no data was available suitable literature was utilized. Thereby, it was ensured that the applicability was granted, e.g. through suitable geographical and time related similarity.

To conduct the LCA, the software SimaPro (version 9.4.0.1) and the database ecoinvent (version 3.8) were utilized. Within ecoinvent, the system model “allocation cut-off by classification” was selected. This database provides an extensive selection of processes including pre-chain emissions in addition to direct emissions. ecoinvent provides the characterization factors to allocate environmental effects to conduct the life-cycle impact assessment (LCIA), which considers for example for the impact category GWP how much greenhouse gas is emitted for every energy and material in- and output collected in the LCI-phase. For the results the method ReCiPe midpoint (hierarchist) [10] is applied. Thereby, as impact categories, GWP (with a time horizon of 100 years, according to the hierarchist view) TE and FRS are selected.

3. Results and Discussion

3.1. Base Case

For the base case, the construction of the subsurface with the boreholes and the surface components are included. This involves the heat exchangers and peak load and redundancy boilers and plant parts. Additionally, the DHN is considered. The extensive LCI can be found in [9], any changes to the original LCI can be found in Table 7 in the appendix.

In Figure 1 the results for the base case are shown. Hereby, the general results are 78.6 g CO_2 eq./kWh for GWP, 399.0 g 1,4-DCB/kWh for TE and 29.3 g oil eq./kWh. It is apparent, that the operation phase dominates the environmental impact for all categories whereas for FRS the construction of the DHN also has a significant impact with 27 %. This is due to the light fuel oil product bitumen that is used for the asphalt which needs to be replaced for the installation of the pipes under streets (see also [9]).

Taking a closer look at the operation phase it is apparent that the main impact comes from the electricity consumption and the peak load and redundancy coverage. The latter has a high impact since it is oil based. The electricity consumption’s high impact is due to the high share of fossil sources like coal and natural gas in the German electricity mix. For the lifetime from 2005 to 2035 this amounts to 55.8 % (electricity mix based on [6] and [11]).The greatest influence of the operation is seen for the GWP: hereby the electricity consumption of the pumps leads to 62.0 % and the peak load and redundancy coverage to 21.2 %. For the TE the peak load coverage and redundancy have the biggest impact with 48.0 % and for FRS the electricity consumption dominates the impact with 43.1 %.

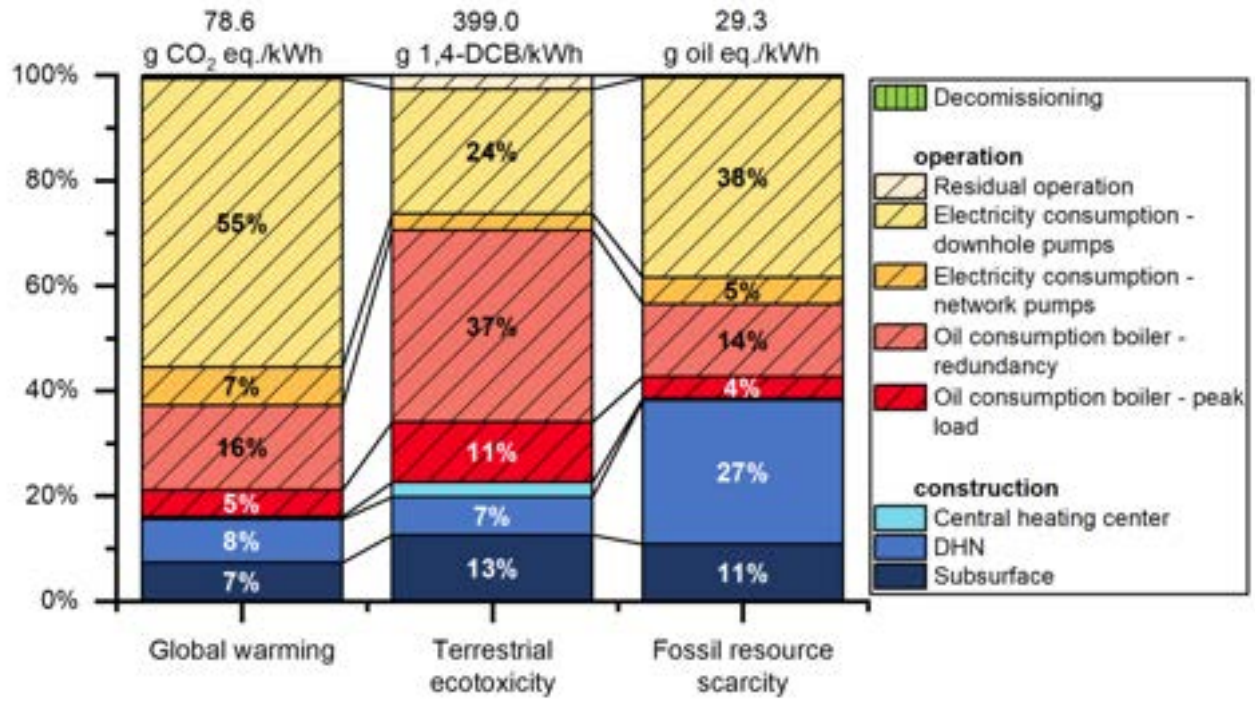

Figure 1. LCA results of a geothermal heat plant with DHN for the operating years of 2005-2035.

With these general results for GWP the threshold of 100 g CO_2/kWh proposed by [3] can be met with ease. They also propose an annual decrease in emissions until net zero 2050. Therefore, strategies should nevertheless be developed to further reduce the environmental impact. Since the single biggest contributors prove to be within the auxiliary energy namely electricity consumption as well as peak load and redundancy

coverage, the impact of these is further examined by the following scenario analyses in the sections 3.2 and 3.3.

3.2. Peak Load Scenarios

Within this section, various technologies for managing peak energy demand are compared, with particular emphasis on those utilizing fuel-based solutions. The comparison is centered around the base case of oil-fuelled boilers for peak energy coverage, contrasted against the conventionally used natural gas alternative. Additionally, consideration is given to the renewable fuel source of Biomethane, which is derived by upgrading biogas through chemical means, increasing its methane content to match that of natural gas [12].

For the use of biomethane two scenarios are created, one with the sole use of biomethane as fuel and the second with a mixture of biomethane and natural gas. The latter is created as a realistic approach since the production volume of biomethane in Germany is limited which is due to being based on agricultural and animal waste as well as energy plants. The latter are in competition for cultivable land for food or feed crops as well as the use of biogas for electricity production (7.8 % of the electricity mix in 2022 [13]) [12,14]. The 10 % value is based on biomethane shares that are already currently commercially offered in the state of Baden-Württemberg in Germany [15]. Furthermore, it also fits within the range (8-12%) Arnold et al. [16] propose as realistic share of biomethane in the German gas grid by 2030. The following Table gives an overview over the different scenarios that are analysed.

Table 2. Peak load scenarios

Scenario	**Base Case**	**Natural gas**	**Biomethane**	**90NG 10BM**
fuel	Light fuel oil	Natural gas	Biomethane	90% natural gas and 10% Biomethane

For the LCI plant parts necessary for using light fuel oil, like the oil storage and catch basin are no longer needed and are therefore excluded. Through the ecoinvent data the gas production and the natural gas grid is considered proportionally. The material and energy input for the boilers are assumed to be the same for the fuel oil and gas, analogous to [17]. Since biomethane is used to substitute natural gas, the same infrastructure as for natural gas (gas network and boilers) is assumed as well as the same emissions for the burning in the boilers. The greenhouse gas emissions for the burning of biomethane, however, are considered as biogenic and are therefore not part of the GWP. The extensive LCI with the selected ecoinvent data for the components and the process of burning of the fuels can be found in the appendix in Table 8. An overview of the relevant parameters and considered infrastructure for the respective scenarios is shown in Table 3. For the scenario with 10 % biomethane and 90 % natural gas the models for natural gas and biomethane from Table 3 are considered proportionally.

Table 3. Parameters for the peak load scenarios with the base case (light fuel oil), natural gas and biomethane

Parameter	**Base case**	**Natural gas**	**Biomethane**
Degree of utilization	91 %[a]	96 %[b]	96 %[c]
Plant components	Boiler	Boiler[d]	Boiler[d]
	chimney	chimney	chimney
Fuel supply	Oil storage and catch basin	Natural gas network	Natural gas network
Direct emissions per kg light fuel oil/m^3 high pressure gas according to ecoinvent process	heat production, light fuel oil, at industrial furnace 1MW	heat production, natural gas, at boiler modulating >100kW	heat production, natural gas, at boiler modulating >100kW[e]

a: degree of utilization for the year 2019, assumed to remain the same over the life time
b: for a modulating, not condensing boiler according to [18]
c: Same value assumed as for natural gas
d: the same inputs are considered as for the oil fuelled boiler analogous to [17]
e: all emitted greenhouse gases are biogenic and are therefore not relevant for the GWP

In Figure 2 the LCA results for the peak load coverage are shown considering the different scenarios. Hereby, only the results for heat generation by the peak load boilers are shown as opposed to the heat generation of the whole geothermal plant.

The results are depicted relative to the oil fuelled base case (BC). The other scenarios are the coverage by natural gas (NG), biomethane (BM) and the realistic scenario with 90 % supply by natural gas and 10 % biomethane (90NG10BM).

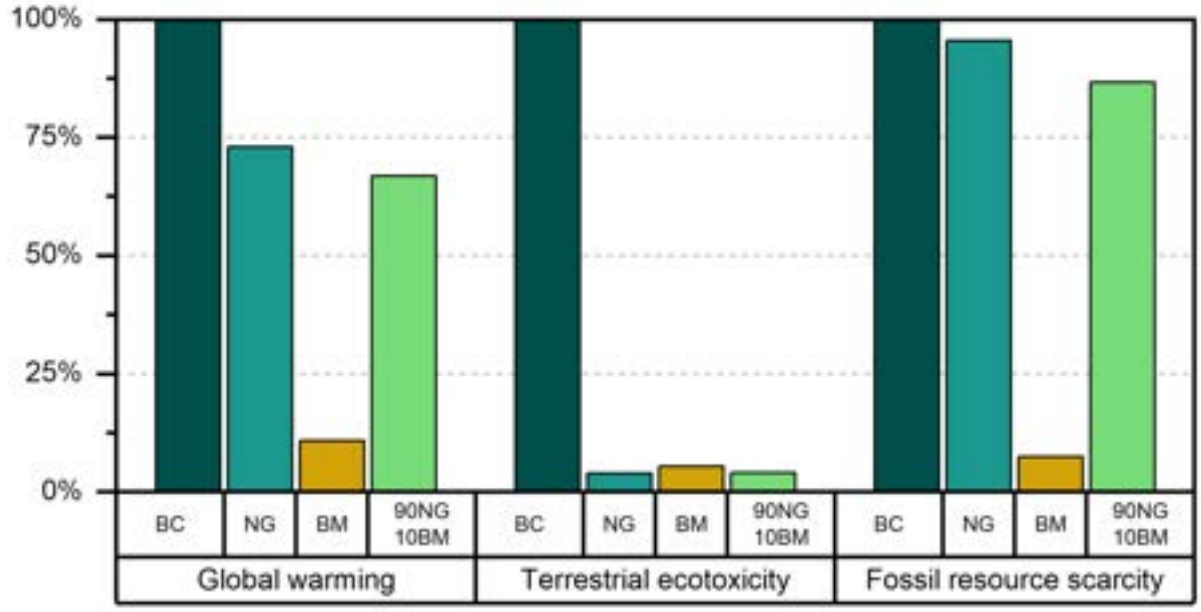

Figure 2. LCA Results of heat generation of different peak load coverage technologies: base case with light fuel oil (BC), natural (NG) and biomethane (BM) as well as a realistic mixture of 90 % natural gas and 10 % biomethane (90NG10BM) relative to the biggest contributor.

The relative results from Figure 2 are also shown in Table 4 as absolute values per kWh generated heat at the plant. In general, all gaseous fuels lead to a reduction of the environmental impact. Beside the higher emissions from burning oil compared to natural gas, this can be partly explained by the difference in utilization factors (that are generally higher for gas boilers than for using oil [19]). Additional contributions are the reduced fossil sources and emissions for biomethane compared to light fuel oil as well as reduced plant components. As expected, the biggest reductions for FRS and GWP are achieved by using biomethane. With the realistic scenario the GWP can be reduced by 33.3 % and the RRS by 13.4 %. For the TE the switch to the gaseous fuel in general leads to the biggest reduction since the oil combustion has a very high TE comparably.

Table 4. Results of the environmental impacts GWP, RE and FRS of the peak load coverage scenarios per kWh produced heat at the boilers (i.e. without DHN heat losses) considering construction, operation and decommissioning of the peak load components

	Base case	**Natural gas**	**Biomethane**	**90ng 10bm**
GWP [g CO_2/kWh]	353.5	257.9	38.2	235.9
TE [g 1,4-DCB]	4497.6	173.0	239.3	179.6
FRS [g oil eq]	110.9	105.8	8.2	96.1

If now the whole heat plant is considered again (see Table 5), with using 100% biomethane a reduction in GWP of 20.4 % can be achieved compared to the base case. Whereas the use of natural gas only reduces the total GWP by 3.2 %. Increasing the amount of biomethane in the gas network would lead to a significant reduction in GWP whereas for TE the switch to either gas greatly decreases the impact (49.4 % for natural gas) with natural gas having a slightly higher reduction potential than pure biomethane. The great effect on the heat plant concerning FRS can be again achieved with biomethane with a reduction of 17.6 %. Since FRS is based on the caloric value of the fossil fuels, the difference between oil and natural gas is mainly due to the higher degree of utilization assumed for the use of natural gas (see Table 3).

Table 5. Results of the environmental impacts GWP, RE and FRS of the peak load coverage scenarios per kWh produced heat by the whole geothermal plant

	Base case	Natural gas	Biomethane	90ng 10bm
GWP [g CO_2/kWh]	78.6	74.1	62.2	73.0
TE [g 1,4-DCB]	399.0	201.8	202.9	201.9
FRS [g oil eq]	29.3	29.1	24.2	28.6

To conclude, switching to natural gas has a small positive impact for GWP and FRS and a significant reduction for TE. Except for TE an increase of biomethane in the gas pipelines significantly decreases the environmental footprint of the plant. Although it has to be considered that the biomethane share in the gas network is dependent on the development of the gas market.

3.3. Renewable Electricity Mix Scenarios

To analyse the ecological potential of changing the consumed electricity mix, the base case is compared to two scenarios with renewable electricity mixes. The base case includes the location-based electricity mix in Germany for the respective electricity demands for each year over the plant's life time of 2005-2035. Whereas the future German electricity mix is obtained from the projection of [20]. To show the difference to a fully renewable mix, the base case is compared to the scenario with the mix of renewable energy of the year 2022 (RE22) [13]. Additionally, as an example of a commercial mix, a scenario containing 90 % hydro and 10 % wind power is created. The average shares of power sources can be found in Table 6.

Table 6. Composition of the examined electricity mixes with the base case displaying the general German electricity mix for the years 2005-2035 considering the differing yearly energy demands of the heat plant over the life time. Future mixes are modelled according to [20]. 90H10W displays an example of the potential of commercially available composition. RE22 is the market of renewable electricity in 2022 according to the German Federal Network Agency [13].

	Share [%]		
Energy source	**Base case**	**90H10W**	**RE22**
Fossil sources	55.8	0	0
Biomass	8.4	0	17.0
Hydro	3.6	90.0	5.3
Wind offshore	6.4	0	10.7
Wind onshore	17.4	10.0	43.3
Solar	7.8	0	23.8
Other renewables	0.6	0	0

In Figure 3 the environmental impacts in regard to GWP, TE and FRS are shown. The results are depicted as normalised to the base case with it being 100 %. With the renewable scenarios a big reduction can be achieved for the GWP with 50.6 % for EE22 and an even bigger reduction for 90H10W with 57.8 %. For FRS there is also a substantial reduction of 40.6 % for EE22 and 42.7 % for 90H10W. The TE is not influenced in the same way. There is only a reduction of 10.8 % for 90H10W and RE22 even exceeds the base case by 13.5 %. This can be explained by looking at the TE of the considered renewable technologies: Solar power has a TE of 3207 g 1.4-DCB/kWh, which is much higher than the other technologies which are located at most in the three-digit range. With this data it is clear that it cannot simply be assumed that environmental compatibility will always be improved by switching to renewable energy sources. Therefore, the technologies must be carefully selected.

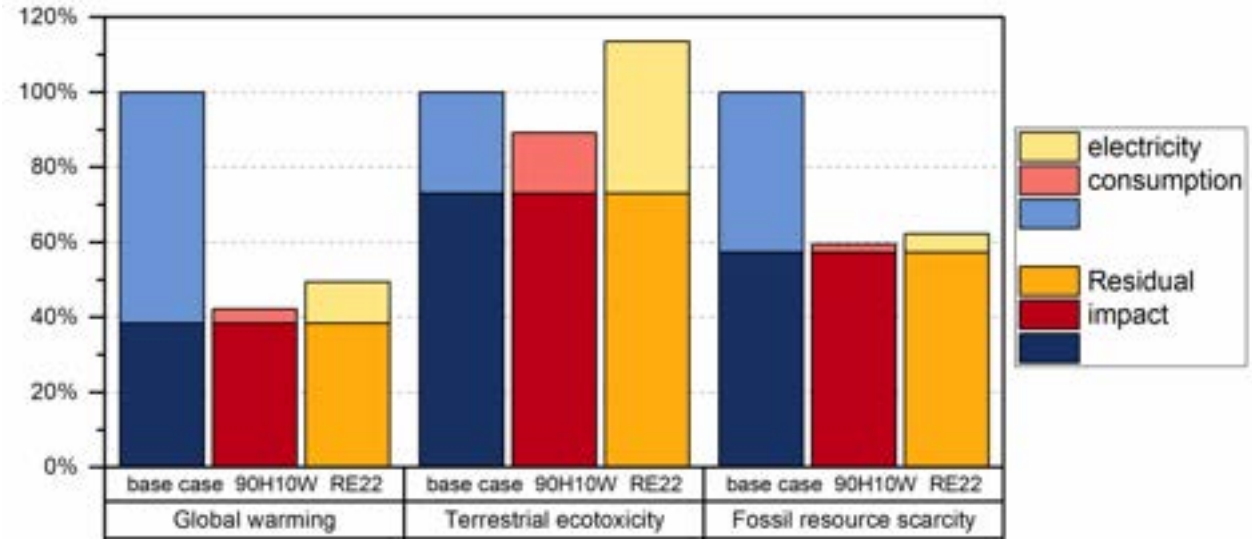

Figure 3. LCA results for the categories GWP TE and FRS for the Variation of the consumed electricity mix; comparison of the German electricity mix and the renewable mix for 2022 RE22 as well as a mix with 90 % hydro power and 10% wind.

The results reveal the potential of choosing an electricity contract with renewable energy. Even though there has to be close look at the composition of the renewable energy mix to ensure a substantial reduction for a holistic environmental improvement.

4. Conclusion

In this study a LCA for a currently operating heat plant in the Southern German Molasse Basin was conducted. Thereby the impact categories GWP, TE and FRS were chosen as well as the method ReCiPe Midpoint (H) [10]. All environmental impacts are related to the functional unit of 1 kWh net thermal energy. The environmental impact of the heat plant amounts to 78.5 g CO_2-eq./kWh, 29.2 g oil-eq./kWh and 399.0 g 1,4-DCB/kWh. The biggest contributor for all categories is the use of auxiliary energy with electricity consumption and peak load coverage by oil boilers. For FRS the DHN also has a significant share with 27.3 %. Therefore, the electricity mix and peak load coverage are analyzed with scenario analyses.

In the base case the electricity is modelled according to the electricity mixes for every year and the demand over the plant's life time. The future mix is modelled according to [20]. For a renewable energy mix the German mix of renewables of 2022 is applied as well as a mix of 90% hydro and 10 % wind power. The biggest reduction is achieved with the scenario 90H10W with 57.8 % for GWP, 10.8 % for TE and 40.5 % for FRS. Surprisingly, the RE22 scenario leads to a TE that is even bigger than the base case due to the high impact of solar power on that category.

For the peak load coverage, the base case with oil fueled boilers is compared to the fuels natural gas, biomethane and a realistic mixture of both with 90 % natural gas and 10 % Biomethane. Peak load coverage with gas always performs better than with oil, with biomethane having the largest effect for GWP and FRS, thus reducing the base case by 20.4% for GWP and 17.6% for FRS. For TE, the reduction by gaseous energy materials is the highest, with natural gas performing slightly better than biomethane with a reduction of 49.4%. The mixed scenario 90NG10BM was investigated, since a supply of pure biomethane from the gas pipelines is unrealistic due to the limited capacity of producing biogas sustainably [21]. Even if the biomethane share is low, significant reductions can still be achieved.

These findings show that deep geothermal heat plants are able to comply with the threshold of 100 g CO_2/kWh by the [3]. Additionally, it also proves the potential of the choice of auxiliary energy in terms of electrical energy mix and peak load coverage to effectively reduce the environmental impact and thus meet the objectives of ongoing GWP reductions until 2050 of the Technical Expert Group. This could be used as incentive for the operators to switch to electricity contracts with renewable sources to further decrease the GWP and FRS.

In future work the potential of peak load coverage other fuels and technologies will be considered. For example in [21] there were also scenarios considered in which the gas demand is covered mainly by e-methane and hydrogen. It would be interesting to investigate these fuels as a basis for peak load. Additionally, other peak load technologies that are not based on fuels should be considered like electric boilers, high-temperature heat pumps or thermal storages.

Additionally more impact categories as suggested in [6] can be considered, especially regarding biodiversity which is also a pressing issue alongside climate change.

Acknowledgments

The funding from the Bavarian State Ministry for Science and the Arts in the framework of the project “Geothermie-Allianz Bayern” is gratefully acknowledged.

Appendix

This study is an extension of [9]. A correspondingly comprehensive LCI of the heat project can be taken from there. In the following, only the modifications are listed in Table 7 and Table 8. The latter also lists the different chosen inputs for the peak load scenarios from section 3.2.

Table 7. Changes to the LCI in comparison to [9].

Parameter	Description	Unit	Value	Source
Plastic sheath pipes	Steel, low-alloyed and drawing of pipes	kg/m DHN	15.27	[22]
	Polyethylene, high density and extrusion, plastic pipes	kg/m DHN	4.43	[22]
	Polyurethane, rigid foam	kg/m DHN	4.01	[22]
	Tap water	kg/m DHN	17.68	[22]
	Sand	kg/m DHN	243.34	[22]
Trench work	Welding: argon, liquid	g/m DHN	30.93	[23]
	Welding: diesel, burned in diesel-electric generating set	MJ/m DHN	2.22	[23]
	Bitumen adhesive compound, hot	kg/m DHN	213.16	[23]
	Diesel, burned in building machine	MJ/m DHN	270.68	[23]
	Waste asphalt	kg/m DHN	149.52	[23]
Transport	Transport, freight, lorry >32 metric ton	tkm/m DHN	51.34	[23]

Table 8. LCI inputs for peak load coverage.

Parameter	Description	Unit	Value	Source
Cruide oil/natural gas boiler	Aluminium, cast alloy	kg	557.05	[18,24]
	Steel, chromium steel 18/8, hot rolled	kg	24880.17	[18,24]
	Stone wool, packed	kg	716.63	[18,24]
	Electricity, medium voltage	kWh	15430.77	[18]
	Heat, district or industrial, natural gas	MJ	88138.46	[18]
	Heat, district or industrial, other than natural gas	MJ	46553.85	[18]
	Transport, freight, lorry 16-32 metric ton, euro3	tkm	1307.69	[18]
	Transport, freight train	tkm	15692.31	[18]
	Transport, freight, lorry 7.5-16 metric ton, euro3	tkm	1307.69	[18]
Oil storage and catch basin	Oil storage, 3000l	p	140.60[a]	[18]
	Transport, freight, lorry 16-32 metric ton, euro3	tkm	6896.55	[18]
	Transport, freight train	tkm	82758.63	[18]
	Transport, freight, lorry 7.5-16 metric ton, euro3	tkm	3416.82	[18]
Chimney	Chimney	m/kWh[b]	1.32E-07	[18]
	Transport, freight, lorry 16-32 metric ton, euro3	tkm/kWh[b]	6.91E-07	[18]
	Transport, freight train	tkm/kWh[b]	8.29E-06	[18]
	Transport, freight, lorry 7.5-16 metric ton, euro3	tkm/kWh[b]	3.29E-09	[18]
Heat production light fuel oil	Light fuel oil	kg/MJ[c]	2.57E-02	Operator
Heat production natural gas	Natural gas, high pressure[d]	m^3/MJ	2.87E-02	[18]
Heat production natural gas	Biomethane, high pressure[d]	m^3/MJ	2.87E-02	[18]

a: scaled to oil consumption for one year (4 GWh for 2019) according to [18]
b: scaled to total heat production through boilers according to [18]
c: MJ produced heat for peak load and redundancy, in total 81.6 GWh. Amount of fuel per MJ according to caloric values and degree of utilization
d: the natural gas grid is included proportionally in the dataset for natural gas and biomethane

1 References

[1] 2021,“Erneuerbare Energien in Zahlen Nationale und internationale Entwicklung im Jahr 2020,” Federal Ministry for Economic Affairs and Energy (BMWi), Dessau-Roßlau.

[2] Keim M., Hamacher T., Loewer M., Molar-Cruz A., Schifflechner C., Ferrand T., Wieland C., Drews M., Zosseder K., Bauer W., Bohnsack D., Heine F., Konrad F., Pfrang D., and Schölderle F., 2020,“Bewertung Masterplan Geothermie,” Lehrstuhl für Energiesysteme.

[3] 2020,“Taxonomy Report: Technical Annex,”

[4] DIN Deutsches Institut für Normung e.V., 2006,“Environmental management – Life cycle assessment – Requirements and guidelines (ISO 14044:2006),” EN ISO 14044:2006.

[5] DIN Deutsches Institut für Normung e.V., 2021,“Environmental management – Life cycle assessment – Principles and framework (ISO 14040:2021-02),” DIN EN ISO 14040:2021-02.

[6] Parisi M. L., Douziech M., Tosti L., Pérez-López P., Mendecka B., Ulgiati S., Fiaschi D., Manfrida G., and Blanc I., 2020,“Definition of LCA Guidelines in the Geothermal Sector to Enhance Result Comparability,” Energies, **13**(13, 3534), pp. 1–18.

[7] Ortner S., Pehnt M., Over, Margarete, Blömer, Sebastian, Ochse S., Ziegler R., Bohn K., Rein M., Möhring P., Westholm H., Sandrock M., Roth T., and Kühne J., 2023,“Dekarbonisierung von Energieinfrastrukturen: Ein politischer Unterstützungsrahmen für das Beispiel Wärmenetze,” CLIMATE CHANGE 08/2021, Dessau-Roßlau.

[8] Oliver-Solà J., Gabarrell X., and Rieradevall J., 2009,“Environmental impacts of the infrastructure for district heating in urban neighbourhoods,” Energy Policy, **37**(11), pp. 4711–4719.

[9] Uhrmann H., Heberle F., and Brüggemann D., 2023, Life Cycle Assessment of an operating geothermal heat project in the Southern German Molasse Basin, *European Geothermal Congress 2022: Proceedings*, European Geothermal Energy Council, ed., pp. 1–9.

[10] Huijbregts M., Steinmann Z., Elshout P. M.F., Stam G., Verones F., Vieira M. D.M., Hollander A., Zijp M., and van Zelm R., 2019. *ReCiPe 2016 v1. 1: A harmonized life cycle impact assessment method at midpoint and endpoint level report I: characterization. RIVM Report 2016-0104a,* 2016th ed.

[11] Icha P., Lauf T., and Kuhs G., 2021. *Entwicklung der spezifischen Kohlendioxid-Emissionen des deutschen Strommix in den Jahren 1990-2020,* 45th ed., Umweltbundesamt, Dessau-Roßlau.

[12] Lauf T., Memmler M., and Schneider S., 2021,“Emissionsbilanz erneuerbarer Energieträger: Bestimmung der vermiedenen Emissionen im Jahr 2020,” CLIMATE CHANGE 71/2021, Dessau-Roßlau.

[13] Federal Network Agency Germany,“market data,” https://www.smard.de/home.

[14] Bettgenhäuser K., Grözinger J., Petersdorff C., and John A.,“Die Rolle von Gas im zukünftigen Energiesystem,” ECOFYS, Köln.

[15] Pehnt M., Weiß U., Fritz S., Jessing D., Lempik J., Mellwig P., Nast M., Bürger V., Kenkmann T., Zieger J., and Steinbach J., 2018. *Final Report on behalf of the Ministry of the Environment, Climate Protection, and the Energy Sector Baden-Württemberg*.

[16] Arnold K., Dienst C., and Lechtenböhmer S., 2010,“Integrierte Treibhausgasbewertung der Prozessketten von Erdgas und industriellem Biomethan in Deutschland,” Environ Sci Eur, **22**(2), pp. 135–152.

[17] Faist-Emmenegger M., Heck T., Jungbluth N., and Tuchschmid M., Eds., 2007. *ecoinvent data v2.0: Teil V: Erdgas*, Swiss Centre for Life Cycle Inventories.

[18] M. Faist Emmenegger, T. Heck, N. Jungbluth, and M. Tuchschmid, Eds., 2007. *ecoinvent data v2.0: Teil V: Erdgas*, Swiss Centre for Life Cycle Inventories.

[19] Ortner S., Pehnt M., Seefeldt F., Rau D., Sahnoun M., Weinert K., Winiewska B., and Oschatz B., 2022,“Untersuchungen zur Weiterentwicklung der Emissionsbilanz erneuerbarer Energieträger im Bereich erneuerbare Wärme: Analyse von Substitutionsfaktoren, Jahresnutzungsgrade und Hilfsenergie,” CLIMATE CHANGE 138/2022, Dessau-Roßlau.

[20] Fattler S., Conrad J., Regett A., Böing F., Guminski A., Greif S., Hübner T., Jetter F., Kern T., Kleinertz B., Murmann A., Ostermann A., Pellinger C., Pichlmaier S., and Schmid T., 2019,“Dynamis - Hauptbericht: Dynamische und intersektorale Maßnahmenbewertung zur kosteneffizienten Dekarbonisierung des Energiesystems,”

[21] Wachsmuth J., Michaelis J., Neumann F., Degünther C., Köppel W., and Zubair A., 2019,“Roadmap Gas für die Energiewende – Nachhaltiger Klimabeitrag des Gassektors,” 12/2019, Dessau-Roßlau.

[22] Biemann K., 2015,“Vergleichende Ökobilanzierung der semi- zentralen Hauswärmebereitstellung aus Holzreststoffen,” Dissertation, Technischen Universität Darmstadt, Darmstadt, https://tuprints.ulb.tu-darmstadt.de/4377.

[23] Grünäugl S., 2020,“Life cycle assessment of Organic Rankine Cycles for geothermal power generation (ORC) considering secondary district heat supply,” Master Thesis, University of Stuttgart, Stuttgart.

[24] “Planungsunterlage - Großkessel 450-5200 kW,”

Utilisation of groundwater heat pumps for the decarbonisation of heating and cooling sector: the analysis of an Italian case study

Luca Socci[a*], Claudio Zuffi[a], Irene Aiello[a], Andrea Rocchetti[a], Daniele Fiaschi[a]

[a] Department of Industrial Engineering -University of Florence, Florence, Italy
* luca.socci@unifi.it, CA

Abstract:

In this paper, the utilisation of groundwater heat pumps for residential heating and cooling purposes is presented. A case study located in Florence (Italy) is discussed. First, a building energy analysis has been performed to obtain the thermal loads. Then three heat pump systems (system 1: air-to-water, 2: groundwater-to-water, 3: surface water-to-water) have been designed and compared in terms of electric energy consumption, taking into account the dynamic changing of boundary conditions of the building. Finally, a Life Cycle Assessment analysis has been conducted to evaluate the environmental impacts of the systems. To ensure a yearly heating energy request of 2 780 kWh (peak load of 5 kW) and a yearly cooling energy request of 630 kWh (peak load of 4.4 kW) the systems present a yearly electricity consumption of 1 088 kW, 770 kW and 872 kW for system 1, 2 and 3 respectively. So the groundwater-to-water solution is the most efficient in terms of energy consumption. Based on LCA evaluation, system 2 is the environmentally less impacting system, with a Climate Change factor of 0.15 kg CO_2 eq/kWh against the 0.21 kg CO_2 eq/kWh of system 1. In terms of single score level, system 2 and system 3 are characterised by a reduction in impacts of about 24 % compared to system 1. The dynamic energy and LCA studies clearly show that the solution based on groundwater exploitation, in this context, is a very effective way to reduce electricity consumption and environmental impacts, confirming that the large-scale implementation of groundwater heat pump systems could be a promising option for the decarbonisation of residential heating and cooling sector.

Keywords:

Groundwater heat pump, Heating&Cooling, Energy-efficiency, Energy-saving, Decarbonisation, Dynamic energy analysis, LCA

1 Introduction

Energy requirements for refrigeration and air conditioning (AC) sectors are becoming wider and wider, with AC systems that account for 20-30 % of the electricity consumption of buildings [1–4]. To obtain large-scale decarbonisation, it is evident that it is necessary to reduce the energy needs of AC systems. The utilisation of efficient heat pumps, instead of the classic thermal power generation devices (e.g. boilers), has represented an important step forward [5]. Heat pumps consume electricity to operate, that in many cases is produced from fossil fuels. To reduce the consumption of this form of primary energy in heat pumps operation, it is possible to implement two main strategies: producing electricity starting from renewable sources (e.g. photovoltaic), and enhancing the efficiency of the system through the utilisation of favourable external thermal sources. This last point is crucial: if the external heat exchanger of a heat pump (evaporator in heating season, condenser in cooling season) works with a source at a temperature close to the one of the user, a consistent increase in the efficiency happens. In this sense, a very promising solution is coupling heat pump devices with ground (or geothermal) sources. This is the concept of a Ground Source Heat Pump (GSHP). At depths of a few meters, the ground temperature is stable during the year and it is in contrast with the trend of air temperatures, as in the hot months ground is cooler than the outdoor air, conversely, in cold months the ground is warmer than the outdoor air. The quasi-constant temperature, quite close to the setpoint temperature of indoor environments, leads to obtaining very high values of the Coefficient Of Performance (COP) of the systems, with consequent energy savings [6]. A GSHP system consists mainly of a ground heat exchanger, a heat pump, and a heating/cooling distribution network [7]. The type of geothermal source used for heat exchange, like ground, groundwater and surface water, defines the type of system: ground heat pump (GHP), groundwater heat pump (GWHP) and surface water heat pump (SWHP) [8]. The last two systems are the object of this study. In a GWHP system, the groundwater is extracted from a water source and it exchanges

heat with the heat pump, then is discharged. A GWHP could be built in different configurations: *open loop with aquifer reinjection*, *standing column wells* and *open loop systems discharging to waste*. In an SWHP there is the presence of a reservoir in which the groundwater is pumped. In this case, there is the possibility to realise an *open loop* or a *closed loop* configuration.
In this paper, the utilisation of groundwater heat pumps for heating and cooling purposes in a residential building located in Florence (Italy) is analysed. The work aims to show, considering real and dynamic boundary conditions, how the exploitation of a natural, renewable and local source such as groundwater could improve the performance of heat pumps. An energy analysis of the building has been performed, in order to obtain the heating and cooling loads necessary to design the systems. Three systems have been studied and compared: a traditional air-to-water heat pump, a groundwater-to-water heat pump and a surface reservoir water-to-water heat pump. With specific dynamic calculations, the energy needings of the three systems have been evaluated. Then, a Life Cycle Assessment analysis has been conducted. The obtained results lead to consider the utilisation of groundwater-driven heat pumps as a very energy-efficient solution in this case study and in general a promising option for the decarbonisation of the residential heating and cooling sector.

2 Materials and methods

The studied building is located in Florence (Italy). The analysis has been conducted assuming a revamping of the existing building envelope, able to bring it to respect the prescriptions of Italian standards [9] in terms of thermal insulation. Three heating/cooling systems are proposed: an air-to-water heat pump (system 1, AHP), a groundwater-to-water heat pump (system 2, GWHP) and a surface reservoir water-to-water heat pump (system 3, SWHP). The system 3 solution has been considered because the building is located in the proximity of a reservoir used for irrigation. Alongside the heating/cooling systems, it is supposed the utilisation of a mechanical ventilation system to ensure high indoor air quality. Two software have been employed to conduct the energy analysis of the building: *Design Builder* and *EC700*. Once the heating and cooling loads have been calculated with these software, they have been used to design the different schemes. Moreover, an hourly dynamic energy analysis (with *Design Builder* and *Matlab*, specifically for the surface reservoir water heat pump) has been performed to obtain the input data necessary to simulate the behaviour of the devices during the heating and cooling season. To evaluate the consumption, a switch-on profile of the systems is defined. In this way, taking into account the presence of people during the day and consequently the real behaviour of a heating/cooling system of a residential building, it has been possible to estimate the yearly consumption of the different schemes. The environmental analysis has been carried out according to ISO 14040 and ISO 14044 standards [10,11], employing the software *OpenLCA* with the *Ecoinvent 3.7* database [12] and following these steps: Goal and scope definition, Life Cycle Inventory (LCI), Life Cycle Impact Assessment (LCIA), Interpretation. The aim was to define which of the three proposed solutions is the least environmentally impactful. The system boundaries are the heating and cooling equipment, considering all necessary devices for the different systems (in particular, for GWHP and SWHP, the pipelines necessary for water withdrawal from the wells and the water reservoir). The functional unit is 1 kWh of the total energy exchanged in the building by the heating and cooling system. This case has been considered a multiproduct system because the product that is generated is both heating and cooling. For this reason, an energy allocation factor equal to 0.81 is assigned, and it represents the produced fraction of heat compared to cold. The LCI has been derived from literature [13] and adequately scaled to the size of the case study. The different piping lengths for GWHP and SWHP have been also appropriately related to this situation. LCIA has been carried out following the Environmental Footprint 3.0 methodology. The analysis focused on the CO_2 emissions produced during the entire life cycle of the three systems. Then to investigate the causes of this impact, a contribution analysis has been conducted. Finally, results have been normalised and weighted to perform a single score comparison.

2.1 Climate and groundwater conditions

The local climatic conditions, necessary for the calculation of thermal loads and simulations, are directly defined by the energy analysis software, based on the indications of ASHRAE and Italian standards. The outdoor air conditions for the heating and cooling design have been set as follows (Table 1).

Table 1. Climatic conditions for heating and cooling design.

Mode			
Heating	T_o	0.0	°C
Cooling	T_o	32.0	°C
	RH_o	45.0	%
	R	0.85	kW

For the cooling design, the climatic conditions are referred to the hour of highest thermal load (deriving from the energy balance of equation (5) presented in the following). Moreover, the temperature of groundwater is assumed constant throughout the year and equal to 15.0 °C.

2.2 Indoor setpoint conditions

The indoor setpoint conditions, ensured during the operativity of the systems, are set as follows (Table 2).

Table 2. Indoor setpoint condition.

Mode			
Heating	T_i	20.0	°C
Cooling	T_i	26.0	°C
	RH_i	50.0	%

For the heating mode, there is not a setpoint value for indoor relative humidity because the systems do not include devices able to control humidity during the heating season. For the cooling mode, it is possible to control also the humidity with the regulation of heat pumps and heat transfer devices (fan coils).

2.3 Characterisation of the building

2.3.1 Geometric and envelope characteristics

The geometric characteristics of the simulated building (Figure 1) are reported in the following Table 3.

Table 3. Geometric characteristics of the building.

Number of floors	2	
Total volume	845.0	m^3
Floor occupied area	210.0	m^2

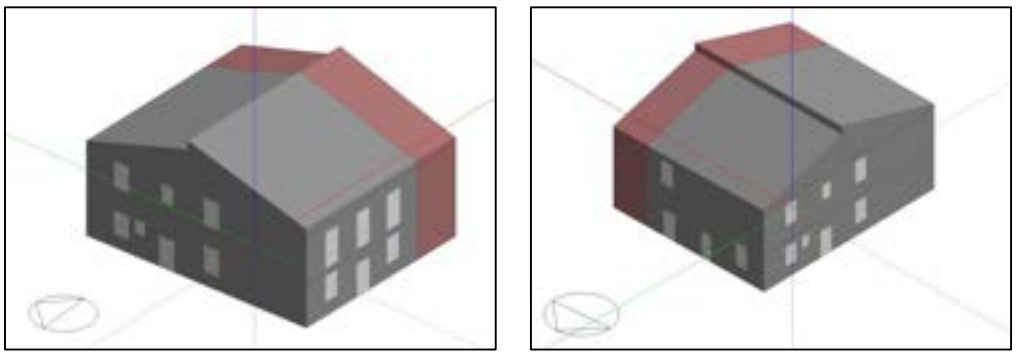

Figure 1. Models of the building (Design Builder).

The characteristics of opaque and transparent elements of the building are reported in the following Table 4.

Table 4. Thermophysical properties of opaque and transparent surfaces.

Element		
External wall		
Thermal transmittance	0.25	$W/m^2/K$
Infrared absorption-emission coefficient	0.9	
Solar radiation absorption coefficient	0.6	
Window (including frames)		
Thermal transmittance	1.0	$W/m^2/K$
Solar radiation transmission coefficient	0.4	

2.3.2 Internal generation, infiltration and ventilation loads

In the calculation of the thermal loads, it is necessary to consider the contributions of internal generation (only for cooling), accidental infiltration and ventilation. The input data are reported in the following Table 5.

Table 5. Heat generation contributions.

Contribution		
Household appliances, electronic devices, lightning		
PD	2.5	W/m^2
People		
OD (full occupancy)	0.03	$people/m^2$
$q_{s,p}$	50.0	W
$q_{l,p}$	50.0	W
Infiltration		
N_{inf}	0.1	vol/h
Ventilation		
$V_{v,p}$	11.0	L/s

The various contributions of thermal loads are calculated as follows:

$$Q_{dev} = PD \cdot S \quad (1)$$

$$Q_p = OD \cdot S \cdot (q_{s,p} + q_{L,p}) \quad (2)$$

$$Q_{inf} = m_{inf} \cdot |j_o - j_i| \quad (3)$$

Concerning the repartition of the terms:

- The internal generation due to appliances and electronic equipment contributes to sensible load.
- People load is divided between sensible and latent.
- Infiltration load is divided between sensible and latent. The value of air changes per hour derived from the accidental infiltration is assumed low due to the refurbishment of the building.
- The ventilation load is evaluated taking into account the presence of people and the air change per person. The effective value of ventilation load depends on the functioning of the air-to-air recuperator, which is explained in the paragraph dedicated to the mechanical ventilation system. This load is divided between sensible and latent.

2.4 Heating and cooling loads and needs

2.4.1 Heating load calculation

The design heating load (calculated in the worst condition) is determined by thermal losses through opaque and transparent surfaces, accidental infiltration and ventilation:

$$Q_h = Q_{bs} + Q_{inf} + Q_v \quad (4)$$

2.4.2 Cooling load calculation

The design cooling load (calculated in the worst condition) is determined by thermal gains through opaque and transparent surfaces, solar radiation, appliances generation loads, people presence, infiltration and ventilation:

$$Q_c = Q_{bs} + Q_r + Q_{dev} + Q_p + Q_{inf} + Q_v \quad (5)$$

2.4.3 Heating and cooling needs throughout the year

Thanks to the dynamic simulation performed by the software, it is possible to calculate the yearly heating and cooling energy needs. For each hour of the simulation, the two software take into account the different contributions of the building energy balances: the heating and cooling energies are the sum of the hourly needings during the respective season.

2.5 Systems description

Three heating/cooling systems have been analysed and compared. Regardless of the thermal sources, they are reversible heat pumps equipped with scroll compressors. The choice of the scroll compressor is dictated by its noiselessness with respect to a reciprocating compressor, making it very suitable in a residential context. All of them have fan coils as distribution terminals: the heat pumps produce hot/cold water that circulates in the indoor water loop and exchanges heat with the indoor air at the fan coils. Moreover, a mechanical ventilation system serves the building, in order to ensure the necessary air changes with outdoor air. A global schematisation of these systems and a general representation of the heat pump schemes are proposed in Figure 2.

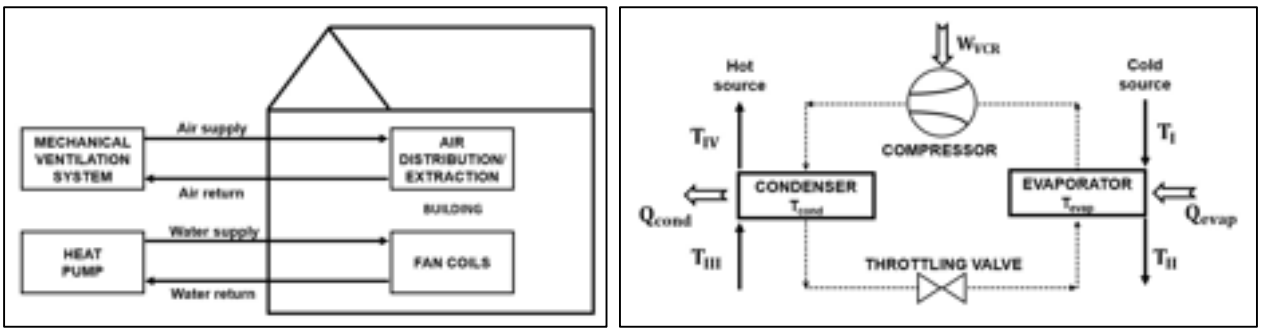

Figure 2. General representation of the systems serving the building (left) and heat pumps simulated in the systems (right).

The evaporator and condenser temperatures are defined by the following equations:

$$T_{evap} = T_{II} - DT_{evap} \quad (6)$$

$$T_{cond} = T_{IV} + DT_{cond} \quad (7)$$

The consumption of the compressor in cooling mode is defined as:

$$W = Q_{evap} / COP_c \quad (8)$$

while in heating mode is:

$$W = Q_{cond} / COP_h \quad (9)$$

Q_{evap} and Q_{cond} correspond to the cooling and heating power exchanged between the heat pump and the internal water loop, so to the requested cooling and heating load. COP has been evaluated taking into account the change in boundary conditions: evaporator and condenser temperatures, evaporator or condenser power. So it is possible to write these general equations for the COP variation:

$$COP_c = F\,(T_{evap}\,,\, T_{cond}\,,\, Q_{evap}) \quad (10)$$

$$COP_h = F\,(T_{evap}\,,\, T_{cond}\,,\, Q_{cond}) \quad (11)$$

The mathematical formulation of COP_c and COP_h, which assumes the form of polynomials, depends on the commercially available models derived from [14].

2.5.1 Air-to-Water Heat Pump (system 1)

In this system:

- In heating mode, the outdoor coil acts as an evaporator taking heat from outdoor air and the indoor coil acts as a condenser releasing heat to the indoor water loop.
- In cooling mode, the outdoor coil act as a condenser releasing heat to outdoor air and the indoor coil acts as an evaporator extracting heat from the indoor water loop.

2.5.2 Groundwater-to-Water Heat Pump (system 2)

In this system:

- In heating mode, the outdoor coil acts as an evaporator taking heat from groundwater and the indoor coil acts as a condenser releasing heat to the indoor water loop.
- In cooling mode, the outdoor coil act as a condenser releasing heat to groundwater and the indoor coil acts as an evaporator extracting heat from the indoor water loop.

This system has 150 m of horizontal pipeline and 30 m of vertical pipeline.

2.5.3 Surface reservoir water-to-Water Heat Pump (system 3)

In this system:

- In heating mode, the outdoor coil acts as an evaporator taking heat from the surface water reservoir and the indoor coil acts as a condenser releasing heat to the indoor water loop.
- In cooling mode, the outdoor coil act as a condenser releasing heat to the water reservoir and the indoor coil acts as an evaporator extracting heat from the indoor water loop.

This system has 300 m of horizontal pipeline.

To perform the dynamic analysis of the heat pump, it is necessary to understand the variation of water reservoir temperature during the system activation. For this purpose, the energy balance of the reservoir is defined as follows [15]:

$$E_{res} = c_w * M_{res} * DT \quad (12)$$

where the reservoir energy content E_{res}, evaluated at each hour of systems activation, depends on the following terms of the thermal balance:

- Thermal power exchanged with the make-up water from the well, with turn-on time defined by the irrigation needs.
- Thermal power received by solar radiation.
- Thermal power exchanged by natural convection with the outdoor air.
- Thermal power exchanged by evaporation through the surface of the reservoir.
- Radiative thermal power in the infrared wavelength exchanged with the outdoor environment.

- Thermal power exchanged by conduction with the walls of the reservoir.
- Thermal power exchanged with the outdoor coil of the heat pump.

The energy balance of the reservoir has been written for each hour of activation of the systems and has been solved with the software Matlab.

2.5.4 Mechanical Ventilation System

The system has been designed taking into account the prescription of Italian standards [16]. The airflow rate, in the case of full occupancy of the building, is defined as:

$$V_v = n_p * V_{v,p} \tag{13}$$

In order to reduce the ventilation load (both in heating and cooling mode), the system has been equipped with an air-to-air recuperator, at which the outdoor air, before entering the building, exchanges heat with the air extracted by indoor environments (Figure 3).

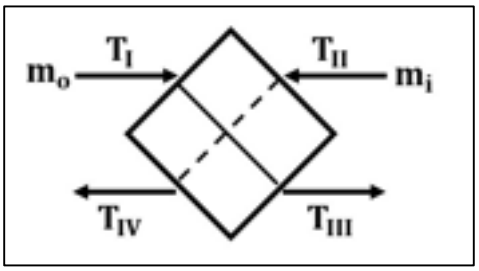

Figure 3. Representation of the air-to-air recuperator of the mechanical ventilation system.

The air-to-air heat exchanger operates on the sensible load, so it is possible to evaluate the temperature of outdoor air exiting the recuperator in heating mode as follows:

$$T_{III} = T_I + \varepsilon * (T_{II} - T_I) \tag{14}$$

and in cooling mode as:

$$T_{III} = T_I - \varepsilon * (T_I - T_{II}) \tag{15}$$

where ε is the efficiency of Kays and London, evaluated knowing that outdoor and indoor air flow rates are equal and with the same specific heat.

The thermal load (heating or cooling) generated by ventilation is equal to:

$$Q_v = m_v \cdot |j_{III} - j_i| \tag{16}$$

The ventilation load in heating mode is only in the sensible form, while it is sensible and latent in cooling mode. The energy consumption of fans for air moving has not been taken into account, due to the fact it is the same in all three systems.

2.5.5 Indoor water loop

The temperatures of the indoor water loop (as presented in the scheme of Figure 2), necessary to maintain the setpoint conditions in heating and cooling mode, are reported in the following Table 6.

Table 6. Temperatures of the indoor water loop.

Mode	Temperature		
Heating	Supply (T_{IV})	45.0	°C
	Return (T_{III})	40.0	°C
Cooling	Supply (T_{II})	7.0	°C
	Return (T_I)	12.0	°C

3 Results and discussion

In this chapter, the yearly performances of the three systems are presented. It is given attention to:

- Electric energy requirements to ensure heating and cooling needs.
- Environmental impacts (considering both the construction and operation of the schemes).

The results have been obtained considering a standard residential utilisation profile of the heating/cooling systems. For all the systems analysed, also the variation of COP (heating and cooling mode) alongside typical days as a function of sources temperatures is reported. The graphs presented for COP do not account for the switching-on profile, but show the behaviour of the systems during an entire day, in order to present the response of the systems to the variation of boundary conditions in a general utilisation of the devices.

3.1 Heating and cooling design loads and energy requirements

For the design of systems, the following peak loads (Table 7) deriving from the resolution of equations (4) and (5), have been obtained:

Table 7. Thermal load contributions for the design of the systems.

Mode	Contribution		
Heating	Q_{bs}	4.2	kW
	Q_{inf}	0.5	k**W**
	Q_v	0.3	kW
	Q_h	**5.0**	**kW**
Cooling	Q_{bs}	0.5	kW
	Q_r	1.7	kW
	Q_{dev}	0.5	kW
	Q_p	0.5	kW
	Q_{inf}	0.4	kW
	Q_v	0.8	kW
	Q_c	**4.4**	**kW**

These values are perfectly similar between Design Builder and EC700. It is useful to note that, during the cooling season, a consistent part of the thermal load depends on solar radiation and ventilation, while the contribution of the surfaces is limited, as expected from a building with an energy-efficient envelope. In terms of necessary heating and cooling energy, the results of Table 8 have been obtained:

Table 8. Yearly thermal energy requirements.

Mode		
Heating	2 780.0	kWh
Cooling	630.0	kWh

The ratio between heating and the sum of heating and cooling requirements is 0.81, which justifies the utilisation of this value for the energy allocation factor in the LCA analysis.

3.2 Air-to-Water heat pump

The design conditions of the system are as follows (Table 9):

Table 9. Design condition for the air-to-water heat pump (system 1).

Mode			
Heating	$T_{II,d}$	-5.0	°C
	$T_{evap,d}$	-10.0	°C
	$T_{IV,d}$	45.0	°C
	$T_{cond,d}$	50.0	°C
	$COP_{h,d}$	2.6	
Cooling	$T_{II,d}$	7.0	°C
	$T_{evap,d}$	2.0	°C
	$T_{IV,d}$	37.0	°C
	$T_{cond,d}$	42.0	°C
	$COP_{c,d}$	3.0	

The changing of outdoor conditions (both in the heating and cooling season) leads to an appreciable variation of COP, as shown in the following Figure 4 referred to the heating and cooling design days.

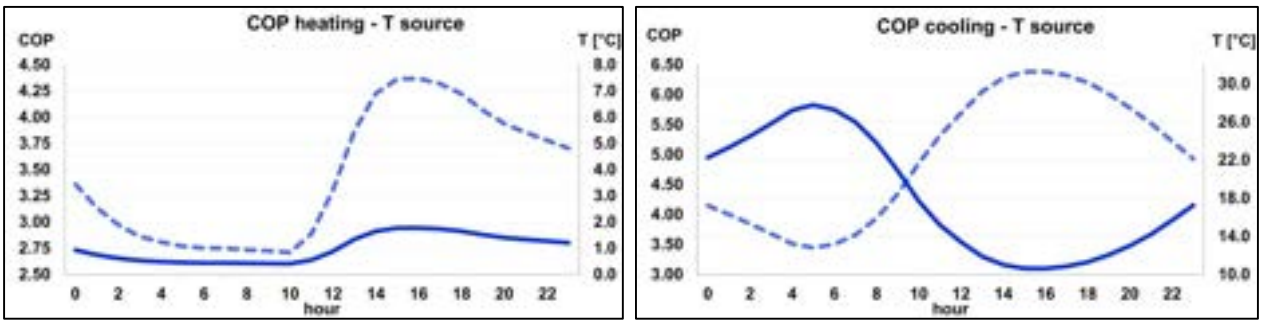

Figure 4. Heating (left) and Cooling (right) COP (left axis, continuous) against source temperature (right axis, dashed), system 1.

It is easy to note that the air-to-air heat pump is particularly penalised in the hours of the cooling season in which the systems should be switched on to ensure the control of thermal loads, with a negative consequence on electricity consumption.

In terms of electric energy consumption, the system presents the following values (Table 10).

Table 10. Electric energy requirements for the air-to-water heat pump (system 1).

Mode	**Energy consumption**	
Heating	915.1	kWh
Cooling	173.0	kWh
TOTAL	1 088.1	kWh

3.3 Groundwater-to-Water heat pump

The design conditions of the system are as follows (Table 11):

Table 11. Design condition for the groundwater-to-water heat pump (system 2).

Mode			
Heating	$T_{II,d}$	12.0	°C
	$T_{evap,d}$	7.0	°C
	$T_{IV,d}$	45.0	°C
	$T_{cond,d}$	50.0	°C
	$COP_{h,d}$	3.9	
Cooling	$T_{II,d}$	7.0	°C
	$T_{evap,d}$	2.0	°C
	$T_{IV,d}$	18.0	°C
	$T_{cond,d}$	23.0	°C
	$COP_{c,d}$	6.4	

The constant temperature of the groundwater throughout the year leads to obtaining a constant value of COP during the heating and cooling season (Figure 5).

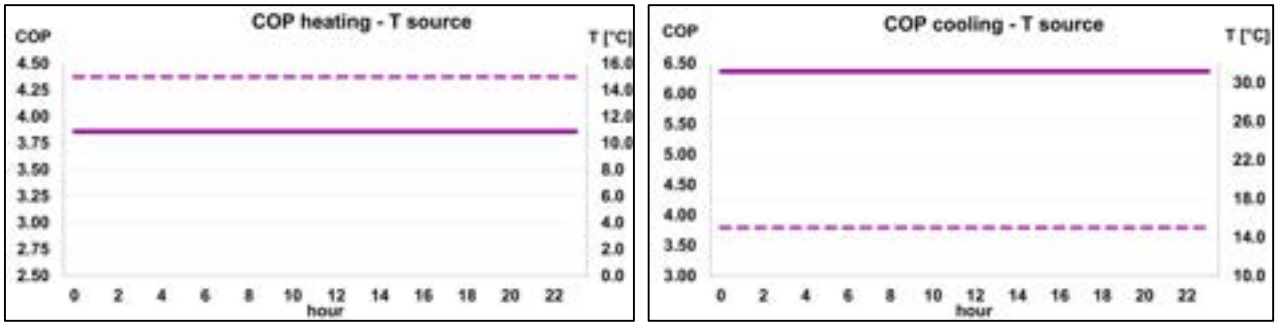

Figure 5. Heating (left) and Cooling (right) COP (left axis, continuous) against source temperature (right axis, dashed), system 2.

In the hours of the highest request for the system, the value of COP remains at the high design value without any influence of the outdoor air. This is the great advantage of a groundwater solution, i.e. the system can work with a very high COP also in the worst conditions of thermal loads. In terms of electric energy consumption, the system presents the following values (Table 12).

Table 12. Electric energy requirements for the groundwater-to-water heat pump (system 2).

Mode	**Energy consumption**	
Heating	679.8	kWh
Cooling	90.2	kWh
TOTAL	770.0	kWh

3.4 Reservoir water-to-Water heat pump

The design conditions of the system are as follows (Table 13):

Table 13. Design condition for the reservoir water-to-water heat pump (system 3).

Mode			
Heating	$T_{II,d}$	5.0	°C
	$T_{evap,d}$	0.0	°C
	$T_{IV,d}$	45.0	°C
	$T_{cond,d}$	50.0	°C
	$COP_{h,d}$	3.1	

Cooling	$T_{II,d}$	7.0	°C
	$T_{evap,d}$	2.0	°C
	$T_{IV,d}$	28.0	°C
	$T_{cond,d}$	33.0	°C
	$COP_{c,d}$	4.6	

The variation of reservoir water temperature is limited with respect to outdoor air, so the fluctuation in COP is quite limited in this case, even if COP is not constant as in the case of direct exploitation of groundwater (Figure 6). Nonetheless, the COP remains high also in the worst conditions for the system, making this technology an energy-efficient solution.

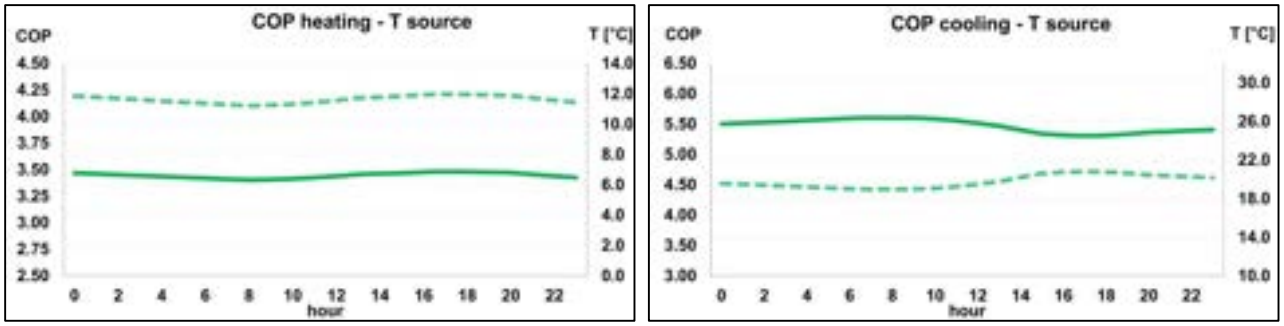

Figure 6. Heating (left) and Cooling (right) COP (left axis, continuous) against source temperature (right axis, dashed), system 3.

In terms of electric energy consumption, the system presents the following values (Table 14).

Table 14. Electric energy requirements for the reservoir water-to-water heat pump (system 3).

Mode	**Energy consumption**	
Heating	764.4	kWh
Cooling	107.2	kWh
TOTAL	871.6	kWh

3.5 Comparison of the energy requirements

Resuming the obtained results, it is possible to clearly show a comparison between the energy consumption of the systems (Figure 7).

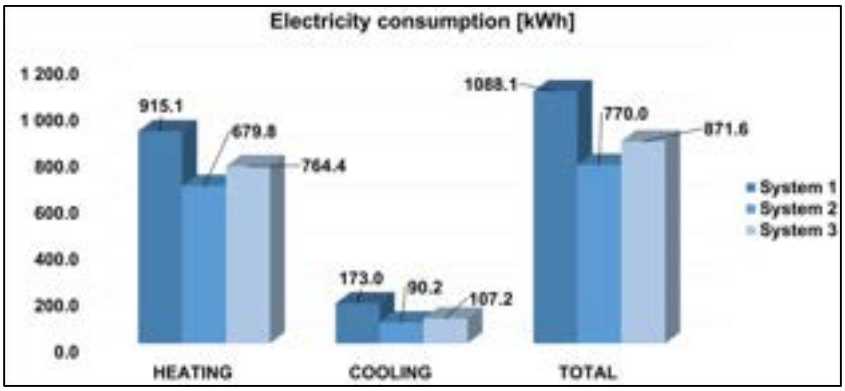

Figure 7. Comparison of electricity consumption for the different systems.

The GWHP (system 2) is the more energy-efficient system, with a yearly electric energy consumption of 770 kWh, which represents a saving of 30 % with respect to a traditional AHP (system 1). The SWHP (system 3), in turn, offers interesting savings (a reduction of 20 % in energy consumption compared to the traditional heat pump). Summing up, if the direct exploitation of groundwater is the most efficient solution in this context, the exploitation through the reservoir might be appropriate where the reservoir is already present, e.g. for irrigation purposes.

3.6 Life Cycle Assessment

The environmental analysis focuses on CO_2 emissions: the Climate Change category is shown in Figure 8. From the obtained results, it is evident that the largest CO_2 emission to the atmosphere is attributable to the AHP system equal to 0.21 kg CO_2 eq/kWh. The second largest system in terms of CO_2 eq emissions is SWHP, with 0.16 kg CO_2 eq/kWh, while GWHP emits slightly less, with 0.15 kg CO_2 eq/kWh.

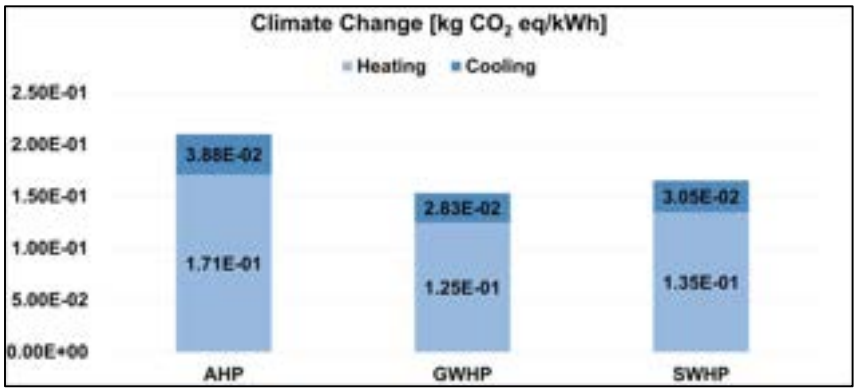

Figure 8. Comparison of the Climate Change LCA category for the different systems.

The contributions analysis (Figure 9) of the environmental impact categories shows that, for all three systems, the main impact comes from the operation phase, particularly in terms of electricity consumption. The construction and commissioning phase has much less impact, except for the categories of HTc, HTnc, and Rumm in which the use of metallic materials assume a great significance and covers about 44.4 %, 47.4 % and 72.2 % of the impacts, respectively. In the case of GWHP and SWHP, the presence of the piping required for water withdrawal assumes additional importance in the environmental impact. Particularly in the case of GWHP, where part of the piping is drilled into the ground to well realisation. Also, to be highlighted is the contribution that the working fluid assumes for the OD category of about 40 % for all three systems.

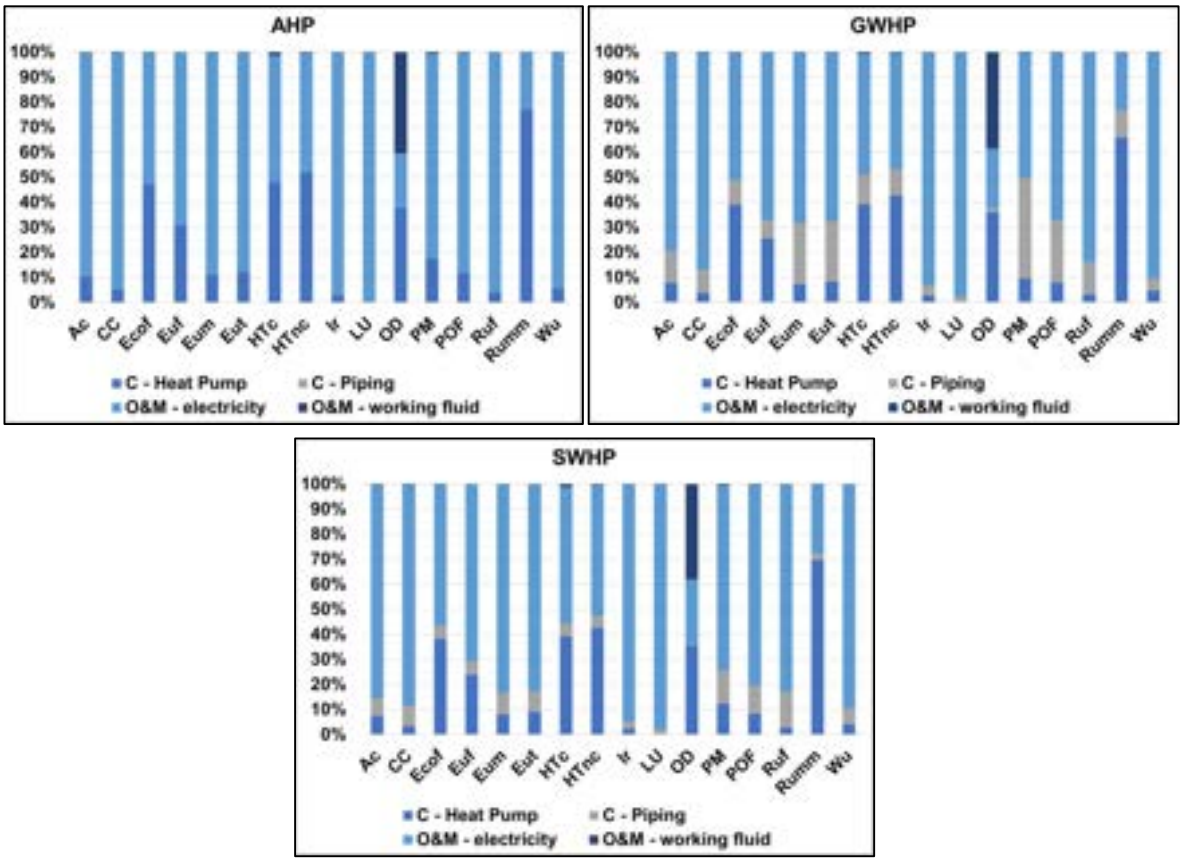

Figure 9 - Contribution analysis of all impact categories for the different systems.

Figure 10 shows the comparison of the three systems at the single score level. The single score shows the overall performance of the three systems. A similar trend to the Climate Change indicator is obtained. Indeed, AHP turns out to be the most impactful system, while GWHP and SWHP are less impacting. A reduction in impacts for both the ground source solutions is evident: about 24 % compared to AHP.

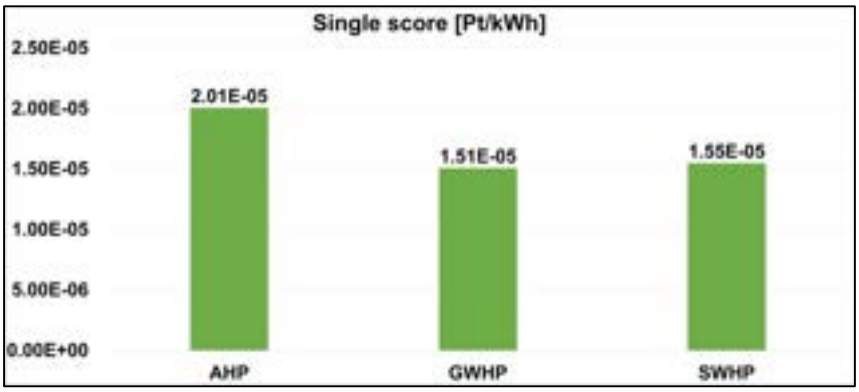

Figure 10 - Single score comparison for the different systems.

4 Conclusions

In this paper, the benefits of using groundwater as a thermal source for residential heat pumps have been discussed. In residential heating and cooling applications heat pumps are widely used, and for the reduction of energy consumption, groundwater represents a very favourable source for the external coils (evaporator in heating mode, condenser in cooling mode) of heat pumps. Three systems have been compared in the context of a specific case study located in Florence (Italy): air-to-water heat pump, groundwater-to-water heat pump and reservoir water-to-water heat pump. For the design of the systems, a detailed energy analysis of the building has been performed, in order to obtain the heating and cooling loads. Then the three systems, of which mathematical models have been presented, have been analysed considering the variation of boundary conditions (thermal loads, sources temperatures), that has been taken into account through a dynamic simulation of the building. Finally, an analysis with Life Cycle Assessment has been performed to show the environmental benefits of the proposed groundwater-based solutions with respect to a traditional heat pump. The analysis has demonstrated that the use of groundwater (direct or through the reservoir) greatly increases the COP (in particular the direct exploitation) of the devices, which results in consistent energy savings. In particular, the dynamic evaluation has shown that: with the groundwater solution it is possible to achieve a saving of 30 % with respect to the traditional air-to-water heat pump, while with the reservoir technology, the saving is 20 %. So the groundwater heat pump is the most energy efficient. Its utilisation is the best choice in terms of energy performance, but in the reality, due to its good results, also the reservoir option could be considered. In particular, a surface water heat pump can be used in all the situations in which the reservoir is already present and could be expensive to build the underground network, or the reservoir is necessary for irrigation needs. LCA analysis confirms, also under the environmental perspective, the advantages of using groundwater. As shown by the focus on the Climate Change category and the comparison to the Single Score, the most impactful system turns out to be AHP, while very little difference is made between the other two systems. GWHP and SWHP allow obtaining a global reduction of impacts of 24 %. The savings achieved with the groundwater solution also suggest a further management strategy for the system. Indeed, as this technology has a much lower electricity consumption than traditional air-to-water ones, it is much easier to integrate it with electricity production from renewable sources such as photovoltaics. In the heaviest situations of thermal or cooling demand of the building, since the groundwater heat pump works at higher COP and therefore lower energy demand, photovoltaic production would be advantaged. Moreover, the LCA analysis of the contributions shows the relevance owned by the electricity that is consumed for every environmental impact, encouraging the utilization of photovoltaic sources. It is therefore evident that, with the perspective of the realisation of *NZEB* buildings that may be integrated into energy communities, the adoption of groundwater technology, where exploitable, is an absolutely desirable strategy.

Nomenclature

Abbreviations		**Subscripts**	
AC	Air Conditioning	bs	building surfaces (opaque and transparent)
AHP	Air to Water Heat Pump	c	cooling
c	specific heat [kJ/kg/K]	cond	condenser
COP	Coefficient Of Performance	d	design condition
DT	Temperature difference [°C]	dev	internal appliances, devices,…
E	Energy [kJ]	evap	evaporator
F	General function of COP	h	heating
GHP	Ground Heat Pump	i	indoor
GSHP	Ground Source Heat Pump	I,II,III,IV	points of devices schematisation
GWHP	Ground Water Heat Pump	inf	infiltration
j	Specific entalphy [kJ/kg]	l	latent heat
LCA	Life Cycle Assessment	o	outdoor
M	Mass [kg]	p	person

LCIA	Life Cycle Impact Assessment	r	solar radiation
LCI	Life Cycle Inventory	res	water reservoir
m	Mass flow rate [kg/s]	s	sensible heat
N	Number of air changes per hour [vol/h]	v	ventilation
n	number of people		
OD	Occupancy Density [W/m^2]		
PD	Power Density [W/m^2]		
Q	Thermal power [kW]		
q	Thermal load/person [kW]		
R	Direct normal solar radiation [kW]		
RH	Relative Humidity [%]		
S	Floor Area [m^2]		
SWHP	Surface Water Heat Pump		
T	Temperature [°C]		
V	Volumetric flow rate [m^3/s]		
W	Electric consumption of heat pump [kW]		
Abbreviations LCA			
Ac	Acidification	Ir	Ionising radiation
CC	Climate change	LU	Land use
Ecof	Ecotoxicity, freshwater	OD	Ozone depletion
Euf	Eutrophication, freshwater	PM	Particulate matter
Eum	Eutrophication, marine	POF	Photochemical ozone formation
Eut	Eutrophication, terrestrial	Ruf	Resource use, fossils
HTc	Human toxicity, cancer	Rumm	Resource use, minerals and metals
HTnc	Human toxicity, non-cancer	Wu	Water use

References

[1] Grazzini G, Milazzo A. Tecnica del Freddo. Esculapio Editore. 2017.

[2] Birol F. World Energy Outlook 2022. International Energy Agency. 2022.

[3] Birol F. Net Zero by 2050 - A Roadmap for the Global Energy Sector. International Energy Agency. 2021.

[4] Birol F. The Future of Cooling. International Energy Agency. 2018.

[5] Abbasi MH, Abdullah B et al. Heat transition in the European building sector: Overview of the heat decarbonisation practices through heat pump technology. Sustainable Energy Technologies and Assessments. 2021. https://doi.org/10.1016/j.seta.2021.101630.

[6] Gondal IA. Prospects of shallow geothermal systems in HVAC for NZEB. Energy and Built Environment 2021. https://doi.org/10.1016/j.enbenv.2020.09.007.

[7] Soltani M, M. Kashkooli F et al. A comprehensive study of geothermal heating and cooling systems. Sustainable Cities and Society. 2019. https://doi.org/10.1016/j.scs.2018.09.036.

[8] Sarbu I, Sebarchievici C. General review of ground-source heat pump systems for heating and cooling of buildings. Energy and Buildings. 2014. https://doi.org/10.1016/j.enbuild.2013.11.068.

[9] Decreto interministeriale 26 giugno 2015. Applicazione delle metodologie di calcolo delle prestazioni energetiche e definizione delle prescrizioni e dei requisiti minimi degli edifici. 2015. *Italian laws and regulations for energy performances of buildings.*

[10] International Organization for Standardization. ISO 14040:2021—Environmental management — Life cycle assessment — Principles and framework.

[11] International Organization for Standardization. ISO 14044:2021 Environmental management - Life cycle assessment - Requirements and guidelines.

[12] Moreno-Ruiz E, Valsasina L et al. Documentation of changes implemented in ecoinvent database v3.6. ecoinvent Association. 2019.

[13] Greening B, Azapagic A. Domestic heat pumps: Life cycle environmental impacts and potential implications for the UK. Energy. 2012. https://doi.org/10.1016/j.energy.2012.01.028.

[14] CoolSelector2 software. Danfoss.

[15] Lovell D, Rickerby T et al. Thermal performance prediction of outdoor swimming pools. Building and Environment. 2019. https://doi.org/10.1016/j.buildenv.2019.106167.

[16] UNI 10339:1995. Impianti aeraulici al fini di benessere. Generalità, classificazione e requisiti. Regole per la richiesta d'offerta, l'offerta, l'ordine e la fornitura. 1995. *Italian laws and regulations for air systems.*

Trade-off between embodied and operational carbon emissions of residential buildings in early design stage

Yijun Zhou [a], Vivian WY Tam [b], and Khoa N. Le [c]

[a] Western Sydney University, School of Engineering, Design and Built Environment, Locked Bag 1797, Penrith, NSW 2751, Australia, 19896117@student.westernsydney.edu.au
[b] Western Sydney University, School of Engineering, Design and Built Environment, Locked Bag 1797, Penrith, NSW 2751, Australia, vivianwytam@gmail.com, CA
[c] Western Sydney University, School of Engineering, Design and Built Environment, Locked Bag 1797, Penrith, NSW 2751, Australia, k.le@westernsydney.edu.au

Abstract:

Buildings are responsible for a significant portion of the global energy use and carbon emissions. There is great potential to reduce a building's environmental impact in the early stages of design. Over the past decade, there has been a concerted effort to create energy-efficient and net-zero buildings by reducing operating energy. However, additional materials and new applications are needed to reduce energy demand. This may result in an increase in embodied carbon, which is the carbon emitted during the materials and construction phase. Since there is a trade-off between embodied and operational environmental environment, it is important to consider both in the design process. However, there is a lack of research that addresses this issue. To help with this challenge, a multi-objective optimization model that combines machine learning, building information modelling, and life cycle assessment has been developed. This model can help in making design decisions that balance embodied and operational carbon emissions. An actual building project has been used to verify the model developed. The findings reveal that early design stage has the potential to save 32.5% emissions for mid-rise buildings in hot summer and cold winter climate zone in China. Moreover, window-to-wall ratio and number of floors largely affecting the trade-off between embodied and operational impacts. The findings of this study can provide low-carbon and energy-efficient design solutions for residential buildings in the early stages of design.

Keywords:

Embodied carbon; Operational carbon; Optimization; Building design.

Nomenclature:

Abbreviations

LCA	-	Life cycle assessment	SVM	-	Support vector machine
BIM	-	Building information modelling	LSSVM	-	Least squares linear machine
HVAC	-	Heating, Ventilation, and Air Conditioning	NSGA-II	-	Non-dominated genetic algorithm II
WWR	-	Window-to-wall ratio	TOPSIS	-	Technique for order preference by similarity to an ideal solution

Symbols

μ	-	Average	R^2	-	Coefficient of determination
Z	-	Standard deviation	a_{i1}	-	low bounds of the i^{th} design variable
$\hat{y}_i$	-	Predicted value by the LSSVM model	a_{i2}	-	up bounds of the i^{th} design variable
$\bar{y}_i$	-	Arithmetic mean of y_i	x_i	-	Input variable
n	-	Number of training examples	x	-	Output variable
∂_i	-	Lagrange multipliers	C	-	Penalty parameter
b	-	Bias term	CO_2-eq	-	Carbon dioxide equivalents

1. Introduction

A significant share of the global negative environmental effects (e.g., use of resources and environmental consequences of releases) are caused by the building sector. The International Energy Agency stated that in 2020, the construction industry accounted for 36% of world energy consumption and 37% of carbon dioxide emissions [1]. The environmental impacts of a building over its life cycle can be divided into embodied environmental impacts and operational environmental impacts. Operational impacts are caused by energy usage during building operation, whereas embodied impacts are connected to the raw material extraction, construction, end-of-life treatments, recycling, and final disposal [2]. The embodied impacts are significant and occasionally equal operational environmental impact levels [3]. It is therefore a pressing need to simultaneously minimize embodied and operational environmental impacts for creating environmentally preferred buildings. However, there is a reciprocal relationship between the embodied and operational environmental impacts. This relationship can be attributed to additional materials and new applications and systems are required to reduce the resources consumption and energy demands during building operational stages [4]. The extra materials and equipment may lead to a decrease of impacts due to operational energy use while increasing embodied environmental impacts. As a result, buildings with energy-efficient measures may cause more total environmental impacts [4,5]. Therefore, it is of great importance to focus on the trade-off between embodied and operational environmental impacts whilst lowering the total environmental impacts.

The environmental impacts of a building over its life cycle are largely influenced by the decisions made during the early stages of design [6]. Creating an eco-friendly building design in the early design practice presents a significant opportunity to lower the total environmental impact of a building and find the optimal trade-off between embodied and operational impacts. However, the early design of a building involves making decisions on numerous design variables, such as floor height, floor area, building shape, building orientation, window-to-wall ratio (WWR), and number of floors. Accordingly, thousands of design alternatives can be generated by varying these design variables. It becomes a significant challenge to determine the most appropriate design that reduces the total environmental impact of a building and achieves an optimal trade-off between embodied and operational impacts. The complexity of building design constraints and the large number of design options make it difficult to find out the optimal design solution.

Life cycle assessment (LCA) is a powerful tool to quantify the environmental impacts of a building over its lifetime [7,8]. On the other hand, building information modelling (BIM) digitally represents the physical and functional characteristics of a facility and related information of the building project [9]. BIM model includes all the necessary information for the assessment of embodied environmental impacts and the simulation of energy demand [10]. BIM applications in the environmental impact assessment of a building enable to improve assessment quality [11]. Moreover, the integration between BIM and LCA has been widely accepted and proven effective for assessing the embodied environmental impact assessment. However, the complexity of assessment process using BIM-LCA integration approaches makes it impractical to identify the optimal design solutions that balance embodied and operational impacts. The repetitive procedures and processes involved in the combined use of BIM and LCA make it challenging to determine the optimal design solutions.

Multi-objective optimization methods allow for different trade-offs between conflicted objectives and have been widely used in the construction industry in a variety of practical topics and contexts. These include, for example, designing building facades [12], selecting building shape [13], and choosing building components or materials such as type of glazing [14] and window type [15]. Multi-objective optimization methods have also been employed to balance the embodied and operational energy in buildings [4]. In the context of building design, multi-objective optimization methods addressed with the parametric design issues [16]. Additionally, multi-objective optimization methods have been applied to address environmental impact topics such as bridge maintenance [17], energy and investment costs management [18], and green building rating systems [19]. For a more comprehensive overview of multi-objective optimization methods applied in the construction industry, see the review articles by Guo and Zhang [20]. The optimization methods have also been used to address other issues such as prefabrication, supply chain, work safety and risk management.

Above discussion reveals that despite the significance, there has been limited focus on the use of multi-objective optimization methods to find the optimal design solutions in linking embodied and operational environmental impacts in early design practice. To address the research gap, this study aims to develop a multi-objective optimization model by using a combination of multi-objective optimization methods and BIM-LCA integration programs to identify optimal solutions that balance the embodied and operational impacts of a building during early design practice. The findings can provide designers with more comprehensive and in-depth understanding on the potentials to save carbon emissions and the relationships between embodied and operational impacts.

2. Research methodology

To fulfil the research aim, this research developed a multi-objective optimization model based on a BIM-LCA integration approach and a meta-based multi-objective optimization method. There are three modules in this developed model: 1) embodied and operational impacts evaluated by a BIM-LCA integration approach, 2) environmental impact prediction based on a machine learning method, and 3) multi-objective optimization of embodied and operational impacts.

2.1. Environmental impact assessment based on integration between BIM and LCA

The first module involves conducting the environmental impact assessment of a building over its life cycle, following a standard process for life cycle assessment outlined in ISO 14040 framework. This process consists of four phases: 1) goal and scope definition, 2) life cycle inventory analysis, 3) life cycle assessment analysis, and 4) life cycle interpretation [21]. In this study, the environmental impact assessment of a building starts with creating a BIM model of the design solutions selected. The goal and scope definition phase includes assumption about the system boundary of life cycle assessment and the building's lifespan. The system boundary in this study includes the product stages (A1-A3), the use stages (B2-B6), and the end-of-life stages (C2-C4), while environmental impacts produced in construction phase (A4) are excluded due to their small proportion of the total environmental impacts [6]. During the life cycle inventory analysis and life cycle assessment phases, the environmental impacts are assessed. Tally is used to assess the embodied impacts by manually matching BIM objects to the building components in Tally. If identical building components cannot be found, similar ones would be used. Moreover, Tally is also used to assess the operational environmental impacts by importing the amount of energy consumption which is simulated by Green Building Studio. Specifically, the physical parameters and thermal properties of the building components, derived from Autodesk Revit database of building components and the common practice in local building projects, are incorporated into the BIM mode to ensure the accuracy of energy simulation. Then, BIM model is transferred into an energy analysis model. Energy analysis parameters are determined such as the operational time of a building, the way of Heating, Ventilation, and Air Conditioning (HAVC) operation. Then, the energy analysis model is imported into Green Building Studio for energy simulation. Green Building Studio is a flexible cloud-based service that uses the DOE2 simulation engine and allows to run building performance simulations to optimize energy efficiency in the design process. In addition, the climate files of the building are set in the performance simulation process. The simulation results are manually input into Tally to assess the operational impacts. In life cycle interpretation phase, the environmental impacts of a building over its life cycle are expressed by environmental impact indicators based on the TRACI 2.1 characterization method [22]. TRACI 2.1 method covers ten different environmental impact indicators by default, such as the global warming potential, non-renewable energy consumption, ozone potential and others. For our calculation, this study considers global warming potential (expressed in the amount of carbon dioxide equivalents (CO_2-eq) to indicate the total environmental impacts of the building.

2.2. Environmental impact prediction by machine learning method

Support vector machine (SVM) developed by Vapnik and Cortes [23], is a machine learning technique based on the statistical learning theory. This technique can solve nonlinear problems very well and is suitable for small sample sizes studies [24]. Least squares linear machine (LSSVM) was developed based on SVM by using a least squares linear system as a loss function to transform the inequality constraints of the optimization problem into equality constraints, thus yielding better performance than an SVM. A training and design of an LSSVM model is an iterative algorithm, and it basically involves four steps: (1) define the problem as the classification or the regression problem, (2) pre-process the input data, (3) determine the model parameters, and (4) validate the model obtained [25]. This study attempts to learn the input-output relationship from the training data, where the inputs are n-dimensional vectors, and the outputs are continuous values. The details about developing the LSSVM model are presented as follows:

The raw data was randomly divided into 80% training data and 20% test data. Given that the units, value domains, physical meanings of independent variables in raw dataset vary substantially, z-score normalisation was performed on raw data to eliminate the influence of different eigenvalue dimensions on the prediction accuracy by applying Equation (1)

$$x' = \frac{x-\mu}{z} \quad (1)$$

Where x denotes the raw data, μ is the average of the sample data, and z represents the standard deviation of the sample data. The processed data follows the standard normal distribution. The average value and the variance of the processed data are 0 and 1 respectively.

The Gaussian kernel function has excellent anti-interference ability [24]. Therefore, Gaussian kernel function Equation (2) was adopted for the prediction model in this study.

$$k(x_i, x) = e^{-\frac{\|x_i - x\|^2}{2\sigma^2}} \quad (2)$$

Where x_i is the input variable, x is the output variable, and σ^2 is the variance of the Gaussian kernel.

Penalty parameter C controls the trade-off between generalization capacity (wide margin width) and the empirical error of the prediction model. Large C leads to small number of misclassifications and consequently to the smaller margin (good generalization capacity) and vice versa [25]. The selection of penalty parameter C and variance σ^2 greatly affects the prediction error of the model. Normally, the parameters were determined by a trial-and-error process.

Cross validation is often used to optimize the selected values of model parameters (i.e., C and σ^2 in this study) in a refined scale. The process is also called tuning, which is generally empirical, with various values for the parameters systematically evaluated, and the combination of values that generate the highest overall accuracy is assumed to be optimal [26]. K-fold cross-validation method was adopted to search for the optimal combination of C and σ^2. Specifically, the sample data is divided into K sample subsets, where one sample data is selected for testing and the other (K-1) samples are used for training. The cross-validation is repeated K times to obtain the optimal parameter values. Accordingly, the LSSVM model can be obtained by using the optimal C and sigma for training.

To the end, the prediction accuracy of the LSSVM model is measured by coefficient of determination (R^2) in this study, which are defined as Equation (3). The higher the R^2, and the less difference between two sets of data.

$$R^2 = 1 - \frac{\sum_{i=1}^{n}(y_i - \hat{y}_i)^2}{\sum_{i=1}^{n}(y_i - \bar{y}_i)^2} \quad (3)$$

Where y_i is the assessment value of i^{th} training example by BIM-LCA integration approaches, $\hat{y}_i$ is the predicted value by the LSSVM model, $\bar{y}_i$ is the arithmetic mean of y_i, and n is the number of training examples passed to LSSVM model.

2.3. Multi-objective optimization based on NSGA-II algorithm

The third module is the multi-objective optimization that deals with the optimization problem related to the environmental impacts of a building.

For this study, the LSSVM-trained model is adopted as the objective functions in the multi-objective optimization process. The relationships between design variables and embodied and operational environmental impacts of buildings are presented as Equation (4):

$$lssvm(x_1, x_2, \dots, x_n) = \sum_{i=1}^{n}(\partial_i - \partial_i^*)\, e^{-\frac{\|x_i - x\|^2}{2\sigma^2}} + b \quad (4)$$

Where $x_1, x_2, \dots, x_n$ are the design variables. ∂_i and ∂_i^* are Lagrange multipliers, b is the bias term, x_i is the input variable, and x is the output variable (i.e., embodied or operational impacts in this study).

Then, the objectives in each design stage are expressed as follows:

$$\begin{cases} \min f_{embodied}(\, lssvm(x_1, x_2, \dots, x_n)) \\ \min f_{operational}(\, lssvm(x_1, x_2, \dots, x_n)) \end{cases} \quad (5)$$

Where $x_1, x_2, \dots, x_n$ are the design variables in early design stage, $f_{embodied}(lssvm(x_1, x_2, \dots, x_n))$ is the embodied environmental impacts of a building, and $f_{operational}(lssvm(x_1, x_2, \dots, x_n))$ is the operational environmental impacts of a building in early design stage.

Constraints on the objective functions are used to ensure the generated solutions reasonable and feasible. The value ranges of design variables according to the design codes, standards and rules were set as the constraints of the objective functions. The constraints on the design variables can be expressed in inequation (6):

$$a_{i1} \le x_i \le a_{i2} \quad (6)$$

Where x_i denotes the i^{th} design variables in each design stage, while a_{i1} and a_{i2} are the low and up bounds, respectively of the i^{th} design variable.

The non-dominated genetic algorithm II (NSGA-II), developed by Deb [27] was adopted to solve the multi-objective optimization problems in this study. The NSGA-II genetic algorithm can be coupled easily with a backbox model and can handle a set of solutions simultaneously allowing to obtain several pareto frontiers in a single run. The optimization model was used to select the optimum building alternatives with minimum embodied and operational environmental impacts. After obtaining the pareto optimal solution set, the technique for order preference by similarity to an ideal solution (TOPSIS), a multi-criteria decision-making approach was employed to the determine the optimal trade-off point. The TOPSIS method figures out the positive-ideal option in which the maximum gain from each of the objectives is taken and the negative-ideal option in which the maximum loss from each of the objectives is taken. Towards the end, the option that is closest to the positive-ideal solution and farthest away from the negative-ideal solution is selected by the TOPSIS method.

3. Case study

The proposed model was verified by using a mid-rise residential building (refer to a residential building between 4 and 8 floors). The purpose of the case study is to identify the optimal design solutions that balance the trade-off between embodied and operational impacts at early design stage. The case selected for this study was adapted from an actual residential apartment built in Chongqing, China. This project is located in a hot summer and cold winter climate zone, which was built in accordance with the Design Code for Residential Buildings [28]. The long sides of the building are facing north and south. The project is an 8-story, reinforced concrete frame building, and the floor height is 2.8m. The construction methods and building elements from the second floor to the seventh floor are the same. Each floor of the building has a single family which owns four bedrooms, a kitchen, a living room, a storeroom, a balcony and two bathrooms. The building has a total above-basement floor area of 1297.12 m^2 with a life expectancy of 50 years. The building project is a typical example of an apartment building in Chongqing, China representing common building materials and construction techniques for walls, floors, and other building components. Figure 1shows the sketches and 3D model of the building.

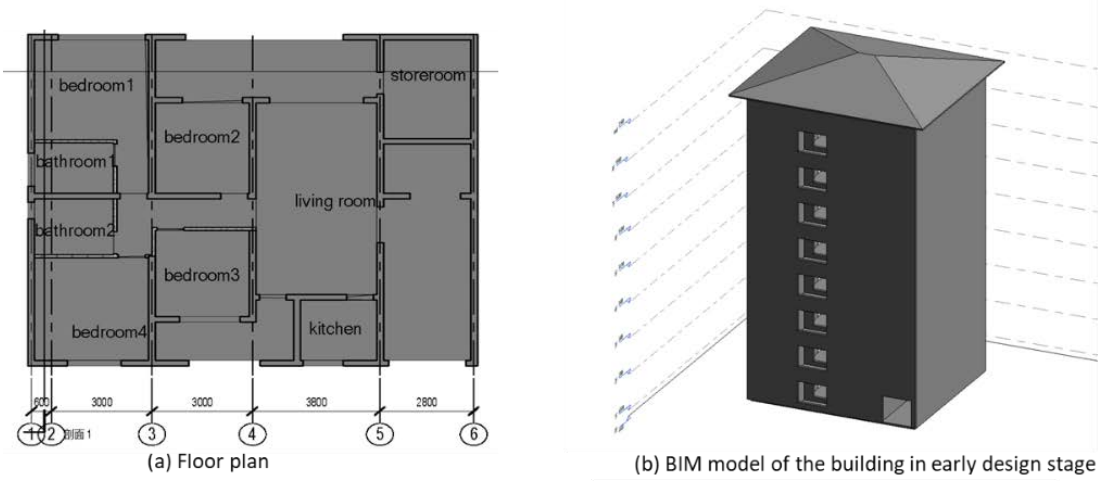

(a) Floor plan (b) BIM model of the building in early design stage

Figure. 1. Sketches and 3D model of the building in early design stage.

There are four design variables affecting the environmental impacts of a building in early design practice [29]. The design variables include: (1) floor height, (2) building orientation, (3) window-to-wall ratio (WWR) and (4) number of floors in early design stage. The variables can be continuous or discrete, and the values or value ranges are determined by national building design and construction standards, regulations and codes [30,31]. The values of the design variables in early design stages are shown in Table 1.

Table 1. Characteristics of design variables for the building in early design stage.

Design variables	Value/value domain	Variable types	Number of options
Floor height	[2.4m, 2.8m]	Continuous	0.1m uniform step (5 options)
Building orientation	[15°, 75°]	Continuous	10° uniform step (7 options)
Window-to-wall ratio	[0.1, 0.5]	Continuous	0.05 uniform step (9 options)
Number of floors	4, 5, 6, 7, 8	Discrete	5 options

4 Results and Discussion

Having examined the design variables and values, possible design alternatives in each design stage are generated by varying design variables. Orthogonal experiment was then conducted to obtain the design samples. In this study, there are 4 design variables and 9 levels in early design stage. Accordingly, 65 design samples were obtained. In referring to the life-cycle environmental impact assessment, BIM models of the design samples were created in Revit. They were then imported into Green Building Studio and Tally for the life-cycle carbon emissions through the BIM-LCA integration approach. The building operating schedule, HVAC system, and outdoor air information are out of the scope of this research, and therefore the building service system is assumed to satisfy the ideal conditions for heating and cooling. As a result, the amount of embodied and operational impacts, expressed by kg CO2eq/m2 for design samples are presented in Figure 2.

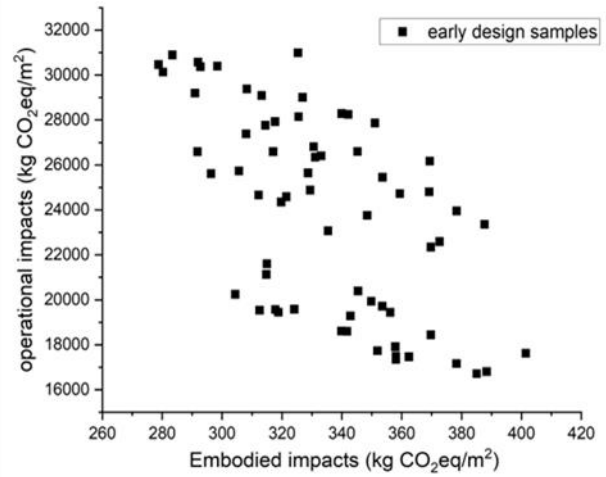

Figure. 2. Environmental impacts of early design alternatives.

As shown in Figure 2, the operational environmental impacts account for a large portion of the life-cycle environmental impacts (over 90% in each design stage). Having obtained the environmental impact assessment results of design samples at each design stage, the MATLAB has been used to train and develop the LSSVM model for predicting the embodied and operational impacts of a building over its design process. 80% of the sample cases (52 cases for early design stage) were used to train the LSSVM model. All inputs and outputs were normalized according to Equation (1). The training results for embodied and operational impact assessment of three design stages are shown in the left of Figure 3. The goodness-of-fit R^2 is 0.97997 for embodied impact assessment and 0.90934 for operational impact in early design stage. They were found very close to 1 for the output studied, thus demonstrating a very good correlation between outputs and target values.

Subsequently, the developed LSSVM model was validated with 13 cases, the rest 20% sample cases. The results of the LSSVM prediction on the testing set are basically consist with the assessment result, as shown in the right of Figure 3. The goodness-of-fit R^2 is 0.9068 and 0.91751 for embodied and operational impact prediction in early design stages, which shows a high prediction accuracy. Therefore, the relationship between design variables and environmental impact established by LSSVM model enables to be used as the objective function of the multi-objective optimization.

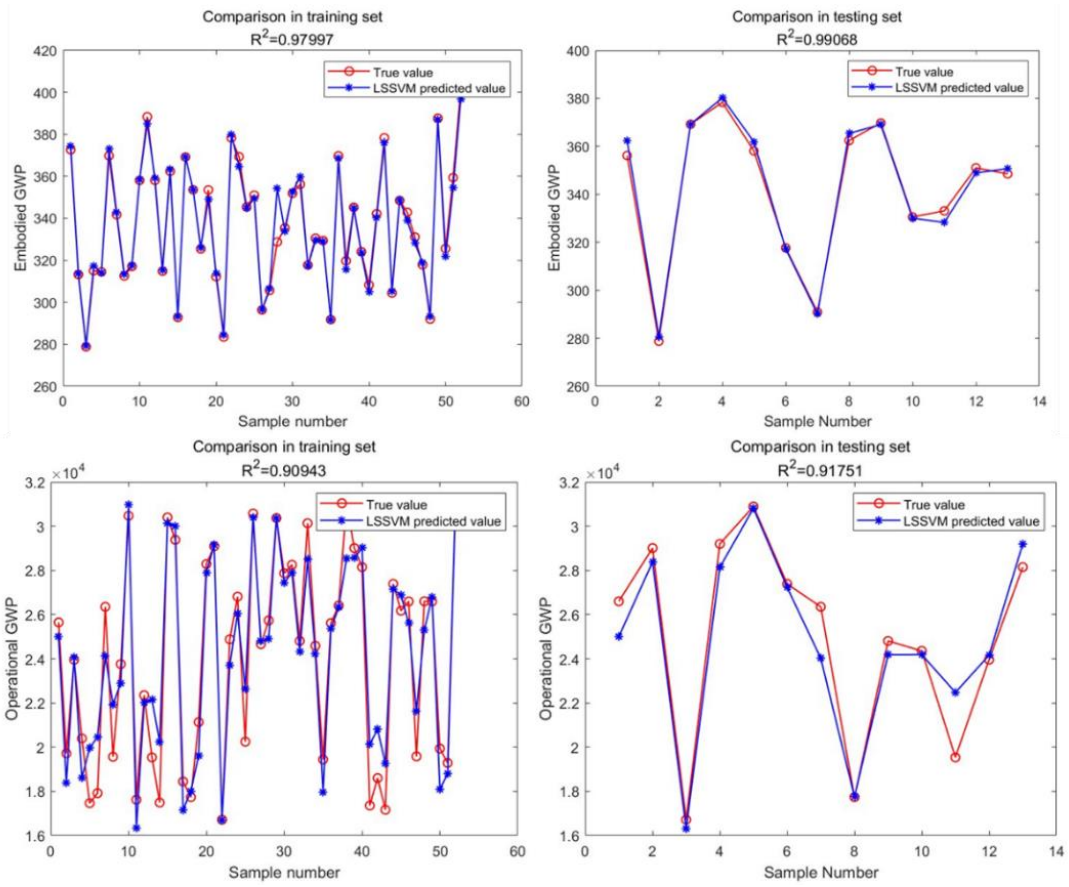

Figure. 3. Environmental impact prediction model.

The combination of LSSVM models and NSGA-II was conducted in Matlab environment to explore the optimal design solution in each design stage. The initial population was set as 100 due for 200 generations based on recommendation. A high mutation rate and a large population size were chosen to avoid getting stuck in local optima. The progress of the objectives was always supervised during the optimization, and if no major improvement could be observed, the algorithm was stopped.

The optimal design solutions are elaborated according to the following optimization cases: (1) Single-objective optimizations for total life-cycle environmental impacts; and (2) A multi-objective optimization considering the operational and the embodied environmental impacts with equal weights. The optimal design solutions are illustrated in Figure 4 and Table 2.

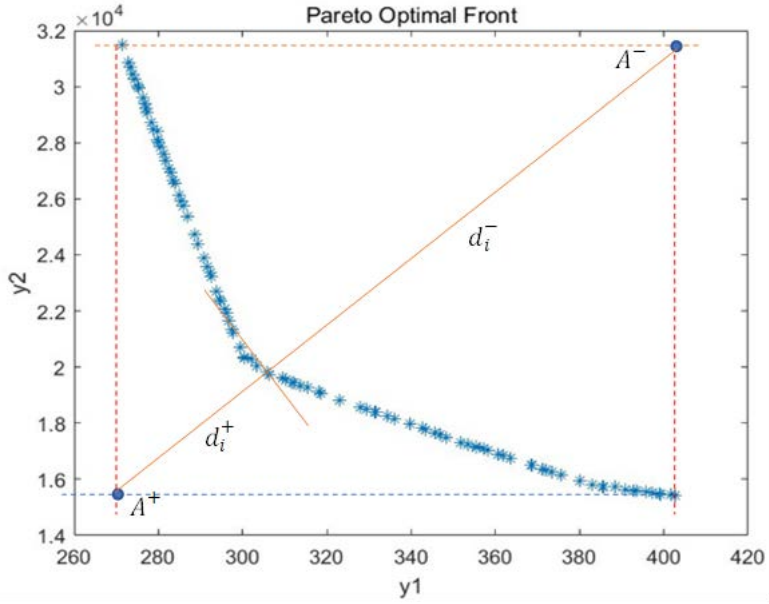

Figure. 4. Pareto optimal front in early design stages.

Table 2. Optimization design solutions.

	Floor height(m)	Orientation (°)	WWR	Number of floors	Embodied impacts	Operational impacts	Total impacts
Original design	2.8	0°	0.25	8	335.38	23070.34	23405.72
Design solution with minimum total environmental impacts	2.8	15°	0.1	4	402.6102	15403	15805.61
Design solution with trade-off between embodied and operational impacts	2.8	15°	0.4	8	322.9659	18831	19153.97

The Pareto frontier in early design stage is illustrated in Figure 4. It indicates that there is a trade-off between embodied and operational environmental impacts in early design stage. As embodied impacts (denoted as y1 in Figure 4) increase, the operational impacts (denoted as y2 in Figure 4) decrease. In referring to the single objective optimization for total life-cycle environmental impacts, the minimum total impact (15805.61 kg CO_2eq/m^2) is obtained in the design option where there are 4 number of floors with floor height of 2.8 m, the WWR is 0.1, and the orientation of building is 15° south to west, as shown in Table 2. The total CO_2eq generated by the optimal design equals to 67.5% of that from the original building design. In other words, it is possible to reduce 32.5% of the environmental impacts for the original design by varying the design parameters in early design practice. The difference between the optimal design solution and the original one lies in the building orientation (15° vs. 0°), WWR (0.1 vs. 0.25) and number of floors (4 vs. 8).

In referring to the trade-off between embodied and operational impacts, the TOPSIS analysis results reveal that the trade-off design solution is the case (number of floors: 8, floor height: 2.8m, orientation: 15° south to west, and WWR: 0.1). The total environmental impact is 19153.97 kg CO_2eq/m^2, which consists of an embodied impact of 322.97 kg CO_2eq/m^2 and an operational impact of 18831 kg CO_2eq/m^2. The operational impact of trade-off design increases by 8.8% while the embodied impact decreases by 25.8%, compared with the original design. Since the trade-off solution intends to simultaneously minimize the embodied and operational impacts of the original design, its total environmental impacts are larger than “the minimum total impacts” (15805.61 kg CO_2eq/m^2). Interestingly, the difference between the “trade-off solution” and the

"solution with minimum total impacts" only lies in the design values of "WWR" and "number of floors" (The floor height and orientation of the building keep constant). This indicates that WWR and number of floors seem to have a strong influence on the trade-off between embodied and operational impacts of a building.

5 Conclusion

This research developed a multi-objective optimization model based on the combined use of BIM-LCA integration approaches, machine learning method and NSGA-II algorithm to find out the balance between embodied and operational impacts of a building in its early design practice. The man conclusion based on the case study are as follows: 1) early design stage has the potential to save 32.5% emissions for mid-rise buildings in hot summer and cold winter climate zone in China. 2) window-to-wall ratio and number of floors largely affecting the trade-off between embodied and operational impacts. Further research needs to investigate other design stages throughout the entire design process. Moreover, future research can also explore other building types in different climate zones.

Acknowledgements

The authors wish to acknowledge the financial support from the Australian Research Council (ARC), Australian Government (No: DP190100559, DP200100057, IH200100010) and the financial support from Sustainable Development Goals Project Allowance Grant in Western Sydney University.

References

[1] IEA. 2021 Global status report for buildings and construction. 2021.

[2] Cavalliere C, Habert G, Dell'Osso GR, Hollberg A. Continuous BIM-based assessment of embodied environmental impacts throughout the design process. J Clean Prod 2019;211:941–52.

[3] Gauch HL, Hawkins W, Ibell T, Allwood JM, Dunant CF. Carbon vs. cost option mapping: A tool for improving early-stage design decisions. Autom Constr 2022;136:104178.

[4] Abbasi S, Noorzai E. The BIM-Based multi-optimization approach in order to determine the trade-off between embodied and operation energy focused on renewable energy use. J Clean Prod 2021;281:125359.

[5] Shadram F, Mukkavaara J. An integrated BIM-based framework for the optimization of the trade-off between embodied and operational energy. Energy Build 2018;158:1189–205.

[6] Basbagill J, Flager F, Lepech M, Fischer M. Application of life-cycle assessment to early stage building design for reduced embodied environmental impacts. Build Environ 2013;60:81–92.

[7] Cavalliere C, Dell'Osso GR, Pierucci A, Iannone F. Life cycle assessment data structure for building information modelling. J Clean Prod 2018;199:193–204.

[8] Najjar M, Figueiredo K, Palumbo M, Haddad A. Integration of BIM and LCA: Evaluating the environmental impacts of building materials at an early stage of designing a typical office building. J Build Eng 2017;14:115–26.

[9] National Institute of Building Sciences. United States-National Building Information Modeling Standard–V.1–P.1:Overview,Principles,and Methododgies. 2007.

[10] Kiss B, Szalay Z. Modular approach to multi-objective environmental optimization of buildings. Autom Constr 2020;111:103044.

[11] Tam VW, Zhou Y, Illankoon C, Le KN. A critical review on BIM and LCA integration using the ISO 14040 framework. Build Environ 2022;213:108865.

[12] Azari R, Garshasbi S, Amini P, Rashed-Ali H, Mohammadi Y. Multi-objective optimization of building envelope design for life cycle environmental performance. Energy Build 2016;126:524–34.

[13] Jalali Z, Noorzai E, Heidari S. Design and optimization of form and facade of an office building using the genetic algorithm. Sci Technol Built Environ 2020;26:128–40.

[14] Taghizade K, Heidari A, Noorzai E. Environmental Impact Profiles for Glazing Systems: Strategies for Early Design Process. J Archit Eng 2019;25:1–12.

[15] Hong T, Kim J, Lee M. A multi-objective optimization model for determining the building design and occupant behaviors based on energy, economic, and environmental performance. Energy

2019;174:823–34.

[16] Hollberg A, Ruth J. LCA in architectural design—a parametric approach. Int J Life Cycle Assess 2016;21:943–60.

[17] Abdelkader EM, Moselhi O, Marzouk M, Zayed T. An exponential chaotic differential evolution algorithm for optimizing bridge maintenance plans. Autom Constr 2022;134:104107.

[18] Abokersh MH, Vallès M, Cabeza LF, Boer D. A framework for the optimal integration of solar assisted district heating in different urban sized communities: A robust machine learning approach incorporating global sensitivity analysis. Appl Energy 2020;267:114903.

[19] Marzouk M, Azab S, Metawie M. BIM-based approach for optimizing life cycle costs of sustainable buildings. J Clean Prod 2018;188:217–26. https://doi.org/10.1016/j.jclepro.2018.03.280.

[20] Guo K, Zhang L. Multi-objective optimization for improved project management: Current status and future directions. Autom Constr 2022;139:104256.

[21] ISO. 14040: Environmental management–life cycle assessment—Principles and framework. vol. 2006. 2006.

[22] Bare J. TRACI 2.0: The tool for the reduction and assessment of chemical and other environmental impacts 2.0. Clean Technol Environ Policy 2011;13:687–96. https://doi.org/10.1007/s10098-010-0338-9.

[23] Cortes C, Vapnik V. Support-vector networks. Mach Learn 1995;628:273–97.

[24] Chen B, Liu Q, Chen H, Wang L, Deng T, Zhang L, et al. Multiobjective optimization of building energy consumption based on BIM-DB and LSSVM-NSGA-II. J Clean Prod 2021;294:126153.

[25] Kecman V. Support Vector Machines – An Introduction. Support Vector Mach. Theory Appl., vol. 177, 2005, p. 1–47.

[26] Ramezan CA, Warner TA, Maxwell AE. Evaluation of sampling and cross-validation tuning strategies for regional-scale machine learning classification. Remote Sens 2019;11.

[27] Deb K, Pratap A, Agarwal S, Meyarivan T. A fast and elitist multiobjective genetic algorithm: NSGA-II. IEEE Trans Evol Comput 2002;6:182–97.

[28] MOHURD. Design Code for Residential Buildings. China: 2011.

[29] Zhou Y, Tam VW, Le KN. Sensitivity analysis of design variables in life-cycle environmental impacts of buildings. J Build Eng 2023;65:105749.

[30] China Institute of Building Standard Design & Research. National Building Design Standard Atlas. 2010.

[31] Chongqing Municipal Commission of Housing and Urban-Rural Development. Chongqing Architectural Atlas. 2016.

ULPGC
Universidad de
Las Palmas de
Gran Canaria

grres ULPGC
group for the research on renewable energy systems

O. Energy, materials, waste and water Resources and footprints

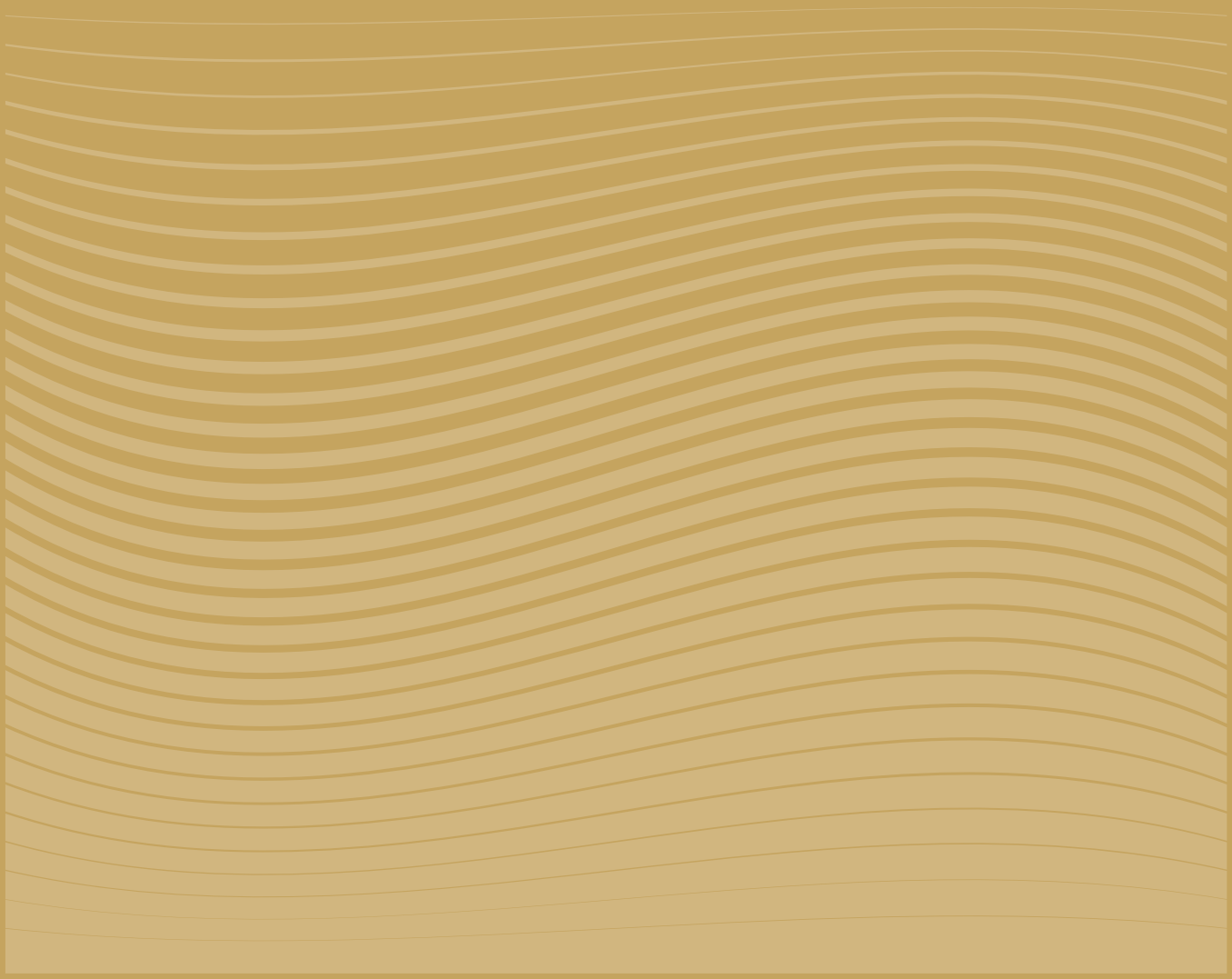

ECOS2023

Energy cost and carbon footprint of metals. Implications for PV-Silicon panels

Jorge Torrubia[a], Alicia Valero[a] and Antonio Valero[a]

[a] Instituto CIRCE (Research Centre for Energy Resources and Consumption) – Universidad de Zaragoza, Zaragoza, Spain, jtorrubia@unizar.es

Abstract:

The demand for low-carbon technologies such as photovoltaic panels, wind turbines or batteries is increasing rapidly due to the energy transition, triggering the demand for metals needed to achieve the sustainable goals. Therefore, it is important to assess the energy consumption and carbon footprint of mining and metal production, as the environmental impact of future energy infrastructures will depend on them. This paper evaluates the energy cost and carbon footprint of one MW of PV panels considering a cradle-to-gate approach from a life-cycle perspective. The focus is on the metals since these are the largest contributors to energy costs (80%), distinguishing between the different stages of production: mining, metal production and the energy cost of the chemicals, and indicating the four most used fuels: coal, diesel, natural gas and electricity. To evaluate the total energy cost and carbon footprint, three different material intensity scenarios are proposed, considering a decrease over time: 2018, 2030 and 2050, and two electricity emissions scenarios: one mainly based on fossil fuels, and another based on renewable electricity. The energy return on investment (EROI) increases from 8.4 to 15.9 and carbon emissions decrease from 40 to 22 gCO_2/kWh, considering the material intensity of 2018 and 2050, respectively. If electricity from renewable sources is used, carbon emissions can be halved, reaching 11 gCO_2eq/kWh with the 2050 material intensity. Therefore, material intensity must be reduced and energy-intensive processes decarbonized to minimize the impacts of future renewable infrastructures.

Keywords:

Energy Cost; Carbon Footprint; Energy Transition; Life cycle assessment; Metal production; Photovoltaic panels.

1. Introduction

Technologies that enable the harnessing of renewable energy contain various metals that facilitate specific functionalities [1]. For instance, one MW of wind energy requires 113 to 132 tons of steel, 1 to 5 tons of copper, 0.5 to 1.6 tons of aluminum and up to 200 kg of REE; while, to manufacture one MW of photovoltaic (PV) panels 60 to 67 tons of steel, 4 to 5 tons of copper, 6 to 8 tons of aluminum and up to 20 kg of Ag are needed. This significant material intensity and the increasing demand for these technologies are triggering the demand for metals in the coming years [2]. Thus, in the case of wind energy, annual material demand is expected to increase by a factor from 2 to 15 in 2050 compared to 2018 values. In the specific case of some metals, such as rare earths elements (REE), the global demand could increase 8-9 times in 2030 and 11-14 times in 2050 compared to 2018 values. The case of solar PV technologies is similar. The most optimistic scenarios indicate a 3 to 8-fold increase in demand for materials by 2050. However, demand for specific metals such as silver or silicon could increase by 4 and 12, respectively [3].

On the other hand, mining and metal production are one of the most energy-intensive industries worldwide. It consumes about 38% of global industrial energy use, 15% of the global electricity use, and 11% of global energy use. This consumption is still based on fossil fuels since it comprises about 19% of global coal and coal products, 5% of global gas, and 2% of global oil supplied [4]. In addition, the energy required in mining is expected to increase in the future due to lower ore grade, finer grain and increasing ore complexity of newly discovered deposits [5,6]. Moreover, the trend of this growth is exponential. For example, a decrease in copper ore of 0.2% to 0.4% requires 7 times more energy [7]. Due to these facts, the energy demand in mining operations could grow 36% by 2035 [4].

Thus, it is observed that manufacturing the infrastructure to achieve the energy transition requires a large amount of metals, which in turn require fossil energy consumption and can generate significant carbon emissions. Other authors have studied this problem from different approaches. One of the most common approaches is through the Energy Return on Investment (EROI). In these studies, EROI at the final energy stage is used to calculate how much of the total energy is required by the energy system to extract, process,

convert and deliver a unit of energy [8–10]. Another approach focuses on life cycle analysis (LCA). It is based on the accounting of the energy required and emissions generated to manufacture and commission an energy system. Generally, this analysis has only been used to estimate the impacts of current technologies in specific case studies [11,12]. One of the advantages of this methodology is that it permits to identify the processes from which the energy consumption or emissions originate [11]. Generally, most energy and emissions are consumed or emitted during the metal extraction and processing [3]. In addition, this methodology also allows the assessment of possible future scenarios with a dynamic approach, although few studies focus on it [13]. Thus, it is possible to establish different variable assumptions such as the material intensity, the energy consumed in the processes or the carbon intensity of the energy system.

In this study we use the life-cycle approach focusing on the energy cost and carbon footprint of the metals needed to manufacture PV panels. The methodology is based on accounting for the resources required for the extraction and production of Ag, Si, Al, Cu, Sn, Fe, and some of their alloys used in steel, such as Cr, Mn, Nb and Ni. The scope covers cradle to gate, i.e., from extraction of raw materials to their use as finished products, in this case, one MW of PV-Silicon panels. In addition, the energy cost is classified by the main energy sources used in mining and metal production: natural gas, diesel, coal, and electricity. Here it also includes the energy and emissions due to the chemicals needed for manufacture. The disaggregation of the processes is sufficient to differentiate the two main stages of metal production: mining and metal production. Thus, it is possible to determine which processes are most critical for decarbonization. Following this idea, two carbon emission scenarios are proposed, depending on electricity's carbon intensity: One based mainly on fossil fuels and the other on renewable energies. The energy used to manufacture PV panels and the energy cost of other materials, such as cement or glass, are also considered. Besides the carbon emission scenarios, three material intensity scenarios are also proposed. Thus, it is possible to study the link between material intensity - energy - carbon emissions, applied to one of the fastest growing technologies, the photovoltaic panels.

2. Data and methodology

Figure 1 shows the main processes and intermediate products required to obtain silver from lead and zinc mines. This Figure is an example to explain the methodology used to calculate the energy cost of metals and the allocation method since there are several different products, such as Pb, Zn or Ag.

As can be observed, each process (M&C and MP in Figure 2) has inputs (materials, energy and chemicals) and outputs (materials for the next process or the final metal). M&C refers to those processes belonging to the mining and concentrating step and MP to those belonging to the metal production step. The cradle-to-gate approach is used; thus, the analysis begins with mining and ends with the product ready for its use in another industry. The reference product is one kg of silver. If there were no co-products, it would be sufficient to sum all the energy (natural gas, diesel, coal and electricity) and chemical resources (also measured in energy cost units) to calculate the energy cost of one kg of the reference product. This is the case for the other metals in this study. But in the silver production more metals are produced simultaneously, which makes it necessary to allocate the silver its corresponding share through an allocation method.

The allocation method depends on the criteria of the authors. Most studies use allocation methods based on the economic benefit provided by the metals. However, its disadvantage is the strong fluctuation of the metal's price in the market [14]. Therefore, this study uses a physical allocation method based on the elements' geological scarcity, which has been successfully used in other studies [15–17]. The main advantage of this method is that the energy or environmental cost of metals is allocated through physical criteria, reflecting their value according to their scarcity in the earth's crust.

The allocation factor is calculated through equation 1, where M_i is the extracted mass of metal i, measured in kg-metal, and CC_i is the concentration of metal i in the earth's crust, measured in kg-metal/kg-crust.

$$Allocation_i\ (\%) = \frac{CC_i^{-1} \cdot M_i}{\sum_{i=1}^{n} (CC_i^{-1} \cdot M_i)} \quad (1)$$

Table 1 lists the parameters used to calculate the allocation factors, which in the case of silver is 12%. Once the allocation of each individual metal es calculated, the allocation of each process can be derived. Thus, the 34% of footprint of the mining and concentration stage is allocated to Pb and Ag, and then the 35.8% of the footprint of the lead production is allocated to Ag, as shown Figure 1.

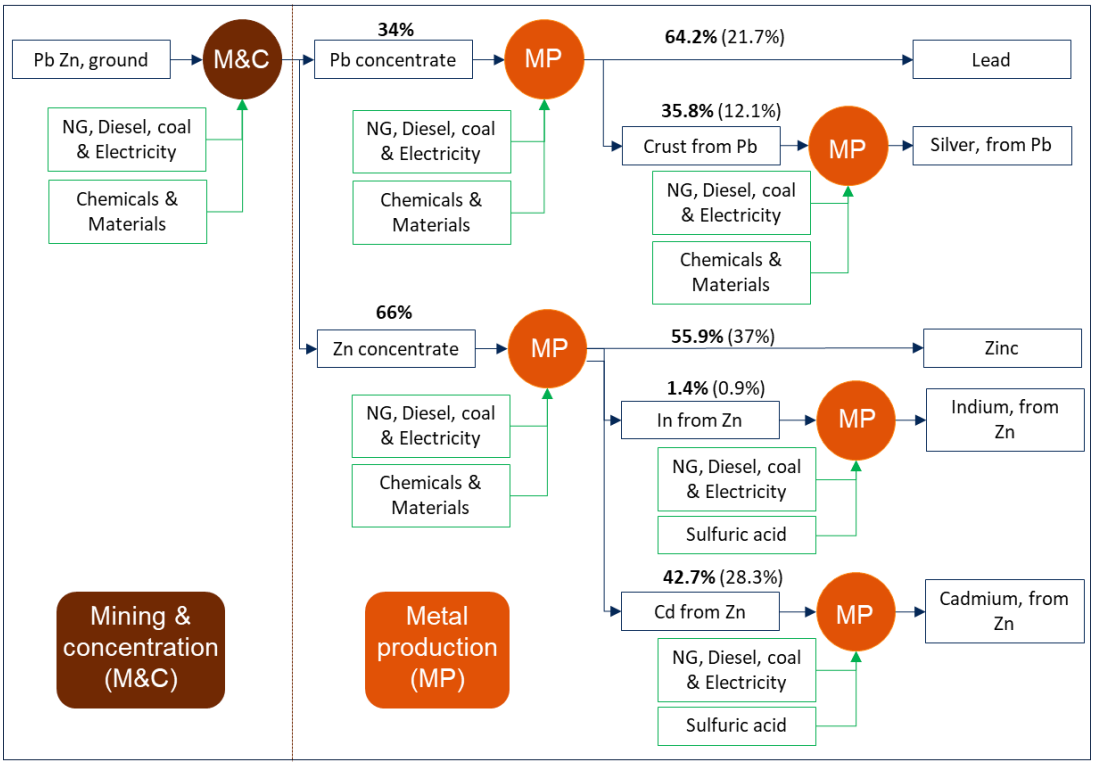

Figure 1. Block flow diagram of silver production from Pb-Zn mines.

Table 1. Mining production, crustal concentration and allocation factors of Pb-Zn mines.

Metal (i)	Mining (M_i) (kg_i)	Crustal concentration (CC_i) $\left(\frac{kg_i}{kg_{crust}}\right)$	Allocation factor
Ag	1	5.0E-08	12%
Pb	717	2.0E-05	22%
Zn	4333	7.1E-05	37%
In	0.08	5.0E-08	1%
Cd	4.6	9.8E-08	28%

As previously discussed, the remaining metals in this study do not require allocation since there are not co-products. The same applies to the calculation of the energy cost of chemicals. The process data inventories were taken from the Ecoinvent database version 3.9.1 [18], except for the Silicon processes, which are from the reference [19].

Once the energy cost is known, separated by fuel type, it is possible to estimate the carbon footprint through equation 2. Where, CF_i is the carbon footprint of metal i, measured in kg CO_2 eq; EC_j the energy cost of fuel j and EF_j is the emission factor of such fuel.

$$CF_i = \sum_{j=1}^{n}(EC_j \cdot EF_j) \quad (2)$$

Table 2 shows the data on the emission factors EF_j used. Two scenarios were established to study the impact on the carbon footprint of a decrease in electricity generation emissions. One scenario is based on fossil fuels; its emission factor is 0.488 kgCO_2eq/kWh. The other is based on renewable sources, and its emission factor is reduced to 0.021 kgCO_2eq/kWh.

Table 2. Emission factors for High Emission Scenario (HES) and Low Emission Scenario (LES)

		Emission factor HES	Emission factor LES	Source
Natural gas	kgCO_2eq/MJ	0.057	0.057	[20]
Diesel	kg CO_2eq/MJ	0.075	0.075	[20]
Coal	kg CO_2eq/MJ	0.1	0.1	[20]
Electricity	kg CO_2eq/kWh	0.488	0.021	[21,22]

The same procedure was used to calculate the energy cost of 1 MW of PV solar panels. Thus, a cumulative sum of all the energy sources needed to manufacture and install is made. In this case, the inventory data were obtained from Ecoinvent database version 3.9.1 [18] and Méndez et al. [12]. In addition, the material

intensity, i.e., the amount of materials that constitute the solar panels, is fundamental to determining their energy cost and, consequently, their carbon footprint. Thus, three material intensity scenarios (Table 3) have been established based on the following study [3], where a decrease in material intensity is estimated for PV panels in 2030 and 2050 compared to 2018. Hence, two electricity emission scenarios and three material intensity scenarios are assessed.

Table 3. Material Intensity of the three scenarios assessed per MW of PV panel

kg/MW PV	Concrete	Plastic	Glass	Steel	Sn	Al	Cu	Si	Ag
2018	60700	8600	46400	67900	139	7500	4600	4000	20
2030	58400	8300	44700	65300	139	7200	4500	2750	6
2050	48600	6900	37100	54300	139	6000	3700	1000	1

To compare the results with the literature, two parameters of the solar panels are calculated: Energy Return of Investment (EROI) and carbon intensity, through equations 3 and 4, respectively.

$$EROI = \frac{Supplied\ energy}{Energy\ cost} = \frac{1MW \cdot t_{operation} \cdot life}{Energy\ cost\ 1MW\ PV} \quad (3)$$

The EROI represents the amount of energy units obtained from an energy system for each unit of energy invested on it, so it has no units. In this case, 1 MW of PV was taken as a reference. Thus, equation 3 shows in the numerator the amount of energy that 1 MW of PV will supply, assuming an operation of 1000 hours per year ($t_{operation}$) for 25 years ($life$). On the other hand, the denominator shows the energy cost required to manufacture and install 1 MW of PV.

$$Carbon\ intensity = \frac{Carbon\ footprint}{Supplied\ energy} = \frac{Carbon\ footprint\ 1MW\ PV}{1MW \cdot h \cdot life} \quad (4)$$

Equation 4 shows the calculation of the carbon intensity, which represents the CO_2 emissions produced by each energy unit. The numerator shows the entire carbon footprint of 1 MW PV measured in g of CO_2. At the same time, the denominator represents all the energy generated by one MW PV (measured in kWh), assuming 1000 hours per year and 25 years of life.

3. Results and discussion

The results of the energy cost and carbon footprint of metals used in a PV panel are presented, discussing their decarbonization possibilities. The specific case of 1 MW of photovoltaic panels is then analyzed.

3.1. Energy cost of metals

Figure 2 shows the energy cost of metals used in photovoltaic panels. The results are ordered from highest to lowest value in MJ/kg. Thus, the most energy-consuming is silver (11,000 MJ/kg), followed by Si (1,400 MJ/kg), Al (75 MJ/kg), Sn (64 MJ/kg), Steel (32 MJ/kg), Cu (23 MJ/kg). In addition, the energy cost is disaggregated into the four most common fuels (natural gas, diesel, coal and electricity), the most important steps (mining and concentration (M&C), and metal production (MP)) and the energy cost of chemicals used these processes.

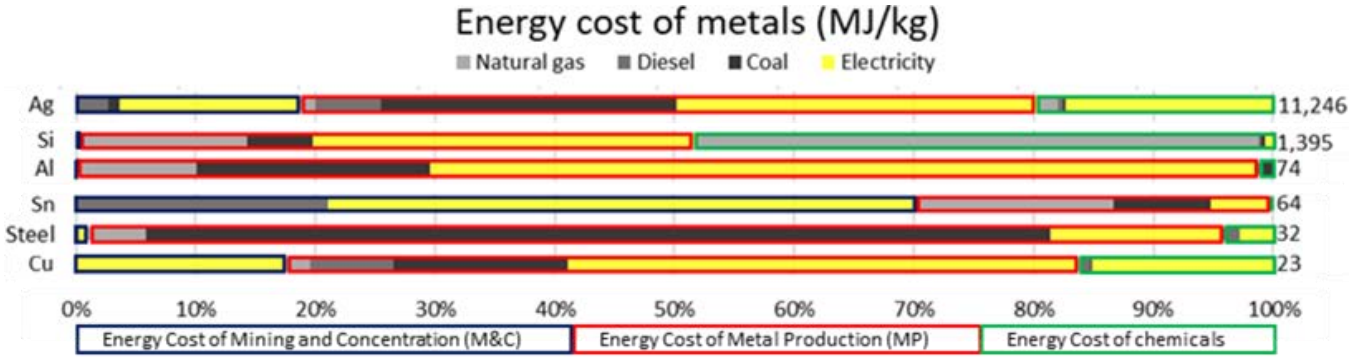

Figure 2. Energy cost of metals used in PV panels.

The mining and concentration step comprises all the processes from the rock extraction until the ore concentrate is obtained. As shown in Figure 2, this step's contribution is considerably lower than the metal production since it is always less than 20%. The exception is the case of Sn, where the M&C contribution is about 70% may be because the underestimation of the amount of chemicals used in this case, which is only 0.25%. On the other hand, for Si, Al and steel (mainly Fe) the contribution is very low (less than 1%) since these elements are very abundant in the earth's crust and therefore, their main energy cost is their metal production. These results are consistent with the literature since, as stated in Norgate et al. [5]: “Mineral

processing & concentration, usually have much less impact than metal extraction and refining in terms of energy".

However, in the future, the energy cost of the mining and concentration step is expected to increase due to two factors: (1) a decrease in ore grade, (2) finer grain of many newly discovered deposits. First, this increase is because additional energy is needed to extract the waste material in low-grade ores [6,23]. Secondly, finer grains require grinding to finer sizes resulting in higher energy consumption [5]. Nevertheless, in some cases, technological improvement may play an important role. For instance, despite the decrease in niobium ore concentration between 2017 and 2019 in Brazil, total energy consumption per kg FeNb was lower in 2019 [24]. However, the exponential trend of energy consumption with decreasing ore grade suggests that increasing energy consumption will prevail despite technological improvements [7]. Thus, for example, a decrease in copper ore grade between 0.2% to 0.4% requires seven times more energy [4].

On the other hand, the energy consumption increase in the mining step need not increase the energy consumption of the metal processing steps since a fixed-grade concentrate is produced in concentrating stage regardless of the initial ore grade [5]. Thus, metal production processes start from the ore concentrate until the elements are produced in their metallic form. This is usually the step with the highest energy consumption, as can be appreciated in Figure 2, and as evidenced the literature [25,26].

In order to verify that the energy cost data are comparable with the literature, Table 4 has been constructed. The "This study" column shows the energy cost results obtained, the "mean" column contains the mean of all the samples from the literature (References column) and the "min", "max" and "SD" columns represent the minimum, maximum and standard deviation, respectively. It is possible to observe that all the metals studied are found between the minimum and maximum (Al, Cu, Fe) or in values close to the minimum (Si, FeCr, FeMn, FeNb) except for Ag and Sn. Instead of comparing the footprint of steel, its more important metallic components (iron and some alloys such as FeCr, FeMn or FeNb) have been compare with literature.

The difference with the Sn results could be due to the underestimation of the energy consumed by the chemicals, as previously explained. This would also reduce the percentage of energy used in mining and concentrating. The reason behind the differences lies in the use of different data inventories. However, in the case of Sn there is only one reference for comparison, so it is not easy to draw accurate conclusions with this comparison.

The case of Ag is different since is a by-product of Pb-Zn, Cu or Au mining. Therefore, allocating the share of costs corresponding to silver in the common processes is necessary, as explained in section 2 data and methodology. Thus, in this case, in addition to using different data inventories, a different allocation system has also been employed. The studies in the literature use an economic allocation, but in this study, we have used the physical allocation described in section 2 data and methodology. This adds more uncertainty in comparing the results. Thus, the higher energy cost of silver in this study may also be because this metal has a lower price relative to its concentration in the earth's crust when compared to its co-produced metals (such as Pb or Zn). However, the impact of this fact on the energy cost of PV panels is low, given the reduced silver content compared to other metals.

Table 4. Comparison of the energy cost of metals with literature

MJ/kg	This study	Mean	Min	Max	SD	Samples	References
Ag	11,246	1,745	210	3,280	2,171	2	[25,27]
Si	1,396	5,242	1,490	9,350	3,039	5	[28,29]
Al	74	169	23	263	66	16	[4,6,25,27,30–34]
Sn	64	321	321	321	--	1	[25]
Cu	23	59	18	168	41	18	[4,6,25,31,35,36]
Steel	32	--	--	--	--	--	--
Fe	24	19	7	30	7	8	[25,31,34]
FeCr	31	62	40	83	30	2	[25,27]
FeMn	20	29	24	34	7	2	[25,31]
FeNb	75	127	82	172	63	2	[25,37]

3.2. Carbon footprint of metals

To estimate the carbon footprint of metals, it is essential to know which type of fuel is used, since each of them has different emissions per unit of energy. For this reason, the fuel types in Figure 2 are discussed below. Firstly, the mining and concentration step and secondly the metal production step, pointing out the difficulties of decarbonization.

3.2.1. Fuels used in Mining and Concentration

In the mining and concentration step, the predominant fuels are diesel and electricity since other fuels never exceed 10%. Diesel is primarily used in heavy mining machinery, such as drilling rigs, trucks, etc. For example, according to Sanjuan-Delmás et al. [36], 99% of the fossil fuels used in a copper mine were diesel in the trucks. Regarding electricity, its main use in mining and concentration step is comminution, a high-energy consumption stage. For instance, comminution uses an average of 15% of the total energy demand of iron production [4]. Another important electricity use is HVAC systems in underground mines [38].

Decarbonization of diesel use is a major challenge. However, some studies [36,39] propose using electric or fuel cell vehicles, but only a few mines currently operate such vehicles, and on a very small scale [40]. On the other hand, decarbonizing electricity is more accessible because renewable energies generate it directly. However, there are two main challenges to decarbonizing electricity from mining operations. The first challenge is integrating renewable energy in remote off-grid mining operations, which usually use fossil fuels for electric generation. However, the number of renewable projects has been increasing. In 2015 there were 600 MW, but by the end of 2019 about 5 GW were projected. But this renewable capacity is still a fraction of the total energy demanded by mining operations, showing a slow-paced development [4]. The second challenge is increasing renewables' share in the grid for connected mining operations.

3.2.2. Fuels used in Metal Processing

As mentioned in the previous section, the metal processing step usually has the highest energy cost. Therefore, its decarbonization would have a greater impact on reducing the carbon footprint. As shown in Figure 2, the most common fossil fuels are natural gas and coal since provide at least 70% of the fossil energy in all the metals. They are used as a source of heat and reducing agents. The use of coal in steel production is noteworthy, as 73% of the total energy comes from this fuel, since its use is inherent to the steel-making process [31].

On the other hand, electricity is mainly used in electrolysis or electrorefining processes. The use of electricity is particularly important in copper and aluminum since contributes to 42% of the total energy cost of copper and 70% in aluminum case. In copper, it is due to its electrorefining stage and in aluminum to the electrolysis process.

Bioreducers and hydrogen are the most promising substitutes for natural gas and hydrogen [26], although with some problems, for example, the sustainable production of bioreductants (such as charcoal) on a global scale, the costs of transporting them or other problems due to their physical characteristics [4]. On the other hand, the use of hydrogen as a reductant is much better in terms of an environmental impact than biomass when it is produced using renewable electricity [41]. However, its generation is still expensive [4], and new infrastructure designed for its use needs to be developed due to its different properties than other fossil fuels [42]. Again, electricity is the most accessible source to decarbonize since metal production plants are usually connected to the grid, not being in remote locations.

3.2.3. Chemical consumption

Chemicals and other auxiliary materials considerably contribute to the energy cost of the processes. This share is significant in the case of Si, Ag and Cu, with a contribution of 48%, 20% and 16%, respectively. In the case of Si, this is mainly because silicon for solar panels must have very high purity, for which a large amount of chemicals is consumed. In the case of Ag and Cu, chemicals are mainly used in electrolysis processes.

In this case, decarbonization depends not on the mining industry but on the chemical industry that provides the products necessary to manufacture metals.

3.2.4. Carbon footprint scenarios

Due to the limitations of substituting fossil fuels (either diesel from mining trucks or coal and natural gas as heat sources and reducing agents in metal processing), this study proposes only the decarbonization of electricity as a first approach to decarbonization. For this purpose, two scenarios are considered: one with high emissions (HES) and the other with low emissions (LES), based on renewable energies. The carbon footprint results are shown in Table 5. The "HES" (high emissions scenario) column shows the results of the scenario in which the electricity has higher emissions; the "LES" (low emissions scenario) column shows the results of the scenario with lower emissions; and the "Diff" column shows the percentage difference between the two scenarios. In addition, a comparison is made with other sources in the literature: the "mean" column shows the mean of all samples; in the "min" column, the minimum; in "max" the maximum; in SD "Standard Deviation", in "simple" the number of samples and finally in “references”, the sources used.

As in Table 4, Table 5 shows that all metals have a carbon footprint in the range of the literature when compared to the "HES" scenario, except for Ag and Sn. The reasons for these exceptions are the same as those explained in section 3.1 above. As seen in Table 5, significant reductions can be achieved just by using renewable energies in electricity generation. The smallest reduction (29%) corresponds to steel due to the large contribution of coal in its energy cost. In addition, the use of coal is inherent in the manufacturing process. However, the footprint of the remaining metals can be reduced from 50% (for Si) to 78.8% (for Cu).

This can have significant implications in the energy transition since using renewable energies in mining reduces the carbon footprint of metals that will later be used in the renewable energy infrastructure, following a feedback process. The following section uses the example of solar panels to expose this idea.

Table 5. Comparison of the carbon footprint in the HES and LES scenarios of metals with literature.

Metal	HES	LES	Diff	Mean	Min	Max	SD	Samples	References
Ag	1333	422	68.4%	283	34	815	301	10	[15,25,43,44]
Si	119	59	50.0%	461	114	775	238	5	[28,29]
Al	8.9	2.2	74.8%	16	5.9	41	9	21	[4,25,30–35,44,45]
Sn	6.8	2.3	65.6%	17	17	17	--	1	[25]
Cu	2.8	0.6	78.8%	5.1	1.1	64.9	9	46	[4,15,25,31,34–36,46]
Steel	3.3	2.3	29.2%	--	--	--	--	--	--
Fe	2.4	1.9	22.3%	3.9	1.2	23.3	7	11	[25,31,34,47]
FeCr	3.5	1.8	48.8%	2.4	2.4	2.4	--	1	[25]
FeMn	2.3	1.1	52.7%	5.2	1.0	9.6	3	10	[25,31,35,43,45]
FeNb	8.8	3.1	64.8%	8.4	5.1	12.5	4	3	[24,25,37]

3.3. Energy cost and carbon footprint of PV Power

Figure 3 shows the Sankey diagram of the energy cost embedded in one MW of solar panels, which amounts to about 10.7 TJ. The diagram allows the analysis by the different stages of the production processes and by the types of fuels. For the first, three phases can be identified:

- Manufacturing and installation: This phase includes all the energy consumption related to the manufacture and installation of a solar panel, but not the energy embedded in the components needed. The energy cost is about 846 GJ, contributing to 7.9% of the total cost.
- Other materials: Besides metals, materials such as concrete or solar glass contribute to energy costs. In this case, they account for 1295 GJ, i.e., 12 % of the total.
- Metals: Metals contribute the most to the energy cost, with 8,623 GJ and 80% of the total. Silicon and steel alone account for 52% and 20% of the total footprint, respectively. Furthermore, the cost of the metals has been divided according to their production steps. As mentioned above, the metal production step is the most important, with 52% of the total cost, followed by the cost due to chemicals, contributing 27%. Finally, the cost of mining is very low, only 0.8%, although, as mentioned in section 3.1, it is expected to grow exponentially in the coming years due to the decrease in ore grades.

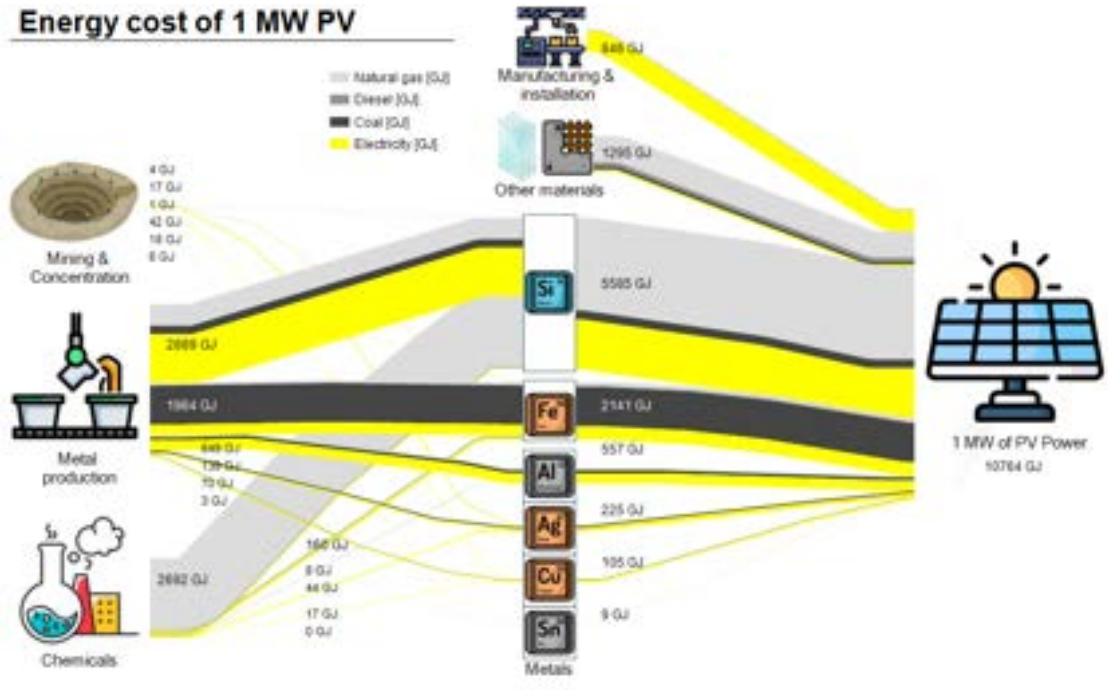

Figure 3. Sankey diagram of energy cost distribution of 1 MW of PV Panels.

Regarding the types of fuels:

- Natural gas is the most consumed fuel (43% of energy), mainly due to the energy cost of chemicals and crystalline silicon production. Another important consumer is manufacturing other materials, such as concrete or solar glass.
- Electricity holds the second highest share (35%). It is used primarily in the solar panel manufacturing process itself, as well as in the production of the metals such as silicon.
- Coal accounts for 19% of the energy cost. Its main use was in steel production, the second largest contributor to the total footprint after silicon.
- Finally, diesel consumption is residual, as it contributes only 2% of the energy cost and is mainly used in mining and concentrating the metals.

Table 6. Material intensity (kg/MW), Energy cost (GJ), Carbon footprint (kg CO_2 (HES & LES), EROI and Carbon Intensity (C.I.) of 1 MW of PV panels according to the contribution of metals or other materials.

		Other materials	Si	Steel	Al	Ag	Cu	Sn	EROI	C.I g/kWh
	kg/MW	115700	4000	67900	7500	20	4600	139	-	-
Case 1	GJ	1,295	5,585	2,141	557	225	105	9	8.4	-
2018	kg CO_2 (HES)	86309	474478	223850	66950	26653	12971	949	-	40.0
	kg CO_2 (LES)	77716	237382	158381	16855	8434	2748	326	-	20.4
	kg/MW	111400	2750	65300	7200	6	4500	139	-	-
Case 2	GJ	1,267	3,840	2,059	535	67	103	9	10.3	-
2030	kg CO_2 (HES)	84317	326204	215278	64272	7996	12689	949	-	32.8
	kg CO_2 (LES)	75940	163200	152316	16181	2530	2688	326	-	16.9
	kg/MW	92600	1000	54300	6000	1	3700	139	-	-
Case 3	GJ	1,141	1,396	1,712	446	11	84	9	15.9	-
2050	kg CO_2 (HES)	75324	118620	179014	53560	1333	10433	949	-	21.9
	kg CO_2 (LES)	67917	59346	126658	13484	422	2210	326	-	11.2

As was done for metals, two scenarios are established, one conventional, with high emissions due to electricity generation, and the other with low emissions. Additionally, three other scenarios are established depending on the demand for materials for photovoltaic generation: one for 2018 and others for 2030 and 2050, based on literature forecasts [3]. The results are shown in Table 6 and the 2018 scenario is the same represented in the Sankey diagram of Figure 3. In addition, the EROI (see section 2 data and methodology) and the carbon intensity (gCO_2/kWh) have been estimated depending on each case. Thus, Table 6 shows the effect of decreasing material intensity in the EROI, which increases from 8.4 in the 2018 scenario to 15.9 with the most optimistic forecasts for the year 2050. The opposite happens with carbon intensity, decreasing from 40 gCO_2/kWh to 22 gCO_2/kWh. These results are obtained only with the reduction of the material intensity. If low-carbon electricity were additionally used, the carbon intensity of solar panels could be halved. That is, from 40 gCO_2/kWh in 2018 scenario, it could decrease to 20 gCO_2/kWh and in 2050 scenario from 22 gCO_2/kWh to 11 gCO_2/kWh. This emission reduction is limited because electricity contributes 35% of energy costs and is the only energy source that reduces emissions according to our assumptions. Therefore, to achieve complete decarbonization, replacing natural gas and coal in metal production processes with other fuels, such as hydrogen, is necessary. However, this would imply the use of more materials, as new infrastructure would need to be developed. Thus, the total energy costs could increase, although it would reduce the carbon footprint. Furthermore, complete substitution should not only occur in the metal industry, but also in the chemical industry, since a large part of natural gas consumption comes from it (Figure 3). This is an example of the strong interconnection between industries and shows that decarbonization of one industry cannot be achieved without decarbonizing others. For instance, manufacturing solar panels with a lower carbon footprint would require reducing the footprint of metal mining, but also reducing the footprint of the chemical industry that supplies it with essential materials for its production.

The results obtained are comparable to those in the literature. EROI only includes the extraction and operation of the energy source, so it is defined as standard [8]. According to Raugei et al. [48], the standard EROI of photovoltaics is between 6 and 12, with numbers on the range from 8 to 10 obtained in this study for the 2018 and 2030 scenarios. Regarding carbon intensity, the 2018 scenario (20 to 40 gCO_2eq/kWh) is comparable to those obtained 25-40 gCO_2eq/kWh by the reference [49].

However, this study has some limitations. First is the quality and detail of the data inventory used. Although results comparable with the literature have been obtained for most of the metals and the solar panels, this has not been the case for some metals such as Sn. In addition, when using the physical allocation, silver has a much higher cost than reported in the literature. However, these deviations have not influenced calculating the PV energy cost much due to the low material intensity of Sn and Ag. Another problem lies in the global

view of this study since the electrical energy mixes vary greatly depending on the regions. However, this study has simplified it by taking two carbon intensity scenarios. In addition, the cost of transportation has not been considered due to the global view. Therefore, in future studies, the estimated origin of the metals should be considered since the energy cost and carbon footprint also depend on it.

Finally, it is important to remark that this study has been limited to studying solar panels. Still, other technologies, such as wind turbines, are required to achieve complete electrification and decarbonization. In addition, studying batteries and electrolyzers (for hydrogen production) is indispensable for continuous electricity supply and for substituting fossil fuels. However, their consideration will decrease the EROI and increase the carbon intensity of the system because, despite consuming a large amount of metals and materials, these technologies do not provide any extra energy.

4. Conclusions

This study estimates silicon solar panels' energy cost and carbon footprint from a life cycle perspective cradle-to-gate. It focuses on the required metals, i.e., Fe, Al, Si, Cu, Ag and Ag, which contribute 80% of the total energy cost together. Si and Fe have the highest contribution with 52% and 20%, respectively, while Al, Ag, Cu and Sn have only 5%, 2%, 1% and 0.1%, respectively. The great impact of Si is not due to its mass contribution (only 2%), but to its high energy cost, which amounts to 1,400 MJ/kg. In contrast, Fe contributes 32% of the mass, but its energy cost is much lower, 32 MJ/kg. The remaining 20% of the cost corresponds to energy consumption due to the manufacture of other materials, such as concrete or glass, and to the manufacture and installation of the photovoltaic panels. At current material intensity, 10.8 TJ is required to produce and install 1 MW, which results in an EROI of 8.4. However, the material intensity of the future PV panels is expected to be lower, which could reduce the energy cost to 8.7 TJ by 2030 and 5.6 TJ by 2050, driving a direct increase in EROI, reaching 10.3 and 15.9, respectively. Nevertheless, it does not consider the effect of the decrease in ore grade, which could lead to an increase in energy consumption in the mining process, and therefore to a decrease in EROI.

On the other hand, the type of fuel and the stage at which it is used is also important, as it indicates the current carbon footprint and the potential ease of decarbonization in the future. Thus, the most consumed fuel is natural gas, accounting for 43% of energy, followed by electricity (35%), coal (19%) and finally diesel (only 2%). Diesel is mainly used in mining, which is the phase that contributes least to the energy costs. Coal has an important share due to steel production. Natural gas owes its contribution mainly to the refining of silicon and the chemical production. And the electricity consumption is the most distributed among all the processes. In addition, two scenarios of electricity system emissions have been established, one with high and the other with low emissions. Under the last scenario, the carbon footprint is reduced by half in all cases of material intensity.

Thus, two variables affect the EROI and the carbon intensity of solar panels: the material intensity and the emissions associated with the types of fuel. Material intensity influences both EROI and carbon intensity. If material intensity decreases, EROI increases and carbon intensity decreases. On the other hand, fuel-related emissions only affect carbon intensity. If the former decreases, the latter also decreases. With the best material intensity and using renewable electricity the carbon intensity is 11gCO_2eq/kWh, thus to achieve an even lower impact it would be necessary to decarbonize all fuels, either through the electrification of processes or the use of alternative fuels such as green hydrogen. In conclusion, future variations in the material intensity and the fuels used in the production of metals, chemicals and other materials will determine the sustainability of future energy sources.

Nomenclature

Ag	Silver
Al	Aluminium
CO_2eq	Carbon Dioxide equivalent emissions
Cu	Copper
EROI	Energy Return on Investment
Fe	Iron
FeCr	Ferro Chromium
FeMn	Ferro Manganese
FeNb	Ferro Niobium
HES	High emissions scenario

LES	Low emissions scenario
M&C	Mining and concentration stage
MP	Metal production stage
Pb	Lead
PV	Photovoltaic
REE	Rare Earth Elements
Si	Silicon
Sn	Tin
Zn	Zinc

References

[1] Bartie N, Cobos-Becerra L, Fröhling M, Schlatmann R, Reuter M. Metallurgical infrastructure and technology criticality: the link between photovoltaics, sustainability, and the metals industry. Mineral Economics 2022;35:503–19. https://doi.org/10.1007/s13563-022-00313-7.

[2] Valero A, Valero A, Calvo G, Ortego A. Material bottlenecks in the future development of green technologies. Renewable and Sustainable Energy Reviews 2018;93:178–200. https://doi.org/10.1016/j.rser.2018.05.041.

[3] Carrara S, Dias Alves P, Plazzotta B, Pavel C. Raw materials demand for wind and solar PV technologies in the transition towards a decarbonised energy system. 2020. https://doi.org/10.2760/160859.

[4] Igogo T, Awuah-Offei K, Newman A, Lowder T, Engel-Cox J. Integrating renewable energy into mining operations: Opportunities, challenges, and enabling approaches. Appl Energy 2021;300. https://doi.org/10.1016/j.apenergy.2021.117375.

[5] Norgate T, Haque N. Energy and greenhouse gas impacts of mining and mineral processing operations. J Clean Prod 2010;18:266–74. https://doi.org/10.1016/j.jclepro.2009.09.020.

[6] Norgate T, Jahanshahi S. Reducing the greenhouse gas footprint of primary metal production: Where should the focus be? Miner Eng 2011;24:1563–70. https://doi.org/10.1016/j.mineng.2011.08.007.

[7] Calvo G, Mudd G, Valero A, Valero A. Decreasing ore grades in global metallic mining: A theoretical issue or a global reality? Resources 2016;5. https://doi.org/10.3390/resources5040036.

[8] Capellán-Pérez I, de Castro C, Miguel González LJ. Dynamic Energy Return on Energy Investment (EROI) and material requirements in scenarios of global transition to renewable energies. Energy Strategy Reviews 2019;26. https://doi.org/10.1016/j.esr.2019.100399.

[9] Diesendorf M, Wiedmann T. Implications of Trends in Energy Return on Energy Invested (EROI) for Transitioning to Renewable Electricity. Ecological Economics 2020;176. https://doi.org/10.1016/j.ecolecon.2020.106726.

[10] Slameršak A, Kallis G, Neill DWO. Energy requirements and carbon emissions for a low-carbon energy transition. Nat Commun 2022;13. https://doi.org/10.1038/s41467-022-33976-5.

[11] Ludin NA, Mustafa NI, Hanafiah MM, Ibrahim MA, Asri Mat Teridi M, Sepeai S, et al. Prospects of life cycle assessment of renewable energy from solar photovoltaic technologies: A review. Renewable and Sustainable Energy Reviews 2018;96:11–28. https://doi.org/10.1016/j.rser.2018.07.048.

[12] Méndez L, Forniés E, Garrain D, Pérez Vázquez A, Souto A, Vlasenko T. Upgraded Metallurgical Grade Silicon for solar electricity production: a comparative Life Cycle Assessment. n.d.

[13] Pehl M, Arvesen A, Humpenöder F, Popp A, Hertwich EG, Luderer G. Understanding future emissions from low-carbon power systems by integration of life-cycle assessment and integrated energy modelling. Nat Energy 2017;2:939–45. https://doi.org/10.1038/s41560-017-0032-9.

[14] International Energy Agency. The Role of Critical Minerals in Clean Energy Transitions. World Energy Outlook Special Report. 2021.

[15] Tuusjärvi M, Vuori S, Mäenpää I. Metal Mining and Environmental Assessments: A New Approach to Allocation. J Ind Ecol 2012;16:735–47. https://doi.org/10.1111/j.1530-9290.2012.00469.x.

[16] Torrubia J, Valero A, Valero A. Beyond metal prices: geological scarcity as a physical cost allocation criterion. The case of Rare Earth Element mining. ECOS 2022 35th International Conference on Efficiency, Cost, Optimization, Simulation and Environmental Impact of Energy Systems, Copenhagen: 2022.

[17] Torrubia J, Magdalena R, Valero A, Valero A. Energy cost and allocation in mining co-production. The case of platinum group metals, nickel and copper. 7th International Conference on Contemporary Problems of Thermal Engineering CPOTE 2022, 20-23 September 2022, Poland, Warsaw: 2022.

[18] https://ecoinvent.org/. Ecoinvent database version 3.9.1 2023. https://ecoinvent.org/the-ecoinvent-database/ (accessed March 7, 2023).

[19] Heidari SM, Anctil A. Country-specific carbon footprint and cumulative energy demand of metallurgical grade silicon production for silicon photovoltaics. Resour Conserv Recycl 2022;180. https://doi.org/10.1016/j.resconrec.2022.106171.

[20] https://ghgprotocol.org/. Fossil fuels emission factors 2023. https://ghgprotocol.org/ (accessed March 7, 2023).

[21] Schlömer S, Bruckner T, Fulton L, Hertwich E, McKinnon A, Perczyk D, et al. Annex III: Technology-specific cost and performance parameters. In: Edenhofer O, Pichs-Madruga R, Sokona Y, Farahani E, Kadner S, Seyboth K, et al., editors. Climate Change 2014: Mitigation of Climate Change. Contribution of Working Group III to the Fifth Assessment Report of the Intergovernmental Panel on Climate Change, Cambride, United Kingdom and New York, NY, USA: Cambridge University Press; 2014.

[22] REN21. 2022 UNECE Renewable Energy Status Report. Paris: 2022.

[23] Wei W, Samuelsson PB, Tilliander A, Gyllenram R, Jönsson PG. Energy consumption and greenhouse gas emissions of nickel products. Energies (Basel) 2020;13. https://doi.org/10.3390/en13215664.

[24] da Silva Lima L, Alvarenga RAF, de Souza Amaral T, de Tarso Gonçalves Nolli P, Dewulf J. Life cycle assessment of ferroniobium and niobium oxides: Quantifying the reduction of environmental impacts as a result of production process improvements. J Clean Prod 2022;348. https://doi.org/10.1016/j.jclepro.2022.131327.

[25] Nuss P, Eckelman MJ. Life cycle assessment of metals: A scientific synthesis. PLoS One 2014;9. https://doi.org/10.1371/journal.pone.0101298.

[26] Hamuyuni J, Tesfaye F, Iloeje CO, Anderson AE. Energy Efficiency and Low Carbon Footprint in Metals Processing. JOM 2022;74:1886–8. https://doi.org/10.1007/s11837-022-05253-9.

[27] Espinosa N, García-Valverde R, Urbina A, Lenzmann F, Manceau M, Angmo D, et al. Life cycle assessment of ITO-free flexible polymer solar cells prepared by roll-to-roll coating and printing. Solar Energy Materials and Solar Cells, vol. 97, Elsevier B.V.; 2012, p. 3–13. https://doi.org/10.1016/j.solmat.2011.09.048.

[28] Fan M, Yu Z, Ma W, Li L. Life Cycle Assessment of Crystalline Silicon Wafers for Photovoltaic Power Generation. Silicon 2020;13:3177–89. https://doi.org/10.1007/s12633-020-00670-4/Published.

[29] Muteri V, Cellura M, Curto D, Franzitta V, Longo S, Mistretta M, et al. Review on life cycle assessment of solar photovoltaic panels. Energies (Basel) 2020;13. https://doi.org/10.3390/en13010252.

[30] Nunez P, Jones S. Cradle to gate: life cycle impact of primary aluminium production. International Journal of Life Cycle Assessment 2016;21:1594–604. https://doi.org/10.1007/s11367-015-1003-7.

[31] van der Voet E, van Oers L, Verboon M, Kuipers K. Environmental Implications of Future Demand Scenarios for Metals: Methodology and Application to the Case of Seven Major Metals. J Ind Ecol 2019;23:141–55. https://doi.org/10.1111/jiec.12722.

[32] Farjana SH, Huda N, Mahmud MAP. Impacts of aluminum production: A cradle to gate investigation using life-cycle assessment. Science of the Total Environment 2019;663:958–70. https://doi.org/10.1016/j.scitotenv.2019.01.400.

[33] Yang Y, Guo Y qi, Zhu W song, Huang J bai. Environmental impact assessment of China's primary aluminum based on life cycle assessment. Transactions of Nonferrous Metals Society of China (English Edition) 2019;29:1784–92. https://doi.org/10.1016/S1003-6326(19)65086-7.

[34] Guzmán JI, Faúndez P, Jara JJ, Retamal C. On the source of metals and the environmental sustainability of battery electric vehicles versus internal combustion engine vehicles: The lithium production case study. J Clean Prod 2022;376. https://doi.org/10.1016/j.jclepro.2022.133588.

[35] Manjong NB, Usai L, Burheim OS, Strømman AH. Life cycle modelling of extraction and processing of battery minerals—a parametric approach. Batteries 2021;7. https://doi.org/10.3390/batteries7030057.

[36] Sanjuan-Delmás D, Alvarenga RAF, Lindblom M, Kampmann TC, van Oers L, Guinée JB, et al. Environmental assessment of copper production in Europe: an LCA case study from Sweden conducted using two conventional software-database setups. International Journal of Life Cycle Assessment 2022;27:255–66. https://doi.org/10.1007/s11367-021-02018-5.

[37] Dolganova I, Bosch F, Bach V, Baitz M, Finkbeiner M. Life cycle assessment of ferro niobium. International Journal of Life Cycle Assessment 2020;25:611–9. https://doi.org/10.1007/s11367-019-01714-7.

[38] Jeswiet J, Archibald J, Thorley U, de Souza E. Energy use in premanufacture (Mining). Procedia CIRP, vol. 29, Elsevier B.V.; 2015, p. 816–21. https://doi.org/10.1016/j.procir.2015.01.071.

[39] Ulrich S, Trench A, Hagemann S. Gold mining greenhouse gas emissions, abatement measures, and the impact of a carbon price. J Clean Prod 2022;340. https://doi.org/10.1016/j.jclepro.2022.130851.

[40] Anglo-American Press releases. Anglo American unveils a prototype of the world's largest hydrogen-powered mine haul truck - a vital step towards reducing carbon emissions over time 2022. https://www.angloamerican.com/media/press-releases/2022/06-05-2022# (accessed March 7, 2023).

[41] Röben FTC, Schöne N, Bau U, Reuter MA, Dahmen M, Bardow A. Decarbonizing copper production by power-to-hydrogen: A techno-economic analysis. J Clean Prod 2021;306. https://doi.org/10.1016/j.jclepro.2021.127191.

[42] Nicoletti G, Arcuri N, Nicoletti G, Bruno R. A technical and environmental comparison between hydrogen and some fossil fuels. Energy Convers Manag 2015;89:205–13. https://doi.org/10.1016/j.enconman.2014.09.057.

[43] Farjana SH, Huda N, Mahmud MAP, Lang C. A global life cycle assessment of manganese mining processes based on EcoInvent database. Science of the Total Environment 2019;688:1102–11. https://doi.org/10.1016/j.scitotenv.2019.06.184.

[44] Farjana SH, Huda N, Parvez Mahmud MA, Saidur R. A review on the impact of mining and mineral processing industries through life cycle assessment. J Clean Prod 2019;231:1200–17. https://doi.org/10.1016/j.jclepro.2019.05.264.

[45] Zhang R, Ma X, Shen X, Zhai Y, Zhang T, Ji C, et al. Life cycle assessment of electrolytic manganese metal production. J Clean Prod 2020;253. https://doi.org/10.1016/j.jclepro.2019.119951.

[46] Farjana SH, Huda N, Mahmud MAP, Lang C. Life-cycle assessment of solar integrated mining processes: A sustainable future. J Clean Prod 2019;236. https://doi.org/10.1016/j.jclepro.2019.117610.

[47] Ferreira H, Leite MGP. A Life Cycle Assessment study of iron ore mining. J Clean Prod 2015;108:1081–91. https://doi.org/10.1016/j.jclepro.2015.05.140.

[48] Raugei M, Fullana-i-Palmer P, Fthenakis V. The energy return on energy investment (EROI) of photovoltaics: Methodology and comparisons with fossil fuel life cycles. Energy Policy 2012;45:576–82. https://doi.org/10.1016/j.enpol.2012.03.008.

[49] http://www.webservice-energy.org/incer-acv. Life cycle impact of photovoltaic systems (INCER-ACV) 2023. http://www.webservice-energy.org/incer-acv (accessed March 7, 2023).

Water saving in electric power generation facilities using the hygroscopic cycle in the subtropical climate

Juan Carlos Ríos-Fernández[a], Roberto Martínez-Pérez[a], Víctor Manuel Fernández-Pacheco[a], Andrés Meana-Fernández[a], Francisco Javier Rubio-Serrano[b], Antonio José Gutiérrez-Trashorras[a]

[a] Department of Energy - University of Oviedo, Gijón, Spain,riosjuan@uniovi.es, martinezroberto@uniovi.es (CA), fernandezpvictor@uniovi.es, andresmf@uniovi.es, gutierrezantonio@uniovi.es

[b] Imasa Technologies (Imatech), Madrid, Spain, fj.rubio@imasatechnologies.com

Abstract:

The sustainability of the electric power generation system worldwide is undoubtedly one of the main challenges of our era. This will be achieved through the massive incorporation of renewable energy sources, but also using highly efficient non-renewable sources. These latest technologies are still necessary today to guarantee the supply of electricity. To optimize its operation in a sustainable way, it is required to minimize both the consumption of primary energy and the water necessary for cooling. In this work, the Hygroscopic Cycle Technology is presented as an alternative to traditional thermal cycles and that allowing to minimize the use of water in refrigeration processes. Thus, assuming the incorporation of this technology to existing thermal power plants in the Canary Islands, cooling water savings were calculated. In this way, the total savings achieved in this subtropical climate amounted to 1.6 Mm^3 annually. A very high value that reinforces the interest of this technological improvement in the thermal processes of thermoelectric plants avoiding the consumption of water.

Keywords:

Hygroscopic Cycle Technology; Energy; Savings in Water Consumption; Sustainability; Thermodynamic Cycles.

1. Introduction

The interest in the use of renewable energies as sources of electricity generation has been strongly increased in recent years. The policies against climate change [1,2] agreed by the main producing and consuming countries of energy, as well as the increase in the price of these raw materials have been decisive. However, electricity production with these "clean" sources has not yet succeeded in displacing traditional energy production using fossil fuels such as coal or gas. Furthermore, in developing countries the use of these traditional energy sources has increased significantly in recent years. According to the Global Electricity Review 2022 [3], the world supply of energy through "clean" sources reached 38%, but nevertheless, there was an unprecedented growth in the level of polluting emissions linked to electricity generation and the energy production with coal. Therefore, the need to improve the efficiency of processes and reduce the environmental impact of power generation with non-renewable sources is paramount. In this direction, the investigations presented in this article are directed and that present an improvement of the thermal cycles used in thermoelectric plants fed with hydrocarbons or coal. The Rankine cycle (RC) used in these plants operates with steam, and despite being a mature technology, due to its wide and extensive use in various industrial processes over time, it still has an improvement rate in its performance. Because of its widespread use, the improvement in efficiency derived from RC constitutes an important global impact in the improvement of energy production processes and in the reduction of related polluting emissions, and also, in the economic viability or increased financial profitability of power plants that use it [4]. In Figure 1 [5], an RC used in thermoelectric installations is represented.

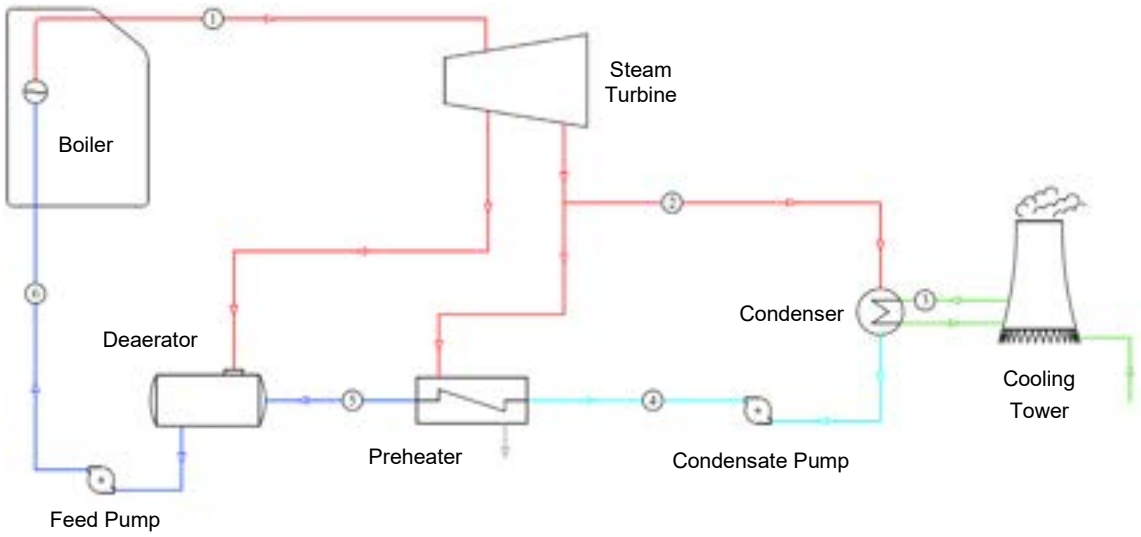

Figure. 1. Diagram of the Rankine Cycle in a thermoelectric power plant.

In this line of cycle improvement [6,7], recent research has focused on reducing irreversibilities and their associated losses, proposing improvements in supercritical, regenerative, superheated, and binary steam cycles. In addition to trying to maintain the quality of the steam above 90% at the outlet of the steam turbine and avoid the entry of steam into the process pumps. Other lines of research have worked on improving efficiency, substituting the pure water used in the cycle with other fluids entering the turbine. Thus, the Organic Rankine Cycle (ORC) appeared [8], which shares its configuration with the traditional RC but is designed to generate work with low-energy heat, with temperatures between 80 and 400 ºC. The ORC [9] uses so-called pure organic fluids, which can be different types of refrigerants and organic compounds. The use of "dry" fluids avoids the need to overheat the steam [10], as is done in the Rankine Cycle Technology (RCT), making the working temperatures and evaporation pressures much lower and increasing the efficiency of the cycle.

Zeotropic mixtures or fluids with different boiling points have also been used in the ORC, but to a lesser extent. The investigations [11,12] carried out comparing the efficiency obtained in the cycle with the use of zeotropic mixtures or dry fluids, have concluded that the use of the former only presents improvements in the efficiency of the process when the operating circumstances are very specific, for example, when the Cooling of water is done at fixed temperatures. However, its use may be interesting based on the growing concern for the environment. An interesting case of zeotropic mixtures is the one formed by ammonia and water and used in the so-called Kalina cycle (KC). This KC presents greater freedom in terms of the composition of the mixture, but its configuration is more complex. However, it is an important alternative [13] to pure ORC due to the use of low heat sources and achieves higher efficiency values due in part to its lower level of irreversibilities. On the other hand [14-18], it also presents limiting factors such as the optimization of the process, the working fluid and the heat sources.

Other cycles [19] that take advantage of the energy from low-medium heat sources are the Goswami cycles (GC), which use binary mixtures. In addition [20], they incorporate mixtures of ammonia and water as a fluid, combined with a RC and an absorption cycle (AC). Other investigations [21] carried out with different zootropic mixtures and working conditions of the RC, have achieved improvements of up to 15% in the performance of the ORC.

Additionally [22], it should be borne in mind the fact that environmental conditions significantly influence the viability of the different types of thermodynamic cycle. From this point of view, the situations of scarcity of water used both in the power generation and cooling processes of the last stages of the cycle, together with high ambient temperatures, can make the application of thermodynamic cycles impossible. This situation of rising temperatures and water scarcity is being aggravated by the current situation caused by climate change. Therefore [23], power generation must be carried out with the least possible use of water, since worldwide electricity generation consumes 10% of the available water, mainly in its cooling stage.

Thus, the so-called Hygroscopic Cycle Technology (HCT) [7,24] arises as an improvement to the traditional thermoelectric generation cycles, improving the thermal efficiency of the cycle, reducing the consumption of cooling water and enabling the implementation of thermal cycles in areas that, due to their high ambient temperatures would make electricity generation very difficult or impossible. In Figure 2 [5], the HCT, which is based on a RC but incorporating improvements in the refrigeration zone to use absorption physicochemical processes, is represented.

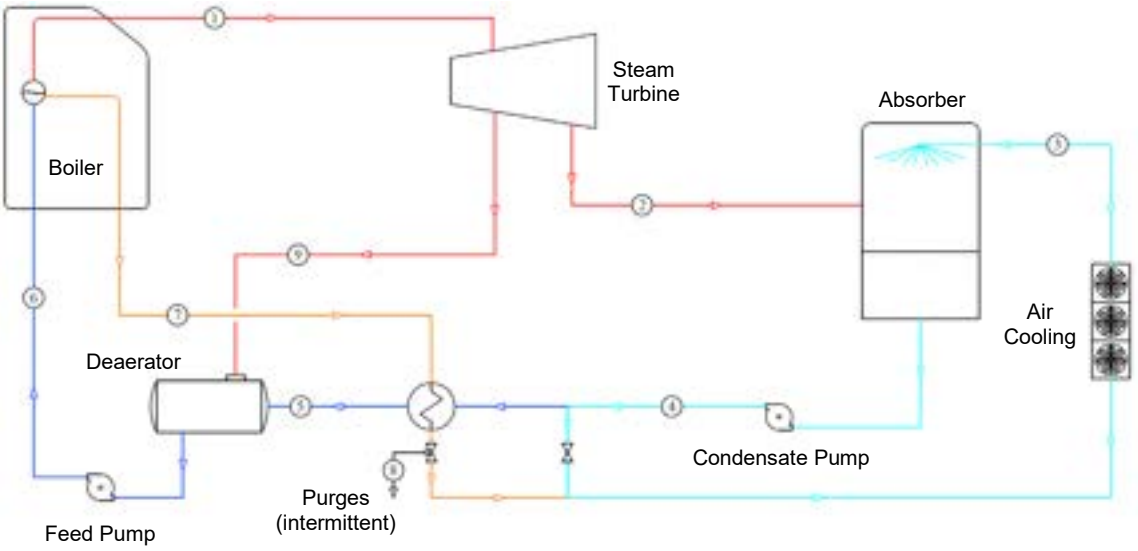

Figure. 2. Diagram of the Hygroscopic Cycle Technology in a thermoelectric power plant.

The HCT [25] uses hygroscopic compounds as part of the working fluids to optimize steam condensation at the turbine outlet through absorption processes. The hygroscopic substances [26] used must meet a series of characteristics to be used in the HCT. They must be non-flammable, have a lower vapor pressure than pure water and therefore less volatile than water, attract surrounding water vapor, and be easily separable to facilitate subsequent vapor desorption (reversible retention). In addition, these substances must be non-toxic and chemically stable under the working conditions of the HCT. The mixtures proposed by [27] consisted of LiBr-H2O as a suitable working fluid for the HCT. This hygroscopic and soluble salt in all stages of the HCT allowed to achieve the best results in the cycle. LiBr [28] increased its solubility considerably with increasing solution temperature. Additionally [26], the separation of the vapor and the hygroscopic compound did not require the use of special desorption technology or additional heat sources. The HCT [29] has already been successfully used in real installations with generated powers between 12.5 MW and 50 MW.

The direct steam condensation process is achieved in the HCT inside the absorber where the pure steam exhaust stream from the turbine (state 2 in Figure 1) is mixed with a solution of hygroscopic compounds in water (state 3 in Figure 1). The improvements [7,30] achieved by this direct condensation are the following:

- Due to the lower condensing pressure necessary at each cooling temperature, the electrical power at the turbine outlet is increased with reference to RC and therefore the general electrical performance of the cycle.
- For a given condensing pressure, the condensing temperature and therefore the cooling temperature are increased. In this way [31], a thermal dissipation of the condensation energy is possible only with air and therefore without the need for the use of water. By not using traditional water-cooling processes in cooling towers, the use of water is avoided and savings are made in cooling tower maintenance.
- At the same time, since the use of cooling water is not necessary, it allows the generation of energy with thermoelectric processes in areas with little water availability.
- Less demand for electrical energy [32] by the cooling system, made up of dry-coolers, since the increase in condensation temperature requires less dissipated thermal energy.

With all these features, the HCT allows improving the traditional RC and increasing electrical efficiency by approximately 2.5%, saving up to 50% in the consumption of demineralized water and additives, reducing investment costs by 5% and 25 % the costs of Operation and Maintenance (O&M) and increase the availability of the technology and its useful life [6]. These characteristics and improvements achieved with HCT technology are of special interest in areas with subtropical climates and possible water scarcity, as is the case in certain areas of the Canary Islands. It must be taken into account that in the Canary Islands the aquifers have been over-exploited, which is why the water table has dropped. As a result [33-36], numerous springs have dried up, wells and galleries have had to be deepened, and the danger of desertification has increased.

Currently [37], the Canary Islands are highly dependent on fossil fuels. According to data from the energy yearbook of the Canary Islands for the year 2021, renewable energies only represent 19.5% of electricity production. The energy is obtained in hundreds of units distributed in gas-fired power plants, diesel engines or steam turbines. Figure 3 shows the dispersion of plants along the islands.

Figure 3. Thermoelectrical power plants and installed capacity in the Canary Islands.

Additionally, a detailed list of these Canarian thermoelectric plants ordered by island with their group type, cooling system, number of units and their power capacity can be found in Table 1.

Table 1. The Canarian thermoelectric plants.

Island	Power Plant	Group Type	Cooling System	Units	Power Capacity (MW)
El Hierro	Llanos Blancos	Diesel	Close cycle desalinated water	10	14.91
Fuerteventura	Las Salinas	Diesel	Open cycle seawater	9	107.92
	Las Salinas	Gas	Adiabatic cooling	3	79.1
Gran Canaria	Jinámar	Diesel	Open cycle seawater	5	84
	Jinámar	Gas	Adiabatic cooling	3	98.45
	Barranco Tirajana	Gas	Adiabatic cooling	6	376
	Jinámar	Steam	Open cycle seawater	2	120
	Barranco Tirajana	Steam	Open cycle seawater	4	320.73
La Gomera	El Palmar	Diesel	Open cycle seawater	6	13.38
	El Palmar	Diesel	Adiabatic cooling	3	7.79
La Palma	Los Guinchos	Diesel	Open cycle seawater	10	82.84
	Los Guinchos	Gas	Adiabatic cooling	1	22.5
Lanzarote	Punta Grande	Diesel	Open cycle seawater	11	199.76
	Punta Grande	Gas	Adiabatic cooling	2	62.5
Tenerife	Candelaria	Diesel	Open cycle seawater	3	36
	Granadilla	Diesel	Open cycle seawater	2	48
	Candelaria	Gas	Adiabatic cooling	3	92.2
	Granadilla	Gas	Adiabatic cooling	6	382.9
	Arona	Gas	Adiabatic cooling	2	50
	Isora	Gas	Adiabatic cooling	1	44
	Candelaria	Steam	Open cycle seawater	2	80
	Granadilla	Steam	Open cycle seawater	4	313.4

For all these reasons, in the present investigation the implementation of HCT in the existing thermoelectric plants and in operation in the different Canary Islands is simulated in order to obtain the potential of water savings for each installation. The application of the HCT is assessed according to the characteristics of each thermal power plant and the specific hydrological needs of the different island areas. All of this would translate into significant environmental savings and would allow the consideration of the use of HCT in areas where the viability of traditional thermoelectric cycles is not feasible or not convenient due to water scarcity.

2. Methodology

The methodology used to calculate the savings obtained with the application of the HCT in the Canary Islands thermoelectric plants consisted of:

1º.The refrigeration system data [38] and the power of the different units were obtained from the environmental declaration of each power generation plant and from the State Registry of Emissions and Polluting Sources [39]. It was also necessary to know the equivalent operating hours. These hours were calculated from the annual production data for each type of plant and island, which are included in the 2021 Canary Islands energy yearbook [37]. These data are shown in Table 2.

Table 2. Equivalent hours and annual production of the Canary thermoelectric plants.

Island	Power Plant	Group Type	Power Capacity (MW)	Annual production (MWh)	Equivalent hours (h)
El Hierro	Llanos Blancos	Diesel	14.91	26 133	1 752.7
Fuerteventura	Las Salinas	Diesel	107.92	477 165	4 421.5
	Las Salinas	Gas	79.1	31.563	399
Gran Canaria	Jinámar	Diesel	84	199 206	2 371.5
	Jinámar	Gas	474.45	1 814 728	3 824.9
	Barranco Tirajana	Gas			
	Jinámar	Steam	440.73	647 519	1 469.2
	Barranco Tirajana	Steam			
La Gomera	El Palmar	Diesel	21.17	71 022	3 354.8
	El Palmar	Diesel			
La Palma	Los Guinchos	Diesel	82.84	238 590	2 880.1
	Los Guinchos	Gas	22.5	499	22.2
Lanzarote	Punta Grande	Diesel	199.76	632 746	3 167.5
	Punta Grande	Gas	62.5	12 581	201.3
Tenerife	Candelaria	Diesel	84	177 029	2 107.5
	Granadilla	Diesel			
	Candelaria	Gas	569.1	1 905 502	3 348.3
	Granadilla	Gas			
	Arona	Gas			
	Isora	Gas			
	Candelaria	Steam	393.4	595 497	1 513.7
	Granadilla	Steam			

2º. In order to obtain the performance of power plants, research developed by [40-43] were considered. In this way, the performances were 34% for the groups with steam, 38% for the groups with gas and 45% for the groups with diesel.

3º. The heat that would have to be dissipated by the cooling system of each plant was obtained by applying equations (1) and (2).

$$\dot{Q}_C = \frac{\dot{W}}{\eta} \quad (1)$$

$$\dot{Q}_F = \dot{Q}_C - \dot{W} \quad (2)$$

Being:

$\dot{Q}_C$: thermal power supplied to the cycle of the plant.

$\dot{Q}_F$: heat rejected by thermal cycle of the plant.

$\dot{W}$: plant power capacity (Table 2).

η: power plant performance. Obtained in previous point 2º.

4º. The necessary water flow for the cooling process was calculated using the following equations and technical data:

$$\dot{Q}_F = \dot{m} \cdot (h_{out} - h_{in}) \quad (3)$$

$$T_{out} = T_{in} + \Delta T \quad (4)$$

Being:

h_{out}: cooling water outlet enthalpy.

h_{in}: cooling water inlet enthalpy.

$\dot{m}$: cooling water mass flow.

T_{in}: cooling water inlet temperature.

T_{out}: cooling water outlet temperature.

ΔT: Temperature difference of the cooling water between the inlet and outlet of the adiabatic cooling equipment. A value of 14 ºC has been taken according to the common industrial values [6].

4º According to [45-46], for processes with open cycle the average consumption of water in thermal power plants such as existing in the Canary Islands (Gas, Diesel or Steam group type) is 0.38 m^3/MWh.

3. Results and conclusions

In this way, the current annual water needs or cooling water consumption (m^3/year) per MWh of each thermoelectric plant in the Canary Islands were obtained and represented in Table 3. For processes with adiabatic coolers, it has been considered that the water consumption was 0.1 percent of the water used in the cooling system [47].

Table 3. Annual water consumption for the cooling system in thermoelectric plants from the Canary Islands.

Island	Power Plant	Water Consumption for the Cooling System (m^3/h)	Equivalent hours (h/year)	Annual Water Consumption for the Cooling System (m^3/year)
El Hierro	Llanos Blancos	5.67	1 752.7	9 930.45
Fuerteventura	Las Salinas	41	4 421.5	181 323.95
	Las Salinas	7.94	399	3 167.78
Gran Canaria	Jinámar	31.92	2 371.5	75 698.28
	Jinámar Barranco Tirajana	47.62	3 824.9	182 144.81
	Jinámar	45.60	1 469.2	246 057.80
	Barranco Tirajana	121.88		
La Gomera	El Palmar	5.08	3 354.8	19 022.10
	El Palmar	0.59		
La Palma	Los Guinchos	31.48	2 880.1	90 663.24
	Los Guinchos	2.26	22.2	50.14
Lanzarote	Punta Grande	75.91	3 167.5	240 441.12
	Punta Grande	6.27	201.3	1 262.79
Tenerife	Candelaria	13.68	2 107.5	127 883.10
	Granadilla	18.24		
	Candelaria Granadilla Arona Isora	57.12	3 348.3	191 257.83
	Candelaria	30.4	1 513.7	226 286.04
	Granadilla	119.1		

Therefore, the minimum potential for savings in water consumption by refrigeration systems would be 1.6 Mm^3 per year. It means that the average minimum water consumption is 0.23 m^3/MWh in thermoelectric plants of the Canary Islands.

All this use of water can be avoided by using the HCT. In this way, the environmental problems associated with the consumption of water for industrial processes or returning water at high temperatures to ecosystems that can be seriously affected, as occurs in open refrigeration systems, would be avoided.

Currently, the total energy generation of the thermoelectric plants of the Canary Islands is 6 829 780 MWh/year. The efficiency is increased by 2.35% when HCT is used instead of traditional Rankine cycle [6]. Therefore, the increment of the total energy generation would be of 160 499.80 MWh/year. In addition to the increase in the efficiency, the application of HCT technology would reduce the costs associated with the maintenance of the cooling systems existing in the current thermoelectric plants in the Canary Islands. On the other hand, the reduction of installation costs would also have been achieved in the new built systems. This economic improvement would reduce the price of energy associated with its generation. Definitely, in the current economic context of high electricity prices it would be very interesting from both a social and a business point of view.

As future work, it is proposed to analyse the economic cost of the incorporation of the HCT in the different plants of the Canary Islands as well as the necessary time to recover the investment.

Nomenclature

$\dot{Q}_C$ heat supplied to the thermal cycle of the plant, kW

$\dot{Q}_F$ heat rejected by thermal cycle of the plant, kW

$\dot{W}$ plant power capacity, kW

h_{out} cooling water outlet enthalpy, kJ/kg

h_{in} cooling water inlet enthalpy, kJ/kg

$\dot{m}$ cooling water mass flow, kg/s

T_{in} cooling water inlet temperature, ºC

T_{out} cooling water outlet temperature, ºC

ΔT temperature difference of the cooling water in the dry-cooler, ºC

Greek symbols

η power plant performance.

Acknowledgments

This work has been supported by the project "Improvement of energy performance of the Hygroscopic Cycle for power production" PID2019-108325RB-I00/AEI/10.13039/501100011033 from the Agencia Estatal de Investigación - Ministerio de Ciencia e Innovación, Spain; and "Severo Ochoa" grant program for training in research and teaching of the Principality of Asturias - Spain (BP20-176). The authors also want to acknowledge the contribution of the Spanish company IMATECH (Imasa Technologies), owner of the Hygroscopic cycle pilot plant, as well as the support from the University Institute of Industrial Technology of Asturias (IUTA), financed by the City Council of Gijón, Spain.

References

[1] International Energy Agency. Global Energy Review. 2021. p. 27.

[2] European Union Commission. 2030 Climate & energy framework. 2020.

[3] Global Electricity Review 2022 - Avaliable at:<https://ember-climate.org/insights/research/global-electricity-review-2022/> [accessed: 11.3.2023]

[4] Sarr J.A.R., Mathieu-Potvin F., Increasing thermal efficiency of Rankine cycles by using refrigeration cycles: A theoretical analysis. Energy Conversion and Management 2016:358–379.

[5] Martínez-Pérez R., Rubio-Serrano F.J., Meana-Fernández, A., Gutiérrez-Trashorras, A.J. Influence of LiBr concentration in the generation of superheated vapor for a Hydroscopic Cycle. International Conference on Renewable Energies and Power Quality (ICREPQ); 2022 July 27-20; Vigo, Spain.

[6] Rubio-Serrano F., Gutiérrez-Trashorras A.J., Soto-Pérez F., Álvarez-Álvarez E., Blanco-Marigorta E. Advantages of incorporating Hygroscopic Cycle Technology to a 12.5-MW biomass power plant. Applied Thermal Engineering 2018:320-327.

[7] Meana-Fernández A., Peris-Pérez B, Gutiérrez-Trashorras A.J., Rodríguez-Artime S., Ríos-Fernández J.C, González-Caballín J.M. Optimization of the propulsion plant of a Liquefied Natural Gas Transport ship. Energy Conversion and Management, 2020;224.113398.

[8] DiGenova K.J., Botros B.B., Brisson J.G. Method for customizing an organic Rankine cycle to a complex heat source for efficient energy conversion, demonstrated on a Fischer Tropsch plant. Applied Energy 2013;102:746–754.

[9] Linke P., Papadopoulos A.I., Seferlis P. Systematic Methods for Working Fluid Selection and the Design, Integration and Control of Organic Rankine Cycles - A Review. Energies,2015;8:4755–4801.

[10] Vanslambrouck B., van den Broek M. and De Paepe M. Organic Rankine cycle versus steam cycle: a thermodynamic comparison. 3rd International Conference: Low Temperature and Waste Heat Use in Communal and Industrial Energy Supply Systems; 2012.

[11] Li Y., Du M., Wu C., Wu S., Liu C. Potential of Organic Rankine Cycle using zeotropic mixtures as working fluids for waste heat recovery. Energy 2014;77:509-519.

[12] Su W., Hwang Y., Deng S., Zhao L., Zhao D. Thermodynamic performance comparison of Organic Rankine Cycle between zeotropic mixtures and pure fluids under open heat source. Energy Conversion and Management 2018;165:720-737.

[13] Wang Y., Tang Q., Wang M., Feng X. Thermodynamic performance comparison between ORC and Kalina cycles for multi-stream waste heat recovery. Energy Conversion and Management 2017;145:482-492.

[14] Campos C.E., Escobar J.C., Venturini O.J., Silva E., Melián V., Marqués D. Lofrano F., Gialluca V. Exergetic and economic comparison of ORC and Kalina cycle for low temperature enhanced geothermal system in Brazil. Applied Thermal Engineering 2013;52:109-119.

[15] Nemati A., Nami H., Ranjbar F., Yari M. A comparative thermodynamic analysis of ORC and Kalina cycles for waste heat recovery: A case study for CGAM cogeneration system. Case Studies in Thermal Engineering 2017;9:1-13.

[16] Roy P., Désilets M., Galanis N., Nesreddine H. and Cayer E. Thermodynamic analysis of a power cycle using a low-temperature source and a binary NH3–H2O mixture as working fluid. International Journal of Thermal Sciences 2010;49:48-58.

[17] Elsayed A., Embaye M., Al-Dadah R., Mahmoud S., Rezk A. Thermodynamic performance of Kalina cycle system 11 (KCS11): feasibility of using alternative zeotropic mixtures. International Journal of Low-Carbon Technologies 2013;8:69-78.

[18] Walraven D., Laenen B., D'haeseleer W. Comparison of thermodynamic cycles for power production from low-temperature geothermal heat sources. Energy Conversion and Management 2013;66:220-233.

[19] Demirkaya G.A., Padilla R.V., Fontalvo A., Bula A. and Goswamy D.Y. Experimental and theoretical analysis of the Goswami cycle operating at low temperature heat sources. Journal of Energy Resources Technology 2018:140(7).

[20] Leveni M., Cozzolino R. Energy, exergy, and cost comparison of Goswami cycle and cascade organic Rankine cycle/absorption chiller system for geothermal application. Energy Conversion and Management, 2021;113598:227.

[21] Chen H., Yogi D., Rahman M.M., Stefanakos E.K. A supercritical Rankine cycle using zeotropic mixture working fluids for the conversion of low-grade heat into power. Energy 2011;36:549-555.

[22] Pinilla-Fernández D.A., Foliaco B., Vásquez-Padilla R., Bula A., González-Quiroga A. High ambient temperature effects on the performance of a gas turbine-based cogeneration system with supplementary fire in a tropical climate. Case Studies in Thermal Engineering 2021;101206:26.

[23] Pan S., Snyder S.W., Packman A.I., Lin Y.J., Chiang P. Cooling water use in thermoelectric power generation and its associated challenges for addressing water-energy nexus. Water-Energy Nexus 2018:26-41.

[24] Rubio Serrano F.J. Ciclo Higroscópico: la evolución eficiente del Ciclo Rankine. Solar News, 2013;45:32-35.

[25] Rubio Serrano F.J. Rankine cycle with absorption step using hygroscopic compounds (WO2010133726A1). World Intellectual Property Organization, Switzerland. 2010.

[26] Rubio-Serrano F.J., Soto-Pérez F., Gutiérrez-Trashorras A.J. Experimental study on the influence of the saline concentration in the electrical performance of a Hygroscopic cycle. Applied Thermal Engineering 2019:165.

[27] Rubio-Serrano F.J., Soto-Pérez F., Gutiérrez-Trashorras A.J. Influence of cooling temperature increase in a hygroscopic cycle on the performance of the cooling equipment. Energy Conversion and Management 2019;112080:200.

[28] Boryta D.A. Solubility of lithium bromide in water between 50. deg. and 100. deg. (45 to 70% lithium bromide). J. Chem. Eng. Data 1970;15(1):142-4.

[29] IMASA Technologies. Avaliable at: <https://imasatechnologies.com/> [accessed 11.3.2023]

[30] Rubio-Serrano F.J., Soto-Pérez F., Gutiérrez-Trashorras A.J., Abad-Ausin G. Comparison between existing Rankine Cycle refrigeration systems and Hygroscopic Cycle Technology. International research conference on sustainable energy, engineering, materials and environment; 2018; Mieres, 25–7.

[31] Rubio Serrano F.J. Saving water in power plants. Power Eng. Int. 2016;24(6).

[32] Rubio-Serrano F.J. An evolution in profitability and efficiency. Power Engineering International 2013;21(9).

[33] De la Fuente J.A., Martel G., Melián G. Plan de Ecogestión del Agua: Gobierno de Canarias; 2013.

[34] Gobierno de Canarias. Ley de Aguas 12/1990, de 26 de julio.

[35] Ministerio de Medio Ambiente, Medio Rural y Marino del Gobierno de España. Resolución de 26 de marzo de 2009, de la Dirección General del Agua, por la que se publica el Convenio de colaboración, entre el Ministerio de Medio Ambiente, y Medio Rural y Marino y la Consejería de Obras Públicas y Transportes del Gobierno de Canarias, para el desarrollo de actuaciones en materia de agua.

[36] Gobierno de Canarias. Orden de 11 de febrero de 2000, por la que se aprueba el Código de Buenas Prácticas Agrarias de la Comunidad Autónoma de Canarias. BO Canarias núm. 23, de 23 de febrero de 2000.

[37] Gobierno de Canarias. Anuario energético de Canarias. 2023.

[38] Endesa. Declaración de impacto ambiental Central Canarias – Available at: <https://www.endesa.com/> [accessed 06.3.2023].

[39] Registro Estatal de Emisiones y Fuentes Contaminantes (PRTR-España). – Available at: <https://prtr-es.es/> [accessed 06.3.2023].

[40] Al-Taha, W. H., Osman, H. A. Performance Analysis of a Steam Power Plant: A Case Study. MATEC Web of Conferences 2018. EDP Sciences 05023

[41] Najjar, Y.S., Abu-Shamleh, A. Performance evaluation of a large-scale thermal power plant based on the best industrial practices. Scientific Reports 2020;10(1):1-9.

[42] Ahmadi, M.H., Alhuyi Nazari, M., Sadeghzadeh, M., Pourfayaz, F., Ghazvini, M., Ming, T., Sharifpur, M. Thermodynamic and economic analysis of performance evaluation of all the thermal power plants: A review. Energy science & engineering 2019;7(1):30-65.

[43] Kanoglu, M., Işık, S.K., Abuşogˇlu, A. Performance characteristics of a diesel engine power plant. Energy Conversion and Management, 2005;46(11-12):1692-1702.

[44] Agencia Estatal de Meteorología (AEMET) Gobierno de España. Valores climatológicos normales. – Available at: <https://www.aemet.es/es/serviciosclimaticos/datosclimatologicos/valoresclimatologicos> [accessed 06.3.2023].

[45] Macknick, J., Newmark, R., Heath, G., Hallett, K. C. Operational water consumption and withdrawal factors for electricity generating technologies: a review of existing literature. Environmental Research Letters. 2012:7(4).

[46] McNabb, D. E. Global Pathways to Water. Sustainability 2019.

[47] Feeley III, T. J., Skone, T. J., Stiegel Jr, G. J., McNemar, A., Nemeth, M., Schimmoller, B., Manfredo, L. (2008). Water: A critical resource in the thermoelectric power industry. Energy, 33(1), 1-11.

A new way to assess the loss of mineral wealth: the case of copper

Jose-Luis Palacios[a], Alicia Valero[b], Óscar Jaime Restrepo Baena [c] and Fabricio Pazmiño[d]

[a] *Departamento de Ingeniería Mecánica, Escuela Politécnica Nacional, Ladrón de Guevara E11-25,Quito 170517, Ecuador; jose.palacios@epn.edu.ec*
[b] *Research Centre for Energy Resources and Consumption (CIRCE) - Universidad de Zaragoza, CIRCE Building – Campus Río Ebro, Mariano Esquillor Gómez, 15, 50018 Zaragoza, Spain; aliciavd@unizar.es*
[c] *School of Mines, Universidad Nacional de Colombia, 050022 Medellín, Colombia*
[d] *Facultad de Geología y Petróleos, Escuela Politécnica Nacional, Ladrón de Guevara E11-25, Quito 170517, Ecuador; fabricio.pazmino@epn.edu.ec*

Abstract:

The search for new electronic appliances, the urgent need for renewable energy technologies and on the multiple uses in the society have produced a high demand for metals. The copper claim has increased significantly in the last centuries. Chile is the world´s largest copper producer. However, the higher production of copper has been accompanied by a considerable decay of ore grades in the Chilean copper mines. That is why it is required to appropriately assess the loss of mineral (LMW) wealth. Methodologies to determine the LMW based on the second law of thermodynamics and the Exergy, have provided valuable information on the scarcity of minerals. The methodology proposed in this paper is based on the simulation of mineral processes for the concentration of copper using HSC from an average mineral composition of the leading in some mines in Chile. One approach to estimating LMW has been utilising the exergy replacement cost (ERC). Although this procedure has been effective in establishing an ultimate scenario of mineral depletion, named Thanatia, it needs to correlate appropriately with the current market conditions to develop a framework for a fairer scheme for the prices of metals. In this paper is proposed a new approach to estimate LMW for the case of copper.

Keywords:

exergy replacement cost (ERC), metal demand, copper, mineral depletion, Exergia

1. Introduction

The transition towards a more sustainable society requires more clean energy technologies, therefore, more minerals and metals are needed. A report of the International Energy Agency [1], it was highlighted the importance of such minerals. Some of them, are categorized as critical for some clean energy technologies. In this report, it is pointed out that the rise of demand for copper and rare earths to more than 40% in the next two decades.

Authors such as Mudd [2]–[6], Craig et. al [7] and Norgate [8] have mentioned the issue of the decline of ore grade in mines over time. In a research [9], the peak production of copper is estimated from 2031 to 2042. A study by Calvo et al. [9] investigated the reduction of ore grades in 25 mines in Chile, Australia, and Peru. The production of these mines accounted for 32% of the total copper production at that time. In addition to this, it was also observed a 25% reduction in average of the ore grade from 2003 to 2013. The decrease in the concentration of copper in mines produced an increase in 46% in energy consumption. On one side, more metals are required, but on the other rich metal deposits have been already extracted. Therefore, the supply of cooper for the next generations is compromised to actions that must be taken for sustainable production in present generations.

In 2020, China had 33,2% of the global share of copper production, and Chile 20,5%. This country had a robust worldwide industry of copper with an essential impact in its economy. In 2020, the share of the copper industry in Chile accounted for 11,2% of its Gross Domestic Product (GDP) [10].

In Chile, the decline of ore grade has been also notorious (Figure 1). The average ore grade in the copper mines was about 1.4% in 1999, which decreased to about 0,6% in 2018.

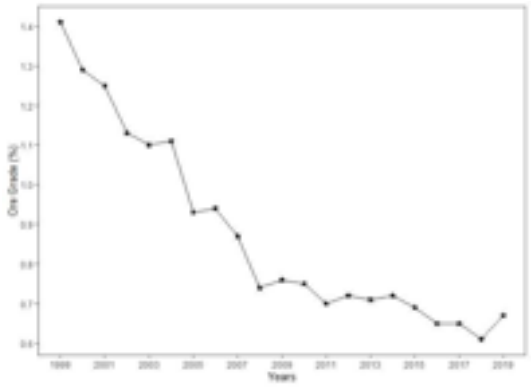

Figure 1. Decline of the average ore-grade of copper mines in Chile.(Calculated based on:[11], [12])

The need for more metals will also produce more extraction of minerals in countries, for example, Chile, where the rich deposits have been already extracted as shown in Figure 1. This will also cause a rapid loss of mineral depletion. It is important to know that mineral endowment was defined by Harris and Agterberg [13] as the amount of metals in a given region. This accumulation of minerals, traded later as commodities, means abundance for a country. Because of the growing need for minerals, they are extensively extracted, producing a loss of mineral wealth (LMW). The LMW represents a quantitative indicator of mineral depletion in that country [6] [37] [38].
As can be seen, it is crucial to have an approach to estimate the LMW. In a publication [17], in this paper is used the exergy replacement cost (ERC) concept to estimate the loss of mineral extraction in 22 countries in Latin America. In this investigation, it was used values of ERC previously reported in [18]. The concept of ERC and its methodological approach will be reviewed in the next section. Nevertheless, this value of ERC for copper will provide a certain sense of the importance of mineral depletion; it fails to give some hints towards a fairer price of minerals.
This paper will provide a new approach based on simulation with HSC Chemistry 9 and HSC Sim software [19] to estimate a new value of ERC for copper as a valuable indicator to evaluate mineral depletion more appropriately.

1.1 The concept of the exergy replacement cost

The traditional way to value minerals has been through the market price. However, prices fluctuate and are unstable because they depend on many factors [19]. Therefore, prices are not sufficient to give an appropriate value to minerals. The mass has been another approach to valuing minerals. Nevertheless, they do not consider the geological scarcity or the difficulty of the production process. An alternative method is using the concept of the exergy replacement cost, which stands for ERC. This concept has its basis on Exergy. For fossil fuels, when they are burned the liberation of energy is accompanied with their higher heating value (HHV) [20], [21].On the other hand, non-fuel minerals are not combustible the HHV is no longer valid. The use of exergy for non-fuel minerals has two perspectives; a traditional way to treat them has been using their chemical exergy. On this perspective, Szargut has published chemical exergy of different elements [22]. These values have been used by Ayres [23], Dewulf et al. [24] and Szargut et al. [15], [25], [26] to evaluate mineral resources. However, this perspective is not valid to allocate the fair value of minerals. A study [28] clearly pointed out the fact by showing that the chemical exergy of precious metal gold is 60 kJ/mol is considerably lower than aluminium 796 kJ/mol. Exergo- ecology, a discipline postulated by Valero [27], can give a more appropriate scheme to value minerals. Physical Geonomics, one Exergoecology´s division, deals with the application of exergy to assess non-fuel minerals. The exergy of minerals has two components: one is related to chemical composition (chemical exergy) and the other is associated with the relative concentration in the Earth´s crust (concentration exergy). The latter makes minerals more valuable than the former. Nature provides a “free bonus” or in economic terms a “hidden cost” just for having minerals concentrated in mines and not dispersed throughout the Earth´s crust. This “free bonus” significantly reduces the costs associated with mining processes. When higher-ore grade mines become depleted, a reduction in this free bonus occurs, leading to an extensive exergy consumption to extract a similar quantity of metal. The bonus provided by nature can be measured through the ERC.
ERC is postulated as the energy that would be required to extract and concentrate a mineral from a completely dispersed state at a crustal concentration (xc) to the conditions of concentration and

composition found in the mine (xm) by using available technology. Thanatia represents a state of total mineral dispersion into the Earth´s crust. Thanatia´s composition is made up of 324 species, 292 minerals and 32 diadochic elements included in the crystal structure of other elements [28], [29].
The exergy required to concentrate minerals from a concentration found in Thanatia (xc) to the average concentration (xm) for different minerals can be found in [18]. This research, will be focused to the ERC for copper. To estimate the ERC for copper, Valero et. al assumed the concentration of copper in the Earth´s crust xc = 6.64x10-5 g/g [30] which corresponds to 0.006 wt-%. Also, an average ore grade assumed xm = 1.67x10-2 (0.5 wt-%) [31]. The ERC for copper reported in [18] was 292 GJ/t-Cu. They considered that 60% of the total energy was for the mining and concentration [32].

1.2 The need of a new approach

The ERC of different minerals were calculated by Valero et al. [32] by observing the behaviour of the decrease of ore grade and increase in energy consumption for some metals, such as cobalt, copper, gold, nickel, and uranium. Valero et al. proposed a function that portrayed the relationship between the energy consumption as a function of the ore grade, Equation (1).

$$E_{(X_m)} = A \,.\, X_m^{-0.5} \quad (1)$$

Where $E_{(X_m)}$ is the energy for the concentration and extraction of minerals at the ore grade (xm), and the coefficient A is determined for each mineral.
In [33] the LMW was estimated for a series of mineral produced in 22 countries in Latin America by using conventional ERC. A remarkable result of this investigation was market prices do not compensate the LMW in the region. As forthcoming, it was established the need to have a scheme to estimate fairer prices for minerals.
The methodology proposed to estimate ERC is limited to the experience of observing historical data of some metals. In this approach, as reported in [34] geological principles prevailed over metallurgical considerations.
An upgrade to the ERC for iron, copper and gold based on simulations of a specialized software HSC Chemestry [35] by considering mineral processing was reported in [36], [37], [38], respectively. These new values of ERC varied in orders of magnitude to the previous ones conveyed in [18]. They differ in the method of calculation from observation to simulation in HSC.
Previous ERC [18] and new ERC for iron, copper and gold [36], [37], [38] are higher values in GJ/t that would lead to numerous errors to estimate a fairer price of minerals. The reason for such magnitude of values is that Thanatia is used as starting point to determine the ERC. Therefore, a new approach is required to have an intermediate scenario that provides more appropriate ERC in this copper case.
This research will be focused to establish this intermediate scenario, which will be described in the next section.

1.3 An intermediate scenario for a new ERC for copper

In order to establish a scenario, first, it is presented an ideal scenario of mineral dispersion in which all minerals are diluted through the Earth´s crust total mineral dispersion named Thanatia. On the other hand, it is described the cut-off grade as the minimum grade in a deposit in which a metal can be economically extracted [39], [40]. Therefore, an intermediate scenario can be found between the concentration of copper in Thanatia and the cut-off grade. In Figure 2, the exergy needed for the concentration of metals is presented as function of the ore grade [28], XB represents the concentration of metal at the beneficiation process (c.a. 99 wt-%), XM the ore grade in mines, for instance, the average ore grade in copper deposits is 0.5 wt-%. Then as the ore-grade decreases, the exergy rises exponentially, Xcut-off the cut-off grade at which the extraction of minerals in deposits is not economically viable. We will consider the cut-off grade for Chile. This value was estimated as average value of 0.2 wt-% of copper [41], [42], [43]. Afterwards, XC is the concentration of metal. As written in section 1.1, in Thanatia de concentration of copper corresponds to 0.006 wt-%. The intermediate scenario (Xin.) of analysis for the new ERC for copper is located between a concentration XC and Xcut-off. For the cut-off grade, since our objective is to estimate a new ERC for copper, we choose Xin for copper at a composition of copper of 0.02 wt-%.
Mine La Escondida, in 2020, produced 30% of the total copper production in Chile [10]. Hence, the model in this paper, will be taken a similar mineral composition to La Escondida as input. A literature review was performed, and the most representative minerals were identified. The most predominant mineralogical composition was based on copper sulphides [44] accompanied by a series of minerals, mostly silicates, as is shown in Table 1.

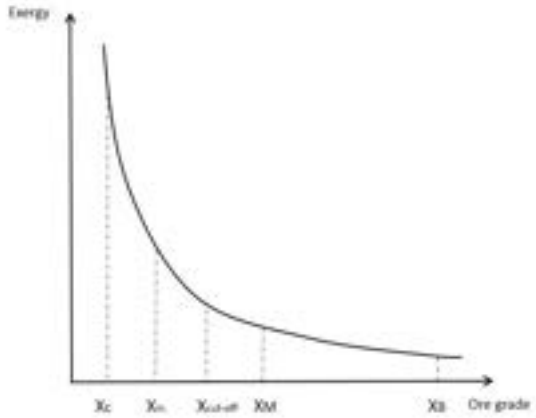

Figure 2. Description of the intermediate scenario for the new ERC for copper.

Estimations were performed on the basis of the abundance of the deposits La Escondida reported in [45], [46]. It was also considered QEMSCAN analysis developed by [47] and [48]. For the model it was allocated each mineral for an average ore-grade of 0.02 wt-% Cu.

2. Methodology

In this section, the stages of determining the new ERC for copper based on HSC Sim 9 [35] are explained.

The target of the model is to estimate the specific energy needed to concentrate copper, in this copper known as the new ERC for copper, from a concentration of copper in the intermediate scenario (0.002 wt-% Cu) to an average concentration in mines (0.5 wt-% Cu). The model was developed to concentrate copper mainly from sulphides, specially Chalcopyrite. Also, the model takes some procedures for the layout reported in previous work to determine ERC from Thanatia [37].

Prior to the model, a literature review was performed [8], [40], as well as state-of-the-art technologies for copper concentration [51]. On the basis of the analysis of operating data for concentrators of copper in La Escondida [57], a flow rate of 6 500 tons per hour was chosen. A top size in the ore feed of 6 E5 µm was considered for the feed.

The new ERC will also consider the energy for ore handling and the concentration of copper. For the ore-handling, it was assumed a minimum distance from an open pit mine to the concentrator so that the fuel consumption per ton of ore prevailed over the distance. For this task, it was supposed a fuel consumption of 0.6 L/ton of rock taken from [58].

The comminution circuit was modelled by following guiding principles reported in [59]. It consisted of three circuits primary crushing, grinding and regrinding. A jaw crusher reduced the 80% of feed particle size (F80) to P80, equal to 10 000 um. Then semi-autogenous (SAG) crushed the rock to 2 000 um Afterwards, a screen is used to separate the oversized particles. The latter went to a pebble mill, where they were reduced to 1 500 um.

During comminution, a fundamental equation to calculate the specific energy required for the mills is Bond´s equation [39], [60] Eq. (2):

$$W = 10\, W_i \left(\frac{1}{\sqrt{P_{80}}} - \frac{1}{\sqrt{F_{80}}} \right) EF_x \qquad (2)$$

where W is the specific energy consumption of the mill (kWh/t), Wi represents the work index (kWh/t), P80 and F80 are the product and feed passing sizes, respectively measured in µm. The last term, EFx is the product of the Rowland efficiency factors, which depend upon mill, size and type of media, type of grinding circuit, etc. [39], [60]–[63]. Then, the theoretical power draw by the mill (kW) is calculated by W x T, where T is the throughput tonnage (t/h) [39].

A hydrocyclone separated the fines to the flotation circuit with F80 lower than 130 um. The coarse of the hydrocyclone went directly into a ball mill that reduced the oversized particles to 600 um. The flotation circuit mainly separated the higher-copper minerals (sulphides), especially Chalcopyrite. To do

this, fast kinetics constants (kf) were set up for Chalcopyrite in the range of 1 to 2.5. These figures were in harmony with values reported in [64] and [65].

The volume and number of cells for the flotation tanks, roughers and scavengers, were established based on data reported by Weiss [51], and Wills and Finch [39].

3. Results and Analysis

The results of the simulations are described in this section. In addition to this, outputs of the model were validated through a comparison between parameters of the comminution and flotation processes with the respective ones found in the literature. As a final point, based on the methodology previously defined in the later section, the specific energy for the concentration of copper from an intermediate scenario (in.) between Thanatia and the cut-off grade, the new ERC for copper is identified.

3.1 Simulation results

From the model, the results were particle size for feed (F80) and output (P80) of the crushers and mills for the comminution processes, Table 1. The reduction ratio (Rr) is calculated by dividing F80 to P80 for every mill. Furthermore, the total reduction ratio is the product of Rr for every mill as specified in [52].

Table 1. Feed and product size, F80 and P80, respectively for the comminution process.

Stage	Equipment	F80 (μm)	P80 (μm)	Reduction ratio (Rr)
Crushing	Primary crusher	15302	10000	2
	SAG mill	4374	2000	2
Grinding	Pebble mill	2968	1500	1
	Ball mill	750	600	2
Re-grinding	HIG mill	131	34	4

The Rr for our model was 32 after the comminution process comes the flotation, which main results of retention time and power consumption are shown in .
Table ***2***.

Table 2. Retention time and power consumption for the flotation process.

Stage	Retention time (min)	Power (kW)
Rougher	14	2250
Scavenger	10	1850
Cleaner	9	185
Scavenger	14	55
Re-cleaner 1	13	75
Scavenger	18	90
Re-cleaner 2	7	150

The outcome of the flotation process had a mass flow rate of 210.10 t/h with a concentration of copper of 0.462%. For the flotation process, the recovery of copper was about 92%, followed by gold 46% and silver 39%.

3.2 Validation of the model

The validation consisted of the comparison between the main results of the model, particularly for comminution and flotation with those reported in the literature. In this sense, for comminution

For the flotation, the parameter for validation was the retention time in flotation. In [51, Ch. 10] the retention time for the roughing circuit was in the range of 13 to 16 minutes. In comparison to the values of our model, they are in the range except for the Cleaner and Re-cleaner 2. They are relatively smaller, nevertheless not so far from the values reported in the literature.

An essential parameter for the validation of the model was final metal recovery. Haque et al. [66] modelled pyro and hydrometallurgical for low-grade copper deposits. In this publication, the recovery of copper was assumed to have a yield between 86% to 89%. The recovery obtained from our model was about 92%. This figure agrees with the previous values reported in the literature. With this comparison, we can see that our model delivers logical and reliable results.

3.3 The new ERC for copper

The energy for comminution depends on the Bond´s work index (Wi), as it was explained in Section 2. In order to have a value that would be used as a reference for faired prices for copper, only one value of the new ERC will be required. Therefore, we assumed an average representative value for Wi equal to 14 kWh/t. This value was in agreement with models for copper in [67].

With these considerations, the power demand for the comminution and the flotation processes was estimated Table 3 .

Table 3. Power draw for comminution and concentration processes.

Stage	Power Demand (MW)	Power Demand (%)
Crushing	10.1	4.3
Grinding	21.3	90.3
Re-grinding	8.2	3.5
Concentration	4.7	2.0
TOTAL	236	100

As can be seen in Table 3, most of the power demand is mostly concentrated in the comminution process (94% approx.). The grinding circuit was the largest consumer.

The specific energy for the concentration process was calculated by following the methodology previously explained, Table 4.

Table 4. Specific energy to concentrate copper from an intermediate scenario.

	Cu concentration (wt-%)	Flow rate (t/h)	Specific Energy (kWh/t)	Specific Energy (MJ/t)
Feed Ore	0.036	6500	36	131
Conc. metal	0.462	220.10	1074	3867

By making a comparison of the average concentration of energy per ton of ore reported for different mines in [58], it can be seen that the value of 36 kWh/t-ore is in the range of those reported for mines such as La Escondida, Michila, Salvador [58]. This also supports that our model delivers reliable results.

In addition to the values of the specific energy shown in Table 5, the ore-handling must be added. For that, a value of 1.2 litres of diesel per ton of rock was considered for the specific fuel consumption. This was reported in [58] as an average value for the energy consumption in the Chuquicamata open-pit mine. The new ERC from the intermediate scenario is shown in Table 5.

Table 5. Specific energy for the concentration of copper from an intermediate scenario in GJ per ton of element.

Phase	Specific Energy (GJ/t)
Ore handling	128
Concentration	3.87
TOTAL	131.87

As can be seen, most of the energy is spent on the transportation of the ore to the concentrator. It is explained because a low ore grade ore (Table 1) is transported.

In Table 6, is made a comparison among values of the exergy replacement cost (ERC) for copper from Thanatia reported in [18]. Also values are compared of ERC based on HSC simulation, considering the starting point Thanatia in [37]. In addition, also is compared the average energy intensity for the Chuquicamata mine from 2000 to 2013, published in [58]. Then it was converted into GJ per ton of copper. Then with this and the exergy replacement cost (ERC) for copper reported in [18], a comparison with the specific energy of the current paper was done, Table 6.

The new ERC for copper is between the ERC from Thanatia in [18] and the specific energy for Chuquicamata [58], Table 8. The new ERC is more than three times the specific energy for Chuquicamata and almost a half of the previous ERC from Thanatia [18]. With regard to the values of

ERC for copper from Thanatia, also based on models in HSC, reported in [37], they differ by one to two orders of magnitude.

Table 6. Comparison of the specific energy of the current work with other reported values in GJ per ton of element.

	Ore	Specific Energy (GJ/t-Cu)	Source
New ERC	Intermediate scenario ($X_{in.}$)	132	current work
Based on HSC-model	Thanatia (X_C)	3100 - 30890	[37]
ERC	Thanatia (X_C)	292	[18]
Chuquicamata		42	[58]

4. Conclusions

More metals are needed to conduct a more sustainable energy transition through renewable energy technologies. The growing need for metal has produced that rich deposits have been exploited. The fact of the mineral exploitation should also be a concern in this path towards a decarbonisation of the society. In this regard, it is vital to have reliable means for the assessment of minerals. One non-conventional way to do this is by applying the concept of the exergy replacement cost (ERC). As a concept ERC has revealed its strengths compared to traditional methods, such as market-price and mass balance. Nevertheless, previous approximations to calculate the ERC for metals do not provide values that can be useful when calculating a market price of metals that consider aspects of mineral depletion. In this regard, the present work is novel in considering an intermediate scenario to estimate a new ERC for a metal widely used and key for an energy transition, copper. In this research, it has been considered an intermediate scenario, one that is located between an approach of total mineral depletion, Thanatia, and the scenario when economic feasibility for the exploitation of metals is not viable, the cut-off ore grade. This research considered the mineralogical composition of a representative copper mine in Chile, La Escondida, as key to developing the intermediate scenario.

The method of calculation of this new ERC for cooper has been based on the use of a reliable software HSC Sim 10.0.7.9 software [35]. This software has been helpful to develop new procedures to estimate ERC a more rigorous approach with mining considerations, as reported in [38].

The new ERC for copper from an intermediate scenario is an appropriate indicator for mineral depletion. It can be helpful to be considered a key indicator of mineral degradation towards the estimation of a fairer scheme for prices. In this scheme is required to have a clear picture on what parameters are the real drives for market prices. They should take into account the more need for energy to extract metals in the near future, as well as the loss of mineral wealth.

A key message of this and previous publications points out the need to give more importance to esteeming current copper deposits, particularly those located in South America. These countries should re-examine their significance as crucial mineral suppliers, particularly when discussing an energy transition.

Acknowledgements

The first author thanks the funding provided by Escuela Politécnica Nacional for the project PIS-19-07. The second author would like to thank to RESET project.

References

[1] International Energy Agency (IEA), “The Role of Critical Minerals in Clean Energy Transitions,” IEA Publ., 2021.

[2] G. M. Mudd, “Global trends in gold mining: Towards quantifying environmental and resource sustainability,” Resour. Policy, vol. 32, no. 1–2, pp. 42–56, 2007, doi: 10.1016/j.resourpol.2007.05.002.

[3] G. M. Mudd, “An analysis of historic production trends in Australian base metal mining,” Ore Geol. Rev., vol. 32, no. 1–2, pp. 227–261, Sep. 2007, doi: 10.1016/J.OREGEOREV.2006.05.005.

[4] G. M. Mudd, “Radon releases from Australian uranium mining and milling projects: assessing the UNSCEAR approach,” J. Environ. Radioact., vol. 99, no. 2, pp. 288–315, Feb. 2008, doi: 10.1016/j.jenvrad.2007.08.001.

[5] G. M. Mudd, “Gold mining in Australia: linking historical trends and environmental and resource sustainability,” Environ. Sci. Policy, vol. 10, no. 7–8, pp. 629–644, Nov. 2007, doi: 10.1016/J.ENVSCI.2007.04.006.

[6] G. M. Mudd, “Global trends and environmental issues in nickel mining: Sulfides versus laterites,” Ore Geol. Rev., vol. 38, no. 1–2, pp. 9–26, Oct. 2010, doi: 10.1016/J.OREGEOREV.2010.05.003.

[7] J. Craig, D. Vaughan, and B. Skinner, Earth resources and the environment, Fourth Edi. Harlow: Pearson Education Limited, 2014.

[8] T. Norgate and S. Jahanshahi, “Low grade ores – Smelt, leach or concentrate?,” Miner. Eng., vol. 23, no. 2, pp. 65–73, Jan. 2010, doi: 10.1016/J.MINENG.2009.10.002.

[9] H. U. Sverdrup, K. V. Ragnarsdottir, and D. Koca, “On modelling the global copper mining rates, market supply, copper price and the end of copper reserves,” Resour. Conserv. Recycl., vol. 87, pp. 158–174, Jun. 2014, doi: 10.1016/J.RESCONREC.2014.03.007.

[10] Comisión Chilena del Cobre, “Anuario de Estadísticas del Cobre y otros Minerales, Yearbook: Copper and other mineral statistics,” p. 161, 2019.

[11] COCHILCO, “Anuario de Estadísticas del Cobre y Otros Minerales 1989-2008,” 2008.

[12] COCHILCO, “Ley Promedio de Mineral de Cobre en la Operaciones Mineras en Chile por Tipo de Proceso,” 2019.

[13] D. P. Harris and F. P. Agterberg, “The appraisal of mineral resources.,” Econ. Geol., vol. 75th Anniv, pp. 897–938, 1981.

[14] G. Calvo, A. Valero, A. Valero, and Ó. Carpintero, “An exergoecological analysis of the mineral economy in Spain,” Energy, vol. 88, pp. 2–8, 2015, doi: 10.1016/j.energy.2015.01.083.

[15] G. Calvo, A. Valero, L. Carmona, and K. Whiting, “Physical Assessment of the Mineral Capital of a Nation: The Case of an Importing and an Exporting Country,” Resources, vol. 4, no. 4, pp. 857–870, 2015, doi: 10.3390/resources4040857.

[16] L. Gabriel Carmona, K. Whiting, A. Valero, and A. Valero, “Colombian mineral resources: An analysis from a Thermodynamic Second Law perspective,” Resour. Policy, vol. 45, pp. 23–28, 2015, doi: 10.1016/j.resourpol.2015.03.005.

[17] A. Valero, A. Valero, J.-L. Palacios, and G. Calvo, “The cost of mineral depletion in Latin America: An exergy based analysis,” in 30th International Conference on Efficiency, Cost, Optimization, Simulation and Environmental Impact of Energy Systems, ECOS 2017, 2017.

[18] G. Calvo, A. Valero, and A. Valero, “Thermodynamic Approach to Evaluate the Criticality of Raw Materials and Its Application through a Material Flow Analysis in Europe,” J. Ind. Ecol., vol. 00, no. 0, pp. 1–14, 2017, doi: 10.1111/jiec.12624.

[19] M. L. C. M. Henckens, E. C. van Ierland, P. P. J. Driessen, and E. Worrell, “Mineral resources: Geological scarcity, market price trends, and future generations,” Resour. Policy, vol. 49, pp. 102–111, 2016, doi: 10.1016/j.resourpol.2016.04.012.

[20] A. Valero and A. Valero, “Exergy of comminution and the Thanatia Earth’s model,” Energy, vol. 44, no. 1, pp. 1085–1093, 2012, doi: 10.1016/j.energy.2012.04.021.

[21] A. Valero and A. Valero, “What are the clean reserves of fossil fuels?,” Resour. Conserv. Recycl., vol. 68, pp. 126–131, 2012, doi: 10.1016/j.resconrec.2012.08.004.

[22] J. Szargut, “Chemical exergies of the elements,” Appl. Energy, vol. 32, no. 4, pp. 269–286, Jan. 1989, doi: 10.1016/0306-2619(89)90016-0.

[23] R. U. Ayres, Energy, Complexity and Wealth Maximization. Springer International Publishing Switzerland: Springer International Publishing, 2016.

[24] J. Dewulf and H. Van Langenhove, “Exergy,” in Renewables-Based Technology, Chichester, UK: John Wiley & Sons, Ltd, 2006, pp. 111–125.

[25] J. Szargut, A. Ziebik, W. Stanek, and A. Valero Delgado, “Towards an international legal reference environment,” in Proceedings of ECOS, 2015, pp. 409–420.

[26] J. Szargut, A. Ziębik, and W. Stanek, “Depletion of the non-renewable natural exergy resources as a measure of the ecological cost,” Energy Convers. Manag., vol. 43, no. 9–12, pp. 1149–1163, Jun. 2002, doi: 10.1016/S0196-8904(02)00005-5.

[27] A. Valero and A. Valero, “Exergoecology: A thermodynamic approach for accounting the Earth’s mineral capital. The case of bauxite-aluminium and limestone-lime chains,” Energy, vol. 35, no. 1, pp. 229–238, 2010, doi: 10.1016/j.energy.2009.09.013.

[28] A. Valero and A. Valero, Thanatia: the destiny of the Earth´s mineral resources. A thermodynamic cradle-to-cradle assessment. Singapore: World Scientific Press, 2014.

[29] A. Valero, A. Valero, and J. Gómez B., “The crepuscular planet. A model for the exhausted continental crust,” Energy, vol. 36, no. 6, pp. 694–707, 2011, doi: 10.1016/j.energy.2010.07.017.

[30] A. Valero, A. Agudelo, and A. Valero, “The crepuscular planet. A model for the exhausted atmosphere and hydrosphere,” Energy, vol. 36, no. 6, pp. 3745–3753, 2011, doi: 10.1016/j.energy.2010.07.017.

[31] D. P. Cox and D. A. Singer, “Mineral deposits Models.” U.S. Geological Survey Bulletin, Denver, USA, p. 400, 1992.

[32] A. Valero, A. Valero, and A. Domínguez, “Exergy Replacement Cost of Mineral Resources,” J. Environ. Account. Manag., vol. 1, no. 2, pp. 147–158, Jun. 2013, doi: 10.5890/JEAM.2013.05.004.

[33] J.-L. Palacios, G. Calvo, A. Valero, and A. Valero, “The cost of mineral depletion in Latin America: An exergoecology view,” Resour. Policy, Jun. 2018, doi: 10.1016/j.resourpol.2018.06.007.

[34] J.-L. Palacios-Encalada, “Beyond a tonnage perspective for the assessment of mineral reources. Focus on Latin America and the Caribbean,” Universidad de Zaragoza, 2019.

[35] A. Garcia, A. Remes, A. Roine, B. Karki, D. Vilaev, and D. Sherstha, “HSC Chemestry 9.” Outotec, 2018.

[36] J.-L. Palacios, I. Fernandes, A. Abadias, A. Valero, A. Valero, and M. A. Reuter, “Avoided energy cost of producing minerals: The case of iron ore,” Energy Reports, vol. 5, 2019, doi: 10.1016/j.egyr.2019.03.004.

[37] J. Palacios, A. Abadias, A. Valero, A. Valero, and M. A. Reuter, “The energy needed to concentrate minerals from common rocks: the case of copper ore,” Energy, vol. 181, pp. 494–503, 2019, doi: 10.1016/j.energy.2019.05.145.

[38] J. Palacios, A. Abadias, A. Valero, A. Valero, and M. A. Reuter, “Producing metals from common rocks : The case of gold,” Resour. Conserv. Recycl., vol. 148, no. February, pp. 23–35, 2019, doi: 10.1016/j.resconrec.2019.04.026.

[39] B. A. Wills and T. Napier-Munn, Will’s Mineral Processing Technology: An introduction to the practical aspects of ore treatment and mineral, no. October. 2006.

[40] W. J. Rankin, Minerals , Metals and Sustainability. Collingwood, Australia: CSIRO, 2011.

[41] J. Cannell, “Geology, Mineralization, Alteration, and Structural Evolution of the El Teniente Porphyry Cu-Mo Deposit,” Econ. Geol., vol. 100, no. 5, pp. 979–1003, Aug. 2005, doi: 10.2113/100.5.979.

[42] Xstrata Canada Corporation, “Mineral Resources and Mineral Reserves, Collahuasi Copper Mine, Tarapacá Region, Chile,” 2011.

[43] R. A. Padilla Garza, S. R. Titley, and F. Pimentel B, “Geology of the Escondida Porphyry Copper Deposit, Antofagasta Region, Chile,” Econ. Geol., vol. 96, no. 2, pp. 307–324, Mar. 2001, doi: 10.2113/GSECONGEO.96.2.307.

[44] COCHILCO, “Sulfuros primarios: desafíos y oportunidades,” 2017.

[45] F. Hervé, M., Sillitoe, R., Wong, C., Fernández, P., Crignola, F., Ipinza, M., Urzúa, “Chapter 3: Geological Overview of the Escondida Porphyry Copper District, Northern Chile,” Soc. Econ. Geol., no. Inc. Special Publication 16, pp. 55–78, 2012.

[46] F. Padilla-Garza, R.A., Titley, S.R., Pimentel, “Geology of the Escondida Porphyry Copper Deposit, Antofagasta Region,” Econ. Geol., vol. 96, pp. 307–324, 2001.

[47] V. Alexandrov, “Impactos Geológicos en el Grado de Liberación de los Sulfuros de Cobre en el Procesamiento Mineral de los Pórfidos Cu-Mo, Distrito Escondida, Región Antofagasta,” universidad de Chile, 2016.

[48] E. Cárdenas del Río, “Caracterización Geoquímica y Mineralógica de Alteraciones Hidrotermales en Pórfido Cuprífero Escondida,” Universidad de Chile, 2015.

[49] S. Northey, S. Mohr, G. M. Mudd, Z. Weng, and D. Giurco, “Modelling future copper ore grade decline based on a detailed assessment of copper resources and mining,” Resour. Conserv. Recycl., vol. 83, pp. 190–201, Feb. 2014, doi: 10.1016/J.RESCONREC.2013.10.005.

[50] M. E. Schlesinger, M. J. King, K. C. Sole, and W. G. Davenport, Extractive Metallurgy of Copper. ELSEVIER, 2011.

[51] E. W. Lindroos and C. U. Keranen, “5. Plants Using Flotation in the Concentration of Iron Ore,” in SME Mineral Processing Handbook, Volume 2., N. L. Weiss, Ed. New York, USA: Society of Mining Engineers of the American Institute of Mining, Metallurgical, and Petroleum Engine, 1985, pp. 20-22-20–33.

[52] Metso, “Basics in minerals processing,” 2015.

[53] C. H. Pitt and M. E. Wadsworth, “Current Energy Requirements in the Copper Producing Industries,” J. Met., pp. 25–34, 1981.

[54] G. R. Ballantyne and M. S. Powell, “Benchmarking comminution energy consumption for the processing of copper and gold ores,” Miner. Eng., vol. 65, pp. 109–114, 2014, doi: 10.1016/j.mineng.2014.05.017.

[55] D. Gray, T. Cameron, and A. Briggs, “Kevitsa Nickel Copper Mine , Lapland , Finland,” Lapland, Finland, 2016.

[56] G. G. Clow, N. L. Lecuyer, D. W. Rennie, and B. J. Y. Scholey, “Technical Report on the Eagle Mine, Michigan, USA,” Toronto, Canada, 2016.

[57] “Escondida Copper, Gold and Silver Mine, Atacama Desert - Mining Technology.” [Online]. Available: https://www.mining-technology.com/projects/escondida/. [Accessed: 13-Apr-2022].

[58] G. Calvo, G. Mudd, A. Valero, and A. Valero, “Decreasing Ore Grades in Global Metallic Mining: A Theoretical Issue or a Global Reality?,” Resources, vol. 5, no. 4, p. 36, 2016, doi: 10.3390/resources5040036.

[59] W. Zhang, “Optimizing performance of SABC comminution circuit of the wushan porphyry copper mine—a practical approach,” Minerals, vol. 6, no. 4, pp. 1–9, 2016, doi: 10.3390/min6040127.

[60] O. I. Skarin and N. O. Tikhonov, “Calculation of the Required Semiautogenous Mill Power based on the Bond Work Indexes,” Eurasian Min., vol. 1, pp. 5–8, 2015.

[61] R. P. (Ronald P. King, Modeling and simulation of mineral processing systems. Butterworth-Heinemann, 2001.

[62] C. A. Rowland, “Selection of rod mills, ball mills, pebble mills, and regrind mills,” in Design and installation of comminution circuits, A. L. Mular and G. V. Jergensen, Eds. Littleton, Colorado USA 80127: Society of Mining Engineers of the American Institute of Mining, Metallurgical, and Petroleum Engineers, 1982, pp. 393–438.

[63] C. A. Rowland, “Selection of rod mills, ball mills, pebble mills, and regrind mills,” in Mineral Processing Pland Desig, Practice, and Control. Proceedings, A. L. Mular and R. B. Bhappu, Eds. Littleton, Colorado USA 80127: Society for Mining, Metallurgy, and Exploration Inc., 2002, pp. 710–728.

[64] J. Duan, D. Fornasiero, and J. Ralston, “Calculation of the flotation rate constant of chalcopyrite particles in an ore,” Int. J. Miner. Process., vol. 72, no. 1–4, pp. 227–237, 2003, doi: 10.1016/S0301-7516(03)00101-7.

[65] M. C. Fuerstenau, G. J. Jameson, R.-H. Yoon, and EBSCOhost., Froth flotation : a century of innovation. Littleton, Colorado USA 80127: Society for Mining, Metallurgy, and Exploration, 2007.

[66] N. Haque, W. Bruckard, and J. Cuevas, “a Techno-Economic Comparison of Pyrometallurgical and Hydrometallurgical Options for Treating High-Arsenic Copper Concentrates,” XXVI Int. Miner. Process. Congr., no. 17, pp. 1908–1923, 2012.

[67] P. Jose-Luis, A. Abadias, A. Valero, A. Valero, and M. Reuter, “The energy needed to concentrate minerals from common rocks: The case of copper ore,” Energy, vol. 181, 2019, doi: 10.1016/j.energy.2019.05.145.

Modeling of thermal conductivity of concrete by using artificial neural networks approaches

Ana Carolina Rosa [a,b], Alejandro Calderón [c], Carles Mateu [d], Assed Haddad [a], Dieter Boer [b]

[a] Programa de Engenharia Ambiental, UFRJ, Universidade Federal do Rio de Janeiro, Rio de Janeiro, 21941-901, Brazil, e-mail: carolinarosa@poli.ufrj.br, assed@poli.ufrj.br
[b] Department of Mechanical Engineering, University Rovira i Virgili, Av. Països Catalans, 26, 43007 Tarragona, Spain, e-mail: dieter.boer@urv.cat
[c] Department of Materials Science and Physical Chemistry, Universitat de Barcelona, Martí i Franquès 1-11, Barcelona 08028, Spain, e-mail: acalderon@ub.edu
[d] Department of Computer Science and Industrial Engineering, University of Lleida, Lleida, Spain, e-mail: carles.mateu@udl.cat

Abstract:

The energy consumption of buildings presents a significant concern, which has led to a demand for building materials with better thermal performance. For this reason, determining the thermal properties of materials is essential information in the search for more energy-efficient materials. However, many time-consuming characterization experiments associated with high costs are required to ensure high accuracy and precision. Thermal conductivity (TC) is among the most relevant properties, which allows for measuring the material's heat transfer resistance. Due to the impracticality of predicting this thermal property in experimental tests, this study seeks to develop a methodology based on artificial neural networks (ANN) to predict the thermal conductivity of different types of concrete through its chemical composition. This work is broken down into two parts. The first one contains a feedforward backpropagation neural network (Multilayer Perceptron, MLP) to predict TC based on 200 experimental data sets of various types of concrete. Then, a Generative Adversarial Network (GAN) is used to expand the size of the training dataset to improve the performance of the first neural network. Currently, the model is implemented in Python, and different ANN structures varying the number of layers and neurons have been tested to find the best accuracy. The MLP model was developed using two hidden layers containing 200-100 neurons. It performed reasonably well on the training and validation dataset with an RMSE of 0.176, 0.183 W/m-K, and R^2 of 0.98 and 0.96, indicating a remarkable consistency between the predicted and the tested results. Furthermore, early GAN results show that it can generate data with reasonable accuracy with R^2 of 0.7. In the near future, we intend to increase the dataset and improve the model. Furthermore, the outcomes from this model can be helpful for the development of materials required for more energy-efficient buildings, providing quantitative information and helping the decision-makers in the construction sector.

Keywords: Artificial neural networks, MLP, GAN, Building materials, Concrete, Thermal conductivity.

1. Introduction

Due to the constant concern about the energy consumption of buildings, there is a growing demand for building materials to improve thermal performance. Utilizing thermal efficiency materials in the construction sector is necessary as they preserve indoor thermal comfort, despite fluctuations in the outdoor environment conditions [1]. Many building materials, such as concrete, masonry, and specific stones, can also be used as thermal energy storage materials. As energy efficiency relies on the material's thermal properties, an accurate prediction of their properties is vital for optimizing their performance in a building.

Concrete is one of the most used materials in construction and as a thermal energy storage material (TES) due to its unique features, such as high compressive strength, heat capacity, and low cost. However, as its chemical composition can vary significantly, its properties can undergo significant variations. For this reason, and in order to be effective as a TES material, it is crucial to have an ideal composition to ensure that its thermal properties meet the required design specifications [2].

Due to the search for more energy-efficient materials, many studies focus on analyzing the thermal properties of construction materials, such as thermal conductivity. This property is essential when evaluating

the ability to transfer and store heat, which is directly related to finding and developing more energy-efficient materials. Therefore, a predictive model that can accurately estimate the thermal behavior of these materials would be beneficial in optimizing their use. In addition, several areas of engineering have used machine learning to perform data processing and analysis tasks due to its high efficiency.

Machine learning (ML) models can be used to develop such predictive models by learning from large datasets and finding patterns that can be used to make predictions. By incorporating ML, the predictive models can adapt to varying conditions and continuously improve their accuracy, making them a valuable tool in optimizing the performance of building materials [3]. Among the machine learning-based models, the Artificial Neural Network (ANN) is one of the most employed ones to solve complex problems and has various applications in several fields [4], [5]. The importance of ANNs lies in their ability to learn and make decisions based on data, which makes them highly valuable in different areas. ANN is composed of a set of networks of interconnected nodes, which work together to learn complex relationships between a group of inputs and outputs, making them well-suited for predicting some values based on a variety of parameters. In this way, ANNs can be used to solve problems that conventional or other computational methods have difficulties [6].

ANNs provide an alternative method for predicting concrete properties that is faster, cheaper, and more accurate than traditional methods. Although it has been applied to properties prediction, a few papers are progressing on models to determine the thermal properties. Additionally, the papers do not have a generalist model, which only focuses on specific types of concrete. This work intends to fill this gap, and the novelty is the development of a methodology using an ANN model to predict the thermal properties of concrete containing different types of materials such as slag, lightweight and recycled aggregates, fibers, and others. For this methodology, a Neural Network model for predicting thermal conductivity will be developed based on the constituents' composition and the concrete's density. The objective of the developed model is to extend it to other building materials, which can improve the performance and efficiency of these materials, making them more effective and cost-efficient.

2. Background

Concrete is a composite material made of cement, water, and fine and coarse aggregates, which let the designers select the components and create mixtures with distinct physical and chemical characteristics [7]. Adjusting these materials and their quantities allows the properties of both fresh and hardened states to be tailored to achieve the design specifications. For this reason, some works have developed an ANN to predict the properties of concrete. Over the years, ANN has been applied to predict different properties of concrete due to its ability to model complex non-linear relationships. After training the neural network, it can predict concrete properties such as compressive strength, slump, and workability with high accuracy. Many works have been published using different structures of a neural network, such as a backpropagation neural network (BPNN) [8], multilayer perceptron (MLP) [9], and radial basis function neural network (RBNN) [10].

Regarding the property predictions, the mechanical properties are the most evaluated, with compressive strength being the most investigated in different machine learning models. For example, Kandiri et al. estimated the compressive strength using a hybrid model of ANN and salp swarm algorithm [11], Abellán-García trained an MLP model to forecast the compressive strength for a given ultra-high-performance concrete (UHPC) mixture design [12]. Besides that, another work also developed an ANN with a feedforward backpropagation algorithm to predict the slump flow and compressive strength of UHPC while incorporating silica fume, limestone powder, recycled glass powder, and FCC [13].

Although many studies are developing new models to predict the properties of concrete, only a few papers investigated thermal conductivity or other thermal properties. Fidan et al. [14] trained different structures of an ANN model to predict thermal conductivity through five parameters – density, compressive strength, tensile strength, porosity, and ultrasonic pulse velocity. The best solution performance was achieved with a neural network with three layers and the following neurons sequence of 5, 25, and 1 in each layer. Sargam et al. [9] evaluated nine machine learning models, and MLP showed the highest prediction accuracy using the maxout activation function and three hidden layers, each containing 100 neurons. Kurpińska et al. [15] also investigated the influence of varying the number of neurons in the hidden layer to forecast the thermal conductivity of lightweight concrete. The model presented a sigmoid function and a structure with four layers: an input layer with two neurons, the first hidden layer varying from 2 to 12, the second hidden layer ranging from 2 to 17, and the output with one neuron. Kursuncu et al. [16] used ANN and ANOVA to investigate the effect of partial replacement of waste marble powder and rice husk ash instead of fine aggregate and cement into foam concrete. The results indicated ANN as the most adequate to estimate the thermal conductivity. Gence et al. [17] compared two neural networks RBNN and MLP to predict the thermal conductivity of concrete with vermiculite and concluded that RBNN had greater accuracy.

Different types of ANNs have been successfully applied to predict the thermal conductivity of concrete. ANN with a backpropagation algorithm is the most popular method for prediction. In order to show the effectiveness of ANN, some comparative studies have been conducted, as listed in Table 1.

Table 1. Comparative studies of different ANN-based methods to predict thermal conductivity.

Reference	ML method	Concrete	Number of inputs	Number of hidden layers	Neurons of hidden layers	Number of outputs	Number of datasets	Activation function	Evaluation criteria
Sargam et al. [18]	MLP	Concrete containing modern constituent materials	3,5,6,8,9,10,13	3	100 100 100	1	213	Maxout	MAE
Fidan et al. [14]	ANN	Concrete	5	1	5,10,15, 20,25	1	132	Tansig	MAE, MAPE, RMSE, R^2
Kurpińska et al. [15]	Backpropagation NN	Lightweight concrete	2	2	2-12 2-17	1	15	Sigmoid	MSE
Kursuncu et al. [16]	ANN	Foam concrete	-	-	-	1	18	Sigmoid	R
Gencel et al. [17]	Radial basis NN / MLP	Concrete with vermiculite	5	1	3	1	20	Non-linear	RMSE, MSE, R
Lee et al. [19]	Backpropagation NN	Concrete	11	2	20 20	1	152	Sigmoid / linear	MSE, R
Ozel and Topsakal [20]	Backpropagation NN	Construction materials	2	1	1	1	110	-	RMSE, R^2

Besides the literature review, a generic bibliometric analysis was performed to identify the most relevant and influential literature in the research domain of the employment of machine learning to predict the properties of concrete, which can facilitate the identification of critical research gaps and areas for future investigation. To proceed with this analysis, VOSviewer was used. It visually represents the research and enables researchers to find insights into the research domain [21]. Consequently, it can lead to more effective development of prediction models of thermal properties.

In order to evaluate the development of the research regarding property predictions using machine learning, a bibliometric study in the Web of Science database was performed. The following query, "concrete" AND "properties" OR "thermal conductivity" AND "machine learning" OR "artificial neural network" OR "ANN", and

search criteria that were used in this bibliometric study summarized a total of 1508 documents that were published between 2000 and 2023. Then, the overall results were inserted in VOSviewer to analyze the keywords present in each paper's title or abstract, which generated the overlay cluster representing the development of the research over the years (Figure 1).

Figure 1 depicts the trend of integrating machine learning techniques with optimization for property prediction over the years, proving that machine learning models are a very actual research line with great expectations of development in this area. Although the ANNs are dated between 2018 and 2019, they are still being explored due to their effectiveness. Although many works employ ANN to predict mechanical properties, it is possible to observe the investigation of some chemical properties.

Therefore, after the literature and the bibliographic review, we noticed a gap in prediction models regarding thermal properties using machine learning models. This study aims to fill this gap and develop a method to predict the thermal conductivity of concrete. Additionally, we intend to build a model for data augmentation that has been used in many fields.

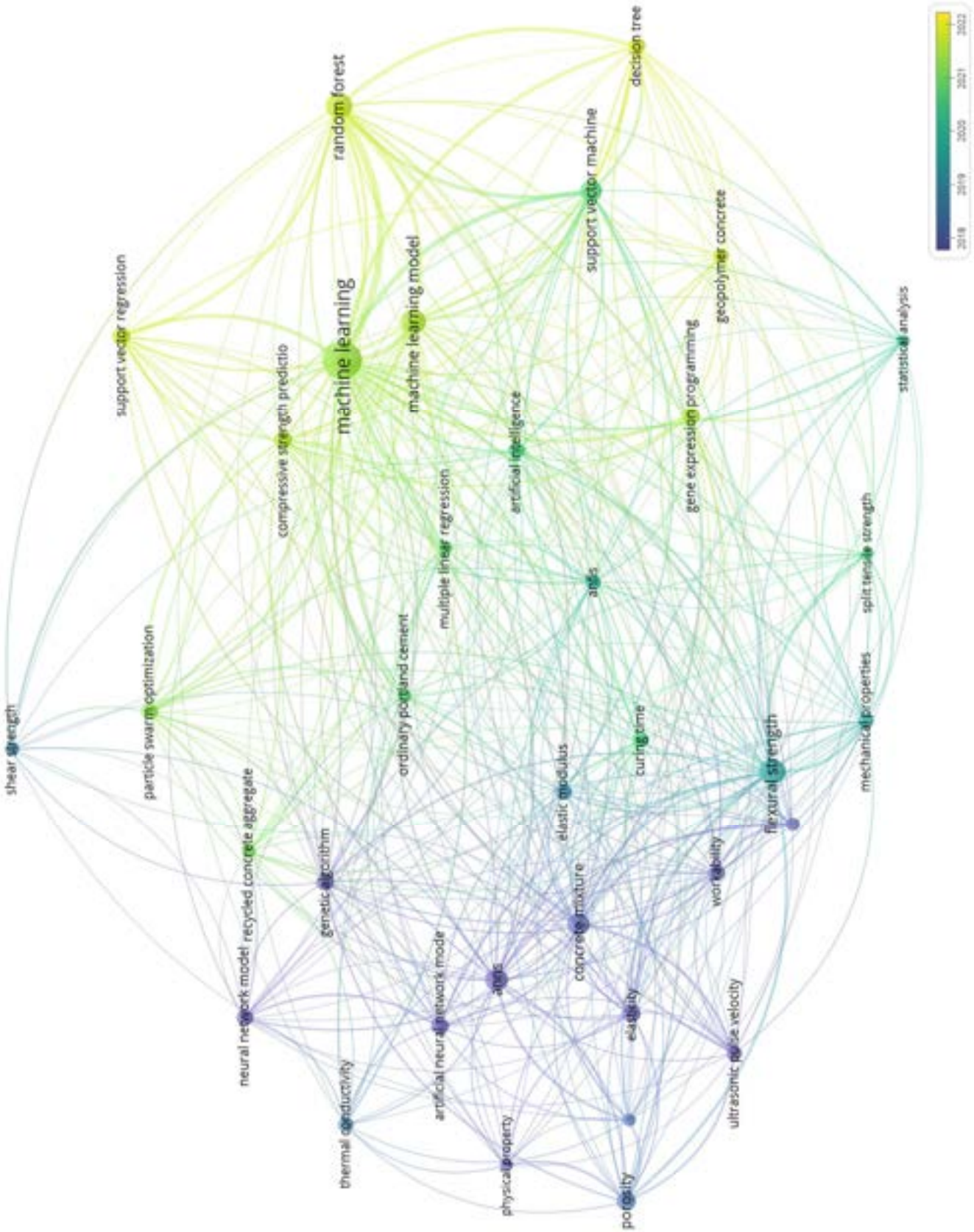

Figure 1. Cluster based on keywords (Overlay visualization).

3. Methodology

The following methodology outlines the development of an ANN model for predicting the thermal conductivity of concrete based on its features, which enables the evaluation of the model potential to foresee this property and shows the efficiency in the prediction speed when compared to the time-consuming experiments, which will provide a reliable model to predict the concrete's thermal conductivity. This methodology is broken down into three steps (Figure 2).

The first one corresponds to the literature review and data collection of a diverse variety of concrete. Collecting the database is the primordial step in building the predictive model, as the ANN will learn from this data. If it presents an inadequate representation of the problem, the model cannot predict the property effectively, thus reducing the model's reliability. Furthermore, for the model to be representative, there must be a sufficiently large amount of data to ensure diversity. In this step, it is necessary to define the dependent and independent variables, that is, to recognize which properties affect the output response of the model. First, the model's inputs and outputs are defined according to the available data and the dependent variables. Then, the available data sets from the literature are organized in a CSV file to develop the ANN model. The second one is related to the general process of building the ANN model to predict thermal conductivity, i.e., the selection of an appropriate neural network architecture for the prediction task, defining the learning rate of the neural network, the number of hidden layers and neurons in each layer, and the metrics to find the best model for the dataset. The last step is analyzing a case study, where the dataset based on previously published works is plugged into the model to evaluate its accuracy. Besides that, a Generative Adversarial Network (GAN) is also developed for data augmentation to improve the model and guarantee a good prediction. Then, both neural networks are implemented to strengthen the final model. Figure 3 summarizes the key steps and the necessary data.

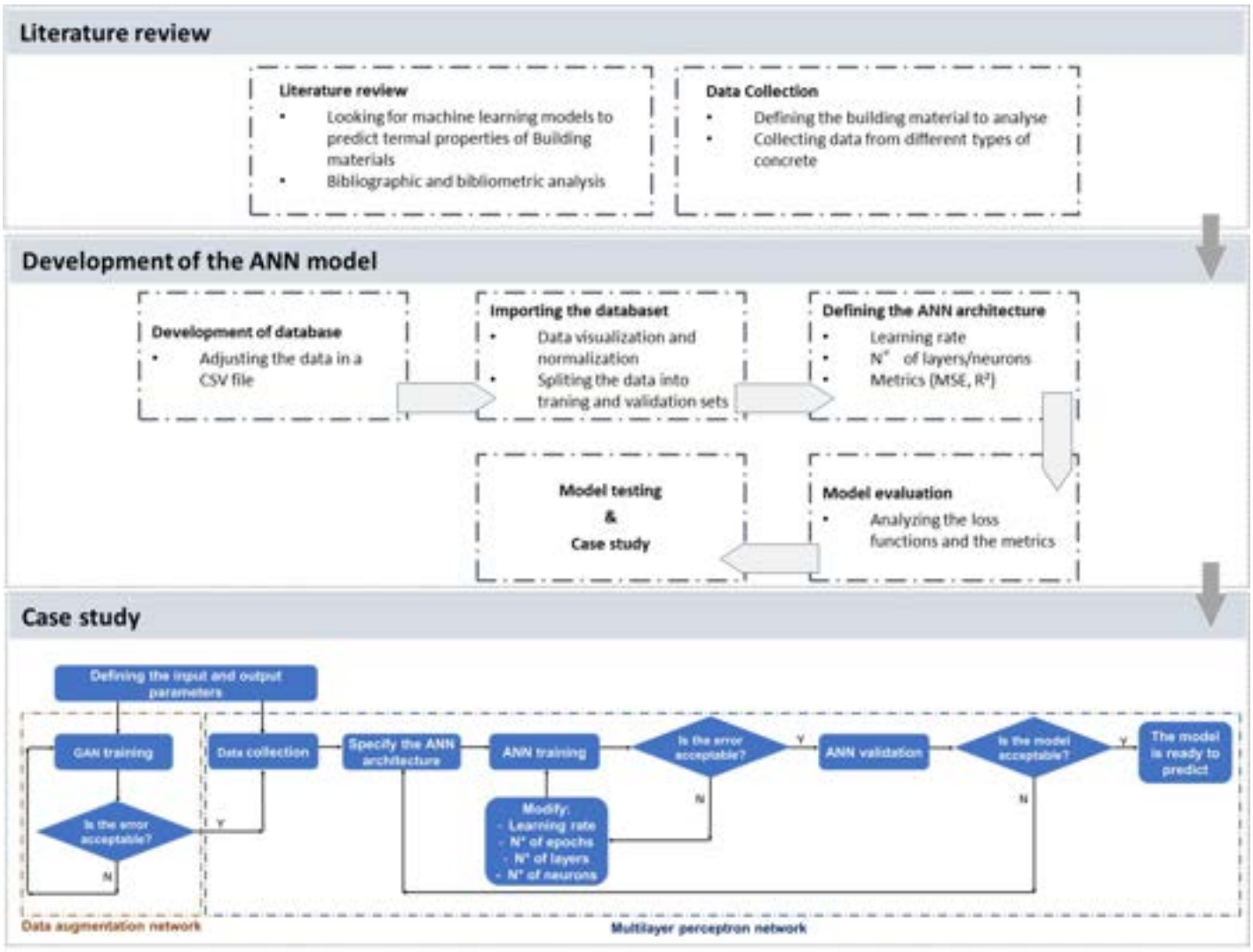

Figure 2. Methodology framework

4. Case study

This case study demonstrates the potential for ANNs to improve the accuracy and efficiency of material property predictions, with important implications for energy-efficient building construction. The case study explores the use of ANNs to predict the thermal conductivity of different types of concrete.

4.1. Database

The database for developing the neural network model was obtained from the literature. This work conducted a comprehensive literature review to create a dataset of 200 points from various relevant articles published in the literature. Furthermore, in order to build an ANN model, data related to the composition and density of each type of concrete were collected and organized to plug into the model. Table 2 presents a sample of the training dataset obtained from the literature.

Table 2. Sample of the training dataset

Density	w/c	Water	Cement	Ceramic powder	Fine agg.	Coarse agg.	Nat. agg.	Fly ash	Silica Fume	Slag	Fiber	Adm.	Splast.	Foam Vol.	TC
1530	0,5	510	1020	0	0	0	0	0	0	0	0	0	0	0	0,6
1530	0,5	510	1020	0	0	0	0	0	0	0	0	0	0	0	0,7
1740	0,33	432	1308	0	0	0	0	0	0	0	0	0	0	0	0,9
1740	0,33	432	1308	0	0	0	0	0	0	0	0	0	0	0	1
2340	0,44	170	387	0	736	1115	0	0	0	0	0	0	0	0	1,1
2340	0,44	170	387	0	736	1115	0	0	0	0	0	0	0	0	1,3
2240	0,49	190	385	0	701	1096	0	0	0	0	0	0	0	0	1,3
2240	0,49	190	385	0	701	1096	0	0	0	0	0	0	0	0	1,4
2260	0,62	183	294	0	701	1236	0	0	0	0	0	0	0	0	1,6
2414	0,62	183	294	0	701	1236	0	0	0	0	0	0	0	0	1,7
1475	0,5	175	350	0	700	250	0	0	0	0	0	0	0	0	1,1
2042	0,5	292	583	0	1167	0	0	0	0	0	0	0	0	0	1,2
1475	0,5	175	350	0	700	250	0	0	0	0	0	0	0	0	1,3
3075	0,5	175	350	0	700	1850	0	0	0	0	0	0	0	0	1,7
1475	0,5	175	350	0	700	250	0	0	0	0	0	0	0	0	1,8
2358	0,48	145	242	0	707	1204	0	60	0	0	0	0	0	0	1,1
2358	0,48	145	242	0	707	1204	0	60	0	0	0	0	0	0	1,1
2358	0,48	145	242	0	707	1204	0	60	0	0	0	0	0	0	1,2
2358	0,48	145	242	0	707	1204	0	60	0	0	0	0	0	0	1,2
2358	0,48	145	242	0	707	1204	0	60	0	0	0	0	0	0	1,3
2349	0,37	161	439	0	621	1128	0	0	0	0	0	0	0	0	1
2349	0,37	161	439	0	621	1128	0	0	0	0	0	0	0	0	1,4

4.2. Artificial Neural Network Model

A neural network is a structure of layers of interconnected artificial neurons, which receive an initial input, process the information, and produce an output. Figure 3 represents a graphical representation of this mechanism. Each input (X_i) is multiplied by the weight (W_i) and summed with each other and added the bias value (b). Then, the result is transferred to the activation function, which adjusts the final output. The essential elements of a neural network are the inputs, outputs, artificial neurons, weights, activation functions, and hidden layers. According to the problem to be solved, these elements are varied until the model obtains outputs closer to the actual values. For example, and the activation functions, there are several possibilities, which are tangent sigmoid (tansig), linear (purelin), tri-angular basis (tribas), radial basis (radbas), and logarithmic sigmoid (logbas) [14]. During training, the complex relationships between the input data and the target values are trained to find specific patterns, and the weights are updated according to the learning technique until the predicted values reach a tolerance limit.

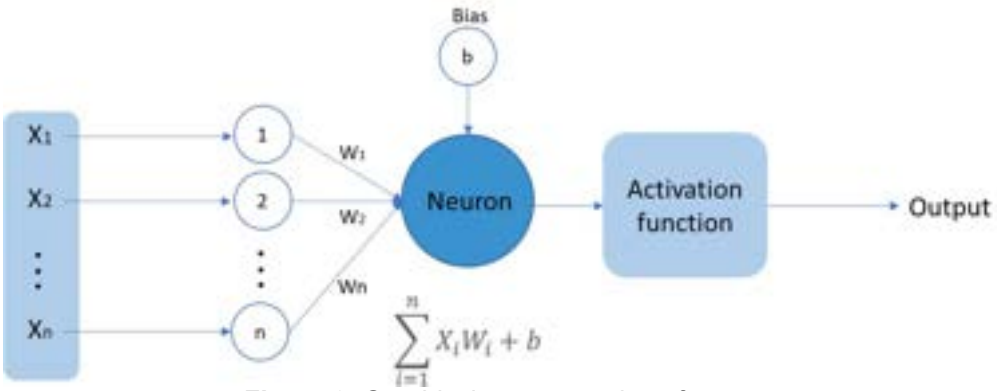

Figure 3. Graphical representation of a neuron

The developed artificial neural network model was built to predict the thermal conductivity of concrete based on chemical properties. To train the ANN with thermal conductivity as the output, this research utilized experimental data reported by previous researchers with thirteen parameters: the water-cement ratio, the unit water weight, the unit cement weight, the unit of ceramic powder, the unit fine aggregate weight, the unit coarse aggregate weight, the unit natural aggregate weight, the unit fly ash weight, the unit silica fume weight, the unit slag weight, the unit fiber weight, the unit superplasticizer weight, and density.

The ANN implemented was a Multilayer perceptron (MLP). It is a feedforward network that consists of an input layer, one or more hidden layers, and an output layer, as shown in Figure 4. Various combinations of network architecture were examined to evaluate the optimum model. The MLP model was built with an input layer with 13 neurons, some hidden layers varying the neurons in each layer, and 1 output layer with 1 neuron. In order to determine the best performance values, different activation functions, neuron numbers, and hidden layers were designed to perform the property prediction. This study tested different activation functions and used the backpropagation algorithm as the learning algorithm because it had been extensively used in previous studies.

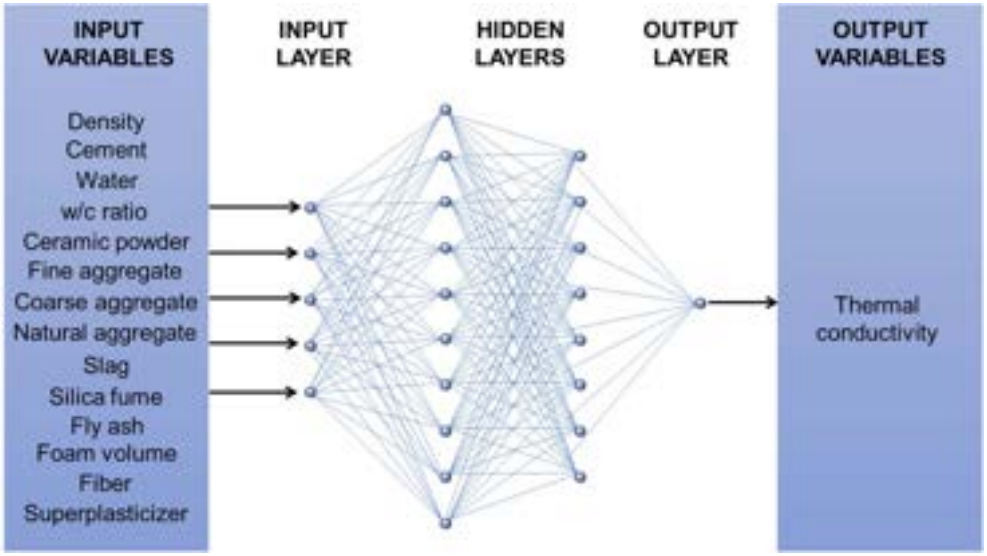

Figure 4. Example of the MLP model

4.3. Generative Adversarial Network

A Generative Adversarial Network (GAN) aims to generate new data based on a real database. The GAN captures the distribution patterns of the real data and creates new examples from this distribution. Its framework comprises two distinct deep neural networks: the generator and the discriminator network, which work together to train the GAN to produce realistic data that are difficult to differentiate between the generated and the data (Figure 5). First, the generator initiates the process, which takes a random noise as an input, creating samples similar to the original dataset. Following this, the discriminator tries to distinguish the data and inform which ones are real or fake. During the training, the generator loss and the discriminator loss are evaluated, allowing the generator to get better and better at producing new artificial data and the discriminator to find if they are real.

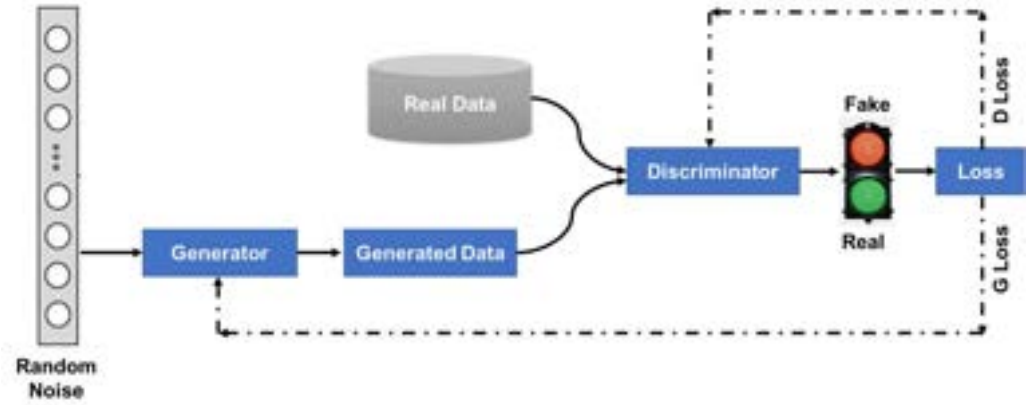

Figure 5. Flowchart of a Generative Adversarial Network (GAN)

5. Results

The first part of this study implemented an MLP model using Fastai, the most updated library to develop neural networks in deep learning. As previously mentioned, the model was developed to predict the thermal conductivity of concrete by utilizing the different compositions and densities as the input parameters.

Firstly, the dataset was plugged into the model and divided into two categories: training (80%), validating, and testing (20%), also used to train the GAN. Then, some features of the model were specified, such as the hyperparameters, metrics, activation, optimization, and loss functions. Table 3 summarizes the main features of this model.

For this study, some hyperparameters were varied during training to achieve the lowest value of the loss function and the highest values of the metrics selected. It used a combination of metrics to compare the model's overall performance. The chosen metrics were the Root Mean Squared Error (RMSE) and the coefficient of determination (R^2); both are frequently adopted to evaluate the prediction quality regarding the variations in the dataset. The learning rate and the number of epochs were kept fixed.

Table 3. Main features of the MLP model

Hyperparameters
Hidden layers = [1, 2, 3, 4]
Batch size = 32
Learning rate = 0.001
Epochs = 40
Metrics
RMSE

R^2
Activation function
ReLU
Optimization function
Stochastic Gradient Descent (SGD)
Loss function
MSE

The numbers of the hidden layers and the neurons have been tested to determine the optimal structure of the ANN model. In order to select the best architecture, it was evaluated the loss function and the metrics. Table 4 displays some of the neural network architecture tested in this work. It can be observed that the best model presents a structure of 2 hidden layers with 200 and 100 neurons, achieving an RMSE of 0.111 W/m.K and R^2 of 0.984 for the training dataset. Regarding the test dataset, the metrics values were 0.183 and 0.96, respectively.

Table 4. Performance indices and metrics of the MLP model

Layers	ANN Architecture	Train Loss	Valid Loss	RMSE	R^2
4	200 – 100	0.083	0.012	0.111	0.984
5	200 – 100 – 50	0.107	0.024	0.155	0.968
5	200 – 100 – 40	0.099	0.037	0.192	0.950
5	200 – 100 – 30	0.087	0.028	0.167	0.960
5	200 – 100 – 20	0.012	0.037	0.191	0.949
6	200 – 100 – 50 – 25	0.102	0.064	0.253	0.918

To the best model evaluated, the loss function versus the number of epochs was analyzed, as seen in Figure 6. Although the number of epochs during the training was set as 40, we can observe the decreasing rate of the loss function over the epochs numbers, and after the setpoint, the loss function tends to be the smallest value in both datasets.

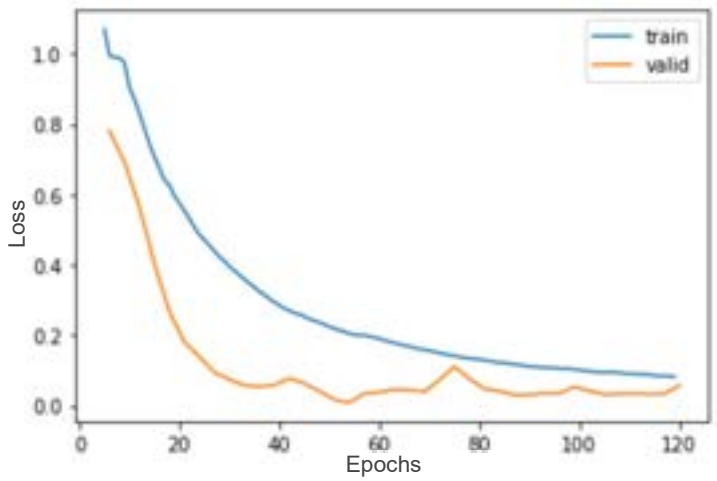

Figure 6. Loss function during the training

Comparing our results with previous works, although the model developed presents an accuracy as high as the other papers, this work brings a greater variety of the constituents of concrete. Fidan et al. [14], using a dataset with 132 entries, developed an ANN with an R^2 performance of 0.996. Sargam et al. [18], the only one to implement a neural network with a larger dataset, presented RMSE and R^2 of 0.117 and 0.964 for the training set and 0.215 and 0.894 for the validation set.

The second part of the study considered the implementation of a GAN for data augmentation. As can be observed in Table 4, increasing the number of layers did not improve the model's learning capacity or performance. If we increase the hidden layers of the model with a small dataset, the model can overfit. For this reason, the metrics and the loss function exhibited higher values. In order to solve this issue, we intend to develop GAN to increase the dataset, creating new synthetic data based on the real data used to develop the MLP model. It will avoid the overfitting process and make the model more robust with extensive dataset training.

This part of the study is broken down into two steps. The first step of GAN training is the generation of a synthetic dataset, and the second is the integration of the MLP and GAN to train the model on both real and artificial datasets. The implementation of GAN used a specific library to create tabular data (Tabgan). The first result showed a promisor result with R^2 of 0.710. The next step of this work will include this new data and verify the performance of the MLP model and if the neural network structure will change.

6. Conclusion

Determining the thermal conductivity of concrete is vital to analyze the thermal behavior of the concrete. Nonetheless, the conductivity value depends on various variables, including composition, porosity, temperature, etc. Thus, a dataset containing the thermal conductivity values of concrete and other parameters related to its composition was developed from published works. This paper proposed a prediction methodology integrating a Multilayer Perceptron (MLP) and Generative Adversarial Network (GAN) models. The first part of the study showed that MLP predictions agree with the thermal conductivity values found in the literature, presenting RMSE and R^2 values of 0.183 and 0.96 for the validation dataset. Therefore, it can be used to predict thermal conductivity with high accuracy. Besides that, the first step of GAN indicated that it could generate reliable synthetic data to be included in the original dataset.

This work is part of a broader effort to develop a methodology for predicting the thermal properties of building materials using ANN. As the contribution of this study, the authors intend to demonstrate the feasibility of the proposed method to predict the thermal conductivity of different types of concrete and show that a GAN model can be used for data augmentation based on a small dataset and present a reliable model. Then, the ultimate goal of this research is to extend the model developed for concrete to other materials, thereby advancing the field of energy efficiency and enabling the development of new energy storage solutions that can meet the growing demands of the future. Additionally, integrating artificial intelligence techniques enhances the intelligence and feasibility of TES systems. By developing models that can predict thermal properties, researchers can improve the performance and efficiency of these materials, making them more effective and cost-efficient. Besides that, the ability to predict the thermal properties of building materials will also facilitate the development of new energy storage solutions that can meet energy demands, ensuring a more sustainable and energy-efficient future for the next generations.

Acknowledgments

The authors would like to acknowledge financial support from the Coordenação de Aperfeiçoamento de Pessoal de Nível Superior (CAPES) - Finance Code 001, Conselho Nacional de Desenvolvimento Científico e Tecnológico (CNPq), Fundação de Amparo à Pesquisa do Estado do Rio de Janeiro (Faperj) 2019-E-26/202.568/2019 (245653), and "Ministerio de Ciencia, Innovación y Universidades" of Spain [PID2021-127713OA-I00, PID2021-123511OB-C32, PID2021-123511OB-C33, PID2021-124139NB-C22 - MCIN/AEI/10.13039/501100011033/FEDER, UE & TED2021-129851B-I00].

References

[1] S. H. Park, J. Chung, M. Souk Yeo, and K. W. Kim, “Evaluation of the thermal performance of a Thermally Activated Building System (TABS) according to the thermal load in a residential building,” *Energy Build*, vol. 73, pp. 69–82, 2014, doi: 10.1016/j.enbuild.2014.01.008.

[2] N. Nwe Htun, S. Sukchai, and S. Hemavibool, “Properties of concrete material for thermal energy storage,” in *International Conference and Utility Exhibition 2014 on Green Energy for Sustainable Development (ICUE 2014)*, N. N. Htun, S. Suckchai, and S. Hemavibool, Eds., Pattaya, Thailand: IEEE, 2014, pp. 1–5.

[3] Z. He, W. Guo, and P. Zhang, “Performance prediction, optimal design and operational control of thermal energy storage using artificial intelligence methods,” *Renewable and Sustainable Energy Reviews*, vol. 156. Elsevier Ltd, Mar. 01, 2022. doi: 10.1016/j.rser.2021.111977.

[4] F. Deng, Y. He, S. Zhou, Y. Yu, H. Cheng, and X. Wu, “Compressive strength prediction of recycled concrete based on deep learning,” *Constr Build Mater*, vol. 175, pp. 562–569, 2018, doi: 10.1016/j.conbuildmat.2018.04.169.

[5] H. Naderpour, A. H. Rafiean, and P. Fakharian, “Compressive strength prediction of environmentally friendly concrete using artificial neural networks,” *Journal of Building Engineering*, vol. 16, no. October 2017, pp. 213–219, 2018, doi: 10.1016/j.jobe.2018.01.007.

[6] Y. Sharifi and M. Hosseinpour, “Compressive strength assessment of concrete containing metakaolin using ANN,” *Journal of Rehabilitation in Civil Engineering*, vol. 8, no. 4, pp. 15–27, 2020, doi: 10.22075/JRCE.2020.19043.1358.

[7] M. A. DeRousseau, J. R. Kasprzyk, and W. V. Srubar, “Computational design optimization of concrete mixtures: A review,” *Cem Concr Res*, vol. 109, no. April, pp. 42–53, 2018, doi: 10.1016/j.cemconres.2018.04.007.

[8] S. R. Salimbahrami and R. Shakeri, “Experimental investigation and comparative machine-learning prediction of compressive strength of recycled aggregate concrete,” *Soft comput*, vol. 25, no. 2, pp. 919–932, 2021, doi: 10.1007/s00500-021-05571-1.

[9] Y. Sargam, K. Wang, and I. H. Cho, “Machine learning based prediction model for thermal conductivity of concrete,” *Journal of Building Engineering*, vol. 34, no. November 2020, p. 101956, 2021, doi: 10.1016/j.jobe.2020.101956.

[10] G. Pazouki, E. M. Golafshani, and A. Behnood, “Predicting the compressive strength of self-compacting concrete containing Class F fly ash using metaheuristic radial basis function neural network,” *Structural Concrete*, no. February, 2021, doi: 10.1002/suco.202000047.

[11] A. Kandiri, E. Mohammadi Golafshani, and A. Behnood, “Estimation of the compressive strength of concretes containing ground granulated blast furnace slag using hybridized multi-objective ANN and salp swarm algorithm,” *Constr Build Mater*, vol. 248, p. 118676, 2020, doi: 10.1016/j.conbuildmat.2020.118676.

[12] J. Abellán-García, “Four-layer perceptron approach for strength prediction of UHPC,” *Constr Build Mater*, vol. 256, 2020, doi: 10.1016/j.conbuildmat.2020.119465.

[13] J. Abellán García, J. Fernández Gómez, and N. Torres Castellanos, “Properties prediction of environmentally friendly ultra-high-performance concrete using artificial neural networks,” *European Journal of Environmental and Civil Engineering*, vol. 0, no. 0, pp. 1–25, 2020, doi: 10.1080/19648189.2020.1762749.

[14] S. Fidan, H. Oktay, S. Polat, and S. Ozturk, “An Artificial Neural Network Model to Predict the Thermal Properties of Concrete Using Different Neurons and Activation Functions,” *Advances in Materials Science and Engineering*, vol. 2019, 2019, doi: 10.1155/2019/3831813.

[15] M. Kurpińska, L. Kułak, T. Miruszewski, and M. Byczuk, “Application of artificial neural networks to predict insulation properties of lightweight concrete,” *Applied Sciences (Switzerland)*, vol. 11, no. 22, Nov. 2021, doi: 10.3390/app112210544.

[16] B. Kursuncu, O. Gencel, O. Y. Bayraktar, J. Shi, M. Nematzadeh, and G. Kaplan, “Optimization of foam concrete characteristics using response surface methodology and artificial neural networks,” *Constr Build Mater*, vol. 337, Jun. 2022, doi: 10.1016/j.conbuildmat.2022.127575.

[17] O. Gencel, F. Koksal, M. Sahin, M. Y. Durgun, H. E. Hagg Lobland, and W. Brostow, “Modeling of thermal conductivity of concrete with vermiculite by using artificial neural Networks approaches,” *Experimental heat transfer*, vol. 26, no. 4, pp. 360–383, 2013, doi: 10.1080/08916152.2012.669810.

[18] Y. Sargam, K. Wang, and I. H. Cho, “Machine learning based prediction model for thermal conductivity of concrete,” *Journal of Building Engineering*, vol. 34, Feb. 2021, doi: 10.1016/j.jobe.2020.101956.

[19] J. H. Lee, J. J. Lee, and B. S. Cho, “Effective Prediction of Thermal Conductivity of Concrete Using Neural Network Method,” *Int J Concr Struct Mater*, vol. 6, no. 3, pp. 177–186, Sep. 2012, doi: 10.1007/s40069-012-0016-x.

[20] C. Ozel and A. Topsakal, “Comparison between ANFIS and ANN for estimation of the thermal conductivity coefficients of construction materials,” 2015. [Online]. Available: www.scientiairanica.com

[21] H. Xu *et al.*, “Application of Artificial Neural Networks in Construction Management: A Scientometric Review,” *Buildings*, vol. 12, no. 7. MDPI, Jul. 01, 2022. doi: 10.3390/buildings12070952.

Exergy cost associated with polymers recycling in vehicles: from qualitative to quantitative indicators

Sofia Russo[a], Alicia Valero[b], Marta Iglesias-Émbil[c], Ricardo Magdalena[d] and Abel Ortego[e]

[a] *CIRCE Institute, Universidad de Zaragoza, Spain, srusso047@gmail.com*
[b] *CIRCE Institute, Universidad de Zaragoza, Spain, aliciavd@unizar.es*
[c] *SEAT-SA, Martorell, Spain, marta-esther.iglesias@seat.es*
[d] *CIRCE Institute, Universidad de Zaragoza, Spain, rmagdalena@unizar.es*
[e] *CIRCE Institute, Universidad de Zaragoza, Spain, aortego@unizar.es*

Abstract

Implementing a recycling route for vehicle plastics surely represents a challenging mission for a company. In general, the recyclability of automotive plastic is influenced by the nature of the polymer (i.e. the material cannot be recycled or recycling would cause deterioration of its properties) or by the lack of an industrial recycling system. In general, there are several technological and economic barriers that must be overcome through design innovation and logistical measures. Based on these factors, an arbitrary scale has been first developed to translate the qualitative indicators into a numerical score that can be useful for comparing different plastic components in a vehicle. Then, the various indicators have been translated in exergy terms, for giving an idea of the order of magnitude of the resources invested in developing the recycling process. Therefore, a new methodology for including critical recycling factors in the total exergy recycling cost is here presented.

Keywords

Exergy, Resource assessment, Recycling, EoL vehicles, Eco-design

1. Introduction

The correct final disposal of End-of-Life Vehicles (ELVs) is still a crucial worldwide issue. At European level, many directives have been implemented in order to regulate the materials used in vehicles and the steps of their end of life (i.e. depollution, dismantling, shredding, and landfill). In particular, the EU Directive 2000/53/EC has set the recycling/recovery target for vehicle to 85% by 2006 and 95% by 2015. This means that from 2015, recovery requirements should achieve the target of at least 95% (with a maximum energy recovery of 10%) and a minimum of 85% of the total material must be reusable and recyclable. The compliance of the EU Directive has been accompanied by a changing in the material composition of cars. According to the EU 2000/53/EC definitions, reuse means “any operation by which components of ELVs are used for the same purpose for which they were conceived”, while recycling means “the reprocessing in a production process of the waste materials for the original purpose or for other purposes but excluding energy recovery”. In this view, plastic materials comply with this standard, since they are theoretically reusable and recyclable. Moreover, their low cost and weight make them even more appealing for cars manufacturers. As a consequence, in the last 10 years, the percentage of plastic in vehicle increased, being the reduction in weight also justified by a decrease in fuel consumption [1]. The current amount of plastic is between 15-17% of the car total weight and 50% of its volume [2]. Currently, the 10% of the global European demand of plastic is for the automotive sector [3][4]. In the last 15 years, an impressive enhancement of End of Life Vehicles (ELVs) occurred, due to the shortening of the cars average life, estimated in 10-12 years [5]. According to a survey delivered by the EU commission [6], the ELVs legally deregistered produce every year between 7 and 8 million tonnes of wastes; anyway, considering also the number of estimated ‘unknown whereabouts’ vehicles, the total increase to 13-15 million tonnes of wastes. Apart from sporadic cases, plastics in ELVs are not recycled. During the pre-shredding phases of depollution and dismantling, the amount of plastic that can be ‘incidentally’ reused (e.g. tyres, bumpers, tanks) does not exceed 25% of the total [7]. Considering an average weight of vehicle of 1250 kg, it means that 150 kg of mixed plastics per

vehicle are discarded, shredded and ultimately landfilled. Therefore, only in EU about 2 millions of tonnes of plastic are dispersed every year due to the automotive sector, approximately 4 kg per person. For comparison, the average production of plastic packaging per year in EU is 31 kg per person [8]. The fact that plastics in vehicle are merely reused or recycled leads to ah huge dispersion of resources. An estimation of the resources embodied in the polymeric content of the ELVs has already be presented in Russo et al. [9], where the concept of Embodied Exergy (EE) is used for assessing the material and energy consumption in each step of polymers production and recycling routes. It resulted that, for the analysed vehicle, about 18.3 GJ of exergy are embodied in the plastic content, only considering the polymers processing and feedstock contribution.

1.1 Recycling practices

The inclusion of recycling in the automotive sector can follow various paths, which can be eventually linked in a closed-loop vision: (i) recycling of plastics to be used in non-automotive applications (i.e. open-loop recycling); (ii) recycling of plastics to be re-integrate in vehicle components (i.e. closed-loop recycling); (iii) integration of recycled plastic from other waste sources, e.g. municipal solid waste (i.e. reverse open-loop recycling. The more diffused practice is the integration of recycled plastic from external sources [10]. However, between the recycling schemes, the closed-loop might assure a predictable and secure source of material, overcoming the problem of scarcity in recycled plastic supply. The recycled material can be used for the same component fabrication or for lower mechanical performance applications. In fact, since mechanical recycling always leads to partial degradation of polymer mechanical properties, solutions have to be adopted. The options are the blending with virgin plastics or the incorporation of additives.

1.2. Recycling issues

Implementing a recycling path for vehicle plastics surely represents a challenging mission for a company. In general, the recyclability of automotive plastic is influenced by the nature of the polymer (i.e. the material cannot be recycled or the recycling would lead to deterioration in its properties) or by the lack of an industrial recycling system. Therefore, there are a series of technological and economic barriers that must be overcome by design innovation and logistic measures**.** A list of the main limits and issues of recycling is reported below.

- ***Compatibility of polymers.*** Nowadays, vehicles contain from 20 to 40 types of polymers [11]. Different polymeric materials are often incompatible at the time of recycling. Mixing of incompatible plastics leads to a recycled material with degraded properties, that cannot be re-used for the same noble application; the tolerance rarely exceeds 2% of contaminants in a mixture; compatibility can change according to the types of polymers [12]. Vehicle parts are practically always made of more than one plastic, but many times this is due to aesthetic reasons. This is the case of the polymer-based surface coatings, films or paint, which are included for obtaining the textile or leather appearance to plastics. Even if the use of compatibility additives is lately gaining attention in recycling practice [], they still represent an extra cost for recyclers and are generally not used, aside from antioxidants.

- ***Use of additives and fillers.*** Additives and fillers are incorporated into the polymers for enhancing mechanical characteristics, strength, fire resistance and for colouring. Additives can hinder the recycling for several reasons: health hazards due to presence of heavy metals and halogens (Br, Cl, F) or incompatibility of different flame retardants; impossible separation of fibres (glass or natural) from the polymer; lack of information on additive composition, which makes impossible the plastic sorting. It is not easy to find information on the degree of tolerance of additives in the recycling process. The fact that many of them are not declared means that the resulting polymer composition is unclear. In addition, given the wide use of additives, the combinations can be multiple and the final composition very varied. For each case, experimental studies must be carried out to quantify the degradation of the material and its possible re-use for different applications. In general, many types of additives migrate from one polymer to another during recycling []. For the purposes of this paper, we will focus on the declared additives found in large quantities in vehicle components: glass fibres, talc, titanium and carbon oxides. The objective is to find out the tolerance range of these additives in the recycling process. The benchmark studies used are as follows. In [13], Pegoretti et al. describe the various recycling alternatives (i.e. mechanical recycling, use of recycled matrices, use of

recycled fibres, use of waste composites, chemical recycling) and provide a literature review on various recycling processes of reinforced polymers. It is highlighted that in mechanical recycling processes the percentage of glass fibres never exceeds 40% of the total polymer matrix, while for talc we report examples with samples up to 20%; data on mechanical characteristics of recycled materials are also reported. The study of Scaffaro et al. [14] focuses more on a review of the various recycling processes of carbon and glass-fibre reinforced polymers and the modification of the mechanical characteristics of the material that affect the field of reuse. Among the results, it is highlighted that recycled composites can be reused for the same applications, when the properties do not change much after recycling, or recycled to applications that require less performance. The main disadvantage lies in the loss of fibre structure and length due to fibre size reduction. The need for milling and grinding steps before the remanufacturing process can also increase the operational cost (even non-standard equipment may be required, able to withstand the wear caused by the fibre during milling). Still, the authors were able to obtain compression-moulded panels with good tensile strength and the same flexural properties as virgin composites by adopting a 'sandwich', multilayer configuration in which virgin material was used as the outer layers and recycled material was used as the core layer. By doing so, 50% of the volume of the virgin material could be replaced by recycled material while maintaining good mechanical properties. An experimental estimation of the additional energy required for the recycling process of PET with 30% glass fibres is given in [15]. In [16], the authors analyse the effect of titanium oxide on the plastic matrix up to concentrations of 12%. A general resume of the allowed additives, in the hypothesis of excellent quality of the recycled products is given in [..]; according to this review, flame-retardants, high concentrations of glass fibres (> 10%), vegetable fibres, nano-particles, pigments with heavy metals are totally not tolerated; small fibres concentrations (< 5%) are partially tolerated, while talc, calcium carbonate, barytes and TiO_2 are admitted for recycling. In general, in order to have noble outlets, i.e. with a property loss <5%, the impurity rate during the sorting process must be <3%. As for carbon, no studies have been found that analyse the criticalities in the recycling phase (apart from the problems of optical separation due to the black colour), so a good tolerance is assumed.

- ***Recycling volumes and dismantling time***. In order to make the recycling process economically viable, consistent recycling volumes of the same polymer have to be achieved. In fact, the investment in dismantling operations must be offset or exceeded by revenues from the sale or reuse of dismantled plastics. Polymer recovery for recycling can take place both upstream and downstream of shredding phase. The degree of precision in polymer recovery at the 'pre-shredding' stage determines the extent and therefore the cost of the dismantling stage. The number of different polymers and vehicle subcomponents, the compatibility of polymers in recycling and the presence of mechanical or adhesive connections between parts of different materials are the influencing factors of the dismantling time. For evaluating the dismantling cost, it would be necessary to have empirical data on dismantling operation and to know the type of dismantling methodology (e.g. manual, mechanized). The energy and monetary cost of the labour could then be accounted with various methodology. As an example, Sciubba et al. [17] have included labour and capital in the exergy assessment.
- ***Supply stability and lack of market demand.*** One of the major limits of plastic recycling is the lack of an industrial and well-assessed market for recycled materials. The relative low-cost of virgin plastic material is still a barrier to the development of a circular economy of plastics, since the costs of installing a new recycling plant is not compensated by the revenues. As consequence, often the companies have doubts about including recycled plastics, because of the concerning of not having stable supply.

1.3. Aim of the analysis

The aim of the present work is to assess methodologies for evaluating the recyclability of polymers in vehicles, including all the factors that influence the process and giving an order of magnitude of the exergy cost associated to recycling of EoL vehicle components. In order to do that, a first qualitative analysis is developed for assessing all the recyclability crucial factors, followed by a translation of some of them into exergy terms.

2. Methodology

2.1. Recyclability table

First, based on the critical factors expressed above, an arbitrary scale (Table 1) has been developed to translate the qualitative indicators into a numerical score that can be useful to compare different polymeric vehicle components. The number of polymers and subcomponents and the compatibility of polymers in recycling influence the dismantling time; the compatibility of additives and fillers in recycling and the presence of adhesives or coatings influence the effective recycling of the polymers, while the compatibility in density separation has an effect on the post-shredding recovering. The scale is arbitrary, decided after empirical attempts in comparing resulting scores for different components. In fact, the main goal is to quantify the qualitative characteristics influencing recyclability and to compare different vehicle parts. For this work, data on vehicle plastic composition have been provided by Seat-SA for a 350 Seat Leon. Four components have been chosen for the analysis: rear bumper, dashboard, floor covering and rear seats. The analysis of vehicle components starts with the identification of the main polymeric materials (present in quantities higher than 1 g) and the main subcomponents containing them. If the same polymer is present but containing different additives, it counts as a different polymer. Resins, adhesives and not-declared additives are not included in the computation of polymers. Then, the recyclability table factors have been identified and a total score from 0 to 5 is assigned to each category. For the compatibility indicators, the main polymers (i.e. the polymers that embodied the majority of the weight) are taken as reference; a weighted average is calculated for assigning the final score, considering that the presence of recycling technologies has a relatively higher importance than the other factor (weight percentages are reported in Table 1). Obviously, this procedure is not based on an absolute criterion, but it is based on common practice and empirical considerations.

Table 1 – Recyclability table for score assigning according to critical factors

	Score	0	1	2	3	4	5
A	**Number of main polymers:** polymeric materials present in quantities higher than 1 g are identified [10%]	≥8	7	6	5	4	≤3
B	**Number of main subcomponents**: only subcomponents containing polymers are considered [10%]	≥16	13-15	10-12	7-9	4-6	≤3
C	**Compatibility of polymers in recycling:** mean value based on the main polymer compatibility with each of the others [10%]	If not compatible		2.5 If limited compatibility for moderate quantities			If 100% compatible
D	**Compatibility of additives and fillers in recycling:** mean value based on the main polymer compatibility with their additives [10%]	Prohibited additive	>60%wg	40-60%wg	20-40%wg	≤20%wg	No additive
E	**Compatibility in density separation:** mean value based on the main polymer compatibility [10%]	Overlapping densities					No overlapping densities
F	**Presence of coatings:** paint and skin can be present and should be chemically removed [10%]	Prohibited coatings	On the main polymer (main part)	On the main polymer (secondary parts)	On the other polymers (main part)	On the other polymers (secondary parts)	No coatings
G	**Presence of adhesives:** adhesives in high quantities can hinder the recycling [10%]	Prohibited adhesives	On the main polymer (main part)	On the main polymer (secondary parts)	On the other polymers (main part)	On the other polymers (secondary parts)	No adhesives
H	**Presence of recycling technologies** for the main polymer for the same application (closed loop) [30%]	No recycling technologies		2.5 If limited technologies are present			Well developed recycling technologies

2.2. Exergy cost of recyclability

The score may be important for a first comparison, but it does not give an idea of the order of magnitude of the energy and resources invested to develop the recycling process. For this reason, the attempt has been trying to translate some indicators using exergy. The initial idea is that all indicators express characteristics that make recycling more difficult and consequently more expensive in terms of resources and money. The recycling routes assessed in [10] referred to 'standard' recycling process, namely they refer to basic polymers (those generally used for packaging), without additives or in percentages compatible with recycling. Due to the lack of information on the effective additional energy burden associated to vehicle dismantling, polymer separation and recovering and coatings and adhesives removal, the analysis has been focused on the recycling of polymers with additives and fillers. According to the review presented in Section 1.2., a set of rules has been chosen as reference for evaluating additives presence in vehicle components and hypothesis of recycling, as presented in Table 2. No declared additives in plastic components are generally lower than 5%, even if it is not possible to know their composition. Concentrations higher than the ones reported in Table are supposed to be not allowed. Therefore, three recycling scenarios are analyzed; every scenario is analyzed in terms of Embodied Exergy in the operations of dismantling of the old vehicle polymeric component and making of the new one, as follows.

Table 2 – Admitted additives and recycling options

Additive		**Recycling**
Talc <20%	Admitted	Polymer 100% recycled
Titanium Dioxide <15%	Admitted	Polymer 100% recycled
Glass fibers <5%	Admitted	Polymer 100% recycled
Glass fibers 5%<GF<40%	Partially admitted	Multilayer - Polymer 50% recycled 50% virgin
No declared additives >5%	Partially admitted	Multilayer - Polymer 50% recycled 50% virgin

- **1st scenario: No recycling.** In case of no recycling all the EE of the polymers in the vehicle component is lost and it is necessary the same amount of EE for remanufacturing them
- **2nd scenario: Recycling only the main polymers in closed-loop,** according to the limitations and the recycling options reported in Table 2. The other polymers are reintroduced as new, so their EE is lost; in case of multilayer configuration, also the EE of the 50% of polymer is lost. The same amount of EE is necessary for remanufacturing them.
- **3rd scenario: Recycling the main polymers in closed-loop and inclusion of recycled polymers from open loops,** according to established markets**.** The EE of the replaced polymers is lost but less exergy is required for their new production, since they come from recycling routes.

In all three cases, the total EE (EE_{tot}) is taken as comparison indicator, being the sum of the EE lost (EE_{lost}) within the old vehicle component and the EE necessary for its new production ($EE_{new\ prod}$), Equation 1.

$$EE_{tot} = EE_{lost} + EE_{new\ prod} \quad (1)$$

In order to perform the calculation the values of EE associated to polymers production and recycling reported in Table 3 are considered [10]. The EE values of production refer to the process only (i.e. from naphtha steam cracking to polymerization), without including the feedstock part or the exergy replacement cost of fuel in the environment. The EE values of recycling refer to standard recycling processes found in literature. The values of EE_{lost} and $EE_{new\ prod}$ were then calculated as the sum of the products of the EE of polymers for the respective quantity in the vehicle part

Table 3 – Production and recycling Embodied Exergy

Polymer	**EE of production (MJ/kg)**	**EE of recycling (MJ/kg)**
PP	39	3
PE	24.3	3
EPM	32.3	11.4
PVC	25.5	1.1
PU	41	5.3
PA	59.3	10.3
PET/PES	51.2	4
SBR	73	11.4
EPDM	55.9	11.4
ABS	69.8	2.3
PC	48.8	3
PMMA	48.8	3

3. Results

3.1. Qualitative indicators

First, the material composition of the four plastic components have been analyzed, mapping the distribution of polymers among the subcomponents. Results are reported in Tables 3-6. If the same polymer is present with different additives, it counts as a different polymer.

Table 3 – Plastic composition and distribution in rear bumper

Rear bumper					
Sub-component	**Material**	**g**	**Additive**	**g**	**TOT**
Main bumper part	PP	2627.3	ND 5%	175.2	2802.5
Diffuser	EPM	725.6	Talc 12%	83.5	809
Mobil guides	EPM	212	Talc 12%	24.4	236.4
Hook cover	EPM	7.5	Talc 12%	0.86	8.4
Screws	PA66	1.9	ND 1.5%	0.03	1.93
Soundproofing	PET	39.6	Titan Dioxide 1%	0.3	39.9
Plaque cover	EPM	464	Talc 5%	53.4	517.4
	PE foam	18.9			18.9
LED housing	PC	12	ND 1.5%	0.2	12.2
Lens	PMMA	4	ND 0.25%	0.1	4.1
Catadioptric lampshade	PMMA	36.4	ND 2%	0.7	37.1
Catadioptric housing	PC+ABS	26.8	ND 1%	0.3	27.1
TOTAL		**4175.9**		**339**	**4514.9**

	PP	**EPM+Talc**	**PMMA**	**PET**	**PC+ABS**	**PE**	**PC**	**PA66**
Tot (g)	2802.5	1571.2	41.2	39.9	27.1	18.9	12.2	1.93
% on total plastic wg	**62.1**	**34.8**	**0.9**	**0.8**	**0.6**	**0.4**	**0.3**	**0.1**

Table 4 – Plastic composition and distribution in dashboard

Dashboard					
Sub-component	**Material**	**g**	**Additive**	**g**	**TOT**
IP Carrier	PP	1106	GF 60%	1843.2	2949.2
	PVC flexible	511.6	ND 6%	62.1	573.7
	PU foam	604.8	ND 1%	6.1	610.9
	PET fibre	6.6			6.6
Airbag bracket	PP	170.4	GF 36%	284	454.4
Central defrost	PP	480.5	Talc 25%	166.9	647.4
IP upper defrost cover	EPM	699.8	GF 25%	243	942.8
Double DIN carrier	PP	257.7	GF 60%	429.5	687.2
Panel drivers lower	EPM	178.2	Talc 15%	32.6	210.8
Panel passenger lower	EPM	144.8	Talc 15%	26.5	171.3
Light switch support	PP	38.4	Talc 25%	13.35	51.75
Kombi support	PP	65.7	GF 60%	65.7	131.4
Manifold Air Distribution	PP	155	Talc 25%	53.8	208.8
Air canal	PE	380.6	ND 1%	2.4	383
Defrost canal	PE	237.6	ND 1%	1.7	239.3
Gasket	PU	1.2	ND 3%	0.03	1.23
Side defrost	EPM	18.2	Talc 15%	3.45	21.65
TOTAL		5057.1		3234.3	**8291.4**

	PP+GF	**PP+Talc**	**EPM+GF**	**PE**	**PU**	**PVC**	**EPM+Talc**	**PET fibre**
Tot (g)	4222.2	907.95	942.8	622.3	612.1	573.7	403.75	6.6
% on total plastic wg	**50.9**	**10.9**	**11.4**	**7.5**	**7.4**	**6.9**	**4.8**	**0.2**

Table 5 – Plastic composition and distribution in floor covering

Floor covering					
Sub-component	**Material**	**g**	**Additive**	**g**	**TOT**
Floor carpet	SBR	48.6	GF 65%	105.2	161.9
			ND	8.1	
	PET fibre	1391	ND 1%	14.05	1405.1
	PE powder	161.1	ND 0.5%	0.8	161.9
Propylat support	PP fibre	575.5	ND 1%	5.8	581.3
	PET fibre	362.7	ND 1%	3.7	366.4
Plastic film	PE	57.2			57.2
Fixing floor carpet	PA66	7.4	GF 30%	3.2	10.76
			ND	0.16	
Cover floor carpet	PA66	8.1	ND 1%	0.12	8.22
TOTAL		**2611.6**		**141.3**	**2752.7**

	PET fibre	**PP fibre**	**PE powder**	**SBR+GF**	**PE**	**PA66+GF**	**PA66**
Tot (g)	1771.5	581.3	161.9	161.9	57.2	10.8	8.2
% on total plastic wg	**64.3**	**21.1**	**5.9**	**5.9**	**2.1**	**0.4**	**0.3**

Table 6 – Plastic composition and distribution in rear seats

Rear seats					
Sub-component	**Material**	**g**	**Additive**	**g**	**TOT**
PU foam	PU foam	2990.46	ND 1.5%	45.4	3036.1
Seats cover	PU foam	63.4	ND 1.5%	1	64.41
	PET fibre	174.1	ND 2.5%	4.6	178.7
	PES fibre	35.96	ND 0.5%	0.2	36.14
	PU	12,77	ND 1.5%	0.2	12.97
	PES fibre	62,01	ND 0.5%	0.3	62.3
	PU	43.3	ND 1.5%	0.7	43.98
	PES fibre	29.4	ND 3%	0.9	30.3
	PU	29.68	ND 5.2%	1.6	31.3
	PU	7.36	ND 1.5%	0.1	7.5
	PET	35.5	ND 4.5%	1.7	37.2
	PU	20.37	ND 3%	0.6	20.97
	PAN fibre	1.01	ND 0.5%	0.05	1.1
	PES fibre	6.77	ND 0.35%	0.02	6.8
	PET fibre	40.18	ND 0.5%	0.02	40.2
	PU	13.3	ND 1.5%	0.2	13.5
	PES	16.77	ND 0.3%	0.04	16.8
	SBR	3.15			3.15
	PU	13.35	ND 1.5%	0.2	13.55
	PES	6.2			6.2
TOTAL		3605.1		57.95	**3663.1**

	PU foam	**PET fiber**	**PES fiber**	**PAN fiber**	**SBR**
Tot (g)	3244.3	256.1	158.5	1,1	3.15
% on total plastic wg	**88.5**	**6.9**	**4.3**	**0.1**	**0.2**

Then, a score is assigned to each component according to the recyclability table. Results are shown in Table 7, where details on the presence of each indicator are reported. An average value is also calculated. According to this scoring, the best component in terms of recyclability is the rear bumper. More detailed comments are reported below.

Table 7 – Results of application of recyclability table

	Rear bumper		Dashboard		Floor covering		Rear seats	
		Score		**Score**		**Score**		**Score**
A	7	2/5	8	0/5	7	1/5	5	3/5
B	11	1/5	14	0/5	5	4/5	2	5/5
C	PP has a limited compatibility with PC+ABS, PA, PMMA and PET and is not compatible with EPM and PE fiber.	1.7/5	PP has a limited compatibility with PVC and PU. PP compatible with PE and not compatible with EPM and PET fiber.	2/5	PET not compatible with any polymer	0/5	PU foam is not compatible with any polymer	0/5
D	Talc, TiO_2 and not declared additives.	4.5/5	Talc admitted and GF not allowed in this percentage.	2.5/5	GF not compatible in this percentage	4.7/5	Only not declared additives in small percentage are present	4/5
E	PP and EPM not compatible	4/5	PP only compatible with PU, PET fiber and PVC	2.5/5	PET not compatible with PA66	4/5	PP has no overlapping densities with other polymers	5/5
F	TiO_2, PU and acrylic resin	1.5/5	No	5/5	PE powder	1/5	Yes	2/5
G	Soundproofing and cover plate	4/5	PU basket	3/5	Plastic film	4/5	Yes	2/5
H	Limited recycling options for EPM+GF	3.75/5	No options for PP+60GF, limited options for EPM+25GF	3.1/5	No closed loop recycling options	0/5	No closed loop recycling options	0/5
	Average value	**3**		**2.4**		**1.9**		**2.1**

3.1.1. Comments

- **Rear bumper.** The main polymer is PP, even if EPM is present in a consistent amount. These two polymers have overlapping densities, so they should be separated before shredding. This means that the diffuser, the mobile guides, the hook cover and the plaque cover should be removed and processed separately. PP has a limited compatibility with the other polymers, even if the level of impurity in recycling should not exceed 2%. For reducing the impurities, some parts should be removed, such as the lens and the catadioptric or the soundproofing. The possibility of dismantling the various parts of the bumper depends on the facility of removing the adhesives and the mechanical junctions. Coatings are present on the surface of the main PP bumper part in a weight percentage of 3.9%; they should be chemically removed before shredding and recycling.
- **Dashboard.** The main recyclable polymer is PP filled with GF or talc, followed by EPM with GF. Since these two polymers have overlapping densities, they should be separated before shredding. Glass fibres content in these percentages hinders the recycling. Even if PP has a limited compatibility with low volumes of PVC and PU, the quantities of PVC and PU are in the same order of magnitude. Flexible PVC and PU foam are all concentrated in the IP carrier subcomponent and they should be separated and recycled separately, as well as PVC and PET fibre contained in the airbag hinge. PU of the gasket could be eventually processed with PP, since they represent an impurity lower than 2%.
- **Floor covering.** This is a component where polymeric materials are mainly used as textiles. The main burdens are represented by the scarce compatibility of PET and PP fibres, the poor practice in polymer fibres recycling and the presence of PE coatings and films. The main material is PET fibre, which is present in the floor carpet and the propylat support. PET is not compatible with PP fibre so these materials should be separated. PE powder used for coating should be removed. Moreover, SBR and PA filled with these percentages of glass fibres are not compatible for recycling and have to be separated and processed separately. Recycling of PET and PP fibres is scarcely diffused, even if the process is possible and some technologies are available; however, many times these materials are reemployed in secondary application (e.g. filling, insulation). For all these reasons, the recoverable volume for this component is pretty low.

- **Rear seats**
  This is a component where polymeric materials are mainly used as fillers (i.e. foam). The main burdens are represented by the absence of closed loop recycling options for PU foam and the scarce compatibility in recycling PU with other polymers. The only advantages are the few number of polymers and sub-components that facilitates the dismantling and the not overlapping density of PU with the other polymers, for an eventually separation after shredding. PU foam can be reused for secondary applications of filling, even if closed loop practices for vehicle applications are not documented.

3.2 Quantitative indicators

The methodology described in Section 2.2 is then applied to the four components, analyzing the three scenarios. Table 8 reports the results of calculation of the lost and new production EE and the total value with an explication for each component. Values of EE are given in MJ.

Table 8 – Results of calculation of EE for the three scenarios

	1st scenario No recycling			**2nd scenario Recycling only the main polymers in closed loop**			**3rd scenario Recycling the main polymers in closed loop and inclusion of recycled polymers from open loops**		
	EE_{lost}	$EE_{new\ prod}$	EE_{tot}	EE_{lost}	$EE_{new\ prod}$	EE_{tot}	EE_{lost}	$EE_{new\ prod}$	EE_{tot}
Rear bumper	154.5	154.5	**309**	42.9	54	**96.9**	42.9	52.1	**95**
	All the EE of the component is lost, and it is necessary the same amount of EE for reproducing it			PP and EPM are recycled in closed loop; PP is totally recycled since 5% of additives are allowed, while recycled EPM is included in percentage of 20/80 ratio; other polymers are reintegrated as new			PP and EPM are recycled in closed loop as in the 2nd scenario; PET is included as recycled material, so their 'first' EE is lost but less exergy is required for their new production		
Dashboard	175.7	175.7	**351.4**	147.2	150	**297.2**	147.2	57.8	**205**
	All the EE of the component is lost, and it is necessary the same amount of EE for reproducing it			PP and EPM cannot be recycled in closed loop with these percentage of GF. Talc is admitted so PP+talc is totally recycled and EPM+talc is included in 20/80 ratio.			PP with GF is included as recycled material (only PP part). EPM is included as recycled in 20%. PET and PE are included as recycled, but not PU and PVC		
Floor covering	122	122	**244**	-	-	-	122	13.3	**135.3**
	All the EE of the component is lost, and it is necessary the same amount of EE for reproducing it			Closed loop recycling is not assessed for the main polymers (PET fiber); SBR cannot be recycled with this percentage of GF			SBR is partially introduced as recycled material (20/80 ratio), while PET and PP fibers and PE are 100% substituted. PA is always included as new material		
Rear seats	152.2	152.2	**304.3**	-	-	-	152.2	132.9	**285.1**
	All the EE of the component is lost, and it is necessary the same amount of EE for reproducing it			Closed loop recycling is not assessed for the main polymers (PU foam)			PU foam is not reccyled in general; only recycled PET/PES can be included		

A graphical representation of the results is shown in Figure 1, while a comparison between the scenarios is presented in Figure 2. The four components have been chosen because they are examples of different cases that can occur when recycling vehicle parts. As expected, there is always a saving in performing some type of recycling; the amount of saving depends on the polymeric composition. In the rear bumper the difference is evident (- 68.6% in the 2nd scenario), since it is composed mainly of PP, which could be completely recycled, and of EPM which can be included in multilayer configuration. ncluding PET from recycled material in the 3rd scenario leads to a further saving of 2%. The step is less evident for the dashboard; here the main polymers, PP and EPM, are present both with talc and GF. Polymers with GF in these percentages cannot be recycled for closed loop application, so only the polymers with talc can be substituted in the second scenario (-16.8% of EE). PET, PE and the polymeric matrix of PP and EPM with GF can be introduced as recycled material in the 3rd scenario, being the saving more evident (-41.6%). The floor covering is an example of component made mainly of textile; in this case the majority of fibers are of PET and PP. Closed loop fiber recycling is not industrially well assessed, so the second scenario is not analyzed. On the other hand, recycling from plastic to fiber is very common, so recycled fibers can be 100%

substituted leading to a saving in 44.5% in the exergy of new production. Finally, rear seats are an example of component made of filler material (i.e. foam) and fibers. Since PU foam is generally not recycled, 2nd scenario is not analyzed; in the 3rd scenario PU is included as new polymer, so that the savings are not so consistent (-6.3%).

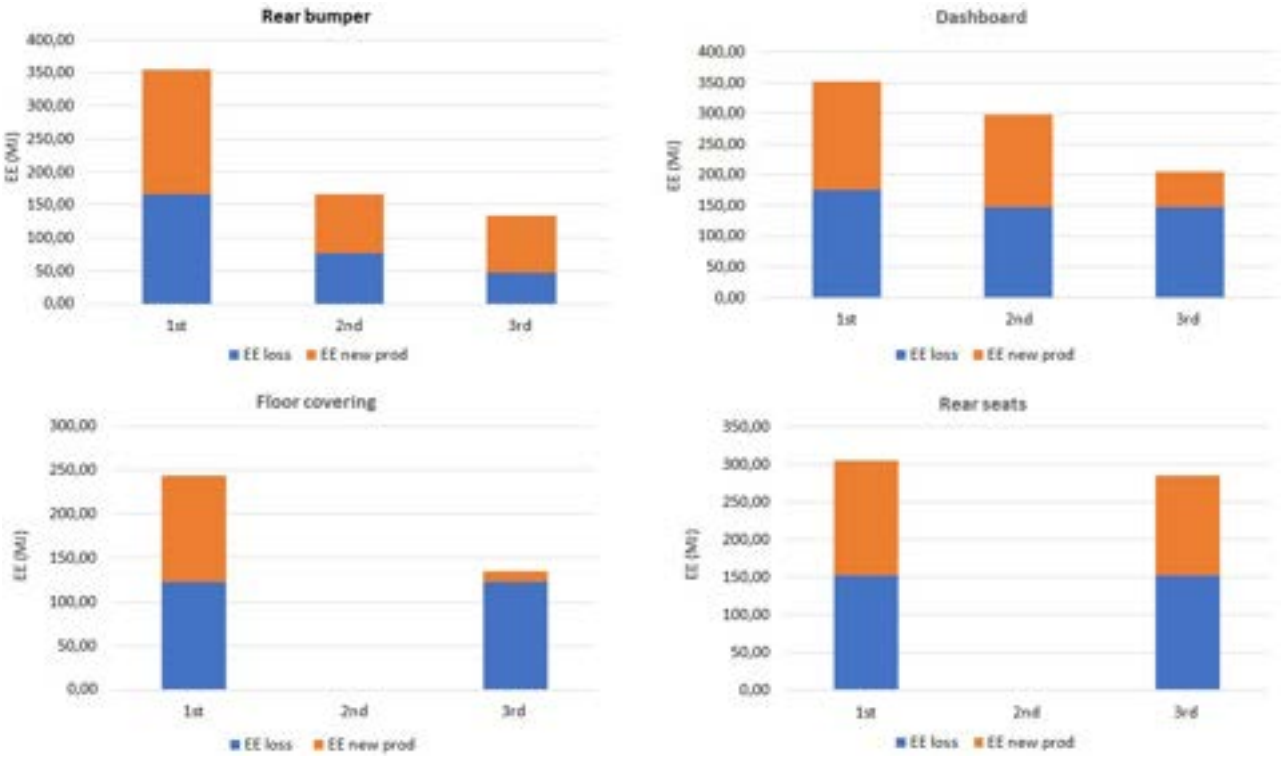

Figure 1 – EE values for the four components in the three scenarios

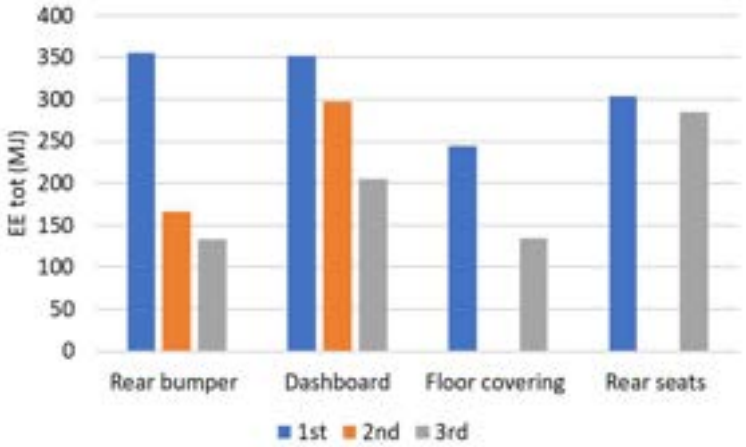

Figure 2 – Comparison between the total EE for the three scenarios

4. Conclusions

The aim of the present work was to assessing methodologies for evaluating the recyclability of polymers in vehicles, including all the factors that influence the process and giving an order of magnitude of the exergy cost associated to recycling of EoL vehicle components. In order to do that, a first qualitative analysis is developed for assessing all the recyclability crucial factors, followed by a translation of some of them into exergy terms. In order to do so, first, based on the critical factors, an arbitrary scale has been developed to translate the qualitative indicators into a numerical score that can be useful to compare different polymeric vehicle components. Then, some of these indicators have been translated using exergy and the values of total EE have been calculated for three recycling scenarios. Results show that, according to the scoring, the best component in terms of recyclability is the rear bumper, due to the high percentage of PP with no additives, while the worst is the floor covering, mainly due to the absence of recycling process for PET fibers. The analysis of the recycling scenarios underlines that savings between 1st and 2nd scenarios are more evident for the rear bumper and floor covering.

[1] Wen Zhang, Jun Xu, Advanced lightweight materials for Automobiles: A review, Materials & Design, Volume 221,2022,110994,ISSN 0264-1275,https://doi.org/10.1016/j.matdes.2022.110994.

[2] Miller, L.; Soulliere, K.; Sawyer-beaulieu, S.; Tseng, S.; Tam, E. Challenges and Alternatives to Plastics Recycling in the Automotive Sector. Materials 2014, 7, 5883–5902.

[3] PlasticEurope. Plastics—The Facts 2020. 2020. Available online: https://www.plasticseurope.org/en/resources/publications/43 12-plastics-facts-2020

[4] CBI Market Intelligence. CBI Product Factsheet: Plastics for Vehicles in the European Union; CBI Market Intelligence: Dutch, The Netherlands, 2016; p. 10

[5] EU Parliament. End of Life Vehicles (ELV) Directive. An Assessment of the Current State of Implementation by Member States; Policy Department: Brussels, Belgium, 2007; p. 69

[6] European Commission. Assessment of the Implementation of Directive 2000/53/EU on End-of-Life Vehicles (the ELV Directive) with Emphasis on the End of Life Vehicles of Unknown Whereabouts; European Commission: Brussels, Belgium, 2017; p. 105.

[7] Santini, A.; Morselli, L.; Passarini, F.; Vassura, I.; Di, S.; Bonino, F. End-of-Life Vehicles management: Italian material and energy recovery efficiency. Waste Manag. 2011, 31, 489–494.

[8] Eurostat. Packaging Waste Statistics. 2018. Available online: https://ec.europa.eu/eurostat/statistics-explained/index.php/ Packaging_waste_statistics

[9] Russo, S.; Valero, A.; Valero, A.; Iglesias-Émbil, M. Exergy-Based Assessment of Polymers Production and Recycling: An Application to the Automotive Sector. Energies 2021, 14, 363. https://doi.org/10.3390/en1402036

[10] Elias Hallack, Nestor Mario Peris, Mattias Lindahl, Erik Sundin, Systematic Design for Recycling Approach – Automotive Exterior Plastics, Procedia CIRP,Volume 105, 2022, Pages 204-209, ISSN 2212-8271, https://doi.org/10.1016/j.procir.2022.02.034

[11] “New Trends In Plastics Consumption In The Automotive Industry – Which Materials Will Be The Winners And Losers?” Adapt Plastics website, accessed in 25/03/2023

[12] Régis Kovacs Scalice , Daniela Beckera, Ramon Cesconetto Silveira, Developing a new compatibility table for design for recycling, Product: Management & Development, Vol. 7 nº 2 December 2009

[13] Alessandro Pegoretti, Recycling concepts for short-fiber-reinforced and particle-filled thermoplastic composites: A review, Advanced Industrial and Engineering Polymer Research, Volume 4, Issue 2, 2021, Pages 93-104, ISSN 2542-5048, https://doi.org/10.1016/j.aiepr.2021.03.004

[14] Scaffaro R, Di Bartolo A, Dintcheva NT. Matrix and Filler Recycling of Carbon and Glass Fiber-Reinforced Polymer Composites: A Review. *Polymers*. 2021; 13(21):3817. https://doi.org/10.3390/polym13213817

[15] Norshah Aizat Shuaib, Paul Tarisai Mativenga, Energy demand in mechanical recycling of glass fibre reinforced thermoset plastic composites, Journal of Cleaner Production, Volume 120, 2016, Pages 198-206, ISSN 0959-6526, https://doi.org/10.1016/j.jclepro.2016.01.070.

[16] Matxinandiarena E, Múgica A, Zubitur M, Yus C, Sebastián V, Irusta S, Loaeza AD, Santana O, Maspoch ML, Puig C, Müller AJ. The Effect of Titanium Dioxide Surface Modification on the Dispersion, Morphology, and Mechanical Properties of Recycled PP/PET/TiO2 PBNANOs. Polymers (Basel). 2019 Oct 16;11(10):1692. doi: 10.3390/polym11101692. PMID: 31623120; PMCID: PMC6835408.

[17] Enrico Sciubba, Exergy-based ecological indicators: From Thermo-Economics to cumulative exergy consumption to Thermo-Ecological Cost and Extended Exergy Accounting, Energy, Volume 168, 2019, Pages 462-476, ISSN 0360-5442, https://doi.org/10.1016/j.energy.2018.11.101.

Magnetic recoverable $Ag_3PO_4/Fe_3O_4/\gamma\text{-}Fe_2O_3$ nanocomposite

Jenifer Vaswani Reboso[1,2,*], Jaime Sadhwani Alonso[1,3], Dunia E. Santiago García[1,4]

(1) Universidad de Las Palmas de Gran Canaria. Escuela de Ingenierías Industriales y Civiles. Dpto. de Ingeniería de Procesos. Campus Universitario de Tafira, 35017 Las Palmas, Spain

(2) Grupo Control Analítico de Fuentes Medioambientales (CAFMA), Instituto Universitario de Estudios Ambientales y Recursos Naturales (i-UNAT), Universidad de Las Palmas de Gran Canaria, 35017 Las Palmas, Spain. e-mail: jenifer.vaswani@ulpgc.es , CA.

(3) Grupo Sistemas Industriales de Eficiencia, Instrumentación y Protección (SEIP), Universidad de Las Palmas de Gran Canaria, 35017 Las Palmas, Spain. e-mail: jimmy.sadhwani@ulpgc.es

(4) Grupo de Fotocatálisis y Espectroscopia para Aplicaciones Medioambientales (FEAM), Departamento de Química, Instituto de Estudios Ambientales y Recursos Naturales (i-UNAT), Universidad de Las Palmas de Gran Canaria, 35017 Las Palmas, Spain. e-mail: dunia.santiago@ulpgc.es

Abstract:

The use of nanomaterials in water treatment is an alternative for the development of new materials that optimize the purification process. Heterogeneous photocatalysis is used for the treatment of wastewaters contaminated with recalcitrant pollutants that cannot be removed in conventionally. Ag_3PO_4 has been reported to use visible light. Another important challenge of heterogeneous photocatalysis is to find a proper support for the photocatalysts to reduce the expense associated with the separation and reuse of these materials. However, the immobilization of the catalyst leads to lower reaction rates because the surface area exposed decreases and the material used as support can also interfere. In the last years, the use of magnetic materials to support photocatalysts has attracted special attention because it allows high surface areas to be exposed. Only few authors have reported the use of Ag_3PO_4/magnetic nanocomposites for photocatalysis and these need to be continued to improve their efficiency. In this work we synthesized Ag_3PO_4 and supported it on Fe_3O_4.
Fe_3O_4 was synthesis at pH 12 by the addition of $FeCl_3$ and $FeCl_2$. The magnetic material was washed with water and dried at 80ºC. Ag_3PO_4 was synthesised over Fe_3O_4 from the reaction between $AgNO_3$ and Na_2HPO_4. The final material was washed, recovered magnetically and dried at 80ºC. For characterization, a SEM and XRD studies were carried out.
Ag_3PO_4 was synthesised and satisfactorily supported over $Fe_3O_4/\gamma\text{-}Fe_2O_3$. The photodegradation of 10 mg·L-1 of methylene blue was achieved, although the apparent reaction rate constant was slightly lower for the magnetic composite than for the Ag_3PO_4 alone. This is explained because the composite contained 48% of the active Ag_3PO_4 material, as depicted form DRX studies.

Keywords:
Photocataysis, wastewater treatment, magnetic nanomaterials,

1. Introduction

Water is a scarce resource and for many countries supply is not enough to satisfy demand. Water resources location and their quality are factors that limit their availability. This problem is further complicated by climate

change, rapid industrialization, population growth and pollution of existing water resources [1]. To solve this question different solutions are proposed which include repairing water distribution infrastructures and conservation of existing water sources. However, these options can not increase resources. Supply water can only be increased beyond hydrological cycle by desalination and water reuse. For this, a series of conventional water treatment technologies are used which include among others: ultraviolet radiation, chemical treatments, distillation and membrane processes (reverse osmosis, ultrafiltration, microfiltration, electrodialysis...), but all of them show specific disadvantages [2].

The continuous deterioration of the environment is a problem with greater relevance every day, and that requires short-term solutions. Most of the harmful contaminants found are anthropogenic compounds that have low biodegradability and therefore cannot be eliminated by conventional treatments. This is the case of the so-called emerging pollutants, which are found in low concentrations in the environment; these have the potential to carry an ecological impact, as well as adverse effects on health [3]. These contaminants include: drugs, additives, pesticides and a wide variety of compounds that, even at low concentrations, can alter endocrine functions [4] and increase the presence of resistant bacteria [5].

Elimination and control of these substances in aqueous media is complex due to their presence in large bodies of water. In recent years, emerging contaminants have been found in practically all the bodies of water studied. In Spain, among others, more than 30 emerging contaminants have been found in groundwater [6], 100 in wastewater treatment plants [7], more than 100 in wastewater already treated in conventional treatment plants [8], several in aquaculture areas [9] and 144 in river water fish [10].

Due to the nature of these contaminants, most have proven to be poorly biodegradable, and cannot be eliminated by conventional purification systems and therefore require advanced oxidation processes for their treatment [11]. Advanced oxidation processes are part of the tertiary treatment of purified water and seek to eliminate compounds that are difficult to biodegrade and reduce microbiological contamination, often with the aim of reusing the water. Among the most common tertiary processes we find ozonation, photocatalysis or membrane filtration, among others.

Based on this situation and nanotechnology development, nanomaterials use for water treatment is an alternative that allows solving drawbacks of methods traditionally used. Due to their new properties nanomaterials can contribute in obtaining stronger, lighter, cleaner and smarter surfaces and systems [12]. They have many applications ranging from automotive and aircraft (for example, reinforced and lighter materials, antifouling paints or more durable pneumatic) to biomedicine (drug released as specific organs, biosensors or prosthesis).

In water treatment, nanotechnology is finding applications through different routes [13] such as the use of large surface area of nanoparticles to adsorb contaminants (they allow retaining a higher rate of contaminants than conventional adsorbent), the use of membranes with nanomaterials (several studies have fixed nanomaterials to different polymer membranes and have obtained a greater water flow than conventional membranes) and the use of catalytic nanoparticles to decompose contaminants (nanomaterials have a higher photoactivity than conventional catalysts). Nanomaterials such as silver nanoparticles [14], TiO_2 nanoparticles and carbon nanotubes [15] have bactericidal effects that make it possible to eliminate microorganisms present in water. They also have better adsorption capacities than conventional adsorbents for low concentrations of heavy metals: porous carbon nanomaterials have been used efficiently for lead, cadmium, nickel and zinc elimination [16]. Another application is oils and organic solvents treatment: SiO_2 nanoparticles fixed to a polysulfone membrane improve antifouling properties and increase permeability from 1.08 to 17.32 $l/m^2 \cdot h$ [17]. On the other hand, boron nitride nano-slides have been shown to adsorb up to 33 times their own weight in oils and organic solvents while repelling water [18]. The use of nanomaterials has also been evaluated for emerging contaminants in water treatment: a combination of titanium dioxide nanotubes on a graphene base eliminates, with the help of the sun, traces of drugs and pesticides that escape from the current purification systems.

Of all the mentioned water treatment processes, we will focus on the use of nanomaterials in heterogeneous photocatalysis.Heterogeneous photocatalysis is used for the treatment of wastewaters contaminated with recalcitrant pollutants that cannot be removed in conventionally. One of the main drawbacks is that most photocatalysts need to be illuminated with wavelengths shorter than 388 nm [19]. Ag_3PO_4 has been reported to use visible light [20]. Another important challenge of heterogeneous photocatalysis is to find a proper support for the photocatalysts to reduce the expense associated with the separation and reuse of these materials. However, the immobilization of the catalyst leads to lower reaction rates because the surface area exposed decreases and the material used as support can also interfere [21]. In the last years, the use of magnetic materials to support photocatalysts has attracted special attention because it allows high surface areas to be

exposed. Only few authors have reported the use of $AgPO_4$/magnetic nanocomposites for photocatalysis [20], [22], [23] and these need to be continued to improve their efficiency.

In this work we synthesized Ag_3PO_4 and supported it on Fe_3O_4, performing the characterization of the synthesized material

2. Bibliometric Analysis

Bibliometric analysis is defined as a statistical evaluation of published scientific documents that enables the measure of the influence of publication in the scientific community.
The data obtained from the bibliometric analysis of the terms "silver nanoparticles" and water treatment are presented below. The scientific database used to search for the terms was Scopus (search conducted on May 23, 2021), and the software used to analyze the results was VOS Viewer®.

A growing trend is observed in the number of documents published as of 2008, with the number of documents published up to that date being less than 200. Regarding the countries with the most publications on this subject, Spain is in position number 10 , with 265 publications. Regarding the research groups or institutions with the greatest scientific production in the field, the first Spanish institution is found in position 23, this being the Higher Council for Scientific Research (CSIC).

However, if we add the term “emerging pollutants” to the previous search, the number of documents is reduced to 454 (from the year 2000 to the present). Thus, up to the year 2010, only 6 references were found in Scopus related to the study of silver nanoparticles for the treatment of emerging contaminants in water. As of that year, the number of documents begins to increase, finding in 2020, 90 documents published on this subject. In this regard, Spain is the fourth country with the most documents (27 documents in total).

Figure 1 shows the bibliometric network obtained from the keywords found in the documents resulting from the search. It is observed that the most commonly used materials for the application of silver nanoparticles are membranes (95 occurrences), graphene oxide (192 occurrences), titanium dioxide (327 occurrences) or magnetite (122 occurrences). Regarding the final application of these materials, we mainly found keywords related to disinfection processes (E. coli, antibacterial activity, etc.), although words related to emerging contaminants (antibiotics, tetracycline) and dyes (blue of methylene, dyes).

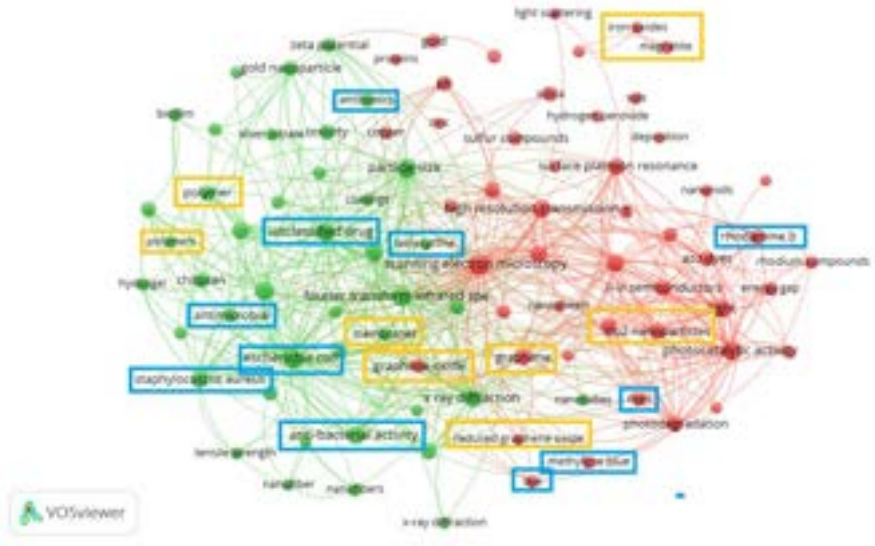

Figure 1. Bibliometric analysis of the terms “silver nanoparticles” and “water treatment”.

3. Experimental

3.1. Sample preparation

Fe_3O_4 nanoparticles were synthesized using a solvothermal method [24], Fe_3O_4 was synthesis at pH 12 by the addition of $FeCl_3$ and $FeCl_2$. The magnetic material was washed with water and dried at 80ºC.

The synthesized Fe_3O4 nanoparticles were then dispersed in distilled water, and added to the NaH_2PO_4 solution (0,15M, pH = 4.12). And then, $AgNO_3$ aqueous solution (0.15 M) was added with drop by drop to the above solution under continuous mechanical vibration, and then the solution was maintained at room temperature and under continuous mechanical vibration for 4 h. The magnetic material was dried at 200ºC.
The as-prepared Fe_3O_4@ Ag_3PO_4 nanoparticles were separated by an external magnetic field, The final material was washed with water to remove excess phosphate ions. The obtained Fe_3O_4@Ag_3PO_4 was separated by an external magnetic field, then dried for 6 h at 80 °C.

3.2. Analysis

Powder X-ray diffraction (XRD) measurements were obtained on an X-ray diffractometer PANalytical Empyrean diffractometer (Cu Kα1, λ = 1.5406 Å). Crystallite sizes were estimated using the Scherrer equationand the fractions of the different phases were obtained from analysis with Match! 3® software.
UV-vis diffuse reflectance spectra (DRS) was measured using a Varian Cary E5 spectrophotometer in the range 200 – 2000 nm.
SEM microscopic observation allowed the visualization of the ground material surface morphology. For scanning electron microscopy (SEM) measurements a Sigma 300 VP FESEM Zeiss instrument was used. It was equipped with energy dispersive X-ray spectroscopy (EDX).

3.3. Degradation experiment

The photocatalytic activities of the samples were evaluated by degradation of MB under a simulated solar lam. A 60 W Hapro Solarium HB175 equipped with four 15 W Philips CLEO fluorescent tubes with emission spectrum from 300 to 400 nm (maximum around 365 nm) and with an average irradiation of about 90 $W \cdot m^{-2}$ was used.. A photocatalyst (0.1 g) was added to an aqueous solution of MB (100 mL, 10mgL−1) at room temperature in air. The suspension was magnetically stirred for 30 min in the dark to establish an adsorption desorption equilibrium to eliminate the influence of adsorption. A lamp was switched on to initiate the reaction. During irradiation, samples were taken at different time intervals for 180 min or until complete degradation was observed. Samples were centrifuged and then the decolorization of MB was measured with a UV–vis spectrophotometer (Cary 60, Varian, USA). To investigate the stability and recyclability of the as-prepared composite magnetic photocatalysts (Fe_3O_4@Ag_3PO_4), recycling experiments were also performed. In the recycling experiments, after the photocatalysts were separated from the solution by an external magnetic field, the remaining solution was removed. Separated photocatalysts were washed five times with distilled water, and then used in the next degradation experiment

4. RESULTS AND DISCUSSION

4.1 Characterization

XRD was used to investigate the phase structures of the samples. Fig. 2. shows typical XRD patterns of the samples at various stages. Fig. 2 shows the XRD pattern of Fe_3O_4 nanoparticles, Fig. 2B shows the XRD pattern of Ag_3PO_4. The successful coating and subsequent crystallization of Ag_3PO_4 and Fe_3O_4 were also confirmed (Fig. 2C).

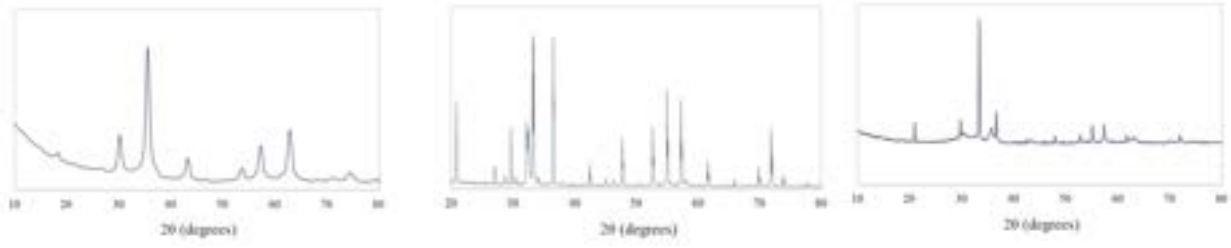

(a) *(b)* *(c)*

Figure 2. XRD patterns of the samples: (a) Fe_3O_4 spheres, (b) Ag_3PO_4, (c) Ag_3PO_4/Fe_3O_4/γ-Fe_2O_3

For the Ag_3PO_4 material alone, DRX studies revealed that 100% Ag_3PO_4 was present. For the magnetic composite, the phases found in DRX studies were Ag_3PO_4 (47,8%), magnetite, Fe_3O_4 (42,6%) and maghemite, γ-Fe_2O3 (9,5%). Although we initially synthesized Fe_3O_4, it is known that this structure can oxidize to γ-Fe_2O_3, also magnetic, even at ambient temperature. The size of the crystals obtained from Ag_3PO_4 is 54 nm and in the case of Fe_3O_4 and γ-Fe_2O_3 crystals it is 18 nm.

Thus, the maghemite crystalline phase (γ-Fe_2O_3) can be intuited in the diffractograms of the catalysts synthesized by calcination in a nitrogen atmosphere. The formation of maghemite can occur as a consequence of the oxidation of magnetite particles, according to equation 1 [25]. This process can occur at room temperature [26], although it usually occurs more favorably in an oxidizing environment above 200 ºC, with the optimum temperature for maghemite formation being between 375-400 ºC [27].

$$2\ Fe_3O_4 + ½\ O_2 \rightarrow 3\ \gamma\text{-}Fe_2O_3 \qquad (1)$$

The SEM image of the $Ag_3PO_4/Fe_3O_4/\gamma\text{-}Fe_2O_3$ composite is shown in Fig. 3.

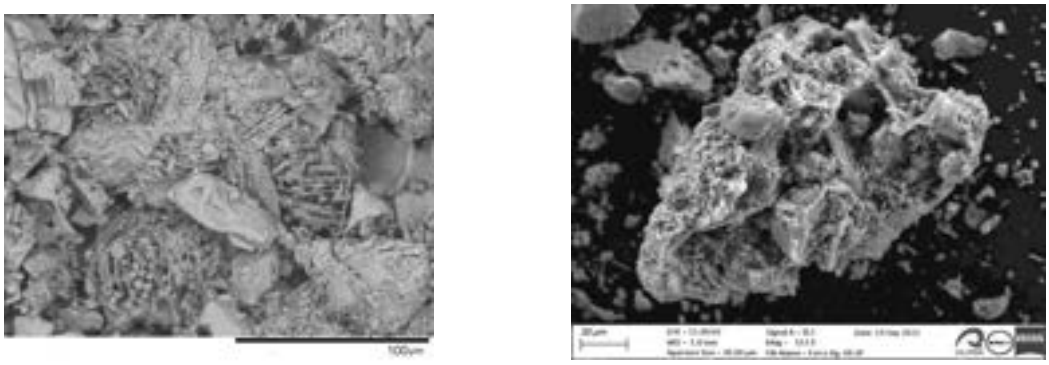

(a) *(b)*

Figure 3. SEM Images of: (a) Ag_3PO_4 (b) $Ag_3PO_4/Fe_3O_4/\gamma\text{-}Fe_2O_3$

It is observed that there is a coating of silver phosphate on the ferromagnetite. Table 1 shows the elemental composition of $Fe_3O_4@Ag_3PO_4$ synthesized material.

Table 1. Composition of $Fe_3O_4@Ag_3PO_4$

Element	Weight %	Atomic %	Error %
O K	38.97	71.81	11.71
P K	9.23	8.78	7.67
Fe K	20.63	10.89	7.56
Ag L	31.17	8.52	6.87

UV–vis absorption spectra of the studied catalysts are depicted in Fig. 4. Pure Ag_3PO_4 absorbs solar energy with a wavelength shorter than approximately 500 nm. In contrast to pure Ag_3PO_4, the absorption edge of $Fe_3O_4@Ag_3PO_4$ and Fe_3O_4 generates red shift, $Fe_3O_4@Ag_3PO_4$ and Fe_3O_4 also exhibit higher absorption in the visible region than the pure Ag_3PO_4.

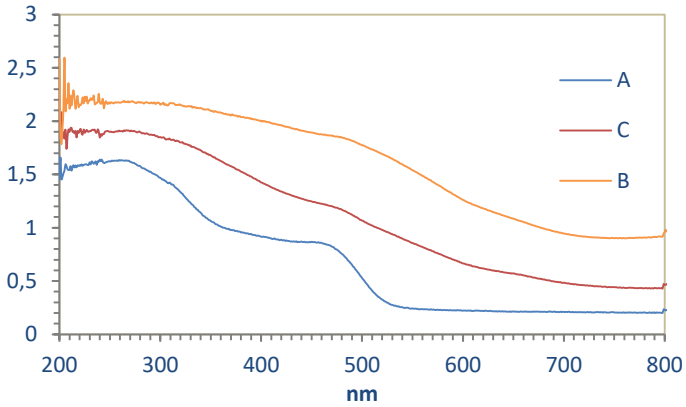

Figure 4. UV–Vis absorption spectra of: (A) pure Ag_3PO_4, (B) pure Fe_3O_4 and (C) $Ag_3PO_4/Fe_3O_4/\gamma\text{-}Fe_2O_3$

The hysteresis curves of the magnetic materials are shown in Fig. 5. We observe that the magnetization saturation is 43 emu·g^{-1} for Fe_3O_4 and 15 emu·g^{-1} for $Ag_3PO_4/Fe_3O_4/\gamma\text{-}Fe_2O_3$.

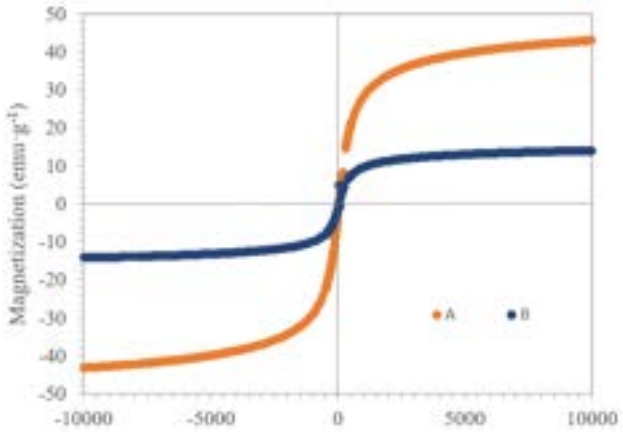

Figure 5. Hysteresis curves of: (A) Fe_3O_4 and (B) $Ag_3PO_4/Fe_3O_4/\gamma\text{-}Fe_2O_3$

4.2 Degradation Experiment

The photocatalytic degradation of MB by $Fe_3O_4@Ag_3PO_4$ under simulated solar irradiation at room temperature was investigated (Fig. 5). For comparison, the Fe_3O_4 and Ag_3PO_4 photocatalyst was also investigated. About 48% of MB was removed by $Fe_3O_4@Ag_3PO_4$ after 180 min irradiation. In contrast, pure Ag_3PO_4 exhibited the highest photocatalytic activity of the catalysts, about 96% of MB within 180 min under simulated solar irradiation.

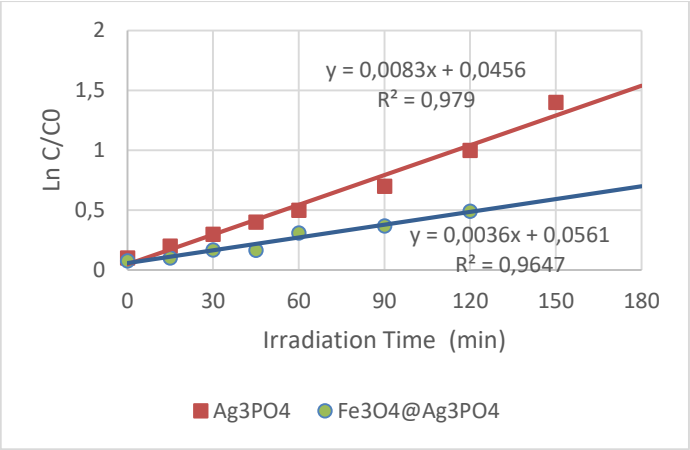

Figure 5. Photocatalytic degradation of MB over Fe_3O_4 spheres, pure Ag_3PO_4 and Fe_3O_4@Ag_3PO_4

The apparent fist-order reaction rate constant for the degradation of methylene blue was 0.0077 min^{-1} for Ag_3PO_4 and 0.0034 min^{-1} for Ag_3PO_4/Fe_3O_4/γ-Fe_2O_3. No photolysis was observed under the studied conditions.

4.3 Separation and reuse

The recyclability of the magnetic photocatalysts was investigated. The Fe_3O_4@Ag_3PO_4 photocatalysts can be rapidly separated under an applied magnetic field in 20 s.

Fig. 6 shows the recyclability of the Fe_3O_4@Ag_3PO_4 for photocatalytic degradation of MB. The degradation activity of Fe_3O_4@Ag_3PO_4 decreased sharply only after 1 cycle.The decoloration efficiency decreased to about 32%, 25%, 19% and 14% for the 2nd, 3rd,4th and 5th degradation cycles, respectively.

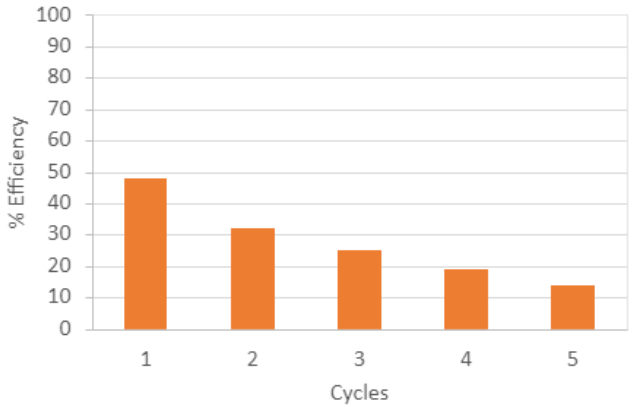

Figure 6. Recyclability of the Fe_3O_4@Ag_3PO_4

Efficiency decreases with reuse, it can be observed that the catalyst darkens due to the photocorrosion of silver by irradiation. This occurs because silver phosphate is slightly soluble in water, and silver ions can react with the generated photoelectrons reducing to elemental silver [28].

5. Conclusions

Ag_3PO_4 was synthesised and satisfactorily supported over Fe_3O_4/γ-Fe_2O_3. The photodegradation of 10 mg·L^{-1} of methylene blue was achieved, although the apparent reaction rate constant was slightly lower for the magnetic composite than for the Ag_3PO_4 alone. This is explained because the composite contained 47.8% of the active Ag_3PO_4 material, as depicted form DRX studies.

Acknowledgments

This research was funded by Fundación Cajadecanarias and Fundación La Caixa through the project “Aplicación de nanopartículas a los procesos de tratamiento de aguas” (NAPLAGUA), with grant number 2021ECO14, Call for Research Projects 2021, with the collaboration of the company Ancor Tecnologica S.L. This project began in February 2022 until February 2024, with José Jaime Sadwani Alonso as the principal investigator.

References

[1] Q. Zaib and H. Fath, “Application of carbon nano-materials in desalination processes,” *Desalin. Water Treat.*, vol. 51, pp. 627–636, Jan. 2012, doi: 10.1080/19443994.2012.722772.

[2] R. Das, M. E. Ali, S. B. A. Hamid, S. Ramakrishna, and Z. Z. Chowdhury, “Carbon nanotube membranes for water purification: A bright future in water desalination.” 2014.

[3] D. Birkholz, S. M. Stilson, and H. S. Elliott, “Analysis of Emerging Contaminants in Drinking Water - A Review,” in *Comprehensive Water Quality and Purification*, vol. 2, 2010, pp. 212–229.

[4] C. García-Gómez, P. Gortáres-Moroyoqui, and P. Drogui, “Contaminantes emergentes: efectos y tratamientos de remoción,” *Química Viva*, vol. 10, no. 2, pp. 96–105, Mar. 2011, [Online]. Available: https://www.redalyc.org/articulo.oa?id=86319141004.

[5] M. Taheran, M. Naghdi, S. K. Brar, M. Verma, and R. Y. Surampalli, “Emerging contaminants: Here today, there tomorrow!,” *Environmental nanotechnology, monitoring & management*, vol. v. 10. Elsevier B.V.

[6] A. Jurado, E. Vàzquez-Suñé, J. Carrera, M. López de Alda, E. Pujades, and D. Barceló, “Emerging organic contaminants in groundwater in Spain: a review of sources, recent occurrence and fate in a European context.,” *Sci. Total Environ.*, vol. 440, pp. 82–94, Dec. 2012, doi: 10.1016/j.scitotenv.2012.08.029.

[7] M. J. M. Bueno, M. J. Gomez, S. Herrera, M. D. Hernando, A. Agüera, and A. R. Fernández-Alba, “Occurrence and persistence of organic emerging contaminants and priority pollutants in five sewage treatment plants of Spain: two years pilot survey monitoring.,” *Environ. Pollut.*, vol. 164, pp. 267–273, May 2012, doi: 10.1016/j.envpol.2012.01.038.

[8] Y. Cabeza, L. Candela, D. Ronen, and G. Teijon, “Monitoring the occurrence of emerging contaminants in treated wastewater and groundwater between 2008 and 2010. The Baix Llobregat (Barcelona, Spain).,” *J. Hazard. Mater.*, vol. 239–240, pp. 32–39, Nov. 2012, doi: 10.1016/j.jhazmat.2012.07.032.

[9] Y. Aminot *et al.*, “Environmental risks associated with contaminants of legacy and emerging concern at European aquaculture areas.” 2019, doi: 10.1016/j.envpol.2019.05.133.

[10] Y. Pico *et al.*, “Contaminants of emerging concern in freshwater fish from four Spanish Rivers,” *Sci. Total Environ.*, vol. 659, pp. 1186–1198, 2019, doi: https://doi.org/10.1016/j.scitotenv.2018.12.366.

[11] A. Gogoi, P. Mazumder, V. K. Tyagi, G. G. Tushara Chaminda, A. K. An, and M. Kumar, “Occurrence and fate of emerging contaminants in water environment,” *A Rev.*, vol. 6, pp. 169–180, Mar. 2018, doi: 10.1016/j.gsd.2017.12.009.

[12] E. Roduner, “Size matters: why nanomaterials are different.,” *Chem. Soc. Rev.*, vol. 35 7, pp. 583–592, 2006.

[13] A. Smith, “Opinion: Nanotech – the way forward for clean water?,” *Filtr. Sep.*, vol. 43, no. 8, pp. 32–33, 2006, doi: https://doi.org/10.1016/S0015-1882(06)70976-4.

[14] T. Ahmed, S. Imdad, K. Yaldram, N. M. Butt, and A. Pervez, “Emerging nanotechnology-based methods for water purification: a review,” *Desalin. Water Treat.*, vol. 52, no. 22–24, pp. 4089–4101, Jul. 2014, doi: 10.1080/19443994.2013.801789.

[15] Q. Li *et al.*, “Antimicrobial nanomaterials for water disinfection and microbial control: potential applications and implications.,” *Water Res.*, vol. 42, no. 18, pp. 4591–4602, Nov. 2008, doi: 10.1016/j.watres.2008.08.015.

[16] J. P. Ruparelia, S. P. Duttagupta, A. K. Chatterjee, and S. Mukherji, “Potential of carbon nanomaterials for removal of heavy metals from water,” *Desalination*, vol. 232, no. 1, pp. 145–156, 2008, doi: https://doi.org/10.1016/j.desal.2007.08.023.

[17] A. L. Ahmad, M. A. Majid, and B. S. Ooi, “Functionalized PSf/SiO2 nanocomposite membrane for oil-in-water emulsion separation,” *Desalination*, vol. 268, no. 1, pp. 266–269, 2011, doi:

https://doi.org/10.1016/j.desal.2010.10.017.

[18] W. Lei, D. Portehault, D. Liu, S. Qin, and Y. Chen, “Porous boron nitride nanosheets for effective water cleaning,” *Nat. Commun.*, vol. 4, no. 1, p. 1777, 2013, doi: 10.1038/ncomms2818.

[19] C. B. Anucha, I. Altin, E. Bacaksiz, and V. N. Stathopoulos, “Titanium dioxide (TiO_2)-based photocatalyst materials activity enhancement for contaminants of emerging concern (CECs) degradation: In the light of modification strategies,” *Chem. Eng. J. Adv.*, vol. 10, p. 100262, 2022, doi: https://doi.org/10.1016/j.ceja.2022.100262.

[20] X. Guo *et al.*, “Performance of magnetically recoverable core–shell Fe3O4@Ag3PO4/AgCl for photocatalytic removal of methylene blue under simulated solar light,” *Catal. Commun.*, vol. 38, pp. 26–30, 2013, doi: https://doi.org/10.1016/j.catcom.2013.04.010.

[21] D. E. Santiago, M. R. Espino-Estévez, G. V González, J. Araña, O. González-Díaz, and J. M. Doña-Rodríguez, “Photocatalytic treatment of water containing imazalil using an immobilized TiO2 photoreactor,” *Appl. Catal. A Gen.*, vol. 498, pp. 1–9, 2015, doi: https://doi.org/10.1016/j.apcata.2015.03.021.

[22] E. Abroshan, S. Farhadi, and A. Zabardasti, “Novel magnetically separable Ag3PO4/MnFe2O4 nanocomposite and its high photocatalytic degradation performance for organic dyes under solar-light irradiation,” *Sol. Energy Mater. Sol. Cells*, vol. 178, pp. 154–163, 2018, doi: https://doi.org/10.1016/j.solmat.2018.01.026.

[23] Z. Liu *et al.*, “The triple-component Ag3PO4-CoFe2O4-GO synthesis and visible light photocatalytic performance,” *Appl. Surf. Sci.*, vol. 458, pp. 880–892, 2018, doi: https://doi.org/10.1016/j.apsusc.2018.07.166.

[24] B. Lv, Y. Xu, H. Tian, D. Wu, and Y. Sun, “Synthesis of Fe3O4\SiO2\Ag nanoparticles and its application in surface-enhanced Raman scattering,” *J. Solid State Chem.*, vol. 183, no. 12, pp. 2968–2973, 2010, doi: https://doi.org/10.1016/j.jssc.2010.10.001.

[25] S. Laurent *et al.*, “Magnetic Iron Oxide Nanoparticles: Synthesis, Stabilization, Vectorization, Physicochemical Characterizations, and Biological Applications,” *Chem. Rev.*, vol. 108, no. 6, pp. 2064–2110, Jun. 2008, doi: 10.1021/cr068445e.

[26] A. Haneda, K. & Morrish, “Magnetite to maghemite transformation in utrafine particles.,” *J. Phys. Colloq.*, vol. 38, pp. 321–323, 1977, doi: https://doi.org/10.1051/jphyscol:1977166.

[27] H. Lepp, “Stages in the oxidation of magnetite,” *Am. Mineral.*, vol. 42, pp. 679–681, 1957.

[28] X. Chen, Y. Dai, and X. Wang, “Methods and mechanism for improvement of photocatalytic activity and stability of Ag3PO4: A review,” *J. Alloys Compd.*, vol. 649, no. C, pp. 910–932, 2015, doi: 10.1016/j.jallcom.2015.07.174.

CONDUCTIVITY ANALYSIS OF ASYMMETRIC POLYSULFONE MEMBRANES FOR CO_2

B. Pascual-Jose[a], Alireza Zare[b], Alberto Puga[b], Jose Antonio Reina[c], M, Giamberini[b], and A. Ribes-Greus[a]

[a] Institute of Technology of Materials (ITM), Universitat Politècnica de València (UPV), Spain, aribes@ter.upv.es
[b] Department of Chemical Engineering (DEQ), Universitat Rovira I Virgili (URV), Tarragona, Spain.
[c] Department of Analytical Chemistry and Organic Chemistry, Universitat Rovira I Virgili (URV), Tarragona, Spain.

Abstract:

Membrane technologies are currently one of the promising strategies to face the continuously increasing CO_2 accumulation in the atmosphere and the associated environmental impact. They have become an alternative for separating and absorbing CO_2 due to their low cost and relatively more straightforward preparation. Polysulfone (PSf) is one of the most common polymers for its commercial availability, processing, and favourable selectivity-permeability characteristics. PSf were blended with a commercial hyperbranched polyethyleneimine Lupasol, modified with benzoyl chloride or phenyl isocyanate with several percentages to improve their performance in terms of direct CO_2 capture. All the membranes were prepared by phase inversion precipitation. The morphology, thermal properties, molecular motion, and conductivity were analyzed. The blended membranes show differences in the microstructure, and the presence of urea and amide groups promoted a considerable increment in the efficiency of the CO_2 capture process compared to the neat membrane due to the enhancement in hydrophilicity and chemical stability. In composite membranes, the absorption capacity is controlled by the conductivity, chemical affinity to CO_2, and morphology of the membranes. The phenyl isocyanate improves the motions of hyperbranched polyethyleneimine in blended membranes facilitating CO_2 direct air capture.

Keywords:
CO_2 air absorption, Asymmetric Polysulfone/hyperbranched polyethyleneimine membranes, morphological, thermal, dielectric, and conductivity analysis.

1. Introduction

Since the beginning of the 21st century, global Greenhouse gas (GHG) emissions have been increasing. GHG traps heat and makes the planet warmer. Human activities such as burning fossil fuels for electricity, heat, and transportation are responsible for almost all of the increase in GHG in the atmosphere over the last 150 years. The Emission Database for Global Atmospheric Research indicated that in only two decades, the global emissions from carbon dioxide have been increasing, rising by approximately 50% of emissions to the atmosphere. If carbon dioxide emissions are not drastically reduced, the increase in temperature is accelerating and is projected to be at the 1.5 °C level within 15 to 20 years. The United Nations International Panel on Climate Change (IPCC) indicated that exceeding a 1.5 °C temperature increase will be catastrophic with consequences of unprecedented flooding, drought, rising sea level, heat waves, and famine [1-2].

There is no single solution to remove carbon dioxide from the air and reduce GHG; no technology is enough to avoid the effects of climate change. Between them, capturing and storing carbon dioxide and its subsequent use may be a possible solution. Nevertheless, this implies that the carbon dioxide must first be captured at atmospheric pressure and stored efficiently.

An interesting technology is a membrane separation-based CO_2 capture system. It uses permeable and semipermeable materials that selectively transport and separate CO_2 from other components in the gas

stream. This separation process is efficient because it does not involve a phase change, leading to low energy consumption. Other advantages over other capture technologies are their compact design and simplicity since adding chemical agents is unnecessary. However, this method also presents disadvantages; it must resist impurities and harden ageing. Recently, a new hybrid technique has been developed; it combines membrane separation and solvent absorption processes with an effective CO_2 absorption in a contactor device. It is also a tiny modular system that can be easily assembled and integrated into other devices [3-6].

Currently, amines are the most efficient and cost-effective materials for carbon dioxide capture. It is commonly mentioned that primary amines are more reactive toward CO_2. However, the basicity of amines is the most critical factor affecting CO_2 capture performance due to the acid/base reaction between CO_2 and amines. Therefore, capturing CO_2 using solid polymeric adsorbents, such as polyamines, is a promising alternative to avoid the problems associated with aqueous amine adsorbents. Amines and aminic compounds have found wide applications as CO_2-removing agents due to the reversible reaction between aminic groups (basic) and CO_2 (acidic). Other commercial options are used Polysulfone (PSf) as basic material because have remarkable hydrolytic stability that sets them apart from other thermoplastics. In addition, it is a high-performance thermoplastic polymer with excellent physical properties at high temperatures. Their characteristics are rigidity, excellent thermal, mechanical, and oxidation resistance, and a high glass transition temperature [6].

This paper aims to increase the performance of Polysulfone membrane contactors by blending comercial PSf with a commercial, hyperbranched polyethylene imine, specifically. Lupasol G20 is a water-soluble polymer; this could prevent membrane preparation from a water coagulation bath as previously described for neat PSf and membrane stability in contact with the storing aqueous. The presence of the basic nitrogen atoms should increase the membrane affinity for carbon dioxide, thus improving its capture and permeability concerning PSf. On the other hand, hyperbranched polyethyleneimine Lupasol G20 is, modified with benzoyl chloride or phenyl isocyanate to enhance the molecular motion and facilitated CO_2 direct air capture. Broadband dielectric spectroscopy (BDS), through the analysis of the molecular motions and the dielectric conductivity, is a suitable technique to determine the reorientation of the permanent dipoles present on the side chains and on the backbone of polymeric materials, which might provide insights into the mobility of the CO_2 in the membranes and tuning the suitable composition of benzoyl chloride or phenyl isocyanate in the blend.

2. Materials and Methods

2.1. Materials and membrane preparation

The used materials are:

Polysulfone (PSf), with a molecular weight of 35,000 Da, was purchased from Sigma-Aldrich.
Lupasol G20, provided by BASF, has a molecular weight of 1300 Da.
Additive 1 is a chemically modifying Lupasol G20 with benzoyl chloride.
Additive 2 is Lupasol G20 chemically modified with phenyl isocyanate.
A phase inversion process at ambient conditions prepared all polysulfone-based membranes. 1-Methyl-2-pyrrolidone (NMP), purchased from Sigma-Aldrich, was used to dissolve 20 g of PSf/G20 mixture (1 and 2,distinctly) so that the total polymer concentration was set at 20% by weight concerning the total weight of the polymer solution. The polymer mixtures were stirred for 48 h. The polymer solutions were then cast on glass support using a 250 µm thick caster blade. Immediately afterward, they were placed in a coagulation bath containing non-solvent water, where the membranes were precipitated by the exchange between the solvent (NMP) and the non-solvent. The resulting flat membranes were removed from the coagulation bath, washed with distilled water, and air-dried overnight [7].

In this way, five different membranes were prepared, one of pure Polysulfone M0, two membranes with 2% and 10% of additive 1 (M1-2%; M1-10%), and two membranes with 2% and 10% of additive 2 (M2-2%; M2-10%).

2.2. Field Emission Scanning Electron Microscopy (FE-SEM)

The surface of the prepared membranes was evaluated through Field Emission Scanning Electron Microscopy (FE-SEM). The membranes, previously vacuum dried, was platinum sputter-coated for 10 s using a Leica EM MED020 coater. Surface electronic micrographs were taken in a Zeiss Ultra 55 at 295 K with a 1 kV voltage.

2.3. Differential scanning calorimetry (DSC)

The surface of the prepared membranes was evaluated through Field Emission Scanning Electron Microscopy (FE-SEM). The membranes, previously vacuum dried, was platinum sputter-coated for 10 s using a Leica EM MED020 coater. Surface electronic micrographs were taken in a Zeiss Ultra 55 at 295 K with a 1 kV voltage.

2.4. Broadband Dielectric Spectroscopy (BDS)

The impedance measurements were conducted using a Novocontrol Broadband Dielectric Impedance Spectrometer (BDS) connected to a Novocontrol Alfa-A Frequency Response Analyzer. All the measurements were obtained under isothermal conditions by increasing in steps by 10 K. The sample electrode assembly (SEA) consisted of two stainless steel electrodes filled with the sample and was directly placed in the cell.

The dielectric spectra were analyzed in terms of the complex permittivity (e*) using as many Havriliak Negami (HN) functions as needed. All the characteristic parameters of each relaxation process were determined as shown in Equation 1:

$$\varepsilon^* = \varepsilon_\infty + \frac{\Delta\varepsilon}{(1 + (i\omega t)^a)^b} \qquad (Eq.1)$$

Where:

τ is the Havriliak-Negami relaxation time. The a and b parameters correspond to the width and asymmetry of the relaxation peak. Δε is the value of the relaxation strength [8-10].

The conductivity response to an applied electric field of a polymer consists mainly of frequency-dependent and frequency-independent components. The former is ascribed to the DC conductivity and shows a frequency independent plateau. In contrast, the latter is attributed to the AC conductivity and is characterized by a high dispersion at higher frequencies. This behaviour can be modelled by the universal dynamic response model, as shown in Equation 2.

$$\sigma(\omega) = \sigma_{DC} + A\omega^n \qquad (Eq.2)$$

3. Results and Discussion

3.1. Morphology

The surface of the samples was analyzed at a microscopic level. Table 1 displays these results. All the membranes present a smooth appearance, with minor roughness marks that could be due to the phase inversion process. The membrane M1-2% shows an active layer with small holes. The back layer of the pure membrane without additive, M0, and the M2-2% membrane, the surface is practically smooth, without any defects. However, the M2-10% membrane presents minor flaws. In contrast, tiny pores are observed along all or part of the surface in membranes with additive 1, M1-2%, and M2-2%.

The cross-section shows that the pure membrane without additive, M0, presents a channel-shaped structure on a porous and dense matrix. In contrast, the channel-shaped structure disappears in the M1-2% membrane, only observing that porous matrix. On the other hand, by increasing the amount of modified Lupasol additive, the morphology of the membrane changes, with the M1-10% membrane showing an evident spongy layer with a much denser layer.

Therefore, it can be affirmed that the morphology of the membrane becomes denser with a higher content of additive 1. The precipitation rate during the phase inversion process predominantly affects the membrane morphology.

Table 1.

Superficial morphology of blended polysulfone membranes

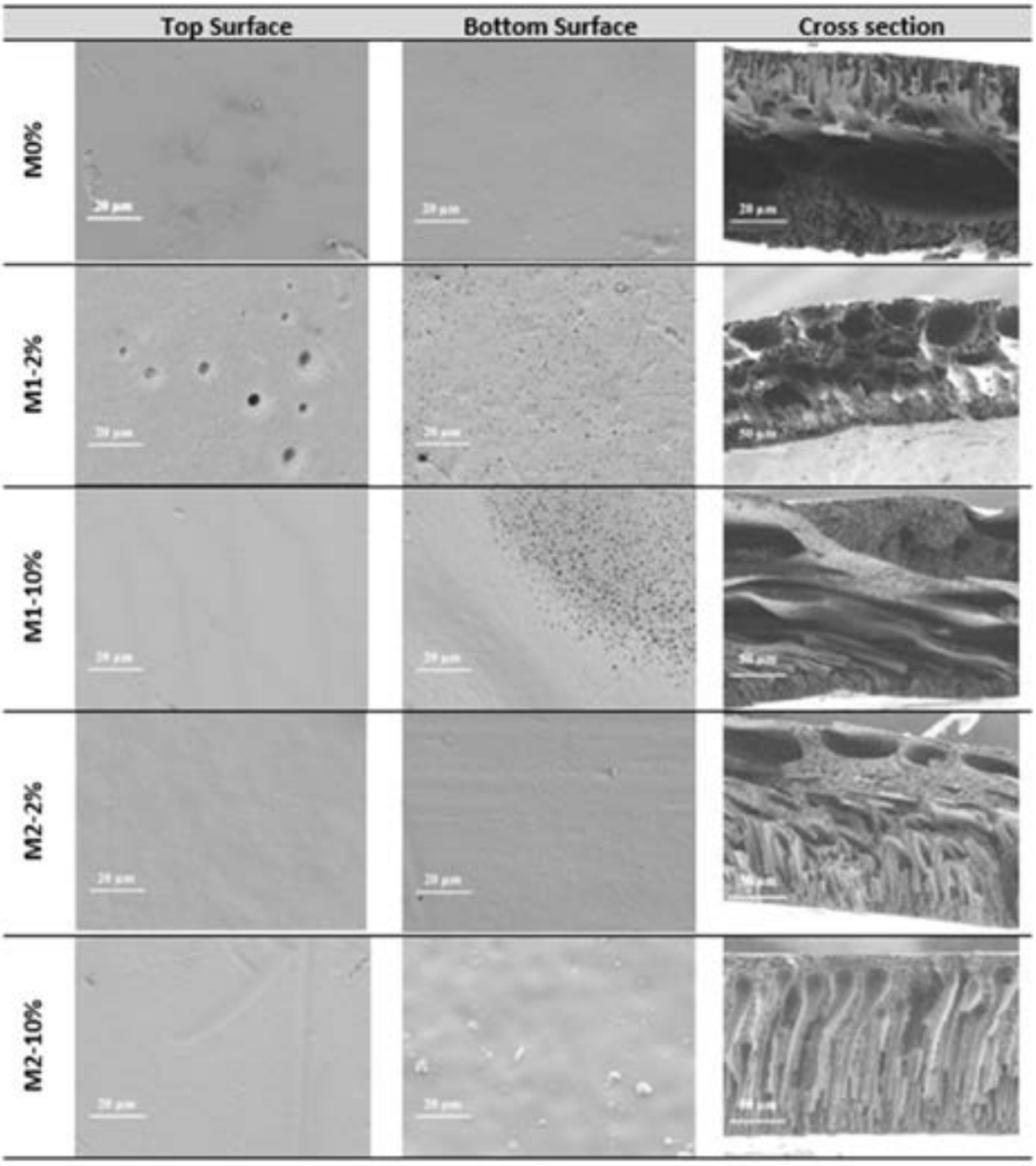

Rapid precipitation is determined by the rapid penetration of the non-solvent into the polymer solution and gives rise to highly asymmetric structures with channel-shaped macrovoids; a slower penetration of the coagulant, and consequently slower precipitation, produce spongy and more symmetrical structures. Thus, the more closely related the polymer and coagulant are, the slower the precipitation and the more symmetrical structures can be expected. The modified Lupasol additive is a relatively hydrophilic and polar polymer; when mixed with PSf, it decreases the polymer solution's precipitation rate [7].

Regarding the samples with additive 2, it can be observed that the M2-2% membrane presents a morphology very similar to the pure sample, M0, with a structure of finger-shaped channels and a dense porous layer. By increasing the additive content, M2-10%, it can be seen that the porous matrix disappears, leaving only the finger-shaped structure for the pores. The number of microvoids remains the same as the modified Lupasol content increases. The membrane's rapid precipitation can explain the pores' internal

structure during phase inversion. This internal structure is due to the rapid penetration of water, as a non-solvent, into the solvent-containing polymer solution.

Consequently, the morphology of the membrane is an asymmetric structure with finger-shaped pores. Since modified M2-10% is a hydrophilic polymer, it should contribute to faster precipitation of PSf-based membranes and leads to a more porous structure, which may enhance CO_2 absorption. Nevertheless, the additive structure and composition favour the interaction and absorption of CO_2.

3.2. Thermal properties

Table 2 presents the glass transition temperatures obtained from the corresponding thermogram in the different heating and cooling scans.

Table 2.
Glass transition temperature values of membranes (M0, M1-2%, M1-10%, M2-2%, and M2-10%).

	1st Heating	Cooling	2nd Heating
	T_g (K)	T_g (K)	T_g (K)
M0	475	452	474
M1-2%	469	437	465
M1-10%	473	446	469
M2-2%	471	444	469
M2-10%	476	447	475

The first heat shows the material with this thermal history. The cooling step imposes a standard thermal trace on the material, so the second heat makes it possible to compare the materials directly. Table 2 shows that glass transition values in the second heating are lower than in the first heating and more uniform among themselves. Considering the DSC curves corresponding to the second heating cycle, it can be observed that the glass transition temperature of the pure membrane without additives, M0, is higher than blended membranes. However, the glass transition temperature increases again as the additive increases. In both cases, the additives have a. Nevertheless, the hyperbranched polyethyleneimine might block the movement of the main chain and reduce the plasticizing effect.

3.3. Analysis of the dielectric spectra

The dielectric relaxation spectrum of each of the membranes (M0, M1-2%, M1-10%, M2-2%, and M2-10%) was studied in terms of loss tangent (tan d), the real and imaginary part of the complex dielectric permittivity (e'), (e'') respectively as a function of frequency and temperature. Figure 1 shows the values of (e ') increase when the temperature increases and the frequency decreases in all the membranes. However, the dielectric spectrum is more complex in the blended membranes due to the motions of hyperbranched polyethyleneimine together with polysulfone chains. It is especially relevant for lower frequencies because the relaxation of both components is more separated.

Figure 2 presents the isothermal dielectric relaxation spectrum in terms of the loss tangent as a function of frequency. Since all isothermal curves are represented on the same scale, the M0 membrane without additive shows higher loss tangent values than M1-2%, M1-10%, and M2-2% additive membranes. Specifically, the loss tangent values are very similar at low temperatures for all the membranes studied. In contrast, the isothermal curves that present the most similar behaviour at high temperatures correspond to the membranes M0, M1-2%, and M1-10%.

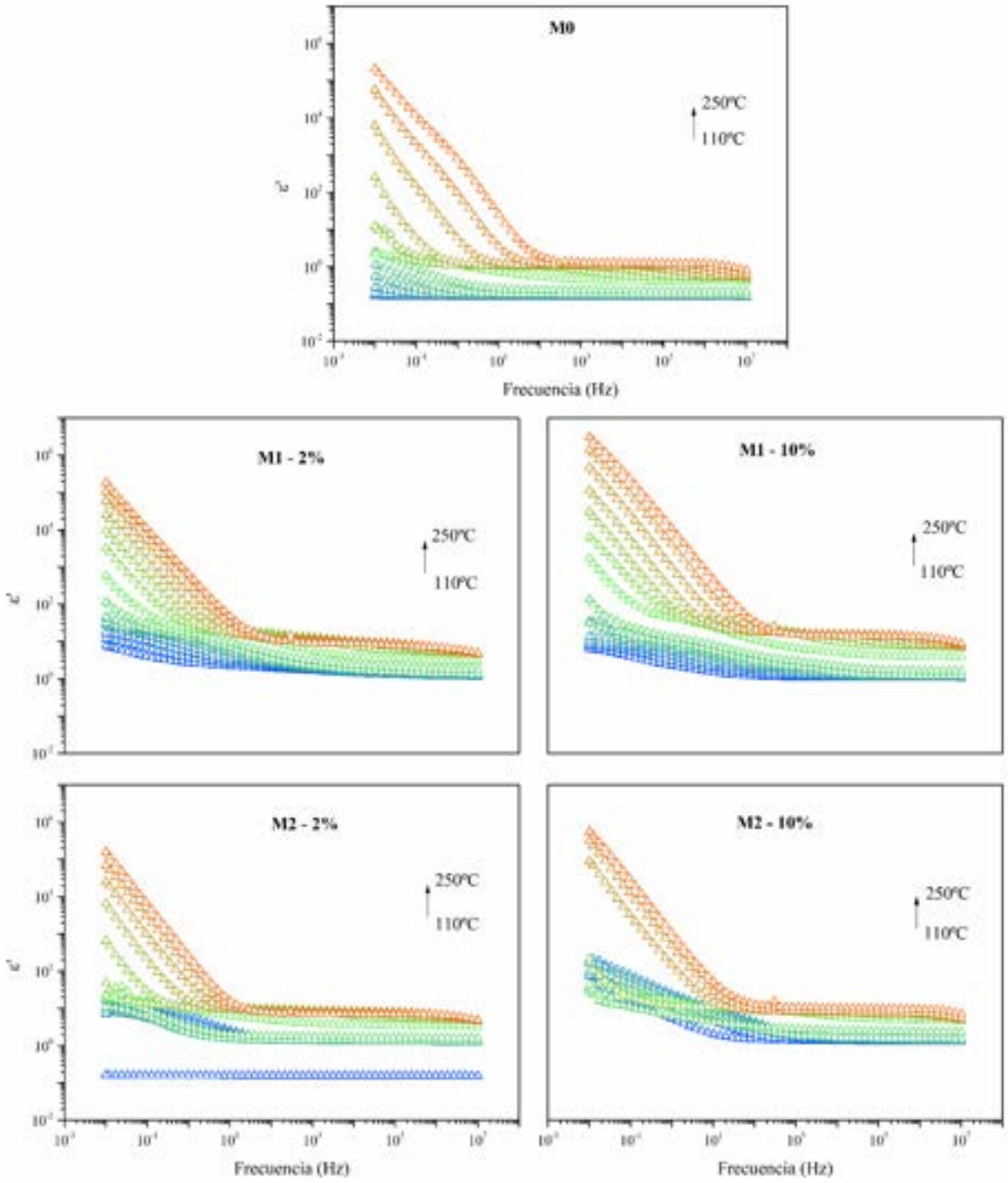

Figure 1. Isothermal curves in terms of the real part (ε') of the complex dielectric permittivity (ε*) for the membranes (M0, M1-2%, M1-10%, M2-2%, and M2-10%).

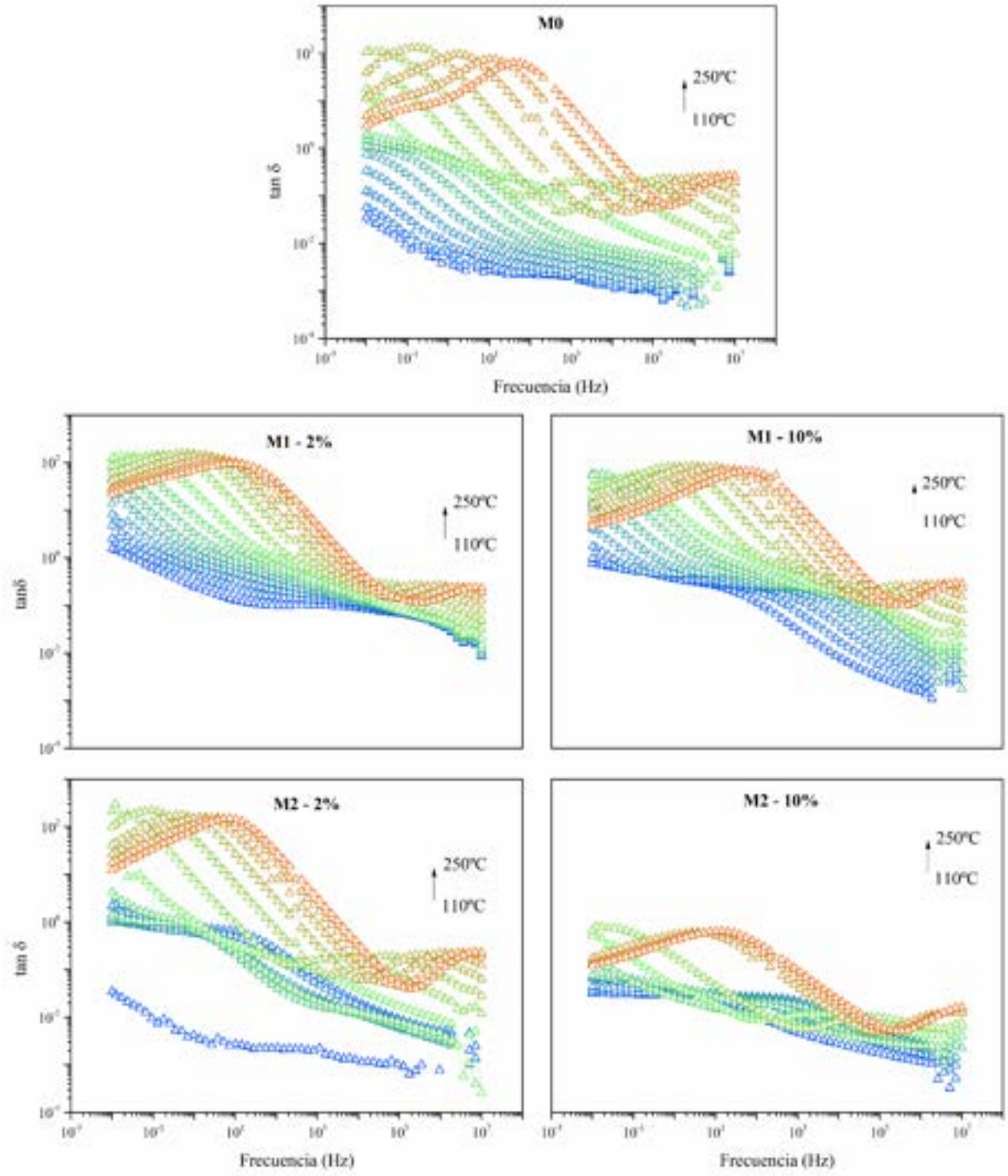

Figure 2. Isothermal curves in terms of the loss tangent (tan δ) for the membranes (M0, M1-2%, M1-10%, M2-2%, and M2-10).

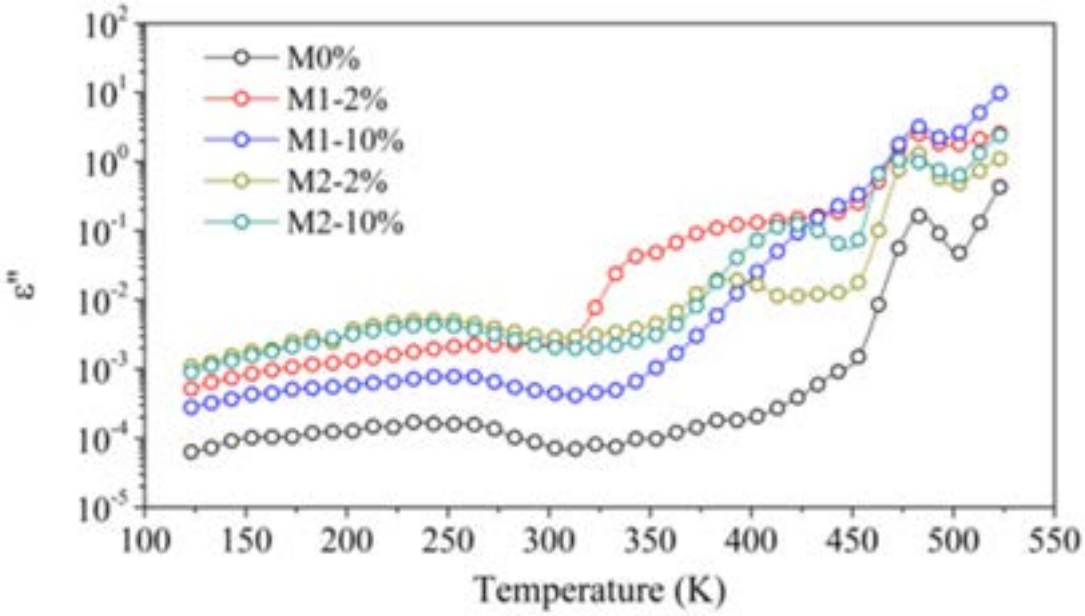

Figure 3. Isochronal curves of the imaginary part (ε'') of the complex permittivity (ε*) of the pure (M0) and blended membranes (M1-2%, M1-10%, M2-2%, M2-10%) at 10 Hz.

Figure 3 presents the dielectric spectrum of the M0 no blended membrane in terms of the imaginary part of the complex permittivity at 10 Hz. Three dielectric relaxation zones γ, ß, and a, with increasing temperature order, are observed to consist of three dielectric relaxations that might be ascribed to motions of local groups and the glass transition of polysulfone (PSf). However, the dielectric spectra of the blended membranes are more complex. Dielectric relaxations corresponding to molecular motions of local and segmental origin of the hyperbranched polyethyleneimine (HPEI) emerge together with the (γ, $ß_{PSf}$, and $α_{PSf}$) dielectric relaxations (transition of polysulfone PSf. The loss factor is higher for the M2-2% and M2-10% membranes than M0, indicating greater mobility of the molecular chains of the mixed membranes.

In order increasing temperature, γ relaxation zone appears between 125K and 223K, and it seems that the loss tangent is independent of the additive concentration in M2-2% and 10%. At higher temperatures, between 393K and 523K, the most prominent relaxations, $α_{PEI}$, and $α_{PSf}$ arise from the motion of the main chains produced by the glass transition of PSU and PEI, respectively. The temperature of $α_{PSf}$ relaxation peak around 483K slightly decreases with the additive concentration, whereas the most remarkable differences appear in the $α_{PEI}$ relaxation. These results confirm the plasticizing effect of hyperbranched polyethyleneimine modified with benzoyl chloride or phenyl isocyanate. The additive imposes fewer steric restrictions on molecular movement. Still, it simultaneously increases the number of chains that can move by plasticizing effect, therefore facilitating the ability of the membrane to diffuse CO_2.

3.4. Analysis of the dielectric spectra

Jonscher's model (Equation 2) quantified the electric conductivity. Table 3 presents the electrical modulus of conductivity, which increases as the temperature increases. Regarding M0, the n-parameter in both regions is equal to 1 and, therefore, is considered the ideal case where long-range pathways for ion transfer are available. Concerning the blended membranes, a more significant dispersion is found regarding the n-parameter.

M1-2% displays the lowest values that are not equal or less than 0.5, which would suggest a high degree of tortuosity, but it reflects that the landscape for ion transfer might not be as favourable as in the case of M1-10%, M2-2%, and M2-10%.

The membranes with phenyl isocyanate additive have the highest values. Note that in this region, the conductivity is higher for the membranes blended with phenyl isocyanate are more polar than benzoyl chloride.

Table 3.
Jonscher's parameters of the pure (M0) and the blended (M1-2%, M1-10%, M2-2%, M2-10%).

	T (K)	σ_{DC} x 10^{15} ($S \cdot cm^{-1}$)	A · 10^{13}	n	R^2
M0%	443	1.7 x 10^1	6.9 x 10^1	1	0.99
	463	1.6 x 10^2	4.3 x 10^1	1	0.99
	503	2.9 x 10^5	3.8 x 10^1	1	0.99
	513	1.5 x 10^6	3.2 x 10^1	1	0.99
M1-2%	373	4.4 x 10^1	1.5 x 10^2	0.86	0.99
	393	2.8 x 10^2	1.7 x 10^2	0.86	0.99
	503	1.1 x 10^7	6.6 x 10^3	0.83	0.99
	513	1.8 x 10^7	2.3 x 10^3	0.89	0.99
M1-10%	373	3.3 x 10^3	1.3 x 10^1	0.95	0.99
	393	1.3 x 10^4	1.7 x 10^1	0.95	0.99
	503	2.5 x 10^7	1.2 x 10^4	0.83	0.99
	513	5.8 x 10^7	5.4 x 10^3	0.89	0.99
M2-2%	373	1.1 x 10^3	4.5 x 10^1	0.96	0.99
	393	1.3 x 10^4	4.9 x 10^1	0.96	0.99
	503	4.3 x 10^6	1.0 x 10^3	0.94	0.99
	513	8.0 x 10^6	1.3 x 10^3	0.93	0.99
M2-10%	373	5.2 x 10^4	4.9 x 10^1	0.96	0.99
	393	3.9 x 10^5	6.2 x 10^1	0.95	0.99
	503	6.0 x 10^6	1.1 x 10^3	0.94	0.99
	513	1.4 x 10^7	1.1 x 10^3	0.94	0.99

The dielectric relaxation spectrum demonstrated that the molecular chain motions of blended membranes are higher than polysulphone membranes. The additive has a plasticizing effect and decreases the glass transition, but this temperature increases as the phenyl isocyanate and benzoyl chloride amount increases. These results agree with the direct air capture CO_2 absorption test carried out in a gas-liquid membrane contactor with the homemade module, as described elsewhere.

Briefly, the prepared membranes were placed in the module, where the top surface was exposed to ambient air by holes in the side of the module. The bottom surface of the flat sheet membrane is in contact with 100 mL of 0.64 M KOH solution as a liquid absorbent in a different flow rate range from 40 to 340 mL/min at room conditions (25 ºC and 1.013 x 10^5 Pa). After one hour, samples were collected, and the absorbed CO_2 amount was determined through a carbon dioxide ion-selective electrode (Hanna HI4105 connected with Thermo Scientific Orion Dual Star pH/ISE Benchtop meter, Thermo Scientific, Waltham, Massacusetts, USA) [11-12].

The CO_2 solubility increases with the addition of modified hyperbranched polyethyleneimine. It is regardless of the additive used (benzoyl chloride or phenyl isocyanate), according to the high affinity of the additive to carbon dioxide. The presence of basic nitrogen enhances the interaction between both molecules. Nevertheless, phenyl isocyanate exhibits higher CO_2 solubility concerning benzoyl chloride. The hyperbranched polyethyleneimine and phenyl isocyanate reaction produce urea groups with more affinities to CO_2. This has been validated through a CO_2 capture device, where a remarkable improvement in comparison with neat PSf (30%) is found. Overall, additive 2 determined better characteristics in terms of CO_2 permeability and capture when compared with additive 1. This information is unpublished (pol.20220773), and the authors are preparing a patent application for the absorption device.

4. Conclusions

Asymmetric polysulfone membranes blending with hyperbranched Lupasol G20 grafted with benzoyl chloride or phenyl isocyanate with 2% and 10%wt were prepared via phase-inversion precipitation to increase their ability for carbon dioxide capture at ambient pressure.

The resulting morphology of the blended membrane presents finger-like macropores together with meso- and micropores and a dense layer, which increases as the additive amount increases. The phenyl isocyanate awards a suitable morphology to improve CO_2 permeability and capture.

The glass transition temperature decreases with the addition of a lower amount of modified hyperbranched polyethyleneimine due to plasticizing effect of the additive. However, this temperature increases as the additive percentage increases.

The dielectric relaxation spectrum demonstrated additives' plasticizing effect and improved the molecular chain motions of blended membranes. The membranes with phenyl isocyanate additive have the highest values of conductivity.

All these results, in turn, indicate the importance of considering all these factors to find the most suitable composition to prepare polysulfone membranes which could favour gas permeation of CO_2.

5. References

[1] Masson-Delmotte, V.; Zhai, P.; Pirani, A.; Connors, S.L.; Péan, C.; Berger, S.; Caud, N.; Chen, Y.; Goldfarb, L.; Gomis, M.I.; et al. (Eds.) IPCC Climate Change 2021: The Physical Science Basis. Contribution of Working Group I to the Sixth Assessment Report of the Intergovernmental Panel on Climate Change; Cambridge University Press: Cambridge, UK, 2021.

[2] IPCC. Global Warming of 1.5 °C; International Panel on Climate Change: Geneva, Switzerland, 2018.

[3] S. Zhao, P.H.M. Feron, L. Deng, E. Favre, E. Chabanon, S. Yan, J. Hou, V. Chen, H. Qi, Status and progress of membrane contactors in post-combustion carbon capture: A state-of-the-art review of new developments, Journal of Membrane Science 511 (2016) 180-206.

[4] M. Rahbari-Sisakht, A.F. Ismail, D. Rana, T. Matsuura, D. Emadzadeh, Carbon dioxide stripping from water through porous polysulfone hollow fiber membrane contactor, Separation and Purification Technology 108 (2013) 119-123.

[5] M. Rahbari-Sisakht, A.F. Ismail, D. Rana, T. Matsuura, D. Emadzadeh, Carbon dioxide stripping from water through porous polysulfone hollow fiber membrane contactor, Separation and Purification Technology 108 (2013) 119-123.

[6] M. Rahbari-Sisakht, A.F. Ismail, D. Rana, T. Matsuura, Effect of novel surface modifying macromolecules on morphology and performance of polysulfone hollow fiber membrane contactor for CO2 absorption, Separation, and Purification Technology 99 (2012) 61-68.

[7] A. Zare, Novel polymeric membrane for artificial photosynthesis, (2022).

[8] S. Havriliak, S. Negami, A complex plane representation of dielectric and mechanical relaxation processes in some polymers, Polymer (Guildf). 8 (1967) 161–210.

[9] Havriliak, S. Negami, A complex plane analysis of a-dispersions in some polymer systems, J. Polym. Sci. Part C Polym. Symp. 14 (1966) 99–117.

[10] J.M. Charlesworth, Deconvolution of overlapping relaxations in dynamic mechanical spectra, J. Mater. Sci. 28 (1993) 399–404.

[11] A. Nogalska, M. Ammendola, B. Tylkowski, V. Ambrogi, R. Garcia-Valls, Ambient CO2 adsorption via membrane contactors Value of assimilation from air as nature stomata, Journal of Membrane Science 546 (2018) 41-49

[12] A. Zare, L. Perna, A. Nogalska, V. Ambrogi, P. Cerruti, B. Tylkowski, R. García-Valls, M. Giamberini, Polymer Blends for Improved CO2 Capture Membranes, Polymers 11(10) (2019) 1662.

Acknowledgments

The authors would like to thank the support of the European Union through the European Regional Development Funds (ERDF) and the Spanish Ministry of Economy, Industry, and Competitiveness for the research projects (PID2020-116322RB-C31) and (PID2020-116322RB-C32).

ULPGC
Universidad de
Las Palmas de
Gran Canaria

grres ULPGC
group for the research on renewable energy systems

P. Digitalization, big data, artificial intelligence in the energy sector

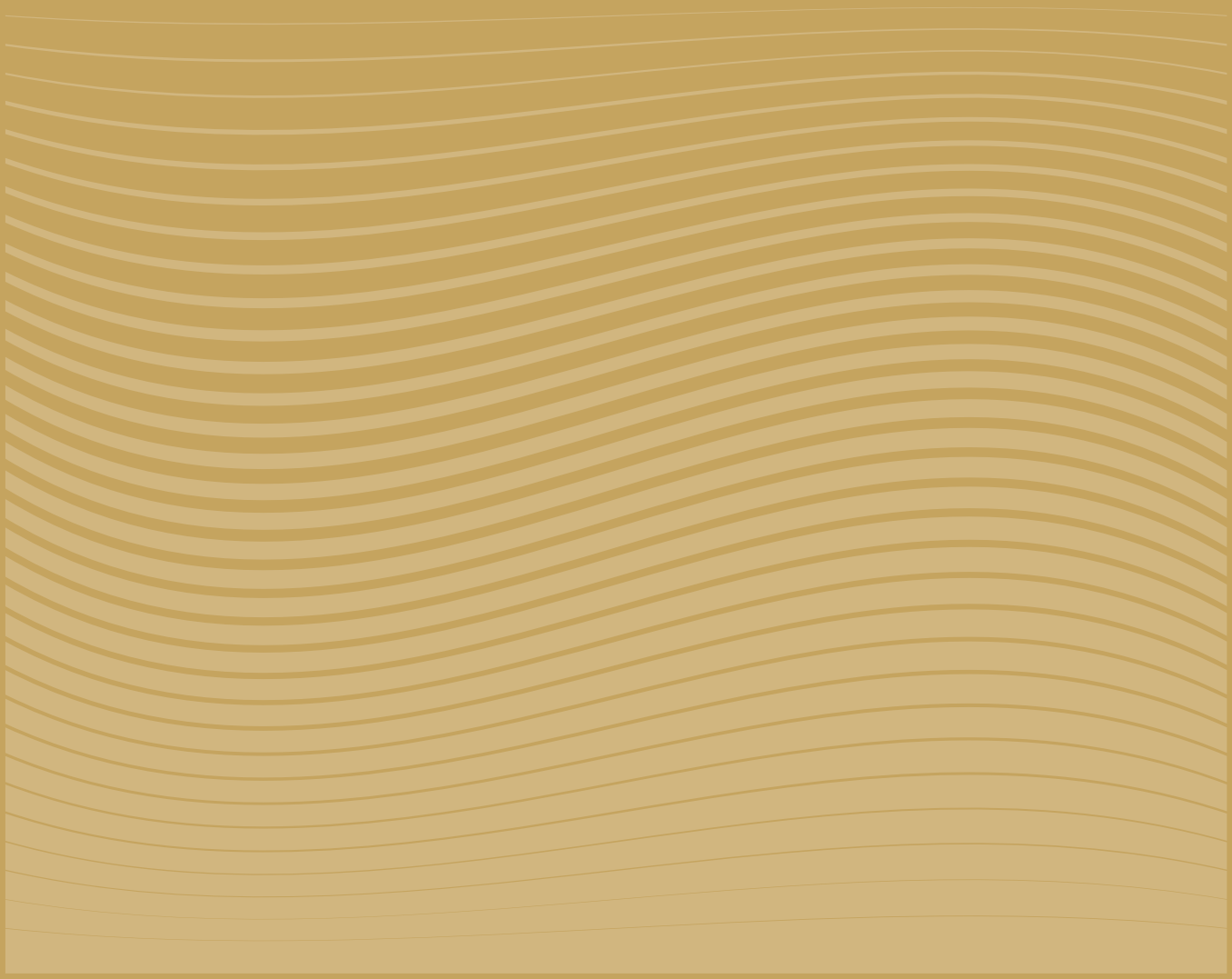

ECOS2023

PROCEEDINGS OF ECOS 2023 - THE 36TH INTERNATIONAL CONFERENCE ON
EFFICIENCY, **C**OST, **O**PTIMIZATION, **S**IMULATION AND ENVIRONMENTAL IMPACT OF ENERGY SYSTEMS
25-30 JUNE, 2023, LAS PALMAS DE GRAN CANARIA, SPAIN

A Novel Deep Learning-Based Technique for Smart Control of Heat Pumps Integrated into Solar District Heating Systems

Youssef Elomari[a], Carles Mateu[b], Marc Marín-Genescà[c], and Dieter Boer[d]

[a] Departament d'Enginyeria Mecànica, Universitat Rovira i Virgili, Av. Paisos Catalans 26, 43007 Tarragona, Spain, youssef.elomari@urv.cat
[b] GREiA Research Group, Department of Computer Science and Industrial Engineering, University of Lleida, 25001 Lleida, Spain, carles.mateu@udl.cat
[b] Departament d'Enginyeria Mecànica, Universitat Rovira i Virgili, Av. Paisos Catalans 26, 43007 Tarragona, Spain, carles.mateu@estudiants.urv.cat
[c] Departament d'Enginyeria Mecànica, Universitat Rovira i Virgili, Av. Paisos Catalans 26, 43007 Tarragona, Spain, marc.marin@urv.cat
[d] Departament d'Enginyeria Mecànica, Universitat Rovira i Virgili, Av. Paisos Catalans 26, 43007 Tarragona, Spain, dieter.boer@urv.cat

Abstract:

District energy systems provide many options for integrating renewable energy sources and energy storage systems into residential and commercial buildings. Solar district heating systems (SDHSs) contribute to the deployment of large-scale solar energy-based technologies. SDHS technical challenges during operation may occur due to not optimal control. Nevertheless, they can be overcome with smart control of an integrated heat pump. To address this problem TRNSYS (transient system simulation) software was used to develop the SDHS model; the system operates by employing a smart control approach for the heat pump, which is coupled to thermal storage tanks for domestic hot water and space heating to meet community demand. The methodological approach has been applied to an SDHS in Madrid (Spain) to provide for the heating demands of a neighbourhood that consists of 280 apartments in order to more effectively illustrate the abilities of the proposed control strategy. The present work focuses on the development of a co-simulation framework based on TRNSYS and Python for offline training of a control strategy based on deep reinforcement learning algorithms for a smart agent that will control the integrated heat pump into SDHS with seasonal storage system. The work will consider the life cycle cost analysis for the technical economic evaluation for the proposed control strategy. Results will show if the heat pump DRL-based control offers significant techno-economic benefits, compared to traditional control strategies.

Keywords:

solar district heating systems, thermal energy storage, heat pump, deep reinforcement learning, life cycle cost analysis

1. Introduction

District energy systems offer various options for integrating energy storage and renewable energy sources into residential and commercial buildings [1]. Solar communities with seasonal thermal energy storage [2] and solar thermal systems [3] are examples of such systems that can facilitate the advancement of fourth and fifth-generation district heating systems [4], [5]. Systems for district heating powered by solar energy help in the deployment of large-scale solar energy-based solutions. In fact, several prosperous large-scale solar district heating systems (SDHSs) are currently in use in nations including Austria, Canada, China, Germany, and Denmark [6]. Tian et al. [7] highlighted two successful large SDHSs. Even though the modeling and design of these systems have been thoroughly studied recently [8], [9], more research is needed to develop advanced control techniques for solar district heating systems.

Techniques for controlling HVAC (heating, ventilation, and air conditioning) are complex due to the way the system's components interact with one another and with the thermal dynamics of buildings. The continuous adjustment of the heating or cooling system while maintaining the comfort levels set by the occupants is one technique to reduce the amount of energy used for space conditioning. The conventional method for control, which is rule-based control (RBC), typically involves simple hysteresis loops that reheat or cool the building every time the temperature reaches a threshold.

Model predictive control (MPC) improves the control technique by allowing the use of predictions from outside variables like the weather, the electricity price, etc. This leads to a wider range and more efficient control compared to RBC. The primary aim is to control building temperature, with cost optimization being a secondary goal. While MPC outperforms RBC regarding its operation capability, it complicates the system and requires the availability of a model that accounts for the system dynamics. Due to the complexity of building thermal dynamics and heterogeneous environment disturbances, the classical rule-based and model-based approaches are frequently ineffective in practice [10].

Another control method is reinforcement learning (RL) which is a model-free approach where the agent learns the optimal action to take by "trial and error" without the need for previous knowledge of the system or process. Model-free methods can operate without a model of the environment [11]. RL techniques can learn by interacting with its environment and do not require any supervision. In recent years and within many fields, RL has become a strong alternative to MPC. The fundamental idea behind RL is that the optimal behavior or action is encouraged by way of a positive reward, while the least desirable action is punished by a negative reward [12], [13].

The drawbacks of conventional RL can be overcome by deep reinforcement learning (DRL), which enhances RL with deep neural networks to approximate the value function and policy function when those are hard to model due to the dimensionality of the problem. Therefore, the DRL approach is more suitable and flexible in terms of control strategies than traditional control approaches. DRL has been utilized extensively in both the business and academic fields, such as, in robotics [14], gaming [15], industrial systems [16], and autonomous vehicles [17].

The present work focuses on the development of a co-simulation framework based on TRNSYS (transient system simulation) and Python for offline training of a control strategy based on deep reinforcement learning algorithms for a smart agent that will control the integrated heat pump and seasonal storage system of a SDHS. The work will consider the life cycle cost analysis for the technical economic evaluation of the proposed control strategy.

2. Materials and method

This section describes the system’s details and the methodology used for system modeling and control.

2.1. Energy system description

An overview of the analyzed systems is presented in Figure 1. The main components of the system are the solar thermal collector (COL), the DHW storage tank (DHWT), a half-buried sensible seasonal storage tank (SST), an auxiliary natural gas heater (AUX), and a water-to-water heat pump unit (HP). This SDHS model was designed and based on the system proposed by Abokersh et al. [18] and Tulus et al. [19].

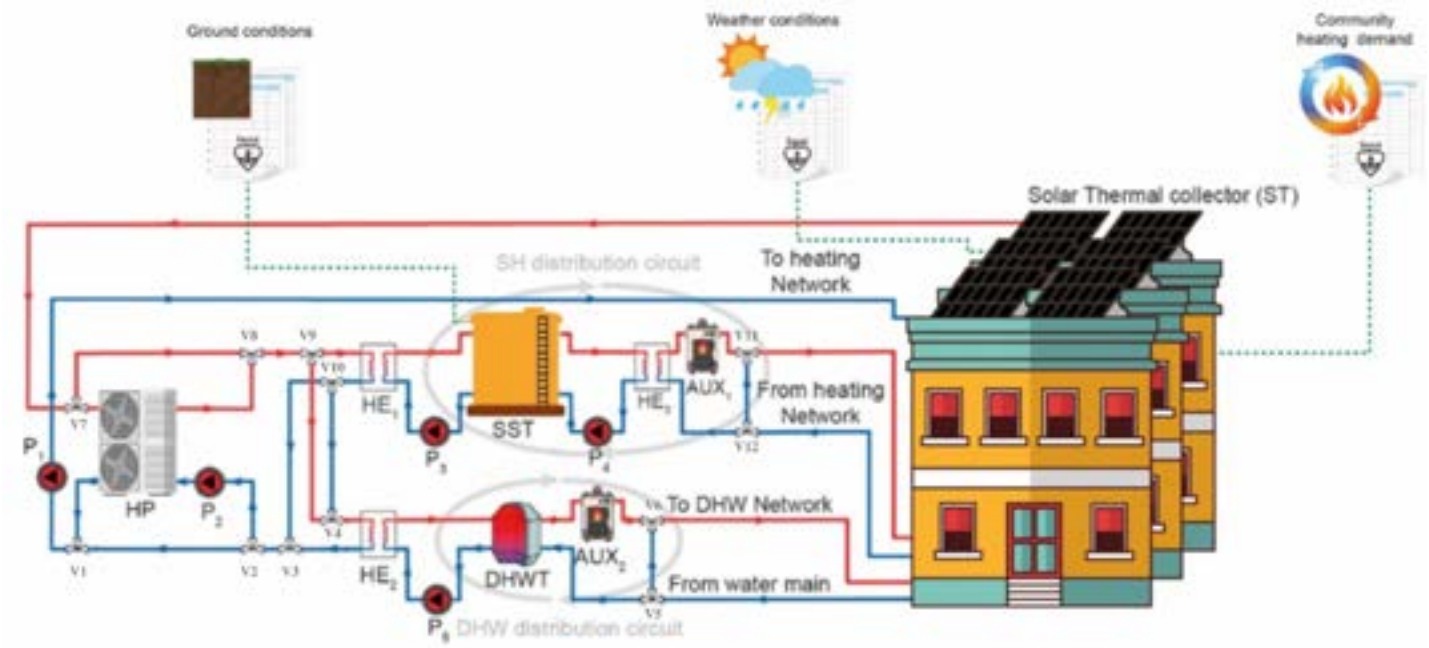

Figure. 1. An overview of the HP with SDHS integration's design.

As seen in Figure 1, the heat pump (HP) functions as a heat source for the SST when connected with the solar field circuit. In this arrangement, the district's space heating (SH) or domestic hot water (DHW) demand can be accomplished efficiently by the thermal energy collected from the COL or it can be stored in the SST. An adequate design of the heat pump that is incorporated in SDHS is required to meet the SH and DHW needs of a hypothetical residential neighbourhood throughout the year. The heat from solar collectors is transferred to the DHWT in the DHW operation mode, with the intervention of P1, P2, and P5 pumps through and switching on the following valves V1, V2, V3, V4, V5, V6, V7, V8, and V9. The AUX2 is activated with the help of V5 and V6, when solar thermal energy is insufficient to meet the demand in the DHW network. The HP unit is inactive while in DHW mode. In SH operation mode, heat is transferred from ST to SST through HE1 using pumps P1, P2, and P3 and valves V1, V2, V3, V8, V9, and V10. Under particular circumstances, the heat generated by the HP is either provided to the SST for charging up the heat stored or delivered directly to the SH. While the daily DHW demand is supplied by the short-term storage DHWT, the SH demand is supplied throughout the winter by the SST. Here, it is crucial to remember that the heat provided for the SH is at a low-temperature level (50 °C), whilst the heat supplied for the DHW is at a high-temperature level (60 °C). Finally, the auxiliary heater acts as a supplement if the solar field, SST, and HP are incapable of providing the required amount of heat.

2.2. Co-simulation TRNSYS-Python framework

TRNSYS (transient system simulation) program is a tool, for simulating an energy system's dynamic behavior. In the simulation studio, TRNSYS's components are linked graphically to solve algebraic and differential equations. The TRNSYS simulation environment's dynamic nature helps to introduce the SHDS model in a more realistic manner. This software does, however, have significant limitations when it comes to the development and optimization of HVAC system control. Some intelligent control algorithms, such as DRL-based control approaches, are inconvenient and difficult to use directly in the built-in software [20].

In order to address this issue, a co-simulation testbed with a SDHS TRNSYS model and DRL-based control approach has been built in order to enable dynamic data transfer and interaction between these two systems as depicted in Figure 2. As DRL-based training requires a large amount of training data, (i.e., of simulations), those simulations would have to be done in parallel to maximize computational resources usage and to reduce the required time for the experimentation. In order to control such simulations and to be able to train the DRL control software, they have been developed, following the de facto standard for DRL training, as a Gym environment [21].

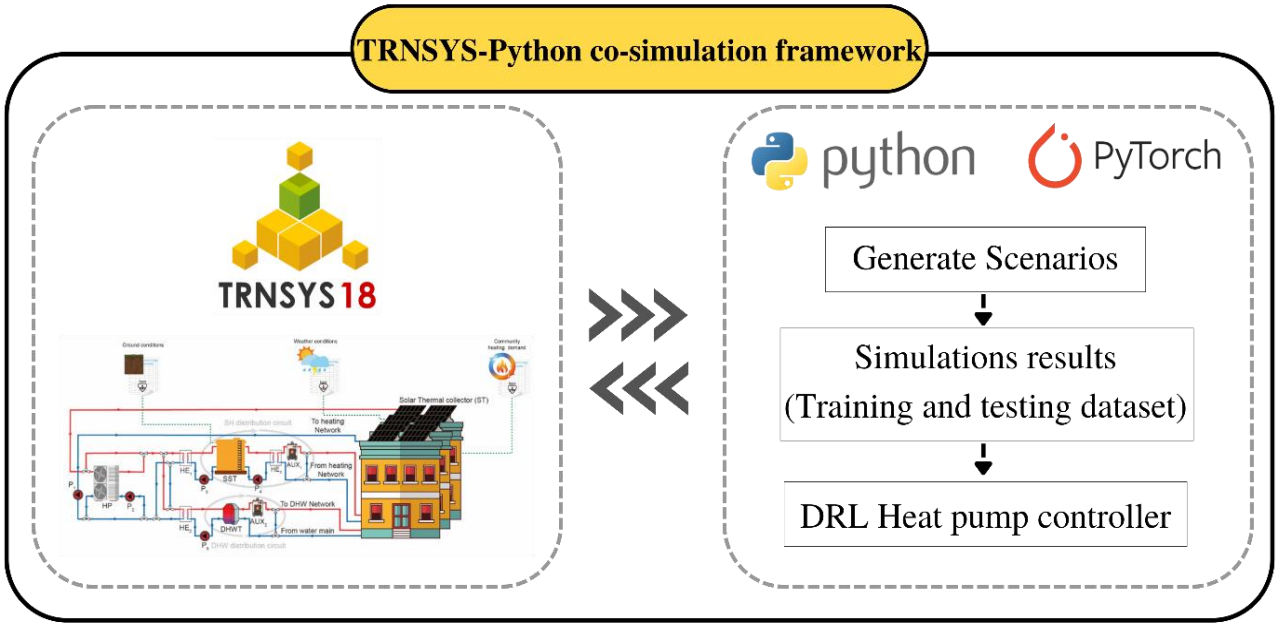

Figure. 2. TRNSYS-Python co-simulation framework.

2.3. Life cycle cost analysis

In the present study, the life cycle costing (LCC) methodology is employed to conduct the economic evaluation of the proposed control strategy of the integrated heat pump integration into a community sized SDHS, which is based on the work of Tulus et al. [19] and Abokersh et al. [18].

The fundamental concept of the LCC technique involves using a future cost approach. This involves calculating the present value of all the expenses incurred over the lifespan of the system, using a discounting method. By adding the initial capital cost (IC), operational cost (OC), maintenance cost (MC), and total equipment replacement cost (RC), we can estimate the net present cost (NPC).

$$NPC = IC + OC + MC + RC \tag{1}$$

The initial capital cost refers to the cost of investment at the beginning of a project. This cost includes the cost of purchasing the equipment, its installation and transportation, as well as any contingencies expenses:

$$IC = (1 + \alpha_{CF}) + \sum_K (PEC_K . FBM_K) \tag{2}$$

In the given equation, PEC_k refers to the initial cost of purchasing equipment unit k, FBM_k represents the bare module factor that takes into account the costs associated with installation and transportation, while α_{CF} is the contingency fees factor. The PEC_k value is adjusted to its present value from the base year (year A) to the year of installation (year B) using the Chemical Engineering Plant Cost Index (CEPCI) [19], with the help of the following equation:

$$PEC_K = PEC_K^{year\ A} \frac{CEPCI^{year\ B}}{CEPCI^{year\ A}} \quad \forall k \tag{3}$$

The operational cost (OC) refers to the total amount of yearly operating expenses that includes the maintenance costs for various equipment units and facilities, the consumption of electricity by hydraulic equipment, and the usage of natural gas by auxiliary heaters. This cost can be stated using the following equation:

$$OC = C_M PWF_M + C_P PWF_P + C_{AUX} PWF_{AUX} \tag{4}$$

In the given equation, C_M, C_P, and C_{AUX} represent the yearly expenses associated with maintenance, hydraulic equipment (such as pumps), and auxiliary consumption costs, respectively. To account for inflation and the time value of money, the present worth factor (PWF) is calculated, taking into consideration the proposed system's lifetime (Ne), inflation rate (i), and discount rate (d), which can be expressed as follows:

$$PWF = \begin{cases} \frac{1}{d-i}\left[1-\left(\frac{1+i}{1-d}\right)^{N_e}\right] & \forall_i \neq d \\ \frac{N_e}{1+i} & \forall_i = d \end{cases} \quad (5)$$

During the operation of the proposed SDHS, certain pieces of equipment have a high rate of depreciation and will require replacement. The cost of replacing them can be calculated using the following equation, which takes into account the present value of the equipment:

$$RC = PVF_n \sum_K (PEC_K . FMB_K) \quad (6)$$

The present value factor of future cash flows in year n is denoted as PVF_n. In this present work, the solar collectors, DHW storage tank, heat pump, heat exchangers, and auxiliary heaters are among the equipment that will require replacement due to their fast depreciation rate over the system's lifetime. PVF_n can be expressed as follows:

$$PVF_n = \frac{(1+i)^n}{(1+d)^n} \quad (7)$$

2.4. Case study

The methodological approach has been applied to an SDHS in Madrid (Spain) to provide for the heating demands of a neighborhood that consists of 10 buildings in order to more effectively illustrate the abilities of the proposed framework. This case study has already been described in a former article where more details can be found [18]. Each building has 28 apartments, each of which has 90 m^2 of usable space [22] and is equipped with a DHW system and radiant underfloor heating system to meet the requirement for space heating (SH) and domestic hot water (DHW) at 50 °C and 60 °C, respectively. Each building requires yearly 191.34 MWh of heating. Based on Tulus et al. [19] and Abokersh et al. [18], the proposed SDHS was previously validated.

2.4.1. Heating demand profiles

In order to compare the proposed DRL-based control strategy to the rule-based control strategy in Abokersh's study [18] the SH and DHW inputs will remain the same. Figure 3 shows the monthly DHW and SH demand for a neighborhood in Madrid that consists of 280 residential apartments.

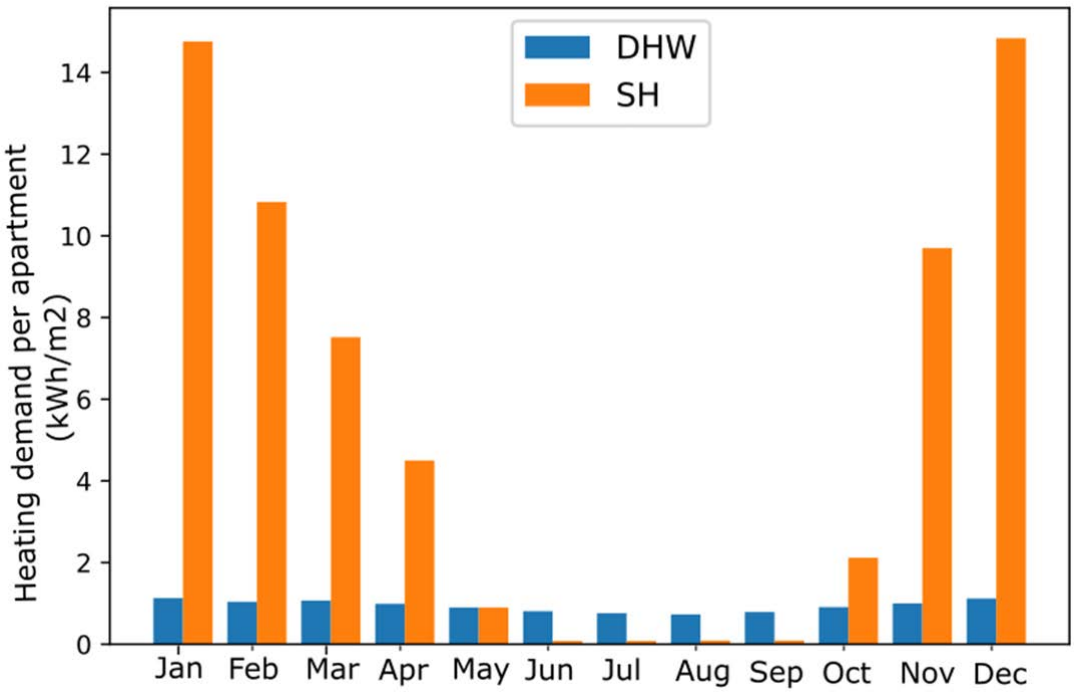

Figure. 3. Demand profiles for domestic hot water and space heating per month for a neighbourhood of 280 apartments in Madrid.

The Energy Plus database is used to gather the weather data for Madrid. This includes the incident solar radiation, ambient temperature, relative humidity, and other pertinent information.

3. Results

In this phase, using the Madrid case study in a residential community of 280 apartments the design variables of various equipment components are taken into account. While formulating the optimization problem, we are testing whether the HP smart control strategies can improve the techno-economic viability of SDHS.

Figure 4 illustrates the optimum system costs for various Net Present Cost terms and payback periods. A clear tradeoff between the proposed objective functions is indicated since the movement from scenario 1 to 5 at both traditional controls (A) and (B) increases the total cost. Thus, Abokersh et al.[18] Pareto's optimal solutions appear to provide a modest economic benefit that provides an opportunity to make improvements on system controlling, which is the objective of our proposed smart control strategy using the deep reinforcement learning algorithm.

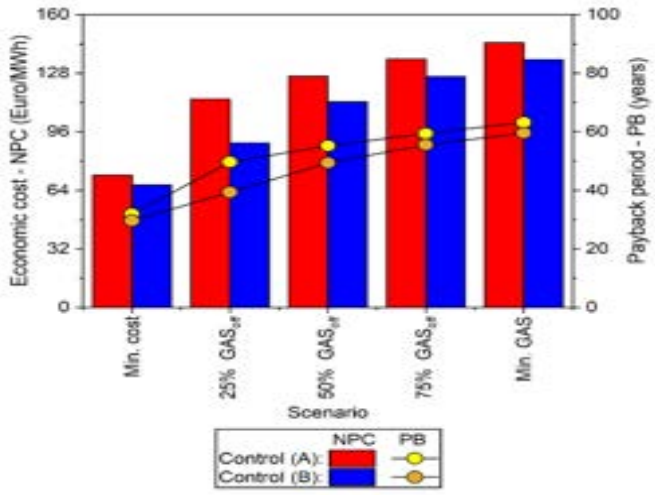

Figure. 4. The economic benefits and the payback period for the optimal Pareto solutions of the HP integrated with SDHS under control strategy (A) and (B) *[18]*.

In addition to calculating the financial gains, the proposed methodology also determines how each technology can operate at its optimal level. Hence, a figure will be illustrated to depict the percentage of grid electricity, fossil fuels (natural gas), and solar energy, following the example in Figure 5.

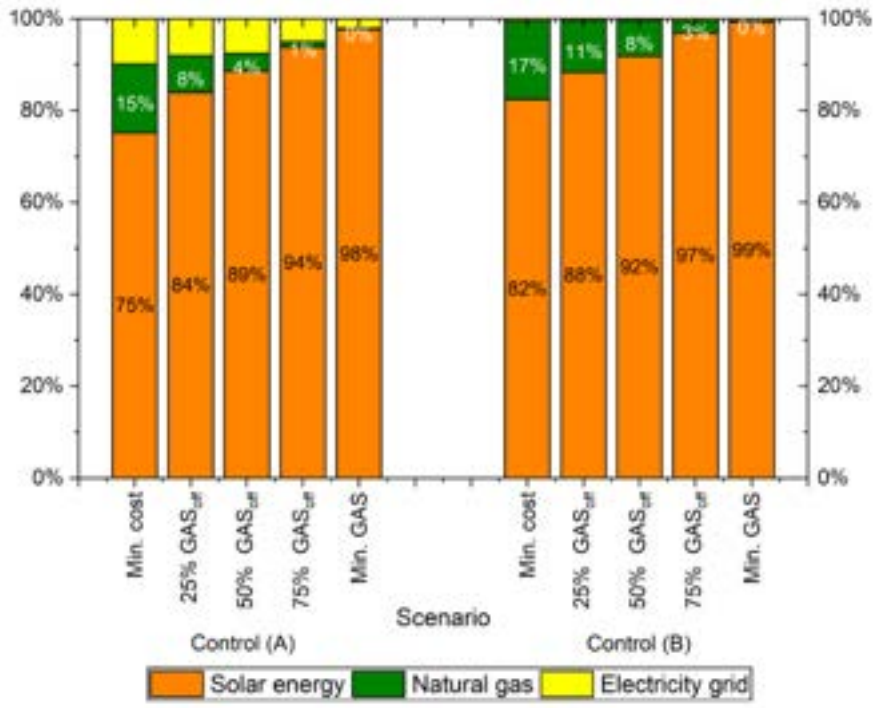

Figure. 5. The share of technologies for the optimal Pareto solutions of the HP integrated with SDHS under control strategy (A) and (B) *[18]*.

We are currently starting the model training and hope to have the results ready when the conference takes place.

4. Conclusions

The current study aims to develop a dynamic model for a solar district heating system (SDHS) integrated with a heat pump in Madrid (Spain), to provide the heating demands of a small community of 280 apartments. A co-simulation framework using TRNSYS, and Python was developed to evaluate the benefits of a smart control strategy based on a deep reinforcement learning algorithm, which will control the heat pump. The current situation can be characterised by concluding the methodology development and initiating the model training. The following step will be to evaluate the control strategy from an economic point of view by way of the life cycle cost analysis.

The aim of this study is to assess the advantages of the proposed smart control strategy using artificial intelligence in terms of technical performance and cost-effectiveness, as well as to determine if the control strategy offers significant benefits over traditional methods. The results of the study could make the solar district heating system a more feasible solution in the market, particularly in light of current policy changes on natural gas prices.

Acknowledgments

The authors would like to acknowledge financial support from the “Ministerio de Ciencia, Innovación y Universidades” of Spain [PID2021-127713OA-I00, PID2021-123511OB-C31, PID2021-123511OB-C33, PID2021-124139NB-C22 - MCIN/AEI/10.13039/501100011033/FEDER, UE & TED2021-129851B-I00].

Nomenclature

AUX	*auxiliary heater fueled by natural gas*
COL	*solar collector field*
DHW	*domestic hot water*
DHWT	*domestic hot water storage*
DL	*deep learning*
DRL	*deep reinforcement learning*
HE	*heat exchanger*
HP	*heat pump*
HVAC	*heating, ventilation, and air Conditioning*
LQR	*linear-quadratic regulator*
MPC	*model predictive control*
P	*centrifugal pump*
RBC	*rule-based control*
RL	*reinforcement learning*
SDHS	*solar district heating system*
SH	*space heating*
SST	*seasonal storage tank*
TES	*thermal energy tank*
TRNSYS	*transient system simulation program*

References

[1] D. Olsthoorn, F. Haghighat, and P. A. Mirzaei, “Integration of storage and renewable energy into district heating systems: A review of modelling and optimization,” *Solar Energy*, vol. 136, pp. 49–64, 2016, doi: 10.1016/j.solener.2016.06.054.

[2] F. M. Rad and A. S. Fung, “Solar community heating and cooling system with borehole thermal energy storage - Review of systems,” *Renewable and Sustainable Energy Reviews*, vol. 60, pp. 1550–1561, 2016, doi: 10.1016/j.rser.2016.03.025.

[3] C. Winterscheid, J. O. Dalenbäck, and S. Holler, “Integration of solar thermal systems in existing district heating systems,” *Energy*, vol. 137, pp. 579–585, 2017, doi: 10.1016/j.energy.2017.04.159.

[4] H. Lund *et al.*, “The status of 4th generation district heating: Research and results,” *Energy*, vol. 164, pp. 147–159, 2018, doi: 10.1016/j.energy.2018.08.206.

[5] S. Buffa, M. Cozzini, M. D’Antoni, M. Baratieri, and R. Fedrizzi, “5th generation district heating and cooling systems: A review of existing cases in Europe,” *Renewable and Sustainable Energy Reviews*, vol. 104, no. June 2018, pp. 504–522, 2019, doi: 10.1016/j.rser.2018.12.059.

[6] D. Tschopp, Z. Tian, M. Berberich, J. Fan, B. Perers, and S. Furbo, “Large-scale solar thermal systems in leading countries: A review and comparative study of Denmark, China, Germany and Austria,” *Appl Energy*, vol. 270, no. January, p. 114997, 2020, doi: 10.1016/j.apenergy.2020.114997.

[7] Z. Tian *et al.*, “Large-scale solar district heating plants in Danish smart thermal grid: Developments and recent trends,” *Energy Convers Manag*, vol. 189, no. October 2018, pp. 67–80, 2019, doi: 10.1016/j.enconman.2019.03.071.

[8] L. Mesquita, D. McClenahan, J. Thornton, J. Carriere, and B. Wong, “Drake Landing solar community: 10 years of operation,” *ISES Solar World Congress 2017 - IEA SHC International Conference on Solar Heating and Cooling for Buildings and Industry 2017, Proceedings*, no. August, pp. 333–344, 2017, doi: 10.18086/swc.2017.06.09.

[9] R. Renaldi and D. Friedrich, “Techno-economic analysis of a solar district heating system with seasonal thermal storage in the UK,” *Appl Energy*, vol. 236, no. October 2018, pp. 388–400, 2019, doi: 10.1016/j.apenergy.2018.11.030.

[10] L. Yu, S. Qin, M. Zhang, C. Shen, T. Jiang, and X. Guan, “A Review of Deep Reinforcement Learning for Smart Building Energy Management,” *IEEE Internet Things J*, vol. 8, no. 15, pp. 12046–12063, 2021, doi: 10.1109/JIOT.2021.3078462.

[11] V. Mnih *et al.*, “Human-level control through deep reinforcement learning,” *Nature*, vol. 518, no. 7540, pp. 529–533, Feb. 2015, doi: 10.1038/nature14236.

[12] V. Mnih *et al.*, “Playing Atari with Deep Reinforcement Learning.”

[13] L. Yu, S. Qin, M. Zhang, C. Shen, T. Jiang, and X. Guan, “Deep Reinforcement Learning for Smart Building Energy Management: A Survey.” [Online]. Available: https://www.researchgate.net/publication/343626535

[14] O. Kotevska *et al.*, “Methodology for Interpretable Reinforcement Learning Model for HVAC Energy Control,” in *Proceedings - 2020 IEEE International Conference on Big Data, Big Data 2020*, Dec. 2020, pp. 1555–1564. doi: 10.1109/BigData50022.2020.9377735.

[15] A. Chen, T. Dewan, M. Trivedi, D. Jiang, A. Aditya, and S. Mohammed, “The Use of Reinforcement Learning in Gaming The Breakout Game Case Study.pdf,” no. April, 2020, doi: 10.36227/techrxiv.12061728.

[16] J. Zhao, C. Yang, W. Dai, and W. Gao, “Reinforcement Learning-Based Composite Optimal Operational Control of Industrial Systems with Multiple Unit Devices,” *IEEE Trans Industr Inform*, vol. 18, no. 2, pp. 1091–1101, 2022, doi: 10.1109/TII.2021.3076471.

[17] J. Kober, J. A. Bagnell, and J. Peters, “Reinforcement learning in robotics: A survey,” *International Journal of Robotics Research*, vol. 32, no. 11, pp. 1238–1274, 2013, doi: 10.1177/0278364913495721.

[18] M. H. Abokersh, M. Vallès, K. Saikia, L. F. Cabeza, and D. Boer, “Techno-economic analysis of control strategies for heat pumps integrated into solar district heating systems,” *J Energy Storage*, vol. 42, 2021, doi: 10.1016/j.est.2021.103011.

[19] V. Tulus, M. H. Abokersh, L. F. Cabeza, M. Vallès, L. Jiménez, and D. Boer, “Economic and environmental potential for solar assisted central heating plants in the EU residential sector: Contribution to the 2030 climate and energy EU agenda,” *Appl Energy*, vol. 236, no. November 2018, pp. 318–339, 2019, doi: 10.1016/j.apenergy.2018.11.094.

[20] H. Zhang, D. Wu, and B. Boulet, “A review of recent advances on reinforcement learning for smart home energy management,” in *2020 IEEE Electric Power and Energy Conference, EPEC 2020*, Nov. 2020. doi: 10.1109/EPEC48502.2020.9320042.

[21] G. Brockman *et al.*, “OpenAI Gym,” Jun. 2016, [Online]. Available: http://arxiv.org/abs/1606.01540

[22] IDAE Secretaría General Departamento de Planificación y Estudios, “Análisis del consumo energético del sector residencial en España INFORME FINAL,” 2011.

Data-driven tool for early building energy performance diagnostic

Olaia Eguiarte[a], Antonio Garrido-Marijuan[b], Iñigo López[c], Noelia Vicente-Gómez[d] Ander Romero-Amorrortu[e]

[a] TECNALIA, Basque Research and Technology Alliance (BRTA), 48160 Derio, Spain, olaia.eguiarte@tecnalia.com, CA,
[b] TECNALIA, Basque Research and Technology Alliance (BRTA), 48160 Derio, Spain, antonio.garridomarijuan@tecnalia.com,
[c] TECNALIA, Basque Research and Technology Alliance (BRTA), 48160 Derio, Spain, inigo.lopez@tecnalia.com,
[d] TECNALIA, Basque Research and Technology Alliance (BRTA), 48160 Derio, Spain, noelia.vicente@tecnalia.com,
[e] TECNALIA, Basque Research and Technology Alliance (BRTA), 48160 Derio, Spain, ander.romero@tecnalia.com,

Abstract:
The building sector is responsible for a large part of the final energy consumption in Europe. One of the most relevant steps in the process of reducing energy consumption in buildings is the energy performance diagnostic. In this paper, a data-driven methodology to obtain early energy performance assessment of commercial buildings using the energy signature approach is used. As a result, a web-dashboard and API that can analyse user data input and produce streamlined outputs like suggestions for energy-saving measures is developed. In order to prove the correct functioning of the tool, a demo site of a commercial building in Dublin has been used.

Keywords:
Data-driven tool, building performance diagnostic, energy signature, commercial buildings

1. Introduction

The building sector is one of the largest consumers of resources at European level in terms of both material and energy aspects throughout all stages of a construction project [1], contributing to 40% of energy consumption and 36% of carbon emissions. An estimated 75% of buildings in the European Union are inefficient, yet only 1% undergoes renovation each year [2]. Non-residential buildings account for approximately 25% of Europe's 25 billion m^2 of useful building floor area, with 28% being wholesale or retail premises, 23% offices, 11% hotels and restaurants, and 4% sports facilities [3]. Commercial landlords often own these types of buildings and rent or lease them to one or more tenants. The split incentive problem is a significant obstacle to energy-efficient renovations in commercially rented buildings, where the benefits of a transaction do not go to the person who pays for it [4]. In this context, it is necessary to develop, test, validate and exploit new business models that lead to greater uptake of Smart Energy Services deployed via performance-based contracting in the commercial rented sector, supported by more accurate and dynamic measurement and verification of energy savings and flexible consumption in order to identify and develop business opportunities.

There are already protocols such as the guide proposed by ASHRAE [5] which set a reference frame for measurement of energy and demand savings of heating, cooling and air-conditioning. In the commercial building context, ASHRAE [6] developed a book providing standardized set of performance measurement protocols that can be applied internationally. Regarding heat load forecasting alternatives for buildings, one of the most suitable alternatives is provided by data-driven demand forecasting models. A wide variety of data-driven models exist and have been successfully implemented for early building performance diagnosis. Moreover, several authors have implemented this approach at district scale [7-9]. Data-driven models can be classified in different groups and one of them is the black-box models, which are purely based on data and statistical techniques with no physical interpretation of the building. In this sense, one of the more common types of black-box models are the energy signature models, which can provide successful results for monthly and seasonal data as demonstrated in several research [10-14]. Energy signature models predict a building's energy consumption based on external climate data. They are usually represented as a graph of overall energy use versus outdoor air temperature [15]. Furthermore, using daily or hourly intervals can provide further insights into typical energy demands in comparison to monthly or weekly patterns, allowing for a more accurate analysis [16].

Therefore, smart solutions are needed to identify potential flexibility opportunities and energy efficiency upgrades with high energy saving potential and communicates estimations of their expected added value to both tenants and building owners.

2. Objectives

This paper presents a new data-driven energy diagnostic approach to identify the most significant energy streams in commercial buildings using a minimal dataset. The algorithms consider general information about the building, such as location, size, usage, and HVAC characteristics, as well as overall facility energy consumption. The diagnostic provides granular data for integration with energy tariffs in real practice, dividing energy use by energy carrier and electricity use by billing schedules. The methodology for the energy use diagnostics is detailed in section 3. The present paper summarizes the work performed, including the development of a user-friendly web-dashboard and Application Programming Interface (API) that allows users to upload specific building information and datasets for early building energy diagnostics. The resulting baseline is cross-referenced against current building performance databases for benchmarking, and key performance metrics are calculated to identify energy-saving measures. Data from a real case study is used to test the algorithms. The outputs from this case study are included in section 6.

3. Methodology

This section details a data-driven methodology approach for carrying out early energy performance diagnostics of commercial buildings by considering energy building signature models. In this case, the developed algorithms are later made available for general use via a web-dashboard and an API. The calculation of the energy signature, the diagnostic requirements and main input and outputs from the developed tool are detailed in following subsections.

3.1. Energy building signature

Energy patterns in buildings are typically represented by one of the behaviours depicted in Figure 1. This model is a general approach to modelling energy loads in buildings and can be considered a good approximation in cases where heating and cooling are provided by the same energy source and where the heating and cooling loads do not overlap in temperature range.

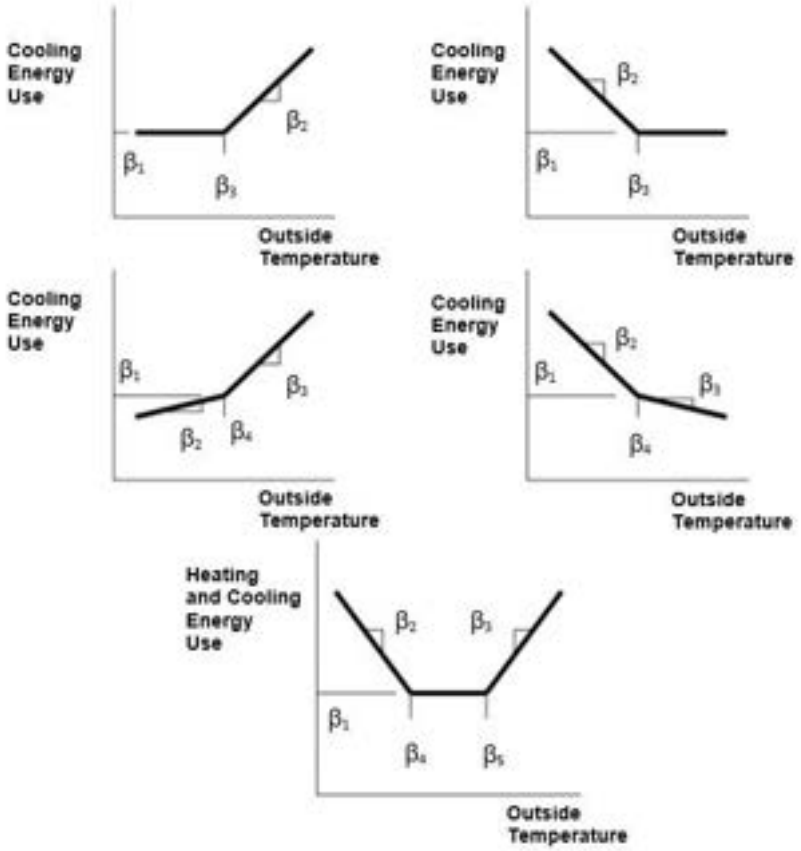

Figure 1. Overall approach to changepoint models. Top row: 3 parameter cooling and heating models. Second row from top: 4 parameter cooling and heating models. Bottom row: five parameter heating and cooling model. Adapted from [17].

Therefore, a regression model has been incorporated to depict the average performance of the commercial buildings on working days. The calculation method chosen to generate the energy signature is a segmented linear regression, in particular, the piecewise regression. Piecewise regression involves fitting a linear regression model to data that has one or more breakpoints where the slope changes. In the Python package used to perform this task, this type of regression follows the approach described by [18], where the breakpoint positions and the linear models are simultaneously fitted using an iterative method. According to [19], the general form of a one breakpoint model is implemented as in Eq. (1). As it is a non-linear relationship, it cannot be solved directly through linear regression. To take a linear approximation it is necessary to use a Taylor expansion around some initial guess for the breakpoint, ψ (0).

$$y = ax + c + \beta(x - \psi)H(x - \psi) + \zeta \quad (1)$$

This results in a linear relationship and thus a new breakpoint estimate, ψ (1), which can be used to perform ordinary linear regression using the stats models Python package [20]. After that, the process must be iterated until the breakpoint estimate converges and the algorithm stops. For multiple breakpoints, the same approach can be used with a multi-variate Taylor expansion around an initial guess for each breakpoint.

The resulted regression will just consider the outdoor temperature but no other significant factors such as solar radiation, occupancy, ventilation, etc. For that reason, 10% upper and lower boundaries are added to account those other aspects.

3.2. Energy use diagnostics

The purpose of the energy use diagnostics is to assess the energy consumption and associated costs of commercial buildings in this case. To adapt the diagnostics to the methodology scope, some requirements have been considered:

- Data sources. Available data sources such as on-site Building Energy Management Systems and data from utilities or energy suppliers.
- Time intervals. The processes should be frequency adaptable to match different time intervals (hourly, monthly data, etc.).
- Subsystems. Assign different energy use to specific areas and/or subsystems in the building.
- Benchmark. Compare energy consumption with other buildings of similar size, configuration, use and climatic conditions.
- Measures. Identify energy-saving measures and determine their potential.

By applying the developed algorithms in section 3.1, a regression with 10% boundaries is obtained. In this case, data located out of that boundary will be considered as misuse energy and some energy saving measures will be given to match the regression boundaries. These measures include optimizing heating and cooling schedules, upgrading lighting systems and heating/cooling equipment, and improving the building envelope.

3.3. Tool description

The above detailed methodology enabling early building performance diagnostics is accessible via a web-dashboard. To ensure user-friendliness, the API facilitates communication with the algorithms by simplifying the underlying calculations and exposing only the necessary objects to stakeholders without requiring knowledge of the operations that occur behind the scenes. Consequently, the web-dashboard enables users to upload specific building information and datasets to obtain early building energy diagnostics through the API, which accesses the developed algorithms.

3.3.1. Input data

To enhance user-friendliness, the input data has been simplified. While additional data such as bank holidays and HVAC characteristics could enable more functionalities and analysis, simplicity has been prioritized to make the application more appealing to potential users. The minimal dataset needed includes the following information.

- Building characteristics:
    - Building location (city): this information will be used to load the weather file of the indicated city or location. The developed API presents a set of 3 preloaded locations; Dublin (Ireland), Madrid (Spain) and Thessaloniki (Greece).
    - Building size (m^2): the total area of the building will be used to normalize its consumption and to compare it to the reference values.
- Energy data with hourly granularity (electricity, natural gas, or other fuels) in kWh.
- Service provided: it is necessary to indicate whether the energy data loaded corresponds to heating, cooling, or heating and cooling.

- Actual building usage:
    - Opening and closing hours.
    - Working days.

3.3.2. Data analysis

Before proceeding to the analysis of the uploaded data, a pre-processing step is performed. This includes a study that analyses the validity of the uploaded data, eliminates possible outliers and erroneous measurement values, transforms the hourly data to a daily frequency and indicates whether the final data quantity, after cleaning, is sufficient for further analysis. If the pre-processing gives satisfactory results, the analysis of the data is performed to generate the building's energy signature.

Three different analysis processes are performed on the uploaded consumption data:

- Non-working hours consumption analysis: based on the hourly frequency data as well as the information provided on days and times of use of the building, a study of the building's consumption is carried out to determine how much is consumed during non-working periods.
- Benchmarking: if the uploaded data cover a whole year, a comparison of the total consumption with the reference values is made.
- Energy signature: daily frequency data is classified according to whether it is a working or non-working day. A piecewise regression is applied in the working day dataset. The information of whether the provided data corresponds to heating, cooling or both is used to determine the number of breakpoints of the regression.

3.3.3. Output

The different results of the analysis are reflected in a graph where the regression line, the 10% boundaries and the uploaded data are shown. The outputs are listed below:

- Energy misuse in non-working hours.
- Energy consumption comparison against reference values.
- Energy signature of the building.
- Qualitative analysis of the building and its system based on the calculated breakpoint in the piecewise regression.

4. User interface of the tool

Figure 2. Web-dashboard, serving as interface between users and algorithms.

As a result of the detailed methodology, an API and web-dashboard were developed. The user interface is linked to the developed algorithms via API. Once the calculations are performed, some recommendations are offered to the user.

This tool allows to users to provide data to obtain an early building performance diagnostics web-dashboard. The user enters the building characteristics through the different available options as shown in Figure 2. As stated above, data must be introduced in hourly frequency.

5. Case study

The proposed methodology is applied to a demo site located in Dublin (Ireland), consisting of six floors with a classical façade constructed in reconstituted stone precast concrete panels. The building was constructed in 1996 and was retrofitted in 2014, after a prolonged period of being unoccupied. After the refurbishment, the building was partially occupied in 2015 for office uses in the following portions of floor area as shown in Table 1. The landlord area includes the ground floor reception, stair cores, toilets, basement level, and subbasement level.

Table 1. Floor areas per occupancy.

	Area (%)	Area (m^2)	Occupancy (persons)
Landlord	29.14%	1,809.00	
Tenant 1 (Investment Services)	43.72%	2,714.36	265
Tenant 2 (Private Banking and Asset Management)	12.97%	805.20	65
Tenant 3 (Hedge Fund)	14.18%	880.44	120

A site survey of the case study building was conducted to gather the necessary information required for applying the tool, such as HVAC system components, occupancy, and schedules information, available monitored data, etc. Due to the building use, there are no energy intensive processes associated to the normal operation of the building. Therefore, main consumptions are related to lighting and HVAC systems. The opening times of the offices are from 8h to 18h from Monday to Friday. There is no occupancy during weekends or holidays. The input data of the case study building have been introduced via the developed web-dashboard as shown in Figure 3.

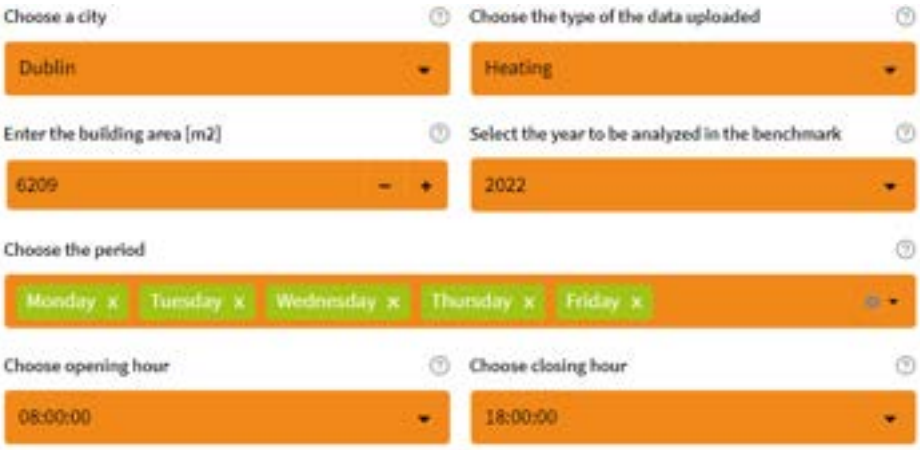

Figure 3. Input data introduced for the Irish demo-site in the web-dashboard.

Apart from input data detailed in Figure 3, heating consumption data (see Figure 4) were also obtained in hourly basis from 26th January 2022 to 14th December 2022 (both included). The boxplot graph shows the statistical distribution of the consumption for each day of the week.

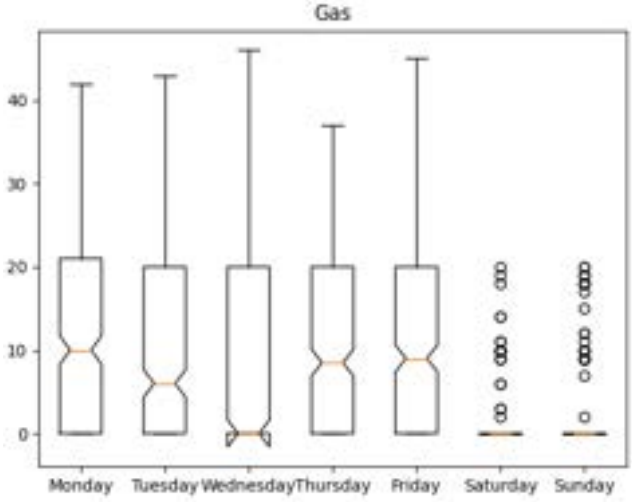

Figure 4. Heating energy consumption distribution during a typical week in the Dublin building.

6. Results

The present section includes the early building diagnostic for a demo site located in Ireland. Once the required input data have been uploaded (see Figure 3), the API provided results analysis as shown in Figure 5. The graphic shown in Figure 5 represents the daily aggregate values of heating consumption (kWh) versus daily average outdoor temperature, where red points belong to weekend and other non-working days. On the other hand, grey points represent heating consumption for working days. As detailed in methodology, 10% upper and lower boundaries have been added to the model and are represented in the graphic with a grey shadow. Data out of this boundary represents energy misuse.

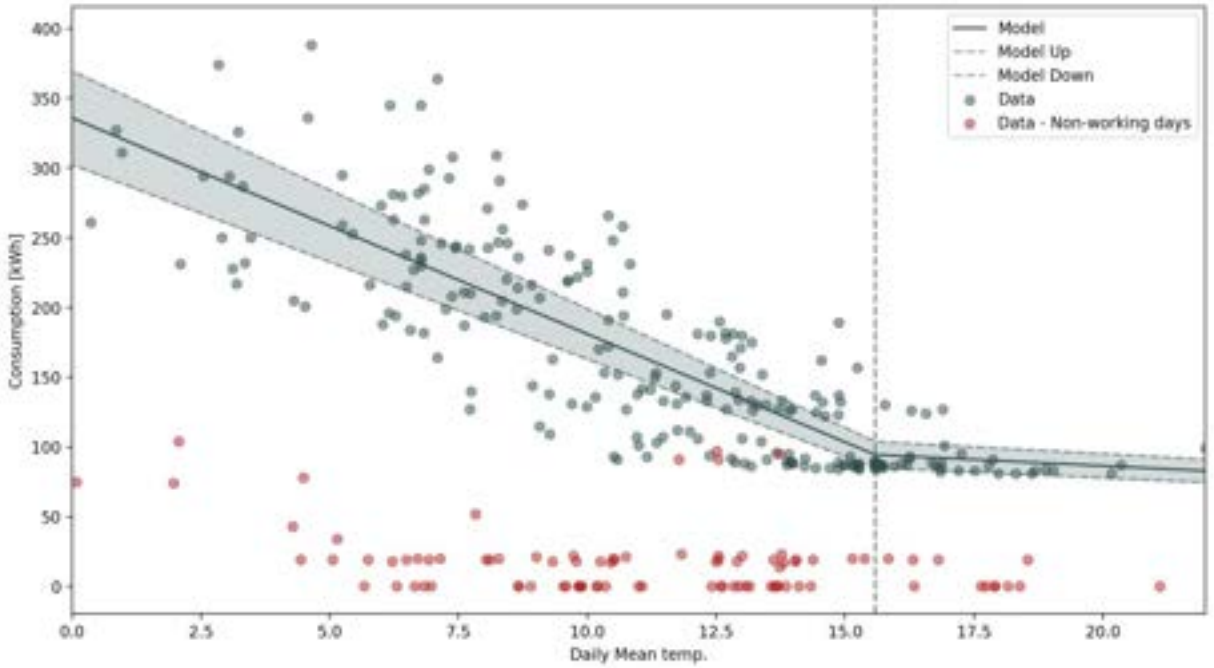

Figure 5. Daily aggregated values of heating consumption (kWh) versus daily average outdoor temperature.

As observed in the figure, heating consumption is weather dependent and increase with low outdoor temperatures. The changepoint corresponding to the regression model take place for a mean outdoor temperature of 15.58ºC. That means that the building heating demand starts for outdoor temperature under 15.58ºC, which could be considered as high. Some consumption peaks have been observed for non-working days (see red dots in Figure 5), which are assumed to be failures on the monitoring system and can be neglected.

7. Conclusions and discussion of results

This paper presents the development of an API and a web-dashboard which allows users for an early building performance diagnostic.

The creation of the API that accesses the developed algorithms highlights the critical role that data availability and synchronization play in this context. The recommended diagnostic procedure heavily relies on utility meters (which are still being delivered with some difficulties) and climate data, which is available from open sources. However, obtaining data from energy sub-meters, building usage, and indoor comfort conditions is still of interest and would significantly enhance performance assessment.

The algorithms created for its implementation in the API have been employed to evaluate the data provided by a commercial demo building in Dublin. The evaluation of this data has been thoroughly presented and analysed in this document to serve as an exemplary case study of the methodology. By application of the developed methodology, it is possible to identify the most significant energy streams in the building using minimal information.

After the application of the regression model, it has been proven that it correctly represents the average performance of the offices during operational days. Data collected in days where the heating consumption is out of a 10% boundary from the model are identified as misuse days and might be separated from non-operational days. Some recommendations can be made based on the analysis performed.

The early building diagnostic outcomes involve the computation of key performance indicators, which enable the automatic identification of energy-saving measures when compared against current building performance databases.

Acknowledgements

This study has been carried out in the context of SmartSPIN project. This project has received funding from the European Union's Horizon 2020 research and innovation programme under grant agreement No 101033744. This publication reflects only the authors' views and neither the Agency nor the Commission are responsible for any use that may be made of the information contained therein.

Nomenclature

c	first segment
H	Heavised step function
x	data
y	data

Greek symbols

α	gradient of the first segment
β	change in gradient from the first to second segments
ξ	noise term
ψ	breakpoint position

References

[1] Fraga-De Cal, B.; Garrido-Marijuan, A.; Eguiarte, O.; Arregi, B.; Romero-Amorrortu, A.; Mezzasalma, G.; Ferrarini, G.; Bernardi, A., «Energy Performance Assessment of Innovative Building Solutions Coming from Construction and Demolition Waste Materials», Materials 2021, 14, 1226. https://doi.org/10.3390/ma14051226

[2] «Energy performance of buildings directive». https://energy.ec.europa.eu/topics/energy-efficiency/energy-efficient-buildings/energy-performance-buildings-directive_en (Accessed on 11th May 2023).

[3] M. Economidou, «Europe's buildings under the microscope», *Building Performance Institute Europe (BPIE)*, otc. 2011, ISBN: 9789491143014

[4] M. Economidou and P. Bertoldi, «Practices to overcome split incentives in the EU building stock», European Council for an Energy Efficient Economy, 2015, ECEEE 2015 Summer Study Proceedings

[5] «ASHRAE Guideline 14-2014: Measurement of Energy, Demand and Water Savings», ASHRAE, 2014

[6] «APMPC ASHRAE Performance Measurement Protocols for Commercial Buildings», ASHRAE, 2010

[7] O. Eguiarte, A. Garrido-Marijuan, R. Garay-Martinez, M. Raud, and I. Hagu, «Data-driven assessment for the supervision of District Heating Networks», *Energy Rep.*, vol. 8, pp. 34-40, dic. 2022, doi: 10.1016/j.egyr.2022.10.212.

[8] A. Garrido-Marijuan, O. Eguiarte, R. Garay-Martinez, M. Raud, and I. Hagu, «Lessons Learnt from Substation Inspection on Low Temperature District Heating Networks», *Environ. Sci. Proc.*, vol. 11, n.º 1, Art. n.º 1, 2021, doi: 10.3390/environsciproc2021011033.

[9] M. Lumbreras *et al.*, «Data driven model for heat load prediction in buildings connected to District Heating by using smart heat meters», *Energy*, vol. 239, p. 122318, ene. 2022, doi: 10.1016/j.energy.2021.122318.

[10] B. Arregi and R. Garay, «Regression analysis of the energy consumption of tertiary buildings», *Energy Procedia*, vol. 122, pp. 9-14, sep. 2017, doi: 10.1016/j.egypro.2017.07.290.

[11] P. Westermann, C. Deb, A. Schlueter, and R. Evins, «Unsupervised learning of energy signatures to identify the heating system and building type using smart meter data», *Appl. Energy*, vol. 264, p. 114715, abr. 2020, doi: 10.1016/j.apenergy.2020.114715.

[12] M. Eriksson, J. Akander, and B. Moshfegh, «Development and validation of energy signature method – Case study on a multi-family building in Sweden before and after deep renovation», *Energy Build.*, vol. 210, p. 109756, mar. 2020, doi: 10.1016/j.enbuild.2020.109756.

[13] L. Belussi and L. Danza, «Method for the prediction of malfunctions of buildings through real energy consumption analysis: Holistic and multidisciplinary approach of Energy Signature», *Energy Build.*, vol. 55, pp. 715-720, dic. 2012, doi: 10.1016/j.enbuild.2012.09.003.

[14] R. Hitchin and I. Knight, «Daily energy consumption signatures and control charts for air-conditioned buildings», *Energy Build.*, vol. 112, pp. 101-109, ene. 2016, doi: 10.1016/j.enbuild.2015.11.059.

[15] FR. Jacobson. «Energy signature and energy monitoring in building energy management systems». *CLIMA 2000 Congress,* Copenhagen, 1985.

[16] G. Nordström, H. Johnsson, and S. Lidelöw, «Using the Energy Signature Method to Estimate the Effective U-Value of Buildings», en *Sustainability in Energy and Buildings*, A. Hakansson, M. Höjer, R. J. Howlett, y L. C. Jain, Eds., en Smart Innovation, Systems and Technologies, vol. 22. Berlin, Heidelberg: Springer Berlin Heidelberg, 2013, pp. 35-44. doi: 10.1007/978-3-642-36645-1_4.

[17] M. T. Paulus, D. E. Claridge, and C. Culp, «Algorithm for automating the selection of a temperature dependent change point model», Energy Build., vol. 87, pp. 95–104, Jan. 2015, doi: 10.1016/j.enbuild.2014.11.033.

[18] V. Muggeo, «Estimating Regression Models with Unknown Break-Points», *Stat. Med.*, vol. 22, pp. 3055-71, oct. 2003, doi: 10.1002/sim.1545.

[19] C. Pilgrim, «piecewise-regression (aka segmented regression) in Python», *J. Open Source Softw.*, vol. 6, n.º 68, p. 3859, dic. 2021, doi: 10.21105/joss.03859.

[20] S. Seabold and J. Perktold, «Statsmodels: Econometric and Statistical Modeling with Python», presented in Python in Science Conference, Austin, Texas, 2010, pp. 92-96. doi: 10.25080/Majora-92bf1922-011.

PROCEEDINGS OF ECOS 2023 - THE 36TH INTERNATIONAL CONFERENCE ON
EFFICIENCY, **C**OST, **O**PTIMIZATION, **S**IMULATION AND ENVIRONMENTAL IMPACT OF ENERGY SYSTEMS
25-30 JUNE 2023, LAS PALMAS DE GRAN CANARIA, SPAIN

Enabling Reinforcement Learning for Flexible Energy Systems through Transfer Learning on a Digital Twin Platform

Carlotta Tubeuf[a], Felix Birkelbach[b], Anton Maly[c], Maximilian Krause[d] and René Hofmann[e]

TU Wien, Institute of Energy Systems and Thermodynamics, Vienna, Austria,
[a] carlotta.tubeuf@tuwien.ac.at, CA
[b] felix.birkelbach@tuwien.ac.at
[c] anton.maly@tuwien.ac.at
[d] maximilian.krause@tuwien.ac.at
[e] rene.hofmann@tuwien.ac.at

Abstract:
Pumped storage power plants compensate for fluctuations in the electricity grid and improve the stability through grid services. By increasing the flexibility of pumped storage power plants, they could compensate fluctuations in an even greater extent and thus accelerate the shift to a fully renewable energy system. One way to do this is to accelerate the switching between operating modes within pumped storage stations. For this, we propose to apply reinforcement learning (RL) to control the start and stop processes within a hydraulic machine. RL has been shown to outperform traditional optimal control methods, however, safety concerns are stalling research on applying RL for process control in safety-sensitive energy systems. To enable the safe and reliable transfer of the algorithm's learning strategy from a virtual test environment to the physical asset, we present a concept for applying RL via a digital twin platform. To demonstrate this concept, we set up a simulation model for the operating behavior during the start and stop processes of a lab-scale pump-turbine and validate it with experimental data. On this virtual representation, we test the application of RL to optimally control the blow-out process within pump-turbines. We present the structure of the deep Q-learning (DQN) RL algorithm we trained and the necessary problem formulations. Our results show that the DQN algorithm is suitable for finding the optimal operating strategy to blow-out the pump-turbine runner. We discuss the viability of our approach for the control of a pump-turbine and outline the next steps to test RL on a lab-scale model machine.

Keywords:
Reinforcement Learning, Digital Twin, Hydro Power, Process Control, Pump-Turbine, Transfer Learning.

1. Introduction

To reach the transition to a clean energy future, renewable energy systems, and especially wind and solar power technologies, will be expanded massively over the next years [1]. The energy sector is thus confronted with the growing share of volatile renewable energy systems in the grid. To balance out fluctuations, other energy sources and storage systems, such as pumped storage power plants, will need to increase not just in capacity but also in flexibility [2].

An approach to make pumped hydro storage systems more flexible is the acceleration of the switching between operating modes of pumped hydro machine units. Pumped storage power plants can be equiped with ternary sets, consisting of a pelton or francis runner and a storage pump, or with reversible pump turbines, where the machine unit can act as a turbine as well as as a pump. When switching from turbine to pump mode in pump-turbines, the runner is typically being blown-out, i.e. the water is being displaced by air, to minimize the start-up torque. This blow-out process is also necessary for both generator types when operating in synchronous condenser mode, which is used for compensating reactive power in the power grid [3].

To reveal optimization potential for faster changes of operating conditions in general and the blow-out process in particular, we propose to use a reinforcement learning (RL) algorithm for process control within the machine unit. RL is a type of machine learning (ML) in which an agent interacts directly with its environment. It aims to learn an optimal decision policy, guided by a scalar reward signal [4]. The application of RL in industrial control settings has received a lot of attention in recent years because it has been shown to outperform traditional optimal control methods [5]. However, safety concerns limit most use cases to simulated environments [6]. While research in the areas of robotics (e.g. [7, 8]) and manufacturing (e.g. [9]) seems to be leveraging the transition

of simulated to real-world applications of RL for process control, the implementation of an RL algorithm to critical infrastructure, such as hydropower systems, is still far from being realized [6].

To enable RL for flexible energy systems, we recently proposed a three-step learning method that uses transfer learning (TL) to transfer a pre-learned RL algorithm via a digital twin (DT) platform from a simple data model over the virtual representation of the machine to the real world machine unit [10]. Based on this method, which will be explained in Section 2.1., we will present the simulation model that was set up to act as the virtual representation of the lab-scale reversible pump-turbine where we plan to test the control of the blow-out process through RL in the future. We then describe the structure of the RL algorithm that we used and discuss our results for implementing the RL agent to control the blow-out process within the simulation model. Finally, we give an outlook on future research and draw a conclusion.

2. Methods

2.1. Reinforcement Learning on a Digital Twin Platform

When operating critical infrastructure, reliability and safety are crucial. Simultaneously, the replacement of standard controllers with RL algorithms to control processes is gaining in attention [6, 11, 12], which may be of interest for continuously revealing optimization potential and automating a flexible operation within energy systems. Hence, to enable the application of RL for process control within safety-sensitive energy systems, requirements for the trustworthiness of the RL algorithm need to be established and satisfied. Therefore, we propose a three-step learning method, that combines the benefits of RL and TL on a DT platform, as presented in our recent journal publication [10]. Figure 1 shows the concept for applying RL on a DT platform.

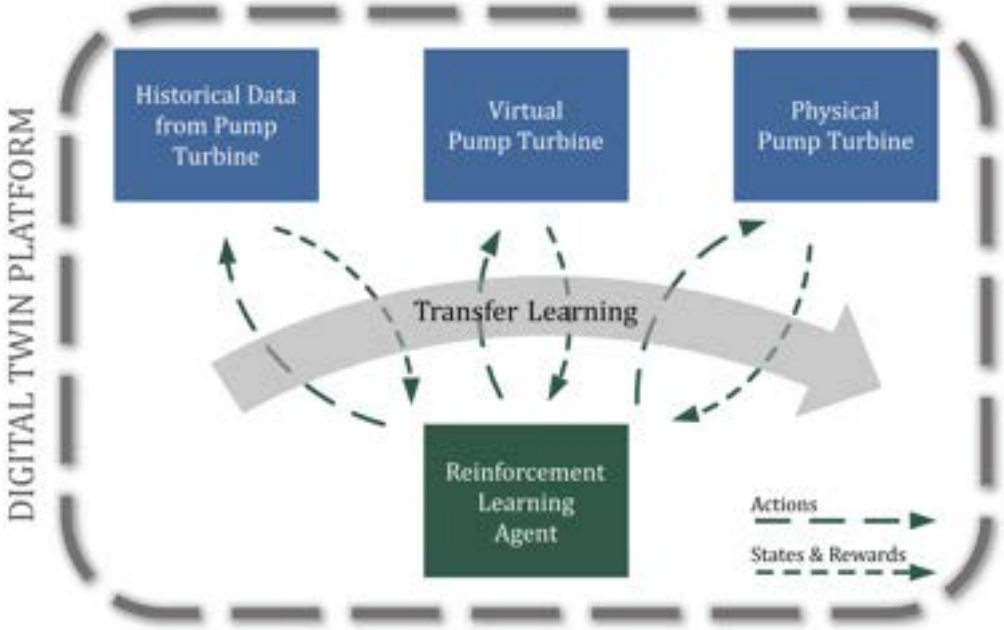

Figure 1: Concept for the application of reinforcement learning (RL) on a digital twin (DT) platform, adapted from [10].

Firstly, pre-training is done with a basic data model, followed by, secondly, training on an exact simulated replica of the actual asset. Thirdly, the pre-learned strategy is being adapted to the real machine unit. This pre-training can substantially reduce technical safety concerns related to learning and operating the actual power system by efficiently limiting the RL agent's action space. Figure 2 shows the general concept of a DT platform, as proposed by Kasper et al. [13], that integrates all three environments for the three-step RL approach: the historical data model, the virtual replication, and the physical unit, allowing TL to be used as a service to continuously enhance the RL agent's strategy.

2.2. Simulation Model

The virtual entity of our DT platform consists of a simulation model of the pump-turbine test rig at the laboratories of the Institute of Energy Systems and Thermodynamics (IET) at TU Wien (see Figure 3). The model pump-turbine consists of seven runner blades and is equipped with 20 guide vanes and 20 stay vanes. The simulation model is built using the Simscape language together with blocks from the Simscape standard libraries within the MATLAB/Simulink environment [14–16]. The model allows for the simulation of various operating

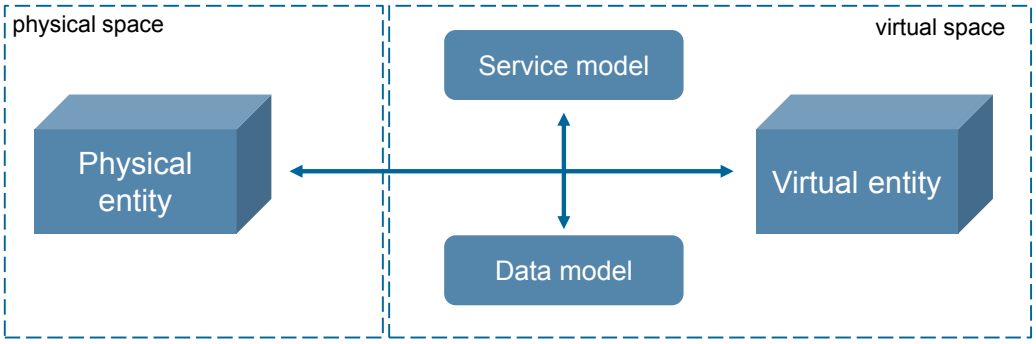

Figure 2: Schematic representation of a generic DT platform, adapted from [13].

Figure 3: Test rig with scale reduced model of a radial pump-turbine at the hydraulic lab of IET, from [10].

conditions. The pump-turbine characteristics were modeled following the assumption of the affinity laws for the behavior of pumps and turbines with variable speeds. Equation 1 describes the linear dependence between the flow rate Q and the rotational speed n, and the cubic relation between n and the pressure difference built up by the pump-turbine Δp_{PT}.

$$\frac{Q_1}{Q_2} = \frac{n_1}{n_2} \approx \sqrt{\Delta p_{\mathrm{PT}}} \tag{1}$$

To make up for deviations between the simulated and the measured values for the flow rate Q, a representative fitting rate η, similar to an efficiency rate, depending on the rotational speed was introduced. The resulting Equation 2 for the pressure difference Δp_{PT} therefore comprises the efficiency rate $\eta(n)$, the scaling factors k_{PT} and k_ω, all compensating for actual flow conditions in the real machine unit, and the angular speed ω.

$$\Delta p_{\mathrm{PT}} = \eta(n) k_{\mathrm{PT}} (\omega - k_\omega)^2 \tag{2}$$

For the calculation of the shaft torque, the experimentally captured Tn- characteristics were directly implemented within the simulation model. To account for the influence of the water level in the draft tube cone on the torque, Equation 3 calculates the shaft torque T by multiplying the measured values T_{ch}, which are dependent on the rotational speed n and the the guide vane opening a, with the fraction between the actual water level x and the maximum water level in the draft tube cone x_{max}.

$$T = \frac{x}{x_{\mathrm{max}}} T_{\mathrm{ch}}(n, a) \tag{3}$$

The simulation model sufficiently replicates the measurements on the real model pump-turbine for the flow rate Q and shaft torque T for different guide vane openings a and rotational speeds n. Figures 4b and 4a show the comparison of the simulated curves with the measured data for the Qn- and Tn-characteristics, respectively.

The relative error for the simulated flow rate compared to the measured data is shown in Figure 5 for an exemplary guide vane opening of a = 30%. The deviations between simulated and measured data are comparable for other guide vane openings. Overall, the model is able to simulate three of the 4-quadrant characteristics (pump, pump brake and turbine) within acceptable relative error tolerances of $\pm$20%. Only when operating as turbine break and reverse pump, the relative error exceeds 20%. As our first use case for enabling increased flexibility within machine operation is on the pump start-up and the operation in synchronous condenser mode,

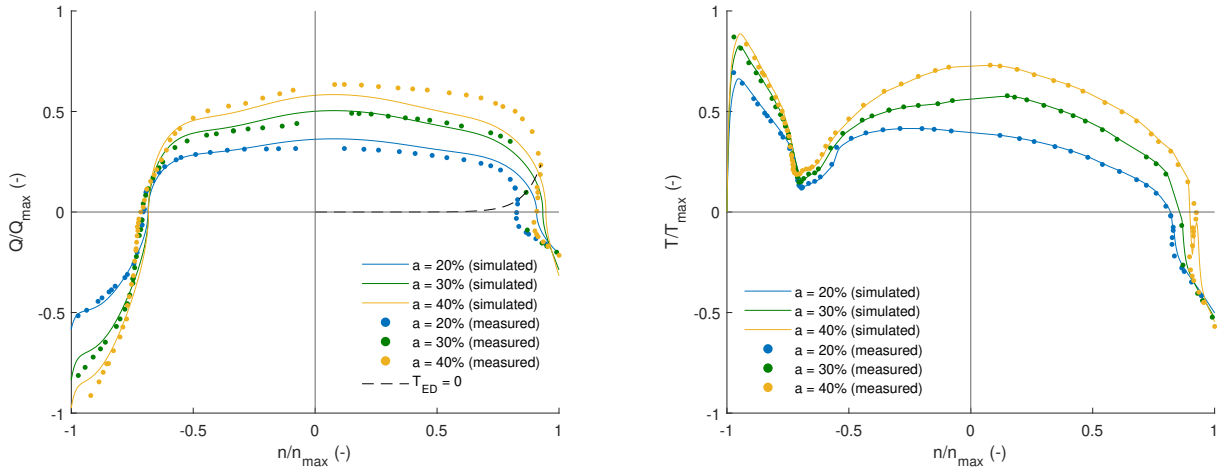

(a) *Qn*-characteristics (b) *Tn*-characteristics

Figure 4: Comparison of *Qn*- and *Tn*-characteristics from measured data with simulated curves for different guide vane openings.

the focus of the simulation is on operation as a pump and the blow-out process with speeds from $-n_{max}$ to around $-0.7n_{max}$. Deviations between the simulated and the experimentally measured data are thus more accepted in the other operation modes, resulting in non-sufficient representation of the operating range below the ”zero torque” ($T_{ED} = 0$), the so called ”S”-characteristic, as it can be seen in Figures 4 and 5. Here, the

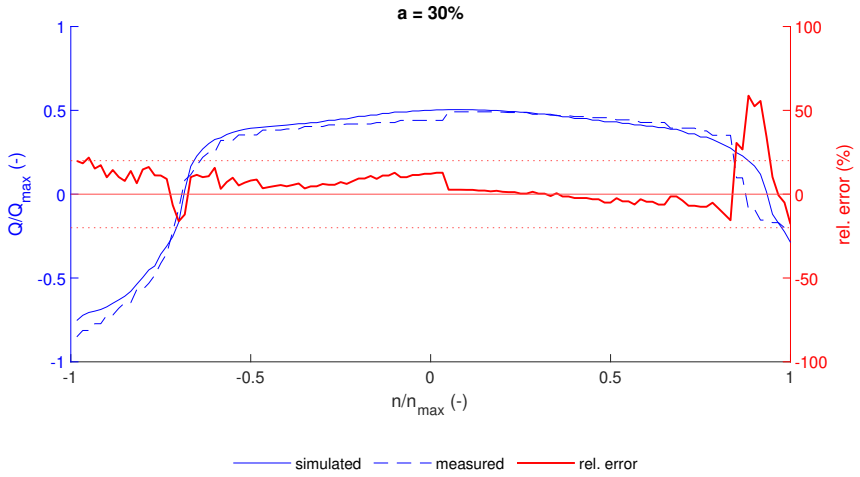

Figure 5: Relative error for the simulated flow rate compared to measurement data.

operating condition is not clearly defined and the area should be avoided in real operation. Nevertheless, the model is easily adaptable and correct representation of all pump-turbine operation modes needs to be ensured before the model is eligible as the complete virtual entity of the DT platform.

The blow-out of the runner is modeled through the lowering of the water level when air is blown into the draft tube. The machine is considered as blown-out as long as the water level is below the threshold $x_{\text{blow-out}}$. If the water level drops too low, air can leak into the tailwater vessel. Therefore, the water level should never fall below the critical level x_{crit}. Figure 6 illustrates the relevant water levels in the model pump-turbine, and Table 1 lists the according values.

2.3. Reinforcement learning algorithm

The objective of an RL agent is to interact with its environment to determine the best possible strategy, which is referred to as the optimal policy [4]. As illustrated in Figure 7, the agent makes a decision on what action to take at each time step t, resulting in a change in the environment. The environment's current state S_t is passed to

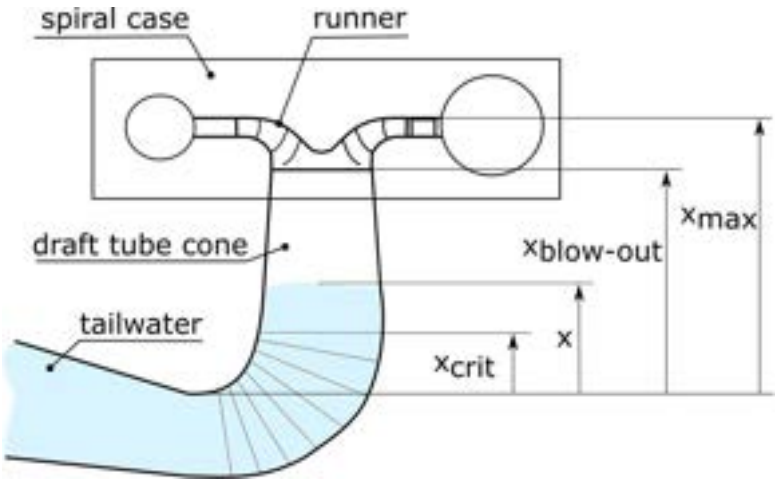

Figure 6: Illustration of relevant water levels inside pump-turbine.

Table 1: Water level values in draft tube of model pump-turbine.

x_{max}	0.807 m
$x_{blow-out}$	0.639 m
x_{crit}	0.227 m

the agent, along with a reward R_t that serves as a measure of the state's quality and provides feedback for the agent's learning algorithm. Based on the observation of the new state, the agent determines the subsequent action. By repeating this sequence, the agent acquires knowledge on how to effectively associate states with actions, with the objective of maximizing the cumulative rewards obtained over time (also known as return G). After a sufficient number of training sessions, this process leads to the development of the optimal policy π^*, with $\pi(A|S)$ indicating the probability of selecting action A when presented with state S [10].

Figure 7: Agent-environment interaction within an RL algorithm, adapted from [4].

During training, an RL algorithm needs to balance between exploring the state space through selecting random actions and exploiting of actions that have already proven to yield high rewards. Only through exploiting on past actions, the agent's performance can be improved. However, prematurely focusing on exploitation may lead to the algorithm settling on a sub-optimal policy [17]. Therefore we use epsilon-greedy exploration following an epsilon decay function. In this way, the exploration probability ϵ decreases continuously during training, ensuring that the agent explores the whole state space in the beginning, but still manages to converge to the optimal policy when training progresses.

For our use case, we use a deep Q-network (DQN) training algorithm, which is a value-based RL algorithm that trains a so-called critic $Q(S, A; \phi)$ with parameters ϕ to predict the return for a given state S and action A. During training, the agent adjusts the parameters in ϕ. When training is finished, the optimal policy can be derived from the trained value function approximator, the critic $Q(S, A)$, with now tuned parameter values ϕ [18]. The general training algorithm for a DQN agent is described in Algorithm 1.

Algorithm 1 Deep Q-Network (DQN) Training Algorithm [18]

Initialize critic Q with random parameter values ϕ
for each episode **do**
  for each training time step **do**
    With probability ϵ select a random action A
    otherwise, select the action, for which the critic value function is greatest:
    $A = \arg\max_A Q(S, A; \phi)$
    Execute action A. Observe the reward R and the next state S'
    Store the experience (S, A, R, S') in the experience buffer
    Sample a random mini-batch of M experiences (S_i, A_i, R_i, S'_i) from the experience buffer
    if S'_i is a terminal state **then**
      Set value function target $y_i = R_i$
    else
      Set $y_i = R_i + \gamma \max_{A'} Q(S'_i, A', \phi)$
    end if
    Update the critic parameters ϕ by one-step minimization of the loss L across all sampled experiences:
    $L = \frac{1}{M} \sum_{i=1}^{M} (y_i - Q(S_i, A_i; \phi))^2$
    Update the probability threshold ϵ for selecting a random action based on the ϵ-decay rate
  end for
end for

3. Results

The goal of our use case is to have the RL algorithm control the blow-out process for pump start-up within the virtual model of our scale reduced pump-turbine in the lab of IET. In doing so, we seek to demonstrate how RL can enhance the flexibility of hydropower systems, by training the agent to minimize the usage of compressed air while blowing out the machine as fast as possible.

As RL algorithm, a DQN agent from the MATLAB Reinforcement Learning Toolbox [18] with the default vector Q-value deep neural network as critic was used. The DQN agent has a discrete action space, $A = [0, 1]$. If the action $A = 0$, no air is blown into the draft tube and if action $A = 1$, air gets blown into the draft tube with a constant pressure of p_{air}. At each time step, the agents receives the state of the environment $S = [x(t), A(t-\Delta t)]$ through a continuous value for the current water level x and the binary value for the previous action A. This informs the agent whether the water level is rising or falling, allowing it to make an informed decision on the next action. The reward at each training step is calculated with a reward function that consists of four weighted terms, as described in Equation 4. Hereby, $R_{\text{waterlevel}}$ is positive if the water level x is between $x_{\text{blow-out}}$ and x_{crit} and negative otherwise. R_{air} accounts for the penalty the agent receives every time $A = 1$, indicating that air is blown into the draft tube cone. $R_{\text{switching}}$ encourages mores stable operation through penalizing the agent whenever it switches the air valve. If the compressor's limit is reached, i.e. if the total mass flow of air blown into the draft tube during the whole training episode reaches the limit of $\dot{m}_{\text{air}} = 1\text{kg}$, the agent receives a high penalty $R_{\text{compressor}}$ and the episode is aborted.

$$R = w_1 R_{\text{waterlevel}} - w_2 R_{\text{air}} - w_3 R_{\text{switching}} - w_4 R_{\text{compressor}} \tag{4}$$

The final cumulative reward, the return, for one training episode can be calculated by summing up over the reward received during each training time step t (Equation 5).

$$G = \sum_{i=1}^{t_{\text{end}}} R(t) \tag{5}$$

All the important parameter and hyperparameter settings for the training of the DQN agent are listed in Table 2. Note that the guide vane opening $a = 1\text{mm}$ and not 0, as it would be expected during the blow-out process. This intentional gap between the guide vanes should indicate leakages, as they are common in real world constructions, leading to air dissipating and therefore the need to repeatedly blow air into the draft tube to remain in blown-out condition.

Figure 8 shows the training progress of the DQN agent for learning how to control the blow-out process while balancing between rapidly reaching and remaining in blown-out operation mode and, simultaneously, minimizing the air mass blown into the draft tube. The large fluctuations for the first 200 training episodes represent the exploration phase of the learning algorithm, during which the agent chooses many random actions to explore the state space and evaluate the value function. As training progresses, the exploration probability ϵ decreases and the average return converges. The drops in the episode return curve in episodes 315 and 433 come from further random action decisions, as the probability for selecting a random action over the action for

Table 2: (Hyper-)Parameter settings for training of the DQN agent.

parameter	symbol	value
simulation options		
maximum simulation time	t_{sim}	120 s
air pressure	p_{air}	8 bar
guide vane opening	a	0.001 m
rotational speed motor-generator	n	0 rpm
agent options		
exploration probability	ϵ	0.5
minimum exploration probability	ϵ_{min}	0.001
exploration probability decay rate	ϵ_{decay}	0.0001
learn rate	γ	0.01
discount factor	α	0.99
mini batch size	M	64
training options		
maximum episodes		1000
averaging window length		20
stop training criterion = average return		91

which the critic value function is greatest, never decreases to 0 but converges to a minimum value ϵ_{min} = 0.1%. During numerous previous training sessions it was discovered that the highest achievable return is limited to G_{max} = 93. Therefore, a return of G_{stop} = 91 averaged over 20 training episodes was chosen as termination criterion. After the 542 training episodes, this criterion was reached and training was stopped.

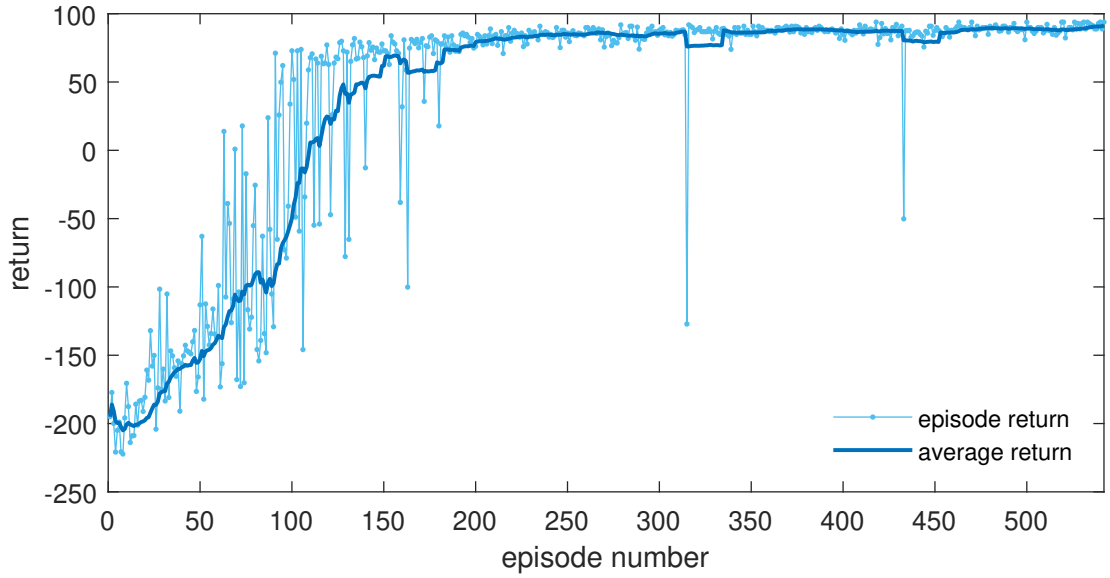

Figure 8: Episode and average return over training episodes.

The simulation results for the blow-out process when controlled by the trained DQN agent are shown in Figure 9. The rotational speed of the motor-generator was set to n = 0rpm, for simulating the machine at standstill. Since a leakage between the rotational guide vanes of a = 1mm was assumed, the flow rate Q is not 0, but a constant water flow of roughly 18 l/s was calculated by the simulation model. The final strategy of the RL algorithm for controlling the blow-out process can be seen in the sub-figures for the action, the mass flow rate and the water level over time. Air gets blown into the draft tube for a certain amount of time (A = 1). Subsequently, the air valve is being closed again (A = 0) and the water level rises again due to leakage effects. When the threshold $x_{\text{blow-out}}$ is reached, the valve opens again (A = 1). This sequence is repeated until the maximum simulation time of t_{sim} = 120s is reached.

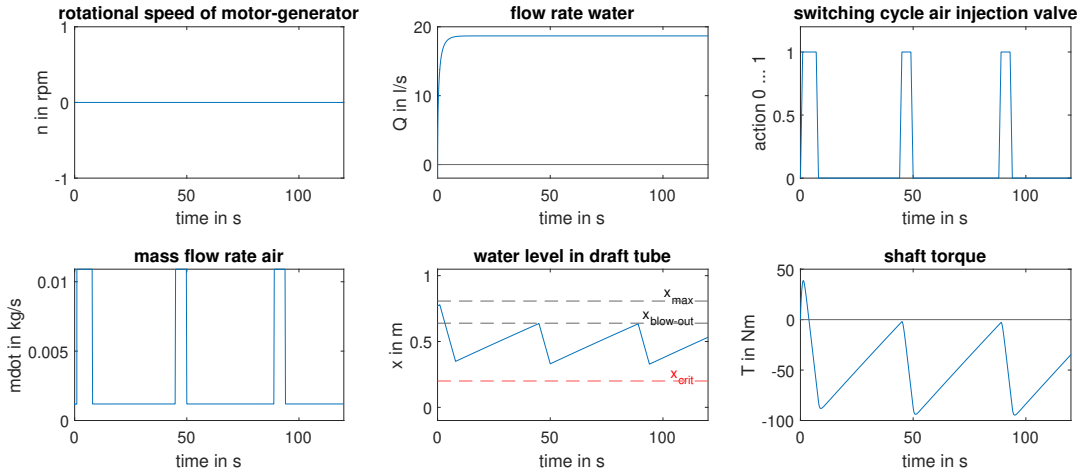

Figure 9: Simulation results for the blow-out process.

4. Discussion

The control of the blow-out process within the simulation model of a model pump-turbine through a DQN RL agent was successfully implemented. However, the algorithm' optimal policy does not yet reveal much optimization potential. Nevertheless it results in a rather logical blow-out sequence that could have also been achieved easily by a simple hysteresis controller. The results therefore show that the DQN agent and our RL problem formulation is suitable for finding the optimal blow-out operation strategy.

Considering that the current water level in the draft tube of the model pump-turbine at our lab facilities is hard to be measured directly, future research will deal with finding a solution for representing the blow-out conditions in the simulation model more accurately. Then, the control of the process will most probably increase in complexity and the optimal policy won't be as straightforward. We assume TL to be beneficial in transferring the DQN agent's policy to handle model adaptations.

Further, in this work we only considered the blow-out process during machine downtime. Blowing out a rotating runner, as it is being done for operation in synchronous condenser mode, may result in different findings. Investigations of different operation parameters are thus recommended and will be a part of our future research.

5. Conclusion

We presented a method to enable the use of RL for process control in pumped hydro storage systems. Concerns for letting a ML algorithm interact with safety-sensitive industrial equipment are among the biggest research barriers for RL for process control. We argue that through the transfer of a pre-learned RL algorithm through the use of a DT platform, safety concerns can be reduced and reliability of the RL algorithm's policy can be increased. In this paper, we showed the first results for the training of a DQN RL agent on a simulation model of a reversible pump-turbine, which acts as the virtual entity of our DT platform. The model was fitted to represent the behavior of a lab-scale model pump-turbine, which is located at the laboratory of the IET at TU Wien with satisfactory accuracy. Training of the RL algorithm was successfully carried out. The results confirm the expected optimal operation of the blow-out process. Future research will address increasing model complexity, exploration of different action and state spaces for the learning of the agent and, ultimately, the transfer of the RL algorithm to the model machine in the lab and use the autonomously learned optimal strategy to control the blow-out process.

Acknowledgments

The authors thank Christian Bauer, head of the Research Unit of Fluid Flow Machinery, for his guidance and advice. The authors acknowledge the support of this work through the women's promotion program of the Faculty of Mechanical and Industrial Engineering (MWBF) at TU Wien.

Abbreviations

DQN Deep Q-Learning

DT Digital Twin

IET Institute of Energy Systems and Thermodynamics, TU Wien

ML Machine Learning

RL Reinforcement Learning

TL Transfer Learning

Nomenclature

a guide vane opening, m

A action

G return

k_{PT} fitting constant, $\mathrm{Pas}^2/\mathrm{rad}^2$

k_ω fitting constant, rad/s

L loss

M mini batch size

$\dot{m}$ mass flow rate, kg/s

n rotational speed, rpm

p pressure, bar

Q flow rate, m^3/s

R reward

S state

t time step, s

t_{sim} simulation time, s

T shaft torque, Nm

T_{ED} torque factor, 1

w weighting factor

x water level, m

y value function

Greek symbols

α discount factor

ϵ exploration probability

ϵ_{decay} exploration probability decay rate

η efficiency

γ learn rate

ϕ Q-learning parameter

Δ difference

ω angular speed, rad/s

Subscripts and superscripts

air air

blow-out blow-out condition

ch characteristic

crit critical

max maximum

min minimum

PT pump-turbine

References

[1] T. Krutzler, H. Wiesenberger, C. Heller, M. Gössl, G. Stranner, A. Storch, H. Heinfellner, R. Winter, M. Kellner, and I. Schindler, "Szenario Erneuerbare Energie 2030 und 2050," tech. rep., Umweltbundesamt, Wien, 2016.

[2] M. Gimeno-Gutiérrez and R. Lacal-Arántegui, "Assessment of the European potential for pumped hydropower energy storage based on two existing reservoirs," *Renewable Energy*, vol. 75, pp. 856–868, Jan. 2015.

[3] A. Maly and C. Bauer, "Experimental investigation of a free surface oscillation in a model pump-turbine," *IOP Conference Series: Earth and Environmental Science*, vol. 774, p. 012068, Jan. 2021. Publisher: IOP Publishing.

[4] R. S. Sutton and A. Barto, *Reinforcement learning: An introduction*. Adaptive computation and machine learning, Cambridge, Massachusetts; London, England: The MIT Press, second edition ed., Jan. 2018.

[5] J. Shin, T. A. Badgwell, K.-H. Liu, and J. H. Lee, "Reinforcement Learning – Overview of recent progress and implications for process control," *Computers & Chemical Engineering*, vol. 127, pp. 282–294, Jan. 2019.

[6] R. Nian, J. Liu, and B. Huang, "A review On reinforcement learning: Introduction and applications in industrial process control," *Computers & Chemical Engineering*, vol. 139, p. 106886, Jan. 2020.

[7] H. Ju, R. Juan, R. Gomez, K. Nakamura, and G. Li, "Transferring policy of deep reinforcement learning from simulation to reality for robotics," *Nature Machine Intelligence*, vol. 4, pp. 1077–1087, Dec. 2022. Number: 12 Publisher: Nature Publishing Group.

[8] E. Salvato, G. Fenu, E. Medvet, and F. A. Pellegrino, "Crossing the Reality Gap: A Survey on Sim-to-Real Transferability of Robot Controllers in Reinforcement Learning," *IEEE Access*, vol. 9, pp. 153171–153187, 2021.

[9] J. Li, D. Pang, Y. Zheng, and X. Le, "Digital Twin Enhanced Assembly Based on Deep Reinforcement Learning," in *2021 11th International Conference on Information Science and Technology (ICIST)*, pp. 432–437, IEEE, 2021.

[10] C. Tubeuf, F. Birkelbach, A. Maly, and R. Hofmann, "Increasing the Flexibility of Hydropower with Reinforcement Learning on a Digital Twin Platform," *Energies*, vol. 16, p. 1796, Jan. 2023. Number: 4 Publisher: Multidisciplinary Digital Publishing Institute.

[11] N. P. Lawrence, M. G. Forbes, P. D. Loewen, D. G. McClement, J. U. Backström, and R. B. Gopaluni, "Deep reinforcement learning with shallow controllers: An experimental application to PID tuning," *Control Engineering Practice*, vol. 121, p. 105046, Apr. 2022.

[12] S. Spielberg, R. Gopaluni, and P. Loewen, "Deep reinforcement learning approaches for process control," in *2017 6th International Symposium on Advanced Control of Industrial Processes (AdCONIP)*, pp. 201–206, May 2017.

[13] L. Kasper, F. Birkelbach, P. Schwarzmayr, G. Steindl, D. Ramsauer, and R. Hofmann, "Toward a Practical Digital Twin Platform Tailored to the Requirements of Industrial Energy Systems," *Applied Sciences*, vol. 12, p. 6981, Jan. 2022. Number: 14 Publisher: Multidisciplinary Digital Publishing Institute.

[14] The MathWorks Inc., "MATLAB version: 9.13 (R2022b)," 2023.

[15] The MathWorks Inc., "Simulink version: 10.6 (R2022b)," 2023.

[16] The MathWorks Inc., "Simscape version: 5.4 (R2022b)," 2023.

[17] J. Langford, “Efficient Exploration in Reinforcement Learning,” in *Encyclopedia of machine learning and data mining* (C. Sammut and G. I. Webb, eds.), Springer Reference, pp. 389–392, New York, NY: Springer, second edition ed., Jan. 2017.

[18] The MathWorks Inc., “Reinforcement Learning Toolbox,” 2023.

PROCEEDINGS OF ECOS 2023 - THE 36TH INTERNATIONAL CONFERENCE ON
EFFICIENCY, **C**OST, **O**PTIMIZATION, **S**IMULATION AND ENVIRONMENTAL IMPACT OF ENERGY SYSTEMS
25-30 JUNE 2023, LAS PALMAS DE GRAN CANARIA, SPAIN

Clustering and typification of urban districts for energy system modelling

Joseph Loustau[a, CA], Dorsan Lepour[a], Cédric Terrier[a] and François Maréchal[a]

[a] EPFL, Lausanne, Switzerland, joseph.loustau@epfl.ch

Abstract:
The interest in Urban Systems has been growing due to the necessary decarbonisation of city energy systems. Decision tools are developed using mathematical optimisation to enable proper decision-making in the transition process. The concept of energy communities - or district energy hub - is expected to have an impact on the energy system at both regional and national scales. However, the shift towards distributed energy systems complexifies the model due to more integrated subsystems and requires larger spatial boundaries to increase self-consumption and decrease grid stresses. The computational power required to model and optimise such systems is to rise drastically.
This work proposes to curtail the large computing needs by typifying the districts of a city, using clustering techniques. Accordingly clustered districts can be optimised by solving a typical district from the group and scaling its solution to the others. The clustering features considered are the districts energetic characteristics: the energy demands on one side, and the endogenous resources on the other. Data are normalised and a principal component analysis is conducted. Two clustering algorithms are investigated: a centroid-based (Kmedoids) and a density-based (GaussianMixture). The ideal number of clusters is determined by maximising the intra-cluster similarity and minimising the inter-cluster similarity, and the final clustering stability is evaluated through the Rand Index.
The method is applied on the case study of a typical European urban area and the two algorithms lead to two distinct typification. The clusterings are used to run an energy hub optimisation for the whole region and the results are compared to the one obtained without archetypes for validation. The results between the two approaches show no significant differences while a considerable computing time reduction is achieved.

Keywords:
Urban energy systems, clustering, energy modelling, energy communities.

1. Introduction

1.1. Background

Among all, the building and construction industry accounts for an estimated 37% of the global operational energy and 37% of the process-related CO_2 emissions, worldwide [1]. Additionally, the world urban population represents 55% of the total and is expected to grow to 6 billion people [2] by 2050 (70% of total). Today, two-thirds of the global energy consumption come from cities, which emit more than 70% of the total greenhouse emissions [2]. Priority needs then to be put on city energy systems decarbonisation. Those considerations lead to a growth of interest in Urban Energy Systems. According to the *Net Zero Emissions (NZE) by 2050* report [3],

decarbonisation should be driven by high electrification. The conventional energy systems (*e.g.* fossil-fuels and boiler for Space Heating (*SH*)) would be replaced by devices and technologies that require renewable energy vectors. In the *NZE* scenario, 1.8 billion heat pumps and 1.2 billion solar thermal systems combined to 7'500 TWh of building-integrated PV would need to be installed [1].
Consequently, the exploitation of local energy resources is expected to grow, shifting the current electrical grid to a more decentralised one; households or organisations will consume energy from the grid at times, while at other times they will produce surplus energy that they can injected into the grid. The installation of energy devices must then be carefully done so that it answers the grid constraints. To ensure the stable operation of the grid at nominal frequency, the grid must always be balanced. While the current system - where few plants are responsible for the production, from the higher voltage level - can easily adapt the plant turbines frequency to keep the balance, with non-drivable inputs on the grid at the low-voltage level, it would be much more difficult to reequilibrate the imbalances [4]. Moreover, high peak production power can also overload the transformers or cause transmission bottlenecks [5]. The grid restrictions make it challenging to determine what technologies should be installed for a building to meet its demand, as optimal solutions depend on the context. Thus, the energy problem must be solved on a case-by-case basis.

To enable good energy-wise policies to help the renewable technologies penetration, an important lever for action is to provide efficient decision tools, able to propose a set of solutions to a specific energy context [6]. The decision-making tools model the system design (*energy hub*) and its possible components and provide an analysis, leaning on mathematical optimisation or simulation. Traditionally, the building is considered as the energy hub perimeter.

1.2. Gaps and contribution

However, to obtain results at a city scale, solving each hub would be too demanding in terms of computational power. To tackle this issue, either the model has to lose accuracy or the data volume must be reduced. [7, 8] developed the use of Machine Learning techniques to cluster the buildings of a city. The building stock is thus simplified using archetypes (i.e. average reconstructed buildings or sample buildings). But, the change towards distributed energy systems encourages the extension of the *energy hub* spatial boundaries so that a higher self-consumption can be achieved, hence releasing some stress over the grid. Indeed, [9] shows that when maximising the electricity generated locally (e.g., solar panels), the interaction of the building energy system with the grid should be lowered. To do so, the *energy hub* considered in this research is the district, which allows interactions between buildings.

This research proposes a method to typify urban districts using clustering techniques, thus combining the benefits of buildings interactions and typification. An application of the method is proposed using the canton of Geneva in Switzerland as a case study.

2. Methods

The method's premise is that by modelling a reduced number of districts, elected as *representative districts*, the results obtained draw the same conclusion as the ones that would be obtained by modelling every districts.
From this premise, the workflow proposed to enable large scale urban energy modelling is described in Figure 1. This paper covers the methods to find the representative districts.

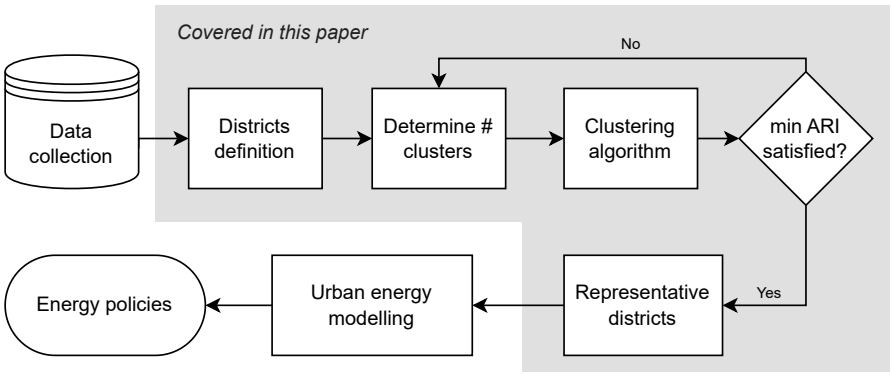

Figure 1: Workflow diagram for large scale urban energy modelling for integrated and distributed systems.

2.1. Definition of a district energy hub

Intuitively, a district is an area. Defining the *District Energy Hub (DEH)* consists in defining its spatial boundaries. A spatial attribute that must be common to all the buildings to consider within the same district is investigated. Because the initial target of the *DEH* is to limit exchanges with the grid, it is necessary that the buildings within the district boundaries can interact. Also, the aggregated load that the transformer has to handle must be taken realistically into account. Hence, the low-voltage transformer is the common attribute within a district in this research.
To be relevant, the clustering is designed so that its input features are the same as the input variables that describe the energy system in the model. A *DEH* is characterised by its infrastructures, the energy imported, the resources, and the on-site energy demands, as detailed in Fig. 2.

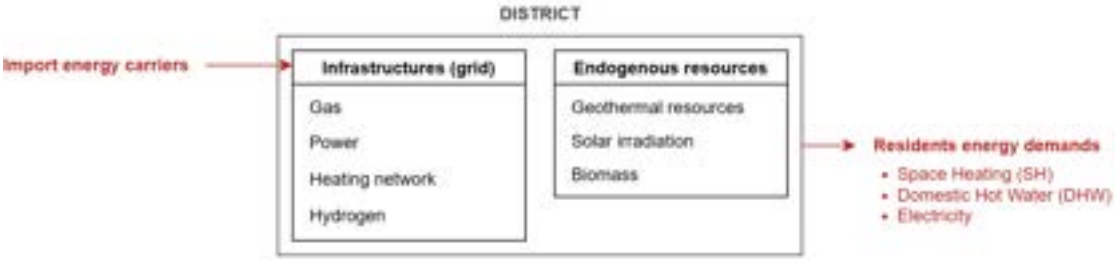

Figure 2: Key characteristics describing a district.

To restrain the number of features and facilitate the solving, the data go through a *Principal Component Analysis (PCA)* before the clustering. A PCA allows reducing a dataset dimensionality while preserving as much of the variability (*i.e.* the statistical information) as possible [10]. It also helps to interpret which features have the most impact on the clustering result. It is implemented in Python, using the *scikit* library.

2.2. Clustering

In *Urban Building Energy Modelling (UBEM)*, the algorithm that comes up most often and that has proven its effectiveness is *Kmeans* [11]. In this method, a derivative of Kmeans is implemented: the *Kmedoids* algorithm. It uses the concept of medoids instead of the mean, which diminishes the influence of the outliers, making it more robust. To make it operational to elliptical distribution, a second algorithm is proposed, the *GaussianMixture* algorithm. Those two algorithms are implemented in Python, using the *scikit-learn* library [12].

2.2.1. *Kmedoids*

Kmedoids require an initial number of clusters to run. If no previous knowledge of the dataset allows knowing this parameter, performance measures are used to determine which number of clusters gives the best result. Three validity indexes are proposed in this method. To put in equations those indexes, the following notation is used:

- The set of clusters $\mathbf{C} = \{C_1, ..., C_I, ..., C_K\}$ with $1 \leq I \leq K$,
- The set of observations $\mathbf{y} = \{y_1, ..., y_i, ..., y_n\}$ with $1 \leq i \leq n$,
- The subset of observations attributed to the cluster $y_i \in C_I$, $i \leq n$, $\mathbf{y_I} = \{y_{I,1}, ..., y_{I,j}, ..., y_{I,n_{C_I}}\}$ with $1 \leq j \leq n_{C_I}$,
- $\bar{y}$ is the centroid of $\mathbf{y}$. Similarly, $\bar{y}_I$ is the centroid of $\mathbf{y_I}$.

- **Elbow index:** the elbow method consists in computing the sum of squared distances (distortion score or inertia (1)) for each point to its assigned centroid [13]. The optimal number of clusters is the one where the drop in the distortion score is the most important.
- **Silhouette index:** for a given observation and $y_{I,j}$, the silhouette score measures the mean distance to all points of its cluster (3a) and compares it to the mean distance to all points of the neighboring cluster (3b). $s(I,j)$ has a score of 1 if $y_{I,j}$ is a perfect match with cluster C_I and a score of -1 with the neighboring cluster. The silhouette index is the mean of all coefficients $s_{I,j}$ (3d).
- **Calinski-Harabasz index:** it estimates the cohesion of clusters. It evaluates the distance from points in a cluster to the centroids and the distance from the centroids to a global centroid (2).

  The elbow index is commonly used. However, according to [14], *CH index* and *silhouette index* are the ones performing the best to evaluate a Kmeans clustering.

$$SS(\mathbf{C}) = \sum_{C_I \in \mathbf{C}} \sum_{y_{I,j} \in \mathbf{y_I}} (y_{I,j} - \bar{y}_I)^2 \quad (1)$$

$$CH(\mathbf{C}) = \frac{n-K}{K-1} \frac{\sum_{C_I \in \mathbf{C}} n_{C_I} \cdot d(\bar{y}_I, \bar{y})}{\sum_{C_I \in \mathbf{C}} \sum_{y_{I,i} \in \mathbf{y_I}} d(y_{I,i}, \bar{y}_I)} \quad (2)$$

$$a(I,j) = \frac{1}{n_{C_I} - 1} \sum_{m \in C_I,\, j \neq m} d(y_{I,j}, y_{I_m}) \quad (3a)$$

$$s(I,j) = \frac{b(I,j) - a(I,j)}{max(a(I,j), b(I,j))} \quad (3c)$$

$$b(I,j) = \min_{J \neq I} \frac{1}{n_{C_J}} \sum_{y_{J,m} \in C_J} d(y_{I,j}, y_{J_m}) \quad (3b)$$

$$S(\mathbf{C}) = \frac{1}{n} \sum_{C_I \in \mathbf{C}} \sum_{y_{I,i} \in C_I} s(I,i) \quad (3d)$$

With this being defined, algorithm 1 is used to determine the optimal number of clusters k_{opt}.

Once k_{opt} is determined, the clustering in itself can be done. It is repeated 500 times and the one with minimal inertia is kept as the final clustering. If the right number of clusters was used, the clustering should be *stable*, *i.e.* observations should be labeled the same way from one iteration to the other. Rand [15] has created an index to evaluate this stability. When two clusterings (obtained from different algorithms or number of clusters) are to be distinguished, the one with the higher Rand index is kept. Moreover, for a clustering to be valid, it should have a minimum level of stability. [16] stated equation (4), defining it depending on the clustering sizes (r and s). If $ARI \leq min\ ARI$, clustering is rejected.

$$min\ ARI = \left[1 - \frac{1}{2}\binom{r+s-1}{2}\left[\binom{r}{2}^{-1} + \binom{s}{2}^{-1}\right]\right]^{-1} \tag{4a}$$

$$if\ r = s:\ min\ ARI = \frac{-r}{3r-2} \tag{4b}$$

2.2.2. *GaussianMixture*

The process is similar to the one for *Kmedoids*. The *GaussianMixture* algorithm needs a number of components and the shape of the covariance matrix to work. Again, if no previous knowledge helps to determine those parameters, scores are used to find them.
Because the *GaussianMixture* relies on probabilities, the best clustering is the one that maximises the likelihood. The likelihood function evaluates the joint probability of observed data as a function of the chosen statistical model. Given a set of n training vectors **y**, the GMM likelihood function can be written as in (5).

However, adding components helps increase the likelihood while it may lead to overfitting the data. Criteria introduce penalty terms on the number of parameters to solve the issue.

- **Akaike Information Criterion (AIC):** defined by (6a), it should be as small as possible. It is an efficient criterion when the model is very complex and is chosen in this context.
- **Bayesian Information Criterion (BIC):** defined by (6b), the BIC should also be as small as possible. It has consistency (meaning it would asymptotically select the candidate model having the correct structure), as its penalty term contains n.

$$p(y \mid \lambda) = \prod^{n} p(y_i \mid \lambda) \tag{5}$$

$$AIC = 2 \cdot ln(k_\lambda) - 2 \cdot ln(\hat{L}) \tag{6a}$$

$$BIC = k \cdot ln(n) - 2 \cdot ln(\hat{L}) \tag{6b}$$

where $\hat{L}$ is the maximised value of the likelihood function of the GMM defined in (5), k the numbers of estimated parameters of the model.

Algorithm 2 describes the steps to determine the key parameters. Once they are selected, as for *Kmedoids*, the Rand index is computed.

2.3. Case study: the Canton of Geneva

In this research, data are collected over the canton of Geneva, an area containing a typical mid-size European city, a peri-urban area, and some rural areas.
The districts are defined according to the LV transformers to which the buildings are connected.

Because the position of transformers is not publicly available, this research uses the synthetic grid approach from the work of [17], which estimates the position of transformers based on the buildings' energy demands. Most of the data concerning buildings comes from **QBuildings**, a database developed at the IPESE laboratory. The buildings data are aggregated over districts and normalised by the total *Energetic Reference Area (ERA)* by district.

3. Results and discussion

The results and discussion seek to demonstrate the applicability of the method developed on a typical European city intending to subsequently run an energy system optimisation model. First, the clusterings obtained with the two algorithms are analysed. Second, the results of the optimisation with and without the clustering are compared to ensure the validity of its use for decision-making purposes.

3.1. Clustering results

3.1.1. Optimal number of clusters

As a first step, the optimal number of clusters should be determined to run the algorithm. Figure 3(a) shows the mean score obtained for each number of clusters for the three indexes and Fig. 3(b) shows the number of occurrences where each number of clusters gives the best score, with the *Kmedoids* algorithm.

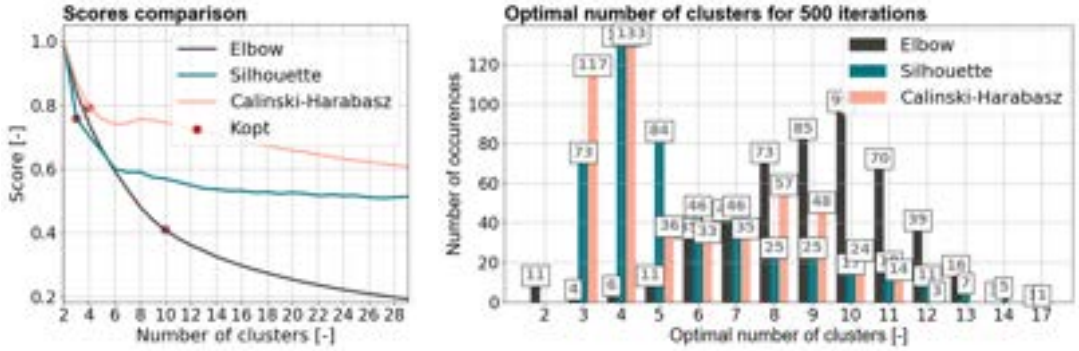

(a) Mean scores obtained for the three indices.

(b) Occurrences where a number of clusters is found optimal.

Figure 3: Results of the optimal number of clusters investigation, Kmedoids, repeated 500 times.

The silhouette and the CH index agree on 2 as the optimal number. However, 2 clusters are insufficient to discriminate between the different optimisation problems that may be posed. Therefore, the next optimum is looked at. According to Fig. 3(a), for CH, the line breaks at 4 and then there is a new local maximum at 8 and for the silhouette index, the break is at 3. This is confirmed by Fig. 3(b). The elbow occurs the most between 8, 9, and 10.

In comparison, Figs. 4(a) and 4(b) indicate an optimal number of clusters between 4, 5, or 6 for the BIC index. The AIC obtains an elbow-like shape curve where the main change of curvature happens at 5 and 8. Note that only the full covariance matrix shape is shown, as it has always obtained the best score.

From those two results, 3, 4, 5, and 8 are the best number of clusters to investigate.

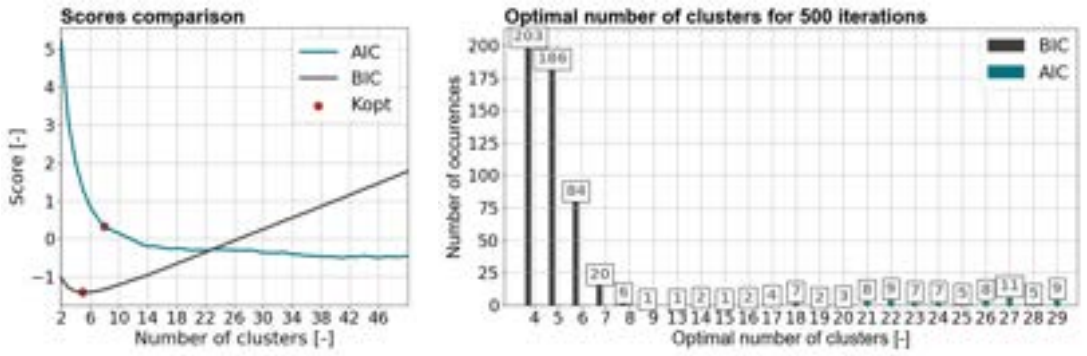

(a) Mean scores obtained for the two indices. (b) Occurrences where a number of clusters is found optimal.

Figure 4: Results of the optimal number of clusters investigation, GaussianMixture, repeated 500 times.

3.1.2. Clustering

With the k_{opt} search results, algorithms are run to compute the Rand index and keep the most stable clustering. Table 1 displays the Rand index computed by repeating the clustering 1000 times, with the different numbers of clusters. The most stable clustering is obtained with the *GaussianMixture* algorithm and in particular when the requested number of clusters is 4 and 5.

Table 1: Rand index by clustering 1000 times, varying number of clusters.

Number of clusters	3	4	5	8
Mixture	-	0.717	0.693	0.399
Kmedoids	0.331	0.383	0.287	0.388

Because they were the best options according to the BIC index and they have a satisfying Rand score, the 4^{th} and 5^{th} options are kept. While doing the clustering with 5 different clusters, it often resulted in an empty 5^{th} cluster. Therefore, 4 different clusters is the selected optimal number. The result of this clustering can be visualised in Fig. 5(a). A heat map from the input features (Fig. 5(b)) is used to understand what differentiates clusters from each other.

Looking at those elements, the clusters can be characterized and described in the following way:

Cluster	DESCRIPTION
1	Districts dominated by industrial, commercial, and administrative buildings
2	Residential belt around the lake, with high buildings density and low solar potential per capita
3	Peri-urban residential buildings, with low ERA density (i.e., single-family detached houses)
4	Peri-urban buildings with important solar availability (high roof on ERA ratio)

The hot water demand, along with the electrical demand, have the biggest influence on the clustering as they can vary a lot according to the building type.

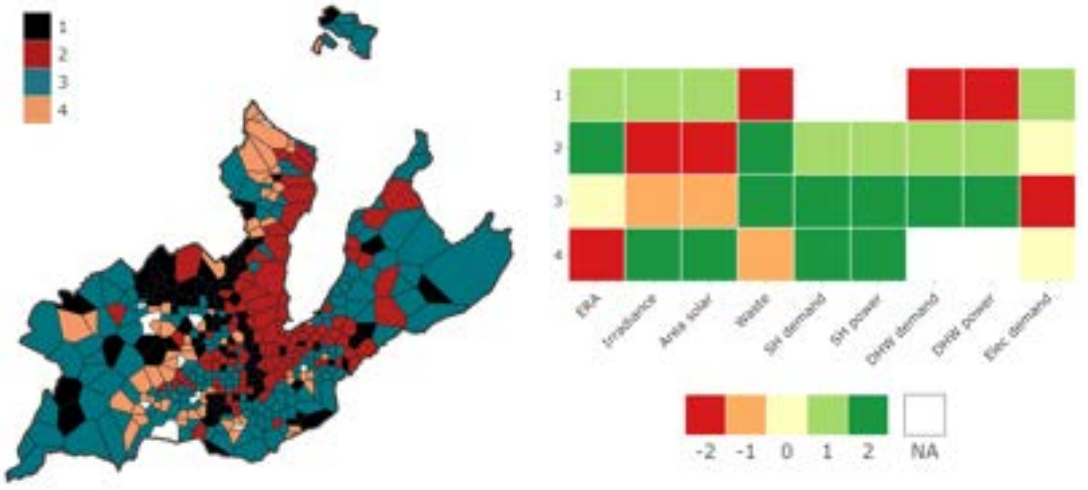

(a) Map of the canton of Geneva coloured by clusters.

(b) Heat map evaluation of each feature for each cluster. Features are evaluated on a scale of -2 to 2.
-2: Very low, -1: Low, 0: Average, 1: High, 2: Very High.
Missing cells correspond to a non-decisive case, indicated by parsed values inside the cluster.

Figure 5: Clustering results and analysis on the canton of Geneva, operated with *GaussianMixture*, 4 components and full covariance matrix.

3.1.3. Comparison of optimisation results with and without district typification

To ensure the validity of the method, one should ensure that when using typical districts to do the optimisation (namely *Representative districts (RD)* approach in what follows), similar results are obtained as the ones where every district has been optimised specifically (*All districts (AD)*).

To do so, the decision variables of the model and the resulting *Key Performance Indicators (KPI)* are compared between the two approaches. The global mean obtained on the canton of Geneva should show no significant distinction. The mean is weighted by the total ERA that each cluster represents for *RD*. The intra-cluster variabilities are also compared to the standard deviation computed over the whole canton.
Using an optimisation tool that models an energy hub and determines the best energy system, finding the optimal energy system for the 468 districts of Geneva took 54h21m23s with *AD* and 48m18s with *RD*, i.e. a reduction in the calculation time of 98.5%. The comparison of their respective decision variables and *KPIs* are shown in Fig.6(a) and Fig.6(b). The major diminishing of the standard deviation for each evaluated metric confirms that the patterns among the inputs that participated to create the district clusters are meaningful as well for patterns in the optimisation results. Moreover, there was no significant difference between the mean obtained using the *AD* or the *RD* approach, with two exceptions: the OPEX and Electrical Heater installation size, which have high variability within the canton. Therefore, it is more difficult to accurately represent these indicators with typical districts.

Nevertheless, the overall results obtained show an excellent performance of the method to facilitate the optimisation of districts over a large scale.

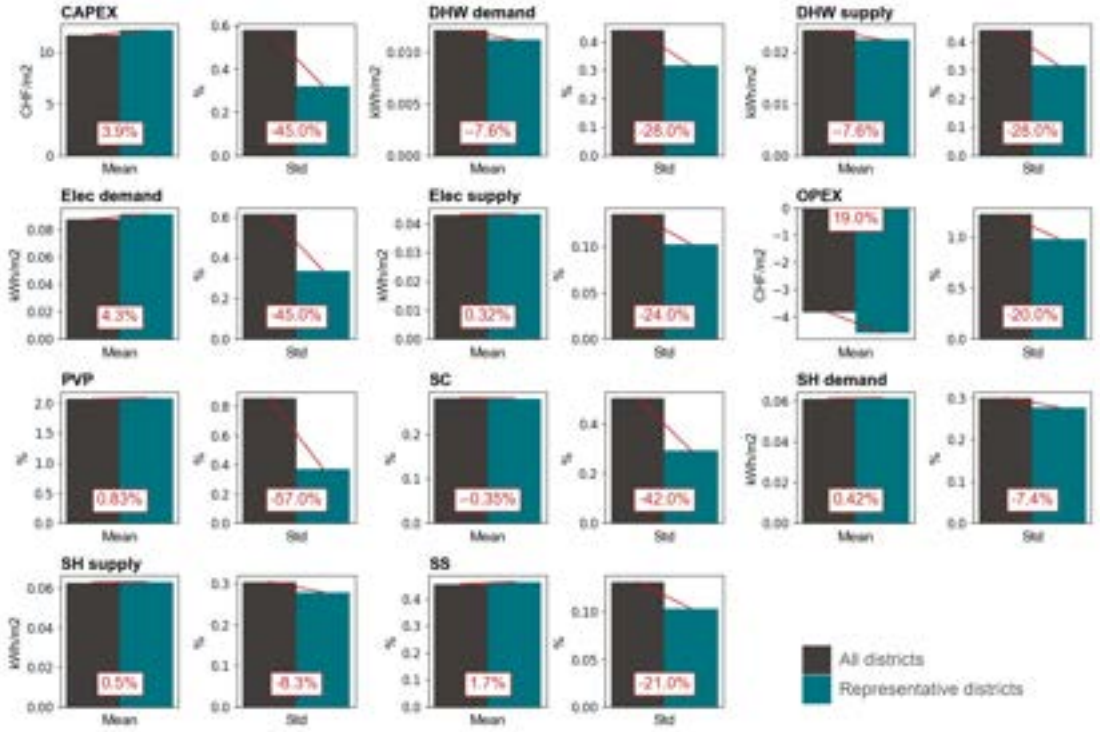

(a) Main KPIs. *CAPEX*=Capital Expenditure, *DHW*=Domestic Hot Water, *Elec*=Electricity, *OPEX*=Operationnal Expenditure, *PVP*=Photovoltaïc Panel Penetration, *SC*=Self-Consumption, *SS*=Self-Sufficiency

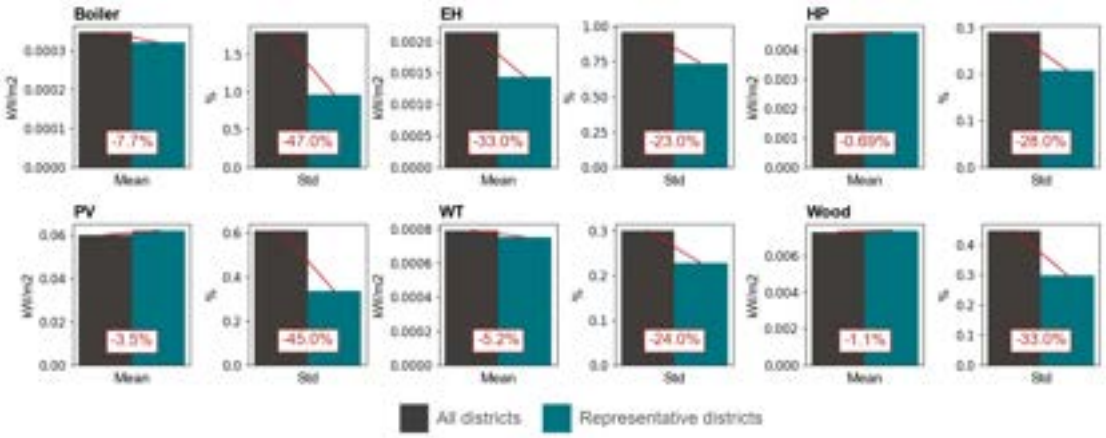

(b) Installed capacity for the energy technologies. *Boiler*=Natural Gas Boiler, *EH*=Electrical Heater, *HP*=Heat Pump, *PV*=Photovoltaïc Panel, *WT*=Water Tank

Figure 6: Comparison of results obtained with the two approaches. *All districts* stands for the results obtained by optimising every district in the canton of Geneva, while *Representative districts* is obtained by running the representative districts and scaling their solution to the districts of their cluster. The figures in red indicate the representative difference between the two approaches.

4. Conclusion

The objective of this paper was to provide a method to enable urban energy modelling at a large scale and high accuracy, for integrated and distributed systems. It uses the concept of archetypes, introduced for buildings, and adapts it to the district scale by defining the low-voltage transformer as the reference energy hub.
The method suggests the use of two clustering algorithms - *Kmedoids* and *GaussianMixture*, depending on the data set - and provided as output the list of the districts labeled by cluster. It was validated on a case study (the canton of Geneva), with the following conclusions:

- It can be delicate to determine the optimal number of clusters;
- The model solving computation time over the whole region was reduced by 98.5%, with respect to the classic approach;
- The results between the two approaches show no significant difference with 4 clusters, although the high variability of certain decisions can lack a good representation with this approach.

The presented work opens up possibilities in the solving of more complex systems at an even larger scale. However, its main limitation is the selected number of clusters, this parameter being the most critical into the analysis of the energy system model results. Therefore, when planning urban energy systems with this method, it will be essential to carry out a correct analysis of the neighbourhood typology.

5. Fundings

The research published in this report was carried out with the support of the Swiss Federal Office of Energy SFOE as part of the SWEET project acronym. The authors bear sole responsibility for the conclusions and the results of the presented publication.

Appendix A Algorithms

Algorithm 1 Find the optimal number of clusters for Kmedoids

Input: A set of observations **y**
Output: A vector $\mathbf{K_{opt}}$ counting the occurrences where a number of clusters has been determined as the best

$\mathbf{K_{opt}} \leftarrow \mathbf{0}$
$Bestscore \leftarrow 0$
for $i \leq 1000$ **do**
  for $k = 2 \leq 30$ **do**
    $\mathbf{C} \leftarrow Kmedoids(\mathbf{y}, n_{medoids} = k)$
    Compute $SS(\mathbf{C})$, $S(\mathbf{C})$ or $CH(\mathbf{C})$
    if $Index \geq Bestscore$ **then**
      $Bestscore \leftarrow Index$
      $k_{best} \leftarrow k$
    end if
  end for
  $\mathbf{K_{opt}}(k_{best}) \leftarrow \mathbf{K_{opt}}(k_{best}) + 1$
end for
return $\mathbf{K_{opt}}$

Algorithm 2 Find the optimal number of clusters for GaussianMixture

Input: A set of observations $\mathbf{y}$

Output: Two vectors $\mathbf{K_{opt}}$ and $\mathbf{Cov_{opt}}$ counting the occurrences where a number of clusters has been determined as the best

$\mathbf{K_{opt}} \leftarrow \mathbf{0}$
$\mathbf{Cov_{opt}} \leftarrow \mathbf{0}$
$Bestscore \leftarrow 0$
for $i \leq 1000$ **do**
  for $k = 2 \leq 30$ **do**
    for $shape \in \{full, diag, tied, spherical\}$ **do**
      $\mathbf{C} \leftarrow GaussianMixture(\mathbf{y}, n_{components} = k, m_{cov} = shape)$
      Compute $AIC(\mathbf{C})$ or $BIC(\mathbf{C})$
      if $Index \leq Bestscore$ **then**
        $Bestscore \leftarrow Index$
        $k_{best} \leftarrow k$
        $shape_{best} \leftarrow shape$
      end if
    end for
  end for
  $\mathbf{K_{opt}}(k_{best}) \leftarrow \mathbf{K_{opt}}(k_{best}) + 1$
  $\mathbf{Cov_{opt}}(shape_{best}) \leftarrow \mathbf{Cov_{opt}}(shape_{best}) + 1$
end for
return $\mathbf{K_{opt}}$, $\mathbf{Cov_{opt}}$

References

[1] United Nations Environment Programme. *2022 Global Status Report for Buildings and Construction: Towards a Zero-emission, Efficient and Resilient Buildings and Construction Sector*. 2022-11. URL: https://wedocs.unep.org/20.500.11822/41133.

[2] World Bank. *Urban development overview*. World Bank. URL: https://www.worldbank.org/en/topic/urbandevelopment/overview (visited on 06/06/2022).

[3] International Energy Agency IEA. *Transition to sustainable buildings: strategies and opportunities to 2050*. Paris: IEA Publ, 2013. 284 pp. ISBN: 978-92-64-20241-2.

[4] Gideon A. H. Laugs, René M. J. Benders, and Henri C. Moll. "Balancing responsibilities: Effects of growth of variable renewable energy, storage, and undue grid interaction". In: *Energy Policy* 139 (Apr. 1, 2020), p. 111203. ISSN: 0301-4215. DOI: 10.1016/j.enpol.2019.111203. URL: https://www.sciencedirect.com/science/article/pii/S0301421519307876 (visited on 06/23/2022).

[5] Karl-Kiên Cao, Johannes Metzdorf, and Sinan Birbalta. "Incorporating Power Transmission Bottlenecks into Aggregated Energy System Models". In: *Sustainability* 10.6 (June 2018). Number: 6 Publisher: Multidisciplinary Digital Publishing Institute, p. 1916. ISSN: 2071-1050. DOI: 10.3390/su10061916. URL: https://www.mdpi.com/2071-1050/10/6/1916 (visited on 06/20/2022).

[6] Shimeng Hao and Tianzhen Hong. "The Application of Urban Building Energy Modeling in Urban Planning". In: *Rethinking Sustainability Towards a Regenerative Economy*. Ed. by Maria Beatrice Andreucci et al. Future City. Cham: Springer International Publishing,

2021, pp. 45–63. ISBN: 978-3-030-71819-0. DOI: 10.1007/978-3-030-71819-0_3. URL: https://doi.org/10.1007/978-3-030-71819-0_3 (visited on 03/07/2023).

[7] Ina De Jaeger et al. “A building clustering approach for urban energy simulations”. In: *Energy and Buildings* 208 (Feb. 1, 2020), p. 109671. ISSN: 0378-7788. DOI: 10.1016/j.enbuild.2019.109671. URL: https://www.sciencedirect.com/science/article/pii/S0378778819313271 (visited on 06/19/2022).

[8] Sara Torabi Moghadam et al. “A new clustering and visualization method to evaluate urban heat energy planning scenarios”. In: *Cities* 88 (May 1, 2019), pp. 19–36. ISSN: 0264-2751. DOI: 10.1016/j.cities.2018.12.007. URL: https://www.sciencedirect.com/science/article/pii/S0264275118307625 (visited on 06/19/2022).

[9] Luise Middelhauve. “On the role of districts as renewable energy hubs”. PhD thesis. 2022.

[10] Ian T. Jolliffe and Jorge Cadima. “Principal component analysis: a review and recent developments”. In: *Philosophical Transactions of the Royal Society A: Mathematical, Physical and Engineering Sciences* 374.2065 (Apr. 13, 2016). Publisher: Royal Society, p. 20150202. DOI: 10.1098/rsta.2015.0202. URL: https://royalsocietypublishing.org/doi/10.1098/rsta.2015.0202 (visited on 05/12/2022).

[11] Chao Wang et al. “Data acquisition for urban building energy modeling: A review”. In: *Building and Environment* 217 (June 1, 2022), p. 109056. ISSN: 0360-1323. DOI: 10.1016/j.buildenv.2022.109056. URL: https://www.sciencedirect.com/science/article/pii/S0360132322002955 (visited on 06/20/2022).

[12] F. Pedregosa et al. “Scikit-learn: Machine Learning in Python”. In: *Journal of Machine Learning Research* 12 (2011), pp. 2825–2830.

[13] M A Syakur et al. “Integration K-Means Clustering Method and Elbow Method For Identification of The Best Customer Profile Cluster”. In: *IOP Conference Series: Materials Science and Engineering* 336 (Apr. 2018), p. 012017. ISSN: 1757-8981, 1757-899X. DOI: 10.1088/1757-899X/336/1/012017. URL: https://iopscience.iop.org/article/10.1088/1757-899X/336/1/012017 (visited on 05/13/2022).

[14] Olatz Arbelaitz et al. “An extensive comparative study of cluster validity indices”. In: *Pattern Recognition* 46.1 (Jan. 2013), pp. 243–256. ISSN: 00313203. DOI: 10.1016/j.patcog.2012.07.021. URL: https://linkinghub.elsevier.com/retrieve/pii/S003132031200338X (visited on 05/13/2022).

[15] William M. Rand. “Objective Criteria for the Evaluation of Clustering Methods”. In: *Journal of the American Statistical Association* 66.336 (Dec. 1, 1971). Publisher: Taylor & Francis _eprint: https://www.tandfonline.com/doi/pdf/10.1080/01621459.1971.10482356, pp. 846–850. ISSN: 0162-1459. DOI: 10.1080/01621459.1971.10482356. URL: https://www.tandfonline.com/doi/abs/10.1080/01621459.1971.10482356 (visited on 05/19/2022).

[16] José E. Chacón and Ana I. Rastrojo. “Minimum adjusted Rand index for two clusterings of a given size”. In: *Advances in Data Analysis and Classification* (Feb. 9, 2022). ISSN: 1862-5355. DOI: 10.1007/s11634-022-00491-w. URL: https://doi.org/10.1007/s11634-022-00491-w (visited on 05/20/2022).

[17] “Countrywide PV hosting capacity and energy storage requirements for distribution networks: The case of Switzerland”. In: *Applied Energy* (2020). Ed. by Rahul Gupta, Fabrizio Sossan, and Mario Paolone. DOI: 10.1016/j.apenergy.2020.116010.

Application of Machine Learning in Energy Systems – a Comparative Analysis of Three Case Studies

Michael Rath[a, b], Naga Lokesh Gunturu Venkata[a], Kiran George[a], Jayares Prince[a]

[a] Bochum University of Applied Sciences, 44801 Bochum, Germany
[b] Fraunhofer Research Institution for Energy Infrastructures and Geothermal Systems IEG, 44801 Bochum, Germany, michael.rath@ieg.fraunhofer.de

Abstract:
The exponential growth in the number of papers published annually in the field of machine learning applications in energy systems presents a challenge to researchers seeking to conduct comprehensive and effective literature reviews. To address this issue, we took a systematic literature review approach with three distinct smaller case studies focusing on the application of machine learning in energy systems, namely:

1. Machine learning in drilling
2. Machine learning for rooftop solar energy potential quantification, and
3. Machine learning in district heating and cooling in the context of seasonal thermal energy storages.

In each case, we employed a systematic literature review methodology. For topic one, we utilized an existing comprehensive review to generate further insights and information. For topics two and three, we used predefined search criteria to conduct relevant publications in a systematic and reproducible manner. We investigate the state of the art of the use of machine learning in these distinct areas of inquiry, thereby facilitating the identification of research gaps. Ultimately, we compare approaches and models utilized in each field, identified common best practices, and propose methods to address potential challenges.

Keywords:
Energy systems, Machine Learning, Drilling, ATES, Roof Potential, Geothermal, Aerial Imaging, Renewable Energy, District heating and cooling, Seasonal Thermal Energy Storage

1. Introduction

Energy systems are the backbone of modern civilization and are critical to promoting environmental, economic, and social sustainability [1]. As energy systems become increasingly complex, they require higher reliability demands and offer greater degrees of freedom for practical enhancement of integrated multi-energy systems [2]. Machine learning-based data-driven models have emerged as a promising approach for significantly improving the overall usage rate of multiple energy sources, especially including renewable energies [3]. Machine learning can capture complicated mechanisms to increase prediction accuracy, make optimal choices based on detailed state information, and reduce computational time needed for energy system optimization [4, 5]. In addition, machine learning has been applied to develop advanced energy storage devices and systems [6]. In this review, we explore three impactful applications of machine learning in energy systems and the challenges and limitations that must be addressed for further progress in this field.

Case Study Approach

We adopt a systematic literature review approach to investigate the state-of-the-art in application of machine learning by conducting three distinct case studies. The aim is to provide valuable insights into the potential of machine learning to solve complex problems across different fields. In the first case study, an analysis of a recent review paper on machine learning in drilling by Li et al. 2022 [7] is conducted to provide additional insights. The second case study focuses on the use of machine learning in rooftop solar energy quantification, while the third case study examines the use of machine learning in district heating and cooling in the context of seasonal thermal energy storages. These case studies showcase the application of machine learning in different sectors, such as load demand forecasting, design, cost, and control optimization. The specific machine learning techniques used, challenges faced, and an outlook in each field are presented. By exploring these case studies, this review paper aims to provide a comprehensive understanding of the state-of-the-art in the application of machine learning and its potential for solving complex problems in various fields. After introducing the applied methodology for each case study and the subsequently chosen selection of papers,

we provide in the results section for each case study a case study results subsection followed by a short case study conclusion and outlook. We conclude with a summarizing conclusion and outlook across the case studies.

2. Methodology

Organizing and planning literature searches is a complex process that requires careful attention to several key categories. These include defining the scope of the literature, conceptualizing the topic, conducting a literature analysis, searching for relevant literature, and developing a research agenda. Various search processes have been introduced to enhance the quality of literature reviews, such as journal and database searches, keyword searches, backward and forward searches, and evaluation of the title and abstract of relevant literature [8]. To ensure effective literature searches, it is also recommended to gain a thorough understanding of the subject matter, test and apply a combination of search parameters, and use seminal sources to build the backbone of the literature review [9]. Our paper employs the Concept Matrix Method [10], which is aligned with these guidelines to ensure accurate and efficient collection, study, and categorization of the survey. In our case studies, we use relevant keywords to conduct literature searches on Google Scholar.

The first case study focuses on machine learning in drilling, which is an enormously active research field. As one can see in Figure 1, the number of papers published per year on machine learning in drilling shows an exponential increase. A very recent and comprehensive review of Li et al.2022 [11] will here be our base of research, whose content we will analyze further in the following.

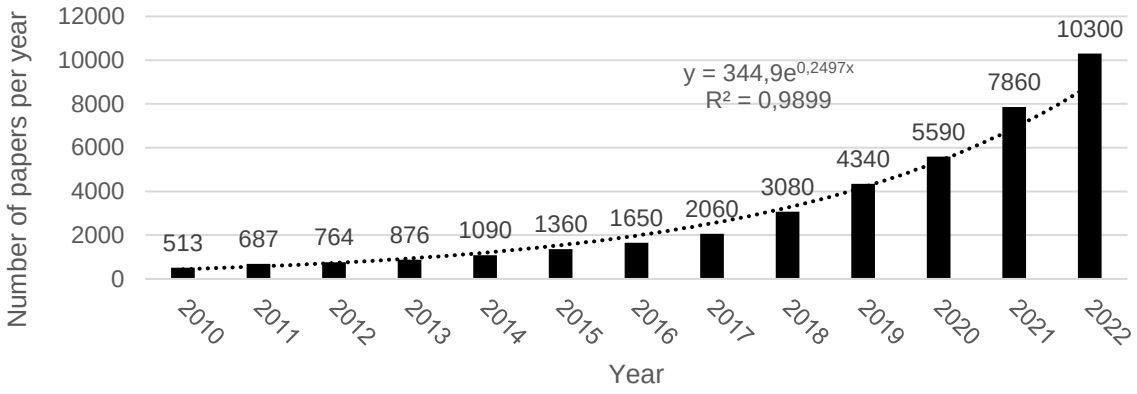

Figure 1: Number of papers published for per year when searching for “machine learning” + “drilling” showing an exponential increase.

The second case study explored the field of solar rooftop potential quantification by finally narrowing down to the search string "machine learning" + "solar energy" + "rooftop" + “quantification” + “urban” + "aerial image" + "geographic information system" (cf. Figure 2).

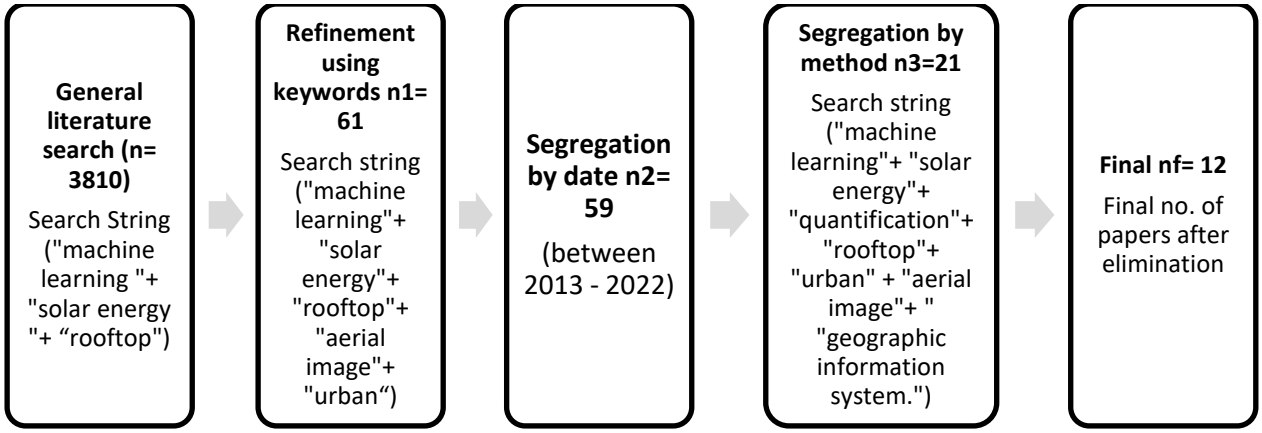

Figure 2: Steps involved in the refinement process for the case of solar rooftop potential quantification using machine learning.

The systematic literature search was undertaken in Google Scholar. Using the search string "machine learning "+ "solar energy "+ “rooftop yielded 3810 papers. The number of results was then reduced by inserting the term "urban" and “aerial image” to the search string to 61, resulting in the search string "machine learning"+ "solar energy"+ "rooftop"+ "aerial image"+ "urban". The results were narrowed down to 59 by excluding publications published on or before 2012. Adding the term "geographic information system" decreased the results to 21 for the search string "machine learning"+ "solar energy"+ "rooftop"+ “quantification” + "urban" + "aerial image"+ "geographic information system", which then where finally reduced to 12 papers due to accessibility (i.e. not open access) and relevance.

During the systematic refinement process, it was observed that there is also an exponential increase in the number of papers published in the research area selected for systematic reviewing for the more general search string "machine learning "+ "solar energy "+ “rooftop" over the years (cf. Figure 3).

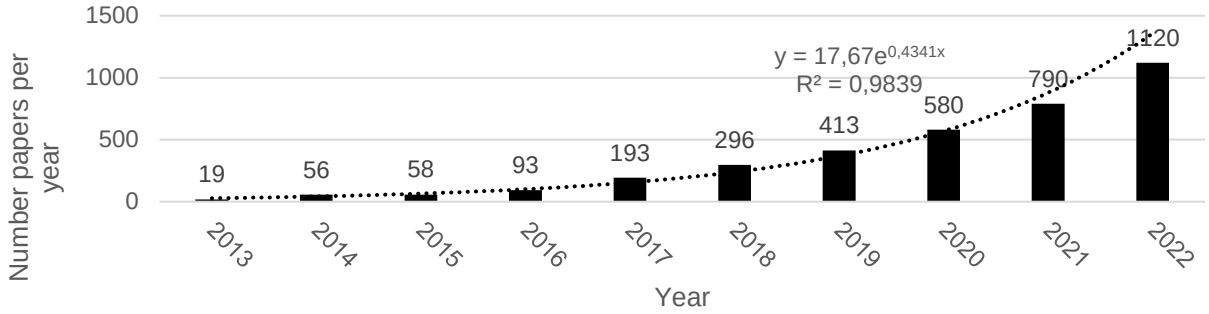

Figure 3: Number of papers published for per year when searching for "machine learning "+ "solar energy "+ “rooftop" showing an exponential increase.

The third case study examined the application of machine learning in district heating and cooling in the context of seasonal thermal energy storages. Be employing the search string "machine learning" + "district heating and cooling" + "seasonal thermal energy storage" and limiting to articles published between 2010 and 2022, we obtained 46 potential articles. Figure 4 displays the number of articles in each year from 2010-2022. The 46 papers were aging reduced to 7 papers based on the following criteria 1. papers that are not open access (21), 2. paper without machine learning application (11), 3. Papers without STES (6), 4. other papers (2), which were not relevant to the study.

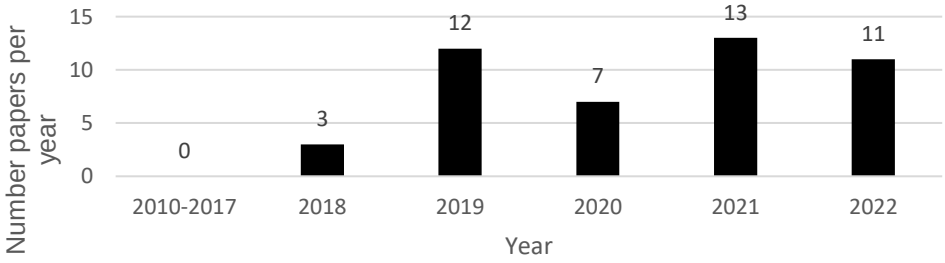

Figure 4: Number of papers published for per year when searching for "machine learning" + "district heating and cooling" + "seasonal thermal energy storage" showing an increase over the years on average.

3. Results

3.1. Machine Learning in Drilling

The application of machine learning or artificial intelligence (AI) has become increasingly prevalent in various industries in recent years [11]. The transition from fossil fuels to renewables to reduce greenhouse gas emissions has led to the rise of renewable energy sectors, such as solar and wind energy, that provide heat and electricity [12,13]. While the share of renewable energy in Europe was 22.2% in 2021 [14], this is still insufficient to meet the renewable energy demands with respect to a climate neutral energy system in the near future [15]. As a result, new technologies are emerging and being developed to support this transition. One sector that requires attention and research to make it a mainstream energy source is geothermal energy, as the energy generation is marginal in both the European Union (3.2%) and Germany (2.5%), despite its potential [16,17,18]. The critical aspect of accessing geothermal energy is developing the reservoir using drilling techniques, which represent nearly 30% to 50% of the costs for a hydrothermal geothermal project and more than half of the total cost on Enhanced Geothermal Systems (EGS) [19]. However, there are also emissions in the drilling process which should be minimized, too [20]. The development of intelligent drilling and

completion technologies using machine learning has shown potential to improve the drilling process's efficiency and accuracy [7]. Our study builds upon the comprehensive literature review conducted by Li et al. [7] and strives to offer insights into the particular domains of drilling where machine learning can be applied, as well as the types of algorithms that can be leveraged for specific tasks to enhance efficiency [7]. Li et al. 2022 [7] cite a total of 160 papers, include a number 137 in their analysis over the research fields (cf. Table 1), from which we further analyze 124 while excluding papers where machine learning is not used.

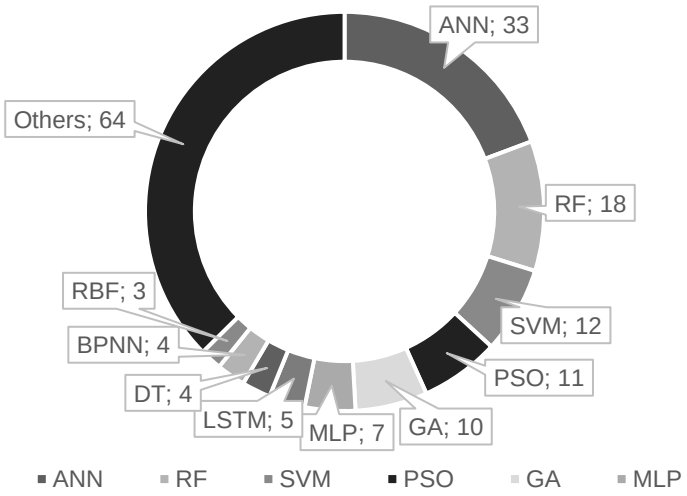

Figure 5: Number of used machine learning algorithms in the 124 papers cited in Li et al. 2022 [7] applying Machine Learning in Drilling

Case Study Results

There are numerous algorithms which have been used in the different papers analyzed by Li et al. 2022 [7] (cf. Figure 5) but among those only five algorithms are highly utilized in most of the fields, which are Artificial Neural Networks (ANN), Random Forests (RF), Support Vector Machine (SVM), Particle swarm optimization (PSO) and Genetic algorithms (GA) (cf. Table 1). These five commonly used algorithms are defined by us based on the repetition and total usage count not less than 10 times across the whole research fields in Li et al. 2022 [7]. Overall, ANNs define the by far most widely used approach and the usage of ANNs is popular in most fields (cf. Figure 6).

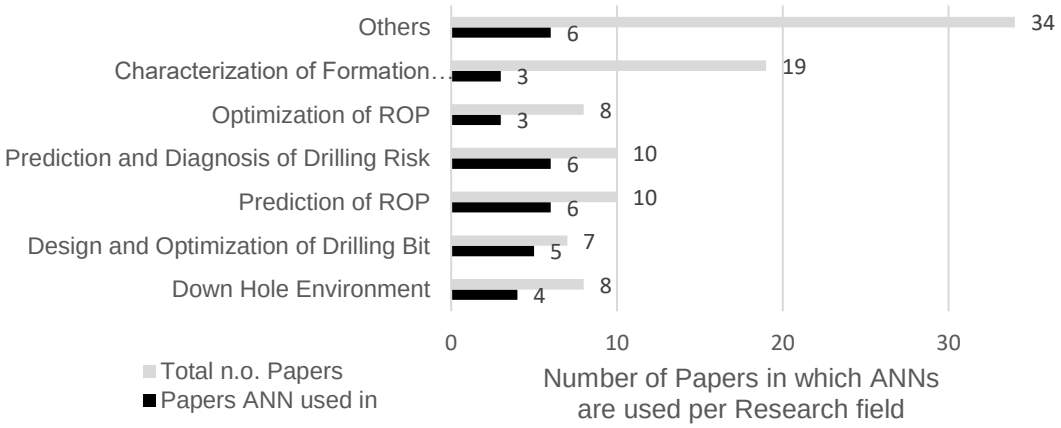

Figure 6: Number of papers per research field in which ANNs were applied in comparison to the total number of papers addressing machine learning in Li et al 2022 [11]

Research Fields	Algorithms				
	ANN	RF	SVM	PSO	GA
Down Hole Environment	4	1	0	0	1
Design and Optimization of Drilling Bit	5	1	0	1	1
Intelligent Prediction of ROP	6	3	3	3	1
Intelligent Optimization of ROP	3	3	0	1	3
Intelligent Design of a well trajectory	0	0	0	1	2
Real time evaluation and optimization of a well trajectory	0	2	0	2	0
Intelligent decision making and control of well trajectory	0	0	0	0	0
Intelligent Characterization of formation properties	3	1	1	0	0
Intelligent Description of wellbore flow behaviour	2	0	1	0	1
Intelligent prediction and diagnosis of drilling risk	6	4	5	1	0
Intelligent control of drilling process	0	0	0	0	0
Intelligent design of hydraulic fracturing	1	1	0	1	1
Intelligent warning and identification of fracturing event	0	1	1	0	0
Productivity prediction and fracturing parameter optimization	1	1	0	0	0
Intelligent completion design and optimization	2	0	1	1	0
Total	33	18	12	11	10

Table 1: Research fields and number of the five most commonly used algorithms in each of these for the analyzed papers from Li et al. [7].

From Table 1, we get an impression of extensively and non-extensively used algorithms in different fields for the five commonly used algorithms. Li et al. [7] analyzed 15 research fields in drilling where machine learning and physical models are used, and from those, whereas 13 fields utilized machine learning for various purposes [7]. Next to the five commonly used algorithms there are few others which are equally often used in some of the research fields, which we want to highlight in the following.

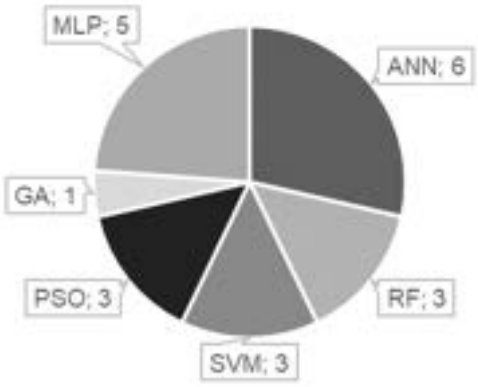

Figure 8: Algorithms used in Prediction of ROP

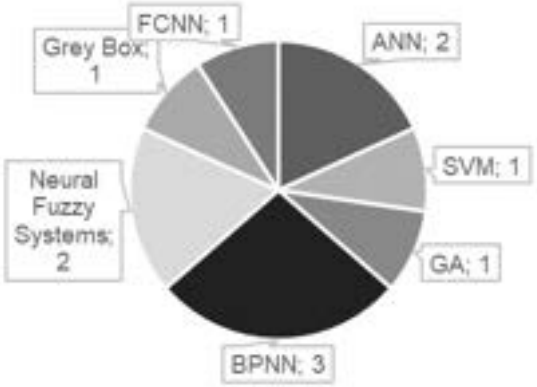

Figure 7: Algorithms used in Wellbore Flow Behavior

From Figure 8, we observe that next to the five widely used algorithms, Multi-Layer Perceptrons (MLP) are commonly applied to predict the rate of penetration (ROP). Back Propagation Neural Networks (BPNN) outnumber the five common algorithms in the field of well bore flow behavior (cf. Figure 7). Of course, there are other fields where utilization algorithms next to the five highlighted ones is common - in any case, to achieve the desired results, multiple algorithms should be tested, and there might be no need to choose an algorithm over another. This analysis gives us an impression on how the different research fields of drilling are commonly approached with machine learning techniques.

Depending on the type of process and thus data (dynamic and static) the selection and application of machine learning models is adapted also with respect to performance and robustness. In the two research fields “control of the drilling process” and “well trajectory design”, physical models and control systems were used for stability, control efficiency of the well, and as a strategy to control the trajectory [7]. There are also few fields where machine learning is partially used or not used at all, but instead, physical based models have been used, mostly to control the well trajectory from real time steerable systems (RSS) [7].

Case study Conclusion and Outlook

The analysis which has been made shows that ANNs are highly used approach in most of the fields, the highest usage of ANNs is in “Intelligent prediction of ROP”, “Intelligent prediction and diagnosis of drilling risk” followed by “Design and optimization of drilling bit” and “Downhole environment perception”. There are few research fields where there is no use of ANNs like “Real time evaluation and optimization of a well trajectory”, “Intelligent design of a well trajectory”, “Intelligent warning and identification of fracturing event” instead other approaches like RF, SVM, PSO were used. As the dominance of ANNs is high one can try implementing them in fields where it has not been used much, yet. Furthermore, RF and SVM approaches were used highly only in “Intelligent prediction and diagnosis of drilling risk” and “Intelligent prediction of ROP”, thus, more studies and implementations could be made in other fields. In the research fields “Intelligent warning and identification of fracturing event” and “Productivity prediction and fracturing parameter optimization” the total use of machine learning is still quite low regarding the total number of papers analyzed by Li et al. 2022 [7], and thus maybe provide good research opportunities for the application of machine learning in drilling.

3.2. Solar Rooftop Potential Quantification

The utilization of solar energy for heat or electricity generation is a highly promising and sustainable alternative to the use of fossil fuels, and the rooftops of buildings represent an underutilized resource for solar power generation [21, 22]. To quantify the potential of rooftop solar energy at a large scale, it is necessary to determine the roof area of buildings that can receive solar radiation, calculate the total solar radiation obtained within the region based on meteorological conditions, and estimate the total solar energy potential with carbon emissions savings and the economic recovery period [23, 25]. However, determining the total roof area can be a challenging task, especially for large regions such as cities or countries [23]. To overcome this challenge, machine learning techniques have been developed to identify and quantify the roof area using aerial and satellite images [24, 26, 28]. This involves collecting initial data from sources such as Google Earth and Copernicus and using semantic segmentation architectures like U-net and Inception-resnet-v2 to identify and segment roofs in the images based on their pixel characteristics [21, 24]. The benefits of utilizing rooftop solar energy are significant, as it enables the local production of renewable power and has enormous potential for reducing greenhouse gas emissions [22, 27]. Studies have shown that rooftop solar energy has the potential to meet a significant portion of a region's energy demands, such as 22% of Europe's energy demand and 15-45% of the energy needs of countries like the United States, Israel, Canada, and Spain [27]. Furthermore, in individual cities like Hong Kong and Seoul, rooftop solar energy has the potential to meet up to 14.2% and 30% of energy demand, respectively [27]. Therefore, there is a clear need to further investigate the potential of rooftop solar energy at a large scale using machine learning and other innovative techniques. This study seeks to provide a systematic literature review of rooftop solar energy measurement based on aerial imaging and machine learning, analyzing various research papers published in this field to compare and address the advantages and disadvantages of different quantification strategies [21, 24, 26, 28]. By doing so, we hope to contribute to the development of more effective methods for quantifying rooftop solar energy potential, which can play a crucial role in the transition from fossil fuels to sustainable energy sources.

Case Study Results

All twelve articles obtained from the systematic literature review process in this study used Google earth as a source for input data. It was also observed that some studies also utilized open-source resources like Copernicus, Open Street Maps (OSM), technical details of PV systems, and aerial pictures accessible using Google Maps' static API. However, the article [24] states that private sources provide high-definition aerial photos for rooftop detection rather than public ones like Google earth.

Semantic segmentation is a major step in the quantification process. It was observed that U-Net is used in most of the studies for semantic segmentation. CNN built on the U-Net is employed, because of its higher performance on small datasets [25]. The paper [26] compared EfficientNet-B3, Inception-resnet-v2, and VGG-19, and Inception-resnet-v2 was chosen due to its superior performance. For semantic segmentation approaches with traditional supervised learning. The article [27] compared three semantic segmentation frameworks: U-Net, PSPNet, and Deeplabv3+ and U-Net was found to be performing better than the others.

In a study conducted by [28] Rooftop Photovoltaic potential has been evaluated using a quick-scan yield prediction technique. It consisted of three primary components. Aerial footage was used to rebuild virtual 3D roof segments for each roof, which were then automatically fitted with PV modules using a fitting algorithm, followed by the calculation of predicted yearly production. After the results were obtained some of the studies had tried to check the accuracy. Twenty randomly chosen roofs were chosen by [29] to compare the model's predictions with estimated real values to assess the findings' accuracy.

Some common challenges in in the application of machine learning for rooftop solar potential quantification are:

- **Failure to identify pre-existing solar panels:**

  As observed in most of the papers, when the roof area was calculated, much research failed to consider pre-existing solar panels. No differentiation between rooftop space and other surfaces is conceivable within building footprints. This can result in incorrect categorization[30]. When we consider a large area with numerous buildings for the study, they can affect the final output. A machine learning model which can identify and discriminate solar panel area from the rest is crucial to obtain correct results. Apart from solar panels, the machine learning model must be able to distinguish objects like water tanks, Chimneys etc.

- **Limited resolution in the available data:**

  Another Challenge faced by semantic segmentation is the least pixel count. Since the least count is restricted to a pixel, if the major portion of pixel is dominated by a particular object, the Machine Learning model identifies the entire pixel to be that object. Most of the studies though uses public sources like Google earth where semantic segmentation can only be done on available images in given course resolution.

- **Failure to identify inclined roofs:**

  Since only the top view is taken into consideration, the calculated roof area of an inclined roof will be always less than the actual value. This can also have a huge impact on the final output. The machine learning model must be taught to consider this factor, while processing the data, as in some research like the one carried out by [31].

Case Study Conclusion and Outlook

We have systematically reviewed papers in the field of application of machine learning rooftop solar energy quantification and One of the major challenges faced in the quantification process is the identification of preexisting solar panels during semantic segmentation. A solution to this was not identified in any of the papers reviewed and could subject to future research.

.

3.3. Machine Learning in District Heating and Cooling in the Context of Seasonal Thermal Energy Storages (STES in DHC)

District heating and cooling (DHC) systems are an important part of the energy sector, providing sustainable solutions to communities. To improve the efficiency of DHC systems, machine learning techniques have been increasingly applied [33]. To supply energy to DHC systems, a source is required, and Seasonal Thermal Energy Storages (STES) can act as an energy source for DHC [34]. STES can help to manage the mismatch between the supply and demand of renewable energy systems, which may occur over seasonal and inter-annual periods. There are four different types of STES: Borehole Thermal Energy Storages (BTES), Aquifer Thermal Energy Storages (ATES), Pit Thermal Energy Storages (PTES), and Tank Thermal Energy Storages (TTES) [35]. Therefore, this study focuses on investigating the application of machine learning in DHC networks with STES, with load/demand prediction, design, and control optimization as the main research categories [33]. This research is motivated by the need to improve the efficiency and reliability of DHC systems while reducing their environmental impact.

Case Study Results

The algorithms used in the seven articles are Artificial neural networks (ANN), genetic algorithms and Non dominant Sorting Genetic Algorithm NGSA-II, which is a multi-objective optimization algorithm which is again the extension of an original NGSA develop by Kalyanmoy Deb in 2022 [4]. Figure 9 gives number of articles used by machine learning methods.

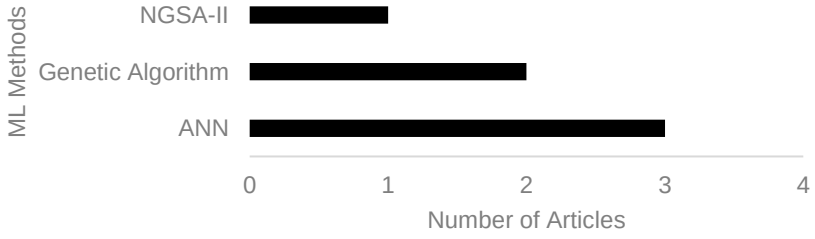

Figure 9: Number of articles with respect to the applied machine learning methods in District Heating and cooling in context of Seasonal Thermal Energy Storages

Various machine learning applications have been applied in different domains, including predictive maintenance, energy demand forecasting, control optimization, and anomaly detection. The papers addressed in this case study had application of machine learning in energy demand forecasting, control optimization, design, and fault detection, specifically in the context of Seasonal Thermal Energy Storages (STES), Aquifer Thermal Energy Storages (ATES), and Borehole Thermal Energy Storages (BTES). However, studies on other types of thermal energy storages, such as Pit Thermal Energy Storages (PTES) and Tank Thermal Energy Storages (TTES), were not present in the papers analyzed and thus not considered in this study. presents the distribution of studies across the various machine learning application categories.

Machine learning applications are applied in differrent ways such as preditcitve maintanence, energy demand forcasting , control optimization, anomaly detection. Here in the study of the selected articles we came accros with the energy demand forecasting, control optimization, design and fault detection. Studies undergo with STES and Aquifer Thermal Energy Storages and Borehole Thermal Enrgy Storages are peformed here, whereas other thermal energy storages such PTES and TTES studies did not show up in the considered papers and are thus neglected. Table 2 shows the three different applied machine learning algorithms in the different categories of application.

Table 2: Applied machine learning algorithms in different categories of application

Category	ANNs	GA	NSGA-II
Energy demand forecasting	1		
Control Optimization		2	1
Design, fault detection	1	1	

Further adressed aspects are:

- In [37], the model predicts the signal of charging and discharging operation and belongs to the category of energy demand forecasting. It was validated to be used in other similar projects; both charging and discharging models have an average accuracy over 95%.
- In [38], optimal based control and model predictive control were applied. MATLAB and a genetic algorithm were used to find an estimate of the global minimum, and a local non-linear minimization routine was used afterwards to refine the calculation.
- In [39], TRNSYS system models and a so-called multi-objective building optimizer (MOBO) are combined to perform the optimization. For this study, the NSGA-II algorithm is used, because it can take care of the constraints, discrete and continuous variables for a multi-objective problem [39].
- In [40], the main objective is to development of a modeling environment able to effectively compare configurational and design choices for multi-energy systems. The core of the Model Predictive Control, that is the optimization function which is Genetic Algorithm, receives information on its settings from the MATLAB organization layer. The role of the Genetic Algorithm is to find the optimal set of instructions for the generation units of the Test Facility for the next prediction horizon. The Genetic Algorithm firstly defines a starting set of instructions following some preset rules. The optimizer then communicates the first set of instructions to the MPC-model.
- In [41], artificial neural networks and geentic algorithms support the fault detection diagnosis. Since the models were trained with laboratory data or data coming from simulations only, they do not achieve a sufficient performance when working with online data. On the other hand, these kind of Fault Detection Diagnosis (FDD) applications show a very promising growth and may be a good option to solve complex FDD problems soon.

In the papers analyzed there are different tools applied for modeling and for data collection. Among these, Transient System Simulation Tool (TRNSYS) seems to be a popular simulation tool within the selected papers which can provide simulated data, if no measured data is available.

Case Study Conclusion and Outlook

The application of machine learning in the energy sector is of utmost importance in the current context. The aim of this study was to provide insights on the use of machine learning in district heating and cooling (DHC) systems, specifically with regards to seasonal thermal energy storages (STES). Despite some research on STES, a comprehensive investigation on this topic remains limited, although Figure 4 depicts an upward trend from 2010 to 2022. The survey highlights the potential field of application of machine learning in various areas such as load demand forecasting, design, fault detection, and control optimization. Artificial Neural Networks

were found to be the most used method due to their superior performance over other machine learning algorithms. Additionally, the TRNSYS simulation tool was predominantly applied for data simulation. Nevertheless, there is a need for more extensive research in the future to better apply machine learning in DHC with STES, including the development of innovative approaches to improve the collection and analysis of data.

4. Discussion and Outlook

This review paper has addressed applications of machine learning in three different energy systems. In all three case studies, we see a smaller to wider range of machine learning models used for various scenarios in developing the technologies, where ANNs are highly utilized machine learning approaches in both STES in DHC and Drilling. The ANN approach seems to have a high accuracy where prediction is involved as in STES in DHC the energy demand forecast model's average accuracy is over 95%, also in drilling a lot of studies were made using ANNs, e.g. in the prediction of ROP and drilling risk. Genetic Algorithms (GA) on the other hand are mostly used in optimization scenarios in both drilling and STES in DHC. However, in the case of rooftop solar quantification, U-Net and inception resnet - v2 is highly used for semantic segmentation as they have higher performance on small datasets compared with others like PSPNet, Deeplabv3+, and VGG-19.

Some of the possible prospects for development and future research in the considered three case studies would:

1. Machine learning in drilling: application of promising machine learning algorithms in fields, where they were not applied, yet (cf. e.g., Table 1).
2. Machine learning for rooftop solar energy potential quantification: developing techniques to identify pre-existing solar panels and improving various methods to recognize inclined roofs.
3. Machine Learning in district heating and cooling in the context of seasonal thermal energy storages: Due to the limited number of studies, there is a good potential for future research on the of application of machine learning in load demand forecasting, design, fault detection, and control optimization.

5. Nomenclature

AI	Artificial Intelligence
ANN	Artificial Neural Network
ATES	Aquifer Thermal Energy Storages
BHA	Bore Hole Assembly
BPNN	Back propagation neural network
BTES	Borehole Thermal Energy Storages
DHC	District heating and Cooling
DT	Decision tree
EGS	Enhanced Geothermal Systems
FCNN	Fully convolutional neural network
FL	Fuzzy logic
GA	Genetic algorithm
LSTM	Long short-term memory neural network
LWD	Logging While Drilling
ML	Machine Learning
MLP	Multi-layer perceptron
MWD	Measured While Drilling
PSO	Particle swarm optimization
PTES	Pit Thermal Energy Storages
RBF	Radial basis function
RF	Random Forest
RSS	Real-Time Steerable System
STES	Seasonal thermal energy storages
SVM	Support Vector Machine
TTES	Tank Thermal Energy Storages

6. References

[1] P. L. Donti and J. Z. Kolter, “Machine Learning for Sustainable Energy Systems,” Annual Review of Environment and Resources, vol. 46, 2021. doi: 10.1146/annurev-environ-020220-061831.

[2] L. Duchesne, E. Karangelos, and L. Wehenkel, “Recent Developments in Machine Learning for Energy Systems Reliability Management,” Proceedings of the IEEE, vol. 108, no. 9, 2020. doi: 10.1109/JPROC.2020.2988715.

[3] D. Sidorov, F. Liu, and Y. Sun, “Machine learning for energy systems,” Energies, vol. 13, no. 18, 2020. doi: 10.3390/en13184708.

[4] A. T. D. Perera, P. U. Wickramasinghe, V. M. Nik, and J. L. Scartezzini, “Machine learning methods to assist energy system optimization,” Appl Energy, vol. 243, 2019. doi: 10.1016/j.apenergy.2019.03.202.

[5] L. Tong, X. Jiang, Z. Wang, and L. Zhang, “Real-time optimal control for district energy systems with machine learning-based models,” Applied Energy, vol. 303, 2022. doi: 10.1016/j.apenergy.2022.117968.

[6] T. Gao and W. Lu, “Machine learning toward advanced energy storage devices and systems,” iScience, vol. 24, no. 1, 2021. doi: 10.1016/j.isci.2020.101936.

[7] G. Li, X. Song, S. Tian, and Z. Zhu, “Intelligent Drilling and Completion: A Review,” Engineering, vol. 18. Elsevier Ltd, pp. 33–48, Nov. 01, 2022. doi: 10.1016/j.eng.2022.07.014.

[8] J. vom Brocke et al., “Reconstructing the giant: on the importance of rigour in documenting the literature search process.” [Online]. Available: www.uni.lihttp://aisel.aisnet.org/ecis2009/161/

[9] J. vom Brocke, A. Simons, K. Riemer, B. Niehaves, R. Plattfaut, and A. Cleven, “Standing on the shoulders of giants: Challenges and recommendations of literature search in information systems research,” Communications of the Association for Information Systems, vol. 37, pp. 205–224, 2015, doi: 10.17705/1cais.03709.

[10] J. Webster and R. T. Watson, “Analyzing the Past to Prepare for the Future: Writing a Literature Review,” 2002.

[11] A. Sircar, K. Yadav, K. Rayavarapu, N. Bist, and H. Oza, “Application of machine learning and artificial intelligence in oil and gas industry,” Petroleum Research, vol. 6, no. 4. KeAi Publishing Communications Ltd., pp. 379–391, Dec. 01, 2021. doi: 10.1016/j.ptlrs.2021.05.009.

[12] “Renewable energy - powering a safer future,” United Nations. https://www.un.org/en/climatechange/raising-ambition/renewable-energy#:~:text=Renewable%20energy%20is%20healthier&text=In%202018%2C%20air%20pollution%20from,also%20air%20pollution%20and%20health. (accessed Mar. 05, 2023).

[13] “Renewable Energy,” Federal Ministry for Economic Affairs and Climate Action, 2018. https://www.bmwk.de/Redaktion/EN/Dossier/renewable-energy.html (accessed Mar. 06, 2023).

[14] “Share of energy consumption from renewable sources in Europe,” European Environment Agency, Oct. 26, 2022. https://www.eea.europa.eu/ims/share-of-energy-consumption-from

[15] Kerstine Appunn, “Sector coupling - Shaping an integrated renewable energy system,” Clean Energy Wire, 2018.

[16] K. McDonnell, L. Molnár, M. Harty, and F. Murphy, “Feasibility study of carbon dioxide plume geothermal systems in Germany−utilising carbon dioxide for energy,” Energies (Basel), vol. 13, no. 10, May 2020, doi: 10.3390/en13102416.

[17] “GEOTHERMAL POWER IN THE COUNTRY OF 100% RENEWABLE ENERGY, ICELAND,” Baseload Power, Dec. 20, 2020. https://baseloadpower.jp/en/geothermal-power-in-the-country-of-100-renewable-energy-iceland/

[18] Ekin İnal, “Geothermal electricity generation in Turkey: Large potential awaiting investors,” Norton Rose Fulbright, Jul. 21, 2020. https://www.nortonrosefulbright.com/de-de/inside-turkey/blog/2020/07/geothermal-electricity-generation-in-turkey-large-potential-awaiting-investors#:~:text=Turkey%20is%20currently%20the%20fourth,of%2048%20plants%20in%20operation. (accessed Mar. 06, 2023).

[19] Dumas P (EGEC), Antics M (GPC IP), and Ungemach P (GPC IP), “GEOELEC - Report on Geothermal Drilling,” 2013.

[20] M. Rizqi Al Asy’ari, J. Tobing, D. Purba, F. R. Fadhillah, S. B. T. Kandou, and D. W. Adityatama, “Carbon Emissions Reduction in Geothermal Drilling Project: A Preliminary Study,” in IOP Conference Series: Earth and Environmental Science, Apr. 2022, vol. 1014, no. 1. doi: 10.1088/1755-1315/1014/1/012017.

[21] D. de B. Soares et al., “Predicting the Solar Potential of Rooftops using Image Segmentation and Structured Data,” May 2021, [Online]. Available: http://arxiv.org/abs/2106.15268

[22] K. Mainzer, S. Killinger, R. McKenna, and W. Fichtner, “Assessment of rooftop photovoltaic potentials at the urban level using publicly available geodata and image recognition techniques,” Solar Energy, vol. 155, 2017, doi: 10.1016/j.solener.2017.06.065.

[23] Z. Huang, T. Mendis, and S. Xu, “Urban solar utilization potential mapping via deep learning technology: A case study of Wuhan, China,” Appl Energy, vol. 250, 2019, doi: 10.1016/j.apenergy.2019.04.113.

[24] J. Park, S. Park, and J. Kang, “Detecting and classifying rooftops with a CNN-based remote sensing method for urban area cool roof application.” [Online]. Available: https://ssrn.com/abstract=4253437

[25] E. Fakhraian, M. Alier, F. V. Dalmau, A. Nameni, and J. C. Guerrero, “The urban rooftop photovoltaic potential determination,” Sustainability (Switzerland), vol. 13, no. 13, Jul. 2021, doi: 10.3390/su13137447.

[26] S. Krapf, N. Kemmerzell, S. K. H. Uddin, M. H. Vázquez, F. Netzler, and M. Lienkamp, “Towards Scalable Economic Photovoltaic Potential Analysis Using Aerial Images and Deep Learning,” Energies (Basel), vol. 14, no. 13, Jul. 2021, doi: 10.3390/en14133800.

[27] D.-Y. Chen, L. Peng, W.-Y. Zhang, Y.-D. Wang, and L.-N. Yang, “Research on Self-Supervised Building Information Extraction with High-Resolution Remote Sensing Images for Photovoltaic Potential Evaluation,” Remote Sens (Basel), vol. 14, no. 21, p. 5350, Oct. 2022, doi: 10.3390/rs14215350.

[28] T. N. C. de Vries et al., “A quick-scan method to assess photovoltaic rooftop potential based on aerial imagery and LiDAR,” Solar Energy, vol. 209, pp. 96–107, Oct. 2020, doi: 10.1016/j.solener.2020.07.035.

[29] A. Boyd, “Mapping Solar PV Potential in Ambleside 2,” 2019.

[30] H. Koch, S. Lechner, S. Erdmann, and M. Hofmann, “Assessing the Potential of Rooftop Photovoltaics by Processing High-Resolution Irradiation Data, as Applied to Giessen, Germany,” Energies (Basel), vol. 15, no. 19, Oct. 2022, doi: 10.3390/en15196991.

[31] M. B. Gergelova, Z. Kuzevicova, S. Labant, S. Kuzevic, D. Bobikova, and J. Mizak, “Roof ś potential and suitability for pv systems based on lidar: A case study of komárno, slovakia,” Sustainability (Switzerland), vol. 12, no. 23, pp. 1–22, Dec. 2020, doi: 10.3390/su122310018.

[32] P. Li et al., “Understanding rooftop PV panel semantic segmentation of satellite and aerial images for better using machine learning,” Advances in Applied Energy, vol. 4, Nov. 2021, doi: 10.1016/j.adapen.2021.100057

[33] C. Ntakolia, A. Anagnostis, S. Moustakidis, and N. Karcanias, “Machine learning applied on the district heating and cooling sector: a review,” Energy Systems, vol. 13, no. 1. Springer Science and Business Media Deutschland GmbH, Feb. 01, 2022. doi: 10.1007/s12667-020-00405-9.

[34] E. Borri, G. Zsembinszki, and L. F. Cabeza, “Recent developments of thermal energy storage applications in the built environment: A bibliometric analysis and systematic review,” Appl Therm Eng, vol. 189, p. 116666, May 2021, doi: 10.1016/j.applthermaleng.2021.116666.

[35] A. Lyden, C. S. Brown, I. Kolo, G. Falcone, and D. Friedrich, “Seasonal thermal energy storage in smart energy systems: District-level applications and modelling approaches,” Renewable and Sustainable Energy Reviews, vol. 167. Elsevier Ltd, Oct. 01, 2022. doi: 10.1016/j.rser.2022.112760.

[36] F. Jimenez, A. F. Gomez-Skarmeta, G. Sanchez, and K. Deb, “An evolutionary algorithm for constrained multi-objective optimization,” in Proceedings of the 2002 Congress on Evolutionary Computation. CEC’02 (Cat. No.02TH8600), pp. 1133–1138. doi: 10.1109/CEC.2002.1004402.

[37] H. Haq, P. Välisuo, L. Mesquita, L. Kumpulainen, and S. Niemi, “An application of seasonal borehole thermal energy system in Finland,” Clean Eng Technol, vol. 2, p. 100048, Jun. 2021, doi: 10.1016/j.clet.2021.100048.

[38] E. Saloux and J. A. Candanedo, “Sizing and control optimization of thermal energy storage in a solar district heating system,” Energy Reports, vol. 7, pp. 389–400, Oct. 2021, doi: 10.1016/j.egyr.2021.08.092.

[39] H. ur Rehman, J. Hirvonen, R. Kosonen, and K. Sirén, “Computational comparison of a novel decentralized photovoltaic district heating system against three optimized solar district systems,” Energy Convers Manag, vol. 191, pp. 39–54, Jul. 2019, doi: 10.1016/j.enconman.2019.04.017.

[40] E. Patrucco, “Executive summary.”

[41] S. Buffa, M. H. Fouladfar, G. Franchini, I. Lozano Gabarre, and M. Andrés Chicote, “Advanced Control and Fault Detection Strategies for District Heating and Cooling Systems—A Review,” Applied Sciences, vol. 11, no. 1, p. 455, Jan. 2021, doi: 10.3390/app11010455.

PROCEEDINGS OF ECOS 2023 - THE 36TH INTERNATIONAL CONFERENCE ON
EFFICIENCY, **C**OST, **O**PTIMIZATION, **S**IMULATION AND ENVIRONMENTAL IMPACT OF ENERGY SYSTEMS
25-30 JUNE 2023, LAS PALMAS DE GRAN CANARIA, SPAIN

Reinforcement Learning for Joint Design and Control of Battery-PV Systems

Marine Cauz[a,b], Adrien Bolland[c], Bardhyl Miftari[c], Lionel Perret[b], Christophe Ballif[a,d], and Nicolas Wyrsch[a]

[a] École polytechnique fédérale de Lausanne (EPFL), Institute of Electrical and Micro Engineering (IEM), Photovoltaics and Thin-Film Electronics Laboratory (PV-Lab), Neuchâtel, Switzerland. Marine.Cauz@epfl.ch, CA.
[b] Planair SA, Yverdon-les-bains, Switzerland
[c] Department of Electrical Engineering and Computer Science, University of Liège, Liège, Belgium
[d] Centre Suisse d'Electronique et de Microtechnique (CSEM), PV-Center, Neuchâtel, Switzerland

Abstract:

The decentralisation and unpredictability of new renewable energy sources require rethinking our energy system. Data-driven approaches, such as reinforcement learning (RL), have emerged as new control strategies for operating these systems, but they have not yet been applied to system design. This paper aims to bridge this gap by studying the use of an RL-based method for joint design and control of a real-world PV and battery system. The design problem is first formulated as a mixed-integer linear programming problem (MILP). The optimal MILP solution is then used to evaluate the performance of an RL agent trained in a surrogate environment designed for applying an existing data-driven algorithm. The main difference between the two models lies in their optimization approaches: while MILP finds a solution that minimizes the total costs for a one-year operation given the deterministic historical data, RL is a stochastic method that searches for an optimal strategy over one week of data on expectation over all weeks in the historical dataset. Both methods were applied on a toy example using one-week data and on a case study using one-year data. In both cases, models were found to converge to similar control solutions, but their investment decisions differed. Overall, these outcomes are an initial step illustrating benefits and challenges of using RL for the joint design and control of energy systems.

Keywords:

Energy systems, Design, Control, RL, MILP.

1. Introduction

1.1. Background and related work

The current transition to renewable energy sources requires rethinking new energy systems, characterized by decentralized and intermittent production. The development of these systems typically occurs in two distinct steps, namely the design and control of these systems. The design problem involves identifying the design variables which are the optimal size of energy system components. The control problem aims to determine the control variables which are the optimal actions to operate the energy system components. Both design and control problem should jointly minimize a cost function and are typically solved sequentially. This paper explores the value of solving the design and control tasks, using a reinforcement learning (RL) method as appropriate design is intrinsically linked to subsequent operation. To evaluate the effectiveness of this approach, its performance are compared with that of the Mixed Integer Linear Programming (MILP) method.

On the one hand, RL is a data-driven approach where an agent learns to make decisions in a dynamic environment through trial-and-error experience. It involves an agent interacting with an environment and receiving feedback in the form of rewards or penalties based on its actions, with the goal of maximizing its cumulative reward over time. On the other hand, Mixed Integer Linear Programming (MILP) is a mathematical optimization technique used to solve problems with linear constraints and integer variables. It involves formulating a mathematical model of the problem and using an optimization algorithm to find the best solution. Both RL and MILP methods will be used to benchmark the results of a one-year time series.

As highlighted in a recent review [1], RL-based approaches have significant potential, yet not fully exploited, in the energy field. Specifically, the review points out that energy systems are typically designed using either MILP or heuristic methods, with RL approaches dedicated to their control. Integrating RL beyond energy flow control would open new interesting research questions. In [2], RL is used to support distributed energy system design due to its flexibility and model-free nature, which allows it to be adapted to different environments at different

scales. However, they did not simultaneously address the dispatch and design problem as a distributed reward problem, as done in this work. Instead, they used a cooperative coevolution algorithm (COCE) to assist the optimization process. Jointly addressing the design and operation of energy systems is a key issue, especially for multi-energy systems, as discussed in [3], where multi-objective evolutionary algorithms (EMOO) and MILP are used to integrate biomass technologies in a multi-energy system. In [4], the focus is on evolution algorithms and their comparison with deep reinforcement learning strategies. After clarifying the fundamental differences between the two approaches, the discussion revolves around their ability to parallelize computations, explore environments, and learn in dynamic settings. The potential of hybrid algorithms combining the two techniques is also investigated, along with their real-world applications.

RL-based frameworks are successfully applied to the operation of energy systems [5], although these methods have not, to the authors' knowledge, been extended to solve real-world design problem in energy system. As reviewed in [6], RL-based frameworks are popular for addressing electric vehicle (EV) charging management, mostly with variants of the DQN algorithm, and outperform other traditional methods. In [7], various deep RL algorithms are benchmarked against rule-based control, model predictive control, and deterministic optimization in the presence of PV generation. The study, which aims to increase PV self-consumption and state-of-charge at departure, demonstrates the potential of RL for real-time implementation. For solving V2G control under price uncertainty, [8] modeled the problem with a Markov Decision Process (MDP) [9], a mathematical framework for modeling system where stochasticity is involved. Additionally, a linear MDP formulation is also used in [10] to address the coordination of multiple charging points at once. Finally in [11], a data-driven approach is defined and evaluated for coordinating the charging schedules of multiple EVs using batch reinforcement learning with a real use case. In conclusion, these studies provide valuable insights and tools for optimizing and improving energy systems, demonstrating the potential of RL to tackle the operation of complex energy systems.

1.2. Contribution

This work aims to evaluate the relevance of jointly designing and controlling an energy system using a deep RL approach. To achieve this purpose, two methods are benchmarked to address jointly the design and control problem of a real-world PV-battery system. The first method, MILP, computes the optimal design and control solution over a sequence of historical data. The second method, RL, computes the optimal design and a control policy through interactions with a simulator by trial and error. The specific RL algorithm used in this study is referred to as Direct Environment and Policy Search (DEPS) [12]. DEPS extends the REINFORCE algorithm [13] by combining policy gradient with model-based optimization techniques to parameterize the design variables. In this framework, an agent looks for the design and control variables that jointly maximize the expected sum of rewards collected over the time horizon of interest. The outcomes of both methods are discussed in the subsequent sections of this paper.

This paper is structured as follows. Section 2. provides two formulations of the energy system, one designed for MILP and the other for RL, and discusses the methodology used to benchmark the results. In Section 3., the outcomes of the study are presented, and these results are discussed in Section 4., with a focus on the potential of RL for joint design and control of energy systems. Finally, the paper concludes with a summary in Section 5..

2. Method

2.1. Problem statement

The study is carried out for the energy system illustrated in Figure 1, whose components are detailed in the subsections below. Overall, the system refers to an office building that has been fitted with a PV installation and a stationary lithium-ion battery to meet its own electricity consumption. Additionally, the building is connected to the electricity grid.

The objective of the study is to jointly propose a design of the PV and battery components, as well as a control strategy of the described energy system in order to minimize the total cost of its ownership. In the following Subsection 2.2., the system is expressed as a mathematical program made-up of constraints and objectives. To be more precise, it is tackled as a Mixed-Integer Linear Program. Subsection 2.3. formulates a surrogate environment as an MDP. The latter represents the same dynamics and rewards as the original problem but the objective is to maximize the sum of rewards gathered over one week on expectation over the 52 weeks of the year of data. By doing so, it allows the use of the RL algorithm and expects the optimal solution to be close to the solution of the original problem. Results are discussed in Section 3.. Finally, for both methods, the energy system is studied over a finite time horizon T, on which all costs are evenly distributed across each time step t. The methodology and the context of the experiments conducted are specified in Subsection 2.4..

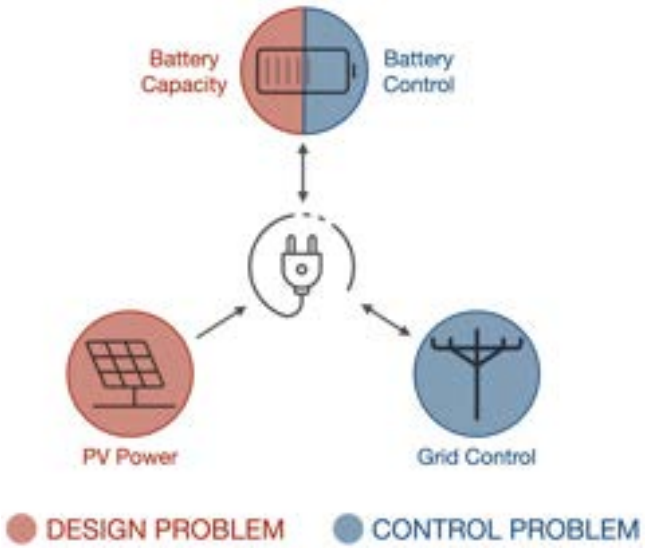

Figure 1: The energy system to be jointly designed and controlled is characterized by an electrical consumption, a battery, a photovoltaic system, and a grid connection. The design problem consists of determining the photovoltaic power and battery capacity, while the control problem aims to regulate the charging and discharging of the battery, as well as the import (resp. export) of electricity to (resp. from) the grid. The overall objective is to meet the electrical consumption needs while minimizing the costs of installing and operating the system.

2.2. Energy system

This subsection describes the physical constraints that apply to the components of the energy system. Theses components, in sequential order, consist of the PV panels, the battery, the electrical load and the power grid. The set of design and control variables and the parameters of the whole system, which is modeled as a discrete-time system, are gathered respectively in Table 1 and 2, respectively.

	Variable	Set	Unit	Description
GRID	P^{IMP}	$\mathbb{R}_+^T$	kW	imported power (from the grid)
	P^{EXP}	$\mathbb{R}_+^T$	kW	exported power (to the grid)
PV	P^{NOM}	$\mathbb{R}_+$	kW_p	nominal power of the PV installation
BATTERY	B	$\mathbb{R}_+$	kWh	nominal capacity of the battery
	SOC	$\mathbb{R}_+^T$	kWh	state of charge of the battery
	P^B	$\mathbb{R}^T$	kW	power exchanged with the battery

Table 1: Set of design and control variables of the energy system studied.

PV system

The objective of the PV installation is to generate electricity on-site to fulfill the local electricity demand. The design of this component is one of the two design variables that will result from the optimization process. The range of the suitable nominal power P^{NOM}, corresponding to its design variable, is set in Eq. (1) and the production at time t is directly proportional to this nominal design variable as shown in Eq. (2). The normalized annual curve $\overline{p}_t^{\text{PROD}}$ corresponds to the actual hourly averaged PV production power of the building.

$$P_{\text{MIN}}^{\text{NOM}} \leq P^{\text{NOM}} \leq P_{\text{MAX}}^{\text{NOM}} \tag{1}$$

$$P_t^{\text{PROD}} = P^{\text{NOM}} \cdot \overline{p}_t^{\text{PROD}} \tag{2}$$

The CAPEX and OPEX values, which are respectively the initial investment and the annual maintenance cost, of the installation are made up of a fixed and a variable part to take account of potential scale effects.

$$\text{CX}_{\text{PV}} = \text{CX}_{\text{PV}}^{\text{FIX}} + \text{CX}_{\text{PV}}^{\text{VAR}} \cdot P^{\text{NOM}} \tag{3}$$

$$\text{OX}_{\text{PV}} = \text{OX}_{\text{PV}}^{\text{FIX}} + \text{OX}_{\text{PV}}^{\text{VAR}} \cdot P^{\text{NOM}} \tag{4}$$

	Parameter	Value	Set	Unit	Description
GRID	$C^{\text{IMP}}_{\text{GRID}}$	1	$\mathbb{R}$	€/kWh	imported electricity price
	$C^{\text{EXP}}_{\text{GRID}}$	-0.05	$\mathbb{R}$	€/kWh	exported electricity price
	C_{GRID}		$\mathbb{R}^T$	€	electricity network cost
	$P^{\text{MAX}}_{\text{GRID}}$	10'000	$\mathbb{R}_+$	kW	grid connection power
PV	$P^{\text{NOM}}_{\text{MIN}}$	0	$\mathbb{R}_+$	kW_p	minimal nominal PV power
	$P^{\text{NOM}}_{\text{MAX}}$	200	$\mathbb{R}_+$	kW_p	maximal nominal PV power
	P^{PROD}		$\mathbb{R}^T_+$	kW	generated PV power
	$\overline{P}^{\text{PROD}}$		$\mathbb{R}^T_+$	kW	expected generated PV power
	$\overline{p}^{\text{PROD}}$		$\mathbb{R}^T_+$	kW	normalised PV power
	L^{PV}	20	$\mathbb{N}$	years	PV lifetime
	R_{PV}		$\mathbb{R}_+$	-	annuity factor
	$\text{OX}^{\text{FIX}}_{\text{PV}}$	3	$\mathbb{R}_+$	€	OPEX PV fixed cost
	$\text{OX}^{\text{VAR}}_{\text{PV}}$	10	$\mathbb{R}_+$	€/kW	OPEX PV variable cost
	$\text{CX}^{\text{FIX}}_{\text{PV}}$	50	$\mathbb{R}_+$	€	CAPEX PV fixed cost
	$\text{CX}^{\text{VAR}}_{\text{PV}}$	200	$\mathbb{R}_+$	€/kW	CAPEX PV variable cost
BATTERY	B_{MIN}	0	$\mathbb{R}_+$	kWh	minimal nominal battery capacity
	B_{MAX}	200	$\mathbb{R}_+$	kWh	maximal nominal battery capacity
	η^{B}	0.9	$]0, 1]$	-	battery efficiency
	L^{B}	30	$\mathbb{N}$	years	battery lifetime
	R_{B}		$\mathbb{R}_+$	-	annuity factor
	$\text{OX}^{\text{FIX}}_{\text{B}}$	5	$\mathbb{R}_+$	€	OPEX Battery fixed cost
	$\text{OX}^{\text{VAR}}_{\text{B}}$	6	$\mathbb{R}_+$	€/kW	OPEX Battery variable cost
	$\text{CX}^{\text{FIX}}_{\text{B}}$	30	$\mathbb{R}_+$	€	CAPEX Battery fixed cost
	$\text{CX}^{\text{VAR}}_{\text{B}}$	110	$\mathbb{R}_+$	€/kW	CAPEX Battery variable cost
SYSTEM	T		$\mathbb{N}$	-	time horizon
	Δt	1	$\mathbb{R}^T_+$	h	time steps
	h_t		$[0 : 23]$	h	hour of the time step
	r	0.05	$\mathbb{R}$	-	discount rate
	P^{LOAD}		$\mathbb{R}^T_+$	kW	uncontrollable electricity consumption
	$\overline{P}^{\text{LOAD}}$		$\mathbb{R}^T_+$	kW	expected electricity consumption

Table 2: Set of parameters of the energy system studied.

Battery

To maximize the potential for on-site self-consumption, a stationary lithium-ion battery is available. The design of this component, corresponding to its capacity B, is the second design variable to determine during the optimization process. This battery capacity can vary in the range of Eq. (5).

$$B_{\text{MIN}} \leq B \leq B_{\text{MAX}} \tag{5}$$

The state of charge variable, SOC_t, changes as a function of the power exchanged with the battery denoted P^B_t. This power is constrained, for charging, by the nominal capacity, Eq. (6), and, for discharging, by the energy stored, Eq. (7). Additionally, the battery efficiency, denoted η^{B}, is assumed identical for both the charging and the discharging processes.

$$P^B_t \leq \frac{\text{B} - \text{SOC}_t}{\Delta t} \qquad \text{if } P^B_t \geq 0 \tag{6}$$

$$P^B_t \geq \frac{-\text{SOC}_t}{\Delta t} \qquad \text{if } P^B_t \leq 0 \tag{7}$$

Knowing the power exchanged with the battery, the state of charge can be updated:

$$\text{SOC}_{t+1} = \begin{cases} \text{SOC}_t + P^B_t \cdot \eta^{\text{B}} \cdot \Delta t & \text{if } P^B_t \geq 0 \\ \text{SOC}_t + \frac{P^B_t}{\eta^{\text{B}}} \cdot \Delta t & \text{if } P^B_t < 0 \end{cases} \tag{8}$$

At the beginning of the optimization, i.e., $t = 0$, the battery SOC is set to half of its capacity value, to initialize the model. Moreover, to avoid any artificial benefit, the final SOC is constrained to be equal to the initial value,

as formulated in Eq. (10).

$$\mathrm{SOC}_{t=0} = \frac{B}{2} \tag{9}$$

$$\mathrm{SOC}_{t=0} = \mathrm{SOC}_{t=T} \tag{10}$$

Similar to the PV plant, the CAPEX and OPEX of the battery consist of both fixed and variable parts.

$$\mathrm{CX_B} = \mathrm{CX_B^{FIX}} + \mathrm{CX_B^{VAR}} \cdot \mathrm{B} \tag{11}$$

$$\mathrm{OX_B} = \mathrm{OX_B^{FIX}} + \mathrm{OX_B^{VAR}} \cdot \mathrm{B} \tag{12}$$

Electrical load

The electrical load used in this project is real data from an office building in Switzerland. This consumption is monitored on an hourly basis and reflects the consumption patterns of office days. This building load power, P_t^{LOAD}, is provided as input and corresponds to an actual measurement sampled by hours over a year.

Electrical grid

To absorb excess solar production or to meet the electricity consumption in the absence of local production, the system is connected to the low-voltage electrical grid. This connection is modeled here as a single balance equation, called the conservation of electrical power, shown in Eq. (13). The power imported from the grid is referred to as P_t^{IMP} and the power injected is referred to as P_t^{EXP}.

$$P_t^{\mathrm{PROD}} + P_t^{\mathrm{IMP}} = P_t^{\mathrm{LOAD}} + P_t^{\mathrm{B}} + P_t^{\mathrm{EXP}} \tag{13}$$

The grid power value at each time t is derived from Eq. 13, and the power limit can be described as follows.

$$0 \leq P_t^{\mathrm{IMP}} \leq P_{\mathrm{GRID}}^{\mathrm{MAX}} \tag{14}$$

$$0 \leq P_t^{\mathrm{EXP}} \leq P_{\mathrm{GRID}}^{\mathrm{MAX}} \tag{15}$$

Based on the import and export power, the total cost of supplying electricity through the network C_{GRID} can be computed.

$$C_{\mathrm{GRID}} = \sum_{t=0}^{T-1} C_{\mathrm{GRID},t} = \sum_{t=0}^{T-1} P_t^{\mathrm{IMP}} \cdot C_{\mathrm{GRID},t}^{\mathrm{IMP}} - P_t^{\mathrm{EXP}} \cdot C_{\mathrm{GRID},t}^{\mathrm{EXP}} \tag{16}$$

Objective function

The objective of this study is to propose a design for the PV and battery components, along with their dispatch, with the aim of minimizing the total cost of ownership. This objective function, of minimizing the overall cost of the system, can be formulated as follows.

$$\min \quad \mathrm{TOTEX} \tag{17}$$

The total cost of the system, denoted TOTEX, is composed of the CAPEX and OPEX of both PV and battery components, as well as the grid cost.

$$\mathrm{TOTEX} = \mathrm{OPEX} + \mathrm{CAPEX} + C_{\mathrm{GRID}} \tag{18}$$

$$\mathrm{OPEX} = \mathrm{OX_{pv}} + \mathrm{OX_B} \tag{19}$$

$$\mathrm{CAPEX} = \mathrm{CX_{pv}} \cdot R_{pv} + \mathrm{CX_B} \cdot R_B \tag{20}$$

The OPEX and grid cost are computed over a finite time period T. However, the CAPEX is an investment cost that is independent of T. To enable the adaptation of the investment cost to the project duration, an annuity factor R adjusts the CAPEX for the finite time horizon T. This annuity factor is computed according to Eq. (21), by taking into account the values of T, the annual discount rate r, and the lifetime L of the component. This formula includes a scaling factor $\frac{T}{8760}$ to adapt R to the period T, based on the assumption that T is expressed in hours since 8760 is the number of hours in a year.

$$R = \frac{r \cdot (1+r)^L}{(1+r)^L - 1} \cdot \frac{T}{8760} \tag{21}$$

2.3. MDP formulation

This section presents an alternative formulation of the problem as a Markov Decision Process (MDP), which is a well-established framework for modeling sequential decision-making problems. This alternative formulation is required for applying DEPS. More precisely, an MDP(S, A, P, R, T), as presented below, consists of the following elements: a finite set of states S, a finite set of actions A, a transition function P, a rewards function R, and a finite time horizon T.

State Space

The state of the system can be fully described by

$$s_t = (h_t, d_t, \mathrm{SOC}_t, \overline{P}_t^{\mathrm{PROD}}, \overline{P}_t^{\mathrm{LOAD}}) \tag{22}$$

$$\in S = \{0, ..., 23\} \times \{0, ..., 364\} \times [0, B] \times \mathbb{R}_+ \times \mathbb{R}_+ \tag{23}$$

- $h_t \in \{0, ..., 23\}$ denotes the hour of the day at time t. The initial value is set to 0.
- $d_t \in \{0, ..., 364\}$ denotes the day of the year at time t. The initial value is set randomly.
- SOC_t is the state of charge of the battery at time t, this value is upper bounded by the nominal capacity of the installed battery B. The value is set initially to a random value during the training process and to half of its capacity during the validation process.
- $\overline{P}_t^{\mathrm{PROD}}$ represents the expected PV power at time t. This value is obtained by scaling normalized historical data $\overline{p}_t^{\mathrm{PROD}}$ with the total installed PV power (P^{NOM}) and considering h_t and d_t values.
- $\overline{P}_t^{\mathrm{LOAD}}$ denotes the expected value of the electrical load at time t. The load profile is determined using historical data that corresponds to the same hour and day as the PV power.

Action Space

The action of the system corresponds to the power exchanged with the battery.

$$\widetilde{a}_t = (\widetilde{P}_t^B) \tag{24}$$

After projecting the action to fall within the acceptable range specified by Eq. (6) and (7), the resulting value is used as a_t, as shown in Eq. (25). This corresponds to the power exchanged with the battery, denoted P_t^B, this value is positive when the battery is being charged and negative when it is being discharged.

$$P_t^B = \begin{cases} \frac{\mathrm{B} - \mathrm{SOC}_t}{\Delta t} & \text{if } \widetilde{P}_t^B > \frac{\mathrm{B} - \mathrm{SOC}_t}{\Delta t} \\ \frac{\mathrm{SOC}_t}{\Delta t} & \text{if } \widetilde{P}_t^B < -\frac{\mathrm{SOC}_t}{\Delta t} \\ P_t^B & \text{otherwise} \end{cases} \tag{25}$$

Transition Function

Each time step t in the system corresponds to one hour, which implies the evolution specified in Eq. (26) of the state variable h and every 24 time steps, the day is incremented by 1.

$$h_{t+1} = (h_t + 1) \bmod 24 \tag{26}$$

$$d_{t+1} = \mathrm{Int}(\frac{h_t + 1}{24}) \tag{27}$$

where the function *Int* takes the integer value of the expression in Eq. (27).

The SOC_t of the battery is updated as Eq. (8), based on the projected action value, and all other state variables are taken from input data.

$$\overline{P}_{t+1}^{\mathrm{PROD}} = \overline{p}_{h_{t+1}, d_{t+1}}^{\mathrm{PROD}} \cdot P^{\mathrm{NOM}} \tag{28}$$

$$\overline{P}_{t+1}^{\mathrm{LOAD}} = \overline{p}_{h_{t+1}, d_{t+1}}^{\mathrm{LOAD}} \tag{29}$$

Reward Function

The reward signal to optimize the agent's actions in RL serves a similar aim as the objective function in the MILP formulation. Therefore, the reward here is the opposite value of the TOTEX defined at Eq. (18). This cost is composed of (i) the investment cost, (ii) the operating cost and (iii) the cost from the purchase and resale of electricity from the grid defined in Eq. (16).

$$r_t = -\mathrm{TOTEX}_t \tag{30}$$

$$= -\mathrm{CAPEX} - \mathrm{OPEX} - C_{\mathrm{GRID},t} \tag{31}$$

$$= -\mathrm{CAPEX} - \mathrm{OPEX} - P_t^{\mathrm{IMP}} \cdot C_{\mathrm{GRID},t}^{\mathrm{IMP}} + P_t^{\mathrm{EXP}} \cdot C_{\mathrm{GRID},t}^{\mathrm{EXP}} \tag{32}$$

where the grid cost is the only time-dependent factor, while CAPEX and OPEX are fixed values for a specific value of P^{NOM} and B.

2.4. Methodology

This subsection discusses the fundamental differences between the two methods (i.e., MILP and RL), along with the experimental protocol that was employed to compare the results. As discussed briefly earlier, although the same problem is aimed to be solved, the methods under study are fundamentally different.

MILP is a method for solving problems that involves optimizing a linear function of variables that are either integer or constrained by linear equalities, as the problem described in Subsection 2.2. The MILP algorithm solves the optimization problem by iteratively adjusting the values of the design and control variables, subject to the constraints, until it finds the optimal solution that maximizes or minimizes the objective function, depending on the problem's goal. This method is applied to the problem described in Subsection 2.2. over a one-year time horizon (T = 8760). The solution is said to be computed with perfect foresight meaning that all variables are selected accounting for the future realization of (normally unknown) events in the time series, providing an optimistic upper bound on the true performance of the control and design. Concretely, the MILP problem is here encoded in the Graph-Based Optimization Modelling Language (GBOML) [14] paired with the Gurobi solver [15].

In contrast, RL is a stochastic optimization method that learns from experience through trials and errors. In this study, we use DEPS [12], an algorithm optimizing design and control variables in an MDP, as the one described in Subsection 2.3., with a finite-time horizon. The agent receives feedback in the form of rewards when it selects a particular design and performs specific actions. The objective of the agent is to maximize the expected cumulative reward, which drives it to learn a design and a control policy. Ideally, as with MILP, the time horizon should be annual, or cover the entire lifetime of the system, taking into account seasonal production and consumption fluctuations and/or equipment aging. However, such extended time horizons are unsuitable for this RL approach. Therefore, to strike a balance between a horizon that is short enough for DEPS and long enough to observe the consequences of decisions on the system, a horizon of T = 168 hours, i.e., 7 days, is defined. Additionally, for each simulation, the initial day is sampled uniformly from the year-long data set and the initial state-of-charge of the battery is also sampled uniformly at random. As the reward is optimized on expectation over all days, the resulting design and control policy is expected to account for the seasonality and other different hazard in the historical data. The DEPS algorithm is trained on a predetermined number of iterations. The PV power and battery capacity values obtained from the last iteration of the algorithm are then taken as the values of the design variables and the final policy is used for the control.

Unlike MILP, the RL method does not secure optimality, therefore the experimental protocol aims to compare both results to see how far the RL solution is from the optimal one. The experimental protocol is conducted in two distinct scenarios to differentiate the impact of adding the design variables in the joint problem. The first control-only scenario (CTR) assessed the control variables when the design variables are fixed. The second scenario, considering both the control and design (CTR & DES) problem, allows for flexibility in designing the battery capacity and PV power, the two design variables. To benchmark the performance of both methods in each scenario (i.e., CTR and CTR & DES), the reward and income value are reported. The reward value is computing according to Eq. (32) for the RL method. To estimate the average reward value for the MILP method, all reward values r_t are averaged over time horizons of T = 168. Comparing the average cumulative reward value of the MILP method to that of the RL method provides a first benchmark for evaluating the performance of both approaches. However, as shown in Eq. (32), only the grid cost is time-dependent, while the CAPEX and OPEX depend solely on investment decisions. Therefore, the income value is defined as the average reward value, but it only includes the grid cost and can be computed as follows:

$$Income = \sum_{t=0}^{T-1} -P_t^{\text{IMP}} \cdot C_{\text{GRID},t}^{\text{IMP}} + P_t^{\text{EXP}} \cdot C_{\text{GRID},t}^{\text{EXP}} \tag{33}$$

Finally, the experiments are performed in two steps. First, to perform a simple comparative study, working on a same finite time horizon T = 168, both methods are conducted using data from a single summer week. Second, the data set is extended to include the one-year data set.

3. Results

The energy system presented in Section 2. is solved using the RL and MILP approaches with parameter values listed in Table 2. To differentiate the performance of the DEPS algorithm for control and design aspects, the study is conducted in two distinct scenarios. The first control-only scenario (CTR) assessed the control aspect for fixed design variables, meaning that the PV power and battery capacity are fixed. The second scenario, considering both the control and design (CTR & DES) aspects, allows for flexibility in designing the battery capacity and PV power. The two following subsections describe the results of the study performed in two steps, over the one-week and one-year data set, respectively.

3.1. A one-week toy example

In order to perform a simple comparative study, both CTR and CTR & DES analyses were conducted using data from a single summer week. This enables to optimize both methods on the same time horizon. This means training the RL algorithm on the same 168 time steps, with an initial day uniformly randomly selected over the week but an initial hour fixed at midnight. Additionally, during the training phase, the battery's initial SOC is uniformly sampled such that the RL algorithm is presented with a large variety of scenarios for improving the quality of the learned policy. The results for both the CTR scenario, where the design variables (i.e., the PV power and battery capacity) are fixed, and the CTR & DES scenario, where the PV and battery design variables are optimized in addition to control, are presented in Table 3.

		Unit	Optimal RL solution	Optimal MILP solution	MILP solution based on RL design
CTR	T	hours	168	168	
	Reward	€	-66	-66	
	Income	€	-30	-30	
CTR & DES	T	hours	168	168	168
	Reward	€	-40	-46	-53
	Income	€	-4	0	-17
	Battery capacity	kWh	62	40	62
	PV power	kWp	41	103	41

Table 3: Results of RL and MILP solutions on one-week data for control-only (CTR) and control and design (CTR & DES) scenarios. T denotes the time horizon in hours, while *income* represents the cost of buying and selling electricity from the grid, *reward* is the average cumulative reward value, and *battery capacity* and *PV power* indicate the values of design variables, which were set to 31.89 kWh and 55.81 kWp, respectively, in the CTR scenario. In the RL model, reward and income values were obtained by reloading the trained model with the determined design variables. Results were computed using an initial state of charge of the battery set to 50% of its capacity for both models. However, the RL model does not take into account the Eq. (10).

3.1.1. RL and MILP optimal objective values are similar in both scenarios but with different designs in the control and design scenario.

Table 3 shows that in the CTR scenario, the results of the RL approach are similar to those of MILP. This confirms that the DEPS algorithm is able to converge to the optimal solution of this specific problem. In the CTR & DES scenario, RL design variables differ from the MILP solution, resulting in an unexpected higher reward value (-40) than the MILP optimal one (-46). A detailed analysis reveals that this unexpected higher value is due to Eq. (10), which is not imposed in the MDP. In order to validate this analysis, the additional grid cost needed to fulfill Eq. (10) has been computed, taking into account the battery's final SOC obtained with the RL approach. As a result, the reward value has increased to -67 (instead of -40). This clearly highlights the importance that Eq. (10) plays in term of overall objective.

3.1.2. The CTR & DES scenario highlights differences in RL and MILP strategies.

It is seen from Table 3 that in the second scenario, the optimal design variables of the RL and MILP solutions differ. Finding different values in design variables shows that the DEPS algorithm is able to identify solutions with comparable reward but using different design strategies. In order to study the sensitivity of the optimal solution, the MILP method was applied by imposing the design variable values obtained with the RL, as it can be seen in the last column of Table 3. This indicates that the RL design solution is less optimal (-53) than the MILP one (-46).

3.2. A one-year case study

Optimal solutions of RL and MILP methods in both scenarios are now computed using data from a full year. The time horizon for the RL algorithm is still equal to $T = 168$, but the starting days are uniformly randomly selected over the year. The RL algorithm is trained over a pre-determined number of 100'000 iterations and the values of the RL design variables considered are the ones from the final iteration. The results are shown in Table 4.

3.2.1. The difficulty of generalizing a policy with stochasticity in the model and on the estimation of the expectation

It can be seen from Table 4 that in both the CTR and CTR & DES scenarios, the optimal reward obtained by the RL method is poorer than the MILP optimal rewards. Furthermore, as depicted in Fig. 2, due to the significant variations in the input data, the reward and income values exhibit substantial fluctuations across

		Unit	Optimal RL solution	Optimal MILP solution	MILP solution based on RL design
CTR	T	hours	168	8760	
	Reward	€	-268	-228	
	Income	€	-220	-196	
CTR & DES	T	hours	168	8760	8760
	Reward	€	-250	-205	-247
	Income	€	-208	-164	-218
	Battery capacity	kWh	44	95	44
	PV power	kWp	57	81	57

Table 4: Results of RL and MILP solutions on one-year data for CTR and CTR & DES scenarios. T denotes the time horizon in hours, while *income* represents the cost of buying and selling electricity from the grid, *reward* is the (expected) cumulative reward value, and *battery capacity* and *PV power* indicate the design variable values, which were set to 64.9 kWh and 63.65 kWp, respectively, in the CTR scenario. The RL solution is based on the trained model to determine the reward and income values, based on an average of 1'000 simulations over T = 168. The MILP solution is computed for a one-year time horizon (T = 8760). Both models use an initial state of charge (SOC) of the battery set to 50% of its capacity. However, the MILP model has an additional constraint specifies in Eq. (10).

iterations.

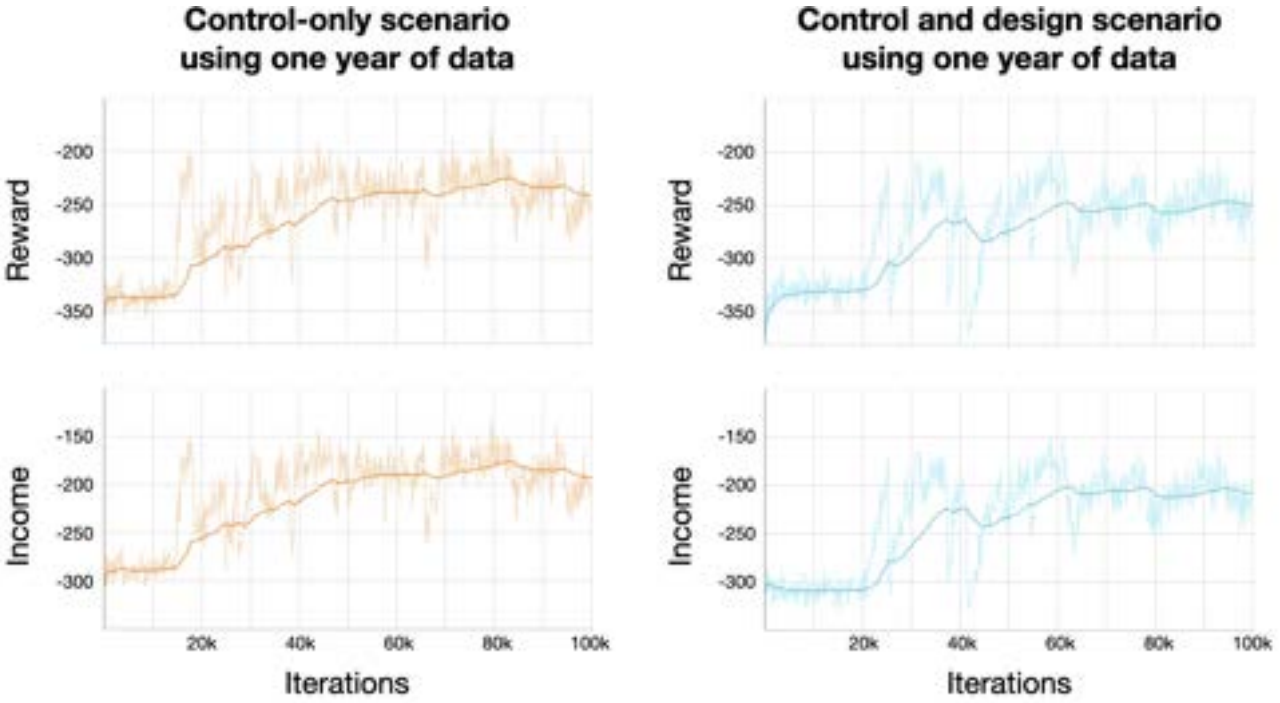

Figure 2: Value of reward and income obtained by the DEPS algorithm at each iteration for both scenarios. The left plots show the reward and income values for the CTR scenario, while the right plot shows the same values for the CTR & DES scenario. The light curve shows the exact values for each time step, while the dark curve displays the corresponding smoothed values. In the CTR scenario, the difference between the reward and income values remains constant at 31.93 due to fixed design variables, with a battery size of 64.9 kWh and a PV power of 63.65 kWp. However, in the CTR & DES scenario, the battery size and PV power output vary from 0 to 200 kWh and kWp, respectively.

During training in the CTR scenario (Fig. 2, left), the RL model achieved maximum reward and income values of -180 and -131, respectively, which are significantly better than the final results obtained from both methods in Table 4. This could suggest that depending on the set of weeks that are averaged at each iteration, it is possible to obtain a better or worse reward. Therefore, it seems important to work with a sufficiently representative number of weeks throughout the year. A similar observation can be made in the CTR & DES scenario, where the maximum reward and income values achieved were -195 and -148, respectively (Fig. 2, right).

3.2.2. The RL method seems to promote lower design variable values

From Table 4 it is also seen that the RL approach seems to promote solutions involving lower values of design variables. To further investigate the reasons underlying this result, the design variables for the evolution of the battery capacity and PV power, during the training process, are reported in Fig. 3 in the CTR & DES scenario.

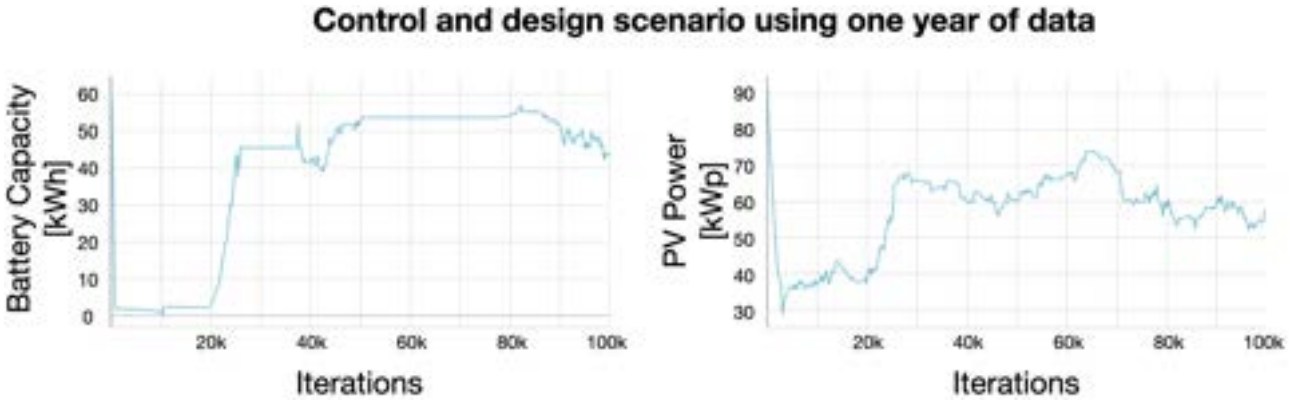

Figure 3: Value of design variables in the RL approach at each iteration, in the CTR & DES scenario. The RL algorithm converges at the final iteration to a battery capacity of approximately 44 kWh and a PV power output of around 57 kWp.

As indicated in Table 2, the design variable values can range from 0 to 200. However, it can be seen that higher values are not explored by the RL method. This latter resulted, at the last iteration, in design variables of 44 kWh for battery capacity and 57 kWp for PV power. During the training phase, the maximum values reached were 59 kWh and 90 kWp for battery capacity and PV power, respectively. This maximal explored battery capacity value is lower than the optimal one found by the MILP approach (95 kWh). Thus, the RL solution of the PV power value is expected to be lower. Indeed, the reward value is penalized if the RL agent injects PV production into the grid, since the cost of exported energy into the grid (C_{grid}^{exp}) is defined as a negative value in Table 2. Consequently, limited battery capacity intrinsically causes a lower PV power value.

4. Discussion

This section discusses the main observations that can be drawn from solving a battery-PV system with both RL and MILP approaches using the one-week and one-year data set.

4.1. The promises of RL for joint design and control of energy systems

The motivation for this study was to explore the potential of RL to enable joint control and design of energy systems. Tables 3 (one-week data) and 4 (one-year data) show that RL provides a solution that is close to the optimal MILP one. This is encouraging as it suggests that despite RL relying on a different optimization strategy, it is able to identify a meaningful solution in a simple case. However, the difference of reward value between MILP and RL increases when integrating design variables to the optimization problem, i.e., CTR & DES scenarios in Tables 3 and 4. Interestingly, the solutions for design variables are consistently smaller in RL as compared to MILP. Furthermore, from Fig. 3, it can be seen that the RL algorithm did not explore higher design variable values in the one-year case study. This observation can be explained by two possibilities: first, DEPS is a local-search method that is thus subject to converging towards local extrema. Once the control policy is too specialised to the investment parameters (under optimization too), these parameters are thus expected to be locally optimal and the algorithm is stuck. Second, the RL algorithms is subject to many hyperparameters to which the final results are sensible, it is possible that a different policy architecture, learning rate, or simply more iterations would ameliorate the performance of the method. Supporting the first explanation is the similarity between the reward values of the RL (-250) and MILP, based on same investments, (-247) approaches for the CTR & DES scenario with T = 8760 (Table 4). Hence, in this specific energy system case study, it could be likely that the RL algorithm did not deem it advantageous to enhance the value of the design variables for either one or both of the two reasons stated.

Overall, these results show that RL provides realistic control and design strategies. Based on this, RL could be used to define new real-time control strategies integrating design constraints, and that are less sensitive to linearization inaccuracies [16], [17]. Given the differences in how uncertainties are accounted for by both methods, RL could also be a better candidate to integrate resources coming with high levels of uncertainty such as electric mobility.

4.2. Technical challenges and future directions

The main technical challenges encountered in this study are essentially the ones inherent to RL methods. First, various parameters need to be tuned: neural network architecture for the policy, the batch size for the optimization, the learning rate, or the different scaling among others. These parameters were tuned by trial and error and would need to be adapted to each new application. For example, the number of layers required in the one-year case study was larger than for the one-week toy example. Second, convergence of the RL method is not guaranteed, and when convergence happens, the solution is not guaranteed to be globally optimal. Third, as illustrated here above for the results of Figure 3, determining the number of iterations (set to 100,000 for the training phase in all our experiments) is also crucial and might affect RL solutions. Therefore, comparing RL and MILP solutions is not trivial because its is difficult to compare perfect foresight with policy based decisions. This should be accounted for when analyzing results from Tables 3 and 4.

From a technical point of view, future work will aim at using more advanced RL methods. In particular, the RL algorithm used here is a modified version of the REINFORCE algorithm [13], which was developed in 1992 and is one of the earliest RL algorithms. Today, more advanced algorithms are available for control problems, which can converge more rapidly or account for infinite time horizons, such as actor-critic algorithms (e.g., PPO [18] and GAE [19]), but are yet to be adapted to joint design and control. In terms of applications, future work will aim to better evaluate the added value of RL by assessing the long-term performance of real-time sized systems. For example, a control framework could be developed to establish an operation strategy for the MILP-sized system. The framework would then be evaluated using several years of real-time data from the same system used for design. The same exercise would be applied to the trained model of the DEPS algorithm and performance obtained from several years of system control would be benchmarked, and the impact of design decisions could be discussed with more perspective.

5. Conclusions

In most studies, MILP is used for the design of energy systems and RL for the control. On the one hand, MILP assumes a perfect foresight of the future and is difficult to generalize to new data. On the other hand, RL methods proved to be efficient in other tasks linked to design and control but not on energy systems. In this study, we assessed the potential of an RL method, DEPS, i.e. an RL algorithm proven efficient for designing and controlling complex systems, for the joint design and control of energy systems.

The energy system studied is a PV-battery system used to answer a real-life demand in order to minimize the overall cost. In order to assess the efficiency of the RL method, we compared the outcomes with those obtained with a MILP. As these two approaches are fundamentally different, the optimization problem was formulated in two distinct ways: first as a MILP and second as an MDP. The methodology and experimental context were clarified to facilitate the discussion of results and have a fair comparison. Both approaches are discussed in terms of their strengths and weaknesses.

The findings show that RL can produce control strategies that are close to optimal, while using different values of design variables. This highlights the potential of RL for joint design and control of energy systems, particularly in scenarios where stochasticity is a key factor. However, the study also highlights the difficulty of tuning and using theses methods. Moving forward, there are several challenges to address, including the need to ensure that the RL solution converges to a global optimum. However, the promising results obtained in this study suggest that RL has the potential to be a valuable tool for jointly designing and controlling energy systems.

References

[1] A. Perera and P. Kamalaruban, "Applications of reinforcement learning in energy systems," *Renewable and Sustainable Energy Reviews*, vol. 137, p. 110 618, Mar. 2021. DOI: 10.1016/j.rser.2020.110618.

[2] A. T. D. Perera, P. U. Wickramasinghe, V. M. Nik, and J.-L. Scartezzini, "Introducing reinforcement learning to the energy system design process," en, *Applied Energy*, vol. 262, p. 114 580, Mar. 2020, ISSN: 0306-2619. DOI: 10.1016/j.apenergy.2020.114580. [Online]. Available: https://www.sciencedirect.com/science/article/pii/S0306261920300921 (visited on 10/24/2022).

[3] S. Fazlollahi and F. Maréchal, "Multi-objective, multi-period optimization of biomass conversion technologies using evolutionary algorithms and mixed integer linear programming (MILP)," en, *Applied Thermal Engineering*, Combined Special Issues: ECP 2011 and IMPRES 2010, vol. 50, no. 2, pp. 1504–1513, Feb. 2013, ISSN: 1359-4311. DOI: 10.1016/j.applthermaleng.2011.11.035. [Online]. Available: https://www.sciencedirect.com/science/article/pii/S1359431111006636 (visited on 11/14/2022).

[4] A. Majid, S. Saaybi, T. Rietbergen, *et al.*, *Deep Reinforcement Learning Versus Evolution Strategies: A Comparative Survey*. May 2021. DOI: 10.36227/techrxiv.14679504.v1.

[5] H. Quest, M. Cauz, F. Heymann, *et al.*, "A 3D indicator for guiding AI applications in the energy sector," en, *Energy and AI*, vol. 9, p. 100 167, Aug. 2022, ISSN: 2666-5468. DOI: 10.1016/j.egyai.2022.100167. [Online]. Available: https://www.sciencedirect.com/science/article/pii/S2666546822000234 (visited on 11/03/2022).

[6] H. M. Abdullah, A. Gastli, and L. Ben-Brahim, "Reinforcement Learning Based EV Charging Management Systems–A Review," *IEEE Access*, vol. 9, pp. 41 506–41 531, 2021, Conference Name: IEEE Access, ISSN: 2169-3536. DOI: 10.1109/ACCESS.2021.3064354.

[7] M. Dorokhova, Y. Martinson, C. Ballif, and N. Wyrsch, "Deep reinforcement learning control of electric vehicle charging in the presence of photovoltaic generation," *Applied Energy*, vol. 301, p. 117 504, Nov. 2021. DOI: 10.1016/j.apenergy.2021.117504.

[8] W. Shi and V. W. Wong, "Real-time vehicle-to-grid control algorithm under price uncertainty," in *2011 IEEE International Conference on Smart Grid Communications (SmartGridComm)*, Oct. 2011, pp. 261–266. DOI: 10.1109/SmartGridComm.2011.6102330.

[9] W. Uther, "Markov Decision Processes," en, in *Encyclopedia of Machine Learning*, C. Sammut and G. I. Webb, Eds., Boston, MA: Springer US, 2010, pp. 642–646, ISBN: 978-0-387-30164-8. DOI: 10.1007/978-0-387-30164-8_512. [Online]. Available: https://doi.org/10.1007/978-0-387-30164-8_512 (visited on 03/10/2023).

[10] Manu Lahariya, N. Sadeghianpourhamami, and Chris Develder, "Computationally efficient joint coordination of multiple electric vehicle charging points using reinforcement learning," [Online]. Available: arXiv:2203.14078.

[11] N. Sadeghianpourhamami, J. Deleu, and C. Develder, "Definition and Evaluation of Model-Free Coordination of Electrical Vehicle Charging With Reinforcement Learning," *IEEE Transactions on Smart Grid*, vol. 11, no. 1, pp. 203–214, Jan. 2020, Conference Name: IEEE Transactions on Smart Grid, ISSN: 1949-3061. DOI: 10.1109/TSG.2019.2920320.

[12] A. Bolland, I. Boukas, M. Berger, and D. Ernst, "Jointly Learning Environments and Control Policies with Projected Stochastic Gradient Ascent," en, *Journal of Artificial Intelligence Research*, vol. 73, pp. 117–171, Jan. 2022, ISSN: 1076-9757. DOI: 10.1613/jair.1.13350. [Online]. Available: https://www.jair.org/index.php/jair/article/view/13350 (visited on 03/07/2023).

[13] R. J. Williams, "Simple statistical gradient-following algorithms for connectionist reinforcement learning," en, *Machine Learning*, vol. 8, no. 3, pp. 229–256, May 1992, ISSN: 1573-0565. DOI: 10.1007/BF00992696. [Online]. Available: https://doi.org/10.1007/BF00992696 (visited on 03/07/2023).

[14] B. Miftari, M. Berger, H. Djelassi, and D. Ernst, "GBOML: Graph-Based Optimization Modeling Language," en, *Journal of Open Source Software*, vol. 7, no. 72, p. 4158, Apr. 2022, ISSN: 2475-9066. DOI: 10.21105/joss.04158. [Online]. Available: https://joss.theoj.org/papers/10.21105/joss.04158 (visited on 03/07/2023).

[15] Gurobi, *Gurobi - The fastest solver*, Library Catalog: www.gurobi.com, 2020. [Online]. Available: https://www.gurobi.com/ (visited on 03/25/2020).

[16] M. Reuß, L. Welder, J. Thürauf, *et al.*, "Modeling hydrogen networks for future energy systems: A comparison of linear and nonlinear approaches," en, *International Journal of Hydrogen Energy*, vol. 44, no. 60, pp. 32 136–32 150, Dec. 2019, ISSN: 0360-3199. DOI: 10.1016/j.ijhydene.2019.10.080. [Online]. Available: https://www.sciencedirect.com/science/article/pii/S0360319919338625 (visited on 10/24/2022).

[17] C. Sánchez, L. Bloch, J. Holweger, C. Ballif, and N. Wyrsch, "Optimised Heat Pump Management for Increasing Photovoltaic Penetration into the Electricity Grid," *Energies*, vol. 12, p. 1571, Apr. 2019. DOI: 10.3390/en12081571.

[18] J. Schulman, F. Wolski, P. Dhariwal, A. Radford, and O. Klimov, *Proximal Policy Optimization Algorithms*, arXiv:1707.06347 [cs], Aug. 2017. [Online]. Available: http://arxiv.org/abs/1707.06347 (visited on 03/12/2023).

[19] J. Schulman, P. Moritz, S. Levine, M. Jordan, and P. Abbeel, *High-Dimensional Continuous Control Using Generalized Advantage Estimation*, arXiv:1506.02438 [cs], Oct. 2018. [Online]. Available: http://arxiv.org/abs/1506.02438 (visited on 03/12/2023).

PROCEEDINGS OF ECOS 2023 - THE 36TH INTERNATIONAL CONFERENCE ON
EFFICIENCY, **C**OST, **O**PTIMIZATION, **S**IMULATION AND ENVIRONMENTAL IMPACT OF ENERGY SYSTEMS
25-30 JUNE 2023, LAS PALMAS DE GRAN CANARIA, SPAIN

Machine-learning-based approximation of the hierarchical model predictive control of multi-use PV-battery systems in non-residential buildings

Laura Maier[a], Sönke Quast[a], Dominik Hering[a] and Dirk Müller[a]

[a] RWTH Aachen University, E.ON Energy Research Center, Institute for Energy Efficient Buildings and Indoor Climate, Aachen, Germany, laura.maier@eonerc.rwth-aachen.de, CA

Abstract:

Model predictive control (MPC) has proven to be a promising method to exploit energy saving potentials in building energy systems. However, they are not widespread in practice due to high hard- and software requirements, high computational effort, and missing trust and know-how among practitioners. Approximate MPC can address these challenges by replacing the hard- and software-intensive optimization program by black box models. Machine learning models such as Artificial Neural Networks or tree-based algorithms have been widely investigated by the scientific community. However, a comparison of Artificial Neural Networks with advanced tree-based models like Random Forest and Gradient Boosting is still missing. In addition, the relation between the models' training and the resulting control performance has not yet been assessed. We close these gaps by investigating the optimal control based on an MPC of a PV-battery system in a non-residential building. The MPC optimizes the battery's power based on a preceding peak load optimization. The MPC is imitated by three machine learning models, namely, an Artificial Neural Network, a Random Forest, and Gradient Boosting, whose performance is subsequently evaluated open- and closed loop. While Gradient Boosting results in the highest open-loop performance with an R^2 of 0.83, it deviates more significantly from the optimal control trajectory than, e.g., the Artificial Neural Network. Nonetheless, Gradient Boosting even outperforms the teacher MPC when considering the system's annuity. This is explained by its ability to push beyond the peak load constraints which are set within the optimization. A rule-based backup controller is, therefore, included for all approximator-based controllers. Based on this, the approximators result in a peak load reduction between 5 % and 7 % compared to the benchmark and a change in annuity between -1 % and 4 % compared to the MPC. To summarize, all approximators can retain most of the MPC's advantages but do not surpass its overall performance.

Keywords:

Approximate Optimal Control, Model Predictive Control, Machine Learning.

1. Introduction

In 2022, the United Nations Environment Program published its global status report for the buildings and construction sector, highlighting the need for immediate action to cut emissions [1]. Following a slowdown caused by the global pandemic, the CO_2 emissions from building operations in 2021 even exceeded their all-time maximum of 2019 by 2 %. When taking into account the emissions of building material production, buildings made up around 37 % of the global CO_2 emissions in 2021 [1]. In addition to investing in refurbishment strategies, optimizing building energy system operation can contribute to the goal of an emission-free building sector by 2050 [1, 2].

Model predictive control (MPC) as a representative of advanced control methods has proven to optimize building operation tremendously. In a review study, Drgoňa et al. [2] find that the realized energy savings range between 15 % and 50 % based on selected case studies [3–6]. MPC is also a valuable method for providing grid flexibility services by, e.g., exploiting price incentives or providing demand response services [2]. The latter is crucial for future grid operation as the building sector will be electrified and, hence, interact with the grid more intensely. However, despite its significant potential MPC is not widespread in practical applications. The reasons lie in the high requirements of hard- and software and data infrastructure, missing know-how among the operating personnel, time-consuming modeling and maintenance, and network and privacy security concerns [2, 7–10]. This is why conventional rule-based and PID controllers are still state-of-the-art in nowadays buildings. A method that bridges the gap between the performance of MPC applications and the simplicity of rule-based controllers is approximate MPC. The idea is to imitate the MPC's output using black box models. The MPC serves as a teacher that generates training data. The implicit MPC-based controller is finally replaced by an explicit controller [11]. The black-box-based explicit controller requires less advanced hard- and software as well as data infrastructure. The used black box models in building energy systems range from

simple linear regression models [9,12], over decision trees [11,13–16] to sophisticated machine learning models like Artificial Neural Networks (ANNs) [11, 17–20]. These so-called approximator-based controllers have proven to retain most of the MPC's performance while significantly reducing the required computational effort and processing time [11]. In this context, decision-tree-based approximators are favorable as they resemble the rule-based controller-like "if-condition-then-action" structure and, hence, promote comprehensibility and address the challenge of missing know-how. However, decision trees tend to overfit data and are very sensitive to input data [21]. Consequently, advanced methods like ANNs are often selected as approximators [11, 19, 20]. High-performing ensemble methods like Random Forest (RF) and Gradient Boosting (GB) can address the decision trees' disadvantages of overfitting. However, to the authors' best knowledge, studies investigating high-performing, tree-based machine learning algorithms like RF and GB in the context of approximate MPC are still missing. Furthermore, even though approximate MPC has been successfully applied to building energy systems, there exists no use case focusing on a grid-connected PV-battery system as a part of a building energy system.

In contrast to that, the scientific community has come up with related methods targeting purely grid-related challenges. Smart grids will play a key role in the energy transition to guarantee safe grid operation. The underlying concept is referred to as the optimal power flow problem, which can focus on AC- and DC-based applications. Here, the main challenge lies in the real-time solution of a highly complex optimization problem that optimizes power flows in a grid, e.g., the optimal power that a set of generators have to produce [22–25]. [23] and [24], e.g., both focus on an AC optimal power flow problem. For example, Zamzam et al. [23] learn the mapping of system loading and optimal generation values using an ANN serving as an input for the subsequent power flow solver. Doing so, they speed up the calculation process by a factor between 8 and 15 while still achieving near-optimal results compared to directly solving the optimal power flow problem. Furthermore, the authors of [24] approximate the cost function and give a feasibility prediction for the AC optimal power flow problem. Again, the accuracy is high and the computational effort is reduced significantly. As approximators, they compare the performance of linear regression, piecewise regression, Gaussian Processes, and ANNs. Apart from that, [22] use graph NNs and [25] test deep NNs, and obtain similar trends for an AC and DC optimal power flow problem, respectively. The aforementioned grid-focused studies all apply their method to simplified use cases and learn the output of static optimal power flow problems. De Jongh et al. [26] are the first to use ANNs to learn a dynamic MPC-based problem of a smart distribution grid. The distribution grid covers 15 nodes and 13 households and considers electric vehicles and heat pumps. The MPC optimizes the power schedule for all flexible devices. The ANN is trained based on a full-year simulation with three months of testing. This time, the closed-loop performance is evaluated and, again, near-optimal results are achieved with a 55 times quicker processing time.

In addition to these aspects, the training process for the approximators differs significantly among the studies. While the grid-focused studies generate randomized training samples using distribution assumptions for their inputs [22,24,25], the building-focused ones tend to use closed-loop operation results [11,12,14]. The training performance is usually evaluated open-loop, i.e., the true and predicted outputs are compared without system interaction. However, it is unclear how the open-loop performance affects the closed-loop one, which we identify as an additional research gap.

1.1. Contributions and structure of this study

To summarize, the state of research highlights that approximate MPC applications are promising for building energy systems. However, we detect a gap in studies focusing on building energy systems while considering their interaction with the grid. In addition, studies are missing that compare sophisticated machine learning models like ANNs to advanced tree-based ones like RF and GB. Furthermore, the scientific literature has not yet presented a detailed investigation of the relation between the open- and closed-loop performance.

This study closes these gaps through the following aspects:

- We present a PV-battery system of a non-residential building in Berlin, Germany (see subsection 2.1.). The battery's operation is optimized based on an MPC, used as teacher MPC, that has been presented in previous work [27] (see subsection 2.2.).
- The teacher MPC is taken as a training basis for three machine learning models, namely, an ANN, an RF, and GB. They are trained based on a full-year simulation of the MPC-controlled system (see subsection 2.4.).
- section 3. presents the open- and closed-loop performance of these approximators, which are used as substitutes for the MPC. For this, we define open- and closed-loop metrics (see subsection 2.5.).
- We finally discuss the relation between the open- and closed-loop performance as well as the comparison of the machine learning models in section 4., conclude our findings (see section 5.), and give an outlook into future work (see section 6.).

By investigating these aspects, we try to answer the two following research questions in the context of approximate MPC:

1. Can advanced tree-based machine learning models outperform the most prominent Artificial Neural Network?
2. Is there a correlation between open- and closed-loop performance?

2. Methodological approach

2.1. Use case: PV-battery system of a non-residential building

The use case is the electrical system of a laboratory and office building in Berlin, Germany. Figure 1 illustrates the central components and their interaction. The energy supply for heating, ventilation, and air conditioning (HVAC) is solely based on electricity. A battery energy storage system aims at reducing potentially arising peak loads and maximizing the electricity generation of the PV power plant. In addition to the demands caused by the HVAC system, the electrical load of the building contains the electricity consumption of the building's, i.e., its tenants', equipment (servers, laboratory equipment, etc.) and lights. The overall system can exchange electricity with the grid.

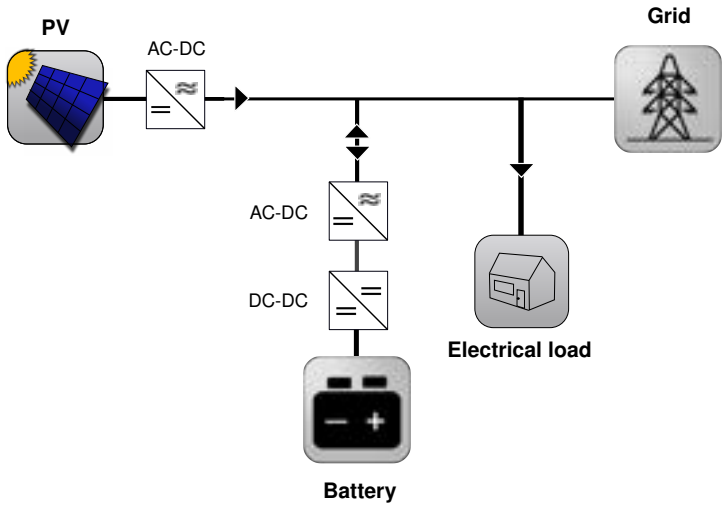

Figure 1: Use case: electrical system setup of the non-residential building including a battery energy storage system, a PV power plant, the building load, and the grid.

The building's electrical loads have been simulated using Modelica as a modeling language. The underlying toolchain to obtain realistic electrical profiles has been presented in [28]. The simulated electrical load is illustrated in Figure 2. The resulting maximum electrical load of the building is 955 kW, the battery's capacity is 2500 kWh and its maximum discharging and charging power is 1250 kW. The PV power plant has a peak power of 500 kWp.

2.2. Model predictive control and data base

In Figure 3, the MPC and AMPC toolchain is illustrated. The target system, which is described in subsection 2.1., is simulated in the modeling language Modelica using the functional mock-up interface. The battery's charging and discharging powers are the manipulated variables that are transferred using the open-source Python package *fmpy*. For every iteration, these manipulated variables are optimized by an mixed-integer linear program (MILP). The MILP is formulated in the Python-based optimization modeling language *Pyomo* [29]. Based on perfect forecast of the disturbances, the battery's state of charge and other state variables, the optimization is solved for two different prediction horizons, resulting in an hierarchical structure. The upper optimization layer is a full-year optimization that determines the optimal electrical peak. This electrical peak is subsequently transferred as a constraint to the second optimization stage that follows the receding horizon scheme. Here, a prediction horizon of 16 h and a timestep of 900 s are applied and the control loop is repeated on an hourly basis. The lower layer optimization optimizes the battery's power based on the PV generation, the building load, as well as economic boundary conditions, such as the electricity price. Since the MPC-based battery operation deals with different sources of revenue, we refer to it as multi-use PV-battery system. Further details on the MILP and the hierarchical MPC are presented in [27].

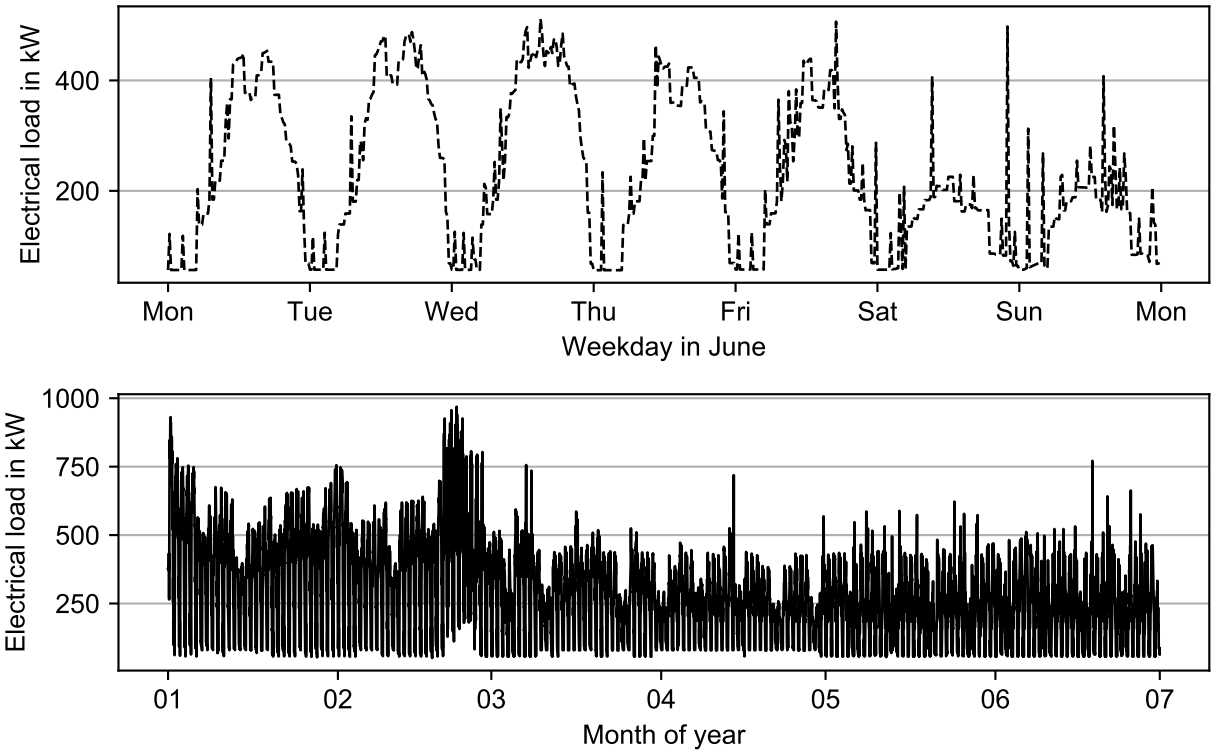

Figure 2: Simulated electrical building load for an exemplary week (top) and the first 6 months (bottom).

The perfectly predicted disturbances comprise:

- **Weather forecasts:** Ambient temperature, global irradiation, and wind speed to compute PV power output based on standardized test reference years [30]
- **Real time electricity prices:** Time-varying EEX electricity prices of 2019 are taken as a basis [31].
- **Electrical building load:** The electricity consumption of the building is simulated in the modeling language Modelica using typical user profiles [28, 32].

This study's aim is to replace the implicit optimization-based controller by an explicit black-box-model-based one. Therefore, we use the open-source machine learning package scikit-learn [33].

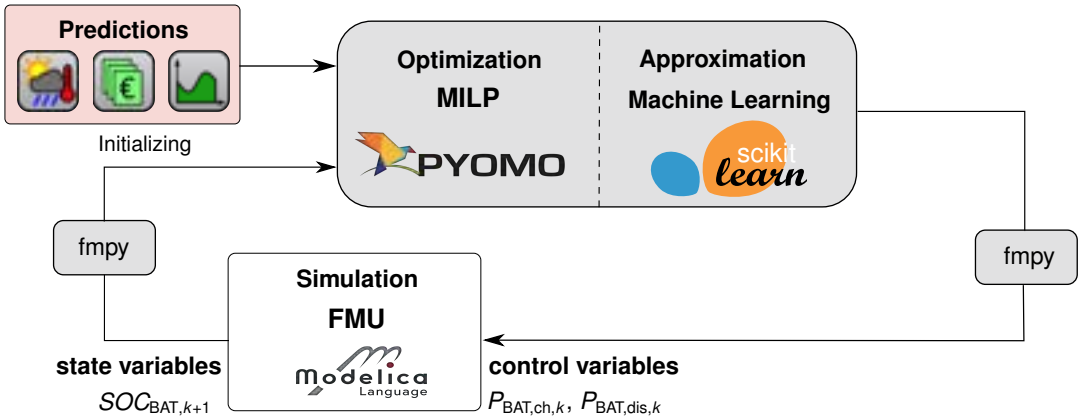

Figure 3: MPC and approximate MPC framework and control loop that calculates the battery's charging $P_k^{BAT,ch}$ and discharging power $P_k^{BAT,ch}$ to the simulation model for each timestep k. Based on measurements like the battery's state of charge SOC_k^{BAT}, the next iteration starts.

2.3. Feature construction and selection

The general approach for approximate MPC is to provide the MPC's input data for the approximator so that it can learn the MPC's output. However, it is recommended to include additional features that support the imitation learning process. For the present study, 14 features have been selected, which are derived based on sensitivity analyses and listed in Table 1. The features comprise measurement data (simulated), set points of a former optimization, synthetic data, and disturbance predictions. The measurements of the previous $k-1$ timestep are used to predict the next timestep's k output. Among these measurements are the simulated battery charging or discharging power, its SOC, the cells' temperatures, the voltage as well as the power from or to the grid. Furthermore, the top layer optimization's computed optimal peak load of timestep k as well as future timesteps serves as input to the approximators. In addition to the measurements, disturbance predictions for 64 timesteps are included, standing for a time period of 16 h, i.e., the MPC's prediction horizon.

Table 1: Overview over features selected to predict the MPC's output.

Feature	timestep	Type
Power of battery (charge or discharge)	k-1	Measurement
State of charge of battery	k-1	Measurement
Temperature of battery cells	k-1	Measurement
Voltage in battery stack	k-1	Measurement
Power to/from grid	k-1	Measurement
Maximum allowed grid demand	k,...,k+63	Optimization set point prediction
Building's electrical load	k,...,k+63	Disturbance prediction
PV electricity generation	k,...,k+63	Disturbance prediction
Electricity price	k,...,k+63	Disturbance prediction
Ratio of building load to maximum allowed grid demand	k,...,k+63	Synthetic (measurement and disturbance prediction)
Ratio of PV generation to building load	k,...,k+63	Synthetic (measurement and optimization set point prediction)
Hour of day	k	Synthetic
Day of week	k	Synthetic
Month of year	k	Synthetic

2.4. Imitation learning process

In approximate MPC applications, the optimization is replaced by an approximated model that imitates the so-called teacher MPC. Machine learning models are the most common approximators in this context. This study deals with a continuous manipulated variable, namely the charging $P_{\text{BAT,ch}}$ and discharging $P_{\text{BAT,dch}}$ power of the battery. We simplify the manipulated variable to P_{BAT}. Due to the continuous nature of the variable, the approximator needs to perform a regression task. The objective of this regression task is to find a regression function $f_\theta : \mathbb{R}^{n_\varepsilon} \rightarrow \mathbb{R}$ that minimizes the squared error between the true manipulated variable P_{BAT} being the MPC's output and the predicted one $\hat{P}_{\text{BAT},k}$ by tuning the parameters θ:

$$\min_{\theta} \sum_{k=1}^{n} (\hat{P}_{\text{BAT},k} - P_{\text{BAT},k})^2, k \in \mathbb{N}, \theta \in \mathbb{R}^{n_\theta} \tag{1}$$

The training data is discretized for each timestep k over the number of relevant samples n.

The regression parameter fitting process is carried out using the open-source Python framework *AddMo* (Automated data-driven modeling) [34]. *AddMo* comprises all relevant steps needed to obtain a well-trained machine learning model. The steps cover the data tuning including data preprocessing, period selection, and feature construction. Subsequently, the tool enables automatic feature selection and hyperparameter tuning. The framework's basis is the open-source machine learning library *scitkit-learn* [33] and covers ANNs, GB, Lasso, RF, and Support Vector Regression as potential model choices. The interested reader is referred to [34] for a more detailed framework presentation.

This study selects ANNs, GB, and RF as approximators as motivated in section 1.

2.5. Open- and closed-loop evaluation scheme

The evaluation includes both the open- and the closed-loop performance of the MPC- and approximator-based controllers. The open-loop performance aims at assessing the approximator's ability to predict the MPC's output, i.e., the charging and discharging power of the battery. As the training process is categorized as supervised machine learning for regression tasks, the coefficient of determination R^2 and the mean absolute

error *MAE* are selected as key performance indicators. Specifically, for each timestep k, the true and predicted output are compared and the respective error metrics are determined. As a simplified initial comparison, these statistical metrics are also computed for the closed-loop operation even though the focus should lie on system- and control-specific metrics and should, thus, be oriented towards the MPC's objectives. For the MPC, the economic evaluation is based on the PV-battery system's annuity. The annuity C_{ANN} simultaneously considers the investment costs (CAPEX, C_{CAPEX}) as well as the operating costs (OPEX,C_{OPEX}). In the context of this study, the following calculation scheme is applied, which is based on the German pricing and regulatory system:

$$C_{\text{ANN}} = f_{\text{AF}} C_{\text{CAPEX}} + C_{\text{OPEX,energy}} + C_{\text{OPEX,power}} \tag{2}$$

$$C_{\text{CAPEX}} = c_{0,\text{PV}} P_{\text{PV,peak}} + c_{0,\text{BAT}} E_{\text{BAT,cap}} \tag{3}$$

$$\begin{aligned} C_{\text{OPEX,energy}} = {} & E_{\text{grid,load}}(c_{k,\text{EEX}} + c_{\text{Tax}} + c_{\text{EEG}}) + E_{\text{grid,BAT}}(c_{k,\text{EEX}} + c_{\text{Tax}} + 0.6 c_{\text{EEG}} \eta_{\text{BAT}}^2) \\ & + 0.4(E_{\text{PV,load}} + E_{\text{BAT,load}}) c_{\text{EEG}} + c_{\text{Network}}(E_{\text{grid,load}} + E_{\text{grid,BAT}}) - E_{\text{BAT,grid}} c_{k,\text{EEX}} - E_{\text{PV,grid}} c_{\text{PV,feedin}} \end{aligned} \tag{4}$$

$$C_{\text{OPEX,power}} = P_{\text{peak}} c_{\text{Peak}} \tag{5}$$

The associated costs of Equation 2 to Equation 5 are listed in Table 2. In the context of this paper, we define costs as positive quantities. In Equation 2, C_{CAPEX} includes the specific investment costs of the battery $c_{0,\text{BAT}}$, the PV power plant $c_{0,\text{PV}}$, including the required DC-DC and DC-AC inverters, respectively (see Equation 3 and Table 2). The battery's investment costs depend on its expected lifetime that is affected by aging. Calendrical and cyclical aging is considered in the simulation model. More specifically, keeping the battery on high SOCs or triggering many cycles leads to a degradation of its capacity and performance. For more details, the interested reader is referred to [27]. The CAPEX are multiplied with the annuity factor f_{AF} that depends on the interest rate i and the observation period T. We assume that all components except for the battery have a lifetime of T. If the battery's lifetime is shorter than the observation period, we consider a price degression d. The operation-related costs are further divided into energy demand- $C_{\text{OPEX,energy}}$ and power-related operating costs $C_{\text{OPEX,power}}$ (see Equation 2). For $C_{\text{OPEX,energy}}$, the energy flows of the PV-battery system, the building, and the grid must be distinguished since different pricing schemes apply. Equation 4 denotes energy flows from source to sink. For example, $E_{\text{grid,load}}$ is the building's consumed electrical energy covered by the grid. In addition to taxes c_{Tax} and network charges c_{Network}, the German pricing scheme includes a charge to support renewable energy sources c_{EEG}, whose quantity depends on the energy source. Therefore, Equation 4 differentiates between flows of the PV power plant, the grid, and the battery. Furthermore, the operation-related costs depend on the EEX market prices of each timestep k. The EEX prices also serve as source of revenue if electrical power is fed back into the grid. As an additional revenue, fed-in electricity from the PV power plant is rewarded with the feed-in price $c_{\text{PV,feedin}}$.

Apart from the purely economic evaluation, this study also focuses on the system's peak load P_{peak} . The system's peak load is taken as an additional metric because the teacher MPC's aims to determine the system's optimal maximum peak load and control the battery's power accordingly. The associated costs are calculated based on a peak power price c_{Peak} (see Equation 5).

Table 2: Assumptions of economic boundary conditions.

Type	Mathematical description	Quantity
Initial invest in battery including DC-DC inverter	$c_{0,\text{BAT}}$	725 €/kWh
Initial invest in PV power plant including DC-AC inverter	$c_{0,\text{PV}}$	1170 €/kWp
Lifetime of battery	T_{BAT}	Simulated
Observation period	T	20 a
Relative price degression	d	6 %/a
Interest rate	i	1.3 %
Real-time pricing	$c_{k,\text{EEX}}$	EEX 2019
PV feed-in pricing	$c_{\text{PV,feedin}}$	6.62 ct /kWh
Tax-related charges	c_{Tax}	3.17 ct /kWh
Network charges	c_{Network}	1.65 ct /kWh
Peak power charges	c_{Peak}	53.53 €/kW

3. Results

The following section presents both the open- and the closed-loop results. The open-loop results stem from comparing the approximator's and the MILP's output regarding the battery's charging and discharging power. Consequently, the control loop is not closed. In contrast, the second part of this section focuses on closed-loop simulation results, for which the approximators are used to control the PV-battery system.

3.1. Open-loop performance

The open-loop analysis compares the predicted output $\hat{P}_{\mathrm{BAT}}$ with the true MPC output P_{BAT} based on a time series comparison. Open-loop training serves as an indicator of how well the machine learning models imitate the controller's output. However, since there is no interaction with the system, we cannot conclude on the closed-loop performance. Figure 4 illustrates the coefficient of determination R^2 as well as the mean absolute error *MAE* for the testing period for both open- and closed-loop operation. For this section, we concentrate on the open-loop results, i.e., the red bars and line graphs. The models are trained based on six months of training data and tested on six months of unseen data. The first half of the year serves as training data, while the second half serves as a testing period. The overall open-loop accuracy is high for all three models. GB results yields the highest R^2 of 0.83 and the lowest *MAE*, while ANN results in the lowest R^2. The ANN and RF yield a similar performance when taking the *MAE* as a basis. However, the ANN's R^2 is slightly lower than the RF's one. Consequently, the GB is favorable from an open-loop performance perspective. Nonetheless, the variations in performance are slight.

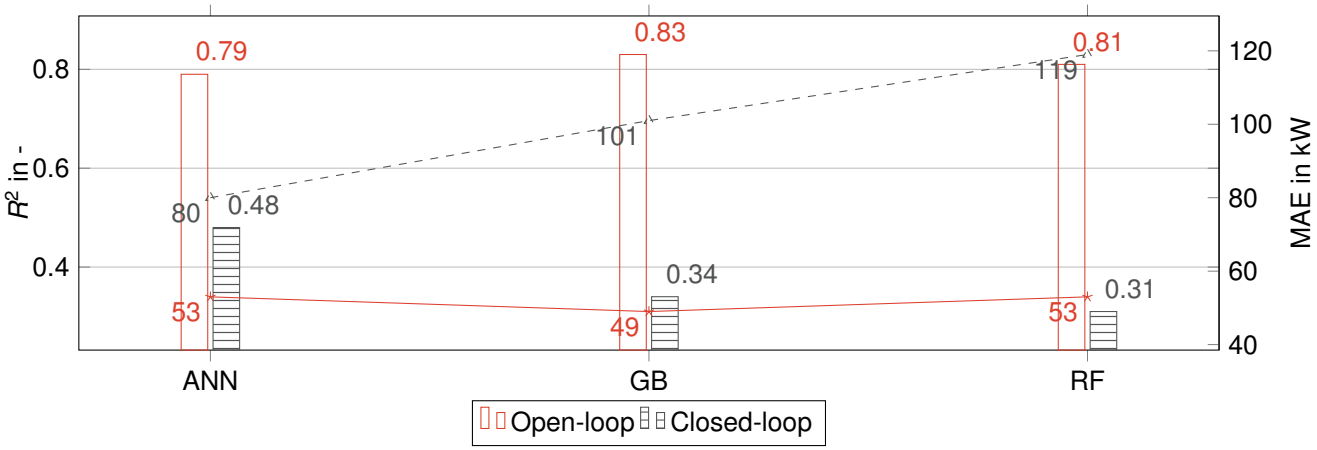

Figure 4: Time-series-based open- and closed-loop prediction results for 6 months training and testing.

3.2. Closed-loop performance

In addition to the open-loop performance not considering any interaction with the simulation model, this section investigates the closed-loop performance. At first, we focus on a purely time-series-based comparison between the open- and closed-loop performance. For this evaluation, Figure 4 also shows the statistical metrics for the closed-loop operation in addition to the open-loop comparison. The data is based on a closed-loop simulation of 6 months, from January to the end of June. The metrics derive from comparing the controllers' outputs, i.e., the battery's set charging and discharging power. The results indicate a different picture compared to the open-loop performance. The ANN clearly outperforms the tree-based models with an R^2 of 0.48 compared to 0.34 for GB and 0.31 for the RF, respectively. The same trend applies to the *MAE*. Based on this, we cannot see any correlation between the open- and the closed-loop performance of the approximators. However, the comparison above is based on time series only and does not consider any MPC performance metrics.

For this reason, we analyze the actual closed-loop performance taking MPC relevant objectives into consideration (see subsection 2.5.). The bar chart on the left of Figure 5 illustrates the resulting annuity of the PV-battery system for the MILP and the approximators, i.e., the ANN-, GB-, and RF-based controller. We like to highlight at this point that the annuities are negative because we mainly consider costs and the rewards through electricity feed-in are small for our use case. The resulting annuity ranges between $-425\,\mathrm{k€}$ for the GB-controlled and $-440\,\mathrm{k€}$ for the ANN-controlled system. Among the approximators, the GB performs best, followed by the RF. The ANN results in the lowest annuity. The GB-controlled system even outperforms the MILP regarding the annuity.

Figure 6 further illustrates the resulting operation for an exemplary week in June. The top plot shows the manipulated variables, namely, the battery's set power for the MILP- and approximator-controlled system. In the middle, the resulting grid load is depicted. As a reference, the optimized peak load is marked, too. A

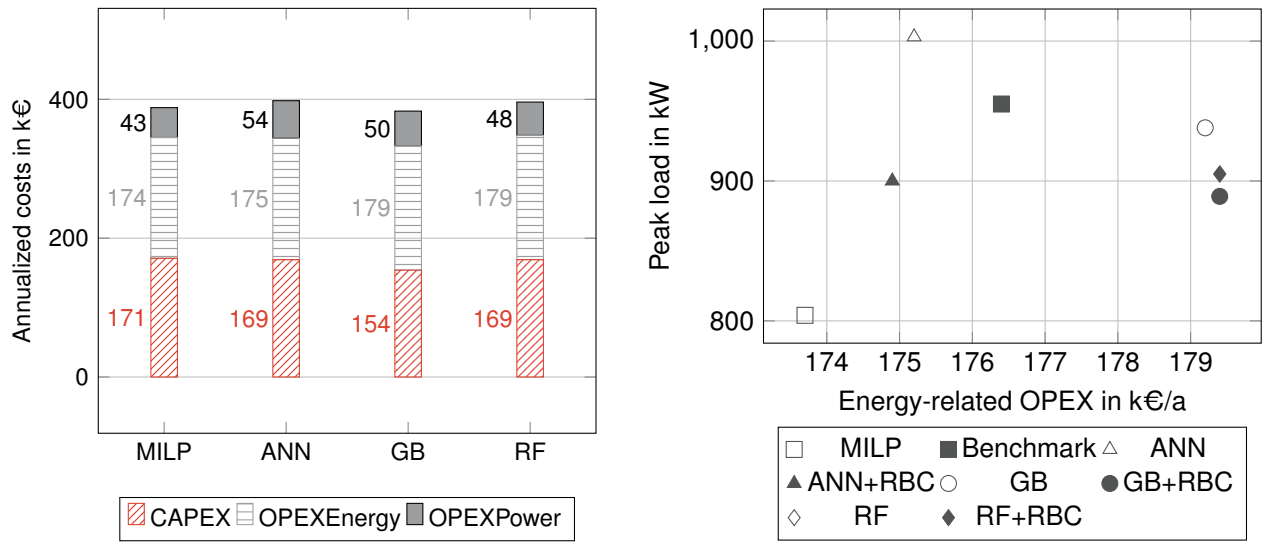

Figure 5: Closed-loop simulation results: The figure illustrates the holistic annuity of the PV-battery system without backup controllers (left) and the comparison of the resulting electrical peak load and demand-related operating costs with (+RBC) and without backup controllers (right).

positive battery power denotes battery charging, while a negative one signifies discharging. Furthermore, positive grid loads denote an energy flow from the grid to the system and vice versa. The bottom part of Figure 6 shows the variable electricity tariff. We observe that the approximators sufficiently imitate the teacher MPC's output. However, the resulting grid load shown in the middle part highlights that some approximators exceed the optimized grid limit. The tendency to overshoot the grid limit applies the most for the ANN-based controller. On the illustrated Saturday afternoon, the ANN lets the battery charge due to low electricity prices. This trend is partially observed for the residual controllers but to a smaller extent. The high charging power results in a grid load exceeding the optimized peak load. This behavior is also present on Thursday and Friday afternoon. Again, the ANN triggers a charging period due to low electricity prices even though the teacher MPC's output is 0 kW. Here, we detect the approximator's correlation between the in- and output without considering the constraints set within the MILP.

Figure 6 highlights the need for an additional backup controller that reinforces the optimized peak. To support the approximators in reducing the peak power, an additional rule-based backup controller is considered. The controller is non-predictive, meaning it relies on present or past measurements of the system. Based on the current grid load and the approximator's output, the rule-based controller limits the battery's set charging or discharging power. The result is depicted on the right-hand side of Figure 5. Here, we illustrate the realized electrical peak load and the energy-related OPEX for two sets of an approximator-controlled, the MILP-controlled system, and a benchmark model. The two sets of approximators consider the machine learning models with and without additional rule-based backup controllers ("X+RBC"). The MILP, i.e., the MPC, runs a pre-optimization for a whole year to determine the optimal peak load. This peak load is 803 kW for the given scenario and a constraint for the MILP. Hence, the MILP does not surpass the optimal peak, so the maximum peak for the 6-months simulation is 803 kW, too. In addition, the MPC also yields the lowest energy-related operating costs $C_{\text{OPEX,energy}}$ of approximately 174 k€. Apart from that, we determine a benchmark model that does not include a battery. We solely include the benchmark model in the right-hand side plot of Figure 5 because the benchmark does not involve an investment in the PV-battery system. Consequently, a comparison based on the annuity is not expedient. The benchmark control does not shift any load and consequently solely depends on the variable electricity price. It yields a peak load of 955 kW and operating costs of 176 k€. Thus, the MPC achieves a peak load reduction of 16 % and a decrease in energy-related operating costs of 1 %. In general, the energy-related operating costs do not vary significantly among the controllers. However, it is noteworthy that high peak loads lead to higher power-related OPEX $C_{\text{OPEX,power}}$. Combining both energy- and power-related OPEX, the MPC results in OPEX savings of 5 %.

In contrast, we observe a great difference in the peak loads. Without integrating a rule-based controller, only the GB- and the RF-based approximators realize a smaller peak load than the benchmark model of 938 kW and 905 kW, respectively. For the RF, the integration of a backup controller has only a negligible effect on the peak load of 0.3 kW. For the GB and the ANN, the effect is more significant. While the peak load is reduced from 938 kW to 889 kW in the case of GB, it decreases from 1003 kW to 900 kW for the ANN. The ANN's tendency to overshoot the peak load is also apparent in Figure 6. Nonetheless, when considering the rule-based controller, the annuities decline by 2 % for the ANN, increase by 0.5 % for GB and by 0.5 % for the RF.

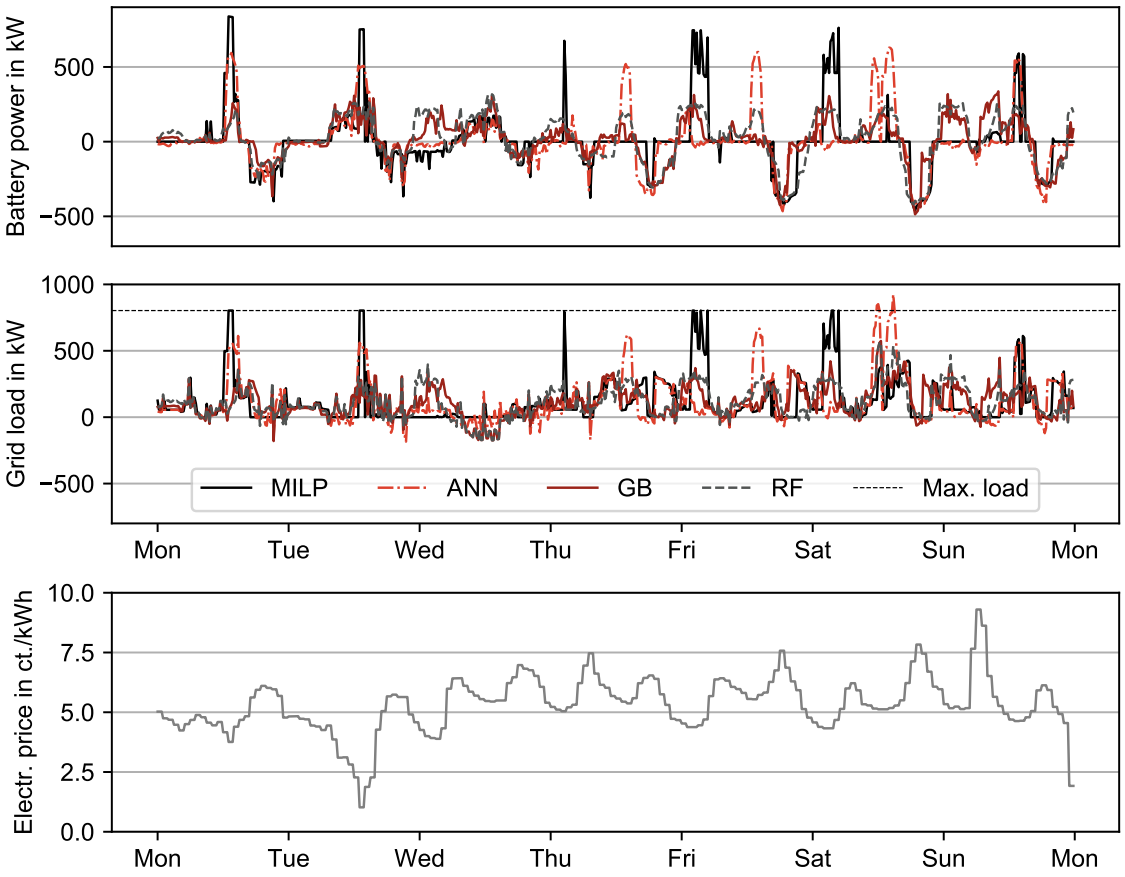

Figure 6: Closed-loop simulation results for the first week in June. The top plot shows the manipulated variables, i.e., the set battery power. In the center, the resulting grid load is depicted. Here, we also mark the optimized peak load as a reference. The bottom plot presents the EEX electricity tariff. The approximators control the system without the rule-based backup controller.

4. Discussion

The results of section 3. highlight that the relation between open- and closed-loop performance is difficult to assess. While a purely time-series-based comparison as shown in Figure 4 supports the conclusion that there is no correlation between open- and closed-loop performance, the subsequent analysis of the MPC-related objectives partially proves the opposite. When considering the annuity, the GB-based controller outperforms the ANN- and RF-based one (see Figure 5). Yet, the GB's resulting battery operation significantly differs from the MILP-based one, which is further supported by the low R^2 of 0.34 and the high *MAE* of 101 kW as illustrated in Figure 4. The ANN realizes the highest conformity with the teacher MPC's set points, which is apparent in Figure 6. Nonetheless, it tends to overshoot the optimized electrical peak due to the correlation with the electricity price. The other machine-learning-based approximators do not adopt this behavior as strongly. This is also why integrating the rule-based backup controller as shown on the right-hand side of Figure 5 has the most significant effect on the ANN-based controller's peak load.

Furthermore, it becomes evident that despite the integration of a rule-based backup controller that reduces the peak load, the optimized peak load of 803 kW is still surpassed by the approximators (see Figure 5). This behavior is explained by the rule-based controller's dependence on past measurements. Consequently, if the building load is higher than the load of the previous timestep, the battery's charging and discharging power in addition to the building load might still exceed the set upper limit. This disadvantage could be mitigated if the rule-based controller was based on building load predictions rather than past measurements. However, integrating these predictions would further increase the approximators' complexity. Still, we see great potential in developing a hybrid approach with a more sophisticated backup controller.

Another aspect is that the GB-based controller seems to slightly outperform its teacher MPC when taking the annuity as a basis (left plot in Figure 5). However, this behavior is only possible because the GB-based controller does not consider the MILP's constraints. A pre-optimization is carried out to obtain the optimal electricity peak. Subsequently, the MILP-based MPC uses this as an upper boundary and manipulates the

charging and discharging powers accordingly. Consequently, the GB extrapolates the defined solution space. Even though the GB-based controller does indeed achieve the lowest annuity, it is still not favorable compared to the MILP from an operator's point of view. It exceeds the optimal peak by approximately 100 kW and results in higher OPEX. Its low annuity mainly derives from low investment costs. The low investment costs are primarily caused by a longer battery lifetime due to reduced cycling and calendrical aging (see subsection 2.5.). When solely focusing on the operation, the ANN- and MILP-based controller are favored.

5. Conclusions

In the present study, we developed an approximate model predictive control approach for a PV-battery system in an office and laboratory building. The study is based on the preceding development of a hierarchical MPC in [27]. The hierarchy is based on prediction horizons so that different time scales can be considered. In the case of the PV-battery system, the MPC aims at optimizing the electrical peak load in a first step and incorporate it in the battery energy management in the second step (see subsection 2.2.). The hierarchical MPC serves as teacher to generate training data for machine learning models. These machine learning models are the approximators that replace the optimization problem after successful training. I.e., they function as controllers instead of the optimization program leading to a speed-up in processing time and lower hard- and software requirements in practice. Since the scientific literature is still missing a comparison of advanced machine learning models in the context of approximate MPC, we investigate an artificial neural network as well as the sophisticated tree-based models Random Forest and Gradient Boosting (see section 1.). In addition to that, we detect a research gap in in-depth analyses of the open- and closed-loop performance of the approximators. In the context of this study, the open-loop performance refers to the purely time-series based comparison of the true, i.e., the MPC output and the predicted, i.e., the approximators' outputs without any system interaction. The closed-loop performance is calculated based on the system interaction between the MPC or the approximators with the target system.

Our results prove that the machine-learning-based approximators all result in relatively high open-loop performances (see Figure 4). While the Gradient Boosting model slightly outperforms the other approximators open-loop, the same trend is not apparent when comparing the closed-loop performance solely based on the respectvie time-series. Here, we compare the MPC's output, i.e., the manipulated variables, with the approximator's one without evaluating the control-oriented metrics as defined in subsection 2.5.. Here, the Artificial Neural Network results in the highest accuracy metrics. When taking into consideration the PV-battery system's annuity, however, the Gradient Boosting model even surpasses the MPC results. The effect that the approximator outperforms its original teacher, is explained by the machine learning models' missing constraints. The MPC considers the maximum electrical peak as a constraint within the optimization. Hence, the MPC does not exceed the pre-optimized peak of 803 kW (see right-hand side of Figure 5). Nonetheless, the MPC performance is still considered the best when taking into account all relevant operation metrics. This behavior can be mitigated by an addtional rule-based backup controller that has been implemented in this study (see right-hand side of Figure 5). The integration of the backup controller results in a decrease in the electrical peak load while achieving almost the same annuity as the purely approximator-controlled system.

All in all, all three approximators result in a reliable closed-loop performance. Even though their control output clearly differs from the MPC's one, they outperform a benchmark model regarding the peak load. No clear relation between open- and closed-loop performance is apparent considering that the approximators all perform best regarding other metrics. Nonetheless, we detect that high open-loop performance supports a robust closed-loop performance. Finally, we go back to the stated research questions in subsection 1.1. as follows:

1. Advanced tree-based machine learning models like Gradient Boosting and Random Forest can outperform Artificial Neural Networks as controllers in an approximate MPC application. In addition, they are favourable from a comprehensibility point of view as they resemble the conventional "if-condition-then-action" structure of rule-based controllers.

2. The open-loop performance is an indicator for a good closed-loop performance, however, no generalizable conclusions can be drawn. A purely time-series-based comparison of controller outputs, i.e., the control trajectory, can be misleading regarding the closed-loop performance.

6. Outlook

The simulative assessment of the PV-battery system is based on a hierarchical MPC with a rolling horizon of 1 h. I.e., the control loop is repeated every hour with a timestep of 15 min and a prediction horizon of 16 h. The approximators, however, learn the in- to output relations based on every timestep, i.e., 15 min. This means that the approximators inheretly learn the model uncertainty of the MPC's process model for 3 out of 4 timesteps. Thus, we recommend future work to use a 1-step MPC to mitigate the model uncertainty. We expect the open-loop performance to increase for this case.

Apart from that, the overall profitability of the PV-battery system is not existent when taking the annuity into account. This is caused by the provided regulatory framework from Germany. Future work should focus on additional sources of revenue such as frequency control reserves. In addition, the interaction with the building energy system should be more closely investigated and synergy effects between the battery and the HVAC system identified.

Acknowledgment

We gratefully acknowledge the financial support by Federal Ministry for Economic Affairs and Climate Action (BMWK), promotional reference 03EN3026C.

References

[1] 2022 Global status report for buildings and construction: Towards a zero-emissions, efficient and resilient buildings and construction sector. Nairobi; 2022.

[2] Drgoňa J, Arroyo J, Cupeiro Figueroa I, Blum D, Arendt K, Kim D, et al. All you need to know about model predictive control for buildings. Annual Reviews in Control. 2020;50:190-232.

[3] Oldewurtel F, Parisio A, Jones CN, Gyalistras D, Gwerder M, Stauch V, et al. Use of model predictive control and weather forecasts for energy efficient building climate control. Energy and Buildings. 2012 Feb;45:15-27. Available from: https://linkinghub.elsevier.com/retrieve/pii/S0378778811004105.

[4] Ma Y, Borrelli F, Hencey B, Coffey B, Bengea S, Haves P. Model Predictive Control for the Operation of Building Cooling Systems. IEEE Transactions on Control Systems Technology. 2012;20(3):796-803.

[5] Sturzenegger D, Gyalistras D, Morari M, Smith RS. Model Predictive Climate Control of a Swiss Office Building: Implementation, Results, and Cost–Benefit Analysis. IEEE Transactions on Control Systems Technology. 2016 Jan;24(1):1-12. Available from: http://ieeexplore.ieee.org/document/7087366/.

[6] Širokỳ J, Oldewurtel F, Cigler J, Prívara S. Experimental analysis of model predictive control for an energy efficient building heating system. Applied energy. 2011;88(9):3079-87.

[7] Cigler J, Gyalistras D, Široký J, Tiet VN, Ferkl L. Beyond theory: the challenge of implementing model predictive control in buildings. Proceedings of 11th Rehva world congress, Clima. 2013;(250).

[8] Prívara S, Cigler J, Váňa Z, Oldewurtel F, Sagerschnig C, Žáčeková E. Building modeling as a crucial part for building predictive control. Energy and Buildings. 2013;56:8-22.

[9] May-Ostendorp PT, Henze GP, Rajagopalan B, Corbin CD. Extraction of supervisory building control rules from model predictive control of windows in a mixed mode building. Journal of Building Performance Simulation. 2013;6(3):199-219.

[10] Domahidi A, Ullmann F, Morari M, Jones CN. Learning decision rules for energy efficient building control. Journal of Process Control. 2014;24(6):763-72.

[11] Drgoňa J, Picard D, Kvasnica M, Helsen L. Approximate model predictive building control via machine learning. Applied Energy. 2018;218:199-216.

[12] May-Ostendorp P, Henze GP, Corbin CD, Rajagopalan B, Felsmann C. Model-predictive control of mixed-mode buildings with rule extraction. Building and Environment. 2011;46(2):428-37.

[13] Klaučo M, Drgoňa J, Kvasnica M, Di Cairano S. Building Temperature Control by Simple MPC-like Feedback Laws Learned from Closed-Loop Data. IFAC Proceedings Volumes. 2014;47(3):581-6.

[14] May-Ostendorp PT, Henze GP, Rajagopalan B, Kalz D. Experimental investigation of model predictive control-based rules for a radiantly cooled office. 2013;19(5):15.

[15] Bursill J, O'Brien L, Beausoleil-Morrison I. Multi-zone field study of rule extraction control to simplify implementation of predictive control to reduce building energy use. Energy and Buildings. 2020 Sep;222:110056. Available from: https://linkinghub.elsevier.com/retrieve/pii/S0378778819335078.

[16] Piscitelli MS, Brandi S, Gennaro G, Capozzoli A, Favoino F, Serra V. Advanced Control Strategies For The Modulation Of Solar Radiation In Buildings: MPC-Enhanced Rule-Based Control. In: Corrado V, Fabrizio E, Gasparella A, Patuzzi F, editors. Proceedings of Building Simulation 2019: 16th Conference of IBPSA. Building Simulation Conference proceedings. IBPSA; 2020. p. 869-76.

[17] Drgoňa J, Picard D, Helsen L. Cloud-based implementation of white-box model predictive control for a GEOTABS office building: A field test demonstration. Journal of Process Control. 2020;88:63-77.

[18] Le K, Bourdais R, Guéguen H. From hybrid model predictive control to logical control for shading system: A support vector machine approach. Energy and Buildings. 2014;84:352-9.

[19] Yang S, Wan MP, Chen W, Ng BF, Dubey S. Experiment study of machine-learning-based approximate model predictive control for energy-efficient building control. Applied Energy. 2021;288:116648.

[20] Lohr Y, Monnigmann M, Klauco M, Kaluz M. Mimicking Predictive Control with Neural Networks in Domestic Heating Systems. In: 2019 22nd International Conference on Process Control (PC19). IEEE; 2019. .

[21] Kuhn M, Johnson K. Applied Predictive Modeling. New York, NY: Springer New York; 2013. Available from: http://link.springer.com/10.1007/978-1-4614-6849-3.

[22] Owerko D, Gama F, Ribeiro A. Optimal power flow using graph neural networks. In: ICASSP 2020-2020 IEEE International Conference on Acoustics, Speech and Signal Processing (ICASSP). IEEE; 2020. p. 5930-4.

[23] Zamzam AS, Baker K. Learning optimal solutions for extremely fast AC optimal power flow. In: 2020 IEEE International Conference on Communications, Control, and Computing Technologies for Smart Grids (SmartGridComm). IEEE; 2020. p. 1-6.

[24] Canyasse R, Dalal G, Mannor S. Supervised learning for optimal power flow as a real-time proxy. In: 2017 IEEE Power & Energy Society Innovative Smart Grid Technologies Conference (ISGT). IEEE; 2017. p. 1-5.

[25] Pan X, Zhao T, Chen M, Zhang S. Deepopf: A deep neural network approach for security-constrained dc optimal power flow. IEEE Transactions on Power Systems. 2020;36(3):1725-35.

[26] de Jongh S, Steinle S, Hlawatsch A, Mueller F, Suriyah M, Leibfried T. Neural Predictive Control for the Optimization of Smart Grid Flexibility Schedules. In: 2021 56th International Universities Power Engineering Conference (UPEC). IEEE; 2021. .

[27] Maier LM, Kühn L, Mehrfeld P, Müller D. Time-based economic hierarchical model predictive control of all-electric energy systems in non-residential buildings. RWTH Aachen University;.

[28] Henn S, Richarz J, Maier L, Ying X, Osterhage T, Mehrfeld P, et al. Influences of usage intensity and weather on optimal building energy system design with multiple storage options. Energy and Buildings. 2022;270:112222.

[29] Hart WE, Watson JP, Woodruff DL. Pyomo: modeling and solving mathematical programs in Python. Mathematical Programming Computation. 2011;3(3):219-60. Available from: https://link.springer.com/article/10.1007/s12532-011-0026-8.

[30] Deutscher Wetterdienst. Wetter und Klima - Deutscher Wetterdienst - Leistungen - Testreferenzjahre (TRY); 18.05.2022. Available from: https://www.dwd.de/DE/leistungen/testreferenzjahre/testreferenzjahre.html.

[31] SMARD — Marktdaten visualisieren; 19.05.2022. Available from: https://www.smard.de/home/marktdaten/?marketDataAttributes=%7B%22resolution%22:%22year%22,%22from%22:1514674800000,%22to%22:1577833199999,%22moduleIds%22:%5B8004169%5D,%22selectedCategory%22:null,%22activeChart%22:true,%22style%22:%22color%22,%22categoriesModuleOrder%22:%7B%7D,%22region%22:%22DE%22%7D.

[32] Sandels C, Brodén D, Widén J, Nordström L, Andersson E. Modeling office building consumer load with a combined physical and behavioral approach: Simulation and validation. Applied Energy. 2016;162:472-85.

[33] Pedregosa F, Varoquaux G, Gramfort A, Vincent M, Thirion B. Scikit-learn: Machine learning in Python. Journal of Machine Learning Research. 2011;12:2825-30. Available from: https://www.jmlr.org/papers/volume12/pedregosa11a/pedregosa11a.pdf?ref=https://githubhelp.com.

[34] Rätz M, Javadi AP, Baranski M, Finkbeiner K, Müller D. Automated data-driven modeling of building energy systems via machine learning algorithms. Energy and Buildings. 2019;202:109384.

PROCEEDINGS OF ECOS 2023 - THE 36TH INTERNATIONAL CONFERENCE ON
EFFICIENCY, **C**OST, **O**PTIMIZATION, **S**IMULATION AND ENVIRONMENTAL IMPACT OF ENERGY SYSTEMS
25-30 JUNE 2023, LAS PALMAS DE GRAN CANARIA, SPAIN

LLEC Energy Dashboard Suite: User Engagement for Energy-Efficient Behavior using Dashboards and Gamification

Eziama Ubachukwu[a], Jana Pick[a], Lea Riebesel[a], Paul Lieberenz[a], Philipp Althaus[a], Dirk Müller[a,b,c], André Xhonneux[a]

[a] Forschungszentrum Jülich GmbH, Institute of Energy and Climate Research, Energy Systems Engineering (IEK-10), Jülich, Germany
[b] JARA-ENERGY, Jülich 52425, Germany
[c] RWTH Aachen University, E.ON Energy Research Center, Institute for Energy Efficient Buildings and Indoor Climate, Aachen 52056, Germany

Abstract:
With growing concerns about climate change and increasing energy costs, energy-efficient use of buildings offers an opportunity to decrease CO_2 emissions and costs. The behavior of building occupants plays a significant role in the process of improving this efficiency both for new and existing buildings. Therefore, we introduce a suite of web-based software applications that aim to encourage energy-efficient building occupant behavior in an office environment under the Living Lab Energy Campus (LLEC) initiative, using the campus of Forschungszentrum Jülich as a demonstration. The suite of applications, developed via a co-design process, provides means to view energy consumption data at various levels of aggregation, and to receive real-time recommendations and incentives for behavior change. Through the *Energy Dashboard*, users can monitor and analyze heating, cooling, and electrical energy consumption at building level. Leveraging IoT-enabled sensors and actuators, *JuControl* offers an interface to view room-specific indoor environmental, heating and ventilation data, and allows occupants to control the room heating by specifying a personal temperature setpoint range. Occupants also receive real-time feedback via recommendations for energy efficiency improvement, alongside periodic behavior evaluation in the form of ratings. The serious game *JuPower* gives users the opportunity to compete in teams to design a CO_2-minimal alternative virtual energy system for the campus, whilst the users' real-world energy-related behavior is translated into in-game effects, thereby providing incentives for energy-efficient behavior via game rewards and social interaction. The interrelations among the applications, deployment strategies, and first outcomes are discussed.

Keywords:
Occupant Behavior, Office Building, Energy Efficiency, Gamification, Serious Game, Energy System Visualization, User Engagement

1. Introduction

In the EU, the building sector contributes 40% of the energy consumption and over 30% of the CO_2 emissions [1], [2]. According to estimations, 75% of the buildings in the EU are energy-inefficient [3].

Within the building sector, occupant behavior has been identified as a key factor in the energy efficiency of buildings and is often implicated in the difference between modeled and actual (post-occupancy) energy consumption of buildings [4, 5, 6]. According to the PROBE studies (Post-occupancy Review of Buildings and their Engineering), this difference is usually a factor of two: the actual consumption is twice the modelled consumption [4, 7]. Similar results are also reported by other studies (e.g. as cited in [8]). Furthermore, in one simulation study of energy behaviors of office occupants with profiles classified as one of austerity, standard, or wasteful, it was estimated that the wasteful profile can use up to 90% more energy than the standard energy profile in a one-person office, while the austerity profile can use up to 50% less energy than the standard profile [9].

Clearly, there is potential for the improvement of energy efficiency in buildings through energy-efficient occupant behaviour. However, there are challenges in engaging occupants and triggering behavior change. First, building occupants in public buildings are usually indifferent to the energy efficiency of their behavior because they are not conscious of their impact on the energy consumption and are not responsible for the energy costs [10]. To solve the consciousness issue, energy consumption should be monitored through measurement data. But this leads to issues of privacy and data security, especially for a country like Germany where privacy is taken more seriously than in most other European countries, with supporting structures like the works

council and Data Protection Officers serving to protect employees from privacy infringements [11, 12, 13, 14].

Furthermore, the issue of occupant apathy to energy consumption in public buildings is not easy to address in a top-down, management-initiated and sustained fashion in a European country like Germany. Only in the light of the energy crisis occasioned by the Russia-Ukraine conflict was there more assertive drive from government to save energy across the country. In spite of this, occupant behavior still requires more intrinsic motivation for its transformation.

In this work, the objective is to develop and test applications that are effective in influencing building occupants' behavior through intrinsic motivation. We focus on occupant interactions with the heating, cooling and air conditioning (HVAC) system in naturally ventilated office buildings under real-world conditions. This work is incorporated in the Living Lab Energy Campus (LLEC), in which a part of the infrastructure of Forschungszentrum Jülich GmbH (FZJ) is transformed to a test-bed for e.g. monitoring and control approaches for future building and district energy systems. Our case study consists of a subset of office buildings in FZJ with different years of construction (ranging from the 1970s up to recently completed buildings), which are representative of the office building stock. Figure 1 gives an overview of the chosen setup in the equipped buildings. All selected buildings, like all FZJ buildings, were already equipped with digital calibrated meters to measure electricity, heating and cooling demand, e.g. for billing purposes. For research purposes, an interface was set up between the facility management's proprietary system and the research ICT platform. In addition, all offices, meeting rooms and kitchenettes in the selected buildings were equipped with wireless indoor air quality sensors (to measure CO_2 concentration, temperature and relative humidity), window and door status sensors, and wireless thermostats. Due to the heterogeneity of the buildings and in order to limit the retrofitting effort in the existing buildings to a sensible level, the sensor network makes use of wireless (EnOcean) sensors. On top of this, a subset of the selected buildings was equipped with wired (KNX) actuators for shading, lighting and underfloor heating control and push buttons with integrated displays. To allow for transfer of the developed approaches to buildings in the outside world, all sensors and actuators used are commercially available. More details can be found in [15].

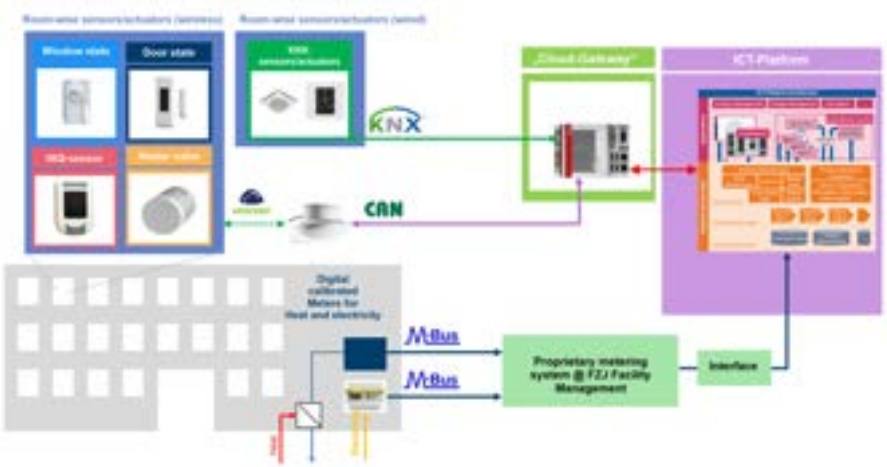

Figure 1: Setup of digital meters, sensors and actuators in buildings

To meet the challenges in bringing about behavior change, we develop applications for building occupants for visualization and control of the building energy system through a human-machine interface (HMI). Additionally, we introduce real-time behavior evaluation and recommendations for the occupants, supported by *gamification* and a serious game. We evaluate the effectiveness of various combinations of these behavior intervention measures. Only initial results from the individual parts of the system are available as at the time of this writing, the fully coupled system has only just been deployed.

1.1. Literature Review

The interaction of occupants with the building and its energy system is the focus of several large-scale studies. For example, the DataFEE project[1] focuses on the development of tools and methods for the analysis of the interaction of occupants with buildings. Likewise, the IEA EBC Annex 66 project [2] and the IEA EBC Annex 79 project [3] focused on modelling occupants and occupancy, as well as the integration of occupancy in building models. Related to these occupant-centric studies, various behavioral intervention projects have

[1] Available at https://www.ebc.eonerc.rwth-aachen.de/cms/E-ON-ERC-EBC/Forschung/Forschungsprojekte2/Projekte-Nutzerverhalten-und-Komfort/ cviyk/DataFEE/?lidx=1

[2] http://www.annex66.org/

[3] Available at https://annex79.iea-ebc.org/

been carried out to address energy efficiency of occupants in buildings. These interventions take one of several forms, including provision of information through visualization, active feedback through various means of communication, and numerous gamification and serious games. One main element for providing information and visual feedback in energy systems is the use of *energy dashboards* [16]. These dashboards provide a Graphical User Interface (GUI) for visualizations regarding energy-related data. Additionally, interactive dashboards provide good User Experience (UX) and encourage interactions with the information being presented. To make such GUIs effective, their design follows Human-machine interface design principles. Rogers, Sharp and Preece [17], who worked extensively on these design principles, highlight the principles of *visibility*, *feedback* and *constraints*. The principle of visibility refers to making actions and functionalities obvious to the user, while the principle of feedback prescribes that the interface should give users notifications when an action has to be performed or has been completed. The principle of constraints refers to limiting user actions in the interface if they are not valid. In the context of energy behavior interventions, these principles encourage the use of energy dashboards. Whilst some studies show that dashboards are beneficial, other studies indicate, however, that visualization alone does not lead to sustainable energy-saving behavior [18, 16]. Most studies related to occupant behavior interventions focus on gamification and serious games.

Gamification is defined as "the use of game design elements in non-game contexts" [19]. A distinction exists between *serious games*, which is the development of full-fledged games for non-entertainment purposes, and gamification, which just involves the use of game elements or "atoms" in an otherwise non-game context [19]. Such game elements include leaderboards, badges, and points. Gamification aims to achieve real-world behavior change by means of an engaging and fun experience.

Several studies have used different gamification concepts with the intention of motivating users to take action for enhanced energy efficiency. In the review by Johnson et al. [20] the authors investigated 25 gamified applications and serious games in the domestic energy consumption sector. The results of the behavioral interventions are classified into four categories: behavioral, cognitive, learning and knowledge acquisition, and user experience. Behavioral interventions refer to real-world and in-game actions and aspirations to save energy, while the cognitive aspect refers to affective and motivational elements, including energy-related opinions, self-awareness about energy saving and motivation to engage in energy-conserving measures. Learning and knowledge acquisition refers to learning effectiveness and knowledge accumulation, and finally user experience refers to the perspective of the user towards the game, including engagement, usability and satisfaction. The results of the majority of the studies (a total of 17 out of 25) fall into more than one result category. The user experience is the most frequent, followed by cognitive, real-world behavioral, knowledge, then in-game behavioral categories.

Across the studies, the results were not exclusively, but mostly, positive. About half of the reviewed interventions explored serious games and the other half explored gamified applications. Among the employed applications were seven mobile apps, nine browser apps and five computer games. While around half of the applications feature integrations with the real world, the others are completely digital without real-world integration.

AlSkaif et al. [21] introduces a conceptual framework based on gamification for residential building user engagement. They classify the framework requirements and link them to corresponding high-level gamification objectives. The five groups of game design aspects implemented are information provision (statistics, messages, tips), rewarding system (electricity bill discounts, virtual currency, prizes/offers/coupons), social connection (competition, collaboration, energy community), user interface (dashboards, leaderboard, progress bar, message box, notifications, degree of control), and performance status (points, badges, levels).

1.2. Research Contributions

The contributions of this paper are as follows. First, we report on various implementations of user behavior interventions with respect to energy efficiency, starting with visualization of energy systems at different levels of spatial granularity, through to provision of a Human-Computer Interface (HCI) for controlling the energy system. Furthermore, we discuss the application of gamification and user behavior evaluation, and the coupling of these to a serious game. When the experimental results are complete, we intend to extensively analyze and discuss the contributions of the various combinations of these interventions to occupant behavior improvement. In this paper, however, we only discuss initial results, since the full-fledged experiment has only been running for a very short time as at the time of writing.

This work is organized as follows: Section 2. describes the purpose and features of the applications developed, Section 3. presents results and discussion of the co-design process of the applications as well as the occupant behavior evaluation. Section4. summarizes and draws a conclusion.

2. Methodology

The LLEC Energy Dashboard suite includes multiple web applications that interact with each other to provide a wide range of functionalities.

2.1. The Energy Dashboard: Visualization of Energy Data

The Energy Dashboard provides an interface through which staff members and visitors can gain insight into the energy demand of the campus. Via the Dashboard, users can view both historical and real-time heating and electricity data at the campus level as well as for individual buildings, see Figure 2.

Additionally, the Dashboard shows operation data of so-called *energy demonstrators*, which are proof-of-concept energy systems for generation, conversion, and storage of renewable energy and waste heat. The goal of the Dashboard is to drive user awareness regarding energy systems in general, as well as to improve the public understanding of the represented systems.

Figure 2: Screenshots of the Energy Dashboard. *Left*: Exemplary building page showing live electricity and thermal demands. *Right*: Comparison of buildings demands for thermal power.

2.1.1. Data

Currently, the two main data measures are electricity and heating demand. Timeseries data for those measurements is visualized on the dashboard at one-minute resolution. The main landing page of the energy dashboard shows the overall consumption of electricity and heating energy for the whole campus using a mix of chart types. This is the highest-level data that is visible on the dashboard. More details for the same consumption data for electricity and heating is also available on the building-level. Via an interactive campus map or a list of building IDs, a single building can be selected to view its data. This data is also available in the form of the same 2-hour-live-chart. Additionally there is a 48-hour historical data bar chart, in which the data is hourly aggregated.

2.1.2. Access rights

One important aspect of the whole framework is data security. There are different levels of access for the energy dashboard, as not all data is visible to every user. Authentication is via Shibboleth, and roles are assigned based on the authenticated user. The basic staff role can view data for the whole campus and single buildings, but buildings in restricted areas on the campus are not available. Admins can escalate their authentication level to view more data like number of sensors reporting for each data point, additional plots, and access to the restricted buildings. The guest role uses login credentials without Shibboleth authentication, and is only permitted to view the campus-level consumption and a special subset of buildings.

2.2. JuControl: Visualization, Control and Gamification

The effects of the behavior of a single office occupant in the context of a whole building are not necessarily directly visible. To account for that, selected buildings were equipped with additional sensors and actuators for data acquisition and control at room level. This allows the collection of more datasets like CO_2 concentration, humidity or window states. The measurement data on room level is visualized via the web-based application *JuControl* (see Figure 3), which is integrated into the Energy Dashboard.

Besides the more detailed visualization of data, *JuControl* also enables users to control actuators in their room via an online interface, in addition to the physical controls available at the actuators themselves.

2.2.1. Automatic heating control

Within LLEC, the equipped rooms form a test-bed for testing different innovative control approaches, e.g. model predictive control-based room controllers. In addition to the control options in the rooms, *JuControl* provides the central user interface for the comfort preferences of the room occupants that are taken into account by

Figure 3: JuControl: Exemplary room view

Figure 4: JuControl: User specific time schedule for the expected presence in the office

the tested automated controls. Regardless of the control algorithms tested, the user interface itself already offers a great deal of savings potential through options that go far beyond the previous manual adjustment of thermostats. Office spaces are usually only used in a clearly limited time frame. Therefore, they offer a good opportunity to save heating energy by lowering the room temperature to an appropriate level while the office is not occupied, for example after working hours and over the weekend. However, for the comfort of employees, it is important to restore the correct temperature within the rooms in time. For this, *JuControl* offers users the ability to create an individual time schedule in which they enter their expected presence; see Figure 4.

In order to accommodate different needs, every user can also define their own comfort temperature range. Based on the schedules of all occupants of an office, *JuControl* then calculates a heating plan for the room. A controller script can query this heating plan via *JuControl*'s API and perform optimal heating control based on the desired temperature setpoints.

2.2.2. Manual control mode

Naturally, an occupant's schedule may not always match the actual presence in the office, for example when the schedule changes temporarily on short notice. For scenarios such as these, the occupant always has the option to switch to "manual control", in which the schedule and the associated desired temperature setpoints are overridden by the manual setting. Manual control can be triggered via the *JuControl* web interface or by physically operating the thermostats. In both cases, the new user-specified setpoint temperature is then targeted by the heating control. After a maximum of 8 hours, the control automatically returns to automatic mode, in which the presence schedule is used once again.

2.2.3. User Consent

Compared to the general building consumption, the parameters measured here are very sensitive data, as they allow drawing direct conclusions about individual persons or small groups of persons. For example, the CO_2 concentration in an office can be used to determine how many people were present in the office at a specific time. The data is only visible to an occupant if all the other occupants of an office agree to the usage of this tool. This poses an additional challenge when users change offices. Basically the following rules are applied: a user only has access to the data of the office they are officially assigned to, and only if all other occupants of this room have given their consent. If someone leaves an office, the person also no longer has access to newly generated data of this office. (However, they can view historical data.) If a new employee joins an office, everyone automatically loses their access rights until this new employee has also agreed to the data processing.

2.2.4. Gamification

JuControl features a gamification section, in which the energy efficiency of occupants' offices is evaluated based on predefined behavioral patterns related to ventilation habits and indoor temperature setpoints. The evaluations, which are currently limited to heating demand, are carried out by *Juracle*, an evaluation engine discussed in Section 2.4.. Corresponding penalties are awarded in the form of "wasted thermal energy" scaled to the size of the FZJ campus. Groups of office rooms compete in teams against groups from the same or other buildings. A leaderboard shows the ranking of teams based on performance and places each room's performance in the context of the team's and global performance. Additionally, a three-color traffic-light feedback system is used to convert the raw energy penalty values to normative feedback that allows occupants to determine if their performance is relatively good or bad.

Social interactions (competitions, teams) have been shown to be key elements of effective gamification [22, 23, 20]. To this end, gamification in *JuControl* is designed around teams and competition. Additionally, the

performance of teams is coupled to a serious game *JuPower*, discussed more in Section 2.3. below. The *JuControl* gamification interface is shown in Figure 5 below.

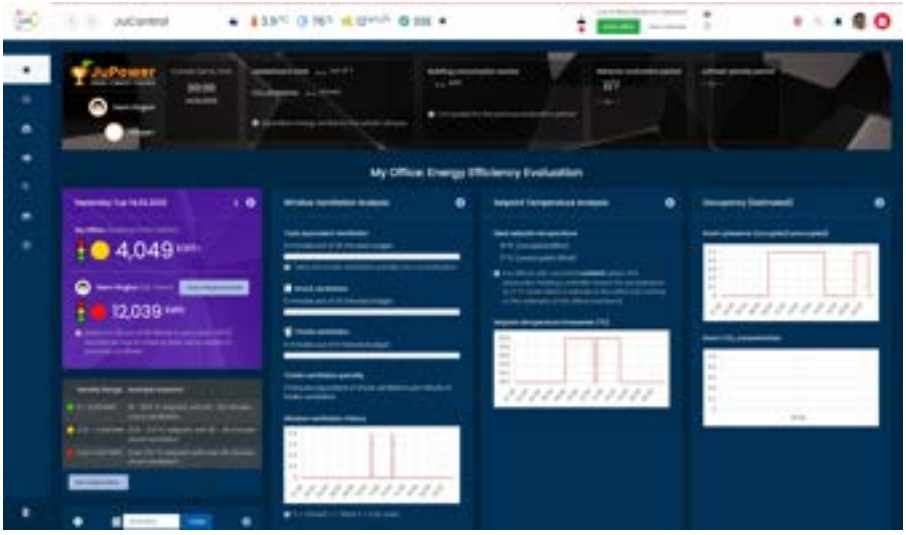

Figure 5: *JuControl* gamification interface showing integration with a serious game, *JuPower* (top dark bar), and evaluations obtained from *Juracle*. The charts show the timeseries for the input quantities for behavior evaluation – window state, setpoint temperature, and presence profile.

2.3. JuPower: A Serious Game

JuPower is a *serious game* developed to enable players appreciate the trade-offs involved in energy system design. A *serious game* is a game developed for non-entertainment purposes, whilst ideally retaining the fun and engaging nature of entertainment games. The purpose of the gamification approach is to engage users and draw attention to the way their behavior affects their energy consumption.

2.3.1. Game design

In the game, the mission for players is to design a more climate-friendly energy supply system for a virtual version of the Forschungszentrum Jülich campus having heating and electricity demand. The electrical demand data is derived from actual historical data for the campus, while the thermal demand data is derived from a mix of Modelica [24] models of the actual buildings developed using the TEASER [25] tool, and historical data. The building models allow players to apply realistic retrofits at a cost in the game.

By design, the default energy source for heating in the virtual campus is an oil boiler, with electrical power being drawn from the virtual electricity grid. This assumption is different in many respects from the actual energy sources in the real campus.

To reduce the CO_2 emissions arising for the supply of energy to the buildings, new installations can be made in the game. Players have a fixed budget with which they can purchase new energy systems and components to replace the default energy system. The resulting energy system for the virtual campus is simulated afterwards for each team, and the teams are ranked continuously based on the total operational CO_2 emissions generated over the simulation period.

2.3.2. Game modes

JuPower admits three different modes of play that can coexist independently. These are:

- Sandbox mode, in which players try out features and learn the system without teams, competitions, or external time pressure. Essentially, the players' game actions and its effects are visible to the player alone.
- Standard game mode, in which players participate in teams in a predefined gameplay instance that is governed by a time schedule. In this mode, outcomes of the real-world behavior evaluation are fed into the game.
- Real-time mode, which is intended for more experienced energy system designers. Here, the game clock is synchronized to the real clock, and boundary condition inputs into the game, like weather and demand data, are derived in real-time from real-world data.

Figure 6: JuPower home page during simulation showing the energy widget (center) and the leaderboard (right).

Figure 7: JuPower simulation page

2.3.3. Gameplay

A game run consists of *game phases*, each of which provides a defined set of interaction opportunities for the players. In the *design phase*, players design an energy system by installing energy system components on a stylized aerial view of the campus via drag-and-drop. The aerial map view faithfully mimics the main features of the landscape of the real campus. Each installation of a component requires cash and real-estate, and is subject to the availability of these resources. Players propose their designs to their teams and cast votes to determine which proposed design is adopted for the team. To enhance coordination and communication amongst players within a team, a rich-text chat functionality with mentions is available in the Proposals page. Furthermore, players tag and optionally describe their designs prior to proposing them.

The *pre-simulation phase* follows the design phase. In this phase, the most-upvoted design is automatically adopted for each team. Based on this design, the operation of the energy system over a certain period is projected by computing the dispatch of the components. The dispatch is the result of a Mixed-Integer Linear Program (MILP) optimization problem, solved using the Gurobi^{TM} [26] solver. Afterwards, the *simulation phase* starts, during which various system data and performance indices are shown in "real game-time" as the simulation progresses. The Key Performance Index (KPI) is the accumulated operational CO_2 emissions, and teams are ranked on a leaderboard based on this KPI. Figure 6 and Figure 7 below show the home page and simulation page, respectively, during simulation. The *post-simulation phase* allows players to take stock and reflect on their design choices.

2.3.4. Coupling with Real-world Behavior Evaluation

The real-world behavior penalties computed as part of the JuControl gamification described above, are transferred to JuPower as additional building demands. Specifically, for each team, the average weekly performance penalty is added to the thermal demand of the buildings in JuPower for that team. This has the effect of a proportional increase in CO_2 emissions in the game, and by extension a worsening of the performance of the energy system in the game.

2.4. Juracle: Occupant Behavior Evaluation Engine

Juracle is an engine that evaluates the thermal energy-related aspects of occupant behavior based on two criteria: window interaction (ventilation) and room heating (temperature setpoint). First, it defines the notion of an ideal occupant, and then computes the deviation of a given instance of occupant behavior from this ideal. Finally, it expresses this deviation in energy terms (kWh) as wasted energy. Two different but related focuses of such a behavior evaluation tool can be identified: behavior modification to conform with some predefined norm, or energy wastage estimation. These two goals are not necessary congruent, since aiming for one could imply violating the other. For example, previous research has shown that *trickle ventilation* during the heating season (i.e. with windows opened only a small angle while hinged on the bottom side) leads to severe energy losses, compared to the so-called *shock ventilation* (with windows fully opened while hinged on the side) [27]. (These multi-modal windows are commonplace in Germany.) However, trickle ventilation leads to more energy wastage only because occupants tend to leave windows in that state for long periods due to its poor efficiency in refreshing the room air, leading to the cooling down of the walls. Evaluation with focus on behavior modification discourages *patterns of behavior* like trickle ventilation, while focus on energy evaluation judges the energy impact of particular instances of behavior that lead to energy wastage.

Effectively, the behavior modification-focused method of intervention tends towards a rule-based system, in which a consistent set of relatively simple rules are defined by which user behavior is judged. These rules do not have to be accurate in the physics sense in its assumptions, but only need to be *self-consistent*, that is – roughly speaking – given similar inputs, they produce similar outputs. On the other hand, model-based systems are more appropriate when the focus is estimating energy wastage. Here, the physical processes

involved and their relationships are represented using laws of physics.

2.4.1. Hybrid Evaluation Model

Juracle uses a hybrid approach: it focuses on the behavior modification goal, and derives a set of physics-informed rules with the following attendant characteristics. First, the ideal occupant is defined in terms of duration of window opening, and the chosen setpoint temperature. A quota is assigned for the ideal occupant and deviations are computed from this quota for real occupants. Secondly, trickle ventilation as a pattern of behavior is discouraged. Therefore a penalty factor scales the trickle ventilation duration to deplete the quota more quickly. Thirdly, the computed deviations based on the measured criteria are applied to a reference model to derive an estimate of the energy "cost" of the deviations (in kWh). Finally, since the rule-based system has fewer parameters than a model-based system, it tends to be more easily scalable than a purely model-based system which has to take into account the variations of the physical properties of the different buildings and interactions.

The penalty derived from *Juracle* is applied to *JuPower* game as a demand increase for which CO_2 emissions must be minimized in the game.

2.5. Experiment Design

In order to evaluate the effectiveness of the suite of applications in concert, an experiment design has been conceived and the experiments are currently ongoing. Some of the questions that the experiment design aims to answer are:

- What are the effects of the behavior evaluation strategy on behavior, both in terms of user actions as compared to the ideal scenario, and in terms of actual energy savings?
- What additional effect does the JuPower serious game have when coupled with behavior evaluation, and what is its stand-alone effect?
- What are the effects of visualization and control, without evaluation?

To this end, the experiment design strategy involves grouping nearly 500 offices across more than ten buildings into teams with various combinations of features enabled for each team. Depending on the set of enabled features, these teams are grouped into independent experiment sets on the basis of feature compatibility. The design of each of these experiment sets provides the potential to answer specific research questions, such as those outlined above.

3. Results and Discussion

The *Energy Dashboard* has been used by more than 1,300 staff members since its release in mid-2020, or about one-fifth of the population of the campus. *JuControl* has been available in one building for well over a year, and has formed a core part of the heating regulation of the rooms in the building. However, as mentioned earlier, the main experimental run and evaluation of the suite of applications only just began, and only limited initial data on user evaluation is available. The *JuPower* game has only been played in test phases, and the development of *Juracle* was only recently concluded. Nevertheless, the results of the evaluations of the apps as stand-alone units are presented in the following sub-sections, covering mainly the user interaction and user experience evaluation and feedback obtained through co-design workshops.

3.1. Co-Design Process

The energy dashboard suite was developed using a co-design process. In this way, future users of the dashboard were actively involved in the development cycle and feedback and results were collected at several points in the process. A total of four co-design workshops targeting different aspects and developmental stages of the Energy Dashboard suite have been carried out, apart from various additional less-structured usability tests. During the co-design workshops, volunteers were granted alpha- and beta-stage access to test the dashboard components and provide feedback on existing features. Furthermore, during the co-design workshop events, potential features and further development concepts were discussed in detail. The results of these four workshops are summarised in the following paragraphs.

3.1.1. Co-Design Results: Energy Dashboard and JuControl

Beyond the standard requirements for user friendliness, the barrier to on-boarding for the applications should be as low as possible. By following a web-based approach, the applications do not require a separate installation step. Additionally, the responsive design that caters to different device sizes and orientations for the Energy Dashboard and *JuControl* made it possible to view these apps on mobile devices and tablets. Furthermore, to ease the burden of password management and mitigate potential security issues related to credentials, we integrated authentication via the institution-wide Shibboleth authentication. Thus, the authentication process was the same for the users as for most other services they access in their regular work.

Figure 8: $C0_2$ health chart developed as a result of feedback from users, in order to understand the values shown.

Figure 9: JuPower screenshot showing main actions and their completion status.

Again, users expressed the wish to have data shown on a spatial granularity level below the campus or building level, i.e. the floor or room level, so that they can reconcile the data to their own contributions. The implementation of this wish was the development of *JuControl*.

Furthermore, given the diverse range of specializations in the campus, it was necessary to not assume a knowledge of energy systems on the part of the users. This meant that all necessary information needed to understand the visualizations were made available in the application. For example, in *JuControl* a health chart is shown alongside the CO_2 concentration for the room, as shown in Figure 8. This was the result of feedback.

Yet again, whilst the applications are designed to maximize user interaction, users expressed fears about the apps being a distraction from work by requiring too much attention. To this end, a notifications management system was developed that allows users to be notified by email about certain events (e.g. when CO_2 concentration is above their defined threshold), or even turn off notifications completely. When the notifications are on, their frequency is throttled.

3.1.2. Co-Design Process for JuPower

For the JuPower game, for which two co-design workshops were conducted, the feedback were received and implemented. In general, the game was well received. Some key aspects are outlined as follows.

First, the game application included a manual that explained the objectives and functionalities in the game. However, multiple test users reported that they found this manual too long and not easily readable, and preferred scan-only help information with relevant information highlighted. In response, we introduced the Quick Start section with selected bolded text that summarized the most important points, alongside visual aids like images and illustrations. In the same vein, to reduce the risk of information overload, an *Actions* widget was introduced, which showed the three main steps involved in the gameplay and their completion status (see Figure 9). Additionally, a short tutorial video of about 15 minutes was made to introduce the main features of the game, which several participants found helpful.

Secondly, since the game usually runs over several weeks, and each stage of user interaction can be spread of several days, it was helpful to notify users of the game phase transitions and impending deadlines by email. The emails contained the relevant description for the phase, and any actions that were necessary were included as clickable links in the email.

Finally, to reduce the cognitive load required to play the game, we reduced the range of component options available to the player in the design of an energy system, based on feedback. Furthermore, the number of exposed parameters for each component was reduced to the bare essentials, in order to make decision making easier for the players.

3.2. Occupant Behavior Evaluation

The main experiment phase of the project for evaluating the energy efficiency of occupant behaviour ran from 13.03.2023 to 28.04.2023 (inclusive). Figure 10 shows the number of offices activated in *JuControl* by occupants (after all occupants in each office digitally granted consent for data visualization), broken down into pre-experiment and experiment periods. In about half of the teams, an activation level of at least 50% was achieved in the end, and more than 70% activation in a quarter of the teams.

Figure 11 below shows the evaluation results for one working week for an office, as well as the team average and the global average of all teams in the experimental group, while Fig 12 compares the average penalties for all teams in the given experimental group for a given working week. The colored regions correspond to a three-color traffic-light rating scheme, in which the energy penalties are assigned to traffic-light colors based on a predefined scheme. The color boundaries are: Green: up to 2,120 kWh; Amber: 2,121 kWh to 4,146 kWh; Red: over 4,146 kWh. The energy penalty value represents the amount of energy *lost* in a day in the campus, if *all offices in FZJ* would have a similar occupant behavior profile as the evaluated office or team.

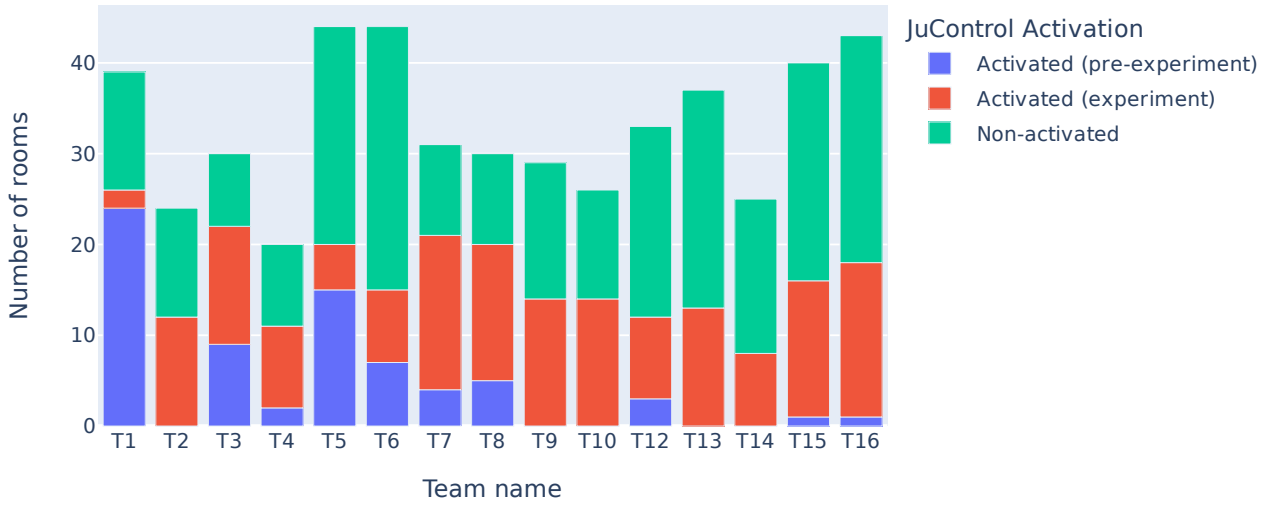

Figure 10: Activation of JuControl in offices by occupants, according to team. The pre-experiment status is shown (blue), along with the additional activation due to the experiment run (red), and non-activated offices (green). Teams T1 and T5 are located in pilot buildings, in which the initial test installations were carried out prior to subsequent extension to other buildings.

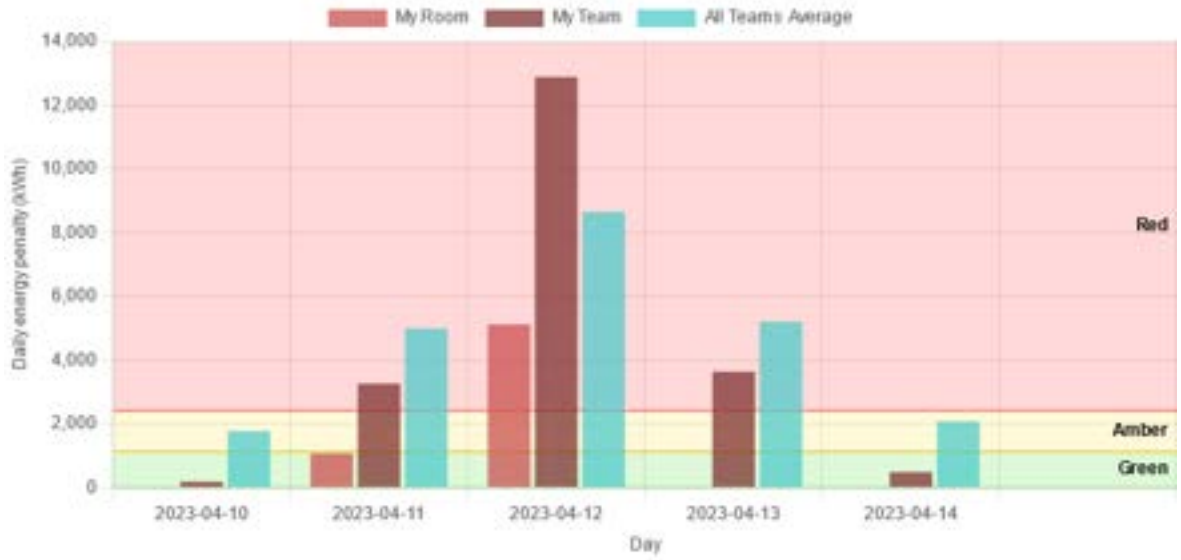

Figure 11: Evaluation penalties for the FZJ campus based on the occupant behaviour for an office (”My Room”), within a team (”My Team”), and for all teams in an experiment group (”All Teams Average”) for one evaluation week (week days).

4. Conclusion

In this paper, a suite of user-facing applications that were developed at Forschungszentrum Jülich to drive user engagement with the overall goal of improving occupant energy behavior was described. With the *Energy Dashboard*, the user has access to building and campus level energy-related data, including consumption data for heating and electricity. Furthermore, comparisons can be made across buildings based on the data. *JuControl* increases the spatial granularity to the room level, and introduces data about other measures like indoor air quality. Furthermore, it enables the control of the occupant's heating energy system. These applications have successfully been used in the field for several months (extending up to 4 years in some cases). The *JuPower* game has been successfully tested and applied in the experiment phase, as well as *Juracle*'s behavior evaluation. In conclusion, the suite of software applications and the strategy of combining and deploying them hold great potential for influencing user behavior towards increased energy efficiency.

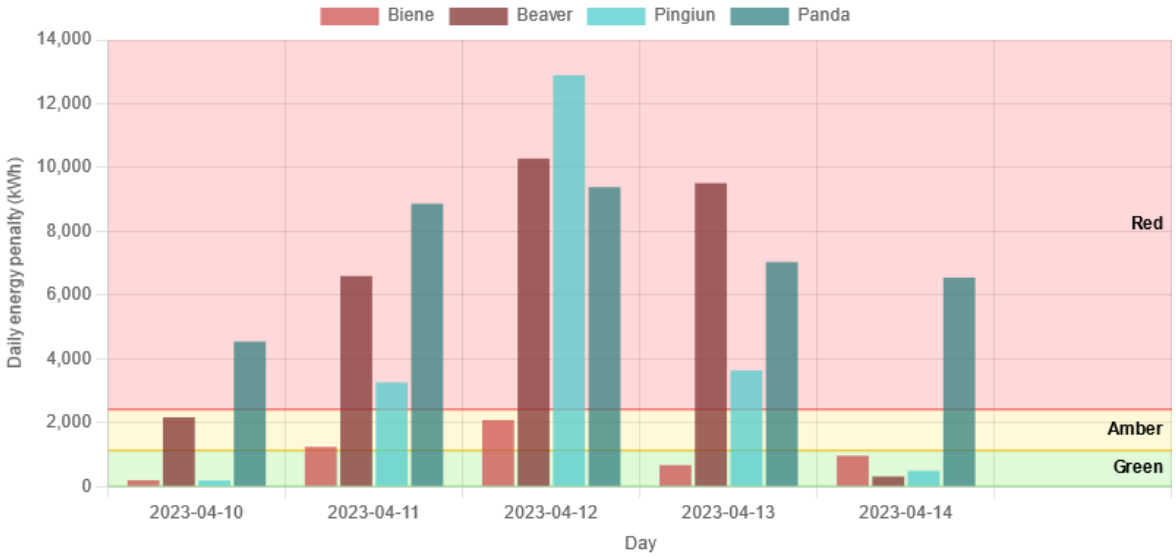

Figure 12: Evaluation penalties for the FZJ campus based on the average occupant behaviour within each team in an experiment group for one evaluation week (week days).

Declaration of Competing Interest

We have no conflict of interest.

Acknowledgements

The authors gratefully acknowledge the financial support by BMWK (German Federal Ministry of Economic Affairs and Climate Action), grant number 03ET1551A and 03EGB0010A.

References

[1] OrbEEt. *D1.2 Specs of SEOR methodology and Enhanced Display Energy Certificates*. Tech. rep. 2017.

[2] European Commission. *Towards reaching the 20% energy efficiency target for 2020, and beyond*. 2017. URL: https://ec.europa.eu/commission/presscorner/detail/en/MEMO%7B%5C_%7D17%7B%5C_%7D162 (visited on 06/15/2020).

[3] European Commission. *COM(2016) 860 ANNEX 1: Accelerating clean energy in buildings*. 2016. URL: https://ec.europa.eu/energy/sites/ener/files/documents/1%7B%5C_%7Den%7B%5C_%7Dannexe%7B%5C_%7Dautre%7B%5C_%7Dacte%7B%5C_%7Dpart1%7B%5C_%7Dv9.pdf (visited on 06/15/2020).

[4] Anna Carolina Menezes et al. "Predicted vs. actual energy performance of non-domestic buildings: Using post-occupancy evaluation data to reduce the performance gap". In: *Applied Energy* 97 (Sept. 2012), pp. 355–364. ISSN: 03062619. DOI: 10.1016/j.apenergy.2011.11.075. URL: http://linkinghub.elsevier.com/retrieve/pii/S0306261911007811%20http://dx.doi.org/10.1016/j.apenergy.2011.11.075.

[5] Karin Schakib-Ekbatan et al. "Does the occupant behavior match the energy concept of the building? - Analysis of a German naturally ventilated office building". In: *Building and Environment* 84 (Jan. 2015), pp. 142–150. ISSN: 03601323. DOI: 10.1016/j.buildenv.2014.10.018.

[6] H. Burak Gunay, William O'Brien, and Ian Beausoleil-Morrison. "A critical review of observation studies, modeling, and simulation of adaptive occupant behaviors in offices". PhD thesis. The University of Gloucestershire, Dec. 2013, pp. 31–47. DOI: 10.1016/J.BUILDENV.2013.07.020. URL: https://www.sciencedirect.com/science/article/pii/S0360132313002187.

[7] B. Bordass et al. "Assessing building performance in use 3: Energy performance of the Probe buildings". In: *Building Research and Information* 29.2 (2001), pp. 114–128. ISSN: 09613218. DOI: 10.1080/09613210010008036.

[8] Valentina Fabi et al. "Occupants' window opening behaviour: A literature review of factors influencing occupant behaviour and models". In: *Building and Environment* 58 (Dec. 2012), pp. 188–198. ISSN: 03601323. DOI: 10.1016/j.buildenv.2012.07.009. URL: http://dx.doi.org/10.1016/j.buildenv.2012.07.009.

[9] Tianzhen Hong and Hung-Wen Lin. *Occupant Behavior: impact on energy use of private offices*. Tech. rep. January. Lawrence Berkeley National Lab.(LBNL), Berkeley, CA (United States), 2012, p. 8. URL: https://www.osti.gov/servlets/purl/1172115%20https://escholarship.org/uc/item/6jp5w8kn%7B%5C#%7Dpage-11.

[10] Andrea Conserva et al. "Selection and assessment of a set of 250 energy efficiency measures integrated in a serious game to promote citizens' behaviour change towards energy efficiency in buildings". In: *12th Conference on Sustainable Development of Energy, Water and Environment Systems* (2017), pp. 1–15.

[11] *Germany: Land of Data Protection and Security – But Why?* 2017. (Visited on 07/06/2020).

[12] Tatjana Zrinski. *EU GDPR vs. German Bundesdatenschutzgesetz – Similarities and Differences*. URL: https://advisera.com/eugdpracademy/knowledgebase/eu-gdpr-vs-german-bundesdatenschutzgesetz-similarities-and-differences/ (visited on 07/06/2020).

[13] Olga Stepanova and Florian Groothuis. *The Privacy, Data Protection and Cybersecurity Law Review - Edition 6: Germany*. 2019. URL: https://thelawreviews.co.uk/edition/the-privacy-data-protection-and-cybersecurity-law-review-edition-6/1210039/germany (visited on 07/06/2020).

[14] Holger Lutz and Simoe Bach. "Employee Monitoring (Germany)". In: *Practical Law* (2019).

[15] Philipp Althaus et al. "Enhancing Building Monitoring and Control for District Energy Systems: Technology Selection and Installation within the Living Lab Energy Campus". In: *Applied Sciences* 12.7 (2022). ISSN: 2076-3417. DOI: 10.3390/app12073305. URL: https://www.mdpi.com/2076-3417/12/7/3305.

[16] Stephanie N. Timm and Brian M. Deal. "Effective or ephemeral? the role of energy information dashboards in changing occupant energy behaviors". In: *Energy Research and Social Science* 19 (2016), pp. 11–20. ISSN: 22146296. DOI: 10.1016/j.erss.2016.04.020. URL: http://dx.doi.org/10.1016/j.erss.2016.04.020.

[17] Yvonne Rogers, Helen Sharp, and Jenny Preece. *Interaction Design: Beyond Human-Computer Interaction*. 3rd. John Wiley & Sons Ltd., 2011. URL: http://eu.wiley.com/WileyCDA/WileyTitle/productCd-0471492787.html.

[18] Nick Verkade and Johanna Höffken. "Is the Resource Man coming home? Engaging with an energy monitoring platform to foster flexible energy consumption in the Netherlands". In: *Energy Research and Social Science* 27 (2017), pp. 36–44. ISSN: 22146296. DOI: 10.1016/j.erss.2017.02.015. URL: http://dx.doi.org/10.1016/j.erss.2017.02.015.

[19] Sebastian Deterding et al. "From game design elements to gamefulness: Defining "gamification"". In: *Proceedings of the 15th International Academic MindTrek Conference: Envisioning Future Media Environments, MindTrek 2011*. 2011, pp. 9–15. ISBN: 9781450308168. DOI: 10.1145/2181037.2181040.

[20] Daniel Johnson et al. "Gamification and serious games within the domain of domestic energy consumption: A systematic review". In: *Renewable and Sustainable Energy Reviews* 73.February 2016 (2017), pp. 249–264. ISSN: 18790690. DOI: 10.1016/j.rser.2017.01.134.

[21] Tarek AlSkaif et al. "Gamification-based framework for engagement of residential customers in energy applications". In: *Energy Research and Social Science* 44.April (2018), pp. 187–195. ISSN: 22146296. DOI: 10.1016/j.erss.2018.04.043. URL: https://doi.org/10.1016/j.erss.2018.04.043.

[22] Frederick Grossberg et al. *Gamified Energy Efficiency Programs*. Tech. rep. February. 2015, p. 73. URL: http://aceee.org/research-report/b1501.

[23] Bunchball. *Enterprise Gamification : The Gen Y Factor*. Tech. rep. 2012, pp. 1–10. URL: https://www.gamification.co/wp-content/uploads/getting-started/White%20Paper%7B%5C_%7DEnterprise%20Gamification%7B%5C_%7DThe%7B%5C_%7DGen%7B%5C_%7DY%7B%5C_%7DFactor%7B%5C_%7D2012.pdf.

[24] The Modelica Association. *Modelica Language*. URL: https://modelica.org/modelicalanguage.html.

[25] Peter Remmen et al. "TEASER: an open tool for urban energy modelling of building stocks". In: *Journal of Building Performance Simulation* 0.0 (), pp. 1–15. DOI: 10.1080/19401493.2017.1283539. URL: http://www.tandfonline.com/doi/abs/10.1080/19401493.2017.1283539.

[26] Gurobi Optimization, LLC. *Gurobi Optimizer Reference Manual*. 2023. URL: https://www.gurobi.com.

[27] Ray Galvin. "Impediments to energy-efficient ventilation of German dwellings: A case study in Aachen". In: *Energy and Buildings* 56 (2013), pp. 32–40. ISSN: 03787788. DOI: 10.1016/j.enbuild.2012.10.020. URL: http://dx.doi.org/10.1016/j.enbuild.2012.10.020.

Online model-based framework for operation and fouling monitoring in a large-scale heat pump

José Joaquín Aguilera [a], Wiebke Meesenburg [a], Wiebke Brix Markussen [b], Benjamin Zühlsdorf [b] and Brian Elmegaard [a]

[a] Department of Civil and Mechanical Engineering, Technical University of Denmark, Kgs. Lyngby, 2800, Denmark, jojap@mek.dtu.dk
[b] Danish Technological Institute, Aarhus C, 8000, Denmark, bez@teknologisk.dk

Abstract:

Heat pump systems are a key technology towards the decarbonisation of district heating systems as they can leverage renewable energy sources and industrial excess heat. Large-scale heat pumps are prone to a variety of faults related to the heat source. Heat exchanger fouling is one of the most common types of faults, which corresponds to the undesired deposition of material on heat transfer surfaces. This fault can be mitigated by the use of different cleaning procedures such as cleaning-in-place. The optimization of the time interval between cleaning periods requires the estimation of the effects of fouling on the heat pump performance, which are often difficult to determine. The present study proposes a framework for online monitoring of a large-scale heat pump affected by evaporator fouling based on a quasi-steady-state simulation model. Model parameters related to the heat transfer coefficients and fouling were repeatedly adjusted by means of a dynamic calibration approach. The framework retrieved operational data from a cloud-based data management system and leveraged existing sensors and controllers in the heat pump. The results indicated that fouling had a larger effect on the thermal resistance than on the pressure drop in the evaporator. The framework also allowed to identify the extent to which a cleaning-in-place system enabled to reduce the evaporator thermal resistance caused by fouling. Overall, the results from the proposed framework showed its potential to describe the operation of the heat pump and to determine the effects of fouling on a real-time basis.

Keywords:

Heat pump, District heating, Fouling, Operation monitoring, Digital twin

1. Introduction

Heat pumps (HPs) are expected to play a major role in the decarbonisation of district heating systems. Today, around 90 % of the global heat supply derives from fossil fuels [1]. HPs enable waste heat recovery and utilization of renewable energy sources. Further, they couple the power and heating sectors, which can support the accommodation of large shares of electric energy from renewable sources in the system. The performance and/or availability of HPs is often negatively affected by faults related to the heat source, as described by HP operators and service providers in [2]. A literature study [3] distinguished fouling in the source side of heat exchangers to be among the most common faults in large-scale HPs. This fault consists of the deposition of material on heat transfer surfaces and in pipes, which can increase the pressure drop and thermal resistance in heat exchangers. As mentioned in [4], the characterization of fouling is challenging, particularly due to uncertainties on the initialization of the deposition process and its growth rate.

Commonly used technologies for the mitigation of fouling are cleaning-in-place (CIP) systems. These include mechanical and chemical cleaning processes [5], which are often off-line i.e. are applied while the heat pump is not in operation. Hence, finding the optimal moment and duration of the CIP activation represents a techno-economic optimization problem. This requires information about the extent to which a particular CIP is able to remove the deposited material as well as information about downtime and CIP implementation costs. A study [6] highlighted the challenge of predicting the thermal resistance attributed to fouling in the source stream heat exchanger of a large-scale wastewater heat pump. This study used data-driven regression models for the prediction of the thermal resistance caused by fouling. The data-driven regressions model were designed for the purpose of optimizing the cleaning procedures.

Physics-based simulation models are useful for the design of HPs and their components, mainly because they are applicable to a wide variety of boundary conditions and system configurations. However, the structure and parametrisation of such models is often fixed and does not adapt to time-dependent variations in the HPs they

represent. Such variations can be caused by faults or wear of components. In order to overcome this limitation, physics-based models may be complemented with numerical models derived from observations or data-driven models for the provision of services for HPs. Examples of such services include fault detection and diagnosis [7,8], operation monitoring [9], and defrosting optimization [10].

The provision of model-based services for HPs used for district heating supply still remains limited. A model-based monitoring and optimization framework has the potential to characterize the operation of a HP for a wide range of operational conditions and identify parameters that could enhance the HP performance. In particular, a thermodynamic model that could adapt its structure based real-time monitored data may enable the characterization of incipient faults affecting the HP, which has not been found in previous studies. The present study aimed at the increase of a HP performance through an improved CIP planning procedure characterized by an automatic model calibration framework. This framework was based on the integration of a physics-based model of the HP with data-driven optimization methods for model calibration.

2. Method

2.1. Case study heat pump

The operation of a two-stage ammonia HP with a design heating capacity of 2 MW was analysed in this study and its layout is shown in Figure 1. The HP is used for the provision of heat at around 68 °C to a local district heating network located in Copenhagen, Denmark. The heat source is industrial wastewater at around 23 °C originated from a biochemical plant. The desuperheater (DSH), condenser, receiver and subcooler (SC) are embedded in a single shell-and-plate heat exchanger unit. The evaporator is also a shell-and-plate heat exchanger and is in direct contact with the industrial wastewater. Each of the two stages in the HP includes a reciprocating compressor and an electronic expansion valve. An open intercooler connects both stages. The HP is controlled by means of the six controllers shown in Figure 1.

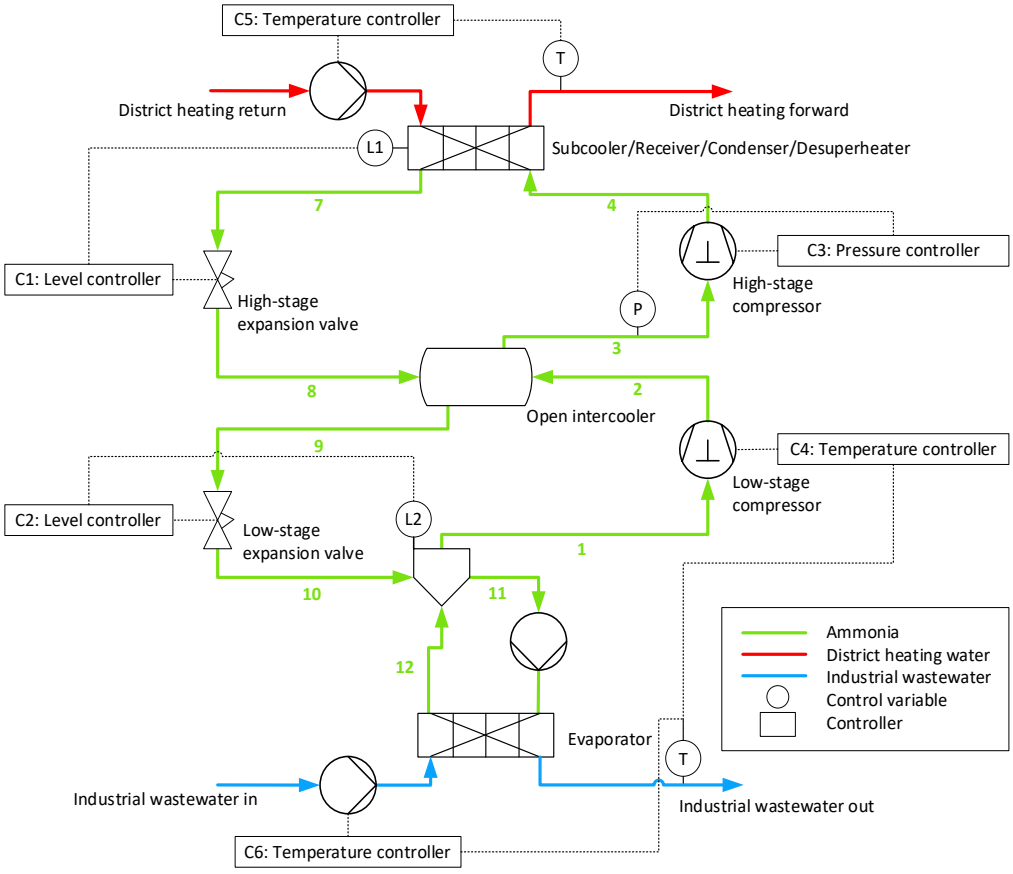

Figure 1: Layout of the two-stage ammonia HP used as case study

The direct contact between the industrial wastewater and the evaporator leads to the presence of fouling in this component, which is mitigated periodically by means of a CIP system. The CIP is used off-line and circulates a chemical solution for the removal of deposited inorganic and organic materials. These materials derived from the industrial processes performed in the biochemical plant. Currently, the frequency of the CIP implementation is defined heuristically by the HP operator based on observations on a decrease in the evaporation pressure (p_e).

2.2. Simulation model

The quasi-steady-state model of the HP shown in Figure 2 was developed in the programming language Python. The model took as input variables the source inlet and outlet temperatures ($T_{source,in}$ and $T_{source,out}$, respectively), the sink inlet temperature ($T_{sink,in}$), the set point for the intermediate pressure ($p_{m,sp}$) as well as the volume flow rates in the source and sink streams (V_{source} and V_{sink}, respectively). The refrigerant states and mass flow rates, heat output and power intake from the HP were determined through an iteration routine that solved the mass and energy balances of the components shown in Figure 2. This was done by the Newton-Raphson method with a tolerance of 10^{-9}, which identified the condensation and intermediate and pressures (p_c, and p_m, respectively), as well as the speed of the low-stage (LS) compressor (N_{LS}). Here, the residuals were the difference between the estimated and real area of the condenser ($A_{cond,calc}$ and A_{cond}), the estimated and real cooling capacity ($\dot{Q}_{source,calc}$ and $\dot{Q}_{source}$) and the LS mass flow rate estimated from the intercooler and the LS compressor models ($\dot{m}_{LS,IC}$ and $\dot{m}_{LS}$). An upper level iteration process enabled to identify the speed of the high-stage (HS) compressor that led to a minimum difference between the intermediate pressure (p_m) and its set point ($p_{m,sp}$). This was performed by the least-squares method with a tolerance of 10^{-5}. The Python module SciPy [11] was used for the implementation of the least-squares method. The refrigerant state calculations were performed with the Coolprop database [12]. The simulation of the quasi-steady-state model was done through multiprocessing, where 10 processing units were used in parallel within a single computer. Here, a simulated period was divided into 10 segments. All segments were simulated by different processors and the guess values were adjusted dynamically within each processor, namely the simulation results from a point in time *i* were used as guess values for the following point *i*+1. As a reference, the simulation of one hour of HP operation (i.e. 60 one-minute data points) required approximately 10 seconds when using multiprocessing an dynamically adjusted guess values, whereas it took around 113 seconds with a single processor and fixed guess values.

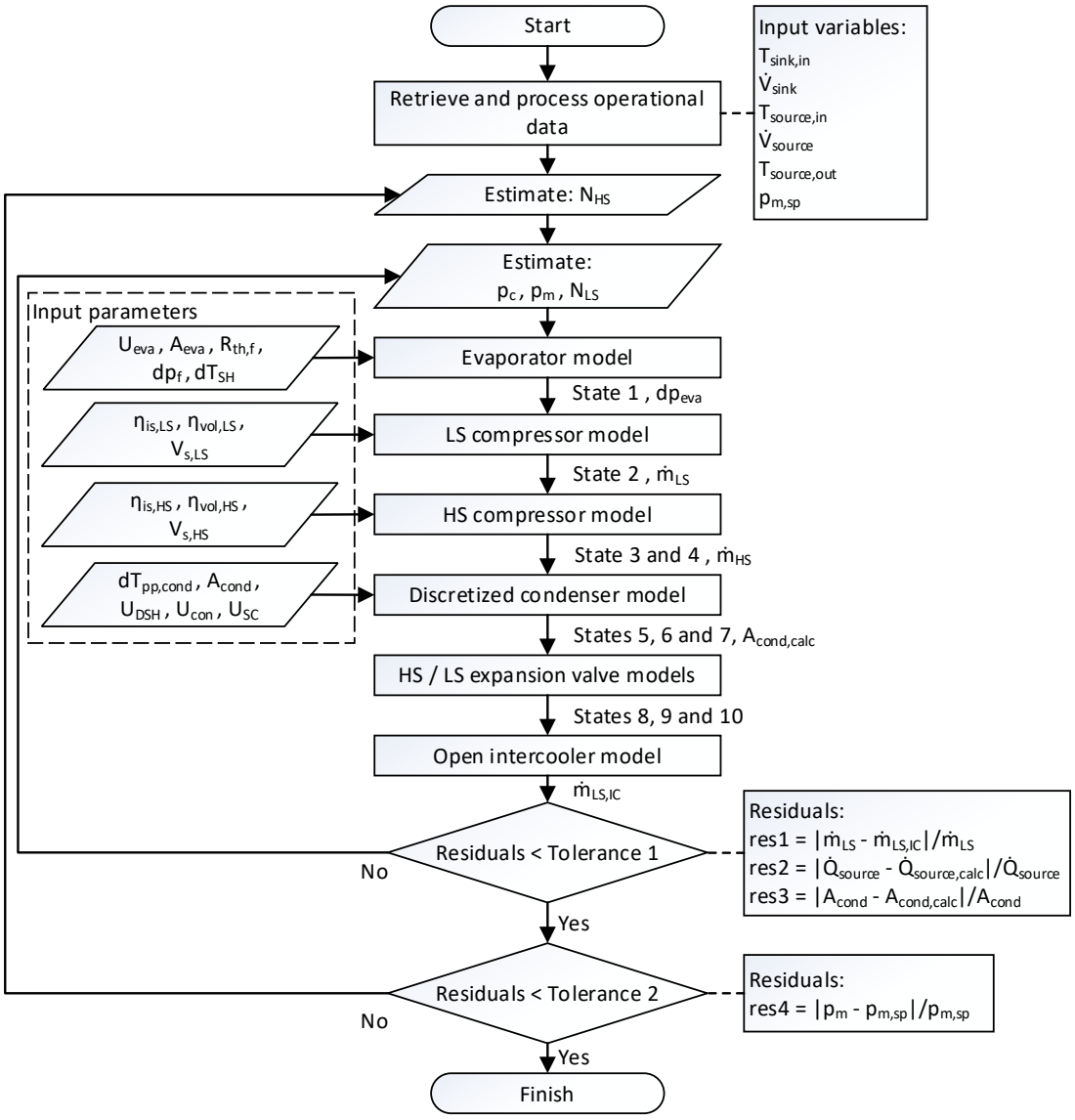

Figure 2: Flow diagram of the HP simulation model

The thermal resistance ($R_{th,f}$) and source stream pressure drop due to fouling (dp_f) were included as input parameters in the evaporator, which were later adjusted based on measurements through the calibration process described in Section 2.3.2. The $R_{th,f}$ was calculated based on Eq. (1), where the thermal resistance of the evaporator under clean conditions ($R_{th,eva,clean}$) was subtracted to the total thermal resistance ($R_{th,eva}$). Both thermal resistances were obtained as the inverse of the UA-value of the evaporator. Similarly, dp_f was determined based on Eq. (2) as the total pressure drop in the evaporator source side (dp_{eva}) minus the source stream pressure drop that was not caused by fouling ($dp_{eva,clean}$). The latter was determined by fitting a quadratic regression model between the volume flow rate in the source stream and the pressure drop in the evaporator right after the CIP was applied. Thereby, the influence of fouling was neglected in such a regression model.

$$R_{\mathrm{th,f}} = 1/\mathrm{UA}_{\mathrm{eva}} - 1/\mathrm{UA}_{\mathrm{eva,clean}} = R_{\mathrm{th,eva}} - R_{\mathrm{th,eva,clean}} \quad (1)$$

$$dp_{\mathrm{f}} = dp_{\mathrm{eva}} - dp_{\mathrm{eva,clean}} \quad (2)$$

The design parameters used in the model are shown in Table 1 and were provided by the HP manufacturer. , the pinch point temperature difference in the condenser ($dT_{pp,cond}$) was assumed to be 5 K. The isentropic and volumetric efficiencies of the compressors (η_{is} and η_{vol}, respectively) were calculated as a function of the compressor speed and the pressure ratios by using polynomials that were determined from information provided by the HP manufacturer.

Table 1: Input parameters used in the simulation model

Component	Input parameter	Symbol	Value	Unit
DSH	Overall heat transfer coefficient	U_{DSH}	230	W/m²K
	Heat transfer area	A_{DSH}	27.8	m²
Condenser	Overall heat transfer coefficient	U_{con}	1210	W/m²K
	Heat transfer area	A_{con}	100.6	m²
	Pinch point temperature difference	$dT_{pp,cond}$	5	K
SC	Overall heat transfer coefficient	U_{SC}	452	W/m²K
	Heat transfer area	A_{SC}	23.1	m²
Evaporator	Overall heat transfer coefficient	U_{eva}	3000	W/m²K
	Heat transfer area	A_{eva}	91.96	m²
	LS suction superheat	dT_{SH}	1	K
Low-stage compressor	Swept volume	$V_{s,LS}$	1018	m³/rev
	Speed	N_{LS}	700-1800	rpm
High-stage compressor	Swept volume	$V_{s,HS}$	532	m³/rev
	Speed	N_{LS}	700-1800	rpm

After the calculation of all the refrigerant states and water outlet temperatures, the model calculated the total heat output ($\dot{Q}_{sink}$) and the coefficient of performance (COP) of the HP based on Eq. (3) and Eq. (4). Here, it was assumed that the specific heat capacity ($c_{p,w}$) and density of water (ρ_w) were constant and equal to 4.18 kJ/(kg·K) and 998 kg/m³, respectively.

$$\dot{Q}_{\mathrm{sink}} = c_{\mathrm{p,w}} \cdot \rho_{\mathrm{w}} \cdot \dot{V}_{\mathrm{sink}} \cdot (T_{\mathrm{sink,out}} - T_{\mathrm{sink,in}}) \quad (3)$$

$$\mathrm{COP} = \dot{Q}_{\mathrm{sink}} / \dot{W}_{\mathrm{total}} \quad (4)$$

2.3. Monitoring framework

The framework proposed in this study consisted of the main components presented in Figure 3. Data from the HP controllers and sensors was accessed by the HP operator through a supervisory control and data acquisition (SCADA) system. The data from the SCADA system was made available to third-party actors through a cloud data management system, which enabled the storage and retrieval of operational data in real-time through an application programming interface (API). Such operational data from the HP was used to calibrate the simulation model described in Section 2.2.

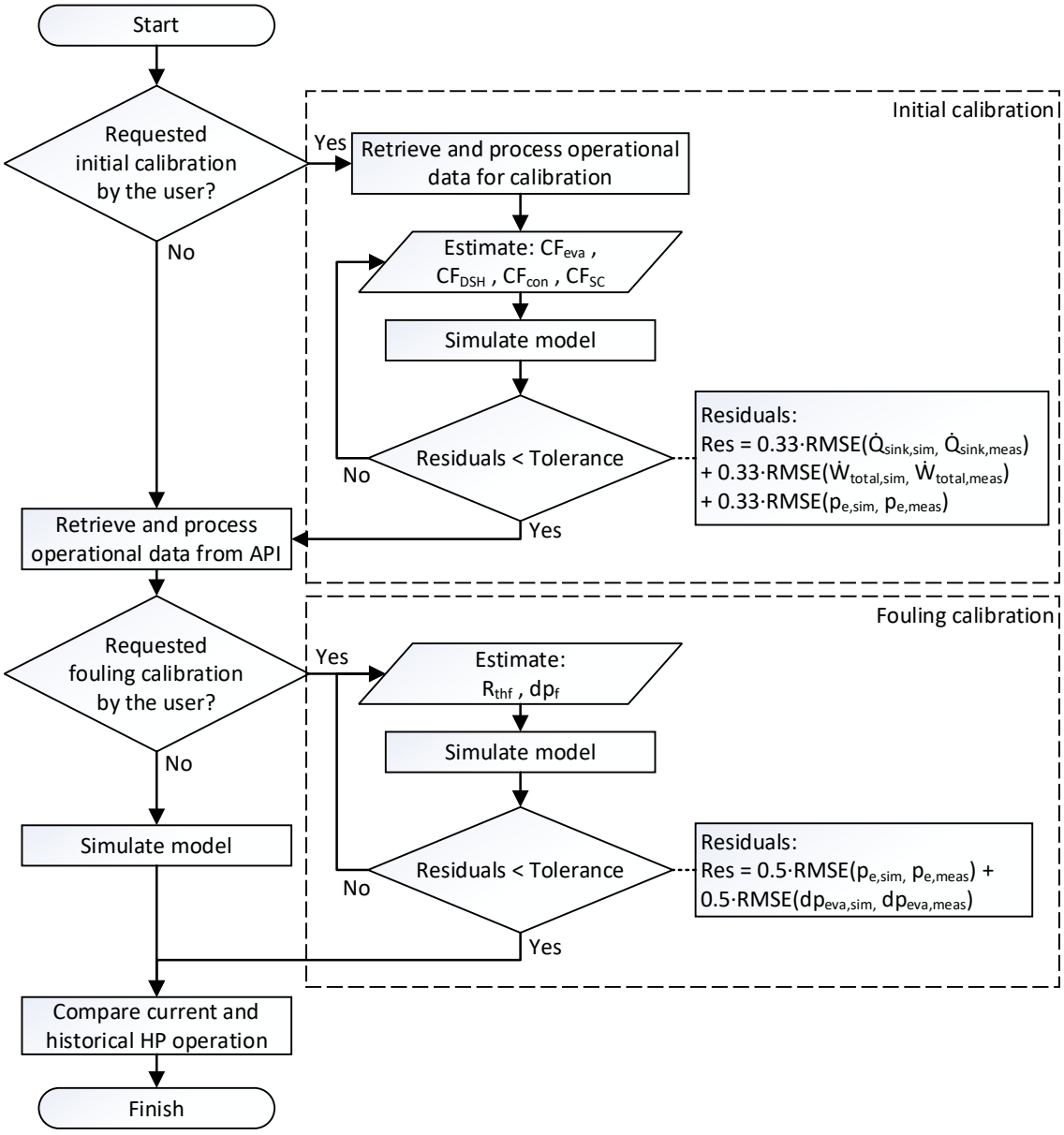

Figure 3: Flow diagram of the proposed monitoring framework

2.3.1. Data retrieval and processing

In the present study, the operational data from the case study HP was retrieved with a one-minute interval. The retrieval and processing of data was performed through Python. Here, the data processing consisted on the calculation of all the refrigerant states shown in Figure 1, for which the Coolprop database was used. This allowed to determine the COP and $\dot{Q}_{sink}$ from the HP by the use of Eq. (3) and Eq. (4). The total operational period included in the present study was 19 days. That period incorporated the activation of the existing CIP system for approximately 3 days, where the HP was not in operation.

2.3.2. Model calibration

Two calibration processes were applied in the proposed framework, namely the initial calibration and fouling calibration processes. The initial calibration was performed based on operational data obtained from the HP manufacturer. Here, the HP was tested under controlled conditions before it was delivered to the end user and thereby fouling was not present. The fouling calibration was based on operational data obtained from the SCADA system through the API. The specific period used for fouling calibration could be selected by the user and should represent periods where is required to analyse the effects of fouling on the HP. In this study, two different operational days were used for fouling calibration, one day before and one day after the CIP implementation. The initial and fouling calibration were comprised of an optimization process where the parameters shown in Table 1 were adjusted. This process minimized the normalized root mean square error (NRMSE) between measured and simulated outputs of interest or calibration targets over a period n, as shown in Eq. (5) and Eq. (6). The normalization was performed through the mean of the measured calibration target over a period n ($\overline{\mathrm{Target}}$). Multiple targets were used in a single optimization process, where each CT was

related to a specific weight (w). The targets for the initial calibration were $\dot{Q}_{sink}$, the total power intake from both compressors ($\dot{W}_{total}$) and the evaporation pressure (p_e), with weights equal to 33.3 % for each target. For the fouling calibration, the targets were the source pressure drop in the evaporator (dp_{eva}) and p_e, where each one had weights equal to 50 %. The weights were determined heuristically were all targets where assumed to have the same relevance.

Table 2: Parameters calibrated in the initial and fouling calibration processes.

Calibration process	Calibration parameter	Symbol	Variation range	Unit
Initial	Correction factor for DSH U-value	CF_{DSH}	0.3 to 1.7	[-]
	Correction factor for condenser U-value	CF_{con}	0.3 to 1.7	[-]
	Correction factor for SC U-value	CF_{SC}	0.3 to 1.7	[-]
	Correction factor for evaporator U-value	CF_{eva}	0.3 to 1.7	[-]
Fouling	Fouling-related evaporator thermal resistance	$R_{th,f}$	0 to 0.02	[K/kW]
	Fouling-related evaporator pressure drop	dp_f	0 to 0.5	[bar]

$$\min f(\text{Parameter}) = \sum_{i=1}^{n} w_i \cdot \text{NRMSE}_i \quad (5)$$

$$\text{NRMSE}_i = \overline{\text{Target}}_{\text{meas}}^{-1} \cdot \sqrt{n^{-1} \cdot \sum_{i=1}^{n} (\text{Target}_{\text{sim,i}}(\text{Parameter}) - \text{Target}_{\text{meas,i}})^2} \quad (6)$$

Time-invariant parameters were adjusted in the initial calibration, which corresponded to correction factors (CFs) for the overall heat transfer coefficients or U-values in the heat exchangers. In the fouling calibration, time-dependent parameters related to fouling were calibrated, namely $R_{th,f}$ and dp_f. The bounds for the calibrated parameters are shown in Table 2. The solution of Eq. (5) and Eq. (6) was obtained through the sequential least squares minimization algorithm available in the SciPy module in Python. The tolerances for both the initial calibration and the fouling calibration process were 10^{-5}.

3. Results

This section shows the results of the proposed monitoring framework, where the operation of the case study HP was monitored and analysed.

3.1. Simulated HP operation

Figure 4 and Figure 5 shows the time-series of the simulated and measured operational variables for a period of 19 days. The initial calibration reduced the difference between simulated and measured COP, $\dot{Q}_{sink}$ and p_e. This difference was reduced even further after the implementation of fouling calibration before the CIP. After the CIP was used, the fouling calibration process reduced the difference between the simulated and measured p_e, but not to the extent seen before the CIP. Moreover, the difference between simulated and measured $\dot{Q}_{sink}$ increased slightly after the second fouling calibration process. The results of the initial calibration process were probably not completely applicable for the period after the CIP, where the effects of fouling on the HP were low. Before the CIP, the mismatch between simulation and measured variables was likely to be lumped into the evaporator thermal resistance attributed to fouling. Regarding the pressure drop in the source stream, only the fouling calibration processes before the CIP led to a higher correspondence between the simulated and measured dp_{source} compared to the period before calibration. This indicated that the CIP did not have a significant effect on the removal of the effect of fouling on the source stream pressure drop.

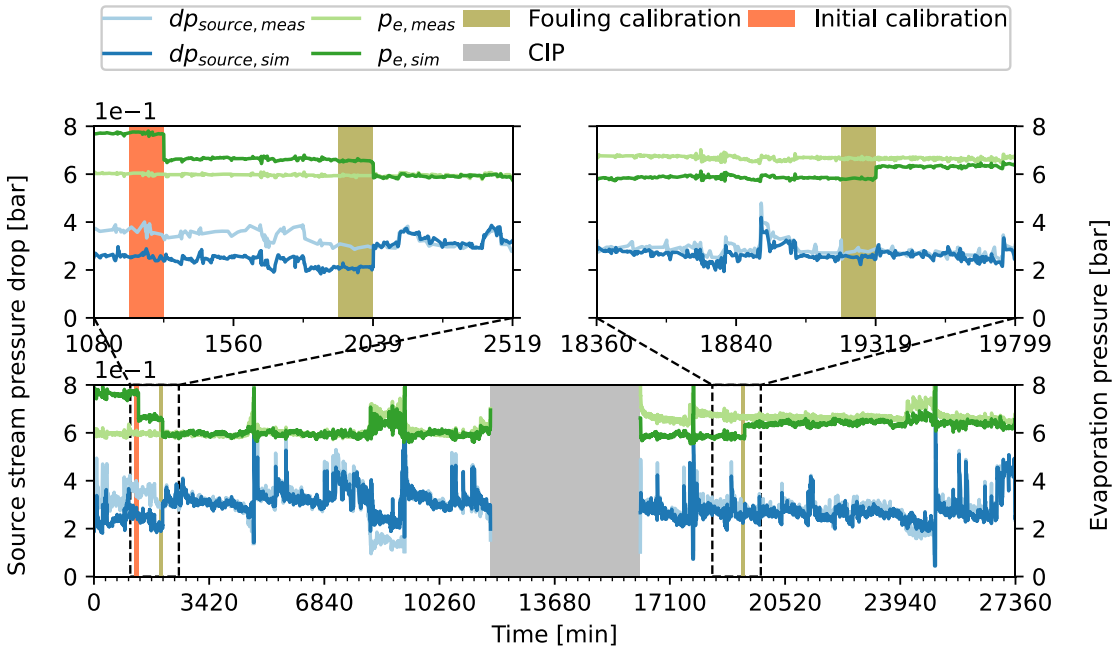

Figure 4: Time-series of the measured and simulated source stream pressure drop as well as evaporation pressure.

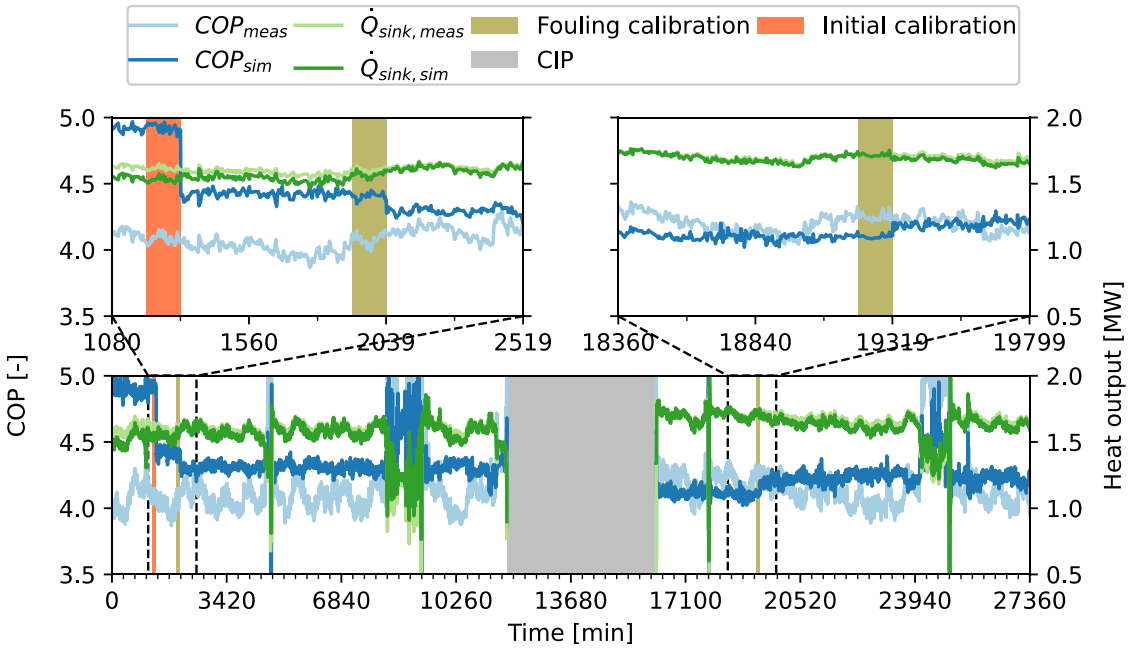

Figure 5: Time-series of the measured and simulated COP as well as heat output.

3.2. Residual analysis

The residuals shown in Figure 6 represent measured operational variables minus their respective simulated values. These residuals were not those presented in Section 2, as they were not normalized and were not used in the iteration processes for simulation (Figure 2) or calibration (Figure 3). The results from Figure 6 indicated that the fouling calibration implemented before the CIP period reduced the absolute value of the residuals related to dp_{eva}, p_e, $\dot{Q}_{sink}$ and $\dot{W}_{total}$. This was also valid for the fouling calibration applied after the CIP, except for dp_{eva}, which did not change significantly as a result of such a calibration. This was possibly an indication the CIP did not have a significant effect over the pressure drop caused by fouling. The initial calibration was observed to have a larger effect on the reduction of the discrepancies between measured and simulated values of COP and $\dot{W}_{total}$. This was expected given that the correction factors for the UA-values were calibrated in the initial calibration process. This led to an improved estimation of the pressure levels in the HP and thereby the total power intake from the compressors. The residuals shown in Figure 6 also showed that the dynamic behaviour of the case study HP was not completely represented by the simulation model. This was observed by the biased patterns in the residuals from the p_e, $\dot{Q}_{sink}$, COP and $\dot{W}_{total}$, which can be seen in Figure 6 at around 8000 min and 24000 min of operation.

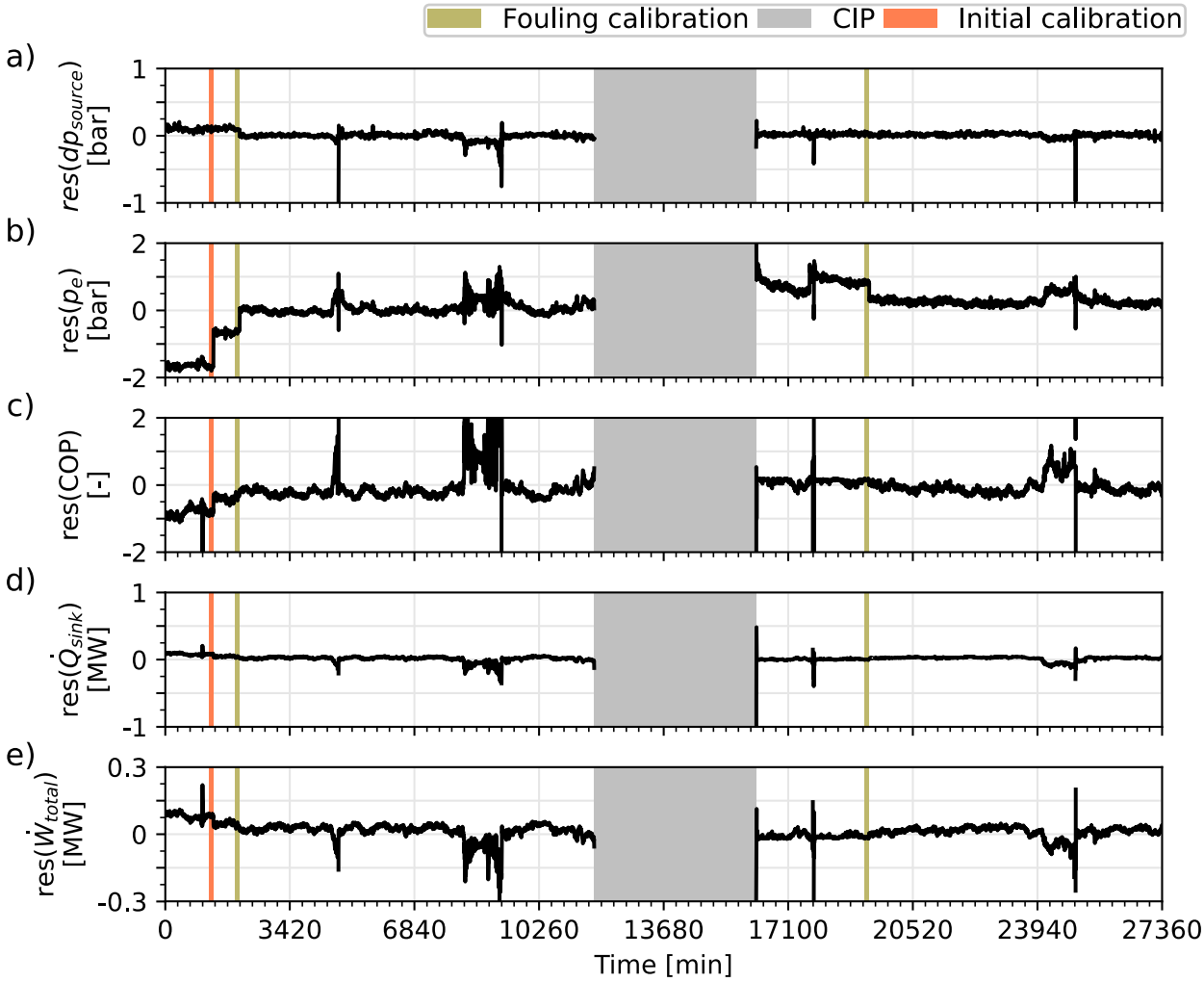

Figure 6: Residuals between simulated and measured operational variables of the HP.

3.3. Calibration results

Table 3 shows the parameters obtained from the calibration processes illustrated in Figures 4, 5 and 6. The calibration results of the correction factors showed that the U-values of the condenser, SC and evaporator presented in Table 1 were over-estimated, whereas they were underestimated for the DSH. This may also relate to a disagreement between the design and actual flow velocities as well as the temperature difference at the pinch point, which was assumed to be 5 K (see Table 1). The correction factors for the other heat exchangers were not significantly adjusted. The results showed that the $R_{th,f}$ and dp_f were reduced significantly as a result of the CIP (around 41 % and 100 %, respectively). However, the value of dp_f represented only around 15 % of the total source stream pressure drop shown in Figure 4. This was in agreement with the limited effect that the fouling calibration had on the calibration of the total source stream pressure drop, observed from the residual analysis shown in Figure 6.

Table 3: Parameters obtained from the calibration processes

Calibration process	Calibration parameter	Symbol	Result value	Unit
Initial	Correction factor for DSH U-value	CF_{DSH}	1.12	[-]
	Correction factor for condenser U-value	CF_{con}	0.96	[-]
	Correction factor for SC U-value	CF_{SC}	0.36	[-]
	Correction factor for evaporator U-value	CF_{eva}	0.47	[-]
Fouling (before CIP)	Fouling-related evaporator thermal resistance	$R_{th,f}$	$2.2 \cdot 10^{-3}$	[K/kW]
	Fouling-related evaporator pressure drop	dp_f	0.09	[bar]
Fouling (after CIP)	Fouling-related evaporator thermal resistance	$R_{th,f}$	0	[K/kW]
	Fouling-related evaporator pressure drop	dp_f	0	[bar]

4. Discussion

The automatic calibration method from the proposed framework reduced the discrepancy between the simulated and measured evaporation pressure, COP, heat output and source pressure drop (see Figures 4, 5 and 6). The results also indicated that the influence of fouling over the source stream pressure drop was significantly lower than the effect over the evaporator thermal resistance and that the CIP implementation led to a larger reduction of the latter than the former.

The relatively short simulation time used by the model applied in this study (around 10 seconds for the simulation of one hour) suggested its applicability for operation and fouling monitoring in a large-scale heat pump on a real-time basis. However, this would require the periodic verification of the validity of multiple factors that affect the simulation and calibration processes. These factors include the tolerances defined for the iteration residuals, the initial guess values and variation ranges for the calibration parameters, the optimization algorithm for NRMSE minimization, the selected calibration targets as well as the size and variability of the time-series data used for calibration. Those factors should be such that the best compromise is found between the required calculation time for calibration and the difference between simulation and measured data.

The results obtained from the proposed framework did not provide an estimation of the amount of deposited material on the heat transfer surface of the evaporator. This can be estimated with dedicated sensing devices for fouling examination such as ultrasonic probes [13] or infrared thermography equipment [14], which are unlikely to be available in large-scale HPs. In this context, the proposed model-based monitoring framework leverages existing sensing devices such as pressure and temperature sensors in the evaporator to estimate the effects of fouling. However, the results from the proposed monitoring framework were not contrasted with measurements from dedicated sensing devices for fouling characterization. This represents an opportunity for future studies.

The disagreements between the outputs of the model and the measured operational variables were probably lumped into the parameters adjusted in the calibration processes. For example, the difference between the heat transfer area of the heat exchangers in the model and in the case study HP was possibly included in the correction factors for the U-values in the model. Moreover, the assumption that those correction factors were calibrated based on an operational period when the evaporator was not affected by fouling due to the CIP usage, was not necessarily correct. Ideally, the initial calibration process should be based on an operational period right after fouling has been completely removed from the evaporator. In the present study, the correction factors obtained from the initial model calibration were also likely to include discrepancies between the model and the HP due to fouling. However, the evaporator of the case study HP could not be dismantled for cleaning, which prevented the complete removal of fouling.

The model used in this study led to a suboptimal representation of the dynamic off-design operation of the HP, which was indicated by the biased patterns observed in the simulation residuals (see Figure 6). It would require the use of a dynamic model to capture most of the dynamics present in a HP. The development of a dynamic simulation model may require information about the volumes and materials of the vessels, control-related parameters, refrigerant charge estimations as well as heat transfer and pressure drop correlations. The development of a quasi-steady-state model does not require such a comprehensive description about the design of a HP. Moreover, the present study focused on fouling monitoring, which often affects the operation of a HP at a slower rate than abrupt faults like the presence of condensed refrigerant in the suction line of a compressor.

The pumps in the secondary streams of the HP were not included in the simulation model. It is expected that the simulation residuals related to the estimation of power intake of such pumps will be reduced after the proposed fouling calibration framework is implemented. Modelling of the pumps could also indicate how the source side pressure drop affects the mass flow rate in the source stream. However, this adds complexity to the model, which may increase the time required for each simulation. Another limitation of the proposed framework was that it only enabled the analysis of historical data from the HP. The authors expect to complement the present version of the framework with forecasting methods that will enable the estimation of the future operation of a HP and the optimization of the time of CIP.

5. Conclusion

A quasi-steady-state simulation model of a heat pump used for district heating supply was calibrated based on operational data obtained from a cloud-based data management system. This framework enabled the estimation of the performance and the effects of fouling on the heat pump, even when the model did not represent accurately the dynamics of such a system. Particularly, the re-calibration of the model based on time-dependant parameters related to fouling allowed to obtain simulation results that were in agreement with measurements over a period of nearly three weeks. This allowed to assess the degree to which a CIP implementation reduced the evaporator thermal resistance and source stream pressure drop caused by fouling. The proposed framework could be used for real-time monitoring of large-scale heat pumps, where the relatively short simulation time achieved, automatic model calibration and leverage of existing sensing devices could be beneficial.

Acknowledgments

This work was funded by EUDP (Energy Technology Development and Demonstration) under the project “Digital twins for large-scale heat pump and refrigeration systems” (project number: 64019-0570).

Nomenclature

Abbreviations

API	application programming interface
CF	correction factor
CIP	cleaning-in-place
HP	heat pump
HS	high-stage
LS	low-stage
(N)RMSE	(normalized) root mean square error
res	residual
SCADA	supervisory control and data acquisition

Letter symbols

A	heat transfer area, m^2
dp	pressure difference, bar
dT	temperature difference, K
$\dot{m}$	mass flow rate, kg/s
N	compressor speed, rpm
$\dot{Q}$	heat flow rate, kW
p	pressure, bar
R	thermal resistance, K/kW
T	temperature, ˚C
U	overall heat transfer coefficient, kW/Km^2
V	volume, m^3
$\dot{V}$	volume flow rate, m^3/s
w	weight, -
$\dot{W}$	power, kW

Greek symbols

ρ	density, kg/m^3
η	efficiency, -

Subscripts and superscripts

c	condensation
calc	calculated
clean	clean
con	condenser
DSH	desuperheater
meas	measurement
e	evaporation
eva	evaporator
f	fouling
h	heat output
in	inlet
is	isentropic
m	intermediate
out	outlet
pp	pinch-point
s	swept
sc	sub-cooler
sim	simulation
sink	sink stream
sp	set point
source	source stream
total	total
th	thermal
vol	volumetric
w	water

References

[1] IEA. The future of heat pumps [Internet]. Paris, France; 2022. Available from: https://www.iea.org/reports/the-future-of-heat-pumps

[2] Aguilera JJ, Meesenburg W, Ommen T, Poulsen JL, Kramer KR, Markussen WB, et al. Operational challenges in large-scale ammonia heat pump systems. In: Proceedings of ECOS 2021: 34th International Conference on Efficiency, Cost, Optimization, Simulation and Environmental Impact of Energy Systems. Taormina, Italy; 2021. p. 12.

[3] Aguilera JJ, Meesenburg W, Ommen T, Markussen WB, Poulsen JL, Zühlsdorf B, et al. A review of common faults in large-scale heat pumps. Renew Sustain Energy Rev [Internet]. 2022 Oct 1 [cited 2022 Aug 18];168:112826. Available from: https://10.0.3.248/J.RSER.2022.112826

[4] Bott TR. Fouling of heat exchangers [Internet]. Amsterdam, The Netherlands: Elsevier Science B.V.; 1995. 524 p. Available from: https://doi.org/10.1016/B978-0-444-82186-7.X5000-3

[5] Pogiatzis T, Ishiyama EM, Paterson WR, Vassiliadis VS, Wilson DI. Identifying optimal cleaning cycles for heat exchangers subject to fouling and ageing. Appl Energy [Internet]. 2012 Jan 1 [cited 2023 Mar 24];89(1):60–6. Available from: https://doi.org/10.1016/j.apenergy.2011.01.063

[6] Meesenburg W, Aguilera JJ, Kofler R, Markussen WB, Elmegaard B. Prediction of fouling in sewage water heat pump for predictive maintenance. In: Proceedings of ECOS 2022: 35th International Conference on Efficiency, Cost, Optimization, Simulation and Environmental Impact of Energy Systems. Copenhagen, Denmark; 2022. p. 12.

[7] Aguilera JJ, Andreas S, Meesenburg W, Ommen T, Markussen WB, Zühlsdorf B, et al. Integration of dynamic model and classification methods for fault detection and diagnosis in a chiller. In: 15th IIR-Gustav Lorentzen conference on Natural Refrigerants [Internet]. Trondheim, Norway; 2022. p. 14. Available from: https://10.0.72.30/iir.gl2022.96

[8] Cui J, Wang S. A model-based online fault detection and diagnosis strategy for centrifugal chiller systems. Int J Therm Sci [Internet]. 2005 Oct 1 [cited 2021 Jun 14];44(10):986–99. Available from: https://10.0.3.248/j.ijthermalsci.2005.03.004

[9] Vering C, Borges S, Coakley D, Krützfeldt H, Mehrfeld P, Müller D. Digital twin design with on-line calibration for HVAC systems in buildings. In: Building Simulation Conference 2021: 17th Conference of IBPSA. Bruge, Belgium; 2021.

[10] Jonas Klingebiel, Göbel S, Venzik V, Mueller D. Evaluation of machine learning methods for optimizing the defrosting process of air-to-water heat pumps. In: 15th IIR-Gustav Lorentzen conference on Natural Refrigerants [Internet]. Trondheim, Norway; 2022. p. 12. Available from: https://10.0.72.30/iir.gl2022.0117

[11] Virtanen P, Gommers R, Oliphant TE, Haberland M, Reddy T, Cournapeau D, et al. SciPy 1.8.0: Fundamental algorithms for scientific computing in Python. Nat Methods [Internet]. 2020;17(3):261–72. Available from: https://doi.org/10.1038/s41592-019-0686-2

[12] Bell IH, Wronski J, Quoilin S, Lemort V. Pure and Pseudo-pure Fluid Thermophysical Property Evaluation and the Open-Source Thermophysical Property Library CoolProp. 2014; Available from: https://10.0.3.253/ie4033999

[13] Bott TR. Biofouling Control with Ultrasound. Heat Transf Eng [Internet]. 2010;21(3):43–9. Available from: https://www.tandfonline.com/action/journalInformation?journalCode=uhte20

[14] Berce J, Zupančič M, Može M, Golobič I. Infrared thermography observations of crystallization fouling in a plate heat exchanger. Appl Therm Eng [Internet]. 2023 Apr 1 [cited 2023 Mar 24];224:120116. Available from: https:///J.APPLTHERMALENG.2023.120116

Robotic system for monitoring pipe wall thickness reduction in nuclear reactors utilizing Digital Twin and Industry 4.0 technologies

Rogério Adas Pereira Vitalli[a] and João Manoel Losada Moreira[b]

Programa de Pós-graduação em Energia
Universidade Federal do ABC, Santo André, Brazil,
[a] rogerio.vitalli@ufabc.edu.br, CA
[b] joao.moreira@ufabc.edu.br

Abstract:

Large thermal electric generation systems based on the Rankine cycle require monitoring the reduction of pipe wall thickness caused by vapor flow due to aging processes such as erosion and accelerated corrosion processes. The inspection difficulties are related to hostile environment (50 ºC and 100 % relative humidity), and spaces with complicated geometry such as pipeline curves and their support structures. This work presents a monitoring program which integrates wall thickness inspections carried out with a robotic system and Industry 4.0 technology to handle collected data and to disseminate information throughout the organization. The robotic system is developed utilizing the digital twin technology, a very realistic virtual modeling scheme which allows interaction with the real-world environment. They include equipment and all the steps to carry out the inspection process. The pipe wall thickness monitoring system is to be utilized in Angra 1 (Brazil) nuclear power plant.

Keywords:

robotics; pipe wall thickness; nuclear power; Digital Twin; Industry 4.0

1. Introduction

In 2025, the Angra 1 nuclear power plant, located in Rio Janeiro state in Brazil, completes 40 years of operation and the owner Eletronuclear requested the Brazilian nuclear regulatory body to extend its operational life and renew the operating license for another 20 years. For life extension, it is necessary to carry out a wide range of plant aging management activities which may end up requiring to replace vessels and pipes which operate under high pressure and do not meet the regulatory agency's criteria to remain in service [1-3]. Large nuclear power plants have hundreds of meters of pipes under this situation and their wall inspection is among the ones more time-consuming procedures, around 300 hours. Erosion and flow accelerated corrosion processes induced by fluid flow are monitored through ultrasound inspections that seek to determine the reduction in pipe wall thickness [4-6].

This work presents the project of pipe inspection automation using a robot integrated with the Industry 4.0 technology through wall thickness measurements using the ultrasound technique. The pipes belong to the secondary system from Angra 1 nuclear power plant, which include those under high pressure connecting the steam generators, turbines, condensers and all associated instrumentation and ancillary systems. The inspection environment is hot and humid (50 degrees Celsius and 100% relative humidity). The field space has complicated geometry and access to inspection locations due to support structures. The pipes have different diameters varying from 50 cm to 65 cm some are straight, and others curved and positioned in horizontal, vertical, or inclined directions. During a shutdown, more than 50,000 measurement points are performed [7,8]

Robotic systems are used in different field applications and environments such as manufacturing activities but also in aerial inspection of structures [9], submarine inspections of structures [10,11] and even rubber tapping in plantations [7]. What they all have in common is that they feature a vehicle-handler system for inspection or other necessary on-site activity. The remotely operated vehicle contains a manipulator support platform, a robotic arm containing in its end effector with specific characteristics to carry out the activity, i.e. sensors to

carry out the measure of interest [12] or the production activity as rubber tapping [13]. To enable the inspection, the vehicle is moved to the designated locations for carrying out the activity. To control the trajectory of the robotic arm, the end-effector normally has sensors for vision and contact with surfaces [14-16].

The digital twin [6] is a project realization concept in which the environment, process or a single physical object is reproduced first in the virtual world and then in the real world. In the case of robotics, its function is to map the main characteristics of the object or physical process previously via virtual simulation and subsequent real implementation whether they are system maintenance [17,18], design and manufacture of products [19–21] or processes [22].

2. Robotic system requirements

It is desirable that the system has a communication interface with intelligence to process the data in the manner established by Eletronuclear and that allows identifying possible locations with thicknesses closer to acceptable limits or simply failures in the process of measuring the thickness of the pipe. In these cases, the robotic system can perform a sweep with more qualified inspection or repeat measurements.

Figure 1 shows the inspection environment in the turbine building of the nuclear power plant Angra 1. Figure 1a shows the current situation of manual thickness measurement. It is necessary to place scaffolding at the various measurement locations so that the technician has access to the measurement locations. It is seen that the environment has a flat floor that allows the movement of a vehicle. Figures 1b and 1c show pipe segments with indications of the places where thickness measurements will be taken and also the difficulty of access due to interference from other equipment and pipes in the vicinity.

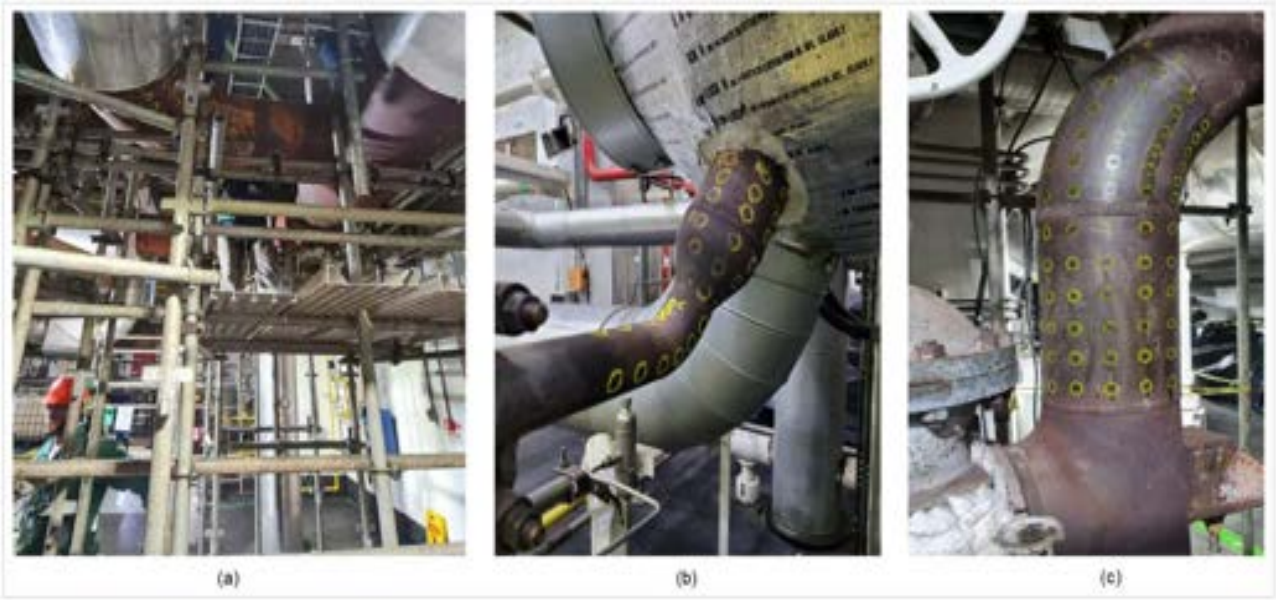

Figure 1. Environment in which measurements of the wall thickness of the pipes in the turbine building are carried out. (a) Flat floor site with scaffolding to allow access to pipes for manual measurements. (b) Pipe segment of different diameters inclined and difficult to access. (c) Piping in vertical position. The yellow circles indicate the locations where thickness measurements are performed using ultrasound.

The industrial manipulator (robotic arm) must be able to access the external wall of the pipe and position the sensor installed in the end-effector in an appropriate way to carry out the measurements. Other sensors present in the end-effector are the contact and distance sensors between the surface that act as the “vision” to avoid collisions with the pipe and the correct positioning of the ultrasound sensor for measurements. A human operator is also foreseen to provide cognitive assistance for vehicle movement and inspection actions. The thickness measurement procedure is as follows: the UROV is moved and parked at certain locations. In

these places, the robotic arm moves and performs inspection on the surface and all thickness measurement procedures.

The vehicle requirements are reduced size to allow access to the different measurement locations and have mechanical strength and space to accommodate the systems of the other two units. Piping access is a great challenge because there are positions where some “elbows” are close to walls and hostile places, making it difficult to position the robotic equipment for measurements in curved surfaces.

3. Robotic system for measuring pipe wall thickness

The Robotic System for Measuring the Wall Thickness of the Secondary Piping of the Angra 1 Nuclear Power Plant (SRME) is composed of 3 units. The first unit, called the Remotely Operated Vehicle Unit (UROV), is a vehicle that can be operated remotely to allow displacement of the SRME to tubes of different diameters and allow thickness measurements. The second unit, called Thickness Measurement Robotic Cell Unit (UMRC), is a robotic work cell indexed in the UROV, equipped with a robotic arm that performs the movements and inspection actions and that has sensors installed that allow the movement of the measurement points and the external measurement of the pipe wall thickness. The third unit, called the Communication, Power Supply and Ancillary Services Unit (UCPA), contains all other SRME systems such as power supply cables, data transmission cables, real-time information, computers and ancillary equipment. The study on automatic thickness measurement uses the GP-7 robot from the manufacturer Yaskawa-Motoman [23]. This robot weighs 34 kg, has a reach of 927 mm horizontally and 1693 mm vertically and has a payload capacity of up to 7 kg. With these attributes, this robot can be used in the field. The robot programming is done using the digital twin technique using the Process Simulate software version 15.1.2.

The Remotely Operated Vehicle Unit (UROV), shown in Figure 2, is designed to access as many pipe runs as possible. The UROV is moved by the human operator to the closest possible location to the measurement point and makes it possible to move the end-effector via remote actuation for displacements in the x-y-z axes for the best positioning of it for carrying out thickness measurements.

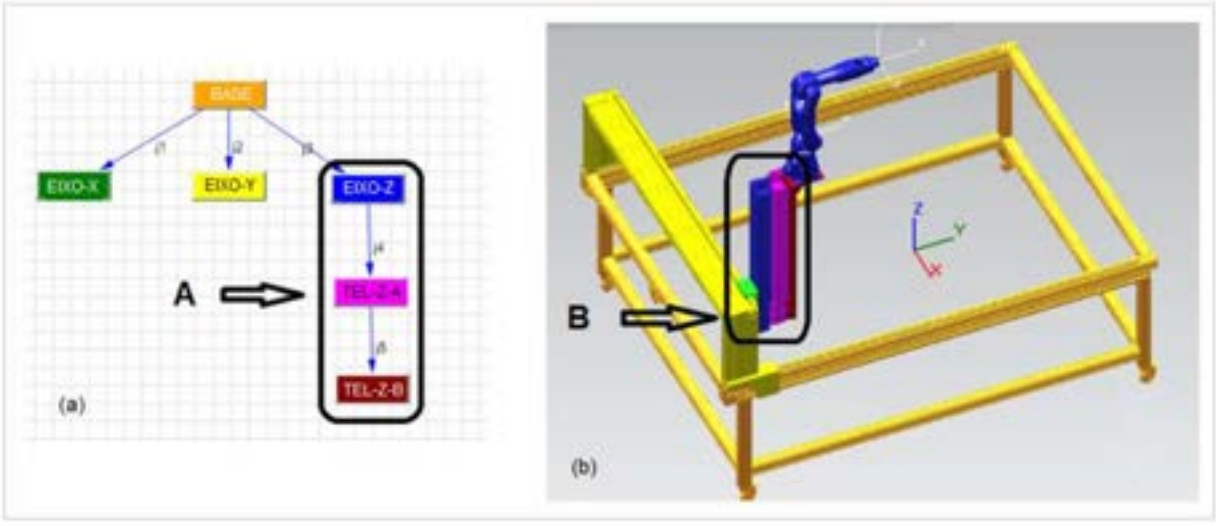

Figure 2. Unit Remotely Operated Vehicle (UROV) with caster system: (a) The X-AXIS describes the horizontal translation movement of the mechanism in the X direction, the Y-AXIS in the Y direction and the Z-AXIS describes the vertical translation movement of the mechanism in the Z direction. The TEL-Z-A-AXIS describes the vertical translation movement of the mechanism in the Z direction with retractable or telescopic articulation and the TEL-Z-B AXIS describes the vertical translation movement of the mechanism in the Z direction with retractable or telescopic articulation telescopic after displacement of the AXIS-TEL-Z-A. (b) In this figure, the yellow color describes the horizontal translation movement of the mechanism in the Y direction, the green color describes the horizontal translation movement of the mechanism in the X direction, and the blue color describes the horizontal translation movement of the mechanism in the X direction. Y direction. In

figures “A” Mathematical modeling in x-y-z by means of horizontal movements, x and y, and telescopic elevation in z with two additional prismatic movements and “B” the corresponding movement of the end-effector on the robotic arm with five degrees of freedom of the measuring robotic cell with teleoperation system.

Figure 3 shows the URMC Robotic Thickness Measuring Cell Unit with a robotic arm having six degrees of freedom to reach a 65 cm diameter pipe and the end-effector. After marking with points offset by 30 degrees, thickness is measured on a 144-point grid. A reservoir installed at the base of the robotic arm with coupling liquid that varies according to the type of material, but is essential to perform the thickness measurement.

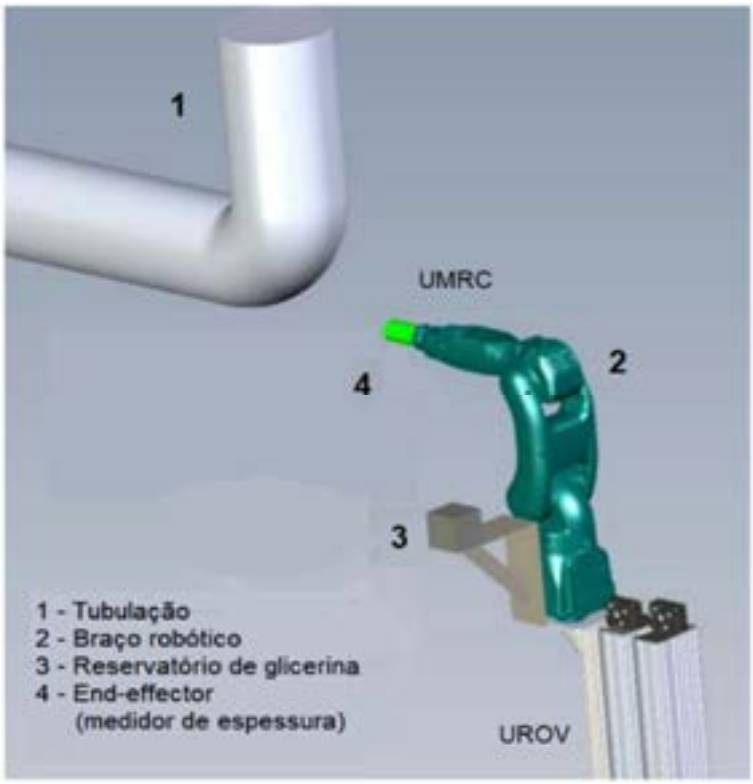

Figure 3. Thickness Measurement Unit (URMC): 1) Piping is where the process of measuring thickness using the ultrasound technique is concentrated and requires the preparation of the surface of the external piping to carry out the measurement, instrumentation, specification and calibration of the ultrasound measurement system point transducer type and surface scanning type ultrasound. 2) Robotic arm and end-effector. 3) Reservoir with coupling liquid. 4) End-effector (thickness gauge) can accurately and quickly measure the thickness of the walls of the pipes at the determined points.

The design challenge consists of integrating thickness measurement, analysis, treatment and storage of information in a safe and reliable way. The industrial robot needs to receive measurements from the electronic transducers of the system that performs the measurement and store them in variables. These variables need to be defined and the technologies that enable Industry 4.0 follow data security protocols and interface communication that can be customized according to the needs of the company, in this case, Eletronuclear.

Robotic manipulators have positioning problems, speeds and forces applied in any type of movement. The definition of the trajectory of the GP-07 robot in three-dimensional space, called direct kinematics, is done with the SIMULATE software. Figure 4 shows the relationship of programming via Digital Twin with the SIMULATE software and the movement of the robotic arm that determines the location of the end-effector. This software uses the Denavit-Hartenberg notation to assign to the robotic system an orthonormal coordinate system for each link of the kinematic chain [4,5,24].

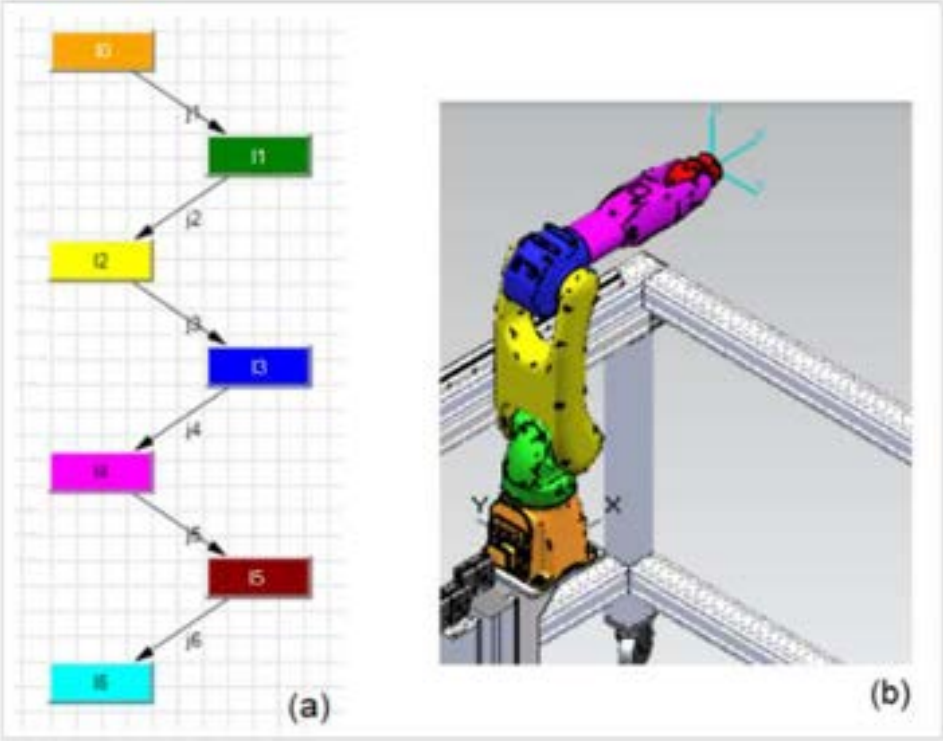

Figure 4. (a), Symbols I0, I1, I2, I3, I4, I5 and I6 in a chain representing the homogeneous transformation matrices according to the Denavit-Hartenberg notation from the base of the robot to axis six, respectively. The symbols J1, J2, J3, J4, J5 and J5 represent the links between the rotation joints of the six degrees of freedom of the robot, respectively. (b) In this figure, the colors of each physical joint of the robot correspond to the same colors as the matrices in figure (a).

The development of the kinematics is done after obtaining the Denavit-Hartenberg parameters of the GP-07 robot [5]. This robot has a reach of 927 mm horizontally and 1693 mm vertically with a payload capacity of up to 7 kg. Once this coordinate system for adjacent links is established, it can be represented by a homogeneous coordinate transformation matrix. With this information, the kinematics of the robotic movement is built, precisely defining the position and orientation of the end-effector next to the surface for carrying out the measurement.

The method used to obtain the results of direct kinematics in virtual space (Digital Twin) showed good precision performing joint, linear, circular and spline interpolated trajectories.

4. Conclusions

To ensure that the prototype results are suitable for the effective use of SRME in Angra 1, all prototype design requirements must take into account the environment where thickness measurements take place in the Turbine Building. This article presents a work stage that considered important aspects of the Angra 1 power plant project. It was possible to model the virtual commissioning activities, transfer all information and project data automatically to the physical project of the SRME. Access to the measurement sites occurs through two movements: the UROV and the UMRC. The UROV is moved by the robotist to the closest possible location to the point of movement. From this point, via remote actuation, the robotist can move the support base of the robotic arm in x-y-z by means of horizontal movements, x and y, and elevation, z.

The second movement is provided by the UMRC robotic arm. This allows greater access to the pipes. The movement of the support base of the robotic arm has a mathematical model with a telescopic concept of the z axis. It is expected a significant productivity gain in this process, as the entire programming of the physical

robot, an important part of the project to carry out the process of measuring the thickness of the pipes, is transferred directly from the virtual project (digital twin) to the real robot.

Acknowledgments

The authors are grateful for the financial and technical support from Eletrobras Termonuclear SA – Eletronuclear, Amazônia Azul Tecnologias de Defesa SA and Fundação Parque de Alta Tecnologia da Região de Iperó – Fundação Pátria.

References

[1] Tugal, H., Cetin K., Petillot Y., Dunnigan M., Erden M. S., Contact-based object inspection with mobile manipulators at near-optimal base locations. Robotics and Autonomous Systems 2023; 161:104345.

[2] Zhou H., Zhang S., Zhang J., Zhang C., Wang S., Zhai Y., Li W., Design, development, and field evaluation of a rubber tapping robot. Journal of Field Robotics 2021; 39:28–54.

[3] Nekoo S. R., Acosta J. A., Heredia G., Ollero A., A benchmark mechatronics platform to assess the inspection around pipes with variable pitch quadrotor for industrial sites. Mechatronics 2021; 79: 102641.

[4] Denavit J., Hartenberg R. S., A Kinematic Notation for Lower-Pair Mechanisms Based on Matrices. Journal of Applied Mechanics 1955; 215–221.

[5] Craig J., Introduction to Robotics: Mechanics and Control. 3rd ed. Cambridge, USA: Pearson; 2004.

[6] Glaessgen E., Stargel D., The Digital Twin Paradigm for Future NASA and U.S. Air Force Vehicles. In Proceedings of the 53rd AIAA/ASME/ASCE/AHS/ASC Structures, Structural Dynamics and Materials Conference, 20th AIAA/ASME/AHS Adaptive Structures Conference, 14th AIAA; 2012 April 23–26, American Institute of Aeronautics and Astronautics, Honolulu, Hawaii, HI, USA.

[7] Zhang H., Ma L., Sun J., Lin H., Thürer M., Digital Twin in Services and Industrial Product Service Systems: Review and Analysis. Procedia CIRP 2019, 83, 57–60

[8] Muszynska M., Szybicki D., Gierlak P., Kurc K., Burghardt A., Uliasz M., Application of Virtual Reality in the Training of Operators and Servicing of Robotic Stations. In Collaborative Networks and Digital Transformation; Camarinha-Matos, L.M., Afsarmanesh, H., Antonelli, D., Eds.; Springer International Publishing: Cham, Germany, 2019; Volume 568, 594–603.

[9] Tao F., Cheng J., Qi Q., Zhang M., Zhang H., Sui F., Digital twin-driven product design, manufacturing and service with big data. Int. J. Adv. Manuf. Technol. 2018, 94, 3563–3576.

[10] Lu Y., Liu C., Wang K. I. K., Huang, H., Xu X., Digital Twin-driven smart manufacturing: Connotation, reference model, applications and research issues. Robot. Comput. Integr. Manuf. 2020, 61, 101837.

[11] Liu J., Du X., Zhou H., Liu X., Ei Li L., Feng F., A digital twin-based approach for dynamic clamping and positioning of the flexible tooling system. Procedia CIRP 2019, 80, 746–749.

[12] Oleksy M., Budzik G., Sanocka-Zajdel A., Paszkiewicz A., Bolanowski M., Oliwa R., Mazur L., Industry 4.0. Part I. Selected applications in processing of polymer materials. Polimery 2018, 63, 531–535.

[13] Stark R., Fresemann C., Lindow K., Development and operation of Digital Twins for technical systems and services. CIRP Ann. 2019, 68, 129–132.

[14] Tao F., Qi Q., Wang L., Nee A.Y.C., Digital Twins and Cyber–Physical Systems toward Smart Manufacturing and Industry 4.0: Correlation and Comparison. Engineering 2019, 5, 653–661.

[15] Vachalek J., Bartalsky L., Rovny O., Sismisova D., Morhac M., Loksik M., The digital twin of an industrial production line within the industry 4.0 concept. In Proceedings of the 2017 21st International Conference on Process Control (PC), Strbske Pleso, Slovakia, 6–9 June 2017; 258–262.

[16] Zhang C., Zhou G., He J., Li Z., Cheng W., A data- and knowledge-driven framework for digital twin manufacturing cell. Procedia CIRP 2019, 83, 345–350.

[17] Baskaran S., Niaki F.A., Tomaszewski M., Gill J.S., Chen Y., Jia Y., Mears L., Krovi V., Digital Human and Robot Simulation in Automotive Assembly using Siemens Process Simulate: A Feasibility Study. Procedia Manuf. 2019, 34, 986–994.

[18] Malik A.A., Bilberg A., Digital twins of human robot collaboration in a production setting. Procedia Manuf. 2018, 17, 278–285.

[19] Kousi N., Gkournelos C., Aivaliotis S., Giannoulis C., Michalos G., Makris S., Digital twin for adaptation of robots' behavior in flexible robotic assembly lines. Procedia Manuf. 2019, 28, 121–126.

[20] Dröder K., Bobka P., Germann T., Gabriel F., Dietrich F., A Machine Learning-Enhanced Digital Twin Approach for Human-Robot-Collaboration. Procedia CIRP 2018, 76, 187–192.

[21] Aivaliotis P., Georgoulias K., Arkouli Z., Makris S., Methodology for enabling Digital Twin using advanced physics-based modelling in predictive maintenance. Procedia CIRP 2019, 81, 417–422.

[22] Zhang Q., Li Y., Lim E., Sun J., Real Time Object Detection in Digital Twin with Point-Cloud Perception for a Robotic Manufacturing Station. ICAC 2022. 27th International Conference on Automation and Computing; 2022 September 1-3, University of the West of England, Bristol, UK.

[23] YASKAWA, Robotics, 2023. Operating manual YRC-1000 GP-07. VI ed. Japan, Kitakyushu: MOTOMAN.

[24] Persson J., Virtual Production Line-Virtual Commissioning [dissertation]. Lund, Sweden: Lund University; 2018 .

Model predictive control with self-learning capability for automated demand response in buildings

Laura Zabala Urrutia[a], Jesus Febres Pascual[b], Estibaliz Pérez Iribarren[c] Raymond Sterling[d], Iker González Pino[e]

[a]Faculty of Engineering of Bilbao, University of the Basque Country UPV/EHU, Bilbao, Spain, laura.zabala@r2msolution.com, CA
[b] R2M Solution Spain, Bilbao, Spain, jesus.febres@r2msolution.com
[c] Faculty of Engineering of Bilbao, University of the Basque Country UPV/EHU, Bilbao, Spain, estibaliz.perezi@ehu.eus
[d] R2M Solution Spain, Bilbao, Spain, raymond.sterling@r2msolution.com
[e] Faculty of Engineering of Bilbao, University of the Basque Country UPV/EHU, Bilbao, Spain, iker.gonzalezp@ehu.eus

Abstract:

This paper presents an optimal management strategy, called *Building Optimizer*, based on a Model Predictive Control (MPC) approach with self-learning capabilities for buildings. This research is framed in the development of an agent-based architecture to provide demand response services in an Energy Community to optimise the management of renewable energy sources and provide grid stability. The proposed MPC is a key enabler of cooperative demand response strategies at community level, ensuring the allocation of an optimal demand profile at each participating member of the community according to an optimal consumption reference defined by a complementary agent at community level. The MPC calculates the optimal setpoints of the HVAC system's terminal units, considering the expected usage of the buildings and the outdoor conditions, and exploiting the building's thermal inertia. The models embedded in the MPC are grey-box models representing a thermal zone of the building. To reduce measurement and model uncertainties, these models incorporate self-learning capabilities implemented as Moving Horizon Estimators that perform a continuous calibration based on real-time operational measurements. This solution allows full automation for model calibration and management of the terminal units. This paper presents a case study in which a baseline MPC with fixed model parameters obtained by an offline calibration is compared to the *Building Optimizer* with self-learning capabilities. The *Building Optimizer* is able to track a requested power consumption providing up to 20% of flexibility compared to the reference consumption without demand management and guaranteeing thermal comfort, at least 98% of the time. For this scenario, the *Building Optimizer* proves more reliable in guaranteeing the thermal comfort and a better match to the requested consumption compared to the baseline MPC. Demand-side management by the MPC can be translated into up to 15% energy shift from peak hours to valley hours.

Keywords:

Optimization; MPC; Building; Energy Community; Demand Response; Self-learning; Renewable Energy

1. Introduction

Building sector represents 40% of European energy consumption, of which 80% is covered by fossil fuels [1]. This sector also accounts for 35% of EU greenhouse gas (GHG) emissions [2]. In consequence, European decarbonization policies and strategies have this sector as one of the most relevant ones [3]. The renewable energy sources (RES) play a fundamental role in this decarbonisation path for switching to greener energy sources and lowering CO2 emissions. However, the increase in the renewable energy share in the energy generation entails some challenges due to the inherent unpredictability and intermittency of RES and the mismatch between the peak production periods and the peak demand periods, which can even lead to grid stability problems [4]. Demand Response (DR), which aims at modifying the consumption load curve, is a crucial tool for RES penetration in the electric system [5]. The residential sector has a great potential for DR that is still unlocked [6]. The residential sector's main end-use, accounting for between 60 and 80% of total energy consumption, is space heating [2]. Thus, there is a huge potential for the application of DR for heating

[7], by exploiting buildings' thermal inertia. Moreover, considering the flexibility of a cluster of buildings, such as a Citizen Energy Community [8] or Renewable Energy Community [9], potentially increases the capacity to exploit flexibility [10]. Several studies focus on Demand response applied at building level. Most of these studies consider electric tariff prices to perform peak shaving actions. They often use *Model Predictive Control* (MPC) technique for the optimal management of the building, a widely used predictive technique for buildings [11]. The MPC uses a predictive model of the building that allows it to anticipate peak demand and take advantage of the building's inertia, thus improving thermal comfort compared to simpler controllers based on PIDs or on/off controllers. It also allows the inclusion of additional targets to be optimized, which opens a wide range of possibilities. The most widely used approach among MPC types is the so-called economic MPC that minimises the power consumption or energy cost consumption [12,13]. Some examples are [14] that manages the cooling demand of a house to reduce the peak periods, and [15] which proposes an economic MPC based on electricity variable prices. Some studies focus on demand response actions instead of a direct reduction on the power, such as [16] in which a hierarchical MPC is used for load shifting in a building, and [17] to perform DR actions at a building taking advantage of installed PV. However, less attention has been paid to DR oriented to a cluster of buildings, such as Energy Communities (EC), as [18] states. A few studies focusing on applying DR actions in an aggregated way can be found, such as [19] and [20]. The challenge for this approach is the scalability of the problem when the number of buildings increases. This paper proposes a solution for an MPC at building level, but which considers objectives at community level by allocating the requested power consumption at household level while guaranteeing the thermal comfort. This enables disaggregating the problem into the optimization of the Community and the building management, alleviating the scalability problem and facilitating the achievement of the community's energy-related objectives.

Another important aspect tackled by this work is the handling of the uncertainties inherent to building modelling. The MPC performance is dependent on the reliability of the embedded model. In the case of the building modelling, this aspect is crucial as many uncertainties are present, especially those derived from the time-variant parameters, occupant behaviour characterisation and measurements [21]. A detailed physical modelling approach that captures all the parameter variations with time is not feasible as this would result in a computationally too expensive model that would not be suitable for optimization purposes. Thus, this paper proposes an approach based on integrating self-learning capabilities to the *Building Optimizer* to cope with these uncertainties in a computationally cheaper way. These capabilities consist of re-calibrating the model parameters during the operation with the latest measured data. This functionality is integrated through the Moving Horizon Estimation (MHE) technique [22], which has proven to give good results in studies such as [23–25].

The novel contributions of this paper include the following:

- An MPC-based solution that goes beyond the typical economic MPC for cost or energy savings. It acts as a key enabler of a cooperative DR solution at community level by managing the demand side and allocating the optimal power consumption at household level that contribute to achieving goals at community level.
- The proposed solution includes self-learning capabilities to reduce the uncertainties of the problem, such as those sources of uncertainty due to the time-variant and uncertain physical characteristics and occupant characteristics.

Finally, the paper is organised as follows: section 2 describes the methodology followed to define the *Building Optimizer*, section 3 describes a case study with the aim of illustrating the contributions of the *Building Optimizer* and section 4 gathers the main conclusions and future work.

2. Methodology

2.1. Agent-based architecture for residential demand response

The proposed MPC with self-learning capabilities for buildings, which is called *Building Optimizer* from this point onwards, is part of an agent-based architecture to provide DR services in an EC to effectively maximise the exploitation of RES and demand-side flexibility and provide grid stability. This multi agent-based architecture includes a Demand Response Optimizer (*DR optimizer*) which deals with both energy supply and demand side in a holistic manner and decides the optimal energy use profile of each household considering EC objectives. This agent-based architecture is proposed in EU HESTIA project, which develops holistic demand response services in European residential communities. The *Building Optimizer* acts as a key enabler, assuring that the optimal energy use calculated by the *DR Optimize*r is allocated at household level while respecting thermal comfort. Thus, the *Building Optimizer* manages the thermal demand in each household to assure they contribute to the EC goals.

To manage the building's thermal demand and assure the optimal consumption allocation, the *Building Optimizer* considers predictions on the weather conditions and estimates the internal heat gains, as both will influence the building's indoor conditions evolution. The *DR Optimizer* provides a day-ahead reference optimal power consumption that the *Building Optimizer* will have to allocate. The *Building Optimizer* solution must also be able to comply with the constraints defined by either the building operator or the users. To complete the

inputs to the *Building Optimizer*, it will also receive real measurements from the system. The general scheme of the solution is presented in Figure 1.

Figure. 1. Building Optimizer's input and output signals.

The *Building Optimizer* is prepared to work in two modes: (1) *explicit mode* with an automated DR actuation, and (2) *implicit mode* through manual DR actions suggested to the users. For the *explicit mode*, the automatic control signal is obtained (scalar value for on/off or modulated signal, depending on the HVAC actuation equipment capabilities). This actuation will cause the room temperature to be adjusted in a way that meets comfort but allows the demand to be reallocated in the requested way. For the *implicit mode*, the optimal temperature profile is translated into DR suggestions to the users. These suggestions would consist of requests to adjust their indoor temperature setpoint, and the users would oversee introducing this new setpoint manually. In this case, the HVAC is not commanded; the low-level controller of the thermostat would be working to operate the HVAC. This paper focuses on the first approach based on the automatic actuation.

An important point to highlight is that the *Building Optimizer* can work as a part of the agent-based optimization architecture with the aim of achieving goals at community level, but it could also be used as a stand-alone solution for building operation. This paper will propose a procedure to generate a reference curve that aims for economic targets at building level.

2.2. Building Optimizer: technical solution definition

The *Building Optimizer* solution must comply with challenging technical requirements as the controlled system is a building, a highly nonlinear system with great inertia and with many uncertainty sources such as internal heat gains.

In this regard, the MPC is a type of controller adequate for this type of application. The MPC is an optimal control strategy that works with a prediction model of the system to be controlled and calculates the optimal setpoints of the controllable units in order to minimise an objective function [26]. In this case, it has a building model embedded and calculates either the optimal indoor temperature setpoint or the HVAC actuator setpoint, depending on the actuation mode. The MPC works with the expected usage and occupancy of the building, forecast and current measurements of the outdoor and indoor conditions and includes user- and system-defined constraints. Even if the MPC optimises the operation in the entire prediction horizon, just the setpoints of the first point are commanded. It works in a closed loop by receiving the real values of the controlled variables and applies the receding horizon control principle.

The MHE is an optimization-based state-estimation technique where the current states and the parameters of the system, henceforth referred to as variables of interest, are inferred based on a finite sequence of past measurements. It uses dynamic optimization and a backward time horizon of measurements to optimally adjust the variables of interest of the problem [27]. The MHE is integrated to work in coordination with the MPC: the MHE is used prior to the execution of the MPC to calibrate the parameters of the model embedded in the MPC. Moreover, in addition to the model parameter estimation, the MHE can also estimate other model variables that are difficult to initialise beforehand or are unmeasurable, which presents a great advantage for building applications.

The following subsection will describe more in detail the main technical parts of the solution: the reduced order models for optimization, the MPC for optimal control, the MHE for self-learning capabilities and the software used for the problem implementation.

2.2.1. Reduced order models for the building and the HVAC

One of the key points in the development of an MPC is the system model that is embedded, as the reliability of the system predictions and the achievement of the control and optimization objectives will directly be impacted by the model accuracy. One of the main challenges is reaching a trade-off between the accuracy of the model (that represents in a detailed and accurate way the dynamics and other complexities of the model) and the computational burden as the optimization problem should be solved in a time that allows real-time application (typically every 15 minutes for this paper's application).

The proposed model considers thermal building envelope, internal heat gains, and heat losses, caused by heat conduction, convection, and ventilation. Modelling is underpinned by calibrated reduced-order data-driven grey box models. The grey-box model used is based on an Resistance-Capacitance (RC) network for a thermal zone defined by [28], which considers both the physical parameters and disturbances that characterise unmeasured inputs, but that can be calibrated with other measured variables. The performance of this model has been demonstrated experimentally in [29].

Figure 2 illustrates the embedded RC network model structure for a single thermal zone. The thermal zone is defined as the area controlled by a thermostat and served by the HVAC, i.e., it can represent several rooms that are controlled by a unique thermostat. T_z is the indoor zone air temperature and T_w is a wall temperature representing averaged behaviours of the enclosures (walls, roof, and floor). T_o is the outdoor air temperature. C_z and C_w represent the respective thermal capacitances of the zone and wall, and R_{zw} and R_{zo} are thermal resistances between the zone air and wall, and between the zone air and outdoor air, respectively. Q_g represents unmeasured internal heat gains. u is the modulation signal for the HVAC system, and Q_{av} the available heat, so the resulting input heat from the HVAC system is Q_u.

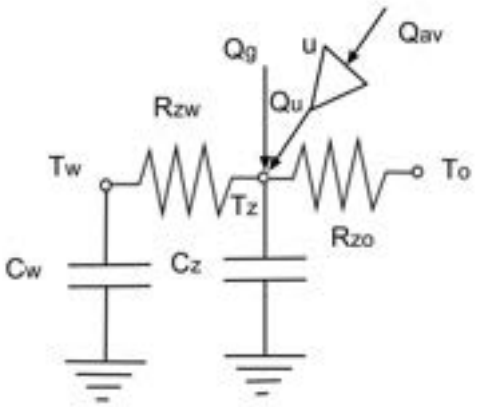

Figure. 2. Reduced order RC model for the building.

Equations (1) and (2) are the corresponding differential equations representing the thermal balance in the zone.

$$C_z \cdot \frac{dT_z}{dt} = \frac{T_w - T_z}{R_{zw}} + \frac{T_o - T_z}{R_{zo}} + Q_g + u \cdot Q_{av}, \quad (1)$$

$$C_w \cdot \frac{dT_w}{dt} = \frac{T_z - T_w}{R_{zw}}, \quad (2)$$

A simplified model for the HVAC is used, consisting of an equation to model the HVAC control, Eq. (3), and the power consumption of the HVAC, Eq. (4). This model will need to be further developed in future work to have a more accurate model of the air conditioning, but the present work focuses on the building part.

$$Q_u = u \cdot Q_{av}, \quad (3)$$

$$P_{HVAC} = \eta \cdot Q_u, \quad (4)$$

where P_{HVAC} is the power consumption of the HVAC and η its efficiency.

2.2.2. Model predictive control for building consumption and indoor conditions management

The dynamic optimization problem defined in the MPC can be formulated as follows:

$$w_{hi}^T e_{hi} + w_{lo}^T e_{lo} \quad (5)$$

subject to:

$$0 = f(\frac{dx}{dt}, x, y, u), \tag{6}$$

$$0 \leq g(\frac{dx}{dt}, x, y, u), \tag{7}$$

Equation (5) is the objective function of the MPC problem and represents the sum of the terms to be minimised through the prediction horizon, in this case, the higher e_{hi} and lower e_{lo}errors of the controlled variables, that is, the indoor temperature in the room and the HVAC power consumption. It is defined based on the l_1-norm so that the absolute difference between the current measured value and the desired target value is computed. This operator does not have a continuous first and second derivative at x=0, but the software used, that is GEKKO, poses the problem in a way that this discontinuity is avoided, as explained in [30]. The lower error is computed as the difference between the variable and the lower bound, and the higher error is defined analogously. When the variable is between the defined limits, there is no penalty.

Equation (6) represents the equality constraints of the problem, derived from the model presented in section 2.2.1, and Eq. (7) the inequality constraints at which the problem is subjected, which consists of physical limits for the variables.

In the problem definition, x represents the state variables, that is, the indoor zone temperature and the wall temperatures: $x^T = [T_z, T_w]^T$. The output is the HVAC power consumption $y = P_{HVAC}$. The manipulated variable is the modulation signal of the HVAC represented by u.

In the problem definition, an important tuning aspect is the weighting factors assignment in the objective function, represented in Eq. (5) by w_{hi} and w_{lo} for each of the variables. These weighting factors enable prioritising either the thermal comfort or the power consumption, and between the lower and higher errors.

The other important tuning factor is the prediction horizon, that is, the length of the forward time window for which the MPC computes the solution.

2.2.3. Moving horizon estimator for incorporating self-learning capabilities

The basic idea of MHE is to minimise the discrepancy between the measured outputs of the system and the outputs predicted (target measurements) by a model of the system, subject to a set of constraints on the states of the system. This is formulated through a dynamic optimization problem, defined as follows:

$$w_{hi}^T e_{hi} + w_{lo}^T e_{lo}, \tag{8}$$

subject to:

$$0 = f(\frac{dx}{dt}, x, y, u), \tag{9}$$

$$0 \leq g(\frac{dx}{dt}, x, y, u), \tag{10}$$

Equation (8) is the objective function of the MHE problem and represents the sum of the terms to be minimised through the backward window of past measurements: the absolute difference between the real measurements of the controlled variables (indoor temperature and HVAC power consumption) and the predicted value with the calibrated model. Both the higher and lower errors are considered, and a dead-band or region around the measurement in which the error is not penalised is included in the problem formulation. This reduces the impact of the noise from the measurements in the model calibration. In this case, the objective function is also defined through the l_1-norm.

Equation (9) represents the equality constraints of the problem, derived from the model presented in section 2.2.1, and Eq. (10) the inequality constraints at which the problem is subjected, which are used to limit and penalise the rate of change of the variables that are adjusted by the MHE and to set absolute bounds.

The most relevant tuning consideration are the weighting of the terms in the objective function (w_{hi}^T and w_{lo}^T) and the length of the time window of past measurements. Including more points in the time window allows the MHE to reconcile the model to more data but also increases computational time.

The outputs of the MHE are the model parameters, R_{zo}, R_{zw}, C_z, C_w, that are *fixed variables*, the available heat for the HVAC system and the estimated internal heat gains. These are the estimated values through the prediction horizon.

2.2.4. Software for problem implementation

Python 3.11 is used to address this development. The algorithms for MHE and MPC have been implemented using the GEKKO library [31] for Python. This library is based on APMonitor [32]. IPOPT is the solver used in the *Building Optimizer*.

3. Results and discussion

This section presents the simulation results of the *Building Optimizer* for a case study.

3.1. Case study description

The presented case study has the following aims:

- Demonstrate that the *Building Optimizer* can guarantee thermal comfort.
- Evaluate to what extent the *Building Optimizer* can adjust to a requested power consumption.
- Evaluate if the *Building Optimizer* incorporating self-learning capabilities outperforms an MPC with fixed model parameters.

In order to assess these points, the case study will consider as a baseline an MPC with fixed parameters, and its performance will be compared to the *Building Optimizer* with self-learning capabilities.

The following subsections present the building that is considered for the case study, the boundary conditions, the uncertainty modelling to generate virtual forecast and the modelling of the flexibility request signal.

3.1.1. Study building description

In order to consider an actual building and to work with realistic values, the values of the case study presented in [28] and [33] are used, consisting of a single-story wood-built house having a floor area of 60m^2 with crawl and roof space. The main thermal characteristics of the building are: $C_z = 1.18\ \left(\frac{kWh}{℃}\right)$, $C_w = 3.99\ (kWh/℃)$, $R_{zo} = 0.48\ (℃/kW)$, $R_{zw} = 7.35\ (℃/kW)$. These values are considered as the real values of the building. The space is considered as a single thermal zone with one thermostat to monitor the indoor temperature and a controllable HVAC that can be modulated through a u signal between 0-100%.

3.1.2. Boundary conditions description

For the weather conditions, the building is considered as located in Bilbao (Spain). The data of the outdoor temperature for February from the Typical Meteorological Year (TMY) of Bilbao (Spain) [34] is used for the simulations, which represents a typical winter heating demand situation.

The internal heat gains of the building are calculated using the ASHRAE standards [35] considering the profile for internal heat gains from people with a Hotel pattern (equivalent to a residential building), assuming the following values: *23.226 m^2/person*, and *73.268 W/person*. The profiles differentiate between weekdays, Saturdays, and Sundays. These profiles are represented in Figure 3.

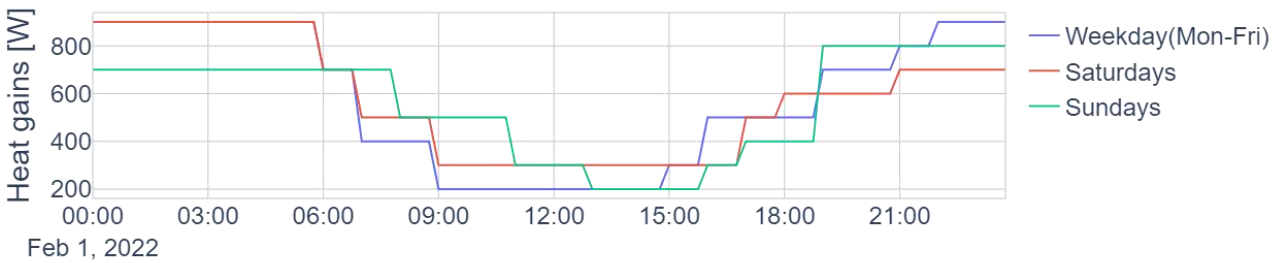

Figure. 3. Internal heat gains hourly profile for weekdays, Saturdays, and Sundays for a residential house.

3.3.3. Forecast uncertainty modelling

Modelling the errors in the weather and internal heat gain predictions is crucial, as they are a great source of uncertainty in the problem and its impact in the solution needs to be assessed.

The uncertainty in the indoor temperature is modelled through an autoregressive model shown in [36]. This generates a realistic error in the outdoor temperature prediction, trying to replicate a low-medium uncertainty scenario. For the error modelling, it is assumed that the outdoor temperature forecast is updated every 24h. Figure 4 shows the real outdoor temperature and the synthetic forecasts for the first week of February.

Figure. 4. Real outdoor temperature for Bilbao for 1-7 February and simulated forecasts.

The internal heat gains profiles for the building are defined based on the ASHRAE profiles shown in section 3.1.2. The difference that can be found between the real occupancy patterns and the ones proposed by ASHRAE are modelled by modifying the ASHRAE curve. White noise is added to the internal heat gains through a gaussian distribution, and it is smoothened so that it resembles a real pattern. The synthetically generated data for the internal heat gains is used as the real profile of the internal heat gains and the ASHRAE profiles are considered as the forecasts for a whole week. Both profiles are illustrated in Figure 5.

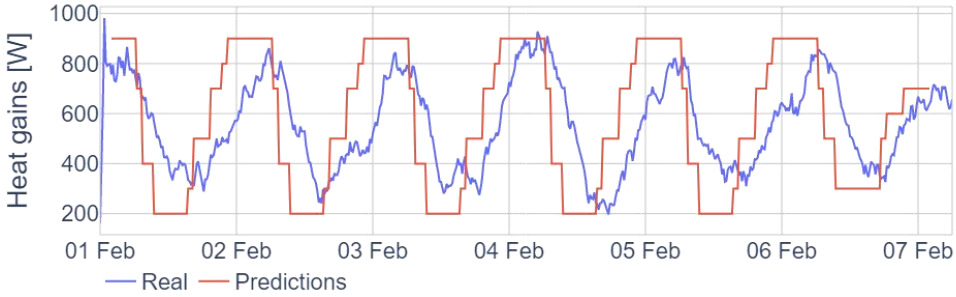

Figure. 5. Simulated internal heat gains for the building and the forecasts.

3.2. Building Optimizer with fixed parameter: model calibration

The Building Optimizer version that integrates an MPC with fixed parameter requires the values of the RC parameters (R_{zo}, R_{zw}, C_z, C_w). An offline calibration is performed to calibrate these parameters based on simulation data of the study building, which is used as if it was operation data. The steps followed for the calibration are:

1. The plant model (building space with the HVAC) is simulated for a whole month with the real parameters from section 3.1.1 and the boundary conditions (weather, internal heat gains) presented in section 3.1.2. The model includes an on/off hysteresis controller, with a constant setpoint of 21.5 ºC, and a dead band of 0.5 ºC for the hysteresis that is used to control the indoor room temperature by calculating the HVAC operation.
2. An offline calibration is performed using the data of a whole week as reference. The fixed values of the model parameters (R_{zo}, R_{zw}, C_z, C_w) are calculated minimising the deviation between the reference values from in Step 1 and the predicted values with the model for the whole week. The problem defined for the MHE is adapted so that it can be used for this calibration. The internal heat gains are set to a fixed value for the whole week. The results are verified by calculating metrics for the errors in the indoor temperature and the HVAC power consumption compared to the reference values.

Different reference errors are calculated for the indoor temperature deviation and the power consumption deviation, as the nature of these variables is different. The temperature is a potential variable, so the most suitable error to be applied to this variable is the *Normalised root-mean-square deviation* (NRMSD), which is defined in Eq. (11).

$$NRMSD(T_z) = \frac{RMSD(T_z)}{T_z^{max} - T_z^{min}} = \frac{\sqrt{\frac{\sum_{t=1}^{T}(\hat{T}_z(t) - T_z(t))^2}{T}}}{T_z^{max} - T_z^{min}}, \quad (11)$$

where $RMSD(T_z)$ is root-mean square deviation of the indoor temperature, T_z^{max} and T_z^{min} are the maximum and minimum value of the indoor temperature, respectively, $T_z(t)$is the real indoor temperature value, $\hat{T}_z(t)$ is the indoor temperature obtained with the calibrated model, and T is total simulation time.

In the case of the power consumed by the HVAC, it is a non-negative scale variable which cannot have negative values, so the mean value is used to normalise the error. Thus, the *Coefficient of Variation of the root-mean-square deviation* (CV(RMSD)) is used as reference, which is described in Eq. (12).

$$CV(RMSD(P_{HVAC})) = \frac{RMSD(P_{HVAC})}{\bar{P}_{HVAC}} = \frac{\sqrt{\frac{\sum_{t=1}^{T}(\hat{P}_{HVAC}(t) - P_{HVAC}(t))^2}{T}}}{\bar{P}_{HVAC}}, \quad (12)$$

where $RMSD(P_{HVAC})$ is root-mean square deviation of the power consumption, $\underline{P}_{HVAC}$ is the mean value of the power consumption, $P_{HVAC}(t)$ is the real power consumption value, and $\hat{P}_{HVAC}(t)$ is the power consumption obtained with the calibrated model.

Table 1. Calibration errors for the building fixed parameter model.

	$NRMSD(T_z)$, %	$CV(RMSD(P_{HVAC}))$, %
Verification, weekdays	20.96%	0.73%
Verification, Saturdays	25.76%	0.72%
Verification, Sundays	14.73%	1.85%
Verification, general	16.50%	1.89%

The errors in the temperature are greater than in the power consumption. This introduces a great uncertainty in the modelling part, especially in the indoor temperature modelling. Nevertheless, the errors in the power consumption are low, which may be due to the simplified HVAC model that makes it easier to be adjusted.

3.3. Flexibility provision evaluation

Both the baseline MPC with the fixed model parameters calculated in section 3.2 and the *Building Optimizer* incorporating the self-learning capabilities are simulated for the same boundary. A simulation of a whole week of February is conducted, with the real and virtually generated forecasts of outdoor temperature, and the synthetic internal gains described in section 3.1.3.

The flexibility request is sent to the *Building Optimizer* through a power consumption reference profile that the optimizer needs to track to allocate the power consumption. This signal, in the solution structure presented in section 2.1 and shown in Figure 1, comes from the DR optimizer. In this case, the signal will be synthetically generated. The procedure explained here also reflects how the *Building Optimizer* can work as a standalone solution by including the generation of the signal as a part of the solution.

The flexibility request is generated considering the Spanish electricity tariff schemes that apply an hourly discrimination and divides the day into the following consumption periods: the peak period (with higher tolls and charges), the flat period (with intermediate values for the costs) and valley periods (with the lowest costs) [36]. The procedure is the following one:

1. The case study model is simulated with the *Building Optimizer* applying just thermal comfort objective, so no actions are taken regarding the power consumption. In this way, a baseline of the typical power consumption in the building is achieved, without demand-side management. This profile is used as a reference for the power consumption.
2. The following assumption is made regarding the flexibility requests that are expected: the power consumption is requested to be reduced in the peak periods, this power consumption should be reallocated in the valley period, and the flat periods should not be modified. This would match with the general requests from the grid point of view but would also be in line with the electric tariff periods, so the benefits would not be just flexibility share increase, but also economic benefits.
3. The baseline power consumption from step 1 is decreased in a percentage in the peak periods, it is maintained in the flat periods, and it increases in the valley. A set of simulations are defined varying the percentage of flexibility request from 10% to 30% by increasing a 5% in each step.

The scenarios requesting different percentages of flexibility are simulated for both the baseline MPC and the *Building Optimizer* incorporating self-learning capabilities.

For the assessment of the thermal comfort guarantee, the thermal discomfort duration is evaluated. This is measured as the percentage of the time that the indoor temperature is outside the defined thermal comfort limits (21-22ºC). The accuracy in the power consumption tracking is evaluated by the deviation compared to the reference curve, using the CV(RMSD) defined in Eq. (12). Table 2 presents these metrics for the different flexibility scenarios. The first simulation day is not considered as it is highly dependant on initialization conditions and does not reflect the normal operation.

Table 2. Temperature and power consumption error comparison for different flexibility scenarios.

Flexibility request	Thermal discomfort duration [%]		Power deviation [%]	
	Baseline MPC	Building Optimizer	Baseline MPC	Building Optimizer
10%	7.07%	0%	2.22%	0%
15%	14.14%	0%	3.31%	3.29%
20%	18.71%	1.25%	7.44%	6.63%
25%	25.37%	8.12%	9.24%	9.35%
30%	31.11%	17.9%	12.1%	12.16%

The results from Table 2 show that the *Building Optimizer* can track the requested power demand with a lower impact in the thermal comfort. It can even reach a 20% flexibility provision with a minimum impact on the thermal comfort (guaranteeing it 98% of the time) and a 25% flexibility provision with a thermal discomfort duration below 10% of the total time. For higher percentage of flexibility requests, there is an accuracy loss in temperature tracking to achieve the other objective of the cost function, that is, the power tracking.

The difference in performance to guarantee thermal comfort between the two analysed scenarios is due to the capacity of the *Building Optimizer* to reduce the uncertainty. The main sources of uncertainty in the problem come from both the inherent uncertainties to the modelling and the input predictions. In the case of the baseline MPC with fixed parameters, the calibrated model parameters present an error when predicting the real building behaviour, as explained in section 3.2. Even if the MPC can reduce this uncertainty using the real measurements of the system, this uncertainty cannot be completely avoided. The *Building Optimizer* tackles this problem by updating the model parameters based on the last real measurements of the system. Regarding the predictions, both scenarios are simulated with outdoor temperature predictions with an uncertainty integrated, which deviates the response from the predicted one. In the case of the internal gains, the baseline MPC uses the predictions of the internal gains from ASHRAE (Figure 5), which introduces a great uncertainty source. On the contrary, the *Building Optimizer* uses the estimated last value of the internal gains by the MHE as prediction. Even if this is an approximation that introduces also considerable uncertainty, this approximation gives better results than using the ASHRAE predictions according to the results.

The scenario for a flexibility request of 20% is analysed to illustrate the performance of both controllers. In Figure 6, the comparison of the indoor temperature of the thermal zone for both the baseline MPC and the *Building Optimizer* is shown, together with the upper and lower thermal comfort limits.

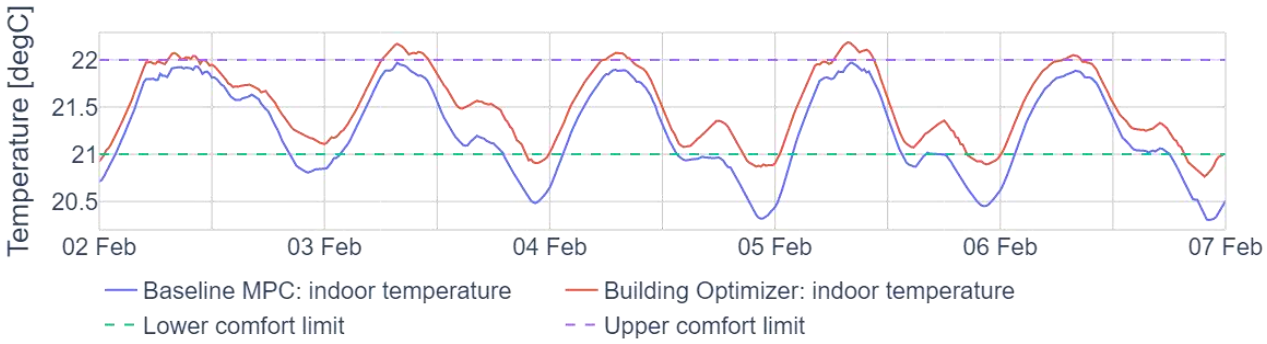

Figure. 6. Indoor temperature with the baseline MPC and the Building Optimizer.

Figure 6 shows how the indoor temperature deviates for longer periods from the thermal comfort conditions in the baseline scenario, for the reasons explained above.

Figure 7 presents the same comparison between the baseline MPC and the *Building Optimizer*, but for the power consumption.

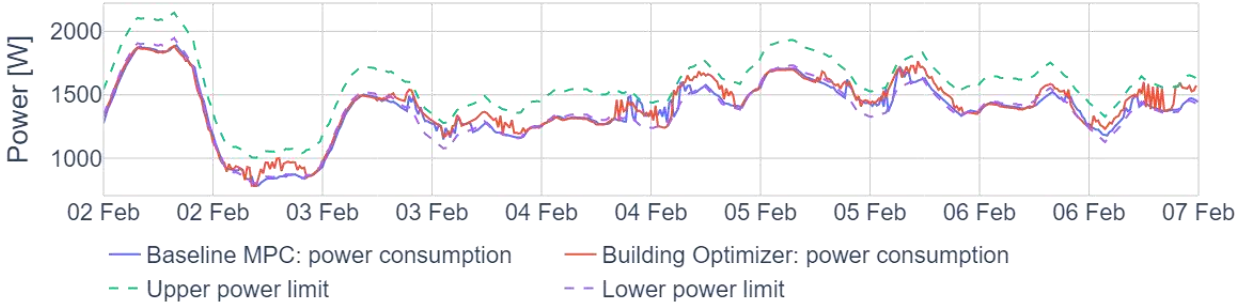

Figure. 7. HVAC power consumption with the baseline MPC and the Building Optimizer.

The power tracking shown in Figure 7 reflets that the power is deviated very similarly in both scenarios. This is the expected conclusion as the calibration errors for the baseline MPC were lower for the power consumption.

Another important aspect to consider is the percentage of energy that is displaced from peak periods to valley periods. This indicator is also a reflection of the ability to perform power shifting actions. This percentage is presented in Table 3.

Table 3. Percentage of energy consumed during peak periods shifted.

Flexibility request scenario	Peak period shifted energy, %
10%	8.06%
15%	11.03%
20%	14.22%
25%	15.21%
30%	16.77%

This reduction in the peak periods could be directly translated into economic benefits and a flexibility provision capacity in accordance with the typical request that may appear from the grid side.

4. Conclusions and future work

In the present work, a control strategy called *Building Optimizer* is developed, consisting of an MPC with self-learning capabilities to manage the thermal demand of a building. The Building optimiser can allocate a requested power consumption in a building while guaranteeing thermal comfort so that an objective at community level is achieved. The capacity for the power consumption management is crucial to integrate demand response in the residential sector, with a great unlocked potential. This boosts the integration of RES in the current energy system as a better match between the intermittent production of renewable sources and the demand at building levels can be achieved. The moving horizon estimation technique is used for incorporating self-learning capabilities, which uses real-time measurements from the plant to recalibrate the model at real time and calculate unmeasurable inputs, such as the internal heat gains. This functionality is relevant for buildings, a system with a wide range of uncertainties due to its characteristics and the occupancy patterns.

A case study is presented for a building represented by a single thermal zone with a controllable HVAC. The performance of an MPC with fixed parameters model is compared to the *Building Optimizer* including the self-learning capabilities. To calibrate the MPC with fixed parameters, a calibration technique is proposed, using the data for a whole week of the study building. A flexibility request scenario is simulated, generating this request through a curve that decreases the power consumption at peak electric prices periods and increases them in valley periods with respect to a reference curve in which demand side management is not performed. The scenario is simulated for different percentages of flexibility request with both the *Building Optimizer* and the fixed-parameter baseline MPC. The simulations are conducted including uncertainty sources in the used predictions for the boundary conditions. It is concluded that 20% is the maximum flexibility at which the deviation in the indoor temperature with respect to the thermal comfort boundaries has a duration lower than 2% of the time. In this scenario, the *Building Optimizer* improves the temperature tracking and the power consumption allocation compared to the baseline MPC, and it can shift up to 14% of the energy that is consumed during peak hours to valley periods. This demonstrates that incorporating self-learning capabilities can improve the performance of this type of controllers.

The studied building is of residential type, but the proposed reduced order model can be extended to other type of buildings, such as commercial buildings or offices. The solution is scalable in terms of the number of buildings, as each building would have its own MPC to ensure that it consumes what is required by the community. The scalability of the solution in terms of the building size and the number of thermal zones to be modelled within the building will be one of the crucial challenges to analyse in further work, as including more thermal zones increases the computational cost of the problem. Future work should expand the inclusion of a more detailed model of the HVAC too.

Acknowledgments

This work has been founded partially funded by Next Generation EU program from the European Union.

This project has received funding from the European Union's Horizon 2020 research and innovation programme under grant agreement No 957823.

Nomenclature

- C thermal capacitance, kWh/(ºC)
- P power, W

Q heat, W

R thermal resistance, ºC/kW

T temperature, °C

u actuation signal, %

w weighting factor, -

x state variables, -

y output variables, -

Greek symbols

η efficiency

Subscripts and superscripts

av available

g internal gains

hi higher

lo lower

o outdoor

u actuation signal

w wall

x states

z thermal zone

References

[1] United Nations Environment Programme. 2022 Global Status Report for buildings and Construction: Towards a Zero-emission, Efficient and Resilient Buildings and Construction Sector. Nairobi: 2022.

[2] European Environment Agency. Greenhouse gas emissions from energy use in buildings in Europe 2022. https://www.eea.europa.eu/ims/greenhouse-gas-emissions-from-energy (accessed February 28, 2023).

[3] European Comission. European Commission-Press release European Green Deal: Commission proposes to boost renovation and decarbonisation of buildings 2021.

[4] International Energy Agency. Getting Wind and Sun onto the Grid: A Manual for Policy Makers. 2017.

[5] D'Ettorre F, Banaei M, Ebrahimy R, Pourmousavi SA, Blomgren EMV, Kowalski J, et al. Exploiting demand-side flexibility: State-of-the-art, open issues and social perspective. Renewable and Sustainable Energy Reviews 2022;165:112605. https://doi.org/10.1016/J.RSER.2022.112605.

[6] Gils HC. Assessment of the theoretical demand response potential in Europe. Energy 2014;67:1–18. https://doi.org/10.1016/J.ENERGY.2014.02.019.

[7] Market Observatory for Energy DE. Quarterly report on European electricity markets. 2022.

[8] DIRECTIVE (EU) 2019/ 944 OF THE EUROPEAN PARLIAMENT AND OF THE COUNCIL - of 5 June 2019 - on common rules for the internal market for electricity and amending Directive 2012/27/ EU. 2019.

[9] European Parliament C of the EU. Directive (EU) 2018/2001 of the European Parliament and of the Council of 11 December 2018 on the promotion of the use of energy from renewable sources (recast) (Text with EEA relevance.) 2018.

[10] Goy S, Finn D. Estimating Demand Response Potential in Building Clusters. Energy Procedia 2015;78:3391–6. https://doi.org/10.1016/J.EGYPRO.2015.11.756.

[11] Prívara S, Cigler J, Váňa Z, Oldewurtel F, Sagerschnig C, Žáčeková E. Building modeling as a crucial part for building predictive control. Energy Build 2013;56:8–22. https://doi.org/10.1016/J.ENBUILD.2012.10.024.

[12] Alqurashi A. The State of the Art in Model Predictive Control Application for Demand Response. Journal of Sustainable Development of Energy, Water and Environment Systems 2022;10. https://doi.org/10.13044/j.sdewes.d9.0401.

[13] Rawlings JB, Angeli D, Bates CN. Fundamentals of economic model predictive control. 2012 IEEE 51st IEEE Conference on Decision and Control (CDC), IEEE; 2012, p. 3851–61. https://doi.org/10.1109/CDC.2012.6425822.

[14] Tang R, Wang S, Xu L. An MPC-Based Optimal Control Strategy of Active Thermal Storage in Commercial Buildings during Fast Demand Response Events in Smart Grids. Energy Procedia 2019;158:2506–11. https://doi.org/10.1016/J.EGYPRO.2019.01.395.

[15] Frahm M, Dengiz T, Zwickel P, Maaß H, Matthes J, Hagenmeyer V. Occupant-Oriented Demand Response with Room-Individual Building Control 2023.

[16] Kim D, Braun JE. MPC solution for optimal load shifting for buildings with ON/OFF staged packaged units: Experimental demonstration, and lessons learned. Energy Build 2022;266:112118. https://doi.org/10.1016/J.ENBUILD.2022.112118.

[17] Mingjun Wei, Zheng O'Neill. Energy Management and Control System for a PV-Battery System to Improve Residential Building Resiliency Under Extreme Weather Conditions. 2023 ASHRAE winter conference, Atlanta: 2023.

[18] Mugnini A, Polonara F, Arteconi A. Demand response strategies in residential buildings clusters to limit HVAC peak demand. E3S Web of Conferences, 2021, p. 09001. https://doi.org/10.1051/e3sconf/202131209001.

[19] Hu M, Xiao F. Quantifying uncertainty in the aggregate energy flexibility of high-rise residential building clusters considering stochastic occupancy and occupant behavior. Energy 2020;194:116838. https://doi.org/10.1016/J.ENERGY.2019.116838.

[20] Iqbal A, Aoki Y, Ninagawa C, Murakawa T. Reactive Power Demand Response for Distribution System with Neighboring Clusters of Building Multi-type Air-conditioners. IEEJ Transactions on Power and Energy 2022;142:306–14. https://doi.org/10.1541/ieejpes.142.306.

[21] Maasoumy M, Razmara M, Shahbakhti M, Vincentelli AS. Handling model uncertainty in model predictive control for energy efficient buildings. Energy Build 2014;77:377–92. https://doi.org/10.1016/J.ENBUILD.2014.03.057.

[22] Eaton AN, Hedengren JD, Eaton AN, Hedengren JD. Overview of Estimation Methods for Industrial Dynamic Systems. n.d.

[23] Simmons CR, Arment JR, Powell KM, Hedengren JD. Proactive energy optimization in residential buildings withweather and market forecasts. Processes 2019;7. https://doi.org/10.3390/PR7120929.

[24] Gates NS, Hill DC, Billings BW, Powell KM, Hedengren JD. Benchmarks for Grid Energy Management with Python Gekko. n.d.

[25] Kim D, Braun JE. Development, implementation and performance of a model predictive controller for packaged air conditioners in small and medium-sized commercial building applications. Energy Build 2018;178:49–60. https://doi.org/10.1016/j.enbuild.2018.08.019.

[26] Drgoňa J, Arroyo J, Cupeiro Figueroa I, Blum D, Arendt K, Kim D, et al. All you need to know about model predictive control for buildings. Annu Rev Control 2020;50:190–232. https://doi.org/10.1016/J.ARCONTROL.2020.09.001.

[27] Rawlings JB. Moving Horizon Estimation. Encyclopedia of Systems and Control, Springer London; 2013, p. 1–7. https://doi.org/10.1007/978-1-4471-5102-9_4-1.

[28] Kim D, Cai J, Braun JE, Ariyur KB. System identification for building thermal systems under the presence of unmeasured disturbances in closed loop operation: Theoretical analysis and application. Energy Build 2018;167:359–69. https://doi.org/10.1016/j.enbuild.2017.12.007.

[29] Kim D, Cai J, Ariyur KB, Braun JE. System identification for building thermal systems under the presence of unmeasured disturbances in closed loop operation: Lumped disturbance modeling approach. Build Environ 2016;107:169–80. https://doi.org/10.1016/j.buildenv.2016.07.007.

[30] Powell KM, Eaton AN, Hedengren JD, Edgar TF. A continuous formulation for logical decisions in differential algebraic systems using mathematical programs with complementarity constraints. Processes 2016;4. https://doi.org/10.3390/pr4010007.

[31] Beal LDR, Hill DC, Abraham Martin R, Hedengren JD. GEKKO optimization suite. Processes 2018;6. https://doi.org/10.3390/pr6080106.

[32] Hedengren JD, Shishavan RA, Powell KM, Edgar TF. Nonlinear modeling, estimation and predictive control in APMonitor. Comput Chem Eng 2014;70:133–48. https://doi.org/10.1016/J.COMPCHEMENG.2014.04.013.

[33] J.J. Bloem, editor. System identification applied to building performance data. European Comission. 1994.

[34] EnergyPlus. EnergyPlus Weather data. Https://EnergyplusNet/Weather n.d. https://energyplus.net/weather (accessed February 15, 2023).

[35] ASHRAE. ASHRAE 90.1-2022 (I-P Edition) Energy Standard for Sites and Buildings Except Low-Rise Residential Buildings (ANSI Approved; IES Co-sponsored). 2022.

[36] Oldewurtel F, Parisio A, Jones CN, Gyalistras D, Gwerder M, Stauch V, et al. Use of model predictive control and weather forecasts for energy efficient building climate control. Energy Build 2012;45:15–27. https://doi.org/10.1016/J.ENBUILD.2011.09.022.

Benchmarking of state-of-the-art machine learning methods for highly accurate thermal load forecasting in district heating networks

Christian Pressa[a], Stefan Leiprecht[a], Fabian Behrens[a], Verena Jetzinger[a], Hendric Popma[a], and Matthias Finkenrath[a]

[a] Kempten University of Applied Sciences, Germany,
e-mail: christian.pressa@hs-kempten.de

Abstract:

Decarbonisation of heat generation has become a priority for district heating network operators. In order to avoid the use of fossil-fired boilers, operators need to know peaks in heat demand in advance. Accurate thermal load forecasting is playing an increasingly important role in this respect.

This paper presents the final results of the research project “deepDHC” (deep learning for district heating and cooling) funded by the German Federal Ministry for Economic Affairs and Climate Action (BMWK). The three-year project focused on systematically benchmarking thermal load forecasts for district heating networks, based on state-of-the-art machine learning methods. The analysis covers a variety of machine learning techniques, such as neural networks – including latest deep learning methods – (e.g. LSTM, TFT, ESN, RC), decision trees (random forests, adaptive boosting, XGB) and statistical methods (SARIMAX). In addition, the impact of combining methods by so-called “stacking” was investigated. Training and validation of the machine learning algorithms was based on historical operating data from the district heating network for the city of Ulm in Germany, in combination with historical weather data, and weather forecasts. Thermal load forecasts – typically for three days ahead – are presented and compared against one another. An automatic tuning routine was developed as part of the project, which enables regular re-training of the machine learning algorithms based on the latest operating data from the heating network. Furthermore, a web interface for real-time forecasting was developed and implemented at the power station.

Keywords:

District heating; load forecasting; machine learning; dispatch optimisation.

1. Introduction

Half of Europe’s entire energy consumption is used for heating and cooling, with 75 percent derived from fossil sources. Thus it is important to provide heat as efficiently as possible, also producing the lowest possible greenhouse gas emissions. District heating networks play a key role in this context, as they are currently used to supply 60 million Europeans with heat.[1] However, with total lengths often spanning several hundred kilometres, supplying district heating networks efficiently presents a considerable challenge. Typically, heating network operators maintain several power plants with different technical and economic features. District heating or cooling can be provided more cost-effectively, efficiently and with fewer emissions, the more precisely the expected load can be estimated. In addition to a comprehensive understanding of individual power plants and a dispatch optimisation strategy, this requires a precise forecast of the thermal loads that can be expected in the network during the next few days. In industrial practice, however, generally only simple forecasting methods with comparably high uncertainties are used for district heating load forecasts

Previously established methods, which are based on typical days or reference load profiles, [2] currently lead to an estimated 15-30 percent load forecasting error rate over a 72-hour horizon. In addition, heating load forecasts have been considerably less intensively studied to date than, for example, electricity load forecasts.

Accurately predicting the district heating load is essential for district heating network operators in order to optimise the utilisation of available power plants, thermal storage facilities and “power-to-heat” plants, thus boosting efficiency. The quality of district heating load forecasting directly impacts plant dispatch quality, making it a critical factor to consider. Nevertheless, quantifying the economic advantage of reducing load forecasting errors is difficult, due to the fact that different load forecasts cannot be relied on to accurately repeat the actual plant dispatch during a specific period. The economic benefit of improved thermal load forecasting was shown in in a previous publication.[3]

New methods in the field of artificial intelligence, especially in machine learning and "deep learning", offer considerable potential for improvement, in particular since machine learning techniques have become easy to deploy due to increasing amounts of training data coupled with cheaper and improved computing power.[4–7]

This work is based on operating data from the district heating network for Ulm, a medium-sized city in southern Germany with about 125,000 inhabitants, as provided by the local utility company “Fernwärme Ulm GmbH” (FUG), which operates a district heating network about 150 km in length supplying some 600,000 MWh of thermal energy per year, equivalent to 45 percent of the city’s heat requirements. Table 1 lists all the major heat generation units operated by FUG. In addition, a pressurised hot water thermal storage of 2,427 m³ volume, equivalent to 150 MWh thermal energy storage capacity, and with 20 MW discharge power, is used.

Table 1. Heat generation units operated by FUG.

Plant type	Thermal load, MW	Electrical load, MW	Fuel type
Biomass CHP plant 1	58	9	Waste wood
Biomass CHP plant 2	25	5	Waste wood
Waste incineration CHP plant	30	11	Waste
Peaking boiler (w/ connection to turbine)	230	15	Coal, gas or oil

2. DeepDHC system structure

The DeepDHC system structure in Figure 1 below shows the developed process for load forecasting. The basis for training the models is historical data on the heat load of the district heating networks, as well as historical and current weather forecasts, which are obtained from the German Meteorological Service (Deutscher Wetterdienst, DWD) and stored in a database. In addition, the weather data currently measured for the Ulm site are obtained from the DWD’s Climate Data Center (CDC) and saved together with the actual district heating load in an hourly resolution. Operational data is rarely available in the correct format or ideal quality. Deviations such as missing measured values, outliers, or data with a different interval (time frames) must be corrected or optimised with statistical methods as part of a pre-processing step. During the machine learning process, features are generated, datasets are divided into test and training data, and the corresponding models are initially trained and optimised. Based on the trained model, a live forecast of the heat load is generated and made available to the power plant operator via a web interface. In addition, an automated learning routine was developed in the project. This routine helps to always provide the best model with optimal parameters, including retraining the forecasting models whenever new training data become available.

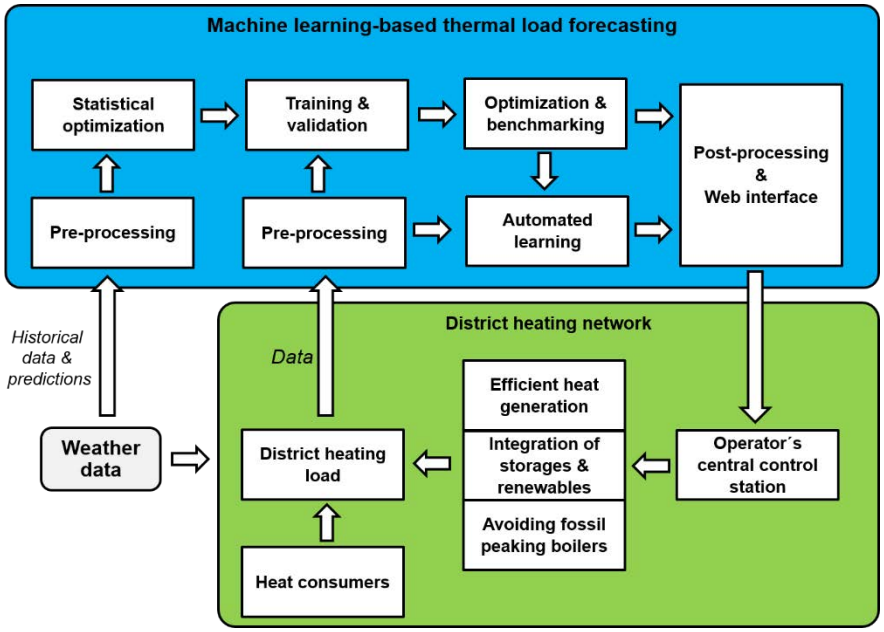

Figure 1. The deepDHC machine learning process for thermal load forecasting

3. Analysed machine learning methods

The objective of this chapter is to provide a concise overview of the analysed machine learning methods, including their characteristics, and to specify the software packages that were used for their implementation.

3.1. Seasonal Auto-Regressive Integrated Moving Average (SARIMAX)

In contrast to neural networks or decision trees, SARIMAX (“Seasonal Auto-Regressive Integrated Moving Average)” is based on statistical calculation models. SARIMAX extends the ARIMA model by adding a

seasonal counterpart to each component.[8] Compared to ARIMA, SARIMIX offers a “seasonal order”, which offers advantages for the type of forecasts examined. There are terms that capture the pattern of the data over a seasonal period, such as a week, a month, or a year. SARIMAX was implemented in this study using the “statsmodels” python library.[9]

3.2. Echo-State Networks (ESN)

Echo-State Networks (ESN) are one of the simplest implementations of a neuron-based reservoir computer. Reservoir computing is a machine learning approach to training recurrent neural networks (RNN). At its core, RNN cells contain an internal memory state which acts as a compact summary of past information. A unique characteristic of the ESN model is its efficiency in terms of the required computing power.[10, 11] Modern machine learning methods are becoming increasingly complex and require increasingly powerful hardware. In contrast, the development of reservoir computers focuses on reducing complexity and solving large machine learning tasks with minimal computing power. Recently, reservoir computers have proven to be a powerful and resource-efficient alternative in the field of classic forecasting of complex dynamic systems.[12] The Python package ReservoirPy was used in implementing this project.[11]

3.3. Next Generation Reservoir Computing (NGRC)

Like the “classic” ESN model, the NGRC model belongs to the group of neuron-based reservoir computers. [12] [13] In the background, a nonlinear vector autoregression (NVAR) algorithm automatically delivers the best possible classic ESN model with the associated hyperparameters. Like the classic ESN model, the NGRC model is very efficient and very easy for the programmer to implement. The Python package ReservoirPy was used in implementing this project.[11]

3.4. Temporal Fusion Transformer (TFT)

In the area of machine learning, transformers are a subtype of neural network. A common obstacle for machine learning algorithms is the inability to handle data in the dimension of time. Commonly, the algorithms weight the relevance of data at each location equally, thus preventing the extraction of usable knowledge in the time dimension. The architecture of the Temporal Fusion Transformer is specialised for performing such time-series prediction tasks. To learn temporal relationships on different scales, TFT uses recurrent layers for local processing and interpretable self-attention layers for long-term dependencies.[14] TFT offers powerful forecasts with customisation options, and unlike other machine learning methods it is not a “black box”. TFT is able to independently recognise dependencies within a data set and also includes tools for selecting relevant or irrelevant features. Originally developed by Google, several TFT implementations are now available. Further details of the TFT-related work in this study have been published separately.[14] The TFT used in this project was implemented using the PyTorch API.[15]

3.5. Long Short-Term Memory (LSTM)

LSTM is a gradient-based, recurrent neural network with feedback connections. LSTM neurons can hold values over any length of time, making them an attractive option for time-series prediction.[16] The standard recurrent neural network (RNN) architecture has difficulties in handling long-term dependencies, more precisely with the ability to adapt to recalling information late in the sequence. LSTM models address this limitation by introducing a memory cell, an internal state that can be updated and read by the network, and "gates" that control the flow of information in and out of the cell. This structure allows the LSTM to selectively store and update information across many time steps, making it well suited for time series forecasting.[16] The LSTM model was implemented using Keras LSTM layers.[17]

3.6. Adaptive Boosting (Adaboost)

Adaptive boosting, also known as AdaBoost, is a machine learning algorithm that belongs to the family of ensemble learning methods. Ensemble methods combine multiple models to improve their predictive power. The basic idea behind AdaBoost is to combine several “weak” learning models into a single “strong” model by iteratively learning from the mistakes of the weak learners. The algorithm can handle non-linear relationships between the input features and the target variable. It is also able to cope with missing data and outliers.[18] AdaBoost was implemented using the scikit-learn library.[19]

3.7. Extreme Gradient Boosting (XGBoost)

XGBoost is an open-source implementation of the decision tree gradient-boosting algorithm. The basic idea of gradient boosting is to train a series of weak models, where each model is trained to correct the previous model’s errors. By iteratively fitting the trees, XGBoost is able to build a highly accurate ensemble of decision trees that can capture complex nonlinear patterns in the data.[20] This ensemble of decision trees is based on gradient tree boosting, i.e. the trees grow sequentially with the knowledge gained from their predecessor. But this method is prone to overfitting, which XGBoost reduces by applying regularisation objects, shrinkage, and feature subsampling. XGBoost was implemented using the open-source python library XGBoost.[21]

3.8. Stacking

With the stacking method, the strengths of multiple individual models are harnessed by combining them into a single meta-model.[22] In this project, different combinations of base forecasting models such as Random Forest, ESN, TFT and LSTM models were analysed. The individual base models' predictions are fed as features into a meta-model, which then makes the final prediction.[22] This can be done in different ways. The stacking methods examined in this project were k-fold variation, bagging and averaging. All three methods were implemented via the scikit-learn library.[19]

4. Data characteristics and their effects on forecasting performance

When assessing a model's ability to make predictions, it is not only the quality of the training data that must be considered, but also its relevance to the current situation. In the context of district heating supply, certain factors influence demand independently of the events that can be planned and modelled. The outbreak of the Covid-19 pandemic was a major unforeseeable event that impacted energy needs, shifting the demand from industrial areas and educational institutions to residential areas. This presents a challenge for cities that operate separate networks for different urban areas, since previous regularities in the data are no longer valid. Additionally, it is uncertain whether the end of an event will restore the previous conditions, or whether changes in energy requirements caused by increased working from home during lockdowns will persist. Old training data may no longer be suitable for training models based on weight adjustments when networks expand or new urban areas are connected, leading to an increase in demand. Seasonal effects, along with the energy consumption of industrial plants that require hot water for their processes, must also be taken into account.

To account for these changes in the model, data must be collected for the altered consumption profile and used to train a new model. In addition to sudden changes such as grid expansion, primary energy shortages, and shifts in user behaviour, long-term global transformations such as climate change must also be considered. These changes occur continuously and can be compensated for with appropriate methods, as described in section 6.

In summary, numerous factors strongly influence the demand presented by a supply network. This project only utilised quantifiable influences to train the models. While it would be possible to incorporate additional data e.g. from climate models, economic forecasts, political events, crisis models, stock prices, and other forms of news into a model, it would be a time-consuming process that would not guarantee long-term improvement. Nevertheless, these factors should be taken into consideration when evaluating and using a forecasting technique. While machine learning models can recognise patterns in data that humans cannot see, it is important to note that there are no conscious trains of thought behind these mathematical models and that only information contained in the machine learning features used can be taken into account.

5. Benchmarking results

Fifteen years of operating and weather data in hourly resolution were used to train the machine learning algorithms. All eight subnetworks in the city of Ulm were analysed, each providing different challenges in terms of demand profiles, data quality and consumer structure. The data used in the following analysis came from a subnetwork of Fernwärme Ulm GmbH spanning a total length of 40 km and representing an annual heat demand of 75 GWh or 1,100 households. Hence a total of 131,400 data sets were used, each consisting of twenty parameters, i.e. measurement data from the district heating network and weather information such as air temperature, wind direction and wind speed. The correlation between individual parameters and the associated district heating load was previously checked by means of a correlation analysis.[23]

When optimising and comparing the quality of forecasting algorithms, the characteristics of the metrics used must be taken into account. In this project, mainly the mean absolute percentage error (MAPE) was investigated because it is easy to interpret and dimensionless. However, a weakness of the MAPE becomes apparent when the forecast values are very low, as during the summer months. The metric is skewed at values close to zero.[24] Therefore, the mean average error (MAE) is used in addition. In the following analysis, the forecasting methods for the heating period winter 2021 (December 2020 and January and February 2021) are examined and compared using the MAPE. This period is also the economically most interesting part of the year for heating network operators. If precise forecasts make it possible to avoid operating fossil-fuelled peaking boilers, the largest proportion of fossil fuels and thus CO_2 emissions can be saved during this period. The bar chart in Figure 2 below shows a final comparison of the forecasting errors of all analysed machine learning algorithms.

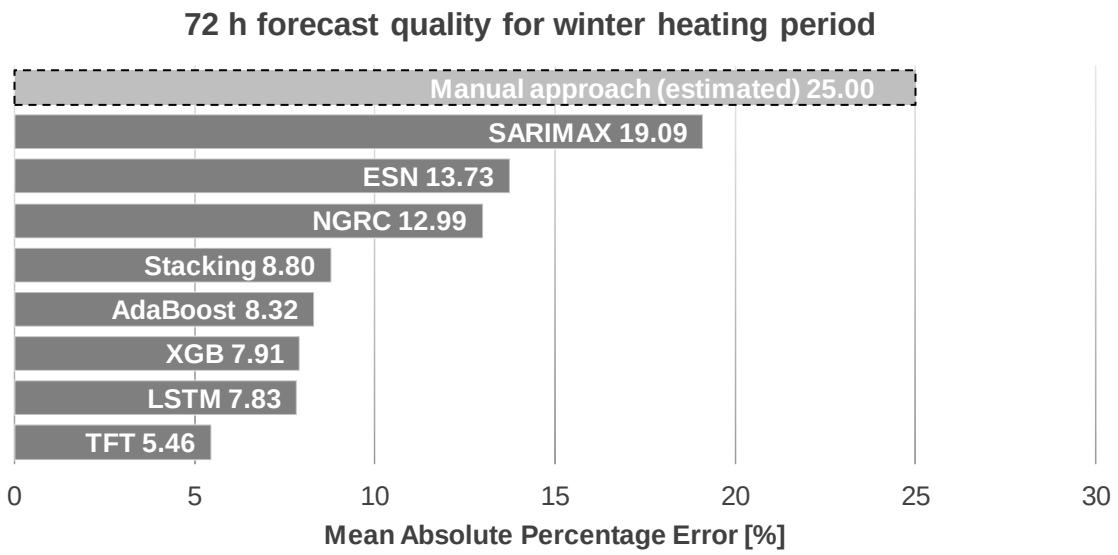

Figure 2. Final results of the 72 h forecast machine learning benchmarking

In the graph above, an estimated error of traditional forecasting methods where no machine learning algorithms is indicated for comparison. Although the SARIMAX model performs only slightly better than the estimated manual approach, it has the advantage of requiring only a small amount of data and still being able to produce a relatively good forecast (3.1 %-8.25 %) for a short time horizon of 12-24 hours (not shown in the graph). However, when predicting over a longer time horizon of 72 hours, the SARIMAX model performs significantly worse, with a MAPE of 19.09%. The NGRC and ESN recurrent neural networks show a similar performance, with NGRC slightly outperforming ESN with a MAPE of 12.99%. Similarly to SARIMAX, these algorithms also have other advantages besides a competitive forecasting error, such as the lower calculation power required and faster training time, which is briefly discussed at the end of this chapter. Throughout the project, it was found that stacking does not necessarily lead to better forecasts than the best individual method. Among the various stacking methods that were examined, such as k-fold variation, bagging, and averaging, simple averaging led to the lowest error value of 8.8%. However, stacking was found to be computationally expensive and required careful tuning of hyperparameters in order to avoid overfitting. Of the examined learning methods, AdaBoost, XGB, and LSTM are amongst the best and most stable, with a forecasting error of around eight percent. The LSTM model, in particular, achieves excellent forecasting quality and has lower memory requirements compared to XGB and AdaBoost, making it one of the most attractive models, but it requires significant implementation effort due to the many hyperparameter options and complex data pre-processing. However, the LSTM model demonstrated excellent adaptability when it was faced with new data. For example in scenarios that were previously unknown to the model, such as the Covid-19 pandemic or the increase in gas prices in 2022, which caused a reduction in heat demand, the LSTM model showed consistent results.

Overall, TFT delivers the best result for the examined subnetwork, with approximately 5.5% MAPE. Figure 3 illustrates the forecasting quality by showing the actual thermal load, the load prediction of the best TFT algorithm, and the percentage deviation for this method over a 72-hour period.

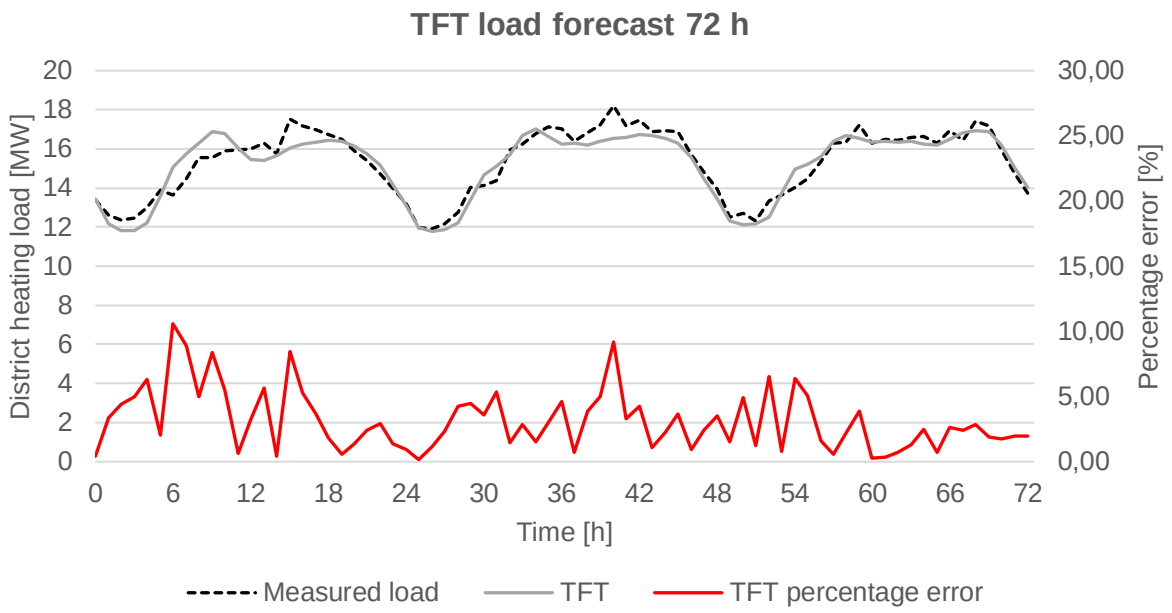

Figure 3. Example of a 72h thermal load forecast using the TFT model.

During live operation at a different grid operator, similar successful forecasting results have been observed. TFT is also one of the most complex algorithms to implement. But on the other hand, TFT offers the ability to predict multiple time series with a single model. If a district heating supplier operates several networks, which is usually the case, a separate model would have to be trained for each network when using a classic machine learning model. With the TFT model, this would no longer be necessary, since the model can assign features to different target predictions by classifying features into groups.[25] As a result, it is only necessary to train a single model for several use cases, which ideally saves time and money.

Benchmarking in terms of calculation power and training time is not straightforward as it depends heavily on the complexity of the model and various other factors such as the size and quality of the data and the hardware used for computation. However, the ESN and NGRC models proved to be exceptionally efficient, even if they do not provide the best forecasting quality. A monthly forecast with approx. 60,000 training data sets can be carried out using a simple office notebook (Intel Core i7-6600U, 16GB RAM, Windows 10) in a period of a few seconds. In comparison, the TFT model computed on a server with comparatively powerful hardware (NVIDIA Quadro RTX 6000 graphics card) needs about 30 minutes for the same training and forecasting process. In addition, the ESN model is very easy to implement and is one of the most user-friendly algorithms analysed.

6. Automated optimisation routine

During the initial setup of each model, various parameters need to be determined such as the choice of subnetwork, training timeframe, and the suitable dataset features. Adjusting the model-specific hyperparameters is usually part of “fine tuning” process, which enables the model to be adapted to the specific network in question. Each district heating network presents its own issues and characteristic properties, such as consumer structure, data quality and consumption patterns (households, industrial customers). A model that delivered very good results for one network might possibly deliver poor to unusable results for a network unknown to the model. Hence a network-specific approach with an automated optimisation routine was developed.

The developed routine is based on a random search algorithm.[26] The best model up to that point is loaded from the database and used as a reference. With the random search method, an n-dimensional parameter space is searched intelligently. By considering the effects of individual changes, parameters with a high impact are examined more intensively. This results in greater efficiency in contrast to a structured grid search. After a comparison, the best model is saved in the database and the process repeated. The system can use this routine to react to changes (network expansions, intensive savings measures, lengthy sub-network failures), in a limited scope, within a few intervals.

6. Live operation and web interface

In addition to benchmarking thermal load forecasting itself, a software system and web interface for live forecasting at the operator's site was developed. This covered a process of data aggregation, including a fully automated routine for regularly fetching required data from different sources, and combining them in a data warehouse. It included a step of screening and cleaning invalid data using methods such as imputation or other replacement strategies. Besides robust backend systems aiding the training and usage of machine learning models, a means of presenting the predictions and additional information to the operator of the district heating network is required. Thus a user-friendly web interface, capable of displaying 72-hour time frames of predictions together with corresponding data for any given date, was developed in cooperation with the district heating system operator. A screenshot of the thermal load forecasting web interface, which was installed at the operator's facilities in summer 2021 and has been in operation since then, is shown in Figure 4 below.

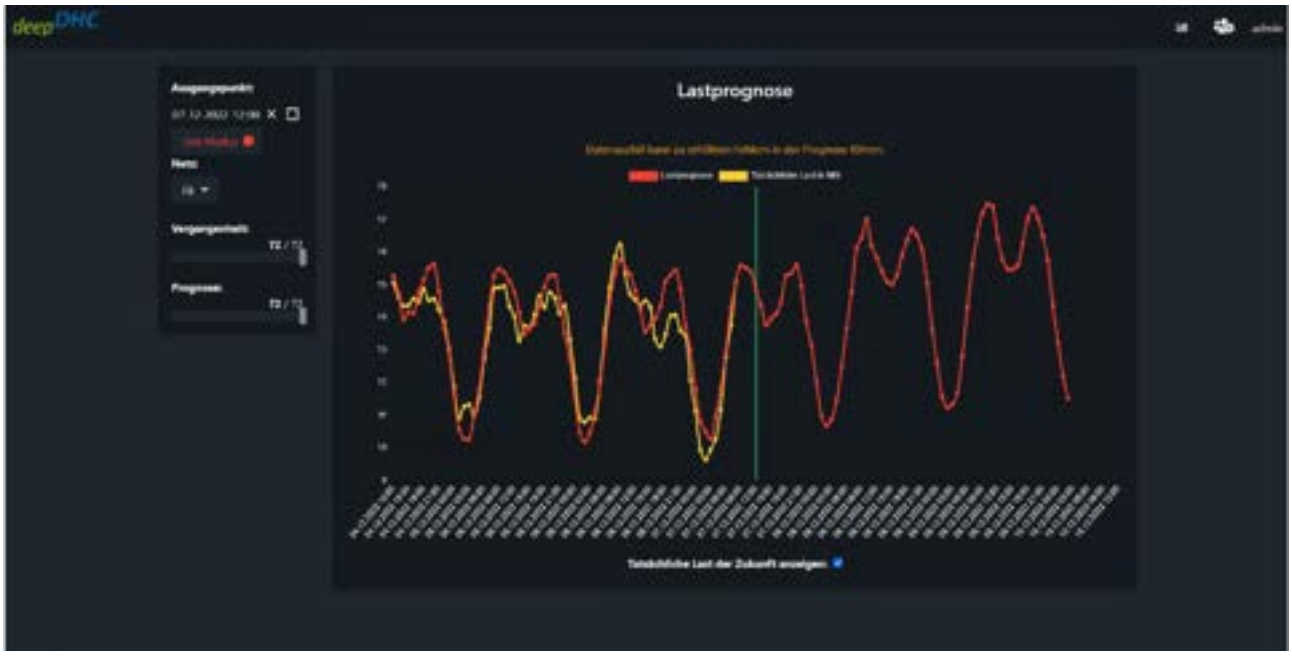

Figure 4. Web-based user interface developed for live operation of load forecasting.

7. DeepDHC user guide

A short guide was created to show the basic steps necessary to implement any of the described models. It is accessible via the code hosting platform GitHub under the following link:

https://github.com/deepDHC/deepDHC-user-guide

This guide will go through an example scenario that will use the historic thermal load and weather data to train a LSTM model. This model will then be saved and loaded from disc to do load predictions for another timeframe. Moreover, it shows how to calculate errors of the predictions compared to the real load demand, thereby providing a brief overview about all basic components needed to create models for district heating demand predictions.

8. Conclusion

The research project deepDHC systematically benchmarked thermal load forecasts using state-of-the-art machine learning methods, such as neural networks, decision trees and statistical methods. The study utilised long-term historical operating data from the district heating network in Ulm, Germany, combined with historical weather data and weather forecasts. Thermal load forecasts were predicted for three days ahead, in comparison against one another, and an automatic tuning routine was developed to retrain machine learning algorithms based on the latest operating data.

A key takeaway from the analysis is that a proper database has at least the same influence on forecasting quality as the model selection. Each and every district heating network is different and requires a model that is tailored to the specific network and database (see "No Free Lunch" theorem [27]).

Over a time period of 72 hours in advance, the developed forecasting tools were able to predict the thermal load within a mean average percentage error of five to eight percent for the investigated district heating subgrid. In summary, the TFT model performs best in the examined subnetwork with respect to forecasting accuracy. An attractive option is also the LSTM model, since it turned out to be computationally more efficient compared to the TFT model, whilst still ranking amongst the best and most stable algorithms in this study.

As part of a plant dispatch optimisation process, the forecasting methods that were analysed in this study can help to operate district heating networks more efficiently and cost-effectively.[3] By developing a web interface, the best analysed forecasting models could be made available for use in live operation and optimisation by the district heating system operator.

Acknowledgments

This work was funded by the German Federal Ministry for Economic Affairs and Climate Action under the funding code 03EN3017, with additional financial and in-kind support from the project partners AGFW, Fernwärme Ulm GmbH and ZAK Energie GmbH. The responsibility for the content of this publication lies with the authors. The authors would like to thank Till Faber and Jonas Brantl for their support during the study.

References

1. Corscadden J., Möhring P, Krasatsenka A. Renewable Energy Sources in District heating and Cooling: EU Level Survey. 2021.
2. VDI 4655: Reference load profiles of residential buildings for power, heat and domestic hot water as well as reference generation profiles for photovoltaic plants 2021.
3. Finkenrath M, Faber T, Behrens F, Leiprecht S. Holistic modelling and optimisation of thermal load forecasting, heat generation and plant dispatch for a district heating network. Energy 2021. doi:10.1016/j.energy.2022.123666.
4. Geysen, D., De Somer, O., Johansson, C., Brage, J., Vanhoudt, D. Operational thermal load forecasting in district heating networks using machine learning and expert advice. Energy and Buildings;2018:144–53.
5. Huang, S., Tang, W., Wu, Q., Li, C. Network constrained economic dispatch of integrated heat and electricity systems through mixed integer conic programming. Energy;2019:464–74.
6. Idowu, S., Saguna, S., Ahlund, C., Schelen, O. Applied machine learning: Forecasting heat load in district heating systems. Energy and Buildings;2016:478–88.
7. Xue, P., Jiang, Y., Zhou, Z., Chen, X., Fang, X., Liu, J. Multi-step ahead forecasting of heat load in district heating systems using machine learning algorithms. Energy. 2019.
8. Fang T, Lahdelma R. Evaluation of a multiple linear regression model and SARIMA model in forecasting heat demand for district heating system. Applied Energy. 2016:544–52.
9. Seabold, Skipper, Perktold J. Statsmodels: Econometric and Statistical Modeling with Python. Proceedings of the 9th Python in Science Conference. 2010.
10. Cortes C., Lawrence N, Lee D., Sugiyama M., Garnett R. Advances in neural information processing systems: Hidden Technical Debt in Machine Learning Systems. NIPS Proceedings. 2015.
11. Trouvain N., Pedrelli L. ReservoirPy. An Efficient and User-Friendly Library to Design Echo State Networks. 2020. https://hal.inria.fr/hal-02595026.
12. Jaurigue L, Lüdge K. Connecting reservoir computing with statistical forecasting and deep neural networks. Nature Communications. 2022.
13. Bollt E. On explaining the surprising success of reservoir computing; 2020.
14. Behrens F, Leiprecht S, Brantl J, Finkenrath M, Behrens F, Leiprecht S, et al. Temporal Fusion Transformer for thermal load prediction in district heating and cooling networks. SIMS Proceedings;2022:333–8. doi:10.3384/ecp192047.
15. Paszke A. et al. PyTorch: An Imperative Style, High-Performance Deep Learning Library. Advances in Neural Information Processing Systems 32. 2019:8024–35.
16. Hochreiter S., Schmidhuber J. Long Short-Term Memory. Neural Computation;1997:1735–80.
17. Chollet F. et al. Keras. Journal of Data Analysis and Information Processing. 2016.
18. Raschka S, Mirjalili V. Machine Learning mit Python und Keras, TensorFlow 2 und Scikit-learn: Das umfassende Praxis-Handbuch für Data Science, Deep Learning und Predictive Analytics. 2021st ed. Frechen: MITP; 2021.
19. Pedregosa et al. Scikit-learn: Machine Learning in Python. JMLR. 2011:2825–30.
20. Chen T, Guestrin C. XGBoost: A Scalable Tree Boosting System. Proceedings of the 22nd ACM SIGKDD International Conference on Knowledge Discovery and Data Mining. 2016:785–94. doi:10.1145/2939672.2939785.
21. xgboost developers. XGBoost Documentation. 2022. xgboost.ai.

22. Wolpert D. Stacked Generalization. Neural Networks. 1992:241–59. doi:10.1016/S0893-6080(05)80023-1.
23. Faber T, Groß J, Finkenrath M. Innovative Lastprognosen mit Deep Learning-Methoden,. EuroHeat & Power;2018:1–2.
24. Barrot C. Methodik der empirischen Forschung. Prognosegütemaße. Wiesbaden: Gabler Verlag; 2007.
25. Lim B., Arik S., Loeff N., Pfister T. Temporal Fusion Transformers for interpretable multi-horizon time series forecasting. International Journal of Forecasting. 2021:1748–64.
26. Mantovani G: et al. Effectiveness of random search in SVM hyper-parameter tuning. International Joint Conference on Neural Networks (IJCNN). 2015:5–8.
27. Wolpert DH. Ubiquity symposium: Evolutionary computation and the processes of life: what the no free lunch theorems really mean: how to improve search algorithms. Ubiquity. 2013;2013:1–15. doi:10.1145/2555235.2555237.

Artificial Intelligence (AI) Based Predictive Maintenance of Waste Heat Recovery System

Sundar Raj Thangavelu[a], Alessio Tafone[b], Imantha Gunasekhara[c], Sivanand Somasundaram[d], Morita Shignore[e]

[a] Nanyang Technological University, Singapore, sundar.rt@ntu.edu.sg CA
[b] Nanyang Technological University, Singapore, alessio.tafone@ntu.edu.sg
[c] Nanyang Technological University, Singapore, Imantha.gunasekhara@ntu.edu.sg
[d] Nanyang Technological University, Singapore, sivanand.s@ntu.edu.sg
[e] Surbana Jurong Consultants Pte Ltd, Singapore, shigenori.morita@surbanajurong.com

Abstract:

Decarbonization and sustainability urge the deployment and utilization of distributed energy systems for high-efficiency gains. The dispatchable devices (gas turbines or diesel engines) are integrated with a waste-to-energy system to harness the energy lost or waste heat and support heat and cold loads. This paper investigates the characteristics of a waste heat recovery system and its performance degradation mechanism to assess its maintenance necessity and optimize maintenance frequency and the associated maintenance and downtime costs. The effectiveness of the waste heat recovery system (WHRS) is regularly estimated using the measured inlet and outlet parameters (flow and temperature) to identify the need for maintenance. The effectiveness changes not only with degradation but also with inlet conditions that deviate from the design conditions. Therefore, the operators are instructed to operate this system at the rated inputs and gauge its actual effectiveness. However, this approach did not provide much information on the root-cause parameters, i.e., the fouling formation and thickness in the shell and tube sides, which are quite important to decide the type of maintenance and the associated cost and duration. This paper studies the performance characteristics of the waste heat recovery system with reference to all critical and influential parameters (i.e., fouling thickness, heat transfer coefficients, and off-design inlet conditions) using a rigorous physics-based model. An AI model was developed using the derived performance characteristics to predict the fouling thickness estimation. The developed prediction model is able to accurately estimate the fouling thickness on the gas and water sides, and the error or deviation is within ±0.3 mm. By deploying this prediction model, the critical parameters can be monitored in real-time, and the performance degradation trajectory paves the way to understand degradation status and estimate the right maintenance time frame to schedule maintenance proactively, considering the maintenance cost and downtime effects.

Keywords:

Waste Heat Recovery; Performance degradation; Fouling Prediction Model; Predictive Maintenance; Sustainability.

1. Introduction

Wide deployments of renewables and distributed energy systems show promising efficiency gains toward decarbonization and sustainability goals. The local power generation reduces transmission and distribution losses, paves the way to harness the waste heat from the dispatchable turbines (gas or diesel) to support thermal loads at a competitive price, and greatly increases the overall energy efficiency ([1], [2]). Unlike turbines and chillers, the waste-heat recovery system, i.e., an apparatus of heat exchangers, is not standard equipment; it is usually passive and primarily designed based on specific process requirements. Over time, the heat exchanger faces fouling issues due to the continuous deposition of impurities or particles on the heat transfer area, which affects efficiency [3]. Most heat exchangers undergo corrective maintenance on a need-based basis or preventive maintenance at periodic intervals. The corrective approach causes equipment downtime and high maintenance costs; preventive maintenance, which proactively entails regular maintenance, does not account for the actual condition of the system and the maintenance needs accurately. This paper focuses on developing a fouling prediction model for waste heat recovery systems (specifically exhaust gas-driven WHRS) to support predictive maintenance planning and reduce maintenance costs and downtime.

1.1 Background – Fouling & Maintenance of Heat Recovery System

Numerous studies have discussed various maintenance methods and their evolution in diverse processes [4]. Corrective or reactive maintenance is a primitive method popularly called "run-to-failure," usually conducted after the system fails, whereas preventive maintenance performs routine periodic inspections to trigger necessary replacement well in advance to avoid any failure. Unlike reactive and preventive maintenance, the predictive approach is more tied to system performance, and it requires concrete measurement to quantify the root cause and key indicators and initiate a suitable maintenance plan. In energy systems, especially in a WHR system, fouling (carbon deposit on the gas side, salt deposit on the water side) occurs gradually over time and affects the heat recovery performance and degrades the system efficiency. The underlying root cause of fouling is the impurities in the inlet streams and their affinity for the heat exchanger surface. Unfortunately, the fouling cannot be measured directly in real-time; some of the available handheld devices support offline measurement that requires perforating the equipment ([5], [6]). Notable studies investigated different heat exchangers and their fouling characteristics. Most of the studies utilized data from experiments and exploited analytical and thermodynamic models. Riverol et al. [7] used a neural network to estimate fouling in a plate heat exchanger for the pasteurization application. The simple neural network (two inputs and one output) developed reads and processes data to detect critical operation conditions and advise on the necessity of cleaning (maintenance). The fouling in heat exchangers and the effect of various factors such as velocity, temperature, concentration, and pH influencing the fouling growth [8]. This study highlighted the variation in fouling thickness over the pipe length. Other possible root causes of fouling are particulates, biological reactions, chemical reactions, corrosion, and decomposition. The NN and RSM models were developed using one-year experimental data to predict the fouling resistance of the crossflow heat exchanger system in a phosphoric acid concentration plant [9]. Elwerfalli et al. [10] estimated the probability of failure in the heat exchangers using risk-based inspection, a ranking matrix, and the associated rectification cost. This approach helps to identify high fouling and plan the shutdown maintenance activity. A few studies investigated the suitability of various machine-learning algorithms for predicting fouling resistance in plate heat exchangers [11]. Interestingly, the focus was mainly on predicting the combined resistance but not the individual resistance and its root cause parameters. Deep learning techniques [12] were adapted to predict the resistance on the gas and water sides as well as the combined resistance with reasonable accuracy. This study considered all critical measurements in the NN model, including flow at fouled conditions, but did not provide much information on translating the derived resistance into maintenance decisions.

Most of the above studies focused on improving the accuracy of the prediction model by using rigorous and sophisticated machine learning and artificial intelligence algorithms using limited real-time data or adequate data from analytical and thermodynamic models. In the majority of processes, upstream processes supply the inlet gas and water; in such cases, fouling mainly imposes an additional pressure drop when the inlet and outlet flow remain the same. This paper aims to study the influence of each measurement (feature) on the prediction results and discover the crucial measurements that can provide acceptable accuracy. Identifying the key inputs prevents needless sensor and instrumentation costs and mainly reduces the complexity of the prediction model to apply in real-world applications. By deploying the prediction model in the process monitoring system, it helps the operator identify the fouling thickness and growth phenomenon regularly. The continuous prediction and monitoring of fouling thickness helps identify the fouling growth rate and type (linear, falling, asymptotic, or saw tooth) [13] that depends on the inlet streams, such as velocity, impurities, and affinities towards the heat exchange surface [14]. By projecting the fouling trend at every time period (monthly or quarterly), the operator can estimate the fouling status for the next time period and decide the need for maintenance activity by comparing it with the tolerance level. Identifying the right time well in advance allows the operator to plan the maintenance activity efficiently, i.e., devise the right maintenance schedule or frequency (washing, purging, antifouling agents, etc.), conduct a cost analysis covering maintenance cost, performance gain cost, and downtime cost, and accordingly trigger the necessary redundancy and alternative operation choices to reduce the production loss.

2. Methodology

2.1 Predictive maintenance concept

The concept of the proposed preventive maintenance methodology for the waste heat recovery system (WHRS) is illustrated in Figure 1. The actual operational data for the duration of a year is the prerequisite for this methodology to model the system's performance and study the effect of scaling parameters. The expected outcome is a maintenance schedule recommendation considering all critical factors such as maintenance cost, downtime effects, and energy efficiency gains. Generally, the actual operation data can

be extracted from the process energy management system (EMS). Data pre-processing is required to remove measurement noise and outliers and mainly extract the required steady-state values from the time-series operation data [15]. In WHRS, the flow, pressure, and temperature of the exhaust gas and water are the critical variables that can be easily measured using appropriate sensors at the inlet and outlet streams. The challenge is measuring the fouling thickness on the interior and exterior of the tubes. Real-time measurement is not possible to measure fouling readily; some of the available hand-held devices require dismantling the system, which is expensive, and regular measurement is not possible [6]. In such cases, leveraging thermodynamic models is very relevant for the user to generate system performance at various inlet, surrounding, and fouling conditions. The minimal computational resources, fast computation, and freedom from measurement noise are additional benefits. Alternatively, in cases of limited operational data, it is good to supplement additional data from thermodynamic models, mainly to account for atypical operation conditions.

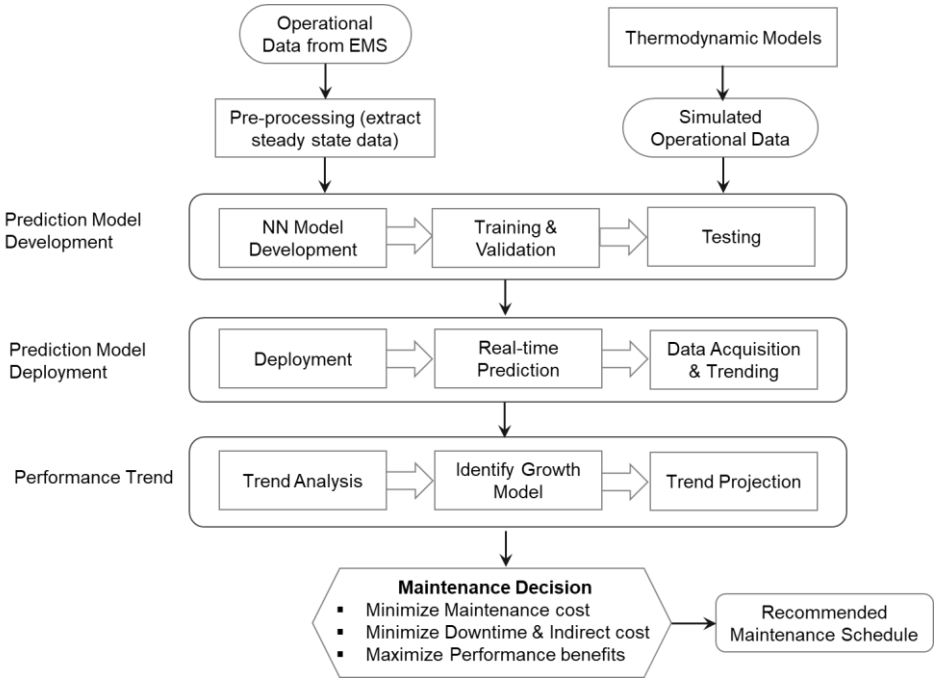

Figure. 1. Schematic of proposed preventive maintenance methodology

Numerous AI-based data-analytic algorithms are emerging to understand and capture system behavior from the data. Interestingly, in certain situations, AI-based data-analytic model development outperforms conventional physics-based models in terms of development time, resources, and prediction accuracy, especially for complex multi-variate systems. However, a data-analytic model requires substantial data for model training, validation, and testing, and the representative data should cover wide ranges to capture the system behavior comprehensively [16].

Deploy the developed data-analytic model in the process EMS and estimate the essential variables using the measurements available in real-time. Of course, the estimated variable may show some variations due to measurement noises, system dynamic behavior, and different inlet conditions. The key takeaway is the trend of the estimated variable on a long run (i.e., on a weekly, monthly, or even quarterly basis) to understand the scaling growth or build-up and performance deterioration trends. Incorporating or configuring a few processing techniques in EMS helps to remove the noise and outliers in the trend so that the system operator can identify the trend and extrapolate for future timeframes of interest. This projection will give an indication of the time when the system performance could fall below the acceptable tolerance and enable the operator to decide the maintenance schedule accordingly. Mainly, this insight or alert comes well in advance so that the operator has adequate time and operation flexibility to plan the maintenance schedule optimally by considering key factors such as system performance, expected downtime, downtime implications, maintenance cost, and benefits.

2.2 WHRS Performance

Figure 2 illustrates a cross-section and elevation view of a tube surface and pinpoints the type of fouling formation on the inner and outer surfaces of the tubes. The exhaust gas flows inside the tube, and water flows outside the tube (i.e., in the shell). Various thermodynamic models, such as the e-NTU method and physics-based ODE and PDE approaches, can estimate heat exchanger performance in diverse inlet scenarios. The e-NTU method [17] is widely employed to estimate the outlet conditions (T_{go} and T_{wo}) of the WHRS for the given inlet conditions (M_g, T_{gi}, M_w, T_{wi}), system (U_{ref}, A), and fouling parameters (t_{shell}, t_{tubes}). The e-NTU model, the pressure drops, and the performance of WHRS are described in Eq. 1 – 11, these equations can be either solved simultaneously using the EES or sequentially and iteratively using MATLAB or Python. The Cp_g and Cp_w represent the heat capacities of exhaust gas and water at their arithmetic mean temperatures. The U_{ref} and U_{calc} refer to the overall heat transfer coefficient of clean and fouled WHSR. The U_{ref} and A are taken from the specification sheet of the pilot plant facility. To simplify and balance the complexity of the thermodynamic model, a few key assumptions were incorporated, such as (i) uniform scaling along the tube length, (ii) fouling causes additional heat resistance and the effect on the heat transfer area is insignificant, and (iii) negligible heat losses to the surrounding area due to perfect insulation on the shell side.

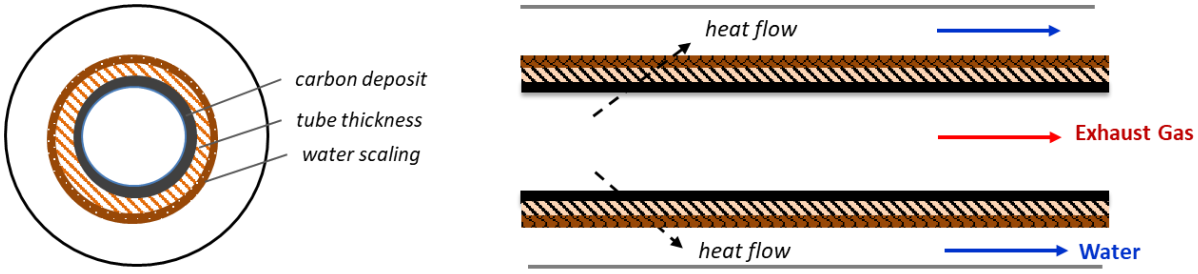

Figure. 2. Cross-section and elevation view of heat exchanger section

$$Q_g = Q_w = Q_{LMTD} \tag{1}$$

$$Q_g = M_g Cp_g\left(T_{gi} - T_{go}\right) \tag{2}$$

$$Q_w = M_w Cp_w (T_{wi} - T_{wo}) \tag{3}$$

$$Q_{LMTD} = U_{calc} A \Delta T_{LMTD} \tag{4}$$

$$Cp_g = \frac{1}{2}\left(Cp_{g,@T_{gi}} + Cp_{g,@T_{go}}\right) \tag{5}$$

$$Cp_w = \frac{1}{2}\left(Cp_{w,@T_{wi}} + Cp_{w,@T_{wo}}\right) \tag{6}$$

$$\Delta T_{LMTD} = \frac{(\Delta T_1 - \Delta T_2)}{ln\left(\frac{\Delta T_1}{\Delta T_2}\right)}, \quad \Delta T_1 = T_{gi} - T_{wi},\ \Delta T_2 = T_{go} - T_{wo} \tag{7}$$

$$\frac{1}{U_{calc}} = \frac{1}{U_{ref}} + \frac{R_{f,g}}{A_i} + \frac{ln\left({D_o}/{D_i}\right)}{2\pi kL} + \frac{R_{f,w}}{A_o} \tag{8}$$

$$P_{go} = P_{gi} - \Delta P_{tubes,foul} \rightarrow \frac{\Delta P_{tubes,foul}}{\Delta P_{tubes,clean}} = \frac{f_f}{f_c}\left(\frac{d_{tubes,clean}}{d_{tubes,foul}}\right)^2 \tag{9}$$

$$P_{wo} = P_{wi} - \Delta P_{shell,foul} \rightarrow \frac{\Delta P_{shell,foul}}{\Delta P_{shell,clean}} = \frac{f_f}{f_c}\left(\frac{d_{eff\_shell,clean}}{d_{eff\_shell,foul}}\right)^2 \tag{10}$$

$$\eta = \frac{Q_{act}}{Q_{opt}} \times 100\% = \frac{Q_{act}}{UA(\overline{T_g} - \overline{T_w})} \times 100\% \qquad \overline{T_g} = \frac{1}{2}\left(T_{gi} + T_{go}\right),\ \overline{T_w} = \frac{1}{2}\left(T_{wi} + T_{wo}\right) \tag{11}$$

Equation 9 and 10 estimate the pressure drop of the gas and water streams (adapted from Kakac et al. [3]). The efficiency of the heat exchanger is the ratio of the actual and optimal heat transfer rates expected in the heat exchanger. The optimal (maximum) heat transfer rate is the product of the UA of the heat exchanger and the arithmetic mean temperature difference (AMTD) of the inlet and outlet streams [18]. Deploying the e-NTU model in the process EMS to estimate the fouling thickness in real-time is challenging because the e-NTU model requires accurate measurement of all critical measurements and computation resources. On the other hand, the AI model can be easily deployed in EMS and is capable of estimating the fouling thickness in real time with minimal computation effort without facing any convergence issues.

2.3 Fouling Prediction Model

The AI-NN architecture (as shown in Figure 3) comprises seven inputs and two outputs used for fouling prediction on the inner (gas fouling) and outer (water fouling) surfaces of the tubes. The inputs (features) are gas flow, gas inlet and outlet temperature, water inlet and outlet temperature, and the pressure drop on the gas and water streams. The water flow remained at its designed condition. The operational data is the requirement for the prediction model development, and the data should cover the board operation range, i.e., all possible operation scenarios such as design and off-design conditions.

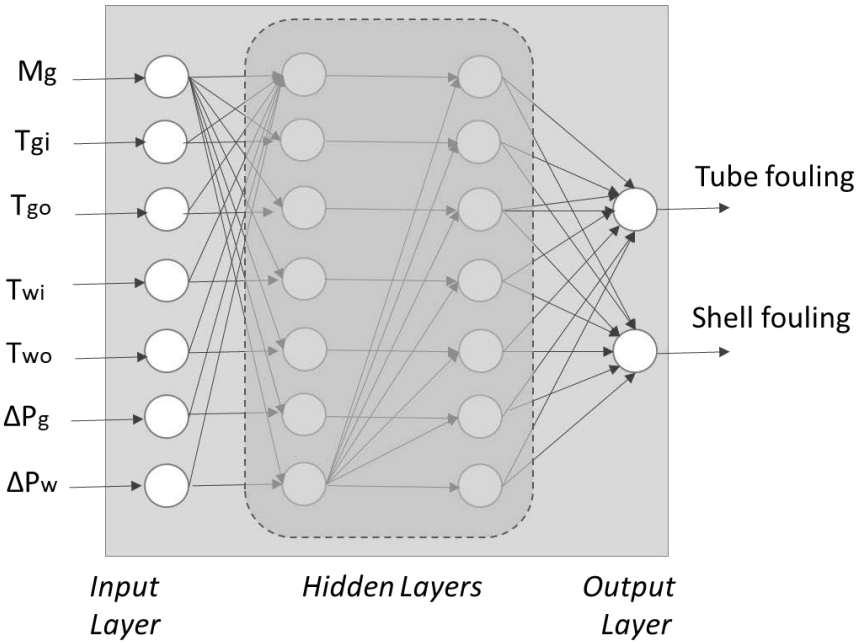

Figure. 3. Schematic of Neural Network architecture used for the fouling prediction.

The number of hidden layers and epochs are the tuneable parameters to balance the model complexity and achieve the desired prediction accuracy. In addition to the fouling prediction, this study aims to understand the importance of inputs (features) and their effects on prediction accuracy. By comprehending the importance of the inputs, they can be categorized as primary and secondary; eventually, the secondary inputs can be either eliminated or wisely chosen to simplify the prediction model and the associated data and instrument requirements without losing the accuracy of fouling prediction. The workability of the proposed methodology will be discussed in the following section using a case study problem.

3. Case Study – Combined Heat & Power (CHP) System

The proposed preventive maintenance methodology is applied in a pilot plant facility at NTU's Experimental Power Grid Centre (EPCG), Singapore. EPGC has a unique test facility, rated above 1 MW of distributed energy resources that allows test-bedding and research, development, and demonstration (RD & D) of a variety of energy technologies. Figure 4 shows the schematic of the integrated electrical and thermal grid facility at EPGC [19]. The generators serve the electrical load, and the exhaust gas from the generators powers the thermal grid to harness waste heat and convert it into useful energy. The thermal grid comprises critical systems such as a WHRS, an adsorption chiller, and thermal storage responsible for recovering waste energy and generating useful forms of thermal energy. The WHRS recovers heat in the form of steam or hot water, depending on the heat potential of the exhaust gas and the type of thermal load. Figure 5 shows a shell and tube heat exchanger as WHRS based on the generator size and the thermal and chemical properties of exhaust gas. The designed WHRS recovers 55%–80% of heat from the exhaust gas, whereas the rest is rejected to the atmosphere, considering the thermodynamic and design limits. The real benefits occur when the heating loads are located near the WHRS; otherwise, the pumping cost needs to be considered. When the generated steam or hot water is higher than the heating loads, either thermal storage is a preferable option to store excess energy for later use or convert it to other forms of useful energy, such as chilled water for air conditioning purposes. This integrated system improves overall energy efficiency by recovering the waste heat from the exhaust gas and converting it into various useful forms of thermal energy [20].

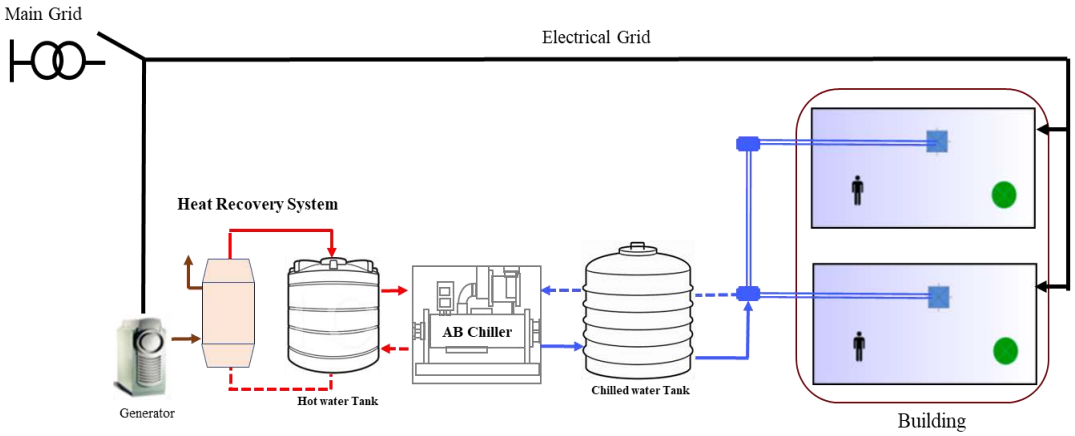

Figure. 4. Schematic of integrated electrical and thermal grids at EPGC

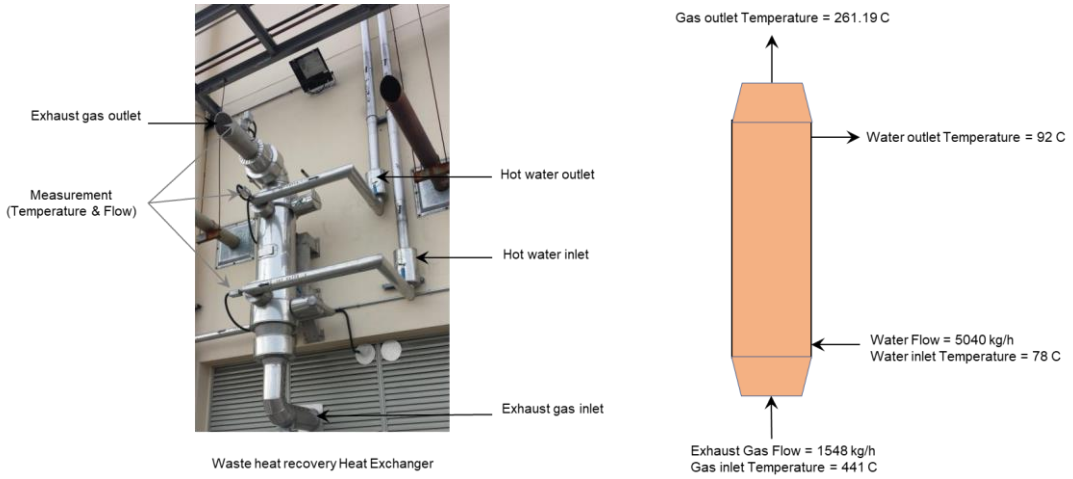

Actual Testbed Design Condition

Figure. 5. Waste heat recovery system: a) Actual system; b) Design conditions

Figure 5 shows the actual WHRS supporting various experiments and testing smart technologies and its design conditions (Table 1). The performance of the WHRS deteriorates over time due to fouling at the inner and outer tubes due to exhaust gas and water, respectively. The carbon and salt deposit builds up gradually, increases the thermal resistance significantly, and reduces the heat transfer between gas and water. The fouling on the interior of the tubes reduces the gas flow area, increases the pressure drop, and influences the back pressure of the generator and its performance. The fouling on the exterior of the tubes reduces the flow area of water and increases the pressure drop and pumping power. Therefore, real-time estimating of fouling is important to understand the system condition and plan maintenance optimally.

Table 1. WHRS designed inlet and outlet properties.

Parameters	Design Condition
Flue gas inlet Flow & Temperature	1548 kg/h and 441 C
Water inlet Flow & Temperature	5040 kg/h and 78 C
Flue gas inlet & outlet pressure	105 and 104.2 kPa
Water inlet & outlet pressure	1000 and 998.5 kPa
Flue-gas fouling factor	0.6 W/mK
Water scaling factor	2.941 W/mK

The actual operational data is the prerequisite for predictive maintenance methodologies. Representative operational data should capture wide operation conditions (i.e., all possible inlet and scaling

cases). Unfortunately, in the actual system, the possibility of collecting broad operational data is difficult because (i) fouling occurs in the long run, (ii) all variables cannot be measured online, especially fouling thickness [6], and (iii) the actual operating range is limited, not wide-ranging. Hence, this study exploits a thermodynamic model to generate complete data under diverse operational conditions.

3.1 WHRS Performance Characteristics and Effects of Fouling

Figure 6 shows the derived outlet condition of WHRS under diverse fouling conditions derived using the e-NTU model. Both carbon deposits and water fouling reduce the heat exchange between exhaust gas and water; therefore, the outlet temperature of exhaust gas increases and the outlet temperature of water decreases compared to the rated outlet condition. The carbon deposit greatly influences the outlet temperature more than water scaling because the heat flows from the gas to the water, and the carbon deposit has low thermal conductivity and imposes high resistance. For example, flue gas resistance is roughly five times higher than that of water. Figure 7 shows the expected performance of the heat exchanger under diverse fouling conditions.

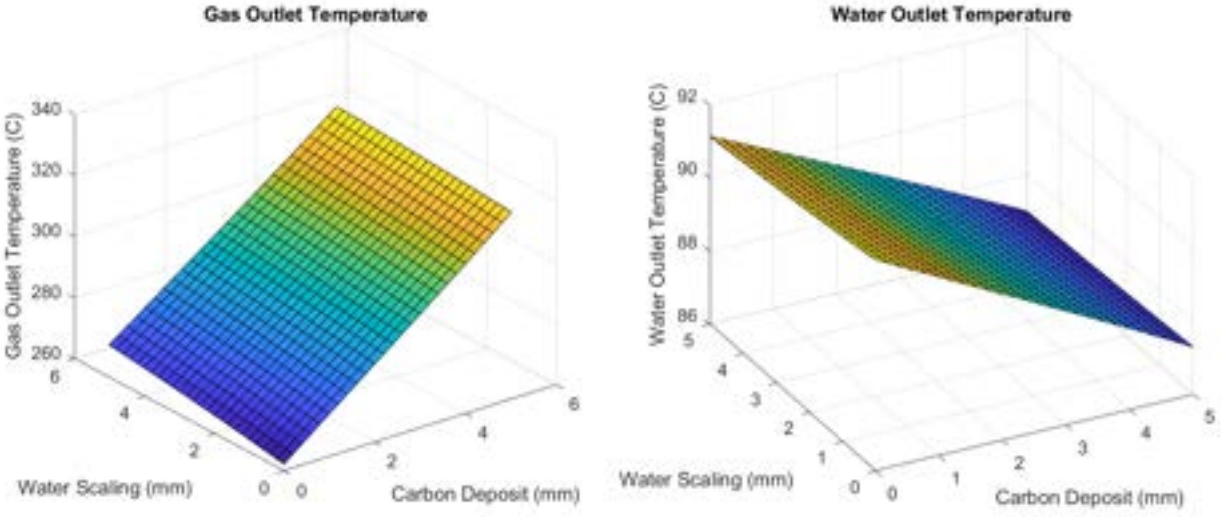

Figure. 6. WHRS performance at diverse fouling (at rated inlet conditions)

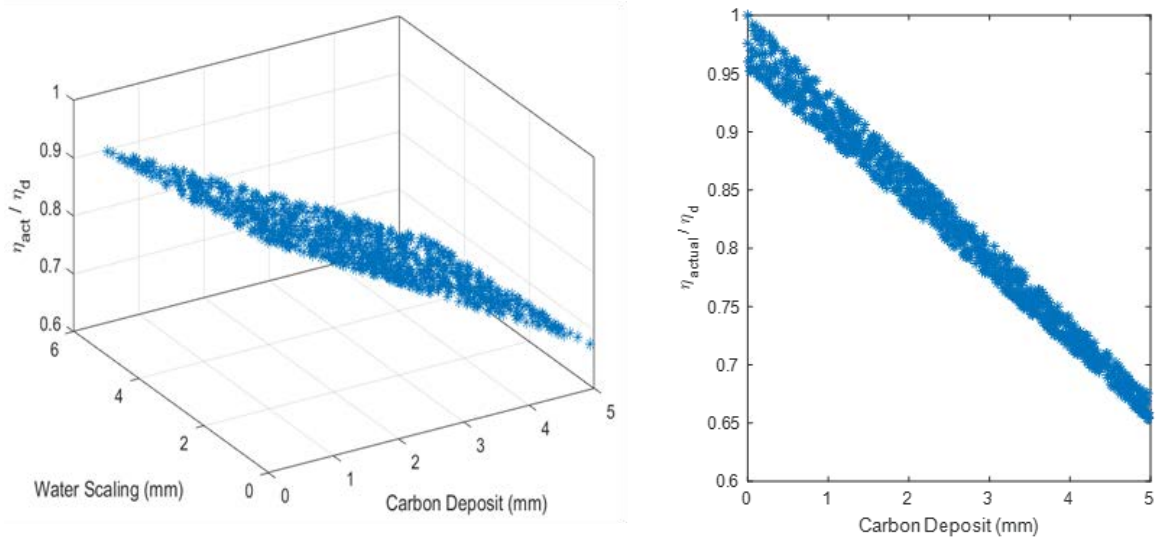

Figure. 7. Normalized performance of WHRS at different fouling (at rated inlet conditions)

In real-world operation, the inlet exhaust gas flow and temperature to the WHRS change with upstream processes such as generator loading and return water conditions. Table 2 shows the operating range

extracted from the historical data of the WHRS. Regrettably, the fouling information is not readily available; therefore, the e-NTU method was exploited to estimate the fouling thickness. The next section will discuss the development of a prediction model to support the predictive maintenance of the WHRS.

Table 2. WHRS Operation Range.

Inlet and outlet streams	Operating range
Flue gas inlet flow	60-100% of designed gas flow
Flue gas inlet temperature	441 – 492.1 C
Water inlet flow	60-100% of designed water flow
Water inlet temperature	78 – 84 C

3.2. AI-NN Fouling Prediction Model

The required performance data was generated for 1000 operational scenarios (uniformly distributed) covering design and off-design conditions, accounting for the actual operation range (as stated in Table 2), and the corresponding fouling estimated by solving the e-NTU model using the EES solver [21]. The AI-NN model with five hidden layers offers acceptable prediction accuracy (R^2 = 99.87% and MSE = 0.005). Figure 8 shows the actual and predicted fouling thickness on the inner and outer tubes (shell sides). The fouling on the inner tube is dominant due to high resistance (as mentioned in Table 1) compared to the fouling on the outer tube. Figure 8c and Figure 8d confirm the error is within an acceptable range and well below ±0.3 mm. To keep in mind, the performance data utilized is smooth; however, in the real application, the actual data may contain instrumentation errors and measurement noises that need to be pre-processed cautiously before applying to the prediction model.

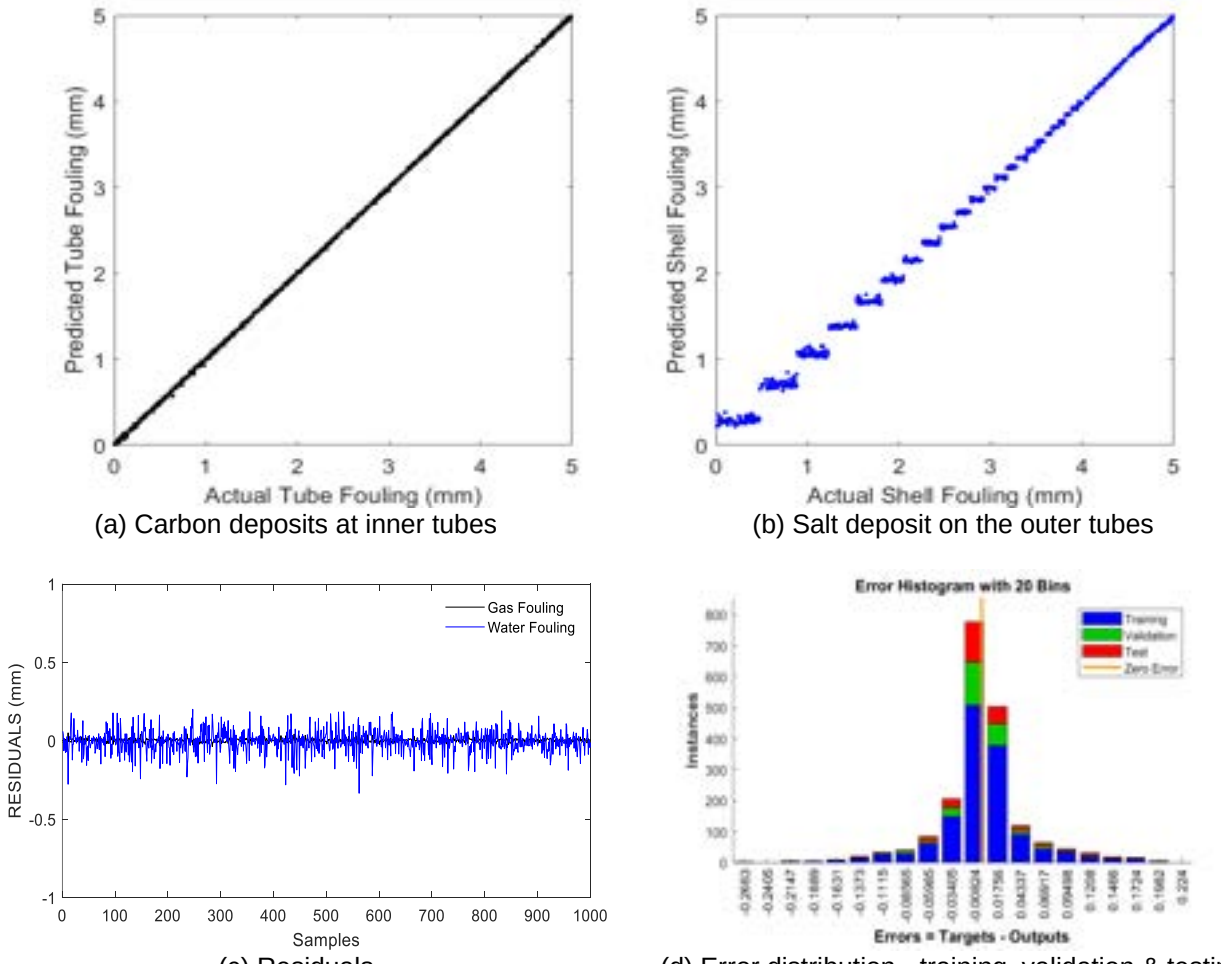

(a) Carbon deposits at inner tubes

(b) Salt deposit on the outer tubes

(c) Residuals

(d) Error distribution - training, validation & testing

Figure. 8. (a) and (b) show the actual and predicted fouling thickness on the tube and shell side. (c) and (d) shows the residuals and prediction error of training, validation, and testing set.

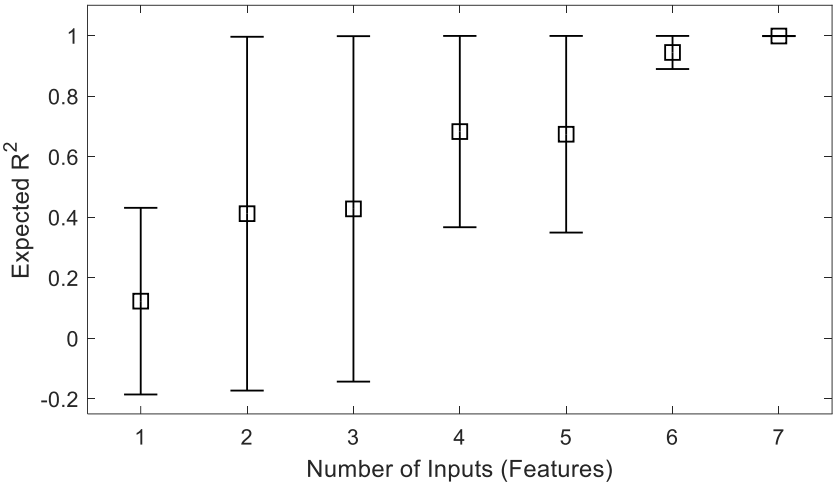

Figure. 9. Number of features and the expected prediction accuracy in regression coefficient.

Even though the above model can predict the fouling thickness accurately, it is essential to understand the importance of each feature to reduce the complexity of the prediction model and operational data requirements. Various recursive feature elimination methods such as random forest, SVM, k-nearest, and neural networks can be useful to study the importance of the features. These methods conduct model training repeatedly and eliminate the weakest feature in each iteration until the specified number of features is reached. The feature selection is purely based on the coefficients; in the case of decision tree-based models (i.e., random forest), the feature selection is based on the importance attribute. This study employed Random Forest for feature selection, which identifies the best feature to split at the next node from a subset of features based on a criterion such as mean squared error, which explains variance reduction to minimize the loss [22]. Figure 9 shows the expected prediction performance when using a different number of features. For example, using three features, the expected prediction performance ranges from 0 to 99.79%.

Table 3. Best features and the expected prediction accuracy

Features	Best Features	R^2 %	MSE x10^{-3}	$\pm\sigma$ mm
1	Tgo	43.08	-	-
2	Tgo and ΔPw	99.59	19.1	6.6
3	Tgo, ΔPw and ΔPg (or Mg)	99.79	9.3	4.1
4	Tgo, ΔPw, ΔPg and Mg	99.87	5.5	2.9
5	Tgo, ΔPw, ΔPg, Mg and Tgi	99.87	5.4	2.9
6	Tgo, ΔPw, ΔPg, Mg, Tgi and Two	99.87	5.4	2.9
7	Tgo, ΔPw, ΔPg, Mg, Tgi, Two and Twi	99.87	5.2	2.8

The best combination of input features offering high prediction accuracy is studied using a feature search algorithm using recursive learning. Table 3 shows the best features and the expected prediction performance; it shows the accuracy improves with the number of features. Especially for this application, a minimum of three features are required to get reasonable accuracy. Using the right number of features would also reduce the data requirements and model complexity. The deployment of the developed prediction model estimates the fouling thickness (on the inner and exterior of the tubes) continuously and aids monitoring and analysis. In the CHP system, fouling occurs slowly over a long period of time; therefore, a minimum of six to twelve months of data is required for complete analysis. Generally, the efficiency of WHRS is a key factor in deciding maintenance. For example, maintenance is activated when the efficiency drops below 20% compared to the design condition. By knowing the actual root cause factors, such as fouling thickness, one can decide on appropriate maintenance methods. The proposed prediction model accurately estimates the root cause factors and their severity, which allows the operator to decide on the right maintenance options and cut down on unnecessary downtime and maintenance costs. Even by knowing the root cause, one can

cautiously redefine the tolerance level (i.e., efficiency losses) considering the dependent process system and costs.

Conclusion

This study proposed a predictive maintenance methodology for waste heat recovery systems to identify an optimal time frame accounting for efficiency loss, maintenance cost, and downtime. An AI-based fouling prediction model is a critical requirement for maintenance methodology and was developed using actual data and supplemented data obtained from the thermodynamic model. The developed model helps identify the root cause and predict the fouling thickness with acceptable accuracy. To simplify the prediction model and data requirements, the importance of each feature and its effects on prediction accuracy were examined. The exhaust gas outlet temperature, the pressure drop of the water and gas streams, and the mass flow of exhaust gas are critical inputs or features required for the AI-based prediction model. Interestingly, the pressure drop data greatly helps the fouling prediction as it inherently accounts for the flow and the effective diameter influenced by the gas and water side fouling. The rest of the features help to improve the prediction accuracy and show a marginal effect. Deploying the developed fouling prediction model in the energy management system provides a fouling trend that greatly supports a project in the future time frame to identify the key time or sweet spot for maintenance accounting, proper redundancy, and mitigation plans.

Acknowledgments

This study is supported under the RIE2020 Industry Alignment Fund-Industry Collaboration Projects (IAF-ICP) Funding Initiative, as well as a cash and in-kind contribution from Surbana Jurong Pte Ltd.

Nomenclature

Acronyms

AI	artificial intelligence
EMS	energy management system
eNTU	effectiveness number of transfer unit method
WHRS	waste heat recovery system
A	heat transfer area, m2
Cp	specific heat, J/(kg K)
d	diameter, m
M	mass flow, kg/s
P	pressure, kPa
ΔP	pressure drop, kPa
Q	heat transfer, W
T	temperature, °C
$\overline{T}$	average temperature, °C
ΔT	temperature difference
U	overall heat transfer coefficient, W/(m^2 K)

Greek symbols

η	heat exchanger efficiency

Subscripts

act	actual heat exchange
calc	fouling condition
g	flue gas
i	inlet
LMTD	log mean temperature difference.
o	outlet
opt	optimal or maximum heat transfer
ref	reference condition
shell	within shell (exterior of tube)
tube	interior of tube
w	water

References

1. Adam Hirsch, Yael Parag, Josep Guerrero, Microgrids: A review of technologies, key drivers, and outstanding issues. Renewable and Sustainable Energy Reviews 2018;90:402-11. https://doi.org/10.1016/j.rser.2018.03.040.
2. Alessio Tafone, Sundar Raj Thangavelu, Shigenori Morita, Alessandro Romagnoli, Design optimization of a novel cryo-polygeneration demonstrator developed in Singapore – Techno-economic feasibility study for a cooling dominated tropical climate. Applied Energy 2023;330(Part B):119916. https://doi.org/10.1016/j.apenergy.2022.119916.
3. Kakaç, S., Liu, H., & Pramuanjaroenkij, A. (2020). Heat Exchangers: Selection, Rating, and Thermal Design, Fourth Edition (4th ed.). CRC Press. https://doi.org/10.1201/9780429469862

4. Raymon van Dinter, Bedir Tekinerdogan, Cagatay Catal, Predictive maintenance using digital twins: A systematic literature review. Information and Software Technology 2022;151:107008. https://doi.org/10.1016/j.infsof.2022.107008.
5. Fouling in Heat Exchangers: Learn Causes, Detection, and Prevention, https://www.csidesigns.com/blog/articles/fouling-in-heat-exchangers (Accessed in Feb 2023)
6. Madhu P.K., R, Subbaiah, J, Krithivasan, K. RF-LSTM-based method for prediction and diagnosis of fouling in heat exchanger. Asia-Pac J Chem Eng 2021;16(5):e2684. https://doi.org/10.1002/apj.2684
7. Riverol, C. and Napolitano, V., Estimation of fouling in a plate heat exchanger through the application of neural networks. J. Chem. Technol. Biotechnol 2005;80:594-600. https://doi.org/10.1002/jctb.1198
8. Hebert Lugo-Granados, Martín Picón Núñez, Modelling scaling growth in heat transfer surfaces and its application on the design of heat exchangers. Energy 2018;160:845-54. ISSN 0360-5442, https://doi.org/10.1016/j.energy.2018.07.059.
9. Jradi, R., Marvillet, C., Jeday, M.R., Analysis and estimation of cross-flow heat exchanger fouling in phosphoric acid concentration plant using response surface methodology (RSM) and artificial neural network (ANN). *Sci Rep* 2022;12(20437). https://doi.org/10.1038/s41598-022-24689-2
10. Elwerfalli A, Alsadaie S, Mujtaba IM. Estimation of Shutdown Schedule to Remove Fouling Layers of Heat Exchangers Using Risk-Based Inspection (RBI). Processes 2021;9(12):2177. https://doi.org/10.3390/pr9122177
11. Kuzucanlı, S. A., Vatansever, C., Yaşar, A. E., & Haktan Karadeniz, Z. (2022). Assessment of fouling in plate heat exchangers using classification machine learning algorithms. CLIMA 2022 Conference. https://doi.org/10.34641/clima.2022.127
12. Sreenath Sundar, Manjunath C. Rajagopal, Hanyang Zhao, Gowtham Kuntumalla, Yuquan Meng, Ho Chan Chang, Chenhui Shao, Placid Ferreira, Nenad Miljkovic, Sanjiv Sinha, Srinivasa Salapaka, Fouling modeling and prediction approach for heat exchangers using deep learning, International Journal of Heat and Mass Transfer 2020;159:120122. https://doi.org/10.1016/j.ijheatmasstransfer.2020.120112
13. Hassan Al-Haj Ibrahim, MATLAB – A Fundamental Tool for Scientific Computing and Engineering Applications – Volume 3, Fouling in Heat Exchangers, Published: September 26th, 2012, DOI: 10.5772/46462
14. Salih Alsadaie., Iqbal M. Mujtaba, Crystallization of calcium carbonate and magnesium hydroxide in the heat exchangers of once-through Multistage Flash (MSF-OT) desalination process, Computers & Chemical Engineering 2019;122:293-305, https://doi.org/10.1016/j.compchemeng.2018.08.033.
15. P. Nunes., J. Santos., E. Rocha., Challenges in predictive maintenance – A review, CIRP Journal of Manufacturing Science and Technology 2023;40:53-67, https://doi.org/10.1016/j.cirpj.2022.11.004.
16. Eleonora Florian, Fabio Sgarbossa, Ilenia Zennaro, Machine learning-based predictive maintenance: A cost-oriented model for implementation. International Journal of Production Economics 2021;236:108114. https://doi.org/10.1016/j.ijpe.2021.108114.
17. Bergman TL Lavine AS Incropera FP DeWitt DP. Fundamentals of Heat and Mass Transfer. 8th ed. New York: Wiley; 2017.
18. Ahmad Fakheri, Efficiency analysis of heat exchangers and heat exchanger networks. International Journal of Heat and Mass Transfer 2014;76: 99-104. https://doi.org/10.1016/j.ijheatmasstransfer.2014.04.027.
19. Thangavelu S.R., Nutkani I.U., Hwee C.M., Myat A., Khambadkone A., Integrated electrical and thermal grid facility - testing of future microgrid technologies. Energies 2015;8(9):10082. http://dx.doi.org/10.3390/en80910082.
20. Sundar Raj Thangavelu, Aung Myat, Ashwin Khambadkone, Energy optimization methodology of multi-chiller plant in commercial buildings. Energy 2017;123: 64-76, https://doi.org/10.1016/j.energy.2017.01.116.
21. S. A. Klein and F. L. Alvarado, “EES-Engineering Equation Solver,” Version 10.834-3D, F-Chart Software, 2023, http://www.fChartSoftware.com
22. Darst B.F., Malecki K.C., Engelman C.D., Using recursive feature elimination in random forest to account for correlated variables in high dimensional data. BMC Genet. 2018 Sep 17;19(Suppl 1):65. doi: 10.1186/s12863-018-0633-8. PMID: 30255764; PMCID: PMC6157185.

PROCEEDINGS OF ECOS 2023 - THE 36TH INTERNATIONAL CONFERENCE ON
EFFICIENCY, **C**OST, **O**PTIMIZATION, **S**IMULATION AND ENVIRONMENTAL IMPACT OF ENERGY SYSTEMS
25-30 JUNE 2023, LAS PALMAS DE GRAN CANARIA, SPAIN

BIM2SIM for hydraulic-focussed Energy Simulations – Automatic Generation of pre parametrized Simulation Models

David Jansen[a], Dominik Hering[a] and Dirk Müller[a]

[a] RWTH Aachen University, E.ON Energy Research Center, Institute for Energy Efficient Buildings and Indoor Climate, Aachen, Germany, david.jansen@eonerc.rwth-aachen.de

Abstract:
The construction of energy-efficient buildings is one of the most important measures to reduce the impact of buildings on our environment. The dynamic simulation of the energy systems of these buildings can improve the design and performance and thus reduce the emissions that impact the environment. However, the process of creating models for dynamic simulations is time-consuming and error-prone. By using already existing digital models from the planning process the process of model generation can partially be automated. This paper presents the tool `bim2sim` and its underlying methodology for the application of automatic model generation for dynamic hydraulic energy system simulation with *Modelica* based in Building Information Modeling models with the open exchange format IFC. The tool is applied to the use case of an example energy system and a manual comparison modeling is performed for the energy system in *Modelica*. The comparison shows that automatic model generation saves a significant amount of time even for comparatively simple systems.

Keywords:
Building Information Modeling, Hydraulic energy simulation, Modelica, Model generation

1. Introduction

Operation of buildings is responsible for 34 % of energy use and 37 % of carbon emissions worldwide [1]. Improving the energy efficiency of building energy systems can help to reduce the environmental impact of buildings. To increase the efficiency of buildings, dynamic simulation models of building energy systems are becoming increasingly important for both design and operation of buildings. However, the generation of these simulation models is a time-consuming process that requires a high level of expertise. Especially because buildings and their energy systems are unique for every building [2]. In order to increase the dissemination of dynamic simulation models in practice, the effort required to create these models must be reduced. The partially automated creation of models on the basis of already existing digital planning data, such as Building Information Modeling (BIM), is a promising approach. In the field of dynamic energy system simulation, however, there are very few approaches that attempt to convert existing BIM models directly into simulation models. By using the open exchange format IFC and the programing language *Python*, this paper presents a tool and the underlying methodologies to achieve a semi automatic model generation of simulation tools based on BIM models.

2. Related Work

The idea of using data models from digital design and, in particular, BIM data is not new. Especially in the field of thermal building simulation, there are already various approaches to avoid redundancy in the double modeling of planning and simulation models [3–7]. In the area of hydraulic-focussed energy simulations or Heating, Ventilation and Air Conditioning (HVAC) simulation in general, the number of existing approaches is smaller. Bazjanac et al. dealt with the issue of transferring HVAC information from IFC in 2002 and 2004 [8] [9]. The presented *IFCtoIDF* tool used EnergyPlus and the IFC2x2 standard, but the tool is not published. Hauer et al. analyze the presentability of HVAC components in the IFC schema [10]. The most important findings are that the IFC schema even in version IFC 4 does not yet provide sufficient options to represent all relevant components of a HVAC system. Accordingly, linked data must be used for a complete description. Furthermore, they give recommendations for possible extensions of the IFC schema with focus on the energy generators. Andriamamonjy et al. present a methodology for deriving thermal building and plant simulations based on the IFC [11]. The IFC is imported to *Python* with *IfcOpenShell* and the output is a *Modelica* simulation model. The focus is on the analysis of different life cycles and planning stages of the building. The approach uses a direct mapping of the BIM data into the *Modelica* library IDEAS. The presented *IFC2Modelica* approach

and its code is not published as an open source project. In his PhD thesis, Pauen invented the TUBES System Ontology (TSO) and the tool IFC2TSO to provide better understanding of the HVAC systems [12].

A necessary aspect to create executable simulation models is the creation of a control for the energy system. In order to represent this control in the simulation model, the control logic itself, as well as the linking of this logic with the signals of the associated sensors and actuators, are necessary.

Benndorf et al. present the implementation of a control in the IFC scheme using the example of a heating curve, a time-controlled volume flow controller and a temperature control. For this purpose, the IFC schema had to be supplemented by own new components. Furthermore, the concept of linked data sources was also used by using the *IfcOwl* schema to establish connectivity with the building automation control. However, it is noted that the use of BIM in the context of building control and automation is just being developed and existing BIM models and modeling tools cannot yet represent control, which is why they had to be subsequently added to the Revit export of the BIM model using *IfcOpenShell*. [13]

Sporr et al. use the IFC data format in their work to develop a methodology for mapping the control of an energy system for building heating. The methodology uses a combination of TRNSYS and Simulink and relies on additionally created data in addition to the IFC, since the IFC does not provide the necessary information on the producer side. [14]

Existing research already covers investigation and usage of BIM-data for simulation model generation in the HVAC domain, but non of the existing approaches was released in form of a public available tool. Furthermore, most approaches are based on the assumption of a perfect IFC model that contains no errors or lacks information. In reality, BIM models are currently often not yet perfect, for three main reasons. Authoring software has shortcomings regarding the export to IFC (1), the IFC format itself has shortcomings as not all relevant components and their semantic data is covered by the current IFC4 standard (2) and last but not least, model creators often do not add the relevant data to the BIM model, especially semantic data is often missing. Based on the existing shortcomings, a new approach is developed that provides an easy extendible and open source approach that works with non-perfect IFC data to create *Modelica* simulation models based on IFC4 data.

3. Methodology

Even though this article focuses on creating hydraulic energy simulations of HVAC systems, we want to give a brief overview on what `bim2sim` can do in general. In short, `bim2sim` is a tool that includes methods and concepts to read data from an IFC file, convert it to a simulation-oriented `meta-class` structure by collecting as much information as possible from the IFC, perform various types of processes and simplifications on the `meta-classes`, and export the results to a simulation model. This process can be used for HVAC simulations as presented here, but we also implemented methods and concepts to perform Building Performance Simulation (BPS) .The basic idea was already published [15] as well as the application on BPS [5, 16].

The workflow that is used specific for HVAC simulation is shown in figure 1. The Computer Aided Design (CAD) model that is created with a BIM authoring software is exported to an IFC model. This IFC model is loaded into `bim2sim` using *IfcOpenShell* and the relevant IFC elements are converted into a `meta-class` structure in *Python*. This `meta-class` structure is designed regarding the needs of the simulation domain. The `meta-class` instances are then transferred into a graph network that allows to run various simplification processes on the HVAC system to make it exportable to a simulation model. In the following sections the different steps are explained in more detail.

3.1. Importing data from IFC

Since two different object types are used in the conversion process, they are formatted differently for better distinction. *IfcElements* are displayed in italics, and *Python* `meta-class elements` are displayed in code style.

To get the relevant information from the IFC file to perform a semi-automatic simulation model generation, we use the *Python* implementation of *IfcOpenShell* to import the IFC data into *Python*. As Amor has shown, the number of entities, and thus the ability to represent systems in IFC, has increased significantly with the release of IFC 4 [17]. For this reason, `bim2sim` supports only IFC 4.

IfcOpenShell allows us not only to get the relevant data for every component but also to get metadata about the authoring software which is needed later in the process to enrich missing data.

3.2. Preliminary Model Check

In the next step we perform a model check against the loaded IFC. First basic validations are performed, e.g. to check that all *IfcElements* have a unique GUID. Subsequently, element specific checks are performed regarding the existence and correctness of attributes (e.g. the capacity of a boiler). In the last step HVAC specific checks are performed. E.g. all *IfcDistributionElements* are checked if they have ports assigned via the *IfcRelConnectsPortToElement* relationship

The results are displayed in form of an interactive HTML report. The goal is that the engineer who is in charge

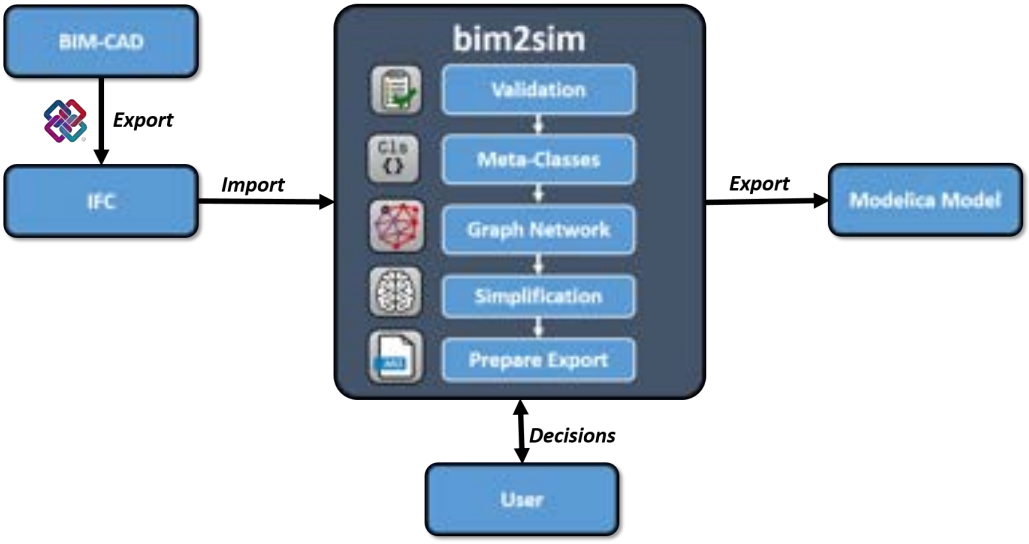

Figure 1: Process of `bim2sim` for HVAC domain.

for the simulations has a document which can be given to the BIM model creator. This document should provide the necessary information about all missing or wrong information inside the IFC model. The BIM model creator can update the IFC export afterwards based on the report.

3.3. Conversion to meta-structure

If the check succeeds the *IfcElements* are converted into the simulation orientated meta structure. This step makes sense, since BIM models for HVAC simulations are still partially insufficiently parameterized. The usage of the meta-structure allows obtaining the relevant information for the simulation from different sources in the IFC. For example, the surface roughness of a pipe can only be taken from the semantic information, but the length and diameter can also be determined via the calculation of the geometry if semantic information is missing. The conversion process consists of two parts. First, the physical instance of the *IfcElement* to be mapped must be identified and second, all relevant information about this class that can be obtained from the BIM data must be collected. The whole process of a `meta-class` element creation for the example of a boiler is shown in figure 2 and is explained in more detail below.

3.3.1. Class mapping

To keep the system modular and easy extendible, we use the class based structure in *Python* to represent each needed element with its own *Python* class. First, we have the base class *IFCBased*, which takes care of general processes such as calculating absolute position and orientation, which is required for all *IfcElements* regardless of their domain. Then we have the *HVACProduct* that inherits from *IfcBased* and adds additional functionality like the connections between ports and elements. This domain specific class is inherited to every element specific class, like the *Boiler* `meta-class`. In this element specific class we define the mapping rules, how to obtain the attributes and additional functions that are required for this process.

The IFC standard uses two information to define an instance of an *IfcElement*: the *IfcElement* itself and the *IfcTypeEnumeration* which allows further specification of the element. In current IFC data, especially in the HVAC domain, we often encounter missing correct declaration of the *IfcElement* and instead dummy classes like *IfcElementProxy* are used. But even if the *IfcElement* is correctly defined, the *IfcTypeEnumeration* is often set to USERDEFINED or completely missing. To overcome these problems and allow `bim2sim` to be used with non-perfect IFC-files, we implemented the possibility to add patterns in the form of regular expressions to look for in the semantic data of the element. This is useful, because even if the *IfcElement* is not correctly defined, the model creator might have entered the relevant information to identify the element as a string in the description of the element.

To make the structure extendible for new elements, these can easily defined as shown in the following example.

```
class Boiler(HVACProduct):
    ifc_types = {'IfcBoiler': ['*', '-EXCLUDING_TYPE']}
    pattern_ifc_type = [
        re.compile('Kessel', flags=re.IGNORECASE),
        re.compile('Boiler', flags=re.IGNORECASE),
    ]
```

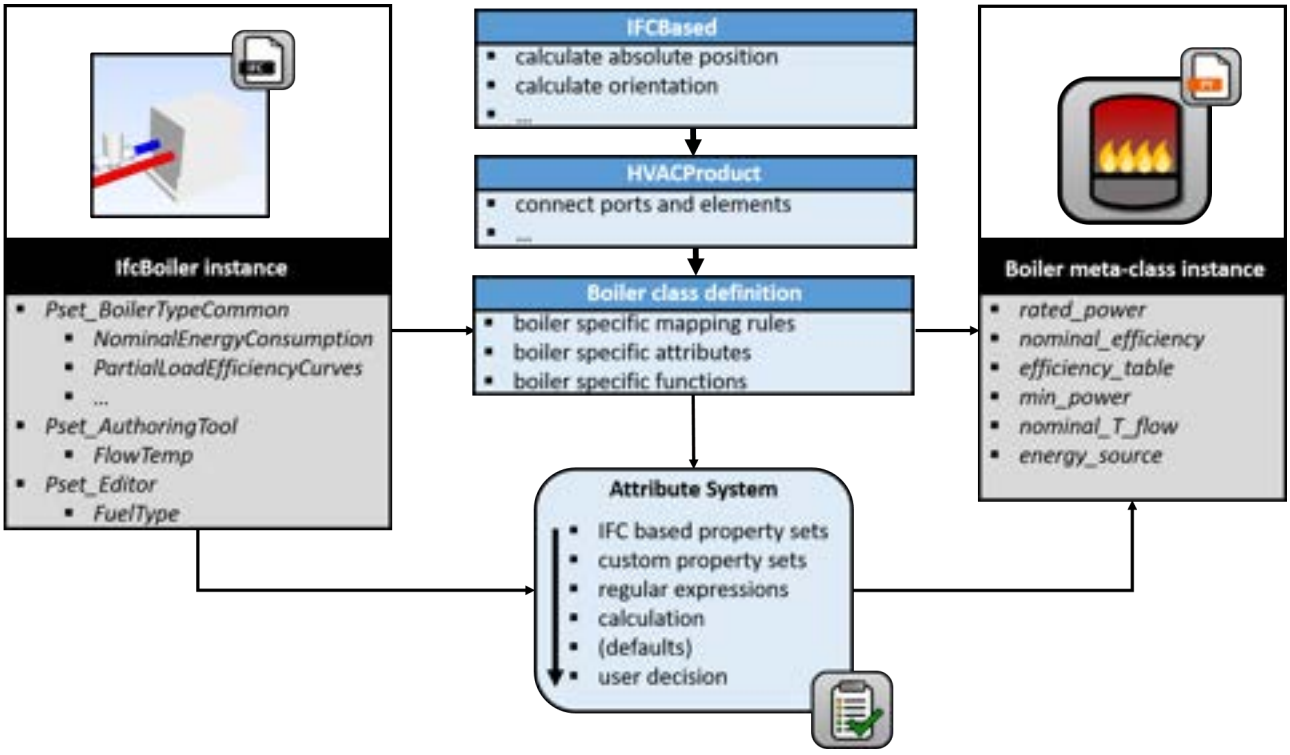

Figure 2: Process of meta class element creation for a boiler.

Based on this definition, the mapping process will first look for elements that are classified as *IfcBoiler* by taking all enumeration types (due to the '*) but the '-EXCLUDING_TYPE' into account. Additionally the process will look for every element that has the strings 'Boiler' or 'Kessel' (german for boiler) in their description. If multiple possible mapping classes are found, a user decision will be triggered.

Based on the defined classes all elements in the IFC will be converted into `meta-class` elements. An overview about all currently implemented classes for HVAC domain and their mapping is listed in Table 1.

Table 1: Mapping between IFC and Meta-structure. *:= all TypeEnumerations are included.

Groups	IFC Element	IfcTypeEnumeration	Meta-Classes
Connections	*IfcDistributionPort*	DUCT, PIPE	`HVACPort`
	IfcDistributionSystem	*	`Medium`
Energy Conversion	*IfcBoiler*	*	`Boiler`
	IfcElectricGenerator	CHP	`CHP`
	-	-	`HeatPump`
	IfcChiller	*	`Chiller`
Hydraulic Distribution	*IfcTank*	STORAGE	`Storage`
	IfcPump	*	`Pump`
	IfcValve	*	`Valve`
	IfcValve	MIXING	`ThreeWayValve`
	IfcPipeSegment	*	`Pipe`
	IfcPipeFitting	*	`PipeFitting`
	IfcPipeFitting	JUNCTION	`Junction`
	IfcDistributionChamberElement	*	`Distributor`
	IfcDistributionSystem	*	`Medium`
Heattransfer	-	-	-
	IfcSpaceHeater	*	`SpaceHeater`
	IfcHeatExchanger	*	`HeatExchanger`
	IfcCoolingTower	*	`CoolingTower`

The *IfcDistributionPort* and *IfcDistributionSystem* have a special role, as they are used to connect the different elements to each other and define the flow direction between the elements. The concept used in IFC to represent connections is shown in figure 3. The `meta-classes` use this concept as well by assigning the respective *HVACPorts* to every `meta-class` element and get additional information about the medium in a circuit from *IfcDistributionSystem*.

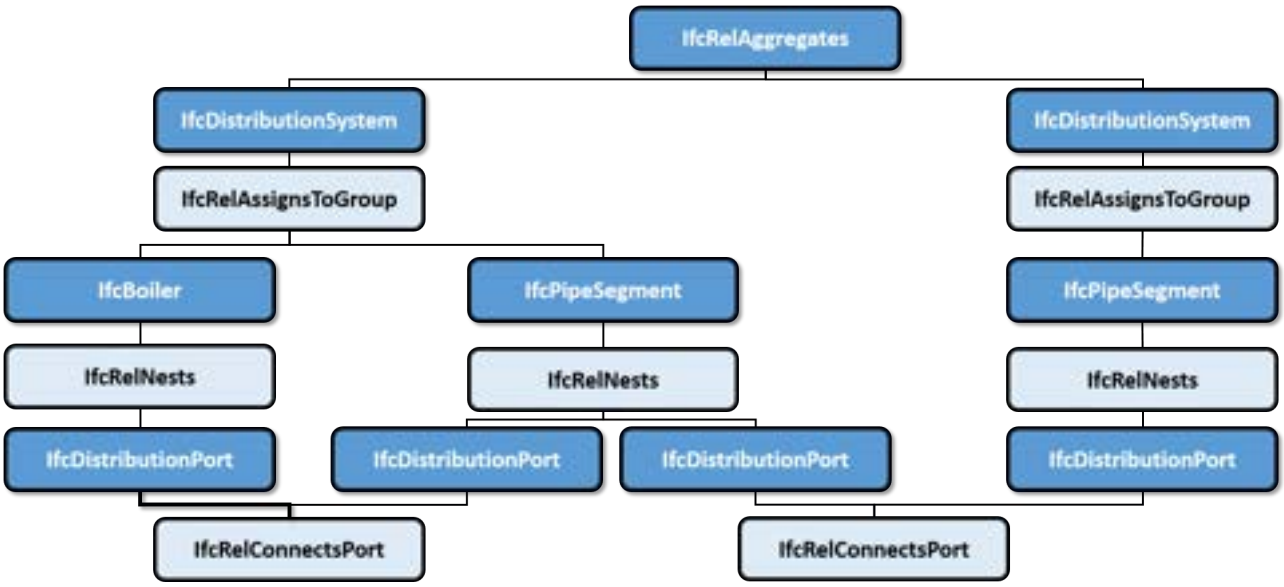

Figure 3: Concept of IFC to represent connections.

It's to mention that due to the fact that the IFC standard does not offer the possibility of directly mapping thermally active components, such as underfloor heating or concrete core activation, are taken care of via the concept of aggregations. Aggregations are explained in more detail in the section 3.4..

3.3.2. Attribute system

The created `meta-class` elements now needs to be filled with the relevant semantic information. On the left side in figure 2, we can see that the *IfcBoiler* provides semantic information included in three *IfcPropertySets* that represent the three different types of property sets that the `bim2sim` tool takes into account.

1. The *Pset_BoilerTypeCommon* as well as the belonging properties are IFC-schema compliant.
2. The *Pset_AuthoringTool* represents a property set that is not IFC schema compliant, but which is nevertheless typical for a specific authoring tool.
3. The *Pset_Editor*, which is a fully custom property set added by an editor. This one is not following any rules.

All three *IfcPropertySets* hold information that are relevant for the simulation model. The first one can be taken directly by implementing the IFC schema into the code. For the second one, additional information for every known export tool needs to be stored. For the last one, regular expressions can be used to find relevant information. Another challenge is that information might be stored implicit, but an additional calculation process is needed to obtain the final data that the simulation model requires.

To obtain all relevant information from the IFC-data we implemented the *Attribute*-system. The *Attribte*-system is a hierarchical approach that searches for a defined information by multiple approaches. The structure in figure 4 shows the usage of the *Attribute*-system to obtain the `nominal_efficiency` and the `rated_power` of the boiler as the IFC standard does not offer pre-defined options to input this data.

In this example, all implemented possibilities to retrieve information from the IFC are covered:

- `default_ps`: get information from property set that is defined in IFC standard
- `functions` and `dependant_attributes`: calculate/convert information into the direct form based on other attributes
- `patterns`: search for attributes based on regular expressions
- `JSON`: an additional file which is used to define typical places where specific authoring tools place information

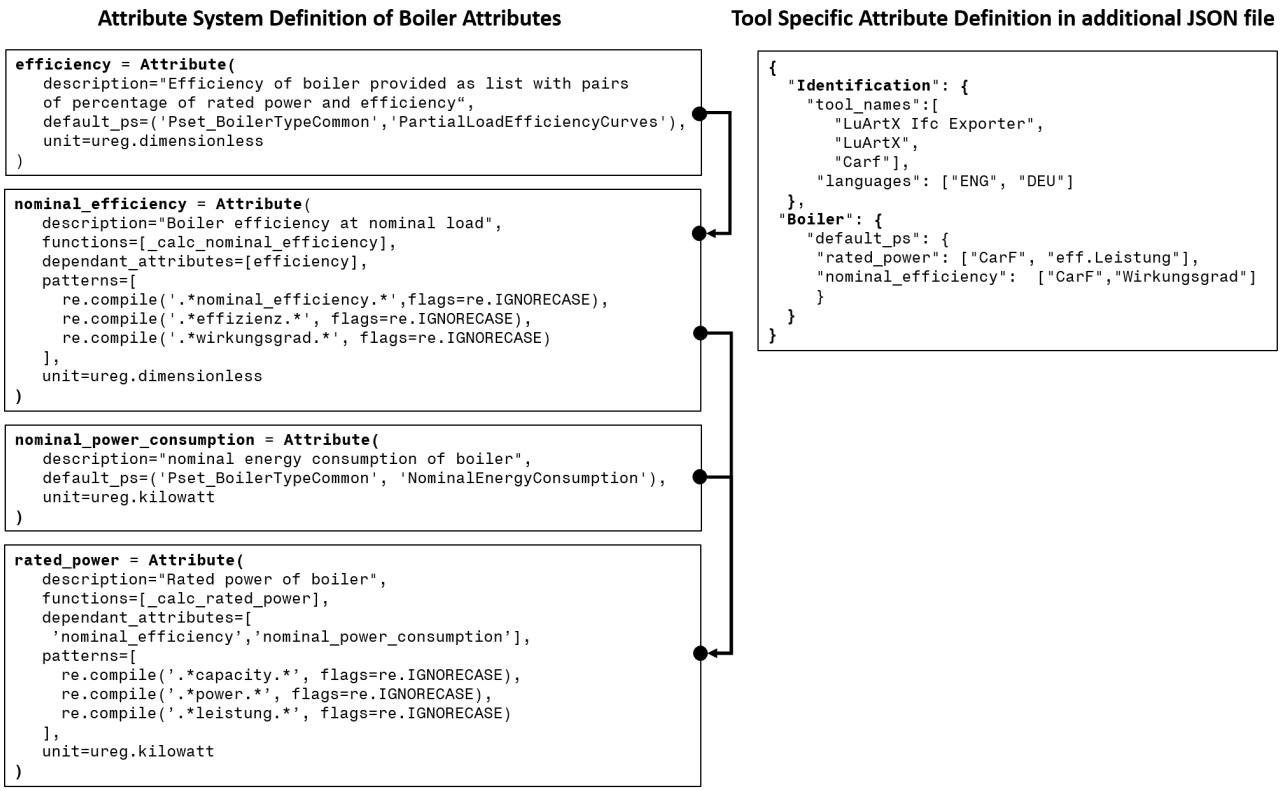

Figure 4: Excerpt of the attribute definition for the boiler `meta-class`.

The IFC-standard only allows defining the efficiency curve as a list of pairs of part load power and part load efficiency, but not `nominal_efficiency` itself. Still, the curve information can be used to calculate the `nominal_efficiency`. The `rated_power` can't be defined in the IFC as well. But based on the calculated `nominal_efficiency` and the `nominal_power_consumption` which can be defined in the IFC, the `rated_power` can be calculated as well.

To meet the goal of being able to generate simulation models even without perfect IFC models, all attributes can also be found in the IFC through the regular expressions as shown. Furthermore, the attribute system searches for dependent properties in the IFC based on the authoring tool defined in `JSON` on the right of the figure. For this purpose, the authoring tool is stored when the IFC file is loaded. As a last option, a user decision is created to retrieve the needed values. However, this is only executed against when the corresponding attribute is needed, either for a calculation of another attribute, or for the export to the simulation model to maximize the level of automation. This is described in more detail in the section 3.5. In addition, the attribute system ensures that all parameters are correctly converted to the specified units, based on the *IfcUnits* specified in the IFC. By using the *Python* package pint [18], it is ensured that later conversions are correct. All these functionalities aren't complex but adding the functionality for all relevant elements in the HVAC domain and in the other domains that `bim2sim` supports without defining a clean, unify and easy to extendible structure would result in non-maintainable code.

3.4. Processing and Simplification

3.4.1. Graph Network Generation

To analyze and simplify the hydraulic circuits the created `meta-classes` and the related HVAC-Ports are converted into a network graph. Network graphs offer the potential to use existing graph algorithms to perform efficient analysis against the hydraulic circuit. `bim2sim` uses two graphs, the `PortGraph` and the `ElementsGraph`. The `PortGraph` uses every `HVACPort` as a node and the edges between the nodes mark the fluid flow between the ports. In the `ElementsGraph` no ports are used, but the elements like a Boiler are the nodes. The `ElementsGraph` graph is an abstraction of the `PortGraph` and is mostly use for visualization. The `PortGraph` is used for most analysis, because it offers information how ports of the same element are connected to each other. This is important as for example a heatpump has four ports, but only two of them are connected with each other in pairs (evaporator and condenser side). `bim2sim` uses the *Python* package *NetworkX* [19] to create network graphs and analyze them.

3.4.2. Aggregations

The concept of `Aggregations` is used in the HVAC part of `bim2sim` to simplify the hydraulic circuit and reduce the numbers of elements to export to the ones relevant for the simulation. This is needed as an export of every `meta-class` instance created based on the IFC directly to a *Modelica* instance would result in an infeasible or at least very slow system of equations in *Modelica*. The simplest example of an `Aggregation` is the `PipeStrand`, which aggregates chains of contiguous connected meta-class elements without junctions to a single `PipeStrand` with an equal total length $l_{total} = \sum_{i=1}^{n} l_i$ and equal diameter $d_m = \sum_{i=1}^{n} l_i \cdot d_i / l_{ges}$. The equivalent parameters are calculated to obtain a simulation model with an equal pressure drop and heat loss. A special case of a `PipeStrand` are coils used for thermal activated building structures, like underfloor heating or concrete core activation. These are specified through the density of pipes (length and number of elements) in a certain area, the distance between the center lines of the pipes.

Using the network graph allows using existing analyze algorithms and classifications. For example, the chain of connected elements can be determined using the degree of the nodes of the graph. The degree of a node is defined as $d_G(v)$ and is calculated based on the number of connections a node has. To find the chain of connected instances without junctions only nodes with a degree of $d_G(v) = [1;2]$ are taken into account which are of the type `Pipe` or `PipeFitting` or `Valve`.

`bim2sim` also includes more advanced aggregations, two of them will be explained in more detail below, the aggregation of parallel pumps and generator cycles. In practice, parallel circuits consisting of several identical pumps are often used in large hydraulic networks for better scalability. In this way, only the required number of pumps can be switched on, depending on the load. For simulation, these parallel circuits can be converted into a single component to reduce the number of equations of the system of equations to be solved and thus the complexity and simulation time of the corresponding model. In 5, the graph network of an example system is shown, which consists of four pumps in the initial state (a), where one of the pumps has a lower power (purple) and three pumps have an identical power (red). There is also a bypass connected in parallel with the four pumps (green).

The algorithm developed allows both a grouping that groups only parallel pumps of the same power and the option to group all parallel pumps. In addition, the an `AggregatedPipeFitting` is also needed, since other connections at the nodes, such as the bypass shown here, should be kept. The result for the case where only pumps of the same power are aggregated is shown in (b), and in addition to the successful aggregation, it also shows that the bypass (green) is still present and the pump with a different power (purple) was not included in the aggregation. The rest of the graph network remains untouched, since only the aggregation for `ParallelPumps` was performed.

Besides just reducing the elements to be represented later in the simulation model, all relevant information is converted into semantic data. In the case of the aggregation `ParallelPump`, these are in particular the total power of the pumps, the combined nominal volume flow as well as the total length and the average diameter of the adjacent pipelines, which are relevant for the pressure loss.

The aggregation `Generators` is relevant because generator circuits consist of many individual components, most of which have no meaning for the simulation or at least do not need to be represented as individual components.

Figure 6 shows the original state of an example in (a). The example consists of a generator circuit with boiler (red), pump (blue), a bypass with valve (green), an expansion tank (purple), and some other pipe elements. The generator circuit is connected to a distributor (gray), to which four other pipe strands are connected, which represent a simplified consumer.

In (b) the result of the aggregation is shown. The simplified consumer circuit with the four pipe elements remains unchanged. However, the generator circuit can be aggregated into a single component, the `GeneratorOneFluid`. This component contains the information about the type and power of the generator, whether there is a separate pump in the circuit, what the power of this pump is, and the information about an existing bypass. Since the expansion tank is not relevant to the simulation, this information is not tracked further. The algorithm can be applied to parallel generators beyond the example shown. In this case, the parallel generators are converted into one generator that provides the total power.

There are limitations in terms of generator types. So far, only algorithms for generators with one external fluid circuit, such as boilers and Combined Heat and Power (CHP), have been included. Generator aggregation for generators with multiple circuits, such as a heat pump, has not yet been created, since mapping a heat pump in the IFC schema is currently only possible with workarounds.

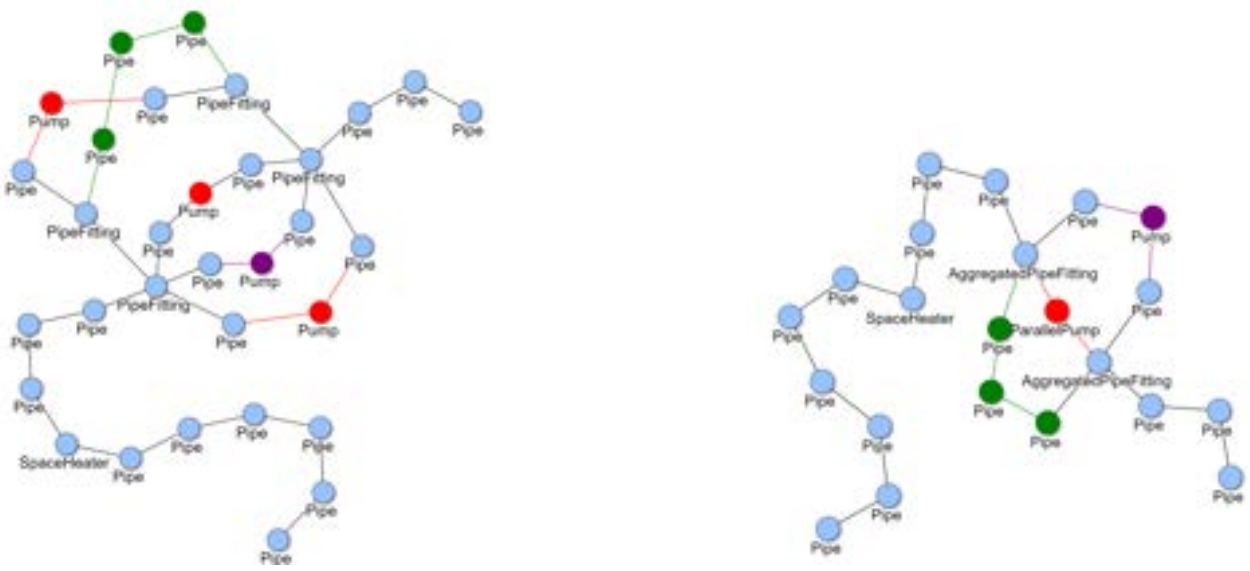

(a) Before Aggregation

(b) After Aggregation

Figure 5: Graph of `meta-class` elements for `ParallelPump` Aggregation

3.5. Exporting to *Modelica*

3.5.1. Export Libraries

The simplified hydraulic network of the `meta-class` elements must now be translated into *Modelica* models in the next step. As introduced before, we implemented a *Plugin* system to allow multiple tools and libraries to take advantage and reuse the concepts that we built with `bim2sim`. Each *Plugin* that uses *Modelica* can build its own export for the used library by creating *Python* classes that inherit from the base instance. In the current version, `bim2sim` holds two *Plugins* for *Modelica* HVAC export: *AixLib* and *HKESim*. *AixLib* is an open source *Modelica* library that holds simulation models for HVAC simulation as well as BPS and is based on the IBPSA core library [20]. *HKESim* is a non-public library used by the ROM Technik company, who significantly contributed to the creation of `bim2sim`. Its focus is on HVAC simulation. Additionally, some basic components are implemented for the *Modelica* Standard Library (MSL).

Every `bim2sim` *Modelica* export class holds information about the path to the *Modelica* model it is exported to, the `bim2sim` instance it represents and the parameters that should be requested before exporting the model. The most basic definition of an export model is as follows:

```
class StaticPipe(StandardLibrary):
    path = "Modelica.Fluid.Pipes.StaticPipe"
    represents = [hvac.Pipe, hvac.PipeFitting, aggregation.PipeStrand]

    def request_params(self):
        self.request_param("length", self.check_length)
        self.request_param("diameter", self.check_diameter)
```

The `self.check_length` and `self.check_diamter` are optional functions to define, to implement plausibility checks against the parameters. Additional functions might but must not be implemented for a basic export. Table 2 shows the current status of which models are used regarding the libraries.

Not all `meta-classes` have a *Modelica* export yet in all libraries, but more export models are currently under development. Furthermore, based on the modular structure, other libraries can be easily added.

3.5.2. Base export instance

To continue the modularity of the built workflow, the export is based on a class structure that can be easily extended. To ensure modularity, we implemented a base class for a *Modelica* export instance that contains the all relevant functionality and can be extended by any *Modelica* instance, regardless of which library it is used in.

Translate *Python* into *Modelica* parameters

Python and *Modelica* both hold the logic for different types of parameters, like boolean, arrays, lists, integers

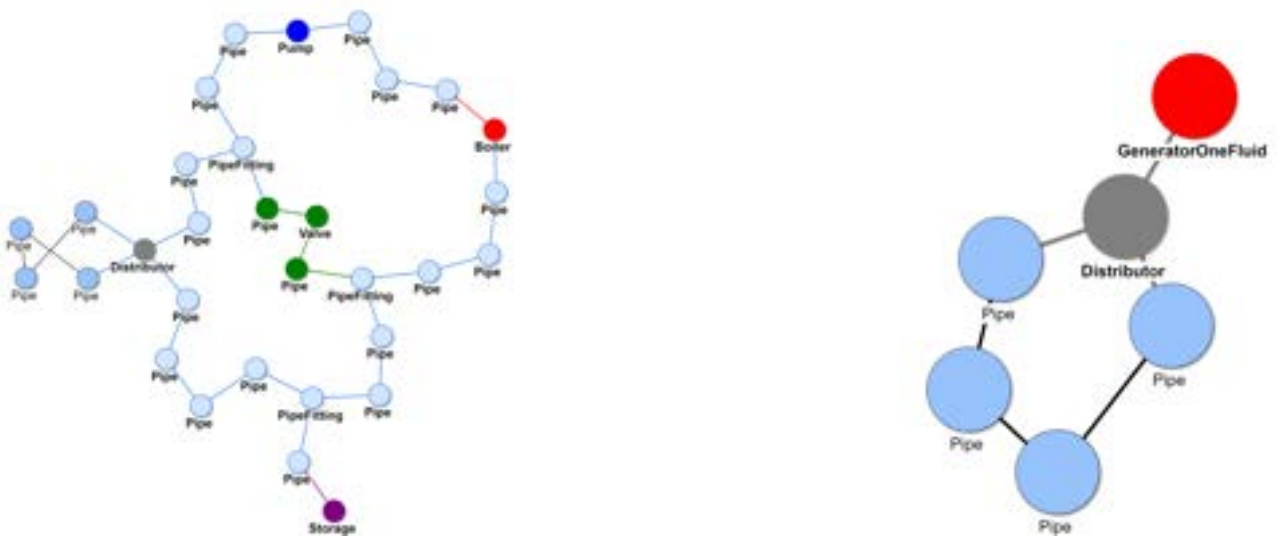

(a) Before Aggregation

(b) After Aggregation

Figure 6: Graph of `meta-class` elements for `Generator` Aggregation

and floats with unit. To keep extensibility simple, the conversion from *Python* to *Modelica* is defined in the base class. The conversion thus subsequently runs in the background and no longer needs to be taken into account when extending a library with new models.

Unit conversion As mentioned, we use the package *Pint* inside *Python* to obtain and maintain the correct units from the IFC file. To ensure that no conversion errors occur, the output unit for the *Modelica* model can be defined. By default, the values obtained from IFC are always converted to SI units during export.

Numerical validation checks These checks allow the definition of value ranges within which individual values may lie. This way, it should be prevented that unphysical values get into the model.

Keep track of corresponding IFC element(s) For traceability between IFC model and *Modelica* simulation model, each *Modelica* component is assigned the GUID of the corresponding IFC object as a parameter.

Parameter request system As written before, not all parameters relevant for the simulation can be extracted from the BIM model for various reasons. Nevertheless, it should be ensured at the time of export that all parameters relevant for the simulation model are available or at least have been requested. At the same time, the number of user inputs should be minimized. To achieve this, only those decisions are queried during the process whose result is needed immediately. An example of this would be the decision of what type an IFC element has if the IFC class is not uniquely defined (e.g. when using *IfcBuildingElementProxy*). Such a decision must be made directly, because it has an impact on the further process. Information that is only required for the final simulation model export will only be executed during export.

This avoids in many cases that parameters, which are no longer relevant for the exported model, are queried. For example, the parameter for the volume of a storage, which is identified during the process as a pressure equalizing vessel that is not relevant for the simulation model. If a user decision is skipped, or a parameter fails the final numerical validity check, that parameter is noted as unknown in the exported model. Thus, it can be directly recognized in the model which parameters have to be reworked.

Translate port logic The AixLib and HKESim as well as the MSL use the *FluidPorts* of the MSL to connect instances with each other. The definition inside *Modelica* is that *Port_a* is the incoming port of a Model and *Port_b* is the outgoing port. The `HVACPort` of the `meta-class` system and the simplified graph network hold the needed information to connect the respective *Modelica* instances with each other during export.

3.5.3. Usage of modules

Table 2 already included the `GeneratorOneFluidModule` and `ConsumerHeatingDistributorModule`. Equivalent to the `aggregations` used in the simplification of the graph network, new module-based models for the AixLib and HKESim libraries are currently implemented for export. These modules are pre-configured combinations of already existing components of the library, which reduce the needed number of parameters to minimum. These modules also contain basic control strategies, which allows the export of almost ready to run simulation models. The basic control strategies however can easily be overwritten by user defined control strategies which can be connected to the BUS connectors of the modules. For AixLib we already implemented a boiler module

Table 2: Current state of `bim2sim` *Modelica* export to different libraries.

Meta-class	AixLib	HKESim	MSL
`Boiler`	X	X	
`GeneratorOneFluidModule`	X		X
`HeatPump`	X		
`Chiller`	X		
`CHP`	X		
`Storage`	X		
`Pump`	X	X	
`Valve`			X
`ThreeWayValve`	X	X	
`Pipe`			X
`PipeFitting`			X
`Junction`	X	X	X
`Distributor`	X	X	
`Radiator`	X	X	
`Consumer`	X		
`ConsumerHeatingDistributorModule`	X	X	

and a consumer module which can be found on GitHub[1]. HKESim won't be discussed because it's an in-house library and not public available.

3.5.4. Export process

The conversion into *Modelica* models is performed based on a dynamic *Mako* template [21]. This template is filled based on the instances and their parameters and connections that are gathered through the previously discussed concepts. During the export, required, but missing parameter trigger decisions to the user. If these decisions are skipped, the parameters will be left empty in the exported simulation model, but a red annotation will be placed on the top level of the model, that gives feedback which parameters are missing. Additionally, the export tries to arrange the *Modelica* instances in a useful pattern, based on the position information from the IFC.

4. Proof of Concept

To prove the functionality of the developed tool, we have created an example use case in cooperation with the software manufacturer LuArtX. This is shown in figure 7 as schematic drawing (a) and screenshot of the IFC model (b).

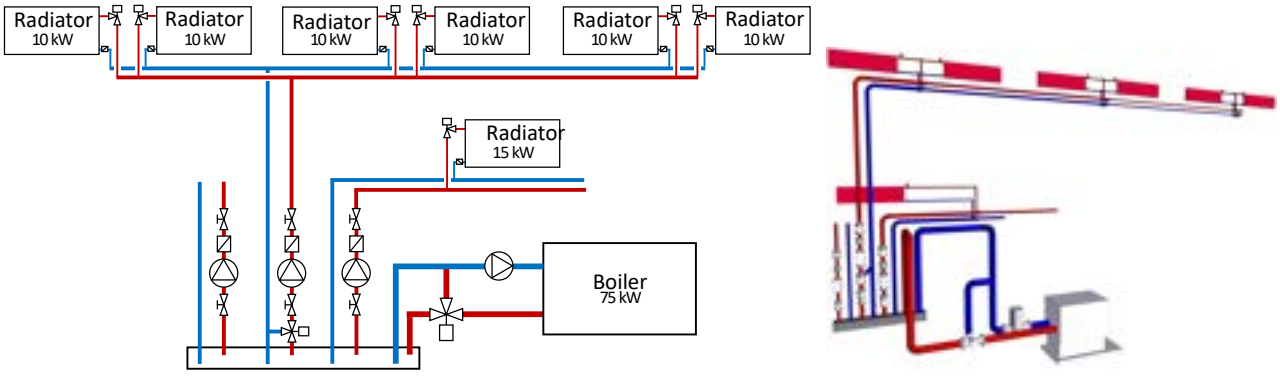

(a) Schematic drawing (b) IFC model

Figure 7: Use case example

The use case consists on the generation side of a boiler for heat generation, a pump, a three-way valve and a bypass for return flow boosting. The consumer side has a distributor, two consumer strands with several

[1] `https://github.com/RWTH-EBC/AixLib/tree/issue1147_ConsumerAndBoiler`

radiators as consumers, of which six radiators are connected in parallel. Each consumer strand has a pump and a valve. One of the consumer strands is an open end and one has a bypass for flow temperature control. The software manufacturer LuArtX improved their CAD software CARF throughout the creation to implement correct export for *IfcPorts*.

Since the creation of *Modelica* models based on plans or 3D models is a common task at the industry partner, both a manual model creation and a partially automated creation by `bim2sim` were performed to demonstrate the potential of the developed tool. The two model exports, both using the in-house library of the industry partner, are shown in figure 8

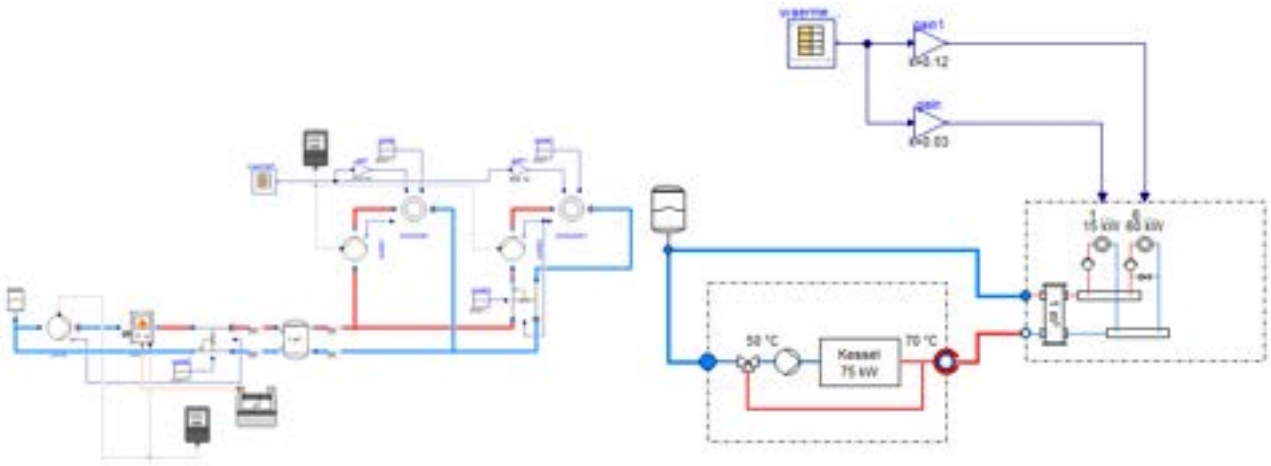

(a) Manual created model

(b) Automatic created model with `bim2sim`

Figure 8: Exported *Modelica* HKESim models

It took a *Modelica* expert from the industry partner 2 hours and 33 minutes (153 minutes) to manually create the model. This includes the understanding of the energy system based on the BIM model, the parameter gathering and entering, modeling in *Modelica* including connections and sensors, creating usage profiles and removing any errors. Creating the simulation model with `bim2sim` took 6 minutes, including adding the missing parameters and demand profiles. This results in a time saving of 95 %.

5. Conclusion

In this paper, the authors presented a brief review of existing approaches in the field of simulation model generation for the HVAC domain based on digital planing data in the form of BIM models. Based on the discovered gap of public available tools which are able to create *Modelica* simulation models based on non-perfect BIM data in form of IFC, the `bim2sim` tool, and it's application for the HVAC domain were introduced. The core of `bim2sim` is the *Python* library with the same. This includes methods easy extendible methods based on orientated programming to convert IFC data into *Modelica* simulation models. The underlying methodology was explained, and the tool was applied to an example use case to prove the concept. The example showed that even for comparatively simple systems, a significant amount of time can be saved.

Currently, the embedded methods are focussed on hydraulic systems. In the future, the authors plan to extend the functionality to duct systems to simulate ventilation as well. Also, the presented use case covered only a small example system. The next step will be bigger systems with multiple generation devices for heating and cooling.

This paper only gives an overview about the functionality and methodology of `bim2sim`. For more information, the authors refer to the GitHub[2] repository, where documentation and the presented example use case can be found.

6. Acknowledgements

The authors gratefully acknowledge the financial support of the German Federal Ministry for Economic Affairs and Energy in the project “BIM2SIM” (project number 03ET1562A) and "BIM2Praxis (project number 3EN1050A). The authors also want to thank the RD department of Rud. Otto Meyer Technik GmbH & Co. KG and especially Christian Warnecke for the extensive contributions to the code.

[2] `https://github.com/BIM2SIM/bim2sim`

References

[1] United Nations Environment Programme. 2022 Global Status Report for Buildings and Construction: Towards a Zero-emission, Efficient and Resilient Buildings and Construction Sector; 2022. Available from: https://wedocs.unep.org/20.500.11822/41133.

[2] Drgoňa J, Arroyo J, Cupeiro Figueroa I, Blum D, Arendt K, Kim D, et al. All you need to know about model predictive control for buildings. Annual Reviews in Control;50:190-232.

[3] Hirth S, Nicolai A. The novel dynamic building energy performance simulation tool SIM-VICUS. vol. 17 of Building Simulation. IBPSA;. p. 0-0. Available from: https://publications.ibpsa.org/conference/paper/?id=bs2021_11116.

[4] Kamel E, Memari AM. Automated Building Energy Modeling and Assessment Tool (ABEMAT). Energy;147:15-24.

[5] Jansen D, Nürenberg M, Müller D. BIM-Basierter Reduced Order Ansatz für Thermische Gebäudesimulationen. In: BauSIM 2020 Proceedings. Verlag der Technischen Universität Graz;. Medium: online Meeting Name: 8. Conference of IBPSA Germany and Austria.

[6] Nytsch-Geusen C, Rädler J, Thorade M, Ribas Tugores C. BIM2Modelica - An open source toolchain for generating and simulating thermal multi-zone building models by using structured data from BIM models;. p. 33-8. 00000. Available from: http://www.ep.liu.se/ecp/article.asp?issue=157%26article=3.

[7] Mediavilla A, Elguezabal P, Lasarte N. Graph-Based methodology for Multi-Scale generation of energy analysis models from IFC. Energy and Buildings;282:112795. Available from: https://www.sciencedirect.com/science/article/pii/S0378778823000257.

[8] Bazjanac, Vladimir, Forester J, Haves, Philip, Sucic, Darko, Xu, Peng. HVAC Component Data Modeling Using Industry Foundation Classes | Building Technology and Urban Systems Division. In: 5th International Conference on System Simulation in Buildings 2002; 2002. .

[9] Bazjanac V, Maile T. IFC HVAC interface to EnergyPlus-A case of expanded interoperability for energy simulation. In: Simbuild;. 00000.

[10] Hauer S, Brès A, Partl R, Monsberger M. An Approach for the Extension of OpenBIM MEP Models with Metadata Focusing on Different Use Cases. In: Proceedings of the 16th IBPSA Conference;. Pages: 189.

[11] Andriamamonjy A, Saelens D, Klein R. An automated IFC-based workflow for building energy performance simulation with Modelica. Automation in Construction. 2018;91:166-81.

[12] Pauen N. Graphbasierte Algorithmen und gesamtheitliche Repräsentation von Systemen der TGA mit BIM und Linked Data [phdthesis];. Available from: https://publications.rwth-aachen.de/record/851025.

[13] Benndorf G, Réhault N, Clairembault M, Rist T, editors. Describing HVAC controls in IFC – Method and application. vol. 122; 2017.

[14] Sporr A, Zucker G, Hofmann R. Automatically Creating HVAC Control Strategies Based on Building Information Modeling (BIM): Heat Provisioning and Distribution. energies. 2020;13:4403.

[15] Jansen D, Fichter E, Richter VE, Barz A, Brunkhorst J, Dahncke M, et al. BIM2SIM - Development of semi-automated methods for the generation of simulation models using Building Information Modeling. In: Proceedings of Building Simulation 2021: 17th Conference of IBPSA;. .

[16] Jansen D, Richter V, Lopez DC, Mehrfeld P, Frisch J, Müller D, et al. Examination of Reduced Order Building Models with Different Zoning Strategies to Simulate Larger Non-Residential Buildings Based on BIM as Single Source of Truth. In: Modelica Conferences;. p. 665-72.

[17] Amor R. Analysis of the Evolving IFC Schema;. .

[18] Pint: makes units easy;. Available from: https://pint.readthedocs.io/en/stable/.

[19] Hagberg A, Schult D, Swart P. Exploring network structure, dynamics, and function using NetworkX. In: Varoquaux G, Vaught T, Millman J, editors. Proceedings of the 7th python in science conference;. p. 11 15.

[20] Maier L, Jansen D, Wüllhorst F, Kremer M, Kümpel A, Blacha T, et al. AixLib: An open-source Modelica library for compound building energy systems from component to district level with automated quality management. submitted to: Journal of Building Performance Simulation.

[21] Bayer M. Mako Templates for Python;. Available from: https://www.makotemplates.org/.

PROCEEDINGS OF ECOS 2023 - THE 36TH INTERNATIONAL CONFERENCE ON
EFFICIENCY, **C**OST, **O**PTIMIZATION, **S**IMULATION AND ENVIRONMENTAL IMPACT OF ENERGY SYSTEMS
25-30 JUNE 2023, LAS PALMAS DE GRAN CANARIA, SPAIN

Evaluation of Graph Neural Networks as Surrogate Model for District Heating Networks Simulation

Taha Boussaid [a, b, *], François Rousset [a], Vasile-Marian Scuturici [b], Marc Clausse [a]

[a] Univ. Lyon, INSA Lyon, CNRS, CETHIL, UMR 5008, F-69621 Villeurbanne, France
[b] Univ. Lyon, INSA Lyon, CNRS, LIRIS, UMR 5205, F-69621 Villeurbanne, France
[*] Corresponding Author, taha.boussaid@insa-lyon.fr

Abstract:

District heating networks have proven their higher conversion efficiency, economic viability and environmental benefits when compared to decentralized and individual heating systems. These benefits are achieved through the ability to incorporate a wide variety of production means, including renewable intermittent sources but also via the use of short-term and/or inter-seasonal storage.
Due to the numerous interactions between these components, their different dynamic aspects and operating constraints, physical simulations are computationally heavy so that running optimization tasks become prohibitively expensive and time consuming. Therefore, new control optimization schemes need to be drawn up to accelerate the predictive control and to facilitate the decision-making process.
In the present work, we assess the application of geometric deep learning as a surrogate modeling framework for district heating simulations. Beyond processing non-Euclidian data, this deep learning approach aims to encode geometric and topological understandings of data as inductive biases in deep learning models. More precisely we trained Graph Neural Networks to emulate a thermo-hydraulic simulator of district heating network. This statistical inference method allows us to drastically reduce simulation time, hence unlocking further optimization loops and parametric space exploration. In addition, their permutation equivariance and stability to perturbations are assessed to discuss their scalability to more complex network topologies and control schemes.

Keywords:

District heating networks simulation, graph neural networks, transient dynamics.

Nomenclature

Letter symbols

c	specific heat, $\mathrm{J/(kgK)}$
T	temperature, K
$\dot{m}$	mass flow rate, $\mathrm{kg/s}$
N	number of nodes
N_b	number of branches
M	incidence matrix, $\in \mathbb{R}^{N \times N_b}$
KS	area independent heat transfer coefficient of pipe, $\mathrm{W/K}$
V	volume of the fluid contained in the control volume, $\mathrm{m^3}$
F_ω	inference function

Greek symbols

$\gamma,\ \phi$	differentiable functions
ω	learnable parameters (weights) of inference function
σ	non-linear activation function

Subscripts and superscripts

i	node i
l	at layer l
t	time-step or learning step
s	relative to soil
b	relative to branches
ext	relative to exterior

1. Introduction

Anthropic activities have increased net greenhouse gas emissions since 2010 in all major sectors (industry, energy, transport, agriculture, construction). A study by IPCC Group III [1] investigated ways to mitigate climate change and reduce greenhouse gas emissions. According to their report, switching from fossil fuels to low-carbon energies is essential to limit climate change. In Europe, the production of heat and cold represents half of the energy consumption and is mainly based on fossil fuels [2]. Since the last century, district heating networks (DHN) have been deployed mainly due to their economical and efficiency benefits. For example, having a joint production process, a higher conversion rate and less maintenance allows to decrease the operating and maintenance costs. Moreover, DHN are well suited for areas of mixed use with strong anchor clients [3]. In recent years, due to the rapid development of renewable energy technologies, the 4th generation of DHN have been identified as a viable option to decarbonize the heat production sector [4, 5]. First, they operate at lower temperatures, hence reducing heat losses and increasing the efficiency of conversion systems. They also take advantage of various heat sources including renewable and recycled ones such as biomass, geothermal, solar thermal, and waste heat. Finally, coupling these sources with thermal energy storage (TES) and optimal control should allow a better peak management. However, the use of TES and various heat sources, some of which are intermittent, adds a new complexity to the system including the stochastic character of some variables such as resources availability, weather conditions and electricity price, which therefore implicitly integrate a predictive character in the control and optimization methods of these systems.

In order to successfully operate these advanced thermal networks, an intelligent control strategy is required. A detailed review on control strategies for DHN can be found in [6]. This study shows that the current tendency is to use hybrid control schemes based on multi-agent systems and model predictive control (MPC). This method falls in two parts: first, solving an operational optimization centrally i.e. energy planning, and then it is distributed to other decentralized agents related to consumers and the different producers connected to the network. This strategy involves the simulation of the dynamic behavior of the considered DHN. In fact, the controller needs to understand and predict the behavior of the system and its response to various scenarios of control variables which requires multiple simulations over variable large time horizons. To accomplish this, accurate models of the network's different components and their interactions are required. Several studies have been carried out to develop numerical models of DHN [7–11]. They can be classified in two main categories: dynamic and pseudo-dynamic models. The latter approach considers only the thermal transient and assumes instantaneous hydraulic changes as fluid dynamic perturbations (i.e. pressure variations) are quickly transferred to the whole network, about 1000 times faster than temperature variations [8]. More importantly, when considering intermittent heat sources like solar thermal, it is crucial to use an adapted small time-step for the simulations. Consequently, this makes running iterative optimization methods computationally heavy and time consuming.

One solution to overcome this limitation is the formulation of a numerically efficient and stable surrogate model of DHN simulations. There are several surrogate modeling approaches [12] such as reduced order models, Gaussian kriging, radial basis functions, etc. But lately and due to extensive research and advances in computing technologies, different studies investigated the application of machine learning algorithms as surrogate models for different engineering systems including energy conversion and distribution processes [13–17]. For example, the study in [16] consisted on training a graph neural network to approximate the optimal solution of power flow optimization problem for electric grids. The results showed that the surrogate model is 10^5 faster than the interior point optimization method and it exhibits much better scalability to larger networks. A tutorial review on using neural network for MPC is given in [17]. More specifically, it highlights the use of recurrent neural networks (RNN) to predict the state of the process model. The authors applied this approach to drive the reactants concentration of a non-isothermal continuous stirred-tank reactor (CSTR) to the optimal steady-state point by controlling heating rate and inlet concentration. It was found that the physics based RNN-MPC system converges faster and requires less computational time.

In the field of DHN design optimization and control, machine learning was applied at two different levels. The first one focuses on predicting the thermal load [18, 19] and the second, more recent, on applying deep reinforcement learning to train autonomous agents to optimal DHN operation [20]. However, to the best author's knowledge, no attempt to formulate a surrogate model of DHN simulation using machine learning have been made. Therefore the primary contributions of this work are as follows:

- A flexible physical pseudo-dynamic simulator of district heating network has been developed based on graph theory.
- To the best author's knowledge, this is the first attempt to apply GNN as surrogate model for physical district heating network transients.
- This approach is validated through the prediction of district heating network behavior as the temperatures evolution in each node of the network.
- Using this framework allows to significantly reduce simulation time from hours to seconds, $\sim 10^4$ faster.

This opens the possibility to further develop quasi instantaneous optimal control schemes.

The remaining of the paper is organised as follows: Section 2. describes the physical model that has been developed to simulate transient dynamics in DHN. Section 3. briefly introduces fundamentals of machine learning with a focus on GNN and the final architecture of our surrogate model. Then, section 4. presents the application case that was chosen to evaluate our approach. Finally, the results, limitations and future developments are presented in section 5.

2. Physical model

The physical model that has been developed is intended to serve as a data generator for DHN simulations similarly to what has been done on the electrical network side with the MATPOWER test cases project [21]. The choice of pseudo-dynamic resolution is justified as the time-step of DHN simulations is generally around one hour and recently minutes with the development of IoT sensors. The hydraulic changes are in fact quick and are transferred to the whole network in a period of time of seconds.
The model has been developed in `Python` language. We used `TESPy` (Thermal Engineering Systems in Python) package [22], an open-source physical solver previously validated on different use cases [23–25]. To simulate steady and transient dynamics of DHN, a customised code layer has been built upon this physical solver. Mainly, the first step consisted on defining the topology of the network using graph theory, then physical properties were assigned to each component in order to run the simulations.

2.1. Graph representation

The topology of each DHN is defined using graph theory. Let $\mathcal{G} = (V, E)$ be a graph with a set of N nodes V and a set of N_b edges E. Physically, the edges are the pipes of the network, while the nodes can be either consumers, producers or distribution/control valves. As the flow direction is an important variable, DHN are represented as directed graphs. Therefore, the simulator needs two variables to completely define the DHN. The first is the *oriented incidence matrix* $M \in \mathbb{R}^{N \times N_b}$, which has a row for each node i and a column for each edge j such as $m_{ij} = 1$ if edge j enters the vertex i, $m_{ij} = -1$ if the edge leaves the node and $m_{ij} = 0$ if the two elements are not connected. The second variable is the *nodes vector* $V_0 \in \mathbb{R}^N$ that defines the type of each node with regard to a predefined set of supported node types schematized in Fig.1.
Currently, the consumer nodes are considered to be heat sinks without modeling the sub-station part, producer nodes can be one of the heat sources implemented at this time: gas boiler, biomass boiler and solar thermal collectors. Finally, two types of distribution valves are modeled, 3 ways valves and cascading consumers valve. The next step is to assign the suitable physical characteristics to each component. The methodology and the physical models implemented are detailed in appendix A.

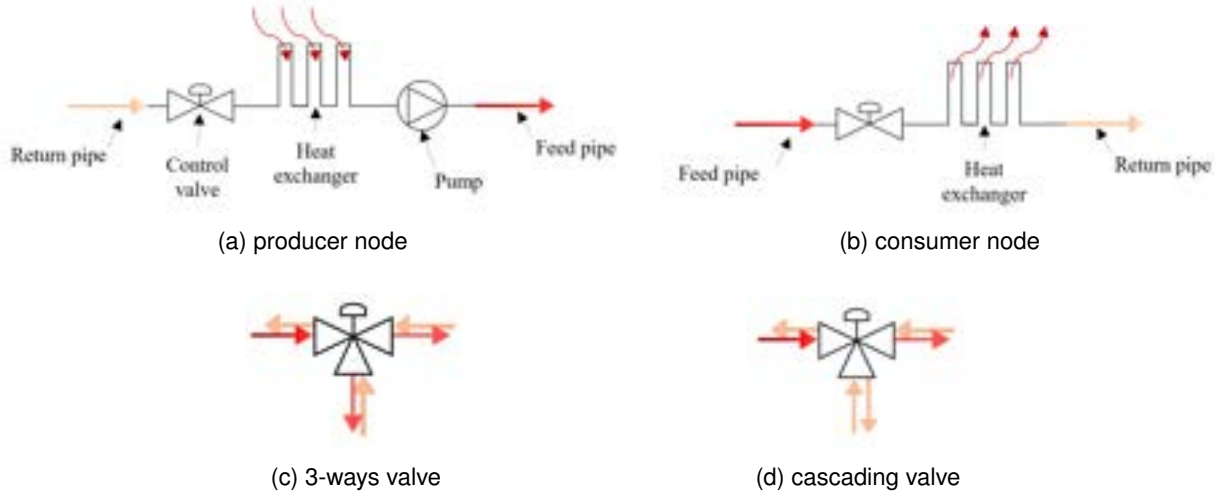

(a) producer node

(b) consumer node

(c) 3-ways valve

(d) cascading valve

Figure 1: The components of each node type supported by the physical simulator

2.2. Numerical methods

Following the graph representation of DHN, the simulator solves the corresponding thermo-hydraulic equations based on the pseudo-dynamic regime assumption. Via a control volume approach, simulating transient dynamics of DHN yields to the following equations for the hydraulic part (see [9]):

$$M \cdot G + G_{ext} = 0, \tag{1}$$

$$M^{\intercal} \cdot P = R \cdot G - W. \tag{2}$$

In Eq.1, $G \in \mathbb{R}^{N_b}$ is the vector containing the flow of each branch, $G_{ext} \in \mathbb{R}^{N}$ the vector containing the extractions or injections of flows that occur at the nodes.
In Eq.2 $R \in \mathbb{R}^{N_b \times N_b}$ is a diagonal matrix containing the hydraulic resistance of each pipe, $W \in \mathbb{R}^{N_b}$ contains the pressure increases due to the work of the pumps and $P \in \mathbb{R}^{N}$ the vector containing the values of the *total pressure* in each node. It should be noted that equations 1 and 2 form a non-linear system given that R depends on G. This system is solved using Newton-Raphson algorithm, G and P being the unknowns of the system.
After the steady hydraulic regime is solved, i.e. the pressure and mass flow rate in each node are known, the thermal transient regime is obtained by following the direction of flow in the network and considering each pipe as a control volume with the outlet temperature as unknown (Fig.8a):

$$\rho c_p V_j \frac{dT_i}{dt} = c_p G_j \left(T_{i-1} - T_i\right) - K S_j \left(\frac{T_{i-1} + T_i}{2} - T_s\right) \tag{3}$$

In case of more than one pipe entering a node i, the temperature of this node is calculated considering a perfect mixture assumption. The heat losses are calculated considering the average temperature of each pipe, this assumption is generally applied in numerical models considering that the temperature drops very slightly along a single pipe segment between two nodes [27]. Formulating Eq.3 for the whole network leads to a linear system that is solved using Euler implicit scheme.

3. Surrogate model

In this section we introduce the surrogate model (SM) architecture that was used for our imitation learning problem. The output of the model can be any variable of interest, but without loss of generality, in this work the SM is trained to predict the evolution of the return temperature at each node given the network topology, its physical characteristics, heat demand and a set of control laws.

3.1. Supervised learning

The aim is to train the SM to emulate the thermo-hydraulic simulator of a DHN. More precisely, let X be the set of inputs given to the physical model and Y the outputs through the physical equations detailed in section 2.2. The SM takes the same inputs and imitate the physical simulator by constructing an *inference function* F_ω such that $Y_\omega = F_\omega(X)$ where ω is a vector of parameters, called weights, that are adjusted during the training step to minimize a specific loss function $\mathcal{L}_\omega$ (i.e. residual function), for example the L_2 norm (i.e. Euclidean norm) $\mathcal{L}_\omega = \|Y_\omega - Y\|_2$.
This is known as a supervised learning problem since we have both the input and output data, unlike unsupervised learning where the goal of the model is to find patterns in the input data to classify them for example. More schematically, the learning process corresponds to an optimization loop where the weights of the model are corrected iteratively in order to reach a global minimum of the loss function as illustrated in Fig.2. The figure also introduces the first *hyper-parameter* of the SM: the learning rate α which modulates the convergence speed of the model.

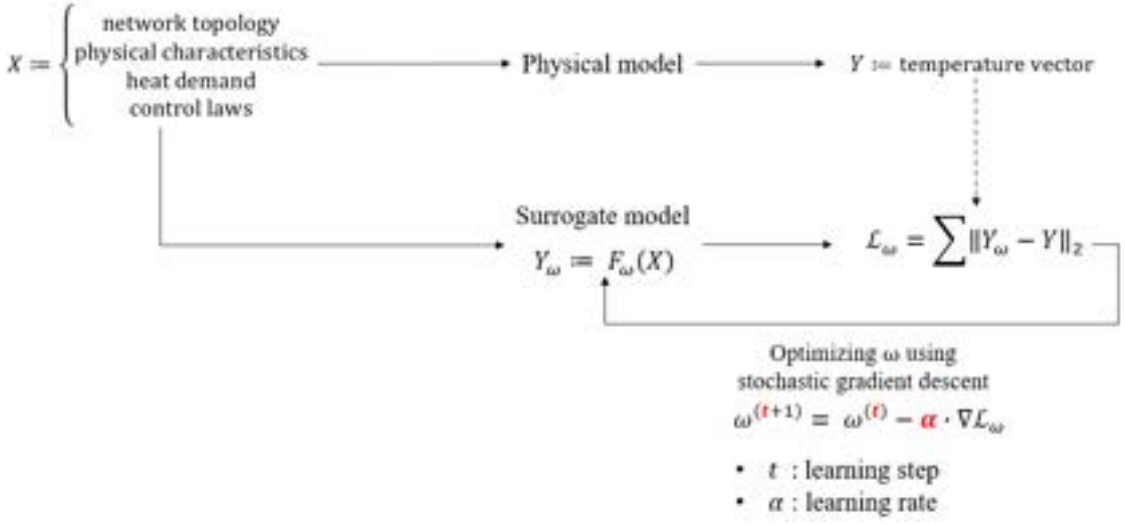

Figure 2: Supervised learning loop of a surrogate model

3.2. Multi-Layer perception networks

The task of constructing the inference function F_ω is an active research area in machine learning. However, deep learning is a particular sub-domain of machine learning where extensive developments are being made continuously. This framework is mainly based on artificial neural networks (ANN) as the learning structure. The simplest ANN is called Multi-Layer Perceptron (MLP) which consists of interconnected layers of artificial neurons, named perceptrons. The neurons in each layer are connected to the neurons in the next layer, forming a directed acyclic graph. Each neuron receives inputs from the neurons in the previous layer, applies a linear transformation to the inputs, and passes the result through a non-linear activation function. The output of a neuron i in layer l is computed as follows:

$$x_i^{(l+1)} = \sigma\left(\sum_{j=1}^{n_l} w_{ij}^{(l+1)} x_j^{(l)} + b_i^{(l+1)}\right), \tag{4}$$

where $x_j^{(l+1)}$ is the output of neuron j in the previous layer, $w_{ij}^{(l+1)}$ is the weight of the connection from neuron j in layer (l) to neuron i in layer $(l+1)$, $b_i^{(l+1)}$ is the bias of neuron i in layer $(l+1)$, n_l is the number of neurons in layer (l) and σ is a non-linear activation function, for example the rectified linear unit function $\texttt{ReLU}(t) = \max(0, t)$. Intuitevely, the activation function either allows the neurons to communicate its output to the next one (i.e. activated) or not when the output does not meet the activation criterion.
Finally, the output of the MLP is the output of the last layer of neurons $\hat{y} = x^{(L)}$. Where $\hat{y}$ is the predicted output, and L is the number of layers in the MLP.

3.3. Graph neural networks

Message passing operation

GNN are a class of neural networks designed to operate on data represented as graphs. GNN aim to learn representations of nodes or the entire graph, which can be used for various tasks such as node classification, node regression, link prediction, etc. The key idea behind GNNs is to iteratively update the representation of each node by aggregating information from its neighboring nodes. This is done by *passing messages* between nodes using a set of learnable parameters. The message passing operation can be formulated as in [28]:

$$\mathbf{x}_i^{(l+1)} = \gamma_\omega\left(\mathbf{x}_i^{(l)}, \bigoplus_{j\in\mathcal{N}(i)} \phi_\omega\left(\mathbf{x}_i^{(l)}, \mathbf{x}_j^{(l)}, \mathbf{e}_{j,i}^{(l)}\right)\right), \tag{5}$$

where $x_i^{(l)}$ is the representation of node i at layer l, $\bigoplus$ a differentiable permutation invariant function (sum, mean, etc.) and $\mathcal{N}(i)$ is the set of neighboring nodes of node i. Finally, γ_ω and ϕ_ω are differentiable functions with learnable weights ω such as MLPs defined in section 3.2. $\mathbf{e}_{j,i}$ is the edge representation connecting node j to node i.
In each layer of a GNN, the representations of all nodes are updated using the message passing operation, resulting in a new set of node representations at the next layer. This process is repeated for multiple layers, allowing the GNN to capture increasingly complex dependencies between nodes. $X^{(l)} = [x_1, \dots x_N]^\intercal$ is the matrix containing the updated representations of the nodes at layer l. If the GNN has L layers, then one has $X^{(0)} = X$ i.e. the initial inputs of the model and $X^{(L)} = Y_\omega$ i.e. the final outputs. For a more guided and detailed presentation on GNN, see [28–30].

Graph attention networks

Graph Attention Networks (GATs) are a type of GNN that uses attention mechanisms to selectively aggregate information from neighboring nodes [31]. The attention mechanism allows GATs to learn different weights for different neighbors of each node, depending on their relevance to the prediction task. Following the definition in Eq.5, the graph attention operation is written as:

$$\mathbf{x}_i^{(l+1)} = \sigma\left(\alpha_{i,i}\mathbf{W}\mathbf{x}_i^{(l)} + \sum_{j\in\mathcal{N}(i)} \alpha_{i,j}\mathbf{W}\mathbf{x}_j^{(l)}\right), \tag{6}$$

where $\alpha_{i,j}$ is the attention coefficient for each neighbor j of node i and σ a non-linear activation function. In a GAT, the representation of each node i at layer l is computed as a *weighted sum* of its neighbors' representations, where the weights are learned using an attention mechanism [31]. The interest of this method here is that physically, nodes in a DHN are first impacted by their upstream neighboring node along the direction of flow, and then by the other nodes in a lesser degree.

4. Study case

4.1. Model architecture

The inference problem shown in Fig.2 involves the use of heterogeneous inputs. Here we will distinguish them according to their static or dynamic character and then according to whether these data are local or global, in other terms whether they are defined at nodes and edges levels or at graph level. First, let $\mathcal{H}$ be the horizon of prediction of the SM and Δt the time-step such that $\mathcal{H} = p \times \Delta t$ and p the number of data points. We define:

- Static nodes attributes: here we simply map the node type to a predefined scalar $\{producers = 0,\ valves = 0.5,\ consumers = 1\}$. This input will be noted $X_s \in \mathbb{R}^N$
- Static edges attributes: as each edge represents a pipe, the attributes are the pipe length L, inner diameter D and its equivalent thermal resistance KS. Subsequently, this variable is noted $E_s \in \mathbb{R}^{N_b \times 3}$.
- Dynamic nodes attributes: it consists of a matrix containing the evolution of heat demand at each node that will be noted $X_d \in \mathbb{R}^{N \times p}$. For distribution valves and producers, the heat demand is computed as the sum of the heat load at their children nodes.
- Global dynamic attributes: this input includes the control signals that affect the whole network, in our case these will be the evolution of the supply temperature $T_s \in \mathbb{R}^p$ and total mass flow rate $G_{tot} \in \mathbb{R}^p$. This input also holds the evolution of the external temperature along the prediction horizon $T_{ext} \in \mathbb{R}^p$.

The network topology is implicitly included during the learning phase via the *adjacency* list that is used by the graph attention operation in order to select the neighbors of each node. Following the above definitions, the SM architecture is in the form of an encoder-processor-decoder as shown in Fig.3. The encoder consists of two MLPs that transform the input data and project it into a latent space where each node is assigned two hidden vectors representing respectively its local attributes (heat demand) and also information from global variables updated with neighbors representations using three graph multi-head attention layers. The processor parts consists on transforming the node hidden representations using three multi-headed attention operations, found to be more efficient than single headed attention in [31]. Finally the decoder is composed of two linear layers that maps the nodes representation to the output space. The model was implement using `Pytorch geometric` library [33].

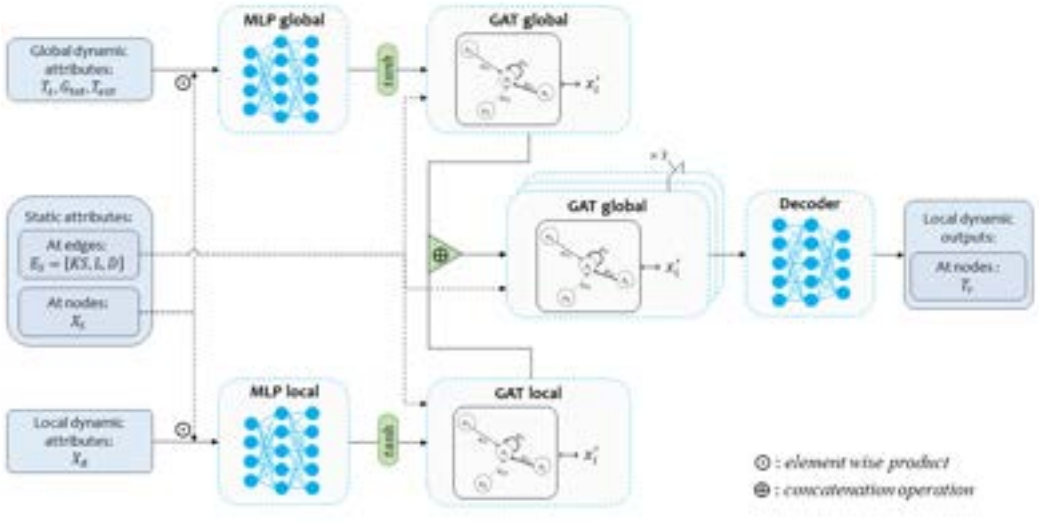

Figure 3: Surrogate model encoder-processor-decoder architecture

4.2. Data generation

In order to assess our approach, we chose to apply it on the academic study case modeled in [32]. This choice is based on the availability of data needed by the physical simulator. The site includes buildings of different usage profiles as shown in Fig.4 where the number under each node indicates its index. Given the annual heat load for each consumer and a typical external temperature variation, we generate an hourly consumption profile for each building using the geometric series approach implemented in `demandlib` library [34], a Python package that allows to create heat profiles from annual values. The supply temperature T_s depends on the outside temperature according to the adapted water law from [35]. For the total flow rate G_{tot}, it is determined

by energy balance over the entire network. The network operation is then simulated for one year with a time step $\Delta t = 600s$. The simulation time is equal to $t_{sim,4c} = 182.1min$ using a four cores CPU processor, which is equivalent to $t_{sim,1c} = 636.2min$ of single core CPU time.
The outputs are time series of $8760 \times 6 = 52560$ data points for each node, representing the evolution of temperatures. Then, we split the data into two datasets, 75% for training and 25% for validation. The horizon of prediction defined in section 4.1. is set to 1 week $= 7 \times 24 \times 6 = 1008$ data points. Thus 39 weeks are used for training and 13 for the validation. Typical values were used for the model hyper-parameters:

- The learning rate α is set to $\alpha_0 = 1 \cdot 10^{-3}$ with an exponential decay factor of $k = 5 \cdot 10^{-4}$, meaning that $\alpha = \alpha_0 \times e^{-kt}$ where t is the epoch number. Therefore, the learning rate is reduced as the training advances which slows down the gradient descent as the loss function approaches its minimum.
- The batch size is the number of samples processed before the model is updated. Here it is set to 8, a compromise between the volume of available data and a large batch size.
- The number of epochs is the number of complete passes through the training dataset. In our case, the model was trained over 200 epochs.
- Finally, L_2 norm was used as the loss function.

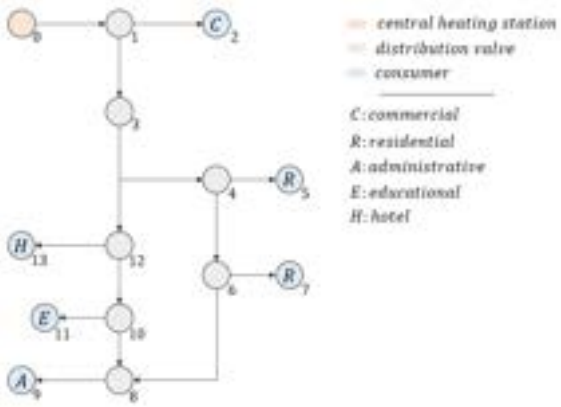

Figure 4: DHN topology of the study case adapted from [32]

5. Results and discussion

After the training phase, the model has been tested on the validation dataset. The root mean squared error (RMSE) is used to evaluate the model performances. It can be seen from table 1 that the error stays below 0.7K for all nodes. Moreover, we report a more visual plot in Fig.5a & 5b for predictions of the node 9, which is an administration building, and the furthest consumer node from the central heating plant. Also, the predictions for node 13, which is a different consumer type, are given in Fig.5c & 5d. More precisely, we plot the normalized temperature (Eq.7), this scaled variable is inherent to the the SM training that fits better with normalized variables (both inputs and outputs) which helps to stabilize the gradient descent step.

$$T^* = \frac{T - T_{min}}{T_{max} - T_{min}}, \tag{7}$$

It can be seen that the prediction results are very close to the values obtained from the physical simulation.

Table 1: RMSE for return temperatures prediction on validation dataset

node	0	1	2	3	4	5	6	7	8	9	10	11	12	13
RMSE (K)	0.5	0.3	0.7	0.2	0.3	0.3	0.5	0.3	0.2	0.1	0.1	0.1	0.1	0.1

The biggest deviations are found at the peaks where the SM underestimates the minimum temperature values and slightly overestimates the maximum values. We also added the Pearson correlation coefficient r that is equal to 0.84 in this case, reflecting a good correlation. The inference time is equal to $t_{inference} = 0.15s$ against $t_{sim,4c} = 2700s$ for the physical simulation on the validation dataset which accounts for approximately 1.8×10^4 time gain.

The regularity observed in the return temperature is the direct effect of the heat profile of the consumer and also the small impact of the control variables that vary quite moderately. Additionally, the same results are shown for node 4 in Figs.5e & 5f. In this case, we observe that the trend is not perfectly fitted while the SM still captures the peak values. Given the scales on both figures, the error, RMSE $= 0.3K$ is still small and acceptable. However, this overestimation of temperature will impact the energy balance on the graph level. This indicates a lack of physical representation in the SM parameters.

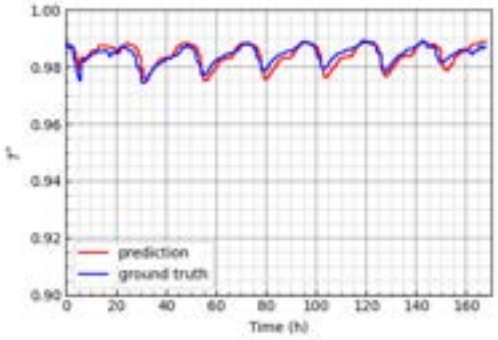

(a) Temperature prediction over 1 week for node 9

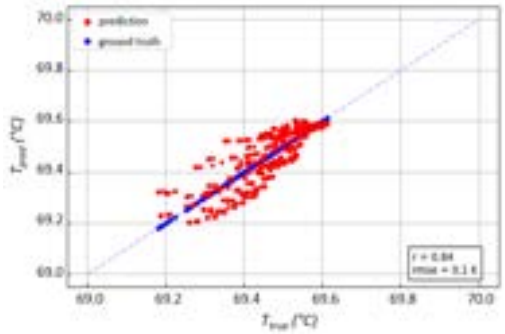

(b) Predicted values as a function of ground truth values for node 9

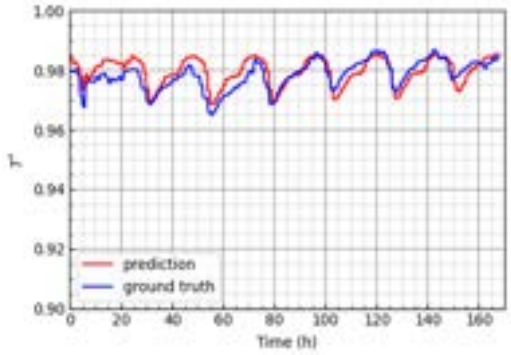

(c) Temperature prediction over 1 week for node 13

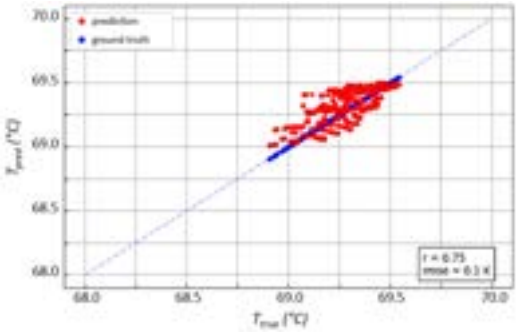

(d) Predicted values as a function of ground truth values for node 13

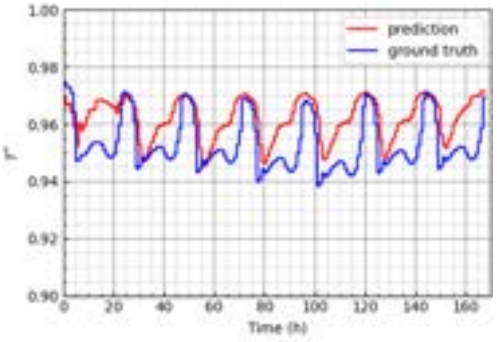

(e) Temperature prediction over 1 week for node 4

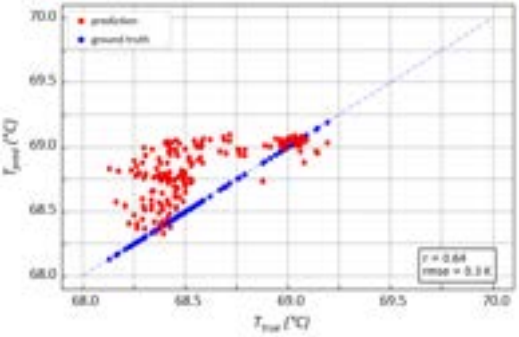

(f) Predicted values as a function of ground truth values for node 4

Figure 5: Example of predictions for nodes 4 (valve), 9 (administration building) and 13 (hotel)

In order to test further the model adaptability and its sensitivity to control laws, we tested it with new simulations where the supply temperature curve and the total mass flow rate were changed more often. Physically, this implied that the return temperature at each node was more affected by the control variables than the heat load itself. The model was not able to capture the correct patterns as illustrated in Fig.6. This limitation originates from an imbalance between the two encoding blocks where the local MLP seems to affects more the prediction. One way of adressing this problem is to incorporate physical laws during the learning phase. More precisely, it is possible to add physical constraints on the predicted values as part of the loss function, in our case this

could be the mass and energy conservation equations that have to be verified at each iteration. Another line of exploration is to use recurrent neural networks such as Gated Recurrent Units (GRU) or Long-Short Term Memory (LSTM) cells that better incorporate the notion of temporality and time dependence into the inference function. Finally, another option is to train the model on more data and different network structures which will allow the SM to better emulates the physical behaviour of DHN.

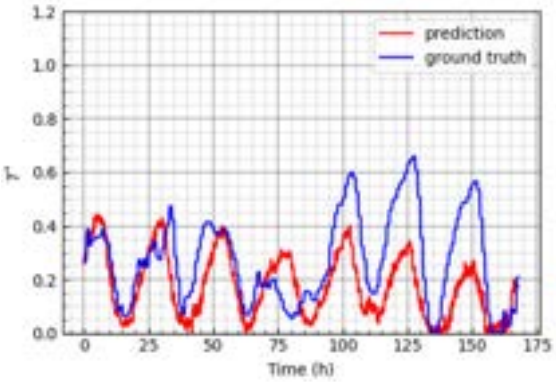

Figure 6: Example of prediction for node 13 (hotel) with a different control law

6. Conclusion

To conclude, the use of geometric deep learning as a surrogate modeling framework for district heating simulations has been evaluated in this study and offers promising results. By leveraging the ability of this approach to process non-Euclidean data and incorporate geometric and topological understandings of data into deep learning models as inductive biases, Graph Neural Networks were trained to emulate a thermo-hydraulic simulator of a district heating network. This statistical inference method has enabled us to significantly reduce simulation time by 10^4 orders of magnitude. Nevertheless, this approach was inadequate to properly capture the physical relations when the control laws are sharper. Therefore, we are currently working on incorporating physical constraints in the surrogate model to alleviate this limitation along with using recurrent structure to leverage more the time dependencies of the data. These improvements will be the subject of a future publication.

7. Acknowledgments

This work was supported by the French Ministry of Higher Education and Research.

References

[1] Masson-Delmotte, V., P. Zhai, H.-O. Pörtner, D. Roberts, J. Skea, P.R. Shukla, A. Pirani, W. Moufouma-Okia, C. Péan, R. Pidcock, S. Connors, J.B.R. Matthews, Y. Chen, X. Zhou, M.I. Gomis, E. Lonnoy, T. Maycock, M. Tignor, and T. Waterfield *IPCC, Summary for Policymakers. In: Global Warming of 1.5℃. An IPCC Special Report on the impacts of global warming of 1.5℃ above pre-industrial levels and related global greenhouse gas emission pathways, in the context of strengthening the global response to the threat of climate change, sustainable development, and efforts to eradicate poverty*. Cambridge University Press 2018, Cambridge, UK and New York, NY, USA, pp. 3-24.

[2] Fleiter, T. *Profile of heating and cooling demand in 2015*. European Union's Horizon 2020; 2017.

[3] Delangle, Axelle and Lambert, Romain SC and Shah, Nilay and Acha, Salvador and Markides, Christos N. *Modelling and optimising the marginal expansion of an existing district heating network*. Energy 2017;140:209-223.

[4] Lund H, Werner S, Wiltshire R, Svendsen S, Thorsen JE, Hvelplund F, Mathiesen BV. *4th Generation District Heating (4GDH): Integrating smart thermal grids into future sustainable energy systems*. Energy. 2014 Apr 15;68:1-1.

[5] Li H, Nord N. *Transition to the 4th generation district heating-possibilities, bottlenecks, and challenges*. Energy Procedia. 2018 Sep 1;149:483-98.

[6] Vandermeulen A, van der Heijde B, Helsen L. *Controlling district heating and cooling networks to unlock flexibility: A review*. Energy. 2018 May 15;151:103-15.

[7] Zheng X, Xu B, Wang Y, You S, Zhang H, Wei S, Wang N. *Hydraulic transient modeling and analysis of the district heating network*. Sustainable Energy, Grids and Networks. 2021 Mar 1;25:100409.

[8] Chertkov M, Novitsky NN. *Thermal transients in district heating systems*. Energy. 2019 Oct 1;184:22-33.

[9] del Hoyo Arce I, López SH, Perez SL, Rämä M, Klobut K, Febres JA. *Models for fast modelling of district heating and cooling networks*. Renewable and Sustainable Energy Reviews. 2018 Feb 1;82:1863-73.

[10] Van der Heijde B, Aertgeerts A, Helsen L. *Modelling steady-state thermal behaviour of double thermal network pipes*. International Journal of Thermal Sciences. 2017 Jul 1;117:316-27.

[11] Guelpa E, Sciacovelli A, Verda V. *Thermo-fluid dynamic model of large district heating networks for the analysis of primary energy savings*. Energy. 2019 Oct 1;184:34-44.

[12] Alizadeh R, Allen JK, Mistree F. *Managing computational complexity using surrogate models: a critical review*. Research in Engineering Design. 2020 Jul;31:275-98.

[13] Sun L, Liu T, Wang D, Huang C, Xie Y. *Deep learning method based on graph neural network for performance prediction of supercritical CO_2 power systems*. Applied Energy. 2022 Oct 15;324:119739.

[14] Fusco F, Eck B, Gormally R, Purcell M, Tirupathi S. *Knowledge-and data-driven services for energy systems using graph neural networks*. In 2020 IEEE International Conference on Big Data (Big Data) 2020 Dec 10 (pp. 1301-1308).

[15] Ryu S, Kim H, Kim SG, Jin K, Cho J, Park J. *Probabilistic deep learning model as a tool for supporting the fast simulation of a thermal–hydraulic code*. Expert Systems with Applications. 2022 Aug 15;200:116966.

[16] Owerko D, Gama F, Ribeiro A. *Optimal power flow using graph neural networks*. In ICASSP 2020 IEEE International Conference on Acoustics, Speech and Signal Processing (ICASSP) 2020 May 4 (pp. 5930-5934).

[17] Ren YM, Alhajeri MS, Luo J, Chen S, Abdullah F, Wu Z, Christofides PD. *A tutorial review of neural network modeling approaches for model predictive control*. Computers & Chemical Engineering. 2022 Aug 13:107956.

[18] Xie J, Li H, Ma Z, Sun Q, Wallin F, Si Z, Guo J. *Analysis of key factors in heat demand prediction with neural networks*. Energy Procedia. 2017 May 1;105:2965-70.

[19] Westermann P, Welzel M, Evins R. *Using a deep temporal convolutional network as a building energy surrogate model that spans multiple climate zones*. Applied Energy. 2020 Nov 15;278:115563.

[20] Zhang B, Ghias AM, Chen Z. *A double-deck deep reinforcement learning-based energy dispatch strategy for an integrated electricity and district heating system embedded with thermal inertial and operational flexibility*. Energy Reports. 2022 Nov 1;8:15067-80.

[21] Birchfield AB, Xu T, Gegner KM, Shetye KS, Overbye TJ. *Grid structural characteristics as validation criteria for synthetic networks.* IEEE Transactions on power systems. 2016 Oct 28;32(4):3258-65.

[22] Witte F, Tuschy I. *Tespy: Thermal engineering systems in python*. Journal of Open Source Software. 2020 May 21;5(49):2178.

[23] Gasanzade F, Witte F, Tuschy I, Bauer S. *Integration of geological compressed air energy storage into future energy supply systems dominated by renewable power sources*. Energy Conversion and Management. 2023 Feb 1;277:116643.

[24] Chen C, Witte F, Tuschy I, Kolditz O, Shao H. *Parametric optimization and comparative study of an organic Rankine cycle power plant for two-phase geothermal sources*. Energy. 2022 Aug 1;252:123910.

[25] Chen X, Hao X. *Exergy analysis of a ground-coupled heat pump heating system with different terminals*. Entropy. 2015 Apr 17;17(4):2328-40.

[26] Wang H, Meng H, Zhu T. *New model for onsite heat loss state estimation of general district heating network with hourly measurements*. Energy conversion and management. 2018 Feb 1;157:71-85.

[27] Fang T, Lahdelma R. *State estimation of district heating network based on customer measurements*. Applied Thermal Engineering. 2014 Dec 5;73(1):1211-21.

[28] Bronstein MM, Bruna J, Cohen T, Veličković P. *Geometric deep learning: Grids, groups, graphs, geodesics, and gauges.* arXiv preprint arXiv:2104.13478. 2021 Apr 27.

[29] Sanchez-Lengeling B, Reif E, Pearce A, Wiltschko AB. *A gentle introduction to graph neural networks*. Distill. 2021 Sep 2;6(9):e33.

[30] Daigavane A, Ravindran B, Aggarwal G. *Understanding convolutions on graphs*. Distill. 2021 Sep 2;6(9):e32.

[31] Veličković P, Cucurull G, Casanova A, Romero A, Lio P, Bengio Y. *Graph attention networks*. arXiv preprint arXiv:1710.10903. 2017 Oct 30.

[32] Belfiore F. *District heating and cooling systems to integrate renewable energy in urban areas*. 8620 EPFL; 2021.

[33] Fey, M., Lenssen, J. E. *Fast Graph Representation Learning with PyTorch Geometric (2019)*. [Computer software]. `https://github.com/pyg-team/pytorch_geometric`

[34] Schachler B, Möller C et al. *demandlib: creating heat and power demand profiles from annual values*. `https://oemof.org/libraries/#demandlib`

[35] Kouhia M, Laukkanen T, Holmberg H, Ahtila P. *District heat network as a short-term energy storage*. Energy. 2019 Jun 15;177:293-303.

Appendix A Adding physical inputs to the simulator

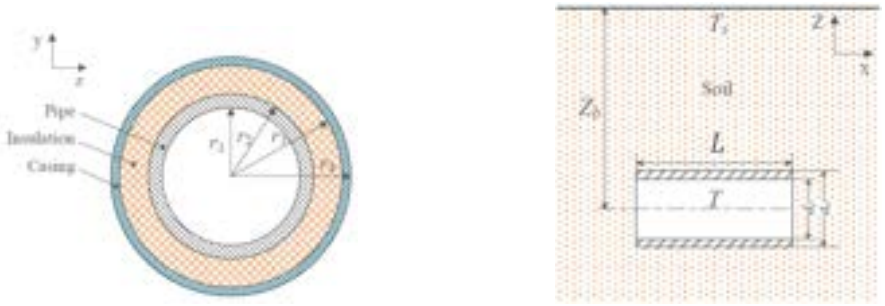

(a) pipe cross section (b) buried pipe

Figure 7: Schematic diagram of an insulated pipe [26]

Once the network topology defined, the physical properties of each component are fed to the model:

- Branches: the *oriented incidence matrix* M allows to create connections between nodes. Each edge corresponds to two pipes, the feeding pipe and the return one. We implement two layers insulated pipes as in [26]. Therefore, all the geometrical quantities $(L, r_1, r_2, Z_b \dots)$ shown in Fig.7 are inputs to the model, in addition to thermal conductivities k and roughness ϵ for determining pressure loss in the pipes.

- Producers: here, the inputs to the model vary depending on the heat source type. As the study case in section 4. considers only gas boiler, the required inputs are $\dot{Q}_{max}$ which is the maximum heat rate of the plant, pr the outlet/inlet pressure, and the isentropic η_s efficiency of the pump coupled to heat source.
- Valves: a quasi-incompressible fluid is assumed, which is always the case for liquids. The fluid flow between the inlet and the outlet of the valve is assumed to be isenthalpic. The flow rate is governed by the equation 8 derived from Bernoulli's law. K_ν is the required input by the model.

$$\dot{V} = K_\nu \sqrt{\Delta P}. \tag{8}$$

- Consumers: similarly the outlet/inlet pressure ratio is needed, and the heat load can be either a scalar if steady state resolution or a vector in the case dynamic simulation.

Finally, the model also needs global inputs that are the external and ground temperatures. The solver comes with its proper verification tools that make sure the system is nor over or under determined. Depending on the resolution scheme and the aim of the simulation, the unknowns of the system have to be chosen carefully. However, and without loss of generality, we will consider the particular case where the DHN is already designed, the variables of our system are the supply temperature at the heat source T_s and the total mass flow rate G_{tot}.

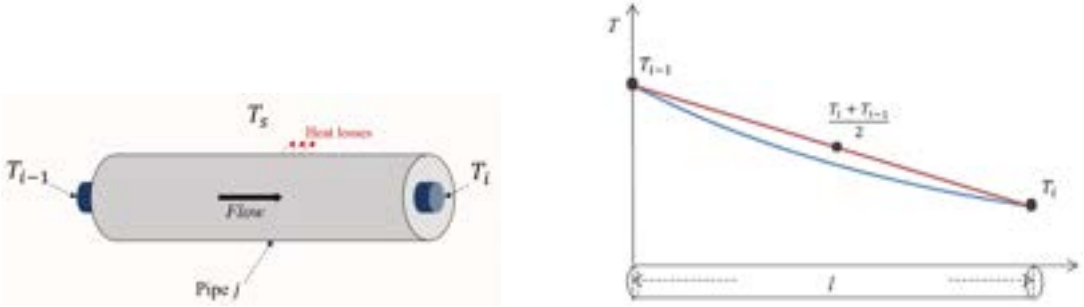

(a) control volume used in thermal transient equation (b) pipe temperature estimation adapted from [27]

Figure 8: Control volume used in Eq.3 and illustration of the error induced by using the average temperature to compute heat losses

Envisioning a Collaborative Energy System Planning Platform for the Energy Transition at the District Level

Lennart Lahrs[a], Pierre Krisam[b], Ulf Hermann[c]

[a] Fraunhofer IEG, Jülich, Germany, lennart.lahrs@ieg.fraunhofer.de
[b] Fraunhofer UMSICHT, Oberhausen, Germany, pierre.krisam@umsicht.fraunhofer.de
[c] Fraunhofer IEG, Jülich, Germany, ulf.herrmann@ieg.fraunhofer.de

Abstract:

Residential and commercial buildings account for more than one-third of global energy-related greenhouse gas emissions. Integrated multi-energy systems at the district level are a promising way to reduce greenhouse gas emissions by exploiting economies of scale and synergies between energy sources. Planning district energy systems comes with many challenges in an ever-changing environment. Computational modelling established itself as the state-of-the-art method for district energy system planning. Unfortunately, it is still cumbersome to combine standalone models to generate insights that surpass their original purpose. Ideally, planning processes could be solved by using modular tools that easily incorporate the variety of competing and complementing computational models. Our contribution is a vision for a collaborative development and application platform for multi-energy system planning tools at the district level. We present challenges of district energy system planning identified in the literature and evaluate whether this platform can help to overcome these challenges. Further, we propose a toolkit that represents the core technical elements of the platform. Lastly, we discuss community management and its relevance for the success of projects with collaboration and knowledge sharing at their core.

Keywords:

Energy System Planning; District Energy Planning Platform; District Data Model; Renewable Energy Integration.

1. Introduction

In the effort to accelerate the transition towards climate neutral energy supply at the district scale, many tools exist that aim to solve individual parts of the district energy system planning process [1], from stochastic occupancy simulation [2, 3] and thermal building simulation [4] via building and district level energy technology sizing [5], to simulations of heat and electrical grids [6, 7]. It is the combination of numerous data sources and tools that is required to provide solutions to the heterogeneous tasks of energy system design.

For each step of the planning process, research is published on how to improve predictions, models and simulations; new models and tools will continue to come. Therefore, whoever wishes to combine tools into a district energy system planning workflow needs to go through continuous efforts to keep up with newly developed tools, improved methods and updated data [8, 9]. The following paragraphs provide an overview of challenges, existing tools and platforms in the field of district energy system planning.

Keirstead et al. [10] review urban energy system models and identify model complexity, data quality and uncertainty, model integration, and policy relevance as the prevailing challenges in urban energy system modelling. They see opportunities in creating an integrated framework where sensitivity analysis, data collection and integration techniques and activity-based modelling, promise advances in the aforementioned challenges. Yazdanie et al. [11] review gaps and solutions for advancing urban energy system and modeling approaches. They state that numerous models and planning tools as well as review articles discussing their features exist, but the gaps and corresponding solution suggestions are rarely discussed. They identify key methodological solutions to be: integrated modeling approaches and comprehensive energy modelling scenarios including social factors and system imperfections and data collection using privacy control, robust and secure communication architecture and improved data sharing platforms.

In between the two review articles, several tools and frameworks have been published, that attempt to solve some of the identified challenges. Bollinger et al. [8] introduce a Holistic Urban Energy Simulation Platform (HUES). They motivate the platform with the need to reuse and integrate existing computational models for urban multi-energy simulation for integrated studies of urban infrastructures. Multi-model ecology is the defining concept of their platform. Fonseca et al. [12] present the CityEnergyAnalyst, a framework for the analysis and optimization of city and district energy systems. It supports the analysis of energy, carbon and financial

benefits of competing design scenarios of optimal distributed generation systems by estimating local energy potentials and simulating energy systems and building energy performance. El Kontar et al. [13] present URBANopt, an open-source software development kit for community and urban district energy modelling. The developers argue that a wide variety of building modeling tools exist, but to address planning problems at an urban scale, these tools need to be combined, which motivates a platform where multiple input formats are supported and this data is mapped onto underlying simulation engines. The combination of modules allows for customized workflows. Wehkamp et al. [14] analyze the challenges of planning and evaluating district energy systems and present a workflow using open-source tools and special purpose models that were demonstrated on a district in northern Germany. The authors identify complex stakeholder structures as an issue requiring further research.

Coming from this state of the literature, we provide a brief overview of the challenges faced in integrated district energy system planning. We then present the components of the collaborative district energy system planning platform as a suitable starting point for further development. Due to the ever-changing landscape of tools under current and future development, we expect different tools to extend or replace the initial toolkit. Finally, we discuss how community management is a potential differentiator between failure and success for this vision.

2. Problem setting

District energy system planning is an interdisciplinary field where planning problems vary widely in terms of the scope to be considered. For clarity, we introduce the system boundaries of district energy systems (DES), which frame the challenges considered in this work. Related literature sometimes refers to urban energy systems (UES), which we consider to be a superset of DES. We address the considered scope of DES planning and the challenges associated with it.

2.1. Considered scope of district energy system planning

Several dimensions need to be considered when planning DES. DES planners have to take into account not only energy conversion, but also policy frameworks, stakeholder interests and business models [10]. Key issues to be addressed during planning include sector coupling, centralized versus decentralized energy supply, demand forecasting, building refurbishment and competing stakeholder interests.

In DES, the energy consumption sectors (e.g. households, commerce, and mobility) as well as the energy supply sectors (e.g. electric power, heat and gas) co-exist. During the planning of energy systems, synergies can be leveraged by considering all sectors at once. Whether it is the use of waste heat from nearby industry or the integration of bi-directional e-mobility into a district power grid, successfully linking the consumption sectors requires the development of appropriate business models, which may be complicated by regulation. Coupling the energy sectors, especially heat and electricity, enables the efficient use of locally generated renewable energy. Therefore, both electricity and district heating networks are crucial for DES planning.

Local energy generation (energy hubs) can play a central role in this [8]. Since conditions vary in each district, various technologies (e.g. heat-pumps, photovoltaic, fuel cells) with different operating and investment costs and both decentralized (building supply) and centralized energy systems (energy hub) should be investigated.

In order to be able to plan DES, the energy demand of the district must be known or determined. Since the available demand data is often incomplete, many methods to generate load profile data have been developed over the recent years [12]. The energy demand depends, among other influences, on building types, type of use, refurbishment status and user preferences [15]. For this reason, optimizing the refurbishment status of the buildings is another important research field and part of a holistic DES planning.

Figure 1 illustrates the system boundaries of DES planning. A district usually consists of a heterogeneous building stock or newly planned buildings. As the type of use and the state of renovation have a strong influence on the energy demand, both are part of the system boundaries. The secure energy supply of the district is guaranteed by transmission networks. In the context of energy transition, heating networks play an increasingly important role, as does the consideration of e-mobility.

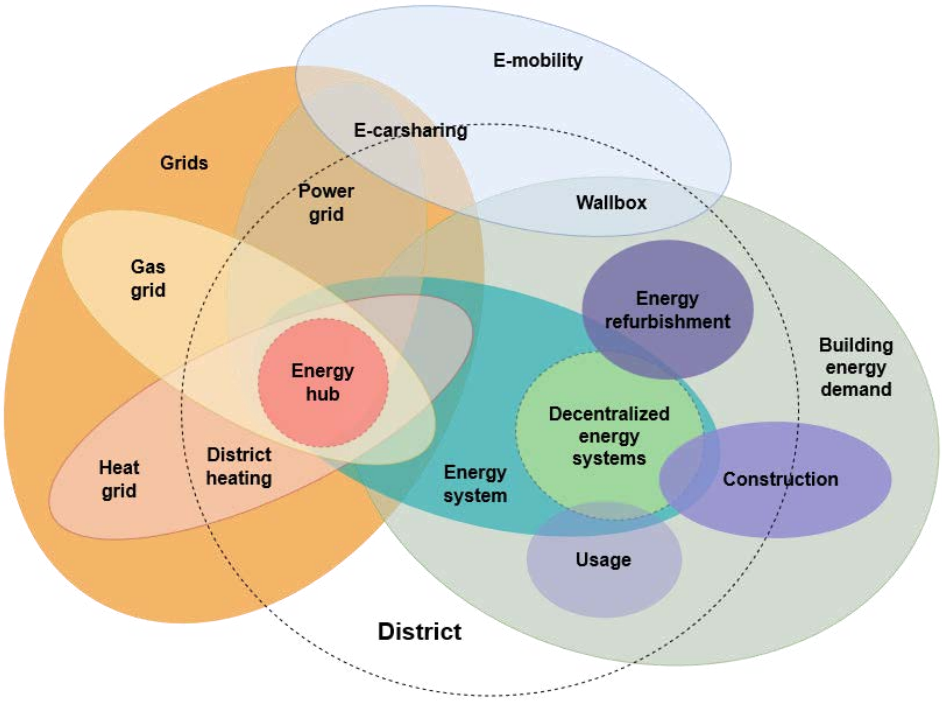

Figure 1. System boundaries of district energy system planning

DES planning is largely influenced by political and institutional decisions. Whether an energy system or business model is economically viable depends not only on technical and economic factors, but also on influences by government subsidies and the regulatory framework; such as carbon pricing or fees and taxes for the use of the electricity grid. Furthermore, many stakeholders are involved in the planning of district projects, such as investors, proprietors, residents, as well as district operators, e.g., residential real estate companies or municipal utilities [14, 16]. In an optimal planning process, all these perspectives are taken into account.

2.2. Challenges of district energy system planning

The various dimensions (e.g. technical, economic and political dimension) of DES planning come with a wide range of challenges. In this section we selected important challenges from the literature and categorized them according to the dimensions of DES planning. Yazdanie et al. [11] reviewed over 30 review studies, over 90 local-scale case studies and 40 surveys and interviews to identify gaps and challenges in energy modeling. Keirstead et al. [10] reviewed 219 papers to analyze approaches, challenges and opportunities of urban energy system models. Wehkamp et al. [14] discussed challenges and tools for planning DES using a German district as a case study. Coming from this extensive collection of challenges in district energy system planning, Table 1 contains clusters of these challenges including an assessment of whether they can be solved through our platform approach. The following paragraphs briefly discusses the most relevant challenges.

Model integration – Numerous models address different dimensions of DES planning. Sensibly combining these existing models, rather than modeling larger and more complex models, is a challenging task. A platform can support this task, e.g. by providing interface standards.

Validating models – Validation of individual models is cumbersome and time-consuming. When models are integrated into generic tools of a platform, they can be evaluated more easily. Furthermore, platform standards and community exchange can improve the validation process of models.

Considering data and geometry heterogeneity – Models require data of different form and levels of granularity. The data exchange between models can thus be hindered. In an integrated platform, a central data model can help with the transferability of data by defining a common standard for models' data requirements.

Handling data gaps and data availability – A common problem in DES planning are data gaps and data availability. This platform can hold a variety of tools for generating synthetic data as well as pre-processed data sets from open data sources. In addition, data preparation done by one user or developer does not need to be redone by a second individual.

Conflicting interests – DES planning centers around conflicting interests. Some models focus on individual perspectives, while others offer multi objective planning. In any case, the more tools are available to compare, the better, different stakeholder interests can be portrayed and represented.

Support for decision making – Decision-makers need reliable and verified results that are presented and visualized in a comprehensible way. By increasing the number of users and benefiting from proof reading of the open-source community, this platform can offer the required level of robustness.

Table 1. Challenges of district energy system planning

	Challenges of DES planning	Platform
Technical and economic challenges	Model integration (combining existing models) [8, 10, 11, 13]	x
	Model complexity and resolution [10–12, 17]	x
	Modelling external factors such as human behavior, economic development and weather [8, 11, 14, 17]	
	Considering novel energy technologies [11, 14]	x
	Improving existing methods [14]	x
	Validating models [8]	x
	Quantifying and handling uncertainty [10, 11, 17]	x
	Considering data and geometry heterogeneity [13, 18]	x
	Balancing model resolution with data availability [17]	
	Handling data gaps and data availability [10, 11, 14, 19]	x
Political and institutional challenges	Conflicting interests [11, 14, 19]	x
	Support for decision making [10–12, 14]	x
	Political uncertainty [10, 17, 19]	
	Sustainable, affordable energy [14, 17]	x
	Energy security [17]	x
	Administrative complexity [19]	x
	Monetizing aggregated flexibility [14]	

The following section presents the tools and technical components of the platform. It also discusses technical considerations that may influence the success of the platform.

3. Platform components

This section presents the components of the platform that would provide a reasonable starting point for the evolving toolkit. This initial collection would be capable of providing meaningful results for standard planning workflows. It would also demonstrate the type of additional methods and tools that could be added in the future. The intention is that the collection of tools and data on the platform will be combined to produce insights beyond the functionality of any individual component. The tools contain data processing logic that leverages various numerical and analytical methods required for DES planning.

The main objectives of the platform are:

- Enabling flexible integration of novel computational methods
- Visualizing planning and optimization interdependencies
- Improving data availability and homogeneity
- Increasing visibility of data uncertainty
- Handling variants and scenarios

The idea of such an initial toolkit is that it can easily be updated, manipulated or replaced, based on the users' and developers' preferences. Each tool is considered a container for many methods to solve a particular problem. Within a tool, a predefined architecture directs researchers and developers, on how new methods can be injected into the tool. The main flow of data would not be altered by switching between methods. The compatibility of tools bases on the commitment to a central data model. To cover the essential elements and processing steps of district planning, we suggest the components displayed in Figure 2. The boxes represent tools and cylinders represent databases; the dashed lines indicate useful extensions, that must not be part of an initial toolset.

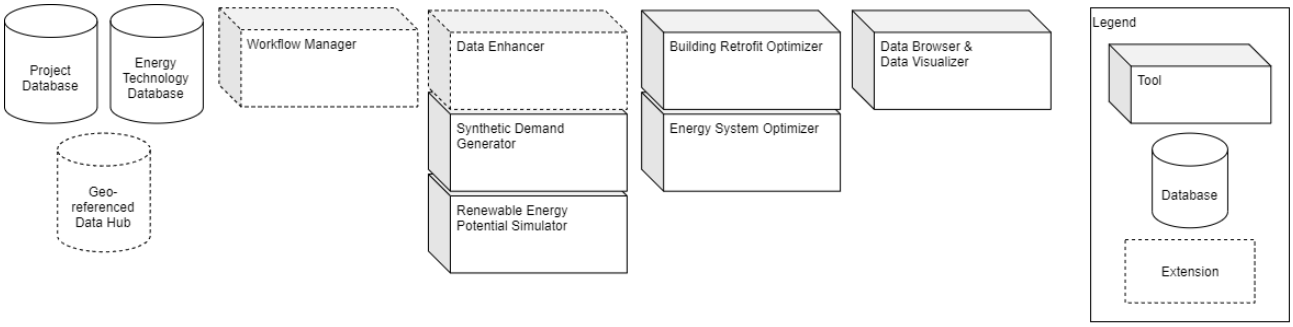

Figure 2. Initial platform toolkit

All tools work with a central district data ontology. The data model is the digital representation of districts including all physical and hypothetical building and energy system components. Tools operate either on a district data object that is transferred between processing steps in an ongoing computation, or they write and read the district data object to and from a database for intermittent processing. The latter would be beneficial for collaborative planning of districts, where multiple planners solve sub-problems successively.

The *Workflow Manager* enforces a structure that separates processing steps programmatically and visually, which improves interpretability and reproducibility. Data sources and functionality can be programmed into the structure of a directed acyclic graph, where nodes represent computations and directed arcs represent information flow and thereby node dependencies. Tools could certainly also be run using a simple script to call the processing steps of the planning problem. This would however result in more heterogeneous planning workflows that would be harder to compare and build upon.

The *Data Enhancer*, *Synthetic Demand Generator* and *Local Energy Potential Quantifier* are all pre-optimization steps, that generate arbitrary data, e.g., timeseries that are fed into energy system simulation and optimization. Usually the available data about existing, and even future buildings is sparse and incomplete. Filling up data gaps using appropriate estimations is therefore a crucial step in the total planning process.

The *Building Retrofit Optimizer* creates plausible retrofit variants by providing adapted building objects to the Synthetic Demand Generator. It either outputs a final optimized retrofit, or it feeds different variants of the building to the proceeding energy system optimization.

The Energy System Optimizer sizes system components based on optimal energy dispatch. This optimization provides answers to the trade-off between decentral and centralized technologies of all energy sectors and thereby defines which form of energy supply dominates. Additional tools could be introduced for more detailed optimizing of heating and electrical grids.

The *Data Browser & Data Visualizer* improve the interpretability of the optimization and simulation results. They output different types of tables, plots and reports, based on the requirements of the audience.

The following paragraphs discuss technical properties of the platform that are not specific to energy system planning, yet greatly affect the quality of the platform and its potential to sustain.

Extendibility – The platform should be easily extendable. By choosing Python as the development language, tools consist of Python packages that run platform independently and are easily updated and shipped to services like the Python Package Index [20]. Interested users, researchers and developers can choose which tools to use, how and where to run them and whether to extend the platform or workflow by some additional or improved functionality. By providing placeholders for typically required tools in district energy planning, it is easy to identify interfaces between processing steps. Documentation can be built into the tools in the form of comments, test cases and demo scripts, and be made available in a web compatible format.

Level of coupling – Introducing a central data model to ensure compatibility comes with advantages and disadvantages. It improves data consistency and integration. This results in fewer errors and inconsistencies while improving efficient development and data flow by reducing transformations. However, a central data model can become very large, having to serve requirements of many different applications. This increases development and maintenance efforts. It further increases the dependency of tools from this data model, which might require updating tools, when updating the data model.

Flexibility and maintainability – Energy system planning is a dynamic environment, where data models and tools regularly need to be updated to cope with novel problems and requirements. Data structures should therefore be flexible enough to cope with unforeseen needs during initial development. Practices that can help are modular data structure components, leveraging industry standards and implementing backward compatibility. Further, the choice of database technology can greatly affect the success of the project due to different levels of flexibility, performance and maintenance effort.

Usability – Usability is to a large extend subjective and experienced differently based on the familiarity with different kinds of interfaces. The main user group is expected to be energy system researchers and engi-

neers who have basic knowledge of Python. We therefore suggest to either provide tools as Python packages, with command line interfaces, or with a graphical user interface. Python has become one of the most popular languages for tools in the energy academic community [21], providing well-designed high-level functions for newly developed tools can be a good balance in terms of usability and flexibility for users familiar with Python. As a high-level programming language, Python makes it easy for beginners to get started, which is important for interested users to start generating results [22]. Due to the expected rapid development in research and application of district energy planning methods and software, this focus on code-based usability is motivated because of the low overhead in interface design. To integrate tools of different languages command line interfaces are sensible. Providing a graphical user interface comes with a higher level of user-friendliness and is particularly useful for presenting a lot of information at once. Developing and maintaining a GUI adds additional work and is therefore expected to be used mostly for result presentation and not necessarily for data processing. Python packages and command line interfaces are also easier to integrate into automation procedures of recurring workflows.

Integrated computing – DES planning quickly becomes computationally demanding. Therefore, we suggest to integrate computational resources into the platform. While the processing and data handling could all be done locally, it would be sensible to integrate computing capacity that supports tools in highly intensive processing tasks. Using a centralized solution can result in lower overhead due to the stronger integration of software and hardware. The data storage could also be hosted on a central machine, which benefits data availability, integration and performance.

The following section discusses community management and its potential influence on the success of the envisioned platform.

4. Platform community management

Open-source community management is the process of building online communities and facilitating active collaboration. This involves engaging community members, moderating communication, facilitating discussion, hosting community events, responding to user questions and generating informational and promotional content [23]. When collaboration and knowledge sharing are at the heart of the project, technical features and robustness do not alone affect the individual's choice to use the platform or to contribute. A platform that builds on the idea of collaborative development requires a community to be engaged and willing to share information, which his particularly sensitive in the early stages of development and research; this requires successful community management [24].

Open-source community management is a topic that has received attention in the context of the most successful open-source projects [24], but to our knowledge it has not been considered a central part in the effort to engage a community of researchers and users of district energy system planning tools. Successful community management can support compatibility of tools and data, bridge the gap between research and application and support active knowledge sharing and sustainable development of the platform. In efforts towards collaborative research and application in district energy system planning, the level of community engagement can be a potential differentiator between failure and success for a collaborative multi-energy system planning platform.

Community management centers around community managers, who connect various groups such as researchers, practitioners, policymakers to facilitate the exchange of experiences, knowledge and best practices and thereby drive innovation and the quality of the platform.

Important aspects of community management are:

- Clear communication of goals, expectations and policies
- Inclusiveness and empathy within the community
- Active engagement of potential contributors
- Decision-making transparency

A collaborative multi-energy system planning platform’s success not only depends on technical aspects, but also on the level of engagement in the community, the user's choice to commit to this platform and potentially contribute themselves, the willingness to share knowledge and the community's ability to make decisions and move forwards. Community management covers these aspects and can help to accelerate research and application of superior methods in district energy system planning.

5. Conclusion

In the context of district energy system planning, we have motivated the need for a collaborative platform to cope with the rapid development of new models and tools by academia and the requirements of practitioners. Due to the interdisciplinary nature of the problem, we expect individual groups to struggle with providing solutions to all elements of the problem. Some platforms exist with fine or major distinctions, of which currently none seems to be established as the status quo for integration for models and tools in district energy

system planning. A platform that is modular and extendable can be the common ground for all parties involved.

Based on existing literature, we see model integration, validating models, considering data and geometry heterogeneity, handling data gaps and data availability, conflicting interests and support for decision making to be the prominent challenges to be solved by the envisioned platform. Concretely, we expect the platform to enable flexible integration of novel computational methods, expose planning and optimization interdependencies, improve data availability and homogeneity, increase visibility of data uncertainty and handle variants and scenarios. For consistent data handling we propose the definition of a central data model as the foundation for tool integration and data consistency. Further, we present a set of essential tools, that we consider indispensable to solve a wide scope of district planning problems.

Fostering openness and effective collaboration potentially is a key differentiator between success and failure of such platforms. Collaboration, communication and decision procedures pose a challenge for ventures like this to thrive in the open-source world. Analyzing these aspects of the problem should be subject of future work.

Setting the groundwork for this vision is a complex task, and no one in the sphere of district energy system planning naturally has the obligation to start. However, it does require an initial definition of standards and interfaces, for this platform to manifest in something tangible. Further, a combination of central guidance and community driven decision making is required to maintain the platform and react to future developments.

Acknowledgments

This paper was written as part of the project ODH@Jülich, which was funded by the Federal Ministry of Education and Research (BMBF).

References

[1] openmod initiative. Open Models. Available at: <https://wiki.openmod-initiative.org/wiki/Open_Models> [accessed 27.02.2023]

[2] Fischer D, Surmann A, Biener W, Selinger-Lutz O. From residential electric load profiles to flexibility profiles – A stochastic bottom-up approach. Energy and Buildings 2020; 224: 110133.

[3] Richardson I, Thomson M, Infield D, Clifford C. Domestic electricity use: A high-resolution energy demand model. Energy and Buildings 2010; 42(10): 1878–87.

[4] EnergyPlus. Available at: <https://energyplus.net/> [accessed 17.01.2023]

[5] Krien U, Schönfeldt P, Launer J, Hilpert S, Kaldemeyer C, Pleßmann G. oemof.solph—A model generator for linear and mixed-integer linear optimisation of energy systems. Software Impacts 2020; 6: 100028.

[6] Lohmeier D, Cronbach D, Drauz SR, Braun M, Kneiske TM. Pandapipes: An Open-Source Piping Grid Calculation Package for Multi-Energy Grid Simulations. Sustainability 2020; 12(23): 9899.

[7] Thurner L, Scheidler A, Schafer F, et al. Pandapower—An Open-Source Python Tool for Convenient Modeling, Analysis, and Optimization of Electric Power Systems. IEEE Transactions on Power Systems 2018; 33(6): 6510–21.

[8] Bollinger LA, Evins R. HUES: A holistic urban energy simulation platform for effective model integration. In: Proceedings of International Conference CISBAT 2015 Future Buildings and Districts Sustainability from Nano to Urban Scale; 2015; 841–6.

[9] Widl E, Cronbach D, Sorknæs P, et al. Expert survey and classification of tools for modeling and simulating hybrid energy networks. Sustainable Energy, Grids and Networks 2022; 32: 100913.

[10] Keirstead J, Jennings M, Sivakumar A. A review of urban energy system models: Approaches, challenges and opportunities. Renewable and Sustainable Energy Reviews 2012; 16(6): 3847–66.

[11] Yazdanie M, Orehounig K. Advancing urban energy system planning and modeling approaches: Gaps and solutions in perspective. Renewable and Sustainable Energy Reviews 2021; 137: 110607.

[12] Fonseca JA, Nguyen T-A, Schlueter A, Marechal F. City Energy Analyst (CEA): Integrated framework for analysis and optimization of building energy systems in neighborhoods and city districts. Energy and Buildings 2016; 113: 202–26.

[13] El Kontar R, Polly B, Charan T, et al. URBANopt: An Open-Source Software Development Kit for Community and Urban District Energy Modeling. In: Building Performance Modeling Conference and SimBuild; 2020.

[14] Wehkamp S, Schmeling L, Vorspel L, Roelcke F, Windmeier K-L. District Energy Systems: Challenges and New Tools for Planning and Evaluation. Energies 2020; 13(11): 2967.

[15] Evins R, Orehounig K, Dorer V. Variability between domestic buildings: the impact on energy use. Journal of Building Performance Simulation 2015; 9(2): 162–75.

[16]Wrobel P, Schnier M, Schill C, Kanngießer A, Beier C, Schill Cornelius S. Planungshilfsmittel: Praxiserfahrungen aus der energetischen Quartiersplanung. Stuttgart: Fraunhofer IRB Verlag: Begleitforschung EnEff:Stadt; 2016. Schriftenreihe EnEff.

[17]Pfenninger S, A. Hawkes, Keirstead J. Energy systems modeling for twenty-first century energy challenges 2014.

[18]Charan T, Mackey C, Irani A, et al. Integration of Open-Source URBANopt and Dragonfly Energy Modeling Capabilities into Practitioner Workflows for District-Scale Planning and Design. Energies 2021; 14(18): 5931.

[19]Cajot S, Peter M, Bahu J-M, Koch A, Maréchal F. Energy Planning in the Urban Context: Challenges and Perspectives. Energy Procedia 2015; 78: 3366–71.

[20]Python Software Foundation. PyPI - The Python Package Index. Available at: <https://pypi.org/> [accessed 24.02.2023]

[21]Groissböck M. Are open source energy system optimization tools mature enough for serious use? Renewable and Sustainable Energy Reviews 2019; 102: 234–48.

[22]Hilpert S, Kaldemeyer C, Krien U, Günther S, Wingenbach C, Plessmann G. The Open Energy Modelling Framework (oemof) - A new approach to facilitate open science in energy system modelling. Energy Strategy Reviews 2018; 22: 16–25.

[23]The Open Source Way 2.0. Available at: <https://www.theopensourceway.org/> [accessed 27.02.2023]

[24]Lee S-YT, Kim H-W, Gupta S. Measuring open source software success. Omega 2009; 37(2): 426–38.

Detection of anomalous energy consumption through clustering techniques: an application to large-scale food retailing activities

Alessandra Ghilardi[a], Guido Francesco Frate[a], Francesca Leonetti[a], Nicola Fredducci[b], Luca Brancolini[c], Lorenzo Ferrari[a]

*[a] Department of Energy, Systems, Territory, and Constructions Engineering University of Pisa, Pisa (PI), Italy, alessandra.ghilardi@phd.unipi.it, guido.frate@unipi.it, f.leonetti1@studenti.unipi.it, lorenzo.ferrari@unipi.it (**CA**)*
[b] Unicoop Firenze, Firenze (FI), Italy, nicola.fredducci@unicoopfirenze.coop.it
[c] Inres Coop, Osmannoro (FI), Italy, luca.brancolini@inres.coop.it

Abstract:

Anomalous energy consumption detection is a valuable strategy for pursuing energy efficiency. In commercial buildings, such as supermarkets, abnormal consumption can occur due to non-adequate equipment, such as lighting devices and refrigeration systems, or non-efficient HVAC plant management. Anomaly detection is usually performed on a single building by comparing its energy consumption to its usual behaviour and applying statistical or artificial intelligence-based techniques. Still, no anomaly emerges if its energy consumption is systematically high (or low). However, a more effective method for detecting anomalies would be to compare the energy consumption of a single building with that of others possessing similar characteristics. This paper then proposes an alternative approach based on clustering analysis. From this perspective, energy consumption data from a group of supermarkets are gathered in clusters to detect which presents abnormal behaviour compared to others with similar characteristics, such as the dimension and external weather conditions. An unsupervised density-based clustering algorithm for outlier detection (DBSCAN) is applied to a pool of 87 supermarkets located in Tuscany (Central Italy) to detect the abnormal ones, considering as input features the floor area, the electrical and thermal consumptions available from monthly bills, the type of the air-conditioning units, and the outdoor temperature. The analysis is performed over three years to detect recurring outliers on an annual and monthly scale to investigate possible seasonal effects. During the three years, approximately 15% of the supermarkets were consistently identified as outliers on both a monthly and annual basis. These findings were subsequently validated through an on-site inspection conducted by the energy manager of the supermarkets, revealing that 50% of the identified outliers exhibited exceptionally high thermal and electrical consumption due to improper plant operation.

Keywords:

Anomaly detection; DBSCAN; Energy efficiency; Unsupervised clustering.

1. Introduction

Pursuing energy efficiency in buildings, industry, transport, and energy supply sectors is one of the central policies imposed by the European Council to meet the 2030 emission targets [1]. Through the years, most attention has been dedicated to reducing energy consumption in the building sector since it is responsible for more than 30% of the CO_2 global emissions [2]. Beyond that, relevant emission cuttings can be achieved by actuating energy efficiency strategies also in the non-residential sector, which includes schools, offices and commercial activities. Non-residential buildings are characterised by higher energy intensities than residential ones and are responsible of the 5% of the total share of CO_2 emissions [3]. This highlights the potential for good energy efficiency practices to have a greater impact. Among this category, food-related commercial activities (i.e., supermarkets) are one of the most energy-intense because of the energy consumption related to space cooling and heating and refrigeration for food preservation [4].

Energy efficiency in existing supermarkets has been pursued mainly by replacing old devices with more efficient ones (HVAC units, refrigeration systems and lighting systems) [5], retrofitting the thermal insulation to minimise thermal losses [6] and implementing renewable generation sources [7]. Although widespread, these strategies often require a significantly high investment cost. On the other hand, efficient strategies for energy consumption management can be cheaper to implement. The most common management strategies involve applying optimal control schemes for HVAC units [8], and the refrigeration units [9] by replacing the traditional

PID control schemes with Model Predictive Control. In addition, the consumption optimization has also been pursued by implementing demand-side management paradigms [10,11].

Besides the cited traditional methods, data-based practices for energy consumption monitoring and fault detection are now gaining interest to make residential and non-residential buildings more efficient. In residential buildings, as well as in supermarkets, a large amount of data is usually collected and stored, thanks to the several measurement sensors spread over the energy plants. Using data for energy monitoring can be beneficial to spot abnormal energy consumption due to suboptimal operation of the HVAC or non-adequate equipment operation (i.e., lighting) [12]. Anomalous energy consumption can be identified using state-of-the-art statistical outlier detection methods, such as z-score [13]. Although statistical methods are effective and easy to implement and interpret, with these techniques, outlier detection is typically driven by a single feature (e.g., the energy consumption time series). More advanced data-driven techniques based on Machine Learning (ML) algorithms allow, instead, to perform the outlier detection over a dataset with multiple features, e.g., considering the weather conditions and the building characteristics beyond the only energy consumption data. So far, most academic research papers focus on using ML for anomalous consumption detection of residential buildings. Still, a similar methodological approach can be applied to commercial activities to investigate its potentiality [14].

AI-based energy monitoring techniques aim to detect anomalous energy consumption. Particularly, Unsupervised Clustering (UC) techniques are gaining interest in the energy sector thanks to their simplicity and the broad range of applicability [15]. Mainly, UC is useful to identify abnormalities only considering the intrinsic behaviour of the energy consumption without knowing a priori if it is normal or not. Several UC techniques for anomalous energy consumption exist, such as k-means clustering [18], Gaussian Mixture Model (GMM) [19] and density-based algorithms [20]. The latter category is particularly suitable for outlier detection since it is based on detecting anomalies by dividing the dataset into clusters with high-density data (regular consumption instances) and clusters with low-density data (abnormal consumption instances) [21]. Local Outlier Factor (LOF), Isolation Forest (IF) and Density-Based Spatial Clustering for Application with Noise (DBSCAN) are the most popular algorithms [22]. Unlike the k-means clustering approaches, density-based algorithms do not require initialising the number of clusters. DBSCAN is particularly suitable for outlier detection, since its capability of clustering data and identifying a specific cluster dedicated to outliers [23]. The clustering emerges from data by setting specific parameters defining each cluster's threshold radius of influence and the minimum number of points that define a cluster. outliers Although setting these parameters can be challenging since they cannot be optimised, some automatic strategies can be applied. DBSCAN found many applications for outliers detection in time series so far [24]. Regarding the energy sector, in [25], the authors propose the DBSCAN algorithm for anomalous energy consumption detection in residential buildings. In this case, the setting of the parameters is automatised, and the clustering results are explanatory and reasonable. Focusing only on time series can bring some limitations, though. Energy consumption patterns, indeed, naturally vary due to seasonal trends, making it hard to distinguish if the wrong operation is systematic or due to an extraordinary change in the boundary conditions (e.g., exceptionally hot or cold seasons). For this reason, authors in [26] perform anomaly detection of a building through a two-step procedure, firstly comparing the building energy consumption with past data and then comparing it with a pool of buildings with similar characteristics.

Given this framework, this work aims to apply the DBSCAN clustering for anomalous energy consumption detection of a group of supermarkets. The paper contribution aims to cover some literature gaps, summarized as follows:

- Despite several papers contributing to this topic, most refer only to residential buildings even though commercial buildings are widespread and their energy consumption is more intense than residential ones. Identifying abnormal consumptions could foster significant energy savings in this context.
- The outlier detection is not performed over a single time series related to a single building but within a pool of supermarkets, defining, then, whether the consumption is normal or abnormal compared to the behaviour of the other supermarkets with similar characteristics (such as the floor area and weather conditions). The clustering is performed both on a monthly and yearly basis, repeating the analysis over three different years. The supermarkets, then, are marked as outliers if their anomaly shows systematically.
- The analysis is performed using consumption data extracted from monthly bills for electricity and gas consumption. Though buildings have several sensors, data collection and management can be expensive. Monthly bills are, instead, easy to collect, making the proposed outlier detection method attractive for situations in which detailed data are unavailable.

2. Case study

The selected case study comprises a group of 108 supermarkets in the Tuscany region, in the north centre of Italy. The group is heterogeneous, including mini-markets (floor area of up to 2000 m^2) and superstores (floor area of up to 5000 m^2). Most of the supermarkets, around 80%, use gas boilers for space heating during the

winter season, while the remaining 20% are equipped with electric heat pumps. The weather conditions mainly determine space heating consumption. The stores are located at latitudes between 42° and 44° N and correspond to specific climatic regions established by the Italian government regulation [27]. Most supermarkets are in the D zone, where heating space is allowed between November 1 and April 15. The remaining are in the E region, characterised by more demanding weather conditions, with an allowed heating season from October 15 to April 15.

The energy management division of the supermarkets provided data about consumption and weather conditions and some characteristics of the building over three years, from 2019 to 2021. The available data are as follows:

- **Electrical consumption data** E_{el}**:** electrical consumption data are provided from the monthly bills. The electrical consumption (kWh) is related to the space air conditioning during the summer and winter seasons (only for those supermarkets that are equipped with electric heat pumps), Medium Temperature (MT) refrigerators for fresh food conservation, Low Temperature (LT) refrigerators for frozen food conservation, lighting devices and food processes (e.g., grocery and bakery).
- **Thermal consumption data** E_{th}**:** The monthly bills also provide thermal consumption data measured with Standard cubic meters (Sm^3). The thermal requirement refers to the space heating (during the winter season) and hot water used by the employees for personal usage and food processing actions. Some supermarkets do not have thermal consumption because the air conditioning is electrified.
- **Buildings data:** The information about the building characteristics consists of the monthly opening hours H_o (for a total of about 4000 h/year) and the floor area A_f.
- **Weather data:** The weather conditions consist of two variables: the outdoor temperature and the outdoor humidity measured through sensors positioned outside the building location. These data are provided with a 15-minute timestep. The weather conditions will be expressed as Heating Degree Days (HDD) and Cooling Degree Days (CDD) (Eq. 1), which give a measure of the heating/cooling demand related to the outdoor temperature and the heating/cooling period. In Eq. (1) $T_{sp,i}$ is the indoor temperature set point for air conditioning, $\bar{T}_{ext,i}$ the outdoor temperature mean value over the day, and N is the number of considered days in the heating/cooling period.

$$HDD = \sum_{i=1}^{N} \max\left(T_{sp,i} - \bar{T}_{ext,i}, 0\right); \qquad CDD = \sum_{i=1}^{N} \max\left(\bar{T}_{ext,i} - T_{sp,i}, 0\right) \tag{1}$$

Figure *1* provides a summary of the sample data ranges. The histograms illustrate the distribution of the data across the group of supermarkets, indicating the number of buildings in the total population (n/n_{tot}) that share similar characteristics.

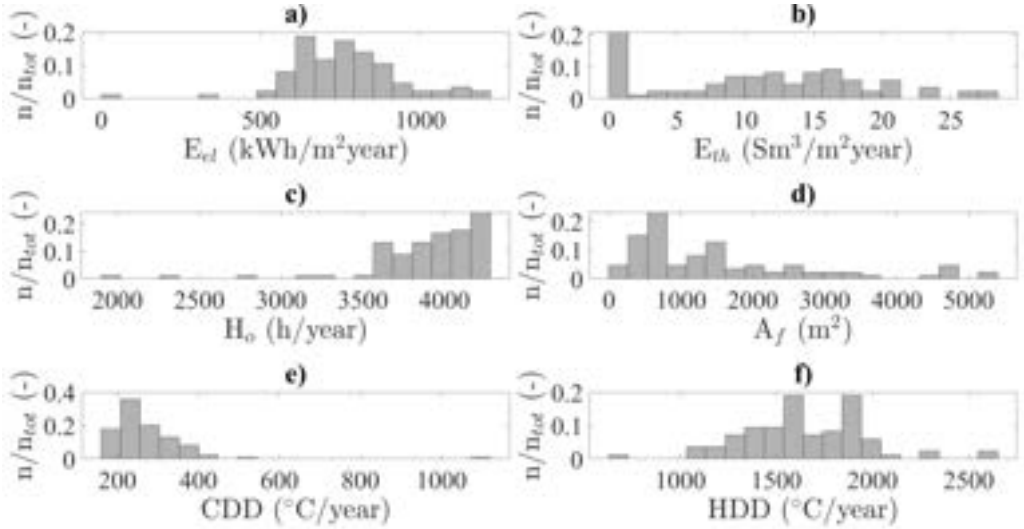

Figure 1. Characteristics of the pool of supermarkets plotted as a fraction of the total supermarkets n/n_{tot}. a) Specific annual electrical consumption E_{el} (kWh/m^2year); b) Specific annual thermal consumption E_{th} (Sm^3/m^2year); c) Annual opening hours Ho (h/year); d) Floor area A_f (m^2) e) Annual Cooling Degree Days CDD (°C/year); f) Annual Heating Degree Days HDD (°C/year).

2.1 Analysed cases

Anomaly detection is performed by considering annual aggregated data and monthly data. The yearly analysis aims to detect which supermarkets have an overall anomaly in energy consumption over the year. Using yearly aggregated data makes this analysis computationally inexpensive and results in the preliminary identification of probable outliers. However, it could also be possible that some supermarkets have abnormal energy consumption only in specific months of the year due to seasonal effects. For example, anomalies could emerge

only during the winter months caused by non-efficient gas boiler usage, while the air conditioning units work correctly in the summer. Monthly analysis can overcome this limit and highlight seasonal effects. For this reason, monthly clustering is also performed even though it is a more computationally expensive analysis since it is repeated every month over three years.

3. Methodology

The methodology section includes the description and preliminary results of the data pre-processing, feature selection, dataset construction and clustering algorithm settings. All the analyses have been realised in Matlab version 2021b.

3.1 Data pre-processing

Pre-process procedures are essential to make raw data usable. Mainly, preliminary operations regarding missing data handling and data aggregation were performed as follows:

- Missing consumption data (both thermal and electric) were not replaced since outlier detection must be performed over actual data to spot anomalies. Supermarkets with missing consumption data were excluded from the analysis, reducing the pool from 108 to 87 supermarkets.
- If possible, missing weather data were interpolated or taken from external databases. Missing periods lower than 24 hours were interpolated linearly. Missing periods longer than one day were replaced with data from the database *IlMeteo.it* [28], which offers historical daily average values for outdoor temperature and humidity. In this case, missing data were replaced with new data, measured not in the proximity of the supermarket but at the closest weather station, usually located in the same municipality.
- Consumption data were aggregated starting from monthly values to obtain yearly global consumption. This operation is necessary to perform monthly and annual clustering to consider seasonal effects, as described in the Case Study Section. Weather data are aggregated into monthly and yearly values starting from the 15-minute time interval measurements.

3.1.1 Feature engineering and feature selection

Few additional features are created starting from the available data to help the clustering algorithm find patterns. The following two features are then created:

- A categorical variable that indicates the air-conditioning plant typology. Supermarkets which use electrical heat pumps for the summer and winter air-conditioning are marked with category E. In contrast, supermarkets which use the gas boiler during the heating season are marked with category EG. Following the standard procedure for categorical variables handling, this feature is processed as a dummy variable [29].
- HDD and CDD. Average values of outdoor air temperature are not particularly meaningful, mainly if the average refers to an extended period (month or year). HDD and CDD, instead, quantify the overall heating/cooling demand, involving the length of the heating/cooling season and the difference between the indoor set point temperature and the outdoor conditions.–Once the set of available variables is defined, feature selection is performed to remove unnecessary data and improve the clustering performance [30]. For this reason, a correlation analysis is performed to identify the more significant features. The feature selection is performed through the evaluation of the Spearman correlation coefficient ρ_s. Spearman correlation coefficient is a statistical measure of the correlation within the variable *x* and *y* based on rank assignment. For the calculation, the values of *x* and *y* are converted into ranks following an ascending or descending order. Then a high correlation score is assigned where a high rank of *x* corresponds to a high rank of *y.* Unlike the Pearson's coefficient, Spearman's is able to calculate the correlation between two variables even if their relationship is not strictly linear. The only assumption is that the relationship has to be monotonic [31]. The calculation of ρ_s is performed as shown in Eq. (2), where D_i^2 is the rank distance between variable *x* and *y*, and N the number of points which constitutes the cluster. The correlation is considered strong when $0.7 \leq |\rho_s| \leq 1$, moderate for $0.3 \leq |\rho_s| < 0.7$ and weak for $|\rho_s| < 0.3$.

$$\rho_s = 1 - 6 \cdot \frac{\sum_{i=1}^{N} D_i^2}{N(N-1)}\,; \qquad D_i = x_i - y_i \tag{2}$$

Correlation analysis is not performed for the yearly aggregated values because no monotonic relationship emerges considering annual data. Correlation analysis is then performed only for the monthly values. Particularly, ρ_s is computed across the following variables:

- Electrical specific consumption E_{el} $(kWh/m^2 month)$
- Thermal specific consumption E_{th} $(Sm^3/m^2 month)$
- Degree Days DD $(°C/month)$. The generic symbol DD refers to HDD for winter months and to CDD for summer months
- Outdoor Relative Humidity RH $(\%)$
- Opening hours H_o (h).

The preliminary results of feature selection are shown in **Figure *2***. The heatmap shows the correlation coefficients ρ_s across the combination of variables for one of the supermarkets as an example. The other supermarkets of the pool showed the same behaviour and are not shown for brevity. As expected, the correlation analysis shows that electrical and thermal consumptions are strongly related to the external temperature conditions (DD). RH showed no correlation with energy consumption, so it is removed from the analysis. Finally, since H_o showed only a moderate correlation with electrical consumption, it was included in the first tests. However, its impact was not significative for the outliers detection, so it was removed in the final dataset. In this plot, the correlation with the floor area was not computed because only one supermarket is considered (so the area does not vary).

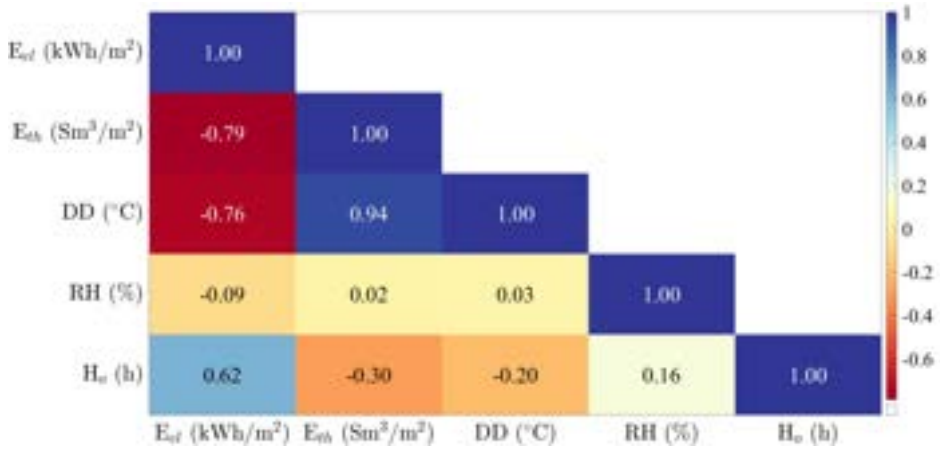

Figure 2. Spearman correlation values for the considered features E_{el}, E_{th}, DD, RH and opening hours. Data are related to one of the supermarkets of the pool as an example.

3.1.2 Dataset construction

As a result of the correlation analysis and considerations given in the previous sections, the annual and monthly datasets are finalised, as **Table *1*** summarises. Finally, each dataset is normalised to ease the clustering procedure. Normalised data are all in the same range, so undesired effects due to different data scales will not affect the clustering results. In this work, data are normalised with the 2-norm approach, in which the Euclidean norm of the variable normalises each data observation (row). Eq. (3) shows the normalisation approach. The generic data x_i is normalised, becoming $x_{i,norm}$, dividing it by the 2-norm, where N is the number of rows of the variable.

$$x_{i,norm} = \frac{x_i}{\left[\sum_{k=1}^{N} |x_k|^2\right]^{1/2}} \quad (3)$$

Table 1. Dataset with selected features for annual and monthly clustering

	Features included in the dataset
Annual clustering	• $E_{el}\ (kWh/m^2 year)$ • $E_{th}\ (Sm^3/m^2 year)$ • $A_f\ (m^2)$ • Air-conditioning units type: E/EG
Monthly clustering	• $E_{el}\ (kWh/m^2 month)$ • $E_{th}\ (Sm^3/m^2 month)$ • $A_f\ (m^2)$ • $DD\ (°C/month)$ • Air-conditioning units type: E/EG

3.2 DBSCAN algorithm

DBSCAN algorithm is an unsupervised clustering technique that identifies high-density regions (normal behaviour) in the k-dimensional space representing the dataset and a few low-density regions where the outliers are located (abnormal behaviour). High-density areas, i.e., the clusters, are defined based on the neighbourhood concept, for which two points are in the same neighbourhood if their distance is below a threshold ε, called the neighbourhood parameter. The pairwise distance from a point to the surrounding ones can be defined in several ways, but the Euclidean distance is used in the analysis. Particularly the

neighbourhood of a point *x,* $N_\varepsilon(\mathrm{x})$, is defined as in Eq. (4), where D is the set of points in the dataset, dist(x,y) is the Euclidean distance between two points *x* and *y,* and ε is the threshold distance [32].

$$N_\varepsilon(\mathrm{x}) = \{\mathrm{y} \in \mathrm{D} | \mathrm{dist}(x,y) \leq \varepsilon\}; \qquad \mathrm{dist}(x,y) = \sqrt[2]{\sum_{i=1}^{N}(x_i - y_i)^2} \tag{4}$$

The cluster definition must include an additional parameter to identify high-density regions correctly. Particularly, $N_\varepsilon(\mathrm{x})$ cannot be constituted by less than a number of points equal to *minPts* (a scalar number ≥ 1). The DBSCAN algorithm operates as represented in **Figure 3**.

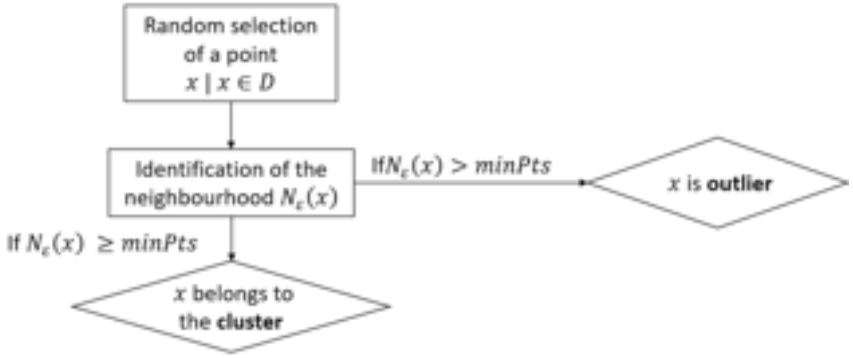

Figure 3. Clustering process using DBSCAN algorithm.

3.2.1 Parameters setting

Since the abnormal energy consumption detection for this case study is unsupervised, the DBSCAN model cannot be trained based on the experience of some previously labelled data which constitute the benchmark (normal or abnormal). For this reason, the parameter setting cannot be optimised by minimising a specified loss function, as happens for supervised cases. The choice of the parameters ε and $minPts$, then, is driven by some specific considerations related to the dataset. However, some general guidelines can be followed to have a proper estimation of suitable values of ε and *minPts*:

- The choice of *minPts* depends on the configuration of the dataset. This work performs a sensitivity analysis varying minPts from 2 to 8. These values are selected considering the size of groups of supermarkets with similar characteristics, like the floor area or the geographical location, in the dataset.
- The choice of ε is based on the method proposed in [33]. To determine a meaningful ε value, the pair-wise distance is calculated from each point in the dataset to all the other *minPts* number of points. The obtained distances are then plotted against the sorted points. Since the number of anomalies is usually limited (i.e., less than 20%), the sorted distances show a typical linear trend for the points in the high-density areas. A fast slope change occurs in the proximity of the so-called "elbow", where the remaining sorted distances are substantial because they are related to the low-density areas (where the outliers are located and the points tend to be distant from each other). The selected ε value, then, is the distance value corresponding to the "elbow*".* Since the results can be affected by the value of ε (i.e., the larger ε, the lower the number of outliers), we performed a sensitivity analysis with different values near the *elbow*, and the results proved to be robust in this range*.* The value selected for ε varies for each simulated case, ranging from 0.0286 to 0.0853.

3.2.2 Key Performance Indicators

The quality of the unsupervised clustering is not quantitative but qualitative since data are not labelled a priori. Results will then be shown with graphical scatter plots to represent clusters and outliers. Despite the limitation of the unsupervised nature of the problem, some additional considerations can prove that one supermarket can be considered an outlier. The clustering analysis is repeated for each year in the dataset (2019-2020-2021) to support this thesis. The number of recurrent outliers is then collected over single or multiple years. Concerning the annual analysis, the fact that a supermarket has been marked as an outlier for more than one year suggests that an issue of some sort occurs systematically.

On the other hand, supermarkets marked as outliers for a single year probably faced some extraordinary operative conditions which never repeated. The same considerations are valid for the monthly clustering. In this case, supermarkets were marked as outliers over one year if they were outliers for at least three months. This value is reasonable because it can reflect seasonal effects due to the heating or cooling periods. Two Key Performance Indicators (KPIs) are then evaluated to quantify the cited results:

- Percentage of outliers n_{out} over 1, 2 or 3 years compared to the total number of supermarkets n_{sup} (Eq. 5):

$$k_{t,sup} = \frac{n_{out}}{n_{sup}} \cdot 100\% \tag{5}$$

- Percentage of outliers over 1, 2 or 3 years compared to the total number of outliers $n_{out,tot}$ (Eq. 6):

$$k_{t,out} = \frac{n_{out}}{n_{out,tot}} \cdot 100\% \quad (6)$$

4. Results and discussion

This session will provide at first step results about the clustering quality by visualising scatter plots with non-anomalous clusters and outliers. After that, the analysis of the KPI will help to understand the supermarkets which showed a systematic anomaly, which can be classified as actual outliers. Finally, the outliers found by the algorithm are verified by plant inspections conducted by the energy manager to validate the clustering results.

4.1 Qualitative clustering

The results of the annual clustering in **Figure *4*** are scattered in a three-dimensional plot that includes the three features defined in the dataset (E_{el}, E_{th} and A_f). The clustering is sensible since the main characteristics of the supermarkets are represented. The regions of the dataset with the highest density are clustered in Group 1 and Group 2. The two clusters are related to supermarkets with electric pumps (category E) and supermarkets with gas boilers (category EG). Smaller clusters indicate limited groups of supermarkets which are similar. Group 3 represents superstores (i.e., most extensive floor areas) with electric heat pumps, while Group 4 concerns superstores with gas boilers for space heating. Outliers emerge beyond regular clusters and are located mostly in low-density regions. Among the whole group of outliers, some show low consumption compared to the average of the surrounding clusters, while others show high consumption. The latter outliers were verified through an on-site plant inspection, finding some explanations for the abnormalities. For example, supermarkets 29, 74 and 51 are outliers because the electrical consumption is abnormal despite the A_f and E_{th} being similar to other supermarkets. In these cases, the anomaly was found to be due to obsolete lighting devices or thermal losses of LT and NT refrigerators that are not closed. The electrical consumption anomalies related to the air-conditioning units are rare since supermarkets of category E are recent, efficient, and monitored. Supermarkets 7, 6 and 45 have abnormal thermal consumption. In these cases, the anomaly is primarily due to sub-optimal operation or out-of-range setpoint temperatures on the heating boilers. Supermarkets of category EG are indeed older than the ones in category E, so the heating plants are not monitored in real-time.

On the other hand, a few supermarkets are marked as anomalous because of lower energy consumption than the neighbourhood, so the on-site inspection was not performed. In some cases, this behaviour is due to the low-quality data, which are partially missing (supermarket 31). In other cases, the low consumption is due to favourable climate conditions during the considered year or the wrong consumption estimation on the bills. The weather conditions effects emerge through the monthly analysis, in which HDD and CDD are used as predictors. **Figure *5*** can also be interpreted qualitatively as for the annual clustering results. In this case, some anomalies can be interpreted thanks to the additional information about the climate conditions. Exceptionally high DD are responsible for some detected abnormalities. For example, supermarkets 76 and 7 have similar DD to many supermarkets of the pool but significantly higher thermal consumption. The heating plants' sub-optimal management set point temperatures can be responsible for these abnormalities. Compared to these, Supermarket 48 is less alarming because it has higher E_{th} due to higher DD. Finally, supermarkets 18 and 25 have lower thermal consumption than the neighbourhood, but this is due to lower DD, indicating that the outdoor temperature was exceptionally lower than usual that month.

4.2 Systematic outliers

The qualitative considerations help support the clustering results, which cannot be compared to a benchmark. Despite this, the interpretation of the results may be impractical as it must be supported by visuals, and every outlier requires some additional effort to be confirmed or denied. Automating this process can be challenging, but iterating the analysis over multiple years can help to strengthen the outlier labelling with more reliability.

Figure *7* highlights the capability of the monthly clustering in understanding systematic seasonal effects that did not emerge from the annual analysis. The analysis is valid for all the months of the year except for September. In this case, data concerning E_{th} of September 2019 were missing, so the statistics could not be computed for this month since the data quality still was not good enough despite data pre-processing. However, the analysis is still relevant for the other eleven months. This graph shows that during winter months, from November to March, a high percentage of supermarkets are outliers over the whole three years. These systematic abnormalities highlight an improper operation of the heating systems, so abnormal consumption in the cold season is highly probable.

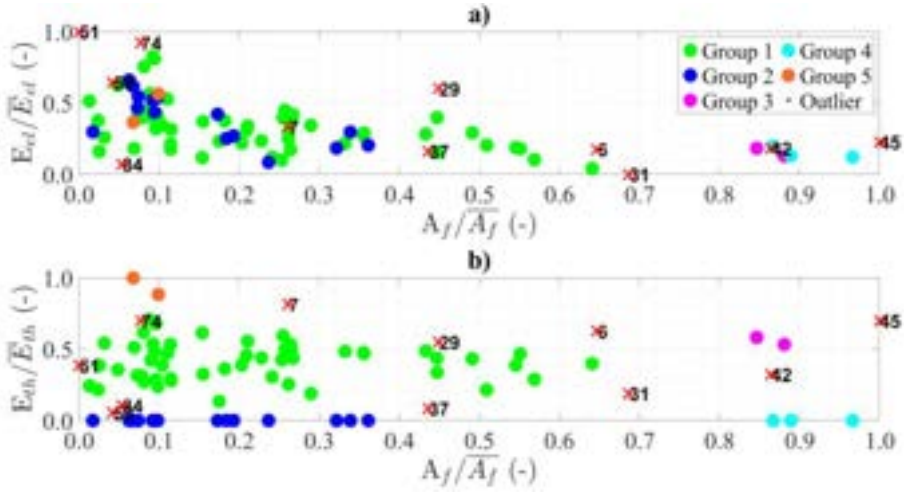

Figure 4. Annual clustering results for the year 2021, as an example. a) Specific electrical consumption Eel versus floor area A_f. b) Specific thermal consumption E_{th} versus floor area. All the variables are normalised with the maximum values $\bar{E}_{el}$, $\bar{E}_{th}$, $\bar{A}_f$ for data privacy. Outliers are marked with red crosses and are associated with a numerical ID.

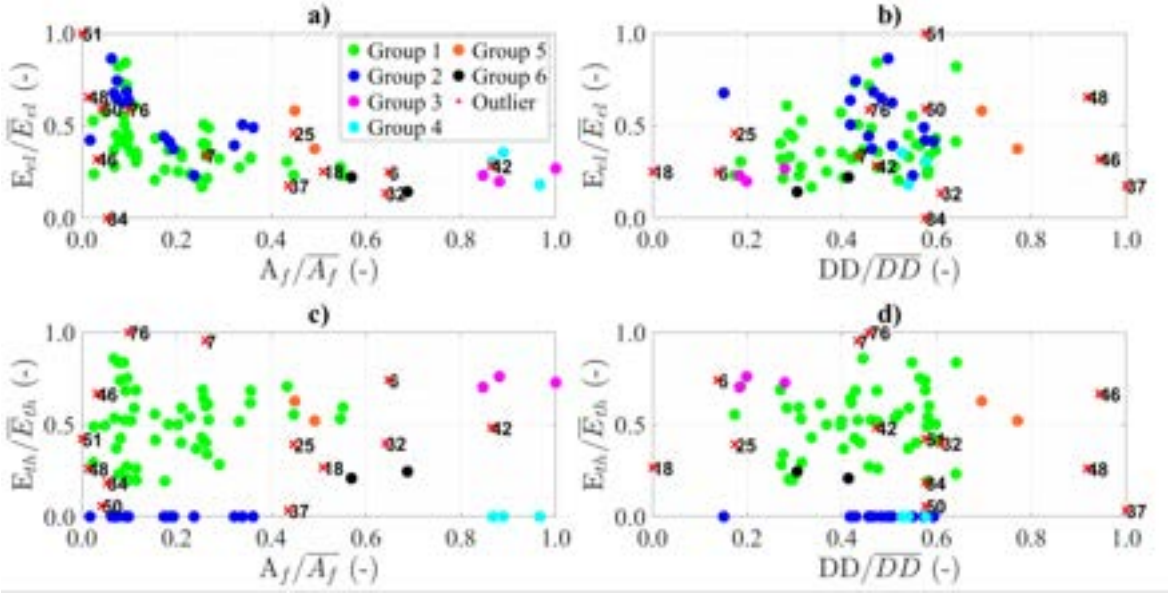

Figure 5. Monthly clustering for January 2021, as an example. a) Specific electrical consumption E_{el} versus floor area A_f. b) Specific electrical consumption E_{el} versus Degree Days DD. c) Specific thermal consumption E_{th} versus floor area A_f. d) Specific thermal consumption Eth versus Degree Days DD. All the variables are normalized with the maximum values $\bar{E}_{el}$, $\bar{E}_{th}$, $\bar{A}_f$ and $\overline{DD}$ for data privacy. Outliers are marked with red crosses and are associated with a numerical ID.

Figure *6* shows how many supermarkets were marked as outliers for 1/3, 2/3 or 3/3 years of the investigated period. Around 10% of the supermarkets had abnormal consumption for only one year over three, highlighting that these abnormalities are not systematic but exceptional. Instead, the green stacked bar highlights the percentage of supermarkets that were marked as outliers for all three years. In this case, since the anomaly is systematic, these supermarkets probably have operating issues related to the consumption of their subsystems. This result is strengthened by comparing the annual and monthly $k_{t,s}$ and $k_{t,out}$ indicators. Regarding 1/3 years and 2/3 years outliers, there are a few differences. The monthly analysis in **Figure *7*** highlighted occasional outliers (orange stacked bar), thanks to its capability of catching seasonal anomalies that cannot appear in the annual analysis, so the results are slightly different. Regarding the 3/3 years abnormalities, yearly and monthly clustering showed almost the same percentage. This result highlights that around 10% of supermarkets in the pool have systematic anomalous consumption that emerges independently from the weather conditions, so it strictly concerns operational issues of the plants. This result is then valuable information for the energy management unit of the supermarkets since it suggests that a plant check is necessary. As a final remark, thanks to this analysis, systematic anomalous supermarkets are marked as outliers with sufficient certainty. The cost of the on-site plant inspection to verify these results and eventually fix the anomaly, then, is justified and can bring to potential savings. **Table 2** provides the validation of the

results through the on-site plant inspection. The 50% of the recurrent outliers proved to have some issues that caused the abnormal consumption, such as the faulty operation of the HVAC units and old lighting equipment. Only in one case the abnormality was caused by a wrong estimation of the monthly bills. The remaining 50% were not found to be outliers, mainly because they were the cases that showed a positive abnormality (i.e., with consumptions lower than supermarkets with similar features).

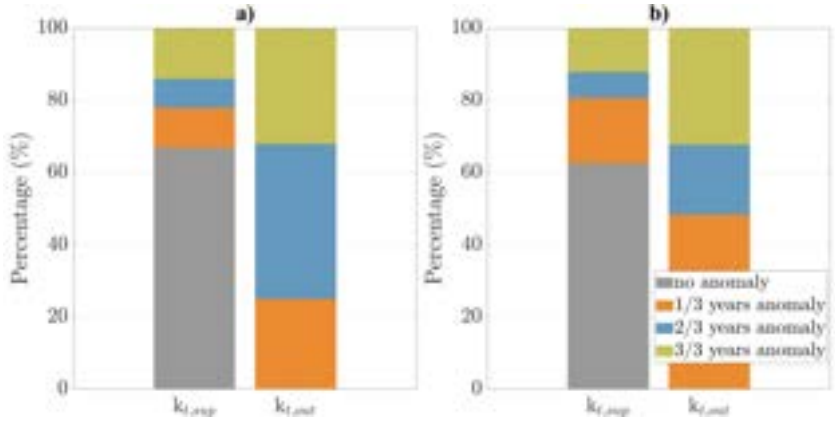

Figure 6. Abnormalities share for a) Annual analysis; b) Monthly analysis.

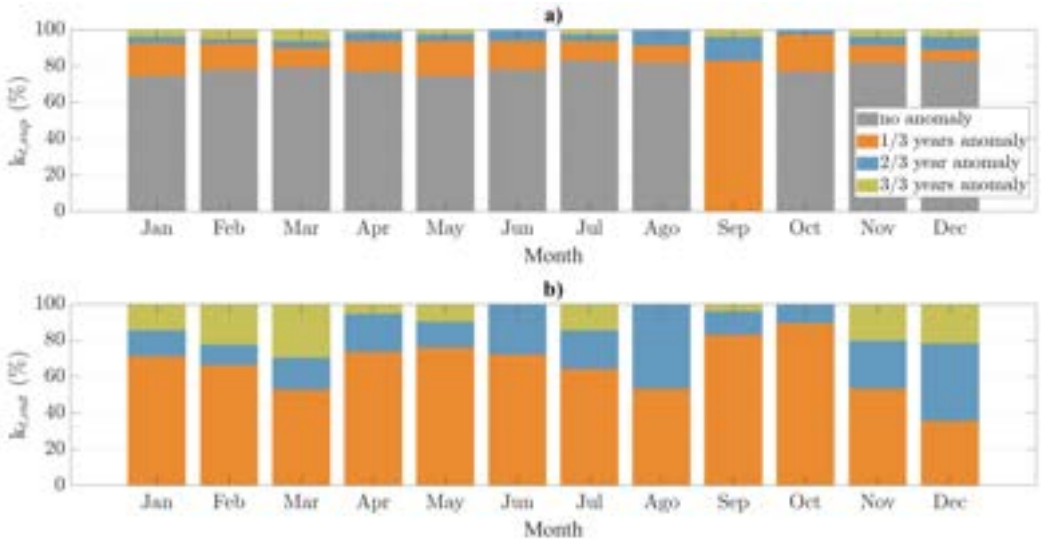

Figure 7. Abnormalities share for monthly analysis for KPIs: a) percentage of outliers among the total number of supermarkets; b) percentage of outliers among the total number of outliers.

Table 2. Results validation for recurrent outliers emerged from the monthly clustering analysis.

Anomalous supermarket	Years of anomaly	Anomaly cause
6	3/3	Old lighting devices; Heating system
7	3/3	Heating system
19	2/3	Heating system
29	3/3	Old lighting devices; HVAC system
30	3/3	Old lighting devices
43	3/3	Heating system
56	3/3	Wrong bill estimation
75	2/3	Heating system

5. Conclusions

The paper investigated the potentialities of using an unsupervised clustering approach for anomalous energy consumption detection in a group of 87 supermarkets in Italy. The final goal of the study was to implement a computationally powerful strategy to identify anomalous supermarkets compared to the others in the group. Unlike standard statistical techniques, this approach helped to identify the outliers considering many features simultaneously, such as thermal and electrical consumptions, the dimensions and weather conditions. The analysis was performed using the DBSCAN algorithm, which is suitable for outlier detection for datasets mainly composed of high-density regions (regular consumptions) and a few low-density regions (abnormalities).

Although this methodological approach had already been applied for anomalous energy consumption detection, it was rarely applied to non-residential buildings, which can easily suffer from non-optimal energy usage because of their higher complexity and energy intensity. In addition, most of the papers performed the outlier detection by comparing one building to its past energy consumption, making it impossible to identify systematic anomalies. The work then tried to bridge these research gaps by observing numerous similar supermarkets, starting from monthly electrical and thermal consumption bills, which are data easy to collect and manage.

Firstly, the results proved that the proposed set of clustering parameters effectively represented the dataset adequately by identifying the main clusters in relation to the air-conditioning plan typology. Once the good quality of the clustering was verified, the annual clustering identified the anomalous supermarkets using consumption data and the floor area as features. After that, weather conditions were embedded in the monthly analysis, which was able to identify the supermarkets that behave anomalously only in particular months due to seasonal effects. Finally, the analyses went beyond the simple labelling as *normal* or *abnormal* consumption by repeating the clustering over the three available years of the dataset. By doing so, supermarkets labelled as outliers over the three years can be considered very likely outliers. Approximately 10 % of the supermarkets of the pool showed an anomaly over 3/3 years. This result was confirmed by comparing the annual and the monthly analyses so that supermarkets systematically affected by significant abnormal energy consumption are identified with improved confidence. This improvement is particularly meaningful since it overcomes the issues of the traditional unsupervised clustering, in which the non-optimal setting of the parameters brings uncertain results. In addition, the monthly analysis highlighted that around 50 % of supermarkets are outliers for only 1/3 years. These supermarkets are not particularly alarming since their abnormality is not systematic and is probably due to non-frequent wrong operation or extreme weather conditions. Repeating the clustering over different time scales and different years then helps to detect the *false positive* outliers and focus the effort on the systematic ones. This result is validated by the on-site inspection of the potential anomalous plants, which proved to have operational issues.

Further improvements could concern the integration of additional features, as far as the data are available (like the occupancy, the type of refrigeration units and so on). In addition, if the supermarkets change during the investigation period, additional characteristics of new equipment could improve the clustering quality. However, since this kind of data is usually difficult to collect, the paper proposes a methodology involving data which are easily accessible.

Acknowledgements

This research has received financial contribution from the Italian Operative National Plan (Piano Operativo Nazionale, PON) in the framework of the project Ricerca e Innovazione 2014−2020 (PON R&I) – Azione IV.6 “Contratti di ricerca su tematiche dell'innovazione e green” (DM MUR 1062/2022).
Prof. Lorenzo Ferrari and Dr. Guido Francesco Frate gratefully acknowledge the financial support of the University of Pisa (UNIPI), in the framework of the Research Project PRA 2022_31: MetOdi per riDurre gli usi di EneRgiA Termica ed Elettrica in ambito civile e industriale (MODERATE).

Nomenclature

AI	Artificial Intelligence
CDD	Cooling Degree Days
DBSCAN	Density-Based Spatial Clustering for Application with Noise
DD	Degree Days
GMM	Gaussian Mixture Model
HDD	Heating Degree Days
HVAC	Heating, Ventilation and Air Conditioning
IF	Isolation Forest
KPI	Key Performance Indicator
LOF	Local Outlier Factor
LT	Low Temperature
minPts	Minimum number of Points
ML	Machine Learning
MT	Medium Temperature
RH	Relative Humidity
UC	Unsupervised Clustering
UD	Unsupervised Detection

Symbols

A	Area
D	Distance
E	Energy consumption
H	Hours
k	Percentage parameter
N	Neighbourhood
n	Number
T	Temperature
x, y	Generic points

Greek symbols

ρ	correlation coefficient
ε	eps parameter

Subscripts and superscripts

el	electrical
ext	external
f	floor
$norm$	normalised
o	opening
out	outlier
s	Spearman
sp	setpoint
sup	supermarkets
th	thermal
tot	total

References

[1] Energy efficiency targets n.d. https://energy.ec.europa.eu/topics/energy-efficiency/energy-efficiency-targets-directive-and-rules/energy-efficiency-targets_en (accessed February 27, 2023).

[2] Ngarambe J, Yun GY, Santamouris M. The use of artificial intelligence (AI) methods in the prediction of thermal comfort in buildings: energy implications of AI-based thermal comfort controls. Energy Build 2020;211:109807. https://doi.org/10.1016/j.enbuild.2020.109807.

[3] World Energy Balances Highlights - Data product - IEA n.d. https://www.iea.org/data-and-statistics/data-product/world-energy-balances-highlights (accessed March 2, 2023).

[4] Monforti F, Dallemand JF, Motola V. Energy use in the EU food sector: State of play and opportunities for improvement Development of long-term energy projections for African countries View project Coal regions in transition View project. 2015. https://doi.org/10.2790/158316.

[5] Ríos Fernández JC, Roqueñí N. Analysis of the potential of Spanish supermarkets to contribute to the mitigation of climate change. Sustain Prod Consum 2018;14:122–8. https://doi.org/10.1016/j.spc.2018.02.003.

[6] Gigoni L, Betti A, Crisostomi E, Franco A, Tucci M, Bizzarri F, et al. Day-Ahead Hourly Forecasting of Power Generation from Photovoltaic Plants. IEEE Trans Sustain Energy 2018;9:831–42. https://doi.org/10.1109/TSTE.2017.2762435.

[7] Franco A, Cillari G. Energy sustainability of food stores and supermarkets through the installation of pv integrated plants. Energies 2021;14. https://doi.org/10.3390/en14185678.

[8] Ge YT, Tassou SA. Control optimizations for heat recovery from CO2 refrigeration systems in supermarket. Energy Convers Manag 2014;78:245–52. https://doi.org/10.1016/j.enconman.2013.10.071.

[9] Hovgaard TG, Larsen LFS, Edlund K, Jørgensen JB. Model predictive control technologies for efficient and flexible power consumption in refrigeration systems. Energy 2012;44:105–16. https://doi.org/10.1016/j.energy.2011.12.007.

[10] Glavan M, Gradišar D, Moscariello S, Juričić Đ, Vrančić D. Demand-side improvement of short-term load forecasting using a proactive load management – a supermarket use case. Energy Build 2019;186:186–94. https://doi.org/10.1016/j.enbuild.2019.01.016.

[11] Coccia G, D'Agaro P, Cortella G, Polonara F, Arteconi A. Demand side management analysis of a supermarket integrated HVAC, refrigeration and water loop heat pump system. Appl Therm Eng 2019;152:543–50. https://doi.org/10.1016/j.applthermaleng.2019.02.101.

[12] Wang A, Lam JCK, Song S, Li VOK, Guo P. Can smart energy information interventions help householders save electricity? A SVR machine learning approach. Environ Sci Policy 2020;112:381–93. https://doi.org/10.1016/j.envsci.2020.07.003.

[13] Seem JE. Using intelligent data analysis to detect abnormal energy consumption in buildings. Energy Build 2007;39:52–8. https://doi.org/10.1016/j.enbuild.2006.03.033.

[14] Miller C, Nagy Z, Schlueter A. A review of unsupervised statistical learning and visual analytics techniques applied to performance analysis of non-residential buildings. Renew Sustain Energy Rev 2018;81:1365–77. https://doi.org/10.1016/j.rser.2017.05.124.

[15] Himeur Y, Ghanem K, Alsalemi A, Bensaali F, Amira A. Artificial intelligence based anomaly detection of energy consumption in buildings: A review, current trends and new perspectives. Appl Energy 2021;287. https://doi.org/10.1016/j.apenergy.2021.116601.

[16] Anil Kumar KS, Chacko AMMO. Clustering Algorithms for Intrusion Detection: A Broad Visualization. ACM Int Conf Proceeding Ser 2016;04-05-Marc:3–6. https://doi.org/10.1145/2905055.2905195.

[17] Ahmed M, Mahmood AN, Islam MR. A survey of anomaly detection techniques in financial domain. Futur Gener Comput Syst 2016;55:278–88. https://doi.org/10.1016/j.future.2015.01.001.

[18] Henriques J, Caldeira F, Cruz T, Simões P. Combining k-means and xgboost models for anomaly detection using log datasets. Electron 2020;9:1–17. https://doi.org/10.3390/electronics9071164.

[19] Ahmed SRA, Al-Barazanchi I, Jaaz ZA, Abdulshaheed HR. Clustering algorithms subjected to K-mean and gaussian mixture model on multidimensional data set. Period Eng Nat Sci 2019;7:448–57. https://doi.org/10.21533/PEN.V7I2.484.

[20] Bhattacharjee P, Mitra P. A survey of density based clustering algorithms. Front Comput Sci 2021;15. https://doi.org/10.1007/s11704-019-9059-3.

[21] Himeur Y, Alsalemi A, Bensaali F, Amira A. Smart power consumption abnormality detection in buildings using micromoments and improved K-nearest neighbors. Int J Intell Syst 2021;36:2865–94. https://doi.org/10.1002/int.22404.

[22] Pereira W, Ferscha A, Weigl K. Unsupervised detection of unusual behaviors from smart home energy data. Lect Notes Comput Sci (Including Subser Lect Notes Artif Intell Lect Notes Bioinformatics) 2016;9693:523–34. https://doi.org/10.1007/978-3-319-39384-1_46.

[23] Fong S, Rehman SU, Aziz K, Science I. DBSCAN : Past , Present and Future 2014:232–8. doi: 10.1109/ICADIWT.2014.6814687.

[24] Jain P, Bajpai MS, Pamula R. A Modified DBSCAN Algorithm for Anomaly Detection in Time-series Data with Seasonality. Int Arab J Inf Technol 2022;19:23–8. https://doi.org/10.34028/iajit/19/1/3.

[25] Yao G, Guo C, Ge Q, Ait-Ahmed M. A practical building energy consumption anomaly detection method based on parameter adaptive setting DBSCAN. Cogn Comput Syst 2021;3:154–68. https://doi.org/10.1049/ccs2.12015.

[26] Arjunan P, Khadilkar HD, Ganu T, Charbiwala ZM, Singh A, Singh P. Multi-user energy consumption monitoring and anomaly detection with partial context information. BuildSys 2015 - Proc 2nd ACM Int Conf Embed Syst Energy-Efficient Built 2015:35–44. https://doi.org/10.1145/2821650.2821662.

[27] Gazzetta Ufficiale n.d. https://www.gazzettaufficiale.it/eli/id/1993/10/14/093G0451/sg (accessed May 11, 2023).

[28] Che tempo faceva a Firenze - Archivio Meteo Firenze » ILMETEO.it n.d. https://www.ilmeteo.it/portale/archivio-meteo/Firenze (accessed March 3, 2023).

[29] Alkharusi H. Categorical Variables in Regression Analysis: A Comparison of Dummy and Effect Coding. Int J Educ 2012;4:202. https://doi.org/10.5296/ije.v4i2.1962.

[30] Chicco G. Overview and performance assessment of the clustering methods for electrical load pattern grouping. Energy 2012;42:68–80. https://doi.org/10.1016/j.energy.2011.12.031.

[31] Hauke J, Kossowski T. Comparison of values of pearson's and spearman's correlation coefficients on the same sets of data. Quaest Geogr 2011;30:87–93. https://doi.org/10.2478/v10117-011-0021-1.

[32] Ester M, Kriegel H-P, Sander J, Xu X. A Density-Based Algorithm for Discovering Clusters in Large Spatial Databases with Noise. Proc 2nd Int Conf Knowl Discov Data Min 1996. https://doi.org/10.11901/1005.3093.2016.318.

[33] DBSCAN - MATLAB & Simulink n.d. https://www.mathworks.com/help/stats/dbscan-clustering.html#mw_4aa35c21-70f7-43a8-b310-1db43ea97eae (accessed March 7, 2023).

PROCEEDINGS OF ECOS 2023 - THE 36TH INTERNATIONAL CONFERENCE ON
EFFICIENCY, **C**OST, **O**PTIMIZATION, **S**IMULATION AND ENVIRONMENTAL IMPACT OF ENERGY SYSTEMS
25-30 JUNE 2023, LAS PALMAS DE GRAN CANARIA, SPAIN

Towards rule extraction for sector-coupled energy systems based on optimization models

David Wackerbauer[a], Thomas Schreiber[a] and Dirk Müller[a]

[a] RWTH Aachen University, E.ON Energy Research Center, Institute for Energy Efficient Buildings and Indoor Climate, Aachen, Germany, david.wackerbauer@eonerc.rwth-aachen.de

Abstract:

Today conventional rule-based control strategies dominate the control of energy systems in urban districts. Due to many interactions in urban districts, commissioning local energy systems and defining rules for optimal setpoint control is a challenge. Currently, expert knowledge based on comparable systems serve as basis to set up increasingly complex controls. Moreover, this process is becoming increasingly challenging due to the growing use of technologies such as heat pumps or storage systems to increase the share of renewable energies in the building energy sector. In academia complex systems are often controlled via computationally intensive methods such as model predictive control. Disadvantages are the complex initial commissioning, high computing demands, and a lack of interpretability of the system's behavior. To capture the complex interrelationships, the proposed method extracts simple rules from artificial optimal control. The energy system is first represented by a mathematical optimization model. The model determines the optimal plant operation for given demand time series. The optimization results are fed into white box machine learning models, such as Decision Tree Classifiers, to determine the revalent influencing factors and dependencies that are decisive for the determined operation. The process yields the relevant variables and setpoints for a simplified rule-based control. The extracted rules for an existing energy system are validated against the existing rule set and the theoretical optimum according to the optimization results by simulation. The rules can be interpreted by technical staff and applied to existing programmable logic controllers. This study introduces a toolchain to automate the creation of rule-based controls for complex energy systems.

Keywords:

rule-based control, optimization, machine learning, energy hub, sector-coupling, district energy system

1. Introduction

In order to achieve the climate targets that have been decided in the European Union, the emissions in CO2 equivalents in the building sector and here in particular also the direct emissions through the heating, cooling and electricity supply must be reduced. [1] To this end, renewable energies are increasingly unsed and integrated into existing energy systems in order to cause fewer emissions from fossil fuels. In the course of the energy transition in the building sector, control of the energy systems play a crucial role, as large potentials are wasted by inefficiency, but also the control of energy systems becomes more complex due to the use of new generation plants, the coupling of sectors and the integration of volatile renewable sources. [2]

The control complexity of an energy system increases with the following characteristics:

- The use of different generators.
- Coupling of sectors and inter-dependencies of sectors and generators.
- Different minimum loads of generators.
- Size and use of storage.
- Integration of own renewable generation such as photovoltaic (PV).
- Variable electricity and gas prices, as well as variable revenues for supply of surplus electricity to the public power grid.
- Utilization of flexibility for grid efficiency in the electricity sector.

Some of the listed factors offer the potential to make the provision of heating, cooling and electricity more efficient and to improve the integration and utilization of renewable energy sources. Due to the complexity of these systems, potentials may remain unused if no benefit is derived from the potentials in practice through simple control strategies.

In practice, the setup of the controls of complex energy hubs [3] that contain different generators coupling the heating, cooling and electricity sectors is an individual and time consuming task. For simple energy systems, containing only few units for energy supply and storage, it is feasible to find a standard procedure that is applicable on multiple reoccurring systems and control problems. With rising complexity and rising demands on the control of modern energy systems there are no normative or systematic procedures to setup the controls. Advanced control strategies, that are promising for complex control tasks, like model predictive control (MPC) or reinforcement learning (RL), have not yet made a leap into broad real world application due to implementation and acceptance barriers. [4] [2] Rule-based-control (RBC) operation is often based on the experience of the technician and individual considerations of the production costs for heating, cooling and electricity by the plants used. These are then implemented by a technician, for example, in the form of a generator sequence control. A common procedure for optimizing the energy system is to evaluate the current operation supported by monitoring and to determine control parameters in an iterative process, to yield satisfactory operation. This is measured and evaluated by the plant operator on the basis of key performance indicators such as the average operating point, efficiencies and prevention of short cycling of the plants.

The present work demonstrates a systematic procedure for deriving feasible operating rules for RBC of a district energy hub, that provides heating, cooling and electricity. The idea is based on the calculation of the theoretical optimum operation by means of mathematical optimization, taking into account dynamic boundary conditions and influencing variables. The results are then analysed in order to derive control rules for the supervisory level of the RBC. This is intended to circumvent barriers of complex control methods such as MPC in order to realize short-term potentials by improving the control of energy hubs in practice.

2. Literature Review

In this section selected sources dealing with rule extraction methods for energy systems in general are used summarize different methods for optimizing RBC systems. Furthermore examples of successful applications are given and challenges are adressed to identify open research questions.

May-Ostendorp et al. have discussed the possibilities of rule extraction from the results of an offline MPC in [5], [6] and [7]. In each case, the goal was temperature control in buildings using extracted rules from a training dataset containing time series data from an offline MPC. A distinction between closed-loop and open-loop learning is introduced in [6]. The closed-loop approach describes how time series data that is extracted from a system with a closed MPC loop with feedback and disturbances from the system is used to train the behavior of this MPC. In the open-loop approach, training is based on optimization results, which are used separately from the system and the actual control. The use cases described by May-Ostendorp et al. each include the building automation system and various parts of the indoor air conditioning system. The generator side is not considered. The derived rules are interpretable and were successfully tested on the building automation system for the studies.

Maier et al. [8] and Yang et al. [9] use Machine Learning (ML) models to approximate the controller behavior of a MPC. This kind of control is also referred to as approximate MPC (AMPC). The methodology of the studies can therefore be classified as closed-loop learning. The primary goal of these studies is to reduce the complexity for implementation in practice. Maier et al. uses a system to supply heating and cooling to a building using a heat pump and thermal storage. With a training data set of 2 years, it was possible to mimic the discrete modes that the MPC specifies for operation. Yang et al. uses a recurrent neural network (RNN) to learn the MPC behavior for a building's HVAC system. While the AMPC model achieves promising cost savings, the MPC is more able at ensuring comfort in the building.

Drgoňa et al. [10] use miltivariate regression algorithms to emulate optimization-based MPC. It is a closed-loop learning approach, which is demonstrated on the example of the control of a multi-zone building. The approximation of MPC yields very good results with the deep time delay neural networks (TDNN) and regression tree (RT) models employed. The application is successfully implemented and demonstrated on embedded hardware in the study.

Domahidi et al. [11] describe rule extraction using a closed-loop approach. Here, binary decision rules are extracted for the supervisory level of a building automation system using the ML models SVM and AdaBoost. Péan et al. [12] compare in their study different control concepts to exploit flexibilities of heat pump systems on the supervisory control level. The use case is the provision of flexibility for the public power grid. Studies with RBC and MPC are compared and it is shown how far RBC can also be used for control with the flexibility objective.

Robillart et al. [13] use the statistical method beta regression to learn from the optimization results. The use case is a residential building which is heated electrically and dynamic electricity tariffs are exploited by load shifting. The results show that the optimal behavior could be reproduced well under drastic reduction of the computing capacity and also outperforms a simple heuristic control.

In their study, Yu et al. [14] use a two-stage ML procedure to extract interpretable rules from a simulated MPC using an EnergyPlus model. Therefore the approach is a closed-loop-learnning procedure. The results of the multi-objective optimization are first clustered by an unsupervised clustering procedure to identify recurrent control decisions. In a second step, a decision tree classification is then used to reassign the clusters to the corresponding initial situations in the space for control. The method shows only slightly lower performance for the control of room air conditioning for the use case compared to the MPC, which serves as a reference.

Kanwar et al. [15] compare a MPC and a RBC approach for a microgrid that includes PV systems and de-centralized storage systems. The control approaches are intended to control the microgrid in such a way that the fluctuating renewable generation is self consumed and the degree of energy utilization is increased via the storage system. The MPC approach shows the best results due to the optimization with included predictions for renewable generation. Here, the rule-based approach consists of if-then-else loops based on engineering considerations that control the system depending on storage levels and electricity prices.

In general, the procedures in the literature can be divided into open-loop and closed-loop procedures as described by May-Ostendorp et al. [6]. The presented studies can also be subdivided with respect to the rule extraction procedure and the applied ML models. On the one hand, there are studies that apply rule mining to directly extract rules and limits for a rule-based system. For this purpose, ML models are used that establish interpretable relationships, such as decision tree classifiers and clustering algorithms. On the other hand, there are studies that aim to approximate the behavior of MPC using the ML models and replace the online MPC with a meta-model, which can significantly reduce the computational effort. For this method, ML models can be implemented on low level hardware to interact and control the energy system. In this case no interpretable relationships between input and output of the controls are given.

The application fields of the literature presented here describe, among others, building energy systems and the supervisory level in the building automation system. The control problems to be solved for RBC partly focus mainly on special problems (control of windows [7]) or the control of individual elements of the energy supply system, such as the utilization of storage units [15]. A research gap is identified that addresses control extraction methods for so called ”multiple input multiple output” (MIMO) problems for the coordination of larger energy systems, such as district energy systems and energy hubs with different generators and the coupling of energy sectors.

This study shall showcase the possibilities by describing the energy hub as a mathematical optimization model for the systematic creation of an optimized RBC. In addition, the comparison with existing RBCs implemented by engineers in practice shows that the methodology can also take other variables into account in order to fulfill requirements such as flexibility for the public grid in a rule-based mannor.

3. Use case

The energy system of the presented use case supplies a city district with heating, cooling and electricity. The generation plants are located in an energy hub, the heating and cooling supply of the buildings in the district is carried out via thermal networks. The district is characterized by mixed use, which includes office buildings, hotels, retail, restaurants, industrial enterprises, sports facilities and cultural institutions. The demand profiles show a high simultaneityof heating and cooling demands throughout the year. The connected industry has a year-round cooling demand. Some of the buildings are supplied with domestic hot water via the local heating network. Therefore a year-round heat and cold supply is provided by the thermal networks and the energy hub. In addition to the energy hub, the system is also connected to the public power grid. Some of the buildings have own additional generators for support, such as decentralized heat pumps, which are, however, neglected in this study and are controlled independently of the energy hub. Decisive for the optimization problem are the thermal and electrical loads, which are supplied by the energy hub to the district.

Figure 1 shows the different sectors and all the supplies and demands, that are located in or connected to the energy hub. The heat supply can be provided by different plants.Two combined heat and power plants (CHP) are available, each with a thermal output of 1111 kW and a nominal electrical output of 851 kW, a gas boiler with a nominal thermal output of 1870 kW, a high-temperature heat pump (HT-HP) with a nominal thermal output of 1284 kW, and an electrical heater (EH) with a nominal thermal output of 250 kW. Cooling is primarily provided by two absorption chillers (AC) with a nominal cooling capacity of 787 kW and a heat demand of 1049 kW nominal each. The ACs are connected to free coolers via a recooling circuit, which can also be used as free coolers at outside temperatures below 0 °C. The ACs are connected to the free coolers via a re-cooling circuit. The re-cooling circuit of the AC also serves as a heat source for the HT-HP. Due to this coupling, the HT-HP can only be used when the chillers are running, which, however, is always the case due to the high year-round cooling demand as long as the free coolers are not used. While the CHP units are decoupled from the heating network via two buffer storages with a total capacity of 24,000 l, all the other heat generation units feed directly into the heating network. Therefore an optimal sceduling of the devices in regard to current demand, efficiency and minimal part load to reduce on/off cycles is crucial for the control of the energy hub.

The structure of the supply system makes it possible to provide both positive and negative flexibility for the public power grid through appropriate control. This is due to the coupling of the electricity and heat sectors via CHP and HT-HP. The flexibility potentials of energy systems are often achieved with temporary measures, such as the utilization of storage facilities and the thermal inertia of buildings. In this context, only limited amounts of energy can be shifted at certain times. The present energy system can also provide permanent flexibility to the public grid depending on the heating, cooling and electricity demands by shifting the load to other generators. This aspect will be discussed in more detail in the result section 5. when considering different electricity and gas prices as an economic incentive.

The current control is based on a generator sequence, which is carried out via the storage levels of the thermal buffer storage. Currently, the CHP are prioritized to provide the base heat load. The HT-HP is switched on manually when the AC are running and there is a heat demand from the local heating network. The gas boiler and electric heater serve as backup and are used manually in certain situations: If the heat demand from the local heating network and the AC exceeds the capacity of the CHP units, a CHP unit is switched off in favor of the gas boiler, since the gas boiler can provide a higher heat output for the gas used. In addition, the gas boiler serves as a redundancy for, among other unplanned downtime, service times of the CHP units. The electric heater has a relatively low output and is also kept in reserve for peak loads. Although the current control system is largely automated, there are still manual interventions and the limits and prioritization of individual generators are adjusted by a technician in the course to manage an economical operation. This is also the motivation for the methodology to implement a mathematically optimized rule-based operation.

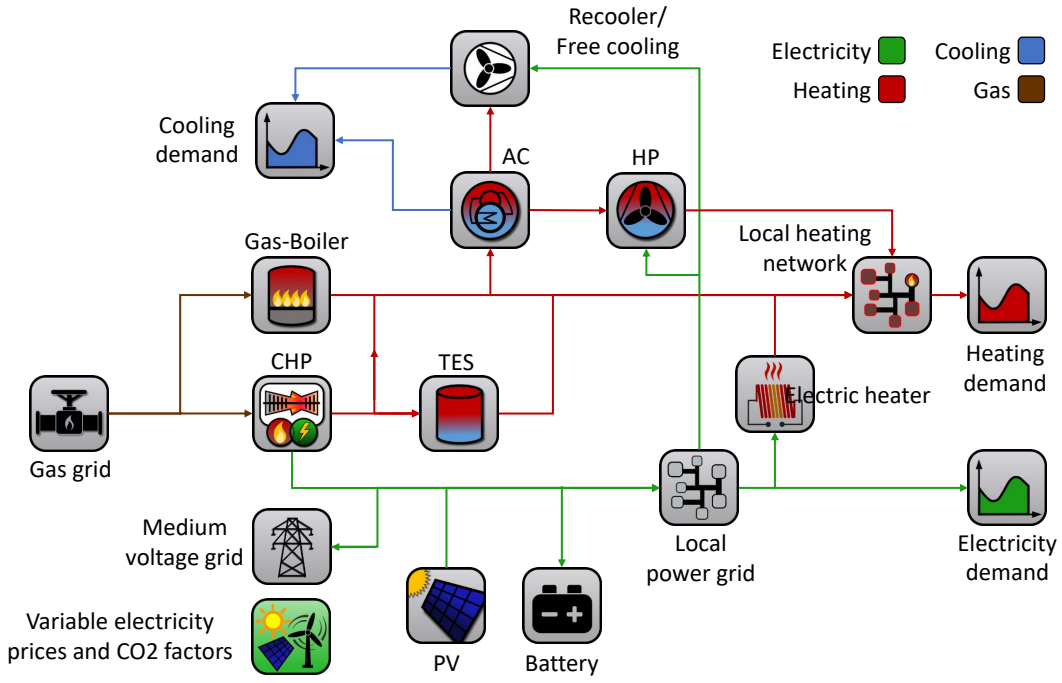

Figure 1: Structure of the sector coupled energy system

4. Methodology

Figure 2 presents the main parts of the methodology. Time series data for heating, cooling and electricity demands, which must be generated by the energy hub serve as input for the optimization model. The time series data must be available for the optimization model in the appropriate temporal resolution. This data can be provided in the form of measurement data from an existing energy system, or from a dynamic building simulation. In addition to the energy requirements, technical and economic constraints are transferred to the optimization model as parameters.

A Mixed Integer Linear Program (MILP) is used as the optimization model. A detailed description of the model is given in section 4.2.. The objective function of the optimization minimizes the operating costs, which, in addition to the costs for purchased electricity and gas, takes into account the revenues for sales to the tenants of the supplied district, as well as lump-sum deductions for start-up costs of the plants and taxes for CO2 emissions. The results of the optimization model are output as a set of time series data per parameter variation. This

contains the current outputs of all plants and storage levels for each time step of the optimization. In addition to these raw data, plant performance indicators such as a start-up counter, energy quantities provided and utilization or average operating points are also outputs.

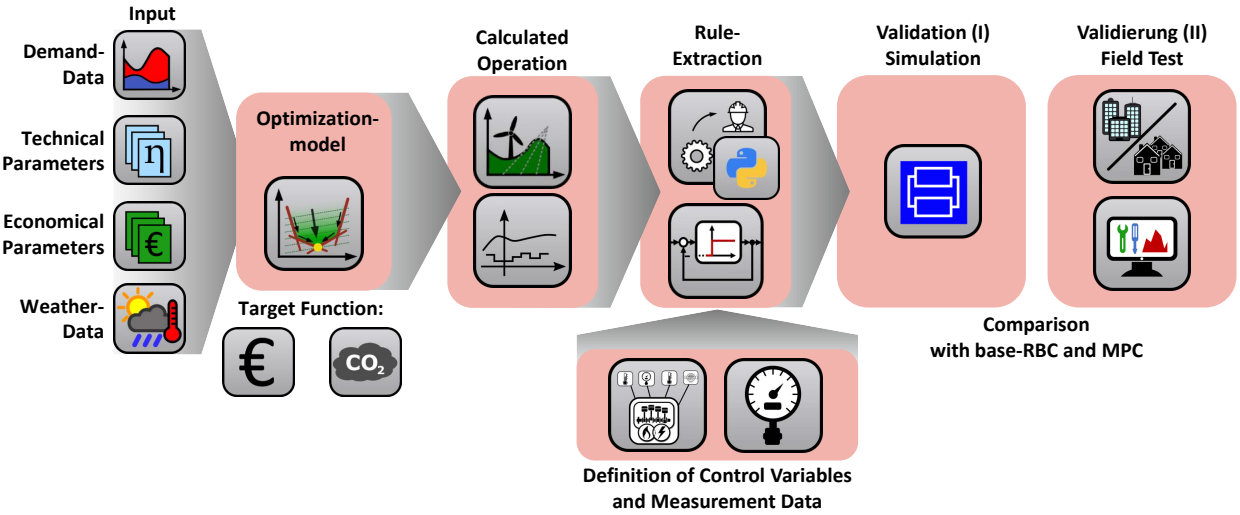

Figure 2: Structure of the Methodology

For the subsequent rule extraction process, the measured datapoints available in the real energy system and the variables to be controlled must be defined. The rule extraction process should use interpretable ML models to establish relationships between the measurable variables and the desired controlled variables for the supervisory level of control of the energy hub implementable by technicians with a corresponding education. In the last step, the rules are validated. On the one hand, an existing simulation model of the energy hub is used, which was implemented in Dymola using the open-source model library AixLib [16]. The comparison can be made in the simulation with the existing RBC of the energy hub, as well as with other control approaches such as an ideal MPC with perfect forecast as an upper-bound comparison. In addition, the rules should also be implemented in practice if they offer potential for improvement compared to the previous mode of operation.

4.1. Data preprocessing

The demand time series for the heating, cooling and electricity demands of the district, which are used for the optimizations, are real measurement data from the project, which were recorded via a monitoring platform. Since cooling can only be provided via the AC, only the heat flow required for the AC, which is recorded via heat meters, is taken into account in order to further simplify the optimization model.

Since data gaps for individual data points occur in the monitoring data set, the time series are subjected to preprocessing. Gaps with a duration of less than 2 hours are closed by the mean value of the adjacent time steps. If a larger gap occurs in one of the time series, the faulty segment removed from the data set. The optimization is then performed for one contiguous segment at a time, with continuity for the thermal storages being maintained by a constraint that the storage levels must be identical at the beginning and the end of each cycle.

4.2. Optimization model

The energy system is formulated as a mathematical optimization problem in Python. The optimization is performed with the commercial solver Gurobi [17]. The coarsest temporal resolution of the underlying measurement data from the real energy system is 15 min. Accordingly, the time step size of the optimization problem is also set to 15 min. The results from the optimization are output as time series data in a structured way.

The main model parameters are described below:

- The thermal and electrical efficiencies of all plants, as well as the coefficient of performance of the HT-HP. The efficiency curve of the gas boiler and the CHP units is approximated by a stepwise linearization, while the EH and the HT-HP are represented by a constant efficiency and coefficient of performance, respectively. Analysis of the measured data shows that the source and sink temperatures of the HT-HP in the application are almost constant, and therefore the assumption of a static COP was assumed to be sufficiently accurate for the case study.
- Minimum partial loads are specified as constraints for all generators.

- Due to the size of the equipment, special consideration must be given to the cost of wear and maintenance due to frequent start-ups. These start-up costs are provided as parameters in the model. The CHP units are the most expensive with 50 EUR per cycle, the gas boiler and the HT-WP with 10 EUR per cycle each and the electric heater with 3 EUR per cycle. The values were estimated with partners from practice.
- Minimum run times for the following components are specified as constraints: The CHP must run for 30 min, the gas boiler and the HT-WP for 15 min each, and the EH for 1 min before they are allowed to be shut down again by the optimization. In addition to the start-up costs, these constraints were chosen to prevent the plants from cycling and to force a solution with longer run times.
- Generator dependencies in the system were specified by constraints: Due to the high temperatures required for the AC, they can only be supplied by the CHP units or the gas boiler.
- The gas connection is limited to a capacity of 5 MW, which is why only two of the gas-fired plants (Two CHP units and one gas boiler) may be operated at a time.
- The costs for the purchase of electricity from the public grid, the purchase of gas, CO2 emission costs and revenues for the sale of surplus electricity to the public grid are each specified by constant parameters. However, the option is provided to run optimizations via a parameter grid variation. These parameters have a sensitive influence on the optimization result and the use of individual generators. Using the parameter-grid, their influence on the results can be displayed for any time-step and later be used in the automated rule extraction.

The parameters listed were implemented according to the manufacturer's specifications.

The procurement prices for electricity and gas were assumed to be constant, but the model is designed to run optimizations for a parameter grid for different electricity, gas and CO2 prices, so that the influence of these costs on the generation sequence can also be mapped at any point in time.

4.3. Rule extraction

The methodology presented in this paper is intended to provide results through the rule extraction procedure that can be interpreted by a technician and used for setting the control in practice. Therefore, only ML methods that allow this form of interpretation are considered. Existing literature provides examples for the use of Decision Tree Classification, Clustering methods, Support Vector Classification and AdaBoost as discussed in 2..

Currently, two ways are being tested to represent the complex dependencies of this MIMO system from the optimization model in a form that can be directly transferred to the automation system in practice. Enabling of generation units depending on the important decision variables such as current heating and cooling demand, as well as electricity and gas costs can be reproduced using Decision Tree Classification. However, the accuracy of the model trained using optimization data does not yet allow conclusions to be drawn about the performance of the control in practice. Validation is still pending. Another possibility is to transfer the optimization results to operating modes that can also be mapped in the automation system. Thus, the data set can be grouped using clustering. The decisive variables and transition conditions between the modes must be determined in a further step.

4.4. Simulation Model

The simulation model to be used for validation of the optimized RBC is implemented in the Modelica language. It is based on physical models of the simulation library AixLib [16] and is modeled by means of plans for the interconnection of the energy hub, as well as the parameters according to the manufacturer's data sheets. Many of the simplifications in the optimization model, which are based on the simplified mathematical description of the system, are more accurately represented in the simulation model. For example, the model uses fluid models that represent the thermodynamic properties of water. Inertias, as well as start-up processes of the plants and temperature wave propagation in the system are taken into account and the temporal triggering in the model is minute-by-minute. The model contains all interfaces for control using logic expressions in Modelica or for integration as a Functional Mockup Unit (FMU) for co-simulation in another environment, e.g. for embedding in a Python program.

5. Results

The optimization model was tested for several years on measured data and for different model parameters to determine their influence. In particular, a systematic variation of variables that change in reality, such as electricity, gas and CO2 certificate prices, is important in order to learn their influence on the basis of the optimization results for improved control.

For the example plots below, the optimization was carried out for a parameter grid of varying electricity and

gas prices. The months of July and December 2021 were used as examples to consider one month in and one month out of the heating period. The plots in figures 3 and 5 each show the relative utilization of the generating units for the heating sector as a percentage. The plots in figures 4 and 6 each show the total operating costs, the revenue generated by selling surplus CHP electricity to the public grid, and the local CO2 emissions generated by the gas-fired plants.

In the month of December, the heat supply for the AC is distributed between the first CHP and the gas boiler depending on the electricity and gas prices. When gas prices are low and electricity prices are high, the first CHP is utilized as much as possible. The second CHP is also partially added when gas prices are low and electricity prices are high. Apparently, the generation of heat and electricity by both CHPs is worthwhile, even if the electricity generation from the CHPs exceeds the captive demand in this case, as shown by the plot of revenues for electricity sales in Figure 4. With increasing gas prices and also decreasing electricity prices, there are parameter pairings that increasingly switch to the gas boiler and also the electric heater for optimal supply. The result is due to the larger amount of heat that can be provided by the gas used through the gas boiler, along with the less economical electricity generation by the CHP units at lower electricity prices. In general, heat generation from the HT-HP is in any case the most economical variant of heat generation for the local heating network, since it is in operation almost continuously high for all variants. Only at the corner of highest electricity costs and lowes gas prices the HT-HP operation is reduced in favor of higher utilization of both CHPs. This is why for the control of the HT-HP, the required waste heat from the AC and sufficient offtake from the local heating network should be decisive and should be preferred to the other generators for heat supply for most cases.

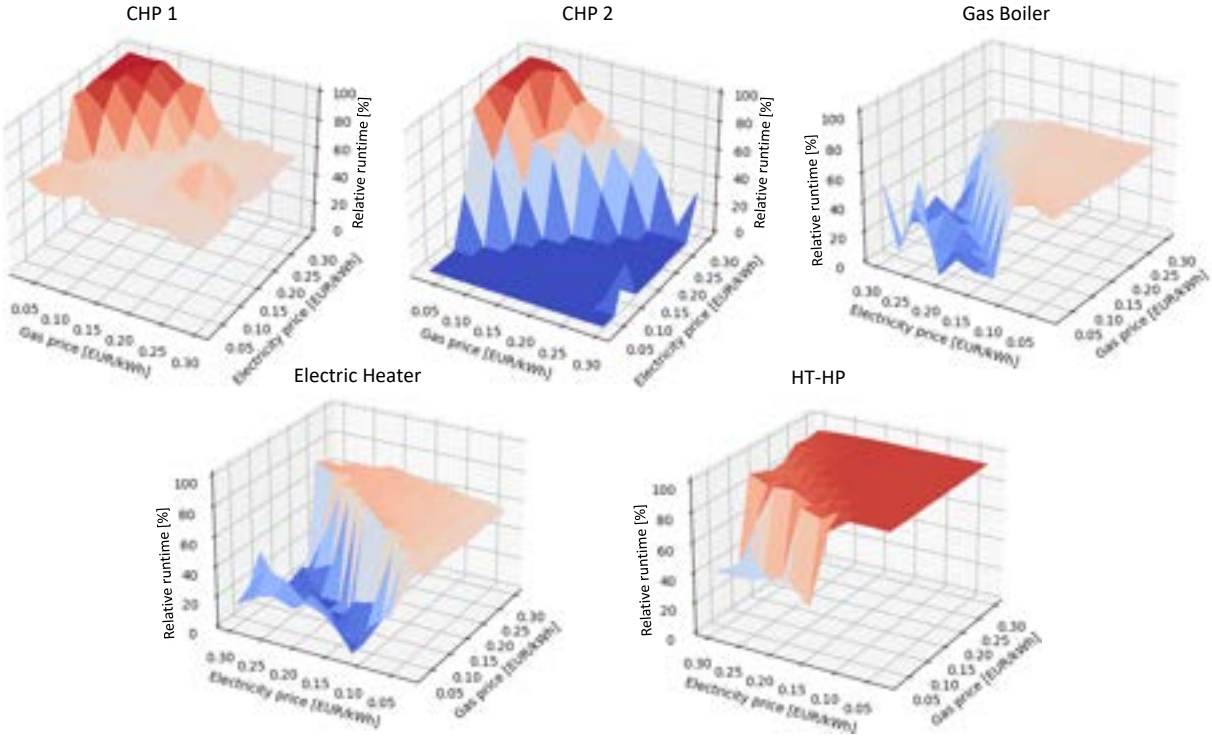

Figure 3: Optimization results for December 2021: Relative runtime of different generators for heating supply

In the month of July, a different generator composition is evident from the plots in figure 5. The share of the second CHP is further reduced for cases of lowest gas prices and highest electricity prices. The gas fueled generators (CHPs and gas boiler) show an only slightly reduced utilization, which is due to the rather constant high temperature heat demand from the ACs that is at a similar level all year round. The heat demand here in July, outside the heating season, is mainly driven by the heat demand of the AC and supplemented from the heat grid only by a small load due to domestic hot water supply. This is clearly evident from the utilization of the HT-HP, which remains at low part load for the entire parameter grid. This can be explained by higher utilization of the generators, which run anyway for the heat supply of the AC, and by the high minimum partial load of the heat pump. Since the heat pump is directly coupled with the heating grid and cannot use a buffer storage volume, a certain minimum demand from the grid is required to operate the HT-HP economically.

The two example months and parameter variations show exemplarily that by a simple analysis of the optimization results rules for the generator enabling can already be derived. In the example, these are dependent on

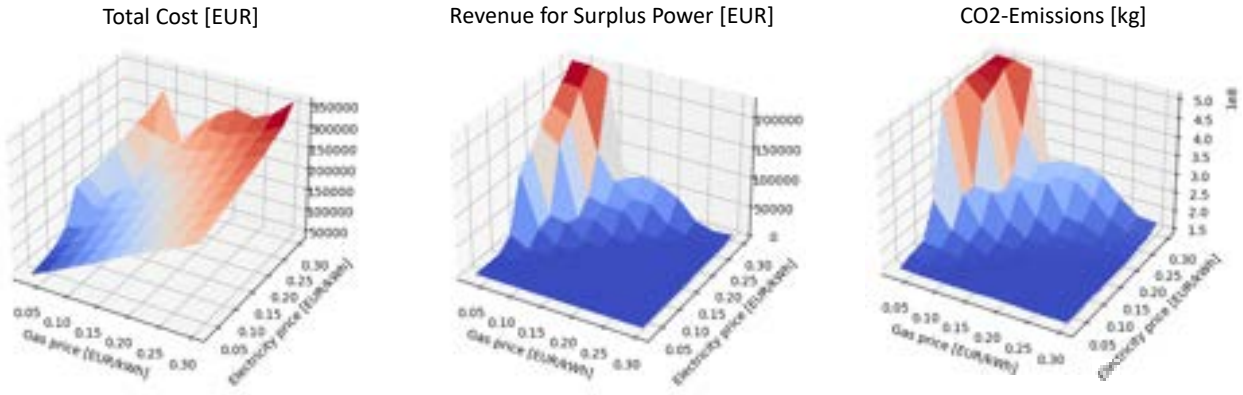

Figure 4: Optimization results for December 2021: Total cost, revenue for surplus power and local CO2-emissions for a parameter-grid of varying gas an electricity costs

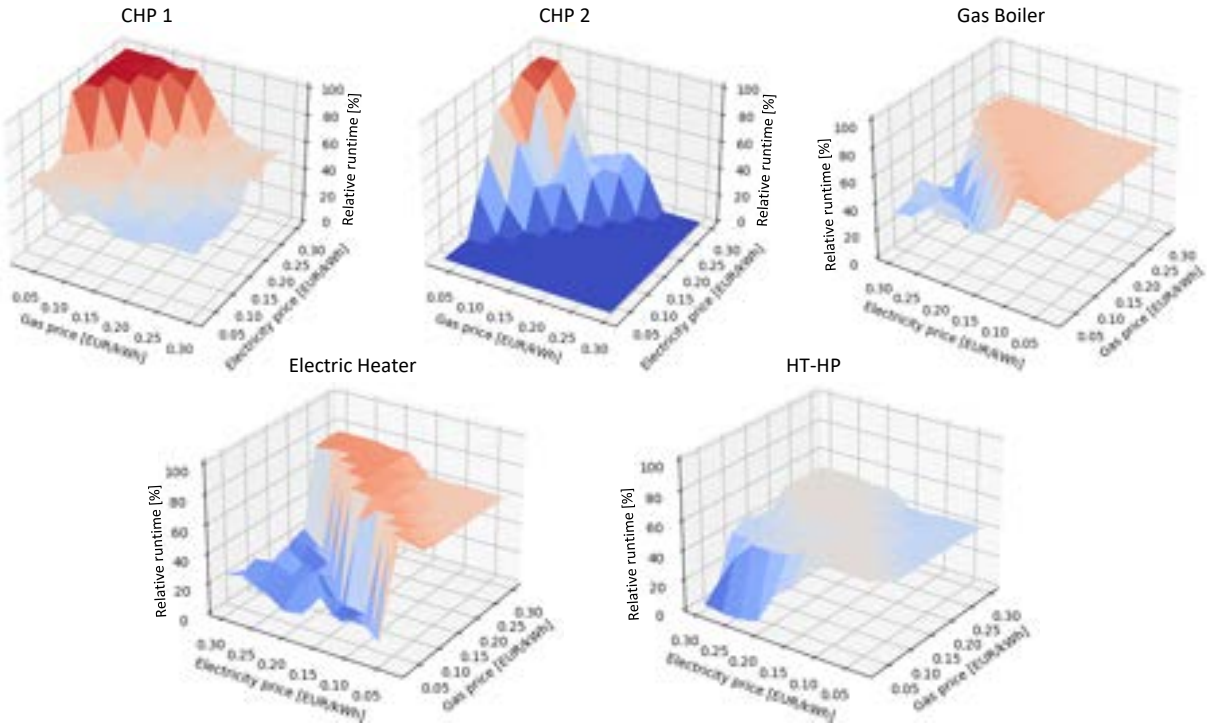

Figure 5: Optimization results for July 2021: Relative runtime of different generators for heating supply

the electricity and gas prices, as well as the season and the correlating heating and cooling demand of the neighborhood and the constraints specified by the model.

The evaluation of different parameter variations shows the dependence of the utilization of individual heat generation plants in the model and the sequence of generators on the influencing variables gas price and electricity price. In particular, if these variables are not fixed in practice by corresponding long-term contracts for periods of time, but are subject to high fluctuations through trading on the energy markets, there is considerable optimization potential here. The previous control-based mode of operation does not include the variable costs described above as decision variables for the control, although in the current situation the prices for electricity purchases and sales are traded directly on the stock exchange. Only gas purchases and CO2 taxes are currently fixed.

6. Summary and Outlook

So far, the study shows the general methodology for systematic optimization of rule-based energy systems using mathematical optimization models. While the mathematical modeling and the representation of the

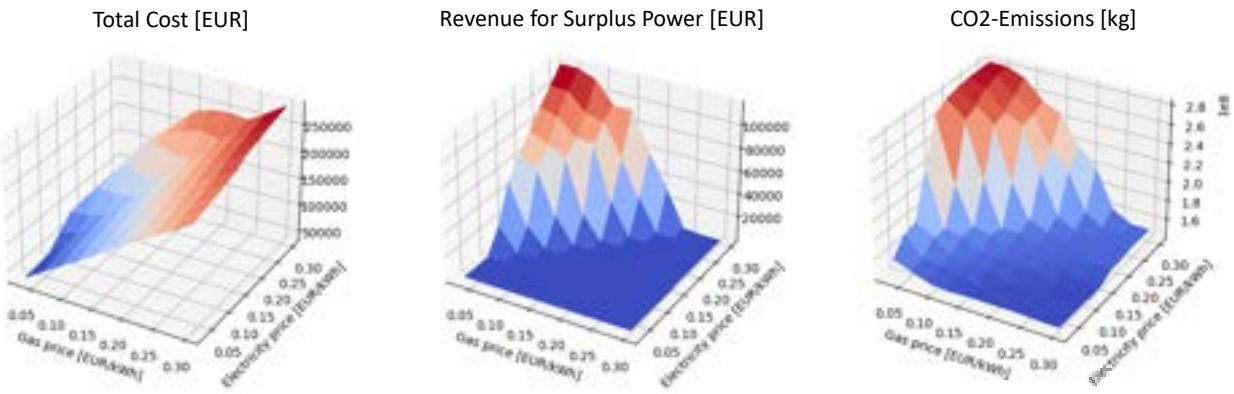

Figure 6: Optimization results for July 2021: Total cost, revenue for surplus power and local CO2-emissions for a parameter-grid of varying gas an electricity costs

energy system using Modelica models have been completed, the automated rule extraction and validation of the entire methodology on simulation and real energy systems are still pending.

The presented methodology can be used to determine the relevant decision variables and extract set-points for an optimized rule-based system, taking into account technical and economic constraints. The iterative procedures for the improvement of rule-based systems, which are common in practice, can be supported by the presented procedure in order to reach an applicable mode of operation faster.

The presented results of the optimization model show exemplarily how the current RBC should be supplemented by further decision variables for the control. Even if validation and the use of automatic control extraction methods are still pending, the influence of variables not yet taken into account in the control, such as the electricity and gas price, can already be derived directly manually.

For systems of high complexity or complex control requirements, the methodology shall also indicate when operation cannot be satisfactorily tuned using a rule-based approach and when it is worth the effort to implement more advanced control strategies, such as MPC.

In further investigations a comparison to conventional RBC and more advanced MPC approaches will be made to demonstrate which of the optimization potentials can already be achieved by an optimized RBC and for which problems more complex controls like MPC are necessary to achieve a satisfying operation.

The influence of the model accuracy of the underlying optimization model on the extracted rules needs to be investigated in more detail. Further studies should show which temporal resolution and properties of the plants i.e. constraints in the optimization model are important for the rule extraction. Provided that the method already delivers satisfactory results for rule-based operation in generic design optimization procedures with lower model accuracy and temporal resolution, this would significantly improve the transferability of the methodology.

In addition, follow-up studies will show whether the accuracy achieved in rule extraction procedures such as clustering or decision tree classification already allows conclusions to be drawn about the performance of the control in reality, or whether it needs to be validated in general.

7. Acknowledgments

We gratefully acknowledge the financial support provided by the BMWK (The Federal Ministry for Economic Affairs and Climate Action), promotional reference 03SBE006A.

References

[1] European Union. *Fit for 55: making buildings in the EU greener* Available at: https://www.consilium.europa.eu/en/policies/green-deal/fit-for-55-the-eu-plan-for-a-green-transition [Last acessed: 27.03.2023].

[2] Drgoňa J., Arroyo J., Figueroa I. C., Blum D., Arendt K., Kim D., Perarnau Ollé E., Oravec J., Wetter M., Vrabie D. L., Helsen L. *All you need to know about model predictive control for buildings*. Annual Reviews in Control 50 (2020); 190–232.

[3] Heimonen I. *Energy-Hub for residential and commercial districts and transport*. Smart City (2015); 70-71.

[4] Cigler J., Gyalistras D., Širokýc J., Tietd V.-N., Ferkla L. *Beyond theory: the challenge of implementing*

Model Predictive Control in buildings. Proceedings of 11th rehva world congress, Clima, Prague, Czech Republic (2013).

[5] May-Ostendorp P. T., Henze G. P., Corbin C. D., Rajagopalan B., Felsmann C. *Model-predictive control of mixed-mode buildings with rule extraction*. Building and Environment 46:2 (2011); 428-437.

[6] May-Ostendorp P. T., Henze G. P., Rajagopalan B., Kalz D. *Experimental investigation of model predictive control-based rules for a radiantly cooled office*. HVAC & R Research 19:5 (2013); 602-615.

[7] May-Ostendorp P. T., Henze G. P., Rajagopalan B., Corbin C. D. *Extraction of supervisory building control rules from model predictive control of windows in a mixed mode building*. Journal of Building Performance Simulation 6:3 (2013); 199-219.

[8] Maier L., Henn S., Mehrfeld P., Müller D. *Approximate Optimal Control for Heat Pumps in Building Energy Systems*. The 34th International Conference on Efficiency, Cost, Optimization, Simulation and Environmental Impact of Energy Systems (2021).

[9] Yang S., Wan M. P., Chen W., Ng B. F., Dubey S. *Experiment study of machine-learning-based approximate model predictive control for energy-efficient building control*. Applied Energy 288 (2021).

[10] Drgoňa J., Picard D., Kvasnica M., Helsen L. *Approximate model predictive building control via machine learning*. Applied Energy 218 (2018); 199-216.

[11] Domahidi A., Ullmann F., Morari M., Jones C. N. *Learning decision rules for energy efficient building control*. Journal of Process Control 24 (2014); 764-772.

[12] Péan T. Q., Salom J., Costa-Castelló R. *Review of control strategies for improving the energy flexibility provided by heat pump systems in buildings*. Journal of Process Control 74 (2019); 35-49.

[13] Robillart M., Schalbart P., Peuportier B. *Derivation of simplified control rules from an optimal strategy for electric heating in a residential building*. Journal of Building Performance Simulation 11:3 (2018); 294-308.

[14] Yu M. G., Pavlak G. S. *Extracting interpretable building control rules from multi-objective model predictive control data sets*. Energy 240 (2022).

[15] Kanwar A., Hidalgo Rodriguez D.,Von Appen J., Braun M. *A Comparative Study of Optimization-and Rule-Based Control for Microgrid Operation*. Power and Energy Student Summit 2015;

[16] Müller D., Lauster M., Constantin A., Fuchs M., Remmen P. *AixLib - An Open-Source Modelica Library within the IEA-EBC Annex 60 Framework*. BauSIM 2016; 3–9.

[17] Gurobi Optimization, available at https://www.gurobi.com

Transfer Learning Mechanism to account Performance Degradation in Gas Turbines with limited Operational Data

Sundar Raj Thangavelu[a], Imantha Gunasekera[b], Alessio Tafone[c], Shigenori Morita[d]

[a] Nanyang Technological University, Singapore, sundar.rt@ntu.edu.sg CA

[b] Nanyang Technological University, Singapore, imantha@ntu.edu.sg

[c] Nanyang Technological University, Singapore, alessio.tafone@ntu.edu.sg

[d] Surbana Jurong Consultants Pte Ltd, Singapore, shigenori.morita@surbanajurong.com

Abstract:

This paper investigates the transfer learning mechanism to improve the prediction accuracy of the energy system model. Artificial intelligence techniques are increasingly being adopted in the energy domain to predict energy system characteristics and performance. However, in many energy systems, the relationship between interested variables and their distributions differs (data and concept drift) with time due to system degradation and aging. There is a requirement for re-training and re-testing AI models to ensure reliable performance over time, which may require extensive latest operational data. Transfer learning helps to confront this challenge by leveraging valuable knowledge from a pre-trained model and reducing the requirement of new operational data significantly. To address these issues, this paper focuses on a gas turbine, a critical energy system widely deployed in diverse applications, and shows performance degradation over its lifetime. The energy model of the gas turbine is a multivariate type that predicts energy efficiency, fuel consumption, and heat energy based on power setpoints and weather conditions. This paper examined transfer learning mechanisms that can capture the latest characteristics of the gas turbine and their effects on prediction accuracy. The developed transfer learning model predicts fuel consumption accurately above 99%, whereas the pre-trained model under-predicts up to 4%, which may lead to suboptimal operation decisions when employed in the scheduling algorithm. Some of the other targets, such as heat energy, show marginal drift, as expected from the gas turbine characteristics. The knowledge gained from the transfer learning mechanism and its efficacy boost assists operational decisions, which helps improve energy efficiency and cost savings.

Keywords:

Transfer Learning; Machine Learning; Distributed Generation, Neural Network, Prediction Energy Model.

1. Introduction

Commercial buildings account for 32% of global energy consumption and are expected to face an annual growth of around 1.3% and 2% for the Organization for Economic Co-operation and Development (OECD) and non-OECD countries [1]. The building sector wastes around 20% of its energy due to faults in energy systems [2,3] which further emphasises the importance of assessing the operational performance of these systems. The increasing trend of energy consumption urges efficient monitoring to improve the efficiency and life span of these systems and reduce carbon footprints and unnecessary downtime. Decarbonization drives distributed energy resources (DER) comprising renewables and local generation to support diverse buildings and communities. Urban communities are moving towards local DERs to gain additional efficiency benefits and strengthen reliability and resilience. Advancements in smart grids, the Internet of Things (IoT) and artificial intelligence (AI) boost adoption to automate and optimize various energy processes. The most common applications in buildings are AI-based energy management systems [4], fault detection and diagnosis [5], and load and renewable forecasting [6]. Traditionally, physics-based models were employed to address these problems and require more specific information about buildings and technologies [7,8]. Now, AI techniques cut short and ease the development and deployment process and offer scalability to larger problems [9] through generalized models. Despite the many advantages of these approaches, a major drawback is the requirement of sufficiently large datasets to produce accurate models [10]. For example, deep learning models not only require large datasets but also extensive training times and computational resources [11], and often compiling

such a dataset can be expensive, time-consuming, and even impractical on certain occasions[12]. This study focuses on developing an AI model of a gas turbine using minimal latest operational data and exploiting most of the information from the pre-trained model.

1.1 Importance of Learning Models

The performance of energy systems degrades over time; some of the performance losses can be recovered through proper maintenance, whereas the non-recoverable losses are due to system wear and tear. Such situations may change the characteristics and performance of the energy system, i.e., the changes in the outputs (dependent variables) for given inputs (independent variables). This process is often referred to as concept drift in literature. It is pre-eminent that predictive models operating in such settings need to account for these changes to retain prediction accuracy. Learning methods are widely used to address some of the performance drift challenges involving data shortages. The learning methods apply a knowledge transfer process and achieve substantial improvements in many domains, including computer vision, natural language processing, speech recognition, bioinformatics, and reinforcement learning [5].

Adaptive learning techniques are applied in dynamic environments where the performance data (system characteristics) varies with time. Adaptive learning consists of four building modules comprising memory, change detection, learning, and loss estimation [13]. The memory module updates the latest information and simultaneously discards irrelevant old information. The change detection module characterises and quantifies concept drift by examining data and its distribution between two-time windows, as well as validating the predicted values with actual measurements. The learning module updates the prediction model through retraining and the incremental method. The retraining mode discards the existing model and develops a new model using both old and new data [14]. In contrast, incremental methods update the current model with the most recent data as it becomes available. The final module is loss estimation, which is related to performance metrics used to estimate the algorithm performance during adaptive learning. Several articles incorporated adaptive learning to account for degradation in their workflow, thus improving the efficiency of systems. These studies focus on batteries and fuel cells, which are prone to significant capacity degradation. Li et al. developed a fuel cell degradation model for a hybrid bus energy management system to account for different decay rates during varying operating conditions [15].

On the other hand, transfer learning uses the knowledge gained in one problem and applies it to a different but related problem, such that the development process is simple and eliminates the need for development from scratch and a complete dataset [16]. Lu et al. applied transfer learning to tackle limited data for improving the thermal load forecasting model and developed a similarity measurement index to select a source task that is most like the target task [17]. Chen et al. [18] proposed a neural network based on control theory for fault detection in actuators and utilized transfer learning to account for degradation in the system. In the context of degrading energy systems, transfer learning aims to update a pre-trained NN model using the latest operation data to capture the changes in the system's behaviour. This type of problem is categorized as domain adaptation, where the model inputs and outputs are still within the same space, but the distribution or system characteristics change due to ageing [19]. Figure 1 shows a general overview of the domain adaptation problem, where the neural network model is developed using a comprehensive dataset, resulting in a pre-trained network. Later, this pre-trained model is adjusted or fine-tuned using the latest dataset to capture the behaviour and performance of the current state of the system. During the finetuning process, the learned weights and biases of the pre-trained model are further adjusted to minimize the loss function in relation to the latest operational data. The fine-tuning process usually leads to shorter training periods because the pre-trained model has already learned useful features.

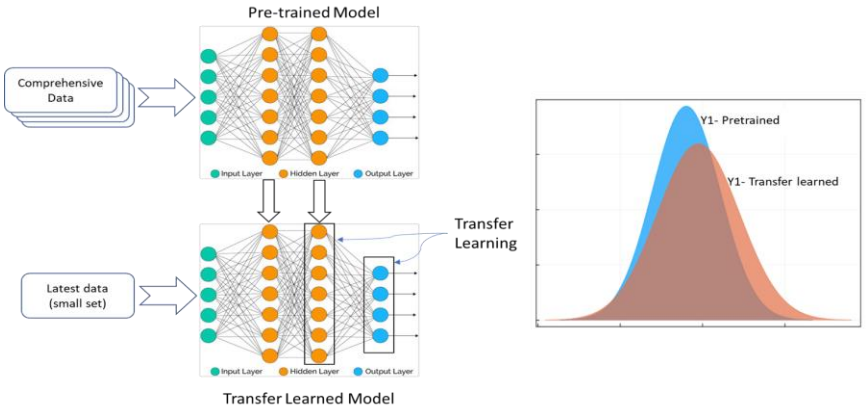

Figure. 1. General schematic of transfer learning for domain adaption problem

In energy systems, transfer learning has been applied to a variety of problems. Liu et al. designed a convolution-based neural network (CNN) to diagnose faults in building chiller plants [5]. Besides transfer learning, other methods solve similar problems involving data limitations; for example, semi-supervised learning takes advantage of unlabeled data together with some labeled data to improve prediction performance [20], but both datasets are required from the same distribution. Multi-view learning leverages multiple different feature sets or views available for additional data description [21]. This study aims to comprehend the transfer learning mechanism and develop transfer learning models to improve the prediction accuracy of the energy system. This study investigates and compares two transfer learning mechanisms that can capture the changes in the energy system characteristics (referred to as data drift) with the limited latest operational data and extract other useful information from the pre-trained model.

2. Methodology - Transfer Learning for Degraded Energy Systems

In degraded energy systems, the transfer learning mechanism is to improve the prediction accuracy of the AI model by using the latest operational data and capitalizing on useful information from the pre-trained AI model. To achieve this, firstly, an AI model was developed using the comprehensive dataset to depict the initial characteristics of the system. Later, this pre-trained model is adjusted to capture the latest characteristics as the performance of the system degrades. The adjusted model is often referred to as the fine-tuned model. In such situations, the dataset representing a degraded system may be limited; however, this requirement is acceptable as this data does not need to represent all characteristics of the system. Figure 2 shows the schematic of the transfer learning mechanism, where data processing is the starting point to extract useful information (i.e., features and targets) from the operational data and eliminate outliers and noise. Develop a multi-layer perceptron neural network (MLP-NN) model to predict energy system behaviour and performance. Data normalization was employed as a pre-processing step to improve model convergence and prediction accuracy, whilst K-Fold cross-validation was used to evaluate model performance considering the network architecture with different hidden units, which defines the complexities of the model that can be varied to achieve desired prediction accuracy. The deployment of the developed NN model in the energy management system supports scheduling algorithms in deriving key operation setpoints and dispatch decisions.

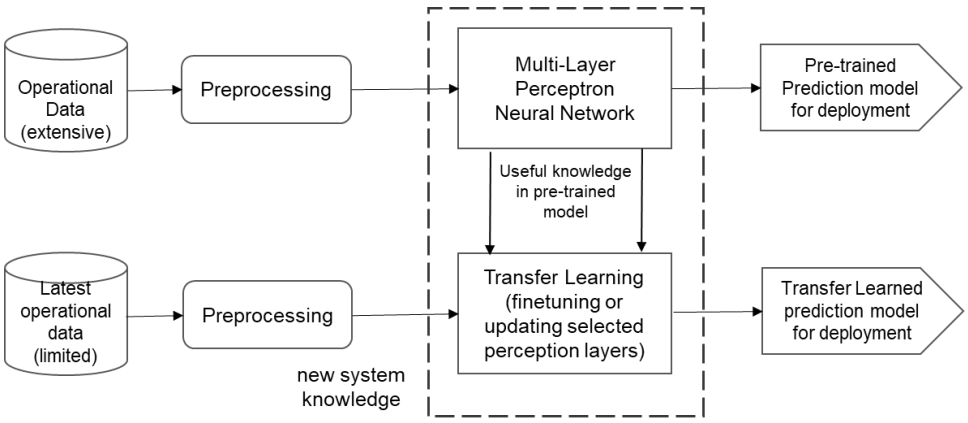

Figure. 2. Schematic of Transfer Learning Mechanism

The performance or prediction accuracy of the developed model is expected to drop over time due to changes in the actual system. Eventually, this model will become obsolete and not useful. Transfer learning helps to revitalise the prediction model using the latest operational (limited) data and critically utilize the useful information from the pre-trained model. Transfer learning can be carried out in different fashions, such as finetuning or updating the coefficients of the output layer or the whole pre-trained NN model using the latest operation data. This mechanism requires less data compared to the NN model developed from scratch. The transfer learning mechanism also helps to include or exclude targets to support any changes in the prediction model requirements. The next section will describe the workability and benefits of the transfer learning mechanism for the energy system application.

3. Case Study – Gas Turbine and Performance Prediction

Generators, renewables, and energy storage are the key distributed energy systems that help to generate, store, and support various forms of electrical and thermal energy. In the long run, some of the DERs show performance degradation due to wear and tear, especially those types of equipment with rotation or fast-moving parts. Even a non-rotating system such as solar PV and batteries shows performance degradation due

to ageing and depreciation of internal components. Interestingly, the solar PV manufacturer provides the expected performance degradation, whereas for other DERs, equipment usage and operation patterns play a dominant role in the performance degradation. This study focuses on gas turbines' critical distributed energy resources, categorized as a dispatchable system where the operation can be easily controlled based on the power requirements to fill the power deficit and synchronize with the grid frequency to absorb the fluctuations. This section will describe the necessity of a transfer learning algorithm for the gas turbine model and its benefits.

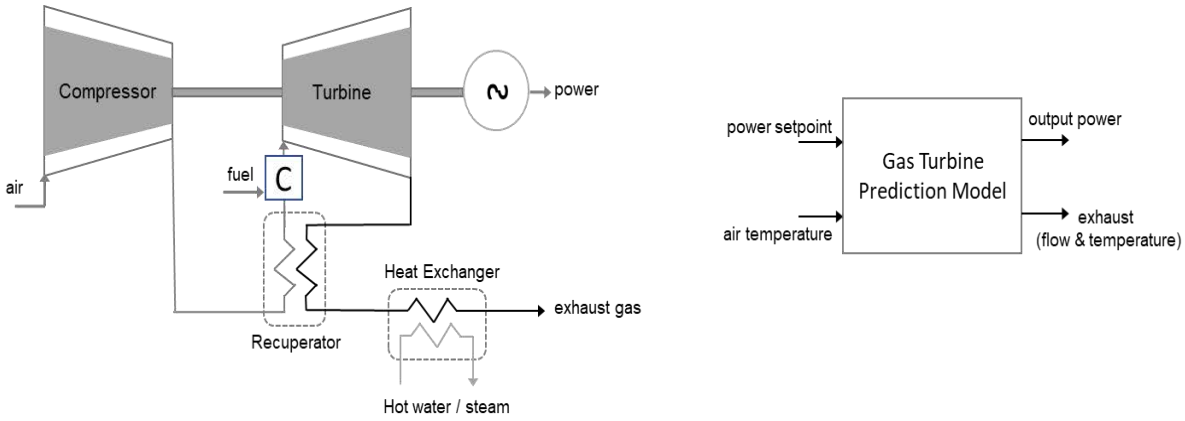

Figure. 3. Schematic of Gas turbine and AI-based prediction model

Gas turbines are widely employed to generate electrical power using clean fossil fuels such as natural gas, and even the waste heat available in the exhaust gas is recovered to support thermal loads. Figure 3 shows the schematic of a gas turbine, where fuel and air drive the turbine to generate power and exhaust gas. The heat energy in the exhaust gas has the potential to produce steam or hot water when diverted through boilers or heat exchangers. The recovered heat energy can be utilized in exhaust-driven absorption chillers to produce chilled water for air conditioning purposes [22]. Gas turbines are available in diverse capacities, ranging from a few kW to over hundred MW scale. Like any other system, a gas turbine provides high efficiency at rated conditions and low efficiency during off-load conditions. The life of the gas turbine is around 150000–200000 hours, or 20 years with regular maintenance and overhauls. Experts and manufacturers confirm that this system shows performance degradation over time; some degradation effects are recoverable through proper and regular maintenance [23], whereas performance degradation due to ageing (due to wear and tear) are permanent and cannot be recovered. Any degradation in performance could result in sub-optimal operation conditions, affect the energy cost, and incur the risk of supply shortages. Therefore, actual performance needs to be accurately accounted for to understand the operation cost of the gas turbine and decide on the right combination of systems for dispatching purposes.

Commonly, performance charts or technical data were widely used to gauge power output, fuel consumption, and fuel cost. Unfortunately, it is quite abstract and covers design conditions at standard temperature and pressure. Experts exploit physics-based models to generate performance charts for diverse conditions [24], this study utilized the gas turbine simulator adapted from TRNSYS to generate the performance data and understand the effect of degradation on the performance factors. TRNSYS is a state-of-the-art commercial simulation tool for industry and academia, based on an object-oriented approach that enables the simulation of the transient behaviour of systems focused on assessing the performance of thermal and electrical energy systems. The software is made up of two main parts: a simulation engine to solve the dynamic mathematical problem and a large library of built-in components or types (e.g., gas turbines, compressors, pumps, mixers, diverters, heat exchangers, etc.), often validated by experimental data. Type 625 has been adopted, utilizing technical data and performance maps of 3.5 MW gas turbines [25]. Exploiting the Type 625 model, the gas turbine performance parameters are derived for diverse output power and inlet air temperatures. Figure 4 shows the performance characteristics of a new gas turbine, where the fuel consumption increases with the output power and the air intake temperature. The air temperature and output power also show an effect on the exhaust gas flow and temperature.

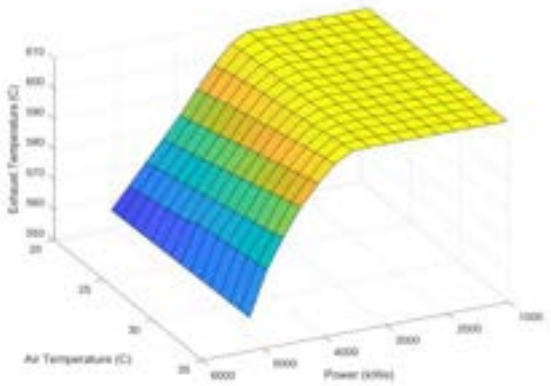

(a) Variation in the exhaust gas temperature

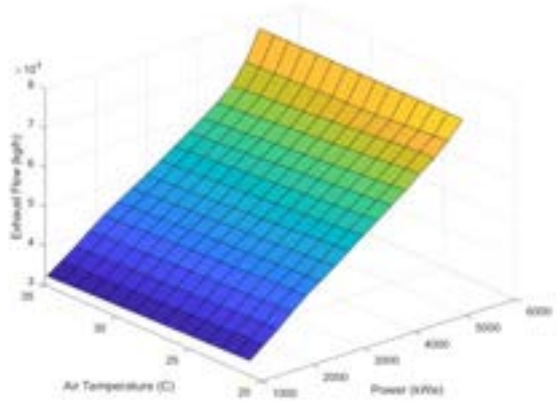

(b) Variation in the exhaust gas flow

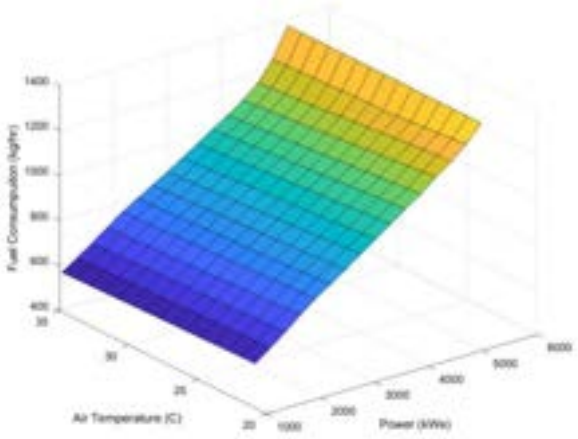

(c) Variation in the fuel consumption

Figure. 4. Performance characteristics of Gas Turbine (without degradation) with reference to part-load behaviour and air intake (ambient) temperature

Model GTD is a multi-layer perceptron (MLP-NN)-based neural network architecture prediction model developed using the performance data (17x15 = 256 data points covering 17 part loads and 15 air temperatures) representing a new gas turbine. Data normalization is applied explicitly to ease the convergence process and prevent any bias due to different data scales. Due to a smaller number of data points, K-Fold cross-validation was employed during training to obtain a more accurate estimate of the model's performance. The model GTD was trained using an ADAM (Adaptive Moment Estimation) optimizer with mean squared error as a loss function. The training epochs and the model complexity (hidden units of 8, 16, 32, and 64 units) are varied to identify the right architecture that provides acceptable accuracy during training and validation. Finally, the Model GTD with 64 hidden units was able to predict the gas turbine outputs with the required accuracy of 0.998 R2 on the validation set.

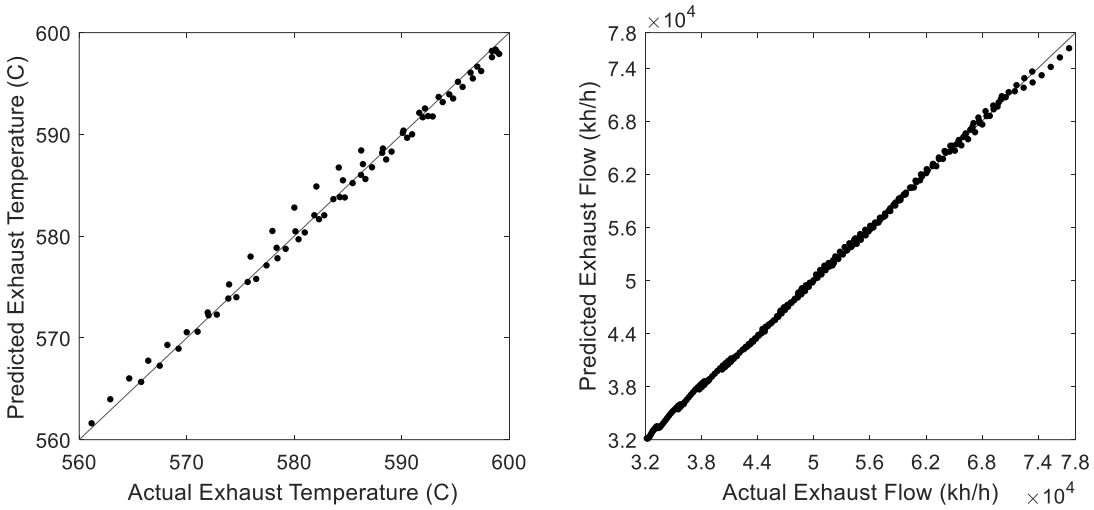

Figure. 5. Actual Exhaust Gas and Model GTD predictions (R2: 99.8%)

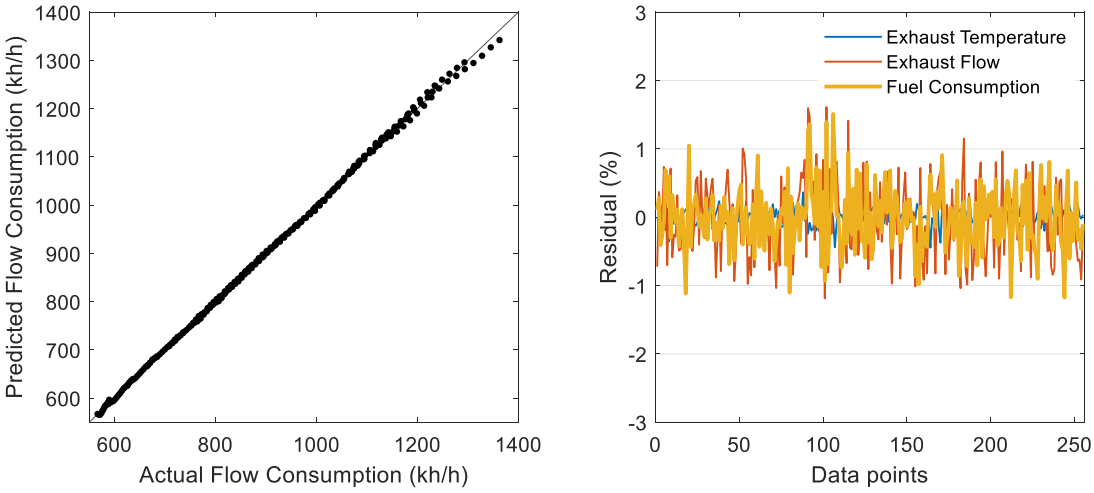

Figure. 6. Actual Fuel consumption and Model GTD predictions (R2: 99.8%)

The accuracy of the developed Model GTD model is shown in Figures 5 and 6. This model helps the scheduling algorithm make optimal operational decisions on an hourly or sub-hourly basis. The normalizers and coefficients, or weights, of the prediction model are preserved for later use.

4. Performance of Pretrained and Transfer Learning Models

The Model GTD prediction is expected to deviate over time because the actual gas turbine characteristics drift due to ageing and degradation. Any inaccuracy in the prediction could lead to suboptimal or inferior scheduling or operation decisions that may result in high energy costs or a potential supply risk. To retain prediction accuracy, a new prediction model needs to be developed from scratch using the latest operational data. In a real application, the gas turbine's operation depends on the loads and operation of other integrated energy systems. Therefore, it is challenging to get the latest performance data over a wide range. The possible collection of real-time operational data is limited and not comprehensive. In such cases, the transfer learning algorithm helps to develop the prediction model for the degraded system by capitalizing on the available information in the pre-trained model and the limited new performance data. This study leverages TRNSYS software to derive the performance data of the degraded gas turbine by applying reported recoverable and non-recoverable performance losses [28]. To account for the practical situation, only a few operational data points (roughly 10% of the 256 data points) of the degraded system were randomly selected for transfer learning.

Previously trained Model GTD (with the same architecture and coefficients) are employed in transfer learning. The key advantage is that the preserved coefficients of the pre-trained model were adjusted instead of learning from a fresh start.

- Model TL1 is the transfer learning model developed by updating the coefficient of the whole pre-trained model (Model GTD) using the latest available operational data.
- Model TL 2 is the transfer learning model developed by updating the output layer coefficient of the pre-trained model using the latest available operational data.

Interestingly, transfer learning requires less effort at around 100 epochs for coefficient adjustment to achieve reasonable predictions.

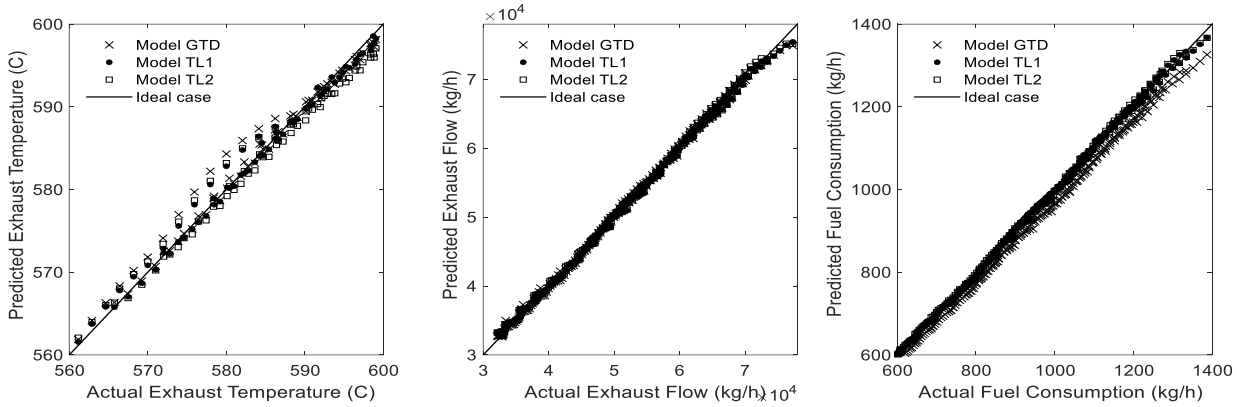

Figure. 7. The actual and predicted gas turbine outputs (exhaust gas temperature, exhaust flow and fuel consumption)

Figure 7 shows the accuracy of three prediction models, Model GTD, Model TL1, and Model TL2, with reference to the latest operational data comprising 256 points. Model GTD failed to predict the gas turbine performance accurately, and it deviates significantly in the fuel consumption estimation (as shown in Figure 8). Even the predicted exhaust temperature values deviated moderately from the actual values. The Model TL1 provides better performance than the Model GTD, and interestingly, the predicted fuel consumption and exhaust gas flow are within the acceptable range. On the other hand, the predicted exhaust gas temperature deviates to a certain extent, especially at partial loads. Model TL2 provides superior performance over Model GTD and Model TL1. The prediction accuracy is around 99.5% (R2), within acceptable limits. Generally, Model TL2 is preferred when the user requirement (output variable or number of output variables) changes or its distribution changes. Consequently, Model TL1 is expected to perform better because all coefficients are adjusted using the latest operational data. Some of the deviations could be due to limited data.

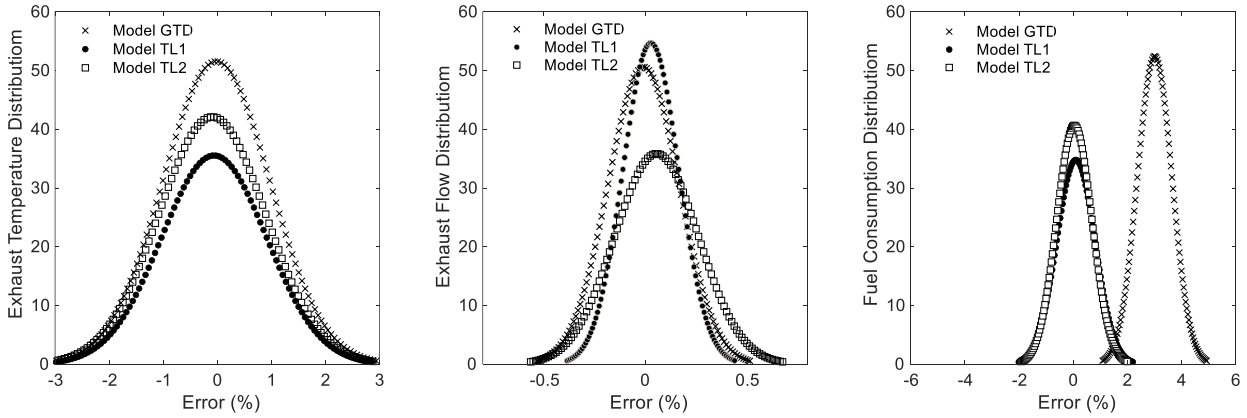

Figure. 8. Error distribution in the predicted gas turbine outputs (exhaust gas temperature, exhaust flow and fuel consumption)

Fuel consumption is the key variable that greatly reflects the operation cost of the gas turbine. Regarding fuel consumption, the performance of Model TL1 and 2 are similar, showing marginal differences at certain data points. Deploying Model TL1 or 2 in the scheduling algorithm can improve operational decisions that lead to improvements in energy efficiency and a reduction in energy costs. Applying transfer learning regularly (once or twice) in a year is important to prevent plant-model mismatches by retaining the accuracy of the prediction model and safeguarding optimal operation decisions. Through careful deployment, this process can be automated to reduce manual involvement by predefining the data extraction, training, and update rules. This approach can be applied to other energy systems, especially those subjected to performance degradation over time, such as chiller systems, heat exchange equipment, etc. In summary, the performance of certain energy systems degrades significantly over time. Not accounting for the performance degradation could lead to suboptimal or inefficient operations of energy systems. While deriving the operational decision, the actual performance characteristics are essential to derive optimal operation set points. Therefore, the prediction model needs to be updated regularly to capture changes in the energy system's characteristics. In this context, transfer learning could assist in retraining or updating the prediction model with the limited operational data to capture and predict the performance of the degrading energy systems.

Conclusion

This study developed transfer learning models for the gas turbine system to improve prediction accuracy by eliminating plant-model mismatch and supporting operational decisions to gain energy and cost savings through efficient operations. The pretrained model cannot predict the degraded system performance and shows significant deviation, which highlights the need for transfer learning. Two transfer learning mechanisms were explored: Model TL1 was obtained by tweaking the coefficients of the whole pre-trained model, and Model TL2 was developed by tweaking the coefficients of the output layer alone. Both mechanisms utilized the latest (and limited) operational data and capitalized on most of the information from the pre-trained model. Interestingly, both models provide better accuracy than the pre-trained model. Comparing transfer learning models, TL2 outperforms TL1, which could be due to limited data availability to fine-tune all coefficients. Deploying Model TL1 or 2 in the scheduling algorithm could reflect the actual performance of the gas turbine and improve the operational or economic dispatch decisions for high energy efficiency and optimal energy cost. This approach can be applied to other energy systems whose performance characteristics are expected to change over time due to ageing and degradation.

Nomenclature

Abbreviations

ADAM	adaptive moment estimation
AI	artificial intelligence
CNN	convolution neural network
DER	distributed energy resources
IoT	internet of things
MLP	multi-layer perceptron
Model GTD	gas turbine model at design condition
Model TL1	transfer learned model by updating the coefficient of the whole pre-trained model
Model TL2	transfer learned model by updating the output layer coefficient of the pre-trained model
NN	neural network
OECD	organization for economic co-operation and development
PV	photovoltaic
R2	coefficient of determination
TL	transfer learning

References

[1] Fan C, Xiao F, Zhao Y. A short-term building cooling load prediction method using deep learning algorithms. Appl Energy 2017;195:222–33. https://doi.org/10.1016/j.apenergy.2017.03.064.

[2] Teke A, Timur O. Assessing the energy efficiency improvement potentials of HVAC systems considering economic and environmental aspects at the hospitals. Renewable and Sustainable Energy Reviews 2014;33:224-235. https://doi.org/10.1016/j.rser.2014.02.002.

[3] Ramesh T, Prakash R, Shukla KK. Life cycle energy analysis of buildings: An overview. Energy Build 2010;42(10):1592-600. https://doi.org/10.1016/j.enbuild.2010.05.007.

[4] Palensky P, Dietrich D. Demand side management: Demand response, intelligent energy systems, and smart loads. IEEE Trans Industr Inform 2011;7(3):381-88. https://doi.org/10.1109/TII.2011.2158841.

[5] Liu J, Zhang Q, Li X, Li G, Liu Z, Xie Y, et al. Transfer learning-based strategies for fault diagnosis in building energy systems. Energy Build 2021;250:111256. https://doi.org/10.1016/j.enbuild.2021.111256.

[6] Chahkoutahi F, Khashei M. A seasonal direct optimal hybrid model of computational intelligence and soft computing techniques for electricity load forecasting. Energy 2017;140:988–1004. https://doi.org/10.1016/j.energy.2017.09.009.

[7] Fadli F, Rezgui Y, Petri I, Meskin N, Ahmad AM, ... Building energy management systems for sports facilities in the Gulf region: a focus on impacts and considerations. Proceedings of 38th International Conference of CIB W78; October 2021, Luxembourg.

[8] Himeur Y, Elnour M, Fadli F, Meskin N, Petri I, Rezgui Y, et al. AI-big data analytics for building automation and management systems: a survey, actual challenges and future perspectives. Springer Netherlands; 2022. https://doi.org/10.1007/s10462-022-10286-2.

[9] Sardianos C, Varlamis I, Chronis C, Dimitrakopoulos G, Alsalemi A, Himeur Y, et al. The emergence of explainability of intelligent systems: Delivering explainable and personalized recommendations for energy efficiency. International Journal of Intelligent Systems 2021;36:656–80. https://doi.org/10.1002/int.22314.

[10] Mirnaghi MS, Haghighat F. Fault detection and diagnosis of large-scale HVAC systems in buildings using data-driven methods: A comprehensive review. Energy Build 2020;229:110492. https://doi.org/10.1016/j.enbuild.2020.110492.

[11] Liu X, Yu W, Liang F, Griffith D, Golmie N. Toward Deep Transfer Learning in Industrial Internet of Things. IEEE Internet Things J 2021;8:12163–75. https://doi.org/10.1109/JIOT.2021.3062482.

[12] Fan C, Liu Y, Liu X, Sun Y, Wang J. A study on semi-supervised learning in enhancing performance of AHU unseen fault detection with limited labeled data. Sustain Cities Soc 2021;70:102874. https://doi.org/10.1016/j.scs.2021.102874.

[13] Gama J, Zliobaite I, Bifet A, Pechenizkiy M, Bouchachia A. A survey on concept drift adaptation. ACM Comput Surv 2014;46(4):1-37. https://doi.org/10.1145/2523813.

[14] Gil Zeira;Oded Maimon; Mark Last; Lior. Change Detection in Classification Models Induced From Time Series Data. Data Mining in Time Series Databases 2004;57:101–25.

[15] Li J, Yang L, Yang Q, Wei Z, He Y, Lan H. Degradation adaptive energy management with a recognition-prediction method and lifetime competition-cooperation control for fuel cell hybrid bus. Energy Convers Manag 2022;271:116306. https://doi.org/10.1016/j.enconman.2022.116306.

[16] Pan SJ, Yang Q. A survey on transfer learning. IEEE Trans Knowl Data Eng 2010;22:1345–59. https://doi.org/10.1109/TKDE.2009.191.

[17] Lu Y, Tian Z, Zhou R, Liu W. A general transfer learning-based framework for thermal load prediction in regional energy system. Energy 2021;217:119322. https://doi.org/10.1016/j.energy.2020.119322.

[18] Chen H, Chai Z, Jiang B, Huang B. Data-Driven Fault Detection for Dynamic Systems with Performance Degradation: A Unified Transfer Learning Framework. IEEE Trans Instrum Meas 2021;70. https://doi.org/10.1109/TIM.2020.3033943.

[19] Zhang Q, Tian Z, Niu J, Zhu J, Lu Y. A study on transfer learning in enhancing performance of building energy system fault diagnosis with extremely limited labeled data. Build Environ 2022;225:109641. https://doi.org/10.1016/j.buildenv.2022.109641.

[20] Zhu X. Semi-Supervised Learning Literature Survey. 2006.

[21] Sun S. A survey of multi-view machine learning. Neural Comput Appl 2013;23:2031–8. https://doi.org/10.1007/s00521-013-1362-6.

[22] Thangavelu SR, Myat A, Khambadkone A. Energy optimization methodology of multi-chiller plant in commercial buildings. Energy 2017;123:64–76. https://doi.org/10.1016/j.energy.2017.01.116.

[23] Amare Fentaye, Aklilu Tesfamichael Baheta, Syed Ihtsham Ul Haq Gilani. Effects of performance deterioration on gas path measurements in an industrial gas turbine ARPN Journal of Engineering and Applied Sciences 2016;11(24):14202-7.

[24] Tafone Alessio, Thangavelu Sundar Raj, Morita Shigenori, Romagnoli Alessandro. Design optimization of a novel cryo-polygeneration demonstrator developed in Singapore – techno-economic feasibility study for a cooling dominated tropical climate. Appl Energy 2023;330:119916.

[25] NovaLT5 | Baker Hughes n.d. https://www.bakerhughes.com/gas-turbines/novalt-technology/novalt5 (accessed March 9, 2022).

ULPGC
Universidad de
Las Palmas de
Gran Canaria

grres ULPGC
group for the research on renewable energy systems

Q. Smart grids and renewables integration. Distributed generation

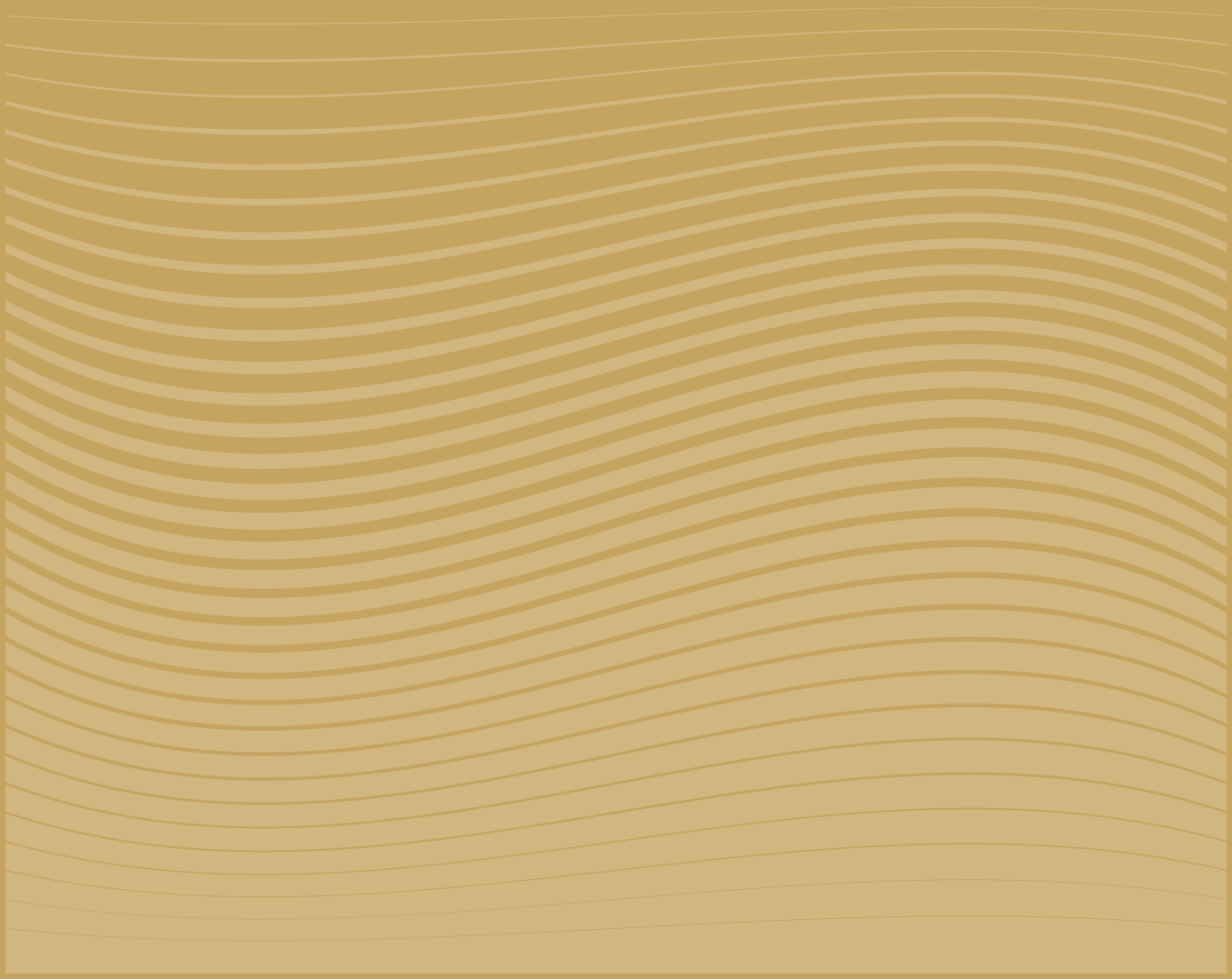

ECOS2023

PROCEEDINGS OF ECOS 2023 - THE 36TH INTERNATIONAL CONFERENCE ON
EFFICIENCY, **C**OST, **O**PTIMIZATION, **S**IMULATION AND ENVIRONMENTAL IMPACT OF ENERGY SYSTEMS
25-30 JUNE 2023, LAS PALMAS DE GRAN CANARIA, SPAIN

Detailed Modeling Framework for Integrated Photovoltaic in Partial Shading Conditions

Justin McCarty[a,b], Christoph Waibel [a], Arno Schlueter[a]

[a] Chair of Architecture and Building Systems, ETH Zurich, Switzerland
[b] corresponding author mccarty@arch.ethz.ch

Abstract:
Building integrated photovoltaic (BIPV) systems are a crucial component of the transition to a low-carbon energy system. However, current simplified models of PV cells and modules used in building and urban energy simulations may not accurately capture the performance of various PV technologies under partial shading conditions. In this paper, we propose a novel framework for modeling parametric BIPV arrays using a high-resolution irradiance grid and a power model that operates from the evaluation of IV-curves at the cell level to the AC to DC conversion in the inverter. This allows us to combine PV modules of varying sizes and electrical configurations based on the selected inverter type, and to capture the operative benefits of multiple types of cell technologies, module designs, and electrical layouts in building-based PV applications. We evaluate the proposed framework by comparing its performance to measurement data and to three other frameworks found in the literature through the simulation of two BIPV façades and a tilted rooftop array. The results show that the proposed framework is necessary to account for partial shading (if present) as well as provide operative details when the type of inverter to be used is in question. Overall, this paper presents a novel framework for modeling the performance of PV cells and modules in building and urban energy simulations, which has significant implications for the design and optimization of building-based PV systems.

Keywords:
Integrated PV, BIPV, Partial Shading, Simulation, Urban.

1. Introduction

Photovoltaics (PV) are becoming increasingly common elements of building and urban energy systems research and optimisation [1, 2, 3]. However, we find that much of the research employs coarse level performance modeling frameworks to parameterise expected PV output. Current standards within research rely on low resolution irradiance estimations and simplistic conversion efficiency methods. These models were originally developed for PV systems that were largely unobstructed and used standard PV modules, such as the arrays found in utility-scale ground mount systems and on rooftops. However, the low cost of PVs and the need for rapid urban energy decarbonisation is leading to their use in environments where the boundary conditions are less than ideal. Due to high degrees of partial shading, heat, and the need for custom module sizing many systems may be installed and produce lower overall system efficiencies than envisioned during planning. This has the potential to translate into less realistic assessments of lifecycle cost and carbon performance at the system scale and grid stability and energy availability at the urban scale. Towards the goal of reducing the performance gap for building and urban energy systems research we compare the results of different PV performance modeling frameworks.

1.1. Objectives

In this paper we demonstrate that a highly detailed performance model can help modelers understand the potential loss in an urban PV system. Additionally, we show that the high level of resolution may not always be necessary and is dependent on the context of the geometry model (i.e. the spatial context of the surface being evaluated). We describe a proposed modeling framework compiled from the literature, compare an initial set of simulated performance indicators from the proposed framework to measured data sets. Then we apply the proposed framework to several theoretical building integrated PV (BIPV) arrays; two façade arrays and one tilted rooftop array. The results of these simulations will be compared to three common frameworks to modeling BIPV performance, briefly described in Table 1. We compare the results in terms of modeling effort and calculated PV yield and outline in which context which modeling resolution is best suited.

1.2. Research Questions and Hypotheses

We ask the following questions with proposed hypotheses for help guide the reporting of the research:

Framework	Description
Surface Face	The surface is divided by a single grid dimension and the center points of each resulting face are used for irradiance simulations. Power is then extracted using a simple power conversion model from the irradiance of the sensor point and the area of the face.
Module Center	The surface is divided by a BIPV array. The center point of the resulting modules are used for irradiance simulations. Power is then extracted using a simple power conversion model from the irradiance of the sensor point and the area of the module.
Cell Center	The modules created by the Module Center framework are further divided into cells. The center point of the resulting cells are used for irradiance simulations. Power is then extracted using the power conversion model from the irradiance of the sensor point and the area of the cell.
Cell IV	The center point of the cells from the Cell Center framework are used for irradiance simulations. Power is then extracted using a single-diode equivalent circuit model from the irradiance of the sensor point and parameters of the selected module/cell.

Table 1: Descriptions of the four modeling frameworks used in the paper.

- Does the proposed framework produce accurate results?
    - Evidence in the literature suggests that the proposed framework is a viable method of predicting the yield of all module types. We aim to improve upon existing methods to bring more flexibility to the framework and providing further clarification of when a more detailed method should be applied over simpler methods.
- In what situations is it recommended to use the proposed framework over simpler methods (e.g. NOCT or performance ratio)?
    - We suspect that surfaces that are subject to mostly diffuse light or mostly direct light are candidates for the simpler methods, while those that see a mixture of direct and diffuse light will not be accurately characterised by these methods and require the more detailed method described in this paper. We expect to see results diverge the most between the *Cell IV* and the other frameworks for the façades while the rooftop arrays will be more consistent between the frameworks.

2. PV Modeling Frameworks

We define a PV performance modeling framework as a set of models and protocols that assist modelers in assessing the power output of a PV array from the definition of the surface to the calculation of performance indicators such as self-consumption (PVSC, i.e. how much of generated electricity is consumed). A framework has three components:

1. Definition of the array geometry through the discretization of a surface.
2. Simulation of the effective irradiance (G_{eff} $[\frac{\text{W}}{\text{m}^2}]$) on the array surfaces.
3. Conversion of the G_{eff} to power (P [W]), either in direct-current (P_{DC}) or alternating current (P_{AC}), typically expressed per timestep which is usually in hours, thus Watt-hours (Wh).

In the following sections we provide a review of the various PV performance modeling frameworks summarised in Table 1. The first group, discussed in Section 2.1. are often found in the literature, vary in their degree of spatial resolution, and utilise one of several power conversion methods. There are often functions of efficiency and performance ratio, to convert G_{eff} into P_{DC}. After reviewing these methods we introduce, in Section 2.2. the proposed high-resolution framework that we have compiled from several sources in the literature. This framework relies on detailed spatially accurate models of module and cell placement, as well as high accuracy irradiance simulations. The power conversion model is a single-diode equivalent circuit model from Bishop (1988) [4] to characterise the electrical attributes of each cell before merging them system wide. It is commonly applied in a less spatially resolute context (i.e. module center points) in power systems modeling for large unobstructed PV arrays.

2.1. Existing module and surface based modeling approaches

The yield from a PV cell is, at its most basic level, a function of the solar irradiance of the cell and the cell's ability to act as a semiconductor through the photovoltaic effect to convert this energy into an electrical charge. In practical terms for a modeling framework this can equate to simply multiply G_{eff} of a module by an efficiency (η) factor associated with the module. This simple conversion can enable very rapid assessment frameworks. Rapid rooftop assessment platforms such as Google's Project Sunroof or Mapdwell have been in place for nearly a decade and rely on a combination of photogrammetry and often proprietary algorithms to estimate the shading on a roof due to nearby objects such as trees or buildings. While these tools do allow individuals to assess their rooftop PV potential quickly and with little to no barriers beyond data availability in their own region. While accessible these tools are not extensible to facades and results for the same location vary greatly between models, suggesting a high degree of inaccuracy is present [5]. In Switzerland a public tool called Sonnenfassade [6] exists for any building in the countries database of 3D models and quickly calculates irradiance using a performance ratio (PR) approach It uses this 3D model of a building along with local climatic data and a shade horizon profile built up of nearby mountains, hills, buildings, and vegetation to estimate the average yearly irradiation value in the middle point of the building's façades. This is then multiplied by the façade area and a PV PR of typically 80% to determine an annual potential yield value.

This was improved upon by Saretta et al. (2020) [7] due to a core inability in distinguishing potential windows and balcony type projections on the façade. The update equation uses three reductions factors to more accurately account for facade area based on a statistical database connected the the building age and type.

While more spatially accurate this approach still relies on the *PR* variable which is difficult to calculate without measured data of a similar system or an accurate model of the system. Additionally, a system's PR varies with time and when considering the dynamics of grid pricing and storage is a key parameter to understand. A temporally resolved approach exists in [8, 9], which employs similar methods to characterise potential irradiance, but does so for each hour of the year through the input of Typical Meteorological Year (TMY) weather data and angular modifiers to model reflection on the glass surface of a PV module. Other models exist as well such as Huld's modification of King's model [10] or the PV Watts method [9]. These methods employ more advanced methods of calculating output from the PV cell that are temperature dependent. To calculate module temperature (T_{mod} [°C]) the nominal operating cell temperature (*NOCT* [°C]) model is often employed [11], shown in Eq. 1, where *NOCT* is a parameter typically given on PV module data sheets and T_{air} ([°C]) is the ambient air temperature, and G_{eff} must be given in $[\frac{\text{mW}}{\text{cm}^2}]$.

$$T_{\text{mod}} = T_{\text{air}} + \frac{NOCT - 20}{80} \cdot G_{\text{eff}} \tag{1}$$

While these models employ more complexity to characterise module performance through various uses of cell temperature, but do not increase the level of detail used for calculating G_{eff}. This increase in spatial resolution can be found in the models employed in urban and building energy modeling tools such as in Fonseca et al. (2016) [12] and Waibel et al. (2017) [13]. These approaches use 3D scenes to simulate irradiance on any number of sensor points. In the former surfaces are discretized using a small amount of sensor points, typically 2-5 m^2 per sensor points, to reduce computation time. Daysim [14], a form of the validated lighting simulation engine Radiance [15], is then used to conduct ray tracing for the sensor points, taking into account any obstructions in the scene along with their reflectivity and transparency. The received irradiance is then used with a variation of Eq. 2 to calculate the yield for an hour of the day. Here G_{STC} is the irradiance during standard test conditions (STC) and $P_{\text{DC,STC}}$ [W] the power output. Similarly the latter framework uses ray tracing and view factors to rapidly assess potential irradiance on a sensor point and use it as input to a variation of Eq. 2.

$$P_{\text{DC}} = \frac{G_{\text{eff}}}{G_{\text{STC}}} \cdot P_{\text{DC,STC}} \left(1 + \gamma \left(T_{\text{mod}} - T_{\text{ref}}\right)\right) \tag{2}$$

These methods improve upon the spatial resolution of the irradiance gathering portion of a necessary PV performance modeling framework, but do not necessarily allow modelers to look at the performance of an array from a module-specific perspective, as they still rely on generic parameters for the type of cell. For module-specific calculations a method such as that employed in EnergyPlus [16] is necessary. The Sandia Performance Model (SPM) [17], utilises module and cell specific parameters to characterise the performance of the module being examined. It is also extended into a larger ecosystem of arrays and systems to account for transmission loss, inverter loss, and other factors such as maintenance to provide a value for system-wide grid-ready power $P_{AC,sys}$. The limitation is that while the SPM uses a cell-based approach of sorts it does not record the current-voltage (IV) curve of the module, just the output power for a timestep. This makes assessing its performance within a larger electrical topology such as a central or string inverter based system difficult as one needs to be able to calculate the maximum power point (MPP) that would come from the inverter or maximum power point tracking device (MPPT).

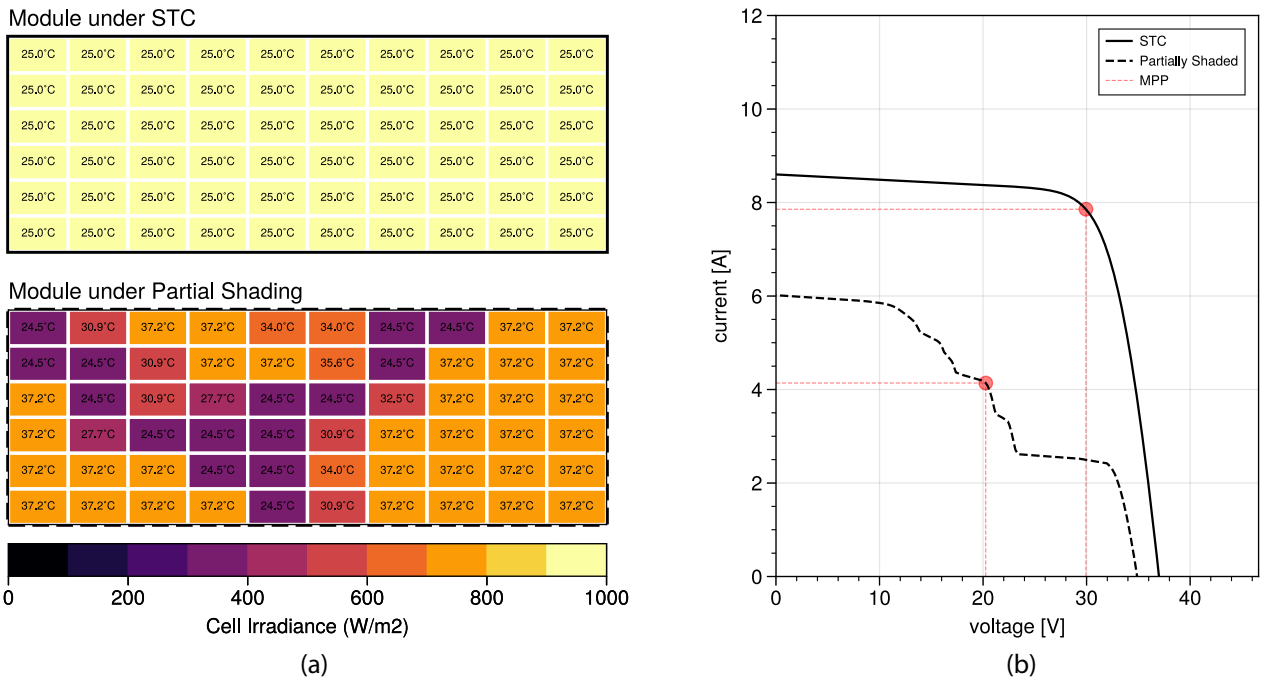

Figure 1: An example of a module under the partial shading of a tree branch (a) and its impact on the IV-curve and power output (b) as compared the a module under standard test conditions. These results were calculated using the proposed framework.

2.2. Existing cell based modeling approaches

When a module is partially shaded, as shown in Figure 1, it operates below optimum. This is due to unshaded cells (high current) reverse-biasing shaded cells (low current) in a string, which leads to overheating in the shaded cells and potential damage, referred to as mismatch. This is mitigated by bypass diodes to reduce the risk of catastrophic failures, but at the expense of total output. It is therefore vital to parameterise these effects in models of PV arrays if they are expected to operate under conditions with a great deal of partial shading. Furthermore, new module types, such as half-cut modules employ less straightforward configurations of cell arrangement and BIPV modules are typically highly customised such that contextualising the cells in module not only in their series placement but also in parallel is necessary to entirely account for the location of bypass diodes.

Additionally, specifying the type of electrical topologies as a part of the modeling framework is necessary to account for the entire impact of partial shading on system performance[18, 19, 20, 21]. This is due to the way in which current and voltage are accumulated when the IV curves of the cells and modules do not match.

Therefore, a highly detailed modeling framework should be able to model the impact of partial shading on a bespoke module's performance as well as throughout a larger electrical topology. Meyers et al. (2017) [22] and Chaudhari et al. (2018) [23] describe a modeling framework for characterising the mismatch in PV cells and modules to better account for partial shading on systems. Walker et al. (2019) [24] developed a workflow to simulate PV modules using a cell-based approach that begins from simulating the irradiance on the cell or an even finer resolution.

Both of the above approaches employ techniques for characterising cell performance that are crucial for modules under highly uneven irradiance such as reverse bias and bypass diodes. Additionally, modelers may want to study arrays with different sized modules (which is common in BIPV design) or explicitly model changes to modules such as front covers for aesthetics, or different bypass diode configurations during parametric optimisation.

3. Methodology, Data, and Tools

In this section we describe the models and methods used to conduct our comparative analysis of PV performance modeling frameworks.

First, we then describe the measured PV yield data (Section 3.1.) to which we compare the proposed framework. For the simulations we use a common monocrystalline module type, Sharp Solar 235Wp (Sharp-NU-U235F2). It was selected due to the availability of its parameters in the California Energy Commission's module

database [1] and it is the sole module found in the measured data. Then, in Section 3.2. the two 3D models that contain the façades and rooftop arrays which we use to compare the performance of the modeling frameworks are described. Then, the four modeling frameworks are summarised. The first (Section 3.3.) is currently common within the literature and employs simpler methods and lower levels of details than the third (Section 3.6.), which is the framework which we are proposing. We also describe the two other levels of detail that operate between these two methods that improve on the spatial resolution of the first, but utilise the same power conversion model; *Module Center* in Section 3.4. and *Cell Center* in Section 3.5..

3.1. Measured Datasets

We use a sub array from a rooftop installation at the United States of America National Institute of Standards and Technology (NIST) to evaulate the performance of the proposed modeling framework's power conversion model. The dataset for the sub array (SC3) is reported on in detail by Boyd (2015) [25]. It contains minute averages for a variety of sensors placed throughout a large rooftop array. The dataset was chosen for its availability and clean data. Ideally the dataset to compare against would be one that is vertically oriented and subject to partial shading. However, to the knowledge of the authors this does not exist. The array comprises of 84 modules of the module mentioned in Section 3.. Of the 84 modules there are seven strings of 12 modules that are combined in parallel to create a single DC output stream. The recorded data from this output was resampled into hourly data and compared against the IV-curve based framework. For the input G_{eff} and T_{cell} we rely on the measured data from within the array. G_{eff} comes from a single silicon reference cell in the array. T_{cell} is a mean value gather from several back-of-module sensors throughout the array. We evaluate the model results using mean absolute error (MAE) and a qualitative comparison of the result distribution.

3.2. 3D Building Geometry

We conduct a comparative analysis between the proposed framework (i.e. *Cell IV*) and the frameworks from the literature to describe the differences in their output and identify situations in which it may not be worth the computational cost of the more detailed method. To make the analysis more relevant to a broader audience we identify two Representative façades to simulate through a clustering analysis of buildings in a district in Zurich Switzerland. A third surface was added as well to compare a minimally obstructed rooftop situation. Clustering was done on building morphology metrics extracted from the urban region following Biljecki et al. (2022) [26]. Principal Component Analysis (PCA) was used to reduce the parameter space before applying a K-Medoids clustering process.[2].

Clustering returned three archetypal buildings, for which the southern-facing façades were extracted. On one of the buildings the extracted façade was unobstructed and it was decided to remove this from the analysis, leaving the two buildings and façades shown in Figure 2. The upper roof section of Building B was used for the roof analysis, where a 30° tilt facing south was assigned to the array. The buildings were modeled in a Rhino/Grasshopper [27] 3D environment and a script was developed to add BIPV and rooftop module arrays with each cell parameterized based on a landscape orientation of the PV module in the NIST dataset. Nearby opaque context was modeled with a 20% reflectivity. A tree exists near one of the residential buildings. This was modeled following Peronato et al. (2018) [28]. The scenes were used for ray-tracing to gather annual irradiance profiles with hourly timesteps.

3.3. Surface-based framework

The existing approach for urban-scale analysis of photovoltaics is to evaluate one or several sensor points on a facade and use those as the basis for the power conversion model. The surface's are discretized using a moderate resolution of two meters between each sensor point to reduce possible error to a negligible amount, as recommended by Peronato et al. (2018) [28]. We remove the area where the window faces intersect with the discretized grid cells to accurately account for the area available to potential PV. In the case of the rooftop array, the flat surface of the roof was split into faces and the center points were assigned the surface normal that would be associated with tilted modules, instead of rotating the faces themselves.

Typically the irradiance simulation would only be done for the sparse sensor points on the surface being analysed. However, due to the stochastic nature of the Radiance engine we use the irradiance map created for the cell-based approach described in a later section. For this we simply take the mean value of the three nearest points to each sensor point on the surface. This irradiance value, for both direct (G_{dir}) and diffuse irradiance (G_{diff}), is used to calculate G_{eff} using Eq. 4 and Eq. 3.

G_{dir} and G_{diff} are simulated for each sensor point using the enhanced 2-Phase ray-tracing method found in Subramanian (2017) [29] using Radiance.[3] They can be modified for any front-covers that an integrated PV module may have using Eq. 3, which in the case of this study is a clear solar glass. Here G_{x0} is the initially calculated irradiance for the sensor point, either direct or diffuse. For f_{loss} a factor is dependant on the colouring

[1] https://www.energy.ca.gov/media/2367

[2] Implementation of the PCA and K-Medoids are from the Python library *scikit-learn*

[3] parameters: -ab 5 -ad 50000 -as 4096 -c 1 -dc 0.75 -dp 512 -dr 3 -ds 0.05 -dt 0.15 -lr 8 -lw 2e-07 -ss 1.0 -st 0.15

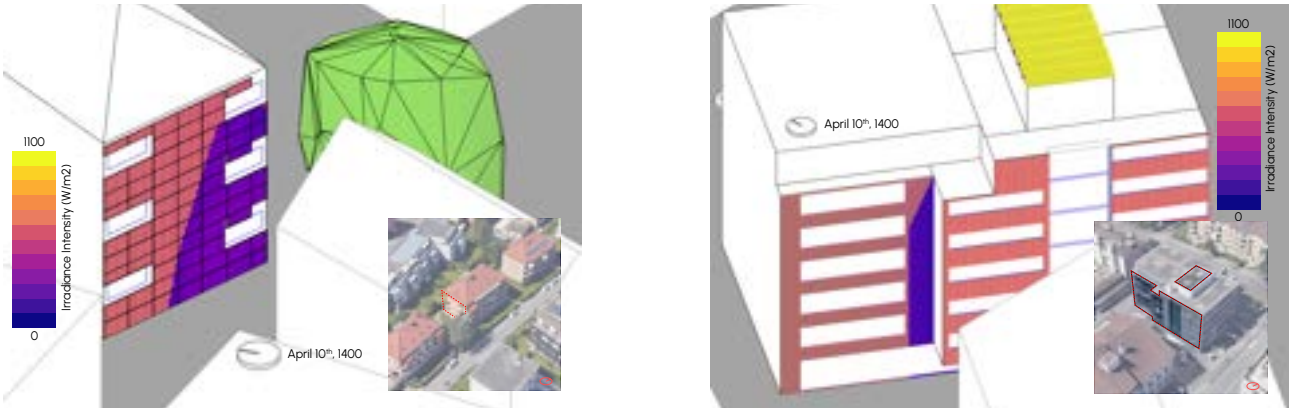

(a) (b)

Figure 2: The two archetypal façades and unobstructed roof (highlighted) used in the study are shown next to their 3D models. In (a) we utilise a lower rise building in the district with a moderately obstructed facade and nearby vegetation. In (b) we utilise a larger facade with more obstruction.

of the front cover and comes from [30].

$$G_x = G_{x0} \cdot (1 - f_{loss}) \tag{3}$$

To calculate G_{eff} for each sensor point we account for the reflectivity of the glass and front cover with an angle of incidence modifier (AOI), shown in Eq. 4 for each timestep based on the location, orientation of the surface, and tilt of the surface.

$$G_{eff} = G_{dir} K(\Theta) + G_{diff} K(60^\circ) \tag{4}$$

K is the angular response factor calculated following Martin and Ruiz (2001) [31], formulated in Eq. 5. K is dependent on Θ and a dimensionless fitting parameter, a_r, which is fixed at 0.17.

$$K = \frac{e^{\frac{1}{a_r}} \left(1 - e^{\frac{\cos(\Theta)}{a_r}}\right)}{e^{\frac{1}{a_r}} - 1} \tag{5}$$

Given G_{eff} of each sensor point, the power conversion model for each hour of the year, shown in Eq. 6, is based on the nominal efficiency of the module(η_{nom}), total surface area available for modules (*area*), and a performance correction dependant on the maximum power temperature coefficient of the module (γ_{ref}) and cell or module temperature (T_{sensor}) which comes from Eq. 1. In this instance we calculate *area* by subtracting the area of windows found within each discretized section the façade from the area of the section. We account for losses in the system due to soiling, cabling, and inverter loss using I_{misc}, which is fixed at 0.10.

$$P_{AC} = \left(\frac{G_{eff}}{G_{stc}} \cdot P_{peak} \cdot [1 + \gamma_{ref} (T_{sensor} - T_{stc})]\right) \cdot (1 - I_{misc}) \tag{6}$$

For the surface-based analysis we calculate P_{peak} using Eq. 7 where $P_{nameplate}$ denotes the standard module capacity, $C_{nameplate}$ denotes the number of cells in a standard module, $A_{nameplate}$ denotes the area of the standard module, and A_{face} denotes the area associated with sensor point in the discretized surface:

$$P_{peak} = \frac{P_{nameplate}}{C_{nameplate}} \cdot \frac{C_{nameplate}}{A_{nameplate}} \cdot A_{face} \tag{7}$$

3.4. Module-based framework

To represent another existing approach to modeling the performance of PV in urban arrays we evaluate simulated performance of modules placed into the surfaces analysed in the previous method. The modules are assessed using a single irradiance sensor point located at the module's center and the power conversion model of Eq. 6, with the only difference being the input for P_{peak} where we employ each module's unique size. The modules are created in a 3D model of the surface which begins by assuming that no windows or impediments exist on the surface. Where they does exist the modules are cut into smaller rectangles. Then we replace A_{face} in Eq. 7 with the area of each individual module.

3.5. Cell-based framework

We increase the resolution of the previous framework by calculating power for the center point of each cell in the array's modules using Eq. 6. The modules modeled in the previous framework are discretized by the cell dimensions, frame width, and spacing between the frame. The input for A_{face} in Eq. 7 is then calculated based on the cell dimensions.

3.6. IV curve-based framework

In this section we describe the proposed modeling framework for high-resolution BIPV analysis that is the focus of this paper. Given the spatially discretized grid from the previous approach we improve the model resolution here by changing the power model. We build on an existing approach for cell-based modeling found in Walker et al. [24]. With this approach we have included a more flexible input for the module type that enables the use of module sizes that are non-standard, which is common in BIPV design and occurs in the 3D models being assessed in this study. With the modules and cells modeled in the 3D space, string connections of modules are built up by first grouping modules of the same cell count into strings. Then the string with the standard module size is split into separate strings with each string having the same modules of the same vertical height. In preparation for the power calculation, each module is assigned four numerical arrays. The first contains the Cartesian position of each cell's center point. The second contains the surface normal of the cells. The third represents to which bypass diode in the module that each cell belongs to. The final is used if a module has multiple sub-modules in parallel, such as in a Half-Cut module, and represents to which sub-module each cell belongs.

G_{eff} is calculated in the same way as the previous framework but is applied to a different power model. The power conversion model is more detailed in this approach as we calculate the IV-curve for each cell. Then, the module IV-curve is compiled based on bypass diodes and string or parallel connections. With each module's IV characteristics, we evaluate the arrays for several electrical topologies: micro-inverter, string inverter, central inverter.

The initial IV-curve for a cell is calculated following Bishop (1988) [4], using Eq. 8. This formulation follows the common single-diode equivalent circuit model that is also applied by EnergyPlus [16] and in the method of Walker et al. (2019) which we build upon. It is assumed that a single cell can be modeled as a portion of the larger module. This is important as the parameters necessary for the single-diode model are typically only given for a module as it was characterised during manufacturer testing. This approach uses the five-parameter input from De Soto et al. (2006) [32]. This uses G_{eff}, T_{cell} (which comes from Eq. 1), the short-circuit temperature coefficient (α_{sc}), diode ideality factor (n_D), number of cells in series (N_{s}), the thermal voltage across the cell (V_{th}), light generated photocurrent at reference conditions ($I_{\text{L,ref}}$), diode reverse saturation current at reference conditions ($I_{0,\text{ref}}$), shunt resistance at reference conditions ($R_{\text{sh,ref}}$), and series resistance at reference conditions ($R_{\text{s,ref}}$). The calculations provided by De Soto et al. produce the diode voltage (V_{d}), photocurrent (I_{L}), saturation current (I_0), series resistance (R_{s}), shunt resistance (R_{sh}), and *nNsVth*. We use the default parameters for breakdown factor (a, 0.0), breakdown voltage (V_{br}, -5.5), and the breakdown exponent (m, 3.28). We include $\frac{d^2}{\mu\tau}$ for completeness, but it is not used in this study as it is only relevant for amorphous silicon cells, therefore it is assigned a value of 0. With the parameters assembled the IV-curve is calculated for each cell, envisioning it as a single module. The resulting curve's V values are divided by the number of cells in series and the I values are divided by the number of cells in parallel.

$$I = I_{\text{L}} - I_0 \left(\exp \frac{V_{\text{d}}}{nN_s V_{\text{th}}} - 1 \right) - \frac{V_{\text{d}}}{R_{\text{sh}}} - \frac{I_{\text{L}} \frac{d^2}{\mu\tau}}{N_s V_{\text{bi}} - V_{\text{d}}} - a \frac{V_{\text{d}}}{R_{\text{sh}}} \left(1 - \frac{V_{\text{d}}}{V_{\text{br}}} \right)^{-\text{m}} \tag{8}$$

This model enables the characterisation of the cell in the second quadrant of the IV-curve plot. This is the characterisation of the reverse-bias potential of the cell. If two cells with mismatched curves are connected in series and operated with the more illuminated cell's maximum power potential, then the less illuminated cell will draw current from the first cell. Thus, the real operation of these cells would require the more illuminated cell to be operated at the level of the lower cell, limiting maximum power potential (MPP). It is this phenomenon that is common in partial shading and we suspect is not well captured in the other three frameworks. Using this approach all cell IV-curves are calculated and first connected in series within each diode pathway, following Kirchoff's circuit laws. Then the various diode pathways of a module are connected in series. If parallel connections exist within the module then these are made to finalise the characterisation of each module's IV-curve.

From here the approach branches to simultaneously evaluate performance of the array using multiple electrical topologies. This is essential for properly characterising MPP in each module as explained earlier, devices under different illumination can limit each other to avoid reverse-bias.

First, individual modules are evaluated using a micro-inverter approach where DC to AC inversion occurs

along with the maximum power point tracking (MPPT). Then, using the same principles of series and parallel connection within the module, strings of modules are connected and the MPPT and inversion is applied to extract MPP for each string. Lastly, strings are connected in parallel to evaluate their power using a single central inverter. We apply a simple 95% inverter efficiency to all inverter operations.

4. Results & Discussion

Here we present and analyse the results of the two portions of the study. First, the proposed modeling framework is evaluated alongside a measured dataset. Second, the simulation results of the proposed framework and surface-based framework are compared.

4.1. Evaluation of High-Resolution Proposed Framework

Figure 3 describes the two power outputs against G_{eff} with a linear curve fitted to the data scatter. Qualitatively, we observe generally good agreement between the two models at lower irradiance levels. However, with higher irradiance levels the proposed model produces a larger P_{DC} response. MAE and root mean squared error (RMSE) of the two data sets is 0.73 kWh, and 1.41 respectively. Additionally, we do not observe in the modeled data very low P_{DC} response at high levels of irradiance, such as seen in the measurement data. We suspect that in this case that much of the measurement array was covered by a shadow, but the censor cell was not. Despite these points the standard deviation and variance of the measurement dataset is lower than that of the model output.

The lack of multiple sensors throughout the array impedes our ability to model the array under heterogeneous conditions, which is likely closer to reality. Factors such as cloud cover that may cover much of the array while the sensor cell is still directly illuminated would then not be captured by the model. This could lead to the over prediction that we witness. Additionally, the proposed framework is meant for vertical facades in an environment with a lot of shading and a only slightly ventilated air cavity between the model and mounting surface. A dataset that contains these attributes would be a better tool to evaluate and eventually validate the proposed framework.

4.2. Comparison of Modeling Frameworks

Here we compare the outputs of the modeling frameworks and discuss their implications for use in larger models. First we evaluate the received irradiance for each framework. Irradiance results for each framework are influenced by the number of sensor points available to the ray-tracing simulation as this allows the ray-tracing to more accurately depict objects that might shade the receiving surface. In Figures 4a-4c we show difference between the irradiance, normalised by available surface area, levels across both of the 3D models through their probability distribution functions. A trend emerges with each in that the *Cell Center* and *Cell IV* framework have overlapping curves, while the *Surface Face* is closely aligned, and the *Module Center* framework contains a time series of larger values. This is due to the self-shading of the array not being captured by the center point on the module, whereas in the *Cell Center* and *Cell IV* a shared sensor grid is used that has many points. The close alignment of the *Surface Face* model is interesting, due to it having many less sensor points. This is worthwhile for future research.

In Figure 5a we show the discretized modules of the Commercial Building's rooftop array. The selected date was chosen for being the hour of the year with the maximum variance amongst the G_{eff} values within each modules, the value being indicated in Table 2. We can see that for the majority of the modules there is a shaded section caused by the module in front. This leads to a high degree of variance across the module. In the case of the *Module Center* the shaded portion of the module is not captured as only the central point is

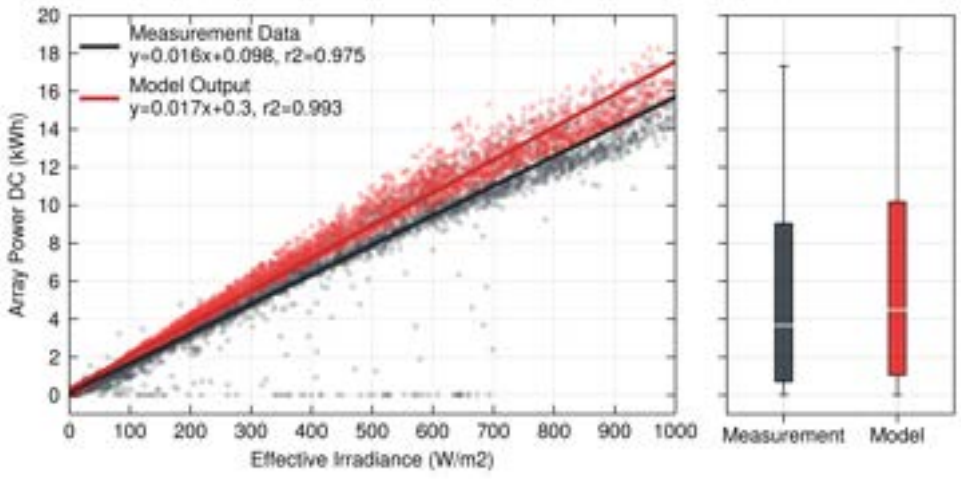

Figure 3: Linear regression of measurement and modeled data where $G_{\text{eff}} > 0$.

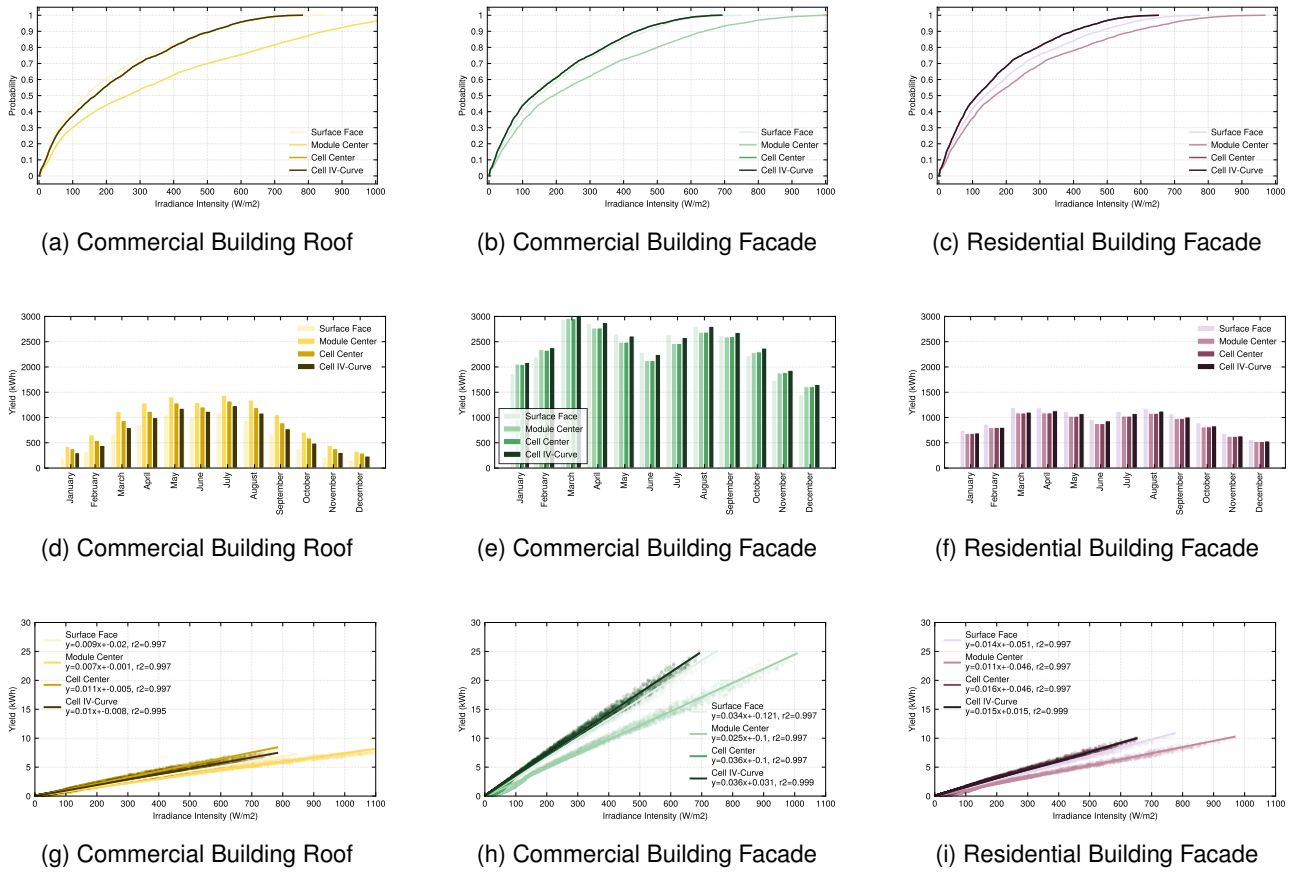

(a) Commercial Building Roof (b) Commercial Building Facade (c) Residential Building Facade

(d) Commercial Building Roof (e) Commercial Building Facade (f) Residential Building Facade

(g) Commercial Building Roof (h) Commercial Building Facade (i) Residential Building Facade

Figure 4: Comparison of the results of the simulations for each of the frameworks. (a-c) The probability distribution function for the irradiance intensity time series (8760 hours) for each of the three surfaces examined. (d-f) Yield comparison resampled for monthly sums. (g-i) Linear regression of the irradiance intensity of the module and the yield for each framework on the three arrays.

sampled to calculate G_{eff}. This inability to capture self-shading extends to the *Surface Face* framework as well, but due to the lack of rotation of the face the total irradiance available to these surfaces is limited anyway.

Looking at the other arrays in Table 2 we see some degree of variance across the modules but with means around 1 and 3 $\frac{W}{m^2}$. This contributes to the yield of the arrays being more consistent amongst the different frameworks, shown in Figures 4e-4f.

Simpler models such as the *Module Center* of *Cell Center* could be used in place of the much more computationally expensive *Cell IV* approach if the conditions for shading are met. In Figures 4g-4i we show linear regression of yield and irradiance intensity on the module. As the variance found in the Commercial Facade and Residential Facade are quite low the regressed models fit the data well. While still a good fit, the lowest r^2 is seen in the *Cell IV* framework of the Commercial Rooftop where, the regression is fit to a wider spread of data points. For the same levels of irradiance intensity different levels of yield are found. This is because the plot shows the irradiance intensity across the entire array, and does not reflect the activity in the modules under mismatch conditions. The results shown for the *Cell IV* framework are those for a system with micro-inverters. This type of electrical topology is able to handle the mismatch conditions well as maximum power (MP) tracking occurs at the module level. We show in Figure 5b the same array conditions in Figure 5a. Here the string inverter system controls the MP of each row of modules independently while the central inverter controls the MP of all modules. We see a drop in the yield if the system is configured with a central inverter due to the need of the system to operate the southern-most row of modules at the same level as the other strings.

Computationally speaking the *Cell IV* approach requires the most setup, although all require the same 3D geometry. From a computational standpoint the *Cell IV* require on average 800 seconds for each simulation of a surface, while the other methods require around 120 seconds.[4]

[4]These numbers come from operating the models on a 2021 Macbook Pro with 8-cores (ARM).

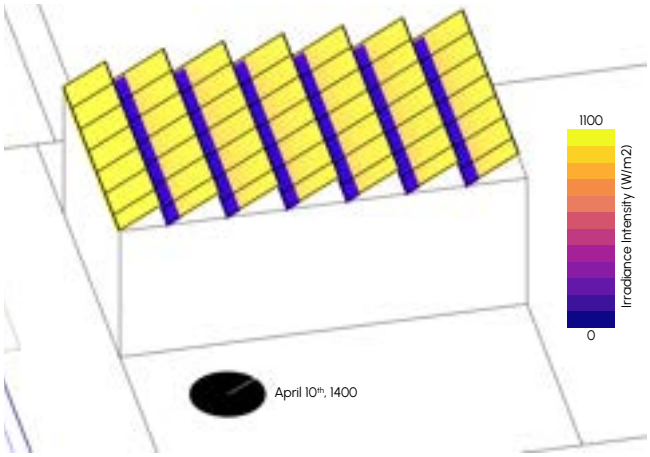

(a)

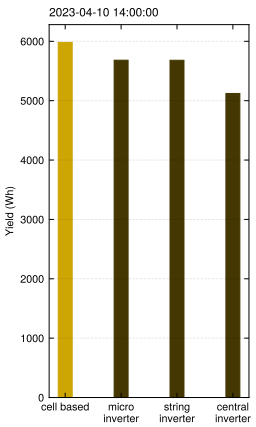

(b)

Figure 5: The irradiance intensity for the rooftop array on the 1st of April at 1400 (a) and the comparison (b) of power output of the array for all three electrical topologies and the *Cell Center* framework

	Commercial Roof	Commercial Facade	Residential Facade
mean	70.355	0.994	3.134
std	76.694	1.363	6.216
min	0.109	0.001	0.004
25%	9.591	0.204	0.345
50%	35.793	0.575	0.94
75%	115.716	1.228	2.087
max	319.586	12.575	55.133

Table 2: The descriptive statistics for the standard deviation found within the effective irradiance (W/m2) for each module's cell points across the year in each of the three arrays.

5. Conclusion

In this paper we proposed a detailed modeling framework for the simulation of building-based PV performance through the characterisation of system-wide IV-curves. This approach is based on existing work in the field with some adjustments to capture a variety of potential electrical topologies. We evaluated this model's performance against measured data and found that the model generally over-predicts, with a mean absolute error of 0.65 kWh. We propose that to better tune the framework a better measurement dataset is needed that can provide a more comprehensive picture of array-wide irradiance and cell temperature characteristics. Additionally, the measurement data should be for vertical arrays under partial shading.

We compared the proposed framework to three common approaches found in the literature. We found that in systems with self shading, the proposed framework is capable of capturing the impact on the modules while surface based and module center based methods are not. The similarly spatially accurate cell center based framework yields similar results, but with less computational expense. The three frameworks found in the literature do not provide a way to compare between electrical topologies, which in the case of partially shaded modules is necessary to evaluate which topology to choose. If you need to analyse different electrical topologies the *Cell IV* framework is necessary.

Beyond this, more research is necessary to compare this framework to the proposed to determine in what cases the more expensive method should be used. We believe though that this suggests that the type of shading cast on the array is important in determining which model is necessary to most accurately predict system yield. Future research should be dedicated to understanding the shading profiles and objects that occlude arrays in order to classify them so we might use the type of shading to select the power conversion model.

Acknowledgments

This research was conducted at the Future Cities Lab Global at ETH Zurich. Future Cities Lab Global is supported and funded by the National Research Foundation, Prime Minister's Office, Singapore under its Campus for Research Excellence and Technological Enterprise (CREATE) programme and ETH Zurich (ETHZ), with additional contributions from the National University of Singapore (NUS), Nanyang Technological University (NTU), Singapore and the Singapore University of Technology and Design (SUTD).

References

[1] Christoph Waibel et al. “Sensitivity analysis on optimal placement of façade based photovoltaics”. In: *Proceedings of the 31st international conference on efficiency, cost, optimization, simulation and environmental impact of energy systems*. ECOS 2018. ISBN: 9789729959646. Guimarães, Portugal: Universidade do Minho., 2018, 12 pp. URL: https://www.dora.lib4ri.ch/empa/islandora/object/empa%3A22695/ (visited on 11/08/2022).

[2] Iris van Beuzekom, Bri-Mathias Hodge, and Han Slootweg. “Framework for optimization of long-term, multi-period investment planning of integrated urban energy systems”. In: *Applied Energy* 292 (2021), p. 14. DOI: 10.1016/j.apenergy.2021.116880. URL: https://doi.org/10.1016/j.apenergy.2021.116880.

[3] Georgios Mavromatidis and Ivalin Petkov. “MANGO: A novel optimization model for the long-term, multi-stage planning of decentralized multi-energy systems”. In: *Applied Energy* 288 (Apr. 15, 2021), p. 116585. ISSN: 0306-2619. DOI: 10.1016/j.apenergy.2021.116585. URL: https://www.sciencedirect.com/science/article/pii/S030626192100129X (visited on 04/11/2022).

[4] J.W. Bishop. “Computer simulation of the effects of electrical mismatches in photovoltaic cell interconnection circuits”. In: *Solar Cells* 25.1 (Oct. 1988), pp. 73–89. ISSN: 03796787. DOI: 10.1016/0379-6787(88)90059-2. URL: https://linkinghub.elsevier.com/retrieve/pii/0379678788900592 (visited on 07/21/2022).

[5] Sergio Castellanos, Deborah A Sunter, and Daniel M Kammen. “Rooftop solar photovoltaic potential in cities: how scalable are assessment approaches?” In: *Environmental Research Letters* 12.12 (Dec. 1, 2017), p. 125005. ISSN: 1748-9326. DOI: 10.1088/1748-9326/aa7857. URL: https://iopscience.iop.org/article/10.1088/1748-9326/aa7857 (visited on 03/06/2023).

[6] SFOE. *Sonnenfassade*. 2020. URL: http://www.sonnendach.ch (visited on 03/29/2022).

[7] Erika Saretta, Pierluigi Bonomo, and Francesco Frontini. “A calculation method for the BIPV potential of Swiss façades at LOD2.5 in urban areas: A case from Ticino region”. In: *Solar Energy* 195 (Jan. 2020), pp. 150–165. ISSN: 0038092X. DOI: 10.1016/j.solener.2019.11.062. URL: https://linkinghub.elsevier.com/retrieve/pii/S0038092X19311624 (visited on 03/13/2022).

[8] JRC. *Photovoltaic Geographical Information System (PVGIS)*. Version 5.2. Mar. 2023. URL: https://re.jrc.ec.europa.eu/pvg_tools/en/ (visited on 03/06/2023).

[9] NREL. *PVWatts Calculator*. Version 8.1.0. Golden, CO, Mar. 2023. URL: https://pvwatts.nrel.gov/ (visited on 03/06/2023).

[10] Thomas Huld et al. “A power-rating model for crystalline silicon PV modules”. In: *Solar Energy Materials and Solar Cells* 95.12 (Dec. 2011), pp. 3359–3369. ISSN: 09270248. DOI: 10.1016/j.solmat.2011.07.026. URL: https://linkinghub.elsevier.com/retrieve/pii/S0927024811004442 (visited on 03/06/2023).

[11] Ronald G. Ross. “Characterization of photovoltaic array performance: An overview”. In: *Solar Cells* 18.3 (Sept. 1986), pp. 345–352. ISSN: 03796787. DOI: 10.1016/0379-6787(86)90133-X. URL: https://linkinghub.elsevier.com/retrieve/pii/037967878690133X (visited on 03/20/2023).

[12] Jimeno A. Fonseca et al. “City Energy Analyst (CEA): Integrated framework for analysis and optimization of building energy systems in neighborhoods and city districts”. In: *Energy and Buildings* 113 (Feb. 2016), pp. 202–226. ISSN: 03787788. DOI: 10.1016/j.enbuild.2015.11.055. URL: https://linkinghub.elsevier.com/retrieve/pii/S0378778815304199 (visited on 03/30/2022).

[13] Christoph Waibel, Ralph Evins, and Jan Carmeliet. “Efficient time-resolved 3D solar potential modelling”. In: *Solar Energy* 158 (Dec. 2017), pp. 960–976. ISSN: 0038092X. DOI: 10.1016/j.solener.2017.10.054. URL: https://linkinghub.elsevier.com/retrieve/pii/S0038092X17309349 (visited on 03/06/2023).

[14] MIT Sustainable Design Lab. *DAYSIM*. original-date: 2016-02-24T16:00:14Z. July 8, 2022. URL: https://github.com/MITSustainableDesignLab/Daysim (visited on 11/23/2022).

[15] LBNL ETA. *Radiance*. Version 5.3. Golden, CO, Sept. 2020. URL: https://github.com/LBNL-ETA/Radiance/releases/tag/012cb178.

[16] NREL. *EnergyPlus*. Version 22.2.0. Golden, CO, Mar. 2023. URL: https://github.com/NREL/EnergyPlus/releases/tag/v22.2.0 (visited on 03/06/2023).

[17] Jay Kratochvil, William Boyson, and David King. *Photovoltaic array performance model*. SAND2004-3535, 919131. Aug. 1, 2004, SAND2004–3535, 919131. DOI: 10.2172/919131. URL: https://www.osti.gov/servlets/purl/919131/ (visited on 03/06/2023).

[18] K. Sinapis et al. “A comprehensive study on partial shading response of c-Si modules and yield modeling of string inverter and module level power electronics”. In: *Solar Energy* 135 (Oct. 2016), pp. 731–741. ISSN: 0038092X. DOI: 10.1016/j.solener.2016.06.050. URL: https://linkinghub.elsevier.com/retrieve/pii/S0038092X16302316 (visited on 03/14/2022).

[19] Chris Tzikas and Gabriela Gómez. “Do Thin Film PV Modules Offer an Advantage Under Partial Shading Conditions?” In: *Proceedings of the 33rd European Photovoltaic Solar Energy Conference and Exhibition*. European Photovoltaic Solar Energy Conference and Exhibition. Amsterdam, the Netherlands: EU PVSEC, Nov. 2017, p. 5.

[20] Simon Ravyts et al. “Impact of photovoltaic technology and feeder voltage level on the efficiency of façade building-integrated photovoltaic systems”. In: *Applied Energy* 269 (July 2020), p. 115039. ISSN: 03062619. DOI: 10.1016/j.apenergy.2020.115039. URL: https://linkinghub.elsevier.com/retrieve/pii/S0306261920305511 (visited on 03/27/2022).

[21] Konstantinos Spiliotis et al. “Electrical system architectures for building-integrated photovoltaics: A comparative analysis using a modelling framework in Modelica”. In: *Applied Energy* 261 (Mar. 2020), p. 114247. ISSN: 03062619. DOI: 10.1016/j.apenergy.2019.114247. URL: https://linkinghub.elsevier.com/retrieve/pii/S0306261919319348 (visited on 03/14/2022).

[22] Bennet Meyers and Mark Mikofski. “Accurate Modeling of Partially Shaded PV Arrays”. In: *2017 IEEE 44th Photovoltaic Specialist Conference (PVSC)*. 2017 IEEE 44th Photovoltaic Specialist Conference (PVSC). June 2017, pp. 3354–3359. DOI: 10.1109/PVSC.2017.8521559.

[23] Chetan Chaudhari et al. “Quantification of System-Level Mismatch Losses using PVMismatch”. In: *2018 IEEE 7th World Conference on Photovoltaic Energy Conversion (WCPEC) (A Joint Conference of 45th IEEE PVSC, 28th PVSEC & 34th EU PVSEC)*. 2018 IEEE 7th World Conference on Photovoltaic Energy Conversion (WCPEC) (A Joint Conference of 45th IEEE PVSC, 28th PVSEC & 34th EU PVSEC). ISSN: 0160-8371. June 2018, pp. 3626–3629. DOI: 10.1109/PVSC.2018.8548107.

[24] Linus Walker, Johannes Hofer, and Arno Schlueter. “High-resolution, parametric BIPV and electrical systems modeling and design”. In: *Applied Energy* 238 (Mar. 2019), pp. 164–179. ISSN: 03062619. DOI: 10.1016/j.apenergy.2018.12.088. URL: https://linkinghub.elsevier.com/retrieve/pii/S0306261918319044 (visited on 03/14/2022).

[25] Matthew T. Boyd. *High-Speed Monitoring of Multiple Grid-Connected Photovoltaic Array Configurations*. NIST TN 1896. National Institute of Standards and Technology, Oct. 2015, NIST TN 1896. DOI: 10.6028/NIST.TN.1896. URL: https://nvlpubs.nist.gov/nistpubs/TechnicalNotes/NIST.TN.1896.pdf (visited on 03/08/2023).

[26] Filip Biljecki and Yoong Shin Chow. “Global Building Morphology Indicators”. In: *Computers, Environment and Urban Systems* 95 (July 2022), p. 101809. ISSN: 01989715. DOI: 10.1016/j.compenvurbsys.2022.101809. URL: https://linkinghub.elsevier.com/retrieve/pii/S0198971522000539 (visited on 11/08/2022).

[27] Robert McNeel \& Associates. *Rhinoceros 3D*. Version Rhino 7.18.22145.08132. May 25, 2022.

[28] Giuseppe Peronato, Emmanuel Rey, and Marilyne Andersen. “3D model discretization in assessing urban solar potential: the effect of grid spacing on predicted solar irradiation”. In: *Solar Energy* 176 (Dec. 1, 2018), pp. 334–349. ISSN: 0038-092X. DOI: 10.1016/j.solener.2018.10.011. URL: https://www.sciencedirect.com/science/article/pii/S0038092X18309861 (visited on 03/13/2022).

[29] Sarith Subramaniam. *Daylighting Simulations with Radiance using Matrix-based Methods*. Berkeley: LBNL Energy Technologies Area, Oct. 2017.

[30] Arne Røyset, Tore Kolås, and Bjørn Petter Jelle. “Coloured building integrated photovoltaics: Influence on energy efficiency”. In: *Energy and Buildings* 208 (Feb. 2020), p. 109623. ISSN: 03787788. DOI: 10.1016/j.enbuild.2019.109623. URL: https://linkinghub.elsevier.com/retrieve/pii/S0378778819322091 (visited on 03/16/2022).

[31] N. Martin and J. M. Ruiz. “Calculation of the PV modules angular losses under field conditions by means of an analytical model”. In: *Solar Energy Materials and Solar Cells* 70.1 (Dec. 1, 2001), pp. 25–38. ISSN: 0927-0248. DOI: 10.1016/S0927-0248(00)00408-6. URL: https://www.sciencedirect.com/science/article/pii/S0927024800004086 (visited on 07/12/2022).

[32] W. De Soto, S. A. Klein, and W. A. Beckman. “Improvement and validation of a model for photovoltaic array performance”. In: *Solar Energy* 80.1 (Jan. 1, 2006), pp. 78–88. ISSN: 0038-092X. DOI: 10.1016/j.solener.2005.06.010. URL: https://www.sciencedirect.com/science/article/pii/S0038092X05002410 (visited on 03/29/2022).

PROCEEDINGS OF ECOS 2023 - THE 36TH INTERNATIONAL CONFERENCE ON
EFFICIENCY, **C**OST, **O**PTIMIZATION, **S**IMULATION AND ENVIRONMENTAL IMPACT OF ENERGY SYSTEMS
25-30 JUNE 2023, LAS PALMAS DE GRAN CANARIA, SPAIN

From local energy communities towards national energy system: a grid-aware techno-economic analysis

Cédric Terrier[a], Joseph Loustau[b] and François Maréchal[c]

[a] EPFL, Sion, Switzerland, cedric.terrier@epfl.ch
[b] EPFL, Sion, Switzerland, joseph.loustau@epfl.ch
[c] EPFL, Sion, Switzerland, francois.marechal@epfl.ch

Abstract:

Energy communities are key actors in the energy transition since they optimally interconnect renewable energy capacities with the consumers. Despite versatile objectives, they usually aim at improving the self-consumption of renewable electricity within low voltage electricity networks to maximize the revenues of the community. In addition, energy communities are an excellent opportunity to supply renewable electricity to regional and national grids. However, effective price signals have to be designed to coordinate the needs of the energy infrastructure with the interests of local stakeholders.

The aim of this paper is to demonstrate the potentials of energy communities at the national level with a bottom-up approach. A district energy system having a building scale resolution is modelled in a mixed integer linear programming problem. The Dantzig-Wolfe decomposition is applied to reduce the computational time. The methodology lies within the framework of renewable energy hub, characterized by a high share of photovoltaic. Both investments into energy capacities and their operation are considered. The model is applied on a set of typical districts and weather locations representative of the whole Switzerland.

The extrapolation to the national scale revealed a heterogeneous photovoltaic potential throughout the country. The actual electricity tariffs promote maximal investment into photovoltaic panels in every region, reaching a capacity of 28 GW and generating 32 TWh per year. Since the forecast national energy need is between 12 and 18 TWh per year, a coordinated design is needed to prevent unnecessary investments. An uncoordinated design increases the total costs of the residential energy system by 31% and curtails 24% of the onsite generated electricity. Moreover, the $CO_{2,eq}$ emission of the unnecessary investment is equivalent to 9% of the actual emissions in the residential sector.

Keywords:

Energy communities; Renewable energy hub; National systems integration; MILP; Multi-objective optimization

1. Introduction

In 2018, the European Parliament has emphasized the role of energy communities in the energy transition and has set up directives to facilitate their creation [1]. Their purpose includes the penetration of renewable energies, the reduction of energy poverty [1], the enhancement of technological acceptance [2] and the improvement of the democratic process [3]. Energy communities aim at supplying the energy needs with high self-consumption of local energy sources. The reduction of the electricity grid reliance prevents costly grid reinforcements, therefore supporting a rapid electrification of the heating and mobility services. By 2050, Photovoltaic (**PV**) installations are expected to represent 50% of the electricity generation capacity worldwide [4]. More specifically, in Switzerland, the electricity demand is expected to reach 55 TWh/yr in 2050, from which 33 TWh/yr will be supplied by hydro power [5, 6]. The remaining electricity will mainly be supplied by PV capacities (11 TWh/yr), wind turbine (4.2 TWh/yr) and geothermal energy (4.3 TWh/yr). The success of PV integration seems to rely on a coordinated integration of energy communities within the infrastructure [1]. The involvement of these actors in investments and operation decisions dictates the energy flows exchanged between the communities and the infrastructure, ultimately affecting the whole energy network structure.

The definition of an energy community is broad but a consensus estimates that it is a local energy system possessing distributed sustainable energy conversion units, both on the supply and demand sides [2]. The concept of energy hub is usually used to model such systems. Multi-energy sources supply a multi-service demand with conversion units being optimally interconnected and operated. Extensive reviews have been carried out on this topic [7, 8]. The scale considered varies from local energy hubs, such as a residential area to

large scale systems including a whole country. Energy communities are usually built at the neighborhood scale since the proximity facilitates the community governance while being large enough to promote an economy of scale. Based on the literature review (Table 1), the scope of the studies mostly consider a single case study on a neighborhood, resulting in a lack of generality. Some studies investigated the broad impact of local residential systems with typical clusters and extrapolation but the scope relied on single building energy system [9, 10]. Therefore, the potential of energy communities to support the energy transition of the overall infrastructure with renewable integration is yet not assessed.

Table 1: Literature review on energy communities: The resolution indicates the considered scale for the investment or demand profiles. The approach shows how the authors handled the complexity of the problem, either by simplifications or by decomposition. The interdependent system feature highlights whether the study considered decision interactions between buildings and between national and local decisions.

Case study		Method		Analysis				
Scope	Resolution	Model	Approach	Regions dependant	National scope	Systemic constraints	Interdependent systems	Reference
Country	Building	MILP	Clustering	✓	✓	✗	✗	[9]
Country	Building	MILP	Clustering	✓	✓	✗	✗	[10]
District	Building	MILP	Pre-selection/profiles	✗	✗	✗	✓	[11]
District	Building	MILP	Profiles	✗	✗	Grid	✗	[12]
District	District	MILP	Profiles	✗	✗	✗	✗	[13]
City	Building	Simulation	Pre-selection	✗	✗	✗	✗	[14]
District	Building	Simulation	Pre-selection/scenario	✗	✗	✗	✗	[15]
District	Building	MILP	Bi-level	✗	✗	✗	✓	[16]
District	District	MILP	Scenario	✗	✗	✗	✗	[17]
District	Building	MILP	Scenario	✗	✗	✗	✗	[18]
District	Building	MINLP	Bi-level	✗	✗	Grid	✓	[19]
District	Building	MILP	Dantzig-Wolfe	✗	✗	✗	✓	[20]
District	Building	MILP	Dantzig-Wolfe	✗	✗	✗	✓	[21]
District	Building	MILP	Profiles	✗	✗	✗	✗	[22]
District	Building	MILP	Benders	✗	✗	✗	✓	[23]
District	Building	MILP	Bi-level	✗	✗	Grid	✓	[24]
District	District	MILP	Rolling horizons + pre-selection	✗	✗	✗	✗	[25]
Country	Building	MILP	Dantzig-Wolfe + clustering	✓	✓	Grid	✓	This paper

Due to its network structure, modeling an energy community at the district scale with building scale resolution usually exceed the computational power. Facing this problem, a popular method is to fix some degrees of freedom by making assumptions and scenarios based on expert knowledge (Table 1). As an example, half of the literature is assuming energy demand profiles or pre-determines the energy system configuration. To promote grid services and renewable energy supply, energy communities should be approached from a service demand perspective rather than an energy demand one. This change of approach is beneficial since it does not assume the type of conversion units [26]. Therefore, it provides flexibility to consider additional constraints, such as the infrastructure capacity or trade-offs between investment and operational costs. In addition, considering each sub-systems within a single optimization reveals the inter-dependency of the decisions and do not force the acceptance of a decision without accounting for the interests of the actors concerned [26]. Therefore, assumptions and scenarios should be considered with care since they tend to oversimplify the view on the problem. Despite the extensive literature existing on the topic of energy communities, a holistic framework is usually not considered.

The main limitations found in the literature are the assumption taken on the type of conversion units installed and the lack of systemic understanding on the role of energy communities. It is yet not clear to which extent these communities can supply renewable electricity to the national energy system considering the actual infrastructure capacity. The performance extrapolation of various local case studies to the national scope is very rare in the literature. Therefore, based on these research gaps, the present study aims at answering the following research questions:

- What are the investment and operation decisions taken within energy communities?
- How does the decisions change with the geographic context?
- What is the potential for energy communities to supply renewable electricity in a country?
- What is the impact to consider the infrastructure capacity constraints?

2. Methodology

The energy community is modelled as a renewable energy hub, being defined as a system optimally interconnecting multi-energy streams and conversion units [27]. Additionally, the energy hub is characterized by a high share of renewable energy and aims at maximizing self-consumption. The renewable energy hub is at the district scale within a low-voltage electricity grid deserved by a low to medium voltage transformer. Service demands of each building, such as domestic hot water, domestic electricity and space heating, are supplied by conversion units and a gas and electricity utility. A mixed integer linear programming (**MILP**) formulation optimizes the investment into conversion units and the operation of the energy system. The main decision variables are the decision to install a unit (binary variables) and the size of the units installed (continuous variables). The conversion units include thermal units (air-water heat pumps, gas boilers, electrical heaters) and storage units (thermal tanks and lithium ion batteries). PV panels are the main source of renewable electricity and can be installed on the roof and facades of buildings. Their orientation is a decision variable as described by Middelhauve et al. [27].

Energy and mass balances as well as heat cascade are the main constraints of the model. Electricity and natural gas balances are applied at the building and district scale, allowing synergies between buildings and between energy carriers. Equation (1a) shows the electricity balance between the building electricity fluxes $\dot{E}^{gr}_{b,p,t}$ and the LV/MV transformer exchanges $E^{tr}_{p,t}$. A positive symbol represents an import of energy and a negative one an export. Decision variables are highlighted with **bold** characters. Additionally, technical constraints are considered to model conversion unit and to account systemic capacity. Constraint (1b) is applied to restrict the power exchanged on the transformer level to a specified value $\dot{E}^{tr,max}$. The electricity balance allows sharing renewable electricity within the community to increase the self-consumption, thus reducing operating costs and minimizing the transformer usage. To reduce computational burdens time series are clustered into typical and extreme operating periods using the K-medoids algorithm. The model consider four sets: buildings B, typical periods P, timesteps of the typical period T and units U. More details on the problem formulation are given in the following thesis [9, 27].

$$\sum_{b \in \mathrm{B}} (\dot{\boldsymbol{E}}^{\boldsymbol{gr,+}}_{\boldsymbol{b,p,t}} - \dot{\boldsymbol{E}}^{\boldsymbol{gr,-}}_{\boldsymbol{b,p,t}}) \cdot d_p \cdot d_t = \boldsymbol{E}^{\boldsymbol{tr,+}}_{\boldsymbol{p,t}} - \boldsymbol{E}^{\boldsymbol{tr,-}}_{\boldsymbol{p,t}} \qquad \forall p \in \mathrm{P}, \quad \forall t \in \mathrm{T} \tag{1a}$$

$$\dot{\boldsymbol{E}}^{\boldsymbol{tr,\pm}}_{\boldsymbol{p,t}} \leq \dot{E}^{tr,max} \qquad \forall p \in \mathrm{P}, \quad \forall t \in \mathrm{T} \tag{1b}$$

2.0.1. Objective functions

The objective functions are described in (2a) to (2e). The total costs (**TOTEX**) encompass operating costs (**OPEX**) and capital costs (**CAPEX**). The OPEX correspond to the annual energy costs and revenues from the utilities. The electricity and gas retail tariffs are respectively $c^{el,+}$ and $c^{ng,+}$ and the feed-in tariff is $c^{el,-}$. The variables E^{tr} and $H^{gr,+}$ correspond to the annual electricity and gas exchanges with the utility at the district level. The CAPEX (Eq. 2c) encompass investments and replacement costs of conversion units. The costs are annualized over an n years horizon with an interest rate i. The investment costs C^{inv} are linearized with fixed ($i^{c1,u}$) and variable ($i^{c2,u}$) costs and multiplied by the bare modulus b^u [9]. The CAPEX is dictated by two decision variables, the decision to install a unit (y^u) and the size installed (f^u). When a conversion unit has a lifetime l_u lower than the project horizon n, the replacement cost is given by the number of replacements R over the horizon n. Multi-objective optimization is performed to evaluate the solution space at the interplay of two conflicting objectives, the operating and capital costs. One objective is upper-bounded by a pre-defined values using an ϵ-constraint while the second objective is minimized. Pareto fronts are generated by varying the ϵ-constraints and by exchanging the objectives constrained and minimized.

$$\boldsymbol{TOTEX} = \boldsymbol{OPEX} + \boldsymbol{CAPEX} \tag{2a}$$

$$\boldsymbol{OPEX} = c^{el,+} \cdot \boldsymbol{E}^{\boldsymbol{tr,+}} - c^{el,-} \cdot \boldsymbol{E}^{\boldsymbol{tr,-}} + c^{ng,+} \cdot \boldsymbol{H}^{\boldsymbol{gr,+}} \tag{2b}$$

$$\boldsymbol{CAPEX} = \frac{i(1+i)}{(1+i)^n - 1} (\boldsymbol{C}^{\boldsymbol{inv}} + \boldsymbol{C}^{\boldsymbol{rep}}) \tag{2c}$$

$$\boldsymbol{C}^{\boldsymbol{inv}} = \sum_{u=1}^{U} b^u \cdot (i^{c1,u} \cdot \boldsymbol{y}^{\boldsymbol{u}} + i^{c2,u} \cdot \boldsymbol{f}^{\boldsymbol{u}}) \tag{2d}$$

$$\boldsymbol{C}^{\boldsymbol{rep}} = \sum_{u=1}^{U} \sum_{r=1}^{R} \frac{1}{(1+i)^{r \cdot l_u}} \cdot (i^{c1,u} \cdot \boldsymbol{y}^{\boldsymbol{u}} + i^{c2,u} \cdot \boldsymbol{f}^{\boldsymbol{u}}) \tag{2e}$$

2.1. Decomposition

The energy community model has a building scale resolution, with case studies up to 100 buildings. Due the network structure and long computation time, the Dantzig-Wolfe decomposition is applied on the original MILP problem. The methodology is described in detail in [27]. The constraint matrix of the original problem is block-angular. Each building energy system represents a subsystem independent from other subsystems except for the resources balance and capacity constraints, being linking constraints. The model is decomposed into two problems: a master problem (**MP**) and several sub problems (**SPs**). Linking constraints, such as energy balances, epsilon constraints or the transformer capacity are included in the MP and represent the district energy system problem. The MP receives building energy system designs from the SPs and selects an optimal configuration for each building by a linear combination of the proposals. Each design account for an investment into conversion units and associated energy flows with the district low voltage grid. Within an iteration loop, the SPs find new design proposals based on price signals sent by the MP. The latter correspond to the dual values of the linking constraints that are inserted in the SPs objective function as Lagrangian multipliers. The SPs are formulated as reduced costs, meaning that a solution with a negative value has the potential to improve the MP objective. The algorithm terminates when the SPs cannot find negative reduced costs.

2.2. Key performance indicators

Key performance indicators (**KPI**) are used to quantify solutions performance. The self-consumption (**SC**) is the share of onsite generated electricity being consumed within the district. The self-sufficiency (**SS**) corresponds to the share of the electricity demand being supplied by onsite generated electricity. PV curtailment is the share of onsite generated electricity being neither self-consumed, nor sold to the grid. Finally, similarly to the total cost, the global warming potential (**GWP**) accounts for both the construction and operation emissions from the consumption of energy resources (3d) as described in [27]. Emissions related to conversion units installation are taken from the Ecoinvent database and are calculated with the method IPCC 2013 and the version 3.6.

$$\mathrm{SC} = (E^{gen} - E^{curt} - E^{tr,-})/E^{gen} \tag{3a}$$

$$\mathrm{SS} = (E^{gen} - E^{curt} - E^{tr,-})/(E^{gen} - E^{curt} - E^{tr,-} + E^{tr,+}) \tag{3b}$$

$$\mathrm{PVC} = E^{curt}/E^{gen} \tag{3c}$$

$$\mathrm{G}^{op} = \sum_{\substack{p\in P \\ t\in T}} \left(g^{el,TR}_{p,t} \cdot (E^{tr,+} - E^{tr,-}) + \sum_{b\in B} g^{ng}_{p,t} \cdot H^{gr,+}_{b,p,t} \right) \tag{3d}$$

2.3. Case Study

Since Switzerland possesses 17'844 LV/MV transformers [28], a kmedoid clustering algorithm is applied to find the most representative districts. The case study is built under a geographic information system (**GIS**) approach to adequately describe the energy demand and sources. Clustering features consider real-estate typologies (heating surface, roof area, service demands, building category, construction year) and geographic ones (annual solar irradiation, average temperature, infrastructure density). Typical Swiss weather profiles had been assessed for each district by Stadler et al. [9]. With this approach, versatile district typologies are considered within a single case study. The five most representative districts are selected for this case study. The representative roof area of each typical district is used for extrapolation to the national scale. Figure 1 presents the distribution of each typical district within Switzerland and Figures 8 to 12 provide a geographical visualization of the district in the Appendix. The present study aims at analysing the impact of energy communities on the national energy system. Therefore, it is assumed that each district in Switzerland is an energy community.

Most data are open source and provided by the Swiss government. The building characteristics, such as the height, heated areas or types of construction come from cantonal and federal Official Buildings Registry [29]. Energy standards such as the envelope heat transfer, building heat capacity and domestic electricity demand as well as the internal and external heat gains are calculated based on Swiss national standard norms [30]. These data are used to build the 1R1C thermal model of the buildings [31]. The outdoor temperature and solar irradiation come from Meteonorm [32]. These time series are clustered into ten typical periods and two extreme periods using k-medoids clustering. The project horizon is 20 years and an interest rate of 2% is taken. The electricity and gas retail tariff are respectively fixed to 0.27 CHF/kWh and 0.14 CHF/kWh and the feed-in tariff is 0.17 CHF/kWh. These values are based on the average energy tariffs in Switzerland for the years 2022-2023 [33]. The carbon content of electricity are taken from [34] and equals 0.1 kg CO_2/kWh$_{el}$ both at the import and export. More details on buildings, units and weather data parameters are detailed in [27].

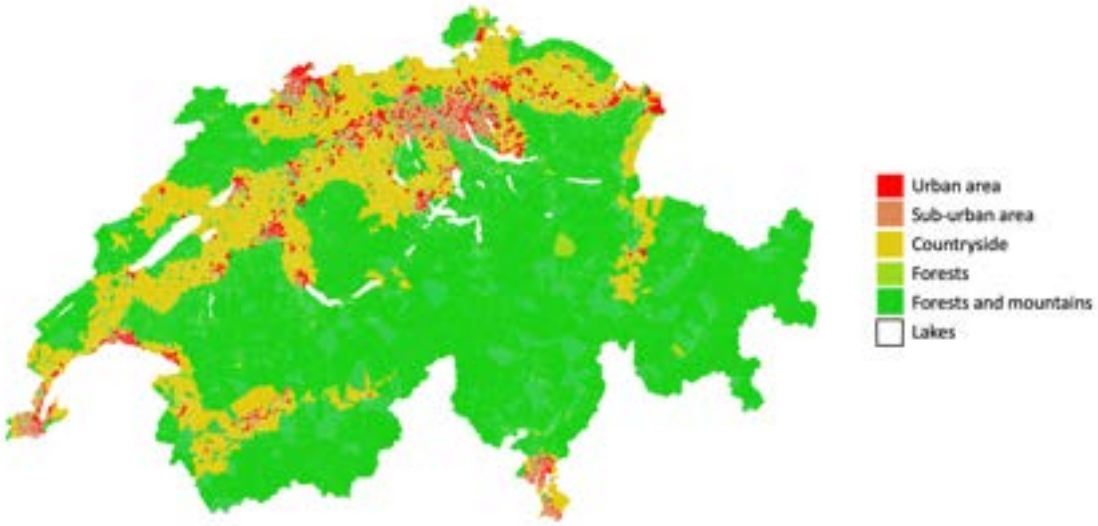

Figure 1: Typical districts distribution in Switzerland. The centroids differentiate the urban and weather typologies of Switzerland.

3. Results and Discussion

The discussion follows two axis. First, the decision trends taken within energy communities are analysed and contextualised with their geographic and urban density characteristics. Multi-objective optimization between the capital and operating costs is performed to extract the solution trends. Then, the solutions are aggregated and extrapolated to the whole country. The potential of energy communities is analysed in terms of renewable electricity supply. Finally, grid constraints and curtailment are applied to assess the cost and energy efficiency impact of a coordinated and uncoordinated investment strategy.

3.1. Region specific Energy Community Investments

Investment trends into energy conversion units are summarized in Figure 2. The investment and operating cost breakdown are presented respectively with red/yellow and green colors. The total cost of the system is located on the right with the blue columns and the revenues from selling electricity corresponds to the white columns. The figure shows the solution spectrum for the typical district 3, representing the countryside districts. The gas boiler solution corresponds to the one with the lowest investment and highest operational cost. The latter is decreased by substituting the base load heat supply from the boiler with a heat pump. Then, the operating costs are further decreased by a progressive investment into solar panels. Due to the profitable electricity tariffs, the energy community reaches net zero operating cost with an average investments into PV units. The operating costs are further decreased by an investment into batteries, allowing a larger investment into PV units and a higher self-consumption. Depending on the interest of the actors, the energy community moves from a passive energy consumer to a renewable electricity supplier for the utility. Similar solution trends are found throughout the other typical districts, even though the magnitude of the investments varies. Figure 3 presents the pareto optimal solutions for each of the typical district. Within the positive operating cost region solutions are similar since they correspond to solutions with few PV integration. Therefore, heating and electricity services are mainly supplied by purchasing energy from the grid and there is no interests into renewable electricity sharing. On the other hand, within the region with high PV integration, the solutions diverge based on the geographic location. The energy community with the lowest operating cost corresponds to the countryside one due to the low building density, large roof surface area and a sufficiently large community allowing economies of scale. On the other side, the district 4 has the highest operating cost, mainly due to the small size of the community. Between the two extremum are located dense urban areas having a large economy of scale but a large energy demand density and small mountain villages with low economies of scale and high thermal demand but large roofs surfaces and high solar irradiation.

3.2. National scale impact of Energy Communities

The electricity tariff of today favors a high implementation of PV. Figure 4 presents a sensitivity analysis on the annual renewable electricity generated by energy communities in Switzerland for a range of feed-in and retail tariffs. Below a certain energy tariff, the PV investment is not profitable due to the affordable electricity cost from the grid. The investment threshold is delimited by the lower black line. On the other side, the up-

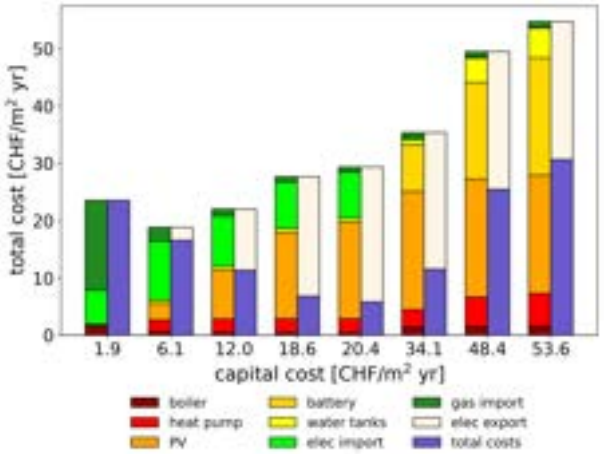

Figure 2: Cost breakdown of the pareto optimal solutions for the district 3 (Figure 11). The left column represents the costs. The right column stacks the total cost (blue) and the electricity revenues (white).

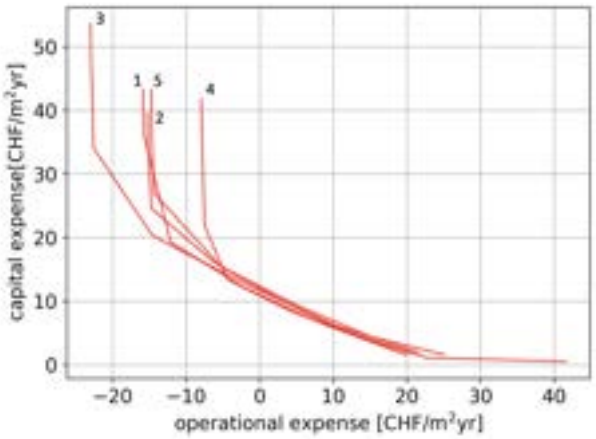

Figure 3: Pareto front for the 5 typical districts. The number refers to the district label in Figures 8 to 12.

per investment limit maps the region where the PV capacity reaches its maximum of 28 GW, representing an annual electricity production of 32 TWh/yr. Since the PV potential varies throughout the typical districts, there exists a spectrum of solutions. First, the district with high solar potential are activated at low electricity tariffs, then investments with lower profitability are activated as the price signals sent by the national infrastructure becomes more attractive. Actual energy tariffs promote a full investment into PV panels, reaching a potential of 32 TWh/yr. However, the optimal PV deployment in Switzerland ranges between 12 and 18 TWh/yr [5, 35]. Therefore, the price incentives should be located in the yellow and green areas. As a conclusion, there is a discordance between the price signals sent by grid operators and the needs of the infrastructure, which could result into costly grid reinforcements or curtailment. Such situations are socially unfair since the former induces costs to customers and the latter might render some investments unprofitable. Ultimately, this conflicting situation might generates mistrust in renewable deployments, therefore in the energy transition. In the following section, the impact of curtailment is analysed in terms of energy efficiency and costs.

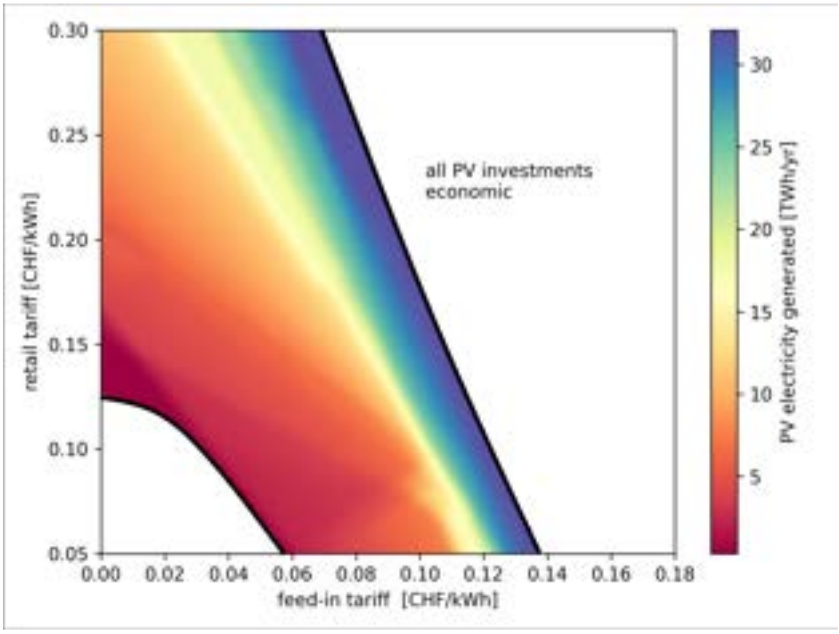

Figure 4: Yearly renewable electricity generation from PV units in energy communities for the whole Switzerland. The electricity supply is presented based on the electricity retail and feed-in tariffs. Data were calculated for the minimum total costs.

To support the analysis, two scenarios are considered. In the first one, an investment decision in PVs and heat pumps is taken today. Then, PV curtailment is applied on the energy system. The operation and investment into batteries are optimized with fixed sizes of PV and heat pump units. In the second scenario, the investment and operation decisions of the overall energy systems are taken considering grid curtailment. Therefore, the PV and heat pump capacities vary with the level of curtailment. The aim of these two scenarios is to assess the impact of grid curtailment on a decision taken today. Figure 5 shows the load duration curve of the electricity fluxes between energy communities and the national grid. The electricity tariffs promote a net export of electricity of 26 TWh/yr, 6 TWh/yr being self-consumed within the communities. The curtailed system reduces by half the maximum export power. In the first scenario, most of the peak is removed while the base load remains stable. This outcome is beneficial for the grid utility since the annual export is less intermittent and decreases to 19 TWh. However, from the perspective of the households, the PV investment is oversized since the optimal export with variable PV capacity would have been 15% lower (dashed red line).

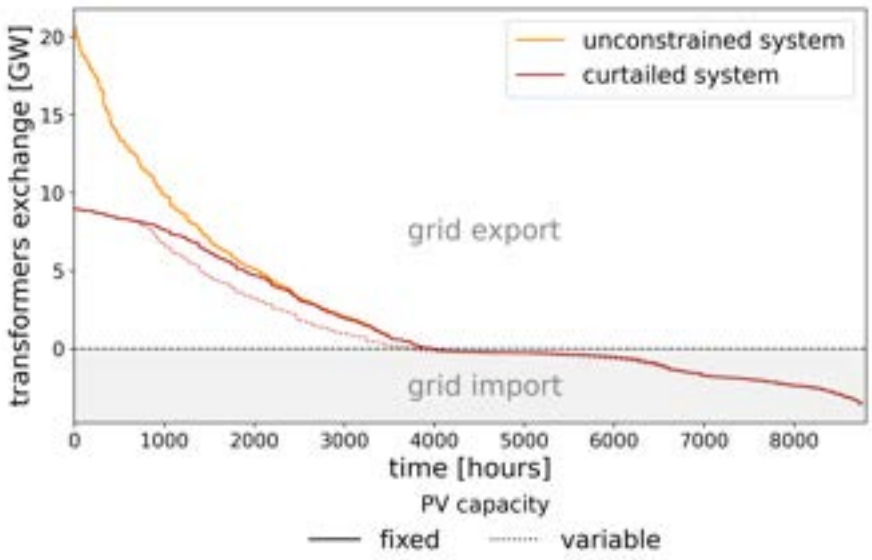

Figure 5: Load duration curve of the electricity imports and exports for energy communities in Switzerland. The unconstrained solution is constrained to reduce the maximum power peaks by half. Two design scenarios are considered, one accounting curtailment in the investment decision (variable PV) and the other one being imposed curtailment after investment decision (fixed PV).

Figures 6 and 7 further detail the energy efficiency, costs and impacts of the two scenarios. They compare metrics to the level of annual electricity export. Based on the renewable needs of the national energy system, an annual electricity export reduction by 8 TWh/yr is needed, decreasing the energy communities exports from 26 TWh/yr to 18 TWh/yr. With a fixed PV design, energy communities invest into batteries to compensate the PV over-investment with self-consumption (Figure 6). For an electricity export reduction of 8 TWh/yr, the battery investment is still not profitable and the SC and SS respectively increase to 18.5% and 50%. In the second scenario, the consideration of the grid capacity in the planning phase decreases the PV capacity by 22%. This decreases the SS from 48% to 46% but increases the SC from 17% to 22% and minimized grid curtailment (5%). The latter is 5 times higher in the first scenario (24%). While a coordinated design promotes self-consumption with a well sized PV capacity, the uncoordinated one reduces export peaks only with curtailment. The energy system is designed to generate large amount of electricity. Therefore, the high presence of renewable electricity in energy communities makes the SS high and the system less flexible to reduce the power peaks with self-consumption.

Since the peak shaving strategy of the second scenario is to decrease the PV capacity, the onsite generated electricity decreases faster with peak reduction compared to the first scenario. To generate the renewable electricity needs of the country, a peak reduction of respectively 41% and 58% is needed in the first and second scenarios (Figure 7). This trend is as well visible on Figure 5 since the scenario with fixed PV capacity has a flatter profile than the one with variable capacity. The oversized PV capacity and curtailment induces a total cost difference of 31% between the two scenarios. The larger amount of electricity sold to the grid in the first scenario do not compensate for the high investment cost on the contrary to the second scenario

where the total costs are balanced between lower electricity revenues and lower investments. From the GWP perspective, both scenarios are usually net negative since they contribute to reduce the carbon content of the grid. At an electricity export reduction of 8 TWh/yr, the scenarios respectively decrease the GWP by -1.5 and -2.1 kg $CO_{2,eq}/m_2$. This has to be contextualised with the actual Swiss GWP of the residential sector, being 6.6 kg $CO_{2,eq}/m_2$ [36]. The difference of 0.6 kg $CO_{2,eq}/m_2$ between the two scenario is due to the embodied carbon content of the PV installation in the first scenario. It represents 9% of the Swiss residential GWP and 1.5% of the direct GWP in the whole country [36].

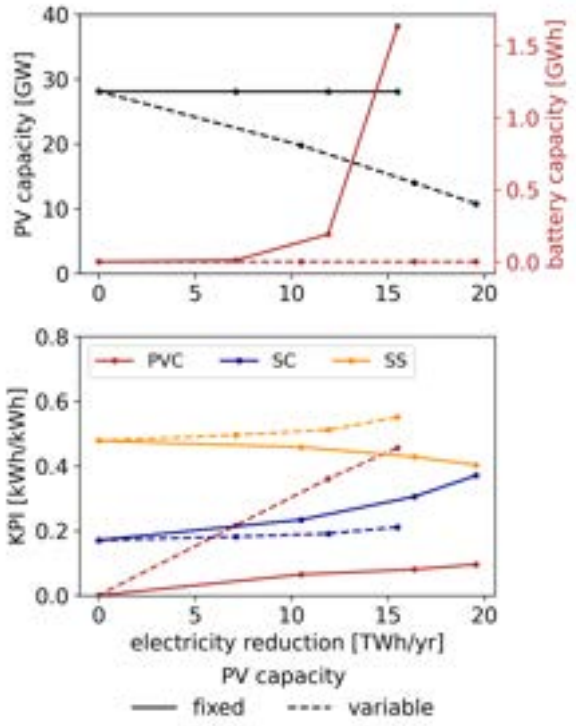

Figure 6: PV and battery capacity with PV indicators for the two scenarios based on the level of electricity export reduction. A reduction by 8 TWh/yr of the unconstrained solution is needed in Switzerland.

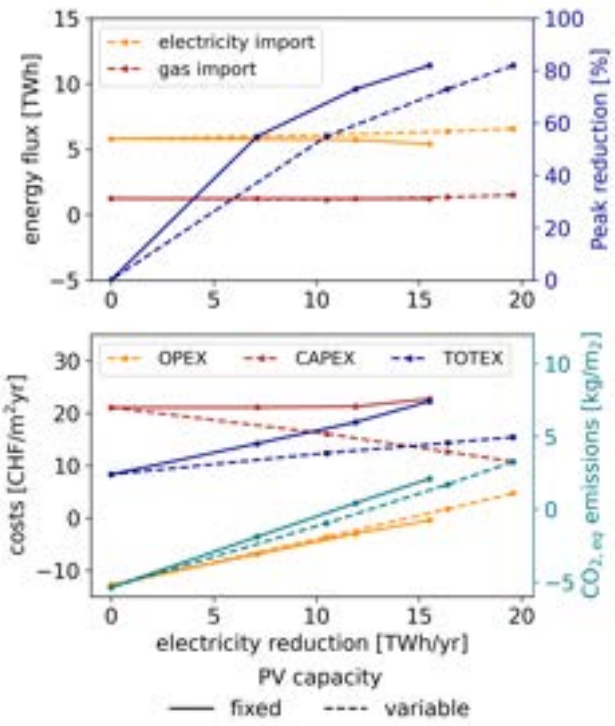

Figure 7: Energy fluxes with the utility, costs and $CO_{2,eq}$ impact metrics. All values are given after extrapolation to the whole country.

4. Conclusion

The objective of this paper was to highlight the decisions trends within energy communities and their integration in the national energy infrastructure. The community is modeled as a renewable energy hub with investment into conversion units. Typical districts are considered to extrapolate the results to the national scale. Multi-objective optimization and grid constraints are applied to meet the renewable electricity supply from the communities to the forecast national needs in 2050. The main outcomes of the study are listed below:

- The investment trends are homogeneous throughout the typical energy communities, even though the investment magnitude into solar panels differs between urban, countryside and isolated areas.
- The PV potential of the residential sector in Switzerland reaches 32 TWh/yr. The associated PV capacity is 28 GW.
- The actual electricity tariffs promote an excessive PV integration in the national electricity system. Based on national guidelines, the annual electricity supply from PV panels could exceed by a factor two the demand, being between 12 and 18 TWh/yr.
- Uncoordinated price signals induce an oversized PV capacity. Grid constraints curtail 24% of the generated electricity and increase by 31% the total costs compared to a coordinated planning, where the energy communities design their energy system based on the needs of the infrastructure. Moreover, the GWP difference between the uncoordinated and coordinated designs represent 9% of the residential total emissions.

The presented results contribute to a better understanding on the decision inter-dependency between small scale actors and national energy systems. The holistic approach encompassing various stakeholders within a single optimization favors a coordinates energy transition and increases the technological acceptance into a decision. Grid operators and national institutions should communicate properly the right price signals to local stakeholders to prevent unfair investments and mitigate costs and emissions. The extension of the work includes a better definition of the national infrastructure, accounting its energy flows and reinforcement costs. To this extent, bi-level and nested decomposition methods have a high potential at linking optimization tools modeling the various decision levels.

5. Fundings

The research published in this report was carried out with the support of the Swiss Federal Office of Energy SFOE as part of the SWEET project acronym. The authors bear sole responsibility for the conclusions and the results of the presented publication.

6. Appendix

Figure 8: Typical district 1: urban area

Figure 9: Typical district 4: forest area

Figure 10: Typical district 2: suburban area

Figure 11: Typical district 3: countryside area

Figure 12: Typical district 5: mountain area

7. Nomenclature

Table 2: Nomenclature Table

Abbreviation	Definition
PV	Photovoltaic
MILP	Mixed Integer Linear Programming
CAPEX	Capital cost
OPEX	Operating cost
TOTEX	Total cost
MP	Master Problem
SP	Sub Problem
KPI	Key Performance Indicator
SC	Self-Consumption
SS	Self-Sufficiency
GWP	Global Warming Potential
GIS	Geographic Information System
$E^{tr,+}$	Electricity import from the low voltage transformer
$E^{tr,-}$	Electricity export to the low voltage transformer
$E^{gr,+}$	Electricity import from the microgrid
$E^{gr,-}$	Electricity export to the microgrid
E^{gen}	Onsite generated electricity
E^{curt}	Curtailed electricity
$H^{gr,+}$	Natural gas import from the gas utility

References

[1] European Parliament. “DIRECTIVE (EU) 2018/ 2001 OF THE EUROPEAN PARLIAMENT AND OF THE COUNCIL - of 11 December 2018 - on the promotion of the use of energy from renewable sources”. en. In: (2018), p. 128.

[2] Henner Busch et al. “Policy challenges to community energy in the EU: A systematic review of the scientific literature”. en. In: *Renewable and Sustainable Energy Reviews* 151 (Nov. 2021), p. 111535. ISSN: 13640321. DOI: 10.1016/j.rser.2021.111535. URL: https://linkinghub.elsevier.com/retrieve/pii/S1364032121008133 (visited on 11/02/2022).

[3] Tineke van der Schoor et al. “Challenging obduracy: How local communities transform the energy system”. en. In: *Energy Research & Social Science* 13 (Mar. 2016), pp. 94–105. ISSN: 22146296. DOI: 10.1016/j.erss.2015.12.009. URL: https://linkinghub.elsevier.com/retrieve/pii/S2214629615300967 (visited on 10/05/2022).

[4] Internation Renewable Energy Agency. “World Energy Transitions Outlook”. In: (2021).

[5] Swiss Federal Office of Energy. *ENERGY STRATEGY 2050, MONITORING REPORT 2019*. Tech. rep. 2019.

[6] Swiss Federal Office of Energy. *Perspectives énergétiques 2050*. Tech. rep. 2913.

[7] Mohammad Mohammadi. “Optimal management of energy hubs and smart energy hubs – A review”. en. In: *Renewable and Sustainable Energy Reviews* (2018).

[8] Yeong-Geon Son et al. “Multi Energy System With an Associated Energy Hub: A Review”. en. In: *IEEE Access* 9 (2021), pp. 127753–127766. ISSN: 2169-3536. DOI: 10.1109/ACCESS.2021.3108142. URL: https://ieeexplore.ieee.org/document/9523745/ (visited on 02/12/2023).

[9] Paul Michael Stadler. “Model-based sizing of building energy systems with renewable sources”. fr. PhD thesis. Lausanne, 2019.

[10] Leander Kotzur et al. “Bottom-up energy supply optimization of a national building stock”. en. In: *Energy and Buildings* 209 (Feb. 2020), p. 109667. ISSN: 03787788. DOI: 10.1016/j.enbuild.2019.109667. URL: https://linkinghub.elsevier.com/retrieve/pii/S0378778819319863 (visited on 06/21/2021).

[11] Auyon Chakrabarti et al. “Optimisation and analysis of system integration between electric vehicles and UK decentralised energy schemes”. en. In: *Energy* 176 (June 2019), pp. 805–815. ISSN: 03605442. DOI: 10.1016/j.energy.2019.03.184. URL: https://linkinghub.elsevier.com/retrieve/pii/S0360544219306048 (visited on 01/26/2022).

[12] Portia Murray, Jan Carmeliet, and Kristina Orehounig. “Multi-Objective Optimisation of Power-to-Mobility in Decentralised Multi-Energy Systems”. en. In: *Energy* 205 (Aug. 2020), p. 117792. ISSN: 03605442. DOI: 10.1016/j.energy.2020.117792. URL: https://linkinghub.elsevier.com/retrieve/pii/S0360544220308999 (visited on 03/12/2022).

[13] Moritz Mittelviefhaus et al. “Optimal investment and scheduling of residential multi-energy systems including electric mobility: A cost-effective approach to climate change mitigation”. en. In: *Applied Energy* 301 (Nov. 2021), p. 117445. ISSN: 03062619. DOI: 10.1016/j.apenergy.2021.117445. URL: https://linkinghub.elsevier.com/retrieve/pii/S0306261921008357 (visited on 03/12/2022).

[14] Alaa Alhamwi et al. “Modelling urban energy requirements using open source data and models”. en. In: *Applied Energy* 231 (Dec. 2018), pp. 1100–1108. ISSN: 03062619. DOI: 10.1016/j.apenergy.2018.09.164. URL: https://linkinghub.elsevier.com/retrieve/pii/S0306261918314752 (visited on 06/21/2021).

[15] Michael Kramer, Akhila Jambagi, and Vicky Cheng. “Bottom-up Modeling of Residential Heating Systems for Demand Side Management in District Energy System Analysis and Distribution Grid Planning”. en. In: (2017), p. 8.

[16] Tetsuya Wakui et al. “Two-stage design optimization based on artificial immune system and mixed-integer linear programming for energy supply networks”. en. In: *Energy* 170 (Mar. 2019), pp. 1228–1248. ISSN: 03605442. DOI: 10.1016/j.energy.2018.12.104. URL: https://linkinghub.elsevier.com/retrieve/pii/S0360544218324708 (visited on 05/25/2021).

[17] Jonathan Reynolds et al. “Operational supply and demand optimisation of a multi-vector district energy system using artificial neural networks and a genetic algorithm”. en. In: *Applied Energy* 235 (Feb. 2019), pp. 699–713. ISSN: 03062619. DOI: 10.1016/j.apenergy.2018.11.001. URL: https://linkinghub.elsevier.com/retrieve/pii/S0306261918317070 (visited on 06/21/2021).

[18] B. Pickering and R. Choudhary. “District energy system optimisation under uncertain demand: Handling data-driven stochastic profiles”. en. In: *Applied Energy* 236 (Feb. 2019), pp. 1138–1157. ISSN: 03062619. DOI: 10.1016/j.apenergy.2018.12.037. URL: https://linkinghub.elsevier.com/retrieve/pii/S0306261918318555 (visited on 06/21/2021).

[19] Samira Fazlollahi, Gwenaelle Becker, and François Maréchal. “Multi-objectives, multi-period optimization of district energy systems: II—Daily thermal storage”. en. In: *Computers & Chemical Engineering* 71 (Dec. 2014), pp. 648–662. ISSN: 00981354. DOI: 10.1016/j.compchemeng.2013.10.016. URL: https://linkinghub.elsevier.com/retrieve/pii/S0098135413003384 (visited on 06/21/2021).

[20] Thomas Schütz et al. “Optimal design of decentralized energy conversion systems for smart microgrids using decomposition methods”. en. In: *Energy* 156 (Aug. 2018), pp. 250–263. ISSN: 03605442. DOI: 10.1016/j.energy.2018.05.050. URL: https://linkinghub.elsevier.com/retrieve/pii/S0360544218308703 (visited on 02/22/2021).

[21] Marco Wirtz et al. “5th generation district heating and cooling network planning: A Dantzig–Wolfe decomposition approach”. en. In: *Energy Conversion and Management* 276 (Jan. 2023), p. 116593. ISSN: 01968904. DOI: 10.1016/j.enconman.2022.116593. URL: https://linkinghub.elsevier.com/retrieve/pii/S0196890422013711 (visited on 01/27/2023).

[22] Carl Haikarainen, Frank Pettersson, and Henrik Saxén. “A decomposition procedure for solving two-dimensional distributed energy system design problems”. en. In: *Applied Thermal Engineering* 100 (May 2016), pp. 30–38. ISSN: 13594311. DOI: 10.1016/j.applthermaleng.2016.02.012. URL: https://linkinghub.elsevier.com/retrieve/pii/S1359431116301387 (visited on 02/03/2023).

[23] Tetsuya Wakui, Moe Hashiguchi, and Ryohei Yokoyama. “Structural design of distributed energy networks by a hierarchical combination of variable- and constraint-based decomposition methods”. en. In: *Energy* 224 (June 2021), p. 120099. ISSN: 03605442. DOI: 10.1016/j.energy.2021.120099. URL: https://linkinghub.elsevier.com/retrieve/pii/S0360544221003480 (visited on 02/03/2023).

[24] Boran Morvaj, Ralph Evins, and Jan Carmeliet. “Optimization framework for distributed energy systems with integrated electrical grid constraints”. en. In: *Applied Energy* 171 (June 2016), pp. 296–313. ISSN: 03062619. DOI: 10.1016/j.apenergy.2016.03.090. URL: https://linkinghub.elsevier.com/retrieve/pii/S0306261916304159 (visited on 02/03/2023).

[25] Javier Silvente et al. “A rolling horizon optimization framework for the simultaneous energy supply and demand planning in microgrids”. en. In: *Applied Energy* 155 (Oct. 2015), pp. 485–501. ISSN: 03062619. DOI: 10.1016/j.apenergy.2015.05.090. URL: https://linkinghub.elsevier.com/retrieve/pii/S0306261915007230 (visited on 02/03/2023).

[26] Caroline Bastholm and Annette Henning. “The use of three perspectives to make energy implementation studies more culturally informed”. en. In: *Energy, Sustainability and Society* 4.1 (Dec. 2014), p. 3. ISSN: 2192-0567. DOI: 10.1186/2192-0567-4-3. URL: https://energsustainsoc.biomedcentral.com/articles/10.1186/2192-0567-4-3 (visited on 11/29/2022).

[27] Luise Middelhauve and Francois Marechal. “About Data Reduction Techniques and the Role of Outliers for Complex Energy Systems”. In: (2022). URL: https://www.sciencedirect.com/science/article/abs/pii/B978032385159650292X.

[28] Rahul Gupta, Fabrizio Sossan, and Mario Paolone. “Countrywide PV hosting capacity and energy storage requirements for distribution networks: The case of Switzerland”. en. In: *Applied Energy* 281 (Jan. 2021), p. 116010. ISSN: 03062619. DOI: 10.1016/j.apenergy.2020.116010. URL: https://linkinghub.elsevier.com/retrieve/pii/S0306261920314537 (visited on 06/13/2021).

[29] Federal Statistical Office. “Federal Register of Buildings and Dwellings”. In: (2019).

[30] SIA. “SIA 380/1:2016 Heizwärmebedarf. Schweizerischer Ingenieur und Architektenverein”. In: (2016).

[31] Luc Girardin. “A GIS-based Methodology for the Evaluation of Integrated Energy Systems in Urban Area”. PhD thesis. EPFL, 2012. DOI: 10.5075/epfl-thesis-5287. URL: http://infoscience.epfl.ch/record/170535/files/EPFL_TH5287.pdf.

[32] J. Remund et al. *METEONORM - Global Meteorological Database for Engineers, Planners and Education*. 2003.

[33] Association des producteurs d’énergie indépendants. *Carte interactive des rétributions*. 2023. URL: https://www.vese.ch/fr/pvtarif/.

[34] Alessio Santecchia. “Enabling renewable Europe through optimal design and operation”. en. In: (2022).

[35] Jonas Schnidrig et al. “A modelling framework for assessing the impact of green mobility technologies on energy systems”. en. In: *34th International Conference on Efficiency, Cost, Optimization, Simulation and Environmental Impact of Energy Systems (ECOS 2021)*. Taormina, Italy: ECOS 2021 Program Organizers, 2022, pp. 928–940. ISBN: 978-1-71384-398-6 978-1-71384-393-1. DOI: 10.52202/062738-0083. URL: http://www.proceedings.com/062738-0083.html (visited on 01/29/2023).

[36] Office fédéral de l’environnement OFEV. “Indicateurs de l’évolution des émissions de gaz à effet de serre en Suisse”. fr. In: (2022).

PROCEEDINGS OF ECOS 2023 - THE 36TH INTERNATIONAL CONFERENCE ON
EFFICIENCY, **C**OST, **O**PTIMIZATION, **S**IMULATION AND ENVIRONMENTAL IMPACT OF ENERGY SYSTEMS
25-30 JUNE 2023, LAS PALMAS DE GRAN CANARIA, SPAIN

Vehicle-to-Grid Coupled Photovoltaic Optimization for Singapore at a District Resolution

Dominic Caviezel[a,*], Christoph Waibel[a,*], Markus Schläpfer[b] and Arno Schlueter[a]

[a] *Architecture and Building Systems (A/S), ETH Zurich, Switzerland, waibel@arch.ethz.ch*
[b] *Civil Engineering and Engineering Mechanics, Columbia University, New York, United States*

Abstract:
This paper investigates the potential of building attached / integrated Photovoltaic (PV) and vehicle-to-grid (V2G) coupling for the city of Singapore. Using the city's 55 planning areas as spatial units, a linear programming (LP) optimization model is developed to determine economically optimal PV scaling and charge/discharge strategies within and across planning areas. Mobility flows between planning areas are assessed using a large set of GPS mobile phone records, from which electric vehicle (EV) schedules are derived. Local electricity demand and solar potentials are modelled using a bottom-up approach based on building geometries and land use information, and loads are calibrated to match measured aggregate city loads. Parametrized assumptions in our model are systematically tested through scenario analysis, including varying carbon taxes, PV system cost, EV penetration, wholesale electricity prices, and local building self-consumption levels. Our study finds significant economic and environmental potential for PV systems, while economic benefits of V2G are strongly scenario dependent but generally limited. This may be explained by the high on-site PV electricity self-consumption potential due to the electricity loads generally exceeding PV generation. However, through the aggregation to the planning area level in our model, local building-resolved mismatches in production and demand were partially flattened, and thus the potential for V2G to act as intermediate storage can be expected to be higher when modelled at a finer spatial resolution. In order to gain further insight, future research could focus on combining large-scale city dynamics with more fine-grained local analysis, e.g., by limiting the analysis to one district only, as well as incorporate explicit grid balancing constraints in the model.

Keywords:
Vehicle-to-grid, Photovoltaic, Linear Programming, District Energy, Optimization.

1. Introduction

Substituting fossil fuel-based energy generation with renewable sources, such as Photovoltaics (PV), and the promotion of electric vehicles (EV), are two of the key measures to decarbonisation [13]. The aim of this paper is therefore to investigate possible synergies between the two technologies, PV and EV, and study the impact on energy-related cost and emissions if vehicle to grid (V2G) technologies were widely adapted at a city scale. V2G relies on bidirectional chargers allowing EVs not only to charge their batteries but also discharge stored electricity back into the grid. In this capacity they can be used as temporary storage devices for excess electricity from renewable sources, participate in electricity arbitrage or even increase grid stability by providing ancillary services.

1.1. V2G at a city scale

With the development of EVs as a potentially low carbon alternative to vehicles with internal combustion engines (ICE), research has investigated their integration into the existing infrastructure. One area of concern is the impact of large-scale EV adoption on grid stability, with studies highlighting the importance of charging speed [25] and grid-related benefits of nighttime off-peak charging [18]. Control schemes can be specifically designed to avoid grid overloads [7], or to optimize for either user preferences or grid cost [23]: When optimizing for user preference (i.e., optimal state-of-charge, SOC, for mobility demand), electricity may be drawn from the grid during peak demand, leading to potential shortage concerns, whereas a grid-cost minimization can relax the load on the power system. Smart charging strategies are therefore central to successfully combine EVs with the intermittent production of renewable energies such as PV. The objective of coordination is often to increase the self-consumption of locally produced PV-electricity by storing excess production in EV-batteries [10].

Further increasing synergies between local production and EVs is attempted through bidirectional charging. Energy stored in the EV battery can be discharged and consumed on site or fed back into the electricity grid

*These authors share first authorship.

(V2G). In this capacity vehicles can deliver stored PV energy at times of high demand or high electricity prices or even provide ancillary grid services. Such concepts have been explored at the level of individual homes [8] or in more aggregated forms such as parking lots [21]. At larger scale and with a focus on generating realistic EV mobility patterns, Lin et al. (2018) [16] developed a multi-agent system to test the impact of different charging schemes on a generated energy hub. By defining the behavior patterns of different agents (EVs, coordinators etc.), an attempt was made to model realistic behavior patterns including parking duration and charge probability. The study found that peak demand increased under uncontrolled charging scenarios, but through coordinating behaviors the demand could be pushed into the valley period. When V2G was employed the overall electricity demand increased significantly, but the operation of a supplementary gas turbine could be reduced and heating and cooling costs fell significantly suggesting synergies between technologies.

V2G analyses at the city scale are scarce in the existing literature. One example is Kobashi et al. (2020) [15], where the authors looked at PV and V2G interactions for the entire city of Kyoto with real world data. A techno-economic analysis was conducted using hourly electricity demand and PV production at a city aggregate resolution. Significant environmental and economic benefits were found when both technologies, PV and V2G, were deployed in conjunction with each other. The study estimates average mobility patterns from survey information and derives gasoline use and park times. However, due to the aggregation to the city level, local mobility patterns or energy demands are not differentiated in the analysis.

1.2. Mobility flows from mobile phone data

Several studies employ mobile phone data to generate mobility patterns. This data can be obtained for a large fraction of the population and is available in locations where other forms of statistics may be limited. Iqbal et al. (2014) [14] demonstrate that mobility flows can be captured in the form of origin-destination matrices using mobile phone Call Detail Records (CDR) and minimal traffic information without the need for detailed demographic and mobility statistics. As such CDR data can also be used for traffic or infrastructure planning in developing countries where data availability is low [9].

Mobile phone data has also been employed in relation to EV technology. Vazifeh et al. (2019) [26] used CDR data of one million users to determine the optimal positioning of charging stations in Boston. To the authors' knowledge Schläpfer et al. (2021) [24] have been the only ones to use mobile phone data to assess local V2G charging and discharging patterns and relate it to V2G infrastructure planning. The data used is not CDR data but collected from a variety of apps. This allows for the implementation of different tracking modes and offers the potential for more complete movement patterns. Using Singapore as case study, the city-state was separated into a grid of 250m-by-250m cells and a trajectory for each user was derived as their recorded locations moved to different cells. From these trajectories aggregate movement patterns were determined which were then translated to EV vehicle movements. Simple, uncoordinated charging schemes were deployed, where users preferably charged their vehicles during the sunny hours and discharge at night, maximizing PV consumption. It was assumed that charging and discharging was possible in any location where a user stayed for more than one hour.

The study found that a large part of the electricity was discharged outside of residential neighborhoods in primarily commercial zones such as the Singapore Downtown Core. This contradicts the assumption that V2G can mainly provide electricity to residential areas and encourages the inclusion of complex mobility patterns in research. Household electricity was estimated and compared to V2G output assuming that 3% of the mobility flows were covered by EVs. It was found that districts could cover up to 40% of the nighttime household demand using V2G, although most districts fell between 10% and 20%. Comparing charging demands to a simple estimate of PV potential found that local PV alone could likely not cover peak charging demands, requiring other solutions such as smart charging or grid imports.

1.3. Contributions

PV and V2G are both essential elements of the Singapore Green Plan 2030 published by five government Ministries as an outline towards the ecological transformation of the city-state [20]. The plan sets several concrete targets to be reached by 2030. Included is the target to increase electric mobility by providing 60'000 EV charging stations throughout the island and the target to install 2 GWp of PV capacity (system peak demand in Singapore by 2030 is projected to be 9 GW [1]). In this context, Singapore provides a good case for studying the integration of PV and V2G. Therefore, the following research questions are investigated in this paper:

- How does the penetration of EVs and V2G technologies affect optimal scaling of building attached / integrated PV systems, as well as cost and emissions of electricity?
- What levels of self-consumption and self-sufficiency can be achieved at a district scale?
- What is the impact of different boundary conditions, including local (i.e. building) self-consumption rates, carbon taxes, PV system cost, EV penetration, and wholesale electricity prices on cost, emissions and PV capacities?

The specific contributions are:

- As compared to Kobashi et al. (2020) [15], we increase the spatial resolution to the district scale in order to capture local effects of a heterogeneous system.
- Building on Schläpfer et al. (2021) [24] as a first assessment of PV and V2G potential, we now investigate economic feasibility in our study.
- Using a similar method for V2G mobility flow assessment, our study includes economic factors to assess feasible PV scaling and optimal charge/discharge patterns in various scenarios.
- We also estimate and implement the full electricity load of Singapore at planning area scale and not just total household demand.
- Finally, building energy demand and PV potentials for rooftops and facades are estimated using bottom up simulations at a high 3D spatio-temporal resolution.

2. Methods

We develop a linear programming (LP) optimization model for the techno-economic investigation of optimal PV scaling and EV charge / discharge schedules at the level of the 55 planning areas of Singapore. The LP is described in section 2.1. and illustrated in Fig. 1. Other methods employed center around the LP to generate following relevant spatio-temporal input data: electricity demand (section 2.2.), solar potentials (section 2.3.), and mobility patterns (section 2.4.).

2.1. Optimization model

The LP model captures electricity, cost, and emission flows for each of the 55 planning areas in Singapore. The temporal resolution is one hour. Calculations are made for one year. However, due to computational constraints only four representative weeks were modeled. These were derived by clustering similar weeks together. Results for each modeled week were then multiplied by the number of weeks in that cluster in order to scale up to a full year. For each district a set of electricity consumers and producers with associated electricity flows was defined. Three main components are included: Buildings, PV Systems, and EVs. Fig. 1 shows the basic structure of the model.

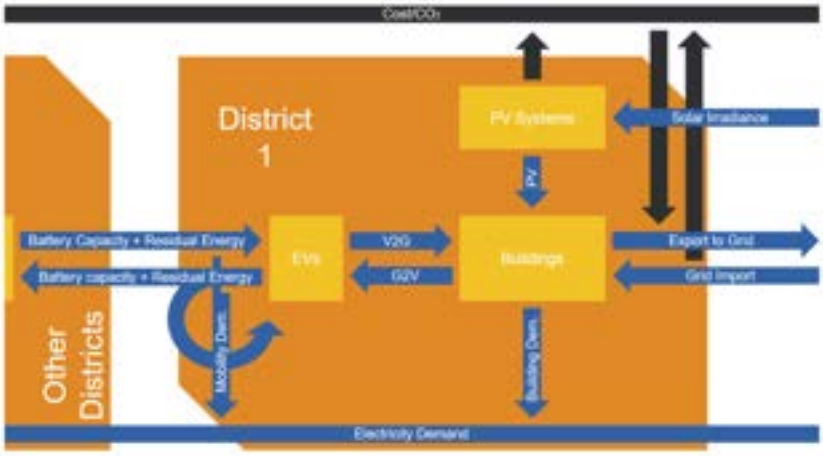

Figure 1: Overview of the LP optimization model. Blue arrows represent electricity flows, black arrows monetary flows and emissions. Yellow boxes represent the main actors contained in the model, orange defines planning area borders.

The majority of consumption in each planning area can be associated to buildings, with modeled demand described in section 2.2.. The main way of meeting the building demand is through grid imports with associated costs and emissions. Alternatively, demand can be met through installed PV systems. Unlike grid imports, PV systems do not incur costs per kWh but rather one time installation and yearly operational costs irrespective of electricity produced. The LP model can optimally scale PV over potential areas, deciding where it is financially viable to install systems. Produced power that exceeds the local demand of a planning area can be exported through the national grid. Exported PV generates revenue. Singapore offers contestable consumers the option to buy and sell electricity at the wholesale electricity price (WEP). For modeling, this WEP was taken as the basis for trading.

The final component represents EVs. When stationary, they can be charged or discharged using V2G. Discharged electricity is fed back into the local energy balance and can be consumed within the planning area

or be exported through the national grid. When EVs drive from one district to another they carry their battery capacity as well as the electricity stored in their battery with them. Since the spatial resolution is the planning area, all EVs in a location at a given time are represented by a single battery and are assumed to have the same state-of-charge (SOC). If an EV enters a district with lower charge, the energy difference is subtracted from the representative battery, and EVs with higher charge add their excess energy to the local battery. Electricity consumed by driving is subtracted from the EVs battery.

The objective function of the LP represents total costs associated with Singapore's electricity flows to meet the total electricity demand and aims to maximize revenue:

$$\max_{x \in \mathbb{R}} (f_{\text{Export}} - f_{\text{Import}} - f_{\text{GridFee}} - f_{\text{PV}}), \quad \text{s.t. } x \in \Omega, \tag{1}$$

where x include operational variables for power flow within and between planning areas and design variables for installed PV per planning area and different orientations (North, East, South, West, roof), and Ω are the system constraints describing the energy balance and technology behavior. f are linear expressions describing revenue generated from generated PV electricity or discharged electricity exported to the grid, as well as cost occurring from imported grid electricity, market support charges on grid transmissions applied to imports and to a fraction of local production to account for local transmission within planning areas, and annualized PV installation cost. Grid carbon emissions are additionally priced with a carbon tax. Prices are obtained from EMC (2022) [6]. A complete formulation and list pf parameters and model constraints can be found in Caviezel (2022) [4]. The model was generated using the `Python` package `Pyomo` and solved using `Gurobi`.

2.2. Building energy demand modeling

The electricity demand for each planning area was modeled with a bottom-up approach using the energy modeling software `City Energy Analyst` (CEA) [11]. The open-source tool can determine different energy related time series for individual buildings based on building attributes, weather input, and site surroundings. A pre-populated database with building archetypes and demand schedules exists for Singapore. For accurate modeling, several attributes were derived for each building in Singapore. For the rest of the variables, CEA-defaults were used.

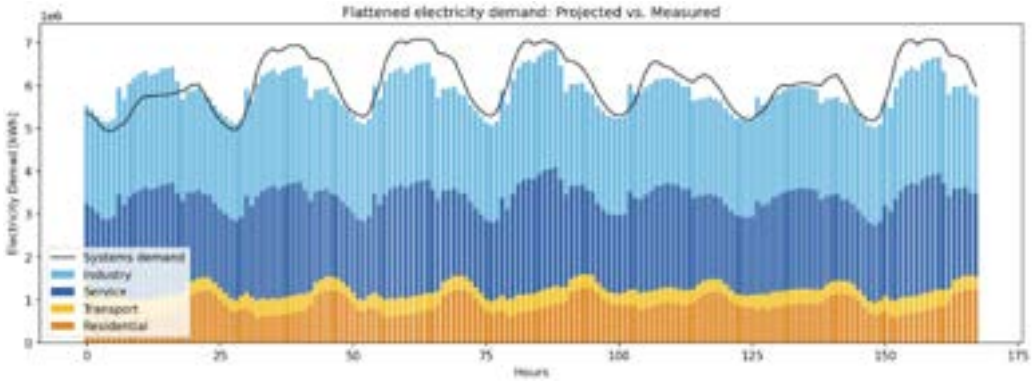

Figure 2: Modeled electricity demand by sector after scaling and amplitude adjustment vs the total systems demand. Period shown is January 1st to January 7th 2019.

2.2.1. Missing building heights

Individual building polygons with height and use type information were obtained from `Open Street Maps` and data from the Urban Redevelopment Authority (URA), resulting in a total of 111'485 buildings. Only 21'755 of the buildings had associated height information. We estimated the height of the remaining buildings using a feed-forward artificial neural network (ANN), using the `Keras` library. After testing different ANN architectures and manually tuning hyper-parameters, the final model resulted in a mean absolute error of 4.64 m and an R-squared value of 0.75, indicating significant correlation. Considering Singapore's large share of high-rise buildings, we consider the error to be acceptable.

2.2.2. Clustering

Due to computational constraints, instead of simulating the 111'485 buildings of Singapore explicitly, we clustered them into groups, similar to the approach taken by Murray et al. (2020) [19]. We used the following 5 attributes for clustering: (i) building use type, (ii) number of attached neighbouring buildings (0, 1, 2 and more), (iii) total floor area, (iv) envelope to volume ratio, and (v) height/distance ratio to neighbouring buildings (sum of the height of each neighbor divided by the distance to that neighbor). The clustering resulted in a total of 445

differentiated groups, representing combinations of the categorical attributes (i) and (ii). For each cluster, the energy demand of the central sample was modeled in CEA and using a typical meteorological year weather file for 2020 as generated from Meteonorm. To represent shading effects, for each modeled building (i.e., cluster centroid), neighboring structures within a 50m radius were included as surroundings.

2.2.3. Calibration

To correct for the mismatch between simulated and actual electricity loads, the load curves were calibrated to measured load curves. We could only find specific hourly loads for the residential sector in Raman & Peng (2021) [22], representing aggregated loads of over 10'000 residential buildings. The demand curves of these measured and aggregated profiles were found to have a smaller amplitude and the evening peak occurred later than in the CEA profiles. Additionally, some days had a morning peak, others did not. The latter were assumed to be weekends when inhabitants did not need to go to work. By adjusting the appliance, lighting and hot water loads in CEA, a custom demand profile was generated which better matches these measured profiles.

The Energy Market Authority (EMA) publishes the annual electricity consumption by sector [3]. The previously generated building demands were summed by sector and compared to these published values. The energy use intensities (EUIs) of service, residential, and industry sectors were scaled to match annual values for 2019, which was chosen as the year before the COVID-19 pandemic, where demand was not yet skewed.

High resolution demand information summed over the entire island is published by EMA in form of half hourly systems demand. After scaling the modeled profiles to match the yearly demand, the systems demand was used to assess hourly load distribution. It was found that the timing of minimum and maximum loads matched well, however the amplitude of the modeled demand curve was much higher than that of the measured systems demand. These differences were corrected by scaling the energy demands around their individual means. Fig. 2 shows the final, adjusted demand for the same period in January 2019. To get local hourly demand curves, the adjusted demands for all buildings in a planning area were summed.

2.3. Solar modeling

Hourly solar irradiation for all building surfaces (roof and façade) was simulated on a 0.7m $\times$ 0.7m grid, resulting in several million hourly solar profiles for the whole city of Singapore. The same weather file as for the building demand simulation is used. Building geometry information was taken from Open Street Maps, and data was kindly provided by researchers from Singapore [2]. The sum of geometrically available surface area per category and planning area was adjusted according to scaling factors found in the SERIS PV Roadmap (2020) [1] in order to get area suited for PV installations. Scaling factors are dependent on building and surface type and were correlated to the sectors assigned in section 2.2.. Since using several million solar profiles would lead to excessive computing cost in the optimization model, solar profiles were clustered into 5 categories (North, South, East, West, roof) for each of the 55 planning areas respectively using k-Medoids. Thus, per district, 5 annual hourly solar profiles were utilized in the PV sizing optimization to represent the bulk aggregate surface areas for each orientation. The software ClimateStudio, which is a plug-in for the CAD program Rhinoceros 3D, was used for simulating solar irradiation. An excerpt of the simulation results is shown in Fig. 5a.

2.4. Mobility patterns generation

To estimate local battery capacity, mobility demand, and the movement of residual energy in EV batteries, mobility patterns were derived. Continuous patterns for one week were generated from a dataset of individual mobile phone logs.

2.4.1. Dataset

A dataset containing mobile phone records collected from September 1st to September 30th, 2020 was obtained from Citydata [5]. During the 30-day period a total of 108'971'459 logs were captured. Each log contains a user ID, GPS coordinates and a timestamp. A total of 1'291'343 unique users are registered. The set covers the whole island of Singapore. The number of logs captured varies throughout the month and throughout each day (Fig. 3 (A)). 4:00 to 5:00 is the hour with least activity. This hour was therefore chosen as starting and ending time for all modeling periods in order to minimize period overlapping activity. The data was collected from users of a wide variety of mobile applications with a geospatial component. Citydata provides application developers with an add-on software component which records anonymized location data. Different tracking modes and log frequencies can be set by developers ranging from "manual" where records must be manually triggered to "HawkEye" with continuous tracking. According to Citydata, around 80% of developers chose "stay detection" which is triggered by the crossing of geofences and thus mainly captures movement (Yeow Leong Lee, personal communication 22.6.2022). The frequency of registrations for individual users varies strongly. Often, bursts of logs are followed by long periods without records. Other users are captured once and then disappear from the dataset (Fig. 3 (B)). Due to the prevalence of "stay detection" tracking, an assumption can be made that in many cases movements are recorded and periods without logs indicate that users remain stationary. The recording mode of individual logs is not indicated in the dataset.

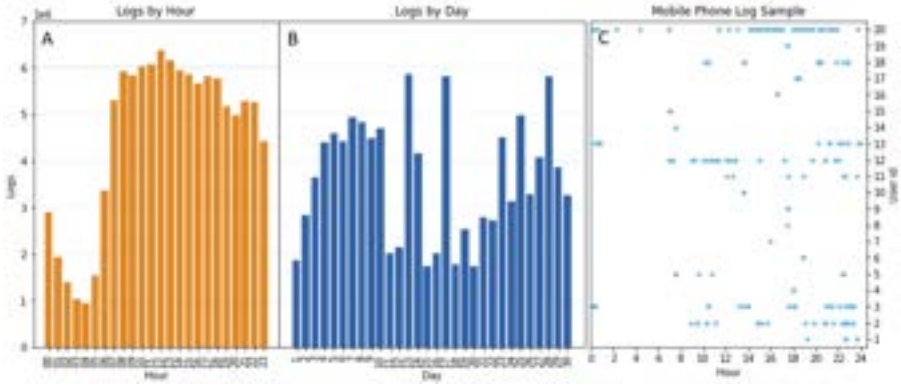

Figure 3: Mobility dataset overview. (A) Cumulative logs contained in the dataset by hour of the day. (B) Cumulative logs by day of the month. (C) Registration times for a random set of users.

Figure 4: (A) Schematic of the routing algorithm. Movement takes place from left to right. Points are classified into route points (orange) or intermediate points (black). (B) An example route generated using OSRM starting at the green waypoint and ending at red. Blue waypoints are routing points, grey ones are intermediate points.

2.4.2. Generating trajectories

In order to generate mobility patterns for a full week, the data was separated into four one-week periods starting on September 2nd, 9th, 16th, and 23rd. Weeks were analyzed separately and later merged. One day before and one after each period were considered for establishing the start and end location of the users. For each time period, only users who had at least one log per day were considered to be reliably tracked and processed further. A total of 56'794 unique IDs remained.

For each user an hourly trajectory was generated. Individual user logs were categorized into route points and intermediate points. The route points were used to determine user trajectories while intermediate points were dropped from further analysis. The first registration of a user in a period was taken as the first route point. Subsequent points were classified as route points if the direct distance to the last route point exceeded 500m or planning area boundaries were crossed. Fig. 4 (A) shows this in a schematic form. Starting with the first orange route point on the left and moving right, points are classified into route points (orange) or intermediate points (black).

Real world driving paths between route points were generated using the open-source routing machine `OSRM` [12]. `OSRM` also provides an estimated driving duration. The registration time of a route point was taken as the arrival time at its location. From this the estimated driving duration was subtracted to get the departure time from the location of the last route point. To match with the time resolution of the LP, users were classified as moving during hourly time steps where they either departed, continued a trip, or arrived at a new destination. During full hours with no movement, users were considered to be stationary and associated with EVs available for charging or discharging. Finally, the routes from all four weeks were combined into one aggregated week. As it is assumed that users follow similar mobility patterns throughout the different weeks, users tracked in multiple weeks were weighted accordingly. Movements by a user included in three of the four weeks were therefore only counted as one third in each of these three weeks.

2.4.3. Anomalies

In occasional cases, logs from individual IDs were observed to jump between far apart locations in very short intervals. In Singapore, car traffic is limited to 90 km/h and the public transport lines do not exceed 100 km/h. A maximum speed of 120 km/h with respect to the direct distance of two log points is therefore set as an upper limit. Logs implying speeds above this threshold are assumed to be GPS anomalies and are not counted as route points. A second anomaly was detected in relation to routing. Occasionally, routes generated by `OSRM` follow long and unintuitive paths between two route points. This is generally the case when points do not follow

the road layout either because the user is taking another mode of transport (e.g. walking or train) or due to GPS inaccuracies. To reduce exaggerated distances and travel times, routes with route distance of more than 2.5 times the direct distance were corrected to have the average ratio between direct distance and route distance. Travel times were adjusted accordingly.

3. Results

3.1. Inputs to Optimization

Fig. 5 and Fig. 6 shows some of the inputs used throughout the studied optimization scenarios. In Fig. 5a, an excerpt of the 3D solar simulation is shown. According to our simulations, PV on buildings can generate up to 15.2 TWh of electricity with 14.2 GWp capacity installed, assuming a conversion efficiency of 20% and an installation threshold of 500 kWh/m^{2}a solar irradiation on surfaces (see Fig. 3 in Waibel et al. 2021 [27] for feasible thresholds in Singapore based on optimization). Alternatively, with a threshold of 750 kWh/m^{2}a, we can achieve a generation potential of 11 TWh and a capacity of 7.5 GWp. This compares well to the SERIS PV roadmap [1], which reports a capacity of 8.6 GWp at 750kWh/m^{2}a threshold, but also including PV on infrastructure and floating PV. The total electricity demand of Singapore for 2019 was reported to be 51.7 TWh, where the industry sectors accounts for 21.5 TWh (41.5%), the commercial and service sectors for 19.3 TWh (37.3%), households for 7.7 TWh (14.8%), and the transport sector for 3.0 TWh (5.8%) [3] (Fig. 6a). Therefore, PV on buildings could potentially cover 21% (750 kWh/m^{2}a threshold) or 29% (500 kWh/m^{2}a threshold) of total annual electricity demand. In this paper, however, the optimization model will decide on the actual PV capacities installed per district.

The annual electricity demand per floor area and planning area is shown in Fig. 6c; the annual solar irradiation is shown in Fig. 6b. Districts dominated by transport have the highest average irradiation of 808 kWh/m2a, followed by Industry with 796 kWh/m2a and Service with 756 kWh/m2a Planning areas with mainly residential buildings have the lowest average solar irradiation per area with 663 kWh/m2a. As for electricity demand, values vary significantly across planning areas, with residential electricity demand intensity being the lowest and industrial the highest.

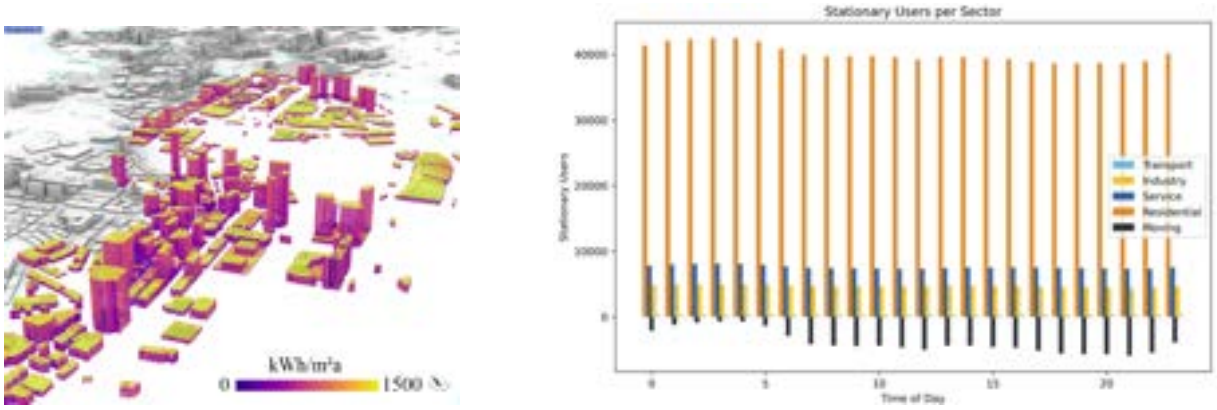

(a) Annual solar irradiation on roof and facades around Downtown Singapore.

(b) Non-stationary users on the negative axis, and stationary users by predominant sector of the planning area they are located in.

Figure 5: Inputs to the optimization: solar potentials and mobility patterns.

Fig. 5b portrays users tracked in the mobility dataset classified as stationary or parked. Planning areas are grouped by predominant sector. Users in motion are plotted on the negative axis. A distinct driving pattern can be observed with lowest activity during the night hours and peaks in the morning and evening. However, shifts of occupancy between sector types throughout the day are minimal. Planning areas of all sector types have their highest occupancy levels at night. These drop during the day. The sum of users is constant, drops in overall stationary users represent users on the move.

3.2. Scenario Analysis

Multiple scenarios were generated by deviating individual parameters from a base scenario. The base scenario reflects targets of the Singapore Green Plan 2030 [20]. Where possible, parameters were modified to represent either current values (low environmental considerations) or targets and predictions for 2040 (high environmental considerations). Amongst others, local self-consumption (LSC) [17] is used as a parameter in our study. It is defined as PV electricity consumed directly by an individual building. Excess electricity needs

to be sent through the local grid, even if it is reconsumed within the same planning area in which case grid charges apply. The LSC factor attempts to correct for this effect by applying scaled grid transmission charges to electricity transferred within a planning area. The charge is applied to all local production (PV and V2G) but is reimbursed when electricity is exported outside of the district, as in this case the full transmission fees are paid in the planning area where the electricity is imported to. In contrast, *district level* self-consumption (SC) is a dependant variable in our study and calculated with $d^{\text{total}}_{w,t,l} = d^{\text{building}}_{w,t,l} + x^{\text{charge}}_{w,t,l} - x^{\text{discharge}}_{w,t,l}$, where x are operational decision variables for charging and discharging batteries (including EVs), d is demand, and w, t, l are indices for week, timestep (hours), and location (district). Detailed and complete parameter values are reported in [4]. Fig. 6d to 6i show the fraction of PV production exceeding local demand at a time of production, district

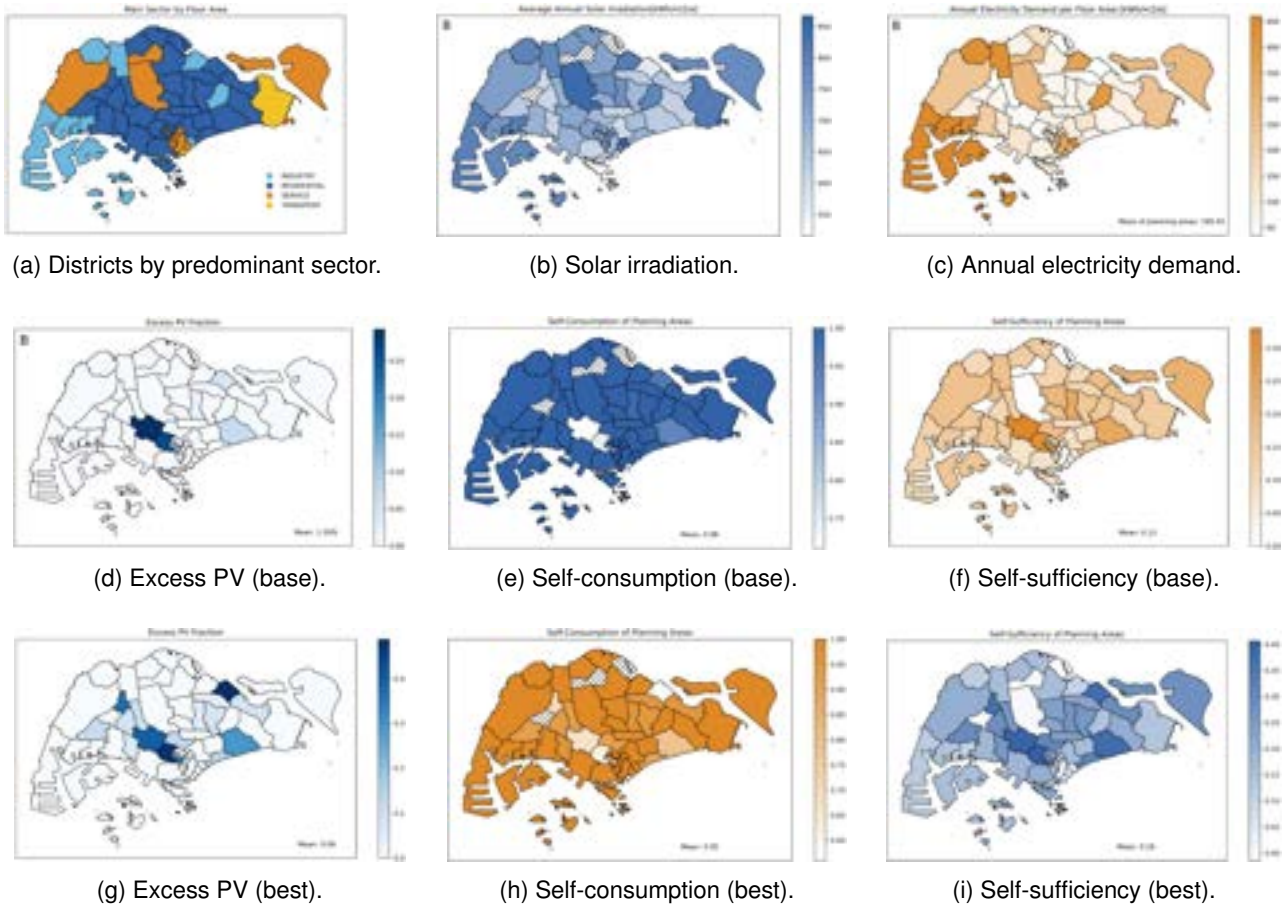

(a) Districts by predominant sector. (b) Solar irradiation. (c) Annual electricity demand.

(d) Excess PV (base). (e) Self-consumption (base). (f) Self-sufficiency (base).

(g) Excess PV (best). (h) Self-consumption (best). (i) Self-sufficiency (best).

Figure 6: Singapore with results shown by planning area. Diagonal lines mark districts where no data was registered.

level self-consumption, SC, and district level self-sufficiency* for the base scenario and an (environmentally) *best case* scenario. In the base scenario a LSC value of 40% is chosen (between typical self-consumption values without storage and values with dedicated storage found in [17]) and in the best case scenario 80% an optimistic value still found in the literature, since Singapore has high demand compared to its PV production capacity. In the base scenario, the prepandemic WEP from 2019 was chosen as a stable baseline. By 2022 the WEP had risen by a factor of 2.8. This was used as a multiplication factor to generate the best case WEP from that in the base scenario. Additionally, full EV-penetration (600'000 EVS) was implemented compared to 10% penetration in the base scenario. In the best case scenario the fraction of excess PV increases to an average of 6% under the best-case scenario with complete utilization of surface potential. All of this is found in predominantly residential planning areas where the average is 10% with values reaching up to 49%. Excess in other sectors is negligible. Self-consumption remains high with 95% and a range from 100% to 56%. Self-sufficiency averages at 18% but can reach levels of 40% in districts where PV production is high compared to local demand. It should be noted that, when running a scenario without V2G, the effect on average planning area self-consumption and self-sufficiency was minimal with V2G increasing self-consumption by about 0.5% and self-sufficiency by 0.03%. This can be explained by the generally already high levels of SC where EV

*Self-consumption represents the fraction of PV consumed locally while self-sufficiency describes the fraction of local demand covered by PV.

electricity demand is negligible in comparison to total electricity demand.

3.2.1. Scenario Comparison

Fig. 7 shows a comparison of all studied scenarios and the difference in system cost, optimal PV capacities, and CO_2 emissions. Following parameters are used in the various scenarios: CO_2 tax in S$/t$CO_2$eq. = 0 (low), 60 (base), 95 (high); EV penetration in number of EVs = 3000 (low), 60'000 (base), 600'000 (high); PV CAPEX = estimates from 2022 (low), 2026 (base), 2031 (high) as from [1]; wholesale electricity price (WEP) = prices from 2019 (base), base $\times$ 2.76 (high), base $\times$ 0.5 (low); LSC in % = 20 (low), 40 (base), 80 (high). Furthermore, some scenarios are calculated with or without PV, and with or without V2G. The colorbar range is set to -30 to +30 %, but numeric values are indicated in the cells.

Results show that increasing LSC made PV systems significantly more viable with investment increasing by 257 Mio S$ or 59%, decreasing self-consumption reduced investment by 42 Mio S$ or 10%. Installed PV capacity reached 8.6 GWp (57% higher than in the base scenario), import related costs decreased significantly and export revenue increased with higher levels of self-consumption. Electricity related CO_2 emissions are reduced by 0.6 Mt/a in a high LSC scenario, while they marginally increase by 0.1 Mt/a in a low LSC scenario. In summary, achieving high degrees of high LSC shows both significant economic and environmental benefits.

In all scenarios PV installations are able to significantly reduce costs and emissions of the Singapore electricity market. The optimal installed capacity determined by the model ranges from 4 to 14 GWp depending on the scenario. Under the base assumptions for 2030, the optimally installed capacity is 5.5 GWp. As such, economically viable PV potential is significantly larger than the 2 GWp capacity targeted set in the Singapore Green Plan 2030 [20]. Under base scenario assumptions PV systems can reduce carbon emissions from electricity generation by around 3 Mt or 15% compared to the same scenario without PV.

The impacts of V2G are strongly scenario dependent. In the base scenario cost reductions due to V2G technology come to only 7 S$ per EV and year. Savings can be increased up to 127.65 S$/EV/a under the best-case scenario. The economic potential of V2G for self-consumption increase and electricity arbitrage is therefore severely limited in all scenarios. Additionally, V2G increases CO_2 Emissions in the base and best-case scenario by increasing the overall electricity imported. Synergies between PV and V2G are minimal although V2G does increase the economically viable PV area in one scenario (High LSC w/o V2G to High LSC scenario).

3.2.2. Demand vs PV production

Fig. 8 shows average hourly building energy demand and PV production with optimal capacities from the base scenario for a predominantly residential, industrial, and service dominated planning area, respectively. It is striking that only in the first district, PV production exceeds demand, while in most other districts PV electricity can only provide a fraction of total demand. Considering that the majority of total electricity demand stems from industry and service/commercial use, most districts will not be able to export PV (also see Fig. 6d and 6g). For the commercial- and service sector, this is due to the constantly high cooling loads throughout the year.

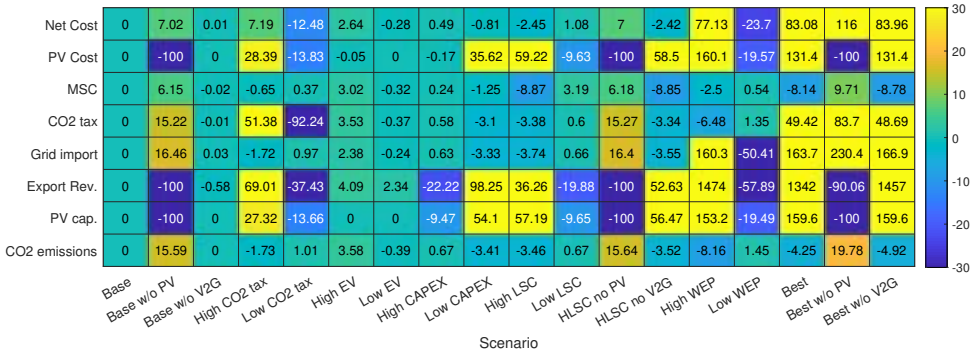

Figure 7: Comparison of all studied scenarios with values shown as % deviation from the base scenario. Net cost = PV Cost + MSC + CO2 tax + Grid import - Export revenue; MSC = market support charge; HLSC = High LSC; WEP = wholesale electricity price.

3.2.3. Charging Schedules

Two modes of EV charging can be differentiated: Charging from the grid and charging using excess PV electricity. The second is defined as charging at times when local PV production exceeds local demand. Average daily charge and discharge patterns for the entire EV fleet of Singapore are shown in Fig. 9, with optimization results for the base scenario in Fig. 9a and for a high LSC scenario in Fig. 9b. In the base scenario, the two charging modes are clearly separated. Grid charging takes place almost exclusively during the night when

electricity prices are low. Excess PV is available during the day but in much smaller quantities. Only 2.21% of charging takes place using excess PV-power. V2G discharging takes place almost exclusively in the hour from 10:00 to 11:00 when electricity prices hit their highest point. The vast majority of annual charging electricity is consumed through driving, a fraction is lost during the charging process. Only 7.2% are discharged back into the grid. In the high LSC scenario, charging still took place primarily during the night and from the grid, however the fraction of charging from excess PV is increased to 18.7%. Discharging was spread more evenly with peaks during the morning and afternoon.

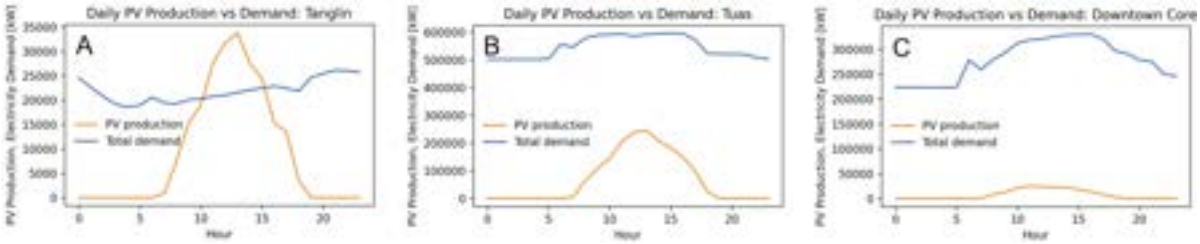

Figure 8: Average hourly building demand and PV production (capacities from base optimization) for three planning areas with three predominant sectors: Tanglin is residential (A), Tuas is industrial (B), Downtown Core is service dominated (C).

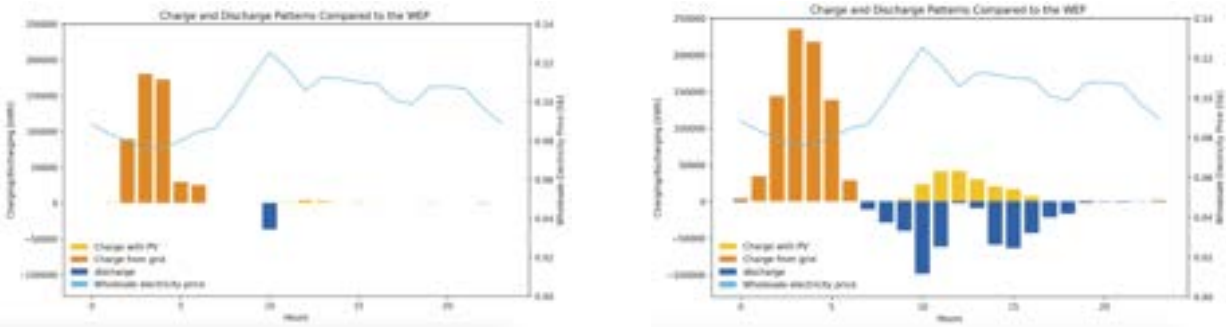

(a) Base scenario.

(b) High self-consumption scenario.

Figure 9: Average daily charging and discharging modes and patterns for EVs.

4. Discussion

Kobashi et al. (2020) [15] found that V2G in combination with PV systems could significantly reduce energy related costs and emissions in Kyoto. The difference in conclusions likely owes to both different model assumptions as well as real differences between the two locations. The most significant difference appears to be the result that local rooftop PV in Kyoto can cover approximately the entire annual electricity demand of the city. This means, times of overproduction are much more frequent and the possibility of storing electricity for later use becomes more valuable compared to this study, where PV generation rarely exceeded local demand. Kyoto is stated to have a rooftop area of 51.1 km^2 and an annual load of 8.1 TWh. In comparison, the area sum of the buildings in Singapore is 90.0 km^2 but the annual demand in 2019 was 51.7 TWh. This means that the demand per roof area is significantly higher in Singapore. Additionally, Kobashi et al. assume that 70% of roof area can be covered by PV whereas scaling factors used in this paper are significantly lower. Additionally, the study aggregates the city to a single unit. No transmission fees within the city are applied.

Schläpfer et al. (2021) [24] used the same mobility dataset and a similar method for extracting mobility patterns for Singapore. They also aggregated to the planning area level and found that for specific planning areas, up to 40% of nighttime *household* electricity demands could be covered by V2G, but for most districts this value was between 10% and 20%. These results were found using a first method assessment relying on a simple charging/discharging scheme where economic effects were excluded. Our study now investigated charging/discharging and PV capacity sizing based on a cost minimization. We found that under base assumptions for 2030 V2G under best case assumptions vehicle discharge made up 4% of the islands total demand (or 26% of *household* demand). However, cost optimal charging took place predominantly from the grid during night hours and discharging happened during the day. As such the transfer from PV electricity produced during the day to the night hours was not observed. Our results show that future work should also increase spatial resolution to better capture local mismatch of demand. This model assumes perfect foresight and focuses on overall economic optimization and not e.g. load balancing or individual benefits to stakeholders. Control schemes operating under bounded information and alternate optimization strategies could be explored.

5. Conclusion

This paper investigated the effects of electric storage from V2G technologies on optimal PV sizing on buildings and associated system costs and operational emissions at the district scale for the city of Singapore. Scenarios were based around the country's climate targets (Singapore Green Plan 2030). Energy and mobility flows were captured in an LP optimization model which defined PV scaling and charge/discharge patterns minimizing total systems cost. Carbon emissions were included in the form of a CO_2 tax. Three main inputs were generated: (i) City scale mobility patterns derived from a large set of mobile phone GPS records, (ii) energy demand at district level modeled using a bottom-up approach, and (iii) PV potentials using building geometries and 3D solar irradiation data. Different levels of local self-consumption were studied in a scenario analysis and compared to a base case.

Average self-consumption at the district level was very high in all scenarios; under base scenario assumptions it was 98% with a self sufficiency rate of 13%. These values were barely affected by V2G. In the best-case scenario with maximum PV installations average sufficiency increased to 18% and self-consumption at planning area scale dropped to 95% but with a significant range. In this scenario V2G was able to increase self-consumption by around 0.5%. Although impacts of V2G were low, the general expected effects were found. V2G was able to increase self-consumption and reduce exports to the grid. Reasons for low impact as compared to other studies are likely twofold. On the one hand Singapore's economically viable building PV potential is low compared to a relatively high demand. This means that PV only exceeds local demand in specific locations and times. Especially residential areas with a demand curve that is low and runs counter to PV production can generate significant overproduction and could be candidates for V2G. On the other hand, through the aggregation to the planning area level, local mismatches in production and demand were partially flattened and thus the potential for V2G to act as intermediate storage was reduced.

In order to gain further insight into the potential of V2G in cities like Singapore, future research could focus on improving mobility demand predictions, and combining large scale city dynamics with more fine-grained local analysis. Investigating additional cities could reveal location based effects. Finally, specific grid dynamics could be modelled explicitly to account for further benefits of V2G such as grid balancing and frequency regulation.

Acknowledgments

This research was conducted at the Future Cities Lab Global at Singapore-ETH Centre and ETH Zurich. Future Cities Lab Global is supported and funded by the National Research Foundation, Prime Minister's Office, Singapore under its Campus for Research Excellence and Technological Enterprise (CREATE) programme and ETH Zurich (ETHZ), with additional contributions from the National University of Singapore (NUS), Nanyang Technological University (NTU), Singapore and the Singapore University of Technology and Design (SUTD). Input was gratefully received from Luis Santos from the Cooling Singapore group at SEC on electricity modeling, and from Dr. Alina Galimshina from the Chair of Sustainable Construction at ETH on embodied emissions of PV systems. Acknowledgement also goes to Citydata for providing the mobility dataset and related support.

References

[1] (SERIS) Solar Energy Research Institute of Singapore. *UPDATE of the Solar Photovoltaic (PV) Roadmap for Singapore*. Tech. rep. 2020. URL: https://www.seris.nus.edu.sg/doc/publications/Update-of-the-Solar-Roadmap-for-Singapore-(March-2020).pdf.

[2] Ayu Sukma Adelia. *Cooling Singapore project, retrieved from Openstreetmap, 2020*.

[3] Energy Market Authority. *Energy Balance*. 2019. URL: ttps://www.ema.gov.sg/singapore-energy-statistics/Ch04/index4 (visited on 03/08/2022).

[4] Dominic Caviezel. "Sizing, Cost, and Emissions of Vehicle to Grid Coupled PV at District Scale". Master Thesis. ETH Zurich, 2022. URL: http://hdl.handle.net/20.500.11850/595017.

[5] CITYDATA.ai. *Mobile Phone Records Singapore*. 2022. URL: https://beta.citydata.ai/company/about (visited on 03/08/2022).

[6] Energy Market Company. *Price Information*. 2022. URL: https://www.emcsg.com/marketdata/priceinformation (visited on 03/08/2022).

[7] Constance Crozier, Thomas Morstyn, and Malcolm McCulloch. "The opportunity for smart charging to mitigate the impact of electric vehicles on transmission and distribution systems". In: *Applied Energy* 268.December 2019 (2020), p. 114973. DOI: 10.1016/j.apenergy.2020.114973. URL: https://doi.org/10.1016/j.apenergy.2020.114973.

[8] Igor Cvetkovic et al. "Future home uninterruptible renewable energy system with vehicle-to-grid technology". In: *2009 IEEE Energy Conversion Congress and Exposition, ECCE 2009*. IEEE, 2009, pp. 2675–2681. DOI: 10.1109/ECCE.2009.5316064.

[9] Merkebe Getachew Demissie et al. “Inferring Passenger Travel Demand to Improve Urban Mobility in Developing Countries Using Cell Phone Data: A Case Study of Senegal”. In: *IEEE Transactions on Intelligent Transportation Systems* 17.9 (2016), pp. 2466–2478. DOI: 10.1109/TITS.2016.2521830.

[10] Reza Fachrizal and Joakim Munkhammar. “Improved photovoltaic self-consumption in residential buildings with distributed and centralized smart charging of electric vehicles”. In: *Energies* 13.5 (2020). DOI: 10.3390/en13051153.

[11] Jimeno A. Fonseca et al. “City Energy Analyst (CEA): Integrated framework for analysis and optimization of building energy systems in neighborhoods and city districts”. In: *Energy and Buildings* 113 (2016), pp. 202–226. DOI: 10.1016/j.enbuild.2015.11.055.

[12] Stephan Huber and Christoph Rust. “Calculate Travel Time and Distance with Openstreetmap Data Using the Open Source Routing Machine (OSRM)”. In: *Stata Journal* 16.2 (2016), pp. 416–423. DOI: 10.1177/1536867X1601600209.

[13] IEA. *Introduction to System Integration of Renewables*. CC BY 4.0. 2020. URL: https://www.iea.org/reports/introduction-to-system-integration-of-renewables (visited on 03/08/2020).

[14] Md Shahadat Iqbal et al. “Development of origin-destination matrices using mobile phone call data”. In: *Transportation Research Part C: Emerging Technologies* 40 (2014), pp. 63–74. DOI: 10.1016/j.trc.2014.01.002. URL: http://dx.doi.org/10.1016/j.trc.2014.01.002.

[15] Takuro Kobashi et al. “On the potential of ”Photovoltaics + Electric vehicles” for deep decarbonization of Kyoto’s power systems: Techno-economic-social considerations”. In: *Applied Energy* 275 (2020), p. 115419. DOI: https://doi.org/10.1016/j.apenergy.2020.115419.

[16] Haiyang Lin et al. “The impact of electric vehicle penetration and charging patterns on the management of energy hub – A multi-agent system simulation”. In: *Applied Energy* 230.May (2018), pp. 189–206. DOI: 10.1016/j.apenergy.2018.08.083. URL: https://doi.org/10.1016/j.apenergy.2018.08.083.

[17] Rasmus Luthander et al. “Photovoltaic self-consumption in buildings: A review”. In: *Applied Energy* 142 (2015), pp. 80–94. ISSN: 03062619. DOI: 10.1016/j.apenergy.2014.12.028. URL: http://dx.doi.org/10.1016/j.apenergy.2014.12.028.

[18] Efstathios E. Michaelides. “Primary energy use and environmental effects of electric vehicles”. In: *World Electric Vehicle Journal* 12.3 (2021). DOI: 10.3390/wevj12030138.

[19] Portia Murray et al. “Optimal transformation strategies for buildings, neighbourhoods and districts to reach CO2 emission reduction targets”. In: *Energy and Buildings* 207 (2020), p. 109569. DOI: 10.1016/j.enbuild.2019.109569. URL: https://doi.org/10.1016/j.enbuild.2019.109569.

[20] Ministry of National Development et al. *SG Green Plan: Our Targets*. 2022. URL: https://www.greenplan.gov.sg/targets (visited on 03/08/2022).

[21] Pedro Nunes, Raquel Figueiredo, and Miguel C. Brito. “The use of parking lots to solar-charge electric vehicles”. In: *Renewable and Sustainable Energy Reviews* 66 (2016), pp. 679–693. DOI: 10.1016/j.rser.2016.08.015. URL: http://dx.doi.org/10.1016/j.rser.2016.08.015.

[22] Gururaghav Raman and Jimmy Chih-Hsien Peng. “Electricity consumption of Singaporean households reveals proactive community response to COVID-19 progression”. In: *Proceedings of the National Academy of Sciences of the United States of America*. Vol. 118. 34. 2021, pp. 1–7. DOI: 10.1073/pnas.2026596118.

[23] Wolf Peter Schill and Clemens Gerbaulet. “Power system impacts of electric vehicles in Germany: Charging with coal or renewables?” In: *Applied Energy* 156.2015 (2015), pp. 185–196. DOI: 10.1016/j.apenergy.2015.07.012. URL: http://dx.doi.org/10.1016/j.apenergy.2015.07.012.

[24] Markus Schläpfer et al. “Using Mobility Patterns for the Planning of Vehicle-to-Grid Infrastructures that Support Photovoltaics in Cities”. In: (2021). arXiv: 2112.15006. URL: http://arxiv.org/abs/2112.15006.

[25] Sriram Vaisambhayana and Anshuman Tripathi. “Study of electric vehicles penetration in Singapore and its potential impact on distribution grid”. In: *2016 Asian Conference on Energy, Power and Transportation Electrification, ACEPT 2016*. IEEE, 2016, pp. 1–5. DOI: 10.1109/ACEPT.2016.7811513.

[26] Mohammad M. Vazifeh et al. “Optimizing the deployment of electric vehicle charging stations using pervasive mobility data”. In: *Transportation Research Part A: Policy and Practice* 121.January (2019), pp. 75–91. DOI: 10.1016/j.tra.2019.01.002. URL: https://doi.org/10.1016/j.tra.2019.01.002.

[27] Christoph Waibel, Shanshan Hsieh, and Arno Schlüter. “Impact of demand response on BIPV and district multi-energy systems design in Singapore and Switzerland”. In: *CISBAT 2021 International Conference Future Buildings and Districts*. Lausanne, Switzerland, 2021.

Quantifying operational flexibility of distributed cross-sectoral energy systems for the integration of volatile renewable electricity generation

Sebastian Berg[a], Lasse Blaume[b] and Benedikt Nilges[c]

[a] *Fraunhofer Institute for Environmental, Safety and Energy Technology UMSICHT, Oberhausen, Germany, sebastian.berg@umsicht.fraunhofer.de, CA*
[b] *Fraunhofer Institute for Environmental, Safety and Energy Technology UMSICHT, Oberhausen, Germany, lasse.blaume@umsicht.fraunhofer.de*
[c] *Institute of Technical Thermodynamics, RWTH Aachen University, Aachen, Germany, benedikt.nilges@ltt.rwth-aachen.de*

Abstract:
As one element of power system transition, distributed cross-sectoral energy systems (DCES) can provide flexibility for the electricity market. So far, no applicable method for quantifying the flexibility potential of DCES operation exists. Nonetheless, by comparing the flexibility demand of the electricity market and the electricity flow between a DCES and the electricity grid it becomes possible to quantify market-serving flexibility of DCES operation. In this work, we categorize aim and scope of already known flexibility quantification methods and develop a new method to assess DCES market-serving flexibility covering residual load (RL). Part of this method is the new developed quantification indicator *Flexibility Deployment Index* (FDI), integrating two factors: The RL of the electricity market and the electricity purchase and feed-in of a DCES. By normalizing both factors, operation of different DCES concepts and scenarios regarding their flexibility can be compared. The developed quantification method is applied in a case study of a hospitals' DCES in Germany. Using a MILP optimization model with different technology concepts and scenarios, we study FDI variation for a fixed tariff, a dynamic tariff and a CO_2-emission-optimized operation. The results of the case study prove that high-capacity combined heat and power units combined with thermal storage units lead to high flexibility provision. Also, the results outline higher flexibility provision in the winter than in the summer period.

Keywords:
Distributed cross-sectoral energy system; Flexibility; Optimized operation; Quantification indicator; Residual load.

1. Introduction and motivation

The aim of this work is to develop a method to quantify the flexibility provision of distributed cross-sectoral energy systems (DCES).

According to [1] flexibility demand results from the difference of electricity power consumption P_{el} and the renewable energy (RE) generation P_{RE} indicated by the residual load (RL) P_{RL} in (1).

$$P_{RL} = P_{el,consumption} - P_{RE,generation} \tag{1}$$

Presently, in the higher-level energy system of Germany, the requirement for flexibility demand of RL is primarily fulfilled by conventional power plants, controllable RE, and storage power plants ([2, 3]). However, with the phasing out of coal and nuclear electricity generation [§ 4 art. 1 cl. 2 KVBG; § 7 art.1 AtG], significant flexibility capacities are going to vanish, leading to the emergence of a potential flexibility gap ([4, 5]).

To address this challenge, one possible solution could be to explore the flexible operation of DCES. However, assessing the flexibility potential of DCES is a non-trivial task due to the absence of a standardized method for evaluating DCES flexibility.

Pina et al. [6] defines energy systems as cross-sectoral when they include at least one polygeneration unit, such as a combined heat and power (CHP) unit, that can be supplemented by additional energy conversion units and storage. These systems are referred to as distributed energy systems (DCES) when they serve as local energy systems. DCES are primarily deployed in industrial, district, and building facilities with high energy demands, such as hospitals, swimming pools, universities, and shopping centers.

DCES primarily serve the energy demand of their respective facilities. Any surplus capacity can be provided to the higher-level energy system. However, since the availability of this capacity is time-dependent due to

the volatile nature of facility demand, the flexibility potential of DCES cannot be accurately measured by their installed generation capacity alone.

To develop a suitable characteristic value we firstly draft an understanding of flexibility in 1.1.. Based on this, we define flexibility of a DCES in 1.2.. We show a literature review giving an overview of existing quantification methods in 1.3.. We present various flexibility indicators and discuss whether they are sufficient for the targeted quantification. Subsequently, we define requirements for a new quantification indicator in 2.1. and deduce and introduce it in 2.2.. In section 2.3., we present a case study in which we performe a plaubility check of the quantification indicator and in 3., we present the results of the case study. In 4., we conclude our results of the study.

1.1. Flexibility in the energy system

In [7–10], flexibility is described as a balancing service for a higher-level energy system. The flexibility purpose is RE market integration and RE curtailment reduction by flexible electricity purchase and electricity feed-in. Load-shifting is a technical implementation to offer this flexibility. Negative load-shifting is characterized by the reduction of electricity generation, increase of load and charging of storage. Positive load-shifting is characterized by the increase of electricity generation, reduction of load and discharging of storage. To gain flexibility by load-shifting the requirements of the higher-level energy system need to be considered.

According to literature, flexibility provision can be divided into different characteristics ranging from capability services up to technical assertions:

1. *Flexibility options* are technologies and operating modes of different fields of function in the energy system that can provide flexibility. In Fig. 1 [11–14] show an overarching definition of these technologies and operating modes and allocate them to the fields of flexible generators, flexible consumers (demand), flexible storage and the expansion of the electricity grid. In this approach the flexibility options cover RL.

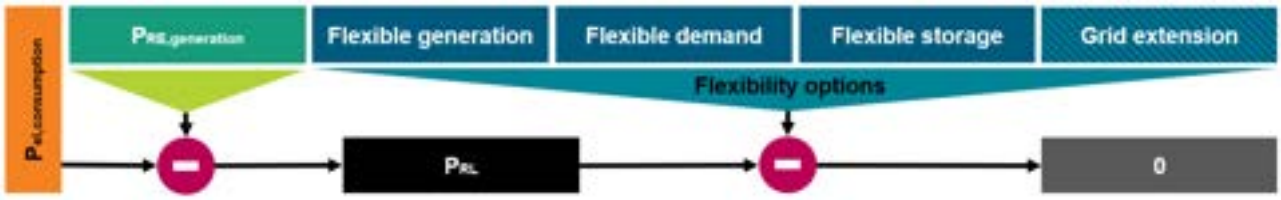

Figure 1: Fields of functions in an energy system with flexibility options covering RL. Figure in accordance with [15].

2. According to [16]], three areas of *flexibility applications* exist. They describe the point of view of a flexibility option:
    - *Market-serving flexibility* does not depend on any physical necessity. It is exercised solely by preferences on the demand side. It comprises of the operation of individual market players, who optimize their operation following an objective function regarding external signals (e. g. electricity price and CO_2 emissions).
    - *System-serving flexibility* is intended to ensure the quality of supply in the electricity grid and thus the security of supply. The main objective is to maintain the frequency by using balancing power for the stability of the system balance of generation and demand. One instrument for providing system-serving flexibility are operating reserves.
    - *Grid-serving flexibility* is provided by the transmission system operators for energy system stability. The focus is on grid congestion management for the interconnected systems and prevention of bottlenecks. In Germany one instrument for providing grid-serving flexibility is e.g. 'Redispatch'.
3. According to [10, 17], flexible operation can be provided on different *flexibility levels* in the energy system - the consumer, producer and storage level.
    - The *consumer level* includes mainly energy demands. Consumer level flexibility can be divided into consumption-side flexibility and load management. These are differentiated by their influence on the energy consumer. The consumption-side flexibility has no influence on the consumer's behavior, as it results from flexibility of the energy supply units on the demand side. In contrast, load management, also called demand-side management (DSM), has an impact on the demand time series and thus has an impact for the consumer and the consumers behavior. The consumer level can also be named *prosumer level*, if the consumer is also able to provide electricity to the grid.

- The *producer level* includes controllable power plants that can be operated flexibly without external constraints.
- The *storage level* includes large-scale storage facilities that can store electrical energy directly or indirectly and thus provide storage flexibility.

4. In [18–20] the term *flexibility potential* is defined as the flexibility that a flexibility option can theoretically provide. [19] differentiates the flexibility potential into the terms technical potential, technically usable potential, socio-technical potential, economic potential and regulatory potential. [18] relates these potential terms to each other according to Fig. 2. In this logic, the differentiation of technical potential from theoretical potential is in accordance with the technical restrictions of the flexibility option. The technical potential is further constrained by the frequency of its flexibility call-ups, defined as the technical usable potential. The technically usable potential is finally reduced to the usable potential by the economic, socio-technical and regulatory potential. The economic restrictions of the technical usable potential are affected by the economic viability of a callable flexibility option, which is mainly characterized by the revenue of selling flexibility services. The socio-technical potential is the willingness of adjusting operation and services for providing flexibility and depend on the extent to which the provision of flexibility leads to restrictions in normal operation or the original intended use of the flexibility option. The regulatory restrictions are defined by legislations of authorities and regulations of market access.

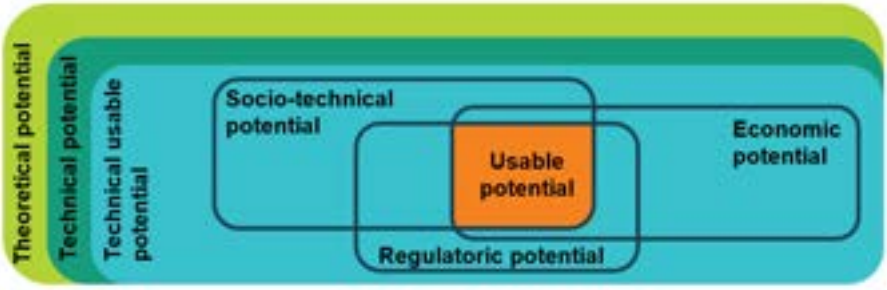

Figure 2: Classification of different flexibility potentials. Figure in accordance with [18].

1.2. Flexibility of a DCES

We classify the flexibility offered by a DCES considering the supply of electricity, heating, and cooling for a facility, and we formulate an understanding of why and how DCES flexibility covers RL.

In this study the DCES is containing energy conversion and storage technologies in the form of a CHP, a gas boiler, a compression chiller (CC) and thermal energy storage units (TES). Every unit represents a flexibility option: The CHP unit, the gas boiler and the CC are flexible generators. The TES are flexible storage units. In the following we consider the entire DCES as one flexibility option. The DCES can thereby provide flexibility to the higher-level energy system by the electricity flows through the public grid connection.

As the focus in this study is on the cost-minimal operation, the flexibility application of the DCES operation can be understood as market-serving flexibility. Though, it should be noted that market-serving flexibility can also be interpreted as system-serving flexibility, as markets for balancing energy exist. According to [21], DCES can also run in a grid-serving manner by considering grid bottlenecks. In this case, they might be installed close to consumers.

The flexibility level of the DCES is the consumer level providing consumption-side flexibility. The DCES offers load-shifting by sector coupling with the CHP and time flexibility with the TES. As no active adjustment of the demand time series exists, DSM is not possible.

In this study, we focus on the usable flexibility potential of the DCES. The economic and regulatory framework conditions are mainly determined by the electricity markets. The socio-technical restrictions are set by the premise that the facility's demand needs to be fulfilled at any time.

Based on this classification we define the flexibility understanding of the DCES in this study in an application context: *Constrained by the socio-technical, regulatory and economic restrictions, the DCES contains a usable flexibility potential of market-serving consumption-side flexibility. The flexibility service does not primarily follow a physical necessity. It follows the optimal operation of the DCES. The optimized operation is controlled by an external signal under the premise that all DCES' facility energy demands are covered at any time. Dependent on the DCES' energy conversion technologies and storage units, the DCES operation covers RL in the higher-level energy system and thus, becomes a flexibility option.*

1.3. Review of flexibility indicators

To quantify the flexibility of DCES, several approaches can be found in literature. These approaches pursue different understandings of flexibility and pursue different flexibility objectives and result in a variety of indicators. However, none of these indicators allows to quantify the previously defined understanding of flexibility covering RL.

The existing indicators are valid for different time periods. Beginning with the quantification of points in time in [24, 26–29, 32], the period of the flexibility provision in [22, 23] and the quantification of a freely selectable period in [22,27,28,30,31,33,34]. The indicators also differ in the use of a reference operation or no reference operation in [22, 24, 26–29, 33, 34]. Based on the different approaches, also the number and types of used parameter varies. As in [22–24] only the time t of a flexibility provision is considered, in [22, 24, 26–29] also the power generation P is taken into account. In [22, 27, 28, 30, 31] both parameters of time and power are combined to quantify flexibility with a parameter of the unit energy E. In [27, 30–34] also external parameters of mostly cost signals and electricity prices are used. A distinction can also be made between relative result values in [24, 26, 27, 31, 33, 34] and absolute result values in [22, 23, 27–30, 32] with parameters of the units time, power, energy or costs.

The indicators from the literature can be categorized into indicators for time flexibility in [22–24], power flexibility in [22, 24–29], energy flexibility in [22, 27, 28, 30, 31], energy efficiency in [27, 28, 32] and the quantification of flexibility through external variables or signals in [27, 30, 31, 33, 34]. The indicators for time flexibility, power flexibility, energy flexibility and energy efficiency focus on flexibility definitions concerning only single energy units or separate energy systems. Only the quantification indicators of flexibility through external variables or signals consider also the higher-level energy system. Though, RL is not considered in any indicator.

2. Method

As no adequate flexibility indicator exists in literature to quantify the above defined flexibility, we determine a new indicator.

2.1. Requirements for a new quantification indicator

The new indicator is intended to quantify to which extend the market-serving flexibility of a DCES covers RL of the higher-level energy system. The indicator should enable a quantification of the usable flexibility potential. The focus is on quantifying the concurrence of the DCES operation with the higher-level energy system. The indicator should be able to distinguish between positive and negative load-shifting at times with high or low RL. Due to the wide range of other possible DCES configurations, it is important that the quantification takes place on the basis of parameters which are applicable for a wide variety of DCES concepts. As the flexibility understanding focuses on the electricity sector, the used parameters should also be electrical values. The indicator should provide comparability of different DCES in different facilities and in different operation modes. Therefore, it is advisable to use normalized values. Usually this leads to an appropriate outcome between zero and one, which also presents the results in an easily and meaningful way. Further, the indicator should work for different quantification periods (QP).

2.2. The flexibility deployment index

We develop the new quantification indicator *Flexibility Deployment Index* (FDI). It consist of different electrical parameters. We consider on the one hand the electrical load-shifting through the grid connection of the DCES to and from the higher-level energy system and on the other hand we consider the RL of the higher-level energy system. Therefore, we set the system boundary around all DCES units and consider the DCES as a black box.

We display the flexibility offer with the load-shifting of the DCES by the *Flexibility Potential Factor* ($F_{DCES,t}$). As can be seen in (2), the $F_{DCES,t}$ includes the electricity purchase P_{pur} and the electricity feed-in P_{in} of the DCES at a time step t within QP as the set of all time steps. To align the power with the capacity of the DCES and its facility's demand, we normalize the power with the maximum and minimum electricity flow in QP. The denominator is determined by a case distinction, depending on whether power is purchased or feed in. If power is fed in (positive numerator), the maximum power feed-in during the QP is used as denominator. If power is purchased (negative numerator), the maximum purchased power in the QP is used as denominator. The $F_{DCES,t}$ has a possible range from -1 to +1, in which -1 represents the maximum possible flexibility potential from negative load-shifting. Conversely, +1 represents the maximum possible flexibility potential from positive load-shifting.

$$F_{DCSE,t} = \frac{P_{in,t} - P_{pur,t}}{|P_{DCSE,max}|} \qquad \text{with } P_{DCSE,max} = \begin{cases} \max\limits_{t \in QP}(P_{in,t}) & \text{if } P_{in,t} - P_{pur,t} > 0 \\ \max\limits_{t \in QP}(P_{pur,t}) & \text{if } P_{in,t} - P_{pur,t} < 0 \end{cases} \tag{2}$$

We display the flexibility demand based on the RL of the higher-level energy system by the *Residual Load Factor* ($F_{RL,t}$). As can be seen in (3), the $F_{RL,t}$ includes the ratio of the RL $P_{RL,t}$ at a time step t to the absolute value of the maximum positive or negative RL $P_{RL,max}$ within QP. For $P_{RL,max}$ we apply a case distinction. If the RL is positive at a time step t, the maximum RL of the QP is used for $P_{RL,max}$. If the RL is negative, the minimum RL of the QP is used for $P_{RL,max}$. Accordingly, the $F_{RL,t}$ differentiates between positive and negative RL. It has a possible range of values from -1 to +1, where -1 corresponds to the maximum need for negative load-shifting and +1 corresponds to the maximum need for positive load-shifting.

$$F_{RL,t} = \frac{P_{RL,t}}{|P_{RL,max}|} \qquad \text{with } P_{RL,max} = \begin{cases} \max\limits_{t \in QP}(P_{RL,t}) & \text{if } P_{RL,t} > 0 \\ \min\limits_{t \in QP}(P_{RL,t}) & \text{if } P_{RL,t} < 0 \end{cases} \tag{3}$$

As a typical DCES provides flexibility services predominantly in a kW or low MW range and the RL is to be classified in a high MW or GW range, normalizing the load-shifting and RL values allows appropriate comparison of the two values resulting in the *FDI*. The comparison of absolute values would lead to very small values, which would impede the comparability. Thereupon, the *FDI* in (4) puts the technical flexibility offer of a DCES $F_{DCES,t}$ and the flexibility demand of the higher-level energy system's RL $F_{RL,t}$ in relation to each other.

$$FDI_t = \begin{cases} 1 & \text{if } FDI_{k,t} > 1 \\ FDI_{k,t} & \text{if } 1 \leq FDI_{k,t} \leq -1 \\ -1 & \text{if } FDI_{k,t} < -1 \end{cases} \qquad \text{with } FDI_{k,t} = \frac{F_{DCSE,t}}{F_{RL,t}} = \frac{P_{in,t} - P_{pur,t}}{P_{DCSE,max}} \times \frac{P_{RL,max}}{P_{RL,t}} \tag{4}$$

A positive value indicates that the DCES load-shifting does support covering RL of the higher-level energy system and a value of + 1 corresponds to maximum possible RL coverage by the DCES. A negative value indicates that the DCES load-shifting does not support covering RL of the higher-level energy system and a value of - 1 corresponds to maximum addition of RL by the DCES. Due to the division of the two factors, an FDI_t greater than 1 would occur in the case that $F_{RL,t}$ is smaller than $F_{DCES,t}$. For this case, the assumption is made that even with a small $F_{RL,t}$, the absolute RL exceeds the absolute power flow of the DCES. Accordingly, in cases where $F_{DCES,t}$ and $F_{RL,t}$ both have a positive or a negative algebraic sign, it results in a positive effect for the higher-level energy system. If the factors have different algebraic signs, the FDI_t is negative.

Averaging the values of FDI_t over the number of all time steps n_{QP} in (5) results in the *average Flexibility Deployment Index* $\overline{FDI}$. It shows the mean *FDI* over the QP resulting in a value between - 1 and + 1.

$$\overline{FDI} = \frac{\sum\limits_{t \in QP} FDI_t}{n_{QP}} \tag{5}$$

2.3. Case study

To apply the defined flexibility indicator, we carry out a case study for the DCES of a hospital in Hattingen, Germany. The hospital includes around 270 beds. Its heat consumption is 4239 MWh and its electricity consumption is 2457 MWh per year. To determine the operation of the DCES, we use a mixed integer linear programming (MILP) optimization model. We create the DCES model with our self-developed optimization tool ESyOpT, which is based on the Python optimization-modelling library Pyomo ([35]) and the open energy modelling framework oemof ([36]). With the mathematical solver Gurobi ([37]) we calculate the optimized operation for the minimum operating costs and for the minimum CO_2 emissions of the optimized electricity and natural gas purchase and feed-in. The demand data is obtained from measurements of the hospital.

We use two different energy system concepts of the DCES in three tariff scenarios. We perform the calculation for one year in a resolution of 15 minutes.

2.3.1. Demand time series

For the input demand time series, we use the electricity, heating and cooling demands of the hospital measured in [38]. The input demand data for one exemplary year has an electricity base load of about 250 kW and an electricity peak load of about 400 kW. The heating base load is about 350 kW in summer and about 650 kW in winter. Cooling is predominantly needed in summer. The cooling base load is around 35 kW at night. During the day the demand rises to a peak of about 75 kW.

2.3.2. Energy system concepts

In the case study we consider two DCES concepts including a CHP, a gas boiler, an emergency cooler, a CC, a TES for heating and a TES for cooling. The unit interdependencies are analyzed in [38]. Depicted

in Table 1, we conceptualize one reference concept (*ref*) and one optimized concept (*opt*), which enables a flexible operation. The *ref* concept includes a CHP with an electrical nominal load of the electrical base load of the hospital. The *opt* concept includes a CHP with an electrical nominal load of the electrical peak load of the hospital.

Table 1: Units and parameters of the concepts in the DCES model.

concepts	$CHP_{nominal\ load}$,		$CHP_{part\ load}$,	gas boiler,	heating TES,	emergency cooler,	CC,	cooling TES,
	kW_{el}	kW_{th}	%	kW_{th}	kWh_{th}	-	kW_{th}	kWh_{th}
ref	250	348	n.a.	1500	n.a.	yes	600	n.a.
opt	400	557	50 - 100	1500	519	n.a.	600	95

2.3.3. Scenario time series

We carry out the optimization for different tariffs. Depicted in Table 2, we use two electricity price tariffs and one tariff, which implies the CO_2 emission factor (EF). Furthermore, for the quantification with the FDI, we use an appropriate RL time series.

2.3.3.1 Optimization tariff scenarios

We optimize the DCES operation according to the minimal costs and the minimal CO_2 emissions. To simulate the actual tariff structures we use a fixed price tariff (*fix*), including a fixed price for electricity and natural gas. To simulate a optimized market-led operation of the DCES, we use a dynamic electricity tariff (*dynamic*) and an *EF* time series of the higher-level energy system.

The *fix* tariff includes a fixed electricity price of 17.9 ct/kWh for electricity purchase and a revenue of 15.5 ct/kWh for electricity feed-in. We adjust the prices to the mean prices of the *dynamic* tariff to keep the same price level. The purchase and feed-in prices vary by taxes and levies.

The *dynamic* tariff includes the German intraday auction market price of 2021 (see Fig. 3a). The mean purchase price is 17.9 ct/kWh and the mean feed-in revenue is 15.5 ct/kWh. The volatility is 1.42 ct/kWh determined by the hourly standard deviation. The purchase and feed-in prices vary by taxes and levies.

The *EF* tariff includes the specific CO_2 emissions of the marginal power plant in the merit order in every time step by the approach of [39] (see Fig. 3a). We use data of [40–42] for the German electricity mix in 2021. Therefore, we use an average marginal EF of 589.1 g_{CO_2}/kWh, which ranks between the EF of conventional gas turbines (EF = 619 g_{CO_2}/kWh) and combined cycle gas turbines (EF = 411 g_{CO_2}/kWh). The maximum EF is 1093 g_{CO_2}/kWh for lignite-fired power plants and the lowest EF is 0 g_{CO_2}/kWh for RE power plants. No EF for the electricity feed-in of the DCES is needed to calculate the optimized operation.

In all tariffs we use a fixed natural gas price of 3.77 ct/kWh with an EF of 201 g_{CO_2}/kWh ([40]).

Table 2: The *fix, dynamic* and *EF* tariffs are the external signals for the optimization model.

tariff	el. purchase	el. feed-in	volatility[a]	natural gas
fix	17.9 ct/kWh	15.5 ct/kWh	-	3.77 ct/kWh
dynamic	ϕ 17.9 ct/kWh	ϕ 15.5 ct/kWh	1.42 ct/kWh	3.77 ct/kWh
EF	ϕ 589.1 g_{CO_2}/kWh	-	90.06 g_{CO_2}/kWh	201 g_{CO_2}/kWh

[a]hourly standard deviation

2.3.3.2 Residual load time series

For calculating the FDI in every timestep, we require the time specific RL (P_{RL}). As the RL depends on the net electricity consumption ($P_{el,consumption}$) and the RE electricity generation ($P_{RE,generation}$), we use consumption and generation data from [43] for 2021. Figure 3b shows the composition of the average RL for the winter time, the summer time and for one year.

3. Results

We calculate the DCES' operation modes of the different concepts and scenarios and determine the FDI for each operation.

3.1. FDI dependency on unit operation and RL demand

We analyze the changes of the FDI_t in accordance with the DCES operation and the RL of the higher-level energy system. Figure 4a shows the DCES electrical key figures in quarter-hourly resolution of the *opt* concept

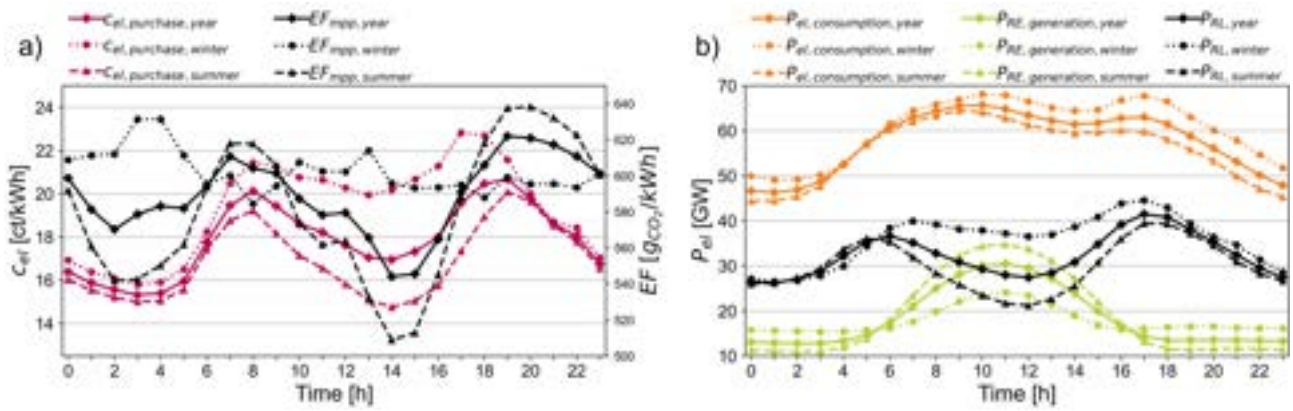

Figure 3: a) Hourly average electricity costs and hourly average EF. b) Composition of the hourly average RL.

in the *EF* tariff and the absolute RL for an exemplary day in winter. Figure 4b shows the corresponding $F_{DCES,t}$ and $F_{RL,t}$ for every time step resulting in the FDI_t.

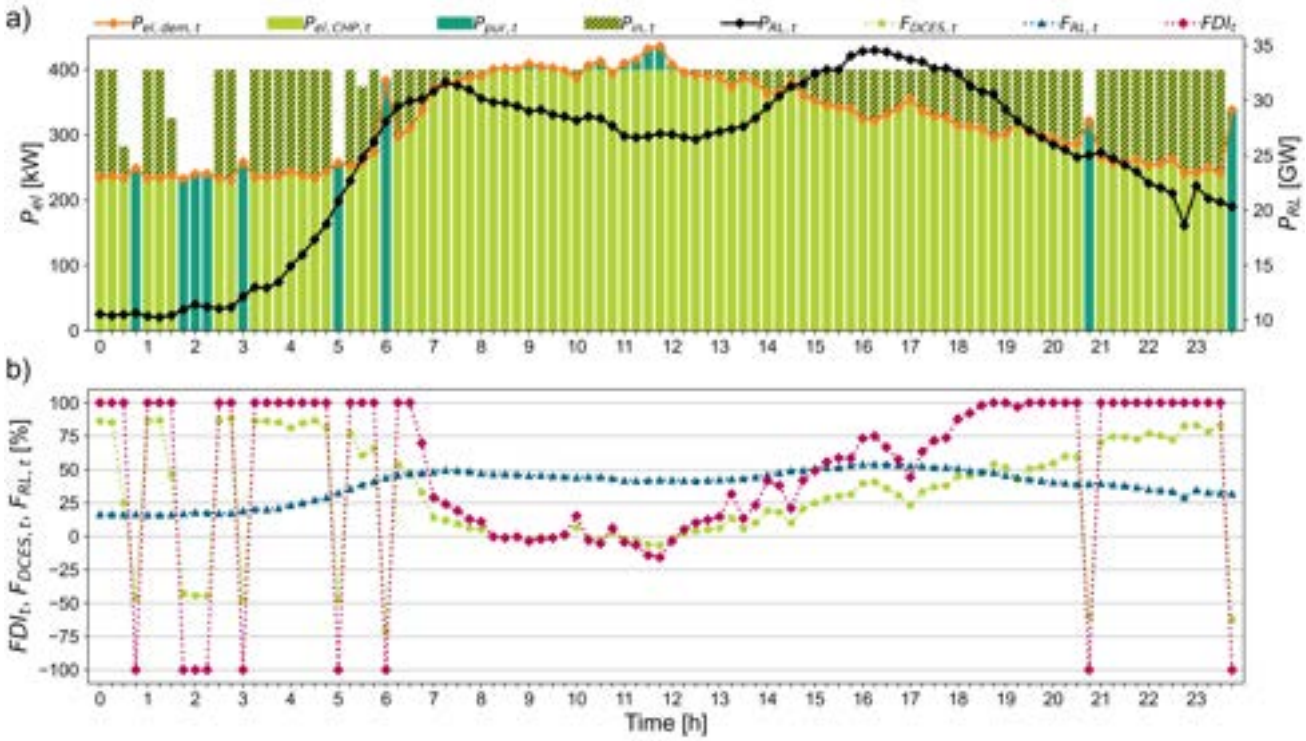

Figure 4: a) The DCES electrical key figures in quarter-hourly resolution of the *opt* concept in the *EF* tariff and the absolute RL for an exemplary day in winter. b) The corresponding $F_{DCES,t}$ and $F_{RL,t}$ for every time step result in the FDI_t.

Due to the high heat demand in winter, the CHP unit operates almost continuously at nominal load. But in some time steps, the CHP operation becomes restricted by the *EF* tariff optimization. This CHP restrictions result in additional electricity purchase. A detailed analysis of the DCES unit operation modes can be found in [38].

Table 3 shows the resulting values of the FDI_t for selected time steps. Among others, in the time steps at 04:00 am and 06:45 am a positive $F_{DCES,t}$ is present resulting from the electricity generation and surplus feed-in. In the cases of no electricity generation at 00:45 am or additional electricity purchase at 11:30 am, the $F_{DCES,t}$ becomes negative. Since the RL is positive for the whole day, the $F_{RL,t}$ is also positive in every time step.

At 06:45 am, the DCES feeds electricity into the public grid and a positive RL exists in the higher-level energy system. This coherency supports covering RL. So, the FDI_t results in a positive value of 69.8%. At 04:00 am, the DCES operation covers the RL even more as now the $F_{DCES,t}$ is greater than the $F_{RL,t}$. The FDI_t is at 100%.

Table 3: FDI_t calculation for single time steps of Figure 4.

Time step, t	$F_{DCES,t}$, %	$F_{RL,t}$, %	FDI_t, %
00:45 am	- 45.9	16.7	- 100
04:00 am	81.2	23.4	100
06:45 am	33.0	47.3	69.8
11:30 am	- 5.9	41.9	- 14.1

A positive $F_{RL,t}$ and a negative $F_{DCES,t}$ result in a negative FDI_t. At 11:30 am, the RL is similar as at 06:45 am, but now the DCES purchases additional electricity from the grid resulting in more RL for the higher-level energy system. So, the FDI_t results in a negative value of - 14.1 %. At 00:45 am, the absolute value of $F_{RL,t}$ is smaller than the absolute value of $F_{DCES,t}$ but with different signs. The FDI_t is at -100%.

3.2. Flexibility assessment over the quantification period

In Fig. 5 we calculate the $\overline{FDI}_{QP}$ of the case study for the winter time, the summer time and one year.

As the *ref* concept contains a CHP with low nominal load and no TES, almost no load-shifting is possible. So, the operation mode in every tariff optimization is the same and the $\overline{FDI}_{QP}$ of the *ref* concept is also the same in all operation modes.

Accordingly, in the *ref* concept electricity feed-in occurs only in a few time steps when the electricity demand is lower as the nominal load of the CHP. In most other cases, electricity is purchased as the demand is mostly higher as the generation. Thus, no differences in operation modes are possible and the FDI is mainly dependent on the facility's demand and the RL. This results in a FDI of -15.4% for one year for the *ref* concept. This result shows that the DCES operation is increasing instead of reducing the RL.

The *opt* concept is useful to cover RL in the QP of one year in all tariffs as the $\overline{FDI}_{year}$ results in positive values. The highest value for $\overline{FDI}_{year}$ is achieved for the operation mode in the *dynamic* tariff, followed by the *EF* and the *fix* tariffs.

The seasonal differences result primarily from the different heating demands of the facility. In the *opt* concept the CHP generates more electricity in the winter time, as it has lower restrictions of its' heat excess. In the summer time, the heat demand of the facility is lower, so the generated electricity by the CHP is lower. This reduces the number of time steps with a positive FDI_t.

In the *opt* concept only slight differences exist between all tariffs. Although the operation mode regarding the *fix* tariff achieves the lowest $\overline{FDI}_{year}$, the $\overline{FDI}_{winter}$ is higher than in the other tariffs. As Pagnier and Jacquod [44] have proven a correlation between the RL and the electricity stock-market price in an energy-only-market, we have expected the highest $\overline{FDI}$ in the optimized operation modes regarding the *dynamic* tariff in every QP. Also, we have expected the $\overline{FDI}$ in the *EF* tariff to be higher than in the *fix* tariff in every QP as the *EF* might be connected with the RL. Though, the $\overline{FDI}_{winter}$ is highest in the *fix* tariff. This gives an indication that although the DCES operations have been optimized according to an external signal that supposedly correlates with the RL, the operations still do not result in an optimized operation mode regarding the RL. Because of the volatility in the *flex* and *EF* tariffs, the data show an arbitrage trading in the optimized operation modes using the TES. This arbitrage trading is at the expense of RL coverage resulting in a lower $\overline{FDI}_{winter}$ compared to the $\overline{FDI}_{winter}$ in the *fix* tariff.

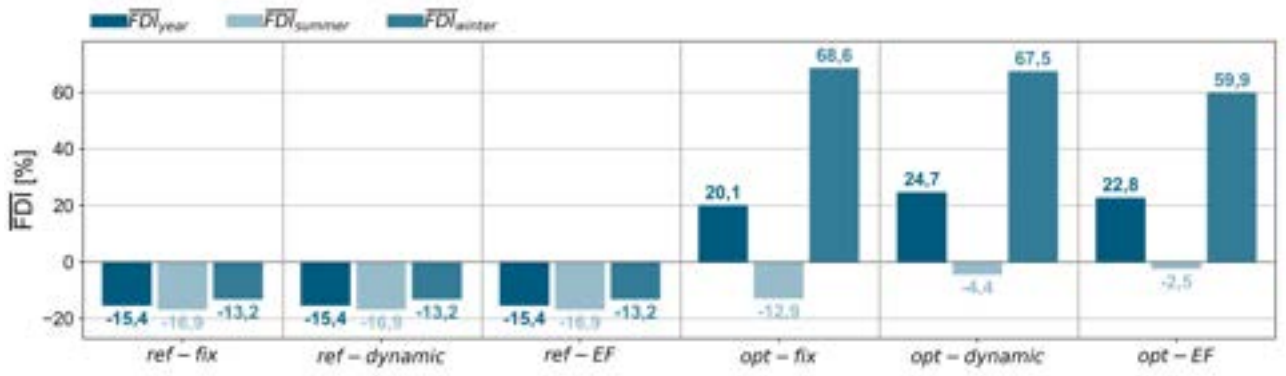

Figure 5: The FDI of relevant QPs for two concepts in three tariff scenarios. The $\overline{FDI}$ is presented for the QP of one year, summer time and winter time.

4. Conclusion and discussion

With the FDI we provide a new method to quantify the flexibility of DCES operation to cover RL of the higher-level energy system. As one element of power system transition optimized DCES operation regarding the best possible FDI might thus cover RL and potentially substitute flexible fossil powered energy plants.

To deduce the FDI, we have outlined different understandings of flexibility and presented a specific definition for flexibility considering the characteristics of a DCES. In this definition we have taken into account the usable flexibility potential of a DCES and its flexibility level as a consumer, respectively a prosumer. We have considered the flexibility of the DCES' operation modes and its connection with the higher-level energy system. We have noted that DCES can be a flexibility option for covering RL in the higher-level energy system with an flexibility potential.

We demonstrated in a case study that regarding the supplied facility's demands and the DCES concept, the DCES might not have a high flexibility potential and therefore a low FDI when storage capacity and electricity generation are low. In this case, the FDI can only be increased by changing the DCES units or the facility's energy demand. We also studied the FDI of a DCES concept with high electricity generation and high storage capacity. In this case, the FDI was higher. As Pagnier and Jacquod [44] have proven a correlation between the RL and the electricity stock-market price in an energy-only-market, it was to be expected that an optimized operation regarding a dynamic tariff might also lead to a higher FDI. Though, the effect was low compared to changing the DCES electricity generation and storage units. Only minor differences between a fix and a dynamic tariff could be noted. Also, the optimization regarding CO_2 emissions of the marginal power plant led only to little changes in the FDI. An optimization regarding the average CO_2 emissions of the electricity mix might lead to a higher FDI, but has to be investigated further. Furthermore, the RL of the higher-level energy system has an influence on the FDI, as it varies regarding the RL curve of the considered QP. It might be helpful to define an appropriate reference QP when using the FDI to compare different DCES operations.

Unlike other flexibility indicators, the FDI allows a quantification without a reference concept. Due to the use of normalized factors it might be valid to compare the FDI of a DCES with other DCES of different facilities including different units (e. g. heat pump, absorption chiller etc.) and variations in capacity within the same higher-level energy system RL scenario. Though, in this study, the FDI was only applied for two DCES concepts of the same facility. Following the principle of the FDI quantification, the method might be adapted for even more energy applications interacting with the higher-level energy system. In this study the method was applied within an energy-only-market and the assertion of the results is directly connected to this kind of market design. Therefore, the presented quantification method needs to be proven in further studies for different DCES concepts, facilities, energy applications and market design.

In summary, the results of the case study show that a higher electricity generation capacity and bigger storage unit capacity in a DCES lead to a higher FDI. With the FDI we have developed an indicator to quantify the flexibility to cover RL regarding the higher-level energy system.

Acknowledgments

This research was supported by the German FEDERAL MINISTRY FOR ECONOMIC AFFAIRS AND CLIMATE ACTION. We thank our partners from STADTWERKE BOCHUM and AUGUSTA KLINIKEN BOCHUM HATTINGEN who provided data and expertise that assisted the research. We also thank our three reviewer for their great insights.

Nomenclature

Abbreviations

CC compression chiller

CHP combined heat and power unit

DCES decentral cross-sectoral energy system

DSM demand-side management

EF emission factor

MILP mixed integer linear programming

QP quantification period

RE renewable energies

RL residual load

TES thermal energy storage

Symbols

c costs, EUR

E electric energy, kWh

EF emission factor, g_{CO_2}/kWh

F_{DCES} flexibility potential factor, $-$

F_{RL} residual load factor, $-$

FDI flexibility deployment index, $-$

$\overline{FDI}$ average flexibility deployment index, $-$

P electric power, kW

n number of time steps, $-$

t time, h

Subscripts

dem demand

el electricity

in feed-in

mpp marginal power plant

pur purchase

References

[1] Schill W. *Residual Load, Renewable Surplus Generation and Storage Requirements in Germany* Deutsches Institut für Wirtschaftsforschung: Berlin, Germany; 2013. ISSN: 1433-0210

[2] Next Kraftwerke GmbH. *Was ist die Residuallast?* Available at: `https://www.next-kraftwerke.de/wissen/residuallast` [accessed 01.02.2023].

[3] SMARD Strommarktdaten. `https://www.smard.de/home` [accessed 01.02.2023].

[4] Stappel M., Gerlach A., Scholz A., Pape C., *The European Power System in 2030: Flexibility Challenges and Integration Benefits. An Analysis with a Focus on the Pentalateral Energy Forum Region.* Kassel, Germany: Fraunhofer IWES, Analysis on behalf of Agora Energiewende; June 2015. Technical Report No.: 067/02-a-2015/En.

[5] Klein K., Killinger S., Fischer D., Streuling C. Kalz D., Salom J., Cubi E. *Comparison of the future residual load in fifteen countries and requirements to grid-supportive building operation*. EuroSun 2016 Oct 11-14; Palma de Mallorca, Spain

[6] Pina E., Lozano M., Serra L. *Assessing the influence of legal constraints on the integration of renewable energy technologies in polygeneration systems for buildings.* Renewable and Sustainable Energy Reviews Vol. 149 111382, 2021. DOI: 10.1016/j.rser.2021.111382

[7] International Energy Agency IEA. *Harnessing Variable Renewables: A Guide to the Balancing Challenge*. OECD Publishing, Paris, 2011, DOI: 10.1787/9789264111394-en

[8] Union of the Electricity Industry EURELECTRIC. *Flexibility and Aggregation. Requirements for their interaction in the market*. Brussels, Belgium. 2014 Jan

[9] Electric Power Research Institute EPRI. *Electric Power System Flexibility. Challenges and opportunities*. Palo Alto, California, USA. 2016 Feb

[10] Lannoye E., Flynn D., O'Malley M. *Evaluation of Power System Flexibility*. In: IEEE Transactions on Power Systems, vol. 27, no. 2, pp. 922-931, May 2012, DOI: 10.1109/TPWRS.2011.2177280

[11] International Renewable Energy Agency IRENA. *Power System Flexibility for the Energy Transition, Part 1: Overview for policy makers*, Abu Dhabi. 2018. ISBN 978-92-9260-089-1

[12] Cruza M., Fitiwib D., Santosa S., Catalãoa J. *A comprehensive survey of flexibility options for supporting the low-carbon energy future* Renewable and Sustainable Energy Reviews 2018 Dec 97 338-353. DOI: 10.1016/j.rser.2018.08.028

[13] Heider A., Reibsch R., Blechinger P., Linke A., Hug G. *Flexibility options and their representation in open energy modelling tools*. Energy Strategy Reviews 2021 Nov 38 100737. DOI: 10.1016/j.esr.2021.100737

[14] Federal Ministry for Economic Affairs and Climate Action BMWK *What exactly are flexibility options?* In: Energiewende Direkt, 2018 Jan 25. Available at: `https://www.bmwi-energiewende.de/EWD/Redaktion/EN/Newsletter/2018/01/Meldung/direkt-account.html` [accessed 13.2.2023].

[15] CONSENTEC Consulting für Energiewirtschaft und -technik GmbH, IAEW Institut für Elektrische Anlagen und Energiewirtschaft RWTH Aachen. *Bewertung der Flexibilitäten von Stromerzeugungs- und KWK-Anlagen*. BDEW Bundesverband der Energie- und Wasserwirtschaft e. V., 2011 Oct `https://www.consentec.de/wp-content/uploads/2011/12/Gutachten_Flexibilisierung_Abschlussbericht.pdf` [accessed 01.03.2023]

[16] Lehmann N., Huber J., Kießling A., *Flexibility in the context of a cellular system model*. In: 16th International Conference on the European Energy Market (EEM); 2019 Sep 18-20; Ljubljana, Slovenia. DOI: 10.1109/EEM.2019.8916358

[17] Böttger D., Becker H., Dreher A., Ganal H., Geiger D., Gerhardt N., HarmsY., Pape C., Pfennig M., Schmitz R., Schön A., Stock S., Ulffers J., Fuchs N., Kost C., Thomsen J., Fouquet D., Große A., Lehnert W., Axthelm W., Stark M. *New Electricity Market Design for the Integration of Fluctuating Renewable Energy Sources*. Fraunhofer Institute for Energy Economics and Energy System Technology (IEE), Fraunhofer Institute for Solar Energy Systems (ISE), Becker Büttner Held Lawyers Auditors Tax Consultants PartGmbB, Analysis on behalf of Bundesverband Erneuerbare Energie e.V. (BEE), German Renewable Energy Federation, Berlin, Germany; Dec 2021.

[18] Kippelt S. *Dezentrale Flexibilitätsoptionen und ihr Beitrag zum Ausgleich der fluktuierenden Stromerzeugung Erneuerbarer Energien [dissertation]* Dortmund, Germany: TU Dortmund; 2018. DOI: 10.17877/DE290R-20341

[19] Langrock T., Achner S., Jungbluth C., Marambio C., Michels A., Weinhard P., Baumgart B., Otto A. *Potentiale regelbarer Lasten in einem Energieversorgungssystem mit wachsendem Anteil erneuerbarer Energien*. Umwelt Bundesamt in Climate Change 19/2015, Sep 2015

[20] Krzikalla N., Achner S., Brühl S. *Möglichkeiten zum Ausgleich fluktuierender Einspeisungen aus erneuerbaren Energien: Studie im Auftrag des Bundesverbandes Erneuerbare Energie*. Bochum, Germany: Ponte Press; 2013. ISBN: 978-392-03286-4-5

[21] Witte J. *Zentrale und dezentrale Elemente im Energiesystem - Der richtige Mix für eine stabile und nachhaltige Versorgung* München, Germany; 2020. ISBN: 978-3-8047-4060-0

[22] Stinner S., Huchtemann K., Müller D. *Quantifying the operational flexibility of building energy systems with thermal energy storages.* In: Applied Energy 181 140–154, 2016. DOI: 10.1016/j.apenergy.2016.08.055

[23] Nuytten T., Claessens B., Paredis K., van Bael J., Six D. *Flexibility of a combined heat and power system with thermal energy storage for district heating.* In: Applied Energy 104 583–591, 2013. DOI: 10.1016/j.apenergy.2012.11.029

[24] Arteconi A., Polonara F. *Assessing the Demand Side Management Potential and the Energy Flexibility of Heat Pumps in Buildings.* In: Energies 11 (7) 1846, 2018. DOI: 10.3390/en11071846

[25] Weidlich A., Zaidi A. *Operational Flexibility of Small-Scale Electricity-Coupled Heat Generating Units.* Technol Econ Smart Grids Sustain Energy 4 8, 2019. DOI:10.1007/s40866-019-0064-2

[26] Yin R., Kara E. C., Li Y., DeForest N., Wang K., Yong T., Stadler, M. *Quantifying flexibility of commercial and residential loads for demand response using setpoint changes*. Applied Energy 2016; 177: 149–164. DOI: 10.1016/j.apenergy.2016.05.090

[27] Finck C., Li R., Kramer R., Zeiler W. *Quantifying demand flexibility of power-to-heat and thermal energy storage in the control of building heating systems*. Applied Energy 2018; 209: 409–425. DOI: 10.1016/j.apenergy.2017.11.036

[28] Reynders G., Diriken J., Saelens D. *Generic characterization method for energy flexibility: Applied to structural thermal storage in residential buildings.* In: Applied Energy 198 192–202 2017 DOI: 10.1016/j.apenergy.2017.04.061

[29] D'hulst R., Labeeuw W., Beusen B., Claessens S., Deconinck G., Vanthournout K. *Demand response flexibility and flexibility potential of residential smart appliances: Experiences from large pilot test in Belgium.* In: Applied Energy 155 79–90, 2015. DOI: 10.1016/j.apenergy.2015.05.101

[30] Coninck R. de, Helsen L. *Quantification of flexibility in buildings by cost curves – Methodology and application.* In: Applied Energy 162 653–665, 2016. DOI: 10.1016/j.a-penergy.2015.10.114

[31] Weiß T., Rüdisser D., Reynders G. *Tool to evaluate the Energy Flexibility in Buildings - A short manual* Technical report from IEA EBC Annex 67 Energy Flexible Buildings; AEE INTEC, Austria; VITO, Belgium; 2019 Jul.

[32] Oldewurtel F., Sturzenegger D., Andersson G., Morari M., Smith R. S. *Towards a standardized building assessment for demand response.* In: 2013 IEEE 52nd Annual Conference on Decision and Control (CDC). 10-1; Florence, Italy; 2013 Dec 10-13.

[33] Le Dréau J., Heiselberg P. *Energy flexibility of residential buildings using short term heat storage in the thermal mass*. Energy 2016; 111: 991–1002. DOI: 10.1016/j.energy.2016.05.076

[34] Junker R. G., Azar A. G., Lopes R. A., Lindberg K. B., Reynders G., Relan R., Madsen H. *Characterizing the energy flexibility of buildings and districts.* In: Applied Energy 225 175–182, 2018. DOI: 10.1016/j.apenergy.2018.05.037

[35] Pyomo. Available at: `https://pyomo.readthedocs.io/` [accessed 18.01.2023]

[36] oemof. Available at: `https://oemof.readthedocs.io/` [accessed 18.01.2023]

[37] Gurobi optimization. Available at: `https://www.gurobi.com/` [accessed 18.01.2023]

[38] Berg S., Blaume L., Goetschkes C. *Unit operation of distributed cross-sectoral energy systems in market-optimized operation* IEEE Xplore In: ETG-Kongress 2023, Kassel , Germany. 2023 Mai 25-26. [to be published]

[39] Baumgärtner N., Delorme R., Hennen M., Bardow A.: *Design of low carbon utility systems: Exploiting timedependent grid emissions for climate friendly demand side management.* In: Applied Energy, 247 (RWTH-2019-04304) 755–765, 2019. DOI: 10.1016/j.a-penergy.2019.04.029

[40] Bundesamt für Wirtschaft und Ausfuhrkontrolle BAFA: *Informationsblatt CO2-Faktoren.* Available at: `https://www.bafa.de/SharedDocs/Downloads/DE/Energie/eew_infoblatt_co2_faktoren_2022.pdf?__blob=publicationFile&v=5`, Version 1.3, 2022. [accessed 10.02.2023]

[41] ENTSO-E: Transparency Platform. `https://transparency.ent-soe.eu/`, [accessed 15.05.2022]

[42] Umweltbundesamt UBA: Datenbank "Kraftwerke in Deutschland" `https://www.umweltbundesamt.de/dokument/datenbank-kraftwerke-in-deutschland`, 2022. [accessed 01.06.2022]

[43] Fraunhofer ISE: Energy-Charts. `https://www.energy-charts.info/index.html?l=de&c=DE`, [accessed 21.06.2022]

[44] Pagnier L., Jacquod P. *How fast can one overcome the paradox of the energy transition? A predictive physico-economic model for the European power grid*. Energy, 157, 2017. DOI: 10.1016/j.energy.2018.05.185.

PROCEEDINGS OF ECOS 2023 - THE 36TH INTERNATIONAL CONFERENCE ON
EFFICIENCY, **C**OST, **O**PTIMIZATION, **S**IMULATION AND ENVIRONMENTAL IMPACT OF ENERGY SYSTEMS
25-30 JUNE 2023, LAS PALMAS DE GRAN CANARIA, SPAIN

Impact of size optimisation on the multi-criteria assessment of local cross-sectoral energy supply concepts

Jana Schneeloch[a] and Mohamed Eldakadosi[b]

[a] *Fraunhofer UMSICHT, Oberhausen, Germany, jana.schneeloch@umsicht.fraunhofer.de, CA*
[b] *Fraunhofer UMSICHT, Oberhausen, Germany, mohamed.eldakadosi@umsicht.fraunhofer.de*

Abstract:
Key elements of the energy system transformation are decentralisation, decarbonisation and sector-coupling. Local energy systems are often customarily designed using heuristics for the technology layout. However, optimisation of the design and operation of energy systems is considered a powerful tool. Therefore, we investigate the influence of an optimised layout and the coupling of the electricity and heat sector on economic, ecological and technological criteria. Three variations from a reference energy concept are regarded for a case study of unrenovated, residential buildings in the city of Düsseldorf, Germany. The concepts supply the heat and electricity demands at different levels of sector-coupling. In a first step, the concepts are mathematically optimised by mixed-integer linear programming with the objective of minimising costs. Afterwards, the results of the criteria metrics are combined in an overall performance score obtained by the Analytic Hierarchy Process. We find that the concepts with an optimised layout do not only have lower costs, but also lead to a significant decarbonisation by several hundreds of kg of CO_2 annually. In the case of optimised layout, heat pump and storage units have smaller capacities. Especially, storages are oversized under the used heuristic. Nevertheless, the photovoltaic units are expanded by up to 300% in comparison to the heuristic layout. We thus find an advantage of the optimised layout on the multi-criteria assessment, even though the optimisation has only an economic objective. The coupling of the heat and electricity sector leads to CO_2 emission savings and a higher self-consumption of the PV energy produced within the system. The coupled system achieves the highest score under the three criteria, irrespective of the building type. The overall best performance under a sensitivity analysis of the criteria weights is found for the sector-coupled concept in the optimised layout.

Keywords:
ECOS Conference; Local energy systems; Mixed-integer linear programming; Multi-criteria assessment; Residential energy supply; Sector-coupling.

1. Introduction

The decentralisation and decarbonisation of national energy systems have been the focus of attention in energy system analysis during the recent years. National targets have been set up by many countries. These targets influence the design of energy systems down to the scale of buildings. Consequently, local energy supply concepts are required to be renewable and efficient. While the building owners and residents have a direct influence on the installation and design of the buildings' energy supply concepts, these building concepts can also be a potential business model for utility companies [1].

When it comes to designing the energy concept, rules of thumb are often taken into account. This form of layout, we call it the *heuristic layout*, can be compared to a layout which results from a mathematical optimisation, which we call the *optimised layout*. A comparison of different layout approaches has been performed by Ogunmodede et al. [2]. The authors found that the technology layout was smaller for the case of optimisation and therefore the system costs were lower. However, the system costs in the *heuristic layout* were already lower than those in the given reference system which corresponded to a fully grid-dependent supply.

Another structural change, that is associated with the transformation of the energy system, is the coupling of energy sectors. It has been shown that the sector-coupling has accelerated the decarbonisation of the European energy system [3]. Thus, we enlarge upon these findings by investigating the effect of sector-coupling on a building scale.

Moreover, the recent shifts in energy system analysis have been accompanied by the need for including multiple criteria in the analysis. Besides economic metrics, further factors have been considered: ecology [4–7], technology [4,6–10], sociology [6,7] or regulatory framework [6]. The use of methods for Multi-Criteria Decision

Analysis (MCDA) to assess energy systems is widely spread [7, 11, 12]. Many studies have thereby applied the Analytic Hierarchy Process (AHP) [4–6, 8–10]. Hence, the energy concepts regarded in this paper are analysed with AHP under multiple criteria.

The aim of this paper is to investigate the multi-criteria behaviour of local energy supply concepts under the aspect of an *optimised layout* and the coupling of the electricity and heat sector. We examine the following questions:

- What impact does an optimised layout have on local energy supply concepts considering economic, ecological and technological criteria?
- How does the coupling of the electricity and the heat sector affect local energy supply concepts in terms of economic, ecological and technological criteria?

In a first step, we describe the methodology of optimisation and assessment used in this paper (Section 2.). Afterwards, we present the case of application and describe the investigated concepts in Section 3. The results of the multi-criteria analysis are shown in Section 4. and discussed in Section 5. Finally, we give a conclusion and outlook in Section 6.

2. Methodology

The methodology of this investigation is described by a two-stage approach. In the first stage, the local energy supply concepts are mathematically optimised under a cost objective. In the second stage, the different optimised concepts are regarded as alternatives and assessed under multiple criteria. Parts of this methodology have already been described in [13].

2.1. Mathematical energy system optimisation

In order to calculate key performance indicators of the concepts, we perform a mathematical optimisation under a cost minimisation objective. The concepts are thereby modelled as Mixed-Integer Linear Programs (MILP) with ESyOpT®, a modelling tool based on the python package oemof-solph [14]. The considered optimisation problems are solved by the Gurobi solver [15] with a branch-and-cut algorithm. The optimisation horizon comprises one year with an hourly resolution.

The python package oemof-solph provides a modular modelling framework of energy systems in which each component, or technology respectively, comes with its own specific constraints for the operation and installation. The energy flows in the system are uniquely set by connections among the components. For the regarded energy concepts of this work, we model the following components: the electricity grid, the gas grid, gas boilers, thermal storages, photovoltaic (PV) modules, batteries and air-water heat pumps. The gas and electricity grids as well as the PV modules are modelled as sources. The PV plant can be used in the building's energy system to meet the electricity demand, but the generated electricity can also be fed into the grid again. The grid feeding is modelled as a sink of the system. The household demands for electricity, space heating and hot water are represented as sinks, too. To implement the other components, we use the class *Transformer* provided by oemof-solph to write our own models.

The gas boiler and the heat pump have an operational constraint on the outflow due to the minimum part load (MPL). This means they can only be operated within the range of the MPL and the nominal power P_{nom}. The gas boiler moreover has a constant efficiency while the heat pump has a time-resolved coefficient of performance (COP) that is dependent on the ambient and the supply temperature, but not on ambient humidity. The COP ranges from 1.53 to 6.40 according to a high-temperature air-water heat pump with a R407c refrigerant [16]. The heat storage is modelled with a capacity-dependent loss [17] and a level-dependent loss [17]. The battery is modelled with a fixed self-discharge loss of 0.025% per day [18] and degradation is not considered. The normalised power output per kW_{peak} of the PV plant is calculated using a pvlib-python model [19]. Data for investment and maintenance cost were taken from studies and market data [20–23].

We distinguish between two optimisation objectives and modelling approaches respectively - a *heuristic layout* and an *optimised layout*. For the case of *heuristic layout*, we perform a dispatch optimisation with a rule of thumb layout of each technology (Section 3.3.). We compare this to the case of an *optimised layout* in which both dispatch and size of the technologies are optimised. The methods differ in their objective function f and the components' set of decision variables.

In the case of a *heuristic layout*, the objective function consists of the annual maintenance and operational costs ($OPEX$) of the concept:

$$min\,(f_{heuristic}) = min\,(OPEX_{annual}) \tag{1}$$

For the case of the *optimised layout*, the objective function consists additionally of the annual investment and installation costs (*CAPEX*) of the concept and therefore equals the total costs (*TOTEX*):

$$min\left(f_{optimised}\right) = min\left(TOTEX_{annual}\right) = min\left(CAPEX_{annual} + OPEX_{annual}\right) \tag{2}$$

The mostly non-linear relations between the components' sizes and their total *CAPEX* are linearised into a fixed term $CAPEX_{fix}$ and a variable term $CAPEX_{variable}$ to be incorporated in the MILP representation. In this manner, scale effects can be considered. The total *CAPEX* are further discounted over the lifetime of the technology to the year of investment, using the weighted average cost of capital (WACC).

$$CAPEX_{annual} = \left(CAPEX_{fix} + CAPEX_{variable} \cdot SIZE\right) \cdot \frac{WACC \cdot (1 + WACC)^{LIFETIME}}{(1 + WACC)^{LIFETIME-1}} \tag{3}$$

The set of decision variables of the *heuristic layout* comprises operational variables $Y_{op}(t)$, which are binary variables indicating whether the component is operating in timestep t, and the power in- and outflow $P_{in/out}(t)$ of the component. The nominal power P_{nom} of the energy supply technologies and the capacity E_{cap} of the storage technologies have to be given for the case of the *heuristic layout* (Section 3.). In the case of the *optimised layout*, however, these variables are optimised as well.

2.2. Multi-criteria decision analysis

The optimised concepts are assessed and ranked under economic, ecological and technological metrics. In order to compare and rank the alternatives by only a single metric, a MCDA method is used. Since we aim at obtaining one performance score for each alternative, we choose a method that follows a Full Aggregation Approach [24]. The method used in this paper is the AHP [10, 25].

In a first step, the metrics for the respective criteria are chosen. Afterwards their preference weights are determined. And finally, the decision metric is determined.

2.2.1. Choice of criteria metrics

The chosen economic metric is the total annual costs ($TOTEX_{annual} = CAPEX_{annual} + OPEX_{annual}$). For the *heuristic layout* the annual *CAPEX* are calculated in the postprocessing of the optimisation using the heuristic sizes of the technologies. In the case of the *optimised layout*, the economic metric corresponds exactly to the objective function.

The chosen ecological metric is the concepts' total annual direct CO_2 emissions which are caused by the grid connections in the modelled energy concepts and do not consider indirect emissions that are caused by production.

The technological metric, the energy performance *EP*, is computed from the self-sufficiency and the self-consumption of the concept. The self-sufficiency *SES* is a measure for the grid-independence. This is calculated as the relative amount of energy produced within the system boundaries (independent from a grid connection) and used for the demands from all the energy in the system which fulfils the demands. A value of 0 indicates a complete dependence on gas and/or electricity grids while a value of 1 indicates a full independence from these grids.

$$SES = \frac{used\ energy\ which\ is\ produced\ within\ the\ systems\ boundaries}{total\ used\ energy} \tag{4}$$

The self-consumption *SEC* gives the ratio of energy produced within the system boundaries and used in it from all the energy produced within the system boundaries. A value of 0 indicates no use of the energy produced within the system boundaries for the system, while a value of 1 indicates full use of the energy produced within the system boundaries for the system.

$$SEC = \frac{used\ energy\ which\ is\ produced\ within\ the\ systems\ boundaries}{total\ energy\ which\ is\ produced\ within\ the\ systems\ boundaries} \tag{5}$$

The *EP* is finally calculated as the average of the two performance indicators:

$$EP = \frac{SES + SEC}{2}. \tag{6}$$

2.2.2. Determination of criteria weights with AHP

The AHP was first introduced by Saaty [25] as a method of measurement with ratio scales. The method can be used for criteria weight determination and alternative assessment. Both are used in this paper. The method's

Table 1: The AHP scale adapted from Saaty [25].

Absolute scale	Definition	Explanation
1	Equal importance	Two activities contribute equally to the objective
3	Moderate importance of one over another	Experience and judgement moderately favour one activity over another
5	Essential or strong importance	Experience and judgement strongly favour one activity over another
7	Very strong importance	An activity is strongly favoured, and its dominance demonstrated in public
9	Extreme importance	The evidence favouring one activity over another is one of the highest possible orders of affirmation
2,4,6,8	Intermediate values between the two adjacent judgements	When compromise is needed

basis is a fundamental scale (Table 1) by which the preferences of the criteria and the alternatives concerning the criteria are identified via pair comparisons. For the determination of the criteria weights, a pair of criteria (i, j) is compared according to the AHP scale. If i is preferred over j, the value in the pair comparison matrix takes the value v_{AHP} from the scale: $a_{ij} = v_{AHP}$, while $a_{ji} = \frac{1}{v_{AHP}}$, and vice versa. Note that all $a_{ii} = 1$. The eigenvector of the first eigenvalue of the pair comparison matrix equates to the criteria weights.

The pairwise comparison of the criteria was performed through a survey in which employees of a local utility company participated. The survey contained a pairwise comparison of economic, environmental and technological criteria. In total, eleven employees of the local utility company filled out the survey and each resulting set of criteria weights was determined using the AHP method and the weights were then averaged. The final set of criteria weights resulted in:

- economic: 0.33,
- ecological: 0.26,
- technological: 0.41,

which were used as default weights for the application of the ranking assessment with the AHP method.

2.2.3. Ranking of alternatives with AHP

The second step of Saaty's method is the ranking of alternatives [25]. In order to perform a ranking of the different alternatives, they are assessed according to the criteria and their weights. If the criterion is qualitative, the algorithm goes equivalent to the process of weight determination (Section 2.2.2.). The alternatives are pairwise compared concerning the criteria according to the AHP scale and the pairwise comparison matrix is built. The first eigenvector of this matrix is calculated for all these qualitative criteria and saved for the next step of the algorithm. The procedure for quantitative criteria deviates from the above-described step in the sense that the normalised vector is built from the alternatives' values for the given criterion. In case the quantitative criterion has a negative ordered scale (meaning, a lower value is preferable), the alternatives' values need to be inverted in a first step, so that the highest value of the normalised vector corresponds to the best parameter value for the given criterion. The matrix of the vectors for all the (qualitative and/or quantitative) criteria is eventually multiplied with the vector of criteria weights. The performance score indicates the multi-criteria metric for each alternative and the ranking of the alternatives follows these performance scores with the best alternative being the one with the highest score.

3. Case study

To illustrate the described methodology, an exemplary case study for unrenovated, residential buildings in the city of Düsseldorf, Germany, is carried out. We take three different typical buildings into account that comprise one flat (single-family house, SFH), eight flats (multi-family house, MFH8) or twenty flats (multi-family house, MFH20), respectively.

3.1. Input data

The assumptions that are made for the annual energy demands and PV potential of each building type are summarised in Table 2. Synthetic load profiles are simulated following VDI 4655 [26]. The norm provides

Table 2: Assumed annual energy demands and PV potential for each building type.

building type	total space heating demand [kWh]	total hot water demand [kWh]	total electricity demand [kWh]	roof area [m^2]
SFH	21000	2800	4000	65
MFH8	56000	9520	14320	175
MFH20	112000	21000	33000	175

reference load profiles of existing residential buildings for ten categories of typical days. These categories are dependent on the seven-day-rolling-average of the ambient temperature, the cloudiness, and the day of the week. Moreover, geographical information is used to multiply the reference profiles by a correction factor. Through the algorithm provided in the norm, the annual demand is distributed over the year accordingly.

The optimisation results are obtained using the test reference year weather data set provided by Deutscher Wetterdienst [27] and historical energy market data. The reference year for the energy market data is the year 2021. We assume a household electricity tariff of 33.7 ct/kWh, a gas tariff of 8.3 ct/kWh and a PV feed-in tariff of 7.3 ct/kWh. For the emission factors of the grid-related direct CO_2 emissions we assume 420 $g\ CO_2/kWh$ [28] for the electricity grid and 201 $g\ CO_2/kWh$ for the gas grid.

3.2. Cross-sectoral local energy supply concepts

The reference energy supply concept (*REF*) consists of an electricity grid connection and a gas boiler with a gas grid connection and a thermal storage to supply electricity, space heating and hot water to residential buildings. A schematic graph of the energy flows in the reference concept is shown in Fig. 1. In our analysis, we first adapt the electricity sector of the reference concept, then the heat sector and finally a combination of both adaptations in order to investigate the effect of sector-coupling. The adaptation in the electricity sector (*EA*) is performed through adding the electricity supply option of PV modules on the buildings' roofs with a battery storage. The adaptation in the heat sector (*HA*) is performed through exchanging the gas boiler with an air-water heat pump. These adapted concepts are shown in Fig. 2. Finally, both sectors are adapted simultaneously in a coupled manner (*SC*) so that the PV power can be used for operating the heat pump. The corresponding energy flows of the coupled concept are shown in Fig. 3.

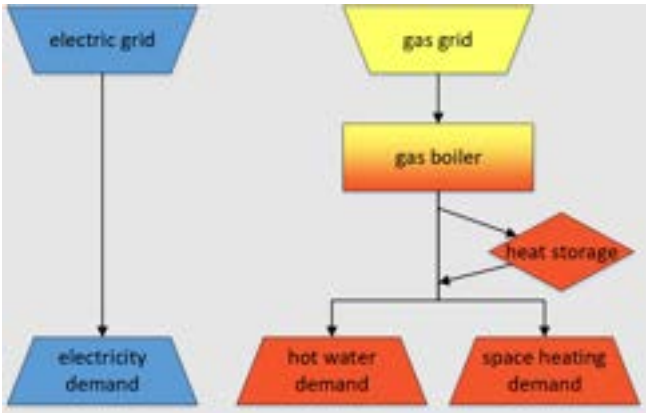

Figure 1: Reference concept (*REF*). The electricity, gas and heat sectors are indicated in blue, yellow and red, respectively.

3.3. Heuristic layout of energy concept technologies

As mentioned in Section 2.1., one of the optimisation approaches is a *heuristic layout* in which the nominal power and capacities of the technologies are kept constant. The heuristics apply to all concepts except for the reference concept. A *heuristic layout* is given for the heat pump, the thermal storage, the PV plant and the battery. A summary of all layouts is given in Table 3.

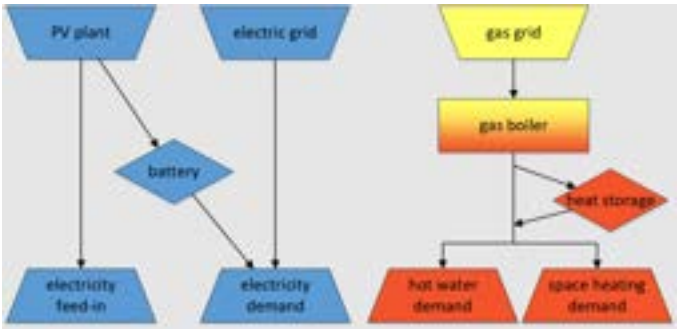

(a) Electricity adapted concept (*EA*).

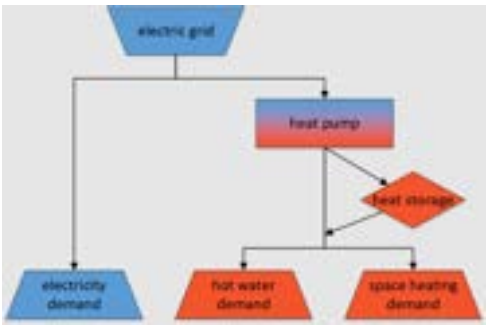

(b) Heat adapted concept (*HA*).

Figure 2: Concepts that have been adapted in one sector. The electricity, gas and heat sectors are indicated in blue, yellow and red, respectively.

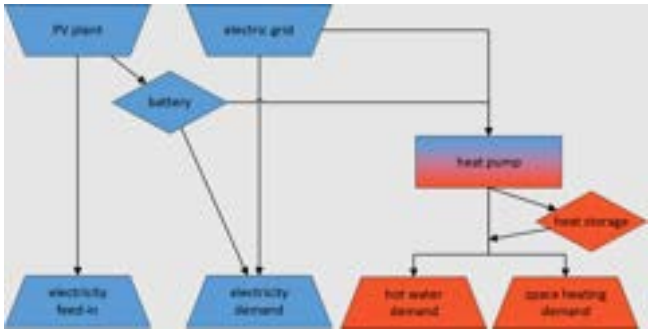

Figure 3: Sector-coupled adapted concept (*SC*). The electricity and heat sectors are indicated in blue and red, respectively.

The heuristic nominal power of the heat pump is computed according to the norm DIN-EN 12831, Supplement 2. According to the norm, the power is dependent on the hours of operation, the heating threshold temperature T_{lim} as well as the ambient temperature T_{amb} and the annual space heating and hot water demands. In this paper, we refer the hours of operation only to the heating period when $T_{amb} < T_{lim}$.

The heuristic to determine the peak power of the PV plant follows the simple rule that 1 kW_{peak} is assumed to be able to produce up to 1000 *kWh* of electricity per year. Therefore, we divide the annual electricity demand by the factor 1000 to determine the PV peak power.

The heuristic for the storage capacities of the thermal storage and the battery corresponds to the layout of a 24h-storage, meaning that the storage capacity is chosen so that an average daily amount of energy in the heating period can be stored. The in- and outflow power of the storages are configured so that the average energy that is necessary in one hour can flow from or to the storage.

4. Results

4.1. Results of the different concepts and building types under the three indicators

The mathematical optimisation of all three concepts has been performed under the two different optimisation objectives and for the three different building types. Additionally, the reference concept was optimised for each building type. This equals to a total of 21 sets of obtained results.

When comparing the implemented sizes of the energy technologies in the case of heuristic layout (HL) with the optimised layout (OL), we find that the storages have smaller capacities in the optimisation than according to the heuristic. We also find that the heat pump does not need as much installed power if the concept is optimised. However, the PV plant is built up to the limiting size of the roofs in the case of optimisation. For the single family house, this corresponds to an amplification of about 300 % in comparison to the HL.

For all 21 sets of concept results, we analyse the three criteria metrics presented in Section 2.2.1. An overview of the distribution of the criteria values is given in the radar charts in Fig. 4. Each axis of the graph represents one criterion and spans the value range of the criterion's metric in the set of results.

Table 3: Heuristic power and capacity of the implemented technologies. (hp=heat pump, tes=thermal storage, ba=battery)

building type	$P_{nom,\ hp}$ [kW]	$P_{peak,\ PV}$ [kW]	$E_{cap,\ tes}$ [m^3]	$P_{in/out,\ tes}$ [kW]	$E_{cap,\ ba}$ [kWh]	$P_{in/out,\ ba}$ [kW]
SFH	14.86	4	2.81	2.72	12.82	0.46
MFH8	40.03	14.32	7.74	7.48	45.91	1.63
MFH20	82.48	33	15.7	15.18	105.79	3.77

The reference concept is found to be the concept yielding the highest CO_2 emissions, irrespective of the building type. This concept, plus the two concepts with the electricity adaptation, lead to $EP = 0$ because they are fully grid-dependent. As expected, we observe for all concepts that the *TOTEX* decrease in the OL by on average 27%. What is more surprising, the CO_2 emissions also decrease by on average 11%. On the contrary, the HL shows a better performance of *EP*. The latter is explained by the high *SEC* in the HL concepts.

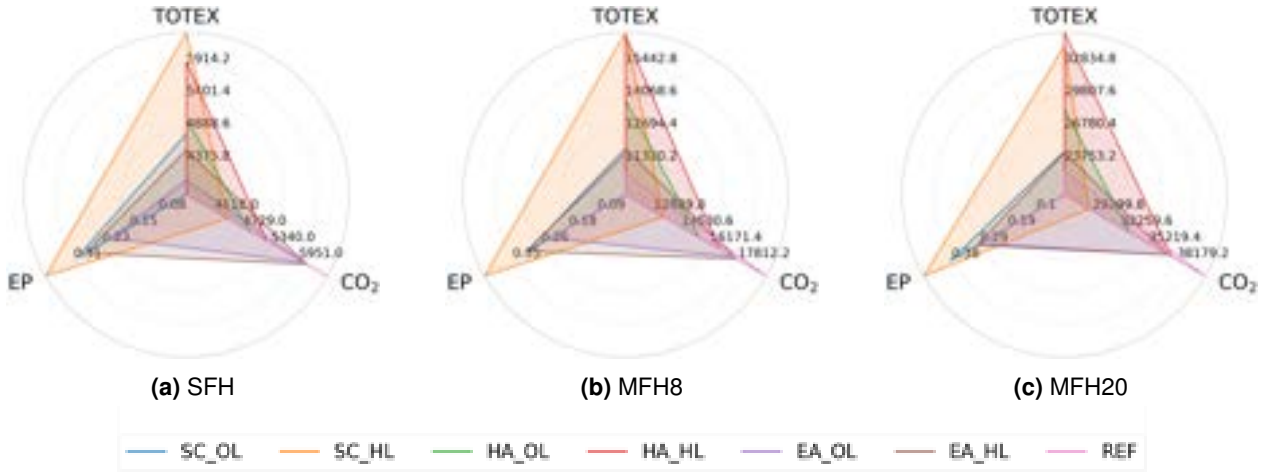

(a) SFH **(b)** MFH8 **(c)** MFH20

Figure 4: Radar charts of the performance of the seven concepts in the three criteria for each building type. The axes are defined by the resulting values from the concepts.

4.2. Results of the AHP ranking for the three building types

In order to condense the information about the concepts, we used the AHP method to determine overall performance scores for each concept. Under the usage of the criteria weights presented in Section 2.2.2., we determine the final rankings as shown in Fig. 5. The ranking orders of the concepts are mostly identical for the different building types. For the MFH20, the ranking order of the two *EA* concepts is swapped. In all cases, the sector-coupled concept with the HL obtains the highest performance score. This is to some extent surprising as it performs worse in the economic and the ecological criterion than the OL of the sector-coupled concept. However, the technological performance is higher than in the OL and it has the highest weight (Section 2.2.2.) and is therefore dominating when the overall performance score is built with AHP.

In the rankings, we also find that the sector-coupled (*SC*) and the electricity adapted (*EA*) concept, in both layout specifications, make the top four positions. On the other hand, the reference (*REF*) concept and the heat adapted (*HA*) concept obtain a significantly lower score. This, again, can be explained by the high weight on the technological criterion and the fact that these three concepts are fully grid-dependent.

4.3. Sensitivity analysis of the criteria weights in the AHP method

The ranking results are highly dependent on the choice of the criteria weights. Therefore, we perform a comprehensive local sensitivity analysis of the criteria weights on the AHP performance score. The criteria weights from the survey are regarded as default weights. Additionally, we vary each weight in the interval [0.0, 1.0] with a step size of 0.1. While varying one weight, the other two weights are adapted while keeping the exact relation that they had in the default weights. The ratio of the economic to ecological weight is 56 : 44, the economic to technological weight is 45 : 55 and the ecological to technological is 39 : 61, respectively.

The resulting graphs are shown in Fig. 6. It is clearly seen how the concepts' performance differs under

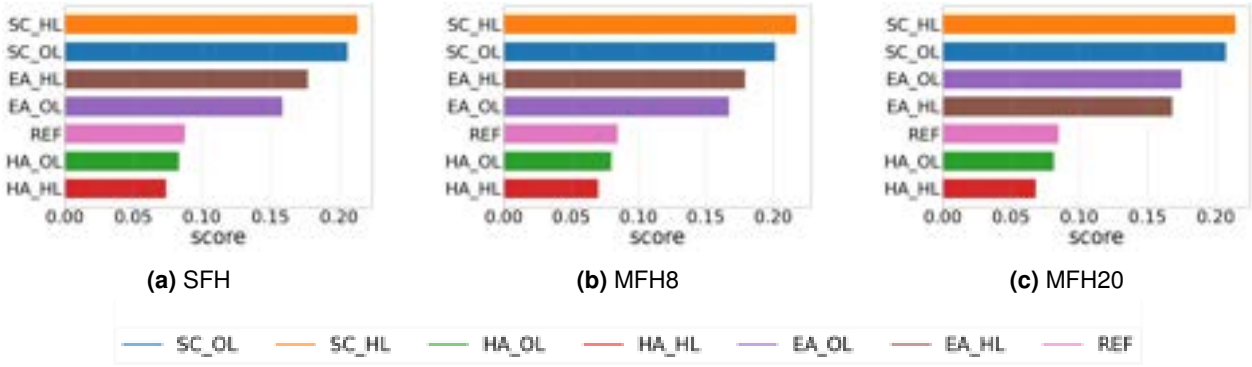

(a) SFH **(b)** MFH8 **(c)** MFH20

Figure 5: AHP Ranking results for each building type.

varying weights. From the graphs, it is noticeable that the scores of the *REF* and *HA* concepts, for the increase in each weight, show opposite trends to the *SC* and *EA* concepts. Moreover, the trends are equal for the economic and ecological weight, while the trends are swapped for the technological weight. However, there is one exception to this observation. The score of the electricity adapted concept in the OL rises with increasing economic weight. From Fig. 4 we see that this concept has either the lowest or second to lowest *TOTEX* (depending on the building type) and therefore the overall score benefits from a higher emphasis on the economic criteria. Another observation is that the value range of the resulting scores is the highest in the case of a high technological weight. This is induced by the value of *EP* = 0 for the three grid-dependent concepts which makes them uncompetitive. On the contrary, for high economic weight or high ecological weight, the scores of all concepts are close to each other.

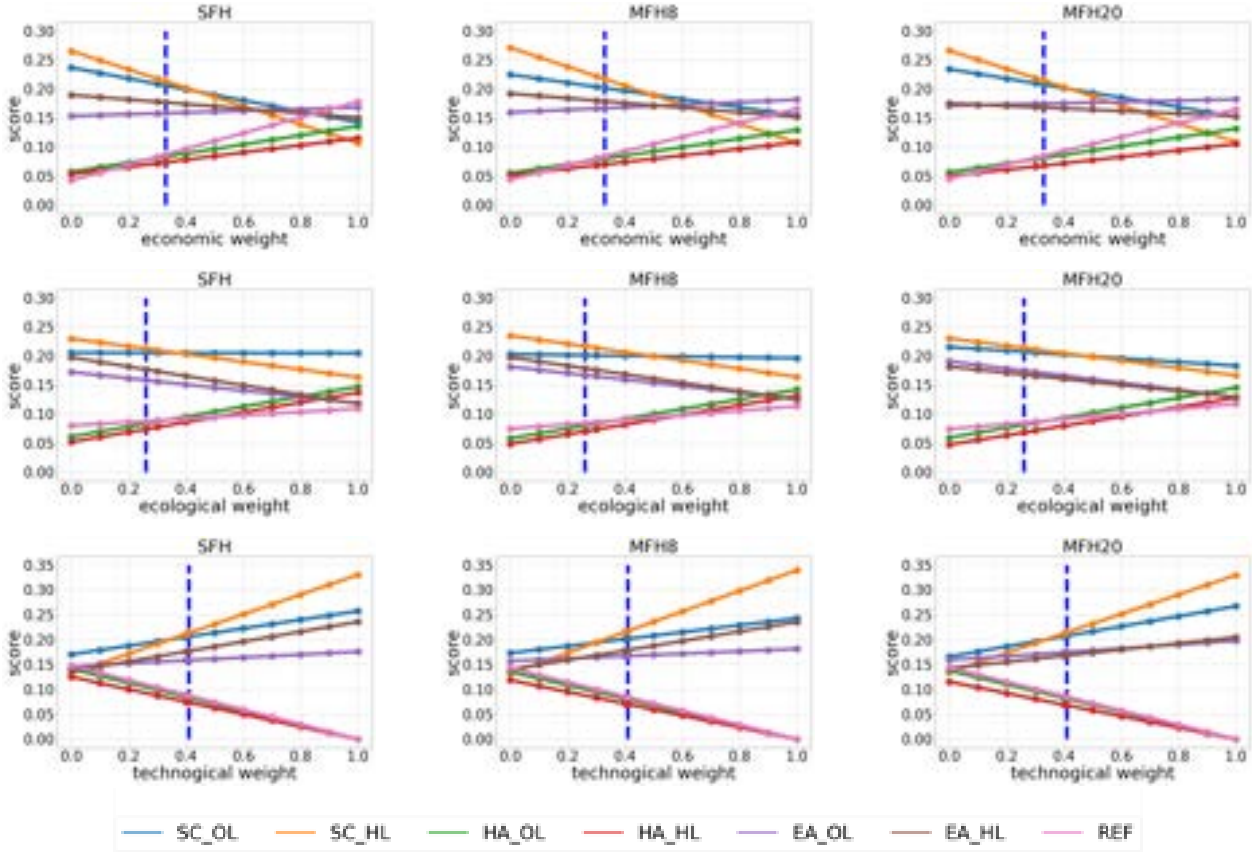

Figure 6: Sensitivity analysis on each criterion for each building type. The blue dashed line in each graph indicates the position of the default weight ranking. The top, middle and bottom row shows the analysis of the economic weight, the ecological weight and the technological weight, respectively.

The results of the sensitivity analysis are further used as a sample for the overall performance analysis of the concepts. The data points of Fig. 6 build a representative set of the concepts' performance results under multiple criteria. Each concept with a corresponding layout choice has been assigned a performance score

and a ranking position under different criteria weight choices. Based on all these ranking positions, including the one corresponding to the default weights, we determine the average ranking positions for each concept. The results of this analysis are summarised in Table 4.

Table 4: Average ranking order of the concepts for each building type.

rank	SFH	MFH8	MFH20
1	SC OL	SC OL	SC OL
2	SC HL	SC HL	SC HL
3	EA HL	EA HL	EA OL
4	EA OL	EA OL	EA HL
5	REF	REF	REF
6	HA OL	HA OL	HA OL
7	HA HL	HA HL	HA HL

The table shows that the *SC* concept in the OL reaches the highest average position in all rankings produced by the sensitivity analysis. Except for the *EA* concept for the SFH and MFH8 building types, all concept alternatives in the OL reach higher average ranking positions than their HL partner concept. The *HA* concept performs worse than the *REF* concept because even though it has lower CO_2 emissions, the extra cost are significant enough to lead to a lower overall performance score for the totality of all regarded weight variations.

5. Discussion

The OL does not only lead to a decrease in total annual costs, but also to a decrease in the total annual direct emissions. This can be explained by the better operational use of the installed energy technologies. In the case of the OL, the installed power/capacity of each technology is perfectly matched to meeting the demands. Since the operational costs and the direct emissions have the same origin - the grids - the reduction of either is directly coupled to the other. The contrary effect is the installation of new technologies for the *EA*, *HA* and *SC* concept, which comes with installation costs. For the *HA*, the heat pump is built with a lower nominal power in the case of optimisation, so that the *TOTEX* are lower for the OL than for the HL. For *EA* and *SC* we observe that the PV is dimensioned much bigger if the layout is optimised. This comes with higher installation costs. However, the storages (battery and heat storage respectively) are installed at lower capacities in the case of an OL. For the *EA* and *SC* concept this balances the higher PV costs out and still, the *TOTEX* decrease for the OL. The strong decrease in installed capacity of the storages if the layout is optimised, shows how much the capacities were overestimated with the used heuristic. The capacities of the storages, moreover, influence the *SEC* and thereby the *EP*. The high capacities in the HL lead to a high *EP*.

The sensitivity analysis of the criteria weights has shown a uniform behaviour of the economic and the ecological criterion. With varying weight, the same concepts show the same behaviour for both criteria. This behaviour is inverted in the technological criterion. The fact that for a high weight on either economic or ecological criterion or a low weight on the technological criterion, the score of all concepts lie closer to each other, shows that the gap between the concepts' performance results mostly from the values of the technological metric and their competitiveness is balanced out if the other metrics have a higher importance.

To answer the second research question, we observe that the two concepts associated with the sector-coupled concept are the two highest ranked for most of the weight variations. Only for a high economic weight, these two concepts obtain lower positions in the ranking. Thus, the coupling of the heat and electricity sector specifically reduces CO_2 emissions and increases the energy performance which leads to a high ranking of the respective concept in the MCDA under the three given metrics.

Finally, the reference concept is found to perform well in the economic criteria as it has low *TOTEX* for all building types, but it shows the worst performance for CO_2 emissions and *EP*. This effect occurs for the given case study because we do not regard installation costs in *REF*. We assume that the gas boiler is already installed and the investment has been made in the past and is not part of the optimisation horizon.

The method used to calculate an average ranking is based on the ranking position that resulted from each weight variation in the sensitivity analysis. A different approach would be to compute the average performance score instead and base the overall ranking on this score. The approach of comparing ranking positions takes equidistant positions between the concepts, while a comparison on performance score could show dominance

between the concepts. However, the ranking position is taken as the supporting indicator for performance of the concepts.

6. Conclusion and outlook

To conclude, we investigated local heat and electricity supply concepts with a different level of coupling the sectors and different layout approaches. We find that the OL decreases the total annual costs by on average 27% and decreases the total annual direct CO_2 emissions by on average 11%. The installation of PV is enforced if the layout is optimised instead of following a rule of thumb. A coupling of the heat and electricity sector leads to CO_2 emission savings and a better energy performance. Between the three different building types we find almost no difference. Yet, the study can be extended towards other building archetypes including non-residential buildings. Furthermore, the energy price markets have recently faced a lot of instabilities. Hence, the robustness of the rankings against different price inputs can be investigated. Lastly, the investigation at hand only refers to the use of one specific MCDA method. However, different methods can lead to different ranking decisions. It can therefore be advised to repeat the analysis with other methods and check if the concepts obtain similar ranking positions.

Acknowledgements

This research has been funded by the research project 'SW.Developer' which is supported by the German Federal Ministry for Economic Affairs and Climate Action (grant 03EN3014A).

Nomenclature

Letter symbols

a	decision matrix
E	energy, kWh
f	objective function
P	power, kW
T	temperature, °C
t	timestep
v	value
Y	binary decision variable

Subscripts and superscripts

amb	ambient
cap	capacity
i	row of the decision matrix
in/out	in- and outflow
j	column of the decision matrix
lim	heating threshold
nom	nominal
op	operational

Abbreviations

AHP	Analytic Hierarchy Process
ba	battery
CAPEX	capital expenditures/investment costs
COP	coefficient of performance
EA	electricity adapted concept
EP	energy performance
HA	heat adapted concept
HL	heuristic layout
hp	heat pump
MCDA	Multi-Criteria Decision Analysis
*MFH*8	multi-family house with eight flats
*MFH*20	multi-family house with twenty flats
MILP	Mixed-Integer Linear Programming
MPL	minimal part load
OL	optimised layout
OPEX	operational expenditures/costs
PV	photovoltaic
REF	reference energy concept
SC	sector-coupled adapted concept
SEC	self-consumption
SES	self-sufficiency
SFH	single-family house with one flat
TOTEX	total expenditures/costs
tes	thermal storage
WACC	weighted average cost of capital

References

[1] Richter M. *Utilities' business models for renewable energy: A review*. Renewable and Sustainable Energy Reviews 2012;16(5):2483–2493.

[2] Ogunmodede O., Anderson K., Cutler D., Newman A. *Optimizing design and dispatch of a renewable energy system*. Applied Energy 2021;287:116527.

[3] Brown, T., Schäfer, M., Greiner, M. *Sectoral Interactions as Carbon Dioxide Emissions Approach Zero in a Highly-Renewable European Energy System*. Energies 2019;12(6):1032.

[4] Dai H., Wang J., Li G., Chen W., Qui B., Yan J. *A multi-criteria comprehensive evaluation method for distributed energy system*. Energy Procedia 2019;158:3748-3753.

[5] Kildienė S., Zavadskas E. K., Tamošaitienė J. *Complex assessment model for advanced technology deployment*. Journal of Civil Engineering and Management 2014;20(2):280-290.

[6] Koubaa Z., Elleuch M.A., Frikha A. *A hybrid tool to combine multi-criterion decision making and economic objective optimization in designing grid connected hybrid energy systems*. In: International Conference on Decision Aid Sciences and Applications (DASA); 2022 Mar 23-25; Chiangrai, Thailand . Available at: http://doi.org/10.1109/DASA54658.2022.9765256.

[7] Witt T., Dumeier M., Geldermann J. *Combining scenario planning, energy system analysis and multi-criteria analysis to develop and evaluate energy scenarios*. Journal of Cleaner Production 2020;242:118414.

[8] Hou J., Wang J., Zhou Y., Lu X. *Distributed energy systems: Multi-objective optimization and evaluation under different operational strategies*. Journal of Cleaner Production 2021;280:124050.

[9] Jing R., Zhu X., Zhu Z., Wang W., Meng C., Shah N., Li N., Zhao Y. *A multi-objective optimization and multi-criteria evaluation integrated framework for distributed energy system optimal planning*. Energy Conversion and Management 2018;166:445-462.

[10] Lazaroiu G. *Multi-criteria decision making in sustainable renewable energy systems*. In: 19th SGEM International Multidisciplinary Scientific GeoConference EXPO Proceedings; 2019 Jun 30-Jul 6; Albena, Bulgaria. Conference Proceedings:19(4.1)Part A.

[11] Cinelli M., Burgherr P., Kadziński M., Słowiński R. *Proper and improper uses of MCDA methods in energy systems analysis*. Decision Support System 2022;163:113848.

[12] Zhang C., Wang Q., Zeng S., Baležentis T., Štreimikienė D., Ališauskaitė-Šeškienė I. *Probabilistic multi-criteria assessment of renewable micro-generation technologies in households*. Journal of Cleaner Production 2019;212:582-592.

[13] Schneeloch J., Rosin L. *Environomic optimisation of local energy concepts for utility companies under the influence of increased energy prices*. In: 13. Internationale Energiewirtschaftstagung (IEWT) an der TU Wien; 2023 Feb 15-17; Vienna, Austria. Available at: http://doi.org/10.24406/publica-1008.

[14] Krien U., Schönfeldt P., Launer J., Hilpert S., Kaldemeyer C., Pleßmann G. *oemof.solph-A model generator for linear and mixed-integer linear optimisation of energy systems*. Software Impacts 2020;6:100028.

[15] Gurobi optimization, LLC. *Gurobi Software* Available at: http://www.gurobi.com/ [accessed 23.2.2023].

[16] Helvetic energy. *Technisches Datenblatt Wärmepumpe AERO AW 23 EVI*. Available at: https://docplayer.org/57833547-Technisches-datenblatt-waermepumpe-aero-aw-23-evi.html [accessed 08.05.2023].

[17] Winkel M. *Simulation und Analyse des kombinierten Einsatzes thermischer Energieausgleichsoptionen zum elektrischen Last- und Erzeugungsmanagement in Wohnsiedlungen [dissertation]*. Bochum, Germany: Ruhr-Universität Bochum; 2015.

[18] Zapf M. *Stromspeicher und Power-to-Gas im deutschen Energiesystem*. Wiesbaden, Germany: Springer Vieweg; 2017.

[19] Stein J., Holmgren, W., Forbess J., Hansen C. *PVLIB: Open Source Photvoltaic Performance Modeling Functions for Matlab and Python*. In: IEEE: Proceedings of the 43rd Photovoltaic Specialists Conference (PVSC); 2016 Jun 5-10; Piscataway, New Jersey. IEEE.

[20] Fraunhofer ISE. *Stromgestehungskosten erneuerbare Energien*. Freiburg, Germany: Fraunhofer Institute for Solar Energy Systems ISE, Energy System Analysis; 2018.

[21] Deutsche Energie-Agentur. *Thermische Energiespeicher für Quartiere*. Berlin, Germany: Deutsche Energie-Agentur GmbH (dena); 2021.

[22] KEA-BW. *Einführung in den Technikkatalog*. Available at `https://www.kea-bw.de/waermewende/wissensportal/technikkatalog` [accessed 10.05.2023].

[23] Professional Energy Consulting. *Stromspeicher Kosten im Jahr 2022*. Available at: `https://pro-ec.de/photovoltaik/stromspeicher-kosten-preise-2022/` [accessed 16.06.2022].

[24] Ishizaka A., Nemery P. *Multi-criteria decision analysis.*. Chicester West Sussex, UK: Wiley; 2013.

[25] Saaty R. *The analytic hierarchy process: what it is and how it is used*. Mathematical Modelling 1987;9(3-5):161-176.

[26] V. e. V. *VDI-Richtlinie 4655*. 2021.

[27] DWD. *Testreferenzjahre (TRY)*. Available at: `https://www.dwd.de/DE/leistungen/testreferenzjahre/testreferenzjahre.html` [accessed 24.1.2023].

[28] Umweltbundesamt. *Strom- und Wärmeversorgung in Zahlen*. Available at: `https://www.umweltbundesamt.de/themen/klima-energie/energieversorgung/strom-waermeversorgung-in-zahlen#Strommix` [accessed 10.05.2023].

Integrated design and operation optimization of multi-energy systems including energy networks

Enrico Dal Cin[a], Gianluca Carraro[b], Andrea Lazzaretto[c], George Tsatsaronis[d], Gabriele Volpato[e], and Piero Danieli[f]

[a] University of Padova, Industrial Engineering Department, Padova, Italy, enrico.dalcin@phd.unipd.it, CA
[b] University of Padova, Industrial Engineering Department, Padova, Italy, gianluca.carraro@unipd.it
[c] University of Padova, Industrial Engineering Department, Padova, Italy, andrea.lazzaretto@unipd.it
[d] Technische Universität Berlin, Chair of Energy Engineering and Environmental Protection, Berlin, Germany, georgios.tsatsaronis@tu-berlin.de
[e] University of Padova, Industrial Engineering Department, Padova, Italy, gabriele.volpato.1@phd.unipd.it
[f] University of Padova, Department of Management and Engineering, Vicenza, Italy, piero.danieli@unipd.it

Abstract:

A multi-energy system is composed of four main subsystems: i) energy conversion, ii) energy transportation, iii) energy supply, and iv) energy storage. Recent works in the literature dealing with the design and operation optimization of multi-energy systems usually include only one of the above-mentioned subsystems at a time and neglect the others or consider them as constraints imposed a priori. That kind of approach may lead to near optimal system configurations. In fact, the global optimum can only be achieved by the synthesis, design and operation optimization of the system in its entirety. Here, a mixed integer linear programming (MILP) approach is proposed to simultaneously optimize the size of the energy conversion and storage plants, the capacity of the energy networks, and the operation of the whole multi-energy system. The objective function consists in minimizing the life cycle cost of the system while imposing an upper bound on greenhouse gas emissions. Moreover, this upper bound can be iteratively reduced to consider increasingly stricter decarbonization targets. A district composed of commercial and residential buildings, with their own electricity and heating demands and operating in a microgrid, is considered as a case study. Heat is provided to the end users via a district heating network, while electricity can be either generated on site or imported from the national grid. Results shows a reduction potential in carbon emissions of 45% for the considered system, together with an 8% reduction of the life cycle cost, with respect to a reference scenario.

Keywords:

Decarbonization; District heating; Microgrid; Multi-energy systems; Optimization.

1. Introduction

The increasing threat of climate change requires timely interventions to drastically reduce the anthropogenic emissions of greenhouse gases By accounting for 75% of the global carbon emissions, the energy sector is the main responsible of global warming. However, the increasing availability at low cost of energy conversion technologies based on Renewable Energy Sources (RES) can pave the way to a deep decarbonization process. To this scope, fostering the distributed generation, electrifying the energy consumption and exploiting the synergies between different final energy sectors, as, for instance, the electricity and heating ones, can play a crucial role in improving the penetration of RES while decreasing the consumption of fossil fuels [1]. All these actions contribute to the development of Multi-Energy Systems (MESs).

A MES is defined as an energy system of any spatial extent (a single building, a district, a city, a nation, …) that involves different types of energy carriers (electricity, heat, fossil fuels, biomass, …) and provide energy in various forms to the end users [2]. It is composed of four main subsystems.

1. Energy conversion. The fleet of the energy conversion plants that provides the end users with the required energy in the required forms.

2. Energy transportation. The energy networks collecting energy from the conversion plants and delivering it to the end users.
3. Energy supply. The end users of the system with their specific energy demands.
4. Energy storage. Components that allow storing energy in different forms in a certain moment and delivering it in a later one. They can be integrated at any level (energy conversion, transportation, supply).

A holistic approach to the study of MESs should consider all the above-mentioned aspects. Thus, the complete optimization of a MES accordingly to a certain objective function should involve three levels of analysis.

1. Synthesis, which targets the topology of the energy networks and the number, type and location within the system of the energy conversion and storage plants required to fulfil the energy demands of the end users.
2. Design, which targets the sizing of the energy conversion and storage plants and the capacity of each branch of the energy networks.
3. Operation, which targets the management of the dispatchable plants, the management of the power and mass flows within the networks, and the application of eventual demand response strategies [3].

Such kind of optimization problems, referred to as Synthesis, Design and Operation (SDO) optimization, is the most complete in the field of energy systems, but also the most challenging to solve, due to the high number of decision variables, either continuous or integer/binary [4].

This paper focuses on MESs at the district level including microgrids and district heating networks (DHNs). An increasing number of works in the recent literature deals with the optimization of such kind of systems. However, most of those works do not embrace a holistic approach but focus on a specific optimization problem (synthesis, design, operation) or a specific aspect of the MES (energy conversion, storage, transportation, supply).

Integrated district energy networks were studied by several authors. Lund et al. [5] highlighted the importance of integrating different energy networks (e.g., district heating, electricity distribution and natural gas supply) at the district level to shape the smart energy system of the future. In this context, decreasing the supply temperature of DHNs (e.g., with 4th and 5th generation DHNs) can facilitate the integration of RES, power to heat technologies and other smart energy systems (e.g., microgrids). Leitner et al. [6] stated that the components required to build up smart energy systems are well known and already available in the market, whereas there is a lack of analyses at a system level. Their study focuses on a modelling and simulation approach for coupled district heating and electrical distribution networks. The DHN is defined by a dynamic thermal-hydraulic model, whereas the electrical distribution network by a quasi-static model. The model is complete but does not involve any kind of optimization, which would probably result in a computational intractability. Other authors, e.g., Nazari-Heris et al. [7], studied the optimal operation of highly integrated MESs involving many energy or energy-related networks (e.g., electricity, heating, natural gas and water networks). However, these models are computationally expensive (they are typically applied to one-day operation) and cannot be applied to the design optimization of those networks. Talebi et al. [8] reviewed the optimization approaches to the design of DHNs and highlighted the relevant role that optimization tools can have in designing district energy systems integrating a high share of RES and energy storage technologies. Moreover, they found out that the most used design optimization techniques are based on numerical approaches, as Mixed Integer Linear or Non-Linear Programming (MILP and MINLP, respectively), or meta-heuristic approaches, as evolutionary or genetic algorithms. Röder et al. [9] developed a MILP optimization framework for the SDO optimization of a DHN. They considered a mixed residential-commercial district in Germany and searched for the cost-optimal topology, capacity, and operation of the DHN supplying all the users of the district. However, they did not optimize the generation and storage sides of the system as they fixed in advance the position, type and capacity of the energy conversion and storage plants providing the network with the required heat, and they did not consider the electricity network.

On the other hand, many authors focused on the optimal design and/or operation of the energy conversion and storage plants supplying a district MES. Rech et al. [10] studied the optimal operation of a fleet of energy conversion plants providing electrical and thermal energy to a mountain village. Heat is generated by means of biomass-fuelled boilers or combined heat and power (CHP) plants, and delivered to the end users via DHN, which is modelled as a black box collecting heat from the generators to fulfil the aggregated heating demand of the village. Ghilardi et al.[11] developed a MILP model for the operation optimization of a University campus MES involving a district heating/cooling network and the thermal management of buildings. They found out considerable advantages in terms of cost reduction, energy saving and integration of RES thanks to the optimal management of the thermal comfort in buildings, the optimal dispatch of the available energy conversion systems and the optimal management of the temperature levels of the district heating/cooling network. In a previous work [12], the authors of the present paper proposed a method for the design and operation multi-objective optimization (economical and environmental) of the energy conversion and storage plants providing electricity and heat to an energy community. Demand response was also applied, but no district energy networks were modelled, assuming that the community members directly interface with the national power grid and fulfil their heating demand autonomously. Wirtz [13] proposed a web tool for the optimal conceptual design

of a district MES generation mix. By means of a Linear Programming (LP) approach, the proposed tool allows defining the optimal size of the energy conversion and storage plants available in an energy hub fulfilling the electricity, heating and cooling demands of the district. Heating and cooling can be also provided via district heating and/or cooling networks. Wirtz et al. [14] also proposed a model for the optimal planning of a 5th generation district heating and cooling network. This model optimizes the design (i.e., the size) of the energy conversion and storage plants available at two levels: i) the energy hub and ii) the end users' buildings, which interface with the heating and cooling network by means of heat pumps and chillers. As a last example, Mashayekh et al. [15] developed an optimization tool for the design of the energy conversion and storage plants supplying a multi energy microgrid involving both electricity and heating networks. The optimization addresses the generation mix selection and sizing, the resource siting and allocation, and the operation scheduling. They found out that considering the spatial distribution of a MES, modelled as a multi nodal system, allows a more realistic assessment of the generation portfolio, which can be otherwise non-optimal if the same system is modelled as a single node.

A lack emerges. On one hand, works dealing with modelling of energy networks either neglect the design of energy conversion and storage systems or build complex models that are not suitable for design optimization procedures. On the other hand, works dealing with design-operation optimization of MESs do not consider the optimization of the topology and capacity of the district energy networks, which are considered only as constraints.

A pioneering work about the SDO optimization of a district MES was proposed by Mehleri et al. [16] and further developed in [17]. In these works, a MILP framework is introduced to optimize the selection (capacity and allocation) and operation of the distributed energy conversion plants supplying the district MES, but also the design (topology and capacity) of a DHN connecting the buildings. However, the weakness of the proposed approach is that the DHN is defined by a set of direct heat exchange connections between two buildings that follow the path of minimum "geometrical distance" (i.e., the straight line connecting two buildings). This is a strong simplification because obstacles that can interrupt the path between two buildings are not considered. A more reliable approach in the design of a network should consider the "geographical distance" between nodes, i.e., the "real" path that a network branch must follow to connect two nodes. Accordingly, a typical approach to DHN design (see, for instance, in [9]) consists in constraining pipelines to follow pre-determined paths, which are usually the streets of the district.

To overcome the above-mentioned weaknesses, this work proposes a holistic MILP approach for the optimal design and operation of a district MES, modelled as a multi-nodal system. The goal consists in finding the size of the available energy conversion and storage plants, the capacity of each branch of the available energy networks, and the operation of the whole system that minimize the life cycle cost of the MES, while fulfilling the energy demands of the end users. Moreover, an environmental constraint is imposed on the maximum amount of carbon dioxide (CO_2) emissions. By iteratively decreasing the value of this constraint, a sort of multi-objective optimization can be carried out, in order to obtain the Pareto front of the cost-optimal system configurations that meet increasingly stricter decarbonization targets. A district located in Padova, Italy, composed of commercial and residential buildings with their own electricity and heating demands, and operating in a microgrid is considered here as a case study to highlight the potentiality of the proposed approach. Heat is provided to consumers via DHN, while electricity can be either generated on site or imported from the national grid.

The novelty introduced in this paper consists in proposing a holistic and integrated method for the design and operation optimization of both conversion/storage plants and energy networks of a MES, while maintaining an accurate representation of the networks, which are modelled with the "geographical distance" criterion, instead of the simplified "minimum geometrical distance" one.

Note that the synthesis problem, i.e., the definition of the topology of the networks and of the number, type and position within the system of the energy conversion and storage plants, is not addressed here. Conversely, the topological data are provided as input to the model. However, the proposed approach is intended as a sub-problem of a wider optimization method that addresses the synthesis problem too, in order to provide a complete SDO optimization tool for district MESs. The idea is to implement the overall SDO problem by means of a two-level evolutionary algorithm, in which the first level deals with the synthesis problem. The topology of the system defined in the first level is then passed to the second level, which deals with the design and operation sub-problem (i.e., the model proposed here). Since the design and operation sub-problem must be run several times for each iteration of the evolutionary algorithm, it must be maintained as simple as possible in order to avoid computational intractability. For this reason, the model presented here is maintained linear by means of proper simplifications of the characteristic curves of the technologies and cost data. A similar two-level approach for the SDO of a district heating system with distributed CHP plants was developed by Casisi et al. [18]. However, they only consider DHN and not the electrical network, and they assume a given topology of the DHN.

The rest of the paper is structured as follows. Section 2 presents the case study, while section 3 presents the developed optimization method. Section 4 discusses the results and, finally, section 5 draws the conclusions.

2. Case study

The case study considers a small mixed residential-commercial district located in Padova, Italy. The district is composed of five buildings (end users), with their own electricity and heating demands, and operates in an autonomous microgrid connected to the national power grid. Heat is provided to the end users via DHN, while electricity can be either generated on site or imported from the national grid. The system is modelled as a multi-nodal MES with 16 nodes in total. Figure 1 shows the layout of the considered system. The buildings located at nodes 3, 5 and 15 are residential buildings, the remaining two (nodes 9 and 11) are commercial buildings. Each building owns a photovoltaic plant (PV) and an electrical energy storage (EES) based on lithium batteries. An energy hub located at node 7 and including a gas-fuelled CHP internal combustion engine (ICE), a gas boiler (BOIL), an air-water heat pump (HP) and a thermal energy storage (TES) feeds the DHN that delivers the required heat to the end users. To maintain the model linear, the operating parameters of the networks are fixed a priori and assumed to remain constant during the operation, as in [9]. This simplification allows modelling the networks by considering only the power or heat flows circulating inside them. The supply and return temperatures of the DHN are set at 70°C and 40°C, respectively. The microgrid voltage is 380V.

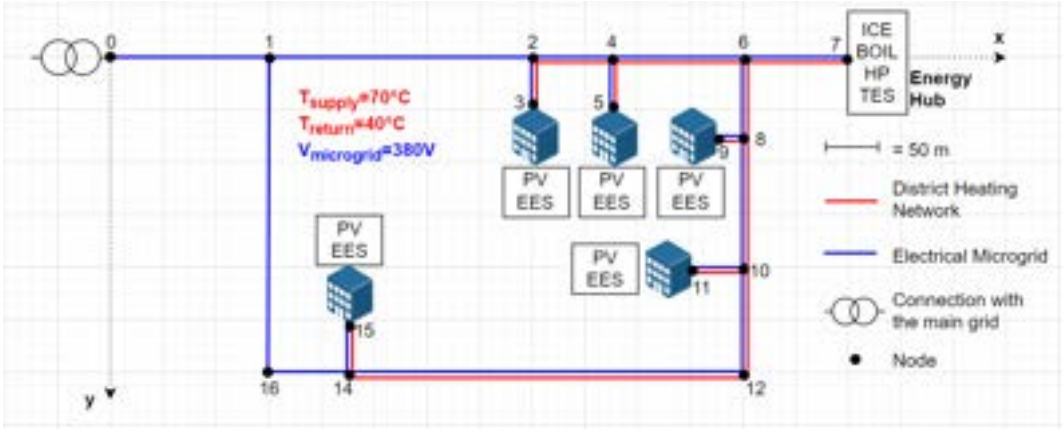

Figure 1 Layout of the multi-energy system considered as case study. The white rectangles contain the conversion and storage plants available at the node where they are located.

The topology of the energy networks can be derived from a geographical map of the district, where the available paths for the network branches are the streets. Accordingly, the layout of the DHN is designed by considering the tree path of "minimum geographical distance" connecting the energy hub to all the end users. In other words, the overall length of the pipelines is minimized, with the constraint of following only the available paths. The same holds true for the electrical microgrid, apart from the inclusion of node 0, which allows the power exchange with the national grid, and the inclusion of the branches between nodes 0-1, 1-2, 2-16 and 14-16, which define a network ring that increases the system reliability.

Table 1 shows the yearly electricity and heating demands of the end users (integral over one year of the hourly demands) and the corresponding demand peaks occurring during the year (maximum values reached by the hourly demands). Since one hour is the time resolution of the model, hourly demands are expressed in unit of power (kW).

Table 1 Yearly electricity and heating demands ($D_{el,year}$ and $D_{th,year}$, respectively) of each end user and aggregated, with the associated demand peaks over the year ($D_{el,peak}$ for electricity, and $D_{th,peak}$ for heating).

Node	$D_{\mathrm{el,year}}$, MWh	$D_{\mathrm{th,year}}$, MWh	$D_{\mathrm{el,peak}}$, kW	$D_{\mathrm{th,peak}}$, kW
3	89.77	73.54	25.0	60.0
5	125.68	98.06	35.0	80.0
9	175.42	20.76	70.0	60.0
11	125.30	17.30	50.0	50.0
15	143.63	122.57	40.0	100.0
Aggregated	659.80	332.23	176.3	344.4

3. Method: MILP optimization

The MILP optimization problem can be formulated in a general form as in Eq. (1) [19].

$$min_{\boldsymbol{x},\boldsymbol{y}}\{f(\boldsymbol{x},\boldsymbol{y}) = \boldsymbol{c}^T\boldsymbol{x} + \boldsymbol{d}^T\boldsymbol{y}\}$$
$$subject\ to\ \boldsymbol{A}\boldsymbol{x} + \boldsymbol{B}\boldsymbol{y} = \boldsymbol{b} \quad (1)$$
$$with\ \boldsymbol{x} \geq 0 \in \Re^{N_x}, \boldsymbol{y} \in \{1,0\}^{N_y}.$$

f is the objective function, $\boldsymbol{c}$ and $\boldsymbol{d}$ are the cost vectors associated with the continuous and binary variables, $\boldsymbol{x}$ and $\boldsymbol{y}$, respectively; $\boldsymbol{A}$ and $\boldsymbol{B}$ are the constraint matrices and $\boldsymbol{b}$ is the vector of the known terms; N_x and N_y indicate the dimension of $\boldsymbol{x}$ and $\boldsymbol{y}$, respectively.

The considered MES is modelled as a multi-nodal system, with $N = 16$ nodes. In the next sections, the constraints, decision variables and objective function of the problem are introduced. The decision variables are highlighted in bold. The subscript $n = 1,2,\dots,N$ refers to the nodes, $k = 1,2,\dots,K$ to the typical days (or cluster centers), and $h = 1,2,\dots,24$ to the hours of the day. The optimization model has been developed in Python and solved with the Gurobi solver.

3.1. Time series aggregation

To be solved, the proposed optimization model requires some time series as input. These are i) the electricity demand of each final user, ii) the heating demand of each final user, iii) the global solar irradiation on the horizontal plane, necessary for calculating the PV generation, and iv) the temperature of the ambient air, necessary for calculating the electrical power consumption of the HP. These time series are available for a reference year subdivided in days with an hourly resolution, for a total of $24 \times 365 = 8760$ timesteps for each time series. However, including the time series in their entirety into the optimization model would result in a computational intractability. In fact, the number of decision variables required to solve the operation problem is proportional to the total number of timesteps. Thus, it is necessary to reduce the total number of timesteps and, in turn, the computational burden.

Following Hoffmann et al. [20], a K-medoids clustering approach is applied here to aggregate time series into typical days, which must be representative of the entire year. The chosen number of typical days is eight. Moreover, the two days of the year having the maximum peak value in i) aggregated electricity demand and ii) aggregated heating demand are added to the clustering process as new cluster centers. Thus, the final number of typical days is $K = 10$. Neglecting the extreme peak periods in defining typical days would lead to underestimate the size of the energy conversion plants, which could not meet the extreme demand peaks occurring during the year. The hourly resolution of the time series is preserved, being each typical day composed of $H = 24$ time steps. In this way, the number of decision variables associated with the operation, proportional to the total number of timesteps, is drastically reduced. In fact, the total number of timesteps is diminished from 8760 to $H \times K = 240$. The time series aggregation also returns the weight w_k of each typical day k (with $k = 1,2,\dots,K$), which corresponds to the number of days of the year represented by that typical day. The Python package "*tsam*" has been utilized for time series aggregation.

3.2. Energy conversion and storage systems

The energy conversion plants are modelled according to [21], the energy storage systems according to [22].

3.2.1. Photovoltaic plant

The electrical power (P_{PV}) generated by a photovoltaic plant, in kW, is given by Eq. (2).

$$P_{PV,n,k,h} = \boldsymbol{C_{PV,n}} \frac{I_{sun,k,h}}{I_{sun,ref}}. \quad (2)$$

$\boldsymbol{C_{PV}}$ is the capacity of the PV plant in kW of peak (kW_p) and is a decision variable, I_{sun} is the global solar irradiation in W/m^2 and is provided as a time series, $I_{sun,ref} = 1000\mathrm{W/m^2}$ is the global solar irradiation in the reference conditions in which the kW_p is defined. It is assumed that 1 kW_p of PV requires 7 m^2 of area.

The PV capacity is bounded in between a minimum value, corresponding, for instance, to the area of a single PV module, and maximum one, corresponding to the entire available area at a node, as reported in Eq. (3).

$$C_{PV,min,n} \leq \boldsymbol{C_{PV,n}} \leq C_{PV,max,n}. \quad (3)$$

If PV is not available at the node n, then $C_{PV,min,n} = C_{PV,max,n} = 0$ and, in turn, $\boldsymbol{P_{PV,n,k,h}} = 0$.

3.2.2. Gas-fuelled internal combustion engine in combined heat and power mode

The fuel (natural gas) consumption (F_{ICE}) of the CHP internal combustion engine (ICE), in kW, and its thermal power (Q_{ICE}), also in kW, are given by Eq. (4) and Eq. (5), respectively, as a linear function of the engine power.

$$F_{ICE,n,k,h} = \boldsymbol{P_{ICE,n,k,h}}\alpha + \boldsymbol{\delta_{ICE,n,k,h}}\beta. \quad (4)$$

$$Q_{ICE,n,k,h} = \boldsymbol{P_{ICE,n,k,h}}\rho + \boldsymbol{\delta_{ICE,n,k,h}}\sigma. \quad (5)$$

$\boldsymbol{P_{ICE}}$ is the electric power in kW and is a decision variable, $\boldsymbol{\delta_{ICE}}$ is a binary decision variable equal to 1 if the ICE is working and equal to 0 otherwise. The linearization coefficients of the ICE characteristic curves are $\alpha = 2.42$, $\beta = 11.0\mathrm{kW}$, $\rho = 1.24$, $\sigma = -1.65\mathrm{kW}$.

The capacity $\boldsymbol{C_{ICE}}$ of the ICE, in kW of nominal electric power, which is a decision variable, is associated with the auxiliary decision variable $\boldsymbol{\vartheta_{ICE}}$ in order to avoid nonlinear constraints [23] of the type $\boldsymbol{P_{ICE}} \leq \boldsymbol{C_{ICE}}\boldsymbol{\delta_{ICE}}$. Equations (6), (7), and (8) bound $\boldsymbol{C_{ICE}}$ and $\boldsymbol{P_{ICE}}$.

$$\boldsymbol{\delta_{ICE,n,k,h}} C_{ICE,min,n} \leq \boldsymbol{\vartheta_{ICE,n,k,t}} \leq \boldsymbol{\delta_{ICE,n,k,h}} C_{ICE,max,n}. \quad (6)$$

$$\left(1 - \boldsymbol{\delta_{ICE,n,k,h}}\right) C_{ICE,min,n} \leq \boldsymbol{C_{ICE,n}} - \boldsymbol{\vartheta_{ICE,n,k,h}} \leq \left(1 - \boldsymbol{\delta_{ICE,n,k,h}}\right) C_{ICE,max,n}. \quad (7)$$

$$\gamma_{ml,ICE} \boldsymbol{\vartheta_{ICE,n,k,h}} \leq \boldsymbol{P_{ICE,n,k,h}} \leq \boldsymbol{\vartheta_{ICE,n,k,h}}. \quad (8)$$

$\gamma_{ml,ICE} = 0.7$ is the ratio between the minimum load at which the ICE can operate and its nominal capacity, and $C_{ICE,min}$ and $C_{ICE,max}$ are the minimum and maximum bounds of the ICE capacity, respectively. If the ICE is not available at the node n, then $C_{ICE,min,n} = C_{ICE,max,n} = 0$ and, in turn, $\boldsymbol{P_{ICE,n,k,h}} = \boldsymbol{F_{ICE,n,k,h}} = \boldsymbol{Q_{ICE,n,k,h}} = 0$.

3.2.3. Gas boiler

The fuel (natural gas) consumption (F_{BOIL}) of the gas boiler (BOIL), in kW, is given in Eq. (9) as a function of the thermal power ($\boldsymbol{Q_{BOIL}}$), in kW, which is a decision variable.

$$F_{BOIL,n,k,h} = \frac{\boldsymbol{Q_{BOIL,n,k,h}}}{\eta_{th,BOIL}}. \quad (9)$$

$\eta_{th,BOIL} = 0.9$ is the boiler efficiency. Equations (10) and (11) bound the thermal power ($\boldsymbol{Q_{BOIL}}$) and the boiler capacity ($\boldsymbol{C_{BOIL}}$), expressed in kW of nominal thermal power, which is another decision variable.

$$C_{BOIL,min,n} \leq \boldsymbol{C_{BOIL,n}} \leq C_{BOIL,max,n}. \quad (10)$$

$$0 \leq \boldsymbol{Q_{BOIL,n,k,h}} \leq \boldsymbol{C_{BOIL,n}}. \quad (11)$$

$C_{BOIL,min,}$ and $C_{BOIL,max}$ are the minimum and maximum bounds of the boiler capacity, respectively. If the boiler is not available at the node n, then $C_{BOIL,min,n} = C_{BOIL,max,n} = 0$ and, in turn, $\boldsymbol{F_{BOIL,n,k,h}} = \boldsymbol{Q_{BOIL,n,k,h}} = 0$.

3.2.4. Air-water heat pump

The electric power consumption (P_{HP}) of the heat pump (HP), in kW, is given in Eq. (12) as a function of the thermal power ($\boldsymbol{Q_{HP}}$), in kW, which is a decision variable.

$$P_{HP,n,k,h} = \frac{1}{COP_{ideal,k,h}} \left(\boldsymbol{Q_{HP,n,k,h}}\mu + \boldsymbol{\delta_{HP,n,k,h}}\omega\right). \quad (12)$$

$\boldsymbol{\delta_{HP}}$ is a binary decision variable equal to 1 if the HP is working and equal to 0 otherwise, $\mu = 1.80$ and $\omega = 2.65$kW are the linearization coefficients of the HP characteristic curves (similarly to the ICE), COP_{ideal} is the coefficient of performance calculated in ideal conditions (Carnot equation) between the ambient temperature T_{amb}, in K, provided as a time series, and the supply temperature T_{supply} of the DHN, in K. Equation (13) shows the ideal coefficient of performance.

$$COP_{ideal,k,h} = \frac{1}{1 - \frac{T_{amb,k,h}}{T_{supply}}}. \quad (13)$$

The capacity ($\boldsymbol{C_{HP}}$) of the HP is a decision variable expressed in kW of nominal thermal power, and is associated with the auxiliary decision variable $\boldsymbol{\vartheta_{HP}}$ to avoid nonlinear constraints. Equations (14), (15), and (16) bound $\boldsymbol{C_{HP}}$ and $\boldsymbol{Q_{HP}}$.

$$\boldsymbol{\delta_{HP,n,k,h}} C_{HP,min,n} \leq \boldsymbol{\vartheta_{HP,n,k,h}} \leq \boldsymbol{\delta_{HP,n,k,h}} C_{HP,max,n}. \quad (14)$$

$$\left(1 - \boldsymbol{\delta_{HP,n,k,h}}\right) C_{HP,min,n} \leq \boldsymbol{C_{HP,n}} - \boldsymbol{\vartheta_{HP,n,k,h}} \leq \left(1 - \boldsymbol{\delta_{HP,n,k,h}}\right) C_{HP,max,n}. \quad (15)$$

$$\gamma_{ml,HP} \boldsymbol{\vartheta_{HP,n,k,h}} \leq \boldsymbol{Q_{HP,n,k,h}} \leq \boldsymbol{\vartheta_{HP,n,k,h}}. \quad (16)$$

$\gamma_{ml,HP} = 0.5$ is the ratio between the minimum load at which the HP can operate and its nominal capacity. $C_{HP,min,}$ and $C_{HP,max}$ are the minimum and maximum bounds of the HP capacity, respectively. If the HP is not available at the node n, then $C_{HP,min,n} = C_{HP,max,n} = 0$ and, in turn, $\boldsymbol{P_{HP,n,k,h}} = \boldsymbol{Q_{HP,n,k,h}} = 0$.

3.2.5. Energy storage systems

The decision variables associated with the thermal energy storage (TES) are its capacity ($\boldsymbol{C_{TES,n}}$), in kWh, the charging heat ($\boldsymbol{Q_{TES,chrg,n,k,h}}$) and discharging heat ($\boldsymbol{Q_{TES,disch,n,k,h}}$), in kW, and the state of charge ($\boldsymbol{SOC_{TES,n,h,k}}$), in kWh. The decision variables associated with the electrical energy storage (EES) are its capacity ($\boldsymbol{C_{EES,n}}$), in kWh, the charging power ($\boldsymbol{P_{EES,chrg,n,k,h}}$) and discharging power ($\boldsymbol{P_{EES,disch,n,k,h}}$), in kW, and the state of charge ($\boldsymbol{SOC_{EES,n,h,k}}$), in kWh. Refer to [22] for the model of energy storage systems. Note that both intra-day and inter-

day storage is allowed. If a storage system is not available at node n, then all the corresponding decision variables are set equal to zero.

3.2.6. Electricity import from/export to the national power grid

The microgrid interfaces with the national power grid at node 0. Here, it is possible to import/export electricity. Thus, two additional sets of decision variables are required: $\boldsymbol{P_{imp,n,k,h}}$, in kW, for import, and $\boldsymbol{P_{exp,n,k,h}}$, in kW, for export. $\boldsymbol{P_{imp,n,k,h}} = \boldsymbol{P_{imp,n,k,h}} = 0$ if $n \neq 0$.

3.3. Energy networks

The system includes $P = 12$ district heating pipelines, and $L = 16$ electrical microgrid lines.

3.3.1. District heating network

For each pipeline p (with $p = 1,2, \dots, P$) connecting two nodes n and m, the decision variables involved in the model of the district heating network (DHN) are: the capacity of the pipeline ($\boldsymbol{C_{DHN,p,nm}}$) connecting the two nodes, in kW, the heat flow from node n to node m ($\boldsymbol{Q_{DHN,nm}}$), in kW, and the heat flow from node m to node n ($\boldsymbol{Q_{DHN,mn}}$), in kW. The heat flows are bounded by the pipeline capacity, as shown in Eq. (17).

$$\boldsymbol{Q_{DHN,nm,k,h}} + \boldsymbol{Q_{DHN,mn,k,h}} \leq \boldsymbol{C_{DHN,p,nm}}. \quad (17)$$

Note that, due to the DHN layout (see Figure 1), heat is constrained to flow from the energy hub (node 7) to the end users (nodes 3, 5, 9, 11, 15). Thus, for each pipeline, the flow in one of the two directions is always zero. If two nodes n and m are not connected by a DHN pipeline, then $\boldsymbol{C_{DHN,p,nm}}$ is not defined, and $\boldsymbol{Q_{DHN,nm,k,h}}$ and $\boldsymbol{Q_{DHN,mn,k,h}}$ are set equal to zero.

3.3.2. Electrical microgrid

For each electric line l (with $l = 1,2, \dots, L$) connecting two nodes n and m, the decision variables involved in the model of the electrical microgrid (EMG) are: the capacity of the network line ($\boldsymbol{C_{EMG,l,nm}}$) connecting the two nodes, in kW, the power flowing from node n to node m ($\boldsymbol{P_{EMG,nm}}$), in kW, and the power flowing from node m to node n ($\boldsymbol{P_{EMG,mn}}$), in kW. The power streams are bounded by the network line capacity, as shown in Eq. (18).

$$\boldsymbol{P_{EMG,nm,k,h}} + \boldsymbol{P_{EMG,mn,k,h}} \leq \boldsymbol{C_{EMG,l,nm}}. \quad (18)$$

If two nodes n and m are not connected by a EMG line, then $\boldsymbol{C_{EMG,l,nm}}$ is not defined, and $\boldsymbol{P_{EMG,nm,k,h}}$ and $\boldsymbol{P_{EMG,mn,k,h}}$ are set equal to zero.

3.4. Energy balances

Two energy balance constraints are imposed for each node, typical day, and time step of the typical day. The "+" sign is assigned to power/heat flows entering a node, the "–" sign to power/heat flows exiting a node.

Equation (19) shows the electrical energy (electricity) balance.

$$-D_{el,n,k,h} - \sum_m \boldsymbol{P_{EMG,nm,k,h}} + \sum_m \boldsymbol{P_{EMG,mn,k,h}}(1 - \lambda_{EMG}) - \boldsymbol{P_{exp,n,k,h}} + \boldsymbol{P_{imp,n,k,h}} - P_{HP,n,k,h} + P_{PV,n,k,h} + \boldsymbol{P_{ICE,n,k,h}} - \boldsymbol{P_{EES,chrg,n,k,h}} + \boldsymbol{P_{EES,disch,n,k,h}} = 0. \quad (19)$$

D_{el} is the hourly electricity demand in kW, m is the set of nodes connected to the node n, $\lambda_{EMG} = 0.02$ is the constant loss factor of the microgrid.

Equation (20) shows the thermal energy (heat) balance.

$$-D_{th,n,k,h} - \sum_m \boldsymbol{Q_{DHN,nm,k,h}} + \sum_m \left[\boldsymbol{Q_{DHN,mn,k,h}}\left(1 - len_{p,nm}\lambda'_{DHN}\right) - len_{p,nm}\lambda''_{DHN}\right] + \boldsymbol{Q_{HP,n,k,h}} + Q_{ICE,n,k,h} - \boldsymbol{Q_{TES,chrg,n,k,h}} + \boldsymbol{Q_{TES,disch,n,k,h}} = 0. \quad (20)$$

D_{th} is the hourly heating demand in kW, m is the set of nodes connected to the node n, len_p is the length of the pipeline in m, $\lambda'_{DHN} = 5.4 \times 10^{-5}\ 1/\mathrm{m}$ and $\lambda''_{DHN} = 7.4 \times 10^{-3}\ \mathrm{kW/m}$ are the linearization coefficients of the district heating losses calculated according to [9] as a function of the pipeline capacity and supply, return and ground temperatures ($T_{supply} = 70°\mathrm{C}$, $T_{return} = 40°\mathrm{C}$, and $T_{ground} = 10°\mathrm{C}$, respectively).

3.5. Objective function

The objective function f, to be minimized, represents the life cycle cost of the system actualized to one-year operation. f is composed of two contributions: f', associated with operation costs, and f'' associated with investment costs. Thus, $f = f' + f''$. f' and f'' are given in Eq. (21) and Eq.(22), respectively.

$$f' = \sum_k w_k \sum_n \sum_h \left[c_{gas}\left(F_{ICE,n,k,h} + F_{BOIL,n,k,h}\right) + c_{el,buy}\boldsymbol{P_{imp,n,k,h}} - c_{el,sell}\boldsymbol{P_{exp,n,k,h}}\right]. \quad (21)$$

$$f'' = \{\sum_n \sum_g [\tau_g (c_{inv,var,g} \boldsymbol{C_{g,n}} + c_{inv,fix,g})]\} + \{\sum_p [\tau_{DHN} len_p (c_{inv,var,DHN} \boldsymbol{C_{DHN,p,nm}} + c_{inv,fix,DHN})]\} +$$
$$\{\sum_l [\tau_{EMG} len_l (c_{inv,var,EMG} \boldsymbol{C_{EMG,l,nm}} + c_{inv,fix,EMG})]\}. \quad (22)$$

w_k is the weight of the typical day k, $c_{gas} = 70€/\text{MWh}$ is the purchasing cost of natural gas, $c_{el,buy} = 200€/\text{MWh}$ is the purchasing cost of electricity from the national grid, and $c_{el,sell} = 50€/\text{MWh}$ is the selling price of electricity to the national grid. The subscript g (with g = PV, ICE, BOIL, HP, TES, EES) refers to the set of energy conversion and storage technologies; $c_{inv,var}$ and $c_{inv,fix}$ are the linearization coefficients of the investment cost of a technology or network (they are reported in Table 2 with their units); $\boldsymbol{C}$ is the capacity (decision variable); len refers to the length of a network branch in m; τ is the actualization factor of a technology or network and is calculated in Eq.(23), where $r = 0.05$ is the interest rate and a is the lifetime of a technology or network (see Table 2).

$$\tau = \frac{r(1+r)^a}{(1+r)^a+1}. \quad (23)$$

Note that operation and maintenance costs of the installed components are not shown in Eq. (22) for simplicity. However, they are included and calculated as a share of the investment cost.

Table 2 Linearized investment cost and lifetime of the energy conversion and storage technologies and energy networks.

Quantity	PV	ICE	BOIL	HP	TES	EES	DHN	EMG
$c_{inv,var}$	1250€/kW	1740€/kW	65€/kW	117€/kW	244€/kWh	880€/kWh	103€/kW/m	34€/kW/m
$c_{inv,fix}$	0€	32050€	1625€	2145€	970€	3495€	0.2€/m	0.05€/m
a, years	20	20	20	20	20	20	40	40

The function Φ defines the CO2 emissions of the system in one year of operation, as shown in Eq. (24).

$$\Phi = \sum_k w_k \sum_n \sum_h [e_{gas}(F_{ICE,n,k,h} + F_{BOIL,n,k,h}) + e_{el,grid} \boldsymbol{P_{imp,n,k,h}}]. \quad (24)$$

$e_{gas} = 197\text{kg/MWh}$ is the direct emission factor of natural gas, $e_{el,grid} = 356\text{kg/MWh}$ is the indirect emission factor associated with the electrical energy withdrawn from the national grid.

A reference scenario is defined by assuming that the aggregated electricity demand of the system is fulfilled by withdrawing electricity from the national grid, whereas the aggregated heating demand is met by burning natural gas in gas boilers. The resulting life cycle cost over one year of operation is $f_{ref} = 135.4\text{k€}$, whereas the CO2 emissions are $\Phi_{ref} = 307.6\text{ton}$.

A global constraint can be imposed on the maximum amount of CO2 emissions, in order to meet certain decarbonization targets. Equation (25) shows such a constraint, where $\varepsilon > 0$ is a fixed parameter.

$$\Phi \leq \varepsilon \times \Phi_{ref}. \quad (25)$$

By iteratively decreasing the value of ε, it is possible to carry out a sort of multi-objective optimization (the so-called ε-constrained multi-objective optimization) in order to obtain the Pareto front of the optimal solutions achieved for increasingly stricter reduction targets in carbon emissions.

4. Results

4.1. Cost-optimal system layout

Initially, the optimization model has been tested without imposing the constraint on CO2 emissions (Eq. (25)). Thus, the obtained results correspond to the cost optimal solution. The resulting value of the objective function, i.e., of the life cycle cost over one year, is $f = 124.3\text{k€}$, which is 8.2% lower than the reference scenario. The operation costs contribute for $f' = 52.1\text{k€}$, whereas the investment costs for $f'' = 72.7\text{k€}$. The total CO2 emissions over one year are $\Phi = 167.8\text{ton}$, which are 45.4% lower than the reference scenario. Hence, a sensible reduction in CO2 emissions results to be economically convenient even without imposing decarbonization targets.

Figure 2 shows the optimal layout of the energy networks, with the capacity of the district heating pipelines and electrical microgrid lines. Table 3 reports the optimal capacity of the energy conversion and storage plants at the node in which they are installed. The capacity of the DHN pipelines decreases by moving from the energy hub towards the end users. This is due to the mono-directionality of the heat flow, which only flows from the hub to the users. Note that the capacity of the DHN is higher than the one strictly required for meeting the heating demand of the end users because of the DHN losses, which have a not negligible impact on the system (79 MWh of losses in one year, more than 20% of the total heating demand). The installed capacity of PV is predominant, with 443.9 kW, for a yearly electricity production of 661.1 MWh that corresponds to a utilization factor of 17% (equivalent hours at the nominal power compared to the 8760 hours of one year). The

installed capacity of the ICE is 57.8 kW, for a yearly electricity production of 198.8 MWh corresponding to a utilization factor of 39%. The gas boiler allows covering the heating demand peaks. Its installed capacity is of 183 kW, for a yearly heat production of 43.6 MWh corresponding to a utilization factor of 3%. The HP covers the heating demand not covered by ICE and BOIL. Its installed capacity is 77.7 kW, for a yearly heat production of 134.2 MWh corresponding to a utilization factor of 20% The installed capacity of TES allows improving the operation flexibility of ICE and HP, thereby increasing their utilization factor. The installed capacity of EES is negligible. The electricity export to the national grid prevails on the electricity import because of the high capacity of PV. This is reflected by how the capacity of the electrical microgrid lines is distributed. In fact, it increases moving from the end users towards node 0, in which the system interfaces with the national grid.

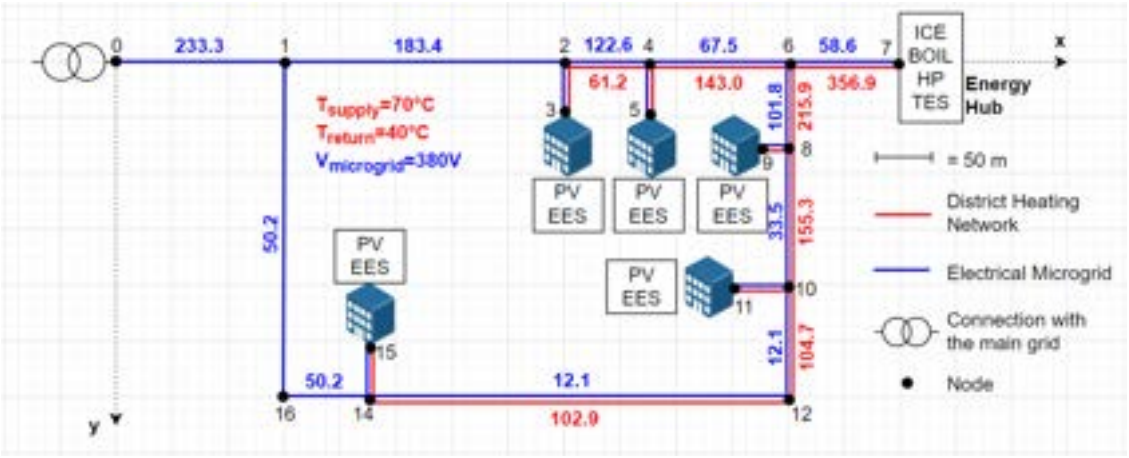

Figure 2 Cost-optimal layout of the energy networks. The capacities of the district heating pipelines and of the microgrid lines, in kW, are shown in red and blue, respectively.

Table 3 Capacity of the installed energy conversion and storage plants.

Node	PV, kW	ICE, kW	BOIL, kW	HP, kW	TES, kWh	EES, kWh
3	100.0	0	0	0	0	0.5
5	100.0	0	0	0	0	0.5
7	8.0	57.8	183.0	77.7	95.1	0
9	95.2	0	0	0	0	0.5
11	48.4	0	0	0	0	3.7
15	92.3	0	0	0	0	0.5

Figure 3 shows the energy balances (electricity and heat) of the whole system over one year, with a daily resolution. It is obtained by replacing each day of the year with the typical day representing it. The predominance, in terms of energy, of PV generation is clear, as also the prevalence of the electricity export compared to import. Globally, 77% of the total electricity demand is covered by electricity generated on site, whereas 37% of the generated electricity is exported. The ICE is more exploited during the cold season because of the contemporary need of electricity and heat by the end users, which makes more effective a CHP operation. The HP share on the daily generation of thermal energy is higher during the warm season, because of the high availability of “free of charge” electricity from PV. However, in absolute terms, the HP generates more in winter, when the heating demand is higher. The role of the boiler in covering the heating demand peaks is clear.

4.2. Variation of the reduction target on carbon emissions

The effect of imposing stricter reduction targets in CO_2 emissions has also been analysed. This corresponds to a decrease in the value of ε in Eq. (25), which represents the share of CO_2 emissions compared to the reference scenario. The cost-optimal system configuration, which does not consider that constraint, already implies a reduction in CO_2 emissions of 45%, corresponding to $\varepsilon = 0.55$. Thus, ε has been varied from 0.55 towards 0. Figure 4a shows the obtained Pareto front. It is evident that, starting from $\varepsilon = 0.55$, the minimization of the life cycle cost and the minimization of the carbon emissions are two contrasting objectives. Thus, reducing ε results in increasing the life cycle cost. It is possible to reduce the CO2 emissions until 120ton/year (60% reduction compared to the reference) while maintaining the economic effectiveness of the system with respect to the reference scenario. Accordingly, a further reduction of ε results in compromising the economic convenience of the proposed system. Moreover, CO_2 emissions cannot be reduced to zero because of the saturation of the PV and EES potentials (i.e., the available area for installing PV and space for installing EES become fully exploited). The minimum value that CO_2 emissions can reach is 69 ton/year, 78% less than in the reference scenario. However, the corresponding life cycle cost is 45% higher than the cost-optimal case.

Figure 4b shows how the capacity of the installed energy conversion and storage plants and largest network branches (EMG line 0-1, DHN pipeline 6-7) varies with ε, i.e., with decreasing CO_2 emissions (the plot should be read from right to left). The most evident result is the progressive increase in PV, HP, EES and EMG capacities. Moving from the cost-optimal system configuration to the minimum emitting one, the PV capacity almost doubles, the HP capacity increases of 130%, the EES capacity increases of more the 100 times, and the EMG capacity increases of 85%. The reason is that PV is the only renewable-based technology available. Thus, the increase in PV capacity is accompanied by an increase in HP capacity, in order to decarbonize the heating demand, and an increase in EES capacity, in order to decarbonize the electricity demand during the hours in which PV generation is not available. The EMG capacity increases too, in order to accommodate the increasing generation surplus from PV. The boiler capacity slowly decreases with decreasing ε. The ICE capacity remains more or less constant, except for a sharply decrease (-91%) to allow the last marginal reduction in CO2emissions. This reflects a sharply increase (+93%) in TES capacity, which is required to improve the flexibility of the HP and, in turn, its utilization factor. The DHN capacity remains constant.

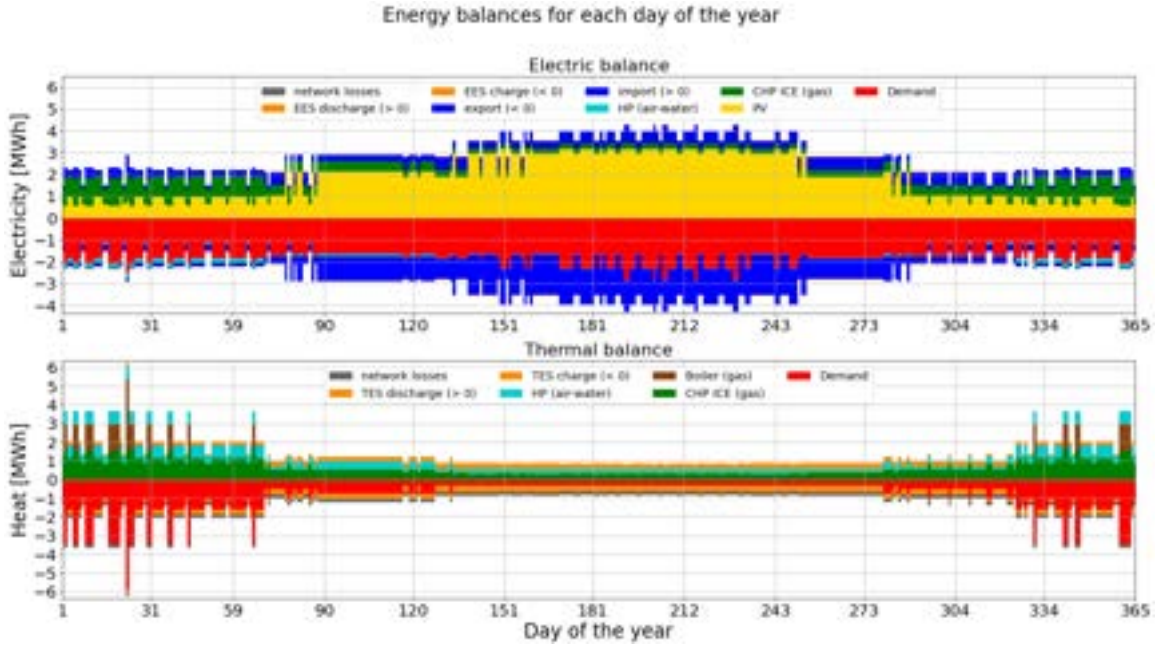

Figure 3 Yearly energy balances of the considered multi energy system with a daily resolution.

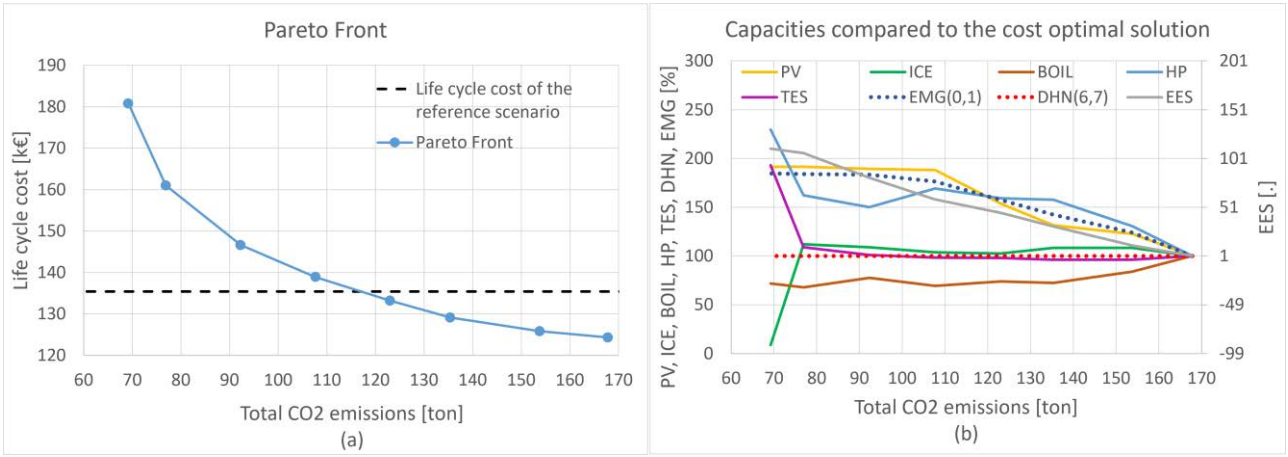

Figure 4 Results of the optimization for increasingly stricter constraints on CO2 emissions: a) Pareto front and b) share of the installed capacities compared to the cost-optimal solution.

5. Conclusions

This paper presents a general method for the design and operation optimization of multi-energy systems integrated with energy networks, with the goal of defining cost-effective system configurations to meet increasingly stricter decarbonization targets. The proposed method makes it possible to concurrently optimize the capacity of the available energy conversion and storage plants, the capacity of each branch of the available networks, and their operation, in order to minimize the life cycle cost of the system for a given cap on carbon

emissions. A district multi-energy system composed of residential and commercial buildings, with their electricity and heating demands, and including a district heating network and an electrical microgrid has been considered as a test case. Without imposing any constraints on CO2 emissions, results show that it is possible to reduce the carbon emissions of the system of 45%, while also decreasing the life cycle cost of 8%, with respect to a reference scenario in which the entire electricity demand is fulfilled by withdrawing electricity from the national grid and the entire heating demand is met by burning natural gas in gas boilers. However, a further decarbonization compromises the cost-effectiveness of the system because of the investments in carbon-neutral technologies and electrical microgrid, the installed capacity of which steeply increases.

The main findings of the study are summarized below.

- Photovoltaic is a promising solution for decarbonizing the electricity demand, by contributing for more than 75% to the total electricity generation. Electrical storage systems are necessary for a deep decarbonization.
- The higher share of photovoltaic generation in deeply decarbonized scenarios requires increasing the capacity of the electrical microgrid up to 85% compared to the cost-optimal system configuration.
- The economic convenience of distributed electricity generation is mainly due to the self-consumption, which approaches 80% of the electricity demand, rather than to selling energy to the national grid.
- Heat pumps are very effective in decarbonizing the heating demand if a surplus of photovoltaic generation is available on site. Their contribution to the thermal power generation approaches 100% in deeply decarbonized scenarios. Moreover, thermal energy storage allows improving their utilization factor.
- Gas-fuelled combined heat and power internal combustion engines can contribute to the decarbonization of both electricity and heating demand in a first phase. However, the scarce heating demand of commercial-residential districts during the warm season sensibly worsens the utilization factor of this technology, which results to be lower than 40%.
- The capacity of the considered tree-shaped district heating network depends only on the heating demand of the end users, thereby remaining unchanged when the decarbonization target varies.

The proposed paper is intended as a part of a wider study aiming at defining a method for the complete synthesis, design and operation optimization of multi energy systems integrated with energy networks. This means that the present work will be further developed in order to include the synthesis of the networks' topology, the selection of the number and type of the energy conversion and storage plants, and their siting within the system into the optimization problem. The idea is to solve the overall synthesis, design and operation problem by means of an evolutionary algorithm, in which the method proposed here is run many times at each iteration for different configurations of the networks' topology and plants' position.

Acknowledgments

The Authors thank "Fondazione Ing. Aldo Gini" of the University of Padova for the economic support.

Project financially supported by BIRD 2019 Research Program of University of Padova (Project BIRD197944)

Nomenclature

Abbreviations

DHN District heating network

EMG Electrical microgrid

MES Multi-energy system

SDO Synthesis, design and operation

Subscripts

g energy conversion and storage technologies (with g = PV, ICE, BOIL, HP, TES, EES)

h hours of the day (with $h = 1, 2, \ldots, 24$)

k typical days or cluster centers (with $k = 1, 2, \ldots, 10$)

l electrical microgrid lines (with $l = 1, 2, \ldots, 16$)

n nodes of the system (with $n = 0, 1, \ldots, 16$) (alternatively, m)

p district heating pipelines (with $p = 1, 2, \ldots, 12$)

References

[1] E. Papadis and G. Tsatsaronis, "Challenges in the decarbonization of the energy sector," *Energy,* vol. 205, p. 118025, 2020. https://doi.org/10.1016/j.energy.2020.118025.

[2] P. Mancarella, "MES (multi-energy systems): An overview of concepts and evaluation models," *Energy,* vol. 65, pp. 1-17, 2014. https://doi.org/10.1016/j.energy.2013.10.041.

[3] G. Volpato, G. Carraro, M. Cont, P. Danieli, S. Rech, and A. Lazzaretto, "General guidelines for the optimal economic aggregation of prosumers in energy communities," *Energy,* vol. 258, p. 124800, 2022. https://doi.org/10.1016/j.energy.2022.124800.

[4] C. A. Frangopoulos, "Recent developments and trends in optimization of energy systems," *Energy,* vol. 164, pp. 1011-1020, 2018. https://doi.org/10.1016/j.energy.2018.08.218.

[5] H. Lund, P. A. Østergaard, T. B. Nielsen, S. Werner, J. E. Thorsen, O. Gudmundsson*, et al.*, "Perspectives on fourth and fifth generation district heating," *Energy,* vol. 227, p. 120520, 2021.

[6] B. Leitner, E. Widl, W. Gawlik, and R. Hofmann, "A method for technical assessment of power-to-heat use cases to couple local district heating and electrical distribution grids," *Energy,* vol. 182, pp. 729-738, 2019. https://doi.org/10.1016/j.energy.2019.06.016.

[7] M. Nazari-Heris, B. Mohammadi-Ivatloo, and S. Asadi, "Optimal operation of multi-carrier energy networks with gas, power, heating, and water energy sources considering different energy storage technologies," *Journal of Energy Storage,* vol. 31, p. 101574, 2020. https://doi.org/10.1016/j.est.2020.101574.

[8] B. Talebi, P. A. Mirzaei, A. Bastani, and F. Haghighat, "A Review of District Heating Systems: Modeling and Optimization," *Frontiers in Built Environment,* vol. 2, 2016. 10.3389/fbuil.2016.00022.

[9] J. Röder, B. Meyer, U. Krien, J. Zimmermann, T. Stührmann, and E. Zondervan, "Optimal Design of District Heating Networks with Distributed Thermal Energy Storages – Method and Case Study," *International Journal of Sustainable Energy Planning and Management,* vol. 31, pp. 5-22, 2021. 10.5278/ijsepm.6248.

[10] S. Rech and A. Lazzaretto, "Smart rules and thermal, electric and hydro storages for the optimum operation of a renewable energy system," *Energy,* vol. 147, pp. 742-756, 2018. https://doi.org/10.1016/j.energy.2018.01.079.

[11] L. M. P. Ghilardi, A. F. Castelli, L. Moretti, M. Morini, and E. Martelli, "Co-optimization of multi-energy system operation, district heating/cooling network and thermal comfort management for buildings," *Applied Energy,* vol. 302, p. 117480, 2021. https://doi.org/10.1016/j.apenergy.2021.117480.

[12] E. Dal Cin, G. Carraro, G. Volpato, A. Lazzaretto, and P. Danieli, "A multi-criteria approach to optimize the design-operation of Energy Communities considering economic-environmental objectives and demand side management," *Energy Conversion and Management,* vol. 263, p. 115677, 2022. https://doi.org/10.1016/j.enconman.2022.115677.

[13] M. Wirtz, "nPro: A web-based planning tool for designing district energy systems and thermal networks," *Energy,* vol. 268, p. 126575, 2023. https://doi.org/10.1016/j.energy.2022.126575.

[14] M. Wirtz, M. Heleno, A. Moreira, T. Schreiber, and D. Müller, "5th generation district heating and cooling network planning: A Dantzig–Wolfe decomposition approach," *Energy Conversion and Management,* vol. 276, p. 116593, 2023. https://doi.org/10.1016/j.enconman.2022.116593.

[15] S. Mashayekh, M. Stadler, G. Cardoso, and M. Heleno, "A mixed integer linear programming approach for optimal DER portfolio, sizing, and placement in multi-energy microgrids," *Applied Energy,* vol. 187, pp. 154-168, 2017. https://doi.org/10.1016/j.apenergy.2016.11.020.

[16] E. D. Mehleri, H. Sarimveis, N. C. Markatos, and L. G. Papageorgiou, "A mathematical programming approach for optimal design of distributed energy systems at the neighbourhood level," *Energy,* vol. 44, pp. 96-104, 2012. https://doi.org/10.1016/j.energy.2012.02.009.

[17] E. D. Mehleri, H. Sarimveis, N. C. Markatos, and L. G. Papageorgiou, "Optimal design and operation of distributed energy systems: Application to Greek residential sector," *Renewable Energy,* vol. 51, pp. 331-342, 2013. https://doi.org/10.1016/j.renene.2012.09.009.

[18] M. Casisi, S. Costanzo, P. Pinamonti, and M. Reini. (2019, Two-Level Evolutionary Multi-objective Optimization of a District Heating System with Distributed Cogeneration. *Energies 12(1),* DOI: *10.3390/en12010114*.

[19] P. Gabrielli, M. Gazzani, E. Martelli, and M. Mazzotti, "Optimal design of multi-energy systems with seasonal storage," *Applied Energy,* vol. 219, pp. 408-424, 2018.

[20] M. Hoffmann, L. Kotzur, D. Stolten, and M. Robinius. (2020, A Review on Time Series Aggregation Methods for Energy System Models. *Energies 13(3)*.

[21] S. Rech, "Smart Energy Systems: Guidelines for Modelling and Optimizing a Fleet of Units of Different Configurations," *Energies,* vol. 12, p. 1320, 2019. doi:10.3390/en12071320.

[22] L. Kotzur, P. Markewitz, M. Robinius, and D. Stolten, "Time series aggregation for energy system design: Modeling seasonal storage," *Applied Energy,* vol. 213, pp. 123-135, 2018. https://doi.org/10.1016/j.apenergy.2018.01.023.

[23] F. Glover, "Improved Linear Integer Programming Formulations of Nonlinear Integer Problems," *Management Science,* vol. 22, pp. 455-460, 1975. http://www.jstor.org/stable/2630109

Multi-objective design optimization of a cryo-polygeneration system in tropical climates - A techno-economic case study for a large-scale utility customer

Alessio Tafone[a], Sundar Raj Thangavelu[b], Shigenori Morita[c], Alessandro Romagnoli[d]

[a] Nanyang Technological University, Singapore, alessio.tafone@ntu.edu.sg
[b] Nanyang Technological University, Singapore, sundar.rt@ntu.edu.sg
[c] Surbana Jurong Pte Ltd, Singapore, shigenori.morita@surbanajurong.com
[d] Nanyang Technological University, Singapore, a.romagnoli@ntu.edu.sg

Abstract:

Small-medium scale decentralized polygeneration systems can provide multiple energy services for urban districts like universities and hospitals, with several energetic, economic and environmental benefits. Indeed, their impact on both energy efficiency, cost and emissions reduction might be disruptive especially in urban districts located in a tropical region, where the cooling demand is approximately stationary throughout the whole year. In this paper a multi-objective optimization model for distributed energy system in tropical climate is presented. The superstructure of the system comprehends a district cooling network that connects the users to medium-scale gas turbine system, solar PV plant, thermal and electrical chiller and a thermal storage. The optimization aims to determine the optimal design structure of the system, the size of each component inside the optimal solution and the optimal operation strategy. The multi-objective optimization is based on a three-level structure: 1) the simulation level developed in TRNSYS; 2) the optimization level based on a pareto-search algorithm developed in Matlab; 3) the Matlab-TRNSYS interface level. In this way the Pareto Front is identified and the possible improvements in both economic and environmental terms can be highlighted. The model has been applied to a specific real case study, namely a polygeneration system to be installed in the NTU campus located in Singapore, and it has been optimized for two different superstructure configurations. The results contribute significantly to developing an efficient and cost-effective energy storage polygeneration system and revealed that the optimized operation of the decentralized energy systems reduces energy costs and CO_2 emissions, as compared with a scenario without integration of renewables and electric energy storage system as well as conventional energy supply systems. Indeed, numerical results show that the Pareto frontier provides good balancing solutions for planners based on economic and sustainability priorities.

Keywords:

Distributed polygeneration system, Design optimization, Cold economy, LNG, Electrical energy storage, Thermal energy storage.

1. Introduction

The energy demand for space heating and cooling is growing faster in buildings and already causing enormous strain on electricity systems in many countries, as well as driving up emissions [1][2]. The sustainability of heating and cooling is of high priority, and the strategy lists to achieve the sustainability goals are decreasing demand, increasing efficiency, and switching to renewable primary energy sources. To this end, the concept of decentralized polygeneration system and microgrid should be recognized as an enabling technology system with great potential. Polygeneration energy systems using multiple energy sources (e.g., wind, biomass, solar) and delivering multiple energy services (i.e., heating, cooling, and electricity) have potential economic and environmental benefits over traditional energy generation systems [3,4]. Indeed, simultaneous production of heating, cooling and power in a combined cooling heating and power system results in higher overall efficiency in comparison with the separate heat and power production [3]. Furthermore, having the energy supply system close to end users offers several other advantages such as lower distribution and transmission cost, less power loss through the transmission and

distribution line, alleviated environmental impacts, and enhanced resilience of the utility grid [5] . Mancarella [3] studied the status of existing models and evaluation methods for performance investigation of multi-energy systems (MES). A complete overview of MES considering various perspectives was provided. Jana et al. [6] presented the status of polygeneration technologies and their capacity to provide a sustainable energy solution. This study highlighted the necessity to conduct more research on multi-criteria optimization of polygeneration systems. Furthermore, the incorporation of innovative storage and generation units in complex polygeneration systems were suggested. A short review on optimization of polygeneration systems in urban applications was presented by Ghaem Sigarchian et al. [7]. The study emphasizes the necessity of further investigation on complex polygeneration systems to achieve results as close as possible to reality. Calise et al. [8] showed that for a combined production of electricity, cooling and heating to satisfy a defined end-user demand, distributed polygeneration systems (DPS) are the most efficient and sustainable way to simultaneously guarantee flexibility and reliability. Indeed, if a high penetration of unpredictable renewable energy sources is thought to be promoted, distributed polygeneration systems could allow to significantly increase the resiliency and flexibility of the power production and distribution networks [9]. Although almost no geographical region is at this stage yet, a potential promising outlook for energy infrastructures would then be a global spread of decentralized energy generation in which larger share of final energy consumption will be produced in a distributed way [10].

Directly responding to this ambitious target, a novel district scale demonstrator has been currently proposed and developed in Singapore [11], aiming to significantly contribute achieving the goal imposed by the country's national agenda on sustainable development [12]. Based on the concept of distributed cryo-polygeneration system, namely an integrated rapidly deployable and highly energy-efficient solution that utilizes cold energy from Liquefied Natural Gas (LNG) and waste heat from power generation, the project might help in meeting the growing energy needs of urbanization and industrialization, especially in tropical and sub-tropical areas. In order to maximize the benefits from the cryo-polygeneration system while still providing the same quality of energy services produced by conventional energy system, the optimal design of the plant layout is necessary and it requires the techno-economic analysis of single components in order to maximize the efficiency of the available energy resources [13]. Indeed, in order to avoid incurring unnecessary costs while still providing the required resilience and reliability, decentralized polygeneration systems require accurate components design [14]. Nevertheless, profitability of the cryo-polygeneration system might not be the only driver for the design optimization of the system: indeed, considering as objective function the CO_2 emission, the optimization might lead to alternative system design. In such a context, a multiobjective approach helps identify balancing solutions to promote participation in the decision-making process and facilitate collective decisions. To this end, a multi-criteria optimization with respect to economic and ecological aspects and thus determination of Pareto optimal solutions has been methodologically developed. In literature the multi-objective optimization of distributed polygeneration systems has been the subject of many researchers within the recent years. Ahmadi et al. [15] presented the thermodynamic modelling and multi-objective optimization of an energy system for the simultaneous generation of electricity, heating, cooling and hot water. Gabrielli et al. [16] analyzed the design of a multi-energy system involving seasonal energy storage and based on a case study in a neighbourhood in Zurich, Switzerland, which is optimized in terms of total annual costs and carbon dioxide emissions. Ghaem Sigarchian et al. [17] applied a multi-objective optimization methodology to a small-scale decentralized polygeneration system: the distributed polygeneration systems reduces both CO_2 emissions and annualized total cost up to 29% and 19%, respectively.

Nevertheless, there seems to be a lack in the literature of studies addressing the optimal operation and design of distributed polygeneration systems in cooling dominated geographical region, as for the urban district in a tropical area characterized by high and uniform temperature and humidity throughout the year. Indeed, although the investigation of energy systems in a cooling dominated context is gaining momentum in literature with few studies highlighting the benefit of district cooling [24] and energy storages in tropical areas [25,26], overall, a systematic and generalized research with an on-site real application on the decarbonization in tropical climate by means of decentralized polygeneration systems is still lacking [24]. In this framework, the present paper aims to go a step further by significantly improving the knowledge on this topic. Indeed, in this paper the multi-objective

optimization model is applied to the cryo-polygeneration concept, and the Pareto frontiers associated to two different system configurations are evaluated. The results of the optimizations can be used to identify the best trade-off solutions. The main objective of the multi-objective optimization is to determine the optimal design (sizing) and the optimal operation strategy for any component within the optimal solution. Indeed, the analysis aims to evaluate the economic and environmental benefits of the integration between gas turbine, PV and energy storage solutions when the optimal synthesis and operation of the whole energy supply system are adopted.

2. Methodology

2.1. Cryo-polygeneration concept

The proposed cryo-polygeneration system concept (developed in TRNSYS) is shown in **Fig. 1**, consisting diverse technologies for electricity and cold energy generation and storage. The electric power is produced from the gas turbines (GT) and photovoltaics (PV) modules whereas the LNG regasification unit (RU), an absorption chiller (ABC) utilizing the waste exhaust heat from the gas turbine and vapour compression water-cooled chillers (WCC) are mainly to support the cooling loads. Cold thermal energy storage (CTES) and battery electrical energy storage (BESS) act as a buffer to complement the unpredictability of renewable energy sources and as a bulk storage to maximize the exploitation of excess thermal energy and electricity. More information regarding the simulation model can be found in Ref.[18].

Two design scenarios are considered to study the economical and environmental benefits of the critical distributed technologies (**Table 1**). The adopted search space values are set according to the demand and the available footprint area for each component. Scenario 1 consists of well-established technologies such as gas turbines, LNG regasification units, thermal (ABC) and electrical (WCC) chillers. In scenario 2, the photovoltaics (PV) system and thermal/electrical energy storage solutions (CTES and BESS) are included to understand the role and impact of renewable combined with energy storage. Conversely, the case where all the demands of the buildings are supplied by the electricity in a grid connected environment is taken as the baseline case scenario (**Fig. 2**). The performance results of this configuration will provide a reference for the two scenarios under investigation.

Table 1 Cryo-polygeneration design case scenarios and optimization search space.

Components	Search Space				
	BC	1	2	Minimum	Maximum
GT	-	✓	✓	0	10000 kW_e
PV	-	-	✓	0	25000 kW_p
BESS	-	-	✓	0	80000 kWh_e
LNG RU	-	✓	✓	-	-
ABC	-	✓	✓	0	15000 kW_c
WCC	✓	✓	✓	0	15000 kW_c
CTES	-	-	✓	0	10000 m^3
Utility Grid (import)	✓	✓	✓	-	-

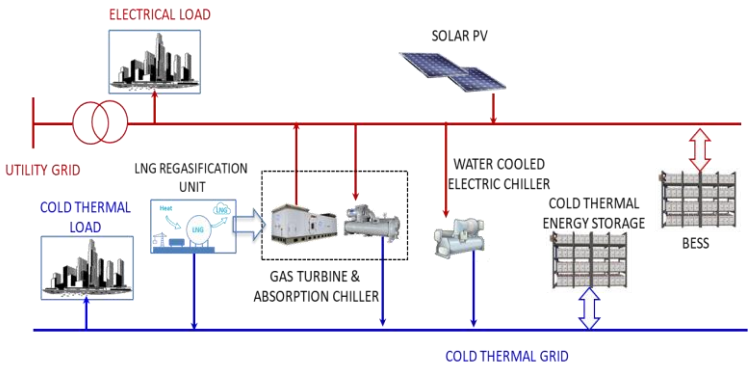

Fig. 1. Superstructure of the Cryo-polygeneration system.

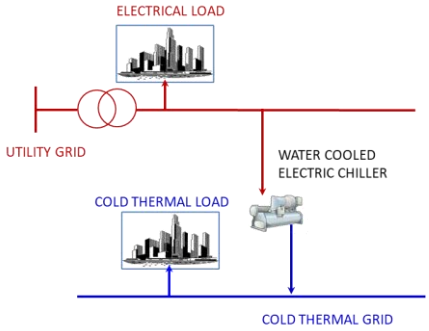

Fig. 2. Superstructure of the baseline case scenario.

2.2. System model

The layouts described in Section 2.1 were dynamically modeled and simulated in TRNSYS environment. TRNSYS is an object-oriented based software that enables to simulate the transient behavior of systems predominantly focused on assessing the performance of thermal and electrical energy systems. The software is made up of two main parts: a simulation engine to solve the dynamic mathematical problem and a large library of built-in components or types (e.g., pumps, mixers, diverters, heat exchangers, etc.), often validated by experimental data. **Fig. 3** shows the cryo-polygeneration system layout implemented in TRNSYS environment: red lines refer to the electricity stream; brown line represents the waste heat flow from the gas turbine to the absorption chiller; green line refers to the LNG stream and blue lines represent chilled water stream.

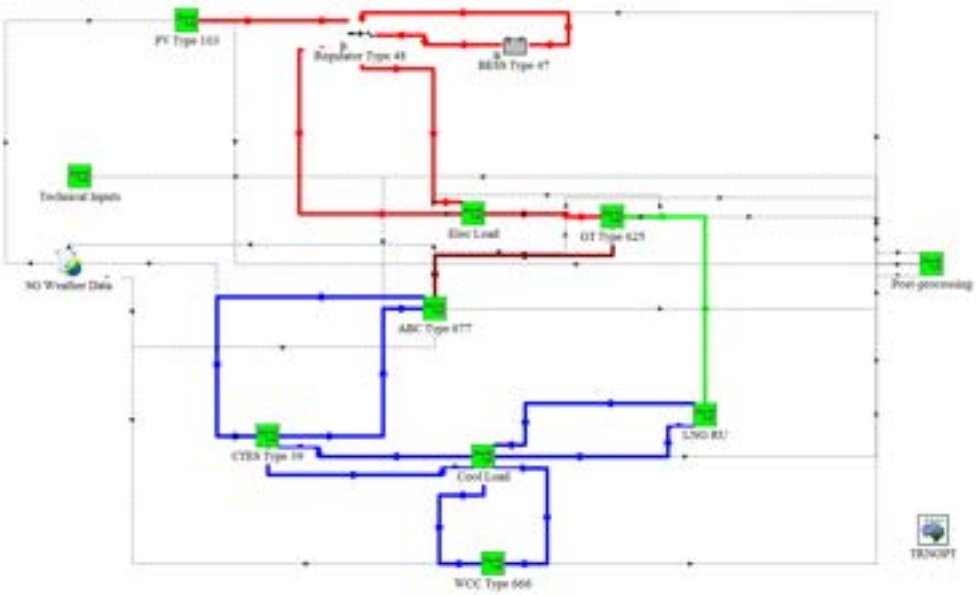

Fig. 3. General layout of the TRNSYS-Cryo-polygeneration system.

2.2. Mathematical problem

Electricity demand and electricity required by vapour compression chiller can be satisfied by grid power, by the electricity provided by the gas turbines, PV, and by the electricity discharged from the BESS. It is assumed that all the electricity provided by GT and PV is self-consumed, while no extra electricity is sold back to the power grid. Space cooling demand can be satisfied by thermal energy provided by the GT through the absorption chiller, vapour compression chillers, and by thermal energy discharged from the CTES.

2.2.1 Decision variables

In the optimization problem, the decision variables include: the existence and sizes of energy devices; operation status (on/off) and energy rates provided by energy devices; capacities of electrical and thermal storage devices; electricity and heat rate input and output to/from electrical and thermal storage devices.

2.2.2 Economic objective function

The total annualized cost (TAC) is the first objective function of the optimization process, a premier economic index taking into account all the expenses during the yearly operational of the project, defined as:

$$TAC = CAPEX_{ann} + OPEX_{UG} + OPEX_{fuel} + OPEX_{O\&M} + OPEX_{CO2} \quad (1)$$

The key parameters for the economic analysis are defined for the different scenarios as follows.

$CAPEX_{ann}$ is the annualized sum of the capital costs, the balance of plants and installation costs of the kth component of the system computed as:

$$CAPEX_{ann} = \sum_k CAPEX_k \cdot CRF_k = \sum_k SC_k \cdot C_k \cdot CRF_k \quad (2)$$

Where SC_k and C_k are the specific capital cost and the capacity of k^{th} component, respectively; CRF is the capital recovery factor of the k^{th} component which takes into account the effect of annual interest rate "i" and the component lifetime "N_k" expressed as:

$$CRF = \frac{i \cdot (1+i)^{N_k}}{(1+i)^{N_k} + 1} \quad (3)$$

$OPEX_{UG}$ accounts for the annual operational cost due to the utilization of the utility grid. It comprises three main factors, namely a) the contracted capacity charge, b) the electricity purchased at a certain electricity tariff *ET,* daily subject to peak and off-peak time periods and c) the use of systems or transmissions costs:

$$OPEX_{UG} = P_{UG,max} \cdot C_{cap,ch} + \int_0^{365} P_{UG} \cdot [ET(t) + UOS(t)] \cdot dt \quad (4)$$

$OPEX_{fuel}$ accounts for the annual operational cost related to the total amount of LNG purchased (m_{LNG}) at a defined price (p_{LNG}):

$$OPEX_{fuel} = \int_0^{365} m_{LNG} \cdot p_{LNG}(t) \cdot dt \quad (5)$$

$OPEX_{O\&M}$ are the annual operational and maintenance costs of the k^{th} component expressed as a fraction ($\phi_{O\&M,k}$) of the total $CAPEX_k$:

$$OPEX_{O\&M} = \sum_k CAPEX_k \cdot \phi_{O\&M,k} \quad (6)$$

As of now, conforming to the Paris Agreement, an increasing number of countries promote energy efficiency measures and the adoption of renewables by including a carbon tax [47,48]. To this end, an operational annual cost related to this tax (taxCO2 expressed in $/tonCO2) is included in the economic analysis as OPEXCO2 computed as:

$$OPEX_{CO2} = \int_{0}^{365} m_{CO2}(t) \cdot tax_{CO2} \cdot dt \quad (7)$$

The key input data for the techno-economic analysis used in this work are depicted in **Table 2**.

Table 2. DES Economic parameters [17,19–23].

Parameter	GT	PV	BESS	LNG RU	ABC	WCC	CTES
SC	1200 \$/kW$_e$	883 \$/kW$_e$	380 \$/kWh$_e$	43.5 \$/kgh	230 \$/kW$_c$	150 \$/kW$_c$	31.8 \$/kWh$_c$
ϕ [%]	3	0.5	1	0.5	2	2	1
Lifetime [years]	30	30	20	30	30	30	30

2.2.3 Emissions objective function

The environmental objective is to minimize the environmental impacts in terms of CO_2 emission from the electricity grid and the consumed fuels. The CO_2 emission due to the use of electricity from the electricity grid is evaluated by multiplying the grid emission factor of the electricity grid (GEF [kg_{CO2}/kWh_e]), and the total amount of electricity purchased from the grid. The carbon intensity of the electricity grid that the cryo-polygenerator is connected to is the amount of CO_2 emission per unit of electricity generated which depends on the fuel mix of Singapore [24]. The CO_2 emission due to the natural gas consumption is evaluated by multiplying the carbon intensity of the fuel, (CI_{NG} [kg_{CO2}/kg_{NG}]), and the total amount of fuel consumption of the cryo-polygenerator system:

$$m_{CO_2} = \int_{0}^{365} P_{UG} \cdot [GEF] \cdot dt + m_{fuel} \cdot CI_{NG} \quad (8)$$

2.2.4 Constraints

The objective function is constrained to the energy balance equation following the rules and limitations of the operating strategies. Some of the critical constraints accounted in the design optimization problem are:

- The electricity and cooling demands are fulfilled at all periods. Otherwise, a high dynamic penalty is imposed on the objective function based on the deviation from the desired value (complete load satisfaction).

- The operation of the gas turbine is prevented below recommended minimum partial load ratio (PLR) to increase its lifetime and decrease the emissions [25]. This constraint is implemented in TRNSYS by a differential controller component limiting the gas turbine operation as follows:

$$0.2 \leq PLR\ (t) \leq 1 \quad (9)$$

- The capacity of the DPS components is limited to the identified optimization search space. The adopted search space values are set according to the demand and the available footprint area for each component.
- The operations of the electrical and thermal energy storage (BESS and CTES) are limited to their maximum and minimum state of charge.
- Revenues from the PV electricity feed-in are not accounted in the TAC equation as it is not within the scope of this work to merely maximize this profit by operating a small power plant. Nevertheless, this component can be further analyzed in future works.

2.2.5 Optimization method

In this section, the general structure of the optimization tool and the optimization technique has been explained. The optimal design (sizing) and operational strategy of the cryo-polygeneration components are based on a three-level configuration. The simulation level (TRNSYS [26]), the “multi-objective genetic algorithm” (gamultiobj) level [27]) and the interface for the communication between those two levels (Matlab [28]). In particular, TRNSYS is dynamic simulation software whose solver calls the subroutines present in the input file and tries to solve the equations for each simulation time step. Gamultiobj is a multi-objective optimization algorithm that minimizes multiple objective functions subject to a set of constraints. The Matlab code developed by the authors acts as an interface between TRNSYS simulator and the “gamultiobj” algorithm and streamlines the optimization process. The multi- objective genetic algorithm in-built in MATLAB, i.e. the gamultiobj function [64], is based on the very popular Non-dominated Sorting Genetic Algorithm – II [27], and is frequently utilized in literature [29] for the accuracy of the Pareto front.

3. Results

This section discusses the optimal DERs capacities obtained for the cryo-polygenerator system and compares the economics and environmental benefits of polygeneration configurations with reference to the base case. The objective functions are estimated by performing TRNSYS simulation for one year with a half an hour time resolution. The electricity and cooling demands are defined on half an hourly basis and are available thanks to smart meters connected directly with the building. Fig. 2 shows representative weekly electrical and cooling demand, a segment of yearly demands considered in this study. Other crucial input data such as fuel price, Singapore weather data, future projections are assumed for all scenarios. The economic analysis was carried out based on 30 years project lifetime. Given those input data, by solving the multi-objective optimization problem, the Pareto front, consisting of the best possible trade-offs between the two objectives, can be obtained. Each point of the Pareto front corresponds to a different operation strategy of the DES. The operators of DESs can choose the operation strategy from the Pareto front based on the economic and environmental priorities.

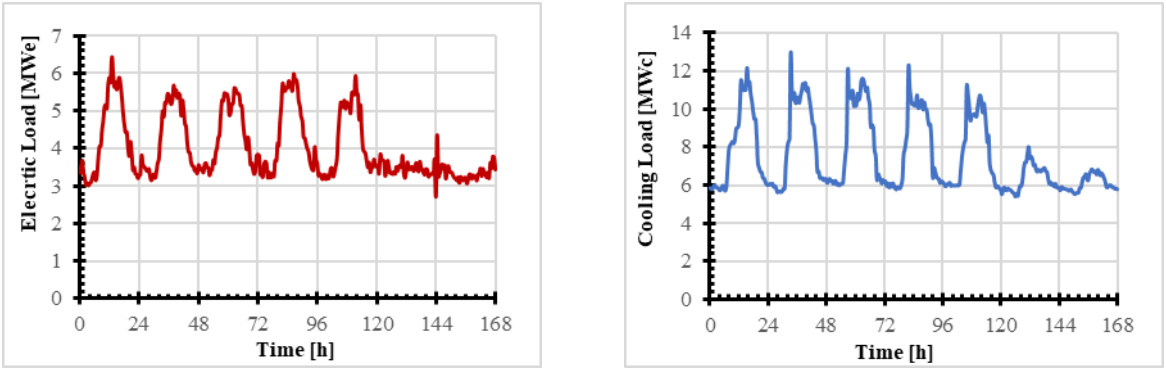

(a) (b)

Fig. 4. Weekly electricity (a) and cooling (b) demands for the building located in NTU campus.

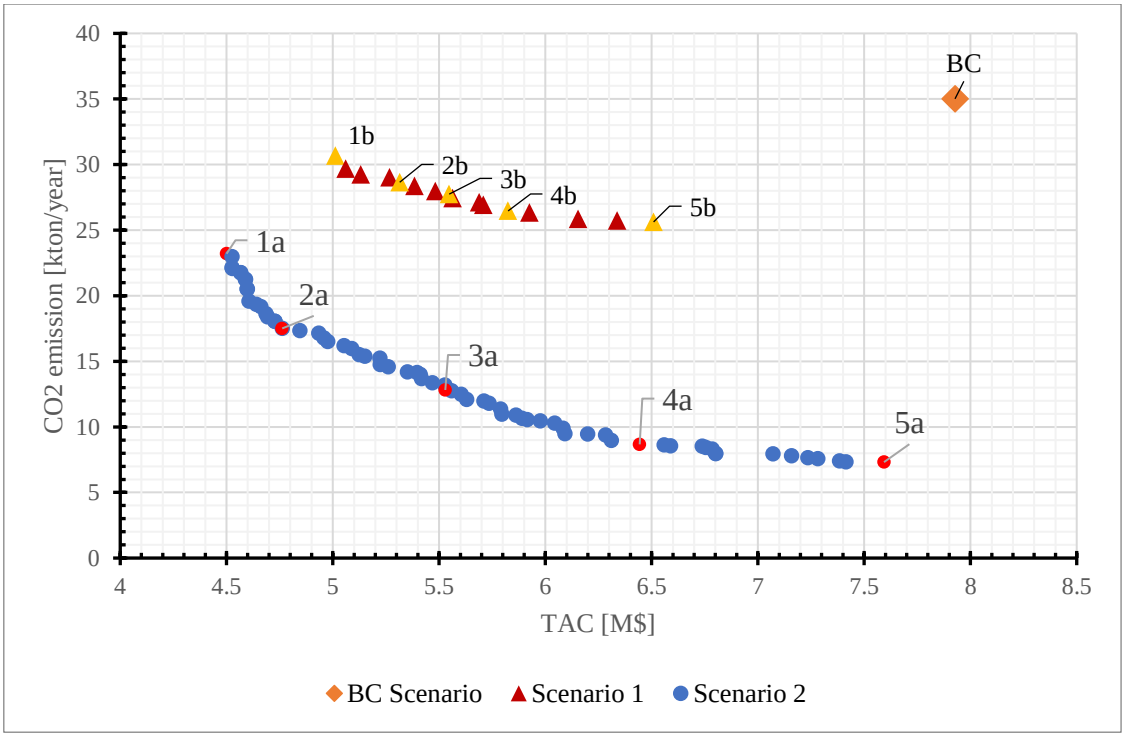

Fig. 5. Pareto front for Scenario 1 and Scenario 2.

In order to understand how the operation strategies of the DES affect the TAC and the CO2 emission, the results at various trade-off points are shown in **Fig. 5** illustrating the Pareto Fronts obtained for both scenarios. For the sake of comparison, the optimal point of operation for the baseline case scenario previously computed in Ref.[18] has been added in **Fig. 5**. Indeed, the baseline scenario represents the business-as-usual configuration where the utility grid provides the electricity to cover the electric and cooling demand and therefore the electricity cost is predominant (≈95 %) compared to all the other TAC cost components. From **Fig. 5**, it can be noticed that for all scenarios the TAC and the carbon emissions are conflicting objectives, i.e. the higher the TAC is the lower the carbon emissions are.

For both scenarios, all the optimal solutions outperform the baseline scenario both in terms of TAC and CO_2 emissions. Furthermore, the optimized solutions of Scenario 1 experience a lower variance of the objective functions compared to scenario 2 with average values of 5.6 MUSD and 27.67 ktonCO$_2$/year for the TAC and CO2 emissions, respectively. The reason for this is the smaller number of available technologies, hence there are less degrees of freedom. Despite a quite evident environmental benefits due to the introduction of renewables and electric energy storage with an average decrease of the CO_2 emissions (13.88 ktonCO$_2$/year), Scenario 2 provides a more diversity pool of optimal solutions with similar average of the TAC compared to Scenario 1. In order to provide a more accurate analysis of the results, for each scenario, component sizes for five different solutions (highlighted in **Fig. 5**) are evaluated. For each solution the component sizes are numerically reported in **Table 3** while the different TAC cost breakdown are plotted in **Fig. 6**-**Fig. 7**. As previously mentioned, Fig. 4 can be utilized by the operators of the cryo-polygeneration system to economically and environmentally assess different design point of the plant, helping thus identifying balancing solution to simultaneously promote cost savings and sustainability. Indeed, by looking at the five different solutions in the two Pareto fronts in **Fig. 5**, it can be noticed that for the same TAC user can choose solution 4a instead of solution 5b to gain ≈66% environmental benefits in terms of carbon emissions. Another potential greener choice would be selecting solution 2a in place of solution 1a to reduce 25% carbon emissions at the expense of only ≈6% increase in TAC.

In Scenario 2, it is evident that, as solutions move towards the carbon emissions objective the capacity of less carbon intensive technologies, such as PV and BESS, is increased, simultaneously reducing the GT capacity. The absorption chiller capacities follow the same trend of the gas turbines with a general decrease due to the reduction of the available waste heat at the GT outlet. As a result, the size of the WCC increases to balance the reduction of the cooling fulfilled by the ABC. Nevertheless, as shown in **Fig. 8a**, reporting the ratio of the current ABC capacity to the potential

ABC capacity exploiting 100 % of the waste heat available (f_{ABC}), it can be seen that it is not anymore economically convenient to enhance the ABC capacity. Indeed, when the PV capacity started to be predominant over the gas turbine, part of the green electricity produced by the PV is conveyed to cover the electricity consumption of the WCC, whose technology is significantly cheaper than absorption chiller. As a result, the maximum available potential capacity of ABC is not fully exploited and the ratio f_{ABC} decreases along the Pareto front. Conversely in Scenario 1 (**Fig. 8b**), since PV is not considered in the optimization search space, the ratio f_{ABC} increases as the GT capacity decreases in order to maximize the exploitation of the available waste heat.

Table 3. Optimal Technologies capacities from Multi-objective optimization for 5 different solutions.

Solutions	P_{GT} [kW_e]	Q_{ABC}[kW_c]	Q_{WCC} [kW_c]	P_{PV} [MW_p]	V_{CTES} [m^3]	C_{EES} [MWh_e]	TAC [M$]	CO2 em [kton/year]
Scenario 2								
1a	4532	8373	6285	6700	4783	2.69	4.50	23.20
2a	3346	6074	10107	14629	3109	3.58	4.76	17.51
3a	2488	3463	10405	20494	3494	21.42	5.53	12.82
4a	2260	2569	10669	22793	3483	50.98	6.44	8.67
5a	2254	2453	11029	22841	3955	73.95	7.59	7.31
Scenario 1								
1b	5389	7862	4742	-	3098	-	5.01	30.68
2b	3895	7238	4763	-	3235	-	5.31	28.65
3b	3375	7217	5298	-	3423	-	5.55	27.75
4b	2682	6084	5379	-	3554	-	5.82	26.47
5b	1754	4085	7646	-	3675	-	6.51	25.63

By evaluating the TAC breakdown of the different optimal points for both Scenarios (**Fig. 6**-**Fig. 7**), different optimal strategies can be identified. Indeed, the analysis of the inhomogeneous distribution of the main cost components' shares within the TAC provides further insights to explain the economic and environmental performance of the cryo-polygeneration system at the different optimal points. Since Scenario 1 relies only on the electricity provided by the GT and the electric grid, the operational costs due to fossil fuels consumption (Fuel_cost) and the ones due to the electric grid (OpexUG and Opex_capacity) are inversely proportional shifting to greener configurations. In addition, due to the decrease of the GT and ABC capacity, the CAPEX share in the TAC tends to decrease as well. Conversely, in Scenario 2, moving from solution 1 to solution 5 characterized by lower CO_2 emissions, the CAPEX becomes predominant with the highest TAC share (≈71 %) followed by operational cost due to the electricity grid (≈15 %). Indeed, in order to guarantee lower CO_2 emissions, the optimization algorithm prefers to enhance the capacity installation of the most expensive technologies such as PV and BESS, at the cost of sacrificing the TAC of the plant exponentially increased with the CAPEX. Simultaneously, despite the highest PV (23 MW_p) and BESS (73 MWh_e) capacities adopted for solution 5, the cryo-polygeneration system does not manage to satisfy the electricity peaks further increasing the necessity to tap into the electricity grid. This is particularly verified for intermediate solutions (2-3) while the operational cost due to the electricity grid starts to decrease for solution 4-5 with the heavily installation of the BESS capacity capable to partially satisfy the peak of the electric demand.

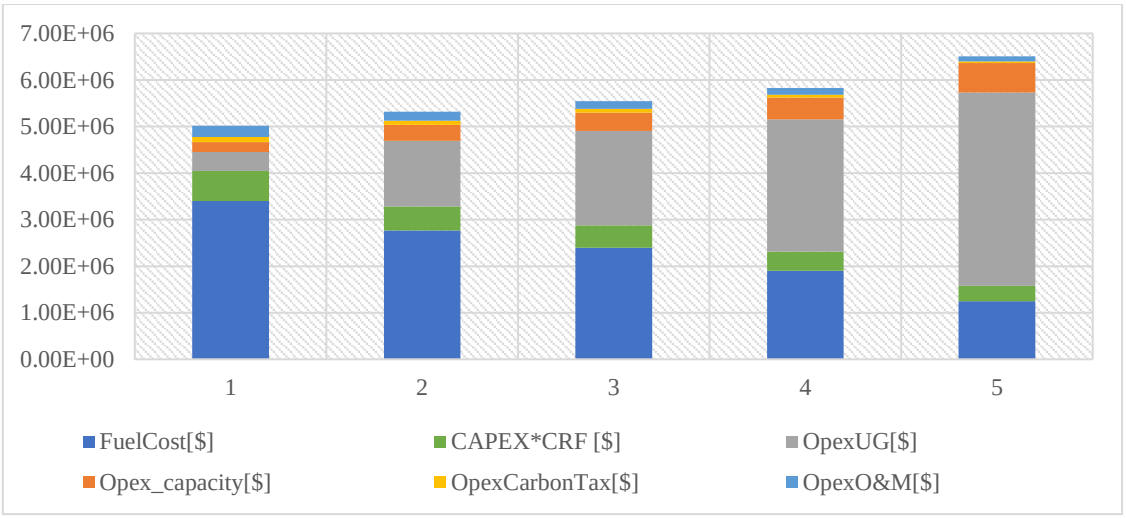

Fig. 6. Costs components of the TAC for Scenario 1.

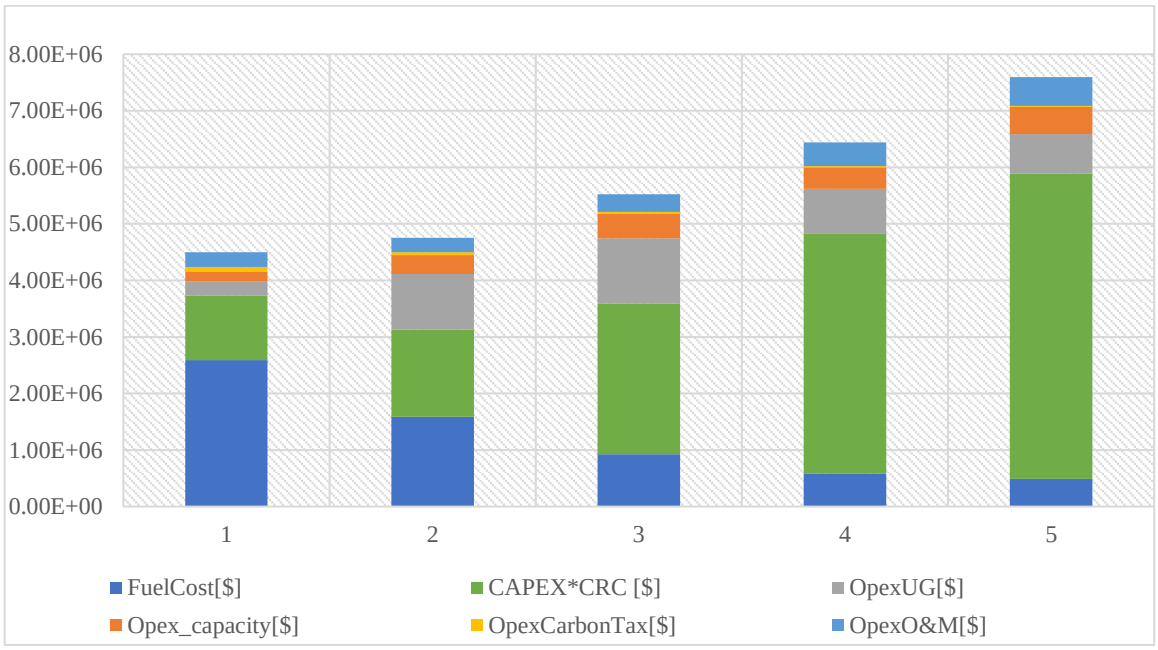

Fig. 7. Costs components of the TAC for Scenario 2.

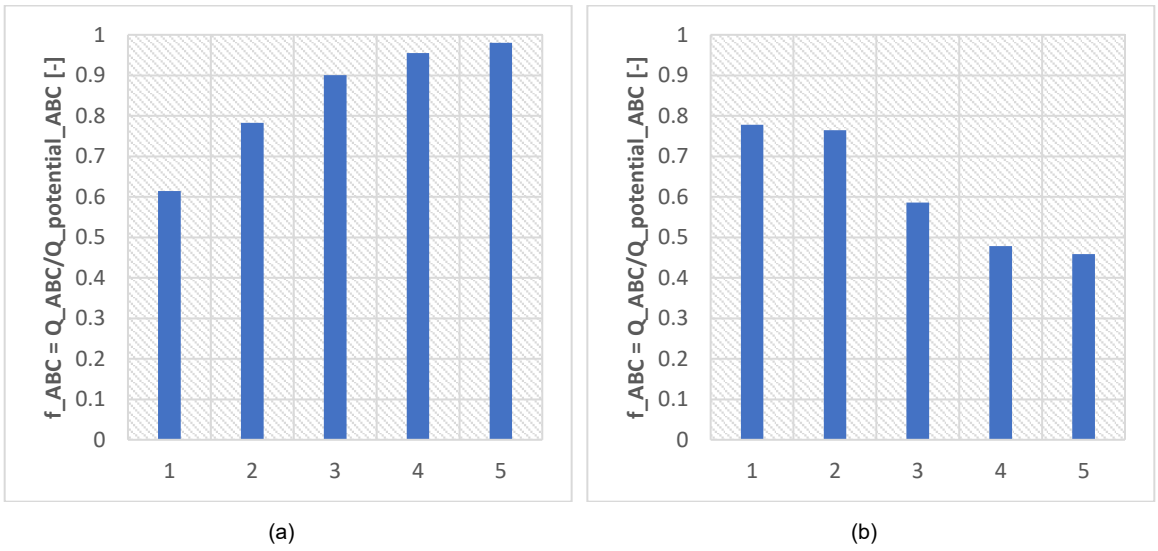

Fig. 8. ABC capacity ratio (f_{ABC}) for Scenario 1 (a) and Scenario 2 (b).

4. Conclusions

This paper discussed a design multi-objective optimization framework of novel cryo-polygeneration systems consisting of different distributed energy resources. The developed model has been applied to a real case study, a cryo-polygeneration system, expected to be operative during 2024 Q1, capable to cover the electric and cooling demand of a building located in a Singaporean university campus (NTU). The results confirm the workability of the framework that effectively determines the best possible trade-offs (Pareto fronts) between the total annualized cost and CO_2 emission. Thus, the operators of DESs can choose the operation strategy from the Pareto front based on their cost and environmental priorities. The results also indicates that the implementation of renewables and electric energy storage in the cryo-polygeneration system (2^{nd} scenario) has significant economic and environmental benefits over the 1^{st} scenario, reducing the total annualized cost and the carbon emissions up to 30 % and 10 %, respectively. Furthermore, in this scenario, by further increasing the PV and BESS capacities, different greener solutions can be achieved, although to the detriment of the total annualized cost due to the current high capital cost of the BESS. In future investigations, the model will analyze the effects of: 1) the island mode scenario; 2) PV electricity exported to the grid; 3) different operating strategies and load characteristics on the performance of cryo-polygeneration systems as well as the design of DES under uncertainty to provide more robust results; 4) the potential carbon emissions related to the construction of the decentralized energy systems.

Acknowledgments

This study is supported under the RIE2020 Industry Alignment Fund – Industry Collaboration Projects (IAF-ICP) Funding Initiative, as well as cash and in-kind contribution from Surbana Jurong Pte Ltd.

Nomenclature

Acronyms		UG	Utility Grid
ABC	Absorption Chiller	UOS	Use of system
AC	Air conditioning	WCC	Water cooled electrical chiller
BC	Baseline Case	*Symbols*	
BESS	Battery energy storage system	η	Efficiency [%]
CAPEX	Capital Cost [$]	i	Discount rate [%]
CRF	Capital Recovery Factor	N	Lifetime project [years]
COP	Coefficient of Performance	φ	CAPEX Fraction [%]
CTES	Cold Thermal Energy Storage	*Subscripts*	
DPS	Distributed Polygeneration System	ann	annualized
EL	Electrical load [kW_e]	base	baseline
ET	Electricity tariff [$/$kWh_e$]	c	cooling
G	Solar irradiance [W/m_2]	ch	charge
GEF	Grid Emission Factor	cap	capacity
GT	Gas Turbine	db	deadband
HE	Heat Exchanger	e	electric
LNG	Liquefied Natural Gas	FL	Full-load
NPV	Net Present Value [$]	imp	imported
OPEX	Operational cost [$]	max	maximum
PES	Primary energy savings	min	minimum
PLR	Partial Load Ratio	NC	Nominal capacity
PV	Photovoltaic system	nom	nominal
RU	Regasification Unit	ref	reference
SC	Specific CAPEX	s	system

STC	Standard test conditions	th	thermal
TAC	Total annualized cost	y	years

References

[1] European Commission. An EU strategy on heating and cooling 2016. vol. 53. 2016.

[2] International Energy Agency (IEA). The Future of Cooling - Opportunities for energy- efficient air conditioning. 2018.

[3] Mancarella P. MES (multi-energy systems): An overview of concepts and evaluation models. Energy 2014;65:1–17. https://doi.org/10.1016/j.energy.2013.10.041.

[4] Mazzoni S, Ooi S, Tafone A, Borri E, Comodi G, Romagnoli A. Liquid Air Energy Storage as a polygeneration system to solve the unit commitment and economic dispatch problems in micro-grids applications. Energy Procedia 2019;158:5026–33. https://doi.org/10.1016/j.egypro.2019.01.660.

[5] Pepermans G, Driesen J, Haeseldonckx D, Belmans R, D'haeseleer W. Distributed generation: definition, benefits and issues. Energy Policy 2005;33:787–98. https://doi.org/10.1016/J.ENPOL.2003.10.004.

[6] Jana K, Ray A, Majoumerd MM, Assadi M, De S. Polygeneration as a future sustainable energy solution – A comprehensive review. Appl Energy 2017;202:88–111. https://doi.org/10.1016/J.APENERGY.2017.05.129.

[7] Ghaem Sigarchian S, Malmquist A, Martin V. The choice of operating strategy for a complex polygeneration system: A case study for a residential building in Italy. Energy Convers Manag 2018;163:278–91. https://doi.org/10.1016/j.enconman.2018.02.066.

[8] Calise F, de Notaristefani di Vastogirardi G, Dentice d'Accadia M, Vicidomini M. Simulation of polygeneration systems. Energy 2018;163:290–337. https://doi.org/10.1016/j.energy.2018.08.052.

[9] López González DM, Garcia Rendon J. Opportunities and challenges of mainstreaming distributed energy resources towards the transition to more efficient and resilient energy markets. Renew Sustain Energy Rev 2022;157:112018. https://doi.org/10.1016/J.RSER.2021.112018.

[10] Burger C, Froggatt A, Mitchell C, Weinmann J. Decentralised Energy - A global game changer. Ubiquity Press 2020. https://doi.org/10.5334/BCF.

[11] Cryo-Polygeneration | Surbana Jurong-NTU Corporate Laboratory | NTU Singapore n.d. https://www.ntu.edu.sg/sj-ntu/research-focus/research-projects/cryo-polygeneration (accessed August 9, 2021).

[12] Singapore Green Plan 2030 n.d. https://www.greenplan.gov.sg/splash (accessed April 5, 2022).

[13] Serra LM, Lozano MA, Ramos J, Ensinas A V., Nebra SA. Polygeneration and efficient use of natural resources. Energy 2009;34:575–86. https://doi.org/10.1016/J.ENERGY.2008.08.013.

[14] Mazzoni S, Sze JY, Nastasi B, Ooi S, Desideri U, Romagnoli A. A techno-economic assessment on the adoption of latent heat thermal energy storage systems for district cooling optimal dispatch & operations. Appl Energy 2021;289:116646. https://doi.org/10.1016/j.apenergy.2021.116646.

[15] Ahmadi P, Rosen MA, Dincer I. Multi-objective exergy-based optimization of a polygeneration energy system using an evolutionary algorithm. Energy 2012;46:21–31. https://doi.org/10.1016/J.ENERGY.2012.02.005.

[16] Gabrielli P, Gazzani M, Martelli E, Mazzotti M. Optimal design of multi-energy systems with seasonal storage. Appl Energy 2018;219:408–24. https://doi.org/10.1016/j.apenergy.2017.07.142.

[17] Sigarchian SG, Malmquist A, Martin V. Design optimization of a complex polygeneration system for a hospital. Energies 2018;11. https://doi.org/10.3390/en11051071.

[18] Tafone A, Raj Thangavelu S, Morita S, Romagnoli A. Design optimization of a novel cryo-polygeneration demonstrator developed in Singapore – Techno-economic feasibility study for a cooling dominated tropical climate. Appl Energy 2023;330:119916. https://doi.org/10.1016/J.APENERGY.2022.119916.

[19] Wirtz M, Hahn M, Schreiber T, Müller D. Design optimization of multi-energy systems using mixed-integer linear programming: Which model complexity and level of detail is sufficient? Energy Convers Manag 2021;240:114249. https://doi.org/10.1016/j.enconman.2021.114249.

[20] Atienza-Márquez A, Ayou DS, Bruno JC, Coronas A. Energy polygeneration systems based on LNG-regasification: Comprehensive overview and techno-economic feasibility. Therm Sci Eng Prog 2020;20:100677. https://doi.org/10.1016/j.tsep.2020.100677.

[21] Renewable Power Generation Costs in 2020 n.d. https://www.irena.org/publications/2021/Jun/Renewable-Power-Costs-in-2020 (accessed March 9, 2022).

[22] DeForest N, Mendes G, Stadler M, Feng W, Lai J, Marnay C. Optimal deployment of thermal energy storage under diverse economic and climate conditions. Appl Energy 2014;119:488–96. https://doi.org/10.1016/j.apenergy.2014.01.047.

[23] Cole W, Frazier AW. Cost projections for utility- scale battery storage. NREL Tech Rep 2019:17.

[24] EMA : Electricity Tariffs n.d. https://www.ema.gov.sg/Residential_Electricity_Tariffs.aspx (accessed January 31, 2019).

[25] Boyce MP. Gas Turbine Engineering Handbook. Gas Turbine Eng Handb 2012. https://doi.org/10.1016/C2009-0-64242-2.

[26] TRNSYS 18 n.d.

[27] Deb K, Pratap A, Agarwal S, Meyarivan T. A fast and elitist multiobjective genetic algorithm: NSGA-II. IEEE Trans Evol Comput 2002;6:182–97. https://doi.org/10.1109/4235.996017.

[28] MATLAB - MathWorks - MATLAB & Simulink n.d. https://www.mathworks.com/products/matlab.html (accessed January 29, 2021).

[29] Rangaiah G, Sharma S, Sreepathi BK. Multi-objective optimization for the design and operation of energy efficient chemical processes and power generation. Curr Opin Chem Eng 2015;10:49–62. https://doi.org/10.1016/J.COCHE.2015.08.006.

Concept of cold generation in a district heating substation by using adsorption heat pumps supported by heat and cold storage units

Wojciech Bujalski[a], Arkadiusz Szczęśniak[b*], Kamil Futyma[c] and Andrzej Grzebielec[d]

[a] Warsaw University of Technology, Warsaw, Poland, Wojciech.Bujalski@pw.edu.pl
[b] Warsaw University of Technology, Warsaw, Poland, Arkadiusz.Szczesniak@pw.edu.pl
[c] Warsaw University of Technology, Warsaw, Poland, Kamil.Futyma@pw.edu.pl
[d] Warsaw University of Technology, Warsaw, Poland, Andrzej.Grzebielec@pw.edu.pl

Abstract:

District heating systems in northern Europe experience large seasonal differences in heat demand, rendering summertime profitability marginal at best. This study discusses a novel concept of a district heating substation that increases heat consumption during the summer period for the purpose of conversion into cold for an air conditioning system. Cold is generated by an adsorption chiller driven by heat from the district heating system. The study numerically models the system and examines its operation during a 24-hour period. The research indicated the need for a cold storage unit to cover cooling demand when ambient temperature limits the operation of the chiller. Additionally, a heat storage unit is required in order to equalize heat consumption from the district heating network.

Keywords:

District heating network, district heating substation, adsorption chillers, PCM storage

1. Introduction

District heating networks (DHNs) are a key element in strategies designed to meet the goals set by the European Union's Renewable Energy Directive [1] as they help deliver reductions in emissions of greenhouse gases among other things. This study deals with bolstering the profitability of DHNs by increasing heat consumption during the summer period [2]. In Poland, the typical heat consumption curve in a DHN is extremely seasonal, with the ratio of summer to winter heat demand being 1:10, as shown in Figure 1 below.

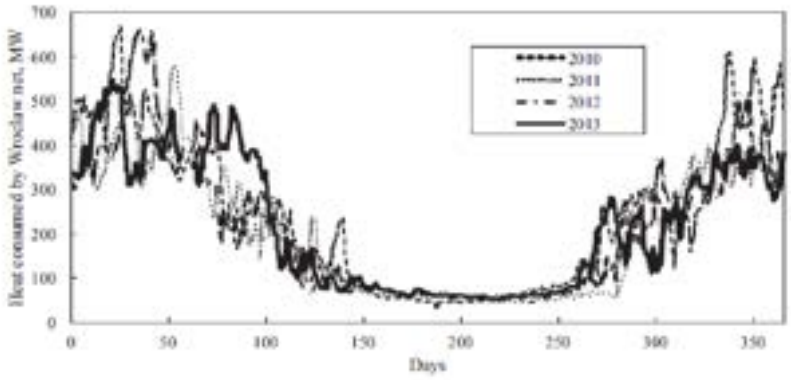

Figure. 1. Annual profile of heat consumption in a mid-sized Polish city, as per Chorowski [3]

Researchers report very similar heat demand profiles in other European countries, e.g., in the Netherlands [4] and Finland [5]. Extreme seasonal fluctuations put the profitability of DHNs into question and this issue is driving research into increasing heat consumption during the summer period. A review of district heating and cooling systems by Lake [6] concluded that DHNs could be enhanced with new technologies. The author cited thermal energy storage and absorption chillers as possible avenues to increase DHN efficiency.

The idea of cold district heating is widely discussed in the available literature [7], which defines it as cold water distribution in the range 10°C to 25°C. Pellegrini [7] notes that water cooling in such systems is done by electric reversible heat pumps. However, these pumps increase electricity consumption and fail to make use of the DHN. In contrast, replacing compressor heat pumps with adsorption refrigeration units boosts summertime consumption of heat thereby reducing summertime heat losses.

Grzebielec et al. [8] examined the possibility of using an adsorption refrigeration unit in a district heating substation (DHS). The authors concluded that it is feasible to use adsorption heat pumps for cold generation, and that this appears to be a promising solution because it uses existing infrastructure for cold generation on the customer's side without requiring long-distance cold transmission. Halon et al. [9] reported on an adsorption heat pump driven by heat from the DHS. The heating temperature was 55°C and the released heat was directed to a rooftop cooling tower.

Wu et al. [10] analyzed a composite heating substation with another type of absorption heat pump with water-LiBr as the working agent and a two-plate heat exchanger. The paper sought to improve the utilization efficiency of geothermal water and the primary supply water.

Another idea of improving DHS efficiency was reported by Turski [2], where the authors compared a 150 kW DHS operating with and without a heat storage accumulator: heat storage accumulators improved the efficiency of the entire heating system by 22%.

McNally et al. [12] experimentally investigated the performance of an adsorption chiller operation in two modes:

- Constant hot water temperature – to represent the DHN.
- Varying hot water temperature – to represent the heat from flat plate solar collectors.

The temperature variations of hot water impacted performance more than the flow variations. Therefore, adsorption chillers are suitable for use with DHNs.

The issue limiting the integration of adsorption chillers for cold generation is the temperature of the heating medium, which is too low for commercial adsorption heat pumps. The temperature of the available heat source could be raised by upgrading the substation with thermal storage tanks linked to renewables [15]. A promising heat storage technology is the PCM storage unit, as it requires 40% less volume than a water-based heat accumulator [13]. Due to a paucity of publicly available information, the potential of PCM heat storage is not widely recognized [14]. The influence of using heat storage with PCM on inlet and outlet temperatures in substations was investigated by Nogaj et al. [15]. The authors examined the integration of PCM with a single-function substation whose thermal power is 150 kW. Once the PCM was integrated, the difference in average return water temperature fell from 7.15K to 2.29K. This allowed the accumulation of 69.5% of excess heat and improved the efficiency of the entire heating system by 22%. The authors concluded the use of PCM accumulators gives potential energy savings of up to 6.7%.

1.1. Paper objective

A review of available literature indicates an opportunity to implement new technologies in DHNs in order to achieve enhanced efficiency. The study models a novel hybrid district heating substation designed to ensure increased summertime heat consumption; the period when heat losses peak due to very low heat consumption. The concept is to supplement the DHS with an adsorption chiller, which will be used to generate cooling for the air conditioning system of a building. The proposed solution uses existing DHN infrastructure for trigeneration and generates cooling directly on site. Thus, heat from the hybrid district heating hub will be used for heating the building in winter, and in summer will drive a chiller for air conditioning needs.

This paper introduces the following novelties:

- Concept of a novel hybrid DHS for cold generation
- Integration of PCM heat and cold storage units for heat load consumption equalization and to provide cold for air conditioning systems in very hot periods.

The concept is verified with a numerical study, which examined system behavior in Polish conditions.

2. Theory

The substation is a key element of the DHN, which is responsible for transferring heat from the medium that circulates in the DHN to the internal heating system inside buildings. Currently, summertime use of heat is very low. Integrating the cooling loop in the DHN would boost summertime heat consumption as it will be used for cold generation by adsorption heat pumps.

The general concept of the hybrid DHS is shown in Figure 1. The main system elements are an adsorption heat pump, DHS heat exchangers, and cold and heat storage units. The idea is to deliver cold for an office air conditioning system. The DHS is tasked primarily with producing cold by means of an adsorption chiller driven by heat from the DHN. The DHS is also equipped with cold and heat storage units. The heat storage unit is used to equalize heat consumption from the DHN, while the cold storage unit covers peak cooling demand

from the storage units. Thus, the installed capacity of the adsorption chiller could be lower in terms of power than the maximum peak power and its operation will be smoother.

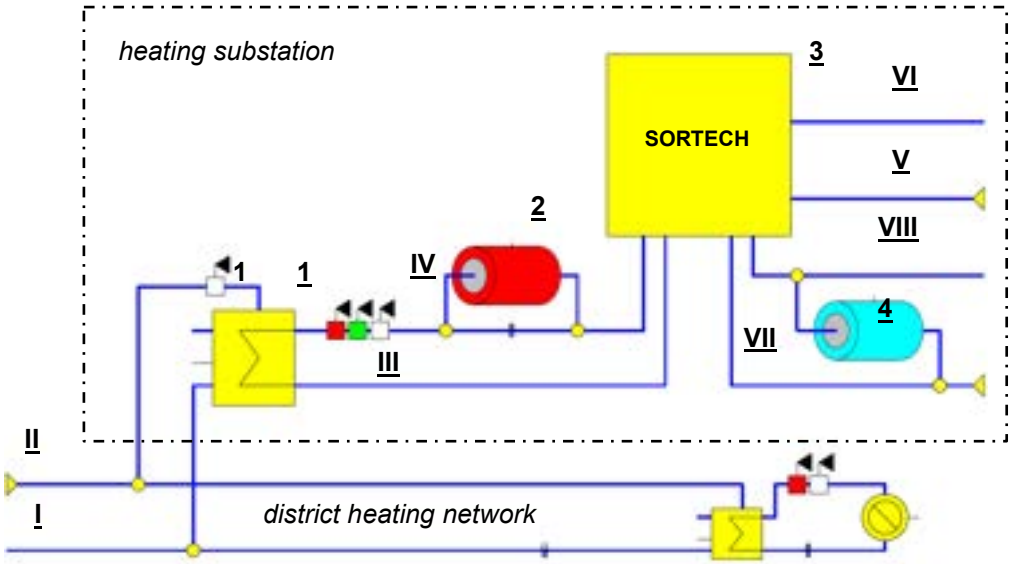

Figure 2. Topology of a hybrid DHS, (1) heat exchanger, (2) PCM for heat storage, (3) adsorption chiller, (4) PCM for cold storage

The thermodynamic parameters for the nominal operating points are shown in the table 1. The points from the table correspond to the above topology diagram.

Table 1. Basic thermodynamic parameters

Point	Temperature	Mass flow rate	Comment
I	65.0°C	10 kg/s	DHS heat supply pipe
II	64.5°C	10 kg/s	DHS return pipe
III	55.0°C	0.607 kg/s	Return pipe
IV	60.0°C	0.607 kg/s	Heat for driving adsorption heat pump
V	28.2°C	1.33 kg/s	Return from dry cooler
VI	25.0°C	1.33 kg/s	Heat for dry cooler
VII	16.0°C	0.806 kg/s	Cold for air conditioning
VIII	14.3°C	0.806 kg/s	Return from air conditioning

For the purpose of this study, we assumed the DHS delivers heat and cold to an office building of total area 142 m^2, total volume 426 m^3 with 6 rooms. Cooling demand is determined by a mathematical model, where the air conditioning is to maintain the interior at a temperature not exceeding 25°C during the summer period. Air temperature inside the rooms changes as per the equation:

$$\frac{\partial T}{\partial t} m \cdot c_p = \dot{Q}_{air} + \dot{Q}_{el} + \dot{Q}_{people} + \dot{Q}_{wall,out} + \dot{Q}_{wall,in} + \dot{Q}_{floor} + \dot{Q}_{ceil} + \dot{Q}_{window} + \dot{Q}_{sun,window}, \quad (1)$$

To simplify the model, $\dot{Q}_{floor}$, $\dot{Q}_{ceil}$ and $\dot{Q}_{wall,in}$ were omitted in the final calculations. The resulting cold demand for the office is shown in Figure 2 below.

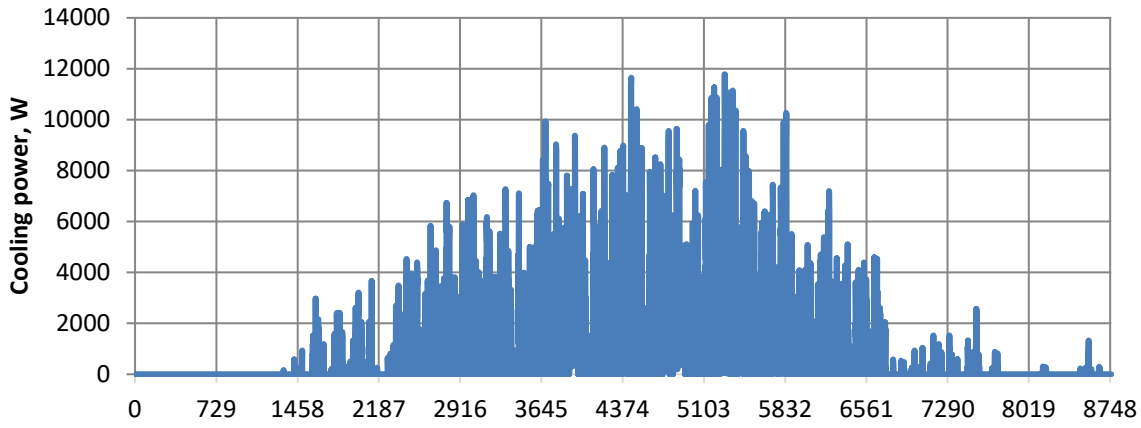

Figure 3. Demand for cooling power of the office building for each hour in the year

To investigate system behavior, the system was modeled in Ebsilon v.15, which is recognized as a robust tool for the simulation of energy systems [11,12]. The topology of the DHS implemented in Ebsilon is shown in Figure 1. The cold is generated by an adsorption chiller, which is driven by heat from the DHN. The DHS operates with SORTECH eco 2.0, which generates cooling water at a temperature of 16°C.

The basic technical data of adsorption heat pump SORTECH, eCoo 2.0 are presented in Table 2.

Table 1. Basic thermodynamic parameters

Parameter	Value
Cooling power	16 kW
Heating power	50 kW
COP	0.65 kW
The temperature of hot water	50 .. 95°C
Recooling water temperature	22 .. 40°C
Cooling water temperature	8 .. 21°C

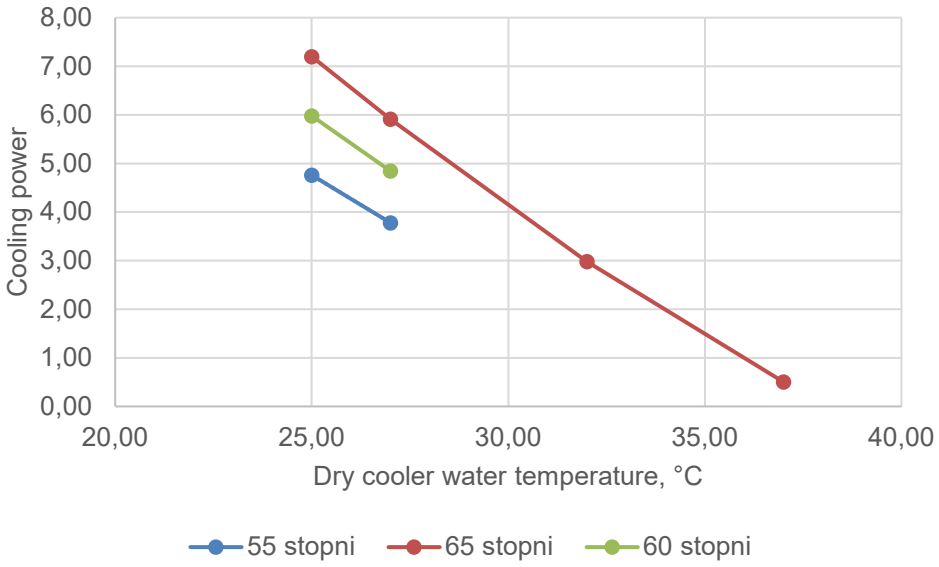

Figure 4. Cooling power of an adsorption chiller as a function of dry cooler water temperature for various temperatures of water in DHS

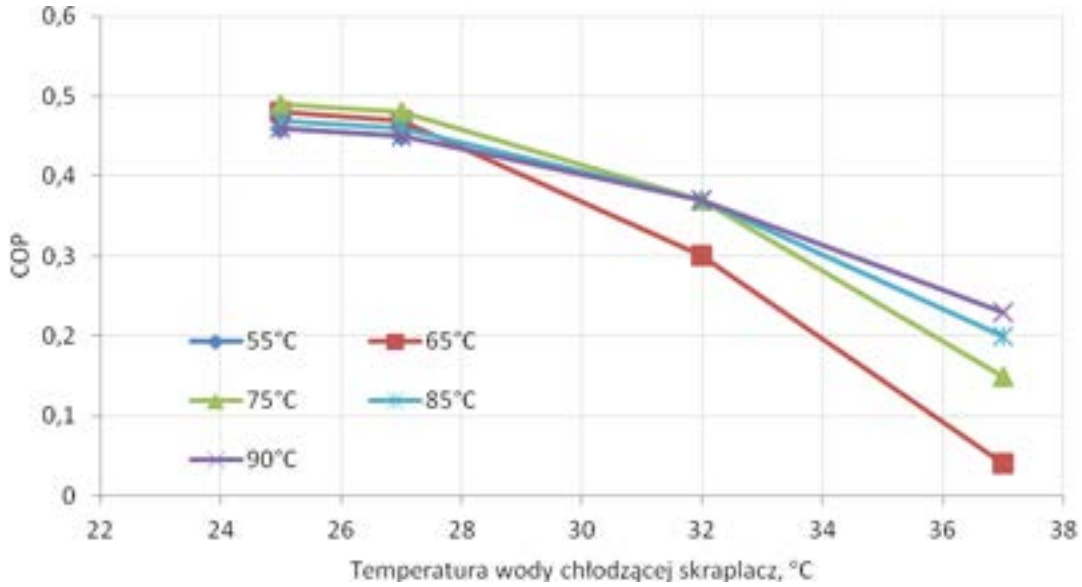

Figure 5. COP of an adsorption chiller as a function of cooling water, for various temperatures of DHS

For simulation purposes, we implemented SORTECH characteristics to determine the performance of an adsorption chiller. The adsorption chiller power as a function of cooling water is shown in Figure 3. The system is driven by the water network at temperature 60°C. Figure 4 shows that the COP of the chiller reaches very low values when the cooler water temperature rises above 34°C. Thus, a higher temperature of the driving source is required in order to increase COP. However, as the driving source is the DHN, it is not always possible to increase the temperature.

The DHS has two PCM storage units for storing heat and cold. CrodaTherm 60 PCM and CrodaTherm 15 were selected for heat and cold storage, respectively. Their storage properties are shown in Fig. 5.

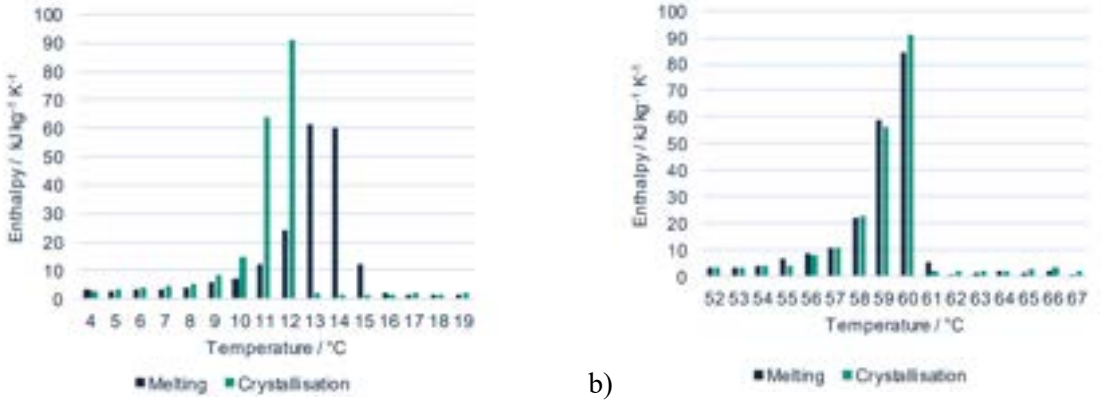

Figure 6. Thermal profile of heat and cold storage units, a) and b) respectively

The PCM storage units are simulated by component 119 Indirect Storage, which calculates the non-steady state heat exchange of the material with the fluid that flows through and around it. Based on the initial state of the temperature field, component 119 calculates the change in the temperature field of the pipe due to a change of the determining factors within a defined period of time. The determining factors are defined by the specification values of the component and by the state variables of the fluid at the component inlet. For the purpose of the study, the characteristics curve for heat and cold storage PCM, respectively, were implemented for this component, as shown in Fig. 5a and 5b.

3.Results

The behavior of the hybrid DHS was tested on operational data from the DHN in the town of Ostrołęka in northeastern Poland. The DHN operates at varying water flow rates and supply temperatures. The design operating temperature is 120/65°C, which corresponds to ambient temperature -20°C. The summertime heating medium is 65°C and the return water is 50°C. The heating medium is water, whose pressure is 0.9 MPa and 0.2 MPa during winter and summer, respectively. The temperature variations with respect to ambient temperature are shown in Fig. 7.

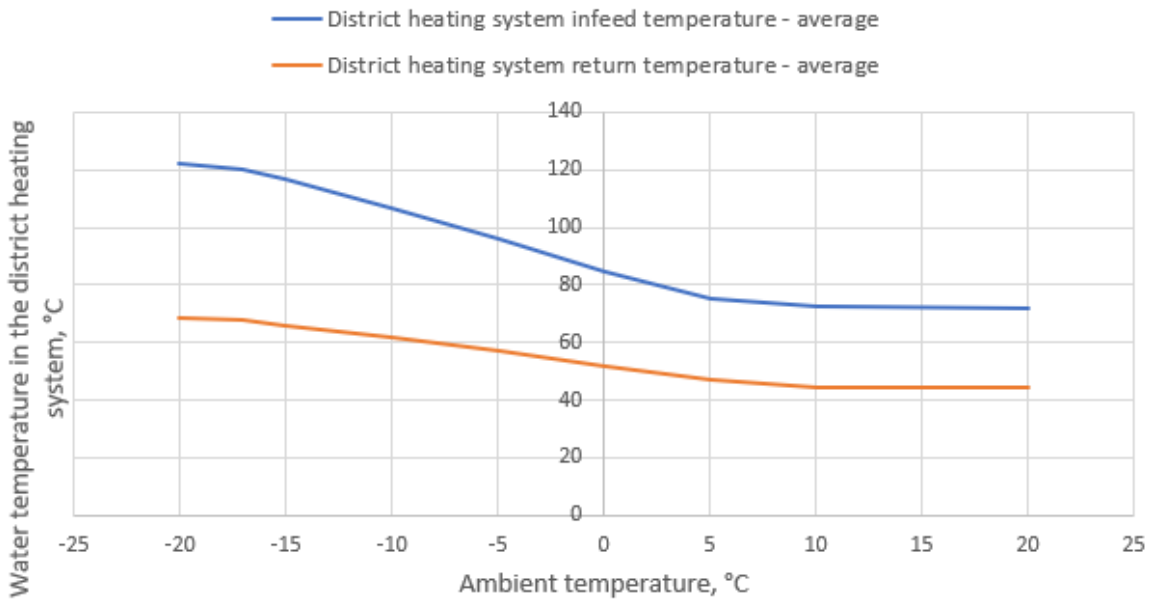

Figure 7. Hot and cold pipe temperature variations as a function of ambient temperature

The behavior of the novel hybrid DHS was examined during a 24-hour sunny summer day operation. Demand for cold and ambient temperature are shown in Figure 6 below.

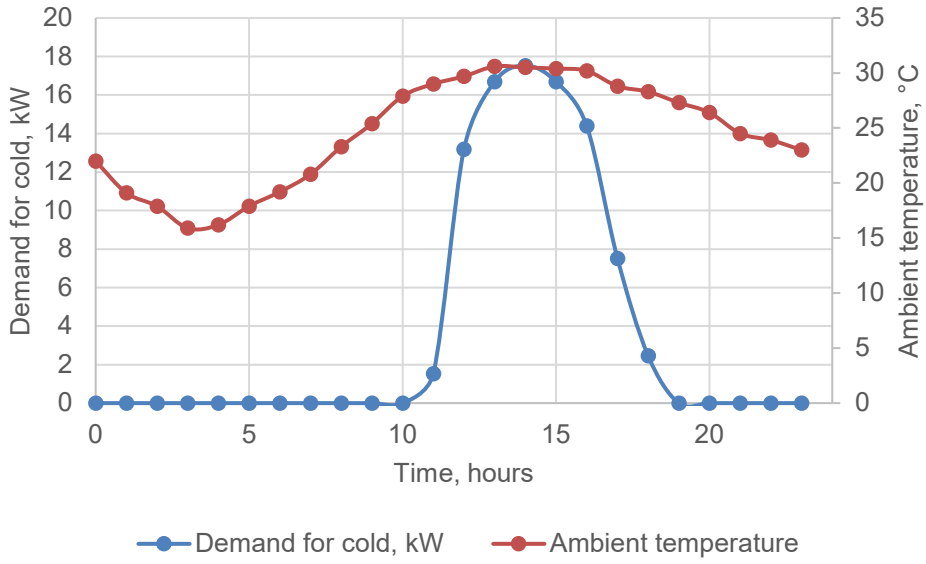

Figure 8. Adsorption chiller power as a function of hour of day

Firstly, the study revealed that the adsorption chiller does not operate when the ambient temperature exceeds 25°C (see Figure 7). Therefore, either the refrigeration technology must change or a cold storage facility is required. A cold storage unit was selected, as it can cover demand for cold during hot periods.

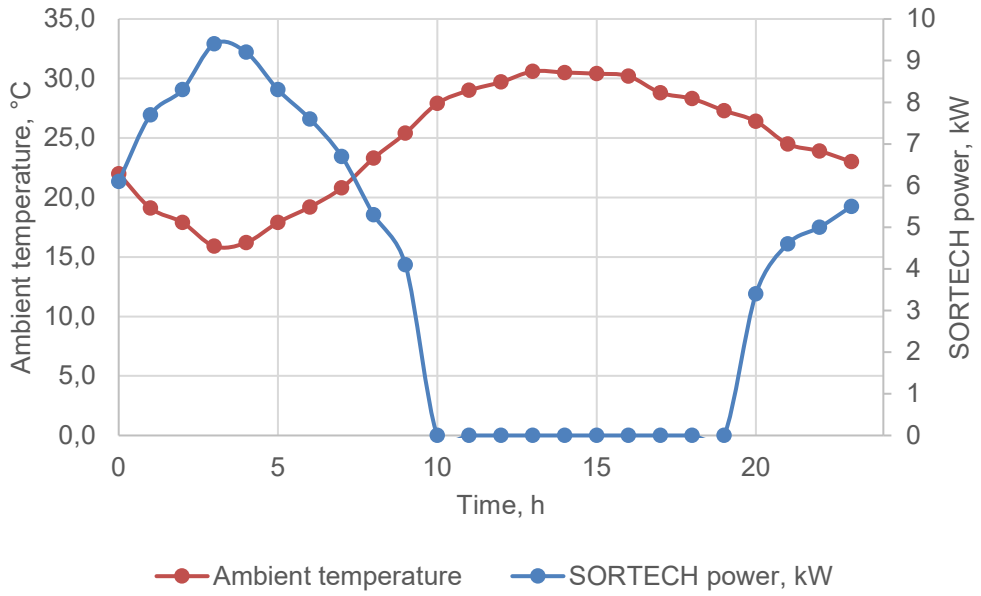

Figure 9. Adsorption chiller power during the day

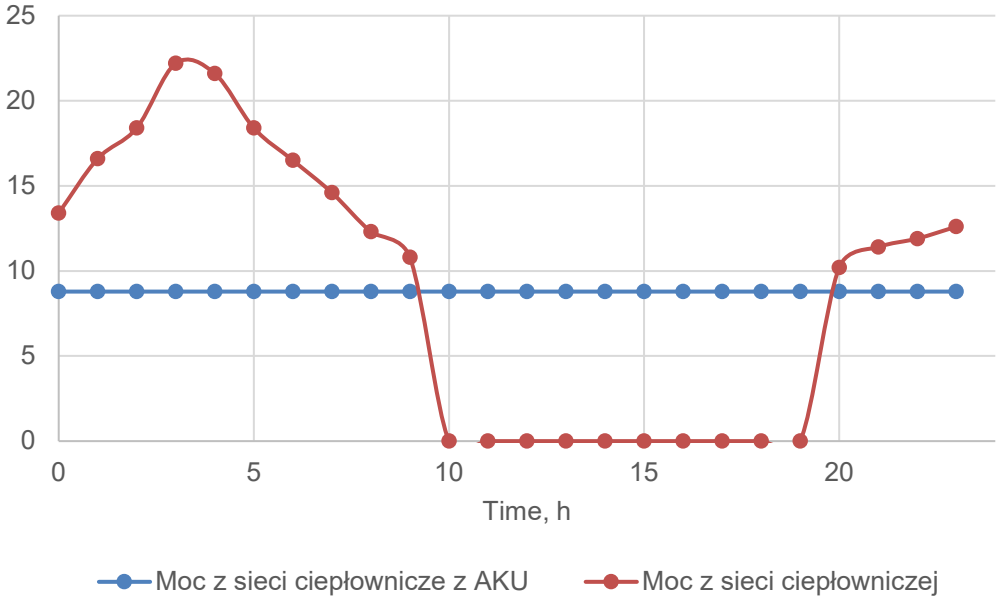

Figure 10 Heat consumption with system with PCM heat storage (blue line) and without (red line)

Figure 10 shows heat consumption from the DHN for two scenarios: operation with and without a heat storage accumulator. The implementation of heat storage enables constant heat consumption by the DHS.

The loading/unloading curves of heat and cold storage units are shown in Figure 9.

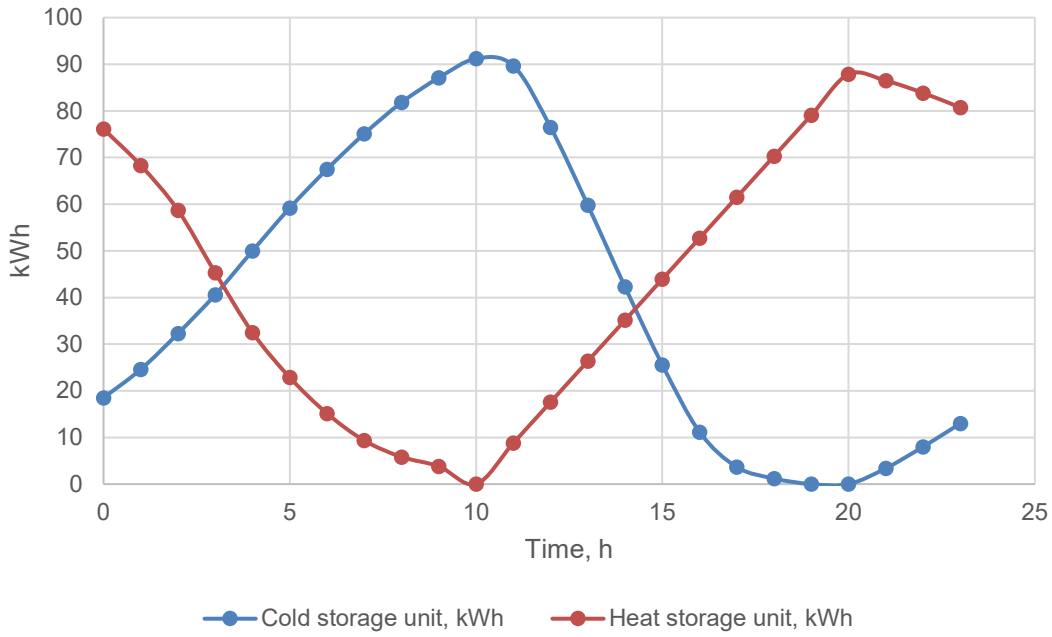

Figure. 11. Loading and unloading curves for heat and cold storage units

The above chart shows that the heat storage units are loaded until 10 am and when the adsorption chiller is unable to operate due to the high ambient temperature, heat storage loading begins (red line).

4. Conclusions

The aim of the research was to examine the concept of a hybrid district heating substation for heat and cold generation. The operation of the DHS was examined using representative data from the system operating in a small city in northeastern Poland, where the summertime temperature of the medium is 65°C. The DHS was assumed to deliver cold for an office air conditioning system. Cold was generated by an adsorption heat pump (SORTECH eCO 2.0) supported by two accumulators: for heat and cold storage.

Operation of the system was simulated across a 24-hour period on a sunny day, when ambient temperature reaches the maximum possible value of 30°C. The examination revealed there is a limiting ambient temperature for the selected adsorption heat pump, i.e., it is unable to operate when the ambient temperature exceeds 25°C, and the cold for the office air conditioning system has to be supplied from the PCM cold storage unit. System operation indicated a need to use a heat storage accumulator to equalize heat consumption, which should reduce summertime heat losses from the DHS.

To conclude, the numerical study proved the concept for the novel hybrid DHS and indicated the operating limits for this technology. The main advantage of our solution is the ability to use existing heating infrastructure to generate cooling with adsorption chillers. This reduces electricity consumption for air conditioning and boosts summertime heat consumption, increasing the efficiency of the DHN. The preliminary study revealed that the modeled DHS is a promising solution to increase heat consumption during the summer period, which should deliver increased profitability for DHNs. However, more detailed study is required to optimize PCM storage tanks and control strategy selection.

ACKNOWLEDGEMENTS

This work was financially supported by the National Research and Development Center in Poland in the framework of the POIR.04.01.04-00-0100/17-00 research project "Innovative heat and cold storage with PCM, operating in a modern installation intended to generate system heat", project acronym: Innostorage.

Nomenclature

DHS	district heating substation
DHN	district heating network

T	indoor temperature
m	mass of the air,
c_p	specific heat of the air,
$\dot{Q}_{air}$	heat exchanged via ventilation,
$\dot{Q}_{el}$	heat gain from electric devices,
$\dot{Q}_{people}$	heat coming from people inside,
$\dot{Q}_{wall,out}$	heat exchanged via convection on the outer walls,
$\dot{Q}_{wall,in}$	heat exchanged via convection on the inner walls,
$\dot{Q}_{floor}$	heat exchanged via convection on the floor,
$\dot{Q}_{ceil}$	heat exchanged via convection on the ceiling,
$\dot{Q}_{window}$	heat exchanged via convection on the windows
$\dot{Q}_{sun,window}$	heat exchanged via solar radiation through the windows.

References

[1] European_Union, Renewable energy directive | Energy, Off. J. Eur. Union. (n.d.). https://ec.europa.eu/energy/topics/renewable-energy/renewable-energy-directive_pl (accessed March 1, 2021).

[2] M. Turski, K. Nogaj, R. Sekret, The use of a PCM heat accumulator to improve the efficiency of the district heating substation, Energy. 187 (2019) 115885. https://doi.org/10.1016/j.energy.2019.115885.

[3] M. Chorowski, Z. Rogala, P. Pyrka, System options for cooling of buildings making use of district heating heat, Int. J. Refrig. 70 (2016) 183–195. https://doi.org/10.1016/j.ijrefrig.2016.06.018.

[4] R. Cuypers, N. Maraz, J. Eversdijk, C. Finck, E. Henquet, H. Oversloot, H. van't Spijker, A. de Geus, Development of a Seasonal Thermochemical Storage System, Energy Procedia. 30 (2012) 207–214.

[5] M. Rämä, S. Mohammadi, Comparison of distributed and centralised integration of solar heat in a district heating system, Energy. 137 (2017) 649–660. https://doi.org/10.1016/j.energy.2017.03.115.

[6] A. Lake, B. Rezaie, S. Beyerlein, Review of district heating and cooling systems for a sustainable future, Renew. Sustain. Energy Rev. 67 (2017) 417–425. https://doi.org/10.1016/j.rser.2016.09.061.

[7] M. Pellegrini, A. Bianchini, The Innovative Concept of Cold District Heating Networks: A Literature Review, Energies 2018, Vol. 11, Page 236. 11 (2018) 236. https://doi.org/10.3390/EN11010236.

[8] A. Grzebielec, A. Rusowicz, M. Jaworski, R. Laskowski, Possibility of using adsorption refrigeration unit in district heating network, Arch. Thermodyn. 36 (2015) 15–24. https://doi.org/10.1515/aoter-2015-0019.

[9] T. Halon, E. Pelinska-Olko, M. Szyc, B. Zajaczkowski, Predicting Performance of a District Heat Powered Adsorption Chiller by Means of an Artificial Neural Network, Energies 2019, Vol. 12, Page 3328. 12 (2019) 3328. https://doi.org/10.3390/EN12173328.

[10] Z. Wu, Y. Wang, S. You, H. Zhang, X. Zheng, J. Guo, S. Wei, Thermo-economic analysis of composite district heating substation with absorption heat pump, Appl. Therm. Eng. 166 (2020) 114659. https://doi.org/10.1016/J.APPLTHERMALENG.2019.114659.

[11] Y. Li, N. Wang, H. Guan, Z. Jia, Y. Zhang, G. Zhao, M. Gao, Optimization study of CO2 capture unit for subcritical coal-fired power generation unit based on Ebsilon and Aspen plus, Energy Convers. Manag. 269 (2022) 116111. https://doi.org/10.1016/J.ENCONMAN.2022.116111.

[12] P. Ziółkowski, P. Madejski, M. Amiri, T. Kuś, K. Stasiak, N. Subramanian, H. Pawlak-Kruczek, J. Badur, Ł. Niedźwiecki, D. Mikielewicz, Thermodynamic Analysis of Negative CO2 Emission Power Plant Using Aspen Plus, Aspen Hysys, and Ebsilon Software, Energies 2021, Vol. 14, Page 6304. 14 (2021) 6304. https://doi.org/10.3390/EN14196304.

Quantifying Demand Flexibilities of Buildings for an optimal Design and Operation of integrated District Energy Systems

Kai Niklas George[a], Michael Rath[a,b], Rolf Bracke[a,c]

[a] Fraunhofer Research Institution for Energy Infrastructures and Geothermal Systems (IEG), Bochum, Germany, kai.george@ieg.fraunhofer.de,
[b] Bochum University of Applied Sciences, Bochum, Germany
[c] Ruhr University Bochum, Bochum, Germany

Abstract:

The EU's ambitious climate targets have highlighted the need for novel methodologies in the integrated energy system planning and the development of sector-coupled operation strategies. In order to balance generation and consumption in the electricity grid with a high share of renewable energies, energy storage potentials have to be utilized across all sectors and new demand-side management strategies have to be developed. The energy storage potentials of buildings could benefit the grid stability and support the exploitation of renewable energy sources. Still, these potentials are not well quantified and are not considered in today's planning methods for district energy systems. This paper presents the derivation of widely applicable linear building models that capture both detailed demand characteristics and storage characteristics from dynamic building simulations, while accounting for thermal comfort. These models are integrated into linear energy system optimization models, enabling the hourly optimization of air source heat pump operation and the heat emittance into the buildings. The resulting approach allows for the quantification of flexibility indicators and provides insights into efficient operation strategies for buildings with varying thermal characteristics. The results indicate that all investigated buildings show economically viable potential for utilizing their thermal flexibility. While well-insulated buildings demonstrate higher potential for longer-lasting preheating and storage periods, still buildings with poor or moderate insulation also offer potential for shorter periods of utilization.

Keywords:

Building demand flexibility; Building simulation; District energy system planning; Energy system optimization.

1. Introduction

With the agreement of the UN Climate Conference in Paris in 2015, 195 parties worldwide agreed to limit global warming to below 2 °C compared to pre-industrial levels and to reduce greenhouse gas emissions worldwide. As a result, with the European Green Deal, the EU has set itself the goal of zero net greenhouse gas emissions by 2050 [1]. This requires far-reaching measures in many areas and a drastic turnaround in the energy sector in particular. In 2019 over 53.1% of total final energy consumption in Germany was required for heating [2], with just 14.9 % coming from renewables [3]. This leaves the heating sector facing a challenging transformation. According to the German Ministry for Economic Affairs and Energy [4], the building sector, was the largest end energy consumer in Germany in 2020 with a share of 43.8 %, consisting of private households as well as commercial, trade and service properties. If the expansion of renewable electricity generation is driven forward, sector coupling technologies such as power-to-heat will strongly increase in importance [5]. Growing shares of renewable energy in the energy system lead to higher fluctuations in the power generation and creates a growing need to adapt the demand to the fluctuating generation. Therefore, demand side management of buildings, districts and district heating networks can play a crucial role in exploiting renewable energy sources.

1.1. State-of-the-art

According to the IEA-EBC Annex 67 [6], energy flexibility of buildings needs to be utilized across a large share of buildings and districts, in order to meet the minimum energy reduction to supply grid services and integrate sufficient amounts of renewable energy. The IEA EBC Annex 67 defines energy flexibility of buildings as: "*the ability to manage demand and generation according to local climate conditions, user needs, and energy network requirements. Energy Flexibility of buildings will thus allow for demand side management / load control and thereby demand response based on the requirements of the surrounding energy networks*." [6]. To provide demand side management, both energy and power adaptions of the demand side are of interest, as well as

the time in which they can be provided [7]. Demand side management includes all measures modifying the demand, including permanent retrofitting measures like renovations [8]. Demand response on the other hand is a subset of demand side management and only covers non-permanent actions, including load shifting and load shedding [8]. In this terminology the energy flexibility of a building is understood as the potential for demand response actions. Therefore, energy flexibility of buildings can be provided on the one hand by storing energy in batteries, in hot water tanks or inside the thermal mass of buildings and on the other hand by shifting the generation in time or by switching to other generation sources [9].

1.2. Flexibility indicators

Reynders et al. [10] review common quantification methods for the flexibility of buildings and identify three common characteristics: *i) temporal flexibility, ii) amplitude of power modulation and iii) the associated costs*. Reynders et al. [11] introduce a generic quantification method for thermal energy flexibility in buildings. As a key indicator they define the available capacity for active demand response C_{ADR} which can be used to quantify upward flexibility and describes the amount of surplus heat, that is additionally emitted into the building before the demand is reduced:

$$C_{ADR} = \int_0^{I_{ADR}} \left(\dot{Q}_{ADR} - \dot{Q}_{Ref}\right) dt. \tag{1}$$

Where I_{ADR} is the duration of the active demand response, $\dot{Q}_{ADR}$ the adapted heat flow during the time of the demand response and $\dot{Q}_{Ref}$ the reference heat flow, that would occur without the demand adaption. They further introduce an efficiency indicator as the ratio between the demand reduction achievable through the demand response event and the additional demand required to achieve the reduced demand:

$$\eta_{ADR} = \frac{Demand\ Reduction}{Add.Demand} = 1 - \frac{\int_0^{\infty} \left(\dot{Q}_{ADR} - \dot{Q}_{Ref}\right) dt}{C_{ADR}}. \tag{2}$$

Kathirgamanathan and Péan et al. [9] analyse three adaptions of these indicators that are used in further literature [12–14]. They find that all indicators show relatively high robustness to different building types, climates and control schemes and consolidate a generic indicator for the available capacity as presented in equation (1). The indicator describing the efficiency of the demand response can vary between different applications and depends on the point of view of the stakeholder. Kathirgamanathan and Péan et al. show that different definitions are necessary to distinguish between downward flexibility, a shift of the generation to later times, and upward flexibility, a shift of the generation to earlier times.

A third indicator introduced by Reynders et al. [11] is the power shifting capability t_δ of the buildings. The power shift $\dot{Q}_\delta$ is described as the difference between the actual heating power during the demand response $\dot{Q}_{ADR}$ and the heating power that would occur during standard operation $\dot{Q}_{ref}$:

$$\dot{Q}_\delta = \dot{Q}_{ADR} - \dot{Q}_{ref}. \tag{3}$$

The power shifting capability t_δ is defined as the duration this shift can be maintained without violating the restrictions of the building zone temperature for thermal comfort:

$$t_\delta = t\left(\dot{Q}_\delta\right). \tag{4}$$

1.3. Quantification of flexibility in buildings

Vandermeulen et al. [15] evaluates the energy flexibility of buildings based on Belgian typologies with the flexibility functions introduced by [6]. They use a resistance-capacitance (RC) building models based on Protopapadaki et al. [16] and the DIN EN ISO 13790, which has been recently replaced by the DIN EN ISO 52016 [17]. Dréau and Heiselberg [18] assess the thermal flexibility of two representative buildings from the Danish building stock using detailed building simulations in EnergyPlus [19]. They show that poorly insulated buildings can still be modulated over a short period of time. Furthermore, they demonstrate that the heating system of well-insulated buildings can be shut off for more than 24 hours and the flexibility potential is highly influenced by the type of insulation and the heating emitter system. Yang et al. [20] analyse the thermal dynamics of low-energy buildings connected to a district heating system using detailed Modelica models. They optimize the strategy to unlock flexibilities inside a building connected to a district heating network using a variable heat price. Nevertheless, the planning of demand side response strategies for district energy systems is still in the beginning and planners and operators are missing the right tools to quantify the flexibilities of their district energy systems and identify potential savings in the energy import costs and investments. In addition to monetary reductions, modelling the flexibility of buildings can also identify more efficient integration strategies of available renewable energy sources.

1.4. Modelling the thermal flexibility of buildings in energy system optimization frameworks

There are lots of existing frameworks and different approaches to optimize the operation or the design of district energy systems. The most common approaches are mixed-integer linear programming (MILP) models and include linear formulations of components like sinks, sources, busses, transformers and storages. This

allows the representation of most elements in an energy system. The application of these frameworks usually requires connecting and parameterizing these components to create the mathematical expression of the overall optimization model. Nevertheless, the structure of only a few abstract components in energy system optimization frameworks has its limitations. When it comes to characterizing flexibilities in the building operation, simple sinks with fixed demand time series are no longer sufficient. Therefore, [21] and [22] introduce a demand model in the optimization framework oemof [23], capable of providing upper and lower capacities for demand responses. Kotzur [24] includes a 5R1C building model in their frameworks that was introduced by [25]. Both use the indoor room temperature as a variable in their models and optimize the temperature inside certain boundaries. It allows a flexible operation of the heating system while integrating one capacity for the whole building. However, as shown in Bacher et al. [26], low order RC models are not always sufficient to represent the thermal dynamics of the buildings. Hence, these methods usually do not take into account the limitations in the power shift, which is caused by the inertia of the heat transfer mechanisms and the time required for the heat to reach the deeper parts of the buildings. This highlights the need for a procedure to estimate these limits and quantify the storage properties of the buildings. Therefore, detailed building models and simulations are necessary to quantify the heat transfer from the room into different layers of the building.

1.5. Quantifying thermal demand flexibilities for a selection of representative buildings

The aim of this paper is to quantify and analyze the thermal demand flexibilities of a selection of representative buildings in Germany, with a focus on utilizing the models in the diverse planning processes of district energy systems. Therefore, a procedure is presented to model thermal flexibilities in buildings for energy system optimization frameworks, using the building database TABULA/episcope [27] and the building simulation standard EN ISO 52016 [17]. The potential of utilizing the flexibility of the building selection is analysed in an existing energy system optimization framework and established flexibility indicators are calculated. By not being oversimplified and yet easy to apply, the method presented in this paper can assist planners of district energy systems to quantify the demand response potentials, identify optimal design and operation strategies or integrate new renewable energy sources more efficiently. This enables the evaluation of thermal flexibilities for diverse applications in the planning of district energy systems.

2. Method

In this section, a procedure is presented to quantify the thermal flexibility of a selection of buildings from the German building stock. First, the chosen buildings analysed in this work are presented. Then, the building simulation model is introduced, that is used to analyse the dynamic heat transfer mechanism for each building. Afterwards, a procedure to determine the thermal storage characteristics of the buildings is presented and the building model for the energy system optimization is displayed. Last, the chosen energy system optimization framework and the modelling approaches to quantify the thermal demand flexibilities of the buildings are presented.

2.1. Building selection

The analysis of heating demand flexibilities in domestic buildings is carried out for a selection of building types in Germany. The building information are based on data from the European building database TABULA/episcope [27]. A single-family house (SFH) built between 1958 and 1968 is chosen as a reference. This type of building accounts for the largest share of all residential buildings in Germany, at around eight percent [28]. In addition, two further SFH are chosen, built before and after the reference building age class. All buildings have a net floor area of 160 m² and are investigated in three states of insulation. The data for geometries, heat transfer coefficients, heat losses and internal heat gains can be found in [27]. Internal solar gains are determined in hourly time steps depending on all transparent surfaces and their tilts and azimuths, using test reference year weather data from the German meteorological service (DWD) for a representative year between 2031 and 2060 [29].

2.2. Building model

To analyse the dynamic characteristics of the buildings and calculate their heating demands, the buildings are modelled and simulated according to DIN EN ISO 52016 [17]. The procedure can be used for residential and non-residential buildings and allows hourly calculations of heating and cooling demands and indoor temperatures. The calculation methods include internal solar gains, ventilation, infiltration and internal heat gains. Each building can be modelled using several zones and opaque and transparent building elements. All opaque building elements are modelled in five nodes, representing the different layers of the components. All layers are set with a heat capacities and heat transfer coefficients depending on the structures of the elements. For the zone and for each node, an energy balance is set up, taking into account the heat transfer mechanisms of conduction, convection and radiation as well as heat storage properties. Effective heat capacities of all building components are assigned according to [17] for average construction types. For simplification, it is assumed that all buildings consist of one heated zone, four walls, two roofs and six window areas, with varying orientations, as well as one floor and one door. Given a certain input, the zone temperature and all node

temperatures can be simulated. To calculate the heating demand required to maintain the set point of the indoor temperature, the energy balance of the zone can be solved for the heating and cooling demand $\dot{Q}_{demand,ref}^{building}(t)$. This modelling approach takes into account the inertia of the heat transfer mechanisms in the different layers of the building elements and is used quantify the heat demand flexibility in the buildings. It further allows to simulate ideal heating and cooling demands for fixed zone temperature setpoints.

2.3. Modelling building and it's flexibility in an energy system optimization framework

Due to diverse building types, building structures and refurbishment conditions, different buildings show varying dynamic characteristics in the heat transfer and the charging of their thermal masses. To quantify all flexibility potentials using the common indicators presented in 1, the demand response events need to be specified. An optimal demand response depends on several factors, including the availability of renewable energy sources, electricity price signals and building parameters such as insulation properties, heat capacities and current temperatures. All these variables influence the quantification of the flexibility indicators. Therefore, the buildings characteristics are integrated in a MILP energy system optimization that allows optimizing the utilization of the buildings flexibility in different applications. To model the heating demand as well as the thermal flexibilities of a building in an energy system optimization framework, a combination of a generic sink and a generic storage is selected. The chosen interconnection is shown in Figure 1. The sink is assigned with a demand time series $\dot{Q}_{demand,ref}^{building}(t)$, resulting from a building simulation based on [17] and taking into account detailed heat transfer mechanisms. The storage component is set to represents the deviation to the normal operation of the building and characterizes the additional heat storage properties and losses. It is therefore referred to as an additional virtual storage (vs). The additional heat losses of the building $\Delta\dot{Q}_{add\_loss}^{building}(t)$ and the losses of the virtual storage $\dot{Q}_{loss}^{vs}(t)$ correspond to the difference between the heating demand at an increased zone temperature $\dot{Q}_{in,increased}^{building}(t)$ and the heating demand at a normal operation $\dot{Q}_{demand,ref}^{building}(t)$:

$$\Delta\dot{Q}_{add\_loss}^{building}(t) = \dot{Q}_{loss}^{vs}(t) = \dot{Q}_{in,increased}^{building}(t) - \dot{Q}_{demand,ref}^{building}(t). \quad (5)$$

The virtual storage component is further defined by a loss rate r_{loss}^{vs}, a nominal storage capacity $C_{nominal}^{vs}$ and a limit in the inflow and outflow power $\dot{Q}_{charging}^{vs}$ and $\dot{Q}_{discharging}^{vs}$. The loss rate r_{loss}^{vs} is the fraction of lost energy per time. The heat losses of the virtual storage $\dot{Q}_{loss}^{vs}(t)$ can therefore be described as the product of the loss rate and the current energy content of the storage $E^{vs}(t)$:

$$\dot{Q}_{loss}^{vs}(t) = r_{loss}^{vs} \cdot E^{vs}(t). \quad (6)$$

Since both, the additional heat losses $\dot{Q}_{loss}^{vs}(t)$ and the storage level $E^{vs}(t)$, show an almost linear dependency on the temperature increase of the zone $\Delta T_{increased}^{Zone}$, the loss rate is assumed to be constant. It can be determined from the ratio between the maximum additional heat loss of the building with a zone temperature of 22 °C ($\dot{Q}_{loss,22°C}^{vs}$) and the storage capacity $C_{nominal}^{vs}$:

$$r_{loss}^{vs} = \frac{\dot{Q}_{loss}^{vs}(t)}{E^{vs}(t)} = \frac{\dot{Q}_{loss,22°C}^{vs}}{C_{nominal}^{vs}}. \quad (7)$$

The storage capacity is set to correspond to the amount of heat that can be stored inside the building and utilized at later times. It is therefore defined as the total heat demand decrease during the discharging event after the system is fully charged and the zone temperature is at its upper limit:

$$C_{nominal}^{vs} = \int_{I_{charged}}^{I_{discharged}} \left(\dot{Q}_{demand,ref}^{building}(t) - \dot{Q}_{in,decreased}^{building}(t)\right) dt. \quad (8)$$

While the heat flow $\dot{Q}_{demand,ref}^{building}(t)$ corresponds to heat demand that is necessary to keep the zone temperature at its lower limit in a static environment, $\dot{Q}_{in,decreased}^{building}(t)$ describes the heat demand that is necessary after the system is fully charged and has reached an equilibrium with a zone temperature at the upper limit. However, not only the storage capacity of buildings varies significantly with the year of construction and the level of insulation, but also the maximum heat flow that can additionally be emitted into the building during the charging process $\dot{Q}_{charging}^{vs}$ and the maximum heating power that can be used again at the discharging process $\dot{Q}_{discharging}^{vs}$ differ depending on the building. During the charging process, a high inflow rate can only be maintained for a short period of time, otherwise the energy cannot be transported into the deeper parts of the building and the zone temperature will exceed its limit. Therefore, a maximum heat input rate needs to be set for the internal storage component as well as a maximum heat output rate.

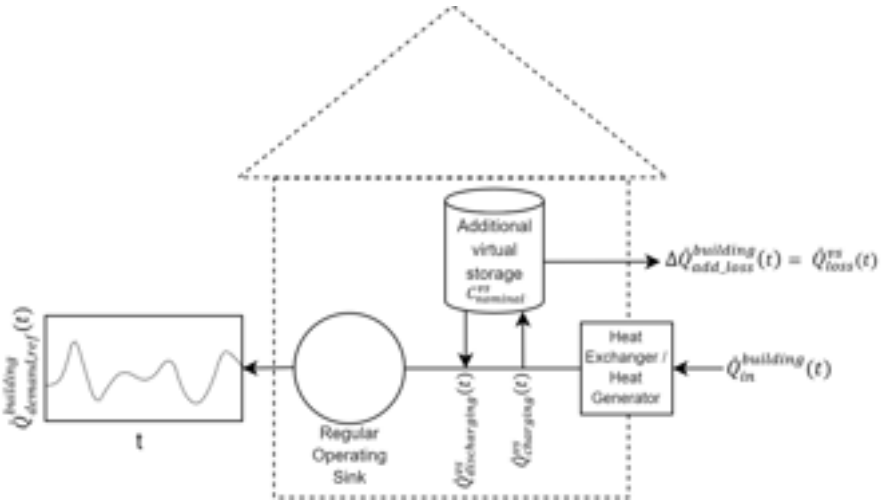

Figure 1. Approach to model the Buildings Demand and Flexibility Characteristics in the Energy System Optimization Framework.

2.4. Quantification of thermal storage characteristics

For the quantification of the storage characteristics of the buildings, building simulations are performed, in which the buildings are exposed to a lift in the indoor temperature setpoint. In this simulation, the ideal heat demand, required to maintain the zone temperature, is determined. Internal solar gains and internal heat gains are neglected in the static test environment, as for the quantification of the additional storage properties it is assumed that their influence on all zone temperature setpoints is equally effective. After an initialization period, to balance all heat transfer mechanisms, the zone temperature setpoint is lifted by a defined maximum temperature lift of 2 K from 20 °C to 22 °C. For another period, the required heat demand is calculated that keeps the zone temperature at the exact defined setpoint. The resulting demand profile defines the maximum heat input that can be emitted into the zone during an active demand response event, without exceeding the indoor temperature limit. Once the system is balanced again, the zone temperature setpoint is reset to 20°C and the reduced heat demand is calculated.

To parameterize the linear storage models of the buildings for the energy system optimization model, the additional storage capacity and the limits on the heating power must be set to constant values. Therefore, seven sets of storage parameters are determined from the simulation. Each set consists of the nominal storage capacity $C_{nominal}^{vs}$, the maximum charging heating power $\dot{Q}_{charging,max}^{vs}$, the maximum discharging heating power $\dot{Q}_{discharging,max}^{vs}$ and the heat loss rate. The sets are selected by varying the relation between the nominal storage capacity and the maximum charging heating power. The resulting relation describes the power shift capability t_δ, the duration in which the buildings can either be heated with the additional maximum charging power $\dot{Q}_{charging,max}^{vs}$ or the heat stored inside the building can be utilized again with the maximum discharging power $\dot{Q}_{discharging,max}^{vs}$, without exceeding the indoor temperature limits. In a linear building model, high power shift capabilities t_δ result in longer charging durations with lower maximum heating powers $\dot{Q}_{charging,max}^{vs}$, whereas low power shift capabilities result in the opposite.

If the power shift capability is fixed and the nominal storage capacity in this work is defined as the usable energy stored inside a building, the capacity can be determined by the product of the maximum discharging heating power $\dot{Q}_{discharging,max}^{vs}$ and the power shift capability t_δ:

$$C_{nominal}^{vs} = \dot{Q}_{discharging,max}^{vs} \cdot t_\delta. \quad (9)$$

For each set of parameters, a separate storage model is set up and used in the energy system optimization. This results in seven different flexible building models that are investigated in the following, representing different characteristics and utilization possibilities of the buildings. The best modelling approaches depend on the exact building type, its insulation, its storage properties and the exact application and are therefore analysed in an energy system optimization model.

2.5. Energy system optimization model

To determine optimal flexibility possibilities, the building characteristics, corresponding to the heating demands and the storage potentials, are integrated in the energy system optimization framework oemof [23]. The objective function is composed of the discounted investment costs of the heat generation plants c_{inv}^{hg} and the electrical energy purchases as shown in equations (10). The main additional constraints are stated in equations (11) - (13). An air source heat pump is selected as the heat generator using a variable coefficient of performance $COP^{hp}(t)$ depending on the outdoor temperature. The coefficient of performance is calculated using the correlations from [30]. The 2020 Day Ahead market prices are used as variable costs for electricity

$c_{el}(t)$. Further constant electricity levies, taxes and duties are neglected. The model optimizes the utilization of the buildings $\dot{Q}^{vs}_{charging/discharging}(t)$, the operation of the heat pump $\dot{Q}^{hp}_{out}(t)$ and the nominal heating power of the heat pump $\dot{Q}^{hp}_{nom}$ to minimize the costs for electricity C_{el} and the investment costs for the heat pump C^{hp}_{inv}:

$$\underset{\dot{Q}^{vs}_{discharging},\dot{Q}^{vs}_{charging},\dot{Q}^{hp}_{out},\dot{Q}^{hp}_{nom}}{\text{minimize}} \quad C_{total} = C_{el} + C^{hp}_{inv} = \sum_{t=0}^{8760} c_{el}(t) \cdot \frac{\dot{Q}^{hp}_{out}(t)}{COP^{hp}(t)} + c^{hp}_{inv} \cdot \dot{Q}^{hp}_{nom} \tag{10}$$

$$s.t. \quad \dot{Q}^{hp}_{out}(t) = \dot{Q}^{building}_{demand,ref}(t) - \dot{Q}^{vs}_{discharging}(t) + \dot{Q}^{vs}_{charging}(t) \tag{11}$$

$$E^{vs}(t) = E^{vs}(t-1) \cdot \left(1 - r^{vs}_{loss}(t)\right) - \dot{Q}^{vs}_{discharging}(t) + \dot{Q}^{vs}_{charging}(t) \tag{12}$$

$$\dot{Q}^{vs}_{discharging}(t) \geq 0 \text{ and } \dot{Q}^{vs}_{charging}(t) \geq 0 \text{ and } \dot{Q}^{hp}_{out}(t) \geq 0 \text{ and } \dot{Q}^{hp}_{nom} \geq 0. \tag{13}$$

The optimization is performed over a period of one year with time steps of one hour. First, for each building type and each state of refurbishment, a single optimization is performed to dimension the heat pump. Then, for each building the operation is optimized without including the investment costs for the heat generator. The results are used to calculate the annual costs reductions for electricity, when the flexibility is utilized, compared to the electricity costs of the same building without a flexible operation. Furthermore, an efficiency for the utilization of the virtual storage $C^{vs}_{nominal}$ is calculated that is based on equation (2). It is defined by the ratio between the total usable heat $\dot{Q}^{vs}_{discharging}$ and the heat that is additionally induced into the building $\dot{Q}^{vs}_{charging}$:

$$\eta_e = \frac{\int_0^{8760} \dot{Q}^{vs}_{discharging}(t)dt}{\int_0^{8760} \dot{Q}^{vs}_{charging}(t)dt}. \tag{14}$$

3. Results

In this section, the results of the individual building simulations and optimizations are introduced and the resulting flexibility indicators are presented. First, the building heating demands are presented under normal conditions without the utilization of their flexibilities. Afterwards, the results of the storage quantification procedure are displayed. Then, for all selected buildings and all storage model approaches the resulting nominal storage capacities, the maximum charging and discharging powers and the power shift capabilities are summarized. Finally, the flexibility efficiencies and the annual electricity cost savings are presented for all individual buildings.

3.1. Building heating demands

Figure 2 shows the heating demand time series $\dot{Q}^{building}_{demand,ref}(t)$ for the reference building in three different states of refurbishment under standard conditions and for a fixed indoor zone temperature. The influence of the insulation is shown in the reduction of the total heat demand as well as the reduced peaks.

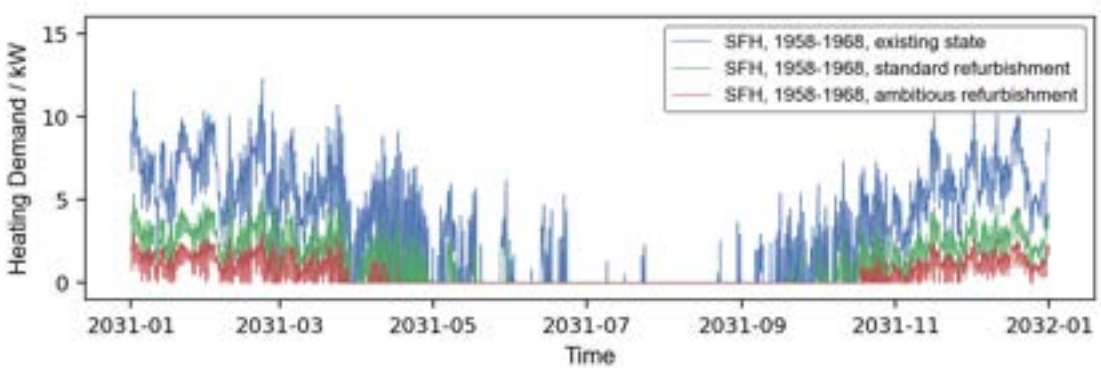

Figure 2. Heating demand time series for the reference single-family house built between 1958 and 1968 in three states of refurbishment, using weather data friom a test reference year from [29].

3.2. Quantification of individual building storage characteristics

Table 1 presents the results of the building simulations in the test environment. With a constant zone temperature of 20° C, each building balances at an individual constant heat demand $\dot{Q}^{building}_{const,20°C}$. When the zone temperature setpoint is raised from 20 °C to 22 °C, all buildings show an increase in the heat demand, that is required to meet the increased zone temperature setpoint. After reaching a maximum value of $\dot{Q}^{building}_{charge,max}$ instantly after the raise of the setpoint temperature, the demand decreases and diverges to a constant value at a zone temperature of 22 °C $\dot{Q}^{building}_{const,22°C} > \dot{Q}^{building}_{const,20°C}$. The profile describes the ideal heat input, that would keep the zone temperature at the upper value of 22 °C. The difference between the upper and lower constant

heat demand $\Delta\dot{Q}_{22°C-20°C}^{building}$ describes the additional heat losses of the building, due to the increased zone temperature. The difference in the heating demand $\Delta\dot{Q}_{22°C-20°C}^{building}$ is nearly constant and almost independent of the ambient temperature, since it only describes the additional losses compared to the heating demand under normal conditions. When the building is in balance again, the zone temperature setpoint is set back to 20 °C and the heat demand decreases in analogy to the lift of the zone temperature setpoint.

Table 1. Overview of the heating power demands in the static test environment of the selected single-family buildings with a net floor area of 160 m² and in dependence of the additional storage model approach.

Building description			Heating power demands / kW				
Building Type	Age class	State of refurbishment	$\dot{Q}_{const,20°C}^{building}$	$\dot{Q}_{const,22°C}^{building}$	$\Delta\dot{Q}_{22°C-20°C}^{building}$	$\dot{Q}_{charge,max}^{building}$	$\dot{Q}_{discharge,max}^{building}$
SFH	1919-1948	Existing state	22.41	24.71	2.30	29.84	17.20
		Standard	7.45	8.32	0.87	14.58	0.0
		Ambitious	4.07	4.61	0.54	10.99	0.0
	1958-1968	Existing state	15.81	17.48	1.67	23.08	10.20
		Standard	6.98	7.81	0.83	14.04	0.0
		Ambitious	3.85	4.38	0.53	10.74	0.0
	2010-2015	Existing state	5.58	6.27	0.69	12.53	0.0
		Standard	4.93	5.57	0.64	11.88	0.0
		Ambitious	3.21	3.68	0.47	10.04	0.0

3.3. Quantification of capacities, maximum charging and discharging powers and power shift capabilities

The results are used to determine the storage nominal capacity $C_{nominal}^{vs}$, the loss rate r_{loss}^{vs} and the maximum additional charging and discharging powers $\dot{Q}_{charging,max}^{vs}$ and $\dot{Q}_{discharging,max}^{vs}$. All parameters are calculated depending on the power shift capability t_δ, as described earlier. The results define the storage properties of the flexible building models that can be integrated in the energy system optimization. Table 2 presents the nominal virtual storage capacities $C_{nominal}^{vs}$ for all buildings and the storage model approaches.

Table **3** shows the corresponding maximum charging and discharging heating powers. Poorly-insulated buildings show their highest usable storage capacity at low power shift capabilities. The SFH built between 1919 and 1948 in an existing state of renovation reaches a nominal storage capacity of 6.58 kWh and a maximum charging power of about 1.28 kW. On the other hand, well-insulated buildings can utilize more capacity when they are charged over a longer period. The building built between 2010 and 2015 with ambitious refurbishments shows the maximum usable storage capacity at a power shift capability of 8 hours and a maximum charging power of 0.91 kW. Each building shows an increase in the utilizable capacity when the state of renovations increases. In the same time, the loss rate decreases due the better insulation of the building envelope.

3.4. Energy system optimization results

The potential of utilizing the heating flexibility is analysed in the energy system optimization model for all building types, using the different sets of parameters for the additional storage component. Figure 3 shows the difference between the optimized heat input and the heat demand without utilizing the flexibility potentials of a single-family house built between 1958 and 1968 in a standard state of renovation. While the green areas correspond to the amount of heat that is additionally emitted into the building compared to the normal operation, the blue areas illustrate the optimized decrease of the heat input. The storage component is parameterized with a nominal storage capacity of 8.78 kWh, a maximum charging power of 2.13 kW, a maximum discharging power of 2.22 kW, and a power shift capability of 4 hours. The optimized heat input is the result of the energy system optimization, which minimizes electricity import costs and leads to fluctuations in the actual zone temperature. It is shown, that the optimized heat input deviates from the original demand during a typical week in the heating period. To validate the modelling approach and the optimized building operation, the optimized heat input is integrated into the building simulation model according to the DIN EN ISO 52016. The resulting zone temperatures from the building simulation are also shown in Figure 3. The temperatures vary between 19.7 °C and 21.75 °C. Figure 4 shows the optimized heat input and the resulting indoor temperature profile in the same week for the same building but without any renovation measures. The amount of energy that can be stored inside the buildings is less, due to higher losses through the building envelope. Still, a few hours during the week can be used to take advantage of a low electricity prices. The indoor room temperatures vary between 19.9 °C and 21.4 °C during the week. The optimal energy storage duration is also less due to the higher loss rate. On the other hand, a single-family house built between 2010 and 2015 in an ambitious state of refurbishment shows a higher potential for electricity cost savings as shown in Figure 5.

Table 2. Overview of the resulting nominal storage capacities of the selected single-family buildings with a net floor area of 160 m² and in dependence of the power shift capability of the additional storage model.

Building description			Nominal storage capacity $C^{vs}_{nominal}$ / kWh						
Building Type	Age class	State of refurbishment	Power shift capability t_δ						
			2 h	3 h	4 h	5 h	6 h	8 h	12 h
SFH	1919-1948	Existing state	5.54	6.38	6.58	6.41	6.05	5.14	3.59
		Standard	7.01	8.3	8.78	8.75	8.42	7.32	4.98
		Ambitious	4.97	7.45	9.93	12.41	11.65	9.99	6.55
	1958-1968	Existing state	6.04	7.05	7.36	7.25	6.92	6.01	4.37
		Standard	7.09	8.39	8.87	8.84	8.5	7.39	5.02
		Ambitious	4.55	6.83	9.11	11.39	13.66	10.7	6.97
	2010-2015	Existing state	6.64	9.96	9.48	9.43	9.04	7.81	5.24
		Standard	5.88	8.82	10.46	10.39	9.95	8.59	5.74
		Ambitious	3.62	5.43	7.25	9.06	10.87	14.45	9.22

Table 3. Overview of the resulting maximum additional charging/discharging heat flows of the selected single-family buildings with a net floor area of 160 m² and in dependence of the power shift capability of the additional storage model.

Building description			Additional max charging/discharging power $\dot{Q}^{vs}_{charge/discharge,max}$/kW						
Building Type	Age class	State of refurbishment	Power shift capability t_δ						
			2 h	3 h	4 h	5 h	6 h	8 h	12 h
SFH	1919-1948	Existing state	2.77	2.13	1.64	1.28	1.01	0.64	0.3
			2.77	2.13	1.64	1.28	1.01	0.64	0.3
		Standard	3.43	2.71	2.15	1.72	1.38	0.9	0.41
			3.51	2.77	2.2	1.75	1.4	0.92	0.41
		Ambitious	3.47	2.75	2.19	1.75	1.41	0.92	0.47
			2.48	2.48	2.48	2.48	1.94	1.25	0.55
	1958-1968	Existing state	3.02	2.35	1.84	1.45	1.15	0.75	0.36
			3.02	2.35	1.84	1.45	1.15	0.75	0.36
		Standard	3.4	2.68	2.13	1.7	1.37	0.89	0.41
			3.55	2.8	2.22	1.77	1.42	0.92	0.42
		Ambitious	3.45	2.74	2.18	1.74	1.4	0.92	0.41
			2.28	2.28	2.28	2.28	2.28	1.34	0.58
	2010-2015	Existing state	3.39	2.68	2.13	1.7	1.36	0.89	0.4
			3.32	3.32	2.37	1.86	1.51	0.98	0.44
		Standard	3.42	2.71	2.15	1.72	1.38	0.9	0.41
			2.94	2.94	2.51	2.1	1.66	1.07	0.48
		Ambitious	3.44	2.72	2.17	1.74	1.39	0.91	0.42
			1.81	1.81	1.81	1.81	1.81	1.81	0.77

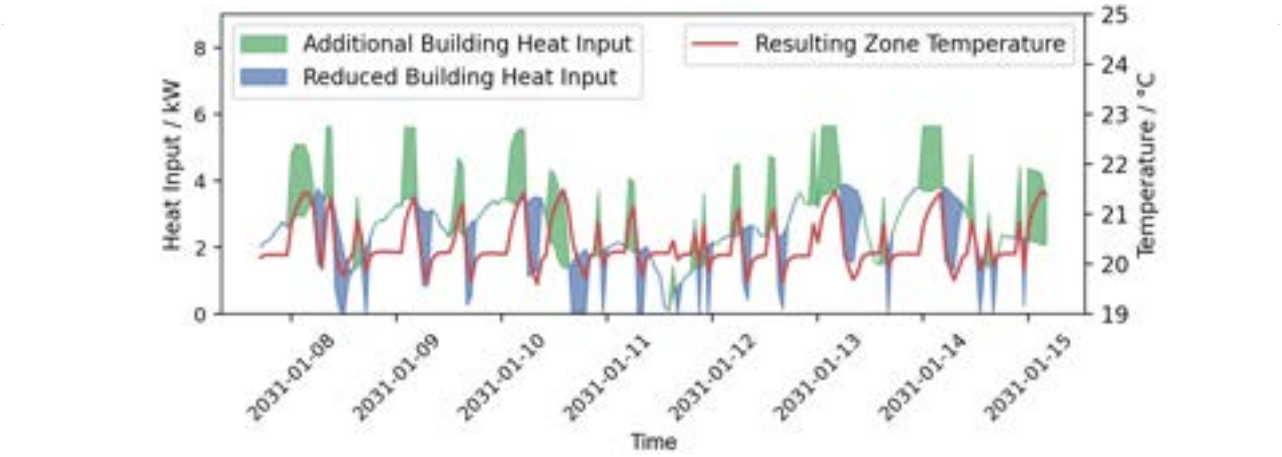

Figure 3. Optimized building heat input and resulting zone temperature in comparison with the heating demand at a constant zone temperature of 20 °C of a single-family household built between 1958 and 1968 in a standard state of renovation. The storage component of the building model is parameterized with a charging duration of 4 hours at full charging power.

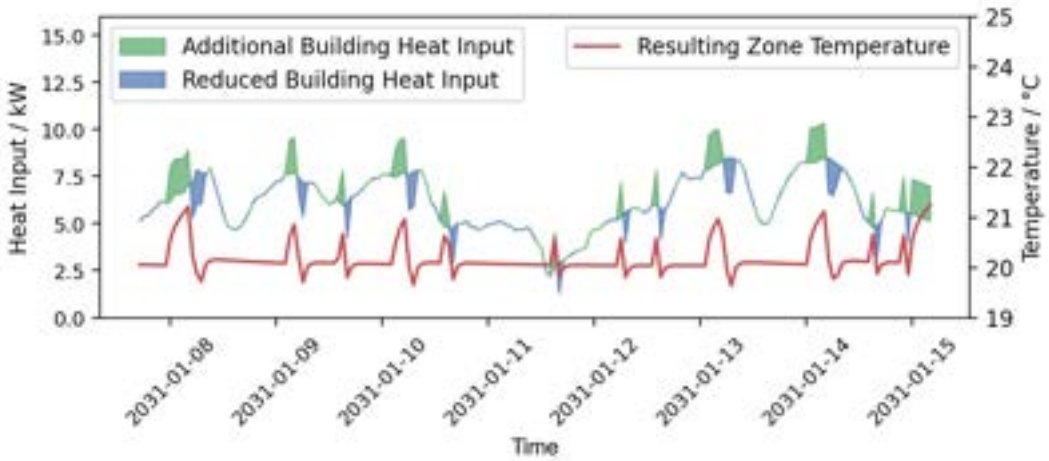

Figure 4. Optimized building heat input and resulting zone temperatures in comparison with the heating demand at a constant zone temperature of 20 °C of a single-family household built between 1958 and 1968 in the original state of renovation. The storage component of the building model is parameterized with a charging duration of 4 hours at full charging power.

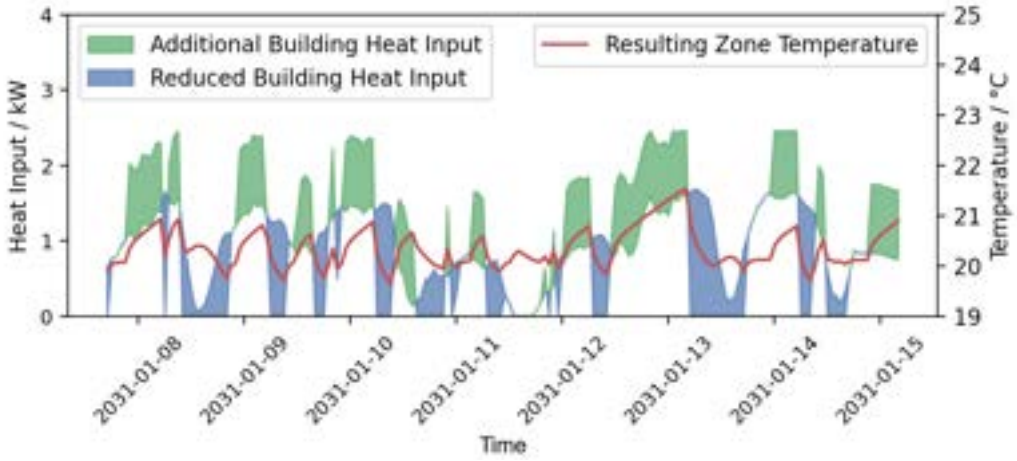

Figure 5. Optimized building heat input and resulting zone temperatures in comparison with the heating demand at a constant zone temperature of 20 °C of a single-family household built between 2010 and 2015 in an ambitious state of renovation. The storage component of the building model is parameterized with a charging duration of 8 hours at full charging power.

3.5. Flexibility quantification of individual buildings

The utilization of the flexibility potentials in the operation of the investigated buildings varies significantly with the building age class and the state of refurbishment. To quantify the flexibility potentials, the flexibility efficiencies and the annual electricity cost savings are calculated for all demand response events during the year. The results are presented in Table 4 and Table 5. The highest annual electricity cost savings of 131.45 € can be reached by the well-insulated building constructed between 2010 and 2015 in its original state, which corresponds to about 12.5% of its original annual electricity costs without utilizing the thermal flexibility. In general, most fairly well-insulated buildings show relatively high saving potentials. It is noteworthy, that the very well insulated buildings have less total electricity cost savings than the worse insulated buildings of the same class, due to the decrease in the total energy demand. The relative annual savings, compared to the costs for electricity without utilizing the thermal flexibility, increase with better insulation for all buildings. The highest utilization efficiencies of the virtual storage are reached by the buildings built between 1919 and 1948 and the building built between 1958 and 1968, both in an ambitious state of refurbishment. In the chosen environment, most buildings show the best efficiency with a power shift capability of 4 hours. Nevertheless, buildings with well-insulated envelopes show an optimal modelling approach using a power shift capability of 6 or 8 hours. Therefore, poorly-insulated buildings with high heat loss rates show higher potentials for short-term energy storage use while well-insulated buildings display higher potentials for longer energy storage durations.

Table 4. Overview of the annual electricity cost savings from the energy system optimization of a SFH with a net floor area of 160 m² and in dependence of the power shift capability of the additional storage model.

Building description			Annual electricity cost savings						
Building Type	Age class	State of refurbishment	Power shift capability t_δ						
			2 h	3 h	4 h	5 h	6 h	8 h	12 h
SFH	1919-1948	Existing state	49.94 € 0.90%	52.50 € 1.00%	45.98 € 0.80%	36.37 € 0.70%	27.36 € 0.50%	15.52 € 0.30%	5.97 € 0.01%
		Standard	102.35 € 6.60%	116.30 € 7.50%	111.75 € 7.20%	98.21 € 6.30%	81.68 € 5.30%	52.14 € 3.40%	18.41 € 1.20%
		Ambitious	61.33 € 9.20%	87.75 € 13.20%	105.41 € 15.90%	114.65 € 17.30%	102.37 € 15.50%	73.17 € 11.00%	29.02 € 4.40%
	1958-1968	Existing state	67.41 € 1.80%	74.66 € 2.00%	68.28 € 1.90%	56.70 € 1.60%	44.97 € 1.20%	26.08 € 0.70%	9.67 € 0.30%
		Standard	102.38 € 7.50%	116.35 € 8.60%	112.46 € 8.30%	99.45 € 7.30%	83.25 € 6.10%	53.52 € 3.90%	19.34 € 1.40%
		Ambitious	54.54 € 9.30%	78.27 € 13.40%	94.50 € 16.20%	103.83 € 17.80%	106.35 € 18.20%	75.41 € 12.90%	30.85 € 5.30%
	2010-2015	Existing state	93.78 € 8.90%	131.45 € 12.50%	119.76 € 11.40%	108.28 € 10.30%	92.30 € 8.80%	60.69 € 5.80%	22.38 € 2.10%
		Standard	79.94 € 8.90%	113.40 € 12.70%	123.87 € 13.90%	114.50 € 12.80%	99.46 € 11.10%	67.23 € 7.50%	25.57 € 2.90%
		Ambitious	40.39 € 9.10%	58.60 € 13.20%	72.14 € 16.30%	80.89 € 18.20%	84.23 € 19.10%	82.23 € 18.50%	38.71 € 8.70%

Table 5. Overview of the demand response efficiencies from the energy system optimization of a SFH with a net floor area of 160 m² and in dependence of the power shift capability of the additional storage model.

Building description			Utilization efficiency of virtual storage η_e / -						
Building Type	Age class	State of refurbishment	Power shift capability t_δ						
			2 h	3 h	4 h	5 h	6 h	8 h	12 h
SFH	1919-1948	Existing state	0.4931	0.486	0.4481	0.4128	0.391	0.32	0.1925
		Standard	0.7592	0.7631	0.753	0.7395	0.7124	0.6738	0.5706
		Ambitious	0.7268	0.7628	0.7758	0.7861	0.7806	0.7609	0.6927
	1958-1968	Existing state	0.6382	0.6255	0.6034	0.5738	0.5384	0.4906	0.3788
		Standard	0.7644	0.7709	0.7644	0.751	0.7329	0.69	0.5896
		Ambitious	0.7177	0.752	0.7658	0.777	0.7837	0.7642	0.7077
	2010-2015	Existing state	0.7607	0.7885	0.7815	0.7737	0.7622	0.7264	0.6372
		Standard	0.7491	0.7782	0.7879	0.7834	0.7762	0.7453	0.6711
		Ambitious	0.6942	0.7282	0.7458	0.7549	0.763	0.7729	0.7513

4. Discussion

In the present work, a modelling approach considering the thermal flexibility of buildings is presented and the flexibility potentials of a selection of representative buildings is quantified. It is shown that the presented building model can be integrated in an energy system optimization framework, in order to help utilizing the flexibility potentials of the individual buildings as well as a building group, district or district heating network. The building model approach used to simulate the buildings takes into account the heat transfer and storage characteristics using five nodes for each opaque building element. However, this approach is still a simplification and the real heat transfer mechanisms may differ from the results in this work. The linear representation of the buildings storage characteristics in the energy system optimisation only accounts for parts of the real flexibility potential and a non-linear representation could lead to better performances of the buildings. In addition, more detailed analyses to quantify the storage parameters are necessary and broader test environments must be implemented to improve the robustness of the models. Nevertheless, the representation of a building using a generic sink and a generic storage component allows the integration in most optimization frameworks and the application in diverse planning processes of different stakeholders, while still allowing to take into account more detailed heating demand analyses. The approach is validated by integrating the optimized heat input in the building simulation model and testing the resulting room temperature to ensure that the specified limits are not exceeded. It is shown that utilizing thermal flexibilities can lead to annual cost reductions in the energy import of up to 130 € for a single-family house built between 2010 and 2015 with a net floor area of 160 m². For the application of the building models and the quantification of their

flexibility in a district energy system or district heating systems, the best performing flexible building models can be chosen and integrated in an optimization model. The best storage model approaches for optimizing the buildings operation depend on the building type and the state of refurbishment. While well-insulated buildings indicate a more economically efficient utilization with longer storage durations and lower charging and discharging heating powers, poorly and moderately insulated buildings show higher potentials in the short-term utilization of their flexibility. Therefore, different building types should also be utilized accordingly. A modern district with 100 buildings built between 2010 and 2015 in a standard state of refurbishment could lead to annual electricity cost reductions of up to 12 300 € if the flexibility potential is utilized. The available storage capacity for this district is up to 1 046 kWh and the possible power shift is 215 kW for the charging event and 251 kW for the discharging event. The annual electricity cost reductions linked to the renovation from the original state to the standard state of renovation without the exploitation of the flexibility are 15 552 €, without including taxes and other fees in the calculation. An exemplary district with 100 SFH, equally distributed in both non-refurbished and standard refurbished condition, can achieve annual electricity cost savings of up 9 550 €, when the flexibility is utilized and provide 772 kWh of virtual storage capacity and 250 kW or 224 kW of power shift during the charging or discharging event. If additional renewable energy from own generation plants, such as photovoltaic systems, can be integrated into the energy system, the savings from exploiting flexibility can be further improved. Investigating the impact of these systems will be part of future studies.

In addition to the findings off the present work, the consideration of thermal flexibilities in the energy system design optimization could lead to savings in the investment costs and identifying efficient and cost-effective operation strategies. The optimization of the energy system can take into account the availability of waste heat, the fluctuating efficiency of heat generation units and the conditions of available heat sources. Utilizing the thermal flexibility of buildings can therefore benefit the integration of local renewable energy sources like wind energy, solar power or waste heat, especially when exploited on a district level. However, since individual households do not have excess to the day-ahead electricity market, the buildings flexibility is most likely to be utilized on a district level or a district heating network. Therefore, new pricing-models for heat must be developed. Yet, in district energy systems and district heating networks, the drawback often lies in the metering devices or the operational control of the buildings. Hence, multi-family buildings might be more likely to be considered to provide flexibility, and therefore the quantification of flexibility should be extended to more building types.

5. Conclusion

The transformation of the heating sector in buildings will face the challenge of integrating fluctuating renewable energy sources to become sustainable. To adjust the heating demand to the volatile generation of renewable energies, it is necessary to use comprehensive methods and tools to quantify the flexibility of the buildings and to incorporate this potential into the diverse planning processes of integrated energy systems, particularly on a district level and for district heating networks. By characterizing the heat transfer dynamics of a selection of buildings with a simulation based on the DIN EN ISO 52016, a generic approach is used to model the building demands and flexibility properties in an energy system optimization framework. By following this procedure, building flexibility indicators can be quantified and appropriate utilization strategies can be identified for individual buildings, building groups, or districts in a variety of applications. Based on a variable day-ahead electricity price and a realistic heat pump coefficient of performance, it is shown how the flexibility of single-family houses can be exploited to reduce energy costs. Depending on the building type and the state of insulation, there are different opportunities for exploitation. When only linear modelling approaches are used, well-insulated buildings tend to be more cost-effective by gradually increasing the heating input and storing the energy for a longer period, while poorly insulated buildings tend to perform better with shorter storage durations and higher charging powers. Still, all investigated buildings show the possibility of cost reductions when utilized and can play an important role in an integrated energy system. Future research should expand the flexibility analysis to include a wider variety of building types and groups. Multi-family buildings, larger apartment blocks, and commercial buildings, in particular, may exhibit different energy flexibility potential and could also play distinct roles in integrating renewable energy into the energy system. Furthermore, energy storage capabilities of district heating networks could be assessed in a similar way and help finding operation strategies or identify optimal supply and return line temperature profiles. In addition to the building analysis, deeper understanding of the flexibility in the operation of the heat generation units and heating emitter systems is necessary. Utilizing flexibilities promises to play an important role in an integrated energy system, especially when exploited on a district level. Until now, the heat generation of large-scale heat pumps in district energy systems mostly covers the base load operation. Nevertheless, the flexible operation of heat generation plants is crucial to leverage variable electricity prices and cope with fluctuating renewable energy sources.

References

[1] Europäische Kommission. The European Green Deal.

[2] Arbeitsgemeinschaft Energiebilanzen e.V. Anwendungsbilanzen zur Energiebilanz Deutschland: Endenergieverbrauch nach Energieträgern und Anwendungszwecken; AGEB Anwendungsbilanzen: Arbeitsgemeinschaft Energiebilanzen e.V.; 2019.

[3] Umweltbundesamt: Umwelt Bundesamt. Energieverbrauch für fossile und erneuerbare Wärme. Available at: <https://www.umweltbundesamt.de/daten/energie/energieverbrauch-fuer-fossile-erneuerbare-waerme#warmeverbrauch-und-erzeugung-nach-sektoren> [accessed 01.04.2021]
[4] Bundesministerium für Wirtschaft und Energie. Energiedaten: Gesamtausgabe. Berlin; 2021.
[5] Sensfuß F, Lux B, Bernath C*, et al.* Langfristszenarien für die Transformation des Energiesystems in Deutschland 3. Kurzbericht: 3 Hauptszenarien. Karlsruhe: Fraunhofer ISI, Karlsruhe; 2021.
[6] Jensen SØ, Marszal-Pomianowska A, Lollini R*, et al.* IEA EBC Annex 67 Energy Flexible Buildings. Energy and Buildings 2017; 155: 25–34.
[7] Junker RG, Azar AG, Lopes RA*, et al.* Characterizing the energy flexibility of buildings and districts. Applied Energy 2018; 225: 175–82.
[8] Guelpa E, Verda V. Demand response and other demand side management techniques for district heating: A review. Energy 2021; 219: 119440.
[9] Kathirgamanathan A, Péan T, Zhang K*, et al.* Towards standardising market-independent indicators for quantifying energy flexibility in buildings. Energy and Buildings 2020; 220: 110027.
[10] Reynders G, Amaral Lopes R, Marszal-Pomianowska A, Aelenei D, Martins J, Saelens D. Energy flexible buildings: An evaluation of definitions and quantification methodologies applied to thermal storage. Energy and Buildings 2018; 166: 372–90.
[11] Reynders G, Diriken J, Saelens D. Generic characterization method for energy flexibility: Applied to structural thermal storage in residential buildings. Applied Energy 2017; 198: 192–202.
[12] Kun Zhang, Michaël Kummert, editors. Potential of building thermal mass for energy flexibility in residential buildings : a sensitivity analysis; 2018.
[13] Kathirgamanathan A, Murphy K, Rosa M de, Mangina E, Finn D, editors. Aggregation of Energy Flexibility of Commercial Buildings; 2018.
[14] Péan T, Torres B, Salom J, Ortiz J, editors. Representation of daily profiles of building energy flexibility; 2018.
[15] Vandermeulen A, Reynders G, van der Heijde B*, et al., editors.* Sources of Energy Flexibility in District Heating Networks: Building Thermal Inertia Versus Thermal Energy Storage in the Network Pipes; 2018.
[16] Protopapadaki C, Reynders G, Saelens D. Bottom-up modelling of the Belgian residential building stock: impact of building stock descriptions. Proceedings of the 9th International Conference on System Simulation in Buildings - SSB2014; 2014.
[17] Deutsches Institut für Normung e.V. DIN EN ISO 52016-1 Energetische Bewertung von Gebaeuden – Energiebedarf für Heizung und Kühlung, Innentemperaturen sowie fühlbare und latente Heizlasten – Teil 1: Berechnungsverfahren (ISO 52016-1:2017); 2018 2018.
[18] Le Dréau J, Heiselberg P. Energy flexibility of residential buildings using short term heat storage in the thermal mass. Energy 2016; 111: 991–1002.
[19] EnergyPlus Documentation - Input Output Reference; 2022 [accessed 20.12.2022] Available at: <https://energyplus.net/assets/nrel_custom/pdfs/pdfs_v22.2.0/InputOutputReference.pdf>.
[20] Yang X, Pan L, Guan W, Ma H, Zhang C. Heat flexibility evaluation and multi-objective optimized control of a low-energy building with district heating. Energy and Buildings 2022; 277: 112523.
[21] Gils HC. Balancing of intermittent renewable power generation by demand response and thermal energy storage 2015.
[22] Zerrahn A, Schill W-P. On the representation of demand-side management in power system models. Energy 2015; 84: 840–5.
[23] Krien U, Schönfeldt P, Launer J, Hilpert S, Kaldemeyer C, Pleßmann G. oemof.solph—A model generator for linear and mixed-integer linear optimisation of energy systems. Software Impacts 2020; 6: 100028.
[24] Kotzur L. Future grid load of the residential building sector. Dissertation.
[25] Schütz T, Schiffer L, Harb H, Fuchs M, Müller D. Optimal design of energy conversion units and envelopes for residential building retrofits using a comprehensive MILP model. Applied Energy 2017; 185: 1–15.
[26] Bacher P, Madsen H. Identifying suitable models for the heat dynamics of buildings. Energy and Buildings 2011; 43(7): 1511–22.
[27] IWU Institut Wohnen und Umwelt. TABULA Calculation Method: Energy Use for Heating and Domestic Hot Water; Reference Calculation and Adaptation to the Typical Level of Measured Consumption; 2013.
[28] Institut Wohnen und Umwelt. Deutsche Wohngebäudetypologie: Beispielhafte Maßnahmen zur Verbesserung der Energieeffizienz von typischen Wohngebäuden; 2. erw. Aufl. Darmstadt: IWU 2015.
[29] Deutscher Wetterdienst (DWD), Bundesamt für Bauwesen und Raumordnung (BBR). Ortsgenaue Testreferenzjahre von Deutschland für mittlere, extreme und zukünftige Witterungsverhältnisse; Handbuch; 2017.
[30] Jesper M, Schlosser F, Pag F, Walmsley TG, Schmitt B, Vajen K. Large-scale heat pumps: Uptake and performance modelling of market-available devices. Renewable and Sustainable Energy Reviews 2021; 137: 110646.

Sensitivity analysis of the Power Demand Uncertainties on the electrical power system optimization models

Sara Fakih[a], Mohamed Tahar Mabrouk[b], Mireille Batton-Hubert[c] and Bruno Lacarrière[d]

[a] IMT Atlantique, Nantes, France, s.fakih995@gmail.com, CA
[b] IMT Atlantique, Nantes, France, Mohamed-tahar.mabrouk@imt-atlantique.fr,
[c] Ecole des Mines de Saint-Etienne, Saint-Etienne, France, batton@emse.fr
[d] IMT Atlantique, Nantes, France, Bruno.lacarriere@imt-atlantique.fr

Abstract:
Accurate estimations of future energy consumption are crucial for decision-makers to better plan the future design and operation of production and distribution systems. The existence of uncertainties in the inputs of the planning process can affect the quality of the model's outcomes and potentially can lead to sub-optimal solutions. This work proposes an investigation of input uncertainties of an Electrical Power System Model (EPSM) based on dynamic linear optimal power flow. The considered model inputs are the electricity demand curves of the buses of the grid. A set of forecasted demand time series is used to generate a probability model of their variability at each time step of the period studied. This probabilistic model is applied to generate the uncertainty of the demand curves and the associated input macro indicators (IMI) which are used to define the experimental design of the sensitivity analysis. The results show that input uncertainties on the demand have significant effects on the results in terms of Levelized Cost of Energy (LCOE) and system design like the installed capacity of Wind Turbines (WT), extracted energy from Classic Generators (CGs), and Battery Energy Storage (BES) location and sizing. In addition, it is shown that the input demand uncertainties can affect the results on the distribution performance parameters like the level of saturation of the different grid branches.

Keywords:
Battery energy storage; Demand Uncertainties; Electrical Grid; Renewable energy sources; Sensitivity analysis.

1. Introduction

Load forecasting models are used to predict future demand behaviors to be used as input for optimal planning models. They rely on long-term expectations for the parameters influencing the load profile (e.g., temperatures, occupancy, behavior, etc.). Therefore, they are likely to give estimations of low accuracy [1]. This could affect the accuracy is the model's output. Thus, there is a need for robust and rigorous techniques that can provide quantifiable information about the impact of uncertainty on model outputs. Sensitivity Analysis (SA) technics incorporate a set of methods that aim to identify the most important input parameters driving the model output variability in addition to the non-influential parameters whose uncertainty can be safely ignored.

In the literature, sensitivity analysis in energy models considers different uncertain input parameters e.g., the intermittent renewable generation, final energy demand, primary energy prices, economic growth, etc. [2]. These uncertain parameters are generally associated with randomness and temporal variability [3]. However, uncertainty in demand estimation introduces additional complexity alongside energy planning scenarios, including Renewable Energy Sources (RES) and Battery Energy Storage (BES) sizing and placement. Under such conditions, it is crucial to understand how demand curves uncertainty affects the optimal design and to identify the most influential uncertain parameters [4].

For the SA of demand curves, two different approaches exist. The first one is the total demand uncertainty applied to the demand patterns directly measured or extracted from the load forecasting models. To assign uncertainty on energy demand profiles, the most commonly used approach is applying Probability Density Function PDF to each time step of the demand time series, like normal distribution [5], uniform distribution [6], etc. The second one is the model-based uncertainty in which the uncertainty is assigned to the input parameters of the load forecasting tool and is propagated to obtain a series of demand patterns. The model-based uncertainty approach is applied in the literature for different types of demand patterns. In Mavromatidis et al. [7], using a building performance simulation tool, the uncertainties are attributed to the building material properties, occupancy patterns, hot water services, ventilation, and climate parameters, etc. Probability distributions are attributed to these parameters (normal, triangular, etc.), and the distribution parameters are then estimated. Thousands of profiles are then extracted and represented in the form of probability distribution to sample them to generate random energy demand profiles for the following study steps. The same approach is applied for the load forecasting model called MOSAIC in [8] developed by the principal French DSO (Enedis [9]), where the input variables are classified into four types: quantitative continuous (local height, coefficient of

performance for heater, temperatures, etc.), qualitative binary (e.g., presence of air conditioner or not), quantitative discrete (e.g., number of occupants) and qualitative nominal (e.g., thermal performance level). The variability range of the parameters are defined, and probability density distributions are attributed to continuous variables. Multiple demand patterns are then extracted from MOSAIC.

Various methods of sensitivity analysis on energy models are performed in the literature while considering the energy demand uncertainty; a local sensitivity analysis is used to study the demand effect on life cycle cost and loss of power supply in Sadeghi et al.[10]. A two-stage elementary effect - variance based technique is developed by Mavromatidis et al. [4] to study the effect of energy demand on the total cost of the system. Many other sensitivity analysis models are developed in [11], [12], [13] and [14], etc. Basically, SA models are classified into three major groups : *1- screening models* that coarse sorting of the most influential inputs from a large number (e.g. Morris method [15]), *2-measure of importance* or quantitative sensitivity indices (e.g. linear regression [16]) and *3- deep exploration of model behavior* that measure the effects of inputs over their total range of variation (e.g., Metamodels-based SA [17]). The selection of the most appropriate method is based on the number of input parameters and the model's complexity.

This paper uses the total demand uncertainty characterization for the extracted curves using the probabilistic techniques presented in [18]. Then Input Macro Indicators IMI are defined to describe these demand curves. The electric demand curves are used as input for the energy planning model that aims to optimally size and place the RES and storage in the existing electrical distribution network. Different indicators are then defined to describe the resulted scenarios aiming to perform the sensitivity analysis. In the studied case, features are assigned to the input curves as macro-parameters indicators and their correlation to the output indicators is studied. Based on the size (the number of model simulations is about 10 times the number of input parameters) and type of the data set, the linear regression (Pearson) is selected for the sensitivity analysis.

2. Methodology

The methodology summarized in Figure 1 aims to investigate the uncertainties in the Electrical Power System Model (EPSM). The EPSM used is the Dynamic Linearized Optimal Power Flow (DLOPF) model detailed in [18]. The model inputs considered are the demand curves. The uncertainties and variability of the demand are first characterized at each time step according to probability models which are used to generate additional demand curves. This set of generated demand profiles are used as inputs of the EPSM on a predefined distribution network to create different planning scenarios. Besides the IMI describing the patterns, output indicators are then determined to help measuring the sensitivity of model's outputs to inputs uncertainties implied by the variability of the demand. Finally, the sensitivity analysis is implemented in order to identify the most effective correlations between the input and output parameters of the model.

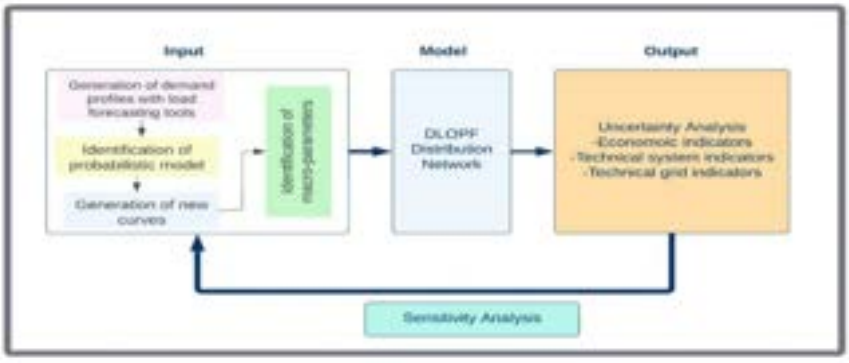

Figure 1. General workflow for uncertainty/sensitivity investigation in EPSM

2.1. Input Data

The electricity demand curves are the input data on which this uncertainty study is based. These curves are generated using a bottom-up load forecasting model called MOSAIC [19]. This tool is based on the characteristics of French loads built from a crossing of different databases: INSEE's residences database (French National Institute on Statistics and Economical Studies; French Distribution System Operators databases).

The total load curves by HTA/BT transformer are generated. For the studied area, MOSAIC simulations are repeated 25 times and therefore 25 curves per HTA/BT substation covering a whole year are obtained. The difference between curves is due to the attributed assumptions from the input data (building parameters,

weather data, etc.). These assumptions contain values and associated probability laws [20]. MOSAIC uses these values and makes random draws, according to the assumptions, to calculate a possible scenario.

The time-dependent uncertainties of the load curves are then characterized using the probability laws tests as explained in [18]. The Gamma law is proved to be the most appropriate law to describe these uncertainties. Then, based on the identified parameters describing the Gamma law at each time step, N=300 load curves are generated for each HTA/BT substation.

The demand curves are generated for one year. Hence, to reduce the simulation time, a clustering method is applied to choose 9 typical days (3 periods of 3 days) representing three different demand levels (high, medium, and low). The variation of the total demand over the 300 cases at each time-step (t) is shown in Figure 2.

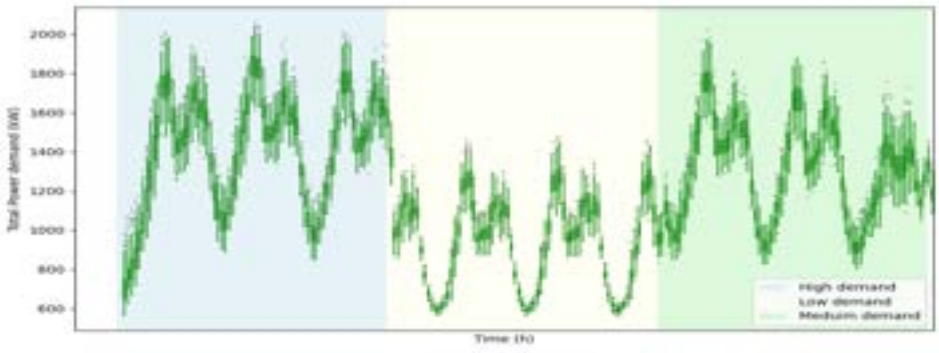

Figure 2. Ranges of variation of the generated energy demand curves

Several input macro indicators can be defined to describe load variation. The chosen parameters are detailed in the followings:

2.1.1.Peak demand values

The peak demand represents the higher demand value recorded in a time frame. The peak demands in each bus (i) are collected for the N_c cases (e) using the following equation (1) where the number of buses $\mathcal{N} = 14$, the time steps $\mathcal{T} = 216$, and the number of cases $N_c = 300$.

$$P_{i,e}^{max} = \max_{t} (P_{i,t,e}) \qquad i \in [1:\mathcal{N}] \quad t \in [1:\mathcal{T}] \quad e \in [1:N_c] \tag{1}$$

2.1.2.Standardized Variances

The variances ($Var_{i,e}$) in load demand curves designates the spread between demand values in each curve. More specifically, variance measures how far each value number in the curve is from the mean (average). The variances are calculated using Eq. (2)

$$Var_{i,e} = \frac{1}{\mathcal{T}} \sum_{t=1}^{\mathcal{T}} (P_{i,t,e} - \frac{\sum_{t=1}^{\mathcal{T}} P_{i,t,e}}{\mathcal{T}}) \tag{2}$$

2.1.3.Duration of maximum loads

The maximum demands are defined here as demands higher than 95% of the total peak demand. The number of hours during which these demands are encountered are defined as maximum durations Du_e.

2.1.4.Total energy demand variation

For that, three different parameters are defined summarizing the total demand in each clustered period (low, medium, and high).

These parameters are calculated using the following formulas Eq. (3)

$$E_e^{lev} = \sum_{t \in \Gamma_{lev}} \sum_{i=1}^{\mathcal{N}} P_{i,t,e} \tag{3}$$

Where $\boldsymbol{lev} \in \{\boldsymbol{Low}, \boldsymbol{Medium}, \boldsymbol{High}\}$ is the demand level and $\boldsymbol{\Gamma_{lev}}$ is the time period corresponding to the demand level $\boldsymbol{lev}$.

2.1.5. Simultaneity factor (Load coincidence)

The simultaneity factor represents how much consumers tend to consume simultaneously. The maximum demand for each bus may not occur at the same time. The ratio of the aggregated maximum demand of the whole network during a particular time to the sum of the maximum demand of individual consumers is called simultaneity factor eq. (4).

$$SF_e = \frac{P_e^{MAX}}{\sum_{i=1}^{Nbus} P_{i,e}^{max}} \tag{4}$$

Where P^{MAX} is the total load maximum value and P_i^{max} is the maximum value of bus i. SF_eranges between 0 and 1 if all peak demands occur at the same time.

2.2. DLOPF model used.

Performing uncertainty and sensitivity analysis requires many simulations (300 in our case). An electrical planning model is used. This DLOPF model takes as initial conditions the Photovoltaic (PV), Wind Turbines (WT), and BES available surfaces and possible locations. The main outputs are the optimal scenario for sizing and placement of PV, WT, and BES in addition to the network simulation with time series variables.

$$min\, F_{obj} = min \frac{\left(\Gamma_{op} + \Gamma_{o\&m}\right) + \Gamma'_{inv}}{\sum_{\boldsymbol{i}=1}^{\mathcal{N}} \sum_{t=1}^{\mathcal{T}} \frac{P_{i,t}^{l}}{(1+ra)^t}} \tag{5}$$

Such that

$$\Gamma'_{inv} = \mathcal{I}^{wt} + \mathcal{I}^{pv} + \mathcal{I}^{st} \tag{6}$$

$$\mathcal{I}^{st} = \sum_{s=1}^{\mathcal{N}^{st}} I^{st}.\boldsymbol{E_{max}^{st}} \tag{7}$$

$$\mathcal{I}^{pv} = \sum_{s=1}^{\mathcal{N}^{pv}} I^{pv}.\boldsymbol{A_s^{pv}} \tag{8}$$

$$\mathcal{I}^{wt} = \sum_{w=1}^{\mathcal{N}^{wt}} I^{wt}.\boldsymbol{R_w^{wt}} \tag{9}$$

$$\Gamma_{op} = \mathcal{C}^{cg} + \mathcal{C}^{vg} + \mathcal{C}^{wt} + \mathcal{C}^{pv} \tag{10}$$

$$\mathcal{C}^{cg} = \sum_{t=1}^{\mathcal{T}} \sum_{c=1}^{\mathcal{N}^{cg}} \frac{C^{cg,p}.\boldsymbol{P_{c,t}^{cg}}.\Delta t + C^{cg,q}.\boldsymbol{Q_{c,t}^{cg}}.\Delta t}{(1+ra)^t} \tag{11}$$

$$\mathcal{C}^{vg} = \sum_{t=1}^{\mathcal{T}} \sum_{i=1}^{\mathcal{N}^{vg}} \frac{(C^{vg,p}.\boldsymbol{P_{i,t}^{vg}}.\Delta t + C^{vg,q}.\boldsymbol{Q_{i,t}^{vg}}.\Delta t)}{(1+ra)^t} \tag{12}$$

$$\mathcal{C}^{wt} = \sum_{t=1}^{\mathcal{T}} \sum_{w=1}^{\mathcal{N}^{wt}} \frac{C^{wt}.\boldsymbol{P_{w,t}^{wt}}.\Delta t}{(1+ra)^t} \tag{13}$$

$$\mathcal{C}^{pv} = \sum_{t=1}^{\mathcal{T}} \sum_{s=1}^{\mathcal{N}^{pv}} \frac{C^{pv}.\boldsymbol{P}_{\boldsymbol{s,t}}^{\boldsymbol{pv}}.\Delta t}{(1+ra)^t} \quad (14)$$

$$\Gamma_{o\&m} = \frac{\sum_{i=1}^{\mathcal{T}}(O^{pv}.\boldsymbol{A}^{\boldsymbol{pv}} + O^{wt}.\boldsymbol{R}^{\boldsymbol{wt}} + O^{cg}.P^{cgT})}{(1+ra)^t} \quad (15)$$

The optimization model used aims to minimize the Levelized Cost of Energy (LCOE) of the system. The objective function is presented by (eq.(5)). It includes the total investment cost (Γ'_{inv}), production cost (Γ_{op}) and operation & maintenance cost ($\Gamma_{\mathrm{o\&m}}$). This sum is divided by the sum of demand ($\mathrm{P}_{\mathrm{i,t}}^{\mathrm{l}}$) (in all buses ($\mathcal{N}$)/ i: bus index $\epsilon\, \mathcal{N}$) for the defined period ($\mathcal{T}$) in years / t: time index $\epsilon\, \mathcal{T}$) over a function of the discount rate of the project (ra).

The total investment cost (Γ'_{inv}) presented by (eq. (6)) considers:

- The batteries investment cost ($\mathcal{I}^{st}$) in (eq. (7) where $\boldsymbol{E}_{\boldsymbol{max}}^{\boldsymbol{st}}$is the maximum energy and I^{ST} is the battery investment cost per unit of capacity.
- The PVs investment cost ($\mathcal{I}^{pv}$) in (eq. (8) where $\mathbf{A}^{\mathbf{pv}}$ is the installed area of PVs is an optimization and I^{pv} is the PV investment cost per unit of surface .
- The WTs investment cost ($\mathcal{I}^{wt}$) in (eq. (9) where $\mathbf{R}^{\mathbf{wt}}$ is the continuous design variable that defines the ratio of installed power capacity to a maximum installable capacity ($\mathbf{R}^{\mathbf{wt}^{\mathbf{max}}}$) of local wind energy and I^{wt} is WT the investment cost of $\mathbf{R}^{\mathbf{wt}^{\mathbf{max}}}$

The total actualized operational costs (Γ_{op}) is represented by Eq. (10). The $\mathcal{C}^{cg}$ is the actualized operational cost of the Classic Generators (CG)s and $\mathcal{C}^{vg}$ is the actualized operational cost of Virtual Generators[1] (VG)s. Solar and wind power operational costs ($\mathcal{C}^{wt}, \mathcal{C}^{pv}$) are supposed to have very low values since they are clean energy sources. The total operational cost for CGs ($\mathcal{C}^{cg}$) is given by eq.(11) where both the sum of active ($\boldsymbol{P}^{\boldsymbol{cg}}$) and reactive ($\boldsymbol{Q}^{\boldsymbol{cg}}$) produced power are multiplied by their corresponding costs ($\mathcal{C}^{cg,p}$ for active and $\mathcal{C}^{cg,q}$ for reactive). Like Eq.(11), Eq.(12) gives the virtual generation cost ($\mathcal{C}^{vg}$). In each bus, virtual generators have generation costs significantly higher than other generators (both $\mathcal{C}^{vg,p}$ and $\mathcal{C}^{vg,q}$). The total operational costs of WTs ($\mathcal{C}^{wt}$) and PVs ($\mathcal{C}^{pv}$) are represented respectively by Eq.(13) and Eq.(14). Γ_{op} is variable according to the energy consumed.

Actualized operation and maintenance cost $\Gamma_{o\&m}$ is given by Eq.(15). It is dependent on the sizing of WTs, PVs and the existing CGs. and their O&M costs (O^{wt}, O^{pv}) in addition to the existing CGs maintenance costs (O^{cg}) multiplied by the total installed power of CGs (P^{cgT}). This cost is a fixed cost for the year regardless of the amount of production. The other equations that form the EPSM model are the linearized power flow equations of the DLOPF. These equations are the same presented in [21] and [18].

3. Case study

A theoretical case study is selected. The chosen topology is a Medium-voltage rural distribution benchmark network shown in

Figure 3. The benchmarking network comprises two separate subnetworks supplied by classic generators located in buses 1 and 12. These subnetworks are connected by buses 8 and 14. In this case, WTs, PVs and BESs could be added to specified buses concerning available surfaces for PVs and the existing potential of WTs. BES systems could also be added within the limit of maximum allowed capacities. This information is detailed in Table 1 with the corresponding costs.

3.1. Output

For the uncertainty analysis step, 300 simulations of the EPSM are performed. Four different types of output indicators are studied:

- Technical indicators of energy production and storage technologies: energy extracted from CG – Installed PVs, WTs capacities – Total produced energy – Batteries capacities.
- Technical grid indicators: branches' saturation levels (Δ_{ij}) – Duration in which this percentage is less than 10% (D_{ij})

[1] [1]Virtual Generators are defined as producers supposed to be added to all the buses to guarantee a feasible solution

- Losses

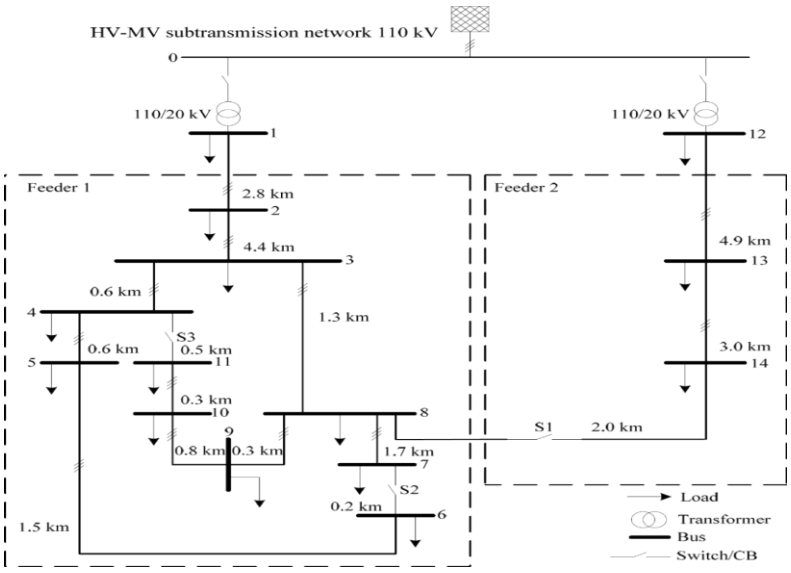

Figure 3: Medium voltage rural distribution benchmark network [22]

Table 1. Summary of buses specifications

Production type	Buses	Maximum capacity	Costs [23]		
			Production ($/MWh fuel)	Investment	O & M ($/MW/yr)
PV	3,4,7,11,13	$A^{pv^{max}} = 800\ \mathrm{m}^2$ $\mathrm{PV_t}$ (peak load) =205 W/m²	$\mathrm{C^{pv}} = 0$	J^{pv} =178 ($/m²)	$\mathrm{O^{pv}} = 8000$
WT	2,3,4,5,10,14	$R^{wt^{max}} = 10$ $\mathrm{WT_t}$ (peak load)=1000 KW	$\mathrm{C^{wt}} = 0$	$\mathrm{J^{wt}}$ = 997 000 $/MW	$\mathrm{O^{wt}} = 33000$
CG	1, 12	20 MW	$\mathrm{C^{cg,p}}, \mathrm{C^{cg,q}} =$ 36	0 (already installed)	$\mathrm{O^{cg}} = 10500$
VG	all buses	10000 KW	$\mathrm{C^{vg,p}}, \mathrm{C^{vg,q}} =$ 10^9	0	0
BES	2,3,4,5,7,9, 10,11,13,14	100 kWh	0	I^{ST}=350 $/kWh	0

3.1.1.Impact on the economic indicator: LCOE

The impact of load data uncertainty on the economic indicator is important since the objective function here is initially based on minimizing the LCOE. The violin plot of Figure 4 represents the shape of the LCOE results from the 300 cases generated above.

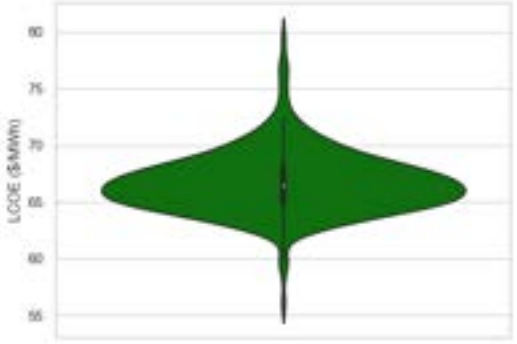

Figure 4. Violin plot for the variation of the levelized cost of energy in the different cases

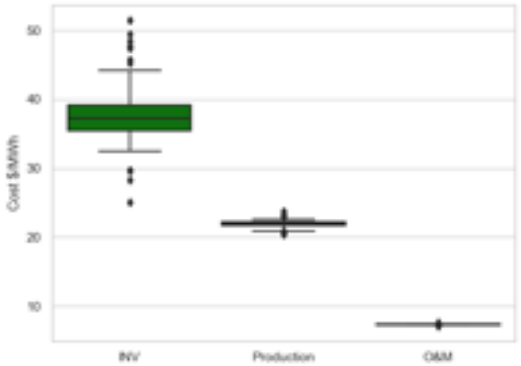

Figure 5. Cost details over the lifetime

The results are centered around the median value (white point) and are almost symmetrically distributed in within -15% and +20% of the variation around the median value. The LCOE analysis revealed that the randomness of the input variables significantly impacts the LCOE and results in a variation of 28 $/MWh which represents millions of dollars over the project lifespan.

The variation in the LCOE is a combination of variations between the investment, production, and O&M costs. These variations are presented in Figure 5. The LCOE variation is mainly due to the investment cost (between 25$/MWh and 51$/MWh) since this includes the investment in WTs, PVs, and batteries. This LCOE is affected to a minor extent by the production cost which is based on the CG production. The O&M cost variation is insignificant compared to others and has a negligible effect on the LCOE.

3.1.2. Technical system indicators

The impact of uncertainties affects the technical indicators of energy production and storage technologies differently. These indicators include the extracted energy from the existing CGs, the installation surface of PVs, the fraction of installed WTs, and the total energy produced in addition to the total installed capacity of the batteries. The results are summarized in the parallel coordinate plots of Figure 6.

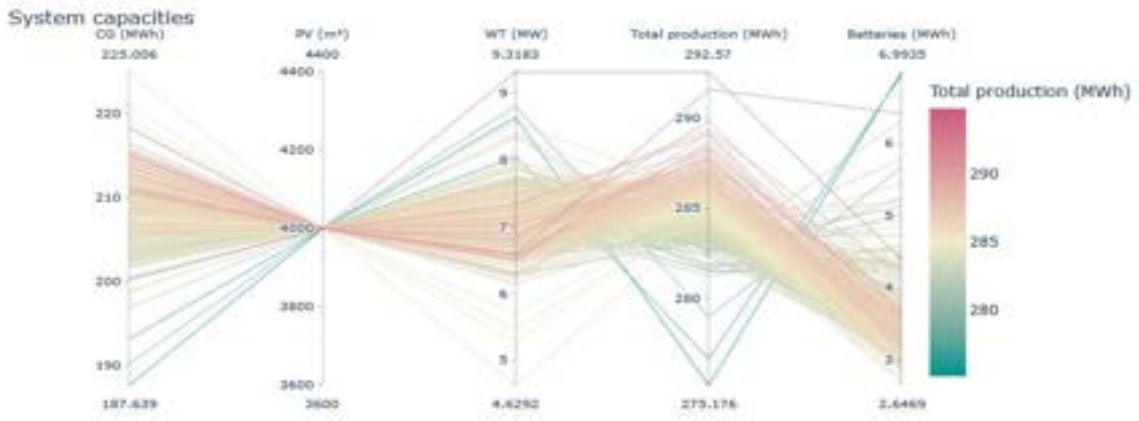

Figure 6. Parallel coordinate plots for the different cases results

The quality of the input data has no effect on the investment cost of the PVs. The installed area is constant at the maximum level for all cases (4000 m²), which means that the model always prioritizes the investment in the cheapest production technology compared to the other sources (CGs and WTs) so that the variations in investment and production amounts will be concentrated in the CGs and WTs. Moreover, substantial variations (16.6%) are shown in the energy extracted from the classic generators (up to 40 MWh) as well as in the installation of WTs (50.2%). The variation in the total production (5.94%) is less important than in the WT and CG since the sum contains both, and this balances the total variation because tracking the extreme points, we notice a maximum energy extracted from CG (225 MWh) that corresponds to a minimum installed WT power (4.6 MW) and a minimum CG (187.6 MWh) corresponds to a significant WT (8.6 MW). The variation in the WTs and PVs that produce intermittent energy induces the variation in the dimensioning of the batteries that aim to compensate for this intermittence. As long as the installed power of PV does not vary, the installed power of WT causes this important variation in the battery installation (62.13%).

3.1.3. Technical grid indicators

To focus on the network itself, technical indicators are used related to the grids, especially the amount of power flowing in the branches. The first indicator is the percentage of saturation of the branches (Δ_{ij}) and the second is the time (D_{ij}) during which the saturation is low and does not exceed 10%.

- The percentage of saturation (Δ_{ij}) in apparent power is calculated using eq.(16)

$$\Delta_{ij}\ (\%) = \frac{S_{ij}}{S_{ij}^{max}} \times 100 \tag{16}$$

The power flow behavior is depicted in **Erreur ! Source du renvoi introuvable.Erreur ! Source du renvoi in trouvable.** for four different branches of one of the 300 simulated cases during the three typical days. In the high demand period, some branches are almost fully saturated, like branch 3-4; this branch also reaches a complete saturation in specific hours in medium (72h to 75h) and low (190h-195h) demand periods. Since this branch transmits power to several other branches, it affects the power delivery to the succeeding buses during these saturation periods, and therefore, it may influence the installation of generation sources to compensate for the lack of power delivery.

Other branches do not reach a saturation point that exceeds 60% of their capacity (e.g., branches 11-4). The maximum Δ_{ij} reached are identified for each branch in the 300 cases. The boxplots of Figure 7 show the repartition of the 300 values attributed to each branch. The uncertainties in input demand do not affect the maximum saturations of the first four branches. The first 3 branches are saturated most of the time because they are responsible for the delivery of energy to other branches. Full saturation is noticed in branches 6-7 also, and it comes back to the non-possibility of installation of RES and BES on bus 6. However, the maximum saturation rates achieved in the other branches vary by ranges of about 5% (12-13, 13-14, etc.).

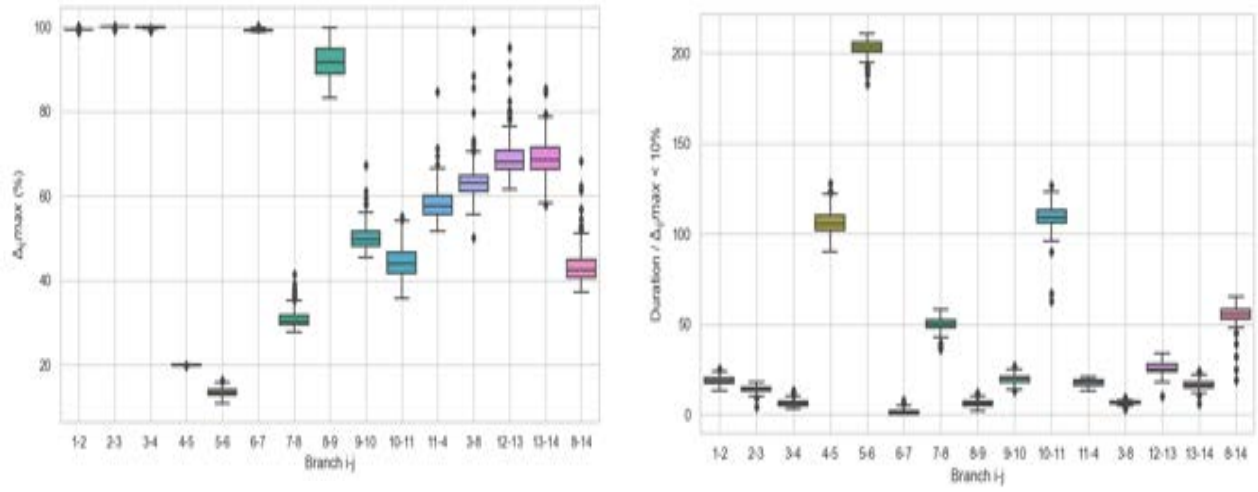

Figure 7. Boxplots of the apparent power saturations (a) and the duration of low saturation (less than 10 %) (b) in each branch

- The duration with very low branch saturation is expressed in eq.(17)

$$D_{ij} = duration\ of\ \ \Delta_{ij} < 10\ \% \qquad (17)$$

The time during which the branches are within 10% of their saturations over the defined duration is considered as a technical indicator for the grid since it concerns the grid's branches dimensioning and their maximum apparent power. The results of the 300 cases are presented in the boxplots of Erreur ! Source du renvoi i ntrouvable. for each branch.

D_{ij} is varying more in the branches where its values are more significant than in those where D_{ij} is about few hours that corresponds to the branches with higher maximum Δ_{ij}. The more the branches are saturated, the less they reach saturation less than 10%. For better understanding, we select the most critical branches (with Δ_{ij}> 80% and D_{ij} < 25 hours). The selected branches are, therefore (1-2, 2-3, 3-4, 6-7 and 8-9). The first branch (1-2) is critical since it is one of the main branches importing power from the classic generators to an important part of the network. The other two branches (2-3 and 3-4) are part of the branch (1-12) that will feed an important part of the network; in addition, they contain RES and BES that satisfy their demands first and transmit as much as possible for the rest of the network. Branches 6-7 and 8-9 are critical because they are connected to buses 6 and 8, where no installation is possible (neither RES nor BES) as shown in **Table *1***. Therefore, these branches deliver power with their maximum capacity to be able to saturate the demand for these buses.

- The grid losses

The grid losses are estimated by calculating the difference between production and demand. The results are presented in the following **Erreur ! Source du renvoi introuvable.**. In most cases, losses have less than 1% o f differences since they vary between 7.1 % and 7.8%. In some cases, losses are at the level of 9.8 %, while minimum observed losses are around 4%.

4. Sensitivity Analysis

The objective of sensitivity analysis is to determine which model parameters are important and their relative impact on the results. This gives insights about the efforts or resources needed to reduce the total uncertainty of the system's forecasts. Among the different SA technics presented in the literature, quantitative tests are made for sensitivity analysis using correlation analysis.

Tests based on correlation analysis.

The Pearson correlation coefficient is widely used in the literature. It measures the association between each input considered separately and the output. A number between -1 and 1 measures the strength and direction of the relationship between two variables. The correlation is given by the eq.(18).

$$r = \frac{\sigma_{xy}}{\sigma_x . \sigma_y} = \frac{\sum_i (x_i - \bar{x})(y_i - \bar{y})}{\sqrt{\sum_i (x_i - \bar{x})^2}\sqrt{\sum_i (y_i - \bar{y})^2}} \qquad i = 1, \dots, N \tag{18}$$

Where N is the number of samples.

The values of r are interpreted as follows [24]:

- Between 0 and 1: a positive correlation exists between variables (strong r > 0.5, moderate 0.3< r < 0.5 and weak 0 < r < 0.3) – when one variable changes, the other variable changes in the same direction.
- 0: No correlation (there is no relationship between the variables)
- Between 0 and -1: a negative correlation exists between variables (strong r < -0.5, moderate -0.3> r > -0.5 and weak 0 > r > -0.3) – when one variable changes, the other variable changes in the opposite direction.

To perform the Pearson correlation test, both variables should be quantitative. They should be normal or a little non-normally distributed. In the studied case, this distribution is visualized by the diagonal of Figure 10. In Pearson correlation tests, choosing a sample size of up to 258 variables means a correlation test with a power 90%, an error 5% and an alternative correlation 0.2 as detailed in the sample size guideline for correlation analysis [25].

The input parameters are therefore $\boldsymbol{P_{i,e}^{max}}$, $\boldsymbol{Var_{i,e}}$, $\boldsymbol{Du_e}$, $\boldsymbol{E_e^{Low}}$, $\boldsymbol{E_e^{Meduim}}$, $\boldsymbol{E_e^{High}}$ and $\boldsymbol{SF_e}$. The output indicators are $LCOE_e$, WT_e, PV_e, BES_e, $losses_e$, $\Delta_{ij,e}$ and $D_e = \sum D_{ij,e}$ with i: bus index, e: case index and ij: branch index. The results of the test of linear relationships between the parameters ($\mathrm{Var_{i,e}}$, $\mathrm{P_{i,e}^{max}}$) and indicators are presented respectively in the following **Erreur ! Source du renvoi introuvable.** and **Erreur ! Source du renvoi introuvable.**. The Pearson correlation index r is calculated for the remaining parameters and represented in Figure 10. The indicator of PVs is excluded since it is demonstrated that the uncertainties do not affect this investment.

From **Erreur ! Source du renvoi introuvable.**, it can be noticed that 4 buses (1,3,10 and 14) have marked an effect of variances on the output indicators. The increased standardized variances of buses 1, 10 and 14 cause an increase in the installed WT power and a decrease in the extracted CG energy. The batteries are affected by the variances in buses 3 and 14. The LCOE increases with the increase of standardized variances of buses 3, 10 and 14. Even if the correlation exists, it is considered weak (r < 0.3). The most influencing bus based on variances is the last one (bus 14) since the increase of load variance in bus 14 also causes an increase in the duration of minor saturations, and a decrease in losses.

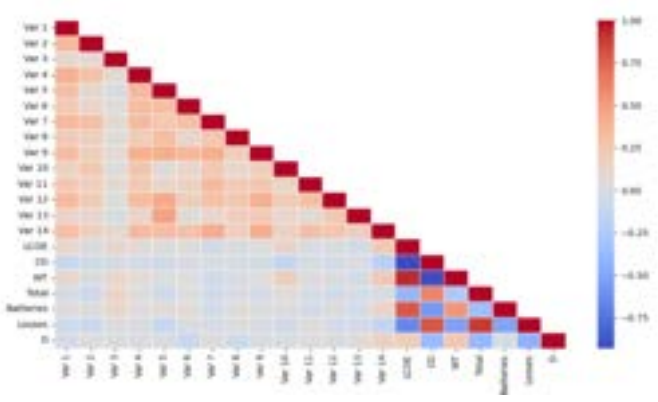

Figure 8. r values resulted from Pearson correlations tests of standardized variances ($Var_{i,k}$) on each bus with the output indicators

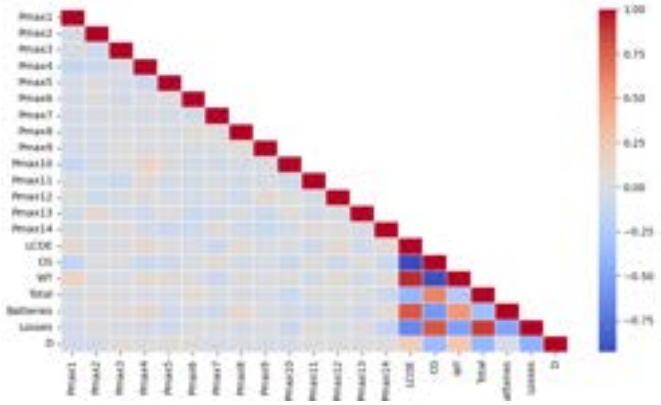

Figure 9. r values resulted from Pearson correlations tests of P^{max} on each bus with the output indicators

In **Erreur ! Source du renvoi introuvable.**, the results show that 4 buses (1,4,8 and 14) could affect the indicators but also with weak correlations (r < 0.15). An increase in the peak power of bus 1 leads to an increase in WT investment and a decrease in CG extraction because this bus conveys power to other buses; when the demand increases, the saturation effect of the branch decreases the quantity conveyed, and consequently the

system invests more in WTs. Increasing the peak power of bus 8 leads to an increase in battery investment since this bus does not contain a RES or BES and is fed from the grid. This increase in peak demand will be compensated by the storage of the power injected into the network, and then more investment in batteries.

The five input macro-parameters correlations with output indicators are displayed in Figure 10. The increase of the first parameter (the maximum duration parameter (Du)) leads to a decrease in the duration with very low branch saturation D_k (r = -0.15). By the fact that as long as the maximum demand values are reached, the low saturations of the branches appear less.

Figure 10. Tests on the different input parameters correlations with the output

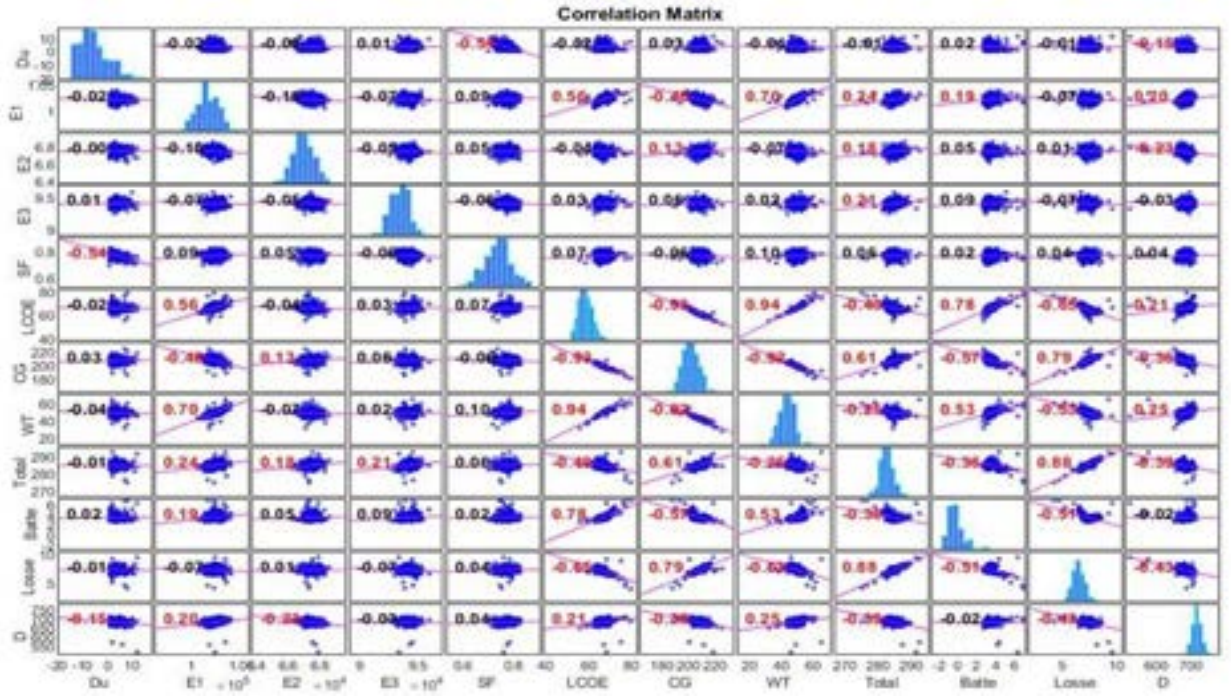

The total energy demands at each demand level calculated by eq.(3) are expressed in Figure 10 respectively by $\mathrm{E1}$ for $\mathrm{E_e^{High}}$, $\mathrm{E2}$ for $\mathrm{E_e^{low}}$ and $\mathrm{E3}$ for $\mathrm{E_e^{Medium}}$. The values of LCOE increase with the high demand total energies $\mathrm{E_e^{High}}$ increasing. Thus, E1 has a strong effect (r = 0.56) on the LCOE, while others have moderate effects (r = -0.04) for E2 and (r = 0.03) for E3. When the total low demand energy $\mathrm{E2}$ increases, the extracted energy from CGs increases also (r = 0.13) which means that this low-level energy is mainly extracted from CGs. This returns to the grid behaviour in the low-demand period when the branch limits are not reached, and the energy from the classic generators can be continuously transmitted. In addition, E2 coincides with a period where renewable energy is less present and therefore increased use of batteries which is less competitive with classic generators. The increasing in $\mathrm{E2}$ also results in a decrease in the $\mathrm{D_k}$ ($\mathrm{r} = -0.23$) because this demand period is the one with a high occurrence of the hours of less than 10% of Δ_{ij}. So, a decrease in the demand increases these durations.

High total energy demand $(E1)$ is the most impactful parameter. An increase in $E1$ leads to a strong increase in investment in WTs ($r = 0.7$) and, therefore, an increase in battery dimensioning ($r = 0.19$). This leads to a decrease in CGs energy extraction ($r = -0.48$) and a significant decrease of the LCOE ($r = -0.5$). An increase in duration D_k is observed ($r = 0.2$). This is because of decentralization of producers (WTs and BES) and the limitation of the transition of the power from CGs, which reduces the saturation of the nearest branches to CGs after recourse to renewables and batteries.

The simultaneity factor (SF) has very weak influences on the indicators ($\mathrm{r} < 0.1$).

The distribution of the parameters is shown in the diagonal of Figure 10. The Gamma test is applied to the output indicators distribution, and the results give p-values lower than 0.05, so the hypothesis of this law is rejected this means that the probabilities of accepting the hypothesis (the data are gamma-distribut) are less than 5% [26].The difference in distributions between the input parameters and the output indicators means that the model does not propagate uncertainties in a linear way between inputs and outputs. The distribution of most parameters is close to a normal distribution as shown in the distributions of E1, E2, E3, SF, CG, Losses, etc. Therefore, the use of Pearson correlations is validated.

5. Conclusions

This paper uses an EPSM model to perform uncertainty and sensitivity analyses. Input macro-parameters were defined to describe an quantify the model's inputs uncertainties. A sensitivity analysis is performed using the correlations between the input parameters and the output indicators to identify the most influential parameters. The results show that the uncertainties have considerable effects on the results. In economic terms, uncertainties lead to a 35% variation range of the LCOE. In terms of system design, there is a need to increase the installed capacity of wind turbines, extract more energy from power plants, and/or install more BES depending on the case. Uncertainties also affect grid saturation in the branches. The analysis enabled the identification of the most important parameter which is the total energy demand during the high demand period (winter), as this parameter strongly affects the defined indicators. This makes this parameter a key parameter in the sizing of RES, BES and thus in the network planning.

Nomenclature

Variables

P	Active power [MW]
Q	Reactive power [MVAr]
F	Objective function
$\mathcal{C}$ / $\mathcal{I}$	Total operational/investment cost by production
Γ	Total cost by category
CC	Capital Cost
A	Installed surface of PV [m²]
R	Ratio of installed WT capacity [MW]
E	Active energy
r	Correlation parameter
Var	Variances
Du	Duration of maximum loads
SF	Simultaneity factor
Δ	Percentage of brunch saturation
D	Duration of less than 10% of brunch saturation

Parameters

C	Elementary operational cost
J	Elementary investment cost
O	Elementary O&M cost
LT	Lifetime
ls	Lifetime of the overall system
ra	Discount rate of the project

Indices and sets

$\mathcal{N}$	Set of buses, $i, j \in \mathcal{N}$
$\mathcal{T}$	Set of all times, $t \in \mathcal{T}$
$\mathcal{B}$	Set of batteries
Nb	Number of batteries
c / u / s / w	Indices of buses with CG/VG/PV/WT
k	Iteration number in DLOPF
inv	Investment
$o\&m$	Operation and maintenance
op	Operational
e	Case index

Upper-scripts

cg / vg	Classic generator/virtual generator
pv / wt / st	Photovoltaic/wind turbines/Storage
b	BES index
l	Load index at a bus
p / q	Active/reactive power
max	Maximum value for the upper limit
low	Low energy levels
$medium$	Medium energy levels

$high$	High energy levels

Acknowledgments

This work was carried out under the auspices of the ValaDoE chair at IMT Atlantique, in partnership with Télécom Paris and Mines Saint Etienne, and was supported by Enedis, Région Pays de la Loire, Nantes Métropole and Akajoule.

References

[1] S. Moret, V. Codina Gironès, M. Bierlaire, et F. Maréchal, « Characterization of input uncertainties in strategic energy planning models », *Appl. Energy*, vol. 202, p. 597-617, sept. 2017, doi: 10.1016/j.apenergy.2017.05.106.
[2] S. F. Santos *et al.*, « Novel Multi-Stage Stochastic DG Investment Planning with Recourse », *IEEE Trans. Sustain. Energy*, vol. 8, nº 1, p. 164-178, janv. 2017, doi: 10.1109/TSTE.2016.2590460.
[3] A. Ehsan et Q. Yang, « State-of-the-art techniques for modelling of uncertainties in active distribution network planning: A review », *Appl. Energy*, vol. 239, p. 1509-1523, avr. 2019, doi: 10.1016/j.apenergy.2019.01.211.
[4] G. Mavromatidis, K. Orehounig, et J. Carmeliet, « Uncertainty and global sensitivity analysis for the optimal design of distributed energy systems », *Appl. Energy*, vol. 214, p. 219-238, mars 2018, doi: 10.1016/j.apenergy.2018.01.062.
[5] R. Mena, M. Hennebel, Y.-F. Li, C. Ruiz, et E. Zio, « A risk-based simulation and multi-objective optimization framework for the integration of distributed renewable generation and storage », *Renew. Sustain. Energy Rev.*, vol. 37, p. 778-793, sept. 2014, doi: 10.1016/j.rser.2014.05.046.
[6] A. Schmoldt, H. F. Benthe, et G. Haberland, « Digitoxin metabolism by rat liver microsomes », *Biochem. Pharmacol.*, vol. 24, nº 17, p. 1639-1641, sept. 1975.
[7] G. Mavromatidis, « Model-based Design of Distributed Urban Energy Systems under Uncertainty », p. 386.
[8] M. R. Font, « ANALYSE DE SENSIbILITE SUR UN MODELE STOCHASTIQUE Pour la PREVISION DEs CONSOMMATIONS ELECTRIQUES », p. 72.
[9] « Enedis | Gestionnaire du réseau de distribution d'électricité ». https://www.enedis.fr/ (consulté le 15 mars 2023).
[10] D. Sadeghi, A. Hesami Naghshbandy, et S. Bahramara, « Optimal sizing of hybrid renewable energy systems in presence of electric vehicles using multi-objective particle swarm optimization », *Energy*, vol. 209, p. 118471, oct. 2020, doi: 10.1016/j.energy.2020.118471.
[11] « Global sensitivity and uncertainty analysis of the levelised cost of storage (LCOS) for solar-PV-powered cooling | Elsevier Enhanced Reader ». https://reader.elsevier.com/reader/sd/pii/S0306261921000854?token=19FF74DD5BF3BF4079BBB8375E018B4BD68EBD20735709B67DA2969AE5C4D5F306631561DBB25A6BD56B206F4D4DAFC6&originRegion=eu-west-1&originCreation=20220822090205 (consulté le 22 août 2022).
[12] M. Ma, H. Huang, X. Song, F. Peña-Mora, Z. Zhang, et J. Chen, « Optimal sizing and operations of shared energy storage systems in distribution networks: A bi-level programming approach », *Appl. Energy*, vol. 307, p. 118170, févr. 2022, doi: 10.1016/j.apenergy.2021.118170.
[13] C. Lythcke-Jørgensen, A. V. Ensinas, M. Münster, et F. Haglind, « A methodology for designing flexible multi-generation systems », *Energy*, vol. 110, p. 34-54, sept. 2016, doi: 10.1016/j.energy.2016.01.084.
[14] A. Mian, « Optimal design methods applied to solar-assisted hydrothermal gasification plants », EPFL, 2016. doi: 10.5075/epfl-thesis-6945.
[15] A. Saltelli, Éd., *Global sensitivity analysis: the primer*. Chichester, England ; Hoboken, NJ: John Wiley, 2008.
[16] G. Saporta, *Probabilités, analyse des données et statistique*. Editions TECHNIP, 2006.
[17] L. L. Gratiet, S. Marelli, et B. Sudret, « Metamodel-Based Sensitivity Analysis: Polynomial Chaos Expansions and Gaussian Processes », in *Handbook of Uncertainty Quantification*, R. Ghanem, D. Higdon, et H. Owhadi, Éd., Cham: Springer International Publishing, 2015, p. 1-37. doi: 10.1007/978-3-319-11259-6_38-1.
[18] S. Fakih, M. T. Mabrouk, M. Batton-Hubert, et B. Lacarriere, « Impact of Uncertainties in Power Demand Estimation on the Optimal Design of Renewable Energy Sources and Storage Systems », in *2022 IEEE 10th International Conference on Smart Energy Grid Engineering (SEGE)*, Oshawa, ON, Canada: IEEE, août 2022, p. 68-73. doi: 10.1109/SEGE55279.2022.9889769.
[19] N. Kong *et al.*, « Long-term forecast of local electrical demand and evaluation of future impacts on the electricity distribution network », *CIRED - Open Access Proc. J.*, vol. 2017, nº 1, p. 2401-2405, oct. 2017, doi: 10.1049/oap-cired.2017.0743.
[20] M. R. Font, « ANALYSE DE SENSIbILITE SUR UN MODELE STOCHASTIQUE Pour la PREVISION DEs CONSOMMATIONS ELECTRIQUES », p. 72.
[21] S. Fakih, M. T. Mabrouk, M. Batton-Hubert, et B. Lacarriere, « Optimal Allocation and Sizing of Renewable Energy Sources and Storage Systems to Support Over-Solicited Electricity Grid », in *2022 6th International Conference on Green Energy and Applications (ICGEA)*, Singapore, Singapore: IEEE, mars 2022, p. 14-21. doi: 10.1109/ICGEA54406.2022.9791941.
[22] « pandapower ». [En ligne]. Disponible sur: https://pandapower.readthedocs.io/en/v2.1.0/networks/cigre.html
[23] Eurostat, « Natural gas price statistics ». [En ligne]. Disponible sur: https://ec.europa.eu/eurostat/statistics-explained/index.php?title=Natural_gas_price_statistics#Natural_gas_prices_for_non-household_consumers
[24] S. Turney, « Pearson Correlation Coefficient (r) | Guide & Examples », *Scribbr*, 13 mai 2022. https://www.scribbr.com/statistics/pearson-correlation-coefficient/ (consulté le 10 octobre 2022).
[25] M. A. Bujang et N. Baharum, « Sample Size Guideline for Correlation Analysis », *World J. Soc. Sci. Res.*, vol. 3, nº 1, p. 37, mars 2016, doi: 10.22158/wjssr.v3n1p37.
[26] S. Mcleod, PhD, « P-Value And Statistical Significance: What It Is & Why It Matters ». 1 mai 2023. [En ligne]. Disponible sur: https://www.simplypsychology.org/p-value.html

PROCEEDINGS OF ECOS 2023 - THE 36TH INTERNATIONAL CONFERENCE ON
EFFICIENCY, **C**OST, **O**PTIMIZATION, **S**IMULATION AND ENVIRONMENTAL IMPACT OF ENERGY SYSTEMS
25-30 JUNE, 2023, LAS PALMAS DE GRAN CANARIA, SPAIN

Smart management for integrated energy systems: tools from communities to regions

Costanza Saletti, Mirko Morini, Agostino Gambarotta

Department of Engineering and Architecture, University of Parma, Parma, Italy
*costanza.saletti@unipr.it **CA**, mirko.morini@unipr.it, agostino.gambarotta@unipr.it*

Abstract:

The novel concept of Smart Energy Systems has emerged over the last decade within the context of the energy transition toward a carbon-free sustainable future. For an energy system to be “smart”, several factors have to converge: (i) a high integration of renewable energy sources, (ii) the flexibility required to deal with their fluctuating nature, (iii) the exploitation of digital technologies and (iv) the cross-sectoral approach that uses synergies between various energy domains (sector coupling). Indeed, the traditional domain-specific energy flows from production to usage are overcome in favor of an integrated approach, in which energy is converted or stored into the most convenient vector. Coupling energy sectors, however, requires smart management and control strategies that are able to drive a system toward minimal energy use (or minimal cost), despite its increased complexity. Furthermore, the advanced management strategy of a smart energy system may vary significantly depending on its spatial dimensions, from the national/regional level to small-scale energy communities or islands. Hence, pointing out the latest progress on smart management is paramount for orienting future research and practice, and fostering the energy transition. This work reviews the available methods and tools for enabling the optimal operation of smart energy systems at different spatial and temporal scales. They are categorized according to relevant features such as the energy vectors and infrastructures involved, the presence of short-term or seasonal storage, the time horizon and specific application. The paper also summarizes research guidelines and drivers for the continuous development and expansion of smart energy systems at all levels. It was found particularly relevant to investigate optimal management at multiple time and space scales at the same time, for exploiting not only synergies between sectors, but also between neighboring communities. The tools should also have the possibility to include additional energy vectors (e.g. different types of chemicals) and their verification in demonstration cases should be promoted.

Keywords:

Control; Hybrid energy systems; Modeling; Optimization; Sector coupling; Smart energy systems; Smart management; System integration.

1. Introduction

Over the last few decades, the decarbonization of all human activities has become a global priority recognized by the international scientific community. Reducing greenhouse gas emissions is indeed a fundamental step to mitigate the effects of human activities on the climate and environment. Being one of the most carbon-intensive areas, the energy sector offers significant room for improvement. To this end, researchers have devoted great efforts in investigating and developing new concepts for the energy sector of the future [1].

In this context, the necessary steps to take are the implementation of energy efficiency actions, and the more rational exploitation of available resources and fuels. Hence, the energy system is progressively undergoing a transition toward a new paradigm, also referred to as sector coupling [2]. This indicates the interconnection between different sectors achieved by integrating multiple energy carriers and exploiting their synergies to enhance overall conversion efficiency. A system with these features is often regarded as an Integrated Energy System (IES) and is shown in Figure 1.

The very first example of this concept was the combined production of heat and electricity within a single plant, i.e. cogeneration unit. This is a high efficiency technology that recovers heat otherwise lost in the environment. Additional steps have been taken with the electrification of heat production and the transport sector.

The rise of new technologies and the possibility to exploit unconventional energy carriers (such as synthetic fuels and chemicals) has led to the integration and interconnection of all energy sectors in a unique circular framework, from the production of electricity to heat at different temperature levels, and even to mobility. While the traditional shape of a generic energy system comprised linear energy flows that were sent from the source directly to the final use, in the new framework the energy flows extracted from the sources can undergo multiple

passages before being used [3]. Some examples of these passages that characterize an IES are 1) conversion into a more cost-effective energy form, 2) accumulation into a storage device, and 3) supply into a distribution network.

The advantages of this new concept, compared to the previous one, are determinant:

- The cross-sectoral approach exploits the synergies between energy domains, so that energy can be transferred in the most convenient form depending on the specific conditions. For example, thermal demand can be translated into electrical demand by means of heat pumps. The deriving heat can be stored (more easily than electricity) or injected into heat distribution infrastructures for supplying entire communities. In parallel, excess electricity (e.g. from renewable sources) can also be converted into a chemical vector through Power-To-Gas systems, to be used at a later time or in a different location.
- An IES presents more degrees of freedom thanks to the different operation possibilities descending from the previous points, thus providing sufficient flexibility to deal with varying conditions.
- The higher flexibility, in turn, makes it possible to reduce the risk of curtailment of non-programmable renewable energy sources, and to operate programmable plants in a more profitable operating range.
- The available local resources can be put at the disposal of a larger community, so that energy can be produced and self-consumed locally, reducing grid losses. An example of this is the constitution of Renewable Energy Communities (REC), according to the recent European legislation.

Although this growing interconnection represents a key part of the energy transition due to the aforementioned benefits, it determines new challenges that deserve to be addressed. The most crucial is that the profitable layout and operation of a given system does not depend only on the single user or single plant, but is highly influenced by the neighboring users and entire infrastructure, including all connected elements and networks.

In this sense, IESs have to become Smart Energy Systems (SES), the definition of which is not limited to the co-operation of different energy infrastructures. A key feature of a SES is that it is planned, designed, operated, or optimized with the aid of dedicated digital tools. In more detail, tools for smart management are particularly relevant for dealing automatically with the complexity of the new paradigm. Indeed, they eliminate the risk of bad operations and relieve operators and technicians from the duty of locally controlling the energy flows of a complex new system for which neither expertise nor data are available.

Until recent years, major efforts have been directed toward the optimization of the electricity sector at all levels, as in the case of REC. Nonetheless, as shown above, the greatest benefits can be enabled by integrating all sectors, especially heat which constitutes at least half of the final energy use in Europe. A recent paper summarizes the development tools for the plant design and control of electro-thermal systems [4]: a system-level framework for the modeling, control, and design of multi-domain systems is defined, with a list of control methods as well as implementation tools (e.g. software and toolboxes). However, the focus is limited to future electrified vehicles. Similarly, Mishra et al. [5] review the technologies for sizing and operating innovative control in renewable integrated energy systems, with the sole focus on stand-alone and grid-connected electricity systems. Here, the term “integrated” is adopted to define an electricity-based system including a wide range of renewable technologies.

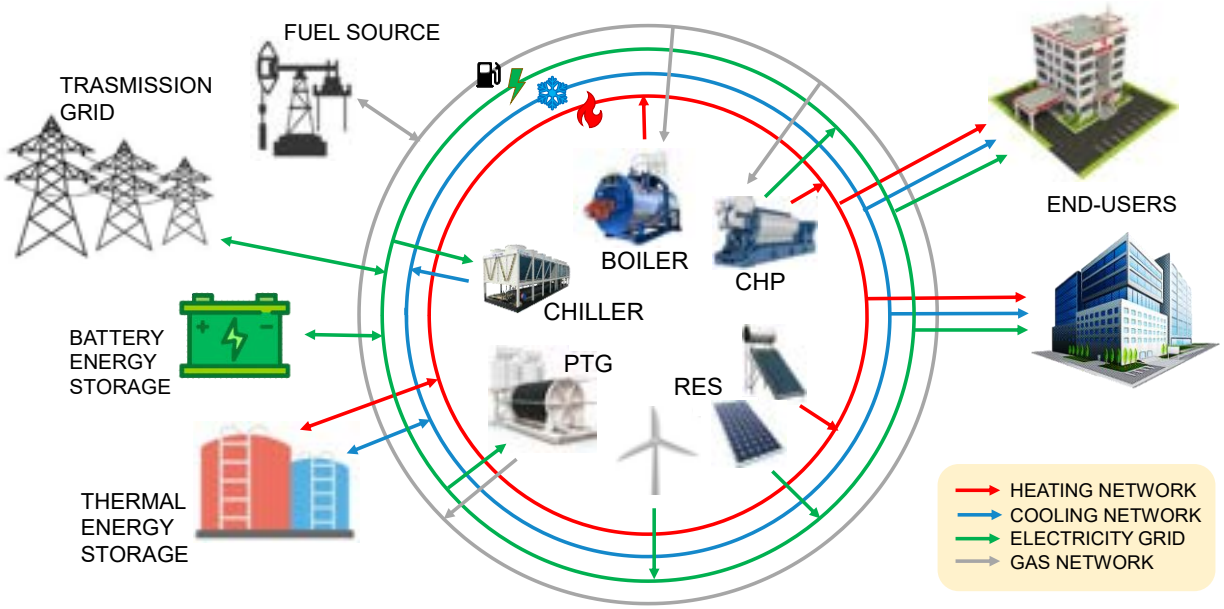

Figure. 1. An example of an integrated energy system in the framework of sector coupling with the electricity, heating, cooling and gas infrastructures. CHP: Combined Heat and Power plant, RES: Renewable Energy Sources, PTG: Power-To-Gas.

Whilst purely electrical infrastructures often have similar features in terms of time scale, due to their very fast dynamics, when coupling different sectors, the differences in time dynamics should be carefully investigated, and also considered in the related optimization tool. In addition, an IES can be implemented in different spatial dimensions, ranging from the IES for an individual building, to its community-scale application, to the whole national energy system of a country. When communities and networks are concerned, there are also large differences in system layouts and network topology.

All these aspects make the development of tools for IES smart management challenging but also critical for the energy transition. Indeed, it is firstly determinant to choose the appropriate tool, algorithm or methodology depending on the desired time or space scale, or even depending on the specific application. Since sector coupling and IES investigation is a rather novel topic, the state-of-the-art research does not offer a detailed overview of these tools. Despite the fact that tools for IES simulation and modeling have been surveyed in [6], to the best of the authors' knowledge, no unique set of tools for smart management exists in the literature.

This paper aims to provide a catalogue of the most recent works that presents tools for optimization and management of IES in the perspective of sector coupling. A particular distinction is made regarding the spatial dimension and time horizon in which each selected tool is supposed to be applied, or offers the greatest benefits. This analysis includes a thorough review of the literature, the selection of the most relevant papers for this purpose, and the extraction of the features of the proposed tools. To restrict the research field, this review aims to give an answer to the following research questions:

- How can smart management be applied to integrated energy systems at different spatial levels?
- Which are the tools that can enable system planning, design, optimization and management when considering different time horizons?

Finally, a set of drivers and guidelines based on the obtained results are given as indications for future research in the field.

2. The concept of sector coupling

2.1. Definition

It can be seen from the literature that a clear contextualization of sector coupling is missing. As noted by Ramsebner et al. [2], the term is often misinterpreted: it is used in a wide range of cases, from the bare inclusion of renewable energy sources, to the coupling of the production of energy and transportation. By contrast, if the scope is restricted to the field of energy production, distribution and utilization, available sources and research works adopt different terms to define the same concept (IES, in the scope of this research).

The focus of this paper is to produce an overview of the tools to achieve the optimal management of IES in the framework of sector coupling. This task is therefore subordinated to the preliminary identification and explanation of the terms used in the literature to refer to IES (as in the meaning given in Section 1). These definitions, which are detailed in Table 1, also represent the main keywords used in the literature search.

With reference to the term "hybrid energy systems" [7], it is worth specifying that, apart from the scope of sector coupling, the term can also identify the following concepts:

- A system in which different conversion units are integrated to pursue the same scope (e.g. supplying electricity). This is the case of renewable energy sources coupled with conventional power plants.
- A system in which different components are integrated within the same power plant to enhance plant efficiency (e.g. fuel cells coupled with gas turbines).

Hence, when analyzing the literature and selecting relevant papers as well as the related tools, particular attention has to be paid to this term.

2.2. Infrastructures

The whole energy system is based on infrastructures that can connect the energy conversion systems with users or storage devices at different scales. These infrastructures are shaped as networks that may have different topologies according to the specific domain. In particular, it is worth mentioning electrical grids, natural gas networks, and heating and cooling networks [8].

Electrical energy and natural gas can be transferred for long distances and then distributed in a widespread manner to the single users. Therefore, in general, these networks are structured with transmission networks (e.g. at high voltage or pressure in order to reduce dissipation) and distribution networks (e.g. where voltage and pressure are progressively decreased toward the users).

Conversely, heat cannot be efficiently transported for more than a few kilometers. Therefore, its production must be close to the users and the networks are only for its distribution. Another peculiarity of heating and cooling networks is that they use a medium for heat distribution (e.g. steam or water) and, therefore, they are composed of supply and return piping.

All these infrastructures were traditionally intended as passive and one-directional, with the energy transferred from a small amount of source points (e.g. power plants) to a high number of sink points (e.g. houses and

factories). Starting from the electrical grid they are becoming progressively more active and bi-directional with an increase in the number of production points and the presence of points that can alternatively be a source or a sink (i.e. the so-called prosumers).

Storage technologies [1] are a key part of the infrastructures, and have become more relevant over the past decades to decouple energy production (often deriving from discontinuous or uncontrollable sources) from its utilization. From the temporal perspective, in this paper the storage technologies are grouped into two categories:

- Short-term storage: this kind of storage technology is characterized by high power but low capacity and therefore it can act over time scales up to one day. It includes, for example, flywheels, batteries and thermal energy storage tanks.
- Long-term storage: this kind of storage technology is characterized by high power and high capacity and can act over time scales from days to months. It comprises, for example, flow batteries, pumped hydro, compressed air, chemicals, seasonal heat storage (e.g. pit thermal energy storage).

Besides the aforementioned energy networks, there is another energy distribution infrastructure, that was traditionally considered disconnected, but which is becoming progressively integrated: fuel for transportation.

2.3. Coupling technologies

Within an IES, the infrastructures described above are connected by means of coupling technologies, which can also be defined as bridging technologies. They are energy conversion units that convert an energy vector into one or more different energy vectors.

Conventional coupling technologies are (i) boilers (i.e. from fuels to heat); (ii) engines (coupled with alternators), which when configurated as cogeneration units can bridge the fuel domain with both the electrical energy and heat domains; and (iii) chillers (i.e. from electrical energy to cooling energy).

The most innovative technologies are heat pumps [1] and Power-To-Gas (PTG). Heat pumps are based on the same working principle of the electric chillers, but in heat pumps the output is the heat that it is delivered at high temperature. Heat pumps can work in a reversible way (i.e. using the electricity to produce heat in winter time and cooling energy in summer time) or they can also have a double effect (i.e. the production of both a cold and warm vector at the same time).

PTG refers to a technology that converts electrical energy into a gaseous fuel (e.g hydrogen or methane). It is therefore composed of an electrolyzer that produces a hydrogen stream, which can be stored or combined with a carbon dioxide stream to feed a reactor for their conversion into methane and water. The water can be removed by condensing it and the methane can be stored or injected into the network.

Table 1. Terms used in the literature to identify integrated energy systems in the context of sector coupling.

Name	Detailed explanation	References
Sector coupling	“The concept of SC encompasses co-production, combined use, conversion, and substitution of different energy supply and demand forms—electricity, heat, and fuels”	[9]
Integrated energy systems	“(IES) combine on-site power generation technologies with technologies for heating and cooling” and “bring together all forms of cooling, heating and power […] combined heat and power […], and cogeneration technologies.”	[10]
Multi-energy systems	“A system designed to allow the operator to choose between multiple energy sources”; and also systems “whereby electricity, heat, cooling, fuels, transport, and so on optimally interact with each other at various levels”	[3,11]
Hybrid energy systems	“Hybrid energy systems are combinations of two or more energy conversion devices (e.g. electricity generators or storage devices), or two or more fuels for the same device, that when integrated, overcome limitations that may be inherent in either.”	[7]
Energy hub	“A unit where multiple energy carriers can be converted, conditioned and stored. It represents an interface between different energy infrastructures and/or loads”	[12]
Smart energy systems	“an integrated holistic focus on the inclusion of more sectors (electricity, heating, cooling, industry, buildings and transportation) and allows for the identification of more achievable and affordable solutions to the transformation into future renewable and sustainable energy solutions”	[8]

By broadening the focus also to the transportation sector, charging infrastructure for electric vehicles can be considered as a bridging technology. It is worth mentioning that this coupling can also enable storage technologies such as Vehicle-to-Grid. This involves batteries of electric vehicles connected to charging stations being provisionally at the disposal of the power grid as storage to aid its operation.

3. Methodology

The methodology adopted to carry out the investigation in this work involved a thorough search of the current scientific literature concerning the subject of integrated energy systems in the framework defined in Section 2.1. The search in international scientific databases was conducted with a combination of keywords to identify both the subject and specific aim of each work. To this end, the keywords defined in Table 1 were in turn combined with keywords such as “optimization”, “control”, “management” and “operation”, in order to restrict the analysis to smart management tools.

Since sector coupling has become a broad topic over the last few years, and research papers have been growing continuously since the first definition, the output of this search was filtered adopting the following criteria for inclusion in the review:

- the paper covers a system with at least two energy vectors or networks;
- the paper presents a novel tool for the design, optimization or management of an IES;
- the spatial scale in which the proposed tool is applied is clearly identified within the scope of the paper;
- the time framework (e.g. time discretization, time horizon) for the application of the proposed tool is clearly determined.

The last two points are particularly relevant to this review. Indeed, the aim of this investigation is to classify the innovative methods and tools that allow an IES to be analyzed and optimized considering the differences that derive from the spatial and temporal dimensions.

To achieve this goal, the selected papers were thoroughly examined to extract their relevant features related to: (i) energy vectors tackled by the proposed tool; (ii) space and time scales; (iii) the presence of storage; (iv) the main aim of the tool; and (v) specific notes on the algorithms or software packages used. In addition, geographical and technical details on the case studies, if present, are noted. The features, divided into categories, are explained in Table 2.

Finally, the deriving information was collected in a broad table that presents an overview of the available studies, in order to:

- View the characteristics of each selected paper;
- Make comparisons between the presented tools;
- Understand which are the most covered aspects and, by contrast, the major gaps that should be tackled by future research;
- Verify if there are tools that tackle more than one feature at the same time, with reference to the same category.

Table 2. Features for the categorization of the selected papers.

Category	Features	Description
Energy vectors	Electricity, heating, cooling, natural gas, hydrogen, steam, other fuels, transportation*	The energy vectors comprised in the IES or included in the tool
Spatial scale	Building, community, city, region, nation or greater (Europe)	The spatial scale of application of the tool, ranging from individual buildings to systems spanning different nations
Time scale	Hours, days, weeks, year, or even multiple years	The time horizon for the investigation performed by the tool
Time discretization	Quarter hours or smaller, hour, day	The time-step for subdivision of the time scale of the tool
Storage	Short-term, long-term	The tool or application considers one or more types of storage, specifying its time scale
Aim of the tool	Simulation, optimization, management, design, long-term planning	Specific aim or aims of the tool (management is related to operation scheduling as well as real-time control)
Algorithms	-	If relevant, this field defines the existing algorithms or software used
Case study	-	If relevant, this field collects the main technical and geographical information of the case studies presented as applications

*Despite being a sector and not an energy vector, transportation was added to consider the aspects of mobility that can be integrated into a broader energy system (e.g. electric vehicles).

It is particularly relevant to consider the last point because, with the growing expansion of IES with different characteristics, it will be necessary to use versatile and multi-scale methods, and not just case-dependent tools that are tailored to a single application. The table of papers obtained in this review makes it possible to identify multi-scale studies (either spatial or temporal) and to verify where room for improvement can be found.

4. Results

The results of the investigation carried out in this work (and outlined in Section 3) are reported in Table 3, which lists the selected papers and the specific features of the proposed tools for the optimal design and operation of IES. The table aims to provide a basis for 1) making comparisons between methods, 2) selecting the most adequate method for a given application, and 3) understanding research gaps and drivers for the future. All these tasks are relevant to the expanding research field of IES.

Overall, 34 papers were selected for the scope of this analysis (and for the sake of space limitations), 4 of which were published before 2020 while the other 30 were published between 2020 and 2023. This distribution reflects the fact that, from the first definitions of sector coupling and IES in the mid 2000s, the number of works has dramatically increased over the last few years. However, it should not be concluded that, before 2020, researchers were not investigating these concepts. This literature search was conducted with precisely identified keywords, most of which were specified quite recently, and broadly adopted by researchers even more recently. Thus, most likely, the tools and methods proposed at earlier times were not labelled with the same definition. In addition, this literature search, which does not presume to be exhaustive, gave priority to more recent works, in order to delineate the latest tools available.

Various useful comments can be drawn from this overview:

- The sectors that are taken into consideration by the most part of papers are electricity, heating (sometimes coupled with cooling in district heating and cooling networks), and natural gas. These infrastructures are indeed the most advanced in current energy systems. However, it is expected that in the future other fuels (e.g. hydrogen, methanol and other non-conventional chemicals) will be an important part of an IES. This highlights a gap that deserves investigation.
- With regard to the building scale, it is common to only consider electricity and heating or cooling, i.e. the vectors that can be distributed internally, while few papers consider natural gas.
- On the contrary, at the scale of a wide region or an entire country, it is more common to include different types of fuels, whereas the aim of the analyses is mainly the optimal planning of capacity development in long-term scenarios (up to 2050). Real-time optimal management of PTG technologies was not found within the scope of this research.
- As already noted, large spatial scales are mainly devoted to simulating the system for future years, planning their development, or determining the optimal capacity and combination of sources for the considered area. In such cases, the time horizon for optimization is at least one year, but the management (with such a long time perspective) is carried out with typical days or typical weeks in the year. Thus, it is not representative of a real-time management tool.
- Investigations at community level are widespread, where community is often viewed as a district with a multiplicity of end-users, but it can also be seen as a set of coordinated power plants feeding a non-specified end-use. Particular attention should be paid to the end-use of each application. In any case, the community is equally analyzed with short time-scales (in the range of days, with the purpose of determining, in the best case, optimal control of the IES) or long time-scales (to schedule the operation of the system over an operating year).
- Storage technologies are almost always taken into consideration, since they enable flexibility and allow the full exploitation of optimal management, planning or design tools. Nevertheless, seasonal storage can be included in very few available tools, and only for those that view a relatively long time horizon.
- Overall, modeling and optimizing all energy sectors with fine discretization in terms of space and time can be computationally demanding. A feasible possibility is to increase the size of the time-steps or to select a few representative periods [13]. This strategy, however, can lead to biases in the generated optimal (or sub-optimal) solution.

An additional result of this research is the in-depth analysis of a selection of tools for each spatial scale, enriched with details on algorithms and case studies, where present. This is reported in Table 4.

It can be noted that a widely used method when dealing with optimal management at building and community scales is Model Predictive Control (MPC), which is an advanced control strategy that requires a model of the system. This feature, promising for the good performance of the management strategy, may make the problem intractable when the number of variables of the system grows. In general, the MILP formulation, a deterministic method that guarantees optimality, is the most used. For larger spatial scales, energy system models and sets of simulations with sensitivity analysis are used to deal with an increase in decision variables.

In light of the above, more studies and systematic reviews will be necessary to further outline the existing bibliography, and to investigate the links and relationship between all the presented features.

Table 3. Relevant features of the tools proposed in the selected papers. E: electricity, H: heating, C: cooling, S: steam, NG: natural gas, H2: hydrogen, OC: other chemicals, M: mobility. ST: short-term, LT: long-term. Sim: simulation, Opt: optimization, Mng: management, Des: design/sizing, Pln: long-term planning.

Paper	Energy vector								Spatial scale	Time scale	Time discretization	Storage			Aim			
	E	H	C	S	NG	H2	OC	M				ST	LT	Sim	Opt	Mng	Des	Pln
[14]	✓	✓	✓		✓				building	hours + day	15 min + 1 h	✓			✓	✓		
[15]	✓	✓	✓						building	days	1 h	✓		✓		✓		
[16]	✓	✓							building	hours	-	✓			✓	✓		
[17]	✓	✓	✓						building	hours + day	1 h	✓			✓	✓		
[18]		✓	✓						building	year	1 h	✓	✓				✓	
[19]	✓	✓	✓						building, community	hours + day	1 h	✓			✓	✓		
[20]	✓	✓	✓						building, community	week	15 min	✓			✓	✓		
[21]	✓	✓	✓	✓	✓				building, community	days + year	15 min + 1 day	✓	✓	✓	✓	✓		
[22]	✓	✓	✓	✓					community	day	1 h	✓			✓	✓		
[23]	✓	✓	✓	✓					community	week + year	1 h	✓			✓	✓		
[13]	✓	✓	✓						community	day + year	15 min	✓			✓	✓	✓	
[24]	✓	✓			✓				community	day	15 min	✓			✓	✓		
[25]	✓	✓	✓						community	week + year	-	✓		✓		✓		
[26]	✓	✓			✓				community	hours + day	1 h	✓			✓	✓		
[27]	✓	✓	✓					✓	community	year	1 h	✓			✓			
[28]	✓	✓				✓			community	day	1 h	✓			✓	✓		
[29]	✓	✓			✓				community	hours + day	mins + 1 hour	✓						
[30]	✓	✓	✓		✓				community	day	1 h	✓			✓	✓		
[31]	✓	✓	✓		✓				community	hours + day	15 min	✓			✓	✓		
[32]	✓	✓							community	hours	15 min	✓			✓	✓	✓	
[33]	✓	✓	✓					✓	community, city	year	1 h	✓					✓	
[34]	✓	✓							community, city	day	15 min	✓			✓	✓		

Paper	Energy vector								Spatial scale	Time scale	Time discretization	Storage		Aim				
	E	H	C	S	NG	H2	OC	M				ST	LT	Sim	Opt	Mng	Des	Pln
[35]	✓	✓	✓		✓	✓			community, city	day	15 min	✓			✓	✓		
[36]	✓	✓						✓	city	year	1 h	✓			✓	✓	✓	
[37]	✓	✓	✓		✓				region	day	1 h				✓	✓		
[38]	✓								region	day	1 h	✓	✓			✓		
[39]	✓	✓						✓	nation	year	1 h	✓		✓	✓		✓	
[40]	✓	✓							nation	-	1 h + 1 day	✓			✓		✓	✓
[41]	✓	✓			✓		✓	✓	nation	multiple years	1 h	✓	✓		✓			✓
[42]	✓	✓							nation	multiple years	1 h	✓			✓			✓
[43]	✓				✓	✓	✓		nation	year	1 h	✓	✓	✓				✓
[44]	✓	✓					✓	✓	nation	multiple years	1 h	✓		✓	✓			
[45]	✓	✓	✓					✓	Europe	week + year	1 h	✓	✓	✓	✓	✓		
[46]	✓	✓				✓		✓	Europe	multiple years	1 h	✓	✓		✓	✓		✓

Table 4. Selected tools for different spatial scales with details regarding algorithms, software and case studies.

Spatial scale	Tool	Case study	Algorithm details
Building	**[17]** Economic MPC with three time scales: (i) scheduling of the next 24 h, (ii) real-time optimization of the next few hours and (iii) set-point tracking	An IES comprising RES, a gas turbine, electric and absorption chillers, a fuel cell, storages	Optimization problems solved in Python based on CasADi (IPOPT and BONMIN solvers)
	[20] MILP scheduling problem for a week, with evaluation of the thermal capacity of building as storage	1) a single building and 2) a university campus in northern Italy, with different IES designs	Optimization formulated with Pyomo and MILP solved with Gurobi solver
Community	**[13]** A two-level optimization: (i) Genetic Algorithm for determining demand side management actions and (ii) storage sizing + IES scheduling with LP	A district multi-energy system with tens of buildings	Optimization formulated and solved with MATLAB (Global Optimization Toolbox)
	[21] MPC with two time scales: (i) yearly scheduling updated every day to consider long-term effects and (ii) real-time unit commitment updated every 15 min	The IES of a hospital in Ferrara (Italy), including its district heating and cooling network	Optimization formulated and solved with MATLAB (Global Optimization Toolbox)
	[25] Multi-model dynamic simulation of the system and sensitivity analysis with different control strategies	A fifth-generation district heating network in Zurich, Switzerland	Model and simulation in IDA ICE
City	**[36]** Linear optimization model considering investment and dispatch within the electricity and heating sector	City of Gothenburg, Sweden, with the addition of electric cars and buses	City Energy Optimization Model
Nation	**[40]** Dispatch sector coupling model for optimal design minimizing energy system costs	The Swiss energy system	Open-source GRIMSEL-AH model
	[42] Balmorel energy system model (assuming a regime of 24 h a day, three days a week, seven representative weeks per year)	Scandinavian countries	Problem formulated in GAMS and solved with CPLEX solver (with great computation effort)
	[45] Soft linking of two models: (i) long-term planning multi-sectorial model and (ii) unit commitment and optimal dispatch model	The European energy system	JRC-EU-TIMES and Dispa-SET (solved with MILP formulation)

From this outline, it is also possible to derive research gaps that should be addressed to improve the smart management of future IES. Three significant drivers for further research are listed below:

- Optimal management of IES is generally tackled with a short time horizon, whereas it should be carried out with more than one time scale, one of which of the order of magnitude of months (up to one year). In this way, the IES control systems are able to account for the effects of long-term storage, large distribution networks and, most of all, storage into chemicals through PTG.
- Optimal management of IES is generally carried out at community level, by means of deterministic optimization algorithms that are subject to a drastic increase in computational time when the size of the system or the number of plants increase. Sector coupling implies indeed that all systems are always connected to neighboring areas. A potential solution to this issue is the decomposition of the problem into communicating sub-problems, each related to a spatial dimension. For this reason, research should focus on tools that consider more than one spatial level and can be implemented with similar features from buildings to wider regions.
- Most available tools for smart management are still at low levels of market readiness, as they are generally demonstrated with simulations or sensitivity analysis. Despite being challenging due to system size, it would be relevant to bring the proposed solutions to demonstration in an operational environment, in order to foster their uptake and see an actual impact on real systems.
- The use of hydrogen and other synthetic fuels produced by surplus electricity should be a determinant part of smart management tools, especially in the perspective of increasing the energy contribution from non-programmable RES.

5. Conclusions

Integrated Energy Systems (IES) have emerged over the last decade within the context of the energy transition toward a carbon-free sustainable future. They provide several advantages in terms of integration of renewable energy sources, system flexibility, and a cross-sectoral approach that uses synergies between various energy domains. However, this new framework requires smart management tools that can automatically drive an IES to optimal operation, overcoming system complexity and lack of expertise. This paper presented an overview of the available tools for the optimization and management of IES in the perspective of sector coupling. The focus of the analysis was to highlight the spatial dimension and time horizon for which the tools were designed. After a thorough review of the literature, the most relevant papers were selected, and their features were extracted and classified in a broad illustrative table. In addition, particularly representative tools for each spatial scale were further illustrated with their algorithm and case study technical details. It was possible to draw conclusions on the most commonly studied energy sectors and methodologies, as well as to identify gaps and guidelines for future improvement. In particular, the following aspects deserve further studies: i) tackling optimal management over multiple time scales (for considering long-term effects and real-time management simultaneously), ii) combining multiple spatial levels through decomposition methods, iii) including synthetic fuel production also at community level, and iv) promoting the demonstration of the tools in real case studies.

Acknowledgments

This work was co-authored by a researcher with a research contract co-funded by the European Union – PON Ricerca e Innovazione 2014-2020 (according to Italian legislation: art. 24, comma 3, lett. a), della Legge 30 dicembre 2010, n. 240 e s.m.i. e del D.M. 10 agosto 2021 n. 1062).

Abbreviations

CHP	Combined Heat and Power
IES	Integrated Energy Systems
MILP	Mixed Integer Linear Programming
MPC	Model Predictive Control
PTG	Power-To-Gas
REC	Renewable Energy Community
RES	Renewable Energy Sources
SES	Smart Energy Systems

References

[1] Rehman OA, Palomba V, Frazzica A, Cabeza LF. Enabling technologies for sector coupling: A review on the role of heat pumps and thermal energy storage. Energies 2021;14. https://doi.org/10.3390/en14248195.

[2] Ramsebner J, Haas R, Ajanovic A, Wietschel M. The sector coupling concept: A critical review. Wiley Interdiscip Rev Energy Environ 2021;10:1–27. https://doi.org/10.1002/wene.396.

[3] Mancarella P. MES (multi-energy systems): An overview of concepts and evaluation models. Energy 2014;65:1–17. https://doi.org/10.1016/j.energy.2013.10.041.

[4] Laird C, Kang Z, James KA, Alleyne AG. Framework for integrated plant and control optimization of electro-thermal systems: An energy storage system case study. Energy 2022;258:124855. https://doi.org/10.1016/j.energy.2022.124855.

[5] Mishra S, Saini G, Saha S, Chauhan A, Kumar A, Maity S. A survey on multi-criterion decision parameters, integration layout, storage technologies, sizing methodologies and control strategies for integrated renewable energy system. Sustain Energy Technol Assessments 2022;52:102246. https://doi.org/10.1016/j.seta.2022.102246.

[6] Widl E, Cronbach D, Sorknæs P, Fitó J, Muschick D, Repetto M, et al. Expert survey and classification of tools for modeling and simulating hybrid energy networks. Sustain Energy, Grids Networks 2022;32:100913. https://doi.org/10.1016/j.segan.2022.100913.

[7] Manwell JF. Hybrid Energy Systems. Encycl Energy 2004:215–29. https://doi.org/10.1201/9781003159421.

[8] Lund H, Østergaard PA, Connolly D, Mathiesen BV. Smart energy and smart energy systems. Energy 2017;137:556–65. https://doi.org/10.1016/j.energy.2017.05.123.

[9] IRENA, IEA, REN21. Renewable Energy Policies in a Time of Transition. 2018.

[10] Mařík K, Schindler Z, Stluka P. Decision support tools for advanced energy management. Energy 2008;33:858–73. https://doi.org/10.1016/j.energy.2007.12.004.

[11] Fabrizio E, Corrado V, Filippi M. A model to design and optimize multi-energy systems in buildings at the design concept stage. Renew Energy 2010;35:644–55. https://doi.org/10.1016/j.renene.2009.08.012.

[12] Geidl M, Koeppel G, Favre-Perrod P. The Energy Hub–A powerful concept for future energy systems. Third Annu. Carnegie Mellon Conf. Electr. Ind. 13-14 March 2007, 2007.

[13] Capone M, Guelpa E, Mancò G, Verda V. Integration of storage and thermal demand response to unlock flexibility in district multi-energy systems. Energy 2021;237. https://doi.org/10.1016/j.energy.2021.121601.

[14] Hu K, Wang B, Cao S, Li W, Wang L. A novel model predictive control strategy for multi-time scale optimal scheduling of integrated energy system. Energy Reports 2022;8:7420–33. https://doi.org/10.1016/j.egyr.2022.05.184.

[15] Brandi S, Gallo A, Capozzoli A. A predictive and adaptive control strategy to optimize the management of integrated energy systems in buildings. Energy Reports 2022;8:1550–67. https://doi.org/10.1016/j.egyr.2021.12.058.

[16] Xiong X, Wu X. Coordinated control of heat-power integrated energy system using zone model predictive control with variable zone width. Appl Therm Eng 2022;217:119270. https://doi.org/10.1016/j.applthermaleng.2022.119270.

[17] Wu L, Yin X, Pan L, Liu J. Economic model predictive control of integrated energy systems: A multi-time-scale framework. Appl Energy 2022;328:120187. https://doi.org/10.1016/j.apenergy.2022.120187.

[18] Shakerin M, Eikeskog V, Li Y, Harsem TT, Nord N, Li H. Investigation of Combined Heating and Cooling Systems with Short-and Long-Term Storages. Sustain 2022;14. https://doi.org/10.3390/su14095709.

[19] Yu Y, Li J, Chen D. Optimal dispatching method for integrated energy system based on robust economic model predictive control considering source–load power interval prediction. Glob Energy Interconnect 2022;5:564–78. https://doi.org/10.1016/j.gloei.2022.10.010.

[20] Ghilardi LMP, Castelli AF, Moretti L, Morini M, Martelli E. Co-optimization of multi-energy system operation, district heating/cooling network and thermal comfort management for buildings. Appl Energy 2021;302:117480. https://doi.org/10.1016/j.apenergy.2021.117480.

[21] Saletti C, Morini M, Gambarotta A. Smart management of integrated energy systems through co-optimization with long and short horizons. Energy 2022;250:123748. https://doi.org/10.1016/j.energy.2022.123748.

[22] Bischi A, Taccari L, Martelli E, Amaldi E, Manzolini G, Silva P, et al. A detailed MILP optimization model for combined cooling, heat and power system operation planning. Energy 2014;74:12–26. https://doi.org/10.1016/j.energy.2014.02.042.

[23] Bischi A, Taccari L, Martelli E, Amaldi E, Manzolini G, Silva P, et al. A rolling-horizon optimization algorithm for the long term operational scheduling of cogeneration systems. Energy 2019;184:73–90. https://doi.org/10.1016/j.energy.2017.12.022.

[24] Roth M, Franke G, Rinderknecht S. Decentralised multi-grid coupling for energy supply of a hybrid bus depot using mixed-integer linear programming. Smart Energy 2022;8:100090. https://doi.org/10.1016/j.segy.2022.100090.

[25] Edtmayer H, Nageler P, Heimrath R, Mach T, Hochenauer C. Investigation on sector coupling potentials of a 5th generation district heating and cooling network. Energy 2021;230:120836. https://doi.org/10.1016/j.energy.2021.120836.

[26] Ju L, Lu X, Yang S, Li G, Fan W, Pan Y, et al. A multi-time scale dispatching optimal model for rural biomass waste energy conversion system-based micro-energy grid considering multi-energy demand response. Appl Energy 2022;327:120155. https://doi.org/10.1016/j.apenergy.2022.120155.

[27] Telle JS, Schlüters S, Schönfeldt P, Hanke B, von Maydell K, Agert C. The optimized integration of temperature-controlled transports into distributed sector-integrated energy systems. Energy Convers Manag 2022;269. https://doi.org/10.1016/j.enconman.2022.116148.

[28] Ye Z, Huang W, Huang J, He J, Li C, Feng Y. Optimal Scheduling of Integrated Community Energy Systems Based on Twin Data Considering Equipment Efficiency Correction Models. Energies 2023;16. https://doi.org/10.3390/en16031360.

[29] Mu Y, Xu Y, Cao Y, Chen W, Jia H, Yu X, et al. A two-stage scheduling method for integrated community energy system based on a hybrid mechanism and data-driven model. Appl Energy 2022;323:119683. https://doi.org/10.1016/j.apenergy.2022.119683.

[30] Ren S, Hu B, Ning L, Xu H, Zhou B, Yang D, et al. Optimal operation of integrated energy system including large-scale controllable industrial loads. Energy Reports 2022;8:938–49. https://doi.org/10.1016/j.egyr.2022.02.131.

[31] Liu C, Wang C, Yin Y, Yang P, Jiang H. Bi-level dispatch and control strategy based on model predictive control for community integrated energy system considering dynamic response performance. Appl Energy 2022;310:118641. https://doi.org/10.1016/j.apenergy.2022.118641.

[32] Zheng B, Wu X. Integrated capacity configuration and control optimization of off-grid multiple energy system for transient performance improvement. Appl Energy 2022;311:118638. https://doi.org/10.1016/j.apenergy.2022.118638.

[33] Perera ATD, Javanroodi K, Wang Y, Hong T. Urban cells: Extending the energy hub concept to facilitate sector and spatial coupling. Adv Appl Energy 2021;3:100046. https://doi.org/10.1016/j.adapen.2021.100046.

[34] Zhang B, Ghias AMYM, Chen Z. A double-deck deep reinforcement learning-based energy dispatch strategy for an integrated electricity and district heating system embedded with thermal inertial and operational flexibility. Energy Reports 2022;8:15067–80. https://doi.org/10.1016/j.egyr.2022.11.028.

[35] Yin L, Zhang B. Relaxed deep generative adversarial networks for real-time economic smart generation dispatch and control of integrated energy systems. Appl Energy 2023;330:120300. https://doi.org/10.1016/j.apenergy.2022.120300.

[36] Heinisch V, Göransson L, Erlandsson R, Hodel H, Johnsson F, Odenberger M. Smart electric vehicle charging strategies for sectoral coupling in a city energy system. Appl Energy 2021;288. https://doi.org/10.1016/j.apenergy.2021.116640.

[37] Zhang A, Zheng Y, Huang H, Ding N, Zhang C. Co-integration theory-based cluster time-varying load optimization control model of regional integrated energy system. Energy 2022;260:125086. https://doi.org/10.1016/j.energy.2022.125086.

[38] Yin L, Li Y. Hybrid multi-agent emotional deep Q network for generation control of multi-area integrated energy systems. Appl Energy 2022;324. https://doi.org/10.1016/j.apenergy.2022.119797.

[39] Herc L, Pfeifer A, Duić N, Wang F. Economic viability of flexibility options for smart energy systems with high penetration of renewable energy. Energy 2022;252. https://doi.org/10.1016/j.energy.2022.123739.

[40] Rinaldi A, Soini MC, Streicher K, Patel MK, Parra D. Decarbonising heat with optimal PV and storage investments: A detailed sector coupling modelling framework with flexible heat pump operation. Appl Energy 2021;282:116110. https://doi.org/10.1016/j.apenergy.2020.116110.

[41] Bogdanov D, Gulagi A, Fasihi M, Breyer C. Full energy sector transition towards 100% renewable energy supply: Integrating power, heat, transport and industry sectors including desalination. Appl Energy 2021;283:116273. https://doi.org/10.1016/j.apenergy.2020.116273.

[42] Bergaentzle C, Gunkel PA. Cross-sector flexibility, storage investment and the integration of renewables: Capturing the impacts of grid tariffs. Energy Policy 2022;164:112937. https://doi.org/10.1016/j.enpol.2022.112937.

[43] Boblenz K, Frank V, Meyer B. Energy system analysis for evaluation of sector coupling technologies. Fuel 2019;254:115658. https://doi.org/10.1016/j.fuel.2019.115658.

[44] Osorio-Aravena JC, Aghahosseini A, Bogdanov D, Caldera U, Ghorbani N, Mensah TNO, et al. The impact of renewable energy and sector coupling on the pathway towards a sustainable energy system in Chile. Renew Sustain Energy Rev 2021;151. https://doi.org/10.1016/j.rser.2021.111557.

[45] Pavičević M, Mangipinto A, Nijs W, Lombardi F, Kavvadias K, Jiménez Navarro JP, et al. The potential of sector coupling in future European energy systems: Soft linking between the Dispa-SET and JRC-EU-TIMES models. Appl Energy 2020;267:115100. https://doi.org/10.1016/j.apenergy.2020.115100.

[46] Bernath C, Deac G, Sensfuß F. Impact of sector coupling on the market value of renewable energies – A model-based scenario analysis. Appl Energy 2021;281. https://doi.org/10.1016/j.apenergy.2020.115985.

Evaluation of Energy Sharing on a Local Energy Market Through Comparison of Energy Management Techniques

Joel David Schölzel[a], Sarah Henn[a], Rita Streblow[a] and Dirk Müller[a]

[a] Institute for Energy Efficient Buildings and Indoor Climate, E.ON Energy Research Center, RWTH Aachen University, Aachen, Germany, joel.schoelzel@eonerc.rwth-aachen.de (CA)

Abstract:

Local energy markets (LEMs) are a promising way to solve the challenges of the increasing extension of decentralized energy systems and to promote the further integration of renewable energy sources. LEMs enable costumers with distributed energy resources to trade and share their electrical energy with each other. In the existing literature, the research focus is mostly on the development and evaluation of specific elements of LEMs, such as bidding strategies or market designs. The paper contributes a comprehensive evaluation of a LEM and the quantification of its benefit regarding the market-based device operation. For the evaluation in terms of financial outcome and local energy exchange, a centralized and a decentralized operation optimization serve as upper and lower references. In centralized optimization, the system boundary comprises the entire neighbourhood. In decentralized optimization, each building is balanced separately. For the LEM, we introduce a distributed market design with the involvement of an auctioneer. We focus there on the implementation of learning bidding strategies and a double-sided auction with non-iterative market clearing rules. For all three energy management techniques, the operating schedules of the devices are determined using mixed-integer linear programming. In several case studies we investigate different neighbourhoods in order to evaluate the influence of different technologies and their penetrations as well as the impact of the building stock in terms of building type and construction year. We evaluate the market outcome with multiple key performance indicators (KPIs) such as the supply- and demand-cover-factor, the total operation costs and the peak load. The results show that total energy costs can be reduced by up to 6.4 %. For the energy exchange, it is shown that the electricity surplus is up to 72 % and the electricity demand of the QUartier decreases by up to 6.8 % compared to the decentralized optimization and increases by up to 14.3 % compared to the centralized optimization. Further, we noted up to 46.2 % higher peak loads.

Keywords:

Local Energy Market, Evaluation, Energy Trading, Optimization Approaches

1. Introduction

For a successful energy transition, the energy supply in neighborhoods has to undergo substantial developments. Two of these developments are the increasing integration of distributed energy resources (DERs) as well as the electrification of the heating and mobility sectors. The end-users are responsible for the purchase of the corresponding devices. LEMs however can promote the further integration of renewable energy sources by giving households financial incentives. Auction-based local energy markets enable the trading and the exchange of energy between producers and consumers within a local area and participating households can reduce their energy costs this way.

For LEMs various market designs have already been developed. They differ with regard to the degree of centralization and topology, which influences the market clearing as well as the decision-making processes of operating and bidding strategies [1, 2]. Market clearing rules which select the admitted participants, determine the trading volumes and prices can be different for LEM. Further, several pricing mechanisms such as uniform pricing or pay-as-bid can be used in electricity markets [3, 4]. Also markets auctions can be divided into different types. These include whether the auction is open-cry or sealed-bid and whether it is one-sided or double-sided [5]. Various bidding strategies with different computation methodologies can be applied for placing promising bids on the market [6].

However, to fully understand the potential benefits and drawbacks of market processes there is a need of finding appropriate evaluation methods. They help to identify the most relevant technical aspects of the market design that increase efficiency and profitability of the electricity trading between consumers and prosumers on LEMs.

Within this work, we propose an evaluation methodology for LEMs in which decentralized and centralized optimization serve as worst-case and best-case references. We specify an auction-based market and a neighborhood of 20 households. The building energy systems (BES) of the households contain of heat pumps (HPs), combined heat and power plants (CHPs), thermal energy storages (TES) as well as photovoltaic (PV) and batteries (BAT). With different scenarios we analyze the influence of the different technology shares and the usage of a price signal for the LEM. We analyze the operation of a neighborhood regarding the energy exchange within and with the superordinate grid, the costs and revenues as well as the the caused emissions.

1.1. Evaluation of Local Energy Markets

The concept of LEMs has gained great traction in recent years for promoting renewable energy and energy efficiency. Evaluations of LEMs are important for understanding the market dynamics like trading volumes within a neighborhood and the resulting prices for the single households. Comprehensive and detailed evaluations are necessary to improve market outcomes in terms of trading efficiency, price fairness and thus cost savings for the households.

Zhou et al. [7] evaluated three different energy sharing mechanisms and two techniques for the convergence of market trading. The used mechanisms were supply-demand-ratio, mid-market rate and bill sharing mechanisms which mainly differ in terms of their iterative pricing. To achieve convergence in trading, change rates of prices and energy volumes were limited and a learning process is involved in the prosumers decision-making process. Three economic indexes and three technical indexes are proposed for the evaluation. The economic KPIs measure the realized overall benefits, the individual benefit compared to trading with fixed tariffs and the income equality within the households. With the technical KPIs the energy exchange with the superordinate grid, the peak power and the electricity demand that is covered by local generation are measured.

Okwuibe et al. [8] analyzed the electricity trading in hierarchical LEMs for different market structures. The market structure differs in the number of layers which result by introducing sub-LEMs that limit the number of trading end-users. Additionally, two market clearing mechanisms which are the double-sided pay-as-bid and the double-sided pay-as-clear are investigated. The different combinations of market structures and market clearing mechanisms are evaluated with KPIs like cost savings through market trading, the internal and external energy exchange, and average trade rate with varying market clearing mechanisms. Finally, the individual savings of different consumer and prosumer types are analyzed.

Sousa et al. [9] gave a comparison of different market designs with differences in the level of centralization and communication structure. A full peer-to-peer, a community-based, and a hybrid peer-to-peer market were analyzed and compared in terms of welfare, total import costs and export revenues to the superordinate grid as well as energy exchange within the market.

El-Baz et al. [10] identified the major factors influencing the market outcome and energy exchange. Several aspects of market design, microgrid configurations and user behavior were investigated for selected scenarios. For example the number of installed PV systems and their capacities are studied. Based on a double-sided auction-based LEM simulation the impact on the market dynamics and energy balance are analyzed and evaluated. For the evaluation, a reference model without a market-based operation is implemented. The four key performance indicators self-sufficiency, self-consumption, peak load and costs were calculated.

Schiera et al. [11] simulated a LEM with two trading systems that differ in terms of the pricing mechanisms. The pricing mechanisms and different member compositions were evaluated regarding the benefits of the neighborhood to identify new considerations in market design. A central mixed-integer linear programming was used as optimization model. The selected member compositions had various penetrations of PV systems and batteries. The results were evaluated with economic and technical indicators like single and total savings, the imported and exported energy as well as the self consumption ratio and the peak-to-average ratio.

Cramer et al. [12] compared an iterative auction-based LEM with a central optimization approach and a self-consumption approach. By aiming to maximize social welfare, an independence indicator is determined that relates self-consumption and traded energy to electricity demand within the neighborhood. This indicator determined for different flexibility levels.

1.2. Contributions

Most papers concentrate on analyzing different market designs to evaluate specific aspects of the design like market structure, market clearing rules or bidding strategies. However, there is a lack of publications that provide comprehensive evaluations of LEM by comparing them with other energy management techniques for neighborhoods. While there are many publications that provide detailed analysis of different market designs with a bunch of KPIs, only few publications deal with LEM using other optimization approaches and these existings ones rather offer superficial/simplified evaluations.

Furthermore, few studies still deal with the participation of flexible heat generators in LEM while most studies focus on the participation of prosumers that have PV systems and batteries.

The main contributions of this paper to research are:

- We implement two operational optimization approaches to evaluate the performance of an auction-based LEM in a comparative and comprehensive way. The decentralized optimization approach provides a lower benchmark without energy trading or coordinated energy exchange. The centralized optimization approach provides a upper benchmark with a controller having all informations.
- We implement an auction-based LEM where individual market participants perform their decision-making processes autonomously without information about other's trading behavior.
- We analyze the impact of the heat generators' shares by varying the number of the corresponding devices.
- We analyze the importance of approaches for shifting consumption and generation to the same times with the exemplary application of a price signal.
- We compare different prosumer types within the neighborhood, namely prosumer with PV systems and batteries and prosumer with CHP.

The following sections are structured as follows. In section 2., we firstly highlight the differences in modeling and balancing of the decentralized and centralized optimization approaches and introduce the evaluated LEM. Afterwards, we present the KPIs and the analyzed scenarios. We compare and evaluate the results on the scenarios in section 3.. The evaluation results finally are discussed and further research needs identified in section 4..

2. Methodology

2.1. Decentral and central optimization approaches

Decentralized optimization and centralized optimization are two different approaches to set-up optimization problems. The key difference between these optimization approaches are the degree of coordination and the decision-making authority. The difference in balance boundaries is shown in figure 1 by the red dashed lines.

Decentralized optimization refers to a scenario where the components or agents act autonomously and communicate with each other only when requested. Decentralized optimization can be more robust and efficient in situations where communication between agents is limited or when the system is large and complex. [1]

Centralized optimization refers to a scenario where a single entity, typically a central controller, collects all relevant information and decides based on that information to optimize the entire system. The central controller has complete control over every entity of the system and can optimize it as a whole. A centralized optimization model can run quickly into high complexity and scalability problems. [1]

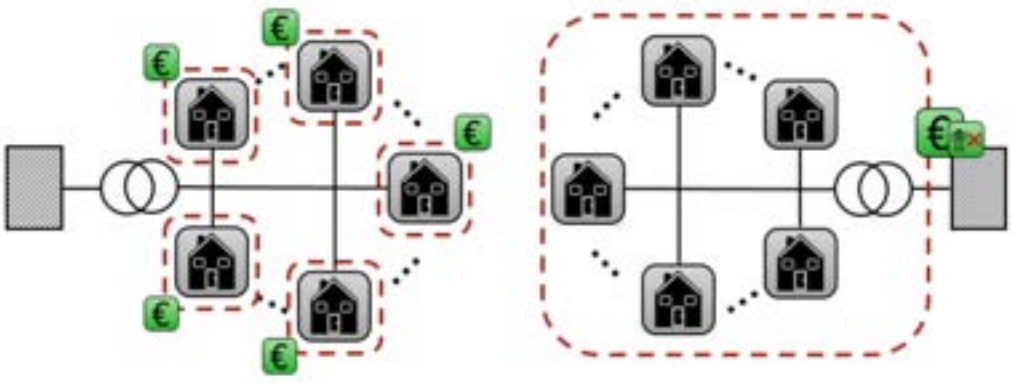

Figure 1: Balance boundaries (red dashed lines) for decentralized optimization (left) and centralized optimization (right)

For the optimal operation of the single BES and the entire neighborhood, we implement mixed-integer linear programs (MILP) of the corresponding systems. The BES model consists of constraints for the minimum and maximum power of the devices as well as for the maximum capacity of the energy storages. The state-of-charge of the storages is inserted as time-coupling constraint. The electricity balance of the BES is given by

equation 1 in which the power of the devices is coupled for every time step t with electrity demand from and the feed-in power into the grid. Thus, we assume that each building is connected to the local distribution network.

$$P_{\text{imp,t}} + P_{\text{PV,t}} + P_{\text{CHP,t}} + P_{\text{BAT,dch,t}} = P_{\text{inj,t}} + P_{\text{HP,t}} + P_{\text{ER,t}} + P_{\text{dom,t}} + P_{\text{BAT,ch,t}} \tag{1}$$

The objective functions of the decentral optimization approach are the minimization of the operational costs incurred from the purchasing minus the revenues for feed-in (equation 2).

$$min \quad C_{\text{BES}} = \Delta t \cdot \sum_{t \in T} (p_{\text{gas}} \cdot P_{\text{gas,t}} + p_{\text{imp}} \cdot P_{\text{imp,t}} - p_{\text{inj}} \cdot P_{\text{inj,t}}) \tag{2}$$

For the modeling of the entire neighborhood, the previously mentioned equations are extended by the electricity purchase and the electricity feed-in of the neighborhood into the superordinate grid level at the grid connection point (GCP) as well as the natural gas purchase (equations 3 - 5).

$$P_{\text{gas,t}} = \sum_{n} P_{\text{n,gas,t}} \tag{3}$$

$$P_{\text{GCP,imp,t}} = \sum_{n} P_{\text{n,imp,t}} \tag{4}$$

$$P_{\text{GCP,inj,t}} = \sum_{n} P_{\text{n,inj,t}} \tag{5}$$

For the centralized optimization approach, the objective function is the minimization of the operating costs and additionally of the peak load. In this case, the operating costs are the purchasing costs minus feed-in revenues at the local network station, because the system boundary includes the entire neighborhood.The peak load is considered in the objective function through a penalty factor (equation 6).

$$min \quad C_{\text{NH}} = \Delta t \cdot \sum_{t \in T} (p_{\text{gas}} \cdot P_{\text{gas,t}} + p_{\text{imp}} \cdot P_{\text{GCP,imp,t}} - p_{\text{inj}} \cdot P_{\text{GCP,inj,t}}) + pen \cdot P_{\text{GCP,inj,t}} \tag{6}$$

2.2. Local Energy Market Model

In this work, we evaluate an auction-based LEM with a hierarchical structure. This structure consists of two levels, the market platform and the operating system, as shown in the figure 2. On the market platform, the auctioneer performs market trading according to predefined rules. On the operating level, the building energy management system of each household determines autonomously the operational schedules of the corresponding devices taking into account a price signal sent by the market platform.

In the first step of the market procedure, each BES performs its operational optimization considering the price signal in the objective function instead of the fixed tariffs. With the information of the external power demand or the energy surplus to be fed into the power grid, the market agents create then the bids. In addition to the amount of energy, these bids also consist of the bid price. The market agents determine the bid price by using a Roth-Erev learning algorithm as bidding strategy. This algorithm combines two principles, namely reinforcing propensities regarding positive outcomes and flattening the learning curve over time. By this, the market agents consider the results of the historical market rounds as well as the success of the bids, which is incorporated into the probability distribution for future bidding [13]. [14, 15] have shown that the Roth-Erev learning algorithm enables the households to achieve promising economic benefits in energy trading.

In the second step, the auctioneer collects all the submitted bids of the supply side and the demand side and sorts them in step functions according to the bid prices. The underlying auction mechanism determines the market clearing price and the clearing quantity based on the received bids. In this work, the uniform pricing mechanism and therefore the intersection of the sorted supply and demand step functions is used to determine the market clearing price and the clearing quantity. [4]

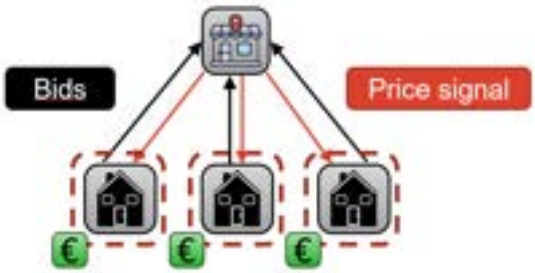

Figure 2: Structure of the local energy market and data exchange during market procedures

After the market clearing, the auctioneer sends the respective market outcome back to the market agents and the successful trades are performed. If in some market rounds there is insufficient local generation to satisfy the demand or excess generation, a superordinate grid with constant tariffs serves as a backup. Finally, a price signal is computed with the supply-demand-ratio mechanism and sent to the BES. This signal indicates, how the price trend for trading is going to develop in the next market rounds. The calculation is based on the hourly values of total supply and demand in the future time steps [7].

2.3. Key Performance Indicators

In this section, we introduce the following KPIs used to analyze the neighborhood operations of the three approaches and to and evaluate the auction-based market trading.

- Single costs and revenues: summed costs and revenues of the individual households within the neighborhood.
- Import and export energy: summed energy quantities imported from and exported to the superordinate grid.
- DCF and SCF: two energetic indicators that are calculated based on load and feed-in profiles of the BES. With them the coverage of the local electrical load by the local electrical generation and the share of self-used generation within the neighborhood are calculated. [16]
- Peak load: incurred during operation measured at the neighborhood's GCP.
- Emissions: caused by device operation in the neighborhood.

2.4. Use Case And Scenarios

To model the neighborhoods, we use our developed tool called "districtgenerator" [17]. It generates the annual profiles of the electrical load and heat demands of each building by using different tools. Using the TEASER tool, envelope areas and building physics parameters are calculated based on building type, floor area and construction year [18]. Additionally, it simulates thermal demands using a 5R1C model, while generating annual electrical load profiles and domestic hot water profiles through stochastic methods [19–21].

The building energy systems within the neighborhood contain electricity based heat generation devices for the heat provision. The single-family houses are equipped either with heat pumps or gas boilers, while the multi-family houses are heated with combined heat and power plants or gas boilers. Accordingly, electricity is also generated locally in the multi-family houses by the combined heat and power plants. Electricity generation at the single-family houses is achieved by PV systems in selected scenarios. Thermal storage and electrical battery storage systems are also taken into account. The technology penetrations vary across the studied scenarios and are presented in table 1.

In this study, we size the heat generators in accordance with german standards [22] and thermal energy storages based on [23]. The PV modules have standard size of 1.65 m^2. In the scenarios with PV systems, there are 20 modules per single-family house with a south orientation and an inclination of 35°, whereby the peak power is 6.38 kW. Furthermore, we use the specified discharge/charge power of 3.4 kW and storage capacity of 5 kWh, which data of commercial batteries.

Scenario	Constr. year	HP	CHP	Boiler	PV	BAT
16 HP	1996	80 %	20 %	0 %	0 %	0 %
8 HP	1996	40 %	20 %	40 %	0 %	0 %
0 HP / 4 CHP	1996	0 %	20 %	80 %	0 %	0 %
8 PV	1996	40 %	0 %	20 %	40 %	0 %
8 PV + BAT	1996	40 %	0 %	20 %	40 %	40 %

Table 1: Selected scenarios with the construction year and the share of devices

For the centralized and decentralized optimization approaches, the purchase electricity price is 42.0 ct/kWh, the feed-in tariffs are 8.2 ct/kWh for PV and 19.28 ct/kWh for CHP. The cost of the gas is 13.4 ct/kWh. For energy trading on the LEM, the purchase electricity price represents the maximum bid price and the feed-in tariffs represent the minimum bid price. We perform the operational optimization approaches and the LEM for a time horizon of an entire year.

For the Roth-Erev learning algorithm, we selected an experimentation parameter of 0.99 and a recency parameter of 0.08. Each scenario was pre-simulated for one year to obtain pre-learned propensities.

3. Results

3.1. Impact of the heat generator shares and the price signal

This section analyzes the summed costs and revenues of the households and the energy exchange at the GCP for different shares of heat pumps. Figure 3 shows the corresponding results. The costs for electricity and gas (dashed bars) as well as the revenues for electricity feed-in (lightened bars) are compared for different shares of heat pumps. Additionally, the electricity supply and feed-in (lightened bars) to the superordinate power grid are considered. The number of heat pumps supplying single-family homes varies, while all four multi-family homes are supplied with CHPs.

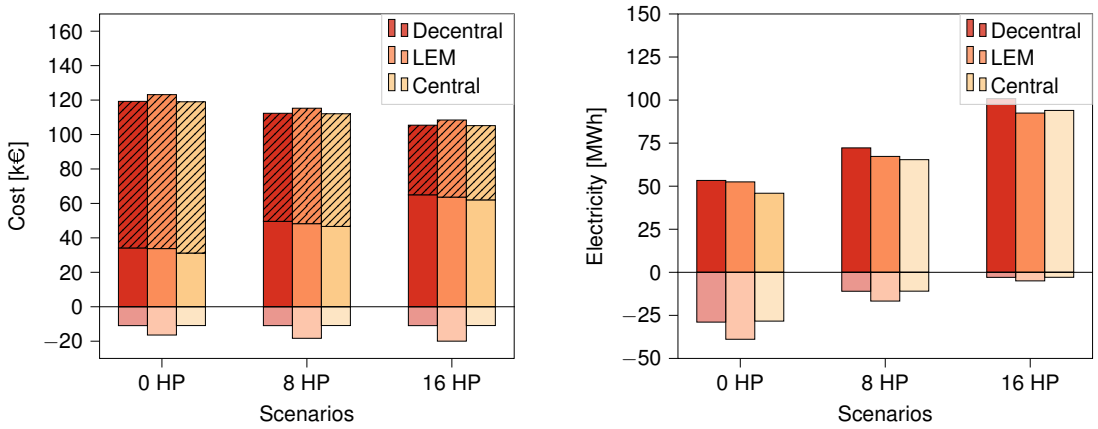

Figure 3: Summed costs and revenues of the households (left) and the energy exchange at the GCP (right) for different shares of heat pumps

In all three scenarios, the summed electricity costs of the households are highest with the decentralized optimization approach, amounting to 34.1 k€, 49.6 k€, and 65.0 k€, respectively. In contrast, the total costs for electricity consumption with the centralized optimization approach are the lowest, amounting to 31.2 k€, 46.6 k€, and 62.0 k€, respectively. Through electricity trading on the LEM, the total costs amount to 33.8 k€, 48.2 k€, and 63.7 k€. Compared to the decentralized optimization approach, the costs are thus reduced by 1.1 % to 2.7 %, while compared to the centralized optimization approach, the costs are 2.7 % to 7.6 % higher. Regarding electricity feed-in, households can achieve the highest compensation through trading on the LEM. These amount to 16.4 k€, 18.3 k€, and 20.0 k€, and are thus up to 83.0 % higher compared to both the decentralized and centralized optimization approach. Noticeable about the results is that the gas costs are highest with 44.8 k€, 67.0 k€ and 89.4 k€ for market-based operation. Thus, compared to the centralized optimization approach, 3.8 % more gas is consumed. Compared to the decentralized optimization approach, gas consumption is up to 10.7 % higher.

The price signal ensures that loads are shifted over time and that heat storages are loaded higher. This increases households' chances of benefiting from lower market prices, but also results in higher energy losses of the heat storages. To compensate these losses, the electricity demand of the heat pumps increases on the

one hand, and on the other hand the gas consumption of the CHPs increases. Furthermore, the operation of the heat pumps is no longer exclusively optimized for favorable outside temperatures to achieve the highest COP, which further increases the electricity demand of the heat pumps.

Another noticeable aspect are the higher revenues for electricity feed-in with an increasing share of heat pumps while the number of CHPs remains constant. The reason is the resulting market clearing prices of the individual scenarios. The average market clearing price is 30.7 ct/kWh in the scenario without heat pumps, 32.8 ct/kWh in the scenario with 8 heat pumps, and 34.2 ct/kWh in the scenario with 16 heat pumps. This increase in the average market price can be explained, on the one hand, by the increased demand for electricity and, on the other hand, by the learning bid strategies. With increased demand and a constant supply on the LEM, bids with higher prices are offered by the learning bidding strategy in the long term to increase the chance of being considered in the market clearing process.

Considering the total energy costs minus the revenues, the LEM performs better up to 1.4 % in the scenario without heat pumps, up to 4.3 % in the scenario with 8 heat pumps, and up to 6.4 % in the scenario with 16 heat pumps. The best result in the last scenario is mainly due to the high revenues. The highest average market price of 34.2 ct/kWh in this scenario, explains the highest revenues, although the number of CHPs and thus the electricity generation remains approximately the same. The high market prices are further an indication that the sellers profit more from energy trading than the buyers, because the difference from the market prices is on average smaller to $p_{\max}$ than to $p_{\min}$.

		CO_2e [t]	Peak load [kW]	SCF [%]	DCF [%]
16 HP	Decentral	148	65	95	35
	LEM	159	95	93	43
	Central	155	63	95	36
8 HP	Decentral	210	40	81	39
	LEM	222	62	77	46
	Central	216	34	81	4
0 HP	Decentral	274	31	49	34
	LEM	287	33	47	40
	Central	280	24	50	38

Table 2: Results of caused emissions, peak load, self-cover-factor and demand-cover-factor

As shown in figure 3, the amounts of electricity fed into the superordinate grid are highest in all three scenarios for the market-based operation. Compared to the centralized optimization approach, these amounts are 37.2 % to 72.0 % higher, and compared to the decentralized optimization approach they are 34.4 % to 69.4 % higher. These results can be explained by the fact that increased load shifts in market-based operation of the CHPs lead to greater heat losses and the compensation of these losses results in increased electricity generation. These results are also reflected in the results of the self-cover-factor as seen in table 2. With a high share of heat pumps, the absolute difference in electricity feed-in between market-based and optimization-based operation is significantly lower. Electricity consumption is up to 6.8 % lower than in the decentralized optimization approach in all scenarios. Compared to the centralized optimization approach, the electricity consumption of the quarter is 14.3 % and 3.0 % higher in scenarios 1 and 2, respectively, while it is 1.6 % lower in scenario 3. These results show that the used price signal improves local electricity consumption, which is also supported by the demand-cover-factors in table 2.

Figure 4 exemplarily shows the course of the residual load for a cold week of scenario 2. During this period, three peak loads can be seen for the decentralized optimization approach. These peak loads are avoided both with the centralized optimization approach and with the market-based operation under usage of the price signal. Nevertheless, the results of the peak loads for the entire seasonal period (table 2) show that the peak loads are significantly higher at individual time steps. This presumably happens when the price signal triggers opposing operational adjustments. Heat pumps collectively shift their electricity consumption to a favorable time step, while the power generation of the CHPs is shifted away from it.

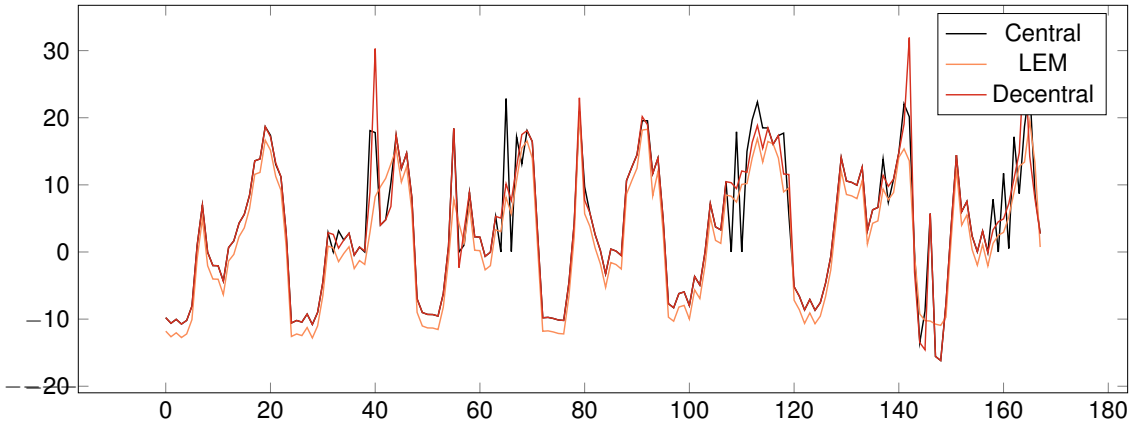

Figure 4: Residualload of the neighborhood at the GCP

3.2. Impact of the PV systems and batteries

The following section analyzes the impact of the electricity generation systems on the market outcomes and electricity exchange of the neighborhood. Scenario 2, in which four CHPs provide electricity generation in the neighborhood, scenario 6, in which six PV systems generate electricity in the neighborhood, and scenario 7, in which BESs have battery storage in addition to PV systems, are compared. In these three scenarios, heat is provided to six single-family homes by heat pumps.

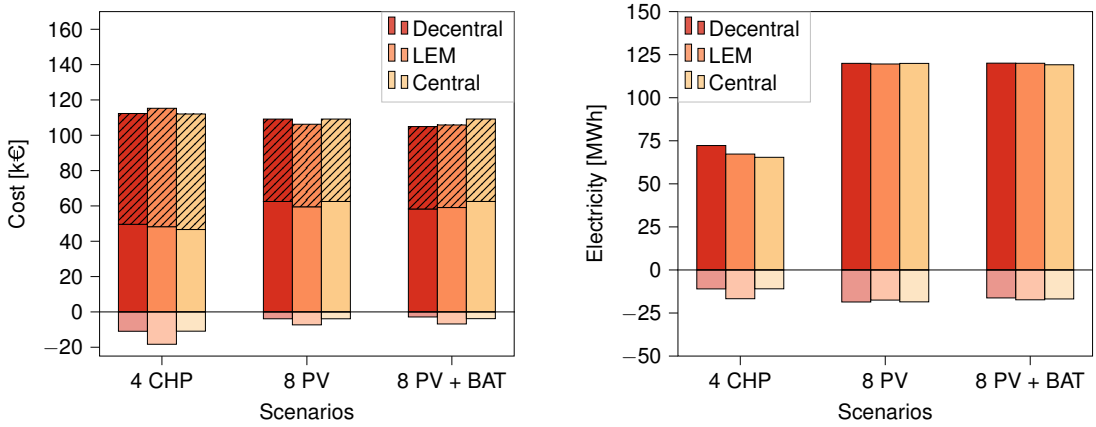

Figure 5: Summed costs and revenues of the households (left) and the energy exchange at the GCP (right)

Figure 5 shows the results of the summed costs and revenues of the households and the energy exchange at the GCP. As seen in the previous section, the revenues are again higher for the scenarios with PV systems with the market-based operation than with the optimization-based operations. While the cost of electricity and gas is slightly lower for the PV scenarios compared to the CHP scenario, the revenues are lower.

Figure 5 further shows that the market-based operation with price signal has only a slight impact on the electricity exchange at the GCP. This is due to the electricity demand of the heat pumps, which exists especially in the cold periods. At these times, however, there is less solar irradiation and thus less power feed-in from the PV systems. Consequently, the potential energy exchange and the trading volume is significantly lower.

		CO_2e [t]	Peak load [kW]	SCF [%]	DCF [%]
4 CHP	Decentral	210	40	81	39
	LEM	222	62	77	46
	Central	216	34	81	41
8 PV	Decentral	175	58	61	19
	LEM	172	57	63	20
	Central	175	47	61	19
8 PV + BAT	Decentral	174	58	53	13
	LEM	172	76	65	19
	Central	174	47	64	20

Table 3: Results of caused emissions, peak load, self-cover-factor and demand-cover-factor

Table 3 shows the remaining results. When comparing operating methods, again that the market-based operation with the usage of the price signal causes significantly increased peak loads. The comparison between generation technologies shows that PV systems causes significantly less emissions, but also results in lower local self-supply and local self-consumption compared to the scenario with CHPs.

4. Conclusions

In this study, we proposed an evaluation of a local energy market by comparing it with a decentralized and a centralized optimization approach. An auction-based LEM with uniform pricing as market clearing process was introduced and learning bidding strategies for the market agents were implemented. To obtain convergence in supply and demand on the market, a price signal was sent to the building energy systems, which served as input to the operational optimization. We examined a neighborhood with single-family and multi-family buildings and analyzed several scenarios with different shares of heat pumps, combined heat and power plants, PV systems and batteries.

We demonstrated that auction-based energy trading can reduce household electricity costs compared to operating the decentralized optimization approach. However, we must emphasize that in the decentralized and centralized optimization approaches, no deviating tariffs for electricity purchase and feed-in were possible. Therefore, it should be examined whether the costs and revenues of the two optimization-based approaches should be allocated with adjusted tariffs in the future in order to improve comparability.

For the overall cost and revenue analysis, the costs and revenues of each household were summed. In the future, a comprehensive evaluation should also examine individual costs and revenues more detailed to determine the fairness of the energy trading.

We have also shown that market-based operation leads to more energy inefficient operation of heat generators. The operation of the heat pumps is no longer geared only to outdoor temperature, and the increased use of heat storage increases heat losses in the neighborhood. Therefore, an indicator should be considered in the future that takes the energetic losses into account.

By using the price signal, we were able to show that the energy exchange and trading compared to decentralized operation can be improved. However, higher maximum peak loads indicate that at individual time steps, load shifting from the generation and demand side can result in opposite directions. Considering that we have used a price signal based only on supply and demand quantity, in the future parameters should include in the calculation of the price signal, which avoid higher peak loads. In addition, to improve energy exchange and trading for auction-based LEM, further techniques for convergence of generation and demand need to be identified and analyzed.

Acknowledgments

We gratefully acknowledge the financial support by Federal Ministry for Economic Affairs and Climate Action (BMWK), promotional reference 03EWB003B.

References

[1] Y. Zhou, J. Wu, C. Long, W. Ming, State-of-the-Art Analysis and Perspectives for Peer-to-Peer Energy Trading, Engineering 6 (7) (2020) 739–753. doi:10.1016/j.eng.2020.06.002.
URL https://linkinghub.elsevier.com/retrieve/pii/S2095809920301405

[2] W. Tushar, C. Yuen, T. Saha, T. Morstyn, A. Chapman, M. J. E. Alam, S. Hanif, H. V. Poor, Peer-to-Peer Energy Systems for Connected Communities: A Review of Recent Advances and Emerging Challenges,

Applied Energy 282 (2021) 116131, arXiv:2011.11118 [cs]. doi:10.1016/j.apenergy.2020.116131.
URL http://arxiv.org/abs/2011.11118

[3] W. E. B. Elbaz, A Bottom-Up Model for Energy Trading Markets and Prosumers Coordination in Microgrids, Ph.D. thesis, Technical University of Munich, Munich, Germany (2018).

[4] S. Nojavan, K. Zare (Eds.), Electricity markets: new players and pricing uncertainties, Springer, Cham, 2020.

[5] L. Maurer, L. Barroso, Electricity Auctions: An Overview of Efficient Practices, The World Bank, 2011. doi:10.1596/978-0-8213-8822-8.
URL http://elibrary.worldbank.org/doi/book/10.1596/978-0-8213-8822-8

[6] M. Prabavathi, R. Gnanadass, Energy bidding strategies for restructured electricity market, International Journal of Electrical Power & Energy Systems 64 (2015) 956–966. doi:10.1016/j.ijepes.2014.08.018.
URL https://linkinghub.elsevier.com/retrieve/pii/S0142061514005444

[7] Y. Zhou, J. Wu, C. Long, Evaluation of peer-to-peer energy sharing mechanisms based on a multiagent simulation framework, Applied Energy 222 (2018) 993–1022. doi:10.1016/j.apenergy.2018.02.089.
URL https://linkinghub.elsevier.com/retrieve/pii/S0306261918302149

[8] G. C. Okwuibe, A. S. Gazafroudi, S. Hambridge, C. Dietrich, A. Trbovich, M. Shafie-khah, P. Tzscheutschler, T. Hamacher, Evaluation of Hierarchical, Multi-Agent, Community-Based, Local Energy Markets Based on Key Performance Indicators, Energies 15 (10) (2022) 3575. doi:10.3390/en15103575.
URL https://www.mdpi.com/1996-1073/15/10/3575

[9] T. Sousa, T. Soares, P. Pinson, F. Moret, T. Baroche, E. Sorin, Peer-to-peer and community-based markets: A comprehensive review, Renewable and Sustainable Energy Reviews 104 (2019) 367–378. doi:10.1016/j.rser.2019.01.036.
URL https://linkinghub.elsevier.com/retrieve/pii/S1364032119300462

[10] W. El-Baz, P. Tzscheutschler, U. Wagner, Evaluation of Energy Market Platforms Potential in Microgrids: Scenario Analysis Based on a Double-Sided Auction, Frontiers in Energy Research 7 (2019) 41. doi:10.3389/fenrg.2019.00041.
URL https://www.frontiersin.org/article/10.3389/fenrg.2019.00041/full

[11] D. S. Schiera, C. De Vizia, A. Zarri, R. Borchiellini, A. Lanzini, E. Patti, L. Bottaccioli, Modelling and techno-economic analysis of Peer-to-Peer electricity trading systems in the context of Energy Communities, in: 2022 IEEE International Conference on Environment and Electrical Engineering and 2022 IEEE Industrial and Commercial Power Systems Europe (EEEIC / I&CPS Europe), IEEE, Prague, Czech Republic, 2022, pp. 1–6. doi:10.1109/EEEIC/ICPSEurope54979.2022.9854537.
URL https://ieeexplore.ieee.org/document/9854537/

[12] W. Cramer, M. Vasconcelos, C. Schmitt, F. Heringer, A. Armstorfer, N. Beg, Engaging Prosumers in Local Energy Market Business Models, in: CIRED 2019 proceedings, Madrid, Spain, 2019, p. 5.

[13] J. Nicolaisen, V. Petrov, L. Tesfatsion, Market power and efficiency in a computational electricity market with discriminatory double-auction pricing, IEEE Transactions on Evolutionary Computation 5 (5) (2001) 504–523. doi:10.1109/4235.956714.
URL http://ieeexplore.ieee.org/document/956714/

[14] S. Bose, E. Kremers, E. M. Mengelkamp, J. Eberbach, C. Weinhardt, Reinforcement learning in local energy markets, Energy Informatics 4 (1) (2021) 7. doi:10.1186/s42162-021-00141-z.
URL https://energyinformatics.springeropen.com/articles/10.1186/s42162-021-00141-z

[15] E. Mengelkamp, P. Staudt, J. Garttner, C. Weinhardt, Trading on local energy markets: A comparison of market designs and bidding strategies, in: 2017 14th International Conference on the European Energy Market (EEM), IEEE, Dresden, Germany, 2017, pp. 1–6. doi:10.1109/EEM.2017.7981938.
URL http://ieeexplore.ieee.org/document/7981938/

[16] D. Müller, A. Monti, S. Stinner, T. Schlösser, Energieoptimiertes Bauen, Tech. rep., Aachen, Germany (May 2017).

[17] S. Henn, T. Beckhölter, J. Schölzel, D. Müller, districtgenerator (September 2022).
URL https://github.com/RWTH-EBC/districtgenerator

[18] P. Remmen, M. Lauster, M. Mans, M. Fuchs, T. Osterhage, D. Müller, TEASER: an open tool for urban energy modelling of building stocks, Journal of Building Performance Simulation 11 (1) (2018) 84–98. doi:10.1080/19401493.2017.1283539.
URL https://www.tandfonline.com/doi/full/10.1080/19401493.2017.1283539

[19] T. Schütz, Optimal Design of Energy Conversion Units and Building Envelopes for Residential Neighborhoods, Ph.D. thesis, RWTH Aachen University, Aachen, Germany (2018).

[20] I. Richardson, M. Thomson, D. Infield, C. Clifford, Domestic electricity use: A high-resolution energy demand model, Energy and Buildings 42 (10) (2010) 1878–1887. doi:10.1016/j.enbuild.2010.05.023.
URL https://linkinghub.elsevier.com/retrieve/pii/S0378778810001854

[21] J. Schiefelbein, J. Rudnick, A. Scholl, P. Remmen, M. Fuchs, D. Müller, Automated urban energy system modeling and thermal building simulation based on OpenStreetMap data sets, Building and Environment 149 (2019) 630–639. doi:10.1016/j.buildenv.2018.12.025.
URL https://linkinghub.elsevier.com/retrieve/pii/S0360132318307686

[22] DIN EN 15450:2007-12, Heizungsanlagen in Gebäuden_- Planung von Heizungsanlagen mit Wärmepumpen; Deutsche Fassung EN_15450:2007, Tech. rep., Beuth Verlag GmbH. doi:10.31030/9854436.
URL https://www.beuth.de/de/-/-/98862901

[23] S. Stinner, K. Huchtemann, D. Müller, Quantifying the operational flexibility of building energy systems with thermal energy storages, Applied Energy 181 (2016) 140–154. doi:10.1016/j.apenergy.2016.08.055.
URL https://linkinghub.elsevier.com/retrieve/pii/S0306261916311424

Towards the introduction of green hydrogen in the energy mix of Mediterranean islands through the integration of wind and solar power: a techno-economic case study

Francesco Superchi[a], Sander Schepers[a,b], Antonis Moustakis[c], George Pechivanoglou[c], Alessandro Bianchini[a]

[a] Department of Industrial Engineering, University of Florence, Florence, Italy, alessandro.bianchini@unifi.it
[b] Department of Mechanical Engineering, Eindhoven University of Technology, Eindhoven, Netherlands, s.h.h.schepers@student.tue.nl
[c] Eunice Energy Group, Athens, Greece, g.pechli@eunice-group.com

Abstract:

Mediterranean islands have always struggled with power supply, with the high cost of electrical submarine cables prompting the pursuing of energy self-sufficiency with renewable energy sources (RES). Despite being clean and sustainable, RES are intermittent and unpredictable, hence the integration of a storage system is crucial to match load with production. Modern batteries are a valuable solution for short term storage, but they are unsuitable for long term storage for both technical and economic reasons. Green hydrogen is among the most promising options to enable a year-long autonomous operation, but it is still an expensive option, with many technical issues that still need to be addressed. One of the key factors hampering a reduction of the levelized cost of green hydrogen (LCOH) is the low number of working hours that an electrolyzer can exploit when connected to low-capacity factor RES. Starting with real production data of a wind turbine and a PV farm in a Mediterranean island, this study aims to assess the optimal combination of wind and solar power to decrease the LCOH (intended as its production cost only) and thus the cost of storage.

The study is made of three steps. First, a comprehensive parametric optimization is carried out to determine the optimal combination of electrolyzer and PV field size to minimize the LCOH produced from the surplus power generated on the island. Secondly, an additional analysis is performed to calculate the minimum PV field expansion required to achieve a complete energy self-sufficiency and to estimate the resulting LCOH in such case. Lastly, the implementation of a fleet of hydrogen buses is proposed to both reduce the carbon footprint of the island transportation system, and further lower the cost of hydrogen production.

Keywords:

Green Hydrogen; Island; Wind; Photovoltaics; Techno-economics; LCOH.

1. Introduction

The focus of the present study is the estimation of the cost of producing green hydrogen on the island of Tilos, as a potential upgrade of the hybrid energy system (HES) currently in use. Nowadays, the system involves a 800-kW wind turbine, a 160-kWp PV field, and a 2.88 MWh battery in proximity of two villages. These villages experience a peak demand of 960 kW during the summer season.

More specifically, the objective is to assess the potential for hydrogen production using the excess power generated by the HES due to the mismatch between intermittent renewable energy production and demand. This excess power is harnessed for water splitting using an alkaline electrolyzer.

The analysis first evaluates the energy deficit and surplus of the HES, initially considering only the RES production and then assessing the storage potentiality. An electrolyzer model is then used to analyze the H_2 production potential from the power excess profiles generated by different scenarios resulting from the upgrade of the PV field. For each simulated couple of increased PV power and electrolyzer sizes, the levelized cost of hydrogen (LCOH) is calculated. Next, the annual hydrogen generation is compared with a preliminary estimation of the amount of hydrogen required to achieve 100% self-sufficiency by reconverting it back to electricity using a fuel cell. The aim is to identify the configuration that produces the cheapest hydrogen in the case a form of seasonal storage is needed. Additionally, this study explores the possibility of using hydrogen excess to power a fleet of buses, which would help in the decarbonization of public transport during the summer

season without imposing an additional strain on the electrical grid. Moreover, it is demonstrated how an increase in the amount of produced hydrogen could further lower the LCOH.

This preliminary assessment aims to evaluate the green hydrogen production potential in remote islands. Those communities may largely benefit from a suitable mean of seasonal storage, due to their highly variable energy demand during the year.

1.1. Tilos project

Tilos belongs to the Greek Non-Interconnected Islands (NIIs) group, i.e., remote communities in the Aegean sea whose electricity requirements have been almost entirely supplied by a local generation based on outdated thermal power stations that rely on diesel and heavy oil [1]. Due to the high solar radiation and pretty high wind speeds that characterize the region, the energy production of the area could be shifted towards a more sustainable generation based on renewable sources. Funded by the European Horizon 2020 project, the hybrid energy system (HES) of Tilos was completed in 2019 and comprises of an Enercon E-53 800-kW wind turbine and a 160-kWp photovoltaic field. In addition, a 2.88-MWh high temperature battery was selected as the storage medium to manage the intermittent energy fluxes from renewable generators [2]. Today, the HES is owned and managed by Eunice Energy Group (EEG), which kindly provided real operational data used for the analyses.

1.2. Green hydrogen production in islands

As a complement to the introduction of RES, green hydrogen and power-to-gas technologies are seen as promising for a variety of applications for the island of Tilos and other similar communities. Due to the significant variation of the electrical energy demand resulting from the seasonal variation of the population, green hydrogen tanks could be in fact a suitable option to store the energy generated in the winter season, when the population is minimum. Then, H_2 can be converted back to electricity during summer when tourists make the population triple.

Several studies have already proven that green hydrogen can be used for seasonal storage. H_2 produced by means of water electrolysis driven by renewable power produced by PV and wind generators can be stored in tanks and, when needed, reconverted into electricity via fuel cells or thermal machines. Lubello et al. [3] assessed the feasibility to utilize hydrogen for long-term storage in energy systems. Despite being inconvenient in normal scenarios, an island could be a suitable candidate for this kind of applications because of its remote location and thus high costs of connection with the main grid. Another viable and promising option is the export of clean fuels. Vilbergsson et al. [4] investigated the potential of producing green hydrogen in remote locations with abundant renewable resources. If electrolysis is utilized to exploit the energy surplus of those communities, a suitable option could also be to export the fuel towards the mainland. Even considering transport, authors proved that hydrogen produced in this way could have a lower environmental impact than yellow hydrogen produced using grid electricity in some European countries.

The possibility of producing hydrogen in a Greek island has been previously investigated by Lykas et al. [5]. The authors performed a dynamic investigation and optimization of a solar-based unit for green hydrogen production by means of a PEM electrolyzer and found that their system can meet the variable demand of an island. The present work builds upon the same main concept and considers a similar location, but different RES generators and another, yet similar, electrolyzer technology, while additional scenarios for hydrogen use are introduced. One factor that may hinder the introduction of this energy vector in islands is the high production cost. To this end, the correct sizing of the hydrogen production plant for an optimal exploitation of all components is key to minimizing the expense. The levelized cost of hydrogen (LCOH) of generating hydrogen from a mix of solar and wind power in different locations with different capacity factors was computed by Tang et al. [6]. In the study, authors calculated the price difference of producing hydrogen in locations with a different availability of renewable sources and proved that LCOH may vary from 7.2 €/kg in low windy areas to 3.5 €/kg if the plant has a high availability of the renewable resource. This result reinforces the interest in investigating the hydrogen production potential of islands, due to their high-RES potential.

1.3. Aims of the study

This study assesses the green hydrogen production potential of the hybrid energy system (HES) of the island of Tilos and the resulting cost for producing it. Figure 1 represents the layout of the considered plant and schematizes how clean power produced by renewable generators, supported by the battery energy storage, satisfy the island load. In addition, the power excess is considered as the input for an alkaline electrolyzer that splits water molecules in oxygen and hydrogen. The hydrogen can then be utilized by users or stored in high pressure tanks for further applications. A first sensitivity analysis on a wide range of electrolyzer sizes and possible PV upgrades was used to assess which configuration can produce hydrogen in Tilos at the lowest cost exploiting the power production excess of the island.

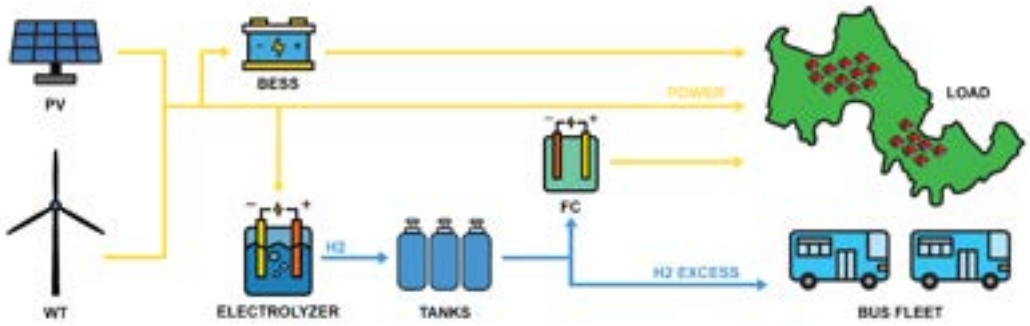

Figure. 1. Tilos HES layout paired with green hydrogen production from power excess and an example of its possible utilization

Then, the possibility of using such hydrogen as seasonal storage is presented, which is supposed to be achieved by means of a fuel cell that converts the gas back to electricity. The hydrogen production capability of different configurations is compared to their hydrogen demand to reach 100% self-sufficiency. The scope is to assess the minimum required upgrade of the PV field to reach total energy independence and to figure out what would be the LCOH in that case. Finally, the LCOH of the hydrogen excess produced by those systems is quantified and a possible exploitation of that excess is proposed. Hydrogen can indeed represent a clean fuel for the decarbonization of the public transport system of the island, and a reduction in the cost of the production excess can make it a competitive fuel with respect to current fossil alternatives.

2. Materials and methods

2.1. Available data

Historical production data of the HES have been made available by EEG, the owner and manager of the system. These data cover eleven months of operation, from November 29th, 2020, to October 29th, 2021, and contain solar production and wind speed measurements sampled with a 1-minute time resolution, directly harvested by the energy management system (EMS). During the first phase of the work available data have been analyzed to produce a consistent input for the hydrogen production model and missing data have been filled. In addition, to carry out relevant production estimations and compare results with literature, a year of operation is required. To address this, PV and wind production datasets were further filled and extended as described in the following section.

2.1.1 Reconstruction of missing data

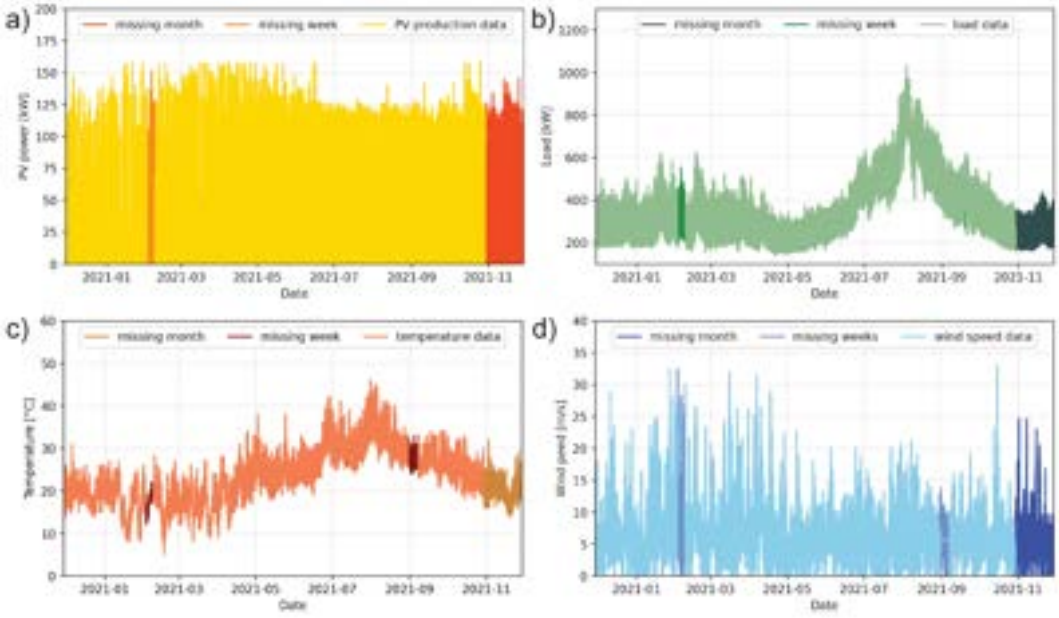

Figure. 2. Time trend during the considered period operation and highlight on reconstructed data related to missing weeks and missing month for a) PV production, b) load, c) ambient temperature, and d) wind speed.

PV power – Regarding the PV production dataset, a linear interpolation was first carried out to fill missing production for hourly periods. This simple yet effective method produced satisfying results for short time intervals. Production data filled using linear interpolation are represented in yellow in Figure 2 (a). The analysis showed that, for each quantity, the period between Feb 2nd and 8th 2021 is missing. To fill this missing spot, a support vector regression (SVR) was applied to find the correlation between the missing data and the value recorded one, two, three and four weeks before. This reconstruction is visible, in orange, in Figure 2 (a). SVR was also applied to reconstruct the missing month from 29th October to 29th November 2021, finding correlations with the previous month and two months prior. The filled month is again visible in Figure 2 (a), in red.

Load and temperature - Load and temperature datasets were cleaned and filled in a similar way. The load dataset was cleaned by abnormal data points. Outliers too far from the moving average of the load time series were removed, as well as isolated missing values given by measurement errors. Then, gaps shorter than 5 hours were again filled by a linear interpolation with satisfying results. After that, short missing periods in the order of days to one week were filled using again SVR trained on the autocorrelation of the series with its own past values. In Figure 2 (b), the resulting reconstructed periods are highlighted in green. Finally, the missing month was reconstructed by means of a multi-layer perceptron regression. Because of the shape of the series, the method was trained on the first 3 months of data. Figure 2 (b) shows the final obtained load trend. The temperature dataset was pre-processed, cleaned, and filled as well. Using the same methods described for the load dataset, missing periods were reconstructed. The whole year temperature time trend is presented in Figure 2 (c).

Wind speed - The wind speed dataset was lacking the same week of February and the final month of November 2021. Due to the small length of the period and low autocorrelation of the wind series, it was chosen to copy measures from previous days to fill the gaps. In this case, an abnormal measure characterized the period between August 31st and September 8th, 2021, for which a constant value was reported for the wind speed, due to a malfunctioning of the acquisition system. Those data were rejected and substituted using the same procedure utilized for the missing week. Then, for the missing month, winter days were sampled from the dataset at random to reconstruct the missing data. Figure 2 (d) reports the wind speed related to the eleven months in light blue, the reconstructed missing weeks in blue, and the reconstructed missing month in dark blue. Finally, via the ideal power curve of the Enercon E-53 800kW wind turbine, the power production was estimated from the obtained wind speed data for the entire year.

2.2. Resource assessment

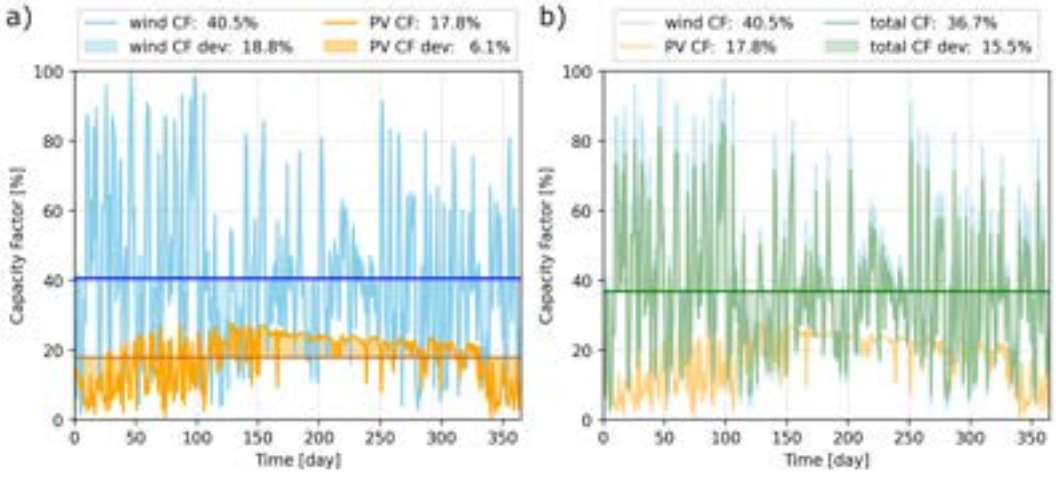

Figure. 3. Daily variation of average capacity factor (CF) and yearly mean value for: a) wind turbine (in blue) and PV field (in orange) and b) hybrid energy system composed by the previous two.

In Figure 3, power production data have been reorganized from January to December, moving the first month of the original dataset to the end, in order to appreciate the seasonal variation of the two resources. Instead of the power production itself from each generator, the energy assessment was based on the generator capacity factor (CF), i.e., the ratio between the actual energy production in each time frame and the energy that the same generator would have produced during the same interval if working at rated power. Figure 3 (a) shows the daily average CF of the wind turbine (in light blue) and PV field (in orange). The CF of the wind turbine is normalized with respect to its nominal power, 800 kW, while the one of the PV is normalized to its peak power of 160 kWp. The dark blue and dark orange flat lines represent the average CF of generators, 40.5% for the WT and 17.8% for the PV. This remarkably high wind capacity factor would in practice be much lower due to the frequent curtailments made by the grid operator to avoid instability problems [7], again proving the need

for a suitable energy storage system. It is apparent how the capacity factor of the PV is higher during the summer season than in the winter season, due to the higher solar radiation and light hours. On the other hand, the wind turbine tends to produce slightly more during winter and spring season. In general, as expected the two resources show a certain degree of complementarity, and their combination may lead to steadier energy productions during the year. Figure 3 (b) shows in green the total CF of the system, given by the sum of power generated by the two resources. Its average value (36.7%) is lower than the one related to the single turbine, but its deviation is lower: 15.5% vs 18.8% of the WT because of the lower variation of the PV (6.1%).

2.2.1 Power surplus and deficit during the year

Figure 4 (a) illustrates the match between the weekly average power production (in black) and the average island demand (in red). As discussed, the weekly average power production shows how the synergy between wind and solar energy makes the power production average almost constant during the year. On the other hand, the island demand is characterized by a clear peak during the summer season, primarily due to the presence of tourists that greatly increase the population of the island and thus its energy needs. Therefore, a considerable power deficit of around 1046 MWh affects summer months. During the rest of the year, especially in the first part, the decrease in the island population creates a power excess of around 1125 MWh.

2.2.2 Battery supported operation

A 2.88 MWh lithium-ion battery is considered to simulate how an electrochemical storage device, close to the actual one installed in the island of Tilos, would shift the power profile. Because of the strong seasonal variation of the island load, the current storage size cannot shift the entire power excess towards the power deficit. In our preliminary estimation, the 2.88 MWh BESS still creates an energy deficit of 755 MWh during summer, and the system reaches 74.9% of self-sufficiency. In that scenario, the power excess of more than 781 MWh created in winter months, when the load is covered by the current RES generation and the battery is already full, has the potential to be converted to hydrogen for seasonal storage. Figure 4 (b) clearly shows how the BESS could fill the gap between surplus and deficit energy, although the daily averaged profile of the delivered power slightly differs from the original one. Thus, a seasonal storage device seems the perfect candidate for meeting this residual requirement.

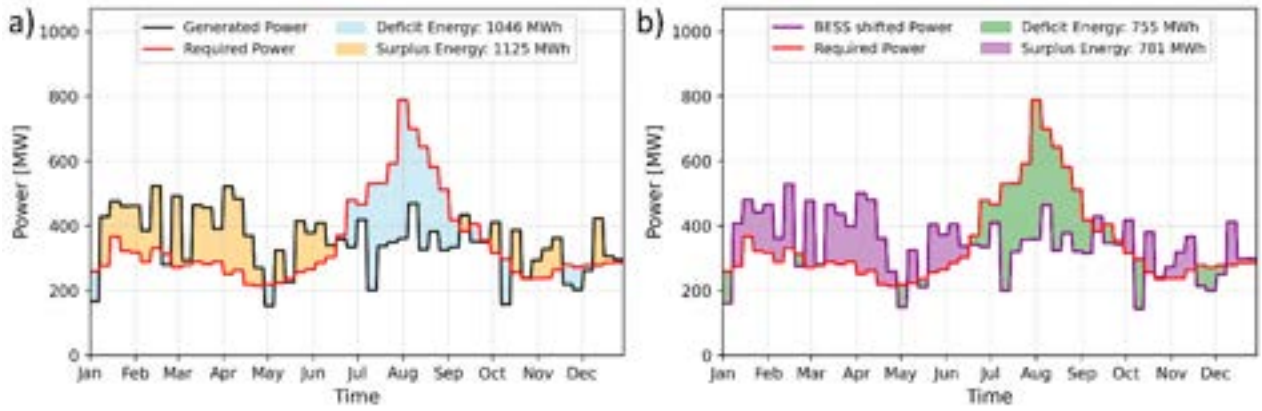

Figure. 4. Match between the daily averaged power production (black line) and the island demand (red line). Highlight on energy surplus (orange/purple areas) and energy deficit (light blue/green areas) for a) RES production and b) BESS-shifted production.

2.3. Green hydrogen production

An in-house alkaline electrolyzer model was developed by some of the authors and was already applied to some other case studies for the green hydrogen production from wind farms [8]. The model was based on the 1MW commercial electrolyzer produced by McPhy, a leading alkaline electrolyzer manufacturer. Since the current Tilos HES has a nominal power of 960 kW, the electrolyzer stack had to be resized to meet the power excess magnitude of the system. Power absorbed by a cell is given by the product of its current and voltage (Eq. 1) and, in this case, corresponds to roughly 9.45 kW. The stack of the commercial 1MW electrolyzer is thus composed of roughly 106 cells connected in series. In this work, customized stacks made by the series connection of a variable number of cells were considered to reach various power levels between 200 kW (22 cells) to 1.5 MW (150 cells), to match the total nominal power level of the HES composed by the wind farm and the PV field.

The operating voltage of the electrolyzer varies due to the performance degradation in time and cool down effect when the H_2 production stops. This time, the main component responsible for the thermal loss, the gas-liquid separator, is scaled according to the considered number of cells to maintain the proper mass flow rate of hydrogen. At each timestep, the conversion factor of the stack is updated according to Eq. 1.

$$\varphi = \frac{H_{2,id}}{I_{id} \cdot n_{cells} \cdot (V_{ideal} + \Delta V_{time,deg} \cdot h_{work} + \Delta V_{Thermal,deg} \cdot (T_{rated} - T_{el}))} \quad (1)$$

To analyze the H_2 exploitation, a fuel cell with a fixed conversion efficiency was considered for the conversion of gas back to electricity. According to IRENA [9], the efficiency of this technology typically ranges between 50 to 68%, thus an average value of 60% was considered for this analysis.

2.5. LCOH

$$LCOH = \frac{\sum_{t=0}^{20} \frac{(CAPEX_t + OPEX_t)}{(1+i)^t}}{\sum_{t=0}^{20} \frac{H_{prod}}{(1+i)^t}} \quad (2)$$

The levelized cost of hydrogen (LCOH) was selected as the main techno-economic metric for comparing different plant layouts. It represents the cost of producing a unit of hydrogen over a selected period of time (20 years in this case) by means of a certain configuration. The LCOH can be computed, according to Eq. 2, as the ratio between the actualized sum of capital (CAPEX) and operating (OPEX) costs and the actualized hydrogen yield of the plant (H_{prod}), considering in this case a discount rate *i* of 6%.

Capital costs (CAPEX) consider the investment cost for the electrolyzer. According to IRENA [9], a 1MW electrolyzer stack has a specific cost of 270 €/kW and accounts for 45% of the total price of the device. Consequently, the electrolyzer price cost was scaled when smaller or bigger stacks were considered, while the balance of plant (BOP) cost was kept constant. CAPEX also includes the substitution costs that must be faced when a part or a whole component must be substituted. The electrolyzer stack has an expected lifetime of 10 years, thus a replacement is expected halfway the plant life.

Operational costs (OPEX) consider instead the necessary maintenance to keep the electrolysis in proper operating conditions, in this case assumed equal to 2.75% of its initial investment. OPEX also accounts for the cost of energy generated by the wind turbine and the PV panels. Since generators first aim to feed the load of the island, only the cost of the consumed energy by the electrolyzer is considered here for the preliminary LCOH calculation, and it was assumed equal to the LCOE of RES. According to IRENA [10], the LCOE was 33 €/MWh for offshore wind and 48 €/MWh for PV in 2021. For this study, because of the energy mix of Tilos HES, such cost was considered equal to 40 €/MWh. Because of the uncertainty and variability of this cost, the present analysis assumed a constant LCOE even when the PV share in the energy mix increases.

Storage, distribution, and utilization costs of the hydrogen have been excluded from the calculation since the scope of the current work is to evaluate the theoretical production cost of H_2 in the island. Possible utilizations of the gas presented in section 3 are studied mainly to assess the required H_2 annual yield, functional to correctly estimate the size of components and key for the LCOH calculation.

3. Results

This section presents the main results related to the hydrogen production potential of several configurations involving different sizes of the photovoltaic field and electrolyzer power levels, assessed by means of the previously described framework. Electrolyzers are fed by the excess power of the HES, after that the wind turbine and the augmented PV field have satisfied the load of the island with BESS support. For each of those configurations, a year of operation was simulated and, together with the amount of hydrogen that each of those can provide, the LCOH and the annual yield were assessed to compare their performance.

3.1. LEVELIZED COST OF HYDROGEN

To provide a general overview of the optimal combination of PV and electrolyzer power to reach the minimum LCOH on the island of Tilos, Figure 5 displays the LCOH for every computed combination of electrolyzer power ranging between 200 and 1400 kW fed by PV power ranging between 0 and 1600 kW, in addition to the fixed 800-kW wind turbine. Inefficient combinations of high PV power and small electrolyzer modules, as well as low PV powers and high electrolyzer power combinations, can be observed in yellow areas. As previously mentioned, it is essential to maintain a right balance between the two to correctly exploit the system.

The area in which combinations lead to the cheapest green hydrogen is characterized by intermediate electrolyzer sizes, between 400 and 800 kW, paired with high PV powers (dark blue region). Overall, increasing the PV size makes the energy surplus high enough to enhance the electrolyzer exploitation and recover the initial investment cost. To optimally utilize the energy surplus of current Tilos HES, a 475-kW electrolyzer should be installed. The analysis shows that a kilogram of hydrogen produced in that way would cost 6.46 €. If the upgrade of the PV field peak capacity is allowed so as to reach the nominal power of the wind turbine of 800 kW, a 520-kW electrolyzer would bring down the price to 5.04 €/kg.

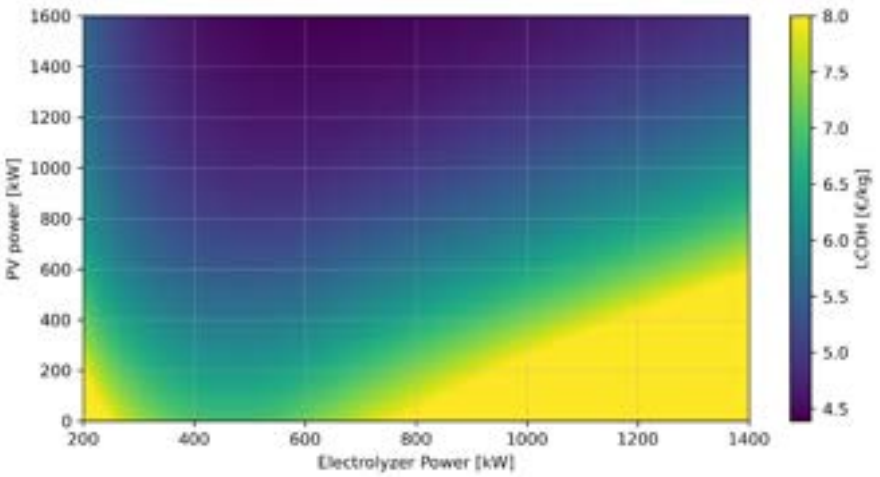

Figure. 5. Colormap showing the levelized cost of hydrogen (LCOH) for each considered combination of electrolyzer and PV power. High LCOH in yellow and low LCOH in dark blue.

It is worth mentioning that the lowest price achieved by the simulation is 4.38 €/kg and given by the combination of a 615-kW electrolyzer with 1600-kWp PV field. However, such a high installed capacity cannot be easily installed in the island. Depending on the hydrogen production requirements that could arise if green gas must be utilized for seasonal storage or other applications, a higher production cost may be acceptable to increase the annual yield. To put those numbers in perspective, the next subsections consider possible uses of green hydrogen.

3.2. HYDROGEN AS SEASONAL STORAGE

This section presents the results of a scenario in which green hydrogen is used as seasonal storage. Hydrogen generated during winter is converted back to electricity during summer to reach 100% energy independence. Figure 6 (a) displays the mass of hydrogen required to reach 100% self-sufficiency (in light blue), varying the installed PV power. Increasing the installed PV capacity generates more renewable power in the summer season, when the demand peaks, leading to an increase of self-consumption. As a result, the required hydrogen curve shows a decreasing trend. The same figure also shows the hydrogen amount that electrolyzers of different sizes (ranging between 0.5 to 1 MW) can produce by exploiting the power excess of the system, always varying the PV capacity.

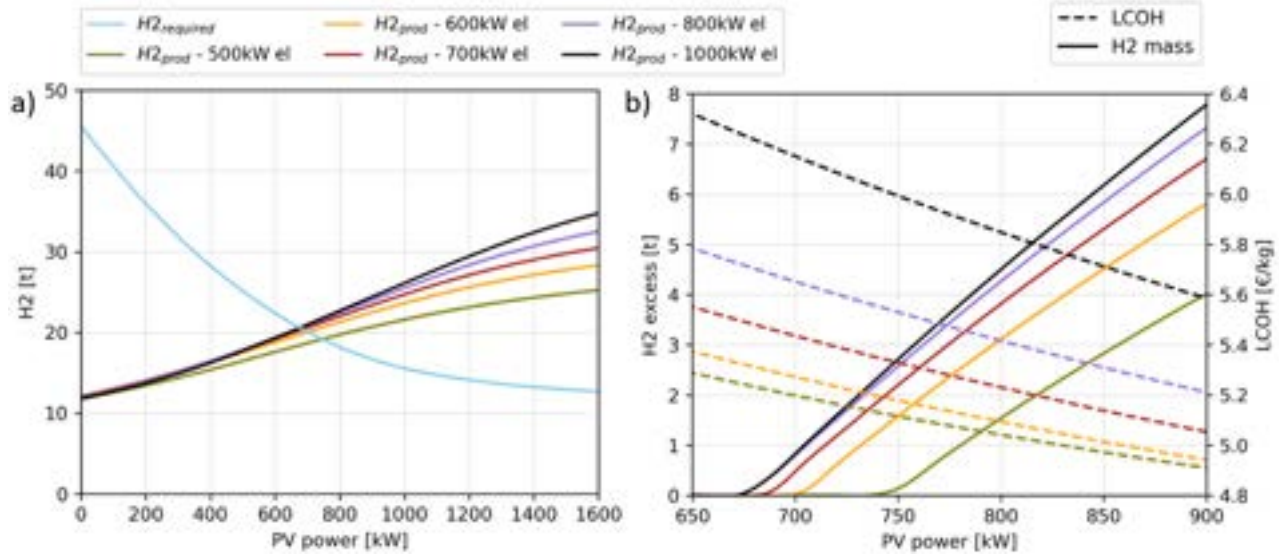

Figure. 6. a) Hydrogen mass required to reach 100 % self-sufficiency (light blue curve) and H_2 production capability from different electrolyzer power varying the PV installed power (line in different colors); b) magnitude (continuous lines) and LCOH (dashed lines) of the hydrogen excess.

With the current HES of Tilos, 37.8 tons of hydrogen would be required to satisfy the energy deficit in summer. However, only 13.6 tons of H_2 can be produced by exploiting the production surplus in winter. This means that, even if hydrogen is employed as a seasonal storage, the system could reach a maximum self-consumption rate of 82.6%, hence requiring a PV field upgrade for full energy independence. The intersection points

between the hydrogen demand and the hydrogen production curves occur at a PV power between 650 and 750 kWp. This is the bare minimum PV power to both increase the self-consumption of the system (up to around 87% without H_2 reconversion) and produce enough hydrogen for the seasonal storage.

After having assessed the required PV upgrade to reach self-sufficiency, Figure 6 (b) focuses on PV capacities ranging from this value up to 900 kWp, slightly higher than the nominal capacity of the wind turbine. In Figure 6 (b), continuous lines show the hydrogen excess that would be produced if the PV capacity is increased, while dashed lines show the resulting costs of hydrogen. Upon examination of the results, an 800-kW electrolyzer is required to achieve total self-sufficiency with the smallest possible PV upgrade. The purple line shows that, coupled with a 675-kWp PV field, this configuration reaches energy independence with an LCOH of 5.66 €/kg.

On the other hand, the green line shows that the configuration that allows reaching 100% self-sufficiency with a lower hydrogen cost (5.11 €/kg) only requires an additional PV upgrade to 750 kWp, since it better exploits a 500kW-only electrolyzer. Dashed lines in Figure 6(b) also show that the increase of the PV power allows for a reduction of the hydrogen cost for all considered electrolyzer levels in addition to the benefit of producing additional hydrogen for other purposes. If the PV power is increased up to 900 kW, a 600-kW electrolyzer can produce almost 6 tons of extra hydrogen at a competitive price of 4.92 €/kg. In the following section, one example of possible use of this extra-production is proposed in the context of a new fleet of buses for a carbon neutral public transport for the island. It is worth remembering that the aim behind the following analysis is to estimate what could be done with extra H_2 that, if correctly justified, may bring to a further reduction in the LCOH.

3.2. HYDROGEN FOR TRANSPORTS

Even today, locally produced green hydrogen may be a cost-competitive fuel in remote islands. Focus of the following calculation is only put on the potential fuel cost, thus excluding the cost of substitution of the current transport fleet, which will represent the topic for future analyses. To calculate the number of hydrogen-fed buses that can be used during the summer season, the existing Solbus was taken as a reference. This bus, with a capacity of 63 passengers, is able of driving 16.39 km on 1 kg of hydrogen [11]. A 7% energy loss was assumed when compressing the hydrogen from 30 to 350 bar, which is the required pressure in the storage tank of the bus. This loss was based on the needed compressor power of a multistage compressor [12]. It is estimated that a bus can drive the whole route on the island 7 times per day. The route was based on the actual bus stops on Tilos. When the bus is only used in the summer season (corresponding to approximately 90 days) the total amount of kilometers driven per year, and thus the required kilograms of hydrogen per year, can be calculated. Figure 7 shows that the number of buses that can drive on the island increases from 0 with a PV power of 700 kW, to 3 or 7 (depending on the electrolyzer size) with a PV power of 900 kW.

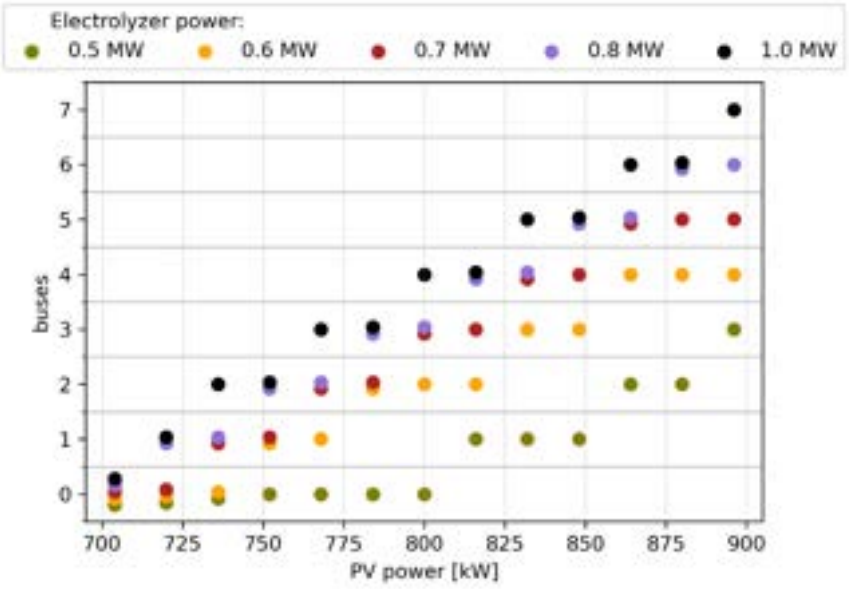

Figure. 7. Number of hydrogen buses that can be powered by the hydrogen surplus coming from different electrolyzer sizes paired with an increasing PV installed power.

Currently, most buses worldwide (including the Greek bus company KTEL) use diesel as a fuel. Assuming a consumption of 24 liters diesel per 100 km [13] would already make the hydrogen competitive with diesel with an average diesel price of €1.81 per liter in Greece [14]. The diesel prices do, however, vary across Greece. On a remote island the price for one liter of diesel is higher than on the mainland. This difference can partially be explained by the extra transportation costs from the Greek mainland to the island. On average petrol prices

are 3-4 cents higher on islands compared to the mainland, or even more for particularly remote islands. The prices for fuel and electricity should probably be higher, but the costs are subsidized and shared by all mainland consumers through a levy on electricity bills [15][16][17]. When hydrogen is produced locally, no transportation costs are required. A rough estimation shows that the cost for hydrogen with an LCOH of 6 €/kg will be around € 37 per 100 kilometers versus € 43.20 for diesel with a cost of € 1.80 per liter. Another advantage of hydrogen over diesel is the fact that a hydrogen bus emits no carbon dioxide or other air pollutant during operation. Different studies show that diesel buses emit over 1.5 kg CO2 per kilometer, which would result in 26.5 tons emission when running 90 days on Tilos. This does not include the transportation from the refinery to the fuel station which might be responsible for an even bigger share of emission [18][19].

Another option to decrease pollution would be to electrify the buses. Hydrogen has however the advantage over electricity that it is produced in winter when there is an electricity surplus. Using electricity would mean that the consumption peak in summer will increase even more. Furthermore, a hydrogen bus does not need to refuel during a day while an electric bus might have to recharge.

4. Discussion and conclusions

The high capacity factors of both the wind turbine and PV field demonstrate the abundance of renewable resources on the island of Tilos. This significantly impacts the competitive LCOH results and highlights the areas' clear potential for H_2 production.

The resulting LCOH was calculated for different scenarios considering both the current system and foreseeable upgrades that could lead to 100% self-sustained operation, and to the decarbonization of the public transport fleet. Table 1 summarizes results of the most remarkable configurations analyzed in the present study.

Table 1. Results from most significant plant configurations: 1) current Tilos' HES, 2) smallest PV upgrade for 100% self-sufficiency, 3) smallest electrolyzer for 100% self-sufficiency, 4) PV upgrade for LCOH abatement and H_2 excess for buses and 5) global lowest LCOH.

Config n°	PV power [kWp]	El. Power [kW]	LCOH [€/kg]	H_2 request [t/y]	H_2 prod. [t/y]	Self-suff. [%]	H_2 excess [t/y]
1	160	475	6.46	37.8	12.7	82	-
2	675	800	5.66	20.3	20.3	100	-
3	750	500	5.11	19.1	19.1	100	-
4	900	600	4.92	16.5	22.5	100	6
5	1600	615	4.38	12.7	28.5	100	15.8

Tilos' HES is equipped with an 800-kW wind turbine and a small 160-kW PV field (Configuration 1). The seasonal variation of the local demand creates a considerable energy deficit during summer, the tourist season. Considering a fuel cell with a conversion efficiency of 60%, it was estimated that more than 37.8 tons of hydrogen are required to achieve 100% self-sufficiency. However, results have shown that an alkaline electrolyzer fed by the power excess of the current HES is able to produce only 12.7 tons of H_2. It is thus evident that there is a need of upgrading the PV field to achieve energy independence. The analysis pointed out that a minimum installed PV power of 675 kWp (Configuration 2) is required to produce the same amount of hydrogen that the island needs. To generate enough hydrogen with this power capacity, an oversized stack of 800 kW must be installed, but this results in a LCOH higher than 5.66 €/kg.

To size the stack correctly, one must consider an additional upgrade of the PV field to 750 kWp (Configuration 3). When paired with a 500-kW electrolyzer, this system achieves 100% self-sufficiency at an LCOH of 5.11 €/kg. Configuration 4 moreover shows that, if it is possible to expand the photovoltaic generator further, excess hydrogen production means a better utilization of the installed electrolyzer and a further reduce the LCOH. A 900-kWp PV field paired with a 600-kW electrolyzer would produce an additional 6 tons of hydrogen at a competitive price of 4.92 €/kg. Without strict limitations on the photovoltaic field expansion, Configuration 5 shows that a high capacity PV field (1600 kWp) could optimally utilize a 615-kW stack and achieve an LCOH of 4.38 €/kg. Results thus show that scaling up components is a suitable strategy to lower the LCOH.

Hydrogen buses have been proposed as a possible use for the excess of hydrogen. Such a fleet could decarbonize the public transport during the touristic season without the introduction of an additional burden to the electric grid, as an electric bus fleet would do. Since their introduction would justify an increase in the hydrogen yield, this technology could contribute to a further decrease of the LCOH. Further developments of the study could include a better assessment of the energy required for hydrogen compression, as well as an estimation of the footprint of the required PV expansion and hydrogen tanks. Furthermore, a variable efficiency fuel cell model, similar to the one employed for the electrolyzer, would produce more accurate results regarding the actual electrical energy coming from the gas-to-power conversion.

Acknowledgments

The Authors would like to acknowledge Eunice Energy Group for providing data of the island of Tilos, as well as the guidance for analyzing them. Thanks are also due to McPhy Energy for providing the constants to calibrate the electrolyzer model.

Nomenclature

$CAPEX$ capital expenditures

CF capacity factor

$LCOH$ levelized cost of hydrogen, €/kg

M mass, kg

P power

PV photovoltaics

WT wind turbine

$OPEX$ operational expenditures

Greek symbols

η efficiency

φ conversion factor, kg/kWh

Subscripts and superscripts

a air

el electrolyzer

id ideal

op operational

PV photovoltaics

WT wind turbine

References

[1] J. K. Kaldellis and D. Zafirakis, 'Prospects and challenges for clean energy in European Islands.The TILOS paradigm', *Renew. Energy*, vol. 145, pp. 2489–2502, Jan. 2020, doi: 10.1016/j.renene.2019.08.014.

[2] J. K. Kaldellis, 'Supporting the Clean Electrification for Remote Islands: The Case of the Greek Tilos Island', *Energ. 2021 Vol 14 Page 1336*, vol. 14, no. 5, pp. 1336–1336, Mar. 2021, doi: 10.3390/EN14051336.

[3] P. Lubello, M. Pasqui, A. Mati, and C. Carcasci, 'Assessment of hydrogen-based long term electrical energy storage in residential energy systems', *Smart Energy*, vol. 8, p. 100088, Nov. 2022, doi: 10.1016/j.segy.2022.100088.

[4] K. V. Vilbergsson, K. Dillman, N. Emami, E. J. Ásbjörnsson, J. Heinonen, and D. C. Finger, 'Can remote green hydrogen production play a key role in decarbonizing Europe in the future? A cradle-to-gate LCA of hydrogen production in Austria, Belgium, and Iceland', *Int. J. Hydrog. Energy*, Feb. 2023, doi: 10.1016/j.ijhydene.2023.01.081.

[5] P. Lykas, E. Bellos, G. Caralis, and C. Tzivanidis, 'Dynamic Investigation and Optimization of a Solar-Based Unit for Power and Green Hydrogen Production: A Case Study of the Greek Island, Kythnos', *Appl. Sci.*, vol. 12, no. 21, Art. no. 21, Jan. 2022, doi: 10.3390/app122111134.

[6] O. Tang, J. Rehme, and P. Cerin, 'Levelized cost of hydrogen for refueling stations with solar PV and wind in Sweden: On-grid or off-grid?', *Energy*, vol. 241, p. 122906, Feb. 2022, doi: 10.1016/j.energy.2021.122906.

[7] J. K. Kaldellis, G. T. Tzanes, C. Papapostolou, K. Kavadias, and D. Zafirakis, 'Analyzing the Limitations of Vast Wind Energy Contribution in Remote Island Networks of the Aegean Sea Archipelagos', *Energy Procedia*, vol. 142, pp. 787–792, Dec. 2017, doi: 10.1016/j.egypro.2017.12.127.

[8] F. Superchi, A. Mati, M. Pasqui, C. Carcasci, and A. Bianchini, 'Techno-economic study on green hydrogen production and use in hard-to-abate industrial sectors', *IOP J. Phys. Conf. Ser.*, 2022.

[9] 'Green hydrogen cost reduction', IRENA, 2020. Accessed: Nov. 14, 2022. [Online]. Available: https://www.irena.org/publications/2020/Dec/Green-hydrogen-cost-reduction

[10] 'Renewable Power Generation Costs in 2021', IRENA, Jul. 2022. [Online]. Available: https://www.irena.org/publications/2022/Jul/Renewable-Power-Generation-Costs-in-2021

[11] R. Nekkers, F. Ex, and J. Van Beckhoven, ‘Hydrogen buses on the Veluwe’, Status report 2BP, Apr. 2020. [Online]. Available: https://www.h2nodes.eu/images/docs/20200416_status_verslag_2BP_Hydrogen_buses_on_the_Veluwe_Eng_.pdf
[12] M. Khan, C. Young, C. Mackinnon, and D. Layzell, ‘Technical Brief: The Techno-Economics of Hydrogen Compression’, Oct. 2021. [Online]. Available: https://transitionaccelerator.ca/techbrief-techno-economics-hydrogen-compression/
[13] A. Al-Mahadin and M. Mustafa, *Utilizing fuel cell technology for Dubai Roads and Transport Authority (RTA)*. 2018, p. 6. doi: 10.1109/ICASET.2018.8376784.
[14] ‘Greece diesel prices, 27-Feb-2023’, *GlobalPetrolPrices.com*. https://www.globalpetrolprices.com/Greece/diesel_prices/ (accessed Mar. 02, 2023).
[15] E. Angelopoulou and H. D. Gibson, ‘The determinants of retail petrol prices in Greece’, *Econ. Model.*, vol. 27, no. 6, pp. 1537–1542, Nov. 2010, doi: 10.1016/j.econmod.2010.07.024.
[16] N. Hatziargyriou, I. Margaris, I. Stavropoulou, S. Papathanassiou, and A. Dimeas, ‘Noninterconnected island systems: The Greek case’, *IEEE Electrification Mag.*, vol. 5, no. 2, pp. 17–27, Jun. 2017, doi: 10.1109/MELE.2017.2685739.
[17] I. Kougias, S. Szabó, A. Nikitas, and N. Theodossiou, ‘Sustainable energy modelling of non-interconnected Mediterranean islands’, *Renew. Energy*, vol. 133, pp. 930–940, Apr. 2019, doi: 10.1016/j.renene.2018.10.090.
[18] A. C. Nix, J. A. Sandoval, W. S. Wayne, N. N. Clark, and D. L. McKain, ‘Fuel economy and emissions analysis of conventional diesel, diesel-electric hybrid, biodiesel and natural gas powered transit buses’, pp. 895–908, Jul. 2011, doi: 10.2495/SDP110741.
[19] J. Merkisz, P. Fuć, P. Lijewski, and J. Pielecha, ‘Actual Emissions from Urban Buses Powered with Diesel and Gas Engines’, *Transp. Res. Procedia*, vol. 14, pp. 3070–3078, Jan. 2016, doi: 10.1016/j.trpro.2016.05.452.

Different allocation mechanisms to distribute the total profits of the Italian Renewable Energy Community

Gabriele Volpato[a] and Gianluca Carraro[a]

[a] University of Padova, Industrial Engineering Department
Via Venezia 1, 35131 Padova, Italy
gabriele.volpato.1@phd.unipd.it, gianluca.carraro@unipd.it

Abstract:

Energy communities could benefit from an optimal match between total energy generation and demand, resulting in economic gains. A main issue is the distribution of the optimal economic gain of an energy community among its members. Several works apply a single criterion of cost/profit allocation within an energy community, neglecting the impact of different criteria on different members. This paper aims at evaluating and comparing two different cost/profit allocation mechanisms, i.e., the cooperative "Shapley value", based on the marginal contributions of members to any coalition within the energy community, and the "Uniform pricing", which relies on a uniform price that is independent of the cooperation among members. According to the Italian legislation, a centralized Renewable Energy Community with virtual energy sharing scheme is analysed. The community encompasses one consumer and two prosumers with shiftable electrical demands that are representative of the tertiary, residential and commercial sectors, and prosumers own photovoltaic plants with/without the electrical storage system. A cooperative model of this energy community is presented, and the daily operational profit is maximized by a Mixed-Integer Non-Linear Programming optimization. Subsequently, the mechanisms of Shapley value and Uniform pricing are applied to allocate the optimal profit of the energy community. Uniform pricing leads to daily profits of 1.95€, 0.69€ and 5.71€ for the tertiary, residential and commercial members, respectively. Conversely, results of the Shapley value are fairer towards prosumers, allocating daily profits of 9.57€ and 3.81€ to the residential and commercial prosumers, and a daily cost of 5.03€ to the tertiary consumer.

Keywords:

Renewable Energy Community; Profit allocation; Cooperative game; Shapley mechanism; Fairness.

1. Introduction

Renewable energy communities (RECs), defined by the recast of the Renewable Energy Directive (RED II) [1], represent a regulatory tool to foster the distributed generation and consumption driven by renewable sources. RECs can help achieve the energetic and environmental targets indicated by the "Fit for 55" document of the European Commission [2] (i.e., renewables share of 40%, increase of energy efficiency by 36% in the final energy consumption and emissions reduction by at least 55% compared to the levels of 1990), beyond leading several economic and social benefits to the European citizens. In the Italian context, the regulation about the technical management of RECs has been recently updated by GSE [3], the Italian Energy Services Operator, while the economic incentives have been defined by ARERA [4], the Italian Regulation Agency for Environment, Network and Energy. In such a context, this paper focuses on the economic benefits associated with the configuration of the Italian REC and of its participants. The current and emerging literature on energy communities is very broad and, for this reason, the literature review in this paper summarizes the main recent works in the following identified fields.

Some works in the literature dealt with business models, policies and modelling techniques that can foster the development of Energy Communities (ECs) [5-7]. Lowitzsch et al. [5] presented a holistic analysis of the already existing and still untapped business models for ECs, identifying different structure and design options (e.g., application technology, cooperating partners, geographical location, types of investors and ownerships etc.). Ceglia et al. [6] assessed the energy, environmental and economic performances of an Italian REC, highlighting its higher electricity self-consumption (till 56%) with respect to other energy-sharing models, e.g., the "System of Efficient Users" (till 12% of electricity self-consumption) that is based on directives released before 2018. Gerundo et al. [7] proposed a methodology to identify potential geographical areas that are

suitable for the development of RECs, while taking into account the constraints of installation for the generation technologies and social benefits as the reduction of the energy poverty.

Other works focused on the optimization of the design and operation of the generation and storage technologies within ECs [8-10]. Cutore et al. [8] conducted a design and operation optimization of a residential REC in Italy to maximize the net-present value (including investment and operational costs) and, then, calculated different indexes to analyse its energetic, environmental and social performances. The centralized configuration of the REC results more profitable compared to the distributed one, because the former exploits only virtual energy sharing that is more incentivized (in the Italian context) compared to physical self-consumption (the distributed configuration can exploit both virtual energy sharing and physical self-consumption). Chang et al. [9] proposed a methodology, based on K-means clustering, to allocate different options of community energy storage among households of an EC, the operational cost of which is minimized by a Mixed-Integer Linear Programming (MILP) optimization. Lazzari et al. [10] developed an optimization framework for the planning and operation of RECs with the aim of increasing their energy sharing. The optimization outcomes, validated with real data of consumption profiles of households in Barcelona, show that a REC with 7 residential users could achieve a self-consumption of 100% and a relevant amount of avoided CO2 emissions till 7 kg/day.

Another relevant issue to be addressed is the distribution of economic benefits (costs or profits) within an EC [11-14]. Casalicchio et al. [11] allocated the total cost saving of a residential EC by applying the Vickrey-Clarke-Groves mechanism that evaluates the contribution of each member to the cost saving of the whole community. This approach is compared to other business allocation criteria by introducing a fairness index that represents the number of members without an economic gain within the community. Zheng et al. [12] analysed the impacts of demand side flexibility and of a Peer-to-Peer (P2P) energy sharing mechanism within an EC, made of commercial prosumers, finding that the P2P strategy could minimize the operational cost by 24.6% compared to a Peer-to-Grid (P2G) operation where each member exchanges energy with the electric grid only. The profit of the EC is distributed among members by the P2P mechanism, which relies on the definition of internal trading prices that depend on the supply-demand ratio of the community. Zatti et al. [13] optimized the capacities of different generation and storage units within an Italian EC comprised of commercial and residential users. The “Shapley value” mechanism, based on a cooperative game theory approach, is applied to allocate the total benefit of the community by quantifying the contributions of members to the economic revenue of any coalition within the community. Siqin et al. [15] formulated a distributionally-robust optimization for the dispatching of a multi-EC system. An improved Shapley value approach was proposed to allocate higher profits to the participants with higher solar PV consumption. Notice that, in the previous papers, a single cost/profit allocation mechanism (e.g., Shapley value) was applied, neglecting the potential results with other allocation criteria.

Vespermann et al. [16] explored different cooperative allocation mechanisms for an EC, including the Shapley value, and analysed their properties of efficiency, individual rationality and stability. Cremers et al. [14] reviewed different applications of the Shapley value for ECs, proposing also a new method (called “Stratified expected value”) to approximate the calculation of the Shapley value in the case of communities of up to 200 prosumers. The authors highlighted the need to further investigate different allocation criteria, other than Shapley, to assess the fairness of the cost/profit distribution within ECs. Li and Okur [17] conducted an operation optimization of an EC and applied Uniform pricing (also called “flat energy pricing method”), time-of-use energy pricing and segmented energy pricing as cost allocation criteria. However, the authors neglected the possible cooperation between the members of the EC and, thus, cooperative allocation mechanisms as the Shapley value were not applied. It is worth highlighting that the above works did not apply both cooperative allocation mechanisms (e.g., Shapley value) and other mechanisms not derived from cooperative game theory.

In the above literature, works dealing with the allocation of economic costs/profits within an EC *i)* apply one single criterion, without assessing the impact of different allocation mechanisms on the benefits of EC members, and/or *ii)* do not compare cooperative allocation mechanisms (e.g., Shapley value) with other mechanisms not based on cooperative game theory (e.g., Uniform pricing). To the best of authors’ knowledge, the application of different allocation criteria for the economic benefit of a REC, according to the Italian framework, represents a first gap in the literature. Moreover, as highlighted in [14], the literature lacks of more in-depth discussions about the fairness of the cost/profit distribution within ECs and, in particular, within RECs. This paper fills in these gaps, and the objective is to present and evaluate two different allocation mechanisms in the context of a REC, i.e., the cooperative “Shapley value” [18] and the “Uniform pricing” criteria [19], with a subsequent insight of the fairness of allocation.

First, a REC with a centralized configuration and a virtual energy sharing scheme, according to the Italian framework, is modelled and its operation is optimized (i.e., the flexible demands of members and the operation of the electrical energy storage system) based on a Mixed-Integer Non-Linear Programming (MINLP) formulation. Subsequently, this work applies the cooperative mechanism Shapley value and the Uniform pricing mechanism to distribute the economic benefits among the members, with the aim of evaluating the differences between these two criteria.

This paper contributes to the current literature with the following novel points:

- Application and comparison of two different allocation criteria, i.e., the cooperative Shapley value and the Uniform pricing, to distribute the total economic profit of an Italian REC among its members;
- Evaluation of how fair is the distribution of economic benefits, based on the Shapley value and the Uniform pricing, within the analysed REC.

The paper is structured as follows. Section 2 describes the Shapley value and Uniform pricing mechanisms. Section 3 reports the mathematical model of the REC, according to the Italian legislation, and the input data for the MINLP optimization. Section 4 discusses the results of the MINLP optimization and subsequent application of Shapley value and Uniform pricing. Conclusions summarize general guidelines retrieved from this work.

2. Materials and method

This Section describes the two cost/profit allocation mechanisms considered in this work, i.e., the cooperative Shapley value (Section 2.1) and the Uniform pricing (Section 2.2). As reported by Berka and Creamer [20] and Gjorgievski et al. [21], the cost/profit allocation within an Energy Community (EC) is an important aspect that is still not exhaustively addressed in the literature. Different allocation mechanisms of the costs/profits of ECs are available in the literature, and they usually refer to approaches from the cooperative game theory or to approaches that define prices for the EC members in relation to their profiles of energy demand [17].

2.1. Shapley value

Game theory is a large field that encompasses techniques to model a group of interacting players [22] under a cooperative or non-cooperative framework. Cooperative games assume that cooperation exists among the players, for example the members of an EC, thus leading to a "grand coalition" of members (e.g., the energy community), with the aim of achieving a common objective (e.g., minimization of the total cost of the EC, improvement of the total renewable self-consumption or self-sufficiency, etc.). On the contrary, the game is non-cooperative when the players pursue independent and, sometimes, conflicting objectives, thus leading to a Nash equilibrium solution. However, this work assumes that the members of an EC can cooperate and, therefore, the focus here is on cooperative games. A cooperative game is defined by a pair *(N,v)*, where *N* refers to the number of players participating into the game, and forming the "grand coalition", while *v(S)* is the "value" function of any possible coalition *S* of players within the grand coalition [23]. The "value" function of a coalition *S* is a mathematical function that takes real values:

$$v(S)\colon 2^N \to R \tag{1}$$

where 2^N represents the set of all coalitions within the grand coalition, included the grand coalition itself and the empty coalition (i.e., the coalition without players). The "value" function represents the "value" in forming the coalition *S*, e.g., the total cost/profit associated with players cooperating in the coalition *S*. In the framework of ECs, notice that the value of the grand coalition corresponds to the total cost/profit of an EC, while the value of the empty coalition is zero. To clarify, consider an EC with three members (players *1,2,3*) that cooperate to minimize the total operational cost. The value of the coalition *{1,2}*, given by the players *1* and *2*, is the total cost of the cooperation between these members, thus neglecting player *3*.

This work adopts the Shapley value as cooperative allocation mechanism because it can lead to a fair distribution of economic gains in a cooperative game. Indeed, this approach allows to allocate higher gains (e.g., higher profits or lower costs) to players that contribute the most to the "value" of all coalitions they could take part in within the grand coalition. According to the Shapley value, the gain, or payoff x_i, allocated to member *i* is calculated as follows:

$$x_i = \sum_{S \subseteq N, i \in S} \frac{(|S|-1)!\,(N-|S|)!}{N!}\big(v(S) - v(S \setminus \{i\})\big) \tag{2}$$

where $|S|$ refers to the size of the coalition *S* and $\big(v(S) - v(S \setminus \{i\})\big)$ is the contribution of member *i* to the value $v(S)$ of coalition *S*. Hence, the Shapley value assigns to each player a payoff that represents his weighted average marginal contribution to the value of any coalition, within the grand coalition, he could take part in. However, the main drawback of the Shapley value, which requires to consider 2^N coalitions, is the computational complexity arising with a high number of players *N*. In the following, a basic example of the Shapley calculation is provided. Let us consider a grand coalition with three players, assuming the values of the 8 (2^N) possible coalitions, where each of these values could be derived by solving a specific cooperative optimization problem with the players involved. Table 1 reports the coalitions analysed and their corresponding assumed "values", where {} represents the empty coalition.

Table 1. Example of a grand coalition with three players, with the "values" of all coalitions.

Coalition	{}	{1}	{2}	{3}	{1,2}	{1,3}	{2,3}	{1,2,3}
Value [€]	0	0	2	3	3	5	6	12

Eq. (2) is applied to compute the Shapley payoff for each of the three players. Player 1 appears in coalitions {1}, {1,2}, {1,3} and {1,2,3} and, therefore, its payoff considers its weighted average marginal contribution to the values of these four coalitions:

$$x_1 = \frac{(1-1)!\,(3-1)!}{3!}\left(v(\{1\}) - v(\{\})\right) + \frac{(2-1)!\,(3-2)!}{3!}\left(v(\{1,2\}) - v(\{2\})\right) + \frac{(2-1)!\,(3-2)!}{3!}\left(v(\{1,3\}) - v(\{3\})\right) + \frac{(3-1)!\,(3-3)!}{3!}\left(v(\{1,2,3\}) - v(\{2,3\})\right) = \frac{1}{3}(0) + \frac{1}{6}(3-2) + \frac{1}{6}(5-3) + \frac{1}{3}(12-6) = \frac{15}{6}$$

Player 2 can participate in coalitions {2}, {1,2}, {2,3} and {1,2,3}, and its payoff is:

$$x_2 = \frac{(1-1)!\,(3-1)!}{3!}\left(v(\{2\}) - v(\{\})\right) + \frac{(2-1)!\,(3-2)!}{3!}\left(v(\{1,2\}) - v(\{1\})\right) + \frac{(2-1)!\,(3-2)!}{3!}\left(v(\{2,3\}) - v(\{3\})\right) + \frac{(3-1)!\,(3-3)!}{3!}\left(v(\{1,2,3\}) - v(\{1,3\})\right) = \frac{1}{3}(2) + \frac{1}{6}(3-0) + \frac{1}{6}(6-3) + \frac{1}{3}(12-5) = 4$$

Player 3 can participate in coalitions {3}, {1,3}, {2,3} and {1,2,3}, and its payoff is:

$$x_3 = \frac{(1-1)!\,(3-1)!}{3!}\left(v(\{3\}) - v(\{\})\right) + \frac{(2-1)!\,(3-2)!}{3!}\left(v(\{1,3\}) - v(\{1\})\right) + \frac{(2-1)!\,(3-2)!}{3!}\left(v(\{2,3\}) - v(\{2\})\right) + \frac{(3-1)!\,(3-3)!}{3!}\left(v(\{1,2,3\}) - v(\{1,2\})\right) = \frac{1}{3}(3) + \frac{1}{6}(5-0) + \frac{1}{6}(6-2) + \frac{1}{3}(12-3) = \frac{11}{2}$$

According to cooperative game theory, this payoff allocation is defined as an “imputation” because it guarantees simultaneously the properties of “efficiency” and “individual rationality”. The property of efficiency ensures that the “value” of the grand coalition is allocated to all players, while the property of individual rationality means that each player benefits from participating into the grand coalition compared to operating as an independent player. In the example above, efficiency is ensured since the sum of payoffs is equal to the “value” of the grand coalition (i.e., 12 €). Moreover, the payoff allocation satisfies the property of individual rationality because the payoff allocated to each player is higher than the “value” of the coalition including only that player (e.g., for player 2, the payoff in the grand coalition is 4 € while its value *v({2})*, as an independent player, is 2 €).

2.2. Uniform pricing

Time-of-use energy pricing, segmented energy pricing and Uniform pricing (also called “flat energy pricing method”) are cost/profit allocation mechanisms, reported by Li et al. [19] and Li and Okur [17], that do not consider the cooperation among EC members. These mechanisms allow to allocate the economic benefits of the EC by defining different prices in relation to the individual energy demands. Time-of-use energy pricing sets high prices in peak hours (i.e., when peak demand occurs) and low prices in off-peak hours (i.e., when low demand occurs), thus promoting load shifting of the energy demands from peak to off-peak hours. Segmented energy pricing establishes a threshold of the energy demand, under which a low price is charged, while a high price is charged above this threshold. Uniform pricing is based on a unique price calculated as the ratio between the total cost (or profit) and the total demand of the EC:

$$c_u = \frac{TC}{\sum_{i=1}^{n}\sum_{t=1}^{T} E_{i,t}} \tag{3}$$

where TC is the total cost (or profit) of the EC and $E_{i,t}$ is the hourly energy demand of member *i*. Uniform pricing mechanism is simple to be implemented and well accepted by network regulators [24].

3. Case study

The Renewable Energy Community (REC) under analysis comprises of three members, one consumer of the tertiary sector and two prosumers that are representative of the residential and commercial sectors. It is assumed that the residential prosumer owns only a Photovoltaic plant (PV), whereas the commercial prosumer owns a PV plant and a battery as electrical storage system. Section 3.1 reports the main equations and constraints associated with the Mixed-Integer Non-Linear Programming (MINLP) optimization model of the Italian REC, developed from a previous work of the authors [25]. Section 3.2 lists the input data of the model.

3.1. Mathematical model of the Renewable Energy Community

The operation of the PV plant of a member *i* is described by Eq. (4):

$$P_{i,t}^{PV} = \eta^{PV} \cdot A_i^{PV} \cdot I_t^{PV} \tag{4}$$

where $P_{i,t}^{PV}$ [kW] is the power generated by the PV plant in time step *t*, η^{PV} [-] is the average efficiency of the PV plant, A_i^{PV} [m^2] is the available PV area and I_t^{PV} [kW/m^2] is the global solar irradiance (on a tilted surface) in time step *t*. In the following, energy and power variables have, respectively, [kWh] and [kW] as units of measurements.

The operation of the battery of a member *i* is given by the following equations and constraints:

$$E_{i,t}^{bat} = E_{i,t-1}^{bat} + P_{i,t}^{bat,c} \cdot \eta^{bat,c} \cdot \Delta t - \frac{P_{i,t}^{bat,d} \cdot \Delta t}{\eta^{bat,d}} \tag{5}$$

$$E_{i,t}^{bat} \leq E_i^{bat,cap} \tag{6}$$

$$P_{i,t}^{bat,c} \leq P_i^{bat,peak} \cdot \delta_{i,t}^{bat,c} \tag{7}$$

$$P_{i,t}^{bat,d} \leq P_i^{bat,peak} \cdot \delta_{i,t}^{bat,d} \tag{8}$$

$$\delta_{i,t}^{bat,c} + \delta_{i,t}^{bat,d} \leq 1 \tag{9}$$

$$E_{i,1}^{bat} = E^{start,end} \cdot E_i^{bat,cap} \tag{10}$$

$$E_{i,24}^{bat} = E_{i,1}^{bat} \tag{11}$$

Eq. (5) describes the energy balance of the battery, where $E_{i,t}^{bat}$, $P_{i,t}^{bat,c}$ and $P_{i,t}^{bat,d}$, $\eta^{bat,c}$ and $\eta^{bat,d}$, and Δt are, respectively, the hourly energy stored in the battery, the hourly charging (*c*) and discharging (*d*) power, the battery charging (*c*) and discharging (*d*) efficiency, and the time step of the MINLP optimization model, i.e., one hour. Constraint (6) states that the hourly energy stored in the battery is bounded by the battery capacity $E_i^{bat,cap}$. Constraints (7)-(8) bound the hourly charging and discharging power of the battery by the maximum value $P_i^{bat,peak}$. The binary variables $\delta_{i,t}^{bat,c}$ and $\delta_{i,t}^{bat,d}$, which make the model non-convex, avoid charging and discharging in the same time step *t*, as indicated by constraint (9). The initial and final energy levels of the battery ($E_{i,1}^{bat}$ and $E_{i,24}^{bat}$) are fixed as ratio of the battery capacity by parameter $E^{start,end}$, as shown in Eqs. (10)-(11).

The shifted electrical demand of each member *i* is subject to the following constraints:

$$\sum_{t=1}^{24} E_{i,t}^{el,shift} = \sum_{t=1}^{24} E_{i,t}^{el} \tag{12}$$

$$E_i^{el,min} \leq E_{i,t}^{el,shift} \leq E_i^{el,max} \tag{13}$$

$$(1 - D^{var}) \cdot E_{i,t}^{el} \leq E_{i,t}^{el,shift} \leq (1 + D^{var}) \cdot E_{i,t}^{el} \tag{14}$$

Eq. (12) states that shifting the hourly electrical demand of a member does not change its total daily electrical demand, where $E_{i,t}^{el,shift}$ and $E_{i,t}^{el}$ are, respectively, the shifted and input electrical demands in time step *t*. Constraints (13) and (14) bound $E_{i,t}^{el,shift}$, where $E_i^{el,min}$, $E_i^{el,max}$ and D^{var} are the hourly minimum and maximum of the input electrical demand and the hourly maximum fraction of the load that can be shifted.

According to the Italian legislation, the members of the centralized REC are directly and separately connected to the same low-medium voltage distribution grid. The energy shared among the members occurs within the distribution grid, in conformity with the concept of “virtual energy sharing” of the Italian REC. The legislation defines two hourly energy balances for the total energy withdrawn from (E_t^{imp}) and injected to (E_t^{exp}) the grid as reported by Eq. (15) and Eq. (16), respectively:

$$E_t^{imp} = \sum_{i=1}^{n} (E_{i,t}^{el,shift} + E_{i,t}^{bat,c}) \tag{15}$$

$$E_t^{exp} = \sum_{i=1}^{n} (E_{i,t}^{PV} + E_{i,t}^{bat,d}) \tag{16}$$

where $E_{i,t}^{PV}$, $E_{i,t}^{bat,c}$ and $E_{i,t}^{bat,d}$ are, respectively, the energy generated by PV, the energy charged and discharged of the battery, for each member *i* in each time step *t*.

The total energy withdrawn from and injected to the grid are limited by the following constraints:

$$E_t^{imp} \leq E^{grid,max} \tag{17}$$

$$E_t^{exp} \leq E^{grid,max} \tag{18}$$

where $E^{grid,max}$ is the maximum allowed energy exchanged with the grid.

The Italian REC benefits from an economic incentive for the "virtual energy shared", $E_{s,t}$, among its members, that is defined as the hourly minimum between E_t^{imp} and E_t^{exp}:

$$E_{s,t} = min(E_t^{imp}, E_t^{exp}) \tag{19}$$

where constraint (19) is non-linear and, therefore, makes the model non-linear.

The REC under analysis aims at maximizing its total daily profit and, therefore, the objective function to be maximized is:

$$c^{REC} = \sum_{t=1}^{24} (E_t^{exp} \cdot c_t^{exp} - E_t^{imp} \cdot c_t^{imp}) + inc_{REC} \cdot \sum_{t=1}^{24} E_{s,t} \tag{20}$$

where c_t^{exp}, c_t^{imp} and inc_{REC} are, respectively, the grid sale price, the grid purchase price and the incentive of the REC (that consists of the sum between a feed-in premium and a feed-in tariff, the latter linked to the avoided network losses within the REC). The first summation represents the difference between the revenue for the energy sold to the grid ($E_t^{exp} \cdot c_t^{exp}$) and the cost for the energy purchased from the grid ($E_t^{imp} \cdot c_t^{imp}$). The last term is the revenue due to the incentive for the virtual energy shared. Notice that the optimal profit of the REC (i.e., the optimal value of the objective function c^{REC}) corresponds to the value of the grand coalition including, as players, all the members of the REC, as explained in Section 2.

3.2. Input data

Figure 1 (a) and (b) show, respectively, the profile of the global solar irradiance on an inclined surface (optimal tilted angle of 38°) for the location of Padua (Italy) derived from the PVGIS database [26], and the profiles of the grid purchase and sale prices [27], in a characteristic day of the spring season. Figure 2 reports the daily electrical demands of the energy users, within the analysed REC, that are representative of the tertiary (consumer "Ter"), residential (prosumer "Res") and commercial (prosumer "Com") sectors [28]. Given the chosen electrical demands, it is worth highlighting that the REC presents a heterogeneous composition that improves its operational flexibility. Table 2 lists the values of other input parameters for the mathematical model described in Section 3.1.

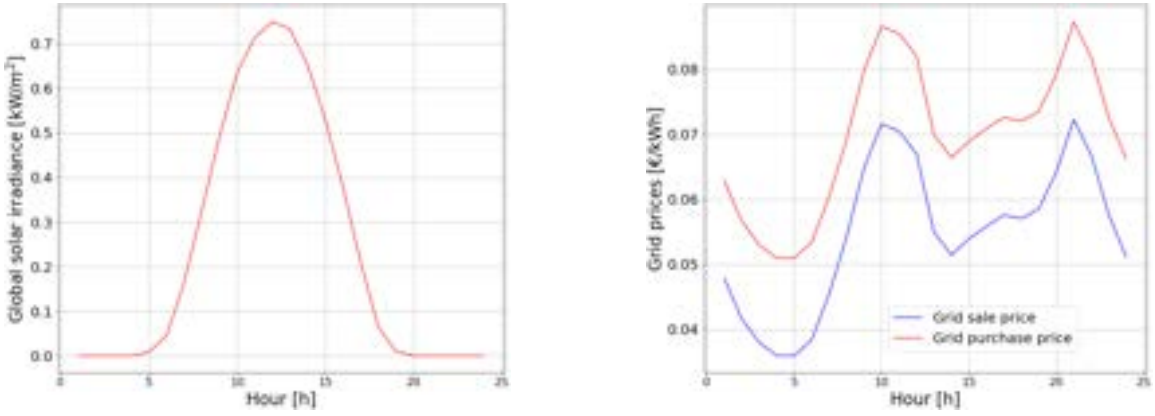

a) *b)*

Figure 1. a) Global solar irradiance on an inclined surface (optimal tilted angle of 38°) in Padua (Italy) and b) grid purchase and sale prices, in a characteristic day of spring.

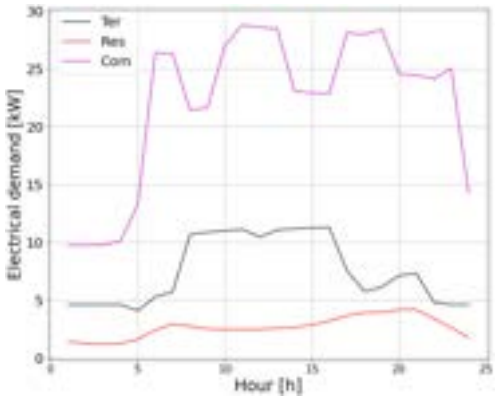

Figure 2. Electrical demands of the tertiary consumer (Ter), residential (Res) and commercial (Com) prosumers.

Table 2. Values of the input parameters in the MINLP optimization.

Parameter	Value	Source
η^{PV} [-]	0.17	assumed
A_i^{PV} [m^2]	60 (Res), 250 (Com)	assumed
$\eta^{bat,c}$, $\eta^{bat,d}$ [-]	0.95	[9]
$E_i^{bat,cap}$ [kWh]	50 (Com)	[29]
$P_i^{bat,peak}$ [kW]	7 (Com)	[29]
$E^{start,end}$ [-]	0.5	assumed
D^{var} [-]	0.1	assumed
$E^{grid,max}$ [kWh]	70	assumed
inc_{REC} [€/kWh]	0.12	[3]

4. Analysis and discussion of results

Section 4.1 reports the results of the Mixed-Integer Non-Linear Programming (MINLP) optimization, conducted on the mathematical model described in Section 3.1, and solved by the Gurobi software [30]. Subsequently, Section 4.2 presents the outcomes of the distribution of the optimal total profit for the REC among the members, by application of the mechanisms of Shapley value and Uniform pricing.

4.1. Optimization results

Figure 3 (a) shows the optimal shifted electrical demands of the tertiary consumer ("Ter"), residential ("Res") and commercial ("Com") prosumers, as well as the total PV power generation for the two prosumers, within the REC. The optimal load shifting of the electrical demand of the commercial prosumer results more evident compared to the other optimal demands, since the commercial prosumer can exploit the electrical battery storage and, thus, has a higher flexibility compared to the other members of the REC. Figure 3 (b) exhibits the optimal operation of the electrical battery storage of the commercial prosumer within the REC, in terms of power charging (red line), power discharging (green line) and energy stored (blue line). Notice that all the shifted electrical demands increase compared to the input demands during hours 7-9 (Figure 3 (a)), when the PV power generation is still low, thus requiring the power discharging of the battery in the same period (Figure 3 (b)). In the middle of the day, during hours 10-15, the total PV power generated is high (maximum value of 39 kW at hour 12), and this allows to charge the battery till almost the maximum capacity (50 kWh) at hour 15. After hour 15 the available PV power decreases and, therefore, power discharging of the battery helps meet the total electrical demand. Figure 4 displays the daily profile of the virtual energy shared within the REC. According to constraint (19) in Section 3.1, the virtual energy shared is defined as the hourly minimum between the total energy withdrawn from the grid (i.e., sum of the total shifted electrical demand and energy charged into the battery) and the total energy injected into the grid (i.e., sum of the total PV energy generation and energy discharged from the battery). At hour 2, the virtual energy shared corresponds to the energy discharged from the battery (7 kWh) that is lower compared to the value of the total shifted electrical demand (17 kWh). At hour 12, the virtual energy shared is the maximum PV energy generated (39 kWh) that is lower compared to the sum between the values of total shifted electrical demand (37 kWh) and energy charged into the battery (7 kWh). Hence, these outcomes demonstrate that a REC with renewable energy plants (as PV) and energy storage systems can effectively exploit the energy sharing and, in turn, achieve higher economic revenues due to the incentive for the energy shared according to the Italian legislation.

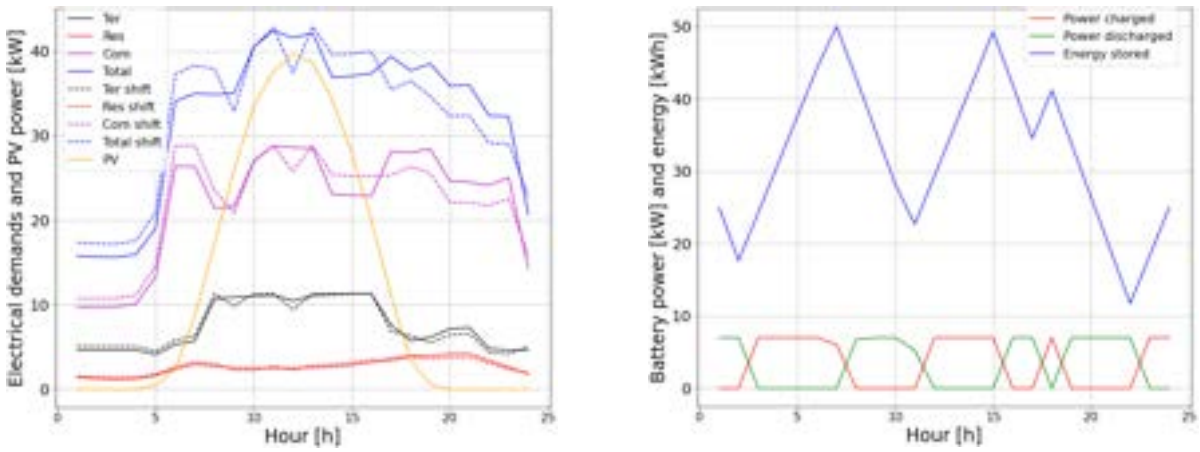

a) *b)*

Figure 3. a) Input and optimal shifted electrical demands of REC members and total PV power generation and b) optimal operation of the battery.

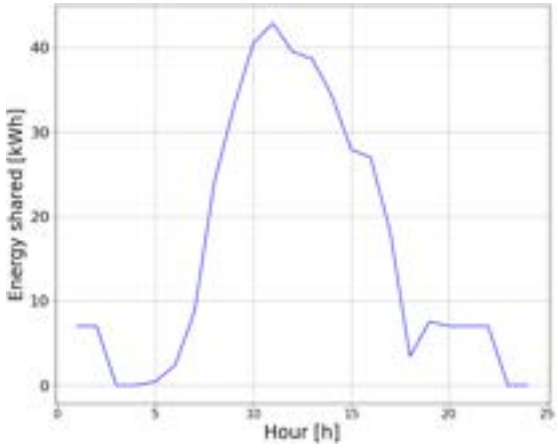

Figure 4. Optimal virtual energy shared in the analysed Italian REC.

4.2. Results of the profit allocation

The Mixed-Integer Non-Linear Programming (MINLP) optimization leads to an optimal daily profit of the REC (optimal value of the objective function, Eq. (20) in Section 3.1) equal to 8.35 €. This total profit is allocated to the members of the REC by applying, separately, the cooperative Shapley value and the Uniform pricing mechanisms, described in Section 2.1 and 2.2, respectively.

The calculation of the Shapley value, according to Eq. (2) in Section 2.1, requires the identification of all coalitions of members within the REC and the computation of their "values" (i.e., the total costs/profits of coalitions, see Section 2.1). In the analysed REC with three members, the 8 possible coalitions are *{}*, *{Ter}*, *{Res}*, *{Com}*, *{Ter, Res}*, *{Ter, Com}*, *{Res, Com}* and *{Ter, Res, Com}*, where the first and last coalitions are, respectively, the empty coalition and the grand coalition that constitutes the REC. *Ter*, *Res* and *Com* refer, respectively, to the tertiary consumer, the residential and commercial prosumers. Notice that the value of the empty coalition is 0, while the value of the grand coalition is the optimal daily profit of the REC (8.35 €). To obtain the value of a specific coalition, it is sufficient to solve the model in Section 3.1 considering only the equations and constraints associated with the members involved in that coalition. For instance, coalition *{Ter, Res}* is made of one consumer (Ter) and one prosumer with only a PV plant (Res), thus the equations and constraints from (5) to (11) (in section 3.1) of the battery energy storage are not used in solving the optimization problem, and the variables of the battery in Eqs. (15)-(16) are not considered as well. Moreover, for coalitions *{Ter}*, *{Res}*, *{Com}*, representing the energy users operating independently, and without cooperation with other community members, the term of energy shared in the objective function (20) is not included. Table 3 reports the "values" calculated for all coalitions within the REC, where negative and positive values refer to net costs and net profits, respectively. For example, the coalition *{Ter}* includes only one consumer, leading to a daily cost of 12.85 €. On the other hand, the coalition *{Res, Com}* is based on the cooperation between the residential and commercial prosumers and, thus, presents the highest daily profit of 20.09 €. Once obtained the values of all coalitions, the formula of the Shapley value (Eq. (2) in Section 2.1) is applied to compute the Shapley payoff of each member of the REC.

The Uniform pricing mechanism is implemented by calculating a uniform price within the REC, as reported in Eq. (3) of Section 2.2, where the numerator is represented by the optimal daily profit of the REC (8.35 €) and the denominator is the optimal shifted demand of the REC. According to Uniform pricing, the payoff of each member is found by multiplying the uniform price with its optimal daily demand.

Table 4 displays the payoffs (positive for profits and negative for costs) allocated to the members of the REC under the Shapley value and Uniform pricing mechanisms. A first outcome is that both allocation mechanisms are efficient (see Section 2.1) because the sum of their payoffs is equal to the optimal daily profit of the REC (8.35 €), i.e., the value of the grand coalition. Both Shapley value and Uniform pricing also guarantee the property of individual rationality and, therefore, all members of the REC have higher gains (higher profits or lower costs) within the REC compared to the case without cooperation. For instance, the tertiary, residential and commercial members have higher daily profits within the REC according to the uniform pricing allocation (profits of 1.95 €, 0.69 € and 5.71 €, respectively, in Table 4) compared to the case in which they operate independently in separate coalitions (costs of -12.85 €, -1.03 €, -22.20 €, respectively, in Table 3). With Uniform pricing all members have daily profits, included the tertiary consumer, while the Shapley allocation shows daily profits for prosumers and a daily cost for the tertiary consumer. Hence, it seems that Uniform pricing is more economically profitable than Shapley value, at least for the tertiary consumer. However, the application of the Shapley value mechanism favours the prosumers of the REC that provide a major contribution in increasing the total daily economic profits, derived from the energy sold to the grid and the incentivised energy shared within the REC. For example, Table 4 shows that the residential prosumer receives the highest payoff, according to Shapley, equal to 9.57 €, highlighting the relevant contribution of this prosumer to the total profit of the REC. Hence, the Shapley value can be considered a fair allocation mechanism in the sense that prosumers, who promote self-consumption and virtual energy sharing within the REC, receive higher payoffs compared to consumers (in any case the latter have economic convenience to be part of the REC instead of operating independently). On the contrary, with the Uniform pricing mechanism, the resulting payoffs are more homogeneous (i.e., all members obtain daily profits) within the REC, without higher rewards to prosumers with respect to consumers.

Table 3. Coalitions of the REC and their calculated "values", which represent daily operational profits (positive) or costs (negative).

Coalition	*{}*	*{Ter}*	*{Res}*	*{Com}*	*{Ter, Res}*	*{Ter, Com}*	*{Res, Com}*	*{Ter, Res, Com}*
Value [€]	0	-12.85	-1.03	-22.20	-6.95	2.70	20.09	8.35

Table 4. Payoffs of all members of the REC according to Shapley value and Uniform pricing.

	Payoffs [€]	
Member	*Shapley value*	*Uniform pricing*
Ter	-5.03	1.95
Res	9.57	0.69
Com	3.81	5.71
Total	8.35	8.35

5. Conclusions

This paper focuses on the issue of costs/profits allocation within the emerging Renewable Energy Communities (RECs). In the current literature, most of the works apply one single allocation mechanism or does not apply and compare different allocation mechanisms that belong to the field of cooperative game theory or other fields. Contrary to the current literature, this work applies two different allocation mechanisms, i.e., the "Shapley value" based on cooperative game theory and the "Uniform pricing", with the aim of evaluating the impact of these mechanisms on the economic benefits of the members of a REC. The cooperative mechanism Shapley value allows to allocate the optimal cost/profit of the community, considering the average marginal contributions of members to the "value" (i.e., total cost or profit) of any coalition of the community in which they could participate. On the other hand, the mechanism of Uniform pricing distributes the optimal cost/profit of the REC by defining a uniform price that is the ratio of the optimal cost/profit and the total electrical demand of the community. This work considers a REC, according to the Italian framework, as case study. The analysed REC includes three members belonging to different sectors, i.e., a tertiary consumer, one residential and one commercial prosumers. The residential prosumer owns only a Photovoltaic (PV) plant (available area of 60 m^2), whereas the commercial prosumer owns a PV plant (available area of 250 m^2) and an electrical battery

storage (capacity of 50 kWh). A Mixed-Integer Non-Linear Programming (MINLP) optimization is carried out to maximize the daily operational profit of the REC under analysis, considering the Italian framework and the related economic incentive for the energy shared. The optimal daily operational profit of 8.35 € of the REC is allocated to the members by applying, separately, the “Shapley value” and “Uniform pricing” mechanisms. Given the payoffs distributed by both Shapley value and Uniform pricing, the three members of the REC always find economically convenient the participation into the community (therefore, higher profits and lower costs) compared to their independent operation, which is characterized by daily costs of 12.85 €, 1.03 € and 22.20 € for the tertiary consumer, residential and commercial prosumers, respectively. Uniform pricing allows to achieve daily profits of 1.95 €, 0.69 € and 5.71 € for the tertiary consumer, residential and commercial prosumers, respectively. On the other hand, the allocation by Shapley value leads to a daily cost of 5.03 € for the tertiary consumer and to daily profits of 9.57 € and 3.81 € for the residential and commercial prosumers, respectively. Eventually, the outcomes of the allocation mechanisms highlight that Uniform pricing can provide more homogeneous payoffs among the members of the REC, whereas Shapley value is fairer towards prosumers (in particular, the residential one), in the sense that “awards” the higher contributions of the prosumers to the optimal daily profit of the REC by giving them higher payoffs than those of consumers. A future research direction of this work could cover the analysis of the economic stability of the REC, strictly dependent on the costs/profits distributed by the implemented allocation mechanisms, to avoid the case of members willing to exit from the REC.

Acknowledgments

The authors thank Professor Andrea Lazzaretto of the University of Padova, for the support in the conceptualization of this work, and “Fondazione Ing. Aldo Gini” of the University of Padova for the economic support provided.

Nomenclature

Com	Commercial
$MINLP$	Mixed-Integer Non-Linear Programming
REC	Renewable Energy Community
Res	Residential
Ter	Tertiary

Subscripts and superscripts

bat	Battery
i	Member of the REC
PV	Photovoltaic

References

[1] Directive (EU) 2018/2001 of the European Parliament and of the Council of 11 December 2018 on the Promotion of the Use of Energy from Renewable Sources (Recast), 2018. https://eur-lex.europa.eu/legal-content/EN/TXT/?uri=uriserv:OJ.L_.2018.328.01.0082.01.ENG. (Accessed 11 May 2022).
[2] European Commission’s Communication, "'Fit for 55': delivering the EU's 2030 Climate Target on the way to climate neutrality" (COM(2021) 550 final), 2021. https://eur-lex.europa.eu/legal-content/EN/TXT/?uri=CELEX:52021DC0550. (Accessed 11 May 2022).
[3] TESTO COORDINATO DEL DECRETO-LEGGE 30 dicembre 2019 n 162 art 42-bis, 2020. https://www.gse.it/servizi-per-te/autoconsumo/gruppi-di-autoconsumatori-e-comunita-di-energia-rinnovabile/documenti. (Accessed 11 May 2022).
[4] ARERA, Autorità di Regolazione per Energia Reti e Ambiente. https://www.arera.it/it/inglese/index.htm. (Accessed 11 May 2022).
[5] J. Lowitzsch, K. Kreutzer, J. George, C. Croonenbroeck, B. Breitschopf, Development prospects for energy communities in the EU identifying best practice and future opportunities using a morphological approach, Energy Policy 174 (2023) 113414.
[6] F. Ceglia, P. Esposito, A. Faraudello, E. Marrasso, P. Rossi, M. Sasso, An energy, environmental, management and economic analysis of energy efficient system towards renewable energy community: The case study of multi-purpose energy community, Journal of Cleaner Production 369 (2022) 133269.
[7] R. Gerundo, A. Marra, A Decision Support Methodology to Foster Renewable Energy Communities in the Municipal Urban Plan, Sustainability 14(23) (2022) 16268.
[8] E. Cutore, R. Volpe, R. Sgroi, A. Fichera, Energy management and sustainability assessment of renewable energy communities: The Italian context, Energy Conversion and Management 278 (2023) 116713.
[9] H.-C. Chang, B. Ghaddar, J. Nathwani, Shared community energy storage allocation and optimization, Applied Energy 318 (2022) 119160.

[10] F. Lazzari, G. Mor, J. Cipriano, F. Solsona, D. Chemisana, D. Guericke, Optimizing planning and operation of renewable energy communities with genetic algorithms, Applied Energy 338 (2023) 120906.
[11] V. Casalicchio, G. Manzolini, M.G. Prina, D. Moser, From investment optimization to fair benefit distribution in renewable energy community modelling, Applied Energy 310 (2022) 118447.
[12] S. Zheng, X. Jin, G. Huang, A.C. Lai, Coordination of commercial prosumers with distributed demand-side flexibility in energy sharing and management system, Energy 248 (2022) 123634.
[13] M. Zatti, M. Moncecchi, M. Gabba, A. Chiesa, F. Bovera, M. Merlo, Energy communities design optimization in the Italian framework, Applied Sciences 11(11) (2021) 5218.
[14] S. Cremers, V. Robu, D. Hofman, T. Naber, K. Zheng, S. Norbu, Efficient methods for approximating the Shapley value for asset sharing in energy communities, Proceedings of the Thirteenth ACM International Conference on Future Energy Systems, 2022, pp. 320-324.
[15] Z. Siqin, D. Niu, M. Li, T. Gao, Y. Lu, X. Xu, Distributionally robust dispatching of multi-community integrated energy system considering energy sharing and profit allocation, Applied Energy 321 (2022).
[16] N. Vespermann, T. Hamacher, J. Kazempour, Access economy for storage in energy communities, IEEE Transactions on Power Systems 36(3) (2020) 2234-2250.
[17] N. Li, Ö. Okur, Economic analysis of energy communities: Investment options and cost allocation, Applied Energy 336 (2023) 120706.
[18] A. Chiş, V. Koivunen, Coalitional game-based cost optimization of energy portfolio in smart grid communities, IEEE Transactions on Smart Grid 10(2) (2017) 1960-1970.
[19] N. Li, R.A. Hakvoort, Z. Lukszo, Cost allocation in integrated community energy systems-A review, Renewable and Sustainable Energy Reviews 144 (2021) 111001.
[20] A.L. Berka, E. Creamer, Taking stock of the local impacts of community owned renewable energy: A review and research agenda, Renewable and Sustainable Energy Reviews 82 (2018) 3400-3419.
[21] V.Z. Gjorgievski, S. Cundeva, G.E. Georghiou, Social arrangements, technical designs and impacts of energy communities: A review, Renewable Energy (2021).
[22] M. Moncecchi, S. Meneghello, M. Merlo, A game theoretic approach for energy sharing in the italian renewable energy communities, Applied Sciences (Switzerland) 10(22) (2020) 1-25.
[23] L. Han, T. Morstyn, M. McCulloch, Incentivizing prosumer coalitions with energy management using cooperative game theory, IEEE Transactions on Power Systems 34(1) (2018) 303-313.
[24] M. Greer, Chapter 8 - Efficient Pricing of Electricity, in: M. Greer (Ed.), Electricity Marginal Cost Pricing, Butterworth-Heinemann, Boston, 2012, pp. 231-262.
[25] G. Volpato, G. Carraro, M. Cont, P. Danieli, S. Rech, A. Lazzaretto, General guidelines for the optimal economic aggregation of prosumers in energy communities, Energy 258 (2022).
[26] Photovoltaic Geographical Information System (PVGIS). https://ec.europa.eu/jrc/en/pvgis. (Accessed 11 May 2022).
[27] Gestore Mercati Energetici. https://www.mercatoelettrico.org/en/default.aspx. (Accessed 11 May 2022).
[28] U.S. Department of Energy. Open EI. Available: https://openei.org/datasets/files/961/pub/. (Accessed 14 March 2023).
[29] L. Colarullo, J. Thakur, Second-life EV batteries for stationary storage applications in Local Energy Communities, Renewable and Sustainable Energy Reviews 169 (2022) 112913.
[30] Gurobi Optimization. https://www.gurobi.com/. (Accessed 11 May 2022).